Edited by
Johannes Buchner, Thomas Kiefhaber

WILEY-VCH

Protein Folding Handbook

Volume 1

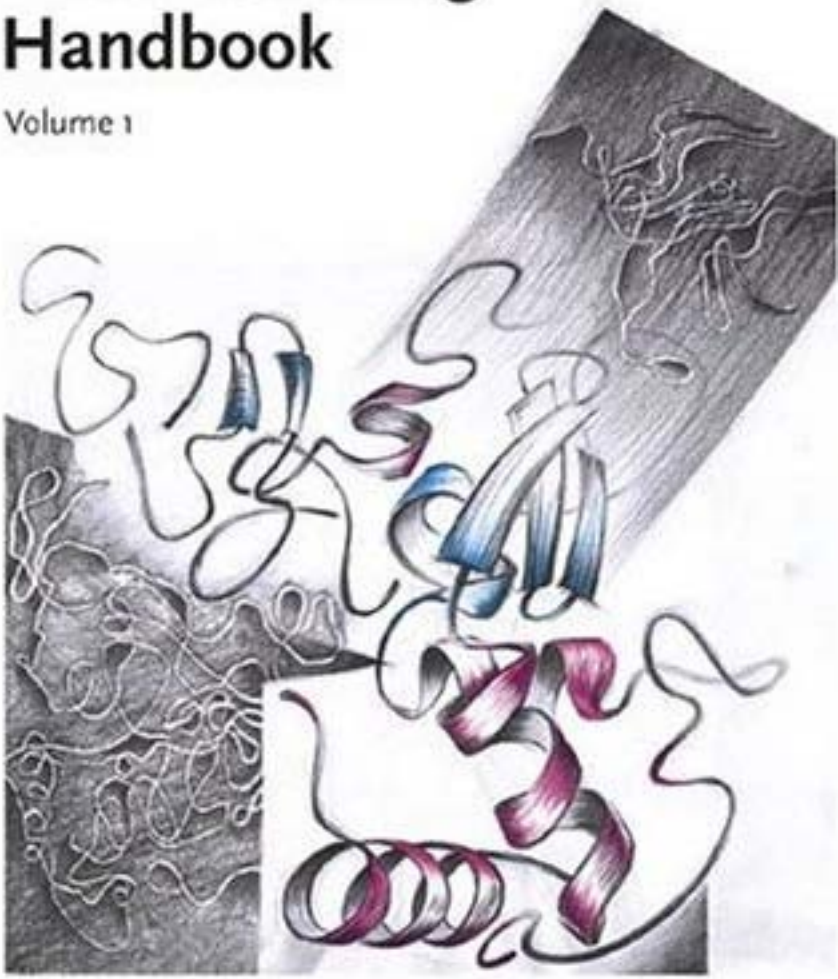

Protein Folding Handbook
Edited by J. Buchner and T. Kiefhaber

Protein Folding Handbook. Part I. Edited by J. Buchner and T. Kiefhaber

ISBN: 3-527-30784-2

Further Titles of Interest

K. H. Nierhaus, D. N. Wilson (eds.)

Protein Biosynthesis and Ribosome Structure

ISBN 3-527-30638-2

R. J. Mayer, A. J. Ciechanover, M. Rechsteiner (eds.)

Protein Degradation

ISBN 3-527-30837-7 (Vol. 1)
ISBN 3-527-31130-0 (Vol. 2)

G. Cesareni, M. Gimona, M. Sudol, M. Yaffe (eds.)

Modular Protein Domains

ISBN 3-527-30813-X

S. Brakmann, A. Schwienhorst (eds.)

Evolutionary Methods in Biotechnology

ISBN 3-527-30799-0

Protein Folding Handbook

Edited by Johannes Buchner and Thomas Kiefhaber

WILEY-VCH Verlag GmbH & Co. KGaA

Editors

Prof. Dr. Johannes Buchner
Institut für Organische Chemie und Biochemie
Technische Universität München
Lichtenbergstrasse 4
85747 Garching
Germany
johannes.buchner@ch.tum.de

Prof. Dr. Thomas Kiefhaber
Biozentrum der Universität Basel
Division of Biophysical Chemistry
Klingelbergstrasse 70
4056 Basel
Switzerland
t.kiefhaber@unibas.ch

Cover
Artwork by Prof. Erich Gohl, Regensburg

Library of Congress Card No.: applied for
A catalogue record for this book is available from the British Library.
Bibliographic information published by Die Deutsche Bibliothek
Die Deutsche Bibliothek lists this publication in the Deutsche Nationalbibliografie; detailed bibliographic data is available in the Internet at http://dnb.ddb.de

Printed in the Federal Republic of Germany.
Printed on acid-free paper.

Typesetting Asco Typesetters, Hong Kong
Printing betz-druck gmbh, Darmstadt
Bookbinding Litges & Dopf Buchbinderei GmbH, Heppenheim

ISBN-13 978-3-527-30784-5
ISBN-10 3-527-30784-2

Contents

Part I, Volume 1

Protein Folding Handbook. Part I. Edited by J. Buchner and T. Kiefhaber

ISBN: 3-527-30784-2

Preface

During protein folding, the linear information encoded in the amino acid sequence of a polypeptide chain is transformed into a defined three-dimensional structure. Although it was established decades ago that protein folding is a spontaneous reaction, a complete understanding of this fundamental process is still lacking. Since its humble beginnings in the fields of biophysical chemistry and biochemistry, the analysis of protein folding and stability has spread into a wide range of disciplines including physics, cell biology, medicine and biotechnology. The recent discovery of the sophisticated cellular machinery of molecular chaperones and folding catalysts which assists protein structure formation in vivo and the analysis of protein folding diseases have added additional twists to the study of protein folding. Consequently, the field has undergone a significant transformation over the last decade.

The increasing interest in protein folding considerably improved our knowledge of the physical principles underlying protein stability and folding and stimulated the development of powerful new techniques for their analysis both in vitro and in vivo. Aspects that had been studied previously in splendid isolation such as basic principles and protein folding diseases are now growing together, experimentally and conceptually.

Over the past years, a number of excellent books on protein folding were published, starting with the famous 'red bible of protein folding' (Jaenicke, 1980). The *Protein Folding Handbook* takes a different approach as it combines in-depth reviews with detailed experimental protocols. Thus, a comprehensive, multi-faceted view of the entire field of protein folding from basic physical principles to molecular chaperones, protein folding diseases and the biotechnology of protein folding – is presented. The *Protein Folding Handbook* intends to provide those who become interested in a specific aspect of protein folding with both the scientific background and the experimental approaches. Ideally, the protocols of the methods sections will allow and stimulate even the novice to boldly enter new experimental territory.

We are grateful to the authors who embarked with us on this endeavour. It was a pleasure to see how, chapter by chapter, the current state of the art in this field emerged and the common themes became apparent.

Finally, we would like to thank Dr. Frank Weinreich from Wiley-VCH for his never-waning efforts to transform our ideas into a book, Prof. Erich Gohl for the cover artwork, Brigitte Heiz-Wyss and Susanne Hilber for excellent assistance and Annett Bachmann and Stefan Walter for help with creating the index.

München and Basel
October 2004

Johannes Buchner
Thomas Kiefhaber

Reference

Jaenicke, R. (1980) Protein Folding. Elsevier, Amsterdam, New York

Contributors of Part I

Hans-Peter Bächinger
Shriners Hospital for Children &
Department of Biochemistry and Molecular Biology
Oregon Health & Science University
3101 SW Sam Jackson Park Road
Portland, OR 97239-3009
USA

Annett Bachmann
Division of Biophysical Chemistry
Biozentrum, University of Basel
Klingelbergstrasse 70
4056 Basel
Switzerland

Jochen Balbach
Biochemie III
Universität Bayreuth
Universitätsstr. 30
95440 Bayreuth
Germany

Robert L. Baldwin
Department of Biochemistry
Stanford University School of Medicine
279 Campus Drive West
Stanford, CA 94305
USA

Hans-Rudolf Bosshard
Department of Biochemistry
University of Zurich
Winterthurerstrasse 190
8057 Zurich
Switzerland

Sonja Braun-Sand
Department of Chemistry
University of Southern California
3620 S. McClintock Ave.
Los Angeles, CA 90089-1062
USA

Philip N. Bryan
Center for Advanced Research in Biotechnology
University of Maryland Biotechnology Institute
9600 Gudelsky Drive
Rockville, MD 20850
USA

Amedeo Caflisch
Department of Biochemistry
University of Zürich
Winterthurerstrasse 190
8057 Zürich
Switzerland

Heiko Carstens
Department für Physik
Ludwig-Maximilians-Universität München
Oettingenstrasse 67
80538 München
Germany

Hong Cheng
Basic Science Division
Fox Chase Cancer Center
333 Cottman Avenue
Philadelphia, PA 19111
USA

Jane Clarke
University Chemical Laboratories
MRC Centre for Protein Engineering
Lensfield Road
Cambridge CB2 1EW
United Kingdom

Monika Davidovic
Department of Biophysical Chemistry
Lund University
22100 Lund
Sweden

Vladimir P. Denisov
Department of Biophysical Chemistry
Lund University
22100 Lund
Sweden

Andrew J. Doig
Department of Biomolecular Sciences
UMIST
PO Box 88
Manchester M60 1QD
United Kingdom

Wolfgang Doster
Department of Physics E13
Technische Universität München
85748 Garching
Germany

Jürgen Engel
Division of Biophysical Chemistry
Biozentrum, University of Basel
Klingelbergstrasse 70
4056 Basel
Switzerland

Neil Errington
Department of Biomolecular Sciences
UMIST
PO Box 88
Manchester M60 1QD
United Kingdom

Alan R. Fersht
Department of Chemistry
University of Cambridge
Lensfield Road
Cambridge CB2 1EW
United Kingdom

Beat Fierz
Division of Biophysical Chemistry
Biozentrum, University of Basel
Klingelbergstrasse 70
4056 Basel
Switzerland

Patrick J. Fleming
Jenkins Department of Biophysics
Johns Hopkins University
3400 N. Charles Street
Baltimore, MD 21218
USA

Josef Friedrich
Department of Physics E14
Technische Universität München
85350 Freising
Germany

Klaus Gast
Institut für Biochemie und Biologie
Universität Potsdam
Karl-Liebknecht-Str. 24–25
14476 Golm
Germany

Yuji Goto
Institute for Protein Research
Osaka University
3-2 Yamadaoka, Suita
Osaka 565-0871
Japan

Gerald R. Grimsley
Dept. of Medical Biochemistry & Genetics
Texas A&M University
College Station, TX 77843-1113
USA

Martin Gruebele
School of Chemistry
University of Illinois, Urbana-Champaign
600 S Mathews Avenue Box 5–6
Urbana, Illinois 61801
USA

Raphael Guerois
DBJC/SBFM
CEA Saclay
91191 Gif-sur-Yvette
France

Nicholas R. Guydosh
Department of Biological Sciences
Stanford University
Stanford, CA 94305-5020
USA

Elisha Haas
Faculty of Life Sciences4
Bar Ilan University
Ramat Gan 52900
Israel

Bertil Halle
Department of Biophysical Chemistry
Lund University
22100 Lund
Sweden

Daizo Hamada
Osaka Medical Center for Maternal and Child Health
840 Murodo, Izumi
Osaka 594-1011
Japan

Heedeok Hong
Department of Molecular Physiology and Biological Physics
University of Virginia
Charlottesville, VA 22908
USA

Teuku M. Iqbalsyah
Department of Biomolecular Sciences
UMIST
PO Box 88
Manchester M60 1QD
United Kingdom

Kiyoto Kamagata
Department of Physics, Graduate School of Science
University of Tokyo
7-3-1 Hongo, Bunkyo-ku
Tokyo 113-0033
Japan

Thomas Kiefhaber
Division of Biophysical Chemistry
Biozentrum, University of Basel
Klingelbergstrasse 70
4056 Basel
Switzerland

Birthe B. Kragelund
Institute of Molecular Biology
University of Copenhagen
Øster Farimagsgade 2 A
1353 Copenhagen
Denmark

Kunihiro Kuwajima
Department of Physics, Graduate School of Science
University of Tokyo
7-3-1 Hongo, Bunkyo-ku
Tokyo 113-0033
Japan

Ramil F. Latypov
Amgen Inc.
Thousand Oaks, CA 91320
USA

George I. Makhatadze
Department of Biochemistry and Molecular Biology
Penn State University College of Medicine
500 University Drive
Hershey, PA 17033-0850
USA

Kosuke Maki
Department of Physics, Graduate School of Science
University of Tokyo
7-3-1 Hongo, Bunkyo-ku
Tokyo 113-0033
Japan

Gennaro Marino
Facoltà die Scienze Biotecnologiche
Università degli Studi di Napoli "Federico II"
Via S. Pansini, 5
80131 Napoli
Italy

Gerald Mathias
Department für Physik
Ludwig-Maximilians-Universität München
Oettingenstr. 67
80538 München
Germany

Joaquim Mendes
EMBL Heidelberg
Meyerhofstrasse 1
69117 Heidelberg
Germany

Kristofer Modig
Institute of Molecular Biology
University of Copenhagen
Øster Farimagsgade 2A
1353 Copenhagen
Denmark

Andreas J. Modler
Institut für Biologie und Biochemie
Universität Potsdam
Karl-Liebknecht-Str. 24-25
14476 Golm
Germany

C. Nick Pace
Dept. of Medical Biochemistry & Genetics
Texas A&M University
College Station, TX 77843-1113
USA

Emanuele Paci
Department of Biochemistry
University of Zürich
Winterthurerstrasse 190
8057 Zürich
Switzerland

Flemming M. Poulsen
Institute of Molecular Biology
Department of Protein Chemistry
University of Copenhagen
Øster Farimagsgade 2 A
1353 Copenhagen
Denmark

Piero Pucci
Dipartimento di Chimica Organica e Biochimica
Università degli Studi di Napoli "Federico II"
Via S. Pansini, 5
80131 Napoli
Italy

Heinrich Roder
Basic Science Division
Fox Chase Cancer Center
333 Cottman Avenue
Philadelphia, PA 19111
USA

George D. Rose
Jenkins Department of Biophysics
Johns Hopkins University
3400 N. Charles Street
Baltimore, MD 21218
USA

Margherita Ruoppolo
Dipartimento di Biochimica e Biotecnologie Mediche
Università degli Studi di Napoli "Federico II"
Via S. Pansini, 5
80131 Napoli
Italy

Ignacio E. Sánchez
Division of Biophysical Chemistry
Biozentrum, University of Basel
Klingelbergstrasse 70
4056 Basel
Switzerland

Christian Schlörb
Institute for Organic Chemistry and Chemical Biology
Center for Biomolecular Magnetic Resonance
Johann Wolfgang Goethe-University
Marie-Curie-Strasse 11
60439 Frankfurt
Germany

Franz Schmid
Biochemisches Laboratorium
Universität Bayreuth
95440 Bayreuth
Germany

J. Martin Scholtz
Dept. of Medical Biochemistry & Genetics
Texas A&M University
College Station, TX 77843-1113
USA

Harald Schwalbe
Institute for Organic Chemistry and Chemical Biology
Center for Biomolecular Magnetic Resonance
Johann Wolfgang Goethe-University
Marie-Curie-Strasse 11
60439 Frankfurt
Germany

Mark S. Searle
School of Chemistry
University of Nottingham
University Park
Nottingham NG7 2RD
United Kingdom

Luis Serrano
EMBL Heidelberg
Meyerhofstrasse 1
69117 Heidelberg
Germany

M. C. Ramachandra Shastry
Basic Science Division
Fox Chase Cancer Center
333 Cottman Avenue
Philadelphia, PA 19111
USA

Lukas K. Tamm
Department of Molecular Physiology and Biological Physics
University of Virginia
Charlottesville, VA 22908
USA

Paul Tavan
Department of Physik
Ludwig-Maximilians-Universität München
Oettingenstrasse 67
80538 München
Germany

Kaare Teilum
Institute of Molecular Biology
University of Copenhagen
Øster Farimagsgade 2 A
1353 Copenhagen
Denmark

Arieh Warshel
Department of Chemistry
University of Southern California
3620 S. McClintock Avenue
Los Angeles, CA 90089-1062
USA

Phil M. Williams
Laboratory of Biophysics and Surface Analysis
University of Nottingham School of Pharmacy
Nottingham, NG7 2RD
United Kingdom

Julia Wirmer
Institute for Organic Chemistry and Chemical Biology
Center for Biomolecular Magnetic Resonance
Johann Wolfgang Goethe-University
Marie-Curie-Strasse 11
60439 Frankfurt
Germany

Markus Zeeb
Biochemie III
Universität Bayreuth
Universitätsstr. 30
95440 Bayreuth
Germany

Part I

1 Principles of Protein Stability and Design

1
Early Days of Studying the Mechanism of Protein Folding

Robert L. Baldwin

1.1
Introduction

Modern work on the mechanism of protein folding began with Chris Anfinsen. He recognized the folding problem, and he asked: How does the amino acid sequence of a protein determine its three-dimensional structure? From this basic question came various research problems, including (1) What is the mechanism of the folding process? (2) How can the three-dimensional structure be predicted from the amino acid sequence? and (3) What is the relation between the folding process in vivo and in vitro? Only the early history of the first problem will be considered here.

The basic facts needed to state the folding problem were already in place before Anfinsen's work. He knew this, well before 1973 when he received the Nobel Prize, and he was somewhat embarrassed about it. In his Nobel address [1], he says in the opening paragraph ''Many others, including Anson and Mirsky in the '30s and Lumry and Eyring in the '50s, had observed and discussed the reversibility of the denaturation of proteins.'' Anfinsen's statement of the folding problem may be dated to 1961 [2], when his laboratory found that the amino acid sequence of ribonuclease A (RNase A) contains the information needed to make the correct four disulfide bonds of the native protein. There are eight –SH groups in the unfolded RNase A chain which could make 105 different S–S bonds. Although in 1961 the reversibility of protein denaturation was recognized by protein chemists, the knowledge that protein denaturation equals protein unfolding had been gained only a few years earlier, in a series of papers from Walter Kauzmann's laboratory, beginning with Ref. [3]. The first protein structure, that of sperm whale myoglobin (2 Å resolution), determined by John Kendrew and his coworkers [4], became available only in 1960. The myoglobin structure confirmed the proposal that proteins possess 3D structures held together by weak, noncovalent bonds, and consequently they might unfold in denaturing conditions. Wu suggested this explanation of protein denaturation as early as 1931 [5].

The other thread in Anfinsen's proposal was, of course, the recognition that protein folding is part of the coding problem. The basic dogma of molecular biology,

Protein Folding Handbook. Part I. Edited by J. Buchner and T. Kiefhaber

ISBN: 3-527-30784-2

"DNA makes RNA makes protein," was already in place in 1958, and Anfinsen knew that the newly synthesized product of RNA translation is an inactive, unfolded polypeptide chain. How does it fold up to become active? In the 1960s and 1970s there was speculation about a code for folding, and some workers even proposed a three-letter code (i.e., three amino acid residues) [6]. Anfinsen proposed a thermodynamic hypothesis [1, 7]: the newly synthesized polypeptide chain folds up under the driving force of a free energy gradient and the protein reaches its thermodynamically most stable conformation. For protein chemists familiar with reversible denaturation, this appeared obvious: what else should drive a reversible chemical reaction besides the free energy difference between reactant and product? But for molecular biologists interested in knowing how an unfolded, newly synthesized protein is able to fold, Anfinsen's hypothesis represented a considerable leap of faith. In fact, biology does introduce subtle complexities, and more is said below about the thermodynamic hypothesis (see Section 1.3). Michael Levitt and Arieh Warshel made a farseeing proposal in 1975: they argued that an unfolded protein folds under the influence of a molecular force field, and someday the folding process will be simulated with the use of a force field [8].

Starting from Anfinsen's insights, this review examines what happened in the 1960s, 1970s, and 1980s to lay the groundwork for the modern study of how proteins fold in vitro. My review ends when the literature balloons out at the end of the 1980s with the study of new problems, such as: (1) experimental study of the transition state, (2) whether hydrophobic collapse precedes secondary structure, (3) the nature of the conformational reactions that allow hydrogen exchange in proteins, (4) using molecular dynamics to simulate the folding process, (5) the speed limit for folding, (6) helix and β-strand propensities, and (7) the mechanism of forming amyloid fibrils. This review is not comprehensive. The aim is to follow the threads that led to the prevalent view at the end of the 1980s. A few references are added after the 1980s in order to complete the picture for topics studied earlier.

1.2 Two-state Folding

An important achievement of early work on the mechanism of protein folding was the recognition that small proteins commonly show two-state equilibrium denaturation reactions and there are no observable intermediates. After the initial observation by Harrington and Schellman in 1956 that RNase A undergoes reversible thermal denaturation [9], at least five laboratories then examined the nature of the unfolding transition curve (see Ref. [10] for references). In the 1950s and 1960s RNase A was widely studied because of its small size (124 residues), purity and availability. The shape of its unfolding transition curve puzzled almost everyone, because the van't Hoff plot of ln K versus $(1/T)$ (K = equilibrium constant for unfolding) is unmistakably curved, which gives a small but observable asymmetry to the unfolding curve. The slope of the van't Hoff plot, $\Delta H/R$ (ΔH = enthalpy of unfolding, R = gas constant) should be constant if ΔH is constant. The typical explanation then was that stable intermediates are present during protein unfolding

and they explain the shape of the unfolding curve. In 1965 John Brandts [10] recognized that the correct explanation for the peculiar shape of the unfolding curve lies in the unusual thermodynamics of protein folding. Brandts argued that the thermodynamics of unfolding is dominated by hydrophobic free energy, as proposed by Walter Kauzmann [11] in 1959. Then there should be a large positive value of ΔC_p for unfolding, which explains the curvature of the van't Hoff plot [10]. ΔC_p is the difference between the heat capacities of the native and denatured forms of a protein, and a large value for ΔC_p causes a strong dependence of ΔH on temperature.

Brandts' proposal that thermal denaturation of RNase A is a two-state reaction without intermediates [10] was strongly supported, also in 1965, by Ginsburg and Carroll [12], who introduced the superposition test for intermediates and found no populated intermediates in the unfolding reaction of RNase A. In the superposition test, two or more normalized unfolding curves are superimposed and tested for coincidence. They are monitored by at least two probes that report on fundamentally different molecular properties, such as specific viscosity that reports on molecular volume and optical rotation that reports on secondary structure.

In 1966 Lumry, Biltonen and Brandts [13] introduced the calorimetric ratio test for intermediates. In this test, the ratio of the calorimetric and van't Hoff values of ΔH should equal 1 if there are no populated intermediates. In the 1970s, after the development of differential scanning calorimetry by Peter Privalov [14], the calorimetric ratio test became widely used as a criterion for two-state folding.

Charles Tanford and his laboratory undertook a wide-ranging study of whether the denaturation reactions of small proteins are truly two-state reactions. In 1968 Tanford summarized the results in a long and widely quoted review [15]. He recognized that conditions must be found in which denatured proteins are completely unfolded, without residual structure, before one can confidently determine if denaturation is a two-state reaction. His laboratory found that 6 M GdmCl (guanidinium chloride) is a denaturant that eliminates residual structure in water-soluble proteins, whereas thermally denatured proteins retain significant residual structure [15]. (Whether or not the residual structure is related to the structure of the native protein was left for future study.) A key finding was that the reversible denaturation reactions of several small proteins are indeed two-state reactions when 6 M GdmCl is the denaturant [15]. This work opened the way to later study of two basic questions: (1) Are there intermediates in protein folding reactions and, if so, how can they be detected? and (2) How can the energetics of protein folding be measured experimentally? In discussing these problems, I use the terms ''unfolded'' and ''denatured'' interchangeably, and a ''denatured'' protein typically has some residual structure that depends on solvent conditions and temperature.

1.3 Levinthal's Paradox

In 1968 Cyrus Levinthal released a bombshell that became known as Levinthal's paradox [16, 17]. He had begun work on prediction of the 3D structures of proteins

from their amino acid sequences. He observed that, if protein folding is truly a two-state reaction without intermediates, then the time needed to fold can be estimated from the time needed to search randomly all possible backbone conformations. Levinthal estimated that the time needed for folding by a random search is far longer than the life of the universe. A plausible conclusion from his calculation is that there must be folding intermediates and pathways [16, 17]. When Levinthal's calculation was repeated in 1992, with the addition of a small free energy bias as the driving force for folding, the time needed to search all conformations by a random search process was reduced to a few seconds [18]. Note, however, that a free energy bias in favor of the native structure is likely to produce intermediates in the folding process, although not necessarily ones that are populated.

In 1969 Levinthal pointed out [17] that, if it has a choice, a protein folds to the structure dictated by the fastest folding pathway and not to the most stable structure, in contrast to Anfinsen's thermodynamic hypothesis. His proposal was confirmed experimentally in 1996 for a protein from the serpin family, whose members form two different stable structures. The folding pathway of the serpin, plasminogen activator inhibitor 1, was found to be under kinetic control [19]. In 1998 Agard and coworkers [20] found that the stability of the folded structure of α-lytic protease appears to be under kinetic control; i.e., the denatured protein is not only kinetically unable to refold but also thermodynamically more stable than the native form [20]. This surprising deduction does not contradict Anfinsen's thermodynamic hypothesis. The enzymatically active form of this protein is formed after complete folding of a much longer polypeptide whose long Pro sequence is cleaved off after folding is complete.

1.4 The Domain as a Unit of Folding

Knowledge that polypeptide chains are synthesized starting from the N-terminus led to speculation that folding begins from the N-terminus of the chain. In 1970, Taniuchi [21] observed that the correct four S–S bonds of RNase A are not formed and the protein remains unfolded if the four C-terminal residues are deleted from the 124-residue polypeptide chain. Consequently, almost the entire polypeptide chain (maybe all of it) is required for stable folding (but see, however, Section 1.10). In 1969 Goldberg [22] found that intracistronic complementation occurs in β-galactosidase via the presence of at least two independently folding units ("globules") in each of the four identical polypeptide chains. In 1973 Wetlaufer [23] found contiguous folded regions in the X-ray structures of several proteins, in some cases apparently connected by flexible linkers. These three observations taken together gave rise to the concept that the domain (~100 amino acids) is the unit of stable folding.

Wetlaufer [23] pointed out that a contiguous folded region of the polypeptide chain is likely to arise from a structural folding nucleus. He noted that a structural nucleus might also serve as a kinetic nucleus for the folding process, with the con-

sequence that successive folding events occur rapidly after the nucleus is formed, so that folding intermediates are never populated. His suggestion was often used in the early 1970s to explain why folding intermediates could not be found. In 1981 Lesk and Rose [24] pointed out that each protein domain can typically be divided into two subdomains, each of which is also folded from a contiguous segment of polypeptide chain – although the subdomains are not separated by flexible linkers. Their observation favors a hierarchic mechanism of folding [24].

In 1974 Goldberg and coworkers [25] proposed domain swapping as the explanation for the concentration-dependent formation of large aggregates of refolding tryptophanase, formed at a critical urea concentration. Their work has been taken as a model for understanding the formation of inclusion bodies and the need for chaperones to improve the yield in many folding reactions. Also in the 1970s Jaenicke and coworkers [26] began a systematic investigation of folding coupled to subunit association in the concentration-dependent folding reactions of oligomeric proteins. These subjects are discussed elsewhere in this book.

1.5 Detection of Folding Intermediates and Initial Work on the Kinetic Mechanism of Folding

Demonstration of two-state equilibrium denaturation by Brandts [10] and by Tanford [15] made clear the difficulty of detecting any folding intermediates that might exist. In 1971, reports of complex kinetics of unfolding/refolding by Ikai and Tanford for cytochrome *c* (cyt *c*) [27] and by Tsong, Baldwin, and Elson for RNase A [28] raised hope that fast-reaction methods would succeed in detecting and characterizing kinetic folding intermediates. Complexity in the refolding kinetics of staphylococcal nuclease (SNase) had already been reported in 1970 [29] from Anfinsen's laboratory (see also Ref. [30]).

Ikai and Tanford used a stopped-flow apparatus to measure the folding kinetics of cyt *c* [27, 31] and hen lysozyme [32]. These studies laid the groundwork for systematic investigation of folding reactions that can be represented by a simple sequential model, $U \leftrightarrow I_1 \leftrightarrow I_2 \leftrightarrow \bullet\bullet\bullet N$, with one unfolded form U, one native form, N, and intervening intermediates. Off-pathway intermediates are described by a branched pathway. A mathematical framework for such studies is given in Ref. [33]. Ikai and Tanford concluded initially that they had evidence for incorrectly folded, off-pathway intermediates in the refolding of cyt *c* [27, 31], but they assumed there was only one unfolded form. Concurrent studies of RNase A refolding showed that two or more unfolded forms are present, which suggested that the same is true of other denatured proteins (see Section 1.6). Ikai and Tanford made a further important contribution by developing tests for stopped-flow artifacts that result from mixing concentrated GdmCl with buffer; this problem was a serious issue at the time. In 1973, when Ikai finished his PhD work, Charles Tanford left the field of folding mechanisms to take up the new study of membrane proteins.

Earlier, in 1968/69, Fritz Pohl began using a slow temperature-jump (''T-jump'')

method, capable of observing kinetic changes only in the time range of seconds and longer, to study the kinetics of protein folding. He reported apparent two-state kinetics for the unfolding/refolding reactions of chymotrypsin [34], trypsin [35], chymotrypsinogen-A [36], and RNase A [36]. He found that the entire kinetic progress curve for unfolding or refolding could be represented by a single exponential time course and the kinetic amplitude agreed with the value expected from the equilibrium unfolding curve. He interpreted his results as showing that folding is highly cooperative, which strengthened the general view that folding intermediates would be very difficult to detect, perhaps impossible. Ikai and Tanford undertook their stopped-flow study of the unfolding/refolding kinetics of cyt *c*, despite Pohl's evidence that the kinetic folding reactions of small proteins are two-state, because Wayne Fish in Tanford's laboratory had evidence suggesting an equilibrium folding intermediate (A. Ikai, personal communication, 2003).

Tsong, Baldwin, and Elson [28, 37] undertook their fast T-jump study (dead time, 10 μs) of the unfolding kinetics of RNase A because they believed that fast kinetics might reveal intermediates in apparent two-state unfolding reactions. Pörschke and Eigen had observed [38] that short RNA helices show unfolding intermediates in the msec time range even though both the major folding and unfolding reactions follow a single exponential time course in the seconds time range. The unfolding kinetics of RNase A could be fitted to a similar type of nucleation-dependent folding model [28, 37, 40]. The model predicts kinetics in which the relative amplitude of the fast unfolding phase increases rapidly with increasing temperature, in agreement with experiment [28, 37]. A fast T-jump study of the unfolding kinetics of chymotrypsinogen-A [40] gave results like those of RNase A, suggesting that the nucleation model might be generally applicable. For chymotrypsinogen, as for RNase A, there is a fast (milliseconds) phase in unfolding, in addition to the slow unfolding reaction (seconds) studied earlier by Pohl [36]. The fast phases in the unfolding of RNase A [28, 37] and of chymotrypsinogen [40] were missed by Pohl [36] because they account for only a few percent of the total kinetic amplitude in his conditions, and because he measured only the slow unfolding reactions. The relative amplitude of the fast unfolding phase approaches 100% at temperatures near the upper end of the thermal unfolding transition of RNase A (see Section 1.6), but of course the total amplitude becomes small.

The T-jump and stopped-flow unfolding studies of RNase A were monitored by tyrosine absorbance [28, 37] and RNase A has six tyrosine residues. Consequently, the fast and slow unfolding reactions of RNase A might be detecting unfolding reactions in different parts of the molecule that occur in different time ranges. This hypothesis was tested and ruled out by studying a chemically reacted derivative of RNase A containing a single, partly buried, dinitrophenyl (DNP) group [41]. The unfolding kinetics monitored by the single DNP group are biphasic, exactly like the kinetics observed by the six tyrosyl groups. Later work by Paul Hagerman (see below) showed that the fast phase in the unfolding of RNase A arises from an unfolding intermediate that is a minor species in the ensemble of unfolded forms.

Thus, in 1973 the stage was set for kinetic studies of the mechanism of protein folding/unfolding. However, three basic questions required answers before folding

mechanisms could be analyzed. (1) Are the observed folding intermediates on-pathway? (2) Are the intermediates partly folded forms or are they completely unfolded, while the complex unfolding/refolding kinetics result from the interconversion of different denatured forms? (3) How can the structures be determined of folding intermediates whose lifetimes are as short as milliseconds?

1.6 Two Unfolded Forms of RNase A and Explanation by Proline Isomerization

In 1973 Garel and Baldwin found that unfolded RNase A contains two different major denatured forms, a fast-folding species (U_F, ~20%) and a slow-folding species (U_S, ~80%) [42] that refolds 50 times more slowly than U_F in some conditions. The two different denatured forms were discovered when refolding was monitored with a probe specific for the enzymatically active protein, namely binding of the specific inhibitor 2′-CMP. Refolding was studied initially after a pH jump (pH 2.0 → pH 5.8) at high temperatures (to obtain complete unfolding at pH 2.0) [42] and later after dilution from 6 M GdmCl [43]. When the unfolding transition is complete in the initial conditions, either at low pH and high temperature [42] or in 6 M GdmCl [43], both the fast and slow kinetic phases of refolding yield native RNase A as product. In 6 M GdmCl, the denatured protein should be completely unfolded and therefore the fast-folding and slow-folding forms correspond to two different denatured species.

In 1976 Hagerman and Baldwin [44] studied the kinetic mechanism of RNase A unfolding by using a stopped-flow apparatus and pH jumps to analyze the unfolding/refolding kinetics as a function of temperature throughout the thermal unfolding zone at pH 3.0. Their analysis is based on a four-species mechanism, $U_S \leftrightarrow U_F \leftrightarrow I \leftrightarrow N$, in which U_S and U_F are the slow-folding and fast-folding forms of the denatured protein discussed above and I is a new unfolding intermediate observed above T_m. Because I is completely unfolded, as judged either by tyrosine absorbance or by enthalpy content [44], I may be labeled instead as U_3 and the unfolding/refolding mechanism written as $U_S \leftrightarrow U_F \leftrightarrow U_3 \leftrightarrow N$. The proportions of U_S:U_F:U_3 in denatured RNase A were predicted in 1976 to be 0.78:0.20:0.02 [44]. Although U_3 was studied initially only as an unfolding intermediate [44], U_3 should be the immediate precursor of N in refolding experiments according to the sequential unfolding/refolding mechanism. This prediction was confirmed next with experiments using a sequential mixing apparatus [45]. U_3 and U_F are populated transiently by unfolding N with a first mixing step and then U_3 and U_F are allowed to refold after a second mixing step. U_3 forms N much more rapidly than U_F does [45], and in 1994 U_3 was detected in the equilibrium population of denatured RNase A species [46].

The 1976 analysis predicts correctly the equilibrium curve for thermal denaturation from the kinetic data [44], and also shows that refolding of U_F and U_S to N must occur by the sequential mechanism $U_S \leftrightarrow U_F \leftrightarrow N$ and not by the split mechanism $U_S \leftrightarrow N \leftrightarrow U_F$. The latter conclusion follows from the behavior of

the kinetic amplitudes when the relative rates of the fast and slow kinetic refolding reactions are varied by changing the temperature [44]. The issue of a sequential versus a split mechanism was tested in a different manner by Brandts and coworkers [47], who were aware of Hagerman's work (see their discussion). They introduced the interrupted unfolding (or "double-jump") experiment in which the species present at each time of unfolding are assayed by refolding measurements.

Brandts and coworkers [47] proposed a proline isomerization model as an explanation for the two different forms of RNase A. Their model includes two separate hypotheses. The first is that the fast-folding and slow-folding forms of a denatured protein are produced by slow cis–trans isomerization of proline peptide bonds after unfolding occurs. The second is that the fast-folding and slow-folding denatured species account entirely for the complex unfolding/refolding kinetics and no structural folding intermediates are populated. Thus, their unfolding/refolding mechanism for a protein with only one proline residue is $N \leftrightarrow U_F \leftrightarrow U_S$. The fast-folding species U_F has the same prolyl isomer (cis or trans) as N and the slow-folding species U_S contains the other prolyl isomer.

Nuclear magnetic resonance (NMR) studies of proline-containing peptides show that the cis:trans ratio of a prolyl peptide bond commonly lies between 30:70 and 10:90, depending on neighboring residues. Because the proline ring sometimes clashes sterically with neighboring side chains, proline peptide bonds (X-Pro) are quite different from ordinary peptide bonds, for which the % cis is only ~0.1–1%. RNase A contains two cis proline residues, as well as as two trans proline residues, and therefore denatured RNase A should have an unusually high fraction of $[U_S]$ (as observed), because the two cis residues isomerize to trans after unfolding and produce U_S species. A later NMR study of the trans → cis isomerization rate of Gly-Pro in water [48] places it in the same time range as the $U_S \leftrightarrow U_F$ reaction of RNase A.

The proline isomerization model of Brandts and coworkers was very persuasive but it proved difficult to test, particularly because one of its two hypotheses turned out to be wrong, namely that no structural intermediates are populated during the kinetics of unfolding or refolding. In 1978 Schmid and Baldwin [49] found that the $U_F \leftrightarrow U_S$ reaction in unfolded RNase A is acid-catalyzed, although very strong acid, >5 M $HClO_4$, is required for catalysis. Very strong acid is needed for the cis → trans isomerization of both prolyl peptide bonds [50] and ordinary peptide bonds, and the slow rate of the $U_F \leftrightarrow U_S$ reaction of RNase A implies that the critical bonds are prolyl peptide bonds rather than ordinary peptide bonds. The high activation enthalpy (~85 kJ mol^{-1}) expected for isomerization of prolyl peptide bonds was found for the $U_F \leftrightarrow U_S$ reaction of denatured RNase A, both in 3.3 M $HClO_4$ and in 5 M GdmCl [49]. The acid catalysis results were widely accepted as evidence that the $U_F \leftrightarrow U_S$ reaction of RNase A is proline isomerization, and the later discovery of prolyl isomerases (see below) ended any doubts. In further work, the role of proline isomerization in protein folding kinetics has been thoroughly analyzed, especially for RNase T1 [51, 52], by combining mutagenesis of specific proline residues with sequential mixing experiments and with accurate measurement and analysis of kinetic amplitudes and relaxation times.

The $U_F \leftrightarrow U_S$ reaction of unfolded RNase A is quite slow ($\sim$1000 s) at 0 °C and it is straightforward to ask whether partial folding precedes proline isomerization at 0 °C. In 1979, Cook, Schmid, and Baldwin [53] tested this issue. They found that that partial folding does precede proline isomerization and they obtained two quite surprising results. (1) The major partly folded form (I_N) has properties closely resembling those of native RNase A (thus, I_N refers to a native-like intermediate). I_N even has RNase A catalytic activity [54]! (2) Not only does proline isomerization occur within the folded structure of I_N, but also the isomerization rate is speeded up in I_N by as much as 40-fold, compared with the rate of the $U_S \leftrightarrow U_F$ reaction in denatured RNase A [53]. These experiments gave the first clear indication that partly folded, noncovalent intermediates are sometimes populated during the kinetic process of protein folding.

Because U_S species fold slowly in physiological conditions, which is likely to make them susceptible to proteolytic cleavage, prolyl isomerases seemed needed to speed up proline isomerization in vivo. Gunter Fischer and coworkers found the first prolyl isomerase and in 1985 they showed that it catalyzes the $U_S \leftrightarrow U_F$ reaction of RNase A [55]. At least three classes of prolyl isomerases are known today. The role of prolyl isomerases in folding in vivo is discussed elsewhere in this book (see Chapter 25).

1.7 Covalent Intermediates in the Coupled Processes of Disulfide Bond Formation and Folding

Disulfide bonds stabilize the folded structures of proteins that contain S–S bonds and, when they are reduced, the protein typically unfolds. This observation was the starting point of Anfinsen's work [2] when he showed that the folding process directs the formation of the four unique S–S bonds of native RNase A. Tom Creighton had the basic insight that S–S intermediates can be covalently trapped, purified by chromatography, and structurally characterized. Because formation of S–S bonds is linked to the folding process, these S–S intermediates should also be folding intermediates. Beginning in 1974, Creighton reported the isolation and general properties of both the one-disulfide [56] and two-disulfide [57] intermediates of the small protein BPTI (bovine pancreatic trypsin inhibitor, 58 residues, three S–S bonds). He later measured the equilibrium constants for forming each of the three S–S bonds in BPTI [58, 59]. For example, he found that the effective concentration of the two –SH groups that form the S–S bond between cysteine residues 5 and 55 is $\sim 10^7$ M [58]. This value is three orders of magnitude higher than the effective concentration of the two adjacent –SH groups in dithiothreitol [58], and it illustrates the rigid alignment of these two –SH groups by the folded structure of BPTI. Later, after the development of two-dimensional NMR made it possible to determine the structures of protein species that are difficult to crystallize, Creighton and coworkers determined the structures of various S–S intermediates of BPTI (see, for example, Ref. [60]). Stabilization of the BPTI structure by a given

S–S bond depends on the effective concentration of the two –SH groups before the bond is formed, and the increase in effective concentration as successive S–S bonds are formed illustrates strikingly how the cooperativity of protein folding operates [58, 59]. The same principle has been used at an early stage in the folding of BPTI to examine the interplay between S–S bond and reverse turn formation [61]. The pathway of disulfide bond formation in BPTI is complex and has been the subject of considerable discussion [62, 63].

Early work [2] from Anfinsen's laboratory showed that nonnative S–S bonds are often formed during the kinetic process in which unfolded RNase A folds and eventually makes the correct S–S bonds. Because the S–S bond is covalent, some mechanism is needed to break nonnative S–S bonds during folding and allow formation of new S–S bonds. Anfinsen and coworkers reported in 1963 that enzymes such as protein disulfide isomerase [7] have a major role in ensuring that correct S–S bonds are formed. The role of disulfide isomerases in folding in vivo is discussed elsewhere in this book (see Chapter 26).

1.8
Early Stages of Folding Detected by Antibodies and by Hydrogen Exchange

Initial studies of the folding of peptide fragments, and also of proteins made to unfold by removing a stabilizing linkage or cofactor, gave the following generalization: the tertiary structures of proteins are easily unfolded and little residual structure remains afterwards. In 1956 Harrington and Schellman [9] found that breaking the four disulfide bonds of RNase A causes general unfolding of the tertiary structure and also destroys the helical structure, which should be local structure that could in principle survive loss of the tertiary structure. In 1968 Epand and Scheraga [64] tested by circular dichroism (CD) whether peptides from helix-containing segments of myoglobin still form helices in aqueous solution. They studied two long peptides and found they have very low helix contents; they did not pursue the problem. In 1969 Taniuchi and Anfinsen [65] made a similar experiment with SNase. They cleaved the polypeptide chain between residues 126 and 127, which causes the protein to unfold. Both fragments 1–126 and 127–149 were found to lack detectable native-like structure by various physical methods, including circular dichroism. For SNase as for RNase A, circular dichroism indicates that the native protein has some helical structure and at that time (1968) the X-ray structure of myoglobin was known [4], which gives the detailed structures of its eight helices. Thus, the overall conclusion from these experiments was that the helical secondary structures of the three proteins are stable only when the tertiary structures are present. In 1971 Lewis, Momany and Scheraga [66] proposed a hierarchic mechanism of folding in which β-turns play a directing role at early stages of folding by increasing the effective concentrations of locally formed structures, such as helices, that later interact in the native structure.

Anfinsen considered it likely that proteins fold by a hierarchic mechanism [1], and he developed an antibody method for sensitively detecting any native-like

structure still present in a denatured protein [67]. His method is simple in principle. He and his coworkers took fragments 1–126 and 99–149 of SNase, which were devoid of detectable structure by physical criteria, and bound them covalently to individual sepharose columns. Antisera were prepared against both native SNase and the two polypeptide fragments, and polyclonal antibodies were purified by immunoabsorption against each homologous antigen. The antibodies developed against native SNase were tested for their ability to cross-react with the two denatured fragments. The results indicate that a weak cross-reaction occurs and a denatured fragment reacts with antibodies made against native SNase as if the denatured fragment exists in the ''native format'' a small fraction ($\sim$0.02%) of the time. These experiments are the forerunner of modern ones in which monoclonal antibodies are made against short peptides, and some of the monoclonal antibodies cross-react significantly with the native protein from which the peptide is derived. In 1975 Anfinsen and coworkers made the converse experiment [68]. They found that antibodies directed against denatured fragments of SNase are able to cross-react with native SNase. They conclude that antibodies made against denatured fragments detect unfolded SNase in equilibrium with native SNase, even though only a tiny fraction of the native protein, less than 0.01%, is found to be unfolded.

In 1979 Schmid and Baldwin [69] developed a competition method for detecting H-bonded secondary structure formed at an early stage in the refolding of denatured RNase A. Native proteins were known at that time, from Linderstrøm-Lang's development of the hydrogen exchange method [70], to contain large numbers of highly protected peptide NH protons. Shortly afterwards, in 1982, NMR hydrogen exchange experiments by Wagner and Wüthrich [71] demonstrated that, as expected, the highly protected peptide NH protons of BPTI are ones involved in H-bonded secondary structure. In this period the exchange rates of freely exchanging, unprotected peptide NH protons were already known from earlier studies of dipeptides by Englander and coworkers [72]. The peptide NH exchange rates are base-catalyzed and the rates become faster above pH 7 than the measured folding rates of the two major U_S species of denatured RNase A.

Thus, the principle of the competition experiment is straightforward [69]. Refolding of denatured, ^{3}H-labeled RNase A is performed at pH values where the rate of exchange-out of the ^{3}H label from denatured RNase A is either faster or slower, depending on pH, than the observed rate of refolding to form native RNase A. (The exchange rates of peptide NH protons in denatured RNase A can be computed from the peptide data [72].) When exchange-out is slower than folding, the folding process traps many ^{3}H-labeled protons. When exchange-out is faster than the formation of native RNase A, the observed folding rate can be used to predict the number of ^{3}H-labeled protons that should be trapped by folding. However, the observed number of ^{3}H-labeled protons trapped by folding is always much larger than the number predicted in this way. Control experiments, made at the same pH values but in the presence of modest GdmCl concentrations added to destabilize folding intermediates, show no trapped ^{3}H label. The first conclusion is that one or more folding intermediates are formed rapidly and they give protection against exchange-out of ^{3}H label. The second conclusion is that some form of early struc-

ture, probably H-bonded secondary structure, is stable before the tertiary structure is formed. In 1980, a more convenient and informative pulse-labeling version of the competition experiment was tested [73] and found superior to the competition method. Methods of resolving and assigning the proton spectra of native proteins were being developed rapidly in the early 1980s and it was evident that the secondary structures of early folding intermediates would be determined by this approach, probably within a few years. A stopped-flow apparatus could be used to trap protected peptide NH protons by means of $^{2}H-^{1}H$ exchange, and 2D ^{1}H-NMR could then be used to determine the structural locations of the protected $N^{1}H$ protons.

1.9 Molten Globule Folding Intermediates

In 1981, Oleg Ptitsyn and coworkers released a bombshell [74] that was comparable in its impact to Levinthal's paradox. They proposed that the folding intermediates everyone had been searching for were sitting under our noses in plain sight, in the form of partly folded structures formed when certain native proteins are exposed to mildly destabilizing conditions. A few proteins were known to form these curious, partly folded, structures, particularly at acid pH. Ptitsyn and coworkers proposed that the partly folded forms, or ''acid forms,'' were structurally related to authentic folding intermediates. The acid forms were supposed to differ from true folding intermediates essentially only by protonation reactions resulting from pH titration to acid pH. The acid forms were found to have surprising properties which suggested that their secondary structures are stable and native-like and their conformations are compact, even though the acid forms lack fixed tertiary structures (for reviews, see Refs [75, 76]). Until then, most workers had taken it for granted that folding intermediates should simply be ''partial replicas'' of native proteins. They should contain some unfolded segments plus some other folded segments whose tertiary and secondary structures are native-like. Later work has verified essential features of Ptitsyn's proposal, although argument about the details continues.

Ptitsyn's background was in polymer physics, and he was accustomed to analyzing problems involving the conformations of polymers. In 1973, he gave his forecast of a plausible model for the kinetic process of protein folding [77], which resembles the 1971 hierarchic mechanism of Scheraga and coworkers [66] but includes also later stages in the folding process. Ptitsyn later used the term ''framework model,'' coined in a 1982 review by Kim and Baldwin [78], to describe his model. In making his 1981 proposal [74], Ptitsyn was impressed by the resemblance between the physical properties of acid forms and the properties he had hypothesized for early folding intermediates. He must also have been impressed by Kuwajima's results for the acid form of α-LA, which revealed some striking properties of acid forms (see below).

The name ''molten globule'' was given to these acid forms by Ohgushi and Wada [79] in 1983: ''globule'' meaning compact, ''molten'' meaning no fixed tertiary

structure. Ohgushi and Wada were studying two acid forms of cyt *c*, which are converted from one form to the other by varying the salt concentration [79, 80].

In 1981 the best studied of these partly folded acid forms was bovine α-lactalbumin (α-LA), which was chosen by Ptitsyn and coworkers [74] for their initial study of an acid form. In 1976 and earlier, Kuwajima and coworkers had analyzed the pH-dependent interconversion between the acid form (or "A-state") and native α-LA [81]. They found a very unusual equilibrium folding intermediate in GdmCl-induced denaturation at neutral pH [81], which by continuity – as the pH is varied – is the same species as the acid form of α-LA. The explanation for this unusual folding intermediate is that native α-LA is a calcium metalloprotein, a property discovered only in 1980 [82]. The 1976 [81] and earlier studies of α-LA were made with the apoprotein in the absence of Ca^{2+}, and the apoprotein is much less stable than the holoprotein. When GdmCl-induced unfolding of the more stable holoprotein is studied in the presence of Ca^{2+}, no stable folding intermediate is observed [76]. The near-UV and far-UV CD spectra of the 1976 folding intermediate [81] reveal some basic properties of molten globule intermediates. The α-LA folding intermediate has no fixed tertiary structure, as judged by its near-UV CD spectrum, but its secondary structure resembles that of native α-LA, as judged by its far-UV CD spectrum. In 1990, when 2D ^{1}H-NMR was used together with ^{2}H–^{1}H exchange to determine the locations and stability of the helices in a few acid forms, the helices were found at the same locations as in the native structures. Particularly clear results were found for the helices in the acid forms of cyt *c* [83] and apomyoglobin [84].

1.10
Structures of Peptide Models for Folding Intermediates

By 1979 a paradox was evident concerning the stability of helices in folding intermediates. The experiments of Epand and Scheraga and of Taniuchi and Anfinsen indicated that the helices of myoglobin [64] and SNase [65] were unstable when the intact polypeptide chains of these proteins were cut into smaller fragments. On the other hand, the ^{3}H-labeling experiments of Schmid and Baldwin [69] indicated that an early folding intermediate – probably a H-bonded intermediate – of RNase A is stable before the tertiary structure is formed. In 1971 Brown and Klee [85] had found partial helix formation by CD at 0 °C in the "C-peptide" of RNase A. C-peptide is formed by cyanogen bromide cleavage at Met13 and contains residues 1–13, while residues 3–12 form a helix in native RNase A.

In 1978, Blum, Smallcombe and Baldwin [86] used the four His residues of RNase A as probes for structure in an NMR study in real time of the kinetics of RNase A folding at pH 2, 10 °C. These are conditions in which the folding rate is sufficiently slow to take 1D NMR spectra during folding. The carbon-bound protons of the imidazole side chains could be resolved by 1D NMR in that period, provided the peptide N^{1}H protons are first exchanged for ^{2}H. By chemical shift, His12 appears to be part of a rapidly formed, folded structure at 10 °C, although it is unfolded at 45 °C, pH 2 [86]. This result suggests that the N-terminal helix of RNase

A is partly folded at low temperatures, in agreement with the C-peptide study of Brown and Klee [85]. An ensuing study by Bierzynski et al. [87] confirmed that temperature-dependent helix formation does occur. Interestingly, C-peptide helix formation was found to be strongly pH dependent with apparent p*K* values, indicating that the ionized forms of His12 and either Glu9 or Glu2 are needed for helix formation [87]. Many peptides later, two specific side-chain interactions were found to contribute substantially to C-peptide helix stability [88]: an amino–aromatic interaction between Phe8 and $His12^{+}$, and a salt bridge between $Glu2^{-}$ and $Arg10^{+}$. Both interactions could be seen in the 1970 X-ray structure of RNase S [89], although the Phe 8•••$His\ 12^{+}$ interaction was not recognized as such in 1970.

In 1989, Marqusee et al. [90] found that alanine-based peptides form stable helices in water without the help of any specific interactions. Because alanine has only a $-CH_3$ side chain, this result indicates that the helix backbone itself is stable in water, although the helix has only marginal stability. Side chains longer than that of Ala detract from, rather than increasing, helix stability. In 1985 Dyson and coworkers [91] found that even reverse turns can be detected in short peptides by ^{1}H-NMR, and 10 years later Serrano and coworkers [92] observed formation of a stable β-hairpin in water. Thus, it is possible for all classes of secondary structure to be present, and to aid in directing the folding process, at very early stages of the folding process.

In 1988 a landmark experiment by Oas and Kim [93] showed that peptides are able to model more advanced folding intermediates. Oas and Kim took two peptides from BPTI: P_α, a 16-residue peptide from residues 43–58 which includes the C-terminal helix, and P_β, a 14-residue peptide from residues 20–33 which includes part of the central β-hairpin. Separately, each peptide appears structureless by physical criteria. When the two peptides are joined by forming the 30–51 S–S bond, both helical and β structures appear. NMR characterization indicates that the 3D structure of the peptide complex resembles that of BPTI [93]. The central question about folding intermediates in that period was [78]: are they formed according to the framework model (secondary structure forms before tertiary structure) or the subdomain model (secondary and tertiary structures form simultaneously in local subdomains)? Before the 1988 experiment of Oas and Kim [93], all evidence seemed to support the framework model. After their experiment, the subdomain model became the focus of much further work.

Acknowledgments

I thank Atsushi Ikai for information and Thomas Kiefhaber for discussion.

References

1 Anfinsen, C. B. (1973). Principles that govern the folding of protein chains. *Science* **181**, 223–230.

2 Anfinsen, C. B., Haber, E., Sela, M., & White, Jr., F. H. (1961). The kinetics of formation of native

ribonuclease, during oxidation of the reduced polypeptide chain. *Proc. NatL Acad. Sci. USA* **47**, 1309–1314.

3 Simpson, R. B. & Kauzmann, W. (1953). The kinetics of protein denaturation. I. The behavior of the optical rotation of ovalbumin in urea solutions. *J. Am. Chem. Soc.* **75**, 5139–5152.

4 Kendrew, J. C., Dickerson, R. E., Strandberg, B. E. et al. (1960). Structure of myoglobin. A three-dimensional Fourier synthesis at 2 Å resolution. *Nature (London)* **185**, 422–427.

5 Wu, H. (1931). Studies on denaturation of proteins. XIII. A theory of denaturation. *Chin. J. Physiol.* **5**, 321–344.

6 Kabat, E. A. & Wu, T. T. (1972). Construction of a three-dimensional model of the polypeptide backbone of the variable region of kappa immunoglobulin light chains. *Proc. Natl Acad. Sci. USA* **69**, 960–964.

7 Epstein, C. J., Goldberger, R. F., & Anfinsen, C. B. (1963). The genetic control of tertiary protein structure: studies with model systems. *Cold Spring Harbor Symp. Quant. Biol.* **28**, 439–444.

8 Levitt, M. & Warshel, A. (1975). Computer simulation of protein folding. *Nature (London)* **253**, 694–698.

9 Harrington, W. F. & Schellman, J. A. (1956). Evidence for the instability of hydrogen-bonded peptide structures in water based on studies of ribonuclease and oxidized ribonuclease. *C.R. Trav. Lab. Carlsberg, Sér. Chim.* **30**, 21–43.

10 Brandts, J. F. (1965). The nature of the complexities in the ribonuclease conformational transition and the implications regarding clathrating. *J. Am. Chem. Soc.* **87**, 2759–2760.

11 Kauzmann, W. (1959). Factors in interpretation of protein denaturation. *Adv. Protein Chem.* **14**, 1–63.

12 Ginsburg, A. & Carroll, W. R. (1965). Some specific ion effects on the conformation and thermal stability of ribonuclease. *Biochemistry* **4**, 2159–2174.

13 Lumry, R., Biltonen, R., & Brandts, J. F. (1966). Validity of the "two-state" hypothesis for conformational transitions of proteins. *Biopolymers* **4**, 917–944.

14 Privalov, P. L. (1979). Stability of proteins. Small globular proteins. *Adv. Protein Chem.* **33**, 167–241.

15 Tanford, C. (1968). Protein denaturation. A. Characterization of the denatured state. B. The transition from native to denatured state. *Adv. Protein Chem.* **23**, 121–282.

16 Levinthal, C. (1968). Are there pathways for protein folding? *J. Chim. Phys.* **65**, 44–45.

17 Levinthal, C. (1969). How to fold graciously. In *Mössbauer Spectroscopy in Biological Systems* (Frauenfelder, H., Gunsalus, I. C., Tsibris, J. C. M., Debrunner, P. G., & Münck, E., eds), pp. 22–24, University of Illinois Press, Urbana.

18 Zwanzig, R., Szabo, A., & Bagchi, B. (1992). Levinthal's paradox. *Proc. Natl Acad. Sci. USA* **89**, 20–22.

19 Wang, Z., Mottonen, J., & Goldsmith, E. J. (1996). Kinetically controlled folding of the serpin plasminogen activator inhibitor 1. *Biochemistry* **35**, 16443–16448.

20 Sohl, J. L., Jaswal, S. S., & Agard, D. A. (1998). Unfolded conformations of α-lytic protease are more stable than its native state. *Nature (London)* **395**, 817–819.

21 Taniuchi, H. (1970). Formation of randomly paired disulfide bonds in des-(121–124)-ribonuclease after reduction and reoxidation. *J. Biol. Chem.* **245**, 5459–5468.

22 Goldberg, M. E. (1969). Tertiary structure of *Escherichia coli* β-D-galactosidase. *J. Mol. Biol.* **46**, 441–446.

23 Wetlaufer, D. B. (1973). Nucleation, rapid folding and globular intrachain regions in proteins. *Proc. Natl Acad. Sci. USA* **70**, 697–701.

24 Lesk, A. M. & Rose, G. D. (1981). Folding units in globular proteins. *Proc. Natl Acad. Sci. USA* **78**, 4304–4308.

25 London, J., Skrzynia, C., & Goldberg, M. E. (1974). Renaturation

of *Escherichia coli* tryptophanase after exposure to 8 M urea: evidence for the existence of nucleation centers. *Eur. J. Biochem.* **47**, 409–415.

26 Jaenicke, R. & Rudolph, R. (1980). Folding and association of oligomeric enzymes. In *Protein Folding* (Jaenicke, R., ed.), pp. 525–546, Elsevier/North Holland, Amsterdam.

27 Ikai, A. & Tanford, C. (1971). Kinetic evidence for incorrectly folded intermediate states in the refolding of denatured proteins. *Nature (London)* **230**, 100–102.

28 Tsong, T. Y., Baldwin, R. L., & Elson, E. L. (1971). The sequential unfolding of ribonuclease A: detection of a fast initial phase in the kinetics of unfolding. *Proc. Natl Acad. Sci. USA* **68**, 2712–2715.

29 Schechter, A. N., Chen, R. F., & Anfinsen, C. B. (1970). Kinetics of folding of staphylococcal nuclease. *Science* **167**, 886–887.

30 Epstein, H. F., Schechter, A. N., Chen, R. F., & Anfinsen, C. B. (1971). Folding of staphylococcal nuclease: kinetic studies of vtwo processes in acid denaturation. *J. Mol. Biol.* **60**, 499–508.

31 Ikai, A., Fish, W. W., & Tanford, C. (1973). Kinetics of unfolding and refolding of proteins. II. Results for cytochrome *c*. *J. Mol. Biol.* **73**, 165–184.

32 Tanford, C., Aune, K. C., & Ikai, A. (1973). Kinetics of unfolding and refolding of proteins. III. Results for lysozyme. *J. Mol. Biol.* **73**, 185–197.

33 Ikai, A. & Tanford, C. (1973). Kinetics of unfolding and refolding of proteins. I. Mathematical analysis. *J. Mol. Biol.* **73**, 145–163.

34 Pohl, F. M. (1968). Einfache Temperatursprung-Methode im Sekunden-bis Stundenbereich und die reversible Denaturierung von Chymotrypsin. *Eur. J. Biochem.* **4**, 373–377.

35 Pohl, F. M. (1968). Kinetics of reversible denaturation of trypsin in water and water-ethanol mixtures. *Eur. J. Biochem.* **7**, 146–152.

36 Pohl, F. M. (1969). On the kinetics of structural transition I of some pancreatic proteins. *FEBS Lett.* **3**, 60–64.

37 Tsong, T. Y., Baldwin, R. L., & Elson, E. L. (1972). Properties of the unfolding and refolding reactions of ribonuclease A. *Proc. Natl Acad. Sci. USA* **69**, 1809–1812.

38 Pörschke, D. & Eigen, M. (1971). Cooperative non-enzymic base recognition. III. Kinetics of the helix-coil transition of the oligoribouridylic-oligoriboadenylic acid system and of oligoriboadenylic acid alone at acid pH. *J. Mol. Biol.* **62**, 361–381.

39 Tsong, T. Y., Baldwin, R. L., & McPhie, P. (1972). A sequential model of nucleation-dependent protein folding: kinetic studies of ribonuclease A. *J. Mol. Biol.* **63**, 453–475.

40 Tsong, T. Y. & Baldwin, R. L. (1972). Kinetic evidence for intermediate states in the unfolding of chymotrypsinogen A. *J. Mol. Biol.* **69**, 145–148.

41 Tsong, T. Y. & Baldwin, R. L. (1972). Kinetic evidence for intermediate states in the unfolding of ribonuclease A. II. Kinetics of exposure to solvent of a specific dinitrophenyl group. *J. Mol. Biol.* **69**, 149–153.

42 Garel, J.-R. & Baldwin, R. L. (1973). Both the fast and slow refolding reactions of ribonuclease A yield native enzyme. *Proc. Natl Acad. Sci. USA* **70**, 3347–3351.

43 Garel, J.-R., Nall, B. T., & Baldwin, R. L. (1976). Guanidine-unfolded state of ribonuclease A contains both fast- and slow-refolding species. *Proc. Natl Acad. Sci. USA* **73**, 1853–1857.

44 Hagerman, P. J. & Baldwin, R. L. (1976). A quantitative treatment of the kinetics of the folding transition of ribonuclease A. *Biochemistry*, **15**, 1462–1473.

45 Hagerman, P. J., Schmid, F. X., & Baldwin, R. L. (1979). Refolding behavior of a kinetic intermediate observed in the low pH unfolding of ribonuclease A. *Biochemistry* **18**, 293–297.

46 Houry, W. A., Rothwarf, D. M., & Scheraga, H. A. (1994). A very fast phase in the refolding of disulfide-intact ribonuclease A: implications for the refolding and unfolding pathways. *Biochemistry* **33**, 2516–2530.

47 Brandts, J. F., Halvorson, H. R., & Brennan, M. (1975). Consideration of the possibility that the slow step in protein denaturation reactions is due to cis-trans isomerism of proline residues. *Biochemistry* **14**, 4953–4963.

48 Cheng, H. N. & Bovey, F. A. (1977). Cis-trans equilibrium and kinetic studies of acetyl-L-proline and glycyl-L-proline. *Biopolymers* **16**, 1465–1472.

49 Schmid, F. X. & Baldwin, R. L. (1978). Acid catlysis of the formation of the slow-folding species of RNase A: evidence that the reaction is proline isomerization. *Proc. Natl Acad. Sci. USA* **75**, 4764–4768.

50 Steinberg, I. Z., Harrington, W. F., Berger, A., Sela, M., & Katchalski, E. (1960). The configurational changes of poly-L-proline in solution. *J. Am. Chem. Soc.* **82**, 5263–5279.

51 Kiefhaber, T. & Schmid, F. X. (1992). Kinetic coupling between protein folding and prolyl isomerization. II. Folding of ribonuclease A and ribonuclease T_1. *J. Mol. Biol.* **224**, 231–240.

52 Mayr, L. M., Odefey, C., Schutkowski, Mike, & Schmid, F. X. (1996). Kinetic analysis of the unfolding and refolding reactions of ribonuclease T1 by a stopped-flow double-mixing technique. *Biochemistry* **35**, 5550–5561.

53 Cook, K. H., Schmid, F. X., & Baldwin, R. L. (1979). Role of proline isomerization in folding of ribonuclease A at low temperatures. *Proc. Natl Acad. Sci. USA* **76**, 6157–6161.

54 Schmid, F. X. & Blaschek, H. (1981). A native-like intermediate on the ribonuclease A folding pathway. 2. Comparison of its properties to native ribonuclease A. *Eur. J. Biochem.* **114**, 111–117.

55 Fischer, G. & Bang, H. (1985). The refolding of urea-denatured ribonuclease A is catalyzed by peptidyl-prolyl cis-trans isomerase. *Biochim. Biophys. Acta* **828**, 39–42.

56 Creighton, T. E. (1974). The single-disulfide intermediates in the refolding of reduced pancreatic trypsin inhibitor. *J. Mol. Biol.* **87**, 603–624.

57 Creighton, T. E. (1974). The two-disulfide intermediates and the folding pathway of reduced pancreatic trypsin inhibitor. *J. Mol. Biol.* **95**, 167–199.

58 Creighton, T. E. (1983). An empirical approach to protein conformation stability and flexibility. *Biopolymers* **22**, 49–58.

59 Creighton, T. E. (1988). Disulfide bonds and protein stability. *BioEssays* **8**, 57–64.

60 van Mierlo, C. P. M., Darby, N. J., Neuhaus, D., & Creighton, T. E. (1991). Two-dimensional ^{1}H nuclear magnetic resonance study of the (5–55) single-disulfide folding intermediate of pancreatic trypsin inhibitor. *J. Mol. Biol.* **222**, 373–390.

61 Zdanowski, K. & Dadlez, M. (1999). Stability of the residual structure in unfolded BPTI in different conditions of temperature and solvent composition measured by disulfide kinetics and double mutant cycle analysis. *J. Mol. Biol.* **287**, 433–445.

62 Creighton, T. E. (1992). The disulfide folding pathway of BPTI. *Science* **256**, 111–112.

63 Weissman, J. S. & Kim, P. S. (1992). Response. *Science* **256**, 112–114.

64 Epand, R. M. & Scheraga, H. A. (1968). The influence of long-range interactions on the structure of myoglobin. *Biochemistry* **7**, 2864–2872.

65 Taniuchi, H. & Anfinsen, C. B. (1969). An experimental approach to the study of the folding of staphylococcal nuclease. *J. Biol. Chem.* **244**, 3864–3875.

66 Lewis, P. N., Momany, F. A., & Scheraga, H. A. (1971). Folding of polypeptide chains in proteins: a proposed mechanism for folding. *Proc. Natl Acad. Sci. USA* **68**, 2293–2297.

67 Sachs, D. H., Schechter, A. N., Eastlake, A., & Anfinsen, C. B. (1972). An immunologic approach to

the conformational equilibria of polypeptides. *Proc. Natl Acad. Sci. USA* **69**, 3790–3794.

68 Furie, B., Schechter, A. N., Sachs, D. H., & Anfinsen, C. B. (1975). An immunological approach to the conformational equilibrium of staphylococcal nuclease. *J. Mol. Biol.* **92**, 497–506.

69 Schmid, F. X. & Baldwin, R. L. (1979). Detection of an early intermediate in the folding of ribonuclease A by protection of amide protons against exchange. *J. Mol. Biol.* **135**, 199–215.

70 Linderstrøm-Lang, K. (1958). Deuterium exchange and protein structure. In *Symposium on Protein Structure* (Neuberger, A., ed.) Methuen, London.

71 Wagner, G. A. & Wüthrich, K. (1982). Amide proton exchange and surface conformation of BPTI in solution. *J. Mol. Biol.* **160**, 343–361.

72 Molday, R. S., Englander, S. W., & Kallen, R. G. (1972). Primary structure effects on peptide group hydrogen exchange. *Biochemistry* **11**, 150–158.

73 Kim, P. S. & Baldwin, R. L. (1980). Structural intermediates trapped during the folding of ribonuclease A by amide proton exchange. *Biochemistry* **19**, 6124–6129.

74 Dolgikh, D. A., Gilmanshin, R. I., Brazhnikov, E. V. et al. (1981). α-Lalbumin: Compact state with fluctuating tertiary structure? *FEBS Lett.* **136**, 311–315.

75 Ptitsyn, O. B. (1995). Molten globule and protein folding. *Adv. Protein Chem.* **47**, 83–229.

76 Kuwajima, K. (1989). The molten globule state as a clue for understanding the folding and cooperativity of globular-protein structure. *Proteins Struct. Funct. Genet.* **6**, 87–103.

77 Ptitsyn, O. B. (1973). The stepwise mechanism of protein self-organization. *Dokl. Nauk SSSR* **210**, 1213–1215.

78 Kim, P. S. & Baldwin, R. L. (1982). Specific intermediates in the folding reactions of small proteins and the mechanism of protein folding. *Annu. Rev. Biochem.* **51**, 459–489.

79 Ohgushi, M. & Wada, A. (1983). 'Molten-globule state': a compact form of globular proteins with mobile side chains. *FEBS Lett.* **164**, 21–24.

80 Kuroda, Y., Kidokoro, S., & Wada, A. (1992). Thermodynamic characterization of cytochrome *c* at low pH. Observation of the molten globule state and of the cold denaturation process. *J. Mol. Biol.* **223**, 1139–1153.

81 Kuwajima, K., Nitta, K., Yoneyama, M., & Sugai, S. (1976). Three-state denaturation of α-lactalbumin by guanidine hydrochloride. *J. Mol. Biol.* **106**, 359–373.

82 Hiraoka, Y., Segawa, T., Kuwajima, K., Sugai, S., & Murai, N. (1980). α-Lactalbumin: a calcium metalloprotein. *Biochem. Biophys. Res. Commun.* **95**, 1098–1104.

83 Jeng, M.-F., Englander, S. W., Elöve, G., Wand, A. J., & Roder, H. (1990). Structural description of acid-denatured cytochrome *c* by hydrogen exchange and 2D NMR. *Biochemistry* **29**, 10433–10437.

84 Hughson, F. M., Wright, P. E., & Baldwin, R. L. (1990). Structural characterization of a partly folded apomyoglobin intermediate. *Science* **249**, 1544–1548.

85 Brown, J. E. & Klee, W. A. (1971). Helix-coil transition of the isolated amino terminus of ribonuclease. *Biochemistry* **10**, 470–476.

86 Blum, A. D., Smallcombe, S. H., & Baldwin, R. L. (1978). Nuclear magnetic resonance evidence for a structural intermediate at an early stage in the refolding of ribonuclease A. *J. Mol. Biol.* **118**, 305–316.

87 Bierzynski, A., Kim, P. S., & Baldwin, R. L. (1982). A salt bridge stabilizes the helix formed by isolated C-peptide of RNase A. *Proc. Natl Acad. Sci. USA* **79**, 2470–2474.

88 Shoemaker, K. R., Fairman, R., Kim, P. S., York, E. J., Stewart, J. M., & Baldwin, R. L. (1987). The C-peptide helix from ribonuclease A considered

as an autonomous folding unit. *Cold Spring Harbor Symp. Quant. Biol.* **52**, 391–398.

89 Wyckoff, H. W., Tsernoglou, D., Hanson, A. W., Knox, J. R., Lee, B., & Richards, F. M. (1970). The 3-dimensional structure of ribonuclease S: interpretation of an electron density map at a nominal resolution of 2 Å. *J. Biol. Chem.* **245**, 305–328.

90 Marqusee, S., Robbins, V. H., & Baldwin, R. L. (1989). Unusually stable helix formation in short alanine-based peptides. *Proc. Natl Acad. Sci. USA* **86**, 5286–5290.

91 Dyson, H. J., Cross, K. J., Houghten, R. A., Wilson, I. A., Wright, P. E., & Lerner, R. A. (1985). The immunodominant site of a synthetic immunogen has a conformational preference in water for a type-II reverse turn. *Nature (London)* **318**, 480–483.

92 Bianco, F. J., Rivas, G., & Serrano, L. (1995). A short linear peptide that folds into a stable β-hairpin in aqueous solution. *Nature Struct. Biol.* **1**, 584–590.

93 Oas, T. G. & Kim, P. S. (1988). A peptide model of a protein folding intermediate. *Nature (London)* **336**, 42–48.

2
Spectroscopic Techniques to Study Protein Folding and Stability

Franz Schmid

2.1
Introduction

Optical spectroscopy provides the standard techniques for measuring the conformational stabilities of proteins and for following the kinetics of unfolding and refolding reactions. Practically all unfolding and refolding reactions are accompanied by changes in absorbance, fluorescence, or optical activity (usually measured as the circular dichroism). These optical properties scale linearly with protein concentration. Spectra and spectral changes can be measured with very high accuracy in dilute protein solutions, and spectrophotometers are standard laboratory equipment. Therefore the methods of optical spectroscopy will remain the basic techniques for studying protein folding. Light absorbance occurs in about 10^{-15} s and the excited states show lifetimes of around 10^{-8} s. Optical spectroscopy is thus well suited for measuring the kinetics of ultrafast processes in folding (e.g., in temperature-jump or pressure-jump experiments).

Proteins absorb and emit light in the UV range of the spectrum. The absorbance originates from the peptide groups, from the aromatic amino acid side chains and from disulfide bonds. The fluorescence emission originates from the aromatic amino acids. Some proteins that carry covalently linked cofactors, such as the heme proteins, show absorbance in the visible range.

In absorption, light energy is used to promote electrons from the ground state to an excited state, and when the excited electrons revert back to the ground state they can lose their energy in the form of emitted light, which is called fluorescence. When a chromophore is part of an asymmetric structure, or when it is immobilized in an asymmetric environment, left-handed and right-handed circularly polarized light are absorbed to different extents, and we call this phenomenon circular dichroism (CD).

The energies of the ground and the activated state depend on the molecular environment and the mobility of the chromophores, and therefore the optical properties of folded and unfolded proteins are usually different. Spectroscopy is a nondestructive method, and, if necessary, the samples can be recovered after the experiments.

Protein Folding Handbook. Part I. Edited by J. Buchner and T. Kiefhaber

ISBN: 3-527-30784-2

This chapter provides an introduction into the spectral properties of amino acids and proteins as well as practical advice for the planning and the interpretation of spectroscopic measurements of protein folding and stability.

2.2 Absorbance

Light absorption can occur when an incoming photon provides the energy that is necessary to promote an electron from the ground state to an excited state. The energy (E) of light depends on its frequency ν ($E = h\nu$) and is thus inversely correlated with its wavelength λ ($E = hc/\lambda$). Light in the 200-nm region has sufficient energy for exciting electrons that participate in small electronic systems such as double bonds. Aromatic molecules have lower lying excited states, and therefore they also absorb light in the region between 250 and 290 nm, which is called the ''near UV'' or ''aromatic'' region of a spectrum. The amino acids phenylalanine, tyrosine, and tryptophan absorb here, as well as the bases in nucleic acids. The aromatic region is used extensively to follow the conformational transitions of proteins and nucleic acids. Light in the visible region of the spectrum can only excite electrons that participate in extended delocalized π systems. Such systems do not occur in normal proteins, but can be introduced by site-specific labeling. The basic aspects of protein absorption are very well covered in Refs [1–6].

The absorbance (A) is related to the intensity of the light before (I_o) and after (I) passage through the protein solution:

$$A = -\log_{10}(I/I_o) \tag{1}$$

The absorbance depends linearly on the concentration of the absorbing molecules in a solution, and absorbance can be measured very easily and with very high accuracy. Therefore absorbance spectroscopy is the most common method for determining the concentration of biological macromolecules in solution. The relation between A and the molar concentration c is given by the Beer-Lambert relationship:

$$A = \varepsilon \times c \times l \tag{2}$$

where l is the pathlength in cm, and ε is the molar absorption coefficient, which can be determined experimentally or calculated for proteins by adding up the contributions of the constituent aromatic amino acids of a protein [7–10].

2.2.1 Absorbance of Proteins

Proteins absorb light in the UV range. As an example, the absorption spectrum of lysozyme is shown in Figure 2.1. The peptide bonds of the protein backbone ab-

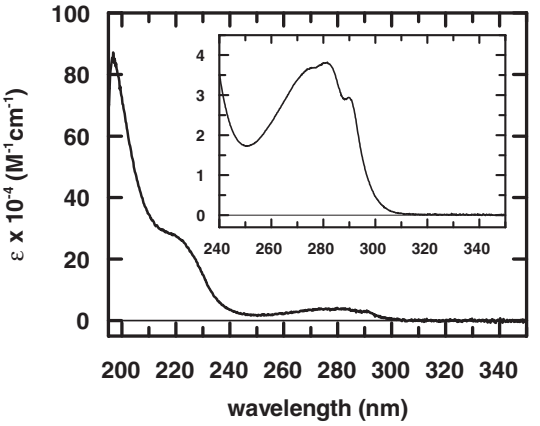

Fig. 2.1. Absorption spectrum of lysozyme. The spectrum was measured at a protein concentration of 0.65 μM in 10 mM K-phosphate buffer pH 7.0, 25 °C, in a 1-cm cell. The inset provides an expanded view of the spectrum in the near-UV region. It was measured with 5.5 μM lysozyme under otherwise identical conditions.

sorb strongly between 180 and 230 nm. Figure 2.1 shows the descending slope of this absorption. The shoulder near 220 nm also contains significant contributions from the aromatic residues of lysozyme. The inset of Figure 2.1 provides an expanded view of the near-UV region of the spectrum. The absorption here is caused by the aromatic side chains of tyrosine, tryptophan, and phenylalanine. Disulfide bonds display a very weak absorbance band around 250 nm. Figure 2.1 emphasizes that proteins absorb much more strongly in the far-UV region than in the near-UV (the "aromatic") region, which is commonly used to measure protein concentrations and to follow protein unfolding.

Spectra of the individual aromatic amino acids are shown in Figure 2.2; their molar absorptions at the respective maxima in the near UV are compared in Table 2.1. The contributions of phenylalanine, tyrosine, and tryptophan to the absorbance of a protein are strongly different. In the aromatic region the molar absorption of phenylalanine ($\lambda_{max} = 258$ nm, $\varepsilon_{258} = 200$ M^{-1} cm^{-1}) is smaller by an order of magnitude compared with those of tyrosine ($\lambda_{max} = 275$ nm, $\varepsilon_{275} = 1400$ M^{-1} cm^{-1}) and tryptophan ($\lambda_{max} = 280$ nm, $\varepsilon_{280} = 5600$ M^{-1} cm^{-1}), and it is virtually zero above 270 nm. The near-UV spectrum of a protein is therefore dominated by the contributions of tyrosine and tryptophan. The shape of the absorbance spectrum of a protein reflects the relative contents of the three aromatic residues in the molecule.

The absorbance maximum near 280 nm is used for determining the concentrations of protein solutions and the 280–295 nm range is used to follow protein unfolding reactions. In this wavelength range only tyrosine and tryptophan contribute to the observed absorbance and to the changes caused by conformational changes. With the distinct fine structure of their absorbance (Figure 2.2) the phenylalanine residues contribute "wiggles" in the 250–260 nm region, and they influence the

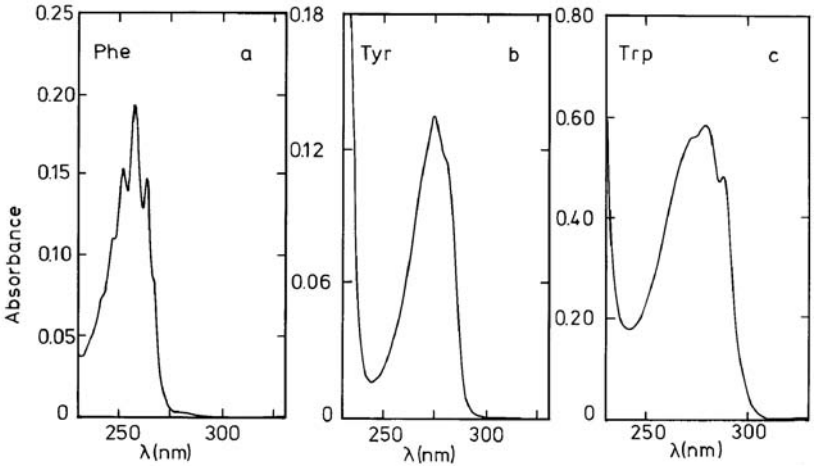

Fig. 2.2. Ultraviolet absorption spectra of the aromatic amino acids in a 1-cm cell in 0.01 M potassium phosphate buffer, pH 7.0 at 25 °C. (a) 1 mM phenylalanine, (b) 0.1 mM tyrosine, (c) 0.1 mM tryptophan. The figure is taken from Ref. [6].

ratio A_{260}/A_{280}, which is often used to identify contaminating nucleic acids in protein preparations.

The aromatic amino acids absorb only below 310 nm, and therefore pure protein solutions should not show absorbance at wavelengths greater than 310 nm. Proteins that are devoid of tryptophan should not absorb above 300 nm (cf. Figure 2.2). A sloping baseline in the 310–400 nm region usually originates from light scattering when large particles, such as aggregates are present in the protein solution. A plot of $\log_{10} A$ as a function of $\log_{10}$ wavelength (above 310 nm) reveals the contribution of light scattering, and the linear extrapolation to shorter wavelength can be used to correct the measured absorbance for the contribution of scattering [5].

Figure 2.3 reflects the strong influence of tryptophan residues on absorbance spectra. It compares the absorption spectra of the wild-type form (Figure 2.3a) and the Trp59Tyr variant (Figure 2.3b) of ribonuclease T1. The wild-type protein

Tab. 2.1. Absorbance and fluorescence properties of the aromatic amino acids[a].

Compound	*Absorbance*		*Fluorescence*		*Sensitivity*
	λ_{max} *(nm)*	ε_{max} *(M^{-1} cm^{-1})*	λ_{max} *(nm)*	$\phi_F{}^b$	$\varepsilon_{max} \times \phi_F{}^b$ *(M^{-1} cm^{-1})*
Tryptophan	280	5600	355	0.13	730
Tyrosine	275	1400	304	0.14	200
Phenylalanine	258	200	282	0.02	4

[a] In water at neutral pH; data are from Ref. [26].
[b] ϕ_F, fluorescence quantum yield.

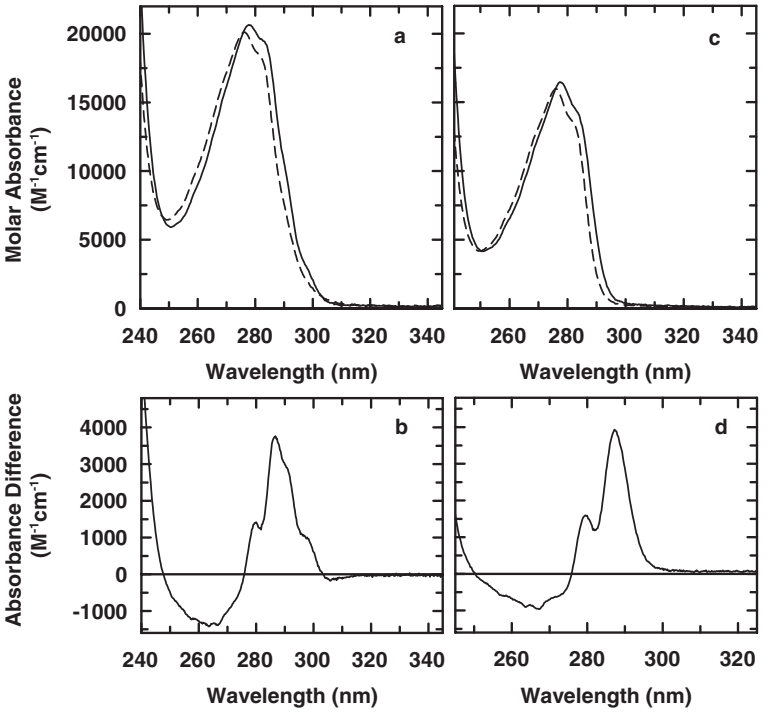

Fig. 2.3. Ultraviolet absorption spectra of a) the wild-type form, and c) the Trp59Tyr variant of ribonuclease T1. The spectra of the native proteins (in 0.1 M sodium acetate, pH 5.0) are shown by the continuous lines. The spectra of the unfolded proteins (in 6.0 M GdmCl in the same buffer) are shown by broken lines. The difference spectra between the native and unfolded forms are shown in b) and d). Spectra of 15 μM protein were measured at 25 °C in 1-cm cuvettes in a double-beam instrument with a bandwidth of 1 nm at 25 °C. The spectra of the native and unfolded proteins were recorded successively, stored, and subtracted. The figure is taken from Ref. [6].

contains one tryptophan and nine tyrosines, the Trp59Tyr variant contains 10 tryosines and no tryptophan. The Trp59Tyr replacement reduces the absorbance in the 280–290 nm region significantly (Figure 2.3c), and the absorbance is essentially zero above 300 nm.

In folded proteins, most of the aromatic residues are buried in the hydrophobic core of the molecule, and upon unfolding they become exposed to the aqueous solvent. The spectral changes that accompany unfolding are dominated by a shift of the absorption spectra of the aromatic amino acids towards lower wavelengths (a blue shift). In addition, small changes in intensity and peak widths are observed as well. The blue shift upon unfolding is typically in the range of 3 nm. It leads to maxima in the difference spectra between native and unfolded proteins in the descending slope of the original spectrum, that is in the 285–288 nm region for tyrosine and around 291–294 nm for tryptophan [11].

Figure 2.3 shows also the spectra for the unfolded forms of the two variants of ribonuclease T1. The difference spectra in Figure 2.3b,d show that the maximal dif-

ferences in absorbance are indeed observed in the descending slopes of the original spectra in the 285–295 nm region. The difference spectrum of the Trp59Tyr variant (Figure 2.3d) shows a prominent maximum at 287 nm. It is typical for proteins that contain tyrosine residues only. In the wild-type protein with its single tryptophan (Figure 2.3b) additional signals are observed between 290 and 300 nm. They originate from the absorbance bands of tryptophan, which are visible as shoulders in the protein spectrum (Figure 2.3a). Difference spectra between the native and the unfolded form, such as those for the variants of ribonuclease T1 in Figure 2.3b,d are observed for most proteins. Generally, these differences are small, but they can be determined with very high accuracy. The contributions of phenylalanine residues to difference spectra are very small. In some cases they are apparent as ripples in the spectral region around 260 nm (cf. Figure 2.3b,d). They are easily mistaken as instrumental noise.

Proteins are usually unfolded by increasing the temperature or by adding destabilizing agents such as urea or guanidinium chloride (GdmCl) (see Chapter 3). These changes not only unfold the protein, but they also influence the spectral properties of the protein solution. The refractive index of the solution decreases slightly with increasing temperature, the protein concentration decreases because the solution expands upon heating, and the ionization state of dissociable groups can change. All these effect are very small, and in combination they often lead to an almost temperature independent protein absorbance in the absence of unfolding.

Chemical denaturants have a significant influence on the absorbances of tyrosine and tryptophan at 287 nm and at 291 nm, respectively, where protein unfolding is usually monitored. The refractive index of the solvent increases as a function of the concentration of GdmCl or urea, which leads to a slight shift to higher wavelengths (a red shift) of the spectra and thus to an increase in absorbance at 287 and 291 nm. A_{291} of tryptophan increases by about 50% when 7 M GdmCl is added. Similar increases are also observed for tyrosine at 287 nm and when urea is used as the denaturant. The GdmCl and urea dependences of tyrosine and tryptophan absorbance are found in Ref. [6]. The spectrum of the unfolded form of a protein and its denaturant dependence can be modeled by mixing tyrosine and tryptophan in a ratio as in the protein under investigation and by measuring the absorbance of this mixture as a function of the denaturant concentration. Such data provide adequate base lines for denaturant-induced unfolding transitions.

The absorbance changes upon unfolding are measured in the steeply descending slopes of the absorbance spectra (cf. Figure 2.3) and consequently they depend on the instrumental settings (in particular on the bandwidth). The reference data must therefore be determined under the same experimental settings as the actual unfolding transition.

2.2.2
Practical Considerations for the Measurement of Protein Absorbance

The solvents used for spectroscopic measurements should be transparent in the wavelength range of the experiment. Water absorbs only below 170 nm, but several of the commonly used buffers absorb significantly already in the region below

Tab. 2.2. Absorbance of various salt and buffer solutions in the far-UV region[a].

Compound		*No absorbance above (nm)*	*Absorbance of a 0.01 M solution in a 0.1-cm cell at:*			
			210 nm	*200 nm*	*190 nm*	*180 nm*
$NaClO_4$		170	0	0	0	0
NaF, KF		170	0	0	0	0
Boric acid		180	0	0	0	0
NaCl		205	0	0.02	>0.5	>0.5
Na_2HPO_4		210	0	0.05	0.3	>0.5
NaH_2PO_4		195	0	0	0.01	0.15
Na-acetate		220	0.03	0.17	>0.5	>0.5
Glycine		220	0.03	0.1	>0.5	>0.5
Diethylamine		240	0.4	>0.5	>0.5	>0.5
NaOH	pH 12	230	≥0.5	>2	>2	>2
Boric acid, NaOH	pH 9.1	200	0	0	0.09	0.3
Tricine	pH 8.5	230	0.22	0.44	>0.5	>0.5
Tris	pH 8.0	220	0.02	0.13	0.24	>0.5
Hepes	pH 7.5	230	0.37	0.5	>0.5	>0.5
Pipes	pH 7.0	230	0.20	0.49	0.29	>0.5
Mops	pH 7.0	230	0.10	0.34	0.28	>0.5
Mes	pH 6.0	230	0.07	0.29	0.29	>0.5
Cacodylate	pH 6.0	210	0.01	0.20	0.22	>0.5

[a] Buffers were titrated with 1 M NaOH or 0.5 M H_2SO_4 to the indicated pH values. Data are from Ref. [6].

230 nm. It is therefore important to select appropriate buffers for measurements in this spectral region and to carefully match buffer concentrations in the sample and the reference cell. Absorbance values of commonly used salt and buffer solutions are found in Table 2.2.

Denaturants such as urea and GdmCl are used in very high concentrations (typically 1–10 M) in protein unfolding experiments. Therefore, the purity of these unfolding agents is of utmost importance. Even impurities in the 1 ppm range are present in the same range of concentration as the protein to be studied (often near 1 μM). Such impurities (such as cyanate in urea solutions) might lead to chemical modifications of the protein. In addition, they may absorb light and thus interfere with the measurement of protein difference spectra.

Solutions for spectroscopy should be filtered through 0.45-μm filters or centrifuged to remove dust particles. For measuring difference spectra such as in protein unfolding studies, a double-beam spectrophotometer and a set of matched quartz cells should be used. The equivalence of two cuvettes is easily tested by placing aliquots of the same solution (e.g., a solution of the protein of interest) into sample and reference cuvette. The difference in absorbance between both cells should ideally be zero (or <0.5% of the measured absorbance) in the wavelength range of interest.

2.2.3 Data Interpretation

Absorbance spectroscopy is an accurate method, but usually spectral changes such as those observed upon protein unfolding cannot be interpreted in molecular terms. The size and shape of difference spectra depends on the nature and the number of the aromatic amino acids as well as on the degree of burial of their side chains in the interior of the native protein. Changes can be assigned to particular aromatic residues only for proteins that carry only a single tyrosine or tryptophan residue, for example, or for mutants that differ from the reference protein only in a single aromatic residue (such as the ribonuclease T1 variants in Figure 2.3).

In the early days of protein spectroscopy there were efforts to determine by difference spectroscopy the number of aromatic residues that are buried in the native protein and become exposed upon unfolding. Donovan [3] presented estimates for the change in absorbance produced by the transfer of a residue from the protein interior to water. He suggested numbers of $-700\ M^{-1}\ cm^{-1}$ at 287 nm for tyrosine and $-1600\ M^{-1}\ cm^{-1}$ at 292 nm for tryptophan. These values were derived by assuming that the transfer from the interior of a protein to an aqueous environment is equivalent to a transfer from 120% ethylene glycol to water. In a protein the absorbance changes upon unfolding depend on the environment of the aromatic residues in the folded protein, which are different for the individual residues, and therefore the numbers given above are, at best, reasonable first approximations.

In summary, the molecular interpretation of absorption differences is often vague. The usefulness of absorption spectroscopy for studies of protein folding rather lies in the favourable properties of absorbance and the ease of the measurements. Absorbance changes linearly with concentration, and even small differences in absorbance can be measured with very high accuracy and reproducibility. Moreover, absorbance can be followed with a very high time resolution after rapid mixing or after perturbations such as a temperature or a pressure jump. Thus, absorbance spectroscopy remains to be a powerful technique for determining the stability of proteins (Chapter 3) and for following the kinetics of protein unfolding and refolding (Chapter 12.1).

2.3 Fluorescence

A molecule emits fluorescence when, after excitation, an electron returns from the first excited state (S_1) back to the ground state (S_0). At about 10^{-8} s, the lifetime of the excited state is very long compared with the time for excitation, which takes only about 10^{-15} s (on the human time scale this would be equivalent to the times of 1 year and 1 second). An excited molecule thus has ample time to relax into the lowest accessible vibrational and rotational states of S_1 before it returns to the ground state. As a consequence, the energy of the emitted light is always smaller

than that of the absorbed light. In other words, the fluorescence emission of a chromophore always occurs at a wavelength that is higher than the wavelength of its absorption.

Electrons can revert to the ground state S_0 also by nonradiative processes (such as vibrational transitions), and in some instances transitions to the excited triplet state T_1 occur. The S_1 to T_1 transition is facilitated by magnetic perturbations, such as the collision of an activated molecule with paramagnetic molecules or with molecules with polarizable electrons. This leads to the phenomenon of fluorescence quenching. Good collisional quenchers are iodide ions, acrylamide, or oxygen. Quenching can also occur intramolecularly, in proteins by the side chains of Cys and His and by amides and carboxyl groups. All conformational transitions that change the exposure to quenchers in the solvent or within the protein will thus lead to fluorescence changes.

Another factor that leads to a decrease in emission is fluorescence resonance energy transfer (FRET), also called Förster transfer. The efficiency of this energy transfer between two chromophores depends, among other factors, on the extent of overlap between the fluorescence spectrum of the donor and the absorption spectrum of the acceptor, and, in particular, on the distance between donor and acceptor.

In combination, these radiationless routes of deactivation compete with light emission, and therefore the quantum yields (ϕ_F) of most chromophores are much smaller than 1. ϕ_F is equal to the ratio of the emitted to the absorbed photons. Its maximal value is thus 1. Good introductions into the principles of fluorescence of biological samples are found in Refs [2, 12, 13].

2.3.1 The Fluorescence of Proteins

The fluorescence of proteins originates from the phenylalanine, tyrosine, and tryptophan residues. Emission spectra for the three aromatic amino acids are shown in Figure 2.4, and their absorption and emission properties are summarized in Table 2.1. The excitation spectra correspond to the respective absorption spectra (Figure 2.2).

The fluorescence intensity of a particular chromophore depends on both its absorption at the excitation wavelength and its quantum yield at the wavelength of the emission. The product $\varepsilon_{max} \times \phi_F$ is thus a good parameter to characterize the fluorescence "sensitivity" of this chromophore. In proteins that contain all three aromatic amino acids, fluorescence is usually dominated by the contribution of the tryptophan residues because its sensitivity parameter is 730, which is much higher than the corresponding values which are 200 for tyrosine and only 4 for phenylalanine (Table 2.1). In proteins, phenylalanine fluorescence is practically not observable, because the other two aromatic residues absorb strongly around 280 nm, where phenylalanine emits, and because its emission is almost completely transferred to tyrosine and tryptophan by FRET.

The fluorescence of tyrosines is often undetectable in proteins that also contain

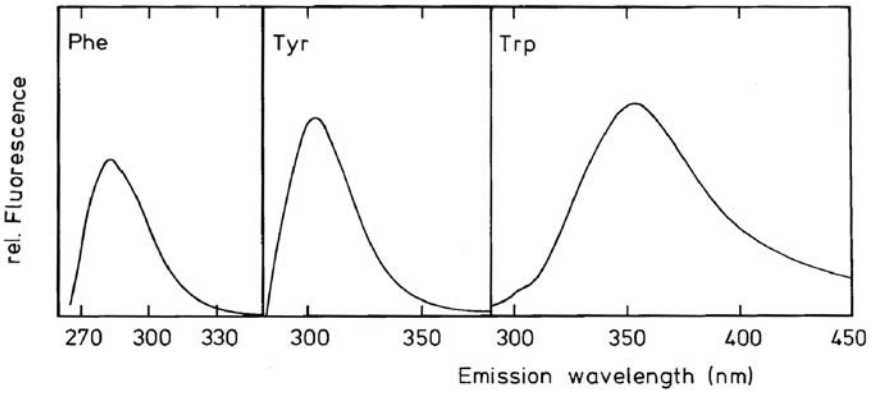

Fig. 2.4. Fluorescence spectra of the aromatic amino acids in 0.01 M potassium phosphate buffer, pH 7.0 at 25 °C. For the measurements, 100 μM phenylalanine, 6 μM tyrosine, and 1 μM tryptophan were used. Excitation was at 257 nm (Phe), 274 nm (Tyr), and 278 nm (Trp). The figure is taken from Ref. [6].

tryptophan, (i) because tryptophan shows a much stronger emission than tyrosine (Table 2.1), (ii) because in folded proteins tryptophan emission is often shifted to lower wavelengths and thus masks the contribution of tyrosine at 303 nm, and (iii) because FRET can occur from tyrosine to tryptophan in the compact native state of a protein [13, 14].

2.3.2
Energy Transfer and Fluorescence Quenching in a Protein: Barnase

The small bacterial ribonuclease barnase provides an instructive example for how strongly protein fluorescence is influenced by the local environment of the chromophores by quenching and by energy transfer, in this case transfer between individual tryptophan residues. Barnase contains three tryptophan residues at positions 35, 71, and 94 (Figure 2.5a). Trp94 is in close contact with His18, Trp71 is about 10 Å away from Tyr92, and Trp35 is about 25 Å away from the other two tryptophan residues. The fluorescence of wild-type barnase increases strongly between pH 6 and pH 9, following a titration curve with an apparent pK of 7.75. This was suggested to reflect the quenching of Trp94 emission by His18.

Fersht and coworkers [15] constructed single mutants of barnase, one in which His18 was mutated to a glycine and then three mutants in which one tryptophan residue at a time was mutated to another aromatic or aliphatic residue. They found that the fluorescence of barnase increased more than 2.5-fold when His17 was mutated to Gly (Figure 2.5b), which suggests that His18 does indeed act as an intramolecular quencher of Trp94 fluorescence. The observed fluorescence increase was, however, much higher than expected under the implicit assumption that all three tryptophan residues contribute equally to the fluorescence of the wild-type protein.

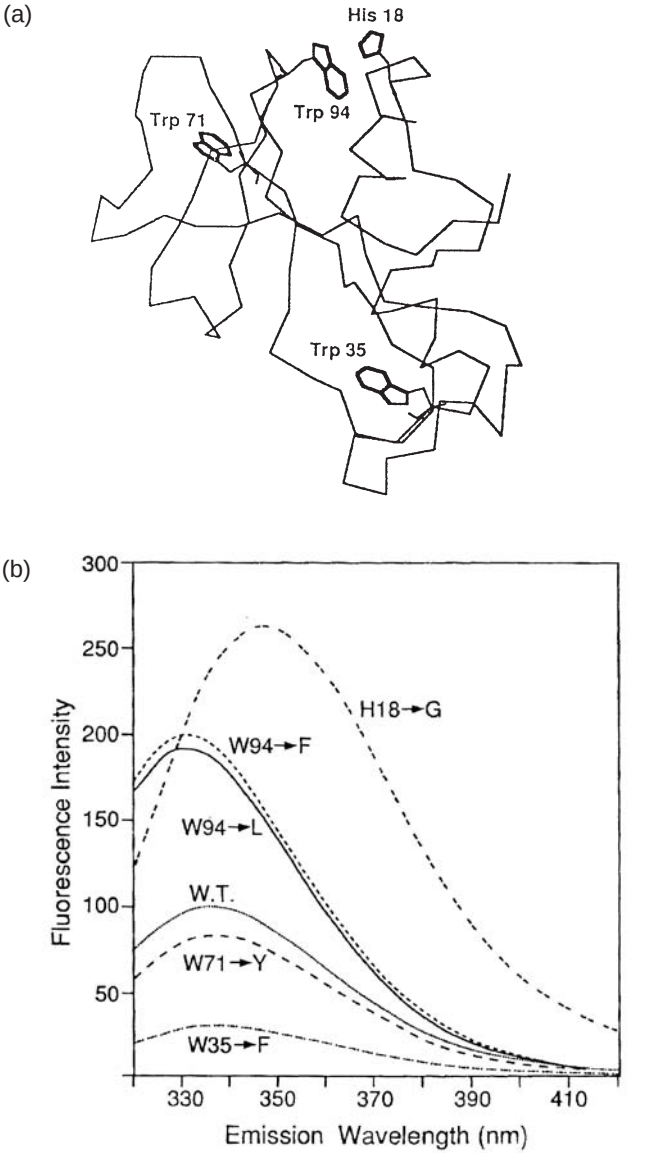

Fig. 2.5. a) The structure of barnase showing the locations of the three Trp residues and of His18. b) Fluorescence emission spectra of barnase and the variants with single mutations of His18 and of its three Trp residues. All spectra were recorded in 10 mM Bis/Tris buffer, pH 5.5 at the same protein concentration of 4 μM. Under these conditions His18 is protonated. The maximal emission of the wild-type protein (W.T.) is set as 100. The figure is taken from Ref. [15].

The subsequent mutations of the individual tryptophan residues revealed that their contributions to the overall fluorescence are indeed strongly different. The Trp35Phe mutation alone decreased the emission by 80% (Figure 2.5b), which indicates that Trp35 is the major contributor to the fluorescence of wild-type barnase, and that the emission of the other two tryptophan residues is largely abolished in the folded protein. Indeed, the replacement of Trp71 by a tyrosine decreased the emission only by 15% (Figure 2.5b). Trp71 is close to Trp94 (Figure 2.5a) and loses most of its emission because of energy transfer to Trp94. Trp94 in turn is efficiently quenched by the neighboring His18. The replacement of Trp94 by Phe or Leu prevents both energy transfer from Trp71 and the quenching of Trp94 by His18. As a consequence, the substitution of Trp94 led to a twofold increase in fluorescence (Figure 2.5b). It reflects the increase in the fluorescence of Trp71, which, in the Trp94Phe variant, no longer loses emission by energy transfer to Trp94.

In summary, this mutational analysis reveals how, in wild-type barnase, Trp71 and Trp94 lose most of their emission via quenching by His18. It demonstrates nicely that protein fluorescence is strongly influenced by energy transfer and by intramolecular quenching, which render fluorescence an excellent probe for protein folding.

2.3.3 Protein Unfolding Monitored by Fluorescence

The extended lifetime of the excited state is a key to understanding the changes that occur during a protein folding transition. As described above, a broad range of interactions or perturbations can influence the fluorophore while it is in the activated state. In particular, singulet-to-triplet inter system crossing can occur, or energy transfer to an acceptor. Fluorescence emission is consequently much more sensitive to changes in the environment of the chromophore than absorption.

The changes in fluorescence during the unfolding of a protein are often very large. In proteins that contain tryptophan both shifts in wavelength and changes in intensity are usually observed. Depending on the environment in the folded protein the tryptophan emission of a native protein can be greater or smaller than the emission of free tryptophan in aqueous solution, and fluorescence can increase or decrease upon unfolding, depending on the protein under investigation. The emission maximum of solvent-exposed tryptophan is near 350 nm, but in a hydrophobic environment, such as in the interior of a folded protein, tryptophan emission occurs at lower wavelengths (indole shows an emission maximum of 320 nm in hexane [16]). As an example the emission spectra of native and of unfolded ribonuclease T1 are shown in Figure 2.6. As mentioned, ribonuclease T1 contains nine tyrosine residues and only one tryptophan (Trp59), which is inaccessible to solvent in the native protein [17].

The fluorescence of the tryptophan residues can be investigated selectively by excitation at wavelengths higher than 295 nm. Tyrosine does not absorb above 295 nm because its absorbance spectrum is blue shifted (as compared with tryptophan, Figure 2.2) and is thus not excited at 295 nm. A comparison of the emission spec-

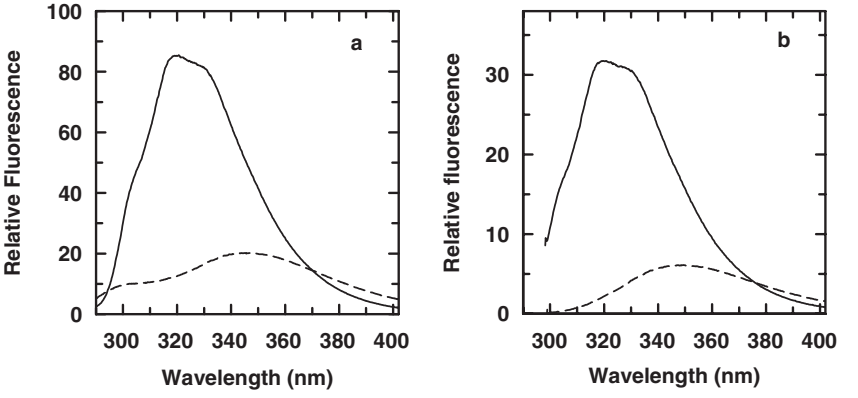

Fig. 2.6. Fluorescence emission spectra of native (——) and of unfolded (-------) ribonuclease T1. Native ribonuclease T1 (1.4 μM) was in 0.1 M sodium acetate pH 5.0, the sample of unfolded protein contained 6.0 M GdmCl in addition. Fluorescence was excited at a) 278 nm and b) 295 nm. The bandwidths were 3 nm for excitation and 5 nm for emission. Spectra were recorded at 25 °C in 1 × 1 cm cells in a Hitachi F-4010 fluorimeter. The figure is taken from Ref. [6].

tra observed after excitation at 280 nm and at 295 nm gives information about the contributions of the tryptophan and the tyrosine residues to the fluorescence of a protein. The data for ribonuclease T1 in Figure 2.6 show that the shapes of the fluorescence spectra observed after excitation at 278 nm and 295 nm are virtually identical. The measured emission originates almost completely from the single Trp59, which is inaccessible to solvent and hence displays a strongly blue-shifted emission maximum near 320 nm. Tyrosine emission is barely detectable in the spectrum of the native protein, because energy transfer to tryptophan occurs. Unfolding by GdmCl results in a strong decrease in tryptophan fluorescence and a concomitant red shift of the maximum to about 350 nm. The distances between the tyrosine residues and Trp59 increase, and energy transfer becomes less efficient. As a consequence, the tyrosine fluorescence near 303 nm becomes visible in the spectrum of the unfolded protein when excited at 278 nm (Figure 2.6a), but not when excited at 295 nm (Figure 2.6b). The examples in Figure 2.6 indicate that, unlike the absorbance changes, the fluorescence changes upon folding can be very large and the contribution of the tryptophan residues can be studied selectively by changing the excitation wavelength. These features, together with its very high sensitivity, make fluorescence measurements extremely useful for following conformational changes in proteins.

Multiple emission bands do not necessarily originate from different tryptophan residues of a folded protein. Figure 2.6 shows that even single tryptophan residues, such as Trp59 of ribonuclease T1 can give rise to several emission bands.

In contrast to ribonuclease T1, where we found a fivefold decrease of tryptophan fluorescence, the fluorescence of the FK 506 binding protein FKBP12 increases about 12-fold upon unfolding [18]. Figure 2.7 shows fluorescence spectra recorded

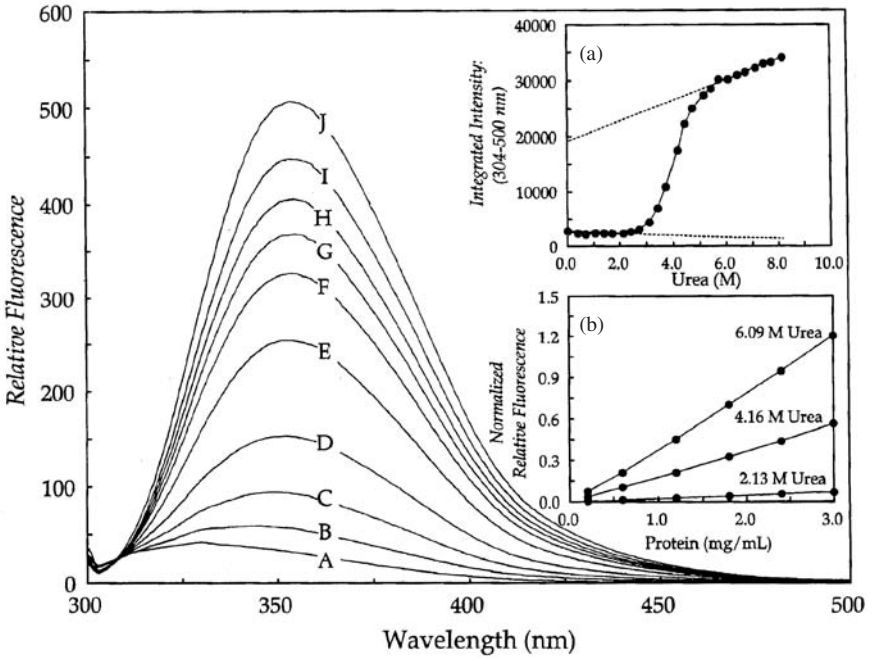

Fig. 2.7. Urea-induced denaturation of FKBP12 measured by intrinsic tryptophan fluorescence at 25 °C. A) Samples containing 50 μM FKBP12 in 75 mM phosphate/25 mM glycine buffer, 1 mM DTT, pH 7.2 and the following concentrations of urea. A)–J) 0.0, 3.1, 3.4, 3.7, 4.1, 4.4, 4.7, 5.1, 6.1, and 7.1 M. Excitation was at 294 nm to minimize inner filter effects. Inset a) Equilibrium unfolding curve based on the integrated emission intensities between 304 and 500 nm. The dashed lines represent linear fits to the pre- and post-transitional baselines. Inset b) A plot of the fluorescence intensity at 350 nm versus protein concentration to examine the linear dependence of the emission on protein concentration. The figure is taken from Ref. [18].

between 0 M and 7.1 M urea. Incidentally both ribonuclease T1 and FKBP12 have a single tryptophan at position 59. The emission of Trp59 of FKBP12 is barely detectable in the folded protein (Figure 2.7), but as soon as the protein enters the transition zone (around 3 M urea, cf. inset a in Figure 2.7) the fluorescence increases strongly and its maximum shifts from 330 nm to 350 nm.

In the experiments shown in Figure 2.7 the fluorescence of the tyrosine residues of FKBP12 was suppressed by exciting Trp59 selectively by light of 294 nm. At this wavelength tyrosine absorption is almost zero (cf. Figure 2.2). In addition, at 294 nm the absorbance of the samples is very low, the inner filter effect (cf. Section 2.3.5) becomes negligible, and the fluorescence emission remains linear over a wide range of protein concentrations (cf. inset b of Figure 2.7).

The fluorescence maximum of tyrosine remains near 303 nm, irrespective of its molecular environment. Therefore the unfolding of proteins that contain only tyrosine is usually accompanied by changes in the intensity, but not in the wavelength of emission. As an example, the fluorescence emission spectra of the Trp59Tyr

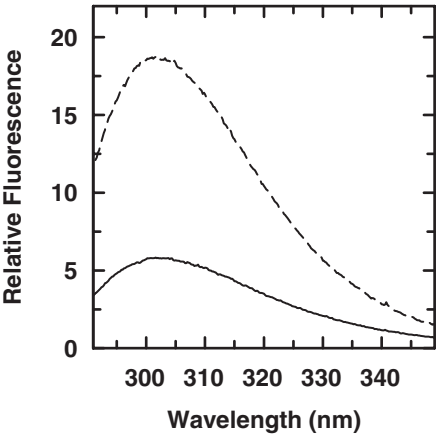

Fig. 2.8. Fluorescence emission spectra of 1.5 μM of the native (——) and of the unfolded (-------) Trp59Tyr variant of ribonuclease T1. This protein contains 10 Tyr residues. The native protein was in 0.1 M sodium acetate, pH 5.0; the unfolded sample contained 6.0 M GdmCl in addition. Fluorescence was excited at 278 nm, the spectra were recorded as in Figure 2.6. The figure is taken from Ref. [6].

variant of ribonuclease T1 in the native and unfolded states are shown in Figure 2.8. A decreased tyrosine fluorescence in the native state (as in Figure 2.8) is frequently observed. It is thought to originate from hydrogen bonding of the tyrosyl hydroxyl group and/or the proximity of quenchers, such as disulfide bonds in the folded state [19].

2.3.4
Environmental Effects on Tyrosine and Tryptophan Emission

The fluorescence of the exposed aromatic amino acids of a protein depends on the solvent conditions. Solvent additives that promote the $S_1 \rightarrow T_1$ transition (such as acrylamide or iodide) quench the fluorescence, and this effect can be used to measure the exposure of tryptophan side chains to the solvent [20].

The fluorescence generally decreases with increasing temperature. This decrease is substantial. To a first approximation, tyrosine and tryptophan emission decrease $\geq$1% per degree increase in temperature [6]. Fluorescence is therefore generally not suited for following the heat-induced unfolding of a protein.

Denaturants such as GdmCl and urea also influence the fluorescence of tyrosine and tryptophan. The dependences on the concentration of GdmCl and urea of tryptophan and tyrosine emission are given in Ref. [6]. As in absorbance experiments (cf. Section 2.2.1) the emission of the unfolded protein can be represented well by an appropriate mixture of tyrosine and tryptophan. The dependence of the emission of this mixture on denaturant concentration is often very useful to determine the baseline equivalent to the unfolded protein for the quantitative analysis of unfolding transition curves.

Protein fluorescence can also be affected by salts. Charged denaturants, such as GdmCl, can thus act in a twofold manner: as a denaturant and as a salt. To identify the salt effect, it is advisable to titrate the protein in control experiments with the appropriate concentrations of NaCl or KCl. Salt effects of GdmCl are often strongest at low GdmCl concentration and thus they can severely affect the baseline of the native protein in equilibrium unfolding experiments.

2.3.5 Practical Considerations

Fluorescence is an extremely sensitive technique, so it is essential to avoid contamination of cuvettes and glassware with fluorescing substances. Deionized and quartz-distilled water should be used and plastic containers should be avoided because they may leach out fluorescing additives. Also, laboratory detergents usually contain strongly fluorescing substances. Fluorescing impurities are easily identified when running buffer controls.

In water, a Raman scattering peak is observed. It originates from the excitation of an O–H vibrational mode of the H_2O molecule, and thus it is present in all aqueous solvents. The Raman peak of water is weak and occurs at a constant frequency difference, not at a constant wavelength difference from the exciting light. The position of the Raman peak as a function of the excitation wavelength can be found in Ref. [6]. After excitation at 280 nm the Raman peak occurs at 310 nm, and therefore it overlaps with the emission spectra of the aromatic amino acids, in particular with tyrosine emission. The Raman peak of the solvent should always be measured separately and subtracted from the measured spectra.

As in absorption spectroscopy impurities and dust particles should be avoided as much as possible and transparent buffers and solvents should be used (cf. Section 2.2). A single dust particle moving slowly through the light beam can cause severe distortions of the fluorescence signal. Continuous stirring during the fluorescence measurement is strongly recommended. Stirring keeps dust particles in rapid motion and thereby minimizes their distorting effect on the signal. In addition it continually transports new protein molecules into the small volume of the cell that is illuminated by the excitation light beam and thereby averages-out photochemical decomposition reactions over the entire sample. Stirring also improves the thermal equilibration in the cuvette, which is important, regarding the strong temperature dependence of fluorescence.

Fluorescence increases with fluorophore concentration in a linear fashion only at very low concentration. Nonlinearity at higher concentration is caused by inner-filter effects. The exciting light is attenuated by the absorption of the protein and of the solvent. The extent of this attenuation depends on the absorbance of the sample at the wavelength of excitation, and therefore it can be varied by a shift in the excitation wavelength. Further attenuation originates from reabsorption of fluorescent light by protein and solvent molecules. This effect is usually small, because the absorption of proteins and solvents beyond 300 nm is almost zero. Inner-filter effects are negligible when the absorbance of the sample at the excitation wave-

length is smaller than 0.1 absorbance units. Additional practical advice on how to measure protein fluorescence is found in Ref. [6].

2.4 Circular Dichroism

Circular dichroism (CD) is a measure for the optical activity of asymmetric molecules in solution and reflects the unequal absorption of left-handed and right-handed circularly polarized light. The CD signals of a particular chromophore are therefore observed in the same spectral region as its absorption bands. A good introduction to the basic principles of CD is provided by Refs [2] and [21].

Proteins show CD bands in two spectral regions. The CD in the far UV (170–250 nm) originates largely from the dichroic absorbance of the amide bonds, and therefore this region is usually termed the amide region. The aromatic side chains also absorb in the far UV and accordingly they also contribute to the CD in this region. These contributions may dominate the spectra of proteins that show a weak amide CD and/or a high content of aromatic residues. The CD bands in the near UV (250–300 nm) originate from the aromatic amino acids and from small contributions of disulfide bonds. Figure 2.9 shows the CD spectra of pancreatic ribonuclease for the native and the denaturant-unfolded forms.

The two spectral regions give different kinds of information about protein structure. The CD in the amide region reports on the backbone (i.e., the secondary) structure of a protein and is used to characterize the secondary structure and changes therein. In particular the α-helix displays a strong and characteristic CD spectrum in the far-UV region. The contributions of the other elements of secondary structure are less well defined. The content of the different secondary structures in a protein can be calculated from its CD spectrum in the amide regions. Methods for these calculations are found in Ref. [22].

The aromatic residues have planar chromophores and are intrinsically symmetric. When they are mobile, such as in short peptides or in unfolded proteins, their CD is almost zero. In the presence of ordered structure, such as in a folded protein, the environment of the aromatic side chains becomes asymmetric, and therefore they show CD bands in the near UV. The signs and the magnitudes of the aromatic CD bands cannot be calculated; they depend on the immediate structural and electronic environment of the immobilized chromophores. Therefore the individual peaks in the complex near-UV CD spectrum of proteins usually cannot be assigned to specific amino acid side chains. However, the near-UV CD spectrum represents a highly sensitive criterion for the native state of a protein. It can thus be used as a fingerprint of the correctly folded conformation.

2.4.1 CD Spectra of Native and Unfolded Proteins

Figure 2.10 shows representative spectra in the far-UV region for all-helical (a), for all-β (b), and for unstructured proteins (c). Helical proteins show rather strong CD

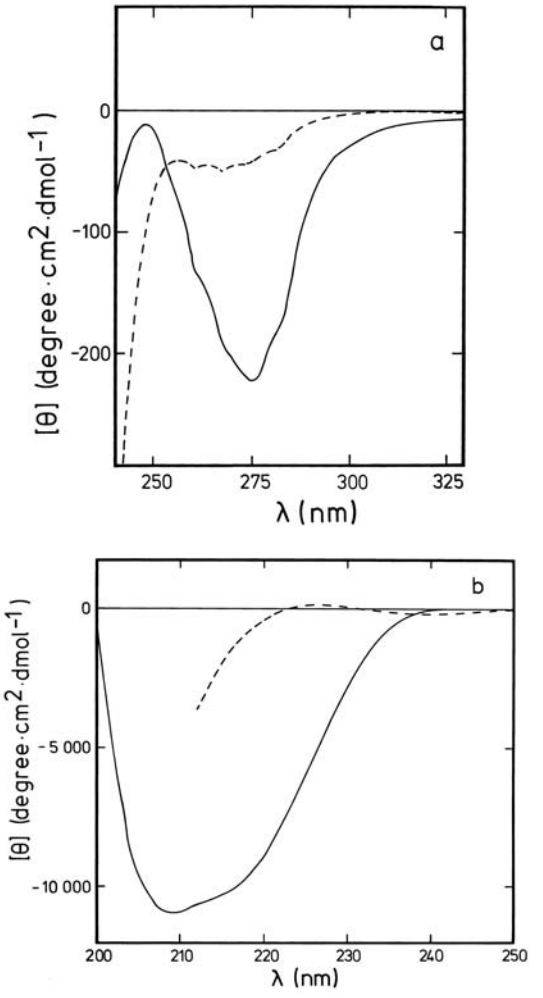

Fig. 2.9. CD spectra of pancreatic ribonuclease (from red deer) at 10 °C in the native (——) and in the unfolded state (-------). The native protein was in 0.1 M sodium cacodylate/HCl, pH 6.0, the unfolded protein was in the same buffer plus 6.0 M GdmCl. a) CD in the aromatic region. The protein concentration was 78 μM in a 1-cm cell. b) CD in the peptide region. 28 μM protein in a 0.1-cm cell. The figure is taken from Ref. [6].

bands with minima near 222 and 208 nm and a maximum near 195 nm. β proteins show weaker and more dissimilar spectra. The shape of the CD spectrum of a β protein depends, among other factors, on the length and orientation of the strands and on the twist of the sheet. Most spectra show, however, a positive ellipticity between 190 and 200 nm. In proteins with helices and sheets usually the helical contributions dominate the CD spectrum. Unordered proteins and peptides show weak CD signals above 210 nm, but a pronounced minimum between 195 and 200 nm.

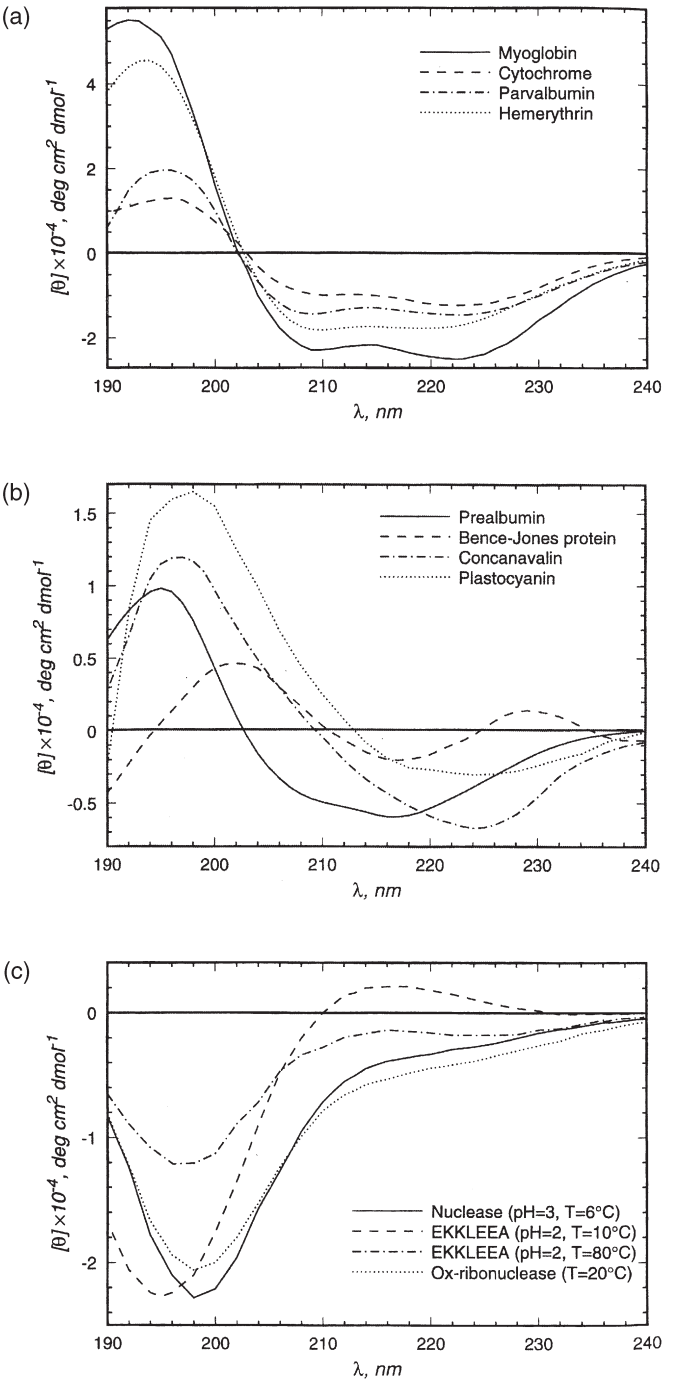

Fig. 2.10. Representative CD spectra of a) helical proteins, b) proteins with β-sheet structure, and c) unordered proteins and peptides. The figure is taken from Ref. [22].

The strong difference near 195 nm between the CD of folded and unfolded proteins should, in principle, provide an ideal probe for monitoring protein unfolding transitions. In practice, however, most unfolding reactions are monitored near 220 nm. Wavelengths below 200 nm are almost never used, because most buffers and virtually all denaturants absorb strongly below 200 nm (Table 2.2), and therefore the advantage of having a strong change in signal is more than offset by the very high background absorbance of the solvent.

The aromatic amino acid side chains absorb not only in the near-UV, but also in the far-UV region [23]. Accordingly, in native proteins they also contribute to the CD in the 180–230 nm region, which has traditionally been ascribed to only the amide bonds in the protein backbone. The aromatic contributions to the far-UV CD are often modest, and for helical proteins it is usually adequate to neglect them in the analyses, because the CD of helices is very strong (cf. Figure 2.10, top). For β proteins with their small and diverse CD signals (cf. Figure 2.10, middle), the aromatic bands can lead to problems and therefore the contents of β structure as calculated from the CD spectra can be seriously wrong. Carlsson and coworkers employed a mutational approach to analyze the contributions of the seven tryptophan residues to the amide CD spectrum of carbonic anhydrase [24]. They found strong contributions of these tryptophan residues to the far-UV spectrum of this protein.

2.4.2 Measurement of Circular Dichroism

The difference between the absorbances of right- and left-handed circularly polarized light of a protein sample is extremely small. In the far-UV region it lies in the range of 10^{-4}–10^{-6} absorbance units in samples with a total absorbance of about 1.0. This requires that less than 0.1% of the absorbance signal be measured accurately and reproducibly. Therefore highly sensitive instruments are necessary and careful sample preparation is important.

CD instruments use a high-frequency photoelectric modulator to generate alternatively the two circularly polarized light components. This leads to an alternating current contribution to the photomultiplier signal that is proportional to the CD of the sample. A detailed description of the principles of CD measurements is found in Refs [6] and [25].

Since the measured CD is so small, an extremely high stability of the CD signal is required. In general the instrument should be allowed to warm up for 30–60 min, and the stability of the baseline with and without the cuvette should be checked regularly.

When CD is measured in the far-UV region particular attention should be paid to a careful selection of solvents and buffers. The contributions of buffers and salts to the total absorbance of the sample should be as small as possible. This poses severe restrictions on the choice of solvents for CD measurements because many commonly used salts and buffers absorb strongly in the far-UV region. Absorbance values for several of them are given in Table 2.2. Common denaturants, such as urea and GdmCl also absorb strongly in the far UV. Therefore they cannot be

used for CD measurements below 210 nm. Oxygen also absorbs in the far UV, but precautions such as purging the cell compartment with nitrogen is necessary only when measurements are performed below 190 nm.

Protein concentration, pathlength and solvent must be carefully selected to obtain good CD spectra and to avoid artifacts. A good signal-to-noise ratio is achieved when the total absorbance is around 1.0. The magnitude of the CD depends on the protein concentration and therefore its contribution to the total optical density of the sample should be as high as possible, and the absorbance of the solvent should be as small as possible. Therefore, for measurements in the far-UV region, short path lengths (0.2–0.01 cm) and increased protein concentrations should be used. Cells of 0.1 cm are usually sufficient for measurements down to about 200 nm. When preparing samples for CD measurements it should be remembered that protein absorbance is about tenfold higher in the far UV when compared with the aromatic region. Artifacts can arise easily from an excessive absorbance of the sample or from light scattering caused by protein aggregates in the sample. Whenever the optical density of the sample becomes too high, the instrument cannot discriminate properly between the right and the left circularly polarized light components, and the CD signal decreases in size. This phenomenon, called absorption flattening, is a serious problem below 200 nm. It is good practice to ascertain that the measured CD is linearly related with path length and protein concentration.

2.4.3 Evaluation of CD Data

CD is recorded either as the difference in absorbance of right- and left-handed circularly polarized light, $\Delta A = A_L - A_R$ or as ellipticity, Θ_{obs}, in degrees. Data in both formats can be converted to the molar values, i.e., to the differential molar circular dichroic extinction coefficient, $\Delta\varepsilon = \varepsilon_L - \varepsilon_R$ and to the molar ellipticity, $[\Theta]$. $\Delta\varepsilon$ and $[\Theta]$ are interrelated by Eq. (3).

$$[\Theta] = 3300 \times \Delta\varepsilon \tag{3}$$

It should be noted that the concentration standards are different for $[\Theta]$ and $\Delta\varepsilon$. $\Delta\varepsilon$ is the differential absorbance of a 1 mol L^{-1} solution in a 1-cm cell, whereas $[\Theta]$ is the rotation in degrees of a 1 dmol cm^{-3} solution and a path length of 1 cm.

CD of proteins in the amide region is usually given as mean residue ellipticity, $[\Theta]_{MRW}$, which is based on the concentration of the sum of the amino acids in the protein solution under investigation. The concentration of residues is obtained by multiplying the molar protein concentration with the number of amino acids. For data in the aromatic region, different units are used in the literature. Frequently, aromatic CD is given as $\Delta\varepsilon$, but $[\Theta]$, based on the protein concentration, and $[\Theta]_{MRW}$, based on the residue concentration are also found.

The molar ellipticity, $[\Theta]$, or the residue ellipticity, $[\Theta]_{MRW}$, are calculated from the measured Θ (in degrees) by using Eqs (4) or (5):

$$[\Theta] = \frac{\Theta \times 100 \times M_r}{c \times l} \tag{4}$$

$$[\Theta]_{MRW} = \frac{\Theta \times 100 \times M_r}{c \times l \times N_A} \tag{5}$$

where Θ is the measured ellipticity in degrees, c is the protein concentration in mg mL^{-1}, l is the pathlength in cm, and M_r is the protein molecular weight. N_A is the number of amino acids per protein. $[\Theta]$ and $[\Theta]_{MRW}$ have the units degrees $\times$ cm^2 $\times$ $dmol^{-1}$. The factor 100 in Eqs (4) and (5) originates from the conversion of the molar concentration to the dmol cm^{-3} concentration unit.

The relation between $[\Theta]$ and $\Delta\varepsilon$, given in Eq. (3) allows an immediate transformation of raw Θ data into ΔA values and vice versa by the relationship: $\Theta = 33(A_L - A_R)$. This implies that a measured ellipticity of 10 millidegrees is equivalent to a ΔA of only 0.0003 absorbance units. Practical aspects of how to measure and analyze CD spectra are discussed in detail in Ref. [6].

The analysis of CD spectra is often used to determine the secondary structure of folded proteins or of folding intermediates. References to computer programs and critical evaluations of the methods can be found in Ref. [22].

References

1 D. B. Wetlaufer, *Adv. Protein Chem.*, **1962**, *17*, 303–421.
2 C. R. Cantor, P. R. Schimmel, *Biophysical Chemistry*. 1980, San Francisco: W. H. Freeman.
3 J. W. Donovan, *Meth. Enzymol.*, **1973**, *27*, 497–525.
4 S. B. Brown, Ultraviolet and visible spectroscopy. In *An Introduction to Spectroscopy for Biochemists*, S. B. Brown, Editor. 1980, Academic Press: London. pp. 14–69.
5 W. Colón, *Meth. Enzymol.*, **1999**, *309*, 605–632.
6 F. X. Schmid, Optical spectroscopy to characterize protein conformation and conformational changes. In *Protein Structure: A practical approach*, T. E. Creighton, Editor. 1997, Oxford University Press: Oxford. pp. 261–298.
7 H. Edelhoch, *Biochemistry*, **1967**, *6*, 1948–1954.
8 S. C. Gill, P. H. von Hippel, *Anal. Biochem.*, **1989**, *182*, 319–326.
9 C. N. Pace, F. X. Schmid, How to determine the molar absorbance coefficient of a protein. In *Protein Structure: A practical approach*, T. E. Creighton, Editor. 1997, Oxford University Press: Oxford. pp. 253–260.
10 C. N. Pace, F. Vajdos, L. Fee, G. Grimsley, T. Gray, *Protein Sci.*, **1995**, *4*, 2411–2423.
11 S. Yanari, F. A. Bovey, *J. Biol. Chem.*, **1960**, *235*, 2818–2826.
12 G. R. Penzer, Molecular emission spectroscopy. In *An Introduction to Spectroscopy for Biochemists*, S. B. Brown, Editor. 1980, Academic Press: London. pp. 70–114.
13 J. R. Lakowicz, *Principles of Fluorescence Spectroscopy*. 1999, New York: Kluwer/Plenum Publishers.
14 P. Wu, L. Brand, *Anal. Biochem.*, **1994**, *218*, 1–13.
15 R. Loewenthal, J. Sancho, A. R. Fersht, *Biochemistry*, **1991**, *30*, 6775–6779.
16 F. W. J. Teale, *Biochem. J.*, **1960**, *76*, 381–387.

17 U. Heinemann, W. Saenger, *Nature*, **1982**, *299*, 27–31.

18 D. A. Egan, T. M. Logan, H. Liang, E. Matayoshi, S. W. Fesik, T. F. Holzman, *Biochemistry*, **1993**, *32*, 1920–1927.

19 R. W. Cowgill, *Biochim. Biophys. Acta*, **1967**, *140*, 37–43.

20 M. R. Eftink, C. A. Ghiron, *Anal. Biochem.*, **1981**, *114*, 199–227.

21 G. D. Fasman, ed. *Circular Dichroism and the Conformational Analysis of Biomolecules*. 1996, Plenum Press: New York.

22 S. Y. Venyaminov, J. T. Yang, Determination of protein secondary structure. In *Circular Dichroism and the Conformational Analysis of Biomolecules*, G. D. Fasman, Editor. 1996, Plenum Press: New York. pp. 69–107.

23 R. W. Woody, A. K. Dunker, Aromatic and cystine side chain circular dichroism in proteins. In *Circular Dichroism and the Conformational Analysis of Biomolecules*, G. D. Fasman, Editor. 1996, Plenum Press: New York. pp. 109–157.

24 P. O. Freskgard, L. G. Martensson, P. Jonasson, B. H. Jonsson, U. Carlsson, *Biochemistry*, **1994**, *33*, 14281–14288.

25 W. C. Johnson, Circular dichroism and its empirical application to biopolymers. In *Methods of Biochemical Analysis*, D. Glick, Editor. 1985, John Wiley: New York. pp. 61–163.

26 M. R. Eftink, Fluorescence techniques for studying protein structure. In *Methods of Biochemical Analysis*, C. H. Suelter, Editor. 1991, John Wiley: New York. pp. 127–205.

3
Denaturation of Proteins by Urea and Guanidine Hydrochloride

C. Nick Pace, Gerald R. Grimsley, and J. Martin Scholtz

3.1
Historical Perspective

The ability of urea to denature proteins has been known since 1900 [1]. Urea is also effective in denaturing more complex biological systems: "A dead frog placed in saturated urea solution becomes translucent and falls to pieces in a few hours" [2]. (It was not reported if frog denaturation is reversible!) The even greater effectiveness of guanidine hydrochloride (guanidinium chloride (GdmCl)) as a protein denaturant was first reported in 1938 by Greenstein [3]. In this chapter we discuss why urea and GdmCl have proven to be so useful to protein chemists and summarize what we have learned over the past 100 years.

Tanford [4] was the first to study quantitatively the unfolding of proteins by urea. The diagram in Figure 3.1 is from Tanford's paper; it shows that when a protein unfolds many nonpolar side chains and peptide groups that were buried in the folded protein are exposed to solvent in the unfolded state. Figure 3.1 also gives the measured values of the free energy of transfer, ΔG_{tr}, of a leucine side chain and a peptide group from water to the solvents shown. Note that ΔG_{tr} of both are negative in the presence of urea and GdmCl. This is true of almost all the constituent groups of a protein, and explains why urea and GdmCl denature proteins, and why GdmCl is a stronger denaturant than urea. It is also clear why both folded and unfolded proteins are generally more soluble in urea and GdmCl solutions than they are in water. Most of this chapter will focus on urea denaturation, however GdmCl denaturation will be discussed where appropriate.

3.2
How Urea Denatures Proteins

Urea is remarkably soluble, 10.5 M, in water at 25 °C. Experimental [5–7] and theoretical studies [8–11] have improved our understanding of urea solutions and how urea and water interact with peptide groups and nonpolar side chains. Based on neutron diffraction studies, Soper et al. [5] show that urea incorporates readily

Protein Folding Handbook. Part I. Edited by J. Buchner and T. Kiefhaber

ISBN: 3-527-30784-2

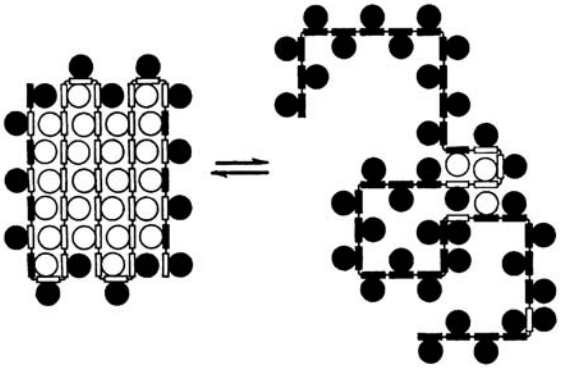

$\Delta G_{tr}(H_2O \rightarrow Solvent)$ (cal/mol)

Solvent	Peptide group	Leu side chain
Urea (2 M)	-70	-110
GdnHCl (2 M)	-135	-210
Ethanol (40%)	+270	-375
Glycerol (20%)	+55	+16
Sucrose (2 M)	+52	+74
Sarcosine (2 M)	+89	+77
TMAO (2 M)	+177	+18

Fig. 3.1. Schematic from Tanford [4] illustrating the changes in accessibility of peptide groups (rectangles) and side chains (circles) on protein unfolding. The closed symbols represent groups that are accessible to solvent and the open symbols represent groups that are not accessible to solvent. See Wang and Bolen [88] for osmolyte, and Pace et al. [56] for denaturant, ΔG_{tr} values.

into water through hydrogen bonding and there is great similarity in the spatial distribution of water around water, urea around water, urea around urea, and water around urea. They estimate that each urea forms ≈5.7 hydrogen bonds. In addition, urea hydrogen bonds with itself, forming chains and clusters in water. (Using a similar approach, Mason et al. [12] show that the Gdm ion has no recognizable hydration shell and is one of the most weakly hydrated cations yet characterized. The Gdm ion can form only three undistorted hydrogen bonds with water.) Urea is nearly three times larger than water, and can form more hydrogen bonds. This may account for the favorable ΔG_{tr} for the transfer of peptide groups from water to urea solutions. This question is considered experimentally and theoretically in Zou et al. [7].

Why ΔG_{tr} values are favorable for the transfer of nonpolar side chains from water to urea solutions was more difficult to explain. Muller [13] suggested that urea molecules replace some of the water molecules in the hydration shell formed around nonpolar solutes, and this changes the hydrogen bonding and van der Waals interactions in such a way as to increase the solubility of the nonpolar sol-

ute. This idea is supported by the experimental results of Soper et al. [5], and by the theoretical calculations of Laidig and Daggett [14].

In the absence of denaturant, Timasheff states [15]: "The fact is that there is no rigid shell of water around a protein molecule, but rather there is a fluctuating cloud of water molecules that are thermodynamically affected more or less strongly by the protein molecule." Crystallographers are able to see some water molecules that are bound tightly enough to be observed, but the fact that no water molecules are observed near many polar groups shows that they do not see them all [16]. When crystal structures are determined in the presence of urea and GdmCl, some denaturant molecules are seen bound to the protein, mainly by hydrogen bonds [17, 18]. These denaturant molecules sometimes link adjacent polar groups on the protein and reduce the conformational flexibility, as shown by a decrease in the temperature factors.

There is also experimental evidence that denaturants (and water) reduce the flexibility of the denatured state by transiently linking parts of the protein molecule through hydrogen bonds to polar groups in the protein [19]. Halle's group has used magnetic relaxation dispersion techniques (MRD) to gain a better understanding of protein hydration at the molecular level (see Chapter 8). For example, Modig et al. [6] summarize:

> ... the urea ^{2}H and water ^{17}O MRD data support a picture of the denatured state where much of the polypeptide chain participates in clusters that are more compact and more ordered than a random coil but nevertheless are penetrated by large numbers of water and urea molecules. These solvent-penetrated clusters must be sufficiently compact to allow sidechains from different polypeptide segments to come into hydrophobic contact, while, at the same time, permitting solvent molecules to interact favorably with peptide groups and with charged and polar side chains. The exceptional hydrogen-bonding capacity and small size of water and urea molecules are likely essential attributes in this regard. In such clusters, many water and urea molecules will simultaneously interact with more than one polypeptide segment and their rotational motions will therefore be more strongly retarded than at the surface of the native protein.

We now have a good understanding of how urea denatures proteins because of careful studies and thoughtful analyses from the labs of Timasheff [20], Record [21], and Schellman [22]. If the excluded volume of the protein is taken into account, the hydrodynamic properties of urea denatured proteins suggest that they approach a randomly coiled conformation [23]. Consequently, the accessible surface area of the denatured state is considerably greater than that of the native state. (This is shown clearly in figure 9 in Goldenberg [23].) Studies by Timasheff [20] and Record [21] have shown that urea binds preferentially to proteins over water, so the concentration of urea near the protein is greater than the concentration in the bulk solvent. Thus, as the urea concentration increases, the denatured state will be favored because it has a much greater surface to interact with the urea (Figure 3.1). Both groups suggest that the dominant contribution is due to preferential binding of urea (or Gdm ions) to the newly exposed peptide groups [20, 21].

Schellman [22] has extended his previous studies to show clearly how osmolytes such as trimethylamine-*N*-oxide (TMAO) or denaturants such as urea act to stabilize or destabilize proteins. The two key factors are the excluded volumes of the cosolvents and their contact interactions with the protein. Because the molecules of interest are all larger than water, the excluded volume effect will always favor the native state. In contrast, contact interactions will generally favor the denatured state. For urea, the contact interaction term is greater than the excluded volume effect, so urea acts as a protein denaturant. For osmolytes, the reverse is true and osmolytes stabilize proteins. Schellman [24] was the first to show that because the direct interaction of urea molecules with proteins is so weak, denaturation should be represented by a solvent exchange mechanism rather than solely by the binding of the denaturant to the protein molecule. His $K_{av} - 1$ term is a measure of the contact interaction for the average site on a protein. For RNase T1, this term is 0.12 for TMAO, 0.22 for urea, and 0.40 for guanidinium ion. The larger value of the contact term reflects the greater preferential binding of the Gdm ion compared to urea, and this is what makes GdmCl a better denaturant than urea [22].

In summary, it is now clear that urea denatures proteins because there is a preferential interaction with urea compared with water, and the denatured state has more sites for interaction. Consequently, proteins unfold as the urea concentration is increased.

3.3 Linear Extrapolation Method

A typical urea denaturation curve is shown in Figure 3.2A. When a protein unfolds by a two-state mechanism, the equilibrium constant, K, can be calculated from the experimental data using:

$$K = [(y)_N - (y)]/[(y) - (y)_D] \quad (1)$$

where (y) is the observed value of the parameter used to follow unfolding, and $(y)_N$ and $(y)_D$ are the values (y) would have for the native state and the denatured state under the same conditions where (y) was measured. In the original analyses of urea denaturation curves [25, 26], log K was found to vary linearly as a function of log [urea] and the slope of the plot was denoted by n, and the midpoint of the curve by $(\text{urea})_{1/2}$ (where $\log K = 0$). These parameters could then be used to calculate the standard free energy of denaturation

$$\Delta G^\circ = -RT \ln K \quad (2)$$

and its dependence on urea concentration using [4]:

$$\mathrm{d}(\Delta G^\circ)/\mathrm{d}(\text{urea}) = RTn/(\text{urea})_{1/2} \quad (3)$$

This equation was used by Alexander and Pace [25] to estimate the differences in

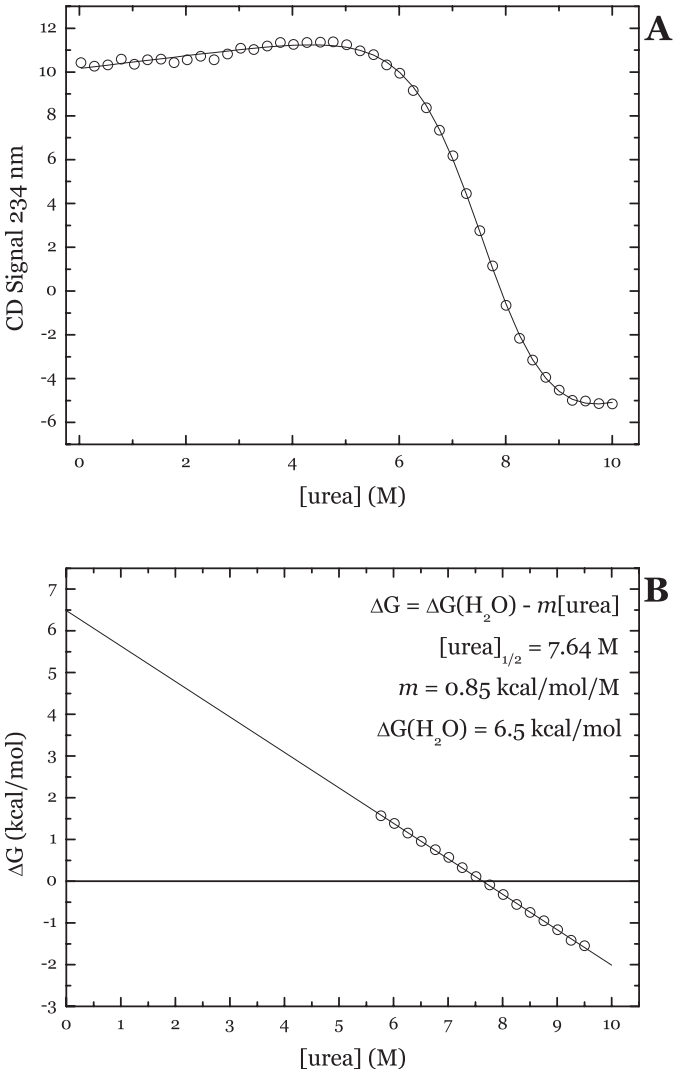

Fig. 3.2. A) Urea denaturation curve for RNase Sa determined at 25 °C, pH 5.0, 30 mM sodium acetate buffer as described by Pace et al. [78]. The solid line is based on an analysis of the data using Eq. (5). B) ΔG as a function of urea molarity. The ΔG values were calculated from the data in the transition region as described in the text. The $\Delta G(H_2O)$ and m-values can be determined by fitting the data in B to Eq. (4), or by analyzing the data in A with Eq. (5).

stability among three genetic variants of a protein for the first time, and was the forerunner of the linear extrapolation method.

The linear extrapolation method (LEM) was first used to analyze urea and GdnHCl denaturation curves by Greene and Pace [27]. When ΔG° is calculated as

a function of urea concentration using data such as those shown in Figure 3.2A, ΔG° is found to vary linearly with urea concentration as shown in Figure 3.2B. Based on results such as these for several proteins, this equation was proposed for analyzing the data:

$$\Delta G = \Delta G(H_2O) - m[\text{urea}] \tag{4}$$

where $\Delta G(H_2O)$ is an estimate of the conformational stability of a protein that assumes that the linear dependence continues to 0 M denaturant, and m is a measure of the dependence of ΔG on urea concentration, i.e., the slope of the plot shown in Figure 3.2B. The same approach has recently been used for measuring the stability of RNA molecules [28].

In the early days, $(y)_N$ and $(y)_D$ were obtained by extrapolating the pre- and posttransition baselines into the transition region, and then using Eq. (1) to calculate K and then ΔG°. However, Santoro and Bolen [29] had a better idea and proposed that nonlinear least squares be used to directly fit data such as those shown in Figure 3.2A. With their approach, six parameters are used to fit the data: a slope and an intercept for the pretransition and posttransition regions, which are generally linear, and $\Delta G(H_2O)$ and m for the transition region, leading to

$$y = \{(y_F + m_F[\text{urea}]) + (y_U + m_U[\text{urea}]) \cdot \exp - ((\Delta G(H_2O) - m \cdot [\text{urea}])/RT)\}$$
$$/(1 + \exp - (\Delta G(H_2O) - m \cdot [\text{urea}])/RT)) \tag{5}$$

where y_F and y_U are the intercepts and m_F and m_U the slopes of the pre- and posttransition baselines, and $\Delta G(H_2O)$ and m are defined by Eq. (4).

The linear extrapolation method is now widely used for estimating the conformational stability of proteins and for measuring the difference in stability between proteins differing slightly in structure. (The original how-to-do-it paper on solvent denaturation [30] has been cited over 1200 times.) In addition, the m-value has taken on a life of its own [31]. These topics will be discussed further below.

3.4 $\Delta G(H_2O)$

The conformational stability of RNase Sa at 25 °C and pH 5 is ~7.0 kcal mol^{-1}. This corresponds to one unfolded molecule for each 135 000 folded molecules ($K = 7.4 \times 10^{-6}$). To study the equilibrium between the folded and unfolded conformations by conventional techniques requires destabilizing the protein so that both conformations are present at measurable concentrations. With urea denaturation this is done by increasing the urea concentration. It is clear from Figure 3.2A that the unfolding equilibrium can be studied only near 7 M urea, and that a long extrapolation is needed to estimate ΔG° in the absence of urea, $\Delta G(H_2O)$. The same is true for thermal denaturation. The unfolding equilibrium can be studied only near 55 °C (Figure 3.3A). Thermal denaturation curves can be analyzed to ob-

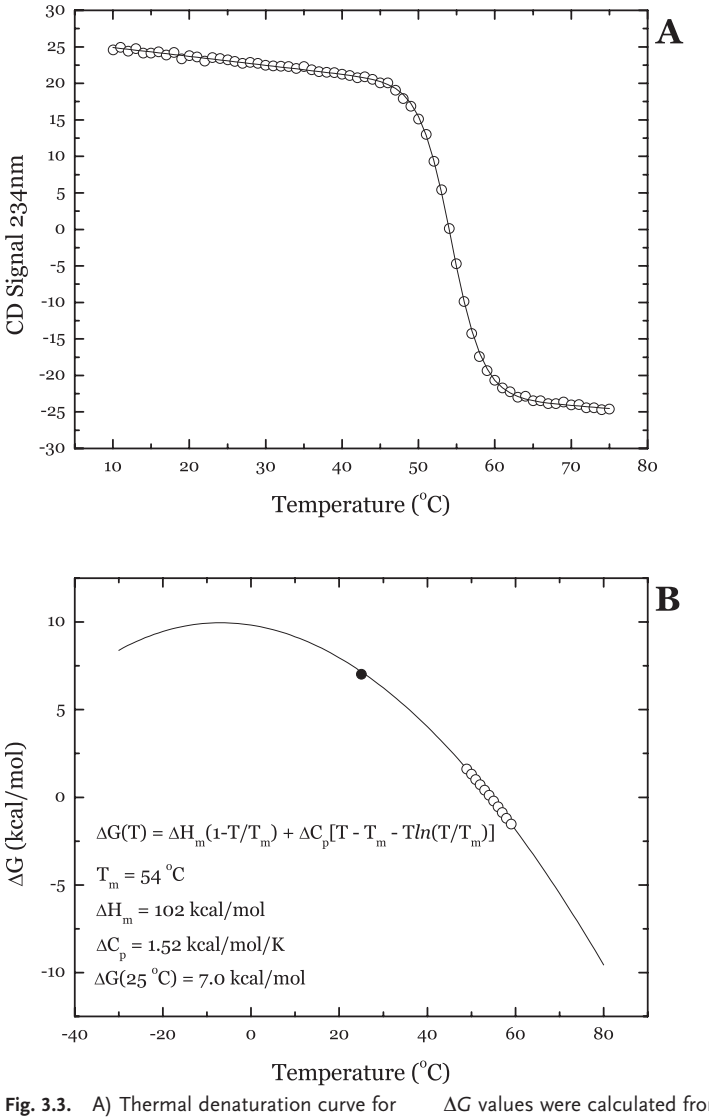

Fig. 3.3. A) Thermal denaturation curve for RNase Sa determined at pH 5.0 in 30 mM sodium acetate buffer as described [78]. The solid line is based on a nonlinear least squares analysis of the data similar to that described for Eq. (5), but for thermal denaturation curves [78]. B) ΔG as a function of temperature. The ΔG values were calculated from data in the transition region as described in the text, and the data were analyzed to determine T_m and ΔH_m as described [78]. The ΔC_p value is from Pace et al. [78]. The ΔG(25 °C) value (filled circle) was calculated using Eq. (6) which is also shown in B.

tain the midpoint of the thermal denaturation curve, T_m, and the enthalpy change at $T_m, \Delta H_m$. These two parameters plus the heat capacity change for folding, ΔC_p, can then be used in the Gibbs-Helmholtz equation [32]:

$$\Delta G(T) = \Delta H_m(1 - T/T_m) + \Delta C_p[T - T_m - T \ln(T/T_m)] \quad (6)$$

to calculate ΔG at any temperature $T, \Delta G(T)$. The temperature dependence of ΔG and the value of $\Delta G(25\ ^\circ C)$ for the denaturation of RNase Sa are shown in Figure 3.3B. Note that the value of $\Delta G(25\ ^\circ C)$ from the thermal denaturation experiment agrees with the $\Delta G(H_2O)$ value from the urea denaturation experiments within experimental error, which is about ± 0.3 kcal mol^{-1} (see Eftink and Ionescu [33] for an excellent discussion of the problems most frequently encountered in analyzing solvent and thermal denaturation curves).

Previously, we used RNase T1 to show that estimates of $\Delta G(T)$ based on DSC experiments were in good agreement with estimates of $\Delta G(H_2O)$ from urea denaturation [34, 35]. In a more recent study using RNase A, we compared $\Delta G(T)$ values from DSC determined in Makhatadze's laboratory with $\Delta G(H_2O)$ values determined using urea denaturation and the LEM [36] in our laboratory. The agreement is remarkably good (Table 3.1). Most recently, we have compared conformational stabilities estimated from hydrogen exchange rates measured under native state conditions with those from thermal or solvent denaturation [37]. Again, the conformational stabilities are in good agreement.

There is considerable experimental evidence that proteins are more extensively unfolded in solutions of urea than they are in water (see, for example, Qu et al.

Tab. 3.1. Comparison of $\Delta G(T)$ values from DSC with $\Delta G(H_2O)$ values from UDC.

pH	*T (°C)*	*T_m[a] (°C)*	*ΔH_m[a] (kcal mol^{-1})*	*$\Delta G(T)$[a] (kcal mol^{-1})*	*$\Delta G(H_2O)$[b] (kcal mol^{-1})*
2.8	17.1	44.9	79.4	5.5	5.4
2.8	21.1	44.9	79.4	4.9	4.9
2.8	24.9	44.9	79.4	4.3	4.3
2.8	27.8	44.9	79.4	3.7	3.5
2.8	25.0	44.9	79.4	4.5	4.3
3.0	25.0	49.1	82.7	5.1	5.2
3.55	25.0	54.5	91.5	6.7	6.4
4.0	25.0	56.1	94.2	7.2	7.3
5.0	25.0	58.6	99.1	8.1	7.9
6.0	25.0	60.3	100.7	8.5	8.6
7.0	25.0	61.8	102.3	8.9	9.1

[a] The $T_m, \Delta H_m$, and $\Delta C_p = 1.15$ kcal mol^{-1} K^{-1} values are from Pace et al. [36]. They were used in Eq. (6) to calculate the $\Delta G(T)$ values.
[b] The first four $\Delta G(H_2O)$ values are from Pace and Laurents [39], and the last five $\Delta G(H_2O)$ values are interpolated from figure 6 in Pace et al. [56].

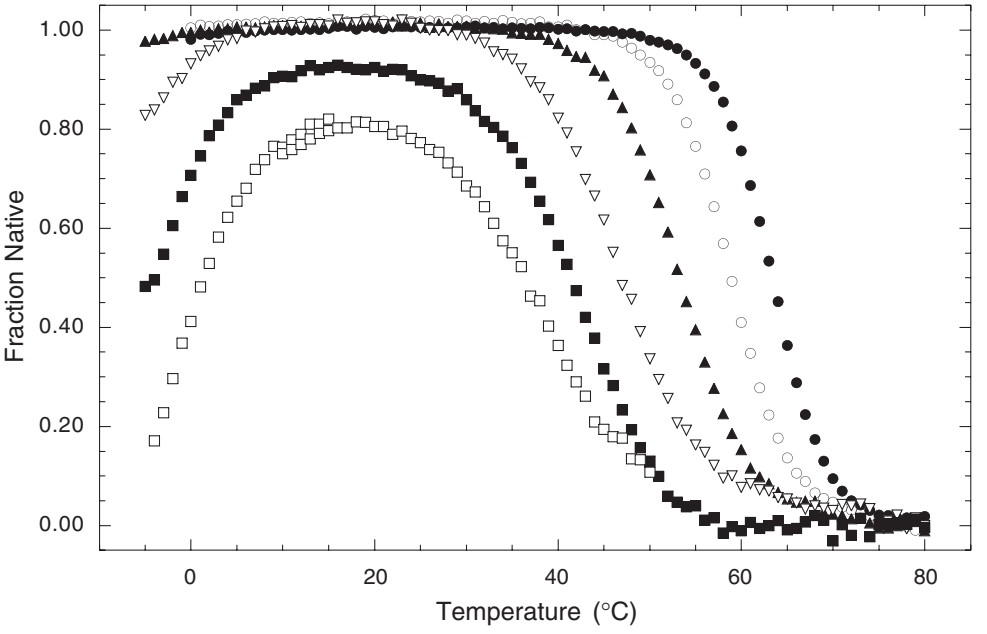

Fig. 3.4. Thermal unfolding curves for *ec*HPr in various urea concentrations at pH 7.0 (10 mM K/P_i) as monitored by the change in ellipticity at 222 nm and converted to fraction folded, f_F. The error on any single point is smaller than the size of the symbol. The urea concentrations are 0 M (filled circle), 1 M (open circle), 2 M (filled triangle), 3 M (open triangle), 3.5 M (filled square), and 4 M (open square). From Nicholson and Scholtz [41].

[38]). Thus, it is surprising that conformational stabilities determined under conditions where the denatured state ensembles differ would be the same. This suggests that the denatured state ensemble that exists under physiological conditions is thermodynamically equivalent to the ensembles that exist after thermal or urea denaturation, even though they do not appear to be structurally equivalent. This is supported by studies where both thermal and urea induced unfolding are used to study the conformational stability of a protein.

This approach had its beginnings in a study that showed that results from thermal and urea denaturation could be combined to get a reasonable estimate of ΔC_p [39]. The method was then extended to characterize the stability of the HPr proteins from *Bacillus subtilis* [40] and *Escherichia coli* [41] as a function of both urea concentration and temperature. Some typical results are shown in Figure 3.4. More recently, Felitsky and Record [42] used this approach to characterize the stability of the Lac repressor DNA-binding domain in the most detailed study of the stability of a protein yet published. A related approach has been described by Ibarra-Molera and Sanchez-Ruiz [43].

The excellent agreement between conformational stabilities based on DSC results and the LEM suggests that the LEM is a reliable method for estimating the

conformational stability of a protein. The Record group has developed an approach for analyzing the results of urea and GdmCl denaturation studies in terms of preferential interaction coefficients that is firmly based on thermodynamics. This method is called the local-bulk domain model and they show that this analysis "justifies the use of linear extrapolation to estimate ($\lesssim$ 5% error) the stability of the native protein in the absence of a denaturation" [21]. The history of this area is summarized in a delightful review titled: "Fifty years of solvent denaturation" by Schellman [44].

Two other methods have been used to analyze urea denaturation curves. They both give estimates of $\Delta G(H_2O)$ that are larger than those based on the LEM. The differences are not large with urea, but they are with GdmCl. One is an extrapolation based on Tanford's model [4] that is discussed in the next section. This method uses ΔG_{tr} values for transfer of the constituent groups of a protein from water to urea solutions. Unfortunately, there is uncertainty in the ΔG_{tr} value to use for a peptide group [38], and this introduces uncertainty into the $\Delta G(H_2O)$ values obtained by this method [45]. Experiments are underway to determine a more reliable value of ΔG_{tr} for a peptide group [7] (Auton and Bolen, personal communication). Makhatadze [46] has shown that the data on which this method is based are consistent with the LEM when urea but not GdnHCl is used as the denaturant.

The other method that can be used to determine $\Delta G(H_2O)$ is the denaturant binding model first used by Aune and Tanford [47]. The plots of log K vs. log [urea] mentioned above show that more urea molecules are bound by the denatured state than by the native state. Also, urea increases the solubility of all of the constituent parts of a protein, and it is possible to account for the enhanced solubility in terms of urea binding, even for leucine side chains (see table XI in Tanford [48]). Thus, it might seem reasonable to try to analyze urea denaturation curves in terms of the denaturant binding model. Generally, all of the urea binding sites are considered identical and independent and $K = 0.1$ is used for the binding constant [30]. However, this is surely not stoichiometric binding and it is unlikely that the binding sites are identical and independent. The enhanced solubility of the model compound data requires "binding constants" in the range 0.05–0.3 [46, 48, 49]. Schellman has shown convincingly that a solvent exchange model is more reasonable than a stoichiometric binding model, and this model is consistent with the LEM. (Schellman's recent article [22] gives references to his earlier work. It is also reviewed in Timasheff's paper [50].)

At first it was puzzling that the LEM worked so well. It seemed likely that there would sometimes be binding sites for urea molecules on folded proteins of at least moderate affinity and this would lead to nonlinearity that would cause the LEM to give erroneous results. Apparently, this rarely occurs. Our understanding of how urea denatures proteins has improved, thanks to the approaches of Timasheff [20], Record [21], and Schellman [22], which all show now why the LEM method works as well as it does.

$\Delta G(H_2O)$ values from GdmCl denaturation studies are less reliable, as pointed out most recently by Makhatadze [46]. This conclusion was reached earlier by Schellman and Gassner [51] who said:

Finally this study as well as a number of others indicates that urea has a number of advantages over guanidinium chloride as far as thermodynamic interactions are concerned. The free energy and enthalpy functions of both proteins and model compounds are more linear; the solutions more ideal; extrapolations to zero concentration are more certain; and least-squares analysis of the data is more stable.

One problem is that the ionic strength cannot be controlled with GdmCl, and this has been shown to affect the results in several studies (see, for example, Ibarra-Molero et al. [52], Monera et al. [53], Santoro and Bolen [54]).

In summary, the agreement between $\Delta G(T)$ values from DSC and thermal denaturation studies and $\Delta G(H_2O)$ values from urea denaturation studies analyzed by the LEM suggests that either method can be used to reliably measure the conformational stability of a protein. In addition, we now have a good understanding of why the LEM works so well.

3.5 *m*-Values

The thermodynamic cycle in Figure 3.5 shows that the dependence of ΔG on denaturant concentration is determined by the groups in a protein that are exposed to solvent in the denatured state, D, but not in the native state, N[4]. In support of this, Myers et al. [55] showed that there is a good correlation between *m*-values and the change in accessible surface area on unfolding. Since $\Delta g_{tr,i}$ values are available for

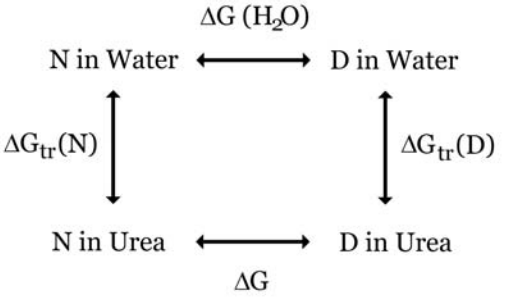

$$\Delta G + \Delta G_{tr}(N) = \Delta G\,(H_2O) + \Delta G_{tr}(D)$$

$$\Delta G - \Delta G\,(H_2O) = \Delta G_{tr}(D) - \Delta G_{tr}(N) = \sum n_i \alpha_i \Delta g_{tr,i}$$

$$\Delta G = \Delta G\,(H_2O) + \sum n_i \alpha_i \Delta g_{tr,i}$$

$$\Delta G = \Delta G\,(H_2O) + (\Delta\alpha) \sum n_i \Delta g_{tr,i}$$

Fig. 3.5. A thermodynamic cycle connecting protein folding in water and urea. N and D denote the native and denatured states, ΔG and $\Delta G(H_2O)$ are defined by Eq. (4), n_i is the total number of groups of type i in the protein, α_i is fraction of groups of type i that are exposed in D but not N, and $\Delta g_{tr,i}$ is the free energy of transfer of groups of type i from water to a given concentration of urea. $\Delta\alpha$ is the average change in exposure of all of the peptide groups and uncharged side chains in the protein [56].

most of the constituent groups in a protein, the equation at the bottom of Figure 3.5 can be used to calculate the dependence of ΔG on denaturant concentration. The *m*-value is an experimental measure of the dependence of ΔG on denaturant concentration. Consequently, for proteins that unfold by a two-state mechanism, $\Delta\alpha$ can be estimated by comparing the calculated and measured *m*-values. Thus, $\Delta\alpha$ is the fraction of buried groups that must become exposed to solvent on unfolding to account for the measured *m*-value [56]. In the original LEM paper [27], this approach was used to estimate $\Delta\alpha$ for four proteins. It was clear that differences among the $\Delta\alpha$ values for individual proteins revealed differences in the accessibility of the denatured state and that these differences depended to some extent on the number and location of the disulfide bonds in the protein.

Interest in *m*-values was stimulated by a series of papers from the Shortle laboratory [57, 58]. (A review of these studies was titled: ''Staphylococcal nuclease: a showcase of *m*-value effects.'' [31].) Their studies of mutants of staphylococcal nuclease (SNase) showed a wide range of *m*-values. Those with *m*-values 5% or more greater than wild type were designated m^+ mutants ($\approx$ 25%) and those with *m*-values 5% or more less than wild type were designated m^- mutants ($\approx$ 50%). Their interpretation was that m^+ mutants unfolded to a greater extent than wild type and vice versa for m^- mutants. These papers were extremely important because they focused attention on the denatured state which had largely been ignored in discussions of protein stability. (Another review from the Shortle lab [58] was titled: ''The denatured state (the other half of the folding equation) and its role in protein stability.'') However, this interpretation is only straightforward if all of the mutants unfold by a two-state mechanism. Shortle and Meeker [57] chose to assume a two-state mechanism to analyze their results even though the m^- mutants did not appear to unfold by a two-state mechanism. It is now clear that some of the m^- mutants unfold by a three-state mechanism [59–62]. The presence of an intermediate state will generally lower the *m*-value [63]. One important consequence of this is that the estimates of $\Delta G(H_2O)$ will be too low when a two-state mechanism is assumed and the mechanism is, in fact, three-state. In the case of the m^- mutant V66L + G88V + G79S, a two-state analysis indicates that this mutant is 3.0 kcal mol^{-1} LESS stable than wild type [57], but a three-state analysis indicates that that this mutant is 0.8 kcal mol^{-1} MORE stable than wild type [60]. This is also true for other m^- mutants [64]. This means that the $\Delta(\Delta G)$ values for the m^- mutants are not correct. Since 50% of the SNase mutants are m^-, this calls into question the interpretation of many of the $\Delta(\Delta G)$ values determined for SNase.

In Table 3.2, we have compiled *m* and $\Delta\alpha$ values for a selection of proteins. In all cases, the folding of the proteins is thought to closely approach a two-state mechanism. The value of $\Delta\alpha$ expected for unfolding a protein depends on the model assumed for the denatured state. If the accessibility of the denatured state is modeled as a tripeptide using the Lee and Richards [65] approach, a value of $\Delta\alpha \approx 0.7$ would be expected. However, if a compact denatured state based on fragments with native-state conformations is assumed, a $\Delta\alpha \approx 0.53$ would be expected [66]. Note in Table 3.2 that most of the $\Delta\alpha$ values are considerably less than 0.53. This suggests that the urea-denatured states of proteins are less completely unfolded than in the hypothetical state that Creamer et al. [66] thought might be a lower limit for

Tab. 3.2. Change in accessibility ($\Delta\alpha$) for urea denaturation calculated from the measured *m*-values using Tanford's model[a].

Protein	*Residues*	*Disulfides*	$(Urea)_{1/2}$	*m*	$\Delta\alpha$
RNase Sa (0K) (pH 7)[b]	96	1	6.44	0.99	0.32
RNase Sa (0K) (pH 3)[b]	96	1	1.48	1.75	0.41
RNase Sa (3K) (pH 7)[b]	96	1	4.07	0.99	0.29
RNase Sa (3K) (pH 3)[b]	96	1	1.47	2.00	0.46
RNase Sa (5K) (pH 7)[b]	96	1	5.31	1.14	0.36
RNase Sa (5K) (pH 3)[b]	96	1	1.30	2.21	0.50
RNase T1[c]	104	2	5.30	1.21	0.32
RNase A[d]	124	4	6.98	1.40	0.35
Lysozyme (Hen)[c]	129	4	6.80	1.29	0.29
SH3 domain[c]	62	0	3.74	0.77	0.34
Calbindin[c]	75	0	5.30	1.13	0.51
HPr (*E. coli*)[e]	88	0	4.32	1.14	0.45
Acyl phosphatase[f]	99	0	4.54	1.25	0.39
λ Repressor[c]	102	0	4.42	1.09	0.38
RNase T1[d]	104	0	3.34	1.64	0.38
FKBP[c]	107	0	4.18	1.46	0.42
Thioredoxin[c]	108	0	6.70	1.30	0.26
Barnase[c]	110	0	4.49	1.94	0.50
Che Y[c]	129	0	3.51	1.60	0.36
FABP[c]	131	0	5.43	1.77	0.40
SNase[g]	149	0	2.56	2.36	0.44
ApoMb[h]	153	0	2.05	2.49	0.47
RNase H[c]	155	0	3.88	1.93	0.35
DHFR (*E. coli*)[c]	159	0	3.10	1.90	0.32
T4 Lysozyme[c]	163	0	6.30	2.00	0.38

[a] Tanford's model is described in Tanford [4] and the details of the approach used to calculate $\Delta\alpha$ are given in Pace et al. [56]. $(Urea)_{1/2}$ values are given in M; *m* values are given in kcal mol^{-1} M^{-1}.
[b] The $(urea)_{1/2}$ and *m*-values are from Shaw [82].
[c] The original reference for these proteins is given in Myers et al. [55].
[d] See Pace et al. [56].
[e] See Nicholson and Scholtz [41].
[f] See Taddei et al. [83].
[g] See Shortle [31].
[h] See Hughson and Baldwin [84].

the compactness of the denatured state at the midpoint of a thermal denaturation curve in water. However, because of uncertainty in the ΔG_{tr} value for a peptide group and for some of the side chains, interpreting the absolute values of $\Delta\alpha$ is hazardous. In contrast, differences among the $\Delta\alpha$ values for individual proteins or for the same protein under different conditions are more trustworthy.

For the proteins without disulfide bonds, the $\Delta\alpha$ values in Table 3.2 range from a low of 0.26 for thioredoxin to a high of 0.51 for calbindin. Thus, if these proteins unfold by a two-state mechanism, calbindin unfolds to a much greater extent than thioredoxin. Barnase also unfolds more completely than most of the other proteins in Table 3.2. In support of this, we have shown that the tryptophan and tyrosine

side chains of urea-denatured barnase are more accessible to a perturbant than those of several other proteins that have lower $\Delta\alpha$ values [67]. The results in Table 3.2 suggest that urea-denatured proteins are not completely unfolded and that they unfold to different extents.

We were surprised to find that for RNases A and T1 [56] and barnase [67], the *m*-value increases markedly as the pH is lowered from 7 to 3. This indicates that the denatured states interact more extensively with urea as the pH is lowered, and we suggested that the denatured state ensemble expands at low pH due to electrostatic repulsion among the positive charges. In support of this interpretation, Privalov et al. [68] have shown that the intrinsic viscosity of unfolded proteins increases at low pH. We have recently obtained results with RNase Sa that provide further support for this idea [69].

RNase Sa is an acidic protein with a pI = 3.5 that contains no lysine residues. We have prepared a triple mutant that we call 3K (D1K, D17K, E41K) with a pI = 6.4, and a quintuple mutant that we call 5K (D1K, D17K, D25K, E41K, E74K) with a pI = 10.2. At pH 3, the estimated net charges are +8 for wild-type RNase Sa, +11 for 3K, and +13 for 5K. The *m*-values for the three proteins at pH 7 and pH 3 are given in Table 3.2. For all three proteins, the *m*-value is considerably greater at pH 3 than at pH 7, and the $\Delta\alpha$ values increase from 0.32 for wild-type RNase Sa to 0.36 for 3K to 0.50 for 5K. This is consistent with an increase in accessibility to denaturant caused by an expansion of the denatured state due to electrostatic repulsion among the positive charges. As the pH increases from 3 to 7, the carboxyl groups are titrated and both negative and positive charges are present. Now attractive charge–charge interactions are possible, and the decrease in the *m*-values suggests that the denatured state ensemble is more compact because of attractive Coulombic interactions. In support of this, the $\Delta\alpha$ value at pH 7 is lowest for 3K where the number of positive and negative charges is almost equal that for wild-type RNase Sa, which has an excess of negative charges, or 5K, which has an excess of positive charges. This and other evidence led us to conclude that long-range electrostatic interactions are important in determining the denatured state ensemble [69].

We suggest that when the hydrophobic and hydrogen bonding interactions that stabilize the folded state are disrupted, the unfolded polypeptide chain rearranges to compact conformations that improve long-range electrostatic interactions. These charge–charge interactions in the denatured state will reduce the net contribution of electrostatic interactions to protein stability but will help determine the denatured state ensemble. If this idea is correct, then long-range charge–charge interactions in the denatured state may play an important role in the mechanism of protein folding.

3.6 Concluding Remarks

Protein denaturants are used for a variety of purposes by protein chemists when they need to solubilize or denature proteins. Urea and GdmCl are the denaturants

most often used. The LEM has proven to be a reliable method for measuring the conformational stability of a protein or the difference in stability between two proteins that differ slightly in structure. In addition, studies of the *m*-values of proteins, especially SNase, have focused attention on the denatured state and we are slowly gaining a better understanding of the denatured state ensemble.

3.7 Experimental Protocols

3.7.1 How to Choose the Best Denaturant for your Study

Both urea and GdmCl will increase the solubility of the folded and unfolded states of a protein. If the denaturant is just going to be used to increase the solubility or unfold your protein of interest, GdmCl is preferred since it is a more potent denaturant and is chemically stable. Guanidinium thiocyanate is an even more potent denaturant than GdmCl and can be used for the same purposes. (The reason for the greater potency is discussed in Mason et al. [12].)

For quantitative studies of protein stability, we previously preferred results from urea and GdmCl unfolding over thermal unfolding studies for several reasons: the product of unfolding seemed to be better characterized, unfolding was more likely to closely approach a two-state mechanism, and unfolding was more likely to be completely reversible. However, in the cases that have been carefully investigated, the two techniques seem to give estimates of $\Delta G(H_2O)$ that are in good agreement [36, 70]. After getting the equipment set up and learning the procedures, either type of unfolding curve can be determined and analyzed in a single day. Consequently, the safest course is to determine both types of unfolding curves whenever possible. Also, we generally prefer urea over GdmCl because salt effects can be investigated, and sometimes reveal interesting information [46, 51, 71, 72].

3.7.2 How to Prepare Denaturant Solutions

Both urea and GdmCl can be purchased commercially in highly purified forms. However, some lots of these denaturants may contain fluorescent or metallic impurities. Methods are available for checking the purity of GdmCl and for recrystallization if necessary [73]. A procedure for purifying urea has also been described [74]. GdmCl solutions are stable for months, but urea solutions slowly decompose to form cyanate and ammonium ions in a process accelerated at high pH [75]. The cyanate ions can react with amino groups on proteins [76]. Consequently, a fresh urea stock solution should be prepared for each unfolding curve and used within the day.

Table 3.3 summarizes useful information for preparing urea and GdmCl stock solutions. We prepare urea stock solutions by weight, and then check the concentration by refractive index measurements using the equation given in Table 3.3. The preparation of a typical urea stock solution is outlined below. Since GdmCl is

Tab. 3.3. Information for preparing urea and GdmCl stock solutions.

Property	*Urea*	*GdmCl*
Molecular weight	60.056	95.533
Solubility (25.0 °C)	10.49 M	8.54 M
d/d_0[a]	$1 + 0.2658W + 0.0330W^2$	$1 + 0.2710W + 0.0330W^2$
Molarity[b]	$117.66(\Delta N) + 29.753(\Delta N)^2 + 185.56(\Delta N)^3$	$57.147(\Delta N) + 38.68(\Delta N)^2 - 91.60(\Delta N)^3$
Grams of denaturant per gram of water to prepare		
6 M	0.495	1.009
8 M	0.755	1.816
10 M	1.103	–

[a] W is the weight fraction denaturant in the solution, d is the density of the solution and d_0 is density of water [85].
[b] ΔN is the difference in refractive index between the denaturant solution and water (or buffer) at the sodium D line. The equation for urea solutions is based on data from Warren and Gordon [86], and the equation for GdmCl solutions is from Nozaki [73].

quite hygroscopic, it is more difficult to prepare stock solutions by weight. Consequently, the molarity of GdmCl stock solutions is generally determined from the refractive index measurement (step 5 below).

Preparation of a urea stock solution This describes the preparation of ~100 mL of ~10 M urea stock solution containing 30 mM MOPS buffer, pH 7.0. We use a top loading balance with an accuracy of about ±0.02 g.

1. Add ≈60 g of urea to a tared beaker and weigh (59.91 g). Now add 0.69 g of MOPS buffer (sodium salt), 1.8 mL of 1 M HCl and ≈52 mL of distilled water and weigh the solution again (114.65 g).
2. Allow the urea to dissolve and check the pH. If necessary, add a weighed amount of 1 M HCl to adjust to pH 7.0.
3. Prepare 30 mM MOPS buffer, pH 7.0.
4. Determine the refractive index of the urea stock solution (1.4173) and of the buffer (1.3343). Therefore, $\Delta N = 1.4173 - 1.3343 = 0.0830$.
5. Calculate the urea molarity from ΔN using the equation given in Table 3.3: M = 10.08.
6. Calculate the urea molarity based on the recorded weights. The density is calculated with the equation given in Table 3.1: weight fraction area $(W) = 59.91/114.65 = 0.5226$; therefore $d/d_0 = 1.148$. Therefore volume = 114.65/1.148 = 99.88 mL. Therefore urea molarity = 59.91/60.056/.09988 = 9.99 M.

3.7.3 How to Determine Solvent Denaturation Curves

Figure 3.2A shows a typical urea unfolding curve for RNase Sa using CD to follow unfolding. We will refer to the physical parameter used to follow unfolding as y

for the following discussion. The curves can be conveniently divided into three regions: (i) The pretransition region, which shows how y for the folded protein, y_F, depends upon the denaturant. (ii) The transition region, which shows how y varies as unfolding occurs. (iii) The posttransition region, which shows how y for the unfolded protein, y_U, varies with denaturant. All of these regions are important for analyzing unfolding curves. As a minimum, we recommend determining four points in the pre- and posttransition regions, and five points in the transition region. Of course, the more points determined the better defined the curve.

With thermodynamic measurements, it is essential that equilibrium is reached before measurements are made, and that the unfolding reaction is reversible. The time required to reach equilibrium can vary from seconds to days, depending upon the protein and the conditions. For example, the unfolding of RNase T1 requires hours to reach equilibrium at 25 °C, as compared to only minutes for RNase Sa. For any given protein, the time to reach equilibrium is longest at the midpoint of the transition and decreases in both the pre- and posttransition regions. To ensure that equilibrium is reached, y is measured as a function of time to establish the time required to reach equilibrium.

To test the reversibility of unfolding, allow a solution to reach equilibrium in the posttransition region and then by dilution return the solution to the pretransition region and measure y. If the reaction is reversible, the value of y measured after complete unfolding should be within $\pm 5\%$ of that determined directly. For many proteins, unfolding by urea and GdmCl is completely reversible. We have left RNase T1 in 6 M GdmCl for over 3 months and found that the protein will refold completely on dilution.

Proteins containing free sulphydryl groups present special problems. If the protein contains only free –SH groups and no disulfide bonds, then a reducing agent such as 10 mM dithiothreitol (DTT) can be added to ensure that no disulfide bonds form during the experiments. For proteins containing both free –SH groups and disulfide bonds, disulfide interchange can occur and this may lead to irreversibility. Disulfide interchange can be minimized by working at low pH [77].

If the unfolding of the protein of interest requires considerable time to reach equilibrium, then each point shown in Figure 3.2A will have to be determined from a separate solution, prepared volumetrically using the best available pipettes. A fixed volume of protein stock solution is mixed with the appropriate volumes of buffer, and urea or GdmCl stock solutions. The protein and buffer solutions are prepared by standard procedures. After the solutions for measurement have been prepared (see the protocol below), they are incubated until equilibrium is reached at the temperature chosen for determining the unfolding curve. After the measurements have been completed, it is good practise to measure the pH of the solutions in the transition region. If the protein equilibrates quickly, as is the case with RNase Sa, titration methods can be used to determine the denaturation curve. This was the method used to obtain the curve in Figure 3.2A. This protocol is described in detail in Pace [78] and Scholtz [40]. If the amount of protein is limited, instruments have been developed to follow the unfolding of a protein simultaneously with several spectral techniques using a single protein solution [79].

Tab. 3.4. Experimental results from a urea denaturation curve[a].

Urea[b] (mL)	*Buffer[c] (mL)*	*Protein[d] (mL)*	*Urea[e] (M)*	θ_{234} *(mdeg)[f]*
0.298	2.152	0.050	1.2	18
0.795	1.655	0.050	3.2	18
1.193	1.257	0.050	4.8	16
1.267	1.183	0.050	5.1	14
1.342	1.108	0.050	5.4	12
1.392	1.058	0.050	5.6	10
1.466	0.984	0.050	5.9	7
1.542	0.909	0.050	6.2	4
1.615	0.835	0.050	6.5	1
1.690	0.760	0.050	6.8	−2
1.740	0.710	0.050	7.0	−4
1.789	0.661	0.050	7.2	−4
1.839	0.611	0.050	7.4	−5
2.087	0.363	0.050	8.4	−5
2.286	0.164	0.050	9.2	−6

[a] Only two or three solutions are shown for the pre- and posttransition regions. In the actual experiment, a total of 32 solutions were prepared and measured.
[b] 10.06 M urea stock solution (30 mM MOPS, pH 7.0).
[c] 30 mM MOPS buffer, pH 7.0.
[d] 5.0 mg mL^{-1} RNase Sa E41H stock solution (30 mM MOPS, pH 7.0).
[e] Urea molarity = 10.06 ((mL urea)/(mL urea + mL protein + mL buffer)).
[f] Circular dichroism measurements at 234 nm using an Aviv 62DS spectropolarimeter.

3.7.3.1 **Determining a Urea or GdmCl Denaturation Curve**

1. Prepare three solutions: a denaturant stock solution, a protein stock solution and a buffer solution.
2. Prepare the sample solutions volumetrically (e.g., with Rainin EDP2 pipettes) in clean, dry test tubes. The solutions made to determine a urea unfolding curve for E41H RNase Sa, along with the resulting CD measurements, are given in Table 3.4.
3. Allow these solutions to equilibrate at the temperature chosen for the experiment until they reach equilibrium. (This is best determined in a separate experiment as described in the text.)
4. Measure the experimental parameter being used to follow unfolding on the solutions in order of increasing denaturant concentration. Leave the cuvette in the spectrophotometer, and do not rinse between samples. Simply remove the old solution carefully with a pasteur pipette with plastic tubing attached to the tip, and then add the next sample. Leaving the cuvette in position improves the quality of the measurements, and the error introduced by the small amount of old solution is negligible.

5. Plot these results to determine if any additional points are needed. If so, prepare the appropriate solutions and make the measurements as described for the original solutions.
6. Measure the pH of the solutions in the transition region.
7. Analyze the results as described below.

3.7.3.2 How to Analyze Urea or GdmCl Denaturant Curves

We assume a two-state folding mechanism for the discussion here (this will be correct for many small globular proteins). Consequently, for any of the points shown in Figure 3.2A, only the folded and unfolded conformations are present at significant concentrations, and $f_F + f_U = 1$, where f_F and f_U represent the fraction protein present in the folded and unfolded conformations, respectively. Thus, the observed value of y at any point will be $y = y_F f_F + y_U f_U$, where y_F and y_U represent the values of y characteristic of the folded and unfolded states, respectively, under the conditions where y is being measured. Combining these equations gives:

$$f_U = (y_F - y)/(y_F - y_U) \tag{A1}$$

The equilibrium constant, K, and the free energy change, ΔG, can be calculated using

$$K = f_U/f_F = f_U/(1 - f_U) = (y_F - y)/(y - y_U) \tag{A2}$$

and

$$\Delta G = -RT \ln K = -RT \ln[(y_F - y)/(y - y_U)] \tag{A3}$$

where R is the gas constant (1.987 cal mol^{-1} K^{-1} or 8.3144 J K^{-1} mol^{-1}) and T is the absolute temperature. Values of y_F and y_U in the transition region are obtained by extrapolating from the pre- and posttransition regions in Figure 3.2A. Usually y_F and y_U are linear functions of denaturant concentration, and a least-squares analysis is used to determine the linear expressions for y_F and y_U.

The calculation of f_U, K, and ΔG from the data in Figure 3.2A is illustrated in Table 3.5. Values of K can be measured most accurately near the midpoints of the curves, and the error becomes substantial for values outside the range 0.1–10. Consequently, we generally only use ΔG values within the range ± 1.5 kcal mol^{-1}. See Eftink and Ionescu [33] and Allan and Pielak [80] for discussions of the problems most frequently encountered in analyzing solvent and thermal denaturation curves.

As discussed above, the simplest method of estimating the conformational stability in the absence of urea, $\Delta G(H_2O)$, is to use the LEM, which typically gives results such as those shown in Figure 3.2B. We strongly recommend that values of $\Delta G(H_2O)$, m, and $[D]_{1/2}$ be given in any study of the unfolding of a protein by

Tab. 3.5. Analysis of a urea denaturation curve[a].

Urea (M)	*y*	y_F	y_U	f_F	f_U	*K*	ΔG (kcal mol^{-1})
6.26	9.16	12.01	−10.53	0.87	0.13	0.14	1.15
6.51	8.38	12.08	−10.22	0.83	0.17	0.20	0.95
6.76	7.35	12.16	−9.88	0.78	0.22	0.28	0.76
7.01	6.17	12.23	−9.55	0.72	0.28	0.39	0.56
7.26	4.45	12.30	−9.23	0.64	0.36	0.57	0.33
7.51	2.75	12.38	−8.91	0.55	0.45	0.83	0.11
7.76	1.15	12.45	−8.58	0.46	0.54	1.16	−0.09
8.01	−0.66	12.52	−8.26	0.37	0.63	1.73	−0.33
8.26	−2.16	12.60	−7.94	0.28	0.72	2.55	−0.56
8.51	−3.14	12.67	−7.61	0.22	0.78	3.53	−0.75
8.75	−3.94	12.74	−7.29	0.17	0.83	4.98	−0.95
9.00	−4.55	12.82	−6.96	0.12	0.88	7.16	−1.17

[a] Data points were from the transition region of the unfolding curve shown in Figure 3.2A.

urea or GdmCl. Remember also that if the LEM is used, one can apply Eq. (5) and use nonlinear least squares [29] to conveniently obtain the unfolding parameters.

3.7.4 Determining Differences in Stability

It is frequently of interest to determine differences in conformational stability among proteins that differ slightly in structure. The structural change might be a single change in amino acid sequence achieved through site-directed mutagenesis, or a change in the structure of a side chain resulting from chemical modification. In Table 3.6, we present results from urea unfolding studies of wild-type RNase Sa and a mutant that differs in amino acid sequence by one residue. Two different methods of calculating the differences in stability, $\Delta(\Delta G)$, are illustrated.

Tab. 3.6. Determining differences in conformational stability[a].

Protein	$\Delta G(H_2O)$[b]	$\Delta(\Delta G)$[c]	*m*[d]	$(Urea)_{1/2}$[e]	$\Delta(Urea)_{1/2}$[f]	$\Delta(\Delta G)$[g]
Wild-type RNase Sa	6.09	–	1170	5.20	–	–
N44 → A RNase Sa	4.12	2.0	1174	3.51	1.69	2.0

[a] Data from Hebert et al. [87].
[b] From Eq. (4), in kcal mol^{-1}.
[c] Difference between the $\Delta G(H_2O)$ values in kcal mol^{-1}.
[d] From Eq. (4), in cal mol^{-1} M^{-1}.
[e] Midpoint of the urea unfolding curve in M.
[f] Difference between the $(urea)_{1/2}$ values in M.
[g] From $\Delta(urea)_{1/2} \times 1172$ (the average of the two *m*-values) in kcal mol^{-1}.

The midpoints of urea, $(\text{urea})_{1/2}$, and thermal, T_m, unfolding curves can be determined quite accurately and do not depend to a great extent on the unfolding mechanism [30]. In contrast, measures of the steepness of urea unfolding curves, *m*, cannot be determined as accurately, and deviations from a two-state folding mechanism will generally change these values. Consequently, differences in stability determined by comparing the $\Delta G(H_2O)$ values can have large errors. However, when comparing completely different proteins or forms of a protein that differ markedly in stability, no other choice is available. This approach is illustrated by the first column of $\Delta(\Delta G)$ values in Table 3.6. There is also danger in drawing conclusions about the conformational stabilities of unrelated proteins based solely on the midpoints of their unfolding curves. For example, lysozyme and myoglobin have similar $\Delta G(H_2O)$ values at 25 °C, but a much higher concentration of GdmCl is needed to denature lysozyme because the *m*-value is much smaller. Likewise, lysozyme and cytochrome *c* are unfolded at about the same temperature, even though lysozyme has a much larger value of $\Delta G(H_2O)$ at 25 °C [81].

A second approach that can be used to determine differences in stability of single-site mutants is to take the difference between $[D]_{1/2}$ values and multiply this by the average of the *m*-values. This is illustrated by the $\Delta(\Delta G)$ values in the last column of Table 3.6. The rationale here is that the error in measuring the *m*-values should generally be greater than any differences resulting from the effect of small changes in structure on the *m*-value. However, substantial differences in *m*-values between proteins differing by only one amino acid in sequence have been observed with some proteins, i.e., SNase, so one must use caution when applying this method.

Acknowledgments

This work was supported by grants GM-37039 and GM-52483 from the National Institutes of Health (USA), and grants BE-1060 and BE-1281 from the Robert A. Welch Foundation. We thank many colleagues and coworkers over the years that have made important contributions to the field of protein folding.

References

1 Spiro, K. (1900). Uber die beeinflussung der eiweisscoagulation durch stickstoffhaltige substanzen. *Z Physiol Chem* 30, 182–199.

2 Ramsden, W. (1902). Some new properties of urea. *J Physiol* 28, 23–27.

3 Greenstein, J. P. (1938). Sulfhydryl groups in proteins. *J Biol Chem* 125, 501–513.

4 Tanford, C. (1964). Isothermal unfolding of globular proteins in aqueous urea solutions. *J Am Chem Soc* 86, 2050–2059.

5 Soper, A. K., Castner, E. W., and Luzar, A. (2003). Impact of urea on water structure: a clue to its properties as a denaturant? *Biophys Chem* 105, 649–666.

6 Modig, K., Kurian, E., Prendergast, G., and Halle, B. (2003). Water and urea interactions with the native and unfolded forms of a β-barrel protein. *Protein Sci* 12, 2768–2781.

7 Zou, Q., Bennion, B. J., Daggett, V., and Murphy, K. P. (2002). The molecular mechanism of stabilization of proteins by TMAO and its ability to counteract the effects of urea. *J Am Chem Soc* 124, 1192–1202.

8 Tsai, J., Gerstein, M., and Levitt, M. (1996). Keeping the shape but changing the charges: A simulation study of urea and its iso-steric analogs. *J Chem Phys* 104, 9417–9430.

9 Tirado-Rives, J., Orozco, M., and Jorgensen, W. L. (1997). Molecular dynamics simulations of the unfolding of barnase in water and 8 M aqueous urea. *Biochemistry* 36, 7313–7329.

10 Sokolic, F. I. A. (2002). Concentrated aqueous urea solutions: A molecular dynamics study of different models. *J Chem Phys* 116, 1636–1646.

11 Bennion, B. J. and Daggett, V. (2003). The molecular basis for the chemical denaturation of proteins by urea. *Proc Natl Acad Sci USA* 100, 5142–5147.

12 Mason, P. E., Neilson, G. W., Dempsey, C. E., Barnes, A. C., and Cruickshank, J. M. (2003). The hydration structure of guanidinium and thiocyanate ions: implications for protein stability in aqueous solution. *Proc Natl Acad Sci USA* 100, 4557–4561.

13 Muller, N. (1990). A model for the partial reversal of hydrophobic hydration by addition of a urea-like cosolvent. *J Phys Chem* 94, 3856–3859.

14 Laidig, K. E. and Daggett, V. (1996). Testing the modified hydration-shell hydrogen-bond model of hydrophobic effects using molecular dynamics simulation. *J Phys Chem* 100, 5616–5619.

15 Timasheff, S. N. (2002). Protein hydration, thermodynamic binding, and preferential hydration. *Biochemistry* 41, 13473–13482.

16 Karplus, P. A. and Faerman, C. (1996). Ordered water in macromolecular structure. *Curr Opin Struct Biol* 4, 770–776.

17 Pike, A. C. W. and Acharya, K. R. (1994). A structural basis for the interaction of urea with lysozyme. *Protein Sci* 3, 706–710.

18 Dunbar, J., Yennawar, H. P., Banerjee, S., Luo, J., and Farber, G. K. (1997). The effect of denaturants on protein structure. *Protein Sci* 6, 1727–1733.

19 Makhatadze, G. I. and Privalov, P. L. (1992). Protein interactions with urea and guanidinium chloride. A calorimetric study. *J Mol Biol* 226, 491–505.

20 Timasheff, S. N. and Xie, G. (2003). Preferential interactions of urea with lysozyme and their linkage to protein denaturation. *Biophys Chem* 105, 421–448.

21 Courtenay, E. S., Capp, M. W., Saecker, R. M., and Record, M. T., Jr. (2000). Thermodynamic analysis of interactions between denaturants and protein surface exposed on unfolding: interpretation of urea and guanidinium chloride m-values and their correlation with changes in accessible surface area (ASA) using preferential interaction coefficients and the local-bulk domain model. *Proteins* Suppl 4, 72–85.

22 Schellman, J. A. (2003). Protein stability in mixed solvents: a balance of contact interaction and excluded volume. *Biophys J* 85, 108–125.

23 Goldenberg, D. P. (2003). Computational simulation of the statistical properties of unfolded proteins. *J Mol Biol* 326, 1615–1633.

24 Schellman, J. A. (1987). Selective binding and colvent denaturation. *Biopolymers* 26, 549–559.

25 Alexander, S. S. and Pace, C. N. (1971). A comparison of the denaturation of bovine-lactoglobulins A and B and goat-lactoglobulin. *Biochemistry* 10, 2738–2743.

26 Pace, C. N. and Tanford, C. (1968). Thermodynamics of the unfolding of β-lactoglobulin A in aqueous urea solutions between 5 and 55. *Biochemistry* 7, 198–208.

27 Greene, R. F. J. and Pace, C. N. (1974). Urea and guanidine hydrochloride denaturation of ribonuclease, lysozyme, alpha-chymotrypsin, and beta-lactoglobulin. *J Biol Chem* 249, 5388–5393.

28 Shelton, V. M., Sosnick, T. R., and Pan, T. (1999). Applicability of urea in the thermodynamic analysis of secondary and tertiary RNA folding. *Biochemistry* 38, 16831–16839.

29 Santoro, M. M. and Bolen, D. W. (1988). Unfolding free energy changes determined by the linear extrapolation method. 1. Unfolding of phenylmetanesulfonyl α-chymotrypsin using different denaturants. *Biochemistry* 27, 8063–8068.

30 Pace, C. N. (1986). Determination and analysis of urea and guanidine hydrochloride denaturation curves. *Methods Enzymol* 131, 266–280.

31 Shortle, D. (1995). Staphylococcal nuclease: a showcase of m-value effects. *Adv Protein Chem* 46, 217–247.

32 Becktel, W. J. and Schellman, J. A. (1987). Protein stability curves. *Biopolymers* 26, 1859–1877.

33 Eftink, M. R. and Ionescu, R. (1997). Thermodynamics of protein unfolding: questions pertinent to testing the validity of the two-state model. *Biophys Chem* 64, 175–197.

34 Yu, Y., Makhatadze, G. I., Pace, C. N., and Privalov, P. L. (1994). Energetics of ribonuclease T1 structure. *Biochemistry* 33, 3312–3319.

35 Hu, C.-Q., Sturtevant, J. M., Thomson, J. A., Erickson, R. E., and Pace, C. N. (1992). Thermodynamics of ribonuclease T1 denaturation. *Biochemistry* 31, 4876–4882.

36 Pace, C. N., Grimsley, G. R., Thomas, S. T., and Makhatadze, G. I. (1999). Heat Capacity Change for Ribonuclease A Folding. *Protein Sci* 8, 1500–1504.

37 Huyghues-Despointes, B. M., Scholtz, J. M., and Pace, C. N. (1999). Protein conformational stabilities can be determined from hydrogen exchange rates. *Nat Struct Biol* 6, 910–912.

38 Qu, Y., Bolen, C. L., and Bolen, D. W. (1998). Osmolyte-driven contraction of a random coil protein. *Proc Natl Acad Sci USA* 95, 9268–9273.

39 Pace, C. N. and Laurents, D. V. (1989). A new method for determining the heat capacity change for protein folding. *Biochemistry* 28, 2520–2525.

40 Scholtz, J. M. (1995). Conformational stability of HPr: the histidine-containing phosphocarrier protein from *Bacillus subtilis*. *Protein Sci* 4, 35–43.

41 Nicholson, E. M. and Scholtz, J. M. (1996). Conformational stability of the *Escherichia coli* HPr protein: test of the linear extrapolation method and a thermodynamic characterization of cold denaturation. *Biochemistry* 35, 11369–11378.

42 Felitsky, D. J. and Record, M. T., Jr. (2003). Thermal and urea-induced unfolding of the marginally stable lac repressor DNA-binding domain: a model system for analysis of solute effects on protein processes. *Biochemistry* 42, 2202–2217.

43 Ibarra-Molero, B. and Sanchez-Ruiz, J. M. (1996). A model-independent, nonlinear extrapolation procdure for the characterization of protein folding energetics from solvent-denaturation data. *Biochemistry* 35, 14689–14702.

44 Schellman, J. A. (2002). Fifty years of solvent denaturation. *Biophys Chem* 96, 91–101.

45 Zhang, O. and Forman-Kay, J. D. (1995). Structural characterization of folded and unfolded states of an SH3 domain in equilibrium in aqueous buffer. *Biochemistry* 34, 6784–6794.

46 Makhatadze, G. I. (1999). Thermodynamics of protein interactions with urea and guanidinium hydrochloride. *J Phys Chem B* 103, 4781–4785.

47 Aune, K. C. and Tanford, C. (1969). Thermodynamics of the denaturation of lysozyme by guanidine hydrochloride II. dependence on denaturant concentration at 25°. *Biochemistry* 8, 4586–4590.

48 Tanford, C. (1970). Protein denaturation. C. Theoretical models

for the mechanism of denaturation. *Adv Protein Chem* 24, 1–95.

49 Liepinsh, E. and Otting, G. (1994). Specificity of urea binding to proteins. *J Am Chem Soc* 116, 9670–9674.

50 Timasheff, S. N. (2002). Thermodynamic binding and site occupancy in the light of the Schellman exchange concept. *Biophys Chem* 101–102, 99–111.

51 Schellman, J. A. and Gassner, N. C. (1996). The enthalpy of transfer of unfolded proteins into solutions of urea and guanidinium chloride. *Biophys Chem* 59, 259–275.

52 Ibarra-Molero, B., Loladze, V. V., Makhatadze, G. I., and Sanchez-Ruiz, J. M. (1999). Thermal versus guanidine-induced unfolding of ubiquitin. An analysis in terms of the contributions from charge–charge interactions to protein stability. *Biochemistry* 38, 8138–8149.

53 Monera, O. D., Kay, C. M., and Hodges, R. S. (1994). Protein denaturation with guanidine hydrochloride or urea provides a different estimate of stability depending on the contributions of electrostatic interactions. *Protein Sci* 3, 1984–1991.

54 Santoro, M. M. and Bolen, D. W. (1992). A test of the linear extrapolation of unfolding free energy changes over an extended denaturant concentration range. *Biochemistry* 31, 4901–4907.

55 Myers, J. K., Pace, C. N., and Scholtz, J. M. (1995). Denaturant m values and heat capacity changes: relation to changes in accessible surface areas of protein unfolding. *Protein Sci* 4, 2138–2148.

56 Pace, C. N., Laurents, D. V., and Thomson, J. A. (1990). pH dependence of the urea and guanidine hydrochloride denaturation of ribonuclease A and ribonuclease T1. *Biochemistry* 29, 2564–2572.

57 Shortle, D. and Meeker, A. K. (1986). Mutant forms of staphylococcal nuclease with altered patterns of guanidine hydrochloride and urea denaturation. *Proteins* 1, 81–89.

58 Shortle, D. (1996). The denatured state (the other half of the folding equation) and its role in protein stability. *FASEB J* 10, 27–34.

59 Gittis, A. G., W. E. Stites, E. E. Lattman. (1993). The phase transition between a compact denatured state and a random coil state in staphylococcal nuclease is first-order. *J Mol Biol* 232, 718–724.

60 Carra, J. H. and Privalov, P. L. (1995). Energetics of denaturation and m values of staphylococcal nuclease mutants. *Biochemistry* 34, 2034–2041.

61 Ionescu, R. M., M. R. Eftink. (1997). Global analysis of the acid-induced and urea-induced unfolding of staphylococcal nuclease and two of it variants. *Biochemistry* 35, 1129–1140.

62 Baskakov, I., Bolen, D. W. (1998). Forcing thermodynamically unfolded proteins to fold. *J Biol Chem* 273, 4831–4834.

63 Pace, C. N. (1975). The stability of globular proteins. *CRC Crit Rev Biochem* 3, 1–43.

64 Carra, J. H., Anderson, E. A., and Privalov, P. L. (1994). Three-state thermodynamic analysis of the denaturation of staphylococcal nuclease mutants. *Biochemistry* 33, 10842–10850.

65 Lee, B. and Richards, F. M. (1971). The interpretation of protein structures: estimation of static accessibility. *J Mol Biol* 55, 379–400.

66 Creamer, T. P., Srinivasan, R., and Rose, G. D. (1997). Modeling unfolded states of proteins and peptides. II. backbone solvent accessibility. *Biochemistry* 36, 2832–2835.

67 Pace, C. N., Laurents, D. V., and Erickson, R. E. (1992). Urea denaturation of barnase: pH dependence and characterization of the unfolded state. *Biochemistry* 31, 2728–2734.

68 Privalov, P. L., Tiktopulo, E. I., Venyaminov, S., Griko Yu, V., Makhatadze, G. I., and Khechinashvili, N. N. (1989). Heat capacity and conformation of proteins in the denatured state. *J Mol Biol* 205, 737–750.

69 Pace, C. N., Alston, R. W., and Shaw, K. L. (2000). Charge–charge interactions influence the denatured state ensemble and contribute to protein stability. *Protein Sci* 9, 1395–1398.

70 Thomson, J. A., Shirley, B. A., Grimsley, G. R., and Pace, C. N. (1989). Conformational stability and mechanism of folding of ribonuclease T1. *J Biol Chem* 264, 11614–11620.

71 Pace, C. N. and Grimsley, G. R. (1988). Ribonuclease T1 is stabilized by cation and anion binding. *Biochemistry* 27, 3242–3246.

72 Yang, M., Ferreon, A. C., and Bolen, D. W. (2000). Structural thermodynamics of a random coil protein in guanidine hydrochloride. *Proteins* Suppl, 44–49.

73 Nozaki, Y. (1972). The preparation of guanidine hydrochloride. In *Methods in Enzymology* (Hirs, C. H. W. and Timasheff, S. N., eds), Vol. 26, pp. 43–50. Academic Press, New York.

74 Prakash, V., Loucheux, C., Scheufele, S., Gorbunoff, M. J., and Timasheff, S. N. (1981). Interactions of proteins with solvent components in 8 M urea. *Arch Biochem Biophys* 210, 455–464.

75 Hagel, P., Gerding, J., Fieggen, W., and Bloemendal, H. (1971). Cyanate formation in solutions of urea. I. Calculation of cyanate concentrations at different temperature and pH. *Biochim Biophys Acta* 243, 366–373.

76 Stark, G. R. (1965). Reactions of cyanate with functional groups of proteins. 3. Reactions with amino and carboxyl groups. *Biochemistry* 4, 1030–1036.

77 Gray, W. R. (1997). Disulfide bonds between cysteine residues. In *Protein Structure: A Practical Approach*, 2nd edn (Creighton, T. E., ed.), pp. 165–186. IRL Press, Oxford.

78 Pace, C. N., Hebert, E. J., Shaw, K. L. et al. (1998). Conformational stability and thermodynamics of folding of ribonucleases Sa, Sa2 and Sa3. *J Mol Biol* 279, 271–286.

79 Saito, Y. and Wada, A. (1983). Comparative study of GuHCl denaturation of globular proteins. I. Spectroscopic and chromatographic analysis of the denaturation curves of ribonuclease A, cytochrome c, and pepsinogen. *Biopolymers* 22, 2105–2122.

80 Allen, D. L. and Pielak, G. J. (1998). Baseline length and automated fitting of denaturation data. *Protein Sci* 7, 1262–1263.

81 Pace, C. N. and Scholtz, J. M. (1997). Measuring the conformational stability of a protein. In *Protein Structure: A Practical Approach*, 2nd edn. (Creighton, T. E., ed.), pp. 299–321. IRL Press, Oxford.

82 Shaw, K. L. (2000). Reversing the net charge of ribonuclease sa. Texas A&M University, PhD dissertation. College Station, TX.

83 Taddei, N., Chiti, F., Paoli, P. et al. (1999). Thermodynamics and kinetics of folding of common-type acylphosphatase: comparison to the highly homologous muscle isoenzyme. *Biochemistry* 38, 2135–2142.

84 Hughson, F. M. and Baldwin, R. L. (1989). Use of site-directed mutagenesis to destabilize native apomyoglobin relative to folding intermediates. *Biochemistry* 28, 4415–4422.

85 Kawahara, K. and Tanford, C. (1966). Viscosity and density of aqueous solutions of urea and guanidine hydrochloride. *J Biol Chem* 241, 3228–3232.

86 Warren, J. R. and Gordon, J. A. (1966). On the refractive indices of aqueous solutions of urea. *J Phys Chem* 70, 297–300.

87 Hebert, E. J., Giletto, A., Sevcik, J. et al. (1998). Contribution of a conserved asparagine to the conformational stability of ribonucleases Sa, Ba, and T1. *Biochemistry* 37, 16192–16200.

88 Wang, A., Bolen, D. W. (1997). A naturally occurring protective system in urea-rich cells: mechanism of osmolyte protection of proteins against urea denaturation. *Biochemistry* 36, 9101–9108.

4
Thermal Unfolding of Proteins Studied by Calorimetry

George I. Makhatadze

4.1
Introduction

Protein folding/unfolding reactions and protein–ligand interactions, like any other chemical reactions, are accompanied by heat effects. At a constant pressure, these heat effects are described by the enthalpy of the process. Temperature-induced changes in the enthalpy of the macroscopic states of a protein are of particular significance. Temperature and enthalpy are coupled extensive and intensive thermodynamic parameters. Thus, the functional relationship between enthalpy and temperature $f = H(T)$ includes all the thermodynamic information on the macroscopic states in the system. This information can be extracted using the formalism of equilibrium thermodynamics.

The enthalpy $H(T)$ function of the system can be determined experimentally from the calorimetric measurements of the heat capacity at constant pressure, $C_p(T)$, of a system over a broad temperature range, as:

$$C_p(T) = \left(\frac{\partial H}{\partial T}\right)_p \quad \text{and thus} \quad H(T) = \int_{T_0}^{T} C_p(T)\,dT + H(T_0) \tag{1}$$

The heat capacity function of a system, $C_p(T)$, is directly measured by differential scanning calorimetry (DSC), making DSC the method of choice to study the conformational stability of biological macromolecules in general and proteins in particular. To study biological macromolecules the DSC instrumentation must satisfy a number of requirements, the most important of which is that measurements must be performed on dilute (< 1 mg mL^{-1}/0.1 weight %) protein solutions to minimize intermolecular interactions, and must use a small volume because in most cases only a few milligrams of protein are available. With these requirements satisfied, the partial heat capacity of a protein in aqueous solution is on the order of 0.03–0.5%, which is measured on the background of more than 99.5% heat capacity of solvent. Contemporary DSC instruments [1, 2] are designed to satisfy these extreme sensitivity, reproducibility, and signal stability requirements (Figure 4.1).

Protein Folding Handbook. Part I. Edited by J. Buchner and T. Kiefhaber

ISBN: 3-527-30784-2

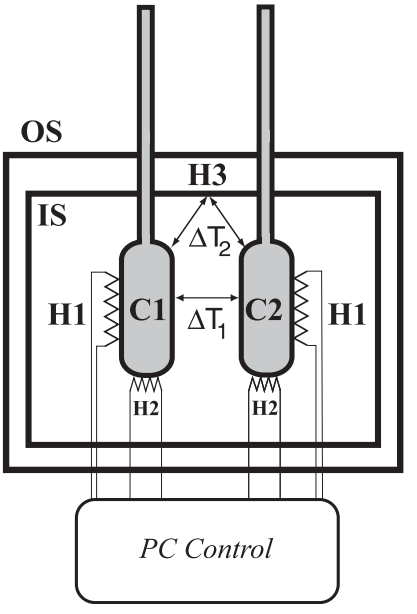

Fig. 4.1. Schematic design of the cell assembly of a contemporary DSC instrument. The matched sample cell (C1) and reference cell (C2) of the total fill type with inlet capillary tubes for filling and cleaning are surrounded by inner (IS) and outer (OS) shields. Two main heating elements (H1) on the cells are supplying electrical power for scanning upward in temperature. The auxiliary heating elements (H2) are activated by a feedback loop to equilibrate the difference in temperatures between cells (i.e., to maintain $\Delta T_1 = 0\ ^\circ C$). Additional heaters (H3) on the inner shield (IS) maintain the temperature difference between the cell and the shield $\Delta T_2 = 0\ ^\circ C$. The feedback loops are controlled by a PC board.

Extreme sensitivity of the instrumentation implies that particular care should be taken over experimental procedures for sample preparation and routine operation of DSC [3, 4]. Some essential considerations for setting up a DSC experiment, and discussion of critical factors are given in Section 4.7. For those interested in collection of numerical data of thermodynamic parameters such as Gibbs free energy change, enthalpy change, heat capacity change, transition temperature etc., two excellent sources of information are Refs [5] and [6].

4.2
Two-state Unfolding

First we consider in details the simplest case – a two-state model of protein unfolding. Some of the more complex cases will be discussed in Section 4.6.

For a monomolecular two-state process:

$$\mathrm{N} \overset{K_\mathrm{U}}{\leftrightarrow} \mathrm{U}$$

the equilibrium constant is defined by the concentrations of protein in the native and unfolded states at a given temperature:

$$K(T) = \frac{[\mathrm{U}]}{[\mathrm{N}]} \tag{2}$$

while the fraction of the molecules in the native, F_N, and unfolded, F_U, states is defined as:

$$F_\mathrm{N}(T) = \frac{[\mathrm{N}]}{[\mathrm{N}] + [\mathrm{U}]} \quad \text{and} \quad F_\mathrm{U}(T) = \frac{[\mathrm{U}]}{[\mathrm{N}] + [\mathrm{U}]} \tag{3}$$

Combining Eqs (2) and (3), the populations of the native and unfolded states are defined by the equilibrium constant as:

$$F_\mathrm{N}(T) = \frac{1}{1 + K(T)} \quad \text{and} \quad F_\mathrm{U}(T) = \frac{K(T)}{1 + K(T)} \tag{4}$$

The equilibrium constant of the unfolding reaction, $K(T)$, on the other hand, is related to the Gibbs energy change upon unfolding as:

$$K(T) = \exp\left(-\frac{\Delta G(T)}{RT}\right) \tag{5}$$

The Gibbs energy of unfolding, $\Delta G(T)$, is defined as:

$$\Delta G(T) = \Delta H(T) - T \cdot \Delta S(T) \tag{6}$$

where $\Delta H(T)$ is the enthalpy change and $\Delta S(T)$ is the entropy changes upon protein unfolding. The temperature dependence of both parameters is defined by the heat capacity change upon unfolding, ΔC_p:

$$\Delta C_\mathrm{p} = \frac{\mathrm{d}\Delta H(T)}{\mathrm{d}T} = T \cdot \frac{\mathrm{d}\Delta S(T)}{\mathrm{d}T} \tag{7}$$

Assuming that ΔC_p is independent of temperature we can write:

$$\Delta H(T) = \Delta H(T_0) + \Delta C_\mathrm{p}(T - T_0) \tag{8}$$

$$\Delta S(T) = \Delta S(T_0) + \Delta C_\mathrm{p} \cdot \ln\left(\frac{T}{T_0}\right) \tag{9}$$

where $\Delta H(T_0)$ and $\Delta S(T_0)$ are the enthalpy and entropy changes at a reference temperature T_0. For a two-state process it is convenient to set the reference temperature at which fractions for the native, F_N, and unfolded, F_U, protein are equal. Correspondingly, at this temperature, which is usually called the transition temperature, T_m, the equilibrium constant is equal to 1 and thus the Gibbs energy is equal to zero:

$$\Delta G(T_m) = -RT \ln K(T_m) = \Delta H(T_m) - T_m \Delta S(T_m) = 0 \tag{10}$$

which allows the entropy of unfolding at T_m to be expressed as:

$$\Delta S(T_m) = \frac{\Delta H(T_m)}{T_m} \tag{11}$$

and the entropy function as

$$\Delta S(T) = \frac{\Delta H(T_m)}{T_m} + \Delta C_p \cdot \ln\left(\frac{T}{T_m}\right) \tag{12}$$

Thus the temperature dependence of the Gibbs energy can be written as:

$$\Delta G(T) = \frac{T_m - T}{T_m} \cdot \Delta H(T_m) + \Delta C_p \cdot (T - T_m) + T \cdot \Delta C_p \cdot \ln\left(\frac{T_m}{T}\right) \tag{13}$$

The importance of Eq. (13) is that if just three parameters, $T_m, \Delta H(T_m)$, and ΔC_p, are known, all thermodynamic parameters $\Delta H, \Delta S$, and ΔG for the two-state process can be calculated for any temperature.

Figure 4.2 shows the temperature dependence of the partial heat capacity, $C_{p,pr}(T)$ of a hypothetical protein. It consists of two terms:

$$C_{p,pr}(T) = C_p^{prg}(T) + \langle C_p(T) \rangle^{exc} \tag{14}$$

where $C_p^{prg}(T)$ is the so-called progress heat capacity (sometimes also called the "chemical baseline") which is defined by the intrinsic heat capacities of protein in different states, and $\langle C_p(T) \rangle^{exc}$ is the excess heat capacity which is caused by the heat absorbed upon protein unfolding. The progress heat capacity for a two-state unfolding can be defined as:

$$C_p^{prg}(T) = F_N \cdot C_{p,N}(T) + F_U \cdot C_{p,U}(T) \tag{15}$$

where $C_{p,N}(T)$ and $C_{p,U}(T)$ are the temperature dependencies of the heat capacities of the native and unfolded states, respectively. It is important to emphasize that the heat capacity of the unfolded state is higher than that of the native state, $C_{p,U} > C_{p,N}$. Extensive studies of the heat capacities of the native and unfolded

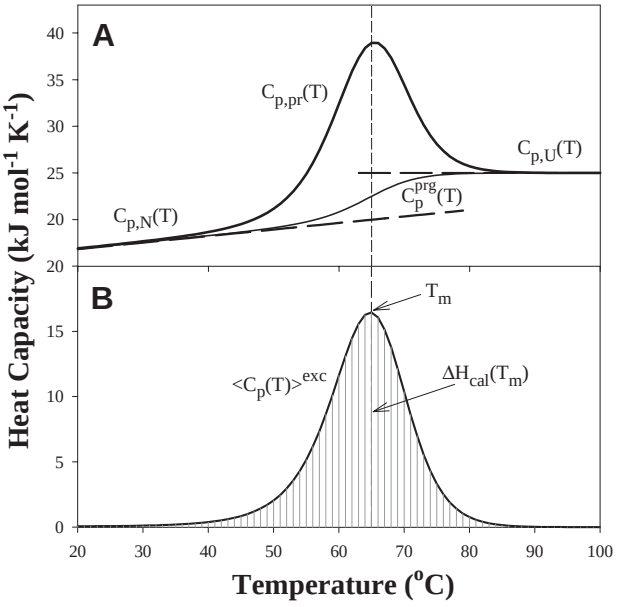

Fig. 4.2. A) Temperature dependence of the partial heat capacity, $C_{p,pr}(T)$, of a hypothetical protein that has the following thermodynamic parameters of unfolding: $T_m = 65$ °C, $\Delta H = 250$ kJ mol^{-1}, $\Delta C_p = 5$ kJ mol^{-1} K^{-1}. $C_{p,N}(T)$ and $C_{p,U}(T)$ are the temperature dependencies of the heat capacities of the native and unfolded states, respectively, and $C_p^{prg}(T)$ is the progress heat capacity (sometimes also called the "chemical baseline"). B) The excess heat capacity, $\langle C_p(T)\rangle^{exc}$, is obtained as a difference between $C_{p,pr}(T)$ and $C_p^{prg}(T)$. The area under $\langle C_p(T)\rangle^{exc}$ is the enthalpy of unfolding, and temperature at which $\langle C_p(T)\rangle^{exc}$ is maximum defines the transition temperature, T_m.

states of small globular proteins have established some general properties [7]. The heat capacity function for the native state appears to be a linear function of temperature with a rather similar slope 0.005–0.008 J K^{-2} g^{-1} when calculated per gram of protein. The absolute values for $C_{p,N}$ vary between 1.2 and 1.80 J K^{-1} g^{-1} at 25 °C. For the unfolded state, the absolute value at 25 °C is always higher than that for the native state ($C_{p,U} > C_{p,N}$) and ranges between 1.85 and 2.2 J K^{-1} g^{-1}. The heat capacity of the unfolded state has nonlinear dependence on temperature. It increases with increase of temperature and reaches a plateau between 60 and 75 °C. Above this temperature $C_{p,U}$ $C_{p,U}$ remains constant with the typical values ranging between 2.1 and 2.5 J K^{-1} g^{-1}.

The excess heat capacity function can thus be calculated as a difference between experimental and progress heat capacities. The excess heat capacity function is very important as it provides the temperature dependence of the fraction of protein in the native and unfolded states:

$$F_N(T) = 1 - F_U(T) = \frac{Q_i(T)}{Q_{tot}} = \frac{\int_0^T \langle C_p(T)\rangle^{exc}\,dT}{\int_0^\infty \langle C_p(T)\rangle^{exc}\,dT} \tag{16}$$

and the temperature dependence of the equilibrium constant

$$K(T) = \frac{\int_T^\infty \langle C_p(T)\rangle^{exc}\, dT}{\int_0^T \langle C_p(T)\rangle^{exc}\, dT} \tag{17}$$

The temperature dependence of the equilibrium constant defines the van't Hoff enthalpy of a two-state process as:

$$\Delta H_{vH} = -R \cdot \frac{d \ln K(T)}{d(1/T)} \tag{18}$$

The area under the $\langle C_p(T)\rangle^{exc}$ is the calorimetric (model independent) enthalpy of unfolding:

$$\Delta H_{cal} = \int_0^\infty \langle C_p(T)\rangle^{exc}\, dT \tag{19}$$

Comparison of the two enthalpies – van't Hoff enthalpy calculated for a two-state transition and model-free calorimetric enthalpy of unfolding – is the most rigorous test of whether protein unfolding is a two-state process [8–11]. If calorimetric enthalpy is equal to van't Hoff enthalpy, $\Delta H_{cal}(T_m) = \Delta H_{vH}(T_m)$, the unfolding process is a two-state process. If calorimetric enthalpy is larger than the van't Hoff enthalpy, $\Delta H_{cal}(T_m) > \Delta H_{vH}(T_m)$, the unfolding process is more complex, such as being not monomolecular or involving intermediate states (see Section 4.6).

Instead of the van't Hoff enthalpy, it is more practical to use the fitted enthalpy of two-state unfolding. This can be done using the following approach. The excess enthalpy function (relative to the native state) is defined as [2, 8]:

$$\langle \Delta H^{exc}\rangle = F_U \cdot \Delta H(T) \tag{20}$$

where $\Delta H(T)$ is the enthalpy difference between native and unfolded states. By definition, the excess heat capacity function is a temperature derivative of the excess enthalpy at constant pressure:

$$\langle \Delta C_p\rangle^{exc} = \frac{\partial \langle \Delta H^{exc}\rangle}{\partial T} = \Delta H \cdot \frac{\partial F_U}{\partial T} \tag{21}$$

Note that the way $\langle C_p(T)\rangle^{exc}$ is defined by Eq. (14), the temperature dependence of ΔH is in the $C_p^{prg}(T)$ function. Combining Eqs (4), (8), and (21) it is easy to show that the excess heat capacity $\langle C_p(T)\rangle^{exc}$ is defined as:

$$\langle C_p(T)\rangle^{exc} = \frac{{\Delta H_{fit}}^2}{R \cdot T^2} \cdot \frac{K}{(1+K)^2} \tag{22}$$

where the enthalpy function is defined as $\Delta H(T)$:

$$\Delta H(T) = \Delta H_{\text{fit}}(T_{\text{m}}) + \Delta C_{\text{p}} \cdot (T - T_{\text{m}}) \tag{23}$$

The experimental partial molar heat capacity function, $C_{\text{p, pr}}(T)$, is then fitted to the following expression:

$$C_{\text{p, pr}}(T) = F_{\text{N}}(T) \cdot C_{\text{p, N}}(T) + \langle C_{\text{p}}(T) \rangle^{\text{exc}} + F_{\text{U}}(T) \cdot C_{\text{p, U}}(T) \tag{24}$$

The heat capacity functions for the native and unfolded states can be represented by the linear functions of temperature as:

$$C_{\text{p, N}}(T) = A_{\text{N}} \cdot T + B_{\text{N}} \tag{25}$$

$$C_{\text{p, U}}(T) = A_{\text{U}} \cdot T + B_{\text{U}} \tag{26}$$

There are seven parameters to fit: $T_{\text{m}}, \Delta H_{\text{fit}}, \Delta C_{\text{p}}, A_{\text{N}}, A_{\text{U}}, B_{\text{N}}$, and B_{U}.

4.3 Cold Denaturation

Initial studies of the thermodynamics of protein unfolding [9, 12–15] done on small globular proteins established that equilibrium protein unfolding is a two-state process, i.e., $\Delta H_{\text{vH}} = \Delta H_{\text{cal}}$ and that the protein unfolding is accompanied by a large positive heat capacity change. Direct consequence of large heat capacity changes upon unfolding is that both enthalpy and entropy functions are strongly temperature dependent which in turn leads to a temperature-dependent Gibbs energy function (Figure 4.3). Both the enthalpy and entropy are expected to be zero at temperature T_{h} and T_{s}. By definition, the slope of temperature dependence of the ΔG function is equal to $-\Delta S$:

$$\frac{\partial \Delta G(T)}{\partial T} = -\Delta S(T)$$

Thus at $T_{\text{s}} \Delta S = 0$ and ΔG has a maximum at T_{s}, so that $\Delta G(T_{\text{s}}) = \Delta H(T_{\text{s}})$. The enthalpy function crosses zero at T_{h}, which is always lower than T_{s} (i.e., $T_{\text{h}} < T_{\text{s}}$), however since $T_{\text{s}} - T_{\text{h}} = \Delta H(T_{\text{s}})/\Delta C_{\text{p}}$, this difference is only a few degrees. There is a simple relationship between T_{h} and the transition temperature T_{m}: $T_{\text{m}} - T_{\text{h}} = \Delta H(T_{\text{m}})/\Delta C_{\text{p}}$.

The fact that ΔG function has a maximum at T_{s} means that it can cross zero at two different temperatures: once at temperature $T_{\text{m}} > T_{\text{s}}$ and again at $T_{\text{m}'} < T_{\text{s}}$. T_{m} is the temperature of denaturation observed upon heating the solution. $T_{\text{m}'}$ is the temperature of protein denaturation upon cooling, the so-called cold denaturation. There is a simple relationship between T_{m} and $T_{\text{m}'}$. The equation $T_{\text{m}'} \approx T_{\text{m}} - 2 \cdot \Delta H(T_{\text{m}})/\Delta C_{\text{p}}$ overestimates the temperature of cold denaturation only by few degrees.

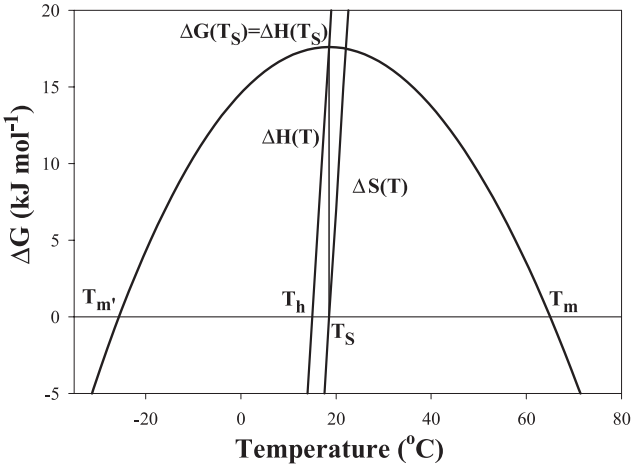

Fig. 4.3. Temperature dependencies of Gibbs energy, ΔG, enthalpy, ΔH, and entropic contribution, $T \cdot \Delta S$, for the same hypothetical protein as in Figure 4.2. Thermodynamics functions were calculated according to equations using the following parameters: $T_m = 65$ °C, $\Delta H = 250$ kJ mol^{-1}, $\Delta\Delta C_p = 5$ kJ mol^{-1} K^{-1}. Other abbreviations: $T_{m'}$ temperature of cold denaturation, T_h temperature at which enthalpy is zero, T_s temperature at which entropy is zero.

Cold denaturation was predicted and later its existence confirmed based on the extrapolation of thermodynamic functions obtained from the study of heat denaturation process [8, 16–19]. Experimental validation of the cold denaturation phenomenon once again demonstrated the power of statistical thermodynamics in the analysis of the conformational properties of proteins.

4.4 Mechanisms of Thermostabilization

From the point of view of applied properties of proteins, two parameters are important – the thermodynamic stability as measured by the Gibbs energy and the thermostability as measured by the transition temperature.

Depending on the relationship between the T_s, T_m and absolute values of ΔG, three extreme models [20–24] account for the increase in ΔG and/or T_m and the relationship between these two parameters (Figure 4.4).

- *Model I* Increase in thermostability is accompanied by little or no change in T_s but with an increase in stability at T_s. This can be achieved by lowering the entropy of unfolding without changes in the enthalpy of unfolding or in ΔC_p.
- *Model II* Increase in thermostability is accompanied by little or no change in T_s and no changes in stability at T_s, but the temperature dependence of ΔG be-

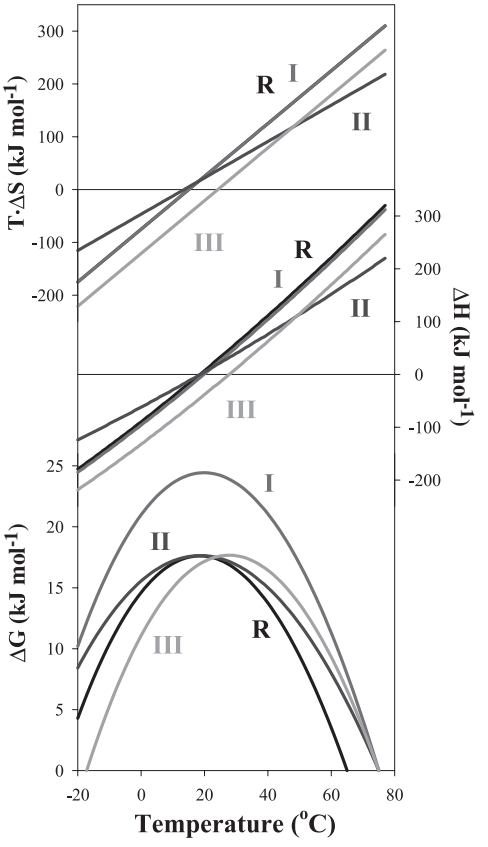

Fig. 4.4. Thermodynamic models for thermostabilization relative to the reference protein. Detailed thermodynamic parameters for the reference protein (R), and models I, II and III are given in Table 4.1.

Tab. 4.1. Thermodynamic parameters used in the simulation of different models for thermostabilization shown in Figure 4.4.

	T_m (°C)	T_s (°C)	ΔC_p (kJ mol^{-1} K^{-1})	$\Delta H(T_m)$ (kJ mol^{-1})	$\Delta G(T_S)$ (kJ mol^{-1})	ΔH(65 °C) (kJ mol^{-1})	$T \cdot \Delta S$(65 °C) (kJ mol^{-1})	$\Delta\Delta G$(65 °C) (kJ mol^{-1})
Reference	65	18	5.00	250	17.6	250	250	0
Model 1	75	19	5.00	300	24.6	250	242	7.9
Model 2	75	18	3.44	212	17.6	177	172	5.6
Model 3	75	27	5.00	254	17.6	204	197	6.6

comes less steep. This can be achieved by lowering ΔC_p, but both enthalpy and entropy will change as well.

- *Model III* Increase in thermostability is accompanied by the increase in T_s but no changes in stability at T_s, or in the temperature dependence of ΔG function. The increase in stability is due to the decrease in both enthalpic and entropic factors, but decrease in $T \cdot \Delta S$ is larger than in ΔH, while ΔC_p remains unchanged.

Of course these three models represent ''extreme'' cases and the real systems can use combination of all three simultaneously. Nevertheless, understanding the contributions of different factors to the thermodynamics of proteins in terms of $\Delta C_p, \Delta H$, and ΔS allows strategies for rational modulation of protein stability and/or thermostability to be designed. These strategies are discussed in the next section.

4.5 Thermodynamic Dissection of Forces Contributing to Protein Stability

The ultimate goal of the field is to be able to understand the determinants of protein stability in such details that will allow the prediction of the stability profile (i.e., ΔG) of any protein under any conditions such as temperature, pH, ionic strength, etc.

For example, the slope of the ΔG dependence on temperature is $-\Delta S$, which in turn is dependent on temperature and this dependence is defined by ΔC_p. Thus one needs to know not only a value for ΔG at one particular temperature, but also $\Delta S, \Delta H$, and ΔC_p to calculate the $\Delta G(T)$ function.

Another potential complexity arises from the fact that ΔG being the difference between the enthalpic (ΔH) and entropic ($T \cdot \Delta S$) terms, is subject to the so-called enthalpy–entropy compensation phenomenon [25–27]. It has been observed in a number of systems that changes in the enthalpy of a system are often compensated by the changes in the entropy in such a way that the resulting changes in ΔG are very small. One particularly striking example of such compensation is the effect of heavy (D_2O) and ordinary light (H_2O) water on protein stability [28]. Heavy water as a solvent provides probably the smallest possible perturbation to the properties H_2O. The stability (ΔG) of proteins in H_2O is very similar to the stability of proteins in D_2O (Figure 4.5). Such similarity in the ΔG values might lead to the conclusion that D_2O did not perturb the properties of the system relative to H_2O. However, if one looks at the corresponding changes in enthalpy (Figure 4.5) and entropy (not shown), it is clear that D_2O has a profound effect on the system, and decreases the enthalpy of unfolding by $\sim$20%. This decrease in enthalpy is accompanied by a decrease in entropy in such a way that the resulting ΔG is largely unchanged.

This result underlines the importance of the analysis of the protein stability in terms of enthalpy, entropy, and heat capacity, so that underlying physicochemical processes are not masked by the enthalpy–entropy compensations. The effect of

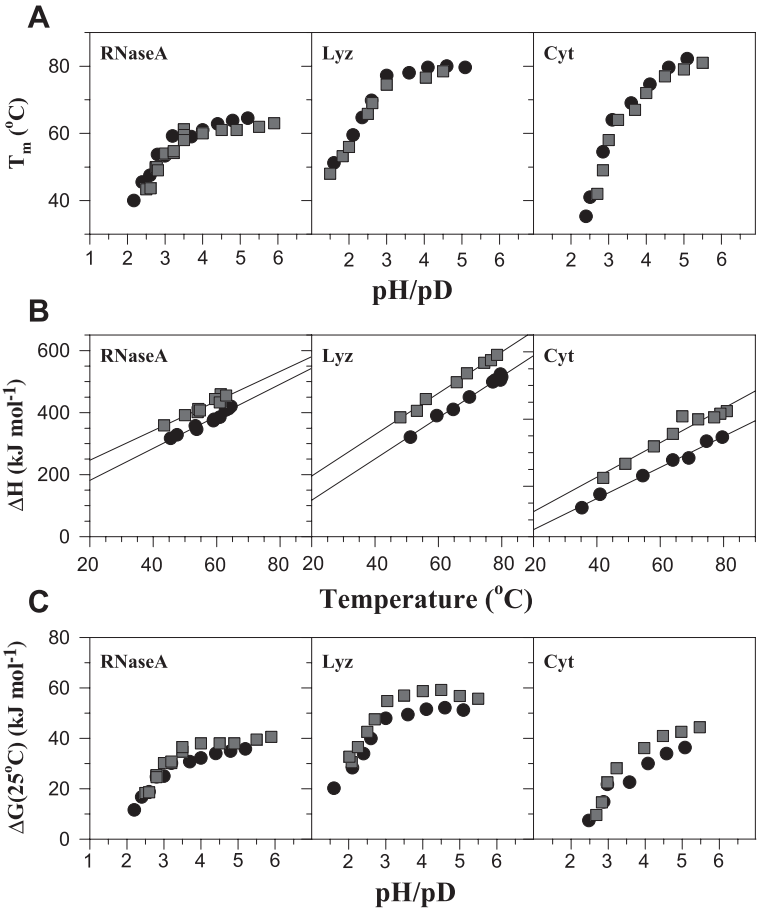

Fig. 4.5. Comparison of the unfolding thermodynamics for three different proteins ribonucleases A (RNaseA), hen-egg white lysozyme (Lyz) and cytochrome *c* (Cyt), in ordinary (H_2O, squares) and heavy (D_2O, circles) water. A) Dependence of the transition temperature, T_m, on the pH/pD. B) Dependence of the enthalpy of unfolding, ΔH, on the transition temperature, T_m. The slopes which represent the heat capacity change upon unfolding (ΔC_p, kJ K^{-1} mol^{-1}) are 4.8 (d-RNase), 5.2 (h-RNase), 6.4 (d-Lyz), 6.7 (h-Lyz), 4.7 (d-Cyt *c*) and 5.5 (h-Cyt *c*). C) Dependence of the Gibbs energy of unfolding at ΔG (25 °C) on the pH/pD. Reproduced with permission from Ref. [28].

D_2O on protein stability also underlines the importance of the solvent (or interactions of protein groups with the solvent) for protein stability. Even such small perturbation in the properties of solvent such as D_2O versus H_2O produces dramatic changes in the enthalpies and entropies of unfolding. Thus in analysis of the factors important for proteins stability one needs to consider not only the interactions between protein groups but also interactions between protein groups and the solvent. The next three sections will discuss the contribution of different types

of interactions to the heat capacity, enthalpy and entropy changes upon protein unfolding.

4.5.1 Heat Capacity Changes, ΔC_p

It is currently believed that the heat capacity changes upon unfolding are entirely defined by the interactions with the solvent of the proteins groups that were buried in the native state but become exposed upon unfolding. Both polar and nonpolar groups seem to contribute although with different sign and magnitude. It appears that nonpolar groups have a large positive contribution to the heat capacity of unfolding, while the polar groups have smaller (for a group of similar size) and negative contribution to ΔC_p. These estimates of ΔC_p for polar and nonpolar groups were obtained from the study of thermodynamics of transfer for model compounds [7, 29–35]. To link the data on model compounds to the results obtained on proteins, the heat capacity changes for model compounds were computed per unit of solvent accessible surface area, and then used as coefficients to calculated the hydration heat capacity for proteins. It has been shown that the ΔC_p values calculated are in a very good agreement with the experimentally determined heat capacity changes for proteins. From this correlation it was concluded that the ΔC_p of protein unfolding is caused exclusively by the hydration and that the disruption of internal interactions in the native state do not contribute to the ΔC_p. This conclusion was in disagreement with the estimates done by Sturtevant [36], who showed that the changes in vibrational entropy of protein upon unfolding should contribute 20–25% to the experimentally observed changes in ΔC_p.

The common belief that ΔC_p is entirely defined by the hydration was questioned by experiments of Loladze et al. [37]. These authors measured experimentally the effects of single amino acid substitutions at fully buried positions of ubiquitin on the ΔC_p of this protein. It was shown that substitution of the fully buried nonpolar residues with the polar ones leads to a decrease in ΔC_p, while the substitutions of fully buried polar residues with nonpolar ones leads to an increase in ΔC_p. These results provided direct experimental support for the model compound data (that indicated difference in the sign for the ΔC_p of hydration for polar and nonpolar groups) to be qualitatively applicable to proteins. Quantitatively, however, the results of substitutions on ΔC_p were not possible to predict based on the model compound data and surface area proportionality. This led to the conclusion that the dynamic properties of the native state also contribute to ΔC_p [37, 38]. At this point quantitative correlation between native state dynamics and ΔC_p awaits experimental validation.

4.5.2 Enthalpy of Unfolding, ΔH

The enthalpy of protein unfolding is positive, which means that enthalpically the native state is favored over the unfolded state. Two major types of interactions can

be considered as a possible source of enthalpy: interactions with the solvent and internal interactions between protein groups in the native state.

Interactions with the solvent by the protein groups newly exposed upon unfolding of the native protein structure are expected to be enthalpically unfavorable (enthalpically hydration of the unfolded state is favored over the hydration of the native state). This follows from the data on the transfer of the model compounds from the gas phase into water; for both polar and nonpolar groups, the enthalpy of transfer is negative [28, 32, 34, 48, 39]. The absolute magnitude of the effects for a polar group and a nonpolar group of the same size is very different. It is far more enthalpically unfavorable to transfer a polar group into water that it is for a nonpolar group. This large difference in the enthalpy of hydration of polar and nonpolar groups in proteins was recently demonstrated experimentally by measuring the effects of nonpolar to polar substitutions at fully buried sites on the enthalpy of unfolding [40].

If the enthalpy of dehydration is unfavorable, it is clear that the internal interactions between protein groups in the native state are enthalpically very stabilizing. The internal interactions are the hydrogen bonding and packing interactions between groups in the protein interior. The packing of the protein core is as good as the packing of organic crystals. Calculations show that the packing density in proteins is very similar to that for organic crystals [41, 42]. Melting or sublimation of a crystal is accompanied by large enthalpy, and one can expect that disruption of packing interactions in the protein interior will also lead to large positive enthalpy. Direct evidence for this was obtained by measuring the effects of substitutions that perturb packing in the protein interior [40]. It was shown that cavity creating substitutions in the protein core led to substantial decrease in the enthalpy of unfolding.

Hydrogen bonding also makes a favorable contribution to the protein stability [43, 44]. The net effect of disruption of hydrogen bonding inside the protein is difficult to measure. However, substitutions that disrupt hydrogen bonding with minimal (but not negligible) perturbations in the packing and hydration indicate that there is a significant enthalpic effect associated with the disruption of internal hydrogen bonds [40]. One needs to keep in mind that this effect is for disruption of hydrogen bonds in the protein interior and does not include the effect of hydration. These two effects are very difficult to estimate separately. The combined effect, i.e., enthalpy of disruption of hydrogen bonds in the protein interior followed by exposure (hydration) of hydrogen bonding groups to the solvent is more straightforward for the experimental analysis. Recent advances in calorimetric instrumentation and the development of novel model systems have provided estimates for the enthalpy of hydrogen bonding upon helix–coil transition [45–47]. The measured value is relatively small ($\sim$3 kJ mol^{-1}) but positive, indicating that the favorable enthalpy of internal hydrogen bonding is larger than the unfavorable enthalpy of hydration.

To summarize, native protein is enthalpically more stable than the unfolded state. Internal interactions (packing and hydrogen bonding) are enthalpically stabi-

lizing, while exposure to the solvent upon unfolding of the buried in the native state groups is enthalpically destabilizing.

4.5.3 Entropy of Unfolding, ΔS

Protein unfolding is accompanied by increase in entropy. This entropy increase is caused by two factors. One factor is the interaction of the newly exposed groups with the solvent in the unfolded state. The other factor is the increase in the number of accessible conformations in the unfolded state relative to the native state. Interactions with the solvent by both polar and nonpolar groups occur with the negative entropy [33, 34, 48]. The molecular details of these effects just start to become clear but in a simplified way they can be described by the increase in order of water molecules around the solute (polar or nonpolar) relative to the bulk water. The molecular mechanism of this ordering is different for polar and nonpolar groups [49]. For a group of the same size, the entropy decrease due to hydration for polar groups appears (based on the model compound study) to be larger than that for the nonpolar groups. Such an effect is expected intuitively, based on consideration that the polar groups will have more ordering effect on the water dipole.

This decrease in entropy due to hydration of protein groups newly exposed to solvent in the unfolded state is overcompensated by the increase (relative to the native state) in the configurational freedom of the polypeptide chain in the unfolded state. There are several different estimates of the magnitude of the configurational entropy in proteins [50–55]. The actual value will probably be strongly context dependent, and will depend on the conformations that can be populated within the unfolded state ensemble.

Overall, hydration of both polar and nonpolar groups (the latter sometimes called hydrophobic effect) entropically favors the native state, while the increase in conformational freedom favors the unfolded state.

On balance, the protein structure is stabilized enthalpically. Large enthalpic stabilization is offset by entropic destabilization, rendering the protein molecule marginally stable [56].

One can only speculate why proteins evolve to be marginally stable. From the biological standpoint, low stability might be advantageous for rapid regulation of protein levels in the cell, because low stability most certainly will facilitate protein degradation by proteases or more complex cellular machineries. Transport of proteins among different cellular compartments involves folding–unfolding and thus low stability will facilitate transport across the membrane [57]. Low stability will probably permit conformational transitions between different functional states, and thus will be advantageous for regulation. Low stability will also have important consequences for the kinetics of folding/unfolding reactions and thus might be important in preventing accumulation of intermediate states that have detrimental properties, such as a tendency to aggregate [57–59].

In discussing protein stability we largely concentrate on the residues that are

buried in the native state as a major source for the stability. Indeed, interactions in the core of the native protein and interactions of these residues with the solvent in the unfolded state provide the dominant effects for protein stability. This does not mean, however, that the surface residues do not contribute to stability [60–63]. They are in most cases not dominant factors defining protein energetics, yet are significantly large relative to the overall protein stability (ΔG) and thus they are important for modulating protein stability and, in the case of charge–charge interactions, enhancing protein solubility.

4.6 Multistate Transitions

In 1978 Biltonen and Freire [8] proposed a universal mechanism for equilibrium unfolding of proteins based on standard statistical thermodynamics approach. They considered a general reaction in which a initial native state, N, undergoes conformational transition to the final unfolded state, U, via a series of intermediate states, I_i:

$$N \leftrightarrow I_1 \leftrightarrow I_2 \cdots \leftrightarrow I_n \leftrightarrow U$$

and showed that the excess enthalpy of the systems (enthalpies of all states in the system relative to the initial state) can be written as:

$$\langle \Delta H^{\mathrm{exc}} \rangle = \sum_{i=0}^{n} F_i \cdot \Delta H_i \tag{27}$$

where F_i is the fractional population of i-th state and ΔH_i is the enthalpy of the i-th state relative to the initial state. Keeping in mind that since

$$\langle \Delta H^{\mathrm{exc}} \rangle = \int_{T_0}^{T} \Delta C_{\mathrm{p}}^{\mathrm{exc}} \cdot \mathrm{d}T \tag{28}$$

knowledge of the excess heat capacity function provides a unique description of the thermodynamic properties of the system. One practical approximation for the multistate transitions is that when the transitions involve many states, it is convenient to assume that the thermodynamic domains behave in an independent manner, with each individual transition approximated by a two-state transition. In such case the excess heat capacity function can be simply written as:

$$\langle \Delta C_{\mathrm{p}}{}^{\mathrm{exc}} \rangle = \sum_{i} \frac{(\Delta H_i)^2}{RT^2} \cdot \frac{K_i}{(1 + K_i)^2} \tag{29}$$

where K_i is the equilibrium constant for the i-th reaction.

The following sections discuss several of the commonest cases for the unfolding process other than the simple two-state case.

4.6.1 Two-state Dimeric Model

In this model only the native dimer, N_2, and unfolded monomer, U, are significantly populated.

$$N_2 \overset{K}{\leftrightarrow} 2 \cdot U$$

The equilibrium constant is then defined as:

$$K = \frac{[U]^2}{[N_2]} \tag{30}$$

where $[N_2]$ and $[U]$ are the concentrations of native dimers and monomers, respectively. The fraction of protein in these two states can be presented as:

$$[N_2] = \tfrac{1}{2} \cdot P_T \cdot F_{N_2} \quad \text{and} \quad [U] = P_T \cdot F_U \tag{31}$$

where F_{N_2} and F_U are the fractions of native dimer and unfolded monomers, respectively, and P_T, the total protein concentration expressed per mole of monomers is:

$$P_T = 2 \cdot [N_2] + [U] \tag{32}$$

Combining Eqs (30) and (32) allows the equilibrium constant to be expressed as a function of total protein concentration and a fraction of unfolded protein as:

$$K = \frac{2 \cdot P_T \cdot {F_U}^2}{1 - F_U} \tag{33}$$

Solving a simple quadratic equation for F_U, we arrive at:

$$F_U = \frac{\sqrt{(K^2 + 8 \cdot P_T \cdot K)} - K}{4 \cdot P_T} \tag{34}$$

The excess enthalpy of the system is related to the enthalpy of unfolding as:

$$\langle \Delta H^{exc} \rangle = F_U \cdot \Delta H(T) \tag{35}$$

which allows calculation of the excess heat capacity function by simple analytical differentiation:

$$\langle \Delta C_p^{exc} \rangle = \frac{\partial \langle \Delta H^{exc} \rangle}{\partial T} = \Delta H \cdot \frac{\partial F_U}{\partial T} = \frac{\Delta H(T)^2}{R \cdot T^2} \frac{F_U \cdot (1 - F_U)}{2 - F_U} \tag{36}$$

Thus the experimental partial molar heat capacity profile can be expressed as:

$$C_{p,pr}(T) = F_N(T) \cdot C_{p,N}(T) + C_p^{exc}(T) + F_U(T) \cdot C_{p,U}(T) \tag{37}$$

where the heat capacity functions for the native and unfolded states are expressed according to Eqs (25–26).

Calculation of the standard thermodynamic quantities such as Gibbs energy, can be done by defining the reference temperature T_m as a temperature at which $F_{N_2} = 0.5$, and thus according to the Eq. (33) the equilibrium constant at this temperature is equal to P_T. The standard Gibbs energy can then be expressed as:

$$\Delta G^0 = \frac{T_m - T}{T_m} \cdot \Delta H(T_m) + \Delta C_p \cdot (T - T_m) + T \cdot \Delta C_p \cdot \ln\left(\frac{T_m}{T}\right) - R \cdot T \cdot \ln K(T_m) \tag{38}$$

It must be emphasized that the ΔG^0 function in this case is refers to a 1 mol L^{-1} concentration of dimers.

4.6.2
Two-state Multimeric Model

For the reaction of unfolding of homo-oligomeric system that occurs without significant population of intermediate states, i.e.

$$N_n \overset{K}{\leftrightarrow} n \cdot U$$

it is easy to show that the excess heat capacity function can be expressed simply as

$$\langle \Delta C_p^{exc} \rangle = \frac{\Delta H(T)^2}{R \cdot T^2} \frac{F_U \cdot (1 - F_U)}{n - F_U \cdot (n - 1)} \tag{39}$$

where n is the order of the reaction. Obviously, for $n = 2$, Eq. (39) is reduced to Eq. (36).

4.6.3
Three-state Dimeric Model

In this model, not only the native dimer, N_2, and the unfolded monomer, U, but also a native monomer, N, are significantly populated.

$$N_2 \overset{K_d}{\leftrightarrow} 2 \cdot N \overset{K_U}{\leftrightarrow} 2 \cdot U$$

Equilibrium constants of dissociation, K_d, and of unfolding, K_U, are then defined as:

$$K_d = \frac{[N]^2}{[N_2]} \quad \text{and} \quad K_U = \frac{[U]}{[N]} \tag{40}$$

where $[N_2], [N]$, and $[U]$ are the concentrations of the native dimers, the native monomers and the unfolded monomers, respectively. The fraction of protein in these three states can be presented as:

$$[N_2] = \tfrac{1}{2} F_{N_2} \cdot P_T \tag{41}$$

$$[N] = F_N \cdot P_T \tag{42}$$

$$[U] = P_T \cdot F_U \tag{43}$$

where F_{N_2}, F_N, and F_U are the fractions of native dimer, native monomer, and unfolded monomer, respectively, and P_T, the total protein concentration expressed per mole of monomers, is:

$$PT = 2[N_2] + [N] + [U] \tag{44}$$

Combining Eqs (40)–(44) allows the equilibrium constants to be expressed as a function of total protein concentration and fractions of native and unfolded protein as:

$$K_d = \frac{2 \cdot {F_N}^2 \cdot P_T}{F_{N_2}} \tag{45}$$

$$K_U = \frac{F_U}{\sqrt{\frac{K_d \cdot F_{N_2}}{2 \cdot P_T}}} \tag{46}$$

Keeping in mind that $F_{N_2} + F_N + F_U = 1$ we can combine Eqs (45) and (46) to get:

$$F_{N_2} = 1 - \sqrt{\frac{K_d \cdot F_{N_2}}{2 \cdot P_T}} - K_U \cdot \sqrt{\frac{K_d \cdot F_{N_2}}{2 \cdot P_T}} \tag{47}$$

Substituting $1 + K_U = q$ and solving the quadratic equation we arrive at the following expressions for the fractions of proteins in the native dimer, native monomer, and unfolded monomer:

$$F_{N_2} = \frac{K_d}{8 \cdot P_T} \cdot \left[\sqrt{q^2 + \frac{8 \cdot P_T}{K_d}} - q \right]^2 \tag{48}$$

$$F_N = \frac{K_d}{4 \cdot P_T} \cdot \left[\sqrt{q^2 + \frac{8 \cdot P_T}{K_d}} - q \right] \tag{49}$$

$$F_U = \frac{K_U \cdot K_d}{4 \cdot P_T} \cdot \left[\sqrt{q^2 + \frac{8 \cdot P_T}{K_d}} - q \right] \tag{50}$$

The excess enthalpy function is defined as:

$$\langle \Delta H^{exc} \rangle = \Delta H_d \cdot F_N + (\Delta H_d + \Delta H_U) \cdot F_U \tag{51}$$

which allows calculation of the excess heat capacity function as a temperature derivative of the excess enthalpy. The corresponding Gibbs energies can be expressed as:

$$\Delta G_d^0 = \frac{T_d - T}{T_d} \cdot \Delta H(T_d) + \Delta C_p \cdot (T - T_d) + T \cdot \Delta C_p \cdot \ln\left(\frac{T_d}{T}\right) - R \cdot T \cdot \ln K(T_d) \tag{52}$$

$$\Delta G_U = \frac{T_m - T}{T_m} \cdot \Delta H(T_m) + \Delta C_p \cdot (T - T_m) + T \cdot \Delta C_p \cdot \ln\left(\frac{T_m}{T}\right) \tag{53}$$

where ΔG_d^0 is the standard Gibbs energy of dissociation of native dimer into native monomers, and ΔG_U is the monomolecular Gibbs energy of unfolding of monomers. For convenience the reference temperatures are defined as follows: T_d is defined as a temperature at which $F_{N_2} = F_N^2$, and thus according to the Eq. (45) the equilibrium constant is equal to $2P_T$; T_m is the temperature at which $F_N = F_U$ and thus the equilibrium constant is equal to 1.

4.6.4
Two-state Model with Ligand Binding

In this model, the native state, N, but not the unfolded state, U, can bind a ligand, L. The ligand does not undergo any conformational transition upon binding.

$$NL \overset{K_d}{\leftrightarrow} N + L \overset{K_U}{\leftrightarrow} U + L$$

The equilibrium constants of dissociation, K_d, and of unfolding, K_U, are then defined as:

$$K_d = \frac{[N] \cdot [L]}{[NL]} \quad \text{and} \quad K_U = \frac{[U]}{[N]} \tag{54}$$

where [NL], [N], [U], and [L] are the concentrations of ligated, and unligated native

states, unfolded state, and free ligand concentration, respectively. The fraction of protein in these three states can be presented as:

$$[\mathrm{N}] = F_{\mathrm{N}} \cdot P_{\mathrm{T}} \tag{55}$$

$$[\mathrm{U}] = F_{\mathrm{U}} \cdot P_{\mathrm{T}} \tag{56}$$

$$[\mathrm{NL}] = F_{\mathrm{NL}} \cdot P_{\mathrm{T}} \tag{57}$$

where the total concentration of the protein, P_{T}, is

$$P_{\mathrm{T}} = [\mathrm{NL}] + [\mathrm{N}] + [\mathrm{U}] \tag{58}$$

Similarly, the total concentration of the ligand, L_{T}, can be expressed as:

$$L_{\mathrm{T}} = [\mathrm{NL}] + [\mathrm{L}] \tag{59}$$

Combining Eqs (54)–(59) allows the equilibrium constants to be expressed as a function of total protein and ligand concentrations and fractions of native and unfolded protein as:

$$K_{\mathrm{d}} = \frac{F_{\mathrm{N}} \cdot (L_{\mathrm{T}} - F_{\mathrm{NL}} \cdot P_{\mathrm{T}})}{F_{\mathrm{NL}}} \tag{60}$$

$$K_{\mathrm{U}} = \frac{F_{\mathrm{U}} \cdot (L_{\mathrm{T}} - F_{\mathrm{NL}} \cdot P_{\mathrm{T}})}{K_{\mathrm{d}} \cdot F_{\mathrm{NL}}} \tag{61}$$

Keeping in mind that $F_{\mathrm{NL}} + F_{\mathrm{N}} + F_{\mathrm{U}} = 1$ we can combine Eqs (60)–(61) and write:

$$F_{\mathrm{NL}} + \frac{K_{\mathrm{d}} \cdot F_{\mathrm{NL}}}{(L_{\mathrm{T}} - F_{\mathrm{NL}} \cdot P_{\mathrm{T}})} + \frac{K_{\mathrm{d}} \cdot K_{\mathrm{U}} \cdot F_{\mathrm{NL}}}{(L_{\mathrm{T}} - F_{\mathrm{NL}} \cdot P_{\mathrm{T}})} = 1 \tag{62}$$

Equation (62) is a simple quadratic equation and can be solved for F_{NL} to give:

$$F_{\mathrm{NL}} = \frac{\sqrt{q^2 - 4 \cdot P_{\mathrm{T}} \cdot L_{\mathrm{T}}} - q}{2 \cdot P_{\mathrm{T}}} \tag{63}$$

where $q = P_{\mathrm{T}} + L_{\mathrm{T}} + K_{\mathrm{d}} + K_{\mathrm{U}} K_{\mathrm{d}}$

The fractions of the unligated native and of the unfolded states can be expressed as:

$$F_{\mathrm{N}} = \frac{K_{\mathrm{d}} \cdot (\sqrt{q^2 - 4 \cdot P_{\mathrm{T}} \cdot L_{\mathrm{T}}} - q)}{2 \cdot L_{\mathrm{T}} \cdot P_{\mathrm{T}} - P_{\mathrm{T}} \cdot (\sqrt{q^2 - 4 \cdot P_{\mathrm{T}} \cdot L_{\mathrm{T}}} - q)} \tag{64}$$

$$F_{\mathrm{U}} = \frac{K_{\mathrm{U}} \cdot K_{\mathrm{d}} \cdot (\sqrt{q^2 - 4 \cdot P_{\mathrm{T}} \cdot L_{\mathrm{T}}} - q)}{2 \cdot L_{\mathrm{T}} \cdot P_{\mathrm{T}} - P_{\mathrm{T}} \cdot (\sqrt{q^2 - 4 \cdot P_{\mathrm{T}} \cdot L_{\mathrm{T}}} - q)} \tag{65}$$

The excess enthalpy function is defined as:

$$\langle \Delta H^{\mathrm{exc}} \rangle = \Delta H_{\mathrm{d}} \cdot F_{\mathrm{N}} + (\Delta H_{\mathrm{d}} + \Delta H_{\mathrm{U}}) \cdot F_{\mathrm{U}} \tag{66}$$

which allows calculation of the excess heat capacity function as a temperature derivative of the excess enthalpy.

The corresponding Gibbs energies can be expressed as:

$$\Delta G_{\mathrm{d}}^{0} = \Delta H(T_0) + \Delta C_{\mathrm{p}} \cdot (T - T_0) - T \cdot \Delta S(T_0) - T \cdot \Delta C_{\mathrm{p}} \cdot \ln\left(\frac{T_0}{T}\right) - R \cdot T \cdot \ln K_{\mathrm{d}}(T_0) \tag{67}$$

$$\Delta G_{\mathrm{U}} = \frac{T_{\mathrm{m}} - T}{T_{\mathrm{m}}} \cdot \Delta H(T_{\mathrm{m}}) + \Delta C_{\mathrm{p}} \cdot (T - T_{\mathrm{m}}) + T \cdot \Delta C_{\mathrm{p}} \cdot \ln\left(\frac{T_{\mathrm{m}}}{T}\right) \tag{68}$$

where $\Delta G_{\mathrm{d}}^{0}$ is the standard Gibbs energy of dissociation, ΔG_{U} is the monomolecular Gibbs energy of unfolding, T_0 is the reference temperature for the dissociation reaction, and T_{m} is the temperature at which $F_{\mathrm{N}} = F_{\mathrm{U}}$ and thus the equilibrium constant is equal to 1. In practice, the ΔG_{U} function is determined from the DSC experiments performed in the absence of the ligand, and then is used to fit the DSC profiles obtained in the presence of ligand.

4.6.5
Four-state (Two-domain Protein) Model

In this model, the protein consists of two interacting domains A and B, each of which unfolds as a two state.

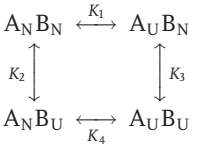

The equilibrium constants for the four reactions can be expressed through the concentrations of four states, native with both A and B domains folded ($A_N B_N$), domain A folded domain B unfolded ($A_N B_U$), domain A unfolded domain B folded ($A_U B_N$), and both domains unfolded ($A_U B_U$), as

$$K_1 = \frac{[A_U B_N]}{[A_N B_N]} \tag{69}$$

$$K_2 = \frac{[A_N B_U]}{[A_N B_N]} \tag{70}$$

$$K_3 = \frac{[A_U B_U]}{[A_U B_N]} \tag{71}$$

$$K_4 = \frac{[A_U B_U]}{[A_N B_U]} \tag{72}$$

It is important to emphasize that the four equilibrium constants are not fully independent since the following relationship is valid $K_1 \cdot K_3 = K_2 \cdot K_4$.

The fraction of each of the four states can be written as:

$$F_{A_N B_N} = \frac{[A_N B_N]}{[A_N B_N] + [A_U B_N] + [A_N B_U] + [A_U B_U]} \tag{73}$$

$$F_{A_U B_N} = \frac{[A_U B_N]}{[A_N B_N] + [A_U B_N] + [A_N B_U] + [A_U B_U]} \tag{74}$$

$$F_{A_N B_U} = \frac{[A_N B_U]}{[A_N B_N] + [A_U B_N] + [A_N B_U] + [A_U B_U]} \tag{75}$$

$$F_{A_U B_U} = \frac{[A_U B_U]}{[A_N B_N] + [A_U B_N] + [A_N B_U] + [A_U B_U]} \tag{76}$$

Combining Eqs (69)–(72) and (73)–(76) we can relate the fraction of individual states to the corresponding equilibrium constants:

$$F_{A_N B_N} = \frac{1}{1 + K_1 + K_2 + K_3} \tag{77}$$

$$F_{A_U B_N} = \frac{K_1}{1 + K_1 + K_2 + K_1 \cdot K_3} \tag{78}$$

$$F_{A_N B_U} = \frac{K_2}{1 + K_1 + K_2 + K_1 \cdot K_3} \tag{79}$$

$$F_{A_U B_U} = \frac{K_1 \cdot K_3}{1 + K_1 + K_2 + K_1 \cdot K_3} \tag{80}$$

Difference in K_1 and K_4 or K_2 and K_3 defines the energy of interaction between domains, ΔG_{int}.

$$K_1 = \frac{K_4}{K_{int}} = \exp\left(-\frac{\Delta G_4 - \Delta G_{int}}{R \cdot T}\right) \tag{81}$$

$$\Delta G_4 = \Delta H(T_A) \cdot \left(1 + \frac{T}{T_A}\right) + \Delta C_{p,A} \cdot (T - T_A - T \cdot \ln(T/T_A)) \tag{82}$$

$$K_2 = \frac{K_3}{K_{int}} = \exp\left(-\frac{\Delta G_3 - \Delta G_{int}}{R \cdot T}\right) \tag{83}$$

$$\Delta G_3 = \Delta H(T_B) \cdot \left(1 + \frac{T}{T_B}\right) + \Delta C_{p,B} \cdot (T - T_B - T \cdot \ln(T/T_B)) \tag{84}$$

$$K_{int} = \exp\left(-\frac{\Delta G_{int}}{R \cdot T}\right) \tag{85}$$

$$\Delta G_{int} = \Delta H_{int} - T \cdot \Delta S_{int} \tag{86}$$

The reference temperatures T_A and T_B are defined as the temperatures at which the each of the two intermediate states, $A_U B_N$ and $A_N B_U$ that have one of the domains unfolded awhile the other one folded, is 50% populated. It is important to emphasize that the energy of interaction as defined above also includes possible conformational changes in each domain upon their interactions.

The excess enthalpy of the system can be written as:

$$\langle \Delta H^{exc} \rangle = (\Delta H_A - \Delta H_{int}) \cdot F_{A_U B_N} + (\Delta H_B - \Delta H_{int}) \cdot F_{A_N B_U} + (\Delta H_A + \Delta H_B - \Delta H_{int}) \cdot F_{A_U B_U} \tag{87}$$

and the excess heat capacity function can be obtained by differentiation.

$$\langle C_p^{exc}(T) \rangle = \frac{\partial \langle \Delta H^{exc} \rangle}{\partial T} = (\Delta H_A - \Delta H_{int}) \cdot \frac{dF_{A_U B_N}}{dT} + (\Delta H_B - \Delta H_{int}) \cdot \frac{dF_{A_N B_U}}{dT} + (\Delta H_A + \Delta H_B - \Delta H_{int}) \cdot \frac{dF_{A_U B_U}}{dT} \tag{88}$$

Note that after one of the domains melts, the interaction energy goes to zero. Thus, ΔG_{int} has apparent effect only on a domain with lower T_m.

4.7 Experimental Protocols

4.7.1 How to Prepare for DSC Experiments

The DSC instrument should be turned on prior to the experiment and several (at least three) baseline scans with both cells filled with the buffer should be recorded. The last two profiles must be overlapping. This establishes the thermal history and verifies that the instrument is working within specifications.

The pre-experiment baseline scans should be done at the scan rate that will be used for the protein scan. The heating rate is one of the most important parameters. Several considerations have to be taken into account. First, the higher the scan rate, the higher the sensitivity of the instrument. The increase in sensitivity is linear with respect to the heating rate (i.e., the sensitivity at a heating rate of 2° min^{-1} is twice as high as that at 1° min^{-1}), but the increase in sensitivity does not mean an increase in the signal-to-noise ratio. Second, if the expected transition is very sharp (e.g., within a few degrees) a high heating rate will affect the shape of the heat absorption profile and lead to an error in the determination of all thermodynamic parameters for this transition. This error will be particularly large for the

transition temperature. Third, the higher the heating rate the less time the system has to equilibrate. So for slow unfolding/refolding processes it is advisable to use low heating rates.

In practice, for small globular proteins exhibiting reversible temperature induced unfolding, a maximal (on most DSC instruments) heating rate of $2^\circ\ \mathrm{min}^{-1}$ is acceptable. For large proteins lower heating rates ($0.5–1^\circ\ \mathrm{min}^{-1}$) are more appropriate. In the case of fibrillar proteins, which usually exhibit very narrow transitions, a heating rate of $0.1–0.25^\circ\ \mathrm{min}^{-1}$ is most suitable.

The purity of the protein sample is very important. Contamination with other proteins, nucleic acids, or lipids can affect both the shape of the calorimetric profiles and the estimation of the thermodynamic parameters of unfolding through the errors in determination of the sample concentration. PAAG electrophoresis, UV/VIS spectroscopy and mass spectroscopy should be used to validate the purity of the protein sample.

Since calorimetric experiments are performed over a broad temperature range, the pH of the buffer should have a small temperature dependence. For this reason for example, very popular ''physiological'' Tris buffer is not the best choice. Glycine, sodium/potassium acetate, sodium/potassium phosphate, sodium cacodilate, and sodium citrate are the buffers of choice.

Equilibration of protein with buffer is a vital part of the sample preparation for calorimetric experiments. One should keep in mind that the DSC instrument measures the heat capacity difference between buffer and protein solutions. Thus any small inequality in the buffer composition will result in an incorrect absolute value and an incorrect slope of the heat capacity profile. The best way to achieve equilibrium between buffer and protein solution is dialysis. The protein sample should be dialyzed against at least two changes of buffer. The buffer solutions should be filtered prior to dialysis using a 0.45 μm filter to eliminate all insoluble material.

Following dialysis, all insoluble particles should be carefully removed from the protein solution. This can be achieved by centrifugation at ~12 000 g in a microcentrifuge for ~15–20 min.

Knowledge of the exact protein concentration *after dialysis* is very important. Among all available methods for determination of protein concentration, spectrophotometric methods seem to be most accurate and rapid. This method requires knowledge of the extinction coefficient of the protein at a given wavelength. The extinction coefficient can be calculated from the number of aromatic residues and disulfide bonds in a protein using an empirical equation [64]:

$$\varepsilon_{280\ \mathrm{nm}}^{0.1\%,\,1\ \mathrm{cm}} = (5690 \cdot N_{\mathrm{Trp}} + 1280 \cdot N_{\mathrm{Tyr}} + 120 \cdot N_{\mathrm{SS}})/\mathrm{MW} \qquad (89)$$

where MW is the molecular weight of the protein in daltons. A more elaborate procedure is described by Pace et al. [65] and improves the accuracy of the calculations. For proteins that do not contain any aromatic residues, the method that is based on absorption of peptide backbone gives fast and accurate results. Light scattering in spectrophotometric measurements of protein concentration can be a significant problem, but can be taken into account using a procedure suggested by Winder and Gent [66].

4.7.2 How to Choose Appropriate Conditions

The most frequent problem in DSC experiments is irreversibility of the unfolding transition. This particularly applies to large proteins that have tendencies to aggregate after unfolding. Sensitivity of contemporary DSC instruments provides reliable heat capacity profiles at concentrations as low as 0.3 mg mL^{-1} for proteins of the molecular range 6–17 kDa. The concentration for larger proteins can be even lower. Low protein concentration leads to decreased probability for aggregation. However, even at low protein concentrations, finding the proper solvent conditions is not a simple task. A rule of thumb is that at a pH value close to the isoelectric point of the protein, aggregation after unfolding is highly probable. High concentrations of neutral salts also promote aggregation. In many cases, aggregation can be avoided by keeping the ionic strength of the solvent very low (10–50 mM) and by using pH values a couple of units away (usually below) from the isoelectric point.

4.7.3 Critical Factors in Running DSC Experiments

Two important pieces of information should be established prior to the analysis of the calorimetric profiles. This will help to decide whether the formalism of equilibrium thermodynamics is applicable to the studied protein:

1. Reversibility of the unfolding transition under several conditions should be examined by rescanning the sample. Reversibility depends on the upper temperature of heating. The unfolding transition can be considered reversible if rescanning after the sample has been heated to the temperature just past the completion of the transition leads to the recovery of at least 85–90% of the initial endotherm. If no endotherm is observed after rescanning, the unfolding reaction is irreversible. Thermodynamic analysis for irreversible transitions is possible only in special cases [11, 67].
2. Equilibrium conditions of reversible unfolding should be examined to find the optimal scan rate that permits establishment of equilibrium between native and unfolded states at all temperatures (i.e., scan rate should not be faster than the folding/unfolding rates). This can be examined by comparing the heat capacity profiles obtained on exactly the same sample at two different heating rates, usually 2° min^{-1} and 0.5° min^{-1}. If the difference in the transition temperature exceeds 0.5–0.7 °C, additional experiments at a lower heating rate (i.e., 0.1° min^{-1}) should be performed and compared with a 0.5° min^{-1} experiment. If there is still a difference in the transition temperature all experiments at a given solvent composition should be performed at several different heating rates and the transition temperatures should be extrapolated to a zero heating rate (for more details see Ref. [68]).

References

1 Plotnikov, V. V., Brandts, J. M., Lin, L. N., & Brandts, J. F. (1997). A new ultrasensitive scanning calorimeter. *Anal Biochem* 250, 237–244.

2 Privalov, G., Kavina, V., Freire, E., & Privalov, P. L. (1995). Precise scanning calorimeter for studying thermal properties of biological macromolecules in dilute solution. *Anal Biochem* 232, 79–85.

3 Lopez, M. M. & Makhatadze, G. I. (2002). Differential scanning calorimetry. *Methods Mol Biol* 173, 113–119.

4 Makhatadze, G. I. (1998). *Measuring protein thermostability by differential scanning calorimetry.* Current Protocols in Protein Chemistry, 2, John Wiley & Sons, New York.

5 Pfeil, W. (1998). *Protein Stability and folding. A collection of thermodynamic data*, Springer, Berlin, Heidelberg, New York.

6 http://www.rtc.riken.go.jp/jouhou/Protherm/protherm.html.

7 Makhatadze, G. I. (1998). Heat capacities of amino acids, peptides and proteins. *Biophys Chem* 71, 133–156.

8 Biltonen, R. L. & Freire, E. (1978). Thermodynamic characterization of conformational states of biological macromolecules using differential scanning calorimetry. *CRC Crit Rev Biochem* 5, 85–124.

9 Privalov, P. L. (1979). Stability of proteins: small globular proteins. *Adv Protein Chem* 33, 167–241.

10 Becktel, W. J. & Schellman, J. A. (1987). Protein stability curves. *Biopolymers* 26, 1859–1877.

11 Sanchez-Ruiz, J. M., Lopez-Lacomba, J. L., Cortijo, M., & Mateo, P. L. (1988). Differential scanning calorimetry of the irreversible thermal denaturation of thermolysin. *Biochemistry* 27, 1648–1652.

12 Lumry, R. & Biltonen, R. (1966). Validity of the "two-state" hypothesis for conformational transitions of proteins. *Biopolymers* 4, 917–944.

13 Jackson, W. M. & Brandts, J. F. (1970). Thermodynamics of protein denaturation. A calorimetric study of the reversible denaturation of chymotrypsinogen and conclusions regarding the accuracy of the two-state approximation. *Biochemistry* 9, 2294–2301.

14 Tsong, T. Y., Hearn, R. P., Wrathall, D. P., & Sturtevant, J. M. (1970). A calorimetric study of thermally induced conformational transitions of ribonuclease A and certain of its derivatives. *Biochemistry* 9, 2666–2677.

15 Privalov, P. L. & Khechinashvili, N. N. (1974). A thermodynamic approach to the problem of stabilization of globular protein structure: a calorimetric study. *J Mol Biol* 86, 665–684.

16 Pace, N. C. & Tanford, C. (1968). Thermodynamics of the unfolding of beta-lactoglobulin A in aqueous urea solutions between 5 and 55 degrees. *Biochemistry* 7, 198–208.

17 Privalov, P. L., Griko Yu, V., Venyaminov, S., & Kutyshenko, V. P. (1986). Cold denaturation of myoglobin. *J Mol Biol* 190, 487–498.

18 Privalov, P. L. (1990). Cold denaturation of proteins. *Crit Rev Biochem Mol Biol* 25, 281–305.

19 Griko, Y. V., Privalov, P. L., Sturtevant, J. M., & Venyaminov, S. (1988). Cold denaturation of staphylococcal nuclease. *Proc Natl Acad Sci USA* 85, 3343–3347.

20 Beadle, B. M., Baase, W. A., Wilson, D. B., Gilkes, N. R., & Shoichet, B. K. (1999). Comparing the thermodynamic stabilities of a related thermophilic and mesophilic enzyme. *Biochemistry* 38, 2570–2576.

21 Hollien, J. & Marqusee, S. (1999). A thermodynamic comparison of mesophilic and thermophilic ribonucleases H. *Biochemistry* 38, 3831–3836.

22 Rees, D. C. & Robertson, A. D. (2001). Some thermodynamic

implications for the thermostability of proteins. *Protein Sci* 10, 1187–1194.

23 Deutschman, W. A. & Dahlquist, F. W. (2001). Thermodynamic basis for the increased thermostability of CheY from the hyperthermophile *Thermotoga maritima*. *Biochemistry* 40, 13107–13113.

24 Makhatadze, G. I., Loladze, V. V., Gribenko, A. V., & Lopez, M. M. (2004). Mechanism of thermostabilization in a designed cold shock protein with optimized surface electrostatic interactions. *J Mol Biol* 336, 929–942.

25 Lumry, R. & Rajender, S. (1970). Enthalpy–entropy compensation phenomena in water solutions of proteins and small molecules: a ubiquitous property of water. *Biopolymers* 9, 1125–1227.

26 Sharp, K. (2001). Entropy–enthalpy compensation: fact or artifact? *Protein Sci* 10, 661–667.

27 Beasley, J. R., Doyle, D. F., Chen, L., Cohen, D. S., Fine, B. R., & Pielak, G. J. (2002). Searching for quantitative entropy–enthalpy compensation among protein variants. *Proteins* 49, 398–402.

28 Makhatadze, G. I., Clore, G. M., & Gronenborn, A. M. (1995). Solvent isotope effect and protein stability. *Nat Struct Biol* 2, 852–855.

29 Makhatadze, G. I. & Privalov, P. L. (1990). Heat capacity of proteins. I. Partial molar heat capacity of individual amino acid residues in aqueous solution: hydration effect. *J Mol Biol* 213, 375–384.

30 Spolar, R. S., Ha, J. H., & Record, M. T., Jr. (1989). Hydrophobic effect in protein folding and other noncovalent processes involving proteins. *Proc Natl Acad Sci USA* 86, 8382–8385.

31 Spolar, R. S., Livingstone, J. R., & Record, M. T., Jr. (1992). Use of liquid hydrocarbon and amide transfer data to estimate contributions to thermodynamic functions of protein folding from the removal of nonpolar and polar surface from water. *Biochemistry* 31, 3947–3955.

32 Baldwin, R. L. (1986). Temperature dependence of the hydrophobic interaction in protein folding. *Proc Natl Acad Sci USA* 83, 8069–8072.

33 Makhatadze, G. I. & Privalov, P. L. (1995). Energetics of protein structure. *Adv Protein Chem* 47, 307–425.

34 Robertson, A. D. & Murphy, K. P. (1997). Protein structure and the energetics of protein stability. *Chem Rev* 97, 1251–1268.

35 Myers, J. K., Pace, C. N., & Scholtz, J. M. (1995). Denaturant m values and heat capacity changes: relation to changes in accessible surface areas of protein unfolding. *Protein Sci* 4, 2138–2148.

36 Sturtevant, J. M. (1977). Heat capacity and entropy changes in processes involving proteins. *Proc Natl Acad Sci USA* 74, 2236–2240.

37 Loladze, V. V., Ermolenko, D. N., & Makhatadze, G. I. (2001). Heat capacity changes upon burial of polar and nonpolar groups in proteins. *Protein Sci* 10, 1343–1352.

38 Cooper, A., Johnson, C. M., Lakey, J. H., & Nollmann, M. (2001). Heat does not come in different colours: entropy-enthalpy compensation, free energy windows, quantum confinement, pressure perturbation calorimetry, solvation and the multiple causes of heat capacity effects in biomolecular interactions. *Biophys Chem* 93, 215–230.

39 Lazaridis, T., Archontis, G., Karplus, M. (1995). Enthalpic contribution to protein stability: insights from atom-based calculations and statistical mechanics. *Adv Protein Chem* 47, 231–306.

40 Loladze, V. V., Ermolenko, D. N., & Makhatadze, G. I. (2002). Thermodynamic consequences of burial of polar and nonpolar amino acid residues in the protein interior. *J Mol Biol* 320, 343–357.

41 Richards, F. M. (1977). Areas, volumes, packing and protein structure. *Annu Rev Biophys Bioeng* 6, 151–176.

42 Fleming, P. J. & Richards, F. M. (2000). Protein packing: dependence

on protein size, secondary structure and amino acid composition. *J Mol Biol* 299, 487–498.

43 Pace, C. N., Shirley, B. A., McNutt, M., & Gajiwala, K. (1996). Forces contributing to the conformational stability of proteins. *FASEB J* 10, 75–83.

44 Myers, J. K. & Pace, C. N. (1996). Hydrogen bonding stabilizes globular proteins. *Biophys J* 71, 2033–2039.

45 Scholtz, J. M., Marqusee, S., Baldwin, R. L., York, E. J., Stewart, J. M., Santoro, M., & Bolen, D. W. (1991). Calorimetric determination of the enthalpy change for the alpha-helix to coil transition of an alanine peptide in water. *Proc Natl Acad Sci USA* 88, 2854–2858.

46 Richardson, J. M., McMahon, K. W., MacDonald, C. C., & Makhatadze, G. I. (1999). MEARA sequence repeat of human CstF-64 polyadenylation factor is helical in solution. A spectroscopic and calorimetric study. *Biochemistry* 38, 12869–12875.

47 Lopez, M. M., Chin, D. H., Baldwin, R. L., & Makhatadze, G. I. (2002). The enthalpy of the alanine peptide helix measured by isothermal titration calorimetry using metal-binding to induce helix formation. *Proc Natl Acad Sci USA* 99, 1298–1302.

48 Yang, A. S., Sharp, K. A., & Honig, B. (1992). Analysis of the heat capacity dependence of protein folding. *J Mol Biol* 227, 889–900.

49 Madan, B. & Sharp, K. (1999). Changes in water structure induced by a hydrophobic solute probed by simulation of the water hydrogen bond angle and radial distribution functions. *Biophys Chem* 78, 33–41.

50 Creamer, T. P. & Rose, G. D. (1992). Side-chain entropy opposes alpha-helix formation but rationalizes experimentally determined helix-forming propensities. *Proc Natl Acad Sci USA* 89, 5937–5941.

51 Doig, A. J. & Sternberg, M. J. (1995). Side-chain conformational entropy in protein folding. *Protein Sci* 4, 2247–2251.

52 Amzel, L. M. (2000). Calculation of entropy changes in biological processes: folding, binding, and oligomerization. *Methods Enzymol* 323, 167–177.

53 Pickett, S. D. & Sternberg, M. J. (1993). Empirical scale of side-chain conformational entropy in protein folding. *J Mol Biol* 231, 825–839.

54 Sternberg, M. J. & Chickos, J. S. (1994). Protein side-chain conformational entropy derived from fusion data – comparison with other empirical scales. *Protein Eng* 7, 149–155.

55 Blaber, M., Zhang, X. J., Lindstrom, J. D., Pepiot, S. D., Baase, W. A., & Matthews, B. W. (1994). Determination of alpha-helix propensity within the context of a folded protein. Sites 44 and 131 in bacteriophage T4 lysozyme. *J Mol Biol* 235, 600–624.

56 Dill, K. A. (1990). Dominant forces in protein folding. *Biochemistry* 29, 7133–7155.

57 Matouschek, A. (2003). Protein unfolding – an important process in vivo? *Curr Opin Struct Biol* 13, 98–109.

58 Doig, A. J. & Williams, D. H. (1992). Why water-soluble, compact, globular proteins have similar specific enthalpies of unfolding at 110 degrees C. *Biochemistry* 31, 9371–9375.

59 Sanchez-Ruiz, J. M. (1995). Differential scanning calorimetry of proteins. *Subcell Biochem* 24, 133–176.

60 Loladze, V. V., Ibarra-Molero, B., Sanchez-Ruiz, J. M., & Makhatadze, G. I. (1999). Engineering a thermostable protein via optimization of charge–charge interactions on the protein surface. *Biochemistry* 38, 16419–16423.

61 Sanchez-Ruiz, J. M. & Makhatadze, G. I. (2001). To charge or not to charge? *Trends Biotechnol* 19, 132–135.

62 Thomas, S. T., Loladze, V. V., & Makhatadze, G. I. (2001). Hydration of the peptide backbone largely defines the thermodynamic propensity scale of residues at the C′ position of the C-capping box of alpha-helices. *Proc Natl Acad Sci USA* 98, 10670–10675.

63 Makhatadze, G. I., Loladze, V. V., Ermolenko, D. N., Chen, X., & Thomas, S. T. (2003). Contribution of surface salt bridges to protein stability: guidelines for protein engineering. *J Mol Biol* 327, 1135–1148.

64 Gill, S. C. & von Hippel, P. H. (1989). Calculation of protein extinction coefficients from amino acid sequence data. *Anal Biochem* 182, 319–326.

65 Pace, C. N., Vajdos, F., Fee, L., Grimsley, G., & Gray, T. (1995). How to measure and predict the molar absorption coefficient of a protein. *Protein Sci* 4, 2411–2423.

66 Winder, A. F. & Gent, W. L. (1971). Correction of light-scattering errors in spectrophotometric protein determinations. *Biopolymers* 10, 1243–1251.

67 Sanchez-Ruiz, J. M. (1992). Theoretical analysis of Lumry-Eyring models in differential scanning calorimetry. *Biophys J* 61, 921–935.

68 Yu, Y., Makhatadze, G. I., Pace, C. N., & Privalov, P. L. (1994). Energetics of ribonuclease T1 structure. *Biochemistry* 33, 3312–3319.

5
Pressure–Temperature Phase Diagrams of Proteins

Wolfgang Doster and Josef Friedrich

5.1
Introduction

One of the most peculiar features of proteins is their marginal stability within a narrow range of thermodynamic conditions. Biologically active structures can be disrupted by increasing or decreasing the temperature, the pressure, the pH or by adding denaturants. By disrupting a structure one can study its architecture and energetics. In this article we focus on the thermodynamic aspects of temperature and pressure denaturation. A variation of temperature inevitably leads to a simultaneous change of entropy and volume through thermal expansion. The advantage of using pressure as a thermodynamic variable is that volume-dependent effects can be isolated from temperature-dependent effects. Just as the increase in temperature drives the system in equilibrium towards states of higher entropy, a pressure increase will bias the ensemble of accessible states towards those with a smaller volume. This is the meaning of le Chatelier's principle. Thus, if the protein has the lower volume in its denatured form, the native structure will become unstable above a critical pressure. Similarly the opposite effect, stabilization of the native state by pressure, is sometimes associated with heat denaturation.

Packing defects in the water-excluding native state, reorganization of the solvent near exposed nonpolar side chains, and electrostriction by newly formed charges act as volume reservoirs which can lower the volume in the unfolded state. While dissociation of oligomeric proteins into subunits occurs at low pressures, i.e., below 200 MPa [1], pressures above 300 MPa are required to denature monomeric proteins. A number of useful review articles on this subject have been published recently (see, for example, Ref. [2]).

The isothermal compressibility of water (0.56/GPa) is quite small. At 11 000 m below sea level and pressures near 100 MPa, the density of water is only 5% higher than at ambient pressure. On the other hand, the density at the freezing transition changes by 9%. Moreover, proteins are 5–10 times less compressible than water. As a result, pressure-induced volume changes in proteins are quite small, typically 0.5% of the total volume at the unfolding transition. For monomeric proteins the difference corresponds approximately to the volume of five water molecules

Protein Folding Handbook. Part I. Edited by J. Buchner and T. Kiefhaber

ISBN: 3-527-30784-2

(5×18 mL mol^{-1}). Thus, minor volume changes often induce large structural rearrangements, where essentially incompressible matter is displaced. Therefore pressure can be a powerful structural gear. On the other hand, the microscopic interpretation of protein volume changes is still one of the difficult and unresolved questions of the field [3, 4].

Part of the problem arises from the fact that the denatured state itself is not very well defined [5]. It is generally assumed that thermal denaturing leads to a random coil state. As to pressure-induced denaturation and cold denaturation, there are indications that the denatured state is still compact and resembles the molten globule state [5–7]. How such a situation can be reconciled with the simple thermodynamic description of protein stability based on a two-state model has to be investigated in each case.

Below we present a thermodynamic frame for describing and interpreting protein stability phase diagrams. The main features are illustrated using our own results obtained with various optical techniques as well as with neutron scattering.

5.2 Basic Aspects of Phase Diagrams of Proteins and Early Experiments

The most striking thermodynamic properties of proteins are related to the hydrophobic effect. These are

- the large and positive heat capacity increment upon unfolding [8–10] and
- the phenomenon of cold denaturation.

The latter was first predicted by Brandts [11, 12] based on studies of heat denaturation on ribonuclease. The transition temperatures for cold denaturation are usually below the freezing point of most aqueous solutions at ambient pressure. However, under high pressure, water remains liquid down to much lower temperatures (-18 °C at 200 MPa, Figure 5.1).

Thus cold denaturation can be studied conveniently at elevated pressures under mild denaturing conditions, without the need to add denaturants.

The phase diagram of water (Figure 5.1) illustrates the relevance of the pressure–temperature plane for locating states of structural stability and for classifying their thermodynamic properties.

The slope of the phase boundary of liquid water and ice I is negative: Increase in pressure extends the stability range of the liquid phase. The slope of the phase boundary is given by the ratio of the negative entropy change and the increase in specific volume at the freezing transition (Eq. (3)). The expansion (+9%) causes substantial damage when biological material is frozen. In contrast, the slope of the liquid to ice III boundary is large and positive, since the corresponding volume change is small and negative. The application of high pressure to the liquid and then cooling into ice III minimizes the damage by volume changes (-3%) at the freezing transition.

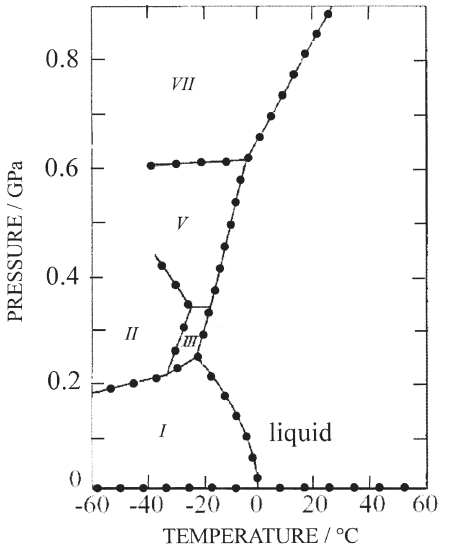

Fig. 5.1. The phase diagram of water: For the boundary from the liquid to hexagonal ice (I) one has $dP/dT = \Delta S/\Delta V < 0$, unlike for the technically relevant modifications, II and III where the volume discontinuity is small.

Proteins, consisting of a few thousand atoms, are mesoscopic objects. Experience and theoretical analysis shows [13] that they can be labeled by well-defined thermodynamic averages, such as the specific heat capacity, the compressibility, and the thermal expansion. The structural reorganization may then be regarded as a change of the macroscopic state of the system. Such changes occur in a highly cooperative manner. Since the native and denatured states of proteins differ not only in heat capacity but also in volume and entropy, the transition between the two states must involve a discontinuity in the first derivatives of the thermodynamic potential. This is the signature of a first-order phase transition. Consequently, the native and denatured states of a single-domain protein may be interpreted as two phases of a macroscopic system, which differ in structural order. For a single protein molecule the transformation can only be abrupt and not gradually. From this point of view a cooperative domain of a protein resembles a crystal, which has, however, a critical size, since it can only exist as a whole. Experimentally, however, one usually deals with protein ensembles.

The properties of the ensemble, which are reflected in the heterogeneity of the characteristic parameters of a protein, such as its energy, structure, compressibility, etc., render some specific features to the denaturing transition compared with phase transitions of thermodynamic systems: The transition is usually rather broad in the variables P or T (e.g., see Figures 5.9 and 5.10). This dispersion of the transition region is directly related to the heterogeneity of the protein ensemble, which has its roots in the fact that a protein, although a large molecule, is not an infinite

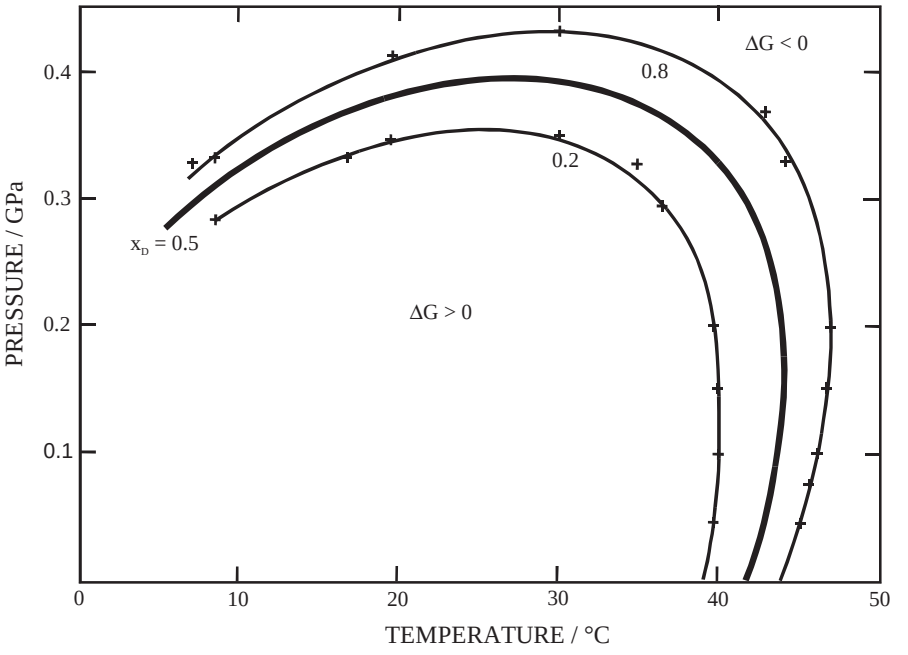

Fig. 5.2. Contours of constant chemical potential $\Delta\mu = \mu_D - \mu_N$ between the denatured (D) and the native (N) state of chymotrypsinogen (after Hawley [14]).

system. The equilibrium constant $K_{DN}(T, P)$ follows from the pressure analog of the van t'Hoff equation with $\partial T \rightarrow \partial P$ and $\Delta S \rightarrow -\Delta V$:

$$\partial(\ln K_{DN})/\partial P = -\Delta V/RT$$

The transition width, determined by the magnitude of the transition volume ΔV, is finite for a mesoscopic protein molecule, in contrast to the zero width of a macroscopic first-order transition.

Hawley, in 1971, was the first to interpret the curve on which the free energy difference between native and unfolded state vanishes as an elliptical phase boundary. This provided a natural explanation for the so-called re-entrant phase behavior of heat and cold denaturation [14]. Figure 5.2 shows the contours of the Gibbs free energy $\Delta G(P, T)$ versus pressure and temperature for chymotrypsinogen. Note that at moderate pressure levels (< 150 MPa), the temperature of heat denaturation increases slightly with pressure. Hence, applying pressure to the thermally denatured protein may actually drive the protein back into the native state. Upon further increasing the pressure, however, unfolding may occur again. In other words, the denatured phase is re-entered, irrespective of the fact that the pressure is monotonously changed. Phase diagrams with this property are called "re-entrant." A similar behavior is found if the temperature is changed. For instance, if one starts out at sufficiently high pressure levels (200 MPa) in the denatured

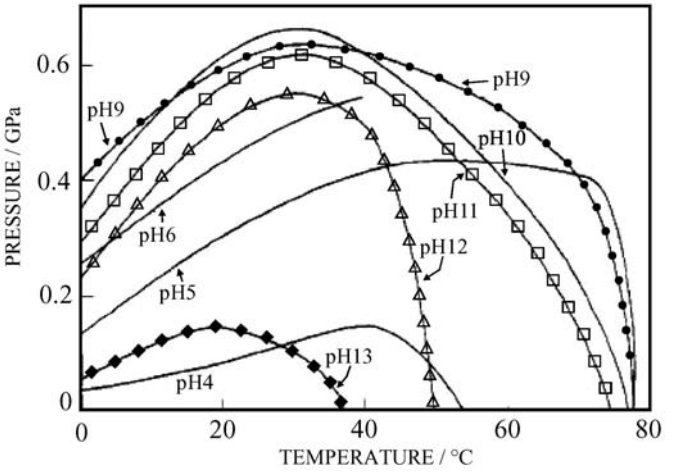

Fig. 5.3. Phase boundaries ($\Delta\mu = 0$) of myoglobin at various pH values, the native state is stable inside the contours, the denatured state outside (after Zipp and Kauzmann [18]).

state and lowers the temperature, one enters the native regime which is, however, left again at even lower temperatures to re-enter the denatured regime again. This latter transition is called "cold denaturation".

Re-entrant phase diagrams of perfect elliptical shape have been observed for liquid crystals by Cladis et al. [15] and by Klug and Whalley [16]. The elliptical shape was analyzed in detail by Clark [16].

In 1973, Zipp and Kauzmann, in a seminal paper, investigated the pressure–temperature–pH phase diagram of myoglobin [18]. They also observed re-entrant behavior, but did not attempt to fit the phase boundaries using ellipses. Depending on pH, the boundaries vary strongly in shape and show nonelliptical distortions, as shown in Figure 5.3.

In recent years, a significant number of studies have suggested diagrams of elliptical shape for protein denaturation or for even more complex units, such as bacteria [19].

The stability phase diagram of proteins and related phenomena have been discussed in several review articles [20, 21, 22].

Our goal is to eludicate the physical basis and thermodynamics of re-entrant protein phase diagrams, the conditions for elliptical shapes, and the limitations of this approach.

5.3
Thermodynamics of Pressure–Temperature Phase Diagrams

The phase equilibrium between the native and the denatured state $N \rightleftharpoons D$ is controlled by the difference in the chemical potentials $\Delta\mu = \mu_D - \mu_N$. The ratio of con-

centrations of the denatured to the native form assuming a dilute solution is given by:

$$K_{DN} = c_D/c_N = \exp(-\Delta\mu/RT) \tag{1}$$

The chemical potential is the driving force that induces transport and transformations of a substance. It is analogous to the electrical potential, which can only induce currents because of charge conservation. Since the concentration of components, water, and protein is fixed (only pressure and temperature are varied), we restrict ourselves to one-component systems. The change $d\mu_i$ with temperature and pressure obeys the Gibbs–Duhem relation for each phase D and N:

$$\begin{aligned} d\mu_N &= -S_N\,dT + V_N\,dP = -RT\,d(\ln c_N/c_0) \\ d\mu_D &= -S_D\,dT + V_D\,dP = -RT\,d(\ln c_D/c_0) \end{aligned} \tag{2}$$

where S_N, S_D and V_N, V_D are the partial molar entropy and volume of the protein in solution in the native and denatured phase, respectively. Since entropy and volume are generally positive quantities, the chemical potential always decreases with increasing temperature, while it increases with increasing pressure, as shown in Figures 5.4 and 5.6. The potentials of two phases, differing in entropy, will thus cross at a particular temperature where a transition to the phase with the lower potential occurs. A similar change in phase will take place with pressure when the volumes of the two phases differ. Thus the more compact phase will be stable at high pressure.

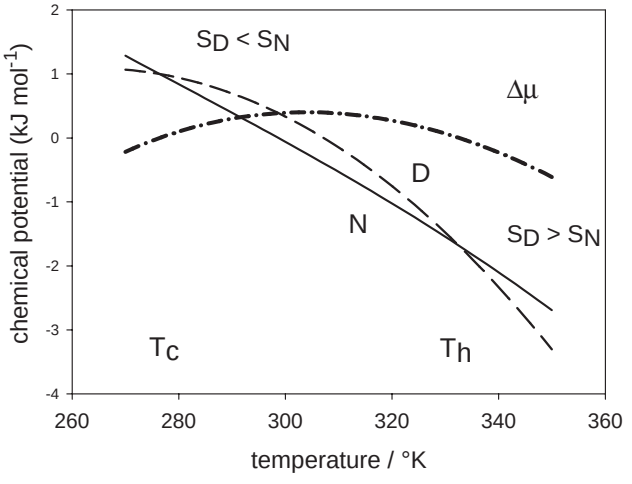

Fig. 5.4. The chemical potentials of the denatured (D) and the native (N) state of myoglobin and the resulting $\Delta\mu$ per mole of amino acid residue. Parameters [25]: $\Delta\mu_{0N} = -0.2$ kJ mol^{-1}, $\Delta\mu_{0D} = 0.2$ kJ mol^{-1}, $\Delta S_C = 14$ J K^{-1} mol^{-1}, $\Delta C_p = 75$ J K^{-1} mol^{-1}. T_H, T_C, and T_M are the temperatures for heat denaturation, for cold denaturation and for maximum stability.

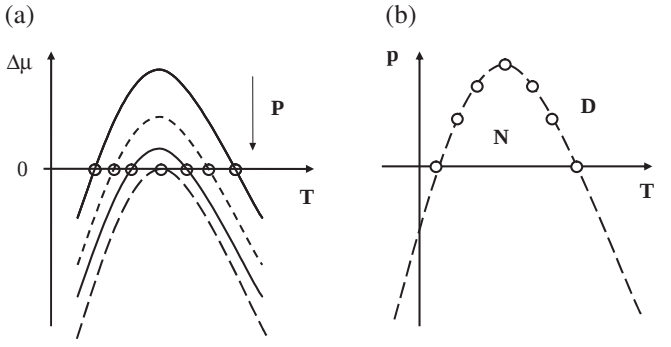

Fig. 5.5. a) Schematic representation of the difference $\Delta\mu = \mu_D - \mu_N$ of the chemical potential as a function of temperature for various pressures as deduced from Figure 5.4. b) The phase boundary as schematically deduced from the various pairs of points with $\Delta\mu = 0$ of Figure 5.5a for negative values of $\Delta V = V_D - V_N$.

For proteins in particular, $S_D > S_N$ at higher temperature because of an excess in configurational entropy of the unfolded chain. Thus μ_D has the more pronounced temperature dependence and will fall below μ_N at T_H, the heat denaturation temperature. For myoglobin it is suggested in Figure 5.4 that the peculiar thermodynamic behavior of proteins arises from the strongly temperature-dependent entropy of the unfolded phase: The slope of $\mu_D(T)$ and thus the entropy $S_D(T)$ decreases with decreasing temperature.

On a microscopic scale this reflects the ordering force of nonpolar groups on surface water molecules. Since the corresponding hydrophobic effect is less pronounced in the native state, S_N is expected to be almost temperature independent. This discrepancy explains why the potential surfaces μ_D and μ_N meet again at T_C, the cold denaturation temperature, as shown in Figure 5.4. The chemical potential difference, $\Delta\mu = \mu_D - \mu_N$, consequently assumes the shape of a convex curve, which is close to an inverted parabola with the maximum at T_M, the temperature of maximum stability (Figure 5.5).

Changes in pressure displace the difference potential surface $\Delta\mu$ vertically, depending on the unfolding volume ΔV as shown in Figure 5.5a.

Since the phase transition occurs at constant chemical potential, $\Delta\mu(P, T) = 0$, or $c_N = c_D$, while pressure and temperature are varied, one derives, from Eq. (2), a differential equation for the phase boundary, the Clausius–Claperon equation:

$$(dP/dT)_{\Delta\mu=0} = \Delta S/\Delta V \tag{3}$$

where $\Delta S = S_D - S_N$ and $\Delta V = V_D - V_N$ can depend on T and P. The phase boundary (Figure 5.5b) will assume the shape of an inverted parabola if the unfolding volume ΔV is negative and constant in P and T. For positive unfolding volumes a regular parabola, open to the high pressure side, would be obtained excluding denaturation by pressure.

The latent quantities ΔS and ΔV are composed of intrinsic contributions of the protein and those of the hydration shell, while the values of bulk water in both phases cancel.

The entropy difference reflects mainly the increase in configurational entropy of the chain, ΔS_C, and the entropy change ΔS_H in the hydration shell, due to exposure of buried residues. The same reasoning applies to the latent volume. Hence, we can write:

$$\begin{aligned} \Delta S &= \Delta S_C + \Delta S_H \\ \Delta V &= \Delta V_C + \Delta V_H \end{aligned} \tag{4}$$

We argue that the closed phase boundaries displayed in Figures 5.2 and 5.3 are the consequence of the variation of ΔS_H and ΔV_H with temperature and pressure due to the hydrophobic effect. Exposure of nonpolar groups upon unfolding tends to immobilize water molecules, thereby decreasing their entropy. This mechanism is strongly temperature dependent. Its experimental signature is the positive heat capacity increment at constant pressure, $\Delta C_p > 0$, of the denatured relative to the native form. In simple terms, to increase the temperature of the unfolded phase requires additional entropy to continuously melt the immobilized water [8–10, 23, 24]. However, above a certain temperature, T_0, approximately 140 °C, the ordering effect has vanished.

Below T_0, the hydration entropy change, $\Delta S_H(T, T_0)$, is rapidly decreasing with decreasing temperature. Assuming ΔC_p to be approximately independent of temperature, one obtains for the change in ''hydration entropy'' [25]:

$$\Delta S_H(T) = \int_{T_0}^{T} \frac{\Delta C_P}{T} dT = -\Delta C_P \cdot \ln\left(\frac{T_0}{T}\right) \tag{5}$$

and thus from Eqs (2)–(5):

$$\Delta\mu = \Delta\mu_0 - (T - T_0) \cdot [\Delta S_C - \Delta C_p \ln(T_0/T)] + \Delta V \cdot P \tag{6}$$

The hydration term $\propto \Delta C_p$ is always negative below T_0, stabilizing the denatured form. This is known as the ''wedging effect'' of water, which softens the native structure. The combined entropy difference ΔS vanishes at the maximum of $\Delta\mu$, at the temperature of maximum stability T_M (Figure 5.4):

$$(\partial\Delta\mu/\partial T)_{T=T_M} = -\Delta S = 0 \tag{7}$$

At T_M the negative hydration entropy ΔS_H just compensates for the positive configurational term ΔS_C:

$$\Delta S_C = \Delta C_p \ln(T_0/T_M) \tag{8}$$

ΔS in Eq. (7) depends on pressure and temperature according to:

$$\mathrm{d}\Delta S(P,T) = (\partial \Delta S/\partial T)\,\mathrm{d}T + (\partial \Delta S/\partial P)\,\mathrm{d}P = (\Delta C_\mathrm{p}/T)\cdot \mathrm{d}T - \Delta\alpha_\mathrm{P}\cdot \mathrm{d}P = 0 \qquad (9)$$

where we have introduced the volume expansion increment $\Delta\alpha_\mathrm{P} = (\partial \Delta V/\partial T)_{\mathrm{P=const}}$.

Equation (9) defines the slope of a boundary $\Delta S(T,P) = \text{constant}$ in the P–T plane:

$$(\mathrm{d}P/\mathrm{d}T)_{\Delta S=\mathrm{const}} = \Delta C_\mathrm{p}/(T\cdot\Delta\alpha_\mathrm{P}) \qquad (10)$$

The special $\Delta S = 0$ line, separating regions of positive and negative transition entropies, is fixed by the condition $(\mathrm{d}P/\mathrm{d}T)_{\Delta\mu=0} = 0$ as shown in Figure 5.11. Since the slope in Figure 5.11 is positive and since both ΔC_p and ΔV are positive, it follows that $\Delta\alpha_\mathrm{P} > 0$. Integrating Eq. (10) yields the effect of pressure on the temperature of maximum stability:

$$T_\mathrm{M} = T_\mathrm{M0}\cdot\exp(P\cdot\Delta\alpha_\mathrm{p}/\Delta C_\mathrm{p}) \qquad (11)$$

For reasonably low pressures one has for the $\Delta S = 0$ line: $T_\mathrm{M} \approx T_\mathrm{M0}\cdot(1 + P\cdot\Delta\alpha_\mathrm{p}/\Delta C_\mathrm{p})$. Expanding the entropic part of the chemical potential (Eq. (6)) about $T_\mathrm{M} \approx T_\mathrm{M0}$ yields an approximate parabola in T with negative curvature (Figure 5.5a):

$$\Delta\mu(T,P) = \Delta\mu_\mathrm{M} - \tfrac{1}{2}\Delta C_\mathrm{p}\cdot(T - T_\mathrm{M})^2/T + \Delta V\cdot P = -RT\ln(c_\mathrm{D}/c_\mathrm{N}) \qquad (12)$$

For $\Delta V < 0$, increasing pressure diminishes the stability range of the native state. If ΔV is constant, one obtains the parabolic pressure–temperature phase diagram, $P(T)_{\Delta\mu=0}$, shown in Figure 5.5b.

Experimental data, like those shown in Figure 5.2, 5.3, and 5.11 suggest a reentrant phase behavior not only as a function of temperature but also as a function of pressure. This leads to a closed or ''ellipsoidal'' phase boundary with ΔV depending on pressure and temperature. The volume of the denatured form, i.e. the slope of $\mu_\mathrm{D}(P)$, in Figure 5.6 increases with decreasing pressure. Thus a second crossing of the D–N potentials may occur at low or even negative pressure denoted by P_L. Thus the unfolded protein is more easily stretched than the compact native state. Moreover, near $P = 0$, a pressure increase will stabilize the native state. In analogy to the temperature (Eq. (7)) we can define a pressure of maximum stability, P_M, according to:

$$(\partial\Delta\mu/\partial P)_{P=P_\mathrm{M}} = \Delta V = 0 \qquad (13)$$

Combining Eqs (4) and (13) shows that the changes in configurational and hydration volume cancel at $P = P_\mathrm{M}$. The small observed unfolding volumes may result from such compensation effects. Equation (13) allows determination of the $\Delta V(P,T) = 0$ line, separating regions of positive and negative volume changes:

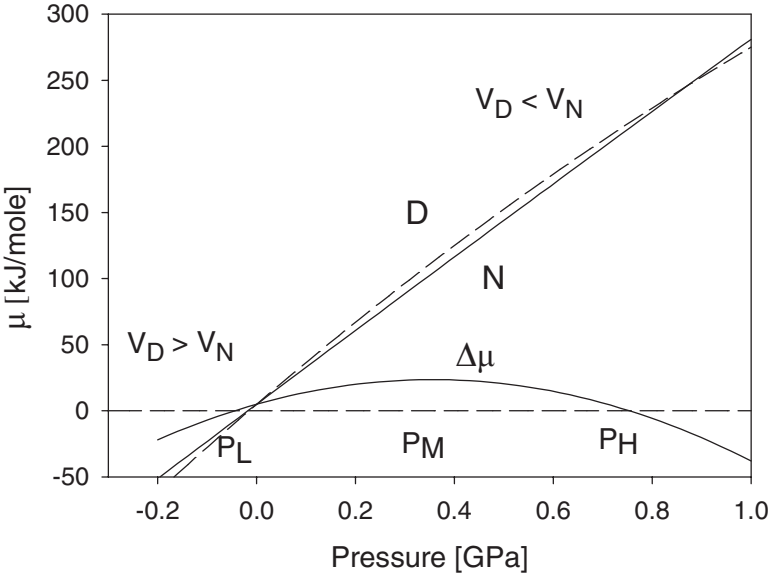

Fig. 5.6. Effect of pressure on the chemical potential $\mu(\div 4)$ for the parameters of cytochrome *c* at 280 K (Table 5.1 and Eq. (12, 17)). The volume of the denatured state decreases with pressure to below the value of the native protein, which leads to a crossing at high pressure P_H. A second crossing occurs at negative pressure P_L. P_M is the pressure of maximum stability.

$$(\partial \Delta V/\partial T)\,\mathrm{d}T + (\partial \Delta V/\partial P)\,\mathrm{d}P = \Delta\alpha_P \cdot \mathrm{d}T - \Delta\beta_T \cdot \mathrm{d}P = 0 \tag{14}$$

thus

$$(\mathrm{d}P/\mathrm{d}T)_{\Delta V=\mathrm{const}} = \Delta\alpha_P/\Delta\beta_T \tag{15}$$

The $\Delta V = 0$ line follows from the additional condition: $(\mathrm{d}P/\mathrm{d}T)_{\Delta\mu=0} = \propto$. For the pressure of maximum stability one obtains:

$$P_M = P_r + (\Delta\alpha_P/\Delta\beta_T)(T - T_r) \tag{16}$$

$\Delta\beta_T$ denotes the increment in the compressibility coefficient: $\Delta\beta_T = -(\partial \Delta V/\partial P)$. T_r denotes an unspecified reference temperature. For second-order phase transitions, sometimes associated with molten globule denaturation [26, 27], there is no discontinuity in the extensive quantities.

Equations (9) and (14) then become the so-called Ehrenfest equations: $(\mathrm{d}P/\mathrm{d}T)_{\Delta S=0} = (\mathrm{d}P/\mathrm{d}T)_{\Delta V=0}$

For most proteins cold denaturation occurs at subzero temperatures in the unstable or supercooled region of the water phase diagram. For this reason cold denaturation was formerly considered to be irrelevant to protein science. Similarly, low-pressure denaturation at $P_L(T)$ occurs for most proteins in a large temperature

range where pressure is negative. Liquids under tension are unstable, although metastable states can exist, since the creation of a new liquid–gas interface involves the crossing of an energy barrier. The first experiments were performed by Berthelot in 1850 using a spinning capillary [28]. Stretched states of water at pressures as low as –280 bars have been observed using the same method [29]. Unfolding experiments with protein solutions at negative pressures still need to be performed. The folding of unstable proteins such as nuclease conA remains incomplete at positive pressure, while negative pressure may further stabilize the native state [30]. At sufficiently high temperature, low-pressure denaturation may occur in the positive range (Figure 5.11) and in this case it is easily accessible experimentally.

Pressure- and temperature-dependent transition volumes originate from finite increments in the partial compressibility $\Delta\beta_T$ and the volume expansion coefficient $\Delta\alpha_P$. Expanding the latent volume ΔV about a reference point (T_r, P_r) yields:

$$\Delta V(P,T) = \Delta V_r - \Delta\beta_T \cdot (P - P_r) + \Delta\alpha_P \cdot (T - T_r) \tag{17}$$

The major part of the change in the compressibility upon global transformations of proteins is due to hydration processes [31]. The greater the hydration, the smaller the partial compressibility of protein and hydration shell. This is the rule for protein solutions at normal temperature and pressure. For native proteins the intrinsic compressibility is as low as that of organic solids [32–34]. The outer surface contribution to the measured partial compressibility is quite negative. Thus complete unfolding leads to a considerable decrease in the partial compressibility due to the loss of intramolecular voids and the expansion of the surface area contacting the bulk water [35]. In this low pressure/high temperature regime $\Delta\beta_T$ is negative, while $\Delta\alpha_P$ is mostly positive. This results in a positive unfolding volume (Eq. (17)) as indicated in Figure 5.6. Consequently moderate pressures stabilize the native state. A number of studies suggest that high-pressure denaturation leads to incomplete unfolding and structures resembling those of molten globule states (MG) [5–7, 36]. The N → MG transition is generally accompanied by an increase in compressibility. The tendency towards a positive $\Delta\beta_T$ at higher pressures due to partial unfolding may lead to the observed negative unfolding volumes. Combining Eqs (12) and (17), the phase boundary $\Delta\mu(T,P) = 0$ with respect to a reference point (T_r, P_r) assumes the form of a second-order hyperface:

$$\begin{aligned} &-\tfrac{1}{2}\Delta C_p \cdot (T - T_r)^2/T - \tfrac{1}{2}\Delta\beta_T \cdot (P - P_r)^2 + \Delta\alpha_P \cdot (T - T_r) \cdot (P - P_r) \\ &\quad - \Delta S_r \cdot (T - T_r) + \Delta V_r \cdot (P - P_r) + \Delta\mu_r = 0 \end{aligned} \tag{18}$$

For approximately constant increments $\Delta C_p, \Delta\beta_T, \Delta\alpha_P$, the phase boundary assumes parabolic ($\Delta\beta_T = 0$), hyperbolic or closed elliptical shapes. The basic condition to obtain an elliptical phase diagram is given by:

$$(\Delta C_p)(\Delta\beta_T) - (\Delta\alpha_P)^2 > 0 \tag{19}$$

Since experiments show that $\Delta C_p > 0$, Eq. (19) requires the compressibility change to be positive: $\Delta\beta_T > 0$. A hyperbolic shape would imply a negative left-hand side in Eq. (19). Thus far only elliptical diagrams, in some cases with distortions (e.g., Figure 5.3) have been discussed. A complete solution would require data in the range where pressure is negative: the data shown in Figure 5.2 are also consistent with a parabolic shape.

5.4 Measuring Phase Stability Boundaries with Optical Techniques

5.4.1 Fluorescence Experiments with Cytochrome *c*

Protein denaturing processes can be investigated with many techniques. The most convenient ones concerning the determination of the whole stability diagram are spectroscopic techniques. Almost all methods have been used: IR, Raman, NMR, absorption and fluorescence spectroscopy. However, data covering complete phase diagrams are quite rare. Some of them were reviewed above. The various techniques have their specific advantages as well as disadvantages. For instance, with vibrational spectroscopy one obtains information on structural changes such as the weakening of the amide I band [20, 21, 37, 38], with NMR one obtains information on hydrogen exchange and the associated protection factors [6] from which conclusions on structural details of the denatured state can be drawn. However, as a rule no information on the structure disrupting mechanism under pressure is obtained. The situation with absorption and fluorescence spectroscopy is different. In optical spectroscopy it is the spectral position and the linewidth of an electronic transition that is measured. From these quantities it is, as a rule, quite difficult to extract any structural information. On the other hand, one obtains detailed information on the interaction of the electronic states with the respective environment. Since these interactions are known in detail, it is possible to extract from their behavior under pressure and temperature changes information on the mechanism of phase crossing.

Compared with other spectroscopic techniques, fluorescence spectroscopy is also the most sensitive. Hence, it is possible to work at very low concentration levels so that aggregation processes can easily be avoided. In most experiments tryptophan is used as a fluorescent probe molecule. With chromoproteins this is, generally speaking, impossible since fast energy transfer to the chromophore quenches the UV fluorescence to a high degree. In the following we describe fluorescence experiments on a cytochrome *c*-type protein in a glycerol/water matrix [39]. The native heme iron was substituted by Zn in order to make the protein strongly fluorescent in the visible range. As a short notation for this protein we use the abbreviation Zn-Cc.

The set-up for a fluorescence experiment is simple and is shown in Figure 5.7.

The sample is in a temperature- and pressure-controlled diamond anvil cell.

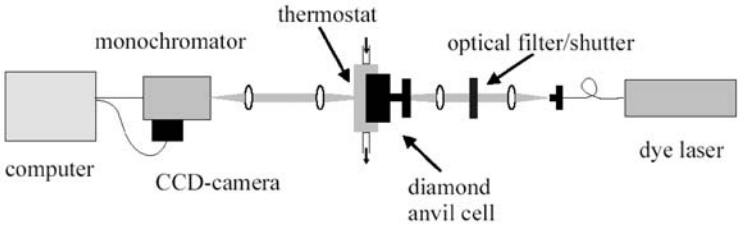

Fig. 5.7. Sketch of a fluorecence experiment for measuring the phase diagram of proteins.

Pressure can be varied up to about 2 GPa. Its magnitude is determined from the pressure shift of the ruby fluorescence, for which reference values can be taken from the literature [40]. The temperature is controlled by a flow thermostat between −20 °C and 100 °C. Excitation is carried out into the Soret band at 420 nm with light from a pulsed dye laser pumped by an excimer laser. The fluorescence is collected in a collinear arrangement, dispersed in a spectrometer and detected via a CCD camera. The quantities of interest for measuring the protein stability phase diagram are the spectral position and the width of the $S_1 \rightarrow S_0$ 00-transition (587 nm, Figure 5.8). Generally speaking the spectral changes for Zn-Cc are rather small. Nevertheless the measured changes of the spectral shifts and widths are accurate within about 3%. Figure 5.8 shows the fluorescence spectrum of Zn-Cc between 550 and 700 nm as it changes with pressure. The sharp line around 695 nm is the fluorescence from ruby.

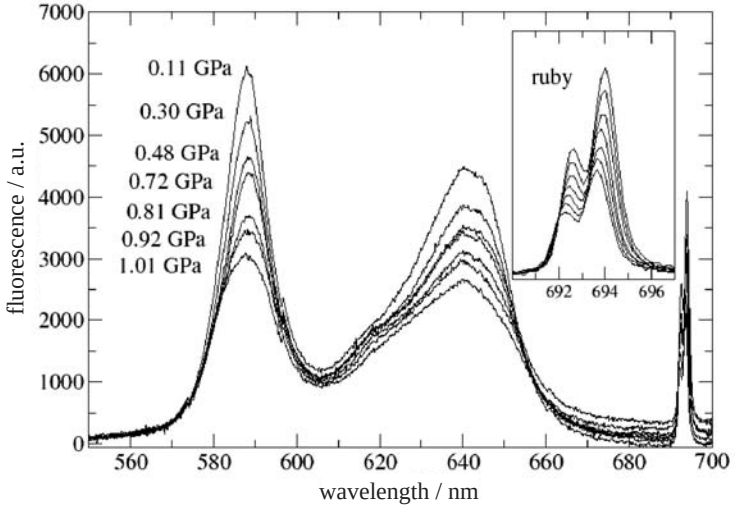

Fig. 5.8. Fluorescence spectrum of Zn-cytochrome *c* in glycerol/water at ambient temperature as it changes with pressure. The stability diagram was determined from the changes of the first and second moment of the 00-band at 584 nm. The fluorescence from ruby is shown as well. It serves for gauging the pressure.

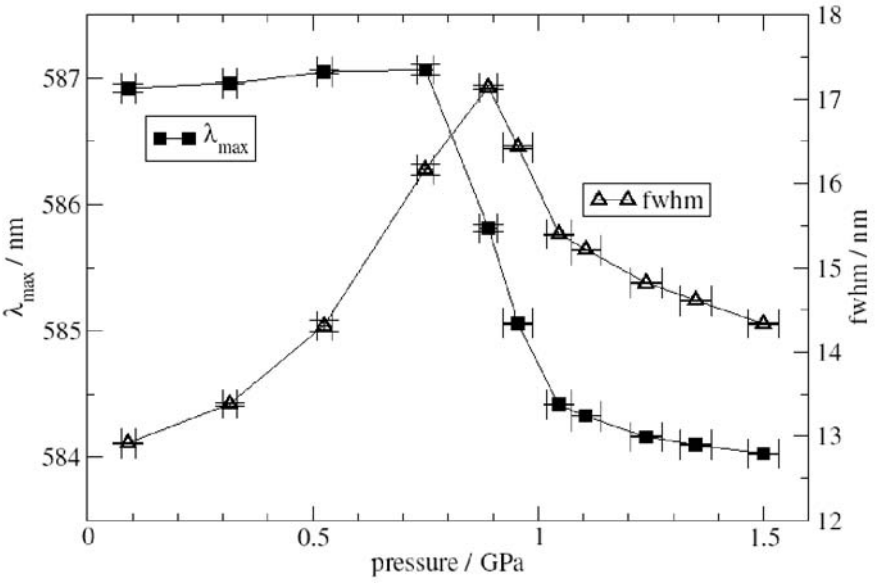

Fig. 5.9. The behavior of first and second moment of the fluorescence under pressure variation at ambient temperature.

5.4.2 Results

Figures 5.9 and 5.10 show typical results for the changes in the first and second moment (position of the maximum and width) of the 00-band under pressure and temperature variation.

If pressure is increased the band responds with a red shift, although a very small one (Figure 5.9). Around 0.75 GPa the red shifting regime changes rather abruptly into a blue shifting regime which levels off beyond 1 GPa. A qualitatively similar behavior is observed for the band shift under a temperature increase: a red shifting phase (in this case more pronounced) is followed by a blue shifting phase (Figure 5.10). Quite interesting is the behavior of the bandwidth: An increase of pressure leads to a rather strong increase in the width (Figure 5.9). This is the usual behavior and just reflects the fact that an increase in density results in an increase in the molecular interactions due to their strong dependence on distance. However, if the pressure is increased beyond about 0.9 GPa, the band all of a sudden narrows. This narrowing levels off beyond about 1 GPa. As can be seen from the figure, the maximum in the bandwidth coincides with the midpoint of the blue shifting regime. The thermal behavior of the bandwidth is different (Figure 5.10): There is no narrowing phase, but there is kind of a kink in the increase of the bandwidth with temperature around 65 °C. Again, this change in the thermal behavior of the width

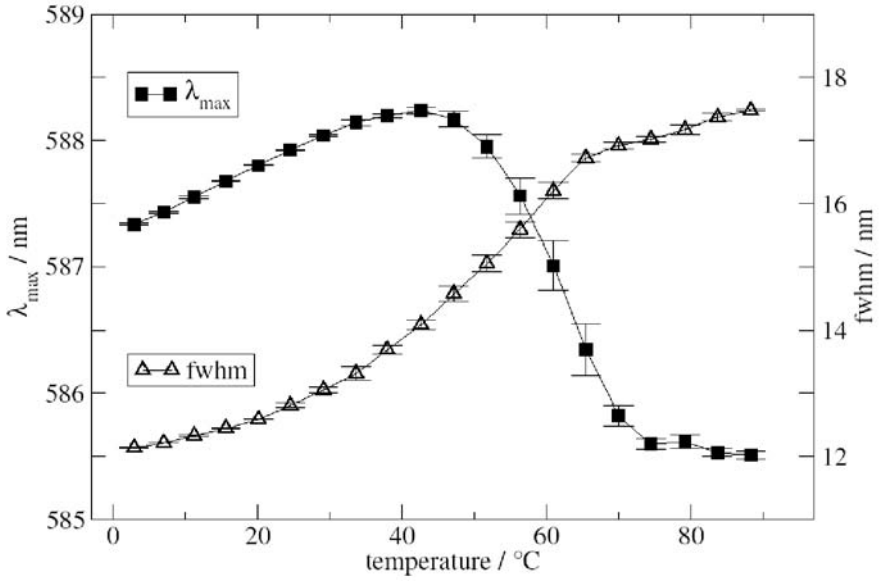

Fig. 5.10. The behavior of the first and second moment of the fluorescence under temperature variation at ambient pressure.

coincides rather well with the midpoint in the thermally induced blue shifting phase.

For measuring the complete phase diagram we performed a series of pressure scans from ambient pressure up to about 1.5 GPa at various temperatures and a series of temperature scans from a few centigrades up to about 90 °C at various pressure levels. The respective pattern of the changes of the fluorescence always showed the sigmoid-like behavior as discussed above. We associate the midpoint of the blue shifting regime with the stability boundary between the native and the denatured state of the protein due to reasons discussed below.

The complete stability diagram is shown in Figure 5.11. The solid line represents an elliptic least square fit to the experimental points. The two solid lines $\Delta S = 0$ and $\Delta V = 0$ cut the stability diagram at points where the volume and the entropy difference change sign (see also Eqs (11) and (16)). For instance, for all data points to the left of the $\Delta S = 0$ line the entropy in the denatured state S_D is smaller than S_N, the entropy in the native state (see below).

Figures 5.12 and 5.13 show specific features of the fluorescence behavior which we want to discuss separately. Figure 5.12 shows the behavior of the first and second moment for cold denaturation at ambient pressure. The point which we want to stress is that the band shift no longer reflects the qualitative change in its behavior. Instead, we observe a blue shift which increases in a nonlinear fashion with decreasing temperature. From such a behavior it is hard to determine a transition

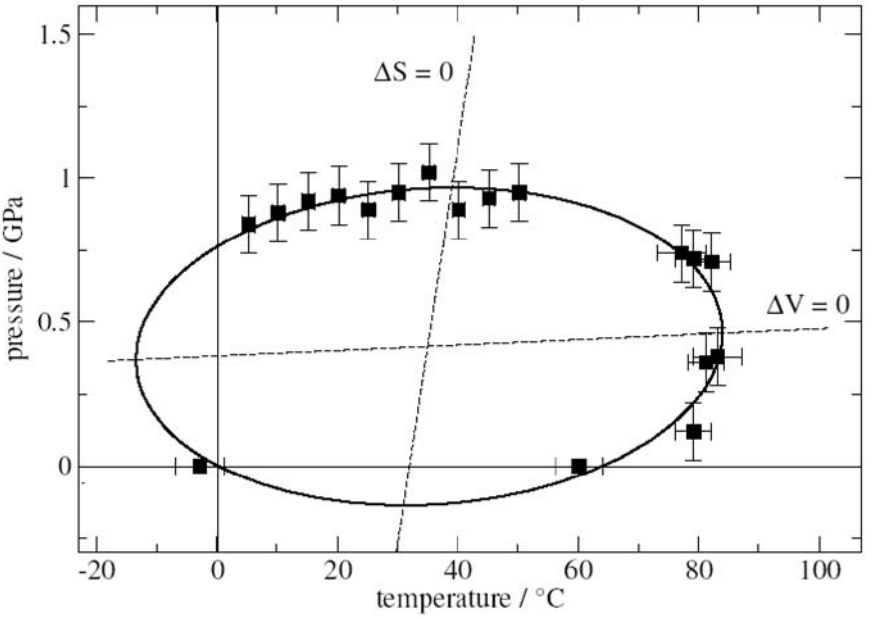

Fig. 5.11. The stability phase diagram of Zn-cytochrome *c*. The solid line is an elliptic least square fit to the data points. The straight lines mark the points where ΔS and ΔV change sign.

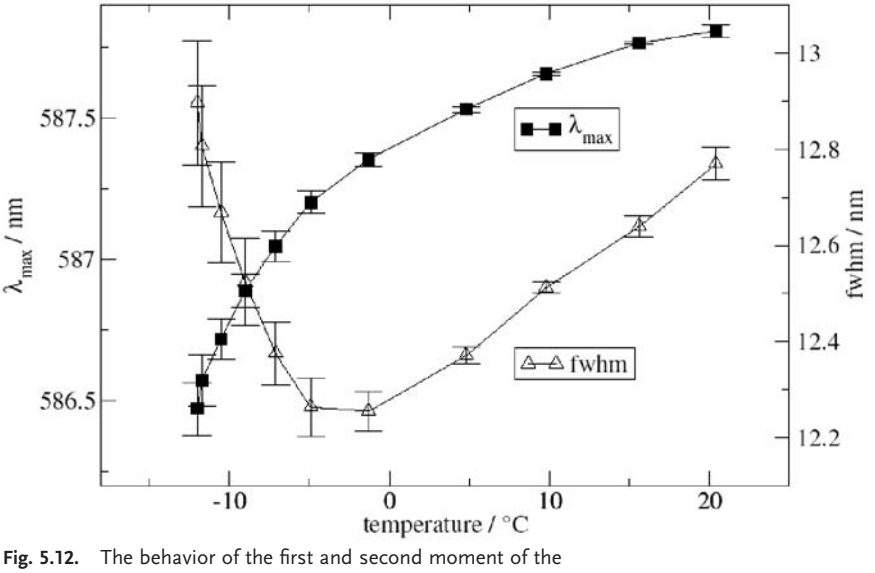

Fig. 5.12. The behavior of the first and second moment of the fluorescence for cold denaturation at ambient pressure.

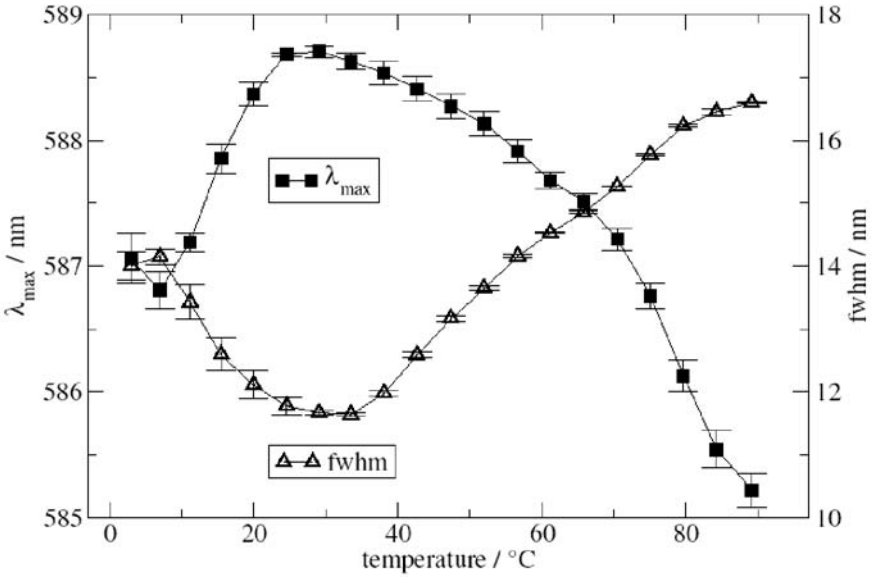

Fig. 5.13. The first and second moment of the fluorescence under a temperature variation at high pressure (0.7 GPa). The pattern shows features characteristic for re-entrant phase crossing.

point. The bandwidth, on the other hand, shows a quite unusual behavior: it narrows with decreasing temperature, but around −3 °C it runs through a minimum and starts broadening upon further decreasing the temperature. The unusual behavior concerns the broadening with decreasing temperature. This broadening obviously originates from an additional state which becomes populated below −3 °C. Naturally, this state must be the denatured state of the protein. Hence, we associate this minimum in the bandwidth with the stability boundary.

The temperature dependence of the moments in Figure 5.13 follows a rather complex pattern. This pattern comes from the re-entrant character of the phase diagram which has been stressed in Section 5.2. At a pressure level of 0.7 GPa, the protein is denatured to a high degree if the temperature is below around 10 °C (see Figure 5.11). Hence, upon increasing the temperature, the protein enters the stable regime. This is most clearly reflected in a narrowing of the bandwidth due to the fact that the denatured state becomes less and less populated At the same time the band maximum undergoes a red shift in line with the observation that the denatured state is blue shifted from the native one. However, around 25 °C the red shifting phase turns into a blue shifting phase, signaling that the protein re-enters the denatured regime. The bandwidth data support this conclusion. Interestingly, the data convey the impression that there are more than just two transitions involved; their nature, however, is not clear.

5.5 What Do We Learn from the Stability Diagram?

5.5.1 Thermodynamics

The eye-catching feature in Figure 5.11 is the nearly perfect elliptic shape of the stability diagram in agreement with the simple model developed in Section 5.3. The elliptic shape implies that the characteristic thermodynamic parameters of the protein, namely the increments of the specific heat capacity, the compressibility and the thermal expansion are rather well-defined material parameters, i.e., do not significantly depend on temperature and pressure. In addition, since the model is based on just two states, we conclude from the elliptic shape that the protein investigated, namely Zn-Cc, can be described as a two-state folder. Applying the Clausius–Clapeyron equation (Eq. (3)) to the elliptic phase boundary, we see that there are distinct points characterized by $(\mathrm{d}P/\mathrm{d}T)_{\Delta\mu=0} = \infty$ and by $(\mathrm{d}P/\mathrm{d}T)_{\Delta\mu=0} = 0$. The former condition separates the regime with positive ΔV from the regime with negative ΔV. The latter one separates the regime with positive ΔS from the regime with negative ΔS (Eqs (7) and (13)).

Let us consider thermal denaturation at ambient pressure. ΔS is definitely positive because the entropy of the chain increases upon denaturation and the entropy of the solvent increases as well. Since the slope of the phase boundary is positive, ΔV must be positive, too. However, moving along the phase boundary, we eventually cross the $\Delta V = 0$ line. For all points above that line, ΔV is negative. In other words: application of pressure destabilizes the native state and favors the denatured state. Below the $\Delta V = 0$-line, ΔV is positive. Accordingly, application of pressure favors the native state.

In a similar way, for all points to the right of the $\Delta S = 0$ line, ΔS is positive. A positive entropy change upon denaturation is what one would straightforwardly expect. However, to the left of the $\Delta S = 0$ line, the entropy change is negative, meaning that the entropy in the denatured state is smaller than in the native state. As was discussed above, the negative entropy change is due to an upcoming ordering of the hydration water as the temperature is decreased: The exposure of hydrophobic groups causes the water molecules in the hydration shell to become more and more immobilized due to the formation of a stronger hydrogen network. Right at the point where the $\Delta S = 0$ line cuts the phase diagram, the chain entropy and the entropy of the hydration shell exactly cancel, as we have stressed above.

There is another interesting outcome from the elliptic shape of the phase diagram: Eq. (19) tells us that the change in the compressibility upon denaturation has to have the same sign as the change in the specific heat. The change in the specific heat is positive meaning that the heat capacity is larger in the unfolded state. As outlined above, this is due to the fact that an increase of the temperature in the denatured state requires the melting of the ordered immobilized hydration shell. Accordingly, $\Delta\beta$ has to be positive, meaning that the compressibility in the denatured state is larger than in the native state. As to the absolute values of

the thermodynamic parameters which determine the phase diagram, they can be determined only if one of the parameters is known. In the following section we will show how the equilibrium constant can be determined as a function of temperature and pressure and how this can be exploited to extract the thermodynamic parameters on an absolute scale.

5.5.2 Determination of the Equilibrium Constant of Denaturation

The body of information that can be extracted from the thermodynamics of protein denaturation reveals surprising details. However, it should be stressed again that all the modeling is based on two important assumptions, namely that folding and denaturing is described within the frame of just two states, N and D, and that these two states are in thermal equilibrium. Neither of these assumptions is straightforward. It is well known that the number of structural states, even of small proteins is, is extremely large [41–47] and the communication between the various states can be very slow so that the establishment of thermal equilibrium is not always ensured. We understand the two-state approximation on the basis of a concept which we call "state lumping." In simple terms this means that the structural phase space can be partitioned into two areas comprising, on the one hand, all the states in which the protein is functioning and, on the other hand, the area in which the protein is dead. We associate the native state N and the denatured state D with these two areas. In order for the "state lumping" concept to work, the immediate consequence is that all states within the two and between the two areas are in thermal equilibrium. Whether this is true or not can only be proven by the outcome of the experiments.

For Zn-Cc this concept seems to hold sufficiently well. In our experiments, typical waiting times for establishing equilibrium were of the order of 20 minutes. In order to make sure that this time span is reasonable, we measured for some points on the phase boundary also the respective kinetics. However, we also stress that at high pressures and low temperatures (left side of the phase diagram, Figure 5.11) we could not get reasonable data and we attributed this to the fact that equilibrium could not be reached within the experimental time window.

Assuming that equilibrium is established and the two-state approximation holds with sufficient accuracy, we can determine the equilibrium constant as a function of pressure and temperature from the fluorescence experiments and from the fact that the phase diagram has an elliptic shape. We proceed in the following way: The fluorescence intensity $F(\lambda)$ in the transformation range is a superposition from the two states N and D with their respective fluorescence maximum at λ_N and λ_D:

$$F(\lambda) = p_N a_N \exp[-(\lambda - \lambda_N)^2/2\sigma_N{}^2] + p_D a_D \exp[-(\lambda - \lambda_D)^2/2\sigma_D{}^2] \qquad (20)$$

where p_N and p_D are the population factors of the two states N and D, a_N and a_D are the respective oscillator strengths. Changes of the temperature or the pressure of the system cause a change in the population factors p_N and p_D which, in turn,

leads to a change in the first moment of $F(\lambda)$, that is in the spectral position of the band maximum, λ_{max}. As to Zn-Cc, we can make use of some of its specific properties: First, the chromophore itself is quite rigid, hence, it is not likely affected by pressurizing or heating the sample. Accordingly, it is safe to assume that the oscillator strengths in the native and in the denatured state are not significantly different from each other. Second, the spectral changes induced by varying the temperature or the pressure are rather small compared to the total width of the long wavelength band (Figure 5.8). In addition, the wavelengths λ_N and λ_D are rather close and well within the inhomogeneous band. As a consequence, the exponentials in Eq. (20) are roughly of the same magnitude irrespective of the value of λ. Along these lines of reasoning, λ_{max} is readily determined from the condition $dF/d\lambda = 0$:

$$\lambda_{max} = p_N(T, P)\lambda_N + p_D(T, P)\lambda_D = p_N(T, p)[\lambda_N - \lambda_D] - \lambda_D \tag{21}$$

The last term on the right hand side of Eq. (21) holds because we restrict our evaluation to an effective two-state system. According to the above equation, the band maximum in the transition region is determined by a population weighted average of λ_N and λ_D. Since λ_N and λ_D depend on pressure and temperature themselves, we have to determine the respective edge values in the transition region. How this is done is shown in Figure 5.14 for thermal denaturation at ambient pressure. Similar figures are obtained for any parameter variation. Having λ_{max} as a function of pressure or temperature from the experiment and knowing the respective edge

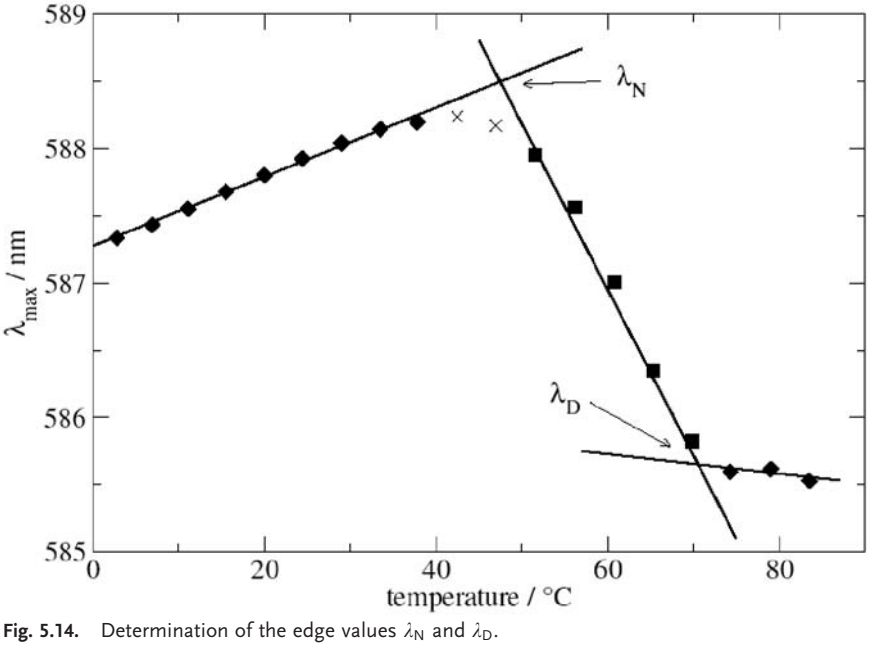

Fig. 5.14. Determination of the edge values λ_N and λ_D.

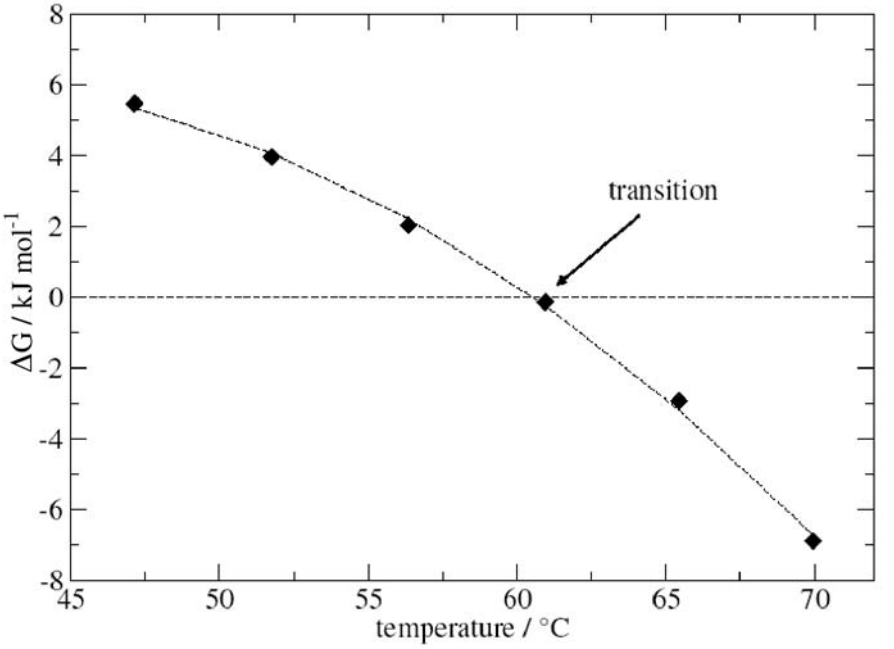

Fig. 5.15. Temperature dependence of the difference of the Gibbs free energy ΔG. (Note that, for a one-component system, $\Delta G/\mathrm{Mol} = \Delta\mu$).

values λ_N and λ_D, the population factors p_N and p_D can readily be evaluated as a function of pressure and temperature using Eq. (21). From the population factors the equilibrium constant K follows immediately:

$$K_{DN}(T,P) = [1 - p_N(T,P)]/p_N(T,P) \tag{22}$$

Once K is known, $\Delta\mu$ (or, equivalently, ΔG mol^{-1}) can be determined as a function of pressure and temperature from Eq. (1). For a fixed pressure, say p_i, $\Delta\mu(T,P_i)$ forms an inverted parabola in T, as was shown in Section 5.3. The same is true for $\Delta\mu(P,T_i)$. So we determined $\Delta\mu(T)$ and $\Delta\mu(P)$ by fitting parabolas to the few data points (Figures 5.15 and 5.16) under the constraints that both branches of these parabolas have to go through the phase boundaries of the stability diagram (Figure 5.11). From the first and second derivative of $\Delta\mu$ with respect to temperature and pressure all the thermodynamic parameters, namely $\Delta V(T,P), \Delta S(T,P)$, $\Delta C_p, \Delta\beta$ and $\Delta\alpha$, can be determined. For Zn-Cc this parameters are listed in Table 5.1. We took ΔC_p from the equilibrium constant because it seems to be the most accurate parameter (Figure 5.15). As a matter of fact our value is rather close to what was measured by Makhatadze and Privalov for unfolding native cytochrome c [10]. All the other parameters are determined from the phase diagram. Note that $\Delta\beta$ has the same sign as ΔC_p, as required for an elliptic shape of the diagram.

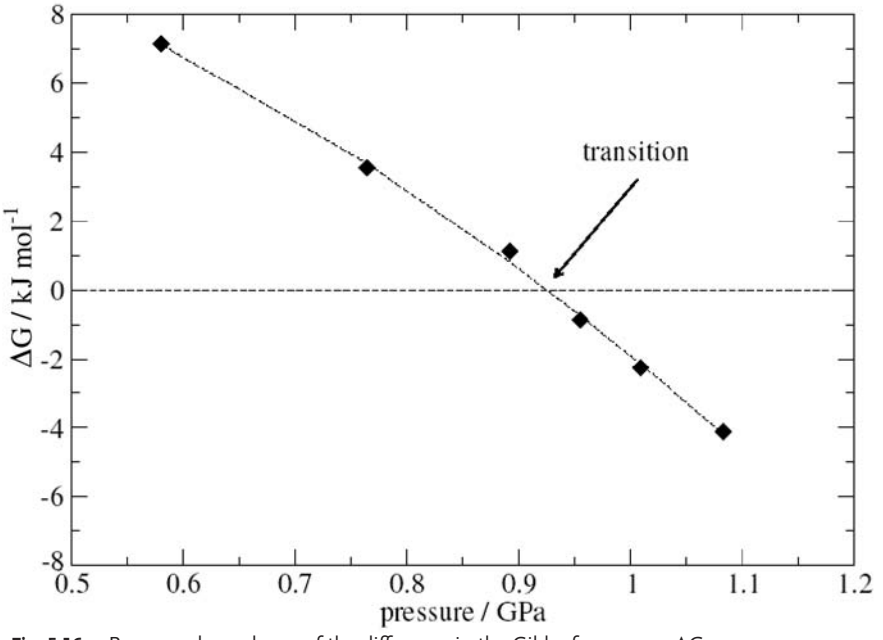

Fig. 5.16. Pressure dependence of the difference in the Gibbs free energy ΔG.

5.5.3 Microscopic Aspects

Having determined the complete set of thermodynamic parameters which govern denaturation of Zn-Cc, we may now proceed with exploring the microscopic driving forces of denaturation. We stress that the pattern in the behavior of the first moment of the fluorescence 00-transition is qualitatively very similar for thermal and pressure denaturation: A red shifting regime upon an increase in both parameters is followed by a blue shifting regime which signals the onset of the transformation range. The solvent shift of an optical transition is mainly determined by

Tab. 5.1. Thermodynamic parameters for the denaturation of Zn-cytochrome *c*.

Parameters	*From the fit*
ΔC_p (kJ mol^{-1} K^{-1})	5.87
$\Delta\beta$ (cm^3 mol^{-1} GPa^{-1})	148.1
$\Delta\alpha$ (cm^3 mol^{-1} K^{-1})	0.139
ΔV (0.91 GPa, 298 K) (cm^3 mol^{-1})	−74.6
ΔS (0.91 GPa, 298 K) (kJ mol^{-1} K^{-1})	−0.263
ΔV (0.1 MPa, 333 K) (cm^3 mol^{-1})	65.0
ΔS (0.1 MPa, 333 K) (kJ mol^{-1} K^{-1})	0.530

two types of interactions, namely the dispersive and the higher order electrostatic interaction (dipole–induced dipole). Both types of interaction are very short ranged. They fall off with distance R as R^{-6}. From the pioneering papers by Bayliss, McRae and Liptay [48–50], it is well known that the dispersive interaction is always red shifting because the polarizability in the excited state is higher than in the ground state. However, electrostatic interactions can cause shifts in both directions, to the red as well as to the blue, depending on how the dipole moment of the chromophore changes in the excited state compared with the ground state Accordingly, in the blue shifting regime, the electrostatic interaction of the probe with its environment obviously increases compared with the dispersive interaction. As a consequence, we conclude that polar groups with a sufficiently large dipole moment have to come close to the chromophore to induce this shift.

As to thermal denaturation, such an interpretation seems to fit quite well into the scenario. Baldwin [23], for instance, could show that thermal denaturation of a protein is remarkably well described in analogy to the solvation of liquid hydrocarbons in water. This ''oil droplet model'' accounts for the temperature dependence of the hydrophobic interaction: The entropic driving force for folding, which comprises the major part of the hydrophobic interaction, decreases as the temperature increases. This driving force is associated with the formation of an ordered structure of the water molecules surrounding the hydrophobic amino acids. At sufficiently high temperature this ordered structure melts away so that the change of the unfolding entropy of the polypeptide chain takes over and the protein attains a random coil-like shape [5]. Since a random coil is an open structure, the chromophore may now be exposed to water molecules. Water molecules have a rather high permanent dipole moment, hence, may become polarized through the electrostatic interaction with the chromophore. Along these lines of reasoning, it seems straightforward that the observed blue shifting regime of the fluorescence in the thermal denaturation of Zn-Cc comes from the water molecules of the solvent. However, as was pointed out by Kauzmann [51], the ''oil droplet model'' has severe shortcomings, despite its success in explaining the specific features of thermal denaturation. It almost completely fails in explaining the specific features of pressure induced denaturation. Pressure denaturation is governed by the volume change ΔV (Section 5.3). In this respect hydrophobic molecules behave quite differently from proteins: ΔV for protein unfolding is negative above a few hundred MPa (see, for instance, Figure 5.11 and discussions in Sections 5.3 and 5.5.1), whereas it is positive in the same pressure range for transfering hydrophobic molecules into water. There are two possible consequences: Either the ''oil droplet model'' is completely wrong, or the pressure denatured state is different from the thermally denatured state.

Indeed, Hummer and coworkers could show that the latter possibility is true [52, 53]. On the basis of their calculations they suggested that, as pressure is increased, the tretrahedral network of H-bonds in the solvent becomes more and more frustrated so that the pressure-induced inclusion of water molecules within the hydrophobic core becomes energetically more and more favorable. As a consequence, the contact configuration between hydrophobic molecules is destabilized by pressure

whereas the solvent-separated contact configuration (a water molecule between two hydrophobic molecules) is stabilized. In simple words this means that water is pressed into the protein, the protein swells but does not completely unfold into a random coil conformation but rather seems to retain major parts of its globular shape. The important conclusion is that pressure denaturation is based on the presence of water. Larger solvent molecules, such as glycerol, can obviously not penetrate the protein, hence may act as stabilizing elements against pressure [54].

It seems that this view on the microscopic aspects of pressure denaturation is convincingly supported by our experiments: First, we stress again that the general pattern in the variation of the first moment with pressure is very similar to the respective variation with temperature. Since, in the latter case, we attributed this pattern to water molecules approaching the chromophore, it is quite natural to associate the pressure-induced pattern with the same phenomenon. Second, the magnitude of the change in the first moments is about the same for thermally and pressure-induced denaturation. Accordingly, the change in the respective interaction has to be very similar. This means, that, on average, the number and the distances of the additionally interacting water molecules have to be the same.

In order to get additional support for this reasoning we performed pressure tuning hole burning experiments [55]. With these experiments it is possible to estimate the size of an average interaction volume of the chromophore with its environment. We found that the respective radius is about 4–5 Å. Accordingly, application of high pressure forces water molecules from the hydration shell into the interior of the protein where they fill the voids around the chromophore in the heme pocket. High-pressure (0.9 GPa) MD simulations (M Reif and Ch Scharnagl, in preparation) are in full agreement with this view of pressure denaturation.

Summarizing this section we state that fluorescence experiments in combination with other optical experiments and computer simulations [22] provide a detailed insight into the processes involved in pressure-induced protein denaturation.

5.5.4
Structural Features of the Pressure-denatured State

From the discussion above it is evident that pressure denaturation leads to a structural state which is different from the respective one obtained by thermal denaturation. It seems that many structural features of the native protein remain preserved under pressure denaturation. Experimental evidence comes from NMR experiments [6], but also from IR experiments [20, 21, 37, 38].

Figure 5.17 shows another experiment [56], namely a neutron-scattering experiment with myoglobin as a target from which the conservation of native structural elements in the denatured state is directly seen. Myoglobin denatures at pH 7 in the range between 0.3 and 0.4 GPa as judged from the optical absorption spectrum of the heme group. The corresponding changes in the protein structure and at the protein–water interface can be deduced from the neutron structure factor $H(Q)$ of a concentrated solution of myoglobin in D_2O (Figure 5.17). Q denotes the length of the scattering vector. The large maximum around $Q = 2\,\text{Å}^{-1}$ arises from O–O cor-

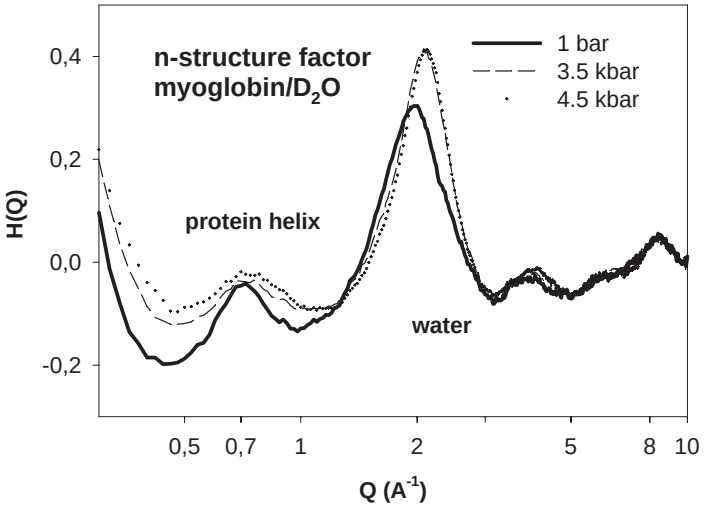

Fig. 5.17. Comparative neutron scattering experiments at ambient pressure and at high pressure. Plotted is the neutron structure factor $H(Q)$ as a function of Q. Data are for myoglobin. The important feature is the partial persistence of the protein helical structure (peak at $Q = 0.7\,\text{Å}^{-1}$) in the pressure-denatured state.

relations of water near the protein interface. This maximum increases with density. The smaller maximum near $Q = 0.7\,\text{Å}^{-1}$ reflects helix-helix correlations. The contrast is provided by the negative scattering length density of the protein hydrogen atoms versus the positive scattering length density of C, N, and O. The most remarkable feature is the persistence of this maximum above the transition at 0.45 GPa, indicating residual secondary structure in the pressure-unfolded form.

5.6 Conclusions and Outlook

Folding and denaturing processes of proteins are extremely complicated due to the complex nature of the protein molecules with their huge manifold of structural states. Hence, it is surprising that some of the characteristic features of equilibrium thermodynamics associated with the folded and denatured state are already revealed on the basis of simple models. Most important in this context is the reduction of the folding and denaturing processes to just two essential states, namely the native state and the denatured state. To reconcile this crude assumption with the large structural phase space, we introduced the concept of ''state lumping.'' Another important approximation concerns the vanishing higher (higher than two) derivatives of the chemical potential, rendering pressure- and temperature-independent state parameters (specific heat, compressibility, thermal expansion) to the protein. The result of these simplifying assumptions is an elliptically shaped

stability phase diagram, provided that the sign of the change in the specific heat capacity and in the compressibility is the same.

Our experiments on the stability of a modified cytochrome *c* in a glycerol/water solvent showed an almost perfect ellipse from which the regimes with positive and negative volume changes as well as positive and negative entropy changes could be deduced. We tried to shed some light on the microscopic aspects responsible for these regimes. A dominant force is the hydrophobic interaction which depends not only on temperature but also on pressure [57]. The characteristic structural features of the pressure-denatured state are different from the respective ones of the thermally denatured state. In both cases, however, water molecules come very close to the chromophore.

As to the open questions in context with the stability phase diagram, we refer to the elliptic shape. So far only closed diagrams have been observed, and in most cases an elliptic shape was an appropriate description. The question comes up how general this observation is and what the microscopic implications are. Admittedly, up to now few experiments have measured the full diagram.

Another problem concerns negative pressure. From an experimental point of view negative pressures as low as −200 bar seem to be feasible. Denaturation under negative pressure, that is under conditions where the relevant interactions are weakened, would add valuable information on pressure-induced denaturing forces.

Finally the role of the solvent has to be addressed in more detail. The solvent may have a dramatic influence on the hydrophobic interaction, the size of the solvent molecules may play an important role in all processes involving pressure, and, last but not least, understanding the influence of the solvent may also shed light on the behavior of membrane proteins.

Acknowledgment

The authors acknowledge financial support from the DFG (FOR 358, A1/2), from the Fonds der Chemischen Industrie (J.F.) and from the Bundesministerium für Bildung und Forschung 03DOE2M1.

Scientific input to this work came from many of our friends. In particular we want to thank J. M. Vanderkooi, H. Lesch, and G. Job and F. Herrmann for the idea to base thermodynamics on entropy and chemical potential.

References

1 G. Weber, H. Drickammer, *Q. Rev. Biophys.* **1983**, *16*, 89–112.
2 Special Issue on "Frontiers in high pressure biochemistry and biophysics", *Biochim. Biophys. Acta* 2002, 1595, Issue 1–2.
3 C. A. Royer, *Biochim. Biophys. Acta* **2002**, *1595*, 201–209.
4 M. Gerstein, C. Gothia, *Proc. Natl Acad. Sci. USA* **1996**, *93*, 10167–10172.
5 A. Fersht, *Structure and Mechanism in Protein Science*, W. H. Freeman, New York, 1999.
6 D. P. Nash, J. Jonas, *Biochemistry* **1997**, *36*, 14375–14383.

7 G. J. A. Vidugiris, J. L. Markley, C. A. Royer, *Biochemistry* **1995**, *34*, 4909–4912.
8 P. L. Privalov, *Adv. Protein Chem.* **1979**, *33*, 167–241.
9 P. L. Privalov, S. J. Gill, *Adv. Protein Chem.* **1988**, *39*, 191–234.
10 G. I. Makhatadze, P. L. Privalov, *Adv. Protein Chem.* **1995**, *47*, 307–425.
11 J. F. Brandts, *J. Am. Chem. Soc.* **1964**, *86*, 4302–4314.
12 J. F. Brandts, *J. Am. Chem. Soc.* **1965**, *87*, 2759–2760.
13 A. Cooper, *Prog. Biophys. Mol. Biol.* **1984**, *44*, 181–214.
14 S. A. Hawley, *Biochemistry* **1971**, *10*, 2436–2442.
15 P. E. Cladis, R. K. Bogardus, W. B. Daniels, G. N. Taylor, *Phys. Rev. Lett.* **1977**, *39*, 720–723.
16 D. D. Klug, E. J. Whalley, *J. Chem. Phys.* **1979**, *71*, 1874–1877.
17 N. A. Clark, *J. Physique* **1979**, *40*, 345–349.
18 A. Zipp, W. Kauzmann, *Biochemistry* **1973**, *12*, 4217–4228.
19 H. Ludwig, W. Scigalla, B. Sojka, in *High Pressure Effects in Molecular Biophysics and Enzymology*, J. L. Markley, D. Northrop, C. A. Royer (Eds), Oxford University Press, Oxford, 1996, 346–363.
20 K. Heremans, L. Smeller, *Biochim. Biophys. Acta* **1998**, *1386*, 353–370.
21 Y. Taniguchi, N. Takeda, in *High Pressure Effects in Molecular Biophysics and Enzymology*, J. L. Markley, D. Northrop, C. A. Royer (Eds), Oxford University Press, Oxford, 1996, 87–95.
22 E. Paci, *Biochim. Biophys. Acta* **2002**, *1595*, 185–200.
23 R. Baldwin, *Proc. Natl Acad. Sci. USA* **1986**, *83*, 8069–8072.
24 R. Baldwin, N. Muller, *Proc. Natl Acad. Sci. USA* **1992**, *89*, 7110–7113.
25 P. L. Privalov, *Biofizika* **1987**, *32*, 742–746.
26 Y. V. Griko, P. Privalov, *J. Mol. Biol.* **1994**, *235*, 1318–1325.
27 Th. Kiefhaber, R. L. Baldwin, *J. Mol. Biol.* **1995**, *252*, 122–132.
28 M. Berthelot, *Ann. Chim.* **1850**, *30*, 232–237.
29 L. J. Briggs, *J. Appl. Phys.* **1950**, *21*, 721–722.
30 M. Eftink, G. Ramsey, in *High Pressure Effects in Molecular Biophysics and Enzymology*, J. Markley, D. Northrop, C. A. Royer (Eds), Oxford University Press, Oxford, 1996, 62.
31 T. V. Chalikian, K. J. Breslauer, *Curr. Opin. Struct. Biol.* **1998**, *8*, 657–664.
32 K. Gekko, H. Noguchi, *J. Phys. Chem.* **1979**, *83*, 2706–2714.
33 B. Gavish, E. Gratton, C. J. Hardy, *Proc. Natl Acad. Sci. USA* **1983**, *80*, 750–754.
34 J. Zollfrank, J. Friedrich, *J. Opt. Soc. Am. B.* **1992**, *9*, 956–961.
35 D. P. Kharakoz, A. P. Sarvazyan, *Biopolymers* **1993**, *33*, 11–25.
36 G. J. A. Vidugiris, C. A. Royer, *Biophys. J.* **1998**, *75*, 463–470.
37 G. Panick, R. Malessa, R. Winter, G. Rapp, K. J. Frye, C. A. Royer, *J. Mol. Biol.* **1998**, *275*, 389–402.
38 H. Herberhold, S. Marchal, R. Lange, C. H. Scheying, R. F. Vogel, R. Winter, *J. Mol. Biol.* **2003**, *330*, 1153–1164.
39 H. Lesch, H. Stadlbauer, J. Friedrich, J. M. Vanderkooi, *Biophys. J.* **2002**, *82*, 1644–1653.
40 M. Eremets, *High Pressure Experimental Methods*, Oxford University Press, Oxford, 1996.
41 J. D. Bryngelson, J. N. Onuchic, N. D. Socchi, P. G. Wolynes, *Proteins Struct. Funct. Genet.* **1995**, *21*, 167–195.
42 H. Frauenfelder, F. Parak, R. D. Young, in *Annu. Rev. Biophys. Chem.* **1988**, *17*, 451–479.
43 H. Frauenfelder, S. G. Sligar, P. G. Wolynes, *Science* **1991**, *254*, 1598–1603.
44 H. Frauenfelder, D. Thorn Leeson, *Nat. Struct. Biol.* **1998**, *5*, 757–759.
45 H. Frauenfelder, *Nat. Struct. Biol.* **1995**, *2*, 821–823.
46 A. E. Garcia, R. Blumenfeld, G. Hummer, J. A. Krummhansl, *Physica D* **1997**, *107*, 225–239.
47 K. A. Dill, H. S. Chan, *Nat. Struct. Biol.* **1997**, *4*, 10–19.
48 N. S. Bayliss, *J. Chem. Phys.* **1950**, *18*, 292–296.

49 N. S. Bayliss, E. G. McRae, *J. Phys. Chem.* **1954**, *58*, 1002–1006.

50 W. Liptay, *Z. Naturforsch.* **1965**, *20a*, 272–289.

51 W. Kauzmann, *Nature* **1987**, *325*, 763–764.

52 G. Hummer, S. Garde, A. E. Garcia, M. E. Paulaitis, L. R. Pratt, *Proc. Natl Acad. Sci. USA* **1998**, *95*, 1552–1555.

53 G. Hummer, S. Garde, A. E. Garcia, M. E. Paulaitis, L. R. Pratt, *J. Phys. Chem.* **1998**, *102*, 10469–10482.

54 A. C. Oliveira, L. P. Gaspart, A. T. Da Poian, J. L. Silva, *J. Mol. Biol.* **1994**, *240*, 184–187.

55 H. Lesch, J. Schlichter, J. Friedrich, J. M. Vanderkooi, *Biophys. J.* **2004**, *86*, 467–472.

56 W. Doster, R. Gebhardt, A. K. Soper, in *Advances in High Pressure Bioscience and Biotechnology*, R. Winter (Ed.), Springer, Berlin, 2003, 29.

57 K. A. Dill, *Biochemistry* **1990**, *29*, 7133–7155.

6
Weak Interactions in Protein Folding: Hydrophobic Free Energy, van der Waals Interactions, Peptide Hydrogen Bonds, and Peptide Solvation

Robert L. Baldwin

6.1
Introduction

Hydrophobic free energy has been widely accepted as a major force driving protein folding [1, 2], although a dispute over its proper definition earlier made this issue controversial. When a hydrocarbon solute is transferred from water to a nonaqueous solvent, or a nonpolar side chain of a protein is buried in its hydrophobic core through folding, the transfer free energy is referred to as hydrophobic free energy. The earlier dispute concerns whether the transfer free energy can be legitimately separated into two parts and the free energy of hydrophobic hydration treated separately from the overall free energy change [3–5]. If the hydrophobic free energy is defined as the entire transfer free energy [5], then there is general agreement that transfer of the nonpolar solute (or side chain) out of water and into a nonaqueous environment drives folding in a major way. A related concern has come forward, however, and scientists increasingly question whether the energetics of forming the hydrophobic core of a protein should be attributed chiefly to packing interactions (van der Waals interactions, or dispersion forces) rather than to burial of nonpolar surface area. This question is closely related to the issue of whether the hydrophobic free energy in protein folding should be modeled by liquid–liquid transfer experiments or by gas–liquid transfer experiments.

The energetic role of peptide hydrogen bonds (H-bonds) was studied as long ago as 1955 [6] but the subject has made slow progress since then, chiefly because of difficulty in determining how water interacts with the peptide group both in the unfolded and folded forms of a protein. Peptide H-bonds are likely to make a significant contribution to the energetics of folding because there are so many of them: about two-thirds of the residues in folded proteins make peptide H-bonds [7]. Peptide backbone solvation can be predicted from electrostatic algorithms but experimental measurements of peptide solvation are limited to amides as models for the peptide group.

This chapter gives a brief historical introduction to the ''weak interactions in protein folding'' and then discusses current issues. It is not a comprehensive review and only selected references are given. The term ''weak interaction'' is somewhat misleading because these interactions are chiefly responsible for the folded struc-

Protein Folding Handbook. Part I. Edited by J. Buchner and T. Kiefhaber

ISBN: 3-527-30784-2

tures of proteins. The problem of evaluating them quantitatively lies at the heart of the structure prediction problem. Although there are methods such as homology modeling for predicting protein structures that bypass evaluation of the weak interactions, de novo methods of structure prediction generally rely entirely on evaluating them. Thus, the problem of analyzing the weak interactions will continue to be a central focus of protein folding research until it is fully solved.

6.2 Hydrophobic Free Energy, Burial of Nonpolar Surface and van der Waals Interactions

6.2.1 History

The prediction in 1959 by Walter Kauzmann [1] that hydrophobic free energy would prove to be a main factor in protein folding was both a major advance and a remarkable prophecy. No protein structure had been determined in 1959 and the role of hydrophobic free energy in structure formation could not be deduced by examining protein structures. The first protein structure, that of sperm whale myoglobin, was solved at 2 Å resolution only in 1960 [8]. On the other hand, the predicted structure of the α-helix [9] given by Pauling and coworkers in 1951, which was widely accepted, suggested that peptide H-bonds would prove to be the central interaction governing protein folding. Peptide H-bonds satisfied the intuitive belief of protein scientists that the interactions governing protein folding should be bonds with defined bond lengths and angles. This is not a property of hydrophobic free energy.

Kauzmann [1] used the ambitious term ''hydrophobic bonds,'' probably aiming to coax protein scientists into crediting their importance, while Tanford [10] introduced the cautious term ''the hydrophobic effect.'' ''Hydrophobic interaction'' has often been used because a factor that drives the folding process should be an interaction. However, hydrophobic interaction is also used with a different meaning than removal of nonpolar surface from contact with water, namely the direct interaction of nonpolar side chains with each other. The latter topic is discussed under the heading ''van der Waals interactions.'' The term ''hydrophobic free energy'' is used here to signify that nonpolar groups help to drive the folding process. Tanford [10] points out that a hydrophobic molecule has both poor solubility in water and good solubility in nonpolar solvents. Thus, mercury is not hydrophobic because it is insoluble in both solvents. Early work leading to the modern view of hydrophobic free energy is summarized by Tanford [11] and a recent discussion by Southall et al. [12] provides a valuable perspective.

6.2.2 Liquid–Liquid Transfer Model

Kauzmann [1] proposed the liquid–liquid transfer model for quantitating hydrophobic free energy. His proposal was straightforward. Hydrophobic molecules

prefer to be in a nonpolar environment rather than an aqueous one and the free energy difference corresponding to this preference should be measurable by partitioning hydrocarbons between water and a nonaqueous solvent. Nozaki and Tanford [13] undertook a major program of using the liquid–liquid transfer model to measure the contributions of nonpolar and partially nonpolar side chains to the energetics of folding. They measured the solubilities of amino acids with free α-COO^- and α-NH_3^+ groups, while Fauchère and Pliska [14] later studied amino acids with blocked end groups, because ionized end groups interfere with the validity of assuming additive free energies of various groups. They measured partitioning of solutes between water and *n*-octanol (saturated with water), which is less polar than the two semi-polar solvents, ethanol and dioxane, used by Nozaki and Tanford [13]. Wimley et al. [15] used a pentapeptide host to redetermine the partition coefficients of the amino acid side chains between water and water-saturated *n*-octanol and they obtained significantly different results from those of Fauchère and Pliska. They emphasize the effect of neighboring side chains (''occlusion'') in reducing the exposure of a given side chain to water. Radzicka and Wolfenden [16] studied a completely nonpolar solvent, cyclohexane, and observed that the transfer free energies of hydrocarbons are quite different when cyclohexane is the nonaqueous solvent as compared to *n*-octanol.

In Figure 6.1 the transfer free energies of model compounds for nonpolar amino

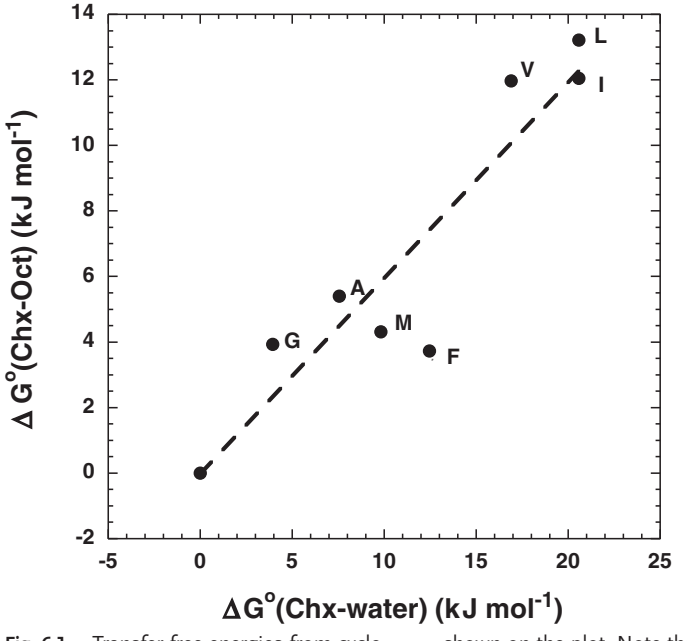

Fig. 6.1. Transfer free energies from cyclohexane to water compared with ones from cyclohexane to water-saturated *n*-octanol (data from Ref. [16]). The model solutes undergoing transfer represent the amino acid side chains shown on the plot. Note that the transfer free energies between cyclohexane and *n*-octanol are more than half as large as those from cyclohexane to water.

acid side chains are compared using either cyclohexane or *n*-octanol as the nonaqueous solvent [16]. If different nonaqueous solvents may be used equally well to model the hydrophobic core of a protein, then the transfer free energies of hydrocarbons from cyclohexane to *n*-octanol should be small compared with the transfer free energies from cyclohexane to water. Figure 6.1 shows this is not the case: the transfer free energies measured between cyclohexane and *n*-octanol are more than half as large as the ones between cyclohexane and water. Thus, these results pose the first serious question about the use of the liquid–liquid transfer model: which nonaqueous solvent should be used to model the hydrophobic core and how valid are the results if no single solvent is a reliable model?

6.2.3
Relation between Hydrophobic Free Energy and Molecular Surface Area

A second important step in quantifying hydrophobic free energy was taken when several authors independently observed that the transfer free energy of a nonpolar solute is nearly proportional to the solute's surface area for a homologous series of solutes [17–19]. This observation agrees with the intuitive notion that the transfer free energy of a solute between two immiscible solvents should be proportional to the number of contacts made between solute and solvent (however, see Section 6.2.6). Lee and Richards [20] in 1971 developed an automated algorithm for measuring the water-accessible surface area (ASA) of a solute by rolling a spherical probe, with a radius equivalent to that of a water molecule (1.4 Å) (10 Å = 1 nm), over its surface. Their work showed how to make use of the surface area of a solute to analyze its hydrophobicity. Proportionality between transfer free energy and ASA does not apply to model compounds containing polar side chains because polar groups interact strongly and specifically with water.

A plot of transfer free energy versus ASA is shown in Figure 6.2 for linear alkanes. The slope of the line for linear (including branched) hydrocarbons is 31 cal mol^{-1} $Å^{-2}$ (1.30 J mol^{-1} nm^{-2}) when partition coefficients on the mole fraction scale [21] are used. Earlier data for the solubilities of liquid hydrocarbons in water are used to provide the transfer free energies. In Figure 6.2 the transfer free energy is nearly proportional to the ASA of the solute. The line does not pass through (0,0), but deviation from strict proportionality is not surprising for small solutes [22].

Hermann [22] points out that linear hydrocarbons exist in a broad range of configurations in solution and each configuration has a different accessible surface area. He also points out [17] that the transfer free energy arises from a modest difference between the unfavorable work of making a cavity in a liquid and the favorable van der Waals interaction between solute and solvent. Consequently, a moderate change in the van der Waals interaction can cause a large change in the transfer free energy. Tanford [10] analyzes the plot of transfer free energy versus the number of carbon atoms for hydrocarbons of various types, and discusses data for the different slopes of these plots.

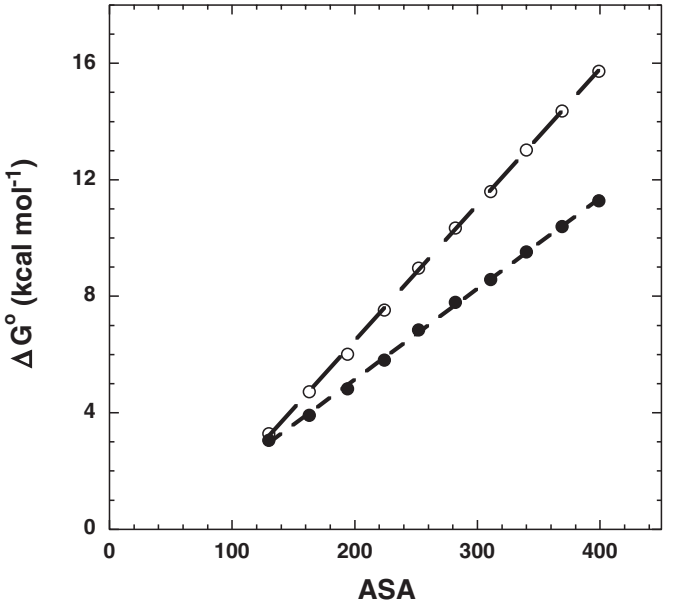

Fig. 6.2. Transfer free energies of linear alkanes (from 1 to 10 carbon atoms) from liquid alkane to water, measured from hydrocarbon solubility in water. They are plotted against water-accessible surface area (ASA in $Å^2$). Data are from Ref. [21]. The uncorrected transfer free energies (filled circles) refer to the mole fraction scale while the corrected values (open circles) refer to the molarity scale and are corrected for the ratio of molecular volumes, solute/solvent, according to Sharp et al. [21]. The data here and in Figure 6.3 are given in kcal mol^{-1} to conform with the literature on this subject. Note that the plots do not pass through 0,0 and note the larger slope (47 cal mol^{-1} $Å^{-2}$) of the corrected plot versus the uncorrected plot (31 cal mol^{-1} $Å^{-2}$).

6.2.4
Quasi-experimental Estimates of the Work of Making a Cavity in Water or in Liquid Alkane

In modern solution chemistry, the solvation free energy of a solute is defined as its transfer free energy from the gas phase into the solvent, when the appropriate standard state concentration (1 M) is used in each phase, as specified by Ben-Naim and Marcus [23]. Gas–liquid transfer free energies are used to analyze the nature of liquid–liquid transfer free energies. The reason for adopting the 1 M standard state concentration in both the gas and liquid phases is to ensure that the density of the solute is the same in both phases at the standard state concentration. Then the transfer free energy gives the free energy change for transferring the solute from a fixed position in the gas phase to a fixed position in the liquid phase [23]. The solute in the gas phase can be treated as an ideal gas [24, 25]

and the nonideal behavior of real gases at 1 M concentration can be omitted from consideration.

Modern theories of solvation indicate that the gas–liquid transfer process can be formally divided into two steps of an insertion model of solvation: see discussion by Lee [24, 25] and basic theory by Widom [26]. In step 1 thermal fluctuations create a cavity in the liquid with a size and shape appropriate for containing the solute. The structure of the liquid undergoes reorganization to make the cavity [24]. In step 2 the solute is inserted into the cavity, van der Waals interactions occur between the solute and the solvent, and the solvent structure undergoes further reorganization at the surface of the cavity. Lee [24] determines quasi-experimental values for the entropy and enthalpy changes in the two steps of the insertion model: (1) making a cavity in the liquid, and (2) inserting the solute into the cavity. Experimental transfer data are used for each of five alkanes undergoing transfer from the gas phase to the liquid phase, either to water or to neat liquid alkane. The transfer thermodynamics then are combined with literature estimates for the van der Waals interaction energies, obtained by Jorgensen and coworkers [27] from Monte-Carlo simulations. The results give quasi-experimental estimates of the enthalpy and entropy changes in each step of the insertion model. Table 6.1 gives these values for the free energy cost of making a cavity to contain the alkane solute both in water and in liquid alkane. The 1977 theory of hydrophobic solvation by Pratt and Chandler [28] divides the process of solvation into the two steps of cavity formation and solute insertion, and the authors consider the rules for separating the solvation process into these two steps. The two steps of dissolving an alkane in water have also been simulated by molecular dynamics and the results analyzed by the free energy perturbation method [29].

The following conclusions can be drawn from Lee's data [24, 25]. (1) The work of making a cavity in water is much larger than in liquid alkane and this difference

Tab. 6.1. Quasi-experimental estimates of the free energy of cavity formation and simulation-based results for van der Waals interaction energies between solvent and solute[a].

Hydrocarbon	ΔG_c*(water)*	ΔG_c*(alkane)*	E_a*(water)*	E_a*(alkane)*
Methane	20.4	9.6	−12.1	−14.7
Ethane	27.7	18.1	−20.1	−26.8
Propane	35.8	23.7	−27.6	−34.4
Isobutane	42.4	24.4	−32.7	−35.1
Neopentane	46.5	27.6	−36.0	−39.6

[a] Values in kJ mol^{-1}. ΔG_c is the free energy cost of making a cavity in the solvent to contain the hydrocarbon solute, from a study by Lee [24]. E_a is the van der Waals interaction energy between solute and solvent; values from Lee [24], based on parameters from a Monte-Carlo simulation study by Jorgensen and coworkers [27]. For water as solvent, conditions are 25 °C, 1 atm; for neat hydrocarbon as solvent, either the temperature or pressure is chosen that will liquefy the hydrocarbon.

is the major factor determining the size of the hydrophobic free energy in liquid–liquid transfer. For example, it costs 46.5 kJ mol^{-1} to make a cavity for neopentane in water but only 27.6 kJ mol^{-1} in liquid neopentane. To understand hydrophobic free energy, it is necessary first of all to understand the free energies of cavity formation in water and in nonpolar liquids. The work of making a cavity in water is large because it depends on the ratio of cavity size to solvent size [30, 31] and water is a small molecule (see Section 6.2.7). It is more difficult to make a cavity of given size by thermal fluctuations if the solvent molecule is small. (2) The work of making a cavity in a liquid is chiefly entropic [24], while the van der Waals interactions between solute and solvent are enthalpic. (3) The van der Waals interaction energy between an alkane solute and water is nearly the same as between the alkane solute and liquid alkane (see Table 6.1). For example, the interaction energies between neopentane and water versus neopentane and liquid neopentane are -36.0 kJ mol^{-1} and -39.6 kJ mol^{-1} [24]. Earlier, Tanford [32] used interfacial tensions to show that the attractive force between water and hydrocarbon is approximately equal, per unit area, to that between hydrocarbon and hydrocarbon. Scaled particle theory predicts well the work of making a cavity either in water or in liquid alkane [24], but it predicts only semi-quantitatively the enthalpy of solvent reorganization for these cavities.

6.2.5
Molecular Dynamics Simulations of the Work of Making Cavities in Water

In 1977 a physico-chemical theory of hydrophobic free energy by Pratt and Chandler [28] already gave good agreement between predicted and observed transfer free energies of linear alkanes, both for gas–liquid and liquid–liquid transfer. Molecular dynamics simulations can be used to obtain the free energy cost of cavity formation in liquids and the results are of much interest because they basically depend only on the specific water model used for the simulations. It should be kept in mind that the physical properties of water used as constraints when constructing water models do not normally include surface tension, and consequently good agreement between the predicted and known surface tension of water is not necessarily to be expected. (For macroscopic cavities, the work of making a cavity equals surface tension times the surface area of the cavity.) In 1982 Berendsen and coworkers [33] determined the free energy of cavity formation in water for cavities of varying size and compared the results to values predicted by scaled particle theory, with reasonable agreement. Remarkably, the comparison with scaled particle theory also gave a value for the surface tension of water close to the known value. Because of the importance of the problem, simulations of cavity formation in water by molecular dynamics continued in other laboratories (see references in [34]). An important result is the development by Hummer and coworkers [34] of an easily used information-theory model to represent the results for water in the cavity size range of interest. Some applications of the information theory model are mentioned below.

6.2.6 Dependence of Transfer Free Energy on the Volume of the Solute

Evidence is discussed in Section 6.2.3 that the transfer free energy is correlated with the surface area (ASA) of the solute. Because it is straightforward to compute ASA [20] from the structure of a peptide or protein, this correlation provides a very useful means of computing the change in hydrophobic free energy that accompanies a particular change in conformation. In recent years, evidence has grown, however, that the transfer free energy of a nonpolar solute depends on its size and shape for reasons that are independent of hydrophobic free energy. In 1990 DeYoung and Dill [35] brought the problem forcibly to the attention of protein chemists by demonstrating that the transfer free energy of benzene from liquid hydrocarbon to water depends on the size and shape of the liquid hydrocarbon molecules. Section 6.2.2 reviews evidence that liquid–liquid transfer free energies depend on the polarity (and perhaps on water content) of the nonaqueous solvent. But in the study by DeYoung and Dill [35] the size and shape of the nonaqueous solvent molecules affect the apparent hydrophobic free energy. A large literature has developed on this subject and recently Chan and Dill [36] have provided a comprehensive review.

Chandler [37] briefly discusses the reason why solvation free energy in water depends on the volume of a sufficiently small nonpolar solute. This dependence can be found in both the information-theory model [34] and the Lum-Chandler-Weeks theory [38] of hydrophobic solvation. Effects of the size and shape of the solute are taken into account in the Pratt and Chandler theory [28].

Stimulated by the results of DeYoung and Dill [35], Sharp and coworkers [21] used a thermodynamic cycle and an ideal gas model to relate the ratio of sizes, solute to solvent, to the transfer free energy for gas–liquid transfer. They conclude that the transfer free energy depends on the ratio of solute/solvent molecular volumes. Their paper has generated much discussion and controversy. In 1994 Lee [39] gave a more general derivation for the transfer free energy, based on statistical mechanics, and considered possible assumptions that will yield the result of Sharp et al. [21].

The Lum-Chandler-Weeks theory of hydrophobic solvation [38] predicts a crossover occurring between the solvation properties of macroscopic and microscopic cavities when the cavity radius is 10 Å. Huang and Chandler [40] point out that the ratio of the work of making a cavity in water to its surface area reaches a plateau value for radii above 10 Å, and this value agrees with the known surface tension of water at various temperatures. On the other hand, the hydrophobic free energy found from hydrocarbon transfer experiments increases slightly with temperature (see Section 6.2.9), implying that the work of making a sufficiently small cavity in water increases with temperature. Chandler [37] explains that these two different outcomes, which depend on solute size, arise naturally from the H-bonding properties of water, because the sheath of water molecules that surrounds a nonpolar solute remains fully H-bonded when the solute is sufficiently small but

not when the solute radius exceeds a critical value. Southall and Dill [41] find that a highly simplified model of the water molecule (the "Mercedes-Benz" model), which reproduces several remarkable properties of water, also predicts such a transition from microscopic to macroscopic solvation behavior.

The question of interest to protein chemists is: should a transfer free energy be corrected for the ratio of solute/solvent volumes or not? Figures 6.2 and 6.3 compare the uncorrected with the volume-corrected plots of transfer free energy versus ASA, for both liquid–liquid transfer (Figure 6.2) and gas–liquid transfer (Figure 6.3). Both correlations show good linearity. However, the hydrophobic free energy corresponding to a given ASA value is substantially larger if the volume-corrected transfer free energy is used (see Ref. [21]). Whether the volume correction should be made remains controversial. Scaled particle theory emphasizes the role of surface area in determining the free energy of cavity formation while the information-theory model [34] and the Lum-Chandler-Weeks theory [38] both emphasize the

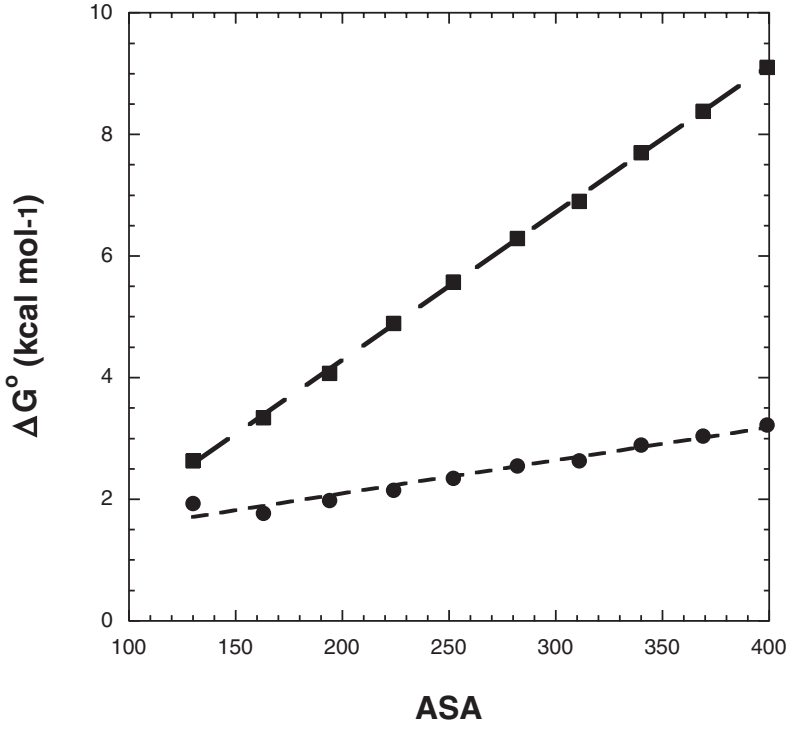

Fig. 6.3. Transfer free energy from the gas phase to liquid water for linear alkanes (from 1 to 10 carbon atoms) plotted against water-accessible surface area (in $Å^2$). Data are from Ref. [21]. The uncorrected transfer free energies (filled circles) refer to the mole fraction scale while the corrected values (filled squares) refer to the molarity scale and are volume-corrected according to Ref. [21]. The slopes of the lines are 5.5 cal mol^{-1} $Å^{-2}$ (uncorrected) and 24 cal mol^{-1} $Å^{-2}$ (corrected).

role of molecular volume. The molecular dynamics simulations of Berendsen and coworkers [33] were interpreted by scaled-particle theory while those of Hummer and coworkers were interpreted by the information-theory model [34], which has much in common with the Lum-Chandler-Weeks theory. Pohorille and Pratt [42] give a detailed discussion of how the scaled particle interpretation [33] may be reconciled with their own analysis.

6.2.7 Molecular Nature of Hydrophobic Free Energy

The molecular nature of hydrophobic free energy has been controversial for a long time [3, 4, 11, 12]. A long-standing proposal, supported by liquid–liquid transfer data at 25 °C [1] and by simulation results [27], is that the arrangement of water molecules in the solvation shell around a dissolved hydrocarbon is entropically unfavorable. Consequently the unfavorable entropy change for dissolving a hydrocarbon in water should provide the driving force for expelling the solute from water. This proposal required modification when it was learned that the hydrophobic free energy found from liquid–liquid transfer is purely entropic only at an isolated temperature near room temperature [43]. Hydrophobic free energy becomes increasingly enthalpy-driven as the temperature increases and it becomes entirely enthalpic upon reaching its maximum value at a temperature above 100 °C (see Section 6.2.9). The characteristic property of hydrophobic free energy that dominates its temperature-dependent behavior is the large positive value of ΔC_p, the difference between the heat capacities of the hydrocarbon in water and in the nonaqueous solvent.

In contradiction to the thesis developed by Kauzmann [1], Privalov and Gill [3, 4] proposed that the hydration shell surrounding a dissolved hydrocarbon tends to stabilize the hydrocarbon in water while the van der Waals interactions between the hydrocarbon solute and the nonaqueous solvent account for the hydrophobicity of the solute. They assume that the van der Waals interaction energy between solute and solvent is large in the nonaqueous solvent compared to water. However, Lee's data (see Table 6.1) show that the large work of making a cavity in water is responsible for the hydrophobic free energy while a hydrocarbon solute makes nearly equal van der Waals interactions with water and with a liquid hydrocarbon [24]. Privalov and Gill coupled two proposals: (1) the van der Waals interactions between nonpolar side chains drive the formation of the hydrophobic core of a protein, and (2) the hydration shell surrounding a dissolved hydrocarbon tends to stabilize it in water. The latter proposal is now widely believed to be incorrect but there is increasing interest in the first proposal.

There are restrictions both on the possible orientations of water molecules in the solvation shell around a hydrocarbon solute and on the hydrogen bonds they form [12]. Models suggesting how these restrictions can explain the large positive values of ΔC_p found for nonpolar molecules in water have been discussed as far back as 1985, in Gill's pioneering study of the problem [44]. Water-containing clathrates of nonpolar molecules surrounded by a single shell of water molecules have been

crystallized and their X-ray structures determined [45]. The water molecules form interconnected 5- and 6-membered rings. Water molecules in ice I are oriented tetrahedrally in a lattice and the oxygen atoms form six-membered rings [45].

In 1985 Lee [30] used scaled particle theory to argue that the low solubilities of nonpolar solutes in water, and the magnitude of hydrophobic free energy, depend strongly on the solute/solvent size ratio, and he reviews prior literature on this subject. Rank and Baker [31] confirmed his conclusion with Monte-Carlo simulations of the potential of mean force between two methane molecules in water. The remarkable temperature-dependent properties of hydrophobic free energy (see Section 6.2.9) are determined, however, chiefly by ΔC_p, which depends on the hydrogen bonding properties of water according to most authors (see Ref. [46]).

6.2.8
Simulation of Hydrophobic Clusters

Formation of the hydrophobic core of a protein during folding must proceed by direct interaction between nonpolar side chains. Yet direct interaction between two hydrocarbon molecules in water is known to be extremely weak (compare Ref. [28]). Benzene dimers or complexes between benzene and phenol in water are barely detectable [47]. Raschke, Tsai and Levitt used molecular dynamics to simulate the formation of hydrophobic clusters, starting from a collection of isolated hydrocarbon molecules in water [48]. Their results give an interesting picture of the thermodynamics of the process. The gain in negative free energy from adding a hydrocarbon molecule to a hydrocarbon cluster in water increases with the size of the cluster until limiting behavior is reached for large clusters. The simulations of cluster formation yield a proportionality between transfer free energy and burial of nonpolar surface area that is similar to the one found from liquid–liquid transfer experiments [48]. The simulation results make the important point that a standard molecular force field is able to simulate the thermodynamics of hydrophobic free energy when a hydrophobic cluster is formed in water [48]. Rank and Baker [49] found that solvent-separated hydrocarbon clusters precede the desolvated clusters found in the interior of large hydrocarbon clusters. Thus, a hydrocarbon desolvation barrier may be important in the kinetics of protein folding [49]. In both simulation studies [48, 49], the authors find that the molecular surface area (defined by Richards [50]) is more useful than water-accessible surface area in analyzing cluster formation.

6.2.9
ΔC_p and the Temperature-dependent Thermodynamics of Hydrophobic Free Energy

Although the gas–liquid transfer model is now often used instead of the liquid–liquid transfer model to analyze hydrophobic free energy, nevertheless thermodynamic data for the transfer of liquid hydrocarbons to water are remarkably successful in capturing basic thermodynamic properties of hydrophobic free energy in protein folding. Figure 6.4A shows ΔH versus temperature for the process

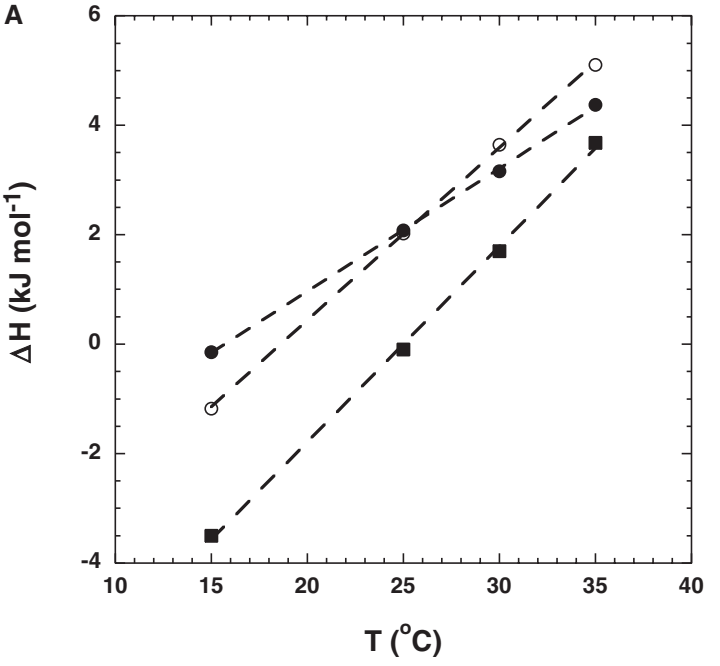

Fig. 6.4. (A) Enthalpy of transfer plotted against temperature for three liquid hydrocarbons (benzene (filled circles), ethylbenzene (open circles) and cyclohexane (filled squares)) undergoing transfer from liquid hydrocarbon to water. Data are from Ref. [51]. Note that the plots are straight lines in this temperature range, where ΔC_p = constant, and ΔH passes through 0 near room temperature.

of transferring three hydrocarbon solutes from neat liquid hydrocarbon to water, taken from the calorimetric study by Gill and coworkers [51]. These results illustrate the large positive values of ΔC_p found when nonpolar molecules are dissolved in water, a property discovered by Edsall [52] in 1935. Although ΔH depends strongly on temperature, ΔC_p (the slope of ΔH versus T) is nearly constant in the temperature range 15–50 °C (see figure 12 of Ref. [3]). ΔC_p decreases perceptibly at temperatures above 50 °C [3, 4].

The following thermodynamic expressions take a simple form when ΔC_p is constant. A strong dependence of ΔH on temperature must be accompanied by a strong dependence of ΔS° on temperature. When ΔC_p is constant, then:

$$\Delta H(T_2) = \Delta H(T_1) + \Delta C_p(T_2 - T_1) \tag{1}$$

$$\Delta S^\circ(T_2) = \Delta S^\circ(T_1) + \Delta C_p T_2 \ln(T_2/T_1) \tag{2}$$

Figure 6.4B compares $\Delta H, T\Delta S^\circ$ and ΔG° as functions of temperature for the transfer of benzene from liquid benzene to water. (The behavior of a liquid alkane,

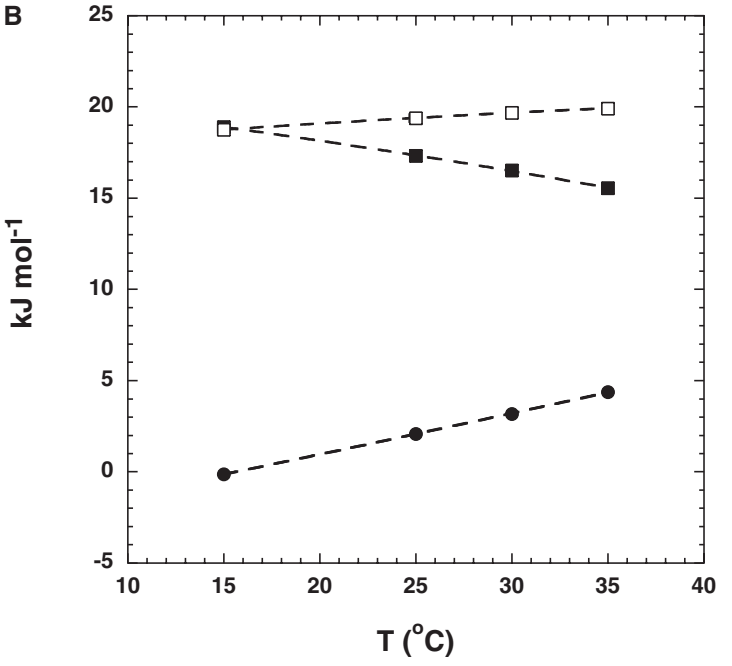

Fig. 6.4. (B) Transfer free energy and the contributions to free energy from ΔH (filled circles) and $T\Delta S$ (filled squares), plotted against temperature, for the transfer of benzene from liquid benzene to water. Data are from Ref. [43]. Note that the relative contribution to ΔG (open squares) from ΔH increases with temperature while the contribution of $T\Delta S$ decreases, and ΔG increases only slightly with temperature. The plots illustrate how entropy–enthalpy compensation affects hydrophobic free energy.

pentane, is fairly similar to that of the aromatic hydrocarbon benzene, see figure 12 of Ref. [3].) Substituting Eqs (1) and (2) into the standard relation

$$\Delta G^\circ = \Delta H - T\Delta S^\circ \tag{3}$$

gives

$$\Delta G^\circ(T_2) = \Delta G^\circ(T_1) + \Delta C_p(T_2 - T_1) - T_2\Delta C_p \ln(T_2/T_1) \tag{4}$$

Equation (4) shows that the ΔC_p-induced changes in ΔH and ΔS° with temperature tend to compensate each other to produce only a small net increase in $-\Delta G^\circ$ as the temperature increases. This property of enthalpy–entropy compensation is one of the most characteristic features of hydrophobic free energy. (ΔG and ΔS depend strongly on the solute concentration and the superscript $^\circ$ emphasizes that ΔG° and ΔS° refer to the standard state concentration.)

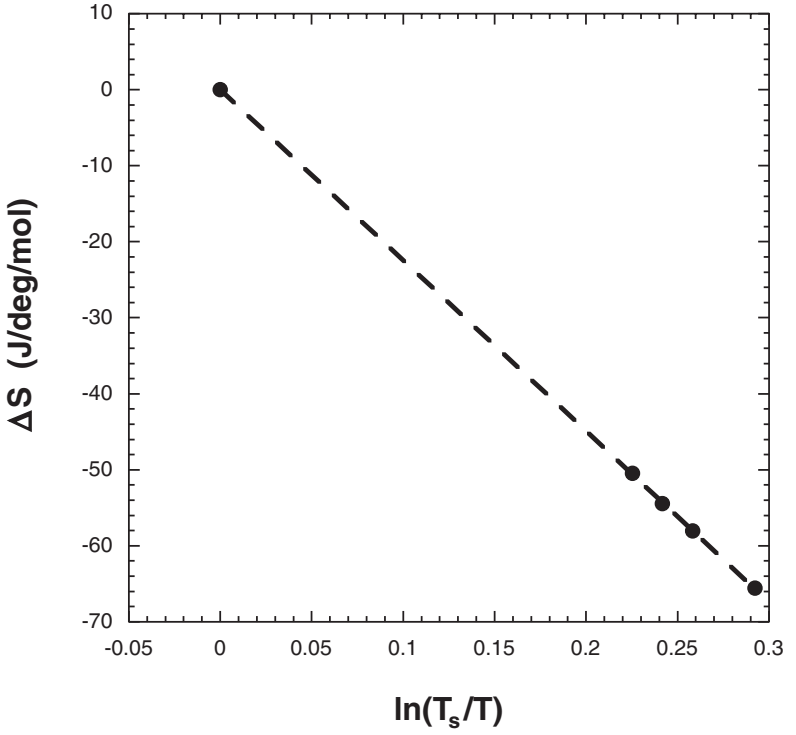

Fig. 6.5. Decrease of $-\Delta S$ towards 0 as temperature (K) approaches T_s (386 K), the temperature at which $\Delta S = 0$. The transfer of benzene from liquid benzene to water is shown. Data are from Ref. [43]. Note the linear decrease in $-\Delta S$ with temperature [43], which depends on using data from the temperature range (15–50 °C) where ΔC_p = constant (see figure 12 of Ref. [3]). $T_s = 386$ K is an average value for several hydrocarbon solutes [43].

Figures 6.4A and 6.4B illustrate some basic thermodynamic properties of hydrophobic free energy as modeled by liquid–liquid transfer. The enthalpy change ΔH is zero near room temperature (the exact temperature depends on the hydrocarbon) and the transfer process is entropy-driven around room temperature. However, as the temperature increases above 25 °C, the transfer process gradually becomes enthalpy-driven. A surprising property is that of entropy convergence: if ΔC_p = constant, then different hydrocarbons share a convergence temperature at which $\Delta S^\circ = 0$ (386 K or 113 °C) [43]. Data taken between 15 and 35 °C are extrapolated linearly versus ln T in Figure 6.5, according to Eqn (2). When the gradual decrease in ΔC_p at temperatures above 50 °C [3] is taken into account by using a curved extrapolation, hydrocarbon data for ΔS° still approach a common value near T_s, the temperature at which the entropy change is 0, which is approximately 140 °C [3, 4]. The property of entropy convergence is predicted both by the information-theory model [53] and scaled particle theory [54].

Privalov [55] discovered in 1979 that values for the specific entropy change on protein unfolding converge near 113 °C when results for some different proteins

are extrapolated linearly versus temperature. His observation, taken together with the entropy convergence shown by hydrocarbon solutes, suggests that the hydrophobic entropy change of a protein unfolding reaction might be removed by extrapolating the total entropy change to T_s for hydrocarbon transfer [43]. However, when Robertson and Murphy [56] analyzed unfolding data from several laboratories, they found more scatter in the data and they did not find a common intercept for the specific entropy change on protein unfolding. The extrapolation offers a possible route to determining the change in conformational entropy on unfolding, one of the basic unsolved problems in protein folding. The hydrophobic contribution to the entropy of unfolding is opposite in sign and, at room temperature, comparable in size to the change in conformational entropy [43].

Schellman [57] points out that there are advantages to using $\Delta G/T$ as an index of stability instead of ΔG itself when considering the temperature dependence of hydrophobic free energy. The low solubilities of hydrocarbons in water have minimum values near room temperature, corresponding to the maximum values of $\Delta G/T$ and to $\Delta H = 0$, whereas ΔG itself increases steadily but slowly with temperature until it reaches a maximum value above 100 °C, at a temperature where $\Delta S = 0$.

A standard test of whether the hydrophobic free energy found from liquid–liquid transfer experiments applies to protein folding experiments is to compare the unfolding free energy change caused by a ''large to small'' mutation with the free energy change predicted from the change in ASA on unfolding. Pace [58] surveyed the literature on this subject (see also Ref. [21]). He concludes there is good agreement provided the proportionality coefficient between $\Delta\Delta G$ and ΔASA is the volume-corrected value 47 cal mol^{-1} Å^{-2} [21]. However, this type of comparison between liquid–liquid transfer and protein folding thermodynamics is complicated by the presence of cavities produced when large-to-small mutations are made [59].

A direct test of the correspondence between liquid–liquid transfer thermodynamics and protein folding is to compare the value of ΔC_p for a protein unfolding experiment with the value predicted from the change in ASA on unfolding. No other factor besides the burial of nonpolar surface area is known to make a significant positive contribution to ΔC_p. This comparison was studied in 1991 by Record and coworkers [60], who found that values of ΔC_p measured in unfolding experiments do agree with the ones predicted from the change in nonpolar ASA on unfolding. The issue became somewhat complicated, however, by contemporary work showing that polar groups (and especially the peptide group) contribute negatively to ΔC_p for unfolding. Makhatadze and Privalov [61] gave extensive model compound data and used them to estimate contributions to the enthalpy and heat capacity changes on unfolding of all groups present in proteins. Freire and coworkers [62] used empirical calibration of protein unfolding data to give the contributions to ΔC_p expected from the changes in polar and nonpolar ASA on unfolding. The issue is seriously complicated, however, by evidence from the study of model compounds that the enthalpies of interaction with water are not related in any simple way to polar ASA: see Table 6.2 and Section 6.3.2. To make progress in analyzing this problem, it is important to get data for the ΔC_p values accompanying unfold-

ing of peptide helices and progress has been reported recently by Richardson and Makhatadze [63].

A long-standing puzzle in comparing the thermodynamics of protein unfolding with those of liquid–liquid transfer has been the unfolding results produced by high pressures [64]. The information-theory model [65] provides new insight into the problem by predicting that water penetrates the hydrophobic cores of proteins during pressure-induced unfolding, as observed experimentally [66], but does not penetrate the hydrophobic cores during thermal unfolding.

6.2.10 Modeling Formation of the Hydrophobic Core from Solvation Free Energy and van der Waals Interactions between Nonpolar Residues

As explained above, solvation free energies of solutes are based on gas–liquid transfer data. They provide an alternative model for the energetics of forming the hydrophobic core of a protein. Compared with the liquid–liquid transfer model, this approach has two major advantages. (1) It considers the van der Waals interactions explicitly, and (2) it avoids the question of which nonaqueous solvent to use for modeling the hydrophobic core. This approach was pioneered by Ooi and Oobatake [67, 68] and by Makhatadze and Privalov [61]. Simonson and Brünger [69] analyze model compound data for gas–liquid transfer. They report that transfer free energies for gas to liquid transfer of cyclic hydrocarbons fall well below the line for linear alkanes when plotted against ASA.

The use of gas–liquid transfer to probe the energetics of folding is illustrated in the cycle shown in Scheme 6.1, in which the native protein (N) is formed by folding the unfolded protein (U) either in the gas phase (g) or in aqueous solution (aq). The cycle is completed by the process of transferring U from aqueous solution to the gas phase and by transferring N from the gas phase back to aqueous solution. Only the nonpolar side chains and nonpolar moieties of polar side chains are considered here. Transfer of the polar peptide NH and CO groups between the gas phase and aqueous solution is considered in Section 6.3.8, together with formation of the peptide H-bonds. The polar moieties of polar side chains are supposed to be fully exposed to water in both U and N, and so their transfer between aqueous solution and the gas phase cancels energetically in steps 1 and 3. The change in conformational entropy when the unfolded polypeptide U folds to the native protein N is supposed to be the same in steps 2 and 4.

In Scheme 6.1, two processes contribute to ΔG°_{UN}, the standard free energy

$$\begin{array}{ccc} \mathrm{U\ (g)} & \Leftarrow (2) \Rightarrow & \mathrm{N\ (g)} \\ \Uparrow\Downarrow (1) & & \Uparrow\Downarrow (3) \\ \mathrm{U\ (aq)} & \Leftarrow (4) \Rightarrow & \mathrm{N\ (aq)} \end{array}$$

Scheme 6.1

change for folding in aqueous solution. Process A is burial (removal from water) of nonpolar side chains (or moieties) in steps 1 and 3, and process B is formation of van der Waals interactions between nonpolar side chains (or moieties) in step 2. Let ΔG_{bur} and ΔG_{vdw} be the contributions to ΔG°_{UN} from processes A and B in Eq. (5).

$$\Delta G^{\circ}_{UN} = \Delta G_{bur} + \Delta G_{vdw} \tag{5}$$

Let ΔASA be the net change in nonpolar solvent-accessible surface area in steps $1 + 3$. Evidence is presented above that ΔG_{bur} can be related to ΔASA even for microscopic cavities. Thus ΔG_{bur} can be represented by

$$\Delta G_{bur} = \beta \Delta \text{ASA} \tag{6}$$

in which β is the proportionality coefficient between ΔG°_{solv} and ASA for alkanes in transfer experiments from the vapor phase to aqueous solution. Figure 6.3 shows good linearity between ΔG°_{solv} and ASA for several alkanes, and β is reasonably constant. However, the value of β changes substantially (from 5.5 to 24 cal mol^{-1} Å^{-2} [21]) when volume-corrected transfer free energy is used. Evaluation of ΔG_{vdw} depends sensitively on parameters that are difficult to determine experimentally, and there is little discussion in the literature of how mutations cause ΔG_{vdw} to vary. See, however, the discussion of ΔG_{vdw} values for selected proteins by Makhatadze and Privalov [61] and note that the *number* of van der Waals contacts is being discussed in mutational studies of packing [70].

For the process of forming the hydrophobic core, ΔG_{vdw} can be estimated approximately in the following manner. First, consider the empirical relation between ΔG°_{UN} and ΔASA given by the liquid–liquid transfer model.

$$\Delta G^{\circ}_{UN} \sim B(\Delta \text{ASA}) \tag{7}$$

In Eq. (7), ΔASA is the net value of ASA buried upon folding and B is the proportionality factor between liquid–liquid transfer free energy and ASA. Combining Eqns (5)–(7) gives:

$$\Delta G_{vdw} \sim (B - \beta)\Delta \text{ASA} \tag{8}$$

The value of $(B - \beta)$ depends on whether or not the volume correction is made to the transfer free energies. If the volume correction is made, then $(B - \beta) = 47 - 25 = 22$ cal mol^{-1} Å^{-2} [21] and ΔG_{vdw} should account for approximately $22/47 = 47\%$ of the free energy change on forming the hydrophobic core. If the volume correction is not made and the mole fraction scale is used for computing transfer free energies, then $(31 - 5)/31$ [21] $= 84\%$, the percentage of ΔG°_{UN} that is assigned to ΔG_{vdw}. This argument follows the one given by Havranek and Harbury [71], who used different numbers for B and β from the ones given by Sharp et al. [21].

Data for the melting of solid crystalline alkanes show that ΔH is substantial and favors the solid alkane, but ΔG for melting is small because there is a substantial ΔS that favors the liquid alkane [72]. These results have been used to argue that a liquid hydrocarbon should model satisfactorily the hydrophobic core of a protein [72], and therefore the van der Waals interactions need not be considered explicitly.

6.2.11 Evidence Supporting a Role for van der Waals Interactions in Forming the Hydrophobic Core

An important role for van der Waals interactions in protein folding is suggested by the unusual close-packed arrangement of the side chains in folded proteins. This argument was pointed out in 1971 by Klapper, who compares the protein core to a wax ball rather than an oil drop [73], and in 1977 by Richards, who compares the protein core to an organic crystal [50]. The fraction of void space in folded proteins is quite small and comparable to that in close-packed spheres, whereas there is a sharp contrast between the small void space in folded proteins and the large void space in nonpolar liquids, as pointed out by these authors. In 1994 Chothia and coworkers [74] made a detailed study of the volumes of aliphatic side chains inside proteins and found they are substantially smaller than in aqueous solution. Water molecules are nevertheless rather well packed around hydrocarbons in aqueous solution and hydrocarbons occupy larger volumes in nonpolar solvents than in water, as pointed out by Klapper [73], who found good agreement between experimental data and predictions based on scaled particle theory.

Stites and coworkers have made extensive mutational experiments on the hydrophobic core of staphylococcal nuclease (SNase) [70, 75] including many single, double, triple, and quadruple mutants. The authors measure interaction energies by taking the difference between the ΔG° values of two single mutants and the double mutant, and so forth. Their overall results suggest that the packing arrangement of nonpolar side chains in the core is an important determinant of SNase stability because favorable interaction energies are associated with certain pairs of residues [75]. They tested this interpretation by constructing seven multiple mutants that were predicted to be hyperstable [75]. The X-ray structures of five mutants were determined. The mutants uniformly show high temperatures for thermal unfolding (T_m). The largest increase in T_m is 22.9 °C and the increase in T_m correlates with the number of van der Waals contacts. The overall results indicate that increased protein stability is correlated with an increased number of van der Waals contacts, and certain pairs of buried side chains make characteristic contributions to the number of van der Waals contacts.

A novel approach to analyzing the thermodynamics of burial of nonpolar side chains in protein folding was undertaken by Varadarajan and coworkers [76, 77]. They measure $\Delta\Delta H$ of folding for mutants with varying extents of burial of nonpolar surface area. Note that $\Delta\Delta H$ should be small near 25 °C for burial of nonpolar surface area, according to liquid–liquid transfer experiments with hydrocarbons (see Figures 6.4A and 6.4B). On the other hand, van der Waals packing interactions

are enthalpy-driven and larger values of $\Delta\Delta H$ are expected if the folding thermodynamics are dominated by packing interactions. The authors are able to measure ΔH directly at fixed temperatures by titration calorimetry for their ribonuclease S system (which is composed of two dissociable species, S-peptide + S-protein) by titrating unfolded S-peptide versus folded S-protein. They determine the X-ray structures of the mutant RNase S species and measure ΔH for folding S-peptide at varying temperatures. They find substantial $\Delta\Delta H$ values for the mutants and conclude that van der Waals packing interactions are responsible; see also the study of cavity mutants of T4 lysozyme by Matthews and coworkers [59].

Zhou and Zhou [78, 79] present an interesting analysis of the energetics of burying different side-chain types. They construct a database of mutational experiments on protein folding from the literature and extract the ''transfer free energy'' contributed by each amino acid side chain to the unfolding free energy: the transfer process is from the folded protein to the unfolded protein in aqueous solution. Then the authors simulate the mutational results by a theoretical analysis based on a potential of mean force, and plot the results as $\Delta\Delta G$ versus ΔASA for each side-chain type. The resulting plots are similar for the various nonpolar amino acids, and the slopes are in the range 25–30 cal mol^{-1} $Å^{-2}$. Interestingly, the plots for polar amino acids are similar in character but have substantially smaller slopes. The authors conclude that it is energetically favorable to fold polar as well as nonpolar side chains, but folding polar side chains contributes less to stability. There should be an energetic penalty if the polar moiety of a side chain is buried without making an H-bond, because the polar group interacts favorably with water (see below).

6.3 Peptide Solvation and the Peptide Hydrogen Bond

6.3.1 History

Interest in the role of the peptide hydrogen bond in stabilizing protein folding took off when Pauling and Corey proposed structures for the α-helix and the parallel and antiparallel β-sheets, and when Schellman analyzed [6] the factors that should determine the stability of the helix backbone in water. He estimated the net enthalpy change for forming a peptide H-bond in water as -1.5 kcal mol^{-1}, based on heat of dilution data for urea solutions [80], and he concluded that an isolated α-helix backbone should be marginally stable in water and might or might not be detectable [6]. Klotz and Franzen [81] investigated by infrared spectroscopy whether H-bonded dimers of *N*-methylacetamide are detectable in water and concluded that they have at best marginal stability: see also a later study of the dimerization of δ-valerolactam [82].

Determination of the first X-ray structures of proteins sparked interest in the problem of whether the peptide sequence for a protein helix can form the helix in water. Initial results based on circular dichroism (CD) (or optical rotatory disper-

sion) spectroscopy were disappointing. In 1968 Epand and Scheraga [83] examined two peptides obtained by cyanogen bromide cleavage from the highly helical protein sperm whale myoglobin and found very low values for the possible helix contents. In 1969 Taniuchi and Anfinsen [84] cleaved staphylococcal nuclease, which has 149 residues, between residues 126 and 127 and found that both fragments 1–126 and 127–149 (each of which has a helix of modest size) were structureless by CD as well as by other physical criteria. In 1969–1971 Klee obtained tantalizing results, suggestive of some helix formation at low temperatures, with the ''S-peptide'' (residues 1–20) [85] and ''C-peptide'' (residues 1–13) [86] of ribonuclease A. (The RNase A helix contains residues 3–12.) The helix problem languished for 11 years, perhaps because of the disappointing results found in the laboratories of Anfinsen and Scheraga. In 1982, Bierzynski et al. [87] used NMR as well as CD spectroscopy to reinvestigate the claim of Brown and Klee [86] and confirmed that partial helix formation occurs. Bierzynski et al. found that helix formation is strongly pH dependent and the pK values indicate that both a His residue and a Glu residue are required for helix formation, thus implicating specific side-chain interactions [87]. Several kinds of helix-stabilizing side-chain interactions were later studied, such as salt bridges, amino–aromatic interactions, and charge–helix dipole interactions [88]. The helix formed by C-peptide or S-peptide has basic properties in common with the protein helix of RNase A: both the peptide and protein helices have the same two helix-stabilizing side-chain interactions and the same helix termination signals. Today hundreds of peptides with sequences derived from proteins form partly stable helices in water [89]. The helix termination signals are well-studied [90] and consistent results are found from protein and peptide helices. The AGADIR algorithm of Muñoz and Serrano [89] fits the helix contents of peptides by statistically evaluating the many parameters describing side-chain interactions and helix propensities.

In 1989 Marqusee et al. [91] found that alanine-rich peptides form stable helices in water without the aid of specific side-chain interactions. Of the 20 natural amino acids, only alanine has this ability [92]. Because alanine has only a $-CH_3$ group for a side chain, this result strongly suggests that the helix backbone itself has measurable stability in water and that side chains longer than alanine somehow destabilize the helix. In 1985 Dyson and coworkers used NMR to detect a reverse turn conformation in a nine-residue peptide [93], and later studied the specific sequence requirements for forming this class of turn in peptides [94]. In 1994 Serrano and coworkers [95] found the β-hairpin conformation in a protein-derived peptide, and other β-hairpin sequences were soon found. Thus, H-bonded secondary structures derived from proteins can in general be studied in peptides in aqueous solution.

Determination of the energetic nature of the peptide H-bond was a chief motivation for the pioneering development in 1979 of a molecular force field by Lifson and coworkers [96]. They concluded that the peptide H-bond is represented to a good first approximation by an electrostatic model based on partial charges residing on the peptide CO and NH groups. Their analysis indicates that the peptide

CO and NH groups interact with water as well as with each other. Solvation of the peptide polar groups has been analyzed by using amides such as *N*-methylacetamide (NMA) as models for the peptide group.

6.3.2 Solvation Free Energies of Amides

In a classic experiment, Wolfenden demonstrated in 1978 that amides interact very strongly with water [97]. He measured the equilibrium distribution of a radioactively labeled amide between aqueous solution and the vapor phase, and calculated its transfer free energy from the vapor phase to aqueous solution. The (hypothetical) standard state concentration of the amide solute is 1 M in the vapor phase as well as in the liquid phase (see Section 6.2.4). Wolfenden and coworkers next measured the transfer free energies of model compounds for amino acid side chains [98]. The ionized forms of the basic and acidic residues are excluded from their study because species containing a full formal charge interact too strongly with water to be measured. Their results show that the interaction of water with amides is stronger than with any of the model compounds representing side chains. Saturated hydrocarbons, which serve as models for the side chains of leucine, isoleucine and valine, are preferentially excluded from aqueous solution and have unfavorable solvation free energies. The basic cause is the large unfavorable work of making a cavity in water, which exceeds the favorable van der Waals interaction energy (see Refs [24, 25] and Section 6.2.4). Figure 6.3 shows a direct proportionality between the transfer free energy ΔG° and ASA for transfer of alkanes from aqueous solution to the vapor phase.

For polar solutes as well as nonpolar solutes, there is an unfavorable work of making a cavity in water for the solute and a favorable van der Waals interaction energy between the solute and water. These effects must be removed from the observed solvation free energy to obtain the interaction free energy between water and the polar groups. Currently the sum of the cavity and van der Waals terms is approximated by experimental data for the transfer free energies of nonpolar solutes, as suggested by Makhatadze and Privalov [61] and Sitkoff et al. [99]. The observed solvation free energy in Eq. (9) is split into two terms: one for the polar groups ($\Delta G(\text{pol})$) and one for the sum of the cavity and van der Waals terms ($\Delta G(\text{np})$). The value of $\Delta G(\text{np})$ in Eq. (10) is taken from the plot of transfer free energy versus ASA for alkanes and the proportionality coefficient β is taken from this plot (Figure 6.3).

$$\Delta G^\circ(\text{obs}) = \Delta G(\text{pol}) + \Delta G(\text{np}) \tag{9}$$

$$\Delta G(\text{np}) = \beta \text{ASA} \tag{10}$$

Values of $\Delta G(\text{pol})$ are given for four amides in Table 6.2, taken from Avbelj et al. [100]. Although the correction term $\Delta G(\text{np})$ is obtained by the approximate procedure of using experimental data for nonpolar solutes, the correction term is fairly

Tab. 6.2. Solvation free energy data for amides as models for the free peptide group[a].

Quantity[b] *(kJ mol^{-1})*	*Acetamide*	*N-methyl-acetamide*	*N,N-dimethyl-acetamide*	*Propionamide*
$\Delta G°$(obs)	−40.58	42.13	−35.73	−39.25
ΔG(np)	8.16	−9.04	9.71	8.87
ΔG(pol)	−48.74	−51.17	−45.44	−48.12
ΔH(obs)	−68.28	−71.42	−69.29	−73.01
ΔH(np)	−19.54	−23.35	−26.15	−22.64
ΔH(pol)	−48.74	−48.07	−43.14	−50.38
ASA(pol) (nm^2)	0.95	0.51	0.32	0.88

[a] Data are from Ref. [100].
[b] $\Delta G°$(obs) is the observed transfer free energy from gas to water. Data are taken from Ref. [100], based on a standard state concentration of 1 M in both the gas and liquid phases and without volume correction. ΔG(np) is the correction for the cavity and van der Waals terms according to Eq. (10) and using the value of β given in Ref. [100] (6.4 cal mol^{-1} Å^{-2}), which is not volume-corrected. ΔG(pol) is the solvation free energy of the polar groups in the amide, found from Eq. (9). The quantities ΔH(obs), ΔH(np) and ΔH(pol) have corresponding meanings and are explained in the text. Values for ΔH(obs) are taken from various calorimetric papers, and references are given in Ref. [100]. ASA(pol) is the value of ASA assigned to the polar groups.

small (9.0 kJ mol^{-1} for *N*-methylacetamide) compared with the observed solvation free energy (−42.1 kJ mol^{-1}) or the value of ΔG(pol) (−51.2 kJ mol^{-1}).

The value of β (Eq. (6)) used by Sitkoff et al. [99] (to obtain values for ΔG(np) in Eq. (10)) is based on transfer free energies that are not volume-corrected [21, 99]. The resulting values of ΔG(pol) (obtained from Eq. (9) for a database of model compounds) have been used to calibrate the PARSE parameter set of the DelPhi algorithm [99] (see Section 6.3.5). For this reason, the values of ΔG(np) in Table 6.1 are based on transfer free energies that are not volume-corrected.

The enthalpy of interaction between the polar groups and water, ΔH(pol), has been obtained [100] from calorimetric data in the literature after approximating ΔH(np) by experimental data for alkanes, as before.

$$\Delta H(\text{obs}) = \Delta H(\text{pol}) + \Delta H(\text{np}) \tag{11}$$

The value for ΔH(obs) in Eq. (11) is found by combining results from two calorimetric experiments. The first experiment yields the heat of vaporization of the liquid amide and the second experiment yields the heat of solution of the liquid amide in water. The value of ΔH(np) is found from the heats of solution, plotted against ASA, of gaseous hydrocarbons in water, for which the heats of solution depend chiefly [24] on the favorable van der Waals interaction energy of the hydrocarbon solute with water.

Some interesting conclusions may be drawn from Table 6.2: (1) The four different amides have similar values for ΔG(pol) and also for ΔH(pol). Although there

is a threefold difference between the values of polar ASA for acetamide and *N*,*N*-dimethylacetamide, their values of ΔG(pol) differ by less than 10%. Thus, the computationally convenient approximation of assuming proportionality between ΔG(pol) and polar ASA [101] is not a satisfactory assumption for amides. The polar groups of an amide interact strongly with water even when they are only partly exposed. (2) The value of ΔG(pol) is nearly equal to the value of ΔH(pol) for each amide, and so the $T\Delta S$(pol) term must be small by comparison. This conclusion is surprising if one expects a large entropy change when water interacts with polar groups. It is not surprising, however, after considering the entropies of hydration of crystalline hydrate salts [102] or the prediction [103] made from the Born equation that ΔG(pol) is almost entirely enthalpic. The basic reason why the entropy term looks small is that the enthalpy term is large. (3) The values of ΔG(pol) are impressively large for amides. NMA is sometimes taken as a model for studying the interaction between water and the peptide group, and its value of ΔG(pol) is -51.2 kJ mol^{-1}. This is a huge value for only one peptide group: $-\Delta G^{\circ}$ for folding a 100-residue protein is typically 40 kJ mol^{-1} or less. Evidently solvation of the peptide group is a major factor in the energetics of folding: see Wolfenden [97] and Makhatadze and Privalov [61].

6.3.3 Test of the Hydrogen-Bond Inventory

Protein chemists often use the H-bond inventory to interpret results of mutational experiments when the experiment involves a change in the number of hydrogen bonds [104, 105]. Experimental data for amides provide a direct test of the H-bond inventory [106]. A key feature of the H-bond inventory is that water (W) is treated as a reactant and the change in the total number of W•••W H-bonds is included in the inventory. When discussing the formation of a peptide H-bond (CO•••HN) in water, the H-bond inventory takes the form of Eq. (12).

$$\mathrm{CO{\bullet\bullet\bullet}W + NH{\bullet\bullet\bullet}W = CO{\bullet\bullet\bullet}HN + W{\bullet\bullet\bullet}W} \tag{12}$$

The peptide NH and CO groups are predicted to make one H-bond each to water in the unfolded peptide, and the CO and NH groups are predicted not to interact further with water after the peptide H-bond is made. Gas phase calculations of H-bond energies indicate that all four H-bond types in Eq. (12) have nearly the same energy [107], -25 ± 4 kJ mol^{-1}, and consequently the net enthalpy change predicted for forming a peptide H-bond in water is 0 ± 4 kJ mol^{-1}. The enthalpy of sublimation of ice has been used to give an experimental estimate of -21 kJ mol^{-1} for the enthalpy of the W•••W H-bond [45].

When a dry molecule of amide (Am) in the gas phase becomes hydrated upon solution in water, the H-bond inventory model postulates that the CO and NH groups each make one H-bond to water and one W•••W H-bond is broken:

$$\mathrm{HN{-}Am{-}CO + W{\bullet\bullet\bullet}W = W{\bullet\bullet\bullet}HN{-}Am{-}CO{\bullet\bullet\bullet}W} \tag{13}$$

Thus, the H-bond inventory predicts a net increase of one H-bond when a dry amide becomes solvated, with a net enthalpy change of -25 ± 4 kJ mol^{-1}. But the experimental enthalpy change for solvating the amide polar groups is ~ -50 kJ mol^{-1} (Table 6.2) and the H-bond inventory fails badly.

6.3.4 The Born Equation

In 1920 Max Born wanted to know why atom-smashing experiments can be visualized in Wilson's cloud chamber [108]: an ion leaves a track of tiny water droplets as it passes through supersaturated water vapor. He computed the work of charging a spherical ion in vacuum and in water, and he treated water as a continuum solvent with dielectric constant D. He gave the favorable change in free energy for transferring the charged ion from vacuum to water as:

$$-\Delta G = (q^2/2r)[1 - (1/D)] \tag{14}$$

in which q is the charge and r is the radius of the ion [109]. This simple calculation answers Born's question: the free energy change is enormous, of the order of -420 kJ mol^{-1} for a monovalent ion transferred to water. Consequently the ion easily nucleates the formation of water droplets. Inorganic chemists – notably W. M. Latimer – realized that Born's equation provides a useful guide to the behavior of solvation free energies. Note that the solvation free energy predicted by Born's equation is inversely proportional to the ionic radius, but which radius should be used? Ions are strongly solvated and the solvated radius is subject to argument. Rashin and Honig [103] argued that the covalent radius is a logical choice and gives consistent results for different monovalent anions and cations. They also point out that one can obtain the enthalpy of solvation from Born's equation and it predicts that, if the solvent is water with a high dielectric constant (near 80), the solvation free energy is almost entirely enthalpy. Quite recently the solvation free energies of monovalent ions have been analyzed by a force field employing polarizable water molecules [110], with excellent agreement between theory and experiment.

6.3.5 Prediction of Solvation Free Energies of Polar Molecules by an Electrostatic Algorithm

The success of the Born equation in rationalizing solvation free energies of monovalent anions and cations suggests that it should be possible to predict the solvation free energies of polar molecules by using an appropriate electrostatic algorithm plus knowledge of the structure and partial charges of the polar molecule. The problem has a long history. Kirkwood and Westheimer [111] developed a theory in 1938, based on a simple geometrical model, that gives the effect of a low dielectric environment within the molecule on the separation between the two pK values of a dicarboxylic acid. The problem was treated later by an electrostatic algorithm that is free from geometrical assumptions about the shape of the molecule

[112]. The latter treatment includes the effect of electrostatic solvation (the ''Born term'') as well as the electrostatic interaction between the two charged carboxylate groups.

Various electrostatic algorithms are in current use [99, 113] today, including one based on using Langevin dipoles [113] to treat the polarization of water molecules in the vicinity of charged groups. The focus here is on the DelPhi algorithm of Honig and coworkers [99], because the PARSE parameter set of DelPhi has been calibrated against a database of experimental solvation free energies for small molecules that includes amides [99]. Thus, DelPhi may plausibly be used to predict the solvation free energies of the polar CO and NH groups of peptides in various conformations. There are no adjustable parameters and the predicted values of electrostatic solvation free energy (ESF) may be compared directly with experiments if suitable data are available. The DelPhi algorithm uses a low dielectric ($D = 2$) cavity to represent the shape of the solute while the partial charges of the solute are placed on a finely spaced grid running through the cavity, and the solvent is represented by a uniform dielectric constant of 80 [99]. The results are calculated by Poisson's equation if the solvent does not contain mobile ions, or by the Poisson-Boltzmann equation if it does.

6.3.6
Prediction of the Solvation Free Energies of Peptide Groups in Different Backbone Conformations

A basic prediction about the electrostatic interactions among polar CO and NH groups in the peptide backbone is that the interactions depend strongly on the peptide backbone conformation [114–116]. The peptide group is normally fixed in the trans conformation while the CO and NH dipoles of adjacent peptide units are aligned antiparallel in the extended β-strand conformation and parallel in the α-helix conformation. When adjacent peptide dipoles are parallel they make unfavorable interactions unless the dipoles are placed end to end, when formation of peptide H-bonds occurs. These simple observations have important consequences, as pointed out especially by Brant and Flory [114, 115] and by Avbelj and Moult [116]. Thus, intrachain electrostatic free energy favors the extended β conformation over the compact α conformation and this factor tends to make β the default conformation in unfolded peptides [114]. There is a very large difference, $\sim$20 kJ mol^{-1}, between the local electrostatic free energy of the α- and β-strand conformations when calculated with $D = 1$ [116]. Nucleation of an α-helix is difficult for this electrostatic reason [115] as well as for the commonly cited loss in backbone conformational entropy: the peptide dipoles in the helix nucleus are parallel and make unfavorable electrostatic interactions. When helix propagation begins and additional H-bonded residues are added onto the helical nucleus, the favorable H-bond energy drives helix formation.

Calculations of polar group solvation (ESF) in peptides [100, 121] using DelPhi show that ESF depends strongly on two factors: the access of solvent to the peptide group and the local electrostatic potential in the peptide chain. Nearby side chains

Tab. 6.3. Calculated solvation free energies of peptide groups in different backbone conformations[a].

Structure[b]	*ESF (kJ mol^{-1})*	*Reference*
Helix, H-bonded, solvent-exposed	−10.5	100
Helix, not H-bonded, solvent-exposed	−39.8	100
β-hairpin, H-bonded, exposed	−10.5	121
β-hairpin, H-bonded, buried	0	121
β-strand[c], not H-bonded, exposed	−35.6	
Polyproline II[b], not H-bonded, exposed	−38.1	

[a] The solvation free energies of the peptide polar groups (CO, NH) are calculated by DelPhi, as explained in the text (see Section 6.3.5). No adjustable parameters are used except those that describe the structure. The calculations listed here are made for all-alanine peptides and they refer to interior peptide groups, not to N- or C-terminal groups.
[b] The H-bonded, solvent-exposed helix refers to the central residue of a 15-residue helical peptide. The solvent-exposed helix, not H-bonded, refers to the central residue of a five-residue peptide in the α-helical conformation ($\phi, \psi = -65°, -40°$). The β-hairpin (H-bonded, solvent-exposed) refers to typical H-bonded residues in a 15-residue peptide with a β-hairpin conformation taken from a segment of the GB1 structure. The solvent-exposed, extended β-strand, not H-bonded ($\phi, \psi = -120°, 120°$) refers to a nine-residue peptide (F. Avbelj and R. L. Baldwin, to be published). The ESF value given here is more negative than the value previously given [100]. The earlier value by accident had a conformation deviating from ($\phi, \psi = -120°, 120°$) because it was used for an Ala to Val substitution and had a conformation suitable for receiving a Val residue. The polyproline II structure (F. Avbelj and R. L. Baldwin, to be published) refers to the central residue of a nine-residue peptide and has ($\phi, \psi = -70°, 150°$).

hinder access of solvent to the peptide group and reduce the negative ESF value. Consequently, helix and β-structure propensities of the different amino acids should depend on the ESF values of the peptide groups [100, 116–118]. The different helix propensities of the amino acids are often attributed instead to the loss in side-chain entropy when an unfolded peptide forms a helix [119]. Because ESF is almost entirely enthalpic (see Table 6.2), these alternative explanations can be tested by determining if the helix propensity differences are enthalpic or entropic. Temperature-dependence results [120] measured for the nonpolar amino acids (see also Ref. [63]) indicate that the helix propensity differences are largely enthalpic.

Table 6.3 gives some ESF values for alanine peptide groups in different backbone conformations. There are several points of interest: (1) A peptide group in a non-H-bonded alanine peptide has substantially different ESF values in the three major backbone conformations β, α_R, and P_{II} (polyproline II). Consequently any analysis based on group additivity that predicts the overall enthalpy change by assigning constant energetic contributions (independent of backbone conformation) to the polar peptide CO and NH groups cannot be valid. The overall enthalpy change con-

tains contributions from both ESF and the local intrachain electrostatic potential (E_{local}) [116–118], both of which depend on backbone conformation. (2) Because ESF depends on the accessibility of water to a peptide group, the N-terminal and C-terminal peptide groups of an all-alanine peptide have more negative ESF values than interior peptide groups. (3) Replacement of Ala by a larger or more bulky residue such as Val [100] changes the ESF not only at the substitution site but also at neighboring sites (Avbelj and Baldwin, to be published). (4) *N*-Methylacetamide, whose ΔG_{pol} (or ESF) is -51.2 kJ mol^{-1} (Table 6.2) is a poor model for the interaction with water of a free peptide group. There is a 16 kJ mol^{-1} difference between the ESF of NMA and that of an alanine peptide group in the β-conformation (Tables 6.2 and 6.3).

6.3.7
Predicted Desolvation Penalty for Burial of a Peptide H-bond

ESF calculations for completely buried peptide groups, with no accessibility to water, show that their ESF values fall to zero [121]. On the other hand, DelPhi calculations for H-bonded and solvent-exposed peptide groups in either the α-helical [100] or β-hairpin [121] conformation show that H-bonded peptide groups interact with solvent and have highly significant ESF values, about -10.5 kJ mol^{-1} for alanine peptides. Of this, -8.5 kJ mol^{-1} is assigned to the peptide CO group and -2 kJ mol^{-1} to the peptide NH group [100]. Consequently, there should be a large desolvation penalty (equal to the ESF of the solvent-exposed, H-bonded peptide group) if a solvent-exposed peptide H-bond becomes completely buried [100, 121]. This deduction agrees with the prediction by Honig and coworkers [122] of an even larger desolvation penalty (16 kJ mol^{-1}) for transferring an amide H-bond in a NMA dimer from water to liquid alkane. Two points of interest for the mechanism of protein folding arise from these ESF calculations. First, the ESF values of H-bonded, solvent-exposed peptide groups are predicted to be a major factor stabilizing molten globule folding intermediates [100, 121]. Second, complete burial of H-bonded secondary structure should involve a substantial desolvation penalty [121]. The size of the penalty depends on how solvated each peptide group is when the secondary structure is solvent-exposed. Neighboring side chains larger or more bulky than Ala reduce the negative ESF of the peptide H-bond.

When Ben-Tal et al. [122] studied the transfer of a H-bonded NMA dimer from water to liquid alkane, they found the formation of the H-bonded dimer in water to be stable by -5 kJ mol^{-1}. Their results give the penalty for forming the H-bond in water and then transferring it to liquid alkane as $-5 + 16 = 11$ kJ mol^{-1}. When their predictions are compared with values for an alanine peptide helix, the results are numerically different (not surprising, in view of the structural difference) but qualitatively the same. Ben-Tal et al. omit the loss in translational and rotational entropy for forming the NMA dimer and their ΔG value of -5 kJ mol^{-1} [122] may be compared with the measured ΔH (-4.0 kJ mol^{-1} [123, 124]) for forming the alanine peptide helix.

Myers and Pace [125] discuss whether or not peptide H-bonds stabilize protein

folding by considering mutational data for H-bonds made between specific pairs of side chains. The ESF studies considered here emphasize the role of context: solvent-exposed peptide H-bonds should stabilize folding but buried H-bonds should detract from stability.

The ESF perspective provides a simple explanation for why alanine, alone of the 20 amino acids in proteins, forms a stable helix in water. The H-bonded, solvent-exposed peptide group in an alanine helix has the most stabilizing ESF value of any nonpolar amino acid except glycine, and glycine fails to form a helix because of the exceptional flexibility of the glycine peptide linkage.

The interaction energy between water and the peptide group is a critical quantity in predicting the structures of membrane proteins from amino acid sequences [126]. Accurate values are needed for the energy of desolvation both of the free and H-bonded forms of the peptide group. The solvent *n*-octanol, which has been used extensively to model the interiors of water-soluble proteins (see Sections 6.2.2 and 6.2.3), has also been used as an experimental model for the lipid bilayer environment of membrane proteins, when measuring transfer free energies of peptides between water and a membrane-like solvent. The small value of the transfer free energy found for the free glycine peptide group transferred from water to water-saturated *n*-octanol (4.8 kJ mol^{-1} [15]) emphasizes the role of the water contained in this solvent, which increases its attraction for the peptide group. Cyclohexane has been used as an alternative solvent that provides a nearly water-free environment when partitioning model compounds [16]. The transfer free energies of amides are much larger in the cyclohexane/water pair than the 4.8 kJ mol^{-1} determined for the peptide group in octanol/water: 25 and 21 kJ mol^{-1} for acetamide and propionamide, respectively [16].

6.3.8 Gas–Liquid Transfer Model

The gas–liquid transfer model has been used in Section 6.2.8 to discuss the respective roles of van der Waals interactions and burial of nonpolar surface area in protein folding (Scheme 6.1). The gas–liquid transfer model can be adapted to discuss the roles of peptide H-bonds and peptide solvation in folding. Scheme 6.2 is written for a simple folding reaction involving only a single peptide H-bond.

Here the conformation of the unfolded form U must be considered because changes in both local electrostatic free energy (E_{local}) and ESF contribute to ΔH

$$\begin{array}{ccccc} U(\gamma)(g) & \Leftarrow(2)\Rightarrow & U(\delta)(g) & \Leftarrow(3)\Rightarrow & N(g) \\ \Uparrow\Downarrow(1) & & \Uparrow\Downarrow(7) & & \Uparrow\Downarrow(4) \\ U(\gamma)(aq) & \Leftarrow(5)\Rightarrow & U(\delta)(aq) & \Leftarrow(6)\Rightarrow & N(aq) \end{array}$$

Scheme 6.2

and they depend on backbone conformation. In order to form the peptide H-bond, a change in peptide backbone conformation must usually take place that involves substantial changes in E_{local} and ESF [116]. The unfolded form U(γ) normally exists as a complex equilibrium mixture of conformations and U(δ) represents the new conformation needed to make the peptide H-bond.

In principle, Scheme 6.2 may be adapted to predict the enthalpy change for forming an alanine peptide helix, whose experimental value is known [123, 124], by assigning provisional values to the different steps. Step 1, desolvating the free peptide group, has $-$ESF = 36 kJ mol^{-1} if the free peptide conformation is an extended β-strand (Table 6.2), and this $-$ESF value gives the contribution to ΔH because ESF and ΔH(pol) are the same within error for amides (Table 6.2). Likewise, solvating the alanine helix in step 4 can be assigned a contribution to ΔH equal to the ESF of the solvent-exposed, H-bonded peptide group, -10.5 kJ mol^{-1} [100]. In step 3, making the peptide H-bond in the gas phase, the H-bond energy has been calculated by quantum mechanics to be -28 kJ mol^{-1} for the H-bonded NMA dimer [122]. Step 3 also contains, however, an additional unknown quantity, the van der Waals interaction energy made in forming the helix backbone. In step 1 there is also an additional problem. The ESF depends not only on the appropriate mixture of backbone conformations (values for α_R, β, and P_{II} are given in Table 6.3), but also on the tendency of a peptide to bend back on itself, which reduces the exposure to solvent of the peptide groups [100]. Likewise, there are unknown – and possibly quite large – changes in E_{local} in both steps 2 and 3. Thus, the puzzle of predicting ΔH even for a simple folding reaction, like that of forming an alanine peptide helix is far from being completely understood.

Nevertheless, the gas–liquid transfer model provides the background for a simple interpretation of the enthalpy of forming the alanine helix. The observed enthalpy of helix formation, ΔH(H-C), can be written as a sum of three terms, and the enthalpy of interaction with water of the helix or of the coil can be approximated by the ESF value, as explained above.

$$\Delta H(\text{H-C}) = \Delta H(\text{hb}) + \Delta H(\text{H-W}) - \Delta H(\text{C-W}) \tag{15}$$

In Eq. (15), H refers to helix, C to coil (the unfolded peptide), W to water and hb to the peptide H-bond. ΔH(H-C) is the observed enthalpy of helix formation in water (-4.0 kJ mol^{-1}, see above). It equals ΔH(hb), the enthalpy of forming the peptide H-bond (-27.6 kJ mol^{-1} [122]), plus ΔH(H-W), the enthalpy of interaction between water and the helix (-10.5 kJ mol^{-1} (see Table 6.3), minus ΔH(C-W), the enthalpy of interaction between water and the coil (unknown, for reasons explained above). The unknown term ΔH(C-W) is found by solving the equation to be $-27.6 - 10.5 + 4.0 = -34.1$ kJ mol^{-1}. This is a reasonable value for the enthalpy of interaction between water and the coil, in view of the ESF values given in Table 6.3 for different unfolded conformations and given also that bending back of the unfolded peptide on itself is likely to reduce the negative ESF value.

Acknowledgments

I thank Franc Avbelj, David Baker, David Chandler, Ken Dill, Pehr Harbury, B.-K. Lee and John Schellman for discussion, and David Chandler, Alan Grossfield, George Makhatadze and Yaoqi Zhou for sending me their papers before publication.

Footnote added in proof

An important paper [127] was overlooked in writing section 6.2.11 on the role of van der Waals interactions in forming the hydrophobic cores of proteins. Loladze, Ermolenko and Makhatadze [127] made a set of large-to-small mutations (e.g., Val → Ala) in ubiquitin and used scanning calorimetry to measure ΔH, $T\Delta S^\circ$ and ΔG° for mutant unfolding. In agreement with a related study by Varadarajan, Richards and coworkers [76, 77], they find that large-to small mutations are characterized chiefly by unfavorable enthalpy changes, and not by the expected unfavorable entropy changes. Surprisingly, they find favorable entropy changes for these mutants, indicating that some kind of loosening of the structure occurs, perhaps at residues lining the cavity surface. Thus, they conclude that burial of nonpolar surface area stabilizes folding primarily by a favorable enthalpy change and not by the favorable change in $T\Delta S^\circ$ predicted by the liquid–liquid transfer model. The measurements are reported at 50 °C [127], where the favorable free energy change for burial of nonpolar surface area given by the liquid–liquid transfer model (Section [6.2.9]) is approximately 30% enthalpy and 70% $T\Delta S^\circ$. The changes in conformational entropy that occur in large-to-small mutants [127] invalidate testing the relation between buried ASA and ΔG° for folding unless the enthalpy changes are also measured and analyzed. There is the further problem of a dependence of $\Delta\Delta G^\circ$ on the size of the cavity, discussed by Matthews and coworkers [59]. Makhatadze and coworkers find values of ΔC_p in these experiments that are too small to be determined accurately [128], in agreement with predictions by the liquid–liquid transfer and other models.

References

1 Kauzmann, W. (1959). Factors in interpretation of protein denaturation. *Adv. Protein Chem.* **14**, 1–63.
2 Dill, K. A. (1990). Dominant forces in protein folding. *Biochemistry* **29**, 7133–7155.
3 Privalov, P. L. & Gill, S. J. (1988). Stability of protein structure and hydrophobic interaction. *Adv. Protein Chem.* **39**, 191–234.
4 Privalov, P. L. & Gill, S. J. (1989). The hydrophobic effect: a reappraisal. *Pure Appl. Chem.* **61**, 1097–1104.
5 Dill, K. A. (1990). The meaning of hydrophobicity. *Science* **250**, 297–298.
6 Schellman, J. A. (1955). The stability of hydrogen-bonded peptide structures in aqueous solution. *C.R. Trav. Lab. Carlsberg Sér Chim.* **29**, 230–259.
7 Stickle, D. F., Presta, L. G., Dill,

K. A., & Rose, G. D. (1992). Hydrogen bonding in globular proteins. *J. Mol. Biol.* **226**, 1143–1159.

8 Kendrew, J. C., Dickerson, R. E., Strandberg, B. E. et al. (1960). Structure of myoglobin. A three-dimensional Fourier synthesis at 2 Å resolution. *Nature* **185**, 422–427.

9 Pauling, L., Corey, R. B. & Branson, H. R. (1951). The structure of proteins: two hydrogen-bonded helical configurations of the polypeptide chain. *Proc. Natl Acad. Sci. USA* **37**, 205–211.

10 Tanford, C. (1980). *The Hydrophobic Effect*, 2nd edn. John Wiley & Sons, New York.

11 Tanford, C. (1997). How protein chemists learned about the hydrophobic factor. *Protein Sci.* **6**, 1358–1366.

12 Southall, N. T., Dill, K. A., & Haymet, A. D. J. (2002). A view of the hydrophobic effect. *J. Phys Chem. B* **106**, 521–533.

13 Nozaki, Y. & Tanford, C. (1971). The solubility of amino acids and two glycine peptides in aqueous ethanol and dioxane solutions. *J. Biol. Chem.* **246**, 2211–2217.

14 Fauchère, J.-L. & Pliska, V. (1983). Hydrophobic parameters π of amino-acid side chains from partitioning of N-acetyl-amino-acid amides. *Eur. J. Med. Chem.* **18**, 369–375.

15 Wimley, W. C., Creamer, T. P., & White, S. H. (1996). Solvation energies of amino acid side chains and backbone in a family of host-guest pentapeptides. *Biochemistry* **35**, 5109–5124.

16 Radzicka, A. & Wolfenden, R. (1988). Comparing the polarities of the amino acids: side-chain distribution coefficients between the vapor phase, cyclohexane, 1-octanol and neutral aqueous solution. *Biochemistry* **27**, 1644–1670.

17 Hermann, R. B. (1972). Theory of hydrophobic bonding. II. The correlation of hydrocarbon solubility in water with solvent cavity surface area. *J. Phys. Chem.* **76**, 2754–2759.

18 Chothia, C. (1974). Hydrophobic bonding and accessible surface area in proteins. *Nature* **248**, 338–339.

19 Reynolds, J. A., Gilbert, D. B., & Tanford, C. (1974). Empirical correlation between hydrophobic free energy and aqueous cavity surface area. *Proc. Natl Acad. Sci. USA* **71**, 2925–2927.

20 Lee, B. & Richards, F. M. (1971). The interpretation of protein structures: estimation of static accessibility. *J. Mol. Biol.* **55**, 379–400.

21 Sharp, K. A., Nicholls, A., Friedman, R., & Honig, B. (1991). Extracting hydrophobic free energies from experimental data: relationship to protein folding and theoretical models. *Biochemistry* **30**, 9686–9697.

22 Hermann, R. B. (1977). Use of solvent cavity area and number of packed molecules around a solute in regard to hydrocarbon solubilities and hydrophobic interactions. *Proc. Natl Acad. Sci. USA* **74**, 4144–4145.

23 Ben-Naim, A. & Marcus, Y. (1984). Solvation thermodynamics of nonionic solutes. *J. Chem. Phys.* **81**, 2016–2027.

24 Lee, B. (1991). Solvent reorganization contribution to the transfer thermodynamics of small nonpolar molecules. *Biopolymers* **31**, 993–1008.

25 Lee, B. (1995). Analyzing solvent reorganization and hydrophobicity. *Methods Enzymol.* **259**, 555–576.

26 Widom, B. (1982). Potential-distribution theory and the statistical mechanics of fluids. *J. Phys. Chem.* **86**, 869–872.

27 Jorgensen, W. L., Gao, J., & Ravimohan, C. (1985). Monte Carlo simulations of alkanes in water. Hydration numbers and the hydrophobic effect. *J. Phys. Chem.* **89**, 3470–3473.

28 Pratt, L. R. & Chandler, D. (1977). Theory of the hydrophobic effect. *J. Chem. Phys.* **67**, 3683–3704.

29 Gallichio, E., Kubo, M. M., & Levy, R. M. (2000). Enthalpy-entropy and cavity decomposition of alkane hydration free energies: Numerical results and implications for theories of hydrophobic solvation. *J. Phys. Chem. B* **104**, 6271–6285.

30 Lee, B. (1985). The physical origin of the low solubility of nonpolar solutes in water. *Biopolymers* **24**, 813–823.

31 Rank, J. A. & Baker, D. (1998). Contributions of solvent-solvent hydrogen bonding and van der Waals interaction to the attraction between methane molecules in water. *Biophys. Chem.* **71**, 199–204.

32 Tanford, C. (1979). Interfacial free energy and the hydrophobic effect. *Proc. Natl Acad. Sci. USA* **76**, 4175–4176.

33 Postma, J. P. M., Berendsen, H. J. C., & Haak, J. R. (1982). Thermodynamics of cavity formation in water: a molecular dynamics study. *Faraday Symp. Chem. Soc.* **17**, 55–67.

34 Hummer, G., Garde, S., García, A., Pohorille, A., & Pratt, L. R. (1996). An information theory model of hydrophobic interactions. *Proc. Natl Acad. Sci. USA* **93**, 8951–8955.

35 DeYoung, L. R. & Dill, K. A. (1990). Partitioning of nonpolar solutes into bilayers and amorphous n-alkanes. *J. Phys. Chem.* **94**, 801–809.

36 Chan, H. S. & Dill, K. A. (1997). Solvation: how to obtain microscopic energies from partitioning and solvation experiments. *Annu. Rev. Biophys. Biomol. Struct.* **26**, 425–459.

37 Chandler, D. (2004). Hydrophobicity: two faces of water. *Nature (London)* **417**, 491–493.

38 Lum, K., Chandler, D., & Weeks, J. D. (1999). Hydrophobicity at small and large length scales. *J. Phys. Chem. B* **103**, 4570–4577.

39 Lee, B. (1994). Relation between volume correction and the standard state. *Biophys. Chem.* **51**, 263–269.

40 Huang, D. M. & Chandler, D. (2000). Temperature and length scale dependence of hydrophobic effects and their possible implications for protein folding. *Proc. Natl Acad. Sci. USA* **97**, 8324–8327.

41 Southall, N. T. & Dill, K. A. (2000). The mechanism of hydrophobic solvation depends on solute radius. *J. Phys. Chem. B* **104**, 1326–1331.

42 Pohorille, A. & Pratt, L. R. (1990). Cavities in molecular liquids and the theory of hydrophobic solubility. *J. Am. Chem. Soc.* **112**, 5066–5074.

43 Baldwin, R. L. (1986). Temperature dependence of the hydrophobic interaction in protein folding. *Proc. Natl Acad. Sci. USA* **83**, 8069–8072.

44 Gill, S. J., Dec, S. F., Olofsson, G., & Wadsö, I. (1985). Anomalous heat capacity of hydrophobic solvation. *J. Phys. Chem.* **89**, 3758–3761.

45 Pauling, L. (1960). *The Nature of the Chemical Bond*, 3rd edn, pp. 468–472. Cornell University Press, Ithaca, NY.

46 Lazaridis, T. (2001). Solvent size versus cohesive energy as the origin of hydrophobicity. *Acc. Chem. Res.* **34**, 931–937.

47 Stellner, K. L., Tucker, E. E., & Christian, S. D. (1983). Thermodynamic properties of the benzene-phenol dimer in dilute aqueous solution. *J. Sol. Chem.* **12**, 307–313.

48 Raschke, T. M., Tsai, J., & Levitt, M. (2001). Quantification of the hydrophobic interaction by simulations of the aggregation of small hydrophobic solutes in water. *Proc. Natl Acad. Sci. USA* **98**, 5965–5969.

49 Rank, J. A. & Baker, D. (1997). A desolvation barrier to cluster formation may contribute to the rate-limiting step in protein folding. *Protein Sci.* **6**, 347–354.

50 Richards, F. M. (1977). Areas, volumes. packing and protein structure. *Annu. Rev. Biophys. Bioeng.* **6**, 151–176.

51 Gill, S. J., Nichols, N. F., & Wadsö, I. (1976). Calorimetric determination of enthalpies of solution of slightly soluble liquids. II. Enthalpy of solution of some hydrocarbons in water and their use in establishing the temperature dependence of their solubilities. *J. Chem. Thermodynam.* **8**, 445–452.

52 Edsall, J. T. (1935). Apparent molal heat capacities of amino acids and other organic compounds. *J. Am. Chem. Soc.* **57**, 1506–1507.

53 Garde, S., Hummer, G., García, A., Paulaitis, M. E., & Pratt, L. R. (1996). Origin of entropy convergence

in hydrophobic hydration and protein folding. *Phys. Rev. Lett.* **77**, 4966–4968.

54 Graziano, G. & Lee, B.-K. (2003). Entropy convergence in hydrophobic hydration: a scaled particle theory analysis. *Biophys. Chem.* **105**, 241–250.

55 Privalov, P. L. (1979). Stability of proteins: small globular proteins. *Adv. Protein Chem.* **33**, 167–241.

56 Robertson, A. D. & Murphy, K. P. (1997). Protein structure and the energetics of protein stability. *Chem. Rev.* **97**, 1251–1267.

57 Schellman, J. A. (1997). Temperature, stability and the hydrophobic interaction. *Biophys. J.* **73**, 2960–2964.

58 Pace, C. N. (1992). Contribution of the hydrophobic effect to globular protein stability. *J. Mol. Biol.* **226**, 29–35.

59 Eriksson, A. E., Baase, W. A., Zhang, X.-J. et al. (1992). Response of a protein structure to cavity-creating mutations and its relation to the hydrophobic effect. *Science* **255**, 178–183.

60 Livingstone, J. R., Spolar, R. S., & Record, M. T. (1991). Contribution to the thermodynamics of protein folding from the reduction in water-accessible nonpolar surface area. *Biochemistry* **30**, 4237–4244.

61 Makhatadze, G. I. & Privalov, P. L. (1993). Contribution of hydration to protein folding. I. The enthalpy of hydration. *J. Mol. Biol.* **232**, 639–659.

62 Gómez, J., Hilser, V. J., Xie, Dong, & Freire, E. (1995). The heat capacity of proteins. *Proteins Struct. Funct. Genet.* **22**, 404–412.

63 Richardson, J. M. & Makhatadze, G. I. (2003). Temperature dependence of the thermodynamics of the helix-coil transition. *J. Mol. Biol.*, **335**, 1029–1037.

64 Kauzmann, W. (1987). Thermodynamics of unfolding. *Nature (London)* **325**, 763–764.

65 Hummer, G., Garde, S., García, A., Paulaitis, M. E., & Pratt, L. R. (1998). The pressure dependence of hydrophobic interactions is consistent with the observed pressure denaturation of proteins. *Proc. Natl Acad. Sci. USA* **95**, 1552–1555.

66 Akasaka, K. (2003). Highly fluctuating protein structures revealed by variable-pressure nuclear magnetic resonance. *Biochemistry* **42**, 10875–10885.

67 Ooi, T. & Oobatake, M. (1988). Effects of hydrated water on protein unfolding. *J. Biochem. (Tokyo)* **103**, 114–120.

68 Oobatake, M. & Ooi, T. (1992). Hydration and heat stability effects on protein unfolding. *Prog. Biophys. Mol. Biol.* **59**, 237–284.

69 Simonson, T. & Brünger, A. T. (1994). Solvation free energies estimated from macroscopic continuum theory: an accuracy assessment. *J. Phys. Chem.* **98**, 4683–4694.

70 Chen, J., Lu, Z., Sakon, J., & Stites, W. E. (2000). Increasing the thermostability of staphylococcal nuclease: implications for the origin of protein thermostability. *J. Mol. Biol.* **303**, 125–130.

71 Havranek, J. J. & Harbury, P. B. (2003). Automated design of specificity in molecular recognition. *Nature Struct. Biol.* **10**, 45–52.

72 Nicholls, A., Sharp, K. A., & Honig, B. (1991). Protein folding and association: insights from the interfacial and thermodynamic properties of hydrocarbons. *Proteins Struct. Funct. Genet.* **11**, 281–296.

73 Klapper, M. H. (1971). On the nature of the protein interior. *Biochim. Biophys. Acta* **229**, 557–566.

74 Harpaz, Y., Gerstein, M., & Chothia, C. (1994). Volume changes on protein folding. *Structure* **2**, 641–659.

75 Chen, J. & Stites, W. E. (2001). Packing is a key selection factor in the evolution of protein hydrophobic cores. *Biochemistry* **40**, 15280–15289.

76 Varadarajan, R., Connelly, P. R., Sturtevant, J. M., & Richards, F. M. (1992). Heat capacity changes for protein-peptide interactions in the ribonuclease S system. *Biochemistry* **31**, 1421–1426.

77 Ratnaparkhi, G. S. & Varadarajan, R. (2000). Thermodynamic and structural studies of cavity formation in proteins suggest that loss of

packing interactions rather than the hydrophobic effect dominates the observed energetics. *Biochemistry* **39**, 12365–12374.

78 Zhou, H. & Zhou, Y. (2002). Stability scale and atomic solvation parameters extracted from 1023 mutation experiments. *Proteins Struct. Funct. Genet.* **49**, 483–492.

79 Zhou, H. & Zhou, Y. (2003). Quantifying the effect of burial of amino acid residues on protein stability. *Proteins Struct. Funct. Genet.* **54**, 315–322.

80 Schellman, J. A. (1955). The thermodynamics of urea solutions and the heat of formation of the peptide hydrogen bond. *C.R. Trav. Lab. Carlsberg, Sér. Chim.* **29**, 223–229.

81 Klotz, I. M. & Franzen, J. S. (1962). Hydrogen bonds between model peptide groups in solution. *J. Am. Chem. Soc.* **84**, 3461–3466.

82 Susi, H., Timasheff, S. N., & Ard, J. S. (1964). Near infrared investigation of interamide hydrogen bonding in aqueous solution. *J. Biol. Chem.* **239**, 3051–3054.

83 Epand, R. M. & Scheraga, H. A. (1968). The influence of long-range interactions on the structure of myoglobin. *Biochemistry* **7**, 2864–2872.

84 Taniuchi, H. & Anfinsen, C. B. (1969). An experimental approach to the study of the folding of staphylococcal nuclease. *J. Biol. Chem.* **244**, 3864–3875.

85 Klee, W. A. (1968). Studies on the conformation of ribonuclease S-peptide. *Biochemistry* **7**, 2731–2736.

86 Brown, J. E. & Klee, W. A. (1971). Helix-coil transition of the isolated amino-terminus of ribonuclease. *Biochemistry* **10**, 470–476.

87 Bierzynski, A., Kim, P. S., & Baldwin, R. L. (1982). A salt bridge stabilizes the helix formed by the isolated C-peptide of RNase A. *Proc. Natl Acad. Sci. USA* **79**, 2470–2474.

88 Baldwin, R. L. (1995). α-Helix formation by peptides of defined sequence. *Biophys. Chem.* **55**, 127–135.

89 Muñoz, V. & Serrano, L. (1994). Elucidating the folding problem of helical peptides using emprical parameters. *Nature Struct. Biol.* **1**, 399–409.

90 Aurora, R. & Rose, G. D. (1998). Helix capping. *Protein Sci.* **7**, 21–38.

91 Marqusee, M., Robbins, V. H., & Baldwin, R. L. (1989). Unusually stable helix formation in short alanine-based peptides. *Proc. Natl Acad. Sci. USA* **86**, 5286–5290.

92 Rohl, C. A., Chakrabartty, A., & Baldwin, R. L. (1996). Helix propagation and N-cap propensities of the amino acids measured in alanine-based peptides in 40 volume percent trifluoroethanol. *Protein Sci.* **5**, 2623–2637.

93 Dyson, H. J., Cross, K. J., Houghten, R. A., Wilson, I. A., Wright, P. E., & Lerner, R. A. (1985). The immunodominant site of a synthetic immunogen has a conformational preference in water for a type-II reverse turn. *Nature (London)* **318**, 480–483.

94 Dyson, H. J., Rance, M., Houghten, R. A., Lerner, R. A., & Wright, P. E. (1988). Folding of immunogenic peptide fragments of proteins in water solution. I. Sequence requirements for the formation of a reverse turn. *J. Mol. Biol.* **201**, 161–200.

95 Blanco, F. J., Rivas, G., & Serrano, L. (1995). A short linear peptide that folds into a stable native β-hairpin in aqueous solution. *Nature Struct. Biol.* **1**, 584–590.

96 Lifson, S., Hagler, A. T., & Dauber, P. (1979). Consistent force field studies of hydrogen-bonded crystals. 1. Carboxylic acids, amides, and the C=O•••H– hydrogen bonds. *J. Am. Chem. Soc.* **101**, 5111–5121.

97 Wolfenden, R. (1978). Interaction of the peptide bond with solvent water: a vapor phase analysis. *Biochemistry* **17**, 201–204.

98 Wolfenden, R., Andersson, L., Cullis, P. M., & Southgate, C. C. B. (1981). Affinities of amino acid side chains for solvent water. *Biochemistry* **20**, 849–855.

99 Sitkoff, D., Sharp, K. A., & Honig, B. (1994). Accurate calculation of

hydration free energies using macroscopic solvent models. *J. Phys. Chem.* **98**, 1978–1988.

100 Avbelj, F., Luo, P., & Baldwin, R. L. (2000). Energetics of the interaction between water and the helical peptide group and its role in determining helix propensities. *Proc. Natl Acad. Sci. USA* **97**, 10786–10791.

101 Eisenberg, D. & McLachlan, A. D. (1986). Solvation energy in protein folding and binding. *Nature (London)* **319**, 199–203.

102 Dunitz, J. D. (1994). The entropic cost of bound water in crystals and biomolecules. *Science* **264**, 670.

103 Rashin, A. A. & Honig, B. (1985). Reevaluation of the Born model of ion hydration. *J. Phys. Chem.* **89**, 5588–5593.

104 Fersht, A. R., Shi, J.-P., Knill-Jones, J. et al. (1985). Hydrogen bonding and biological specificity analysed by protein engineering. *Nature (London)* **314**, 235–238.

105 Fersht, A. R. (1987). The hydrogen bond in molecular recognition. *Trends Biochem. Sci.* **12**, 301–304.

106 Baldwin, R. L. (2003). In search of the energetic role of peptide H-bonds. *J. Biol. Chem.* **278**, 17581–17588.

107 Mitchell, J. B. O. & Price, S. L. (1991). On the relative strengths of amide•••amide and amide•••water hydrogen bonds. *Chem. Phys. Lett.* **180**, 517–523.

108 Galison, P. (1997). *Image and Logic*, p. 68, University of Chicago Press, Chicago.

109 Born, M. (1920). Volumen und Hydrationswärme der Ionen. *Z. Physik* **1**, 45–48.

110 Grossfield, A., Ren, P., & Ponder, J. W. (2003). Ion solvation thermodynamics from simulation with a polarizable force field. *J. Am. Chem. Soc.* **125**, 15671–15682.

111 Kirkwood, J. G. & Westheimer, F. H. (1938). The electrostatic influence of substituents on the dissociation constants of organic acids. *J. Chem. Phys.* **6**, 506–512.

112 Rajasekaran, E., Jayaram, B., & Honig, B. (1994). Electrostatic interactions in aliphatic dicarboxylic acids: a computational route to the determination of pK shifts. *J. Am. Chem. Soc.* **116**, 8238–8240.

113 Florian, J. & Warshel, A. (1997). Langevin dipoles model for ab initio calculations of chemical processes in solution: parameterization and application to hydration free energies of neutral and ionic solutes and conformational analysis in aqueous solution. *J. Phys. Chem. B* **101**, 5583–5595.

114 Brant, D. A. & Flory, P. J. (1965). The configuration of random polypeptide chains. II. Theory. *J. Am. Chem. Soc.* **87**, 2791–2800.

115 Brant, D. A. & Flory, P. J. (1965). The role of dipole interactions in determining polypeptide configurations. *J. Am. Chem. Soc.* **87**, 663–664.

116 Avbelj, F. & Moult, J. (1995). Role of electrostatic screening in determining protein main chain conformational preferences. *Biochemistry* **34**, 755–764.

117 Avbelj, F. & Fele, L. (1998). Role of main-chain electrostatics, hydrophobic effect and side-chain conformational entropy in determining the secondary structure of proteins. *J. Mol. Biol.* **279**, 665–684.

118 Avbelj, F. (2000). Amino acid conformational preferences and solvation of polar backbone atoms in peptides and proteins. *J. Mol. Biol.* **300**, 1335–1359.

119 Creamer, T. P. & Rose, G. D. (1994). α-Helix-forming propensities in peptides and proteins. *Proteins Struct. Funct. Genet.* **19**, 85–97.

120 Luo, P. & Baldwin, R. L. (1999). Interaction between water and polar groups of the helix backbone: an important determinant of helix propensities. *Proc. Natl Acad. Sci. USA* **96**, 4930–4935.

121 Avbelj, F. & Baldwin, R. L. (2002). Role of backbone solvation in determining thermodynamic *β* propensities of the amino acids. *Proc. Natl Acad. Sci. USA* **99**, 1309–1313.

122 Ben-Tal, N., Sitkoff, D., Topol, I. A., Yang, A.-S., Burt, S. K., & Honig, B.

(1997). Free energy of amide hydrogen bond formation in vacuum, in water, and in liquid alkane solution. *J. Phys. Chem. B* **101**, 450–457.

123 Lopez, M. M., Chin, D.-H., Baldwin, R. L., & Makhatadze, G. I. (2002). The enthalpy of the alanine peptide helix measured by isothermal titration calorimetry using metal-binding to induce helix formation. *Proc. Natl Acad. Sci. USA* **99**, 1298–1302.

124 Goch, G., Maciejczyk, Oleszczuk, M., Stachowiak, D., Malicka, J., & Bierzynski, A. (2003). Experimental investigation of initial steps of helix propagation in model peptides. *Biochemistry* **42**, 6840–6847.

125 Myers, J. K. & Pace, C. N. (1996). Hydrogen bonding stabilizes globular proteins. *Biophys. J.* **71**, 2033–2039.

126 Jayasinghe, S., Hristova, K., & White, S. H. (2001). Energetics, stability and prediction of transmembrane helices. *J. Mol. Biol.* **312**, 927–934.

127 Loladze, V. V., Ermolenko, D. N., & Makhatadze, G. I. (2002). Thermodynamic consequences of burial of polar and nonpolar amino acid residues in the protein interior. *J. Mol. Biol.* **320**, 343–357.

128 Loladze, V. V., Ermolenko, D. N., & Makhatadze, G. I. (2001). Heat capacity changes upon burial of polar and nonpolar groups in proteins. *Protein Sci.* **10**, 1343–1352.

7
Electrostatics of Proteins: Principles, Models and Applications

Sonja Braun-Sand and Arieh Warshel

7.1
Introduction

The foundation of continuum (classical) electrostatic theory was laid in the early eighteenth century and formulated rigorously by the Maxwell equations. Unfortunately, this formal progress and the availability of analytical solutions of a few simple cases have not provided proper tools for calculations of electrostatic energies in proteins. Here one is faced with electrostatic interactions in microscopically small distances, where the concepts of a dielectric constant are problematic at best. Furthermore, the irregular shape of protein environments made the use of analytical models impractical. Nevertheless, the realization that some aspects of protein action must involve electrostatic interactions led to the emergence of simplified phenomenological models [1, 2] that could provide in some cases a useful insight (see below).

The availability of X-ray structures of proteins and the search for concrete quantitative results led to the emergence of modern, microscopically based studies of electrostatic effects in proteins (see below). These studies and subsequent numerical continuum studies led to the gradual realization that the electrostatic energies provide by far the best structure function correlator for proteins and other macromolecules (Section 7.6). However, the overwhelming impact of macroscopic concepts still leads to major confusions in the field and to oversimplified assumptions. Here the problem can be reduced by focusing on relevant validation studies (Section 7.5).

This review will consider the above issues and try to lead the reader from concepts to models and to applications, pointing out pitfalls and promising directions. General background material can also be found in the following reviews [3–9].

7.2
Historical Perspectives

The basis for all electrostatic theories is Coulomb's law, which expresses the reversible work of bringing two charges (Q_i and Q_j) together by:

Protein Folding Handbook. Part I. Edited by J. Buchner and T. Kiefhaber

ISBN: 3-527-30784-2

$$\Delta W = 332 Q_i Q_j / r_{ij} \tag{1}$$

Where the free energy is given in kcal mol^{-1}, the distance in Å, and Q in atomic units (au). Manipulations of this led to the general macroscopic equation [10]:

$$\mathbf{V}\mathbf{E} = 4\pi\rho \tag{2}$$

where $\mathbf{E}$ is the macroscopic electric field and ρ is the charge density ($\rho(\mathbf{r}) = \sum_i Q_i(\delta(\mathbf{r} - \mathbf{r}_i))$). Further manipulation, using the fact that the field $\mathbf{E}$ can be expressed as a gradient of a scalar potential, U, gives:

$$\mathbf{E} = -\mathbf{V}U \tag{3}$$

which leads to the Poisson equation:

$$\nabla^2 U(r) = -4\pi\rho(r) \tag{4}$$

Assuming that the effects which are not treated explicitly can be represented by a dielectric constant, ε, leads to:

$$\mathbf{V}\varepsilon(r)\mathbf{V}U(r) = -4\pi\rho(\mathbf{r}) \tag{5}$$

When ions are presented in the solution around our system and when the ion distribution is described by the Boltzmann distribution we obtain rather some approximation, the linearized Poisson–Boltzmann (PB) equation:

$$\mathbf{V}\varepsilon(\mathbf{r})\mathbf{V}U(\mathbf{r}) = -4\pi\rho(\mathbf{r}) + \kappa^2 U \tag{6}$$

where κ is the Debye–Hückel screening parameter. The major problem with these ''rigorous'' equations is their physical foundation. Not only that the continuum assumptions are very doubtful on a molecular level, but the nature of the dielectric constant in this equation is far from being obvious when applied to heterogeneous environments. Nevertheless, the early history of protein electrostatics has been marked by the emergence of phenomenological models [2, 11]. Perhaps the most influential model was the Tanford Kirkwood (TK) model [2] that describes the protein as a sphere with a uniform dielectric constant. The validity of this model was not obvious since it was formulated before the elucidation of the structure of proteins. However, subsequent analysis by Warshel and coworkers [12] indicates that the model ignores one of the most important physical aspects of protein electrostatics, the self-energy of the charged groups (the energy of forming these charges in the given protein site). This problem was not obvious at the time of the formulation of the TK model, when it was thought that the ionizable groups reside on the surface of the protein). However, this assumption was found to be incorrect in key cases. Nevertheless, the TK model is repeatedly invoked as a physically reasonable model, where only the assumption of a spherical shape is considered as a rough approximation. Interestingly, even today we find cases where the self-energy

term is neglected [13]. Another fundamental problem of the early phenomenological models was the selection of the protein dielectric constant. This problem remains a major issue in modern continuum models (see Section 7.4).

The emergence of modern electrostatic models can probably be traced to the work of Warshel and Levitt [14]. In this work it was realized that the only way to reach clear conclusions about enzyme catalysis is to obtain quantitative estimates of the corresponding electrostatic energies. This meant that any concept about the dielectric constant of proteins would generate nonunique conclusions about the origin of enzyme catalysis. The best way to overcome this problem was to abandon the concept of a dielectric constant and to develop a simplified microscopic model that included all feasible microscopic contributions. The solvent was modeled by an explicit grid of Langevin dipoles (LD) and the protein was modeled explicitly, taking into account its permanent and induced dipoles, as well as a limited reorganization (by energy minimization).

The resulting protein dipoles Langevin dipoles (PDLD) model was the first model to capture correctly the physics of protein electrostatics. In fact, the microscopic perspective of the PDLD microscopic model has been the best guarantee against the traps of the continuum concepts (see below).

The introduction of discretized continuum (DC) models [4, 15, 16] and the inherent respect to the authoritative continuum equations (e.g., Eqs (2)–(6)) led to a wide acceptance of DC models. In fact, many workers have no problem accepting the questionable continuum description while questioning more microscopic models (see Section 7.3.2). This trend was not slowed down by the identification of major conceptual problems that were pointed out and resolved by the use of microscopic models [3, 7, 12, 17]. More specifically, early DC models overlooked self-energy, ignored the key role of the protein permanent dipoles [17] and used unjustified dielectric constants [3, 19]. However, the so-called continuum models kept evolving and becoming more and more microscopic and in many respects converging to the PDLD and its semi-macroscopic version, the PDLD/S-LRA model (see below). At present we have a wide range of almost reasonable electrostatic models, but there is still major ignorance about the nature and the meaning of different aspects of these models (e.g., the dielectric constant). Some of these issues will be clarified in Sections 7.3 and 7.4. At any rate, it is important to realize here that almost any conceptual problem of the continuum models have been resolved and clarified by the use of microscopic concepts. Perhaps the best example is the elucidation of the nature of the protein dielectric constant [3, 19].

Early, insightful observations of Perutz [20] and others (see, for example, Refs [21–23]) have indicated that electrostatic interactions must play an important role in biology. However, it was the development of computational methods and their successful applications that led to the realization that electrostatic energies provide the best structure–function correlation for proteins [18]. This has been demonstrated in studies of a wide range of properties that will be considered in Section 7.6. However, in some cases it took major effort to convince the scientific community of the importance of electrostatic contributions to different effects. For example, some workers invoked entropic and dynamic effects as crucial factors, even in cases

of charge formation, such as redox and ionization processes. This assumption may have reflected unfamiliarity with the fact that electrostatic free energies involve entropy changes, and that averaging over configurations is an integral part of the proper evaluation of electrostatic free energies rather than an inherent dynamic effect. In some important cases, such as enzyme reactions, it was impossible to assess the importance of electrostatic effects without developing quantitative models. Here the use of macroscopic estimates led repeatedly to the conclusion that electrostatic effects cannot play a major role in catalysis (see, for example, Ref. [24]).

7.3 Electrostatic Models: From Microscopic to Macroscopic Models

Although the progress in studies of electrostatic effects is sometimes taken to be synonymous with that in continuum approaches [25], in fact a wide range of modeling approaches exist (Figure 7.1), each with its own scope and limitations. This includes, of course, the aforementioned difficulty of analyzing continuum results without the use of microscopic models. Thus, it is important to understand the relationship between various approaches, spanning a range from continuum dielectrics to all-atom classical representations and quantum mechanical models. For example, there is a surprising degree of confusion regarding dipolar models that bridge the all-atom and continuum dielectric models. Below we will consider the key classes of electrostatic models and discuss their current scope and limitations.

7.3.1 All-Atom Models

An all-atom model describes a system as a collection of particles that interact via a quantum mechanical potential surface or the corresponding classical force field. Although such approaches can be quite rigorous, adequate convergence may sometimes not be achieved even with nanosecond simulations, particularly for macromolecules. One of the most significant ''unresolved'' issues in atomistic simulations is the proper representation of an infinite system, which is critical for the proper treatment of long-range electrostatic effects. Periodic boundary conditions, although appropriate in nonpolar systems for nonelectrostatic problems or in molecular crystals [26], cannot produce truly infinite noncrystalline systems without artifacts when long-range electrostatic interactions are significant. It is only now becoming commonly appreciated that the Ewald method for periodic boundary conditions gives divergent solvation energies for the same solute depending on the size of the simulated system [27]. Correction formulas for specific charge distributions [28] do not provide a general solution (see discussion in Ref. [29]). As demonstrated elsewhere [29–31], problems do not exist in simulations that use spherical boundary conditions and utilize the local reaction field (LRF) approach [32].

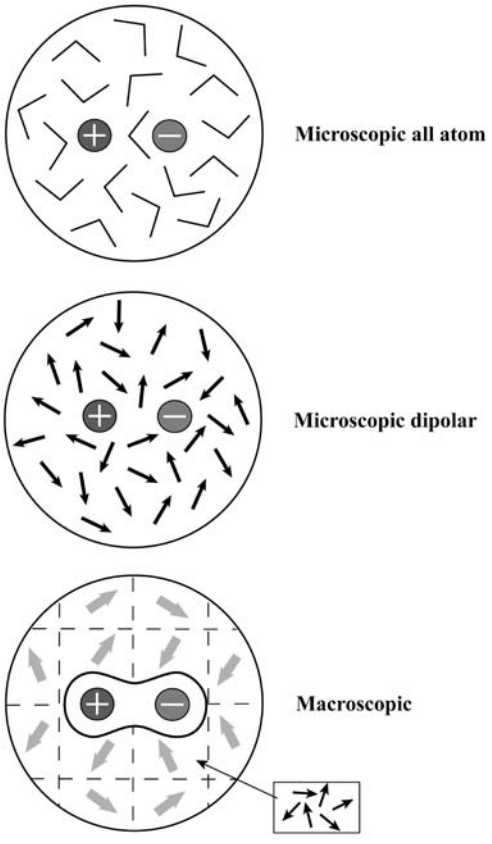

Fig. 7.1. The three main options for representing the solvent in computer simulation approaches. The microscopic model uses detailed all-atom representation and evaluates the average interaction between the solvent residual charges and the solute charges. Such calculations are expensive. The simplified microscopic model replaces the time average dipole of each solvent molecule by a point dipole, while the macroscopic model is based on considering a collection of solvent dipoles in a large volume element as a polarization vector.

Spherical boundary conditions offer an obvious alternative that is more physically consistent than the Ewald methods. There is no spurious periodicity; a spherical region of atomic representation is surrounded by a simplified region. Because the simplified outer region is far from the focal point of the simulation, its effect can be made to be indistinguishable from that of an atomistic representation. The issues involved in constructing proper boundaries for spherical models are logical and obvious. The most important requirement is that the system will maintain proper polarization at and around the boundaries [33]. This requirement, which is far more important than the physically trivial requirement of maintaining proper

heat flow by stochastic boundaries [34], has been solved by the surface constraint all-atom solvent (SCAAS) model [35].

It is important to reemphasize here that the problem is not the well-known bulk contribution from the surrounding of the simulation sphere [36], which has been implemented repeatedly in simulation studies (see, for example, Refs [37] and [38]), but the polarization at the microscopic boundaries of the simulation sphere.

With reasonable boundary conditions and proper long-range treatment, one may use all-atom models for evaluation of electrostatic free energies. Here the most obvious approach is the free energy perturbation (FEP) approach [39, 40] which involves a gradual change of the solute charge from zero to its actual value $Q = Q_0$ using a mapping potential of the form (see, for example, Refs [39] and [41]):

$$V_m = V(Q = 0)(1 - \lambda_m) + V(Q_0)\lambda_m \tag{7}$$

and then evaluating the corresponding free energy change by:

$$\exp\{-\Delta G(\lambda_m \rightarrow \lambda_{m+1})\beta\} = \langle \exp\{-(V_{m+1} - V_m)\beta\} \rangle_{V_m} \tag{8}$$

where $\langle\ \rangle_{V_m}$ designates a molecular dynamics (MD) average over V_m and $\beta = 1/k_B T$. A very useful alternative approach is the linear response approximation (LRA) where the free energy is given by [42]:

$$\Delta G(Q = 0 \rightarrow Q_0) = \tfrac{1}{2}[\langle V(Q_0) - V(Q = 0) \rangle_{V(Q_0)} + \langle V(Q_0) - V(Q = 0) \rangle_{V(Q=0)}] \tag{9}$$

Although the use of the FEP and LRA approaches is very appealing, it still involves major convergence problems and a relatively small number of systematic studies (see, for example, Refs [39] and [43–45]).

7.3.2 Dipolar Lattice Models and the PDLD Approach

The most natural simplification of all-atom polar models involves the representation of molecules or groups as dipoles. Dipolar models have a long history in the theory of polar solvents and in providing the fundamental microscopic basis of electrostatic theories. Simulations with sticky dipoles [46] and formal studies [47] addressing the origin of the dipolar representation have been recently reported. The nature of the Brownian dipole lattice (BDL) and Langevin dipole (LD) models and their relationship to continuum models has been established [48]. This study indicated that continuum solvation models are the infinite dipole density limit of a more general dipolar representation, and that their linearity is a natural consequence of being at that limit (although the discreteness of dipole lattice models is not equal to that of continuum models [49]). It was also found that the linearity of a continuum model is a direct consequence of being the infinite density limit of a dipolar model. An instructive conclusion of the above studies is the finding that

the solvation behavior of the LD model is identical to that of the more rigorous BDL model. This is significant since a version of the LD model, the protein dipoles Langevin dipoles (PDLD) model, has been used extensively to treat electrostatics in macromolecules [3]. PDLD is probably the first to properly treat macromolecular electrostatics.

At this point it might be useful to readdress the criticism of the PDLD model by some workers who have little difficulties accepting macroscopic models as a realistic description of macromolecules. Some of this criticism involved selective citation of incorrect arguments (see discussion in footnote 21 of Ref. [43]). Unfortunately the criticism continues despite the obvious conclusions of repeated rigorous studies of dipolar lattices [49] and related models (for example, see the recent excellent study of Borgis and coworkers [50]). An instructive example is the suggestion [51] that the PDLD model of Ref. [14] did not evaluate self-energies and that this model is in fact macroscopic in nature and that it is physically equivalent to the use of a finite-difference grid within DC methods. These assertions are incorrect both in presentation of facts and in interpretation of the physics of dipolar solvents. It should be clear by now that a grid of dipoles with finite spacing or the equivalent system of polar molecules on a lattice is not equivalent to the numerical grid used in evaluating the electrostatic potential in DC approaches (see the clear analysis of footnote 26 of Ref. [43]).

Another more recent example is the attempt to support the argument that the LD and DC models are equivalent, which was advanced by Ref. [8]. This work stated ''the LD model is not only analogous to the continuum model (as stated many times in the literature), but identical to the continuum model in its discrete approximation,'' continuing ''to our knowledge this rigorous equivalence was only pointed out very recently [50].'' Not only does this reflect a clear misunderstanding of the conclusions of Ref. [50], but it also overlooks the rigorous finding of Ref. [49], where it was found that the LD and DC models have different structural features even at the *limit* of infinitely small spacing. Only with a regular cubic grid of linearized Langevin dipoles and with a Clausius-Mossotti based local polarizability one can move, at the limit of infinitely small spacing, from the LD to the DC limit.

In considering the difference between the LD and continuum philosophies, it should be realized that the original LD model, with its finite spacing, has always been a simplified microscopic model. Insisting on the clear physical features of the model (i.e., the clear identification of each grid point as a discrete particle) has been the reason for the fact that the PDLD model did not fall into all the traps that plagued continuum studies of proteins. For example, looking at the microscopic interactions led immediately to the explicit considerations of the protein permanent dipoles rather than to the futile attempt of representing them by a low dielectric constant. At any rate, saying that the LD model (or other dipolar model) is equal to a continuum model is like saying that an all-atom model is equal to a continuum model. Finally, if the reader is still confused at this point by the suggestion that the LD model is a continuum model [8, 51], it is useful to point out that macroscopic models involve scaling by a dielectric constant but no such scaling is used in the PDLD model.

7.3.3 The PDLD/S-LRA Model

The PDLD model and other microscopic models do not involve any dielectric constant. While this is a conceptual strength it is also sometimes a practical "weakness" since they involve the balance between very large contributions, which is hard to obtain without a perfect convergence. In some cases it is possible to assume that the balance must exist and to represent this balance by scaling the results with a dielectric constant (see Section 7.4). Such a philosophy leads to semi-macroscopic models, which are obviously more stable (but not necessarily more reliable) than the corresponding microscopic models. A promising way to exploit the stability of the semi-macroscopic models, and yet to keep a clear physical picture, is the semi-macroscopic version of the PDLD model (the PDLD/S model [52]). The PDLD/S model takes the PDLD model and scales the corresponding contributions by assuming that the protein has a dielectric constant ε_p. Now, in order to reduce the unknown factors in ε_p it is useful to move to the PDLD/S-LRA model, where the PDLD/S energy is evaluated within the LRA approximation with an average on the configurations generated by MD simulation of the charged and the uncharged states (see Refs [19, 37, 43]). In this way one uses MD simulations to automatically generate protein configurations for the charged and uncharged forms of the given "solute" and then average these contributions according to Eq. (9). This treatment expresses the free energy of moving a charge from water to the protein active site, which is given by [42]:

$$\Delta\Delta G_{sol}^{w\to p} = \tfrac{1}{2}[\langle \Delta U^{w\to p}(Q=0\to Q=Q_0)\rangle_{Q_0} + \langle \Delta U^{w\to p}(Q=Q_0)\rangle_{Q=0}] \qquad (10)$$

where

$$\Delta U^{w\to p} = [\Delta\Delta G_p^w(Q=0\to Q=Q_0) - \Delta G_Q^w]\left(\frac{1}{\varepsilon_p}-\frac{1}{\varepsilon_w}\right) + \Delta U_{Q\mu}^p(Q=Q_0)\frac{1}{\varepsilon_p} \qquad (11)$$

Here ΔG_Q^w is the solvation energy of the given charge in water, $\Delta\Delta G_p^w$ is the change in the solvation energy of the entire protein (plus its bound charge) upon changing this charge from its actual value (Q_0) to zero. $\Delta U_{Q\mu}$ is the microscopic electrostatic interaction between the charge and its surrounding protein polar groups (for simplicity we consider the case when the interaction with the protein ionizable groups is treated in a separate cycle (see, for example, Ref. [43]) with the effective dielectric constant ε_{eff} of Section 7.3.5. Now we bring here the explicit expression of Eq. (11), since to the best of our knowledge it provides the clearest connection between microscopic quantities such as $\Delta\Delta G_p^w$ and $\Delta U_{Q\mu}$ and semi-macroscopic treatments. In fact, the PDLD/S treatment without the LRA treatment converges to the PB treatment and thus provides the clearest connection between PB treatments and microscopic treatments, allowing one to demonstrate the exact nature of ε_{eff} (see, for example, Ref. [19] and Section 7.4). At any rate, it is important to keep in mind

that the LRA considerations of Eq. (10) treat the protein reorganization explicitly, and this reduces the uncertainties about the magnitude of ε_p. It is also important to mention that the recently introduced molecular mechanics PB surface area (MM-PBSA) model [53] is basically an adaptation of the PDLD/S-LRA idea of MD generation of configurations for implicit solvent calculations, while only calculating the average over the configurations generated with the charged solute (the first term of Eq. (9)).

7.3.4 Continuum (Poisson-Boltzmann) and Related Approaches

Continuum solvent models have become a powerful tool for calculations of solvation energies of large solutes in solutions. Here one solves the Poisson equation or related equations [54] numerically [15, 16]. However, these treatments need more than the solvent dielectric, ε_s, to be useful. Solvation energy depends on the chosen solute cavity radius much more strongly than it does on ε_s. In addition to solute size, the cavity radius must absorb the effect of local structure near the solute. Consistent studies [49] showed that the cavity radius depends on the degree of solvent discreteness, even though the solute "size," as defined by an exclusion radius, is invariant. Also, a "cavity-in-a-continuum" description of solvation is physically inconsistent for discrete (i.e., real) solvents, leading to Born radii that depend on purely nonstructural factors [49, 55]. Thus, one cannot treat the cavity size as a transferable parameter that can be used in different dielectrics or in a given dielectric under even moderately different conditions.

PB approaches for studies of protein electrostatics represent the solvent and the protein by two dielectric constants (ε_p and ε_s, respectively) and solve numerically Eqs (5) or (6). Although these approaches became extremely popular, they involve significant conceptual and practical problems. Purely macroscopic (continuum) models are entirely inadequate for proteins because they miss the crucial local polarity defined largely by the net orientations of protein permanent dipoles rather than by a dielectric constant [7, 52]. The effect of these dipoles (sometimes called "back field"; see Ref. [43]) is now widely appreciated. Thus, most current "continuum" models are no longer macroscopic but semi-macroscopic and therefore potentially reliable. Their reliability depends, however, on properly selecting the "dielectric constant" ε_p (see below) for the relevant protein region. Despite recent suggestions that the reliability of continuum methods can be increased by configurational averaging [19], such averaging still does not capture the crucial protein reorganization effect (see Section 7.4).

The popularity of continuum models may be due to the belief that the formulation of the PB equation must reflect some fundamental physics and that the criticism of such models only address minor points that can be "fixed" in one way or another. The discussion of conceptually trivial issues such as the linear approximation of the second term in Eq. (6) often created the feeling that this is the true problem in such models. In fact, the real unsolved problem is the fact that the results depend critically on ε_p, whose value cannot be determined uniquely (see Sec-

tion 7.4). Another reason for the acceptance of PB models has been the use of improper validation, addressing mainly trivial cases of surface groups where all macroscopic models would give the same results (see Section 7.5). At any rate, PB models (see, for example, Ref. [56]) are becoming more and more microscopic, borrowing ideas from the semi-macroscopic PDLD/S-LRA model.

7.3.5 Effective Dielectric Constant for Charge–charge Interactions and the GB Model

Electrostatic energies in proteins can be formulated in terms of a two-step thermodynamic cycle. The first step involves the transfer of each ionized group from water to its specific protein site where all other groups are neutral, and a second step where the interaction between the ionized groups is turned on [19]. Thus, we can write the energy of moving ionized groups from water to their protein site as:

$$\Delta G = \sum_{i=1}^{N} \Delta G_i + \sum_{i>j} \Delta G_{ij} \tag{12}$$

where the first and second terms correspond to the first and second steps, respectively. ΔG_i, which represents the change in self-energies of the i-th ionized group upon transfer from water to the protein site, can be evaluated by the PDLD/S-LRA approach with a relatively small ε_p. However, the charge–charge interaction terms (the ΔG_{ij}) are best reproduced by using a simple macroscopic Coulomb's-type law:

$$\Delta G_{ij} = 332 Q_i Q_j / r_{ij} \varepsilon_{ij} \tag{13}$$

where ΔG is given in kcal mol^{-1}, r_{ij} in Å and ε_{ij} is a relatively high distance-dependent dielectric constant [3, 12]. The dielectric constant ε_{ij} can be described by (e.g., Ref. [12]):

$$\varepsilon(r_{ij}) = 1 + \varepsilon' \lfloor 1 - \exp(-\mu r_{ij}) \rfloor \tag{14}$$

Although the fact that ε_{ij} is large has been supported by mutation experiments (e.g., [57, 58]) and conceptual considerations [3], the use of Eq. (13) is still considered by many as a poor approximation for PB treatments (without realizing that the PB approach depends entirely on an unknown ε_p). Interestingly, the so-called generalized Born (GB) model, whose usefulness is now widely appreciated [59], is basically a combination of Eq. (13) and the Born energy of the individual charges. Thus, the GB model is merely a version of an earlier treatment [3]. More specifically, as pointed out originally by Warshel and coworkers [3, 60], the energy of an ion pair in a uniform dielectric medium can be written as [3]:

$$\Delta G_{ij} = 332 Q_i Q_j / r_{ij} + \Delta G_{sol} = \Delta G_{sol}^{\infty} + 332 Q_i Q_j / r_{ij} \varepsilon \tag{15}$$

where the free energies are given in kcal mol^{-1} and the distances in Å. ΔG_{sol} is the solvation energy of the ions and ΔG^{∞}_{sol} is the solvation of the ions at infinite separation. Equation (15) gives (see also Ref. [3]):

$$\begin{aligned}\Delta G_{sol} &= \Delta G^{\infty}_{sol} - (332 Q_i Q_j / r_{ij})(1 - 1/\varepsilon) \\ &= -166[(Q_i^2/a_i + Q_j^2/a_j) + (2Q_i Q_j / r_{ij})](1 - 1/\varepsilon) \end{aligned} \quad (16)$$

where the a_i and a_j are the Born's radii of the positive and negative ions, respectively. Equation (16) with some empirical modifications leads exactly to the GB treatment [61]. Thus, the widely accepted GB treatment is in fact a glorified Coulomb's law treatment [7]. Nevertheless, it is instructive to note that the GB approximation can also be obtained by assuming a *local* model where the vacuum electric field, $\mathbf{E}_0$, and the displacement vector, $\mathbf{D}$, are identical [62]. This model, which can be considered as a ''local Langevin Dipole model'' [50] or as a version of the noniterative LD model, allows one to approximate the energy of a collection of charge and to obtain (with some assumptions about the position dependence of the dielectric constant) the GB approximation.

It should be noted that the simple derivations of the GB approximation are valid for homogeneous media with a high dielectric (e.g., the solvent around the protein). This can be problematic when one considers models where the protein has a low dielectric constant and when we are dealing with transfer of charges from water to the protein environment. Fortunately, it is reasonable to use a large ε for the second term in Eq. (15), even for protein interiors (see discussion of ε_{ij} of Eq. (14)). Here again, the main issue is the validity of Eq. (13) and not its legitimization by the seemingly ''rigorous'' GB formulation. It is also important to realize that a consistent treatment should involve the replacement of ΔG^{∞}_{sol} by the ΔG^{+} and ΔG^{-} of the ions in their specific protein site when ε_p is different from ε_w.

7.4 The Meaning and Use of the Protein Dielectric Constant

As demonstrated in the validation studies of Ref. [19], the value of the optimal dielectric constant depends drastically on the model used. This finding might seem a questionable conclusion to readers who are accustomed to the view that macroscopic models have a universal meaning. This might also look strange to some workers who are experienced with microscopic statistical mechanics, where ε is evaluated in a unique way from the fluctuations of the total dipole moment of the system (see below). Apparently, even now, it is not widely recognized that ε_p has little to do with what is usually considered as the protein dielectric constant. That is, as was pointed out and illustrated by the conceptual analysis of Warshel and Russell [3], the value of the dielectric constant of proteins is entirely dependent on the method used to define this constant and on the model used. Subsequent studies [5, 19, 63] clarified this fact and established its validity. As stated in these

studies the dependence of ε_p on the model used can be best realized by considering different limiting cases. That is, when all the interactions are treated explicitly, $\varepsilon = 1$; when all but induced dipoles are included explicitly, $\varepsilon = 2$ [3]; and when the solvent is not included explicitly, $\varepsilon > 40$ (although this is a very bad model). When the protein permanent dipoles are included explicitly but their relaxation (the protein reorganization) and the protein induced dipoles are included implicitly, the value of ε_p is not well defined. In this case ε_p should be between 4 and 6 for dipole–charge interactions and >10 for charge–charge interactions [64, 65].

One may clearly argue that there is only one "proper" dielectric constant, which is the one obtained from the fluctuation of the average dipole moment [6, 63, 66–68]. However this protein dielectric constant ($\varepsilon = \bar{\varepsilon}$) is not a constant because it depends on the site considered [63, 66]. More importantly (see above), $\bar{\varepsilon}$ cannot be equal to ε_p, where the simplest example is the use of explicit models where $\varepsilon_p = 1$. Detailed analysis of this issue is given in Ref. [69]. At any rate, it is still useful to review what has been learned on the nature of $\bar{\varepsilon}$. Apparently it has been found [63] that the value of $\bar{\varepsilon}$ can be significantly larger than the traditional value ($\bar{\varepsilon} \cong 4$) deduced from measurements of dry proteins and peptide powders [70, 71] or from simulations of the entire protein, rather than a specific region (see, for example, Ref. [63]). In fact, the early finding of $\bar{\varepsilon} = 4$, which was obtained from a gas phase study [71], ignored the large effect of the solvent reaction field (see analysis and discussion in Ref. [63]). The larger than expected value of $\bar{\varepsilon}$ was attributed to the fluctuations of ionized side chains [8, 66, 67]. However, consistent simulations [63] that included the reaction field of the solvent gave $\bar{\varepsilon} \cong 10$ in and near protein active sites, even in the absence of the fluctuations of the ionized residues. This established that the fluctuations of the protein polar groups and internal water molecules contribute significantly to the increase in $\bar{\varepsilon}$. In view of this finding it might be instructive to address recent suggestions [8] that the calculations of reference [63] did not converge. Apart from the problematic nature of this assertion it is important to realize that the SCAAS model used in Ref. [63] converges much faster than any of the periodic models (and the corresponding very large simulation systems) used in the alternative "converging" studies mentioned in Ref. [8]. In fact the convergence of $\bar{\varepsilon}$ in reference [63] was examined by longer runs and by using alternative formulations. Obviously, there is a wide intuitive support for the idea that $\bar{\varepsilon}$ in protein active sites cannot be large unless it reflects the effect of ionized surface groups. However, the scientific way to challenge the finding of Ref. [63] is to repeat the calculations of $\bar{\varepsilon}$ in the *active site* of trypsin (rather than the whole protein) and to see if the conclusions of Ref. [63] reflect convergence problems. Unfortunately, no such attempt to repeat the calculations of Ref. [63] (or to study $\bar{\varepsilon}$ in other active sites with and without ionizable surface groups) has been reported. Finally, it is important to realize that recent experimental studies [73, 74] provided a clear support to the finding that $\bar{\varepsilon}$ is large in active sites even when they are far from the protein surface.

In view of the above analysis, and despite the obvious interest in the nature of $\bar{\varepsilon}$, it should be recognized that $\bar{\varepsilon}$ is not so relevant to electrostatic energies in proteins. Here one should focus on the energies of charges in their specific environ-

ment and the best ways for a reliable and effective evaluation of these energies. Unfortunately, $\bar{\varepsilon}$ does not tell us in a unique way how to determine the ε_p of semi-macroscopic models. For example (see also above), obtaining $\varepsilon_p = 1$ in a fully microscopic model, or $\varepsilon_p = 2$ in a model with implicit induced dipoles has nothing to do with the corresponding $\bar{\varepsilon}$. The best way to realize this point is to think of charges in a water sphere (our hypothetical protein) surrounded by water. In such a model $\bar{\varepsilon} \cong 80$, whereas microscopic models of the same system with implicit induced dipoles will be best described by using $\varepsilon_p = 2$. Of course, one may argue that the entire concept of a dielectric constant is invalid in the heterogeneous environment of proteins [14]. However, because fully microscopic models are still not giving sufficiently precise results, it is very useful to have reasonable estimates using implicit models and in particular semi-macroscopic models. Thus, it is justified to look for optimal ε_p values after realizing, however, what these parameters really mean. Even the use of a consistent semi-macroscopic model such as the PDLD/S-LRA does not guarantee that the corresponding ε_p will approach a universal value. For example, in principal the PDLD/S-LRA model should involve $\varepsilon_p = 2$, because all effects except the effect of the protein-induced dipoles are considered explicitly. However, the configurational sampling by the LRA approach is not perfect. The protein reorganization energy is probably captured to a reasonable extent [69], but the change in water penetration on ionization of charged residues is probably not reproduced in an accurate way. This problem is particularly serious when we have ionized groups in nonpolar sites in the interior of the proteins. In such cases we have significant changes in water penetration and local conformations during the ionization process, (as indicated by the very instructive study of Ref. [75]) but these changes might not be reproduced in standard simulation times.

The fact that ε_{eff} for charge–charge interactions is large has been pointed out by several workers [12, 76, 77]. However, this important observation was not always analyzed with a clear microscopic perspective. Mehler and coworkers [76, 78] argued, correctly, that $\varepsilon_{eff}(r)$ is a sigmoid function with a large value at relatively short distances based on classical studies of $\varepsilon(r)$ in water [79–81]. Similarly, it has been assumed by Jonsson and coworkers [77] that electrostatic interactions in proteins can be described by using a large ε_{eff} for charge–charge interactions. Now, although we completely agree that ε_{eff} is large in many cases and we repeatedly advanced this view [3], we believe that the reasons for this are much more subtle. That is, the finding of a particular behavior of ε in water might be not so relevant to the corresponding behavior in proteins (in principle, ε_{eff} in proteins can be very different from ε_{eff} in water). Here the remarkable reason why ε_{eff} is large, even in proteins, was rationalized in Ref. [3], where it was pointed out that the large ε_{eff} must reflect the compensation of charge–charge interactions and solvation energy in proteins (see, for example, figure 4 in Ref. [64]). It seems to us that the understanding of this crucial compensation effect is essential for the understanding of ε_{eff} in proteins.

Finally, it might be useful to comment on the perception that somehow the macroscopic dielectric of a given region in the protein can still be used to provide a general description of the energetics of changes in the same region. The funda-

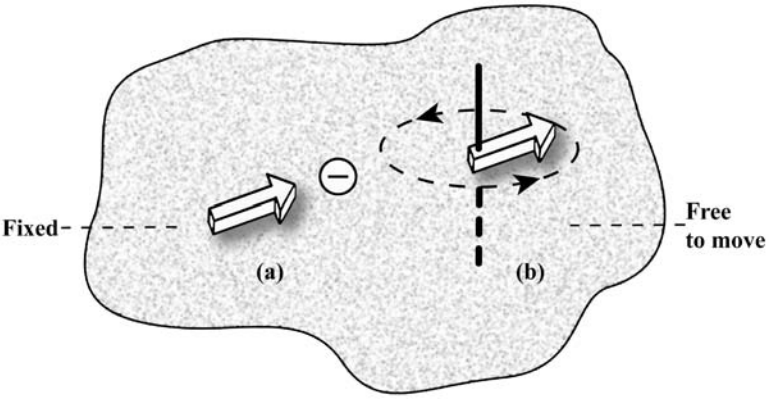

Fig. 7.2. A single macroscopic dielectric constant (which is evaluated by some microscopic prescription) cannot be used to reproduce the energetics of charges in proteins in a unique way. The figure considers a hypothetical site with a relatively fixed and freely rotated dipoles. Using the same ε_p for both dipoles will underestimate the effect of μ_a and overestimate the effect of μ_b.

mental problem with such an assertion is demonstrated in Figure 7.2. This figure considers a typical site with an internal site with two dipolar groups, one fixed (preorganized) and the other free to rotate. Since this is an internal site, the leading term in semi-macroscopic treatments will be the $\boldsymbol{U}_{\mathbf{Q}\boldsymbol{\mu}}/\varepsilon_p$ term of Eq. (11). Now, one of the best ways to estimate ε_p is to calculate the reorganization energy (λ) for the given charges [8, 69]. Using this ε_p (for $\boldsymbol{U}_{\mathbf{Q}\boldsymbol{\mu}}/\varepsilon_p$) for the interaction between site (a) to the charge will underestimate the corresponding free energy contribution, while using it for site (b) will overestimate this interaction. The same problem will occur if we use $\bar{\varepsilon}$ evaluated from the dipolar fluctuations in the site that includes the dipoles and the charge. Furthermore, if the site involves an ion pair instead of a single ionized group we will need a different ε_p to reproduce the energy of this ion pair.

7.5 Validation Studies

As discussed above, the conceptual and practical problems associated with the proper evaluation of electrostatic energies in proteins are far from trivial. Here the general realization of the problems associated with different models has been slow in part because of the use of improper validation approaches. For example, although it has been realized that pK_a value calculations provide an effective way for validating electrostatic models, [3, 39, 44, 72, 75, 78, 82, 83] most studies have focused mainly on the pK_a values of surface groups. Unfortunately, these pK_a values can be reproduced by many models, including those that are fundamentally incorrect [7]. Thus, the commonly used benchmarks may lead toward unjustified

conclusions about the nature of electrostatic effects in proteins. It has been pointed out [7, 19, 75] that ionizable groups in protein interiors should provide a much more discriminating benchmark because these groups reside in a very heterogeneous environment, where the interplay between polar and nonpolar components is crucial. For example, an ionizable group in a true nonpolar environment will have an enormous pK_a shift, and such a shift cannot be reproduced by models that assume a high dielectric in the protein interior. Similarly, a model that describes the protein as a uniform low dielectric medium, without permanent dipoles, will not work in cases where the environment around the ionizable group is polar [3].

The problems with nondiscriminating benchmarks were established in Ref. [19] and are reillustrated in Figure 7.3. This figure considers the pK_a values of acidic and basic groups and correlates the results obtained by the modified TK (MTK) model with the corresponding observed results. The figure gives the impression

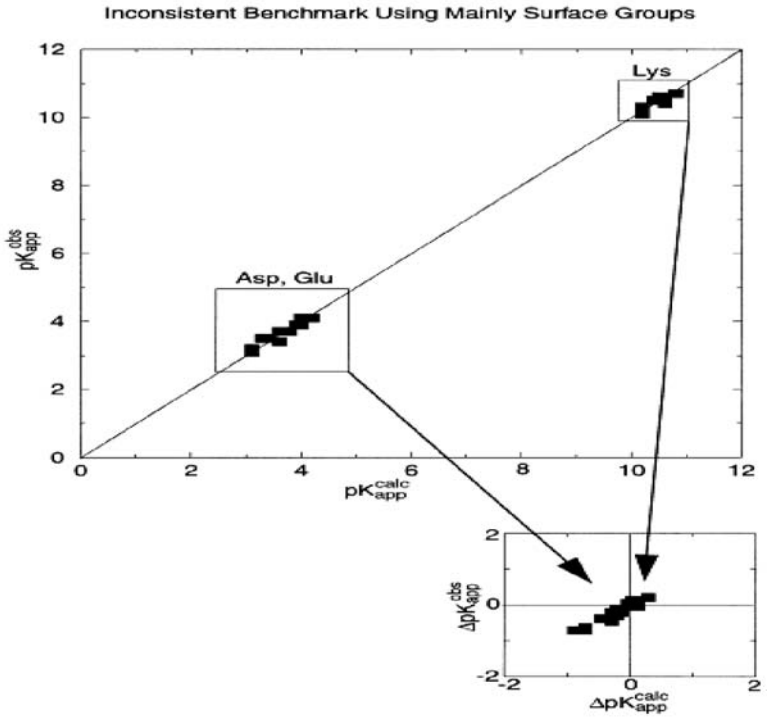

Fig. 7.3. The correlation between the calculated and observed pK_a values gives a nondiscriminative benchmark that only involves surface groups. The figure considers Asp, Glu, and Lys residues on the surfaces of lysozyme and ribonuclease but includes only those residues with $pK^{obs}_{app} < 1$. The calculated pK_a values are evaluated by the MTK(S) model with $\varepsilon_p = 40$ and $\varepsilon_{eff} = 80$. As seen from the figure, we obtain seemingly impressive results for this benchmark, but when the results are displayed as ΔpK_a, it becomes clear that we have simply a poor benchmark where $\Delta pK_a \approx 0$ and any model that produces a small pK_a shift looks like an excellent model.

that the MTK is an excellent model, but the same agreement would be obtained for any model that uses a large ε since most surface groups have very small ΔpK_a so that Asp and Glu have $pK_a \approx 4$ and all Lys have $pK_a \approx 10$. Thus, as emphasized in the inset in the figure, we are dealing with a very small amount of relevant information and probably the best correlation would have been obtained with the trivial null model when $\Delta pK_a = 0$ for all surface groups.

In view of the above example, it is very important to validate electrostatic models by using discriminative benchmarks (DBM) with $\Delta pK_a > 2$ and to use the same philosophy for other electrostatic properties. The use of a DBM in pK_a calculations [19] has been found to be extremely useful in demonstrating the range of validity and the proper dielectric of different models.

7.6 Systems Studied

7.6.1 Solvation Energies of Small Molecules

Modeling of almost any biological process requires one to know the solvation free energy of the relevant reacting system in aqueous solutions. Thus for example, calculations of binding energies compare the solvation energy of the ligand in its protein site to the corresponding solvation energy in solution. Early attempts to estimate solvation energies (see, for example, Refs [84] and [85]) were based on the use of the Born's or Onsager's model with basically arbitrary cavity radius. The first attempts to move toward quantitative evaluation of solvation energies can be divided into two branches. One direction involves attempts to examine quantum mechanically the interaction between the solute and a single solvent molecule [86, 87]. The other direction that turns out to be more successful involves the realization that quantitative evaluation of solvation free energies requires parameterization of the solute solvent van der Waals interaction in a complete solute solvent system [33] and evaluation of the interaction between the solvent and many (rather than one) solvent molecules.

Although such an empirical approach was considered initially as having "too many parameters" it was realized eventually that having an atom-solvent parameter for each type of the solute atoms is the key requirement in any quantitative semiempirical solvation model. The same number of parameters exists now in more recent continuum solvation models [54, 88, 89] and in all-atom models [35, 40, 41, 90]. At any rate, it took significant time (see Ref. [91]) until the realization that with any solvation model with a given set of solute charges, the most crucial step is the parameterization of the solute–solvent repulsion term (or the corresponding atomic radius).

Now assuming that we have reasonable atomic parameters the next requirement is to obtain converging results with the given modeling method (all-atom solvent simplified solvent model, PB model, GB model, etc.). Here the general progress is

quite encouraging, as is apparent from the results reported by many research groups.

FEP calculations have focused on the proper treatment of ionized groups and the role of proper boundary conditions [27, 28, 92]. Recently, the validity of the LRA treatment in solvation calculations was explored [93], and the LRA formalism was used in a quantum mechanical treatment [94]. LD calculations were found to give accurate results when incorporated into quantum mechanical models [95, 96] and similar success was reported in continuum [54, 97] and GB [98] studies. All of these models apparently give similar accuracy once properly parameterized. The deviation from experiments in special cases probably reflects the neglected charge transfer to the solvent.

The fact that the calculations of solvation energies of small molecules in solution give reasonable results does not guarantee reasonable results for the solvation energies of charged (or other) ligands in proteins. This issue will be addressed in subsequent sections. Another interesting and important issue is the solvation energy of the entire macromolecule. Here the options are, in principle, reasonable. One can use the LD model, PB model and GB model. The problem is, however, to get quantitative results. Some attempts will be considered in Section 7.6.10.

7.6.2
Calculation of pK_a Values of Ionizable Residues

The electrostatic energy of ionizable residues in proteins plays a major role in most biological processes including enzymatic reactions, proton pumps, and protein stability. Calculation of pK_a values of ionizable groups in proteins provides a stringent test of different models for electrostatic energies in proteins [3]. Calculations of pK_a values by all-atom FEP approaches have been reported in only a few cases [39, 45]. Recent works include studies of the pK_a of metal-bound water molecules [99] and proton transfer in proteins [100]. All-atom LRA calculations [43, 44] were also reported: the error range of the all-atom models is still somewhat disappointing, although the inclusion of proper long-range treatments and induced dipoles leads to some improvements [43, 45]. Remaining problems might reflect insufficient sampling of protein configurations and solvent penetration. PDLD/S-LRA calculations [19, 43] gave encouraging results with $\varepsilon_p = 4$. Although the LRA treatment accounts at least formally for the protein reorganization, the limit of $\varepsilon_p = 2$ (which would be expected from a ''perfect'' model with implicitly induced dipoles) has not been reached, since apparently some of this reorganization and/or water penetration is not captured in the computer time used in the simulations.

Semi-macroscopic ''continuum'' (i.e., PB) models, (which now include the protein permanent dipoles and the self-energy term [12]) also often give reasonable results (e.g., [72, 101, 102]). Yet most PB models do not treat the effect of the protein reorganization explicitly, and the so-called multi-conformation continuum electrostatic (MCCE) model [56] (which has been inspired by the LRA approach) only considers the reorganization of polar side chains instead of performing a

proper LRA treatment on all the protein coordinates. Another problem with current PB models is the assumption that the same ε_p should be used in accounting for the effect of the protein dipoles and in providing the screening for charge-charge interactions [19, 43]. This requirement led to inconsistency that can only be demonstrated by the use of discriminating benchmarks for both self-energies and charge–charge interactions. Although it is extremely important to continue to use DBM with large ΔpK_a in attempts to further explore the validity of different electrostatic models, it is important to realize that the trend in pK_a changes can be captured by models that focus more on charge–charge interactions than on the self-energy term or by models that estimate the self-energy term by empirical considerations [78].

It might be useful to point here to the perception that the need for averaging over the protein configurations is the main problem in continuum calculations of pK_a values [103–105]. First, the obvious need for proper configurational averaging in free energy calculations should not be confused, as done in several cases (e.g., [106]), with dynamics effects. Second, and perhaps more importantly, most attempts of configurational averaging involve only one charge state. This corresponds to only one charge state in the LRA treatment (Eq. (9)) and thus to incorrect estimates of the relevant charging free energy. Here it would help to recognize that a proper LRA averaging, rather than a simple average on one charge state, is essential for formally correct pK_a calculations.

Overall, we believe that a more complete consensus about the validity of different models for pK_a calculations will be obtained when the microscopic models start to give stable quantitative results. Here the comparison of the microscopic and semi-macroscopic models (as was done in Ref. [43]) will be particularly useful.

7.6.3
Redox and Electron Transport Processes

Electron transport processes are involved in key energy transduction processes in living systems (most notably photosynthesis). Such processes involve changes in the charges of the donor and acceptor involved, and thus are controlled by the electrostatic energies of the corresponding charges and the reorganization energies involved in the charge transfer process. Here the challenge is to evaluate the redox energies, and the reorganization energies using the relevant protein structure. Probably the first attempt to address this problem was reported by Kassner [107], who represented the protein as a nonpolar sphere. The idea that such a model can be used for analyzing redox properties held up for a significant time (see discussion in Refs [108–115]). However, Warshel and coworkers have shown by using the PDLD model [116, 117] that the evaluation of redox potentials must take into account the protein permanent dipoles, and the penetration of water molecules. The role of the protein permanent dipoles has been most clearly established in subsequent studies of iron–sulfur proteins [118, 119]. Another interesting factor is the effect of ionized groups on redox potentials. The effect of ionized residues

can usually be described well using Coulomb's law with a large effective dielectric constant [12, 57, 58].

Microscopic estimates of protein reorganization energies have been reported [57, 69, 120] and used very effectively in studies of the rate constants of biological electron transport. This also includes studies of the nuclear quantum mechanical effect, associated with the fluctuations of the protein polar groups (for review see Ref. [121]). PB studies of redox proteins have progressed significantly since the early studies that considered the protein as a nonpolar sphere (see above). These studies (e.g., [108, 111, 122–124]) started to reflect a gradual recognition of the importance of the protein permanent dipoles, although some confusion still exists (see discussion in Refs [108] and [114]).

Recent studies reported quantum mechanical evaluation of the redox potentials in blue copper proteins [125], but even in this case it was found that the key problem is the convergence issue, and at present semi-macroscopic models give more accurate results than microscopic models.

7.6.4 Ligand Binding

A reliable evaluation of the free energy of ligand binding can potentially play a major role in designing effective drugs against various diseases (e.g., [126]). Here we have interplay between electrostatic, hydrophobic, and steric effects, but accurate estimates of the relevant electrostatic contributions are still crucial.

In principle, it is possible to evaluate binding free energies by performing FEP calculations of the type considered in Eqs (7) and (8), for "mutating" the ligand to "nothing" in water and in the protein active site. This approach, however, encounters major converence problems, and at present the reported results are disappointing except in cases of very small ligands. Alternatively one may study in simple cases the effect of small "mutations" of the given ligand [40], for example replacement of NH_2 by OH. However, when one is interested in the absolute binding of medium-size ligands, it is essential to use simpler approaches. Perhaps the most useful alternative is offered by the LRA approach of Eq. (9), and augmented by estimates of the nonelectrostatic effects. That is, the LRA approach is particularly effective in calculating the electrostatic contribution to the binding energy [42, 127, 128]. With this approximation one can express the binding energy as

$$\Delta G_{\text{bind}} = \tfrac{1}{2}[\langle U^{\text{p}}_{\text{elec},l}\rangle_l + \langle U^{\text{p}}_{\text{elec},l}\rangle_{l'} - \langle U^{\text{w}}_{\text{elec},l}\rangle_l - \langle U^{\text{w}}_{\text{elec},l}\rangle_{l'}] + \Delta G^{\text{nonelec}}_{\text{bind}} \qquad (17)$$

where $U^{\text{p}}_{\text{elec},l}$ is the electrostatic contribution for the interaction between the ligand and its surrounding; p and w designate protein and water, respectively; and l and l' designate the ligand in its actual charge form and the "nonpolar" ligand where all the residual charges are set to zero. In this expression the terms $\langle U_{\text{elec},l} - U_{\text{elec},l'}\rangle$, which are required by Eq. (9), are replaced by $\langle U_{\text{elec},l}\rangle$ since $U_{\text{elec},l'} = 0$. Now, the evaluation of the nonelectrostatic contribution $\Delta G^{\text{nonelec}}_{\text{bind}}$ is still very challenging,

since these contributions might not follow the LRA. A useful option, which was used in Refs [42] and [127], is to evaluate the contribution to the binding free energy from hydrophobic effects, van der Waals, and water penetration. Another powerful option is the so-called linear interaction energy (LIE) approach [93]. This approach adopts the LRA approximation for the electrostatic contribution but neglects the $\langle U_{\mathrm{elec},l}\rangle_{l'}$ terms. The binding energy is then expressed as:

$$\Delta G_{\mathrm{bind}} \approx \alpha\lfloor\langle U^{\mathrm{p}}_{\mathrm{elec},l}\rangle_l - \langle U^{\mathrm{w}}_{\mathrm{elec},l}\rangle_l\rfloor + \beta\lfloor\langle U^{\mathrm{p}}_{\mathrm{vdW},l}\rangle_l - \langle U^{\mathrm{w}}_{\mathrm{vdW},l}\rangle_l\rfloor \tag{18}$$

where α is a constant that is around 1/2 in many cases and β is an empirical parameter that scales the van der Waals (vdW) component of the protein–ligand interaction. A careful analysis of the relationship between the LRA and LIE approaches and the origin of the α and β parameters is given in Refs [127].

More implicit models can, of course, estimate the binding energy. This includes the use of the PDLD/S-LRA model for both the electrostatic and nonelectrostatic components (see Refs [42] and [127]) and the PB approach augmented by estimates of the hydrophobic contributions using the calculated surface area of the ligand (e.g., [128, 129]).

The idea that conformational averaging is useful for calculations of binding energies seems quite obvious, generally understood and widely used [53]. What is much less understood and somehow still ignored by a large part of the computational community is the realization that a proper LRA treatment requires averaging on both the charged (or polar) and nonpolar states of the ligand. The frequently neglected average on the nonpolar state (the second term of Eq. (9)) plays a crucial role in proteins as it reflects the effect of the protein preorganization. The role of this term in binding calculations has been discussed in Ref. [127] and its importance has been illustrated in an impressive way in studies of the fidelity of DNA polymerase [130].

7.6.5 Enzyme Catalysis

Understanding enzyme catalysis is a subject of major practical and fundamental importance [131–134]. The development of combined quantum mechanical/molecular mechanics (QM/MM) computational models (e.g., [14, 131, 134–140]) that allow enzymatic reactions to be simulated provided a way for quantifying the main factors that contribute to enzyme catalysis. QM/MM studies, including those conducted by the empirical valence bond (EVB) method [132], helped to establish the proposal [141] that the electrostatic effects of preorganized active sites play a major role in stabilizing the transition states of enzymatic reactions [142]. In fact, there is now growing appreciation of this view (e.g., [143, 144]). Simulation approaches that focus on the electrostatic aspects of enzyme catalysis (i.e., the difference between the stabilization in the enzyme and solution) appear to give much more quantitative results than those that focus on the quantum mechanical aspects of the problem but overlook the proper treatment of long-range effects (see discussion in Ref. [145]). In fact, some problems can be effectively treated even

by PB approaches (see, for example, Ref. [146]) without considering quantum mechanical issues. Some studies focus on the role of the diffusion step of enzyme catalysis [147, 148]. As pointed out, however (e.g., [149]), these effects are trivial compared with the electrostatic effect of enzymes in actual chemical steps. Interestingly, evaluation of activation free energies of enzymatic reactions appeared to be simpler, in terms of the stability of the corresponding results, than other types of electrostatic calculations such as binding free energies (see discussion in Ref. [150]). This apparent advantage that has been exploited for a long time in EVB studies (see, for example, Ref. [131]) is now being reflected in molecular orbital QM/MM studies [134, 137, 151].

7.6.6 Ion Pairs

Ion pairs play a major role in biological systems and biological processes. This includes the "salt bridges" that control the Bohr effect in hemoglobin [152], ion pair type transition states [132], ion pairs that help in maintaining protein stability (see Section 7.6.9), ion pairs that play crucial roles in signal transduction (Section 7.6.6) and ion pairs that play a major role in photobiological processes [153]. Reliable analysis of the energetics of ion pairs in proteins presents a major challenge and has been the subject of significant conceptual confusions (see discussions in Refs [3] and [12]). The most common confusion is the intuitive assumption that ion pairs are more stable in nonpolar environments rather than less stable in nonpolar environments (see analysis in Refs [154] and [155]). Excellent examples of this confusion are provided even in recent studies (e.g., [156]) and in most of the desolvation models (e.g., [157–159]) which are based on the assumption that enzymes destabilize their ground states by placing them in nonpolar environments. However, as has been demonstrated elsewhere (e.g., [132, 150]) enzymes do not provide nonpolar active sites for ion pair type ground states (they provide a very polar environment that stabilizes the transition state).

In general it is important to keep in mind that ion pairs are not stable in nonpolar sites in proteins. Thus most ion pairs in proteins are located on the surface, and those key ion pairs that are located in protein interiors are always surrounded by polar environments [132]. Forcing ion pairs between amino acids to be in nonpolar environments usually results in the conversion of the pair to its nonpolar form (by a proton transfer from the base to the acid).

The energetics of specific ion pairs in proteins has been studied by microscopic FEP calculations [160, 161] and by semi-macroscopic calculations [19, 37, 52, 162, 163]. However, we only have very few systematic validation studies. An instructive example is the study of Hendsch and Tidor [164] and its reanalysis by Schutz and Warshel [19]. That is, Ref. [164] used a PB approach with a low value of ε_p. This might have led to nonquantitative results. That is, in the case of T4 lysozyme, the calculated energies for $Asp70^0 \ldots His31^+ \rightarrow Asp70^- \ldots His31^+$ and for $Asp70^- \ldots His31^0 \rightarrow Asp70^- \ldots His31^+$ were -0.69 kcal mol^{-1} and -0.77 kcal mol^{-1}, respectively. This should be compared with the corresponding ob-

served values (-4.7 and -1.9 kcal mol^{-1}) or the values obtained in Ref. [19] (-4.7 and -2.2 kcal mol^{-1}). Similarly, the estimate of 10 kcal mol^{-1} destabilization of the Glu11-Arg45 ion pair in T4 lysozyme seems to be a significant overestimate relative to the result of $\sim$3 kcal mol^{-1} obtained by the current PDLD/S-LRA study. It is significant that the Asp70$^-$ ... His31$^+$ ion pair does not appear to destabilize the protein. That is, the energy of moving the ion pair from infinite separation in water to the protein site (relative to the corresponding energy for a nonpolar pair) was found here to be around zero compared with the 3.46 kcal mol^{-1} obtained in Ref. [164]. The origin of difference between the two studies can be traced in part to the estimate of the stabilizing effect of the protein permanent dipoles (the $V_{Q\mu}$ term in Ref. [19] and $\Delta G_{\text{protein}}$ in Ref. [164]). The ~-5 kcal mol^{-1} $V_{Q\mu}$ contribution found by the PDLD/S-LRA calculation corresponds to a contribution of only ~-0.26 kcal mol^{-1} in Ref. [164]. This might be due to the use of an approach that does not allow polar groups to reorient in response to the charges of the ion pair. It is exactly the stabilizing effect of the protein polar groups that plays a crucial role in stabilizing ion pairs in proteins. Clearly, the estimate of the energetics of ion pairs depends crucially on the dielectric constant used and models that do not consider the protein relaxation explicitly must use larger ε_p than the PDLD/S-LRA model.

Obviously, it is essential to have more systematic validation studies considering internal ion pairs with well-defined structure and energy. In this respect, it is useful to point out that the instructive statistical analysis reported so far (e.g., [165]) may involve similar problems as those mentioned in Section 7.5, since it does not consider a discriminative database; it includes mainly surface groups rather than ion pairs in protein interiors.

7.6.7
Protein–Protein Interactions

Protein–protein interactions play a crucial role in many biological systems, including in signal transduction [166], energy transduction [167], different assembly processes (e.g., [22]) and electron transport [168, 169]. Here again it seems that electrostatic effects are the most important factor in determining the nature and strength of the interaction between protein surfaces.

Calculations of protein–protein interactions are very challenging, particularly because of the large surfaces involved and the large structural changes upon binding. Considering the protein reorganization upon binding is particularly challenging and an LRA study that tried to accomplish this task for the Ras/RAF system [65] did not succeed to obtain quantitative results. However, a much simpler approach that evaluated charge–charge interaction by the effective dielectric constant of Eq. (14) gave encouraging results for the effect of mutations of the binding energy between the two proteins [65].

Recent studies of the binding of Barnase and Barstar [170] also indicate that the results are very sensitive to the dielectric model used. This study identified problems associated with the use of PB with different standard dielectric constant models.

7.6.8
Ion Channels

The control of ion permeation by transmembrane channels underlies many important biological functions (e.g., [171]). Understanding the control of ion selectivity by ion channels is basically a problem in protein electrostatics (e.g., [172, 173]) that turns out to be a truly challenging task. The primary problem is the evaluation of the free energy profile for transferring the given ion from water to the given position in the channel. It is also essential to evaluate the interaction between ions in the channel if the ion current involves a multi-ion process [174]. Early studies of ion channels focused on the energetics of ions in the gramicidine channel [175, 176]. The solution of the structure of the KscA potassium channel [177] provided a model for real biological channels and a major challenge for simulation approaches. Some early studies provided a major overestimate of the barriers for ion transport (e.g., [178, 179]) and the first reasonable results were obtained by the FEP calculations of Åqvist and Luzhkov [180]. These calculations involved the LRF long-range treatment and the SCSSA boundary conditions that probably helped in obtaining reliable results. Microscopic attempts to obtain the selectivity difference between K^+ and Na^+ were also reported [181]. However, these attempts did not evaluate the activation barriers for the two different ions and thus could not be used in evaluating the difference in the corresponding currents. Furthermore, attempts to evaluate the so-called potential of mean force (PMF) for ion penetration, that have the appearance of truly rigorous approaches, have not succeeded to reproduce the actual PMF for moving the ions from water to the channel (see discussion in Ref. [174]).

A promising alternative that appears to be quite effective in capturing the energetics of ion transport through the KcsA channel has been provided by the semi-macroscopic PDLD/S-LRA approach. This approach has provided activation barriers that reproduced the difference between the currents of Na^+ and K^+ [182]. Here it is important to point out that the LRA treatment of the PDLD/S-LRA approach has been crucial for the reproduction of the K^+/Na^+ selectivity. That is, without the LRA or related treatments it is impossible to capture the change in the protein (channel) structure upon change from K^+ to Na^+. This presents a major challenge to PB attempts to reproduce ion selectivity. It is also important to note that the evaluation of ion current by Langevin Dynamics or related approaches requires a very fast evaluation of the relevant electrostatic energies at different configurations of the transferred ions. Here the use of the PDLD/S-LRA approach and the distance dependence of the dielectric constant of Eq. (14) was found to be quite effective [174].

7.6.9
Helix Macrodipoles versus Localized Molecular Dipoles

The idea that the macroscopic dipoles of α-helices provide a critical electrostatic contribution [183, 184] has gained significant popularity and appeared in many

proposals. The general acceptance of this idea and the corresponding estimates (see below) is in fact a reflection of a superficial attitude. That is, here we have a case where the idea that microscopic dipoles (e.g., hydrogen bonds and carbonyls) play a major role in protein electrostatics [3] is replaced by a problematic idea that macrodipoles are the source of large electrostatic effects. The main reason for the acceptance of the helix-dipole idea (except the structural appeal of this proposal) has probably been due to the use of incorrect dielectric concepts. That is, estimates of large helix-dipole effects [184–188] involved a major underestimate of the corresponding dielectric constant and the customary tendency to avoid proper validation studies. Almost all attempts to estimate the magnitude of the helix-dipole effect have not been verified by using the same model in calculations of relevant observables (e.g., pK_a shift and enzyme catalysis). The first quantitative estimate of the effect of the helix dipole [189] established that the actual effect is due to the first few microscopic dipoles at the end of the helix and not to the helix macrodipole. It was also predicted that neutralizing the end of the helix by an opposing charge will have a very small effect and this prediction was confirmed experimentally [190].

An interesting recent examples of the need for quantitative considerations of the helix-dipole effect has been provided by the KcsA K^+ channel. The instructive study of Roux and MacKinnon [191] used PB calculations with $\varepsilon_p = 2$ and obtained an extremely large effect of the helix dipoles on the stabilization of the K^+ ion in the central cavity (~ -20 kcal mol^{-1}). However, a recent study [182] that used a proper LRA procedure in the framework of the PDLD/S-LRA approach gave a much smaller effect of the helix macrodipole (Figure 7.4). Basically, the use of $\varepsilon_p = 2$ overestimates the effect of the helix dipole by a factor of 3 and the effect is rather localized on the first few residues.

7.6.10 Folding and Stability

The study of protein folding by simulation approaches dates back to the introduction of the simplified folding model in 1975 [192]. This model, which forms the base for many of the current folding models, demonstrated for the first time that the folding problem is much simpler than previously thought. The simplified folding model and the somewhat less physical model developed by Go [193], which are sometimes classified as off-lattice and on-lattice models, respectively, paved the way for major advances in studies of the folding process and the free energy landscape of this process (e.g., [194–197]). Further progress has been obtained in recent years from all-atom simulation of peptides and small proteins (e.g., [198–200]). Some of these simulations involved the use of explicit solvent models and most involved the use of implicit solvation models ranging from GB type models [198], to the Langevin dipole model [200]. Interesting insights have been provided by the idea of using a simplified folding model as a reference potential for all-atom free energy simulation [200], but the full potential of this approach has not been exploited

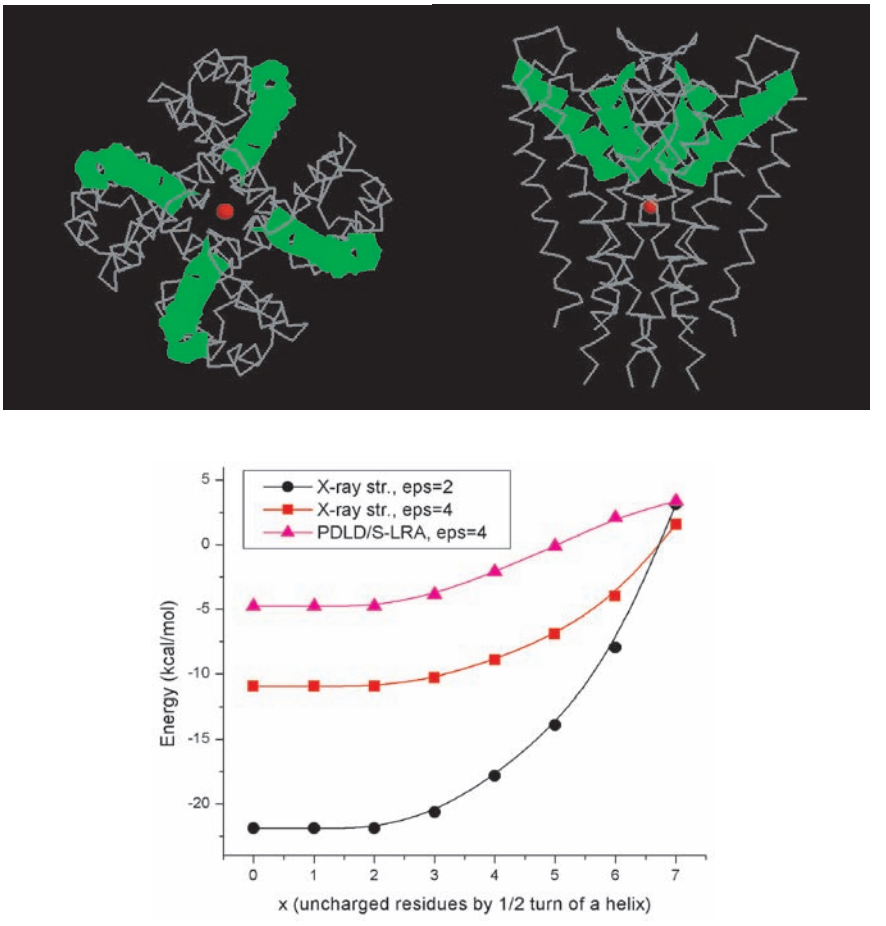

Fig. 7.4. Examination of the effect of the helix dipoles of the KcsA ion channel (upper panel) on a K^+ ion in the central cavity. The lower panel presents the contribution of the residues in the four helices as a function of the dielectric treatment used. It is shown that the use of $\varepsilon_p = 2$ drastically overestimates the contribution of the macrodipoles, which is evaluated more quantitatively with the PDLD/S-LRA treatment.

yet. Another promising direction has been offered by the use of a large amount of distributed computing resources [201].

At present it seems that simplified folding models describe quite well the average behavior of all-atom models (e.g., [200]), although more systematic studies are needed. The use of implicit solvent models also looks promising but here again there is a clear need for detailed validation studies focusing on observed electrostatic energies.

Despite the progress in studies of the folding process, we do not have yet a clear understanding of the factors that determined protein stability. Early insight-

ful considerations [20] argued that electrostatic effects must play a major role in controlling protein stability. Other workers emphasized hydrophobic effects and disulfide bridges, yet no consensus has been reached. Here it might be useful to consider the current situation with regards to the role of electrostatic contributions to thermal stability. Experimental studies of mesophilic, thermophilic, and hyperthermophilic proteins have provided an excellent benchmark for studies of the relationship between electrostatic energy and protein stability (e.g., [202, 203]). In general, the number of charged residues increases in hyperthermophiles, and thus can be considered as a stabilizing factor. However, the effect of ionized residues [164] and polar groups [204] has been thought to lead to destabilization bases on continuum studies (e.g., [164]). A notable example is the study of Hendsch and Tidor [164]. This study concluded that internal salt bridges tend to destabilize proteins, but as discussed in Section 7.6.6, this study did not reproduce the relevant observed energies. On the other hand, some studies (e.g., [205–208]) seem to support the idea that charged residues may help to optimize protein stability. The problem in reaching clear conclusions is closely related to the uncertainty about the value of ε_p in PB and related treatments. Here we have a competition between desolvation penalties, stabilization by local protein dipoles, and charge–charge interactions. The situation is relatively simple when one deals with a hypothetical hydrophobic protein (the original TK model). In this case, as was shown first in Ref. [12], both isolated ions and ion pairs become unstable in the "protein" interiors. The situation becomes, however, much more complex in real proteins where charges are stabilized by polar groups (e.g., [17]). Here the balance between charge–charge interactions and self-energy may depend drastically on the assumed ε_p. As stated in previous sections, it seems to us that different ε_p should be used for charge–charge interactions and self-energies. The above point can be clarified by writing the contribution of the ionizable residues to the folding energy as:

$$\Delta G^{\text{elec}}_{\text{fold}} = \Delta G^{\text{elec}}_{f} - \Delta G^{\text{elec}}_{uf} = -2.3RT \sum_i Q_i^{(f)} (\text{p}K^{\text{p}}_{i,\text{int}} - \text{pH}) + \frac{1}{2}\sum_{i\neq j} Q_i^{(f)} Q_j^{(f)} \left(\frac{332}{r_{ij}^{(f)} \varepsilon_{\text{eff}}(r_{ij}^{(f)})} \right) - \sum_i Q_i^{(uf)} (\text{p}K^{\text{w}}_{\text{a},i} - \text{pH}) - \frac{1}{2}\sum_{i>j} Q_i^{(uf)} Q_j^{(uf)} \left(\frac{332}{80 r_{ij}^{(uf)}} \right) \tag{19}$$

where f and uf designate, respectively, the folded and unfolded form of the protein, and the Qs are the charges of the ionized groups in their particular configuration. The above expression is based on our previous description of the electrostatic free energies of ionization states in proteins [209] and on the simplified approximation that considered the charges in the unfolded state as being fully solvated by water. If we assume that the same groups are ionized in the folded state, we can get a simpler expression:

$$\Delta G_{\text{fold}}^{\text{elec}} \approx -2.3RT \sum_i Q_i (\text{p}K_{i,\text{int}}^{\text{p}} - \text{p}K_{i,\text{w}}^{\text{w}}) + 166 \sum_{i>j} Q_i Q_j \left[\frac{1}{r_{ij}^{(f)} \varepsilon_{ij}^{(f)}} - \frac{1}{80 r_{ij}^{(\text{uf})}} \right] \quad (20)$$

The first term in Eq. (20) represents the change of self-energy upon moving the given charge from water to the protein active site, and the second term represents the effect of charge–charge interaction. Now, in general the ε_{p} for the first term and the ε_{eff} of the second term are quite different, and this makes the analysis complicated. At any rate, our preliminary analysis [210] evaluated the relative folding energies of two proteins expressed from the cold shock protein B (CspB) family, expressed by the mesophilic bacterium *Bacillus subtilis* [211] and the thermophilic bacterium *Bacillus caldolyticus*. This study obtained different trends with different ε_{p} and ε_{eff}, and reproduced the increased stability of the thermophilic protein with $\varepsilon_{\text{p}} = 8$ and $\varepsilon_{\text{eff}} = 20$. It seems to us, however, that this issue must be subjected to very careful validation studies, focusing in particular on the reproduction of the observed pK_{a} values of the proteins under consideration. Relevant benchmarks can be obtained in part from available experimental studies.

7.7 Concluding Remarks

Electrostatic effects play a major role in almost all biological processes. Thus, accurate evaluation of electrostatic energies is a key to quantitative structure function analysis [18]. Here the key to further progress is expected to depend on wider recognition of the importance of proper validation studies and on the increase in accuracy of microscopic calculations. That is, in many cases the focus on trivial properties of surface groups lead to entirely incorrect views of the validity of different models. Another worrisome direction is the tendency to validate different implicit models by their ability to reproduce PB results. For example, GB calculations are frequently verified by comparing them to the corresponding PB calculations. This implies a belief that the PB results represent the correct electrostatic energies, overlooking the fact that these calculated energies depend critically on an undefined dielectric constant. Consistent validations and developments of reliable models must involve comparisons to relevant experimental results. Proper verification of semimacroscopic models might also involve a comparison to microscopic results but in many cases these results do not reach proper convergence. Here the wider realization of the importance of long-range effects, boundary conditions and convergence issues are expected to help in increasing the accuracy of microscopic models. The continuing increase in computational resources will also play a key role in providing more accurate electrostatic energies.

Recent studies of electrostatic energies in proteins have repeatedly focused on the formal validations of PB and related approaches, while focusing on the contribution of the solvent around the protein. This focus, however, seems to overlook and sometimes ignore a key issue. That is, the PB and GB approaches provide ex-

cellent models for the effect of the solvent around the protein. The problem, however, is the effect of the protein and the proper ε_p. Here we cannot use any formal justification since our results depend drastically on a somewhat arbitrary parameter (i.e., ε_p).

Although this review presents a somewhat critical discussion of different semi-macroscopic approaches, it does not mean that such approaches are not useful. That is, as long as the difficulties of obtaining reliable results by microscopic approaches persist one must resort to semi-macroscopic approaches. Such approaches are also essential in studies of problems that require fast evaluation of the relevant electrostatic energies (e.g., the folding problem). The results obtained by semi-macroscopic models are expected to become more accurate with a better understanding of the protein dielectric ''constant''.

Acknowledgments

This work was supported by NIH grants GM 40283 and 24492, and NSF grant MCB-0003872. We are grateful to Mitsunori Kato for the work presented in Figure 7.4.

References

1 Linderstrom-Lang, K., The ionization of proteins. *C. R. Trav. Lab. Carlsberg*, 1924; **15**: 29.
2 Tanford, C. and J. G. Kirkwood, Theory of protein titration curves. I. General equations for impenetrable spheres. *J. Am. Chem. Soc.*, 1957; **79**: 5333–5339.
3 Warshel, A. and S. T. Russell, Calculations of electrostatic interactions in biological systems and in solutions. *Q. Rev. Biophys.*, 1984; **17**: 283–421.
4 Sharp, K. A. and B. Honig, Electrostatic interactions in macromolecules: theory and applications. *Annu. Rev. Biophys. Biochem.*, 1990; **19**: 301–332.
5 Warshel, A. and J. Åqvist, Electrostatic energy and macromolecular function. *Annu. Rev. Biophys. Biochem.*, 1991; **20**: 267–298.
6 Nakamura, H., Roles of electrostatic interaction in proteins. *Q. Rev. Biophys.*, 1996; **29**: 1–90.
7 Warshel, A. and A. Papazyan, Electrostatic effects in macromolecules: fundamental concepts and practical modeling. *Curr. Opin. Struct. Biol.*, 1998; **8**: 211–217.
8 Simonson, T., Electrostatics and dynamics of proteins. *Rep. Prog. Phys.*, 2003; **66**(5): 737–787.
9 Davis, M. E. and J. A. McCammon, Electrostatics in biomolecular structure and dynamics. *Chem. Rev.*, 1990; **90**: 509–521.
10 Jackson, J. D., *Classical Electrodynamics*, 3rd edn. New York: John Wiley & Sons, 1999, 808.
11 Linderstrom-Lang, K., On the ionization of proteins. *C. R. Trav. Lab. Carlsberg*, 1924; **15**: 1.
12 Warshel, A., S. T. Russell, and A. K. Churg, Macroscopic models for studies of electrostatic interactions in proteins: limitations and applicability. *Proc. Natl Acad. Sci. USA*, 1984; **81**: 4785–4789.
13 Chung, S. H. and S. Kuyucak, Ion channels: recent progress and prospects. *Eur. J. Biochem.*, 2002; **31**: 283–293.
14 Warshel, A. and M. Levitt, Theoretical studies of enzymic reactions:

dielectric, electrostatic and steric stabilization of the carbonium ion in the reaction of lysozyme. *J. Mol. Biol.*, 1976; **103**: 227–249.

15 Orttung, W. H., Polarizability of density of inert-gas atom pairs. 1. *J. Phys. Chem.*, 1985; **89**: 3011–3016.

16 Warwicker, J. and H. C. Watson, Calculation of the electric potential in the active site cleft due to alpha-helix dipoles. *J. Mol. Biol.*, 1982; **157**: 671–679.

17 Warshel, A., What about protein polarity? *Nature*, 1987; **333**: 15–18.

18 Warshel, A., Electrostatic basis of structure-function correlation in proteins. *Acc. Chem. Res.*, 1981; **14**: 284–290.

19 Schutz, C. N. and A. Warshel, What are the dielectric "constants" of proteins and how to validate electrostatic models. *Proteins*, 2001; **44**: 400–417.

20 Perutz, M. F., Electrostatic effects in proteins. *Science*, 1978; **201**: 1187–1191.

21 Matthew, J. B., P. C. Weber, F. R. Salemme, and F. M. Richards, Electrostatic orientation during electron-transfer between flavodoxin and cytochrome-c. *Nature*, 1983; **301**(5896): 169–171.

22 Bloomer, A. C., J. N. Champness, G. Bricogne, R. Staden, and A. Klug, Protein disk of tobacco mosaic-virus at 2.8 Å resolution showing interactions within and between subunits. *Nature*, 1978; **276**(5686): 362–368.

23 Vernon, C. A., Mechanisms of hydrolysis of glycosides and their relevance to enzyme-catalyzed reactions. *Proc. R. Soc. Lond. B Biol.*, 1967; **167**(1009): 389–401.

24 Thoma, J. A., Separation of factors responsible for lysozyme catalysis. *J. Theor. Biol.*, 1974; **44**: 305–317.

25 Schaefer, M., M. Sommer, and M. Karplus, pH-dependence of protein stability: absolute electrostatic free energy differences between conformations. *J. Phys. Chem. B*, 1997; **101**: 1663–1683.

26 Dufner, H., S. M. Kast, J. Brickmann, and M. Schlenkrich, Ewald summation versus direct summation of shifted-force potentials for the calculation of electrostatic interactions in solids – a quantitative study. *J. Comput. Chem.*, 1997; **18**: 660–675.

27 Figueirido, F., G. S. Del Buono, and R. M. Levy, On the finite size corrections to the free energy of ionic hydration. *J. Phys. Chem. B.*, 1997; **101**(29): 5622–5623.

28 Hummer, G., L. R. Pratt, and A. E. Garcia, Free energy of ionic hydration. *J. Phys. Chem.*, 1996; **100**: 1206–1215.

29 Sham, Y. Y. and A. Warshel, The surface constrained all atom model provides size independent results in calculations of hydration free energies. *J. Chem. Phys.*, 1998; **109**: 7940–7944.

30 Aqvist, J., Comment on transferability of ion models. *J. Phys. Chem.*, 1994; **98**(33): 8253–8255.

31 Aqvist, J. and T. Hansson, Analysis of electrostatic potential truncation schemes in simulations of polar solvents. *J. Phys. Chem. B*, 1998; **102**(19): 3837–3840.

32 Lee, F. S. and A. Warshel, A local reaction field method for fast evaluation of long-range electrostatic interactions in molecular simulations. *J. Chem. Phys.*, 1992; **97**: 3100–3107.

33 Warshel, A., Calculations of chemical processes in solutions. *J. Phys. Chem.*, 1979; **83**: 1640–1650.

34 Brooks III, C. L. and M. Karplus, Deformable stochastic boundaries in molecular dynamics. *J. Chem. Phys.*, 1983; **79**: 6312–6325.

35 King, G. and A. Warshel, A surface constrained all-atom solvent model for effective simulations of polar solutions. *J. Chem. Phys.*, 1989; **91**(6): 3647–3661.

36 Kirkwood, J. G., Theory of solutions of molecules containing widely serparated charges with special application to zwitterions. *J. Chem. Phys.*, 1934; **2**: 351–361.

37 Lee, F. S., Z. T. Chu, and A. Warshel, Microscopic and semi-microscopic calculations of electrostatic energies in proteins by the POLARIS and ENZYMIX programs. *J. Comput. Chem.*, 1993; **14**: 161–185.

38 Alper, H. and R. M. Levy, Dielectric and thermodynamic response of generalized reaction field model for liquid state simulations. *J. Chem. Phys.*, 1993; **99**(12): 9847–9852.

39 Warshel, A., F. Sussman, and G. King, Free energy of charges in solvated proteins: microscopic calculations using a reversible charging process. *Biochemistry*, 1986; **25**: 8368–8372.

40 Kollman, P., Free energy calculations: applications to chemical and biochemical phenomena. *Chem. Rev.*, 1993; **93**: 2395–2417.

41 Warshel, A., Dynamics of reactions in polar solvents, semiclassical trajectory studies of electron-transfer and proton-transfer reactions. *J. Phys. Chem.*, 1982; **86**: 2218–2224.

42 Lee, F. S., Z. T. Chu, M. B. Bolger, and A. Warshel, Calculations of antibody-antigen interactions: microscopic and semi-microscopic evaluation of the free energies of binding of phosphorylcholine analogs to McPC603. *Protein Eng.*, 1992; **5**: 215–228.

43 Sham, Y. Y., Z. T. Chu, and A. Warshel, Consistent calculations of pK_a's of ionizable residues in proteins: semi-microscopic and macroscopic approaches. *J. Phys. Chem. B*, 1997; **101**: 4458–4472.

44 Delbuono, G. S., F. E. Figueirido, and R. M. Levy, Intrinsic pK(a)s of ionizable residues in proteins – an explicit solvent calculation for lysozyme. *Proteins*, 1994; **20**(1): 85–97.

45 Saito, M., Molecular dynamics free-energy study of a protein in solution with all degrees of freedom and long-range Coulomb interactions. *J. Phys. Chem.*, 1995; **99**: 17043–17048.

46 Liu, Y. and T. Ichiye, The static dielectric-constant of the soft sticky dipole model of liquid water – Monte Carlo simulation. *Chem. Phys. Lett.*, 1996; **256**: 334–340.

47 Coalson, R. D. and A. Duncan, Statistical mechanics of a multipolar gas: a lattice field theory approach. *J. Phys. Chem.*, 1996; **100**: 2612–2620.

48 Papazyan, A. and A. Warshel, Continuum and dipole-lattice models of solvation. *J. Phys. Chem.*, 1997; **101**: 11254–11264.

49 Papazyan, A. and A. Warshel, Effect of solvent discreteness on solvation. *J. Phys. Chem. B*, 1998; **102**: 5248–5357.

50 HaDuong, T., S. Phan, M. Marchi, and D. Borgis, Electrostatics on particles: phenomenological and orientational density functional theory approach. *J. Chem. Phys.*, 2002; **117**(2): 541–556.

51 Schaefer, M. and M. Karplus, A comprehensive analytical treatment of continuum electrostatics. *J. Phys. Chem.*, 1996; **100**: 1578–1599.

52 Warshel, A., G. Naray-Szabo, F. Sussman, and J.-K. Hwang, How do serine proteases really work? *Biochemistry*, 1989; **28**: 3629–3673.

53 Kollman, P. A., I. Massova, C. Reyes, B. et al., Calculating structures and free energies of complex molecules: combining molecular mechanics and continuum models. *Acc. Chem. Res.*, 2000; **33**: 889–897.

54 Tomasi, J., B. Mennucci, R. Cammi, and M. Cossi, *Quantum Mechanical Models for Reactions in Solution, in Computational Approaches to Biochemical Reactivity* (G. Naray-Szabo, and A. Warshel, Eds.). Dordrecht: Kluwer Academic Publishers, 1997, 1–102.

55 Papazyan, A. and A. Warshel, A stringent test of the cavity concept in continuum dielectrics. *J. Chem. Phys.*, 1997; **107**(19): 7975–7978.

56 Georgescu, R. E., E. G., Alexov, and M. R. Gunner, Combining conformational flexibility and continuum electrostatics for calculating pK(a)s in proteins. *Biophys. J.*, 2002; **83**(4): 1731–1748.

57 Alden, R. G., W. W. Parson, Z. T. Chu, and A. Warshel, Calculations of electrostatic energies in photosynthetic reaction centers. *J. Am. Chem. Soc.*, 1995; **117**: 12284–12298.

58 Johnson, E. T. and W. W. Parson, Electrostatic interactions in an integral membrane protein. *Biochemistry*, 2002; **41**: 6483–6494.

59 Bashford, D. and D. A. Case, Generalized born models of

macromolecular solvation effects. *Annu. Rev. Phys. Chem.*, 2000; **51**: 129–152.

60 Luzhkov, V. and A. Warshel, Microscopic models for quantum mechanical calculations of chemical processes in solutions: LD/AMPAC and SCAAS/AMPAC calculations of solvation energies. *J. Comput. Chem.*, 1992; **13**: 199–213.

61 Still, W. C., A. Tempczyk, R. C. Hawley, and T. Hendrickson, Semianalytical treatment of solvation for molecular mechanics and dynamics. *J. Am. Chem. Soc.*, 1990; **112**: 6127–6129.

62 Borgis, D., N. Levy, and M. Marchi, Computing the electrostatic free-energy of complex molecules: The variational Coulomb field approximation. *J. Chem. Phys.*, 2003; **119**(6): 3516–3528.

63 King, G., F. S. Lee, and A. Warshel, Microscopic simulations of macroscopic dielectric constants of solvated proteins. *J. Chem. Phys.*, 1991; **95**: 4366–4377.

64 Sham, Y. Y., I. Muegge, and A. Warshel, The effect of protein relaxation on charge-charge interactions and dielectric constants of proteins. *Biophys. J.*, 1998; **74**: 1744–1753.

65 Muegge, I., T. Schweins, R. Langen, and A. Warshel, Electrostatic control of GTP and GDP binding in the oncoprotein p21 ras. *Structure*, 1996; **4**: 475–489.

66 Simonson, T. and C. L. Brooks, Charge screening and the dielectric constant of proteins: Insights from molecular dynamics. *J. Am. Chem. Soc.*, 1996; **118**: 8452–8458.

67 Pitera, J. W., M. Falta, and W. F. van Gunsteren, Dielectric Properties of Proteins from Simulation: The Effects of Solvent, Ligands, pH, and Temperature. *Biophys. J.*, 2001; **80**: 2546–2555.

68 Simonson, T., D. Perahia, and A. T. Brunger, Microscopic theory of the dielectric properties of proteins. *Biophys. J.*, 1991; **59**: 670–690.

69 Muegge, I., P. X. Qi, A. J. Wand, Z. T. Chu, and A. Warshel, The reorganization energy of cytochrome c revisited. *J. Phys. Chem. B*, 1997; **101**: 825–836.

70 Harvey, S. and P. Hoekstra, Dielectric relaxation spectra of water adsorbed on lysozyme. *J. Phys. Chem.*, 1972; **76**: 2987–2994.

71 Gilson, M. and B. Honig, The dielectric constant of a folded protein. *Biopolymers*, 1986; **25**: 2097–2119.

72 Antosiewicz, J., J. A. McCammon, and M. K. Gilson, Prediction of pH-dependent properties of proteins. *J. Mol. Biol.*, 1994; **238**: 415–436.

73 Cohen, B. E., T. B. McAnaney, E. S. Park, Y. N. Jan, S. G. Boxer, and L. Y. Jan, Probing protein electrostatics with a synthetic fluorescent amino acid. *Science*, 2002; **296**(5573): 1700–1703.

74 Borman, S., Fluorescent probe for proteins: nonnatural amino acid used to investigate electrostatic properties within proteins. *Chem. Eng. News*, 2002; **80**(24): 30.

75 Garcia-Moreno, B., J. J. Dwyer, A. G. Gittis, E. E. Lattman, D. S. Spencer, and W. E. Stites, Experimental measurement of the effective dielectric in the hydrophobic core of a protein. *Biophys. Chem.*, 1997; **64**: 211–224.

76 Mehler, E. L. and G. Eichele, Electrostatic effects in water-accessible regions of proteins. *Biochemistry*, 1984; **23**: 3887–3891.

77 Penfold, R., J. Warwicker, and B. Jonsson, Electrostatic models for calcium binding proteins. *J. Phys. Chem. B*, 1998; **108**: 8599–8610.

78 Mehler, E. L. and F. Guarnieri, A self-consistent, microscopic modulated screened Coulomb potential approximation to calculate pH-dependent electrostatic effects in proteins. *Biophys. J.*, 1999; **75**: 3–22.

79 Debye, P. J. W. and L. Pauling, The inter-ionic attraction theory of ionized solutes. IV. The influence of variation of dielectric constant on the limiting law for small concentrations. *J. Am. Chem. Soc.*, 1925; **47**: 2129–2134.

80 Webb, T. J., The free energy of hydration of ions and the electro-

striction of the solvent. *J. Am. Chem. Soc.*, 1926; **48**: 2589–2603.

81 Hill, T. L., The electrostatic contribution to hindered rotation in certain ions and dipolar ions in solution iii. *J. Chem. Phys.*, 1944; **12**: 56–61.

82 Russell, S. T. and A. Warshel, Calculations of electrostatic energies in proteins; the energetics of ionized groups in bovine pancreatic trypsin inhibitor. *J. Mol. Biol.*, 1985; **185**: 389–404.

83 Honig, B., Sharp, K., Sampogna, R., Gunner, M. R., and Yang, A. S., On the calculation of pKas in proteins. *Proteins*, 1993; **15**: 252–265.

84 Kosower, E. M., *Introduction to Physical Organic Chemistry*, 1968, Wiley, New York.

85 Mataga, N. and T. Kubota, *Molecular Interactions and Electronic Spectra.*, 1970, M. Dekkar, New York.

86 Pullman, A. and B. Pullman, New paths in the molecular orbital approach to solvation in biological molecules. *Q. Rev. Biophys.*, 1975; **7**: 506–566.

87 Jorgensen, W. L., Ab initio molecular orbital study of the geometric properties and protonation of alkyl chloride. *J. Am. Chem. Soc.*, 1978; **100**: 1057–1061.

88 Cramer, C. J. and D. G. Truhlar, General parameterized SCF model for free energies of solvation in aqueous solution. *J. Am. Chem. Soc.*, 1991; **113**: 8305–8311.

89 Honig, B., K. Sharp, and A.-S. Yang, Macroscopic models of aqueous solutions: biological and chemical applications. *J. Phys. Chem.*, 1993; **97**: 1101–1109.

90 Åqvist, J., Ion-water interaction potentials derived from free energy perturbation simulations. *J. Chem. Phys.*, 1990; **94**: 8021–8024.

91 Warshel, A. and Z. T. Chu, Calculations of solvation free energies in chemistry and biology, in *ACS Symposium Series: Structure and Reactivity in Aqueous Solution. Characterization of Chemical and Biological Systems* (D. G. Truhlar, Ed.). Washington, DC: ACS, 1994, p. 72–93.

92 Figueirido, F., G. S. Delbuono, and R. M. Levy, On finite-size effects in computer simulations using the Ewald potential. *J. Chem. Phys.*, 1995; **103**: 6133–6142.

93 Åqvist, J. and T. Hansson, On the validity of electrostatic linear response in polar solvents. *J. Phys. Chem.*, 1996; **100**: 9512–9521.

94 Orozco, M. and F. J. Luque, Generalized linear-response approximation in discrete methods. *Chem. Phys. Lett.*, 1997; **265**: 473–480.

95 Florián, J. and A. Warshel, Langevin dipoles model for ab initio calculations of chemical processes in solution: parameterization and application to hydration free energies of neutral and ionic solutes, and conformational analysis in aqueous solution. *J. Phys. Chem. B*, 1997; **101**(28): 5583–5595.

96 Malcolm, N. O. J. and J. J. W. McDouall, Assessment of the Langevin dipoles solvation model for Hartree-Fock wavefunctions. *Theochem-J. Mol. Struct.*, 1996; **336**: 1–9.

97 Marten, B., K. Kim, C. Cortis, R. A. et al., New model for calculation of solvation free energies: correction of self-consistent reaction field continuum dielectric theory for short-range hydrogen bonding effects. *J. Phys. Chem.*, 1996; **100**: 11775–11788.

98 Hawkins, G. D., C. J. Cramer, and D. G. Truhlar, Parametrized models of aqueous free-energies of solvation based on pairwise descreening of solute atomic charges froma dielectric medium. *J. Phys. Chem.*, 1996; **100**: 19824–19839.

99 Fothergill, M., M. F. Goodman, J. Petruska, and A. Warshel, Structure-energy analysis of the role of metal ions in phosphodiester bond hydrolysis by DNA polymerase I. *J. Am. Chem. Soc.*, 1995; **117**(47): 11619–11627.

100 Åqvist, J. and M. Fothergill, Computer simulation of the

triosephosphate isomerase catalyzed reaction. *J. Biol. Chem.*, 1996; **271**: 10010–10016.

101 Beroza, P. and D. R. Fredkin, Calculation of amino acid pK(a)s in a protein from a continuum electrostatic model: Method and sensitivity analysis. *J. Comput. Chem.*, 1996; **17**(10): 1229–1244.

102 Koumanov, A., H. Ruterjans, and A. Karshikoff, Continuum electrostatic analysis of irregular ionization and proton allocation in proteins. *Proteins*, 2002; **46**(1): 85–96.

103 You, T. J. and D. Bashford, Conformation and hydrogen ion titration of proteins: a continuum electrostatic model with conformational flexibility. *Biophys. J.*, 1995; **69**: 1721–1733.

104 van Vlijmen, H. W. T., M. Schaefer, and M. Karplus, Improving the accuracy of protein pK(a) calculations: Conformational averaging versus the average structure. *Proteins*, 1998; **33**(2): 145–158.

105 Zhou, H. X. and M. Vijayakumar, Modeling of protein conformational fluctuations in pK(a) predictions. *J. Mol. Biol.*, 1997; **267**(4): 1002–1011.

106 Wendoloski, J. J. and J. B. Matthew, Molecular-dynamics effects on protein electrostatics. *Proteins*, 1989; **5**(4): 313–321.

107 Kassner, R. J., Effects of non polar environments on the redox potentials of heme complexes. *Proc. Natl Acad. Sci. USA*, 1972; **69**: 2263–2267.

108 Zhou, H.-X., Control of reduction potential by protein matrix: lesson from a spherical protein model. *J. Biol. Inorg. Chem.*, 1997; **2**: 109–113.

109 Bertini, I., G. Gori-Savellini, and C. Luchinat, Are unit charges always negligible? *J. Biol. Inorg. Chem.*, 1997; **2**: 114–118.

110 Mauk, A. G. and G. R. Moore, Control of metalloprotein redox potentials: what does site-directed mutagenesis of hemoproteins tell us? *J. Biol. Inorg. Chem.*, 1997; **2**: 119–125.

111 Gunner, M. R., E. Alexov, E. Torres, and S. Lipovaca, The importance of the protein in controlling the electrochemistry of heme metalloproteins: methods of calculation and analysis. *J. Biol. Inorg. Chem.*, 1997; **2**: 126–134.

112 Naray-Szabo, G., Electrostatic modulation of electron transfer in the active site of heme peroxidases. *J. Biol. Inorg. Chem.*, 1997; **2**: 135–138.

113 Armstrong, F. A., Evaluations of reduction potential data in relation to coupling, kinetics and function. *J. Biol. Inorg. Chem.*, 1997; **2**: 139–142.

114 Warshel, A., A. Papazyan, and I. Muegge, Microscopic and semimacroscopic redox calculations: what can and cannot be learned from continuum models. *J. Biol. Inorg. Chem.*, 1997; **2**: 143–152.

115 Rogers, N. K. and G. R. Moore, On the energetics of conformational-changes and pH dependent redox behavior of electron-transfer proteins. *FEBS Lett.*, 1988; **228**(1): 69–73.

116 Churg, A. K., R. M. Weiss, A. Warshel, and T. Takano, On the action of cytochrome c: correlating geometry changes upon oxidation with activation energies of electron transfer. *J. Phys. Chem.*, 1983; **87**: 1683–1694.

117 Churg, A. K. and A. Warshel, Control of redox potential of cytochrome c and microscopic dielectric effects in proteins. *Biochemistry*, 1986; **25**: 1675–1681.

118 Stephens, P. J., D. R. Jollie, and A. Warshel, Protein control of redox potentials of iron-sulfur proteins. *Chem. Rev.*, 1996; **96**: 2491–2513.

119 Swartz, P. D., B. W. Beck, and T. Ichiye, Structural origins of redox potentials in Fe–S proteins-electrostatic potentials of crystal structures. *Biophys. J.*, 1996; **71**: 2958–2969.

120 Yelle, R. B. and T. Ichiye, Solvation free-energy reaction curves for electron-transfer in aqueous solution – theory and simulation. *J. Phys. Chem. B*, 1997; **101**: 4127–4135.

121 Warshel, A. and W. W. Parson, Dynamics of biochemical and biophysical reactions: insight from computer simluations. *Q. Rev. Biophys.*, 2001; **34**: 563–670.

122 Rabenstein, B., G. M. Ullmann, and

E. W. Knapp, Energetics of electron-transfer and protonation reactions of the quinones in the photosynthetic reaction-center of *Rhodopseudomonas viridis*. *Biochemistry*, 1998; **37**(8): 2488–2495.

123 Noodleman, L., T. Lovell, T. Q. Liu, F. Himo, and R. A. Torres, Insights into properties and energetics of iron-sulfur proteins from simple clusters to nitrogenase. *Curr. Opin. Chem. Biol.*, 2002; **6**(2): 259–273.

124 Teixeira, V. H., C. M. Soares, and A. M. Baptista, Studies of the reduction and protonation behavior of tetraheme cytochromes using atomic detail. *J. Biol. Inorg. Chem.*, 2002; **7**(1–2): 200–216.

125 Olsson, M. H. M., G. Hong, and A. Warshel, Frozen density functional free energy simulations of redox proteins: computational studies of the reduction potential of plastocyanin and rusticyanin. *J. Am. Chem. Soc.*, 2003; **125**: 5025–5039.

126 Muegge, I. and M. Rarey, Small molecule docking and scoring, in *Reviews in Computational Chemistry* (D. B. Boyd, Ed.). New York: Wiley-VCH, John Wiley and Sons, 2001, 1–60.

127 Sham, Y. Y., Z. T. Chu, H. Tao, and A. Warshel, Examining methods for calculations of binding free energies: LRA, LIE, PDLD-LRA, and PDLD/S-LRA calculations of ligands binding to an HIV protease. *Proteins*, 2000; **39**: 393–407.

128 Madura, J. D., Y. Nakajima, R. M. Hamilton, A. Wierzbicki, and A. Warshel, Calculations of the electrostatic free energy contributions to the binding free energy of sulfonamides to carbonic anhydrase. *Struct. Chem.*, 1996; **7**: 131–137.

129 Froloff, N., A. Windemuth, and B. Honig, On the calculation of binding free energies using continuum methods – application to MHC class-I protein–peptide interactions. *Protein Sci.*, 1997; **6**(6): 1293–1301.

130 Florian, J., M. F. Goodman, and A. Warshel, Theoretical investigation of the binding free energies and key substrate-recognition components of the replication fidelity of human DNA polymerase *β*. *J. Phys. Chem. B*, 2002; **106**: 5739–5753.

131 Warshel, A., Computer simulations of enzyme catalysis: methods, progress, and insights. *Annu. Rev. Biophys. Biomech.*, 2003. **32**: 425–443.

132 Warshel, A., *Computer Modeling of Chemical Reactions in Enzymes and Solutions*. New York: John Wiley & Sons, 1991, 236.

133 Fersht, A., *Structure and Mechanism in Protein Science. A Guide to Enzyme Catalysis and Protein Folding*. New York: W.H. Freeman and Co., 1999, 631.

134 Field, M., Stimulating enzyme reactions: challenges and perspectives. *J. Comput. Chem.*, 2002; **23**: 48–58.

135 Bash, P. A., M. J. Field, R. C. Davenport, G. A. Petsko, D. Ringe, and M. Karplus, Computer simulation and analysis of the reaction pathway of triosephosphate isomerase. *Biochemistry*, 1991; **30**: 5826–5832.

136 Hartsough, D. S. and K. M. Merz, Jr., Dynamic force field models: molecular dynamics simulations of human carbonic anhydrase II using a quantum mechanical/molecular mechanical coupled potential. *J. Phys. Chem.*, 1995; **99**: 11266–11275.

137 Alhambra, C., J. Gao, J. C. Corchado, J. Villà, and D. G. Truhlar, Quantum mechanical dynamical effects in an enzyme-catalyzed proton transfer reaction. *J. Am. Chem. Soc.*, 1999; **121**: 2253–2258.

138 Martí, S., J. Andrés, V. Moliner, E. Silla, I. Tunon, and J. Bertran, Transition structure selectivity in enzyme catalysis: a QM/MM study of chorismate mutase. *Theor. Chem. Acc.*, 2001; **105**: 207–212.

139 Mulholland, A. J., G. H. Grant, and W. G. Richards, Computer modelling of enzyme catalysed reaction mechanisms. *Protein Eng.*, 1993; **6**: 133–147.

140 Singh, U. C. and P. A. Kollman, A combined ab initio quantum mechanical and molecular mechanical method for carrying out simulations on complex molecular systems:

applications to the $CH_3Cl + Cl^-$ exchange reaction and gas phase protonation of polyethers. *J. Comput. Chem.*, 1986; **7**(6): 718–730.

141 Warshel, A., Energetics of enzyme catalysis. *Proc. Natl Acad. Sci. USA*, 1978; **75**: 5250–5254.

142 Warshel, A., Electrostatic origin of the catalytic power of enzymes and the role of preorganized active sites. *J. Biol. Chem.*, 1998; **273**: 27035–27038.

143 Roca, M., S. Marti, J. Andres et al., Theoretical modeling of enzyme catalytic power: Analysis of "cratic" and electrostatic factors in catechol O-methyltransferase. *J. Am. Chem. Soc.*, 2003; **125**(25): 7726–7737.

144 Cannon, W. R. and S. J. Benkovic, Solvation, reorganization energy, and biological catalysis. *J. Biol. Chem.*, 1998; **273**(41): 26257–26260.

145 Naray-Szabo, G., M. Fuxreiter, and A. Warshel, Electrostatic basis of enzyme catalysis, in *Computational Approaches to Biochemical Reactivity*. Dordrecht: Kluwer Academic, 1997, 237–294.

146 Van Beek, J., R. Callender, and M. R. Gunner, The contribution of electrostatic and van der Waals interactions to the stereospecificity of the reaction catalyzed by lactate-dehydrogenase. *Biophys. J.*, 1997; **72**: 619–626.

147 Fisher, C. L., D. E. Cabelli, R. A. Hallewell, P. Beroza, E. D. Getzoff, and J. A. Tainer, Computational, pulse-radiolytic, and structural investigations of lysine-136 and its role in the electrostatic triad of human Cu, Zn superoxide dismutase. *Proteins*, 1997; **29**: 103–112.

148 Antosiewicz, J., J. A. McCammon, S. T. Wlodek, and M. K. Gilson, Simulation of charge-mutant acetylcholinesterases. *Biochemistry*, 1995; **34**: 4211–4219.

149 Fuxreiter, M. and A. Warshel, Origin of the catalytic power of acetylcholinesterase: computer simulation studies. *J. Am. Chem. Soc.*, 1998; **120**: 183–194.

150 Warshel, A., J. Villà, M. Štrajbl, and J. Florián, Remarkable rate enhancement of orotidine 5′-monophosphate decarboxylase is due to transition state stabilization rather than ground state destabilization. *Biochemistry*, 2000; **39**: 14728–14738.

151 Cui, Q., M. Elstner, E. Kaxiras, T. Frauenheim, and M. Karplus, A QM/MM implementation of the self-consistent charge density functional tight binding (SCC-DFTB) method. *J. Phys. Chem. B*, 2001; **105**: 569–585.

152 Perutz, M. F., J. V. Kilmartin, K. Nishikura, J. H. Fogg, P. J. G. Butler, and H. S. Rollema, Identification of residues contributing to the Bohr effect of human-hemoglobin. *J. Mol. Biol.*, 1980; **138**(3): 649–670.

153 Warshel, A. and N. Barboy, Energy storage and reaction pathways in the first step of the vision process. *J. Am. Chem. Soc.*, 1982; **104**: 1469.

154 Warshel, A., Charge stabilization mechanism in the visual and purple membrane pigments. *Proc. Natl Acad. Sci. USA*, 1978; **75**: 2558.

155 Warshel, A., Calculations of enzymic reactions: calculations of pK_a, proton transfer reactions, and general acid catalysis reactions in enzymes. *Biochemistry*, 1981; **20**: 3167–3177.

156 Jordan, F., H. Li, and A. Brown, Remarkable stabilization of zwitterionic intermediates may account for a billion-fold rate acceleration by thiamin diphosphate-dependent decarboxylases. *Biochemistry*, 1999; **38**(20): 6369–6373.

157 Dewar, M. J. S. and D. M. Storch, Alternative view of enzyme reactions. *Proc. Natl Acad. Sci. USA*, 1985; **82**: 2225–2229.

158 Crosby, J., R. Stone, and G. E. Lienhard, Mechanisms of thiamine-catalyzed reactions. Decarboxylation of 2-(1-carboxy-1-hydroxyethyl)-3,4-dimethylthiazolium chloride. *J. Am. Chem. Soc.*, 1970; **92**: 2891–2900.

159 Lee, J. K. and K. N. Houk, A proficient enzyme revisited: the predicted mechanism for orotidine monophosphate decarboxylase. *Science*, 1997; **276**: 942–945.

160 Hwang, J.-K. and A. Warshel, Why ion pair reversal by protein

engineering is unlikely to succeed. *Nature*, 1988; **334**: 270.

161 Cutler, R. L., A. M. Davies, S. Creighton et al., Role of arginine-38 in regulation of the cytochrome c oxidation-reduction equilibrium. *Biochemistry*, 1989; **28**: 3188–3197.

162 Barril, X., C. Aleman, M. Orozco, and F. J. Luque, Salt bridge interactions: stability of the ionic and neutral complexes in the gas phase, in solution, and in proteins. *Proteins*, 1998; **32**(1): 67–79.

163 Warshel, A. (Ed.), *Computational Approaches to Biochemical Reactivity. Understanding Chemical Reactivity.* Dordrecht: Kluwer Academic Publishers, 1997, 379.

164 Hendsch, Z. S. and B. Tidor, Do salt bridges stabilize proteins – a continuum electrostatic analysis. *Protein Sci.*, 1994; **3**(2): 211–226.

165 Kumar, S. and R. Nussinov, Relationship between ion pair geometries and electrostatic strengths in proteins. *Biophys. J.*, 2002; **83**(3): 1595–1612.

166 Nassar, N., G. Horn, C. Herrmann, A. Scherer, F. McCormick, and A. Wittinghofer, The 2.2 Å crystal structure of the ras-binding domain of the serine/threonine kinase c-Raf1 in complex with Rap1A and a GTP analogue. *Nature*, 1995; **375**: 554–560.

167 Menz, R. I., J. E. Walker, and A. G. W. Leslie, Structure of bovine mitochondrial F1-ATPase with nucleotide bound to all three catalytic sites: implications for the mechanism of rotary catalysis. *Cell*, 2001; **106**: 331–341.

168 Flock, D. and V. Helms, Protein–protein docking of electron transfer complexes: cytochrome c oxidase and cytochrome c. *Proteins*, 2002; **47**(1): 75–85.

169 Victor, B. L., J. B. Vicente, R. Rodrigues et al., Docking and electron transfer studies between rubredoxin and rubredoxin: oxygen oxidoreductase. *J. Biol. Inorg. Chem.*, 2003; **8**(4): 475–488.

170 Dong, F., M. Vijayakumar, and H.-X. Zhou, Comparison of Calculation and Experiment Implicates Significant Electrostatic Contributions to the Binding Stability of Barnase and Barstar. *Biophys. J.*, 2003; **85**: 49–60.

171 Hille, B., *Ion Channels of Excitable Membranes*, 3rd edn. Sunderland, MA: Sinauer Associates, 2001, 814.

172 Eisenman, G. and R. Horn, Ionic selectivity revisted: the role of kinetic and equilibrium processes in ion permeation through channels. *J. Membr. Biol.*, 1983; **50**: 1025–1034.

173 Eisenman, G. and O. Alvarez, Structure and function of channels and channelogs as studied by computational chemistry. *J. Membr. Biol.*, 1991; **119**(2): 109–132.

174 Burykin, A., C. N. Schutz, J. Villa, and A. Warshel, Simulations of ion current in realistic models of ion channels: the KcsA potassium channel. *Proteins*, 2002; **47**: 265–280.

175 Åqvist, J. and A. Warshel, Energetics of ion permeation through membrane channels. Solvation of Na^+ by gramicidin A. *Biophys. J.*, 1989; **56**: 171–182.

176 Jordan, P. C., Microscopic aproaches to ion transport through transmembrane channels. The model system gramicidin. *J. Phys. Chem.*, 1987; **91**: 6582–6591.

177 Morals-Cabral, J. H., Y. Zhou, and R. MacKinnon, Energetic optimization of ion conduction rate by the K^+ selectivity filter. *Nature*, 2001; **414**: 37–42.

178 Shrivastava, I. H. and M. S. P. Sansom, Simulations of ion permeation through a potassium channel: molecular dynamics of KcsA in a phospholipid bilayer. *Biophys. J.*, 2000; **78**: 557–570.

179 Allen, T. W., S. Kuyucak, and S. H. Chung, Molecular dynamics study of the KcsA potassium channel. *Biophys. J.*, 1999; **77**: 2502–2516.

180 Åqvist, J. and V. Luzhkov, Ion permeation mechanism of the potassium channel. *Nature*, 2000; **404**: 881–884.

181 Luzhkov, V. and J. Aqvist, K^+/Na^+ selectivity of the KcsA potassium

channel from microscopic free energy perturbation calculations. *Biochim. Biophys. Acta Protein Struct. Mol.*, 2001; **36446**: 1–9.

182 Burykin, A., M. Kato, and A. Warshel, Exploring the origin of the ion selectivity of the KcsA potassium channel. *Proteins*, 2003; **52**: 412–426.

183 Wada, A., The alpha-helix as an electric macro-dipole. *Adv. Biophys.*, 1976; **9**: 1–63.

184 Hol, W. G. J., P. T. V. Duijnen, and H. J. C. Berendson, Alpha helix dipole and the properties of proteins. *Nature*, 1978; **273**: 443–446.

185 Roux, B., S. Berneche, and W. Im, Ion channels, permeation and electrostatics: insight into the function of KcsA. *Biochemistry*, 2000; **39**(44): 13295–13306.

186 Daggett, V. D., P. A. Kollman, and I. D. Kuntz, Free-energy perturbation calculations of charge interactions with the helix dipole. *Chem. Scripta*, 1989; **29A**: 205–215.

187 Gilson, M. and B. Honig, The energetics of charge–charge interactions in proteins. *Proteins*, 1988; **3**: 32–52.

188 Vanduijnen, P. T., B. T. Thole, and W. G. J. Hol, Role of the active-site helix in papain, an abinitio molecular-orbital study. *Biophys. Chem.*, 1979; **9**(3): 273–280.

189 Åqvist, J., H. Luecke, F. A. Quiocho, and A. Warshel, Dipoles localized at helix termini of proteins stabilize charges. *Proc. Natl Acad. Sci. USA*, 1991; **88**(5): 2026–2030.

190 Lodi, P. J. and J. R. Knowles, Direct evidence for the exploitation of an alpha-helix in the catalytic mechanism of triosephosphate isomerase. *Biochemistry*, 1993; **32**(16): 4338–4343.

191 Roux, B. and R. MacKinnon, The cavity and pore helices the KcsA K^+ channel: Electrostatic stabilization of monovalent cations. *Science*, 1999; **285**: 100–102.

192 Levitt, M. and A. Warshel, Computer simulation of protein folding. *Nature*, 1975; **253**(5494): 694–698.

193 Go, N., Theoretical-studies of protein folding. *Annu. Rev. Biophys. Biol.*, 1983; **12**: 183–210.

194 Onuchic, J. N., P. G. Wolynes, Z. Luthey-Schulten, and N. D. Socci, Toward an outline of the topography of a realistic protein-folding funnel. *Proc. Natl Acad. Sci. USA*, 1995; **92**: 3626–3630.

195 Godzik, A., J. Skolnick, and A. Kolinski, Simulations of the folding pathway of triose phosphate isomerase-type-alpha/beta barrel proteins. *Proc. Natl Acad. Sci. USA*, 1992; **89**(7): 2629–2633.

196 Karanicolas, J. and C. L. Brooks, The structural basis for biphasic kinetics in the folding of the WW domain from a formin-binding protein: Lessons for protein design? *Proc. Natl Acad. Sci. USA*, 2003; **100**(7): 3954–3959.

197 Dill, K. A., Dominant forces in protein folding. *Biochemistry*, 1990; **29**: 7133–7155.

198 Simmerling, C., B. Strockbine, and A. E. Roitberg, All-atom structure prediction and folding simulations of a stable protein. *J. Am. Chem. Soc.*, 2002; **124**(38): 11258–11259.

199 Snow, C. D., N. Nguyen, V. S. Pande, and M. Gruebele, Absolute comparison of simulated and experimental protein-folding dynamics. *Nature*, 2002; **420**(6911): 102–106.

200 Fan, Z. Z., J. K. Hwang, and A. Warshel, Using simplified protein representation as a reference potential for all-atom calculations of folding free energies. *Theor. Chem. Acc.*, 1999; **103**: 77–80.

201 Shirts, M. and V. S. Pande, Computing – Screen savers of the world unite! *Science*, 2000. **290**(5498): 1903–1904.

202 Hollien, J. and S. Marqusee, Structural distribution of stability in a thermophilic enzyme. *Proc. Natl Acad. Sci. USA*, 1999; **96**(24): 13674–13678.

203 Usher, K. C., A. F. A. De la Cruz, F. W. Dahlquist, R. V. Swanson, M. I. Simon, and S. J. Remington, Crystal structures of CheY from *Thermotoga maritima* do not support conventional

explanations for the structural basis of enhanced thermostability. *Protein Sci.*, 1998; **7**(2): 403–412.

204 Honig, B. and A. S. Yang, Free-energy balance in protein-folding. *Adv. Protein Chem.* 1995; **46**: 27–58.

205 Xiao, L. and B. Honig, Electrostatic contributions to the stability of hyperthermophilic proteins. *J. Mol. Biol.*, 1999; **289**(5): 1435–1444.

206 Ibarra-Molero, B. and J. M. Sanchez-Ruiz, Genetic algorithm to design stabilizing surface-charge distributions in proteins. *J. Phys. Chem. B*, 2002; **106**(26): 6609–6613.

207 Giletto, A. and C. N. Pace, Buried, charged, non-ion-paired aspartic acid 76 contributes favorably to the conformational stability of ribonuclease T-1. Biochemistry, 1999; **38**(40): 13379–13384.

208 Grimsley, G. R., K. L. Shaw, L. R. Fee et al., Increasing protein stability by altering long-range coulombic interactions. *Protein Sci.*, 1999; **8**(9): 1843–1849.

209 Warshel, A., Conversion of light energy to electrostatic energy in the proton pump of *Halobacterium halobium*. Photochem. Photobiol., 1979; **30**: 285–290.

210 Schutz, C. N. and A. Warshel, unpublished results.

211 Willimsky, G., H. Bang, G. Fischer, and M. A. Marahiel, Characterization of Cspb, a *Bacillus subtilis* inducible cold shock gene affecting cell viability at low temperatures. *J. Bacteriol.*, 1992; **174**(20): 6326–6335.

8
Protein Conformational Transitions as Seen from the Solvent: Magnetic Relaxation Dispersion Studies of Water, Co-solvent, and Denaturant Interactions with Nonnative Proteins

Bertil Halle, Vladimir P. Denisov, Kristofer Modig, and Monika Davidovic

8.1
The Role of the Solvent in Protein Folding and Stability

During the course of three billion years of evolution, proteins have adapted to their aqueous environments by exploiting the unusual physical properties of water [1] in many ways. The solvent therefore play a central role in the noncovalent interactions responsible for the unique three-dimensional structures of native globular proteins. The most important example of this is the hydrophobic effect [2, 3], which provides the main driving force for protein folding (see Chapter 6). The thermodynamic stability of native proteins, conferred by numerous but weak noncovalent interactions, is marginal [4]. Even a small variation in external conditions can therefore cause denaturation, that is, a partial or complete loss of the native polypeptide conformation. Proteins can be denatured by a variety of perturbations [5]: thermal (see Chapter 4), pressure (see Chapter 5), electrostatic (see Chapter 7), or solvent composition (see Chapters 3 and 24). Because each perturbation alters the balance of stabilizing forces in a different way, a given protein may adopt a variety of nonnative states with distinct properties.

A fundamental understanding of protein folding and stability, including the mechanism of action of denaturants and co-solvents, must be based on studies of the structure, solvation, and energetics of nonnative proteins at a level of detail comparable with what has been achieved for native proteins [6]. Because of their complexity, nonnative proteins need to be examined from different vantage points using several techniques. Most experimental studies have focused on the properties of the polypeptide chain, such as its degree of compactness and secondary structure content. Inferences about solvation have usually been indirect – where the peptide chain is not, there is solvent – or have relied on uncertain premises. The current view of nonnative protein solvation derives largely from calorimetric (see Chapter 4), volumetric, and other macroscopic measurements, the interpretation of which is highly model dependent.

Computer simulations can, in principle, give a detailed picture of nonnative protein solvation (see Chapter 32), but suffer from two serious limitations. First,

Protein Folding Handbook. Part I. Edited by J. Buchner and T. Kiefhaber

ISBN: 3-527-30784-2

because molecular dynamics trajectories cannot (yet) be extended to the time scales where proteins unfold, the experimentally studied nonnative equilibrium states of proteins are inaccessible. Second, protein conformational equilibria are governed by small free energy differences involving hundreds of noncovalent interaction sites. Even minor inaccuracies in the (mostly empirical) force field model can thus produce unacceptably large accumulated errors. At the other extreme, qualitative insights into protein folding are sought from ''minimalist'' models. Because such models describe the solvent implicitly or, at best, in a highly idealized manner, they cannot be expected to capture the subtle thermodynamics of real proteins.

As one of the few methods that directly probes water molecules interacting with proteins, water ^{17}O magnetic relaxation dispersion (MRD) [7, 8] has been used extensively to study both the internal and surface hydration of native proteins [9–11]. In recent years, the MRD method has also been applied to nonnative proteins, yielding new information about the interaction of water (^{17}O and ^{2}H MRD) and co-solvent (^{2}H and ^{19}F MRD) molecules with proteins denatured by heat, cold, acid, urea, guanidinium chloride, or trifluoroethanol. In the following, we summarize the results of these MRD studies, which, in most cases, indicate that nonnative proteins are more structured and less solvent exposed than commonly believed. Relevant aspects of MRD methodology and data analysis are described at the end of this chapter. More comprehensive and technical accounts of biomolecular MRD are available [7, 8].

8.2 Information Content of Magnetic Relaxation Dispersion

MRD investigations of protein solutions usually entail measurements of the longitudinal relaxation rate, R_1, for a nuclear isotope, such as ^{2}H, ^{17}O, or ^{19}F, belonging to a solvent molecular species. These R_1 measurements are performed as a function of the resonance frequency, ν_0, which is determined by the strength of the applied static magnetic field. A data set, $R_1(\nu_0)$, covering two or more frequency decades is referred to as a dispersion profile. The MRD profile can provide quantitative information about several aspects of native and nonnative proteins, such as (i) long-lived association of water, denaturant, and co-solvent molecules with the protein, (ii) global exposure of the protein to water and other solvent components, (iii) the hydrodynamic volume of the protein, and (iv) side chain flexibility (via order parameters of labile hydrogens). Unlike high-resolution NMR spectroscopy (see Chapter 21), the MRD method is equally applicable to native and nonnative proteins, to small and large proteins, and to high and low (even subzero) temperatures (or other high-viscosity samples).

In the MRD context, a ''long-lived association'' usually means a residence time longer than 1 ns. The origin of this operational definition is that a correlation time of 1 ns produces a dispersion centered around 100 MHz, which is the highest resonance frequency for low-γ nuclei such as ^{2}H and ^{17}O achievable with present-day superconducting NMR magnets. Fortuitously, the 1 ns residence time also hap-

pens to be a convenient dividing line between solvent molecules buried in internal cavities, which typically have residence times in the range 10^{-8}–10^{-4} s at room temperature [9, 10], and solvent molecules interacting with the external protein surface, the vast majority of which have residence times in the range 10^{-11}–10^{-10} s at room temperature [9–11]. The MRD profile yields the quantity $N_\beta {S_\beta}^2$, the product of the number of long-lived solvent molecules, N_β, and their mean-square orientational order parameter ${S_\beta}^2$, a number in the range 0–1.

Nearly all globular proteins contain buried water molecules in the native state, on average one per 25 amino acid residues [12]. These internal water molecules are conserved to the same extent as the amino acid sequence and must therefore be essential for function [13]. Not all protein cavities of sufficient size are occupied by water molecules. To compensate for the favorable intermolecular interactions in bulk water, the cavity must allow for at least two (more commonly, three or four) hydrogen bonds with the internal water molecule. (Two exceptions to this "rule" would be a large cavity occupied by an internally hydrogen-bonded water cluster and a cavity with a large electric field, produced by nearby ionized side chains.) However, the long residence time of internal water molecules is not a consequence of these hydrogen bonds (which are also present in the bulk solvent), but result from trapping by the protein structure. The quantity $N_\beta {S_\beta}^2$ thus reflects the structural integrity of the protein. For a completely unfolded protein in a random-coil conformation, we expect that $N_\beta {S_\beta}^2 = 0$. If the locations of the buried water molecules are known in the native protein (from the crystal structure), then an observed difference in $N_\beta {S_\beta}^2$ between native and nonnative forms gives an indication of the structural integrity at the corresponding locations in the protein. Similar considerations apply to other solvent species.

The MRD profile also yields a measure of the global solvent exposure of the protein in the form of the quantity $N_\alpha \rho_\alpha$, the product of the number of dynamically perturbed, but short-lived (< 1 ns), solvent molecules, N_α, and their rotational retardation factor, $\rho_\alpha = \tau_\alpha / \tau_{\text{bulk}} - 1$. Because the dynamic perturbation of the solvent is short-ranged, only solvent molecules in direct interaction with the protein surface are significantly perturbed [10]. The correlation time τ_α can therefore be interpreted as the mean rotational correlation time for solvent molecules in contact with the protein surface. Technically, τ_α is the integral of the time correlation function for the second-rank Legendre polynomial [7]. However, because ρ_α involves the ratio $\tau_\alpha / \tau_{\text{bulk}}$, it is independent of the rank and can be compared directly with results obtained by other methods. The number of solvent molecules of species S in contact with the protein surface can be expressed as $N_\alpha^{\text{S}} = N_{\text{S}} \theta_{\text{S}}$, where N_{S} is the total number of S sites (that can be occupied simultaneously) on the protein surface and θ_{S} is the mean occupancy of these sites by S molecules. The number of sites can be estimated from geometric considerations as $N_{\text{S}} = A_{\text{P}}^{\text{S}} / a_{\text{S}}$, where A_{P}^{S} is the surface area of the protein accessible to S molecules and a_{S} is the mean surface area occupied by one S molecule at the protein surface. In the case of water (S = W), A_{P}^{W} is the usual solvent-accessible surface area computed with a probe radius of 1.4 Å and a_{W} is approximately 15 Å^2. For a 15 kDa protein, N_{W} is about 500.

The MRD-derived quantity $N_\alpha \rho_\alpha$ can thus provide information about the global

solvent exposure of the protein in different states. If water is the only solvent component, then $\theta_W = 1$ and N_α^W is proportional to the water-accessible surface area A_P^W. Consequently, N_α^W should increase when the protein unfolds. However, the MRD profile does not monitor solvent accessibility directly; an observed change in $N_\alpha\rho_\alpha$ may also be due to a variation in the retardation factor ρ_α. For native proteins, the average τ_α is dominated by a relatively small number of water molecules located in surface pockets, where the geometric constraints prevent the cooperative motions that are responsible for the fast rotational and translational dynamics in bulk water [9–11]. If these surface pockets are disrupted in the unfolded protein, ρ_α will be smaller than for the native protein. On the other hand, water molecules that penetrate a (partially) unfolded protein, perhaps in the form of hydrogen-bonded water chains or small clusters, may be more strongly motionally retarded than water molecules at the fully exposed (convex) surface of the native protein. Because of this interpretational ambiguity, the quantity $N_\alpha\rho_\alpha$ can only provide bounds on the solvent exposure (based on an assumption about ρ_α) or on the rotational retardation (based on an assumption about N_α). On the other hand, penetrating solvent molecules may become long-lived, in which case they contribute to the parameter $N_\beta S_\beta^2$.

For solvent-denatured proteins, we must also deal with the complication of preferential solvation [14, 15]. In other words, N_α^S is determined not only by the solvent-accessible area of the protein, but also by the competition for this area by water and co-solvent molecules. The occupancy θ_S, which describes this competition, can be estimated from the known activities of both solvent species and the (usually unknown) co-solvent binding constant (which may differ between native and nonnative states).

The third parameter provided by an MRD profile is the correlation time τ_β, which is the characteristic time for orientational randomization of long-lived solvent molecules trapped within the protein. In general, this randomization occurs by two parallel and independent processes: rotational diffusion of the protein, with rotational correlation time τ_R, and escape of the solvent molecule from the protein, with mean residence time τ_S (the inverse of the dissociation rate constant). Mathematically, this is expressed as $\tau_\beta = \tau_R\tau_S/(\tau_R + \tau_S)$. Therefore, if $\tau_S \gg \tau_R$, as is often the case, the observed correlation time τ_β can be identified with the rotational correlation time τ_R of the protein. For native globular proteins, τ_R is usually described by the Stokes-Einstein-Debye equation, $\tau_R = \eta_0 V_H/(k_B T)$, where η_0 is the viscosity of the solvent (not the solution!) and V_H is an effective hydrodynamic volume. If the protein were a smooth sphere that did not perturb the solvent ($\rho_\alpha = 0$), then V_H would simply be the protein volume. However, a real protein sweeps out a larger volume when it rotates than does a compact sphere of the same volume. Furthermore, it perturbs the motion of adjacent solvent molecules. The former effect can be handled by molecular hydrodynamics, where the hydrodynamic equations are solved for the actual protein structure, specified in atomic detail [16]. The second effect can be incorporated by assigning a higher viscosity to the hydration layer [17]. An empirical approach [17], which predicts τ_R with similar accuracy, is to set

$V_H = 2V_0$, where V_0 is the protein volume obtained from the partial specific volume, v_P, that is, $V_0 = v_P M_P / N_A$.

MRD exploits trapped solvent molecules as intrinsic probes of protein rotational diffusion. It would thus appear that τ_R cannot be determined for an unfolded protein without long-lived solvent molecules. However, water ^2H MRD monitors not only water molecules but also the labile hydrogens in the protein that exchange sufficiently rapidly (usually meaning residence times < 1 ms) with water hydrogens. Under most conditions (pH and temperature being the critical variables), the labile hydrogen contribution is sufficient to produce a ^2H dispersion even in the absence of long-lived water molecules. For native proteins, τ_R can be determined by several other techniques besides MRD, for example, ^{15}N spin relaxation and fluorescence depolarization.

Under conditions where $\tau_\beta = \tau_R$, which is always the case for the labile-hydrogen contribution to the ^2H dispersion, the correlation time yields the hydrodynamic volume of the protein. However, for extensively unfolded proteins, V_H is an apparent volume that cannot be related to protein structure in a simple way. The Stokes-Einstein-Debye relation between τ_R and V_H is only valid for a rigid and nearly spherical protein. In the random-coil limit, the rotational dynamics would have to be described by a distribution of correlation times, as in the Rouse-Zimm theory [18]. Because a flexible protein exhibits internal rotational modes with shorter correlation times than for the rigid protein, the apparent V_H does not necessarily increase when the protein expands. This complication limits the diagnostic value of τ_R. Another confounding factor is that unfolding leads to increased exposure of nonpolar groups, which may cause the denatured protein to self-associate. However, these complications notwithstanding, the correlation time τ_β always provides a lower bound on the residence time τ_S for the long-lived solvent molecules responsible for the dispersion. As such, it defines the time scale on which the local structural integrity of the protein is probed.

8.3 Thermal Perturbations

8.3.1 Heat Denaturation

The first water ^2H and ^{17}O MRD study of heat denaturation examined bovine pancreatic ribonuclease A (RNase A) [19], which is known to undergo a reversible and cooperative thermal unfolding at neutral or acidic pH. However, some studies have indicated that the conformational transition may not be truly two-state. The thermally denatured state of RNase A appears to be relatively compact and is further unfolded on reduction of the four disulfide bonds.

MRD profiles have been recorded at seven temperatures in the interval 4–65 °C at pH 2.0 and 4.0 (all pH values quoted in this chapter are uncorrected for H_2O/

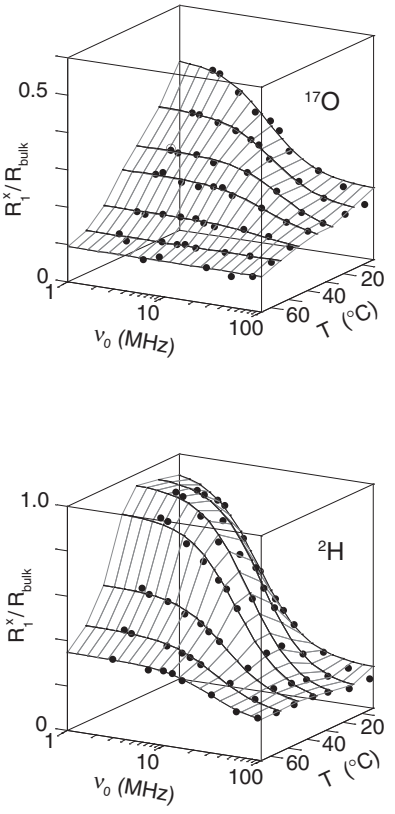

Fig. 8.1. Water ^{17}O (top) and ^{2}H (bottom) MRD profiles from 3.8 mM solution of ribonuclease A in D_2O at pH 2.0 and seven temperatures from 4 to 65 °C [19]. The vertical axis shows the excess relaxation rate $R_1^x = R_1 - R_{bulk}$, normalized by R_{bulk} to remove most of the trivial (viscosity-related) temperature dependence. The ^{17}O dispersion curves are three-parameter fits according to Eq. (8).

D_2O isotope effects). Figure 8.1 shows the MRD data obtained at pH 2, where the transition midpoint T_m is 31 °C according to CD measurements. For the native protein, observed at low temperatures, the MRD profiles yield $N_\beta S_\beta^2 = 2.3 \pm 0.1$, which requires at least three long-lived water molecules (since $S_\beta^2 \leq 1$). The crystal structure of RNase A reveals six water molecules partly buried in surface pockets, but no deeply buried water molecules. The ^{17}O MRD profile from the native protein must be due to some or all of these six water molecules. The absence of ^{17}O dispersion at high temperatures indicates a loss of persistent native structure at the locations of these hydration sites.

If the conformational transition involves only two states, then $N_\beta S_\beta^2$ yields the fraction native protein at any temperature (see Eq. 17). Figure 8.2a compares this with the native-state fraction derived from CD measurements. The MRD and CD results agree on the width (ΔT) of the transition, but T_m is 5–10 °C higher in the

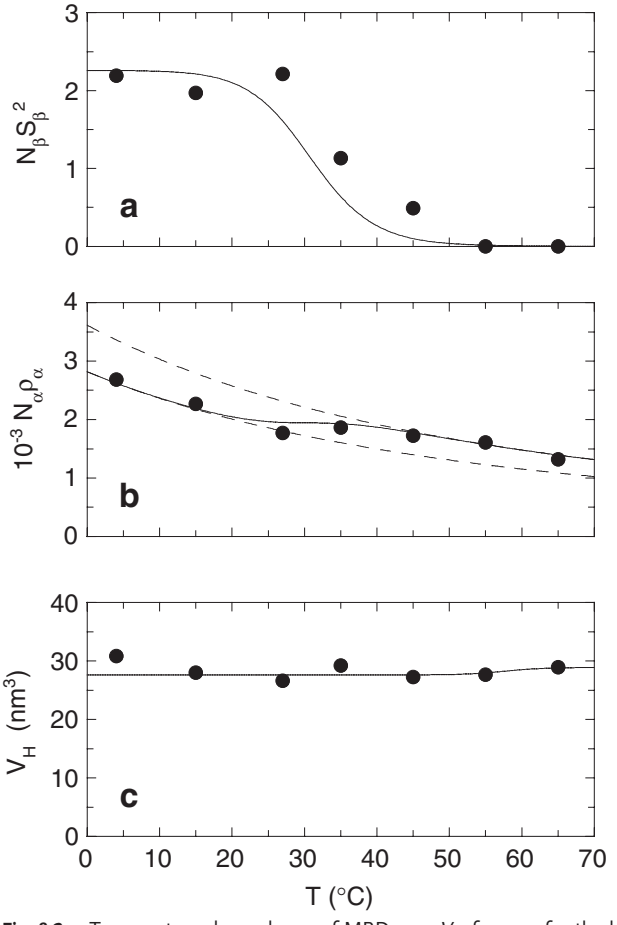

Fig. 8.2. Temperature dependence of MRD parameters derived from water ^{17}O and ^{2}H MRD profiles from 3.8 mM solution of ribonuclease A in D_2O: a) $N_\alpha\rho_\alpha$ from $\alpha(^{17}O)$ at pH 2.0; b) $N_\beta S_\beta^2$ from $\beta(^{17}O)$ at pH 2.0; and c) V_H from τ_β for the labile-hydrogen contribution to the ^{2}H dispersion at pH 4.0 [19]. The curves correspond to a two-state transition with transition midpoint and width as determined by CD measurements at 222 and 275 nm.

MRD data. This shift indicates that the transition is not truly two-state and that the first step does not affect the tertiary structure that maintains the 3–6 long-lived hydration sites. On the other hand, the MRD data rule out a scenario with an intermediate state extensively permeated by long-lived water molecules.

Figure 8.2b shows the surface hydration parameter $N_\alpha\rho_\alpha$ derived from the ^{17}O MRD profiles. The solid curve is a fit based on the two-state model with T_m and ΔT fixed at the values determined by CD measurements. Since the rotational retardation factor ρ_α involves a ratio of correlation times that may have different activation energies, it is expected to vary with temperature (dashed curves in Figure

8.2b). The fit in Figure 8.2b yields an activation enthalpy of 12 ± 2 kJ mol^{-1} for τ_α/τ_{bulk} $(= \rho_\alpha + 1)$, in the range found for the hydration of small organic molecules. For the native state, the fit yields $N_\alpha\rho_\alpha = (1.8 \pm 0.1) \times 10^3$ at 27 °C. The number of water molecules in contact with the native protein surface can be estimated as $N_\alpha = A_P^W/a_W \approx 460$ (see Section 8.2), whereby $\rho_\alpha = 3.9 \pm 0.2$. This value is similar to what has been found for many other native proteins (at 27 °C), but is about twice as large as the ρ_α value obtained for amino acids and other small organic molecules [9–11]. The larger ρ_α value for proteins can be understood if τ_α, which typically is an average over some 500 water molecules in contact with the protein surface, has a sizable contribution from a small number of water molecules with a relatively large dynamic retardation. If ρ_α has the same temperature dependence in the native and denatured states, then the MRD data yield $N_\alpha(U)\rho_\alpha(U)/N_\alpha(N)\rho_\alpha(N) = 1.3 \pm 0.2$. Although this result does not allow us to infer how much the individual factors N_α and ρ_α differ between the two states, it restricts the possible scenarios.

Calorimetric studies showing that the heat capacity of thermally denatured proteins is essentially the same as that of the constituent amino acid side chains (see Chapter 4) have been taken to imply that thermally denatured RNase A is extensively unfolded and that the nonpolar side chains forming the native hydrophobic core are fully hydrated [20, 21]. Changes in the apparent molar volume and adiabatic compressibility on thermal denaturation of RNase A have also been attributed to extensive exposure of nonpolar side chains [22]. For complete unfolding (to an extended β conformation), the solvent-accessible area of RNase A increases by a factor 2.4 (see Chapter 20), but the topological constraints imposed by the four disulfide bonds reduce this factor to 1.9 [23]. To be consistent with a 1.9-fold area increase, the MRD results require that $\rho_\alpha = 2.6$ in the denatured state, 33% less than for the native state. A smaller rotational retardation in the denatured state would be expected if the strongly retarded surface sites in the native state are absent. However, extensive solvent penetration of the partly unfolded protein may well increase ρ_α.

The ^{2}H MRD profiles in Figure 8.1 also reflect the thermal unfolding transition, but differ qualitatively from the ^{17}O profiles in two respects. First, a sizable ^{2}H dispersion remains even at 65 °C, where the native state has negligible population. Second, the ^{2}H dispersion amplitude increases markedly with temperature outside the transition region. These are the hallmarks of a labile hydrogen contribution. A detailed analysis of the ^{2}H MRD profiles confirms that they are dominated by rapidly exchanging hydrogens in the 11 carboxyl and 31 hydroxyl groups of RNase A. This analysis also indicates that the orientational order parameters of the O–D bonds in these groups are strongly reduced in the transition, as expected from the greater conformational flexibility in the unfolded state [19].

The correlation time τ_β associated with the labile hydrogen contribution to the ^{2}H dispersion can be identified with the rotational correlation time τ_R of RNase A, which therefore can be determined also for the denatured state. To remove the trivial (via η/T) temperature dependence in τ_R, we consider the variation of the hydrodynamic volume V_H as the protein unfolds. Figure 8.2c shows V_H derived in this way from ^{2}H MRD data at pH 4.0, where $T_m = 58$ °C according to CD mea-

surements. Thus all temperatures but the two highest refer to the native state, where $V_H = 27.6 \pm 1.0\ nm^3$, in reasonable agreement with the value 30.5 nm^3 determined by ^{15}N relaxation at pH 6.4, 25 °C (and sixfold lower protein concentration) [24]. Remarkably, V_H is not significantly different at 65 °C, where the protein is 94% denatured according to CD. Presumably, this invariance is a result of compensating effects on the rotational dynamics of polypeptide expansion and flexibility (see Section 8.2).

In summary, the MRD data show that the 3–6 long-lived hydration sites in native RNase A are disrupted in the thermally denatured state. While the denatured protein lacks structural integrity on the 10 ns time scale at these sites, it is much more compact (less solvent exposed) than the maximally unfolded disulfide-intact protein. This picture is consistent with other observations, indicating substantial residual structure in the heat-denatured state of RNase A.

8.3.2 Cold Denaturation

For most proteins, the temperature-dependent free energy difference, $\Delta G(T)$, between denatured and native states exhibits negative curvature at all (accessible) temperatures, with maximum thermal stability at or near ambient temperature. Such a parabolic stability profile is predicted by macroscopic thermodynamics if the isobaric heat capacity difference, ΔC_P, is positive and temperature-independent. This simplified analysis also predicts that $\Delta G(T) = 0$, not only at the heat denaturation midpoint T_m, but also at a lower temperature, T'_m, identified as the midpoint of an exothermic cold denaturation [25]. Heat denaturation is readily understood as the result of thermal excitation of the numerous disordered configurations of the polypeptide chain. While the molecular details of cold denaturation remain obscure, it is usually attributed to a weakening of the hydrophobic effect caused by the temperature-dependent structure of bulk water [25]. If this notion is correct, cold denaturation might hold the key to understanding the major driving force for protein folding.

Studies of cold denaturation are hampered by the fact that, for most proteins, T'_m is predicted to be well below the freezing point of water. This obstacle can be circumvented by increasing T'_m and/or preventing ice formation. The most common strategy is to expose the protein to a second (nonthermal) perturbation, typically a few kilobars of hydrostatic pressure or a moderate denaturant concentration, which lowers the $\Delta G(T)$ curve, thereby raising T'_m and lowering T_m. Both pressure elevation and co-solvent addition also depress the freezing point of the water (to −19 °C at 2 kbar). However, this approach has a serious drawback: even if the secondary perturbation does not denature the protein at ambient temperature, the relative importance of the two simultaneous perturbations is difficult to establish. Thus, for example, the term pressure-assisted cold denaturation merely indicates that temperature was the experimental variable, but does not imply that the low temperature is more important than the high pressure in determining the properties of the resulting nonnative state. In other words, it is important to distinguish denaturation occurring at low temperature from denaturation caused by the low temperature.

To study cold denaturation per se for proteins with $T'_m < 0$ °C, the aqueous solvent must be maintained in a metastable, supercooled state. By careful water treatment and judicious choice of (small) sample containers to eliminate ice nucleation sites, water can be supercooled to about −20 °C [26]. A more robust method is to subdivide the protein solution into micrometer-sized emulsion droplets, the vast majority of which remain unfrozen down to the homogeneous nucleation temperature of −38 °C (for H_2O) [27]. While sample emulsification interferes with most scattering and spectroscopic measurements, it poses little or no problem for MRD studies.

Cold denaturation of bovine β-lactoglobulin (βLG) has been observed by several methods, using denaturants [28–30] or elevated pressure [31] to bring T'_m into a more accessible range. This 162-residue β-barrel protein is dimeric at physiological pH, but is essentially monomeric at pH < 3 in the absence of salt [32]. Remarkably, βLG is more stable towards urea denaturation at pH 2 than at neutral pH. Calorimetric, ^{1}H NMR and CD studies of βLG at pH 2 in the presence of 4 M urea (which raises T'_m to about 20 °C) indicate that cold denaturation involves an intermediate with disrupted tertiary structure, which unfolds extensively at temperatures close to 0 °C [28, 29]. However, SAXS, hydrogen exchange and heteronuclear NMR measurements at 0 °C (pH 2.5, 4 M urea) indicate a rather compact structure (27% increase of the radius of gyration) with a residual, native-like β-hairpin structure (stabilized by one of the two disulfide bonds) [30]. All these studies, as well as the MRD studies to be discussed, refer to isoform A of βLG.

Crystal structures of βLG identify two water molecules trapped in small cavities. In addition, the β barrel contains a large, elongated, hydrophobic cavity that can bind retinol, fatty acids and other nonpolar ligands. One crystal structure indicates that the ligand-free cavity is occupied by a hydrogen-bonded string of five water molecules [33]. Consequently, we expect that βLG contains at least two, but possibly more, long-lived water molecules. This structure-based prediction is consistent with ^{17}O MRD studies of native βLG (0.9 mM, pH 2.5) at 10 °C, yielding $N_\beta S_\beta^2 = 2.2 \pm 0.2$ [34]. In addition, the MRD results reveal several water molecules with a correlation time of 2–3 ns, tentatively assigned to partially buried hydration sites in small surface pockets and/or in the large binding pocket.

Lowering of the temperature to −1 °C does not affect $N_\beta S_\beta^2$ significantly (see Figure 8.3), indicating that the native protein structure remains intact at this temperature. However, addition of 4 M urea virtually eliminates the ^{17}O dispersion at −1 °C, as expected from earlier studies of urea-assisted cold denaturation [28–30]. The MRD result, $N_\beta S_\beta^2 = 0.3 \pm 0.2$, indicates a native fraction on the order of 10% under these conditions. In the absence of urea and at temperatures down to −1 °C, the rotational correlation time τ_R of βLG, derived from the ^{2}H MRD profile (with a large contribution from labile hydrogens), agrees quantitatively (after η/T scaling) with expectations based on hydrodynamic modeling [17] and ^{15}N relaxation [35]. This provides further evidence for a native structure under these conditions. For the denatured protein in 4 M urea at −1 °C, the ^{2}H correlation time τ_β is 30% shorter than the τ_R expected for the native protein, even though SAXS measurements indicate a twofold volume expansion in the denatured state [30]. This

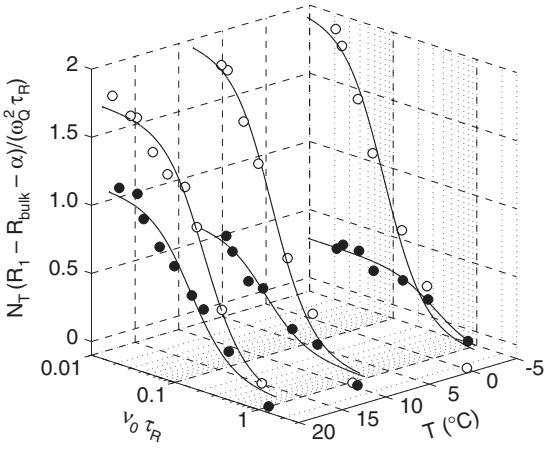

Fig. 8.3. Water ^{17}O MRD profiles from 0.9 mM solutions of β-lactoglobulin A (pH 2.5, 52% D_2O) at 19.4, 10.2 and −1.1 °C [34]. The solvent is salt-free water (open circles) or 4 M urea (solid circles). The vertical axis shows the β-dispersion part of the relaxation rate, $R_1 - R_{bulk} - \alpha$, normalized by $\omega_Q^2 \tau_R / N_T$ to remove the trivial dependence on viscosity and temperature. This reduced quantity approaches $N_\beta S_\beta^2$ at low frequencies. The curves are three-parameter fits according to Eq. (8).

shortening of the correlation time shows that the denatured protein does not undergo rigid body rotational diffusion. Rather, it exhibits internal reorientational motions on a range of time scales (shorter than the rigid body τ_R), as expected for labile hydrogens in unfolded polypeptide segments.

To examine whether βLG can be cold denatured in the absence of urea, water ^2H and ^{17}O MRD profiles have been recorded on emulsified samples down to −20 °C [34]. Control experiments yield identical MRD profiles before and after emulsification, justifying the neglect of βLG interactions with the interface of the 10 μm diameter emulsion droplets. The MRD data show no evidence of a cold denaturation, but indicate that the native structure persists down to at least −20 °C (see Figure 8.4). Indeed, after normalization to remove the trivial temperature dependence via τ_R, the ^{17}O MRD profiles exhibit little variation from 27 °C to −20 °C. The ^2H profiles do have reduced amplitude at low temperatures, but this can be accounted for by the slower labile hydrogen exchange.

In summary, MRD shows that βLG is extensively denatured in 4 M urea at −1 °C, in agreement with previous studies. However, even though the conventional thermodynamic analysis indicates that the midpoint temperature for cold denaturation of βLG in the absence of urea should be about −20 °C, the MRD data indicate that the native protein structure persists down to this temperature. This suggests that the standard thermodynamic analysis is incomplete and that the observed denaturation at low temperature in the presence of urea may not be driven primarily by the temperature dependence of the water structure, which is the usual explanation of cold denaturation.

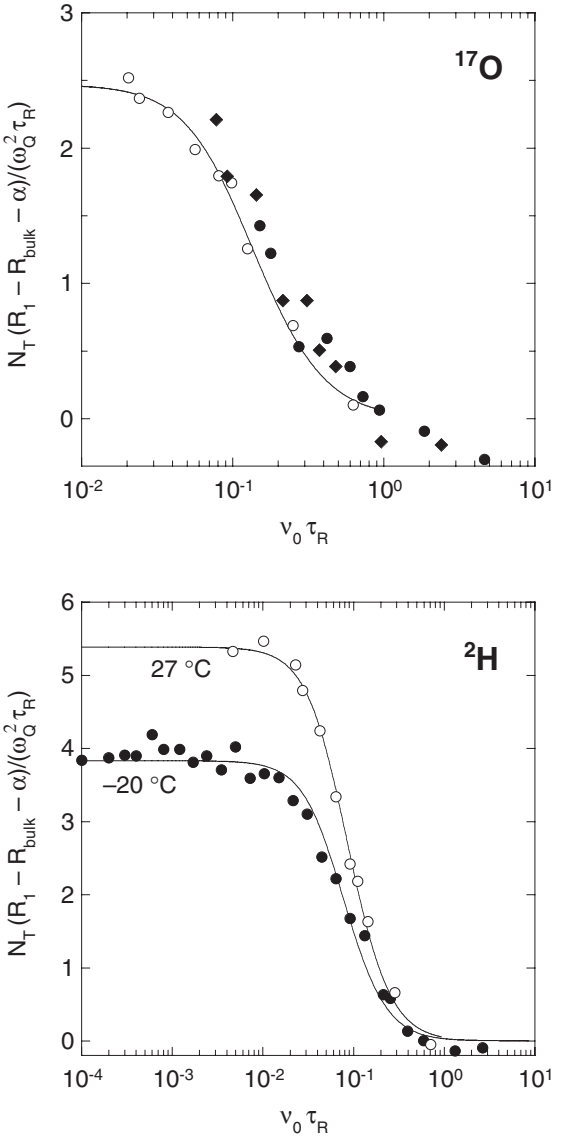

Fig. 8.4. Water ^{17}O (top) and ^{2}H (bottom) MRD profiles from emulsified 0.8 mM solutions of β-lactoglobulin A (pH 2.7, 50–100% D_2O) at 27 °C (open circles), −10 °C (solid diamonds) and −20 °C (solid circles) [34]. The relaxation rate has been reduced as in Figure 8.3. The curves are three-parameter fits (to the 27 °C data in the case of ^{17}O) according to Eq. (8).

8.4
Electrostatic Perturbations

Ionizable side chains contribute to protein stability via their mutual Coulomb interactions and via ionic solvation effects, that is, the charge-dependent part of side-chain interactions with the polarizable environment, including water, co-solvents, salt and buffer ions, and the rest of the protein (see Chapter 7). This contribution to protein stability can be manipulated by changing the net charge of side chains, by means of pH titration or site-directed mutagenesis, or by adding salt to the solvent. In contrast to thermal or solvent denaturation, pH titration or mutation of an ionizable side chain is a localized perturbation. However, because the Coulomb interaction is long-ranged, the effect of the perturbation is not necessarily local.

Whereas some proteins remain in the native state even at extreme pH values, others undergo a cooperative transition to a compact globular state with disordered ("molten") side chains, but with native-like secondary structure and backbone fold (see Chapter 23). This so-called molten globule (MG) state is thought to be an equilibrium analog of a universal kinetic intermediate on the protein folding pathway [36]. If the native protein is regarded as an (irregular) crystal, one would expect the MG state to be favored by high temperature. However, in most reported studies, the MG state has been induced by nonthermal perturbations. In particular, many proteins adopt MG-like states when some or all carboxylate groups are neutralized.

MG proteins are remarkably compact. Typically, the radius of gyration is only 10–30% larger than for the native state [36]. Nevertheless, if the MG is modeled as a uniformly expanded version of the native protein, this corresponds to a volume expansion factor of 1.3–2.2. Even for a small protein, the inferred difference in volume between the native and MG states translates into several hundred water molecules. However, it is not clear whether the additional volume of the MG protein is, in fact, occupied by water. This issue, which is of vital importance for the understanding of the MG state, has been addressed by water ^{17}O MRD studies of the acid MG states of three proteins [37].

Among these proteins is α-lactalbumin (αLA), which at pH 2 adopts a conformation that has come to be regarded as the paradigmatic molten globule [36]. The crystal structure of native (human) αLA shows six potentially long-lived water molecules. Two of these coordinate the bound Ca^{2+} ion, residing in a cavity between the α and β domains that traps three additional water molecules. The ^{17}O MRD profile (see Figure 8.5) from native (bovine) αLA yields $N_\beta S_\beta^2 = 3.4 \pm 0.2$, indicating a residence time between 10 ns and a few microseconds (at 27 °C) for at least four, and perhaps all six, of these water molecules. For the MG state at pH 2, $N_\beta S_\beta^2 = 1.8 \pm 0.2$, corresponding to at least two long-lived water molecules. This observation demonstrates that the structural integrity of the MG state is sufficient to trap at least two long-lived water molecules. Because the Ca^{2+} ion is no longer bound at pH 2, the difference in $N_\beta S_\beta^2$ between the native and MG states might be fully accounted for by the loss of the two calcium-coordinated water molecules. However, since the MRD data do not reveal water locations, we cannot say if the long-lived water molecules in the MG state correspond to native hydration sites.

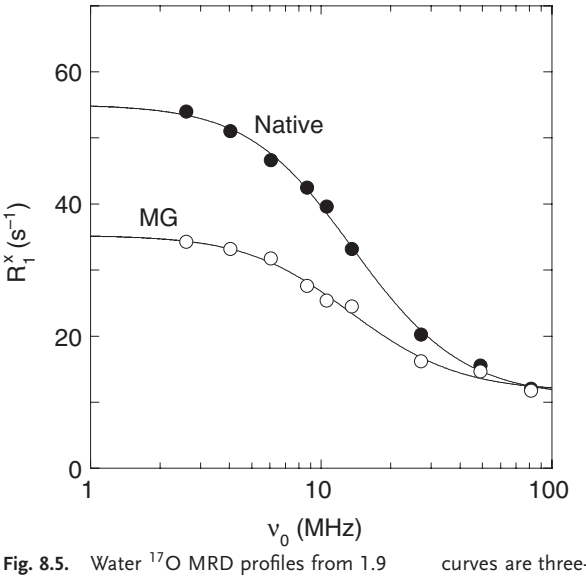

Fig. 8.5. Water ^{17}O MRD profiles from 1.9 mM solutions of bovine α-lactalbumin (D_2O, 27 °C) at pH 8.4 (native) and 2.0 (molten globule, MG) [37]. The vertical axis shows the excess relaxation rate $R_1^x = R_1 - R_{bulk}$. The curves are three-parameter fits according to Eq. (8). The presence of the MG state at pH 2.0 was verified by the characteristic CD profile and loss of the upfield methyl resonances in the ^1H NMR spectrum.

The convergence at high frequencies of the native and MG profiles (see Figure 8.5) implies that the two states have very similar surface hydration parameter. Indeed, the fits yield $N_\alpha\rho_\alpha = (1.8 \pm 0.1) \times 10^3$ for the native state and $(1.9 \pm 0.1) \times 10^3$ for the MG state. From the solvent-accessible area of the native protein, we estimate $N_\alpha = 450$ and thus $\rho_\alpha = 4.0 \pm 0.3$, a typical value for native globular proteins. Low-temperature MRD studies of protein hydration and ^{17}O relaxation studies of small-solute hydration suggest that $\rho_\alpha = 1$–2 for the vast majority of the water molecules in contact with the protein surface [11]. The ρ_α values of 4–5 typically found for native proteins must therefore be dominated by a small subset of hydration sites with strongly rotationally retarded water molecules. If these special hydration sites are abolished in the MG state, ρ_α would be substantially smaller than for the native protein. In this case, the invariance of $N_\alpha\rho_\alpha$ observed for αLA must be accidental, the reduction of ρ_α being precisely canceled by an increase of N_α due to a greater solvent exposure in the MG state. This additional solvent exposure could reflect extensive water penetration of the MG protein. This scenario would be consistent with a strictly geometric interpretation of the 35–60% reported increase of the hydrodynamic volume for the MG state, leading to the conclusion that 270 water molecules penetrate the interior of the αLA molten globule [38]. However, later measurements have indicated a significantly smaller expansion of the αLA MG (see below). Moreover, as the hydrodynamic volume reflects the vis-

cous energy dissipation associated with protein motion, it depends, not only on protein geometry, but also on water dynamics at the protein surface, as manifested in ρ_α and in the local viscosity [17].

The observed invariance of $N_\alpha\rho_\alpha$ may also be interpreted, in a more restrictive way, as resulting from the invariance of each of the quantities N_α and ρ_α. In this interpretation, the expansion of the MG must be explained without invoking water penetration. Recent reports indicate that the αLA MG is even more compact than previously thought. From NMR diffusion measurements a volume expansion of $20 \pm 4\%$ [39] or $22 \pm 5\%$ [40] has been reported and the fluorescence anisotropy decay of the three tryptophan residues indicates even smaller values of 12–18% [41]. These results should be compared with the typical 15% expansion on melting of crystals of small organic molecules [42]. Considering also that native proteins are typically 4% more densely packed than small-molecule crystals [42], a 20% expansion of αLA upon ''melting'' of the side chains seems plausible. In this view, which also appears to be consistent with calorimetric data [43, 44], the weakening of the attractive van der Waals interactions in the protein core is compensated by the configurational entropy associated with alternative side chain packings without the need to invoke a significant amount of water penetration.

Although the individual factors N_α and ρ_α in the product $N_\alpha\rho_\alpha$ cannot be determined from MRD data alone, the interpretational ambiguity for αLA might be resolved by investigating other proteins. If the $N_\alpha\rho_\alpha$ invariance observed for αLA is an accidental result of large compensating changes in N_α and ρ_α, then it is unlikely to be a universal phenomenon. On the other hand, if the generic MG state has an expanded and dynamic but dry core and a native-like surface, then neither N_α nor ρ_α would change much in the native to MG transition and their product should be nearly invariant for most MG proteins. This latter scenario is supported by the MRD data available so far [37]. Thus, for human carbonic anhydrase (CA) in form II (homologous with the bovine B form), the ^{17}O MRD profiles yield $N_\alpha\rho_\alpha = (7.0 \pm 0.4) \times 10^3$ for the native state at pH 9.0 and $(6.9 \pm 0.3) \times 10^3$ for the MG state at pH 3.0 [37]. With $N_\alpha = 770$ estimated from the solvent-accessible area of the native protein, this yields a rotational retardation factor ρ_α of 9.1 ± 0.5, twice as large as for most other native proteins. This large value is attributed to the unusual prevalence in CA of hydrated surface pockets and, possibly, to internal motions of the large number of long-lived buried water molecules ($N_\beta S_\beta^2 = 8$–9 for both the native and the MG state). The observed state invariance of the large $N_\alpha\rho_\alpha$ value (for a protein of this size) suggests that strongly motionally retarded water molecules occupy surface pockets also in the MG state of CA.

A different picture emerged from a ^1H NMR study of (bovine) CA in the native (pH 7.2), MG (pH 3.9) and urea-denatured (pH 7.2) states [45]. Magnetization transfer between water and protein protons was observed on the 100 ms time scale in the MG state, but not in the native or denatured states. This finding was taken as evidence for a much greater hydration (due to extensive water penetration) for the MG state than for the other two states. However, a more plausible explanation is that the observed magnetization transfer is relayed by the roughly 50 hydroxyl and carboxyl protons present in CA at pH 3.9, which exchange with water protons

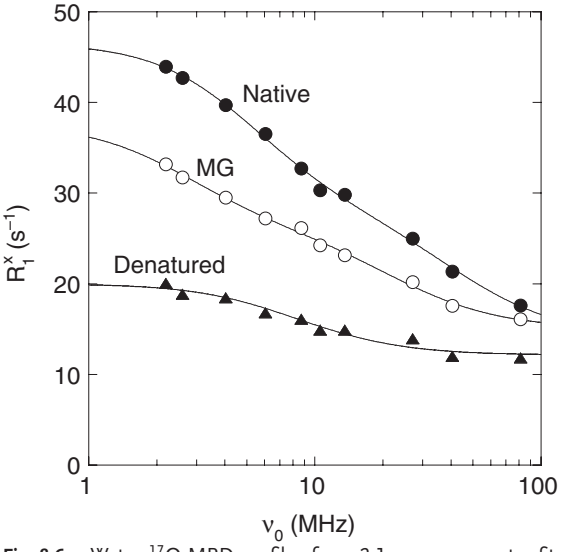

Fig. 8.6. Water ^{17}O MRD profiles from 2.1 mM solutions of equine apomyoglobin (D_2O, 27 °C) at pH 5.9 (native), 4.2 (molten globule, MG) and 2.2 (denatured) [37]. The vertical axis shows the excess relaxation rate $R_1^x = R_1 - R_{bulk}$. The curves are three- or five-parameter fits according to Eq. (8) or its bilorentzian generalization. The presence of the MG state at pH 4.2 was verified by the characteristic CD profile and loss of the upfield methyl resonances in the ^1H NMR spectrum.

within 100 ms at pH 3.9, but are either titrated (carboxyl) or exchange too slowly (hydroxyl) at pH 7.2 [46].

Also for apomyoglobin (apoMb), the ^{17}O MRD profiles for the native (pH 5.9) and MG (pH 4.2) states converge at high frequencies (see Figure 8.6), yielding $N_\alpha\rho_\alpha = (2.1 \pm 0.4) \times 10^3$ for the native state (corresponding to $\rho_\alpha = 4.0 \pm 0.8$) and $(2.2 \pm 0.2) \times 10^3$ for the MG state [37]. The MG state of apoMb has a high helix content and native-like fold [47], but, with about 70% larger hydrodynamic volume than native apoMb, it is less compact than the αLA MG. A uniform volume expansion by 70% can hardly be achieved without water penetration. However, the observed 20% increase in hydrodynamic radius [48] and radius of gyration [49] could be produced by a smaller expansion of the core (as for αLA) and some protrusion of polypeptide segments from fraying helices and termini [49]. Because water does not penetrate the core and water in contact with protruding polypeptide segments should not be much rotationally retarded ($\rho_\alpha = 1$–2, as for small molecules), this picture of the MG structure is compatible with the observed $N_\alpha\rho_\alpha$ invariance.

Myoglobin has an exceptionally large amount of internal cavities, some of which contain disordered water molecules [50]. The exchange of these buried water molecules among internal hydration sites may be responsible for the observed high-frequency dispersion with a correlation time of a few nanoseconds. The MRD profiles in Figure 8.6 were thus fitted with a bilorentzian dispersion function. It is

apparent from the MRD profiles that the number of long-lived water molecules is comparable in the native (at least three) and MG (at least two) states.

At pH 2 in the absence of salt, apoMb is extensively unfolded with 50% larger radius of gyration than in the native state [49]. This contrast with αLA, which forms an MG under these conditions, presumably due to the conformational constraints imposed by the four disulfide bonds (there are no disulfide bonds in apoMb). Another factor contributing to this difference may be the 80% higher surface charge density (ratio of net charge to solvent-accessible area) in apoMb. The ^{17}O MRD profile from apoMb at pH 2 (see Figure 8.6) exhibits a small dispersion ($N_\beta S_\beta^2 = 0.3 \pm 0.1$), probably due to a small fraction of coexisting MG state. Even though the acid-denatured state should be much more solvent exposed (larger N_α) than the native or MG states, it has a smaller $N_\alpha\rho_\alpha$ of $(1.8 \pm 0.1) \times 10^3$. This implies that, on average, water penetrating the unfolded protein is considerably less rotationally retarded (smaller ρ_α) than water at the surface of the native or MG proteins. With $N_\alpha \approx 1300$ computed from the solvent-accessible area of the fully extended polypeptide chain [51] we obtain a lower bound of $\rho_\alpha \approx 1.4$, similar to the rotational retardation for small organic molecules [11]. Because the polypeptide chain cannot be fully solvent exposed even in the denatured state of apoMb, ρ_α should be somewhat larger, but still substantially smaller than the value of 4–5 typical for native proteins. The 15% reduction in $N_\alpha\rho_\alpha$ on acid denaturation of apoMb contrast with the 30% increase on heat denaturation of RNase A at pH 2 (see Section 8.3.1). This difference may result from the four disulfide bonds in RNase A, which force the denatured protein to adopt more compact conformations, where the penetrating water molecules are more strongly rotationally retarded.

In summary, ^{17}O MRD data from three proteins show that the MG state has the same value for the surface hydration parameter $N_\alpha\rho_\alpha$ as in the native state. The possibility that, for all three proteins, this invariance is the result of an accidental near-perfect compensation of a large increase in N_α (due to extensive water penetration of the MG structure) and a corresponding decrease in ρ_α seems unlikely because the native (and, presumably, MG) structures of the proteins are very different: apoMb is mainly α-helical, CA mainly β-sheet, and αLA contains one α and one β domain. Furthermore, the rotational retardation factor ρ_α for native CA is a factor 2.3 larger than for the other two proteins. An accidental compensation would therefore require an exceptionally large water penetration of the MG state of CA. For these reasons, we believe that the MRD data support the picture of a dry molten globule, with little or no water penetration of the protein core and with native-like surface hydration. This view is further supported by the finding that the MG and native states have a comparable number of long-lived water molecules trapped within the protein structure.

To the extent that the MG state plays the role of a kinetic folding intermediate, the MRD results also provide new insights into the mechanism of protein folding. Notably, they indicate that the cooperative transition from the MG to the native state is not accompanied (or driven) by water expulsion. Consequently, this transition only involves the locking in of the side chains in the native conformation, with the consequent entropy loss being compensated mainly by more favorable van der

Waals interactions in the more densely packed protein core. Furthermore, the presence of some long-lived water molecules in the MG state suggests that some or all of the internal water molecules that stabilize the native protein by extending the hydrogen bond framework are already in place when the native tertiary structure is fully formed. This underscores the important role of internal water molecules, not only in stabilizing the native protein, but also in shaping the energy landscape that governs the folding process.

8.5 Solvent Perturbations

Early work suggested that whereas thermally denatured proteins tend to be relatively compact and may retain some native-like structure, proteins exposed to high concentrations of denaturants like urea or guanidinium chloride (and disulfide reduction) are essentially structureless random coils [5]. This view of solvent denatured proteins has received support from SAXS measurements, showing that, for many proteins, solvent denaturation roughly doubles the radius of gyration. The picture of the denatured state as a fully unfolded, and thus fully solvent-exposed, polypeptide chain is also implicit in the widely used solution transfer approach to protein stability [23]. However, because a theta solvent does not exist for a heteropolymer, it is clear that the random-coil model is, at best, an approximation. In fact, a growing body of experimental evidence for the survival of significant amounts of residual structure under the harshest denaturing conditions [52, 53] suggests that the random-coil model is, in many cases, far from reality.

The phenomenon of solvent denaturation raises two fundamental questions: (i) What is the structure (in a statistical sense) of the denatured protein? and (ii) What is the mechanism whereby denaturants destabilize native proteins? Because protein stability results from the free energy difference between native and denatured states, the second problem cannot be fully solved without an answer to the first question [54]. While detailed information about polypeptide conformation in denatured states is beginning to emerge, our knowledge about the other side of the coin – the solvent – remains incomplete and indirect. Solvent denaturation is obviously a result of altered protein–solvent interactions, but there is little consensus about the precise thermodynamic and structural role of the solvent. At the high denaturant concentrations commonly used, nearly all water molecules interact directly with the denaturant. Solvent denaturation thus interferes directly with the main driving force for protein folding – the hydrophobic effect [2–5]. Moreover, a mixed solvent in contact with a protein is, in general, spatially inhomogeneous. In other words, the protein may exhibit preferential solvation, preferential solvent penetration, and differential denaturant "binding" in the native and denatured states [14, 15]. Through these complex phenomena, the structural and mechanistic aspects of solvent denaturation are inextricably linked. To make progress, we need to take a closer look at the solvent.

8.5.1 Denaturation Induced by Urea

Despite the widespread use of urea in studies of protein stability and folding thermodynamics [2, 5, 23] (see Chapter 3), the molecular mechanism whereby urea unfolds proteins has not been established. In particular, it is not clear whether urea acts directly by binding to the polypeptide, indirectly by perturbing solvent-mediated hydrophobic interactions, or by a combination of these mechanisms. The direct mechanism is made plausible by the structural similarity between urea and the peptide group, suggesting that urea–peptide interactions, like peptide–peptide interactions, can compete favorably with water–peptide interactions. If this is the case, then solvent denaturation can be driven simply by the exposure of more binding sites in the denatured protein [55]. The indirect mechanism is supported by the observation that urea enhances the solubility of not-too-small nonpolar solutes or groups [56, 57] and, by implication, weakens the hydrophobic stabilization of the folded protein.

The available structural data on urea–protein interactions are limited and, with few exceptions [58], are restricted to native proteins [59–61]. Explicit solvent simulations cannot access the time scales on which solvent-induced protein unfolding takes place and have only provided information about urea–protein interactions in the native state or in partially unfolded states at very high temperatures [62, 63]. The MRD method is an ideal tool for investigating solvent denaturation. By exploiting different nuclear isotopes, water–protein and denaturant–protein interactions can be monitored simultaneously across the unfolding transition. So far, the MRD method has been used to study urea denaturation of two proteins, β-lactoglobulin (see Section 8.3.2) and intestinal fatty acid-binding protein (I-FABP) [64].

I-FABP is a 15 kDa cytoplasmic protein with a β clam structure composed of 10 antiparallel strands that enclose a very large (500–1000 $Å^3$) internal cavity. Lipids are thought to enter the cavity via a small "portal" lined by two short α-helices. In the apo form, the cavity is occupied by 20–25 water molecules [65]. The internal and external hydration of native I-FABP in both apo and holo forms have been characterized in detail by ^{17}O and ^{2}H MRD [66, 67]. A three-parameter fit (see Eq. (8)) to the low-frequency part (β dispersion) of the ^{17}O MRD profile at 27 °C yields $N_\beta S_\beta^2 = 2.4 \pm 0.3$ and $\tau_\beta = 6.8 \pm 0.5$ ns [64, 66]. The correlation time τ_β agrees quantitatively with the (η/T scaled) rotational correlation time τ_R of native I-FABP as determined by ^{15}N NMR relaxation [68] and fluorescence depolarization [69].

The MRD profile also exhibits a high-frequency dispersion (labeled γ), which is only partly sampled at 27 °C. The γ dispersion is produced by the 20–25 water molecules in the binding cavity, which exchange among internal hydration sites on a time scale of 1 ns. This intra-cavity exchange has also been seen in molecular simulations [70, 71]. Because these water molecules remain in the cavity for periods longer than τ_R, they also contribute to the β dispersion. Therefore [67], $N_\beta S_\beta^2 = N_I S_I^2 + N_C S_C^2 A_C^2$, where the subscripts I and C refer to singly buried water

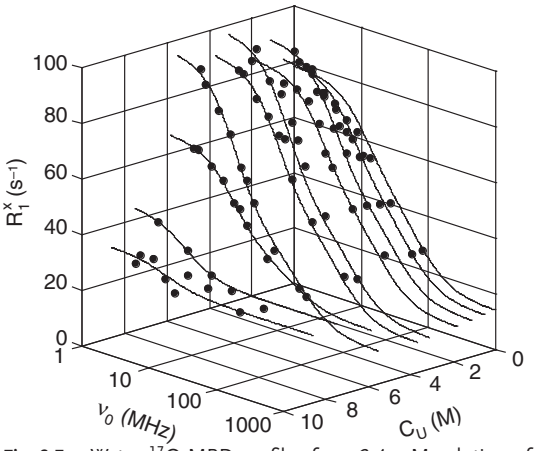

Fig. 8.7. Water ^{17}O MRD profiles from 2.4 mM solution of apo I-FABP at pH 7.0 (52% D_2O, 27 °C) and 10 different urea concentrations in the range 0–8.6 M [64]. The vertical axis shows the excess relaxation rate $R_1^x = R_1 - R_{bulk}$.

molecules and water molecules in the large binding cavity, respectively. The local, root-mean-square order parameters for these two classes of hydration sites are denoted by S_I and S_C, while the anisotropy parameter A_C is, roughly speaking, a measure of the nonsphericity of the cavity shape [67]. A detailed analysis [65–67] indicates that the β dispersion has contributions from the 20–25 cavity water molecules as well as from an isolated water molecule (known as W135) buried near a hydrophobic cluster at the turn between β-strands D and E. This internal water molecule is conserved across the family of lipid-binding proteins and must therefore contribute importantly to the stability of the native protein [72]. Because the hydrophobic cluster at the D–E turn forms early on the folding pathway, W135 can be used as an MRD marker for this (un)folding event.

Figure 8.7 shows ^{17}O MRD profiles from the apo form (without bound fatty acid) of I-FABP at 10 different urea concentrations, $C_U = 0$–8.6 M [64]. An examination of the dispersion parameters shows that the maximum seen in Figure 8.7 is due to an increase of $N_\beta S_\beta^2$ by nearly one unit in the range 0–3 M urea, where CD data indicate that the protein is fully native (see Figure 8.8a). Whereas the CD data are well described by a two-state model, the MRD data thus signal the presence of an intermediate state. This result conforms with the detection, by ^{1}H–^{15}N HSQC NMR, of an intermediate with maximum population in the range of 2.0–3.5 M urea [73].

The MRD data yield a significantly higher denaturation midpoint ($C_{1/2} = 6.5$ M) than the CD data (5.1 M). Again, this is consistent with ^{1}H–^{15}N HSQC NMR spectra [73], demonstrating that native-like structural elements persist up to 6.5 M urea, where CD and fluorescence data suggest that the protein is fully denatured. The observation of a substantial ^{17}O dispersion at 6.5 M urea implies that the residual protein structure is sufficiently permanent to trap water molecules for pe-

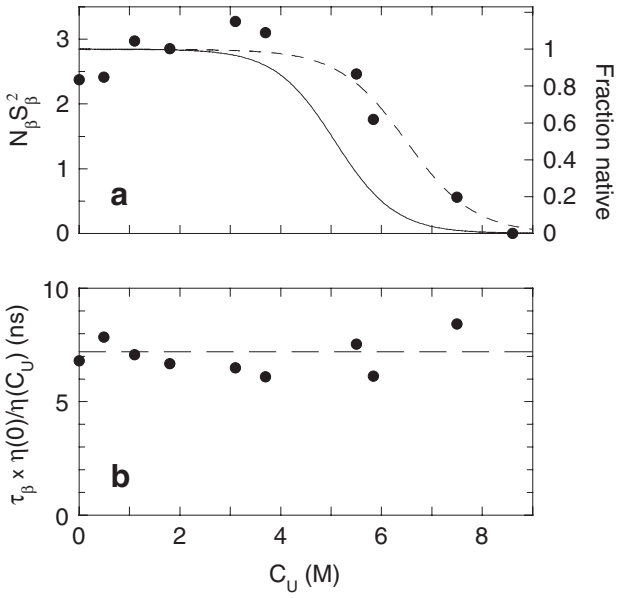

Fig. 8.8. Urea concentration dependence of MRD parameters for apo I-FABP, derived from the ^{17}O MRD profiles in Figure 8.7 [64]. a) $N_\beta S_\beta^2$ and the two-state fit (dashed curve). The solid curve and the right-hand axis refer to the apparent fraction native protein, derived from 216 and 222 nm CD data (12 μM I-FABP) and a fit based on the standard two-state linear free energy model. b) The correlation time τ_β, viscosity-corrected to remove the effect of urea on the hydrodynamic friction. The dashed line corresponds to the independently determined rotational correlation time of native I-FABP.

riods longer than 10 ns. This residual structure may be related to the equilibrium folding intermediate detected at $C_U = 4$–7 M by ^{19}F NMR on fluorinated Trp82 [74], the backbone NH of which donates a hydrogen bond to the long-lived internal water molecule (W135) in the D–E turn. The vanishing of $N_\beta S_\beta^2$ at 8.6 M urea (see Figure 8.8a) therefore indicates that the binding cavity has collapsed and that the hydrophobic cluster at the D–E turn has disintegrated.

In contrast to $N_\beta S_\beta^2$, the correlation time τ_β, when corrected for the variation in solvent viscosity, is virtually independent of urea concentration (see Figure 8.8b). In the absence of urea, τ_β can be identified with the rotational correlation τ_R of the protein. The viscosity-corrected τ_β should therefore reflect any global changes in protein structure upon denaturation. However, the disappearance of the ^{17}O dispersion at 8.6 M urea shows that there are no long-lived water molecules in the fully denatured protein. For a two-state denaturation, the frequency-dependent part of R_1 would thus be entirely due to the native protein fraction (see Eq. (17)). The invariance of τ_β in Figure 8.8b then indicates that the overall structure of the native state is essentially independent of urea concentration. This conclusion is consistent with studies of BPTI [60] and hen lysozyme [59, 61], showing that the native protein structure is virtually unaffected by high urea concentrations. On the

other hand, MRD and other data reveal intermediate states in the urea denaturation of I-FABP. The observed invariance of τ_β thus also requires the hydrodynamic volume of the intermediate species to be similar to the native state.

The third piece of information obtained from a three-parameter fit (see Eq. (8)) to (the low-frequency part of) the ^{17}O MRD profile is the surface hydration parameter $N_\alpha\rho_\alpha$. For native I-FABP, the interpretation of this quantity is complicated by water exchange among hydration sites in the large binding cavity, which contributes to $N_\alpha\rho_\alpha$ to roughly the same extent as the rotational retardation of some 460 water molecules in contact with the external protein surface. However, in the denatured state of I-FABP, present at 8.6 M urea, the binding cavity has collapsed. Under these conditions, $N_\alpha\rho_\alpha$ is governed by solvent exposure, preferential solvation, and rotational retardation. While it is impossible to separate these effects, some conclusions can be drawn with the aid of independent data. Thus, if the urea-binding constant K_U is assumed to lie in the range 0.05–0.2 M^{-1}, we obtain $N_S\rho_S = (4.6–9.4) \times 10^3$ (see Section 8.7.2.6; the subscript S refers to the external protein surface). If the urea denatured state of I-FABP resembled a fully solvent-exposed polypeptide chain, we would expect $\rho_S \approx 1.3$ [11, 37] and $N_S \approx 1250$ (based on the solvent-accessible area of the fully unfolded protein). The $N_S\rho_S$ value predicted for the fully unfolded polypeptide chain is thus a factor 3–6 smaller than the experimental result. Because N_S cannot exceed the estimate for the unfolded chain, it follows that the rotational retardation factor ρ_S for urea denatured I-FABP is substantially larger than expected for a fully unfolded structure. This is expected to be the case if the denatured protein is penetrated by water strings or clusters that interact simultaneously with several polypeptide segments. In other words, the MRD data indicate that denatured I-FABP is considerably more compact than a random coil even in 8.6 M urea. This conclusion is in line with recent reports of residual native-like structure in 8 M urea for staphylococcal nuclease [52] and hen lysozyme [53].

Because the expected value of $N_S\rho_S$ is similar for the native ($460 \times 4.0 = 1.8 \times 10^3$) and fully unfolded ($1250 \times 1.3 = 1.6 \times 10^3$) states, it is clear that this quantity is not related to protein structure in a simple way. Nevertheless, one can easily imagine denatured protein structures where $N_S\rho_S$ would have much smaller or larger values. Experimental $N_S\rho_S$ values thus provide valuable information, even if a unique structural interpretation is precluded. For example, if the relative change in $N_S\rho_S$ on going from the native to the denatured state varies substantially among different proteins (of similar size) or for different denaturation agents, then we can expect a corresponding variation in the properties of the denatured states. For the two urea denatured proteins that have been investigated by MRD, βLG and I-FABP, the relative change in $N_S\rho_S$ is 100–300%. This may be contrasted with the much smaller changes of 30% for heat denatured RNase A (see Section 8.3.1) and −15% for acid-denatured apoMb (see Section 8.4). While the molecular basis of these results remains to be clarified, the very much larger change in $N_S\rho_S$ for urea-denatured proteins can hardly be explained by more extensive unfolding or solvent exposure (larger N_S). More likely, the dramatic increase in $N_S\rho_S$ reflects a stronger rotational retardation (larger ρ_S) of water molecules that penetrate urea

denatured proteins. Ultimately, this must be related to the perturbations involved. Thermal and electrostatic perturbations can be viewed as general driving forces for protein expansion, where a configurational entropy gain or a reduction of Coulomb repulsion pays the free energy price for penetration by weakly interacting (with small ρ_S) water molecules. Solvent perturbations act more locally, for example, by replacing intramolecular hydrogen bonds by protein–solvent hydrogen bonds. Solvent molecules will thus penetrate the protein only if they can interact favorably with the polypeptide (leading to a large ρ_S). To elaborate this view, we need to know the relative affinity of water and urea for the interior of the unfolded protein as well as for the surface of the native protein.

Information about urea–protein interactions can be obtained from ^{2}H MRD. When the solvent contains urea and D_2O, hydrogen exchange distributes the ^{2}H nuclei uniformly among water and urea molecules. The ^{2}H magnetization therefore reports on both species. Separate water and urea resonance peaks are observed only at high magnetic fields and neutral pH, where water–urea hydrogen exchange is slow on the chemical shift time scale. Nevertheless, because the exchange remains in the slow to intermediate regime on the relaxation time scale, the individual water and urea ^{2}H relaxation rates can be determined also at low fields from a quantitative analysis of the biexponential ^{2}H magnetization recovery [64].

Whereas the water ^{2}H and ^{17}O MRD profiles yield a similar picture of I-FABP hydration, the urea ^{2}H MRD profile (see Figure 8.9) provides new information

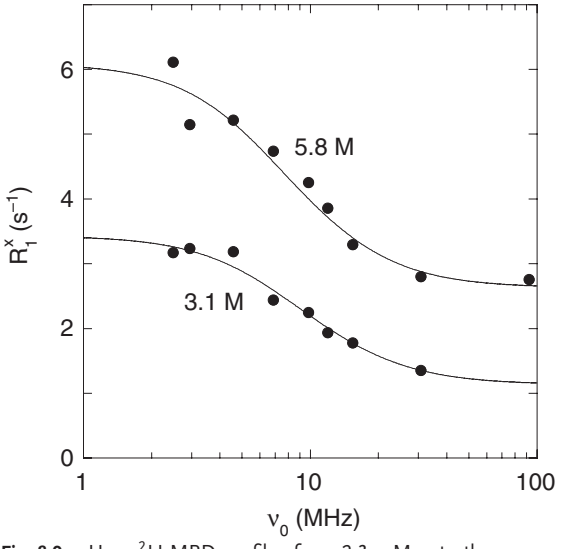

Fig. 8.9. Urea ^{2}H MRD profiles from 2.3 mM solutions of apo I-FABP at pH 7.0 (52% D_2O, 27 °C) and two different urea concentrations [64]. The vertical axis shows the excess urea ^{2}H relaxation rate $R_1^x = R_1 - R_{bulk}$, normalized to the same urea/protein mole ratio ($N_T^U = 1470$, corresponding to $C_U = 3.1$ M) to remove the trivial dependence on urea concentration. The curves are three-parameter fits according to Eq. (8).

about denaturant–protein interactions. As for the water dispersions, the urea correlation time τ_β can be identified with the tumbling time τ_R of the protein. In principle, the species giving rise to the urea dispersion could be either bound urea or labile hydrogens in the protein. However, at pH 7 hydrogen exchange between protein and urea, whether direct or water mediated, is slow on the relaxation time scale [60, 64]. Consequently, the urea ^{2}H dispersion, observed at all investigated urea concentrations from 3.1 to 7.5 M, provides direct evidence for urea binding to I-FABP with a residence time between 10 ns and 200 μs.

The fits to the urea ^{2}H profiles yield $N_\beta S_\beta^2$ values in the range 0.5–1.0. These dispersions might result from urea molecules trapped in the binding cavity, but then $N_\beta S_\beta^2$ should decrease with increasing urea concentration and vanish at $C_U = 7.5$ M, where the CD data indicate that the cavity is disrupted (see Figure 8.8a). Since $N_\beta S_\beta^2$ actually increases (slightly) with C_U, this possibility can be ruled out. It can therefore be concluded that both the native and denatured forms of I-FABP contain at least one specific urea-binding site. This finding raises the possibility that strong urea binding contributes significantly to the unfolding thermodynamics, thus compromising the linear extrapolation method widely used to determine the stability of the native protein in the absence of urea [23].

The high urea concentrations needed to denature proteins implies that weak binding to many sites is involved. Information about such interactions is contained in the MRD parameter $N_\alpha \rho_\alpha$, which can be attributed to urea molecules in short-lived (< 1 ns) association with the external protein surface. Taking into account exchange averaging over coexisting native and denatured proteins (see Eq. (17)) as well as preferential solvation effects (see Eq. (18)), it can be shown [64] that the $N_\alpha \rho_\alpha$ results are consistent with urea-binding constants in the range 0.05–0.2 M^{-1} and a similar rotational retardation for urea and water in the denatured protein.

To summarize, the urea ^{2}H and water ^{17}O MRD data support a picture of the denatured state where much of the polypeptide chain participates in clusters that are more compact and more ordered than a random coil but nevertheless are penetrated by large numbers of water and urea molecules. These solvent-permeated clusters must be sufficiently compact to allow side chains from different polypeptide segments to come into hydrophobic contact, while, at the same time, permitting solvent molecules to interact favorably with peptide groups and with charged and polar side chains. The exceptional hydrogen-bonding capacity and small size of water and urea molecules are likely to be essential attributes in this regard. In such clusters, many water and urea molecules will simultaneously interact with more than one polypeptide segment and their rotational motions will therefore be more strongly retarded than at the surface of the native protein. While the hydrogen-bonding capacity per unit volume is similar for water and urea, the 2.5-fold larger volume of urea reduces the entropic penalty for confining a certain volume of solvent to a cluster. The energetics and dynamics of solvent included in clusters is expected to differ considerably from solvent at the surface of the native protein. This view is supported by the slow water and urea rotation in the denatured state, as deduced from the MRD data.

8.5.2 Denaturation Induced by Guanidinium Chloride

Guanidinium chloride (GdmCl) is among the most potent denaturants and, at high concentrations, is thought to induce extensive unfolding of most proteins [5]. Like urea and water, GdmCl has a high hydrogen-bonding potential, but it is also a strong electrolyte. GdmCl thus introduces an electrostatic perturbation by screening Coulomb interactions. Being a salt, GdmCl should have a weaker affinity than urea for the protein interior, which is less polarizable than the bulk solvent. Consequently, GdmCl may denature proteins by a different mechanism than urea, and the resulting denatured states may exhibit qualitative differences.

Water ^{17}O MRD studies of GdmCl denaturation have been carried out on four proteins: bovine α-lactalbumin (αLA), hen lysozyme (HEWL), ribonuclease A (RNase A), and human carbonic anhydrase [37]. The first three of these proteins are of similar size (about 14 kDa) and they are all stabilized by four disulfide bonds. In fact, HEWL is structurally homologous with αLA, but lacks the strongly bound Ca^{2+} ion. According to the crystal structures, all three proteins have 6–7 potentially long-lived water molecules, but in αLA two of these coordinate the Ca^{2+} ion and in RNase A none of the water molecules is deeply buried. In accordance with these structure-based predictions, the ^{17}O MRD profiles for the native proteins (see Figure 8.10) show that $N_\beta S_\beta^2$ is largest for αLA, 3.4 ± 0.2, decreasing to 2.7 ± 0.4 for HEWL and 2.3 ± 0.3 for RNase A. The amplitude of the dispersion steps differs more than $N_\beta S_\beta^2$ because the correlation time τ_β shows the same trend among the proteins. In particular, the relatively short residence time of the buried water molecules in RNase A reduces τ_β by a factor of 2 compared with the other two proteins (see Section 8.3.1). The surface hydration parameter $N_\alpha \rho_\alpha$ has similar values for the three native proteins, yielding rotational retardation factors ρ_α in the typical range 4.0–4.5.

Surprisingly, all three proteins exhibit dispersions at high GdmCl concentrations, where conventional methods indicate that they are extensively unfolded. The residual $N_\beta S_\beta^2$ is 0.4 ± 0.1 for αLA and HEWL and 0.2 ± 0.1 for RNase A, and the correlation time τ_β is about 5 ns (the difference from the native state is barely significant). These findings demonstrate unequivocally that the extensively solvent-denatured states of these proteins trap at least one, and more if $S_\beta^2 \ll 1$, long-lived water molecules. The residence time of these water molecules, that is, the time spent within the protein before they escape into the bulk solvent, must be longer than 5 ns but shorter than 1–10 μs (the upper bound depends on the value of S_β^2).

For all three proteins, the dispersion disappears when the four disulfide bonds are broken by dithiothreitol reduction (see Figure 8.10). This indicates that the long-lived water molecules in the denatured proteins are trapped by persistent structures stabilized by the disulfide bonds. In accord with this view, no ^{17}O dispersion was observed for the solvent denatured state (4 M GdmCl) of human carbonic anhydrase (form II), which lacks disulfide bonds [37]. The MRD results are also consistent with NMR diffusion measurements on bovine αLA at 5 °C, showing

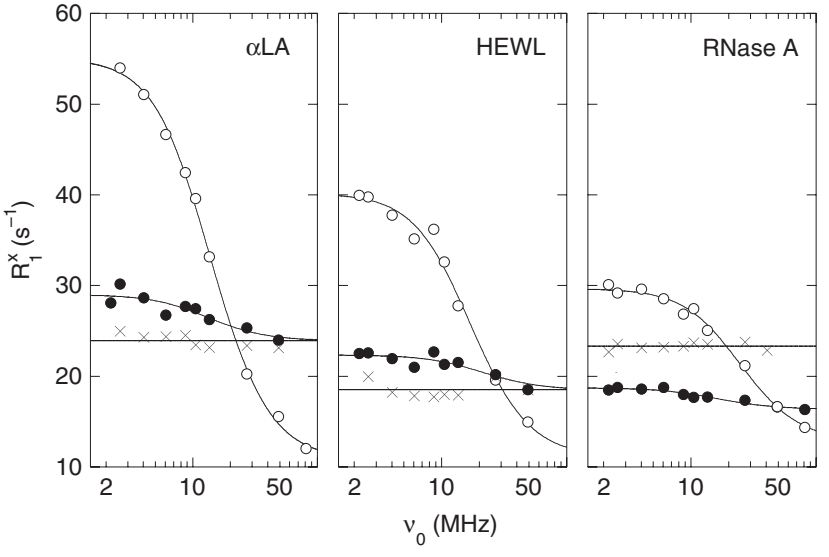

Fig. 8.10. Water ^{17}O MRD profiles from native and denatured states of bovine α-lactalbumin (1.9 mM αLA, pH 8.4 native, pH 7.0 denatured), hen lysozyme (7.0 mM HEWL, pH 4.4 native, pH 5.0 denatured), and ribonuclease A (3.8 mM RNase A, pH 4.0), all at 27 °C [37]. The MRD profiles refer to the native (open circles), denatured (filled circles) and reduced-denatured (crosses) protein. The solvent was D_2O and the GdmCl concentration for the denatured states was 4.4 M (αLA), 7.0 M (HEWL), or 4.0 M (RNase A). The vertical axis shows the excess relaxation rate $R_1^x = R_1 - R_{bulk}$, scaled to the same water/protein mole ratio ($N_T = 28\,500$) for all three proteins. The curves are three-parameter fits according to Eq. (8).

that the hydrodynamic volume of the native protein expands by 120 ± 10% in the disulfide-intact denatured state (6 M GdmCl) and by 380 ± 20% on disulfide reduction (without GdmCl) [40].

As judged by the ^{17}O MRD data in Figure 8.10, the reduced–denatured states of the three proteins are very similar with regard to hydration and are therefore likely to have similar configurational statistics. (The smaller excess relaxation for HEWL can be attributed to the higher GdmCl concentration. When HEWL and αLA are both studied at 7 M GdmCl, nearly identical MRD profiles are obtained for the denatured states.) However, the disulfide-intact reduced states are markedly different. For the structurally homologous αLA and HEWL, disulfide reduction has virtually no effect on the surface hydration parameter $N_\alpha\rho_\alpha$ (see Figure 8.10). This is an unexpected result, because disulfide reduction is accompanied by a large expansion of the hydrodynamic volume of αLA [40]. Because the invariance of $N_\alpha\rho_\alpha$ under disulfide reduction has only been observed for two structurally related proteins, and is not seen for RNase A, it may result from an accidental compensation of a sizeable increase in N_α by a corresponding decrease in ρ_α. For RNase A, $N_\alpha\rho_\alpha$ increases by 42 ± 2% when the four disulfide bonds are broken (see Figure 8.10). The MRD

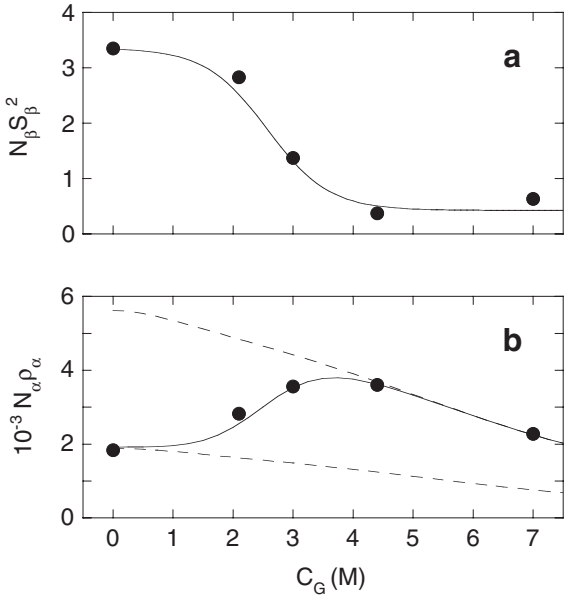

Fig. 8.11. Guanidinium chloride concentration dependence of a) $N_\beta S_\beta^2$ and b) $N_\alpha \rho_\alpha$, derived from ^{17}O MRD profiles for 1.9 mM disulfide-intact α-lactalbumin at pH 7 and 27 °C [37]. The solid curves resulted from a simultaneous two-state fit based on Eqs (17) and (18) and the standard linear free energy model. The dashed curves show the effect on $N_\alpha \rho_\alpha$ for the native and denatured states of replacing water by GdmCl.

data thus indicate that the hydration of the disulfide-intact denatured state is more native-like for RNase A than for the other two proteins (smaller N_α and/or ρ_α). This is consistent with reports of substantial residual helix content and aromatic side chain clustering in GdmCl denatured RNase A.

For a quantitative analysis of MRD data from solvent-denatured proteins, it is necessary to take preferential solvation effects into account (see Section 8.7.2.6). This requires MRD data to be recorded at several denaturant concentrations. In the case of GdmCl, this has been done for αLA (see Figure 8.11) [37]. The analysis of these data shows that the variation of the MRD parameters $N_\beta S_\beta^2$ and $N_\alpha \rho_\alpha$ with the GdmCl concentration is well described by the standard two-state linear free energy model [23]. The coincidence of the $N_\beta S_\beta^2$ and $N_\alpha \rho_\alpha$ transitions shows that the release of the long-lived water molecules from the native protein occurs in the same cooperative unfolding event as the influx of short-lived water molecules into the expanded denatured state. The apparent two-state behavior also shows that the MG intermediate, which is maximally populated at GdmCl concentrations of 2–3 M, cannot have a much larger number (N_β) of long-lived water molecules than the native state. The fit to the combined $N_\beta S_\beta^2$ and $N_\alpha \rho_\alpha$ data yields a midpoint GdmCl concentration of 2.6 $\pm$ 0.2 M and an *m*-value of 4.8 $\pm$ 1.7 kJ mol^{-1} M^{-1}. The close agreement of these values with those derived from the far-UV CD measurements

[75] indicates that the major hydration changes upon GdmCl denaturation are correlated with the disruption of secondary structure.

The fit in Figure 8.11 yields an average GdmCl binding constant $K_G = 0.16 \pm 0.07\ M^{-1}$, in good agreement with calorimetrically determined values for HEWL and RNase A [76, 77]. For the denatured state (see the upper dashed curve in Figure 8.11b), we obtain $N_S\rho_S = 5.6 \times 10^3$. This value is a factor 3.8 larger than expected for the fully hydrated polypeptide chain (based on the maximum solvent-accessible area and $\rho_S = 1.3$). Water molecules interacting with the GdmCl denatured state of αLA are thus much more dynamically perturbed (larger ρ_S) than water molecules in contact with a fully exposed polypeptide chain. This suggests that a substantial fraction of the water molecules that penetrate the denatured protein interact strongly with several polypeptide segments and, therefore, that the structure of the denatured state contains relatively compact domains. The finding that $N_S\rho_S$ is unaffected by reduction of the four disulfide bonds in αLA (see Figure 8.10) implies that the compact domains are not due to topological constraints, although the loss of the residual dispersion suggests that these domains become more dynamic. As viewed from the solvent, the GdmCl denatured state of αLA appears to be similar to the urea-denatured state of I-FABP (see Section 8.5.1).

In summary, the MRD data show that loss of specific internal water sites and influx of external solvent are concomitant with disintegration of secondary structure (as seen by CD), consistent with the view that disruption of α-helices and β-sheets is promoted by water acting as a competitive hydrogen bond partner [78]. The large rotational retardation inferred for the denatured state suggests that water penetrating the GdmCl denatured protein differs substantially from the hydration shell of a fully exposed polypeptide chain. Taken together with the residual dispersion from the denatured state of all three investigated proteins, this suggests that even strongly solvent-denatured proteins contain relatively compact domains. This is consistent with the finding that mutations can exert their destabilizing effects directly on the denatured state [54]. Furthermore, for αLA and HEWL, disulfide bond cleavage appears to affect the flexibility of the denatured protein more than its compactness. The MRD data thus suggest that, even under extremely denaturing conditions, proteins are far from the idealized random-coil state.

8.5.3
Conformational Transitions Induced by Co-solvents

Fluorinated alcohols, such as 2,2,2-trifluoroethanol (TFE), are known to stabilize regular secondary structure, in particular α-helices, in peptides and to trigger a cooperative transition to an open helical structure in many proteins [79] (see Chapter 24). Apparently, TFE allows amino acid residues to manifest their intrinsic helical propensity, which may be suppressed by nonlocal interactions in the native protein [79–81]. Bovine βLG has been widely used as a model for studies of the alcohol-induced $\beta \rightarrow \alpha$ transition in proteins (see Chapter 24). The 48% α-helix content predicted theoretically greatly exceeds the 7% found in the crystal structure of βLG [82], consistent with the finding that isolated βLG fragments may adopt non-

native helical structure in aqueous solution and invariably do so in the presence of TFE [83, 84]. βLG undergoes a $\beta \rightarrow \alpha$ transition in the range 15–20% TFE, with the helix content increasing from 7% in the native protein (N) to 60–80% in the helical state (H) at 30% TFE. Several studies indicate that the TFE-induced structural transformation is best described as a three-state equilibrium, $N \leftrightarrow I \leftrightarrow H$, with the intermediate state (I) being most populated around 15–20% TFE [85, 86]. (Section 8.3.2, which deals with urea and cold denaturation of βLG, contains further references to the structure and hydration of native βLG.)

Although the effects of TFE on peptides and proteins have been thoroughly studied, no consensus has emerged about the underlying molecular mechanisms. Most studies have focused on peptides, where the relevant equilibrium involves unstructured and helical forms: $U \leftrightarrow H$. One may then ask whether TFE shifts the equilibrium by stabilizing the H form or by destabilizing the U form, or both. It is frequently assumed that the peptide is preferentially solvated by TFE, that is, that TFE accumulates near the peptide–solvent interface. Direct evidence for such preferential solvation has recently come from intermolecular NOE measurements and molecular simulations [87–89]. Whether the principal effect of TFE is to strengthen intrapeptide hydrogen bonds (because TFE is a less polar solvent than water and a less potent hydrogen bond competitor) or to weaken hydrophobic interactions among side chains (by displacing water and modifying its structure) is less clear.

Because the TFE-induced $N \leftrightarrow H$ equilibrium in proteins does not involve the unfolded state, the thermodynamics and mechanism may differ considerably from the peptide case. While CD and high-resolution NMR studies have elucidated the dependence of protein secondary structure on TFE concentration, little direct information is available about the critical role of protein solvation in TFE/water mixtures. Molecular dynamics simulations on the time scale of the $N \rightarrow H$ transition are not yet feasible and the only reported intermolecular NOE study (on hen egg white lysozyme at pH 2) detected TFE binding in the active site but did not provide quantitative results on preferential solvation or solvent penetration [90].

The MRD method has been used to monitor the interactions of water and TFE with βLG in native and TFE-induced nonnative states at pH 2.4 (where βLG is monomeric) [91]. Water ^{2}H and ^{17}O MRD profiles measured at 4 °C (see Figure 8.12) are bilorentzian, that is, a γ dispersion has to be added to Eq. (8), with the exception of the ^{17}O profile at 30% TFE, which only exhibits a γ dispersion. In the absence of TFE, the ^{2}H and ^{17}O profiles yield essentially the same correlation times: $\tau_\beta = 16$–17 ns, as expected for rotational diffusion of monomeric βLG [35], and $\tau_\gamma = 3$–4 ns, which reflects exchange of (partly) buried water molecules. The ^{17}O dispersion amplitude parameters are $N_\beta S_\beta^2 = 2.2 \pm 0.8$, consistent with the presence of two fully buried water molecules in all crystal structures of βLG, and $N_\gamma S_\gamma^2 = 9 \pm 6$, attributed to water molecules in deep surface pockets and/or in the large binding cavity. The surface hydration parameter $N_\alpha \rho_\alpha$ corresponds to $\rho_\alpha = 5.3 \pm 1.8$, slightly above the typical range. The ^{2}H MRD data contain a substantial contribution from the hydroxyl group of TFE and from about 50 carboxyl and hydroxyl hydrogens in βLG, in fast exchange with water hydrogens at pH 2.4. The ^{2}H

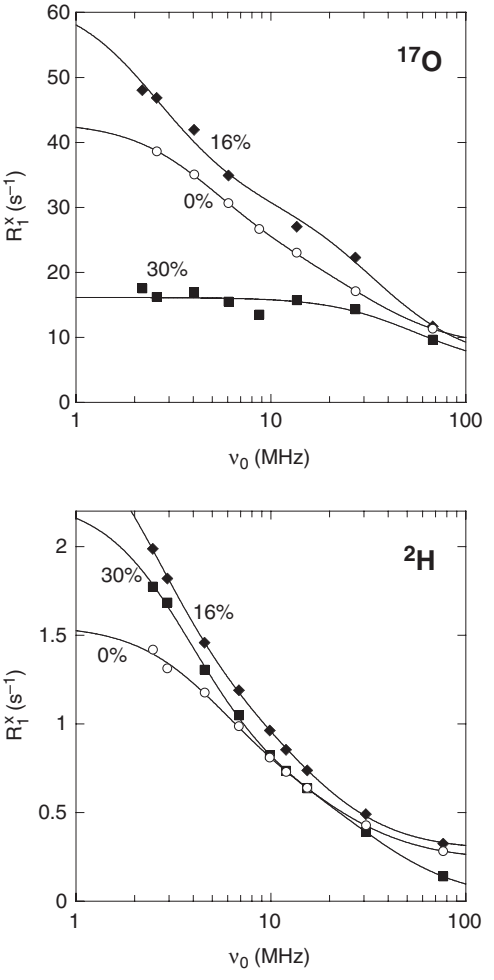

Fig. 8.12. Water ^{17}O (top) and ^{2}H (bottom) MRD profiles from 0.5 mM solutions of β-lactoglobulin A (25–50% D_2O, 4 °C, pH 2.4) at the indicated TFE concentrations [91]. The vertical axis shows the excess relaxation rate $R_1^x = R_1 - R_{bulk}$, scaled to the same water/protein mole ratio ($N_T^W = 103\,600$) for all samples. The curves are three-parameter (^{17}O, 30% TFE) or five-parameter (all other profiles) fits according to Eq. (8) or its bilorentzian generalization.

profile can thus provide the tumbling time (and hydrodynamic volume) of the protein even in the absence of long-lived water molecules.

Analysis of the 4 °C data in Figure 8.12 shows that the effect of adding 16% TFE is essentially to increase the viscosity (thereby increasing τ_β), whereas $N_\beta S_\beta^2$ is hardly affected. This indicates that βLG retains a compact native-like structure at 16% TFE and 4 °C, consistent with the finding that the $^{1}H-^{15}N$ heteronuclear single-quantum coherence (HSQC) NMR spectrum of βLG in 15% TFE is close

to that of native βLG at temperatures below 15 °C [85]. However, at 27 °C, 16% TFE should be close to the midpoint of the N ↔ H transition, where the I state is highly populated [82, 83, 86]. The correlation time, $\tau_\beta = 24 \pm 4$ ns, then exceeds the rotational correlation time, $\tau_R = 14.6$ ns, predicted for the native protein at this solvent viscosity. This implies that the hydrodynamic volume of the protein has increased by 65 ± 30%, consistent with the prevalent view of the TFE-induced helical state as a relatively open assembly of weakly interacting helical segments [82]. A substantial structural change is also signaled by a fourfold reduction of $N_\beta S_\beta^2(^{17}O)$, indicating that the long-lived hydration sites are largely disrupted.

At 30% TFE, the protein should be fully converted to the H state at 27 °C [82, 83, 86]. Consistent with this expectation, τ_β is about twice as long as the τ_R predicted for the native protein, implying a correspondingly large expansion of the protein. A progressive expansion of βLG in going from 0 to 16 to 30% is also indicated by the continued decrease of $N_\beta S_\beta^2$ for both nuclei. The small value $N_\beta S_\beta^2(^{17}O) = 0.14 \pm 0.05$ presumably reflects several weakly ordered water molecules that penetrate the open H state. At 4 °C, however, the ^{17}O profile only exhibits a γ dispersion (see Figure 8.12), indicating that the nonnative state in 30% TFE undergoes significant structural change between 4 and 27 °C.

TFE–protein interactions can be monitored by ^{19}F MRD (see Section 8.7.2.4). The ^{19}F profiles in Figure 8.13, recorded at 27 °C, demonstrate long-lived binding of TFE to βLG at 7% and 21% TFE. The correlation time τ_β of the Lorentzian dispersion is 7 ± 1 ns at 7% TFE and 4 ± 1 ns at 21% TFE, several-fold shorter than the τ_β values derived from the corresponding ^2H profiles. This implies (see Eq. (4))

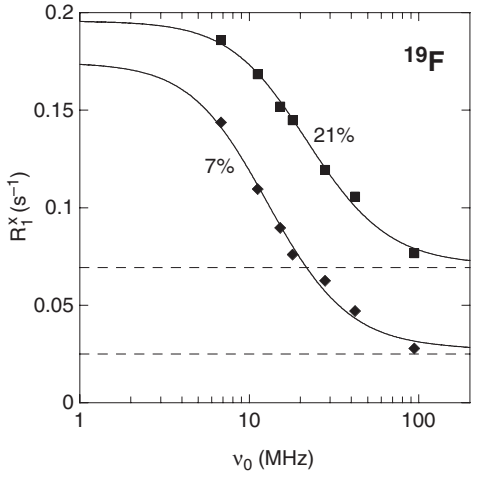

Fig. 8.13. Trifluoroethanol ^{19}F MRD profiles from 1.0 mM solutions of β-lactoglobulin A (50% D_2O, 4 °C, pH 2.4) at the indicated TFE concentrations [91]. The vertical axis shows the excess relaxation rate $R_1^x = R_1 - R_{bulk}$, scaled to the same TFE/protein mole ratio ($N_T^{TFE} = 970$) for both samples. The curves are three-parameter fits according to Eq. (8) and the dashed lines indicate the high-frequency (α) plateau.

that the residence time of TFE molecules bound to βLG is in the range 5–10 ns at 27 °C. The ^{19}F parameter $N_\beta S_\beta^2$ is 4.5 and 6 at the two concentrations, indicating that βLG contains at least five such long-lived TFE molecules. (Since S_β^2 may be well below its rigid-binding limit of 1, the number N_β might be an order of magnitude larger.)

According to CD and high-resolution NMR studies [82, 83, 85, 86], βLG retains its native structure at 7% TFE, whereas at 21% TFE the I and H states are present at roughly equal populations without any coexisting native protein. The ^{19}F MRD results thus suggest that $N_\beta S_\beta^2$ is nearly the same in the native and TFE-induced states. However, the TFE-binding sites are not necessarily the same in the different protein states. In fact, judging by the strong variation of the ^{2}H and ^{17}O profiles with TFE concentration, this is highly improbable. A more likely scenario is that the native state has a relatively small number of long-lived binding sites with large S_β^2, whereas the I and H states are penetrated by a considerably larger number of less ordered TFE molecules.

As for water, TFE residence times in the nanosecond range cannot be rationalized solely in terms of favorable hydrogen bonds and other noncovalent interactions. These interactions are also present in the bulk solvent, where molecular motions take place on a picosecond time scale. Instead, long residence times result from trapping of solvent molecules within the protein structure. In the native protein at 7% TFE, the most likely sites for long-lived TFE molecules are the small surface pockets and large binding cavity seen in the crystal structures. If the water molecules that occupy these pockets in the absence of TFE have residence times of order 100 ps, TFE binding should be accompanied by a reduction of $N_\alpha\rho_\alpha$ in the ^{17}O profile. Although ^{17}O data at 7% TFE are not available, such a reduction is indeed seen at 16% TFE.

Addition of 30% TFE reduces $N_\alpha\rho_\alpha(^{17}\mathrm{O})$ by a factor 4 (at both temperatures), even though the expanded state of βLG should have a larger solvent-accessible area than the native state. If this is due to replacement of water by TFE at the protein surface, it should be accompanied by an increase in $N_\alpha\rho_\alpha(^{19}\mathrm{F})$. This is indeed observed: $N_\alpha\rho_\alpha(^{19}\mathrm{F})$ increases from 150 ± 20 at 7% TFE to 350 ± 90 at 21% TFE. Because TFE is a poor hydrogen bond acceptor and interacts only weakly with peptides, we expect ρ_α to be smaller for TFE than for water. The $N_\alpha\rho_\alpha(^{19}\mathrm{F})$ values are therefore consistent with several hundred TFE molecules at the protein surface. On purely geometrical grounds, we estimate that about 225 TFE molecules are needed to cover the surface of native βLG. In the expanded state, this number would be larger. On the other hand, if water and TFE were uniformly distributed throughout the solvent, then only about 30 TFE molecules would make contact with the (native) protein surface at 21% TFE. To account for $N_\alpha\rho_\alpha(^{19}\mathrm{F}) = 350$, we would then need a retardation factor of about 10, which is clearly unrealistic. The ^{19}F MRD data thus indicate that βLG has a strong preference for solvation by TFE. This is in accord with the two- to threefold TFE enrichment in the surface layer of peptides in 30% TFE seen in several simulations [87–89].

In summary, the transformations N → I → H at 27 °C are found to be accompanied by a progressive expansion of the protein and loss of specific long-lived hydra-

tion sites. The observation of ^{17}O and ^{19}F dispersions when the protein is in the H state demonstrates long-lived association of water (> 40 ns) and TFE (5–10 ns) with the expanded protein. These long residence times indicate that solvent molecules penetrate the protein matrix. The number of long-lived internal TFE molecules is $\sim 5/S_\beta^2$, with S_β^2 in the range 0–1. In the N $\rightarrow$ H transition, the surface hydration parameter decreases by a factor 4, while the corresponding TFE parameter increases by a factor 2 between 7 and 21% TFE. The MRD data are consistent with a strong accumulation of TFE at the surface as well as in the interior of the protein. The ^{19}F MRD data also demonstrate long-lived binding of several TFE molecules in the native protein, presumably by displacement of water molecules in deep surface pockets. At 4 °C, βLG is much less affected by TFE. The protein remains in the native state in the presence of 16% TFE, but adopts a nonnative structure at 30% TFE. This nonnative structure is not penetrated by long-lived water molecules, but presumably contains internal TFE molecules.

8.6 Outlook

During the past 5 years, the MRD method has been used to study proteins in a variety of nonnative states induced by thermal, electrostatic, and solvent perturbations. By focusing on the solvent, the MRD method provides a unique perspective on protein folding and stability and a valuable complement to techniques that probe the conformation and dynamics of the polypeptide chain. While the quantitative interpretation of MRD data is not always straightforward, the underlying theoretical framework of nuclear spin relaxation is rigorous. In general, the MRD method yields clear-cut information about long-lived protein–solvent interactions, while inferences about the more transient surface solvation tend to be more model dependent. Given the high complexity of the investigated systems, one cannot hope that a single technique will provide all the answers. MRD applications to nonnative proteins are still in an early exploratory phase and further studies are needed to establish the generality of the (sometimes unexpected) results obtained so far. MRD studies of nonnative proteins should not only be extended to a larger set of proteins, they can also be used to examine other types of denaturants and co-solvents as well as different perturbations, including pressure-denatured proteins.

8.7 Experimental Protocols and Data Analysis

8.7.1 Experimental Methodology

The term magnetic relaxation dispersion (MRD) refers to the frequency dependence of spin relaxation rates arising from thermal molecular motions. In a typical

MRD experiment, the longitudinal spin relaxation time, T_1, is measured as a function of the resonance frequency, ν_0, and the plot of the relaxation rate, $R_1 = 1/T_1$, versus ν_0 is known as the dispersion profile. The MRD profile resolves the total fluctuation amplitude of the so-called spin-lattice coupling (the interaction that couples the nuclear spin to the molecular degrees of freedom) into contributions from motions on different time scales. This distribution of motional frequencies, called the spectral density function, is the essential information provided by spin relaxation experiments on liquid samples [92]. In most MRD experiments, the probing frequency is controlled by the strength of the static magnetic field applied during the evolution period. The MRD method provides direct access to the spectral density over a wide frequency range: 2–3 decades can be covered with multiple-field measurements (MF-MRD), while 4–6 decades can be accessed with the field-cycling technique (FC-MRD). This allows molecular motions on a wide range of time scales to be studied. At the low (detection) fields used in most MRD studies, only relatively abundant low-molecular-weight species, such as water, co-solvents, and salt ions, can be studied [8].

8.7.1.1 Multiple-field MRD

In bulk water at room temperature, the dispersion is centered at 45 GHz. However, current NMR magnet technology only provides access to frequencies below 1 GHz. In aqueous solutions of globular proteins with molecular weights in the range 5–50 kDa, on the other hand, long-lived (> 1 ns) interactions of water molecules or co-solvents with the protein give rise to a dispersion in the range 1–100 MHz, which is accessible with conventional NMR spectrometers. Typically, the dispersion profile is the result of relaxation measurements at three or four magnetic fields in the range 2.35–14.1 T, using several NMR spectrometers equipped with fixed-field cryomagnets, combined with measurements at 5–10 fields in the range 0.1–2 T, using a dedicated MRD instrument: a tunable, multi-channel NMR spectrometer equipped with an iron-core electromagnet and a variable external field-frequency lock.

To determine the three parameters defining a Lorentzian dispersion, accurate relaxation data covering approximately two frequency decades are needed. By maintaining a high (> 100) signal-to-noise ratio at all fields, the longitudinal relaxation rate can usually be determined with an accuracy of 0.5% using the 180–τ–90 inversion recovery pulse sequence with standard phase cycling and carefully calibrated pulse length. An accurate and robust procedure for temperature calibration and control is vital for reducing systematic errors in MRD experiments. Parallel measurements on a reference sample with a known temperature-dependent (but frequency-independent) relaxation rate is a reliable temperature check.

8.7.1.2 Field-cycling MRD

For large proteins or subzero temperatures (as in studies of cold denaturation), the dispersion profile is shifted to frequencies below the accessible range of MF-MRD. At these low frequencies, MRD studies can only be performed with the field-cycling (FC) technique [93, 94]. FC-MRD differs fundamentally from MF-MRD in

that the static field is varied during the course of an individual relaxation experiment. The principal limitations of FC-MRD are the relatively low maximum attainable field and the time required to switch the field, factors that have so far precluded FC-MRD studies of fast-relaxing nuclei. Due to their different strengths and weaknesses, the MF-MRD and FC-MRD techniques complement each other.

The initial nonequilibrium polarization required for a longitudinal relaxation experiment can be created either by manipulating the spin state populations with a coherent radiofrequency magnetic field without altering the spin energy levels, as in an MF-MRD experiment at a fixed magnetic field, or by changing the level spacing without altering the populations, as in the cyclic field variation performed in FC-MRD. In either case, the nonequilibrium state should preferably be established (by the radiofrequency pulse or the static field switch) in a time that is short compared with the longitudinal relaxation time T_1. Field switching can be accomplished mechanically or electronically. The mechanical approach, where the sample is pneumatically shuttled between two magnetic fields, has the advantage that the detection field can be provided by a high-field cryomagnet, with consequent improvements in sensitivity and resolution. However, the long shuttling time (typically on the order of 100 ms) limits the mechanical approach to samples with relatively slow relaxation. With electronic switching of the magnet current, the maximum field is usually in range 0.5–2 T, but the field switching rate may be 100 T s^{-1} or higher, allowing measurements of T_1 values in the millisecond range.

8.7.1.3 Choice of Nuclear Isotope

For MRD studies of protein hydration, three stable nuclides are available: ^1H, ^2H, and ^{17}O (disregarding the radioactive ^3H isotope). The first MRD studies of protein solutions employed the ^1H isotope, which has the highest sensitivity and the widest accessible frequency range. These advantages, however, are offset by serious drawbacks. Most importantly, ^1H relaxation generally contains a potentially confounding contribution from labile protein protons in rapid exchange with water protons. Due to proton exchange catalysis, this contribution is more pronounced away from neutral pH and in the presence of buffers. In the past, exchange-averaged labile proton contributions to ^1H MRD data have frequently been unjustifiably ignored. Despite having two orders of magnitude lower receptivity and one order of magnitude faster relaxation than ^1H, the ^2H isotope can be used for water MRD studies (both MF and FC). Due to the shorter intrinsic relaxation time, ^2H is less susceptible than ^1H to labile hydrogen exchange averaging. Nevertheless, rapidly exchanging protein deuterons can dominate water ^2H relaxation at low and high pH values and can never be neglected a priori.

Unlike the hydrogen isotopes, water ^{17}O does not exchange with protein atoms on the relaxation time scale and therefore reports exclusively on water molecules. An observed water ^{17}O dispersion in the 1–100 MHz range is therefore indisputable evidence for water molecules in long-lived association with the protein. Due to the low natural abundance of the ^{17}O nuclide, ca. 20 mM in water, isotope-enriched water is essential for accurate MRD work. ^{17}O-enriched H_2O and D_2O is commercially available at enrichment levels up to at least 60%. The fast quadrupo-

lar relaxation of ^{17}O allows for efficient signal averaging and, in combination with the small magnetic moment, makes ^{17}O much less susceptible than ^{1}H to paramagnetic impurities.

For MRD studies of denaturants and co-solvents, the nuclides ^{2}H and ^{19}F have been used so far. The ^{2}H isotope is particularly convenient when the studied molecule can be deuterated at nonlabile positions, as with DMSO-d_6 in H_2O [95]. However, even species with labile deuterons can be studied, for example, urea-d_4 in D_2O [64], provided that the (pH- and temperature-dependent) hydrogen exchange with water is not too fast. Fluorinated co-solvents, like trifluoroethanol [91], can be studied by ^{19}F MRD. Like ^{1}H, the ^{19}F nuclide has a predominantly dipolar relaxation mechanism. Because T_1 is long (several seconds) for these spin-1/2 nuclei, paramagnetic O_2 makes a significant contribution to the dispersion profile. This contribution can be eliminated by O_2 purging of the protein solution with Ar or N_2 gas.

8.7.2 Data Analysis

8.7.2.1 Exchange Averaging

In MRD studies of protein solutions, the observed nucleus usually resides in a mobile solvent molecule that can diffuse between the bulk solvent region and one or more sites on (or in) the protein. Spin relaxation is then influenced by molecular motions at two levels. At the level of spin dynamics, translational diffusion transfers magnetization between microenvironments with different local relaxation rates. If sufficiently fast, such diffusional exchange leads to spatial averaging of the local relaxation rates. At the level of time correlation functions, molecular rotation (and translation, in the case of intermolecular couplings) averages out the anisotropic nuclear coupling and thus determines the local spin relaxation rates.

The theoretical framework for analyzing relaxation data from nuclei exchanging between two or more states or regions is well established. The simplest description of exchange averaging of the longitudinal relaxation rate in a protein solution yields for the excess relaxation rate, $R_1^x(\omega_0)$, that is, the relaxation rate $R_1(\omega_0)$ measured on the protein solution minus the rate R_{bulk} measured on a protein-free reference sample,

$$R_1^x(\omega_0) \equiv R_1(\omega_0) - R_{\mathrm{bulk}} = f_\alpha(R_\alpha - R_{\mathrm{bulk}}) + \sum_k \frac{f_{\beta k}}{\tau_k + 1/R_{1\beta k}(\omega_0)} \qquad (1)$$

where $\omega_0 = 2\pi\nu_0$ is the resonance frequency in angular frequency units. The first (α) term in Eq. (1) refers to nuclei residing in molecules that have so short-lived encounters with the protein that the local relaxation rate is frequency independent throughout the investigated frequency range. The second (β) term is due to nuclei in molecules that associate with the protein for sufficiently long periods (usually meaning > 1 ns) that their local relaxation rate is frequency dependent within the investigated frequency range. Such long-lived encounters generally involve

well-defined sites, each characterized by a mean residence time τ_k and a local longitudinal relaxation rate $R_{1k}(\omega_0)$. At any time, a fraction $f_\beta = \sum_k f_{\beta k}$ of the nuclei reside in such sites. The simple form of the second term in Eq. (1) is valid provided that $f_{\beta k} \ll 1$ and $R_{1\beta k} \gg R_{\text{bulk}}$. This is nearly always the case in MRD studies of protein solutions.

8.7.2.2 Spectral Density Function

Spin relaxation of nuclides with spin quantum number $I \geq 1$, like $^2\text{H}(I = 1)$ and $^{17}\text{O}(I = 5/2)$, is induced by the coupling of the nuclear electric quadrupole moment with fluctuating electric field gradients [92]. The local relaxation rate, $R_{1\beta k}(\omega_0)$, can then be expressed as

$$R_{1\beta k}(\omega_0) = 0.2J_{\beta k}(\omega_0) + 0.8J_{\beta k}(2\omega_0) \tag{2}$$

This expression is exact for ^2H and an excellent approximation for ^{17}O. The spectral density function, $J(\omega)$, is the cosine transform of the time autocorrelation function for the fluctuating electric field gradient. For a small molecule rigidly bound to a protein undergoing spherical-top rotational diffusion, it has the Lorentzian form

$$J_{\beta k}(\omega) = \omega_{\text{Qk}}^2 \frac{\tau_{\beta k}}{1 + (\omega\tau_{\beta k})^2} \tag{3}$$

The effective correlation time $\tau_{\beta k}$ is determined by the residence time τ_k in site k and the rotational correlation time τ_R of the biomolecule according to

$$\frac{1}{\tau_{\beta k}} = \frac{1}{\tau_\text{R}} + \frac{1}{\tau_k} \tag{4}$$

The quadrupole frequency ω_Q depends on the spin quantum number, the quadrupole coupling constant, and the asymmetry parameter of the electric field gradient tensor. For ^2H and ^{17}O in water, $\omega_\text{Q} = 8.7 \times 10^5\ \text{s}^{-1}$ and $7.6 \times 10^6\ \text{s}^{-1}$, respectively [7]. Equation (3) is readily generalized to nonspherical proteins with symmetric-top rather than spherical-top rotational diffusion. However, for globular proteins, the effect of anisotropic rotational diffusion on the shape of the relaxation dispersion is usually negligible.

In general, small molecules are not rigidly attached to the protein on the time scale (τ_R) of protein tumbling, but undergo restricted local rotational motions on time scales short compared with τ_R. If these local motions are much faster than the global motion (with correlation time $\tau_{\beta k}$) and the highest investigated MRD frequency, then the generalization of Eq. (3) is [96]

$$J_{\beta k}(\omega) = \omega_{\text{Qk}}^2 \left\{ (1 - S_{\beta k}^2)\tau_{\beta k}^{\text{loc}} + S_{\beta k}^2 \frac{\tau_{\beta k}}{1 + (\omega\tau_{\beta k})^2} \right\} \tag{5}$$

where $\tau_{\beta k}^{\text{loc}}$ is an effective correlation time for the local restricted rotation. Furthermore, $S_{\beta k}$ is the generalized second-rank orientational order parameter for site k,

which has a maximum value of unity for a rigidly attached molecule. When this spectral density is substituted into Eq. (2), we obtain

$$R_{1\beta k}(\omega_0) = R_{\beta k}^{\mathrm{loc}} + b_k \tau_{\beta k} \left[\frac{0.2}{1 + (\omega_0 \tau_{\beta k})^2} + \frac{0.8}{1 + (2\omega_0 \tau_{\beta k})^2} \right] \tag{6}$$

where $R_{\beta k}^{\mathrm{loc}} = \omega_{\mathrm{Q}k}^2 (1 - S_{\beta k}^2) \tau_{\beta k}^{\mathrm{loc}}$ and $b_k = (\omega_{\mathrm{Q}k} S_{\beta k})^2$. Using this expression for $R_{1\beta k}(\omega_0)$, we can manipulate Eq. (1) into the usual fast-exchange form, but with renormalized parameters:

$$R_1^{\mathrm{x}}(\omega_0) = \alpha + \sum_k f_{\beta k} b_k' \tau_{\beta k}' \left[\frac{0.2}{1 + (\omega_0 \tau_{\beta k}')^2} + \frac{0.8}{1 + (2\omega_0 \tau_{\beta k}')^2} \right] \tag{7}$$

where $\alpha = f_\alpha (R_\alpha - R_{\mathrm{bulk}}) + \sum_k f_{\beta k} R_{\beta k}^{\mathrm{loc}}$ and we have assumed that $f_\beta \ll 1$ and $R_{\beta k}^{\mathrm{loc}} \tau_k \ll 1$. Furthermore, we have introduced the renormalized parameters $b_k' = b_k / [1 + R_{1\beta k}(0)\tau_k]^{1/2}$ and $\tau_{\beta k}' = \tau_{\beta k} / [1 + R_{1\beta k}(0)\tau_k]^{1/2}$. Equation (7) shows that a given site produces a Lorentzian dispersion profile even outside the fast-exchange regime. With increasing residence time τ_k, the dispersion shifts to higher frequency ($\tau_{\beta k}' < \tau_{\beta k}$) and the dispersion step is reduced in magnitude ($b_k' < b_k$), but the shape remains Lorentzian (to an excellent approximation). However, if several sites with different effective correlation times $\tau_{\beta k}$ contribute, then the dispersion profile will be stretched out over a wider frequency range.

If all sites have the same effective correlation time $\tau_{\beta k}$, which is the case if $\tau_k \gg \tau_{\mathrm{R}}$ for all sites, and if also all sites are in the fast-exchange regime, meaning that $R_{1\beta k}(0)\tau_k \ll 1$, then Eq. (7) reduces to

$$R_1^{\mathrm{x}}(\omega_0) = \alpha + \beta \tau_\beta \left[\frac{0.2}{1 + (\omega_0 \tau_\beta)^2} + \frac{0.8}{1 + (2\omega_0 \tau_\beta)^2} \right] \tag{8}$$

where $\beta = \sum_k f_{\beta k} b_k$. The dispersion profile is then fully characterized by the three parameters α, β, and τ_β. In the fast-exchange regime, sites of a particular type k contribute to the β parameter a quantity $f_{\beta k} b_k = N_{\beta k} (\omega_{\mathrm{Q}k} S_{\beta k})^2 / N_{\mathrm{T}}$, where $N_{\beta k}$ is the number of small (water or co-solvent) molecules bound to k-sites and N_{T} is the total number of such molecules, both counted per protein molecule. Usually, $\omega_{\mathrm{Q}k}$ can be taken from solid-state data, while N_{T} is obtained from the sample composition (which requires an accurate determination of the protein concentration). The dispersion amplitude parameter β thus provides the molecular quantity

$$N_\beta S_\beta^2 = \frac{\beta N_{\mathrm{T}}}{\omega_{\mathrm{Q}}^2} \tag{9}$$

Here, $N_\beta = \sum_k N_{\beta k}$ is the total number of small molecules in long-lived (> 1 ns) association with the protein and S_β is their root-mean-square order parameter. Because $0 \le S_\beta^2 \le 1$, the quantity $N_\beta S_\beta^2$ furnishes a lower bound on the number N_β.

The number N_α of perturbed but short-lived solvent molecules is usually very much larger than the number N_β of long-lived molecules. We can then neglect the

local-motion contribution to α from the long-lived molecules. The high-frequency amplitude parameter α thus provides the molecular quantity

$$N_\alpha \rho_\alpha = \frac{\alpha N_T}{R_{bulk}} \tag{10}$$

where $\rho_\alpha = R_\alpha / R_{bulk} - 1 = \tau_\alpha / \tau_{bulk} - 1$ is a measure of the increase of the rotational correlation time τ_α for the N_α perturbed molecules relative to the rotational correlation time τ_{bulk} of the same molecule in the bulk solvent. The quantity ρ_α, known as the rotational retardation factor, is an average over all N_α short-lived solvation sites. The dynamic solvent perturbation is short-ranged [10], so that ρ_α differs significantly from zero only for molecules that interact directly with the surface. If the solvent is pure water, the number N_α can therefore be estimated by dividing the solvent-accessible surface area of the protein by the mean area occupied by a water molecule, usually taken as 15 Å^2 (see Section 8.2).

8.7.2.3 **Residence Time**

The MRD profile separates contributions from interaction sites with long and short residence times τ_k. The observation of a dispersion step demonstrates unambiguously that a fraction of the nuclei reside in sites with correlation times on the order of the inverse dispersion frequency. To contribute maximally to the relaxation dispersion, a site k must have a residence time τ_k much longer than the rotational correlation time τ_R of the biomolecule, but much shorter than the zero-frequency local relaxation time, $1/R_{1\beta k}(0)$. If $R_{1\beta k}(0) \gg R^{loc}_{\beta k}$, as is usually the case, these conditions are expressed by the inequalities

$$\tau_R \ll \tau_k \ll \frac{1}{b_k \tau_R} \tag{11}$$

which may be said to define the MRD residence time window. Of course, sites that do not obey these inequalities may still contribute to the dispersion, but do so with less than the maximum contribution $f_{\beta k} b_k \tau_R$. If $R^{loc}_{\beta k}$ is neglected, violation of the right-hand (fast-exchange) inequality in Eq. (11) reduces the effective dispersion amplitude parameter and the effective correlation time by the relative amounts

$$\frac{\beta'_k}{\beta_k} = \left[\frac{1 + \tau_R/\tau_k}{1 + \tau_R/\tau_k + b_k \tau_R \tau_k}\right]^{1/2} \tag{12}$$

$$\frac{\tau'_{\beta k}}{\tau_R} = \frac{1}{[(1 + \tau_R/\tau_k)(1 + \tau_R/\tau_k + b_k \tau_R \tau_k)]^{1/2}} \tag{13}$$

For residence times on the central plateau of the MRD window, only lower and upper bounds on τ_k can be established, as expressed by the inequalities in Eq. (11). On the wide flanks of the MRD window, however, τ_k can be quantitatively determined. On the short-τ_k flank, this requires independent information about τ_R. If the τ_β value deduced from the MRD profile is much smaller than τ_R, then it can be

directly identified with the residence time τ_k without the need for an accurate estimate of τ_R. In contrast, determination of residence times comparable to τ_R requires knowledge of the precise value of τ_R. This can be obtained from ^{1}H or ^{2}H MRD data, which generally contain contributions from labile protein hydrogens (with $\tau_k \gg \tau_R$).

Longer residence times can be determined on the long-τ_k flank of the MRD window. According to Eqs (12) and (13), τ_k can be obtained from either β'_k or $\tau'_{\beta k}$, since $\beta'_k/\beta_k = \tau'_{\beta k}/\tau_R = (1 + b_k\tau_R\tau_k)^{-1/2}$ in this regime. To determine τ_k at a given temperature, τ_R and b_k must be known. From a variable-temperature MRD study, b_k (assumed to be temperature independent) and the activation enthalpy of τ_k can be determined if τ_R is taken to scale as η/T (as expected for rotational diffusion). If τ_R is known at one temperature, τ_k is obtained at all investigated temperatures [97].

8.7.2.4 ^{19}F Relaxation

The ^{19}F nuclei in a partially fluorinated co-solvent molecule, such as trifluoroethanol (TFE), are relaxed by fluctuating magnetic dipole–dipole interactions involving ^{19}F–^{19}F and ^{19}F–^{1}H pairs. In place of Eq. (2), we then have [91, 92]

$$R_{1\beta k}(\omega_0) = 0.2J^{FF}_{\beta k}(\omega_F) + 0.8J^{FF}_{\beta k}(2\omega_F) + 0.1J^{FH}_{\beta k}(\omega_H - \omega_F) + 0.3J^{FH}_{\beta k}(\omega_F) + 0.6J^{FH}_{\beta k}(\omega_H + \omega_F) \quad (14)$$

where ω_F and ω_H are the ^{19}F and ^{1}H angular resonance frequencies. The dipolar spectral density functions $J^{FF}_{\beta k}(\omega)$ and $J^{FH}_{\beta k}(\omega)$ are given by Eq. (5), but with the quadrupole frequency ω_Q replaced by the dipole-coupling frequencies ω_{FF} and ω_{FH}. For the TFE molecule, the ^{19}F amplitude parameters α and $\beta = \beta_{FF} + \beta_{FH}$ are given by [91]

$$\alpha = \frac{R_{bulk}}{N_T^{TFE}} N_\alpha \rho_\alpha \quad (15)$$

$$\beta_{FF} = 2 \times \frac{3}{2} \frac{\omega^2_{FF}}{N_T^{TFE}} N_\beta S^2_\beta \quad (16a)$$

$$\beta_{FH} = 2 \frac{\omega^2_{FH}}{N_T^{TFE}} N_\beta S^2_\beta \quad (16b)$$

where N_T^{TFE} is the TFE/protein mole ratio and $N_\alpha, \rho_\alpha, N_\beta$, and S_β now refer to TFE rather than to water. The factor 2 in Eq. (16) appears because each ^{19}F nucleus is dipole coupled to two other ^{19}F nuclei in the CF_3 group or to two protons in the adjacent CH_2 group. The factor 3/2 in Eq. (16a) reflects cross-relaxation within a homonuclear pair of dipole-coupled nuclei. The dipole-coupling frequencies ω_{FF} and ω_{FH} in Eq. (16) refer to bound TFE molecules that tumble with the protein and are averaged over the much faster internal rotation of the CF_3 group. From the molecular geometry of TFE, one obtains $\omega_{FF} = -3.39 \times 10^4$ rad s^{-1} and $\omega_{FH} = 2.39 \times 10^4$ rad s^{-1}.

At high magnetic fields, it is necessary to include a contribution to ^{19}F relaxation from rotational modulation of the anisotropic ^{19}F shielding tensor and at high temperatures there may also be a contribution from the so-called spin-rotation mechanism [92]. Under certain conditions it may also be necessary to include the effect of intermolecular dipole–dipole couplings.

8.7.2.5 Coexisting Protein Species

Under conditions where significant populations of two or more protein states are present simultaneously, the relaxation theory must be generalized. Typically, the observed solvent molecules exchange rapidly (on the relaxation time scale) between solvation sites on the protein (in different states) and the bulk solvent. The observed (excess) relaxation rate is then simply a population-weighted average. For example, for coexisting native (N) and unfolded (U) states:

$$R_1^x = x_N R_1^x(N) + (1 - x_N) R_1^x(U) \tag{17}$$

where x_N is the fraction native protein. It follows from Eq. (8), that the high-frequency amplitude parameter α may be expressed as a population-weighted average in the same way. In principle, the observed (β) dispersion is a population-weighted superposition of dispersions from the native and unfolded states. In practice, the rotational correlation times (τ_R) of the native and (partially) unfolded states are often sufficiently similar that the dispersion profile can be accurately described by a single Lorentzian. Also the amplitude parameter β can then be expressed as a population-weighted average. Of course, if the long-lived solvent sites have been lost in the unfolded state, then only the native state contributes to the β parameter.

8.7.2.6 Preferential Solvation

In MRD studies of solvent-induced denaturation, the variation of the native protein fraction x_N with the denaturant concentration C_D may be obtained from the usual assumption that the free energy of unfolding varies linearly with C_D [23]. It then follows that $x_N = 1/(1 + K_U)$, with the unfolding constant $K_U = \exp[m(C_D - C_{1/2})/(RT)]$, where the parameters $C_{1/2}$ and m characterize the midpoint and slope, respectively, of the N → U transition [23].

The denaturant concentration not only controls the N ↔ U equilibrium; it also affects the number of water (N_α^W) and denaturant (N_α^D) molecules in contact with the protein surface (in each state). The molecular parameters $N_\alpha^W \rho_\alpha^W$ and $N_\alpha^D \rho_\alpha^D$ derived from the MRD parameters α^W and α^D by means of Eq. (10) can be decomposed into contributions from individual protein states as in Eq. (17), but now also the numbers N_α^W and N_α^D depend on C_D. This dependence can be handled by the solvent-exchange model [14], where denaturant binding to the protein surface is described thermodynamically as a one-to-one exchange with water. The denaturant occupancy averaged over all binding sites is then given by

$$\theta_D = \frac{K_D a_D^c}{a_W^x + K_D a_D^c} \tag{18}$$

where K_D is an effective denaturant binding constant (with units M^{-1}), a_D^c is the denaturant activity on the molarity scale, and a_W^x is the water activity on the mole fraction scale. We then write $N_\alpha^D(N) = \mathcal{N}_D(N)\theta_D(N)$ and $N_\alpha^W(N) = \mathcal{N}_W(N)[1 - \theta_D(N)]$ along with analogous expressions for the unfolded (U) state. Here, $\mathcal{N}_D(N)$ and $\mathcal{N}_W(N)$ are the number of sites on the surface of the native protein that can be occupied by denaturant and water molecules, respectively. Because a denaturant molecule is larger than a water molecule, we allow these numbers to be different. This may be regarded as an ad hoc generalization of the one-to-one solvent exchange model.

References

1 Eisenberg, D. and Kauzmann, W. (1969). *The Structure and Properties of Water*. Clarendon, Oxford.

2 Kauzmann, W. (1959). Some factors in the interpretation of protein denaturation. *Adv. Protein Chem.* **14**, 1–63.

3 Tanford, C. (1980). *The Hydrophobic Effect*, 2nd edn, Wiley, New York.

4 Dill, K. A. (1990). Dominant forces in protein folding. *Biochemistry* **29**, 7133–7155.

5 Tanford, C. (1968). Protein denaturation. Part A. Characterization of the denatured state. *Adv. Protein Chem.* **23**, 121–282.

6 Shortle, D. (1996). Structural analysis of non-native states of proteins by NMR methods. *Curr. Opin. Struct. Biol.* **6**, 24–30.

7 Halle, B., Denisov, V. P., and Venu, K. (1999). Multinuclear relaxation dispersion studies of protein hydration. In *Biological Magnetic Resonance* (Krishna, N. R. and Berliner, L. J., eds), Vol. 17, pp. 419–484, Kluwer/Plenum, New York.

8 Halle, B. and Denisov, V. P. (2001). Magnetic relaxation dispersion studies of biomolecular solutions. *Methods Enzymol.* **338**, 178–201.

9 Denisov, V. P. and Halle, B. (1996). Protein hydration dynamics in aqueous solution. *Faraday Discuss.* **103**, 227–244.

10 Halle, B. (1998). Water in biological systems: the NMR picture. In *Hydration Processes in Biology* (Bellisent-Funel, M.-C., ed.), pp. 233–249, IOS Press, Dordrecht.

11 Modig, K., Liepinsh, E., Otting, G., and Halle, B. (2004). Dynamics of protein and peptide hydration. *J. Am. Chem. Soc.* **126**, 102–114.

12 Williams, M. A., Goodfellow, J. M., and Thornton, J. M. (1994). Buried waters and internal cavities in monomeric proteins. *Protein Sci.* **3**, 1224–1235.

13 Baker, E. N. (1995). Solvent interactions with proteins as revealed by X-ray crystallographic studies. In *Protein–Solvent Interactions* (Gregory, R. B., ed.), pp. 143–189, M. Dekker, New York.

14 Schellman, J. A. (1994). The thermodynamics of solvent exchange. *Biopolymers* **34**, 1015–1026.

15 Timasheff, S. N. (2002). Protein hydration, thermodynamic binding, and preferential hydration. *Biochemistry* **41**, 13473–13482.

16 Garcia de la Torre, J., Huertas, M. L., and Carrasco, B. (2000). Calculation of hydrodynamic properties of globular proteins from their atomic-level structure. *Biophys. J.* **78**, 719–730.

17 Halle, B. and Davidovic, M. (2003). Biomolecular hydration: from water dynamics to hydrodynamics. *Proc. Natl Acad. Sci. USA* **100**, 12135–12140.

18 Doi, M. and Edwards, S. F. (1986). *The Theory of Polymer Dynamics*. Clarendon, Oxford.

19 Denisov, V. P. and Halle, B. (1998). Thermal denaturation of ribonuclease A characterized by water ^{17}O and ^{2}H magnetic relaxation dispersion. *Biochemistry* **37**, 9595–9604.

20 Privalov, P. L., Tiktopulo, E. I., Venyaminov et al. (1989). Heat capacity and conformation of proteins in the denatured state. *J. Mol. Biol.* **205**, 737–750.

21 Privalov, P. L. and Makhatadze, G. I. (1990). Heat capacity of proteins. II. Partial molar heat capacity of the unfolded polypeptide chain of proteins: protein unfolding effects. *J. Mol. Biol.* **213**, 385–391.

22 Tamura, Y. and Gekko, K. (1995). Compactness of thermally and chemically denatured ribonuclease-A as revealed by volume and compressibility. *Biochemistry* **34**, 1878–1884.

23 Myers, J. K., Pace, C. N., and Scholtz, J. M. (1995). Denaturant *m* values and heat capacity changes: relation to changes in accessible surface areas of protein unfolding. *Protein Sci.* **4**, 2138–2148.

24 Cole, R. and Loria, J. P. (2002). Evidence for flexibility in the function of ribonuclease A. *Biochemistry* **41**, 6072–6081.

25 Privalov, P. L. (1990). Cold denaturation of proteins. *Crit. Rev. Biochem. Mol. Biol.* **25**, 281–305.

26 Sabelko, J., Ervin, J., and Gruebele, M. (1998). Cold-denatured ensemble of apomyoglobin: implications for the early steps of folding. *J. Phys. Chem. B* **102**, 1806–1819.

27 Rasmussen, D. H. and MacKenzie, A. P. (1973). Clustering in supercooled water. *J. Chem. Phys.* **59**, 5003–5013.

28 Griko, Yu. V. and Privalov, P. L. (1992). Calorimetric study of the heat and cold denaturation of β-lactoglobulin. *Biochemistry* **31**, 8810–8815.

29 Griko, Yu. V. and Kutyshenko, V. P. (1994). Differences in the processes of β-lactoglobulin cold and heat denaturations. *Biophys J.* **67**, 356–363.

30 Katou, H., Hoshino, M., Kamikubo, H., Batt, C. A., and Goto, Y. (2001). Native-like β-hairpin retained in the cold-denatured state of bovine β-lactoglobulin. *J. Mol. Biol.* **310**, 471–484.

31 Valente-Mesquita, V. L., Botelho, M. M., and Ferreira, S. T. (1998). Pressure-induced subunit dissociation and unfolding of dimeric β-lactoglobulin. *Biophys. J.* **75**, 471–476.

32 Sakurai, K., Oobatake, M., and Goto, Y. (2001). Salt-dependent monomer-dimer equilibrium of bovine β-lactoglobulin at pH 3. *Protein Sci.* **10**, 2325–2335.

33 Jameson, G. B., Adams, J. J., and Creamer, L. K. (2002). Flexibility, functionality and hydrophobicity of bovine β-lactoglobulin. *Int. Dairy J.* **12**, 319–329.

34 Davidovic, M. and Halle, B., manuscript in preparation.

35 Uhrinova, S., Smith, M. H., Jameson, G. B., Uhrin, D., Sawyer, L., and Barlow, P. N. (2000). Structural changes accompanying pH-induced dissociation of the β-lactoglobulin dimer. *Biochemistry* **39**, 3565–3574.

36 Arai, M. and Kuwajima, K. (2000). Role of the molten globule state in protein folding. *Adv. Protein Chem.* **53**, 209–282.

37 Denisov, V. P., Jonsson, B.-H., and Halle, B. (1999). Hydration of denatured and molten globule proteins. *Nature Struct. Biol.* **6**, 253–260.

38 Kharakoz, D. P. and Bychkova, V. E. (1997). Molten globule of human α-lactalbumin: hydration, density, and compressibility of the interior. *Biochemistry* **36**, 1882–1890.

39 Redfield, C., Schulman, B. A., Milhollen, M. A., Kim, P. S., and Dobson, C. M. (1999). α-Lactalbumin forms a compact molten globule in the absence of disulfide bonds. *Nature Struct. Biol.* **6**, 948–952.

40 Balbach, J. (2000). Compaction during protein folding studied by real-time NMR diffusion experiments. *J. Am. Chem. Soc.* **122**, 5887–5888.

41 Chakraborty, S., Ittah, V., Bai, P., Luo, L., Haas, E., and Peng, Z. (2001). Structure and dynamics of the α-lactalbumin molten globule:

fluorescence studies using proteins containing a single tryptophan residue. *Biochemistry* **40**, 7228–7238.

42 Harpaz, Y., Gerstein, M., and Chothia, C. (1994). Volume changes on protein folding. *Structure* **2**, 641–649.

43 Griko, Yu. V., Freire, E., and Privalov, P. L. (1994). Energetics of the α-lactalbumin states: a calorimetric and statistical thermodynamic study. *Biochemistry* **33**, 1889–1899.

44 Griko, Yu. V. (2000). Energetic basis of structural stability in the molten globule state: α-lactalbumin. *J. Mol. Biol.* **297**, 1259–1268.

45 Kutyshenko, V. P. and Cortijo, M. (2000). Water–protein interactions in the molten-globule state of carbonic anhydrase b: an NMR spin-diffusion study. *Protein Sci.* **9**, 1540–1547.

46 Liepinsh, E., Otting, G., and Wüthrich, K. (1992). NMR spectroscopy of hydroxyl protons in aqueous solutions of peptides and proteins. *J. Biomol. NMR* **2**, 447–465.

47 Eliezer, D., Yao, J., Dyson, H. J., and Wright, P. E. (1998). Structural and dynamic characterization of partially folded states of apomyoglobin and implications for protein folding. *Nature Struct. Biol.* **5**, 148–155.

48 Gast, K., Damaschun, H., Misselwitz, R., Müller-Frohne, M., Zirwer, D., and Damaschun, G. (1994). Compactness of protein molten globules: temperature-induced structural changes of the apomyoglobin folding intermediate. *Eur. Biophys. J.* **23**, 297–305.

49 Kataoka, M., Nishii, I., Fujisawa, T., Ueki, T., Tokunaga, F., and Goto, Y. (1995). Structural characterization of the molten globule and native states of apomyoglobin by solution X-ray scattering. *J. Mol. Biol.* **249**, 215–228.

50 Osterman, A., Tanaka, I., Engler, N., Niimura, N., and Parak, F. G. (2002). Hydrogen and deuterium in myoglobin as seen by a neutron structure determination at 1.5 Å resolution. *Biophys. Chem.* **95**, 183–193.

51 Creamer, T. P., Srinivasan, R., and Rose, G. D. (1995). Modeling unfolded states of peptides and proteins. *Biochemistry* **34**, 16245–16250.

52 Shortle, D. and Ackerman, M. S. (2001). Persistence of native-like topology in a denatured protein in 8 M urea. *Science* **293**, 487–489.

53 Klein-Seetharaman, J., Oikawa, M., Grimshaw, S. B., et al. (2002). Long-range interactions within a nonnative protein. *Science* **295**, 1719–1722.

54 Shortle, D. (1996). The denatured state (the other half of the folding equation) and its role in protein stability. *FASEB J.* **10**, 27–34.

55 Schellman, J. A. (1987). Selective binding and solvent denaturation. *Biopolymers* **26**, 549–559.

56 Wetlaufer, D. B., Malik, S. K., Stoller, L., and Coffin, R. L. (1964). Nonpolar group participation in the denaturation of proteins by urea and guanidinium salts. Model compound studies. *J. Am. Chem. Soc.* **86**, 508–514.

57 Shimizu, S. and Chan, H. S. (2002). Origins of protein denatured state compactness and hydrophobic clustering in aqueous urea: Inferences from nonpolar potentials of mean force. *Proteins* **49**, 560–566.

58 Dötsch, V. (1996). Characterization of protein–solvent interactions with NMR-spectroscopy: The role of urea in the unfolding of proteins. *Pharm. Acta Helv.* **71**, 87–96.

59 Lumb, K. J. and Dobson, C. M. (1992). ^{1}H nuclear magnetic resonance studies of the interaction of urea with hen lysozyme. *J. Mol. Biol.* **227**, 9–14.

60 Liepinsh, E. and Otting, G. (1994). Specificity of urea binding to proteins. *J. Am. Chem. Soc.* **116**, 9670–9674.

61 Pike, A. C. W. and Acharya, K. R. (1994). A structural basis for the interaction of urea with lysozyme. *Protein Sci.* **3**, 706–710.

62 Tirado-Rives, J., Orozco, M., and Jorgensen, W. L. (1997). Molecular dynamics simulations of the unfolding of barnase in water and 8 M aqueous urea. *Biochemistry* **36**, 7313–7329.

63 Caflisch, A. and Karplus, M. (1999).

Structural details of urea binding to barnase: a molecular dynamics analysis. *Structure* **7**, 477–488.

64 Modig, K., Kurian, E., Prendergast, F. G., and Halle, B. (2003). Water and urea interactions with the native and unfolded forms of a β-barrel protein. *Protein Sci.* **12**, 2768–2781.

65 Scapin, G., Gordon, J. I., and Sacchettini, J. C. (1992). Refinement of the structure of recombinant rat intestinal fatty acid-binding apoprotein at 1.2-Å resolution. *J. Biol. Chem.* **267**, 4253–4269.

66 Wiesner, S., Kurian, E., Prendergast, F. G., and Halle, B. (1999). Water molecules in the binding cavity of intestinal fatty acid binding protein: Dynamic characterization by water ^{17}O and ^{2}H magnetic relaxation dispersion. *J. Mol. Biol.* **286**, 233–246.

67 Modig, K., Rademacher, M., Lücke, C., and Halle, B. (2003). Water dynamics in the large cavity of three lipid-binding proteins monitored by ^{17}O magnetic relaxation dispersion. *J. Mol. Biol.* **332**, 965–977.

68 Hodsdon, M. E. and Cistola, D. P. (1997). Ligand binding alters the backbone mobility of intestinal fatty acid-binding protein as monitored by ^{15}N NMR relaxation and ^{1}H exchange. *Biochemistry* **36**, 2278–2290.

69 Frolov, A. and Schroeder, F. (1997). Time-resolved fluorescence of intestinal and liver fatty acid binding proteins: Role of fatty acyl CoA and fatty acid. *Biochemistry* **36**, 505–517.

70 Likic, V. A. and Prendergast, F. G. (2001). Dynamics of internal waters in fatty acid binding protein: Computer simulations and comparison with experiments. *Proteins* **43**, 65–72.

71 Bakowies, D. and van Gunsteren, W. F. (2002). Simulations of apo and holo-fatty acid binding protein: Structure and dynamics of protein, ligand and internal water. *J. Mol. Biol.* **315**, 713–736.

72 Likic, V. A., Juranic, N., Macura, S., and Prendergast, F. G. (2000). A ''structural'' water molecule in the family of fatty acid binding proteins. *Protein Sci.* **9**, 497–504.

73 Hodsdon, M. E. and Frieden, C. (2001). Intestinal fatty acid binding protein: the folding mechanism as determined by NMR studies. *Biochemistry* **40**, 732–742.

74 Ropson, I. J. and Frieden, C. (1992). Dynamic NMR spectral analysis and protein folding: identification of a highly populated folding intermediate of rat intestinal fatty acid-binding protein by ^{19}F NMR. *Proc. Natl Acad. Sci. USA* **89**, 7222–7226.

75 Kuwajima, K., Nitta, K., Yoneyama, M., and Sugai, S. (1976). Three-state denaturation of α-lactalbumin by guanidine hydrochloride. *J. Mol. Biol.* **106**, 359–373.

76 Makhatadze, G. I. and Privalov, P. L. (1992). Protein interactions with urea and guanidinium chloride. A calorimetric study. *J. Mol. Biol.* **226**, 491–505.

77 Schellman, J. A. and Gassner, N. C. (1996). The enthalpy of transfer of unfolded proteins into solutions of urea and guanidinium chloride. *Biophys. Chem.* **59**, 259–275.

78 Barron, L. D., Hecht, L., and Wilson, G. (1997). The lubricant of life: a proposal that solvent water promotes extremely fast conformational fluctuations in mobile heteropolypeptide structure. *Biochemistry* **36**, 13143–13147.

79 Buck, M. (1998). Trifluoroethanol and colleagues: cosolvents come of age. Recent studies with peptides and proteins. *Q. Rev. Biophys.* **31**, 297–355.

80 Thomas, P. D. and Dill, K. A. (1993). Local and nonlocal interactions in globular proteins and mechanisms of alcohol denaturation. *Protein Sci.* **2**, 2050–2065.

81 Jasanoff, A. and Fersht, A. R. (1994). Quantitative determination of helical propensities from trifluoroethanol titration curves. *Biochemistry* **33**, 2129–2135.

82 Shiraki, K., Nishikawa, K., and Goto, Y. (1995). Trifluoroethanol-induced stabilization of the α-helical structure of β-lactoglobulin: implica-

tion for non-hierarchical protein folding. *J. Mol. Biol.* **245**, 180–194.

83 Hamada, D., Kuroda, Y., Tanaka, T., and Goto, Y. (1995). High helical propensity of the peptide fragments derived from β-lactoglobulin, a predominantly β-sheet protein. *J. Mol. Biol.* **254**, 737–746.

84 Kuroda, Y., Hamada, D., Tanaka, T., and Goto, Y. (1996). High helicity of peptide fragments corresponding to β-strand regions of β-lactoglobulin observed by 2D NMR spectroscopy. *Folding Des.* **1**, 255–263.

85 Kuwata, K., Hoshino, M., Era, S., Batt, C. A., and Goto, Y. (1998). $\alpha \rightarrow \beta$ transition of β-lactoglobulin as evidenced by heteronuclear NMR. *J. Mol. Biol.* **283**, 731–739.

86 Mendieta, J., Folqué, H., and Tauler, R. (1999). Two-phase induction of the nonnative α-helical form of β-lactoglobulin in the presence of trifluoroethanol. *Biophys. J.* **76**, 451–457.

87 Fioroni, M., Díaz, M. D., Burger, K., and Berger, S. (2002). Solvation phenomena of a tetrapeptide in water/trifluoroethanol and water/ethanol mixtures: a diffusion NMR, intermolecular NOE, and molecular dynamics study. *J. Am. Chem. Soc.* **124**, 7737–7744.

88 Díaz, M. D., Fioroni, M., Burger, K., and Berger, S. (2002). Evidence of complete hydrophobic coating of bombesin by trifluoroethanol in aqueous solution: an NMR spectroscopic and molecular dynamics study. *Chem. Eur. J.* **8**, 1663–1669.

89 Roccatano, D., Colombo, G., Fioroni, M., and Mark, A. E. (2002). Mechanism by which 2,2,2-trifluoroethanol/water mixtures stabilize secondary-structure formation in peptides: a molecular dynamics study. *Proc. Natl Acad. Sci. USA* **99**, 12179–12184.

90 Martinez, D. and Gerig, J. T. (2001). Intermolecular $^{1}H\{^{19}F\}$ NOEs in studies of fluoroalcohol-induced conformations of peptides and proteins. *J. Magn. Reson.* **152**, 269–275.

91 Kumar, S., Modig, K., and Halle, B. (2003). Trifluoroethanol-induced $\beta \rightarrow \alpha$ transition in β-lactoglobulin: hydration and cosolvent binding studied by ^{2}H, ^{17}O, and ^{19}F magnetic relaxation dispersion. *Biochemistry* **42**, 13708–13716.

92 Abragam, A. (1961). *The Principles of Nuclear Magnetism.* Clarendon, Oxford.

93 Noack, F. (1986). NMR field-cycling spectroscopy: principles and applications. *Prog. NMR Spectrosc.* **18**, 171–276.

94 Anoardo, E., Galli, G., and Ferrante, G. (2001). Fast field-cycling NMR: applications and instrumentation. *Appl. Magn. Reson.* **20**, 365–404.

95 Jóhannesson, H., Denisov, V. P., and Halle, B. (1997). Dimethyl sulfoxide binding to globular proteins: a nuclear magnetic relaxation dispersion study. *Protein Sci.* **6**, 1756–1763.

96 Halle, B. and Wennerström, H. (1981). Interpretation of magnetic resonance data from water in heterogeneous systems. *J. Chem. Phys.* **75**, 1928–1943.

97 Denisov, V. P., Peters, J., Hörlein, H. D., and Halle, B. (1996). Using buried water molecules to explore the energy landscape of proteins. *Nature Struct. Biol.* **3**, 505–509.

9
Stability and Design of α-Helices

Andrew J. Doig, Neil Errington, and Teuku M. Iqbalsyah

9.1
Introduction

Proteins are built of regular local folds of the polypeptide chain called secondary structure. The α-helix was first described by Pauling, Corey, and Branson in 1950 [1], and their model was quickly supported by X-ray analysis of hemoglobin [2]. Irrefutable proof of the existence of the α-helix came with the first protein crystal structure of myoglobin, where most secondary structure is helical [3]. α-Helices were subsequently found in nearly all globular proteins. It is the most abundant secondary structure, with ≈30% of residues found in α-helices [4]. In this review, we discuss structural features of the helix and their study in peptides. Some earlier reviews on this field are in Refs [5–11].

9.2
Structure of the α-Helix

A helix combines a linear translation with an orthogonal circular rotation. In the α-helix the linear translation is a rise of 5.4 Å per turn of the helix and a circular rotation is 3.6 residues per turn. Side chains spaced $i, i+3$, $i, i+4$, and $i, i+7$ are therefore close in space and interactions between them can affect helix stability. Spacings of $i, i+2$, $i, i+5$, and $i, i+6$ place the side chain pairs on opposite faces of the helix, avoiding any interaction. The helix is primarily stabilized by $i, i+4$ hydrogen bonds between backbone amide groups.

The conformation of a polypeptide can be described by the backbone dihedral angles ϕ and ψ. Most ϕ, ψ combinations are sterically excluded, leaving only the broad β region and narrower α region. One reason why the α-helix is so stable is that a succession of the sterically allowed α, ϕ, ψ angles naturally position the backbone NH and CO groups towards each other for hydrogen bond formation. It is possible that a succession of the most stable conformation of an isolated residue in a polymer with alternative functional groups could point two hydrogen bond donors or acceptors towards each other, making secondary structure formation un-

Protein Folding Handbook. Part I. Edited by J. Buchner and T. Kiefhaber

ISBN: 3-527-30784-2

favourable. One reason why polypeptides may have been selected as the polymer of choice for building functional molecules is that the sterically most stable conformations also give strong hydrogen bonds.

The residues at the N-terminus of the α-helix are called N′-N-cap-N1-N2-N3-N4 etc., where the N-cap is the residue with nonhelical ϕ, ψ angles immediately preceding the N-terminus of an α-helix and N1 is the first residue with helical ϕ, ψ angles [12]. The C-terminal residues are similarly called C4-C3-C2-C1-C-cap-C′ etc. The N1, N2, N3, C1, C2, and C3 residues are unique because their amide groups participate in $i, i+4$ backbone–backbone hydrogen bonds using either only their CO (at the N-terminus) or NH (at the C-terminus) groups. The need for these groups to form hydrogen bonds has powerful effects on helix structure and stability [13]. The following rules are generally observed for N-capping in α-helices: Thr and Ser N-cap side chains adopt the *gauche*$^-$ rotamer, hydrogen bond to the N3 NH and have ψ restricted to $164 \pm 8°$. Asp and Asn N-cap side chains either adopt the *gauche*$^-$ rotamer and hydrogen bond to the N3 NH with $\psi = 172 \pm 10°$, or adopt the *trans* rotamer and hydrogen bond to both the N2 and N3 NH groups with $\psi = 107 \pm 19°$. With all other N-caps, the side chain is found in the gauche$^+$ rotamer so that the side chain does not interact unfavorably with the N-terminus by blocking solvation and ψ is unrestricted. An $i, i+3$ hydrogen bond from N3 NH to the N-cap backbone C=O is more likely to form at the N-terminus when an unfavorable N-cap is present [14].

Bonds between sp^3 hybridized atoms show preferences for dihedral angles of $+60°$ (*gauche*$^-$), $-60°$ (*gauche*$^+$) or $180°$ (*trans*). Within amino acid side chains the preferences for these rotamers varies between secondary structures [15–18]. Within the α-helix, rotamer preferences vary greatly between different positions of N-cap, N1, N2, N3, and interior [14, 19]. At helix interior positions, the *gauche*$^+$ rotamer is usually most abundant (64%), followed by *trans* (33%) with *gauche*$^-$ very rare (3%), though considerable variations are seen. For example, Ser and Thr are *gauche*$^-$ 19% and 14% of the time, respectively, as their hydroxyl groups can hydrogen bond to the helix backbone in this conformation. The β-branched side chains Val, Ile, and Thr are the most restricted with *gauche*$^+$ very common.

9.2.1 Capping Motifs

The amide NH groups at the helix N-terminus are satisfied predominantly by side chain hydrogen bond acceptors. In contrast, carbonyl CO groups at the C-terminus are satisfied primarily by backbone NH groups from the sequence following the helix [13]. The presence of such interactions would therefore stabilize helices. A well-known interaction is helix capping, defined as specific patterns found at or near the ends of helices [12, 20–24]. The patterns involve hydrogen bonding and hydrophobic interactions as summarized in Table 9.1.

A common pattern of capping at the helix N-terminus is the capping box. Here, the side chain of the N-cap forms a hydrogen bond with the backbone of N3 and,

Tab. 9.1. The most common capping motifs at α-helix termini.

Sequence	*Related position*	*Designation*	*Interactions*	*References*
N-capping				
p-XXp	N-cap → N3	Capping box	Reciprocal H-bonds between residues at N-cap and N3, where S/T at N-cap and E at N3 are the most frequently observed residues	24, 25
hp-XXph	N′ → N4	Expanded capping box/Hydrophobic staple	Reciprocal H-bonds between residues at N-cap and N3 accompanied by hydrophobic interactions between residues at N′ and N4	26, 298
hP-XXVh	N′ → N4	Pro-box motif	N-cap Pro residues are usually associated with Ile and Leu at N′, Val at N3 and a hydrophobic residue at N4	28
C-capping				
hXp-XGh	C3 → C″	Schellman motif	H-bonds between C″ NH and the C3 CO at and between C′ NH and C2 CO, respectively accompanied by hydrophobic interaction between C3 and C″	31, 223
hXp-XGp	C2 → C″	α_L motifs	As The Schellman motif but H-bond between C′ NH and C3 CO where C″ polar	32
X-Pro	C-cap → C′	Pro-capping motif	A stabilizing electrostatic interaction of the residues at positions C-cap and Pro at C′ with the helix macrodipole	34

p, polar amino acids; h, hydrophobic amino acids; X, any amino acids;
P, proline; G, glycine.

reciprocally, the side chain of N3 forms a hydrogen bond with the backbone of the N-cap [25]. The definition of the capping box was expanded by Seale et al. [26] to include an associated hydrophobic interaction between residues N′ and N4 and is also known as a ''hydrophobic staple'' [27]. A variant of the capping box motif, termed the ''big'' box with an observed hydrophobic interaction between nonpolar side chain groups in residues N4 and N″ (not N′) [26].

The Pro-box motif involves three hydrophobic residues and a Pro residue at the N-cap [28]. The N-cap Pro residue is usually associated with Ile or Leu at position N″, Val at position N3, and a hydrophobic residue at position N4. This motif is arguably very destabilizing since it discourages helix elongation due to the low N-cap preference of Pro [29] and the poor helix propagation parameter value of Val [30]. This suggests that the Pro-box motif will not specially contribute to protein stability but to the specificity of its fold.

The two primary capping motifs found at helix C-termini are the Schellman and the α_L motifs [31–33]. The Schellman motif is defined by a doubly hydrogen-bonded pattern between backbone partners, consisting of hydrogen bonds between

the amide NH at C″ and the carbonyl CO at C3 and between the amide NH at C′ and the carbonyl CO at C2, respectively. The associated hydrophobic interaction is between C3 and C″. In a Schellman motif, polar residues are highly favored at the C1 position and the C′ residue is typically glycine.

If C″ is polar, the alternative α_L motif is observed. The α_L motif is defined by a hydrogen bond between the amide NH at C′ and the carbonyl CO at C3. As in the Schellman motif, the C′ residue is typically glycine, which adopts a positive value of ϕ dihedral angle. However, the hydrophobic interaction in an α_L is heterogeneous, occurring between C3 and any of several residues external to the helix ($C^{3\prime}$, $C^{4\prime}$, or $C^{5\prime}$) [32].

A statistical analysis of the protein crystal structures database detected another possible C-cap local motif, designated Pro C-capping [34]. Certain combinations of X-Pro pairs, in which residue X is the C-cap and the Pro is at position C′, are more abundant than expected. The aliphatic (Ile, Val, and Leu) and aromatic residues (Phe, Tyr, and Trp), together with Asn, His, and Cys are the most favored residues accompanying Pro at position C′.

A notable difference between the N- and C-terminal motifs is that at the N-terminus, helix geometry favors side chain-to-backbone hydrogen bonding and selects for compatible polar residues [14, 19]. Accordingly, the N-terminus promotes selectivity in all polar positions, especially N-cap and N3 in the capping box. In contrast, at the C-terminus, side chain-to-backbone hydrogen bonding is disfavored. Backbone hydrogen bonds are satisfied instead by posthelical backbone groups. The C-terminus need only select for C′ residues that can adopt positive values of the backbone dihedral angle ϕ, most notably Gly [32].

9.2.2 Metal Binding

In general, the stabilization of folded forms can be achieved by reducing the entropy by cross-linking, such as via metal ions. Another way to stabilize helix conformations, especially in short peptides, is to introduce an artificial nucleation site composed of a few residues fixed in a helical conformation. For example, the calcium-binding loop from EF-hand proteins saturated with a lanthanide ion promotes a rigid short helical conformation at its C-terminus region [35].

Metal ions play a key structural and functional role in many proteins. There is therefore interest in using peptide models containing metal complexes. In stabilizing proteins, the rule of thumb in metal–ligand binding is that ''hard metals'' prefer ''hard ligands''. For example Ca and Mg prefer ligands with oxygen as the coordinating atoms (Asp, Glu) [36]. In contrast, soft metals, such as Cu and Zn, bind mostly to His, Cys, and Trp ligands and sometimes indirectly via water molecules [37].

In studies of helical peptide models, soft ligands have been mostly used. In the presence of Cd ions, a synthetic peptide containing Cys-His ligands $i, i+4$ apart at the C-terminal region promoted helicity from 54% to 90%. The helicity of a sim-

ilar peptide containing His-His ligands increased by up to 90% as a result of Cu and Zn binding [38]. The addition of a *cis*-Ru(III) ion to a 6-mer peptide, Ac-AHAAAHA-NH_2, changed the peptide conformation from random coil to 37% helix [39]. An 11-residue peptide was converted from random coil to 80% helix content by the addition of Cd ions, although the ligands used were not natural amino acids but aminodiacetic acids [40]. As(III) stabilizes helices when bound to Cys side chains spaced $i, i+4$ by -0.7 to -1.0 kcal mol^{-1} [41].

9.2.3 The 3_{10}-Helix

3_{10}-Helices are stabilized by $i, i+3$ hydrogen bonds instead of the $i, i+4$ bonds found in α-helices, making the cylinder of the 3_{10}-helix narrower than α and the hydrogen bonds nonlinear. About 3–4% of residues in crystal structures are in 3_{10}-helices [4, 42], making the 3_{10}-helix the fourth most common type of secondary structure in proteins after α-helices, β-sheets, and reverse turns. Most 3_{10}-helices are short, only 3 or 4 residues long, compared with a mean of 10 residues in α-helices [4]. 3_{10}-Helices are commonly found as N- or C-terminal extensions to an α-helix [4, 43, 44]: Strong amino acid preferences have been observed for different locations within the interiors [42] and N- and C-caps [14] of 3_{10}-helices in crystal structures.

The 3_{10}-helix is being recognized as of increasing importance in isolated peptides and as a possible intermediate in α-helix formation [45, 46]. It has been proposed that peptides made of the standard 20 L-amino acids can form 3_{10}-helices [47], or at least populate a significant amount of 3_{10}-helix at their N- and C-termini. The fraction of 3_{10}-helix present in a helical peptide is strongly sequence dependent [48, 49]. 3_{10}-helix formation can be induced by the introduction of a $C_{\alpha,\alpha}$-disubstituted α-amino acid, of which α-aminoisobutyric acid (AIB) is the prototype. For most amino acids, the α-helical geometry ($\phi = -57^\circ$, $\psi = -70^\circ$) is of lower energy than the 3_{10} geometry ($\phi = -49^\circ$, $\psi = -26^\circ$). There is no disallowed region between the α and 3_{10} conformations in the Ramachandran plot, and a peptide can therefore be gradually transformed from one helix to the other [50].

9.2.4 The π-Helix

In contrast to the widely occurring α- and 3_{10}-helices, the π-helix is extremely rare. The π-helix is unfavorable for three reasons: its dihedral angles are energetically unfavorable relative to the α-helix [51, 52], its three-dimensional structure has a 1 Å hole down the center that is too narrow for access by a water molecule, resulting in the loss of van der Waals interactions, and a higher number of residues (four) must be correctly oriented before the first $i, i+5$ hydrogen bond is formed, making helix initiation more entropically unfavorable than for α- or 3_{10}-helices. The π-helix may be of more than theoretical interest [53–57].

9.3 Design of Peptide Helices

The first protein crystal structures showed an abundance of α-helices, leading to speculation whether peptide fragments of the helical sequences could be stable in isolation. Since isolated helices lack hydrophobic cores, this question could be rephrased to ask whether the amide–amide hydrogen bond is strong enough to oppose the loss of conformational entropy arising from restricting the peptide into a helical structure [58]. Early estimates of these terms suggested that hydrogen bonds were not strong enough and this was confirmed by peptide studies of helices from myoglobin [59] and staphylococcal nuclease [60], which found no helix formation. Early estimates of helix/coil parameters from a host–guest system (see Section 9.3.1) suggested that polypeptides would need to be hundreds of residues long to form stable helices. Hence, the earliest work on peptide helices was on long homopolymers of Glu or Lys, which show coil-to-helix transitions on changing the pH from charged to neutral. The neutral polypeptides are metastable and prone to aggregation, ultimately to β-sheet amyloid [61].

A conflicting result was found by Brown and Klee in 1971 [62], who reported that the C-peptide of ribonuclease A, which contains the first 13 residues of the protein and which forms a helix in the protein, was helical at 0 °C. This observation was not followed up for 10 years until extensive work on the sequence features responsible for helix formation in this peptide, and in the larger S-peptide, was performed by Baldwin and coworkers [63–73], while NMR studies by Rico and coworkers precisely defined the helical structure [74–82]. Some important features responsible for the helicity of the C-peptide that emerged from this work included an $i, i+4$ Phe-His interaction, an $i, i+3$ Glu-His salt bridge, an unusual $i, i+8$ Glu-Arg salt bridge that spanned two turns of the helix and a helix termination signal at Met. The stabilizing effects of salt bridges were inferred from pH titrations and circular dichroism (CD), where a decrease in helicity was seen when a residue participating in a salt bridge was neutralized. Quantification of these features in terms of a free energy was not possible at that time, as helix/coil theory that included side-chain interactions and termination signals (caps) had not been developed.

Perhaps the most interesting result from the C- and S-peptide work was the importance of Ala. The replacement of interior helical residues with Ala was stabilizing, indicating that a major reason why this helix was folded in isolation was the presence of three successive alanines from positions 4–6. This led to the successful design of isolated, monomeric helical peptides in aqueous solution, first containing several salt bridges and a high alanine content, based on $(EAAAK)_n$ [83–84] and then a simple sequence with a high alanine content solubilized by several lysines [85]. These "AK peptides" are based on the sequence $(AAKAA)_n$, where n is typically 2–5. The Lys side chains are spaced $i, i+5$ so they are on opposite faces of the helix, giving no charge repulsion and may be substituted with Arg or Gln to give a neutral peptide. Hundreds of AK peptides have been studied, giving most of the results on helix stability in peptides (see below). The Alanines in the

$(EAAAK)_n$ type peptides may be removed entirely; E_4K_4 peptides, with sequences based on $(EEEEKKKK)_n$ or EAK patterns are also helical, stabilized by large numbers of salt bridges [8, 86–88].

9.3.1 Host–Guest Studies

Extensive work from the Scheraga group has obtained helix/coil parameters using a host–guest method. Long random copolymers were synthesized of a water-soluble, nonionic guest (poly[N^5-(3-hydroxypropyl)-L-glutamine] (PHPG) or poly[N^5-(4-hydroxybutyl)-L-glutamine] (PHBG)), together with a low (10–50%) content of the guest residue. Using the s and σ Zimm-Bragg helix/coil parameters (see below) for the host homopolymer, it was possible to calculate those for the guest using helix/coil theory as a function of temperature. The results from the host–guest work are in disagreement with most of those from short peptides of fixed sequence (see below).

9.3.2 Helix Lengths

Helix formation in peptides is cooperative, with a nucleation penalty. Helix stability therefore tends to increase with length, in homopolymers at least. As the length of a homopolymer increases, the mean fraction helix will level off below 100% as long helices tend to break in two. In heteropolymers, observed lengths are highly sequence dependent. As helices are at best marginally stable in monomeric peptides in aqueous solution, they are readily terminated by the introduction of a strong capping residue or a residue with a low intrinsic helical preference.

The length distribution of helices in peptides is very different to proteins [4]. Most helices are short, with 5–14 residues most common. There is a general trend for a decrease in frequency as the length increases beyond 13 residues. Helix lengths longer than 25 are rare. This is a consequence of the organization of proteins into domains of similar size, rather than showing different rules for stability; helices do not extend beyond the boundaries of the domain and so terminate. There is also a preference to have close to an integral number of turns so that their N- and C-caps are on the same side of the helix [89].

9.3.3 The Helix Dipole

The secondary amide group in a protein backbone is polarized with the oxygen negatively charged and hydrogen positively charged. In a helix the amides are all oriented in the same direction with the positive hydrogens pointing to the N-terminus and negative oxygens pointing to the C-terminus. This can be regarded as giving a positive charge at the helix N-terminus and a negative charge at the helix C-terminus [90–92]. In general, therefore, negatively charged groups are stabi-

lizing at the N-terminus and positive at the C-terminus, as shown by numerous titrations that measure helix content as a function of pH and amino acid preferences for helix terminal positions. An alternative interpretation of these results is that favored side chains are those that can make hydrogen bonds to the free amide NH groups at N1, N2, and N3 or free CO groups at C1, C2, and C3 [93]. Charged groups can form stronger hydrogen bonds than neutral groups, thus providing an alternative rationalization of the pH titration results. These hypotheses are not mutually exclusive, as a charged side chain can also function as a hydrogen bond acceptor or donor. A free energy simulation of Tidor [94] suggested that helix-stabilizing interactions, as a result of a Tyr → Asp substitution at an N-cap site, arose from hydrogen-bonding interactions from its direct hydrogen-bonding partners, and from more distant electrostatic interactions with groups within the first two turns of the helix.

Measurements of the amino acid preferences for the N-cap, N1, N2, and N3 positions in the helix allow a comparison to be made of the relative importance of helix-dipole and hydrogen-bonding interactions [29, 95–97]. The helix-dipole model implies that the side chains most favored at the helix N-terminus are those with a negative charge while positive charges are disfavored. A pure hydrogen-bonding model implies that favored side chains are those that can make hydrogen bonds to the free amide NH groups at N1, N2, and N3. In general, the N-cap results suggest that hydrogen bonding is more important than helix-dipole interactions; the best N-caps are Asn, Asp, Ser, and Thr [29], which can accept hydrogen bonds from the N2 and N3 NH groups [14]. Glu has only a moderate N-cap preference despite its negative charge. In contrast, N1, N2, and N3 results suggest that helix-dipole interactions are more important. The contrasting results between the different helix N-terminal positions can be rationalized by considering the geometry of the hydrogen bonds. N-cap hydrogen bonds are close to linear [14] and so are strong, while N1 and N2 hydrogen bonds are close to 90° [19], making them much weaker. Helix-dipole effects are likely to be present at all sites, as also shown by every pH titration where a more negative side chain is favored over a more positive side chain, but this can be overwhelmed by strong hydrogen bonds, as at the N-cap. In the absence of strong hydrogen bonds, helix-dipole effects dominate. Hydrogen bonds can therefore make a substantial contribution to protein stability, but only if their geometry is close to linear (as it is for backbone to backbone hydrogen bonds in α-helices and β-sheets).

9.3.4 Acetylation and Amidation

A simple, yet effective, way to increase the helicity of a peptide is to acetylate its N-terminus [22, 98]. This is readily done with acetic anhydride/pyridine, after completion of a peptide synthesis, but before cleavage of the peptide from the resin and deprotection of the side chains. Acetylation removes the positive charge that is present at the helix terminus at low or neutral pH; this would interact unfavor-

ably with the positive helix dipole and free N-terminal NH groups. The extra CO group from the acetyl group can form an additional hydrogen bond to the NH group, putting the acetyl at the N-cap position. This has a strong stabilizing effect by approximately 1.0 kcal mol^{-1} compared with alanine [29, 30, 99]. The acetyl group is one of the best N-caps. We found only Asn and Asp to be more stabilizing [29].

Amidation of the peptide C-terminus is achieved by using different types of resin in solid-phase peptide synthesis, resulting in the replacement of COO^- with $CONH_2$. This is similar structurally to acetylation: the helix is extended by one hydrogen bond and an unfavorable charge–charge repulsion with the helix dipole is removed. The energetic benefit of amidation is rather smaller, however, with the amide group being no better than Ala and in the middle if the C-cap residues are ranked in order of stabilization effect [29]. As most helical peptides studied to date are both acetylated and amidated, and acetylation is more stabilizing than amidation, the helicity of peptides is generally skewed so that residues near the N-terminus are more helical than those near the C-terminus. Acetylation and amidation are often also beneficial in removing a pH titration that can obscure other effects.

9.3.5
Side Chain Spacings

Side chains in the helix are spaced at 3.6 residues per turn of the helix. Side chains spaced at $i, i+3$, $i, i+4$, and $i, i+7$ are therefore close in space and interactions between them can affect helix stability. Spacings of $i, i+2$, $i, i+5$, and $i, i+6$ place the side chain pairs on opposite faces of the helix, avoiding any interaction. Care must therefore be taken to avoid unwanted interactions when designing helices. For example, we studied these peptides to determine the energetics of the Phe-Met interaction [100]:

F7M12 Ac-YGAAKAFAAKAMAAKAA-NH_2
F8M12 Ac-YGAAKAAFAKAMAAKAA-NH_2

The control peptide F7M12 has Phe and Met spaced $i, i+5$ where they cannot interact; F8M12 moves the Phe one place towards the C-terminus so that Phe and Met are spaced $i, i+4$ where they can form a noncovalent interaction. The increase in helix content was used to derive the Phe-Met interaction energy. These sequences are not ideal, however. F7M12 contains a Phe-Lys $i, i+3$ interaction that is replaced by a Lys-Phe $i, i+3$ interaction in F8M12. If either of these are stabilizing or nonstabilizing the Phe-Met $i, i+4$ energy will be in error. While this problem is likely to be small, in this case at least, our more recent designs try to minimize such potential problems. For example, the following peptides, designed to measure Ile-Lys $i, i+4$ energies, do not introduce or remove an unwanted $i, i+3$ spacing [101]:

IKc Ac-AK<u>I</u>AAAA<u>KI</u>AAAA<u>K</u>AKAGY-NH_2
IKi Ac-AKA<u>I</u>AAA<u>K</u>A<u>I</u>AAA<u>K</u>AKAGY-NH_2

9.3.6 Solubility

Lack of peptide solubility can be a problem. Peptides designed to be helices can even become highly insoluble amyloid with a high β-sheet content. We have occasionally found that alanine-based peptides designed to be helical instead form amyloid, though this may only take place after several years storage in solution. The measurement of interactions in a helix will be compromised by peptide oligomerization so it is generally essential to check that the peptides are monomeric. This can be done rigorously by sedimentation equilibrium, which determines the oligomeric state of a molecule in solution. This is difficult, however, with the short peptides often used, as their molecular weights are at the lower limit for this technique. A simpler method is to check a spectroscopic technique that depends on peptide structure, most obviously CD, as a function of concentration. If the signal depends linearly on peptide concentration across a large range, including that used to study the peptide structure, it is safe to assume that the peptide is monomeric. For example, if helicity measurements are made at 10 μM, CD spectra can be acquired from 5 μM to 100 μM. An oligomer that does not change state, such as a coiled-coil, across the concentration range cannot be excluded, however. Light scattering can detect aggregation. A monomeric peptide should have a flat baseline in a UV spectrum outside the range of any chromophores in the peptide. In stock solutions of a peptide with a single tyrosine isolated from the helix region by Gly should have $A_{300}/A_{275} < 0.02$ and $A_{250} < A_{275} < 0.2$ [102].

Consideration of solubility is essential when designing helical peptides. While Ala has the highest helix propensity and would provide an ideal theoretical background for substitutions, poly(Ala) is insoluble. Solubility can be achieved most easily by including polar side chains spaced $i, i + 5$ in the sequence where they cannot interact. Lys, Arg, and Gln are used most often for this purpose. Gln may be preferred if unwanted interactions with charged Lys or Arg may be a problem, but some AQ peptides lack sufficient solubility and AQ peptides are less helical. We have found that it is not easy to predict peptide solubility. For example, 20 peptides with sequence Ac-XAAAAQAAAAQAAGY-NH_2, where X is all the amino acids encoded by the genetic code, were all soluble [95]. However, when the homologous peptide Ac-AAAAAAQAAAAQAAAAQGY-NH_2 was synthesized to study the N2 position it tended to aggregate. The Gln side chains were therefore replaced with Lys, giving no further problems [96].

The spacing of side chains in the helix is best visualized with a helical wheel, to ensure that the designed helix does not have a nonpolar face that may lead to dimerization. The following web pages provide useful resources for this:

http://www.site.uottawa.ca/~turcotte/resources/HelixWheel/
http://marqusee9.berkeley.edu/kael/helical.htm

9.3.7
Concentration Determination

An accurate measurement of helix content depends on an accurate spectroscopic measurement and, equally importantly, peptide concentration. This is usually achieved by including a Tyr side chain at one end of the peptide. The extinction coefficient of Tyr at 275 nm is 1450 M^{-1} cm^{-1} [103]. If Trp is present, measurements at 281 nm can be used where the extinction coefficient of Trp is 5690 M^{-1} cm^{-1} and Tyr 1250 M^{-1} cm^{-1} [104]. Phe absorbance is negligible at this wavelength. These UV absorbances are ideally made in 6 M GuHCl, pH 7.0, 25 °C, though we have found very little variation with solvent so measurements in water are identical within error. The main source of error is in pipetting small volumes; this is typically around 2%. Pipetting larger volumes with well-maintained fixed volume pipettors can help minimize this error, which may well be the largest when measuring a percentage helix content by CD.

Though the inclusion of aromatic residues is required for concentration determination, this can have the unwanted side effect of perturbing a CD spectrum, leading to an inaccurate measure of helix content. A simple solution to this is to separate the terminal Tyr from the rest of the sequence by one or more Gly residues [105]. If the aromatic residues must be included within the helical region, the CD spectrum should be corrected to remove this perturbation (see later).

9.3.8
Design of Peptides to Measure Helix Parameters

Numerous peptides have been studied to measure the forces responsible for helix formation (see below). In general, one or more peptides are synthesized that contain the interaction of interest, while all other terms that can contribute to helix stability are known. The helix content of the peptide is measured and the statistical weight of the interaction is varied until predictions from helix/coil theory match experiment. The weight of the interaction (and hence its free energy, as $-RT$ ln(weight)) is then known. In practice it is wise to also synthesize a control peptide that lacks the interaction, but is otherwise very similar. The helix content of this peptide should be predictable from helix/coil theory using known parameters. For example, Table 9.2 gives sequences of control and interaction peptides used to measure Phe-Lys $i, i+4$ side-chain interaction energies [106]. The FK control peptide has no $i, i+4$ side-chain interactions and all the helix/coil weights for these residues are known. The helicity predicted by SCINT2 [30] for this peptide is in close agreement with experiment. This is an important confirmation that the helix/coil model and the parameters used are accurate. The discrepancy between prediction and experiment for the FK interaction peptide is because this peptide contains two Phe-Lys $i, i+4$ side-chain interactions whose weights are assumed to be 1 (i.e., $\Delta G = 0$). If the Phe-Lys weight is changed to 1.3, the prediction agrees with experiment. Hence ΔG (Phe-Lys) $= -RT \ln 1.3 = -0.14$ kcal mol^{-1}.

It is important to minimize the error in determining helix/coil parameters. Errors can be calculated by assuming an error in measurement of % helix ($\pm$3% is

Tab. 9.2. Peptides designed to measure the energetics of the Phe-Lys interaction.

Peptide name	*Sequence*	*Experimental helicity*	*Predicted nelicity (no side-chain interaction)*	*Phe-Lys weight to fit experiment*	*ΔG (Phe-Lys) kcal mol^{-1}*
FK control	Ac-AAAKFAAAAKFAAAAKAKAGY-NH_2	35.4%	35.6	N/A	N/A
FK interaction	Ac-AAAKAFAAAKAFAAAKAKAGY-NH_2	41.1%	34.6	1.3	−0.14

reasonable) and refitting the results across this experimental error range. For the case above, ΔG (Phe-Lys) was calculated for 38.1% and 44.1% helix, giving a range of -0.05 to -0.18 kcal mol^{-1}. This is a remarkably small error range, resulting from the high sensitivity of helix content to a small change in helix stability. This sensitivity can be maximized by including multiple identical interactions; here the FK interaction peptide has two Phe-Lys interactions, for example. The helix contents of the control and interaction peptides should be close to 50%. This may be difficult to achieve if the residues being used have low helix preferences. The best way to maximize sensitivity is to calculate it in advance using possible sequences, helix/coil theory, an error of $\pm 3\%$ and guessing a sensible value for the interaction energy. The interaction of interest can be placed at various positions in the peptide, its length can be changed by adding further AAKAA sequences, terminal residues such as a Tyr can be moved, and solubilizing side chains can be changed. Peptide design can be lengthy, considering sensitivity and solubility, but is a valuable process. The complex nature of the helix/coil equilibrium with frayed conformations highly populated means that considerable variations can be seen for apparently small changes, such as moving an interaction towards one terminus of a sequence.

9.3.9
Helix Templates

A major penalty to helix formation is the loss of entropy arising from the requirement to fix three consecutive residues to form the first hydrogen bond of the helix. Following this nucleation, propagation is much more favored as only a single residue need be restricted to form each additional hydrogen bond. A way to avoid this barrier is to synthesize a template molecule that facilitates helix initiation, by fixing hydrogen bond acceptors or donors in the correct orientation for a peptide to bond in a helical geometry. The ideal template nucleates a helix with an identical geometry to a real helix. Kemp's group applied this strategy and synthesized a proline-like template that nucleated helices when a peptide chain was covalently attached to a carboxyl group (Figure 9.1a) [107–111]. The template is in an equilibrium between *cis* and *trans* isomers of the proline-like part of the molecule. Only the *trans* isomer can bond to the helix so helix content is determined by measuring the *cis*/*trans* ratio by NMR. Bartlett et al. reported on a hexahydroindol-4-one template (Figure 9.1b) [112] that induced 49–77% helicity at 0 °C, depending on the method of determination, in an appended hexameric peptide. Several other templates were less successful and could only induce helicity in organic solvents [113–115]. Their syntheses are often lengthy and difficult, partly due to the challenging requirement of orienting several dipoles to act as hydrogen bond acceptors or donors.

9.3.10
Design of 3_{10}-Helices

Peptides can be induced to form 3_{10}-helix by the incorporation of a significant amount of disubstituted C_α amino acids, of which the simplest is α-aminoisobuty-

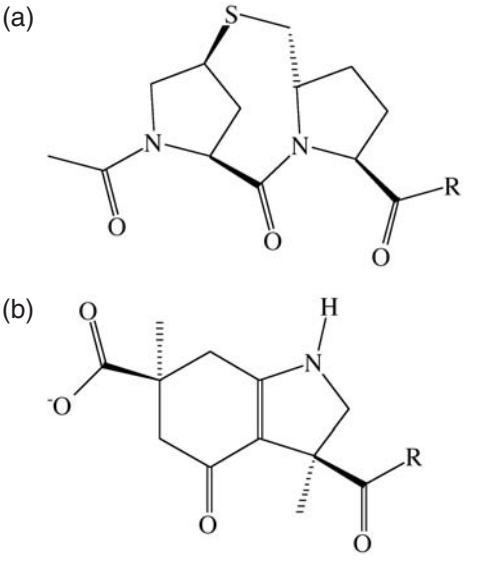

Fig. 9.1. Helix templates. a) Kemp, b) Bartlett.

ric acid (Aib) [116–119]. The presence of steric interactions from the two methyl groups on the α-carbon in AIB results in the 3_{10} geometry being energetically favored over the α. Peptides rich in $C_{\alpha,\alpha}$-disubstituted α-amino acids are readily crystallized and many of their structures have been solved (reviewed in Refs [50] and [120]). Aib is conformationally restricted so that shorter Aib-based helices are more stable than Ala-based α-helices [121]. Many examples of helix stabilization or 3_{10}-helix formation by Aib have been reported. The $\alpha/3_{10}$ equilibrium has been studied in peptides. Yokum et al. [122] synthesized a peptide composed of $C_{\alpha,\alpha}$-disubstituted α-amino acids that forms mixed 3_{10}-/α-helices in mixed aqueous/organic solvents. Millhauser and coworkers have studied the $3_{10}/\alpha$ equilibrium in peptides by electron spin resonance (ESR) and nuclear magnetic resonance (NMR) [47, 49, 123, 124] and argued that mixed 3_{10}-/α-helices are common in polyalanine-based helices. Yoder et al. [125] studied a series of L-(αMe)-Val homopolymers and showed that their peptides can form coil, 3_{10}-helix, or α-helix depending on concentration, peptide length, and solvent. Kennedy et al. [126] used Fourier transform infrared (FTIR) spectroscopy to monitor 3_{10}- and α-helix formation in poly(Aib)-based peptides. Hungerford et al. [127] synthesized peptides that showed an α to 3_{10} transition upon heating. 3_{10}-Helices have also been proposed as thermodynamic intermediates where helical peptides of moderate stability exist as a mixture of α- and 3_{10}-structures [45, 128].

Guidelines for the inclusion of the 20 natural amino acids in 3_{10}-helices can be taken from their propensities in proteins, both at interior positions [42] and at N-caps [14]. These are similar, but not identical to α preferences. Side-chain interactions in the 3_{10}-helix are spaced $i, i+3$, with $i, i+4$ on opposite sides of the helix.

This offers scope to preferentially stabilize 3_{10} over α, by including stabilizing $i, i+3$ interactions and $i, i+3$ repulsions. As the 3_{10}- and α-helix structures are so similar, with only a small change in backbone dihedral angle, peptides designed to form 3_{10}-helix are likely to form a mixture of 3_{10} and α, with a central α segment and 3_{10} at the helix termini common. This complex equilibrium, and the spectroscopic similarity of α and 3_{10} makes the analysis of these peptides difficult.

9.3.11 Design of π-helices

To our knowledge, no peptide has yet been made that forms π-helix. There are 4.4 side chains per turn of the π-helix, so $i, i+5$ interactions may weakly stabilize π-helix over α. Given the other strongly destabilizing features of the π-helix, however, we doubt whether this effect will ever be strong enough. We expect that no peptide composed of the 20 natural amino acids will ever fold to a monomeric π-helix in aqueous solution. We are willing to back up this prediction, but in view of the outcome of the Paracelsus challenge [129, 130], we are taking the advice of George Rose [131] and offering only an ''I Met the π-Helix Challenge'' T-shirt as a prize.

9.4 Helix Coil Theory

Peptides that form helices in solution do not show a simple two-state equilibrium between a fully folded and fully unfolded structure. Instead they form a complex mixture of all helix, all coil or, most frequently, central helices with frayed coil ends. In order to interpret experiments on helical peptides and make theoretical predictions on helices it is therefore essential to use a helix/coil theory that considers every possible location of a helix within a sequence. The first wave of work on helix/coil theory was in the late 1950s and early 1960s and this has been reviewed in detail by Poland and Scheraga [132]. In 1992, Qian and Schellman [133] reviewed current understanding of helix/coil theories. Our review covered the extensive development of helix/coil theory since this date [134].

The simplest way to analyze the helix/coil equilibrium, still occasionally seen, is the two-state model where the equilibrium is assumed to be between a 100% helix conformation and 100% coil. This is incorrect and its use gives serious errors. This is because helical peptides are generally most often found in partly helical conformations, often with a central helix and frayed, disordered ends, rather than in the fully folded or fully unfolded states.

9.4.1 Zimm-Bragg Model

The two major types of helix/coil model are (i) those that count hydrogen bonds, principally Zimm-Bragg (ZB) [135] and (ii) those that consider residue conforma-

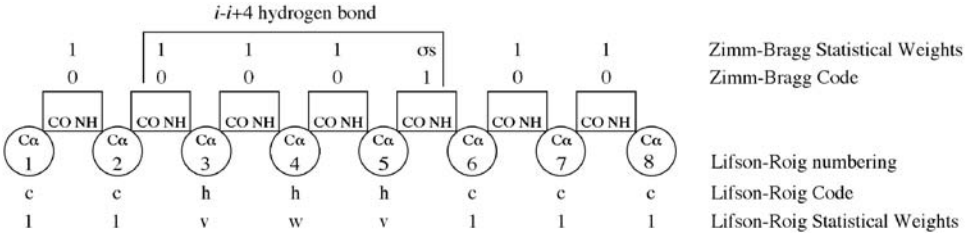

Fig. 9.2. Zimm-Bragg and Lifson-Roig codes and weights for the α-helix.

tions, principally Lifson-Roig [136]. In the ZB theory the units being considered are peptide groups and they are classified on the basis of whether their NH groups participate in hydrogen bonds within the helix. The ZB coding is shown in Figure 9.2. A unit is given a code of 1 (e.g., peptide unit 5 in Figure 9.2) if its NH group forms a hydrogen bond and 0 otherwise. The first hydrogen-bonded unit proceeding from the N-terminus has a statistical weight of σs, successive hydrogen bonded units have weights of s and nonhydrogen-bonded units have weights of 1. The s-value is a propagation parameter and σ is an initiation parameter. The most fundamental feature of the thermodynamics of the helix/coil transition is that the initiation of a new helix is much more difficult than the propagation of an existing helix. This is because three residues need to be fixed in a helical geometry to form the first hydrogen bond while adding an additional hydrogen bond to an existing helix require that only one residue is fixed. These properties are thus captured in the ZB model by having σ smaller than s. The statistical weight of a homopolymeric helix of a N hydrogen bonds is σs^{N-1}. The cost of initiation, σ, is thus paid only once for each helix while extending the helix simply multiplies its weight by one additional s-value for each extra hydrogen bond.

9.4.2 Lifson-Roig Model

In the LR model each residue is assigned a conformation of helix (h) or coil (c), depending on whether it has helical ϕ, ψ angles. Every conformation of a peptide of N residues can therefore be written as a string of N c's or h's, giving 2^N conformations in total. Residues are assigned statistical weights depending on their conformations and the conformations of surrounding residues. A residue in an h conformation with an h on either side has a weight of w. This can be thought of as an equilibrium constant between the helix interior and the coil. Coil residues are used as a reference and have a weight of 1. In order to form an $i, i+4$ hydrogen bond in a helix three successive residues need to be fixed in a helical conformation. M consecutive helical residues will therefore have $M-2$ hydrogen bonds. The two residues at the helix termini (i.e., those in the center of chh or hhc conformations) are therefore assigned weights of v (Figure 9.2). The ratio of w to v gives the approximately the effect of hydrogen bonding (1.7:0.036 for Ala [30]

or $-RT \ln(1.7/0.036) = -2.1$ kcal mol^{-1}). A helical homopolymer segment of M residues has a weight of $v^2 w^{M-2}$ and a population in the equilibrium of $v^2 w^{M-2}$ divided by the sum of the weights of every conformation (i.e., the partition function). In this way the population of every conformation is calculated and all properties of the helix/coil equilibrium evaluated. The LR model is easier to handle conceptually for heteropolymers since the w and v parameters are assigned to individual residues. The substitution of one amino acid at a certain position thus changes the w- and v-values at that position. In the ZB model the initiation parameter σ is associated with several residues and s with a peptide group, rather than a residue. It is therefore easier to use the LR model when making substitutions. Indeed, most recent work has been based on this model.

A further difference is that the ZB model assigns weights of zero to all conformations that contain a chc or chhc sequence. This excludes a very large number of conformations that contain a residue with helical ϕ, ψ angles but with no hydrogen bond. In LR theory, these are all considered. The ZB and LR weights are related by the following formulae [133]: $s = w/(1 + v)$; $\sigma = v^2/(1 + v)^4$.

The complete helix/coil equilibrium is handled by determining the statistical weight for every possible conformation that contains a helix plus a reference weight of 1 for the coil conformation. Each conformation considered in the helix/coil equilibrium is given a statistical weight. This indicates the stability of that conformation, with the higher the weight, the more probable the conformation. Weights are defined relative to the all coil conformation, which is given a weight of 1. The statistical weight of a conformation can thus be regarded as an equilibrium constant relative to the coil; a weight >1 indicates the conformation is more stable than coil, <1 means less stable and 1 means equally stable. The population of each conformation is given by the statistical weight of that conformation divided by the sum of the statistical weights for every conformation (i.e., the partition function). Thus the greater the statistical weight, the more stable the conformation.

The key to using helix/coil theory is the partition function. All the properties of a system at equilibrium are contained within the partition function, which makes it very valuable. Partition functions are extremely powerful concepts in statistical thermodynamics since they include all properties of an equilibrium. Any property of the equilibrium can be extracted from the partition function by applying the appropriate mathematical function. This is analogous to quantum mechanics where any property can be determined from a system by applying an operator function to a wavefunction. In this case the properties could be the mean number of hydrogen bonds, the mean helix length, the probability that each residue is within a helix etc. In particular, the mean number of residues with a weight x is given by $\partial \ln Z/\partial \ln x$. Circular dichroism is commonly used to give the mean helix content of a helical peptide, namely the fraction of residues that have a weight of w. LR-based models can thus be related to experimental data by equating the measured mean helix content to $(\partial \ln Z/\partial \ln x)/N$, where N is the number of residues in the peptide. Statistical weights can be regarded as equilibrium constants for the equilibrium between coil and the structure (as the reference coil weight is defined as 1). They can therefore be converted to free energies as $-RT \ln$(weight).

Equations for partition functions are determined as follows: Write a table of the conformations and assigned statistical weights for residues. For the Lifson-Roig model, the weights of a residue depend on its conformation and the weights of its two neighboring residues as follows:

Conformation	*Weight of central residue in triplet*
ccc	1
cch	1
chc	v
chh	v
hcc	1
hch	1
hhc	v
hhh	w

The same information is rewritten in the form of a matrix (M):

$$\mathrm{M} = \begin{array}{c} \\ \mathrm{h\bar{h}} \\ \mathrm{h\bar{c}} \\ \mathrm{c\bar{h}} \\ \mathrm{c\bar{c}} \end{array} \begin{array}{c} \begin{array}{cccc} \bar{\mathrm{h}}\mathrm{h} & \bar{\mathrm{h}}\mathrm{c} & \bar{\mathrm{c}}\mathrm{h} & \bar{\mathrm{c}}\mathrm{c} \end{array} \\ \begin{pmatrix} w & v & 0 & 0 \\ 0 & 0 & 1 & 1 \\ v & v & 0 & 0 \\ 0 & 0 & 1 & 1 \end{pmatrix} \end{array}$$

For each triplet, the state of the left-most residue is shown at the start of each row in the matrix. The state of the right-most residue in each triplet is shown at the end of the top of each column. The state of the center residue of each triplet is shown as the barred residue in both the rows and columns. When the states of the center residues differ (i.e., one is c while the other is h), the entry in the matrix is zero. Otherwise, the matrix gives the weight, taken from the table. This apparently simple change in presentation now (amazingly) allows the generation of the partition function (Z) for a polypeptide of N residues as:

$$\mathrm{Z} = \begin{pmatrix} 0 & 0 & 1 & 1 \end{pmatrix} \mathrm{M}^N \begin{pmatrix} 0 \\ 1 \\ 1 \\ 1 \end{pmatrix}$$

The end vectors are present to ensure that the first and last residues in the peptide cannot have a w-weighting. A w-weighting indicates that the residue is between two residues that hydrogen bond to each other and this is impossible for terminal residues. Further extensions to helix/coil theory are dealt with in the same way, by defining residue weight assignments, rewriting as a matrix and determining end vectors. The work may be made easier by combining any identical columns. For

example, the Lifson-Roig matrix above has identical third and fourth columns so can be simplified to a 3×3 matrix:

$$\mathrm{M} = \begin{array}{c} \\ \mathrm{h}\bar{\mathrm{h}} \\ \mathrm{h}\bar{\mathrm{c}} \\ \mathrm{c}(\mathrm{h} \cup \mathrm{c}) \end{array} \begin{array}{c} \begin{array}{ccc} \bar{\mathrm{h}}\mathrm{h} & \bar{\mathrm{h}}\mathrm{c} & \bar{\mathrm{c}}(\mathrm{h} \cup \mathrm{c}) \end{array} \\ \begin{pmatrix} w & v & 0 \\ 0 & 0 & 1 \\ v & v & 1 \end{pmatrix} \end{array}$$

Here, $\mathrm{h} \cup \mathrm{c}$ shows the residues being combined. The matrix entries for the combined positions are the entries for the noncombined entries, with zero being discounted if combined with a nonzero entry. New end vectors are now required, as their lengths must be the same as the order of the square matrix.

9.4.3
The Unfolded State and Polyproline II Helix

The treatment of peptide conformations is based on Flory's isolated-pair hypothesis [137]. This states that while ϕ and ψ for a residue are strongly interdependent, giving preferred areas in a Ramachandran plot, each ϕ, ψ pair is independent of the ϕ, ψ angles of its neighbors. Pappu et al. examined the isolated-pair hypothesis in detail by exhaustively enumerating the conformations of poly(Ala) chains [138]. Each residue was considered to populate 14 mesostates, defined by ranges of ϕ, ψ values. By considering all 14^N mesostate strings, all conformations were considered for up to seven alanines. The number of allowed conformations was found to be considerably fewer than the maximum, thus showing that the isolated-pair hypothesis is invalid. The chains mostly populate extended or helical conformations as many partly helical conformations are sterically disallowed. Such effects are not included in helix/coil theories, thus presenting a considerable challenge for the future. Helix/coil theories assign the same weight (1) to every coil residue; steric exclusion means that these should vary and be lower than 1 in many cases.

The polyproline II helix may well be an important conformation for unfolded proteins [139–148]. In particular, denatured alanine-rich peptides may form polyproline II helix [143, 148, 149]. It may therefore be valid to consider residues in helical peptides to be in three possible states (helix, coil, or polyproline II), rather than two (helix or coil). No current helix/coil model takes this into account. A scale of amino acid preferences for the polyproline II helix has recently been published [150].

9.4.4
Single Sequence Approximation

Since helix nucleation is difficult, conformations with multiple helical segments are expected to be rare in short peptides. In the one-, or single-, helical sequence approximation, peptide conformations containing more than one helical segment are assumed not to be populated and are excluded from the partition function

(i.e., assigned statistical weights of zero). As peptide length increases, the approximation is no longer valid since multiple helical segments can be long enough to overcome the initiation penalty. The single sequence approximation will also break down when a sequence with a high preference for a helix terminus is within the middle of the chain. The error from using the single sequence approximation will therefore show a wide variation with sequence and could be potentially serious if a sequence has a high preference to populate more than one helix simultaneously. Conformations with two or more helices may also often include helix–helix tertiary interactions that are ignored in all helix/coil models.

9.4.5 N- and C-Caps

In the original LR model weights are assigned to residues in the center of hhh triplets (a weight of w for propagation) or in the center of chh or hhc triplets (a weight of v for initiation). Residues in all other triplets have weights of 1. LR-based models have been extended by assigning weights to additional conformations. N-capping can therefore be included in LR theory be assigning a weight of n to the central residue in a cch triplet [99]. Similarly, the C-cap is the first residue in a nonhelical conformation (c) at the C-terminus of a helix. C-cap weights (c-values) are assigned to central residues in hcc triplets. Application of the model to experimental data where the C-terminal amino acid of a helical peptide was varied, allowed the determination of the c-values and hence free energies of C-capping (as $-RT \ln c$) of all the amino acids [29].

A problem with the original definitions of the capping weights above is that they apply to isolated h or hh conformations that are best regarded as part of the random coil. A helical hydrogen bond can only form when a minimum of three consecutive h residues are present. Andersen and Tong [151] and Rohl et al. [9] therefore changed the definition of the N-cap to apply only to the c residue in a chhh quartet. The N-cap residues in chc or chhc conformations have weights of zero in the Andersen-Tong model and 1 in the Rohl et al. model.

9.4.6 Capping Boxes

The N-terminal capping box [25] includes a side chain–backbone hydrogen bond from N3 to the N-cap $(i, i-3)$. This is included in the LR model by assigning a weight of w^*r to the chhh conformation, where r is the weight for the Ser backbone to Glu side chain bond [9].

9.4.7 Side-chain Interactions

As helices have 3.6 residues per turn, side chains spaced $i, i+3$ or $i, i+4$ are close in space. Side-chain interactions are thus possible when four or five consecutive

residues are in a helix. They are included in the LR-based model by giving a weight of w^*q to hhhh quartets and w^*p to hhhhh quintets. The side-chain interaction is between the first and last side chains in these groups; the w weight is maintained to keep the equivalence between the number of residues with a w weighting and the number of backbone helix hydrogen bonds [100].

Scholtz et al. [152] used a model based on the one-helical-sequence approximation of the LR model to quantitatively analyze salt bridge interactions in alanine-based peptides. Only a single interaction between residues of any spacing was considered, though this was appropriate for the sequences they studied. Shalongo and Stellwagen [153] also proposed incorporating side-chain interaction energies into the LR model, using a clever recursive algorithm.

9.4.8
N1, N2, and N3 Preferences

The helix N-terminus shows significantly different residue frequencies for the N-cap, N1, N2, N3, and helix interior positions [12, 19, 154, 155]. A complete theory for the helix should therefore include distinct preferences for the N1, N2, and N3 positions. In the original LR model, the N1 and C1 residues are both assigned the same weight, v. Shalongo and Stellwagen [153] separated these as v_N and v_C. Andersen and Tong [151] did the same and derived complete scales for these parameters from fitting experimental data, though some values were tentative. The helix initiation penalty is $v_N{}^*v_C$ and so v_N and v_C values are all small (≈ 0.04).

We added weights for the N1, N2, and N3 (*n1*, *n2*, and *n3*) positions as follows [156]: The *n1* value is assigned to a helical residue immediately following a coil residue. The penalty for helix initiation is now $n1.v$, instead of v^2, as v remains the C1 weight. An N2 helical residue is assigned a weight of $n2.w$, instead of w. The weight w is maintained in order to keep the useful definition of the number of residues with a w weighting being equal to the number of residues with an $i, i+4$ main chain–main chain hydrogen bond. The *n2* value is an adjustment to the weight of an N2 residue that takes into account the structures that can be adopted by side chains uniquely at this position. Similarly, an N3 residue is now assigned the weight $n3.w$, instead of w.

9.4.9
Helix Dipole

Helix-dipole effects were added to the LR model by Scholtz et al. [152], though they used the one-sequence approximation so that only one or no dipoles in total are present. In LR models helix-dipole effects are subsumed within other energies. For example, N-cap, N1, N2, and N3 energies will include a contribution from the helix-dipole interaction so the energy of interaction of charged groups at this position with the dipole should not be counted in addition.

9.4.10
3_{10}- and π-Helices

The Lifson-Roig formalism can easily be adapted to describe helices of other cooperative lengths [157]. The fundamental difference between a 3_{10}-helix and an α-helix is that the 3_{10}-helix has an $i, i+3$ hydrogen-bonding pattern rather than the $i, i+4$ pattern characteristic of the α-helix. For a given number of units in helical conformations, a 3_{10}-helix will consequently have one more hydrogen bond than an α-helix. To include this difference in the 3_{10}-helix theory, one of the α-helical-initiating residues (i.e., the central unit of either the $h_\alpha h_\alpha c$ or the $ch_\alpha h_\alpha$ triplet) must become a 3_{10}-helix-propagating residue. We arbitrarily chose to assign the propagating statistical weight, w_τ, to the central unit of the $h_\tau h_\tau c$ triplet such that helix propagating unit i is associated with the hydrogen bond formed between the CO of peptide $i-2$ and the NH of peptide $i+1$. The remainder of the statistical weights applicable to the α-helix/coil theory are maintained.

The models described above for the α-helix/coil and 3_{10}-helix/coil transitions can be combined to describe an equilibrium including pure α-helices, pure 3_{10}-helices, and mixed α-/3_{10}-helices [157]. In this model, three conformational states are possible, 3_{10}-helical (h_τ), α-helical (h_α), and coil (c). The pure 3_{10}-helix and the mixed α-/3_{10}-helix models were subsequently extended to include side-chain interactions [158]. Sheinerman and Brooks [128] independently produced a model for the α/3_{10}/coil equilibrium, based on the ZB formalism, rather than the LR model. They similarly extend the classification of conformations from α/coil to α/3_{10}/coil.

In a π-helix, formation of an $i, i+5$ hydrogen bond requires that four units be constrained to the π-helical conformation, h_π. The π subscript designates the conformation and weights describing the π-helix, whose dihedral angles are distinct from α- and 3_{10}-helices. Assigning statistical weights to individual units requires consideration of the conformations of the unit itself and its three nearest neighbors [157]. The initiating statistical weight, v_π, is assigned to a helical unit when one or more of its two N-terminal and nearest C-terminal neighbors are in the coil conformation. The definition of helix-initiating units as the two N-terminal and one C-terminal units of each helical stretch is again arbitrary. Units in a π-helical conformation with three helical neighbors are assigned the propagating statistical weight, w_π. A π-helix propagating residue, i, is thus associated with the hydrogen bond between the NH of residue $i+2$ and the CO of residue $i-3$.

9.4.11
AGADIR

AGADIR is an LR-based helix/coil model developed by Serrano, Muñoz and coworkers. The original model [159] included parameters for helix propensities excluding backbone hydrogen bonds (attributed to conformational entropy), backbone hydrogen bond enthalpy, side-chain interactions, and a term for coil weights at the end of helical sequences (i.e., caps). The single-sequence approximation was used. The original partition function assumed that many helical conformations did not exist, as all conformations in which the residue of interest is not part of a helix

were excluded [100, 159]. These were corrected in a later version, AGADIRms, which considers all possible conformations [160]. If AGADIR and LR models are both applied to the same data, to determine a side-chain interaction energy, for example, the results are similar, showing that the models are now not significantly different [160, 161]. The treatment of the helix/coil equilibrium differs in a number of respects from the ZB and LR models and these have been discussed in detail in by Muñoz and Serrano [160]. The minimal helix length in AGADIR is four residues in an h conformation, rather than three. The effect of this assumption is to exclude all helices which contain a single hydrogen bond; only helices with two or more hydrogen bonds are allowed. In practice, this probably makes little difference as chhhc conformations are usually unfavorable and hence have low populations. Early versions of AGADIR considered that residues following an acetyl at the N-terminus or preceding an amide at the C-terminus were always in a c conformation; this was changed to allow these to be helical [162].

The latest version of AGADIR, AGADIR1s-2 [162], includes terms for electrostatics [162], the helix dipole [162, 163], pH dependence [163], temperature [163], ionic strength [162], N1, N2, and N3 preferences [164], and capping motifs such as the capping box, hydrophobic staple, Schellman motif, and Pro-capping motif [162]. The free energy of a helical segment, $\Delta G_{\text{helical-segment}}$, is given by

$$\Delta G_{\text{helical-segment}} = \Delta G_{\text{Int}} + \Delta G_{\text{Hbond}} + \Delta G_{\text{SD}} + \Delta G_{\text{dipole}} + \Delta G_{\text{nonH}} + \Delta G_{\text{electrost}},$$

which are terms for the energy required to fix a residue in helical angles (with separate terms for N1, N2, N3, and N4), backbone hydrogen bonding, side-chain interactions excluding those between charged groups, capping, and helix-dipole interactions, respectively. Electrostatic interactions are calculated with Coulomb's equation. Helix-dipole interactions were all electrostatic interactions between the helix dipole or free N- and C-termini and groups in the helix. Interactions of the helix dipole with charged groups located outside the helical segment were also included. pH-dependence calculations considered a different parameter set for charged and uncharged side chains and their pK_a values. The single sequence approximation (see above) is used again, unlike in AGADIRms. This means that it must not be used for full protein sequences, though this has been done, even if they do not have any tertiary interactions.

AGADIR is at present the only model that can give a prediction of helix content for any peptide sequence, thus making it very useful. It can also predict NMR chemical shifts and coupling constants. In order to do this it must include estimates of all the terms that contribute to helix stability, notably the 400 possible $i, i+4$ side-chain interactions. Since only a few of these interactions have been measured accurately, the terms used cannot be precise. Further determination of energetic contributions to helix stability is therefore still needed.

9.4.12 Lomize-Mosberg Model

Lomize and Mosberg also developed a thermodynamic model for calculating the stability of helices in solution [165]. Interestingly, they extended it to consider helices in micelles or a uniform nonpolar droplet to model a protein core environ-

ment. Helix stability in water is calculated as the sum of main chain interactions, which is the free energy change for transferring Ala from coil to helix, the difference in energy when replacing an Ala with another residue, hydrogen bonding and electrostatic interactions between polar side chains and hydrophobic side-chain interactions. An entropic nucleation penalty of two residues per helix is included. Different energies are included for N-cap, N1–N3, C1–C3, C-cap, hydrophobic staples, Schellman motifs, and polar side-chain interactions, based on known empirical data at the time (1996). Hydrophobic interactions were calculated from decreases in nonpolar surface area when they are brought in contact. Helix stability in micelles or nonpolar droplets are found by calculating the stability in water then adding a transfer energy to the nonpolar environment.

9.4.13
Extension of the Zimm-Bragg Model

Following the discovery of short peptides that form isolated helices in aqueous solution, Vásquez and Scheraga extended the ZB model to include helix-dipole and side-chain interactions [166]. The model is very general as it can include interactions of any spacing within a single helix. It was applied to determine $i, i+4$ and $i, i+8$ interactions. Long-range interactions, beyond the scope of LR models, can thus be included. Roberts [167] and Gans et al. [88] also refined the ZB model to include side-chain interactions.

9.4.14
Availability of Helix/Coil Programs

Some Lifson-Roig based helix/coil models are available at http://www.bi.umist.ac.uk/users/mjfajdg/HC.htm. We recommend SCINT2 for peptides with side-chain interactions (freely available from us). If no side-chain interactions are present, CAPHELIX is identical and simpler to run. If N1, N2, or N3 preferences are important in your sequence N1N2N3 can be used. If the peptide contains side-chain interactions that have not been well characterized (which is the case for the great majority of sequences) AGADIR can be run at http://www.embl-heidelberg.de/Services/serrano/agadir/agadir-start.html. In our experience, SCINT2 or CAPHELIX are more accurate at predicting helix contents of alanine-based control peptides than AGADIR (see Refs [101] and [106] for examples), though AGADIR can be applied to many more sequences. The Andersen version of an LR-based helix/coil is at http://faculty.washington.edu/nielshan/helix/.

9.5
Forces Affecting α-Helix Stability

9.5.1
Helix Interior

Since the advent of crystal structures of proteins it had been noticed that some amino acids appeared frequently in α-helices and others less frequently [168, 169].

For example alanine and leucine are abundant, whereas proline and glycine appear rarely. As more of this kind of information became available a helix propensity scale was derived [170] and eventually allowed prediction of the location of α-helices (and other structures) in folded proteins from their sequence [171].

Different approaches have been used in order to determine the helical propensity or preference of individual amino acids. Scheraga and coworkers used a host–guest strategy (see Section 9.3.1) to derive values for the helical preference of various amino acid residues [172, 173]. This has been carried out for all 20 naturally occurring amino acids [174]. This work has been criticized as the host side chains can interact with each other [175]. The introduction of a guest residue thus removes host–host interactions and replaces them with PHBG–guest or PHPG–guest side-chain interactions that may obscure the intrinsic helix propensities. We believe that helix propensities are best evaluated in an alanine background, where no side-chain interactions can affect the helix stability.

Rohl et al. [30] used many alanine-based peptides with the general sequences Ac-$(AAKAA)_m$Y-NH_2 (or with Q instead of K) to measure interior helix propensities. Substitutions in the helix interior and subsequent measures of helicity using CD spectroscopy in both water and 40% (v/v) trifluoroethanol (TFE) allowed both the calculation of the Lifson-Roig *w* parameter and stabilization energy for all 20 amino acids (see Table 9.3). Kallenbach and coworkers also used synthetic peptides

Tab. 9.3. Helix propagation propensities and free energies of amino acids in water.

Amino acid	*ΔG° (helix) (kcal mol^{-1})*	*w value*
Ala	−0.27	1.70
Arg^+	−0.052	1.14
Leu	0.095	0.87
Met	0.25	0.65
Lys^+	0.019	1.00
Gln	0.28	0.62
Glu	0.21	0.70
Ile	0.44	0.46
Trp	0.69	0.29
Ser	0.52	0.40
Tyr	0.42	0.48
Phe	0.73	0.27
Val	0.77	0.25
His	0.57	0.36
Asn	0.69	0.29
Thr	0.95	0.18
Cys	0.64	0.32
Asp	0.52	0.40
Gly	1.7	0.048
Pro	>3.8	<0.001

From Ref. [30].

of the form succinyl-YSEEEEKAKKAXAEEAEKKKK-NH_2 where substitutions at X allowed determination of helix stabilising energies for common amino acids [87]. Stellwagen and coworkers made substitutions in position 9 of Ac-Y$(EAAAK)_3$A-NH_2 [84]. These agree well with the alanine-based peptide work described previously [30, 176].

Other groups have investigated helical propensities and stabilization using whole protein methods. Blaber et al. [177–179] used mutagenesis in the helices of phage T4 lysozyme to study the structural effects of substitutions of amino acids. With the exception of substituting proline, they found that no substitutions significantly distorted the helix backbone. $\Delta\Delta G$ values correlated well (71–93%) with model peptide studies and with studies on the frequency of amino acid occurrence in protein structures [171]. Fersht and coworkers used a similar method with barnase to study the effect of replacing Ala32 of the second helix in this protein with the other 19 naturally common amino acids [180]. They used reversible urea denaturation to measure free energies of unfolding.

O'Neil and DeGrado [181] used substitutions into an α-helical two-stranded coiled-coil system to deduce helix-forming tendencies of common amino acids, through the design of a peptide that forms a noncovalent α-helical dimer, which is in equilibrium with a randomly coiled monomeric state. The α-helices in the dimer contain a single solvent-exposed site that is surrounded by small, neutral amino acid side chains. Each of the commonly occurring amino acids was substituted into this guest site, and the resulting equilibrium constants for the monomer–dimer equilibrium were determined to provide a list of free energy difference $(\Delta\Delta G^0)$ values. Again these values show good agreement with those of other groups working in different model systems.

In 1998 Pace and Scholtz [182] gathered information from many different sources and derived a scale for the propensity of each amino acid in the helix interior. This is summarized in Table 9.4. The values are in $\Delta(\Delta G)$ relative to alanine as zero. Alanine was taken as zero as it is generally (though not universally) agreed that this amino acid has the highest helical propensity. Shown for comparison in Table 9.5 are the *s* values from the Zimm-Bragg model as derived by the Scheraga group [174]. Both tables are ranked in terms of descending helical propensity.

As can be seen from Tables 9.4 and 9.5, the two series do not agree on even the relative helical propensities of the amino acid residues. The data summarized by Pace and Scholtz shows alanine having the highest helix propensity and all other residues having lower values (a positive $\Delta(\Delta G)$ value relative to Ala). Both series show proline and glycine to have the lowest helical propensity (highest $\Delta(\Delta G)$ value or lowest *s* value. The most controversial of these differences over the years has been that of alanine. Host–guest analysis showing alanine to be effectively helix-neutral has been supported by data from some other groups, notably the templated helices of Kemp and coworkers [107]. Several efforts have been made to try to explain this discrepancy, including implication of the charged groups used to solubilize the alanine-based peptides [183, 184], but little reconciliation has been achieved. The use of template-nucleated helices has been criticized by Rohl et al. [185] who argued that the low apparent helix propensity of alanine is a conse-

Tab. 9.4. Summary of other experimental helix propensities (relative to alanine).

Amino acid	*Helix propensity (ΔΔG) (kcal mol^{-1})*
Ala	0.00
Arg^{+}	0.21
Leu	0.21
Met	0.24
Lys^{+}	0.26
Gln	0.39
Glu	0.40
Ile	0.41
Trp	0.49
Ser	0.50
Tyr	0.53
Phe	0.54
Val	0.61
His	0.61
Asn	0.65
Thr	0.66
Cys	0.68
Asp	0.69
Gly	1.00
Pro	3.16

From Ref. [182].

quence of properties of the template–helix junction. However, recent work by Kemp and coworkers [186] may at last settle the controversy. Using templates to investigate the helix-forming tendency of polyalanine, these workers extended the length of the polyalanine beyond the previous limit of six residues. Below six residues, both this group and Scheraga's had low helix propensities for alanine (see above) but when the limit of six was exceeded, a dramatic increase in helix propensity was observed. For chains with less than six alanines, $w = 1.03$, in agreement with both Kemp and Scheraga's earlier experimental results. For chains with 6–9 alanines, $w = 1.15$ and for more than 10 Alanines, w is 1.26. This indicates that there is a length-dependent term in the helicity of polyalanine and that the charged groups are not having the effect previously ascribed to them. These values for longer polyalanine sequences are also much more consistent with values published by other groups.

9.5.2 Caps

Serrano and Fersht [20] explored the capping preferences at the N-cap by mutating Thr residues at the N-cap of two helices in barnase. They found that negatively

Tab. 9.5. Helical propensity values from host–guest studies.

Amino acid	*s (20 °C)*
Glu	1.35
Met	1.2
Leu	1.14
Ile	1.14
Trp	1.11
Phe	1.09
Ala	1.07
Arg+	1.03
Tyr	1.02
Cys	0.99
Gln	0.98
Val	0.95
Lys+	0.94
His	0.85
Thr	0.82
Asn	0.78
Asp	0.78
Ser	0.76
Gly	0.59
Pro	0.19

From Ref. [174].

charged residues were favored at the N-cap with a rank order of Asp > Thr > Glu > Ser > Asn > Gly > Gln > Ala > Val. Interestingly, their result conflicted with the statistical survey result that Asn is one of the most frequently found N-caps in proteins [12]. Experimentally Asn destabilized the helices by 1.3 kcal mol^{-1} relative to Thr. The rank order of amino acids N-cap preferences in T4 lysozyme was found to be Thr > Ser > Asn > Asp > Val = Ala > Gly [21]. They suggested that Asn can be inherently as good an N-cap as Ser or Thr, but it requires a change in backbone dihedral angles of N-cap residues, which might be altered in native proteins as the results of tertiary contacts. Indeed Asn is the most stabilizing residue at N-cap in a peptide model in the absence of tertiary contacts and other side-chain interactions (see below).

The Kallenbach group [187] substituted several amino acids at the N-cap position in peptide models in the presence of a capping box. They found that Ser and Arg are the most stabilizing residues with $\Delta\Delta G$ relative to Ala of −0.74 and −0.58 kcal mol^{-1}, respectively, whilst Gly and Ala are less stabilizing. The results are in agreement with the results of Forood et al. [23], who found that the trend in α-helix inducing ability at the N-cap is Asp > Asn > Ser > Glu > Gln > Ala. A more comprehensive work to determine the preferences for all 20 amino acids at the N-cap position used peptides with a sequence of NH_2-XAKAAAAKAAAAKAAGY-$CONH_2$ [22, 29, 99]. N-Capping free energies ranged from Asn (best) to Gln (worst) (Table 9.6).

Tab. 9.6. Amino acid propensities at N- and C-terminal positions of the helix.

Residue	*ΔΔG relative to Ala for transition from coil to the position (kcal mol^{-1})*												
	N-cap	*N1*		*N2*		*N3*		*C3*	*C2*		*C1*	*C-cap*	*C′*
	29[a]	*95*[b]	*164; 188*[c]	*96*[d]	*164; 188*[e]	*97*[f]	*164; 188*[g]	*189*[h]	*190*[i]	*189*[j]	*189*[k]	*29*[l]	*299*[m]
A	0	0	0	0	0	0	0	0	0	0	0	0	0
C°												0.2	
C$^-$	−1.4	1.0		0.9									
D°		0.5		0.7								0.2	0.3
D$^-$	−1.6	0		−0.2		1.1							
E°		1.0		−0.2								−0.4	0.3
E$^-$	−0.7	0.1		−0.4		0.6						−0.5	
F	−0.7	1.4		0.9		1.3			0.6				0.1
G	−1.2	1.0	0.7		0.4		0.8	2.1	1.0	0.6	0.4	0.1	−1.1
H°	−0.7	0.7		0.8		2.6							
H$^+$												−0.2	−0.9
I	−0.5	0.5	0.4	0.6	0.5	0.7	0.5	0.2	0.2	0.4	0.5		1.5
K$^+$	0.1	0.7		0.9		0.9						−0.1	−0.1
L	−0.7	0.4	0.2	0.5	0.5	0.8	0.4		0.1			−0.1	
M	−0.3	0.5	0.1	0.7	0.3	0.7	0.4		0.1			−0.3	0.1
N	−1.7		0.6	1.7	0.7		0.7	0.5	0.7	0.4	0.3	0.1	−0.4
P	−0.4	0.6	0.5										1.2
Q	2.5	0.5	0.3	0.5	0.3	1.2	0.2	0.2	−0.02	0.2	0.05	−0.5	−0.1
R$^+$	−0.1	0.7		0.8								−0.4	−0.2
S	−1.2	0.4	0.4	0.7	0.5	1.1	0.6	0.6	0.5	0.7	0.5	0.8	0.3
T	−0.7	0.5	0.5	0.5	0.5	1.2	0.6	0.8	0.6	0.5	0.8		1.1
V	−0.1	0.6		0.5	0.4		0.4	0.3	0.4	0.7	0.6	0.9	1.6
W	−1.3	0.4		0.8		4.0							0.7
Y	−0.9					1.2						−2.2	

[a] NH_2-*X*AKAAAAKAAAAKAAGY-$CONH_2$
[b] CH_3CO-*X*AAAAQAAAAQAAGY-$CONH_2$
[c] CH_3CO-*X*AAAAAAARAAARGGY-NH_2
[d] CH_3CO-A*X*AAAAKAAAAKAAGY-$CONH_2$
[e] CH_3CO-A*X*AAAAAAARAAARGGY-NH_2
[f] CH_3CO-AA*X*AAAAKAAAAKAGY-$CONH_2$
[g] CH_3CO-AA*X*AAAAAARAAARGGY-NH_2
[h] NH_2-YGGSAKEAAARAAAA*X*AA-$CONH_2$
[i] Substitution of residue 32 (C2 position) of α-helix of ubiquitin.
[j] NH_2-YGGSAKEAAARAAAAA*X*A-$CONH_2$
[k] NH_2-YGGSAKEAAARAAAAAA*X*-$CONH_2$
[l] CH_3CO-YGAAKAAAAKAAAAKA*X*-COOH
[m] Substitution of residue 35 (C′ position) of α-helix of ubiquitin.

We have used a similar approach using peptide models to probe the preferences at N1 [95], N2 [96], and N3 [97] using peptides with sequences of CH_3CO-XAAAA-QAAAAQAAGY-$CONH_2$, CH_3CO-AXAAAAKAAAAKAAGY-$CONH_2$ and CH_3CO-AAXAAAAKAAAAKAGY-$CONH_2$, respectively. The results have given N1, N2,

and N3 preferences for most amino acids for these positions (Table 9.6) and these agree well with preferences seen in protein structures, with the interesting exception of Pro at N1. Petukhov et al. similarly obtained N1, N2, and N3 preferences for nonpolar and uncharged polar residues by applying AGADIR to experimental helical peptide data, and found almost identical results [164, 188]. The complete sequences of peptides used can be seen in the table footnote. In general, at N1, N2, and N3, Asp and Glu as well as Ala are preferred, presumably because negative side chains interact favorably with the helix dipole or NH groups while Ala has the strongest interior helix preference.

Although it is also unique in terms of the presence of unsatisfied backbone hydrogen bonds, the C-terminal region is less explored experimentally. The C-terminus of the α-helix tends to fray more than the N-terminus, making C-terminal measurements less accurate. Preferences at the C-cap position differ from those at the N-cap. At the N-terminus, the helix geometry favors side chain-to-backbone hydrogen bonding, so polar residues are preferred [14, 19]. At the C-terminus unsatisfied backbone hydrogen bonds are fulfilled by interactions with backbone groups upstream of the helix. Zhou et al. [48] found that Asn is the most favored residue at the C-cap followed by Gln > Ser∼Ala > Gly∼Thr. Forood et al. [23] tested a limited number of amino acids at the C-terminus (C1) finding a rank order of Arg > Lys > Ala. Doig and Baldwin [29] determined the C-capping preferences for all 20 amino acids in α-helical peptides. The thermodynamic propensities of some amino acids at C′, C-cap, C1, C2, and C3 are also included in Table 9.6 [189, 190].

9.5.3 Phosphorylation

Phosphoserine is destabilizing compared with serine at interior helix positions [191, 192]. We investigated the effect of placing phosphoserine at the N-cap, N1, N2, N3, and interior position in alanine-based α-helical peptides, studying both the −1 and −2 phosphoserine charge states [193]. Phosphoserine stabilizes at the N-terminal positions by as much as 2.3 kcal mol^{-1}, while it destabilizes in the helix interior by 1.2 kcal mol^{-1}, relative to serine. The rank order of free energies relative to serine at each position is N2 > N3 > N1 > N-cap > interior. Moreover, −2 phosphoserine is the most preferred residue known at each of these N-terminal positions. Experimental pK_a values for the −1 to −2 phosphoserine transition are in the order N2 < N-Cap < N1 < N3 < interior. Phosphoserine can form stabilizing salt bridges to arginine [192].

9.5.4 Noncovalent Side-chain Interactions

Many studies have been performed on the stabilizing effects of interactions between amino acid side chains in α-helices. These studies have identified a number of types of interaction that stabilize the helix including salt bridges [83, 86, 88, 152, 194–198], hydrogen bonds [152, 198–200], hydrophobic interactions [100, 201–

203], basic/aromatic interactions [106, 204], and polar/nonpolar interactions [101]. The stabilizing energies of many pairs in these categories have been measured, though some have only been analyzed qualitatively. As described earlier, residue side chains spaced $i, i+3$ and $i, i+4$ are on the same face of the α-helix, though it is the $i, i+4$ spacing that receives most attention in the literature, as these are stronger. A summary of stabilizing energies for side-chain interactions is given in Table 9.7. We give only those that have been measured in helical peptides with the side-chain interaction energies determined by applying helix/coil theory. Almost all are attractive, with the sole exception of the Lys-Lys repulsion.

9.5.5
Covalent Side-chain interactions

Lactam (amide) bonds formed between NH_3^+ and CO_2^- side chains can stabilize a helix, acting in a similar way to disulfide bridges in a protein by constraining the side chains to be close, reducing the entropy of nonhelical states [205]. Lactam bridges between Lys-Asp, Lys-Glu, and Glu-Orn spaced $i, i+4$ have been introduced into analogs of human growth hormone releasing factor [206], and proved to be stabilizing with Lys-Asp most effective. The same Lys-Asp $i, i+4$ lactam was stabilizing in other helical peptide systems [207–210], while Lys-Glu $i, i+4$ lactam bridges were less effective [211]. Two overlapping Lys-Asp lactams were even more stabilizing [212]. The effect of the ring size formed by the lactam was investigated by replacing Lys with ornithine or (*S*)-diaminopropionic acid. A ring size of 21 or 22 atoms was most stabilizing (a Lys-Asp $i, i+4$ lactam is 20 atoms) [206]. Lactams between side chains spaced $i, i+7$ [213, 214] or $i, i+3$ [214]; [215], spanning two or one turns of the helix have also been reported. $i, i+7$ disulfide bonds have been introduced into alanine-based peptides, using (D)- and (L)-2-amino-6-mercaptohexanoic acid derivatives [216]. Strongly stabilizing effects were observed.

Some interesting recent work has shown that helix formation can be reversibly photoregulated. Two cysteine residues are cross-linked by an azobenzene derivative which can be photoisomerized from *trans* to *cis*, causing a large increase or decrease in the helix content of the peptide, depending on its spacing [217–219].

9.5.6
Capping Motifs

Although the N-terminal capping box sequence stabilizes helices by inhibiting N-terminal fraying, it does not necessarily promote elongation unless accompanied by favorable hydrophobic interactions as in a "hydrophobic staple" motif [220, 221]. The nature of the capping box stabilizing effect thus not only arises from reciprocal hydrogen bonds between compatible residues, but also from local interactions between side chains, helix macrodipole-charged residue interactions and solvation [222].

Despite statistical analyses revealing that Schellman motifs are observed more frequently that expected at the helix C-terminus, this motif populates only transi-

Tab. 9.7. Summary of side-chain interaction energies from literature.

Interaction	*ΔΔG (kcal mol^{-1})*	*Reference*
Ile-Lys $(i, i+4)$	−0.22	101
Val-Lys $(i, i+4)$	−0.25	101
Ile-Arg $(i, i+4)$	−0.22	101
Phe-Met $(i, i+4)$	−0.8	100
Met-Phe $(i, i+4)$	−0.5	100
Gln-Asn $(i, i+4)$	−0.5	200
Asn-Gln $(i, i+4)$	−0.1	200
Phe-Lys $(i, i+4)$	−0.14	106
Lys-Phe $(i, i+4)$	−0.10	106
Phe-Arg $(i, i+4)$	−0.18	106
Phe-Orn $(i, i+4)$	−0.4	204
Arg-Phe $(i, i+4)$	−0.1	106
Tyr-Lys $(i, i+4)$	−0.22	106
Glu-Phe $(i, i+4)$	−0.5	300
Asp-Lys $(i, i+3)$	−0.12	227
Asp-Lys $(i, i+4)$	−0.24	227
Asp-His $(i, i+3)$	>-0.63	301
Asp-His $(i, i+4)$	>-0.63	301
Asp-Arg $(i, i+3)$	−0.8	302
Glu-His $(i, i+3)$	−0.23	227
Glu-His $(i, i+4)$	−0.10	227
Glu-Lys $(i, i+3)$	−0.38	152
Glu-Lys $(i, i+4)$	−0.44	152
Phe-His $(i, i+4)$	−1.27	198
Phe-Met $(i, i+4)$	−0.7	203
His-Asp $(i, i+3)$	−0.53	198
His-Asp $(i, i+4)$	−2.38	241
His-Glu $(i, i+3)$	−0.45	227
His-Glu $(i, i+4)$	−0.54	227
Lys-Asp $(i, i+3)$	−0.4	227
Lys-Asp $(i, i+4)$	−0.58	227
Lys-Glu $(i, i+3)$	−0.38	227
Lys-Glu $(i, i+4)$	−0.46	227
Lys-Lys $(i, i+4)$	+0.17	196
Leu-Tyr $(i, i+3)$	−0.44	153
Leu-Tyr $(i, i+4)$	−0.65	153
Met-Phe $(i, i+4)$	−0.37	203
Gln-Asp $(i, i+4)$	−0.97	199
Gln-Glu $(i, i+4)$	−0.31	152
Trp-Arg $(i, i+4)$	−0.4	300
Trp-His $(i, i+4)$	−0.8	161
Tyr-Leu $(i, i+3)$	−0.02	153
Tyr-Leu $(i, i+4)$	−0.44	153
Tyr-Val $(i, i+3)$	−0.13	153
Tyr-Val $(i, i+4)$	−0.31	153
Arg $(i, i+4)$ Glu $(i, i+4)$ Arg	−1.5	303
Arg $(i, i+3)$ Glu $(i, i+3)$ Arg	−1.0	303
Arg $(i, i+3)$ Glu $(i, i+4)$ Arg	−0.3	303
Arg $(i, i+4)$ Glu $(i, i+3)$ Arg	−0.1	303
Phosphoserine-Arg $(i, i+4)$	−0.45	192

ently in aqueous solution but it is formed in 30% TFE [223]. This might be due to the C-terminus being very frayed and the increase of helical content contributed from this motif is small. Energetically this motif is not very favorable due to the entropic cost of fixing a Gly residue at the position C′. The Schellman motif is believed to be a consequence of helix formation and does not involve α-helix nucleation [224]. The α_L motif seems to be more stable than the alternative Schellman motif [221].

9.5.7 Ionic Strength

Electrostatic interactions between charged side chains and the helix macrodipole can stabilize the helix [92, 102, 225]. The interactions are potentially quite strong, but are alleviated by the screening effects of water, ions, and nearby protein atoms. In theory, increasing ionic strength of the solvent (up to 1.0 M) should stabilize the helix through interactions with α-helix dipole moments by shifting the equilibrium between α-helix and random coil, which has a random orientation of the peptide dipoles [226]. The energetics of the interaction between fully charged ion pairs can be diminished by added salt and completely screened at 2.5 M NaCl [197, 227]. In peptides containing side chain-to-side-chain interactions, the effect of ion pairs and charge/helix-dipole interactions cannot be clearly separated. There are, however, indications that the interactions of charged residues with the helix macrodipole are less affected than those between charged side chains [227, 228]. In coiled-coil peptides, salt also affects hydrophobic residues by strengthening their interactions at the coiled-coil interface. This can be explained through alterations of the peptide–water interactions at high salt concentration. However, this requires a strong kosmotropic anion to accompany the screening cation [229].

9.5.8 Temperature

Thermal unfolding experiments show that the helix unfolds with increasing temperature [230–232]. There is no sign of cold denaturation, as seen with proteins. Enthalpy and entropy changes for the helix/coil transition are difficult to determine as the helix/coil transition is very broad, precluding accurate determination of high- and low-temperature baselines by calorimetry [230]. Nevertheless, isothermal titration calorimetric studies of a series of peptides that form helix when binding a nucleating La^{3+}, find ΔH for helix formation to be -1.0 kcal mol^{-1} [135, 233], in good agreement with the earlier work.

9.5.9 Trifluoroethanol

Peptides with sequences of helices in proteins usually show low helix contents in water. An answer to this problem is to add TFE (2,2,2-trifluoroethanol) to induce

helix formation [234–237]. For many peptides, the concentration of TFE used to increase the helix content is only up to 40% [234–236, 238, 239]. TFE may act by shielding CO and NH groups from the water solvent while leading to hydrogen bond formation between them. The conformational equilibrium thus shifts toward more compact structures, such as the α-helical conformation [184]. The mechanism involves interaction between TFE and water with several interpretations. One view suggests that TFE indirectly disrupts the solvent shell on α-helices [240, 241]. Another view proposes that TFE destabilizes the unfolded species and thereby indirectly enhances the kinetics and thermodynamics of folding of the coiled coil [242]. A more compromising view suggests that TFE forms clusters in water solution, which at lower concentration pulls the water molecules from the surface of proteins. At higher concentration, TFE clusters associate with appropriate hydrophobic side chains reducing their conformational entropy and switch the conformation at TFE concentration $>$ 40% [243].

The propagation propensities of all amino acids increase variably in 40% TFE relative to water. The propagation propensities of the nonpolar amino acids increase greatly in 40% TFE whilst other amino acids propensity increase uniformly. However, glycine and proline are strong helix breakers in both in water and 40% TFE solvents [30]. In addition, 40% TFE dramatically alters electrostatic (and polar) interactions and increases the dependence of helix propensities on the sequence [244].

9.5.10 pK_a Values

Evaluation of pK_a values of titrable amino acids in a peptide sequence can be used to analyze the strength of the possible interaction they form in water. pK_a shifts of charged residues at the helix termini are significant because they can potentially interact with unsatisfied hydrogen bonds of the NH groups and CO group at the N-terminus and C-terminus, respectively, or the helix dipole. The pK_a values can be measured accurately from the change in ellipticity across a broad range of pH. The asymptotic values of the ellipticities for the different protonation states are fitted to a Henderson-Hasselbach equation to calculate the pK_a.

In general, the pK_a values of Glu and His at N1–N3 are normal compared with those in model compounds. In contrast, Asp and Cys have shifted pK_a to lower values [95, 96, 102, 152, 225, 245–248]. An exception for negatively charged residues at the N-cap is that they have a lower pK_a [29]. This may be because side chains at the N-cap can form strong hydrogen bonds to NH groups of N2 and N3, while the bonds formed by side chains at N1, N2, and N3 are much weaker [14, 19].

The negatively charged residues at higher pH destabilize helices when at the C-cap [29]. The increased pK_a may result from an unfavorable electrostatic interaction with the C-terminal dipole or partial negative charges on the terminal CO groups.

9.5.11
Relevance to Proteins

Many of the features studied in peptide helices are also applicable to proteins and can be used to rationally modify protein stability or to design new helical proteins. Helices in proteins are often found on the surface with one face exposed to solvent and the other buried in the protein core. Helix propensities and side-chain interactions measured in peptides are thus directly applicable to the solvent-exposed face. Substitutions at buried positions are much more complex and tertiary interactions also make major contributions to stability. Tertiary interactions at helix termini are rare; nearly all side-chain interactions are local [14]. Preferences for capping sites and the first and last turn of the helix are therefore applicable to most protein helices. The feature of protein helices of amphiphilicity, reflected in possession of a hydrophobic moment [249], is irrelevant to monomeric isolated helices.

9.6
Experimental Protocols and Strategies

9.6.1
Solid Phase Peptide Synthesis (SPPS) Based on the Fmoc Strategy

Solid phase synthesis was first described by Merrifield [250]. It depends on the attachment of the C-terminal amino acid residue to a solid resin, the stepwise addition of protected amino acids to a growing peptide chain covalently bound to the resin and finally the cleavage of the completed peptide from the solid support. This cyclical process is repeated until the chain assembly process is completed (Figure 9.3).

To select the appropriate resin for the synthetic target, several key features of the linker have to be taken into consideration, for example racemization-free synthetic attachment of the first amino acid residue and resulting C-terminal functionality [251]. A key choice is whether to have a C-terminal amide or carboxyl group, as this is determined by the resin.

The Fmoc (9-fluorenylmethoxycarbonyl) group is the α-amino-protecting group, which is widely used in solid state peptide synthesis for its adaptability to linkers, resin, and cleavage chemistries [252, 253]. Other amino-protecting groups, e.g., BOC (*t*-butyloxycarbonyl), are also commonly used, but only the strategy using Fmoc will be covered here. The procedure can be done either manually or automatically in a peptide synthesizer. Here we describe the procedure of manual peptide synthesis using Fmoc chemistry on a 0.1 mmol scale. There are many other methods in peptide synthesis using different procedures and chemicals [251].

9.6.1.1 Equipment and Reagents

- A sintered glass funnel and a vacuum flask connected to water vacuum pump.
- A high speed centrifuge and centrifuge tubes.
- Freeze dryer with suitable jar.

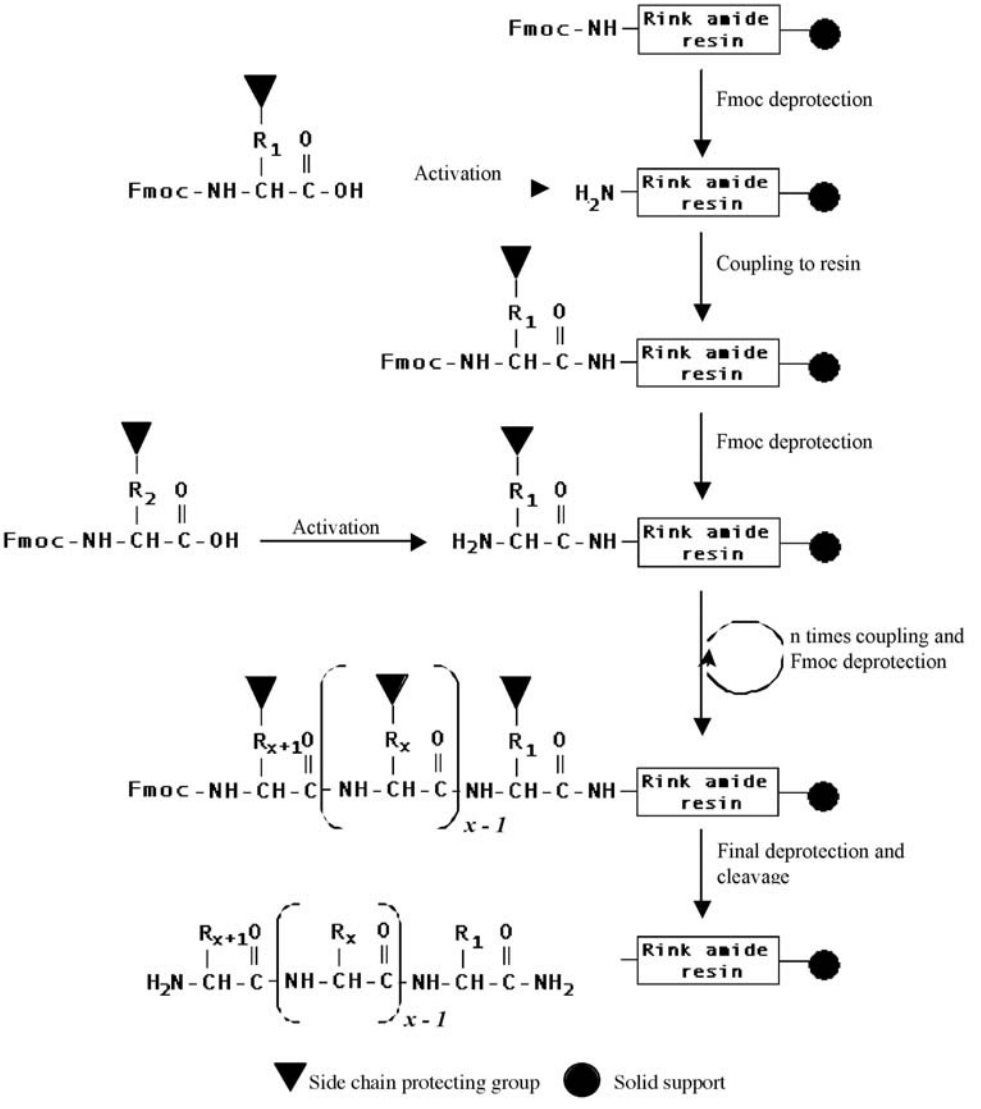

Fig. 9.3. Schematic diagram of peptide chain assembly.

- Rink amide resin 100–200 mesh (other resins can be used depending on the C-terminal functionality required, for example Wang resin is used to give C-terminal carboxyl).
- Deprotecting agent: 20% piperidine in DMF (dimethylformamide).
- Activating/coupling agents:
  - −0.45 M HBTU (2-(1H-benzotriazole-1-yl)-1,1,3,3-tetramethyluronium hexafluoro phosphate) dissolved in a solution of HOBt (1-hydroxy-1H-benzotriazole) in DMF. HATU, HCTU or TBTU are popular alternatives
  - −2 M DIEA (*N*,*N*,diisoprophylethylamine)

- NMP (*N*-methylpyrrolidone)
- DCM (dichloromethane)
- Diethyl ether
- Pyridine
- Acetic anhydride
- TFA (trifluoroacetic acid)
- TIS (triisopropyl silane) as scavengers (the choice of scavenger depends on peptide sequence)
- Fmoc-protected amino acids. Certain side chains contain functional groups that can react with free amine groups during the formation of the amide bond. Therefore, it is important to mask the functional groups of the amino acid side chain. The following side chain protecting groups are compatible with TFA cleavage (see Section 9.6.1.4):

Fmoc-Arg(Boc)	Fmoc-Cys(Acm)	Fmoc-Lys(Boc)
Fmoc-Arg(Mtr)	Fmoc-Cys(Trt)	Fmoc-Lys(Fmoc)
Fmoc-Arg(Pbf)	Fmoc-Gln(Tmob)	Fmoc-Lys(Mtt)
Fmoc-Arg(Pmc)	Fmoc-Gln(Trt)	Fmoc-Ser(tBu)
Fmoc-Asn(Tmob)	Fmoc-Glu(OtBu)	Fmoc-Thr(tBu)
Fmoc-Asn(Trt)	Fmoc-His(Boc)	Fmoc-Tyr(tBu)
Fmoc-Asp(OtBu)	Fmoc-His(Trt)	

9.6.1.2 **Fmoc Deprotection and Coupling**

1. Place Fmoc-protected Rink amide resin in a clean sintered glass funnel. For a resin with a loading 0.67 mmol g^{-1} use:

$$\frac{0.1 \text{ mmol}}{0.67 \text{ mmol}} = 0.15 \text{ g of resin}$$

   (using a 0.1 mmol scale).
2. Block the bottom end of the funnel with a stopper (e.g., use a tiny rubber bung). Immerse the resin in NMP for several minutes to make it swell. Remove the stopper temporarily; drain the solution from the funnel by applying suction with water vacuum pump.
3. Add 2 mL of 20% piperidine to the resin, leave it for 20 min, swirl occasionally to deprotect the base labile α-amino Fmoc group of carboxyamidated C-terminus Rink amide resin.
4. Drain the solution from the funnel by applying suction with water vacuum pump. Then wash unprotected resin with NMP several times. Make sure the resin is very clean from the previous reagent.
5. In a vial, dissolve Fmoc-protected amino acids in 2 mL of 0.45 M HBTU/HOBt in DMF, mix for about 5 min. Then add 1 mL of 2 M DIEA. The reagents will

activate the carboxyl group of the amino acid and couple it to the resin. The first amino acid to use is the one at the C-terminus. Use a 10× molar excess of the amino acid compared with the resin, for example 0.300 g of protected amino acid with MW of 300 g mol^{-1} to give 10 mmol of amino acid.
6. Transfer the solution to unprotected resin in the funnel. Leave it for 0.5–3 h, depending on the difficulty of coupling (note: β-branched amino acids sometimes need longer coupling time, i.e., overnight). Swirl the mixture frequently.
7. Repeat step 4.
8. If necessary, do a Kaiser test (see below), a quantitative ninhydrin procedure [254, 255], on a small amount of the peptide resin to check the completeness of the coupling process. Wash the beads with methanol before conducting the Kaiser test.

Continue cyclical process (repeat steps 3–8) of Fmoc deprotection and coupling until the last residue left with a free N-terminus.

9.6.1.3 Kaiser Test

The principle of the Kaiser test is that free amines react with ninhydrin to form a violet colored-compound (Ruhemann's purple). The following procedure is only applicable for Fmoc chemistry.

1. Add 2–3 mL methanol and 2–3 drops acetic acid to a test tube, and dry using a vacuum evaporator.
2. Add a few resin beads to the test tube.
3. Add 4 drops phenol/ethanol (80 g in 20 mL), 8 drops KCN/pyridine (1 mM diluted with 100 mL), and 4 drops ninhydrin/ethanol (500 mg in 10 mL). Do the same to a test tube without resin as a blank.
4. Incubate at 100 °C for 5 min.
5. After heating is completed, remove the tube and immediately add 4.8 mL of 60% ethanol for a final volume of 5 mL, vortex and let the beads settle to the bottom of the tube.
6. Pipette the sample into cuvette and read the absorbance of the sample (including the blank) at 570 nm. Use 60% ethanol to zero the spectrophotometer.
7. Calculate the μmol g^{-1} of amine as follows:

$$\mu\text{mol g}^{-1} = \frac{[(\text{Abs}_{\text{sample}} - \text{Abs}_{\text{blank}}) \times \text{dilution (mL)}]10^6}{\text{Extinction coefficient} \times \text{sample weight (mg)}}$$

where, dilution = 5 mL and extinction coefficient = 15 000 M^{-1} cm^{-1}
8. Calculate the percent coupling as follows:

$$\%\ \text{coupled} = \frac{[1 - \text{amine } (\mu\text{mol g}^{-1})]}{10^3 \times \text{substitution (mmol g}^{-1})} \times 100$$

Substitution can be calculated as follows (for Fmoc-Asp(OtBu) on 0.67 mmol g^{-1} Rink amide resin):

$$\frac{1000 \text{ mmol mol}^{-1}}{0.67 \text{ mmol g}^{-1}} = 1492 \text{ g mol}^{-1}$$

$$\text{Fmoc-Asp(OtBu)} = 411 \text{ g mol}^{-1}$$

$$-H_2O = -18 \text{ g mol}^{-1}$$

$$\text{Total} = 1885 \text{ g mol}^{-1}$$

$$\text{Substitution} = \frac{1000 \text{ mmol mol}^{-1}}{1885 \text{ g mol}^{-1}} = 0.53 \text{ mmol g}^{-1}$$

For an easier qualitative observation, the beads remain white and the solution yellow after heating (step 4) indicates a complete reaction. In contrast, a dark blue color on the beads and in the solution indicates an incomplete reaction (positive test). If free amino groups remain, the resin should be subjected again to coupling reaction (repeat Fmoc deprotection and coupling procedure using the same amino acid) or acetylation (see Section 9.6.1.4) to increase the purity of the final product.

9.6.1.4 **Acetylation and Cleavage**

1. Wash the peptide resin with about 10 mL each of DMF and DCM and further wash with methanol. Apply some suction using a water vacuum pump to dry the peptide resin.
2. When needed (otherwise go to step 4), the free N-terminus of the peptide is acetylated by adding acetylation solution consisting of 2.3 mL DMF, 0.1 mL acetic anhydride, and 0.12 mL pyridine to the peptide resin and leave for 30 min. Swirl occasionally.
3. Remove the acetylation solution from the peptide resin by applying some suction, wash the peptide resin three times each with about 10 mL of DMF and DCM.
4. In a tube, suspend the peptide resin in 5 mL cleavage solution containing 4.75 mL TFA, 125 µL H_2O and 125 µL TIS and leave for at least 3 h with an occasional swirl. The later serves as scavengers to protect the peptide from carbocations of amino acid side chain-protecting groups generated during cleavage, which can lead to side reactions. The exact choice of scavengers depends on the amino acids present.
5. Place the peptide resin back into the sintered glass funnel (use clean flask), apply some suction and collect the filtrate. Wash the resin twice with 5 mL of DCM and pool the filtrate.
6. Reduce the volume of the filtrate containing the peptide to about 0.5–1.0 mL by blowing compressed air/nitrogen onto the filtrate.

9.6.1.5 Peptide Precipitation

1. Drop concentrated filtrate into about 30 mL of dry, ice-cold diethyl ether in centrifuge tube. Keep the solution overnight at −20 °C for the precipitate to develop.
2. Centrifuge the resulting precipitate at 10 000 rpm for 10 min at 4 °C.
3. Wash the pellet three times with 30 mL of fresh dry, ice-cold diethyl ether and repeat step 2.
4. Evaporate the ether from the pellet by placing the centrifuge tube in warm water.
5. Dissolve dried pellet containing crude peptide in 5 mL of water, freeze it in dry ice and freeze dry overnight. Crude peptide is ready for HPLC purification.

9.6.2 Peptide Purification

9.6.2.1 Equipment and Reagents

- HPLC system equipped with C18 reverse phase analytical columns (250 × 10 mm, 5 μm).
- Acetonitrile containing 0.1% TFA.
- Deionized water containing 0.1% TFA.

9.6.2.2 Method

1. Wash the column thoroughly by running through 95% acetonitrile for at least 20 min.
2. When using a UV detector, set the detector wavelength at 214 nm.
3. Equilibrate the column with 5% H_2O for 10 min before the purification run.
4. Load the crude peptide sample dissolved in deionized water and start a linear gradient run. The amount of peptide loaded depends on its concentration. A typical run usually consist of two eluents which are mixed using a linear gradient with a flow rate which will give a 0.5% to 1.0% change per minute.
5. From the chromatogram obtained, optimize the conditions for further purification. This allows the change in flow rate and eluents composition across the elution time. If necessary, the collected fractions can be further purified using isocratic conditions.[1]
6. Inject sample again and start a new linear gradient run with optimized conditions.

1) For example, if a peptide elutes out at 30% aqueous acetonitrile (0.1% TFA) (from linear gradient run), a lower concentration of acetonitrile is chosen as the eluent for isocratic run (e.g., 28% (0.1% TFA) aqueous acetonitrile). The peptide peak will come out 4–5 min after the solvent peak under isocratic conditions.

7. Pool fractions of the suspected peptide[2] and analyze by mass spectrometry.[3]
8. When it is confirmed by the mass spectrometry results, collect the desired fractions several times, followed by lyophilization and storage at −20 °C for further use.[4]

9.6.3 Circular Dichroism

Circular dichroism (CD) is a very useful technique for obtaining secondary structural information on proteins and peptides. This area has been extensively reviewed in the past two decades in relation to both folding and secondary structure determination. Greenfield [256] has reviewed methods of obtaining structural information from CD data. This covers the advantages and pitfalls of each technique and experimental considerations, such as how the wavelength range of data acquisition affects the precision of conformation determination, how precisely must the protein concentration be determined for each method to give reliable answers and what computer resources are necessary to use each method. Manning [257] has reviewed various applications of CD spectroscopy to the study of proteins including analysis of denaturation curves, calculation of secondary structure composition, observation of changes in both secondary and tertiary structure and characterization of folding intermediates. The excellent book *Circular Dichroism and the Conformational Analysis of Biomolecules* [258] covers a wide range of applications of CD in detail, including a review of CD applied to α-helices by Kallenbach and coworkers [8].

In CD, the sample is illuminated with left and right circularly polarized light and the difference in absorbance of each component of the light is measured. Typically this is expressed as change in absorbance (ΔA) or as the ellipticity of the beam exiting the sample (ε, in millidegrees). This signal is proportional to the concentration of the sample, the optical path length of the cell or cuvette and the proportion of the sample exhibiting chiral behavior.

2) The crude peptide obtained from the synthesis will contain many by-products which are a result of deletion or truncated peptides as well as side products stemming from cleaved side chains or oxidation during the cleavage and deprotection process.
3) The peptides mass can be verified by low resolution, electrospray ionization (ESI) or MALDI mass spectrometry. ESI allows the peptide sample, which is dissolved in acetonitrile/water (0.1% TFA) after HPLC purification, to be directly analyzed without further treatment. For small molecules ($<$ 2000 Da) ESI typically generates singly or doubly charged gaseous ions, while for large molecules ($>$ 2000 Da) the ESI process typically gives rise to a series of multiply charged species.
4) It is recommended to first dissolve the peptide in sterile distilled or deionized water. Sonication can be applied if necessary to increase the rate of dissolution. If the peptide is still insoluble (e.g., peptides containing multiple hydrophobic amino acid residues), addition of a small amount of dilute (approximately 10%) acetic acid (for basic peptides) or aqueous ammonia (for acidic peptides) can facilitate dissolution of the peptide. For long-term storage of peptides, lyophilization is highly recommended. Lyophilized peptides can be stored for years at temperatures of −20 °C or lower with little or no degradation. Peptides in solution are much less stable. Peptides containing methionine, cysteine, or tryptophan residues can have limited storage time in solution due to oxidation. These peptides should be dissolved in oxygen-free solvents or stored with a reducing agent such as DTT.

Two conditions are necessary for obtaining a circular dichroism signal: The sample must be optically active or chiral and there must be a chromophore near to the chiral center.

9.6.4 Acquisition of Spectra

There are several considerations when obtaining spectra, some instrumental, others concerned with sample preparation etc.

9.6.4.1 Instrumental Considerations

Nitrogen flushing

This is essential for several reasons. The xenon lamps used in CD spectrometers have a quartz envelope so if oxygen is present when running, a lot of ozone can be generated. This has health and safety implications for users and can also be severely detrimental to mirror surfaces in the instrument. Oxygen also absorbs UV light below 195 nm. For these reasons, a flow of at least 3 L min^{-1} of clean dry nitrogen should be used at higher wavelengths, with increased flow if the wavelength is to approach 180 nm. Below this level (not available in most lab instruments) a flow of up to 50 L min^{-1} may be necessary. The flow should be started several minutes before the spectra are to be collected. When opening the sample holder compartment, keep the lid open for only a short time to help with flushing.

Scanning parameters

The criteria for selecting scanning parameters for CD spectrophotometers are essentially those for more common UV-visible spectrophotometers. There are five basic selections to be made:

1. Response time. The signal-to-noise ratio of the system is in proportion to the integration time so the easiest way to improve the quality of spectra is to increase the response time. When measuring model helical peptides response times in the region of 1 s are common.
2. Bandwidth or slit width. Setting the width of the slits can also be used to decrease noise level in spectra. The width should be as large as possible but comparable to the natural bandwidth of the bands to be scanned. Scanning parameters for α-helices would typically have bandwidths in the 1 nm region.
3. Scanning speed. The scanning speed selection is important, as speeds that are too high will tend to distort the obtained spectra. The maximum scanning speed is obtained from the bandwidth:response time ratio, so with a 1 nm slit and 1 s response time the maximum speed would be 1 nm s^{-1} or 60 nm min^{-1}. Slower scan speeds will give better quality spectra but obviously take longer times.
4. Data density/pitch. This is the measurement interval or number of data points per nm wavelength. This has no effect on noise in the spectrum, but it is advisable to choose a large number of data points if there will be postaccumulation processing such as curve fitting or filtering to reduce noise.

5. Averaging or accumulation. A further way to reduce the signal-to-noise ratio in spectra is to accumulate several spectra and average them. Noise will reduce as the square root of the number of accumulations, e.g., four accumulations will reduce noise by a factor of two, nine by a factor of three. The main effect is on short-term random noise. Long-term noise such as temperature drifts will not be compensated for in this way.

9.6.5 Data Manipulation and Analysis

CD data are usually expressed as an ellipticity (θ) or delta absorbance (ΔA). These are easily interconvertable as $\Delta A = \theta/32980$. Ellipticity is also converted to molar ellipticity ($[\theta]$) as follows:

$$[\theta] = \theta/(10 \times C \times l)$$

$$[\theta] = \theta M/(1000 \times c \times l)$$

Here θ is ellipticity in millidegrees, C is molar concentration (mol dm^{-3}), l is cell path length (cm), M is molecular weight (g mol^{-1}), and c is weight concentration (g mL^{-1}). $[\theta]$ is expressed in deg cm^{-2} $dmol^{-1}$. With peptides and proteins the mean residue molar ellipticity is often used. This replaces the C in the above equation with C_r, where $C_r = (1000 \times n \times c_g)/M_r$. Here M_r is the molecular weight of the species, n is the number of peptide bonds, and c_g is the macromolecular concentration (g mL^{-1}).

An example of a peptide helix CD spectrum is shown in Figure 9.4. To obtain the fraction of the peptide/protein that has α-helical secondary structure the mean residue molar ellipticity at 222 nm is most commonly used, as there is a strong helical minimum here and the coil signal is very small. There are several equations that

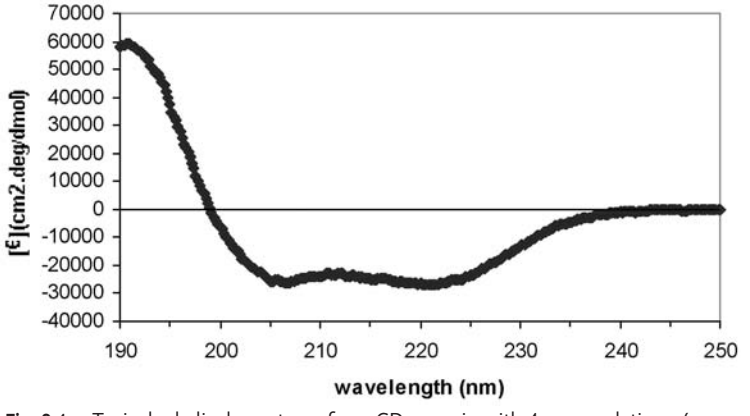

Fig. 9.4. Typical α-helical spectrum from CD spectroscopy. Measured using a Jasco J-810 spectrophotometer at 0.1 °C, data resolution 0.2 nm, Bandwidth 1 nm, scan speed 20 nm/min with 4 accumulations (averages). Model peptide – at 90 μM in 1 mm path length cell. Sequence: Ac-AKAAAAKAAAASAAAAKAAGY-NH_2.

can be used for this purpose. The equation below is a long-established equation for this purpose.

$$f_H = (\theta_{OBS} - \theta_C)/(\theta_H - \theta_C)$$

Here f_H is the average fraction of helix content, θ_C is the mean residue ellipticity when the peptide is 100% coil, θ_H is the mean residue ellipticity when the peptide is 100% helical and θ_{OBS} is the observed mean residue molar ellipticity from CD measurements. θ_C and θ_H can be calculated from empirical formulae below derived by Luo and Baldwin [259] where T is temperature (°C) and N_r is the chain length in residues. The value of 3 in the length correction $(1–3/N_r)$ is the number of backbone CO groups in a carboxyamidated peptide that are not hydrogen bonded.

$$\theta_C = 2220 - 53T$$

$$\theta_H = (-44000 + 250T)(1 - 3/N_r)$$

As can be seen from the equations above, accurate determination of protein/peptide concentration is essential for determination of secondary structure content from CD measurements. Any errors in this value will propagate throughout the calculation. Colorimetric assays such as those of Bradford, Lowry, and the BCA (bicinchonic acid) are not accurate enough for this purpose. Spectroscopic (UV absorbance) methods are much better if a reasonable chromophore is present as they are rapid and nondestructive of sample. However, the absorbance maxima and extinction coefficient of chromophores can be environmentally sensitive and so for example, a Trp residue in helical or β-sheet conformation may give a different reading to one in random coil conformation. Extinction coefficients usually quoted are for residues in free solution or fully solvent exposed, therefore for the best accuracy, concentration should be corrected for this, usually involving serial dilution in 6 M guanidinium chloride and comparison with the same dilutions in water (see Section 9.3.7).

A further complication with spectrum measurement and helix content evaluation is the presence of aromatic residues within the helix. In our own model peptides we usually employ tyrosine as a concentration marker but place a glycine (commonly known as a helix-breaker residue) between this and the helical region of the peptide [105]. Aromatic side chains can lead to greatly altered estimates of helix content from θ_{222} measurements. Tyrosine, depending upon the rotamer present, can alter the θ_{222} by up to 4000 deg cm^{-2} $dmol^{-1}$ [106]. The effect on CD measurements of aromatic side chains has long been known [105, 260, 261] and is due to the contributions of electronic transitions in the aromatic groups [262] and favorable interactions with the backbone. Several methods have been proposed and used for correcting CD spectra for this effect. One of the most common is to compute the expected spectrum using the matrix method of Bayley, Nielsen, and Schellman [263]. In this the band intensities are derived directly from transition dipole moments (electronic and magnetic) via the rotational strength of each ex-

cited state of the peptide. With model peptides the nonaromatic residues are commonly modeled as alanine to simplify the calculations (see, e.g., Andrew et al. [106]).

Other methods for estimation of secondary structure content involve deconvolution of entire CD spectra. These methods are based upon data from high-quality structure files for which secondary structure content is accurately known or use iterative fitting methods.

Dichroprot (available at http://dicroprot-pbil.ibcp.fr/Documentation_dicroprot.html) is a commonly used program using deconvolution/fitting analysis. It is based mainly upon the work of Sreerama and Woody [264]. They derived a self-consistent procedure fitting sums of spectra of different secondary structures to the experimental spectrum to obtain estimates of secondary structure content.

9.6.5.1 Protocol for CD Measurement of Helix Content

1. Cell path length and sample concentration. This combination should be chosen to give a maximum absorbance of roughly 0.8, this includes all species in the solution, i.e., solvent, buffer salts, etc. as well as the protein/peptide in question. A good starting point in our hands is a peptide concentration of roughly 20 μM with a path length of 1 mm.
2. Baseline measurement for correction. During the same work session as the spectrum for the peptide/protein solution is measured a blank spectrum should be taken with the same cell containing the solvent, buffer salts, etc. at the same concentrations (preferably dialyzed to equilibrium against the peptide solution). Ideally this would give a ΔA value of zero across the spectrum but practically this is rarely the case and so correction is needed by subtraction of this spectrum from the experimental one(s).
3. Measurement time, slit width and data resolution and averaging. These parameters should be set according to the criteria outlined above so as to reduce noise and prevent distortion of the signal. In our experience scan rates of 20 nm min^{-1} with a slit width of 1 nm, response time of 1 s, data resolution of 0.2 nm and 4–6 averages give spectra of good quality for analysis.
4. Spectral range. To check for helical character a spectrum from 250 or 260 nm to 190 or 180 nm is sufficient. α-Helices give a characteristic spectrum (Figure 9.4) with minima at around 222 and 208 nm and a maximum around 190 nm.

9.6.6 Aggregation Test for Helical Peptides

9.6.6.1 Equipment and Reagents

- Circular dichroism spectrometer. See Figure 9.4 text for CD parameters.
- Quartz cuvette
- Peptide with a range of concentration between 5 μM and 500 μM in an appropriate buffer. Notes: Avoid using a buffer that absorbs at far UV wavelength. Typical buffer used is phosphate buffer 5–10 mM containing NaCl 5–10 mM.

9.6.6.2 Method

1. Record UV CD spectra of the buffer.
2. Record UV CD spectra of each peptide.
3. Subtract the average buffer reading from the average peptides readings.
4. Convert the unit of ellipticity (mdeg) to mean residual ellipticity.
5. Aggregation does not occur if the mean residual ellipticities of the peptides are independent of concentration.

9.6.7 Vibrational Circular Dichroism

Circular dichroism can also be performed in the vibrational region of the spectrum. In vibrational CD (VCD) the characteristic transitions of the amide group are resolved well from most other transition types [265]. VCD has important properties due to the local character of vibrational excitations. Overlap with aromatic modes is avoided as aromatic side chains are locally nonchiral and do not couple strongly to amides. Vibrational couplings are also short-range in nature, mostly to the next residue and dipole moments are not strong. This leads to more local structure sampling than in conventional CD [258, 266]. For peptides, empirical correlations between secondary structures and bandshapes were first developed over 20 years ago, mainly for peptides in nonaqueous solvents. A key determination was that the amide band VCD depended on peptide chain conformation and not on other functional groups. The main bandshape criterion was the helical chirality of the backbone [267]. Proteins with a high α-helical content tend to have negative signals in the amide II band with maximum negativity at around 1515–1520 cm^{-1}. As β-sheet content increases a three-featured pattern $(+ - +)$ appears in the amide I band and amide II intensity drops [268].

VCD equipment is now available commercially [269] though most measurements have been performed with modified dispersive or FTIR absorbance spectrometers. The commercial instruments give high-quality data for nonaqueous solutions of small molecules but aqueous solution work is highly demanding, especially in determining baselines and related artifacts [265]. Improvements are continually being made in these instruments in terms of polarization modulation and birefringence effects [269, 270] and so data continue to improve.

9.6.8 NMR Spectroscopy

The full theory and practise of NMR spectroscopy is well beyond the scope of this review. Many reviews of this technique and its application to secondary structure determination exist already. Secondary structure determination by NMR techniques does not require a full three-dimensional structural analysis as does X-ray crystallography. Knowledge of the amide and α proton chemical shifts are in principle all that is necessary, although if this information is available it is likely that nearly complete assignments of side chain protons are also available. While obtain-

ing the sequential resonance assignments is a laborious task, the NMR method is perhaps the most powerful method of secondary structure determination without a crystal structure. Unlike CD and other kinds of spectroscopy, NMR secondary structure determination does not give an average secondary structure content but assigns secondary structures to different parts of the peptide chain.

Several parameters from NMR are needed for unambiguous structure assignments. A mixture of coupling constants, nuclear Overhauser effect (NOE) distances, amide proton exchange rates and chemical shifts may be necessary.

Coupling constants are through-bond or scalar (often called J-coupling) quantities, J-couplings between pairs of protons separated by three or fewer covalent bonds can be measured. The value of a three-bond J-coupling constant contains information about the intervening torsion angle. Unfortunately in general, torsion angles cannot be unambiguously determined from such information since as many as four different torsion angle values correlate with a single coupling constant value. Similar relationships can be determined between the three-bond coupling constant between the α proton and the β proton(s) yielding information on the value of the side chain dihedral angle $\chi 1$. Constraints on the dihedral angles ϕ and $\chi 1$ are important structural parameters in the determination of protein three-dimensional structures by NMR.

The three-bond coupling constant between the intraresidual α and amide protons (^{3}JHαHN) is the most useful for secondary structure determinations as it can be directly related to the backbone dihedral angle ϕ (Table 9.8). Unfortunately there is no three-bond proton coupling that can be related to the angle ψ.

9.6.8.1 Nuclear Overhauser Effect

The other major source of structural information comes from through space dipole–dipole coupling between two protons. This is the nuclear Overhauser effect or NOE. The intensity of an NOE is proportional to the inverse of the sixth power of the distance separating the two protons and is usually observed if two protons are separated by <5 Å. The NOE is therefore a sensitive probe of short intramolecular distances. They are categorized according to the location of the two protons involved in the interaction. Intraresidual NOEs are between protons within the same amino acid residue whereas sequential, medium, and long-range NOEs are between protons on residues sequentially adjacent, separated by up to three resi-

Tab. 9.8. Typical coupling constants and ϕ angles for different secondary structures.

Secondary structure	ϕ *(degrees)*	^{3}*JHαHN (Hz)*
Right-handed α-helix	−57	3.9
Right-handed 3/10-helix	−60	4.2
Antiparallel β-sheet	−139	8.9
Parallel β-sheet	−119	9.7
Left-handed α-helix	57	6.9

dues, and separated by four or more residues in the polypeptide sequence. A network of these short interproton distances form the backbone of three-dimensional structure determination by NMR.

A number of short (< 5 Å) distances are fairly unique to secondary structural elements. For example, α-helices are characterized by short distances between certain protons on sequentially neighboring residues (e.g., between backbone amide protons, dNN, as well as between β protons of residue i and the amide protons of residue $i + 1$, dBN). Helical conformations result in short distances between the α proton of residue i and the amide proton of residues $i + 3$ and to a lesser extent $i + 4$ and $i + 2$. These $i + 2$, $i + 3$, and $i + 4$ NOEs are collectively referred to as medium range NOEs while NOEs connecting residues separated by more than five residues are referred to as long-range NOEs. Extended conformations (e.g., β-strands), on the other hand, are characterized by short sequential, dAN, distances. The formation of sheets also results in short distances between protons on adjacent strands (e.g., dAA and dAN).

9.6.8.2 Amide Proton Exchange Rates

More information on secondary structure can be obtained from the rate of exchange of the amide proton. The regular hydrogen-bonded secondary structures "protect" amide protons involved in them as evidenced by their significantly reduced amide proton exchange rates with the solvent (H_2O). Although nearly all polypeptide amide protons are involved in hydrogen bonds in a globular protein [43], those in regular secondary structures appear to be longer lived. For example, after placing a lyophilized sample of BPTI into D_2O, many amide protons are completely replaced with deuterons within 1 h. Over the next several hours, the amide protons in the N-terminal and then the C-terminal helix also completely exchange. However, some amide protons participating in the central antiparallel sheet are still present after several months. Rohl and Baldwin [271] compared CD and amide exchange measurements as tools for studying helix content in peptides as well as helix/coil transition parameters, over a broad range of helix contents. They showed that helix/coil transition theory did fit both CD and exchange data independently. However, the helix contents measured by exchange are larger than those measured by CD. To bring the techniques into agreement they showed that the assumption that the intrinsic chemical exchange rate in the helix is the same as the exchange rate measured for short unstructured model peptides was incorrect. Modifying this assumption allowed the CD and NH exchange data to be described by the same set of helix parameters and also indicated that the intrinsic exchange rate in the presence of helical structure is reduced approximately 17% relative to the rates measured in unstructured models.

9.6.8.3 ^{13}C NMR

Spera and Bax [272] have used ^{13}C NMR to study secondary structure assignment, helix distribution, capping parameters, and thermal transitions of helical peptide systems. Spera and Bax derived an empirical relationship between backbone conformation and in combination with high-resolution X-ray structures for which ^{13}C chemical shift assignments were available. Stellwagen and coworkers [273–275]

have used the same C_α, C_β ^{13}C chemical shifts to study thermal transitions in model peptides to compare Lifson-Roig theory predictions of helicity with experimental values. They showed that mean helix content as measured by CD coincided with that measured by ^{13}C NMR using the mean of all individual fitted transitions of the carbonyl residues. Using the carbonyl, C_α or C_β chemical shifts for a particular residue all gave the same melting temperature and width of thermal transition, although their chemical shift changes upon melting differed in both magnitude and sign. This suggests that each residue acts as a cooperative unit in helix formation. They also indicated that there are more interactions than simply backbone hydrogen bonds at the helix termini, as these appeared less frayed than Lifson-Roig theory would predict.

Detailed treatments of using these parameters are well established in the literature and it is beyond the scope of this current article to treat them in further detail [272, 276, 277].

9.6.9
Fourier Transform Infrared Spectroscopy

Another increasingly popular method for secondary structure determination is Fourier transform infrared spectroscopy (FTIR). There are many descriptions of the basis of IR spectroscopy in the literature [278, 279] and so we will not expand upon that area here.

With proteins/peptides there are nine characteristic absorbance bands produced by the amide functionality. These are named amides A, B, I, II ... VII. Of these, amides I and II are the major bands of interest. The amide I band (between 1600 and 1700 cm^{-1}) is mainly associated with the C=O stretching vibration (70–85%) and is directly related to the backbone conformation. Amide II results from the N–H bending vibration (40–60%) and from the C–N stretching vibration (18–40%). Amide II, a more complex, conformationally sensitive band, is found in the 1510 and 1580 cm^{-1} region. Unfortunately the contribution of side chains also occurs in the same region as the amide I and II bands. Only nine of the 20 common amino acids in proteins have significant absorbance in this region and these are Asp, Asn, Glu, Gln, Lys, Arg, Tyr, Phe and His. The contributions of these side chains must be accounted for before using the amide I and II bands for secondary structure determination. Fortunately this has been well investigated by Venyaminov and Kalnin [280].

9.6.9.1 Secondary Structure

A large number of synthetic polypeptides have been used for the characterization of infrared spectra for proteins with a defined secondary structure content. For example, polylysine adopts random, β-sheet or α-helical structures depending upon conditions of temperature and pH of the solution [281]. Experimental and theoretical work on a large number of synthetic polypeptides has provided insights on the variability of the frequencies for each structure. The large amount of data published by Krimm and Bandekar [282] give an insight in the nature of the amide bond.

For α-helical structures the mean frequency was found to be 1652 cm^{-1} for the amide I and 1548 cm^{-1} for the amide II absorption [283]. The half-width of the α-helix bands depends on the stability of the helix. For the most stable helices, the half-width of about 15 cm^{-1} corresponds with a helix/coil transition free energy of more than 300 cal mol^{-1}. Other α-helices display half-widths of 38 cm^{-1} and helix/coil transition free energies of about 90 cal mol^{-1}. The pioneering work of Byler and Susi [284] on spectral deconvolution has allowed much more detailed analysis of FTIR spectra in terms of secondary structure assignment.

There is a wealth of information that can be used to derive structural information by analyzing the shape and position of bands in the amide I region of the spectrum. The presence of a number of amide I band frequencies have been correlated with the presence of α-helical, antiparallel and parallel β-sheets and random coil structures [285–287]. It is now well accepted that absorbance in the range from 1650 to 1658 cm^{-1} is generally associated with the presence of α-helix in aqueous environments. Precise interpretation of bands in this region are difficult because there is significant overlap of the helical structures with random structures. One way to resolve this issue is to exchange the hydrogen from the peptide N–H with deuterium. If the protein contains a significant amount of random structure, the H–D exchange will result in a large shift in the position of the random structure (will now absorb at around 1646 cm^{-1}) and only a minor change in the position of the helical band. Beta-sheet vibrations have been shown to absorb between 1640 and 1620 cm^{-1} (though there is considerable disagreement on assignments for parallel and antiparallel β-sheets). Absorbances centered at 1670 cm^{-1} have been assigned to β-turns, or simply "turns" by some investigators.

9.6.10
Raman Spectroscopy and Raman Optical Activity

Raman spectroscopy is based on the Raman effect, which is the inelastic scattering of photons by molecules. The Indian physicist, C. V. Raman, discovered the effect in 1928 [288]. The Raman effect comprises a very small fraction, about 1 in 10^7, of the incident photons. In Raman scattering, the energies of the incident and scattered photons are different. Raman spectroscopy is another vibrational mode technique as the incoming photon promotes a vibrational oscillation from the ground state to a virtual, nonstationary state or, if the vibration is already in the virtual state, it can cause relaxation to the ground state. Raman spectroscopy comes in various guises such as difference, Fourier transform and resonance Raman spectroscopy, details of which can be found elsewhere [289, 290]. As with FTIR spectroscopy, we are measuring and assigning vibration bands with these techniques and it is the amide bands from peptide bonds that give most information regarding secondary structure (see Tables 9.9 and 9.10 for details). It is the precise positions of the amide I and III bands that are sensitive to secondary structure [291]. Correlations between these frequencies are widely noted in the literature (see, for example, Ref. [292]). Table 9.10 gives some examples of helix-related bands.

The amide III vibration and the $C_\alpha H$ bending vibration in UV Raman resonance spectroscopy are very sensitive to the amide backbone configuration [293]. The var-

Tab. 9.9. Ranges for wavenumbers and vibration assignments for amide vibrations (from Ref. 297).

Band name	*Wavenumber (cm^{-1})*	*Approximate description*
Amide A	3250–3300	N–H stretching
Amide I	1630–1700	C=O stretching
Amide II	1510–1570	N–H deformation
Amide III	1230–1330	N–H/C–H deformation
Amide IV	630–750	O=C–N deformation
Amide V	700–750	N–H out-of-plane deformation
Amide VI	~600	C=O out-of-plane deformation

From Ref. [297].

ious contributing signals are mixed when ψ is around 120°, i.e., for "random coil" and β-sheet conformations, but are unmixed at ψ values around 60° (α-helix conformation). This may allow the extraction of amide ψ angles from UV resonance Raman spectra [293].

Raman optical activity (ROA) measures vibrational optical activity. This is due to the small difference in the intensity of Raman scattering from chiral molecules in right and left circularly polarized incident light [142]. The technique is routinely applicable to biomolecules in aqueous environments but requires relatively large amounts of sample (typically 20–100 mg mL^{-1}) [142]. It can provide new information about solution dynamics as well as structure which is complementary to that obtained from more conventional optical spectroscopic techniques described above. Reviews of the theory of ROA can be found in the literature [294, 295] and are beyond the scope of this review.

ROA gives useful information regarding protein/peptide secondary structure in aqueous solution as the signals in the spectrum tend to be dominated by bands from the peptide backbone. Additionally it is sensitive to dynamic aspects of the structure and so can give information on mobile regions and nonnative states. Side chain bands are also present in the spectra though much less prominently. The extended amide III band [296, 297] is very useful in ROA as it is very sensitive to geometry, being composed of coupling between N–H and C_α-H deformations. A good description and review of secondary structure assignments from ROE spectra is given by Barron et al. [142].

Tab. 9.10. Raman amide I and III vibrations related to α-helical structure.

Location (cm^{-1})	*Assignment*	*information*
1655 ± 5	Amide C=O stretch	α-helix in water
1632	Amide C=O stretch	α-helix in D_2O
1661 ± 3	Amide C=O stretch	α-helix in D_2O
>1275	Amide III (weak)	α-helix (nothing below 1275 cm^{-1})

9.6.11 pH Titrations

9.6.11.1 Equipment and Reagents

- Circular dichroism spectrometer
- Quartz cuvette with a path length of 1 cm equipped with a magnetic bar
- A pH meter with a small-sized electrode
- A magnetic stirrer
- Peptide at a concentration such that the aggregation does not occur (typically 20–30 μM) dissolved in an appropriate buffer. Notes: Avoid using buffers that absorb at far UV wavelengths. Typical buffer used in pH titration contains 10 mM NaCl, 1 mM sodium phosphate, 1 mM sodium borate, and 1 mM sodium citrate.
- Concentrated HCl and NaOH

9.6.11.2 Method

1. Record UV CD spectra of the buffer at 222 nm.
2. Record UV CD spectra of the peptide at the starting pH. Typical parameters of CD measurement are as in Aggregation test protocol.
3. Record UV CD spectra after pH adjustments that are made by the addition of either NaOH or HCl. Record volume of acid or alkali added.
4. Subtract the average buffer reading from the average peptides readings.
5. Convert the unit of ellipticity (mdeg) to mean residual ellipticity. Note the concentration will decrease as acid or alkali is added.
6. Plot $[\theta]_{222}$ versus pH.
7. Fit the data to a Henderson-Hasselbach equation depending on the number of titrable groups in the peptide. For one apparent pK_a, the value is given by:

$$[\theta]_{222\mathrm{nm}} = [\theta]_{222,\,\mathrm{high\_pH}} \times \left(1 - \frac{1}{1 + 10^{\mathrm{pH}-\mathrm{p}Ka}}\right) + [\theta]_{222,\,\mathrm{low\_pH}} \times \left(\frac{1}{1 + 10^{\mathrm{pH}-\mathrm{p}Ka}}\right)$$

where $[\theta]_{222,\,\mathrm{highpH}}$ and $[\theta]_{222,\,\mathrm{lowpH}}$ are the molar ellipticities measured at 222 nm at the titration end points at high and low pH.

The equation for two different pK_a values is:

$$[\theta]_{222\mathrm{nm}} = [\theta]_{222,\,\mathrm{mid\_pH}} \times \left(1 - \frac{1}{1 + 10^{\mathrm{pH}-\mathrm{p}Ka1}}\right) + [\theta]_{222,\,\mathrm{low\_pH}} \times \left(\frac{1}{1 + 10^{\mathrm{pH}-\mathrm{p}Ka1}}\right) + [\theta]_{222,\,(\mathrm{mid\_pH}-\mathrm{high\_pH})} \times \left(1 - \frac{1}{1 + 10^{\mathrm{pH}-\mathrm{p}Ka2}}\right)$$

where, pK_a1 and pK_a2 are the pK_a values measured for the acid–base equilibrium at low and high pH, respectively. $[\theta]_{222,\,\mathrm{highpH}}$, $[\theta]_{222,\,\mathrm{midpH}}$, and $[\theta]_{222,\,\mathrm{lowpH}}$ are the molar ellipticities measured at 222 nm at the titration end points at high, mid, and low pH. $[\theta]_{222\mathrm{mid\_pH}-\mathrm{high\_pH}}$ is the change in molar ellipticity associated with pK_a2.

Acknowledgments

We thank all our coworkers in this field, namely Avi Chakrabartty, Carol Rohl, Buzz Baldwin, Tod Klingler, Ben Stapley, Jim Andrew, Eleri Hughes, Simon Penel, Duncan Cochran, Nicoleta Kokkoni, Jia Ke Sun, Jim Warwicker, Gareth Jones, and Jonathan Hirst. Current work in our lab on helices is supported by the Wellcome Trust (grant references 057318 and 065106). TMI thanks the Indonesian government for a scholarship.

References

1 Pauling, L., Corey, R. B., and Branson, H. R. (1951). The structure of proteins: two hydrogen-bonded helical configurations of the polypeptide chain. *Proc. Natl Acad. Sci. USA* 37, 205–211.

2 Perutz, M. F. (1951). New X-ray evidence on the configuration of polypeptide chains. *Nature* 167, 1053–1054.

3 Kendrew, J. C., Dickerson, R. E., Strandberg, B. E. et al. (1960). Structure of myoglobin. *Nature* 185, 422–427.

4 Barlow, D. J. and Thornton, J. M. (1988). Helix geometry in proteins. *J. Mol. Biol.* 201, 601–19.

5 Scholtz, J. M. and Baldwin, R. L. (1992). The mechanism of α-helix formation by peptides. *Annu. Rev. Biophys. Biomol. Struct.* 21, 95–118.

6 Baldwin, R. L. (1995). α-helix formation by peptides of defined sequence. *Biophys. Chem.* 55, 127–35.

7 Chakrabartty, A. and Baldwin, R. L. (1995). Stability of α-helices. *Adv. Protein Chem.* 46, 141–76.

8 Kallenbach, N. R., Lyu, P., and Zhou, H. (1996). CD spectroscopy and the helix-coil transition in peptides and polypeptides. In *Circular Dichroism and the Conformational Analysis of Biomolecules* G. D. Fasman, editor, Plenum Press, New York, 201–59.

9 Rohl, C. A. and Baldwin, R. L. (1998). Deciphering rules of helix stability in peptides. *Meth. Enzymol.* 295, 1–26.

10 Andrews, M. J. I. and Tabor, A. B. (1999). Forming stable helical peptides using natural and artificial amino acids. *Tetrahedron* 55, 11711–43.

11 Serrano, L. (2000). The relationship between sequence and structure in elementary folding units. *Adv. Protein Chem.* 53, 49–85.

12 Richardson, J. S. and Richardson, D. C. (1988). Amino acid preferences for specific locations at the ends of α helices. *Science* 240, 1648–52.

13 Presta, L. G. and Rose, G. D. (1988). Helix signals in proteins. *Science* 240, 1632–41.

14 Doig, A. J., MacArthur, M. W., Stapley, B. J., and Thornton, J. M. (1997). Structures of N-termini of helices in proteins. *Protein Sci.* 6, 147–55.

15 MacGregor, M. J., Islam, S. A., and Sternberg, M. J. E. (1987). Analysis of the relationship between side-chain conformation and secondary structure in globular proteins. *J. Mol. Biol.* 198, 295–310.

16 Swindells, M. B., MacArthur, M. W., and Thornton, J. M. (1995). Intrinsic ϕ, ψ propensities of amino acids derived from the coil regions of known structures. *Nat. Struct. Biol.* 2, 596–603.

17 Dunbrack, R. and Karplus, M. (1994). Conformational analysis of the backbone-dependent rotamer preferences of protein side-chains. *Nat. Struct. Biol.* 1, 334–9.

18 Dunbrack, R. L. (2002). Rotamer libraries in the 21(st) century. *Curr. Opin. Struct. Biol.* 12, 431–40.

19 Penel, S., Hughes, E., and Doig, A. J. (1999). Side-chain structures in the first turn of the α-helix. *J. Mol. Biol.* 287, 127–43.

20 Serrano, L. and Fersht, A. R. (1989). Capping and α-helix stability. *Nature* 342, 296–9.

21 Bell, J. A., Becktel, W. J., Sauer, U., Baase, W. A., and Matthews, B. W. (1992). Dissection of helix capping in T4 lysozyme by structural and thermodynamic analysis of six amino acid substitutions at Thr 59. *Biochemistry* 31, 3590–6.

22 Chakrabartty, A., Doig, A. J., and Baldwin, R. L. (1993). Helix capping propensities in peptides parallel those in proteins. *Proc. Natl Acad. Sci. USA* 90, 11332–6.

23 Forood, B., Feliciano, E. J., and Nambiar, K. P. (1993). Stabilization of α-helical structures in short peptides via end capping. *Proc. Natl Acad. Sci. USA* 90, 838–42.

24 Dasgupta, S. and Bell, J. A. (1993). Design of helix ends. Amino acid preferences, hydrogen bonding and electrostatic interactions. *Int. J. Pept. Protein Res.* 41, 499–511.

25 Harper, E. T. and Rose, G. D. (1993). Helix stop signals in proteins and peptides: the capping box. *Biochemistry* 32, 7605–9.

26 Seale, J. W., Srinivasan, R., and Rose, G. D. (1994). Sequence determinants of the capping box, a stabilizing motif at the N-termini of α-helices. *Protein Sci.* 3, 1741–5.

27 Muñoz, V. and Serrano, L. (1995). The hydrophobic-staple motif and a role for loop residues in α-helix stability and protein folding. *Nat. Struct. Biol.* 2, 380–385.

28 Viguera, A. R. and Serrano, L. (1999). Stable proline box motif at the N-terminal end of α-helices. *Protein Sci.* 8, 1733–42.

29 Doig, A. J. and Baldwin, R. L. (1995). N- and C-capping preferences for all 20 amino acids in α-helical peptides. *Protein Sci.* 4, 1325–36.

30 Rohl, C. A., Chakrabartty, A., and Baldwin, R. L. (1996). Helix propagation and N-cap propensities of the amino acids measured in alanine-based peptides in 40 volume percent trifluoroethanol. *Protein Sci.* 5, 2623–37.

31 Schellman, C. (1980). The αL conformation at the ends of helices. *Protein Folding* 53–61.

32 Aurora, R., Srinivasan, R., and Rose, G. D. (1994). Rules for α-helix termination by glycine. *Science* 264, 1126–30.

33 Aurora, R. and Rose, G. D. (1998). Helix capping. *Protein Sci.* 7, 21–38.

34 Prieto, J. and Serrano, L. (1997). C-capping and helix stability: the Pro C-capping motif. *J. Mol. Biol.* 274, 276–88.

35 Siedlecka, M., Goch, G., Ejchart, A., Sticht, H., and Bierzynski, A. (1999). α-Helix nucleation by calcium-binding peptide loop. *Proc. Natl Acad. Sci. USA* 96, 903–8.

36 Jernigan, R., Raghunathan, G., and Bahar, I. (1994). Characterisation of interactions and metal-ion binding-sites in proteins. *Curr. Opin. Struct. Biol.* 4, 256–63.

37 Alberts, I. L., Nadassy, K., and Wodak, S. J. (1998). Analyisis of zinc binding sites in protein crystal structures. *Protein Sci.* 7, 1700–16.

38 Ghadiri, M. R. and Choi, C. (1990). Secondary structure nucleation in peptides – transition-metal ion stabilized α-helices. *J. Am. Chem. Soc.* 112, 1630–2.

39 Kise, K. J. and Bowler, B. E. (2002). Induction of helical structure in a heptapeptide with a metal cross-link: Modification of the Lifson-Roig Helix-Coil theory to account for covalent cross-links. *Biochemistry* 41, 15826–37.

40 Ruan, F., Chen, Y., and Hopkins, P. B. (1990). Metal ion enhanced helicity in synthetic peptides containing unnatural, metal-ligating residues. *J. Am. Chem. Soc.* 112, 9403–4.

41 Cline, D. J., Thorpe, C., and Schneider, J. P. (2003). Effects of As(III) binding on α-helical structure. *J. Am. Chem. Soc.* 125, 2923–9.

42 Karpen, M. E., De Haset, P. L., and Neet, K. E. (1992). Differences in the

amino acid distributions of 3_{10}-helices and α-helices. *Protein Sci.* 1, 1333–42.

43 Baker, E. N. and Hubbard, R. E. (1984). Hydrogen bonding in globular proteins. *Prog. Biophys. Mol. Biol.* 44, 97–179.

44 Némethy, G., Phillips, D. C., Leach, S. J., and Scheraga, H. A. (1967). A second right-handed helical structure with the parameters of the Pauling-Corey α-helix. *Nature* 214, 363–5.

45 Millhauser, G. L. (1995). Views of helical peptides – a proposal for the position of 3_{10}-helix along the thermodynamic folding pathway. *Biochemistry* 34, 3872–7.

46 Bolin, K. A. and Millhauser, G. L. (1999). α and 3_{10}: The split personality of polypeptide helices. *Acc. Chem. Res.* 32, 1027–33.

47 Miick, S. M., Martinez, G. V., Fiori, W. R., Todd, A. P., and Millhauser, G. L. (1992). Short alanine-based peptides may form 3_{10}-helices and not α-helices in aqueous solution. *Nature* 359, 653–5.

48 Zhou, H. X. X., Lyu, P. C. C., Wemmer, D. E., and Kallenbach, N. R. (1994). Structure of C-terminal α-helix cap in a synthetic peptide. *J. Am. Chem. Soc.* 116, 1139–40.

49 Fiori, W. R. and Millhauser, G. L. (1995). Exploring the peptide 3_{10}-helix/α-helix equilibrium with double label electron spin resonance. *Biopolymers* 37, 243–50.

50 Toniolo, C. and Benedetti, E. (1991). The polypeptide 3_{10}-helix. *Trends Biochem. Sci.* 16, 350–3.

51 Ramachandran, G. N. and Sasisekharan, V. (1968). Conformation of polypeptides and proteins. *Adv. Protein Chem.* 23, 283–437.

52 Low, B. W. and Grenville-Wells, H. J. (1953). Generalized mathematical relations for polypeptide chain helixes. The coordinates for the π helix. *Proc. Natl Acad. Sci. USA* 39, 785–801.

53 Shirley, W. A. and Brooks, C. L. (1997). Curious structure in "canonical" alanine based peptides. *Proteins: Struct. Funct. Genet.* 28, 59–71.

54 Lee, K. H., Benson, D. R., and Kuczera, K. (2000). Transitions from α to π helix observed in molecular dynamics simulations of synthetic peptides. *Biochemistry* 39, 13737–47.

55 Weaver, T. M. (2000). The π-helix translates structure into function. *Protein Sci.* 9, 201–6.

56 Morgan, D. M., Lynn, D. G., Miller-Auer, H., and Meredith, S. C. (2001). A designed Zn2+-binding amphiphilic polypeptide: Energetic consequences of π-helicity. *Biochemistry* 40, 14020–9.

57 Fodje, M. N. and Al-Karadaghi, S. (2002). Occurrence, conformational features and amino acid propensities for the π-helix. *Protein Eng.* 15, 353–8.

58 Baldwin, R. L. (2003). In search of the energetic role of peptide hydrogen bonds. *J. Biol. Chem.* 278, 17581–8.

59 Epand, R. M. and Scheraga, H. A. (1968). *Biochemistry* 7, 2864–72.

60 Taniuchi, J. H. and Anfinsen, C. B. (1969). *J. Biol. Chem.* 244, 2864–72.

61 Spek, E. J., Gong, Y., and Kallenbach, N. R. (1995). Intermolecular interactions in a helical oligo- and poly(L-glutamic acid) at acidic pH. *J. Am. Chem. Soc.* 117, 10773–4.

62 Brown, J. E. and Klee, W. A. (1971). *Biochemistry* 10, 470–6.

63 Bierzynski, A., Kim, P. S., and Baldwin, R. L. (1982). A salt bridge stabilizes the helix formed by isolated C-peptide of ribonuclease A. *Proc. Natl Acad. Sci. USA* 79, 2470–4.

64 Kim, P. S., Bierzynski, A., and Baldwin, R. L. (1982). A competing salt-bridge suppresses helix formation by the isolated C-peptide carboxylate of Ribonuclease A. *J. Mol. Biol.* 162, 187–99.

65 Kim, P. S. and Baldwin, R. L. (1984). A helix stop signal in the isolated S-peptide of ribonuclease A. *Nature* 307, 329–34.

66 Shoemaker, K. R., Kim, P. S., Brems, D. N. et al. (1985). Nature of the charged-group effect on the stability of the C-peptide helix. *Proc. Natl Acad. Sci. USA* 82, 2349–53.

67 Strehlow, K. G. and Baldwin, R. L. (1989). Effect of the substitution Ala-

Gly at each of 5 residue positions in the C-peptide helix. *Biochemistry* 28, 2130–3.

68 Osterhout, J. J., Baldwin, R. L., York, E. J., Stewart, J. M., Dyson, H. J., and Wright, P. E. (1989). H-1 NMR studies of the solution conformations of an analog of the C-peptide of ribonuclease-A. *Biochemistry* 29, 7059–64.

69 Shoemaker, K. R., Fairman, R., Schultz, D. A. et al. (1990). Side-chain interactions in the C-peptide helix – Phe8–His12^{+}. *Biopolymers* 29, 1–11.

70 Fairman, R., Shoemaker, K. R., York, E. J., Stewart, J. M., and Baldwin, R. L. (1990). The Glu2–Arg10+ side-chain interaction in the C-peptide helix of ribonuclease A. *Biophys. Chem.* 37, 107–19.

71 Strehlow, K. G., Robertson, A. D., and Baldwin, R. L. (1991). Proline for alanine subsitutions in the C-peptide helix of ribonuclease A. *Biochemistry* 30, 5810–14.

72 Fairman, R., Armstrong, K. M., Shoemaker, K. R., York, E. J., Stewart, J. M., and Baldwin, R. L. (1991). Position effect on apparent helical propensities in the C-peptide helix. *J. Mol. Biol.* 221, 1395–401.

73 Blanco, F. J., Jimenez, M. A., Rico, M., Santoro, J., Herranz, J., and Nieto, J. L. (1992). The homologous angiogenin and ribonuclease N-terminal fragments fold into very similar helices when isolated. *Biochem. Biophys. Res. Commun.* 182, 1491–8.

74 Rico, M., Nieto, J. L., Santoro, J., Bermejo, F. J., and Herranz, J. (1983). H1-NMR parameters of the N-terminal 13-residue C-peptide of ribonuclease in aqueous-solution. *Org. Magn. Res.* 21, 555–63.

75 Gallego, E., Herranz, J., Nieto, J. L., Rico, M., and Santoro, J. (1983). H1-NMR parameters of the N-terminal 19-residue S-peptide of ribonuclease in aqueous-solution. *Int. J. Pept. Protein Res.* 21, 242–53.

76 Rico, M., Nieto, J. L., Santoro, J., Bermejo, F. J., Herranz, J., and Gallego, E. (1983). Low temperature H1-NMR evidence of the folding of isolated ribonuclease S-peptide. *FEBS Lett.* 162, 314–19.

77 Rico, M., Gallego, E., Santoro, J., Bermejo, F. J., Nieto, J. L., and Herranz, J. (1984). On the fundamental role of the Glu2^{-} . . . Arg10^{+} salt bridge in the folding of isolated ribonuclease A S-peptide. *Biochem. Biophys. Res. Commun.* 123, 757–63.

78 Nieto, J. L., Rico, M., Jimenez, M. A., Herranz, J., and Santoro, J. (1985). Amide H1-NMR study of the folding of ribonuclease C-peptide. *Int. J. Biol. Macromol.* 7, 66–70.

79 Nieto, J. L., Rico, M., Santoro, J., and Bermejo, J. (1985). NH resonanaces of ribonuclease S-peptide in aqueous solution – low temperature NMR study. *Int. J. Pept. Protein Res.* 25, 47–55.

80 Santoro, J., Rico, M., Nieto, J. L., Bermejo, J., Herranz, J., and Gallego, E. (1986). C13 NMR spectral assignment of ribonuclease S-peptide – Some new structural information about its low temperature folding. *J. Mol. Struct.* 141, 243–8.

81 Rico, M., Herranz, J., Bermejo, J. et al. (1986). Quantitative interpretation of the helix coil transition in RNase A S-peptide. *J. Mol. Struct.* 143, 439–44.

82 Rico, M., Santoro, J., Bermejo, J. et al. (1986). Thermodynamic parameters for the helix coil thermal transition of ribonuclease S-peptide and derivatives from H1 NMR data. *Biopolymers* 25, 1031–53.

83 Marqusee, S. and Baldwin, R. L. (1987). Helix stabilization by Glu^{-} . . . Lys^{+} salt bridges in short peptides of de novo design. *Proc. Natl Acad. Sci. USA* 84, 8898–902.

84 Park, S. H., Shalongo, W., and Stellwagen, E. (1993). Residue helix parameters obtained from dichroic analysis of peptides of defined sequence. *Biochemistry* 32, 7048–53.

85 Marqusee, S., Robbins, V. H., and Baldwin, R. L. (1989). Unusually stable helix formation in short alanine based peptides. *Proc. Natl Acad. Sci. USA* 86, 5286–90.

86 Lyu, P. C., Marky, L. A., and Kallen-

bach, N. R. (1989). The role of ion-pairs in α-helix stability – 2 new designed helical peptides. *J. Am. Chem. Soc.* 111, 2733–34.

87 Lyu, P. C., Liff, M. I., Marky, L. A., and Kallenbach, N. R. (1990). Side-chain contributions to the stability of α-helical structure in peptides. *Science* 250, 669–73.

88 Gans, P. J., Lyu, P. C., Manning, P. C., Woody, R. W., and Kallenbach, N. R. (1991). The helix-coil transition in heterogeneous peptides with specific side chain interactions: Theory and comparison with circular dichroism. *Biopolymers* 31, 1605–14.

89 Penel, S., Morrison, R. G., Mortishire-Smith, R. J., and Doig, A. J. (1999). Periodicity in α-helix lengths and C-capping preferences. *J. Mol. Biol.* 293, 1211–19.

90 Wada, A. (1976). The α-helix as an electric macro-dipole. *Adv. Biophys.* 9, 1–63.

91 Hol, W. G. J., van Duijnen, P. T., and Berendsen, H. J. C. (1978). The α-helix dipole and the properties of proteins. *Nature* 273, 443–6.

92 Aqvist, J., Luecke, H., Quiocho, F. A., and Warshel, A. (1991). Dipoles located at helix termini of proteins stabilize charges. *Proc. Natl Acad. Sci. USA* 88, 2026–30.

93 Zhukovsky, E. A., Mulkerrin, M. G., and Presta, L. G. (1994). Contribution to global protein stabilization of the N-capping box in human growth hormone. *Biochemistry* 33, 9856–64.

94 Tidor, B. (1994). Helix-capping interaction in λ Cro protein: a free energy simulation analysis. *Proteins: Struct. Funct. Genet.* 19, 310–23.

95 Cochran, D. A. E., Penel, S., and Doig, A. J. (2001). Contribution of the N1 amino acid residue to the stability of the α-helix. *Protein Sci.* 10, 463–70.

96 Cochran, D. A. E. and Doig, A. J. (2001). Effects of the N2 residue on the stability of the α-helix for all 20 amino acids. *Protein Sci.* 10, 1305–11.

97 Iqbalsyah, T. M. and Doig, A. J. (in press). Effect of the N3 residue on the stability of the α-helix. *Protein Sci.* 13, 32–39.

98 Decatur, S. M. (2000). IR spectroscopy of isotope-labeled helical peptides: Probing the effect of N-acetylation on helix stability. *Biopolymers* 180–5.

99 Doig, A. J., Chakrabartty, A., Klingler, T. M., and Baldwin, R. L. (1994). Determination of free energies of N-capping in α-helices by modification of the Lifson-Roig helix-coil theory to include N- and C-capping. *Biochemistry* 33, 3396–403.

100 Stapley, B. J., Rohl, C. A., and Doig, A. J. (1995). Addition of side chain interactions to modified Lifson-Roig helix-coil theory: application to energetics of phenylalanine-methionine interactions. *Protein Sci.* 4, 2383–91.

101 Andrew, C. D., Penel, S., Jones, G. R., and Doig, A. J. (2001). Stabilising non-polar/polar side chain interactions in the α-helix. *Proteins: Struct. Funct. Genet.* 45, 449–55.

102 Huyghues-Despointes, B. M., Scholtz, J. M., and Baldwin, R. L. (1993). Effect of a single aspartate on helix stability at different positions in a neutral alanine-based peptide. *Protein Sci.* 2, 1604–11.

103 Brandts, J. R. and Kaplan, K. J. (1973). Derivative spectroscopy applied to tyrosyl chromophores. Studies on ribonuclease, lima bean inhibitor, and pancreatic trypsin inhibitor. *Biochemistry* 10, 470–6.

104 Edelhoch, H. (1967). Spectroscopic determination of tryptophan and tyrosine in proteins. *Biochemistry* 6, 1948–54.

105 Chakrabartty, A., Kortemme, T., Padmanabhan, S., and Baldwin, R. L. (1993). Aromatic side-chain contribution to far-ultraviolet circular dichroism of helical peptides and its effect on measurement of helix propensities. *Biochemistry* 32, 5560–5.

106 Andrew, C. D., Bhattacharjee, S., Kokkoni, N., Hirst, J. D., Jones, G. R., and Doig, A. J. (2002). Stabilising interactions between aromatic and basic side chains in α-helical peptides and proteins. Tyrosine effects on helix circular dichroism. *J. Am. Chem. Soc.* 124, 12706–14.

107 Kemp, D. S., Boyd, J. G., and Muendel, C. C. (1991). The helical s-constant for alanine in water derived from template-nucleated helices. *Nature* 352, 451–4.

108 Kemp, D. S., Allen, T. J., and Oslick, S. L. (1995). The energetics of helix formation by short templated peptides in aqueous solution. 1. Characterization of the reporting helical template Ac-HE1(1). *J. Am. Chem. Soc.* 117, 6641–57.

109 Groebke, K., Renold, P., Tsang, K. Y., Allen, T. J., McClure, K. F., and Kemp, D. S. (1996). Template-nucleated alanine-lysine helices are stabilized by position-dependent interactions between the lysine side chain and the helix barrel. *Proc. Natl Acad. Sci. USA* 93, 4025–9.

110 Kemp, D. S., Oslick, S. L., and Allen, T. J. (1996). The structure and energetics of helix formation by short templated peptides in aqueous solution. 3. Calculation of the helical propagation constant *s* from the template stability constants t/c for Ac-Hel(1)-Ala(*n*)-OH, $n = 1$–6. *J. Am. Chem. Soc.* 118, 4249–55.

111 Kemp, D. S., Allen, T. J., Oslick, S. L., and Boyd, J. G. (1996). The structure and energetics of helix formation by short templated peptides in aqueous solution. 2. Characterization of the helical structure of Ac-Hel(1)-Ala(6)-OH. *J. Am. Chem. Soc.* 118, 4240–8.

112 Austin, R. E., Maplestone, R. A., Sefler, A. M. et al. (1997). Template for stabilization of a peptide α-helix: Synthesis and evaluation of conformational effects by circular dichroism and NMR. *J. Am. Chem. Soc.* 119, 6461–72.

113 Arrhenius, T. and Satterthwait, A. C. (1990). *Peptides: Chemistry, Structure and Biology*: Proceedings of the 11th American Peptide Symposium, ESCOM, Leiden.

114 Muller, K., Obrecht, D., Knierzinger, A. et al. (1993). *Perspectives in Medicinal Chemistry*, pp. 513–531, Verlag Chemie, Weinheim.

115 Gani, D., Lewis, A., Rutherford, T. et al. (1998). Design, synthesis, structure and properties of an α-helix cap template derived from N-[(2S)-2-chloropropionyl]-(2S)-Pro-(2R)-Ala-(2S,4S)-4-thioPro-OMe which initiates α-helical structures. *Tetrahedron* 54, 15793–819.

116 Aleman, C. (1997). Conformational properties of α-amino acids disubstituted at the α-carbon. *J. Phys. Chem.* 101, 5046–50.

117 Sacca, B., Formaggio, F., Crisma, M., Toniolo, C., and Gennaro, R. (1997). Linear oligopeptides. 401. In search of a peptide 3_{10}-helix in water. *Gazz. Chim. Ital.* 127, 495–500.

118 Tanaka, M. (2002). Design and conformation of peptides containing α,α-disubstituted α-amino acids. *J. Synth. Org. Chem. Japan* 60, 125–36.

119 Lancelot, N., Elbayed, K., Raya, J. et al. (2003). Characterization of the 3_{10}-helix in model peptides by HRMAS NMR spectroscopy. *Chem. Eur. J.* 9, 1317–23.

120 Karle, I. L. and Balaram, P. (1990). Structural characteristics of α-helical peptide molecules containing Aib residues. *Biochemistry* 29, 6747–56.

121 Banerjee, R. and Basu, G. (2002). A short Aib/Ala-based peptide helix is as stable as an Ala-based peptide helix double its length. *ChemBiochem* 3, 1263–6.

122 Yokum, T. S., Gauthier, T. J., Hammer, R. P., and McLaughlin, M. L. (1997). Solvent effects on the 3_{10}-/α-helix equilibrium in short amphipathic peptides rich in α,α-disubstituted amino acids. *J. Am. Chem. Soc.* 119, 1167–8.

123 Millhauser, G. L., Stenland, C. J., Hanson, P., Bolin, K. A., and van de Ven, F. J. M. (1997). Estimating the relative populations of 3_{10}-helix and α-helix in Ala-rich peptides. A hydrogen exchange and high field NMR study. *J. Mol. Biol.* 267, 963–74.

124 Fiori, W. R., Lundberg, K. M., and Millhauser, G. L. (1994). A single carboxy-terminal arginine determines the amino-terminal helix conformation of an alanine-based peptide. *Nat. Struct. Biol.* 1, 374–7.

125 Yoder, G., Polese, A., Silva, R. A.

G. D. et al. (1997). Conformation characterization of terminally blocked L-(αMe)Val homopeptides using vibrational and electronic circular dichroism. 3_{10}-Helical stabilization by peptide-peptide interaction. *J. Am. Chem. Soc.* 119, 10278–85.

126 Kennedy, D. F., Crisma, M., Toniolo, C., and Chapman, D. (1991). Studies of peptides forming 3_{10}- and α-helices and β-bend ribbon structures in organic solution and in model biomembranes by Fourier transform infrared spectroscopy. *Biochemistry* 30, 6541–8.

127 Hungerford, G., Martinez-Insua, M., Birch, D. J. S., and Moore, B. D. (1996). A reversible transition between an α-helix and a 3_{10}-helix in a fluorescence-labelled peptide. *Angew. Chem. Int. Ed. Engl.* 35, 326–9.

128 Sheinerman, F. B. and Brooks, C. L. (1995). 3_{10}-Helices in peptides and proteins as studied by modified Zimm-Bragg theory. *J. Am. Chem. Soc.* 117, 10098–103.

129 Rose, G. D. and Creamer, T. P. (1994). Protein-folding – predicting predicting. *Proteins: Struct. Funct. Genet.* 19, 1–3.

130 Dalal, S., Balasubramanian, S., and Regan, L. (1997). Protein alchemy: Changing β-sheet into α-helix. *Nat. Struct. Biol.* 4, 548–52.

131 Rose, G. D. (1997). Protein folding and the paracelsus challenge. *Nat. Struct. Biol.* 4, 512–14.

132 Poland, D. and Scheraga, H. A. (1970). *Theory of Helix-Coil Transitions in Biopolymers*. Academic Press, New York and London.

133 Qian, H. and Schellman, J. A. (1992). Helix/coil theories: A comparative study for finite length polypeptides. *J. Phys. Chem.* 96, 3987–94.

134 Doig, A. J. (2002). Recent advances in helix-coil theory. *Biophys. Chem.* 101–102, 281–93.

135 Zimm, B. H. and Bragg, J. K. (1959). Theory of the phase transition between helix and random coil in polypeptide chains. *J. Chem. Phys.* 31, 526–35.

136 Lifson, S. and Roig, A. (1961). On the theory of the helix-coil transition in polypeptides. *J. Chem. Phys.* 34, 1963–74.

137 Flory, P. J. (1969). *Statistical Mechanics of Chain Molecules*. Wiley, New York.

138 Pappu, R. V., Srinivasan, R., and Rose, G. D. (2000). The Flory isolated-pair hypothesis is not valid for polypeptide chains: Implications for protein folding. *Proc. Natl Acad. Sci. USA* 97, 12565–70.

139 Tiffany, M. L. and Krimm, S. (1968). New chain conformations of poly(glutamic acid) and polylysine. *Biopolymers* 6, 1379–82.

140 Krimm, S. and Tiffany, M. L. (1974). The circular dichroism spectrum and structure of unordered polypeptides and proteins. *Israel J. Chem.* 12, 189–200.

141 Woody, R. W. (1992). Circular dichroism and conformations of unordered polypeptides. *Adv. Biophys. Chem.* 2, 37–79.

142 Barron, L. D., Hecht, L., Blanch, E. W., and Bell, A. F. (2000). Solution structure and dynamics of biomolecules from Raman optical activity. *Prog. Biophys. Mol. Biol.* 73, 1–49.

143 Blanch, E. W., Morozova-Roche, L. A., Cochran, D. A. E., Doig, A. J., Hecht, L., and Barron, L. D. (2000). Is polyproline II helix the killer conformation? A Raman optical activity study of the amyloidogenic prefibrillar intermediate of human lysozyme. *J. Mol. Biol.* 301, 553–63.

144 Smyth, E., Syme, C. D., Blanch, E. W., Hecht, L., Vasak, M., and Barron, L. D. (2000). Solution structure of native proteins irregular folds from Raman optical activity. *Biopolymers* 58, 138–51.

145 Syme, C. D., Blanch, E. W., Holt, C. et al. (2002). A Raman optical activity study of the rheomorphism in caseins, synucleins and tau. *Eur. J. Biochem.* 269, 148–56.

146 Rucker, A. L. and Creamer, T. P. (2002). Polyproline II helical structure in protein unfolded states: Lysine peptides revisited. *Protein Sci.* 11, 980–5.

147 Shi, Z. S., Woody, R. W., and Kallenbach, N. R. (2002). Is polyproline II a major backbone conformation in unfolded proteins? *Adv. Protein Chem.* 62, 163–240.

148 Pappu, R. V. and Rose, G. D. (2002). A simple model for polyproline II structure in unfolded states of alanine-based peptides. *Protein Sci.* 11, 2437–55.

149 Shi, Z., Olson, C. A., Rose, G. D., Baldwin, R. L., and Kallenbach, N. R. (2002). Polyproline II structure in a sequence of seven alanine residues. *Proc. Natl Acad. Sci. USA* 99, 9190–5.

150 Rucker, A. L., Pager, C. T., Campbell, M. N., Qualis, J. E., and Creamer, T. P. (2003). Host-guest scale of left-handed polyproline II helix formation. *Proteins: Struct. Funct. Genet.* 53, 68–75.

151 Andersen, N. H. and Tong, H. (1997). Empirical parameterization of a model for predicting peptide helix/coil equilibrium populations. *Protein Sci.* 6, 1920–36.

152 Scholtz, J. M., Qian, H., Robbins, V. H., and Baldwin, R. L. (1993). The energetics of ion-pair and hydrogen-bonding interactions in a helical peptide. *Biochemistry* 32, 9668–76.

153 Shalongo, W. and Stellwagen, E. (1995). Incorporation of pairwise interactions into the Lifson-Roig model for helix prediction. *Protein Sci.* 4, 1161–6.

154 Argos, P. and Palau, J. (1982). Amino acid distribution in protein secondary structures. *Int. J. Pept. Protein Res.* 19, 380–93.

155 Kumar, S. and Bansal, M. (1998). Dissecting α-helices: position-specific analysis of α-helices in globular proteins. *Proteins* 31, 460–76.

156 Sun, J. K., Penel, S., and Doig, A. J. (2000). Determination of α-helix N1 energies by addition of N1, N2 and N3 preferences to helix-coil theory. *Protein Sci.* 9, 750–4.

157 Rohl, C. A. and Doig, A. J. (1996). Models for the 3_{10}-helix/coil, π-helix/coil, and α-helix/3_{10}-helix/coil transitions in isolated peptides. *Protein Sci.* 5, 1687–96.

158 Sun, J. K. and Doig, A. J. (1998). Addition of side-chain interactions to 3_{10}-helix/coil and α-helix/3_{10}-helix/coil theory. *Protein Sci.* 7, 2374–83.

159 Muñoz, V. and Serrano, L. (1994). Elucidating the folding problem of helical peptides using empirical parameters. *Nat. Struct. Biol.* 1, 399–409.

160 Muñoz, V. and Serrano, L. (1997). Development of the multiple sequence approximation within the AGADIR model of α-helix formation: comparison with Zimm-Bragg and Lifson-Roig formalisms. *Biopolymers* 41, 495–509.

161 Fernández-Recio, J., Vásquez, A., Civera, C., Sevilla, P., and Sancho, J. (1997). The tryptophan/histidine interaction in α-helices. *J. Mol. Biol.* 267, 184–97.

162 Lacroix, E., Viguera, A. R., and Serrano, L. (1998). Elucidating the folding problem of α-helices: local motifs, long-range electrostatics, ionic-strength dependence and prediction of NMR parameters. *J. Mol. Biol.* 284, 173–91.

163 Muñoz, V. and Serrano, L. (1995). Elucidating the folding problem of helical peptides using empirical parameters. II. Helix macrodipole effects and rational modification of the helical content of natural peptides. *J. Mol. Biol.* 245, 275–96.

164 Petukhov, M., Muñoz, V., Yumoto, N., Yoshikawa, S., and Serrano, L. (1998). Position dependence of non-polar amino acid intrinsic helical propensities. *J. Mol. Biol.* 278, 279–89.

165 Lomize, A. L. and Mosberg, H. I. (1997). Thermodynamic model of secondary structure for α-helical peptides and proteins. *Biopolymers* 42, 239–69.

166 Vásquez, M. and Scheraga, H. A. (1988). Effect of sequence-specific interactions on the stability of helical conformations in polypeptides. *Biopolymers* 27, 41–58.

167 Roberts, C. H. (1990). A hierarchical nesting approach to describe the stability of α helices with side chain interactions. *Biopolymers* 30, 335–47.

168 Guzzo, A. V. (1965). The influence of amino acid sequence on protein structure. *Biophys. J.* 5, 809–22.

169 Davies, D. R. (1964). A correlation between amino acid composition and protein structure. *J. Mol. Biol.* 9, 605–9.

170 Chou, P. Y. and Fasman, G. D. (1974). Conformational parameters for amino acids in helical, b-sheet and random coil regions calculated from proteins. *Biochemistry* 13, 211–21.

171 Chou, P. Y. and Fasman, G. D. (1978). Empirical predictions of protein conformation. *Annu. Rev. Biochem.* 47, 251–76.

172 Von Dreele, P. H., Poland, D., and Scheraga, H. A. (1971). Helix-coil stability constants for the naturally occurring amino acids in water. I. Properties of copolymers and approximate theories. *Macromolecules* 4, 396–407.

173 Von Dreele, P. H., Lotan, N., Ananthanarayanan, V. S., Andreatta, R. H., Poland, D., and Scheraga, H. A. (1971). Helix-coil stability constants for the naturally occurring amino acids in water. II. Characterization of the host polymers and application of the host-guest technique to random poly-(hydroxypropylglutamine-co-hydroxybutylglutamine). *Macromolecules* 4, 408–17.

174 Wojcik, J., Altmann, K. H., and Scheraga, H. A. (1990). Helix-coil stability constants for the naturally occurring amino acids in water. XXIV. Half-cysteine parameters from random poly-(hydroxybutylglutamine-co-S-methylthio-L-cysteine). *Biopolymers* 30, 121–34.

175 Padmanabhan, S., York, E. J., Gera, L., Stewart, J. M., and Baldwin, R. L. (1994). Helix-forming tendencies of amino acids in short (hydroxybutyl)-L-glutamine peptides: An evaluation of the contradictory results from host-guest studies and short alanine-based peptides. *Biochemistry* 33, 8604–9.

176 Chakrabartty, A., Kortemme, T., and Baldwin, R. L. (1994). Helix propensities of the amino acids measured in alanine-based peptides without helix-stabilizing side-chain interactions. *Protein Sci.* 3, 843–52.

177 Blaber, M., Zhang, X.-J., and Matthews, B. W. (1993). Structural basis of amino acid α-helix propensity. *Science* 260, 1637–40.

178 Blaber, M. W., Baase, W. A., Gassner, N., and Matthews, B. W. (1993). Structural basis of amino acid α-helix propensity. *Science* 260, 1637–40.

179 Blaber, M., Zhang, X. J., Lindstrom, J. D., Pepiot, S. D., Baase, W. A., and Matthews, B. W. (1994). Determination of α-helix propensity within the context of a folded protein: sites 44 and 131 in bacteriophage-T4 lysozyme. *J. Mol. Biol.* 235, 600–24.

180 Horovitz, A., Matthews, J. M., and Fersht, A. R. (1992). α-Helix stability in proteins. II. Factors that influence stability at an internal position. *J. Mol. Biol.* 227, 560–8.

181 O'Neil, K. T. and DeGrado, W. F. (1990). A thermodynamic scale for the helix-forming tendencies of the commonly occurring amino acids. *Science* 250, 646–51.

182 Pace, C. N. and Scholtz, J. M. (1998). A helix propensity scale based on experimental studies of peptides and proteins. *Biophys. J.* 75, 422–7.

183 Vila, J., Williams, R. L., Grant, J. A., Wojcik, J., and Scheraga, H. A. (1992). The intrinsic helix-forming tendency of L-alanine. *Proc. Natl Acad. Sci. USA* 89, 7821–5.

184 Vila, J. A., Ripoll, D. R., and Scheraga, H. A. (2000). Physical reasons for the unusual α-helix stabilization afforded by charged or neutral polar residues in alanine-rich peptides. *Proc. Natl Acad. Sci. USA* 97, 13075–9.

185 Rohl, C. A., Fiori, W., and Baldwin, R. L. (1999). Alanine is helix-stabilizing in both template-nucleated and standard peptide helices. *Proc. Natl Acad. Sci. USA* 96, 3682–7.

186 Kennedy, R. J., Tsang, K.-Y., and Kemp, D. S. (2002). Consistent helicities from CD and template t/c data for N-templated polyalanines:

progress toward resolution of the alanine helicity problem. *J. Am. Chem. Soc.* 124, 934–44.

187 Lyu, P. C., Zhou, H. X. X., Jelveh, N., Wemmer, D. E., and Kallenbach, N. R. (1992). Position-dependent stabilizing effects in α-helices – N-terminal capping in synthetic model peptides. *J. Am. Chem. Soc.* 114, 6560–2.

188 Petukhov, M., Uegaki, K., Yumoto, N., Yoshikawa, S., and Serrano, L. (1999). Position dependence of amino acid intrinsic helical propensities II: Non-charged polar residues: Ser, Thr, Asn, and Gln. *Protein Sci.* 8, 2144–50.

189 Petukhov, M., Uegaki, K., Yumoto, N., and Serrano, L. (2002). Amino acid intrinsic α-helical propensities III: Positional dependence at several positions of C-terminus. *Protein Sci.* 11, 766–77.

190 Ermolenko, D. N., Richardson, J. M., and Makhatadze, G. I. (2003). Noncharged amino acid residues at the solvent-exposed positions in the middle and at the C terminus of the α-helix have the same helical propensity. *Protein Sci.* 12, 1169–76.

191 Szalik, L., Moitra, J., Krylov, D., and Vinson, C. (1997). Phosphorylation destabilizes α-helices. *Nat. Struct. Biol.* 4, 112–14.

192 Liehr, S. and Chenault, H. K. (1999). A comparison of the α-helix forming propensities and hydrogen bonding properties of serine phosphate and α-amino-γ-phosphonobutyric acid. *Bioorg. Med. Chem. Lett.* 9, 2759–62.

193 Andrew, C. D., Warwicker, J., Jones, G. R., and Doig, A. J. (2002). Effect of phosphorylation on α-helix stability as a function of position. *Biochemistry* 41, 1897–905.

194 Horovitz, A., Serrano, L., Avron, B., Bycroft, M., and Fersht, A. R. (1990). Strength and co-operativity of contributions of surface salt bridges to protein stability. *J. Mol. Biol.* 216, 1031–44.

195 Merutka, G. and Stellwagen, E. (1991). Effect of amino acid ion pairs on peptide helicity. *Biochemistry* 30, 1591–4.

196 Stellwagen, E., Park, S.-H., Shalongo, W., and Jain, A. (1992). The contribution of residue ion pairs to the helical stability of a model peptide. *Biopolymers* 32, 1193–200.

197 Huyghues-Despointes, B. M., Scholtz, J. M., and Baldwin, R. L. (1993). Helical peptides with three pairs of Asp-Arg and Glu-Arg residues in different orientations and spacings. *Protein Sci.* 2, 80–5.

198 Huyghues-Despointes, B. M. and Baldwin, R. L. (1997). Ion-pair and charged hydrogen-bond interactions between histidine and aspartate in a peptide helix. *Biochemistry* 36, 1965–70.

199 Huyghues-Despointes, B. M., Klingler, T. M., and Baldwin, R. L. (1995). Measuring the strength of side-chain hydrogen bonds in peptide helices: the Gln.Asp $(i, i+4)$ interaction. *Biochemistry* 34, 13267–71.

200 Stapley, B. J. and Doig, A. J. (1997). Hydrogen bonding interactions between Glutamine and Asparagine in α-helical peptides. *J. Mol. Biol.* 272, 465–73.

201 Padmanabhan, S. and Baldwin, R. L. (1994). Tests for helix-stabilizing interactions between various nonpolar side chains in alanine-based peptides. *Protein Sci.* 3, 1992–7.

202 Padmanabhan, S. and Baldwin, R. L. (1994). Helix-stabilizing interaction between tyrosine and leucine or valine when the spacing is $i, i+4$. *J. Mol. Biol.* 241, 706–13.

203 Viguera, A. R. and Serrano, L. (1995). Side-chain interactions between sulfur-containing amino acids and phenylalanine in α-helices. *Biochemistry* 34, 8771–9.

204 Tsou, L. K., Tatko, C. D., and Waters, M. L. (2002). Simple cation-p interaction between a phenyl ring and a protonated amine stabilizes an α-helix in water. *J. Am. Chem. Soc.* 124, 14917–21.

205 Taylor, J. W. (2002). The synthesis and study of side-chain lactam-bridged peptides. *Biopolymers* 66, 49–75.

206 Campbell, R. M., Bongers, J., and Felxi, A. M. (1995). Rational design, synthesis, and biological evaluation of novel growth-hormone releasing-factor analogs. *Biopolymers* 37, 67–8.

207 Chorev, M., Roubini, E., McKee, R. L. et al. (1991). Cyclic parathyroid-hormone related protein antagonists – lysine 13 to aspartic acid 17 [I to (I + 40] side-chain to side-chain lactamization. *Biochemistry* 30, 5968–74.

208 Osapay, G. and Taylor, J. W. (1992). Multicyclic polypeptide model compounds. 2. Synthesis and conformational properties of a highly α-helical uncosapeptide constrained by 3 side-chain to side-chain lactam bridges. *J. Am. Chem. Soc.* 114, 6966–73.

209 Bouvier, M. and Taylor, J. W. (1992). Probing the functional conformation of Neuropeptide-T through the design and study of cyclic analogs. *J. Med. Chem.* 35, 1145–55.

210 Kapurniotu, A. and Taylor, J. W. (1995). Structural and conformational requirements for human calcitonin activity – design, synthesis, and study of lactam-bridged analogs. *J. Med. Chem.* 38, 836–47.

211 Osapay, G. and Taylor, J. W. (1990). Multicyclic polypeptide model compounds. 1. Synthesis of a tricyclic amphiphilic α-helical peptide using an oxime resin, segment-condensation approach. *J. Am. Chem. Soc.* 112, 6046–51.

212 Bracken, C., Gulyas, J., Taylor, J. W., and Baum, J. (1994). Synthesis and nuclear-magnetic-resonance structure determination of an α-helical, bicyclic, lactam-bridged hexapeptide. *J. Am. Chem. Soc.* 116, 6431–2.

213 Chen, S. T., Chen, H. J., Yu, H. M., and Wang, K. T. (1993). Facile synthesis of a short peptide with a side-chain-constrained structure. *J. Chem. Res.* (S) 6, 228–9.

214 Zhang, W. T., and Taylor, J. W. (1996). Efficient solid-phase synthesis of peptides with tripodal side-chain bridges and optimization of the solvent conditions for solid-phase cyclizations. *Tetrahedron Lett.* 37, 2173–6.

215 Luo, P. Z., Braddock, D. T., Subramanian, R. M., Meredith, S. C., and Lynn, D. G. (1994). Structural and thermodynamic characterization of a bioactive peptide model of apolipoprotein-E–side-chain lactam bridges to constrain the conformation. *Biochemistry* 33, 12367–77.

216 Jackson, D. Y., King, D. S., Chmielewski, J., Singh, S., and Schultz, P. G. (1991). General approach to the synthesis of short α-helical peptides. *J. Am. Chem. Soc.* 113, 9391–2.

217 Kumita, J. R., Smart, O. S., and Woolley, G. A. (2000). Photo-control of helix content in a short peptide. *Proc. Natl Acad. Sci. USA* 97, 3803–8.

218 Flint, D. G., Kumita, J. R., Smart, O. S., and Wolley, G. A. (2002). Using an azobenzene cross-linker to either increase or decrease peptide helix content upon trans-to-cis photoisomerization. *Chem. Biol.* 9, 391–7.

219 Kumita, J. R., Flint, D. G., Smart, O. S., and Woolley, G. A. (2002). Photo-control of peptide helix content by an azobenzene cross-linker: steric interactions with underlying residues are not critical. *Protein Eng.* 15, 561–9.

220 Jiménez, M. A., Muñoz, V., Rico, M., and Serrano, L. (1994). Helix stop and start signals in peptides and proteins. The capping box does not necessarily prevent helix elongation. *J. Mol. Biol.* 242, 487–96.

221 Kallenbach, N. R. and Gong, Y. X. (1999). C-terminal capping motifs in model helical peptides. *Bioorg. Med. Chem.* 7, 143–51.

222 Petukhov, M., Yumoto, N., Murase, S., Onmura, R., and Yoshikawa, S. (1996). Factors that affect the stabilization of α-helices in short peptides by a capping box. *Biochemistry* 35, 387–97.

223 Viguera, A. R. and Serrano, L. (1995). Experimental analysis of the Schellman motif. *J. Mol. Biol.* 251, 150–60.

224 Gong, Y., Zhou, H. X., Guo, M., and Kallenbach, N. R. (1995). Structural analysis of the N- and C-termini in a peptide with consensus sequence. *Protein Sci.* 4, 1446–56.

225 Armstrong, K. M. and Baldwin, R. L. (1993). Charged histidine affects α-helix stability at all positions in the helix by interacting with the backbone charges. *Proc. Natl Acad. Sci. USA* 90, 11337–40.

226 Scholtz, J. M., York, E. J., Stewart, J. M., and Baldwin, R. L. (1991). A neutral water-soluble, α-helical peptide: The effect of ionic strength on the helix-coil equilibrium. *J. Am. Chem. Soc.* 113, 5102–4.

227 Smith, J. S. and Scholtz, J. M. (1998). Energetics of polar side-chain interactions in helical peptides: Salt effects on ion pairs and hydrogen bonds. *Biochemistry* 37, 33–40.

228 Lockhart, D. J. and Kim, P. S. (1993). Electrostatic screening of charge and dipole interactions with the helix backbone. *Science* 260, 198–202.

229 Jelesarov, I., Durr, E., Thomas, R. M., and Bosshard, H. B. (1998). Salt effects on hydrophobic interaction and charge screening in the folding of a negatively charged peptide to a coiled coil (leucine zipper). *Biochemistry* 37, 7539–50.

230 Scholtz, J. M., Marqusee, S., Baldwin, R. L. et al. (1991). Calorimetric determination of the enthalpy change for the α-helix to coil transition of an alanine peptide in water. *Proc. Natl Acad. Sci. USA* 88, 2854–8.

231 Yoder, G., Pancoska, P., and Keiderling, T. A. (1997). Characterization of alanine-rich peptides, Ac-(AAKAA)n-GY-NH2 (n) 1–4), using vibrational circular dichroism and fourier transform infrared conformational determination and thermal unfolding. *Biochemistry* 36, 5123–33.

232 Huang, C. Y., Klemke, J. W., Getahun, Z., DeGrado, W. F., and Gai, F. (2001). Temperature-dependent helix-coil transition of an alanine based peptide. *J. Am. Chem. Soc.* 123, 9235–8.

233 Goch, G., Maciejczyk, M., Oleszczuk, M., Stachowiak, D., Malicka, J., and Bierzynski, A. (2003). Experimental investigation of initial steps of helix propagation in model peptides. *Biochemistry* 42, 6840–7.

234 Nelson, J. W. and N. R., K. (1986). Stabilization of the ribonuclease S-peptide α-helix by trifluoroethanol. *Proteins: Struct. Funct. Genet.* 1, 211–17.

235 Nelson, J. W. and N. R., K. (1989). Persistence of the α-helix stop signal in the S-peptide in trifluoroethanol solutions. *Biochemistry* 28, 5256–61.

236 Sonnichsen, F. D., Van Eyk, J. E., Hodges, R. S., and Sykes, B. D. (1992). Effect of trifluoroethanol on protein secondary structure: an NMR and CD study using a synthetic actin peptide. *Biochemistry* 31, 8790–8.

237 Waterhous, D. V. and Johnson, W. C. (1994). Importance of environment in determining secondary structure in proteins. *Biochemistry* 33, 2121–8.

238 Jasanoff, A. and Fersht, A. R. (1984). Quantitative determination of helical propensities. Analysis of data from trifluoroethanol titration curves. *Biochemistry* 33, 2129–35.

239 Albert, J. S. and Hamilton, A. D. (1995). Stabilization of helical domains in short peptides using hydrophobic interactions. *Biochemistry* 34, 984–90.

240 Walgers, R., Lee, T. C., and Cammers-Goodwin, A. (1998). An indirect chaotropic mechanism for the stabilization of helix conformation of peptides in aqueous trifluoroethanol and hexafluoro-2-propanol. *J. Am. Chem. Soc.* 120, 5073–9.

241 Luo, P. and Baldwin, R. L. (1999). Interaction between water and polar groups of the helix backbone: An important determinant of helix propensities. *Proc. Natl Acad. Sci. USA* 96, 4930–5.

242 Kentsis, A. and Sosnick, T. R. (1998). Trifluoroethanol promotes helix formation by destabilizing backbone

exposure: Desolvation rather than native hydrogen bonding defines the kinetic pathway of dimeric coiled coil folding. *Biochemistry* 37, 14613–22.

243 Reiersen, H. and Rees, A. R. (2000). Trifluoroethanol may form a solvent matrix for assisted hydrophobic interactions between peptide sidechains. *Protein Eng.* 13, 739–43.

244 Myers, J. K., Pace, N., and Scholtz, J. M. (1998). Trifluoroethanol effects on helix propensity and electrostatic interactions in the helical peptide from ribonuclease T1. *Protein Sci.* 7, 383–8.

245 Nozaki, Y. and Tanford, C. (1967). Intrinsic dissociation constants of aspartyl and glutamyl carboxyl groups. *J. Biol. Chem.* 242, 4731–5.

246 Kyte, J. (1995). *Structure in Protein Chemistry*, Garland Publishing, New York and London.

247 Kortemme, T. and Creighton, T. E. (1995). Ionisation of cysteine residues at the termini of model α-helical peptides. Relevance to unusual thiol pKa values in proteins of the thioredoxin family. *J. Mol. Biol.* 253, 799–812.

248 Miranda, J. J. (2003). Position-dependent interactions between cysteine and the helix dipole. *Protein Sci.* 12, 73–81.

249 Eisenberg, D., Weiss, R. M., and Terwilliger, T. C. (1982). The helical hydrophobic moment: a measure of the amphiphilicity of a helix. *Nature* 299, 371–4.

250 Merrifield, R. B. (1963). Solid phase peptide synthesis. I. The synthesis of a tetrapeptide. *J. Am. Chem. Soc.* 85, 2149–54.

251 White, P. D. and Chan, W. C. (2000). Fmoc solid phase peptide synthesis. A practical approach (Hames, B. D., ed.), pp. 9–40. Oxford University Press, Oxford.

252 Carpino, L. A. and Han, G. Y. (1970). The 9-fluorenylmethoxycarbonyl function, a new base-sensitive amino-protecting group. *J. Am. Chem. Soc.* 92, 5748–9.

253 Carpino, L. A. and Han, G. Y. (1972). The 9-fluorenylmethoxycarbonyl amino-protecting group. *J. Org. Chem.* 37, 3404–9.

254 Kaiser, E., Colescott, R. L., Bossinger, C. D., and Cook, P. I. (1970). Color test for detection of free terminal amino groups in the solid-phase synthesis of peptide. *Anal. Biochem.* 34, 595–8.

255 Sarin, V. K., Kent, S. B. H., Tam, J. P., and Merrifield, R. B. (1981). Quantitative monitoring of solid-phase peptide synthesis by the ninhydrin reaction. *Anal. Biochem.* 117, 147–57.

256 Greenfield, N. J. (1996). Methods to estimate the conformation of proteins and polypeptides from circular dichroism data. *Biochemistry* 235, 1–10.

257 Manning, M. C. (1993). ACS Symposium Series, Vol. 516, pp. 33–52, OUP, New York.

258 Fasman, G. D. (1996). *Circular Dichroism and the Conformational Analysis of Biomolecules*. Plenum Press, New York.

259 Luo, P. and Baldwin, R. L. (1997). Mechanism of helix induction by trifluoroethanol: a framework for extrapolating the helix-forming properties of peptides from trifluoroethanol/water mixtures back to water. *Biochemistry* 36, 8413–21.

260 Strickland, E. H. (1974). Thermodynamics and dynamics of histidine-binding protein, the water-soluble receptor of histidine permease. *CRC Crit. Rev. Biochem.* 2, 113–74.

261 Manning, M. C. and Woody, R. W. (1989). Theoretical study of the contribution of aromatic side chains to the circular dichroism of basic bovine pancreatic trypsin inhibitor. *Biochemistry* 28, 8609–13.

262 Woody, R. W., Dunker, A. K., and Fasman, G. D. (1996). In *Circular Dichroism and the Conformational Analysis of Biomolecules* (Fasman, G. D., ed.), pp. 109–157. Plenum Press, New York.

263 Bayley, P. M., Nielsen, E. B., and Schellman, J. A. (1969). The rotatory properties of molecules containing two peptide groups. *J. Phys. Chem.* 73, 228–43.

264 Sreerama, N. and Woody, R. W. (1993). A self-consistent method for the analysis of protein secondary structure from circular dichroism. *Anal. Biochem.* 209, 32–44.

265 Keiderling, T. A. (2002). Protein and peptide secondary structure and conformational determination with vibrational circular dichroism. *Curr. Opin. Struct. Biol.* 6, 682–8.

266 Keiderling, T. A. (2002). In *Circular Dichroism: Principles and Applications* (Berova, N., Nakanishi, K., and Woody, R. A., eds), pp. 621–666. Wiley-VCH, New York.

267 Tanaka, T., Inoue, K., Kodama, T., Kyogoku, Y., Hayakawa, T., and Sugeta, H. (2001). Conformational study on poly[γ-(α-phenethyl)-L-glutamate] using vibrational circular dichroism spectroscopy. *Biopolymers* 62, 228–34.

268 Baumruk, V., Pancoska, P., and Keiderling, T. A. (1996). Predictions of secondary structure using statistical analyses of electronic and vibrational circular dichroism and Fourier transform infrared spectra of proteins in H_2O. *J. Mol. Biol.* 259, 774–91.

269 Nafie, L. A. (2000). Dual polarization modulation: a real-time, spectral multiplex separation of circular dichroism from linear birefringence spectral intensities. *Appl. Spectros.* 54, 1634–45.

270 Hilario, J., Drapcho, D., Curbelo, R., and Keiderling, T. A. (2001). Polarization modulation Fourier transform infrared spectroscopy with digital signal processing: comparison of vibrational circular dichroism method. *Appl. Spectros.* 55, 1435–47.

271 Rohl, C. A. and Baldwin, R. L. (1997). Comparison of NH exchange and circular dichroism as techniques for measuring the parameters of the helix-coil transition in peptides. *Biochemistry* 36, 8435–42.

272 Spera, S. and Bax, A. (1991). Empirical correlation between protein backbone conformation and Cα and Cβ ^{13}C nuclear magnetic resonance chemical shifts. *J. Am. Chem. Soc.* 113, 5490–2.

273 Shalongo, W., Dugad, L., and Stellwagen, E. (1994). Distribution of helicity within the model peptide Acetyl$(AAQAA)_3$ amide. *J. Am. Chem. Soc.* 116, 8288–93.

274 Shalongo, W., Dugad, L., and Stellwagen, E. (1994). Analysis of the thermal transitions of a model helical peptides using C-13 NMR. *J. Am. Chem. Soc.* 116, 2500–7.

275 Park, S.-H., Shalongo, W., and Stellwagen, E. (1998). Analysis of N-terminal Capping using carbonyl-carbon chemical shift measurements. *Proteins: Struct. Funct. Genet.* 33, 167–76.

276 Wuthrich, K. (1986). *NMR of Proteins and Nucleic Acids*, John Wiley and Sons, New York.

277 Kilby, P. M., van Eldick, L. J., and Roberts, G. C. K. (1995). Nuclear magnetic resonance assignments and secondary structure of bovine S100β protein. *FEBS Lett.* 363, 90–6.

278 Campbell, I. D. and Dwek, R. A. (1984). *Biological Spectroscopy.* Benjamin Cummings, Menlo Park, CA.

279 Brey, W. S. (1984). *Physical Chemistry and its Biological Applications.* Academic Press, New York.

280 Venyaminov, S.-Y. and Kalnin, N. N. (1990). Quantitative IR Spectrophotometry of peptide compounds in water (H_2O) solutions. 2. Amide absorption-bands of polypeptides and fibrous proteins in α-coil, β-coil, and random coil conformations. *Biopolymers* 30, 1243–57.

281 Susi, H., Timasheff, S. N., and Stevens, L. (1967). Infra-red spectrum and protein conformations in aqueous solutions. *J. Biol. Chem.* 242, 5460–6.

282 Krimm, S. and Bandekar, J. (1986). Vibrational spectroscopy and conformation of peptides, polypeptides and protein. *Adv. Protein Chem.* 38, 181–364.

283 Nevskaya, N. A. and Chirgadze, Y. N. (1976). Infrared spectra and resonance interactions of amide-I and II vibration of α-helix. *Biopolymers* 15, 637–48.

284 Byler, D. M. and Susi, H. (1986).

Examination of the secondary structure of proteins by deconvolved FTIR spectra. *Biopolymers* 25, 469–87.

285 Yang, W.-J., Griffiths, P. R., Byler, D. M., and Susi, H. (1985). Protein Conformation by Infra-red spectroscopy – Resolution enhancement by Fourier self deconvolution. *Appl. Spectros.* 39, 282–7.

286 Susi, H. and Byler, D. M. (1988). Fourier deconvolution of the Amide-I Raman band of proteins as related to conformation. *Appl. Spectros.* 42, 819–25.

287 Kato, K., Matsui, T., and Tanaka, S. (1987). Quantitative estimation of α-helix coil content in bovine sreum albumin by Fourier transform-infrared spectroscopy. *Appl. Spectros.* 41, 861–5.

288 Raman, C. V. and Krishnan, K. S. (1928). A new type of secondary radiation. *Nature* 121, 501–2.

289 Hendra, P. J., Jones, C., and Warnes, G. (1991). *Fourier Transform Raman Spectroscopy.* Ellis Horwood, Chichester.

290 Callender, R., Deng, H., and Gilmanshin, R. (1998). Raman difference studies of protein structure and folding, enzymatic catalysis and ligand binding. *J. Raman Spectros.* 29, 15.

291 Withnall, R. (2001). Protein-Ligand Interactions: structure and spectroscopy (Harding, S. E. and Chowdhry, B. Z., eds). Oxford University Press, Oxford.

292 Peticolas, W. L., ed. (1995). *Vibrational Spectra: Principles and Aplications with Emphasis on Optical Activity.* Vol. 246. *Methods in Enzymology* (Sauer, K., ed.). Academic Press, New York.

293 Asher, S. A., Ianoul, A., Mix, G., Boyden, M. N., Karnoup, A., Diem, M., and Schweitzer-Stenner, R. (2001). Dihedral ψ angle dependence of the amide III vibration: A uniquely sensitive UV resonance Raman secondary structural probe. *J. Am. Chem. Soc.* 123, 11775–81.

294 Polavarapu, P. L. (1998). *Vibrational Spectra: Principles and Applications with Emphasis on Optical Activity.* Elsevier, Amsterdam.

295 Nafie, L. A. (1997). Infrared and Raman vibrational optical activity: Theoretical and experimental aspect. *Annu. Rev. Phys. Chem.* 48, 357–86.

296 Ford, S. J., Wen, Z. Q., Hecht, L., and Barron, L. D. (1994). Vibrational Raman optical-activity of alanyl peptide oligomers – a new perspective on aqueous-solution conformation. *Biopolymers* 34, 303–13.

297 Diem, M. (1993). *Introduction to Modern Vibrational Spectroscopy*, Wiley, New York.

298 Muñoz, V. and Serrano, L. (1995). Analysis of $i, i+5$ and $i, i+8$ hydrophobic interactions in a helical model peptide bearing the hydrophobic staple motif. *Biochemistry* 34, 15301–6.

299 Thomas, S. T., Loladze, V. V., and Makhatadze, G. I. (2001). Hydration of the peptide backbone largely defines the thermodynamic propensity scale of residues at the C′ position of the C-capping box of α-helices. *Proc. Natl Acad. Sci. USA* 98, 10670–5.

300 Shi, Z., Olson, C. A., Bell, A. J., and Kallenbach, N. R. (2002). Nonclassical helix-stabilizing interactions: C–H . . . O H-bonding between Phe and Glu side chains in α-helical peptides. *Biophys. Chem.* 101–2, 267–79.

301 Luo, R., David, L., Hung, H., Devaney, J., and Gilson, M. K. (1999). Strength of solvent-exposed salt-bridges. *J. Phys. Chem. B* 103, 366–80.

302 Marqusee, S. and Sauer, R. T. (1994). Contributions of a hydrogen bond/salt bridge network to the stability of secondary and tertiary structure in lambda repressor. *Protein Sci.* 3, 2217–25.

303 Shi, Z., Olson, C. A., Bell, A. J., and Kallenbach, N. R. (2001). Stabilization of α-helix structure by polar side-chain interactions: Complex salt bridges, cation π interactions and C–H . . . O–H bonds. *Biopolymers* 60, 366–80.

10
Design and Stability of Peptide β-sheets

Mark S. Searle

10.1
Introduction

The pathway by which the polypeptide chain assembles from the unfolded, ''disordered'' state to the final active folded protein has been the subject of intense investigation. Hierarchical models of protein folding emphasize the importance of local interactions in restricting the conformational space of the polypeptide chain in the search for the native state. These nuclei of structure promote interactions between different parts of the sequence leading ultimately to a cooperative rate-limiting step from which the native state emerges [1–4]. Designed peptides that fold autonomously in water (α-helices and β-sheets) have proved extremely valuable in probing the relationship between local sequence information and folded conformation (the stereochemical code) in the absence of the tertiary interactions found in the native state of proteins. This has allowed intrinsic secondary structure propensities to be investigated in isolation, and enabled the nature and strength of the weak interactions relevant to a wide range of molecular recognition phenomena in chemistry and biology to be put on a quantitative footing.

While the literature is rich in studies of α-helical peptides [5–8], water-soluble, nonaggregating monomeric β-sheets have emerged relatively recently [9–11]. For reasons of design and chemical synthesis, these are almost exclusively antiparallel β-sheets, although others have used nonnatural linkers to engineer parallel strand alignments [12–14]. Here we focus on contiguous antiparallel β-sheet systems. Autonomously folding β-hairpin motifs, consisting of two antiparallel β-strands linked by a reverse β-turn (Figure 10.1), represent the simplest systems for probing weak interactions in β-sheet folding and assembly, although more recently a number of three- and four-stranded β-sheet structures have been described. From this growing body of data, key factors have come into focus that are important in rational design. The following will be considered: the role of the β-turn in promoting and stabilizing antiparallel β-sheet formation; the role of intrinsic backbone ϕ, ψ propensities in preorganizing the extended conformation of the polypeptide chain; the role of cooperativity in β-sheet folding and stability and in the propagation of

Protein Folding Handbook. Part I. Edited by J. Buchner and T. Kiefhaber

ISBN: 3-527-30784-2

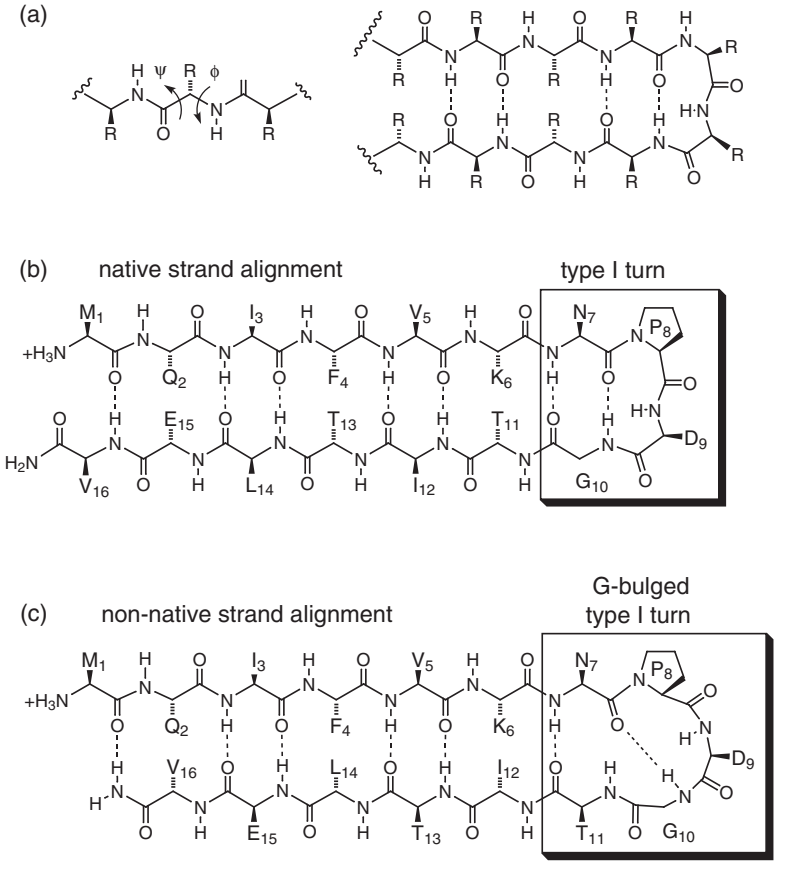

Fig. 10.1. a) Beta-strand alignment and interstrand hydrogen bonds in an antiparallel β-hairpin peptide; R groups represent amino acid side chains, main chain ϕ and ψ angles are shown. N-terminal β-hairpin of ubiquitin in which the native TLTGK turn sequence has been replaced by the sequence NPDG. b) Native strand alignment giving rise to a type I NPDG turn. c) Nonnative strand alignment with a G-bulged type I turn (NPDGT).

multistranded β-sheets, and quantitative approaches to estimating the energetics of β-sheet stability and folding.

10.2
β-Hairpins Derived from Native Protein Sequences

The early focus on peptides excised from native protein structures provided the first insights into autonomously folding β-hairpins, preceding the more rational approach to β-sheet design. Peptides derived from tendamistat [15], B1 domain of

protein G [16, 17], ubiquitin [18, 19], and ferredoxin [20] showed that these sequences could exist in the monomeric form without aggregating, but that in most cases they showed a very limited tendency to fold in the absence of tertiary contacts. The use of organic co-solvents appeared to induce native-like conformation [17, 18, 20]. The study by Blanco et al. [20] of a peptide derived from the B1 domain of protein G provided the first example of native-like folding in water of a fully native peptide sequence. In contrast, the studies of hairpins isolated from the proteins ubiquitin and ferredoxin, which are structurally homologous to the G B1 domain (all form an α/β-roll fold) showed these to be unfolded in water [18, 20]. More recent studies of the native ubiquitin peptide have now revealed evidence for a small population of the folded state in water [21], while a β-turn mutation has been shown to significantly enhance folding [22].

The apparent lack of evidence for folding of the peptide derived from residues 15–23 of tendamistat (YQSWRYSQA) [15], and from the N-terminal sequence of ubiquitin (MQIFVKTLTGKTITLEV) [19] led to partial redesign of the sequence to enhance folding through modification to the β-turn sequence by introducing an NPDG type I turn, which is the most common type I turn sequence in proteins. Thus, in the former peptide SWRY was replaced by NPDG [15], and in the latter the G-bulged type I turn TLTGK was replaced by NPDG [19]. By introducing this tight two-residue loop across PD it was envisaged that both hairpins would be stabilized. This was certainly the case, however, the most striking observation was that both peptides folded into nonnative conformations with a three-residue G-bulged type I turn (PDG) reestablished across the turn (Figure 10.1b and c). These initial studies in rational redesign led to strikingly irrational results, prompting a much more systematic approach to β-hairpin design. The above results revealed that the β-turn sequence, which dictates the preferred backbone geometry, appears to be an important factor in dictating the β-strand alignment. From the protein folding viewpoint, as demonstrated by the redesigned ubiquitin hairpin sequence, it is evident that one important role of the native turn sequence may be to preclude the formation of nonnative conformations that may be incompatible with formation of the native state.

10.3 Role of β-turns in Nucleating β-hairpin Folding

The systematic classification of β-turns in proteins reveals a wide variety of geometries and sizes of loop [22–24]. For the design of β-hairpins, the emphasis has been on incorporation of the smallest turn sequence possible to limit the entropic destabilization effects. While two-residue type I and type II turns are generally common in β-turns, the backbone conformation (ϕ and ψ torsion angles) of a two-residue type I or type II turn results in a local left-handed twist, which is not compatible with the right-handed twist found in protein β-sheets. Consequently, these turns are less commonly found between contiguous antiparallel β-strands. However, the

diastereomeric type I′ and II′ turns have the ϕ and ψ angles complementary to the right-handed twisted orientation of the β-strands. These conclusions appear to rationalize, at least in part, the above observations with β-turn modifications introduced into the β-hairpins of tendamistat and ubiquitin. The introduced NPDG type I turn is not compatible with the right-handed twist of the β-strands resulting in a refolding to a more flexible G-bulged type I turn.

The work of Gellman et al. [25] has shown the importance of backbone ϕ, ψ angle preferences for the residues in the turn sequence by comparing the stability of a number of β-hairpin peptides derived from the ubiquitin sequence (MQIFVKSXXKTITLVKV) containing either XX = L-Pro-Xaa or D-Pro-Xaa. Replacing L-Pro with D-Pro switches the twist from left-handed (type I or II) to right-handed (type I′ or II′), making the latter compatible with the right-handed twist of the two β-strands. NMR data (Hα shifts and long-range nuclear Overhauser effects (NOEs)) indicate that each of the D-Pro containing peptides showed a significant degree of folding, whereas the L-Pro analogs appeared to be unfolded. Similar conclusions were drawn from studies of a series of 12-mers containing XG turn sequences, with X = L-Pro or D-Pro [26].

A number of natural L-amino acids are commonly found in the α_L region of conformational space and are compatible with the type I′ or II′ turn conformation. Statistical analyses from a number of groups have identified Xaa-Gly as a favored type I′ turn. A number of studies have used the Asn-Gly sequence to design β-hairpin motifs and have demonstrated a high population of the folded structure with the required turn conformation and strand alignment [27–32]. The work by de Alba et al. [28] identified two possible conformations of the peptide ITSYNGKTYGR. The NOE data appear to be compatible with rapidly interconverting conformations involving an YNGK type I′ turn and a NGKT type II′ turn, each giving a distinct pattern of cross-strand NOEs. Ramirez-Alvarado et al. [27] also described an NG-containing 12-mer (RGITVXGKTYGR; X = N), which they subsequently extended to a series of hairpins to examine the correlation between hairpin stability and the database frequency of occurrence of residues in position X [29]. Using nuclear magnetic resonance (NMR) and circular dichroism (CD) measurements they concluded that X = Asn > Asp > Gly > Ala > Ser in promoting hairpin folding, in agreement with the intrinsic ϕ, ψ preferences of these residues. Despite extensive analysis of NG type I′ turns in the protein database (PDB), it is still not entirely clear why Asn at the first position is so effective in promoting turn formation. There is no evidence for specific side chain to main chain hydrogen bonds that might stabilise the desired backbone conformation, although specific solvation effects cannot be ruled out [30].

Evidence that the NG turn is able to nucleate folding in the absence of cross-strand interactions was demonstrated in a truncated analog of one designed 16-residue β-hairpin sequence KKYTVSINGKKITVSI (***β*1** in Figure 10.2), in which the sequence was shortened to SINGKKITVSI, lacking the N-terminal six residues [30]. Evidence from NOE data showed that the turn was significantly populated with interactions observed between Ser6 Hα ↔ Lys11 Hα and Ile7 NH ↔ Lys10

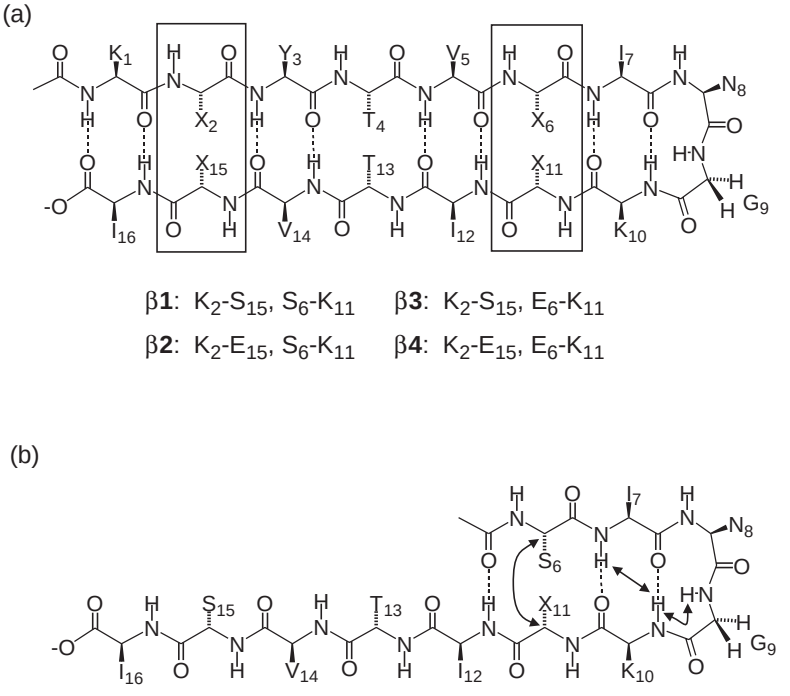

Fig. 10.2. Structure of the 16-residue β-hairpin sequence ***β*1**, and mutants ***β*2**, ***β*3** and ***β*4** in which cross-strand salt bridges (Lys-Glu) have been introduced at position X_2-X_{15} and X_6-X_{11}. In b), hairpin ***β*1** has been truncated by removing the N-terminal hydrophobic residues (1–5). The resulting peptide still shows the ability to fold around the turn sequence as evident from medium range NOEs (indicated by arrows) that show that the INGK sequence is adopting a type I′ NG turn.

NH (Figure 10.2b) that are only compatible with a folded type I′ turn around NG. Two destabilized β-hairpin mutants (KKYTVSINGKKITKSK with electrostatic repulsion between the N- and C-terminal Lys residues, and KKATASINGKKITVSI with the loss of key hydrophobic residues in one strand) showed no evidence from NMR chemical shift data for cross-strand interactions; however, careful examination of NOE data revealed evidence for NG turn nucleation [30]. Titration with organic co-solvent showed both peptides to fold significantly, indicating that the turn sequence probably already predisposes the peptide to form a β-hairpin but that favorable cross-strand interactions are required for stability.

The work of de Alba et al. convincingly illustrated this principle in a series of six hairpin sequences (10-mers) where strand residues were conserved but turn sequences varied [28]. Using a number of NMR criteria they were able to show that changes in turn sequence could result in a variety of turn conformations including two residue 2:2 turns, 3:5 turns and 4:4 turns (see earlier nomenclature

[22–24]), with different pairings of amino acid side chains. As with the earlier examples cited with the turn modification described for hairpins derived from tendamistat and ubiquitin, the bulged-type I turn (3:5 turn) appears to be an intrinsically stable turn with the necessary right-handed twist. Together these data strongly support a model for hairpin folding in which the turn sequence strongly dictates its preferred conformation, and that strand alignment, cross-strand interactions and subsequently conformational stability are dictated by the specificity of the turn.

10.4 Intrinsic ϕ, ψ Propensities of Amino Acids

Statistical analyses of high-resolution structures in the PDB have provided significant insights into residue-specific intrinsic backbone ϕ, ψ preferences in polypeptide chains. A novel approach presented by Swindells et al., was to determine ϕ, ψ propensities of different residues in nonregular regions of protein structure where backbone geometry is free of interactions associated with regular hydrogen bonded β-sheet or α-helical secondary structure [33]. The striking observation is that in this context ϕ and ψ angles (see Figure 10.3) are far from randomly distributed, and that most occupy regions of Ramachandran space associated with regular secondary structure. The observed ϕ, ψ distributions for individual residues has been taken as representative of those found in denatured states of proteins providing the basis of a ''random coil'' state from which residue-specific NMR parameters ($^3J_{NH\text{-}H\alpha}$ and NOE intensities) can be derived as a reference state for folding studies [34, 35]. While β-propensity is found to vary significantly from one residue to the next, context-dependent effects also appear to play an important part [36].

While V, I, F, and Y, for example, have a high intrinsic preference to be in the β-region of the Ramachandran plot where steric interactions with flanking residues are minimized, their conformation is relatively insensitive to the nature of the flanking residues. In contrast, small or unbranched side chains have a higher preference for the α-helical conformation, however, this preference can be significantly modulated by its neighbors through a combination of steric and hydrophobic interactions, as well as both repulsive and attractive electrostatic interactions. General effects of flanking residues (grouped as α-like or β-like, reflecting ϕ, ψ propensities) on the central residue of a XXX triplet are illustrated in Figure 10.4a as an average over all residues at the central position. More specific effects are also shown for Ser, Val, and Lys (Figure 10.4b–d). With Ser, for example, having bulky flanking residues either side with high β-propensity (denoted $\beta S\beta$, where β could be V, I, F or Y), significantly increases the β-propensity of the Ser residue to minimize the steric repulsion between the two bulky neighboring residues [36]. Thus, intrinsic structural propensities appear to be highly context dependent.

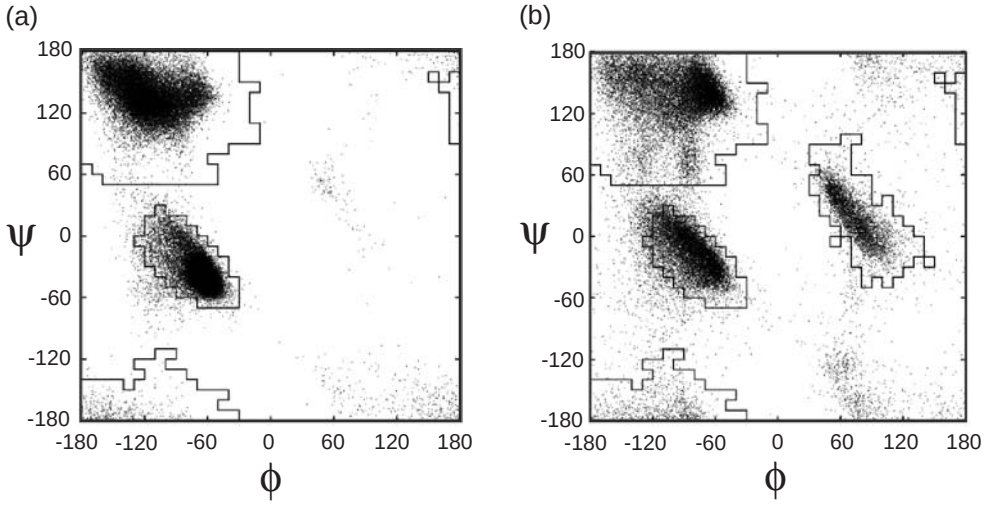

Fig. 10.3. Ramachandran plots of residue backbone ϕ and ψ angles taken from a database of 512 high-resolution protein X-ray structures showing: a) residues in regular β-sheet (ϕ, ψ: $-120^\circ, 120^\circ$) and α-helix (ϕ, ψ: $-60^\circ, 60^\circ$), and b) residues in the irregular coil regions of the same structures (ϕ, ψ: $60^\circ, 0^\circ$ is the α_L region of conformational space mainly occupied by Gly). The distribution in b) shows that residues have a natural propensity to occupy the α and β regions of conformational space even when they are not involved in regular protein secondary structure. Taken from Ref. [36].

This statistical framework has been extended to a number of experimental systems to examine the extent to which isolated β-strand sequences (in the absence of secondary structure interactions) are predisposed by the primary sequence to adopt an extended β-like conformation. The isolated 8-mer (GKKITVSI), corresponding to the C-terminal β-strand of the hairpin ***β*1** (Figure 10.2; KKYTVSIN<u>GKKITVSI</u>), was examined by NMR analysis of $^3J_{NH\text{-}H\alpha}$ values and backbone NOE intensities. Surprisingly, many of these parameters are similar to those for the folded hairpin despite the monomeric nature of the 8-mer [32, 36]. In an analogous study of the C-terminal strand of the ubiquitin hairpin described above [21, 37], similarly large deviations of coupling constants and NOE intensities from random coil values suggested that the isolated β-strands are partially preorganized into an extended conformation supporting a model for hairpin folding which may not require a significant further organisation of the peptide backbone, a factor that may contribute significantly to hairpin stability. Several studies of denaturated states of proteins have also highlighted the influence of neighboring residues in modulating main chain conformational preferences [38–41], and the importance of residual structure in the unfolded state in guiding the conformational search to the native state [42, 43].

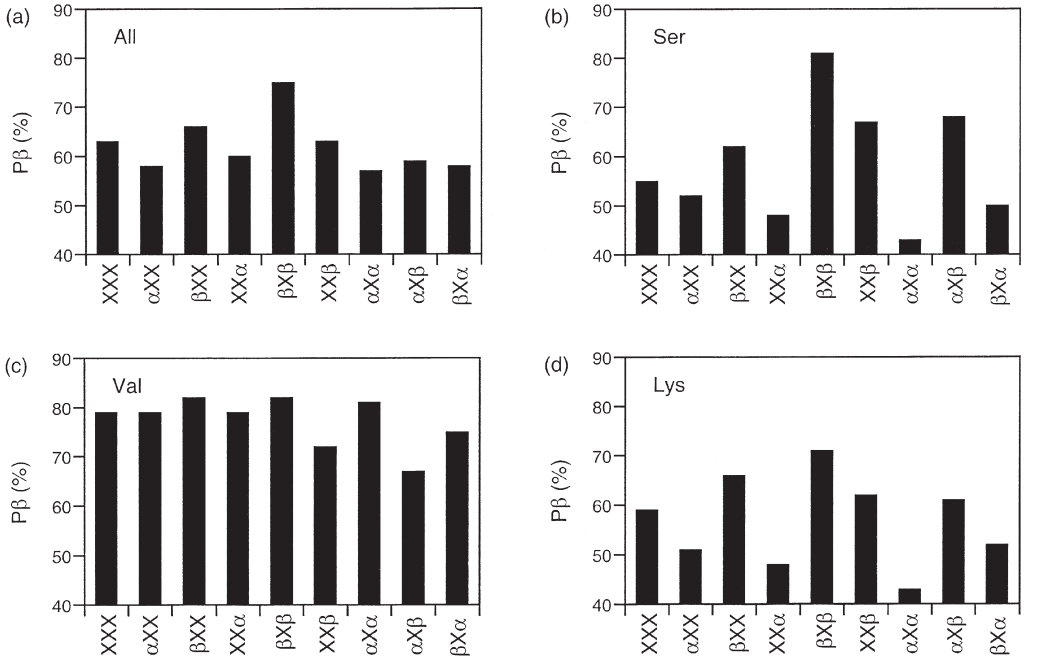

Fig. 10.4. Effects of neighboring residues on residue β-propensities within the triplets XϕX calculated from the data in Figure 10.3b. The β-propensity of residue ϕ is a measure of the number of times a particular residues is found in the β-region of the Ramachandran plot as a fraction of the total distribution between α- and β-space $[\beta/(\alpha+\beta)]$. The context dependence of the β-propensity is estimated by considering the nature of the neighboring residue (X) (X = any residue, α is a residue that prefers the α-helical region – Asp, Glu, Lys, or Ser, β is a residue that prefers the β-sheet region – Ile, Val, Phe, or Tyr). The effects of neighboring residues on the average β-propensity is shown in (a), specific effects on Ser (b), Val (c) and Lys (d) are also shown. While Val is relatively insensitive to the nature of the flanking residues, the smaller Ser residue can be forced to adopt a higher β-propensity if it has bulky neighbors. Thus, the intrinsic β-propensity of a particular residue is highly context dependent. Taken in part from Ref. [36].

10.5
Side-chain Interactions and β-hairpin Stability

There is a strong case, at least in the context of isolated peptide fragments, that the origin of the specificity of β-hairpin folding is largely dictated by the conformational preferences of the turn sequence. However, the stability of the folded state has been attributed to interstrand hydrogen bonding and/or hydrophobic interactions, though which dominates is still a matter of debate. Ramirez-Alvarado et al. [27] reported that the population of the folded state of the hairpin RGITVNGKTYGR was significantly diminished by replacing residues on the N-terminal

strand, and then the C-terminal strand, by Ala. The loss of stability was attributed firstly to a reduction in hydrophobic surface burial, but also due to the intrinsically lower β-propensity of Ala, the latter contributing through an adverse conformational entropy term. To compensate for this de Alba et al. [44] described a family of hairpins derived from the sequence IYSNSDGTWT. The effects of residue substitutions in the first three positions was examined while maintaining the overall β-character of the two strands. Several favorable cross-strand pair-wise interactions were identified that were apparent in earlier, and more recent, PDB analysis of β-sheet interactions [45, 46]. For example, Thr-Thr and Tyr-Thr cross-strand pairs produced stabilizing interactions, whilst Ile-Thr and Ile-Trp had a destabilizing effect. Other studies of Ala substitution in one β-strand have similarly highlighted hydrophobic burial as a key factor in conformational stability [30], while the observation of large numbers of side chain NOEs have been used as evidence for hydrophobic stabilization in water (see below) [19, 25–27, 30].

10.5.1 Aromatic Clusters Stabilize β-hairpins

The first example of a natural β-hairpin sequence that folded autonomously in water (residues 41–56 of the B1 domain of protein G) identified an aromatic-rich cluster of residues that appears to impart considerable stability [17]. The interstrand pairing of Trp/Val and Tyr/Phe has subsequently been exploited in the design of a number of model hairpin systems, in particular to examine the relationship between the position of this stabilizing cluster and the β-turn sequence. The separation between the loop sequence and cluster strongly influences stability and the extent of participation in β-sheet forming interactions (Figure 10.5a). In an isomeric family of 20-mers (peptides **1**, **2**, and **3**), all of which contain exactly the same residue composition, the most stable hairpin is that in which the smallest cost in conformational entropy is paid to bring the cluster together, i.e., where the cluster is closest to the loop sequence [47]. This arrangement results in the largest Hα chemical shift deviations, indicating a well-formed core; however, the terminal residues show a lower propensity to fold. Thus, there exists a strong interplay between the two key stabilizing components of the hairpin. A statistical model was developed to rationalize the experimental observations and estimate the free energy change versus the number of peptide hydrogen bonds formed (Figure 10.5b).

It is a well-known phenomenon that α-helical peptides become more stable as the length increases, reflecting the fact that while helix nucleation is energetically unfavorable, the propagation step has a small net increase in stability. In β-hairpin systems, Stanger et al. [48] suggest that this may not be the case. There is some evidence for an increase in stability as strands lengthen from five to seven residues, however, further extension (to nine) does not lead to a further stability increment, suggesting that there may be an intrinsic limit to strand length. Since the choice of

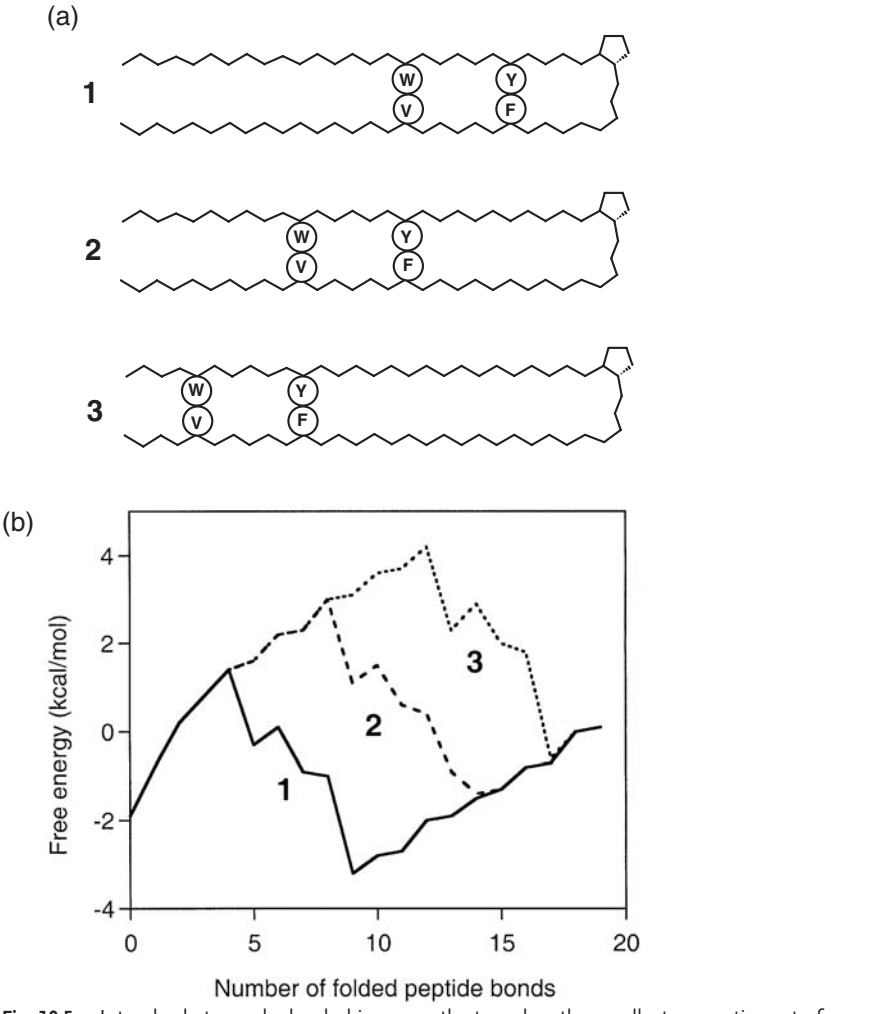

Fig. 10.5. Interplay between hydrophobic cluster and turn position in a family of isomeric β-hairpins. The distance of the WVYF cluster from the turn is shown in (a) for peptides **1**, **2**, and **3**. A statistical mechanical model was used to estimate the free energy of folding for the three peptides according to the number of peptide hydrogen bonds formed and the relative position of the stabilizing hydrophobic cluster (b). Thus, peptide **1**, which has the hydrophobic cluster closest to the turn, has the smallest energetic cost of forming the cluster which then significantly stabilizes this core motif, but leads to fraying of the N- and C-termini. In contrast, in the case of peptide **3**, there is a large energy penalty in ordering the peptide backbone to bring the residues of the cluster together. Overall the core hairpin is less stable but more residues are involved in ordered structure. Adapted from Ref. [47].

Tab. 10.1. trpzip β-hairpin peptides, sequences and stability.

β-hairpin	*Sequence*	*Turn type*	T_m	ΔH (kJ mol^{-1})
trpzip1	SWTWEGNKWTWK	(Type II′ turn)	323	−45.4
trpzip2	SWTWENGKWTWK	(Type I′ turn)	345	−70.6
trpzip3	SWTWE^{D}PNKWTWK	(Type II′ turn)	352	−54.8

sequence extension in this study was limited to an all Thr extension or an alternating Ser-Thr $(ST)_n$ extension the conclusions should be viewed with caution. Since cross-strand Ser/Ser and Thr/Thr pairings do not bury very much hydrophobic surface area, it is not surprising perhaps that cross-strand side-chain interactions may only just compensate for the entropic cost of organizing the peptide backbone. Studies with other more favorable pairings may be enlightening.

Undoubtedly the most successfully designed structural motif to date has been the tryptophan zipper (trpzip) motif [49], whose stability exceeds substantially all those already described. The design is based around stabilizing nonhydrogen-bonded cross-strand Trp-Trp pairs (Table 10.1).

The most successful designs involved two such Trp-Trp pairs which NMR structural analysis reveals are interdigitated in a zipper-like manner stabilized through face–face offset π-stacking giving a compact structure (Figure 10.6). This arrangement of the indole rings results in a pronounced signature in the CD spectrum with intense exciton-coupling bands at 215 and 229 nm indicative of interactions between aromatic chromophores in a highly chiral environment (see Figure 10.7). The high sensitivity of the CD bands permits thermal denaturation curves to be determined with high sensitivity, in contrast to other β-sheet systems where only small changes in the CD spectrum at 216 nm are evident, resulting in poor signal-to-noise. The thermal unfolding curves are sigmoidal and reversible, fitting to a two-state folding model (Figure 10.7).

The trpzip hairpins 1, 2, and 3 show high T_m values (see Table 10.1) with folding strongly enthalpy driven. Changing the turn sequence (GN versus NG versus D-PN) has a significant impact on stability. The unfolding curve for trpzip2 with the NG type I′ turn gives the most cooperative unfolding transition and appears to be the most stable of the three at room temperature, despite other studies that suggest that the unnatural D-PN (type II′) turn is the most stabilizing [25]. Clearly, context-dependent factors are at work. Also, the strongly enthalpy-driven signature for folding is different to that reported previously for other systems [32], reflecting differences in the nature of the stabilizing interactions which in the case of the trpzip peptides involve π–π stacking interactions. Despite the fact that the trpzip hairpins represent a highly stabilized motif, no such examples have been found in the protein structure database. The authors suggest that on steric grounds it may be difficult to accommodate the trpzip motif within a multistranded β-sheet or through packing against other structural elements.

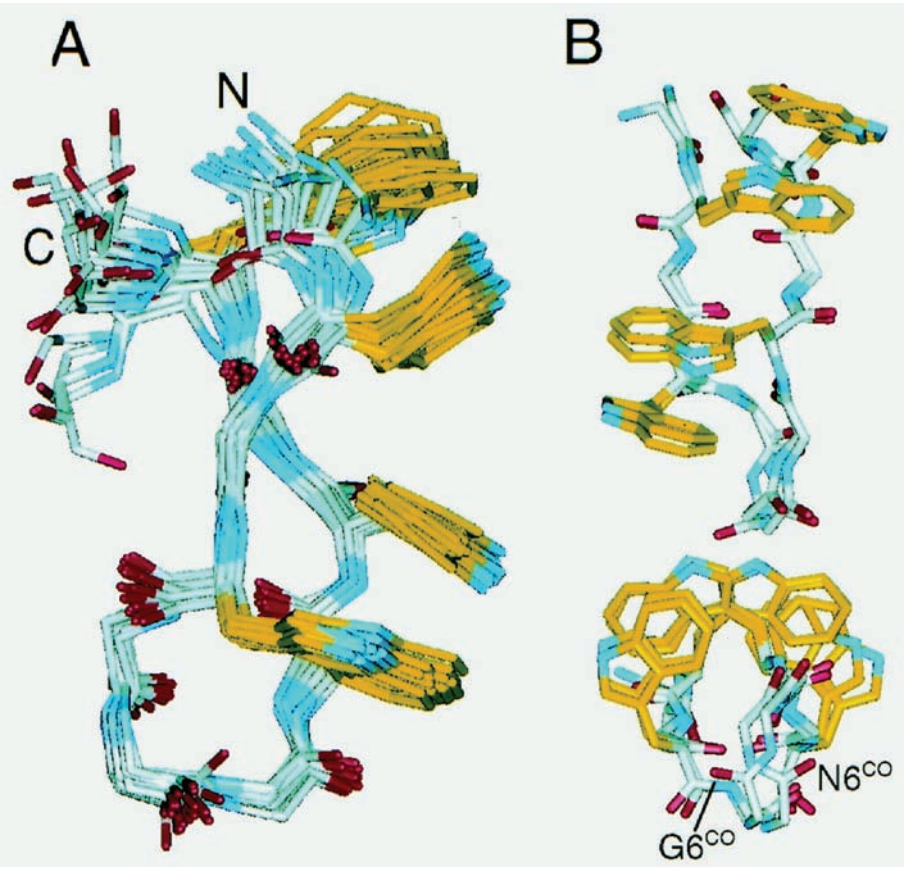

Fig. 10.6. NMR structures of trpzips 1 and 2. A) Ensemble of 20 structures of trpzip1 (residues 2–11) showing the relative orientations of the indole rings. B) Overlay of trpzip 1 and 2 aligned to the peptide backbone of residues 2–5 and 8–11 (top), and rotated by 90° for the end-on view of the indole rings. The backbone carbonyl of residue 6 is labeled to illustrate the different turn geometries of the two hairpins (type II′ and type I′). Taken from Ref. [49].

10.5.2
Salt Bridges Enhance Hairpin Stability

The high abundance of salt bridges on the surface of hyperthermophilic proteins [50, 51], together with examples of rational enhancement of protein stability through redesign of surface charge, has strongly implicated ionic interactions as a stabilizing force [52, 53]. In model peptides that are only weakly folded in water, the relative importance of ionic versus hydrophobic interactions in stabilizing local

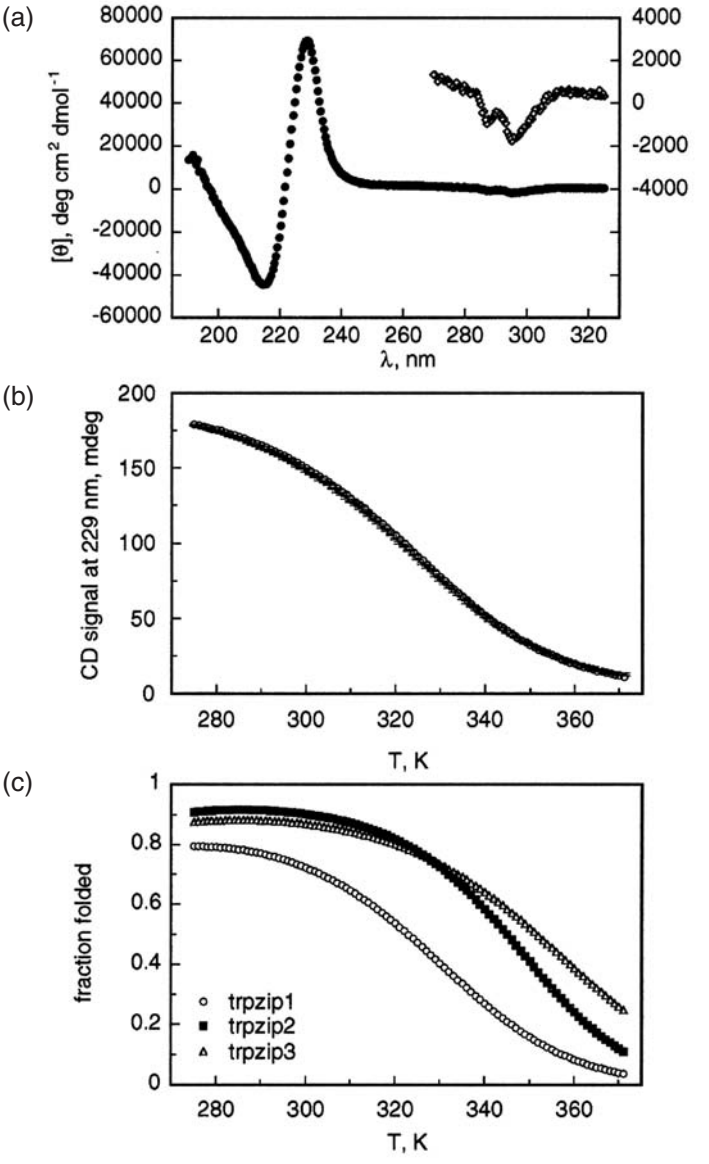

Fig. 10.7. Folding data for trpzips 1 to 3 determined from near- and far-UV CD spectra. a) CD spectrum of trpzip 1, with inset of near-UV CD showing buried aromatic residues (10-fold expansion). b) Reversible thermal denaturation of trpzip 1 monitored by CD at 229 nm (unfolding and refolding curves overlayed). c) Temperature dependence of folding for trpzips 1 to 3 plotted as fraction folded. Taken from Ref. [49].

secondary structure has been less well investigated in terms of a detailed quantitative description. To this end, peptide ***β*1** (Figure 10.2) was mutated to introduce Lys-Glu salt bridges at two positions within the hairpin involving substitution of Ser → Glu: one salt bridge is postioned adjacent to the β-turn, while the other involves residues close to the N- and C-termini (see Figure 10.2) [54]. Using NMR chemical shift data from Hα resonances we have estimated the net contribution to stability from these two interactions. Although the contribution to stability in each case is small, Hα chemical shifts are extremely sensitive to small shifts in the population of the folded state, as evident from the ΔδHα data in Figure 10.8. On this basis, the individual contributions of these two interactions was estimated (K2-E15, peptide ***β*2**, and E6-K11, peptide ***β*3**) compared with their K2-S15 and S6-K11 counterparts (peptide ***β*1**) and found to be similar (-1.2 and -1.3 kJ mol^{-1} at 298K). When the two salt bridges are introduced simultaneously into the hairpin sequence (***β*4**), the energetic contribution of the two interactions together (-3.6 kJ mol^{-1}) is significantly greater than the sum of the individual interactions. This effect is readily apparent from the large increase in ΔδHα values in Figure 10.8, indicating that the contribution of a given interaction appears to depend on the relative stability of the system in which the interaction is being measured. Similar observations have been reported using a disulfide cyclized β-hairpin scaffold [55]. The indication is that the strength of the interaction appears to depend on the degree of preorganization of the β-hairpin template that pays varying degrees of the entropic cost in bringing the pairs of side chains together.

This is more clearly illustrated by the schematic representation shown in Figure 10.9a that shows the thermodynamic cycle indicating the effects on stability of the introduction of each mutation. Thus, the energetic contribution of the S15/E15 mutation could be measured either from ***β*1** ↔ ***β*2** or from ***β*3** ↔ ***β*4**. The values obtained are quite different, the latter suggesting that the interaction is more favorable (-1.2 versus -2.3 kJ mol^{-1}). This appears to correlate with the fact that the stability of ***β*3** is greater than ***β*1** and that the degree of preorganization of the former determines the energetic contribution of the interaction. The same principle is evident when determining the energetics of the E6-K11 interaction. This can be estimated from ***β*1** ↔ ***β*3** or ***β*2** ↔ ***β*4**. Again, the energetics are quite different (-1.3 versus -2.4 kJ mol^{-1}) with the larger contribution from the ***β*2** ↔ ***β*4** pair, where the intrinsic stability of the ***β*2** reference state is higher.

The NMR data show that the folded conformation of ***β*4** is highly populated ($> 70\%$) giving rise to an abundance of cross-strand NOEs (Figure 10.9b) [55]. On the basis of 173 restraints (NOEs and torsion angle restraints from $^{3}J_{NH\text{-}H\alpha}$ values) we have calculated a family of structures compatible with the NMR data (Figure 10.9c). The large number of van der Waals contacts between hydrophobic residues (V, I, and Y) evident from the NOE data leads us to conclude that hydrophobic interactions still provide the overall driving force for folding with structure and stability further consolidated by additional Coulombic interactions from the salt bridges. CD melting curves for hairpin ***β*4** in water and various concentrations of methanol (Figure 10.10) show the same characteristics described above from temperature-dependent NMR data for ***β*1**: a shallow melting curve for ***β*4** in water

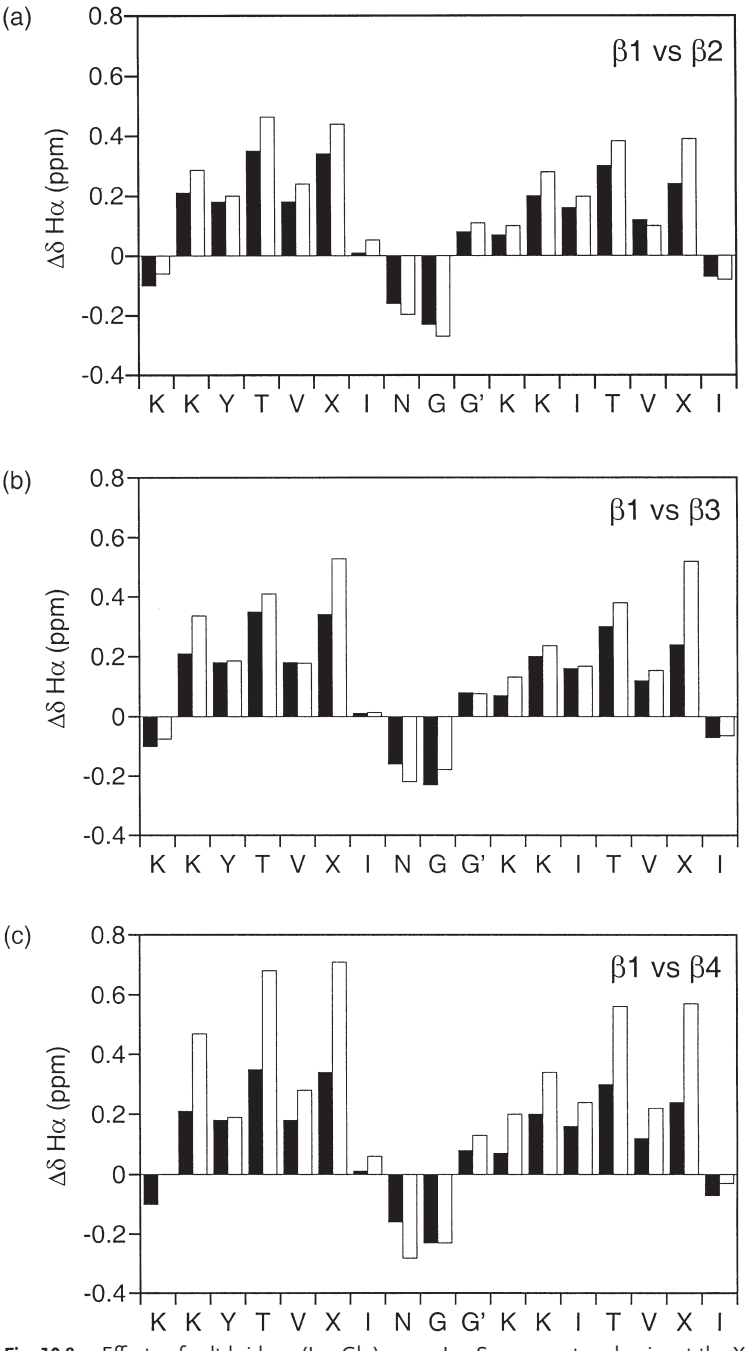

Fig. 10.8. Effects of salt bridges (Lys-Glu) on β-hairpin stability. Hα chemical shift deviation from random coil values (Δδ Hα values) for β-hairpin peptides ***β*2** to ***β*4** compared with those of the reference hairpin peptide ***β*1** containing Lys-Ser cross-strand pairs at the X_2-X_{15} and X_6-X_{11} mutation sites (see Figure 10.2). a) ***β*1** versus ***β*2**; b) ***β*1** versus ***β*3**, and c) ***β*1** versus ***β*4**. All data at 298K and pH 5.5. Taken from Ref. [54].

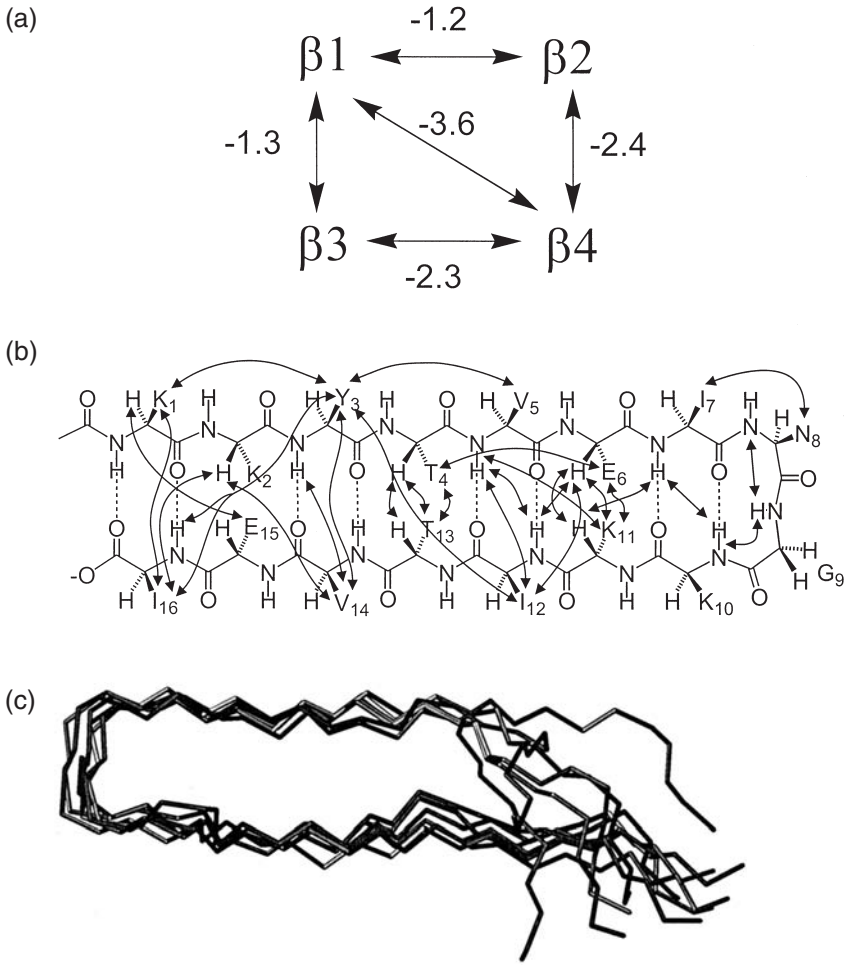

Fig. 10.9. a) Thermodynamic cycle showing the context-dependent energetic contribution to hairpin stability of each electrostatic interaction in the ***β*1** to ***β*4** family of hairpins (Figure 10.2) by comparing relative hairpin stabilities at 298K determined from NMR chemical shift data; $\Delta\Delta G$ values are shown for Lys-Glu interactions at pH 5.5. The stabilizing contribution of each salt bridge is context dependent, showing some degree of cooperativity between the two mutation sites according to the degree of preorganization of the hairpin structure. b) Shematic illustration of the abundance of cross-strand NOEs in hairpin peptide ***β*4**. c) Family of five NMR structures of hairpin ***β*4** showing the peptide backbone alignment, with some fraying at the N- and C-termini. Taken from Ref. [54].

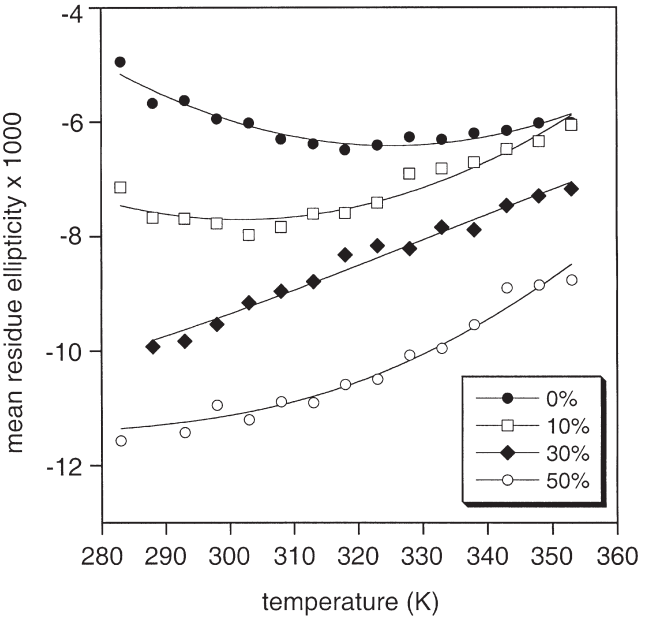

Fig. 10.10. CD melting curves for ***β4*** at various concentrations (% v/v) of MeOH, as indicated. The nonlinear least squares fit is shown in each case from which thermodynamic data for folding were determined (see Ref. [54]). The change in heat capacity on folding in 30% and 50% aqueous methanol is assumed to be zero; there is evidence for cold-denaturation in water and 10% methanol. Taken from Ref. [54].

with evidence for cold denaturation is consistent with the hydrophobic interaction again providing the dominant driving force for folding ($\Delta H = +11.9$ kJ mol^{-1} and $\Delta S = +38$ J K^{-1} mol^{-1}), while folding becomes strongly enthalpy driven in 50% aqueous methanol ($\Delta H = -39.8$ kJ mol^{-1} and $\Delta S = -106$ J K^{-1} mol^{-1}).

10.6
Cooperative Interactions in β-sheet Peptides: Kinetic Barriers to Folding

Folding kinetics for a β-hairpin derived from the C-terminus of the B1 domain of protein G have been described from measurements of tryptophan fluorescence following laser-induced temperature-jump [56, 57]. Kinetic analysis of this peptide (and a dansylated analogue) reveals a single exponential relaxation process with time constant 3.7 ± 0.3 μs. The data indicate a single kinetic barrier separating folded and unfolded states, consistent with a two-state model for folding. Subsequently, the authors developed a statistical mechanical model based on these observations, describing the stability in terms of a minimal numbers of parameters: loss of conformational entropy, backbone stabilization by hydrogen bonding and forma-

tion of a stabilizing hydrophobic cluster between three key residues. This model seems sufficient to reproduce all of the features observed experimentally, with a rough, funnel-like energy landscape dominated by two global minima representing the folded and unfolded states. The formation of the hydrophobic cluster appears to be a key folding event. Nucleation by the turn seems most likely, consistent with experimental measurements of loop formation on the timescale of $\sim$1 μs [58]. However, simulation studies by others suggest that folding may proceed by hydrophobic collapse followed by rearrangement to form the hydrophobic cluster, with hydrogen bonds then propagating outward from the cluster in both directions [59]. Such a model does not appear to require a turn-based nucleation event.

10.7 Quantitative Analysis of Peptide Folding

Quantitative analysis of the population of folded β-sheet structures in solution still presents a challenge, largely as a consequence of uncertainties in limiting spectroscopic parameters for the fully folded state. Far UV-CD has been considered to be unreliable as a consequence of the complicating influence of the β-turn conformation and possibly aromatic residues, where present [10]. Added to this, the CD spectrum of β-sheet is intrinsically weak compared with α-helical secondary structure. The trpzip peptides [49] represent the exception to the rule, as discussed above. The use of NMR parameters (Hα chemical shifts, $^3J_{NH\text{-}H\alpha}$ values and NOE intensities) to quantify folded populations has been discussed [9–11, 32, 60]. NMR offers the advantage that several independent parameters can be used in quantitative analysis to provide a consensus picture of the folded state. There still appear to be significant discrepancies between CD analysis and NMR, with peptides that appear to be significantly folded by NMR giving rise to a largely random coil CD spectrum. One interpretation of this observation is that in aqueous solution the peptides fold as a collapsed state with an ill-defined hydrogen bonding network dominated by side-chain interactions. Interestingly, in many cases the addition of organic co-solvents changes the CD spectrum dramatically. The interpretation of co-solvent-induced folding is also subject to some uncertainty. Does trifluorethanol or methanol actually significantly perturb the equilibrium between the folded and unfolded states (induce folding), or do these solvents exert their influence by changing the nature of the folded state such as to stabilize interstrand hydrogen bonding interactions without significantly changing the folded population? The latter hypothesis would appear to more readily account for the observation of solvent-induced effects on the CD spectrum, and finds some support from studies of cyclic β-hairpin analogs where the folded population is fixed, but whose CD spectrum undergoes large solvent-induced changes [60].

The use of cyclic β-hairpin analogs has been exploited in a number of studies to generate a fully folded NMR reference state for comparison with the folding of acyclic analogs [61, 62]. Backbone cyclization through amide bond formation or

through a disulfide bridge seem to work equally well. Such an approach has been used effectively to measure the thermodynamics of folding of a short hairpin carrying a motif of aromatic residues [62]. The cyclic analogs show a much higher stability than their acyclic counterparts, including significant protection from amide H/D exchange due to enforced interstrand hydrogen bonding. While peptide cyclization seems a worthwhile approach to defining the fully folded state, there may also be some caveats to this approach that have not been tested. When conformational constraints (β-turns) are imposed at both ends of the structure this may affect the intrinsic twist of the two β-strands, resulting in a more pronounced twist in the cyclic analog than in the acyclic hairpin. Further, the latitude for conformational dynamics in the fully folded state will also be different. Both of these factors are likely to influence Hα shifts chemical shifts to some degree.

10.8 Thermodynamics of β-hairpin Folding

The number of β-hairpin model systems is expanding rapidly with a greater focus now on quantitative analysis and thermodynamic characterization. The thermodynamic signature for the folding of **β1** (Figure 10.2) presents an insight into the nature of the stabilizing weak interactions in various solvent milieu [30, 32]. **β1** exhibits the property of cold denaturation, with a maximum in the stability curve occurring at 298K as judged by changes in Hα chemical shift (Figure 10.11a). Such pronounced curvature is clear evidence for entropy-driven folding accompanied by a significant change in heat capacity. Both of these thermodynamic signatures are hallmarks of the hydrophobic effect contributing strongly to hairpin stability. More recent studies by Tatko and Waters [63] have also shown that cold denaturation effects can be observed for simple model peptides, consistent with substantial changes in heat capacity on folding. Further examination of folding in the presence of methanol co-solvent shows that the signature changes such that folding becomes strongly enthalpy driven, and that in 50% aqueous methanol the temperature–stability profile is indicative of the absence of any significant contribution of the hydrophobic effect to folding [32]. The population of the folded state appears to be enhanced by methanol, reflecting similar observations in helical peptides where the phenomenon has been attributed to the effects of the co-solvent destabilizing the unfolded peptide chain so promoting hydrogen bonding interactions in the folded state.

It is unlikely that the folded state of a model β-hairpin peptide resembles a β-sheet in a native protein, with the former sampling a much larger number of conformations of similar energy stabilized by a fluctuating ensemble of transient interactions. IR analysis of the amide I band of **β1** does not show significant differences in the region expected for β-sheet formation ($\approx 1630\ cm^{-1}$) from data on a nonhydrogen-bonded short reference peptide [64]. However, this band does appear under aggregating conditions (Figure 10.11b). In other cases, IR spectral fea-

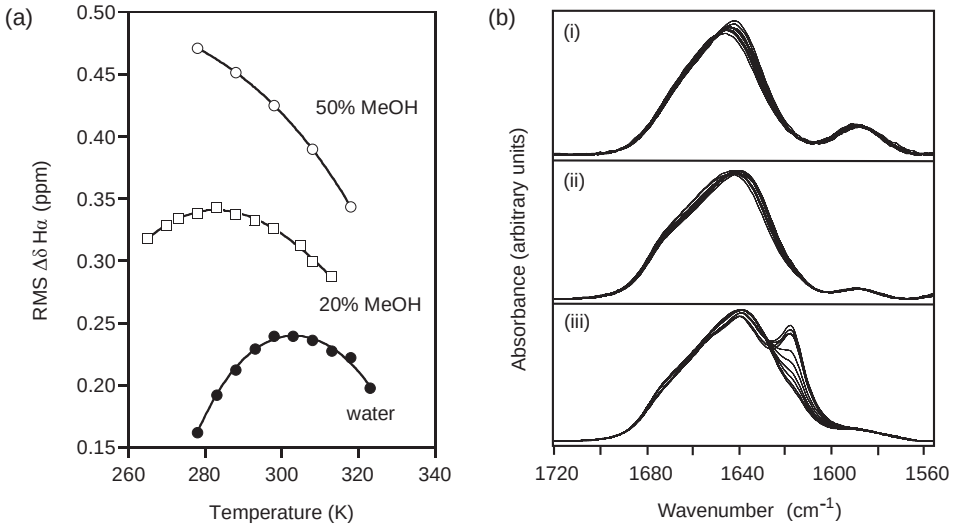

Fig. 10.11. a) Temperature-dependent stability of the hairpin peptide ***β*1** (see Figure 10.2) at pH 5.5 in water, 20% methanol and 50% methanol. Temperature is plotted against the RMS value for the deviation of Hα chemical shifts from random coil values, assuming a two-state folding model. In water the peptide shows "hot" and "cold" denaturation, but in 50% methanol the folded population increases at low temperature. The best fits to the three sets of data are shown; in water folding is slightly entropy-driven with a large negative ΔC°_{p} value, while in 50% methanol folding is strongly enthalpy-driven with ΔC°_{p} close to zero. In 20% methanol the values are in between. (Reproduced with permission from the *Journal of the American Chemical Society* [32]). b) Variable-temperature FTIR spectra of i) 2 mM aqueous solution of the 8-mer peptide GKKITVSI (C-terminal β-strand of hairpin ***β*1**); ii) 2 mM solution of β-hairpin peptide ***β*1**; iii) 10 mM solution of ***β*1**, all in the temperature range 278–330 K and in D_2O solution, pH 5.0 (uncorrected). In iii) the band that appears around 1620 cm^{-1} is formed irreversibly indicative of peptide aggregation. Reproduced from Ref. [64].

tures characteristic of β-hairpins have been shown to form reversibly at relatively high peptide concentrations [65]. Similarly, β-hairpins that appear to be well folded on the basis of various NMR criteria seem to be weakly folded by CD analysis [60]. This discrepancy has been attributed largely to weak interstrand hydrogen bonding interactions in the folded state. Indeed, molecular dynamics simulations using ensemble-averaging approaches or time-averaged NOEs tend to de-emphasize the role of hydrogen bonding between the peptide backbone of the two strands, but emphasize the role of hydrophobic side chains interactions [30, 66, 67]. In all cases described, side chain NOEs across the β-strands support such interactions, however, cross-strand backbone NOEs only imply the possibility of hydrogen bonds since weakly populated folded states lead to only small NH ↔ ND protection factors in water.

In studies (both calorimetric and NMR) of the folding of the C-terminal hairpin from the B1 domain of protein G, enthalpy-driven folding is observed in water

[68]. In contrast with the above data, where the stabilizing hydrophobic interactions involved aliphatic side chains, here an aromatic cluster is responsible for folding. A strongly enthalpy-driven transition is also apparent for the trpzip motifs described above [49] all of which is consistent with π–π interactions stabilizing β-hairpin structures through fundamentally electrostatic interactions rather than through only solvophobic effects. Studies of a designed β-hairpin system, also carrying the same motif of three aromatic residues, demonstrate qualitatively similiar enthalpy-driven folding [62], while the thermodynamics of the N-terminal hairpin component of a designed three-stranded antiparallel β-sheet enables similar conclusions to be drawn (see further below) [69]. The difference in the thermodynamic signature for aliphatic versus aromatic side-chain interactions has been suggested to have its origins in enthalpy–entropy compensation effects, such that enthalpy-driven interactions may be fundamentally a consequence of tighter interfacial interactions, giving rise to stronger electrostatic (enthalpic) interactions [62]. More recent work by Tatko and Waters [70] probing the energetics of aromatic–aliphatic interactions in hairpins suggests that there is a preference for the self-association of aromatics over aromatic–aliphatic interactions, and that the unique nature of this interaction may impart some degree of sequence selectivity. The limited data available from such systems suggest that the thermodynamic driving force for β-hairpin folding is highly dependent on the nature of the side-chain interactions involved. Further quantitative analysis of peptide folding is required to substantiate these hypotheses.

10.9 Multistranded Antiparallel β-sheet Peptides

The natural extension of the earlier studies on β-hairpin peptides was to design three- and four-stranded antiparallel β-sheets using the design principles already discussed, focusing on the importance of turn sequence in defining stability and strand alignment, and employing motifs of interacting side chains already identified to impart stability. An overriding question concerns the extent to which cooperative interactions perpendicular to the strand direction are important in stabilizing these structures (see Figure 10.12a); in other words, how good is a preorganized β-hairpin motif at templating the interaction of a third strand. Several studies have attempted to address this important question. The earliest study described a 24-residue peptide incorporating two NG turns (KKFTLSING KKYTISNG KTYITGR) that showed little evidence for folding in water but was significantly stabilised in aqueous methanol solutions [71, 72]. By comparison with a 16-residue β-hairpin analog consisting of the same C-terminal sequence (GKKYTISNG KTYITGR), it was possible to show that the Hα shift perturbations for the C-terminal β-hairpin were greater in the presence of the interactions of the third strand. Subsequent design strategies, incorporating the D-Pro-Gly loop, together with other Asn-Gly-containing turn sequences have illustrated that it is possible to design structures that fold in water [69, 73–75], some of which show a degree of

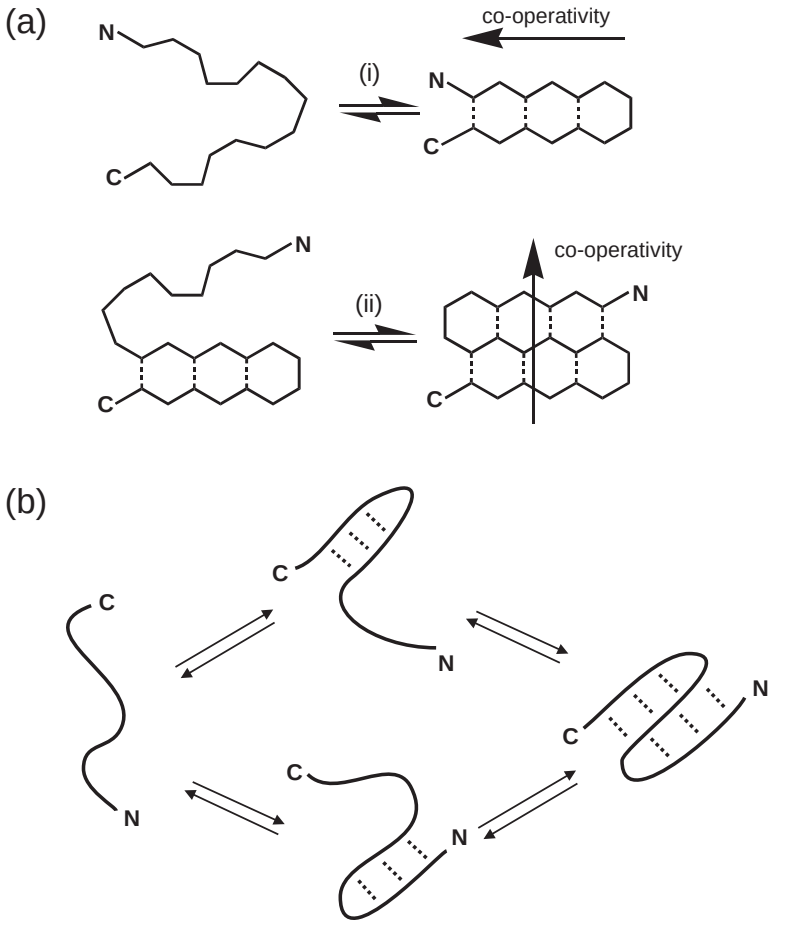

Fig. 10.12. a) Models for the folding of β-hairpin and three-stranded β-sheet peptides illustrating the possibility of cooperative interactions being propagated parallel i) and perpendicular ii) to the β-strand direction. b) Four-state model for the folding of a three-stranded antiparallel β-sheet peptide showing the presence at equilibrium of the unfolded state and partially folded states in which the C-terminal β-hairpin is formed but the N-terminus is disordered, the N-terminal β-hairpin is formed but the C-terminus is disordered, and the fully folded state. The preformed hairpins can act as templates for the folding of the third strand.

cooperative stabilization between different strands. Other studies have reported peptides that fold to three- (and four-) stranded β-sheets in organic solvents [76], but a quantitative dissection of stabilizing interactions between β-strands has not been presented. Redesign of the three-stranded Betanova, following earlier work [74], reported the use of an automated approach using the algorithm PERLA (protein engineering rotamer library algorithm) to define stabilizing and destabilizing

single and multiple-residue mutations producing incremental increases in stability over the original design of up to ~4 kJ mol^{-1} [77]. Schenck and Gellman [73] demonstrated cooperative interactions using their D-ProGly to L-ProGly switch, the latter destabilizing one hairpin component selectively. From chemical shift analysis they showed that the individual β-hairpins are cooperatively stabilized by the presence of the third strand. De Alba et al. [75] also reported a designed β-sheet system, but were unable to find convincing evidence for cooperative stabilization of either hairpin by the third strand.

It is clear that folding is not a highly cooperative process in these peptide systems. Thus, the folded three-stranded β-sheet is more than likely in equilibrium with populations of the individual hairpins and the unfolded state (see Figure 10.12b). One quantitative study of cooperative interactions between the strands of a three-stranded β-sheet [69] was based on a designed system incorporating a previously studied β-hairpin with the third strand capable of forming a stabilizing motif of aromatic residues (Figure 10.13a), similar to that already described [17, 62]. The earlier study of the isolated C-terminal β-hairpin showed cold denaturation [30], approximating to two-state unfolding. In the designed three-stranded system, the same hairpin component shows the same cold denaturation profile, however, the N-terminal hairpin (sharing a common central strand) showed increased folding at low temperature. While the first process is characterized by entropy-driven folding, the latter is enthalpy-driven (Figure 10.13b). Clearly, two different thermodynamic profiles are not consistent with a single two-state folding model, but the data could be rationalized in terms of a four-state model in which the individual hairpins with an unfolded tail are also populated (Figure 10.12b). Examination of the folding of the isolated C-terminal hairpin, and comparison of the data with that of the three-stranded analog, shows good evidence that the C-terminal hairpin is cooperatively stabilized by the interaction of the third strand, even though overall folding is not highly cooperative. The data in Figure 10.13b show the temperature dependence of the splitting of the Gly Hα resonances in the two NG turns. Larger values indicate a higher folded population. The splitting for G17 is greater in the three-stranded sheet than for the isolated C-terminal hairpin, while many Hα resonances are further downfield shifted than in the isolated hairpin. The temperature dependence of the stability shows the C-terminal hairpin in both cases to undergo cold denaturation. The N-terminal hairpin carrying the aromatic motif of residues increases in population at low temperature; fitting the data shows the former to be entropy driven and the latter enthalpy driven [69]. Entropic factors seem to be the likely explanation for the small cooperative stabilization effect on the C-terminal hairpin (< 2 kJ mol^{-1}), with each hairpin providing a possible template against which the third strand can interact. With one strand preorganized, the entropic cost of association of an additional strand is largely confined to the associating strand [73, 78]. The nature of the folded state is unlikely to compare with that of a β-sheet in a native protein, more likely, hydrophobic contacts between side chains stabilize a collapsed conformation where interstrand hydrogen bonds may play a minor stabilizing role. These ''loosely'' defined interactions between side chains,

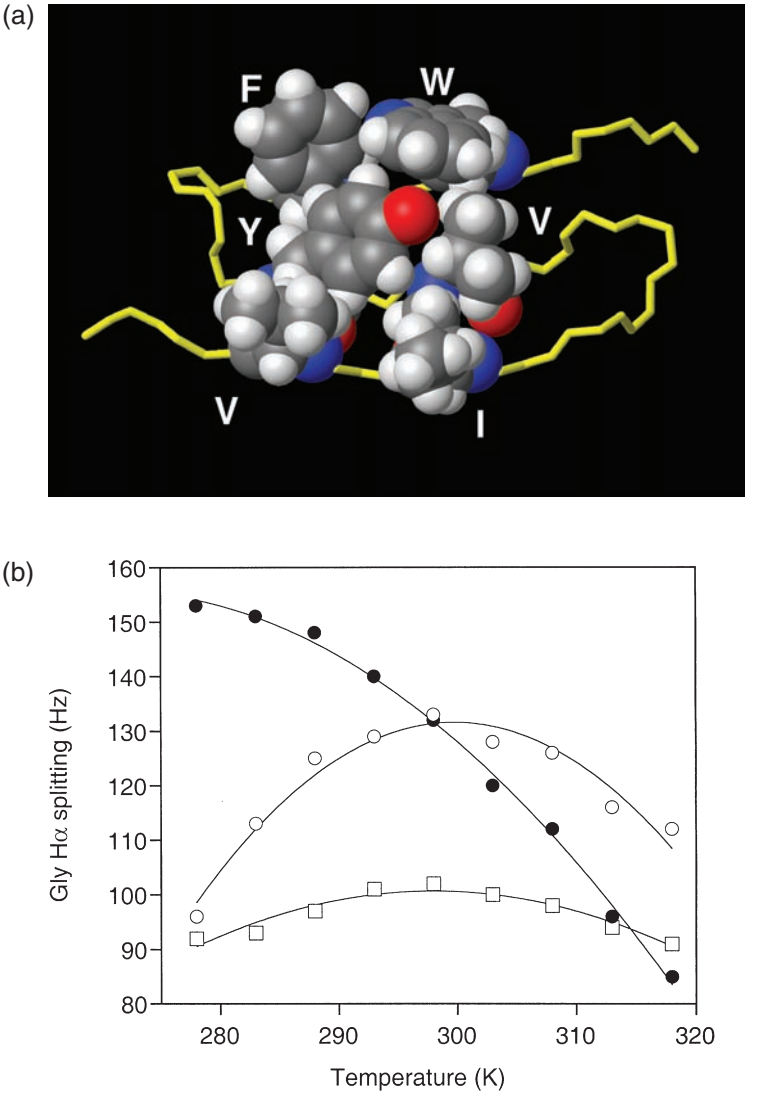

Fig. 10.13. a) Mean NMR structure of the fully folded state of the three-stranded antiparallel β-sheet structure of sequence KGEWTFVNG[9]KYTVSING[17]KKITVSI showing the core cluster of hydrophobic residues (underlined). b) Temperature-dependent stability profiles for the various β-hairpin components of the three-stranded sheet using the Hα splitting of Gly9 and Gly17 in the two β-turns: Gly9 (filled circles), Gly17 (open circles). Gly17 (open squares) in the isolated C-terminal hairpin peptide (G[9]KYTVSING[17]KKITVSI) is also shown. A larger Gly Hα splitting indicates a higher population of the folded hairpin. Different profiles for Gly9 and Gly17 in the three-stranded sheet show that the peptide cannot be folding via a simple two-state model involving only random coil and fully folded peptide. The data have been fitted assuming the four-state model shown in Figure 10.12b. Reproduced from Ref. [69].

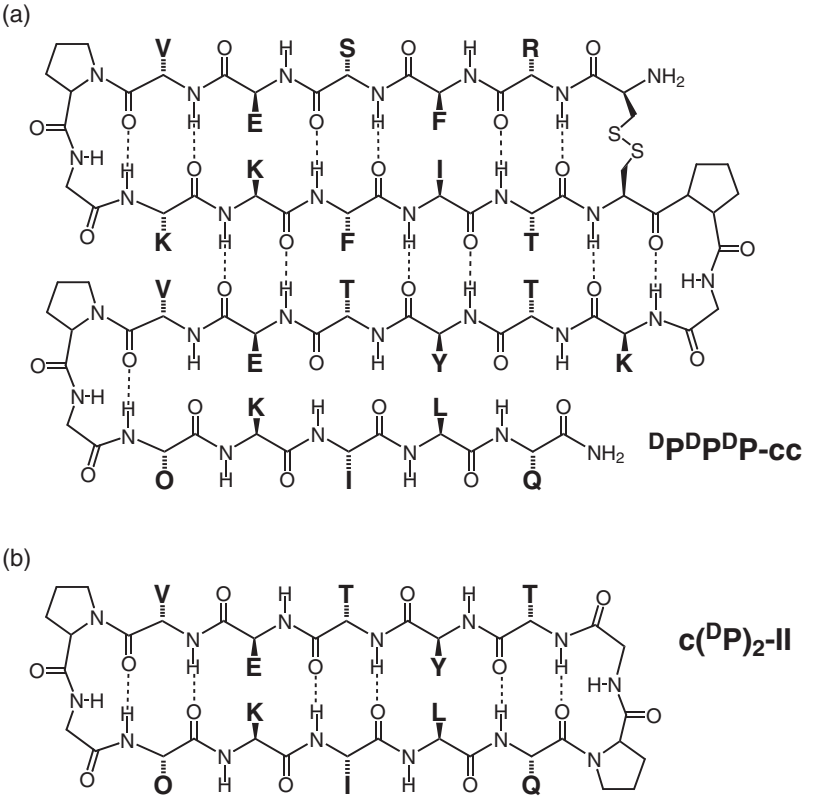

Fig. 10.14. Structure of the four-stranded β-sheet peptide **^{D}P^{D}P^{D}P-cc** (a), and the cyclic reference peptide **c(^{D}P)$_2$-II** (b) used for estimating limiting values for the fully folded state of the C-terminal hairpin of **^{D}P^{D}P^{D}P-cc**. Adapted from the work of Ref. [78].

rather than a native-like "crystalline" array of hydrogen bonds, may explain why cooperative interactions have only a small effect on overall stability because only a small energy barrier separates the folded from partially or fully unfolded states.

Several of the above studies have attempted to address the issue of whether cooperative interactions are propagated orthogonal to the strand direction as the number of β-strands increases. Gellman and coworkers have examined the influence of strand number on antiparallel β-sheet stability in designed three- and four-stranded structures (see Figure 10.14), using the D-Pro-Gly β-turn sequence to define β-turn position and strand length. The results are not dissimilar to those described above; a third strand stabilizes an existing two-stranded β-sheet by ~2 kJ mol^{-1}, while a fourth strand seems to confer a similar small stability increment [79].

10.10
Concluding Remarks: Weak Interactions and Stabilization of Peptide β-Sheets

In contrast to the highly cooperative folding behavior characteristic of native globular proteins, simple model β-sheet systems, which lack defining tertiary interactions, do not possess this characteristic. The limited number of three- and four-stranded β-sheet peptides so far described confirms this, although some evidence for cooperative interactions between β-strands have been presented and rationalized on the basis of the entropic benefits associated with adding an additional β-strand to a preformed template. In all cases to date, it seems that designed three- and four-stranded β-sheet structures are in equilibrium with their partially folded β-hairpin components. This is an indication that the energy landscape is relatively flat unlike that for most native proteins where there is a significant energy difference between the single native structure and other conformations. It is interesting to look at examples of the smallest known β-sheet proteins and make comparisons with the designed systems described above.

The WW domains [80–82] form a single folded motif consisting of three strands of antiparallel β-sheet but with well-defined tertiary interactions arising from folding back of the N- and C-termini to form a small compact hydrophobic core. This defining feature appears to allow the WW domains to fold co-operatively despite their small size (some as small as 35 residues) (Figure 10.15). Apart from the desire to be able to design molecules to order with specific tailored properties, the model β-sheet systems described have enabled considerable progress to be made in testing our understanding of the basic design principles of β-sheets and fundamental aspects of weak interactions.

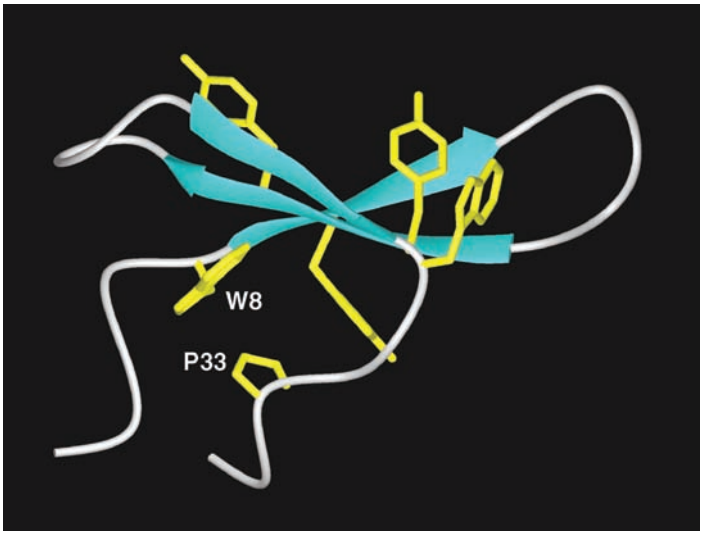

Fig. 10.15. NMR structure of the WW domain of the formin binding protein (PDB code: 1EOI), consisting of a three-stranded antiparallel β-sheet motif; the side chains of conserved residues are shown with tertiary contacts evident between W8 and P33.

References

1 Honig, B. *J. Mol. Biol.* **1999**; *293*, 283–93.
2 Brockwell, D. J., Smith, D. A., Radford, S. E. *Curr. Opin. Struct. Biol.* **2000**; *10*, 16–25.
3 Baldwin, R. L., Rose, G. *Trends Biochem. Sci.* **1999**; *24*, 26–76.
4 Baldwin, R. L., Rose, G. *Trends Biochem. Sci.* **1999**; *24*, 77–83.
5 Chakrabartty, A., Baldwin, R. *Adv. Protein Chem.* **1995**; *46*, 141–76.
6 Munoz, V., Serrano, L. *J. Mol. Biol.* **1995**; *245(3)*, 275–96.
7 O'Neil, K. T., Degrado, W. F. *Science* **1990**; *250(4981)*, 646–51.
8 Hill, R., Degrado, W. *J. Am. Chem. Soc.* **1998**; *120(6)*, 1138–45.
9 Gellman, S. H. *Curr. Opin. Chem. Biol.* **1998**; *2*, 717–25.
10 Ramirez-Alvarado, M., Kortemme, T., Blanco, F. J., Serrano, L. *Bio-org. Med. Chem.* **1999**; *7*, 93–103.
11 Searle, M. S. *J. Chem. Soc. Perkin Trans.* **2001**; *2*, 1011–20.
12 Kemp, D. S., Bowen, B. R., Meundel, C. C. *J. Org. Chem.* **1990**; *55*, 4650–7.
13 Nowick, J. S., Smith, E. M., Pairish, M. *Chem. Soc. Rev.* 1996; 401–15.
14 Diaz, H., Tsang, K. Y., Choo, D., Espina, J. R., Kelly, J. W. *J. Am. Chem. Soc.* **1993**; *115*, 3790–1.
15 Blanco, F. J., Jimenez, M. A., Herranz, J., Rico, M., Santoro, J., Nieto, J. L. *J. Am. Chem. Soc.* **1993**; *115*, 5887–9.
16 Blanco, F. J., Rivas, G., Serrano, L. *Nat. Struct. Biol.* **1994**; *1*, 584–90.
17 Blanco, F. J., Jimenez, M. A., Pineda, A., Rico, M., Santoro, J., Nieto, J. L. *Biochemistry* **1994**; *33*, 6004–14.
18 Cox, J. P. L., Evans, P. A., Packman, L. C., Williams, D. H., Woolfson, D. N. *J. Mol. Biol.* **1993**; *234*, 483–92.
19 Searle, M. S., Williams, D. H., Packman, L. C. *Nat. Struct. Biol.* **1995**; *2*, 999–1006.

20 Searle, M. S., Zerella, R., Williams, D. H., Packman, L. C. *Protein Eng.* **1996**; *9*, 559–65.

21 Zerella, R., Evans, P. A., Ionides, J. M. C. et al. *Protein Sci.* **1999**; *8*, 1320–31.

22 Zerella, R., Chen, P. Y., Evans, P. A., Raine, A., Williams, D. H. *Protein Sci.* **2000**; *9*, 2142–50.

23 Sibanda, B. L., Blundell, T. L., Thornton, J. M. *J. Mol. Biol.* **1989**; *206*, 759–77.

24 Hutchinson, E. G., Thornton, J. M. *Protein Sci.* **1994**; *3*, 2207–16.

25 Haque, T. S., Gellman, S. H. *J. Am. Chem. Soc.* **1997**; *119*, 2303–4.

26 Stanger, H. E., Gellman, S. H. *J. Am. Chem. Soc.* **1998**; *120*, 4236–7.

27 Ramirez-Alvarado, M., Blanco, F. J., Serrano, L. *Nat. Struct. Biol.* **1996**; *3*, 604–12.

28 De Alba, E., Jimenez, M. A., Rico, M. *J. Am. Chem. Soc.* **1997**; *119*, 175–83.

29 Ramirez-Alvarado, M., Blanco, F. J., Niemann, H., Serrano, L. *J. Mol. Biol.* **1997**; *273*, 898–912.

30 Griffiths-Jones, S. R., Maynard, A. J., Searle, M. S. *J. Mol. Biol.* **1999**; *292*, 1051–69.

31 Maynard, A. J., Searle, M. S. *J. Chem. Soc. Chem. Commun.* 1997; 1297–8.

32 Maynard, A. J., Sharman, G. J., Searle, M. S. *J. Am. Chem. Soc.* **1998**; *120*, 1996–2007.

33 Swindells, M. B., Macarthur, M. W., Thornton, J. M. *Nat. Struct. Biol.* **1995**; *2*, 596–603.

34 Fiebig, K. M., Schwalbe, H., Buck, M., Smith, L. J., Dobson, C. M. *J. Phys. Chem.* **1996**; *100*, 2661–6.

35 Smith, L. J., Bolin, K. A., Schwalbe, H., Macarthur, M. W., Thornton, J. M., Dobson, C. M. *J. Mol. Biol.* **1996**; *255*, 494–506.

36 Griffiths-Jones, S. R., Sharman, G. J., Maynard, A. J., Searle, M. S. *J. Mol. Biol.* **1998**; *284*, 1597–609.

37 Jourdan, M., Griffiths-Jones, S. R., Searle, M. S. *Eur. J. Biochem.* **2000**; *267*, 3539–48.

38 Neri, D., Billeter, M., Wider, G., Wuthrich, K. *Science* **1992**; *257*, 1559–63.

39 Frank, M., Clore, G. M., Gronenborn, A. *Protein Sci.* **1995**; *4*, 2605–15.

40 Buckler, D., Haas, E., Sheraga, H. *Biochemistry* **1995**; *34*, 15965–78.

41 Shortle, D. *FASEB J.* **1996**; *10*, 27–34.

42 Klein-Seetharaman, J., Oikawa, M., Grimshaw, S. B. et al. *Science* **2002**; *295*, 1719–22.

43 Shortle, D., Ackerman, M. S. *Science* **2001**; *293*, 487–9.

44 De Alba, E., Rico, M., Jimenez, M. A. *Protein Sci.* **1997**; *6*, 2548–60.

45 Wouters, M. A., Curmi, P. M. G. *Protein Struct. Funct. Genet.* **1995**; *22*, 119–31.

46 Hutchinson, E. G., Sessions, R. B., Thornton, J. M., Woolfson, D. N. *Protein Sci.* **1998**; *7*, 2287–300.

47 Espinosa, J. F., Munoz, V., Gellman, S. H. *J. Mol. Biol.* **2001**; *306*, 397–402.

48 Stanger, H. E., Syud, F. A., Espinosa, J. F., Giriat, I., Muir, T., Gellman, S. H. *Proc. Natl Acad. Sci. USA* **2001**; *98*, 12105–20.

49 Cochran, A. G., Skelton, N. J., Starovasnik, M. A. *Proc. Natl Acad. Sci. USA* **2001**; *98*, 5578–83.

50 Karshikoff, A., Ladenstein, R. *Trends Biochem. Sci.* **2001**; *26*, 550–6.

51 Kumar, S., Nussinov, R. *Cell. Mol. Life Sci.* **2001**, *58*, 1216–33.

52 Takano, K., Tsuchimori, K., Yamagata, Y., Yutani, K. *Biochemistry* **2000**, *39*, 12375–81.

53 Loladze, V. V., Ibarra-Molero, B., Sanchez-Ruiz, J., Makhatadze, G. I. *Biochemistry* **1999**, *38*, 16419–23.

54 Ciani, B., Jourdan, M., Searle, M. S. *J. Am. Chem. Soc.* **2003**; *125*, 9038–47.

55 Russell, S. J., Blandl, T., Skelton, N. J., Cochran, A. G. *J. Am. Chem. Soc.* **2003**; *125*, 388–95.

56 Munoz, V., Thompson, P. A., Hofrichter, J., Eaton, W. A. *Nature* **1997**; *390*, 196–199.

57 Munoz, V., Henry, E. R., Hofrichter, J., Eaton, W. A. *Proc. Natl Acad. Sci. USA* **1998**; *95*, 5872–9.

58 Hagen, S. J., Hofrichter, J., Szabo, A., Eaton, W. A. *Proc. Natl Acad. Sci. USA* **1996**; *93*, 11615–17.

59 Dinner, A. R., Lazaridis, T., Karplus, M. *Proc. Natl Acad. Sci. USA* **1999**; *96*, 9068–73.

60 Lacroix, E., Kortemme, T., Lopez de la Paz, M., Serrano, L. *Curr. Opin. Struct. Biol.* 1999; 487–93.

61 Synd, F. A., Espinosa, J. F., Gellman, S. H. *J. Am. Chem. Soc.* **1999**; *121*, 11577–8.

62 Espinosa, J. F., Gellman, S. H. *Angew. Chem.* **2000**; *39*, 2330–3.

63 Tatko, C. D., Waters, M. L. *J. Am. Chem. Soc.* **2004**; *126*, 2018–2034.

64 Colley, C. S., Griffiths-Jones, S. R., George, M. W., Searle, M. S. *J. Chem. Soc. Chem. Commun.* 2000; 593–4.

65 Hilario, J., Kubelka, J., Keiderling, T. A. *J. Am. Chem. Soc.* **2003**; *125*, 7562–7574.

66 Ma, B., Nussinov, R. *J. Mol. Biol.* **2000**; *296*, 1091–104.

67 Wang, H., Sung, S.-S. *Biopolymers* **1999**; *50*, 763–76.

68 Honda, S., Kobayashi, N., Munekata, E. *J. Mol. Biol.* **2000**; *295*, 269–78.

69 Griffiths-Jones, Searle, M. S. *J. Am. Chem. Soc.* **2000**; *122*, 8350–6.

70 Tatko, C. D., Waters, M. L. *J. Am. Chem. Soc.* **2002**; *124*, 9372–3.

71 Sharman, G. J., Searle, M. S. *J. Chem. Soc. Chem. Commun.* 1997; 1955–6.

72 Sharman, G. J., Searle, M. S. *J. Am. Chem. Soc.* **1998**; *120*, 5291–300.

73 Schenck, H. L., Gellman, S. H. *J. Am. Chem. Soc.* **1998**; *120*, 4869–70.

74 Kortemme, T., Ramirez-Alvarado, M., Serrano, L. *Science* **1998**; *281*, 253–6.

75 De Alba, E., Santoro, J., Rico, M., Jimenez, M. A. *Protein Sci.* **1999**; *8*, 854–65.

76 Das, C., Raghothama, S., Balaram, P. *J. Am. Chem. Soc.* **1998**; *120*, 5812–13; Das, C., Raghothama, S., Balaram, P. *Chem. Commun.* 1999; 967–8.

77 Lopez de la Paz, M., Lacroix, E., Ramirez-Alvarado, M., Serrano, L. *J. Mol. Biol.* **2001**; *312*, 229–46.

78 Finkelstein, A. V. *Proteins* **1991**; *9*, 23–7.

79 Syud, F. A., Stanger, H. E., Schenck Mortell, H. et al. *J. Mol. Biol.* **2003**; *326*, 553–68.

80 Macias, M. J., Gervais, V., Civera, C., Oschkinat, H. *Nat. Struct. Biol.* **2000**; *7*, 375–9.

81 Koepf, E. K., Petrassi, H. M., Ratnaswamy, G., Huff, M. E., Sudol, M., Kelly, J. W. *Biochemistry* **1999**; *38*, 14338–51.

82 Kanelis, V., Rotin, D., Forman-Kay, J. D. *Nat. Struct. Biol.* **2001**; *8*, 407–12.

11
Predicting Free Energy Changes of Mutations in Proteins

Raphael Guerois, Joaquim Mendes, and Luis Serrano

The ability to predict with good accuracy the effect of mutations on protein stability or complex formation is needed in order to design new proteins, as well as to understand the effect of single nucleotide polymorphisms on human health. In the following sections we will summarize what is known and can be used for this purpose. We will start by describing the forces that act on proteins, an understanding of which is a prerequisite to understanding the following section dealing with prediction methods. Finally we will briefly summarize other possible unexpected results of making mutants, such as changes in "in vivo" stability or inducing protein aggregation.

11.1
Physical Forces that Determine Protein Conformational Stability

In this section, we will briefly discuss the physical forces that determine the conformational stability of proteins. This section is intended to serve as a basis for the understanding of the following sections, and no effort has been made to comprehensively cover the relevant literature. However, many excellent reviews that thoroughly cover this topic have been written, several of which are cited in the titles to the various subsections for the interested reader; more specific references are given in the text.

11.1.1
Protein Conformational Stability [1]

Under physiological conditions, proteins exist in a biologically active state (the native (N) state), which is in dynamic equilibrium with a biologically inactive state (the denatured (D) state). The relative thermodynamic stability of the N state with respect to the D state is measured by the folding free energy: $\Delta G_{fold} = G_N - G_D$. Although G_N and G_D are individually large numbers, ΔG_{fold} is always small – typically on the order of 5–20 kcal mol^{-1}. This cancellation of large values is due

Protein Folding Handbook. Part I. Edited by J. Buchner and T. Kiefhaber

ISBN: 3-527-30784-2

to enthalpy–entropy compensation. The N state of proteins is, therefore, only marginally stable with respect to the D state, this stability being determined by a delicate balance between the forces that stabilize the N state and those that stabilize the D state.

11.1.2 Structures of the N and D States [2–6]

A detailed understanding of protein conformational stability requires that the structures of all microstates involved be known. Since the N and D states contribute on the same footing to ΔG_{fold}, the structures of both states are, in principle, required.

The N state of proteins consists of a compact structure in which the polypeptide chain folds up upon itself. This structure is frequently described as a single, unique conformation, which is a feature typical of proteins, compared with synthetic polymers. It is this feature that allows the structure of the N state to be determined experimentally with high accuracy, using methods such as X-ray crystallography and nuclear magnetic resonance (NMR) spectroscopy. However, the N state corresponds more accurately to an ensemble of structurally very similar conformations, which manifests itself experimentally as flexibility. Two levels of flexibility can be distinguished [7]: vibrational flexibility, corresponding to structural fluctuations within the same energy well on the energy hypersurface, and conformational flexibility, corresponding to structural transitions between different energy wells. Vibrational flexibility can be observed, for example, in the atomic B-factors of high-resolution X-ray models, whereas conformational flexibility can be observed in these models in the alternative rotamer conformations adopted predominantly by surface side chains.

In contrast to the N state, little is known structurally about the D state of proteins. Proteins can be denatured by a variety of means, including extremes of high or low temperatures, extremes of pH, addition of organic solvents, and addition of chemical denaturants. However, the denatured state relevant to determining protein stability is that which exists in equilibrium with the N state under physiological conditions. It has been extremely difficult to observe this state experimentally, since it exists at very low concentration relative to the N state. Initially, the D state was conceived of as an ensemble of structurally very diverse, totally unfolded conformations of the polypeptide chain, which are highly solvated. These conformations were believed to be completely random and, therefore, the ensemble would be devoid of any structural features, i.e., a random coil state. This conception was based on data from a variety of experimental methods that indicate that almost all tertiary and secondary structure present in the N state is disrupted upon denaturation (probed by fluorescence, UV absorption, and near-UV circular dichroism), and that the polypeptide chain expands to a size approximately equal to that expected for a random coil (probed by viscometry, gel filtration, and small angle X-ray scattering). However, several inconsistencies with the random coil model of the D state appeared: (i) significant amounts of secondary structure can

be detected in the D state of some proteins using far-UV circular dichroism even under relatively strong denaturing conditions, (ii) the D state of some proteins is only slightly expanded relative to the N state and much more compact than would be expected for a random coil, (iii) some single-point mutations can drastically alter the compactness of the D state, and (iv) the free energy change arising from some point mutations cannot be rationalized when a random coil model is assumed.

In relation to point (iv), point mutants have been found for which the folding enthalpy is reduced to less than 50% of the wild-type value and the folding entropy increases to a value that almost perfectly compensates the enthalpy change, such that there is practically no difference in ΔG_{fold} of the mutant and wild-type proteins [8]. But by definition, there are no side chain–side chain interactions in a random coil state and, therefore, the change in free energy of the D state accompanying mutation depends only on the identity of the mutated residue in the mutant and wild-type proteins, and not on the particular amino acid sequence; as such, under the random coil assumption, the change in stability produced by a mutation can be rationalized based solely on the structure of the N state. However, to explain the changes in enthalpy and entropy in these mutants solely in terms of effects on the native state requires (1) more than half of the chemical bonds stabilizing the wild type N state to be broken in the mutant N state, and (2) an enormous increase in the vibrational entropy of the mutant N state in order to avoid raising its free energy. Crystallographic studies of the N state of many mutant proteins have invariably shown only modest changes in atomic coordinates and thermal B-factors, making this interpretation highly implausible.

A wealth of studies over the past decade or so have made considerable steps forward in elucidating the structure of the D state. These studies are based on a variety of NMR experiments. In contrast to other spectroscopic and hydrodynamic studies mentioned above, which yield data that correspond to a global property of the protein, NMR spectroscopy provides information about individual residues. The most important of these studies have directly observed the D state under physiological conditions. This has been accomplished by destabilizing the N state relative to the D state, such that both exist in similar concentrations or the D state predominates. The destabilization has been achieved by particular pH conditions [9, 10], a single-point mutation [11, 12], or the deletion of residues at the N- and C-termini [5, 13–15]. The conclusion of these studies is that considerable amounts of secondary structure exist in the D state. This structure can be either native-like or nonnative-like. It is not persistent but, rather, fluctuating. It can exist up to high concentrations of chemical denaturants, but eventually melts out at very high concentrations. Recent studies using paramagnetic probes or residual dipolar couplings have found that, in addition to local secondary structure, a considerable amount of nonlocal structure exists in the D state. For some proteins, the D state appears to adopt the same overall topology of the N state. This nonlocal structure persists even at very high concentrations of denaturant [16]. In the scope of protein engineering it was shown that the specific destabilization of nonnative residual structure in the denatured state could bring about a dramatic stabilization in an SH3 domain [17].

The current conception of the D state under physiological conditions is that of a highly compact ensemble with considerable local and nonlocal structure, which, for some proteins, may already be poised to adopt the N state. The recent systematic survey of 21 well-characterized proteins based on kinetics and protein engineering data also strongly suggests that a majority of proteins studied so far follow such behavior [18].

11.1.3 Studies Aimed at Understanding the Physical Forces that Determine Protein Conformational Stability [1, 2, 8, 19–26]

A large number of studies have been undertaken to assess the relative importance of different physical forces in stabilizing the N and D states of proteins. Two types of study have been performed: (1) studies in which ΔG_{fold} is decomposed into the respective ΔH_{fold} and ΔS_{fold} components and these in turn into various component forces, and (2) studies in which the change in ΔG_{fold} produced by point mutations is decomposed into component forces. These studies provided many important insights and improved the understanding of protein conformational stability considerably. However, some of their conclusions are still very controversial. The controversy arises from several factors: (i) the large enthalpy–entropy compensation accompanying folding leads to a very small ΔG_{fold}, the consequence of which is that a small error in the estimation of a particular force can lead to a stabilizing force being interpreted as being destabilizing, or vice versa, (ii) the impossibility of uniquely decomposing experimental thermodynamic quantities into intramolecular and solvation contributions, (iii) the limited knowledge of the structural details of the D state and the lack of adequate models for it, and (iv) the considerable plasticity of the N state, i.e., its ability to readjust structurally to accommodate point mutations. In spite of the controversy, since ΔG_{fold} is always small, even forces that contribute only a few kcal mol^{-1} make a large contribution to ΔG_{fold} and, thus, tip the balance in favor of the N state or of the D state. Therefore, as a general conclusion that has emerged mainly from mutant studies, each protein uses a different strategy to tweak this stability of the N state, taking advantage of small increases in stability afforded by a particular type of force.

11.1.4 Forces Determining Conformational Stability [1, 2, 8, 19–27]

In their natural environment, most globular proteins are immersed in an aqueous medium. As such, to understand the conformational stability of proteins it does not suffice to consider the intramolecular interactions of the polypeptide chain in the N and D states. One must also consider the intermolecular interactions between the polypeptide chain in each of these states with the water molecules of the aqueous medium, as well as the alterations in the interactions of the water molecules among themselves induced by the presence of the protein. These latter interactions, which contain both enthalpic and entropic components, are usually

all collected together in the solvation free energy. Apart from the intramolecular interaction energy and the solvation free energy, one must also take into account the entropy of the N and D states when attempting to understand protein conformational stability.

11.1.5 Intramolecular Interactions

The intramolecular interactions that stabilize the N and D states of a protein are predominantly nonbonded forces. Bonded forces are essential for maintaining the covalent structure of the polypeptide chain, but are less important in determining stability.

11.1.5.1 van der Waals Interactions

The core of proteins in the N state is very densely packed – as dense as in organic crystals. As such, intramolecular van der Waals interactions are very important in stabilizing this state. Since the D state is significantly expanded with respect to the N state, intramolecular van der Waals interactions should be much fewer and weaker because it is a short-ranged interaction and, therefore, should play a much less important role in stabilizing this state.

11.1.5.2 Electrostatic Interactions

Charge–charge interactions Electrostatic interactions between charged groups in proteins can only contribute significantly to ΔG_{fold} if they are nonlocal, i.e., between groups on residues significantly separated in sequence. For neighboring residues, the free energy should be very similar in both the N and D states because charged groups are usually highly exposed in the N state as well.

Salt bridges form in the N state between groups of opposite charge that are in direct contact and simultaneously establish hydrogen bonds with each other. It is frequently argued that buried salt bridges cannot stabilize the N state because the energy gained by the electrostatic interaction, even though high due to the interior of the protein having a low dielectric constant, cannot compensate for the dehydration of two charged groups. However, recent calculations suggest that salt bridges with favourable geometry are likely to be stabilizing anywhere in the protein [28]. On the other hand, it is frequently argued that salt bridge formation at the surface of the protein cannot contribute much to the stability of the N state, because the energy gained by the electrostatic interaction in the aqueous medium of high dielectric constant cannot compensate for the loss of side chain entropy involved in fixing the side chains in the correct orientation for the salt bridge to form. However, if most of the entropy of the side chains is already lost prior to the formation of the salt bridge due to packing with other side chains at the surface, then salt bridge formation does not lead to an entropy loss and is considerably stabilizing.

On a similar note, entropic cooperativity can occur when networks of surface salt bridges are formed. Thus, although formation of the first salt bridge requires the

loss of entropy of the two side chains involved, formation of a second salt bridge from a third residue to the already bridged pair requires only loss of the entropy of one side chain. Salt bridge networks are very common in hyperthermophilic proteins, and are thought to be important in stabilizing the N state of these proteins [1].

Long-ranged electrostatic interactions between groups not directly involved in a salt bridge with each other can also contribute to stabilize or destabilize the N state relative to the D state. Thus, too many charges of the same type at the surface of the protein destabilize the N state with respect to the D state, because in the more expanded D state the like charges are further apart and repel each other less strongly. On the other hand, some studies indicate that the distribution of charges at the surface of the protein can be optimized such that the overall long-ranged electrostatic interactions stabilize the N state [29–31].

It is frequently difficult to predict the effect of mutations that aim at increasing protein stability by optimizing electrostatic interactions among charged groups on the surface of the N state of the protein. In fact, the stability increase can be considerably smaller than predicted and, in some cases, a decrease in stability is observed when an increase was predicted. These results suggest that favorable charge–charge interactions occur in the D state, and that the free energy of this state may be decreased even more than that of the N state by the mutations in charged residues that had aimed at improving the electrostatics of the N state [32].

Hydrogen bonding The N state of proteins is extensively hydrogen bonded and intramolecular hydrogen bonding is an important interaction in stabilizing this state. In the D state, intramolecular hydrogen bonds are not persistent and, therefore, probably do not contribute significantly to the stability of this state. Most hydrogen bonds in proteins involve strong hydrogen bond donors and acceptors, and are of type N–H•••O and O–H•••O. However, there is some structural evidence that the α-hydrogen of the polypeptide backbone can participate in C–H•••O hydrogen bonds, which, although somewhat weaker, could make a significant contribution to the stability of the N state [33, 34].

Dipole interactions Molecular mechanic calculations indicate that intramolecular dipole–dipole interactions between polar groups not directly hydrogen bonded to each other can contribute substantially to stabilizing the N state of proteins [22]. These interactions were also found to represent a major stabilizing interaction in the D state, using an extended chain conformation as a model for this state [22]. It is possible that this would also be the case if a more realistic model of the D state were used, since this state is currently thought to contain considerable local and nonlocal structures similar to that in the N state (see above).

Intramolecular charge–dipole interactions can also contribute significantly to stabilizing the N state of proteins. Thus, mutating a residue at the C-terminus of an α-helix to a positively charged amino acid, or mutating a residue at the N-terminus of an α-helix to a negatively charged amino acid, is found to stabilize the

N state of the protein through charge–dipole interactions between the charged residues and the net dipole moment of the helix. Presumably, in these cases, the helix is not formed or only partially formed in the D state and, therefore, the charge–dipole interactions either do not exist or are much weaker in this state.

Aromatic interactions The aromatic groups of aromatic residues have a net electric quadrupole moment. This arises from the electronic distribution being concentrated above and below the aromatic plane, leading to a net negative charge above and below this plane and a net positive charge within the plane and on the aromatic hydrogen atoms. The quadrupole moment is responsible for the particular interactions in which aromatic groups are involved.

Aromatic groups in direct contact can interact with each other through aromatic–aromatic interactions. Two stabilizing geometries are found in proteins: in one, the hydrogen atoms at the edge of one group point towards the center of the other, in the other the two aromatic planes are stacked on top of each other parallel but off-centered. Intramolecular aromatic–aromatic interactions can be considerably strong and can stabilize the N state of proteins significantly. In fact, aromatic residues exist most frequently in the core of native proteins and are in contact with each other more frequently than random.

Aromatic groups can also be involved in cation–π interactions within proteins [35]. In this interaction, a positive ion is in close proximity to the negative partial charge at the center of the aromatic ring, thus interacting favorably with the quadrupole moment. Intramolecular cation–π interactions can contribute considerably to the stability of the N state of proteins.

The aromatic hydrogen atoms can also interact with the sulfur atom of Cys and Met residues through a kind of weak hydrogen bond as has been experimentally shown [36].

Aromatic groups can also participate in a variety of hydrogen bonds of differing strengths [37].

11.1.5.3 Conformational Strain

Conformational strain is a consequence of bonded forces. Presumably, in the D state of proteins strained conformations do not exist because it is expanded and very flexible. Conformational strain can, however, occur in the tightly packed N state of proteins when: (i) a torsion angle or a bond angle deviates significantly from its equilibrium value, (ii) the side chain rotamer selected in the N state is not the one of lowest local energy, and (iii) there is overlap between atoms leading to steric repulsion. The first two of these are coined χ-strain and rotamer strain by Penel and Doig [38], and can make a considerable contribution to destabilizing the N state of proteins. These two types of strain can totally counterbalance the stabilizing effect of a disulfide bridge if this is under strain in the N state. As for the third type of strain, mutations that attempt to fit too large a residue into an internal cavity of a protein can result in so much atomic overlap that the protein does not fold. In less dramatic cases, it can lead to a significant decrease in the stability of the N state.

11.1.6
Solvation

The effects of solvation on protein conformational stability can be quantified through the solvation free energy of the N and the D states, defined as the free energy of transferring the polypeptide chain in each of these states from vacuum into aqueous solution. The free energies of transfer of model compounds indicate that the solvation of polar and charged groups in proteins is strongly favorable, that of aromatic groups is slightly favorable, and that of aliphatic groups is unfavorable. The favorable solvation of polar and charged groups is due to a negative enthalpy associated with favorable van der Waals interactions, hydrogen bond formation, and dipole–dipole or charge–dipole interactions with the solvent molecules. The slightly favorable solvation of aromatic groups is also enthalpic in origin and arises from favorable van der Waals and weak hydrogen bonds to the solvent molecules. The unfavorable solvation of aliphatic groups is due to the hydrophobic effect. This is a complex effect, which is still not completely understood. At room temperature, it is predominantly entropic in nature, involving the ordering of water molecules around the solute, but at other temperatures has both entropic and enthalpic contributions. The solvation data from these model compounds indicates that the solvation of polar and aromatic groups stabilizes the D state more than the N state, because in the D state such groups are more exposed to solvent. In contrast, solvation of aliphatic groups strongly destabilizes the D state with respect to the N state, because a large fraction of these groups is buried in the protein core in the N state but considerably exposed in the D state.

11.1.7
Intramolecular Interactions and Solvation Taken Together

A change in a thermodynamic quantity of folding, such as ΔG_{fold}, ΔH_{fold}, or ΔS_{fold}, resulting from a point mutation cannot be decomposed experimentally into the effects of intramolecular interactions and those of solvation. Therefore, it is common to assess the importance of the combined effects of intramolecular interactions and solvation on protein stability, of the different classes of chemical groups. Aliphatic groups stabilize the N state and destabilize the D state because they form more and stronger intramolecular van der Waals interactions and are excluded from solvent in the core of the protein in the N state. It is frequently argued that the stabilization afforded by the intramolecular van der Waals interactions in the N state is almost exactly offset by the intermolecular van der Waals interactions of the polypeptide chain with water in the D state (contained in the solvation free energy). Therefore, van der Waals interactions as a whole would not contribute to protein conformational stability, and the stability afforded by aliphatic groups is due to the destabilizing effect of hydrophobic solvation in the D state. However, the enthalpy of dissolution of organic crystals in water (as a model of the unfolding of the densely packed protein core) is unfavorable.

Privalov and coworkers have interpreted this result as indicating that the van der Waals interactions in the crystal are stronger than between the organic molecule

and water, as a consequence of the much less dense, open structure of water, which leads to fewer and weaker contacts than in the crystal [39]. They extend this explanation to protein stability, arguing that the intramolecular van der Waals interactions in the N state are stronger than the intermolecular van der Waals interactions with water in the D state and, therefore, van der Waals interactions are an important force in stabilizing the N state. However, based on molecular dynamics simulations, Karplus and coworkers suggested a different interpretation of the dissolution data [22]. They find that the intramolecular van der Waals interaction energy in the crystal is approximately the same as the intermolecular van der Waals energy of interaction between the organic molecule and water. Therefore, they argue that van der Waals interactions hardly contribute to protein conformational stability, and that the unfavorable enthalpy of dissolution results from changes in water structure associated with cavity formation.

Although, the net contribution of aliphatic groups is to destabilize the D state through the hydrophobic effect and to stabilize the N state through van der Waals interactions, in some mutants an inverse hydrophobic effect has been observed for very exposed hydrophobic residues in the N state [40]. This has been interpreted as resulting from the hydrophobic residues being more buried in the D state than in the N state.

Aromatic groups probably stabilize the N state more than they do the D state, because they are most frequently buried in the N state establishing favorable intramolecular van der Waals and aromatic interactions, which strongly outweigh the slightly favorable solvation when exposed in the D state. In fact, the very unfavorable free energies of transfer of aromatic compounds from the pure liquid into water, in spite of their favorable solvation free energy, is thought to result from the much more favorable aromatic–aromatic interactions in the pure liquid.

There is still controversy on the contribution of polar groups to protein conformational stability. Some authors defend that the favorable solvation of these groups when exposed to solvent in the D state almost exactly cancels the favorable intramolecular hydrogen bond and dipolar interactions they establish in the N state, and therefore their net contribution to ΔG_{fold} is practically zero. Other authors argue that the intramolecular interactions of the polar groups in the N state outweigh their favorable solvation in the D state, and conclude that polar group interactions contribute about the same to ΔG_{fold} as do the interactions of aliphatic and aromatic groups. Whatever its net contribution to protein stability, hydrogen bonding is always important for achieving a specific fold, since any unsatisfied hydrogen bond donor or acceptor group in the N state of the protein largely destabilizes this state with respect to the D state, in which such groups establish hydrogen bonds with water molecules.

11.1.8 Entropy

The entropy of the D state of proteins is considerably larger than that of the N state, because it consists of a structurally much more diverse ensemble of conformations. As such, entropy stabilizes the D state with respect to the N state. One

may consider the entropy of a polypeptide chain to be composed of backbone entropy and side chain entropy, although they are coupled.

Mutants that change the entropy of the backbone in the D state can affect conformational stability substantially. Thus, Xaa-Gly mutations lead to an increased flexibility of the D state, which corresponds to an increase in entropy and, consequently a decrease in G_D. Since the mutation does not affect the entropy of the N state to the same degree, G_N is approximately constant. Therefore, ΔG_{fold} decreases in absolute value, representing a decrease in the stability of the N state with respect to the D state. Xaa-Pro mutations induce exactly the opposite effect. Thus, they lead to a decreased flexibility of the D state, with a consequent decrease in entropy and associated increase in G_D. ΔG_{fold} increases in absolute value, representing an increase in the stability of the N state with respect to the D state. Xaa-Cys mutations designed to form additional disulfide bridges can also drastically reduce the entropy of the D state, thus enhancing stability [41]. However, the disulfide bridge must have the correct geometry in the N state, otherwise conformational strain can totally offset the gain in stabilization afforded by the reduction in entropy of the D state.

The change in side chain entropy upon folding is thought to be a major factor determining α-helix and β-sheet propensities of the various amino acids. The conformational freedom of side chains is lost to a differing degree upon folding from the D to the N state. In the D state, side chains are considerably flexible and can probably access most rotamer states. However, particular interactions in the D state can limit the conformational freedom of side chains [42]. In the N state, totally buried side chains and side chains involved in salt bridges, for example, have very little conformational freedom. However, totally exposed residues may maintain most of the freedom they had in the D state, whereas partially exposed residues may have an intermediate flexibility. Although it is frequently assumed, when interpreting protein conformational stability, that side chain entropy is totally lost upon folding, the differing degrees of side chain flexibility in the N state as well as in the D state should be considered to gain a detailed understanding of the effect of side chain entropy on stability. Clearly, this will only be totally feasible with the advent of more realistic models of the D state.

11.1.9 Cavity Formation

The effect of cavity-forming mutations on protein conformational stability can be difficult to interpret, since it involves a simultaneous change of several interactions. If a hydrophobic cavity that is accessible to solvent is formed, there will be a reduction in the number of intramolecular van der Waals interactions and the exposure of a hydrophobic surface to solvent. All other factors held constant, such mutations will, in general, be destabilizing. If a polar cavity is formed, it is frequently observed that structural water molecules fill the cavity in the mutant. If the group deleted from the wild-type protein was polar, the water molecule(s) may substitute for its interactions and there may be no change in stability. However, if

the deleted group was hydrophobic, the exposure of polar groups to solvent, which in the wild-type protein had unsatisfied hydrogen bonding, and the removal of an exposed hydrophobic group will, in general, lead to a stabilization of the mutant.

11.1.10 Summary

Many different forces participate in determining the final stability of a protein, which results from the sum of these forces in the native and denatured states. In general terms, entropy favors the denatured state, while desolvation of apolar groups, van der Waals interactions, hydrogen bonds, and electrostatic interactions favor the native state. Experimentally it has been very difficult to assign absolute values to all these terms, since any mutation will affect many of these terms simultaneously. Thus, breaking a buried H-bond by mutating a Ser into Ala not only breaks the H-bond but also changes the solvation properties of the denatured state, produces a cavity in the native state, and reduces the van der Waals interactions in this state. The native structure can relax, thereby increasing backbone entropy locally, while decreasing side chain entropy by eliminating one degree of freedom of the Ser residue. As a consequence, when protein scientists speak of the H-bond contribution, or of the hydrophobic contribution of an amino acid group, they are not speaking in pure physical terms, but rather are just referring to the main contributor to the interactions being analyzed. Studies over many different proteins and mutants show that all forces contribute to protein stability and that different proteins could use different combinations of forces to achieve stability. In fact, and contrary to what many groups have postulated, it has been shown that it is easier to stabilize a protein through substitutions on the surface than in the protein core [43–45]. A good example of how regular folded structures can be achieved without using hydrophobic amino acids is the formation of β-sheet amyloid fibrils by poly-Gln polypeptides [46]. In this case without any doubt the H-bonding and van der Waals interactions dominate over the hydrophobic contribution.

11.2 Methods for the Prediction of the Effect of Point Mutations on in vitro Protein Stability

11.2.1 General Considerations on Protein Plasticity upon Mutation

Over the past 20 years the protein engineering method was used as an efficient means to probe the chemistry underlying protein structure and interactions. The large amount of thermodynamic data obtained experimentally offers an appealing support for the development and assessment of predictive methods that estimate the effect of point mutation on protein stability. On average, single deletion or conservative point mutations can alter the stability of a protein by 10–20% of its total

stability (the upper limit is around 50% of the total stability) and is supposed not to cause too drastic changes in the three-dimensional structure. The observation that the structure is little affected by single deletion or conservative point mutations has been obtained from extensive works of different groups that have systematically solved the structure of the mutated protein [47–52]. The mutation of buried residues is expected to be most deleterious to protein structure and is discussed briefly here. As regards mutants in which a chemical group is deleted, slight adjustments usually partially accommodate changes in side-chain volume, but only to a limited degree [53–55]. In fact, it appears that full compensations are unlikely because it is difficult to reconstitute the equivalent set of interactions that were present in the wild-type structure (Figure 11.1). In the case of a new group inserted in a protein core, the changes in structure tend to accommodate the introduced side chains by rigid-body displacements of groups of linked atoms, achieved through relatively small changes in torsion angles (Figure 11.2). It is rare, for instance, that a side chain close to the site of substitution changes to a different rotamer [56].

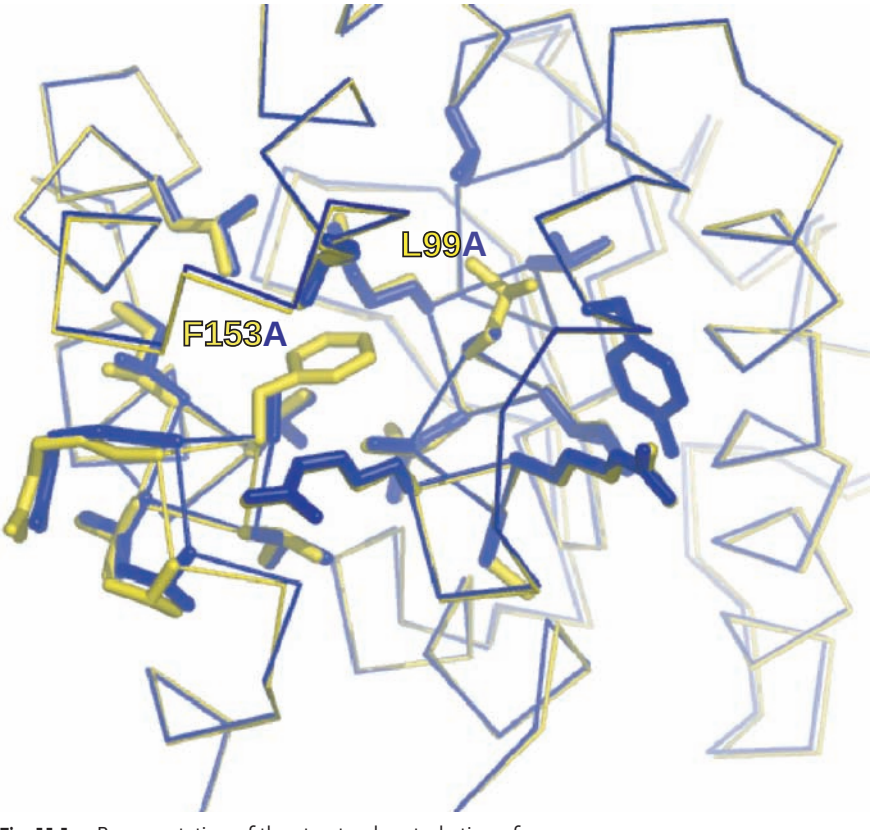

Fig. 11.1. Representation of the structural perturbation of side-chains in the core of the T4 lysozyme upon deletion of chemical groups. The wild-type (PDB: 4LZM) is in yellow and the mutant F153A and L99A (PDB: 1L89) is in blue.

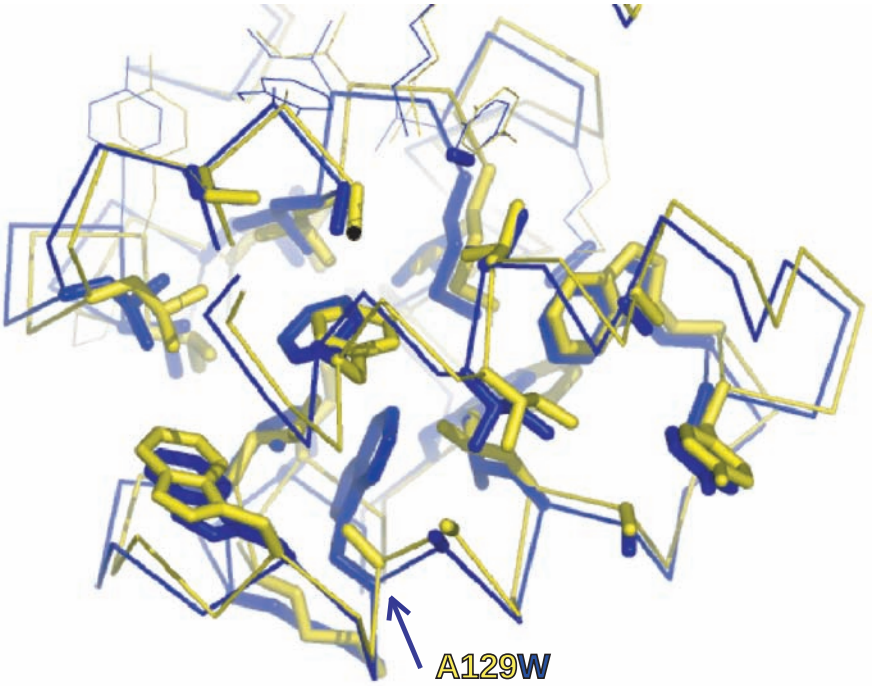

Fig. 11.2. Representation of the structural perturbation of side-chains in the core of the T4 lysozyme upon insertion of chemical groups. The wild-type (PDB: 4LZM) is in yellow and the mutant A129W (PDB: 1QTD) is in blue.

In a sense these observations are consistent with the fact that proteins in their native state are in a deep energy well. Alternative structures are higher in energy and not populated as long as the destabilization effect is limited. Only when several side chains are mutated at one time are wider rearrangements observed in the set of interactions that stabilize protein structure [55, 57]. In cases of extreme perturbation (such as the insertion of amino acids inside a helix), experimental observations reveal an amazing plasticity of proteins that can successfully change and adapt their structures (Figure 11.3, see p. 358) [58]. Such modifications are still far from being predicted by computational methods. Yet, for the majority of the point mutants considered by the predictive algorithms, the assumption that the structure does not undergo large changes is a reasonable one, although some exceptions have also been shown [59].

11.2.2 Predictive Strategies

A wide range of different strategies exist to account for the effect of point mutations on protein stability [60]. The methods can be divided into three classes: (i) statistically based methods (SEEF) that rely on the analysis of either sequence or

structure databases to transform probabilities into energies, (ii) protein engineering based methods (EEEF), which are empirically based methods that take advantage of thermodynamic data obtained on protein mutants, and (iii) physically based methods (PEEF) that rely on the derivation of energy terms from model compounds and of rigorous treatment of thermodynamics to calculate free energy changes upon mutation. In the following we consider each of the three approaches, analyzing the bases and limits of their current predictive power and attempting to draw out the critical features that should be implemented for future progress.

11.2.3 Methods

11.2.3.1 From Sequence and Multiple Sequence Alignment Analysis

Several works suggest that the information obtained from multiple sequence alignments could be converted into knowledge-based potentials helpful for guiding protein engineering. Indeed, sequence profiles include in an implicit manner a combination of important protein traits, such as stability, structural specificity, and solubility. For instance, protein engineering experiments based the predictive approach solely on multiple sequence alignments to achieve a successful stabilization of several protein folds [61, 62]. Looking at the reason for the success of this strategy, it was observed that in 25% of the cases the increase in stability could be explained by an enhanced propensity of the substituted residue for the local backbone conformation at the mutated site [61]. This conclusion was reached based on the predictions of local structures using the I-sites library [63]. It would be interesting to use libraries of local structures such as the I-sites library [63] or strategies such as those used in AGADIR [64] to account implicitly for the energetic properties of local structures that cannot be described adequately by the basic α or β secondary structure classes. This may also be an interesting way to calculate the energy of the unfolded state when some residual structure is likely to be formed. However, used as a unique source of information, multiple sequence alignments are unlikely to provide quantitative estimates of the effect of a mutation on protein stability. Yet, if the structure of the protein target is unknown they become the only useful method for rationally modifying the sequence (and might be useful to improve the sample properties as shown in the field of structural genomics [65]).

11.2.3.2 Statistical Analysis of the Structure Databases

Statistical potentials derived from the protein structure database have been widely used in the field of protein structure prediction. As mentioned by Lazaridis and Karplus [66], they have the advantage of being quick to compute, of accounting implicitly for complex effects that may be difficult to consider otherwise, and of perhaps being less sensitive to errors or atom displacement in the protein structure. In the case of protein design however, pairwise statistical potentials for residue–residue interactions may not be adequate for the structural stringency that is required [67, 68]. An elegant method has been developed that may overcome this limitation [69]. A four-body statistical potential, SNAPP, was developed based on the Delaunay tesselation of protein structure. The protein structure is divided into

tetrahedra whose edges represent all nearest neighbors of side chain centroids. Quite strong correlations were obtained in the prediction of point mutations of hydrophobic core residues. Yet as discussed further, prediction of the effect of point mutations on buried hydrophobic residues is not the most difficult to achieve. Simple counting methods were shown to perform quite well also [70]. The tessellation strategy might be more difficult to extend to surface accessible positions and a four-body potential method might be less successful for polar residues.

Statistical potentials based on the linear combination of database-derived potentials such as the PoPMuSiC algorithm have also been shown to have good predictive power, especially at fully exposed locations in proteins [71–73]. This program (accessible at http://babylone.ulb.ac.be/popmusic/) was successfully used to guide the engineering of an α_1-antitrypsin protein [74] and helped to identify that cation–π interactions are likely to play a key role in the ability of proteins to undergo domain swapping [75]. The latter is an interesting example of how database-derived potentials can reveal the role of specific interaction types that would have not been detected with atomic potentials that do not explicitly integrate this type of interaction.

11.2.3.3 **Helix/Coil Transition Model**

The evolution of the algorithms based on the helix/coil transition model illustrates beautifully the extent to which the field of prediction could benefit from protein engineering data. Because of its apparent simplicity, the helix structure has long been recognized to be an excellent model for understanding the fundamentals of protein structure and folding and for probing the effects of mutations on protein stability. The fact the helices are mainly stabilized through local interactions prompted many groups to tackle the analysis of small helical peptides whose sequences could be extensively varied. Short monomeric peptides present less context dependence than proteins. As mentioned in the previous section, changes in local interactions are also likely candidates to contribute to the stability of the native state and the denatured ensemble. Such systems have been successfully used to dissect the contribution of local interactions to helix stability (for reviews see Refs [76] and [77]), and have then been used to analyze β-hairpin and β-sheet formation (for a review see Ref. [77]).

Nowadays spectroscopic analysis, either by circular dichroism (CD) or nuclear magnetic resonance (NMR), has been carried out for a large number of short peptides encompassing helices of natural proteins. While short-range interactions are not enough to determine a single definite helix structure in a peptide, they do determine helix propensities, experimentally observed as helical populations in peptides that are different for every sequence and for each residue in the peptide. Thus, accurate predictions of helix stability require a statistical mechanics approach in which all the possible helical conformations in a peptide and all the energy contributions are taken into account. Its simplest version, postulated by Zimm and Bragg [78], used equilibrium constants characteristic of each amino acid to represent the nucleation and elongation of helical segments. Later versions of the helix/coil transition theory algorithms include detailed interaction terms such as capping interactions, side chain–side chain interactions, $i, i+3$ and $i, i+4$ electrostatic effects, interaction of charged groups with the helix dipole, etc. (for reviews see Refs

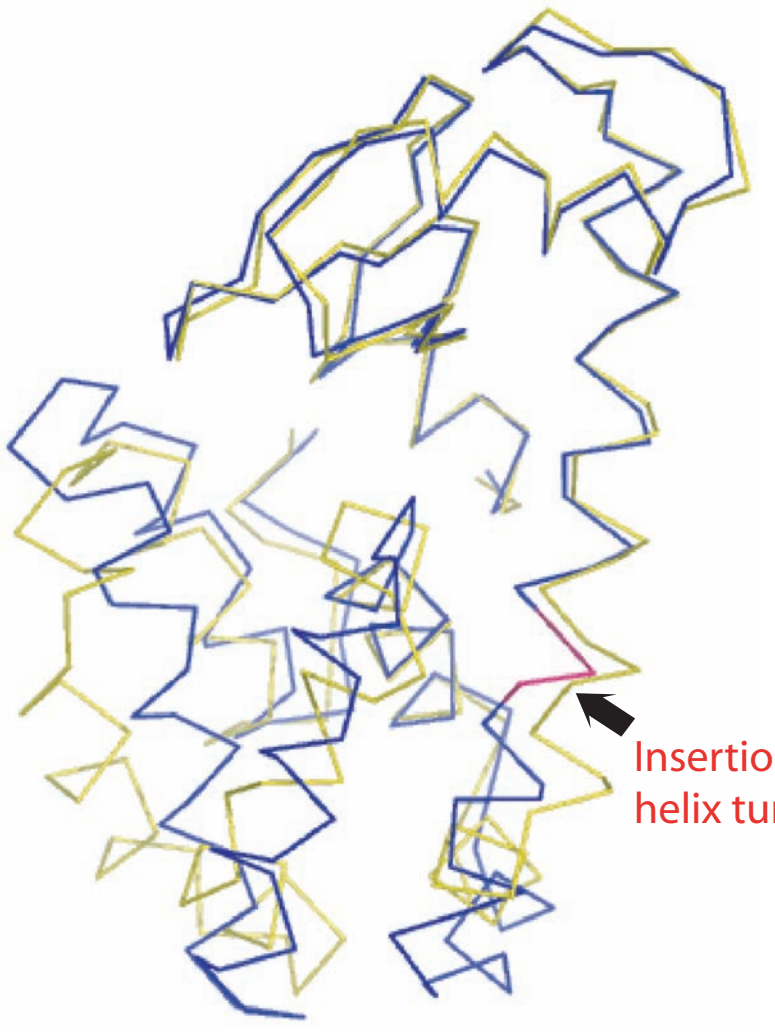

Fig. 11.3. Representation of the structural perturbation induced by the insertion of a triplet of amino acids inside a helix of the T4 lysozyme. The wild-type (PDB: 4LZM) is in yellow and the mutant (PDB: 1L74) is in blue with the inserted region in red.

[76, 77, 79, 80]). These terms have been introduced, either to follow experimental data [64, 76, 81–86], or to correspond to the statistical analysis of the protein database [84]. The latest version of one of these algorithms, AGADIR1s-2, includes: local motifs, a position dependence of the helical propensities for some of the 20 amino acids, an electrostatic model that takes into consideration all electrostatic interactions up to 12 residues in distance in the helix and random coil conformations

and the effect of ionic strength [64]. This algorithm predicts with an overall standard deviation value of 6.6% (maximum helix is 100%), the CD helical content of 778 peptides (223 correspond to wild-type and modified protein fragments), as well as the conformational shifts of the C H protons, and the ^{13}C and ^{15}N J coupling values (web access at http://www.embl-heidelberg.de/Services/serrano/agadir/agadir-start.html). The important point for our discussion here is that these methods, originally developed to predict the properties of peptides, could also be used to predict the effect of mutation on protein stability. Several experimental results are now confirming that the use of AGADIR could help understanding or designing the effect of mutations on protein stability [43–45].

The development of an AGADIR-like program for the quantitative prediction of β-hairpin stability has been somewhat less successful than in the case of helices. Several nonaggregating peptides exhibiting a large amount of β-hairpin structure were studied in the 1990s and allowed experimental analysis of the specific interactions both at the turn regions and in the strands [87–91]. In general, a good correlation was found between the experimental data and the statistical analysis of the protein database. As more experimental information is available, the description of hairpin formation in a beta/coil transition algorithm might be undertaken. However, due to the complexity of the interactions present in β-sheets, a residue-based empirical description such as the one used in AGADIR is unlikely to be successful. For example, the energetic contribution of a pairwise interstrand side-chain interaction appears to be dependent on the face of the β-sheet on which it is located, and intrinsic propensities are likely to display a significant position dependence along the strands as well as in the different turn positions, and will vary for the different turn types. Furthermore parallel β-sheets will differ in their properties from the antiparallel β-sheets. Taken together, these different contributions would yield a huge number of parameters to be experimentally determined for any empirical model of β-sheet formation.

As suggested in the next section, a rational approach to quantitatively predict the effect of mutations on β-hairpin and β-sheet stability will be more successful if, in addition to the residue based description used in AGADIR, an atomic-based description is included. Simple peptide models adopting β-hairpin and conformations hence constitute crucial systems for testing and refining such algorithms.

11.2.3.4 **Physicochemical Method Based on Protein Engineering Experiments**

The physicochemical reasoning methods originate from the rationalization of results obtained from a large quantity of protein engineering data. They have been designed from the assembly of empirical rules that are likely to reflect most of the stability variations in proteins observed upon mutation. The resolution of more than 100 crystal structures of point mutants and the creation of databases gathering all available mutant information such as the Protherm [92] or ASEdb [93] databases constituted decisive steps in pushing forward a large-scale validation of these predictive strategies. We have identified four independent methods recently published that tackled the challenge of developing tools for predicting $\Delta\Delta G$ upon any type of mutation: the SPMP [94, 95], the FOLD-X energy function (FOLDEF) [96]

(accessible on the web at http://fold-x.embl-heidelberg.de), the Kortemme et al. method [97], and the Lomize et al. method [98].

The aim of these methods is to estimate free energies from a single structural conformation. This means that they not only consider the potential energies associated with the interactions but also integrate effects such as the protein conformational entropy or the solvation. Because the exploration of the conformational space is limited in these methods, much of these effects have to be accounted for in an implicit manner. Also, the structure of the denatured state is not taken into account explicitly, rather interactions with close neighbours are neglected. Hence, in these methods, an initial fitting procedure is required to adjust the weights of the various explicit and implicit contributions to protein stability. In the training procedure, the structures of the mutants were either modeled from the wild-type structure (FOLDEF, Kortemme et al.) or obtained from experimentally determined X-ray structures (SPMP, Lomize et al.). The fact that most mutations are conservative (involving the deletion or the substitution of chemical groups) prevents large modeling issues.

Table 11.1 summarizes the major factors included in the methods and briefly presents the way the energetic contributions were implemented. A global agreement is reached between all the methods regarding the minimal set of terms that are to be considered. For each term, however, depending on the method, a variable number of parameters were used in the fit. Apart from the work by Lomize et al., in which the different interactions were independently fitted with respect to the atom types (18 parameters all in all), the total number of adjustable parameters is around 8.

A major feature of these methods is that the amplitudes of the various terms are scaled with respect to the solvent proximity. The scaling factor is calculated either from the accessible surface area or the density of protein atoms, which are two highly correlated parameters. In the case of the entropy terms (derived from statistical analyses of the structures database) the scaling accounts implicitly for the fact that, at the surface, side chains or backbone loops are more flexible. In the FOLD-X algorithm, this conformational entropy is also dependent on the existence of hydrogen bond interactions that are likely to freeze the conformations.

The contributions of the solvation effects (derived or consistent with model compound analysis) appear to be approximated in a reasonable manner by the use of the scaling factors. Penalties associated with the burial of polar groups represent the largest contribution to the destabilization of the protein tested in these methods. The implicit treatment of solvation effects is, however, questioned to account for the effect of so-called structural water (or water bridges), which are water molecules making more than two hydrogen bonds with the protein atoms. In the SPMP and FOLD-X methods, an explicit treatment of water bridges was found absolutely required for predicting the $\Delta\Delta G$ of mutants in which a water bridge had been altered. The SPMP method detailed the effect of water even further by considering explicitly the entire water shell network surrounding the protein [99]. This method relied on the X-ray structure of the mutants obtained at very low temperature so that the thermal fluctuations do not impede the observation of water molecules

network around the protein. When the structure of the mutant is not known, a fast predictive method for positioning the water molecules is required. The one proposed in [100] was for instance adapted in the FOLD-X method. It is important to note that in their study, Kortemme et al. suggested that the method they used for hydrogen bond calculation allowed an implicit treatment of the effect of these structural water molecules [97].

The role and the way to compute the effects of hydrogen bonds in protein stability has been a matter of debate for some years [101, 102]. In all the methods based on protein engineering analysis, an explicit consideration of the hydrogen bond with distance and angular constraints was used. Other recent studies also suggest that, in order to score a unique structural conformation, the angular and distance constraints inherent to the formation of hydrogen bonds are better modeled by a specific expression than by a global term accounting for all the electrostatic interactions [103, 104].

Different databases were used to test these potentials, which makes a ranking comparison between the methods rather difficult. For the FOLDEF, SPMP, and Kortemme et al. methods a precision ranging from 0.7 to 1 kcal mol^{-1} of standard deviation between prediction and experiments was obtained. The fourth method (Lomize et al.) produced very low rmsd errors between theoretical and experimental (0.4 kcal mol^{-1} and 0.57 kcal mol^{-1} for the training database or the blind test database respectively). Yet the mutant databases used in the latter studies were limited to fully buried residues (test carried out on solvent accessible residues led to mean unsigned errors of 1.4 kcal mol^{-1}) and the blind test database was restricted to 10 point mutants.

Interestingly, each method has specifically focused on at least one term of the energy function: (i) the SPMP method has developed specific analyses for explicit water molecules, (ii) the FOLD-X focused on the way entropy penalties are applied, (iii) the Kortemme et al. method derived a distance and angular dependent expression for hydrogen bonds, and (iv) the Lomidze et al. method used a specific Lennard Jones potential for each atom type interaction. A combination of these specific developments may push forward the current limits of the predictive algorithms. The way hydrogen bonds strength and charge–charge electrostatic interactions are modulated with solvent accessibility and with long-range interactions is probably one of the lines of improvement that can still be achieved in these methods. Yet, to be precise enough, this improvement will require the inclusion of side chain or backbone conformational exploration as was already partly included in the Kortemme et al. method.

An interesting test case to those questions has been proposed in the study of a surface salt bridge K11/E34 in ubiquitin and of the mutant in the reverse orientation E11/K34 [31]. It is clearly shown that long-range interactions contribute to the strength of these salt bridges and that a simple model can predict the effect of the surrounding on this type of interaction. Another track for improvement is related to the selection of the mutants tested in the fitting procedure. The fitting of the adjustable parameters tends to prioritize mutants with a larger $\Delta\Delta G$. Contexts or interactions that involve smaller $\Delta\Delta G$ or interactions that are little represented in the

Tab. 11.1. Summary of the implementation of the energetic factors included in four different methods for predicting free energy changes upon mutation.

	SPMP	*FOLD-X*	*Kortemme et al.*	*Lomize et al.*
Number of adjustable parameters	9	8	8	18
Training database	54 mut. with X-ray structures	339 mut.	743 mut.	106 mut. with X-ray structures
Blind test database	56 mut. with X-ray structures	667 mut. + 82 in complexes	371 mut. + 233 in complexes	10 mut. with X-ray structures
Excluded mutations	High B-factor residues	None	None	Water-accessible residues
Accessibility estimation	ASA based	Protein atomic density from the atom volumic contact parameter	Protein atomic density	ASA based
Van der Waals	None	Set by the atom volumic contact (atomic density)	Lennard-Jones with two parameters for attractive and repulsive terms	Lennard-Jones like. Nine terms depending on atom types
Solvation	ASA-based model (2 parameters)	Derived from average of model compounds analysis	Lazaridis, and Karplus solvation model	ASA-based model (five parameters)
Explicit hydrogen bond	Distance-dependent value. Three terms depend on protein or water interactions	Constant value. Fitted	Angular, distance, and solvent-accessible dependence. Different terms for backbone and side chains. Four parameters	10–12 Lennard-Jones like potential. Three terms depending on atom types
Electrostatics except H-bonds	None	Coulombic dielectric constant varying with atomic density	Coulombic dielectric constant varying with interatomic distance	None
Backbone entropy	Two-states propensity α/β	Propensities from Ramachandran plot statistics	Propensities from Ramachandran plot statistics	None

Side chain entropy	Yes. From statistical table	Yes. From statistical table	None	Yes. From statistical analysis (α/β differences)
Explicit water	Yes from X-ray	Yes. Position of water bridges predicted	None	None
Cavity	Yes	None	None	None
Other specificities		Helix capping term Helix dipole term	Allows side chain flexibility (Monte-Carlo)	Explicit account of torsion strains in side chains

database may tend to be underoptimized. For instance, in the case of mutations made at the surface of a protein, the amplitudes of $\Delta\Delta G$ are on average smaller than those for the buried ones. Also, mutations which alter the cap of a helix or the partners of a structural water are relatively rare, but their corresponding $\Delta\Delta G$ can be quite large. In all those cases, the fitting procedure is likely to limit the optimization of the parameters. A strategy to improve the current algorithms might be to restrict the databases to mutants that specifically address certain classes of interactions, such as the interaction with water bridges or the very solvent exposed ones.

11.2.3.5 Methods Based only on the Basic Principles of Physics and Thermodynamics

These methods use a combination of basic principles of physics and thermodynamics to reproduce with the highest fidelity possible the complex balance of interactions occurring in proteins. With respect to the more empirical methods described above, they restrict as far as possible the number of implicit terms they have to consider in the calculation. The great interest of such approaches is that the origin of any perturbation can then be analyzed and understood in the greatest detail. In principle, the free energy change between two states can be determined by evaluating the partition function in each state. In molecular systems as complex as proteins, however, one cannot sample thoroughly the conformational space to obtain accurate free energies. One of the strategies used instead is to break the change into many smaller steps, so that the free energy change for each step is evaluated by perturbation or thermodynamic integration methods [105–107].

In this method, the ΔG between a state A and B can be expressed with respect to the Hamiltonian of each state, H_A and H_B by defining a λ factor so that

$$H(\lambda) = \lambda H_B + (1 - \lambda) H_A \tag{1}$$

as follows:

1. Using the free energy perturbation method,

$$\Delta G = G_B - G_A = \sum_{\lambda=0}^{1} -RT \ln\langle e^{-\Delta H'/RT}\rangle_\lambda, \quad \text{where } \Delta H' = H_{\lambda+d\lambda} - H_\lambda \tag{2}$$

2. Using the thermodynamic integration method,

$$\Delta G = \int_{\lambda=0}^{\lambda=1} \left\langle \frac{\partial H}{\partial \lambda} \right\rangle_\lambda d\lambda \tag{3}$$

This methodology has been applied to a wide range of free energy calculations dedicated to the study of enzymatic reactions, conformational changes, binding of proteins, nucleic acids or small molecules [108], and also of the effects of muta-

tions on protein stability. Compared with other fields of application, the estimation of protein stability is relatively difficult. Indeed, contrary to the analysis of binding between macromolecules, the estimation of the ΔG of folding requires the energy calculation of a highly flexible and still poorly characterized state, the denatured state ensemble.

Since the early 1990s, molecular dynamics strategies coupled to free energy calculations have been used to analyze the stability changes of about 30 different point mutations in experimentally studied proteins [109–119]. The agreements between experimental and predictions have been good in the large majority of the cases observed, although significant discrepancies could also be observed [120]. The importance of the denatured state in the free energy calculation has been highlighted in many of the most recent calculations. It supports the experimental observation of the existence of residual structure, often with native like properties, in the denatured state of protein as reported in the first section. The systematic calculations carried out on 10 different mutants of chymotrypsin inhibitor 2 (CI2), with various conditions for the representation of the denatured protein emphasize the importance of considering a proper denatured state structure ensemble [118]. This analysis illustrates that when the denatured state is taken into account in the calculation, the predictions are much more successful (correlation going from 0.68 to 0.82). Besides, depending on the model, either an extended tripeptide or a more realistic full-length simulated structure of the denatured state, clear improvements in the simulations could be obtained. Hence, in the case of the hydrophobic mutations considered there, the quality of the prediction was shown to depend on the model of the denatured state.

Similarly, the works by Kitao's group [114, 116] showed a better agreement between experimental values and theory when they changed their reference state from a pentapeptide with an extended conformation to a more realistic pentapeptide model with the native like conformation.

As stated above, the advantage of molecular dynamics simulations or alternative methods that are based on the basic principle of physics is that they allow a detailed inspection of the origin of the stabilization or destabilization. Yet, the way free energies can be divided into energy (such as Lennard Jones, electrostatic, etc.) or residue terms is not a trivial issue. Several theories regarding the path dependence of the free energy components have been advanced [107, 121–125]. Under controlled conditions and proper choice of the λ coupling parameter it seems possible to extract some meaningful information. Unexpected results were observed, for instance, in the case of mutations involving apolar residues. The reason for the loss of stability in the V57A mutant in CI2 or the L56F mutant in T4 lysozyme could be interpreted as a larger variation in the electrostatic component. These particular mutants were not well predicted by the empirical-based methods and this fact emphasizes the advantage of mixing various approaches to get further insight in the origin of protein stabilization or destabilization.

Because it is based on molecular dynamics simulation, the free energy calculation method can account for the change in structure provoked by a mutation and does not depend on the assumption that the structure is unchanged upon muta-

tion. Yet compared with the less sophisticated empirical methods the computer time required to run a calculation on one mutant is several orders of magnitude larger. The most exhaustive study is still limited to eight to ten mutants. It would, however, be of great interest to get results from the calculation of a larger number of point mutants so that a statistical estimation of the error made by these methods could be more easily made. To speed up and overcome the sampling problems mixed strategies using Monte-Carlo sampling coupled to molecular dynamics have been proposed [117].

It is also important to mention alternative strategies using optimized methods for extensive sampling of the side chain conformational space. In this case however the backbone is considered rigid. Instead of extracting free energies from molecular dynamic simulation, these methods account for the conformational entropy component by an extensive sampling of side chain conformations. Different levels of sophistication in the force field can be included in these methods [126–128]. For instance the method in Ref. [128] included an implicit solvation term that allowed the calculation of a large number of point mutants not only at solvent-buried positions but also at solvent-exposed ones. This line of research is, to our view, one of the most promising for the prediction of the effect of point mutation on protein stability since it combines a high sampling quality and a force field that can depend both on physical and statistical terms to achieve the highest prediction rate.

11.3 Mutation Effects on in vivo Stability

A frequently forgotten aspect of proteins is that in general they need to perform their function in vivo. The cell has evolved a series of mechanisms to ensure the removal of proteins that have already carried out their function or of polypeptide chains that are faulty at synthesis or become misfolded. Thus there are some cryptic signals in proteins that are recognized by a cell and determine the half-life of a protein or target for destruction. Knowing about these signals is important since they could determine the outcome of an experiment (i.e., yield, protein activity, etc.).

In general these signals could be classified as follows: (1) N-terminal rules, (2) C-terminal rules, and (3) PEST sequences. However, it is possible that many other spurious signals exist and result in rapid degradation of an otherwise stable protein.

11.3.1 The N-terminal Rule

The N-end rule relates the in vivo half-life of a protein to the identity of its N-terminal residue. Similar but distinct versions of the N-end rule operate in all organisms examined, from mammals to fungi and bacteria. In eukaryotes, the N-end rule pathway is a part of the ubiquitin system. In *Escherichia coli*, three genes

Tab. 11.2. The N-end rule in *E. coli* and *Saccharomyces cerevisiae*.

Residue X in X-gal	*In vivo half-life of X-βgal (min)*	
	***In* E. coli**	***In* S. cerevisiae**
Arg	2	2
Lys	2	3
Phe	2	3
Leu	2	3
Trp	2	3
Tyr	2	10
His	>600	3
Ile	>600	30
Asp	>600	3
Glu	>600	30
Asn	>600	3
Gln	>600	10
Cys	>600	>1200
Ala	>600	>1200
Ser	>600	>1200
Thr	>600	>1200
Gly	>600	>1200
Val	>600	>1200
Pro	?	?
Met	>600	>1200

Approximate in vivo half-lives of X-β-galactosidase (βgal) proteins in *E. coli* at 36 °C [130] and in *S. cerevisiae* at 30 °C ([131, 132]). A question mark at Pro indicates its uncertain status in the N-end rule (see text).

From Ref. [129].

have been identified, *clpA*, *clpP*, and *aat*, as part of the degradation machinery involved in the N-terminal rule. In Table 11.2 we show data for the half-life of a protein having different N-terminal amino acids. For a review see Ref. [129].

11.3.2 The C-terminal Rule

In *E. coli* it has been found that when the ribosome encounters a problem in protein synthesis it attaches a 11 amino acid peptide (the ssrA degradation tag) to the C-terminus of the stalled protein chain and then the protein is released and targeted for degradation by the ClpX system [133]. Consequently it has been found that proteins containing an unstructured C-terminal segment with a hydrophobic amino acid at the C-terminus could be targeted for degradation by the ClpX machinery and that the efficiency of the degradation is related to the hydrophobic composition of the last five amino acids [134].

11.3.3
PEST Signals

Polypeptide regions rich in proline (P), glutamic acid (E), serine (S), and threonine (T) (PEST) target intracellular proteins for destruction [135]. Attachment of PEST sequences to proteins results in the fusion protein being degraded from 2- to almost 40-fold faster than the parental molecule [136].

11.4
Mutation Effects on Aggregation

When making a mutation or designing a protein, a frequently forgotten aspect is that the folded protein is in equilibrium with the denatured state and more important that the denatured state, or folding intermediates, can lead to aggregation. It is important at this point to make the distinction with the random process of precipitation, which is related to issues of solubility and does not appear to alter the structure of the proteins, as is seen for example by salting out using ammonium sulfate salts.

Protein aggregation has long been thought of as an unspecific process caused by the formation of nonnative contacts between protein folding intermediates. This view was supported by the wide variation of morphologies of aggregates that were observed by techniques such as electron microscopy and atomic force microscopy. Spectroscopically, two major types of aggregates are observed: the ones that involve the formation of β-sheet [137] and the ones that retain the native spectrum [138], although in a few cases helical aggregates can also be found. Both principal forms of initial aggregates can ultimately be converted to amyloid-like fibers that are invariably rich in cross-beta structure [137]. It seems therefore that nearly all proteins when aggregating will end up in a universal cross-beta structure but that the mechanism of getting there is determined by the competition between retaining the native structure and forming cross-β contacts.

Mutations that favor protein aggregation can be classified into those that destabilize the protein and increase the concentration of aggregation prone species (denatured and intermediate conformations) [139], or those that increase per se the tendency of an amino acid sequence to aggregate [140]. Analysis of the effect of different mutations on the aggregation tendency of unfolded Acp and other peptides [141] has illustrated the importance of secondary structure propensity, hydrophobicity, and charges in the process.

Recently, a statistical mechanics algorithm, TANGO, based on simple physicochemical principles of β-sheet formation extended by the assumption that the core regions of an aggregate are fully buried, has been developed to predict protein aggregating regions. TANGO predicts with surprisingly good accuracy the regions experimentally described to be involved in the aggregation of 176 peptides of over 20 proteins. The predictive capacities of TANGO are further illustrated by two examples: the prediction of the aggregation propensities of Aβ1–40 and Aβ1–42 and in

several disease-related mutations of the Alzheimer's β-peptide as well as the prediction of the aggregation profile of human acyl phosphatase. Thus, by capturing the energetics of structural parameters observed to contribute to protein aggregation and taking into account competing conformations, like α-helix and β-turn formation, it is possible to identify protein regions susceptible of promoting protein aggregation. The success of TANGO shows that the underlying mechanism of cross-β formation aggregates is universal [142]. It is expected that improvements of this or similar algorithms developed by other groups in conjunction with other software used to measure the impact of mutations on protein stability will allow us to design new proteins taking into account all the states and interactions.

References

1 Vieille, C. and Zeikus, G. J. (2001). Hyperthermophilic enzymes: sources, uses, and molecular mechanisms for thermostability. *Microbiol Mol Biol Rev* 65, 1–43.

2 Dill, K. A. (1990). Dominant forces in protein folding. *Biochemistry* 29, 7133–55.

3 Dill, K. A. and Shortle, D. (1991). Denatured states of proteins. *Annu Rev Biochem* 60, 795–825.

4 Shortle, D. (1996). The denatured state (the other half of the folding equation) and its role in protein stability. *FASEB J* 10, 27–34.

5 Shortle, D. (2002). The expanded denatured state: an ensemble of conformations trapped in a locally encoded topological space. *Adv Protein Chem* 62, 1–23.

6 Millett, I. S., Doniach, S., and Plaxco, K. W. (2002). Toward a taxonomy of the denatured state: small angle scattering studies of unfolded proteins. *Adv Protein Chem* 62, 241–62.

7 Karplus, M., Ichiye, T., and Pettitt, B. M. (1987). Configurational entropy of native proteins. *Biophys J* 52, 1083–5.

8 Sturtevant, J. M. (1994). The thermodynamic effects of protein mutations. *Curr Opin Struct Biol* 4, 69–78.

9 Kortemme, T., Kelly, M. J., Kay, L. E., Forman-Kay, J., and Serrano, L. (2000). Similarities between the spectrin SH3 domain denatured state and its folding transition state. *J Mol Biol* 297, 1217–29.

10 Lietzow, M. A., Jamin, M., Jane Dyson, H. J., and Wright, P. E. (2002). Mapping long-range contacts in a highly unfolded protein. *J Mol Biol* 322, 655–62.

11 Klein-Seetharaman, J., Oikawa, M., Grimshaw, S. B. et al. (2002). Long-range interactions within a nonnative protein. *Science* 295, 1719–22.

12 Mayor, U., Grossmann, J. G., Foster, N. W., Freund, S. M., and Fersht, A. R. (2003). The denatured state of Engrailed Homeodomain under denaturing and native conditions. *J Mol Biol* 333, 977–91.

13 Ackerman, M. S. and Shortle, D. (2002). Molecular alignment of denatured states of staphylococcal nuclease with strained polyacrylamide gels and surfactant liquid crystalline phases. *Biochemistry* 41, 3089–95.

14 Mok, Y. K., Kay, C. M., Kay, L. E., and Forman-Kay, J. (1999). NOE data demonstrating a compact unfolded state for an SH3 domain under non-denaturing conditions. *J Mol Biol* 289, 619–38.

15 Choy, W. Y. and Forman-Kay, J. D. (2001). Calculation of ensembles of structures representing the unfolded state of an SH3 domain. *J Mol Biol* 308, 1011–32.

16 Shortle, D. and Ackerman, M. S. (2001). Persistence of native-like topology in a denatured protein in 8 M urea. *Science* 293, 487–9.

17 Mok, Y. K., Elisseeva, E. L., Davidson, A. R., and Forman-Kay, J. D. (2001). Dramatic stabilization of an SH3 domain by a single substitution: roles of the folded and unfolded states. *J Mol Biol* 307, 913–28.

18 Sanchez, I. E. and Kiefhaber, T. (2003). Hammond behavior versus ground state effects in protein folding: evidence for narrow free energy barriers and residual structure in unfolded states. *J Mol Biol* 327, 867–84.

19 Creighton, T. E. (1991). Stability of folded conformations. *Curr Opin Struct Biol* 1, 5–16.

20 Matthews, B. W. (1991). Mutational analysis of protein stability. *Curr Opin Struct Biol* 1, 17–21.

21 Fersht, A. R. and Serrano, L. (1993). Principles of protein stability derived from protein engineering experiments. *Curr Opin Struct Biol* 3, 75–83.

22 Lazaridis, T., Archontis, G., and Karplus, M. (1995). Enthalpic contribution to protein stability: insights from atom-based calculations and statistical mechanics. *Adv Protein Chem* 47, 231–306.

23 Makhatadze, G. I. and Privalov, P. L. (1995). Energetics of protein structure. *Adv Protein Chem* 47, 307–425.

24 Honig, B. and Yang, A. S. (1995). Free energy balance in protein folding. *Adv Protein Chem* 46, 27–58.

25 Jaenicke, R., Schurig, H., Beaucamp, N., and Ostendorp, R. (1996). Structure and stability of hyperstable proteins: glycolytic enzymes from hyperthermophilic bacterium *Thermotoga maritima*. *Adv Protein Chem* 48, 181–269.

26 Pace, C. N., Shirley, B. A., McNutt, M., and Gajiwala, K. (1996). Forces contributing to the conformational stability of proteins. *FASEB J* 10, 75–83.

27 Creighton, T. E. (1993). *Proteins: Structures and Molecular Properties*, 2nd edn. W. H. Freeman and Co., New York.

28 Kumar, S. and Nussinov, R. (1999). Salt bridge stability in monomeric proteins. *J Mol Biol* 293, 1241–55.

29 Martin, A., Kather, I., and Schmid, F. X. (2002). Origins of the high stability of an in vitro-selected cold-shock protein. *J Mol Biol* 318, 1341–9.

30 Torrez, M., Schultehenrich, M., and Livesay, D. R. (2003). Conferring thermostability to mesophilic proteins through optimized electrostatic surfaces. *Biophys J* 85, 2845–53.

31 Makhatadze, G. I., Loladze, V. V., Ermolenko, D. N., Chen, X., and Thomas, S. T. (2003). Contribution of surface salt bridges to protein stability: guidelines for protein engineering. *J Mol Biol* 327, 1135–48.

32 Pace, C. N., Alston, R. W., and Shaw, K. L. (2000). Charge-charge interactions influence the denatured state ensemble and contribute to protein stability. *Protein Sci* 9, 1395–8.

33 Scheiner, S., Kar, T., and Gu, Y. (2001). Strength of the Calpha H•••O hydrogen bond of amino acid residues. *J Biol Chem* 276, 9832–7.

34 Chamberlain, A. K. and Bowie, J. U. (2002). Evaluation of C–H•••O hydrogen bonds in native and misfolded proteins. *J Mol Biol* 322, 497–503.

35 Pletneva, E. V., Laederach, A. T., Fulton, D. B., and Kostic, N. M. (2001). The role of cation-pi interactions in biomolecular association. Design of peptides favoring interactions between cationic and aromatic amino acid side chains. *J Am Chem Soc* 123, 6232–45.

36 Viguera, A. R. and Serrano, L. (1995). Side-chain interactions between sulfur-containing amino acids and phenylalanine in alpha-helices. *Biochemistry* 34, 8771–9.

37 Scheiner, S., Kar, T., and Pattanayak, J. (2002). Comparison of various types of hydrogen bonds involving aromatic amino acids. *J Am Chem Soc* 124, 13257–64.

38 Penel, S. and Doig, A. J. (2001). Rotamer strain energy in protein

helices – quantification of a major force opposing protein folding. *J Mol Biol* 305, 961–8.

39 Makhatadze, G. I. and Privalov, P. L. (1995). Energetics of protein structure. *Adv Protein Chem* 47, 307–425.

40 Bowler, B. E., May, K., Zaragoza, T., York, P., Dong, A., and Caughey, W. S. (1993). Destabilizing effects of replacing a surface lysine of cytochrome c with aromatic amino acids: implications for the denatured state. *Biochemistry* 32, 183–90.

41 Matsumura, M. and Matthews, B. W. (1991). Stabilization of functional proteins by introduction of multiple disulfide bonds. *Methods Enzymol* 202, 336–56.

42 Choy, W. Y., Shortle, D., and Kay, L. E. (2003). Side chain dynamics in unfolded protein states: an NMR based 2H spin relaxation study of delta131delta. *J Am Chem Soc* 125, 1748–58.

43 Munoz, V., Cronet, P., Lopez-Hernandez, E., and Serrano, L. (1996). Analysis of the effect of local interactions on protein stability. *Fold Des* 1, 167–78.

44 Villegas, V., Zurdo, J., Filimonov, V. V., Aviles, F. X., Dobson, C. M., and Serrano, L. (2000). Protein engineering as a strategy to avoid formation of amyloid fibrils. *Protein Sci* 9, 1700–8.

45 Taddei, N., Chiti, F., Fiaschi, T. et al. (2000). Stabilisation of alpha-helices by site-directed mutagenesis reveals the importance of secondary structure in the transition state for acylphosphatase folding. *J Mol Biol* 300, 633–47.

46 Scherzinger, E., Lurz, R., Turmaine, M. et al. (1997). Huntingtin-encoded polyglutamine expansions form amyloid-like protein aggregates in vitro and in vivo. *Cell* 90, 549–58.

47 Takano, K., Scholtz, J. M., Sacchettini, J. C., and Pace, C. N. (2003). The contribution of polar group burial to protein stability is strongly context-dependent. *J Biol Chem* 278, 31790–5.

48 Takano, K., Yamagata, Y., and Yutani, K. (2001). Contribution of polar groups in the interior of a protein to the conformational stability. *Biochemistry* 40, 4853–8.

49 Takano, K., Yamagata, Y., and Yutani, K. (2003). Buried water molecules contribute to the conformational stability of a protein. *Protein Eng* 16, 5–9.

50 Takano, K., Yamagata, Y., Funahashi, J., Hioki, Y., Kuramitsu, S., and Yutani, K. (1999). Contribution of intra- and intermolecular hydrogen bonds to the conformational stability of human lysozyme. *Biochemistry* 38, 12698–708.

51 Yamagata, Y., Kubota, M., Sumikawa, Y., Funahashi, J., Takano, K., Fujii, S., and Yutani, K. (1998). Contribution of hydrogen bonds to the conformational stability of human lysozyme: calorimetry and X-ray analysis of six tyrosine → phenylalanine mutants. *Biochemistry* 37, 9355–62.

52 Matthews, B. W. (1995). Studies on protein stability with T4 lysozyme. *Adv Protein Chem* 46, 249–78.

53 Takano, K., Yamagata, Y., Fujii, S., and Yutani, K. (1997). Contribution of the hydrophobic effect to the stability of human lysozyme: calorimetric studies and X-ray structural analyses of the nine valine to alanine mutants. *Biochemistry* 36, 688–98.

54 Eriksson, A. E., Baase, W. A., Zhang et al. (1992). Response of a protein structure to cavity-creating mutations and its relation to the hydrophobic effect. *Science* 255, 178–83.

55 Baldwin, E., Xu, J., Hajiseyedjavadi, O., Baase, W. A., and Matthews, B. W. (1996). Thermodynamic and structural compensation in "size-switch" core repacking variants of bacteriophage T4 lysozyme. *J Mol Biol* 259, 542–59.

56 Liu, R., Baase, W. A., and Matthews, B. W. (2000). The introduction of strain and its effects on the structure and stability of T4 lysozyme. *J Mol Biol* 295, 127–45.

57 Gassner, N. C., Baase, W. A., and Matthews, B. W. (1996). A test of the "jigsaw puzzle" model for protein folding by multiple methionine substitutions within the core of T4 lysozyme. *Proc Natl Acad Sci USA* 93, 12155–8.

58 Vetter, I. R., Baase, W. A., Heinz, D. W., Xiong, J. P., Snow, S., and Matthews, B. W. (1996). Protein structural plasticity exemplified by insertion and deletion mutants in T4 lysozyme. *Protein Sci* 5, 2399–415.

59 Consonni, R., Santomo, L., Fusi, P., Tortora, P., and Zetta, L. (1999). A single-point mutation in the extreme heat- and pressure-resistant sso7d protein from sulfolobus solfataricus leads to a major rearrangement of the hydrophobic core. *Biochemistry* 38, 12709–17.

60 Mendes, J., Guerois, R., and Serrano, L. (2002). Energy estimation in protein design. *Curr Opin Struct Biol* 12, 441–6.

61 Rath, A. and Davidson, A. R. (2000). The design of a hyperstable mutant of the Abp1p SH3 domain by sequence alignment analysis. *Protein Sci* 9, 2457–69.

62 Wang, Q., Buckle, A. M., and Fersht, A. R. (2000). Stabilization of GroEL minichaperones by core and surface mutations. *J Mol Biol* 298, 917–26.

63 Bystroff, C. and Baker, D. (1998). Prediction of local structure in proteins using a library of sequence-structure motifs. *J Mol Biol* 281, 565–77.

64 Lacroix, E., Viguera, A. R., and Serrano, L. (1998). Elucidating the folding problem of alpha-helices: local motifs, long-range electrostatics, ionic-strength dependence and prediction of NMR parameters. *J Mol Biol* 284, 173–91.

65 Pedelacq, J. D., Piltch, E., Liong, E. C. et al. (2002). Engineering soluble proteins for structural genomics. *Nat Biotechnol* 20, 927–32.

66 Lazaridis, T. and Karplus, M. (2000). Effective energy functions for protein structure prediction. *Curr Opin Struct Biol* 10, 139–45.

67 Betancourt, M. R. and Thirumalai, D. (1999). Pair potentials for protein folding: choice of reference states and sensitivity of predicted native states to variations in the interaction schemes. *Protein Sci* 8, 361–9.

68 Thomas, P. D. and Dill, K. A. (1996). An iterative method for extracting energy-like quantities from protein structures. *Proc Natl Acad Sci USA* 93, 11628–33.

69 Carter, C. W., Jr., LeFebvre, B. C., Cammer, S. A., Tropsha, A., and Edgell, M. H. (2001). Four-body potentials reveal protein-specific correlations to stability changes caused by hydrophobic core mutations. *J Mol Biol* 311, 625–38.

70 Serrano, L., Kellis, J. T., Jr., Cann, P., Matouschek, A., and Fersht, A. R. (1992). The folding of an enzyme. II. Substructure of barnase and the contribution of different interactions to protein stability. *J Mol Biol* 224, 783–804.

71 Gilis, D. and Rooman, M. (2000). PoPMuSiC, an algorithm for predicting protein mutant stability changes: application to prion proteins. *Protein Eng* 13, 849–56.

72 Gilis, D. and Rooman, M. (1997). Predicting protein stability changes upon mutation using database-derived potentials: solvent accessibility determines the importance of local versus non-local interactions along the sequence. *J Mol Biol* 272, 276–90.

73 Gilis, D. and Rooman, M. (1996). Stability changes upon mutation of solvent-accessible residues in proteins evaluated by database-derived potentials. *J Mol Biol* 257, 1112–26.

74 Gilis, D., McLennan, H. R., Dehouck, Y., Cabrita, L. D., Rooman, M., and Bottomley, S. P. (2003). In vitro and in silico design of alpha1-antitrypsin mutants with different conformational stabilities. *J Mol Biol* 325, 581–9.

75 Dehouck, Y., Biot, C., Gilis, D., Kwasigroch, J. M., and Rooman, M. (2003). Sequence-structure signals of

3D domain swapping in proteins. *J Mol Biol* 330, 1215–25.

76 Chakrabartty, A. and Baldwin, R. L. (1995). Stability of alpha-helices. *Adv Protein Chem* 46, 141–76.

77 Serrano, L. (2000). The relationship between sequence and structure in elementary folding units. *Adv Protein Chem* 53, 49–85.

78 Zimm, B. H. and Bragg, J. K. (1959). Theory of the phase transition between helix and random coil in polypeptide chains. *J Chem Phys* 31, 526–535.

79 Munoz, V. and Serrano, L. (1995). Helix design, prediction and stability. *Curr Opin Biotechnol* 6, 382–6.

80 Doig, A. J. (2002). Recent advances in helix-coil theory. *Biophys Chem* 101–102, 281–93.

81 Lifson, S. and Roig, A. (1961). On the helix-coil transition in polypeptides. *J Chem Phys* 34, 1963–74.

82 Lomize, A. L. and Mosberg, H. I. (1997). Thermodynamic model of secondary structure for alpha-helical peptides and proteins. *Biopolymers* 42, 239–69.

83 Andersen, N. H. and Tong, H. (1997). Empirical parameterization of a model for predicting peptide helix/coil equilibrium populations. *Protein Sci* 6, 1920–36.

84 Misra, G. P. and Wong, C. F. (1997). Predicting helical segments in proteins by a helix-coil transition theory with parameters derived from a structural database of proteins. *Proteins* 28, 344–59.

85 Munoz, V. and Serrano, L. (1994). Elucidating the folding problem of helical peptides using empirical parameters. *Nat Struct Biol* 1, 399–409.

86 Munoz, V. and Serrano, L. (1995). Analysis of $i, i+5$ and $i, i+8$ hydrophobic interactions in a helical model peptide bearing the hydrophobic staple motif. *Biochemistry* 34, 15301–6.

87 Ramirez-Alvarado, M., Blanco, F. J., and Serrano, L. (1996). De novo design and structural analysis of a model beta-hairpin peptide system. *Nat Struct Biol* 3, 604–12.

88 de Alba, E., Rico, M., and Jimenez, M. A. (1997). Cross-strand side-chain interactions versus turn conformation in beta-hairpins. *Protein Sci* 6, 2548–60.

89 Ramirez-Alvarado, M., Blanco, F. J., Niemann, H., and Serrano, L. (1997). Role of beta-turn residues in beta-hairpin formation and stability in designed peptides. *J Mol Biol* 273, 898–912.

90 de Alba, E., Rico, M., and Jimenez, M. A. (1999). The turn sequence directs beta-strand alignment in designed beta-hairpins. *Protein Sci* 8, 2234–44.

91 Lacroix, E., Kortemme, T., Lopez de la Paz, M., and Serrano, L. (1999). The design of linear peptides that fold as monomeric beta-sheet structures. *Curr Opin Struct Biol* 9, 487–93.

92 Gromiha, M. M., Uedaira, H., An, J., Selvaraj, S., Prabakaran, P., and Sarai, A. (2002). ProTherm, thermodynamic database for proteins and mutants: developments in version 3.0. *Nucleic Acids Res* 30, 301–2.

93 Thorn, K. S. and Bogan, A. A. (2001). ASEdb: a database of alanine mutations and their effects on the free energy of binding in protein interactions. *Bioinformatics* 17, 284–5.

94 Takano, K., Ota, M., Ogasahara, K., Yamagata, Y., Nishikawa, K., and Yutani, K. (1999). Experimental verification of the 'stability profile of mutant protein' (SPMP) data using mutant human lysozymes. *Protein Eng* 12, 663–72.

95 Funahashi, J., Takano, K., and Yutani, K. (2001). Are the parameters of various stabilization factors estimated from mutant human lysozymes compatible with other proteins? *Protein Eng* 14, 127–34.

96 Guerois, R., Nielsen, J. E., and Serrano, L. (2002). Predicting changes in the stability of proteins and protein complexes: a study of more than 1000 mutations. *J Mol Biol* 320, 369–87.

97 Kortemme, T. and Baker, D. (2002).

A simple physical model for binding energy hot spots in protein-protein complexes. *Proc Natl Acad Sci USA* 99, 14116–21.

98 Lomize, A. L., Reibarkh, M. Y., and Pogozheva, I. D. (2002). Interatomic potentials and solvation parameters from protein engineering data for buried residues. *Protein Sci* 11, 1984–2000.

99 Funahashi, J., Takano, K., Yamagata, Y., and Yutani, K. (2002). Positive contribution of hydration structure on the surface of human lysozyme to the conformational stability. *J Biol Chem* 277, 21792–800.

100 Pitt, W. R. and Goodfellow, J. M. (1991). Modelling of solvent positions around polar groups in proteins. *Protein Eng* 4, 531–7.

101 Honig, B. and Yang, A. S. (1995). Free energy balance in protein folding. *Adv Protein Chem* 46, 27–58.

102 Myers, J. K. and Pace, C. N. (1996). Hydrogen bonding stabilizes globular proteins. *Biophys J* 71, 2033–9.

103 Kortemme, T., Morozov, A. V., and Baker, D. (2003). An orientation-dependent hydrogen bonding potential improves prediction of specificity and structure for proteins and protein–protein complexes. *J Mol Biol* 326, 1239–59.

104 Morozov, A. V., Kortemme, T., and Baker, D. (2003). Evaluation of models of electrostatic interactions in proteins. *J Phys Chem B* 107, 2075–90.

105 Beveridge, D. L. and DiCapua, F. M. (1989). Free energy via molecular simulation: applications to chemical and biomolecular systems. *Annu Rev Biophys Biophys Chem* 18, 431–92.

106 Kollman, P. A. (1993). Free energy calculations: applications to chemical and biochemical phenomena. *Chem Rev* 93, 2395–417.

107 Brady, G. P. and Sharp, K. A. (1995). Decomposition of interaction free energies in proteins and other complex systems. *J Mol Biol* 254, 77–85.

108 Wang, W., Donini, O., Reyes, C. M., and Kollman, P. A. (2001). Biomolecular simulations: recent developments in force fields, simulations of enzyme catalysis, protein–ligand, protein–protein, and protein–nucleic acid noncovalent interactions. *Annu Rev Biophys Biomol Struct* 30, 211–43.

109 Tidor, B. and Karplus, M. (1991). Simulation analysis of the stability mutant R96H of T4 lysozyme. *Biochemistry* 30, 3217–28.

110 Prevost, M., Wodak, S. J., Tidor, B., and Karplus, M. (1991). Contribution of the hydrophobic effect to protein stability: analysis based on simulations of the Ile-96----Ala mutation in barnase. *Proc Natl Acad Sci USA* 88, 10880–4.

111 Sneddon, S. F. and Tobias, D. J. (1992). The role of packing interactions in stabilizing folded proteins. *Biochemistry* 31, 2842–6.

112 Yamaotsu, N., Moriguchi, I., Kollman, P. A., and Hirono, S. (1993). Molecular dynamics study of the stability of staphylococcal nuclease mutants: component analysis of the free energy difference of denaturation. *Biochim Biophys Acta* 1163, 81–8.

113 Yamaotsu, N., Moriguchi, I., and Hirono, S. (1993). Estimation of stabilities of staphylococcal nuclease mutants (Met32 → Ala and Met32 → Leu) using molecular dynamics/free energy perturbation. *Biochim Biophys Acta* 1203, 243–50.

114 Sugita, Y., Kitao, A., and Go, N. (1998). Computational analysis of thermal stability: effect of Ile → Val mutations in human lysozyme. *Fold Des* 3, 173–81.

115 Sugita, Y. and Kitao, A. (1998). Improved protein free energy calculation by more accurate treatment of nonbonded energy: application to chymotrypsin inhibitor 2, V57A. *Proteins* 30, 388–400.

116 Sugita, Y. and Kitao, A. (1998). Dependence of protein stability on the structure of the denatured state: free energy calculations of I56V mutation in human lysozyme. *Biophys J* 75, 2178–87.

117 Pitera, J. W. and Kollman, P. A. (2000). Exhaustive mutagenesis in

silico: multicoordinate free energy calculations on proteins and peptides. *Proteins* 41, 385–97.

118 Pan, Y. and Daggett, V. (2001). Direct comparison of experimental and calculated folding free energies for hydrophobic deletion mutants of chymotrypsin inhibitor 2: free energy perturbation calculations using transition and denatured states from molecular dynamics simulations of unfolding. *Biochemistry* 40, 2723–31.

119 Funahashi, J., Sugita, Y., Kitao, A., and Yutani, K. (2003). How can free energy component analysis explain the difference in protein stability caused by amino acid substitutions? Effect of three hydrophobic mutations at the 56th residue on the stability of human lysozyme. *Protein Eng* 16, 665–671.

120 Spencer, D. S. and Stites, W. E. (1996). The M32L substitution of staphylococcal nuclease: disagreement between theoretical prediction and experimental protein stability. *J Mol Biol* 257, 497–9.

121 Mark, A. E. and van Gunsteren, W. F. (1994). Decomposition of the free energy of a system in terms of specific interactions. Implications for theoretical and experimental studies. *J Mol Biol* 240, 167–76.

122 Smith, P. A. and van Gunsteren, W. F. (1994). When are free energy components meaningful? *J Phys Chem* 98, 13735–40.

123 Boresch, S., Archontis, G., and Karplus, M. (1994). Free energy simulations: the meaning of the individual contributions from a component analysis. *Proteins* 20, 25–33.

124 Boresch, S. and Karplus, M. (1995). The meaning of component analysis: decomposition of the free energy in terms of specific interactions. *J Mol Biol* 254, 801–7.

125 Brady, G. P., Szabo, A., and Sharp, K. A. (1996). On the decomposition of free energies. *J Mol Biol* 263, 123–5.

126 Lee, C. and Levitt, M. (1991). Accurate prediction of the stability and activity effects of site-directed mutagenesis on a protein core. *Nature* 352, 448–51.

127 Lee, C. (1994). Predicting protein mutant energetics by self-consistent ensemble optimization. *J Mol Biol* 236, 918–39.

128 Mendes, J., Baptista, A. M., Carrondo, M. A., and Soares, C. M. (2001). Implicit solvation in the self-consistent mean field theory method: sidechain modelling and prediction of folding free energies of protein mutants. *J Comput Aided Mol Des* 15, 721–40.

129 Varshavsky, A. (1996). The N-end rule: functions, mysteries, uses. *Proc Natl Acad Sci USA* 93, 12142–9.

130 Tobias, J. W., Shrader, T. E., Rocap, G., and Varshavsky, A. (1991). The N-end rule in bacteria. *Science* 254, 1374–7.

131 Bachmair, A., Finley, D., and Varshavsky, A. (1986). In vivo half-life of a protein is a function of its amino-terminal residue. *Science* 234, 179–86.

132 Bachmair, A. and Varshavsky, A. (1989). The degradation signal in a short-lived protein. *Cell* 56, 1019–32.

133 Flynn, J. M., Levchenko, I., Seidel, M., Wickner, S. H., Sauer, R. T., and Baker, T. A. (2001). Overlapping recognition determinants within the ssrA degradation tag allow modulation of proteolysis. *Proc Natl Acad Sci USA* 98, 10584–9.

134 Flynn, J. M., Neher, S. B., Kim, Y. I., Sauer, R. T., and Baker, T. A. (2003). Proteomic discovery of cellular substrates of the ClpXP protease reveals five classes of ClpX-recognition signals. *Mol Cell* 11, 671–83.

135 Rogers, S., Wells, R., and Rechsteiner, M. (1986). Amino acid sequences common to rapidly degraded proteins: the PEST hypothesis. *Science* 234, 364–8.

136 Loetscher, P., Pratt, G., and Rechsteiner, M. (1991). The C terminus of mouse ornithine decarboxylase confers rapid degradation on dihydrofolate reductase. Support for the pest hypothesis. *J Biol Chem* 266, 11213–20.

137 Dobson, C. M. (2002). Getting out of shape. *Nature* 418, 729–30.

138 Bousset, L., Thomson, N. H., Radford, S. E., and Melki, R. (2002). The yeast prion Ure2p retains its native alpha-helical conformation upon assembly into protein fibrils in vitro. *EMBO J* 21, 2903–11.

139 Booth, D. R., Sunde, M., Bellotti, V. et al. (1997). Instability, unfolding and aggregation of human lysozyme variants underlying amyloid fibrillogenesis. *Nature* 385, 787–93.

140 Chiti, F., Taddei, N., Bucciantini, M., White, P., Ramponi, G., and Dobson, C. M. (2000). Mutational analysis of the propensity for amyloid formation by a globular protein. *EMBO J* 19, 1441–9.

141 Chiti, F., Stefani, M., Taddei, N., Ramponi, G., and Dobson, C. M. (2003). Rationalization of the effects of mutations on peptide and protein aggregation rates. *Nature* 424, 805–8.

142 Fernandez-Escamilla, A. M., Rousseau, F., Schymkowitz, J., and Serrano, L. (2004). Prediction of sequence-dependent and mutational effects on the aggregation of peptides and proteins. *Nat Biotechnol* 22, 1302–1306.

Part I

2 Dynamics and Mechanisms of Protein Folding Reactions

12.1
Kinetic Mechanisms in Protein Folding

Annett Bachmann and Thomas Kiefhaber

12.1.1
Introduction

The understanding of protein folding landscapes requires the characterization of local saddle points (transition states) and minima (intermediates) on the free energy surface between the ensemble of unfolded states and the native protein. This chapter discusses experimental approaches to analyze kinetic data for protein folding reactions, to identify folding intermediates and to assign their role in the folding process. Chapter 12.2 will describe methods used to obtain thermodynamic and structural information on transition states. The methods discussed in these chapters mainly use concepts from classical reaction kinetics and from physical organic chemistry to analyze the dynamics of protein folding and unfolding. It could be argued that these methods may not be applicable to the protein folding process, which represents a conformational search on a complex multidimensional free energy surface. However, results from a variety of different studies suggest that efficient folding proceeds through partially folded intermediates and that protein folding in solution encounters major free energy barriers. In addition, protein folding transition states are usually structurally well-defined local maxima along different testable reaction coordinates [1] (see Chapter 12.2). This suggests that we can indeed derive information on protein folding barriers using the classical concepts.

12.1.2
Analysis of Protein Folding Reactions using Simple Kinetic Models

The aim of kinetic studies is trying to find the minimal model capable of describing the experimental data by ruling out as many alternative models as possible. It is thereby assumed that the mechanism involves a finite number of kinetic species that are separated by energy barriers significantly larger than the thermal energy ($>5k_BT$), but each kinetic species may consist of different conformations in rapid equilibrium. Thus, the transitions between large ensembles of states can be treated

Protein Folding Handbook. Part I. Edited by J. Buchner and T. Kiefhaber

ISBN: 3-527-30784-2

using classical reaction kinetics and the interconversion between two species, X_i and X_j, can be described with microscopic rate constants for the forward (k_{ij}) and reverse (k_{ji}) reactions

$$X_i \underset{k_{ji}}{\overset{k_{ij}}{\rightleftharpoons}} X_j \tag{1}$$

12.1.2.1
General Treatment of Kinetic Data

Experimental studies on the mechanism of protein folding have focused mainly on monomeric single domain proteins as model systems. Folding of oligomeric proteins and multidomain proteins is discussed in Chapter 27 and Chapter 2 in Part II. Folding kinetics of monomeric proteins have the major advantage that all observed reactions are of first order. Consequently, the time-dependent change in intensity of an observed signal (P) can be represented as a sum of n exponentials with observable rate constants (λ_i) and corresponding amplitudes (A_i)

$$P_t - P_\infty = \sum_{i=1}^{n} A_i \cdot e^{-\lambda_i t} \tag{2}$$

where P_t is the observed intensity at time t and P_∞ is the intensity at $t \to \infty$. The apparent rate constants, λ_i, are functions of the microscopic rate constants, k_{ij}, which depend on external parameters like temperature, pressure, and denaturant concentration. The amplitudes A_i additionally depend on the initial concentrations of the kinetic species (see Protocols, Section 12.1.6). Generally, any kinetic mechanism with n different species connected by first-order reactions results in $n-1$ observable rate constants. Applied to protein folding with fixed initial (U) and final (N) state the observation of $n-1$ apparent rate constants thus indicates the presence of $n-2$ transiently populated intermediate states. A more detailed treatment of the analysis of kinetic data in protein folding is given in Refs [2] and [3] and general treatments of kinetic mechanisms are given in Refs [4] and [5].

12.1.2.2
Two-state Protein Folding

Experimental investigations have revealed simple two-state folding with single exponential folding and unfolding kinetics for more than 30 small proteins (Figure 12.1.1; for an overview see Ref. [6]):

$$U \underset{k_u}{\overset{k_f}{\rightleftharpoons}} N \tag{3}$$

where k_f and k_u are the microscopic rate constants for the folding and unfolding reactions, respectively. The single observable macroscopic rate constant (λ) for this

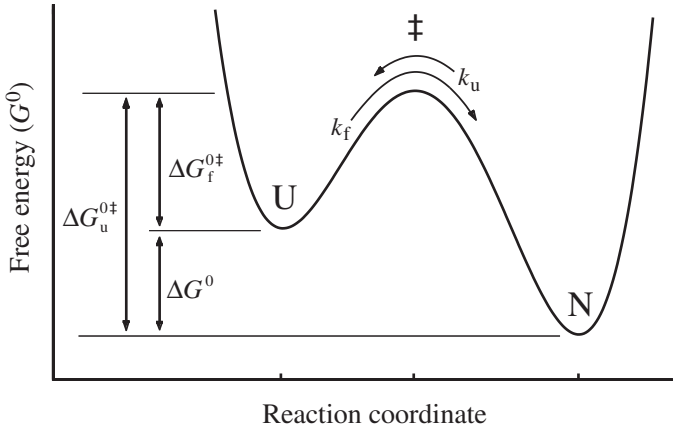

Fig. 12.1.1. Free energy profile for a hypothetical two-state protein folding reaction. The ground states U and N are separated by a free energy barrier with the transition state as point along the reaction coordinate with the highest free energy. The activation free energies for passing the barrier from U or N, $\Delta G_f^{\circ‡}$ and $\Delta G_u^{\circ‡}$, respectively, are reflected in the microscopic rate constants k_f or k_u (see Eq. (8)).

mechanism is readily derived as

$$\lambda = k_f + k_u \tag{4}$$

The equilibrium of the reaction is determined by the flows from the native state N to the unfolded state U and vice versa:

$$k_f \cdot [U]_{eq} = k_u \cdot [N]_{eq} \tag{5}$$

and the equilibrium constant (K) for folding is

$$K := \frac{[N]_{eq}}{[U]_{eq}} = \frac{k_f}{k_u} \tag{6}$$

A straightforward parameter that can be inferred from two-state behavior is the free energy for folding (ΔG°) which is connected by the van't Hoff relation with the equilibrium constant (K)

$$\Delta G^\circ = -RT \cdot \ln(K) = -RT \cdot \ln\left(\frac{[N]_{eq}}{[U]_{eq}}\right) = -RT \cdot \ln\left(\frac{k_f}{k_u}\right) \tag{7}$$

Thus, protein stability can be measured in two different ways, either by equilibrium methods or by kinetic measurements. The agreement between the free energies for folding inferred from equilibrium and kinetic measurements is commonly used as a test for two-state folding (see Figure 12.1.2).

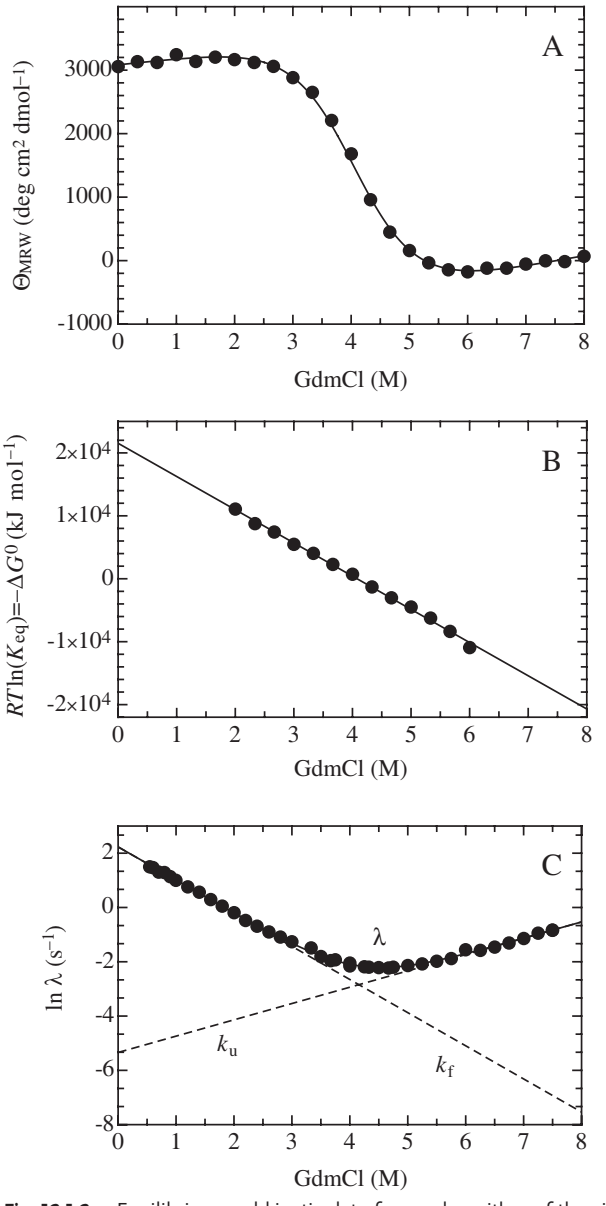

Fig. 12.1.2. Equilibrium and kinetic data for two-state tendamistat folding and unfolding at pH 2.0. A) GdmCl-induced equilibrium transition of wild-type tendamistat at pH 2.0 measured by far-UV circular dichroism. B) Plot of RT ln K_{eq} for the data in the transition region result in a linear dependency on the denaturant concentration. The slope corresponds to $-m_{eq}$ (see Eq. (11)). C) GdmCl dependence of the logarithm of the single observable folding rate constant ($\lambda = k_f + k_u$) gives a V-shaped profile commonly termed a chevron plot. This reveals a linear dependence between [GdmCl] and the $\ln(k_{f,u})$ as indicated by the dashed lines. The values for K_{eq} and m_{eq} derived from kinetic (panel C) and equilibrium data (panel B) are identical, which is a strong support for a two-state folding mechanism.

The same formalism can be applied to obtain information on the free energy of activation ($\Delta G^{\circ\ddagger}$) for a reaction using transition state theory

$$k = k_0 \cdot e^{-\Delta G^{\circ\ddagger}/RT} \tag{8}$$

where k_0 is the pre-exponential factor and represents the maximum rate constant for a reaction in the absence of free energy barriers. Combination of Eqs (6) and (8) allows us to gain information on the free energy changes along the reaction coordinate (see Figure 12.1.1).

$$\Delta G^{\circ} = \Delta G_f^{\circ\ddagger} - \Delta G_u^{\circ\ddagger} \tag{9}$$

In the original Eyring theory the pre-exponential factor corresponds to the frequency of a single bond vibration [7, 8]:

$$k_0 = \kappa \frac{k_B T}{h} \approx 6 \cdot 10^{12}\ s^{-1} \text{ at } 25\ ^{\circ}C \tag{10}$$

where κ represents the transmission coefficient, which is usually set to 1. Since protein folding involves formation and breakage of weak intramolecular interactions rather than changes in covalent bonds, the Eyring prefactor will not be useful for the analysis of protein folding reactions. The pre-exponential factor for protein folding reactions will be strongly influenced by intrachain diffusion processes but will also depend on the location of the transition state on the free energy landscape and on the nature of the rate-limiting step for a particular protein. It is likely around 10^7–$10^8\ s^{-1}$ [9]. This is discussed in detail in Chapter 22.

Experimental analysis of protein folding reactions usually makes use of the effect of chemical denaturants like urea and GdmCl on the rate and equilibrium constants (see Chapter 3). Empirically, a linear correlation between the denaturant concentration ([D]) and both the equilibrium free energy (ΔG°) [10, 11] and the activation free energies [12] for folding ($\Delta G_f^{\circ\ddagger}$) and unfolding ($\Delta G_u^{\circ\ddagger}$) is found (Figure 12.1.2). Accordingly, for two-state folding a plot of the logarithm of the single observable (apparent) rate constant, λ, vs. [D] yields a V-shaped curve, commonly called chevron plot [13, 14] (Figure 12.1.2C). This plot gives information on the refolding reaction at low denaturant concentrations (the refolding limb) and information on the unfolding reaction at high denaturant concentrations (the unfolding limb). Accordingly, proportionality constants, m_x, are defined as

$$m_{eq} = \frac{\partial \Delta G^{\circ}}{\partial [\text{Denaturant}]} \tag{11}$$

$$m_{f,u} = \frac{\partial \Delta G_{f,u}^{\circ\ddagger}}{\partial [\text{Denaturant}]} \tag{12}$$

Since the m_{eq}-values were shown to be proportional to the changes in accessible surface area (ASA) upon unfolding of the protein [15], the kinetic m-values are believed to reflect the changes in ASA between the unfolded state and the transition

state (m_f) and the native state and the transition state (m_u). This can be used to characterize the solvent accessibility of a protein folding transition state (see Chapter 12.2).

The *m*-values allow an extrapolation of the data to any given denaturant concentration using

$$\Delta G^{\circ}(D) = \Delta G^{\circ}(H_2O) + m_{eq} \cdot [D] \quad (13)$$

$$\Delta G_f^{\circ\ddagger}(D) = \Delta G_f^{\circ\ddagger}(H_2O) + m_f \cdot [D] \quad (14)$$

$$\Delta G_u^{\circ\ddagger}(D) = \Delta G_u^{\circ\ddagger}(H_2O) + m_u \cdot [D] \quad (15)$$

where (H_2O) denotes the values in the absence of denaturant and (D) those at a given denaturant concentration [D]. Combining Eq. (9) with Eqs (13)–(15) shows that the comparison of the kinetic and equilibrium free energies and *m*-values provides a tool to test for the validity of the two-state mechanism (see Figure 12.1.2):

$$\Delta G^{\circ}(H_2O) = \Delta G_f^{\circ\ddagger}(H_2O) - \Delta G_u^{\circ\ddagger}(H_2O) \quad (16)$$

and

$$m_{eq} = m_f - m_u \quad (17)$$

12.1.2.3 Complex Folding Kinetics

For simple two-state folding reactions the microscopic rate constants are readily obtained from the chevron plot (cf. Figure 12.1.2) and the properties of the transition barriers can be analyzed using rate equilibrium free energy relationships [1, 16–19] (REFERs; see Chapter 12.2). However, folding of most proteins is more complex with several observable rate constants. These complex folding kinetics can have different origins. The transient population of partially folded intermediates, which frequently occurs under native-like solvent conditions (i.e., at low denaturant concentrations), will lead to the appearance of additional kinetic phases (see Section 12.1.3.2) and to a downward curvature in the chevron plot (Figure 12.1.3A) [13, 20–23]. Kinetic coupling between two-state folding and slow equilibration processes in the unfolded state provides another source for multiphasic folding kinetics [2, 24, 25] (Section 12.1.3.1). Since these possible origins for complex folding kinetics have far-reaching effects on the molecular interpretation of the kinetic data it is crucial to discriminate between them and to elucidate the origin of complex kinetics. With the knowledge of the correct folding mechanism the microscopic rate constants (k_{ij}) connecting the individual states can be determined.

12.1.2.3.1 Heterogeneity in the Unfolded State

The unfolded state of a protein consists of a large ensemble of different conformations which are in rapid equilibrium, and can thus be treated as a single kinetic

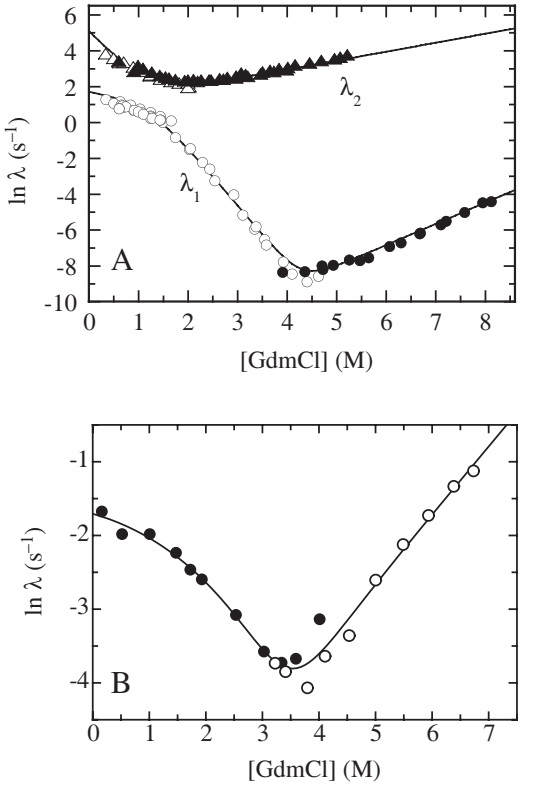

Fig. 12.1.3. Different origins for curvatures in chevron plots: A) Population of a transient intermediate during folding of hen egg white lysozyme. At low denaturant concentrations two rate constants are observed in refolding (λ_2 and λ_1; open triangles and open circles). For unfolding of native lysozyme a single kinetic phase is observed (filled circles). λ_2 at higher denaturant concentrations (filled triangles) corresponds to unfolding of the intermediate and can only be detected when the intermediate is transiently populated by a short refolding pulse and then unfolded at high denaturant concentrations in sequential mixing experiments [52] (interrupted refolding experiments). B) Chevron plot for ribonuclease T1 W59Y. The curvature in the refolding limb at low denaturant concentrations is caused by kinetic coupling between prolyl isomerization and protein folding [24, 25]. Only the slowest refolding phase is shown. The fraction of faster folding molecules with all prolyl peptide bonds in the native conformation could not be detected since the experiments were carried out by manual mixing. Data for lysozyme were taken from Ref. [52] and data for RNase T1 were taken from Ref. [25].

species as long as their interconversion is faster than the kinetic reactions leading to the native state. Studies on the time scale of intrachain diffusion in unfolded polypeptide chains in water showed that these processes occur on the 10–100 ns time scale [9, 26], which is significantly faster than protein folding reactions [27, 28]. On the other hand, slow interconversion reactions between the different unfolded conformations lead to kinetic heterogeneity. This was first observed by Garel

and Baldwin [29] who showed that both fast and slow refolding molecules exist in unfolded ribonuclease A (RNase A). In 1975 Brandts and coworkers [30] showed with their classical double jump experiments that slow and fast folding forms of RNase A are caused by a slow equilibration process in the unfolded state and proposed *cis–trans* isomerization at Xaa-Pro peptide bonds as the molecular origin (see Chapter 1). This was confirmed later with proline mutations [31] and catalysis of the slow reactions by peptidyl-prolyl *cis-trans* isomerases [32]. The fast folding molecules have all Xaa-Pro peptide bonds in their native isomerization states, whereas slow-folding molecules contain nonnative prolyl isomers, which have to isomerize to their native isomerization state during folding. This isomerization process is slow with time constants ($\tau = 1/\lambda$) around 10–60 s at 25 °C, which usually limits the folding reaction of the unfolded molecules with nonnative prolyl isomers (see Chapter 25). Since the equilibrium population of the *cis* isomer in Xaa-Pro peptide bonds is between 7 and 36%, depending on the Xaa position, [33] all proteins with prolyl residues should show a significant population of slow folding molecules. Prolyl isomerization has indeed been observed in folding of many proteins [34]. Whenever folding and proline isomerization have similar rate constants or when folding is slower than isomerization, a pronounced curvature is observed in the refolding limb of the chevron plot, which looks similar to the effect of transiently populated intermediates (Figure 12.1.3B). The effect of prolyl isomerization on folding kinetics and its identification as a rate-limiting step is discussed in detail in Chapter 10 in Part II. The effect on chevron plots is treated quantitatively in Refs [2, 35, 36].

In addition to prolyl isomerization also nonprolyl peptide bond isomerization has recently been shown to cause slow parallel folding pathways [37, 38]. *Cis–trans* isomerization of nonprolyl peptide bonds has long been speculated to cause slow steps in protein folding, since it is an intrinsically slow process with a high activation energy [30, 33]. The large number of peptide bonds in a protein leads to a significant fraction of unfolded molecules with at least one nonnative *cis* isomer, although the *cis* isomer is only populated to about 0.15% in equilibrium in the unfolded state [39]. Studies on a slow folding reaction in a prolyl-free tendamistat variant revealed that folding of about 5% of unfolded molecules is limited by the *cis–trans* isomerization of nonprolyl peptide bonds [38] (Figure 12.1.4). The slow equilibrium between *cis* and *trans* nonprolyl peptide bonds in the unfolded state was revealed by double jump experiments [38] (see also Chapter 25). In these experiments (Figure 12.1.4C) the protein is rapidly unfolded at high denaturant concentrations often in combination with low pH. After various times, unfolding is stopped by dilution to refolding conditions. The resulting folding kinetics are monitored by spectroscopic probes. If a slow isomerization reaction in the unfolded state occurs, the slow folding molecules will be formed slowly after unfolding. Thus, the amplitude of the slow reaction will increase with unfolding time as observed for the proline free tendamistat variant shown in Figure 12.1.4C. Figure 12.1.4 further reveals that nonprolyl isomerization has a rate constant around 1 s^{-1}, which is significantly faster than prolyl peptide bond isomerization. This is in accordance with rate constants for nonprolyl isomerization measured in model

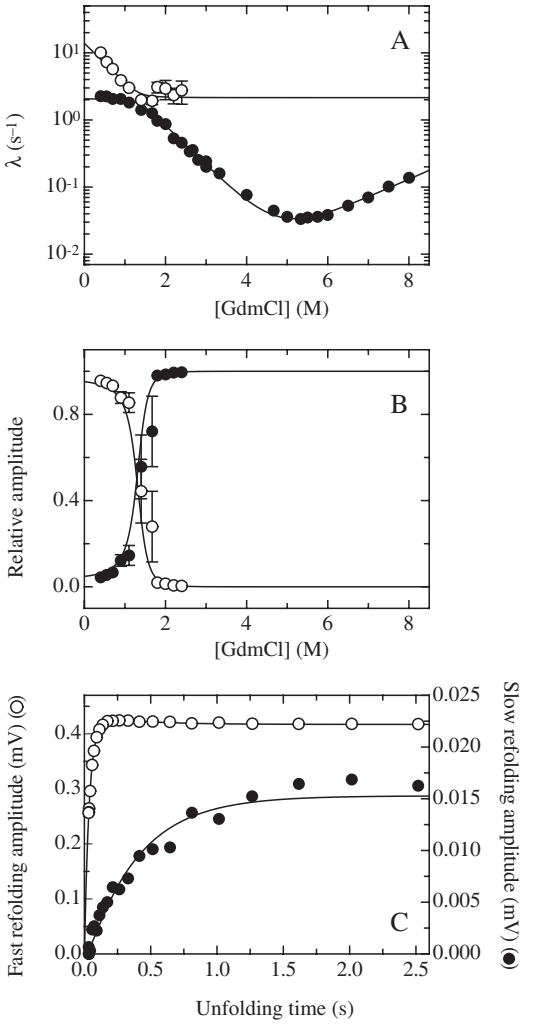

Fig. 12.1.4. Complex folding kinetics caused by nonprolyl *cis–trans* isomerization in the unfolded state of a proline-free variant of tendamistat. GdmCl dependence of the apparent rate constants, λ_1 (open circles), λ_2 (filled circles) for folding and unfolding (A) and the respective refolding amplitudes (A_1 (open circles), A_2 (filled circles) are shown. The lines in panels A and B represent the global fit of both apparent rate constants and amplitudes to the analytical solution of a linear three-state model. The fit reveals a GdmCl-independent isomerization reaction and a GdmCl-dependent folding reaction (see Ref. [38]). C) Double jump experiments to detect the slow isomerization process in the unfolded state. Appearance of the fast-refolding (open circles) and the slow-refolding (filled circles) molecules during unfolding. Native protein was unfolded at high denaturant concentrations for the indicated time. Under the applied conditions unfolding was complete after 150 ms. After various unfolding times refolding was initiated by a second mixing step and the amplitudes of the two refolding reactions (open circles, filled circles) in the presence of 0.8 M GdmCl (cf. panel A) were measured. The results show that the slow-refolding phase (filled circles) is formed slowly in the unfolded state whereas the fast-refolding phase is formed with the same time constant as that with which unfolding of tendamistat occurs. Data were taken from Ref. [38].

peptides [39]. The results on the effect of nonprolyl isomerization on protein folding imply that isomerization at non prolyl peptide bonds will dramatically effect folding of large proteins. For a protein with 500 amino acid residues more than 50% of the unfolded molecules have at least one nonnative peptide bond isomer. Since the isomerization rate constant is around 1 s^{-1}, it will mainly affect the early stages of folding and folding of fast folding proteins [38].

Another cause of kinetic heterogeneity in the unfolded state was identified in cytochrome *c*, where parallel pathways were shown to be due to the exchange of the heme ligands in the unfolded state [40–42] (see Chapter 15).

12.1.2.3.2 **Folding through Intermediates**

As discussed above, the number of kinetic species, n, is related to the number of observable rate constants, $n - 1$, and thus, with unfolded and native state as the initial and final states, the number of intermediates is given by $n - 2$. Thus, for a single observable rate constant there are no intermediates, corresponding to two-state folding. The observation of two apparent rate constants indicates a single intermediate, etc. It should be noted that these considerations only apply if there is a kinetically homogeneous unfolded state with rapidly interconverting conformations. In the case of heterogeneous populations of unfolded molecules separated by slow interconversion reactions like prolyl isomerization, the number of observable rate constants is additionally correlated with the number of unfolded species. In the following we will describe experiments that allow the elucidation of mechanisms of fast folding molecules (i.e., of molecules with all Xaa-Pro bonds in the native isomerization state).

The first step in elucidating a folding mechanism is the determination of the number of exponentials, i.e., the number of observable rate constants, λ_i, needed to describe the kinetics. In principle, the number of observable rate constants should not depend on the probe used to monitor the folding reaction, as observed for lysozyme refolding shown in Figure 12.1.5, which shows the same two observable rate constants measured by a number of different probes. However, some reactions may not cause a signal change in a specific probe, if , for example, an intermediate shows the same spectral properties as the native or unfolded state. Thus, kinetics should be monitored using different probes. In addition, it is crucial to test for burst-phase reactions (i.e., for processes occurring within the experimental dead-time) (Figure 12.1.5). These reactions are observed for many proteins during refolding at low denaturant concentrations and are usually caused by a considerable compaction of the polypeptide chain [43, 44] (Figure 12.1.5E) and concomitant formation of significant amounts of secondary structure [45] (see Chapter 23). Whether rapid collapse represents a distinct step on a folding pathway or whether it is the response of the unfolded state to the change in solvent conditions upon refolding is currently under discussion. Results on the folding of α-lactalbumin [46–48], apo-myoglobin [49], and lysozyme [44] suggest that burst-phase intermediates unfold cooperatively, indicating that they are separated by a barrier from the ensemble of random coil conformations, which are populated at high denaturant concentrations. To test for aggregation side reactions during refolding, which

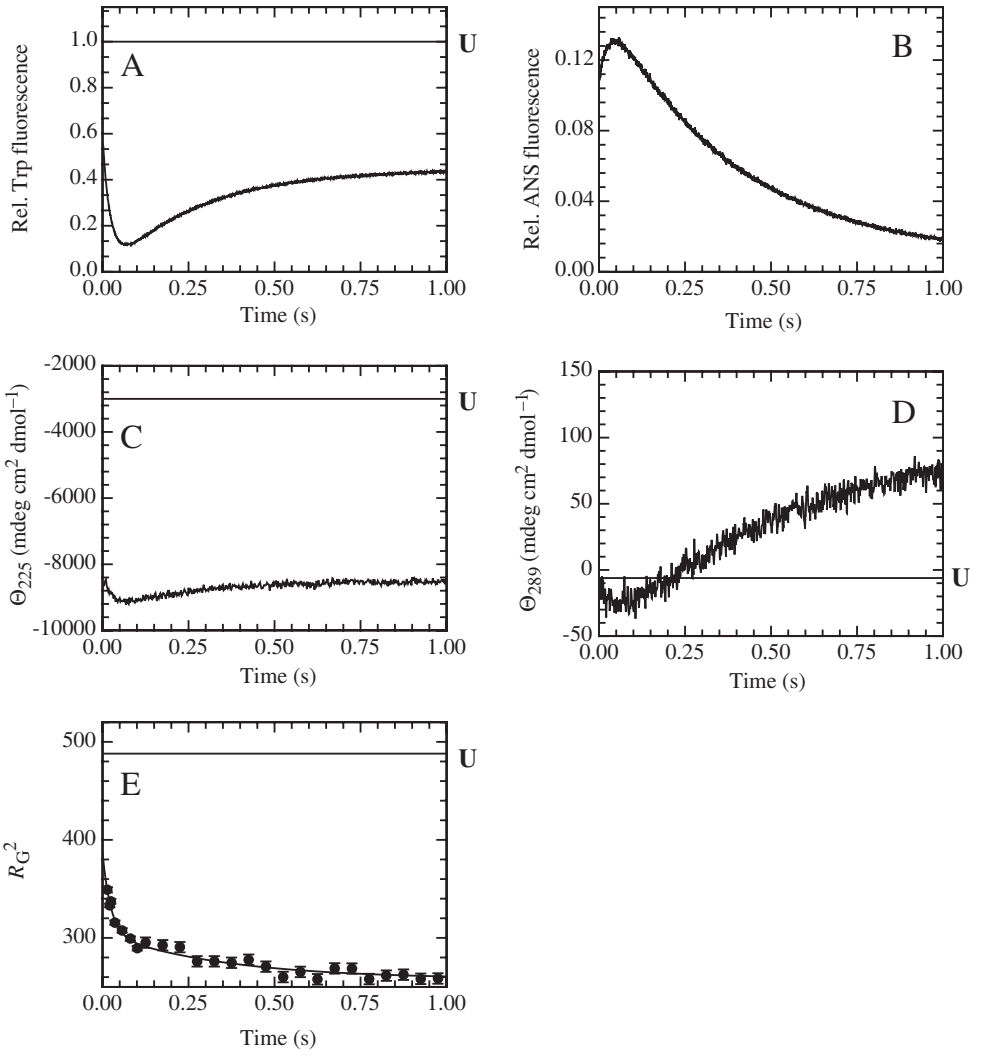

Fig. 12.1.5. Lysozyme refolding observed with different probes: A) Intrinsic tryptophan fluorescence above 320 nm after excitation at 280 nm; B) ANS fluorescence; C) far-UV circular dichroism at 225 nm; D) near-UV circular dichroism at 289 nm; E) changes in radius of gyration measured by small-angle X-ray scattering (SAXS). The lines of constant signal represent the signal of the unfolded state. The traces are recorded at 23 °C, pH 5.2. Data in panels A–D were recorded by stopped-flow mixing. SAXS data were recorded by continuous-flow and stopped-flow mixing. All data can be fitted globally with $\lambda_2 = 34\ s^{-1}$; $\lambda_1 = 4.3\ s^{-1}$ demonstrating that all probes detect the same two kinetic phases. In addition, major signal changes in the dead time of mixing are detected by all probes except near-UV CD, indicating a fast reaction that cannot be resolved by the experiments (burst phase with $\lambda > 2000\ s^{-1}$). Data were taken from Refs [43] and [44].

are occasionally also observed for small proteins, [50], the concentration dependence of the folding reaction should be tested.

The next step in determining a folding mechanism is to locate the intermediates on the folding pathway. If a single folding intermediate is observed two apparent rate constants will be observed for all possible three-state mechanisms shown in Scheme 12.1.1.

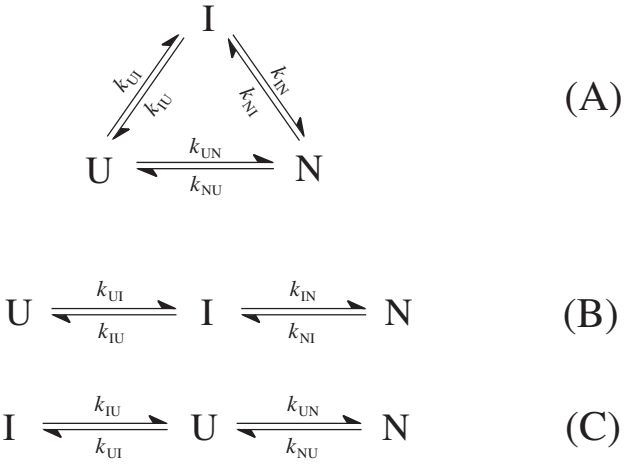

Scheme 12.1.1

The triangular mechanism shown in panel A represents the general three-state model whereas mechanisms B (on-pathway intermediate) and C (off-pathway intermediate) represent special cases of mechanism A with one of the three equilibria between the individual states being too slow to influence the kinetics. Thus, if only mechanisms B or C are considered for a particular protein, the assumption is made that one of the equilibration processes between the three states is significantly slower than the other two. A consequence from the mathematical analysis of the mechanisms shown in Scheme 12.1.1 is that the two observable rate constants for the triangular mechanism cannot be simply related to individual microscopic rate constants but are functions of several microscopic rate constants (see Protocols, Section 12.1.6). Thus it is essential to elucidate the correct folding mechanism and to determine all microscopic rate constants in order to draw conclusions on the individual transition states between the kinetic species.

Since all mechanisms shown in Scheme 12.1.1 give rise to two experimentally observable rate constants, it is impossible to exclude the triangular mechanism on the basis of direct spectroscopic measurements of the folding kinetics. However, in the triangular mechanism the native molecules are produced in both the faster and the slower kinetic phase whereas in the on-pathway mechanism the native state is produced with a lag phase. Thus, discrimination between these mechanisms requires to specifically monitor the time course of the native state. Experiments,

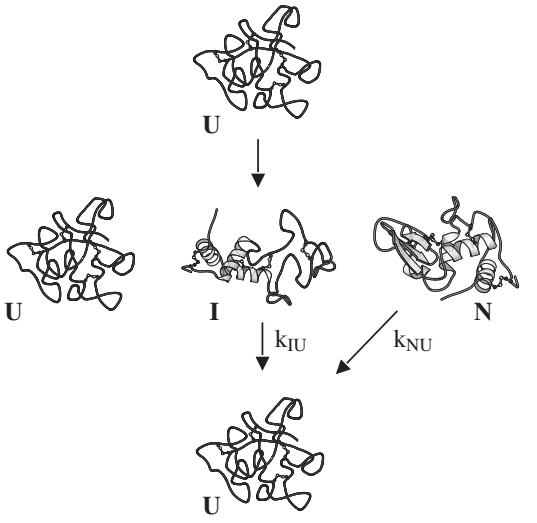

Fig. 12.1.6. Principle of interrupted refolding experiments to measure the time course of the population of a folding intermediate (I) and of native proteins (N) starting from completely unfolded protein (U). The experiments are described in detail in the text.

which selectively measure the population of the individual kinetic species during folding, have been introduced by Schmid [51] and were initially used to detect slow and fast folding pathways during RNase A folding. They are commonly termed interrupted refolding experiments. These experiments make use of the fact that each state of the protein has its characteristic stability and unfolding rate constant. Interrupted refolding experiments consist of two consecutive mixing steps (Figure 12.1.6). In a first step refolding is initiated from completely unfolded protein. The folding reaction is allowed to proceed for a certain time (t_i) after which the solution is transferred to a high concentration of denaturant. This results in the unfolding of all native molecules and of partially folded states which have accumulated during the refolding step. Each state (N or I) is identified by its specific unfolding rate constant at high concentrations of denaturant, where unfolding is virtually irreversible, so that little kinetic coupling occurs. The amplitudes of the observed unfolding reactions reflect the amounts of the respective species present at time (t_i) when refolding was interrupted. Thus, varying the time (t_i) allowed for refolding gives the time course of the populations of native protein and of the intermediate during the folding process. With the use of highly reproducible sequential mixing stopped-flow instruments these experiments also became feasible on a faster time scale and allow the discrimination between sequential and triangular folding mechanism on fast folding pathways [22, 52].

The discrimination between the off-pathway mechanism and the triangular mechanism is usually difficult, since also in the off-pathway model some mole-

cules may fold directly from U to N, depending on the ratio of the rate constants k_{UN} and k_{UI} [52]. The discrimination between these mechanisms usually requires analysis of the denaturant dependence of all folding and unfolding rate constants in combination with the time course of the different species [52]. The data are then fitted to the analytical solutions of the differential equations describing the different models. For folding reactions of monomeric proteins all reactions are of first order and the analytical solutions of the differential equations can be obtained for mechanisms with four species or less. These solutions are derived in many kinetic textbooks and rate constants and amplitudes for three-state and four-state mechanisms are given in Refs [24] and [52]. The solutions for the three-state models in Scheme 12.1.1 are given in the Protocols (Section 12.1.6.1–12.1.6.3). A particularly useful source for the analytical solution of a vast number of different kinetic mechanisms is the article by Szabo [4]. For more complex mechanisms numerical methods have to be applied to analyze the data. As an example for the discrimination between the different kinetic models shown in Scheme 12.1.1, the elucidation of the folding mechanism of lysozyme will be discussed in detail in Section 12.1.3.

12.1.2.3.3 **Rapid Pre-equilibria**

The analysis for mechanisms B and C in Scheme 12.1.1 simplifies when equilibration between U and I occurs on a much faster time scale than folding to the native state [53, 54]. In this case, formation of the intermediate can be treated as a rapid pre-equilibrium. The apparent rate constants for mechanism B (on-pathway intermediate) can thus be approximated by

$$\lambda_1 = k_{UI} + k_{IU}, \quad \lambda_2 = \frac{1}{1 + 1/K_{UI}} k_{IN} + k_{NI} \quad \text{with } K_{UI} = \frac{k_{UI}}{k_{IU}} \tag{18}$$

and for mechanism C (off-pathway intermediate) as

$$\lambda_1 = k_{UI} + k_{IU}, \quad \lambda_2 = \left(1 - \frac{1}{1 + 1/K_{UI}}\right) k_{UN} + k_{NU} \tag{19}$$

where $1/(1 + (1/K_{UI}))$ represents the fraction of intermediate ($f(I)$) in the pre-equilibrium. Since I is productive in mechanism B and nonproductive in mechanism C, the rate of formation of N depends on $f(I)$ and $1 - f(I)$, respectively. Due to the commonly observed strong denaturant dependence of the microscopic rate constants, the simplifications made above might not be valid at some denaturant concentrations. Therefore, the simplified treatment of the data should only be performed if formation and unfolding of the intermediate is significantly faster than the k_{IN} and k_{NI} under all experimental conditions. Otherwise, the exact solutions of the three state model must be used to fit the data [52] (see Protocols, Section 12.1.6).

Under conditions where the simplifications given in Eqs (18) and (19) hold and the triangular mechanism has been ruled out, these equations can provide a simple tool for identifying off-pathway intermediates. Destabilization of the intermedi-

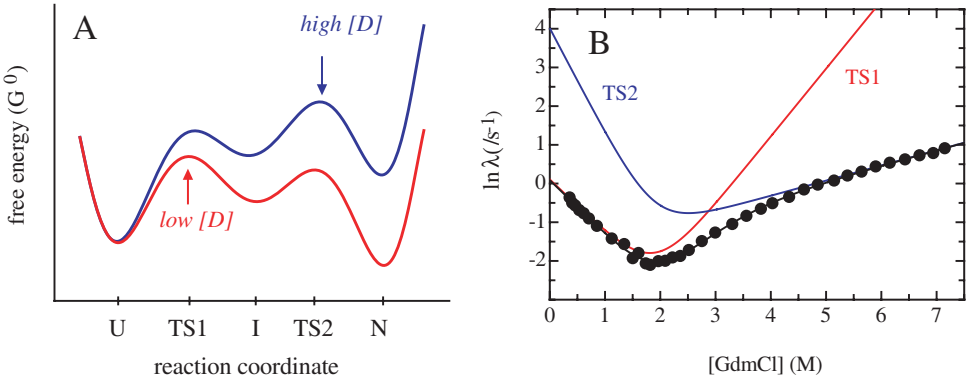

Fig. 12.1.7. Transition barrier for apparent two-state folding through a high-energy intermediate and the consequences on the shape of the chevron plot. A) The reaction coordinate of tendamistat comprises two discrete transition states and a high-energy intermediate. B) A single folding rate constant is observed which shows a kink in the denaturant dependence of the chevron-plot which indicate the switch between the two alternative transition states [57]. The black line represents a fit of the data to a three-state model as described in the Protocols (Eqs (35)–(42)). The lines labeled TS1 and TS2 correspond to constructed chevron plots for the two transition states. Data were taken from Ref. [57].

ate leads to a larger fraction of productive (unfolded) molecules in the off-pathway model. Thus, addition of denaturant will speed up folding, when the resulting destabilization of the intermediate exceeds the deceleration of the U → N reaction. As a consequence, an increase in the folding rate with increasing concentrations of denaturant points to the transient accumulation of an off-pathway intermediate. This behavior has been observed for intermediates trapped by nonnative disulfide bonds, [55] by nonnative proline isomers [56] and by nonspecific aggregation [50].

12.1.2.3.4 Folding through an On-pathway High-energy Intermediate

Many apparent two-state folders were shown to fold through on-pathway high-energy intermediates, which cannot be detected directly with spectroscopic methods, since they are less stable than N and U [57, 58] (Figure 12.1.7A). Their existence can be inferred from kinks in chevron plots, which are not accompanied by additional kinetic phases nor by burst-phase reactions [1, 18, 19, 57–61]. Figure 12.1.7B shows such a kink in the chevron plot for a tendamistat variant [57]. The changing slope in the unfolding limb of the chevron plot indicates the existence of two consecutive transitions states, TS1 and TS2, and a "hidden" high-energy intermediate (I^*; see Chapter 12.2) and thus provides an effective way to identify on-pathway intermediates [1, 18, 19, 57–61]. The detection of a high-energy on-pathway intermediate results in a linear three-state model:

$$U \underset{k_{IU}}{\overset{k_{UI}}{\rightleftharpoons}} I^* \underset{k_{NI}}{\overset{k_{IN}}{\rightleftharpoons}} N \qquad (20)$$

The kinetics at a single denaturant concentration cannot be distinguished from two-state folding (Eq. (3)). However, the presence of a kink in the chevron plot and the resulting altered slope at high denaturant concentrations allows a characterization of both transition states [57] (see Protocols, Section 12.1.6.4). Since I^* does not become populated at any conditions, its stability can not be determined. However, the difference in free energy between both transition states ($\Delta G^{\circ}_{TS2/TS1}$) and the difference in their ASA ($m_{TS2} - m_{TS1}$) can be obtained by fitting the GdmCl dependence of $\ln \lambda$ to the analytical solutions of the three-state model shown in Eq. (20) (see Protocols, Section 12.1.6.4). Figure 12.1.7B shows the results of a three-state fit for the kinked chevron and the constructed chevron plots for the individual transition states for the tendamistat variant.

12.1.3 A Case Study: the Mechanism of Lysozyme Folding

In the following, we will use lysozyme as a case study to discuss how sequential mixing experiments in combination with the denaturant dependence of the apparent rate constants allow a quantitative analysis of complex folding kinetics and the determination of all microscopic rate constants.

12.1.3.1 Lysozyme Folding at pH 5.2 and Low Salt Concentrations

Lysozyme consists of two structural subdomains, the α-domain with exclusively α-helical structure and the β-domain with predominantly β-structure [62, 63]. Starting from GdmCl-unfolded disulfide intact protein, large changes in far-UV CD and fluorescence signals are observed within the first millisecond of refolding [43, 44, 64, 65] (Figure 12.1.5A–D). Time-resolved small angle X-ray scattering experiments show that this burst-phase reaction leads to a globular state, with a significantly smaller radius of gyration (R_G) than the unfolded protein [43, 44] (Figure 12.1.5E). In a subsequent reaction, with a time constant of 30 ms (at pH 5.2 and 20 °C), an intermediate state (I_N) is formed, as observed by strong quenching in tryptophan fluorescence to a level below that of the native state [43, 44, 66], by an increase in the far-UV CD signal [64, 65], by small changes in near-UV CD [44] and by a further compaction of the polypeptide chain [43, 44]. Pulsed hydrogen/deuterium exchange experiments showed that this intermediate has native-like helical structure in the α-domain whereas the β-sheet structures are not formed [67]. The intermediate converts to the native state with a relaxation time of about 400 ms. Double-jump experiments showed that the slow folding reaction of lysozyme is not caused by slow equilibration processes coupled to the folding reaction [52] (Figure 12.1.8A). There had been controversial reports as to the role of I_N in the folding process and it remained unclear whether it represents an obligatory intermediate on the folding pathway for all lysozyme molecules [66, 67]. In addition, a reaction on the 10 ms time scale was observed in pulsed hydrogen exchange experiments [67–69], which leads to formation of molecules with native hydrogen

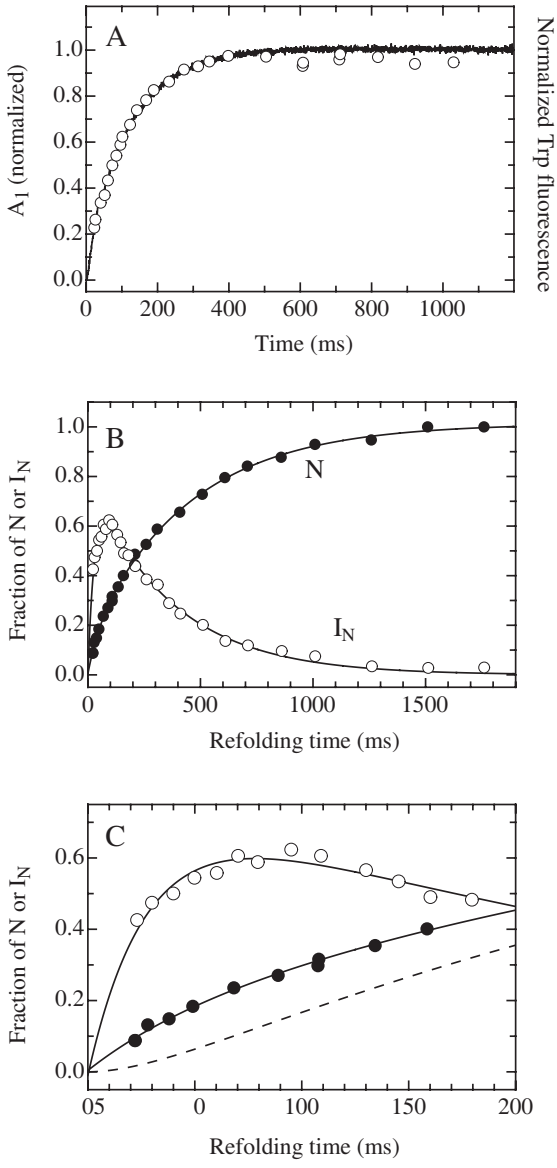

Fig. 12.1.8. Double jump (A) and interrupted refolding experiments (B, C) for lysozyme folding at pH 5.2. Double jump experiments show that amplitude of the slow folding reaction (A_1, open circles) is formed with the same time constant as that at which unfolding of native lysozyme occurs. For comparison the unfolding kinetics directly monitored by the change in intrinsic Trp fluorescence is shown (solid line). B) Time course of the population of native lysozyme, N (filled circles) and of the kinetic intermediate, I_N (open circles) measured in interrupted refolding experiments. C) The early time region of the kinetics shows that the faster process ($t = 30$ ms) produces both native molecules and the partially folded intermediate I_N. The lag phase for formation of N, expected for a linear on-pathway model shown in Scheme 12.1.1B (---), is not observed. Data were taken from Ref. [52].

bonding network and was thus proposed to produce an intermediate with native-like hydrogen bonding network [70]. However, this reaction was not observed with any other spectral probe or in SAXS experiments (see Figure 12.1.5), which obscured its interpretation.

The observation of two apparent rate constants (treating the burst-phase collapse as a pre-equilibrium uncoupled from the slower reactions) cannot rule out any of the mechanisms shown in Scheme 12.1.1. However, comparing mechanism A with mechanisms B and C offers a simple way to distinguish obligatory from nonobligatory folding intermediates. In the case of an obligatory intermediate, all molecules have to fold through this state, resulting in a lag phase in the formation of native molecules [5]. Direct spectroscopic measurements or measurements of changes in R_G are not able to monitor formation of native lysozyme directly, since changes in spectroscopic and geometric properties occur in all folding steps (see above). Further, the use of inhibitor binding to detect formation of active lysozyme did not give any clear-cut results since binding is too slow under the applied experimental conditions [22, 66]. Thus, interrupted refolding experiments were used to monitor the time course of native protein and of I_N. Two unfolding reactions were observed in interrupted refolding experiments [22, 52]. One of them corresponds to the well-characterized unfolding kinetics of native lysozyme, and a second much faster one corresponds to unfolding of the intermediate (see Figure 12.1.6). The faster reaction is only observed at short and intermediate refolding times but is not observed when native lysozyme is unfolded. The collapsed state unfolds too fast under all conditions to be measured by stopped-flow unfolding. The results show that the intermediate is not obligatory for lysozyme folding, since no lag phase in forming native lysozyme is observed [22] (Figure 12.1.8B,C). Rather, formation of I_N and formation of 20% of the native molecules occur with the faster kinetic phase ($\tau = 30$ ms). The slower process ($\tau = 400$ ms) reflects the interconversion of the intermediate to the native state, resulting in the remaining 80% of the molecules folding to the native state [22, 52]. As discussed above, identical apparent rate constants for forming the intermediate and native molecules on a fast pathway are expected, since any three-state model gives rise to only two observable rate constants.

The lack of an initial lag phase during formation of native lysozyme ruled out a linear on-pathway model, but it could not distinguish between the triangular model and the off-pathway model [22]. Performing a least-squares fit of the denaturant dependence of the two apparent rate constants to the analytical solutions of both models (see Protocols, Section 12.1.6) revealed that only the triangular model was able to describe the data [52] (Figure 12.1.9). In the case of the off-pathway model, unfolding of the intermediate should become the rate-limiting step for folding at very low denaturant concentrations. This would predict an increase in the folding rate with increasing denaturant concentration, which was, however, not observed (Figure 12.1.9). Fitting the data to the circular three-state model allowed the determination of all six microscopic rate constants (Figure 12.1.10). For this analysis it was crucial to know the unfolding rate constant of the intermediate at high denaturant concentrations (λ_2 in Figures 12.1.3A and 12.1.9). Since unfolding of

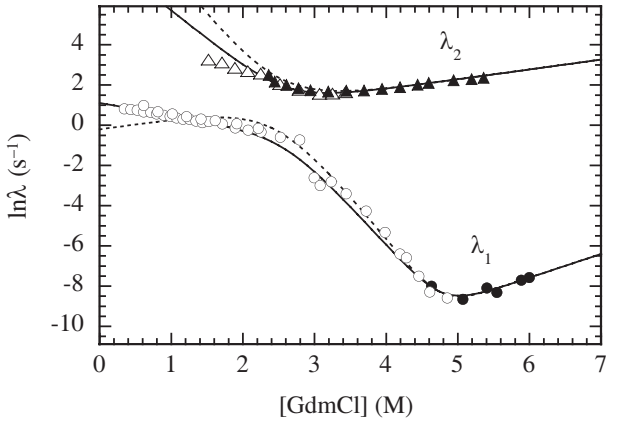

Fig. 12.1.9. GdmCl dependence of the apparent rate constants of lysozyme folding at pH 5.2. λ_2 (open and filled triangles) and λ_1 (open and filled circles) are fit to the analytical solutions of the triangular model (Scheme 12.1.1A, —) and to the linear off-pathway model (Scheme 12.1.1C, ----). The fits show that the off-pathway model is not able to describe the data. To increase the stability of the inter-mediate and thus allow a better distinction between the on- and the off-pathway model the experiments were carried out in the presence of 0.5 M Na_2SO_4. Data were taken from Ref. [52].

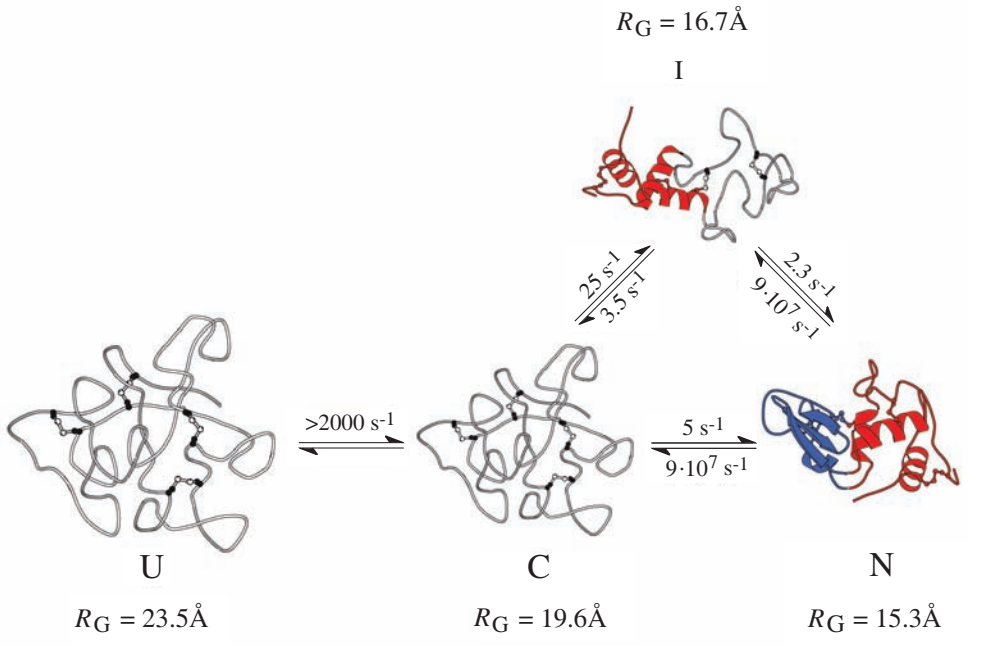

Fig. 12.1.10. Folding mechanism of lysozyme at pH 5.2 and low salt concentrations obtained by analyzing a large number of experimental data using various probes to detect refolding (see Figure 12.1.5), the GdmCl dependence of λ_1 and λ_2 (Figure 12.1.3A) and the results from interrupted refolding experiments (Figure 12.1.8B,C). Adapted from Refs [3], [43] and [52].

native lysozyme is single exponential at high denaturant concentrations and determined by λ_1, the faster rate constant (λ_2) had to be obtained in sequential mixing experiments [52]. In these experiments the intermediate was populated by a short (100 ms) refolding pulse and then unfolded at high denaturant concentrations to yield λ_2 (see Figure 12.1.6).

The triangular folding mechanism for lysozyme raises the question for the origin for the kinetic partitioning into a fast direct pathway and a slow pathway through I_N at the stage of the collapsed state. Fluorescence and NMR measurements revealed nonnative short- and long-range interactions around Trp residues in denaturant-unfolded lysozyme [44, 71] and in the collapsed state [43]. These interactions involve Trp62 and Trp63 which are located in the β-domain and may cause distinct subpopulations in the collapsed state and prevent structure formation in the β-domain of part of the collapsed molecules. This model is supported by the folding kinetics of a W62Y mutant, which has weakened hydrophobic interactions in the unfolded state and shows faster folding kinetics [72]. Also replacement of Trp108 by tyrosine accelerates folding of lysozyme [72] supporting a model of nonnative short-range and long-range interactions, which prevent fast folding of the β-domain.

The final conundrum in the folding mechanisms of lysozyme at pH 5.2 was the origin of the 10 ms reaction that was only observed in pulsed hydrogen exchange experiments [67–69]. This reaction was interpreted as formation of a native-like intermediate with secondary structure formed both an the α- and β-domains [70]. It is very difficult to imagine formation of a native-like state to occur without changes in any spectroscopic parameters. A quantitative analysis of all reactions occurring during the pulsed hydrogen exchange experiments revealed, however, that the 10 ms reaction is an artifact of incomplete hydrogen exchange, which was misinterpreted as fast protection of protons [73]. The reason for the incomplete exchange was an acceleration of all folding rate constants and a change in the folding mechanism under the conditions of the exchange pulse (pH 9–10; see below). The determination of the folding mechanism and all microscopic rate constants for folding and unfolding under the conditions of the exchange pulse allowed a quantitative calculation of the exchange kinetics expected on the basis of the rate constants determined from spectroscopic probes. All microscopic rate constants for all conditions applied during the exchange experiments and the rate constants for H/D exchange of the individual amide protons in lysozyme [74] were used to calculate exchange kinetics. The results quantitatively reproduced the experimentally measured time course of amide occupancy when the folding rate constants from spectroscopic experiments (Figures 12.1.3A and 12.1.5) were used [73]. This showed that no kinetic phases in addition to the ones observed by spectroscopic probes are required to quantitatively explain the hydrogen exchange kinetics.

12.1.3.2
Lysozyme Folding at pH 9.2 or at High Salt Concentrations

The procedure described above to elucidate the three-state mechanism for lysozyme folding at pH 5.2 can also be applied to elucidate the mechanism of more

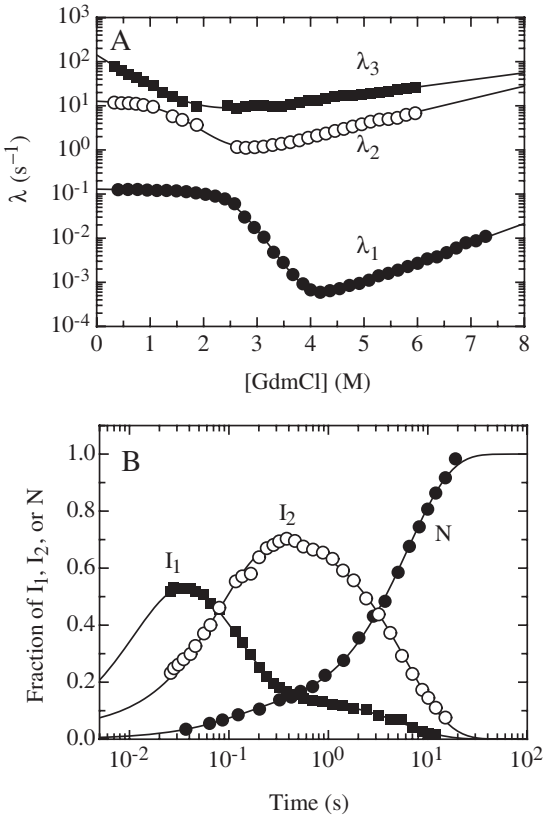

Fig. 12.1.11. Folding of lysozyme at pH 9.2. A) Effect of GdmCl on the three apparent rate constants λ_1, λ_2, and λ_3 measured by a combination of single and sequential mixing experiments [73]. B) Time course of the two kinetic intermediates and the native state during refolding at 0.6 M GdmCl. A global fit to the mechanism shown in Scheme 12.1.3 can describe the data (solid lines in all panels) and allowed all the microscopic rate constants to be determined (see Scheme 12.1.3).

complex folding reactions with more than one intermediate. For lysozyme folding, a third kinetic reaction is observed at high salt concentrations [75] and at high pH (>8.5) [73], indicating the stabilization of an additional intermediate under these conditions. Thus, a four-state model with an additional rapid pre-equilibrium is required to describe the folding kinetics under these conditions. Again interrupted refolding experiments were able to monitor the time course of the population of all intermediates and of native molecules (Figure 12.1.11B). Together with the denaturant dependence of all three rate constants obtained from single and sequential mixing stopped-flow refolding and unfolding experiments (Figure 12.1.11A) this allowed the identification of the minimal kinetic mechanism for lysozyme folding under these conditions. The results showed that the additional intermediate induced at high salt concentrations or at high pH is located on a third parallel folding pathway. The four-state mechanisms shown in Schemes 12.1.2 and 12.1.3

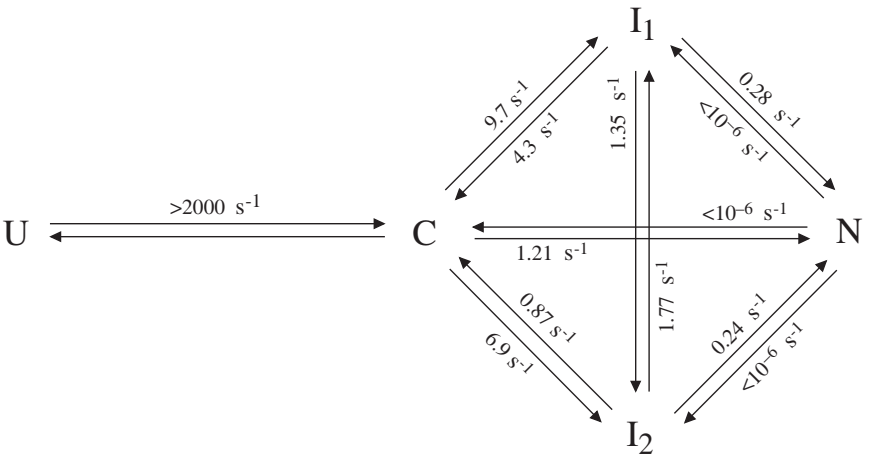

Scheme 12.1.2. Mechanism and rate constants for lysozyme folding at pH 5.2 in the presence of 0.85 M NaCl. Adapted from Ref. [75].

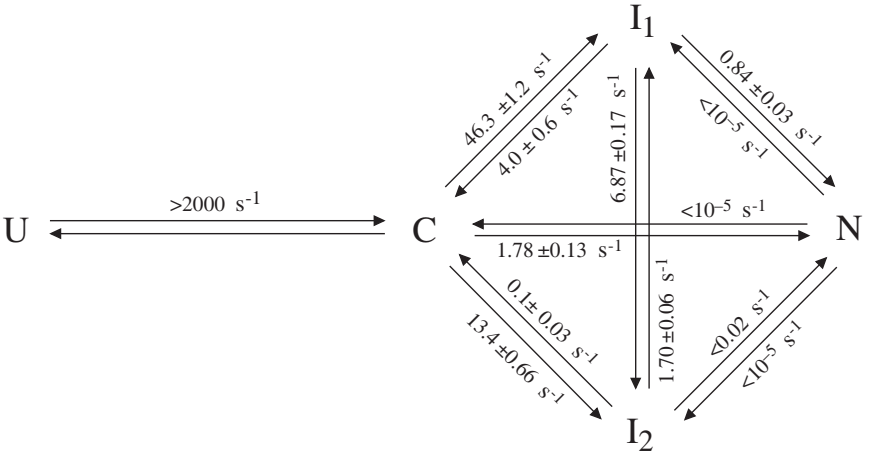

Scheme 12.1.3. Mechanism and rate constants for lysozyme folding at pH 9.2. Adapted from Ref. [73]

show the minimal models describing lysozyme folding at pH 9.2 and high salt concentrations, respectively. In addition the microscopic rate constants obtained from global fits of all data are shown.

This case study demonstrates the need for methods capable of detecting the time course of individual kinetic species during the folding process. Direct spectroscopic measurements are usually not able to provide this information. In addition, the folding studies on lysozyme show that for complex reactions it is usually impossible to assign experimentally observed rate constants directly to individual steps on folding pathways, since they are complex functions of several microscopic rate constants. In order to determine all microscopic rate constants for a mechanism it

is essential to combine results from interrupted refolding experiments and from the denaturant-dependence of all observable folding and unfolding reactions in a global fit to the solutions of various possible models (see Protocols, Section 12.1.6).

12.1.4 Non-exponential Kinetics

Non-exponential kinetics were first reported by Kohlrausch [76] for the relaxation of glass fibers after stretching. He described a broad distribution of relaxation times covering time scales of several orders of magnitude. Such non-exponential kinetics can be treated with a stretched exponential term of the kind

$$A = A_0 e^{-(k \cdot t)^{\beta}} \tag{21}$$

The stretch factor (β) indicates a time-dependent change in the rate constant (k), with $\beta = 1$ corresponding to the special case of single exponential kinetics. The kinetics become increasingly stretched with decreasing β. Stretched exponential behavior, which has also been referred to as ''strange'' kinetics [77], has recently been observed both in theoretical [78, 79] and in experimental work on biological systems [80]. The best-studied experimental model is the structural relaxation of myoglobin at low temperature [80] or at high solvent viscosity [81]. A prerequisite for strange kinetics is a rough energy landscape with significant barriers between a large number of local minima [78]. Thus, it was argued that protein folding reactions might exhibit stretched behavior, under conditions where local minima on the folding landscape become stabilized (e.g., at low temperature). Up to date there are only a few experimental reports on strange kinetics in protein folding, which describe the refolding of ubiquitin [82], phosphoglycerate kinase [82], and a WW domain at low temperature [83] measured in laser temperature-jump experiments on the microsecond time scale. The difficulty of unambiguously assigning the observed kinetics to stretched behavior may be seen from the fact that the kinetics only cover about 2.5 orders of magnitudes of life-times and can also be described by the sum of two or three exponentials. Nevertheless, these first indications of non-exponential behavior in protein folding on the very fast time scale provide an interesting new aspect to the understanding of energy landscapes for protein folding (see Chapter 14 for a more detailed discussion of non-exponential kinetics in protein folding).

12.1.5 Conclusions and Outlook

A quantitative treatment of folding kinetics is a prerequisite for elucidating mechanisms of protein folding. We have seen that concepts from classical reaction kinetics can be applied to protein folding as long as different ensembles of states are separated by significant barriers ($>5kT$). In most cases a discrimination between different folding mechanisms is not possible without the determination of

the time course of native molecules. Thus, interrupted refolding experiments in combination with the complete denaturant dependence of all observable rate constants should be routinely used to analyzed complex folding reactions.

12.1.6
Protocols – Analytical Solutions of Three-state Protein Folding Models

12.1.6.1
Triangular Mechanism

The most general three-state mechanism is the triangular model is given by

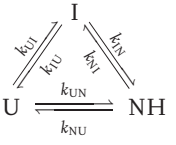

(22)

The characteristic equation for this mechanism is

$$f(\lambda) = \lambda^2 - \lambda(k_{UI} + k_{IU} + k_{UN} + k_{NU} + k_{NI} + k_{IN}) + (\gamma_1 + \gamma_2 + \gamma_3) = 0 \tag{23}$$

with

$$\begin{aligned}\gamma_1 &= k_{NI}k_{IU} + k_{NU}k_{IU} + k_{IN}k_{NU}\\ \gamma_2 &= k_{NU}k_{UI} + k_{UI}k_{NI} + k_{UN}k_{NI}\\ \gamma_3 &= k_{UI}k_{IN} + k_{IU}k_{UN} + k_{UN}k_{IN}\end{aligned} \tag{24}$$

The apparent rate constants, λ_1 and λ_2 are the solution of Eq. (23) and are given by:

$$\lambda_{1,2} = \frac{-B \pm \sqrt{B^2 - 4C}}{2} \tag{25}$$

with $B = -(k_{UN} + k_{NU} + k_{UI} + k_{IU} + k_{IN} + k_{NI})$ and $C = \gamma_1 + \gamma_2 + \gamma_3$.

The time-dependent behavior of the different kinetic species for refolding starting from the unfolded state ($U_0 = 1$; $I_0 = 0$; $N_0 = 0$) is given by

$$\begin{aligned}U(\mathrm{t}) &= U_0\left(\frac{\lambda_1(k_{UN} + k_{UI}) - (\gamma_2 + \gamma_3)}{\lambda_1(\lambda_1 - \lambda_2)}\mathrm{e}^{-\lambda_1 t} + \frac{\gamma_2 + \gamma_3 - \lambda_2(k_{UN} + k_{UI})}{\lambda_2(\lambda_1 - \lambda_2)}\mathrm{e}^{-\lambda_2 t} + \frac{\gamma_1}{\lambda_1\lambda_2}\right)\\ I(\mathrm{t}) &= U_0\left(\frac{\gamma_2 - k_{UI}\lambda_1}{\lambda_1(\lambda_1 - \lambda_2)}\mathrm{e}^{-\lambda_1 t} + \frac{k_{UI}\lambda_2 - \gamma_2}{\lambda_2(\lambda_1 - \lambda_2)}\mathrm{e}^{-\lambda_2 t} + \frac{\gamma_2}{\lambda_1\lambda_2}\right)\\ N(\mathrm{t}) &= U_0\left(\frac{\gamma_3 - k_{UN}\lambda_1}{\lambda_1(\lambda_1 - \lambda_2)}\mathrm{e}^{-\lambda_1 t} + \frac{k_{UN}\lambda_2 - \gamma_3}{\lambda_2(\lambda_1 - \lambda_2)}\mathrm{e}^{-\lambda_2 t} + \frac{\gamma_3}{\lambda_1\lambda_2}\right)\end{aligned} \tag{26}$$

where $U(t)$, $I(t)$, and $N(t)$ represent the concentrations of the respective species at a given time t. The pre-exponential factors give the amplitude of the observable rate constant (see Eq. (2)) for monitoring the time course of the respective species and the constant terms represent the equilibrium concentrations of each species. The principle of microscopic reversibility provides an additional constraint for fitting the experimental data to the triangular mechanism

$$\frac{k_{UI} + k_{IN} + k_{NU}}{k_{IU} + k_{NI} + k_{UN}} = 1 \tag{27}$$

The time-dependent behavior of the different species for starting from the native state ($N_0 = 1;\ U_0 = 0;\ I_0 = 0$) or from the intermediate ($I_0 = 1;\ U_0 = 0;\ N_0 = 0$) are obtained by substituting the respective microscopic rate constant in Eq. (26).

12.1.6.2 On-pathway Intermediate

$$U \underset{k_{IU}}{\overset{k_{UI}}{\rightleftharpoons}} I \underset{k_{NI}}{\overset{k_{IN}}{\rightleftharpoons}} N \tag{28}$$

The characteristic equation for the on-pathway mechanism is given by

$$f(\lambda) = \lambda^2 - \lambda \cdot (k_{UI} + k_{IU} + k_{IN} + k_{NI}) + (k_{UI}k_{IN} + k_{UI}k_{NI} + k_{IU}k_{NI}) = 0 \tag{29}$$

The apparent rate constants, λ_1 and λ_2 are the solution of Eq. (29) (see Section 12.1.6.1). The time-dependent behavior of the different kinetic species for refolding starting from the unfolded state ($U_0 = 1;\ I_0 = 0;\ N_0 = 0$) is given by

$$\begin{aligned}
U(t) &= U_0\left(\frac{k_{UI}(\lambda_1 - k_{IN} - k_{NI})}{\lambda_1(\lambda_1 - \lambda_2)}e^{-\lambda_1 t} + \frac{k_{UI}(k_{NI} + k_{IN} - \lambda_2)}{\lambda_2(\lambda_1 - \lambda_2)}e^{-\lambda_2 t} + \frac{k_{NI}k_{IU}}{\lambda_1\lambda_2}\right)\\
I(t) &= U_0\left(\frac{k_{UI}(k_{NI} - \lambda_1)}{\lambda_1(\lambda_1 - \lambda_2)}e^{-\lambda_1 t} + \frac{k_{UI}(\lambda_2 - k_{NI})}{\lambda_2(\lambda_1 - \lambda_2)}e^{-\lambda_2 t} + \frac{k_{UI}k_{NI}}{\lambda_1\lambda_2}\right)\\
N(t) &= U_0\left(\frac{k_{UI}k_{IN}}{\lambda_1(\lambda_1 - \lambda_2)}e^{-\lambda_1 t} + \frac{-k_{UI}k_{IN}}{\lambda_2(\lambda_1 - \lambda_2)}e^{-\lambda_2 t} + \frac{k_{UI}k_{IN}}{\lambda_1\lambda_2}\right)
\end{aligned} \tag{30}$$

For initial conditions $I_0 = 1;\ U_0 = 0;\ N_0 = 0$ we yield

$$\begin{aligned}
U(t) &= I_0\left(\frac{k_{IU}(k_{NI} - \lambda_1)}{\lambda_1(\lambda_1 - \lambda_2)}e^{-\lambda_1 t} + \frac{k_{IU}(\lambda_2 - k_{NI})}{\lambda_2(\lambda_1 - \lambda_2)}e^{-\lambda_2 t} + \frac{k_{NI}k_{IU}}{\lambda_1\lambda_2}\right)\\
I(t) &= I_0\left(\frac{(k_{UI} - \lambda_1)(k_{NI} - \lambda_1)}{\lambda_1(\lambda_1 - \lambda_2)}e^{-\lambda_1 t} + \frac{(\lambda_2 - k_{NI})(k_{UI} - \lambda_2)}{\lambda_2(\lambda_1 - \lambda_2)}e^{-\lambda_2 t} + \frac{k_{UI}k_{NI}}{\lambda_1\lambda_2}\right)\\
N(t) &= I_0\left(\frac{k_{IN}(k_{UI} - \lambda_1)}{\lambda_1(\lambda_1 - \lambda_2)}e^{-\lambda_1 t} + \frac{k_{IN}(\lambda_2 - k_{UI})}{\lambda_2(\lambda_1 - \lambda_2)}e^{-\lambda_2 t} + \frac{k_{UI}k_{IN}}{\lambda_1\lambda_2}\right)
\end{aligned} \tag{31}$$

The solutions for starting from the native state ($N_0 = 1;\ U_0 = 0;\ I_0 = 0$) are the same as for starting from the unfolded state with replacing the respective microscopic rate constants in Eq. (30).

12.1.6.3 Off-pathway Mechanism

$$\mathrm{I} \underset{k_{\mathrm{UI}}}{\overset{k_{\mathrm{IU}}}{\rightleftharpoons}} \mathrm{U} \underset{k_{\mathrm{NU}}}{\overset{k_{\mathrm{UN}}}{\rightleftharpoons}} \mathrm{N} \tag{32}$$

The characteristic equation for the off-pathway mechanism is given by

$$f(\lambda) = \lambda^2 - \lambda(k_{\mathrm{UI}} + k_{\mathrm{IU}} + k_{\mathrm{UN}} + k_{\mathrm{NU}}) + (k_{\mathrm{IU}}k_{\mathrm{UN}} + k_{\mathrm{IU}}k_{\mathrm{NU}} + k_{\mathrm{UI}}k_{\mathrm{NU}}) = 0 \tag{33}$$

The apparent rate constants, λ_1 and λ_2 are the solution of Eq. (33) (see Section 12.1.6.1). The time-dependent behavior of the different kinetic species for refolding starting from the unfolded state ($U_0 = 1;\ I_0 = 0;\ N_0 = 0$) is given by

$$\begin{aligned}
U(\mathrm{t}) &= U_0\left(\frac{(k_{\mathrm{IU}} - \lambda_1)(k_{\mathrm{NU}} - \lambda_1)}{\lambda_1(\lambda_1 - \lambda_2)}\mathrm{e}^{-\lambda_1 t} + \frac{(\lambda_2 - k_{\mathrm{NU}})(k_{\mathrm{IU}} - \lambda_2)}{\lambda_2(\lambda_1 - \lambda_2)}\mathrm{e}^{-\lambda_2 t} + \frac{k_{\mathrm{IU}}k_{\mathrm{NU}}}{\lambda_1\lambda_2}\right) \\
I(\mathrm{t}) &= U_0\left(\frac{k_{\mathrm{UI}}(k_{\mathrm{NU}} - \lambda_1)}{\lambda_1(\lambda_1 - \lambda_2)}\mathrm{e}^{-\lambda_1 t} + \frac{k_{\mathrm{UI}}(\lambda_2 - k_{\mathrm{NU}})}{\lambda_2(\lambda_1 - \lambda_2)}\mathrm{e}^{-\lambda_2 t} + \frac{k_{\mathrm{NU}}k_{\mathrm{UI}}}{\lambda_1\lambda_2}\right) \\
N(\mathrm{t}) &= U_0\left(\frac{k_{\mathrm{UN}}(k_{\mathrm{IU}} - \lambda_1)}{\lambda_1(\lambda_1 - \lambda_2)}\mathrm{e}^{-\lambda_1 t} + \frac{k_{\mathrm{UN}}(\lambda_2 - k_{\mathrm{IU}})}{\lambda_2(\lambda_1 - \lambda_2)}\mathrm{e}^{-\lambda_2 t} + \frac{k_{\mathrm{IU}}k_{\mathrm{UN}}}{\lambda_1\lambda_2}\right)
\end{aligned} \tag{34}$$

The solutions for starting from the native state ($N_0 = 1;\ U_0 = 0;\ I_0 = 0$) or from the intermediate ($I_0 = 1;\ U_0 = 0;\ N_0 = 0$) are obtained in the same way as discussed in Section 12.1.6.2.

12.1.6.4 Folding Through an On-pathway High-Energy Intermediate

Apparent two-state folding through a high-energy intermediate (see Figure 12.1.7A) can be described by a three-state on-pathway model

$$\mathrm{U} \underset{k_{\mathrm{IU}}}{\overset{k_{\mathrm{UI}}}{\rightleftharpoons}} \mathrm{I}^* \underset{k_{\mathrm{NI}}}{\overset{k_{\mathrm{IN}}}{\rightleftharpoons}} \mathrm{N} \tag{35}$$

As discussed above, the kinetics of folding through a high-energy intermediate cannot be distinguished from two-state folding, when monitored at a single denaturant concentration. However, the presence of a kink in the chevron plot and the resulting altered slope at high denaturant concentrations (Figure 12.1.7B) allows a characterization of both transition states [57]. Comparing two-state folding (Eq. (3))

with Eq. (35) allows the rate constants k_f and k_u to be expressed for apparent two-state folding as a function of the microscopic rate constants k_{ij} for the three-state model for the different regimes shown in Figure 12.1.7A. At low denaturant concentrations (TS1 limit) formation of the high-energy intermediate (k_{UI}) is rate-limiting for folding ($k_{UI} \ll k_{IN}$) and thus we can approximate k_f in the TS1 limit ($k_f(TS1)$) as

$$k_f(TS1) = k_{UI} \tag{36}$$

The unfolding reaction in the TS1 limit requires going through I^*. Since I^* is higher in free energy than N ($k_{NI} \ll k_{IN}$) and TS1 represents the highest barrier, the crossing of transition state 2 can be treated as a pre-equilibrium. Thus, k_u in the TS1 limit ($k_u(TS1)$) is given by

$$k_u(TS1) = \frac{k_{NI}}{k_{IN}} k_{I^*U} = k_{NI} \left(\frac{k_{IN}}{k_{IU}}\right)^{-1} \tag{37}$$

For folding and unfolding at high denaturant concentrations TS2 represents the highest barrier (TS2 limit). Thus, in analogy to Eqs (36) and (37), k_f and k_u can be expressed in the TS2 limit as:

$$k_f(TS2) = \frac{k_{UI}}{k_{IU}} k_{IN} = k_{UI} \frac{k_{IN}}{k_{IU}} \tag{38}$$

$$k_u(TS2) = k_{NI} \tag{39}$$

These considerations show that the presence of a kink in the chevron plot allows the determination of the ratio k_{IU}/k_{IN}, which is equivalent to the equilibrium constant between the two transition states ($K_{TS1/TS2}$) and can be converted into the difference in free energy between the two transition states ($\Delta G^\circ_{TS1/TS2}$)

$$k_{IN}/k_{IU} = K_{TS1/TS2} = e^{-(1/RT)(\Delta G^{\circ\ddagger}(TS2) - \Delta G^{\circ\ddagger}(TS1))} = e^{-\Delta G^\circ_{TS2/TS1}/RT} \tag{40}$$

Accordingly, the stability of I^* cannot be determined, since it does not become populated, but the difference in free energy between both transition states ($\Delta G^\circ_{TS2/TS1}$) can be obtained. It should be noted that this analysis does not make any assumptions on the stability of the hypothetical intermediate besides that it is always less stable than U and N. Fitting the GdmCl dependence of ln λ to the analytical solutions of the three-state model (Eq. (29)) with λ_1 and λ_2 given by Refs [4] and [24]

$$\lambda_{1,2} = \frac{-B \pm \sqrt{B^2 - 4C}}{2} \tag{41}$$

with

$$B = -(k_{UI} + k_{IU} + k_{IN} + k_{NI})$$
$$C = k_{UI}(k_{IN} + k_{NI}) + k_{IU}k_{NI} \quad (42)$$

therefore allows the determination of k_{UI} and k_{NI} and their denaturant dependencies m_{UI} and m_{NI}, respectively. It further yields the parameters k_{IN}/k_{IU} and $m_{IN} - m_{IU}$. Since only the ratios k_{IN}/k_{IU} and $m_{IN} - m_{IU}$ are defined for folding through a high-energy intermediate, these ratios have to be used for data fitting [57]. Folding through a high-energy intermediate shows apparent two-state behavior and thus only the smaller one of the two apparent rate constants (λ_1) should have the complete folding and unfolding amplitude ($A_1 = 1$) whereas $A_2 = 0$ (see Ref. [57]).

Acknowledgments

We thank Manuela Schätzle and Beat Fierz for comments on the manuscript and all members of the Kiefhaber lab for help and discussion.

References

1 Sánchez, I. E. & Kiefhaber, T. (2003). Hammond behavior versus ground state effects in protein folding: evidence for narrow free energy barriers and residual structure in unfolded states. *J. Mol. Biol.* 327, 867–884.
2 Kiefhaber, T. (1995). Protein folding kinetics. In *Methods in Molecular Biology, Vol. 40: Protein Stability and Folding Protocols* (Shirley, B. A., ed.), pp. 313–341. Humana Press, Totowa, NJ.
3 Bieri, O. & Kiefhaber, T. (2000). Kinetic models in protein folding. In *Protein Folding: Frontiers in Molecular Biology* 2nd edn (Pain, R., ed.), pp. 34–64. Oxford University Press, Oxford.
4 Szabo, Z. G. (1969). Kinetic characterization of complex reaction systems. In *Comprehensive Chemical Kinetics* (Bamford, C. H. & Tipper, C. F. H., eds), Vol. 2, pp. 1–80. 7 vols. Elsevier Publishing Company, Amsterdam.
5 Moore, J. W. & Pearson, R. G. (1981). *Kinetics and Mechanisms.* John Wiley & Sons, New York.
6 Jackson, S. E. (1998). How do small single-domain proteins fold? *Folding Design* 3, R81–R91.
7 Eyring, H. (1935). The activated complex in chemical reactions. *J. Chem. Phys.* 3, 107–115.
8 Evans, M. G. & Polanyi, M. (1935). Some applications of the transition state method to the calculation of reaction velocities, especially in solution. *Trans. Faraday Soc.* 31, 875–885.
9 Krieger, F., Fierz, B., Bieri, O., Drewello, M. & Kiefhaber, T. (2003). Dynamics of unfolded polypeptide chains as model for the earliest steps in protein folding. *J. Mol. Biol.* 332, 265–274.
10 Greene, R. F. J. & Pace, C. N. (1974). Urea and guanidine-hydrochloride denaturation of ribonuclease, lysozyme, alpha-chyomtrypsinn and beta-lactoglobulin. *J. Biol. Chem.* 249, 5388–5393.
11 Santoro, M. M. & Bolen, D. W. (1988). Unfolding free energy changes determined by the linear extrapolation method. 1. Unfolding of

phenylmethanesulfonyl alpha-chymotrypsin using different denaturants. *Biochemistry* 27, 8063–8068.

12 Tanford, C. (1970). Protein Denaturation. Part C. Theoretical models for the mechanism of denaturation. *Adv. Prot. Chem.* 24, 1–95.

13 Ikai, A., Fish, W. W. & Tanford, C. (1973). Kinetics of unfolding and refolding of proteins. II. Results for cytochrome c. *J. Mol. Biol.* 73, 165–184.

14 Matthews, C. R. (1987). Effect of point mutations on the folding of globular proteins. *Methods Enzymol.* 154, 498–511.

15 Myers, J. K., Pace, C. N. & Scholtz, J. M. (1995). Denaturant m values and heat capacity changes: relation to changes in accessible surface areas of protein unfolding. *Protein Sci.* 4, 2138–2148.

16 Leffler, J. E. (1953). Parameters for the description of transition states. *Science* 117, 340–341.

17 Leffler, J. E. & Grunwald, E. (1963). *Rates and Equilibria of Organic Reactions.* Dover, New York.

18 Jencks, W. P. (1969). *Catalysis in Chemistry and Enzymology.* McGraw-Hill, New York.

19 Sánchez, I. E. & Kiefhaber, T. (2003). Non-linear rate-equilibrium free energy relationships and Hammond behavior in protein folding. *Biophys. Chem.* 100, 397–407.

20 Ikai, A. & Tanford, C. (1973). Kinetics of unfolding and refolding of proteins. I. Mathematical Analysis. *J. Mol. Biol.* 73, 145–163.

21 Tanford, C., Aune, K. C. & Ikai, A. (1973). Kinetics of unfolding and refolding of proteins. III. Results for lysozyme. *J. Mol. Biol.* 73, 185–197.

22 Kiefhaber, T. (1995). Kinetic traps in lysozyme folding. *Proc. Natl Acad. Sci. USA* 92, 9029–9033.

23 Khorasanizadeh, S., Peters, I. D. & Roder, H. (1996). Evidence for a three-state model for protein folding from kinetic analysis of ubiquitin variants with altered core residues. *Nat. Struct. Biol.* 3, 193–205.

24 Kiefhaber, T., Kohler, H. H. & Schmid, F. X. (1992). Kinetic coupling between protein folding and prolyl isomerization. I. Theoretical models. *J. Mol. Biol.* 224, 217–229.

25 Kiefhaber, T. & Schmid, F. X. (1992). Kinetic coupling between protein folding and prolyl isomerization. II. Folding of ribonuclease A and ribonuclease T1. *J. Mol. Biol.* 224, 231–240.

26 Bieri, O., Wirz, J., Hellrung, B., Schutkowski, M., Drewello, M. & Kiefhaber, T. (1999). The speed limit for protein folding measured by triplet-triplet energy transfer. *Proc. Natl Acad. Sci. USA* 96, 9597–9601.

27 Bieri, O. & Kiefhaber, T. (1999). Elementary steps in protein folding. *Biol. Chem.* 380, 923–929.

28 Kubelka, J., Hofrichter, J. & Eaton, W. A. (2004). The protein folding speed limit. *Curr. Opin. Struct. Biol.* 14, 76–88.

29 Garel, J. R. & Baldwin, R. L. (1973). Both the fast and slow folding reactions of ribonuclease A yield native enzyme. *Proc. Natl Acad. Sci. U.S.A.* 70, 3347–3351.

30 Brandts, J. F., Halvorson, H. R. & Brennan, M. (1975). Consideration of the possibility that the slow step in protein denaturation reactions is due to *cis-trans* isomerism of proline residues. *Biochemistry* 14, 4953–4963.

31 Kiefhaber, T., Grunert, H. P., Hahn, U. & Schmid, F. X. (1990). Replacement of a cis proline simplifies the mechanism of ribonuclease T1 folding. *Biochemistry* 29, 6475–6480.

32 Lang, K., Schmid, F. X. & Fischer, G. (1987). Catalysis of protein folding by prolyl isomerase. *Nature* 329, 268–270.

33 Reimer, U., Scherer, G., Drewello, M., Kruber, S., Schutkowski, M. & Fischer, G. (1998). Side-chain effects on peptidyl-prolyl cis/trans isomerization. *J. Mol. Biol.* 279, 449–460.

34 Balbach, J. & Schmid, F. X. (2000). Proline isomerization and its catalysis

in protein folding. In *Protein Folding: Frontiers in Molecular Biology* (Pain, R., ed.). Oxford University Press, Oxford.

35 Kiefhaber, T., Quaas, R., Hahn, U. & Schmid, F. X. (1990). Folding of ribonuclease T1. 1. Existence of multiple unfolded states created by proline isomerization. *Biochemistry* 29, 3053–3061.

36 Kiefhaber, T., Quaas, R., Hahn, U. & Schmid, F. X. (1990). Folding of ribonuclease T1. 2. Kinetic models for the folding and unfolding reactions. *Biochemistry* 29, 3061–3070.

37 Odefey, C., Mayr, L. & Schmid, F. X. (1995). Non-prolyl cis/trans peptide bond isomerization as a rate-determinig step in protein unfolding and refolding. *J. Mol. Biol.* 245, 69–78.

38 Pappenberger, G., Aygün, H., Engels, J. W., Reimer, U., Fischer, G. & Kiefhaber, T. (2001). Nonprolyl cis peptide bonds in unfolded proteins cause complex folding kinetics. *Nat. Struct. Biol.* 8, 452–458.

39 Scherer, G., Kramer, M. L., Schutkowski, M., Reimer, U. & Fischer, G. (1998). Barriers to rotation of secondary amide peptide bonds. *J. Am. Chem. Soc.* 120, 5568–5574.

40 Colon, W., Wakem, L. P., Sherman, F. & Roder, H. (1997). Identification of the predominant non-native histidine ligand in unfolded cytochrome c. *Biochemistry* 36, 12535–12541.

41 Yeh, S.-R., Takahashi, S., Fan, B. & Rousseau, D. L. (1998). Ligand exchange in unfolded cytochrome c. *Nat. Struct. Biol.* 4, 51–56.

42 Yeh, S.-R. & Rousseau, D. L. (1998). Folding intermediates in cytochrome c. *Nat. Struct. Biol.* 5, 222–228.

43 Segel, D., Bachmann, A., Hofrichter, J., Hodgson, K., Doniach, S. & Kiefhaber, T. (1999). Characterization of transient intermediates in lysozyme folding with time-resolved small angle X-ray scattering. *J. Mol. Biol.* 288, 489–500.

44 Bachmann, A. & Kiefhaber, T. (2002). Test for cooperativity in the early kinetic intermediate in lysozyme folding. *Biophys. Chem.* 96, 141–151.

45 Kuwajima, K. (1989). The molten globule state as a clue for understanding the folding and cooperativity of globular-protein structure. *Proteins Struct. Funct. Genet.* 6, 87–103.

46 Wu, L. C., Peng, Z.-Y. & Kim, P. S. (1995). Bipartite structure of the α-lactalbumin molten globule. *Nat. Struct. Biol.* 2, 281–286.

47 Wu, L. C. & Kim, P. S. (1998). A specific hydrophobic core in the α-lactalbumin molten globule. *J. Mol. Biol.* 280, 175–182.

48 Luo, Y. & Baldwin, R. L. (1999). The 28–111 disulfide bond contrains the a-lactalbumin molten globule and weakens its cooperativity of folding. *Proc. Natl Acad. Sci. USA* 96, 11283–11287.

49 Luo, Y., Kay, M. S. & Baldwin, R. L. (1997). Cooperativity of folding of the apomyoglobin pH 4 intermediate studied by glycine and proline mutations. *Nat. Struct. Biol.* 4, 925–929.

50 Silow, M. & Oliveberg, M. (1997). Transient aggregates in protein folding are easilty mistaken for folding intermediates. *Proc. Natl Acad. Sci. USA* 94, 6084–6086.

51 Schmid, F. X. (1983). Mechanism of folding of ribonuclease A. Slow refolding is a sequential reaction via structural intermediates. *Biochemistry* 22, 4690–4696.

52 Wildegger, G. & Kiefhaber, T. (1997). Three-state model for lysozyme folding: triangular folding mechanism with an energetically trapped intermediate. *J. Mol. Biol.* 270, 294–304.

53 Hill, T. L. (1974). The sliding filament model of contraction of striated muscle. *Progr. Biophys. Mol. Biol.* 28, 267–340.

54 Hill, T. L. (1977). *Free Energy Transduction in Biology.* Academic Press, London.

55 Weismann, J. S. & Kim, P. S. (1991). Reexamination of the folding of BPTI: predominance of native intermediates. *Science* 253, 1386–1393.

56 Kiefhaber, T., Grunert, H. P., Hahn, U. & Schmid, F. X. (1992).

Folding of RNase T1 is decelerated by a specific tertiary contact in a folding intermediate. *Proteins Struct. Funct. Genet.* 12, 171–179.

57 Bachmann, A. & Kiefhaber, T. (2001). Apparent two-state tendamistat folding is a sequential process along a defined route. *J. Mol. Biol.* 306, 375–386.

58 Sánchez, I. E. & Kiefhaber, T. (2003). Evidence for sequential barriers and obligatory intermediates in apparent two-state protein folding. *J. Mol. Biol.* 325, 367–376.

59 Jencks, W. P. (1980). When is an intermediate not an intermediate? Enforced mechanisms of general acid-base catalyzed, carbonation, carbanion, and ligand exchange reactions. *Acc. Chem. Res.* 13, 161–169.

60 Kiefhaber, T., Bachmann, A., Wildegger, G. & Wagner, C. (1997). Direct measurements of nucleation and growth rates in lysozyme folding. *Biochemistry* 36, 5108–5112.

61 Walkenhorst, W. F., Green, S. & Roder, H. (1997). Kinetic evidence for folding and unfolding intermediates in staphylococcal nuclease. *Biochemistry* 36, 5795–5805.

62 Blake, C. C. F., Koenig, D. F., Mair, G. A., North, A. C. T., Phillips, D. C. & Sarma, V. F. (1967). Structure of hen egg-white lysozyme. *Nature* 206, 757–761.

63 Blake, C. C. F., Mair, G. A., North, A. C. T., Phillips, D. C. & Sarma, V. F. (1967). On the conformation of the hen egg-white lysozyme molecule. *Proc. R. Soc. B* 167, 365–377.

64 Kuwajima, K., Hiraoka, Y., Ikeguchui, M. & Sugai, S. (1985). Comparison of the transient folding intermediates in lysozyme and α-lactalbumin. *Biochemistry* 24, 874–881.

65 Chaffotte, A. F., Guillou, Y. & Goldberg, M. E. (1992). Kinetic resolution of peptide bond and side-chain far-UV CD during folding of HEWL. *Biochemistry* 31, 9694–9702.

66 Itzhaki, L. S., Evans, P. A., Dobson, C. M. & Radford, S. E. (1994). Tertiary interactions in the folding pathway of hen lysozyme: kinetic studies using fluorescent probes. *Biochemistry* 33, 5212–5220.

67 Radford, S. E., Buck, M., Topping, K. D., Dobson, C. M. & Evans, P. A. (1992). Hydrogen exchange in native and denatured states of hen egg-white lysozyme. *Proteins* 14, 237–248.

68 Miranker, A. D., Robinson, C. V., Radford, S. E., Aplin, R. T. & Dobson, C. M. (1993). Detection of transient protein folding populations by mass spectroscopy. *Science* 262, 896–900.

69 Matagne, A., Chung, E. W., Ball, L. J., Radford, S. E., Robinson, C. V. & Dobson, C. M. (1998). The origin of the α-domain intermediate in the folding of hen lysozyme. *J. Mol. Biol.* 277, 997–1005.

70 Kulkarni, S. K., Ashcroft, A. E., Carey, M., Masselos, D., Robinson, C. V. & Radford, S. E. (1999). A near-native state on the slow refolding pathway of hen lysozyme. *Protein Sci.* 8, 35–44.

71 Klein-Seetharaman, J., Oikawa, M., Grimshaw, S. B., Wirmer, J., Duchardt, E., Ueda, T., et al. (2002). Long-range interactions within a nonnative protein. *Science* 295, 1719–1722.

72 Rothwarf, D. M. & Scheraga, H. A. (1996). Role of non-native aromatic and hydrophobic interactions in the folding of hen egg white lysozyme. *Biochemistry* 35, 13797–13807.

73 Bieri, O. & Kiefhaber, T. (2001). Origin of apparent fast and non-exponential kinetics of lysozyme folding measured in pulse labeling experiments. *J. Mol. Biol.* 310, 919–935.

74 Bai, Y., Milne, J. S., Mayne, L. & Englander, W. (1993). Primary structure effects on peptide group hydrogen exchange. *Proteins Struct. Funct. Genet.* 17, 75–86.

75 Bieri, O., Wildegger, G., Bachmann, A., Wagner, C. & Kiefhaber, T. (1999). A salt-induced intermediate is on a new parallel pathway of lysozyme folding. *Biochemistry* 38, 12460–12470.

76 Kohlrausch, R. (1847). Über das

Dellmann'sche Elektrometer. *Ann. Phys. Chem.* 11, 353–405.

77 Shlesinger, M. F., Zaslavsky, G. M. & Klafter, J. (1993). Strange kinetics. *Nature* 363, 31–37.

78 Saven, J. G., Wang, J. & Wolynes, P. G. (1994). Kinetics of protein folding: The folding dynamics of globally connected rough energy landscapes with biases. *J. Chem. Phys.* 101, 11037–11043.

79 Skorobogatiy, M., Guo, H. & Zuckermann, M. (1998). Non-Arrhenius behavior in the realaxation of model proteins. *J. Chem. Phys.* 109, 2528–2535.

80 Austin, R. H., Beeson, K. W., Eisenstein, L., Frauenfelder, H. & Gunsalus, I. C. (1975). Dynamics of ligand binding to myoglobin. *Biochemistry* 14, 5355–5373.

81 Hagen, S. J., Hofrichter, J. & Eaton, W. A. (1995). Protein kinetics in a glass at room temperature. *Science* 269, 959–962.

82 Sabelko, J., Ervin, J. & Gruebele, M. (1999). Observation of strange kinetics in protein folding. *Proc. Natl Acad. Sci. USA* 96, 6031–6036.

83 Yang, W. Y. & Gruebele, M. (2003). Folding at the speed limit. *Nature* 423, 193–197.

12.2 Characterization of Protein Folding Barriers with Rate Equilibrium Free Energy Relationships

Thomas Kiefhaber, Ignacio E. Sánchez, and Annett Bachmann

12.2.1 Introduction

The characterization of barriers and mechanisms of chemical reactions has a long tradition in physico-organic chemistry [1]. Several concepts have been developed to gain information on the structural and thermodynamic properties of transition states. Rate equilibrium free energy relationships (REFERs) have proved to be a powerful tool for the characterization of the properties and the shape of free energy barriers. REFERs have also been applied to the study of complex biochemical reactions like enzyme kinetics [2]. This chapter will show how REFERs can be used to gain information on free energy barriers for protein folding reactions and will discuss results in terms of a general picture of the properties of protein folding transition states. This analysis implies that protein folding encounters major free energy barriers which separate ensembles of different kinetic states on the free energy landscape. This assumption seems to be supported by experimental results (see Chapter 12.1).

12.2.2 Rate Equilibrium Free Energy Relationships

For many reactions in organic chemistry the changes in activation free energy ($\Delta G^{\circ\ddagger}$) induced by changes in solvent conditions or by modifications in structure are linearly related to the corresponding change in equilibrium free energy (ΔG°) between reactant and product [3]. A proportionality constant, α_x, was defined by Leffler to quantify the energetic sensitivity of the transition state relative to the ground states with respect to a perturbation, ∂x [3]:

$$\alpha_x = \frac{\partial \Delta G^{\circ\ddagger}/\partial x}{\partial \Delta G^{\circ}/\partial x} \tag{1}$$

where α_x is a measure for the position of the transition state along the reaction co-

Protein Folding Handbook. Part I. Edited by J. Buchner and T. Kiefhaber

ISBN: 3-527-30784-2

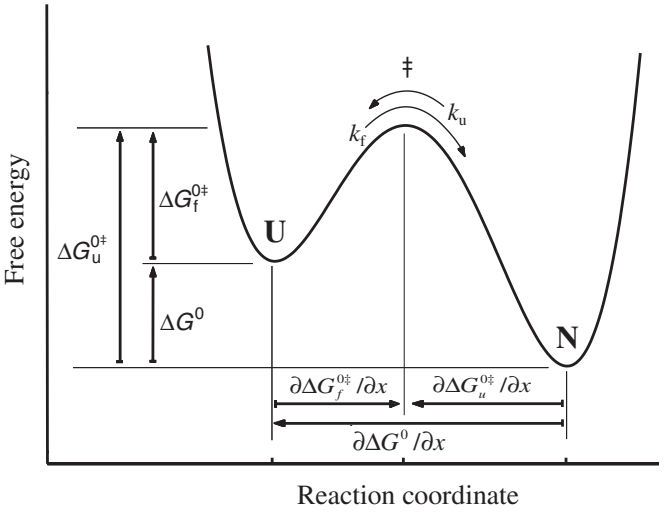

Fig. 12.2.1. Free energy profile for a two-state folding reaction. The sensitivity of the reaction to changes in a parameter ∂x as a test for the respective reaction coordinate according to the Leffler postulate (see Eq. (1)) are indicated.

ordinate probed by ∂x and it can be used to gain structural and thermodynamic information on the transition state. If $\alpha_x = 1$ the transition state has the same property as the product and for $\alpha_x = 0$ it has the same properties as the educt. Figure 12.2.1 shows the relationship between the equilibrium free energies and the activation free energies for a two-state reaction as well as the relationship between $\partial\Delta G^\circ/\partial x$ and $\partial\Delta G^{\circ‡}/\partial x$. Obviously, $\partial\Delta G^\circ/\partial x$ is a measure for the length of the reaction coordinate, whereas $\partial\Delta G^{\circ‡}/\partial x$ is a measure for the respective change between the educt and the transition state. Frequently used perturbations are changes in pressure, temperature, or structure, which will yield information on the position of the transition state in respect to its volume, its entropy, or its interactions at the site of structural change, respectively (see below). Since these relationships are empirical rather than rigorously derived from the laws of thermodynamics they are commonly termed "extrathermodynamic relationships" [1].

For many reactions the α_x-values are constant over a broad range of ΔG° indicating little effect of the perturbations on the structure of the transition state (linear REFERs) [1]. This can be used to infer structural and thermodynamic properties of a transition state (see Section 12.2.2.1). For other reactions, α_x is sensitive to changes in ΔG° which leads to nonlinear REFERs indicating changes in the position of the transition state relative to the ground states (cf. Figure 12.2.1). It was shown that the characterization of nonlinear REFERs can give valuable information on the mechanism of a reaction and on the shape of the transition barrier since nonlinearities can have different origins: (1) a movement of the position of

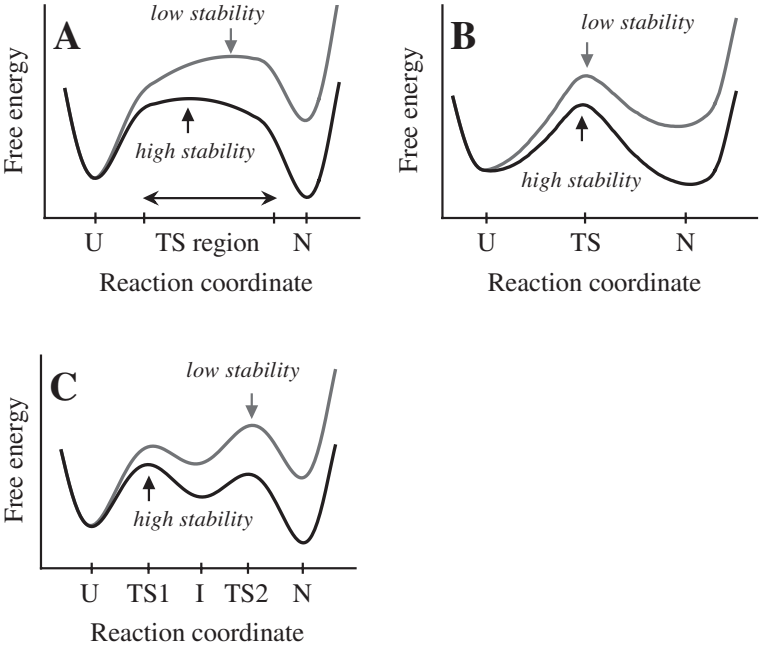

Fig. 12.2.2. Schematic representation of the response of different types of free energy barriers to the same perturbation. The position of the transition state along the reaction coordinate is more sensitive to the perturbation if the free energy shows a broader maximum (A) than if the maximum is narrow (B). An apparent movement of the position of the transition state can also be due to a switch between consecutive transition states on a linear pathway (C). The position of the highest point along the barrier region is indicated by an arrow.

the transition state along a broad barrier region (Hammond behavior; Figure 12.2.2A,B) [4, 5]; (2) a change in the rate-limiting step on a sequential pathway (Figure 12.2.2C) [1]; (3) a change in the mechanism of the reaction due to a switch between parallel pathways [1]; or (4) structural changes in the ground state(s) (ground state effects) [6]. If the rate-limiting step (Figure 12.2C) or the mechanism of a reaction changes, a discrete jump in the position of the transition state along the reaction coordinate will be observed. A gradual transition state movement (Figure 12.2.2A) will result in a rather smooth structural shift of the position of transition state upon perturbation. Detailed analysis of nonlinear REFERs have been widely used to characterize the shape of free energy barriers and to elucidate reaction mechanisms in organic chemistry and of complex biochemical reactions like the catalytic mechanisms of enzymes [2]. In the following, we will discuss how these concepts can be applied to characterize the barriers for protein folding reactions and results from linear and nonlinear REFERs will be presented.

12.2.2.1

Linear Rate Equilibrium Free Energy Relationships in Protein Folding

REFERs for protein folding reactions can be derived using various perturbations. Let us consider the Gibbs fundamental equation

$$\mathrm{d}\Delta G^\circ = \Delta V^\circ \,\mathrm{d}p - \Delta S^\circ \,\mathrm{d}T + \sum \Delta\mu_\mathrm{i}^\circ \,\mathrm{d}n_\mathrm{i} \tag{2}$$

where $\Delta G^\circ, \Delta V^\circ, \Delta S^\circ$, and $\sum \Delta\mu_\mathrm{i}^\circ$ are the differences in Gibbs free energy, volume, entropy, and chemical potential, respectively, between the unfolded and the native states. In protein folding the most common perturbation of chemical potential is the addition of chemical denaturants (D) like urea and guanidinium chloride (GdmCl), which were shown to have a linear effect on ΔG° [7, 8] (see Chapters 3 and 12.1). Including the empirically observed effect of a chemical denaturant, Eq. (2) can be written as

$$\mathrm{d}\Delta G^\circ = \Delta V^\circ \,\mathrm{d}p - \Delta S^\circ \,\mathrm{d}T + m \cdot [\mathrm{D}] \tag{3}$$

Assuming a free energy barrier between the unfolded and the native protein, the Gibbs equation can be applied to the activation free energies of the folding ($\Delta G_\mathrm{f}^{\circ\ddagger}$) and unfolding ($\Delta G_\mathrm{u}^{\circ\ddagger}$) reaction:

$$\mathrm{d}\Delta G_{\mathrm{f,u}}^{\circ\ddagger} = \Delta V_{\mathrm{f,u}}^{\circ\ddagger} \,\mathrm{d}p - \Delta S_{\mathrm{f,u}}^{\circ\ddagger} \,\mathrm{d}T + m_{\mathrm{f,u}} \cdot [\mathrm{D}] \tag{4}$$

since $\Delta G_\mathrm{f}^{\circ\ddagger}$ and $\Delta G_\mathrm{u}^{\circ\ddagger}$ were also shown to be linearly dependent on [D] [9] (see also Chapter 12.1). Combining Eqs (1)–(3) shows that different properties of the transition state and thus different reaction coordinates can be probed by applying REFERs to protein folding. α_p and α_T-values can be obtained by changes in pressure at constant temperature or changes in temperature at constant pressure, respectively [10, 11].

$$\alpha_\mathrm{p} = \frac{\partial\Delta G_\mathrm{f}^{\circ\ddagger}/\partial p}{\partial\Delta G^\circ/\partial p} = \frac{\Delta V_\mathrm{f}^{\circ\ddagger}}{\Delta V^\circ} \tag{5}$$

$$\alpha_\mathrm{T} = \frac{\partial\Delta G_\mathrm{f}^{\circ\ddagger}/\partial T}{\partial\Delta G^\circ/\partial T} = \frac{\Delta S_\mathrm{f}^{\circ\ddagger}}{\Delta S^\circ} \tag{6}$$

This gives information on the volume and on the entropy of the transition state, respectively. From Eq. (6) we can further calculate the change in enthalpy for formation of the transition state using the Gibbs-Helmholtz equation. The value of α_T changes with temperature due to the change in molar heat capacity ($\Delta C_\mathrm{p}^\circ$) typically associated with protein folding reactions [12]. This allows the definition of another reaction coordinate [13]

$$\alpha_C = \frac{\Delta C_{p(f)}^{\circ\ddagger}}{\Delta C_p^{\circ}} \tag{7}$$

α_C allows the characterization of a transition state in terms of its relative solvent exposure, since ΔC_p° mainly arises from differences in interactions of the protein with the solvent [14].

For two-state folding the logarithm of the single observable apparent rate constant, λ ($\lambda = k_f + k_u$) vs. chemical denaturant concentration yields a V-shaped curve [15, 16], commonly called a chevron plot (Figure 12.2.3B, see also Chapter 12.1). This plot gives information on the refolding reaction at low denaturant concentrations (the refolding limb) and information on the unfolding reaction at high denaturant concentrations (the unfolding limb). The V-shaped form of the chevron plot is the result of linear changes in $\Delta G_f^{\circ\ddagger}$ and $\Delta G_u^{\circ\ddagger}$ with denaturant concentration. Since ΔG° is also linearly dependent on denaturant concentration (Figure 12.2.3A), the proportionality constants, m_x, are defined as:

$$m_{eq} = \frac{\partial \Delta G^{\circ}}{\partial [\text{Denaturant}]} \tag{8}$$

$$m_{f,u} = \frac{\partial \Delta G_{f,u}^{\circ\ddagger}}{\partial [\text{Denaturant}]} \tag{9}$$

This allows us to use the m_f- and m_{eq}-values to calculate a denaturant-induced REFER to obtain α_D [9] according to

$$\alpha_D = \frac{\partial \Delta G_f^{\circ\ddagger} / \partial [\text{Denaturant}]}{\partial \Delta G^{\circ} / \partial [\text{Denaturant}]} = \frac{m_f}{m_{eq}} \tag{10}$$

α_D reflects the relative sensitivity of the transition state to changes in denaturant concentration. Since the m_{eq}-value was shown to be proportional to the changes in accessible surface area upon unfolding of the protein [17], α_D is interpreted as the relative amount of accessible surface area buried in the transition state and is expected to correlate with α_C [17].

A practical way to analyze REFERs and to test for linearity is to plot the rate constant for folding (k_f) vs. the equilibrium constant (K_{eq}) determined under the same conditions. The slope of this plot (Leffler plot) gives α_x. As an example, Figure 12.2.3C shows a Leffler plot of the effect of GdmCl concentration on k_f and K_{eq} for tendamistat folding. The refolding and unfolding limbs of the chevron plot for tendamistat are perfectly linear over the complete range of denaturant concentrations (Figure 12.2.3B) and thus also the slope of the Leffler plot is constant between 0 and 8 M GdmCl with an α_D-value of 0.67 $\pm$ 0.02. This indicates that 67% of the change in accessible surface area (ASA) between U and N has already occurred in the transition state. The same results will be obtained by plotting $\Delta G^{\circ\ddagger}$ vs. ΔG°, as in the original Leffler formalism (cf. Figure 12.2.5). However, calculation of absolute values for $\Delta G_f^{\circ\ddagger}$ requires the knowledge of the pre-exponential fac-

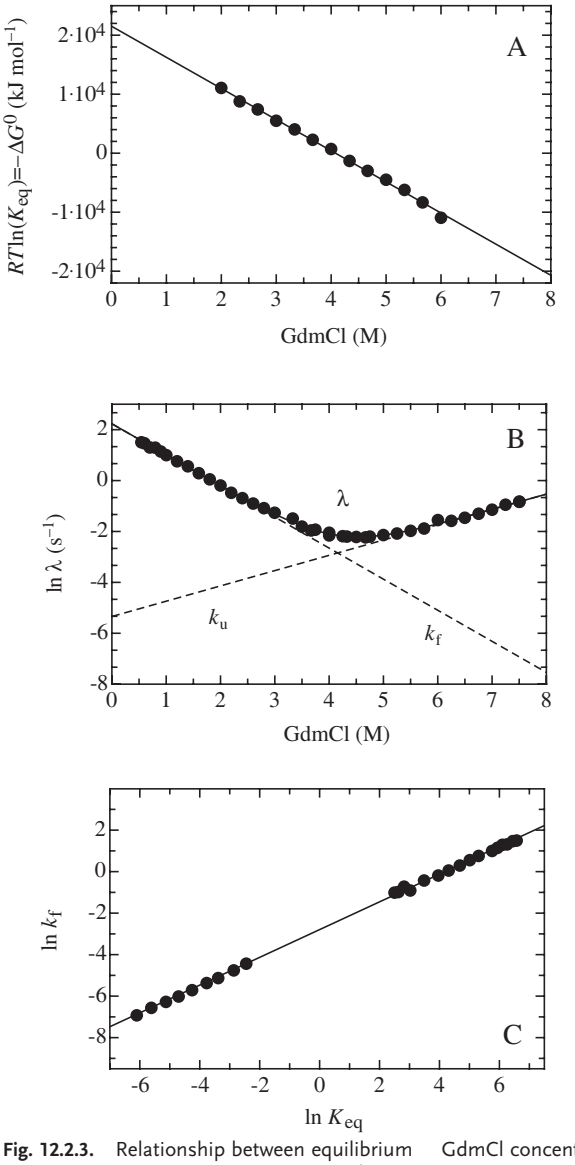

Fig. 12.2.3. Relationship between equilibrium (ΔG°) and activation free energies ($\Delta G^{\circ\ddagger}$) for tendamistat folding at pH 2. A) Change in $-\Delta G^\circ$ with GdmCl concentration calculated using the equilibrium constant determined from the data shown in Chapter 12.1, Fig. 12.1.2A. B) Effect of GdmCl on the apparent folding rate constant ($\lambda = k_f + k_u$). The V-shaped plot is commonly termed "chevron plot" and allows calculation of k_f and k_u as indicated (cf. Eqs (8) and (9) and Chapter 12.1. C) Leffler plot comparing the effect of GdmCl concentration on the equilibrium constant (K_{eq}) and folding rate constant (k_f) calculated from the data shown in panels A and B. The slope corresponds to the α_D-value and a linear fit (solid line) gives a value of 0.67. The folding rate constant (k_f) under unfolding conditions was calculated from the unfolding rate constant (k_u) using $k_f = K_{eq} \cdot k_u$. Only data from the linear regions of the chevron plot ($|\ln K_{eq}| > 2$) were used since near the minimum of the chevron plot both k_f and k_u significantly contribute to λ.

tor for folding. This will not influence the slope of the Leffler plot but it poses some uncertainty on the absolute value of $\Delta G_f^{\circ\ddagger}$.

Other solvent additives such as alcohols (2,2,2-trifluoroethanol), polyols (glycerol, sugars), salts (Na_2SO_4, NaCl), and D_2O as solvent can also lead to a change in protein stability and can therefore be used to define the corresponding α-values [10, 11] (see Table 12.2.1). Specific ligand binding is another source of changes in protein stability and thus allows characterization of the transition state [9]. Many proteins specifically bind ions, substrates, or cofactors, and all bind hydrogen ions at ionizable side chains, which can be used to compare the effect on kinetics and thermodynamics. The changes in free energy upon binding are commonly proportional to the logarithm of the ligand concentration and can be used to determine an α_L-value [18–23], which represents the ligand-binding ability of the transition state.

Equations (5)–(7) and (10) can be considered as medium- or solvent-induced REFERs. A detailed structural information on interactions formed in the transition state can be obtained by analyzing structure-induced REFERs [16, 24, 25], which compare the effect of amino acid replacements introduced by site-directed mutagenesis on $\Delta G_f^{\circ\ddagger}$ and ΔG°.

$$\alpha_S = \phi_f = \frac{\partial \Delta G_f^{\circ\ddagger}/\partial \text{Structure}}{\partial \Delta G^\circ/\partial \text{Structure}} \tag{11}$$

α_S, which is commonly called ϕ_f in protein folding, reports on the energetics of the interactions formed by a side chain with the rest of the protein in the transition state relative to the native state (see Chapter 13). The free energy of the unfolded state serves as a reference. Usually, only a single-point mutation is made at an individual position to calculate a ϕ_f-value, which is a major source for uncertainty in ϕ_f-value analysis and does not allow to test for linearity in the REFER [26]. To gain more detailed information on the interactions in the transition state of a certain amino acid side chain, multiple mutations at the same site should be analyzed in a Leffler plot. Figure 12.2.4 shows a Leffler plot of 14 mutations at position 24 of the fyn SH3 domain. The data reveal a linear REFER over a 400-fold change in K_{eq} (16 kJ mol^{-1} change in protein stability) and give a ϕ_f-value (slope of the plot) of 0.33 ± 0.01. Similar results were obtained for two other sites in SH3 domains [26–28]. In addition to analyzing ϕ_f-values for a single residue (ϕ_f^i), information on larger parts of the protein can be obtained by determining the ϕ_f-value using all residues in a protein [29] ($\langle \phi_f^{prot} \rangle$; Figure 12.2.5) or in substructures such as subdomains or individual secondary structure elements [30].

It should be noted that the type of REFERs described here are commonly termed ''Brønsted plots'' in protein folding literature, which is misleading. ''Brønsted plots'' were originally used to relate the effect of a change in the rate constant of an acid- or base-catalyzed reaction to the dissociation constant of the catalyst [31]. The rate equilibrium relationships considered here are rather Leffler-type relationships, since they directly relate the rate constants of a reaction to the equilibrium constants of the *same* reaction [3].

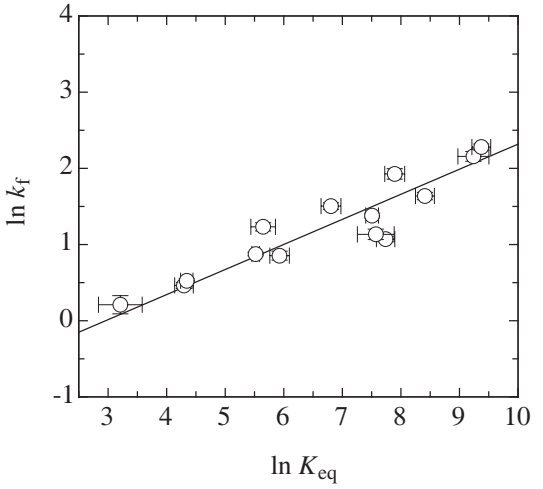

Fig. 12.2.4. Structure-induced Leffler plot for multiple mutations at position 24 of the fyn SH3 domain. The line corresponds to a linear fit of the data and gives a slope (ϕ_f-value) of 0.33 ± 0.01. The relationship between k_f and K_{eq} is linear over the complete stability range indicating negligible effect of the mutations on transition state structure even for highly destabilizing mutants. Data were taken from Ref. [28] and the plot was adapted from Ref. [26].

12.2.2.2

Properties of Protein Folding Transition States Derived from Linear REFERs

The most popular REFER in protein folding studies is the study of the effect of denaturants on rate and equilibrium constants (see Figure 12.2.3). Experimentally

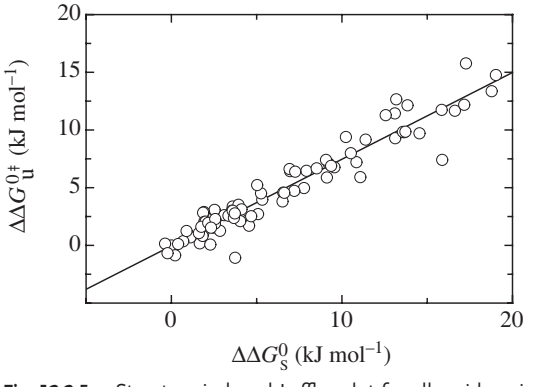

Fig. 12.2.5. Structure-induced Leffler plot for all residues in CI2 to determine the average ϕ_f-value ($\langle\phi_f\rangle$). The line represents a linear fit of the data. Since $\Delta G_u^{\circ\ddagger}$ is plotted vs. ΔG_S° the slope corresponds to $1 - \langle\phi_f\rangle$. The plot was adapted from Ref. [26] and data were taken from Ref. [30].

determined α_D-values are usually native-like with values between 0.6 and 1, indicating that protein folding transition states have a rather native-like ASA. Temperature and pressure have less frequently been used to determine REFERs in protein folding and are more difficult to interpret since both have large and compensating effects on the solvent, on the protein and on solvent–protein interactions. The most straightforward parameter to interpret is the α_C-values derived from heat capacity changes (Eq. (7)), which reflects the interactions of the solvent (water) with the protein. All reported α_C-values are also native-like but generally slightly lower than α_D-values. Analysis of the effect of temperature further revealed both entropic and enthalpic contributions to protein folding barriers at room temperature. However, due to the large changes in $\Delta C^{\circ\ddagger}_{p(f)}$ these values are strongly temperature dependent. Even fewer data are available for the effect of pressure on protein folding transition states. High-pressure stopped-flow measurements on tendamistat revealed a rather native-like volume of the transition state with an α_p-value of 0.6, which increases with increasing denaturant concentration (see Section 12.2.3.1).

Structural information on the properties of transition states from ϕ_f $(= \alpha_S)$-value analysis has been obtained for several proteins (see Chapter 13). A major problem in these studies is the small data set at a single position with usually just a single mutation and the wild-type protein determining a REFER. It was recently shown that ϕ_f-values from such a two-point analysis are highly inaccurate if the stability change of a mutation ($\Delta\Delta G^\circ_S$) is smaller than 6–7 kJ mol^{-1} [26]. This uncertainty is in part due to intrinsic statistical errors, which should, however, give reliable ϕ_f-values for $|\Delta\Delta G^\circ_S| > 3$ kJ mol^{-1} for high-quality data sets [26]. The additional uncertainty in ϕ_f-values probably arises from changes in the structure of the unfolded state, which is observed in many mutants [11, 26] (see Section 12.2.4.1). This not only changes the structure of the ground state but very likely also influences the pre-exponential factor for folding by changing the dynamics of the unfolded state [32, 33]. The contributions from these effects will be more pronounced for mutations with small $|\Delta\Delta G^\circ_S|$ [26].

The results from reliable ϕ_f-values give a picture of transition states as distorted native states for the major part of a protein (diffuse transition states) or for large substructures (polarized transitions states). For diffuse transition states the ϕ_f-values are around 0.1–0.5 throughout the structured regions of the protein and average ϕ_f-values are between 0.2 and 0.4, indicating partial formation of the native set of interactions [26]. For these proteins a Leffler plot of all mutations throughout the protein usually gives a linear REFER supporting a structurally homogeneous transition state (Figure 12.2.5). In proteins with polarized transition states ϕ_f-values are significantly higher (up to 0.8) in a large substructure of a protein whereas they are 0 or close to 0 in other parts. These results suggest that the formation of the native topology for the whole protein or for a large substructure of the protein is a major part of the rate-limiting step in folding of small single domain proteins and might explain the correlation between the contact order and protein folding rate constants [34, 35]. The results contradict a nucleation-condensation model with a small structural nucleus formed by a few specific interactions in the transition state [36].

In ϕ_f-value analysis structural changes are typically introduced in amino acid side chains and the results consequently report on side-chain interactions although they are commonly interpreted in terms of secondary structure. Replacement of alanine by glycine residues, which leads to a more flexible backbone, was recently suggested to give information on the backbone interactions in the transition state [37]. However, side-chain interactions may also be changed upon replacing an amino acid by glycine and it thus questionable whether these ϕ_f-values are indicative of secondary structure formation. To gain more information on the secondary structure in protein folding transition states it will be necessary to introduce isosteric changes into the amino acid backbone. A backbone ϕ_f-value analysis using cytochrome *c* as well as monomeric and dimeric versions of GCN4 investigated amide deuterated proteins and gave ϕ_f-values around 0.5. This was interpreted as formation of 50% of the hydrogen bonds in the transition state [38]. However, this result is also compatible with formation of all native backbone hydrogen bonds at reduced strength, which would be compatible with the results on the diffuse nature of protein transition states from side chain ϕ_f-value analysis [26]. This discussion reveals a major problem in the quantitative interpretation of fractional ϕ_f-values, which may originate in formation of partial interactions in a single ensemble of transition states or in parallel pathways with different degrees of structure formation in the different transition states. However, there is no evidence for parallel pathways in the majority of proteins (see Section 12.2.4.2), which, for most proteins, favors the model of a native-like transition state topology throughout the protein with weakened interactions [26, 34, 35]. However, as discussed in Section 12.2.4.2, parallel pathways would be difficult to detect if they have similar α_x-values [11].

12.2.3
Nonlinear Rate Equilibrium Free Energy Relationships in Protein Folding

As pointed out above, the characterization of nonlinear REFERs can give information on various properties of the transition barriers. In the following we will first describe methods to detect and to analyze nonlinearities in REFERs and will then discuss the possible origins of nonlinear REFERs in more detail. Finally, results from nonlinear REFERs will be discussed in terms of general properties of protein folding barriers.

12.2.3.1
Self-Interaction and Cross-Interaction Parameters

Jencks and coworkers [5] proposed self-interaction and cross-interaction parameters as practical ways to detect and to analyze nonlinear REFERs. A self-interaction parameter (p_x) is the direct measure for a curvature in a REFER caused by a shift in the position of the transition state along the reaction coordinate with changing ΔG° upon a perturbation ∂x:

$$p_x = \frac{\partial \alpha_x}{\partial \Delta G_x^\circ} = \frac{\partial^2 \Delta G^{\circ\ddagger}}{(\partial \Delta G_x^\circ)^2} \tag{12}$$

By definition, a shift in the position of the transition state towards the destabilized state (e.g., as a result of Hammond behavior or due to sequential barriers) will give a positive p_x-value.

For a folding reaction perturbed by addition of denaturant or destabilized by mutations, the corresponding self-interaction parameters p_D and p_S are [10, 11]:

$$p_D = \frac{\partial \alpha_D}{\partial \Delta G_D^\circ} = \frac{\partial^2 \Delta G^{\circ\ddagger}}{(\partial \Delta G_D^\circ)^2} \tag{13}$$

$$p_S = \frac{\partial \phi_f}{\partial \Delta G_S^\circ} = \frac{\partial^2 \Delta G^{\circ\ddagger}}{(\partial \Delta G_S^\circ)^2} \tag{14}$$

Thus, in the denaturant-induced Leffler plot shown in Figure 12.2.3C, a positive p_D-value will result in a downward curvature (transition state becomes more native-like with decreasing protein stability) and a negative p_D-value would result in an upward curvature. The same curvatures would consequently be observed in the chevron plots.

The use of self-interaction parameters in the analysis of transition state movements is often not sensitive enough, because the energy range of the measurements is too narrow or the curvatures are too small [5]. A more sensitive test for transition state movements is provided by cross-interaction parameters [5], which measure changes in the position α_x of the transition state of a reaction (measured using the perturbation ∂x) caused by a second perturbation ∂y:

$$p_{xy} = \frac{\partial \alpha_x}{\partial \Delta G_y^\circ} = \frac{\partial^2 \Delta G^{\circ\ddagger}}{(\partial \Delta G_x^\circ)(\partial \Delta G_y^\circ)} = \frac{\partial \alpha_y}{\partial \Delta G_x^\circ} = p_{yx} \tag{15}$$

For nonlinear REFERs the value of α_x changes with the amount of a second perturbation ∂y, resulting in a nonzero p_{xy}-value. A shift in the position of the transition state towards the destabilized state will yield positive p_{xy}-values.

For tendamistat, the denaturant dependence of the folding reaction was measured at different pressures [39]. This allowed the calculation of the pressure/denaturant cross-interaction parameter (p_{Dp}). Figure 12.2.6 shows equilibrium transition curves and chevron plots at pressures between 20 and 1000 bar. Increasing pressure destabilizes tendamistat leading to a shift of the GdmCl-induced unfolding transition to lower GdmCl concentrations (Figure 12.2.6A) and indicating that the native state has a larger volume than the unfolded state. Interestingly, the volume of the transition state exceeds the volume of the native state at high denaturant concentrations as indicated by a decrease in the unfolding rate constant with increasing pressure above 5 M GdmCl (Figure 12.2.6B). This scenario is not treated in the original Leffler formalism, which assumes that the properties of the transition state are between those of the reactants and the products. The

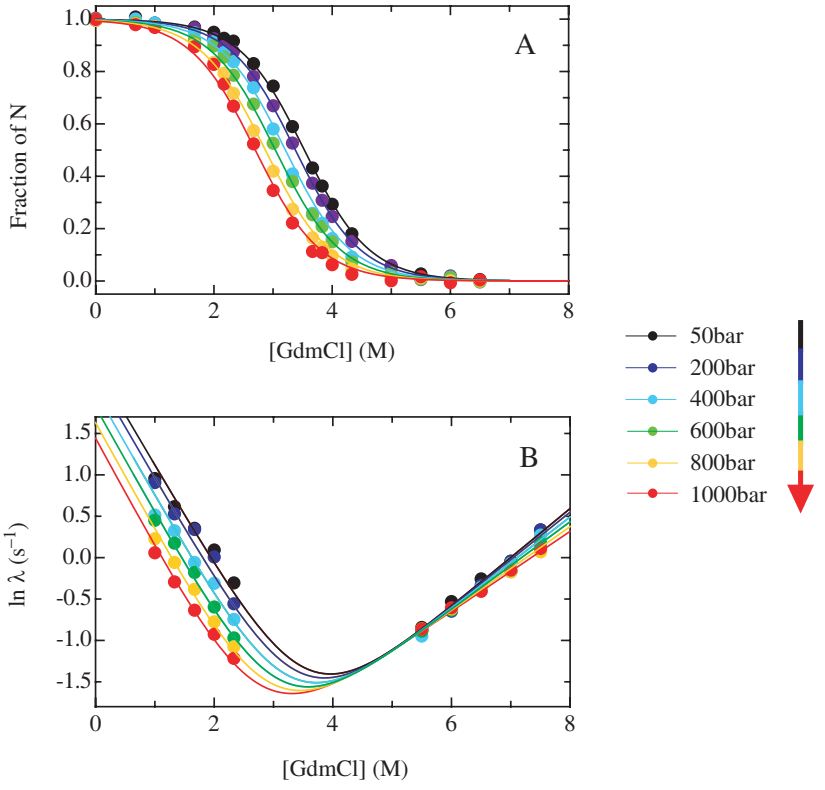

Fig. 12.2.6. Effect of pressure on A) the GdmCl-induced unfolding transition and B) the GdmCl dependence of the apparent rate constant for tendamistat folding at pH 2. The lines represent global fits of the data with $\partial m_f/\partial p = \partial \Delta V_f^{\circ\ddagger}/\partial[\text{GdmCl}] = 2.5 \pm 0.6$ cm^3 mol^{-1} M^{-1}. Data and fits were taken from Ref. [39].

denaturant/pressure-induced nonlinear activation free energy relationships in tendamistat indicate a transition state movement towards a less solvent-exposed structure when the protein is destabilized [39]. The data were used to calculate the denaturant/pressure cross-interaction parameter

$$p_{Dp} = \frac{\partial \alpha_D}{\partial \Delta G_p^\circ} = \frac{\partial^2 \Delta G^{\circ\ddagger}}{(\partial \Delta G_p^\circ)(\partial \Delta G_D^\circ)} = \frac{\partial \alpha_p}{\partial \Delta G_D^\circ} = p_{pD} \tag{16}$$

Figure 12.2.7 shows the effect of $\partial \Delta G_p^\circ$ on the α_D-value for the denaturant/pressure-dependent folding data shown in Figure 12.2.5. The α_D-value increases significantly with decreasing stability indicating a positive p_{Dp}-value (Figure 12.2.7A). Figure 12.2.7B shows that the effect of $\partial \Delta G_p^\circ$ is only observed in the kinetic m-values while m_{eq} is unchanged due to compensating changes in m_f and m_u. This indicates a true denaturant/pressure-induced transition state movement.

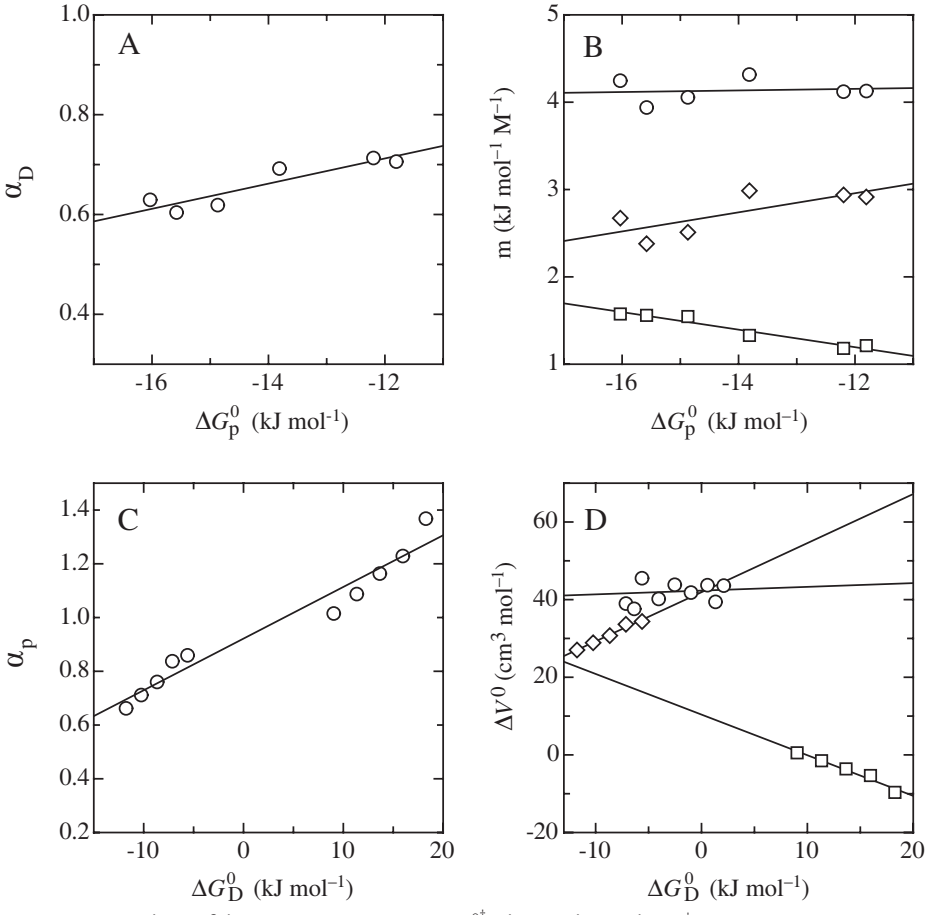

Fig. 12.2.7. Analysis of the pressure-denaturant cross-interaction parameter p_{pD} and p_{Dp} for tendamistat folding at pH 2 (see Figure 12.2.6). Panels A and B show the effect of $\partial\Delta G_p^\circ$ on α_D (A) and on m_{eq} (open circles), m_f (diamonds), and m_u (squares), respectively. Panels C and D show the effect of $\partial\Delta G_D^\circ$ on α_p (C) and on ΔV° (circles), $\Delta V_f^{\circ\ddagger}$ (diamonds), and $\Delta V_u^{\circ\ddagger}$ (squares), respectively. As expected for real Hammond behavior, the same effect is observed for $\partial\alpha_D/\partial\Delta G_p^\circ \partial\alpha_p/\partial\Delta G_D^\circ$ and for $\partial\alpha_p/\partial\Delta G_D^\circ$, i.e., $p_{pD} = p_{Dp}$; $V = 0.025 \pm 0.006$ mol/kJ. The original data used to construct the cross-interaction parameters are shown in Figure 12.2.6 and were taken from Ref. [39].

As postulated by Eq. (16) the same effect is observed when the effect of $\partial\Delta G_D^\circ$ on the α_p-value is analyzed (Figure 12.2.7C,D). Here a change in α_p is caused by compensating changes in $\Delta V_f^{\circ\ddagger}$ and $\Delta V_u^{\circ\ddagger}$ with constant ΔV°.

In mutational studies the changes in $\Delta G^{\circ\ddagger}$ and ΔG° are usually determined as a function of the denaturant concentration for each mutant. This directly allows the calculation of the denaturant/structure cross-interaction parameter (p_{DS}) [10, 11].

$$p_{DS} = \frac{\partial \alpha_D}{\partial \Delta G_S^\circ} = \frac{\partial^2 \Delta G^{\circ\ddagger}}{(\partial \Delta G_S^\circ)(\partial \Delta G_D^\circ)} = \frac{\partial \phi_f}{\partial \Delta G_D^\circ} = p_{SD} \tag{17}$$

p_{DS} tests whether changes in the stability of the native state caused by mutations ($\partial \Delta G_S^\circ$) have an effect on the relative solvent exposure of the transition state for folding (α_D).

If the effect of a change in structure by mutation is tested in the background of the wild type (∂Structure) and of another variant (∂Structure′), we can calculate a structure/structure cross-interaction parameter.

$$p_{SS'} = \frac{\partial \phi_f^S}{\partial \Delta G_{S'}^\circ} \tag{18}$$

$p_{SS'}$ indicates whether ϕ_f ($= \alpha_S$) changes when the protein stability is altered by an additional mutation [10, 11, 40].

These considerations show that various self-interaction and cross-interaction parameters can be used to detect and to analyze nonlinear REFERs along different reaction coordinates. In the following, several possible origins of nonlinear REFERs will be discussed.

12.2.3.2 Hammond and Anti-Hammond Behavior

According to the Hammond postulate the position of a transition state is shifted towards the ground state that is destabilized by the perturbation. Accordingly, α_x increases if the native state is destabilized relative to the unfolded state, which will lead to curvatures in REFERs. In principle, Hammond behavior should be observed for any transition state. If the free energy landscape in the vicinity of the transition state is a broad and smoothly curved maximum, α_x will be strongly influenced by changes in protein stability [5] (Figure 12.2.2A). If the transition region represents a rather narrow free energy maximum on the reaction coordinate, the changes in α_x will usually be too small to be detected experimentally [5] (Figure 12.2.2B). The sensitivity of α_x to changes in protein stability can thus be used to obtain information on the broadness of the free energy barriers.

It is worth discussing Thornton's theoretical explanation of transition state movements [41]. It assumes that the transition state is a saddle point in the energy landscape of the reaction. It represents an energy maximum in the direction of the reaction coordinate and an energy minimum in all other directions. A second assumption is that the potential for each vibrational mode of the molecule can be approximated by a quadratic function. The vibration of the reacting bond(s), the one(s) that are formed or broken in the reaction, is considered to be parallel to the reaction coordinate. Since the transition state is located at a maximum of the parabolic potential along the reaction coordinate, it will shift towards the destabilized state if a linear free energy perturbation is applied (Figure 12.2.2A). All other vibra-

tional modes of the molecule are considered to be perpendicular to the reaction coordinate. For those, the transition state is at the minimum of the parabolic potential, which will shift towards the stabilized side of the coordinate if a linear perturbation is applied (Figure 12.2.2B). These are the two ''reacting bond rules'' in the IUPAC nomenclature [42], which are sometimes referred to as ''Hammond effect'' and ''anti-Hammond effect.'' The effect of the perturbation on the structure of the transition state will be the sum of the individual effects on all coordinates. This theory is valid for any transition state along the reaction coordinate and does not require the product to have nearly the same energy content as the transition state. Significant movements of the transition state (i.e., both Hammond and anti-Hammond behavior) are thus expected if the energy landscape around it has a smooth curvature and different regions become limiting after a perturbation [5] (e.g., in reactions taking place with a continuum of mechanisms or when the free energy would consist of a continuum of consecutive states with different structure but similar free energy) (Figure 12.2.2A). A perturbation will not yield an observable change in the position of the maximum along the coordinate if the transition state of a reaction is a narrow free energy maximum in the reaction coordinate (Figure 12.2.2B). In organic reactions the transition state movements probed by different perturbations can be decoupled (i.e., a certain p_x or p_{xy} can have a positive value while others are zero). For these reactions the experimental reaction coordinates x and y describe the formation or breakage of different covalent bonds in a very direct way and thus x and y can change from totally synchronous to totally asynchronous [5]. In protein folding many noncovalent protein–protein, protein–solvent, and solvent–solvent interactions are formed and broken during the reaction and many ''microscopic'' reaction coordinates are averaged into the various ''macroscopic'' α_x-values, which therefore are likely to be highly correlated. Thus, the different p_x- and p_{xy}-values should generally be coupled in protein folding reactions if they are due to global structural changes in the transition state (i.e., transition state movements should be observable with independent perturbations) [10].

12.2.3.3 Sequential and Parallel Transition States

Nonlinear REFERs provide a unique tool to characterize complex transition state regions and especially to distinguish between sequential and parallel reaction pathways [1]. If destabilization of the native state leads to a shift in the rate-limiting step to a more native-like transition state (larger α_x; Figure 12.2.2C) a discrete change in α_x-value will be observed. This will lead to downward kink in the chevron plot and consequently also in the Leffler plot (positive p_D-value). Such a behavior implies that an on-pathway high-energy intermediate is ''hidden'' on the free energy landscape, which is not directly detectable due to its low stability relative to the native and unfolded state (see Figure 12.2.2C). Figure 12.2.9A shows chevron plots between 5 °C and 45 °C for a tendamistat variant that exhibits a nonlinear unfolding limb. The α_D-value changes from 0.4 at low denaturant concentration

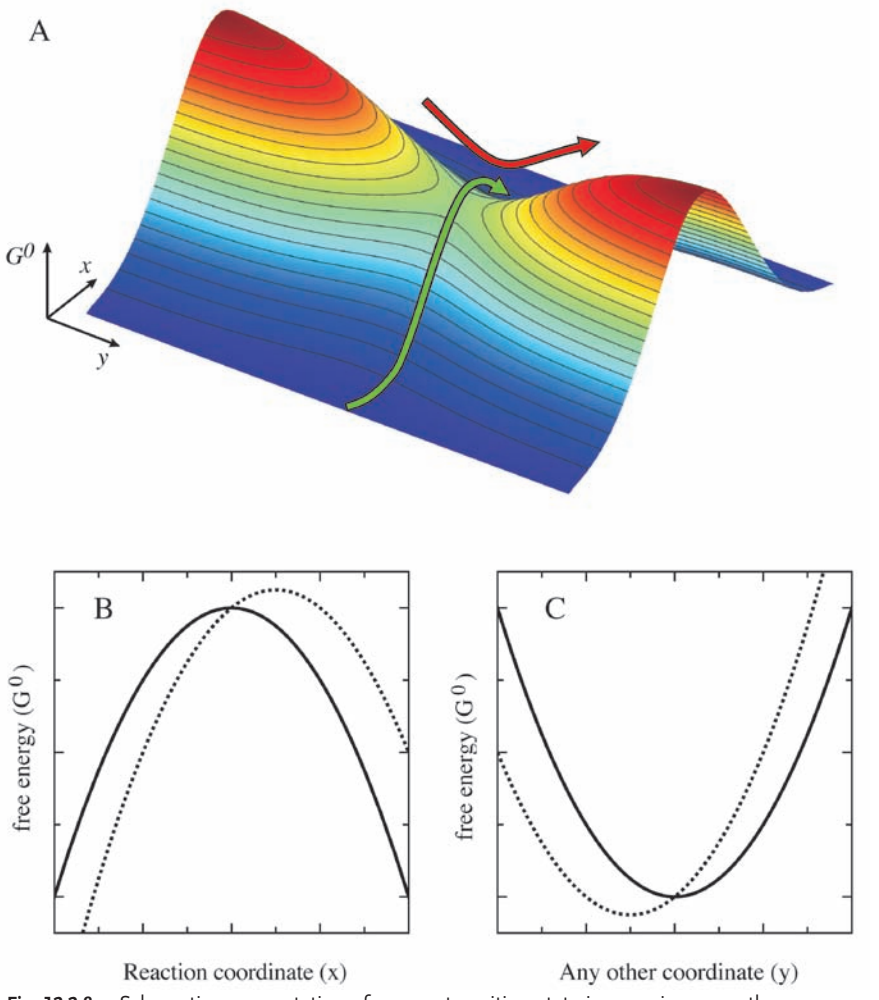

Fig. 12.2.8. Schematic representation of a simple transition region (A) and illustration of Thornton's first (B) and second reacting bond rule (C). The energy landscape in the vicinity of a transition state is approximated by a parabolic potential, both before (continuous line) and after (dotted line) a linear perturbation. B) In the direction of the reaction coordinate (green trajectory in panel A) the transition state is a maximum on the energy landscape, which will shift towards the state that is destabilized. C) In a direction perpendicular to the reaction coordinate (red trajectory in panel A) the transition state is a minimum on the energy landscape, which will shift towards the state that is stabilized. Panels B and C were adapted from Ref. [41].

(< 2 M GdmCl) to 0.9 at high denaturant concentrations (>5 M GdmCl). At high and low denaturant concentrations the chevron plots are linear, indicating a denaturant-induced switch between two distinct transition states [43]. This suggests a sequential folding model with consecutive transition states and a metastable high

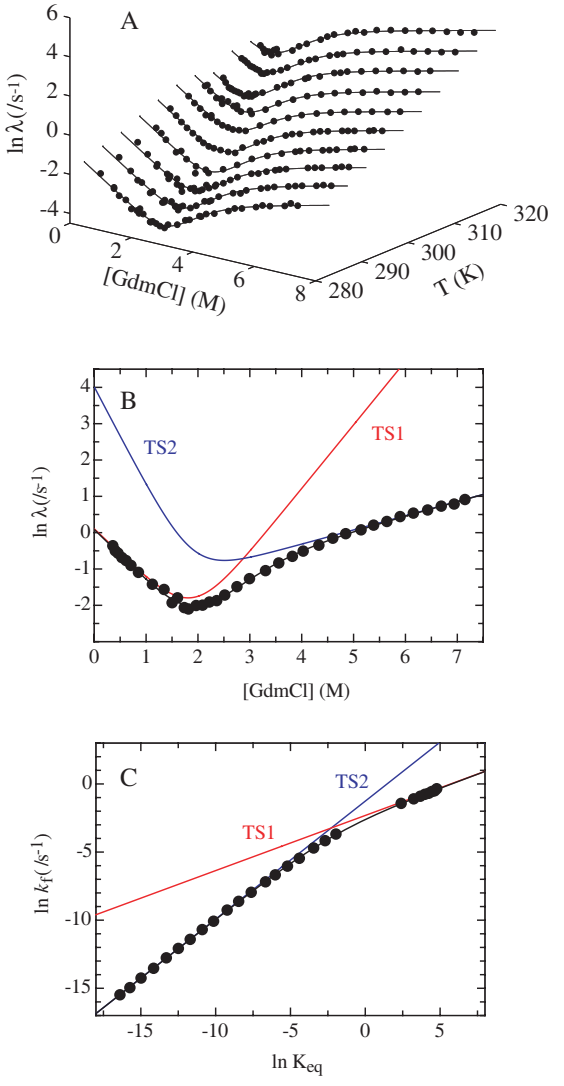

Fig. 12.2.9. Nonlinear rate equilibrium free energy relationship for folding of the tendamistat C45A/C73A variant caused by two consecutive transition states with a high-energy intermediate (cf. Figure 12.2.2C.). A) Temperature dependence of the chevron plots indicating a kink in the unfolding limb. B) Chevron plot at 25 °C. The black line represents a fit to a linear three-state mechanism with a high-energy intermediate (see Chapter 12.1). The thin lines represent hypothetical chevron plots for two-state folding limited either by the early transition state (TS1) of the late transition state (TS2). Plots were adapted from Ref. [43]. C) Leffler plot of the data shown in panel B. The kink in the chevron plots causes a downward kink in the Leffler plot. The red and the blue lines represent hypothetical Leffler plots for the early transition state (TS1 with $\alpha_D = 0.45$) and for the late transition state (TS2 with $\alpha_D = 0.88$), respectively. The folding rate constants (k_f) under unfolding conditions were calculated from the unfolding rate constant (k_u) using $k_f = K_{eq} \cdot k_u$. Data in the region $|\ln K_{eq}| < 2.5$ were not used since here both k_f and k_u significantly contribute to the apparent rate constant (λ).

energy intermediate (Figure 12.2.2B). Figure 12.2.9B shows the chevron plot at 25 °C with the fit of the data to a three-state model with a high-energy intermediate (see Chapter 12.1). This allows information to be gained on both transition states. Figure 12.2.9C shows the same data displayed as a Leffler plot, also showing a clear kink in the slope from 0.4 to 0.9 from going from low to high protein stability. Thus, a kink in the Leffler plot with a positive p_x value provides a simple way to show that an intermediate is on-pathway if the intermediate is higher in free energy than the unfolded and the native state. As discussed in Chapter 12.1, an on-pathway intermediate is more difficult to distinguish from an off-pathway intermediate when it is more stable than the unfolded state and thus becomes populated to detectable amounts. Depending on the α-values of the consecutive transition states and on the rate constants it might be difficult to distinguish a kink from a gradual shift in the position of the transition state caused by Hammond behavior.

If folding occurs through parallel pathways, the reaction with the most native-like transition state will be most sensitive to a reduced stability of the native state and an alternative parallel pathway with a more unfolded-like transition state may become rate limiting with increasing denaturant concentrations. This will lead to a decrease in α_x with decreasing protein stability resulting in a negative p_x-value. Thus parallel pathways will lead to an upward kink in the chevron plot (Figures 12.2.10A,B) and consequently also in the Leffler plot (Figure 12.2.10C,D) [11]. This phenomenon is sometimes referred to as anti-Hammond behavior in the protein folding literature [30, 44] but should be clearly distinguished from genuine anti-Hammond behavior discussed in Section 12.2.3.2, which is based on the property of a single barrier (see Figure 12.2.8).

12.2.3.4
Ground State Effects

Changes in the length of the reaction coordinate due to structural changes in the native or unfolded protein caused by the effects of a mutation or by a change in solvent conditions (ground state effects) can easily be mistaken for genuine transition state movement [6, 10, 11]. Both phenomena have similar effects on the experimentally observable REFERs in Leffler plots but they are based on completely different free energy barriers. Figure 12.2.11 illustrates the difference between Hammond behavior and ground state effects, showing as an example the effect of a change in protein stability caused by mutations ($\partial\Delta G^\circ_S$) on the location of the transition state in terms of its ASA measured in Chevron plots (α_D-value). This corresponds to the determination of a structure/denaturant cross-interaction parameter (p_{SD}) defined in Eq. (17). The reference conditions of the wild-type protein are given in Figure 12.2.11D. In the case Figure 12.2.11B the mutation leads to a transition state movement along the reaction coordinate relative to both ground states. The length of the reaction coordinate is unchanged (i.e., the structure of both ground states is not affected by the mutation, or both states are affected to the same extent). This scenario is in accordance with Hammond behavior if we as-

sume that the native state is destabilized by the mutation. Figure 12.2.11C and D show apparent transition state movements caused by ground state effects. In both cases the absolute position and the structure of the transition state remains unchanged but the structure of either the unfolded state (Figure 12.2.11C) or of the native state (Figure 12.2.11D) changes, which leads to a change in length of the reaction coordinate. In this case an apparent transition state movement will be observed if the position of the transition state is normalized against the length of the reaction coordinate. This demonstrates that the characterization of transition state movements requires the determination of the effects of a perturbation on the rate constants for the forward and backward reaction, on the equilibrium constant and on the length of the reaction coordinate. The effect on the length of the reaction coordinate can easily be tested by determining the effect of ∂x on the respective equilibrium properties. In the case discussed above, the length of the reaction coordinate is reflected by m_{eq}.

The same considerations apply for other self- and cross-interaction parameters. For pressure- and temperature-induced REFERs the length of the reaction coordinate can be tested by determining the effect of ΔV°, and $\Delta S^\circ/\Delta C_p^\circ$, respectively. Changes in these parameters with ∂x indicate ground state effects induced by the change in conditions or by mutation. Structural changes in the unfolded state should also be detectable by NMR spectroscopy. However, it would be very time consuming to determine NMR structures of the unfolded state of each mutant and would not directly allow a correlation with the observed ground state effects, since they are defined by changes in free energy.

Figure 12.2.12 shows the results of a test for ground states effects and transition state movement in mutants of the Sso7d SH3 domain (Figure 12.2.12 upper panels) and for CI2 (Figure 12.2.12 lower panels). The effect of a change in ΔG° induced by mutations ($\partial \Delta G_S^\circ$) on the α_D-values and on the m_{eq}-, m_f-, and m_u-values are shown. Both proteins show increasing α_D-values with decreasing protein stability in accordance with Hammond behavior. However, the origins for the changing α_D-values are different in the two proteins. In the SH3 domain the m_{eq}-value changes significantly upon mutation, indicating structural changes it at least one of the ground states. The value of m_f changes by the same amount as m_{eq} while m_u is essentially independent of protein stability. This is seen more clearly in a plot of m_f and m_u vs. m_{eq}, which shows that m_f correlates with m_{eq} whereas m_u is virtually independent of m_{eq} (Figure 12.2.13A). This indicates that the structure of the transition state does not move relative to the structure of the native state (cf. Figure 12.2.11). The increase in m_{eq}- and m_f-values point at the disruption of interactions in the unfolded state upon mutation which leads to a less compact unfolded state. These results show that the apparent shift in the position of the transition state along the reaction coordinate seen for the SH3 domain is a ground state effect on the unfolded state rather than Hammond behavior. Structural changes in the unfolded state can be rationalized in the light of recent results on residual structure of unfolded proteins (see Section 12.2.4.1). These interactions may be disrupted by mutations and thus lead to changes in the m_{eq}-values [11].

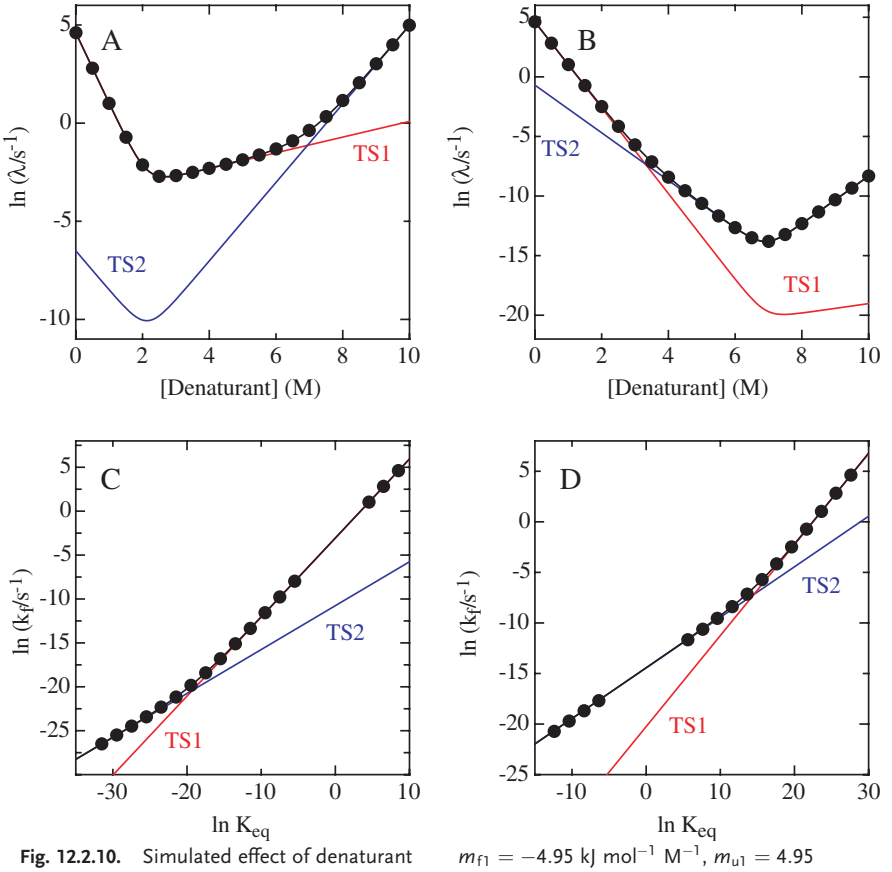

Fig. 12.2.10. Simulated effect of denaturant concentration on the apparent rate constant (filled circles and black line) for the folding of a protein through two parallel pathways with the transition states TS1 and TS2. The individual chevron plots corresponding to folding over TS1 and TS2 are shown. For two parallel pathways with the folding and unfolding rate constants of k_{f1}, k_{u1} (for TS1) and k_{f2}, k_{u2} (for TS2) the single observable rate constant (λ) is given by the sum of the two apparent rate constants ($\lambda_1 = k_{f1} + k_{u1}$ and $\lambda_2 = k_{f2} + k_{u2}$) for the parallel pathways: $\lambda = \lambda_1 + \lambda_2$. Data were simulated with the rate constants for folding and unfolding of A) $k_{f1} = 0.0015\ s^{-1}$, $k_{u1} = 3 \cdot 10^{-7}\ s^{-1}$; $k_{f2} = 100\ s^{-1}$; $k_{u2} = 0.02\ s^{-1}$ and B) $k_{f1} = 5\ s^{-1}$, $k_{u1} = 3 \cdot 10^{-7}\ s^{-1}$; $k_{f2} = 100\ s^{-1}$; $k_{u2} = 0.02\ s^{-1}$. The m_i-values ($m_i = RT(\partial \ln k_i / \partial[\text{Denaturant}])$) were $m_{f1} = -4.95$ kJ mol^{-1} M^{-1}, $m_{u1} = 4.95$ kJ mol^{-1} M^{-1}; $m_{f2} = -8.92$ kJ mol^{-1} M^{-1}; $m_{u2} = 0.99$ kJ mol^{-1} M^{-1} in both cases. This corresponds to α_D-values of 0.5 and 0.9 for TS1 and TS2, respectively. The plots show that significantly different α_D-values for the two parallel pathways are required to obtain a clear nonlinearity. Panels C and D show Leffler plots of the data displayed in panels A and B, respectively. Both Leffler plots show a clear upward kink indicating the shift between the two parallel pathways. The red and blue lines represent hypothetical Leffler plots for the two parallel pathways with α_D-values of 0.5 (TS1) and 0.9 (TS2). Data in the region $|\ln K_{eq}| < 2.5$ were not used since here both k_f and k_u significantly contribute to the apparent rate constant (λ).

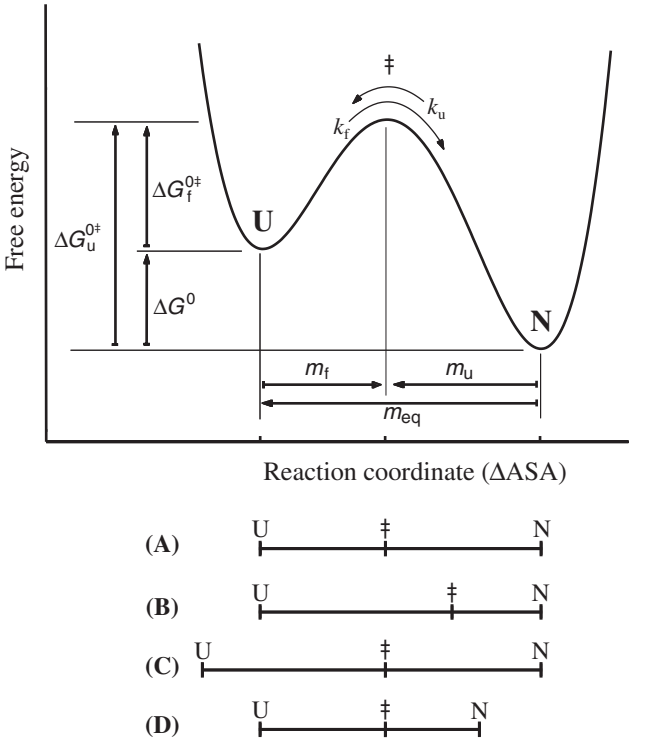

Fig. 12.2.11. Schematic representation of the possible effect of a perturbation on the position of the ground states and on the transition state along a reaction coordinate probed by the change in denaturant concentrations (∂[Denaturant]). The reference conditions (A) are compared with real Hammond behavior (B) and with apparent transition state movements caused by ground state effects due to changes in the structure of the unfolded (C) and native state (D). In all three cases (B–D) the position of the transition state will change by the same amount relative to the ground states (i.e., identical $p_{DS} = \partial\alpha_D/\partial\Delta G_S^\circ$ values). However, for genuine Hammond behavior (B) m_{eq} will not be affected by mutation and m_f and m_u will show compensating changes. Changes in the ASA of the ground states (C, D) will lead to changes in m_{eq}.

In CI2 a change in stability results in opposing effects on m_f and m_u accompanied by a significant change in the m_{eq}-values. The small change in m_u indicates a minor transition state movement in addition to a large ground state effect. As for the SH3 domain, m_f correlates with m_{eq} whereas m_u is independent of m_{eq}, indicating that mutations in CI2 also change the structure of the unfolded state with little effect on native state and transition state (Figure 12.2.13C). An example for genuine transition state movement without additional ground state effects is the nonzero pressure/denaturant cross-interaction parameter for tendamistat folding shown in Figures 12.2.6 and 12.2.7. Here the ΔV° and m_{eq} are independent of denaturant concentration and pressure, respectively.

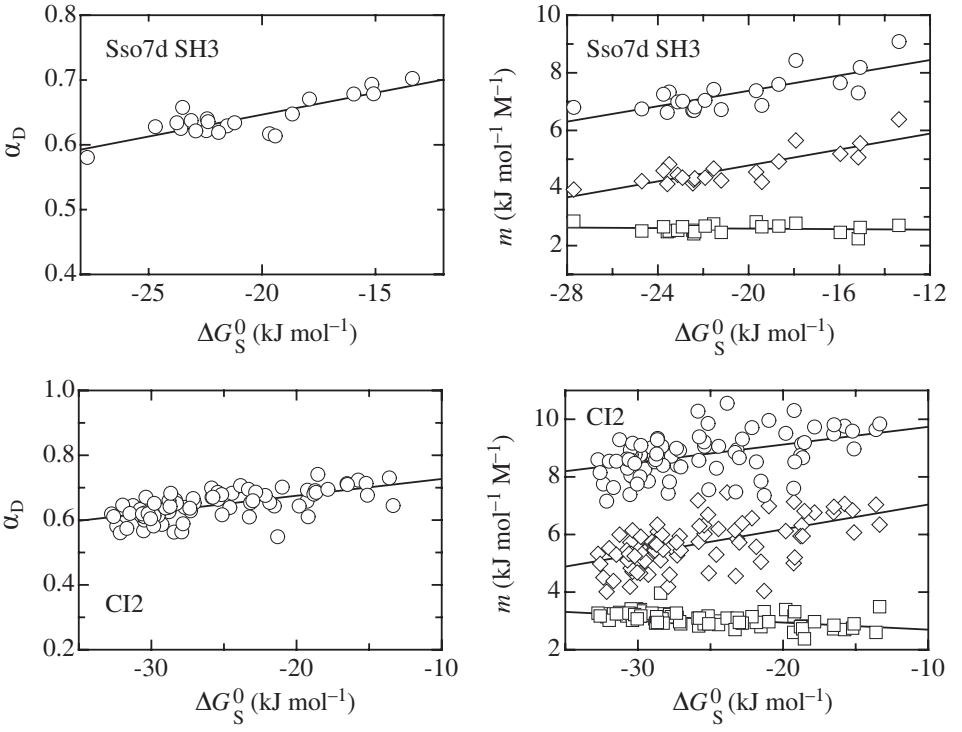

Fig. 12.2.12. Effect of changes in ΔG°_S on α_D (left panels) and on m_{eq} (open circles), m_f (diamonds) and $-m_u$ (squares; right panels) for the Sso7d SH3 domain and for CI2. Linear fits of the data show that in both proteins α_D, m_{eq}, and m_f are sensitive to changes in ΔG°_S, whereas $-m_u$ is constant for Sso7d SH3 and slightly changing in the opposite direction as m_f for CI2. This indicates that the effect of mutations ΔG°_S on α_D is caused by ground state effects on the unfolded state in Sso7d SH3 and by major ground state effects in addition to small Hammond behavior in CI2. Plots were adapted from Ref. [11], and constructed based on data from Refs [29, 87].

12.2.4
Experimental Results on the Shape of Free Energy Barriers in Protein Folding

12.2.4.1
Broadness of Free Energy Barriers

From the observation of nonlinear chevron plots for apparent two-state folders [45, 46] and from changing α_D-values in mutants of several proteins [45–48] it was originally concluded that folding of many proteins shows Hammond behavior and thus a single broad barrier region with a continuum of states with similar free energy was proposed (Figure 12.2.1A). As discussed above for tendamistat (Figure 12.2.9), the frequently observed curvature in chevron plots may also be caused by a switch between a few consecutive narrow barriers on a sequential folding path-

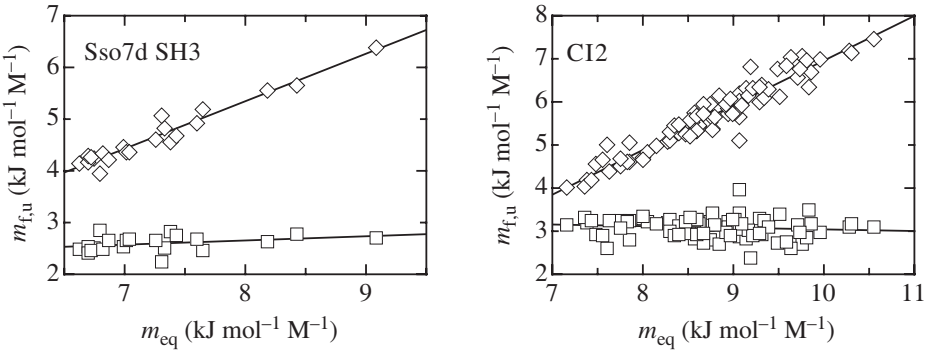

Fig. 12.2.13. Correlation of the changes in m_{eq} with changes in m_u (squares) and m_f (diamonds) for Sso7d SH3 and CI2. Linear fits of the data indicate that the variation in m_{eq} is correlated with the changes in m_f whereas m_u is only little affected by changes in m_{eq}. Correlation coefficients between m_f and m_{eq} are 0.97 for Sso7d SH3 and 0.95 for CI2. The correlations coefficients between m_u and m_{eq} are 0.34 Sso7d SH3 and −0.12 for CI2. Plots were adapted from Ref. [11].

way (Figure 12.2.2C) [43, 49–51]. Analysis of curved chevron plots reported for a large number of different proteins showed that a sequential folding model with consecutive transition states and at least one metastable high-energy intermediate is in better accordance with experimental data than a gradual transition state movement along a broad barrier [51]. This suggests that folding of many apparent two-state folders proceeds along a few defined consecutive barriers and through high-energy intermediates.

In ϕ_f-value analysis the folding and unfolding rate constants of mutants are typically obtained from chevron plots. This allowed a test for ground state effect and Hammond behavior in a large number of variants in several proteins by investigating the effect of the mutation on α_D, and the kinetic and equilibrium m-values as shown in Figure 12.2.12 [10, 11]. The analysis revealed that in about half of the proteins that have been extensively mutagenized the position of the transition state changes with mutation in accordance with apparent Hammond behavior (increased α_D-value with decreased protein stability; cf. Figure 12.2.12). However, the large majority of proteins with apparent transition state movement showed the same behavior as the SH3 domain displayed in Figure 12.2.12, indicating that the change in the position of the transition state is due to ground state effects on the structure of the unfolded state and not caused by genuine Hammond behavior [11]. In these proteins the structure of the transition state does not move relative to the structure of the native state (constant m_u-values), indicating that both the native state and the transition state are structurally well-defined and robust against mutations. In contrast, both the m_{eq}- and the m_f-values increase with decreasing in protein stability, which argues for a disruption of interactions in the unfolded state upon mutation leading to a less compact unfolded state.

Structural changes in the unfolded state can be rationalized in the light of the increasing evidence for residual structure of unfolded proteins. Recently, several

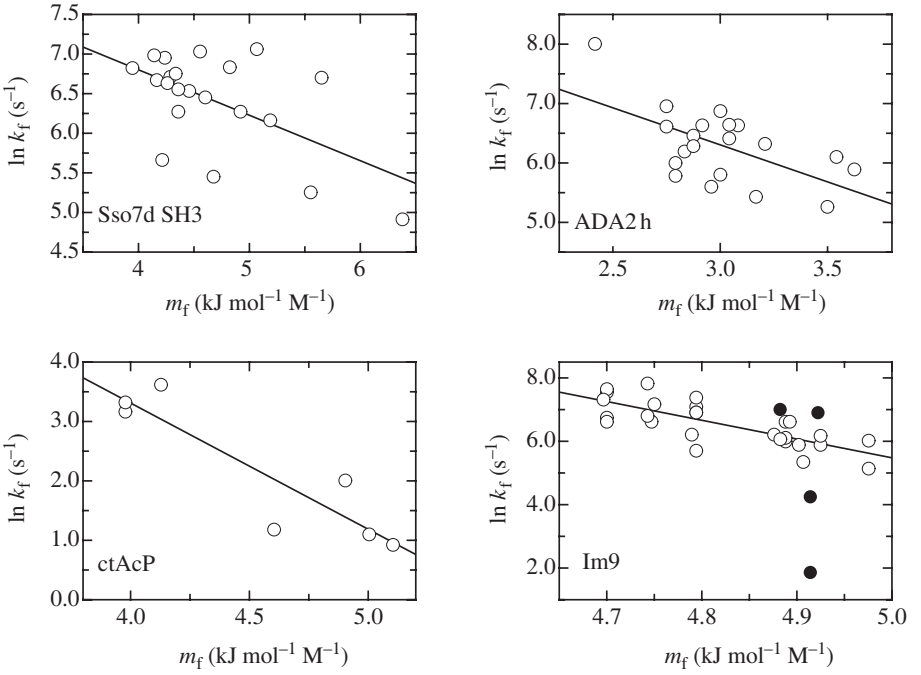

Fig. 12.2.14. Effect of changes in m_f on ln k_f for Sso7d SH3, ADA2h, ctAcP, and Im9 which exhibit ground state effects on the unfolded state. The filled symbols indicate mutants that have significantly different m_f-values and are thus likely to have a different rate-limiting transition stats. The correlation coefficients are −0.57, −0.59, −0.90, and −0.77, respectively. Plots were adapted from Ref. [11]. Original data used to calculate the correlations were taken from Refs [75, 87–89].

high-resolution NMR studies have shown that both native-like and nonnative-like interactions are present in unfolded states of several proteins [52–63] (see also Chapter 21). These interactions may be disrupted by mutations and thus lead to changes in the m_{eq}-values [32]. Only for a few proteins like CI2 weak Hammond behavior is observed, which is usually accompanied by significantly stronger ground state effects (Figures 12.2.12 and 12.2.13).

The presence of interactions in the unfolded state that are sensitive to mutation raises the question of which way these interactions influence the rate of protein folding. Figure 12.2.14 shows the correlation between the rate constant for folding (k_f) and the folding m-value (m_f) for four proteins (Ss07d SH3, ADAh2, ctAcP, and Im9) [11]. These proteins show significantly decreased folding rates with increasing m_{eq}- and m_f-values (significance of correlation larger than 90%). The same effect was observed for CI2, protein G, and protein L [11]. None of the proteins shows increased folding rates with increasing m_f and m_{eq} values.

Obviously, the disruption of residual structure in the unfolded state on average slows down folding, although the structure of the transition state is unchanged. This has three important consequences. First, it shows that the majority of the

residual interactions in the unfolded state of these proteins are also present in the transition state. The presence of interactions in the unfolded state that are not present in the transition state would result in an energetic cost for the folding reaction, since the unfolded state would be stabilized relative to the transition state. This would lead to increased folding rates when these interactions are destabilized, which is not observed. The data do not allow, however, discrimination between native and nonnative interactions. Since ϕ-value analysis showed that transition states commonly contain a subset of the native interactions at reduced strength, our results indicate that the residual interactions in the unfolded state of these seven proteins are predominantly native-like. The second consequence of the results is that residual interactions in unfolded proteins can accelerate folding. It has been proposed that the accumulation of native-like structure in the unfolded state should stabilize the unfolded state relative to the transition state and therefore slow down folding [64]. This reasoning assumes, however, that the free energy of the transition state is independent of the strength of a specific interaction in the unfolded state, which can only be assumed for interactions that are not present in the transition state. Changes in stability of an interaction will affect the free energies of the unfolded state and of the transition state, if the interaction is present in both states. The destabilization and disruption of residual interactions obviously has on average a stronger effect on the free energy of the transition state compared with the unfolded state. This indicates that the interactions are stronger in the transition state than in the unfolded state and thus more sensitive to mutations. The third conclusion from these results is that a subset of the interactions present in the transition state for folding can be directly pointed out from structural studies on the unfolded state.

As discussed in Section 12.2.3.2, transition state movements in protein folding should be highly correlated since different reaction coordinates should be sensitive to protein–protein and protein–solvent interactions in the transition state. Transition state movements should thus show up in different p_x- and p_{xy}-values. Analysis of other self- and cross-interaction parameters in available folding data (Table 12.2.1) indicates the absence of genuine transition state movements for folding of most of the proteins [11]. Out of 21 investigated proteins only CI2 showed a small but coherent transition state movement. These results suggest that Hammond behavior is not common in protein folding reactions. Most protein folding transition states seem to be robust, conformationally restricted maxima in the free energy landscape and, similar to native states, they usually do not undergo extensive structural rearrangements upon mutation or changes in solvent conditions. These results argue for the generality of free energy landscapes with a limited number of sequential but structurally well-defined transition states in apparent two-state folding. The clearest examples for significant transition states movement is the effect of pressure and denaturant on the transition state for tendamistat folding (Figures 12.2.6 and 12.2.7). Due to the lack of other data on pressure-induced REFERs and the scarcity of data on temperature-induced REFERs it is difficult to judge whether transition state movements are frequently induced by perturbants other than denaturant or mutation.

Tab. 12.2.1. Proteins for which more than one self- or cross-interaction coefficient can be determined. A p_x or p_{xy}-value is considered to be larger (> 0) or smaller (< 0) than zero if it differs from zero in more than two standard deviations.

Protein	$p_D = \frac{\partial \alpha_D}{\partial \Delta G^\circ_D}$	$p_S = \frac{\partial \phi_f^{prot}}{\partial \Delta G^\circ_S}$	$p_{DS} = \frac{\partial \alpha_D}{\partial \Delta G^\circ_S}$	$p_{DT} = \frac{\partial \alpha_D}{\partial \Delta G^\circ_T}$	$p_{DpH} = \frac{\partial \alpha_D}{\partial \Delta G^\circ_{pH}}$	$p_{Dp} = \frac{\partial \alpha_D}{\partial \Delta G^\circ_p}$	$p_{DGl} = \frac{\partial \alpha_D}{\partial \Delta G^\circ_{Gl}}$	$p_{ST} = \frac{\partial \phi_f^i}{\partial \Delta G^\circ_T}$	$p_{SpH} = \frac{\partial \phi_f^i}{\partial \Delta G^\circ_{pH}}$	$p_{SS'} = \frac{\partial \phi_f^i}{\partial \Delta G^\circ_{S'}}$
ACBP [74]	$\cong 0$	$\cong 0$	>0							
ADA2h [75]	$\cong 0$	$\cong 0$	>0							
Barnase [30, 44, 47, 48, 76, 77]	>0	<0 for helix 1	>0 for core	>0				>0 for helix 1		<0 for helix 1
CI2 [29, 45, 48]	>0 for some mutants	$\cong 0$	>0	>0				>0		
CspB [78]	>0 for some mutants		$\cong 0$							
CTL9 [23]	$\cong 0$				$\cong 0$					
FKBP12 [79, 80]	>0 for some mutants	$\cong 0$	$\cong 0$	$\cong 0$						
NTL9 [21, 81]	$\cong 0$			$\cong 0$	$\cong 0$					
Protein L [82–84]	$\cong 0$	$\cong 0$	$\cong 0$	$\cong 0$			$\cong 0$			
Spectrin SH3 [40, 85]	>0	$\cong 0$	$\cong 0$		$\cong 0$				$\cong 0$	$\cong 0$
Tendamistat [39, 43, 86]	>0 for some mutants			>0 for some mutants	$\cong 0$	>0				

In several proteins, some mutations lead to discrete jumps in the position of the transition state in a p_{DS} analysis. This indicates changes in the rate-limiting step of the folding process [11] and might be due to parallel folding pathways or to consecutive barriers on a sequential pathway [10, 11]. Sequential pathways with a few discrete transition states are in agreement with the results from the analysis of proteins with nonzero p_D-values as discussed above. The existence of multiple consecutive barriers may further explain transition state movements observed only with some p_x- or p_{xy}-values. If two consecutive transition states have a very similar α_x-value in that particular reaction coordinate, the range of experimentally accessible perturbations may lie in a region where the switch between the two transition states occurs. Therefore, conditions where only one of the transition states is limiting may be missed. This will show up as an apparent gradual movement of the transition state position [39, 43].

12.2.4.2 Parallel Pathways

Theoretical studies on protein-like model heteropolymers suggested a highly heterogeneous transition state ensemble with a manifold of parallel routes leading to the native state [65, 66]. In this case a perturbation should affect the substates of the transition state ensemble to different degrees. The free energy of more native-like transition states would be more strongly increased when the native state is destabilized, which would lead to an apparent movement to more unfolded-like transition states (see Figure 12.2.10). This would result in negative self- and cross-interaction parameters in our data analysis. The same reasoning applies to a scenario with defined parallel pathways of similar free energy leading to the native state (Figure 12.2.10). At least three parallel pathways were described for lysozyme folding. In this case one (low salt conditions) or two of the pathways (high salt conditions) transiently populate an intermediate, which facilitated the detection and characterization of the parallel routes [67] (see Chapter 12.1).

The clearest example for two parallel pathways in two-state folding came from a titin domain, where a clear upward curvature in the chevron plot was reported [68]. The existence of two parallel pathways was also deduced for folding of a variant of GCN4, a dimeric coiled-coil [22] with an engineered Zn^{2+}-binding site. In this case the presence of Zn^{2+} induced a parallel pathway detected by an upward curvature in the Leffler plot. Negative p_S- and $p_{SS'}$-values also indicated parallel pathways for the formation of the first helix of barnase [30, 44] and negative $p_{SS'}$-values were also found for protein G [69]. The analysis of other two-state folders did not detect any additional negative p_x- and p_{xy}-values. The lack of evidence for negative p_x- and p_{xy}-values in the majority of proteins could indicate that parallel folding pathways are rare or that they have transition states with similar α_x-values. This would lead to only minor shifts in the apparent position of the transition state which would escape detection in our data analysis.

Negative p_x-values observed for helix 1 in barnase (negative p_S-value) [44] and for the titin domain (negative p_D-value) [70] were originally interpreted as anti-

Hammond behavior. However, a more detailed analysis of the effects revealed that in both proteins the negative p_x-values are compatible with parallel pathways [11, 68]. Up to date there is no clear example for anti-Hammond behavior for protein folding reactions supporting the picture of narrow and defined transition state regions.

12.2.5 Folding in the Absence of Enthalpy Barriers

Theoretical models have proposed that folding is an energetically downhill process limited only by entropic barriers [71]. Zwanzig treated protein folding as a rapid barrier-less equilibration reaction between many unfolded conformations linked to a barrier-less escape process, which can only take place from a limited number of unfolded conformations or ''escape states'' [72], similar to the flow out of a bath tub. Simulation of the dynamic behavior of such a system shows that single exponential kinetics result when the transitions between the different unfolded states are fast and the number of escape states is small compared with the total number of unfolded conformations. This process can thus not be distinguished experimentally from two-state folding kinetics with an energy barrier. A more general treatment of the effect of entropy barriers on chemical dynamics shows that single exponential kinetics should always be observed (at least for reactions in solution) in the absence of energetic (enthalpic) barriers, as long as entropic barriers exist [73]. These considerations highlight the difficulties in discriminating between different folding models on the basis of single exponential behaviour, since the same experimentally observed kinetics can result from different folding landscapes.

12.2.6 Conclusions and Outlook

A quantitative treatment of folding kinetics is a prerequisite for elucidating mechanisms of protein folding. Even simple kinetics, like single exponential behavior can be caused by a variety of different folding landscapes. Therefore the interplay between theoretical models and experimental results is essential in the effort to understand protein folding. We have seen that concepts from classical reaction rate theory developed for simple chemical reactions can be applied to protein folding. Analysis of self-interaction and cross-interaction parameters prooved to be useful tools to detect nonlinear REFERs in protein folding. This gave valuable information on the shape of free energy barriers and thus on the mechanism of protein folding. The analysis of transition state movements in a large number of well-characterized proteins using self-interaction and cross-interaction parameters shows that Hammond behavior is rare in protein folding reactions, indicating that folding transition states are narrow regions on the free energy landscape which are robust against perturbations. Apparent transition state movements detected by p_{DS} cross-interaction parameters are in most proteins due to ground state effects and

are most commonly caused by structural changes in the unfolded state. This supports the presence of residual structure in unfolded proteins. The analysis of the denaturant-induced REFERs for a large number of proteins further supports sequential folding pathways with obligatory high-energy intermediates as a simple and general explanation for curvatures in chevron plots. This suggests that apparent two-state folding and folding through transiently populated intermediates share similar free energy landscapes with consecutive barriers on sequential pathways. The major difference between two-state and multistate folding is the relative stability of partially folded intermediates.

Up to date mainly mutational analysis in combination with denaturant dependence of folding rate constants has been applied to characterize protein folding barriers. It will be interesting to see whether protein folding transition states are also robust along other reaction coordinates, which can be probed by changes in pressure, temperature and by ligand binding or protonation of specific side chains. In addition, more experimental results on backbone interactions in the transition state and on the existence of parallel transition states will be required to get a more complete picture of the structure of protein folding transition states and on the properties of the free energy barriers.

Acknowledgments

We thank Andi Möglich for preparing Figure 12.2.8A, Manuela Schätzle and Beat Fierz for comments on the manuscript and all members of the Kiefhaber lab for help and discussion.

References

1 Leffler, J. E. & Grunwald, E. (1963). *Rates and Equilibria of Organic Reactions*. Dover, New York.
2 Jencks, W. P. (1969). *Catalysis in Chemistry and Enzymology*. McGraw-Hill, New York.
3 Leffler, J. E. (1953). Parameters for the description of transition states. *Science* 117, 340–341.
4 Hammond, G. S. (1955). A correlation of reaction rates. *J. Am. Chem. Soc.* 77, 334–338.
5 Jencks, W. P. (1985). A primer for the Bema Hapothle. An empirical approach to the characterization of changing transition-state structures. *Chem. Rev.* 85, 511–527.
6 Farcasiu, D. (1975). The use and misuse of the Hammond postulate. *J. Chem. Ed.* 52, 76–79.
7 Greene, R. F. J. & Pace, C. N. (1974). Urea and guanidine-hydrochloride denaturation of ribonuclease, lysozyme, alpha-chyomtrypsinn and beta-lactoglobulin. *J. Biol. Chem.* 249, 5388–5393.
8 Santoro, M. M. & Bolen, D. W. (1988). Unfolding free energy changes determined by the linear extrapolation method. 1. Unfolding of phenylmethanesulfonyl alpha-chymotrypsin using different denaturants. *Biochemistry* 27, 8063–8068.
9 Tanford, C. (1970). Protein denaturation. Part C. Theoretical models for the mechanism of denaturation. *Adv. Protein Chem.* 24, 1–95.
10 Sánchez, I. E. & Kiefhaber, T.

(2003). Non-linear rate-equilibrium free energy relationships and Hammond behavior in protein folding. *Biophys. Chem.* 100, 397–407.

11 Sánchez, I. E. & Kiefhaber, T. (2003). Hammond behavior versus ground state effects in protein folding: evidence for narrow free energy barriers and residual structure in unfolded states. *J. Mol. Biol.* 327, 867–884.

12 Pohl, F. M. (1976). Temperature-dependence of the kinetics of folding of chymotrypsinogen A. *FEBS Lett.* 65, 293–296.

13 Chen, B. L., Baase, W. A. & Schellman, J. A. (1989). Low-temperature unfolding of a mutant of phage T4 lysozyme. 2. Kinetic investigations. *Biochemistry* 28, 691–699.

14 Privalov, P. L. & Makhatadze, G. I. (1992). Contribution of hydration and non-covalent interactions to the heat capacity effect on protein unfolding. *J. Mol. Biol.* 224, 715–723.

15 Ikai, A., Fish, W. W. & Tanford, C. (1973). Kinetics of unfolding and refolding of proteins. II. Results for cytochrome c. *J. Mol. Biol.* 73, 165–184.

16 Matthews, C. R. (1987). Effect of point mutations on the folding of globular proteins. *Methods Enzymol.* 154, 498–511.

17 Myers, J. K., Pace, C. N. & Scholtz, J. M. (1995). Denaturant m values and heat capacity changes: relation to changes in accessible surface areas of protein unfolding. *Protein Sci.* 4, 2138–2148.

18 Kuwajima, K. (1989). The molten globule state as a clue for understanding the folding and cooperativity of globular-protein structure. *Proteins Struct. Funct. Genet.* 6, 87–103.

19 Sancho, J., Meiering, E. M. & Fersht, A. R. (1991). Mapping transition states of protein unfolding by protein engineering of ligand-binding sites. *J. Mol. Biol.* 221, 1007–1014.

20 Tan, Y. J., Oliveberg, M. & Fersht, A. R. (1996). Titration properties and thermodynamics of the transition state for folding: comparison of two-state and multi-state folding pathways. *J. Mol. Biol.* 264, 377–389.

21 Luisi, D. L. & Raleigh, D. P. (2000). pH-dependent interactions and the stability and folding kinetics of the N-terminal domain of L9. Electrostatic interactions are only weakly formed in the transition state for folding. *J. Mol. Biol.* 299, 1091–1100.

22 Krantz, B. A. & Sosnick, T. R. (2001). Engineered metal binding sites map the heterogeneous folding landscape of a coiled coil. *Nat. Struct. Biol.* 8, 1042–1047.

23 Sato, S. & Raleigh, D. P. (2002). pH-dependent stability and folding kinetics of a protein with an unusual alpha-beta topology: the C-terminal domain of the ribosomal protein L9. *J. Mol. Biol.* 318, 571–82.

24 Goldenberg, D. P., Frieden, R. W., Haack, J. A. & Morrison, T. B. (1989). Mutational analysis of a protein-folding pathway. *Nature* 338, 127–32.

25 Fersht, A. R., Matouschek, A. & Serrano, L. (1992). The folding of an enzyme. I. Theory of protein engineering analysis of stability and pathway of protein folding. *J. Mol. Biol.* 224, 771–782.

26 Sánchez, I. E. & Kiefhaber, T. (2003). Origin of unusual phi-values in protein folding: Evidence against specific nucleation sites. *J. Mol. Biol.* 334, 1077–1085.

27 Mok, Y. K., Elisseeva, E. L., Davidson, A. R. & Forman-Kay, J. D. (2001). Dramatic stabilization of an SH3 domain by a single substitution: roles of the folded and unfolded states. *J. Mol. Biol.* 307, 913–928.

28 Northey, J. G., Maxwell, K. L. & Davidson, A. R. (2002). Protein folding kinetics beyond the phi value: using multiple amino acid substitutions to investigate the structure of the SH3 domain folding transition state. *J. Mol. Biol.* 320, 389–402.

29 Itzhaki, L. S., Otzen, D. E. & Fersht, A. R. (1995). The structure of

the transition state for folding of chymotrypsin inhibitor 2 analyzed by protein engineering methods: evidence for a nucleation-condesation mechanism for protein folding. *J. Mol. Biol.* 254, 260–288.

30 Fersht, A. R., Itzhaki, L. S., elMasry, N. F., Matthews, J. M. & Otzen, D. E. (1994). Single versus parallel pathways of protein folding and fractional formation of structure in the transition state. *Proc. Natl Acad. Sci. USA* 91, 10426–10429.

31 Brønsted, J. N. & Pedersen, K. J. (1924). *Z. physikal. Chem.* 108, 185–.

32 Klein-Seetharaman, J., Oikawa, M., Grimshaw, S. B., Wirmer, J., Duchardt, E., Ueda, T., et al. (2002). Long-range interactions within a non-native protein. *Science* 295, 1719–1722.

33 Krieger, F., Fierz, B., Bieri, O., Drewello, M. & Kiefhaber, T. (2003). Dynamics of unfolded polypeptide chains as model for the earliest steps in protein folding. *J. Mol. Biol.* 332, 265–274.

34 Makarov, D. E., Keller, C. A., Plaxco, K. W. & Metiu, H. (2002). How the folding rate constant of simple single-domain proteins depends on the number of native contacts. *Proc. Natl Acad. Sci. USA* 99, 3535–3539.

35 Makarov, D. E. & Plaxco, K. W. (2003). The topomer search model: A simple quanitative theory of two-state protein folding kinetics. *Protein Sci.* 12, 17–26.

36 Vendruscolo, M., Paci, E., Dobson, C. M. & Karplus, M. (2001). Three key residues form a critical contact network in a protein folding transition state. *Nature* 409, 641–645.

37 Sato, S., Religa, T. L., Daggett, V. & Fersht, A. R. (2004). Testing protein-folding simulations by experiment: B domain of protein A. *Proc. Natl Acad. Sci. USA* 101, 6952–6956.

38 Krantz, B. A., Moran, L. B., Kentsis, A. & Sosnick, T. R. (2000). D/H amide kinetic isotope effects reveal when hydrogen bonds form during protein folding. *Nat. Struct. Biol.* 7, 62–71.

39 Pappenberger, G., Saudan, C., Becker, M., Merbach, A. E. & Kiefhaber, T. (2000). Denaturant-induced movement of the transition state of protein folding revealed by high pressure stopped-flow measurements. *Proc. Natl Acad. Sci. USA* 97, 17–22.

40 Martinez, J. C., Pisabarro, M. T. & Serrano, L. (1998). Obligatory steps in protein folding and the conformational diversity of the transition state. *Nat. Struct. Biol.* 5, 721–9.

41 Thornton, E. R. (1967). A simple theory for predicting the effects of substituent changes on transition-state geometry. *J. Am. Chem. Soc.* 89, 2915–2927.

42 Müller, P. (1994). Glossary of terms used in physical organic chemistry. *Pure Appl. Chem.* 66, 1077–1184.

43 Bachmann, A. & Kiefhaber, T. (2001). Apparent two-state tendamistat folding is a sequential process along a defined route. *J. Mol. Biol.* 306, 375–386.

44 Matthews, J. M. & Fersht, A. R. (1995). Exploring the energy surface of protein folding by structure-reactivity relationship and engineered proteins: Observation of Hammond behavior for the gross structure of the transitions state and anti-hammond behavior for structural elements for unfolding/folding of barnase. *Biochemistry* 34, 6805–6814.

45 Oliveberg, M., Tan, Y.-J., Silow, M. & Fersht, A. R. (1998). The changing nature of the protein folding transition state: implications for the free-energy profile for folding. *J. Mol. Biol.* 277, 933–943.

46 Silow, M. & Oliveberg, M. (1997). High-energy channeling in protein folding. *Biochemistry* 36, 7633–7637.

47 Matouschek, A. & Fersht, A. R. (1993). Application of physical organic chemistry to engineered mutants of proteins: Hammond postulate behavior in the transition state of protein folding. *Proc. Natl Acad. Sci. USA* 90, 7814–7818.

48 Matouschek, A., Otzen, D. E.,

Itzhaki, L., Jackson, S. E. & Fersht, A. R. (1995). Movement of the transition state in protein folding. *Biochemistry* 34, 13656–13662.

49 Kiefhaber, T., Bachmann, A., Wildegger, G. & Wagner, C. (1997). Direct measurements of nucleation and growth rates in lysozyme folding. *Biochemistry* 36, 5108–5112.

50 Walkenhorst, W. F., Green, S. & Roder, H. (1997). Kinetic evidence for folding and unfolding intermediates in staphylococcal nuclease. *Biochemistry* 36, 5795–5805.

51 Sánchez, I. E. & Kiefhaber, T. (2003). Evidence for sequential barriers and obligatory intermediates in apparent two-state protein folding. *J. Mol. Biol.* 325, 367–376.

52 Evans, P. A., Topping, K. D., Woolfson, D. N. & Dobson, C. M. (1991). Hydrophobic clustering in nonnative states of a protein: interpretation of chemical shifts in NMR spectra of denatured states of lysozyme. *Proteins* 9, 248–266.

53 Neri, D., Billeter, M., Wider, G. & Wüthrich, K. (1992). NMR determination of residual structure in a urea-denatured protein, the 434-repressor. *Science* 257, 1559–1563.

54 Logan, T. M., Theriault, Y. & Fesik, S. W. (1994). Structural characterization of the FK506 binding protein unfolded in urea and guanidine hydrochloride. *J. Mol. Biol.* 236, 637–648.

55 Smith, C. K., Bu, Z. M., Anderson, K. S., Sturtevant, J. M., Engelman, D. M. & Regan, L. (1996). Surface point mutations that significantly alter the structure and stability of a protein's denatured state. *Protein Sci.* 5, 2009–2019.

56 Sari, N., Alexander, P., Bryan, P. N. & Orban, J. (2000). Structure and dynamics of an acid-denatured protein G mutant. *Biochemistry* 39, 965–977.

57 Wong, K. B., Clarke, J., Bond, C. J., Neira, J. L., Freund, S. M., Fersht, A. R. & Daggett, V. (2000). Towards a complete description of the structural and dynamic properties of the denatured state of barnase and the role of residual structure in folding. *J. Mol. Biol.* 296, 1257–1282.

58 Teilum, K., Kragelund, B. B., Knudsen, J. & Poulsen, F. M. (2000). Formation of hydrogen bonds precedes the rate-limiting formation of persistent structure in the folding of ACBP. *J. Mol. Biol.* 301, 1307–1314.

59 Kortemme, T., Kelly, M. J., Kay, L. E., Forman-Kay, J. D. & Serrano, L. (2000). Similarities between the spectrin SH3 domain denatured state and its folding transition state. *J. Mol. Biol.* 297, 1217–1229.

60 Garcia, P., Serrano, L., Durand, D., Rico, M. & Bruix, M. (2001). NMR and SAXS characterization of the denatured state of the chemotactic protein CheY: implications for protein folding initiation. *Protein Sci.* 10, 1100–1112.

61 Choy, W. Y. & Forman-Kay, J. D. (2001). Calculation of ensembles of structures representing the unfolded state of an SH3 domain. *J. Mol. Biol.* 308, 1011–1032.

62 Kazmirski, S. L., Wong, K. B., Freund, S. M., Tan, Y. J., Fersht, A. R. & Daggett, V. (2001). Protein folding from a highly disordered denatured state: the folding pathway of chymotrypsin inhibitor 2 at atomic resolution. *Proc. Natl Acad. Sci. USA* 98, 4349–4354.

63 Yi, Q., Scalley-Kim, M. L., Alm, E. J. & Baker, D. (2000). NMR characterization of residual structure in the denatured state of protein L. *J. Mol. Biol.* 299, 1341–1351.

64 Fersht, A. R. (1995). Optimization of rates of protein folding: The nucleation-condensation mechanism and its implications. *Proc. Natl Acad. Sci. USA* 92, 10869–10873.

65 Guo, Z. & Thirumalai, D. (1995). Kinetics of protein folding: nucleation mechanism, time scales, and pathways. *Biopolymers* 36, 83–102.

66 Wolynes, P. G., Onuchic, J. N. & Thirumalai, D. (1995). Navigating the folding routes. *Science* 267, 1619–1620.

67 Bieri, O., Wildegger, G., Bachmann, A., Wagner, C. &

Kiefhaber, T. (1999). A salt-induced intermediate is on a new parallel pathway of lysozyme folding. *Biochemistry* 38, 12460–12470.

68 Wright, C. F., Lindorff-Larsen, K., Randles, L. G. & Clarke, J. (2003). Parallel protein-unfolding pathways revealed and mapped. *Nat. Struct. Biol.* 10, 658–662.

69 Nauli, S., Kuhlman, B. & Baker, D. (2001). Computer-based redesign of a protein folding pathway. *Nat. Struct. Biol.* 8, 602–605.

70 Fowler, S. B. & Clarke, J. (2001). Mapping the folding pathway of an immunoglobulin domain: structural detail from Phi value analysis and movement of the transition state. *Structure (Camb.)* 9, 355–366.

71 Wolynes, P. G. (1997). Folding funnels and energy landscapes of larger proteins within the capillarity approximation. *Proc. Natl Acad. Sci. USA* 94, 6170–6175.

72 Zwanzig, R. (1997). Two-state models for protein folding. *Proc. Natl Acad. Sci. USA* 94, 148–150.

73 Zhou, H.-X. & Zwanzig, R. (1991). A rate process with an entropic barrier. *J. Chem. Phys.* 94, 6147–6152.

74 Kragelund, B. B., Osmark, P., Neergaard, T. B., Schiodt, J., Kristiansen, K., Knudsen, J. & Poulsen, F. M. (1999). The formation of a native-like structure containing eight conserved hydrophobic residues is rate limiting in two-state protein folding of ACBP. *Nat. Struct. Biol.* 6, 594–601.

75 Villegas, V., Martinez, J. C., Avilés, F. X. & Serrano, L. (1998). Structure of the transition state in the folding process of human procarboxypeptidase A2 activation domain. *J. Mol. Biol.* 283, 1027–1036.

76 Matouschek, A., Matthews, J. M., Johnson, C. M. & Fersht, A. R. (1994). Extrapolation to water of kinetic and equilibrium data for the unfolding of barnase in urea solutions. *Protein Eng.* 7, 1089–1095.

77 Dalby, P. A., Oliveberg, M. & Fersht, A. R. (1998). Movement of the intermediate and rate determining transition state of barnase on the energy landscape with changing temperature. *Biochemistry* 37, 4674–4679.

78 Perl, D., Holtermann, G. & Schmid, F. X. (2001). Role of the chain termini for the folding transition state of the cold shock protein. *Biochemistry* 40, 15501–15511.

79 Fulton, K. F., Main, E. R., Daggett, V. & Jackson, S. E. (1999). Mapping the interactions present in the transition state for unfolding/folding of FKBP12. *J. Mol. Biol.* 291, 445–461.

80 Main, E. R. G., Fulton, K. F. & Jackson, S. E. (1999). Folding pathway of FKBP12 and characterization of the transition state. *J. Mol. Biol.* 291, 429–444.

81 Kuhlman, B., Luisi, D. L., Evans, P. A. & Raleigh, D. P. (1998). Global analysis of the effects of temperature and denaturant on the folding and unfolding kinetics of the N-terminal domain of the protein L9. *J. Mol. Biol.* 284, 1661–1670.

82 Scalley, M. L. & Baker, D. (1997). Protein folding kinetics exhibit an Arrhenius temperature dependence when corrected for the temperature dependence of protein stability. *Proc. Natl Acad. Sci. USA* 94, 10636–10640.

83 Plaxco, K. W. & Baker, D. (1998). Limited internal friction in the rate-limiting step of a two-state protein folding reaction. *Proc. Natl Acad. Sci. USA* 95, 13591–13596.

84 Kim, D. E., Fisher, C. & Baker, D. (2000). A breakdown of symmetry in the folding transition state of protein L. *J. Mol. Biol.* 298, 971–984.

85 Martinez, J. C. & Serrano, L. (1999). The folding transition state between SH3 domains is conformationally restricted and evolutionarily conserved. *Nat. Struct. Biol.* 6, 1010–1016.

86 Schönbrunner, N., Pappenberger, G., Scharf, M., Engels, J. & Kiefhaber, T. (1997). Effect of pre-formed correct tertiary interactions on rapid two-state tendamistat folding: evidence for hairpins as initiation sites

for β-sheet formation. *Biochemistry* 36, 9057–9065.

87 Guerois, R. & Serrano, L. (2000). The SH3-fold family: experimental evidence and prediction of variations in the folding pathways. *J. Mol. Biol.* 304, 967–982.

88 Taddei, N., Chiti, F., Fiaschi, T., Bucciantini, M., Capanni, C., Stefani, M., et al. (2000). Stabilisation of alpha-helices by site-directed mutagenesis reveals the importance of secondary structure in the transition state for acylphosphatase folding. *J. Mol. Biol.* 300, 633–647.

89 Friel, C. T., Capaldi, A. P. & Radford, S. E. (2003). Structural analysis of the rate-limiting transition states in the folding of Im7 and Im9: similarities and differences in the folding of homologous proteins. *J. Mol. Biol.* 326, 293–305.

13
A Guide to Measuring and Interpreting ϕ-values

Nicholas R. Guydosh and Alan R. Fersht

13.1
Introduction

Arguably the most important state to characterize on a folding pathway, and indeed in any reaction, is the transition state. But, its ephemeral existence and composition of unstable interactions render conventional tools inadequate in determining an atomic level structure. But the structures of many transition states have been solved using protein engineering techniques developed over the last two decades: ϕ-value analysis [1, 2]. The folding pathways for numerous proteins have now been experimentally characterized with ϕ-values [1, 3–5]. These data have in turn been used for benchmarking molecular dynamics simulations of protein folding [6].

This chapter outlines the basic theory behind a ϕ-value analysis and discusses how structural information is derived from it. This includes a discussion on choosing mutations for minimizing error in calculations. The techniques for measuring the thermodynamic and kinetic parameters used to compute ϕ-values are also presented.

13.2
Basic Concept of ϕ-Value Analysis

The concept of ϕ-value analysis grew out of extensive study on structure–activity relationships used throughout organic chemistry and enzymology. These techniques include Brønsted analysis to analyze covalent bond formation and protein engineering methods to quantify noncovalent bond formation in enzymic transition states [7, 8]. Indeed, all the basic principles for analyzing protein folding were laid down in studies analysing the noncovalent interactions that stabilize the transition state for the formation of tyrosyl adenylate catalyzed by the tyrosyl-tRNA synthetase [2]. Small perturbations are made to the molecule that cause small changes in structure and hence thermodynamic and kinetic properties.

These perturbations take the form of systematic point mutations of amino acids

Protein Folding Handbook. Part I. Edited by J. Buchner and T. Kiefhaber

ISBN: 3-527-30784-2

in a ϕ-value analysis. Kinetic and thermodynamic data from these mutants are then used to determine the extent of native-like interactions formed in a protein folding transition state. For the wild-type protein and each mutant, two quantities are required: the free energy stability of the native state with respect to the denatured state (ΔG_{N-D}) and rate of folding from the denatured state to the native state (rate constant k_f).

The stability change for the folding reaction upon mutation is defined as

$$\Delta\Delta G_{N-D} = \Delta G_{N-D} - \Delta G_{N'-D'} \quad (1)$$

Here, ΔG_{N-D} typically ranges from -3 to -15 kcal mol^{-1} for small, single-domain proteins. The primed terms represent the quantities for the mutant.

Next, transition state theory can be applied to kinetic rate constants for folding to obtain the energetic difference between denatured and transition states, in terms of exponential prefactors. When taking the ratio of the rate constants for the mutant and wild-type proteins (k'_f and k_f, respectively), the prefactors cancel, with the assumption that they do not change upon mutation. This gives an expression for $\Delta\Delta G_{TS-D}$ as

$$\Delta\Delta G_{TS-D} = \Delta G_{TS-D} - \Delta G_{TS'-D'} = RT \ln \frac{k'_f}{k_f} \quad (2)$$

The notation is as before, but with TS symbolizing the transition state. The ratio of these two values is then defined as ϕ.

$$\phi = \frac{\Delta\Delta G_{TS-D}}{\Delta\Delta G_{N-D}} \quad (3)$$

The value of ϕ is simply a measure of the destabilization of the transition state relative to the denatured state, normalized to the destabilization between the ground states. A value of 1 indicates that the native and transition states have energies that are perturbed equally upon mutation. A value of 0 indicates that the perturbation to the ground and transition states is isoenergetic. Structurally, a ϕ-value of 1 corresponds to native-like interactions for the mutated residues in the transition state. A ϕ-value of 0 corresponds to denatured-like interactions of the mutated residues in the transition state.

For example, consider a deletion mutation of Ile to Val, where the deleted methyl group exists between two helices. If the helices have native-like packing at this position in the transition state, the expectation would be that the mutation has isoenergetic effects on the transition and native states. The rate of folding would be reduced, giving $\phi = 1$. If the helices are not packed in the transition state, the expectation would be that the rate of folding does not change, giving $\phi = 0$. This is illustrated in Figure 13.1.

Choice of mutation is crucial. For the value of ϕ to have any meaning in relation to the native folding pathway, mutations must not change the pathway for folding

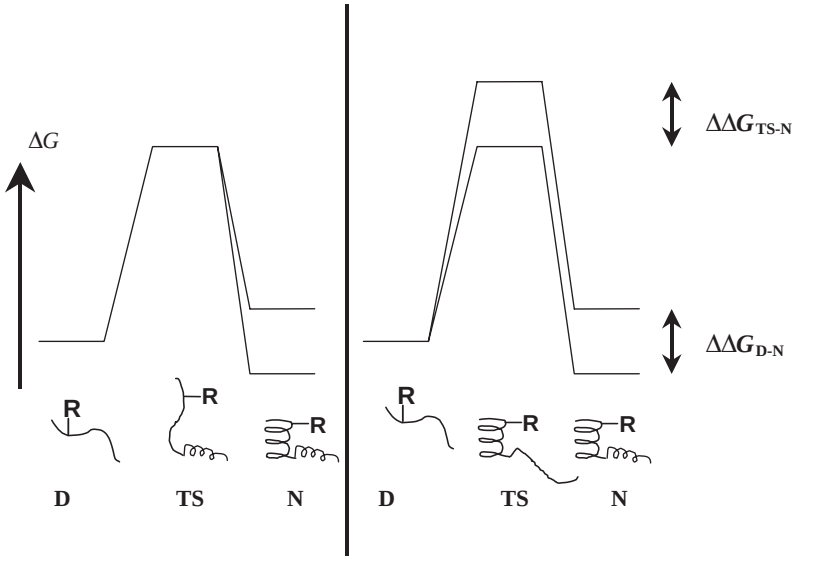

Fig. 13.1. Graphical representation of ϕ-value analysis. The panel on the left signifies a ϕ-value of 0. The residue R is not structured in the transition state. The panel on the right signifies a ϕ-value of 1. The residue is structured in the transition state.

or introduce new interactions. Ideally, they should not rearrange the structure of the protein around the site of mutation in either the denatured or native states, though information can still be obtained if these latter two conditions are not met (see below). Mutations found to have minimal effects on the pathway and structure are small, hydrophobic deletions without change in stereochemistry ("nondisruptive deletions" [2]). By making mutations such as Ile to Val, Thr to Ser, Ala to Gly, Leu to Ala, or Phe to Ala, cavities are created in the hydrophobic core, leaving the folding pathway largely the same. Correlation between native state stability and points of contact of the deleted atoms within a small, 6-Å radius supports the assumption that the structural region probed is defined locally around the deleted atoms [9].

More radical mutations, particularly those affecting electrostatic interactions, are more difficult to interpret because new, unpredictable interactions are introduced, which could be taking place more distant from the site of interest. In cases where these sorts of mutations are not possible, the residue of interest can be first truncated to Ala and then to Gly, to get some idea of the role of that particular position to the transition state.

Mutation of Ala to Gly is a special case because the Gly amino acid is much more conformationally flexible about its ϕ and ψ bond angles. Such a mutation not only probes the effect of the deleted steric bulk of the alanine methyl group, but also backbone conformational flexibility at the site of mutation. Estimates for

the conformational entropy contribution of Gly are $\sim$1 kcal mol^{-1}, which can be a significant percentage of a protein's typical stability [10, 11]. By carefully making Ala to Gly mutations, the role of backbone flexibility can be probed. Along with other single methyl group deletions (Ile to Val and Thr to Ser), Ala to Gly mutations can probe secondary structural interactions. The extent of formation of the hydrophobic core can be probed by larger deletions from fully buried residues.

The stability of mutated proteins is an indicator of possible error in computation of ϕ-values. Mutants that have a stability change (ΔG_{N-D}) of less than $\sim$0.6 kcal mol^{-1} run the risk of producing ϕ-values with significant error since the ratio used to compute ϕ is of two small numbers. Similarly, mutations that substantially destabilise the protein are of concern because larger energetic changes are more likely to contain significant structural changes.

13.3 Further Interpretation of ϕ

To get a better understanding of the interpretation of ϕ, thermodynamic cycles for the folding and unfolding reactions can be written as shown in Figure 13.2. Here, D represents the denatured state, N the native state, and TS the transition state. The primed states are those corresponding to the mutant.

Using the cycle below to rearrange Eq. (3), we can then rewrite the definition of ϕ

$$\phi = \frac{\Delta\Delta G_{TS-D}}{\Delta\Delta G_{N-D}} = \frac{\Delta G_{TS'-TS} - \Delta G_{D'-D}}{\Delta G_{N'-N} - \Delta G_{D'-D}} \tag{4}$$

where the notation is as before. Here, the term $\Delta G_{D'-D}$ is simply the change in denatured state relative free energy upon mutation. Since the denatured state is unstructured for the most part, this term reflects the change in solvation and conformational entropy of the denatured state as a result of a mutation. This term is often negligible for small hydrophobic deletions. However, in cases where polar or

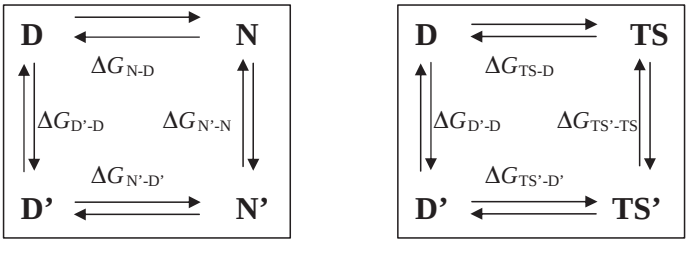

Fig. 13.2. Thermodynamic cycles between the denatured state (D) and transition state (TS), or native state (N) for a wild-type (unprimed) and mutant (primed) protein.

charged groups are exchanged for hydrophobic groups, solvation energies are no longer simply fractions of a kcal, as in the case of hydrophobic deletions [5]. Cases where glycine is deleted or introduced also introduce conformational entropy terms that are of similar magnitude [11].

There are two cases, as given earlier, of simple interpretation. When $\Delta G_{TS'-TS} = \Delta G_{N'-N}$, $\phi = 1$. Here, the native and transition states are equally perturbed. Whether or not the denatured state energy, $\Delta G_{D'-D}$, changes is not critical. Structurally, the residues mutated have the same structural interactions in the transition and native states.

In the second case, $\Delta G_{TS'-TS} = \Delta G_{D'-D}$ and $\phi = 0$. In this situation, changes in interactions in the native state are largely not important (so long as they do not change the folding pathway). Since the energy $\Delta G_{D'-D}$ is often very small, the transition and denatured state mutated atoms have the same unstructured form. However, it could also indicate equal breakdown of residual structure in the denatured and transition states. In such a case, however, the interpretation is the same: native interactions do not form until a position past the transition state on the folding pathway.

Fractional ϕ-values are more difficult to interpret. In one simplifying case, some speculation can be made. When the energy of solvation for a particular mutation is zero ($\Delta G_{D'-D} = 0$), the expression for ϕ simplifies to $\Delta G_{TS'-TS}/\Delta G_{N'-N}$. This is the case when the particular mutation is buried within the protein and makes no contact with solvent. This fractional ϕ-value is interpreted as an indication of a partially formed structure in the transition state. However, the energetics of the structural interactions is unlikely to be simply linear, so exact structural interpretation is difficult. Some ϕ-values are close to 0 or 1 in value, making interpretation easier. Fractional values are more likely to suggest partial structure formation when they appear in groups within a particular region of a protein structure, such as the hydrophobic buried core.

A large number of ϕ-values that are fractional over a specific region of a protein structure can help rule out the possibility of parallel folding pathways: one with ϕ-values around 1 and one with ϕ-values around 0 [12]. This is most readily accomplished by graphically plotting the ϕ-value data. Data are plotted with ΔG_{TS-D} on the vertical axis and ΔG_{N-D} on the horizontal axis (or $\Delta \ln k_{D-N}$ against $\Delta \ln K_{D-N}$). Points that fall onto a linear plot likely fold with the mutated atoms structured to a similar extent in the transition state. If more mutations are made in the same element of structure, the expectation is that points continue to fall on the same line. However, in the case of multiple pathways, additional mutations, which stabilize the native state of the protein to a greater or lesser extent, may favor one of the folding pathways and change the slope of the line to a new value.

Beyond multiple pathways, it is also important to rule out the possibility of the addition of new interactions upon mutation. In such a situation, a double mutant cycle can elucidate the problem. A known interaction between two residues is broken by mutating each residue in separate experiments and then both residues in a double mutant experiment [13]. A rough estimate of the energy of interaction be-

tween residues can be made, giving some indication of possible structural rearrangements upon mutation.

Occasionally, uncanonical ϕ-values (greater than 1 or less than 0) are reported. Such cases can be explained by an overpacked, and hence destabilized hydrophobic core, which may be preferentially stabilized in comparison to the transition state when a deletion mutant is made. Such problems are more common in engineered sequences [14, 15]. Nonnative interactions in the transition state can also lead to these sorts of unconventional ϕ-values.

It should also be noted that ϕ-values are not limited to characterization of the transition state. It is also possible to determine ϕ-values for intermediates along the folding pathway, substituting ΔG_{I-D} for ΔG_{TS-D} in Eq. (3), where I represents the intermediate state. In the case of the barnase, ϕ-value analysis of the intermediate showed a structure consistent with the complete folding mechanism assembled from NMR studies on the denatured state and ϕ-values determined of the transition state [16].

Thus far, discussion of ϕ-values has focused on the forward, folding reaction. It should be noted, however, that the reverse (unfolding) reaction also has an associated ϕ-value, which can be understood with a similar analysis. For a simple two-state reaction, this is simply $1 - \phi$ for folding. Often, this unfolding ϕ-value is simpler to compute, because intermediate states are most likely to occur between the denatured state and transition state, which affect the rate of folding and not unfolding. The unfolding pathway from the folded state to the transition state is more typically a first-order reaction that can be readily determined by fitting the unfolding arm of a chevron plot (see below).

13.4 Techniques

Protein stability is frequently measured using either chemical or thermal means to allow the protein to undergo denaturation under equilibrium conditions [17]. In general, the two methods for determining changes in stability upon mutation provide similar results for canonical two-state folding proteins.

Thermal denaturation is typically measured using differential scanning calorimetry (DSC). Fitting a DSC trace (or a trace created by spectroscopically following a thermal unfolding curve) will provide the enthalpy (ΔH_{N-D}) and entropy (ΔS_{N-D}), as well as a precise measure of the melting temperature, T_m. The entropy and enthalpy here are assumed to be at the melting temperature. Such a fit is best done with knowledge of the specific heat capacity change during folding (ΔC_P). If the change in stability upon mutation is approximated to be temperature independent, the following equation can be used to calculate it.

$$\Delta\Delta G_{D-N} \approx \Delta T_m \Delta S_{D-N} = \frac{\Delta T_m}{T_m} \Delta H_{D-N} \tag{5}$$

In a spectroscopically followed chemical denaturation using urea or guanidinum chloride as a denaturant, the free energy change with the concentration of denaturant is taken to be linear.

$$\Delta G_{D-N} = m_{D-N}([D]_{50\%} - [D]) \tag{6}$$

Similar to the thermal unfolding case, fits to denaturation curves will provide two numbers: the *m*-value (m_{D-N}) and midpoint of the denaturation ($[D]_{50\%}$). The *m*-value is usually taken to be a constant that scales with the change in solvent-accessible surface area of the protein upon unfolding. Often, the mutated and wild-type proteins have negligible differences in *m*-values, given that so few atoms are deleted. However, significant errors can be introduced when the stability is extrapolated to zero denaturant concentration. To minimize this error, the average *m*-value is computed. This is then multiplied against the change in the denaturation midpoint (a precisely determined value like the change in T_m) to give the change in stability upon mutation.

$$\Delta\Delta G_{D-N} \approx 0.5(m_{D-N} + m'_{D-N})\Delta[D]_{50\%} \tag{7}$$

The kinetics of protein folding can be followed using numerous techniques: stopped flow and continuous flow mixing, temperature jump, and NMR line-broadening analysis. As before, spectroscopic probes such as circular dichroism or tryptophan fluorescence can be used to indicate the population of folded and unfolded protein. The observed rate in the folding reaction is k_{obs} and is the sum of the folding and unfolding rate constants: $k_f + k_u$. It is typically taken as a function of denaturant concentration and plotted as a v-shaped chevron plot.

As in the equilibrium situation, a linear *m*-value is used to describe the dependence of the energetics of folding and unfolding on denaturant concentration.

$$\Delta G_{TS-D} \propto m_{TS-D}[D] \tag{8a}$$

$$\Delta G_{TS-N} \propto m_{TS-N}[D] \tag{8b}$$

where m_{TS-N} and m_{TS-D} are the kinetic *m*-values. Summation of the kinetic *m*-values should give the equilibrium *m*-value. A common explanation for any shortfall is the existence of intermediate states on the folding pathway. The ratio of the kinetic *m*-value to the equilibrium *m*-value gives a measure of the solvent exposure, or compactness, of the transition state. This information, in the form of Tanford β, defined below as β_T, is complementary to the ϕ-value, which is a structurally more specific measure of transition state structure.

$$\beta_T = \frac{m_{TS-N}}{m_{D-N}} \tag{9}$$

Application of transition state theory to Eq. (8) gives equations describing the dependence of rate on denaturant concentration, [D]

$$\ln k_f = \ln k_f^{H_2O} - m_{TS-D}[D] \quad (10a)$$

$$\ln k_u = \ln k_u^{H_2O} + m_{TS-N}[D] \quad (10b)$$

where $k_f^{H_2O}$ and $k_u^{H_2O}$ are the rate constants for folding and unfolding, respectively, in the absence of denaturant. These equations describe the characteristic chevron plot of k_{obs} as a function of denaturant concentration. Deviations from a v-shaped plot with two linear arms, representing the folding and unfolding parts of the reaction, are strong indicators that the folding reaction is more complicated than a simple two-state process. Further, it should be understood that a v-shaped chevron plot cannot alone be taken as evidence for a two-state transition without first fitting it to a standard equation and recovering reasonable values for kinetic constants. Fitting the entire plot also reduces error that may be present in single rate constant at a particular denaturant concentration.

The particular denaturant concentration used for computation of ϕ-values is not critical in the case of a two-state folding protein, where the value of the Tanford β does not change upon mutation and the folding pathway is unchanged. In general, it is wisest to compute values of $\Delta\Delta G_{TS-D}$ at a variety of denaturant concentrations to observe whether the folding pathway changes with denaturant concentration [18]. In cases where intermediate states are believed to exist between the denatured and transition states, it may be best to use values exclusively at high denaturant concentrations or to simply fit the unfolding arm of the chevron plot with a linear fit, since such intermediates are contributing little to the observed rate constant, k_{obs}, at high denaturant concentration.

13.5 Conclusions

The method described here for carrying out a ϕ-value analysis is the only experimental method available for atomic level structural information of folding transition states. Extensive ϕ-value analyses have been carried out on the proteins barnase and chymotrypsin inhibitor 2 [1, 3–5]. The transition state structural information obtained in such studies, when combined with molecular dynamics simulation and NMR structural information, can then be used to determine the complete, atomistic picture of protein folding [19]. As computing power further improves to bring simulated folding temperatures into agreement with experimental temperatures, a combination of ϕ-value analysis and computational techniques will be essential for increasing the repertoire of proteins for which the complete, atomistic folding pathway is known.

References

1 Fersht, A. R., Matouschek, A. & Serrano, L. The folding of an enzyme I. Theory of protein engineering analysis of stability and pathway of protein folding. *J. Mol. Biol.* 224, 771–782 (1992).

2 Fersht, A. R., Leatherbarrow, R. J. & Wells, T. N. Quantitative-analysis of structure activity relationships in engineered proteins by linear free-energy relationships. *Nature* 322, 284–286 (1986).

3 Itzhaki, L. S., Otzen, D. E. & Fersht, A. R. The structure of the transition state for folding of chymotrypsin inhibitor 2 analysed by protein engineering methods: evidence for a nucleation-condensation mechanism for protein folding. *J. Mol. Biol.* 254, 260–288 (1995).

4 Matouschek, A., Jr., Kellis, J. T. K., Serrano, L. & Fersht, A. R. Mapping the transition state and pathway of protein folding by protein engineering. *Nature* 340, 122–126 (1989).

5 Otzen, D. E., Itzhaki, L. S., ElMasry, N. F., Jackson, S. E. & Fersht, A. R. Structure of the transition state for the folding/unfolding of the barley chymotrypsin inhibitor 2 and its implications for mechanisms of protein folding. *Proc. Natl Acad. Sci. USA* 91, 10422–10425 (1994).

6 Mayor, U., Guydosh, N. R., Johnson, C. M., Grossmann, J. G., Sato, S., Jas, G. S., Freund, S. M. U., Daggett, U. & Fersht, A. R. The complete folding pathway of a protein from nano-seconds to microseconds. *Nature* 421, 863–867 (2003).

7 Fersht, A. R. Dissection of the structure and activity of the tyrosyl-tRNA synthetase by site-directed mutagenesis. *Biochemistry* 26, 8031–8037 (1987).

8 Carroll, F. A. *Perspectives on Structure and Mechanism in Organic Chemistry.* Brooks/Cole Publishing, London (1998).

9 Jackson, S. E., Moracci, M., elMasry, N., Johnson, C. M. & Fersht, A. R. Effects of cavity-creating mutations in the hydrophobic core of chymotrypsin inhibitor 2. *Biochemistry* 32, 11259–11269 (1993).

10 Serrano, L., Neira, J.-L., Sancho, J. & Fersht, A. R. Effect of alanine versus glycine in α-helices on protein stability. *Nature* 356, 453–455 (1992).

11 Burton, R. E., Huang, G. S., Daugherty, M. A., Calderone, T. L. & Oas, T. G. The energy landscape of a fast-folding protein mapped by Ala-Gly Substitutions. *Nature Struct. Biol.* 4, 305–310 (1997).

12 Fersht, A. R., Itzhaki, L. S., ElMasry, N. F., Matthews, J. M. & Otzen, D. E. Single versus parallel pathways of protein folding and fractional formation of structure in the transition state. *Proc. Natl Acad. Sci. USA* 91, 10426–10429 (1994).

13 Matouschek, A. & Fersht, A. R. Protein engineering in analysis of protein folding pathways and stability. *Methods Enzymol.* 202, 82–112 (1991).

14 Viguera, A. R., Vega, C. & Serrano, L. Unspecific hydrophobic stabilization of folding transition states. *Proc. Natl Acad. Sci. USA* 99, 5349–5354 (2001).

15 Ventura, S., Vega, M. C., Lacroix, E., Angrand, I., Spagnolo, L. & Serrano, L. Conformational strain in the hydrophobic core and its implications for protein folding and design. *Nature Struct. Biol.* 9, 485–493 (2002).

16 Bond, C. J., Wong, K. B., Clarke, J., Fersht, A. R. & Daggett, V. Characterization of residual structure in the thermally denatured state of barnase by simulation and experiment: description of the folding pathway. *Proc. Natl Acad. Sci. USA* 9, 13409–13413 (1997).

17 Fersht, A. *Structure and Mechanism in Protein Science.* W.H. Freeman and Company, New York (1998).

18 Matouschek, A., Otzen, D. E., Itzhaki, L. S., Jackson, S. E. & Fersht, A. R. Movement of the position of the transition state in protein folding. *Biochemistry* 17, 13656–13662 (1995).

19 Daggett, V. & Fersht, A. R. The present view of the mechanism of protein folding. *Nature Rev. Mol. Cell Biol.* 4, 497–502 (2003).

14
Fast Relaxation Methods

Martin Gruebele

14.1
Introduction

In a chemical system at equilibrium, the forward and backward reactions occur at the same rate. For a simple two-state reaction D ⇄ F, the equilibrium concentrations and rate coefficients are thus related by the equilibrium "constant" $K_{eq} = [F]/[D] = k_f/k_d$. The quotation marks are warranted because K_{eq} is not really a constant, it depends on the environment of the chemical system. According to Le Châtelier, an endothermic reaction shifts towards higher concentrations of product when the temperature is raised, thus raising K_{eq}. Similarly, a reaction producing a reduced-volume product shifts towards the product when pressure is applied. As a final example, addition of a denaturant such as urea or guanidinium hydrochloride to a protein solution (see Chapter 3) favors exposure of hydrophobic surfaces, and would increase the concentration of denatured state D (the reactant in the equations shown above).

The sensitivity of K_{eq} to the environment can be exploited to study reaction rates. The idea behind relaxation methods is straightforward: If a parameter such as temperature, pressure, or denaturant concentration is switched to a new value so rapidly that the chemical system cannot respond during the switching process, the subsequent relaxation towards equilibrium can be monitored. This idea was first turned into a practical experimental technique by Manfred Eigen and coworkers [1]. Eigen received the 1967 Nobel prize in chemistry for this work.

Two ingredients are required to make a relaxation experiment work: a fast initiation step and a fast detection scheme. Protein folding has been initiated by pressure jumps, temperature jumps, electrochemical potential jumps, sudden binding/unbinding of substrates, and denaturant jumps, to name just the most prominent examples [2–4]. Optical probes have contributed the bulk of fast detection methods, including infrared and visible absorption, Raman scattering, X-ray scattering, fluorescence, and circular dichroism [4, 5].

What is "fast" in the context of protein folding? A somewhat arbitrary but commonly used definition is given here: Beginning in the 1980s, a number of protein-folding reactions were investigated by stopped-flow mixing with a time resolution

Protein Folding Handbook. Part I. Edited by J. Buchner and T. Kiefhaber

ISBN: 3-527-30784-2

of ca. 1 ms. It was found that many proteins have an unresolved burst phase, even though the complete folding process may require from milliseconds to seconds [6]. More recently, proteins and peptides have been discovered that fold completely on the submillisecond time scale, so none of the folding kinetics can be resolved by conventional stopped-flow techniques [7]. Relaxation techniques were developed to break the ''ms-barrier,'' and so processes in the nanosecond to microsecond range will be considered ''fast.'' Relaxation and other fast techniques have proved that none of the elementary events for folding take more than a millisecond, and far more stringent limits on the time scales have been set in the meantime.

Fast relaxation studies of biologically relevant systems have a long history. Eigen himself had studied imidazole protonation by 1960 [8]. Flynn and coworkers studied the association of proflavine in 1972 by laser temperature jump [9]. Holzwarth and coworkers studied lipid phase transitions [10] and dye–DNA binding in the 1980s, and Turner's group extensively investigated relaxation of nucleic acid oligomers in the 1980s [11]. Submillisecond relaxation was first applied to peptide and protein folding in the 1990s [12–16], including photolysis-induced, temperature, electrochemical [17], and later pressure jumps [3].

The relaxation experiments discussed here are not to be confused with dielectric relaxation spectroscopy [18], which does not involve a sudden initiation step, or with NMR relaxation experiments [7], which can study protein folding kinetics on a microsecond time scale via analysis of the lineshapes. These, as well as stopped-flow techniques and submillisecond continuous flow techniques are discussed in Chapter 23.

14.2 Techniques

14.2.1 Fast Pressure-Jump Experiments

Pressure (or solvent density) is a useful variable for controlling protein folding. Although folded proteins are more compact than unfolded proteins in terms of radius of gyration, the cores are not perfectly packed and the unfolded state generally has a smaller partial volume of solvation than the folded state. According to Le Châtelier's principle, proteins thus unfold at higher pressure, and this generally occurs at pressures of $1–5 \times 10^8$ Pa. Increased pressure also raises the cold-denaturation temperature of proteins and decreases the heat-denaturation temperature. To a first approximation, the folding–unfolding phase diagram can be derived from a quadratic expansion of the free energy in T and P. Supporting evidence shows that in the low-pressure regime, the stability of some proteins is actually enhanced by pressure [19, 20] (see Chapter 5).

A number of kinetic studies using pressure relaxation with millisecond or slower time resolution have been reported [21]. Submillisecond time resolution was achieved by Schmid and coworkers [3], who used a piezoelectric driver design first

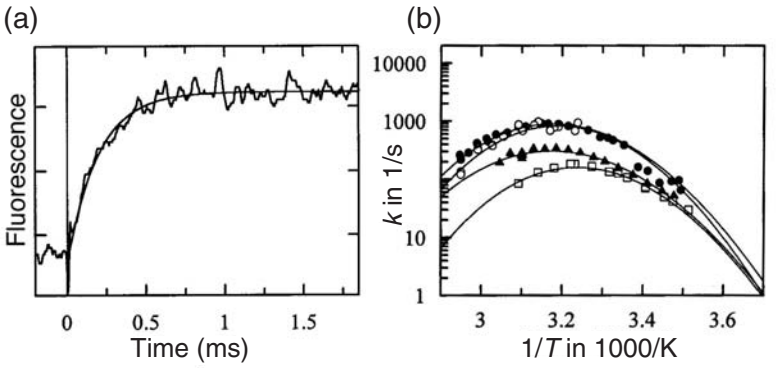

Fig. 14.1. a) Refolding of 6 μM *Bc*-Csp after a pressure jump from 100 to 3 bar at 75.3 °C. b) Arrhenius plot of the microscopic rate constant k of refolding of (open circle) wild-type *Bs*-CspB and the (filled circle) Phe27Ala, (triangle) Phe17Ala, and (square) Phe15Ala variants. From Ref. [3].

proposed by Clegg et al. [22] In this design, a sample contained in a 2 mm bore sapphire ring covered on each side by a flexible membrane is compressed in $<$100 μs by a piezoelectric element. Pressure changes up to 10^7 Pa can be achieved in both directions, and can be maintained essentially indefinitely. The sapphire ring provides optical access around the whole sample.

A prototypical result is shown in Figure 14.1 [3]. The cold shock protein from *Bacillus subtilis* relaxes in as little as 41 μs via an apparent two-state mechanism. (How to obtain folding rates from relaxation rates is briefly discussed in the protocols, and in Chapter 12.1.) The unfolding rate is Arrhenius-like (a straight line on a ln k versus $1/T$ plot), but the folding rate is highly curved with a maximum rate at the temperature of maximum hydrophobicity.

14.2.2 Fast Resistive Heating Experiments

The first successful fast temperature-jump relaxation experiments were based on resistive heating. Hoffman developed an instrument capable of 50 ns time resolution in high ionic strength solvents [23]. Commercial instruments (DIA-LOG) are available based on the work of Jovin and coworkers [24]. These instruments have a time resolution of $<$5 μs under physiologically relevant conditions (low ionic strength solvent).

In a resistive temperature jump, a 10–50 nF capacitor at about 500 V is discharged into a $\approx$1 ml sample cell. The risetime of the jump depends on solvent conductivity, and ranges down to 1 μs in solutions at a moderate ionic strength yielding 100 Ω cell resistance.

A prototypical result obtained by heating the cold-denatured protein barstar in about 5 μs is shown in Figure 14.2 [14, 25]. Two phases are resolved in the unfold-

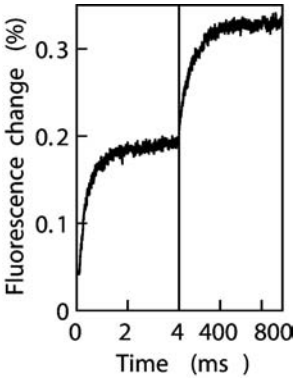

Fig. 14.2. Biphasic submillisecond and millisecond relaxation of barstar, showing accumulation of an intermediate ensemble. From Ref. [14].

ing reaction, so a minimal scheme involving a denatured state D, intermediate state I and folded state N could be constructed. A mutational phi-value analysis reveals the differing contributions of amino acid side chains to the stability of the intermediate state. More recent work on WW domain and homeodomain folds has revealed two-state refolding times as fast as 19 μs [26–30]. A study of *Drosophila* calmodulin, which folds in approximately 100 μs, confirms a behavior also seen in slower folding proteins [31, 32]: the unfolding rate is Arrhenius-like (linear plot of $\ln k$ vs. $1/T$ with negative slope), indicating that the transition state free energy shifts with the folded state, and implying that the transition state is not very different structurally from the folded state.

14.2.3
Fast Laser-induced Relaxation Experiments

Lasers can be used to induce relaxation via a variety of photochemical and photophysical processes. A substrate can be removed by photolysis, thereby causing rearrangements of the binding protein. Redox agents or proton donors can be light-activated, changing the oxidation or protonation state of a protein. Disulfide bridges or other linkages can be broken, releasing the strain of a nonnative conformation. Other photochemical processes include pH jumps and dissociation of unnatural amino acids. Among photophysical processes, chromophore relaxation has been used to study the folding speed limit, and the most commonly used is heating of the solvent (temperature jump). We discuss these approaches in turn.

14.2.3.1 **Laser Photolysis**

Laser photolysis was first used by Eaton and coworkers to induce protein refolding [12]. They used the increase of protein stability when the CO ligand is photodissociated to induce folding events. The same group also induced a ''protein quake'' by

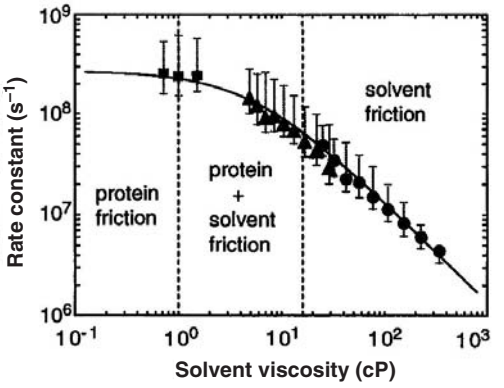

Fig. 14.3. Rate constant of myoglobin relaxation as a function of solvent viscosity. An inverse relationship holds except at the very lowest viscosities. From Ref. [33].

ligand dissociation [33]. By laser-dissociating CO from myoglobin in glycerol/water mixtures ranging in viscosity from 0.7 to 300 cP, they were able to show that protein self-friction contributes ≈1 cP (mPa s) to the effective viscosity in a Kramer's theory for the folding rate (Figure 14.3). (See Experimental Protocols and Chapter 22 for more details on Kramer's theory.)

14.2.3.2 **Electrochemical Jumps**

Electrochemical jumps were pioneered by Gray, Winkler and coworkers [17, 34–38]. In these experiments, redox active complexes (often based on Ru^{2+} ions) reduce a prosthetic group (such as the heme group in cytochrome *c*). Depending on the choice of complex, the electron transfer reaction can be complete in under 1 μs. The fastest redox agents are typically limited to <1 ms by charge recombination.

Barrier-limited refolding has been studied in cytochrome *c* by reducing unfolded ferricytochrome in ca. 3 M GuHCl buffer. Under these denaturant conditions, ferricytochrome *c* is more stable in the unfolded state, but ferrocytochrome *c* is more stable in the folded state; the protein refolds after the electron transfer occurs, with the fastest phase observed of 40 μs duration [17, 37]. Because electron transfer processes can be tuned to have large negative free energies, they can also be used to probe submicrosecond processes corresponding to diffusional motions of proteins (see also "Chromophore Excitation" below) [38]. Figure 14.4 shows the 250 ns contact time obtained under highly denaturing conditions between a ruthenium complex bound to histidine 33 of cytochrome *c*, and a zinc-modified porphyrin 15 residues away. After applying a steric correction, the authors estimate a ≈60 ns contact formation rate.

14.2.3.3 **Laser-induced pH Jumps**

Laser-induced pH jumps rely on changes of the pK_a induced by electronic excitation. Systems have been developed in which the pH is lowered through the reac-

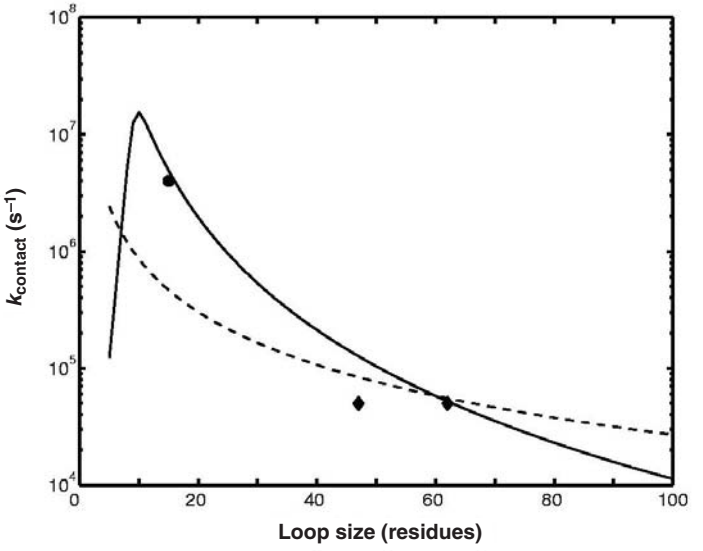

Fig. 14.4. Rates of tertiary contact formation in denatured cyt *c* have been extracted from measurements of ET rates in Ru(His33)-Zn-cyt *c* (filled circle [Gdm_HCl] = 5.4 M, temperature = 22 °C, 15-residue loop). The solid line is from the Camacho-Thirumalai theory, the dashed line from the Szabo model. From Ref. [38].

tion $AH \rightarrow A^- + H^+$, and where the pH is raised through the recombination $A^- + H^+ \rightarrow AH$ [39, 40]. The bimolecular recombination process is generally diffusion limited, so the original pH is reestablished upon deexcitation of the chromophore. This occurs within 10 s of microseconds at concentrations useful for protein-folding studies. Some reactions also yield stable photoproducts following a reaction of the photoproduced anion (e.g., *ortho*-nitrosobenzoic acid = *o*-NBA), so the pH is stable after the jump [41].

Recent pH-jump relaxation studies investigated the formation of the molten globule intermediate of apomyoglobin using *o*-NBA [42, 43]. The two observed kinetic processes were attributed to histine imidazole (fast) and carboxylate (slow) protonation by one set of authors, while the others found a significant denaturant-induced reduction in the slower rate process.

14.2.3.4 **Covalent Bond Dissociation**

Covalent bond dissociation overcomes the main limitation of the two previous approaches: the need for denaturant tuning. In order to poise the protein at the brink of (un)folding, so substrate removal or electron transfer can have a large effect, molar quantities of denaturant often need to be added. By photolyzing disulfide bridges used to constrain peptide or protein structure to a nonnative state, experiments can be carried out in denaturant-free buffer. This has been applied to the recombination dynamics of aminothiotyrosine "unnatural" amino acids in model peptides: the aqueous sample can be photolyzed at 270 nm with a femtosecond or

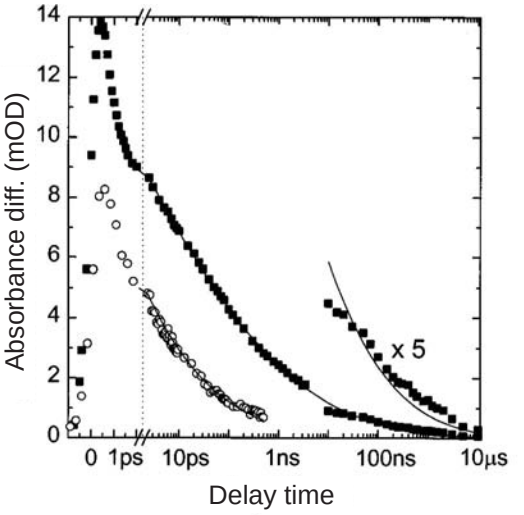

Fig. 14.5. Decay of thiyl radical absorbance in the 17-mer peptide discussed in the text. The dynamics can be fitted by powerlaws $t^{-\alpha}$ with α near 0.1. From Ref. [44].

picosecond pulse [44, 45]. Disulfide bridges cleave by a directly dissociative process of <1 ps duration, providing an enormous dynamic range over which two point correlations of the thiyl termini can be studied. Figure 14.5 shows the relaxation of an alanine-rich 17-mer initially cyclized by a disulfide bridge. The relaxation process is highly nonexponential and extends from picoseconds to microseconds.

14.2.3.5 **Chromophore Excitation**

Chromophore excitation has been used as a direct probe of the fastest diffusive events that can occur during protein folding [46–51]. A typical example would be diffusion of a peptide loop until end-to-end contacts are formed. In such experiments, a chromophore is excited at $t = 0$. The chromophore excitation then relaxes, but the relaxation rate is accelerated by quenching when the peptide loop forms contacts. Experiments quenching tryptophan triplet states with cysteine have yielded loop contact times ranging from 40 to 140 ns as the chain length is increased from 5 to 20 [49, 50]. Experiments utilizing triplet–triplet energy transfer between thioxanthone and naphtyl groups have yielded even shorter times of 20 ns for small loops [48, 51]. Such experiments are described in more detail in Chapter 22.

14.2.3.6 **Laser Temperature Jumps**

Laser temperature jumps are perhaps the most commonly used relaxation method for peptide and protein folding experiments [5, 13, 15, 16, 30, 52–66]. The first successful laser temperature-jump studies of chemical reactions were carried out in the 1970s, but the technique was not applied to protein folding until 20 years later.

Laser temperature-jumps can achieve dead times as short as 2 ps [13]. The lower limit is imposed by the need for thermal equilibration of the solvent after a specific solvent mode has been excited by the laser. (Backbone modes of the protein should of course not equilibrate, since one wishes to observe them after the temperature jump.) The achievable temperature jumps generally lie in the range of 5–30 K, sufficient to cause large changes in protein K_{eq} values. Most laser temperature-jump experiments are carried out with nanosecond heating pulses in the 1.5–1.9 μm range to pump directly H_2O or D_2O stretching vibrations, which thermalize within the nanosecond pump profile. These wavelengths can be obtained from Nd:YAG lasers Raman-shifted in hydrogen (1.9 μm) or methane (1.5 μm) [67], or by difference frequency generation in $LiNbO_3$ crystals [53]. Fast temperature jumps can potentially cause pressure and temperature fronts to propagate through the sample, but such effects can be mitigated by using the proper counterpropagating pumping geometry, initial temperature, pump spot size, and a noncollinear detection method [67].

Protein unfolding, peptide relaxation, and protein refolding were initially observed by laser temperature jumps in the mid-1990s [13, 15, 16]. In apomyoglobin, formation of the hydrophobic AGH helical core happened 5 orders of magnitude faster (<10 μs) than complete refolding of the protein, resolving the burst phase seen by stopped-flow kinetics [6, 16]. Small peptides of well-defined secondary structure exhibit even faster kinetics [15, 55, 68–72]. Figure 14.6 shows the relaxation kinetics of a β-hairpin and of a short helix, common motifs in protein secondary structure. Analysis of the hairpin data is compatible with formation of the turn as a rate-limiting step [70], although models with early interstrand contacts have similar time scales [73]. The helix data use ^{13}C isotopic labeling to dissect local peptide kinetics, and confirms nonexponential dynamics previously observed for nonnatural helical polymers and expected from helix formation models [71, 74, 75].

Two-state and more complex folding mechanisms of larger proteins have also been observed by laser temperature jumps. Phi value and other mutation analyses (see Chapter 13) have been reported [59], as well as solvent-tuning studies [76]. Like resistive temperature-jump experiments and temperature-dependent pressure jumps, laser temperature-jump studies have shown strong curvatures in Arrhenius plots for the folding rate of fast folders [59]. Figure 14.7 illustrates laser temperature jumps of proteins with the relaxation kinetics of two very fast folding λ-repressor fragment mutants [65]. All mutants of this molecule with >50 μs folding times exhibit single exponential kinetics, while all mutants with $\tau < 50$ μs, irrespective of the location of the mutations, exhibit an additional fast phase lasting for a few microseconds.

14.2.4
Multichannel Detection Techniques for Relaxation Studies

Relaxation experiments are easily combined with a large variety of single-channel probes such as integrated fluorescence [14], one-color absorption [77], photoacous-

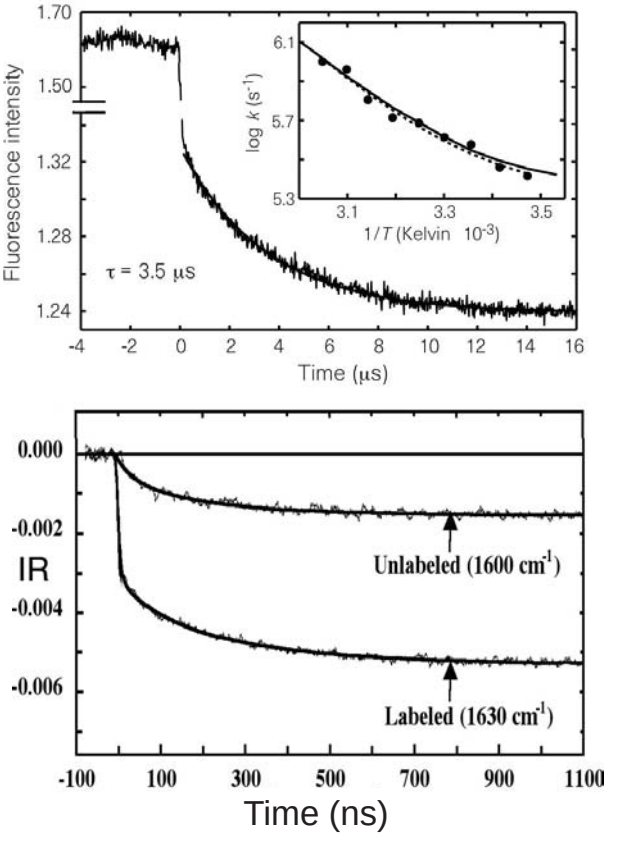

Fig. 14.6. Relaxation response of 16-mer beta hairpin (top) and of unlabeled and ^{13}C-labeled helix peptides (bottom), showing a significant change in the fast-phase amplitude. From Refs [69] and [71].

tic spectroscopy [42], or transient gratings [43]. Here multichannel techniques will be described in more detail. Multichannel techniques provide an array of data at each kinetic measurement, such as a full infrared spectrum or a time-resolved fluorescence decay. They can extract additional information not available when only rate constants from a single probe are used to characterize folding. These probes address different aspects of protein structure.

14.2.4.1 Small Angle X-ray Scattering or Light Scattering

This can be used to characterize protein compactness by plotting the intensity vs. scattering vector. Time-resolved Kratky plots can follow the evolution from highly denatured to globular states, and the radius of gyration can be used as a single measure of protein compactness. These detection techniques have achieved submillisecond resolution when combined with mixing techniques (see Chapter 15)

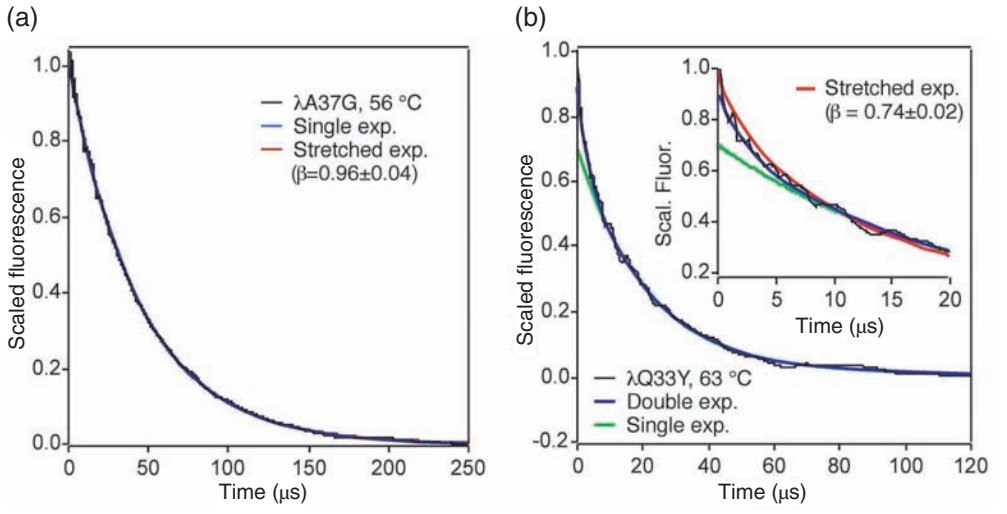

Fig. 14.7. a) Relaxation of a very fast folding mutant of lambda-repressor fragment (Y22W/Q33Y/G46A/G48A), showing deviation from single exponential relaxation below 5 μs. b) The slower Y22W/Q33Y/A37G mutant follows single-exponential relaxation with high precision. From Ref. [65].

[78], but they have not been combined with the relaxation experiments described here.

14.2.4.2 **Direct Absorption Techniques**

These have been applied to submillisecond protein folding in the infrared and visible [12, 31, 79] IR bands at ≈1650 cm^{-1} (amide I′) and ≈1300 cm^{-1} (amide III′) are sensitive to overall secondary structure, with specific signatures for native and solvated α-helices, β-sheets, and aggregates. Three approaches have been developed for obtaining mid-infrared spectra with submicrosecond time resolution from relaxation experiments. In the scanning method, a high-resolution laser is tuned across the spectral region in steps, and a relaxation experiment is performed at each step [15]. In step-scan FTIR, a Fourier-transform infrared spectrometer is stopped at regular intervals in the scan of its moveable mirror, and a kinetic transient is collected at n points in time. The resulting n interferograms can be Fourier-transformed to yield the infrared spectrum at each of the n kinetic time intervals [80]. In the third technique, a nanosecond-spaced sequence of broadband infrared pulses is generated by a femtosecond laser, sent through the sample after relaxation has initiated protein kinetics once, and finally dispersed onto an array detector [81]. Perhaps the most common use of IR techniques has been in time-resolved secondary structure melting via the amide I′ band of both peptides and proteins. Experiments have shown the existence of a new α-helical signature [53], ascribed to a solvated helix that occurs during unfolding. Particularly noteworthy is the fast

secondary structure loss examined in detail for the folded and several partially folded forms of apomyoglobin [5].

In the near-IR and visible region, the local environment of prosthetic groups such as heme (Soret band at ≈420 nm) or side chains such as tyrosine [31] can be probed. Parallel data collection is possible with a broadband excitation source, such as a femtosecond Ti:Sapphire laser or fluorescence from a laser-pumped dye (typically 50–100 nm bandwidth) dispersed onto an array detector. This again has the advantage that the entire absorption spectrum is collected after a single relaxation event. The first submillisecond measurements of diffusional dynamics of a protein (cytochrome *c*) were carried out using absorption measurements and laser photolysis (see above) in 1993 [12]. Recently the method has been used to study the dissociation dynamics of light-harvesting complexes into dimer and monomer subunits (see Chapter 14.5 for precautions in the analysis of such relaxation) [64].

Some relaxation experiments (e.g. temperature jumps and pressure jumps) can induce significant variations in the solvent refractive index. In such cases, great care must be taken when applying direct absorption to detect protein kinetics, as the probe beam may wander or may be lensed as it passes through the solvent [64].

14.2.4.3 Circular Dichroism and Optical Rotatory Dispersion

These techniques measure the difference in absorbance or refractive index of left and right circularly polarized light due to chirality of the absorber. Two regions are of particular interest for studying protein backbones and side chains: at 250–300 nm, asymmetries in the environment of aromatic side chains cause CD or ORD signals; at 190–230 nm, absorption of the amide group probing the backbone itself leads to distinctive CD signals for random coils (small or positive from 210 to 220 nm), sheets (negative peak near 215 nm), and helices (two negative peaks at 208 and 222 nm). Nanosecond time-resolution methods have been developed for relaxation experiments: a highly elliptically polarized probe pulse (to avoid birefringence artifacts) is passed through the sample and modulated between left- and right-handed, then analyzed by a linear polarizer. This is repeated with different time delays after initiation of relaxation to yield a kinetic transient, and then at different wavelengths to yield a spectrum. The method has been used to directly measure the appearance of secondary structure on a nanosecond time scale in model peptides as well as microsecond time scale formation of some secondary structure in cytochrome *c* [82–85].

14.2.4.4 Raman and Resonance Raman Scattering

These have been used to determine both secondary structure content [86, 87] and changes in the local environment of prosthetic groups [88]. UV pulses near 210 nm resonantly excites amide electronic states of the backbone, creating scattered light about 5 nm away that can be selected by a monochromator (corresponding to the 1300 cm^{-1} amide III band). Pumping the Soret band of heme near 400 nm yields a combination of vibrational peaks very sensitive to ligation, and specific side chain vibrational modes can also be probed [88]. It is worth noting here that this

detection technique has been applied extensively to fast folding coupled with continuous mixers (Chapter 15) [89]. Compared with absorption techniques, Raman and fluorescence emission have an important advantage: their relatively isotropic light collection makes them less sensitive to refractive index fluctuations and other variations in the sample induced by the initiation step. In addition, neither the probe beam nor the scattered Raman light are absorbed by the aqueous solvent, and Raman is an inherently parallel probe technique which does not require scanning to obtain an entire spectrum. The main disadvantage is that dispersed Raman spectra are quite weak. Intense pump lasers can help, but photodamage must then be taken into account [88].

14.2.4.5 **Intrinsic Fluorescence**

Intrinsic fluorescence can be used to probe solvent exposure, motional anisotropy, the formation of specific tertiary contacts via quenching, and pair distances via engineered quenchers. Intrinsic fluorescence of proteins without prosthetic groups is due to the aromatic residues [90]. Tryptophan fluorescence dominates at 290–300 nm excitation, but tyrosine fluorescence has also been detected in fast relaxation experiments [56, 63]. Tryptophan fluorescence can be quenched by short-range electron or proton energy transfer (1–5 Å) from/to protonated histidine, cysteine and a few other side chains [91], or by longer range Förster energy transfer [92] (10–50 Å) to heme, nitrotyrosine, and cysteines derivatized with acceptor dyes [93]. This results in a decrease of the fluorescence lifetime from as long as 10 ns to as short as 0.1 ns, making tryptophan a useful probe of tertiary contact formation [42, 94]. Tryptophan fluorescence shifts from $\lambda_{max} \approx 350$ nm to ≈ 330 nm upon burial in the hydrophobic core, and quenchers such as acrylamide can also be used to probe solvent accessibility in fast relaxation experiments [95]. A number of proteins hyperfluoresce during the initial stage of denaturation, indicating that fluorescence intensity is a very sensitive probe of the native-like packing [96, 97].

Instruments capable of detecting an entire fluorescence spectrum every 100 ns, and an entire fluorescence decay every 14 ns have been designed for use with relaxation experiments [67, 98]. The resulting series of fluorescence spectra or fluorescence decays at nanosecond intervals require parallel data analysis methods, such as singular value decomposition (see Chapter 14.5) [99]. The advantage compared with an analysis of the rate constants only is that general inferences about the structural changes of the protein can be drawn. For example, a change in fluorescence lifetime unaccompanied by a wavelength shift indicates that tryptophan is coming into contact with a quencher, but without being desolvated.

14.2.4.6 **Extrinsic Fluorescence**

Extrinsic fluorescence or phosphorescence can be used to extract structural information in the form of pair-distances. The protein is labeled with a fluorescent donor dye, and with an acceptor that may or may not be fluorescent. Distances between donor and acceptor can be extracted using the Förster resonant energy trans-

fer (FRET) theory, although some caution is required when attempting to extract quantitative results because assumptions about orientational effects are often necessary. FRET techniques and single molecule techniques are described in detail in Chapter 17.

14.3 Protein Folding by Relaxation

14.3.1 Transition State Theory, Energy Landscapes, and Fast Folding

A general overview of the classical transition state theory and Kramer's theory as applied to protein folding is given in Chapters 12.1 and 22. Here certain aspects of energy landscape theory addressed by fast folding experiments are described in more detail.

Figure 14.8 illustrates the connection between folding funnels, folding free energy surfaces, and smoothed free energy surfaces for folding. Energy landscape theory, based on random heteropolymer theory with an energetic bias towards the native state [100, 101], posits that the energy of a protein gradually decreases as it becomes more compact. This gives a plot of energy versus configurational entropy per residue the funnel-like shape shown in Figure 14.8 (column 1).

Superimposed on the funnel shape are energy fluctuations caused by interactions of the backbone, side chain, and solvent if some coordinates are not averaged over, but kept as reaction coordinates '*x*'. Nonnative interactions over a wide energy scale are the main cause of landscape roughness. Among the largest of these is the classic example of proline *cis–trans* barrier (other side chains can also create conformational traps; see Chapter 25) [102, 103]. Although proline isomerization is not a necessary feature of folding [104, 105], even proteins whose energy landscape has been smoothed by design as much as possible retain some roughness [65]. This is so because not all nonnative interactions can be removed – in the language of energy landscapes, a residual frustration persists [106]. A typical examples of such an unavoidable residual interaction would be the steric clashes of different side chains [107, 108].

Among the traps on the funnel (assumed to have a Gaussian depth-distribution in random-energy theory) some can be rather deep [109], thus qualifying for specific treatment as ''intermediates'' rather than a statistical treatment. The best example is the noncoincidence between chain collapse and core drying – the latter a transition where water molecules are squeezed from the protein core. A larger energy fluctuation is shown at the entrance of the top funnel in Figure 14.8. Rapidly formed folding intermediates are discussed further in a separate section below.

Free energies are related to energies and entropies by $F = E - TS$, and so the funnel can be transformed into a picture more amenable for experimental work, which is generally carried out at constant temperature, not at constant entropy. Of

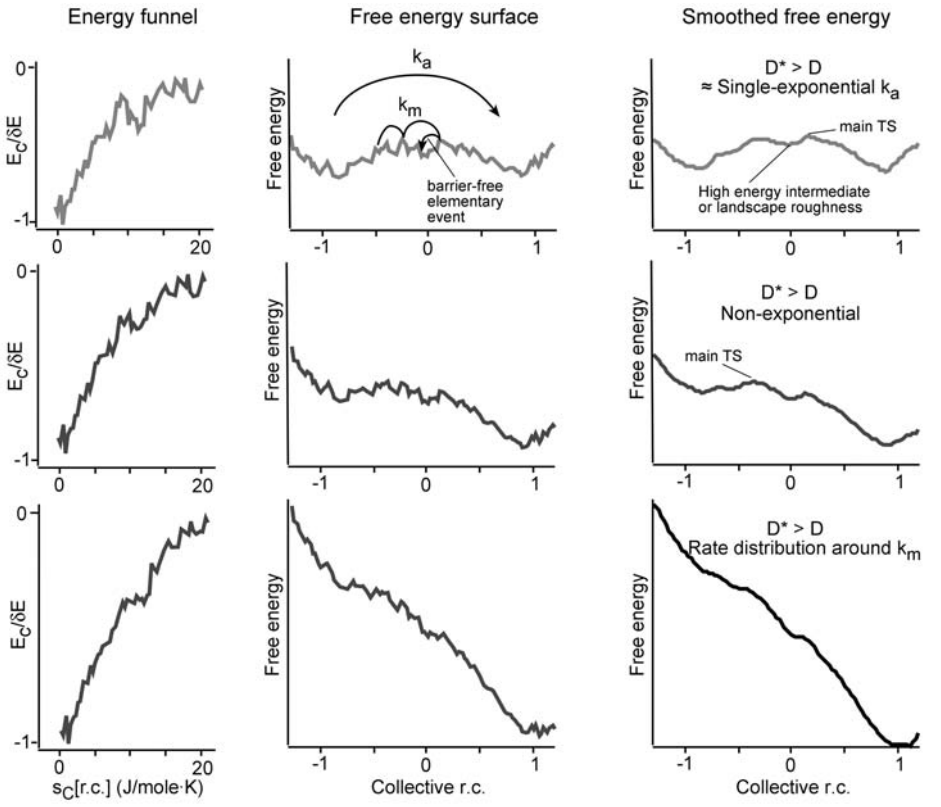

Fig. 14.8. Folding energy landscapes, free energy reaction plots, and smoothed free energy plots in one dimension. From top to bottom, the native bias increases. Important points and types of transitions are annotated, r.c. stands for reaction coordinate.

course the computation of the Gibbs free energy is somewhat more involved because it depends on enthalpy and total entropy (not energy and configurational entropy alone). The middle column of Figure 14.8 shows an example with a reaction coordinate linearly related to the configurational entropy.

The three free energy surfaces shown differ by the degree of compensation between energy and entropy. If entropy reduction during collapse is not fully compensated by contacts, a barrier results (top middle in Figure 14.8). In addition the free energy surface has a rough structure, and some of the local minima may be sufficiently prominent to deserve classification as "intermediates" or "high-energy intermediates" [110, 111]. The two are distinguished simply by whether the intermediate comes within 2–3 $k_B T$ of the denatured or native states (is populated), or not. The top middle case is very common in relaxation studies of small proteins [3, 14, 16, 26, 28, 31, 53, 57, 59].

It is not obvious that a free energy surface such as the one in the top middle of Figure 14.8 should give rise to single exponential kinetics. As surmised by Creighton and discussed by Zwanzig it does, if the interconversion among pairs of states is fast compared to traversing the bottleneck to the folded state [112, 113]. In that case, the activated folding rate coefficient k_a is much smaller than the diffusional time scale k_m for moving among the local minima, allowing the protein to equilibrate locally on the surface compared to the time scale required for barrier crossing. The local diffusion events characterized by k_m occur among the unavoidable minima left over when the protein is "minimally frustrated". Computations using Go models have shown that the free energy fluctuations caused by minimal frustration are generally $<3\ k_B T$" [114–116]. The three arrows in Figure 14.8 show part of a sequence of events occurring on the time scale k_m. Because of the residual roughness of the free energy surface, k_m is slower [65] than the fastest events the backbone can undergo (such as formation of a hairpin or the collision of two residues in a random peptide of length N in a θ-solvent tuned to eliminate all barriers) [15, 48, 49, 51, 68, 117]. A lower limit on k_m is set by such elementary-event peptide experiments, and ranges from $k_e = (10–100\ \text{ns})^{-1}$, depending on peptide length and residue composition.

In the large barrier case (Figure 14.8 top) only k_a can be observed, not k_m. This leads to an ambiguity in using transition state-like theories, which contain two time scales: the prefactor, and the smaller rate coefficient, which differs from the prefactor by a Boltzmann factor (see Chapter 12.1 and equation 3 in Section 14.5.4.1). The choice of prefactor then depends on how we treat the free energy surface: on the rough free energy surface in the top middle of Figure 14.8, we would use $(10–100\ \text{ns})^{-1}$, and treat the small barrier crossings caused by frustration explicitly as an additional free energy barrier. On the smoothed free energy surface to the right, we would use k_m as our slower prefactor, which has been shown to correspond to a renormalization of the diffusion constant to a smaller value D^* [118]. Experimentally, this renormalization factor can be derived by combining peptide relaxation studies [48, 68] and protein relaxation studies. For lambda repressor, it turns out to be about 40, equivalent to residual free energy fluctuations of $0.6\ k_B^2 T^2$ caused by frustration [65].

Can k_m be measured directly? The middle and lower rows of Figure 14.8 show what happens when the energy and entropy decrease are better compensated in the funnel: the free energy barrier disappears. In the completely downhill case on a rough surface, Zwanzig has shown with well-defined assumptions (see below) that the kinetics can be exponential, but with the renormalized slower diffusion constant D^* [118]. In the intermediate case (center row of Figure 14.8), the assumption that $k_m \gg k_a$ discussed earlier breaks down when the main barrier becomes comparable to the minimal roughness of the free energy surface in one dimension [56, 65, 119]. Both time scales can then be observed simultaneously by relaxation experiments with proteins engineered to fold downhill in a few microseconds, yielding a value of $k_m = (2\ \mu\text{s})^{-1}$ for the case of lambda repressor [65]. Explicit calculations for lambda repressor [120], as well as general theoretical calculations also yield speed limits in the 0.5–2 μs range [121].

The speed limit k_m is not a universal quantity, but depends on the complexity of the protein's fold or "topology," as it is often referred to in the folding literature. The reason is that more complex proteins have to undergo more elementary events to fold and are also more likely to be subject to residual frustration [114, 119]. For example, the most optimized fast-folding sequence for a two-helix bundle should fold faster (<1 μs) than the most optimized 8-helix myoglobin fold (>7 μs). This has been expressed in a relationship between the contact order (average loop length between to native contacts) and logarithm of the rate constant [122, 123]; a rigorous analysis must also include chain-length effects [124]. ln k vs. contact order is usually plotted for any two-state folders at hand, resulting in a large amount of scatter (2–3 orders of magnitude) along the vertical axis. The analysis outlined above shows that one should use instead the largest value of k_m, obtained with the most optimized sequence for a given fold, i.e., the actual speed limit of a fold subject to minimal frustration. Measurements of the fastest folding rates will allow a more quantitative experimental analysis of the rate–contact order relationship by revealing the degree of energetic frustration a given sequence imparts on a fold.

Changing the bias of the free energy by optimizing folding conditions has an effect even when a significant barrier persists. Consider the top and middle cases in Figure 14.8, and imagine for the moment that the barriers in the middle case are still significant (by making the denatured minimum a bit deeper). Then the top transition state is "late," and the middle transition state is "early." Whether one describes the motion of the transition state as a smooth shift [125], or as a switch across a high-energy intermediate [111], depends on the degree of smoothing applied to the free energy surface. Thus it is necessary to define a rule for how much the free energy surface should be smoothed in kinetic descriptions. A useful rule is that the smoothing should leave intact minima deeper than 2–3 $k_B T$, since this is the crossover where fast relaxation experiments and Langevin simulations have shown Kramer's exponential rate theory to be applicable [65]. This degree of smoothing removes the roughness caused by minimal frustration, but leaves more pronounced intermediates intact. When smaller barriers have to be treated (middle right in Figure 14.8), Langevin simulations are required to obtain the correct dynamics on the one-dimensional potential [65, 126].

One can choose to not apply any coarse-graining at all, and pick the classical value $k_B T/h \approx 300$ fs for the prefactor [28], along with an atomic scale motion as the reaction coordinate. In such a description of the kinetics, the reaction coordinate can change dramatically from realization to realization (e.g., in a series of MD simulations, each successive folding trajectory has a different atomic-level reaction coordinate at the free energy maximum). Thus, a structural justification for smoothing of the free energy surface is to apply smoothing until a consistent set of collective coordinates emerges.

The question then arises: how many coordinates should be used for a good description – are the one-dimensional cartoons in Figure 14.8 sufficient? As discussed earlier, Zwanzig has shown that with certain assumptions, even diffusion on a rough surface can be treated as an exponential process [118]. A one-dimensional reaction coordinate (such as the plot in Figure 14.8 bottom) is an

important assumption invoked to derive exponential diffusive behavior [118] $n > 1$ dimensions more easily accommodate the local minima needed so that a single bottleneck does not necessarily control the dynamics, and anomalous diffusion can result in stretched exponential or power-law dynamics [45, 127, 128]. In these nonexponential models, randomly distributed local minima of the free energy surface lead to ''logarithmic oscillations'' superimposed on the smooth nonexponential dynamics. These oscillations are analogous to the steps observed in multiexponential fits, and attributed to specific intermediates there. The conceptual difference between the two approaches hinges on either enumerating the fewest local minima needed to fit the data, or considering the entire hierarchy of minima constrained by scaling laws. The current computational and experimental evidence shows that at most a few coordinates should be required to accommodate the local minima necessary for robust nonexponential kinetics. For example, for a tetrapeptide investigated by Becker and coworkers [129, 130], two coordinates provided a rather complete description of the folding dynamics.

Experimental data, with few exceptions [44], are not highly nonexponential and can be fitted equally well by multiexponentials and logarithmic oscillations [56, 58]. This is partly due to the limited dynamic time range of experimental data. However, phosphoglycerate kinase data under a wide range of conditions always fits on average to stretched exponentials [63]. There is no a priori reason why a single trap should always yield rates that approximate a stretched exponential, whereas the hierarchical trap model naturally explains this because traps of many depths coexist. Both types of models agree that addition of denaturants will either smooth out the surface or raise the energy of traps in the barrier region, resulting in more exponential kinetics. This is observed experimentally [63]. It has also been shown experimentally that cold denaturation has a similar smoothing effect [56].

In a very recent experiment on λ-repressor, early time deviations from exponential kinetics are ascribed to diffusion events, but the deviation itself can be fitted by a stretched exponential with $\beta \geqslant 0.7$, again favoring a low-dimensional surface for the diffusion process [65]. No firm limits can be set at present, but it appears that at most a handful of collective reaction coordinates should be sufficient to describe folding processes rather completely.

14.3.2 Viscosity Dependence of Folding Motions

Viscosity effects on folding rates provide important clues to the mechanism. This is discussed in detail in Chapter 22, but a few observations from relaxation studies are worth reemphasizing here. A proper discussion requires at least Kramer's theory [131] because the same solvent–protein coupling both activates the protein for reaction and slows down the reaction when the coupling (and hence the viscosity) becomes large.

Viscogenic agents, such as sucrose or ethylene glycol, can affect both the prefactor ($\sim\eta^{-1}$ in the strongly damped Kramer's regime) and free energy barriers, as well as the compactness of the denatured state. Early observations of submillisecond refolding kinetics indicated a decrease of the rate with increasing viscosity, but

did not compensate for barrier effects [16, 33, 132]. Recent work has carefully calibrated the free energy at different viscogen concentrations, finding that the viscosity dependence of the prefactor is very close to η^{-1} [133–135]. These authors also make the argument that barriers are required to protect the native state from continuous unfolding, supported by the recent observation that very fast folding proteins without a substantial free energy barrier are aggregation prone [65].

There has been an ongoing discussion of deviations from Kramer's strongly damped regime caused by self-friction of the protein molecule during folding [16, 33]. Such deviations have been modeled by phenomenological equations of the type $k \sim (\eta + \eta_0)^{-1}$ or $k \sim \eta^{-d}$ where $d < 1$. Small peptides indeed have a length-dependent viscosity dependence, with powers deviating from -1 to as low as -0.8 [136]. In larger proteins, the evidence generally favors the simple Kramer's result. Some of the insights from simulation are discussed further below.

14.3.3 Resolving Burst Phases

As discussed in the section on transition states, some local minima in the free energy surface are deep enough to be amenable to individual analysis by relaxation experiments. Even when they lie at high energy, they can have subtle effects on the folding kinetics [137]. It has been postulated that a discrepancy between the time scale for collapse and the time scale for desolvation of the protein core could give rise to compact but solvated globular states [138]. Fast relaxation experiments support this general idea. An intermediate with native-like quenching of the apomyoglobin AGH helices forms on a microsecond time scale, and amide exchange experiments show that parts of this intermediate are protected, while others are still undergoing rapid exchange [6, 16]. Several nonnative forms of apomyoglobin have been investigated by Dyer and coworkers, and some have been shown to form a compact core at the diffusion limit [76]. Resistive temperature-jump experiments have been used to study the biphasic folding of barstar. Phi-value analysis shows that two of the helices consolidate rapidly ($\approx$300 μs), but a fluorescence shift towards a native-like structure requires nearly a second [25].

The question of the barrier height separating the unfolded state from the intermediate has been discussed extensively in the literature. Stretched- or multiexponential formation of a folding intermediate of the two-domain protein phosphoglycerate kinase indicates that for one of the two domains, the formation of the intermediate is limited by a hopping process on a rough free energy surface, rather than by a single barrier crossing [56, 63]. This is also supported by the observation that cold denaturation, which should smooth out the free energy surface, brings the kinetics back towards single-exponential folding. More work has been done using flow techniques (see Chapter 15 for details): Using a prefactor of 50 ns (to include free energy landscape roughness in the activation barrier) yields values below 8 $k_B T$ for molecules such as cytochrome *c* or ubiquitin [138–141]. It has been argued that in many cases, no barrier beyond residual roughness exists [56, 142, 143], or that these barriers come after the main transition state [144, 145]. In one

case, it has also been convincingly shown that the intermediate contains significant nonnative structure, but nonetheless has direct access to the native state [146].

14.3.4
Fast Folding and Unfolded Proteins

It has long been known that unfolded states contain sequence-dependent residual structure [147]. As discussed in Chapters 20 and 21, this has come to be much better understood in recent years. Residual unfolded structure is particularly important when interpreting fast relaxation experiments: the barriers are small, and changes in the unfolded structural ensembles can have a major effect on folding kinetics [31, 148]. For example, a variety of relaxation experiments have shown that unfolding rates tend to have ''normal'' linear Arrhenius plots, while folding rates have highly curved plots (see for example Figure 14.1). This has been taken as a sign that transition states remain relatively native like upon temperature tuning [31, 32], while the unfolded state becomes more native-like at low temperature. The effect of unfolded states on the rate constant can be reduced, by making them equally rigid at all temperatures. In that case motions of the transition state make a larger contribution to the rate turnover effect. Many natural proteins that are not highly optimized for folding probably fall in this category.

When the contributions of the unfolded state to the rate are not too large, a continuous analog of Φ-value analysis (see Chapter 13) can be used to analyze protein folding. This has the advantage that arbitrarily small perturbations can be applied, while mutations apply a defined-size perturbation [59]. Denaturant, pressure, and temperature have been tuned to this effect [57, 125, 137]. By itself, tuning thermodynamic variables provides no structural information, but when combined with mutations, structural information can be revealed. One useful application of continuous tuning is to test mutations for ''conservativeness'': a mutant with a very different temperature dependence of the free energy from the wild type is less likely to be a conservative mutation one wishes to use in Φ-value analysis [59].

The bottom line is this: whenever unfolded states are significantly altered by any perturbation, whether it is a mutation or the change of a thermodynamic variable, caution must be exercised when using free energy derivative analysis [32, 119]. An example in the case of temperature has already been given above, and is discussed in more detail in Ref. [148]. As an example of a mutation, truncation of a large side chain to a smaller side chain may reduce a nonnative interaction in the unfolded state, causing apparent shifts in Φ-values that are not related to changes in the transition state [32]. The characterization of unfolded proteins has only scratched the surface so far, but the number of experiments characterizing unfolded states of proteins is steadily increasing.

14.3.5
Experiment and Simulation

A hierarchy of simulation techniques has been used to describe fast relaxation data, some of which are described in more detail in Chapters 32 and 33. At the

simplest level, master equations are used, such as the n-state kinetic schemes discussed throughout this volume [4, 149]. Two common ones, prototypical of fast folding and association reactions, are discussed in more detail in the Experimental Protocols (Chapter 14.5). Their breakdown, outlined qualitatively earlier in the discussion, is also discussed more mathematically in terms of linear response theory [150], which explains rigorously when the transition from activated kinetics to the molecular time scale $(k_m)^{-1}$ occurs. More sophisticated kinetic schemes, which provide a more microscopic treatment of the dynamics by including large numbers of states, have yielded insights into the formation of small segments of secondary structure, as well as the folding of proteins [70, 113, 123, 151]. These models trace their ancestry to classic treatments of secondary structure such as the Zimm-Bragg model [152]. An important concept in such models is how many groups of states can independently undergo a transition. In ''single sequence approximations,'' native-like stucture must spread out from a single locus. In ''n-sequence approximation'' models, more sites are allowed where native structure can form [123]. The latter models yield lower barriers, and are generally in close accord with full theoretical treatments and experimental data.

Motion on continuous folding free energy surfaces can be treated by Langevin dynamics, revealing some interesting behavior. For example, it has been shown that small minima in the barrier region can actually accelerate folding if they increase the local curvature at the barriers [126]. Simulations on smoothed downhill surfaces such as Figure 14.8 (middle right) have verified nonexponential decays with renormalized diffusion constants ranging as small as $D^* \approx 0.00016$ nm^2 ns^{-1}, considerably smaller than the free diffusion constant for a small segment of secondary structure, in accord with analytical models [65].

Lattice models [116, 153–155] have proved very fruitful in comparison with fast folding experiments. Originally two-dimensional and allowing only for two types of residues, they have been extended to include more residue types and different lattice geometries [156, 157], for example to describe nonexponential helix relaxation kinetics [74]. Lattice models were among the first to show that proteins could fold via a rapid non-cooperative collapse, followed by crossing a relatively small barrier [155].

Off-lattice models are useful because they still coarse-grain the folding problem, thus making larger systems accessible, yet they do so with fewer restrictions than lattice models [158]. The viscosity dependence of folding reactions has been investigated by Klimov and Thirumalai in a model coupling a coarse-grained model of the protein with Langevin dynamics to represent the solvent. In agreement with several experiments, the normal Kramer's regime ($k \sim \eta^{-1}$) provides a good fit for α-helical and β-sheet peptides [159]. There are however certain conditions where a fractional power smaller than -1 can occur [160]. Off-lattice models have also revealed a rough free energy surface which can give rise to nonexponential kinetics [114, 127].

Molecular dynamics (MD) simulation has become an increasingly important tool for protein folding, as fast relaxation time scales and the capabilities of MD simulation on large computers are beginning to merge on the microsecond time scale [161]. A detailed overview is given in Chapters 32 and 33; here a few examples of

direct comparisons between fast relaxation experiments and MD simulation illustrate the synergy between them. The first detailed comparisons were made for unfolding rates extrapolated to higher temperature to match nanosecond time scale MD simulations. Excellent agreement between the extrapolated experimental and simulated unfolding time scales, as well as transition state structures was obtained [28, 162]. Folding rates are more challenging, but have become accessible with the development of very fast folding mini-proteins. A recent study compared 700 μs of trajectories of the molecule BBA5 with thermodynamic and kinetic data, and obtained good agreement for the folding rate constant and equilibrium constant [61]. The simulation shows that BBA5 does not fold via a single pathway, but by a funnel-like coalescence of secondary structures towards the native minimum. One caveat in this study is that folding was observed as a rare event in thousands of nanosecond-long trajectories, rather than in a few longer trajectories. MD simulations have also proved useful in providing a microscopic mechanism for experimental relaxation studies [66, 163]. They have also revealed that the free energy surface of denatured proteins is indeed complex, as also inferred from analytical models: [164]. Brooks and coworkers, and other groups, have found a rich structure of traps and nonnative local minima in two-dimensional free energy plots [165]. Figure 14.9 shows a one-dimensional plot for the 12-mer hairpin trpzip2 computed by Swope and coworkers. The free energy plot for this system at 250–300 K is reminiscent of the random free energy surface plot in Figure 14.8 (middle right): a plateau of denatured local minima, separated by a small barrier from the native state.

14.4 Summary

Fast relaxation experiments are testing predictions of the free energy landscape theory [166], such as roughness of the free energy surface and downhill folding.

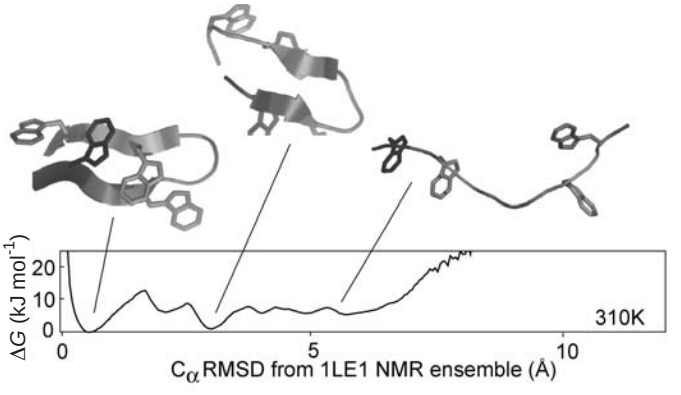

Fig. 14.9. Free energy surface for the hairpin trpzip2 with the C_α RMS deviation from the native state as one-dimensional reaction coordinate. The unfolded state is a plateau with multiple shallow minima, like the middle case in Figure 14.8 and the fitted surface for lambda repressor in Ref. [4].

They have directly measured the time scales of elementary folding processes, including secondary structure formation and loop formation. The low barriers of fast folding proteins allow their free energy surfaces to be explored beyond the native and unfolded basins. Experimental folding kinetics and molecular dynamics simulations are meeting in the nanosecond to microsecond regime.

14.5 Experimental Protocols

The following protocols provide some more technical information on laser temperature-jump relaxation experiments, and specific references where more information can be found.

14.5.1 Design Criteria for Laser Temperature Jumps

Water absorption in the 1.5 μm region is about 200 m^{-1}, limiting pathlengths to about 250 μm in single pass, or 500 μm in counterpropagating geometry, if a temperature uniformity of 10% is to be maintained in a 10 °C temperature jump. About 100 mJ of near infrared light is required to achieve sufficiently large temperature differentials. This output level can be obtained from a 1.5 m long Raman cell at 20 atm (2×10^6 Pa) of methane, with a collimated input beam diameter of 0.5 cm and input power levels of 500 mJ. Currently, an unamplified single-oscillator Nd:YAG laser is capable of meeting these specifications without requiring optical isolation to prevent feedback from reflections into the laser cavity. Care needs to be taken in the choice of optics: $\geq$3 mm sapphire or $\geq$6 mm fused silica windows with 1.06 μm antireflection coating are sufficient to withstand the pressure and laser intensity. In designing a Galilean (convex/concave lens) beam telescope, one must keep in mind that at 500 mJ, even second-surface reflections on optical curvatures can focus down to a damaging level. Upon output, a Pellin-Broca or equilateral glass prism can be used to separate the YAG fundamental from the Raman-shifted light. An IR image intensifier and Kodak Linagraph paper provide convenient means of tracing the Raman beam, which can be split in a 50:50 beam splitter for a counterpropagating pump geometry. For heating purposes, the beam needs to be brought to ca. 1–2 mm diameter when interacting with the cell. This can be achieved at the beamwaist of a long-focal length lens (ca. 1 m), or by placing a shorter lens sufficiently close to the sample so the focus lies beyond the sample. Because of the Fourier-transform property of focusing, the resulting beamprofile is generally of much higher quality than the original beamprofile, as verified by knife-edge measurements or a CCD camera.

The following two temperature-jump calibration methods are straightforward to implement: $A \approx 1.5$ μm wavelength diode laser beam can be chopped, sent through the sample, and demodulated by a lock-in amplifier. The change in water absorbance can simply be calibrated by reading diode transmission changes over

the desired temperature interval. Alternatively, tryptophan or NATA at pH 7 have a well-defined temperature dependence of the fluorescence lifetime, which can be measured if a fast lifetime detector is included in the system. A convenient way of reducing jump size is to use D_2O/H_2O mixtures (this can also be applied to D_2O jumps when using H_2 Raman-shifted 1.9 μm light), or to use thin films of water, so the laser system does not need to be adjusted. Additional details (superseded by the above information when different) can be found in Refs [67] and [55].

14.5.2 Design Criteria for Fast Single-Shot Detection Systems

In a single-shot detection system, the light source either provides sufficiently short pulses so that fluorescence decays can be directly resolved, enough bandwidth so a full absorption spectrum can be measured, and sufficiently high pulse repetition rates that kinetics can be fully resolved. Currently, the most convenient laser systems for excitation are mode-locked Ti:sapphire lasers pumped by intracavity-doubled diode-pumped YAG lasers. Such systems easily achieve 1 W average output power in <100 fs pulses at ca. 80 MHz pulse repetition rate. They are tunable in the 750–950 nm wavelength range, as well as at half, third, and quarter wavelengths by nonlinear sum-frequency generation (with maximum output levels typically 200 mW, 50 mW, and 10 mW, respectively). This provides at least 10^4 photon/pulse, or $1{:}10^2$ shot noise. Systems with sufficiently high bandwidth can also be difference-frequency generated in silverthiogallatre crystals to produce up to 200 cm^{-1} bandwidth mid-infrared pulses (1000–1800 cm^{-1}) [81]. Commercial lasers and sum-frequency generators are available.

The most important distinction between detection by transmission or by fluorescence lies in the allowed cell pathlength. Backround absorption in mid-IR absorption, even in D_2O, limits pathlengths to 50–100 μm. In addition, a thermal lens created by the variation of the refractive index about the ca. 1–2 mm diameter heating profile limits the pathlength in transmission experiments to <100 μm. The effect can be minimized by heating an at least 10× larger diameter of the sample than is probed, but even this precaution is not sufficient when cell pathlengths significantly >100 m are used.

Fluorescence detection is less sensitive. To avoid polarization artifacts, the pump beam should be depolarized and fluorescence should be detected at the magic angle. However, artifacts caused by cavitation (formation of vapor bubbles) during large temperature jumps are generally a more severe limiting factor. Light guides filled with a UV-transmitting fluid can be used in lieu of lens-based imaging optics to collect the fluorescent output. Models with f-ratios as large as 0.8 and diameters ≤4 mm are available, allowing efficient collection of the fluorescence and piping to remote detection systems.

Details of the electronics of a detector which can detect a fluorescence decay every 14 ns with a 500 ps risetime are given in Ref. [67], details of a detector which can collect an entire fluorescence spectrum from 300 to 400 nm every 100 ns are given in Ref. [98], and details of a detector that can detect a mid-IR spectrum of

200 cm^{-1} with 300 ns time resolution are given in Ref. [81]. Additional circuit diagrams and software are available from the author.

For experiments with cold-denatured proteins, the choice of cell is critical to avoid freezing supercooled samples because of nucleation on cell defects. In extruded fused silica cells, temperatures as low as −15 °C are routinely possible in water, and −20 °C have been observed. Such cells are available in pathlengths from 0.3 mm to 1 mm. The author has observed laser-induced temperature jumps between two temperatures below freezing without nucleation. Cell temperaures are most conveniently adjusted by thermoelectric coolers (for fast adjustment) in combination with a recirculating bath.

14.5.3
Designing Proteins for Fast Relaxation Experiments

Three design criteria have proved particularly useful in increasing the refolding rate of protein mutants:

1. Increase unfolded structure: this leads to a more structured unfolded state. For example, Oas has replaced glycine residues in helical positions 46 and 48 of lambda repressor fragment λ_{6-85} by alanines, thereby greatly increasing the folding rate [167].
2. Eliminate functional residues: a significant fraction of the energetic frustration in proteins probably comes from functional residues that are not optimal for folding. For example, replacing the distal histidine in apomyoglobin by a phenylalanine increases the folding significantly [168], and grafting the shorter FBP WW loop onto the Pin WW domain increases the folding rate by a factor of 3 [169].
3. Decrease the contact order: simplifying the fold reduces residual roughness of the free energy. As a rough guide, 2–3 helix bundles can be expected to reach a speed limit around 0.5 μs (W. F. DeGrado, private comminication, 2003), 5 helix bundles around 1–2 μs [65], and 8 helix bundles around 2–5 μs [52]. The time scales observed thus far for beta-rich proteins are somewhat longer (e.g., ≥1 μs for a simple double-stranded hairpin) [69].

14.5.4
Linear Kinetic, Nonlinear Kinetic, and Generalized Kinetic Analysis of Fast Relaxation

Many complicated kinetic schemes can arise in the discussion of relaxation experiments [170] (see Chapter 22). Here we discuss in detail three cases that illustrate the type of information that can be extracted, and the pitfalls that arise in the analysis. Other cases can be found in texts on reaction kinetics. Only kinetic schemes are discussed here; the actual analysis of raw experimental data is discussed in the next protocol.

14.5.4.1 The Reaction D ⇄ F in the Presence of a Barrier

This case corresponds to the reversible folding of a monomeric protein. Rate differential equations can be used with rate coefficients given by Kramer's theory:

$$\frac{d[D]}{dt} = -k_f[D] + k_d[F] \quad \text{with } [D] + [F] = P_{tot}. \tag{1}$$

The solution to this equation, using the equilibrium constant $K_{eq} = F_{eq}/D_{eq} = k_f/k_d$, is given by

$$[D] = D_{eq} + (D_0 - D_{eq})e^{-(k_f+k_d)t} \tag{2}$$

Kramer's version of transition state theory (which allows for recrossings of the barrier induced by the solvent) yields a forward rate constant [131]

$$k_f = \nu^{\dagger}[\eta(T)]e^{-\Delta G^{\dagger}/kT} \tag{3}$$

where the barrier crossing prefactor $\nu^{\dagger}$ depends on the solvent viscosity η. ($\nu^{\dagger}$ generally decreases with increasing solvent viscosity. It may level off at small solvent viscosities because the protein self-friction becomes dominant. It may even decrease with decreasing solvent viscosity because the solvent–reactant collisions no longer are strong enough to activate the reactant when the solvent viscosity is very low; this ''inverted Kramer's'' regime has not been observed during protein folding.)

According to the rate law given above, the kinetics remain single exponential for any size relaxation; the forwards and backwards rate coefficients can be extracted independently if the equilibrium constant is known. However, under certain conditions nonsingle exponential kinetics can be observed: if the relaxation significantly changes the properties of the states D or F, and if their spectroscopic signatures change, then the populations before the jump are no longer local equilibrium populations. As a result, rapid relaxation within the states D and F may be observed before the barrier crossing kinetics [56].

14.5.4.2 The Reaction $2A \rightleftarrows A_2$ in the Presence of a Barrier

This is a prototype case for protein association reactions studied by relaxation experiments, such as the assembly/disassembly equilibrium of a light-harvesting complex containing multiple subunits. Assuming again that rate is limited by barrier crossing, one can write the differential equation

$$\frac{d[A]}{dt} = -k_a[A]^2 + 2k_d[A_2] \quad \text{with } [A] + 2[A_2] = A_{tot} \tag{4}$$

whose solution, with the initial condition $[A](t = 0) = A_0$ and $[A_2](t = 0) = 0$ can be written in compact form as

$$[A](t) = \frac{k'}{k_f}\tanh\left(k't + \tanh^{-1}\frac{k_b + A_0k_f}{k'}\right) - \frac{k_b}{k_f}, \quad k' = \sqrt{k_b^2 + 2k_bk_fA_0} \tag{5}$$

(Note that this evaluates to a real quantity even in cases where $(k_b + A_0k_f)/k' > 1$.) Clearly the functional form of the kinetics is not single exponential, and the shape

of the relaxation actually depends on the initial concentration A_0. This differs from the case above, where the relaxation remains exponential for any initial condition, no matter how far from equilibrium.

If this system is near equilibrium however, then the relaxation becomes single exponential. This can be seen most easily by writing the rate equation in terms of $[A] = \delta A + A_{eq}$, where δA represents the small deviation of the concentration from the equilibrium value. Neglecting quadratic terms in δA, the rate equation is approximated by

$$\frac{d\delta A}{dt} \approx (-2k_f A_{eq} + k_b)\delta A \tag{6}$$

and by using mass conservation and the equilibrium constant $K_{eq} = A_{2,eq}/A_{eq} = k_f/2k_b$ the solution becomes

$$\delta A = \delta A_0 e^{-kt}, \quad \text{where } k = \sqrt{k_b^2 + 4A_{tot}k_b k_f} \tag{7}$$

Thus the rate constant depends on the concentration, but the kinetics are single exponential. By varying the concentration, the forwards and backwards rate coefficients can be extracted independently.

14.5.4.3 The Reaction D ⇄ F at Short Times or over Low Barriers

The phenomenological description of two-state kinetics above is satisfactory when applied to large barrier crossings at sufficiently long times. At short times, especially when the barrier is not very large compared with $k_B T$, simple rate theories no longer apply. This is true for the more sophisticated Kramer's model (which includes perturbation of the solute free energy by the solvent explicitly), as well as for the classical transition state theory. There are several related reasons for this failure.

At very short times, the rate coefficient k_f is no longer a constant [150]. At $t = 0$, its value $k_f(0)$ must be greater than the value at long times. The reason is that at $t = 0$, barrier recrossings and other diffusive motions that reduce the rate coefficient have not yet had a chance to occur. A more complete theory has been developed in the linear response limit (i.e., for small relaxation jumps). The rate coefficient then becomes

$$k_f(t) = \min\langle v(t=0)\delta(RC(t=0) - RC_0)n_F(t)\rangle/\chi_F \tag{8}$$

In this equation, RC is a reaction coordinate. RC_0 is the position along the reaction coordinate that separates the states D and F (the position of the transition state in conventional transition state theory). n_F is the folded population obtained by integrating over the population from reaction coordinate $RC_0 \approx 0$ towards the F side of the free energy surface. δ is the Dirac delta function so only trajectories at $RC = 0$ are counted. v is the velocity of the protein trajectory along the reaction coordinate.

min<> indicates that an average over many trajectories is to be performed and minimized by moving RC_0.

If the folding barrier is very low, a substantial fraction of the protein population occupies the barrier region. Also, transitions among denatured states are no longer fast compared to transitions over the barrier region. If the spectroscopic signature of the activated population differs from that of the states D and F, a sizable kinetic amplitude will be observed for motions of this population. The relaxation of such a population is faster than the barrier-limited rate, but not arbitrarily fast. At a minimum, it is limited by free diffusion of the backbone, a process known to require 10–100 ns per contact for peptides of 10–100 chain length [48]. As discussed by Zwanzig, it may be slowed down further by roughness of the free energy surface. In his one-dimensional model, the diffusion constant on a rough surface is slowed down by a factor $\exp[-(\varepsilon/k_B T)^2]$, where ε is the root-mean-squared barrier height [118].

The barrier-free relaxation time scale for intermediate populations (termed "molecular time scale" by kineticists and "speed limit" in the protein folding community) determines when the rate coefficient $k_f(t)$ becomes a rate "constant" [150].

14.5.5 Relaxation Data Analysis by Linear Decomposition

Relaxation data can contain a single channel of information, or multiple channels. Linear decomposition techniques are very convenient for analyzing multichannel data [67, 98, 99]. For example, when an infrared spectrum shifts at successive kinetic time points, there are generally far fewer independent spectra than time points – in the case of a rigorous two-state folder, only two spectra. Linear decomposition techniques such as singular value decomposition can extract such "basis spectra" while minimizing assumptions about the nature of the fluorescence spectrum (λ) or fluorescence decays (t').

14.5.5.1 Singular Value Decomposition (SVD)

Both fluorescence decay transients and fluorescence/infrared spectra may be thought of as $m \times n$ matrices whose n columns track the spectroscopic profile (as a function of λ or t'), and whose m rows track the kinetics (as a function of t = kinetic time). SVD reduces this matrix to a set of n basis functions that describe the profile, n singular values which describe the importance of each profile to the total signal, and n vectors of length m that describe how each of the basis functions contributes to the kinetic signal as a function of time t.

Pronounced singular values up to $n' \leq n$ indicate that at least an n'-state kinetic model is required to account for the data quantitatively. n' sets a lower limit on the complexity of the kinetics because some intermediates may have spectral signatures similar to reactant or product. For example, a double-exponential decay guarantees that the kinetics are not two-state, but it does not guarantee that the kinetics are three-state.

14.5.5.2 χ-Analysis

When the thermodynamic data for a folding reaction as a function of temperature (or some other variable) can be represented by a cooperative two-state folding model, the following question becomes relevant: Are the folding kinetics those of an activated two-state system, and hence single exponential? In that case the reaction proceeds as

$$\mathrm{D} \rightleftarrows \mathrm{N}, \quad [\mathrm{D}](t) = ([\mathrm{D}]_0 - [\mathrm{D}]_\infty)e^{-kt} + [\mathrm{D}]_\infty \tag{9}$$

A similar question can be asked if a long-lived intermediate I is formed from D because the reaction $D \rightleftarrows I$ is then a quasi-two-state reaction. The χ-fit is a powerful tool to test these questions without making any assumptions about the functional form of the fluorescence decays or spectra of D, N (or I).

The practical implementation of the procedure for time-resolved fluorescence decays requires two steps. (In the following discussion, λ may replace t' in any formula, if spectra are analyzed instead of decays.) First, two fluorescence profiles f_1 and f_2 are constructed. f_1 represents the fluorescence profile as a function of λ or t' just after initiation of the kinetics. f_2 represents the fluorescence long after initiation of the kinetics.

The sampled data matrix $f(t, t')$ has m rows indexed by t and n columns indexed by t' or λ. Each row of f is fitted by linear least-squares to a combination of the two basis spectra f_1 and f_2, which themselves are functions of t' or λ:

$$f(t, t' \text{ or } \lambda) = a_1(t)f_1(t' \text{ or } \lambda) + a_2(t)f_2(t' \text{ or } \lambda) \tag{10}$$

The function χ_1 is then defined as:

$$\chi_1(t) = \frac{a_1(t)}{a_1(t) + a_2(t)} \tag{11}$$

It describes how the shape of the fluorescence profile evolves from a more unfolded signature towards a more folded signature, independent of the signal amplitude. This function has three important properties, which make it an excellent choice for representing folding kinetics. It approaches a signal-to-noise ratio limited only by the Poisson statistics of photon numbers in each laser shot (like ideal fluorescence intensity analysis); it is immune to laser intensity fluctuations (like fluorescence lifetime analysis); it allows one to extract species populations for two-state folders, and distinguishes two-state from multi-state folding (unlike amplitude or lifetime analysis). Further details are discussed in Ref. [98].

Acknowledgments

The author was supported by NSF grant MCB-0316925 while this work was prepared, and would like to thank the research groups who have generously allowed

figures from their publications to be used in this work. Additional material for this review was taken from other primary literature publications by the author listed in the references.

References

1 Eigen, M. & Maeyer, L. D. (1963). Relaxation methods. In *Technique of Organic Chemistry* (Weissberger, A., ed.), pp. 895–1054. Interscience, New York.

2 Valentine, J. S. (1998). Special Issue on Protein Folding. In *Acc. Chem. Research* (Valentine, J. S., ed.), Vol. 31, pp. 697–780.

3 Jacob, M., Holtermann, G., Perl, D. et al. (1999). Microsecond folding of the cold shock protein measured by a pressure-jump technique. *Biochemistry* 38, 2882–91.

4 Gruebele, M. (1999). The physical chemistry of protein folding. *Annu. Rev. Phys. Chem.* 50, 485–516.

5 Callender, R. & Dyer, D. B. (2002). Probing protein dynamics using temperature jump relaxation spectroscopy. *Curr. Opin. Struct. Biol.* 12, 628–33.

6 Jennings, P. & Wright, P. (1993). Formation of a molten globule intermediate early in the kinetic folding pathway of apomyoglobin. *Science* 262, 892–5.

7 Huang, G. S. & Oas, T. G. (1995). Submillisecond folding of monomeric λ repressor. *Proc. Natl Acad. Sci. USA* 92, 6878–82.

8 Eigen, M., Hammes, G. G. & Kustin, K. (1960). Fast reactions of imidazole studied with relaxation spectrometry. *J. Am. Chem. Soc.* 82, 3482–3.

9 Turner, D. H., Flynn, G. W., Lundberg, S. K., Faller, L. D. & Sutin, N. (1972). Dimerization of proflavin by the laser Raman temperature-jump method. *Nature* 239, 215–17.

10 Holzwarth, J. F., Eck, V. & Genz, A. (1985). Iodine laser temperature-jump: relaxation processes in phospholipid bilayers on the picosecond to millisecond time-scale. In *Spectroscopy and the Dynamics of Molecular Biological Systems* (Bayley, P. M. & Dale, R. E., eds), pp. 351–377. Academic Press, London.

11 Williams, A. P., Longfellow, C. E., Freier, S. M., Kierzek, R. & Turner, D. H. (1989). Laser temperature-jump, spectroscopic, and thermodynamic study of salt effects on duplex formation by dGCATGC. *Biochemistry* 28, 4283–91.

12 Jones, C. M., Henry, E. R., Hu, Y. et al. (1993). Fast events in protein folding initiated by pulsed laser photolysis. *Proc. Natl Acad. Sci. USA* 90, 11860–64.

13 Phillips, C. M., Mizutani, Y. & Hochstrasser, R. M. (1995). Ultrafast thermally induced unfolding of RNase A. *Proc. Natl Acad. Sci. USA* 92, 7292–6.

14 Nölting, B., Golbik, R. & Fersht, A. R. (1995). Submillisecond events in protein folding. *Proc. Natl Acad. Sci. USA* 92, 10668–72.

15 Williams, S., Causgrove, T. P., Gilmanshin, R. et al. (1996). Fast events in protein folding: helix melting and formation in a small peptide. *Biochemistry* 35, 691–7.

16 Ballew, R. M., Sabelko, J. & Gruebele, M. (1996). Direct observation of fast protein folding: The initial collapse of apomyoglobin. *Proc. Natl Acad. Sci. USA* 93, 5759–64.

17 Pascher, T., Chesick, J. P., Winkler, J. R. & Gray, H. B. (1996). Protein folding triggered by electron transfer. *Science* 271, 1558–60.

18 Schwarz, G. & Seelig, J. (1968). Kinetic properties and the electric field effect of the helix-coil transition of poly(γ-benzyl L-glutamate) determined from dielectric relaxation measurements. *Biopolymers* 6, 1263–77.

19 Hawley, S. A. (1971). Reversible pressure-temperature unfolding of chymotrypsinogen. *Biochemistry* 10, 2436–42.

20 Royer, C. A. (2002). Revisiting volume changes in pressure-induced protein unfolding. *Biochim. Biophys. Acta* 1595, 201–9.

21 Desai, G., Panick, G., Zein, M., Winter, R. & Royer, C. A. (1999). Pressure-jump Studies of the Folding/Unfolding of trp Repressor. *J. Mol. Biol.* 288, 461–7.

22 Clegg, R. M., Elson, E. L. & Maxfield, B. W. (1975). New technique for optical observation of the kinetics of chemical reactions perturbed by small pressure changes. *Biopolymers* 14, 883–7.

23 Hoffman, G. W. (1971). A nanosecond temperature-jump apparatus. *Rev. Sci. Instrum.* 42, 1643–7.

24 Rigler, R., Rabl, C. R. & Jovin, T. M. (1974). A temperature-jump apparatus for fluorescence measurements. *Rev. Sci. Instrum.* 45.

25 Nölting, B., Golbik, R., Neira, J. L., Soler-Gonzalez, A. S., Schreiber, G. & Fersht, A. R. (1997). The folding pathway of a protein at high resolution from microseconds to seconds. *Proc. Natl Acad. Sci. USA* 94, 826–30.

26 Ferguson, N., Johnson, C. M., Macias, M., Oschkinat, H. & Fersht, A. (2001). Ultrafast folding of WW domains without structured aromatic clusters in the denatured state. *Proc. Natl Acad. Sci. USA* 98, 13002–7.

27 Ferguson, N., Pires, J. R., Toepert, F. et al. (2001). Using flexible loop mimetics to extend Phi-value analysis to secondary structure interactions. *Proc. Natl Acad. Sci. USA* 98, 13008–13.

28 Mayor, U., Johnson, C. M., Daggett, V. & Fersht, A. R. (2000). Protein folding and unfolding in microseconds to nanoseconds by experiment and simulation. *Proc. Natl Acad. Sci. USA* 97, 13518–22.

29 Gillespie, B., Vu, D. M., Shah, P. S. et al. (2003). NMR and temperature-jump measurements of de novo designed proteins demonstrate rapid folding in the absence of explicit selection for kinetics. *J. Mol. Biol.* 4.

30 Mayor, U., Guydosh, N. R., Johnson, C. M. et al. (2003). The complete folding pathway of a protein from nanoseconds to microseconds. *Nature* 421, 863–7.

31 Rabl, C. R., Martin, S. R., Neumann, E. & Bayley, P. M. (2002). Temperature jump kinetic study of the stability of apo-calmodulin. *Biophys. Chem.* 101, 553–464.

32 Sanchez, I. E. & Kiefhaber, T. (2003). Hammond behavior versus ground state effects in protein folding: Evidence for narrow free energy barriers and residual structure in unfolded states. *J. Mol. Biol.* 327, 867–84.

33 Ansari, A., Jones, C. M., Henry, E. R., Hofrichter, J. & Eaton, W. A. (1992). The role of solvent viscosity in the dynamics of protein conformational changes. *Science* 256, 1796–8.

34 Mines, G. A., Pascher, T., Lee, S. C., Winkler, J. R. & Gray, H. B. (1996). Cytochrome c folding triggered by electron transfer. *Chem. Biol.* 3, 491–7.

35 Wittung-Stafshede, P., Gray, H. B. & Winkler, J. R. (1997). Rapid formation of a four-helix bundle, cytochrome b_{562} folding triggered by electron transfer. *J. Am. Chem. Soc.* 119, 9562–3.

36 Telford, J. R., Wittung-Stafshede, P., Gray, H. B. & Winkler, J. R. (1998). Protein folding triggered by electron transfer. *Acc. Chem. Res.* 31, 755–63.

37 Lee, J. C., Gray, H. B. & Winkler, J. R. (2001). Cytochrome c′ folding triggered by electron transfer: fast and slow formation of four-helix bundles. *Proc. Natl Acad. Sci. USA* 98, 7760–4.

38 Chang, I. J., Lee, J. C., Winkler, J. R. & Gray, H. B. (2003). The protein-folding speed limit: Intrachain diffusion times set by electron-transfer rates in denatured Ru(NH3)(5)(His-33)-Zn-cytochrome c. *Proc. Natl Acad. Sci. USA* 100, 3838–40.

39 Gutman, M., Huppert, D. & Pines, E. (1981). The pH jump: a rapid

modulation of pH of aqueous solutions by a laser pulse. *J. Am. Chem. Soc.* 103, 3709–13.

40 Pines, E. & Huppert, D. (1983). pH jump: a relaxation approach. *J. Phys. Chem.* 87, 4471–8.

41 George, M. V. & Scaiano, J. C. (1980). Photochemistry of o-nitrobenzaldehyde and related studies. *J. Phys. Chem.* 84, 492–5.

42 Abbruzzetti, S., Crema, E., Masino, L. et al. (2000). Fast events in protein folding: Structural volume changes accompanying the early events in the N → I transition of apomyoglobin induced by ultrafast pH jump. *Biophys. J.* 78, 405–15.

43 Choi, J., Hirota, N. & Terazima, M. (2001). Enthalpy and volume changes on the pH jump process studied by the transient grating technique. *Anal. Sci.* 17, s13–s15.

44 Volk, M., Kholodenko, Y., Lu, H. S. M., Gooding, E. A., DeGrado, W. F. & Hochstrasser, R. M. (1997). Peptide conformational dynamics and vibrational stark effects following photoinitiated disulfide cleavage. *J. Phys. Chem.* 101, 8607–16.

45 Metzler, R., Klafter, J., Jortner, J. & Volk, M. (1998). Multiple time scales for dispersive kinetics in early events of peptide folding. *Chem. Phys. Lett.* 293, 477–84.

46 Hagen, S. J., Hofrichter, J., Szabo, A. & Eaton, W. A. (1996). Diffusion-limited contact formation in unfolded cytochrome c: Estimating the maximum rate of protein folding. *Proc. Natl Acad. Sci. USA* 93, 11615–17.

47 Hagen, S. J., Hofrichter, J. & Eaton, W. A. (1997). Rate of intrachain diffusion of unfolded cytochrome c. *J. Phys. Chem. B* 101, 2352–65.

48 Bieri, O. & Kiefhaber, T. (1999). Elementary steps in protein folding. *Biol. Chem.* 380, 923–9.

49 Lapidus, L. J., Eaton, W. A. & Hofrichter, J. (2000). Measuring the rate of intramolecular contact formation in polypeptides. *Proc. Natl Acad. Sci. USA* 97, 7220–5.

50 Lapidus, L., Eaton, W. & Hofrichter, J. (2001). Dynamics of intramolecular contact formation in polypeptides: distance dependence of quenching rates in room temperature glass. *Phys. Rev. Lett.* 87.

51 Bieri, O. & Kiefhaber, T. (2000). Kinetic models in protein folding. In *Mechanisms of Protein Folding*, 2nd edn (Pain, R. H., ed.), Vol. 32, pp. 34–64. Oxford University Press, Oxford.

52 Ballew, R. M., Sabelko, J. & Gruebele, M. (1996). Observation of distinct nanosecond and microsecond protein folding events. *Nat. Struct. Biol.* 3, 923–6.

53 Gilmanshin, R., Williams, S., Callender, R. H., Woodruff, W. H. & Dyer, R. B. (1997). Fast events in protein folding: Relaxation dynamics of secondary and tertiary structure in native apomyoglobin. *Proc. Natl Acad. Sci. USA* 94, 3709–13.

54 Thompson, P. A., Eaton, W. A. & Hofrichter, J. (1997). Laser temperature jump study of the helix reversible arrow coil kinetics of an alanine peptide interpreted with a 'kinetic zipper' model. *Biochemistry* 36, 9200–10.

55 Dyer, R. B., Gai, F., Woodruff, W. H., Gilmanshin, R. & Callender, R. H. (1998). Infrared studies of fast events in protein folding. *Acc. Chem. Res.* 31, 709–16.

56 Sabelko, J., Ervin, J. & Gruebele, M. (1999). Observation of strange kinetics in protein folding. *Proc. Nat. Acad. Sci. USA* 96, 6031–6.

57 Crane, J. C., Koepf, E. K., Kelly, J. W. & Gruebele, M. (2000). Mapping the transition state of the WW domain beta sheet. *J. Mol. Biol.* 298, 283–92.

58 Leeson, D. T., Gai, F., Rodriguez, H. M., Gregoret, L. M. & Dyer, R. B. (2000). Protein Folding on a Complex Energy Landscape. *Proc. Natl Acad. Sci. USA* 97, 2527–32.

59 Jäger, M., Nguyen, H., Crane, J., Kelly, J. & Gruebele, M. (2001). The folding mechanism of a β-sheet: The WW domain. *J. Mol. Biol.* 311, 373–93.

60 Gulotta, M., Gilmanshin, R., Buscher, T. C., Callender, R. H. & Dyer, R. B. (2001). Core formation in

apomyoglobin: probing the upper reaches of the folding energy landscape. *Biochemistry* 40, 5137–43.

61 Snow, C., Nguyen, H., Pande, V. & Gruebele, M. (2002). Absolute comparison of simulated and experimental protein folding dynamics. *Nature* 420, 102–6.

62 Osváth, S. & Gruebele, M. (2003). Proline can have opposite effects on fast and slow protein folding phases. *Biophys. J.* 85, 1215–22.

63 Osváth, S., Sabelko, J. & Gruebele, M. (2003). Tuning the heterogeneous early folding dynamics of phosphoglycerate kinase. *J. Mol. Biol.* 333, 187–99.

64 Pandit, A., Ma, H., Stokkum, I. v., Gruebele, M. & Grondelle, R. v. (2003). The time resolved dissociation reaction of the light-harvesting 1 complex of Rhodospirillum rubrum, studied with an infrared laser-pulse temperature jump. *Biochemistry* 41, 15115–20.

65 Yang, W. & Gruebele, M. (2003). Folding at the speed limit. *Nature* 423, 193–7.

66 Nguyen, H., Jäger, M., Gruebele, M. & Kelly, J. (2003). Tuning the free-energy landscape of a WW domain by temperature, mutation and truncation. *Proc. Natl Acad. Sci. USA* 100, 3948–53.

67 Ballew, R. M., Sabelko, J., Reiner, C. & Gruebele, M. (1996). A single-sweep, nanosecond time resolution laser temperature-jump apparatus. *Rev. Sci. Instrum.* 67, 3694–9.

68 Eaton, W. A., Muñoz, V., Thompson, P. A., Henry, E. R. & Hofrichter, J. (1998). Kinetics and dynamics of loops, α-helices, β-hairpins, and fast-folding proteins. *Acc. Chem. Res.* 31, 745–53.

69 Muñoz, V., Thompson, P. A., Hofrichter, J. & Eaton, W. A. (1997). Folding dynamics and mechanism of β-hairpin formation. *Nature* 390, 196–9.

70 Muñoz, V., Henry, E. R., Hofrichter, J. & Eaton, W. A. (1998). A Statistical Mechanical Model for β-Hairpin Kinetics. *Proc. Natl Acad. Sci. USA* 95, 5872–9.

71 Huang, C. Y., Getahun, Z., Wang, T., DeGrado, W. F. & Gai, F. (2001). Time-resolved infrared study of the helix-coil transition using C-13-labeled helical peptides. *J. Am. Chem. Soc.* 123, 12111–12.

72 Getahun, Z., Huang, C. Y., Wang, T., Leon, B. D., DeGrado, W. F. & Gai, F. (2003). Using nitrile-derivated amino acids as infrared probes of local environment. *J. Am. Chem. Soc.* 125.

73 Klimov, D. K. & Thirumalai, D. (2000). Mechanisms and kinetics of beta-hairpin formation. *Proc. Natl Acad. Sci. USA* 97, 2544–9.

74 Yang, W., Prince, R., Sabelko, J., Moore, J. S. & Gruebele, M. (2000). Transition from exponential to nonexponential kinetics during formation of an artificial helix. *J. Am. Chem. Soc.* 122, 3248–9.

75 Hummer, G., Garcia, A. E. & Garde, S. (2000). Conformational diffusion and helix formation kinetics. *Phys. Rev. Lett.* 85, 2637–40.

76 Gilmanshin, R., Callender, R. H. & Dyer, R. B. (1998). The core of apomyoglobin E-form folds at the diffusion limit. *Nat. Struct. Biol.* 5, 363–5.

77 Low, D. W., Winkler, J. R. & Gray, H. B. (1996). Photoinduced oxidation of microperoxidase-9: generation of ferryl and cation-radical prophyrins. *J. Am. Chem. Soc.* 118, 117–20.

78 Pollack, L., Tate, M. W., Darnton, N. C., Knight, J. B., Gruner, S. M., Eaton, W. A. & Austin, R. H. (1999). Compactness of the denatured state of a fast-folding protein measured by submillisecond small-angle X-ray scattering. *Proc. Natl Acad. Sci. USA* 96, 10115.

79 Gilmanshin, R., Callender, R. H., Dyer, R. B. & Woodruff, W. H. (1998). Fast event in protein folding: the time evolution of primary processes. *Annu. Rev. Phys. Chem.* 49, 173–202.

80 Wang, J. & El-Sayed, M. A. (1999). Temperature jump-induced secondary structural change of the membrane

protein bacteriorhodopsin in the premelting temperature region: a nanosecond time-resolved Fourier transform infrared study. *Biophys. J.* 76, 2777–83.

81 Ma, H., Ervin, J. & Gruebele, M. (2003). Multichannel, single-sweep infrared detection for nanosecond relaxation kinetics experiments. *Rev. Sci. Inst.* 75, 486–491.

82 Chen, E. F. & Kliger, D. S. (1996). Time-resolved near UV circular dichroism and absorption studies of carbonmonoxymyoglobin photolysis intermediates. *Inorg. Chim. Acta* 242, 149–58.

83 Chen, E. F., Goldbeck, R. A. & Kliger, D. S. (1997). Nanosecond time-resolved spectroscopy of biomolecular processes. *Annu. Rev. Biophys. Biomol. Struct.* 26, 327–55.

84 Chen, E., Wood, M. J., Fink, A. L. & Kliger, D. S. (1998). Time-resolved circular dichroism studies of protein folding intermediates of cytochrome c. *Biochemistry* 37, 5589–98.

85 Chen, E. F., Gensch, T., Gross, A. B., Hendriks, J., Hellingwerf, K. J. & Kliger, D. S. (2003). Dynamics of protein and chromophore structural changes in the photocycle of photoactive yellow protein monitored by time-resolved optical rotatory dispersion. *Biochemistry* 42, 2062–71.

86 Lednev, I. K., Karnoup, A. S., Sparrow, M. C. & Asher, S. A. (1999). α-Helix peptide folding and unfolding activation barriers: a nanosecond UV resonance study. *J. Am. Chem. Soc.* 121, 8074–86.

87 Lednev, I. K., Karnoup, A. S., Sparrow, M. C. & Asher, S. A. (1999). Nanosecond UV resonance raman examination of initial steps in α-helix secondary structure evolution. *J. Am. Chem. Soc.* 121, 4076–7.

88 Yamamoto, K., Mizutani, Y. & Kitagawa, T. (2000). Nanosecond temperature jump and time-resolved Raman study of thermal unfolding of ribonuclease A. *Biophys. J.* 79, 485–95.

89 Yeh, S., Han, S. & Rousseau, D. L. (1998). Cytochrome c Folding and Unfolding: A Biphasic Mechanism. *Acc. Chem. Res.* 31, 727–36.

90 Lakowicz, J. R. (1986). Fluorescence studies of structural flucturations in macromolecules as observed by fluorescence spectroscopy in the time, lifetime, and frequency domains. In *Methods in Enzymology*, Vol. 131, pp. 518–567. Academic Press, New York.

91 Chen, Y. & Barkley, M. D. (1998). Toward understanding tryptophan fluorescence in proteins. *Biochemistry* 37, 9976–82.

92 Förster, T. (1948). Zwischenmolekülare Energiewanderung und Fluoreszenz. *Ann. Physik* 2, 55–75.

93 Rischel, C. & Poulsen, F. M. (1995). Modification of a specific tyrosine enables tracing of the end-to-end distance during apomyoglobin folding. *FEBS Lett.* 374, 105–9.

94 Ballew, R. M. (1996). Direct observation of fast protein folding: distinct nanosecond and microsecond events in the folding of apomyoglobin. Thesis, University of Illinois.

95 Gruebele, M., Sabelko, J., Ballew, R. & Ervin, J. (1998). Laser temperature jump induced protein refolding. *Acc. Chem. Res.* 31, 699–707.

96 Garcia, P., Desmadril, M., Minard, P. & Yon, J. M. (1995). Evidence for residual structures in an unfolded from of yeast phosphoglycerate kinase. *Biochemistry* 34, 397–404.

97 Ervin, J., Larios, E., Osvath, S., Schulten, K. & Gruebele, M. (2002). What causes hyperfluorescence: Folding intermediates or conformationally flexible native states? *Biophys. J.* 83, 473–83.

98 Ervin, J., Sabelko, J. & Gruebele, M. (2000). Submicrosecond real-time fluorescence detection: application to protein folding. *J. Photochem. Photobiol.* B54, 1–15.

99 Henry, E. R. & Hofrichter, J. (1992). Singular value decomposition: application to analysis of experimental data. *Methods Enzymol.* 210, 129–92.

100 Bryngelson, J. D. & Wolynes, P. G. (1987). Spin glasses and the statistical mechanics of protein folding. *Proc. Natl Acad. Sci. USA* 84, 7524–8.

101 Onuchic, J. N., Wolynes, P. G., Luthey-Schulten, Z. & Socci, N. D. (1995). Toward an outline of the topography of a realistic protein folding funnel. *Proc. Natl Acad. Sci. USA* 92, 3626–30.

102 Kiefhaber, T., Schmid, F. X., Willaert, K., Engelborghs, Y. & Chaffotte, A. (1992). Structure of a rapidly formed intermediate in ribonuclease T1 folding. *Protein Sci.* 1, 1162–72.

103 Pappenberger, G., Aygun, H., Engels, J. W., Reimer, U., Fischer, G. & Kiefhaber, T. (2001). Nonprolyl cis peptide bonds in unfolded proteins cause complex folding kinetics. *Nat. Struct. Biol.* 8, 452–8.

104 Kelley, R. F. & Richards, F. M. (1987). Replacement of proline-76 with alanine eliminates the slowest kinetic phase in thioredoxin folding. *Biochemsitry* 26, 6765–74.

105 Plaxco, K. W., Guijarro, J. I., Morton, C. J., Pitkeathly, M., Campbell, I. D. & Dobson, C. M. (1998). The folding kinetics and thermodynamics of the Fyn-SH3 domain. *Biochemistry* 37, 2529–37.

106 Onuchic, J. N., Luthey-Schulten, Z. & Wolynes, P. G. (1997). Theory of protein folding: the energy landscape perspective. *Annu. Rev. Phys. Chem.* 48, 545–600.

107 Pappu, R. V., Srinivasan, R. & Rose, G. D. (2000). The Flory isolated-pair hypothesis is not valid for polypeptide chains: Implications for protein folding. *Proc. Natl Acad. Sci. USA* 97, 12565–70.

108 Bromberg, S. & Dill, K. A. (1994). Side-chain entropy and packing in proteins. *Protein Sci.* 3, 997–1009.

109 Bryngelson, J. D. & Wolynes, P. G. (1989). Intermediates and barrier crossing in random energy model (with applications to protein folding). *J. Phys. Chem.* 93, 6902–15.

110 Kim, P. S. & Baldwin, R. L. (1990). Intermediates in the folding reactions of small proteins. *Annu. Rev. Biochem.* 59, 631–60.

111 Bachmann, A. & Kiefhaber, T. (2001). Apparent two-state tendamistat folding is a sequential process along a defined route. *J. Mol. Biol.* 306, 375–86.

112 Creighton, T. E. (1988). Toward a better understanding of protein folding pathways. *Proc. Natl Acad. Sci. USA* 85, 5082–6.

113 Zwanzig, R. (1997). Two-state models of protein folding kinetics. *Proc. Natl Acad. Sci. USA* 94, 148–50.

114 Nymeyer, H., García, A. E. & Onuchic, J. N. (1998). Folding funnels and frustration in off-lattice minimalist protein landscapes. *Proc. Natl Acad. Sci. USA* 95, 5921–8.

115 Plotkin, S. S., Wang, J. & Wolynes, P. G. (1997). Statistical mechanics of a correlated energy landscape model for protein folding funnels. *J. Chem. Phys.* 106, 2932–48.

116 Go, N. (1983). Theoretical studies of protein folding. *Annu. Rev. Biophys. Bioeng.* 12, 183–210.

117 Thompson, P. A., Eaton, W. A. & Hofrichter, J. (1997). Laser temperature jump study of the helix × coil kinetics of an alanine peptide interpreted with a 'kinetic zipper' model. *Biochemistry* 36, 9200–10.

118 Zwanzig, R. (1988). Diffusion in a rough potential. *Proc. Natl Acad. Sci., USA* 85, 2029–30.

119 Shea, J. E., Onuchic, J. N. & C L Brooks, I. (2000). Energetic frustration and the nature of the transition state ensemble in protein folding. *J. Chem. Phys.* 113, 7663–71.

120 Portman, J. J., Takada, S. & Wolynes, P. G. (2001). Microscopic theory of protein folding rates. II. Local reaction coordinates and chain dynamics. *J. Chem. Phys.* 114, 5082–96.

121 Thirumalai, D., Klimov, D. K. & Dima, R. I. (2002). Insights into specific problems in protein folding using simple concepts. *Adv. Chem. Phys.* 120, 35–76.

122 Alm, E. & Baker, D. (1999). Prediction of protein-folding mechanisms from free energy landscapes derived from native structures. *Proc. Natl Acad. Sci. USA* 96, 11305–10.

123 Muñoz, V. & Eaton, W. A. (1999).

A simple model for calculating the kinetics of protein folding from three-dimenstional structures. *Proc. Natl Acad. Sci. USA* 96, 11311–16.

124 Koga, N. & Takada, S. (2001). Roles of native topology and chain-length scaling in protein folding: a simulation study with a Go-like model. *J. Mol. Biol.* 313, 171–80.

125 Silow, M. & Oliveberg, M. (1997). High-energy channeling in protein folding. *Biochemistry* 36, 7633–7.

126 Wagner, C. & Kiefhaber, T. (1999). Intermediates can accelerate protein folding. *Proc. Natl Acad. Sci. USA* 96, 6716–21.

127 Skorobogatiy, M., Guo, H. & Zuckerman, M. (1998). Non-Arrhenius modes in the relaxation of model proteins. *J. Chem. Phys.* 109, 2528–35.

128 Metzler, R., Klafter, J. & Jortner, J. (1999). Hierarchies and logarithmic oscillations in the temporal relaxation patterns of proteins and other complex systems. *Proc. Natl Acad. Sci. USA* 96, 11085–9.

129 Becker, O. M. & Karplus, M. (1997). The topology of multidimensional potential energy surfaces: theory and application to peptide structure and kinetics. *J. Chem. Phys.* 22, 1495–517.

130 Becker, O. M. (1998). Principal coordinate maps of molecular potential energy surfaces. *J. Comput. Chem.* 19, 1255–67.

131 Kramers, H. A. (1940). Brownian motion in a field of force and the diffusion model of chemical reactions. *Physica* 7, 284.

132 Plaxco, K. W. & Baker, D. (1998). Limited internal friction in the rate-limiting step of a two-state protein folding reaction. *Proc. Natl Acad. Sci. USA* 95, 13591–6.

133 Jacob, M., Schindler, T., Balbach, J. & Schmid, F. X. (1997). Diffusion control in an elementary protein folding reaction. *Proc. Natl Acad. Sci. USA* 94, 5622–7.

134 Jacob, M., Geeves, M., Holtermann, G. & Schmid, F. X. (1999). Diffusional barrier crossing in a two-state protein folding reaction. *Proc. Natl Acad. Sci. USA* 94, 5622–7.

135 Bhattacharyya, R. P. & Sosnick, T. R. (1999). Viscosity dependence of the folding kinetics of a dimeric and monomeric coiled coil. *Biochemistry* 38, 2601–9.

136 Bieri, O., Wirz, J., Hellrung, B., Schutkowski, M., Drewello, M. & Kiefhaber, T. (1999). The speed limit of protein folding measure by triplet-triplet energy transfer. *Proc. Natl Acad. Sci. USA* 96, 9597–601.

137 Pappenberger, G., Saudan, C., Becker, M., Merbach, A. E. & Kiefhaber, T. (2000). Denaturant-induced movement of the transition state of protein folding revealed by high-pressure stopped-flow measurements. *Proc. Natl Acad. Sci. USA* 97, 17–22.

138 Khorasanizadeh, S., Peters, I. & Roder, H. (1996). Evidence for a three-state model of protein folding from kinetic analysis of ubiquitin variants with altered core residues. *Nat. Struct. Biol.* 3, 193–205.

139 Shastry, M. C. R. & Roder, H. (1998). Evidence for barrier-limited protein folding kinetics on the microsecond time scale. *Nat. Struct. Biol.* 5, 385–92.

140 Hagen, S. J. & Eaton, W. A. (2000). Two-state expansion and collapse of a polypeptide. *J. Mol. Biol.* 297, 781–9.

141 Qin, Z., Ervin, J., Larios, E., Gruebele, M. & Kihara, H. (2002). Formation of a compact structured ensemble without fluorescence signature early during ubiquitin folding. *J. Phys. Chem. B* 106, 13040–6.

142 Finkelstein, A. V. & Shakhnovich, E. I. (1989). Theory of cooperative transitions in protein molecules. ii. phase diagram for a protein molecule in solution. *Biopolymers* 28, 1681–94.

143 Parker, M. J. & Marqusee, S. (1999). The cooperativity of burst phase reactions explored. *J. Mol. Biol.* 293, 1195–210.

144 Englander, S. W., Sosnick, T. R., Mayne, L. C., Shtilerman, M., Qi, P. X. & Bai, Y. (1998). Fast and slow folding in cytochrome c. *Acc. Chem. Res.* 31, 767–74.

145 Krantz, B. A. & Sosnick, T. R. (2000). Distinguishing between two-state and three-state models for ubiquitin folding. *Biochemistry* 39, 11696–701.

146 Capaldi, A. P., Shastry, M. C. R., Kleanthous, C., Roder, H. & Radford, S. E. (2001). Ultrarapid mixing experiments reveal that Im7 folds via an on-pathway intermediate. *Nat. Struct. Biol.* 8, 68–72.

147 Miller, W. G. & Goebel, C. V. (1968). Dimensions of protein random coils. *Biochemistry* 7, 3925–34.

148 Ervin, J. & Gruebele, M. (2002). Quantifying protein folding transition states with Phi-T. *J. Biol. Phys.* 28, 115–28.

149 Pain, R. H., ed. (2000). *Mechanisms of Protein Folding*, Vol. 32. *Frontiers in Molecular Biology*. Oxford University Press, Oxford.

150 Berne, B. J. (1993). Theoretical and numerical methods in rate theory. In *Activated Barrier Crossing: Applications in Physics, Chemistry and Biology* (Hänggi, P. & Fleming, G. R., eds), pp. 82–119. World Scientific, Singapore.

151 Muñoz, V. (2002). Thermodynamics and kinetics of downhill protein folding investigated with a simple statistical mechanical model. *Int. J. Quantum Chem.* 90, 1522–8.

152 Poland, D. & Scheraga, H. A. (1970). *Theory of Helix-Coil Transitions in Biopolymers*, Academic Press, New York.

153 Dill, K. A. (1985). Theory for the folding and stability of globular proteins. *Biochemistry* 24, 1501–9.

154 Yue, K., Fiebig, K. M., Thomas, P. D., Chan, H. S., Shakhnovich, E. I. & Dill, K. A. (1995). A test of lattice protein folding algorithms. *Proc. Natl Acad. Sci. USA* 92, 325–9.

155 Shakhnovich, E., Farztdinov, G., Gutin, A. M. & Karplus, M. (1991). Protein folding bottlenecks: a lattice Monte Carlo simulation. *Phys. Rev. Lett.* 67, 1665–8.

156 Onuchic, J. N., Nymeyer, H., Garcia, A. E., Chahine, J. & Socci, N. D. (2000). The energy landscape theory of protein folding: Insights into folding mechanisms and scenarios. *Adv. Protein Chem.* 53, 87–152.

157 Kaya, H. & Chan, H. S. (2000). Energetic components of cooperative protein folding. *Phys. Rev. Lett.* 85, 4823–6.

158 Guo, Z. & Thirumalai, D. (1996). Kinetics and thermodynamics of folding of a de novo designed four-helix bundle protein. *J. Mol. Biol.* 263, 323–43.

159 Klimov, D. K. & Thirumalai, D. (1997). Viscosity dependence of the folding rates of proteins. *Phys. Rev. Lett.* 79, 317–20.

160 Srinivas, G., Yethiraj, A. & Bagchi, B. (2001). Nonexponentiality of time dependent survival probability and the fractional viscosity dependence of the rate in diffusion controlled reactions in a polymer chain. *J. Chem. Phys.* 114, 9170–8.

161 Duan, Y. & Kollman, P. A. (1998). Pathways to a protein folding intermediate observed in a 1-microsecond simulation in aqueous solution. *Science* 282, 740–4.

162 Ladurner, A. G., Itzhaki, L. S., Daggett, V. & Fersht, A. R. (1998). Synergy between simulation and experiment in describing the energy landscape of protein folding. *Proc. Natl Acad. Sci. USA* 95, 8473–8.

163 Karanicolas, J. & III, C. L. B. (2003). The structural basis for biphasic kinetics in the folding of the WW domain from a formin-binding protein: lessons for protein design. *Proc. Natl Acad. Sci. USA* 100, 3954–9.

164 Kaya, H. & Chan, H. S. (2000). Polymer principles of protein calorimetric two-state cooperativity. *Proteins Struct. Funct. Genet.* 40, 637–61.

165 Shea, J. & Brooks, C. L. (2001). From folding theories to folding proteins: a review and assessment of simulation studies of protein folding and unfolding. *Annu. Rev. Phys. Chem.* 52, 499–535.

166 Clementi, C., Nymeyer, H. & Onuchic, J. N. (2000). Topological and energetic factors: What deter-

mines the structural details of the transition state ensemble and "en-route" intermediates for protein folding? An investigation for small globular proteins. *J. Mol. Biol.* 298, 937–53.

167 Burton, R. E., Huang, G. S., Daugherty, M. A., Calderone, T. L. & Oas, T. G. (1997). The energy landscape of a fast-folding protein mapped by Ala → Gly Substitutions. *Nat. Struct. Biol.* 4, 305–10.

168 Garcia, C., Nishimura, C., Cavagnero, S., Dyson, H. J. & Wright, P. E. (2000). Changes in the apomyoglobin folding pathway caused by mutation of the distal histidine residue. *Biochemistry* 39, 11227–37.

169 Jäger, M., Nguyen, H., Kelly, J. & Gruebele, M. (2003). Redesigning the turns of WW domain: the function-folding relationship. Submitted.

170 Fersht, A. (1999). *Structure & Mechanism in Protein Science: A Guide to Enzyme Catalysis and Protein Folding.* WH Freeman, New York.

15
Early Events in Protein Folding Explored by Rapid Mixing Methods

Heinrich Roder, Kosuke Maki, Ramil F. Latypov, Hong Cheng, and M. C. Ramachandra Shastry

15.1
Importance of Kinetics for Understanding Protein Folding

As with any complex reaction, time-resolved data are essential for elucidating the mechanism of protein folding. Even in cases where the whole process of folding occurs in a single step, which is the case for many small proteins [1], the kinetics of folding and unfolding provide valuable information on the rate-limiting barrier. The effects of temperature and denaturant concentration give insight into activation energies and solvent-accessibility of the transition state ensemble, and by measuring the kinetic effects of mutations, one can gain more detailed structural insight [2–4]. If the protein folding process occurs in stages, i.e., if partially structured intermediate states accumulate, kinetic studies can potentially offer much additional insight into the structural and thermodynamic properties of intermediate states and intervening barriers [5–9]. Rapid mixing techniques have played a prominent role in kinetic studies of protein folding [5–7, 10–12]. The combination of quenched-flow techniques with hydrogen exchange labeling and NMR has proven to be particularly fruitful for the structural characterization of transient folding intermediates [13–15].

Theoretical models and computer simulations describe the process of protein folding in terms of a diffusive motion of a particle on a high-dimensional free energy surface [16–18]. This ''landscape'' description of protein folding predicts that a protein can choose among a large number of alternative pathways, which eventually converge toward a common free energy minimum corresponding to the native structure. In contrast, the time course of protein folding monitored by optical and other experimental probes generally shows relaxation kinetics with one or a few exponential phases, which are adequately described in terms of a simple kinetic scheme with a limited number of populated states (the chemical kinetics description). These apparently conflicting models can be consolidated if the free energy surface is divided into several regions (basins) separated by substantial free energy barriers due to unfavorable enthalpic interaction or entropic factors (conformational bottlenecks). The protein can rapidly explore conformational space within each basin corresponding to a broad ensemble of unfolded or partially folded states,

Protein Folding Handbook. Part I. Edited by J. Buchner and T. Kiefhaber

ISBN: 3-527-30784-2

but has to traverse substantial kinetic barriers before entering another basin. This type of free energy surface can thus give rise to multi-exponential folding kinetics.

Dissecting the sequence of structural events associated with the folding of a protein poses formidable technical challenges. Important structural events occur on the microsecond time scale, which cannot be accessed by conventional kinetic techniques, such as stopped-flow mixing. Temperature-jump and other rapid perturbation methods have shown that isolated helices and β-hairpins form and decay over a time window ranging from about 50 ns to several microseconds [19–23], which is short compared with the time it takes to complete the process of folding, even for the most rapidly folding proteins (reviewed in Ref. [24]). While these results demonstrate that secondary structure formation is not the rate-determining step in folding, they do not rule out the possibility that these elementary structural events affect the overall rate of folding if they represent energetically unfavorable, but obligatory, early steps. Recent advances in rapid mixing techniques combined with structurally informative spectroscopic probes made it possible to resolve conformational events on the submillisecond time scale preceding the rate-limiting step in the folding of globular proteins [25–27]. Historically, some of the earliest rapid kinetic measurements with millisecond time resolution used a continuous-flow arrangement combined with absorbance measurements of the reaction progress at different points downstream [28]. However, continuous-flow experiments were later replaced by the more versatile and economic stopped-flow experiment, which can be coupled with a wide range of spectroscopic probes to monitor reactions with millisecond time resolution [29, 30]. Continuous-flow techniques have experienced a renaissance in recent years due to advances in mixer design and detection methods, which made it possible to push the time resolution into the microsecond time range [25, 26, 31, 32]. By coupling an efficient capillary mixer with a digital camera, we can routinely extend fluorescence- or absorbance-based kinetic measurements to times as short as 50 μs, which has yielded a wealth of new insight into early stages of protein folding [33–40]. Other techniques make use of two or more consecutive mixing steps in order to prepare the system in a particular initial state (double-jump stopped-flow), or to execute multiple reaction steps in sequence (quenched-flow). If a reaction can be quenched by manipulating solution conditions (e.g., pH) or lowering temperature, quenched-flow or freeze-quench protocols can be used in combination with slower analytical techniques, such as NMR, electron paramagnetic resonance (EPR), or mass spectrometry [41]. To achieve efficient turbulent mixing conditions requires high flow rates and relatively large channel dimensions, which can consume substantial amounts of material. A promising alternative to turbulent mixing with improved sample economy uses hydrodynamic focusing to mix solutions under laminar flow conditions [42, 43].

15.2
Burst-phase Signals in Stopped-flow Experiments

In many cases, stopped-flow and quenched-flow measurements of protein folding reactions show evidence for unresolved rapid processes occurring within the dead

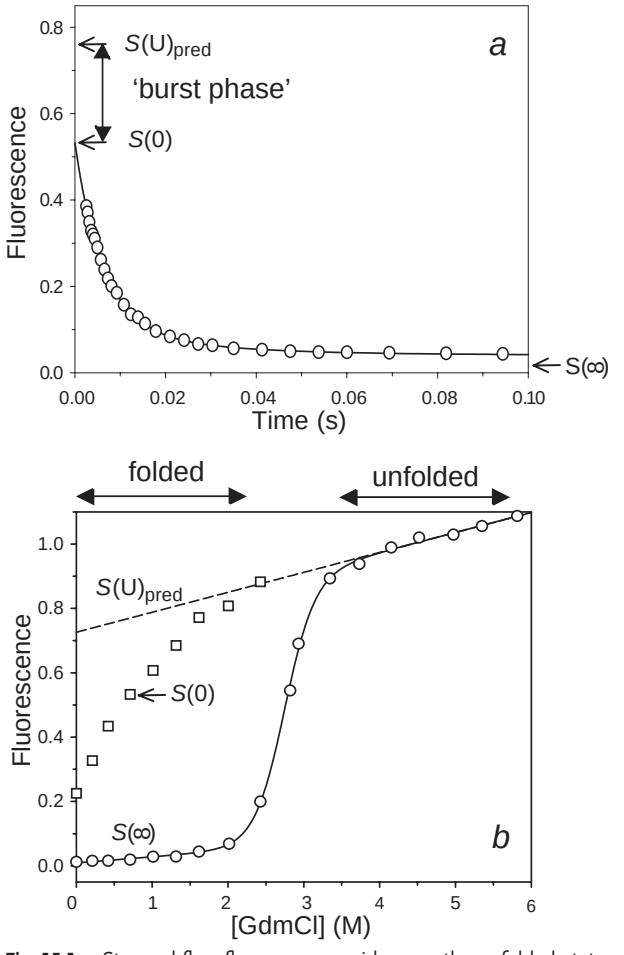

Fig. 15.1. Stopped-flow fluorescence evidence for an unresolved rapid process (burst phase) during folding of cyt *c* (pH 5, 10 °C). a) Tryptophan fluorescence changes during refolding of acid-unfolded cytochrome *c* (pH 2, ~15 mM HCl) at a final GdmCl concentration of 0.7 M. The initial signal $S(0)$ at $t = 0$ (determined on the basis of a separate dead-time measurement) falls short of the signal for the unfolded state under refolding conditions, $S_{pred}(U)$, obtained by linear extrapolation of the unfolded-state baseline (see dashed line in b). b) Effect of the denaturant concentration on the initial (squares) and final (circles) fluorescence signal, $S(0)$ and $S(\infty)$, measured in a series of stopped-flow refolding experiments at different final GdmCl concentration.

time (e.g., Refs [44, 45–49]). This is illustrated by Figure 15.1, which shows the kinetics of refolding of horse cytochrome *c* (cyt *c*) measured by stopped-flow fluorescence along with equilibrium fluorescence data vs. denaturant concentration [50]. The protein was unfolded by addition of 4.5 M guanidine hydrochloride (GdmCl), which lies in the baseline region above the cooperative unfolding transition (Figure 15.1b). The refolding reaction was triggered by sixfold dilution with buffer (0.1 M

sodium acetate, pH 5), resulting in a final GdmCl concentration of 0.75 M, well within the folded baseline region. The data points in Figure 15.1a were recorded by sampling the fluorescence emission above 325 nm (using a glass cutoff filter) at logarithmically spaced time intervals. The first time point corresponds to the instrumental dead time of 2.5 ms, which was calibrated using a standard test reaction [51] (see Appendix). The observed time course describes a double-exponential decays (solid line) consisting of a major phase with a time constant of about 8 ms and a minor one with a time constant in the 100 ms range.

Extrapolation of the observed kinetics back to $t = 0$ yields the initial signal, $S(0)$, which is compared in Figure 15.1b (arrow) with the equilibrium unfolding transition plotted on the same fluorescence scale (relative to unfolded cyt *c* at 4.5 M GdmCl). The initial signal observed in this and a series of additional stopped-flow experiments at different final GdmCl concentrations is consistently below the relative fluorescence of the unfolded state, $S_{\mathrm{pred}}(\mathrm{U})$, predicted by linear extrapolation from the unfolded baseline region to lower GdmCl concentrations (dashed line in panel b). The difference between the predicted and observed initial amplitude, $S_{\mathrm{pred}}(\mathrm{U}) - S(0)$, often called the burst phase, reflects conformational events occurring within the dead time of the stopped-flow experiment. Similar observations on many different proteins using various spectroscopic parameters gave clear evidence for the existence of rapid conformational events that cannot be resolved with conventional mixing techniques, and provided a strong incentive for the development of faster methods for triggering and observing structural changes during the first millisecond of refolding.

15.3 Turbulent Mixing

Most rapid mixing schemes rely on turbulent mixing to achieve complete mixing of two (or more) solutions. Mixers of various design are in use ranging from a simple T-arrangements to more elaborate geometries, such as the Berger ball mixer [52]. The goal is to achieve highly turbulent flow conditions in a small volume. The turbulent eddies thus generated can intersperse the two components down to the micrometer distance scale. However, the ultimate step in any mixing process relies on diffusion in order to achieve a homogeneous mixture at the molecular level. Given that the diffusion time t varies as the square of the distance r over which molecules have to diffuse, it takes a molecule with a diffusion constant $D = 10^{-5}$ cm^2 s^{-1} about 1 ms to diffuse over a distance of 1 μm ($t = r^2/D$). Thus, the mechanical mixing step has to intersperse the two components on a length scale of less than 1 μm in order to achieve submillisecond mixing times. The onset of turbulence is governed by the Reynolds number, *Re*, defined as

$$Re = \rho v d/\eta \tag{1}$$

where ρ is the density (g cm^{-3}), v is the flow velocity (cm s^{-1}), d describes the characteristic dimensions of the channel (cm), and η is the viscosity of the fluid (e.g.,

0.01 poise for water at 20 °C). To maintain turbulent flow conditions in a cylindrical tube, *Re* has to exceed values of about 2000.

Turbulence is important not only for achieving efficient mixing, but also for maintaining favorable flow conditions during observation. In stopped-flow and quenched-flow experiments, turbulent flow insures efficient purging of the flow lines. In continuous-flow measurements, turbulent flow conditions in the observation channel lead to an approximate ''plug flow'' profile, which greatly simplifies data analysis compared to the parabolic profile obtained under laminar flow conditions. The time resolution of a rapid mixing experiment is governed not only by the mixing time, which in practice is difficult to quantify, but also the delay between mixing and observation. The effective delay between initiation of the reaction and the first reliably measurable data point is defined as the dead time, Δt_d. In both stopped- and continuous-flow experiments, any unobservable volume (dead volume), ΔV, between the point where mixing is complete and the point of observation contributes an increment $\Delta t = \Delta V/(dV/dt)$ to the dead time (dV/dt is the flow rate). Additional contributions to the effective dead time include the time delay to stop the flow and any artifacts that can obscure early parts of the kinetic trace (see Appendix).

Increasing the flow rate promotes more efficient mixing by generating smaller turbulent eddies, and yields shorter time delays Δt, and thus should lead to shorter dead times. However this trend does not continue indefinitely. Aside from practical problems due to back pressure and, in the case of stopped-flow measurements, various stopping artifacts, the time resolution of a rapid mixing experiment is ultimately limited by cavitation phenomena [53]. Under extreme conditions, the pressure gradients across turbulent eddies can become so large that the solvent begins to evaporate, forming small vapor bubbles that can take a long time to dissolve. The result is an intensely scattering plume that makes meaningful detection of the kinetic signal virtually impossible.

15.4 Detection Methods

The design principles and performance tests of common rapid mixing instruments, including a typical commercially available stopped-flow apparatus and the continuous-flow instrument developed in our laboratory [26], are described in the Appendix. A major strength of rapid mixing methods is that they can be combined with a wide range of detection methods. Table 15.1 lists common detection methods used in rapid mixing studies of the kinetics of folding, which are illustrated here with selected examples.

15.4.1 Tryptophan Fluorescence

The fluorescence emission properties of tryptophan and tyrosine side chains provide information on the local environment of these intrinsic chromophores.

Tab. 15.1. Common detection methods used in kinetic studies of protein folding.

Method	*Probe*	*Properties probed*	*Sensitivity*
Fluorescence	Trp, Tyr	Solvent shielding, tertiary contacts (quenching)	+++
	ANS	Hydrophobic clusters, collapse	+++
	FRET	Donor–acceptor distance	++
Absorbance	Trp, Tyr, cofactors	Polarity, solvent effects	++
Far-UV CD	Peptide bond	2° structure	–
Near-UV CD	Tyr, Trp, cofactor	Side-chain packing, moblity	–
Vibrational IR res. Raman	Peptide bond, cofactor	2° structure metal coordination	+
SAXS	Heavy atoms	Size (R_G), shape	–

For example, a fully solvent-exposed tryptophan in the denatured state of a protein typically shows a broad emission spectrum with a maximum near 350 nm and quantum yield of ~0.14, similar to that of free tryptophan or its derivative, NATA. Burial of the tryptophan side chain in an apolar environment within the native state or a compact folding intermediate can result in a substantial blue-shift of the emission maximum (by as much as 25 nm) and enhanced fluorescence yield. These changes are a consequence of the decrease in local dielectric constant and shielding from quenchers, such as water and polar side chains. In other cases, close contact with a polar side chain or backbone moiety gives rise to a decrease in fluorescence yield upon folding. Most polar amino acid side chains (as well as main chain carbonyl and the terminal amino and carboxyl groups) are known to quench tryptophan fluorescence, probably via excited-state electron or proton transfer [54, 55]. Thus, the straightforward measurement of fluorescence intensity vs. folding or unfolding time can provide useful information on solvent accessibility and proximity to quenchers of an individual fluorescence probe. Complications due to the presence of multiple fluorophores can be avoided by using mutagenesis to replace any additional tryptophans (see, for example, Refs [56, 57]). Because Trp is a relatively rare amino acid, proteins with only one tryptophan are not uncommon; in the case of Trp-free proteins, a unique fluorophore can be introduced by using site-directed mutagenesis (see, for example, Refs [58, 59]).

The use of tryptophan fluorescence to explore early stages of protein folding is illustrated by our recent results on staphylococcal nuclease (SNase) [60] shown in Figure 15.2. A variant with a unique tryptophan fluorophore in the N-terminal β-barrel domain (Trp76 SNase) was obtained by replacing the single typtophan in wild-type SNase, Trp140, with His in combination with Trp substitution of Phe76. The fluorescence of Trp76 is strongly enhanced and blue-shifted under native conditions relative to the denatured state in the presence of urea (Figure 15.2a), indicating that upon folding the indole ring of Trp76 moves from a solvent-exposed location to an apolar environment within the native structure. An intermediate state with a fluorescence emission spectrum similar to, but clearly distinct from the

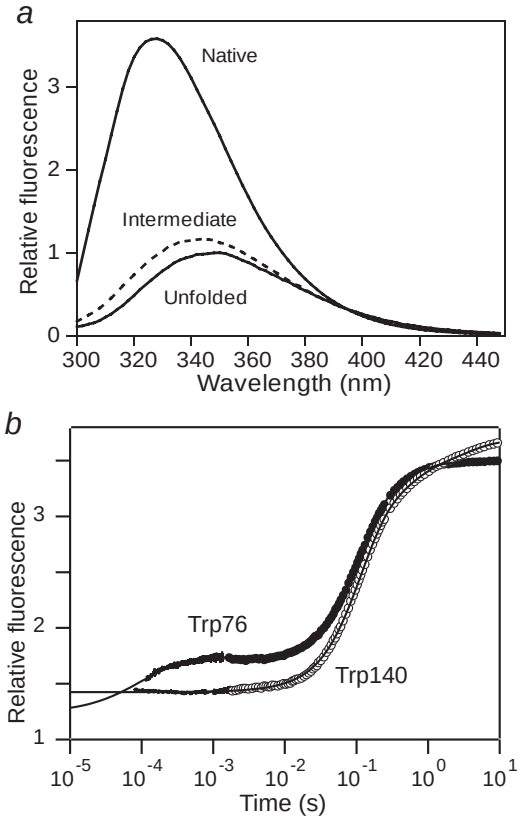

Fig. 15.2. Folding mechanism of SNase probed by tryptophan fluorescence. a) Fluorescence emission spectra of the Trp76 variant of SNase under native and denaturing conditions (solid) and a folding intermediate populated at equilibrium (dashed). The spectrum of the intermediate was determined by global analysis of the fluorescence spectra as a function of urea concentration (pH 5.2, 15 °C). b) Time course of folding (triggered by a pH jump from 2 to 5.2) for WT* SNase (Trp140) and a single-tryptophan variant (Trp76) measured by continuous-flow ($< 10^{-3}$ s) and stopped-flow ($> 10^{-3}$ s) fluorescence.

native state was detected in equilibrium unfolding experiments (dashed line in Figure 15.2a). In contrast to WT* SNase (P47G, P117G and H124L background), which shows no changes in tryptophan fluorescence prior to the rate-limiting folding step (~100 ms), the F76W/W140H variant shows additional changes (enhancement) during an early folding phase with a time constant of about 80 μs (Figure 15.2b). The fact that both variants exhibit the same number of kinetic phases with very similar rates confirms that the folding mechanism is not perturbed by the F76W/W140H mutations. However, the Trp at position 76 reports on the rapid formation of a hydrophobic cluster in the N-terminal β-sheet region while the wild-type Trp140 is silent during this early stage of folding.

15.4.2 ANS Fluorescence

Valuable complementary information on the formation of hydrophobic clusters at early stages of folding can be obtained by using 1-anilino-8-naphthalene-sulfonic acid (ANS) as extrinsic fluorescence probe [61–63]. Figure 15.3 illustrates this with recent results on the Trp76 variant of SNase introduced above [60]. Panel a shows continuous-flow measurements of the enhancement in ANS fluorescence that accompanies early stages of SNase folding under native conditions (U → N),

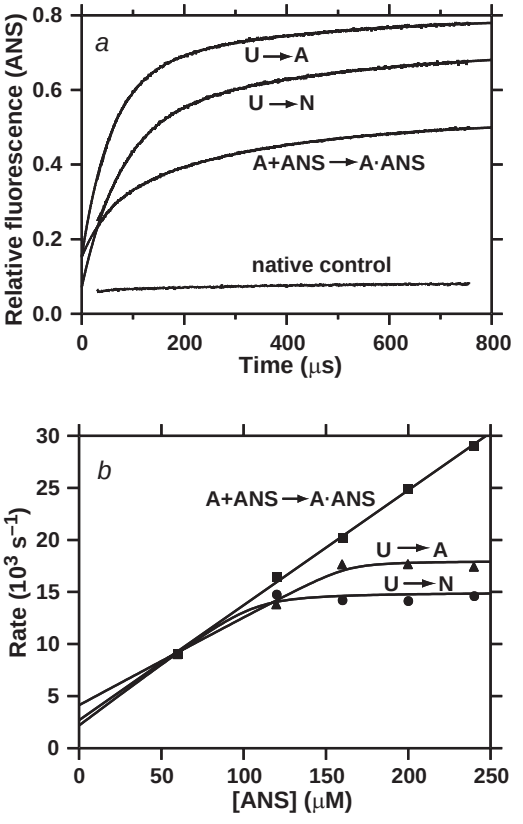

Fig. 15.3. An early folding event in Trp76 SNase detected by ANS fluorescence. a) ANS fluorescence changes during ANS binding/folding of Trp76 SNase measured by continuous-flow experiments at 15 °C in the presence of 160 μM ANS. U → A: Salt concentration jump from 0 M to 1 M KCl at pH 2.0; U → N: refolding induced by a pH-jump from 2.0 to 5.2; A + ANS → A · ANS: ANS binding kinetics in the presence of 1 M KCl at pH 2.0; native control: ANS binding kinetics under the native condition (pH 5.2). b) ANS concentration dependence of the rates for the major (fast) kinetic phases observed during the U → A (triangles), U → N (filled circles), and A + ANS → A · ANS (filled squares) reactions.

and during formation of the A-state, the compact acid-denatured state of SNase (U → A). Also shown is the kinetics of ANS binding to the preformed A-state. While the rate of ANS binding to the A-state shows the linear dependence on ANS concentration characteristic of a second-order binding process (panel b), the rates observed under refolding conditions (both to the native state and compact A-state) level off at ~120 μM ANS. The limiting ANS-independent rate at higher concentrations thus is due to an intramolecular conformational event that precedes ANS binding. The rate of this process closely matches that of the earliest phase detected by intrinsic fluorescence of Trp76 (Figure 15.3b), confirming that both processes reflect a common early folding step. The results are consistent with the rapid accumulation of an ensemble of states containing a loosely packed hydrophobic core involving primarily the β-barrel domain. In contrast, the specific interactions in the α-helical domain involving Trp140 are formed only during the final stages of folding.

15.4.3 FRET

Fluorescence resonant energy transfer (FRET) can potentially give more specific information on the changes in average distance between fluorescence donors and acceptors. For example, cyt *c* contains an intrinsic fluorescence donor–acceptor pair, Trp59 and the covalently attached heme group, which quenches tryptophan fluorescence via excited-state energy transfer [64]. We have made extensive use of this property to characterize the folding mechanism of cyt *c* [14, 50, 65], including the initial collapse of the chain on the microsecond time scale [33, 34].

We recently combined ultrafast mixing experiments with FRET in order to monitor large-scale structure changes during early stages of folding of acyl-CoA-binding protein (ACBP), a small (86-residue) four-helix bundle protein [38]. ACBP contains two tryptophan residues on adjacent turns of helix 3, which served as fluorescence donors, and an AEDANS fluorophore covalently attached to a C-terminal cystein residue was used as an acceptor (Figure 15.4a). Earlier equilibrium and kinetic studies, using intrinsic tryptophan fluorescence, showed a cooperative unfolding transition and single-exponential (un)folding kinetics consistent with an apparent two-state transition. Even when using continuous-flow mixing to measure intrinsic tryptophan fluorescence changes on the submillisecond time scale (Figure 15.4b), we found only minor deviations from two-state folding behavior. However, when we monitored the fluorescence of the C-terminal AEDANS group while exciting the tryptophans, we observed a large increase in fluorescence during a fast kinetic phase with a time constant of 80 μs, followed by a decaying phase with a time constant ranging from about 10 ms to 500 ms, depending on denaturant concentration (Figure 15.4c). The large enhancement in FRET efficiency is attributed to a major decrease in the average distance between helix 3 and C-terminus of ACBP. The fact that the early changes are exponential in character suggests that the initial compaction of the polypeptide is limited by an energy barrier rather than chain diffusion. The subsequent decrease in AEDANS fluorescence during the final stages

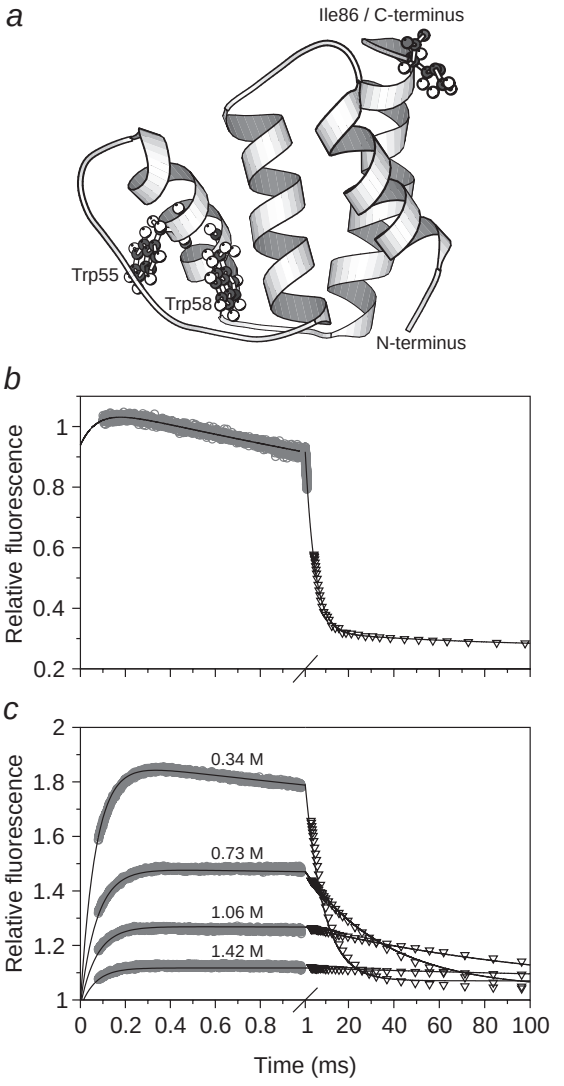

Fig. 15.4. FRET-detection of an early folding intermediate in a helix-bundle protein, ACBP. a) Ribbon diagram of ACBP, based on an NMR structure. The two tryptophan residues and the mutated C-terminal isoleucine are shown in ball and stick. The two lower panels show refolding kinetics of unmodified ACBP (b) and AEDANS-labeled ACBP,I86C (c) in pH 5.3 buffer containing 0.34 M GdmCl at 26 °C. In both panels data from continuous-flow (open circles) and stopped-flow (open triangles) experiments were matched and combined.

of folding is attributed to a sharp decrease in the intrinsic fluorescence yield of the two tryptophans due to intramolecular quenching.

The specific side-chain interactions responsible for quenching are established only in the close-packed native structure and are not present during the initial

folding event. These observations indicate that the early (80 μs) folding phase marks the formation of a collapsed, but loosely packed and highly dynamic ensemble of states with overall dimensions (in terms of fluorescence donor–acceptor distance) similar to that of the native state. Accumulation of partially structured states with some native-like features may facilitate the search for the native conformation. Because of their short lifetime and low stability, such intermediates can easily be missed by conventional kinetic techniques, whereas the continuous-flow FRET technique offers the temporal resolution and structural sensitivity to detect even marginally stable intermediates populated during early stages of folding.

15.4.4 Continuous-flow Absorbance

Although fluorescence is inherently more sensitive, our capillary mixing instrument can also be adapted for continuous-flow absorbance measurements on the microsecond time scale. The fully transparent flow cell used for fluorescence measurements is replaced with a custom-made partially opaque absorbance flow cell of the same dimensions (0.25 mm pathlength). Relatively uniform illumination with minimal changes to the optical arrangement (see Figure 15.16) was achieved by using a 2-mm fluorescence cuvette filled with a highly turbid suspension (non-dairy creamer works well) as scattering cell. As in fluorescence measurements, a complete reaction profile can be recorded in a single 2–3 s continuous-flow run by imaging the flow channel onto the CCD chip. Using the reduction of 2,6-dichlorophenolindophenol (DCIP) by ascorbic acid as a test reaction ([66]; see Appendix), we measured dead times as short as 40 μs at the highest flow rate tested (1.1 mL s^{-1}).

To validate the technique, we measured the changes in heme absorbance in the Soret region (~360–430 nm) associated with the folding of oxidized horse cyt *c*. The reaction was initiated by a rapid jump from pH 2, where the protein is fully unfolded, to pH 4.7, where folding occurs rapidly with minimal complications due to non-native histidine-heme ligands. A series of kinetic traces covering the time window from 40 μs to ~1.5 ms were measured at different wavelengths spanning the Soret region (Figure 15.5). A parallel series of stopped-flow experiments (data not shown) was performed under matching conditions to extend the data to longer times (2 ms to 10 s). Global fitting of the family of kinetic traces to sums of exponential terms yielded three major kinetic phases with time constants of 65 μs, 500 μs, and 2 ms, respectively, consistent with accumulation of two intermediate species, I_1 and I_2, with absorbance properties distinct from both the initial (U) and final (N) states. In previous continuous-flow fluorescence measurements on horse cyt *c* [33, 34], we also observed three kinetic phases with very similar time constants, indicating that a basic four-state mechanism is sufficient to describe the folding process of cyt *c* in the absence of complications due to nonnative heme ligation and other slow events, such as *cis–trans* isomerization of peptide bonds.

15.4.5
Other Detection Methods used in Ultrafast Folding Studies

Continuous-flow measurements have been coupled with several other biophysical techniques, including resonance Raman spectroscopy [25], CD [67, 68], EPR [69, 70], and SAXS [27, 68, 71, 72]. In their pioneering work, Takahashi et al. [25] used resonance Raman spectroscopy to monitor changes in heme coordination during folding of cyt *c* on the submilliscond time scale. Their findings confirmed and extended prior results on the involvement of heme ligation in folding of cyt *c*, based on stopped-flow absorbance and fluorescence measurements [73–75].

CD spectroscopy in the far-UV (peptide) region provides an overall measure of secondary structure content, and is thus an especially valuable technique for protein folding studies (see, for example, Refs [44, 45]). However, the low inherent sensitivity of the technique, together with various flow artifacts, such as strain-induced birefringence, has limited the resolution of stopped-flow CD measurements to the 10-ms time range [76]. Akiyama et al. [67] were able to extend the time resolution down to the 400 μs range by coupling an efficient turbulent mixer (T-design) with a commercial CD spectrometer. Their continuous-flow measurements of CD spectral changes in the far-UV region revealed the formation of (helical) secondary structure during the second and third (final) stage of cyt *c* folding. The same group recently designed a mixer/flow-cell assembly with a dead time as short as 160 μs for continuous-flow SAXS measurements on a synchrotron [68, 72]. They were thus able to follow the changes in size (radius of gyration, R_g) and shape (pair distribution derived from scattering profiles) associated with refolding of acid-denatured cyt *c* under conditions similar to those used in our absorbance measurements (Figure 15.5). The intermediate formed within their dead time, which corresponds to the product of the 65 μs process in Figure 15.5, is substantially more compact ($R_g \sim 20$ Å) than the acid-denatured state ($R_g = 24$ Å). This finding clearly shows that cyt *c* undergoes a partial chain collapse during the initial folding phase, confirming earlier fluorescence data [33, 77].

15.5
A Quenched-Flow Method for H-D Exchange Labeling Studies on the Microsecond Time Scale

H-D exchange labeling experiments coupled with NMR detection [13–15, 78, 79] are important sources of structural information on protein folding intermediates. These experiments generally rely on commercial quenched-flow equipment to carry out two or three sequential mixing steps, which limits the time resolution to a few milliseconds or longer. In order to push the dead time of quenched-flow measurements into the microsecond time range, we made use of our highly efficient capillary mixers [26]. The device (illustrated in Figure 15.6a) uses a quartz capillary mixer similar to that used for optical measurements (see Appendix), but without observation cell, in order to generate a homogeneous mixture of solutions

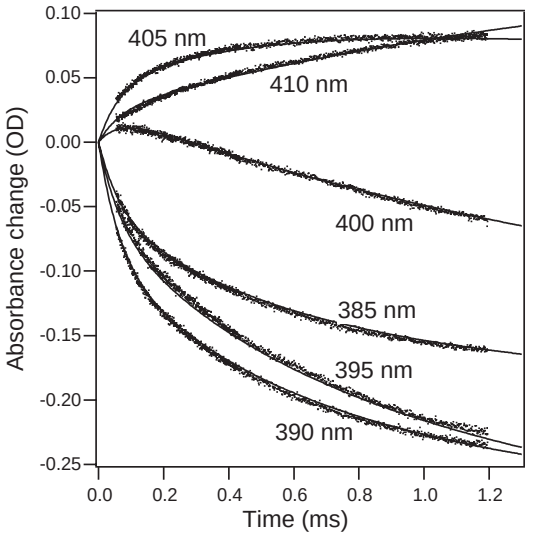

Fig. 15.5. Initial stages of refolding of acid-denatured oxidized cyt *c* at pH 5 monitored by continuous-flow absorbance measurements at different wavelengths spanning the Soret heme absorbance band. The lines represent a global fit of a four-state folding mechanism to the family of kinetic traces.

A and B. The mixture emerges from the capillary as a fine (200 μm diameter) jet with a linear velocity of up to 40 m s^{-1} at the highest flow rate used (1.25 mL s^{-1}). A second mixing event can be achieved simply by injecting the jet into a test tube containing a third solution C; the extremely high flow velocity ensures very efficient mixing.

To determine the dead time (i.e., the shortest delay between the two mixing events), we carried out a series of H-D exchange experiments on a pentapeptide (YGGFL). Rapid exchange of the backbone amide protons with solvent deuterons was achieved by mixing an H_2O solution of the peptide with fivefold excess of D_2O buffered at pH* 9.7 (uncorrected pH meter reading). The exchange reaction was quenched by injecting the mixture into ice-cooled acetate buffer at pH* 3. Under these quench conditions, the rate of exchange for some of the peptide NH groups (Gly3, Phe4, and Leu5) is sufficiently slow (10, 45, and 70 min, respectively) to determine their residual NH intensity by recording one-dimensional ^1H NMR spectra. Figure 15.6b shows the results of a series of experiments in which the capillary was raised from direct contact with the quench solutions to a distance of about 40 mm corresponding to a ''time-of-flight'' of ~1 ms. For Gly3 and Phe4, exponential fits of the decay in residual NH intensity with the incremented time delay yields exchange rates of 5600 and 4400 s^{-1}, respectively, in agreement with published intrinsic exchange rates [80] (the rate of the C-terminal amide group is too slow to be measurable over a 1-ms time window, and the Gly2 NH continues to

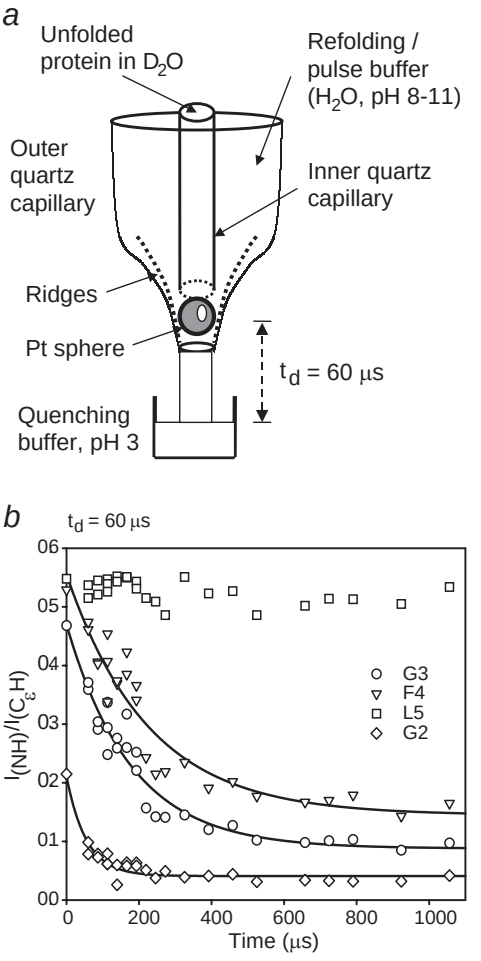

Fig. 15.6. A capillary mixing device for quenched-flow measurements on the microsecond time scale. a) A capillary mixer similar to that described in the Appendix (Figure 15.16), but without flow cell, is used to generate a fast free-flow jet. A second mixing event occurs upon impact of the jet with a quench buffer solution. b) Quenched-flow NMR measurement of the H-D exchange reaction of backbone NH groups of a model peptide (YGLFG). Extrapolation of the exponential decay in normalized NH resonance intensity (solid curves) yields an estimated dead time of 60 μs.

exchange under quench conditions). Extrapolation of the fits up to the NH intensity expected at $t = 0$ (measured in a separate control) indicates that the first measurement corresponds to an effective exchange time of 60 ± 10 μs, thus defining the dead time of the measurement. We used a similar set-up to measure the protection of amide protons at early times of refolding of β-lactoglobulin [37].

15.6
Evidence for Accumulation of Early Folding Intermediates in Small Proteins

15.6.1
B1 Domain of Protein G

Observation of a burst-phase signal, such as that shown in Figure 15.1, suggested deviations from two-state behavior for many proteins, including some small ones [7, 9, 81]. An illustrative example is the 57-residues B1 domain of protein G (GB1), which is among the smallest globular protein domains that do not depend on disulfide bonds or metals for stabilization (Figure 15.7a). Like many other small proteins [1], GB1 was initially thought to fold according to a two-state mechanism [82]. However, continuous-flow fluorescence measurements of the GB1 folding kinetics showed clear deviations from the first-order (single-exponential) kinetics expected for a simple two-state reaction [35]. The time course of refolding from the GdmCl-denatured state revealed a prominent exponential phase with a time constant of 600–700 μs followed by a second, rate-limiting process with a time constant of 2 ms or longer, depending on denaturant concentration (Figure 15.7b). The fast phase dominates the kinetics at low denaturant concentrations and accounts for the total fluorescence change associated with the burial of Trp43 upon folding, including the previously unresolved burst-phase signal [83]. In Figure 15.8, the rates of the two observable folding phases and the corresponding amplitudes are plotted vs. denaturant concentration. The biphasic kinetics of folding observed over a range of GdmCl concentrations can be modeled quantitatively on the

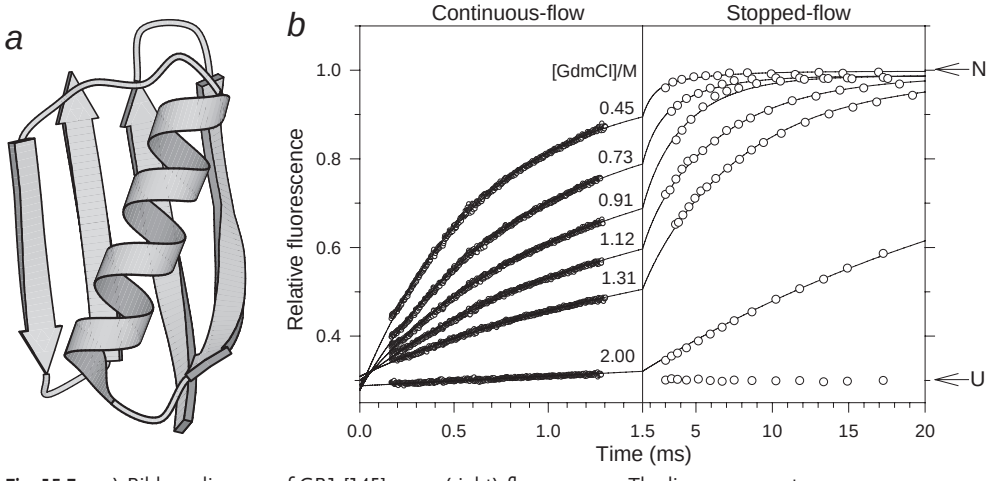

Fig. 15.7. a) Ribbon diagram of GB1 [145]. b) Folding kinetics of GB1 at different final GdmCl concentrations in the presence of 0.4 M sodium sulfate (pH 5.0, 20 °C) monitored by continuous-flow (left) and stopped-flow (right) fluorescence. The lines represent double-exponential fits to the the combined traces, which are normalized with respect to the native state.

basis of a three-state folding mechanism (Scheme 15.1),

$$U \underset{k_{iu}}{\overset{k_{ui}}{\rightleftharpoons}} I \underset{k_{ni}}{\overset{k_{in}}{\rightleftharpoons}} N$$

Scheme 15.1

where I represents an ensemble of intermediate states with native-like fluorescence properties (i.e., Trp43 is buried). Alternative mechanisms with nonproductive or nonobligatory intermediates lead to somewhat poorer fits of the data at low denaturant concentration, but cannot be ruled out definitively on the basis of available data (see Section 15.7.4 and Chapter 12.1).

The dependence of elementary rate constants, k_{ij}, on denaturant concentration c (dashed lines in Figure 15.8) is governed by the following relationship

$$\ln k_{ij} = \ln {k_{ij}}^0 + ({m_{ij}}^{\ddagger}/RT) \times c \tag{2}$$

where ${k_{ij}}^0$ represents the elementary rate constant in the absence of denaturant, and ${m_{ij}}^{\ddagger}$ describes its dependence on denaturant concentration (kinetic m-value). The system of linear differential equations describing Scheme 15.1 was solved by determining the eigenvalues and eigenvectors of the corresponding rate matrix, using standard numeric methods [84, 85]. Although a three-state kinetic mechanism can be solved analytically (see, for example, Ref. [86]), the rate-matrix approach has the advantage that it can be readily expanded to more complex first-order kinetic mechanisms. After optimizing the four elementary rate constants and corresponding m-values, the two observable rates (eigenvalues) and associated amplitudes predicted by the model (solid lines in Figure 15.8) simultaneously fit both the observed rate profile (log(rate) vs. GdmCl concentration) and kinetic amplitudes at each denaturant concentration, as well as the midpoint and slope of the equilibrium unfolding transition (diamonds in panel b).

The three-state mechanism explains the kinetic behavior at low (< 1 M) and intermediate (1–3 M) GdmCl concentrations in terms of two distinct kinetic limits reminiscent of the EX1 and EX2 limits of hydrogen exchange [87]. At low denaturant concentration, the intermediate is stable and transiently populated (the free energy of I in Figure 15.8c is lower than that of U), and the rate of the slower folding phase approaches the elementary rate constant of the final folding step, k_{IN}. At the same time, the fast (submillisecond) folding phase gains amplitude at the expense of the slow (rate-limiting) phase. At intermediate denaturant concentrations, the intermediate is destabilized (Figure 15.8c) and no longer accumulates. However, if I is an obligatory intermediate, the observed folding rate approaches the limiting value $k_f = K_{UI} \times k_{IN}$, where $K_{UI} = k_{UI}/k_{IU}$ is the equilibrium constant of the U $\leftrightarrow$ I transition. Thus, the sharp decrease in the net folding rate as the denaturant concentration approaches the midpoint of the unfolding transition is explained in terms of the unfavorable U $\leftrightarrow$ I pre-equilibrium involving a high-energy intermediate.

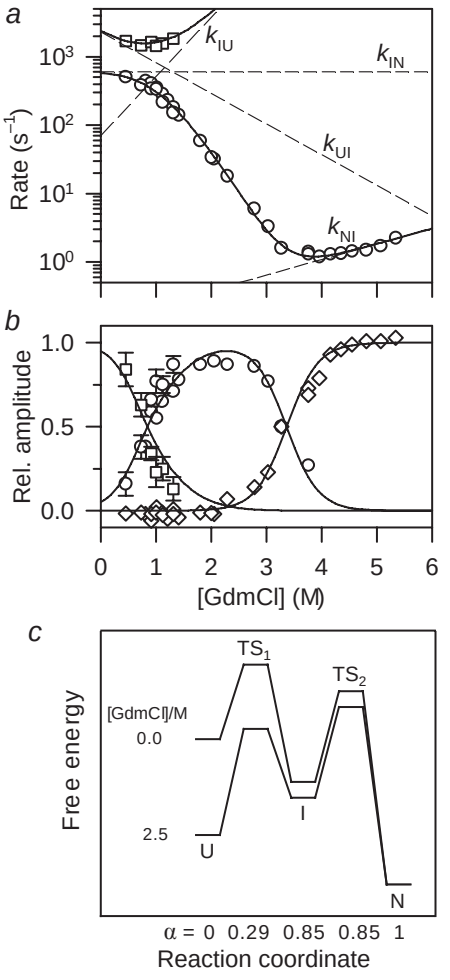

Fig. 15.8. GdmCl-dependence of the rate constants (a) and kinetic amplitudes (b) of the fast (squares) and slow (circles) kinetic phases observed during folding of GB1. (c) Free energy diagrams for folding of GB1 under conditions where the intermediate, I is well populated (0 M) and unstable (2.5 M GdmCl). α represents the change in solvent-accessible surface area relative to the unfolded state U.

Three-state analysis of a complete set of kinetic data, such as that of GB1 reported by Park et al. [35], provides a comprehensive description of the folding mechanism in terms of the size of the free-energy barriers separating the intermediate from the unfolded and native states (labeled TS_1 and TS_2 in Figure 15.8c) and the stability of the intermediate ($\Delta G = -RT \ln(k_{UI}/k_{IU})$. In addition, the denaturant dependence of the four elementary rate constants provides valuable insight into the changes in solvent-accessible surface area associated with each transition. In Figure 15.8c, each state and intervening transition state is labeled with the cor-

responding α-value (sometimes called β_T in reference to Tanford [88]) obtained by the cumulative kinetic *m*-values with respect to the total equilibrium *m*-value. According to this analysis, the initial barrier, TS_1, represents a well solvated ensemble of states ($\alpha = 0.29$) while both I and TS_2 are nearly as solvent-shielded as the native state ($\alpha = 0.85$). The relative changes in fluorescence associated with the two folding phases of GB1 provide additional insight into the structural properties of the intermediate. The large increase in fluorescence during the fast phase (Figure 15.7b), which accounts for nearly all of the fluorescence change at equilibrium, indicates that Trp43 becomes largely buried already during the initial phase of folding. Given the central location of Trp43 at the interface between the C-terminal β-hairpin and the α-helix, this indicates that the intermediate contains a well-developed hydrophobic core.

Krantz et al. recently questioned the validity of our analysis and argued that the folding kinetics of GB1 should be modeled as a two-state process [89]. However, this requires that the complete time course of folding can be fitted by a single exponential. In contrast, we find that a satisfactory fit of our combined continuous- and stopped-flow data requires two exponential phases, while a single exponential fit leads to nonrandom residuals of the order of 10%, which is unacceptable, given the quality of the data (Figure 15.9). It should be noted that the two phases differ sufficiently in rate ($>$ 3.5-fold) to make their separation unambiguous. This conclusion is strengthened by the absence of additional, slower phases in GB1, which contains no proline residues. Reanalyzing a manually digitized version of our data, Krantz et al. [89] were able to fit single exponentials to the separate continuous-flow and stopped-flow traces, but obtained different rates for the two experiments, which confirms our conclusion that the overall kinetics is biphasic. Below 1 M GdmCl, where the slower phase of our double-exponential fit levels off (Figure 15.8), the apparent rate obtained by single-exponential fitting continues to increase, approximating the linear chevron behavior of a two-state system.

This phenomenon is explained by the fact that the approximate rate obtained by fitting a single exponential represents a weighted average of the rates obtained by double-exponential fitting (see next section). Because the fast phase dominates at low and the slow phase at higher denaturant concentrations, the result is a relatively linear rate profile. We further note that the population of the intermediate becomes negligible at GdmCl concentrations approaching the transition region, resulting in an apparent two-state unfolding equilibrium. Thus, contrary to Krantz et al. [89], the predicted equilibrium behavior cannot be used to discriminate between the two models. Finally, the folding kinetics of GB1 was found to be independent of protein concentration [83], indicating that intermolecular interactions are not involved in stabilizing the intermediate.

15.6.2 Ubiquitin

The 76-residue α/β protein ubiquitin is another well-studied small protein for which three-state folding behavior has been reported under some conditions. Khor-

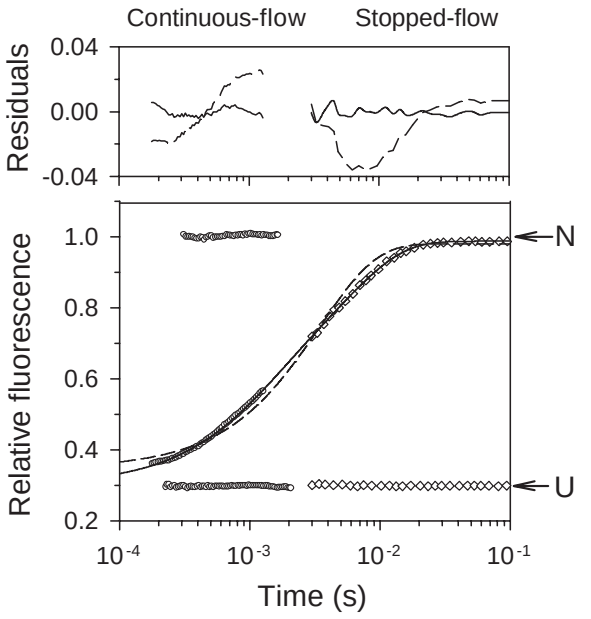

Fig. 15.9. Folding kinetics of GB1 at 1.12 M GdmCl (pH 5.0, 20 °C, 0.4 M sodium sulfate) monitored by continuous-flow (circles) and stopped-flow (diamonds) fluorescence. Single- and double-exponential fits and residuals are shown with solid and dashed lines, respectively.

asanizadeh et al. [48, 58] found deviations from two-state behavior in the folding kinetics of a tryptophan-containing ubiquitin variant (F45W mutant), including a downward curvature in the rate profile (log(rate) vs. [denaturant] plot) and a concomitant drop in the relative amplitude of the main folding phase at low denaturant concentration. They were able to account for both phenomena (rollover and burst phase) in terms of a three-state mechanism ($U \leftrightarrow I \leftrightarrow N$) with an obligatory on-path intermediate. As detailed above for GB1, this simple kinetic mechanism explains the leveling-off of the rate constant and diminishing amplitude of the principal (rate-limiting) folding phase at GdmCl concentrations below 1 M. However, without direct observation of the inferred fast folding phase, it is not possible to rule out alternative mechanisms with off-path or non-obligatory intermediates (further discussed in Section 15.7.3). Moreover, the uncertainty in the burst-phase amplitude is substantial if the main observable folding phase approaches the dead time of the kinetic experiment, which is the case for ubiquitin under stabilizing conditions. Krantz and Sosnick [90] remeasured the folding kinetics of F45W ubiquitin, using a stopped-flow instrument with a dead time of ~1 ms. They found a linear rate profile for the main folding phase and no indications of a burst phase, and concluded that our earlier evidence for a folding intermediate was based on fitting artifacts.

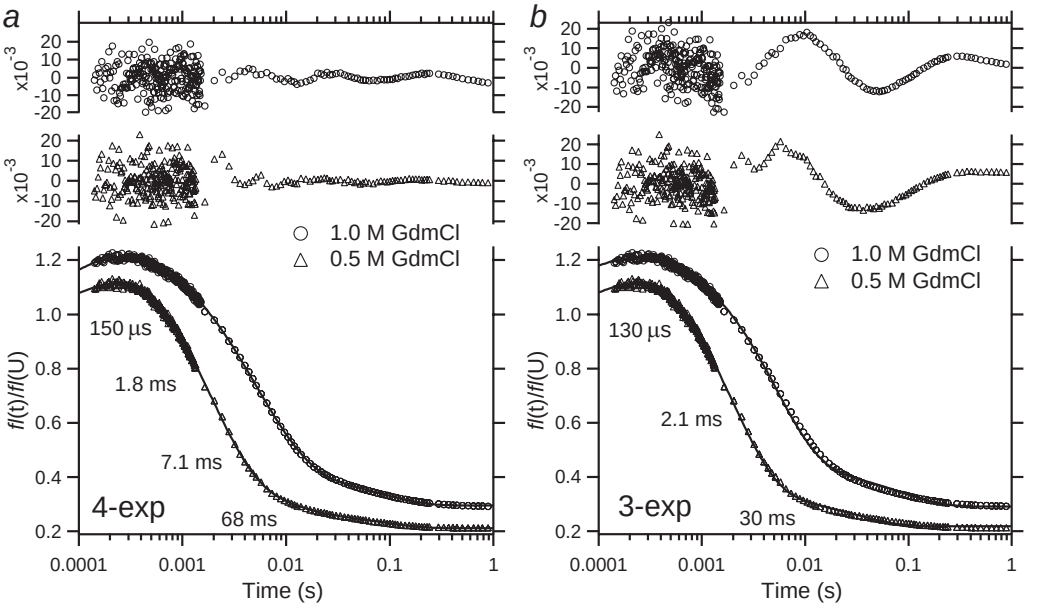

Fig. 15.10. Comparison of quadruple (a) and triple (b) exponential fitting of the kinetics of refolding of F45W ubiquitin at final GdmCl concentrations of 0.5 and 1.0 M (pH 5, 25 °C). Fluorescence traces measured in continuous- and stopped-flow experiments were normalized with respect to the unfolded protein in 6 M GdmCl. The residuals (top two traces in each panel) indicate that four exponentials are required to obtain a satisfactory fit of the data over the time window shown.

In an effort to settle this debate, we recently revisited the folding kinetics of F45W ubiquitin, combining continuous-flow fluorescence measurements with stopped-flow experiments with an improved dead time, which allowed us to continuously monitor the time course of folding from about 100 µs to 100 s (see Figure 15.10a for two representative kinetic traces). The initial increase in fluorescence relative to the GdmCl-unfolded state with a time constant of 150 µs becomes more pronounced in the presence of sodium sulfate (data not shown) and is consistent with a decrease in the solvent accessibility of the fluorophore, Trp45, at an early stage of folding. However, further studies are required to determine whether this process reflects formation of a folding intermediate or a less specific collapse event. The subsequent fluorescence decay is attributed to intramolecular quenching of Trp45 fluorescence upon folding [91].

A thorough kinetic analysis, using multi-exponential fitting functions, indicates that a minimum of four distinct phases are required to obtain a satisfactory fit of the data over the 0.1–1 s time window (Figure 15.10a); a minor additional fluorescence decay at longer times has been attributed to proline isomerization [58]. In contrast, if we use only three exponentials (including one increasing and two decaying phases) to fit the data over the same time window, we obtain non-random

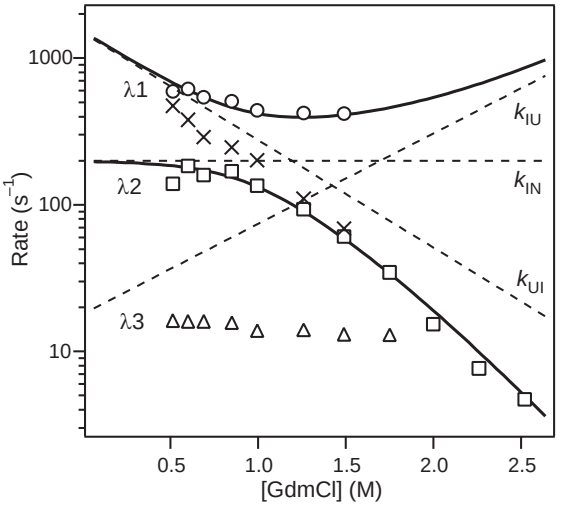

Fig. 15.11. Expanded region of the rate profile (log rate versus [GdmCl]) for the two main phases (circles and squares) and a minor slower phase (triangles) observed during folding of F45W ubiquitin (pH 5, 25 °C). The solid lines show the rates predicted by a three-state model, and the dashed lines indicate the elementary rate constants used. The X-symbols show the apparent rates obtained by triple-exponential fitting (Figure 15.10b).

residuals with amplitudes much larger than the scatter of the data points (Figure 15.10b). Under the most stabilizing conditions studied (0.5 M GdmCl), a satisfactory fit of the main fluorescence decay between 300 μs to 10 ms requires two distinct phases, λ_1 and λ_2, with time constants $\tau_1 = 1.8$ and $\tau_2 = 7.1$ ms, respectively. A fourth phase ($\tau_3 \sim 70$ ms) is necessary to account for a minor decay observed between 20 and 200 ms. The fact that both the rate and amplitude of λ_3 are essentially independent of denaturant concentration points toward a heterogeneous process, perhaps involving a minor population of molecules containing nonnative (*cis*) proline isomers.

A plot of the rate constants for the three decaying phases vs. GdmCl concentration (Figure 15.11) shows a pronounced rollover for λ_2 (squares) with a denaturant-independent regime below 0.75 M followed by a linear decrease above 1 M GdmCl, whereas λ_1 shows a shallow upward curvature. As in the case of GB1 (Figure 15.8), this behavior is fully consistent with a three-state mechanism (Scheme 15.1). Figure 15.11 also shows the apparent rates for the main decaying phase obtained by fitting only three exponentials (symbol *x*). Since they represent an average of λ_1 and λ_2 weighted according to the relative amplitudes, they continue to increase with decreasing GdmCl concentration below 1 M. Thus, the controversy whether an intermediate accumulates during folding of ubiquitin boils down to a rather subtle curve-fitting problem.

In our initial study, we detected only the slower process, λ_2, which exhibits the rollover and missing-amplitude effects indicative of a burst-phase intermediate

[48]. By extending their stopped-flow measurements to shorter times (~1 ms), Krantz and Sosnick [90] obtained a faster rate without apparent rollover corresponding to a weighted average of the two underlying processes. In a recent stopped-flow study, Went et al. [92] found that F45W ubiquitin exhibits three-state folding kinetics under some conditions (in the presence of GdmCl or urea plus salt) and two-state behavior under other conditions (in the presence of urea at low ionic strength). They further report that the folding kinetics of F45W ubiquitin (unmodified N-terminus) varies with protein concentration, suggesting that transient association may stabilize the intermediate. All of these observations, including our earlier findings on the effects of core mutations [48], can be explained by the presence of a marginally stable intermediate, which affects the kinetics of folding only under sufficiently stabilizing conditions.

15.6.3 Cytochrome *c*

Cyt *c* has played a central role in the development of new kinetic approaches for exploring early events in protein folding. The presence of a covalently attached heme group in this 104-residue protein (Figure 15.12) serves as a useful optical marker, and its redox and ligand binding properties provide unique experimental opportunities for rapid initiation and observation of folding [19, 25, 93]. Its sole tryptophan residue, Trp59, is located within 10 Å of the heme iron (Figure 15.12), resulting in efficient fluorescence quenching through a Förster-type energy transfer mechanism. Strongly denaturing conditions (e.g., 4.5 M GdmCl, or acidic pH

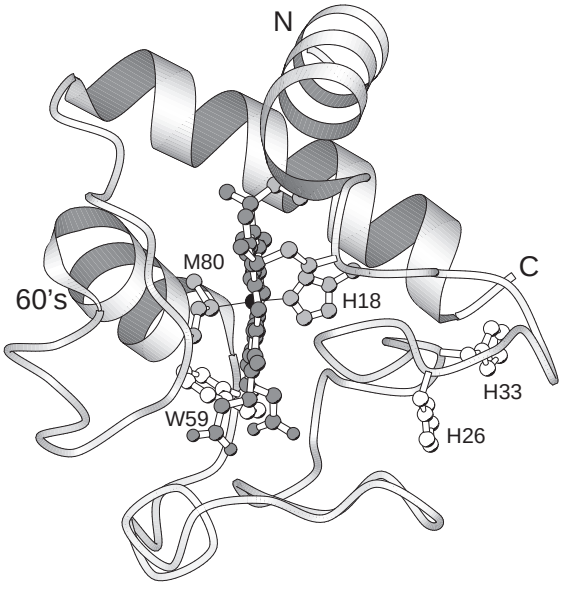

Fig. 15.12. Ribbon diagram of horse cytochrome *c*, based on the crystal structure [146].

at low ionic strength) result in a large increase in Trp59 fluorescence (up to ~60% of that of free tryptophan in water) indicative of an expanded chain conformation with an average tryptophan–heme distance greater than 35 Å [32, 64]. While numerous studies have shown that folding of oxidized cyt *c* is accompanied by changes in coordination of the heme iron [14, 25, 45, 50, 73, 74, 94–96], these complications can be largely avoided by working at mildly acidic pH (4.5–5) where the protein is still stable, but histidine residues are protonated and no longer can bind to the heme iron [73, 97].

Our capillary mixing apparatus [26] enabled us to resolve the entire fluorescence-detected folding kinetics of cyt *c*, including the elusive initial collapse of the chain [33]. Figure 15.13a shows the decay in Trp59 fluorescence observed during refolding of acid-unfolded cyt *c* (pH 2, 10 mM HCl) induced by a pH jump to native conditions (pH 4.5, 22 °C). The continuous-flow data covering the time range from 45 μs to ~1 ms are accurately described by a biexponential decay with a major rapid phase (time constant 59 ± 6 μs) and a minor process in the 500 μs range. This fit extrapolates to an initial fluorescence of 1.0 ± 0.05 (relative to the acid-unfolded protein) at $t = 0$, indicating the absence of additional, more rapid fluorescence changes that remain unresolved in the 45 μs dead time. The same data are plotted in Figure 15.13b on a logarithmic time scale, along with a stopped-flow trace measured under matching conditions, which accounts for the final 10% of the total fluorescence change.

The combined kinetic trace covers six orders of magnitude in time and accounts for the complete change in Trp59 fluorescence associated with refolding of cyt *c*. An Arrhenius plot of the rate of the initial phase (Figure 15.13a, inset) yields an apparent activation enthalpy of 30 kJ mol^{-1}, which is significantly larger than that expected for a diffusion-limited process [98]. In subsequent laser T-jump studies, Hagen, Eaton and colleagues [77, 99] detected a relaxation process with similar rates and activation energy, confirming the presence of a free energy barrier between unfolded and collapsed conformations of cyt *c*.

In other continuous-flow experiments, we measured the kinetics of folding of cyt *c* starting from either the acid-unfolded (pH 2, 10 mM HCl) or the GdmCl-unfolded state (4.5 M GdmCl, pH 4.5 or pH 7), and ending under various final conditions (pH 4.5 or pH 7 and GdmCl concentrations from 0.4 to 2.2 M) [33]. In each case, we observed a prominent initial decay in fluorescence with a time constant ranging from 25 to 65 μs. In particular, the rate of the initial phase, measured under the same final conditions (pH 4.5, 0.4 M GdmCl), was found to be independent of the initial state (acid- or GdmCl-unfolded). These observations clearly indicate that a common rate-limiting step is encountered during the initial stages of cyt *c* folding. The large amplitude of the initial phase (as much as 70% of the total change in fluorescence under strongly native conditions) is consistent with the formation of an ensemble of compact states, which was confirmed in subsequent small-angle X-ray (SAXS) studies [71, 72].

Using their continuous-flow CD instrument to follow refolding of acid-denatured cyt *c* after a dead time of ~400 μs, Akiyama et al. [67] observed significant changes in the far-UV region during the 500 μs and 2 ms folding phases of cyt

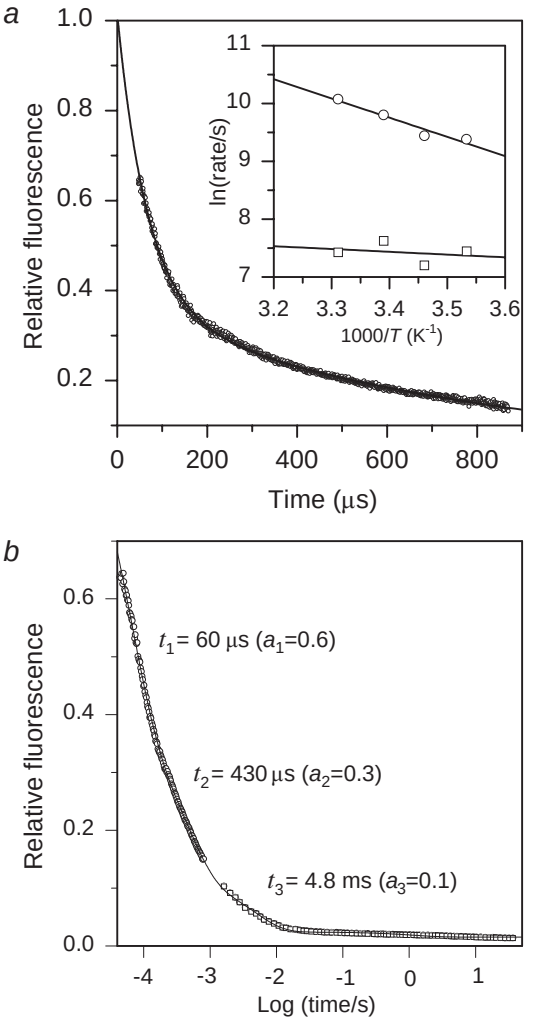

Fig. 15.13. Refolding kinetics of acid-unfolded cyt *c* at pH 4.5, 22 °C [33]. a) Submillisecond kinetics measured by continuous-flow mixing, indicating heme-induced quenching of Trp59 fluorescence associated with chain collapse. Inset: Arrhenius plot for the rates of the major (circles) and the minor (squares) submillisecond phases. b) Combined plot of continuous-flow and stopped-flow kinetic traces measured under identical conditions. The time constants and relative amplitudes (in parenthesis) are indicated for the three major phases.

c, indicating that most of the native helical secondary structure is acquired during the second and third (final) stages of folding. Extrapolation of the CD signal at 222 nm to shorter times indicated that the product of the 60 μs collapse phase is about 20% more helical than the GdmCl-unfolded state, but has a similar helix content as the acid-unfolded state. In their subsequent continuous-flow SAXS

measurements, Akiyama et al. [72] found that a partially collapsed cyt *c* intermediate ($R_g = 20.5$ Å) accumulates within the 160 μs dead time of their experiment, which corresponds to a significant compaction relative to the acid-denatured state ($R_g = 24$ Å). In a subsequent phase on the millisecond time regime, the protein passes through a second, more compact intermediate ($R_g = 18$ Å) before reaching the native state ($R_g = 13.9$ Å). These findings confirm that cyt *c* undergoes a major chain collapse during the initial folding phase on the 10–100 μs time scale detected in previous continuous-flow and T-jump measurements of the heme-induced quenching of Trp59 fluorescence [33, 77, 99].

15.7 Significance of Early Folding Events

15.7.1 Barrier-limited Folding vs. Chain Diffusion

In Sections 15.4 and 15.6, we presented continuous-flow results on the folding kinetics of five proteins (GB1, cyt *c*, ubiquitin, ACBP, and SNase) all of which show significant fluorescence changes in one or more rapid phases on the submillisecond time scale that precede the rate-limiting folding step [33, 35, 36, 38, 60]. Other examples include the bacterial immunity protein Im7 [36], which will be discussed further in Section 15.7.3, cytochrome c_{551} from *Pseudomonas aeruginosa* [39], β-lactoglobulin [37] and the Y92W mutant of ribonuclease A (Welker, Maki, Shastry, Juminaga, Bhat, Roder & Scheraga, submitted). For most proteins (GB1, ubiquitin, Im7, β-lactoglobulin, SNase, and RNase), we observed an increase in Trp fluorescence during the fast phase, which we attribute to the burial of the tryptophan fluorophores within an apolar environment. For three proteins (cyt *c*, cytochrome c_{551}, and ACBP), we measured a large increase in energy transfer efficiency during the fast phase, confirming that these early conformational events include a large-scale collapse of the polypeptide chain. Thus, we conclude that for all of these structurally diverse proteins, major conformational changes, including a large-scale collapse of the chain, precede the rate-limiting step in folding. In every case the initial phase follows an exponential time course, indicating that a discrete free energy barrier separates the ensemble of compact states from the more expanded ensemble of unfolded states. In contrast, if the collapse of the polypeptide chain were a continuous process governed by diffusive dynamic, as predicted for homopolymers [100], it would be characterized by a broad distribution of time constants likely to give rise to nonexponential ('distributed') kinetics [16, 101].

In fact, Sabelko et al. [102] observed such distributed folding kinetics in temperature-jump experiments under conditions where folding can proceed downhill from a saddle point in the free energy surface. While the observation of exponential kinetics may not always be a sufficient condition for the presence of an activation barrier [103], the case for a barrier-limited process is strengthened considerably if the process also exhibits a significant activation enthalpy, as observed

for cyt *c* [33]. Moreover, comparison of the pH-induced folding traces of cyt c monitored by Trp59 fluorescence (Figure 15.13) and heme absorbance (Figure 15.5) indicates that the time constant of the initial phase is independent of the probe used (59 ± 6 μs by fluorescence compared to 65 ± 4 μs by absorbance), which strongly supports the presence of a barrier (a diffusive collapse process is likely to lead to probe-dependent kinetics).

The existence of a prominent free energy barrier between expanded and compact states justifies the description of the initial folding events in terms of a model involving an early folding intermediate. The first large-scale conformational change during folding can, thus, be described as a reversible two-state transition. The finding that the rate of collapse in cyt *c* is insensitive to initial conditions [33] suggests that the barrier may represent a general entropic bottleneck encountered during the compaction of the polypeptide chain, which is consistent with the moderate activation enthalpy associated with the initial transition (Figure 15.13). Bryngelson et al. [16] classified this type of folding behavior as a ''type I'' scenario where a free energy barrier arises because of the unfavorable reduction in conformational entropy, which can be compensated by favorable enthalpic and solvent interactions only during the later stages of collapse.

15.7.2 Chain Compaction: Random Collapse vs. Specific Folding

Although denatured proteins often retain far more structure than expected for a random coil polymer [104], they are substantially more expanded than the native state [105]. The folding process therefore must be accompanied by a net decrease in chain dimensions. However, there are persistent controversies surrounding the question whether chain contraction occurs prior to or concurrent with the rate-limiting folding step, and whether compact states are the result of random hydrophobic collapse or a more specific structural events. Our earlier conclusion that the optical changes on the submillisecond time scale (burst-phase events) seen for cyt *c* and many other proteins [7, 9] reflect the formation of productive folding intermediates has been challenged by Englander and coworkers [106, 107] on the basis of fluorescence and CD measurements on two heme-containing peptide fragments of cyt *c* (residues 1–65 and 1–80, respectively). Although the fragments are unable to assume a folded structure, they nevertheless show rapid (<ms) denaturant-dependent fluorescence and far-UV CD changes resembling the burst-phase behavior of the intact polypeptide chain (cf. Figure 15.1).

Assuming that the fragments remain fully unfolded under all conditions, Sosnick et al. [106, 107] concluded that both the optical properties of the fragments and the burst-phase changes seen during refolding of intact cyt *c* reflect a rapid solvent-dependent readjustment of the unfolded polypeptide chain rather than formation of partially folded states. However, this conclusion is inconsistent with our observation that refolding of both GdmCl- and acid-denatured cyt *c* is accompanied by an exponential fluorescence decay [33], which indicates that the ensemble of states formed on the submillisecond time scale are separated by a free energy barrier from the unfolded states found immediately after adjustment of the solvent

conditions. That these states are not just part of a broad distribution of more or less expanded denatured conformations is further supported by the observation of nonrandom amide protection patterns [79]. Apparently, both the full-length and truncated forms of cyt *c* can assume a compact ensemble of states upon lowering of the denaturant concentration. This leads to the prediction that the fragments will also exhibit an exponential fluorescence change on a time scale similar to the intact protein (40–60 μs at 22 °C and GdmCl concentrations of 0–0.4 M [33]). This prediction was recently confirmed by Qiu et al. [99], who observed an exponential relaxation process with a time constant of 20–30 μs at room temperature and a substantial activation energy (60–70 kJ mol^{-1}) for the 1–65 and 1–80 fragments of cyt *c*, using a laser T-jump apparatus.

In a subsequent study on ribonuclease A (RNase A), Englander and colleagues [108] reported that the GdmCl-dependence of the CD signal for the fully disulfide-reduced form closely matches the initial kinetic amplitude observed in stopped-flow refolding experiments on the protein with all four disulfide bonds intact. As in the case of the cyt *c* fragments, Qi et al. [108] assumed that reduced RNase remains in a random denatured state even under nondenaturing solvent conditions, which needs to be explored further. As an alternative interpretation, we again suggest that both in the presence and absence of disulfide bonds, RNase A rapidly forms a nonrandom ensemble of states, which is consistent with the shallow, but distinctly sigmoidal GdmCl dependence of the far-UV CD signal [108]. Since the native RNase A structure relies on disulfide bonds for its stability, folding of the reduced form cannot proceed beyond this early intermediate while the oxidized protein continues to fold to the native state.

15.7.3
Kinetic Role of Early Folding Intermediates

Several small proteins exhibit two-state behavior under certain conditions (e.g., elevated denaturant concentration, destabilizing mutations), but show evidence for populated intermediates (burst phase and/or nonlinear rate profiles) under other, more stabilizing, conditions [32, 38, 48, 58, 93, 109–111]. Thus, apparent two-state behavior can be considered a limiting cases of a multistate folding mechanism with unstable (high-energy) intermediates [48]. On the other hand, there are many well-documented examples of small proteins that show two-state folding behavior even under stabilizing conditions (reviewed in Refs [1, 112]). In several cases, the rate of folding at low denaturant concentrations was found to extend into the submillisecond time range and could be resolved only by methods such as NMR lineshape analysis [113, 114], electron transfer triggering [115], pressure-jump [116] or temperature-jump techniques [24].

While these findings clearly indicate that many small proteins can fold rapidly without going through intermediates, there is little support for the notion that early intermediates slow down the search for the native conformation [74, 117, 118], except in cases where they contain features inconsistent with the native fold, such as nonnative proline isomers, metal ligands [73, 74, 119], or intermolecular interactions [120]. In fact, solution conditions that favor accumulation of inter-

mediates, such as low denaturant concentrations or stabilizing salts, generally accelerate the overall rate of folding [7]. Moreover, mutations that destabilize or abolish early intermediates often result in much slower rates of folding (see, for example, Refs [48, 121, 122]), which is a strong indication that they are productive states. Although continuous-flow results are fully consistent with Scheme 15.1 [33, 35, 38], it has been difficult to rigorously demonstrate that early intermediates are obligatory states on a direct path to the native state.

Alternative mechanisms involving formation of nonproductive states (Scheme 15.2) or mechanisms with parallel pathways and nonobligatory intermediates (Scheme 15.3) can be ruled out only if (i) the two transitions are kinetically coupled (i.e., they have similar rates), (ii) both phases are directly observable and kinetically resolved, and (iii) the experimental probe used to monitor folding can discriminate native from intermediate and unfolded populations. Under these circumstances, the transient accumulation of an obligatory intermediate leads to a detectable lag in the appearance of the native population whereas an off-path intermediate gives rise to a rapid increase in the population of N during the initial phase. Clear evidence for such a lag phase was obtained in a stopped-flow fluorescence study on a proline-free variant of staphylococcal nuclease [123].

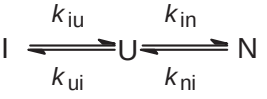

Scheme 15.2

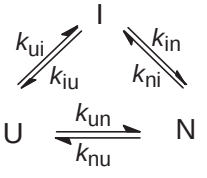

Scheme 15.3

On the other hand, a thorough kinetic analysis, using a double-jump protocol, indicated that a late intermediate during folding of lysozyme is nonobligatory [124]. Other efforts to detect a lag phase during folding of interlukin-1β [125, 126] and apomyoglobin [127] were inconclusive because of the disparate time scales of early and rate-limiting folding events. In order to determine the kinetic role of early folding intermediates, it is necessary to directly measure the population of native molecules on the submillisecond time scale, either by double-jump experiments or via a specific spectroscopic probe for the native state.

A particularly favorable protein for investigating the kinetic importance of early folding intermediates is the bacterial immunity protein Im7, an 86-residue protein with a simple four-helix bundle structure (Figure 15.14a). Radford and colleagues have previously shown that Im7 populates a hyperfluorescent intermediate during

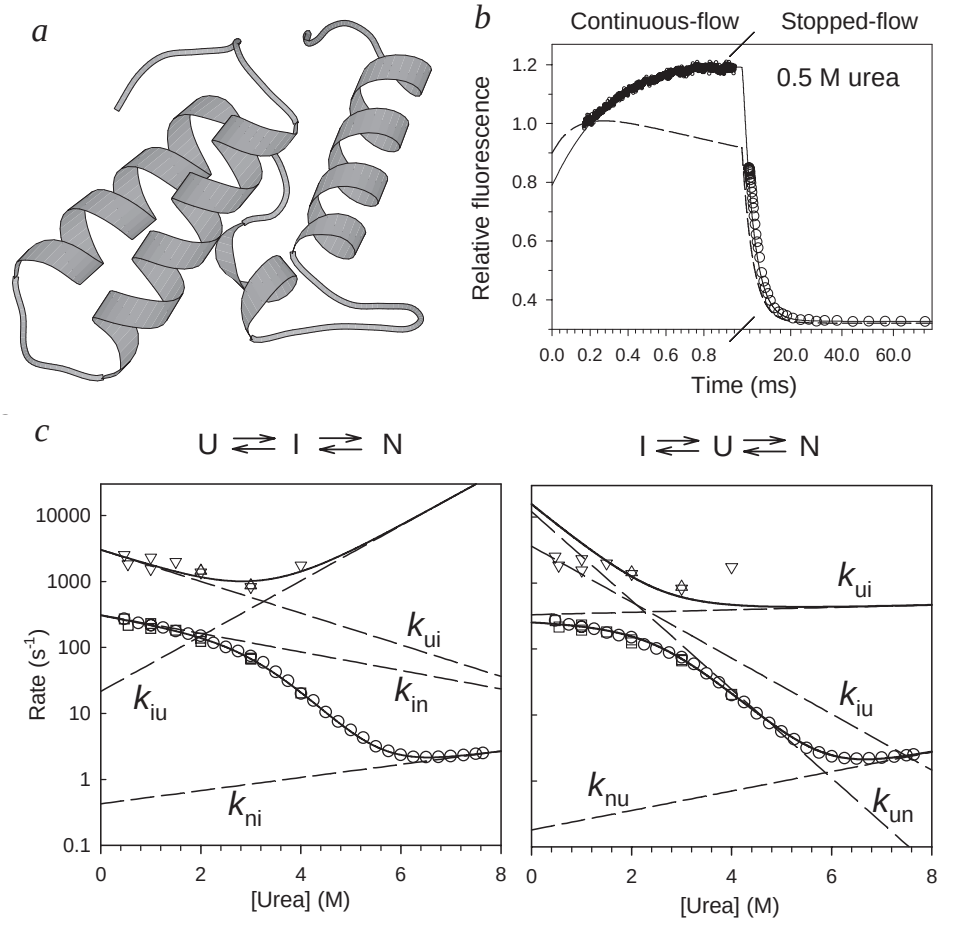

Fig. 15.14. Kinetic mechanism of Im7 folding. a) Ribbon diagram of Im7. b) Representative kinetic trace measured by continuous-flow (●) and stopped-flow (○) fluorescence. The kinetics at this and all other urea concentrations measured is accurately predicted by on on-pathway mechanism (solid line) while schemes with off-pathway intermediates fail to reproduce the data (dashed line). c) Observed (symbols) and predicted (solid lines) rates of folding and unfolding, based on mechanisms with on-pathway (left) and off-pathway (right) intermediates. Dashed lines indicate the corresponding elementary rate constants.

the 2.5-ms dead time of their stopped-flow instrument. However, the data could be fitted equally well to models involving either on- or off-pathway intermediates. Capaldi et al. extended these measurements into the microsecond time range [36], using our continuous-flow mixing instrument to detect the changes in fluorescence of a single tryptophan (Trp75) associated with folding under various conditions (Figure 15.14b). The initial increase in fluorescence above the level of the denatured state in 6 M urea over the 100 μs to 1 ms time range is consistent with the rapid formation of a compact state resulting in a solvent-shielded environment for

Trp75. The native structure is formed within a few milliseconds or longer (depending on the final concentration of urea), which is accompanied by partial quenching of Trp75 fluorescence due to close contact with a histidine. The tight kinetic coupling of the two folding events, together with the distinct fluorescence properties of the three conformational states involved, allowed us to discriminate among various possible kinetic mechanisms. The time course of folding predicted by solving the kinetic equations corresponding to the on-path mechanism (Scheme 15.1) accurately describes the observed behavior (Figure 15.14b, solid line). By contrast, the off-path mechanism (Scheme 15.2) failed to reproduce the data, especially at low urea concentrations where the intermediate is well populated (Figure 15.14b, dashed line). Likewise, the quality of the fits does not improve when a second, parallel pathway is introduced (Scheme 15.3) and deteriorates when more than 25% of the flux bypassed the intermediate.

These findings were further confirmed by a more detailed analysis of the dependence of the two observable rate constants on urea concentration (Figure 15.14c). While Scheme 15.1 reproduces all of the kinetic data, there are major discrepancies in the rate of the fast phase predicted by Schemes 15.2 and 15.3, which can thus be ruled out.

By eliminating alternative mechanisms, we have thus been able to show that accumulation of a compact intermediate on the submillisecond time scale is a productive and obligatory event in folding of Im7 [36]. This supports the notion that rapid formation of compact states can facilitate the search for the native conformation. Interestingly, a recent mutation study revealed that the Im7 folding intermediate contains non-native tertiary interactions among the three major α-helices, A, B and D, while the short helix C forms only during the final stages of folding [128]. Apparently, intermediates can be kinetically productive even if they contain some structural features not found in the final native state.

15.7.4 Broader Implications

Table 15.2 lists the time constants of the earliest folding phase measured by continuous-flow fluorescence for some of the proteins discussed in this chapter along with their size and structural type. The initial folding times vary by an order of magnitude, but show no apparent correlation with protein size. This argues against the notion that the early stages of folding are dominated by a nonspecific hydrophobic polymer collapse, in which case the rate of the initial phase would depend primarily on the size of the hydrophobic core and would be insensitive to structural details.

There appears to be no simple relationship between the time scale of early folding events and secondary structure content. For example, the β-sheet containing proteins, GB1 and SNase, are near opposite ends of the time range, and Im7 has a $\sim$fivefold slower initial rate compared to the structurally similar ACBP. Thus, the individual structural and topological features have a profound effect already during early stages of folding.

The finding that the earliest detectable folding event in GB1 domain is an order

Tab. 15.2. Comparison of the time constants of the initial folding phase with protein size and secondary structure type for proteins with multi-state folding kinetics.

Protein	*Residues*	*Structure type*	*τ (initial)/μs*	*Ref.*
GB1	57	α/β	600	35
ACBP	86	α	80	38
Im7	87	α	450	36
cyt *c*	104	α	60	33
SNase (F76W)	149	α/β	75	60

of magnitude slower than that of cyt *c* may well be related to the fact that GB1 contains β-sheet structure (Figure 15.7a) while cyt *c* is primarily α-helical (Figure 15.12). With its parallel pairing of β-strands from opposite ends of the chain, GB1 has a relatively high contact order, a metric of fold complexity that was found to correlate with the logarithm of the folding time of proteins with two-state mechanisms [129]. Such a trend is not expected for proteins with multistate folding mechanisms, since the rate-limiting step in structurally and kinetically more complex proteins is likely to involve structural events unrelated to the overall fold, such as side chain packing and specific tertiary interactions. However, if compact early intermediates have a native-like chain topology, one might expect a correlation between the time constant of the initial phase and contact order. Some of the trends seen in Table 15.2 are consistent with this idea. For instance, cyt *c* and ACBP have low contact order and collapse much faster than GB1, which has the highest contact order among the proteins studied. The surprisingly fast initial phase of SNase (75 μs) in comparison to the much smaller GB1 (600 μs) may be related to the fact that the folding step in SNase detected by Trp76 and ANS fluorescence reflects a relatively local structural event within its antiparallel β-barrel domain, whereas the fluorescence of Trp43 in protein G may report on a more global conformational change involving the parallel pairing of N- and C-terminal β-strands.

Finally, we note that several small proteins (or isolated domains of larger proteins) can complete the process of folding on a comparable time scale as the early stages of folding for some of the multistate proteins discussed here (see, for example, Refs [130–133]; see Ref. [24] for a review). The underlying conformational events may be similar, but the fast-folding two-state proteins can directly reach the native state in a concerted collapse/folding event while most proteins encounter additional steps after crossing the initial barrier.

Appendix

A1 Design and Calibration of Rapid Mixing Instruments

A1.1 Stopped-flow Equipment

In a typical stopped-flow experiment, a few hundred microliters of solution are delivered to the mixer via two syringes driven by a pneumatic actuator or stepper-

motors. Total flow rates in the range of 5–10 mL s^{-1} with channel diameters of the order of 1 mm insure turbulent flow conditions ($Re > 5000$). After delivering a volume sufficient to purge and fill the observation cell with freshly mixed solution, the flow is stopped abruptly when a third syringe hits a stopping block, or by closing a valve. Commercial instruments can routinely reach dead times of a few milliseconds. Recent improvements in mixer and flow-cell design by several manufacturers of stopped-flow instruments resulted in dead times well under 1 ms.

The upper end of the time scale that can be reliably measured in a stopped-flow experiment is determined by the stability of the mixture in the flow cell, which is limited by convective flow or diffusion of reagents in and out of the observation volume. For slow reactions with time constants longer than a few minutes, manual mixing experiments are generally more reliable. Stopped-flow mixing is usually coupled with real-time optical observation using absorbance (UV through IR), fluorescence emission or circular dichroism spectroscopy, but other biophysical techniques, including fluorescence lifetime measurements [134, 135], NMR [136, 137], and small-angle X-ray scattering (SAXS; [138]), have also been implemented.

The interpretation of stopped-flow data requires a careful calibration of the instrumental dead time by measuring a pseudo-first-order reaction tuned to the time scale of interest (i.e., a single-exponential process with a rate-constant approaching the expected dead time) and an optical signal matching the application. Common test reactions for absorbance measurements include the reduction of 2,6-dichlorophenolindophenol (DCIP) or ferricyanide by ascorbic acid [66].

A convenient test reaction for tryptophan fluorescence measurements is the irreversible quenching of *N*-acetyltryptophanamide (NATA) by *N*-bromosuccinimide (NBS). For fluorescence studies in or near the visible range, one can follow the pH-dependent association of the Mg^{2+} ion with 8-hydroxyquinoline, which results in a fluorescent chelate [139], or the binding of the hydrophobic dye 1-anilino-8-naphthalene-sulfonic acid (ANS) to bovine serum albumin (BSA), which is associated with a large increase in fluorescence yield [140].

As a practical example, Figure 15.15 shows a series of DCIP absorbance measurements at several ascorbic acid concentrations used to estimate the dead time of our Bio-Logic SFM-4 stopped-flow instrument equipped with a FC-08 microcuvette accessory (Molecular Kinetics, Indianapolis, IN, USA). The reaction was started by mixing equal parts of DCIP (0.75 mM in water at neutral pH, where the dye is stable) with L-ascorbic acid at pH 2 at final concentrations ranging from 6 to 25 mM. Absorbance changes measured at 525 nm, near the isosbestic point between the acidic and basic forms of DCIP, are plotted relative to the absorbance of the reactant in water, measured in a separate control (Figure 15.15, inset). After the flow comes to a full stop, the absorbance decays exponentially with a rate constants of about 290, 780, and 1400 s^{-1} at ascorbate concentrations of 6, 14, and 25 mM, respectively, which is consistent with a pseudo-first-order reduction process with a second-order rate constant $k'' \approx 5.7 \times 10^5$ s^{-1} M^{-1}.

At shorter times, the exponential fits intersect at an absorbance $\Delta A = 0$, which corresponds to the level of the oxidized DCIP measured in the control. The delay between this intercept and the first data point that joins the fitted exponential pro-

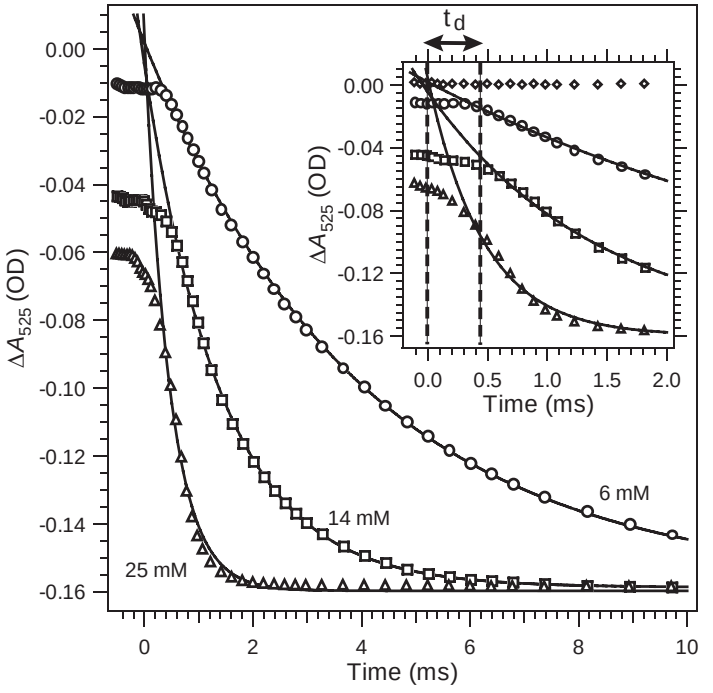

Fig. 15.15. Estimation of the dead time of stopped-flow absorbance measurement on a Biologic SFM-4 instrument with FC-08 microcuvette accessory, using the reduction of DCIP by ascorbic acid as a test reaction. Equal parts of DCIP in water (pH 7) and sodium ascorbate (pH 2) at final concentrations of 6 (circles), 14 (squares) and 25 mM (triangles) were mixed at a total flow rate of 12 mL s^{-1}. The inset shows an expanded plot at early times with dashed lines indicating the dead time (~0.5 ms). Absorbance changes at 525 nm are plotted relative to the absorbance of a control (diamonds) measured by mixing DCIP with 10 mM HCl.

vides an estimate of the instrumental dead time, $t_d = 0.55 \pm 0.1$ ms. Alternatively, the dead time can be estimated from the signal level of the continuous-flow regime prior to closure of the stop valve, I_{cf}, using the following equation:

$$t_{cf} = -\ln[(I_{cf} - I_\infty)/(I_0 - I_\infty)]/k \qquad (3)$$

where I_∞ is the baseline at long times, I_0 is the signal of the reactant (in this case, DCIP mixed with an equal volume of water), and k is the first-order rate constant obtained by exponential fitting. Note that t_{cf} does not account for the finite stop time and other stop-related artifacts, and is thus always shorter than t_d, which explains why some manufacturers of stopped-flow instruments prefer to cite t_{cf} over the more realistic operational dead time, t_d. In the present example, Eq. (3) yields t_{cf} in the range of 0.25 and 0.4 ms, compared with $t_d \approx 0.55$ ms obtained by the extrapolation (Figure 15.15).

A1.2 Continuous-flow Instrumentation

In a continuous-flow experiment, the reaction is again triggered by turbulent mixing, but, in contrast to stopped-flow, the progress of the reaction is sampled under steady-state flow conditions as a function of the distance downstream from the mixer [141, 142]. This avoids artifacts related to arresting the flow and makes it possible to use relatively insensitive detection methods. Thus, continuous-flow measurements can achieve shorter dead times compared to stopped-flow, but this comes at the expense of sample economy. Most earlier versions of this experiment involved point-by-point sampling of the reaction profile while maintaining constant flow at high rates (several ml/s for a conventional mixer). The prohibitive amounts of sample consumed limited the impact of continuous-flow techniques until advances in mixer design made it possible to achieve highly efficient mixing at lower flow rates [26, 31, 32, 143], and an improved detection scheme allowed simultaneous recoding of a complete reaction profile in a few seconds [26]. These developments lowered both the dead time and sample consumption by at least an order of magnitude, and made routine measurements on precious samples with dead times as short as 50 μs possible.

In 1985, Regenfuss et al. [31] described a capillary jet mixer consisting of two coaxial glass capillaries with a platinum sphere placed at their junction. The reaction progress was monitored in a free-flowing jet, using conventional photography to measure fluorescence vs. distance from the mixer. Measurements of the binding kinetics of ANS to BSA indicated that dead times less than 100 μs can be achieved with this mixer design. More recently, several laboratories reported continuous-flow resonance Raman and fluorescence studies of enzyme and protein folding reactions on the submillisecond time scale, using machined mixers with dead-times of about 100 μs [25, 32, 143]. More widespread use of these methods has been hampered by a number of technical and experimental difficulties. Continuous-flow experiments involving a free-flowing jet [31, 32, 143, 144] are fraught with difficulties due to instability and scattering artifacts. The use of a conventional camera with high-speed monochrome film for fluorescence detection is inadequate due to the low sensitivity of the film in the UV region, limited dynamic range and the nonlinearity of the film response. Finally, prohibitive sample consumption makes continuous-flow experiments that record a kinetic trace one point at a time feasible only for highly abundant proteins [25, 67, 72, 97].

We were able to overcome many of these limitations by combining a highly efficient quartz capillary mixer, based on the design of Regenfuss et al. [31], with a flow cell and an improved detection system involving a digital camera system with a UV-sensitized CCD detector [26]. A diagram of the experimental arrangement is shown in Figure 15.16. Two Hamilton syringes driven by an Update (Madison, WI, USA) quenched-flow apparatus deliver the reagents to be studied at moderate pressure (< 10 atm) into each of the two coaxial capillaries. The outer capillary consists of a thick-walled (6 mm o.d., 2 mm i.d.) quartz tube, which is pulled to a fine tip ($\sim$200 μm i.d. at the end), using a glassblowing lathe or a simple gravity method. The inner capillary (360 μm o.d., 150–180 μm i.d., purchased from Polymicro Technologies, Phoenix, AZ, USA) with a $\sim$250 μm platinum sphere suspended at the end is positioned inside the tapered end of the outer capillary.

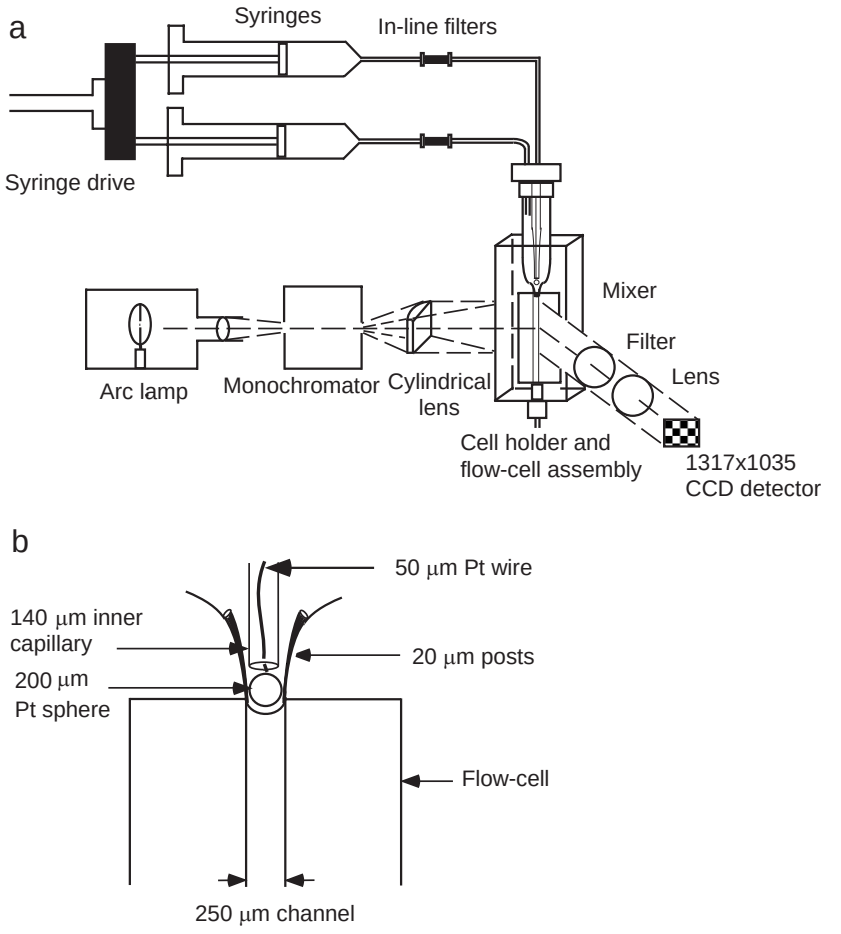

Fig. 15.16. Continuous-flow capillary mixing apparatus in fluorescence mode. a) Schematic diagram of the solution delivery system, mixer, observation cell and optical arrangement. b) Expanded view of the mixer/flow cell assembly.

The sphere is formed by melting the end of 50 μm diameter platinum wire. Thin glass rods fused to the inner wall of the outer capillary (tapering down to diameter of ~20 μm) prevent the sphere from plugging the outlet. The reagents are forced through the narrow gap between the sphere and the outer wall where mixing occurs under highly turbulent flow conditions. The fully homogeneous mixture emerging from the mixer is injected into the 250 μm × 250 μm flow channel of a fused-silica observation cell (Hellma) joined to the outer capillary by means of a hemispherical ground-glass joint. Typical flow rates are 0.6–1.0 mL s^{-1} resulting in a linear flow velocities of 10–16 m s^{-1} through the 0.25 × 0.25 mm^2 channel of the observation cell.

The reaction progress in a continuous-flow mixing experiment is measured by recording the fluorescence profile vs. distance downstream from the mixer (Figure

15.16). A conventional light source consisting of an arc lamp (we currently use a 350 W Hg arc lamp in a lamp housing from Oriel, Stratford, CT, USA), collimating optics and monochromator, is used for fluorescence excitation. Relatively uniform illumination of the flow channel over a length of 10–15 mm is achieved by means of a cylindrical lens. A complete fluorescence vs. distance profile is obtained by imaging the fluorescent light emitted at a 90° angle onto the CCD detector of a digital camera system (Micromax, Roper Scientific, Princeton, NJ, USA) containing a UV-coated Kodak CCD chip with an array of 1317 × 1035 pixels. The camera is equipped with a fused silica magnifying lens and a high-pass glass filter or a band-pass interference filter to suppress scattered incident light.

Figure 15.17 illustrates a typical continuous-flow experiment, using the quenching of NATA by NBS as a test reaction. The upper panels show raw data obtained by averaging the intensity across the flow channel vs. the distance d downstream from the mixer. Panel a shows the intensity profile for the quenching reaction, $I_e(d)$, at final NATA and NBS concentrations of 40 μM and 4 mM, respectively (mixing 1 part of 440 μM NATA in water with 10 parts of 4.4 mM NBS in water). Panel b shows the distribution of incident light intensity, $I_c(d)$, measured by mixing the same NATA solution with water. Panel c shows the scattering background, $I_b(d)$, measured by passing water through both capillaries. Panel d shows the corrected kinetic trace, $fl_{rel}(t)$, obtained according to

$$fl_{rel} = (I_e - I_b)/(I_c - I_b) \tag{4}$$

Distance was converted into time on the basis of the known flow rate (0.8 mL s^{-1} in this example), the cross-sectional area of the flow channel (0.0625 mm^2) and the length of the channel being imaged (12.5 mm, or 9.5 μm per pixel). The signal measured at points below the entrance to the flow channel are well fitted by a single-exponential decay. The trace at $fl_{rel} = 1$ in panel d of Figure 15.17 represents a control for the mixing efficiency measured as follows. The 440 μM NATA stock solution used in the experiment above was diluted 11-fold with water and filled into both syringes. The continuous-flow trace recorded at the same flow rate was then background-corrected and normalized according to Eq. (3), using the I_c trace recorded previously in which the same NATA solution was diluted 11-fold in the capillary mixer. Immediately after entering the flow channel, the ratio approaches unity, indicating that NATA is completely mixed with water. Alternatively, mixing efficiency could be assessed using a very fast reaction completed within the dead time, such as the quenching of tryptophan (or NATA) by sodium iodide.

To estimate the dead time of the continuous-flow experiment, we measured the pseudo-first-order NATA-NBS quenching reaction at a final NATA concentration of 40 μM and several NBS concentrations in the range 2–32 mM. Figure 15.18a shows a semilogarithmic plot of the relative fluorescence, fl_{rel}, calculated according to Eq. (3), along with exponential fits (solid lines). Since $fl_{rel} = 1$ corresponds to the unquenched NATA signal expected at $t = 0$, the intercept of the fits with $fl_{rel} = 1$ indicates the time point $t = 0$ where the mixing reaction begins. The delay between this point and the first data point that falls onto the exponential fit corresponds to

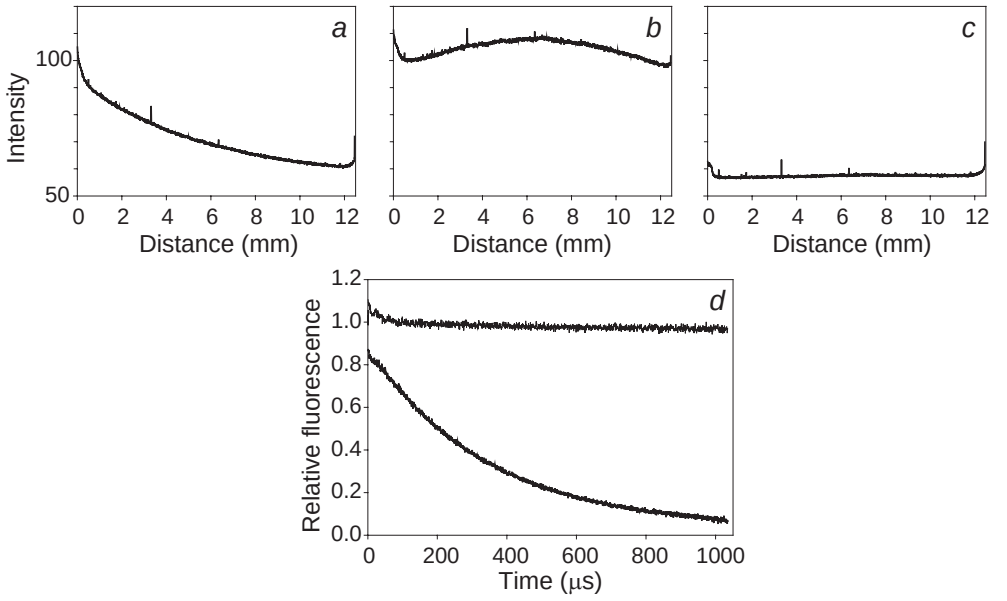

Fig. 15.17. A typical continuous-flow mixing experiment. The upper panels show raw intensity profiles vs. distance from the mixing region. a) Raw kinetic trace (NATA mixed with NBS). b) Fluorescence control (NATA mixed with water). c) Scattering background (water deliverd from both syringes). Panel d shows the corrected kinetic trace calculated according to Eq. (3).

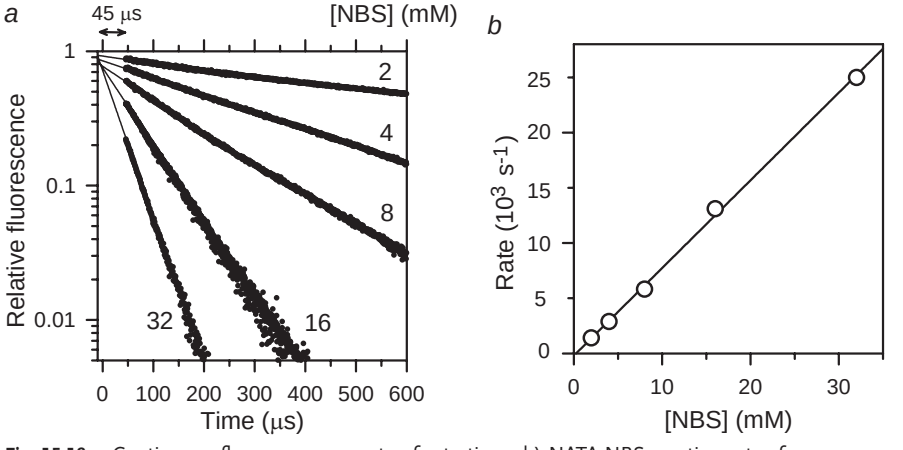

Fig. 15.18. Continuous-flow measurements of the quenching of NATA fluorescence by NBS used to determine the experimental dead-time. a) Semi-logarithmic plot of NATA fluorescence (> 324 nm) vs. time at several NBS concentrations. b) NATA-NBS reaction rates from exponential fitting of the data in panel a vs. NBS concentration. Linear regression (line) yields a second-order rate constant of 7.9 10^5 M^{-1} s^{-1}.

the dead time of the experiment, Δt_d, which in this example is 45 ± 5 μs. In Figure 15.18b, the rate constants obtained by exponential fitting are plotted as a function of NBS concentration. The slope of a linear fit (solid line) yields a second-order rate constant for the NBS-induced chemical quenching of NATA of 7.9×10^5 M^{-1} s^{-1}, which is consistent with data obtained by stopped-flow measurements at lower NBS concentration [51]. This agreement, together with the linearity of the second-order rate plot (Figure 15.18b), demonstrates the accuracy of the kinetic data.

Acknowledgments

This work was supported by grants GM56250 and CA06927 from the National Institutes of Health, grant MCB-079148 from the National Science Foundation, and an Appropriation from the Commonwealth of Pennsylvania.

References

1 Jackson, S. E. (1998). How do small single-domain proteins fold? *Fold. Des.* 3, R81–R91.
2 Matthews, C. R. (1987). Effect of point mutations on the folding of globular proteins. *Meth. Enzymol.* 154, 498–511.
3 Matouschek, A., Kellis, J. T., Jr., Serrano, L. & Fersht, A. R. (1989). Mapping the transition state and pathway of protein folding by protein engineering. *Nature* 340, 122–126.
4 Jackson, S. E., elMasry, N. & Fersht, A. R. (1993). Structure of the hydrophobic core in the transition state for folding of the chymotrypsin inhibitor-2: A critical test of the protein engineering method of analysis. *Biochemistry* 32, 11270–11278.
5 Matthews, C. R. (1993). Pathways of protein folding. *Annu. Rev. Biochem.* 62, 653–683.
6 Evans, P. A. & Radford, S. E. (1994). Probing the structure of folding intermediates. *Curr. Opin. Struct. Biol.* 4, 100–106.
7 Roder, H. & Colón, W. (1997). Kinetic role of early intermediates in protein folding. *Curr. Opin. Struct. Biol.* 7, 15–28.
8 Baldwin, R. L. & Rose, G. D. (1999). Is protein folding hierarchic? II. Folding intermediates and transition states. *Trends Biochem. Sci.* 24, 77–83.
9 Roder, H., Elöve, G. A. & Shastry, R. M. C. (2000). Early stages of protein folding. In *Mechanisms of protein folding* (Pain, R. H., ed.), pp. 65–104. Oxford University Press, New York.
10 Tanford, C., Aune, K. C. & Ikai, A. (1973). Kinetics of unfolding and refolding of proteins III. Results for lysozyme. *J. Mol. Biol.* 73, 185–197.
11 Kim, P. S. & Baldwin, R. L. (1982). Specific intermediates in the folding reactions of small proteins and the mechanism of protein folding. *Annu. Rev. Biochem.* 51, 459–489.
12 Roder, H. & Shastry, M. C. R. (1999). Methods for exploring early events in protein folding. *Curr. Opin. Struct. Biol.* 9, 620–626.
13 Roder, H. & Wüthrich, K. (1986). Protein folding kinetics by combined use of rapid mixing techniques and NMR observation of individual amide protons. *Proteins* 1, 34–42.
14 Roder, H., Elöve, G. A. & Englander, S. W. (1988). Structural characterization of folding intermediates in cytochrome c by H-exchange labelling and proton NMR. *Nature* 335, 700–704.
15 Udgaonkar, J. B. & Baldwin, R. L. (1988). NMR evidence for an early

framework intermediate on the folding pathway of ribonuclease A. *Nature* 335, 694–699.

16 Bryngelson, J. D., Onuchic, J. N., Socci, N. D. & Wolynes, P. G. (1995). Funnels, pathways, and the energy landscape of protein folding: A synthesis. *Proteins* 21, 167–195.

17 Dobson, C. M. & Karplus, M. (1999). The fundamentals of protein folding: bringing together theory and experiment. *Curr. Opin. Struct. Biol.* 9, 92–101.

18 Onuchic, J. N. & Wolynes, P. G. (2004). Theory of protein folding. *Curr. Opin. Struct. Biol.* 14, 70–75.

19 Jones, C. M., Henry, E. R., Hu, Y. et al. (1993). Fast events in protein folding initiated by nanosecond laser photolysis. *Proc. Natl Acad. Sci. USA* 90, 11860–11864.

20 Callender, R. H., Dyer, R. B., Gilmanshin, R. & Woodruff, W. H. (1998). Fast events in protein folding: the time evolution of primary processes. *Annu. Rev. Phys. Chem.* 49, 173–202.

21 Gruebele, M. (1999). The fast protein folding problem. *Annu. Rev. Phys. Chem.* 50, 485–516.

22 Eaton, W. A., Munoz, V., Hagen, S. J. et al. (2000). Fast kinetics and mechanisms in protein folding. *Annu. Rev. Biophys. Biomol. Struct.* 29, 327–359.

23 Huang, C. Y., He, S., DeGrado, W. F., McCafferty, D. G. & Gai, F. (2002). Light-induced helix formation. *J. Am. Chem. Soc.* 124, 12674–12675.

24 Kubelka, J., Hofrichter, J. & Eaton, W. A. (2004). The protein folding 'speed limit'. *Curr Opin Struct Biol* 14, 76–88.

25 Takahashi, S., Yeh, S.-R., Das, T. K., Chan, C.-K., Gottfried, D. S. & Rousseau, D. L. (1997). Folding of cytochrome *c* initiated by submillisecond mixing. *Nature Struct. Biol.* 4, 44–50.

26 Shastry, M. C. R., Luck, S. D. & Roder, H. (1998). A continuous-flow capillary mixer to monitor reactions on the microsecond time scale. *Biophys. J.* 74, 2714–2721.

27 Pollack, L., Tate, M. W., Darnton, N. C. et al. (1999). Compactness of the denatured state of a fast-folding protein measured by submillisecond small-angle x-ray scattering. *Proc. Natl Acad. Sci. USA* 96, 10115–10117.

28 Hartridge, H. & Roughton, F. J. W. (1923). The velocity with which carbon monoxide displaces oxygen from combination with heamoglobin. I. *Proc. R. Soc. (Lond.) B Biol. Sci.* 94, 336–367.

29 Gibson, Q. H. & Milnes, L. (1964). *Biochem. J.* 91, 161.

30 Chance, B. (1964). *Rapid Mixing and Sampling Techniques in Biochemistry.* (Chance, B., Eisenhardt, R. H., Gibson, Q. H. & Lonberg-Holm, K. K., Eds), Academic Press, New York.

31 Regenfuss, P., Clegg, R. M., Fulwyler, M. J., Barrantes, F. J. & Jovin, T. M. (1985). Mixing liquids in microseconds. *Rev. Sci. Instrum.* 56, 283–290.

32 Chan, C.-K., Hu, Y., Takahashi, S., Rousseau, D. L., Eaton, W. A. & Hofrichter, J. (1997). Submillisecond protein folding kinetics studied by ultrarapid mixing. *Proc. Natl Acad. Sci. USA* 94, 1779–1784.

33 Shastry, M. C. R. & Roder, H. (1998). Evidence for barrier-limited protein folding kinetics on the microsecond time scale. *Nature Struct. Biol.* 5, 385–392.

34 Shastry, M. C. R., Sauder, J. M. & Roder, H. (1998). Kinetic and structural analysis of submillisecond folding events in cytochrome *c*. *Acc. Chem. Res.* 31, 717–725.

35 Park, S.-H., Shastry, M. C. R. & Roder, H. (1999). Folding dynamics of the B1 domain of protein G explored by ultrarapid mixing. *Nature Struct. Biol.* 6, 943–947.

36 Capaldi, A. P., Shastry, R. M. C., Kleanthous, C., Roder, H. & Radford, S. E. (2001). Ultra-rapid mxing experiments reveal that Im7 folds *via* an on-pathway intermediate. *Nature Struct. Biol.* 8, 68–72.

37 Kuwata, K., Shastry, R., Cheng, H. et al. (2001). Structural and kinetic

characterization of early folding events in beta-lactoglobulin. *Nature Struct. Biol.* 8, 151–155.

38 Teilum, K., Maki, K., Kragelund, B. B., Poulsen, F. M. & Roder, H. (2002). Early kinetic intermediate in the folding of acyl-CoA binding protein detected by fluorescence labeling and ultrarapid mixing. *Proc. Natl Acad. Sci. USA* 99, 9807–9812.

39 Gianni, S., Travaglini-Allocatelli, C., Cutruzzola, F., Brunori, M., Shastry, M. C. & Roder, H. (2003). Parallel pathways in cytochrome c(551) folding. *J. Mol. Biol.* 330, 1145–1152.

40 Khan, F., Chuang, J. I., Gianni, S. & Fersht, A. R. (2003). The kinetic pathway of folding of barnase. *J. Mol. Biol.* 333, 169–186.

41 Johnson, K. A. (1995). Rapid quench kinetic analysis of polymerases, adenosinetriphosphatases, and enzyme intermediates. *Meth. Enzymol.* 249, 38–61.

42 Knight, J. B., Vishwanath, A., Brody, J. P. & Austin, R. H. (1998). Hydrodynamic focusing on a silicon chip: Mixing nanoliters in microseconds. *Phys. Rev. Lett.* 80, 3863–3866.

43 Pabit, S. A. & Hagen, S. J. (2002). Laminar-flow fluid mixer for fast fluorescence kinetics studies. *Biophys. J.* 83, 2872–2878.

44 Kuwajima, K., Yamaya, H., Miwa, S., Sugai, S. & Nagamura, T. (1987). Rapid formation of secondary structure framework in protein folding studied by stopped-flow circular dichroism. *FEBS Lett.* 221, 115–118.

45 Elöve, G. A., Chaffotte, A. F., Roder, H. & Goldberg, M. E. (1992). Early steps in cytochrome c folding probed by time-resolved circular dichroism and fluorescence spectroscopy. *Biochemistry* 31, 6876–6883.

46 Jennings, P. A. & Wright, P. E. (1993). Formation of a molten globule intermediate early in the kinetic folding pathway of apomyoglobin. *Science* 262, 892–895.

47 Jones, B. E. & Matthews, C. R. (1995). Early intermediates in the folding of dihydrofolate reductase from *Escherichia coli* detected by hydrogen exchange and NMR. *Protein Sci.* 4, 167–177.

48 Khorasanizadeh, S., Peters, I. D. & Roder, H. (1996). Evidence for a three-state model of protein folding from kinetic analysis of ubiquitin variants with altered core residues. *Nature Struct. Biol.* 3, 193–205.

49 Walkenhorst, W. F., Edwards, J. A., Markley, J. L. & Roder, H. (2002). Early formation of a beta hairpin during folding of staphylococcal nuclease H124L as detected by pulsed hydrogen exchange. *Protein Sci* 11, 82–91.

50 Colón, W., Elöve, G. A., Wakem, L. P., Sherman, F. & Roder, H. (1996). Side chain packing of the N- and C-terminal helices plays a critical role in the kinetics of cytochrome *c* folding. *Biochemistry* 35, 5538–5549.

51 Peterman, B. F. (1979). Measurement of the dead time of a fluorescence stopped-flow instrument. *Anal. Biochem.* 93, 442–444.

52 Berger, R. L. & Chapman, H. F. (1968). High resolution mixer for the study of the kinetics of rapid reactions in solution. *Rev. Sci. Instrum.* 39, 493–498.

53 Zeff, B. W., Lanterman, D. D., McAllister, R., Roy, R., Kostelich, E. J. & Lathrop, D. P. (2003). Measuring intense rotation and dissipation in turbulent flows. *Nature* 421, 146–149.

54 Chen, Y. & Barkley, M. D. (1998). Toward understanding tryptophan fluorescence in proteins. *Biochemistry* 37, 9976–9982.

55 Van Gilst, M., Tang, C., Roth, A. & Hudson, B. (1994). Quenching interactions and nonexponential decay: Tryptophan 138 of bacteriophage T4 lysozyme. *Fluorescence* 4, 203–207.

56 Clark, P. L., Weston, B. F. & Gierasch, L. M. (1998). Probing the folding pathway of a beta-clam protein with single-tryptophan constructs. *Fold. Des.* 3, 401–412.

57 Shao, X. & Matthews, C. R. (1998). Single-tryptophan mutants of monomeric tryptophan repressor: optical spectroscopy reveals nonnative structure in a model for an early folding intermediate. *Biochemistry* 37, 7850–7858.

58 Khorasanizadeh, S., Peters, I. D., Butt, T. R. & Roder, H. (1993). Folding and stability of a tryptophan-containing mutant of ubiquitin. *Biochemistry* 32, 7054–7063.

59 Eftink, M. R. & Shastry, M. C. R. (1997). Fluorescence methods for studying kinetics of protein-folding reactions. *Meth. Enzymol.* 278, 258–286.

60 Maki, K., Cheng, H., Dolgikh, D. A., Shastry, M. C. & Roder, H. (2004). Early events during folding of wild-type staphylococcal nuclease and a single-tryptophan variant studied by ultrarapid mixing. *J. Mol. Biol.* 338, 383–400.

61 Stryer, L. (1968). Fluorescence spectroscopy of proteins. *Science* 162, 526–533.

62 Semisotnov, G. V., Rodionova, N. A., Kutyshenko, V. P., Ebert, B., Blanck, J. & Ptitsyn, O. B. (1987). Sequential mechanism of refolding of carbonic anhydrase B. *FEBS Lett.* 224, 9.

63 Engelhard, M. & Evans, P. A. (1995). Kinetics of interaction of partially folded proteins with a hydrophobic dye: evidence that molten globule character is maximal in early folding intermediates. *Protein Sci.* 4, 1553–1562.

64 Tsong, T. Y. (1974). The Trp-59 fluorescence of ferricytochrome c as a sensitive measure of the over-all protein conformation. *J. Biol. Chem.* 249, 1988–1990.

65 Colón, W. & Roder, H. (1996). Kinetic intermediates in the formation of the cytochrome *c* molten globule. *Nature Struct. Biol.* 3, 1019–1025.

66 Tonomura, B., Nakatani, H., Ohnishi, M., Yamaguchi-Ito, J. & Hiromi, K. (1978). Test reactions for a stopped-flow apparatus. Reduction of 2,6-dichlorophenolindophenol and potassium ferricyanide by L-ascorbic acid. *Anal. Biochem.* 84, 370–383.

67 Akiyama, S., Takahashi, S., Ishimori, K. & Morishima, I. (2000). Stepwise formation of alpha-helices during cytochrome c folding. *Nature Struct. Biol.* 7, 514–520.

68 Uzawa, T., Akiyama, S., Kimura, T. et al. (2004). Collapse and search dynamics of apomyoglobin folding revealed by submillisecond observations of α-helical content and compactness. *Proc. Natl Acad. Sci. USA* 101, 1171–1176.

69 Grigoryants, V. M., Veselov, A. V. & Scholes, C. P. (2000). Variable velocity liquid flow EPR applied to submillisecond protein folding. *Biophys. J.* 78, 2702–2708.

70 DeWeerd, K., Grigoryants, V., Sun, Y., Fetrow, J. S. & Scholes, C. P. (2001). EPR-detected folding kinetics of externally located cysteine-directed spin-labeled mutants of iso-1-cytochrome c. *Biochemistry* 40, 15846–15855.

71 Pollack, L., Tate, M. W., Finnefrock, A. C. et al. (2001). Time resolved collapse of a folding protein observed with small angle x-ray scattering. *Phys. Rev. Lett.* 86, 4962–4965.

72 Akiyama, S., Takahashi, S., Kimura, T. et al. (2002). Conformational landscape of cytochrome c folding studied by microsecond-resolved small-angle x-ray scattering. *Proc. Natl Acad. Sci. USA* 99, 1329–1334.

73 Elöve, G. A., Bhuyan, A. K. & Roder, H. (1994). Kinetic mechanism of cytochrome c folding: involvement of the heme and its ligands. *Biochemistry* 33, 6925–6935.

74 Sosnick, T. R., Mayne, L., Hiller, R. & Englander, S. W. (1994). The barriers in protein folding. *Nature Struct. Biol.* 1, 149–156.

75 Colón, W., Wakem, L. P., Sherman, F. & Roder, H. (1997). Identification of the predominant non-native histidine ligand in unfolded cytochrome *c*. *Biochemistry* 36, 12535–12541.

76 Kuwajima, K. (1996). Stopped-flow

circular dichroism. In *Circular Dichroism and the Conformational Analysis of Biomolecules* (Fasman, G. D., Ed.). Plenum Press, New York.

77 Hagen, S. J. & Eaton, W. A. (2000). Two-state expansion and collapse of a polypeptide. *J. Mol. Biol.* 297, 781–789.

78 Gladwin, S. T. & Evans, P. A. (1996). Structure of very early protein folding intermediates: new insights through a variant of hydrogen exchange labelling. *Fold. Des.* 1, 407–417.

79 Sauder, J. M. & Roder, H. (1998). Amide protection in an early folding intermediate of cytochrome *c*. *Fold. Des.* 3, 293–301.

80 Bai, Y., Milne, J. S. & Englander, S. W. (1993). Primary structure effects on peptide group exchange. *Proteins* 17, 75–86.

81 Clarke, A. R. & Waltho, J. P. (1997). Protein folding pathways and intermediates. *Curr. Opin. Biotechnol.* 8, 400–410.

82 Alexander, P., Orban, J. & Bryan, P. (1992). Kinetic analysis of folding and unfolding the 56 amino acid IgG-binding domain of streptococcal protein G. *Biochemistry* 31, 7243–7248.

83 Park, S.-H., O'Neil, K. T. & Roder, H. (1997). An early intermediate in the folding reaction of the B1 domain of protein G contains a native-like core. *Biochemistry* 36, 14277–14283.

84 Benson, S. W. (1960). The foundations of chemical kinetics. In *Advanced Topics in Chemistry*, 1st edn, p. 725. McGraw-Hill, New York.

85 Pogliani, L. & Terenzi, M. (1992). Matrix formulation of chemical reaction rates. *J. Chem. Educ.* 69, 278–280.

86 Sanchez, I. E. & Kiefhaber, T. (2003). Evidence for sequential barriers and obligatory intermediates in apparent two-state protein folding. *J. Mol. Biol.* 325, 367–376.

87 Hvidt, A. & Nielsen, S. O. (1966). Hydrogen exchange in proteins. *Adv. Protein Sci.* 21, 287–386.

88 Tanford, C. (1968). Protein denaturation. *Adv. Protein Chem.* 23, 121–282.

89 Krantz, B. A., Mayne, L., Rumbley, J., Englander, S. W. & Sosnick, T. R. (2002). Fast and slow intermediate accumulation and the initial barrier mechanism in protein folding. *J. Mol. Biol.* 324, 359–371.

90 Krantz, B. A. & Sosnick, T. R. (2000). Distinguishing between two-state and three-state models for ubiquitin folding. *Biochemistry* 39, 11696–11701.

91 Laub, P. B., Khorasanizadeh, S. & Roder, H. (1995). Localized solution structure refinement of an F45W variant of ubiquitin using stochastic boundary molecular dynamics and NMR distance restraints. *Protein Sci.* 4, 973–982.

92 Went, H. M., Benitez-Cardoza, C. G. & Jackson, S. E. (2004). Is an intermediate state populated on the folding pathway of ubiquitin? *FEBS Lett.* 567, 333–338.

93 Pascher, T., Chesick, J. P., Winkler, J. R. & Gray, H. B. (1996). Protein folding triggered by electron transfer. *Science* 271, 1558–1560.

94 Brems, D. N. & Stellwagen, E. (1983). Manipulation of the observed kinetic phases in the refolding of denatured ferricytochromes c. *J. Biol. Chem.* 258, 3655–3660.

95 Muthukrishnan, K. & Nall, B. T. (1991). Effective concentrations of amino acid side chains in an unfolded protein. *Biochemistry* 30, 4706–4710.

96 Hammack, B., Godbole, S. & Bowler, B. E. (1998). Cytochrome *c* folding traps are not due solely to histidine-heme ligation: Direct demonstration of a role for N-terminal amino group-heme ligation. *J. Mol. Biol.* 275, 719–724.

97 Yeh, S.-R., Takahashi, S., Fan, B. & Rousseau, D. L. (1997). Ligand exchange during cytochrome *c* folding. *Nature Struct. Biol.* 4, 51–56.

98 Hagen, S. J., Hofrichter, J., Szabo, A. & Eaton, W. A. (1996). Diffusion-limited contact formation in unfolded cytochrome *c*: Estimating the maximum rate of protein folding. *Proc. Natl Acad. Sci. USA* 93, 11615–11617.

99 Qiu, L., Zachariah, C. & Hagen, S. J. (2003). Fast chain contraction during protein folding: "foldability"

and collapse dynamics. *Phys Rev Lett* 90, 168103.

100 Dill, K. A., Bromberg, S., Yue, K. et al. (1995). Principles of protein folding – a perspective from simple exact models. *Protein Sci.* 4, 561–602.

101 Nymeyer, H., Garcia, A. E. & Onuchic, J. N. (1998). Folding funnels and frustration in off-lattice minimalist protein landscapes. *Proc. Natl Acad. Sci. USA* 95, 5921–5928.

102 Sabelko, J., Ervin, J. & Gruebele, M. (1999). Observation of strange kinetics in protein folding. *Proc. Natl Acad. Sci. USA* 96, 6031–6036.

103 Hagen, S. J. (2003). Exponential decay kinetics in "downhill" protein folding. *Proteins* 50, 1–4.

104 Shortle, D. (2002). The expanded denatured state: an ensemble of conformations trapped in a locally encoded topological space. *Adv. Protein Chem.* 62, 1–23.

105 Tanford, C., Kawahara, K. & Lapanje, S. (1967). Proteins as random coils. I. Intrinsic viscosities and sedimentation coefficients in concentrated guanidine hydrochloride. *J. Am. Chem. Soc.* 89, 729–749.

106 Sosnick, T. R., Mayne, L. & Englander, S. W. (1996). Molecular collapse: the rate-limiting step in two-state cytochrome c folding. *Proteins* 24, 413–426.

107 Sosnick, T. R., Shtilerman, M. D., Mayne, L. & Englander, S. W. (1997). Ultrafast signals in protein folding and the polypeptide contracted state. *Proc. Natl Acad. Sci. USA* 94, 8545–8550.

108 Qi, P. X., Sosnick, T. R. & Englander, S. W. (1998). The burst phase in ribonuclease A folding and solvent dependence of the unfolded state. *Nature Struct. Biol.* 5, 882–884.

109 Choe, S. E., Matsudaira, P. T., Osterhout, J., Wagner, G. & Shakhnovich, E. I. (1998). Folding kinetics of villin 14T, a protein domain with a central beta-sheet and two hydrophobic cores. *Biochemistry* 37, 14508–14518.

110 Ferguson, N., Capaldi, A. P., James, R., Kleanthous, C. & Radford, S. E. (1999). Rapid folding with and without populated intermediates in the homologous four-helix proteins Im7 and Im9. *J. Mol. Biol.* 286, 1597–1608.

111 Gorski, S. A., Capaldi, A. P., Kleanthous, C. & Radford, S. E. (2001). Acidic conditions stabilise intermediates populated during the folding of Im7 and Im9. *J. Mol. Biol.* 312, 849–863.

112 Ivankov, D. N., Garbuzynskiy, S. O., Alm, E., Plaxco, K. W., Baker, D. & Finkelstein, A. V. (2003). Contact order revisited: influence of protein size on the folding rate. *Protein Sci* 12, 2057–2062.

113 Huang, G. S. & Oas, T. G. (1995). Submillisecond folding of monomeric λ repressor. *Proc. Natl Acad. Sci. USA* 92, 6878–6882.

114 Burton, R. E., Huang, G. S., Daugherty, M. A., Fullbright, P. W. & Oas, T. G. (1996). Microsecond protein folding through a compact transition state. *J. Mol. Biol.* 263, 311–322.

115 Wittung-Stafshede, P., Lee, J. C., Winkler, J. R. & Gray, H. B. (1999). Cytochrome b562 folding triggered by electron transfer: approaching the speed limit for formation of a four-helix-bundle protein. *Proc. Natl Acad. Sci. USA* 96, 6587–6590.

116 Jacob, M., Holtermann, G., Perl, D. et al. (1999). Microsecond folding of the cold shock protein measured by a pressure-jump technique. *Biochemistry* 38, 2882–2891.

117 Creighton, T. E. (1994). The energetic ups and downs of protein folding. *Nature Struct. Biol.* 1, 135–138.

118 Fersht, A. R. (1995). Optimization of rates of protein folding: the nucleation-condensation mechanism and its implications. *Proc. Natl Acad. Sci. USA* 92, 10869–10873.

119 Roder, H. & Elöve, G. A. (1994). Early stages of protein folding. In *Mechanisms of Protein Folding: Frontiers in Molecular Biology* (Pain, R. H., Ed.), pp. 26–55. Oxford University Press, New York.

120 Silow, M. & Oliveberg, M. (1997). Transient aggregates in protein folding are easily mistaken for folding

intermediates. *Proc. Natl Acad. Sci. USA* 94, 6084–6086.

121 Matouschek, A., Serrano, L. & Fersht, A. R. (1994). Analysis of protein folding by protein engineering. In *Mechanisms of Protein Folding: Frontiers in Molecular Biology* (Pain, R. H., Ed.), pp. 137–159. Oxford University Press, Oxford.

122 Raschke, T. M., Kho, J. & Marqusee, S. (1999). Confirmation of the hierarchical folding of RNase H: a protein engineering study. *Nature Struct. Biol.* 6, 825–831.

123 Walkenhorst, W. F., Green, S. M. & Roder, H. (1997). Kinetic evidence for folding and unfolding intermediates in Staphylococcal nuclease. *Biochemistry* 63, 5795–5805.

124 Kiefhaber, T. (1995). Kinetic traps in lysozyme folding. *Proc. Natl Acad. Sci. USA* 92, 9029–9033.

125 Heidary, D. K., Gross, L. A., Roy, M. & Jennings, P. A. (1997). Evidence for an obligatory intermediate in the folding of interleukin-1β. *Nature Struct. Biol.* 4, 725–731.

126 Jennings, P., Roy, M., Heidary, D. & Gross, L. (1998). Folding pathway of interleukin-1 beta. *Nature Struct. Biol.* 5, 11.

127 Tsui, V., Garcia, C., Cavagnero, S., Siuzdak, G., Dyson, H. J. & Wright, P. E. (1999). Quench-flow experiments combined with mass spectrometry show apomyoglobin folds through and obligatory intermediate. *Protein Sci.* 8, 45–49.

128 Capaldi, A. P., Kleanthous, C. & Radford, S. E. (2002). Im7 folding mechanism: misfolding on a path to the native state. *Nature Struct. Biol.* 9, 209–216.

129 Plaxco, K. W., Simons, K. T. & Baker, D. (1998). Contact order, transition state placement and the refolding rates of single domain proteins. *J. Mol. Biol.* 277, 985–994.

130 Myers, J. K. & Oas, T. G. (2001). Preorganized secondary structure as an important determinant of fast protein folding. *Nature Struct. Biol.* 8, 552–558.

131 Qiu, L., Pabit, S. A., Roitberg, A. E. & Hagen, S. J. (2002). Smaller and faster: the 20-residue Trp-cage protein folds in 4 micros. *J. Am. Chem. Soc.* 124, 12952–12953.

132 Mayor, U., Guydosh, N. R., Johnson, C. M. et al. (2003). The complete folding pathway of a protein from nanoseconds to microseconds. *Nature* 421, 863–867.

133 Zhu, Y., Alonso, D. O., Maki, K. et al. (2003). Ultrafast folding of alpha3D: a de novo designed three-helix bundle protein. *Proc. Natl Acad. Sci. USA* 100, 15486–15491.

134 Beechem, J. M., James, L. & Brand, L. (1990). Time-resolved fluorescence studies of the protein folding process: new instrumentation, analysis and experimental approaches in time-resolved laser spectroscopy in biochemistry. *SPIE Proc.* 1204, 686–698.

135 Jones, B. E., Beechem, J. M. & Matthews, C. R. (1995). Local and global dynamics during the folding of *Escherichia coli* dihydrofolate reductase by time-resolved fluorescence spectroscopy. *Biochemistry* 34, 1867–1877.

136 Balbach, J., Forge, V., van Nuland, N. A. J., Winder, S. L., Hore, P. J. & Dobson, C. M. (1995). Following protein folding in real time using NMR spectroscopy. *Nature Struct. Biol.* 2, 865–870.

137 Frieden, C. (2003). The kinetics of side chain stabilization during protein folding. *Biochemistry* 42, 12439–12446.

138 Segel, D. J., Bachmann, A., Hofrichter, J., Hodgson, K. O., Doniach, S. & Kiefhaber, T. (1999). Characterization of transient intermediates in Lysozyme folding with time resolved small-angle X-ray scattering. *J. Mol. Biol.* 288, 489–499.

139 Brissette, P., Ballou, D. P. & Massey, V. (1989). Determination of the dead time of a stopped-flow fluorometer. *Anal. Biochem.* 181, 234–238.

140 Gibson, Q. H. & Antonini, E. (1966). Kinetics of heme–protein intractions. In *Hemes and Hemeproteins* (Chance, B., Estabrook, R. W. & Yonetani, T.,

Eds), pp. 67–78. Academic Press, New York.

141 Hartridge, H. & Roughton, F. J. W. (1923). Method of measuring the velocity of very rapid chemical reactions. *Proc. R. Soc. (Lond.): A Math. Phys. Sci.* 104, 376–394.

142 Gutfreund, H. (1969). *Meth. Enzymol.* 16, 229–249.

143 Takahashi, S., Ching, Y.-c., Wang, J. & Rousseau, D. L. (1995). Microsecond generation of oxygen-bound cytochrome c oxidase by rapid solution mixing. *J. Biol. Chem.* 270, 8405–8407.

144 Paeng, K., Paeng, I. & Kincaid, J. (1994). Time-resolved resonance raman spectroscopy using a fast mixing device. *Anal. Sci.* 10, 157–159.

145 Gallagher, T., Alexander, P., Bryan, P. & Gilliland, G. L. (1994). Two crystal structures of the B1 immunoglobulin-binding domain of streptococcal protein G and comparison with NMR. *Biochemistry* 33, 4721–4729.

146 Bushnell, G. W., Louie, G. V. & Brayer, G. D. (1990). High-resolution three-dimensional structure of horse heart cytochrome c. *J. Mol. Biol.* 214, 585–595.

16
Kinetic Protein Folding Studies using NMR Spectroscopy

Markus Zeeb and Jochen Balbach

16.1
Introduction

The mechanism by which polypeptides fold to their native conformation remains an area of active research in structural biology. Our understanding of the protein folding reaction and the deduction of protein folding models has been strongly influenced by the data accessible at the time when they were formulated. During all stages of progression in our understanding of protein folding, nuclear magnetic resonance (NMR) spectroscopy played an important role. NMR combines high spatial resolution with dynamic and kinetic analyses on an enormous time scale ranging from picoseconds to days (Figure 16.1). Therefore, NMR has emerged as an especially fruitful technique to study the protein folding reaction on molecular grounds.

The first milestones were certainly the use of NMR to define the distributions of deuterons at labile sites of proteins. Site-specific H/D exchange experiments [1, 2] and the calculation of protection factors revealed the thermodynamics of local and global unfolding of the native state as well as protein folding intermediates [3]. These states show distinct protection factors at different denaturant concentrations [4]. The determination of proton occupancies on a residue level by NMR following quenched-flow pulse labeling experiments provided important information about the structure formation during the first steps in protein folding [5–7].

Early direct NMR investigations of protein folding included studies of the equilibrium conversion between the native and the unfolded state at elevated temperatures, high denaturant concentrations, or extreme pH values [8, 9]. These experiments provided insights into the cooperativity and thermodynamics of protein folding. Additionally, NMR spectroscopy of nonnative states emerged. Although the system is at equilibrium, the rates of conversion between different states of folding can be determined by NMR spectroscopy [10]. Low rates in the range between 0.1 s^{-1} and 10 s^{-1} can be determined directly by NMR exchange spectroscopy. Fast processes on a microsecond to millisecond time scale affect the relaxation of the NMR active nuclei by chemical exchange contributions to the transversal relaxation rates (Figure 16.1). Therefore, the microscopic un- and re-

Protein Folding Handbook. Part I. Edited by J. Buchner and T. Kiefhaber

ISBN: 3-527-30784-2

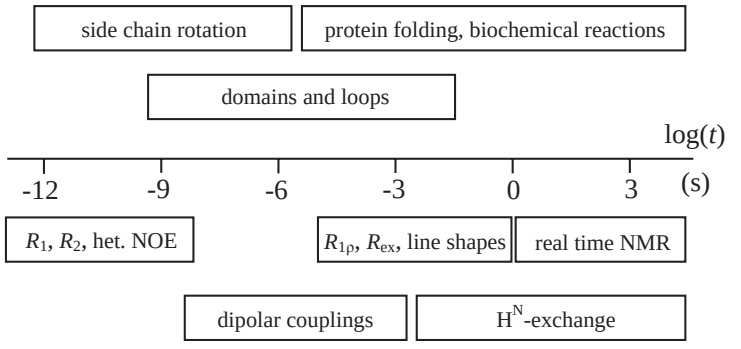

Fig. 16.1. Logarithmic NMR time scale. Illustration of accessible protein motions and reactions by the respective NMR technique: R_1, spin-lattice relaxation rate; R_2, spin-spin relaxation rate; het. NOE, heteronuclear Overhauser enhancement; $R_{1\rho}$, relaxation in the rotating frame; R_{ex}, chemical exchange contribution to R_2; line shapes, line shape analysis of proton resonances; dipolar couplings, residual dipolar couplings in different alignment media; H^N-exchange, proton–deuterium exchange of amide protons.

folding rates are accessible by line shape analyses of NMR resonances [11, 12], from ^{15}N $R_{1\rho}$ relaxation rates [13], from ^{15}N transverse cross-correlation relaxation rates [14], or from ^{15}N R_2 relaxation dispersion experiments [15]. These fast folding rates can be well predicted by the diffusion-collision model for several small proteins [16] or derived experimentally by extrapolating the denaturant dependence of the un- and refolding rates from stopped-flow experiments to 0 M denaturant [12, 14]. Recently, the analysis of residual dipolar couplings measured in different alignment media have allowed the determination of the dynamics between nanoseconds and milliseconds and filled the gap between very fast and slower motions of proteins [17, 18]. All these methods have in common that the populations of unfolded and folded polypeptide chains are at equilibrium but differ in their chemical shifts of the NMR active nuclei. During the detection or delay times in the pulse sequence (between about 1 ms and 1 s), fluctuations between the populations cause additional contributions to the natural relaxation of the different states from Brownian motions. These contributions can be converted into un- and refolding rates.

Nonequilibrium reactions can be directly followed in the NMR probe, where rates above 5 min^{-1} require a stopped-flow device to be observable. Since very early NMR studies of protein reactions in ''real time'' several of these devices have been designed [19–21]. Unfolding and refolding of proteins can be initiated by rapid mixing of solutions inside the NMR spectrometer with short experimental dead times [22–25]. One very powerful approach has been to use ^{19}F NMR to study proteins with ^{19}F-labeled tryptophan residues and a data collection started within 100 ms of the initiation of the mixing. Distinct steps of the folding reaction of dihydrofolate reductase could be resolved by these pioneering studies by Frieden and coworkers [23, 26, 27]. Recently, this method was successfully applied to resolve

the consecutive steps of folding and assembly of the two-domain chaperone PapD using a 5-mm ^{19}F cryoprobe [28].

Very slow protein folding reactions, such as those limited by isomerization of peptidyl-prolyl bonds [29] can be initiated by manual mixing [30–33] and followed by the sequential accumulation of one-dimensional spectra. These studies revealed important information about the properties of intermediates during un- and refolding. An extension to two-dimensional techniques has been possible in a few cases, to increase the number of specific spin labels in well-resolved NMR spectra [34]. Most recently, Mizuguchi et al. succeeded in recording a series of 3D NMR spectra during the refolding reaction of apoplastocyanin [35] and were able to resolve changes of distances between protons during refolding.

For several proteins denaturant-induced unfolding transitions monitored by NMR uncovered equilibrium intermediates, which were silent in circular dichroism (CD)- or fluorescence-detected transitions [36–38]. This demonstrates the unique sensitivity of the chemical shifts of NMR resonances towards the local environment even in poorly structured protein states. Many features of the molten globule state, the archetypal protein folding intermediate, have been characterized by NMR spectroscopy [39] and especially the close correspondence between equilibrium and kinetic molten globules [40].

The use of NMR spectroscopy to study protein folding has been extensively reviewed [9, 23, 41–49]. The first part of this chapter concentrates on the developments of real-time NMR spectroscopy during the last 5 years in following very slow protein folding reactions. Earlier achievements have been already reviewed [24, 50, 51]. The very rapid development of the interpretation of NMR relaxation data in terms of micro- and millisecond motions during the last few years has been excellently reviewed [10]. Based on this theoretical background the second part of this contribution will focus on the derivation of millisecond protein folding rates from NMR relaxation experiments.

16.2 Following Slow Protein Folding Reactions in Real Time

The development of 1D and 2D real-time NMR experiments focuses on generally suitable methods of studying the structural and dynamic changes occurring during the protein folding reaction. A relatively simple mixing device has turned out to be very useful and generally applicable to initiate folding reactions, because no modifications of the spectrometer or the probe head are required [24]. This device has recently been optimized to reduce the dead time of mixing from 800 ms [40] down to tens of milliseconds (Figure 16.2) [25]. Typically, 50 μL of unfolded protein at high denaturant concentrations are injected into 250–450 μL refolding buffer already present in the NMR tube inside the magnet. To avoid premature mixing of the denatured protein with the refolding buffer and with the solvent in the tube that connects to the syringe, the solutions are separated by two air bubbles. Pushing the syringe located outside the magnet by 10 bar results in a complete mixing

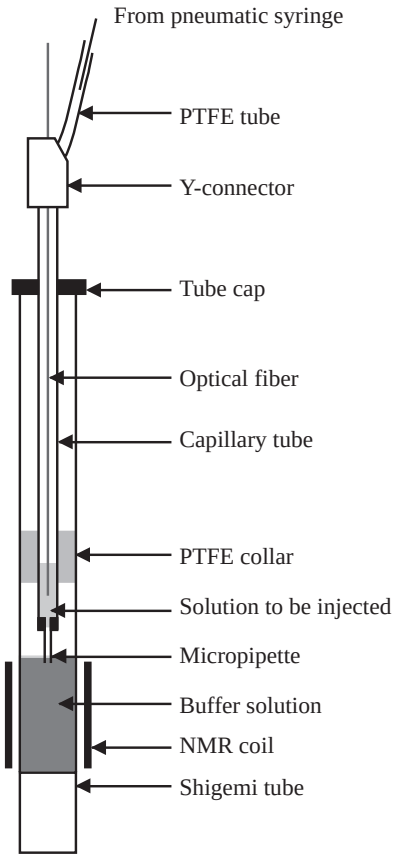

Fig. 16.2. Schematic representation of the rapid mixing device used for real-time NMR experiments. The NMR tube in the probe of the spectrometer contains the refolding or unfolding buffer, which is separated from the denatured or native protein solution, respectively, in the micropipette and capillary tube by an air bubble to avoid mixing of the solutions before injection. The transfer line to the syringe, which is outside the magnet, has to be filled with solvent and the piston is pneumatically triggered by 10 bar for a rapid transfer of the protein solution into the NMR tube.

within the active volume of the detection coil of the probe head during the dead time of the device (for further details see Section 16.6.1). Most presented examples in this report are multiscan NMR experiments with proteins, which require a relaxation period of at least 300 ms between scans for a sufficient build-up of polarization. Therefore, the present dead time of this simple stopped-flow mixing device is satisfactory.

The first proteins studied by real-time NMR employing such a device were bovine α-lactalbumin (α-LA) and hen lysozyme [24]. α-LA was particularly suitable for setting up the device [40], because it is a well-defined system for many aspects

of protein folding and its folding kinetics can be varied over several orders of magnitude by control of the Ca^{2+} concentration of the solution [52, 53]. The folding reaction is initiated by changing the solvent conditions such as the pH [54, 55] or the concentration of denaturants [40, 56] or stabilizing agents [57, 58]. Subsequently, various NMR techniques can be applied to monitor the change of different properties of the polypeptide chain during the folding reaction. In the simplest case, a series of 1D spectra follows the rapid mixing step, allowing kinetic studies for processes with rates below 0.1 s^{-1}. These 1D real-time NMR experiments have been successfully applied to more than a dozen proteins: bovine α-LA [40, 59, 60], ribonuclease T1 of *Aspergillus oryzae* [61], human CDK inhibitor $P19^{INK4d}$ [38], phosphocarrier HPr of *Escherichia coli* [62], SH3 domain of phosphatidylinositol 3′-kinase [63], human muscle acylphosphatase [64], French bean apoplastocyanin [32], thioredoxin of *E. coli* [33], rat intestinal fatty acid binding protein [23], dihydrofolate reductase of *E. coli* [27], bovine pancreatic ribonuclease A [31], hen lysozyme [25, 65, 66], chymotrypsin inhibitor 2 [67], barnase [67], barstar [68, 69], staphylococcal nuclease [70], yeast prion Sup35 [71], HIV I protease [72, 73] as well as peptides [74]. All studies make use of distinct chemical shifts for the different states changing with time, to determine the kinetics of the respective protein folding reaction. The dispersion of the resonances and the line width can also be used to distinguish possible folding intermediates from the unfolded and folded state. The appearance of 1D spectra of folding intermediates range between mainly unfolded, molten-globule-like, and native-like. Intermediate populations below 5% of the protein molecules are difficult to detect.

Figures 16.3 and 16.4 illustrate one example for the use of 1D real-time NMR spectroscopy to study the refolding of $P19^{INK4d}$, human cyclin D-dependent kinase inhibitor [38]. After dilution from 6 M to 2 M urea two fast refolding phases produce 83% of native molecules during the dead time of the NMR experiment. These two fast phases have been revealed by stopped-flow far-UV circular dichroism spectroscopy during the formation of the five native ankyrin repeats comprising ten α-helices. Refolding of the remaining 17% of unfolded molecules is retarded by a slow *cis*/*trans* isomerization of prolyl residues resulting in a refolding rate of 0.017 s^{-1}. This slow phase can be accelerated by the prolyl isomerase cyclophilin 18 from the cytosol of *E. coli*. The native population of $P19^{INK4d}$ can be directly detected by the high-field shifted resonance at 0.7 ppm. To analyze the decay of the unfolded population at 0.9 ppm or 1.45 ppm, the native contribution to the 1D spectra has to be subtracted [38, 61]. First, this subtraction revealed identical un- and refolding rates. Secondly, each 1D spectrum can be represented by a linear combination of the spectrum of the unfolded and the folded population. This suggests that no further intermediate gets significantly populated during this final folding event of $P19^{INK4d}$ and that the polypeptide chain cannot form a native-like ordered structure prior to the prolyl isomerization.

A similar analysis was possible for the S54G/P55N variant of ribonuclease T1 from *Aspergillus oryzae* [61, 75]. About 15% of the unfolded S54G/P55N-RNase T1 molecules contain the native *cis* prolyl peptide bond Tyr38-Pro39 and fold to the native state within the dead time of the NMR experiment. They give rise to a burst

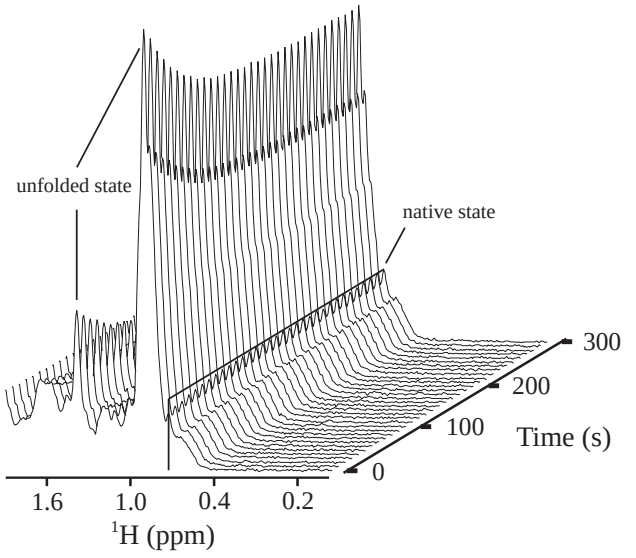

Fig. 16.3. Stacked plot of the high field region of the 1D ^{1}H NMR spectra at different times of refolding. Human CDK inhibitor P19^{INK4d} in 50 mM Na-phosphate pH 7.4 (10% ^2H_2O) at 15 °C was refolded by a tenfold dilution from 6 M urea to yield a final urea concentration of 2 M. For this representation two 1D experiments with four transients were averaged to yield a resolution of 11 seconds per spectrum. Resonances of the unfolded and native state are indicated and the integral of the latter is plotted in Figure 16.4a.

of all resonances of the native state in the very first spectrum recorded after initiation of the refolding reaction. The refolding of the remaining 85% unfolded molecules is very slow and limited in rate by the *trans* → *cis* isomerization of Pro39. In contrast to the above-mentioned example of P19^{INK4d}, where the molecules were largely unfolded before the very slow rate-limiting step, S54G/P55N-RNase T1 rapidly forms a folding intermediate arrested at this stage of folding because of the nonnative prolyl peptide bond. The major fraction of their intensities decays with a rate of 1.4×10^{-4} s^{-1} at 10 °C, which is very close to the formation of the native state with a rate constant of 1.25×10^{-4} s^{-1}. A minor fraction (about 7%) reveals 50 times higher rates and belongs to a second shorter-lived intermediate. The entire dataset could be decomposed according to the time dependence of a basis set of 1D spectra of the native state, the major intermediate I^{39t} and the minor intermediate (for a detailed description see Ref. [61]). The dispersion and line widths of the resonances indicated that the long-lived intermediate I^{39t} has a defined tertiary structure already close to the native state, but several resonances of I^{39t} revealed not-yet-native chemical shifts. The shorter lived transient species is mainly unstructured.

These examples of S54G/P55N-RNase T1 and P19^{INK4d} substantiate that nonnative prolyl peptide bonds can either prevent the formation of native protein or can arrest the protein in an already well-structured but not-yet-native conformation.

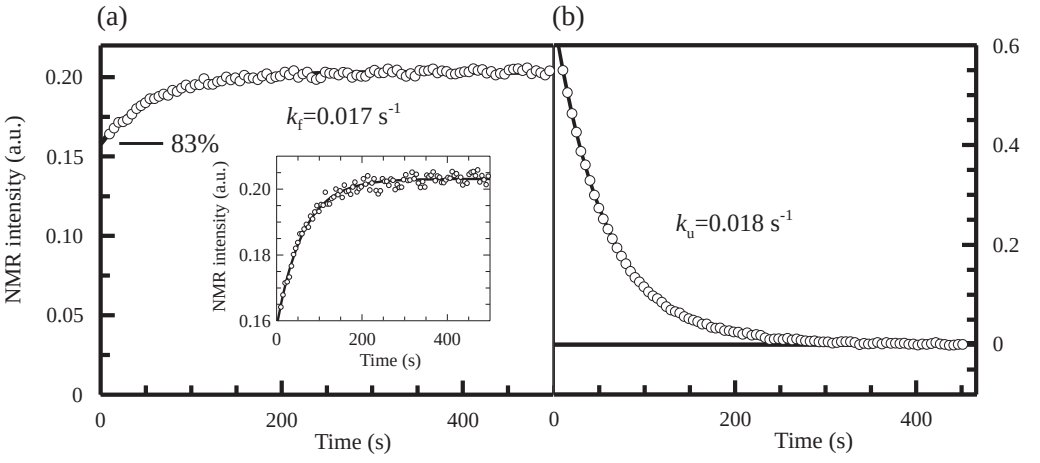

Fig. 16.4. Folding kinetics of P19^{INK4d} extracted from the experiment depicted in Figure 16.3. a) The build-up of the native state is represented by the integral of the NMR intensities between 0.65 ppm and 0.70 ppm. The continuous line corresponds to a single exponential fit with a rate constant of 0.017 s^{-1} and a burst phase in the dead time of the experiment of 83%. The inset shows the same data with enlarged ordinate. b) Decay of the contribution of the unfolded state to the NMR spectra. A single exponential fit was applied to the integral of the NMR signals between 0.78 ppm and 0.90 ppm and reveals a rate constant of 0.018 s^{-1}, which is shown as a continuous line. Prior to the integration, the native component was subtracted from every 1D spectrum (see Section 16.6.1).

Therefore, for a protein function in the cell several levels of regulation based on prolyl peptide bonds are possible. Ubiquitous peptidyl prolyl isomerases with and without substrate specificity have been identified and proposed as key for this kind of regulation [29, 76]. Most recently that kind of a proline-driven conformational switch has been structurally characterized [77, 78].

A particularly important approach to the characterization of transient protein folding intermediates is to monitor nuclear Overhauser effects (NOEs) between protons of these states and how they evolve during the folding process. NOEs can, in principle, be converted into interproton distances, which is the basis for structure determination of proteins by NMR spectroscopy. The molten globule state formed rapidly after initiation of refolding of α-LA can be studied by real-time 1D NOE experiments [57]. Although the resolution of the spectrum is limited, the overall NOE on the aliphatic proton resonances as a consequence of saturating all aromatic resonances can be measured. It had been shown previously that this approach works for the A-state of α-LA, which is populated at equilibrium at pH 2 [55]. The intensity of the steady-state NOE of the kinetic molten globule observed transiently during refolding at pH 7.0 is already 80% of the steady-state NOE intensity of the native state. This is even larger than the value of 70% measured previously for the equivalent NOE effect in the A-state at equilibrium. The average radius of the species formed after initiation of folding can be estimated from the

steady-state NOE to be within 4% of that of the native state [57]. This experiment shows that the folding of α-LA involves the rapid formation of a highly collapsed but partially disorganized molten globule, which subsequently reorganizes slowly to form the fully native state mainly by packing of the side chains.

Additional evidence for a native-like compactness of the molten globule of α-LA came from 1D real-time NMR diffusion experiments [56]. This method allows the determination of the hydrodynamic radius of kinetic folding intermediates. The experiment is based on a pulsed field gradient spin echo pulse sequence to determine the diffusion coefficient of molecules in liquids [79, 80]. The latter can subsequently be converted into the effective hydrodynamic radius for nonspherical molecules (R_h) such as proteins (for further details see Section 16.6.1 and Refs [81, 82]). The application of these spin echoes during refolding of α-LA from 6 M GdmHCl revealed R_h of the kinetic molten globule, which is only 8% larger than the R_h of apo α-LA [56]. The equivalent experiment was performed during refolding of S54G/P55N-RNase T1 and showed that R_h of the I^{39t} intermediate is only about 5% larger than the radius of the native state [75]. Consequently, the major compaction of the extended unfolded polypeptide chain occurs before the rate-limiting folding step regardless whether the side chains are already in a well-defined conformation (S54G/P55N-RNase T1) or not (α-LA).

In parallel to the successful formation of the native state, polypeptide chains can follow misfolding pathways. This failure of proteins to fold correctly or to remain folded is implicated in the onset of a range of diseases [83, 84]. To characterize these misfolding reactions, it is necessary to use a variety of complementary spectroscopic methods. Real-time NMR spectroscopy can be used to study the association and aggregation of proteins in solution by monitoring the aggregation-competent but still soluble states during these processes. Carver and coworkers used α-LA as a model system to study protein aggregation, which occurs during unfolding of the protein by reducing its four disulfide bonds. They initiated the aggregation reaction by rapid mixing of apo α-LA or holo α-LA with a large excess of the reducing agent dithiothreitol (DTT) [85–87]. Reduction of the disulfide bonds promotes unfolding of α-LA through several well-characterized intermediate states, which expose hydrophobic surfaces prone to aggregation. The well-dispersed NMR spectrum of the native apo protein gets lost during the dead time of the experiment (1.2 s) after the addition of DTT. The first obtained spectrum shows broad resonances with significantly reduced signal intensity and resembles the molten globule or A-state of α-LA. After several minutes the resonance intensity disappears since aggregation occurs leading to substantial precipitation out of the solution with an apparent rate of 1.5×10^{-3} s^{-1} at 37 °C. Aggregation can be significantly decelerated and precipitation totally prevented by adding chaperones such as α-crystallin [85, 87] or clusterin [86] to the refolding buffer of the real-time NMR experiment. Both chaperones bind to the aggregation competent monomeric molten globule state of apo α-LA and therefore stabilize the protein. Reduction and concomitant aggregation of holo α-LA is less efficiently prevented by α-crystallin because it is only partially reduced and more structured compared with the fully reduced and disordered form of apo α-LA. Additionally, holo α-LA precipitates more

rapidly, which is important for the chaperone action of α-crystallin, since it is much more efficient with slowly precipitating species [87].

Solution aggregation of acid-denatured cold shock protein A (CspA) from *E. coli* is also a very slow process, which results in formation of insoluble fibrils [88]. Several 2D $^{1}H-^{15}N$ heteronuclear single-quantum coherence (HSQC) spectra, ^{15}N relaxation experiments and even four 3D HSQC-NOESY spectra can be recorded during this self-assembly process. A combined analysis of these data reveal that mainly residues from the β-strands of CspA monitor a fast exchange on the NMR chemical shift time scale between acid-denatured monomers and soluble aggregates during the lag phase of aggregation. During the exponential phase of aggregation the first three β-strands are predominantly involved in the association process.

The aggregation of the prion-determining region of the NM domain of Sup35 in yeast, $Sup35^{5-26}$, has been followed recently by 1D real-time NMR spectroscopy [71]. As expected, only signals originating from soluble peptide molecules are visible in the spectra and after 80 min 50% of the peptide became insoluble. Adding catalytic amounts of Hsp104 prevents aggregation for about 80% of the peptide molecules by binding to the hexameric/tetrameric species of $Sup35^{5-26}$ and releasing intermediate and monomeric species. These conclusions could be drawn because binding of Hsp104 causes significant changes of chemical shifts of several tyrosine resonances. Based on these resonances, the molecular weight of the $Sup35^{5-26}$ oligomers could be estimated by NMR diffusion experiments.

In photo-CIDNP (chemically induced dynamic nuclear polarization) NMR experiments, the polarization of solvent-exposed protons is induced more rapidly than the natural spin-lattice relaxation via a dye excited by a laser flash [89]. This method reduces the time required to polarize spins transferred into the NMR probe from a lower field region of the magnet [66]. Together with the very small portion of the sample illuminated by the laser beam, the dead time of the device shown in Figure 16.2 can be further reduced [25]. The strength of the photo-CIDNP approach, however, is not only in its time resolution but also in its spectral resolution. The latter is significantly improved because the induced polarization for example by flavin mononucleotide as dye is only generated in a limited number of residues (tyrosine, tryptophan, and, under some conditions, histidine). Moreover, polarization occurs only when these residues are accessible to the photoexcited dye molecules in the solution, enabling the environment of individual residues to be probed directly in real time during folding. Hen lysozyme for example forms initially (after 30 ms experimental dead time) a relatively disordered collapsed state with largely buried tryptophan residues [25, 66]. The structurally closely related bovine α-LA also forms very early a collapsed state during refolding, which very closely resembles the photo-CIDNP spectrum of the pH 2 molten globule state of this protein [59, 60]. Subsequently, a reorganization of these aromatic residues occurs during the course towards the fully native proteins in both cases.

Histidine residues only get excited by the photo-CIDNP process when the protein contains no tryptophan residues or when all tryptophan residues are buried and the histidine residues are exposed. These very rare conditions are met by the histidine-containing phosphocarrier protein HPr from *E. coli*. The wild-type pro-

tein contains no tryptophan and tyrosine residues, giving rise to several well-resolved histidine resonances in the photo-CIDNP spectrum [90]. In several tryptophan-containing variants of HPr no histidine resonances of the native and unfolded state were detectable because of the exposed Trp. Directly after refolding has been initiated, in most variants the Trp side chain was buried and some His residues could be transiently excited by the dye until the native conformation was formed.

16.3 Two-dimensional Real-time NMR Spectroscopy

A major limitation of 1D NMR experiments with proteins is, of course, the low resolution due to severe signal overlap. Therefore, only a few well-resolved resonances allow a detailed analysis with molecular resolution. In many cases the general appearance of the 1D spectrum rather than single resonances is analyzed. Thus, current work focuses on the extension of real-time NMR experiments to utilize the power of multidimensional NMR in kinetic experiments. Very slow folding reactions can be directly followed by sequentially recorded 2D spectra such as 2D $^{1}H-^{15}N$ HSQC spectra [34]. An equivalent proton–nitrogen correlation spectrum can be recorded in much less time (in about 200 s per 2D spectrum) if a heteronuclear multiple-quantum coherence (HMQC) pulse sequence is used in combination with Ernst angle pulses [56, 91]. During the refolding of S54G/P55N-RNase T1 from 6 M GdmHCl at 1 °C, for example, a series of 128 of these fast-HMQC spectra could be recorded [75]. After correction for the dead time events, the complete 2D spectrum of the kinetic folding intermediate I^{39t} could be obtained. The spectrum exhibits the same dispersion of the resonances and the same line widths as the spectrum of the native state, indicating a well-defined tertiary structure of I^{39t}. The backbone resonances of 22 (out of 104) residues of I^{39t} show native chemical shifts and identify therefore regions in which a native environment is already present in the intermediate state. For 66 backbone amide probes, which differ in chemical shifts between the native state and I^{39t}, single exponential refolding kinetics could be extracted from the 2D real-time NMR experiment. All showed the same time constant within experimental error indicating that the *trans* → *cis* isomerization of Pro39 fully synchronizes the rate-limiting step of refolding, which is the transition of not-yet-native regions in I^{39t} towards the native conformation. Interestingly, amide protons in not-yet-native environments are not only located close to the nonnative *trans* Tyr38-Pro39 peptide bond, but are spread throughout the entire protein.

The slowest step during the refolding of barstar, the intracellular inhibitor of barnase, is also dominated by the formation of a *cis* peptidyl prolyl bond of Tyr47-Pro48 in the native state [92, 93]. A set of 16 2D $^{1}H-^{15}N$ HSQC spectra recorded in real time revealed that the intermediate with the *trans* Tyr47-Pro48 bond has a predominantly native-like conformation [68]. Only the *trans* prolyl peptide bond and three residues in close proximity to Pro48 rearrange upon complete refolding.

Therefore, this intermediate is silent in conventional CD and fluorescence spectra. Addition of cyclophilin from the human cytosol leads to a rapid interconversion of the *trans* intermediate to the native form within the dead time of the NMR experiment. This helped to identify not-yet-native backbone amides in the intermediate by calculating double difference spectra. In contrast to the intermediate of S54G/P55N-RNase T1, where a nonnative prolyl peptide bond prevented the formation of a native conformation at various close and remote sites, the intermediate of barstar tolerates such a peptide bond and therefore affects the conformation only locally.

The collagen triple helix folds slowly, on a time scale of minutes to hours, making this system amenable to 2D real-time NMR monitoring of the kinetics of peptide fragments (see reviews [49, 50]). Triple helix formation of these peptides can be initiated by rapid cooling of the sample from 50 °C to 10 °C. Residues located at the termini exhibit rates and folding kinetics that are distinct from residues in the central region of the peptide. The NMR data are consistent with an association/nucleation mechanism at the peptide termini and subsequent propagation [34]. The slow propagation results most likely from the conversion of a mixed *cis*/*trans* ensemble of numerous imino acids of the monomers to the final all-*trans* form in the triple helix [94]. A recent 2D real-time NMR study of peptides comprising 18 residues from human collagen type I proved that both the nucleation at the C-terminus and the propagation towards the N-terminus are limited by *cis*/*trans* isomerizations of imide bonds [95]. These peptides contained ^{15}N spin labels at various positions along the sequence, allowing a detailed analysis of consecutive steps during folding of the collagen triple helix. Point mutations known from collagen diseases such as osteogenesis imperfecta, which can be easily included in these model peptides, revealed during which steps misfolding events occur [49, 96].

The collagen triple helix formation was further investigated by residue-specific real-time NMR diffusion experiments [97]. This very powerful 2D development of the 1D real-time diffusion experiment described above also allows determination of the diffusion coefficient and therefore the association states of unfolded, folded, and kinetic intermediates with transient lifetimes simultaneously. The authors could confirm their previous results from the kinetic studies that early nucleated trimers are well ordered only at the C-terminus and that the zipper-like propagation follows in the expected direction.

As mentioned above, a major limitation of 1D experiments is of course the limited resolution of the spectra. Series of 2D experiments, on the other hand, are time demanding, because the acquisition time of each 2D dataset requires at least several minutes. Therefore, we developed methods to reconstruct the kinetic history of folding reactions from a single 2D NMR spectrum recorded during the entire time course of the reaction [54, 61]. This information arises because different time courses of the respective protein states modulate the line widths and intensities of their NMR resonances differently. In general, 2D NMR spectra are recorded by incrementing a time delay between the preparation and observation pulses while a series of free induction decays (FIDs) is recorded. If a chemical re-

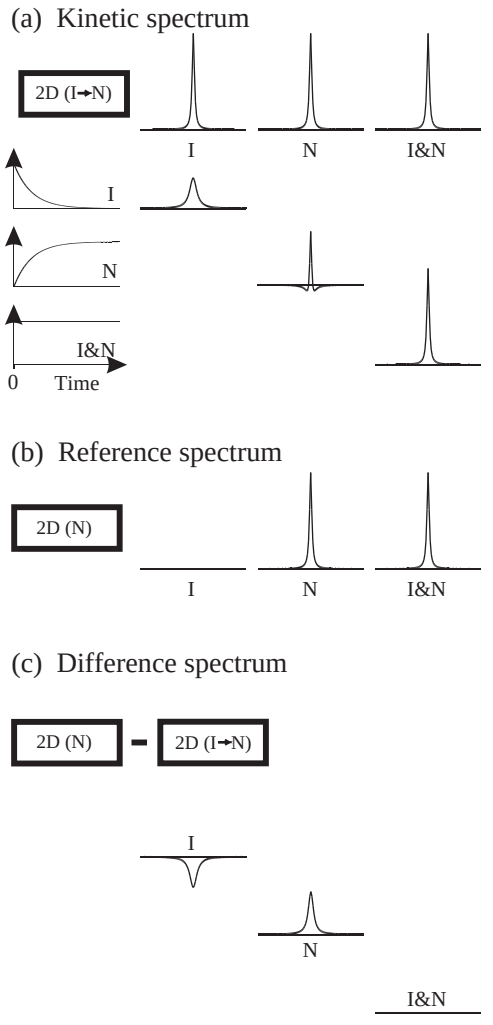

Fig. 16.5. Schematic line shapes and intensities in the indirect dimension F1 for different cross-peaks in a) the kinetic spectrum recorded during the refolding reaction, b) the reference spectrum of the native state after refolding, and c) the result of subtracting the kinetic spectrum from the reference spectrum.

action occurs during the accumulation of data in the experiment, it influences the amplitude of the different signals recorded at various incrementation times. This modulation determines both the line shape and intensity of the cross-peaks in the resulting 2D spectrum, namely in the indirect dimension (Figure 16.5). The principle and effectiveness of this strategy have been demonstrated for α-LA using a $^{1}H-^{15}N$ HSQC experiment [54]. The resonances of the native state of α-LA showed in the kinetic spectrum the expected lower intensities and negative components in

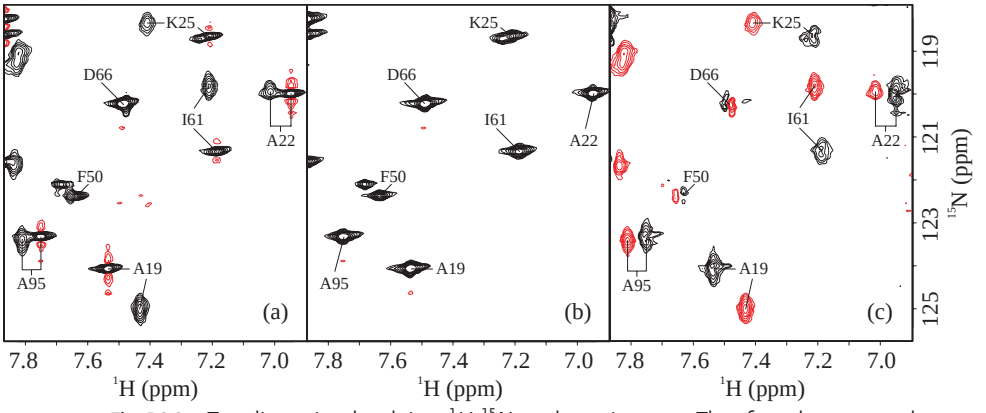

Fig. 16.6. Two-dimensional real-time ^{1}H-^{15}N HSQC spectra of S54G/P55N-RNase T1 recorded during and after the refolding reaction from 6 M GdmHCl at 15 °C. Section of a) the kinetic HSQC, b) the reference HSQC of the native protein, and c) the difference spectrum between the kinetic HSQC and the reference HSQC. Positive NMR intensities in (a) and (c) are indicated with black lines, negative signals by red lines. D66 and F50 are in a native region of the intermediate. The cross-peaks of the amide protons depict equivalent chemical shifts, sharp lines and equivalent intensities in the intermediate and the native state. Therefore, the cross-peaks are present in (a) and (b) and cancel out in the difference spectrum (c). A19, A22, K25, I61, and A95 are in a nonnative environment in the intermediate and depict different chemical shifts as well as line broadening. These cross-peaks of the intermediate state are absent in (b) and show negative intensities in (c). Correspondingly, the emerging cross-peaks of the native state can be identified by the two flanking negative components along the ^{15}N dimension in (a) and reveal positive cross-peaks in (c).

the wings of the peaks compared to the reference spectrum (see the line shapes and intensities of N in panel (a) in the schematic illustration in Figure 16.5). In the special case of α-LA, only very few signals of the molten globule (represented by I in Figure 16.5) are observable, because most resonances are widened.

All three line shapes shown in panel (a) of Figure 16.5 could be experimentally observed in a single 2D real-time ^{1}H–^{15}N-HSQC NMR experiment during the refolding of S54G/P55N-RNase T1 from 6 M GdmHCl at 15 °C [98]. The resonances of F50 and D66 show native chemical shifts in the folding intermediate I^{39t} in both, the ^{1}H and ^{15}N dimension of the spectrum. Thus, sharp lines have been observed in the 2D real-time NMR experiment (Figure 16.6a) along the ^{15}N dimension. For A19, A22, K25, I61, and A95, the resonances of I^{39t} differ in their chemical shifts from the final native state and therefore depict line broadening along the indirect F1 dimension. The corresponding resonances of the native state can be identified by the two flanking negative components along the ^{15}N dimension (negative intensities are shown in red in Figure 16.6a).

Beside identification and assignment of the resonances of transient species, real-time 2D NMR can be used to determine folding kinetics from these described line shapes (see Section 16.6.3) [54, 61]. Here, the key aspect is that folding kinetics can

be monitored residue-by-residue to identify regions of the peptide chain that fold cooperatively according to kinetic arguments. Towards this end, the rate constants from each secondary structure element of α-LA have been determined and it was concluded that the closely packed native environment of the main-chain amide groups of different residues is achieved cooperatively, and with the same kinetics as observed for the side chains [54].

This approach was further developed for homonuclear 2D techniques, where we mainly use the line shape analysis to assign the resonances and NOEs to the respective state of folding. Cross-peaks in a conventional 2D NOESY spectrum reveal protons that are closer than about 5 Å apart. This distance information is used as constraints in structure calculations. Therefore, the obvious goal is the development of NMR experiments to determine NOEs between protons in transient protein folding intermediates to gain high-resolution structural data. The time requirements for well-resolved 2D and 3D NOESY spectra are about 10-fold above the recording time for respective heteronuclear correlation spectra. Rates of amide proton exchange could be determined from a set of 2D NOESY spectra (with a recording time of 5.2 min per spectrum), but both the resolution and the signal-to-noise ratio was very poor in these experiments [99].

Very detailed distance information, however, can be extracted from a single 2D NOESY spectrum recorded during very slow folding reactions with time constants of at least 30 min. Such an experiment was measured during the first 10 hours of refolding of S54G/P55N-RNase T1 at 10 °C to further characterize the major folding intermediate I^{39t} [61]. Three kinds of NOEs can be differentiated in this kinetic 2D NOESY according to the observed F1 line shape of respective cross-peaks. As illustrated in Figure 16.5: (i) NOEs between protons, which are close to each other only in the intermediate state but not in the native state, are specified as nonnative NOEs. They show decaying intensities during the refolding reaction because the concentration of the intermediate decreases. This results in an apparent line broadening of the respective cross-peaks. (ii) NOEs between protons that are close in space only in the native state exhibit increasing intensities during refolding as the native protein is formed. These cross-peaks show distinct line shapes as described above with two flanking negative components [54]. (iii) Native NOEs already present in the intermediate state also exist in the native state, of course, and are therefore specified as native-like NOEs. Their intensity does not change during the entire recording of the spectra so that the intensity and the line shape remain unchanged.

To classify the NOEs to one of the three groups, every single NOE cross-peak has to be compared with the respective signal in the reference NOESY experiment by means of intensity and line shape, which is very time consuming. Therefore, a method was developed to convert the line shape information of each cross-peak into positive and negative intensities [61]. A reference spectrum has to be recorded immediately after the refolding reaction and the kinetic spectrum has to be subtracted afterwards. The result is shown schematically in Figure 16.5c and experimentally in Figure 16.6c for the 2D real-time $^{1}H-^{15}N$ HSQC. Along these lines, the above-mentioned kinetic NOESY was subtracted from a reference NOESY of

the native protein to facilitate the classification of NOE effects. This approach, in principle, allows the 3D structure of a protein folding intermediate to be determined. About 200 NOEs have been analyzed for a detailed characterization of the I^{39t} intermediate of S54G/P55N-RNase T1 [61]. They revealed, for example, that the β-strands involved in disulfide bonds already have the native conformation in I^{39t} as well as the N-terminal half of the α-helix. The C-terminal half of the α-helix has a not-yet-native conformation together with many other regions interspersed among the native-like sections of this protein folding intermediate. This very detailed structural information about I^{39t} considerably extended the qualitative picture we got by just comparing its chemical shifts with the native state as discussed above.

16.4 Dynamic and Spin Relaxation NMR for Quantifying Microsecond-to-Millisecond Folding Rates

Most folding reactions are too fast to be monitored directly by real-time NMR spectroscopy, because the time required to record one 1D ^{1}H spectrum of a protein is at least 100 ms. For signal-to-noise reasons, usually more than one scan is needed with an interscan delay for sufficient relaxation of excitable magnetization of at least 300 ms. Therefore, not more than three 1D scans are possible within one second after a sufficient fast mixing to initiate refolding. Reactions with time constants below 500 ms cause line broadening of the proton resonances in 1D spectra, but even with a fast stopped-flow mixing device only single-scan experiments are possible, which is not very practicable for protein NMR [21]. Interleaved methods with different delay times after mixing to record the first 1D spectrum as well as continuous-flow experiments require very large amounts of protein, because NMR with biological samples works at millimolar concentrations, and are therefore rare [55, 66, 100].

Because of these technical problems of nonequilibrium experiments, fast protein folding reactions have been measured under equilibrium conditions. Fluctuations on a 10 ms to 10 μs time scale between two or more states, where the NMR active nuclei experience different chemical environments, have profound effects on the shape and position of their resonances [101]. For proteins, the analysis of line shapes has been used to study ligand binding, local fluctuations as well as global fluctuations such as complete un- and refolding of the polypeptide chain (a very good overview and references are given in Ref. [10]). One major drawback during the quantification of NMR line shapes in terms of intrinsic unfolding and refolding rates is that a folding model has to be assumed. In most cases simple two-state protein folding systems have been studied or an apparent two-state model such as free and complexed protein has been applied to analyze the line shapes. The first protein folding system that could be quantitatively studied by dynamic NMR spectroscopy on the above-mentioned time scale was the N-terminal domain of phage λ repressor, λ_{6-85} [11]. The urea dependence of the intrinsic un- and refolding rate

constants could be determined between 1.3 M and 3.2 M urea with a maximum value for $k_f = 1200\ s^{-1}$ and a minimum value for $k_u = 100\ s^{-1}$ at 1.3 M urea. From a linear extrapolation of the chevron plot to 0 M urea, $k_f{}^0 = 3600 \pm 400\ s^{-1}$ and $k_u{}^0 = 27 \pm 6\ s^{-1}$ have been obtained. Later, Oas et al. verified these extrapolated rates by ^1H transverse relaxation experiments (see below) [12]. Typically, the resonances of aromatic protons are analyzed in ^2H_2O samples with completely exchanged amide protons, because only then can the former resonances between 6 and 11 ppm be assigned for both folded and unfolded state. These chemical shifts are needed at any urea concentration for an accurate line shape analysis (see Section 16.6.2). According to a two-state folding mechanism, only aromatic resonances of the folded and unfolded state are present within this region. In the case of λ_{6-85}, which contains only two tyrosine and two phenylalanine residues, the entire aromatic region of the 1D spectra could be simulated at any urea concentration (for example by using the program ALASKA [102]), which significantly increases the reliability of the extracted folding rates [12].

The cold shock protein CspB from *Bacillus subtilis* also follows a two-state folding mechanism with $k_f{}^0 = 1070 \pm 20\ s^{-1}$ and $k_u{}^0 = 12 \pm 7\ s^{-1}$ at 25 °C and 0 M urea [103]. From a urea transition monitored by 1D NMR in ^2H_2O, the resonance of His29$^{\varepsilon 1}$ could be used to determine unfolding and refolding rates between 2.9 M and 5.6 M urea (Figures 16.7 and 16.8). The simulation of the line shape and the position of this resonance according to the extracted parameters closely resembles the experimental data and is depicted in the right panel of Figure 16.7. The extrapolated folding rates from the dynamic NMR experiment ($k_f{}^0 = 1490 \pm 370\ s^{-1}$ and $k_u{}^0 = 16 \pm 3\ s^{-1}$) correspond nicely to the rates derived from the stopped-flow fluorescence experiments. The Tanford factors $\beta_T = m_f/(m_f + m_u)$ obtained from the linear slopes of log k_f and log k_u versus urea concentration (Fig-

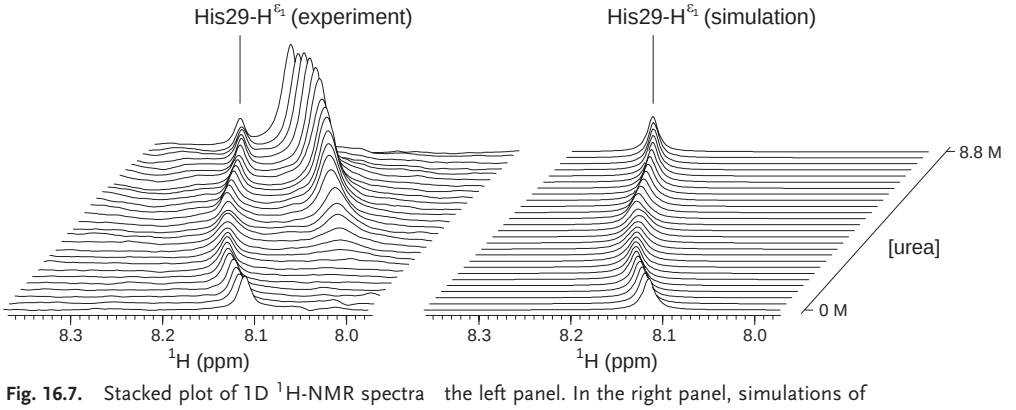

Fig. 16.7. Stacked plot of 1D ^1H-NMR spectra of a complete urea-induced unfolding transition of CspB from *B. subtilis* in ^2H_2O at 25 °C. Experimental 1D spectra of the His29$^{\varepsilon 1}$ resonance in the low field region is shown in the left panel. In the right panel, simulations of the 1D spectra using the extracted and extrapolated folding rates from the line shape analysis described in Section 16.6.2 at the respective urea concentration are depicted.

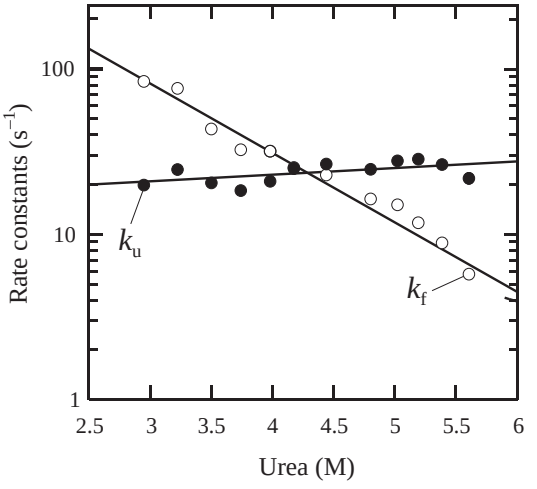

Fig. 16.8. Urea dependence of the folding rates of CspB determined by the line shape analysis approach applied to the 1D ^{1}H-NMR spectra of His29$^{\varepsilon 1}$ in ^2H_2O (Figure 16.7). The logarithm of k_f and k_u in the transition region (between 2.9 ppm and 5.6 ppm) is plotted versus the urea concentration. The linear slope of the continuous lines represents the *m*-value of refolding and unfolding (m_f, m_u) from which the Tanford value β_T is derived with 0.9. Extrapolation to the absence of denaturant reveals folding rates of $k_f{}^0 = 1490 \pm 370\ s^{-1}$ and $k_u{}^0 = 16 \pm 3\ s^{-1}$.

ure 16.8) are 0.9 from both the NMR and fluorescence experiment and indicate that the activated state of unfolding of CspB still resembles the native state in the accessibility to the solvent [103].

The folding and unfolding kinetics of the N-terminal domain of the ribosomal protein L9 have been measured at temperatures between 7 °C and 85 °C and between 0 M and 6 M guanidine deuterium chloride. The joint analysis of stopped-flow fluorescence (between 7 °C and 55 °C) and dynamic NMR data (between 55 °C and 85 °C) revealed thermodynamic parameters of the activated state of folding [104, 105]. The dynamic NMR data were required because the apparent folding rate constant for the latter temperature range was 700–3000 s^{-1} too high for traditional stopped-flow experiments. Following the same lines a small all-helix protein psbd41 could be analyzed by the line shape approach revealing maximum folding rates of 21 600 s^{-1} and maximum unfolding rates of 24 600 s^{-1} [106].

The upper time limit for dynamic NMR to study protein folding reactions are tens of microseconds if the difference in chemical shift of an NMR nuclei between the unfolded and native state is sufficient (at least 500 Hz). Raleigh and coworkers found refolding rates between 3×10^4 s^{-1} and 2×10^5 s^{-1} in a thermal unfolding transition of the villin headpiece, which confirmed experimentally recent all-atoms molecular dynamics calculations to simulate protein folding reactions (see Ref. [107] and references therein). A similar link between theory and experiment was possible for the three-helix bundle-forming B-domain of staphylococcal protein A.

Dynamic NMR analyses revealed folding rate constants of 120 000 s^{-1}, which are in good agreement with predictions from diffusion–collision theory [108].

One limitation of the use of dynamic NMR to study fast protein folding rates is that reliable rates can only be obtained from the central region of denaturant- or temperature-induced unfolding transitions, where at least 15% of both states are populated. The wide linear extrapolation of log k_f to conditions with a maximal population of the native state might miss nonlinear effects such as a ''roll-over'' under strong native conditions. One way to bypass this problem is the use of NMR relaxation data to determine protein folding rates. If the rates of interconversion are on the millisecond-to-microsecond time scale and large chemical shift differences between the states are present, transverse relaxation rates can be sensitive to the presence of the minor conformation with populations as low as 1% [10].

One early application was the direct determination of folding rates of the λ repressor head piece λ_{6-85} under strong native conditions by ^1H transverse relaxation using a 1D Carr-Purcell-Meiboom-Gill (CPMG)-based spin echo pulse sequence (see Section 16.6.4) [12]. The chemical exchange contribution (R_{ex}) to the transverse relaxation rate (R_2) leads to an apparent increase of the latter from which the folding rates can be extracted. At 0 M urea the authors found for λ_{6-85} $k_f = 4000 \pm 340\ s^{-1}$ and $k_u = 32 \pm 3.2\ s^{-1}$, which is in good agreement with the values obtained by extrapolation from the line shape analysis ($k_f = 4900 \pm 600\ s^{-1}$ and $k_u = 30 \pm 4.6\ s^{-1}$).

Most current applications facilitate CPMG-based ^{15}N-relaxation measurements to determine the chemical exchange contribution R_{ex} to R_2. The advantage of this approach is that 2D $^1H-^{15}N$ correlation spectra are used to extract the relaxation rates. Therefore, R_{ex} can be determined on a residue-by-residue basis to discriminate for example local and global unfolding of the peptide chain. The calculation of k_f and k_u from R_{ex} requires some further parameters to be determined beforehand (see Section 16.6.4). Among several approaches to determine the R_{ex} contributions to R_2 (such as an extended Lipari-Szabo approach, $R_{1\rho}$ measurements, or the interference of dipolar $^1H-^{15}N$ and ^{15}N chemical shift anisotropy relaxation), R_2 dispersion experiments are the most popular ones (for an overview and further literature see Ref. [10]). The basic idea is that the R_{ex} contributions to R_2 can be modulated in a CPMG-based sequence by varying the delay time τ_{cp} between consecutive 180° pulses on the ^{15}N nuclei (see Section 16.6.4). The so-called dispersion curve is a plot of R_2 over $1/\tau_{cp}$ (Figure 16.9). At very small $1/\tau_{cp}$ values, the transverse ^{15}N relaxation rate R_2 contains the full contribution of R_{ex} and at high $1/\tau_{cp}$ values no R_{ex} contributions are present. Therefore, the difference between R_2 at the lowest and highest $1/\tau_{cp}$ value provides an estimate for R_{ex}. Fitting of the entire dispersion curve reveals the apparent folding rate k_{ex}, which is the sum of k_f and k_u. If the two-state model is valid and the equilibrium constant under the respective conditions is known explicit values for k_f and k_u can be calculated [10, 12, 13]. R_2 dispersion curves depend on the magnetic field strength [109] and therefore a joint fit of data obtained at various field strengths decreases the errors of the derived dynamic parameters.

Figure 16.9 shows the ^{15}N R_2 dispersion curves for A32 of the cold shock protein

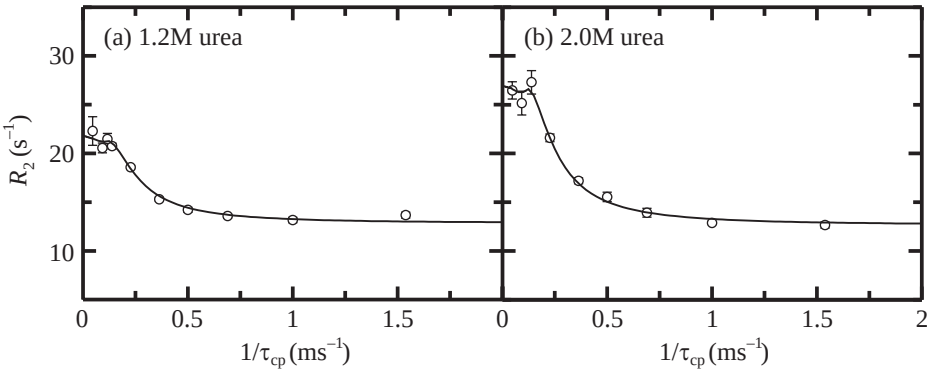

Fig. 16.9. Relaxation dispersion curves of A32 of CspB from *B. subtilis* in 90% H_2O/10% ^2H_2O at 25 °C. Values for $R_2(1/\tau_{cp})$ in the presence of a) 1.2 M and b) 2 M urea at $B_0 = 14.1$ T (60.8 MHz ^{15}N frequency) are depicted. The solid lines represent fits of the data to Eq. (10) with the known difference in ^{15}N chemical shifts between the cross-peaks of A32 in native and unfolded CspB (119 Hz and 122 Hz for 1.2 M and 2 M urea, respectively) as well as the population of the native state (0.96 and 0.89, respectively). It revealed k_f (217 s^{-1} at 1.2 M urea and 124 s^{-1} at 2.0 M urea) and k_u (9.8 s^{-1} at 1.2 M urea and 15 s^{-1} at 2.0 M urea).

CspB at 1.2 M urea and 2.0 M urea with native populations of 0.96 and 0.89, respectively. From a urea transition under NMR detection and from ZZ-exchange spectra [110] the difference in chemical shifts of the A32 backbone amide resonances between the native and unfolded state at the two urea concentrations are known (119 Hz and 122 Hz, respectively). The analysis of the dispersion curves according to the protocol described below (see Section 16.6.4) reveals k_{ex} (227 s^{-1} at 1.2 M urea and 139 s^{-1} at 2.0 M urea) and subsequently k_f (217 s^{-1} at 1.2 M urea and 124 s^{-1} at 2.0 M urea) and k_u (9.8 s^{-1} at 1.2 M urea and 15 s^{-1} at 2.0 M urea) in good agreement with the rates from conventional stopped-flow folding experiments under fluorescence detection [103]. In principle, this kind of NMR relaxation experiment can be used to measure chevron plots of proteins on a residue-by-residue basis, which should be very useful to map the transition state of folding in terms of homogeneity or heterogeneity and to determine the cooperativity within the folding peptide chain.

Several applications of ^{15}N and ^{13}C R_2 dispersion curves have been reported to determine rates of local motions under strong native conditions [109, 111–115]. In this case, two conformations have to be assumed in this region of the protein to gain apparent rates of interconversion. Additionally, the populations of the two conformations and the difference in chemical shifts of the respective nuclei have to be extracted entirely from the NMR relaxation data, which makes this kind of analysis very difficult and might limit the interpretation of the data.

Studies of global two-state folding–unfolding reactions allow an accurate determination of folding rates from R_2 dispersion experiments, because the populations of the native and unfolded state under the respective conditions can be determined

experimentally [13, 15, 116]. Additionally, the differences of their chemical shifts are accessible from independent NMR experiments or can be at least extrapolated (see also Section 16.6.4). For global unfolding reactions all resonances of the protein should show R_2 dispersion curves as long as these differences are above 2 Hz, which makes joint fittings possible. In the case of the N-terminal SH3 domain of the *Drosophila* protein drk, on top of the global unfolding reaction, a local conformational exchange process of the unfolded state could be revealed by a systematic analysis of ^{15}N R_2 dispersion data [15]. For the de novo designed dimeric four-helix bundle protein α_2D, refolding rates of $(4.7 \pm 0.9) \times 10^6$ M^{-1} s^{-1} and unfolding rates of 15 ± 3 s^{-1} could be determined for this bimolecular reaction from ^{13}C R_2 dispersion curves [116]. The $^{13}C^{\alpha}$ chemical shifts for unfolded and folded forms of α_2D indicate that the ensemble of unfolded states includes transiently structured helical conformations.

16.5 Conclusions and Future Directions

NMR spectroscopy is an important, well-established technique in structural studies of protein folding. We have highlighted here in Sections 16.2 and 16.3 the use of NMR to follow protein folding in real-time mode, where the reaction occurs within the NMR spectrometer. The step from 1D real-time NMR to 2D real-time NMR dramatically increased the accessible structural information about protein folding and misfolding reactions. Recently, the first 3D real-time NMR experiment following the refolding of apoplastocyanin, as mentioned above, has been described [35]. The authors were able to follow structure-specific NOEs in a series of 12 3D $^1H-^{15}N$ HSQC-NOESY-HSQC spectra. Local and long-range interactions in the native apoplastocyanin are formed simultaneously, consistent with highly cooperative formation of the native structure. One future direction to increase the dimensionality without increasing the recording time per spectrum might be the use of real-time G-matrix Fourier transform (GFT) NMR spectroscopy [117]. Another recent experimental development that might become fruitful in the near future is the induction of un- and refolding reactions inside the NMR tube by pressure-jump experiments [118]. Here several transitions can be accumulated, because the un- and refolding under high and low pressure, respectively, is reversible and does not require mixing of solutions. All the presented real-time NMR experiments are powerful methods for the characterization of the aggregation-competent conformation of proteins on misfolding pathways [87, 88]. Thus, we expect key information about malfunctioning protein folding reactions and pathological fibril formation to be revealed in the near future. These novel methodologies will further increase the versatility of real-time NMR.

Our studies of the I^{39t} intermediate of S54G/P55N-RNase T1 allow us to explore experimentally parts of the energy landscape for the refolding of this protein. These free energy landscapes calculated from molecular simulations can be put up by simple progress coordinates such as the number of native contacts (Q) and

the radius of gyration [119]. From real-time NOESY experiments we can count the number of native and nonnative NOEs for I^{39t} resulting in a Q value of 0.6. The hydrodynamic radius of I^{39t} was calculated from real-time NMR diffusion experiments to be only 5% above R_h of the native state. The relative Gibbs free energy of I^{39t} was determined from the protection factors of 45 amide protons derived from a competition between refolding and H/D exchange under NMR detection [75]. The intermediate has already gained 40% of the total Gibbs free energy change during refolding of 36.6 kJ mol^{-1}, which is the global minimum of the native state with $Q = 1$. I^{39t} has a well-defined tertiary structure, implying that only a very narrow ensemble of states is present at this very deep local minimum of the funnel. As predicted [45, 120], NMR can provide very detailed contributions combining experiment and theory within the new view of protein folding.

Recent developments have gone one step further in this direction. On the one hand, extremely long molecular dynamics (MD) simulations became possible by using clusters of thousands of computers [121, 122]. On the other hand, dynamic NMR spectroscopy can reveal experimentally folding rates of proteins up to 200 000 s^{-1} [107]. At such high rates, several folding–unfolding interconversions occur during the now accessible length of one MD simulation. Therefore the gap between experiments and simulations has been closed and many exciting new insights into the elementary steps of protein folding can be expected in the near future.

16.6 Experimental Protocols

16.6.1 How to Record and Analyze 1D Real-time NMR Spectra

Refolding experiments are typically started with a dilution of a protein solution in high concentrations of denaturants. Here, the protein solution has to be injected into the refolding buffer, which is already present in the NMR tube (see Figure 16.2). For a rapid change of the pH for starting the folding reaction, the protein is already in the NMR tube and the respective puffer has to be injected. The concentrations and pH values of buffer of the protein sample and of the injected buffer have to be properly adjusted beforehand. Low pH values (< pH 2) can be achieved by titrating the protein sample with HCl or DCl without buffer. Typically, final protein concentrations between 0.5 mM and 1 mM are used.

16.6.1.1 Acquisition

One-dimensional real-time NMR experiments start with the initiation of the protein folding reaction inside the NMR spectrometer. If reactions are followed with time constants of seconds, fast mixing devices are required with dead times below 100 ms [25, 123]. A dead time around 1 s can be achieved with a much simpler device, which needs a pneumatically driven gas-tight syringe (Hamilton, Bonaduz,

Switzerland) working between 8 bar and 10 bar [24]. Dead times between 2 s and 5 s are possible by the same device but manual pulling of the syringe. In the latter case, after the first shot, 50 μL should be sucked back in the syringe and pulled again to gain a homogeneous mixture in the NMR tube. For 2D real-time NMR, this has to be performed during the dummy scans before recording the spectrum. For 1D applications, the shots can occur during the first 1D spectra, which allows the first spectrum to be selected without mixing artifacts. For a fast recovery of the shim system, one shot should be performed in advance with the same buffers and volumes but with a test protein such as commercially available bovine α-lactalbumin or hen lysozyme. After this shot with the NMR tube in the magnet, a proper matching and tuning of the probe head is possible, as well as shimming of the field. For the actual experiment a tube with exactly the same geometry has to be used. Due to the induced field inhomogeneity during the mixing process the lock signal should be electronically increased by using a very high ''lock gain'' to avoid unlocking at the beginning of the experiment. For denaturant-induced refolding experiments, urea should be used in preference to GdmCl if the stability of the protein allows a choice, because the salt properties of GdmCl reduce the sensitivity of NMR coils significantly. For experiments in ^2H_2O, no suppression of the residual resonances of the denaturant (between 6 ppm und 6.7 ppm) is needed if the protons of urea and GdmCl have been properly exchanged against deuterons by several cycles of solving in ^2H_2O and freeze drying. A suppression of these signals can even be avoided for experiments in H_2O, if temperatures above 20 °C are used. The fast chemical exchange between the protons of water and of the denaturant causes an effective saturation transfer and suppression of water is sufficient. At lower temperatures, the water resonance can be suppressed for example by a WATERGATE sequence [124] and the resonance of the denaturant by an off-resonance presaturation during the relaxation delay between scans [38].

16.6.1.2 **Processing**

Conventional 1D NMR data processing can be applied to each of the series of 1D experiments. It is most convenient to run a pseudo 2D experiment by storing the 1D spectra in one serial file and to apply the Fourier transformation of this file only in the F2 dimension. The phase correction should be the same for all 1D spectra and the values for zero order and first order should be determined for the last 1D dataset of the real-time NMR experiment. If possible, only a zero order polynomial function should be used for baseline correction and pivot baseline points should be selected manually in regions where no signals occur during the entire NMR experiment.

16.6.1.3 **Analysis**

After the mixing dead time constant buffer and temperature conditions are reached and the chemical shift position of the resonances of the different protein states are fixed because we are usually working in the slow exchanging regime. Thus, well-resolved resonances can be integrated within identical limits in every 1D spectrum to obtain input data for the kinetic analyses. Each 1D spectrum is a

sum of spectra of the respective protein populations present at the time point of recording. The kinetic information obtained from well-resolved resonances of these states allows a reconstruction of the full 1D spectrum of every state [38, 61]. Usually the final native state has the largest deviations from random coil chemical shifts and well-resolved resonances of aromatic residues or high field shifted CH_2 and CH_3 groups are unique for this state. Secondly, a 1D spectrum with a very good signal-to-noise ratio can be recorded after the reaction has finished. This spectrum has to be scaled according to the refolding kinetics of the native state, which has been determined from the integrals of its well-resolved resonances. This scaled 1D spectrum has to be subtracted from every 1D spectrum of the real-time NMR experiment. This step eliminates all contributions of the native state to the 1D spectra. If a two-state reaction is analyzed, the remaining NMR intensity represents entirely the 1D spectrum of the population from which the reaction has started. Now, these 1D spectra can be averaged to get a decent 1D spectrum of this state. Secondly, the decay kinetics should reveal the same rate constant as the build-up of the native state. Thirdly, this approach allows determination of the result of fast folding events during the dead time of the NMR experiment, which cause a burst of one of these two states [38, 61]. Finally, the 1D contributions of the decaying population can be eliminated in a second subtraction step by scaling the above-mentioned averaged 1D spectrum according to the decay kinetics. If the two-state approximation is valid, no residual NMR intensity should be obtained [38]. It is a sensitive test to add all 1D spectra after the second subtraction step. In the case of RNase T1, this test showed a third protein species populated only by 7% at the beginning of the refolding reaction [61]. Its full 1D spectrum and time course could be determined by analyzing the remaining NMR intensities after the second subtraction step.

16.6.1.4 Analysis of 1D Real-time Diffusion Experiments

The diffusion coefficient of proteins in protein folding reactions can be determined by PFG-SLED NMR experiments [79–82]. If the diffusion delay in this stimulated echo experiments remains constant, Eq. (1) can be fitted to measured NMR intensities $I(g)$ at various gradient strength g.

$$I(g) = A \cdot \exp(-dg^2) \tag{1}$$

The diffusion delay (for example 30 ms) and the variation of the gradient strength (a constant gradient pulse length between 5 ms and 10 ms are common) have to be adjusted before the real-time NMR experiment to make sure that the intensities of the protein signals decay by more than 50% at the highest gradient strength. If dioxan is used as internal standard at 3.6 ppm, a modified version of Eq. (1) has to be used [14] and a dioxan signal should remain for at least half of the varied gradient strengths. A fit of Eq. (1) to the Gaussian decay curves (gradient strength plotted against NMR intensity) reveals d, which is proportional to the diffusion coefficient of the protein. d can be converted into the hydrodynamic radius R_h of the protein by assuming R_h of dioxan of 2.12 Å [14, 82]. From the empiric correlations $R_h =$

$4.75 \times N^{0.29}$ and $R_h = 2.21 \times N^{0.57}$ the hydrodynamic radius determined by NMR diffusion experiments can be estimated from the number of residues N of a globular folded protein and an unfolded peptide chain, respectively [82].

For the determination of the hydrodynamic radius of a transient protein folding intermediate in 1D real-time NMR diffusion experiments, a set of diffusion experiments have to be recorded during the refolding reaction [56, 75]. The gradient strength has to be varied continuously between low and high values typically in 10 steps. For a two-state model, where the intermediate forms in the dead time of the time-resolved NMR experiment, the total intensity of all protein resonances $I(g,t)$ in Eq. (2) depend on the known gradient strength g at every time point t. The relative populations of the intermediate and the native state can be calculated from the known reaction rate constant k. The differences in the relaxation rates between the intermediate and the native state are reflected in the respective amplitudes A_I and A_N.

$$I(g,t) = A_I \cdot \exp(-d_I g^2) \cdot \exp(tk) + A_N \cdot \exp(-d_N g^2) \cdot (1 - \exp(tk)) \quad (2)$$

From d_I the hydrodynamic radius of the folding intermediate can be determined via the internal standard dioxan or from the ratio d_I/d_N the extend of compaction of the intermediate compared to the native state.

16.6.2
How to Extract Folding Rates from 1D Spectra by Line Shape Analysis

For an accurate line shape analysis the system under investigation has to fulfill several requirements. Most important is the existence of a two-state folding process where only folded (N) and unfolded (U) protein molecules are present at equilibrium and in the kinetics at all denaturant concentrations (Eq. (3)). Additionally it is important that the analyzed resonance signals are well resolved throughout the entire equilibrium transition and do not overlap with other resonances. In rare cases, where only few resonances are in a narrow region of the 1D spectra under all conditions, the entire 1D spectrum can be simulated to overcome signal overlap problems [12, 102]. Denaturation of the protein can be achieved either by successively adding chaotropic agents (for example urea, guanidinium chloride) or by increasing the temperature or by a combination of both. A small difference between the resonance frequency of the native and unfolded state (below 100 Hz) allows a determination of folding time constants of tens of milliseconds, whereas a difference above 1500 Hz can cover time constants in a submillisecond range. This difference can be varied for the same system by using different field strengths [107]. Since the exchange between the two states is in the fast exchange regime in respect to the NMR chemical shift time scale ($(k_f + k_u) > \Delta\nu$) only one resonance is detectable over the entire transition with a line shape and resonance frequency that represents the relative populations.

$$N \underset{k_f}{\overset{k_u}{\rightleftharpoons}} U \quad (3)$$

16.6.2.1 Acquisition

NMR spectra of high quality at reasonably high protein concentrations (ensure the absence of aggregation) with a very good signal-to-noise ratio should be obtained with at least 256 transients and 4096 complex points. Small receiver gains should be used to avoid disadvantageous baseline effects. To prevent saturation of ^1H with long spin-lattice relaxation times (t_1) the recycle delay between individual transients should be at least 3 s. This ensures that the magnetization reaches the Boltzmann equilibrium. Using ^2H_2O as solvent for the protein and deuterated buffers should be preferred because a selective suppression of individual resonances (for example from water or denaturants) reduces the quality of the fit by producing resonance intensities, which are not proportional to the protein populations as well as baseline problems. For example the WATERGATE sequence can effectively suppress the solvent signal but has a nonlinear excitation profile at the edges of the spectral window. Therefore, resonances that undergo a change in chemical shift during the unfolding transition are not excited equally throughout the entire transition. If chemically induced denaturation of the protein is achieved by adding urea or guanidinium chloride the exchangeable ^1H are substituted by NMR nonactive ^2H, which reduces the solvent suppression scheme to residual water. Therefore, a long presaturation pulse with a duration of 1–1.5 s on the water signal is sufficient. To minimize the residual water one should also perform several deuteration steps of the denaturation agent and the protein before mixing the sample. Another advantage of ^2H_2O is that the exchangeable ^1H of the protein, namely the amide protons, are not detectable, which greatly reduces spectral overlap in the low field region of the ^1H spectrum (6–11 ppm). Thus, well-resolved resonances of ^1H of the aromatic amino acids Phe, Tyr, Trp, and His can be used to perform the line shape analysis approach. High-field shifted resonances in the native state have the disadvantage that these protons cluster at their random coil positions in the unfolded state.

16.6.2.2 Processing

The NMR data are converted to Felix format or to equivalent processing software such as NMR pipe, XEASY, etc. The data must be dc-offset corrected and zero-filled once in respect to the acquired complex points. No window function should be applied to prevent distortion of the original line shape of the resonance. If a window function is required, only a single-exponential function can be used, which increases the adjustable T^*_{2N} and T^*_{2U}. Individual spectra are separately phase corrected because a correct phasing is essential for the extraction of reliable rates in the further analysis. Baseline correction of each spectrum in the region around the resonance of interest is also performed manually. The order of the polynomial function depends on the quality of the baseline but should be invariant for all spectra. The referencing of the ^1H spectrum to an internal standard like dioxane, DSS, or TSP is recommended. The choice of the standard should depend on the denaturation method (chaotropes, pH, temperature) due to different properties of the respective compound and on the distance between the resonance frequency of the standard and the resonance of interest to avoid unwanted disturbance. To reduce

the amount of data the spectra are truncated to the region of the analyzed signal and the real data points are saved in an ASCII format.

16.6.2.3 **Analysis**

The line shape analysis can be performed with any standard processing software like Sigmaplot (SPSS Inc.), Kaleidagraph (Synergy software), or Grafit (Erithacus software), which is capable of nonlinear least square fitting using the Levenberg-Marquardt algorithm. Especially for this purpose Oas and coworkers designed the ALASKA package, which is based on Mathematica [102]. This package is also very useful for simulating complete aromatic 1D ^{1}H spectra. The formalism to determining folding rates from line shape analysis (Eq. (4)) was introduced by Oas and coworkers [11], and is only applicable when the two-state approximation (Eq. (3)) is fulfilled. In Eq. (4), $I(v)$ represents the intensity as a function of the frequency v and C_0 is a normalization constant, which is proportional to the protein concentration. $I(v)$ also depends on the population of the native and unfolded state (p_N, p_U), the apparent spin–spin relaxation times of the resonance in the respective state under nonexchanging conditions (T^*_{2N}, T^*_{2U}), the resonance frequency of both states (v_N, v_U) and the refolding and unfolding rate constant (k_f, k_u).

$$
\begin{aligned}
I(v) &= \frac{C_0}{P^2+R^2}\cdot\left(P\cdot\left(1+\tau\cdot\left(\frac{p_N}{T^*_{2U}}+\frac{p_U}{T^*_{2N}}\right)\right)+Q\cdot R\right)\\
P &= \tau\cdot\left(\left(\frac{1}{T^*_{2N}T^*_{2U}}\right)-4\pi^2\cdot\Delta v^2+\pi^2\cdot(\delta v)^2\right)+\frac{p_N}{T^*_{2N}}+\frac{p_U}{T^*_{2U}}\\
Q &= \tau\cdot(2\pi\cdot\Delta v-\pi\cdot\delta v\cdot(p_N-p_U))\\
R &= 2\pi\cdot\Delta v\cdot\left(1+\tau\cdot\left(\frac{1}{T^*_{2N}}+\frac{1}{T^*_{2U}}\right)+\pi\cdot\delta v\cdot\tau\cdot\left(\frac{1}{T^*_{2U}}-\frac{1}{T^*_{2N}}\right)\right)\\
&\quad+\pi\cdot\delta v\cdot(p_N-p_U)\\
\Delta v &= (v_N+v_U)/2\quad \delta v=(v_N-v_U)\quad \tau=(k_f-k_u)^{-1}\\
p_N &= k_f\cdot\tau\quad p_U=k_u\cdot\tau
\end{aligned}
\tag{4}
$$

In the following, the line shape analysis procedure is described step by step.

1. The apparent transverse relaxation rates of the resonance in the native and unfolded state (T^*_{2N}, T^*_{2U}) have to be determined. Therefore, the signal of the fully native or unfolded protein, respectively, is simulated with a function corresponding to an absorptive Lorentzian signal ($I(v)=C_0R_2/\{R_2^2+(v_i-v)\}$) where $R_2=1/T_2^*$ and v_i represents the chemical shift of the signal.
2. The dependence of the resonance frequency of the signal of the native and the unfolded state from the denaturant concentration or the temperature is also required. Thus, the resonance frequency of the respective signal in the spectra under nonexchanging conditions (that is in the beginning of the baselines of the transition under strong native and strong nonnative conditions) is measured.

Assuming a linear dependence of the resonance frequency on the denaturant concentration or the temperature the actual resonance frequency of the signal of the native and the unfolded state (v_N, v_U) under all conditions can be calculated by a linear extrapolation method.

3. With the determined parameters ($T_{2N}^*, T_{2U}^*, v_N, v_U$) the simulation of the resonance signals in the transition region with Eq. (4) reveals the normalization constant C_0 and the folding rates (k_f, k_u) for every individual 1D spectrum (Figures 16.7 and 16.8). Most reliable results are obtained if the population of both states is above 15%.
4. The error estimated by the Levenberg-Marquardt algorithm is not very meaningful. Therefore usually a systematic variation of k_f and k_u around their fitted values gives a much more realistic error. A comparison of the residuals between the calculated and experimental line shapes reveals errors typically around 10% [11, 104, 107].

16.6.3 How to Extract Folding Rates from 2D Real-time NMR Spectra

In principle, there are two ways to determine folding rates by 2D real-time NMR. First, a series of individual 2D NMR experiments can be recorded during the folding reaction, which reveals cross-peaks with increasing or decreasing intensities depending on the respective state. This method is useful if the folding reaction is slow enough to record a set of reasonably good 2D spectra. The processing of these spectra follows standard protocols. Individual cross-peaks can be integrated in every 2D spectrum or its maximum can be used to determine the folding rates [75]. The second method to obtain folding rates from 2D real-time NMR spectra is, in terms of acquisition, even more straightforward but processing and analysis are more complex. Technically, only a single 2D NMR spectrum is recorded during the entire refolding reaction, which has been initiated by a rapid mixing device (see Section 16.6.1). This has the advantage that significantly more transients and t_1-increments can be recorded compared with the first method and therefore the signal-to-noise ratio and spectral resolution in the indirect dimension is much higher. As discussed in Section 16.3, the folding reaction leads to different line shapes and intensities of cross-peaks assigned to the respective species (Figure 16.5 and Figure 16.6). Comparing the kinetic experiment with a reference experiment under identical conditions after the reaction is finished reveals three different read-outs. Cross-peaks of the starting conformation (for example the intermediate or unfolded state) lose intensity during the reaction and exhibit line broadening. Cross-peaks of the emerging final state (for example the native state) show increasing intensities accompanied by characteristic line shape in the indirect dimension. Finally, cross-peaks with invariant chemical shifts in the starting and the final conformation depict constant intensity and narrow line widths. The assignment of individual cross-peaks to the respective species can be achieved by using the different line shape, which works nicely for 2D $^1H-^{15}N$ HSQC spectra (Figure 16.6). In the case of 2D NOESY or 2D TOCSY spectra this approach becomes very time consum-

ing because hundreds of cross-peaks have to be analyzed and signal overlap can alter the expected theoretical line shapes. A more straightforward procedure is to subtract the kinetic experiment from the reference experiment, revealing positive or negative intensities for the final or starting state, respectively. Cross-peaks with invariant chemical shifts show the same intensity in both experiments and cancel out. A mathematical description is provided below. The power of this method was shown for 2D ^{1}H-^{1}H NOESY [61] and 2D ^{1}H-^{15}N HSQC experiments [54] and can theoretically be extended to any other two- or three-dimensional NMR experiment.

16.6.3.1 Acquisition

Basically, one single 2D or 3D NMR experiment is recorded after initiation of the refolding reaction depending on the time constant of the folding reaction. Since the folding kinetics modulates the FIDs of the indirect dimension a reasonable number of t_1-increments should be recorded to achieve high spectral resolution. The dead time of the experiment can be greatly reduced by using a mixing device (see Section 16.6.1) because tuning and matching of the probe and shimming as well as temperature calibration can be performed before starting the reaction. No modifications of standard pulse programs are needed.

16.6.3.2 Processing

The NMR data can be converted and analyzed by any standard processing software. The FIDs in both dimensions should be zero-filled once and an apodization in the time domain applied. Only single-exponential window functions can be used if a quantitative line shape analysis is to be performed to extract protein folding rates.

16.6.3.3 Analysis

The assignment of each cross-peak to the respective state can be achieved by analyzing the different line shapes. For a more straightforward assignment of the cross-peaks a simple subtraction method can be used. The complex FID for a signal with a frequency offset v' and an apparent transversal relaxation rate constant R_2^* is given by Eq. (5).

$$\mathrm{F}(t) = A \cdot \exp\{2\pi \mathrm{i} v' t) \cdot \exp\{-R_2^* t\} \tag{5}$$

As discussed before, three cases of modulation of the FID in the indirect dimension are possible and are defined by Eq. (6) with the assumption that k is the rate constant of a two-state transition.

$$\begin{aligned} \mathrm{G}^1(t) &= \exp(-kt\} \\ \mathrm{G}^2(t) &= 1 - \exp(-kt\} \\ \mathrm{G}^3(t) &= 1 \end{aligned} \tag{6}$$

Fourier transformation of the respective products $\mathrm{S}^{\mathrm{x}} = \mathrm{G}^{\mathrm{x}}(t)\mathrm{F}(t)$ yield the following real parts in the frequency domain (Eq. (7)).

$$\mathrm{Re}\{\mathrm{FT}[\mathrm{S}^1(t)]\} = A \cdot \left[\frac{R_2^* + k}{(R_2^* + k)^2 + 4\pi^2(\nu - \nu')^2}\right]$$

$$\mathrm{Re}\{\mathrm{FT}[\mathrm{S}^2(t)]\} = A \cdot \left[\frac{\frac{1}{R_2^*}}{1 + \left(\frac{1}{R_2^*}\right)^2 \cdot 4\pi^2(\nu - \nu')^2} - \frac{R_2^* + k}{(R_2^* + k)^2 + 4\pi^2(\nu - \nu')^2}\right]$$

$$\mathrm{Re}\{\mathrm{FT}[\mathrm{S}^3(t)]\} = A \cdot \left[\frac{\frac{1}{R_2^*}}{1 + \left(\frac{1}{R_2^*}\right)^2 \cdot 4\pi^2(\nu - \nu')^2}\right] \tag{7}$$

Subtracting the three equations (Eq. (7)) from the reference experiment of the fully native protein reveals Eq. (8), which corresponds to the three different read-outs discussed above.

$$\mathrm{Re}\{\mathrm{FT}[\mathrm{S}^1(t)]\} = -A \cdot \left[\frac{R_2^* + k}{(R_2^* + k)^2 + 4\pi^2(\nu - \nu')^2}\right]$$

$$\mathrm{Re}\{\mathrm{FT}[\mathrm{S}^2(t)]\} = A \cdot \left[\frac{R_2^* + k}{(R_2^* + k)^2 + 4\pi^2(\nu - \nu')^2}\right]$$

$$\mathrm{Re}\{\mathrm{FT}[\mathrm{S}^3(t)]\} = 0 \tag{8}$$

The refolding rate is obtained from the 2D NMR spectra (for example ^{1}H-^{1}H NOESY, ^{1}H-^{15}N HSQC) by a two-step line shape analysis procedure. For this approach the 1D spectrum in the indirect dimension has to be extracted from the two-dimensional matrix of the kinetic and reference experiment, respectively. In the first step, the resonance signal of the reference spectrum is fitted with the real part of the Fourier transformed function $\mathrm{S}^3(t)$ of Eq. (7), which yields the amplitude, R_2^* and ν' of the native signal under equilibrium conditions (Figure 16.10a). In the second step, the resonance signal of the native state in the kinetic experiment is fitted by $\mathrm{Re}\{\mathrm{FT}[\mathrm{S}^2(t)]\}$ of Eq. (7) using the determined R_2^* and ν' as fixed parameters (Figure 16.10b). The thus derived apparent folding rate k has to be further scaled because the time scale of the acquisition of the indirect dimension ($t_{\mathrm{dwell}} = 1/2SW_{\mathrm{indirect}}$ with SW_{indirect} as the spectral width in the incremented dimension) and the "real" time resolution between two points in the FID of the indirect dimension (that is the explicit time between two sequential t_1-increments, $t_{1\mathrm{D}}$, which is the total length of the refolding experiment divided by the number t_1-increments) differ. The actual refolding rate k_{f} can therefore be calculated by Eq. (9):

$$k_{\mathrm{f}} = k \cdot \frac{k_{\mathrm{dwell}}}{k_{1\mathrm{D}}} \tag{9}$$

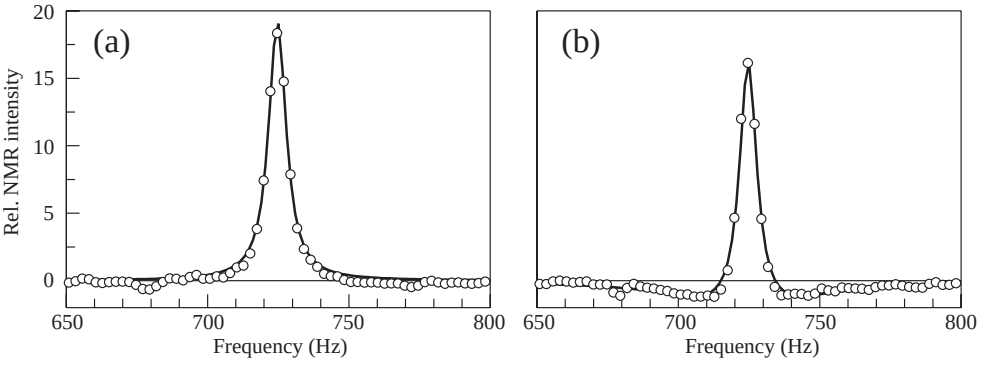

Fig. 16.10. Line shape analysis of A19 from S54G/P55N-RNase T1. The folding reaction at 15 °C was followed by 2D ^{1}H-^{15}N NMR correlation spectroscopy. a) The ^{15}N 1D NMR spectrum of A19 in the native state (trace along in the indirect F1 dimension from the reference spectrum (Figure 16.6b)). The continuous line represents the fit of the data to Re{FT[$S^3(t)$]} of Eq. (7) (see Section 16.6.3), which reveals R_2^* and ν' with 23.4 s^{-1} and 725 Hz, respectively. b) The equivalent ^{15}N 1D NMR spectrum of A19 from the kinetic ^{1}H-^{15}N HSQC experiment (Figure 16.6a). The resonance shows the characteristic line shape with the two flanking negative components. Fitting the data to Re{FT[$S^2(t)$]} of Eq. (7) with constant R_2^* and ν' from (a) reveals the continuous line and a rate k of 130.6 s^{-1}. The actual folding rate k_f is then calculated by Eq. (9) and yields 4.3×10^{-4} s^{-1}.

An alternative way to determine the rate constant k of folding would be a simulation of cross-sections of the resonances of individual residues along the indirect F1 dimension [54, 125]. For this purpose the cross-sections from the kinetic 2D spectrum can be simulated by multiplying the respective cross-section from the reference spectrum with a single-exponential function prior to the second Fourier transformation of the 2D data set.

16.6.4
How to Analyze Heteronuclear NMR Relaxation and Exchange Data

As described in the preceding sections, the determination of explicit un- and refolding rates requires a protein that follows a two-state folding model. One of the first applications of R_2 relaxation dispersion curves to study fast folding reactions was performed by homonuclear 1D ^{1}H NMR spectroscopy [12]. To overcome the limitations of 1D NMR like severe spectral overlap, more recently heteronuclear 2D relaxation methods have been established [10], which provide many site-specific probes. Therefore, a further requirement is to enrich the protein under investigation with the NMR active heteronuclei ^{15}N and/or ^{13}C.

One common approach is the measurement of so-called ^{15}N R_2 dispersion curves. Despite the high spectral resolution of the 2D ^{1}H-^{15}N correlation spectra used to determine the R_2 relaxation rates there are some further advantages of this method in respect to the above-mentioned 1D experiments (for example line shape analysis, see Section 16.6.2). First, the determination of the R_2 rates is

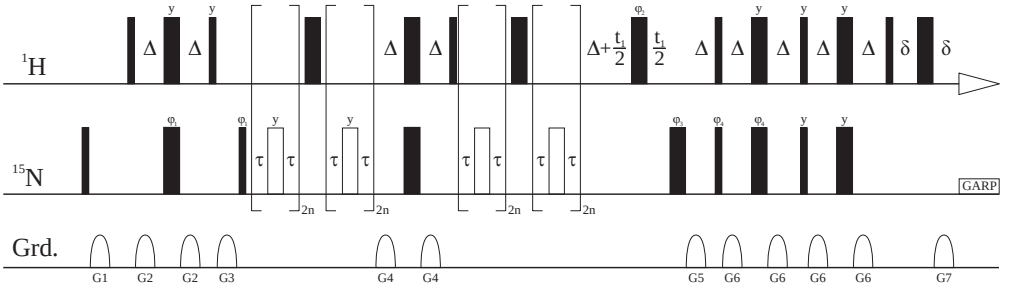

Fig. 16.11. Pulse sequence of a relaxation-compensated ^{15}N CPMG experiment for the determination of conformational and chemical exchange. Variation of τ ($\tau = \tau_{cp}/2$) and a successive determination of R_2 for each τ_{cp} reveals the so called R_2 relaxation dispersion curves (Figure 16.9). Narrow and wide black bars depict 90° and 180° pulses, respectively. The wide white bars represent 180° ^{15}N pulses in the spin echo sequence. All pulses are *x*-phase unless indicated otherwise and gradients are shown as half-ellipsoids. Spectra for initial intensities are obtained by omitting the sequences in brackets. For more experimental details and theoretical description see Ref. [132].

straightforward and robust, because instrument effects such as magnetic field inhomogeneities might introduce significant errors in 1D line shape analyses. More important, it is possible to extract folding rates down to a population of one state of about 1%. The major drawback of this method is the time-consuming acquisition. R_2 rates are usually measured with pulse sequences based on the Carr-Purcell-Meiboom-Gill (CPMG) spin echo element ($[\tau - 180° - \tau]_n$) with $\tau_{cp} = 2 \times \tau$ [126, 127]. An example of a useful pulse sequence and further description is provided in Figure 16.11. Principally, the spin echo element contains a single 180° pulse on the nuclei of interest, which is separated by two equivalent delays $\tau = \tau_{cp}/2$. Contributions from chemical exchange (R_{ex}) to R_2 can be effectively eliminated by the CPMG sequence if the exchange process is on a slower time scale in respect to the delay time τ_{cp}. For very short τ_{cp} values (that is the fast pulsing limit) only very fast processes on a picosecond to nanosecond time scale contribute to the apparent R_2 value, which is R_2^0. However, if τ_{cp} is made long enough that multiple folding/unfolding events occur during τ_{cp}, chemical exchange R_{ex} contributes to R_2: $R_2 = R_2^0 + R_{ex}$. Therefore, a dispersion of R_2 regarding R_{ex} can be generated by a variation of τ_{cp}.

16.6.4.1 Acquisition

High-quality heteronuclear 2D NMR spectra can be recorded with pulse sequences as shown in Figure 16.11. The recycle delay between individual transients should be as long as possible and at least 1 s. For each 2D ^{1}H-^{15}N spectrum at least 128 t_1-increments in the indirect dimension should be acquired with 16–32 transients for each t_1-increment depending on the protein concentration. The relaxation delay using a fixed spin echo delay τ_{cp} has to be varied by multiple repetition of the spin echo sequence. This relaxation delay (calculated by $4 \times (2n \times (2\tau + \tau_{180(N)})) + 2 \times \Delta + \tau_{180(N)} + \tau_{90(H)}$ according to Figure 16.11, where $\tau_{180(N)}$ and $\tau_{90(H)}$ denote

the length of the 180° pulse on ^{15}N and the 90° pulse on ^{1}H, respectively) varies typically between 10 ms and 250 ms. The decay of the intensity for an accurate determination of R_2 should be defined by at least six different relaxation delays with a minimal loss of 80% of the initial intensity.

16.6.4.2 Processing

The 2D NMR data can be processed with any available processing software such as Felix, NMR pipe, XEASY, etc. and follows closely standard protocols. The FID is zero-filled once in both dimensions and any window function can be applied before Fourier transformation. Normally phase correction in the ^{1}H dimension remains constant over sequentially acquired data sets if the pulse program is not changed. Phase correction in the indirect dimension should be avoided by properly adjusting the first t_1-increment. The spectral resolution in the indirect dimension can be enhanced by linear prediction methods especially if only 128 t_1-increments are recorded. A baseline correction can also be performed. However, most important is that all spectra are processed identically to minimize uncertainties of the extracted peak intensities.

16.6.4.3 Analysis

For the determination of the R_2 rates for every τ_{cp} value the fitting of the intensity decay curve is applicable with a single exponential function without offset ($I = A\exp(-R_2 t)$) and can be performed using any standard software. However, the programs of Palmer and coworkers such as CURVEFIT and for further analysis CPMGfit (http://cpmcnet.columbia.edu/dept/gsas/biochem/labs/palmer/software/modelfree.html) are strongly recommended because they are specially designed for this purposes and due to the extensive error analysis by various methods such as Monte-Carlo or jack-knife simulations [128, 129]. The derived R_2 values are plotted on the ordinate of the R_2 dispersion curve (see Figure 16.9). The exchange rate k_{ex} and the chemical exchange contribution R_{ex} to R_2 can be derived by fitting Eq. (10) to the R_2 dispersion curves [10, 130]. This formalism represents the general phenomenological description of R_2 of site N in Eq. (3), which is independent of the exchange regime (slow, intermediate or fast in respect of the NMR chemical shift time scale) as well as the present population ratio.

$$R_2(1/\tau_{cp}) = \frac{1}{2}\left(R_{2N} + R_{2U} + k_{ex} - \frac{1}{\tau_{cp}}\cosh^{-1}[D_+\cosh(\eta_+) - D_-\cosh(\eta_-)]\right) \tag{10}$$

with

$$D_\pm = \frac{1}{2}\left[\pm 1 + \frac{\psi + 2\Delta\omega^2}{\sqrt{\psi^2 + \zeta^2}}\right]; \quad \eta_\pm = \frac{\tau_{cp}}{\sqrt{2}}\sqrt{\pm\psi + \sqrt{\psi^2 + \zeta^2}}$$

$$\psi = (R_{2N} - R_{2U} - p_N k_{ex} + p_U k_{ex})^2 - \Delta\omega^2 + 4 p_N p_U k_{ex}^2$$

$$\zeta = 2\Delta\omega \cdot (R_{2N} - R_{2U} - p_N k_{ex} + p_U k_{ex})$$

$$R_{ex} = \Delta R_2(0,\infty) = R_2(1/\tau_{cp} \to 0) - R_2(1/\tau_{cp} \to \infty)$$
$$= \frac{1}{2}\left\{\sqrt{\psi + \Delta\omega^2} - \frac{1}{\sqrt{2}}\sqrt{\psi + \sqrt{\psi^2 + \zeta^2}}\right\}$$

where $\Delta\omega$ is the difference of the ^{15}N chemical shift of the cross-peak between the native and the unfolded state ($\Delta\omega = 2\pi\Delta\nu$ with $\Delta\nu$ given in Hz), p_N and p_U the population of the respective state and $\tau_{cp} = 2 \cdot \tau$ as well as $k_{ex} = k_f + k_u$. $\Delta\omega$ defines the exchange regime for a given k_{ex} ($k_{ex} < \Delta\omega$: slow exchange; $k_{ex} \approx \Delta\omega$: intermediate exchange; $k_{ex} > \Delta\omega$: fast exchange). A less complex approximation was proposed by Ishima and Torchia, which is valid for all time scales if $p_N \gg p_U$ (Eq. (11)).

$$R_2(1/\tau_{cp}) = R_2(1/\tau_{cp} \to \infty) + p_N p_U \Delta\omega^2 k_{ex}/[k_{ex}^2 + (p_N^2\Delta\omega^4 + 144/\tau_{ex}^4)^{1/2}] \quad (11)$$

This expression is especially helpful to estimate the expected contributions of R_{ex} to R_2 for a protein folding system, where kinetic rates and populations are already available. If R_{ex} is smaller than 2 Hz, dispersion curves become very difficult to analyze. If R_{ex} exceeds significantly 2 Hz, errors for the folding rates can drop below 10%.

The precise determination of $\Delta\omega$ is essential for the reliability of the extracted parameters, which could be achieved by recording for example a denaturant-induced unfolding transition followed by a series of ^1H-^{15}N HSQC spectra. Therein, nuclei in the slow exchange regime depict a cross-peak for each state. Unfolding transition data have the advantage that the dependence of the chemical shifts from the concentration of the denaturant can be determined. The same holds for temperature-induced transitions. A straightforward assignment of the unfolded state can be performed by correlating the cross-peaks of the native and the unfolded state via the respective exchange cross-peaks in a 2D ZZ-exchange spectrum [110]. However, only a fraction of amide protons can be assigned by this method due to severe spectral overlap of the cross-peaks of the unfolded state with the exchange cross-peaks or by exhibiting fast or intermediate exchange phenomena (such as averaged chemical shifts or extreme line broadening). If the chemical exchange rates are below 0.1 s^{-1}, no exchange cross-peaks in a 2D ZZ-exchange spectrum are observed, which requires a time-consuming assignment of the unfolded state by other methods [131].

In many cases, $\Delta\omega$ cannot be determined directly. In this case, $\Delta\omega$ has to become an adjustable parameter during the fitting procedure. If dispersion curves at two magnetic fields are available, reliable interconversion rates can be extracted, if the populations are known or if the populations can be estimated within certain limits. Here, typical errors of the rates are around 30%. A global fit of all dispersion curves might help to estimate the populations [115]. Extremely good dispersion curves are required if the populations have to be adjusted as well during the fit and an iterative scheme has to be developed to successively reduce the lower and upper limits for the respective parameters.

Acknowledgments

We thank F. X. Schmid and C. M. Dobson for many stimulating discussions about protein folding and real-time NMR. This research was supported by grants from the Deutsche Forschungsgemeinschaft (Ba 1821/2-1; Ba 1821/3-1), the ARC program of the Deutscher Akademischer Austauschdienst, the INTAS-2001 program, and the SON UMR in Utrecht (HPRI-CT-2001-00172).

References

1 Wagner, G., Wüthrich, K. *J. Mol. Biol.* 1982, *160*, 343–361.
2 Wand, A. J., Roder, H., Englander, S. W. *Biochemistry* 1986, *25*, 1107–1114.
3 Englander, S. W., Sosnick, T. R., Englander, J. J., Mayne, L. *Curr. Opin. Struct. Biol.* 1996, *6*, 18–23.
4 Bai, Y. W., Sosnick, T. R., Mayne, L., Englander, S. W. *Science* 1995, *269*, 192–197.
5 Radford, S. E., Dobson, C. M., Evans, P. A. *Nature* 1992, *358*, 302–307.
6 Udgaonkar, J. B., Baldwin, R. L. *Nature* 1988, *335*, 694–699.
7 Roder, H., Elöve, G. A., Englander, S. W. *Nature* 1988, *335*, 700–704.
8 Dobson, C. M., Evans, P. A. *Biochemistry* 1984, *23*, 4267–4270.
9 Roder, H. *Methods Enzymol.* 1989, *176*, 446–473.
10 Palmer, A. G., III, Kroenke, C. D., Loria, J. P. *Methods Enzymol.* 2001, *339*, 204–238.
11 Huang, G. S., Oas, T. G. *Proc. Natl Acad. Sci. U.S.A.* 1995, *92*, 6878–6882.
12 Burton, R. E., Huang, G. S., Daugherty, M. A., Fullbright, P. W., Oas, T. G. *J. Mol. Biol.* 1996, *263*, 311–322.
13 Vugmeyster, L., Kroenke, C. D., Picart, F., Palmer, A. G., III, Raleigh, D. P. *J. Am. Chem. Soc.* 2000, *122*, 5387–5388.
14 Zeeb, M., Jacob, M. H., Schindler, T., Balbach, J. *J. Biomol. NMR* 2003, *27*, 221–234.
15 Tollinger, M., Skrynnikov, N. R., Mulder, F. A., Forman-Kay, J. D., Kay, L. E. *J. Am. Chem. Soc.* 2001, *123*, 11341–11352.
16 Myers, J. K., Oas, T. G. *Annu. Rev. Biochem.* 2002, *71*, 783–815.
17 Meiler, J., Peti, W., Griesinger, C. *J. Am. Chem. Soc.* 2003, *125*, 8072–8073.
18 Meiler, J., Prompers, J. J., Peti, W., Griesinger, C., Brüschweiler, R. *J. Am. Chem. Soc.* 2001, *123*, 6098–6107.
19 Grimaldi, J., Baldo, J., McMurray, C., Sykes, B. D. *J. Am. Chem. Soc.* 1972, *94*, 7641–7645.
20 Grimaldi, J. J., Sykes, B. D. *J. Am. Chem. Soc.* 1975, *97*, 273–276.
21 Kühne, R. O., Schaffhauser, T., Wokaun, A., Ernst, R. R. *J. Magn. Reson.* 1979, *35*, 39–67.
22 McGee, W. A., Parkhurst, L. J. *Anal. Biochem.* 1990, *189*, 267–273.
23 Frieden, C., Hoeltzli, S. D., Ropson, I. J. *Protein Sci.* 1993, *2*, 2007–2014.
24 van Nuland, N. A. J., Forge, V., Balbach, J., Dobson, C. M. *Acc. Chem. Res.* 1998, *31*, 773–780.
25 Mok, K. H., Nagashima, T., Day, I. J., Jones, J. A., Jones, C. J., Dobson, C. M., Hore, P. J. *J. Am. Chem. Soc.* 2003, *125*, 12484–12492.
26 Hoeltzli, S. D., Frieden, C. *Biochemistry* 1996, *35*, 16843–16851.
27 Hoeltzli, S. D., Frieden, C. *Biochemistry* 1998, *37*, 387–398.
28 Bann, J. G., Pinkner, J., Hultgren, S. J., Frieden, C. *Proc. Natl Acad. Sci. USA* 2002, *99*, 709–714.
29 Balbach, J., Schmid, F. X. In *Mechanisms of Protein Folding*; 2nd edn; Pain, R. H., Ed.; Oxford

University Press: Oxford, 2000; pp 212–237.
30 Blum, A. D., Smallcombe, S. H., Baldwin, R. L. *J. Mol. Biol.* 1978, *118*, 305–316.
31 Kiefhaber, T., Labhardt, A. M., Baldwin, R. L. *Nature* 1995, *375*, 513–515.
32 Koide, S., Dyson, H. J., Wright, P. E. *Biochemistry* 1993, *32*, 12299–12310.
33 Wishart, D. S., Sykes, B. D., Richards, F. M. *Biochim. Biophys. Acta* 1993, *1164*, 36–46.
34 Liu, X. Y., Siegel, D. L., Fan, P., Brodsky, B., Baum, J. *Biochemistry* 1996, *35*, 4306–4313.
35 Mizuguchi, M., Kroon, G. J., Wright, P. E., Dyson, H. J. *J. Mol. Biol.* 2003, *328*, 1161–1171.
36 Ropson, I. J., Frieden, C. *Proc. Natl Acad. Sci. USA* 1992, *89*, 7222–7226.
37 Russell, B. S., Melenkivitz, R., Bren, K. L. *Proc. Natl Acad. Sci. USA* 2000, *97*, 8312–8317.
38 Zeeb, M., Rösner, H., Zeslawski, W., Canet, D., Holak, T. A., Balbach, J. *J. Mol. Biol.* 2002, *315*, 447–457.
39 Kuwajima, K., Arai, M. In *Mechanisms of Protein Folding*; 2nd edn; Pain, R. H., Ed.; University Press: Oxford, 2000; pp 138–174.
40 Balbach, J., Forge, V., van Nuland, N. A. J., Winder, S. L., Hore, P. J., Dobson, C. M. *Nat. Struct. Biol.* 1995, *2*, 865–870.
41 Englander, S. W., Mayne, L. *Annu. Rev. Biophys. Biomol. Struc.* 1992, *21*, 243–265.
42 Baldwin, R. L. *Curr. Opin. Struct. Biol.* 1993, *3*, 84–91.
43 Shortle, D. R. *Curr. Opin. Struct. Biol.* 1996, *6*, 24–30.
44 Dyson, H. J., Wright, P. E. *Annu. Rev. Phys. Chem.* 1996, *47*, 369–395.
45 Onuchic, J. N. *Proc. Natl Acad. Sci. USA* 1997, *94*, 7129–7131.
46 Clarke, A. R., Waltho, J. P. *Curr. Opin. Biotechnol.* 1997, *8*, 400–410.
47 Dyson, H. J., Wright, P. E. *Nat. Struct. Biol.* 1998, *5 Suppl.*, 499–503.
48 Barbar, E. *Biopolymers* 1999, *51*, 191–207.
49 Baum, J., Brodsky, B. *Curr. Opin. Struct. Biol.* 1999, *9*, 122–128.
50 Baum, J., Brodsky, B. *Fold Des.* 1997, *2*, R53–60.
51 Dobson, C. M., Hore, P. J. *Nat. Struct. Biol.* 1998, *5 Suppl.*, 504–507.
52 Ikeguchi, M., Kuwajima, K., Mitani, M., Sugai, S. *Biochemistry* 1986, *25*, 6965–6972.
53 Kuwajima, K. *FASEB J.* 1996, *10*, 102–109.
54 Balbach, J., Forge, V., Lau, W. S., van Nuland, N. A. J., Brew, K., Dobson, C. M. *Science* 1996, *274*, 1161–1163.
55 Balbach, J., Forge, V., Lau, W. S., Jones, J. A., van Nuland, N. A., Dobson, C. M. *Proc. Natl Acad. Sci. USA* 1997, *94*, 7182–7185.
56 Balbach, J. *J. Am. Chem. Soc.* 2000, *122*, 5887–5888.
57 Forge, V., Wijesingha, R. T., Balbach, J., Brew, K., Robinson, C. V., Redfield, C., Dobson, C. M. *J. Mol. Biol.* 1999, *288*, 673–688.
58 Kühn, T., Schwalbe, H. *J. Am. Chem. Soc.* 2000, *122*, 6169–6174.
59 Maeda, K., Lyon, C. E., Lopez, J. J., Cemazar, M., Dobson, C. M., Hore, P. J. *J. Biomol. NMR* 2000, *16*, 235–244.
60 Wirmer, S. L., Kühne, T., Schwalbe, H. *Angew. Chem* 2001, *113*, 4378–4381.
61 Balbach, J., Steegborn, C., Schindler, T., Schmid, F. X. *J. Mol. Biol.* 1999, *285*, 829–842.
62 van Nuland, N. A. J., Meijberg, W., Warner, J., Forge, V., Scheek, R. M., Robillard, G. T., Dobson, C. M. *Biochemistry* 1998, *37*, 622–637.
63 Guijarro, J. I., Morton, C. J., Plaxco, K. W., Campbell, I. D., Dobson, C. M. *J. Mol. Biol.* 1998, *276*, 657–667.
64 van Nuland, N. A. J., Chiti, F., Taddei, N., Raugei, G., Ramponi, G., Dobson, C. M. *J. Mol. Biol.* 1998, *283*, 883–891.
65 Laurents, D. V., Baldwin, R. L. *Biochemistry* 1997, *36*, 1496–1504.
66 Hore, P. J., Winder, S. L., Roberts, C. H., Dobson, C. M. *J. Am. Chem. Soc.* 1997, *119*, 5049–5050.

67 Killick, T. R., Freund, S. M., Fersht, A. R. *FEBS Lett.* 1998, *423*, 110–112.

68 Killick, T. R., Freund, S. M., Fersht, A. R. *Prot. Sci.* 1999, *8*, 1286–1291.

69 Bhuyan, A. K., Udgaonkar, J. B. *Biochemistry* 1999, *38*, 9158–9168.

70 Kautz, R. A., Fox, R. O. *Protein Sci* 1993, *2*, 851–858.

71 Narayanan, S., Bosl, B., Walter, S., Reif, B. *Proc. Natl Acad. Sci. USA* 2003, *100*, 9286–9291.

72 Panchal, S. C., Bhavesh, N. S., Hosur, R. V. *FEBS Lett.* 2001, *497*, 59–64.

73 Panchal, S. C., Hosur, R. V. *Biochem. Biophys. Res. Commun.* 2000, *269*, 387–392.

74 Reimer, U., Scherer, G., Drewello, M., Kruber, S., Schutkowski, M., Fischer, G. *J. Mol. Biol.* 1998, *279*, 449–460.

75 Steegborn, C., Schneider-Hassloff, H., Zeeb, M., Balbach, J. *Biochemistry* 2000, *39*, 7910–7919.

76 Yaffe, M. B., Schutkowski, M., Shen, M., Zhou, X. Z., Stukenberg, P. T., Rahfeld, J. U., Xu, J., Kuang, J., Kirschner, M. W., Fischer, G., Cantley, L. C., Lu, K. P. *Science* 1997, *278*, 1957–1960.

77 Brazin, K. N., Mallis, R. J., Fulton, D. B., Andreotti, A. H. *Proc. Natl Acad. Sci. USA* 2002, *99*, 1899–1904.

78 Mallis, R. J., Brazin, K. N., Fulton, D. B., Andreotti, A. H. *Nat. Struct. Biol.* 2002, *9*, 900–905.

79 Stejskal, E. O., Tanner, J. E. *J. Chem. Phys.* 1965, *42*, 288–292.

80 Gibbs, S. J., Johnson, C. S., Jr. *J. Magn. Reson.* 1991, *93*, 395–402.

81 Jones, J. A., Wilkins, D. K., Smith, L. J., Dobson, C. M. *J. Biomol. NMR* 1997, *10*, 199–203.

82 Wilkins, D. K., Grimshaw, S. B., Receveur, V., Dobson, C. M., Jones, J. A., Smith, L. J. *Biochemistry* 1999, *38*, 16424–16431.

83 Dobson, C. M. *Trends Biochem. Sci.* 1999, *24*, 329–332.

84 Raso, S. W., King, J. In *Mechanisms of Protein Folding*; 2nd edn; Pain, R. H., Ed.; Oxford University Press: Oxford, 2000; pp 406–428.

85 Lindner, R. A., Kapur, A., Carver, J. A. *J. Biol. Chem.* 1997, *272*, 27722–27729.

86 Poon, S., Treweek, T. M., Wilson, M. R., Easterbrook-Smith, S. B., Carver, J. A. *FEBS Lett.* 2002, *513*, 259–266.

87 Carver, J. A., Lindner, R. A., Lyon, C., Canet, D., Hernandez, H., Dobson, C. M., Redfield, C. *J. Mol. Biol* 2002, *318*, 815–827.

88 Alexandrescu, A. T., Rathgeb-Szabo, K. *J. Mol. Biol.* 1999, *291*, 1191–1206.

89 Hore, P. J., Broadhurst, R. W. *Prog. NMR Spectrosc.* 1993, *25*, 345–402.

90 Canet, D., Lyon, C. E., Scheek, R. M., Robillard, G. T., Dobson, C. M., Hore, P. J., van Nuland, N. A. *J. Mol. Biol.* 2003, *330*, 397–407.

91 Ross, A., Salzman, M., Senn, H. *J. Biomol. NMR* 1997, *10*, 389–396.

92 Schreiber, G., Fersht, A. R. *Biochemistry* 1993, *32*, 11195–11203.

93 Golbik, R., Fischer, G., Fersht, A. R. *Protein Sci.* 1999, *8*, 1505–1514.

94 Mayo, K. H., Parra-Diaz, D., McCarthy, J. B., Chelberg, M. *Biochemistry* 1991, *30*, 8251–8267.

95 Buevich, A. V., Dai, Q. H., Liu, X., Brodsky, B., Baum, J. *Biochemistry* 2000, *39*, 4299–4308.

96 Bhate, M., Wang, X., Baum, J., Brodsky, B. *Bichemistry* 2002, *41*, 6539–6547.

97 Buevich, A. V., Baum, J. *J. Am. Chem. Soc.* 2002, *124*, 7156–7162.

98 Hagn, F. Diplom thesis, Universität Bayreuth, 2003.

99 Morikis, D., Wright, P. E. *Eur. J. Biochem.* 1996, *237*, 212–220.

100 Winder, S. L. PhD thesis, University of Oxford, 1997.

101 Sandström, J. *Dynamic NMR Spectroscopy*; Academic Press: New York, 1982.

102 Burton, R. E., Busby, R. S., Oas, T. G. *J. Biomol. NMR* 1998, *11*, 355–360.

103 Schindler, T., Herrler, M., Marahiel, M. A., Schmid, F. X. *Nat. Struct. Biol.* 1995, *2*, 663–673.

104 Kuhlman, B., Boice, J. A., Fairman, R., Raleigh, D. P. *Biochemistry* 1998, *37*, 1025–32.

105 Kuhlman, B., Luisi, D. L., Evans, P. A., Raleigh, D. P. *J. Mol. Biol.* 1998, *284*, 1661–1670.

106 Spector, S., Raleigh, D. P. *J. Mol. Biol.* 1999, *293*, 763–768.

107 Wang, M., Tang, Y., Sato, S., Vugmeyster, L., McKnight, C. J., Raleigh, D. P. *J. Am. Chem. Soc.* 2003, *125*, 6032–6033.

108 Myers, J. K., Oas, T. G. *Nat. Struct. Biol.* 2001, *8*, 552–558.

109 Millet, O., Loria, J. P., Kroenke, C. D., Pons, M., Palmer, A. G. *J. Am. Chem. Soc.* 2000, *122*, 2867–2877.

110 Farrow, N. A., Zhang, O., Forman-Kay, J. D., Kay, L. E. *J. Biomol. NMR* 1994, *4*, 727–734.

111 Akke, M., Liu, J., Cavanagh, J., Erickson, H. P., Palmer, A. G., III. *Nat. Struct. Biol.* 1998, *5*, 55–59.

112 Ishima, R., Wingfield, P. T., Stahl, S. J., Kaufman, J. D., Torchia, D. A. *J. Am. Chem. Soc.* 1998, *120*, 10534–10542.

113 Mulder, F. A., van Tilborg, P. J., Kaptein, R., Boelens, R. *J. Biomol. NMR* 1999, *13*, 275–288.

114 Mulder, F. A., Mittermaier, A., Hon, B., Dahlquist, F. W., Kay, L. E. *Nat. Struct. Biol.* 2001, *8*, 932–935.

115 Mulder, F. A., Hon, B., Mittermaier, A., Dahlquist, F. W., Kay, L. E. *J. Am. Chem. Soc.* 2002, *124*, 1443–1451.

116 Hill, R. B., Bracken, C., DeGrado, W. F., Palmer, A. G. *J. Am. Chem. Soc.* 2000, *122*, 11610–11619.

117 Kim, S., Szyperski, T. *J. Am. Chem. Soc.* 2003, *125*, 1385–1393.

118 Kitahara, R., Royer, C., Yamada, H., Boyer, M., Saldana, J. L., Akasaka, K., Roumestand, C. *J. Mol. Biol.* 2002, *320*, 609–628.

119 Brooks, C. L. *Acc. Chem. Res.* 2002, *35*, 447–454.

120 Dobson, C. M., Sali, A., Karplus, M. *Angew. Chem. Int. Ed. Engl.* 1998, *37*, 868–893.

121 Snow, C. D., Nguyen, H., Pande, V. S., Gruebele, M. *Nature* 2002, *420*, 102–106.

122 Zagrovic, B., Snow, C. D., Shirts, M. R., Pande, V. S. *J. Mol. Biol.* 2002, *323*, 927–937.

123 Hoeltzli, S. D., Ropson, I. J., Frieden, C. *Tech. Prot. Chem.* 1994, *V*, 455–465.

124 Piotto, M., Saudek, V., Sklenar, V. *J. Biomol. NMR* 1992, *2*, 661–665.

125 Helgstrand, M., Härd, T., Allard, P. *J. Biomol. NMR* 2000, *18*, 49–63.

126 Carr, H. Y., Purcell, E. M. *Phys. Rev.* 1954, *94*, 630–638.

127 Meiboom, S., Gill, D. *Rev. Sci. Instrum.* 1958, *29*, 688–691.

128 Mandel, A. M., Akke, M., Palmer, A. G., III *J. Mol. Biol.* 1995, *246*, 144–163.

129 Palmer, A. G., III, Rance, M., Wright, P. E. *J. Am. Chem. Soc.* 1991, *113*, 4371–4380.

130 Carver, J. P., Richards, R. E. *J. Magn. Reson.* 1972, *6*, 89–105.

131 Yao, J., Chung, J., Eliezer, D., Wright, P. E., Dyson, H. J. *Biochemistry* 2001, *40*, 3561–3571.

132 Loria, J. P., Rance, M., Palmer, A. G. *J. Am. Chem. Soc.* 1999, *121*, 2331–2332.

17
Fluorescence Resonance Energy Transfer (FRET) and Single Molecule Fluorescence Detection Studies of the Mechanism of Protein Folding and Unfolding

Elisha Haas

Abbreviations

AMP, adenosine 5′-monophosphate; ANS, anilino naphthalene sulfonate; ATP, adenosine triphosphate; AK, *E. Coli* adenylate kinase (EC 2.7.4.3); BPTI, bovine pancreatic trypsin inhibitor; (1-n)BPTI, N^{a}MNA-Arg^{1}-N^{e}-DA-coum-lys^{n}-BPTI; DA, donor and acceptor, D, donor; DA-coum, 7-(dimethylamino-(-coumarin-4-yl-acetyl; DTT, dithiothriethol; *E*, transfer efficiency (%); EED, end-to-end distance; FRET, resonance energy transfer; FWHM, full width at half maximum; GdmCl, guanidinium hydrochloride; LI, local interaction; LID, a domain in AK; MNA, 2-methoxynaphthyl-1-methylenyl; NLI, nonlocal interaction; PGK, phosphoglycerate kinase; PMT, photomultiplier tube; RNase A, ribononuclease A; R(1-n)BPTI, reduced (1-n)BPTI; R-BPTI, reduced BPTI; Tris, tris-(hydroxymethyl)aminomethane.

17.1
Introduction

An ideal folding experiment would yield the distributions of the coordinates of each atom or residue in a protein molecule at each time interval during the transition from any ensemble of nonnative conformers to the ensemble of native conformers. The ideal time resolution (i.e., the length of the time interval) should be defined by the rates of motions of the chain segments, within the nanosecond to microsecond time regime. While such an experiment is not feasible with present-day techniques, methods for the determination of intramolecular distances with subnanosecond time resolution provide significant though partial information. This determination can be achieved through the development of methods based on distance-dependent interactions between selected main-chain or side-chain atoms or dipoles.

Multidimensional NMR spectroscopy of isotopically labeled protein samples has the potential for the rapid determination of solution structures of partially folded protein molecules (see Chapter 16). Although the first method of choice, multidimensional NMR spectroscopy has three primary limitations that restrict the appli-

Protein Folding Handbook. Part I. Edited by J. Buchner and T. Kiefhaber

ISBN: 3-527-30784-2

cability of 2D and 3D NMR spectroscopy in folding research: limited sensitivity (millimolar concentrations are required while unfolded and partially folded proteins are very insoluble); limited time resolution and the short interaction length which is limited to less than 5 Å. The second method of choice is the optical analog of the measurements of the magnetic dipole–dipole interactions. Measurements of dynamic nonradiative excitation energy transfer (FRET) [1–6], which is based on the distance-dependent interactions between excited state dipoles, can be applied for the determination of long-range distances between amino-acyl residues in partially folded proteins with the following capabilities: close to the ideal time resolution; very high sensitivity up to the single molecule detection, over distances of molecular dimensions (10–100 Å); and the ability to recover distributions of intramolecular distances in transient ensembles of refolding protein molecules within the fast folding transitions. With these capabilities, FRET measurements can help answer some of the central questions in the problem of protein folding as described in the next section.

17.2 What are the Main Aspects of the Protein Folding Problem that can be Addressed by Methods Based on FRET Measurements?

17.2.1 The Three Protein Folding Problems

The term ''protein folding'' covers three different general phenomena: (a) the transition of the backbone to its native fold, known as the *chain entropy problem*; (b) the stabilization of the native fold, that is *the stability problem*; and (c) the refolding of the protein molecule to different conformations in response to small changes of the solution conditions, ligand binding, membrane insertion, or protein–protein interactions. This is known as *the function problem*.

17.2.1.1 The Chain Entropy Problem

The first protein folding problem refers primarily to the reduction of the conformational entropy of the main chain. According to the experimental data [7], the backbone entropy loss is a factor of almost 3 times greater than the factor of side-chain packing. Therefore protein folding is largely a backbone conformational transition process, rather than the process of side-chain ordering and packing.

A central difficulty of the chain entropy problem lies in the unknown nature of the 1D to 3D information translation in transferring amino-acyl sequence information to the native protein conformation. The information processing cannot occur in a sequential symbol by symbol fashion, but must operate simultaneously using remote parts of the sequence, and hence is essentially a nonlocal, collective process rather than the trivial translation of a message [8]. Moreover all along the folding pathways, the folding intermediates and the transient, partially ordered states of protein molecules form ensembles that can be characterized by distributions of

intramolecular distances. The following parameters best characterize the conformational transitions: the means; the widths; the number of subpopulations; and the shapes of the distributions of the intramolecular distances. Time-resolved FRET (trFRET) measurements of double-labeled protein samples can yield these parameters. Both ensemble and single molecule FRET experiments were applied in studies targeted to the chain entropy problem.

Three common stages compose the folding transition of most proteins. These stages can occur sequentially or in parallel. The hydrophobic collapse is the first stage of folding. In this stage, a question of much interest is asked: is the collapse a general nonspecific solvent exclusion process which reduces the volume and hence the conformational space available for the protein molecules, or is the collapse a specifically directed transition in which specific subdomain structures are formed? The second stage of folding is the formation of secondary and tertiary structures according to the balance of local and nonlocal, native and nonnative interactions (see Chapters 6 and 7) [9]. Most proteins are very complex systems made of multiple structural elements. The search for the timing of formation of such native or nonnative structural elements during the first two folding stages either as a function of time or as a function of the solution conditions is another major challenge of experimental folding research. It calls for methods for determination of distributions of intramolecular distances in the protein molecule either in the kinetic or equilibrium transitions. The third stage of folding is final packing of side chains and secondary structure elements.

In the unfolded or partially folded states, protein molecules undergo rapid conformational fluctuations. Changes in these parameters are another characteristic that reflect the progress of the folding of chain elements. The lifetime of the excited states of donor probes in trFRET experiments (nanoseconds) define time windows that enable the detection of rapid fluctuations of intramolecular distances both in the ensemble and in the single molecule modes. Slower fluctuations can be detected by single molecule FRET spectroscopy or autocorrelation analysis of intensity fluctuations of double-labeled protein samples.

FRET experiments can address also the question of the extent of randomness of protein molecule structures in the presumably unfolded or denatured states (see Chapter 20). Small bias from statistical coil distributions of intramolecular distances can serve as a sensitive measure of subdomain structures in otherwise unfolded protein molecules. Such bias is of particular interest in the context of the so-called ''natively unfolded'' proteins (see Chapter 8 in Part II). These proteins appear to be unfolded by some measurements, but might demonstrate partial order that is difficult to detect by other measurements.

This chapter will focus mainly on the first problem with some reference to the third problem.

17.2.1.2 **The Function Problem: Conformational Fluctuations**

A protein molecule may be regarded as a ''system'' in the thermodynamic sense, immersed in a solvent ''bath'' [10]. The number of degrees of freedom of a protein and its volume are relatively small (although still amounting to several thousands).

The protein molecule, may therefore be regarded as a ''small system'' [10]. In small systems, fluctuations are an inherent characteristic, and such systems may spend a substantial amount of time in states quite different from the average conformation.

The extent of fluctuations was estimated, at least qualitatively, from measurable thermodynamic properties. For example, the heat capacity of a system is linked to fluctuations in energy through the following relation [10]:

$$\langle \partial E^2 \rangle = k_B T^2 C_V \tag{1}$$

Where $\langle \partial E^2 \rangle$ is the mean squared energy fluctuation, related to the second moment of energy distribution, k_B is the Boltzmann constant, T is the absolute temperature, and C_V is the heat capacity at constant volume. A typical heat capacity for proteins is approximately 0.3 cal K^{-1} g^{-1} [11], and for a 25 000 Da protein this leads to a root-mean-squared fluctuation of 35 kcal mol^{-1}. This number should be compared to the common average free energy of stabilization of the folded states of proteins, ~10–15 kcal mol^{-1} [12].

The dynamics of protein molecules do not have one typical time scale, and there is a hierarchy of time scales for motions of different structural elements in a protein. The fastest motions are those of side chains that occur on the picosecond time scale, while slow, large scale conformational changes may take microseconds to be completed [13]. The investigation of the functional properties of many proteins, especially enzymes, still relies on relatively slow kinetic techniques [14]. Ensemble trFRET and single molecule FRET spectroscopy are best posed to detect and characterize such fluctuations.

In short, the sensitivity, the time and spatial resolution, the specificity of measurements of structural elements, the option of measurements of distributions of intramolecular distances and their rapid fluctuations by the ensemble trFRET and single molecule FRET experiments, makes FRET a powerful tool in protein folding research. The currently limited extent of applications of this approach is probably a result of the complex procedure involved in the biochemistry and chemistry of site specific labeling of the protein samples. The following sections contain the theoretical background of the FRET experiments, the principles of their applications in folding research, and the essential control experiments that should support the data analyses of these experiments.

17.3 Theoretical Background

17.3.1 Nonradiative Excitation Energy Transfer

Nonradiative transfer of excitation energy requires some interaction between a donor molecule and an acceptor molecule. This transfer can occur if at least some

vibronic levels in the donor have the same energy as the corresponding transitions in the acceptor. Energy transfer can result from different interaction mechanisms. The interactions may be Coulombic and/or due to intermolecular orbital overlap. The Coulombic interactions consist of long-range dipole–dipole interactions (Förster's mechanism) and short-range multipolar interactions. In the energy transfer process, the initially excited electron on the donor, D, returns to ground state orbital on D, while simultaneously an electron on the acceptor, A, is promoted to an excited state. For permitted transitions on D and A, the Coulombic interaction is predominant, even at short distances. This is the case of the singlet-singlet transfer:

$$^1D^* + {}^1A \rightarrow {}^1D + {}^1A^*$$

which is effective over a long interaction range (up to 80–100 Å). For forbidden transitions on D or A, the Coulombic interaction is negligible and the exchange mechanism is dominant. Here, the interaction is effective only at short distances (< 10 Å) because the interaction requires the overlap of the molecular orbitals. This is the case of triplet–triplet transfer

$$^3D^* + {}^1A \rightarrow {}^1D + {}^3A^* \quad \text{and} \quad {}^3D^* + {}^1A \rightarrow {}^1D + {}^1A^*$$

where the transitions $T_1 \rightarrow S_o$ in D and $S_o \rightarrow T_1$ on A are forbidden (Figure 17.1).

Two main mechanisms are relevant in the context of the application of energy transfer in protein folding research: The Förster mechanism for long-range interactions, and the triplet–triplet transfer for the detection of short-range interactions.

17.3.2 What is FRET? The Singlet–Singlet Excitation Transfer

The term fluorescence resonance energy transfer (FRET) is commonly used to describe singlet–singlet energy transfer via a mechanism based on long-range dipole–dipole resonance coupling[1] [1].

Classically, it is possible to approximate the donor and the acceptor molecules by idealized oscillating dipoles (or higher order multipoles). The electric field surrounding the emitting oscillating dipole is expressed by equation that includes several terms [15] (page 158 in ref. [15]). At distances as large as the wavelength, the term that contributes the radiation of energy dominates. At shorter distances the other terms that describe the electric field surrounding the oscillating dipole dominate. An acceptor chromophore positioned close to the donor will therefore

1) The acronym FRET denoting fluorescence resonance energy transfer is incorrect because the transfer does not involve any fluorescence but the electronic excitation energy of the donor. This mechanism does not depend on the fluorescence properties of the acceptor. The correct term should be EET, representing "electronic energy transfer" or "excitation energy transfer" or RET for "resonance energy transfer." However, since the literature is saturated with the term FRET, we will use it.

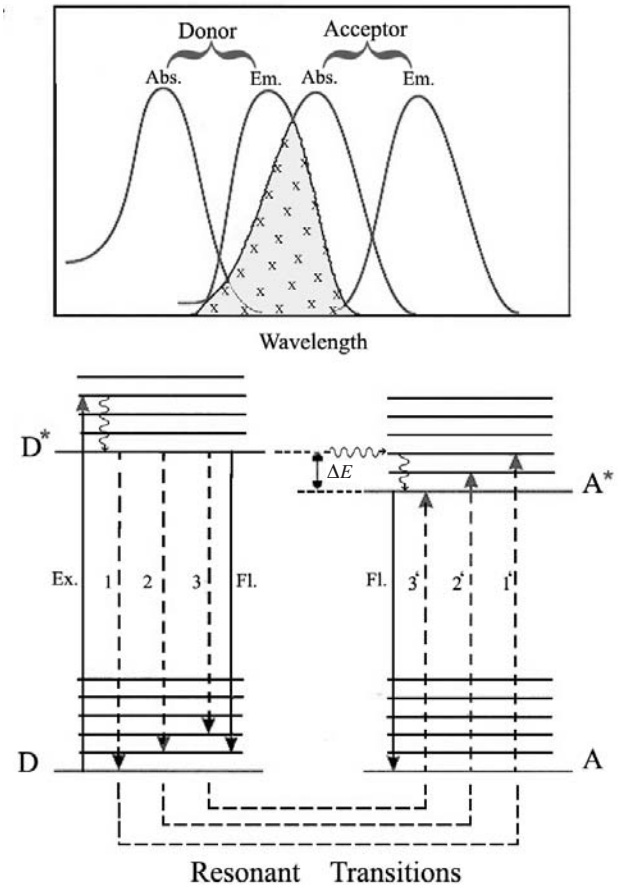

Fig. 17.1. Energy level diagram demonstrating the mechanism of resonance coupling of the nonradiative transitions in the donor and acceptor probes under conditions where the vibrational relaxation is faster than the energy transfer (very weak coupling). The nonradiative transitions are shown in dashed lines and the radiative transitions are shown as continuous vertical lines. The upper inset shows a scheme of the corresponding absorption and emission spectra of the probes and the overlap integral.

be affected by the components of the field that do not contribute to the radiation of energy.

17.3.3 Rate of Nonradiative Excitation Energy Transfer within a Donor–Acceptor Pair

A molecule in an electronically excited state (donor) can transfer its excitation energy to another molecule (acceptor) [1] provided that the pair fulfills several conditions [20]: (a) The energy donor must be luminescent; (b) the emission spectrum

of the donor should have some overlap with the absorption spectrum of the acceptor; and (c) the distance between the two probes should not exceed an upper limit (usually within the range of up to 80 Å). The transfer is readily observed when two different probes are involved, but transfer within a homogeneous population of chromophores can occur. This transfer was detected already in 1927 by Perrin by the loss of polarization of the emitted light [16]. The theory for the mechanism of long-range nonradiative energy transfer was developed by Förster with both classical and quantum mechanical approaches. In both approaches, the interaction is assumed to be of the dipole–dipole type between the energy donor and acceptor [1]. Förster considered two neighboring, electrically charged classical mechanical oscillators coupled through weak electrostatic interactions. This coupling is analogous to two resonating pendulums that are weakly coupled mechanically and exchange oscillation energy back and forth. Förster assumed that only the donor oscillator is initially vibrating. Classically, the donor oscillator will lose energy via radiation and nonradiative exchange with the acceptor provided that they are close enough. The two dipoles, of dipole moment μ (an approximation) interact over distance R with interaction energy

$$E_{\text{int}} \approx \kappa\mu^2/n^2R^3 \tag{2}$$

where κ is the orientation factor (see below) and n is the refractive index of the medium. Förster calculated the distance between the two oscillators where the time for radiative emission of a classical oscillator $\tau_{\text{rad}} \approx 3hc^2/\mu^2\omega^2$ and the time for exchange of energy between the two oscillators $\tau_{\text{int}} \approx h/E_{\text{int}} = hn^2R^3/\kappa\mu^2$ are equal. Here $R \equiv R_o$ when $\tau_{\text{rad}} = \tau_{\text{int}}$. R_o, also known as the Förster critical distance, is the distance between the donor and the acceptor, where half of the energy that would have otherwise been emitted by the donor is transferred to the acceptor. Spectral broadening by very rapid dephasing of the molecular excitation energies lengthens the time considerably for the exchange of energy between the weakly coupled oscillators, and this leads to smaller R_o values. Förster calculated the probability of full overlap of the spectral regions of the two oscillators and w, the probability that the energies of both oscillators are simultaneously nearly the same within the small interaction energy E_{int}. This probability is $w = (\Omega'/\Omega)(E_{\text{int}}/h\Omega)$, where Ω and Ω' are respectively the spectral width (assumed to be the same for both probes) and the overlap spectral region (the second term is the probability that frequency within the broadband frequencies, Ω, will fall within the relatively narrow bandwidth of E_{int}/h). The rate of transfer calculated without this dephasing correction ($1/\tau_{\text{int}} \approx \kappa\mu^2/hn^2R^3$) is then multiplied by w to give the rate of transfer with real systems:

$$K_T \approx 1/\tau'_{\text{int}} = w/\tau_{\text{int}} = \mu^4\kappa^2\Omega'/(h^2n^4R^6\Omega^2) \tag{3}$$

Here, we see that the correction for the spectral broadening in real systems gives the famous R^6 dependence of the rate of excitation energy transfer on the interchromophoric distance.

By solving the distance R_o where $\tau_{rad} = \tau'_{int}$, Förster calculated the dependence of R_o on the characteristics of the two probes:

$$R_o^6 = 3(c^3/\omega^3)\mu^2\kappa^2(\Omega'/\Omega^2)(1/hn^4) = 9(\lambda^6/2\pi(\kappa^2/n^4)(\Omega'/\Omega^2)(1/\tau_{rad})) \tag{4}$$

where $\tau_{rad} = 3hc^3/\mu^2\omega^3$ replaces μ^2 and $c = \lambda\omega/2\pi$. The most relevant feature of this derivation in the context of application of FRET methods in folding research is the $1/R^6$ dependence of the FRET efficiency. This strong distance dependence derives from the distance dependence of the interaction energy of a dipole on $1/R^3$ which is multiplied by the correction for the dephasing of the two spectra. The strict requirement for exact resonance between the two interacting dipoles means that overlapping narrower (line) spectra can exchange energy over larger distances. Förster emphasized that although the transfer mechanism depends on exchange of excitation energy quanta, it is essentially a resonance mechanism and hence the classical approximation gives satisfactory results. Förster published his rigorous quantum mechanical derivation in 1948 and showed that the original classical derivation included all the essentials of process [1].

An alternative classical derivation by Steinberg et al. [17] also assumes an interaction between two idealized oscillating dipoles. Let us denote the donor dipole by $f = f_o \sin 2\pi\nu t$ where f_o is the amplitude, t is time, and ν is the frequency of oscillations. The fields surrounding such an oscillating dipole are given in polar coordinates as follows:

$$\begin{aligned}
E_r &= 2\left[\frac{f_o}{D_e}\cos\theta\right]\left[\frac{2\pi\nu}{r^2c/n}\cos 2\pi\nu\left(t-\frac{r}{c/n}\right)+\frac{1}{r^3}\sin 2\pi\nu\left(t-\frac{r}{c/n}\right)\right]\\
E_\theta &= \left[\frac{f_0}{D_e}\sin\theta\right]\left[-\frac{(2\pi\nu)^2}{r(c/n)^2}\sin 2\pi\nu\left(t-\frac{r}{c/n}\right)+\frac{2\pi\nu}{r^2c/n}\cos 2\pi\nu\left(t-\frac{r}{c/n}\right)\right.\\
&\qquad\left.+\frac{1}{r^3}\sin 2\pi\nu\left(t-\frac{r}{c/n}\right)\right]\\
H_\phi &= \left[\frac{f_0}{(D_e\mu)^{1/2}}\sin\theta\right]\left[-\frac{(2\pi\nu)^2}{r(c/n)^2}\sin 2\pi\nu\left(t-\frac{r}{c/n}\right)+\frac{2\pi\nu}{r^2c/n}\cos 2\pi\nu\left(t-\frac{r}{c/n}\right)\right]\\
E_\phi &= H_r = H_\theta = 0
\end{aligned} \tag{5}$$

where E and H are the electric and magnetic fields, respectively. The subscripts r, θ and ϕ denote components along the r, θ and ϕ spherical coordinates, respectively; D_e and μ are respectively, the dielectric constants and magnetic permeability of the medium; n is the refractive index of the medium, and c is the velocity of light in vacuum. Only components whose Poynting's vector $[(c/4\pi)(E \times H)]$ is nonzero carry radiative energy flux. Only the first terms of E_θ and H_ϕ, which show $1/r$ dependence contribute to the energy flux radiated from the oscillating dipole over complete cycle of oscillation. The other terms carry energy from the dipole to the field and back in an oscillatory way, with zero net radiative flux. At distances

shorter than the wavelength of the emitted radiation, the $1/r^3$ terms in E_θ and E_r are the dominant ones in magnitude, but they do not carry a net flux of energy. An acceptor molecule positioned at such short distances from the oscillating dipole is affected predominantly by the field components which do not contribute to the radiation field. Therefore the excitation transfer has no effect on the shape of the emission spectrum of the donor. The transferred energy is drawn from the field components that exchange energy with the oscillating dipole.

The dipole–dipole interaction that leads to the transfer of excitation energy is very weak, usually of the order of ~2–4 cm^{-1}, while the spectroscopic energies that are transferred are much higher, ~15 000–40 000 cm^{-1}.

Based on the above discussion, which identifies the short-range components of the dipole field, the rate of energy transfer can be calculated. Several treatments lead to the same results. Förster's theory describe the rate of energy transfer for an isolated pair of chromophores which fulfill the requirements for energy transfer by the dipole–dipole interaction to be

$$k_T = \frac{9(\ln 10)\kappa^2 \Phi_D^o}{128\pi^5 N_A' r^6 \tau_D^o} \int_0^\infty f(\lambda)\varepsilon(\lambda)\lambda^4 \, d\lambda \tag{6}$$

$$k_T = \frac{1}{\tau_D^o}\left(\frac{R_o}{r}\right)^6 \tag{6a}$$

where $\kappa = \cos\theta_{DA} - 3\cos\theta_D \cos\theta_A = \sin\theta_D \sin\theta_A \cos\varphi - 2\cos\theta_D \cos\theta_A$ (θ_{DA} is the angle between the donor and the acceptor dipoles; θ_D and θ_A are respectively the angles between the donor and the acceptor dipoles and the line joining their centers and φ is the angle between the projections of the transition moments on the plane perpendicular to the line through the centers (Figure 17.2). κ^2 can in principle assume values from 0 (perpendicular transition moments) to 4 (collinear

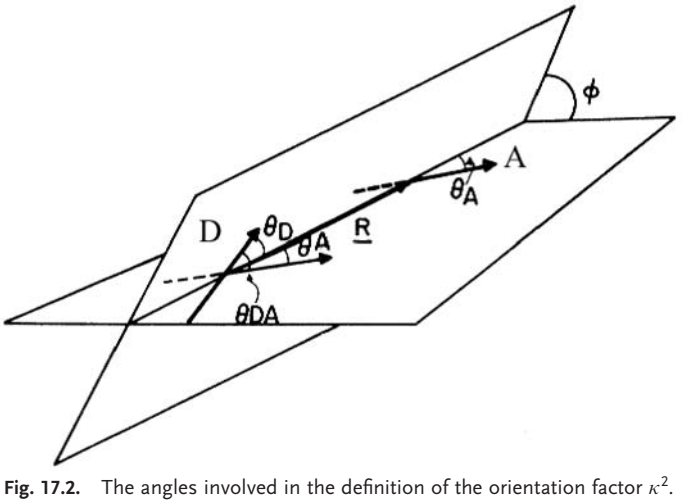

Fig. 17.2. The angles involved in the definition of the orientation factor κ^2.

transition moments), or 1 when the transition moments are parallel)); Φ_D^0 and τ_D^0 are respectively the quantum yield and the fluorescence lifetime of the donor in the absence of an acceptor; r is the distance between the centers of the two dipoles (donor and acceptor); N'_A is Avogadro's number per mmole, $f(\lambda)$ is the fluorescence intensity of the donor in the range λ to $\lambda + d\lambda$ normalized so that $\int_0^\infty f(\lambda)\,d\lambda = 1$ and $\varepsilon(\lambda)$ is the absorption coefficient of the acceptor at the wavelength λ. In Eq. (6), r and λ are in centimeters, $\varepsilon_A(\lambda)$ in $cm^2\ mol^{-1}$, and $J(\lambda)$ in $cm^6\ mol^{-1}$. When those units are used R_o is defined by Eq. (7) and is given by:

$$R_o^6 = 8.8 \times 10^{-28} \Phi_D^o \kappa^2 n^{-4} J \tag{7}$$

where J is the overlap integral in Eq. (6). The energy transfer process competes with the spontaneous decay of the excited state of the donor, characterized by the rate constant $k_D^o = 1/\tau_D^o$. If $\varepsilon_A(\lambda)$ is given in $cm^{-1}\ mol^{-1}$ L units, then $R_o^6 = 8.8 \times 10^{-25} \Phi_D^o \kappa^2 n^{-4} J$. Thus the probability ρ for the donor to retain its excitation energy during the time t after excitation is given by:

$$-\left(\frac{1}{\rho}\right)\frac{d\rho}{dt} = \frac{1}{\tau_D^o} + \frac{1}{\tau_D^o}\left(\frac{R_o}{r}\right)^6 \tag{8}$$

and the efficiency of E of energy transfer is expressed by:

$$E = \frac{R_o^6}{R_o^6 + r^6} \tag{9}$$

R_o is thus the inter-dipole distance at which the transfer efficiency (and the donor lifetime) is reduced to 50% and has the strongest dependence on changes of that distance (Figure 17.3).

There is strong experimental support for Förster's equations (Eqs (6)–(9)) (reviewed by Steinberg [4]. Weber and Teal [18], and Latt et al. [19] showed the dependence on the overlap integral. The R^{-6} dependence was demonstrated by Stryer and Haugland [20].

Equation (9) shows that the distance between a donor and an acceptor can be determined by measuring the efficiency of transfer, provided that r is not too different from R_o and that all molecules in the sampled ensemble share the same intramolecular distance. If this is not the case, an average distance r_{av} that would be extracted from the measured transfer efficiency does not correspond to any simple average distance.

The efficiency of energy transfer is independent of the value of the lifetime of the excited state of the donor. Efficient energy transfer can occur even for ''long life'' excited states (e.g., for phosphorescence emission) provided that the quantum yield of emission is reasonably high. Such transfer phenomena has been observed. Equations (8) and (9) thus define the characteristic time and distance ranges (''windows'') in which the transfer efficiency, E, is most sensitive to conformational transitions and their rates (Figure 17.3). Typical values available for probes that are used in protein chemistry are in the range of 10–80 Å and down to picosecond

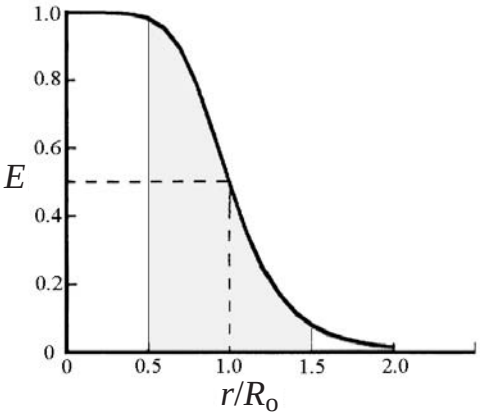

Fig. 17.3. Variation of the transfer efficiency, *E*, as a function of the distance between the donor and the acceptor probes. The shadowed range represents the limits of the distance range where reliable measurements of distances are possible.

time intervals. Many conformational changes and processes in proteins occur in these intervals. Hence it is in the hands of the researcher to design the experiments with the time and distance resolutions most suitable for each molecular question.

17.3.4 The Orientation Factor

Distance determination by measurements of transfer efficiencies is complicated by the strong dependence of the probability for energy transfer on the orientation of the interacting dipoles. Therefore knowledge of the orientation factor, κ^2, is essential for applications of FRET in studies of protein folding. When the two dipoles undergo rapid orientational averaging during the lifetime of the excited state of the donor, the orientation factor can be averaged to yield the numerical value of 2/3.

The large span of possible κ^2 values, between 0 and 4, makes it the primary source of uncertainty in distance determination by FRET measurements.

The main uncertainties that should to be eliminated in FRET-based folding experiments are (a) the question whether changes in transfer efficiencies during folding are caused by changes of intramolecular distances or merely by changes of the orientation of the probes and (b) in time-resolved FRET experiments, multi-exponential decay of the donor emission can result from the distribution of either the distances or the orientations. Various approaches were proposed for the reduction of these uncertainties and the determination of the range of possible error in distance determination. Dale et al. [21–23] reported the most extensive studies in which they utilized the partial rotations of the chromophores (as revealed by their emission anisotropy) to estimate limits for the range that κ^2 can

assume. In cases where the distance between the donor and the acceptor does not change appreciably during the time that the transfer takes place, it is possible to derive a $\langle\kappa^2\rangle_{\min}$ and a $\langle\kappa^2\rangle_{\max}$ from anisotropy measurements. This procedure is based on assumptions that the two probes can be represented by single oscillating dipoles whose orientations fluctuate (e.g., wobble) within a cone and that the orientation of the axis of the cone also fluctuates. κ^2 values can be averaged over the corresponding range of orientations. Rapid reorientation during the lifetime of the excited state of the donor is reflected in the anisotropy measurements and therefore can be estimated experimentally for each preparation. The average κ^2 will depend on "depolarization factors" that are (averages of) second-rank Legendre polynomials of a cosine of a polar angle θ between 0 and π. The depolarization factors have the form:

$$d_\theta = \frac{1}{2}\cos^2\theta - \frac{1}{2} \Rightarrow -\frac{1}{2} \le d_\theta \le 1 \tag{10}$$

or

$$\langle d_\theta \rangle = \left\langle \frac{1}{2}\cos^2\theta - \frac{1}{2} \right\rangle \Rightarrow -\frac{1}{2} \le \langle d_\theta \rangle \le 1 \tag{10a}$$

where the brackets denote a weighted average over the range of angles covered by θ during times that are brief as compared to the average transfer time. The depolarization factors are derived from the anisotropy values under each experimental setup and solution conditions (for details of all the angles taken into account see Dale et al. [22, 23] and Van der Meer [6], pp. 55–83).

An ideal case, where full averaging is an intrinsic characteristic of the system, is achieved with atom probes, such as lanthanides and chelated transitions metal ions [5, 24–26]. An alternative approach to this problem is based on the fact that many chromophores show mixed polarizations in their spectral transitions (i.e., their absorption and emission across the relevant spectral range of overlap involves a combination of two or more incoherent dipole moments). The physical basis for this phenomenon has been discussed by Albrecht [27]. Its manifestation is well known in the observation that the limiting anisotropy of many organic probes used in FRET experiments is lower than the theoretically predicted upper limit. Haas et al. [26] showed that the occurrence of mixed polarizations in the energy donor and acceptor may markedly limit the range of possible values that κ^2 can assume and thus in favorable conditions alleviate the problem of the orientation factor in FRET experiments. The fact that any one of the two probes has two or more transition dipole moments involved in the transfer mechanism eliminates the extreme values that κ^2 can assume. It is equivalent to ultrafast rotation of an ideal dipole over the very wide range of orientations and hence to fast averaging. This effect, when considered in planning FRET experiments by using probes that show a high degree of internal depolarization, can reduce the κ^2-related uncertainties to the range of the other common experimental uncertainties.

A table was prepared of the possible range of values of κ^2 corresponding to the experimentally observed anisotropy values for the donor and the acceptor. An improved approximation of the value of κ^2 is obtained when the contribution of the rotation of the whole molecule to the emission anisotropy of the probes is first subtracted from the observed anisotropy. This procedure can be achieved when the anisotropy decay is determined and the analysis shows the relative amplitude associated with the decay component corresponding to the molecular rotational diffusion.

This procedure produces a distribution $P(\kappa^2)\mathrm{d}(\kappa^2)$ which is the probability that the orientation factor assumes a value between κ^2 and $\kappa^2 + \mathrm{d}(\kappa^2)$ for a frozen system of randomly oriented donor–acceptor pairs. As expected, the extreme values of κ^2 are eliminated even for moderate values of emission anisotropy of the probes. When the emission anisotropy of both the donor and the acceptor is relatively low, $P(\kappa^2)$ attains its maximal value at κ^2 close to 2/3. This is the case for many common probes which have high levels of mixed polarization, such as aromatic probes and derivatives of naphthalene.

The uncertainty in r can be further reduced by employing two independent FRET experiments. In these experiments different pairs of probes are used for FRET determination of the distance between one pair of sites in a protein molecule.

The tables given in Ref. [26] can be used for the evaluation of the probable range of uncertainty in the distances estimated from FRET experiments for pairs of probes based on measurements of their anisotropies.

17.3.5
How to Determine and Control the Value of R_o?

The distance range for the statistically significant determination of distances for each pair is defined by the characteristics of the probes and is given by the R_o value. Equation (9) shows that the limits of that range are $r = R_o \pm 0.5R_o$ (Figure 17.3). Maximal sensitivity of the FRET effect to small changes in r is observed when $r = R_o$. Therefore optimal design of FRET experiments includes a selection of a pair of probes that have an R_o value close to the expected r value.

R_o depends on four parameters which are characteristic of each pair of probes (Eq. (6)). These parameters were discussed critically by Eisinger, Feuer, and Lamola [28]. Modulation of the value of R_o of any specific pair in order to adjust it to the expected r value, is limited to a narrow range due to the sixth power of relation of R_o and the spectroscopic constants of the probes. Equation (6) shows that the donor quantum yield Φ_D^o and the overlap integral parameters are the most readily available for manipulation to modulate the R_o value.

17.3.6
Index of Refraction n

The values used for n to calculate R_o for a pair of probes attached to a protein molecule vary widely, from 1.33 to 1.6. Eisinger, Feuer, and Lamola [28] recommended

using the value $n = 1.5$ in the region of spectral overlap of the aromatic amino acids in proteins.

17.3.7 The Donor Quantum Yield Φ_D^o

Φ_D^o should be determined for each probe when attached to the protein molecule at the same site used for the FRET experiment. Many experiments showed that the Φ_D^o is affected by both the site of attachment of the probes and by modifications at other sites in the protein molecule; by attachment of an acceptor at second sites; by changes of solvent conditions; and by ligand binding or folding/unfolding transitions. Therefore R_o should be determined repeatedly after changes in the conditions to avoid misinterpretation of changes of R_o as changes of r. The R_o depends on the sixth root of Φ_D^o and is therefore not very sensitive to uncertainties in Φ_D^o. Nevertheless, this same dependence limits the range that R_o can be manipulated. For instance, a twofold decrease Φ_D^o would result in ~9% decrease of R_o. Increasing Φ_D^o without a change of probes usually requires change of solvent and therefore is not very useful in folding studies; but Φ_D^o can be decreased by adding quenching solute without a change of solvent.

Frequently bound donor probes may have few modes of interactions with the macromolecular environment in the ground or in the electronically excited state. In such a case, each subpopulation which has a different lifetime also has a different R_o, as indicated in Eqs (6) and (7).

17.3.8 The Spectral Overlap Integral J

The most effective variation of R_o is available by selecting probes according to the overlap of their spectra. The value of J depends on the local environment of the probes. As a rule, absorption spectra vary relatively little with a change of solvent, temperature, or local environment, but emission spectra may be very sensitive to such changes of the local environment of the probes. An example of this dependence is the fluorescence of indole derivatives [29]. The selection of probes with narrow emission and absorption spectra and with high extinction coefficients of the acceptor can yield high R_o values.

17.4 Determination of Intramolecular Distances in Protein Molecules using FRET Measurements

Clear presentation of theoretical background for the methods described below may be found in the monographs by Valeur [30], Lakowicz [31], Van Der Mear [6], and numerous reviews such as Refs [4, 32–35] published in the past 40 years.

17.4.1 Single Distance between Donor and Acceptor

The Förster resonance energy transfer can be used as a spectroscopic ruler in the range 10–100 Å. Measurements can be conducted under equilibrium conditions or in the kinetics mode during conformational transitions. Distances shorter than 8–10 Å should be avoided since short-range multipoles contribute interactions which have different distance dependence.

E can be defined analogously to the quantum efficiency in terms of the rates of elementary competing processes of de-excitation of the donor excited states:

$$E = k_{\text{ret}} / \left(k_{\text{ret}} + k_{\text{fl}} + \sum k_{\text{i}} \right) \tag{11}$$

where $k_{\text{ret}}, k_{\text{fl}}$, and $\sum k_{\text{i}}$ are respectively the rate constants of FRET, fluorescence, and all other competing modes of de-excitation of the donor's first singlet excited state. E can be effectively monitored by observing the effect of the acceptor on either the lifetime of the donor excited state or on emission quantum efficiency. To evaluate E one must compare $\tau_{\text{D}}^{\text{o}}$ or $\Phi_{\text{D}}^{\text{o}}$ (in the absence of an acceptor) and the donor lifetime τ_{D} or quantum efficiency Φ_{D} in the presence of an acceptor.

Determination of distances via determination of FRET efficiency, E, is possible via a determination of the decrease of donor emission or an enhancement of the acceptor emission by steady state and time-resolved methods.

$$r = \left(\frac{1}{E} - 1 \right)^{1/6} R_{\text{o}} \tag{12}$$

Due to the comparative nature of this mode of determination of E, the concentrations of the probes (and hence the labeled protein molecules) and their microenvironments must be the same for all samples in every set of measurements.

17.4.1.1 Method 1: Steady State Determination of Decrease of Donor Emission

The competition of the FRET process results in decreased quantum yield of the donor emission:

$$E = 1 - \frac{\Phi_{\text{D}}}{\Phi_{\text{D}}^{\text{o}}} \tag{13}$$

since only relative quantum yields are to be determined, Eq. (13) can be written directly in terms of single wavelength donor emission intensities at wavelengths where the acceptor emission intensity is negligible:

$$E = 1 - \frac{A(\lambda_{\text{D}})}{A_{\text{D}}(\lambda_{\text{D}})} \frac{I_{\text{D}}(\lambda_{\text{D}}, \lambda_{\text{D}}^{\text{em}})}{I_{\text{D}}^{\text{o}}(\lambda_{\text{D}}, \lambda_{\text{D}}^{\text{em}})} \tag{14}$$

The factor A/A_D corrects for the absorption by the acceptor. This method can be readily applied at the single molecule level.

17.4.1.2 Method 2: Acceptor Excitation Spectroscopy

The most direct mode of determination of E, independent of correction factors or differences in concentrations, can be achieved via measurements of acceptor excitation spectra. In this procedure, the acceptor excitation spectra of three samples should be measured under the same solution conditions. These spectra are: (a) The acceptor excitation spectrum of the double-labeled protein (labeled by both the donor and the acceptor), $I_A(\lambda_D, \lambda_A^{em})$; (b) the excitation spectrum of the acceptor in the absence of a donor, using protein sample labeled by the acceptor alone, $I_{ref\,0}(\lambda_D, \lambda_A^{em})$ (a reference for $E = 0$); and (c) the excitation spectrum of the acceptor attached to a double-labeled (donor and acceptor) model compound where E is well known under the conditions of the measurements $I_{ref\,1}(\lambda_D, \lambda_A^{em})$. The acceptor excitation spectra of the three samples monitored at an acceptor emission wavelength (with negligible donor emission contribution) are then normalized at the acceptor excitation wavelength. E can then be obtained with high accuracy by

$$E = \frac{I_A(\lambda_D, \lambda_A^{em}) - I_{ref\,0}(\lambda_D, \lambda_A^{em})}{I_{ref\,1}(\lambda_D, \lambda_A^{em}) - I_{ref\,0}(\lambda_D, \lambda_A^{em})} \tag{15}$$

There is no need for additional independent measurements and exact knowledge of the concentrations or instrumental corrections. (Further reduced noise can be achieved by using the ratio of the area under the excitation spectra in the donor absorption range.) Therefore, this is the preferred method for the determination of E by steady state methods. Non-FRET mechanisms of quenching of the donor might affect the determination of E by method 1. Control experiments should be performed that confirm that the missing donor emission intensity is observed in the acceptor emission. Such non-FRET change of the donor emission does not affect the determination of E by method 2. Both steady state methods might be affected by the inner filter effect and care must be taken to account for changes in emission intensity changes due to that effect.

17.4.2 Time-resolved Methods

Time-resolved emission of the donor or the acceptor fluorescence provides direct information on the transfer rates independent of the concentrations, as this information is in the shape of the fluorescence decay curves, and not in the amplitudes. The donor and the acceptor fluorescence decay curves contain additional information not available from the steady state measurements. This information, which can be extracted directly by proper analytical procedures, is of particular interest for folding studies. An analysis of time-resolved FRET experiments can resolve conformational subpopulations and distributions of distances and fast conformational changes on the nanosecond time scales.

17.4.3
Determination of from Donor Fluorescence Decay Rates

Equation (11) can be rewritten:

$$1/\tau_D = 1/\tau_D^o + k_{ret} \tag{16}$$

and Eq. (13) can be replaced by

$$E = 1 - \frac{\tau_D}{\tau_D^o} \tag{17}$$

and

$$r = \frac{R_o}{(\tau_D/\tau_D^o - 1)^{1/6}} \tag{18}$$

when a nonexponential decay of the donor alone (τ_D^o) is observed, a common situation due to heterogeneity of microenvironments, average lifetime values can be used to calculate E, provided that the deviation from monoexponentiality is moderate:

$$E = 1 - \frac{\langle \tau_D \rangle}{\langle \tau_D^o \rangle} \quad \text{where } \langle \tau \rangle = \sum_i \alpha_i \tau_i \Big/ \sum_i \alpha_i \tag{19}$$

when the heterogeneity of the decay rates is enhanced by the FRET effect, then the use of Eq. (18) might yield only an approximation of an average intramolecular distance. In such a case, distribution analysis accompanied by appropriate control experiments should be applied.

17.4.4
Determination of Acceptor Fluorescence Lifetime

The concentration of excited acceptor probes, $A^*(t)$, after a δ-pulse excitation at the donor excitation wavelength, obeys the following rate law:

$$\frac{dA^*(t)}{dt} = k_{ret} D^*(t) - (1/\tau_A^o) A^*(t) \tag{20}$$

where $D^*(t)$ is the time dependent concentration of excited donor probes. Under ideal conditions, where there is no direct excitation of the acceptor, and the donor decay is single-exponential, the time dependent excited acceptor concentration, $A^*(t)$, shows a "growing in" component (marked by the negative pre-exponent). Under the initial condition that $D^*(t = 0) = D^*(0)$, the time dependence of the

concentration of excited acceptor probes follows a nonexponential decay law,

$$A^*(t) = \frac{D^*(0)k_{\text{ret}}}{1/\tau_{\text{D}} - 1/\tau_{\text{A}}^{\text{o}}}\left[\text{e}^{-t/\tau_{\text{A}}^{\text{o}}} - \text{e}^{-t/\tau_{\text{D}}}\right] \tag{21}$$

This expression is typical of an excited state reaction where the second exponent is equal to the decay of the donor excited state that produces the acceptor excited states. The pre-exponential factor of the donor excited state is the same as for the first exponent, but is negative. Therefore the measurement of the acceptor decay under excitation of the donor is an important control experiment which confirms that any reduction of the donor excited state lifetime is due to the FRET mechanism, and that the distance determination is valid.

In practice, direct excitation of the acceptor to create a subpopulation, $A^*(0) = A^*(t = 0)$, of directly excited acceptor probes at $t = 0$, cannot be avoided in most cases. Consequently, Eq. (21) should be rewritten to add the decay of this subpopulation:

$$A^*(t) = \left[\frac{D^*(0)k_{\text{ret}}}{1/\tau_{\text{D}} - 1/\tau_{\text{A}}^{\text{o}}} + A^*(0)\right]\text{e}^{-t/\tau_{\text{A}}^{\text{o}}} - \frac{D^*(0)k_{\text{ret}}}{1/\tau_{\text{D}} - 1/\tau_{\text{A}}^{\text{o}}}\text{e}^{-t/\tau_{\text{D}}} \tag{22}$$

17.4.5
Determination of Intramolecular Distance Distributions

Distance determination by means of steady state or time-resolved measurements using Eqs (13) or (18) is valid for single molecule experiments or when all molecules in an ensemble share the same D–A distance during the time of the data collection. However, a situation where all molecules in an ensemble of partially folded molecules share the same intramolecular distances is quite rare, and an equilibrium distribution of intramolecular distances, $N_{\text{o}}(r)$, with finite FWHM is the rule. In most folding experiments, the FRET efficiency determined by steady state measurements is averaged over the efficiencies of all fractions in the distribution,

$$\langle E \rangle = \int_0^\infty N_{\text{o}}(r)\frac{R_{\text{o}}^6}{R_{\text{o}}^6 + r^6}\text{d}r \tag{23}$$

where $N_{\text{o}}(r)\,\text{d}r$ is the fraction of molecules with D–A pairs at distance r to $r + \text{d}r$. It is not possible to evaluate $N_{\text{o}}(r)$ from single steady state measurement. Cantor and Pechukas [36] suggested the use of a series of measurements where the same ensemble would be labeled by different pairs of probes, characterized by different R_{o} values for each experiment. A single time-resolved experiment contains all the information needed for the determination of $N_{\text{o}}(r)$.

Consider the time dependence of a sample of the labeled molecules in which the donor has been excited at time $t = 0$ by a very short pulse of excitation light. At the moment of excitation, the intramolecular distance probability distribution (IDD) of

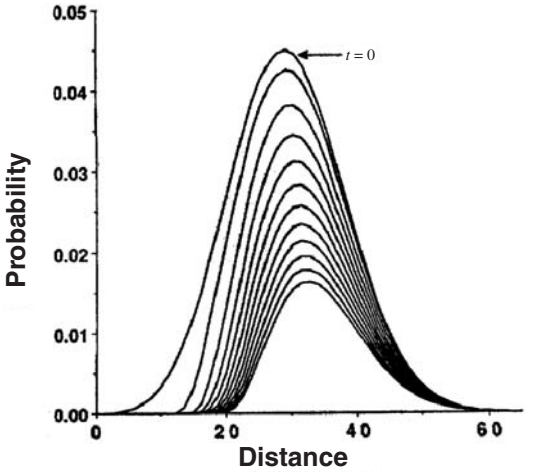

Fig. 17.4. Demonstration of the perturbation of the shape of the intramolecular distance distribution by the energy transfer effect. Simulation of the time dependence of an intramolecular distance distribution of the excited state donor subpopulation, $N^*(r,t)$, starting at time $t = 0$ with subsequent time intervals every 0.4 ns ($R_o = 27$ Å, $\tau = 6.0$ ns) without diffusion. The shift of the mean of the distribution to longer distances and the depletion of the short distance fractions as a function of time is demonstrated.

the sample of molecules with excited state donor probe, which is selected at random by the excitation pulse, $N^*(r,0)$, is congruent with the equilibrium distance distribution of the whole population, $N_o(r)$ (within a proportionality factor). The rate of decay of the donor excited state in the fraction of labeled protein molecules which are characterized by a short D–A distance is nonlinearly accelerated relative to the corresponding rate observed for labeled molecules with larger D–A distances. This is due to the $1/r^6$ dependence of the dipole–dipole interactions. Figure 17.4 shows the rapid depletion of the lower end fractions of $N^*(r,t)$.

The net effect is (a) the generation of a virtual concentration gradient (within the original Gaussian boundaries); (b) a time-dependent shift of the mean of the time-dependent distance distribution of the sample of protein molecules with excited donor probe, $N^*(r,t)$, to larger intramolecular distances; and (c) an enhanced rate of decay of the excited state of the donor probe. This effect can be illustrated as an equivalent of optical ''hole burning'' in the distance probability distribution. When the intramolecular distances are unchanged during the lifetime of the excited state of the donor, the decay kinetics of the donor emission of the entire population of molecules with excited donor is multiexponential,

$$i(t) = k \int_0^\infty N_o(r) \exp\left[-\frac{t}{\tau_D^o}\left(1 + \left(\frac{R_o}{r^6}\right)^6\right)\right] dr \qquad (24)$$

where k is a proportionality factor. Knowledge of R_o, and τ_D^o enables the extraction of $N_o(r)$ from the multiexponential decay curve, $i(t)$.

17.4.6

Evaluation of the Effect of Fast Conformational Fluctuations and Determination of Intramolecular Diffusion Coefficients

As a result of the optically generated "concentration gradient" within the envelope of the equilibrium distribution, the random Brownian motion of the labeled segments causes a net transfer of molecules with excited donor probe to the short distance fractions. This rapid exchange between distance fractions has no effect on the shape of the equilibrium distance distribution, $N_o(r)$, and the molecules transferred to the shorter distances thus have enhanced transferred probability. This phenomenon can be viewed as a process of diffusion under the conformational force field which governs the equilibrium IDD [17, 37, 38]. Within the ensemble of labeled protein molecules whose donor was excited at the time $t = 0$, the fast conformational fluctuations act towards restoration of the equilibrium distribution, an effect that is well visible in the simulation shown in Figure 17.5. The Brownian fluctuations of segments incorporated in a complex molecule such as a globular protein, or even an unfolded polypeptide, are probably not purely random walks. Yet, in the absence of specific knowledge of the modes of motion, one can approximate these motions using a Fick equation. This is the basis for derivation of Eq. (25) which considers both the energy transfer reaction term, $k(r)$, and the restoration force by the diffusion term. Equation (25) is the basis for the experimental data analysis [37]:

$$\frac{\partial \bar{N}_i(r,t)}{\partial t} = \frac{D}{N_0(r)} \times \frac{\partial}{\partial r}\left[N_0(r)\frac{\partial}{\partial r}\bar{N}_i(r,t)\right] - k_i(r)\bar{N}_i(r,t) \tag{25}$$

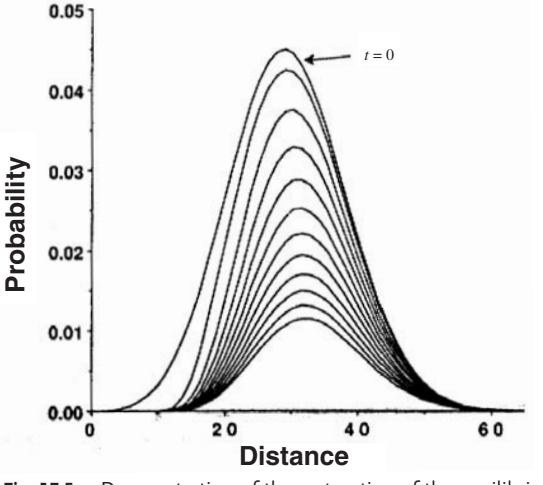

Fig. 17.5. Demonstration of the restoration of the equilibrium intramolecular distance distribution by the diffusion effect. The simulation shown in Figure 17.4 was repeated with nonzero value of the diffusion coefficient, $D = 20 \times 10^{-7}$ cm^2 s^{-1}. The replenishment of the short distance fractions is demonstrated.

where i denotes the ith species of the donor fluorescence decay (in the absence of an acceptor), $N^*{}_i(r, o) = N_0(r)$ (the equilibrium distance distribution); $N^*{}_i(r, t)\,dr$ is the probability for molecules with an excited state species i of the donor to have an intramolecular distance in the range r to $r + dr$ and $\bar{N}_i(r, t) = N^*{}_i(r, t)/N_0(r)$. D is defined as the intramolecular diffusion coefficient of the segments carrying the two probes; τ_i and α_i are respectively the lifetime and the normalized pre-exponential factor of the excited state of the ith species of the donor in the absence of an acceptor. $k_i(r)$, the reaction term, includes the spontaneous emission rate and the Förster energy transfer rate:

$$k_i(r) = \frac{1}{\tau_i} + \frac{1}{\tau_r}\left(\frac{8.79 \times 10^{-25} n^{-4} \kappa^2 J}{r^6}\right) \tag{26}$$

τ_r is the radiative lifetime of the donor, and the other terms were defined in Eqs (6) and (6a). Equation (26) considers the variation of R_o due to variations of the donor quantum yield Φ_D^0. This is represented by the ratio of the donor lifetime components and the radiative lifetime, which is assumed to be independent of local environmental effects.

The solution of Eq. (25) is obtained by numerical methods. Since the boundaries are chosen in such a way that the distribution function is very small at both the upper and lower extreme distances, reflective boundary conditions are arbitrarily used [39]:

$$[\delta \bar{N}(r, t)/\delta r]_{r=r_{min}, r_{max}} = 0 \tag{27}$$

$i_c^D(t)$, the calculated fluorescence decay curve of the donor is readily obtained from $\bar{N}(r, t)$ by the relationship [37]

$$i_c^D = m \int_{r_{min}}^{r_{max}} N_0(r) \left[\sum_i \alpha_i \bar{N}_i(r, t)\right] dr \tag{28}$$

where m is a constant and α_i is the pre-exponential factor of the ith excited state species of the donor in the absence of an acceptor.

The ideal case is such that the fluorescence decay of the donor in the absence of an acceptor is monoexponential. In such a case, all molecules share one value of R_o and the sum in Eq. (28) reduces to one term and the reactive term, $k_i(r)$ (Eq. (26)), can be replaced by a simpler expression:

$$k(r) = -1/\tau[1 + (R_o/r)^6] \tag{29}$$

In a case where the diffusion rate is known to be negligible on the time scale of the lifetime of the excited state of the donor, the Fick term in Eq. (25) is zero and $N_o(r)$ can be derived directly from an analysis of the donor decay curve. In such a case, Eq. (25) can be replaced by [17]:

$$i_c^D(t) = k \int_0^\infty N_o(r)(\exp -k(r))\,dr \tag{30}$$

17.5 Experimental Challenges in the Implementation of FRET Folding Experiments

Practical implementation of the FRET approach in protein folding experiments either in the ensemble or the single molecule modes involves three very different steps:

1. Design and preparation of pure homogenous structurally and functionally intact double-labeled protein samples.
2. Spectroscopic determination of transfer efficiencies and fluorescence decay profiles of the probes and control experiments.
3. Data analysis.

17.5.1 Optimized Design and Preparation of Labeled Protein Samples for FRET Folding Experiments

A minimum of at least two, and more often three labeled protein species should be prepared for each well controlled, folding FRET experiment. These are (a) a double-labeled (by both donor and acceptor) mutant; (b) a single donor-labeled mutant (at the same site as in (a)); and (c) a single acceptor-labeled mutant (at the same site as in the double-labeled mutant) (optional). An ideal folding FRET experiment would employ three homogeneously ($> 97\%$) labeled samples of the model protein where the donor and the acceptor probes would be selectively attached to selected residues. In this ideal experiment, the following requirements should be satisfied: (a) the distance between the two selected sites should be sensitive to changes most relevant to the working hypothesis to be tested by the planned experiments; (b) the structure and function of the labeled protein derivatives should be unperturbed or minimally perturbed; (c) the mechanism of folding (kinetics and equilibrium transitions) should be undisturbed; (d) the probes should be of small size and preferably close to the main chain; and (e) the probes should have ideal spectroscopic characteristics that would make the detection and data analysis free of corrections factors.

Like everything in life, ideal experimental systems are good for dreams only, proteins are rarely totally unaffected by chemical or mutational modifications; the sites that are most desirable for insertion of the probes are in many cases also critical for folding mechanism and the spectroscopically ideal probes are usually also very large. Therefore, the design process is a matter of optimization, not maximization.

The compositional and structural homogeneity as well as the extent of perturbation of the folding mechanism; the structure; the function (activity) and stability of each labeled preparation should be monitored by standard methods. The extent of perturbation is an important factor in the evaluation of the FRET results. Occasionally modified protein molecules are found to be unsuitable for planned experiments due to very strong perturbations. Consequently, an alternative modification design should be attempted. The concern for purity cannot be overemphasized since background or impurity fluorescence can drastically distort the results of distance determinations.

Incomplete labeling of the two reference single-labeled mutants in each set should not prohibit the use of the preparation in FRET experiments, provided that the extent of labeling is known. Even incomplete labeling of the double-labeled mutant can be tolerated in ensemble steady state or time-resolved detected experiments, provided that the extent of labeling is known, and (in some cases) does not exceed 15–20% of single-labeled molecules. The strict requirements of complete labeling and accurate knowledge of the extent of labeling is relaxed in single molecule FRET experiments. In these measurements, it is possible to discard single molecule records that do not show both the donor and the acceptor emission during data processing.

The main spectral characteristics that should be considered in the design of FRET experiments are as follows: (1) R_o of the selected pair should be as close as possible to the expected mean distance between the two labeled sites (including the linker of the probes); (2) the orientation of the probes should be averaged during the lifetime of the fluorescence of the excited state of the donor; (3) in case of time-resolved ensemble experiments, the ratio $\tau_D/\tau_A \geq 3$; (4) photostability; (5) minimal environmental sensitivity of the spectral characteristics; (6) large Stokes shifts of the acceptor to achieve minimal overlap of the emission spectra of the donor and the acceptor; (7) a high extinction coefficient of the donor to be able to study the folding in very dilute solutions (where aggregation problems are minimized) and in particular in the case of single molecule detection experiments. Ideal probes are rare and therefore some of the spectral characteristics are compromised. Under such circumstances, control experiments should accompany the FRET measurements in order to reduce experimental uncertainties.

17.5.2
Strategies for Site-specific Double Labeling of Proteins

Site-specific labeling can be achieved by six basic strategies:

1. Use of natural probes, the tyrosine or tryptophan residues and a few prosthetic groups. Site-directed mutagenesis can be applied for the preparation of single tryptophan mutants and generation of sites for attachment of the acceptor by insertion of cysteine or other residues [33, 40, 41].
2. Nonselective chemical modification of reactive side chains and chain terminal reactive groups (amine, carboxyl, and mainly sulfhydryl groups) combined with high resolution or affinity chromatography separation methods.
3. Solid phase synthesis of protein fragments and conformationally assisted ligation of two synthetic peptide fragments, or of a genetically truncated protein fragment and a synthetic complementing fragment can be applied for efficient site-specific labeling of proteins. Total synthesis of labeled protein molecules is applicable for medium-size proteins (e.g., the total synthesis of chymotrypsin inhibitor 2 (CI2) [42]).
4. Production of edited mutants with no more than one pair of exposed reactive side chains, preferably cysteine residues, at the desired sites, followed by chemical modification and chromatographic separation.

5. Cell-free protein synthesis and the use of edited tRNAs and edited genetic code for the incorporation of nonnatural amino acids into selected sites in the chain [43].
6. Enzyme-catalyzed insertion of fluorescent substrates taking advantage of the specificity and mild conditions of the enzymatic reaction [44].

Strategy 1 avoids the potential artifacts caused by labeling procedures and uncertainties such as the labeling ratio. On the other hand, the main limitations of using the natural probes are the limited arsenal of available probes; their less than ideal spectral characteristics; the limited range of R_o values that can be achieved using them, and the fact that most proteins contain several Trp and Tyr residues. Applications of strategy 2 are limited to small proteins or proteins where a limited number of the reactive side chains can be found [45]. Nitration of tyrosine residues was also successfully applied in few cases [49, 50]. Strategy 5 is the ultimate one, which achieves full freedom for the designer of protein derivatives best suited for testing well-defined working hypotheses. This strategy will most probably become the method of choice in the field of spectroscopic research of protein folding [43, 51]. The limited scope of application of this approach at the present time is mainly due to the very sophisticated and multistep operations involved and the low yields. These yields are limiting only in the case of measurements of folding kinetics, where many samples are employed (e.g., stopped-flow double kinetics experiments). In most FRET folding experiments, the sensitivity of the fluorometric detection systems makes this method satisfactory and promising. Strategy 6 is not of general use due to the limited number of known suitable enzymatic reactions and the multiplicity of the reactive side chains. The well-documented catalysis of peptide bond synthesis by proteolytic enzymes was applied (for C-terminal labeling of RNase A [44]) but it is not easy to apply as a general method. Transglutaminase catalysis of insertion of primary amino groups attached to fluorescent probes was also attempted [46–48] but the development of strategy 4 offers a simpler route.

Strategy 4 is currently the most practical approach for several reasons: first, exposed cysteine residues are rare, and in many proteins these residues can be replaced by Ser or Ala residues without major perturbations of structure and function. Thus, most proteins can be engineered to have two exposed sulfhydryl side chains. Second, the arsenal of sulfhydryl reactive pairs of probes covering a wide range of spectroscopic characteristics and R_o values is abundant, and the experimental design can be optimized to meet a wide variety of distances and labeling conditions. Third, these reagents can be selectively targeted at the cysteine residues and huge amounts of-labeled mutants suitable for kinetic experiments can be produced [40, 52–57].

17.5.3
Preparation of Double-labeled Mutants Using Engineered Cysteine Residues (strategy 4)

Although reagents for selective alkylation of sulfhydryl residues are available, the challenge here is to develop methods for selective modification of each one of the

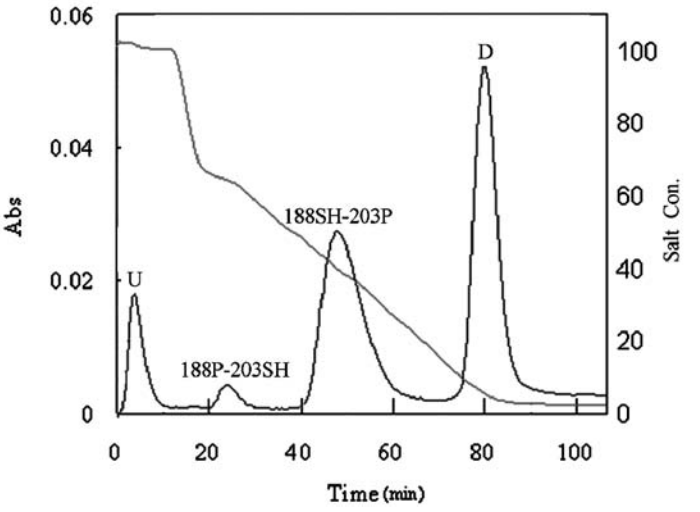

Fig. 17.6. The first step in preparation of a set of labeled AK mutants for trFRET experiments (labeling strategy 4). An engineered AK mutant with two engineered cysteine residues at sites 188 and 203 was prepared and reacted with 1-iodo-acetamido-methyl-pyrene. The reaction was allowed to proceed for 24 hours. The excess reagent was removed by dialysis and the solution was equilibrated with 0.5 M $(NH_4)_2SO_4$ in 20 mM Tris pH 7.5. The reaction mixture was then applied to a phenyl-sepharose column (1 cm diameter, height 7 cm) equilibrated with the same salt solution. The column was eluted with a gradient of decreasing salt concentration. The four fractions that were well resolved were: unlabeled protein (U), the two single labeled proteins (188P-203SH where only cysteine 188 was labeled, 188SH-203P where only cysteine 203 was labeled) and a double-labeled fraction (D). The main product, 188SH-203P, was later on reacted with an acceptor reagent to produce the double-labeled protein. The differential reactivity of the two engineered cysteine residues is demonstrated.

two reactive sulfhydryl groups in the same protein molecule (Figures 17.6 and 17.7).

Submilligram amounts of labeled proteins can suffice for a full set of FRET experiments under equilibrium conditions. Such minute amounts of site-specific double-labeled protein samples can be prepared, based on high-resolution chromatography, i.e. chromatography of a mixture of the possible products, following a nonselective reaction of two-cysteine mutants with a fluorescent reagent. Homogeneous double-labeled products can be obtained in a second cycle of reaction and separation. Hundred-fold larger preparations of labeled proteins are needed for stopped-flow double-kinetic experiments. In this case, it is desirable to develop methods in which the selectivity is achieved by differential reactivity of selected sites on the protein molecule. A general systematic procedure was developed for high-yield selective labeling of each one of two cysteine residues in mutant protein molecules [57, 58]. The determination of individual reaction rate constants of the engineered SH groups and the optimization of reaction conditions enabled high yields (70–90%) of the preparation of pure, site-specific double-labeled AK mutant.

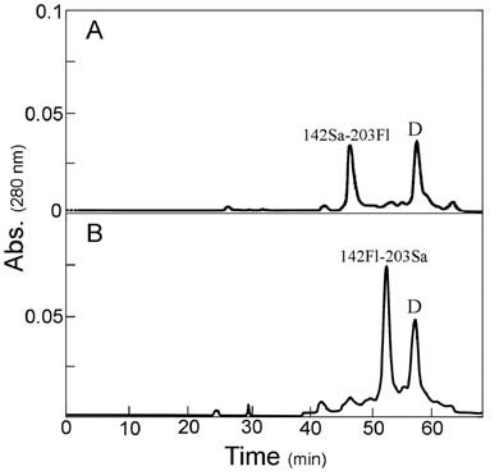

Fig. 17.7. Preparation of site-specific double-labeled AK with two engineered cysteine residues (142 and 203) in a single reaction step (strategy 4). The 10-fold reactivity of cysteine 203 relative to the reactivity of cysteine 142 enabled the preferred labeling of residue 203. The reaction mixture was separated on a Mono-Q ion exchange column (0.5 × 5 cm). Two preparations are shown: A) the acceptor (Fl) was reacted first (equimolar ratio of dye to protein, 2.5 h) and then a 10-fold excess of the donor reagent (Sa) and concentrated GdmCl (to a final concentration of 2 M) were added. After 2.5 h at room temperature. The reaction was stopped by addition of 50-fold excess DTT and dialyzed into 20 mM Tris pH 8.0 before the chromatography. B) The same procedure was repeated, except that the probes reagents were added in the reversed order. Single separation step gave the pure double-labeled products in both cases.

These high yields make some otherwise difficult experiments feasible, such as the double kinetics time-resolved FRET measurements [59, 60].

Jacob et al. [58] improved the prediction of the rates of reactions of engineered cysteine residues at selected sites in a protein. They based this on the observed correlation between reactivity of engineered sulfhydryl groups and the effect of neighboring charged groups (due to dependence of its pK_a), and the freedom of rotation of the side chain. The selectivity of the labeling reaction can be further enhanced by local increase or reduction of reactivity of selected side chains by means of conformational effects. Solvent composition (organic solvents, salt components, and pH) and temperature are the most common variables that can differentially affect the reaction rate constants of selected side chains. Drastic effects can be obtained by ligand binding (substrates, inhibitors, and protein–protein interactions). In this work, the ratio of the reaction rate constants was examined only under a range of temperatures and salt concentrations.

The level of homogeneity required for spectroscopic measurements makes the chromatographic separation steps indispensable. Separation of the reaction products can be enhanced when one of the labels is either charged or very hydrophobic. Yet, either hydrophobicity or extra electrostatic charges can affect the folding path-

way of proteins and can be a disadvantage when the modifications are made for structural studies. Affinity chromatography was also used for separating multiple-labeled protein derivatives [45, 61]. It is also possible to use a mixed disulfide resin for separation of fractions with free cysteine residues in the process of labeling two-cysteine mutants. The single-labeled mutants that are used for the reference measurements can be prepared by straightforward labeling of single cysteine mutants. Caution must be taken since in several cases it was shown that the spectroscopic properties of a probe attached at one site on a protein are significantly modified when the second cysteine was inserted at the second site for the double labeling. In this case, it is desirable to use the corresponding single-labeled protein sample of the two-cysteine mutant in which the second cysteine residue is blocked by a nonfluorescent alkylation reagent such as iodoacetamide.

17.5.4
Possible Pitfalls Associated with the Preparation of Labeled Protein Samples for FRET Folding Experiments

Important issues associated with the sample preparations include: (a) the specificity and the extent of labeling; (b) the purity of the labeled samples; and (c) possible effects of the labeling procedures and modifications on the stability, activity, solubility, and folding mechanisms.

(a) Incomplete specificity of the labeling might prohibit meaningful interpretation of trFRET data, since the reference measurements might not be faithful to the double-labeled samples. Consequently, distributions of labeled products might be interpreted as distributions of distances. In principle, under conditions where the extent of distribution of labeling sites is known, it should be possible to adjust the model in the analysis algorithm and resolve subpopulations of distance distributions. This, however, might be possible only under very limited circumstances, and since it requires the addition of parameters in the analysis, the uncertainties might become too high.

(b) Two types of impurities are of concern here: the first is the presence of fluorescent impurities and background emission, and the second is incomplete labeling. As long as the background emission is not too high (ca. $< 20\%$ of the signal), and the emission can be determined independently (control experiments), reliable distance determination is possible by careful subtraction of the background emission. Incomplete labeling of the single-labeled samples should not interfere with analysis of trFRET data. Analysis of data collected with double-labeled samples that contain fractions of single-labeled molecules can be achieved as long as an independent analytical procedure is employed to determine the size of such fractions and that these fractions do not exceed about 25% of the molecules. Consider the results of a FRET measurement using a preparation where a donor–acceptor labeled protein sample contains 20% molecules labeled with donor only, without acceptor. A long lifetime component would be observed in the decay of the donor fluorescence, and this can erroneously be interpreted as a fraction of molecules with long intramolecular distance (''unfolded subpopulation''). When the size of

such a fraction is known this decay component can be considered and the correct distance distribution can be recovered. Less strict requirements apply in preparations made for single molecule FRET measurements. Data collected from molecules which lack one of the probes in a double-labeled preparation can be easily recognized and discarded without bias of the computed distributions.

(c) By definition, chemical or mutational modifications of any protein molecule are a perturbation, which should be minimized. Naturally, the modified proteins are different from the native ones, which is not a matter of concern unless the experiments are aimed at studying specific aspects of the folding of a specific protein. In many folding studies, the more important concern regarding the modification is that in a series of modified mutants of any model protein the perturbations should be similar in all mutants. Such common perturbation enables reliable multiprobe test of the cooperativity and steps of the folding mechanism where each pair probes the folding of the same model protein at a selected section of the chain (e.g., secondary structure elements, loops, and nonlocal interactions). Structural perturbations can be minimized by the proper choice of labeling sites and probes. Rigorous control experiments for determination of the extent of perturbation due to the modifications are mandatory. Control experiments can include the determination of biological activities; the detection of structural properties such as CD, IR, and other spectral characteristics and rates of refolding.

17.6 Experimental Aspects of Folding Studies by Distance Determination Based on FRET Measurements

17.6.1 Steady State Determination of Transfer Efficiency

17.6.1.1 Donor Emission

The most commonly used method for steady state determination of transfer efficiency is based on the determination of the extent of quenching of donor emission in the double-labeled samples (Eqs (12)–(14)). Emission of the donor is recorded at a wavelength range free of acceptor emission and then $E = 1 - I_{DA}/I_D$ where I_{DA} and I_D are the donor emission intensities in the presence and absence of an acceptor respectively. Both intensities should be normalized to the same donor concentration. It may be difficult to determine the concentration of the donor in the presence of an acceptor. This difficulty (which is eliminated in the time-resolved experiment) was solved by enzymatic digestion of each sample after determination of I_{DA}. A second emission intensity measurement immediately after the digestion thus provides I_{DA} and an internal reference [62]. The FRET interaction does not affect the shape of the spectra of the probes. Therefore, nonlinear least squares fitting of the absorption and emission spectra of the double- and single-labeled samples can be used to overcome the concentration normalization problem [63]. The nonlinear least squares fitting of the entire emission spectral ranges can improved

the accuracy of transfer efficiency calculations when the donor and acceptor emissions overlap [34, 64].

17.6.1.2 Acceptor Excitation Spectroscopy

The most direct and error-free determination of FRET efficiency by steady state experiments is obtained when the excitation spectra of the acceptor recorded for three samples are normalized (at the acceptor excitation range) and superimposed (Eq. (15)). The three samples (and corresponding spectra) are (a) the acceptor single-labeled mutant (I_A^{ex}), (b) the double-labeled mutant (I_{DA}^{ex}), and (c) a special double-labeled reference of well documented transfer efficiency, E_{ref} (preferably a compound in which the two probes are very close, $E_{ref} = 1.0$) (I_{ref}^{ex}). The integrated areas under the three curves in the donor excitation wavelength range provides the transfer efficiency free of instrumental artifacts and concentration normalization:

$$E = \frac{I_{DA}^{ex} - I_A^{ex}}{E_{ref} I_{ref}^{ex} - I_A^{ex}} \tag{31}$$

17.6.2 Time-resolved Measurements

Equations (17)–(19) are used for the determination of the average FRET efficiency by time-resolved measurements. The main technical advantage of this measurement is that there is no need to know the concentrations of the proteins and the accuracy of the lifetime measurements surpasses that of the steady state intensity measurements. Intramolecular distances can be obtained from measurements of the average transfer efficiency only for very uniform structures.

The shape of fluorescence decay curves of the probes in time-resolved FRET experiments contain detailed information on heterogeneity of the ensembles of protein molecules and are therefore much more effective in the folding research. The scheme shown in Figure 17.8 demonstrates the application of trFRET in folding research. The fluorescence decay of the donor (and the acceptor as well) contain the information on the distribution of the distance between the two labeled sites and that can be used for characterization of the conformational state of the labeled protein molecule at equilibrium and during the folding/unfolding transitions.

The technology of time-resolved fluorescence measurements reached a level of maturity during the last quarter of the twentieth century. During this period, the main technological developments that promoted the art of time-resolved measurements to a stage of stable and routine analytical method were (a) the implementation of tunable picosecond laser sources (at present mainly the titanium sapphire solid state lasers); (b) the development of very fast and sophisticated single photon counting devices and the phase modulation instruments; and (c) the development of efficient algorithms for global data analysis. Fluorescence decay can be detected either by the single-photon counting method or by the phase modulation method, and in principle, both methods are equivalent. While phase experiments are rela-

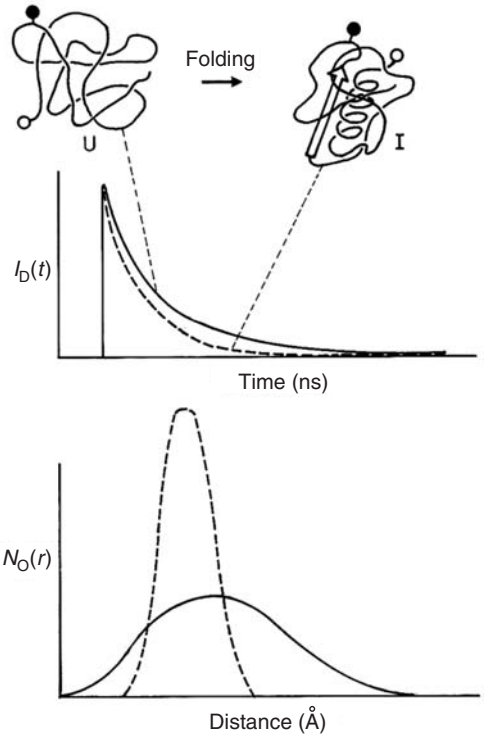

Fig. 17.8. A scheme of the application of the time-resolved energy transfer experiments for determination of conformational changes in globular protein. The scheme describes a hypothetical two states folding transition in a globular protein. The corresponding time domain signals, the decay curves of the donor in the two states, are shown in the center of the scheme. The two corresponding intramolecular distance distributions derived from the time domain data, are shown in the lower section. This scheme is a simulation of the detection of a formation of a nonlocal interaction, indicated by a transition from a broad to a narrow distribution with a smaller mean distance.

tively easy to perform, single-photon counting techniques offer more straightforward methods for incorporation of acceptor decay curves in the analysis and easier control of background subtraction and other corrections.

A standard current state of the art setup for time-correlated single-photon counting measurements includes:

1. An excitation source: a picosecond mode-locked Ti:sapphire laser pumped by a high-power diode laser equipped with broadband optics and a pulse selector which is used to reduce the basic 76 or 80 MHz pulse rate to 1–10 MHz (according to the lifetime of the probes). The laser output is frequency-tripled by a flexible second and third harmonics generator. Such systems can be tuned over ranges from 230 nm to 330 nm, 400 nm to about 500 nm, and 720 nm to above 1000 nm and produce trains of 1.6 ps pulses (before doubling) with minimal drift.

2. A spectrometer which includes a thermostated cell holder equipped with stirring device; a double Fresnel rhomb at the excitation side; a polarizer at the emission side; a double 1/8 meter subtractive monochromator and cooled microchannel plate PMT detector biased at −3200 V.
3. A single-photon counting board (e.g., SPC 630, Becker & Hickel GmbH) fed via an preamplifier and triggered by a photodiode. The response of such system yields a pulse width of 20–30 ps.

17.7 Data Analysis

The basic procedure used for analysis of experiments follows the common practice of analysis of time-resolved experiments. The basic procedure is based on a search for a set of free parameters. These are the parameters of the distribution function; the diffusion coefficient; the fluorescence lifetimes and their associated preexponents. A calculated donor emission impulse response, $i_c^D(t)$ is obtained via numerical solution of Eqs (25)–(28) or (30). The acceptor impulse response, $i_c^A(t)$, is obtained by the convolution of, $N_A(t)$, the calculated population of molecules. The acceptor probes are excited at time t either via the FRET mechanism or via direct excitation, with the acceptor fluorescence lifetime (in the absence of FRET), $i_A(t)$,

$$i_c^A(t) = N_A(t) \otimes i_A(t) \tag{32}$$

A calculated fluorescence decay of the donor, $F_D(t)$, is obtained by the convolution of the donor impulse response with the system response,

$$F_D(t) = k_D(\lambda_{em})[I(t, \lambda_{ex}, \lambda_{em}) \otimes i_c^D(t)] \tag{33}$$

where $k_D(\lambda_{em})$ represents the emission spectral contour of the donor relative to the acceptor and $I(t, \lambda_{ex}, \lambda_{em})$ represents the experimentally measured instrument response function at this particular optical setup (excitation and emission wavelengths setting, monochromator setting, detector spectral response, etc.). A calculated acceptor decay curve, $F_A(t)$, is similarly obtained by:

$$F_A(t) = k_A(\lambda_{em})[i_c^A(t) \otimes I(t, \lambda_{ex}, \lambda_{em})] \tag{34}$$

The final calculated fluorescence decay profile is therefore,

$$F_{calc}(t, \lambda_{ex}, \lambda_{em}) = F_A(t) + F_D(t) \tag{35}$$

Several computational methods were developed for the search of the set of free parameters of $N_o(r)$ and D. This yields the theoretical impulse response, which when convoluted with the system response, yields $F_{calc}(t, \lambda_{ex}, \lambda_{em})$ best fitted to the experimentally recorded fluorescence decay curves $F_{exp}(t, \lambda_{ex}, \lambda_{em})$ [65, 66]. This procedure is inherently difficult since the analysis of any multiexponential

decay curve is a mathematically ''ill defined'' problem [67, 68]. The quality of fit of the experimental and calculated curves is judged by the minimization to the χ^2 value of the fit and the randomness of the deviations [68, 69].

The differential Eq. (25) does not have a simple general analytical solution (except for specific cases). Consequently, a numerical solution based on the finite difference (FA) method [70, 71] was applied. Therefore the currently most common practice is the use of model distribution functions for $N_o(r)$ with a small number of free parameters. The model used in the experiments described below is a Gaussian distribution ($N_o(r) = C4\pi r^2 \exp -a(r-\mu)^2$ where a and μ are the free parameters which determine the width and the mean of the distribution respectively and C is a normalization factor). Correlations between the free parameters, mainly a, μ and D, searched in the curve-fitting procedure leave a range of uncertainties in these values. This uncertainty is being routinely reduced by global analysis of multiple independent measurements. In particular, coupled analysis of the fluorescence decay of both the donor and the acceptor probes contributes over-determination of the free parameters. This over-determination is sufficient to allow simultaneous determination of both the parameters of the equilibrium intramolecular distance distribution and the diffusion coefficients, despite the strong correlation between those parameters [38].

The information content of the decay curves of the two probes is not redundant. Due to the r^{-6} dependence of the transfer probability, the fluorescence decay of the donor is insensitive to contributions from the conformers with intramolecular distance $r \ll R_o$ (fast decay). The contribution of these conformers is well detected in the fluorescence decay of the acceptor. On the other hand, the contributions of the fractions of the distance distributions characterized by intramolecular distance $r > R_o$, are well detected by the donor decay and are less weighted in the acceptor fluorescence decay. Both simulations and experiments have shown the following: with the present level of experimental noise of the time-resolved experiments a ratio of fluorescence lifetimes of the donors and the acceptors, $\tau_D/\tau_A \geq 3$ is a necessary condition for reliable simultaneous determination of the parameters of the intramolecular distribution functions and the associated intramolecular diffusion coefficients. Several curve-fitting procedures are available, the most widely used are based on the well-known Marquardt-Levenberg algorithm [38].

Maximum entropy method (MEM) is also applied to the analysis of time-resolved fluorescence [72] and FRET experiments [73]. This analysis is independent of any physical model or mathematical equation describing the distribution of lifetimes. Whatever methods are used for data analysis, the best fit must be tested by the statistical tests. Fine details of the distance distributions can be extracted from each experiment depending on the level of systematic and random noise of the system.

The routine global analysis procedure includes joint analysis of at least one set of four fluorescence decay curves of the probes attached to the protein. Two measurements are conducted on a double-labeled molecule, containing one donor and one acceptor: (a) The ''DD-experiment,'' determination of τ_D the fluorescence decay of the donor in the presence of FRET (excitation at the donor excitation wavelength

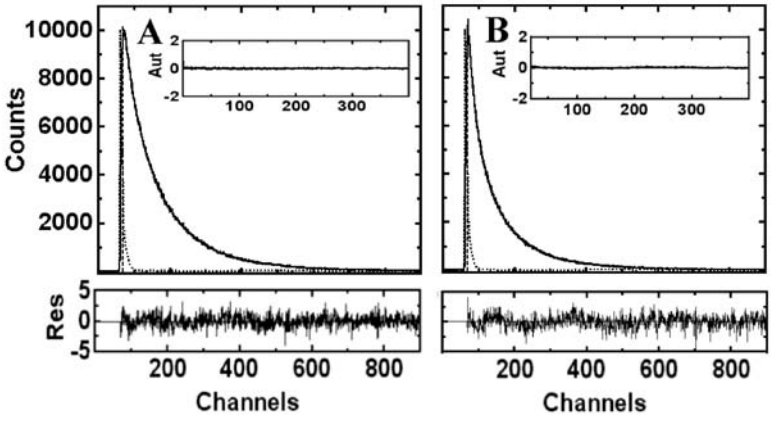

Fig. 17.9. Representative pair of donor fluorescence decay curves used for determination of intramolecular distance distributions in a labeled RNase A mutant. A) Fluorescence decay curves for the tryptophan residue in W^{76}-RNase A (the "D"-experiment) and B) the fluorescence decay of the tryptophan residue in (76–124)-RNase A in the reduced under folding conditions (R_N state) in 40 mM phosphate buffer, pH 7.0, 20 mM DTT (the "DD" experiment) at room temperature. Excitation wavelength 297 nm and emission at 360 nm (bandwidth for emission was 2 nm). (. . .) the system response to excitation pulse, (---) the experimental trace of the tryptophan fluorescence pulse, and (—) the best fit theoretical curves obtained by the global analysis. The "DD" experiment was fit to a theoretical curve based on the distribution of distances [31]. The residuals of the fits (Res) are shown in the lower blocks, and the autocorrelation functions of the residuals [$C(t)$] are presented for each curve in the upper right inset. The χ^2 obtained in this experiment was 2.02 (reproduced with permission from ref. 40).

and detection at the donor emission wavelength); and (b) The "DA-experiment," determination of τ_A, the acceptor emission in the presence of FRET, with excitation at the donor excitation range, and detection of the acceptor emission at the long wavelength range (Figure 17.9). Two internal reference measurements for determination of the probes lifetime when attached to the same corresponding sites as in the double-labeled mutant but in the absence of FRET. (c) The "D-experiment" is a measurement of τ_D^o, the emission of the donor in the absence of an acceptor, using protein molecule labeled by the donor alone; and (d) the "A-experiment" is a measurement of τ_A^o, the decay of the acceptor emission in the double-labeled protein, excited directly at a wavelength where the donor absorption is negligible or using a protein preparation labeled by the acceptor only.

When collected under the same laboratory conditions (optical geometry, state of the instrument, time calibration, linearity of the response, and solution parameters) used for the first two experiments, the D- and A-experiments serve as "internal standards" for the time calibration of this experiment and the dependence of the spectroscopic characteristics of the probes applicable for the specific labeled sites and experimental conditions of the FRET experiments. These on-site obtained data contribute to the elimination of most possible sources of experimental uncertainty due to variations between independent measurements and conditions.

Why monitor the FRET effect twice, both at the donor and at the acceptor end? Brand and his students [66] showed that this over-determination significantly reduces the uncertainty in the values of the free parameters, searched by curve-fitting procedures. The Brand group introduced the concept of global analysis in the field of time-resolved fluorescence measurements and showed that every additional independent data set that is globally analyzed, further reduces the statistical uncertainty in the most probable values of the searched parameters. Beechem and Haas [38] showed that the global analysis of sets of donor and acceptor decay curves can reduce the uncertainty in the values of the parameters of the distance distributions and their associated diffusion coefficients. Both a shift of the mean and reduction of the width of a distance distribution as well as an enhanced rate of the intramolecular diffusion can cause similar reduction of the donor fluorescence lifetime. The fine differences between the two mechanisms appear in the shape of the decay curves and hence the combined analysis of the donor and the acceptor decay curves can resolve the two mechanisms.

17.7.1 Rigorous Error Analysis

The statistical significance of the value of any one of the free parameters that is determined by any curve-fitting method can be evaluated by a rigorous analysis procedure. In this procedure the iterative curve-fitting procedure is repeated while the select parameter is fixed and the other free parameters adopt values that yield the best possible fit under the limitation of that fixed value of the selected parameter. This procedure can be repeated for a series of values of the selected parameter, and the limits of acceptable values can be determined by the statistical tests and the selected thresholds, in particular those of the χ^2-values (Figure 17.10). This procedure, if repeated for every free parameter, actually generates projections of the χ^2 hypersurface on specific axes in the parameter space. Error limits at any required significance level can then be determined using an F-test [38].

This procedure considers all correlations between the parameters. The evaluation of each analysis and of the significance of the parameters is based on four indicators: (1) The global χ^2-values; (2) the distributions of the residuals; (3) the autocorrelation of the residuals; and (4) the error intervals of the calculated parameters obtained by the rigorous analysis procedure. In addition, each ''DD-experiment'' is analyzed by multiexponential (three or four exponentials) decay model. The χ^2-values obtained in these analyses serve for evaluation of the significance of the χ^2-values obtained for each set of experiments in the global analysis, based on the solution of Eqs (25)–(28) and (32)–(35).

17.7.2 Elimination of Systematic Errors

The linearity of the systems and possible effects of systematic errors are routinely checked by measurements of the fluorescence decay of well-defined standard ref-

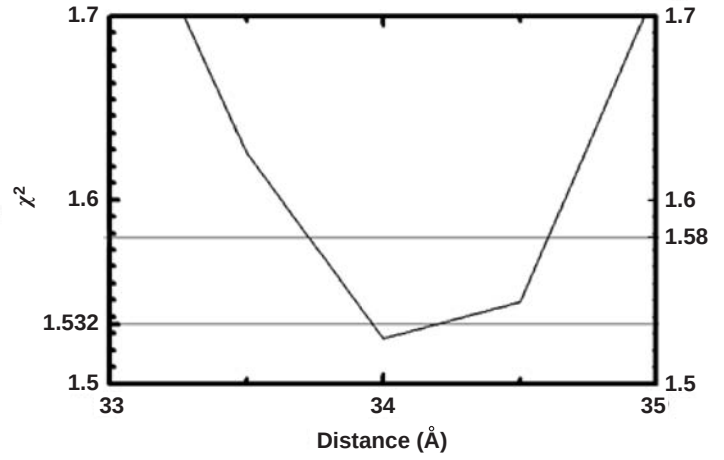

Fig. 17.10. χ^2 surface obtained in rigorous analysis of a typical trFRET experiment for determination of intramolecular distance distribution in double-labeled adenylate kinase mutant labeled at residues 154 and 203. Global analysis was repeated for several fixed values of the intramolecular mean distance and all other parameters were allowed to change. The ranges of one and two standard deviations at χ^2 values of 1.53 and 1.58 respectively are shown and can be used for determination of the uncertainty range for the mean of the distance distribution.

erence materials (e.g., anthracene in cyclohexane). The fluorescence parameters of the reference materials (monoexponential decay of the fluorescence, lifetimes, quantum yields, and spectra) are well known and can be used for testing and fine tuning of the response of the instruments (mainly linearity, time calibration, and dynamic range). Possible effects of other potential systematic errors, introduced by non-FRET effects of conformational changes on the spectral parameters of the probes (e.g., environmental sensitivity, spectral shifts, or quenching) are eliminated by inclusion of the two reference protein derivatives in each experiment. In practice, the error ranges obtained for the mean of the distance distributions determined by trFRET experiments were minimal ($\Delta r < \pm 1$ Å), and the highest uncertainty was encountered in the values of the diffusion parameters.

17.8
Applications of trFRET for Characterization of Unfolded and Partially Folded Conformations of Globular Proteins under Equilibrium Conditions

17.8.1
Bovine Pancreatic Trypsin Inhibitor

Bovine pancreatic trypsin inhibitor (BPTI) (Figure 17.11) is a small, stable globular protein of 58 amino-acyl residues, including four lysyl residues and three disulfide bonds [74, 75]. Four double-labeled BPTI samples were prepared for measure-

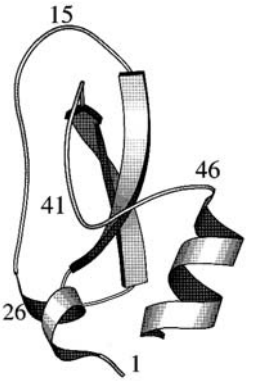

Fig. 17.11. The crystal structure of BPTI, a stable, single folding unit protein. The N-terminus was the site of attachment of the donor probe, 2-methoxy-naphthyl-methylenyl (MNA), and the acceptor, 7-dimethyl-amino-coumarin-4-carboxymethyl (DA-coum), was attached to the lysine residues (15, 26, 41, and 46 in four different preparations), thus labeling a series of monotonically increasing chain length.

ments of a series of increasing chain segmental lengths between the N-terminus (attachment of the donor) and residues 15, 26, 41, and 46 (sites of acceptor attachment) [45].

Relatively narrow distributions with mean distances close to those expected, based on the crystal structure, were obtained for all four-labeled BPTI samples in the native state. This result confirmed the validity of the distance calibration and the orientational averaging of the probes.

17.8.2 The Loop Hypothesis

Reduced BPTI in 6 M GdmCl is fully denatured [75, 76], but under these conditions the mean of the four intramolecular distance distributions did not show monotonous increase as a function of labeled chain length [77]. The mean distances were reduced by raising the temperature from 4 °C to 60 °C. These results are an indication of conformational bias of the distribution even under drastic denaturing conditions (i.e., the protein was partially unfolded). The strong temperature dependence of the mean distances is cold unfolding transition [78] and an indication that the structures that exist in the denatured state are probably stabilized by hydrophobic interactions. Moreover, at least two, one native-like and one unfolded, subpopulations were distinguished in the distributions of end-to-end distances of each segment. The sizes of the two subpopulations were temperature- and denaturant concentration-dependent [79] (i.e., transition to more folding conditions increased the native like subpopulation and reduced the unfolded one).

These observations led to *the loop hypothesis*, which states that loop formation by specific nonlocal interactions (NLIs) prior to the formation of secondary struc-

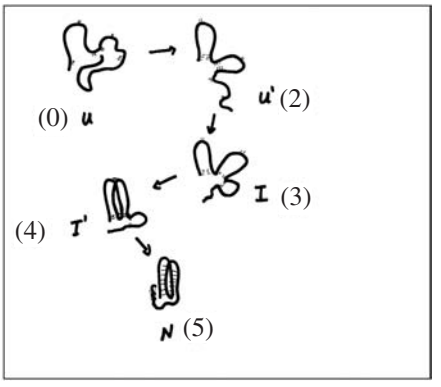

Fig. 17.12. The loop hypothesis. A scheme of a protein molecule with several groups of residues that form nonlocal interactions is shown. A hypothetical pathway is shown where after formation of four nonlocal interactions the chain fold is native-like and the last step of packing all the local interactions completes the folding transition.

tures can be a key factor both in the solution of the Levinthal paradox and in determining the steps which direct the folding pathway [79] (Figure 17.12). The loops, generated by loose cross-links between specific clusters of residues separated by long chain stretches, may bias the intramolecular distance distributions and reduce the chain entropy and the volume of the searched conformational space. The observation of the cold unfolding of the intramolecular loops [77] led to the suggestion that the main interaction between these clusters should be hydrophobic. These long loops define the basic folding unit and thus BPTI is composed of two folding units [79]. A similar mechanism was recently suggested by Klein-Seetharaman et al. [80] based on the NMR study of the denatured state of lysozyme. This specificity of the interactions is in agreement with Lattman and Rose [81], who suggested that a specific stereochemical code directs the folding. FRET experiments can be designed to locate those interactions, and site-directed mutagenesis can be used to test the hypotheses of the role of specific residues in the formation of the NLIs. Berezovsky et al. [82, 83] analyzed the crystal structures of 302 proteins in search for native loop structures. They showed that protein structure can be viewed as a compact linear array of closed loops. Furthermore, they proposed that protein folding is a consecutive looping of the chain with the loops ending primarily at hydrophobic nuclei.

17.8.3 RNase A

Navon et al. [40] applied this same experimental approach to the study of the unfolded and partially folded states of reduced ribonuclease A (RNase A). RNase A represents a higher level of complexity in the folding problem. The chain length is twice that of BPTI (124 residues). Buckler et al. labeled the C-terminus of RNase

A with a donor and attached the acceptor to residues 104, 61, or 1, one at a time. This set of pairs of labeling sites spans the full length, one half of the length of the chain and the C-terminal segment [44, 84]. Navon prepared 11 double-labeled RNase A mutants to probe the folding transitions in the C-terminal subdomain of the protein.

The pattern of the dependence of the means of the end-to-end distance distributions of the labeled segments in the RNase A mutants on the number of residues in each segment resembled the pattern of the segment length dependence of the corresponding Cα-Cα distances in the crystal structure of the molecule. But the width of the distributions was large, an indication for very weak bias by nonlocal interactions.

The distance distribution between the C-terminal residue (residue 124) and residue 76 (a 49-residue chain segment) was another example whereby two subpopulations were resolved. The distributions represent an equilibrium between native-like and unfolded conformers (Figure 17.13). The same equilibrium was found for the chain segment between residues 76 and 115.

The intramolecular segmental diffusion coefficients obtained by Buckler et al. [84] correlated well with the conformational states of the chain. In the native state, only the distance between the two chain termini showed rapid nanosecond fluctuations; in the presence of 6 M GdmCl, the shorter segments also underwent rapid intramolecular distance fluctuations which were further enhanced by the reduction of the disulfide bonds. This demonstrates that the segmental intramolecular diffusion coefficients can be determined and used as another parameter for monitoring specific changes of the states of folding intermediates.

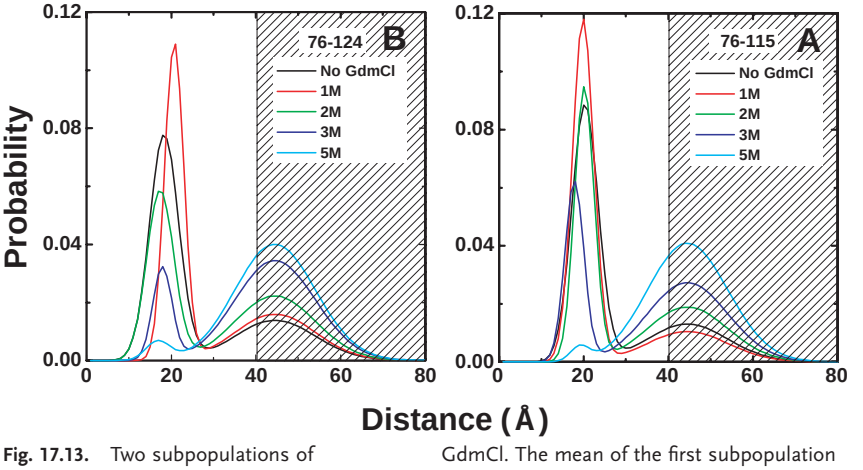

Fig. 17.13. Two subpopulations of intramolecular distance distribution between residues 76 (tryptophan residue, the donor) and 124 (engineered cysteine residue labeled by an aminocoumarin derivative, the acceptor) in the C-terminal subdomain of reduced RNase A were resolved by the trFRET experiment (in 40 mM HEPES buffer pH 7.0, 20 mM DTT, and 5 mM EDTA) with increasing concentrations of GdmCl. The mean of the first subpopulation was close to that of the native state; the mean of second subpopulation was much larger, but could not be determined with a high degree of accuracy due to the smaller R_0. The ratio of the unfolded subpopulations increased from 30% in HEPES buffer to 95% at 6 M GdmCl (Reproduced with permission from ref. 40).

17.8.4
Staphylococcal Nuclease

Brand and coworkers [85, 86] used a similar approach in a search for structural subpopulations and chain dynamics in the compact thermally denatured state of staphylococcal nuclease mutant. Two subpopulations were found in the distribution of distances between residues 78 and 140 in the heat-denatured state. At the highest temperatures measured, both the apo- and holoenzyme showed compact and heterogeneous populations in which the nonnative subpopulation was dominant. The asymmetry found in the distribution of distances between Trp140 and a labeled Cys45 in the destabilized mutant K45C at room temperature (native state) was attributed to static disorder. Partial cold unfolding or chemical denaturation reduced the asymmetry of the distribution and its width. This effect was analyzed in terms of the nanosecond dynamic flexibility of the protein molecule.

17.9
Unfolding Transition via Continuum of Native-like Forms

Lakshmikanth et al. [73] and their collaborators employed the strength of the multiple pairs trFRET experiments to reveal multiple transitions in the unfolding of a small protein. Lakshmikanth et al. [73] used a maximum entropy method for determination of the distributions of intramolecular distances between Trp53 and the trinitrobenzoic acid moiety attached to Cys82 in the bacterial RNase inhibitor barstar. They found that the equilibrium unfolding transition of native barstar occurs through a continuum of native-like conformers. They also concluded that the swelling of the molecule as a function of denaturant concentration to form a molten globule state is separated from the unfolded state by a free energy barrier. This is another demonstration of the effectiveness of FRET-detected folding experiments in the multiple probe test of the cooperativity of folding/unfolding transitions.

17.10
The Third Folding Problem: Domain Motions and Conformational Fluctuations of Enzyme Molecules

Lakowicz and coworkers [41, 89–93] applied frequency domain FRET methods in experiments that focused on the third folding problem, the functional refolding of various proteins. Residues Met25 and Cys98 in rabbit skeletal troponin C located at the N- and C-terminal domains respectively were labeled by a donor and acceptor. At pH 7.5 and in the presence of Mg^{2+}, the mean distance was close to 15 Å and the FWHM was 15 Å, a flexible structure. The addition of calcium caused an increase of the average distance to 22 Å and a decrease of the width by 4 Å, a transition to an extended and more uniform ensemble of conformers. At pH 5.2, the conformation of troponin C is further extended with an average distance of 32 Å,

and a narrower FWHM of only 7 Å. Similar results were obtained in the complex of troponin C and troponin I. This finding is a good example of the application of the FRET methods in studies of conformational changes involved in functional refolding of proteins.

Vogel et al. [94, 95] developed applications of FRET measurements in studying conformational transitions of membrane peptides and proteins.

The unique feature of proteins is that they have probably evolved to couple between conformational fluctuations and the specific tasks they perform [96, 97]. A prominent example of this principle is the enzymes that can be viewed as machines designed to accelerate chemical transformations by dynamic adaptation of specific binding sites to metastable transition states [98–100]. This can be achieved by a combination of structural flexibility (fluctuations) and a design that allows a limited number of modes of motion [101]. This is manifested in enzymes called transferases which catalyze the transfer of charged groups. Upon substrate binding, these molecules undergo structural changes to screen the active center from water to avoid abortive hydrolysis [102, 103] and catalyze the transfer reaction.

X-ray analysis of enzyme crystals revealed large-scale structural changes associated with substrate binding. These and diffuse X-ray scattering data suggest that domain displacement induced by substrate binding represents a unique mechanism for the formation of the enzyme active center [102, 104].

The dynamic trFRET and the single molecule FRET experiments go beyond existing methods. These experiments are usually able to describe the full conformational space for a specific mode of motion. Moreover, the FRET experiments provide dynamic information which is essential for understanding how the intramolecular interactions (which are programmed in the sequence information of the protein) control the modes of motion that compose the directed conformational change.

Two phosphoryl transfer enzymes were studied as model systems: yeast phosphoglycerate kinase (PGK) [105], which catalyzes the phosphoryl transfer from (1,3)-diphosphoglyceric acid to an ADP molecule, and *E. coli* adenylate kinase (AK) which catalyzes the phosphoryl transfer reaction ($MgATP + AMP \leftrightarrow MgADP + ADP$) [106].

The PGK molecule is made of two distinct domains and a domain closure was postulated as the simple mechanism that brings the two substrates into contact (closure of a 10 Å distance) [107]. A mutant PGK was prepared in which one probe was attached to residue 135 (the N-terminal domain) and the second to residue 290 (C-terminal domain). A very wide distribution was obtained from trFRET measurements of the apo form of the labeled PGK molecule. This is an indication of the multiplicity of conformations. Substrates binding induced an increase in the mean of the distributions (increased interdomain distance) and as expected, reduced the FWHM.

The crystal structure of *E. coli* AK shows three distinct movable domains. A comparison of the crystal structures (Figure 17.14) representing the enzyme in different ligand forms revealed large structural changes [108–110]. Very wide distance distributions were obtained for the distances between both minor domains and

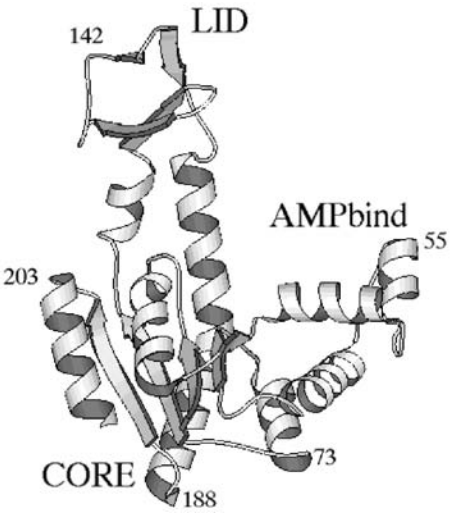

Fig. 17.14. Ribbon diagram of the crystal structure of apo-AK from *E. coli* (1ake) (generated with the program MOLSCRIPT). The sites of attachment of the probes are marked.

the CORE domain in the apo-AK. This an indication for multiple conformers separated by small energy barriers. Furthermore, the crystal structure is only very poorly populated in the apo-AK. Moreover, the wide distributions also include the partial population of the closed conformers, where the interdomain distance is already similar to that of the holoenzyme. This is in support of a select-fit mechanism of the coupling of the domain closure conformational change and the binding of either substrates. Binding of each one of the substrates is associated with substantial reduction of the mean and width of the distributions, as expected for the domain closure mechanism. The interdomain distance distributions observed for the complexes of the two enzymes with their substrates were narrower, i.e., the flexibility is restricted towards a more uniform structure in solution. The folding of the holoenzyme differs from that of the apoenzyme due to the additional interactions between the pairs of the domains and substrate. Electrostatic interactions (see chapter 7) probably contribute a major part of the extra stabilization of the structures of holo-phosphoryl transferases studied here.

17.11
Single Molecule FRET-detected Folding Experiments

The long-range goal of protein folding research is the elucidation of the principles of the solution of the chain entropy problem, i.e., the guided construction of the native structure. Imagine a dream experiment that would create a movie that fol-

lows a polypeptide chain during its transition from an unordered state to the native state. Single molecule FRET spectroscopy, based on site-specific labeling and the recent advances in laser technology and pinhole optics, makes this dream a reality. It is already possible to continuously monitor trajectories of changes of intramolecular distances in single protein molecules over periods of few seconds. This ultra high sensitivity helps us arrive as closely as possible to the ultimate analytical resolution. Trajectories collected for series of double-labeled protein mutants that monitor various distances in the protein molecule can report the order of formation of the various structures in the protein and their transitions. This type of experiment can add important insights relevant to the central folding questions, but the folding transition is inherently a stochastic process. Therefore, we cannot deduce any general principle from observations of single molecules at any resolution. Consequently, the principles of the mechanism of the folding transition must be investigated in the behavior of the ensembles, not in the individual molecules. So how do the amazing modern achievements of single molecule FRET spectroscopy serve the goals of protein folding research beyond the knowledge gained by the ensemble studies?

Individual trajectories of single molecule FRET spectroscopy can be grouped to generate both distributions of intramolecular distances and rates of their transitions. So why bother with the tedious, noisy single molecule detection, when trFRET can produce the ensemble distributions with much higher signal-to-noise ratio? The extra value of the distributions constructed from individual trajectories of single molecules can be described as follows: (a) these model-free distributions represent the true statistics of the sample trajectories; (b) subpopulations of protein molecules which may differ in the extent of the conformation space that they populate can be resolved; and (c) slow (longer than the span of a lifetime of a donor-excited state) conformational transitions and fluctuations within an equilibrium conformational space can be recorded and analyzed. This subject is of much interest for studies of conformational dynamics of unfolded and partially folded protein molecules.

The dynamic aspects of single molecule FRET really distinguish it from the ensemble trFRET experiments. So, why not quit the ensemble trFRET experiments and concentrate efforts on the promotion of single molecule FRET folding experiments? In general, the folding problem is multidimensional and therefore, a combination of complementary methods is essential. At present, the main limitations of single molecule FRET folding experiments are: (a) limited time resolution; (b) difficulties in performing perturbation initiated fast kinetics experiments; (c) the contribution of shot noise which affects the observed width of the distributions; (d) the problem of immobilization; and (e) quantitative analyses. Quantitative analyses of single molecule FRET experiments are inherently difficult due to the comparative nature of the measurements. Reference trajectories for the determination of variables that are essential input for the analyses of FRET experiments (e.g., determination of I_D, Φ_D^0, or τ_D^o) and control experiments for the non-FRET contributions, such as molecular orientations or non-FRET dye quenching, are difficult to match with individual FRET measurements. Therefore, it seems that a combina-

tion of ensemble and single molecule experiments are and will be the appropriate way to proceed.

17.12 Principles of Applications of Single Molecule FRET Spectroscopy in Folding Studies

In principle, reversible folding–unfolding transitions of single protein molecules can be studied at equilibrium. Through the selection of experimental equilibrium conditions, whereby protein molecules can reversibly cross the barriers between folded and unfolded conformations, single molecule FRET detection allows direct observation of the type of the transitions.

Several recent single molecule FRET studies which employed this strategy were reported. Weiss and coworkers [42] studied the folding of a double-labeled mutant of the two-state folder chymotrypsin inhibitor 2 (CI2) under several partially unfolded conditions (GdmCl concentrations). Subpopulations of folded and unfolded molecules were clearly resolved in this experiment, and their relative contributions under varied denaturant concentrations matched the ensemble denaturation curve. Eaton and coworkers [111, 112] obtained distributions of the folded and unfolded subpopulations of another two-state fast folder, the cold shock protein of *Thermotoga maritime* (Csp*Tm*).

Haran and coworkers [113] developed an elegant confinement technique. This technique enabled them to record relatively long (few seconds) trajectories of the time dependence of an intramolecular distance (between residues 73 and 203) in the CORE domain of *E. coli* adenylate kinase under partially folding conditions. Folding and unfolding transitions appeared in experimental time traces as correlated steps in donor and acceptor fluorescence intensities. The size of the spontaneous fluctuations in FRET efficiency shows a very broad distribution. This distribution which peaks at a relatively low value indicates a preference for small-step motion on the energy landscape. The time scale of the transitions is also distributed, and although many transitions are too fast to be time-resolved here, the slowest transitions may take >1 s to complete. These extremely slow changes during the folding of single molecules highlight the possible importance of correlated, non-Markovian conformational dynamics (Figure 17.15).

17.12.1 Design and Analysis of Single Molecule FRET Experiments

17.12.1.1 How is Single Molecule FRET Efficiency Determined?

In a typical single molecule FRET experiment, the single molecule emission intensities at the donor detector and acceptor detector are measured simultaneously (I_D and I_A). These raw intensities are integrated in time according to the desired time resolution. The problem of obtaining time trajectories of single molecules was solved by implementing two basic strategies: (a) free diffusing molecules in solution in which all the photons emitted in a burst (while the molecule is diffusing

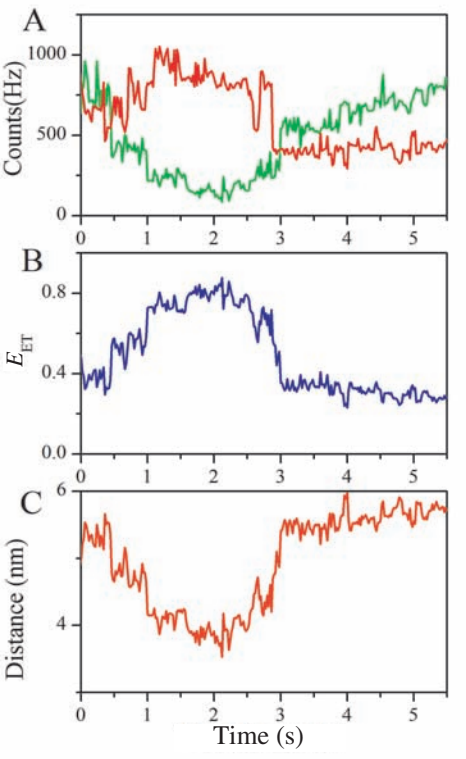

Fig. 17.15. Time-dependent signals from single AK molecules labeled at residues 73 and 203 showing slow folding or unfolding transitions. A) Signals showing a slow folding transition starting at ~0.5 s and ending at ~2 s. The same signals display a fast unfolding transition as well (at ~3 s). The acceptor signal is shown in red, and the donor is shown in green. B) FRET efficiency trajectory calculated from the signals in A. C) The interprobe distance trajectory showing that the slow transition involves a chain compaction by only 20%. The distance was computed from the data presented in trace B using a Förster distance $R_o = 49$ Å.

through the excitation volume) are summed to obtain I_D and I_A; (b) immobilized [114], or confined single molecules [113] in which the photon flux is continuously recorded at time resolution determined by the bining intervals, and $I_D(t)$ $I_A(t)$ are recorded. Following various corrections and filtering techniques (distinguish real molecular signal from noise, correction for leakage of signals due to overlap of spectra) the transfer efficiency, E, is calculated by

$$E(t) = I_A/(I_A + \beta I_D) \tag{36}$$

where β is a correction factor that depends on the quantum yields of the donor and the acceptor and the detection efficiencies of the two channels.

17.12.1.2 The Challenge of Extending the Length of the Time Trajectories

An ideal single molecule FRET folding experiment depends on the ability to follow the temporal trajectory of a single functional biological molecule for a long time under biologically relevant conditions, unperturbed by a trapping method. The free diffusion method which relies on random transit of refolding molecules in the small observation volume (sometimes termed ''burst spectroscopy''), avoid any perturbation at the expense of the limitation of the length of the time trajectories to milliseconds. While this technique is very powerful in separating subpopulations and fast conformational dynamics, the free diffusion approach is not suitable for recording the temporal trajectories of the conformational transitions of individual molecules over extended (seconds) periods. Extended observation periods of individual molecules are important for the identification of slow or rare dynamic events. To enable observation periods for timespans much longer than allowed by diffusion, it is necessary to isolate and immobilize molecules. Several immobilization methods have been reported. Methods whereby the protein molecules were directly attached to a solid surface suffer from the influence of the surface interactions. Entrapment in the pores of poly(acrylamide) [115] or agarose [115] gels was also found to be useful for single molecule immobilization with reduced surface interactions. Haran and coworkers [113, 116] trapped single protein molecules in surface-tethered unilamellar lipid vesicles (Figure 17.16). The vesicles are large enough (~100 nm in diameter) to allow encapsulated protein molecules to diffuse freely within them. Yet because the vesicles are immobilized to a solid

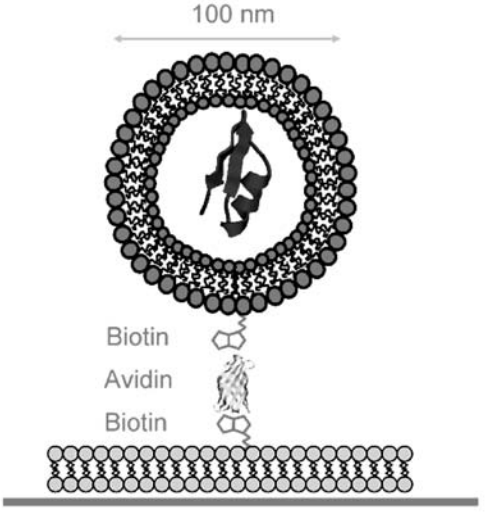

Fig. 17.16. Scheme of the methodology used for surface tethering of single molecule-containing liposomes. Large unilamellar lipid vesicles, each encapsulating a single protein molecule, were attached to a glass-supported lipid bilayer, using biotin-avidin chemistry.

surface, the proteins remain localized within the illuminating laser beam. Therefore, it is possible to record single molecule conformational transitions trajectories whose duration are limited by the photostability of the probes.

17.12.2 Distance and Time Resolution of the Single Molecule FRET Folding Experiments

The distance resolution of the single molecule folding experiments is determined by the characteristics of the pair of dyes and the signal-to-noise ratio, which depends also on the hardware. The scale of the distance determination is defined by the Förster critical distance, R_o, uncertainties in the value of R_o are contributed by the dependence of the parameters of Eq. (6). Uncertainties in the absolute distance calibration are of secondary importance in this case, the main interest in these experiments is in the fast fluctuations of the intramolecular distances due to folding/unfolding transitions. The overlap integral, the dipole orientations, and the donor quantum yield are frequently environmental sensitive, and hence are affected by the time dependent conformational changes. It is impossible to measure trajectories of those parameters simultaneously with the measurements of the FRET trajectories and hence fluctuations of R_o values limit the resolution of the determination of conformational transitions. In addition, in the unfolded or partially unfolded states, most protein molecules undergo conformational fluctuations on time scales shorter than the photon integration time (whether "bining" or burst duration). This can bias the apparent distances towards shorter end. Equation (9) shows that maximal distance resolution is obtained when the interprobe distance, r, equals R_o. An enhanced signal-to-noise ratio of the photon detection, which is essential for reduced uncertainty of the distance determination, calls for the use of dyes with high quantum yields and high extinction coefficients. These in turn contribute to high R_o values, and reduced resolution at the folded states of the proteins, where the distances are reduced. Most of the pairs used to date have R_o values of almost 50 Å. Thus care must be taken in the interpretation of intensity fluctuations results when distances less than 30 Å are involved. A detailed discussion of the signal-to-noise versus distance resolution was presented by Deniz et al. [117].

The time resolution of the single molecule FRET experiments is determined by the photon emission rate. With the current sensitive detection systems the main limiting factor is the extent of the triplet state population which is dependent on the excitation beam intensity and oxygen and triplet quencher agent concentrations [118, 119]. With present-day probes the practical time resolution in determination of trajectories of conformational transitions is in the millisecond range.

At present, the technology of single molecule FRET experiments is in its infancy. Therefore, we have good reason to expect significant further increases of distance and time resolution. The current reported experiments are very promising.

17.13
Folding Kinetics

17.13.1
Steady State and trFRET-detected Folding Kinetics Experiments

A dream folding kinetics experiment (see Chapters 12–15) would be one that would produce a time-dependent series of 3D structures. These structures constitute the transition of an ensemble of molecules from an unfolded state under folding conditions to the folded state. The experiment would probably initiate at very low-resolution blurred 3D images and gradually the profiles would become more resolved and the structures become visible. Would this change to more resolved structures be uniform for the whole molecule or would different folding nuclei or focal points become visible at different time points? FRET-detected rapid kinetic experiments were designed in a search for folding intermediates, the order of formation of structural elements, and the interactions that stabilize them. An analysis of such a dream experiment would hopefully reveal the order of structural transitions and formation of structural elements along very broad and gradually narrowing pathways to the native state. These might hopefully enable inference of the basic principles of the master design of the folding transitions. If such a dream experiment could be combined with site-directed perturbation mutagenesis, it might also be possible to search for the "sequence signals," i.e., inter-residue interactions that stabilize and lock structural elements, either in parallel, simultaneously, or sequentially.

Steady state and trFRET-detected kinetics experiments are far from such dream experiments, but these FRET experiments display some unique qualities that justify the preparative efforts of production of site-specifically labeled protein samples. The goal of these experiments is production of time series of distributions of selected key intramolecular distances (e.g., distances between structural elements). Such series can enable characterization of the transient structures of folding intermediates. The range of detected distances; the time resolution; the direct structural interpretation of the spectroscopic signals; the real time detection and the ability to determine transient distributions of distances add to the kinetic FRET experiment's unique strength.

Both steady state and time-resolved detection were applied together with any method of fast initiation of the folding or unfolding transition, e.g., stopped flow, continuous flow, and T-jump.

17.13.2
Steady State Detection

The ensemble mean transfer efficiency can be detected continuously by rapid recording of the donor emission, or the acceptor emission, or both. As in the case of equilibrium experiments, at least two traces should be recorded: (a) the donor emission ($I_{DD}(t)$) or the acceptor emission ($I_{DA}(t)$) of the double-labeled protein; and (b) the donor or the acceptor emission in the absence of FRET, ($I_D(t)$) or

$(I_A(t))$ respectively. Then,

$$\langle E(t) \rangle = 1 - \frac{I_{DD}(t)}{I_D(t)}$$

quantitative determination of $E(t)$ through detection of the acceptor emission can be performed using Eq. (15), provided that the reference of constant transfer efficiency is available. Elegant examples of steady state FRET monitoring of the kinetics of folding were reported, and the text below describes some representative examples (see Chapter 15).

Eaton and Hofrichter [120, 121] used ultrarapid mixing continuous-flow method to study the submillisecond folding of the chemically denatured cytochrome *c*. Fluorescence quenching due to excitation energy transfer from the tryptophan to the heme was used to monitor the distance between these groups. The biphasic microsecond kinetics were interpreted as a barrier-free, partial collapse to a new equilibrium unfolded state at the lower denaturant concentration. This was followed by a slower crossing of a free energy barrier, separating the unfolded and folded states.

A similar experiment was reported by Roeder and coworkers [122, 123] (see Chapter 15) who studied the early conformational events during refolding of acyl-CoA binding protein (ACBP), an 86-residue α-helical protein. The continuous-flow mixing apparatus was used to measure rapid changes in tryptophan-dansyl FRET. Although the folding of ACBP was initially described as a concerted two-state process, the FRET signal revealed the formation of an ensemble of states on the 100 μs time scale. The kinetic data are fully accounted for by three-state mechanisms with either on- or off-pathway intermediates. The intermediates accumulate to a maximum population of 40%, and their stability depended only on weakly denaturant concentrations, which is consistent with a marginally stable ensemble of partially collapsed states. These experiments demonstrate the strength of fast kinetics FRET measurements, and can reveal and characterize transient accumulation of intermediate states in the folding of a protein considered to have apparent two-state folding mechanisms.

Beechem and coworkers [124, 125] studied the complex unfolding transition of the two-domain protein yeast phosphoglycerate kinase (PGK) using the multiple distances determination approach. Real-time determination of multiple intramolecular distances in the PGK molecule during the unfolding transition was achieved by means of steady state FRET-detected stopped-flow experiments. A series of six site specifically double-labeled PGK mutants was prepared using engineered tryptophan and cysteine residues (''strategy 1''). The unfolding of PGK was found to be a sequential multistep process (native $\rightarrow I_1 \rightarrow I_2 \rightarrow$ unfolded) with rate constants of 0.30, 0.16, and 0.052 s^{-1}, respectively (from native to unfolded). Six intramolecular distance vectors were resolved for both the I_1 and I_2 states. The transition from the native to I_1 state could be modeled as a large hinge-bending motion, in which both domains ''swing away'' from each other by almost 15 Å. As the domains move apart, the C-terminal domain rotates almost 90° around the hinge region connecting the two domains, while the N-terminal domain remains intact during the native to I_1 transition. This elegant set of measurements demon-

strates the potential structural details that can be obtained by FRET determination of multiple intramolecular distances during the unfolding/refolding transitions of protein molecules.

Udgaonkar and Krishnamoorthy and their coworkers used multisite trFRET in a study of the unfolding intermediates in the unfolding transition of barstar [87, 88]. Four different single cysteine-containing mutants of barstar with cysteine residues at positions 25, 40, 62, and 82 were studied. Four different intramolecular distances were measured by steady state detection of the donor emission intensity and multiple, coexisting conformers could be detected on the basis of the time dependence of the apparent mean distances. The authors concluded that during unfolding the protein surface expands faster than, and independently of, water intrusion into the core. Like the works reported previously for the larger proteins, the multisite FRET study of Barstar showed that noncooperative folding, which is not observed by routinely used spectroscopic methods, can be found in unfolding of small proteins as well.

Another application of a multiple-distance probe study of folding of a small two-state protein was recently reported by Magg and Schmid [126]. *Bacillus subtilis* cold shock protein (Bc-CspB) folds very rapidly in a simple two-state mechanism. Magg and Schmid measured the shortening of six intramolecular distances during stopped-flow-initiated refolding by means of steady state FRET. Six mutants labeled by the pair Trp-1,5-AEDANS were prepared by means of labeling strategy 1. The calculated $R_o = 22$ Å fit well with the native dimensions of this small protein. Two pairs of sites were found to have the same inter-residue distance in both the native and the unfolded states. For four donor/acceptor pairs, the probed apparent mean intramolecular distances shorten with almost identical very rapid rates and thus, the two-state folding of this protein was confirmed. At the same time, more than 50% of the total increase in energy transfer upon folding occurred prior to the rate-limiting step. This finding reveals a very rapid collapse before the fast two-state folding reaction of Bc-Csp, and suggests that almost half of the shortening of the intramolecular distances upon folding of Bc-Csp has occurred before the rate-limiting step.

Fink and coworkers [126] used a similar labeling strategy and studied both the equilibrium and transient stopped-flow refolding intermediates of *Staphylococcus* nuclease by means of steady state FRET. The results indicate that there is an initial collapse of the protein in the deadtime of the stopped-flow instrument (regain 60% of the native FRET signal) which precedes the formation of the substantial secondary structure. The distance determination shows similar structures in the equilibrium and transient intermediates.

17.13.3
Time-resolved FRET Detection of Rapid Folding Kinetics: the "Double Kinetics" Experiment

The transient transfer efficiencies determined by steady state detection of the fluorescence intensities of the donor or the acceptor probes report rapid changes of dis-

tances. But since the conformations found in ensembles of partially folded protein molecules are inherently heterogeneous, the mean transfer efficiency (Eq. (12)) cannot be used for the determination of any meaningful mean distances. The mean and width of the distributions of distances in these rapid changing ensembles of partially folded protein molecules can be determined by rapid recording of time-resolved fluorescence decay curves of the probes. This was achieved by the ''double kinetics'' experiment.

The ''double kinetics'' [59, 127, 129] folding/unfolding experiments combine fast initiation of folding/unfolding transitions by rapid change of the solvent synchronized with the very rapid determination of fluorescence decay curves [129]. Single pulse detection enables the determination of fluorescence decay curves in less than a microsecond per curve, with a satisfactory signal-to-noise ratio. This enables us to determine time-dependent transient intramolecular distance distributions, IDD(t). Two time regimes are involved in this experimental approach: first is the duration of the conformational transition, the ''*chemical time regime*'' (t_c), (microseconds to seconds) and the second the ''*spectroscopic time regime*'', (t_s), the nanosecond fluorescence decay of the probes. This experimental approach is designed to reveal the course of the development of IDD(t)s with millisecond or submillisecond time resolution (depending on the time resolution of the folding initiation technique). Combining this instrumental approach with the production of a series of protein samples, site-specifically labeled with donor and acceptor pairs, enables the characterization of the backbone fold and flexibility in transient intermediate states, during the protein folding transitions.

The challenge here is twofold: first, to collect fluorescence decay curves with a sufficiently high signal-to-noise ratio to enable determination of statistically significant parameters of the IDD(t); and second, to synchronize the refolding initiation device with the probe pulsed laser source. A stopped-flow double kinetics device based on a single photon counting method was developed by Beechem and coworkers [127] and applied for the determination of transient anisotropy decays. This approach utilized only one photon in several pulses and hence required both a very large number of stopped-flow experiments, and an amount of labeled protein. A system developed by Ratner et al. [59] based on low-frequency (10 MHz) laser pulses and fast digitizer oscilloscope, overcomes this difficulty (Figure 17.17). The current time resolution of the spectroscopic time scale, t_s, in this mode of double kinetics experiment is 250 ps. Up to 20 fluorescence decay curves can be measured with an acceptable signal-to-noise ratio within a single stopped-flow run. The single pulse detection of fluorescence decay curves can be synchronized with several methods of rapid initiation of refolding or unfolding, e.g., stopped-flow and laser-induced temperature jump.

17.13.4
Multiple Probes Analysis of the Folding Transition

The multiple probe test, in which a variety of probes of secondary and tertiary structures are applied to monitor the unfolding/refolding kinetics (see Chapters 2

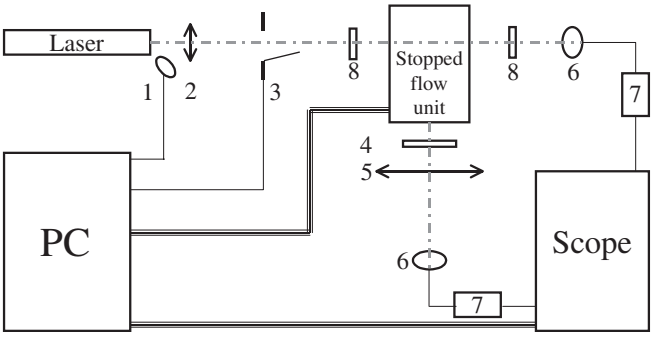

Fig. 17.17. Scheme of double kinetics device in the stopped flow configuration. The laser is a Quata-Ray high finesse OPO YAG Laser (Spectra-Physics, CA, USA), the stopped-flow unit is DX17MV (Applied photophysics, UK), the scope is Infinium 1.5 GHz oscilloscope (Hewlett-Packard, CA, USA), 1 and 5: lenses; 2: fast photodiode (Hamamatsu, Japan); 3: shutter; 4: bandpass filter; 6: biplanar phototubes (R1193U-03 Hamamatsu, Japan); 7: preamplifiers C 5594 (Hamamatsu, Japan); 8: attenuating filters.

and 12), has proved to be useful in distinguishing between parallel and sequential mechanisms. The determination of distributions of selected intramolecular distances by means of a series of double-labeled mutants of the model protein enables the determination of the time dependence of the formation of secondary structure elements; the formation of loops; changes of subdomain structures, and overall compaction of the chain at high time resolution. Changes of the mean and the width of distributions of intramolecular distances in protein molecules during the initial phases of the folding transitions can reveal weak energy bias (see Chapter 6). This favors conformational trends that affect the direction of the folding process. Very few and very weak interactions between chain elements may affect the shape of the distributions at the earliest phases of the folding. From such findings we can ask: Are such interactions effective during the initial collapse making it a biased change of conformation, rather than a random compaction driven only by solvent exclusion mechanism? Are those interactions local or nonlocal?

Ratner et al. [128] applied the double kinetics experiment in studying the early folding transitions of the CORE domain of *E. coli* adenylate kinase (AK) (Figure 17.14). Using the double-mixing stopped-flow mode of the double kinetics experiment the intramolecular distance distributions of a series of double-labeled AK mutants were determined in the unfolded state (in 1.8 M GdmCl). This occurred immediately after the change to refolding conditions (2–5 ms after dilution of denaturant), and upon completion of the refolding transition. This series of experiments was motivated by two questions. First, what is the extent of structure formation in different parts of the chain at the earliest detected intermediate state? And second, do secondary structure elements appear during folding prior to the formation of tertiary folds of the chain? What is the role of local and nonlocal interactions in the earliest phases of folding? This work is in progress, but the results obtained

to date with several double-labeled mutants indicate the following: 5 ms after being transferred from unfolded to refolded states in a double-mixing unfolding/refolding cycle, the distributions of distances between two pairs of sites which measure the full length of secondary structure elements in the protein (pairs 169–188, an α-helix and pair 188–203, a β-sheet) maintain the same shape as found in the unfolded state (Figure 17.18). Native intramolecular distance distributions of these two segments are found only after 3 s. This finding shows that at least these secondary structure elements are formed only very late in the folding transition. Do tertiary structure elements appear in the CORE domain at an earlier time? Preliminary experiments in which the distances between residues 18 and 203, indicate that this may be the case, and this question remains under investigation.

Data obtained through multiple FRET experiments can reflect the complexity of the folding transition, but simultaneously help resolve some common principles of the resolution of this complexity. Those are the principles that enable the transition of ensembles of protein molecules from states characterized by multiple conformations to the native state characterized by narrow distributions of conformations.

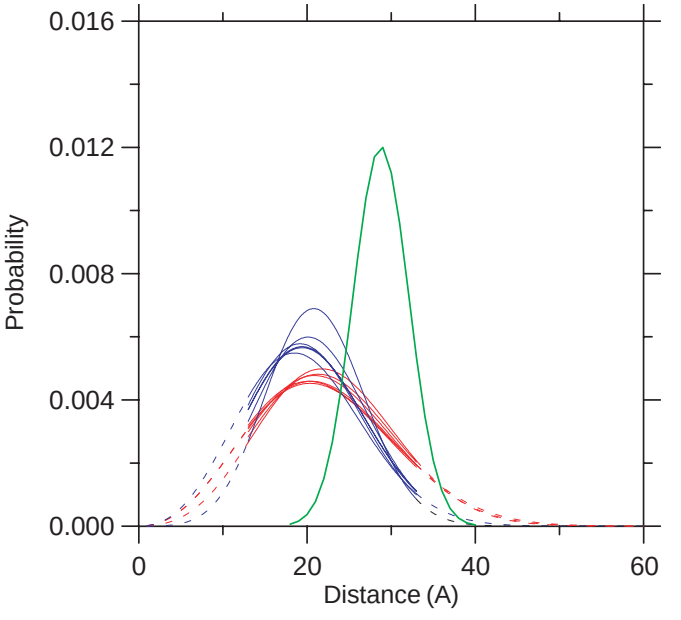

Fig. 17.18. Sets of transient distance distribution between residues 169 and 188 in AK in the denatured state (blue traces), in the 5 ms refolding intermediate state (red traces) and in the native state (after 3 s, green trace). The protein was denatured in 1.8 M GdmCl for 100 s and then the denaturant was diluted to final concentration of 0.3 M. Repeated traces are shown in order to demonstrate the range of experimental uncertainty in the parameters of the distributions. This experiment shows that in the early folding steps the helical segment between residues 169 and 188 (Figure 17.15) is unfolded, very similar to its state in the high denaturant concentration.

17.14 Concluding Remarks

The problem of folding and dynamics of globular proteins is a multidimensional problem. The structures of refolding protein molecules should be characterized by multiple distances and time constants. No single method can provide the full description of the structure and dynamics of a protein molecule in solution. X-ray crystallography and multidimensional NMR measurements are the most informative methods for determination of the average equilibrium conformations of protein molecules. It seems that deciphering the mechanism that overcomes the three folding problems depends on studies of the processes rather than the structures alone. That is where spectroscopy is indispensable.

The elementary steps in all the transitions of the protein molecules are the random fluctuations. Therefore the proteins evolved to have multiple conformations, distributions of the active structures, and combinations of multiple modes of motions. Modulation of these distributions of conformations and modes of motions is the basis for generation of vectorial process from Brownian elementary steps and control of the processes. Therefore it is essential to study the molecular processes at the population level as well as at the single molecule level.

The proposed loop hypothesis raises the next question: where is the information for the nonlocal interactions that form the loops? Our working hypothesis is that pairs of small clusters of mainly hydrophobic residues located on widely separated chain segments, carry the genetic message for the non-local interactions. Therefore an important future direction in FRET applications in folding research is the preparation of series of double-labeled mutants combined with ''perturbation mutations,'' mutations that perturb putative nonlocal interactions. The effect of such mutations on the shape of the time- or denaturant-dependent intramolecular distance distributions is expected to be an adequate test of this hypothesis. It seems that a complete understanding of the folding and action of globular proteins will always require a combination of approaches. Ensemble and single molecule FRET measurements can be a major component in the arsenal of proposed methods.

The modern laser and detector technologies opened a wide window of time and wavelength regimes for probing the processes involved in the folding transition and changes of conformations of proteins in action. The development of protein engineering and advanced separation methods has enabled rational design of protein mutants suitable for experiments designed to answer specific questions. It is the unique combination of these recent advances in three different disciplines as well as new computational techniques that may lead to quantitative analysis of the basic processes. The development of the double kinetics method is an example of combination with a synchronization experiment. Additional technologies such as pressure or temperature jumps will enable determination of detailed correlations between dynamics (both local and global) and the folding transition.

Future development of the applications of FRET methods in folding research will probably be based on the current methods with few new directions. We can expect further improvement of signal-to-noise ratio, distance and time resolution, compu-

tational methods of analysis of decay curves, determination of single molecule fluorescence decay rates, methods for preparations of series of multiple distances and the sensitivity of the detection at the level of single molecule level.

Future developments should strive to advance fours aspects of the FRET measurements: (a) the sensitivity of the detection method, (b) the modes of measurements, (c) the biochemical technology of site-specific labeling, and (d) development of new fluorescent probes.

(a) Future directions of the spectroscopic methods can further improve the signal-to-noise ratio for detection of distributions of distances; subpopulations and improved time resolution. Enhancement of the time resolution and dynamic range of single pulse detection will enhance the applications of the double kinetics approach. It is conceivable that faster collection of multiple single molecule trajectories will be achieved. Development of new confinement methods and new methods for ultrafast changes of the solution conditions at the microscopic level for single molecule detection experiments will hopefully enable determination of transient distributions of selected distances during the folding transitions of model proteins.

(b) Future modes of measurements will probably include further development of the double kinetics approach, use of multiparametric measurements including anisotropy measurements, time-resolved spectra and further development of pressure-jump, temperature-jump, pH-jump, and other perturbation modes.

(c) A major future progress in accomplishment of the promising potential of FRET methods in folding research can be gained by investing research efforts in the development of the biochemical methodology of high-yield site-specific labeling methods. The current specific aims of these developmental efforts should be: new methods for selection of nonperturbing modifications of protein molecules, new methods for efficient purification of labeled products and development of new selective reagents. It is expected that the cell-free proteins synthesis methods will become much more widely used.

(d) The main limitation of single molecule FRET spectroscopy in folding research is the photobleaching of the probes. Major developmental efforts for synthesis of photostable probes or methods for reduction of the photo-oxygenation reactions are needed. Parallel efforts for development of probes of smaller volume and pairs of wider ranges of R_o-values are also essential for enhancement of the future applications of FRET spectroscopy in folding research. The current state of the art is very advanced and that is the basis of optimism that these developments are feasible.

Acknowledgments

The author was privileged to work for a long time with a group of devoted and enthusiastic scientists, collaborators and students, who contributed to many aspects of the projects cited in this chapter. Their contributions are deeply acknowledged. The approach described here was influenced by the initiative which was started

as early as 1968 by E. Katzir-Katchalsky, Izhak Steinberg, and Meir Wilchek who realized at that time the potential of using this approach in the study of protein conformational dynamics. The author had the privilege of working under their guidance in the early 1970s. This work was supported by the grants from NIH Institute of General Medical Sciences, United States-Israel Binational Science Foundation (BSF), Equipment Grants and Research Grants from the Fund for Basic Research of the Israeli Academy of Sciences (ISF) and the German-Israel foundation (GIF).

References

1 Förster, T. H. (1948). Zwischen Molekulare Energie Wanderung und Fluoreszenz. *Ann Phys (Leipzig)* 2, 55–75.
2 Förster, T. H. (1959). Transfer mechanisms of electronic excitation. *Discuss Faraday Soc* 27, 7–17.
3 Förster, T. H. (1965). Delocalized excitation and excitation transfer. In *Modern Quantum Chemistry, Istanbul lectures Part III: Action of Light and Organic Crystals* (Sinaonglu, O., ed.), pp. 93–137. Academic Press, New York.
4 Steinberg, I. Z. (1971). Long-range nonradiative transfer of electronic excitation energy in proteins and polypeptides. *Annu Rev Biochem* 40, 83–114.
5 Stryer, L., Thomas, D. D. & Meares, C. F. (1982). Diffusion-enhanced fluorescence energy transfer. *Annu Rev Biophys Bioeng* 11, 203–222.
6 Van Der Meer, W. B., Coker, G. III, & Chen, S. Y. S. (1994). *Resonance Energy Transfer Theory and Data*. VCH Publishers, New York.
7 Makhatadze, G. I. & Privalov, P. L. (1996). On the entropy of protein folding. *Protein Sci* 5, 507–510.
8 Plotkin, S. S. & Onuchic, J. N. (2002). Understanding protein folding with energy landscape theory. Part II: Quantitative aspects. *Q Rev Biophys* 35, 205–286.
9 Ferguson, N. & Fersht, A. R. (2003). Early events in protein folding. *Curr Opin Struct Biol* 13, 75–81.
10 Cooper, A. (1984). Protein fluctuations and the thermodynamic uncertainty principle. *Prog Biophys Mol Biol* 44, 181–214.
11 Privalov, P. L. & Potekhin, S. A. (1986). Scanning microcalorimetry in studying temperature-induced changes in proteins. *Methods Enzymol* 131, 4–51.
12 Creighton, T. E. (1993). *Proteins: Structure and Molecular Properties*, 2nd edn. W.H. Freeman, New York.
13 Careri, G., Fasella, P. & Gratton, E. (1979). Enzyme dynamics: the statistical physics approach. *Annu Rev Biophys Bioeng* 8, 69–97.
14 Fersht, A. R. (1985). *Enzyme Structure and Mechanism*, 2nd edn. W.H. Freeman, New York.
15 Slater, J. C. & Frank, N. H. (1947). *Electromagnetism*. McGraw, New York.
16 Perrin, J. (1927). Fluorescence et induction moleculaire par sesonance. *C R Hebd Seances Acad Sci* 184, 1097–1100.
17 Steinberg, I. Z., Haas, E. & Katchalsky-Katzir, E. (1983). Long-range non-radiative transfer of electronic excitation energy. In *Time Resolved Spectroscopy in Biochemistry* (Cundall, R. B. & Dale, R. E., eds), pp. 411–451. Plenum Publishing, New York.
18 Weber, G. & Teal, F. J. W. (1959). *Discuss Faraday Soc* 27, 134–151.
19 Latt, S. A., Cheung, H. T. & Blout, E. R. (1965). Energy transfer. A system with relatively fixed donor-acceptor separation. *J Am Chem Soc* 87, 995–1003.

20 Stryer, L. & Haugland, R. P. (1967). Energy transfer: a spectroscopic ruler. *Proc Natl Acad Sci USA* 58, 719–726.

21 Eisinger, J. & Dale, R. E. (1974). Letter: interpretation of intramolecular energy transfer experiments. *J Mol Biol* 84, 643–647.

22 Dale, R. E. & Eisinger, J. (1976). Intramolecular energy transfer and molecular conformation. *Proc Natl Acad Sci USA* 73, 271–273.

23 Dale, R. E., Eisinger, J. & Blumberg, W. E. (1979). The orientational freedom of molecular probes. The orientation factor in intramolecular energy transfer. *Biophys J* 26, 161–193.

24 Selvin, P. R. & Hearst, J. E. (1994). Luminescence energy transfer using a terbium chelate: improvements on fluorescence energy transfer. *Proc Natl Acad Sci USA* 91, 10024–10028.

25 Mersol, J. V., Wang, H., Gafni, A. & Steel, D. G. (1992). Consideration of dipole orientation angles yields accurate rate equations for energy transfer in the rapid diffusion limit. *Biophys J* 61, 1647–1655.

26 Haas, E., Katchalski-Katzir, E. & Steinberg, I. Z. (1978). Effect of the orientation of donor and acceptor on the probability of energy transfer involving electronic transitions of mixed polarization. *Biochemistry* 17, 5064–5070.

27 Albrecht, A. C. (1960). Forbidden characterizing allowed electronic transitions. *J Chem Phys* 33, 156.

28 Eisinger, J., Feuer, B. & Lamola, A. A. (1969). Intramolecular singlet excitation transfer. Applications to polypeptides. *Biochemistry* 8, 3908–3915.

29 Cortijo, M., Steinberg, I. Z. & Shaltiel, S. (1971). Fluorescence of glycogen phosphorylase b. Structural transitions and energy transfer. *J Biol Chem* 246, 933–938.

30 Valeur, B. (2002). *Molecular Fluorescence Principles and Applications*. Wiley-VCH, Weinheim.

31 Lakowicz, J. R. (1999). *Principles of Fluorescence Spectroscopy*, 2nd edn. Kluwer Academic/Plenum, New York.

32 Stryer, L., Thomas, D. D. & Carlsen, W. F. (1982). Fluorescence energy transfer measurements of distances in rhodopsin and the purple membrane protein. *Methods Enzymol* 81, 668–678.

33 Wu, P. & Brand, L. (1994). Resonance energy transfer: methods and applications. *Anal Biochem* 218, 1–13.

34 Clegg, R. M. (1992). Fluorescence resonance energy transfer and nucleic acids. *Methods Enzymol* 211, 353–388.

35 Clegg, R. M. (1996). Fluorescence resonance energy transfer. In *Fluorescence Imaging Spectroscopy and Microscopy* (Wang, X. F. & Herman, B., eds), Chemical Analysis Series Vol. 137, pp. 179–252. John Wiley & Sons, New York.

36 Cantor, C. R. & Pechukas, P. (1971). Determination of distance distribution functions by singlet-singlet energy transfer. *Proc Natl Acad Sci USA* 68, 2099–2101.

37 Haas, E., Katchalsky-Katzir, E. & Steinberg, I. Z. (1978). Brownian motion of the ends of oligopeptide chains in solution as estimated by energy transfer between the chain ends. *Biopolymers* 17, 11–31.

38 Beechem, J. M. & Haas, E. (1989). Simultaneous determination of intramolecular distance distributions and conformational dynamics by global analysis of energy transfer measurements. *Biophys J* 55, 1225–1236.

39 Chandrasekhar, S. (1943). Stochastic problems in physics and astronomy. *Rev Mod Phys* 15, 1–89.

40 Navon, A., Ittah, V., Landsman, P., Scheraga, H. A. & Haas, E. (2001). Distributions of intramolecular distances in the reduced and denatured states of bovine pancreatic ribonuclease A. Folding initiation structures in the C-terminal portions of the reduced protein. *Biochemistry* 40, 105–118.

41 Lakowicz, J. R., Kusba, J., Szmacinski, H. et al. (1991). Resolution of end-to-end diffusion coefficients and distance distributions of flexible molecules using fluorescent donor-acceptor and donor-quencher pairs. *Biopolymers* 31, 1363–1378.

42 Deniz, A. A., Laurence, T. A., Beligere, G. S. et al. (2000). Single-molecule protein folding: diffusion fluorescence resonance energy transfer studies of the denaturation of chymotrypsin inhibitor 2. *Proc Natl Acad Sci USA* 97, 5179–5184.

43 Liu, D. R., Magliery, T. J., Pastrnak, M. & Schultz, P. G. (1997). Engineering a tRNA and aminoacyl-tRNA synthetase for the site-specific incorporation of unnatural amino acids into proteins in vivo. *Proc Natl Acad Sci USA* 94, 10092–10097.

44 Buckler, D. R., Haas, E. & Scheraga, H. A. (1993). C-terminal labeling of ribonuclease A with an extrinsic fluorescent probe by carboxypeptidase Y-catalyzed transpeptidation in the presence of urea. *Anal Biochem* 209, 20–31.

45 Amir, D. & Haas, E. (1987). Estimation of intramolecular distance distributions in bovine pancreatic trypsin inhibitor by site-specific labeling and nonradiative excitation energy-transfer measurements. *Biochemistry* 26, 2162–2175.

46 Takashi, R. (1988). A novel actin label: a fluorescent probe at glutamine-41 and its consequences. *Biochemistry* 27, 938–943.

47 Folk, J. E. & Chung, S. I. (1985). Transglutaminases. *Methods Enzymol* 113, 358–375.

48 Fink, M. L., Chung, S. I. & Folk, J. E. (1980). Gamma-glutamylamine cyclotransferase: specificity toward epsilon-(L-gamma-glutamyl)-L-lysine and related compounds. *Proc Natl Acad Sci USA* 77, 4564–4568.

49 Tcherkasskaya, O., Ptitsyn, O. B. & Knutson, J. R. (2000). Nanosecond dynamics of tryptophans in different conformational states of apomyoglobin proteins. *Biochemistry* 39, 1879–1889.

50 Rischel, C., Thyberg, P., Rigler, F. & Poulsen, F. M. (1996). Time-resolved fluorescence studies of the molten globule state of apomyoglobin. *J Mol Biol* 257, 877–885.

51 Santoro, S. W., Anderson, J. C., Lakshman, V. & Schultz, P. G. (2003). An archaebacteria-derived glutamyl-tRNA synthetase and tRNA pair for unnatural amino acid mutagenesis of proteins in Escherichia coli. *Nucleic Acids Res* 31, 6700–6709.

52 Haran, G., Haas, E., Szpikowska, B. K. & Mas, M. T. (1992). Domain motions in phosphoglycerate kinase: determination of interdomain distance distributions by site-specific labeling and time-resolved fluorescence energy transfer. *Proc Natl Acad Sci USA* 89, 11764–11768.

53 Pennington, M. W. (1994). Site-specific chemical modification procedures. *Methods Mol Biol* 35, 171–185.

54 Sinev, M. A., Sineva, E. V., Ittah, V. & Haas, E. (1996). Domain closure in adenylate kinase. *Biochemistry* 35, 6425–6437.

55 Sinev, M., Landsmann, P., Sineva, E., Ittah, V. & Haas, E. (2000). Design consideration and probes for fluorescence resonance energy transfer studies. *Bioconjug Chem* 11, 352–362.

56 Ortiz, J. O. & Bubis, J. (2001). Effects of differential sulfhydryl group-specific labeling on the rhodopsin and guanine nucleotide binding activities of transducin. *Arch Biochem Biophys* 387, 233–242.

57 Ratner, V., Kahana, E., Eichler, M. & Haas, E. (2002). A general strategy for site-specific double labeling of globular proteins for kinetic FRET studies. *Bioconjug Chem* 13, 1163–11670.

58 Jacob, M. H., Amir, D., Ratner, V. & Haas, E. Straightforward selective protein modification by predictions and utilizing reactivity differences of surface cysteine residues. (in preparation)

59 Ratner, V. & Haas, E. (1998). An instrument for time resolved monitoring of fast chemical transitions: application to the kinetics of refolding of a globular protein. *Rev Sci Instrum* 69, 2147–2154.

60 Ratner, V., Sinev, M. & Haas, E. (2000). Determination of intramolecular distance distribution during protein folding on the millisecond timescale. *J Mol Biol* 299, 1363–1371.

61 Amir, D., Levy, D. P., Levin, Y. & Haas, E. (1986). Selective fluorescent labeling of amino groups of bovine pancreatic trypsin inhibitor by reductive alkylation. *Biopolymers* 25, 1645–1658.

62 Epe, B., Woolley, P., Steinhauser, K. G. & Littlechild, J. (1982). Distance measurement by energy transfer: the 3′ end of 16-S RNA and proteins S4 and S17 of the ribosome of *Escherichia coli*. *Eur J Biochem* 129, 211–219.

63 Flamion, P. J., Cachia, C. & Schreiber, J. P. (1992). Non-linear least-squares methods applied to the analysis of fluorescence energy transfer measurements. *J Biochem Biophys Methods* 24, 1–13.

64 Brand, L. (1992). *Methods in Enzymology* (Brand, L. & Johnson, L. M., eds), Vol. 210.

65 Beechem, J. M. & Brand, L. (1985). Time-resolved fluorescence of proteins. *Annu Rev Biochem* 54, 43–71.

66 Ameloot, M., Beechem, J. M. & Brand, L. (1986). Simultaneous analysis of multiple fluorescence decay curves by Laplace transforms. Deconvolution with reference or excitation profiles. *Biophys Chem* 23, 155–171.

67 Lanczos, C. (1956). *Applied Analysis*, pp. 272–304. Prentice Hall, Engelwood Cliffs.

68 Bevington, P. R. (1969). *Data Reduction and Error Analysis for the Physical Sciences*. McGraw-Hill, New York.

69 Grinvald, A. & Steinberg, I. Z. (1974). On the analysis of fluorescence decay kinetics by the method of least-squares. *Anal Biochem* 59, 583–598.

70 Ames, W. F. (1977). *Ames, William F. Numerical Methods for Partial Differential Equations*, 2nd edn. Academic Press, New York.

71 Press, W. H., Flannery, B. P., Teukolski, S. A. & Vetterling, W. F. (1989). *Numerical Recipes: The Art of Scientific Computing*. Cambridge University Press, Cambridge.

72 Brochon, J. C. (1994). Maximum entropy method of data analysis in time-resolved spectroscopy. *Methods Enzymol* 240, 262–311.

73 Lakshmikanth, G. S., Sridevi, K., Krishnamoorthy, G. & Udgaonkar, J. B. (2001). Structure is lost incrementally during the unfolding of barstar. *Nat Struct Biol* 8, 799–804.

74 Deisenhofer, J. & Steigmann, W. (1975). Crystallographic refinement of the structure of bovine pancreatic trypsin inhibitor at 1.5 A resolution. *Acta Crystallogr* B31, 238.

75 Creighton, T. E. (1978). Experimental studies of protein folding and unfolding. *Prog Biophys Mol Biol* 33, 231–297.

76 Gussakovsky, E. E. & Haas, E. (1992). The compact state of reduced bovine pancreatic trypsin inhibitor is not the compact molten globule. *FEBS Lett* 308, 146–148.

77 Gottfried, D. S. & Haas, E. (1992). Nonlocal interactions stabilize compact folding intermediates in reduced unfolded bovine pancreatic trypsin inhibitor. *Biochemistry* 31, 12353–12362.

78 Griko, Y. V., Privalov, P. L., Sturtevant, J. M. & Venyaminov, S. (1988). Cold denaturation of staphylococcal nuclease. *Proc Natl Acad Sci USA* 85, 3343–3347.

79 Ittah, V. & Haas, E. (1995). Nonlocal interactions stabilize long range loops in the initial folding intermediates of reduced bovine pancreatic trypsin inhibitor. *Biochemistry* 34, 4493–4506.

80 Klein-Seetharaman, J., Oikawa, M., Grimshaw, S. B. et al. (2002). Long-range interactions within a nonnative protein. *Science* 295, 1719–1722.

81 Lattman, E. E. & Rose, G. D. (1993). Protein folding – what's the question? *Proc Natl Acad Sci USA* 90, 439–441.

82 Berezovsky, I. N., Grosberg, A. Y. & Trifonov, E. N. (2000). Closed loops of nearly standard size: common basic element of protein structure. *FEBS Lett* 466, 283–286.

83 Berezovsky, I. N., Kirzhner, V. M., Kirzhner, A. & Trifonov, E. N. (2001). Protein folding: looping from hydrophobic nuclei. *Proteins* 45, 346–350.

84 Buckler, D. R., Haas, E. & Scheraga, H. A. (1995). Analysis of the structure of ribonuclease A in native and partially denatured states by time-resolved noradiative dynamic excitation energy transfer between site-specific extrinsic probes. *Biochemistry* 34, 15965–15978.

85 Wu, P. G., James, E. & Brand, L. (1993). Compact thermally-denatured state of a staphylococcal nuclease mutant from resonance energy transfer measurements. *Biophys Chem* 48, 123–133.

86 Wu, P. & Brand, L. (1994). Conformational flexibility in a staphylococcal nuclease mutant K45C from time-resolved resonance energy transfer measurements. *Biochemistry* 33, 10457–10462.

87 Sridevi, K. & Udgaonkar, J. B. (2003). Surface expansion is independent of and occurs faster than core solvation during the unfolding of barstar. *Biochemistry* 42, 1551–1563.

88 Sridevi, K., Lakshmikanth, G. S., Krishnamoorthy, G. & Udgaonkar, J. B. (2004). Increasing stability reduces conformational heterogeneity in a protein folding intermediate ensemble. *J Mol Biol* 337, 699–711.

89 Cheung, H. C., Wang, C. K., Gryczynski, I. et al. (1991). Distance distributions and anisotropy decays of troponin C and its complex with troponin I. *Biochemistry* 30, 5238–5247.

90 Cheung, H. C., Gryczynski, I., Malak, H., Wiczk, W., Johnson, M. L. & Lakowicz, J. R. (1991). Conformational flexibility of the Cys 697-Cys 707 segment of myosin subfragment-1. Distance distributions by frequency-domain fluorometry. *Biophys Chem* 40, 1–17.

91 Lakowicz, J. R., Wiczk, W., Gryczynski, I., Szmacinski, H. & Johnson, M. L. (1990). Influence of end-to-end diffusion on intramolecular energy transfer as observed by frequency-domain fluorometry. *Biophys Chem* 38, 99–109.

92 Lakowicz, J. R., Kusba, J., Wiczk, W., Gryczynski, I., Szmacinski, H. & Johnson, M. L. (1991). Resolution of the conformational distribution and dynamics of a flexible molecule using frequency-domain fluorometry. *Biophys Chem* 39, 79–84.

93 Eis, P. S. & Lakowicz, J. R. (1993). Time-resolved energy transfer measurements of donor-acceptor distance distributions and intramolecular flexibility of a CCHH zinc finger peptide. *Biochemistry* 32, 7981–7993.

94 Vogel, H., Nilsson, L., Rigler, R., Voges, K. P. & Jung, G. (1988). Structural fluctuations of a helical polypeptide traversing a lipid bilayer. *Proc Natl Acad Sci USA* 85, 5067–5071.

95 Vogel, H., Nilsson, L., Rigler, R. et al. (1993). Structural fluctuations between two conformational states of a transmembrane helical peptide are related to its channel-forming properties in planar lipid membranes. *Eur J Biochem* 212, 305–313.

96 Bennett, W. S. & Huber, R. (1984). Structural and functional aspects of domain motions in proteins. *CRC Crit Rev Biochem* 15, 291–384.

97 Huber, R. & Bennett, W. S., Jr. (1983). Functional significance of flexibility in proteins. *Biopolymers* 22, 261–279.

98 Warshel, A. & Aqvist, J. (1991). Electrostatic energy and macromolecular function. *Annu Rev Biophys Biophys Chem* 20, 267–298.

99 Jencks, W. P. (1975). Binding energy, specificity, and enzymic catalysis: the circe effect. *Adv Enzymol Relat Areas Mol Biol* 43, 219–410.

100 Fersht, A. R. (1998). *Structure and Mechanism in Protein Science: A Guide to Enzyme Catalysis and Protein Folding*. W. H. Freeman, New York.

101 Bialek, W. & Onuchic, J. N. (1988). Protein dynamics and reaction rates: mode-specific chemistry in large molecules? *Proc Natl Acad Sci USA* 85, 5908–5912.

102 Schulz, G. E. (1991). Mechanisms of enzyme catalysis from crystal structure analyses. *Ciba Found Symp* 161, 8–22; discussion 22–27.

103 Anderson, C. M., Zucker, F. H. & Steitz, T. A. (1979). Space-filling

models of kinase clefts and conformation changes. *Science* 204, 375–380.

104 Pavlov, M., Sinev, M. A., Timchenko, A. A. & Ptitsyn, O. B. (1986). A study of apo- and holo-forms of horse liver alcohol dehydrogenase in solution by diffuse x-ray scattering. *Biopolymers* 25, 1385–1397.

105 Watson, H. C., Walker, N. P., Shaw, P. J. et al. (1982). Sequence and structure of yeast phosphoglycerate kinase. *EMBO J* 1, 1635–1640.

106 Noda, L. (1973). Adenylate kinase. In *The Enzymes* (Boyer, P. D., ed.), Vol. 8, pp. 279–305. Academic Press, New York.

107 Banks, R. D., Blake, C. C., Evans, P. R. et al. (1979). Sequence, structure and activity of phosphoglycerate kinase: a possible hinge-bending enzyme. *Nature* 279, 773–777.

108 Muller, C. W., Schlauderer, G. J., Reinstein, J. & Schulz, G. E. (1996). Adenylate kinase motions during catalysis: an energetic counterweight balancing substrate binding. *Structure* 4, 147–156.

109 Muller, Y. A., Schumacher, G., Rudolph, R. & Schulz, G. E. (1994). The refined structures of a stabilized mutant and of wild-type pyruvate oxidase from *Lactobacillus plantarum*. *J Mol Biol* 237, 315–335.

110 Muller, C. W. & Schulz, G. E. (1992). Structure of the complex between adenylate kinase from *Escherichia coli* and the inhibitor Ap5A refined at 1.9 A resolution. A model for a catalytic transition state. *J Mol Biol* 224, 159–177.

111 Schuler, B., Lipman, E. A. & Eaton, W. A. (2002). Probing the free-energy surface for protein folding with single-molecule fluorescence spectroscopy. *Nature* 419, 743–747.

112 Lipman, E. A., Schuler, B., Bakajin, O. & Eaton, W. A. (2003). Single-molecule measurement of protein folding kinetics. *Science* 301, 1233–1235.

113 Rhoades, E., Gussakovsky, E. & Haran, G. (2003). Watching proteins fold one molecule at a time. *Proc Natl Acad Sci USA* 100, 3197–3202.

114 Talaga, D. S., Lau, W. L., Roder, H. et al. (2000). Dynamics and folding of single two-stranded coiled-coil peptides studied by fluorescent energy transfer confocal microscopy. *Proc Natl Acad Sci USA* 97, 13021–13026.

115 Dickson, R. M., Cubitt, A. B., Tsien, R. Y. & Moerner, W. E. (1997). On/off blinking and switching behaviour of single molecules of green fluorescent protein. *Nature* 388, 355–358.

116 Boukobza, R. S. & Haran, G. (2001). Immobilization in surface-tethered lipid vesicles as a new tool for single biomolecule spectroscopy. *J Phys Chem B* 105, 12165–12170.

117 Deniz, A. A., Dahan, M., Grunwell, J. R. et al. (1999). Single-pair fluorescence resonance energy transfer on freely diffusing molecules: observation of Forster distance dependence and subpopulations. *Proc Natl Acad Sci USA* 96, 3670–3675.

118 Ha, T., Enderle, T., Chemla, D. S., Selvin, P. R. & Weiss, S. (1997). Quantum jumps of single molecules at room temperature. *Chem Phys Lett* 271, 1–5.

119 Veerman, J. A., Garcia-Parajo, M. F., Kuipers, L. & van Hulst, N. F. (1999). Time-varying triplet state lifetimes of single molecules. *Phys Rev Lett* 83, 2155–2158.

120 Chan, C. K., Hu, Y., Takahashi, S., Rousseau, D. L., Eaton, W. A. & Hofrichter, J. (1997). Submillisecond protein folding kinetics studied by ultrarapid mixing. *Proc Natl Acad Sci USA* 94, 1779–1784.

121 Eaton, W. A., Munoz, V., Thompson, P. A., Chan, C. K. & Hofrichter, J. (1997). Submillisecond kinetics of protein folding. *Curr Opin Struct Biol* 7, 10–14.

122 Teilum, K., Kragelund, B. B. & Poulsen, F. M. (2002). Transient structure formation in unfolded acyl-coenzyme A-binding protein observed by site-directed spin labelling. *J Mol Biol* 324, 349–357.

123 Teilum, K., Maki, K., Kragelund, B. B., Poulsen, F. M. & Roder, H. (2002). Early kinetic intermediate in

the folding of acyl-CoA binding protein detected by fluorescence labeling and ultrarapid mixing. *Proc Natl Acad Sci USA* 99, 9807–9812.

124 Lillo, M. P., Szpikowska, B. K., Mas, M. T., Sutin, J. D. & Beechem, J. M. (1997). Real-time measurement of multiple intramolecular distances during protein folding reactions: a multisite stopped-flow fluorescence energy-transfer study of yeast phosphoglycerate kinase. *Biochemistry* 36, 11273–11281.

125 Lillo, M. P., Beechem, J. M., Szpikowska, B. K., Sherman, M. A. & Mas, M. T. (1997). Design and characterization of a multisite fluorescence energy-transfer system for protein folding studies: a steady-state and time-resolved study of yeast phosphoglycerate kinase. *Biochemistry* 36, 11261–11272.

126 Magg, C. & Schmid, F. X. (2004). Rapid collapse precedes the fast two-state folding of the cold shock protein. *J Mol Biol* 335, 1309–1323.

127 Jones, B. E., Beechem, J. M. & Matthews, C. R. (1995). Local and global dynamics during the folding of Escherichia coli dihydrofolate reductase by time-resolved fluorescence spectroscopy. *Biochemistry* 34, 1867–1877.

128 Ratner, V., Kahana, E. & Haas, E. (2002). The natively helical chain segment 169–188 of *Escherichia coli* adenylate kinase is formed in the latest phase of the refolding transition. *J Mol Biol* 320, 1135–1145.

129 Ballew, R. M., Sabelko, J. & Gruebele, M. (1996). Direct observation of fast protein folding: the initial collapse of apomyoglobin *Proc Natl Acad Sci USA* 93, 5759–5764.

18
Application of Hydrogen Exchange Kinetics to Studies of Protein Folding

Kaare Teilum, Birthe B. Kragelund, and Flemming M. Poulsen

18.1
Introduction

Amide hydrogen exchange is one of the most useful methods for obtaining site-specific information about hydrogen bond formation and breaking in the folding protein. In particular, the method allows study of the individual amides in the peptide chain, and for this reason the method has very wide applications in studies of the protein folding mechanism.

Hydrogen exchange is a chemical exchange reaction between labile hydrogen atoms chemically bound to either nitrogen, oxygen, or sulfur atoms. The exchange reaction occurs most commonly between these labile hydrogen atoms in molecules dissolved in a solvent that itself contains labile hydrogen atoms like water. Obviously this type of exchange reaction can take place for many atoms in a protein molecule dissolved in water, where several types of labile hydrogen can exchange with the water hydrogen atoms. The hydrogen atoms that potentially engage in hydrogen exchange typically also have the potential for hydrogen bond formation. The chemistry of the hydrogen exchange reaction is a proton transfer reaction, which requires the release of the hydrogen atom. For this reason the hydrogen exchange reaction can be used to monitor hydrogen bond formation and breaking. In proteins hydrogen bonds involving the peptide backbone amides and carbonyls are the most important structural element in secondary structure formation. Therefore by studying the hydrogen exchange reaction of the individual amides in the folding peptide information becomes available regarding the hydrogen bond formation of the individual segments in the protein folding process. Similarly information about the stability and the kinetics of the hydrogen bonding segments in the peptide chain can be obtained by measuring the hydrogen exchange reaction in native conditions.

The kinetics of hydrogen exchange in proteins can be studied directly by nuclear magnetic resonance (NMR) spectroscopy using solvent saturation transfer or the magnetic relaxation rate to study very fast reactions. Slower reactions can be studied by letting the exchange reaction replace a hydrogen atom in the dissolved

Protein Folding Handbook. Part I. Edited by J. Buchner and T. Kiefhaber

ISBN: 3-527-30784-2

molecule by deuterium from deuterium oxide solvent. This replacement can be measured directly by ^{1}H NMR spectroscopy because the NMR active ^{1}H is replaced by the ^{2}H, which is not detectable at the proton NMR frequency. Also the exchange can be measured by mass spectrometry in combination with enzymatic degradation because the molecular mass increases by introduction of the deuteron.

The amide hydrogen exchange reaction has been widely used ever since it was first described as a method for obtaining structural information about the peptide backbone in proteins [1]. Although the methods for measuring the hydrogen exchange were developed at a time where no three-dimensional structures were known, it was being used to describe the content of secondary structures in proteins [2, 3]. However, very early in the history of the method it became clear that the method also carried information about the dynamics of protein structures [4]. In particular after the first three-dimensional structures of proteins had been determined by X-ray crystallography it was realized that amide hydrogen exchange carried the message of dynamics. The compact and firmly packed globular protein structures contained interior amides in the secondary structure, which had no surface contact [5]. Nevertheless, these buried amides were found to be subject to exchange with solvent hydrogen, indicating that these amides do get in contact with solvent and suggesting that dynamic processes had to bring the interior in contact with an exterior water molecule.

Amide hydrogen exchange kinetics was originally measured by methods that were only able to record bulk exchange using either infrared spectroscopy or tritium hydrogen exchange. This meant that the measured exchange was a result of the contribution from all exchanging amides in the protein. The method therefore did not allow measurements of exchange rates at specific sites in the protein. Protein NMR spectroscopy changed this dramatically [6, 7]. With assigned NMR signals from essentially all amide groups in the peptide backbone and access to the three-dimensional structure of the protein molecule in question, hydrogen exchange kinetics could be rationalized and understood in a molecular context that was not available previously. The study of hydrogen exchange using NMR spectroscopy is the key to making the exchange kinetics of protein structures useful.

In the days before NMR spectroscopy was being applied in hydrogen exchange several mechanisms were proposed to explain the observation that amides in the centers of molecules were exchanged [8], however, many NMR studies of the thermodynamics and kinetics of individual hydrogen exchange reactions in many proteins have led to the widely agreed view that individual amides in globular proteins are exposed to exchange with solvent hydrogen atoms by a number of mechanisms. Some amides exchange by local openings, others by subglobular openings and finally the most interior amides exchange by cooperative global protein unfolding.

The latter group of amides exchanging by global unfolding has received considerable attention because it has been proposed that the study of these may provide information about the protein folding and unfolding events in native conditions [9–13]. Considering that the folded state and the unfolded state are in chemical

equilibrium, this equilibrium will for most proteins be strongly shifted towards the folded form in native conditions. However, since both states have to be populated in all conditions, even in native conditions a small fraction of molecules will be of the unfolded form. If the mechanism of hydrogen exchange for a specific amide group is by global unfolding, the kinetics of the exchange reaction will carry information about the rate constants of folding and unfolding in native conditions. This consideration has stimulated much interest in the use of hydrogen exchange in native conditions to exploit the nature of the protein folding/unfolding equilibrium.

The group around Linderstøm-Lang suggested a simple, two-step mechanism for hydrogen exchange [1, 4]. The first step is the equilibrium between the closed state and the open state and the second step is the chemical exchange reaction occurring from the open state. Therefore, when the mechanism of exchange for a given amide group is by protein folding/unfolding, the rate constants for opening and for closing would be equivalent to those of folding and unfolding, provided the folding is a simple two-state process. Hence there would be an obvious interest in determining these rate constants. A paragraph in this chapter will address some of the methods used to extract the rate constants of the opening and closing reactions in particular conditions favoring such measurements. The simplest condition is to measure the amide hydrogen exchange kinetics when the rate-determining step in the reaction mechanism is the opening rate, in which case the amide hydrogen exchange rate is simply the unfolding rate [13, 14]. Another method applies the measurement of the hydrogen exchange rates at a set of different pH values at which the chemical exchange rate from the open form is known. The measurement of the amide hydrogen exchange kinetics in an array of pH values provide a sample of data that subjected to nonlinear fitting can provide the two rate constants for the opening and closing reactions [10, 15]. A paragraph in this chapter will describe examples of the application of this type of analysis to several model proteins and present the results of these analyses.

Another approach which is being used to bridge the gap between amide hydrogen exchange in native-like conditions and in denaturing conditions is to study the rate of exchange as a function of a denaturing agent [9, 15–17]. As the concentration of denaturant increases, the unfolding equilibrium constant will typically increase, bringing a larger and larger proportion of the molecules of the unfolded form, resulting in faster amide hydrogen exchange. The study of individual amides has for several proteins shown that the kinetics of the exchange of groups of amides has typical patterns that reflect the mechanism of exchange and allow the distinction between exchange by local, subglobal, or cooperative global exchange mechanisms.

Amide hydrogen exchange has been a very useful tool for measuring the formation of hydrogen bonds during protein folding. The quenched-flow and pulse-labeling techniques, which combine rapid mixing techniques with analysis by NMR spectroscopy or mass spectrometry, have had a great impact on outlining the routes of protein folding [18–26]. These techniques allow determination of the kinetics of the formation of a protected state for individual amides through-

out the peptide chain. These methods are extremely powerful because the information they provide has both a structural and kinetic implication.

For an understanding of the folding of proteins, the unfolded state of the peptide chain has been subject to several studies because many studies have indicated the existence of structure in the otherwise unfolded peptide chain. Such structures are of interest because they may be labile precursors of the formation of native structures. Again, amide hydrogen exchange is one method of probing the presence of residual structure in the unfolded state, structures in the molten globule and other folding intermediates by comparison of the exchange kinetics with the exchange rates predicted for the random coil conformation of the peptide [9, 12, 15, 27–43].

The study of protein folding is focused on understanding the thermodynamic and structural routes of a peptide chain transforming from the unfolded state to the folded state, identifying secondary and tertiary interactions in the transition states and intermediates. Amide hydrogen exchange in combination with NMR spectroscopy has played a considerable role in monitoring and describing these states of protein folding. It should be kept in mind, however, that the method of amide hydrogen exchange is an indirect way of detecting the progress of protection of an amide hydrogen atom towards exchange with solvent. The method has no way of providing information regarding the chemical and structural nature of the protection. Therefore, careful evaluation is recommended when structural interpretations of transition states and intermediates based on the results of amide exchange are presented in their own right. The literature has several examples of opposite interpretations of amide hydrogen exchange results. For instance it has been proposed that the slow exchanging core of amides in the interior of a protein is the folding nucleus of proteins [44, 45]. This view has been opposed on the grounds of thermodynamic considerations and by examples of experimental evidence of proteins for which the folding nucleus and the core of slowly exchanging amides did not coincide [46, 47]. It has been suggested that pathways of protein folding may be determined by detection of on-pathway intermediates [48]. Many of the intermediates of protein folding have been identified by ultra-fast kinetic measurements or indirectly detected in the dead time of rapid mixing experiments and recorded by spectroscopic techniques, which do not provide information about the structure of the intermediate. The coincidence of the measures of thermodynamic parameters describing the intermediate and those describing native state hydrogen exchange kinetics have been used to couple such observations [12]. However, even the presence or absence of an on-pathway intermediate in barnase, as determined by amide hydrogen exchange studies in combination with a large number of very carefully conducted folding studies, has turned out to be controversial [11, 49–52].

Nevertheless, amide hydrogen exchange is a powerful tool in studies of protein folding, and used with care the combined results of kinetic and native state hydrogen exchange measurements with other spectroscopic measurements can provide important information about protein folding.

The field of amide hydrogen exchange in protein folding has been reviewed many times, most recently in Refs [53–57].

18.2
The Hydrogen Exchange Reaction

The exchange of amide hydrogen with hydrogen atoms from water is a catalyzed reaction [58]. The catalyst can be the basic hydroxide ion, the neutral water molecule, or the acid hydroxonium ion. The initial step in the reaction is the formation of a transient complex between the reactive group and the catalyst through a hydrogen bond. Subsequently the labile proton is transferred to the catalyst in the complex and the complex is dissociated. The replacement of the hydrogen atom with a hydrogen atom from the solvent molecule represents the hydrogen solvent exchange reactions. This implies that amide hydrogen exchange is pH dependent (Figure 18.1).

18.2.1
Calculating the Intrinsic Hydrogen Exchange Rate Constant, k_{int}

In an unstructured polypeptide, the rate of exchange of an amide hydrogen with solvent depends on the pH, temperature, ionic strength, the isotopes (H or D), and the chemical nature of the neighboring amino acid side chains. Taking these factors into account, intrinsic hydrogen exchange rates of amide hydrogen in pro-

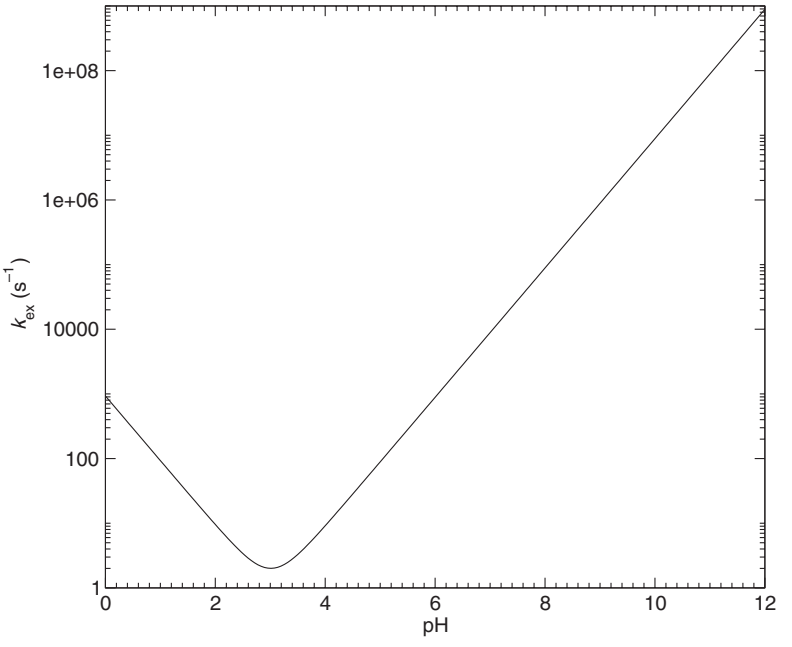

Fig. 18.1. Variation with pH of the amide hydrogen exchange rate, k_{ex}, of poly-D,L-alanine. At pH below 3 acid catalysis dominates. Above pH 3 base catalysis dominates.

Tab. 18.1. Exchange rates of poly-D,L-alanine under various conditions.

Isotopes	*Additive*	*Temp (K)*	*log k_A*	*log k_B*	*log k_W*	*Ref.*
H in D_2O	0.5 M KCl	278	1.19	9.90	−2.5	59
H in D_2O	No salt	293	1.62	10.05	−1.5	136
H in D_2O	0.1 M NaCl	293	1.50	9.66	−1.28	137
D in H_2O	No salt	293	1.40	9.87	−1.6	136
D in 91% H_2O	0.55 M GdmCl	293		10.00		33
H in D_2O	2.0 M GdmCl/0.1 M NaCl	293	1.64	10.01	−1.69	137
H in D_2O	4.0 M GdmCl/0.1 M NaCl	293	1.43	10.05	−1.84	137
H in D_2O	6.0 M GdmCl/0.1 M NaCl	293	1.22	9.78	−1.72	137
D in H_2O	8.0 M urea/0.1 M NaCl	293	2.43	8.52	−1.77	137

The rate constants are in units of M^{-1} min^{-1}.

teins, k_{int}, can be calculated according to:

$$k_{int} = k_A A_L A_R [H^+] + k_B B_L B_R [OH^-] + k_W B_L B_R \quad (1)$$

where k_A, k_B, and k_W are second-order rate constants for acid, base, and water catalyzed hydrogen exchange in poly-D,L-alanine (PDLA). These rate constants have been measured under different conditions and are listed in Table 18.1. When calculating k_{int}, a PDLA reference close to the actual experimental conditions should be chosen. In Eq. (1), A_L, A_R, B_L, and B_R are factors correcting the PDLA rates for effects of neighboring side chains other than Ala (Table 18.2) [59]. Different factors for acid and base catalysis should be used. Thus, A_L and A_R are used to correct k_A, whereas B_L and B_R are used to correct k_B and k_W. The L and R subscripts correspond to whether the amide is to the left or to the right of the side chain (see Figure 18.2 for definition of left and right in this situation). Note that the correction factors for left and right in Table 18.2 are different. For calculation of $[OH^-]$ from a pH meter reading, the pK_W values of Covington et al. [60] in H_2O and D_2O at 278 K and 293 K are listed in Table 18.3.

The temperature difference between the temperature under the reference conditions, T_{ref}, and the actual temperature of the experiment, T, is corrected from the Arrhenius equation for each of the reference rate constants k_A, k_B, and k_W according to:

$$k(T) = k(T_{ref}) \exp(-E_a(T^{-1} - T_{ref}^{-1})R^{-1}) \quad (2)$$

where E_a is the activation energy and R is the gas constant. E_a is 14, 17, and 19 kcal mol^{-1} for k_A, k_B, and k_W respectively. These E_a values correct the second-order rate constants k_A, k_B, and k_W and the autoprotolysis constants of H_2O or D_2O.

For example, calculate k_{int} in H_2O for the amide hydrogen in the sequence -Phe-NH-Gly- at low salt, pH 7, and 298 K.

From Table 18.1 the PDLA reference for D-exchange in H_2O with no salt at 293 K is chosen. Thus, $k_A = 10^{1.40}$ M^{-1} min^{-1}, $k_B = 10^{9.87}$ M^{-1} min^{-1}, and $k_W = 10^{-1.6}$

Tab. 18.2. Effect of amino acid side chains on hydrogen exchange rates of neighboring amide hydrogens.

Side chain	*Acid catalysis*		*Base catalysis*	
	log A_L	*log A_R*	*log B_L*	*log B_R*
Ala	0.00	0.00	0.00	0.00
Arg	−0.59	−0.32	0.08	0.22
Asn	−0.58	−0.13	0.49	0.32
Asp(COO^-)	(0.9)[1]	0.58	−0.30	−0.18
Asp(COOH)	(−0.9)	−0.12	0.69	(0.6)
Cys (red)	−0.54	−0.46	0.62	0.55
Cys (ox)	−0.74	−0.58	0.55	0.46
Gly	−0.22	0.22	0.27	0.17
Gln	−0.47	−0.27	0.06	0.20
Glu(COO^-)	(−0.9)	0.31	−0.51	−0.15
Glu(COOH)	(−0.6)	−0.27	0.24	0.29
His			−0.10	0.14
His^+	(−0.8)	−0.51	(0.8)	0.83
Ile	−0.91	−0.59	−0.73	−0.23
Leu	−0.57	−0.13	−0.58	−0.21
Lys	−0.56	−0.29	−0.04	0.12
Met	−0.64	−0.28	−0.01	0.11
Phe	−0.52	−0.43	−0.24	0.06
Pro (*trans*)		−0.19		−0.24
Pro (*cis*)		−0.85		0.60
Ser	−0.44	−0.39	0.37	0.30
Thr	−0.79	−0.47	−0.07	0.20
Trp	−0.40	−0.44	−0.41	−0.11
Tyr	−0.41	−0.37	−0.27	0.05
Val	−0.74	−0.30	−0.70	−0.14
N-term (NH_3^+)		−1.32		1.62
C-term (COO^-)	0.96		(−1.8)	
C-term (COOH)	(0.05)			

[a] Numbers in brackets are determined with low accuracy [59].
Adapted from Bai et al. [59].

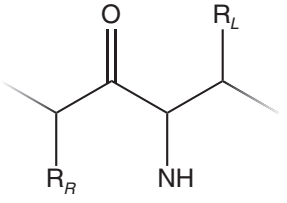

Fig. 18.2. Left and right in Table 18.2 are defined relative to an amino acid side chain. To correct the hydrogen exchange rate of an amide to the right of side chain R_R and to the left of side chain R_L the PDLA reference rate has to be corrected with the "R" value of side chain R_R and the "L" value of side chain R_L.

Tab. 18.3. Autoprotolysis constants (pK_W) of H_2O and D_2O.

Temp (K)	*278*	*293*
H_2O	14.734	14.169
D_2O	15.653	15.049

From Covington et al. [60].

M^{-1} min^{-1}. The amide is to the right of Phe, so from Table 18.2 $A_R = 10^{-0.43}$ and $B_R = 10^{0.06}$. The amide is to the left of Gly, so $A_L = 10^{-0.22}$ and $B_L = 10^{0.27}$. From Table 18.3 we get $pOH = pK_W - pH = 15.049 - 7 = 8.049$. Calculating the acid, base, and water terms in Eq. (1) separately gives:

$$k_{acid} = 10^{(1.40-0.22-0.43-7)}\ min^{-1} = 5.6 \times 10^{-7}\ min^{-1}$$

$$k_{base} = 10^{(9.87+0.27+0.06-8.049)}\ min^{-1} = 141.6\ min^{-1}$$

$$k_{water} = 10^{(-1.6+0.27+0.06)}\ min^{-1} = 53.7 \times 10^{-3}\ min^{-1}$$

Each term must be corrected for the temperature difference between the reference conditions and the experimental conditions according to Eq. (2) and added to get k_{int}. However, k_{acid} and k_{water} are negligible compared with k_B and only the base term need be considered:

$$k_{int} = 141.6\ min^{-1} \exp\left(\frac{-17\ kcal \cdot mol^{-1}((298\ K)^{-1} - (293\ K)^{-1})}{1.987 \times 10^{-3}\ kcal \cdot mol^{-1}\ K^{-1}}\right)$$

$$= 231.1\ min^{-1}$$

Hydrogen exchange rates may also be calculated using the web-service "Sphere" from Heinrich Roders laboratory at: http://www.fccc.edu/research/labs/roder/sphere.

Protection factors, P, are defined as the ratio of the calculated intrinsic exchange rate of an amide in the unstructured environment, k_{int}, to the observed rate constant of exchange, k_{obs}, from the folded, intermediate, or unfolded state. Protection factors are calculated individually for each backbone amide and are regarded as a tool to predict the degree of structural protection against exchange, $P = k_{int}/k_{obs}$ (see also Section 18.4.3).

18.3 Protein Dynamics by Hydrogen Exchange in Native and Denaturing Conditions

The hydrogen exchange reactions of amides in native state globular proteins are a result of dynamic processes. From simple measurements of direct amide exchange

rates and the subsequent calculation of protection factors (see Section 18.1), the stability and hydrogen bond structure of stable, populated, equilibrium protein folding intermediates of several proteins have been described. Typically, the amides of a protein in its stable native state are protected against exchange and the rates are reduced by factors in the order of 10^6 to 10^{10}, whereas the intermediate states have protection factors in the order of 10^1 to 10^3 [43, 61–64]. For a few proteins studied at high concentrations of chemical denaturants, for example in 8 M urea, protection factors of less than five have been determined [38, 65].

At equilibrium under native conditions, a fraction of the protein population will occupy high-energy intermediate and unfolded states, and this provides an excellent opportunity to map the structure of protein folding intermediates in native conditions, even when sparsely populated. The amide hydrogen exchange process is a suitable process, since any perturbation of the native state stability occurring from a change in any equilibrium in the direction of populating folding/unfolding intermediates or the unfolded state will result in a change in the observed exchange rate. The perturbation of the equilibrium can occur by changing the pH of the sample, by addition of small amounts of chemical denaturants, or by changing the temperature. Information about global and local folding rates and populations of intermediates in the protein folding reactions are all available from equilibrium hydrogen exchange measurements. In the following studies, it is of importance that the native state is always the most populated state.

18.3.1 Mechanisms of Exchange

Amides are protected against exchange either because they are involved in a hydrogen bond or because they are placed in a hydrophobic environment [66]. Exchange of hydrogen-bonded amides requires opening of the hydrogen bond and separation of donor and acceptor by at least 5 Å [67]. The breakage of any given hydrogen bond can occur by three different mechanisms, each of which can be identified by the use of the "Native State Hydrogen Exchange" strategy [9] described below. Either the hydrogen bond is broken as a consequence of a cooperative global unfolding process or by cooperative local unfolding reactions exposing sets of hydrogen bonds [8, 53, 68]. The third possibility for exposure to solvent is by noncooperative (limited) local fluctuations, which only expose one amide proton at a time for exchange [67, 69]. In a globular, native protein the amide hydrogen exchange rate monitored for a particular amide proton will be a result of the sum of exchange by all three mechanisms.

18.3.2 Local Opening and Closing Rates from Hydrogen Exchange Kinetics

Independent of the three mechanisms for exchange described above, and neglecting any populations of intermediates, the amide exchange reaction can be described by a two-step reaction (Figure 18.3) [1, 70]. The first step opens the amide

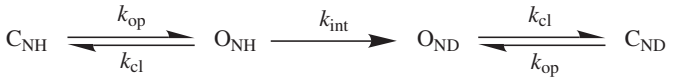

Fig. 18.3. The Linderstrøm-Lang model for hydrogen exchange in a protein dissolved in a deuterated medium. An amide may either be found in hydrogen protected state C, or in a hydrogen exchange competent state O. Conversion between C and O is a reversible first-order process with the rate constants k_{op} and k_{cl} for the opening and closing reactions, respectively. From the open state amide hydrogen may exchange with solvent deuterium in a pseudo first-order process with the rate constant k_{int} (see also Section 18.2.1).

from a closed hydrogen exchange protected form, C_{NH}, to an exchange competent form, O_{NH}, described by the first-order rate constants k_{op} and k_{cl}. The second step is a pseudo first-order reaction where the amide hydrogen exchanges with solvent deuterium with the rate constant k_{int} (see also Section 18.2.1). In a hydrogen exchange experiment little or no solvent hydrogen is present and rehydrogenation can be neglected.

As the amide exchange process is strongly pH dependent, the rates of segmental opening and closing of a giving amide, k_{op} and k_{cl}, can be determined quantitatively from measurements of the observed hydrogen exchange rate, k_{obs}, as a function of pH. For several proteins it has been shown that the most slowly exchanging amide protons have opening and closing rates corresponding to the global folding and unfolding rates determined by standard stopped-flow kinetic techniques [71, 72], and this fact opens a route to determine protein folding kinetics by equilibrium hydrogen exchange measurements.

18.3.2.1 The General Amide Exchange Rate Expression – the Linderstrøm-Lang Equation

Without making any assumptions to the relative measures of the three rate constants k_{op}, k_{cl}, and k_{int}, a general expression for the observed exchange rate constant for a given amide hydrogen in a protein can be derived from the kinetic equations (Eqs (3) and (4)) describing the reaction scheme above as follows:

$$\frac{d[C_{NH}]}{dt} = -k_{op}[C_{NH}] + k_{cl}[O_{NH}] \tag{3}$$

$$\frac{d[O_{NH}]}{dt} = k_{op}[C_{NH}] - (k_{int} + k_{cl})[O_{NH}] \tag{4}$$

with the biphasic solutions:

$$[C_{NH}](t) = A_{C0} + A_{C1}e^{-\lambda_1 t} + A_{C2}e^{-\lambda_2 t} \tag{5}$$

$$[O_{NH}](t) = A_{O0} + A_{O1}e^{-\lambda_1 t} + A_{O2}e^{-\lambda_2 t} \tag{6}$$

where A_{x0} is the equilibrium concentration of species x, and A_{x1} and A_{x2} are the amplitudes of the two phases. The rate constants for these phases are given by:

$$\lambda_1 = \frac{1}{2}(k_{op} + k_{cl} + k_{int} - ((k_{op} + k_{cl} + k_{int})^2 - 4k_{op}k_{int})^{1/2}) \quad (7)$$

and

$$\lambda_2 = \frac{1}{2}(k_{op} + k_{cl} + k_{int} + ((k_{op} + k_{cl} + k_{int})^2 - 4k_{op}k_{int})^{1/2}) \quad (8)$$

In a hydrogen exchange experiment λ_2 is generally larger than 10 s^{-1} and the fast phase described by this rate constant will be over in the dead time of the experiment, which typically will be measured in minutes. Thus, only λ_1 will be observed and $k_{obs} = \lambda_1$. This general description of the amide exchange rate was first described by Linderstrøm-Lang [1] and is applicable under all conditions.

18.3.2.2 Limits to the General Rate Expression – EX1 and EX2

In a stable protein under conditions favoring the native state $k_{cl} \gg k_{op}$, Eq. (7) may be reduced as follows using that $(1 - x)^{1/2} \approx 1 - x/2$ for $x \ll 1$:

$$\begin{aligned} k_{obs} &\approx \frac{1}{2}\left(k_{cl} + k_{int} - (k_{cl} + k_{int})\left(1 - \frac{4k_{op}k_{int}}{(k_{cl} + k_{int})^2}\right)^{1/2}\right) \\ &\approx \frac{1}{2}\left(k_{cl} + k_{int} - (k_{cl} + k_{int})\left(1 - \frac{2k_{op}k_{int}}{(k_{cl} + k_{int})^2}\right)\right) = \frac{k_{op}k_{int}}{k_{cl} + k_{int}} \end{aligned} \quad (9)$$

Two limiting cases of Eq. (9) may be considered. If $k_{int} \gg k_{cl}$, which is typical under alkaline conditions, Eq. (9) reduces to:

$$k_{obs} \approx k_{op} \quad (10)$$

This is the EX1 limit [4, 70, 73, 74]. In this limit the amide will exchange in every opening event as the rate-limiting step will be the conformational opening from the closed form. In the EX1 limit, the observed rate of exchange, k_{obs}, directly gives k_{op}.

If $k_{cl} \gg k_{int}$, Eq. (9) reduces to:

$$k_{obs} \approx k_{int}k_{op}/k_{cl} = k_{int}K_{op} \quad (11)$$

This is the EX2 limit [4, 73, 74]. In the EX2 limit the amide will not exchange in every opening event as closing competes with exchange. From the observed rate of exchange, k_{obs}, and the intrinsic exchange rate, k_{int}, the equilibrium constant for opening, K_{op}, may be obtained.

From Eqs (10) and (11) it is seen that if k_{op} and k_{cl} are both pH independent, k_{obs} for amides under EX1 conditions is also independent of pH. k_{obs} for amides under EX2 conditions will be pH dependent through the pH dependence of k_{int}. Taking the logarithm of Eqs (10) and (11) yields:

$$\log k_{obs} = \log k_{op} \tag{12}$$

for EX1, and

$$\log k_{obs} = \log k_{int} + \log K_{op} = pH - pK_W + \log B_L + \log B_R + \log k_B + \log K_{op} \tag{13}$$

for EX2. Thus, in a plot of log k_{obs} versus pH a slope of zero will reflect an amide with exchange in the EX1 limit and a slope of one will reflect an amide with exchange in the EX2 limit (Figure 18.4).

For a given protein, the residue-dependent variations of k_{op}, k_{cl}, and k_{int} will result in observed exchange rates varying over several orders of magnitudes. For a given amide in a fixed amino acid sequence, a set of simulations of the observed exchange rate, k_{obs}, with different opening and closing rates is shown in Figure

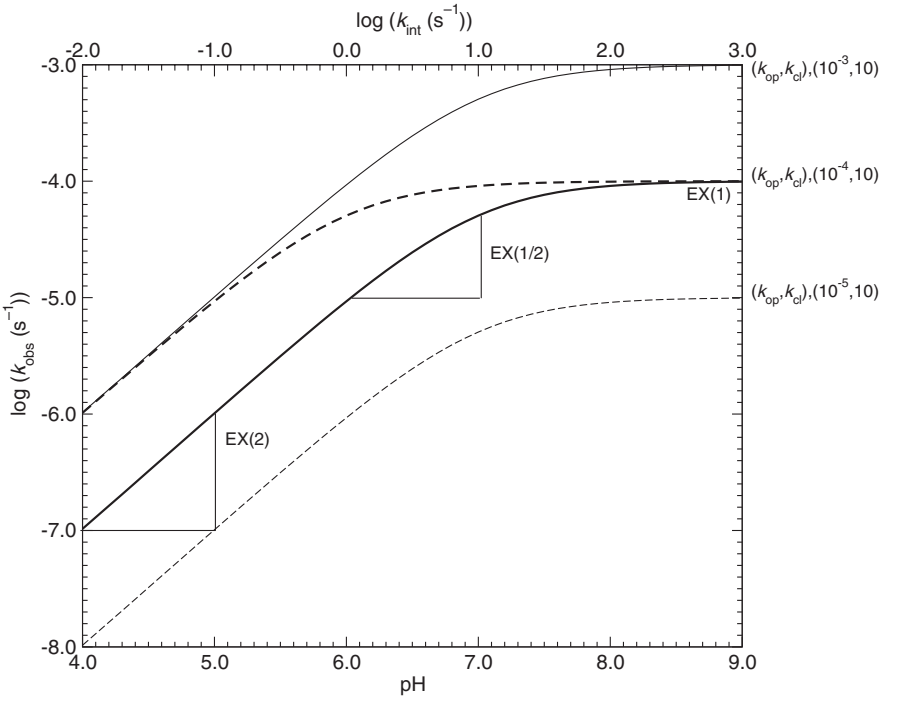

Fig. 18.4. Simulated pH dependence of k_{obs} for amide exchange according to Eq. (7). Data are simulated in the pH range from pH 4.0 to pH 10.0 for the situation that only the base-catalyzed reaction is active and the rate constants k_{op} and k_{cl} are not pH dependent. The chemical exchange rate $k_{int} = 10^8\ s^{-1}\ M^{-1} \times 10^{(pH-14)}$ M expected for the amide in the sequence Ala-NH-Ala is on the top axis. The three situations of exchange are illustrated in the figure: EX2 (pH dependence = 1), EX(1/2) (0 < pH dependence < 1), and EX1 (no pH dependence).

18.4. Four lines are shown representing simulated pH-dependent exchange in four different situations with different values of k_{op} and k_{cl}. The variation in k_{op} will shift the value for the observed rate constant, log k_{obs}, by a simple transposition where increasing k_{op} (and/or k_{int}) shift log k_{obs} to higher values (bold solid line to thin solid line). Variation in k_{cl} will change the profile of the line and increasing k_{cl} will shift log k_{obs} to the left and lead to exchange in the EX1 limit at lower pH (bold solid line to bold dashed line).

EX1 limit: $k_{obs} = k_{op}$ $(k_{cl} \ll k_{int})$
EX2 limit: $k_{obs} = K_{op}k_{int}$ $(k_{cl} \gg k_{int})$

18.3.2.3 The Range between the EX1 and EX2 Limits

In the range between the two limits, the simplifications of the general rate expression as in the EX1 and EX2 limits are not applicable. This range, which has often been ignored, is referred to here as the EX(1/2) range [75]. The change from EX2 to EX1 exchange appears in the alkaline pH range, where k_{int} is large. For amides with exchange kinetics in the EX(1/2) range there is a unique possibility to determine the rate constants k_{op} and k_{cl} simply by nonlinear least squares fitting to the pH dependence of the exchange kinetics using the general expression (Eq. (7)) for k_{obs}.

A nonlinear fitting analysis of Eq. (7) can unambiguously determine k_{op} without any assumptions other than the reaction scheme of Figure 18.3, whereas k_{cl} and k_{int} are too strongly correlated to be determined. If it is assumed that a site-specific random coil rate constant [59] can be applied as k_{int}, the experimental data for a given residue can initially determine k_{op} and subsequently k_{op} and k_{int} are used to determine k_{cl}, or k_{op} and k_{cl} can be determined directly in a two-parameter fit where it is assumed that k_{int} is known [10, 14, 76]. It has been argued that the intrinsic rate constant does not apply to exchange by local fluctuations or local unfolding mechanisms, as these open structures does not resemble the random coil peptides [77]. In these cases only the opening rate, k_{op}, can be determined unambiguously.

18.3.2.4 Identification of Exchange Limit

When the rate constants k_{op} and k_{cl} are themselves pH dependent, the method of determining these from the pH dependence of the amide hydrogen exchange kinetics is clearly not valid. It is therefore important to distinguish between hydrogen bond amides for which the two rate constants are not affected by pH from those for which they are. For an amide with no change in stability with pH, the pH dependence of the exchange kinetics, $\alpha_{pH} = \Delta \log k_{obs}/\Delta pH$ reflect directly the exchange mechanism, such that for an EX2 amide which experiences no pH-induced change in stability, $\alpha_{pH} = 1$, for an EX1 amide the exchange is independent of pH ($\alpha_{pH} = 0$) and for an amide with exchange in the (EX1/2) limit, $0 < \alpha_{pH} < 1$. If the stability is increasing with pH, log k_{obs} will for an EX2 amide increase by less than 1 per unit of pH ($\alpha_{pH} < 1$) and for an EX1 amide α_{pH} will be

negative. If the stability is decreasing with pH, the pH dependence will be larger than one for an EX2 amide ($\alpha_{pH} > 1$) and larger than zero for an EX1 amide ($\alpha_{pH} > 0$). An amide that has $\alpha_{pH} < 1$ is therefore either an EX2 amide whose environment is stabilizing with increasing pH, an EX1 amide that is destabilizing with increasing pH, or an amide that exchanges in the EX(1/2) range. When determining the segmental opening and closing rate constants, k_{op} and k_{cl}, these issues must be considered. One way is to assure that exchange takes place by EX1 mechanism at higher pH and by EX2 mechanism at lower pH. Optical techniques may also be invoked to determine the global stability with pH.

pH dependence of k_{obs} and resulting exchange limits When the rate constants k_{op} and k_{cl} are not themselves pH dependent, amides exchanging in the EX(1/2) range can easily be distinguished from amides in the EX1 and the EX2 range by the slope $\alpha_{pH} = \Delta \log k_{obs}/\Delta pH$ of the pH dependence of the hydrogen exchange kinetics.

EX2 amides $\alpha_{pH} = 1$
EX1 amides $\alpha_{pH} = 0$
EX(1/2) amides α_{pH} is between 0 and 1

18.3.2.5 Global Opening and Closing Rates and Protein Folding

Analysis of protein amide exchange by use of the general Linderstrøm-Lang equation together with in-depth analysis of individual segmental opening and closing rates, k_{op} and k_{cl}, have been reported for only six proteins: lysozyme [76], acyl-coenzyme A binding protein (ACBP) [75], turkey ovomucoid third domain (OMTKY3) [10], hisactophilin [78], Csp A [79], and ubiquitin [13]. Either the general rate expression has been applied in the analysis to determine k_{op} and k_{cl} directly, or a combined analysis of exchange under both EX2 or EX1 conditions have provided measures of K_{op} ($= k_{op}/k_{cl}$) and k_{op}, respectively [80].

Global unfolding reactions of the proteins are always more rare than local unfolding reactions. Rates of amide exchange by global unfolding correspond commonly to rates of global unfolding measured by optical techniques. Regardless of the method used, either fitting to the general expression Eq. (7), to the simplified expression for stable proteins Eq. (9), or by combining measurements obtained under both EX1 and EX2 conditions, the opening rate constant, k_{op}, can be determined with high precision.

Determination of k_{cl} is highly dependent on the precision of k_{int} as these are greatly correlated, and when fitting to the reduced expression it is important that the amide do exchange in the EX2 limit. Thus, any local structure will tend to cause k_{int} to be overestimated, k_{cl} to be underestimated, and any pH-dependent change in exchange mechanism will be accumulated as errors in the determination of k_{cl}. The local closings are much faster than the global closing, and k_{cl} are larger for the slowly exchanging amides, resulting from the globally open form being more long lived than the locally open forms. No correlations of either opening or closing rates with overall protein stability have been noticed.

18.3.3 The "Native State Hydrogen Exchange" Strategy

The structure and stability of exchange-competent states, which also includes the structure and stability of low populated, partially unfolded states of a protein, can be deduced and investigated using the "Native State Hydrogen Exchange" strategy [9, 69, 81]. In this strategy, the denaturant dependence of hydrogen exchange rates is measured under EX2 conditions such that the denaturant concentration is varied only in the range favoring the native state. Through the perturbations of the equilibrium between the folded state and any unfolded state by chemical denaturants or by temperature, the dominant exchange process for a given amide can be mapped and cooperative units in protein unfolding, the so-called native-like partially unfolded forms, PUFs (see below) [9] can be located. Importantly, no information regarding the order of the folding reaction can be provided by this strategy, as kinetic mechanisms cannot be derived from an equilibrium analysis [47, 82]. It has been of some debate whether the slow-exchanging amides identify the protein folding nucleus. There seems only to be a correlation for a subset of proteins [44, 83] and certainly not for others [54, 84]. It must be stressed that the order of events cannot be determined from equilibrium measurements. Only when independent and complementary kinetic folding experiments are provided can distinctions between on- and off-pathway intermediates be made.

In the EX2 regime of exchange, the transient equilibrium constant for the opening reaction, K_{op}, can be used to calculate the apparent free energy of exchange (or opening), ΔG_{HX}, (or ΔG_{op}) as

$$\Delta G_{HX} = -RT \ln K_{op} \tag{14}$$

Earlier studies have demonstrated that the free energy of unfolding is linearly dependent on the concentrations of denaturant [85–87], which is expressed as

$$\Delta G_{unf} = \Delta G^{\circ}_{unf} - m[\text{denaturant}] \tag{15}$$

where m is a measure of the change in exposed surface area upon unfolding and ΔG°_{unf} is the unfolding free energy at 0 M denaturant (see Chapters 12.1, 12.2 and 13). The exchange can be regarded as a sum of two different processes [8, 68]. First, exchange can occur as a result of local fluctuations that do not expose additional surface area upon exchange and that are independent of the concentration of denaturant. Secondly, exchange can occur as a result of an unfolding reaction, which can be either global or local, depends on the concentration of denaturant, and exposes additional surface area. These two processes can be separately defined and the free energy of opening described as the sum of the processes.

$$\Delta G_{HX} = -RT \ln(K_{unf} + K_{fluc}) \tag{16}$$

The equilibrium constant for unfolding can be rewritten as

$$K_{\text{unf}} = \exp\left(\frac{-\Delta G^{\circ}_{\text{unf}} + m[\text{denaturant}]}{RT}\right) \tag{17}$$

Combining Eqs (16) and (17), an expression for the free energy of exchange that accounts for both fluctuation and unfolding mechanisms for exchange is obtained as

$$\Delta G_{\text{HX}} = -RT \ln\left(\exp\left(\frac{-\Delta G_{\text{fluc}}}{RT}\right) + \exp\left(\frac{-\Delta G^{\circ}_{\text{unf}} + m[\text{denaturant}]}{RT}\right)\right) \tag{18}$$

A set of simulations of the different mechanisms of exchange according to the expression above is shown in Figure 18.5. Four different amide-exchange profiles with increasing concentrations of denaturant converted to exchange free energies are illustrated. The four different profiles have the following characteristics:

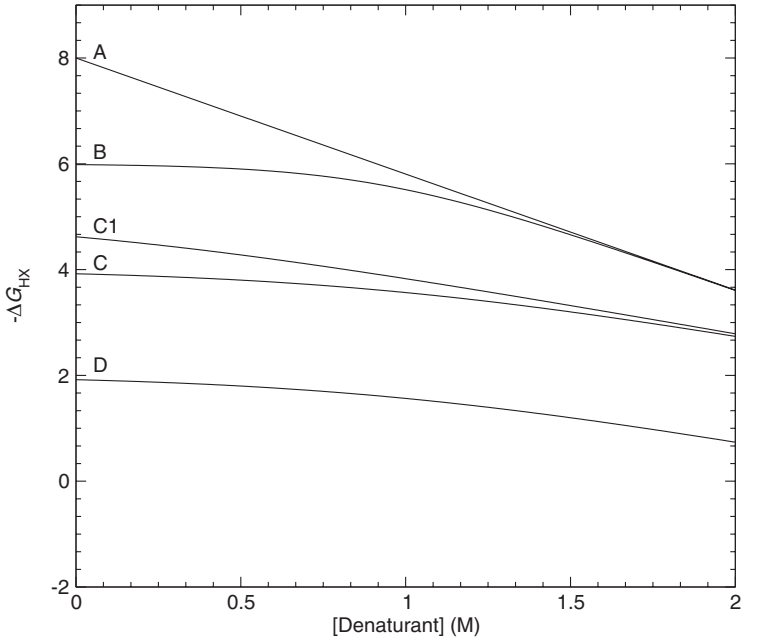

Fig. 18.5. Simulation of different hydrogen exchange mechanisms according to Eq. (18). For amide A the slope of the line (*m*) equals the *m*-value from equilibrium unfolding studies monitoring global unfolding (for example fluorescence and CD spectroscopy). For amide A, hydrogen exchange takes place entirely by global unfolding mechanism, and this has the highest free energy determined for the protein. Amide B has an *m*-value of zero at low concentration of denaturant and thus exchange is due to local fluctuations. The exchange is governed by global unfolding at higher denaturant concentrations. The curve coincide with the curve of amide A. Amides C and C1 shift to local unfolding with increasing denaturant concentration and merge to a common isoenergetic unfolding reaction and is part of the same cluster in the structure. Amide D is an example where global unfolding is never the dominating mechanism of exchange (Adapted from Ref. [135].)

- *Amide A: Global unfolding.* Amide hydrogen exchange takes place by global unfolding and represents the highest free energy at 0 M guanidinium chloride (GdmCl) determined in the protein. The slope of the line equals the *m*-value in Eq. (18) and corresponds to the *m*-value obtained from classical equilibrium unfolding studies using, for example, circular dichroism (CD) or fluorescence spectroscopy.
- *Amide B: Local fluctuations to global unfolding.* At low concentrations of denaturant, this amide exchange by local fluctuations. This is seen by the *m*-value of zero. At higher concentrations of denaturant, there is a shift for amide B to exchange by global unfolding, with an *m*-value equal to the *m*-value determined from CD or fluorescence.
- *Amide C and C1: Local fluctuations → local unfolding.* At low denaturant concentration amides C and C1 exchange by local fluctuations. At intermediate denaturant concentrations amides C and C1 exchange through local unfolding events with similar change in free energy (see below (PUF)). At higher concentrations of denaturant (>2 M) it is expected that both C and C1 will exchange by global unfolding and their lines will merge with the lines for A and B.
- *Amide D: Local unfolding.* For this amide global unfolding is never the dominating mechanism of exchange in the shown region of denaturant concentrations. This amide exchanges predominantly by local unfolding.

When fitting to Eq. (18), three parameters are determined: the *m*-value (slope), $\Delta G^{\circ}_{\mathrm{unf}}$, which is the free energy of exchange at 0 M denaturant (extrapolated intercept *y*-axis, dotted line), and ΔG_{fluc}, which is the free energy arising from fluctuations. The *m*-value provides direct information on the amide exchange mechanism: Fluctuation mechanisms are characterized by *m*-values of zero or very low *m*-values, local unfolding mechanisms have intermediate *m*-values lower than the *m*-values describing global unfolding, and finally global unfolding mechanisms give *m*-values equal to the *m*-values determined by global unfolding monitored by spectroscopic measures.

18.3.3.1 Localization of Partially Unfolded States, PUFs

Perturbation of the structural equilibrium of a protein by chemical denaturants or by temperature as described above allows mapping of the hydrogen exchange processes for the determination of a structural localization of independent unfolding units. This is done through identification of amides for which the exchange free energies merge to a common isoenergetic line different to the global unfolding line, for example the amides C and C1 of Figure 18.5. A set of such amides, whose exchange free energies, ΔG_{HX}, merge to a common isoenergetic line, originate from the same structural unfolding unit and have been termed a partially unfolded form (PUF) [9]. These unfolded forms of a protein identified from hydrogen exchange measurements have the slowest exchanging amides and generally have a strong dependence on the concentration of chemical denaturant, whereas the fastest exchanging amides are much less dependent on the concentration of denaturant, and require less unfolding of the protein to exchange. For many amides the

predominant exchange mechanism at 0 M denaturant is by local fluctuations [67, 88] and since these forms of the exchange competent amides are still highly structured ($m \approx 0$), caution must be taken in interpretation of the results. Again, exchange must occur by the EX2 mechanism in the entire range of denaturant concentrations.

The native state hydrogen exchange strategy has identified both kinetic folding intermediates [12] and partially unfolded forms for several proteins of various structures and with different folding characteristics. PUFs have been identified in proteins known to form kinetic transient intermediates as cytochrome *c* [9, 89], ribonuclease H [29, 64], apomyoglobin [90], and T4 lysozyme [91] and for other proteins as well such as ribonuclease A [69, 92], cytochrome b_{562} [93], barstar [94], and staphylococcus nuclease [95]. The PUFs observed are in some cases similar to the kinetic folding intermediates observed by optical techniques [9, 64, 89] and also cooperative unfolding units with regions of individual ΔG_{HX} and *m*-values which represent segments of structure with different intrinsic stabilities, have been localized. For some proteins the absence of any common isoenergetic lines [15, 47, 96, 97] has raised the question of whether the intermediate forms need necessarily to be discrete states (U and I) or if they rather exist as a continuum of states ($U_1 \ldots U_N$) [98, 99]. Some of these proteins fold and unfold in simple two-state reactions without any intermediate forms when investigated with optical techniques. But for barnase and thioredoxin, where kinetic pulse-labeling techniques (see Section 18.4) have identified intermediates, the lack of PUFs are puzzling. It may be due to a change in exchange mechanism from EX2 to EX1 [47] or to destabilization of the intermediates at higher denaturant concentrations.

In many cases, the highest possible energy of opening, ΔG_{HX}, typically derived from the slowest exchanging amides, is found to be equal to the global unfolding energy, ΔG_U. In some cases, however, ΔG_{HX} has been found to be larger than ΔG_U, [77, 97, 100], and this discrepancy has been termed "super protection". This super protection of the most protected amides has been ascribed to several origins: overestimation of k_{int} from residual structure in the open state [101], interference with EX1 behavior [47, 102], *cis–trans* proline isomerization [77], increased stability in D_2O [103], or a nonlinear dependence of the stability with denaturant concentration leading to increased stability at 0 M denaturant [104–107]. The discrepancy is still under debate.

18.4
Hydrogen Exchange as a Structural Probe in Kinetic Folding Experiments

Following the protein folding reaction by hydrogen exchange in combination with NMR and mass spectrometry is a great supplement to the more general optical detection techniques such as fluorescence and CD. Fluorescence only measures the environment of a single or a few tryptophans, and far-UV CD measures an average of the conformation of all peptide bonds. In contrast to this, hydrogen exchange reports on all amide protons involved in hydrogen bonds or amide protons pro-

tected by a hydrophobic environment and in combination with 2D NMR, resolution at the residue level is achievable. In combination with mass spectrometry, hydrogen exchange may report on the heterogeneity of the sample and to some extent sequence-specific information can also be provided by this detection method.

At present, two methods for measuring hydrogen bond formation during the course of the protein folding process are employed; folding/hydrogen exchange competition and pulse labeling hydrogen exchange.

18.4.1 Protein Folding/Hydrogen Exchange Competition

The folding/exchange competition method was developed in Baldwin's laboratory and used to measure bulk hydrogen–tritium exchange [18, 108, 109]. Subsequently, the method was refined by Roder and Wüthrich to using hydrogen–deuterium exchange and NMR to detect exchange of amide hydrogen atoms of individual amides [110]. First, a deuterated unfolded protein is mixed with a hydrogenated refolding buffer under conditions where hydrogen exchange is fast enough to compete with the protein folding reaction. After a period of time, t_{pulse}, exchange is quenched by mixing with a buffer that lowers pH and thus slows hydrogen exchange, and the protein is allowed to completely fold to the native state before analysis (see Figure 18.6 for an outline of the method). If a hydrogen bond is formed during t_{pulse}, deuterium will become trapped in the structure. The amount of deuterium at a specific amide position depends on the rate by which the hydrogen bond is formed at this site, on the stability of this hydrogen bond and on the intrinsic exchange rate, k_{int}, of the amide in the particular conditions of the experiment.

The degree of hydrogen bond formation is determined from the amount of trapped deuterium. This can be measured by NMR spectroscopy by measuring the amount of incorporated proton at a given amide position from the peak volume of the H^N,N cross-peak in a HSQC spectrum or of the H^N,H^α cross-peak in a COSY spectrum. In order to compare the measured proton incorporation the volume, V, of a peak from an amide that becomes protected must be normalized to the volume, V_{ref}, of one or more peaks that do not become protected. This value is then normalized to the corresponding intensities (V_c and $V_{c,ref}$) measured in a uniformly labeled control sample and corrected for the fraction of H_2O, f_{H_2O}, in the labeling buffer. The resulting proton occupancy I can then be expressed:

$$I = \frac{V/V_{ref}}{V_c/V_{c,ref}} f_{H_2O}^{-1} \tag{19}$$

In the pH interval of an exchange/folding competition experiment the hydrogen exchange is dominated by base catalysis. By varying the pH of the refolding/exchange buffer, the intrinsic exchange rate of the individual amides, k_{int}, may be changed according to:

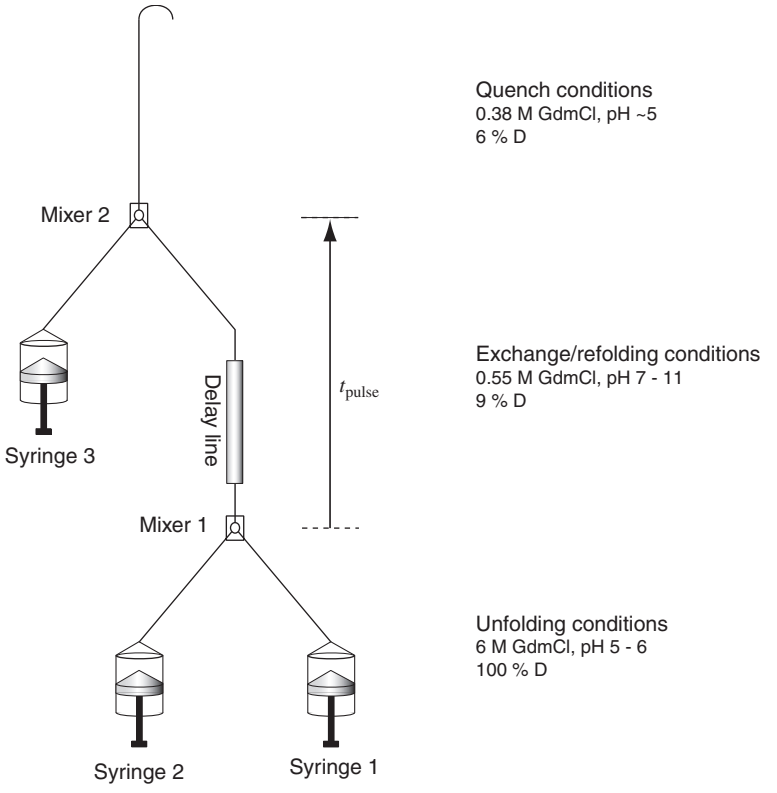

Fig. 18.6. Outline of the folding/exchange competition experiment. The experiment is carried out in a three-syringe quenched flow apparatus. Syringe 1 contains fully deuterated protein in 100% D_2O under conditions favoring the unfolded state. In mixer 1 the protein is diluted with 10 volumes of hydrogenated folding and exchange buffer from syringe 2. A series of experiments where pH of the refolding buffer is varied in the range from ~7 to ~11 is performed. Hydrogen exchange and protein folding competes while the protein flows from mixer 1 to mixer 2. After a period of time, t_{pulse} the sample reaches mixer 2 where quench buffer is added from syringe 3. The pH is now lowered to 5 or less and hydrogen exchange becomes slow. The sample is collected and desalted prior to analysis by NMR.

$$k_{int} = k_B B_L B_R [OH^-] \tag{20}$$

In the following, exchange occurs in a hydrogenated medium and it is assumed that all labile proton sites in the protein initially are deuterated. The equations can readily be modified for the reverse situation. As pH (and thus $[OH^-]$) does not change in a hydrogen exchange experiment, the hydrogen exchange process will be pseudo first-order and the change in proton occupancy, I, can be described by a single exponential decay described by Eq. (21). I is a function of both the length of the pH pulse, t_{pulse}, and of pH (through k_{int}):

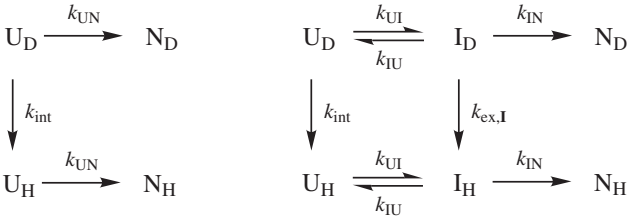

Fig. 18.7. Models of folding and hydrogen exchange of proteins following two- and three-state folding mechanisms. **U** is the unfolded state, **I** an intermediate state, and **N** the native state. Hydrogen exchange may occur directly from the **U**-state, which is supposed to be unstructured, with a rate k_{int}. Exchange from the **I**-state may occur due to local fluctuations with a rate constants $k_{ex,I}$. It is assumed that no hydrogen exchange takes place from an amide in the native state **N**. Back exchange from H to D is not considered due to high excess of H in the exchange medium. It is also assumed that there is no flux away from **N** (i.e., $k_{NU} \approx 0$ and $k_{NI} \approx 0$) as the experiments are conducted under native conditions.

$$I = 1 - \exp(-k_{int} t_{pulse}) \tag{21}$$

If a hydrogen bond is formed to an amide in a two-state process (Figure 18.7) the proton occupancy may be found from the following rate equations. Remember that $\mathbf{U}_H$ is allowed to fold to $\mathbf{N}_H$ before measuring the proton occupancy so we are interested in $[\mathbf{U}_H] + [\mathbf{N}_H]$.

$$\frac{d[\mathbf{U}_D]}{dt} = -(k_{int} + k_{UN})[\mathbf{U}_D] \tag{22}$$

$$\frac{dI}{dt} = \frac{d([\mathbf{U}_H] + [\mathbf{N}_H])}{dt} = k_{UN}[\mathbf{U}_D] \tag{23}$$

Solving Eqs (22) and (23) with the assumption that all protein is found as U_D for $t_{pulse} = 0$ yields:

$$I = \frac{k_{int}}{k_{UN} + k_{int}}(1 - \exp(-(k_{UN} + k_{int})t_{pulse})) \tag{24}$$

The proton occupancy versus pH curve of an amide that gets protected from exchange will thus be shifted to the right of the curve calculated for an unstructured amide using Eq. (21) (Figure 18.8). Selecting $t_{pulse} \gg 1/(k_{UN} + k_{int})$ Eq. (24) reduces to:

$$I = \frac{k_{int}}{k_{UN} + k_{int}} \tag{25}$$

By fitting the measured proton occupancies to Eqs (24) or (25) the rate of structure (hydrogen bond) formation, k_{UN}, can be obtained.

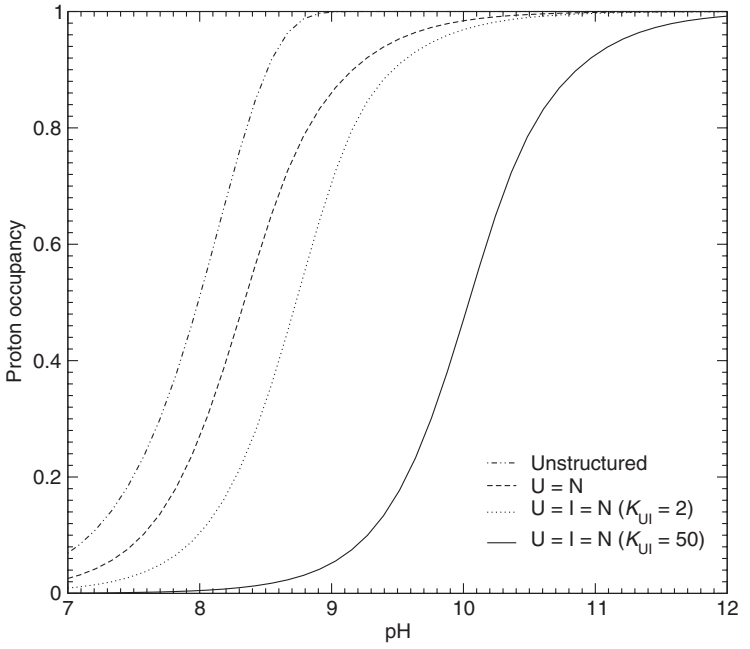

Fig. 18.8. Simulated proton occupancy profiles from a protein folding/hydrogen exchange competition experiment. ($\cdot - \cdot \cdot \cdot -$) exchange from an unprotected amide with $k_{int} = 1.67 \times 10^8$ s^{-1} M^{-1} [OH$^-$] according to Eq. (21); ($- - -$) exchange from an amide in a two-state process with $k_{UN} = 50$ s^{-1}, $k_{int} = 1.67 \times 10^8$ s^{-1} M^{-1} [OH$^-$] according to Eq. (24); ($\cdots$) exchange from an amide in a three-state process with $K_{UI} = 2$, $k_{IN} = 50$ s^{-1}, $k_{int} = 1.67 \times 10^8$ s^{-1} M^{-1} [OH$^-$], and $k_{ex,I} = 0$ according to Eq. (29); (——) exchange from an amide in a three-state process with $K_{UI} = 50$, $k_{IN} = 50$ s^{-1}, $k_{int} = 1.67 \times 10^8$ s^{-1} M^{-1} [OH$^-$], and $k_{ex,I} = 0$ according to Eq. (29).

For a protein that folds through an intermediate (Figure 18.7), the folding/competition protocol can be used to estimate the stability of the hydrogen bonds formed in the intermediate. If $k_{UI}, k_{IU} \gg k_{int}, k_{IN}$, **U** and **I** can be approximated to be in equilibrium at all times. Thus $[\mathbf{U}] = 1/(1 + K_{UI})([\mathbf{U}] + [\mathbf{I}])$ and $[\mathbf{I}] = K_{UI}/(1 + K_{UI})([\mathbf{U}] + [\mathbf{I}])$. The rate equations become:

$$\frac{d[\mathbf{N}_D]}{dt} = k_{IN}[\mathbf{I}_D] = \frac{k_{IN}K_{UI}}{1 + K_{UI}}([\mathbf{U}_D] + [\mathbf{I}_D]) \tag{26}$$

$$\begin{aligned}\frac{d([\mathbf{U}_D] + [\mathbf{I}_D])}{dt} &= -k_{int}[\mathbf{U}_D] - (k_{IN} + k_{ex,\mathbf{I}})[\mathbf{I}_D] \\ &= -\frac{k_{int} + (k_{IN} + k_{ex,\mathbf{I}})K_{UI}}{1 + K_{UI}}([\mathbf{U}_D] + [\mathbf{I}_D])\end{aligned} \tag{27}$$

$$\frac{d[\mathbf{X}_H]}{dt} = k_{int}[\mathbf{U}_D] + k_{ex,I}[\mathbf{I}_D] = \frac{k_{int} + K_{UI}k_{ex,I}}{1 + K_{UI}}([\mathbf{U}_D] + [\mathbf{I}_D]) \tag{28}$$

where $\mathbf{X}_H$ is any hydrogenated state ($[\mathbf{X}_H] = [\mathbf{U}_H] + [\mathbf{I}_H] + [\mathbf{N}_H]$). During measurement of the proton occupancy I only the **N** state is observed and essentially all hydrogenated species will be found in this state. Thus $[\mathbf{X}_H]$ is equivalent to I. Solving these equations yields the following expression for I:

$$I = \frac{k_{int} + K_{UI}k_{ex,\mathbf{I}}}{k_{int} + K_{UI}(k_{IN} + k_{ex,\mathbf{I}})}\left(1 - \exp\left(-\frac{K_{UI}(k_{IN} + k_{ex,\mathbf{I}}) + k_{int}}{K_{UI} + 1}t_{pulse}\right)\right) \tag{29}$$

I is a function of both pH (through the pH dependence of k_{int}) and t_{pulse}. If $k_{ex,\mathbf{I}} \gg k_{IN}$ or $k_{int} \gg K_{UI}k_{IN}$ insignificant amounts of protein will reach the native state **N** during the exchange period, t_{pulse}, and Eq. (29) is often simplified to:

$$I = 1 - \exp(-k_{app,\mathbf{I}}t_{pulse}) \tag{30}$$

where $k_{app,\mathbf{I}} = k_{int}/P_{app}$ with the apparent protection factor, $P_{app} = \frac{K_{UI} + 1}{K_{UI}k_{ex,\mathbf{I}}/k_{int} + 1}$. If $k_{ex,\mathbf{I}} \ll k_{int}$ only little exchange occurs directly from **I** and $P_{app} \approx 1 + K_{UI}$. If no protection from hydrogen exchange is present in **I**, $k_{ex,\mathbf{I}} = k_{int}$ and $P_{app} = 1$. Great care should be taken when using the simplified Eq. (30). Indeed, Gladwin and Evans [33] and Bieri and Kiefhaber [111] have stressed the importance of accounting for later folding events (i.e. the flux to **N**) in folding competition experiments. In a study of early folding intermediates in lysozyme and ubiquitin Gladwin and Evans simplified Eq. (29) by considering the **U** and **I** states as a single denatured state **D** in which some protecting structure may be formed. A two-state reaction scheme as in Figure 18.7 was used to describe the situation and an expression analogous to Eq. (24) can be obtained by setting $k_{ex} = (k_{int} + K_{UI}k_{ex,\mathbf{I}})/(K_{UI} + 1)$ and $k_f = K_{UI}k_{IN}/(K_{UI} + 1)$ in Eq. (29):

$$I = \frac{k_{ex}}{k_f + k_{ex}}(1 - \exp(-(k_f + k_{ex})t_{pulse})) \tag{31}$$

where k_f is the apparent folding rate and k_{ex} is the apparent exchange rate from **D**. In order to describe the protective structure in **D**, a protection factor or inhibition factor, k_{int}/k_{ex}, was reported [33].

An important prerequisite for good estimates of the stability of folding intermediates from the folding/exchange competition protocol is that the stability and kinetics of the folding process have low pH dependence. If the stability of an intermediate changes significantly with pH analysis of the data is not straightforward [111].

18.4.2
Hydrogen Exchange Pulse Labeling

Whereas the folding/exchange competition experiment has proven very useful for characterizing early folding intermediates, the protocol does not have the time resolution required for characterizing the time course of a protein folding process with multiple kinetic phases. The hydrogen exchange pulse labeling experiment is the choice for studying the time course of hydrogen bond formation. The hydrogen

exchange pulse labeling protocol was developed on RNase A by Udgaonkar and Baldwin [112] and on cytochrome *c* by Roder et al. [19]. The great advantage of this technique is its capacity to take a ''snap shot'' on the millisecond timescale of the hydrogen bonds as they evolve during folding. The pulse labeling experiment consists of three steps: folding, the exchange pulse, and the quench as outlined in Figure 18.9. The similarity with the folding/competition experiment is obvious. The only differences are the initial extra mixing stage, the folding period prior to the labeling pulse and the choice of pH in the various steps.

In a two-state folding experiment the following will occur: pH is low (5–6) during the folding step and $k_{UN} \gg k_{int}$. Therefore, exchange will be negligible for short folding times. During the exchange pulse, pH is raised as much as possible considering the stability of the protein (typically pH 10–11) and $k_{int} \gg k_{UN}$. Now, all deuterated amides that are not forming a protective structure will exchange and become protonated. In the last step pH is lowered to 5 or less whereby $k_{UN} \gg k_{int}$, and exchange is again negligible compared with folding. Folding is now allowed to go to completion. This mixing sequence will result in trapped deuterium at amides sites that have formed hydrogen bonds in the folding step, and will be observed as decreased signals of these amides in proton NMR spectra. The proton occupancy (and thus the NMR signal) will decrease as a function of the folding time, t_{fold}, with a rate equal to k_{UN}. If intermediates are present, additional phases will be observed just as with any other probe.

For an intermediate formed within the dead time of a hydrogen exchange pulse labeling experiment, a folding/exchange competition experiment can be conducted as described above to determine the stability of the structures formed [33]. If the intermediate forms later during folding the stability can be estimated by varying the pH of the exchange pulse in the pulse labeling experiment keeping the folding time, t_{fold}, constant. In this way the intermediate is allowed to populate before the folding/exchange competition is initiated [113].

The advantage of both hydrogen exchange pulse labeling and hydrogen exchange/folding competition in combination with NMR over direct spectroscopic techniques is that the kinetics of structure formation can be resolved at the residue level. Two points should, however, be kept in mind when interpreting the results of hydrogen exchange pulse labeling experiments. First, only amides that are highly protected in the native state are suitable probes. Hydrogens, which are only marginally protected or not protected at all, will exchange with the solvent during sample handling and analysis. Secondly, the experiment cannot distinguish between the formation of native and nonnative hydrogen bonds. If hydrogen bond formation is detected in an intermediate state, information from several experiments must be considered in order to characterize the hydrogen bonds as native or nonnative.

18.4.3
Protection Factors in Folding Intermediates

In order to characterize hydrogen bonds identified in intermediates by hydrogen exchange labeling techniques, protection factors are often reported. For the native

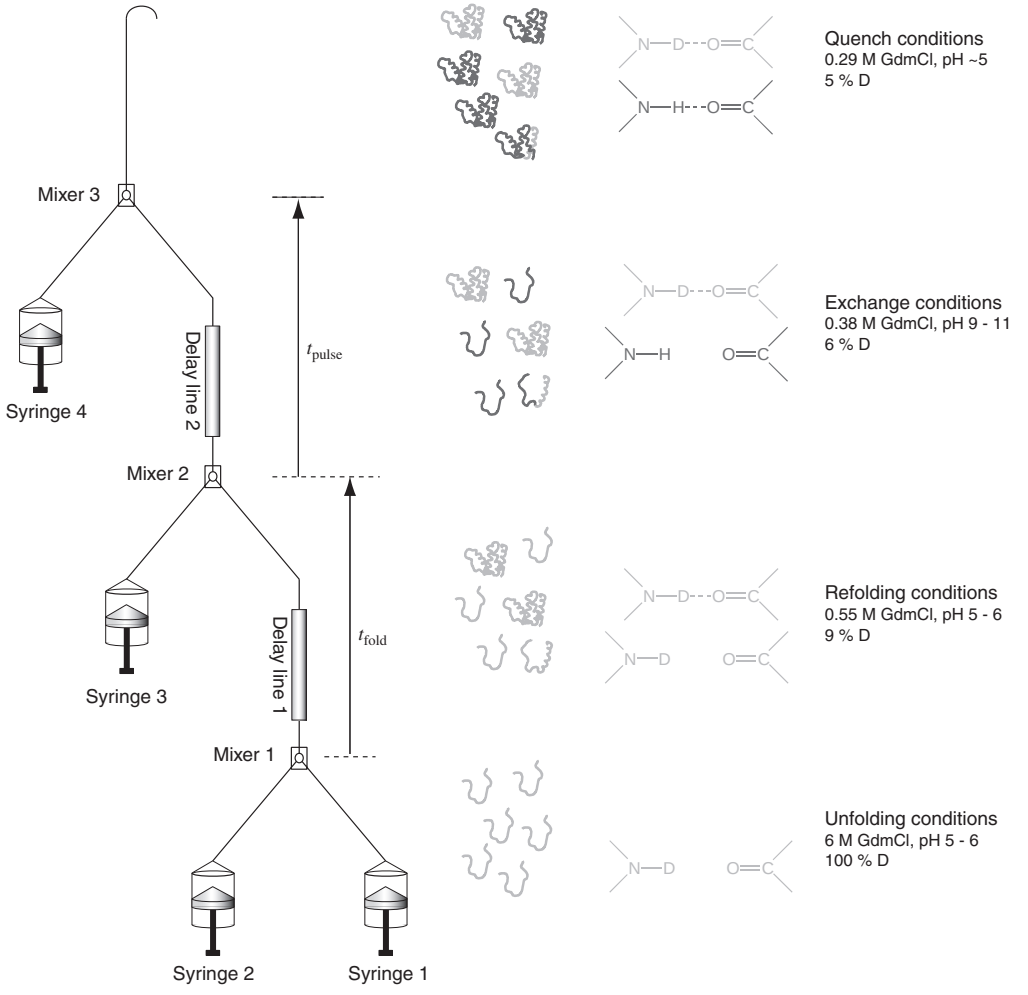

Fig. 18.9. Outline of the quenched flow hydrogen exchange pulse labeling experiment. The experiment is carried out in a four-syringe quenched flow apparatus. Syringe 1 contains fully deuterated protein in deuterated buffer under conditions favoring the unfolded state. In mixer 1 the protein is diluted with 10 volumes of hydrogenated refolding buffer. The protein is allowed to fold while it flows from mixer 1 to mixer 2. The folding time will thus be dependent on the volume between mixers 1 and 2 and the flow rate. At mixer 2 five volumes of hydrogen exchange buffer with high pH is added from syringe 3. At high pH hydrogen exchange is fast and deuterium at amides not engaged in hydrogen bonds will exchange with hydrogen from the solvent. After a period of time, t_{pulse} the sample reaches mixer 3 where quench buffer is added from syringe 4. The pH is now lowered to 5 or less and hydrogen exchange becomes slow. The result is a snapshot of the hydrogen bonds formed at mixer 2 as amides engaged in hydrogen bonds at this point will be labeled with deuterium. The sample is collected and desalted prior to analysis by NMR.

state, the protection factor is defined as $P = k_{int}/k_{obs}$ (Section 18.2.1). In analogy to this, a structural protection factor $P_{struc} = k_{int}/k_{ex,\mathbf{I}}$ can be defined, where $k_{ex,\mathbf{I}}$ is the apparent rate of hydrogen exchange directly from **I** [114]. P_{struc} thus reports on the stability and local fluctuations of structure in **I**-like protection factors for the native state. In P_{struc}, exchange through preceding unfolding of **I** to **U** is not considered. In order to get a reliable measure of P_{struc} it is important to be able to separate the exchange from the **I**-state from unfolding to and exchange from the **U**-state. This may be achieved if the **I**-state only converts slowly to the **U**-state compared with the exchange directly from **I**, or if previous knowledge of the folding kinetics allows for correction of the contribution to exchange from other states. An example of measurement of P_{struc} for two intermediates in the refolding of RNase A has been reported by Houry and Scheraga, who used an ingenious double jump hydrogen exchange protocol to selectively populate two different intermediates and measure the hydrogen exchange from these [114, 115].

Another way of defining a protection factor for early folding intermediates is as an apparent protection factor, $P_{app} = k_{int}/k_{app,\mathbf{I}}$ [114], which was introduced in the discussion of Eq. (30). In this definition, the apparent exchange rate k_{app}, which includes both direct exchange and exchange through unfolding processes, is considered. P_{app} is thus closely related to the overall stability of a hydrogen bond formed in an intermediate state including both the direct exchange and unfolding events. Often P_{app} is more easily measured than P_{struc}, as the contributions from the structure in **I** and the folding events do not have to be dissected.

18.4.4
Kinetic Intermediate Structures Characterized by Hydrogen Exchange

The hydrogen exchange labeling techniques described above have been used to characterize kinetic folding intermediates in numerous proteins. Both transient intermediates formed very early in the folding process and more stable intermediates formed later during folding have been observed by hydrogen exchange labeling.

One of the most well-studied systems is cytochrome *c* (cyt *c*) [116]. Three kinetic phases of the folding process have been characterized by tryptophan fluorescence [19, 117]. The fastest phase occurring within the dead time of conventional stopped-flow techniques was characterized by rapid mixing continuous-flow kinetic experiments and has a time constant of 50 μs [117]. The structures formed in this initial phase have been characterized by folding/hydrogen exchange competition. Sauder and Roder [26] found that several amides from three segments of the polypeptide that form α-helices in the folded state acquire significant protection from hydrogen exchange with the solvent within 2 ms of folding in 0.3 M GdmCl. Apparent protection factors in the range from 1.5 to 8 relative to exchange in cyt *c* unfolded in 2.5 M GdmCl were observed. Larger protection factors of 5–8 were observed in the helical regions forming side-chain interactions between the N- and C-terminal helices in the native structure. These protection factors agree well with the protection factors of 4–5 expected from stopped-flow experiments [26]. The lower protection factors of 1.5–5 were observed at the helical ends, suggesting

exchange through local fluctuations in these regions in the intermediate. The following phase in the folding of cyt *c* has a time constant of 20 ms, during which the structure in the N- and C-terminal helices consolidates. Tight native-like packing of these two helix fragments in the intermediate probably stabilizes the hydrogen bonds. The major fraction of the protein population reaches the native state from the late intermediate by organizing the structure around the heme with a time constant of 370 ms [19].

Lysozyme has also been extensively studied. Folding experiments at pH 5.2 showed a dead-time burst followed by two exponential phases using a variety of detection techniques with time constants of 25 ms and 340 ms respectively [118]. By folding/hydrogen exchange competition, protection factors of 2–15 in the burst phase were observed for amides constituting the α-domain in the native structure [33]. Hydrogen exchange pulse labeling resolved the kinetics of the hydrogen bond formation and showed that the amides in the α-domain become significantly protected in a kinetic phase with varying time constants of 7 ms to 60 ms for the different amides. The β-domain acquires protection in a later phase with a time constant of around 400 ms [22]. The range of time constants observed for the formation of protective structure in the α-domain apparently disagrees with kinetics measured by optical detection. However, simulation of the hydrogen exchange shows, when taking the folding kinetics of lysozyme during the exchange pulse at pH 9.5 into account, that the experimental data are in agreement with the proposed triangular folding model for lysozyme [111, 119]. The results on lysozyme stress the importance of thorough comparison of data from different techniques.

In the case of apomyoglobin, hydrogen exchange pulse labeling was used to identify the order of helix formation [41]. It was found that helices A, G, and H and a part of helix B form very fast within the dead time of the experiment. The rest of helix B forms stable structure at a later stage followed by helix C, the CD loop, and helix E, which dock as a late event in the folding process [41]. Leghemoglobin, which is a distant homolog of myoglobin (13% sequence identity), has also been studied by hydrogen exchange pulse labeling [120]. Like apomyoglobin, apoleghemoglobin forms a substantial amount of helical structure within the dead time of an ordinary stopped-flow experiment. Interestingly, the hydrogen exchange pulse labeling experiment showed that helices E, G, and H are structured in the burst phase intermediate whereas the A and B helices are not. It has thus been demonstrated that though apomyoglobin and apoleghemoglobin both fold through a compact intermediate with helical structure, the order in which the helices form and dock are different [120]. These results have contributed to the discussion about evolutionary conservation in protein folding [121–124] and show that the details of the folding process need not be evolutionary conserved.

On β-lactoglobulin, hydrogen exchange pulse labeling experiments have been performed using both conventional quench-flow mixing and ultra-rapid mixing. By this approach it was possible to resolve the kinetics of the hydrogen bond formation from 240 μs to 1 s [125]. It has been found that during folding of β-lactoglobulin some nonnative helical structure is formed [125, 126]. By hydrogen

exchange labeling the location of this transient structure was mapped to the N-terminal part of the protein, which forms a β-strand in the native structure. It was suggested that this nonnative structure protects the N-terminal part of the protein from aggregation during folding until most of the sheet, of which this strand is a part, has formed.

For several other proteins, both well-defined (RNase A [112, 115, 127], barnase [128], and RNase H from *E. coli* [129] and *Thermus thermophilus* [130]) and transient low-stability intermediates (protein G [131] and ACBP [132]) have been observed by hydrogen exchange pulse labeling techniques.

18.5 Experimental Protocols

18.5.1 How to Determine Hydrogen Exchange Kinetics at Equilibrium

The following experiment can be used to measure directly the amide exchange kinetics from any protein state at equilibrium. Typically exchange of hydrogen is measured with solvent deuterium, so any buffers used need to be deuterated before use.

18.5.1.1 Equilibrium Hydrogen Exchange Experiments

For each condition, samples of 0.5–2 mM protein in H_2O are adjusted to the desired pH and freeze dried repeatedly. After the final freeze drying, the protein is dissolved in the appropriate volume (300 or 600 μL) of 99.99% D_2O. For native state hydrogen exchange the desired concentration of deuterated denaturant in deuterated buffer is also included. The concentration of denaturant is always measured by refractive index [133, 134] and all pH measurements in D_2O are normally reported as direct meter readings. The sample is readjusted, if necessary, to the desired pH and transferred to a cold NMR tube to slow exchange. This is immediately placed in the spectrometer, which in advance has been tuned and calibrated using a similar sample. Acquisition of the first experiment is initiated when the desired sample temperature is obtained. Series of two-dimensional $^{15}N-^{1}H$ HSQC spectra, or COSY spectra if ^{15}N-labeled protein is unavailable, are recorded with good resolution for each sample. Peak integrals are measured and decay curves of peak integrals with time are fitted to an exponential three-parameter decay of the form

$$I(t) = I(\infty) + I(0)\exp(-k_{obs}t) \tag{32}$$

where $I(t)$ is the cross-peak intensity at time t after addition of D_2O to the lyophilized protein, $I(0)$ is the cross peak intensity at time zero, $I(\infty)$ is the final cross-peak intensity, and k_{obs} is the observed exchange rate constant. The time, t, is taken

as the midpoint of the NMR data acquisition for each data point. For amides with incomplete exchange in the time course of the experiment, $I(\infty)$ is omitted from the fit. Values and standard deviations of $I(\infty), I(0)$, and k_{obs} are obtained from nonlinear fitting procedures, and the uncertainties obtained on peak integrals are conveniently included.

18.5.1.2 Determination of Segmental Opening and Closing Rates, k_{op} and k_{cl}

Determination of the site-specific rate constants k_{op} and k_{cl} of the pre-exchange equilibrium can be determined from the pH dependence of the experimentally determined k_{obs}. Two different approaches can be applied. In the first approach, exchange is measured under both EX2 (to provide measures of k_{op}/k_{cl}) and EX1 (measures k_{op}) conditions and the result are combined to get k_{cl}. This of course requires that the protein is stable in high alkaline conditions and that k_{int} can be applied directly. For amides with exchange in the EX(1/2) regime, nonlinear fitting of experimental data to Eq. (7) or (9) are performed as described.

18.5.1.3 Determination of ΔG_{fluc}, m, and ΔG°_{unf}

In exchange experiments measured as a function of denaturant, values for $\Delta G_{fluc}, m$, and ΔG°_{unf} are obtained in a nonlinear fitting procedure to ΔG_{HX} as a function of denaturant concentration as described by Eq. (18). The only assumptions are that the unfolding free energies are linearly dependent on the concentration of denaturant and that exchange is within the EX2 limit.

18.5.2 Planning a Hydrogen Exchange Folding Experiment

The following is a general protocol for a folding/competition hydrogen exchange and a hydrogen exchange pulse labeling experiment. The protocol describes a deuterated protein that exchanges with solvent hydrogen. The reverse experiment can also be done. Modifications may be necessary to meet potential problems of protein stability and solubility. If ^{15}N-labeled protein is available it is desirable to use due to the increased sensitivity and simplicity and a better water suppression of a HSQC spectrum compared with a COSY spectrum.

18.5.2.1 Determine a Combination of t_{pulse} and pH_{pulse}

For the pulse labeling experiment the first step is to choose a suitable pH for the labeling pulse and a suitable labeling time. pH should be as high as possible but still well within the stability range of the protein. t_{pulse} should be long enough to ensure full (>99%) exchange of the amide with the lowest intrinsic exchange rate, k_{int}, calculated as described in Section 18.2.1. Typically, pH is in the range from 9 to 10.5 and t_{pulse} in the range of 5 ms to 20 ms.

18.5.2.2 Setup Quench Flow Apparatus

A rapid mixing apparatus (Bio-Logic SFM-400 or similar) has to be configured. For folding/exchange competition experiments the apparatus has to be configured in a

two-mixer mode whereas the pulse labeling experiment require three mixers. The easiest way of making proper mixing sequences is to use the manufactures software, which calculates the aging times in the delay lines at the chosen flow rates. In the pulse labeling experiment the apparatus must be operated in either of two modes. In a continuous flow mode the folding time depends on the flow rate and the volume of the first delay line. In interrupted mode the flow is stopped when the first delay line has been filled with mixed protein/refolding buffer. In this mode varying the length of the time the flow is stopped varies the folding time.

In a folding/exchange competition experiment the volume of the solutions in each step will typically be 1:10:5 (protein:refolding/exchange buffer:quench buffer). In the pulse labeling hydrogen exchange experiment the mixing ratio will be 1:10:5:5 (protein:refolding buffer:exchange buffer:quench buffer).

18.5.2.3 **Prepare Deuterated Protein and Chemicals**

Deuterated protein is prepared by several rounds of incubation in D_2O and freeze drying. If the protein is sensitive to freeze drying hydrogen may be exchanged with deuterium by thorough dialysis. Amide hydrogens that are very stable towards exchange may exchange when the protein is unfolded in deuterated GdmCl. It is a good idea to check the completeness of the exchange by NMR. Deuterated GdmCl is prepared simply by several rounds of incubation in D_2O and freeze drying.

18.5.2.4 **Prepare Buffers and Unfolded Protein**

The buffers mentioned below are suggestions, which will give proper pH in the various mixing steps; other buffers and pH values can, however, be chosen. The important issue to consider for the choice of buffers and experimental conditions is that the desired pH value is obtained in each mixing step. Prior to the hydrogen exchange step pH should be low (around 5) to ensure minimal hydrogen exchange. In the actual hydrogen exchange step pH is varied in the folding/exchange competition experiments. It should be as high as the stability of the protein allows in the hydrogen exchange pulse labeling experiment to ensure complete exchange of nonhydrogen bonded amides during the short exchange pulse. In the last mixing step, hydrogen exchange has to efficiently quenched. This is achieved by low pH (again around 5).

For a folding/exchange competition experiment the following solutions are suggested:

- Unfolded deuterated protein in 20 mM Na-acetate, 6 M deuterated GdmCl, pH 5.3 (in D_2O)
- Refolding/exchange buffer at varying pH from 7.5 to 11 (for example 20 mM HEPES (pH 6.8–8.2), 20 mM BICINE (pH 7.6–9.0), 20 mM CHES (pH 8.6–10.0), and 20 mM CAPS (pH 9.7–11.1))
- Quench buffer: 0.5 M Na-acetate, pH 4.8.

For a pulse labeling experiment the following solutions are suggested:

- Unfolded deuterated protein in 20 mM Na-acetate, 6 M deuterated GdmCl, pH 5.3 (in D_2O)
- Refolding buffer: 20 mM Na-acetate, pH 5.3
- Exchange buffer: 200 mM Na-borate, pH 11.0
- Quench buffer: 300 mM Na-acetate, pH 3.3.

18.5.2.5 Check pH in the Mixing Steps

It is important to check the pH at each step in the mixing sequence by performing manual mixing of the solutions in the right ratios on the bench. The check should be performed for each new batch of solutions as small variations in the buffer solutions may shift pH. If the desired pH is not obtained adjust pH of the appropriate buffer.

18.5.2.6 Sample Mixing and Preparation

The mixing apparatus is filled with the solutions. Let the solutions temperature equilibrate before the mixing is carried out. For each sample, enough protein for a proper NMR spectrum to be recorded in about 2 hours should be collected. Some loss of protein during the subsequent steps must be expected, but around 5 mg protein per sample (depending on the protein) is usually sufficient for a $^{1}H,^{15}N$ HSQC. If ^{15}N-labeled protein is unavailable more protein is needed to get the same signal-to-noise ratio from a COSY spectrum.

The samples should be put on ice immediately, and all subsequent steps should be carried out on ice or in the cold to minimize further hydrogen exchange. The samples are concentrated to approximately 1 mL and diluted with H_2O at pH 5 to 10 mL. This is repeated three times to dilute buffer and denaturant components. Finally, the sample is concentrated to 540 µL, 60 µL D_2O is added, and pH is adjusted. It is important to choose a low pH value (around 5) for the NMR samples in order to minimize hydrogen exchange during acquisition of the NMR spectrum.

The sample should be analyzed by NMR as soon as possible. It is our experience that samples kept on ice for up to 3 hours give good results. It is thus possible to prepare two samples in parallel. Longer storage of samples is undesirable. Record a spectrum with good resolution and signal-to-noise in 2–3 hours.

18.5.3 Data Analysis

Transform the spectra and integrate each amide cross-peak. Choose a set of well-resolved cross-peaks that show no protection against hydrogen exchange as reference peaks. Calculate the proton occupancy I according to Eq. (19). In a folding/exchange competition experiment plot I as a function of pH and fit the data to

Eq. (30) or (31) depending on which assumptions apply to the system under investigation. In a hydrogen exchange pulse labeling experiment plot the data against t_{fold} and fit the data to one or more exponential decays.

Acknowledgments

We would like to thank Flemming Hofmann Larsen, Wolfgang Fieber, and Jens Kaalby Thomsen for suggestions and for critically reading the manuscript.

References

1 Linderstrøm-Lang, K. (1955). Deuterium exchange between peptides and water. *Chem. Soc. Spec. Publ.* **2**, 1–20.

2 Hvidt, A. (1955). Deuterium exchange between ribonuclease and water. *Biochim. Biophys. Acta* **18**, 306–308.

3 Blout, E. R., Deloze, C. & Asadourian, A. (1961). Deuterium exchange of water-soluble polypeptides and proteins as measured by infrared spectroscopy. *J. Am. Chem. Soc.* **83**, 1895.

4 Hvidt, A. (1973). Isotope hydrogen exchange in solutions of biological macromolecules. In *Dynamic aspects of conformation changes in biological macromolecules* (Sadron, C., ed), pp. 103–115, Reidel and Dordrect, Holland.

5 Richards, F. M. (1979). Packing defects, cavities, volume fluctuations, and access to the interior of proteins – including some general-comments on surface-area and protein-structure. *Carlsberg Res. Commun.* **44**, 47–63.

6 Masson, A. & Wuthrich, K. (1973). Proton magnetic resonance investigation of the conformational properties of the basic pancreatic trypsin inhibitor. *FEBS Lett.* **31**, 114–118.

7 Campbell, I. D., Dobson, C. M., Jeminet, G. & Williams, R. J. (1974). Pulsed NMR methods for the observation and assignment of exchangeable hydrogens: application to bacitracin. *FEBS Lett.* **49**, 115–119.

8 Woodward, C. K. & Hilton, B. D. (1979). Hydrogen exchange kinetics and internal motions in proteins and nucleic acids. *Annu. Rev. Biophys. Bioeng.* **8**, 99–127.

9 Bai, Y., Sosnick, T. R., Mayne, L. & Englander, S. W. (1995). Protein folding intermediates: native-state hydrogen exchange. *Science* **269**, 192–197.

10 Arrington, C. B. & Robertson, A. D. (1997). Microsecond protein folding kinetics from native-state hydrogen exchange. *Biochemistry* **36**, 8686–8691.

11 Chu, R. A., Takei, J., Barchi, J. J. & Bai, Y. (1999). Relationship between the native-state hydrogen exchange and the folding pathways of barnase. *Biochemistry* **38**, 14119–14124.

12 Parker, M. J. & Marqusee, S. (2001). A kinetic folding intermediate probed by native state hydrogen exchange. *J. Mol. Biol.* **305**, 593–602.

13 Sivaraman, T., Arrington, C. B. & Robertson, A. D. (2001). Kinetics of unfolding and folding from amide hydrogen exchange in native ubiquitin. *Nat. Struct. Biol.* **8**, 331–333.

14 Roder, H., Wagner, G. & Wuthrich, K. (1985). Amide proton exchange in proteins by EX1 kinetics: studies of the basic pancreatic trypsin inhibitor at variable p2H and

temperature. *Biochemistry* **24**, 7396–7407.

15 Itzhaki, L. S., Neira, J. L. & Fersht, A. R. (1997). Hydrogen exchange in chymotrypsin inhibitor 2 probed by denaturants and temperature. *J. Mol. Biol.* **270**, 89–98.

16 Xu, Y., Mayne, L. & Englander, S. W. (1998). Evidence for an unfolding and refolding pathway in cytochrome c. *Nat. Struct. Biol.* **5**, 774–778.

17 Viguera, A. R. & Serrano, L. (2003). Hydrogen-exchange stability analysis of Bergerac-Src homology 3 variants allows the characterization of a folding intermediate in equilibrium. *Proc. Natl. Acad. Sci. USA* **100**, 5730–5735.

18 Kim, P. S. & Baldwin, R. L. (1980). Structural intermediates trapped during the folding of ribonuclease A by amide proton exchange. *Biochemistry* **19**, 6124–6129.

19 Roder, H., Elove, G. A. & Englander, S. W. (1988). Structural characterization of folding intermediates in cytochrome c by H-exchange labelling and proton NMR. *Nature* **335**, 700–704.

20 Miranker, A., Radford, S. E., Karplus, M. & Dobson, C. M. (1991). Demonstration by NMR of folding domains in lysozyme. *Nature* **349**, 633–636.

21 Miranker, A., Robinson, C. V., Radford, S. E., Aplin, R. T. & Dobson, C. M. (1993). Detection of transient protein folding populations by mass spectrometry. *Science* **262**, 896–900.

22 Radford, S. E., Dobson, C. M. & Evans, P. A. (1992). The folding of hen lysozyme involves partially structured intermediates and multible pathways. *Nature* **358**, 302–307.

23 Lu, J. & Dahlquist, F. W. (1992). Detection and characterization of an early folding intermediate of T4 lysozyme using pulsed hydrogen exchange and two-dimensional NMR. *Biochemistry* **31**, 4749–4756.

24 Briggs, M. S. & Roder, H. (1992). Early hydrogen-bonding events in the folding reaction of ubiquitin. *Proc. Natl. Acad. Sci. USA* **89**, 2017–2021.

25 Baldwin, R. L. (1993). Pulsed H/D-exchange studies of folding intermediates. *Curr. Opin. Struct. Biol.* **3**, 84–91.

26 Sauder, J. M. & Roder, H. (1998). Amide protection in an early folding intermediate of cytochrome c. *Fold. Des.* **3**, 293–301.

27 Fong, S., Bycroft, M., Clarke, J. & Freund, S. M. (1998). Characterisation of urea-denatured states of an immunoglobulin superfamily domain by heteronuclear NMR. *J. Mol. Biol.* **278**, 417–429.

28 Neira, J. L., Itzhaki, L. S., Otzen, D. E., Davis, B. & Fersht, A. R. (1997). Hydrogen exchange in chymotrypsin inhibitor 2 probed by mutagenesis. *J. Mol. Biol.* **270**, 99–110.

29 Chamberlain, A. K. & Marqusee, S. (1998). Molten globule unfolding monitored by hydrogen exchange in urea. *Biochemistry* **37**, 1736–1742.

30 Chamberlain, A. K. & Marqusee, S. (1997). Touring the landscapes: partially folded proteins examined by hydrogen exchange. *Structure* **5**, 859–863.

31 Hosszu, L. L., Craven, C. J., Parker, M. J., Lorch, M., Spencer, J., Clarke, A. R. & Waltho, J. P. (1997). Structure of a kinetic protein folding intermediate by equilibrium amide exchange. *Nat. Struct. Biol.* **4**, 801–804.

32 Roder, H. & Colon, W. (1997). Kinetic role of early intermediates in protein folding. *Curr. Opin. Struct. Biol.* **7**, 15–28.

33 Gladwin, S. T. & Evans, P. A. (1996). Structure of very early protein folding intermediates: new insights through a variant of hydrogen exchange labelling. *Fold. Des.* **1**, 407–417.

34 Schulman, B. A., Redfield, C., Peng, Z. Y., Dobson, C. M. & Kim, P. S. (1995). Different subdomains are most protected from hydrogen

exchange in the molten globule and native states of human alpha-lactalbumin. *J. Mol. Biol.* **253**, 651–657.

35 Udgaonkar, J. B. & Baldwin, R. L. (1995). Nature of the early folding intermediate of ribonuclease A. *Biochemistry* **34**, 4088–4096.

36 Jones, B. E. & Matthews, C. R. (1995). Early intermediates in the folding of dihydrofolate reductase from Escherichia coli detected by hydrogen exchange and NMR. *Protein Sci.* **4**, 167–177.

37 Kotik, M., Radford, S. E. & Dobson, C. M. (1995). Comparison of the refolding of hen lysozyme from dimethyl sulfoxide and guanidinium chloride. *Biochemistry* **34**, 1714–1724.

38 Buck, M., Radford, S. E. & Dobson, C. M. (1994). Amide hydrogen exchange in a highly denatured state. Hen egg-white lysozyme in urea. *J. Mol. Biol.* **237**, 247–254.

39 Alexandrescu, A. T., Ng, Y. L. & Dobson, C. M. (1994). Characterization of a trifluoroethanol-induced partially folded state of alpha-lactalbumin. *J. Mol. Biol.* **235**, 587–599.

40 Alexandrescu, A. T., Evans, P. A., Pitkeathly, M., Baum, J. & Dobson, C. M. (1993). Structure and dynamics of the acid-denatured molten globule state of alpha-lactalbumin: a two-dimensional NMR study. *Biochemistry* **32**, 1707–1718.

41 Jennings, P. A. & Wright, P. E. (1993). Formation of a molten globule intermediate early in the kinetic folding pathway of apomyoglobin. *Science* **262**, 892–896.

42 Radford, S. E., Buck, M., Topping, K. D., Dobson, C. M. & Evans, P. A. (1992). Hydrogen exchange in native and denatured states of hen egg-white lysozyme. *Proteins* **14**, 237–248.

43 Jeng, M. F. & Englander, S. W. (1991). Stable submolecular folding units in a non-compact form of cytochrome c. *J. Mol. Biol.* **221**, 1045–1061.

44 Woodward, C. K. (1993). Is the slow exchange core the protein folding core? *Trends Biochem. Sci.* **18**, 359–360.

45 Woodward, C. K. (1994). Hydrogen exchange rates and protein folding. *Curr. Opin. Struct. Biol.* **4**, 112–116.

46 Bai, Y. (1999). Equilibrium amide hydrogen exchange and protein folding kinetics. *J. Biomol. NMR* **15**, 65–70.

47 Clarke, J. & Fersht, A. R. (1996). An evaluation of the use of hydrogen exchange at equilibrium to probe intermediates on the protein folding pathway. *Fold. Des.* **1**, 243–254.

48 Baldwin, R. L. (1996). On-pathway versus off-pathway folding intermediates. *Fold. Des.* **1**, R1–R8.

49 Clarke, J., Hounslow, A. M., Bycroft, M. & Fersht, A. R. (1993). Local breathing and global unfolding in hydrogen exchange of barnase and its relationship to protein folding pathways. *Proc. Natl. Acad. Sci. USA* **90**, 9837–9841.

50 Matouschek, A., Kellis, J. T., Jr., Serrano, L., Bycroft, M. & Fersht, A. R. (1990). Transient folding intermediates characterized by protein engineering. *Nature* **346**, 440–445.

51 Fersht, A. R. (2000). A kinetically significant intermediate in the folding of barnase. *Proc. Natl. Acad. Sci. USA* **97**, 14121–14126.

52 Takei, J., Chu, R. A. & Bai, Y. (2000). Absence of stable intermediates on the folding pathway of barnase. *Proc. Natl. Acad. Sci. USA* **97**, 10796–10801.

53 Englander, S. W. (2000). Protein folding intermediates and pathways studied by hydrogen exchange. *Annu. Rev. Biophys. Biomol. Struct.* **29**, 213–238.

54 Clarke, J. & Itzhaki, L. S. (1998). Hydrogen exchange and protein folding. *Curr. Opin. Struct. Biol.* **8**, 112–118.

55 Englander, S. W., Mayne, L., Bai, Y. & Sosnick, T. R. (1997). Hydrogen exchange: the modern legacy of Linderstrøm-Lang. *Protein Sci.* **6**, 1101–1109.

56 Dyson, H. J. & Wright, P. E. (1996). Insights into protein folding from NMR. *Annu. Rev. Phys. Chem.* **47**, 369–395.

57 Raschke, T. M. & Marqusee, S. (1998). Hydrogen exchange studies of protein structure. *Curr. Opin. Biotechnol.* **9**, 80–86.

58 Eigen, M. (1964). Proton transfer acid-base catalysis + enzymatic hydrolysis. I. Elementary processes. *Angew. Chem. Int. Ed. Engl.* **3**, 1.

59 Bai, Y., Milne, J. S., Mayne, L. & Englander, S. W. (1993). Primary structure effects on peptide group hydrogen exchange. *Proteins* **17**, 75–86.

60 Covington, A. K., Robinson, R. A. & Bates, R. G. (1966). The Ionization Constant of Deuterium Oxide from 5 to 50°. *J. Phys. Chem.* **70**, 3820–3824.

61 Alexandrescu, A. T., Dames, S. A. & Wiltscheck, R. (1996). A fragment of staphylococcal nuclease with an OB-fold structure shows hydrogen-exchange protection factors in the range reported for ''molten globules''. *Protein Sci.* **5**, 1942–1946.

62 Guijarro, J. I., Jackson, M., Chaffotte, A. F., Delepierre, M., Mantsch, H. H. & Goldberg, M. E. (1995). Protein folding intermediates with rapidly exchangeable amide protons contain authentic hydrogen-bonded secondary structures. *Biochemistry* **34**, 2998–3008.

63 Yamasaki, K., Yamasaki, T., Kanaya, S. & Oobatake, M. (2003). Acid-induced denaturation of Escherichia coli ribonuclease HI analyzed by CD and NMR spectroscopies. *Biopolymers* **69**, 176–188.

64 Chamberlain, A. K., Handel, T. M. & Marqusee, S. (1996). Detection of rare partially folded molecules in equilibrium with the native conformation of RNaseH. *Nat. Struct. Biol.* **3**, 782–787.

65 Mori, S., van, Z. & Shortle, D. (1997). Measurement of water-amide proton exchange rates in the denatured state of staphylococcal nuclease by a magnetization transfer technique. *Proteins* **28**, 325–332.

66 Spyracopoulos, L. & O'Neil, J. D. J. (1994). Effect of a Hydrophobic Environment on the Hydrogen Exchange Kinetics of Model Amides Determined by 1H-NMR Spectroscopy. *J. Am. Chem. Soc.* **116**, 1395–1402.

67 Milne, J. S., Mayne, L., Roder, H., Wand, A. J. & Englander, S. W. (1998). Determinants of protein hydrogen exchange studied in equine cytochrome c. *Protein Sci.* **7**, 739–745.

68 Woodward, C. K. & Hilton, B. D. (1980). Hydrogen isotope exchange kinetics of single protons in bovine pancreatic trypsin inhibitor. *Biophys. J.* **32**, 561–575.

69 Mayo, S. L. & Baldwin, R. L. (1993). Guanidinium chloride induction of partial unfolding in amide proton exchange in RNase A. *Science* **262**, 873–876.

70 Hvidt, A. & Nielsen, S. O. (1966). Hydrogen exchange in proteins. *Adv. Prot. Chem.* **21**, 287–386.

71 Orban, J., Alexander, P., Bryan, P. & Khare, D. (1995). Assessment of stability differences in the protein G B1 and B2 domains from hydrogen-deuterium exchange: comparison with calorimetric data. *Biochemistry* **34**, 15291–15300.

72 Huyghues-Despointes, B. M., Scholtz, J. M. & Pace, C. N. (1999). Protein conformational stabilities can be determined from hydrogen exchange rates. *Nat. Struct. Biol.* **6**, 910–912.

73 Frost, A. A. & Pearson, R. G. (1953). *Kinetics and mechanisms* John Wiley, New York.

74 Hvidt, A. (1963). A discussion of the pH dependence of the hydrogen-deuterium exchange of proteins. *C. R. Trav. Lab. Carlsberg* **34**, 299–317.

75 Kragelund, B. B., Heinemann, B., Knudsen, J. & Poulsen, F. M. (1998). Mapping the lifetimes of local opening events in a native state protein. *Protein Sci.* **7**, 2237–2248.

76 Pedersen, T. G., Thomsen, N. K.,

Andersen, K. V., Madsen, J. C. & Poulsen, F. M. (1993). Determination of the rate constants k1 and k2 of the Linderstrøm-Lang model for protein amide hydrogen exchange. A study of the individual amides in hen egg-white lysozyme. *J. Mol. Biol.* **230**, 651–660.

77 Bai, Y., Milne, J. S., Mayne, L. & Englander, S. W. (1994). Protein stability parameters measured by hydrogen exchange. *Proteins* **20**, 4–14.

78 Houliston, R. S., Liu, C., Singh, L. M. & Meiering, E. M. (2002). pH and urea dependence of amide hydrogen-deuterium exchange rates in the beta-trefoil protein hisactophilin. *Biochemistry* **41**, 1182–1194.

79 Rodriguez, H. M., Robertson, A. D. & Gregoret, L. M. (2002). Native state EX2 and EX1 hydrogen exchange of Escherichia coli CspA, a small beta-sheet protein. *Biochemistry* **41**, 2140–2148.

80 Arrington, C. B. & Robertson, A. D. (2000). Microsecond to minute dynamics revealed by EX1-type hydrogen exchange at nearly every backbone hydrogen bond in a native protein. *J. Mol. Biol.* **296**, 1307–1317.

81 Englander, S. W. (1998). Native-state HX. *Trends Biochem. Sci.* **23**, 378.

82 Clarke, J., Itzhaki, L. S. & Fersht, A. R. (1997). Hydrogen exchange at equilibrium: a short cut for analysing protein-folding pathways? *Trends Biochem. Sci.* **22**, 284–287.

83 Li, R. & Woodward, C. (1999). The hydrogen exchange core and protein folding. *Protein Sci.* **8**, 1571–1590.

84 Chi, Y. H., Kumar, T. K., Kathir, K. M., Lin, D. H., Zhu, G., Chiu, I. M. & Yu, C. (2002). Investigation of the structural stability of the human acidic fibroblast growth factor by hydrogen-deuterium exchange. *Biochemistry* **41**, 15350–15359.

85 Shortle, D. (1995). Staphylococcal nuclease – a showcase of *m*-value effects. *Adv. Prot. Chem.* 217–247.

86 Tanford, C. (1970). Protein denaturation. C. Theoretical models for the mechanism of denaturation. *Adv. Prot. Chem.* **24**, 1–95.

87 Schellman, J. A. (1987). The thermodynamic stability of proteins. *Annu. Rev. Biophys. Biophys. Chem.* **16**, 115–137.

88 Huyghues-Despointes, B. M., Pace, C. N., Englander, S. W. & Scholtz, J. M. (2001). Measuring the conformational stability of a protein by hydrogen exchange. *Methods Mol. Biol.* **168**, 69–92.

89 Bai, Y. & Englander, S. W. (1996). Future directions in folding: the multi-state nature of protein structure. *Proteins* **24**, 145–151.

90 Feng, Z., Butler, M. C., Alam, S. L. & Loh, S. N. (2001). On the nature of conformational openings: native and unfolded-state hydrogen and thiol-disulfide exchange studies of ferric aquomyoglobin. *J. Mol. Biol.* **314**, 153–166.

91 Llinas, M., Gillespie, B., Dahlquist, F. W. & Marqusee, S. (1999). The energetics of T4 lysozyme reveal a hierarchy of conformations. *Nat. Struct. Biol.* **6**, 1072–1078.

92 Juneja, J. & Udgaonkar, J. B. (2002). Characterization of the unfolding of ribonuclease A by a pulsed hydrogen exchange study: evidence for competing pathways for unfolding. *Biochemistry* **41**, 2641–2654.

93 Fuentes, E. J. & Wand, A. J. (1998). Local dynamics and stability of apocytochrome b562 examined by hydrogen exchange. *Biochemistry* **37**, 3687–3698.

94 Bhuyan, A. K. & Udgaonkar, J. B. (1998). Two structural subdomains of barstar detected by rapid mixing NMR measurement of amide hydrogen exchange. *Proteins* **30**, 295–308.

95 Loh, S. N., Prehoda, K. E., Wang, J. & Markley, J. L. (1993). Hydrogen exchange in unligated and ligated staphylococcal nuclease. *Biochemistry* **32**, 11022–11028.

96 Yi, Q., Scalley, M. L., Simons, K. T.,

Gladwin, S. T. & Baker, D. (1997). Characterization of the free energy spectrum of peptostreptococcal protein L. *Fold. Des.* **2**, 271–280.

97 Bhutani, N. & Udgaonkar, J. B. (2003). Folding subdomains of thioredoxin characterized by native-state hydrogen exchange. *Protein Sci.* **12**, 1719–1731.

98 Parker, M. J. & Marqusee, S. (1999). The Cooperativity of Burst Phase Reactions Explored. *J. Mol. Biol.* **293**, 1195–1210.

99 Parker, M. J. & Marqusee, S. (2000). A statistical appraisal of native state hydrogen exchange data: evidence for a burst phase continuum? *J. Mol. Biol.* **300**, 1361–1375.

100 Swint-Kruse, L. & Robertson, A. D. (1995). Hydrogen bonds and the pH dependence of ovomucoid third domain stability. *Biochemistry* **34**, 4724–4732.

101 Neira, J. L. & Fersht, A. R. (1999). Exploring the folding funnel of a polypeptide chain by biophysical studies on protein fragments. *J. Mol. Biol.* **285**, 1309–1333.

102 Perrett, S., Clarke, J., Hounslow, A. M. & Fersht, A. R. (1995). Relationship between equilibrium amide proton exchange behavior and the folding pathway of barnase. *Biochemistry* **34**, 9288–9298.

103 Parker, M. J. & Clarke, A. R. (1997). Amide backbone and water-related H/D isotope effects on the dynamics of a protein folding reaction. *Biochemistry* **36**, 5786–5794.

104 Makhatadze, G. I. & Privalov, P. L. (1992). Protein interactions with urea and guanidinium chloride. A calorimetric study. *J. Mol. Biol.* **226**, 491–505.

105 Johnson, C. M. & Fersht, A. R. (1995). Protein stability as a function of denaturant concentration: ther thermal stability of barnase in the presence of urea. *Biochemistry* **34**, 6795–6804.

106 Shortle, D., Meeker, A. K. & Gerring, S. L. (1989). Effects of denaturants at low concentrations on the reversible denaturation of staphylococcal nuclease. *Arch. Biochem. Biophys.* **272**, 103–113.

107 Nozaki, Y. & Tanford, C. (1970). The solubility of amino acids, diglycine, and triglycine in aqueous guanidine hydrochloride solutions. *J. Biol. Chem.* **245**, 1648–1652.

108 Brems, D. N. & Baldwin, R. L. (1985). Protection of amide protons in folding intermediates of ribonuclease A measured by pH-pulse exchange curves. *Biochemistry* **24**, 1689–1693.

109 Schmid, F. X. & Baldwin, R. L. (1979). Detection of an early intermediate in the folding of ribonuclease A by protection of amide protons against exchange. *J. Mol. Biol.* **135**, 199–215.

110 Roder, H. & Wüthrich, K. (1986). Protein folding kinetics by combined use of rapid mixing techniques and NMR observation of individual amide protons. *Proteins* **1**, 34–42.

111 Bieri, O. & Kiefhaber, T. (2001). Origin of apparent fast and non-exponential kinetics of lysozyme folding measured in pulsed hydrogen exchange experiments. *J. Mol. Biol.* **310**, 919–935.

112 Udgaonkar, J. B. & Baldwin, R. L. (1988). NMR evidence for an early framework intermediate on the folding pathway of ribonuclease A. *Nature* **335**, 694–699.

113 Elöve, G. A. & Roder, H. (1991). Structure and Stability of Cytochrome c Folding Intermediates. In *Protein Refolding* (Georgiou, G. & de Bernardez-Clark, E., eds), pp. 50–63, American Chemical Society, Washington.

114 Houry, W. A., Sauder, J. M., Roder, H. & Scheraga, H. A. (1998). Definition of amide protection factors for early kinetic intermediates in protein folding. *Proc. Natl. Acad. Sci. USA* **95**, 4299–4302.

115 Houry, W. A. & Scheraga, H. A. (1996). Sturcture of a Hydrophobically Collapsed Intermediate in the Conformational Folding Pathway of Ribonuclease A Probed by Hydrogen-

Deuterium Exchange. *Biochemistry* **35**, 11734–11746.

116 Shastry, M. C. R., Sauder, J. M. & Roder, H. (1998). Kinetic and Structural Analysis of Submillisecond Folding Events in Cytochrome *c*. *Acc. Chem. Res.* **31**, 725.

117 Shastry, M. C. & Roder, H. (1998). Evidence for barrier-limited protein folding kinetics on the microsecond time scale. *Nat. Struct. Biol.* **5**, 385–392.

118 Itzhaki, L. S., Evans, P. A., Dobson, C. M. & Radford, S. E. (1994). Tertiary interactions in the folding pathway of hen lysozyme: kinetic studies using fluorescent probes. *Biochemistry* **33**, 5212–5220.

119 Kiefhaber, T. (1995). Kinetic traps in lysozyme folding. *Proc. Natl. Acad. Sci. USA* **92**, 9029–9033.

120 Nishimura, C., Prytulla, S., Jane, D. H. & Wright, P. E. (2000). Conservation of folding pathways in evolutionarily distant globin sequences. *Nat. Struct. Biol.* **7**, 679–686.

121 Larson, S. M., Ruczinski, I., Davidson, A. R., Baker, D. & Plaxco, K. W. (2002). Residues participating in the protein folding nucleus do not exhibit preferential evolutionary conservation. *J. Mol. Biol.* **316**, 225–233.

122 Plaxco, K. W., Larson, S., Ruczinski, I., Riddle, D. S., Thayer, E. C., Buchwitz, B., Davidson, A. R. & Baker, D. (2000). Evolutionary conservation in protein folding kinetics. *J. Mol. Biol.* **298**, 303–312.

123 Mirny, L. A. & Shakhnovich, E. I. (1999). Universally conserved positions in protein folds: reading evolutionary signals about stability, folding kinetics and function. *J. Mol. Biol.* **291**, 177–196.

124 Kragelund, B. B., Poulsen, K., Andersen, K. V., Baldursson, T., Krøll, J. B., Neergård, T. B., Jepsen, J., Roepstorff, P., Kristiansen, K., Poulsen, F. M. & Knudsen, J. (1999). Conserved residues and their role in the structure, function, and stability of acyl-coenzyme A binding protein. *Biochemistry* **38**, 2386–2394.

125 Kuwata, K., Shastry, R., Cheng, H., Hoshino, M., Batt, C. A., Goto, Y. & Roder, H. (2001). Structural and kinetic characterization of early folding events in beta-lactoglobulin. *Nat. Struct. Biol.* **8**, 151–155.

126 Hamada, D., Segawa, S. & Goto, Y. (1996). Non-native alpha-helical intermediate in the refolding of beta-lactoglobulin, a predominantly beta-sheet protein. *Nat. Struct. Biol.* **3**, 868–873.

127 Udgaonkar, J. B. & Baldwin, R. L. (1990). Early folding intermediate of ribonuclease A. *Proc. Natl. Acad. Sci. USA* **87**, 8197–8201.

128 Bycroft, M., Matouschek, A., Kellis, J. T., Serrano, L. & Fersht, A. R. (1990). Detection and characterization of a folding intermediate in barnase by NMR. *Nature* **346**, 488–490.

129 Raschke, T. M. & Marqusee, S. (1997). The kinetic folding intermediate of ribonuclease H resembles the acid molten globule and partially unfolded molecules detected under native conditions. *Nat. Struct. Biol.* **4**, 298–304.

130 Hollien, J. & Marqusee, S. (2002). Comparison of the folding processes of T. thermophilus and E. coli ribonucleases H. *J. Mol. Biol.* **316**, 327–340.

131 Kuszewski, J., Clore, G. M. & Gronenborn, A. M. (1994). Fast folding of a prototypic polypeptide: the immunoglobulin binding domain of streptococcal protein G. *Protein Sci.* **3**, 1945–1952.

132 Teilum, K., Kragelund, B. B., Knudsen, J. & Poulsen, F. M. (2000). Formation of hydrogen bonds precedes the rate-limiting formation of persistent structure in the folding of ACBP. *J. Mol. Biol.* **301**, 1307–1314.

133 Nozaki, Y. (1972). The Preparation of Guanidine Hydrochloride. *Methods Enzymol.* **26**, 43–50.

134 Pace, C. N. (1986). Determination and analysis of urea and guanidine hydrochloride denaturation curves. *Methods Enzymol.* **131**, 266–280.

135 Thomsen, J. K. (2001). Ph.D. Thesis, University of Copenhagen.

136 Connelly, G. P., Bai, Y., Jeng, M.-F. & Englander, S. W. (1993). Isotope Effects in Peptide Group Hydrogen Exchange. *Proteins* **17**, 87–92.

137 Loftus, D., Gbenle, G. O., Kim, P. S. & Baldwin, R. L. (1986). Effects of denaturants on amide proton exchange rates: a test for structure in protein fragments and folding intermediates. *Biochemistry* **25**, 1428–1436.

19
Studying Protein Folding and Aggregation by Laser Light Scattering

Klaus Gast and Andreas J. Modler

19.1
Introduction

The term laser light scattering is used here for recent developments in both static light scattering (SLS) and dynamic light scattering (DLS). In principle, DLS can be performed with conventional light sources [1], however, laser light is mandatory in practice, and recent progress in laser technology has greatly improved the capability of both DLS and SLS.

Static or "classical" light scattering, which attains molecular parameters from the angular and concentration dependence of the time-averaged scattering intensity, was one of the main tools for the determination of molecular mass in the middle of the last century. However by the 1970s the method had somewhat lost its significance when it became possible to measure the molecular mass of proteins and other small biological macromolecules with high precision by electrospray ionization (ESI) or matrix-assisted laser desorption/ionization (MALDI) mass spectrometry. Furthermore these alternative methods required less material and less careful preparation of the samples. SLS is now restoring its popularity due mostly to significant technical improvements. Well-calibrated instruments equipped with lasers and sensitive solid-state detectors allow precise measurements over a wide range of particle masses (10^3–10^8 kDa) using sample volumes of the order of 10 μL. The coupling with separation devices (e.g., size exclusion or other chromatographic techniques and field-flow fractionation) has provided the biomolecular community with a powerful molecular analyzer, particularly for polydispersed materials.

The advent of DLS in the early 1970s led to great expectations concerning the study of dynamic processes in solution. A readily measurable quantity by this procedure is the translational diffusion coefficient of macromolecules from which the hydrodynamic Stokes radius R_S can be calculated. Up to the 1990s, however, the method appeared to be experimentally much more difficult than SLS. Laboratory-built or commercially available DLS photometers consisted of gas lasers, expensive, huge correlation electronics and subsequent data evaluation was tedious because of severe requirements on computation: powerful online computers were not gener-

Protein Folding Handbook. Part I. Edited by J. Buchner and T. Kiefhaber

ISBN: 3-527-30784-2

ally available. The first "compact" devices (DLS-based particle sizers) were only applicable to strongly scattering systems. This situation has fundamentally changed during the last 10 years. A sophisticated single-board correlator, which can be easily plugged into a desktop computer, is essentially the only additional element needed to upgrade an SLS to a DLS instrument.

As a consequence of these developments, laser light scattering can now be considered as a standard laboratory method. Several compact instruments are on the market, which are valuable tools for protein analysis. Nevertheless, for special applications, including also particular studies of protein folding and aggregation, a more flexible laboratory-built set-up assembled of commercially available components is preferred.

We would like to stress that laser light scattering investigations are entirely noninvasive and can be done under any solvent conditions. However, the measurements must be done with solutions that are free of undesired large particles and bubbles. Particular care has to be taken with proteins that absorb light in the visible region. It is worth mentioning that SLS measurements can also be performed using conventional fluorescence spectrometers including stopped-flow fluorescence devices in the case of kinetic experiments.

Important information in the case of protein folding studies can be obtained especially from DLS, which yields the molecular dimensions of proteins in terms of the Stokes radius. However, the combined application of SLS and DLS is very useful for distinguishing changes in the dimensions of individual protein molecules due to molecular folding or association.

In this review we will first deal with the measurement of hydrodynamic dimensions, intermolecular interactions, and the state of association of proteins in differently folded states. The application of kinetic laser light scattering to the study of folding kinetics is also discussed. A special section is dedicated to the study of protein aggregation accompanying misfolding. Useful protocols for some standard applications of light scattering to protein folding studies are listed in Section 19.6.

19.2 Basic Principles of Laser Light Scattering

19.2.1 Light Scattering by Macromolecular Solutions

Much of the experimental methodology, skilful practice, and basic theoretical approaches for static light scattering had already been developed in the first half of the last century. The birth of dynamic light scattering can be dated to the middle of the 1960s, and the next decade yielded much of the fundamental groundwork on the principles and practice of DLS from researchers in the fields of physics, macromolecular biophysics, biochemistry, and biology. This short introduction to both methods is an attempt to supply fellow researchers who are not familiar with these techniques with an intuitive understanding of the basic principles and the

applicability to protein folding and aggregation problems. We will therefore only recall some of the more fundamental equations. A more detailed understanding can be achieved on the basis of numerous excellent textbooks (see, for example, Refs [2–7]).

The theory of light scattering can be approached from the so-called single-particle analysis or density fluctuation viewpoint. The single-particle analysis approach, which will be used here, is simpler to visualize and is adequate for studying the structure and dynamics of macromolecules in diluted solutions. The fluctuation approach is appropriate for studying light scattering in liquids. Furthermore, it is useful to distinguish light scattering from small particles and molecules (of $d < \lambda/20$) and large particles, whose maximum dimension, d, are comparable to or larger than the incident wavelength λ (the wavelength of blue-green light is about 500 nm). The former case is easier to handle, but much information about the structure is not accessible. Proteins used for folding studies entirely fulfill the conditions of the first case, provided we exclude large protein complexes or aggregates. The concepts of light scattering from small particles in vacuum can be applied to the scattering of macromolecules in solution by considering the excess of different quantities (e.g., light scattering, polarizibility, refractive index) of macromolecules over that of the solvent.

The strength of the scattering effect primarily depends on the polarizibility α of a small scattering element, which might be the molecule itself if it is sufficiently small. Larger molecules are considered as consisting of several scattering elements. The oscillating electric field vector $\vec{E}_0(t,\vec{r}) = \vec{E}_0 \cdot e^{-i(\omega t - \vec{k}_0 \cdot \vec{r})}$ of the incident light beam induces a small oscillating dipole with the dipole moment $\vec{p}(t) = \alpha \cdot \vec{E}(t)$. ω is the angular frequency and $\vec{k}_0$ is the wave vector with the magnitude $|\vec{k}_0| = 2\pi \cdot n_0/\lambda$. This oscillating dipole re-emits electromagnetic radiation, which has the same wavelength in the case of elastic scattering. The intensity of scattered light at distance r is

$$I_S = \frac{4\pi^4 n_0^4}{\lambda^4} \cdot \frac{\alpha^2}{r^2} \cdot I_0 \tag{1}$$

where λ is the wavelength in vacuum, n_0 is the refractive index of the surrounding medium and $I_0 = |\vec{E}_0|^2$ is the intensity of the incident vertically polarized laser beam. Equation (1) differs only by a constant factor for the case of unpolarized light. In general, the scattered light is detected at an angle θ with respect to the incident beam in the plane perpendicular to the polarization of the beam (Figure 19.1). The wave vector pointing in this direction is $\vec{k}_S$, where $\vec{k}_0$ and $\vec{k}_S$ have the same magnitude.

Of particular importance is the vector difference $\vec{q} = \vec{k}_0 - \vec{k}_S$, the so-called scattering vector, which determines the spatial distribution of the phases $\phi_i = \vec{q} \cdot \vec{r}_i$ of the scattered light wave emitted by individual scattering elements i (Figure 19.1). The magnitude of $\vec{q}$ is $q = (4\pi \cdot n/\lambda) \sin(\theta/2)$. The phases play an essential role in the total instantaneous intensity, which results from the superposition of light waves emitted by all scattering elements within the scattering volume v defined by

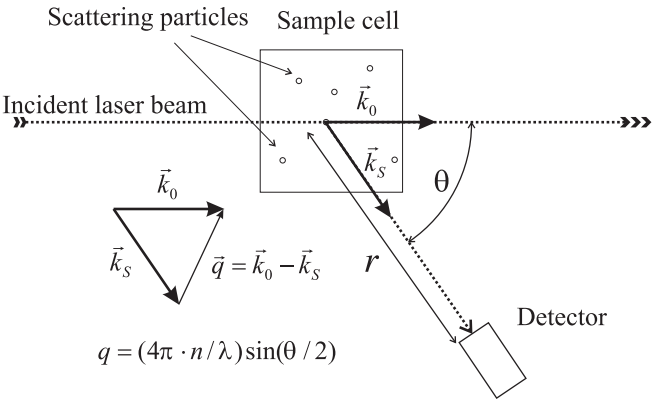

Fig. 19.1. Schematic diagram of the optical part of an light scattering instrument.

the primary beam and the aperture of the detector. The instantaneous intensity fluctuates in time for nonfixed particles, like macromolecules in solution, due to phase fluctuations $\phi_i(t) = \vec{q} \cdot \vec{r}_i(t)$ caused by changes in their location $\vec{r}_i(t)$.

SLS measures the time average of the intensity, thus the term "time-averaged light scattering" would be more appropriate, although "static light scattering" appears the accepted convention now. SLS becomes q-dependent for large particles when light waves emitted from scattering elements within a individual particle have noticeable phase differences.

DLS analyses the above-mentioned temporal fluctuations of the instantaneous intensity of scattered light. Accordingly, DLS can measure several dynamic processes in solution. It is evident that only those changes in the location of scattering elements lead to intensity fluctuations that produce a sufficiently large phase shift. This is always the case for translational diffusion of macromolecules. The motion of segments of chain molecules and rotational motion can be studied for large structures. Rotational motion of monomeric proteins and chain dynamics of unfolded proteins are practically not accessible by DLS.

19.2.2
Molecular Parameters Obtained from Static Light Scattering (SLS)

The expression for the light scattering intensity from a macromolecular solution can be derived from Eq. (1) by summation over the contributions of all macromolecules in the scattering volume v and substituting the polarizability α by related physical parameters. The latter can be done by applying the Clausius-Mosotti equation to macromolecular solutions, which leads to $n^2 - n_0^2 = 4\pi \cdot N' \cdot \alpha$, where n and n_0 are the refractive indices of the solution and the solvent, respectively. N' is the number of particles (molecules) per unit volume and can be expressed by $N' = N_A \cdot c/M$. N_A is Avogadro's number, c and M are the weight concentration and the molecular mass (molar mass) of the macromolecules, respectively. Using

the approximation $n + n_0 \sim 2n_0$ we get $n^2 - n_0^2 \sim 2n_0 \cdot (\partial n/\partial c) \cdot c$. $\partial n/\partial c$ is the specific refractive index increment of the macromolecules in the particular solvent. The excess scattering of the solution over that of the solvent $I_{ex} = I_{solution} - I_{solvent}$ of noninteracting small molecules is then

$$I_{ex} = \frac{4\pi^2 n_0^2 (\partial n/\partial c)^2}{\lambda^4 N_A} \cdot \frac{v}{r^2} \cdot c \cdot M \cdot I_0 = H \cdot \frac{v}{r^2} \cdot c \cdot M \cdot I_0 \tag{2}$$

The optical constant $H = 4\pi^2 n_0^2 (\partial n/\partial c)^2/\lambda^4 N_A$ depends only on experimental parameters and the scattering properties of the molecules in the particular solvent, which is reflected by $\partial n/\partial c$. The exact knowledge of $\partial n/\partial c$, the dependence of n on protein concentration in the present case, is very important for absolute measurements of the molecular mass. For proteins in aqueous solvents of low ionic strength it is about 0.19 $cm^3\ g^{-1}$ and practically does not depend significantly on the amino acid sequence. However, it is markedly different in solvents containing high concentrations of denaturants.

The instrument parameters in Eq. (2) can be eliminated by using the Rayleigh (excess) ratio $R_q = (I_{ex}/I_0)(r^2/v)$. In practice, R_q of an unknown sample is calculated from the scattering intensities of the sample and that of a reference sample of known Rayleigh ratio R_{ref} by

$$R_q = R_{ref} \cdot f_{corr} \cdot (I_{ex}/I_{ref}) \tag{3}$$

where f_{corr} is an experimental correction factor accounting for differences in the refractive indices of sample and reference sample [5]. In the more general case including intermolecular interactions and large molecules, which have a refractive index n_p and satisfy the condition $4\pi(n_p - n_0)d/\lambda \ll 1$ of the Rayleigh-Debye approximation, static light scattering data are conveniently presented by the relation

$$\frac{H \cdot c}{R_q} = \frac{1}{M \cdot P(q)} + 2A_2 \cdot c \tag{4}$$

$P(q)$ is the particle scattering function, which is mainly expressed in terms of the product $q \cdot \overline{R_G}$, where $\overline{R_G} = \langle R^2 \rangle^{1/2}$ is the root mean square radius of gyration of the particles. Analytical expressions for $P(q)$ are known for different particle shapes, whereas instead of R_G also other characteristic size-dependent parameters are used (e.g., length L for rods or cylinders). In the limit $q \cdot \bar{R}_G \ll 1$, the approximation $P(q)^{-1} = 1 + (q \cdot \bar{R}_G)^2/3$ can be used to estimate $\bar{R}_G$ from the angular dependence of R_q. A perceptible angular dependence of the scattering intensity can only be expected for particles with $R_G > 10$ nm. Thus, light scattering is not an appropriate method to monitor changes of R_G during unfolding and refolding of small monomeric proteins. A substantial angular dependence is observed for large protein aggregates, however.

The concentration dependence of the right hand side of Eq. (4) yields the second virial coefficient A_2, which reflect the strength and the type of intermolecular interactions. The usefulness of measuring A_2 will be discussed below. A_2 is positive for

predominant repulsive (covolume and electrolyte effects) and negative for predominant attractive intermolecular interactions.

In general, both extrapolation to zero concentration and zero scattering angle ($q = 0$) are done in a single diagram (Zimm plot) for calculations of M from Eq. (4). The primary mass "moment" or "average" obtained is the weight-average molar mass $M = \sum_i c_i M_i / \sum_i c_i$ in the case of polydisperse systems. This has to be taken into consideration for proteins when monomers and oligomers are present. Molar masses of proteins used in folding studies (i.e., $M < 50\,000$ g mol^{-1}) can be determined at 90° scattering angle because the angular dependence of R_q is negligible. Measurements at different concentration are mandatory, however, because remarkable electrostatic and hydrophobic interactions may exist under particular environmental conditions. In the following, the values of parameters measured at finite concentration are termed apparent values, e.g., M_{app}.

19.2.3 Molecular Parameters Obtained from Dynamic Light Scattering (DLS)

Information about dynamic processes in solution are primarily contained in the temporal fluctuations of scattered electric field $\vec{E}_s(t)$. The time characteristics of these fluctuations can be described by the first-order time autocorrelation function $g^{(1)}(\tau) = \langle \vec{E}_s(t) \cdot \vec{E}_s(t+\tau) \rangle$. The brackets denote an average over many products of $\vec{E}_s(t)$ with its value after a delay time τ. $g^{(1)}(\tau)$ is only accessible in the heterodyne detection mode, where the scattered light is mixed with a small portion of the incident beam on the optical detector. This experimentally complicated detection method must be used if particle motions relative to the laboratory frame, e.g., the electrophoretic mobility in an external electric field, are measured. The less complicated homodyne mode, where only the scattered light intensity is detected, is normally the preferred optical scheme. This has the consequence that only the second-order intensity correlation function $g^{(2)}(\tau) = \langle I(t) \cdot I(t+\tau) \rangle$ is directly available. Under particular conditions, which are met in the case of light scattering from dilute solutions of macromolecules, the Siegert relation $g^{(2)}(\tau) = 1 + |g^{(1)}(\tau)|^2$ can be used to obtain the normalized first-order correlation function $g^{(1)}(\tau)$ from the measured $g^{(2)}(\tau)$. Analytical forms of $g^{(1)}(\tau)$ have been derived for different dynamic processes in solution. As we have already indicated above only translational diffusional motion essentially contributes to the fluctuations of the scattered light in the case of monomeric proteins and we can reasonably neglect rotational effects. $g^{(1)}(\tau)$ for identical particles with a translational diffusion coefficient D has the form of an exponential

$$g^{(1)}(\tau) = e^{-q^2 \cdot D \cdot \tau} \tag{5}$$

D is related to the hydrodynamic Stokes radius R_S by the Stokes-Einstein equation

$$R_S = \frac{k \cdot T}{6\pi \cdot \eta \cdot D} \tag{6}$$

where k is Boltzmann's constant, T is the temperature in K, and η is the solvent viscosity. $g^{(1)}(\tau)$ for a polydisperse solution containing L different macromolecular species (or aggregates) with masses M_i, diffusion coefficients D_i and weight concentrations c_i is

$$g^{(1)}(\tau) = \left(\sum_{i=1}^{L} a_i \cdot e^{-q^2 \cdot D_i \cdot \tau} \right) \Big/ S \tag{7a}$$

where $S = \sum_{i=1}^{L} a_i$ is the normalization factor. The weights $a_i = c_i \cdot M_i = n_i \cdot M_i^2$ reflect the $c \times M$ dependence of the scattered intensity (see Eq. (2)). n_i is the number concentration (molar concentration) of the macromolecular species. Accordingly, even small amounts of large particles are considerably represented in the measured $g^{(1)}(\tau)$. The general case of an arbitrary size distribution, which results in a distribution of D, can be treated by an integral

$$g(\tau) = \left(\int a(D) \cdot e^{-q^2 \cdot D \cdot \tau} \, dD \right) \Big/ S \tag{7b}$$

Equation (7b) has the mathematical form of a Laplace transformation of the distribution function $a(D)$. Thus, an inverse Laplace transformation is needed to reconstruct $a(D)$ or the related distribution functions $c(D)$ and $n(D)$. This is an ill-conditioned problem from the mathematical point of view because of the experimental noise in the measured correlation function. However, there exist numerical procedures termed "regularization", which allow a researcher to obtain stabilized, "smoothed" solutions. A widely used program package for this purpose is "CONTIN" [8]. Nevertheless, the distributions obtained can depend sensitively on the experimental noise and parameters used during data evaluation procedure in special cases. Thus, it might be more appropriate to use simpler but more stable data evaluation schemes like the method of cumulants [9], which yields the z-averaged diffusion coefficient $\bar{D}$ and higher moments reflecting the width and asymmetry of the distribution. $\bar{D}$ can be obtained simply from the limiting slope of the logarithm of $g^{(1)}(\tau)$, viz. $\bar{D} = -q^{-2} \cdot \frac{d}{d\tau} (\ln|g^{(1)}(\tau)|)_{\tau \to 0}$. This approach is very useful for rather narrow distributions.

D, like M, exhibits a concentration dependence, which is usually written in the form

$$D(c) = D_0(1 + k_D \cdot c) \tag{8}$$

where k_D is the diffusive concentration dependence coefficient, which can be used to characterize intermolecular interactions. However, k_D differs from A_2. The concentration dependence of D and other macromolecular parameters was discussed in more detail by Harding and Johnson [10]. Extrapolation to zero protein concentration yielding D_0 is essential in order to calculate the hydrodynamic dimensions in terms of R_S for individual protein molecules.

19.2.4
Advantages of Combined SLS and DLS Experiments

Many of the modern laser light scattering instruments allow both SLS and DLS to be measured in one and the same experiment. This experimental procedure is more complicated, since the optimum optical schemes for SLS and DLS are different. Briefly, DLS needs focused laser beams and only a much smaller detection aperture can be employed because of the required spatial coherence of the scattered light. This reduces the SLS signal and demands higher beam stability.

Combined SLS/DLS methods have two main advances for protein folding studies. The first one concerns the reliability of measurements of the hydrodynamic dimensions during folding or unfolding. The observed changes of R_S could partly or entirely result from an accompanying aggregation reaction, which can be excluded if the molecular mass remains essentially constant.

The second advantage is the capacity to measure molecular masses of proteins in imperfectly clarified solutions that contain protein monomers and an unavoidable amount of aggregates. This situation is often met, for example during a folding reaction or when the amount of protein is too small for an appropriate purification procedure. In this case, SLS alone would measure a meaningless weight average mass. The Stokes radii of monomers and aggregates are mostly well separated, allowing the researcher to estimate the weighting a_i for monomers and aggregates fitting the measured $g^{(1)}(\tau)$ by Eq. (7a). Knowledge of the weighting allows the contributions of monomers and aggregates to the total scattering intensity to be distinguished and, therefore, the proper molecular mass of the protein to be obtained.

19.3
Laser Light Scattering of Proteins in Different Conformational States – Equilibrium Folding/Unfolding Transitions

19.3.1
General Considerations, Hydrodynamic Dimensions in the Natively Folded State

The molecular parameter of interest in folding studies is primarily the hydrodynamic Stokes radius R_S. Additional direct estimations of the molecular mass from SLS data are recommended to check whether the protein is and remains in the monomeric state during folding or unfolding. Formation of a dimer of two globular subunits could easily be misinterpreted as a swollen monomer since its Stokes radius is only larger by a factor of 1.39 than that of the monomer [11]. Hydrodynamic radii in the native state have been measured for many proteins. For globular proteins, a good correlation with the mass or the number of amino acids was found [12] (see also below). This has encouraged some researchers and manufacturers of commercial DLS devices to estimate M from R_S. This procedure has to be

applied with great care and clearly contradicts the application of DLS to folding studies.

For correct estimations of molecular dimensions in terms of R_S before and after a folding transition, extrapolation of D to zero protein concentration should be done before applying Eq. (6). The concentration dependence of D indicated by k_D possibly changes during unfolding/refolding transitions as it is shown in Figure 19.2 for thermal unfolding of RNase T1. Strong changes in k_D are often observed

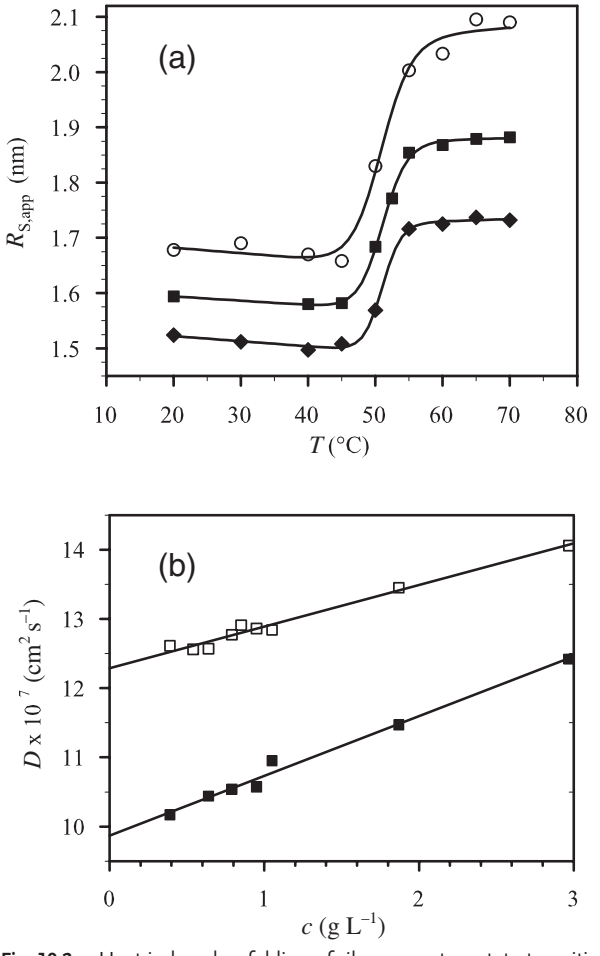

Fig. 19.2. Heat-induced unfolding of ribonuclease T1 in 10 mM sodium cacodylate, pH 7, 1 mM EDTA. a) Temperature dependence of the apparent Stokes radius at concentrations of 0.8 mg mL^{-1} (open circles), 1.9 mg mL^{-1} (filled squares), and 3.9 mg mL^{-1} (filled diamonds). The continuous lines were obtained by nonlinear least squares fits according to a two-state transition yielding $T_m = 51.0 \pm 0.5$ °C and $\Delta H_m = 497 \pm 120$ kJ mol^{-1} (average over all three fits). b) Concentration dependence of the diffusion coefficient D at 20 °C (open square) and 60 °C (filled square). Linear fits to the data yield the diffusive concentration dependence coefficient k_D (see text).

in the case of pH-induced denaturation. Apparent Stokes radii, $R_{S,app}$, are measured if extrapolation is not possible due to certain experimental limitations.

19.3.2 Changes in the Hydrodynamic Dimensions during Heat-induced Unfolding

The first DLS studies of the thermal denaturation of proteins were reported by Nicoli and Benedek [13]. These authors investigated heat-induced unfolding of lysozyme in the pH range between 1.2 and 2.3 and different ionic strength. The size transition coincided with the unfolding curve recorded by optical spectroscopic probes. The average radius increased by 18% from 1.85 to 2.18 nm. The same size increase was also found for ribonuclease A (RNase A) at high ionic strength. The proteins had intact disulfide bonds.

A good candidate for thermal unfolding/refolding studies is RNase T1, since the transition is completely reversible even according to light scattering criteria [14]. The unfolding transition curves measured at three different protein concentrations at pH 7 are shown in Figure 19.2a. The concentration dependence of D in the native and unfolded states is shown in Figure 19.2b. The increase of the diffusive concentration dependence coefficient from 49 to 87 mL g^{-1} on the transition to the unfolded state indicates a strengthening of the repulsive intermolecular interactions. The Stokes radii obtained after extrapolation to zero protein concentration are 1.74 nm and 2.16 nm for the native and unfolded states, respectively. The corresponding increase in R_S of 24% is somewhat larger than those for lysozyme and RNase A. This might be due to the fact that RNase T1 differs in the number and position of the disulfide bonds as compared with lysozyme and RNase A.

The thermal unfolding behavior of the wild-type λ Cro repressor (Cro-WT) is more complex, but it allows us to demonstrate the advantage of combined SLS/DLS experiments. The native Cro-WT is active in the dimeric form. Spectroscopic and calorimetric studies [15] (and references cited therein) revealed that thermal unfolding proceeds via an intermediate state. The corresponding changes of the apparent Stokes radius and the relative scattering intensity, which reflects changes in the average mass, are quite different at low and high concentrations (Figure 19.3). At low concentration, Cro-WT first unfolds partly, but remains in the dimeric form between 40 °C and 55 °C according to the increase in R_S between 40 °C and 55 °C and the nearly constant scattering intensity. Above 55 °C, both R_S and the relative scattering intensity decrease due to the dissociation of the dimer. At high concentration, the increase of R_S during the first unfolding step is much stronger and is accompanied by an increase in the scattering intensity. This is due to the formation of dimers of partly unfolded dimers. At temperatures above 55 °C, dissociation into monomers is indicated by the decrease of both R_S and scattering intensity. The transient population of a tetramer is a peculiarity of thermal unfolding of Cro-WT.

Unfortunately, many proteins aggregate upon heat denaturation, thus preventing reliable measurements of the dimensions.

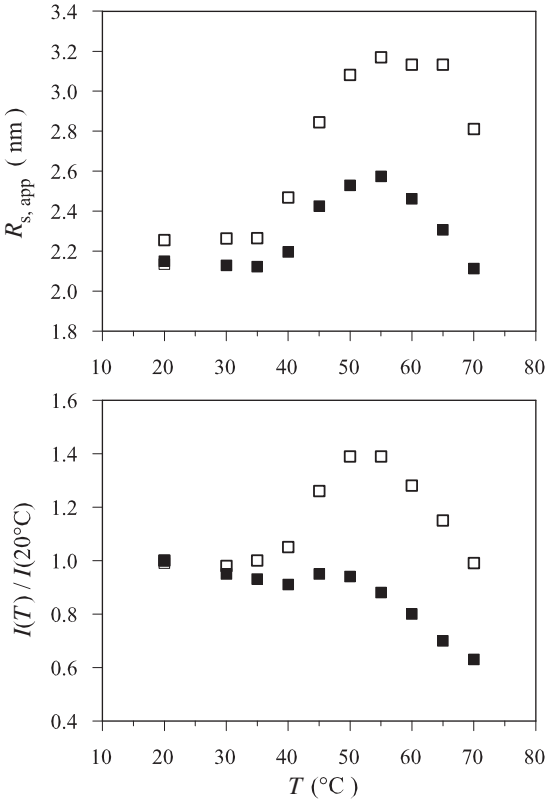

Fig. 19.3. Heat-induced unfolding and association/dissociation of Cro repressor wild-type at 1.8 mg mL^{-1} (filled squares) and 5.8 mg mL^{-1} (open squares) in 10 mM sodium cacodylate, pH 5.5.

19.3.3
Changes in the Hydrodynamic Dimensions upon Cold Denaturation

Since the stability curves for proteins have a maximum at a characteristic temperature, unfolding in the cold is a general phenomenon [16]. However, easily attainable unfolding conditions in the cold exist only for a few proteins. Cold denaturation under destabilizing conditions was reported for phosphoglycerate kinase from yeast (PGK) [17, 18] and barstar [19, 20]. The increases in R_S upon cold denaturation for PGK [18] and barstar (unpublished results) are shown in Figure 19.4. The size increase is a three-state transition in the case of PGK, because of the independent unfolding of the two domains in the cold. Both proteins aggregate on heating preventing to compare the results with those for heat-induced unfolding.

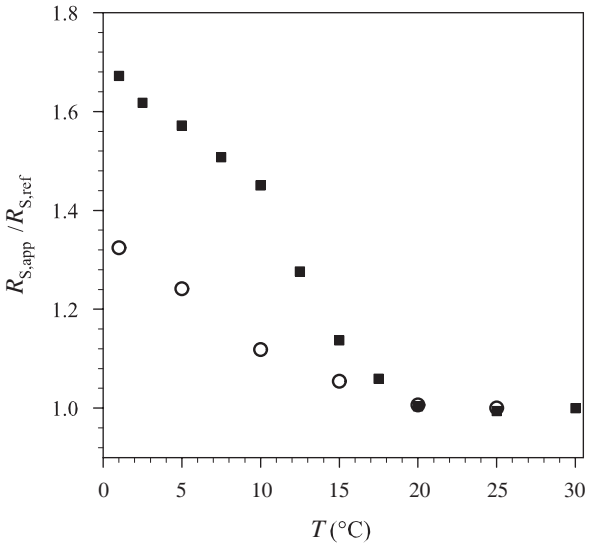

Fig. 19.4. Relative expansion, $R_{S,app}/R_{S,ref}$, upon cold denaturation for barstar (pseudo wild-type), 2.4 mg mL^{-1}, in 50 mM Tris/HCl, pH 8, 0.1 M KCl, 2.2 M urea (open circles) and phosphoglycerate kinase from yeast, 0.97 mg mL^{-1}, in 20 mM sodium phosphate, pH 6.5, 10 mM EDTA, 1 mM DTT, 0.7 M GdmCl (filled squares). $R_{S,ref}$ is the Stokes radius in the reference state at the temperature of maximum stability under slightly destabilizing conditions.

19.3.4
Denaturant-induced Changes of the Hydrodynamic Dimensions

Before the advent of DLS, most data relating to the hydrodynamic dimensions of proteins under strongly denaturing conditions had been obtained by measuring intrinsic viscosities [21]. In a pioneering DLS experiment on protein denaturation, Dubin, Feher, and Benedek [22] studied the unfolding transition of lysozyme in guanidinium chloride (GdmCl). These authors meticulously analyzed the transition at 31 GdmCl concentrations between 0 M and 6.4 M in 100 mM acetate buffer, pH 4.2, at a protein concentration of 10 mg mL^{-1}. It was found that $R_{S,app}$ increases during unfolding by 45% and 86% in the case of intact and reduced disulfide bonds, respectively. Meanwhile, the hydrodynamic dimensions at high concentrations of GdmCl have been measured for many proteins lacking disulfide bonds by using DLS. The results will be discussed below in connection with scaling (i.e., power) laws, which can be derived from this data. Here we consider briefly the influence of disulfide bonds and temperature on the dimensions of proteins in the highly unfolded state. Such experiments were done with RNase A [23]. Figure 19.5 shows the temperature dependence of the relative dimensions ($R_{S,app}/R_{S,native}$) for RNase A with intact and with reduced disulfide bonds. The slight compaction with increasing temperature is typical for proteins in highly unfolded states: for example, similar results are obtained with RNase T1 (Figure 19.5). Surprisingly, RNase

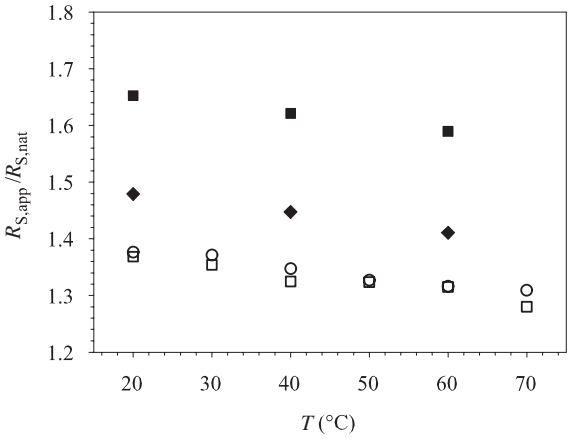

Fig. 19.5. Temperature dependence of the relative expansion $R_{S,app}/R_{S,nat}$ of RNase A and RNase T1 in the unfolded state at high concentrations of GdmCl. RNase T1, 2.2 mg mL^{-1}, in 10 mM sodium cacodylate, pH 7, 1 mM EDTA, 5.3 M GdmCl (open circles), RNase A, 2.9 mg mL^{-1}, in 50 mM MES, pH 5.7, 1 mM EDTA, 6 M GdmCl (open squares), and RNase A (broken disulfide bonds), 2.9 mg mL^{-1}, in 50 mM MES, pH 6.5, 1 mM EDTA, 6 M GdmCl (filled squares). RNase A, 2.5 mg mL^{-1}, with broken disulfide bonds is highly unfolded even in the absence of GdmCl (filled diamonds).

A without disulfide bonds is already unfolded in the absence of GdmCl and has larger dimensions than RNase A with intact disulfide bonds in 6 M GdmCl.

19.3.5
Acid-induced Changes of the Hydrodynamic Dimensions

Many proteins can be denatured by extremes of pH, and most of the studies on this have focused on using acid as denaturant. Proteins respond very differently to acidic pH. For example, lysozyme remains native-like, some other protein adopt the molten globule conformation with hydrodynamic dimensions about 10% larger than in the native state, and many proteins unfold into an expanded conformation. Fink et al. [24] have introduced a classification scheme for the unfolding behavior under acidic conditions. The molecular mechanisms of acid denaturation have been studied in the case of apomyoglobin by Baldwin and co-workers [25]. The dimensions of selected acid-denatured proteins are listed below in Table 19.1. Some proteins are more expanded in the acid-denatured than in the chemical-denatured state, e.g., PGK ($R_{S,unf}/R_{S,native} = 2.49$) and apomyoglobin ($R_{S,unf}/R_{S,native} = 2.05$). Furthermore, those proteins exhibit strong repulsive intermolecular interactions, as reflected by large values of k_D (e.g., 550 mL g^{-1} for PGK at pH 2). This means, that D_{app} is twice as large as D_0 at a concentration of about 2 mg mL^{-1}. This underlines the importance of extrapolation of the measured quantity to zero protein concentration.

Tab. 19.1. Stokes radii R_S, relative compactness $R_S/R_{S,\,native}$, and diffusive concentration dependence coefficients k_D of selected proteins in differently folded states determined by DLS.

Protein/state	R_S*(nm)*	$R_S/R_{S,\,native}$	k_D *(mL g^{-1})*	*References*
Bovine α-lactalbumin				
Native state (holoprotein)	1.88		−7	29
Unfolded state (5 M GdmCl)	2.46	1.31	−9	29
A-state (pH 2, 50 mM KCl)	2.08	1.11	15	29
Molten globule (neutral pH)	2.04	1.09	62	29
Molten globule (15% v/v TFE)	2.11	1.12	−100	33
TFE-state (40% v/v TFE)	2.25	1.20	−10	33
Kinetic molten globule	1.99	1.06	−60	33
PGK				
Native state	2.97		0.8	44
Unfolded state (2 M GdmCl)	5.66	1.91	–	44
Cold denatured state (1 °C, 0.7 M GdmCl)	5.10	1.72	–	44
Acid denatured state (pH 2)	7.42	2.50	552	34
TFE-state (50% v/v TFE, pH 2)	7.76	2.61	1030	34
Apomyoglobin				
Native state	2.09		26	30
Acid denatured (U-form, pH 2)	4.29	2.05	520	30
Molten globule (I-form, pH 4)	2.53	1.21	104	30
RNase T1				
Native state	1.74		49	14
Unfolded state (5.3 M GdmCl)	2.40	1.38	–	14
Heat denatured (60 °C)	2.16	1.24	87	14
RNase A				
Native state	1.90		≈0	56
Unfolded state (6 M GdmCl, nonreduced SS)	2.60	1.37	–	56
Unfolded state (6 M GdmCl, reduced SS)	3.14	1.65	–	56
TFE-state (70% v/v TFE)	2.28	1.20	15	33
Barstar				
Native state	1.72		5	87
Unfolded state (6 M urea)	2.83	1.65	50	87
Cold-denatured state (1 °C, 2.2 M urea)	2.50	1.45	−3	87

Experimental errors were omitted for brevity. Errors in R_S are typically less than ±2%. Errors in k_D are of the order of ±10% except for k_D values close to zero.
For exact solvent conditions we refer to the original literature.

19.3.6
Dimensions in Partially Folded States – Molten Globules and Fluoroalcohol-induced States

From the wealth of partly folded states existing for many proteins under different destabilizing conditions, DLS data obtained for some particular types will be considered here. Molten globule states [26–28] have been most extensively studied

(see Chapter 23). DLS data on the hydrodynamic dimensions were published for the molten globule states of two widely studied proteins, α-lactalbumin [29] and apomyoglobin [30]. The results including data for the kinetic molten globule of α-lactalbumin are shown in Table 19.1. Data also exist on the geometric dimensions in terms of the radius of gyration, R_G, for both α-lactalbumin [31] and apomyoglobin [30, 32] in different conformational states.

Only a few DLS studies on the hydrodynamic dimension of proteins in aqueous solvents containing structure-promoting substances like trifluoroethanol (TFE) and hexafluoroisopropanol (HFIP) have been reported so far. The Stokes radii at high fluoroalcohol content, at which the structure stabilizing effect saturates, are very different for various proteins. An increase in R_S of only about 20% was found for α-lactalbumin and RNase A [33] with intact disulfide bonds. By contrast, PGK at pH 2 and 50% (v/v) TFE has a Stokes radius $R_S = 7.76$ nm exceeding that of the native state by a factor of 2.6 [34]. According to the high helical content estimated from CD data and the high charge according to the large value of k_D it is conceivable that the entire PGK molecule consists of a long flexible helix. Fluoroalcohols may have a different effect at low volume fractions. In the case of α-lactalbumin, a molten globule-like state was found at 15% (v/v) TFE [33]. This state revealed a native-like secondary structure and a Stokes radius 10% larger than that of native protein. Furthermore, strong attractive intermolecular interactions were indicated by a large negative diffusive concentration dependence coefficient, $k_D = -100$ mL g^{-1}, which result presumably from the exposure of hydrophobic patches in this state. k_D was close to zero both in the absence and at high percentage of TFE.

19.3.7
Comparison of the Dimensions of Proteins in Different Conformational States

The hydrodynamic dimensions in different equilibrium states of five proteins frequently used in folding studies are summarized in Table 19.1. Some general rules become evident from these data, e.g., heat-denatured proteins are relatively compact as compared with those denatured by high concentration of denaturants or cold-denatured proteins. In this connection, a particular class of proteins should be mentioned, namely the so-called intrinsically unstructured proteins [35] (see Chapter 8 in Part II). These proteins are essentially unfolded according to their CD spectra and have much larger Stokes radii under physiological conditions than $R_{S,glob}$ expected for a globular proteins of the same molecular mass. Typical examples are prothymosin α and α-synuclein, with relative dimensions R_S/R_{glob} of 1.77 [36] and 1.52 (unpublished results), respectively.

19.3.8
Scaling Laws for the Native and Highly Unfolded States, Hydrodynamic Modeling

A systematic dependence of the hydrodynamic dimensions on the number of amino acids N_{aa} or molecular mass M can be established for the dimension of

globular proteins in the native state and also for proteins lacking disulfide bonds in the unfolded state induced by high concentrations of GdmCl or urea. Scaling (i.e., "power") laws for native globular proteins have been published by several authors. Damaschun et al. [37] obtained the relation $R_S[nm] = 0.362 \cdot N_{aa}^{1/3}$ on the basis of the Stokes radii calculated for more than 50 globular proteins deposited in the protein databank. Uversky [38] found the dependence $R_S[nm] = 0.0557 \cdot M^{0.369}$ using experimental data from the literature and Stokes radii measured with a carefully calibrated size exclusion column (this is consistent with $R_S[nm] = 0.325 \cdot N_{aa}^{0.369}$ for a mean residue weight of 119.4 g mol^{-1}). An advantage of DLS is that no calibration of the methods is needed. The relation between R_S and N_{aa} determined by Wilkins et al. [39] is $R_S[nm] = 0.475 \cdot N_{aa}^{0.29}$. The scaling laws for the native state are useful for the classification of proteins for which the high-resolution structure is not known or cannot be obtained. Deviation from the scaling law indicates that the protein has no globular shape or does not adopt a compactly folded structure under the given environmental conditions.

In contrast to the native state, proteins in unfolded states populate a large ensemble of configurations, which are restricted only by the allowed ϕ, ψ angles and nonlocal interactions of the polypeptide chain. In the absence of (or at balanced) nonlocal interactions (i.e., in the unperturbed or theta state), polypeptide chains behave as random chains and their conformational properties can be described by the rotational isomeric state theory [40]. Whether or not unfolded proteins are indeed true random chains is a matter of debate [41]. The dimension of a denatured protein is an important determinant of the folding thermodynamics and kinetics [42]. Thus, the chain length dependence of the hydrodynamic dimension in the form of scaling laws is an important experimental basis for the characterization of unfolded polypeptide chains.

A first systematic analysis of the chain length dependence of the hydrodynamic dimensions was done by Tanford et al. [43] by measuring the intrinsic viscosities of unfolded proteins. The Stokes radii measured by DLS [44] for 12 proteins denatured by high concentrations of GdmCl are shown in Figure 19.6. From the data the scaling law $R_S[nm] = 0.28 \cdot N_{aa}^{0.5}$ was obtained. Scaling laws were also published by other authors. Uversky [38] derived $R_S[nm] = 0.0286 \cdot M^{0.502}$ (corresponding to $R_S[nm] = 0.315 \cdot N_{aa}^{0.502}$) from Stokes radii measured by size exclusion chromatography. Wilkins et al. [39] found $R_S[nm] = 0.221 \cdot N_{aa}^{0.57}$ using Stokes radii mostly measured by pulse field gradient NMR. By analysing published Stokes radii measured by different methods Zhou [42] obtained the relation $R_S[nm] = 0.2518 \cdot N_{aa}^{0.522}$.

Two aspects that are closely related to measurements of the hydrodynamic dimensions of proteins are hydrodynamic modeling [45, 46] and the hydration problem [47, 48]. Particularly for globular proteins, both are important for the link between high-resolution data from X-ray crystallography or NMR and hydrodynamic data. Protein hydration appears as an adjustable parameter in recent hydrodynamic modeling procedures [49]. The average values over different proteins are 0.3 g water per g protein or in terms of the hydration shell 0.12 nm. Model calculations are also in progress for unfolded proteins [42].

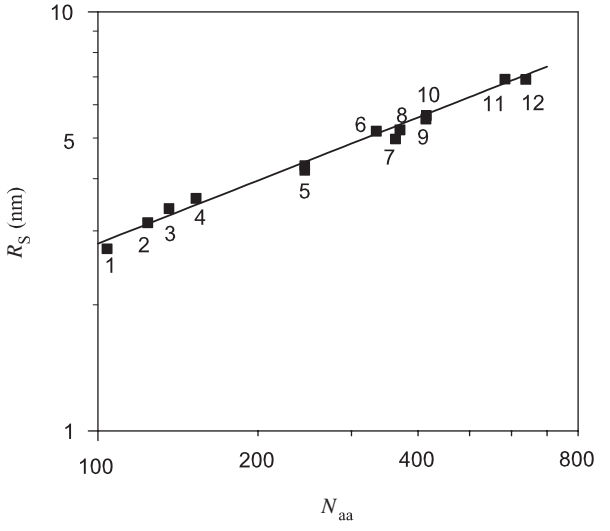

Fig. 19.6. Stokes radii R_S of 12 proteins unfolded by 6 M GdmCl in dependence on the number of amino acid residues N_{aa}. The linear fit yields the scaling law $R_S[nm] = 0.28 \cdot N_{aa}^{0.5}$. 1: apocytchrome *c*, 2: staphylokinase, 3: RNase A, 4: apomyoglobin, 5: chymotrypsinogen A, 6: glyceraldehydes-3-phosphate dehydrogenase, 7: aldolase, 8: pepsinogen, 9: streptokinase, 10: phosphoglycerate kinase, 11: bovine serum albumin, 12: DnaK. Disulfide bonds, if existing in native proteins, were reduced.

19.4
Studying Folding Kinetics by Laser Light Scattering

19.4.1
General Considerations, Attainable Time Regions

An important characteristic of the folding process is the relation between compaction and structure formation. Therefore, it is intriguing to monitor compactness during folding by measuring the Stokes radius using DLS, which is the fastest among the hydrodynamic methods. Furthermore, R_S and also the radius of gyration, R_G, are direct measures of the overall molecular compactness. The first studies of this kind were measurements of the compaction during lysozyme refolding by continuous-flow DLS [50]. In general, the basic experimental techniques of continuous- and stopped-flow experiments can also be applied for laser light scattering. There are no restrictions from general physical principles concerning the accessible time range for SLS. The data acquisition time T_A, which is needed to obtain a sufficiently high signal-to-noise ratio (S/N), depends solely on the photon flux and can be minimized by increasing the light level. However, there are two fundamental processes that limit the accessible time scales in the case of DLS. These problems are discussed in detail by Gast et al. [51] and will be outlined only briefly in this chapter.

First, unlike other methods including SLS, the enhancement of the signal is not sufficient to increase the (S/N), since the measured signal is itself a statistical quantity. At light levels above the shot-noise limit the signal-to-noise ratio of the measured time correlation function depends on the ratio of T_A to the correlation time τ_C of the diffusion process by $(S/N) = (T_A/\tau_C)^{1/2}$. τ_C is of the order of tens of microseconds for proteins, leading to a total acquisition time $T_A \sim 5$–10 s in order to achieve an acceptable (S/N). This time can be shortened by splitting it into N_S ''shots'' in a stopped-flow experiment. $N_S = 100$ is an acceptable value leading to acquisition times of 50–100 ms during one ''shot.'' This corresponds to the time resolution in the case of the stopped-flow technique.

The second limiting factor becomes evident when the continuous-flow method is used. Excellent time resolutions have been achieved with this method in the case of fluorescence measurements [52] and small-angle X-ray scattering [53, 54]. Continuous-flow experiments are especially useful for slow methods, since the time resolution depends only on the aging time between mixer and detector and not on the speed of data acquisition. Increasing the flow speed in order to get short aging times also reduces the resting time of the protein molecules within the scattering volume. However, to avoid distortions of the correlation functions, this time must be longer than the correlation time corresponding to the diffusional motion of the molecules. This limits the flow speed to about 15 cm s^{-1} under typical experimental conditions [51], resulting in aging times of about 100 ms. The benefit of continuous-flow measurements over stopped-flow measurements does not exist for DLS. Thus, DLS is only suitable for studying late stages of protein folding in the time range > 100 ms. However, this time range is important for folding and oligomerization or misfolding and aggregation (see Section 19.5). Two examples for the compaction of monomeric protein molecules during folding will be now be considered.

19.4.2
Hydrodynamic Dimensions of the Kinetic Molten Globule of Bovine α-Lactalbumin

The hydrodynamic dimensions of equilibrium molten globule states are well characterized (Table 19.1). It is interesting to compare the dimensions in these states with that of the kinetic counterpart. Stopped-flow DLS investigations [29] were done with the Ca^{2+}-free apoprotein, which folds much slower than the holoprotein. The time course of the changes of the apparent Stokes radius at a protein concentration of 1.35 mg mL^{-1} is shown in Figure 19.7a. Measurements at different protein concentrations (Figure 19.7b) revealed the ''sticky'' nature of the kinetic molten globule as compared to the completely unfolded and refolded states. The kinetic molten globule appears to be slightly more compact than the equilibrium molten globules. The dimensions of the natively folded apo- and the holoprotein are practically the same. The changes of the dimensions of holo α-lactalbumin were measured later by time-resolved X-ray scattering [55].

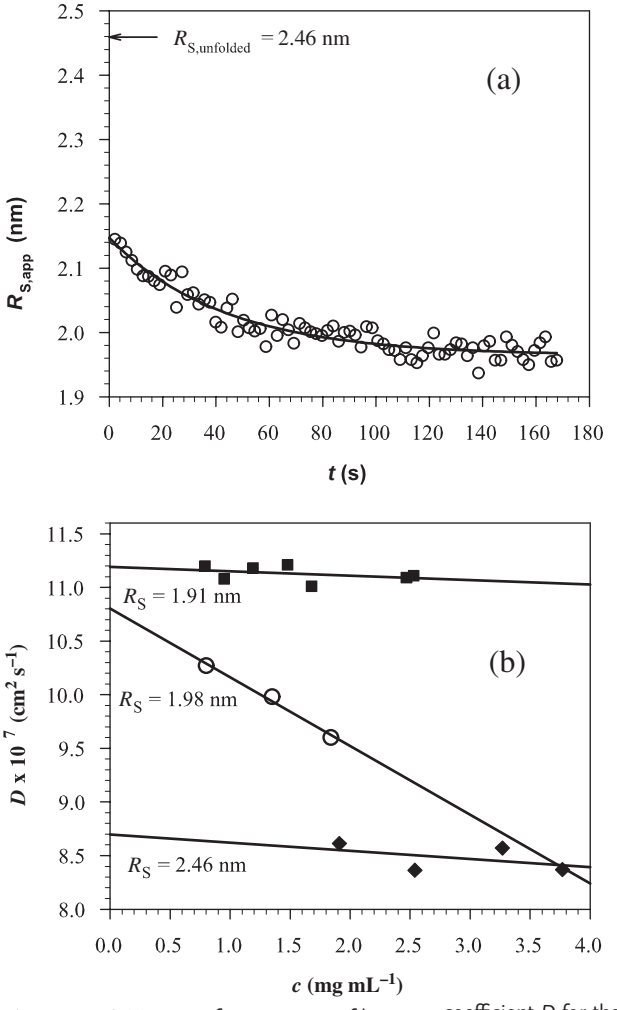

Fig. 19.7. a) Kinetics of compaction of bovine α-lactalbumin after a GdmCl concentration jump from 5 M to 0.5 M, final protein concentration 1.35 mg mL^{-1}, 50 mM sodium cacodylate, pH 7, 50 mM NaCl, 2 mM EGTA, $T = 20$ °C. The data can be fitted by a single exponential with a decay time $\tau = 43 \pm 6$ s. b) Concentration dependence of the diffusion coefficient D for the apoform of bovine α-lactalbumin under native conditions (filled squares), in the presence of 5 M GdmCl (filled diamonds), and for the kinetic molten globule (open circles). The buffer was same as in (a). The Stokes radii obtained from D extrapolated to zero concentration are shown.

19.4.3
RNase A is Only Weakly Collapsed During the Burst Phase of Folding

In the previous section, it was demonstrated that α-lactalbumin collapses very rapidly into the molten globule with dimensions close to that of the native state. A dif-

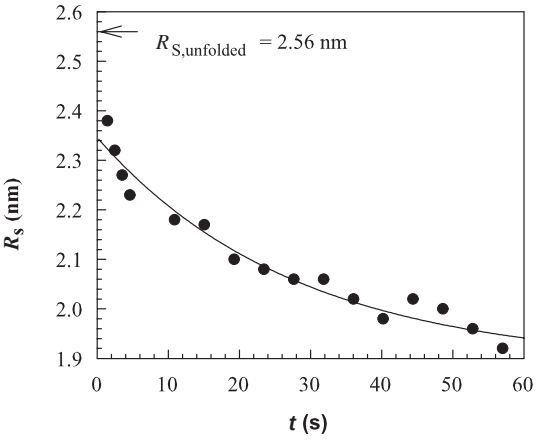

Fig. 19.8. Kinetics of compaction of RNase A after a GdmCl concentration jump from 6 M to 0.67 M, final protein concentration 1.9 mg mL^{-1}, 50 mM sodium cacodylate, pH 6, $T = 10\,^{\circ}C$. The single exponential fit yields a decay time $\tau = 28 \pm 5$ s.

ferent folding behavior was observed for RNase A [56]. The Stokes radius of RNase is 2.56 nm in the unfolded state at 6 M GdmCl and decreases only to 2.34 nm during the burst phase (Figure 19.8). Most of the compaction towards the native state occurs at later stages in parallel with the final arrangement of secondary structure and the formation of tertiary structure.

19.5 Misfolding and Aggregation Studied by Laser Light Scattering

19.5.1 Overview: Some Typical Light Scattering Studies of Protein Aggregation

Misfolding and aggregation of proteins have been regarded for a long time as undesirable side reactions and the importance of these processes became evident only recently in connection with recombinant protein technology and the observation that the development of particular diseases correlates with protein misfolding and misassembly [57]. The basic principles of protein aggregation have been considered for example by De Young et al. [58].

Light scattering is the most sensitive method in detecting even small amounts of aggregates in macromolecular solutions. From the numerous applications of light scattering to aggregation phenomena only a few selected applications to proteins will be discussed briefly before turning to the more special phenomenon of the combined processes of misfolding and aggregation.

Light scattering studies of aggregation are mostly kinetic experiments. In contrast to the kinetic schemes discussed in Section 19.4, measurements of the intensity, which indicate the increase in the particle mass, are preferred in this case. Typical experiments of this kind have been reported by Zettlmeissl et al. [59], who studied the aggregation kinetics of lactic dehydrogenase using a stopped-flow laser light scattering apparatus. These authors thoroughly investigated the effect of enzyme concentration on the kinetics of aggregation and obtained an apparent reaction order of 2.5 from the concentration dependence of the initial slopes of the light scattering signal. Fast aggregation events in the millisecond time range during refolding of interleukin 1β were measured by Finke et al. [60] using a stopped-flow fluorescence device for the kinetic light scattering experiments.

Many light scattering investigations have been done in connection with heat-induced aggregation of proteins. Jøssang et al. [61] studied the aggregation kinetics of human immunoglobulins by measuring the increase in the relative mass and the relative Stokes radius. From the changes of both quantities the authors obtained quite detailed information about the aggregation process, which could be consistently described by Smoluchowski's coagulation theory [62]. The heat aggregation of the β-lactoglobulin protein was very intensively investigated by light scattering [63–65]. These studies are examples of very careful light scattering investigations of protein aggregation. In many of these studies size-exclusion chromatography has been used in addition to light scattering. This is very important in order to follow the consumption of the initial species (mostly monomers) during aggregation (see below). Monomer consumption cannot be easily derived from light scattering data, since the measured weight averaged mass is dominated by the growing large particles.

If the protein aggregates or polymerization products become large enough, further structural information about the growing species can be obtained from the angular dependence of the light scattering intensity. A careful analysis of fibrin formation using stopped-flow multiangle light scattering was reported by Bernocco et al. [66].

An interesting question is: how can protein aggregation be influenced? Suppression of citrate synthase aggregation and facilitation of correct folding has been demonstrated by Buchner et al. [67] using a commercial fluorometer as a light scattering device.

19.5.2 Studying Misfolding and Amyloid Formation by Laser Light Scattering

19.5.2.1 Overview: Initial States, Critical Oligomers, Protofibrils, Fibrils

Conformational conversion of proteins into misfolded structures with an accompanying assembly into large particles, mostly of fibrillar structure called amyloid, is presently an expanding field of research. In this section of the review we will try to sketch the potentials and limits of laser light scattering for elucidating these processes. It is clear beforehand that SLS and DLS are best applied for this purpose mostly in conjunction with other methods, particularly with those sensitive to

changes in secondary structure (CD, FTIR, NMR) and methods giving evidence of the morphology of the growing species such as electron microscopy (EM) and/or atomic force microscopy (AFM). Nevertheless, we will concentrate mainly upon the contribution from the light scattering studies in the following.

Amyloid formation comprises different stages of particle growth. The information that can be obtained from light scattering experiments strongly depends on the quality of the initial state [68]. A starting solution containing essentially the conversion competent monomeric species is a prerequisite for studies of early stages involving the formation of defined oligomers, later called critical oligomers, and protofibrillar structures. These structures became interesting recently because of their possible toxic role. The size distributions and the kinetics of formation of these rather small particles can be characterized very well by light scattering. A careful experimental design (e.g., multi-angle light scattering or model calculations regarding the angular dependence of the scattered light intensity) is needed for the characterization of late products such as large protofibrils or long "mature" fibrils. The problems involved in light scattering from long fibrillar structures have been discussed in a review article by Lomakin et al. [69]. Quantitative light scattering studies of fibril formation have been reported for a few protein systems. Some of them will be discussed now.

19.5.2.2 Aggregation Kinetics of Aβ Peptides

Aβ peptide is the major protein component found in amyloid deposits of Alzheimer's patients and comprises 39–43 amino acids. The first light scattering investigations of Aβ aggregation kinetics were reported by Tomski and Murphy [70] for synthetic Aβ(1–40). According to their SLS and DLS data, these authors modeled the assembly kinetics as formation of rods with a diameter of 5 nm built up from spontaneously formed small cylinders consisting of eight Aβ monomers. The kinetic aggregation model was based on Smoluchowski's theory in the diffusion-limited case. Later, the same group [71] studied the concentration dependence of the aggregation process. They found that a high molecular weight species is formed rapidly when Aβ(1–40) is diluted from 8 M urea to physiological conditions. The size of this species was largest and constant at the lowest concentration (70 μM), while it was smaller and was growing with time at higher concentrations. Furthermore, dissociation of Aβ monomers from preformed fibrils was observed.

Detailed light scattering investigations of Aβ(1–40) fibrillogenesis in 0.1 M HCl have been reported by Lomakin et al. [72–74]. Aβ(1–40) fibrillization was found to be highly reproducible at low pH. In a review article [69], these authors thoroughly analyzed the requirements to obtain good quantitative data of the fibril length from the measured hydrodynamic radius. Adequate measurements can be done if the fibril length does not exceed about 150 nm. Rate constants for fibril nucleation and elongation were determined from the measured time evolution of the fibril length distribution. The initial fibril elongation rate varied linearly with the initial peptide concentration c_0 below a critical concentration $c^* = 0.1$ mM and was constant above c^*. From these observations particular mechanisms for

Aβ fibril nucleation were derived. Homogeneous nucleation within small ($d \sim 14$ nm) Aβ micelles was proposed for $c_0 > c^*$ and heterogeneous nucleation on seeds for $c < c_0$. From the temperature dependence of the elongation rate an activation energy of 23 kcal mol^{-1} was estimated for the proposed monomer addition to fibrils.

Finally, it should be mentioned that reproducibility of Aβ fibrillogenesis in vitro is a serious problem in general due to possible variations in the starting conformation and the assembly state of the Aβ preparations [68].

19.5.2.3 Kinetics of Oligomer and Fibril Formation of PGK and Recombinant Hamster Prion Protein

Presently more than 60 proteins and peptides are known that form fibrillar structures under appropriate environmental conditions. Many of these proteins are not related to any disease. Particularly interesting are those which have served as model proteins in folding studies and could also be good candidates for studying basic principles of structure conversion and amyloid formation. The potentials of laser light scattering for this purpose will be demonstrated here for PGK from yeast and recombinant prion protein from Syrian hamster, ShaPrP$^{90-232}$. A well-defined conversion competent state free of any ''seeds'' can be achieved for these proteins under specific environmental conditions thus allowing studies of early stages of misfolding and aggregation.

Conversion of PGK starts from a partially folded state at pH 2, at and above room temperature and in the presence of defined amounts of salt [34]. The time dependence of the relative increases in the average mass and the average Stokes radius after adding Na-TCA are shown in Figure 19.9a. Two growth steps are clearly visible. The mass and size transition curves scale linearly with concentration [75]. Thus, the growth process is a second-order reaction. Both growth steps can be well described within the framework of Smoluchowski's coagulation theory. During the first stage, clustering towards oligomers consisting of about 8–10 PGK molecules occurs. These oligomers, termed ''critical oligomers'', assemble into protofibrillar structures during the second stage. Such a behavior could be inferred from the relation between mass and size (Figure 19.9c), which yields an idea of the dimensionality of the growth process. Electron microscopy at selected growth stages have confirmed this idea [75]. The mutual processes of growth and secondary structure conversion were analyzed by relating the increase in mass to the changes in the far-UV CD [75].

Recombinant PrP^C can be converted into a β-rich aggregated structure at low pH and under destabilizing conditions [76–78]. The relative changes in the mass and size for ShaPrP$^{90-232}$ in sodium phosphate, pH 4.2, after a GdmCl concentration jump from 0 M to 1 M are shown in Figure 19.9b. The aggregation process resembles that of PGK with respect to the occurrence of a well-populated oligomeric state. The transient size maximum during oligomer formation is an indication of a concentration dependent overshoot phenomenon. Extrapolation of this size maximum to zero protein concentration yielded an octamer as the smallest oligomer

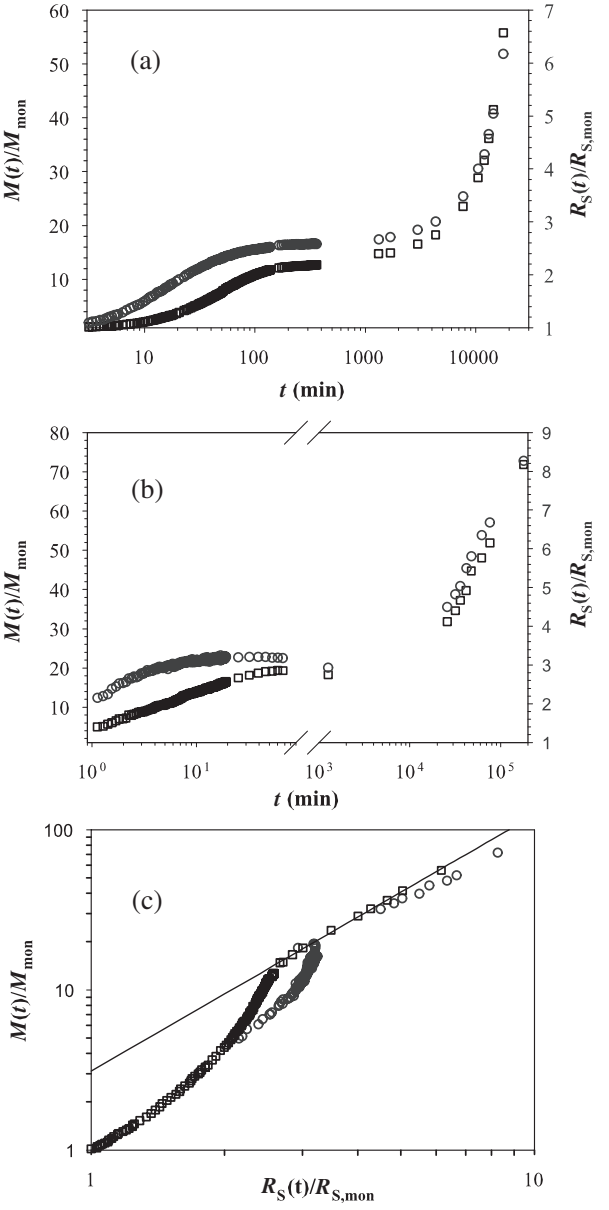

Fig. 19.9. Amyloid assembly of PGK and recombinant Syrian hamster PrP^{90-232}. a) Relative increases in mass (squares) and Stokes radius (circles) during assembly of PGK, $c = 2.7$ mg mL^{-1}, into fibrillar structures in 10 mM HCl, pH 2, 9.1 mM sodium trichloroacetate, $T = 20$ °C. Structural conversion was initiated by adding sodium trichloroacetate. M_{mon} and $R_{S,mon}$ are the molecular mass and the Stokes radius of the monomer, respectively. b) Relative increases in mass (squares) and Stokes radius (circles) during assembly of recombinant Syrian hamster PrP^{90-232}, $c = 0.59$ mg mL^{-1}, in 20 mM sodium acetate, pH 4.2, 50 mM NaCl, 1 M GdmCl, 20 °C. Structural conversion was initiated by a GdmCl concentration jump from 0 to 1 M. c) Dimensionality plots, $M(t)/M_{mon}$ versus $R_S(t)/R_{S,mon}$ for the data shown in (a) and (b) for PGK (squares) and Syrian hamster PrP^{90-232} (circles), respectively. The fit for the data of PGK corresponds to a dimensionality of 1.6.

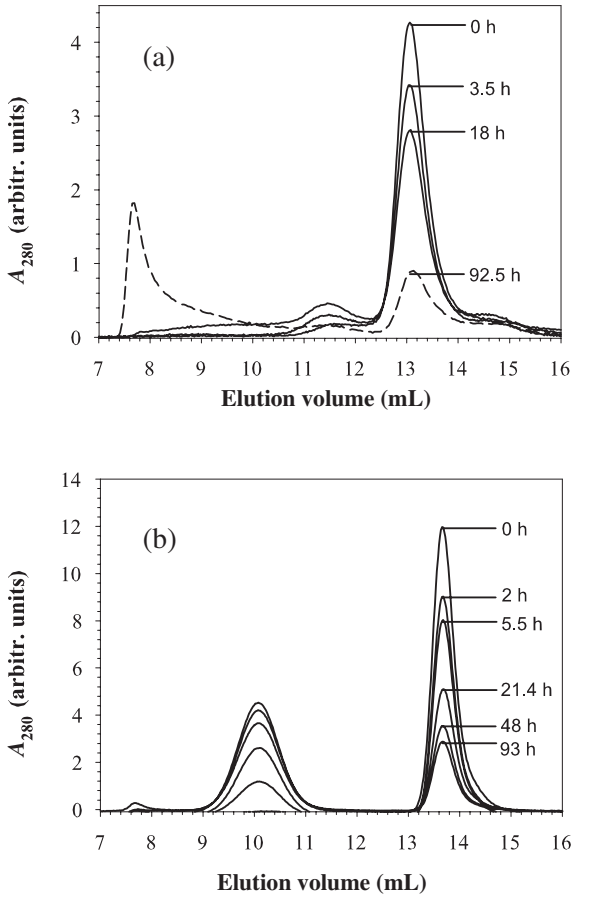

Fig. 19.10. Amyloid assembly monitored by size-exclusion chromatography. a) PGK ($c = 0.14$ mg mL^{-1}, 10 mM HCl, pH 2, 190 mM NaCl) and b) recombinant Syrian hamster PrP$^{90-232}$ ($c = 0.08$ mg mL^{-1}, in 20 mM sodium acetate, pH 4.2, 50 mM NaCl, 1 M GdmCl) at room temperature. The conversion process was triggered either by addition of salt (PGK) or GdmCl (prion protein), respectively.

[79]. The subsequent slow increases in size and mass result from the formation of protofibrillar structures [79]. The change in particle morphology is again indicated by a kink in the dimensionality plot (Figure 19.9c).

The concentration dependence of the growth process revealed remarkable kinetic differences as compared to PGK according to the estimated apparent reaction order of 3. The differences in the formation of the critical oligomers are well documented by size exclusion chromatography (Figure 19.10). Different oligomeric states can be detected during aggregation of PGK, while only monomers and the critical oligomer (octamer) are populated in the case of ShaPrP$^{90-232}$. Accordingly, the octamer is the smallest stable oligomer. Complementary FTIR and CD

studies [79] have led to the conclusion that the misfolded secondary structure is stabilized within the octamer. The sole appearance of monomers and octamers and/or higher oligomers tells us that the dimensionality of the first growth process in the case of ShaPrP$^{90-232}$ (Figure 19.9c) is due to changes in the population of two discrete species.

Kinks in the dimensionality plot are also observed when various growth stages are not clearly separated in plots of M and R_S versus time (Figure 19.9a,b) because of comparable growth rates. This is a clear advantage of this data representation. However, one must be careful in relating the (apparent) dimensionality derived from these plots to simple geometrical models.

19.5.2.4 Mechanisms of Misfolding and Misassembly, Some General Remarks

Viewed from the perspective of chemical kinetics amyloid formation is a complex polymerization reaction, since assembly into amyloid fibrils is accompanied by secondary structure rearrangement into a predominant β-sheet structure. β-sheet strands are needed for association at the edges of monomeric subunits to build up the fibrillar end products [80]. This is in marked contrast to polymerization reactions of low-molecular-weight compounds, where the monomers possess already the functional groups for polymerization at initiation of the reaction [81] and to polymerization of proteins like actin, microtubulin [82], and sickle cell hemoglobin [83]. In the latter cases the proteins possess the assembly-competent structure immediately after the start of the reaction. These processes are usually interpreted in the framework of a nucleation polymerization mechanism [82, 83]. This interpretation has been overtaken to rationalize the kinetics of amyloid formation [84] and only little attention has been paid to the relation between secondary and quaternary structure formation in models of amyloid fibril assembly. The latest model proposals have put their focus especially on this point and have emphasized the population of intermediate long-lived oligomeric assemblies on the pathway to amyloid fibrils [75, 85].

19.6 Experimental Protocols

19.6.1 Laser Light Scattering Instrumentation

19.6.1.1 Basic Experimental Set-up, General Requirements

The experimental set-up for light scattering measurements in macromolecular solutions is relatively simple (Figure 19.1). A beam of a continuous wave (cw) laser is focused into a temperature-stabilized cuvette. A temperature stability better than ± 0.1 °C is required for DLS experiments because of the temperature dependence of the solvent viscosity. The scattered light intensity is detected at one or different scattering angles using either photomultiplier tubes or avalanche photodiode detectors (APD). Though photomultiplier tubes have still some advantages, an impor-

tant feature of APDs is the much higher quantum yield (>50%) within the wavelength range of laser light between 400 and 900 nm.

The expense of a light scattering system depends essentially on the type of the laser and the complexity of the detection system. For example, simple systems detect the light only at 90° or in the nearly backward scattering direction, while sophisticated devices are able to monitor the scattered light simultaneously at many selectable scattering angles. An important feature is the construction of the sample cell holder, which should allow the use of different cell types. As discussed earlier, for folding studies and molecular weight determinations of proteins detection at one scattering angle is sufficient. Multi-angle detection is recommended for studies of protein assembly, when the size of the formed particles exceeds about 50 nm.

A criterion for choosing the appropriate cell type is the decision between batch and flow experiments and the available amount of protein. Batch experiments require the lowest amount of substance, since standard microfluorescence cells with volumes of the order of 10 μL can be used. These cells have the further advantage that the protein concentration can be measured in the same cell. Flow-through cells, which are essential for stopped-flow experiments and on-line coupling to particle separation devices, like HPLC, FPLC, and field-flow fractionation, are also useful for batch experiments in the following respect. A direct connection of these cell to a filter unit are the best way to obtain perfectly cleaned samples.

The cells must be cleaned first by flushing a large amount of water and solvent through the filter and the cell. The protein sample is then applied without removing the filter unit. Several cell types can be used including standard fluorescence flow-through cells, sample cells used in stopped-flow systems, or special flow-through cells provided by manufacturers of light scattering equipments. Most of these flow cells have the disadvantage of a restricted angular range. An exception is the cell used in the Wyatt multiangle laser light scattering (MALLS) device. Cylindrical cells in connection with an index matching bath have to be used for precise measurements at different, particularly small scattering angles.

In the case of SLS experiments, measurements of the photocurrent with subsequent analog-to-digital conversion as well as photon-counting techniques are used. The latter technique is preferred in DLS experiments. An appropriate correlation electronics is no longer a problem for modern dynamic light scattering devices since practically ideal digital correlators can be built up.

The minimum protein concentration needed in a DLS experiment depends on the molecular mass and the optical quality of the instrument, particularly on the available laser power. But, even at sufficiently high laser power of about 0.5 W the experiments become impractical below a certain concentration. This happens when the excess scattering of the protein solution falls below the scattering of pure water, e.g., for a protein with $M = 10$ kDa at concentrations below 0.25 mg mL^{-1}. Thus, DLS experiments can be done without special efforts at concentrations satisfying the condition $c \times M \geq 5$ kDa mg mL^{-1}. For SLS experiments the value of $c \times M$ can be about one order of magnitude lower.

Removal of undesired contaminations, such as dust, bubbles, or other large par-

ticles, is a crucial step in preparing samples for light scattering experiments. Large particles can readily removed by membrane filters having pore sizes of about 0.1 μm or by centrifugation at 10 000 *g* or higher, while size-exclusion chromatography or similar separation techniques have to be applied when a protein solution contains oligomers or small aggregates only slightly larger than the monomeric protein. Fluids used to clean the scattering cell must also be free of all particulates.

In an SLS experiment, the time-averaged scattering intensities of solvent, solution, and reference sample (scattering standard) have to be measured. Data evaluation has to be done according to Eqs (3) and (4). Commercial instruments are in general equipped with software packages that generate Zimm plots according to Eq. (4). Additionally, the software contains the Rayleigh ratios for scattering standards at the wavelength of the instrument. A widely used scattering standard is toluene. The Rayleigh ratios of toluene and other scattering standards at different wavelength are given in Ref. [5]. Instrument calibration can also be done using an appropriate protein solution. However, the protein must be absolutely monomeric under the chosen solvent conditions.

DLS measurements demand slightly more experience concerning experiment duration and data evaluation. Calibration is not needed. The basis for obtaining stable and reliable results is an adequately measured correlation function. A visual inspection of this primary data is recommended before any data evaluation is done. The signal-to-noise ratio that is needed depends on the complexity of the system under study. For example, short measurement times are acceptable only in the case of unimodal narrow size distributions, when a noisy correlation function can be well fitted by a single exponential. In practise, two data evaluation schemes are mainly used, the method of cumulants [9] yielding an average Stokes radius and the second and third moments of the size distribution and/or the approximate reconstruction of the size distribution by an inverse Laplace transformation, mostly using the program CONTIN [8]. The corresponding software packages are available from the author or are provided by the manufacturers of the instruments. CONTIN allows the reconstruction of a distribution function in terms of scattering power, weight concentration, or number (molar) concentration. Though the latter two types are more instructive, they should only be calculated when a reasonable particle shape can be anticipated within the considered size range.

19.6.1.2 Supplementary Measurements and Useful Options

For the estimation of the molecular mass from SLS, and the diffusion coefficient and the Stokes radius from DLS, additional physical quantities are required. For the calculation of the optical constant in Eq. (2) the refractive index of the solvent and the refractive index increment of the protein in the particular solvent must be known. The former can be measured easily by an Abbe refractometer, whereas an differential refractometer is needed for precise measurements of $\partial n/\partial c$. Measurements of $\partial n/\partial c$ are often more expensive than the light scattering experiment itself. A comprehensive collection of $\partial n/\partial c$ values can be found in [86]. $\partial n/\partial c = 0.19$ mL g^{-1} is a good approximation for proteins in aqueous solution at moderate (<200 mM) salt concentrations.

For calculations of R_S from DLS data via Eq. (6) the dynamic viscosity η of the solvent must be known. η can be obtained from the kinematic viscosity ν (e.g., measured by an Ubbelohde type viscometer) and the density ρ (measured by a digital densitometer, e.g., DMA 58, Anton Paar, Austria) by $\eta = \nu \times \rho$.

A very useful option for light scattering instruments is the on-line coupling with FPLC, HPLC, or field-flow fractionation (FFF) and a concentration detector, which might be a UV absorption monitor or a refractive index detector. This allows direct measurements of M during the flow. In the case of known $\partial n/\partial c$ for the particular solvent conditions, the molecular mass can be obtained from the output signals of the SLS and refractive index detectors by $M = k_e \times (\partial n/\partial c)^{-1} \times (\text{output})_{SLS}/(\text{output})_{RI}$, where k_e is the instrument calibration constant. A parallel estimation of R_S is possible, when the scattering is strong enough allowing a sufficiently precise DLS experiment during a few minutes.

A further option is the coupling to a mixer allowing kinetic light scattering experiments. Two schemes can be used. Either a mixing device is coupled to a light scattering apparatus equipped with a flow cell [66] or the light scattering apparatus is built-up around a stopped-flow device originally constructed for fluorescence detection [56].

19.6.1.3 Commercially Available Light Scattering Instrumentation

There are several companies that produce light scattering instruments and optional units. Many of them have taken into consideration the special demands for studies on protein solutions. Accordingly, most of the systems can handle very small sample volumes, have the sensitivity to study low concentrations of monomeric proteins, and can work in batch and flow mode. For those who are interested in applying SLS and DLS to folding and aggregation studies we have listed several companies and the corresponding websites in alphabetic order.

- ALV-Laservertriebsgesellschaft m.b.H., Germany: http://www.alvgmbh.de
- Brookhaven Instruments Corporation, USA: http://www.bic.com
- Malvern Instruments Ltd., UK: http://www.malvern.co.uk
- Precision Detectors, USA: http://www.lightscatter.com
- Proterion Corporation, USA (formerly Protein Solutions): http://www.proterion.com
- Wyatt Technology Corporation, USA: http://www.wyatt.com, visit also *http://www.wyatt.de*

19.6.2 Experimental Protocols for the Determination of Molecular Mass and Stokes Radius of a Protein in a Particular Conformational State

The purpose of the protocols is to demonstrate critical steps of combined SLS/DLS measurements. If a commercial instrument with sophisticated data evaluation software is used, the individual steps may be involved, but slightly differently arranged in the software protocol. The protocols are based on the assumption that the in-

strument provides an average over time T of the scattered intensity $\overline{I_T}$ and a set of N normalized correlation functions $g^{(2)}(\tau, T_A)$ calculated during an accumulation time T_A and is equipped with the software to reconstruct the size distribution (CONTIN or similar packages).

Protocol 1

Determination of the apparent molecular mass M_{app}, diffusion coefficient D_{app}, and the corresponding Stokes radius R_{app} of a protein at a given concentration c_P at 20 °C.

Equipment and reagents

- SLS/DLS instrument with thermostatted cell holder
- UV spectrophotometer, preferentially single-beam instrument
- Abbe-type refractometer
- Flow-through cell for fluorometry, light path 1.5 mm ($V = 25$ μL, e.g., Hellma 176.152) and ultra-microfluorescence cell, light path 1.5 mm ($V = 12$ μL, e.g., Hellma 105.252).
- Whatman filter Anotop and Anodisc, $d = 10$ mm, pore size 0.1 μm with appropriate filter holders, syringes 1–2 mL (laboratory centrifuge and pipettes for method B).
- Suitable buffer, e.g., 50 mM Tris/HCl, pH 8, 100 mM KCl (the viscosity $\eta =$ 1.018 cP at 20 °C is not very different from that of water, $\eta = 1.002$ cP).

(A) Measurements with flow-through cells

1. Prepare the protein solution of the required concentration (suitable range 1–5 mg mL^{-1}).
2. Wet the Anotop filter with distilled water and connect it to the flow-through cell (do not disconnect until the end of the experiment).
3. Flush at least 5 mL distilled water through filter and cell.
4. Insert the cell into the light scattering instrument and check for purity (the scattering intensity must be very low and "spikes" in intensity should be totally absent. Otherwise, repeat step 3.
5. Fill a syringe with 1–2 mL buffer and flush it through filter and cell (note that the actual dead volume of filter and cell is larger than the specified volume of the cell).
6. Insert the cell into the light scattering instrument and measure the scattering intensity of the buffer, $\overline{I}_{T,\,buffer}$. In some cases, it could be useful to run a short DLS experiment in order to check that the baseline is flat.
7. Measure the scattering intensity of the reference sample (toluene) in a separate cuvette of similar geometry.

8. Insert the flow-through cell with buffer into the UV spectrometer and measure the blank spectrum (note that the center height of the cell fits both the SLS/DLS and UV spectrophotometer).
9. Measure the refractive index of the buffer with the Abbe-type refractometer.
10. Flush about 1 mL protein solution slowly through filter and cell in order to replace the buffer by the protein solution (the protein solution that has passed filter and cell can be used to prepare a sample of lower concentration).
11. Measure the absorption spectrum of the protein solution in the flow-through cell, subtract the blank spectrum, and calculate the actual protein concentration in the cell on the basis of known extinction coefficients.
12. Insert the cell into the SLS/DLS instrument and start data acquisition. It is recommended to record the correlation function not in a single long run, but rather by superposition of N short runs (of about 10 s). This enables one to get a better overview about the stability and quality of the sample. Furthermore, good acquisition software allows to discard distorted runs. Though a correlation function is clearly built up within 10 s, it is mostly too noisy for adequate data evaluation.
13. Store all data and prepare data evaluation by entering additional parameters like temperature, refraction index, and viscosity.
14. Data evaluation, especially estimations of size distribution, should be done immediately giving the chance to continue the experiment. This could be useful if the resulting size distribution is still very unstable against variation in data evaluation parameters.
15. The size distribution should consist of one dominating peak in the present case. Otherwise, the protein is strongly prone to aggregation. The influence of stable aggregates of clearly distinct size can be eliminated in many cases as discussed at the end of Section 19.2.
16. Calculate M using Eqs (2), (3), and (4), the Rayleigh ratio of the reference sample (the value depends on the wavelength used in the instrument), and $\partial n/\partial c = 0.19$ mL g^{-1}.

(B) Measurements with ultra-microfluorescence cells

Although Scheme A is superior from the light scattering point of view, a rather large amount of protein is needed. This can be circumvented by using ultra-micro cells. Here, we repeat only those steps that concern the preparation of buffer and protein solutions. Two approaches are applicable.

(B1) Preparation using micro-filter units

Several manufacturers (e.g. Proterion Corporation or Wyatt Technology Corporation) deliver micro-filter holder for Anodisc filter membranes with dead volumes less than 10 μL. This allows sample volumes as small as 25 μL to be filtered. The following steps have to be done.

1. Insert a dry filter membrane into the filter holder and wet the filter with buffer and filter about 100 μL buffer.
2. Flush the fluorescence cell with a strong nitrogen stream in order to remove any dust.
3. Filter about 50 μL buffer into the cell and check for purity in the light scattering instrument. Do the same measurements with the buffer and reference sample as indicated under Scheme A. (Empty the cell, wash is with distilled water, dry it with ethanol (Uvasol) and nitrogen and repeat steps 2 and 3 if dust or bubbles can be detected.)
4. Empty the cell carefully (washing and drying is not necessary) and filter about 25 μL protein solution into the cell.
5. Close the cell, determine the concentration and measure SLS and DLS as under Scheme A.
6. This procedure is nearly as good as filtration according to Scheme A, but the presence of dust and bubbles cannot be totally excluded.

(B2) Preparation by centrifugation

This procedure has to be applied when only about 15 μL of protein solution are available and differs from Scheme B1 only by step 4. The protein solution centrifugated about 15 min at 10 000 *g* or more has to be transferred into the scattering cell. An alternative is careful centrifugation within the scattering cell (note that ultra-micro cells are rather expensive!).

Protocol 2

Determination of the molecular mass, diffusion coefficient D, Stokes radius R_S and virial coefficients of a protein in a particular state.

This experimental procedure is a repetition of the sequences given in Protocol 1 for at least four protein concentrations. Scheme A is recommended, whereas a stock solution of 1 mL with the highest concentration is needed.

Additional data evaluation concerns extrapolation of $(H \times c)/R_q$ (Eq. (4) with $P(q) \approx 1$) and D to zero protein concentration.

Acknowledgments

The authors are grateful to Stephen Harding, University Nottingham, for valuable comments and suggestions.

References

1 Jakeman, E., Pusey, P. N. & Vaughan, J. M. (1976). Intensity fluctuation light-scattering spectroscopy using a conventional source. *Optics Commun.* **17**, 305–308.
2 Huglin, M. (1972). *Light Scattering*

from Polymer Solutions, Academic Press, New York.

3 Kratochvil, P. (1987). *Classical Light Scattering from Polymer Solutions*, Elsevier, Amsterdam.

4 Schmitz, K. S. (1990). *An Introduction to Dynamic Light Scattering by Macromolecules*. Academic Press, New York.

5 Chu, B. (1991). *Laser Light Scattering*. Academic Press, New York.

6 Brown, W. (1993). *Dynamic Light Scattering*. Claredon Press, Oxford.

7 Berne, B. J. & Pecora, R. (2000). *Dynamic Light Scattering with Applications to Chemistry, Biology, and Physics*. Dover Publications, Mineola, New York.

8 Provencher, S. W. (1982). CONTIN – a general-purpose constrained regularization program for inverting noisy linear algebraic and integral-equations. *Com. Phys. Commun.* **27**, 229–242.

9 Koppel, D. E. (1972). Analysis of macromolecular polydispersity in intensity correlation spectroscopy: the method of cumulants. *J. Chem. Phys.* **57**, 4814–4820.

10 Harding, S. E. & Johnson, P. (1985). The concentration dependence of macromolecular parameters. *Biochem. J.* **231**, 543–547.

11 Garcia Bernal, J. M. & de la Torre, J. G. (1981). Transport-properties of oligomeric subunit structures. *Biopolymers* **20**, 129–139.

12 Claes, P., Dunford, M., Kenney, A. & Penny, V. (1992). An on-line dynamic light scattering instrument for macromolecular characterization. In *Laser Light Scattering in Biochemistry* (Harding, S. E., Sattelle, D. B. & Bloomfield, V. A., eds), pp. 66–76. Royal Society of Chemistry, Cambridge.

13 Nicoli, D. F. & Benedek, G. B. (1976). Study of the thermal denaturation of lysozyme and other globular proteins by light-scattering spectroscopy. *Biopolymers* **15**, 2421–2437.

14 Gast, K., Zirwer, D., Damaschun, H., Hahn, U., Müller-Frohne, M., Wirth, M. & Damaschun, G. (1997). Ribonuclease T1 has different dimensions in the thermally and chemically denatured states: a dynamic light scattering study. *FEBS Lett.* **403**, 245–248.

15 Fabian, H., Fälber, K., Gast, K., Reinstadler, D., Rogov, V. V., Naumann, D., Zamyatkin, D. F. & Filimonov, V. V. (1999). Secondary structure and oligomerization behavior of equilibrium unfolding intermediates of the lambda Cro repressor. *Biochemistry* **38**, 5633–5642.

16 Privalov, P. L. (1990). Cold denaturation of proteins. *Crit. Rev. Biochem. Mol. Biol.* **25**, 281–305.

17 Griko, Y. V., Venyaminov, S. Y. & Privalov, P. L. (1989). Heat and cold denaturation of phosphoglycerate kinase (interaction of domains). *FEBS Lett.* **244**, 276–278.

18 Damaschun, G., Damaschun, H., Gast, K., Misselwitz, R., Müller, J. J., Pfeil, W. & Zirwer, D. (1993). Cold denaturation-induced conformational changes in phosphoglycerate kinase from yeast. *Biochemistry* **32**, 7739–7746.

19 Agashe, V. R., Udgaonkar, J. B. (1995). Thermodynamics of denaturation of barstar: evidence for cold denaturation and evaluation of the interaction with guanidine hydrochloride. *Biochemistry* **34**, 3286–3299.

20 Wong, K. B., Freund, S. M. V. & Fersht, A. R. (1996). Cold denaturation of barstar: H-1, N-15 and C-13 NMR assignment and characterisation of residual structure. *J. Mol. Biol.* **259**, 805–818.

21 Tanford, C. (1968). Protein denaturation. *Adv. Protein Chem.* **23**, 121–282.

22 Dubin, S. B., Feher, G. & Benedek, G. B. (1973). Study of the chemical denaturation of lysozyme by optical mixing spectroscopy. *Biochemistry* **12**, 714–719.

23 Nöppert, A., Gast, K., Müller-Frohne, M., Zirwer, D. & Damaschun, G. (1996). Reduced-denatured ribonuclease A is not in a compact state. *FEBS Lett.* **380**, 179–182.

24 Fink, A. L., Calciano, L. J., Goto, Y., Kurotsu, T. & Palleros, D. R. (1994). Classification of acid denaturation of proteins: intermediates and unfolded states. *Biochemistry* **33**, 12504–12511.

25 Barrick, D., Hughson, F. M. & Baldwin, R. L. (1994). Molecular mechanism of acid denaturation – the role of histidine-residues in the partial unfolding of apomyoglobin. *J. Mol. Biol.* **237**, 588–601.

26 Ptitsyn, O. B. (1995). Molten globule and protein folding. *Adv. Protein Chem.* **47**, 83–229.

27 Arai, M. & Kuwajima, K. (2000). Role of the molten globule state in protein folding. *Adv. Protein Chem.* **53**, 209–282.

28 Kuwajima, K. & Arai, M. (2000). The molten globule state: the physical picture and biological significance. In *Mechanisms of Protein Folding* (Pain, R. H., ed.), pp. 138–174. Oxford University Press, Oxford.

29 Gast, K., Zirwer, D., Müller-Frohne, M. & Damaschun, G. (1998). Compactness of the kinetic molten globule of bovine alpha-lactalbumin: a dynamic light scattering study. *Protein Sci.* **7**, 2004–2011.

30 Gast, K., Damaschun, H., Misselwitz, R., Müller-Frohne, M., Zirwer, D. & Damaschun, G. (1994). Compactness of protein molten globules: temperature-induced structural changes of the apomyoglobin folding intermediate. *Eur. Biophys. J.* **23**, 297–305.

31 Kataoka, M., Kuwajima, K., Tokunaga, F. & Goto, Y. (1997). Structural characterization of the molten globule of alpha-lactalbumin by solution x-ray scattering. *Protein Sci.* **6**, 422–430.

32 Kataoka, M., Nishii, I., Fujisawa, T., Ueki, T., Tokunaga, F. & Goto, Y. (1995). Structural characterization of the molten globule and native states of apomyoglobin by solution X-ray scattering. *J. Mol. Biol.* **249**, 215–228.

33 Gast, K., Zirwer, D., Müller-Frohne, M. & Damaschun, G. (1999). Trifluoroethanol-induced conformational transitions of proteins: insights gained from the differences between alpha-lactalbumin and ribonuclease A. *Protein Sci.* **8**, 625–634.

34 Damaschun, G., Damaschun, H., Gast, K. & Zirwer, D. (1999). Proteins can adopt totally different folded conformations. *J. Mol. Biol.* **291**, 715–725.

35 Wright, P. E. & Dyson, H. J. (1999). Intrinsically unstructured proteins: Re-assessing the protein structure-function paradigm. *J. Mol. Biol.* **293**, 321–331.

36 Gast, K., Damaschun, H., Eckert, K., Schulze-Forster, K., Maurer, H. R., Muller, F. M., Zirwer, D., Czarnecki, J. & Damaschun, G. (1995). Prothymosin alpha: A biologically active protein with random coil conformation. *Biochemistry* **34**, 13211–13218.

37 Damaschun, G., Damaschun, H., Gast, K., Misselwitz, R., Zirwer, D., Gührs, K. H., Hartmann, M., Schlott, B., Triebel, H. & Behnke, D. (1993). Physical and conformational properties of staphylokinase in solution. *Biochim. Biophys. Acta* **1161**, 244–248.

38 Uversky, V. N. (1993). Use of fast protein size-exclusion liquid-chromatography to study the unfolding of proteins which denature through the molten globule. *Biochemistry* **32**, 13288–13298.

39 Wilkins, D. K., Grimshaw, S. B., Receveur, V., Dobson, C. M., Jones, J. A. & Smith, L. J. (1999). Hydrodynamic radii of native and denatured proteins measured by pulse field gradient NMR techniques. *Biochemistry* **38**, 16424–16431.

40 Flory, P. J. (1969). *Statistical Mechanics of Chain Molecules.* John Wiley & Sons, New York.

41 Baldwin, R. L. & Zimm, B. H. (2000). Are denatured proteins ever random coils? *Proc. Natl Acad. Sci. USA* **97**, 12391–12392.

42 Zhou, H. X. (2002). Dimensions of denatured protein chains from

hydrodynamic data. *J. Phys. Chem.* **106**, 5769–5775.

43 Tanford, C., Kawahara, K. & Lapanje, S. (1966). Proteins in 6 M guanidine hydrochloride. Demonstration of random coil behavior. *J. Biol. Chem.* **241**, 1921–1923.

44 Damaschun, G., Damaschun, H., Gast, K. & Zirwer, D. (1998). Denatured states of yeast phosphoglycerate kinase. *Biochemistry (Moscow)* **63**, 259–275.

45 Byron, O. (2000). Hydrodynamic bead modeling of biological macromolecules. *Methods Enzymol.* **321**, 278–304.

46 Garcia de la Torre, J., Huertas, M. L. & Carrasco, B. (2000). Calculation of hydrodynamic properties of globular proteins from their atomic-level structure. *Biophys. J.* **78**, 719–730.

47 Harding, S. E. (2001). The hydration problem in solution biophysics: an introduction. *Biophys. Chem.* **93**, 87–91.

48 Halle, B. & Davidovic, M. (2003). Biomolecular hydration: From water dynamics to hydrodynamics. *Proc. Natl Acad. Sci. USA* **100**, 12135–12140.

49 Garcia de la Torre, J. (2001). Hydration from hydrodynamics. General considerations and applications of bead modelling to globular proteins. *Biophys. Chem.* **93**, 159–170.

50 Feng, H. P. & Widom, J. (1994). Kinetics of compaction during lysozyme refolding studied by continuous-flow quasielastic light scattering. *Biochemistry* **33**, 13382–13390.

51 Gast, K., Zirwer, D. & Damaschun, G. (2000). Time-resolved dynamic light scattering as a method to monitor compaction during protein folding. In *Data Evaluation in Light Scattering of Polymers* (Helmstedt, M. & Gast, K., eds), pp. 205–220. Wiley-VCH, Weinheim.

52 Shastry, M. C. R., Luck, S. D. & Roder, H. (1998). A continuous-flow capillary mixing method to monitor reactions on the microsecond time scale. *Biophys. J.* **74**, 2714–2721.

53 Segel, D. J., Bachmann, A., Hofrichter, J., Hodgson, K. O., Doniach, S. & Kiefhaber, T. (1999). Characterization of transient intermediates in lysozyme folding with time-resolved small-angle X-ray scattering. *J. Mol. Biol.* **288**, 489–499.

54 Pollack, L., Tate, M. W., Darnton, N. C., Knight, J. B., Gruner, S. M., Eaton, W. A. & Austin, R. H. (1999). Compactness of the denatured state of a fast-folding protein measured by submillisecond small-angle x-ray scattering. *Proc. Natl Acad. Sci. USA* **96**, 10115–10117.

55 Arai, M., Ito, K., Inobe, T., Nakao, M., Maki, K., Kamagata, K., Kihara, H., Amemiya, Y. & Kuwajima, K. (2002). Fast compaction of alpha-lactalbumin during folding studied by stopped-flow X-ray scattering. *J. Mol. Biol.* **321**, 121–132.

56 Nöppert, A., Gast, K., Zirwer, D. & Damaschun, G. (1998). Initial hydrophobic collapse is not necessary for folding RNase A. *Folding Des.* **3**, 213–221.

57 Jaenicke, R. & Seckler, R. (1997). Protein misassembly in vitro. *Adv. Protein Chem.* **50**, 1–59.

58 De Young, L. R., Dill, K. A. & Fink, A. L. (1993). Aggregation of globular proteins. *Acc. Chem. Res.* **26**, 614–620.

59 Zettlmeissl, G., Rudolph, R. & Jaenicke, R. (1979). Reconstitution of lactic dehydrogenase. Noncovalent aggregation vs. reactivation. 1. Physical properties and kinetics of aggregation. *Biochemistry* **18**, 5567–5571.

60 Finke, J. M., Roy, M., Zimm, B. H. & Jennings, P. A. (2000). Aggregation events occur prior to stable intermediate formation during refolding of interleukin 1 beta. *Biochemistry* **39**, 575–583.

61 Jossang, T., Feder, J. & Rosenqvist, E. (1985). Heat aggregation kinetics of human IgG. *J. Chem. Phys.* **82**, 574–589.

62 Smoluchowski, M. v. (1917). Versuch einer mathematischen Theorie der Koagulationskinetik kolloider Lösungen. *Z. Phys. Chem.* **92**, 129–168.

63 Aymard, P., Nicolai, T., Durand, D. & Clark, A. (1999). Static and dynamic scattering of beta-lactoglobulin aggregates formed after heat-induced denaturation at pH 2. *Macromolecules* **32**, 2542–2552.

64 Le Bon, C., Nicolai, T. & Durand, D. (1999). Kinetics of aggregation and gelation of globular proteins after heat-induced denaturation. *Macromolecules* **32**, 6120–6127.

65 Bauer, R., Carrotta, R., Rischel, C. & Ogendal, L. (2000). Characterization and isolation of intermediates in beta-lactoglobulin heat aggregation at high pH. *Biophys. J.* **79**, 1030–1038.

66 Bernocco, S., Ferri, F., Profumo, A., Cuniberti, C. & Rocco, M. (2000). Polymerization of rod-like macromolecular monomers studied by stopped-flow, multiangle light scattering: Set-up, data processing, and application to fibrin formation. *Biophys. J.* **79**, 561–583.

67 Buchner, J., Schmidt, M., Fuchs, M., Jaenicke, R., Rudolph, R., Schmid, F. X. & Kiefhaber, T. (1991). GroE facilitates refolding of citrate synthase by suppressing aggregation. *Biochemistry* **30**, 1586–1591.

68 Fezoui, Y., Hartley, D. M., Harper, J. D., Khurana, R., Walsh, D. M., Condron, M. M., Selkoe, D. J., Lansbury, P. T., Fink, A. L. & Teplow, D. B. (2000). An improved method of preparing the amyloid beta-protein for fibrillogenesis and neurotoxicity experiments. *Amyloid* **7**, 166–178.

69 Lomakin, A., Benedek, G. B. & Teplow, D. B. (1999). Monitoring protein assembly using quasielastic light scattering spectroscopy. *Methods Enzymol.* **309**, 429–459.

70 Tomski, S. J. & Murphy, R. M. (1992). Kinetics of aggregation of synthetic beta-amyloid peptide. *Arch. Biochem. Biophys.* **294**, 630–638.

71 Murphy, R. M. & Pallitto, M. R. (2000). Probing the kinetics of beta-amyloid self-association. *J. Struct. Biol.* **130**, 109–122.

72 Lomakin, A., Chung, D. S., Benedek, G. B., Kirschner, D. A. & Teplow, D. B. (1996). On the nucleation and growth of amyloid beta-protein fibrils: Detection of nuclei and quantitation of rate constants. *Proc. Natl Acad. Sci. USA* **93**, 1125–1129.

73 Lomakin, A., Teplow, D. B., Kirschner, D. A. & Benedek, G. B. (1997). Kinetic theory of fibrillogenesis of amyloid beta-protein. *Proc. Natl Acad. Sci. USA* **94**, 7942–7947.

74 Kusumoto, Y., Lomakin, A., Teplow, D. B. & Benedek, G. B. (1998). Temperature dependence of amyloid beta-protein fibrillization. *Proc. Natl Acad. Sci. USA* **95**, 12277–12282.

75 Modler, A. J., Gast, K., Lutsch, G. & Damaschun, G. (2003). Assembly of amyloid protofibrils via critical oligomers – a novel pathway of amyloid formation. *J. Mol. Biol.* **325**, 135–148.

76 Hornemann, S. & Glockshuber, R. (1998). A scrapie-like unfolding intermediate of the prion protein domain PrP(121–231) induced by acidic pH. *Proc. Natl Acad. Sci. USA* **95**, 6010–6014.

77 Morillas, M., Vanik, D. L. & Surewicz, W. K. (2001). On the mechanism of alpha-helix to beta-sheet transition in the recombinant prion protein. *Biochemistry* **40**, 6982–6987.

78 Baskakov, I. V., Legname, G., Baldwin, M. A., Prusiner, S. B. & Cohen, F. E. (2002). Pathway complexity of prion protein assembly into amyloid. *J. Biol. Chem.* **277**, 21140–21148.

79 Sokolowski, F., Modler, A. J., Masuch, R., Zirwer, D., Baier, M., Lutsch, G., Moss, D. A., Gast, K. & Naumann, D. (2003). Formation of critical oligomers is a key event during conformational transition of recombinant Syrian hamster prion protein. *J. Biol. Chem.* **278**, 40481–40492.

80 Richardson, J. S. & Richardson, D. C. (2002). Natural beta-sheet proteins use negative design to avoid edge-to-edge aggregation. *Proc. Natl Acad. Sci. USA* **99**, 2754–2759.

81 Flory, P. J. (1953). *Principles of Polymer Chemistry*. Cornell University Press, Ithaca.
82 Oosawa, F. & Asakura, S. (1975). *Thermodynamics of the Polymerization of Protein*. Academic Press, London.
83 Eaton, W. A. & Hofrichter, J. (1990). Sickle cell hemoglobin polymerization. *Adv. Protein Chem.* **40**, 63–279.
84 Jarrett, J. T. & Lansbury, P. T., Jr. (1993). Seeding "one-dimensional crystallization" of amyloid: a pathogenic mechanism in Alzheimer's disease and scrapie? *Cell* **73**, 1055–1058.
85 Serio, T. R., Cashikar, A. G., Kowal, A. S., Sawicki, G. J., Moslehi, J. J., Serpell, L., Arnsdorf, M. F. & Lindquist, S. L. (2000). Nucleated conformational conversion and the replication of conformational information by a prion determinant. *Science* **289**, 1317–1321.
86 Theisen, A., Johann, C., Deacon, M. P. & Harding, S. E. (2000). *Refractive Increment Data-book*. Nottingham University Press, Nottingham.
87 Gast, K., Modler, A. J., Damaschun, H., Kröber, R., Lutsch, G., Zirwer, D., Golbik, R. & Damaschun, G. (2003). Effect of environmental conditions on aggregation and fibril formation of barstar. *Eur. Biophys. J.* 32, 710–723.

20
Conformational Properties of Unfolded Proteins

Patrick J. Fleming and George D. Rose

20.1
Introduction

The protein folding reaction, U(nfolded) ⇄ N(ative), is a reversible disorder ⇄ order transition. Proteins are disordered (U) at high temperature, high pressure, extremes of pH, or in the presence of denaturing solvents; but they fold to uniquely ordered, biologically relevant conformers (N) under physiological conditions. This folding transition is highly cooperative such that individual molecules within the population are predominantly fully folded or fully unfolded; partially folded chains are transitory and rare. Notably, no covalent bonds are made or broken during folding/unfolding; in effect, the transition is simply a re-equilibration in response to changes in temperature, pressure, pH, or solvent conditions. Currently, there are more than 20 000 examples of native proteins in the protein databank. In contrast, the unfolded population, by its very nature, resists ready structural characterization. In this sense, the folding reaction might be more appropriately denoted as ? ⇄ N.

This chapter traces thinking about the unfolded state from Pauling's and Wu's early suggestions in the 1930s, through the work of Tanford and Flory in the 1960s to the present moment. Early work gave rise to the random coil model for the unfolded state, as described below. Confirmatory findings established this model as the conceptual anchor point for thinking about unfolded proteins – until recently, perhaps. In the past few years, results from both theory and experiment indicate the existence of conformational bias in the unfolded state, a condition that is not addressed by the random coil model. If unfolded conformers are biased toward their native conformation sufficiently, then the random coil model is likely to be superseded by newer, more specific models. Though controversial, such a conceptual shift appears to be underway, as we attempt to describe.

20.1.1
Unfolded vs. Denatured Proteins

The term unfolded protein is generic and inclusive, and it can range from protein solutions in harsh denaturants to protein subdomains that undergo transitory ex-

Protein Folding Handbook. Part I. Edited by J. Buchner and T. Kiefhaber

ISBN: 3-527-30784-2

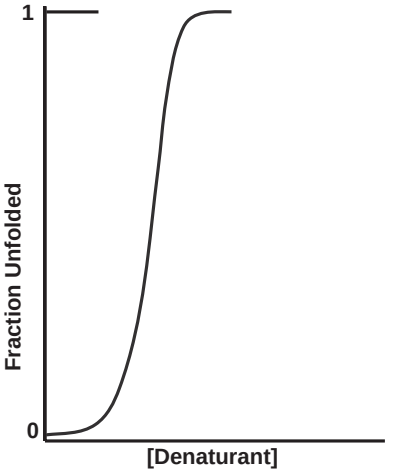

Fig. 20.1. The folding transition. The folding reaction of a typical, small biophysical protein is a highly cooperative, all-or-none transition. At the transition midpoint, half the ensemble is folded and half is unfolded; the population of partially folded/unfolded molecules is negligible. In this idealized plot of an actual experiment [37], the population is followed by a conformational probe (e.g., circular dichroism or fluorescence) as a function of denaturant concentration. Upon addition of sufficient denaturant, the probe signal reaches a plateau, indicating that the transition is complete.

cursions from their native format via spontaneous fluctuations. While conceptually complete, this range is too diverse to be practically useful, and it requires further specification. Accordingly, the field has focused more specifically on denatured proteins, the population of unfolded conformers that can be studied at equilibrium under high concentrations of denaturing solvents, high temperature, high pressure, high/low pH, etc. Early experiments of Ginsburg and Carroll [37] and Tanford [93] demonstrate that such conditions can give rise to a defined equilibrium population in which the unfolding transition is complete (Figure 20.1). In this chapter, we use both terms and rely on the context for specificity.

20.2 Early History

The fact that protein molecules can undergo a reversible disorder $\rightleftarrows$ order transition originated early in the last century, in ideas proposed by Wu [29, 101] and Mirsky and Pauling [59]. Both papers propose that a theory of protein structure is tantamount to a theory of protein denaturation. In particular, these authors recognized that many disparate physical and chemical properties of proteins are abolished coordinately upon heating. This was unlikely to be mere coincidence. Both Wu and Mirsky and Pauling hypothesized that such properties are a consequence of the protein's structure and are abolished when that structure is melted. Their hypothesis was later confirmed by Kauzmann and Simpson [86], at which

point the need for an apt characterization of the melt became clear, and protein denaturation emerged as a research discipline.

A widely accepted view assumes that unfolded polypeptide chains can explore conformational space freely, with constraints arising only from short-range local restrictions and longer range excluded volume effects. To a good first approximation, short-range local restrictions refer to repulsive van der Waals interactions between sequentially adjacent residues (i.e., steric effects) captured by the well-known Ramachandran map for a dipeptide [70]. Longer range excluded volume effects also refer to repulsive van der Waals interactions, in this case those between nonbonded atoms that are distant in sequence but juxtaposed in space as the chain wanders at random along a Brownian walk in three dimensions [32, 91]. This random coil model has conditioned most of the thinking in the field.

It is important to realize that the random coil model need not imply an absence of residual structure in the unfolded population. Kauzmann's famous review raised the central question about structure in the unfolded state explicitly [45]:

> ***For instance, one would like to know the types of structures actually present in the native and denatured proteins. . . . The denatured protein in a good solvent such as urea is probably somewhat like a randomly coiled polymer, though the large optical rotation of denatured proteins in urea indicates that much local rigidity must be present in the chain (p. 4).***

20.3 The Random Coil

A chain molecule is a freely jointed random coil if it traces a random walk in three-dimensional space, in incremental steps of fixed length. The random coil model has enjoyed a long and successful history in describing unfolded proteins. By definition, a random coil polymer has no strongly preferred backbone conformations because energy differences among its sterically accessible backbone conformations are of order ~kT. Accordingly, the energy landscape for such a polymer can be visualized as an ''egg crate'' of high dimensionality, and a Boltzmann-weighted ensemble of such polymers populates this landscape uniformly.

More than others, this elegant theory was developed by Flory [33], pp. 30–31; [17], pp. 991–996) and advanced by Tanford [91–93], who demonstrated that proteins denatured in 6 M guanidinum chloride (a strong denaturant) appear to be structureless, random chains. Tanford's pioneering studies established a compelling framework for interpreting experimental protein denaturation that would survive largely unchallenged for the next 30 years.

Often, the term random coil is used synonymously with the freely jointed chain model (described below), in which there is no correlation between the orientation of two chain monomers at any length scale. That is, configurational properties of a freely jointed chain, such as its end-to-end distance, are Gaussian distributed at all

chain lengths. In practice, no actual polymer chain is freely jointed. More realistic models, such as Flory's rotational isomeric-state model, have Gaussian-distributed chain configurations only in the infinite chain limit ([33], pp. 30–31; [17], pp. 991–996). These distinctions notwithstanding, the main characteristic of the random coil holds in all cases, both ideal and real: the unfolded state is structurally featureless because the number of available conformers is large and the energy differences among them are small.

20.3.1 The Random Coil – Theory

Statistical descriptions are the natural way to characterize a large heterogeneous population, such as an ensemble of unfolded proteins. A few key ideas are mentioned here, but they are no substitute for the many excellent treatments of this subject [17, 18, 24, 32, 33].

The fundamental model is the freely jointed chain (or freely jointed random coil or random flight), a linear polymer of n adjoining links, each of fixed length, with complete freedom of rotation at every junction (Figure 20.2). From this definition, it follows that the angles at link junctions (i.e., bond angles) are completely uncorrelated. This model is completely general because it neglects chemical constraints, and therefore its scope is not restricted to any particular type of polymer chain. However, additional constraints such as chain thickness or hindered bond rotation can be added as appropriate, resulting in more specific models. What can be said about a polymer chain that is devoid of chemistry?

The freely jointed chain is equivalent to Brownian motion with a mean free path of fixed length, as described by Einstein-Smoluchowski theory [30]. The basic relationship governing both freely jointed chains and Brownian particles is:

$$\sqrt{\langle r^2 \rangle} = l\sqrt{n} \tag{1}$$

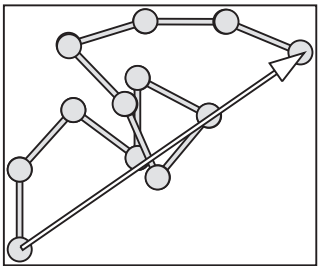

Fig. 20.2. A freely jointed chain. The chain is comprised of links, each of fixed length, l, with freedom of rotation at every junction. For a chain of n links, the vector from the beginning to the end, $\vec{r}_n$, (shown as the long arrow) is given by summing the links, $\vec{l}_i$: $\vec{r}_n = \sum_{i=1}^{n} \vec{l}_i$ and $|\vec{l}_i| = l$.

where $\sqrt{\langle r^2 \rangle}$ is the root-mean-square end-to-end distance (see Figure 20.2), l is the link length, and n is the number of links in the polymer. In other words, the distance between termini increases as the square root of the number of chain links: doubling the distance requires four times as many links.

The end-to-end distance measures the size of a polymer coil. Another such measure is the radius of gyration, R_G, the root-mean-square distance of link termini from their common center of gravity:

$$R_G^2 = \left[\frac{1}{n+1}\right] \sum_{i=0}^{n} R_{Gi}^2 \tag{2}$$

where R_{Gi} is the distance of link i from the center of gravity and n is the number of links in the polymer. According to a theorem of Lagrange in 1783, R_G can be rewritten in terms of the individual link vectors, r_{ij}, without explicit reference to the center of gravity ([33], appendix A).

$$R_G^2 = \frac{1}{2n^2} \sum_{i=1}^{N} \sum_{j=1}^{N} r_{ij}^2 \tag{3}$$

The two measures are related:

$$\langle R_G^2 \rangle = \frac{\langle r^2 \rangle}{6} \quad \text{as } n \to \infty \tag{4}$$

For a freely jointed chain, the values of such configurational measures are Gaussian distributed.

Of course, no real chain is freely jointed. The chemical bonds in real chains restrict motion; bond rotations are never random. Also, each link of a real chain occupies a finite volume, thereby reducing the free volume accessible to remaining links. Accordingly, ideal chains descriptions must be modified if they are to accommodate such real-world constraints.

A strategy for accommodating restricted bond motion is to depart from physical chain links and instead re-represent the chain as though it were comprised of longer, uncorrelated virtual links. The idea underlying this strategy is as follows: a short chain segment (e.g., a dipeptide) is somewhat rigid [70], but a sufficiently long segment is flexible. Therefore, the chain becomes flexible at some length between the dipeptide and the longer peptide. This leads to the idea of an effective segment, $l_{effective}$, also called a Kuhn segment, the length scale at which chain segments approach independent behavior and correlated orientations between them dwindle away. A chain of length L contains $L/l_{effective}$ Kuhn segments and can be approximated as a freely jointed chain of Kuhn segments:

$$\langle r^2 \rangle = l_{\text{effective}}^2 \frac{L}{l_{\text{effective}}} = l_{\text{effective}} L \tag{5}$$

A closely related idea is defined in terms of the chain's persistence length, the length scale over which correlations between bond angles "persist". In effect, the chain retains a "memory" of its direction at distances less than the persistence length. Stated less anthropomorphically, the energy needed to bend the chain through a 90° angle diminishes to $\sim kT/2$ at its persistence length, and thus ambient-temperature fluctuations can randomize the chain direction beyond this length. The size of a Kuhn segment is approximately two persistence lengths (i.e., directional correlations die away in either direction).

Current models strive to capture the properties of real chains with more detail than idealized, freely jointed chains can provide. For example, no actual chemical bond is a freely swiveling joint. To treat bond restrictions more realistically, Flory devised the rotational isomeric state approximation ([33], p. 55), in which bond angles are restricted to discrete values, chosen to correspond to known potential minima (e.g., gauche$^+$, gauche$^-$, and trans).

A real polymer chain cannot evade itself. Inescapably, the volume occupied by a chain element is excluded from occupancy by other chain elements. Otherwise, a steric clash would ensue: nonbonded atoms cannot occupy the same space at the same time. This excluded volume effect is substantial for proteins and results in a major departure from ideal chain dimensions (Eqs (1)–(4)).

As real polymers fluctuate, contracted coils have more opportunities to experience excluded volume steric clashes than expanded coils, perturbing the chain toward larger dimensions than those expected for ideal polymers.

Chain dimensions are also perturbed by the nature of the solvent. A good solvent promotes chain expansion by favoring chain:solvent interactions over chain:chain interactions. Conversely, a poor solvent promotes chain contraction by favoring chain:chain interactions over chain:solvent interactions. Flory introduced the idea of a Θ-solvent in which, on average, chain:chain interactions exactly counterbalance chain:solvent interactions, leading to unperturbed chain behavior. He pointed out that the notion of a Θ-solvent for a liquid is analogous to the Boyle point for a real gas, the temperature at which a pair of gas molecules follow an ideal isotherm because repulsion arising from volume exclusion is compensated exactly by mutual attraction ([33], p. 34).

Flory provided a simple relationship that relates the coil dimensions to solvent quality [33]. For a random coil polymer with excluded volume, the radius of gyration, R_G, is given by:

$$R_G = R_0 n^{\nu} \tag{6}$$

where R_0 is a constant that is a function of the chain's persistence length, n is the number of links, and ν is the scaling factor of interest that depends on solvent

quality. Values of ν range from 0.33 for a collapsed, spherical molecule in poor solvent through 0.5 at the Θ-point (Eq. (1)) to 0.6 in good solvent.

Protein molecules are amphipathic, and their interactions with solvent are complex. However, on balance, denaturing agents such as urea and guanidinum chloride can be considered good solvents. Using Eq. (6), the degree to which unfolded proteins are random coil polymers in denaturing solvents can assessed by measuring ν, the main topic of Section 20.3.2.

20.3.1.1 The Random Coil Model Prompts Three Questions

The random coil model set the stage for much of the contemporary theoretical work on unfolded proteins. A key question was brought into sharp focus by Levinthal [51]: if the random coil model holds, how can an unfolded protein discover its native conformation in biological real time? In particular, if unfolded protein molecules wander freely in a vast and featureless energy landscape, with barriers of order ~kT, then three related questions arise:

1. *The kinetic question*: How does a protein discover its native conformation in biological real time? If restricted solely to the two most populated regions for a dipeptide, a 100-residue backbone would have $2^{100} \cong 10^{30}$ conformers. With bond rotations of order 10^{-13} s, the mean waiting time en route to the native conformation would be prohibitive just for the backbone. In actuality, experimentally determined folding times range from milliseconds to seconds.
2. *The thermodynamic question*: How does a protein compensate for the large conformational entropy loss on folding? With $2^{100} \cong 10^{30}$ conformers, the entropic price required to populate a single conformation $\cong 30 \times R \ln(10) \cong 40$ kcal mol^{-1} at room temperature, a conservative estimate.
3. *The dynamic question*: How does a protein avoid meta-stable traps en route to its native conformation? An equivalent way of asking this question is: why do proteins have a unique native conformation instead of a Boltzmann-distributed ensemble of native conformations?

Many investigators have sought to provide answers to these questions. Two notable examples are mentioned here, though only in bare outline.

20.3.1.2 The Folding Funnel

Following earlier work of Frauenfelder et al. [2], who suggested an analogy between proteins and spin glasses, Wolynes and coworkers introduced the notion of a folding funnel [16] to describe the progress of a protein population that traverses its energy landscape en route to the folded state. The favorable-high-entropy, unfavorable-high-energy unfolded state is conceptualized as a wide funnel mouth, while the unfavorable-low-entropy, favorable-low-energy native state corresponds to a narrow funnel spout. According to this conception, sloping funnel walls guide the population downhill toward the folded state from any starting point, answering question 1. During this downhill trajectory, lost entropy is progressively compensated by favorable pairwise interactions, answering question 2. Finally, meta-stable

traps can be avoided if the funnel walls are sufficiently smooth [23], answering question 3. As a corollary, it is postulated that evolutionary pressures screen protein sequences, selecting those which can fold successfully in a funnel-like manner [94]. The folding funnel evokes a graphic portrait of folding dynamics and thermodynamics but is not intended to address specific structural questions, such as whether a region of interest will be helix or sheet.

20.3.1.3 Transition State Theory

Fersht and coworkers imported transition state theory from small molecule chemical reactions into protein folding [43]. Akin to the folding funnel, transition state kinetics focus on the entire population, with the transition state species pictured at the top of an energy barrier which separates U from N. But, unlike the folding funnel, only a few key residues comprise the organizational "tipping point", viz., those that participate in the transition state.

Questions 1–3 are not at issue for small molecule chemical reactions: (1) the mean waiting time for a reaction to occur depends upon a bond vibration, (2) after barrier crossing, the process is steeply downhill, and (3) intermediates between reactant and product are unstable because bond making/breaking energies are large. To the degree that the transition state approximation holds for protein folding [10], similar answers will obtain.

Transition state theory, expressed in the Eyring rate equation, transforms time-dependent kinetics into time-independent thermodynamics via an internal ticking clock: the rate of product formation depends upon the frequency of vibration of a critical bond. In contrast, no covalent bonds are made or broken in a folding reaction, and structure accretion is incremental and hierarchic en route from U to N [9, 10]. Not surprisingly then, the application of transition state theory to protein folding is complex [20].

Confidence in the application of the transition state approximation to protein folding comes from its success in describing simplified folding reactions [25] and the thermal unfolding of a β-hairpin [60]. However, recent work also illustrates the complexities. The transition state can be shifted dramatically without changing a protein's amino acid sequence [82, 100]. In simulations, the folding reaction can produce a broad ensemble of transition states instead of a single, well-defined species [50]. This blurring of the lines is further compounded by other work showing that the transition state resembles nearby folding intermediates [46] or is simply a distorted form of the native state [77].

20.3.1.4 Other Examples

The preceding examples illustrate how the random coil model has informed current thinking about unfolded proteins and the folding transition. The search for answers to the three questions has motivated other studies as well. In yet another example that focuses on question 3, Sali et al. [74, 75] analyzed the density of states in lattice simulations of folding and found a large energy gap – the e-gap – separating the native state (i.e., the ground state) from the nearest nonnative state (i.e., the 1st excited state). This finding rationalizes the predominance of the native state.

20.3.1.5 Implicit Assumptions from the Random Coil Model

Unfolded state models utilized in computer simulations often incorporate random coil assumptions implicitly. Four such assumptions are mentioned here.

1. The unfolded landscape is smooth. If the energy differences among sterically accessible backbone conformations are of order ~kT, the landscape will be devoid of kinetic traps and conformational bias. This assumption simplifies strategies for exploring the unfolded state in simulations.
2. The isolated-pair hypothesis is valid. Lattice models provide a way to count conformational alternatives explicitly, and they have been used extensively [18]. Most often, residues are represented as single lattice points (i.e., all residues are sterically equivalent on a lattice). Consequently, residue-specific steric restrictions beyond the dipeptide are either underweighted or ignored. This practice is valid to the degree that local steric repulsion does not extend beyond nearest chain neighbors, an assumption made explicit in Flory's isolated-pair hypothesis [33], which posits that each ϕ, ψ pair is sterically independent.
3. The Go approximation holds. A simplifying idea, introduced by Go [38], computes the energy of a conformation by rewarding native-like contacts while ignoring nonnative contacts, i.e., fortuitous nonnative contacts are not allowed to develop into kinetic traps. For simulations, this is a useful artifice that can be rationalized in a featureless landscape, where nonnative contacts dissolve as easily as they form.
4. Peptide backbone solvation is uniform. In other words, solvent water does not induce conformational bias in the unfolded state. If the interaction with water were energetically favored by some particular backbone conformation(s), then the unfolded landscape would be preferentially populated by these favored conformers, in violation of the featureless, random coil model.

These four assumptions are examined in Section 20.4.

20.3.2 The Random Coil – Experiment

Is a denatured protein aptly described as a random coil? It was Charles Tanford's experimental work that convinced the field. In numerous studies, Tanford demonstrated that proteins denatured in 6 M guanidinum chloride (GdmCl) have coil dimensions that obey simple scaling laws, consistent with random coil behavior. His masterful review of protein denaturation in *Advances in Protein Chemistry* [91, 92] is required reading for anyone interested in this topic.

In essence, the experimental strategy involves measuring coil dimensions for unfolded proteins in solution, fitting them to Eq. (6), and determining whether the scaling exponent, ν, is consistent with a random coil polymer with excluded volume in good solvent. The excluded volume can be obtained directly from any practical technique that depends upon the colligative properties of the polymer solu-

tion, such as osmotic pressure. Using such techniques, concentration-dependent deviations from ideality arising from solute:solvent interactions are measured. To extract the excluded volume, the chemical potential of the polymer solution is expanded as a power series in solute concentration – the virial expansion. For purely repulsive interactions, the molar excluded volume is given by the second virial coefficient [78]. As mentioned above, excluded volume increases chain dimensions, with ν ranging from 0.33 for a collapsed, spherical molecule in poor solvent through 0.5 at the Θ-point to 0.6 in good solvent.

Tanford documented many experimental pitfalls [91]. His investigations emphasized the importance of eliminating any potential residual structure in the unfolded protein by showing that the unfolding transition is complete. In fact, some residual structure is evident in heat-denatured proteins [3], but it can be eliminated in 6 M GdmCl. He also cautioned that the radius of gyration alone is an insufficient criterion for assessing random coil behavior, pointing out that a helical rod and a random polypeptide chain have similar values of R_G at chain lengths approximating those of ribonuclease and lysozyme.

20.3.2.1 Intrinsic Viscosity

In classic studies, Tanford used the intrinsic viscosity to determine coil dimensions. The intrinsic viscosity of a protein solution measures its effective hydrodynamic volume per gram in terms of the specific viscosity ([98], chapter 7). In particular, if η is the viscosity of the solution and η_0 is the viscosity of solvent alone, the specific viscosity, $\eta_{sp} = (\eta - \eta_0)/\eta_0$, is the fractional change in viscosity produced by adding solute. While η_{sp} is the quantity of interest, it is expressed in an experimentally inconvenient volume fraction concentration scale. This is remedied by converting to the intrinsic viscosity, $[\eta]$, which is η_{sp} normalized by the protein concentration, c, at infinite dilution: $[\eta] = \lim_{c \to 0}\left(\frac{\eta_{sp}}{c}\right)$. Specific viscosity is a pure number, so intrinsic viscosity has units of reciprocal concentration, milliliters per gram.

The intrinsic viscosity is not a viscosity per se but a viscosity increment owing to the volume fraction of solution occupied by the protein, like η_{sp}. It measures the hydrated protein volume, which will be much larger for randomly coiled molecules than for compactly folded ones; $[\eta]$ scales with chain length, n. The dependence of $[\eta]$ on n is conformation dependent, and Tanford took advantage of this fact. The relevant equation is:

$$[\eta] = Kn^{x} \tag{7}$$

where K is a constant that depends upon the molecular weight, but only slightly. Intrinsic viscosity is closely related to R_G, and Eqs (6) and (7) have a similar form. If unfolded proteins retain residual structure, each in their own way, the relation between $[\eta]$ and n is expected to be idiosyncratic. Conversely, a series of proteins that conform to Eq. (7) is indicative of random coil behavior.

In fact, for a series of 15 proteins denatured in GdmCl, a plot of $\log[\eta]$ vs. $\log n$ describes a straight line with slope 0.666, the exponent in Eq. (7) ([91], figure 6). The linearity of this series and the value of the exponent are strong evidence in favor of random coil behavior.

20.3.2.2 SAXS and SANS

Small angle X-ray scattering (SAXS) can be used to measure the radius of gyration, R_G, directly [58]. Molecules in a protein solution scatter radiation like tiny antennae ([99], chapter 7). In idealized situations, particles scatter independently (Rayleigh scattering), but significant interference occurs when intramolecular distances are of the same order as the wavelength of incident radiation, λ. This is the situation that obtains when proteins are irradiated with X-rays, and it is the basis for all experimental scattering techniques that yield R_G. In this case, the quantity of interest is $P(\theta)$, the ratio of measured intensity to the intensity expected for independent scattering by particles much smaller than λ, as a function of the scattering angle, θ. For a solution of scatterers,

$$P(\theta) = \frac{1}{n^2}\sum_{i=1}^{N}\sum_{j=1}^{N}\frac{\sinh r_{ij}}{hr_{ij}} \tag{8}$$

where n is the number of scattering centers, r_{ij} is the distance between any pair of centers i and j, and h is a function of the wavelength and scattering angle:

$$h = \frac{4\pi}{\lambda}\sin\frac{\theta}{2} \tag{9}$$

The double sum over all scattering centers is immediately reminiscent of Eq. (3), in which R_G is rewritten in terms of individual vectors, without explicit reference to their center of gravity. Van Holde et al. ([99], p. 321) show that

$$P(\theta) = \frac{1}{n^2}\sum_{i=1}^{N}\sum_{j=1}^{N}(1) - \frac{h^2}{6n^2}\sum_{i=1}^{N}\sum_{j=1}^{N}r_{ij}^2 \tag{10}$$

where the first term is unity and R_G is directly related to the double sum in the second term, as in Eq. (3).

Millett et al. used SAXS to determine R_G for a series of proteins under both denaturing and native conditions ([58], table I and fig. 4). Disulfide cross-links, if any, were reduced in the denatured species. Their experimentally determined values of R_G were fit to Eq. (6), giving values of $\nu = 0.61 \pm 0.03$ for the denatured proteins and $\nu = 0.38 \pm 0.05$ for their native counterparts (Figure 20.3). These values are remarkably close to those expected from theory, viz., $\nu = 0.6$ for a random coil with excluded volume in good solvent and $\nu = 0.33$ for a collapsed, spherical molecule in poor solvent.

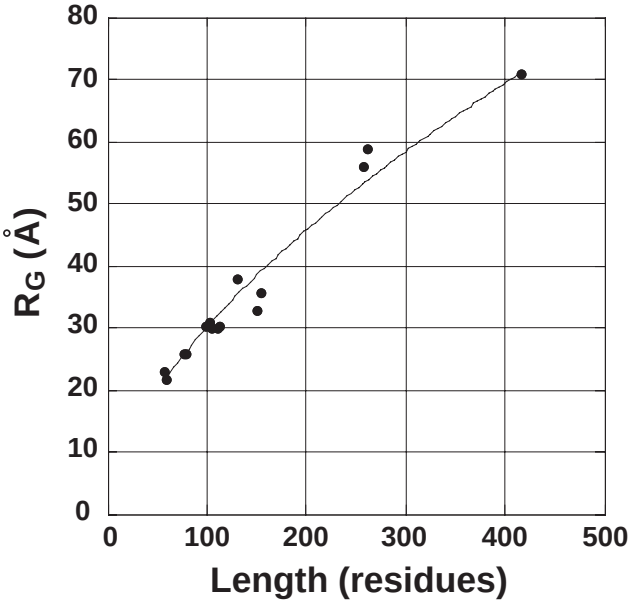

Fig. 20.3. The relationship between chain length and the radius of gyration, R_G, for a series of denatured proteins is well described by Eq. (6). Data points were taken from table 1 in [58], obtained using SAXS. The fitted curve has a value of $\nu = 0.61 \pm 0.03$, in close agreement with theory. This figure reproduces the one in Millett et al. ([58], fig. 4), but with omission of outliers.

The SAXS data provide the most compelling evidence to date in favor of the random coil model for denatured proteins.

20.4 Questions about the Random Coil Model

The random coil model would seem to be on firm ground at this point. However, recent work from both theory and experiment has raised new questions about the validity of the model – questions that provoke considerable controversy. Are they mere quibbles, or are they the prelude to a deeper understanding of the unfolded state?

Familiarity conditions intuition. At this point, the random coil model has conditioned our expectations for several decades. Should we be surprised that the dimensions of unfolded proteins are well described by a single exponent? Size matters here. As Al Holtzer once remarked, a steel I-beam behaves as a Gaussian coil if you make it long enough. But, at relevant length scales, the fact that proteins and polyvinyl behave similarly is quite unanticipated. After all, proteins adopt a unique folded state, whereas nonbiological polymers do not.

Flory emphasized this difference [33]: "Synthetic analogs of globular proteins are unknown. The capability of adopting a dense globular configuration stabilized by self-interactions and of transforming reversibly to the random coil are characteristics peculiar to the chain molecules of globular proteins alone" (p. 301).

The new questions center around the possibility of conformational bias and/or residual structure in unfolded proteins [11], even those unfolded in strong denaturing solvents like 6 M GdmCl [68]. We turn now to this discussion.

20.4.1 Questions from Theory

Superficially, the question of whether polypeptide chains are true random coils seems amenable to straightforward analysis by computer simulation. In principle, chains of n residues could be constructed, one at a time, using some plausible model (e.g., the Flory rotational isomeric model) to pick backbone dihedral angles. The coil dimensions and other characteristics of interest could then be analyzed by generating a suitable population of such chains. In practice, the excluded volume problem precludes this approach for chains longer than $\sim$20 residues, where the likelihood of encountering a steric clash increases sharply, killing off nascent chains before they can elongate. Naively, one might think that the problem can be solved by randomly adjusting offending residues until the clash is relieved, but this tactic biases the overall outcome. In fact, the only unbiased tactic is to rebuild the chain from scratch, resulting almost invariably in other clashes at new sites for chain lengths of interest. Such problems have thwarted attempts to analyze the unfolded population via simulation and modeling.

20.4.1.1 The Flory Isolated-pair Hypothesis

Nearly all theoretical treatments of the unfolded state assume that local steric repulsion does not extend beyond nearest chain neighbors. This simplifying assumption was made explicit in Flory's isolated-pair hypothesis ([33], p. 252), which posits that each ϕ, ψ pair is sterically independent of its neighbors.

Recently, the isolated-pair hypothesis was tested by exhaustive enumeration of all sterically accessible conformations of short polyalanyl chains [66]. To count, ϕ, ψ space was subdivided into a uniform grid. Every grid square, called a mesostate, encloses a $60^\circ \times 60^\circ$ range of ϕ, ψ values, with 36 mesostates in all. Each such mesostate was sampled extensively and at random to determine whether alanyl dipeptides with ϕ, ψ values in this range are sterically allowed. Only 14 mesostates are populated; the remaining 22 mesostates experience ubiquitous steric clashes throughout their entire range. Reconstruction of allowed ϕ, ψ space from mesostate sampling recreates the dipeptide map [70] and provides an acceptance ratio for each mesostate (Figure 20.4). The acceptance ratio, Λ_i, is the fraction of sterically allowed samples for mesostate i, ranging from 0 to 1.

These Λs were then used to test the isolated-pair hypothesis. Specifically, short polypeptide chains of length $n = 3 \ldots 7$ were tested by enumerating all possible strings over the 14 allowed mesostates and sampling them extensively. If the iso-

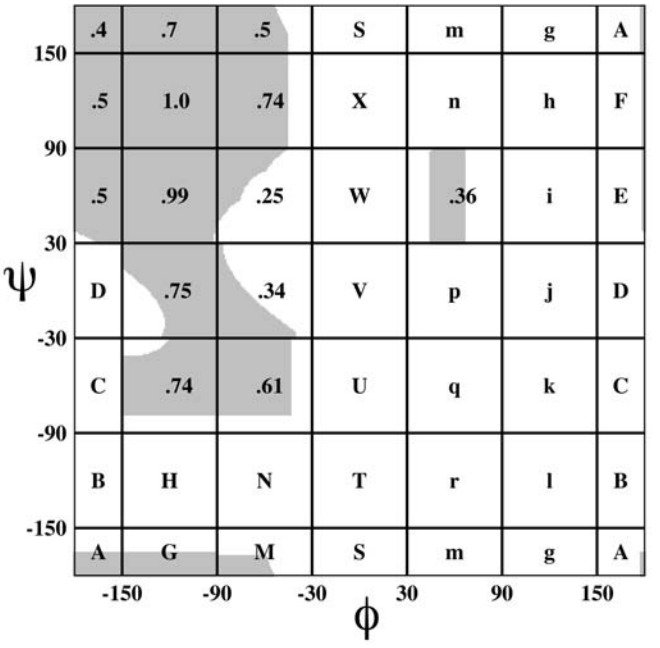

Fig. 20.4. Testing the Flory isolated-pair hypothesis. ϕ, ψ space for a dipeptide was subdivided into 36 alphabetically labeled coarse-grain grid squares, called mesostates. Treating the atoms as hard spheres, a Ramachandran plot (shown in gray) was computed by generating 150 000 randomly chosen ϕ, ψ conformations within each mesostate and testing for steric collisions [65]. Twenty-two meso-states have no allowed population; in each of these cases, every ϕ, ψ value results in a steric collision. In the 14 remaining mesostates, the fraction of sterically allowed samples, $0 < \Lambda_i \leq 1$, was determined, as shown.

lated-pair hypothesis holds, then ϕ, ψ angles in each mesostate are independent, and the fraction of sterically allowed conformers for each string is given by the product of individual acceptance ratios, $\prod_i^n \Lambda_i$. But, if there are steric clashes between nonnearest neighbors in the string, then $\Lambda_{\text{string}} < \prod_i^n \Lambda_i$, invalidating the hypothesis.

From this analysis, the isolated-pair hypothesis was found to be valid in the upper left quadrant of ϕ, ψ space but invalid in all other allowed regions. This finding makes sense physically: upon adopting ϕ, ψ values from the upper left quadrant, the chain is extended, like a β-strand, and nonnearest neighbors are separated. However, with ϕ, ψ values from any of the remaining five allowed mesostates (see Figure 20.4), the chain is contracted, like a helix or turn, and nonnearest neighbors are juxtaposed, enhancing opportunities for steric interference.

The failure of the isolated-pair hypothesis for short peptides ($n = 7$) challenges the random coil model, possibly in a major way. Steric restrictions obtain in the

folded and unfolded states alike. The failure of the hypothesis for contracted chains implies that such conformers will be reduced selectively in the unfolded state, resulting in a population that is more extended than random coil expectations. Structurally, this shift in the population will result in a more homogeneous ensemble of unfolded conformers, and thermodynamically, it will reduce the entropy loss accompanying folding. But is it significant?

Studies of van Gunsteren et al. [97] and Sosnick and his colleagues [104] concur that the size of conformational space that can be accessed by unfolded molecules is restricted in peptides. However, Ohkubo and Brooks [63] argue that restrictions become rapidly insignificant as chain lengths grow beyond $n \cong 7$, with negligible consequences for the random coil model.

In an inventive approach to the problem, Goldenberg simulated populations of protein-sized chains [39] by adapting a standard software package that generates three-dimensional models from NMR-derived distance constraints. He analyzed the resultant unfolded state population using several measures, including coil dimensions, and found them to be well described as random coils. A note of caution is in order, however, because a substantial fraction of the conformers generated by this method fall within sterically restricted regions of ϕ, ψ space ([39], table 1).

20.4.1.2 Structure vs. Energy Duality

Often, the complex interplay between structure and energy has confounded simulations. Small changes in structure can give rise to large changes in energy, and conversely. From a structural point of view, two conformers are distinguishable when their ϕ, ψ angles differ. From a thermodynamic point of view, two conformers are indistinguishable when they can interconvert via a spontaneous fluctuation.

This structure–energy duality has contributed confusion to the Levinthal paradox (Section 20.3.1.1) and many related size estimates of the unfolded population because a single energy basin can span multiple conformers. For example, most sterically accessible conformers of short polyalanyl chains in good solvent [66] are quite extended, as expected in the absence of stabilizing intramolecular interactions. The ϕ, ψ values for these conformers are densely distributed over a broad region in the upper left quadrant of the ϕ, ψ map, as shown in Figure 20.5. When energy differences among these structures are calculated using a simple soft-sphere potential, the population partitions largely into two distinct energy basins, one that includes β-strands and another that includes polyproline II helices [65]. All conformers within each basin can interconvert spontaneously at room temperature (i.e., $\Delta A_{i,j} \leq RT$ at 300 K, where $\Delta A_{i,j}$ is the Helmholtz free energy difference between any two conformers, i and j, R is the universal gas constant and T the temperature in Kelvin). Thus, apparent structural diversity is reduced to two thermodynamically homogeneous populations.

20.4.1.3 The "Rediscovery" of Polyproline II Conformation

More than three decades ago, Tiffany and Krimm proposed that disordered peptides are comprised of left-handed polyproline II (P_{II}) helical segments inter-

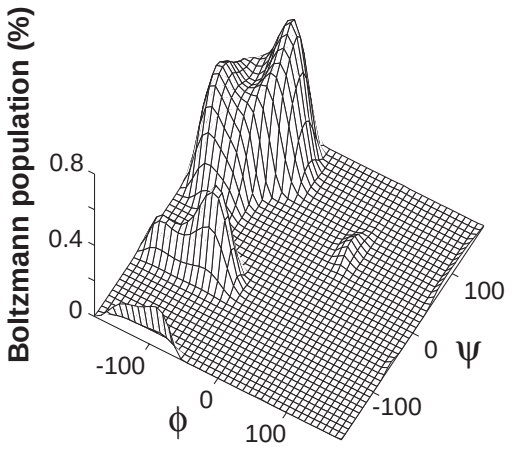

Fig. 20.5. A single energy basin can span multiple conformers. Most sterically accessible conformers of short polyalanyl chains in good solvent are extended. Using a soft-sphere potential, the Boltzmann-weighted population for the alanyl dipeptide is predominantly in the upper left quadrant of ϕ, ψ space and partitions into two distinct energy basins, one that includes polyproline II helices (larger) and another that includes β-strands (smaller) [65]. At 300 K, conformers with each basin interconvert spontaneously.

spersed with bends [95, 96]. They were led to this prescient proposal by the similarity between the optical spectra of P_{II} helices and nonprolyl homopolymers. Even earlier, Schellman and Schellman had already argued that the spectrum of unfolded proteins was unlikely to be that of a true random coil [79]. Following these early studies, the ensuing literature disclosed a noticeable similarity between the spectra of P_{II} and unfolded proteins, but such suggestive hints failed to provoke widespread interest – until recently. See Shi et al. for a thorough review [84].

The designation "polyproline" can be misleading. The circular dichroism (CD) spectrum, characteristic of actual polyproline or collagen peptides, has a pronounced negative band near 200 nm and a positive band near 220 nm. However, similar spectra can be obtained from peptides that are neither "poly" [54] nor proline-containing [96].

The P_{II} conformation is a left-handed helix with three residues per turn ($\phi, \psi \cong -75°, +145°$), resulting in three parallel columns spaced uniformly around the long axis of the helix. This helix has no intrasegment hydrogen bonds, and, in solution, significant fluctuations from the idealized structure are to be expected. The P_{II} conformation is forced by sterics in a polyproline sequence, but it is adopted readily by proline-free sequences as well [21].

Only three repetitive backbone structures are sterically accessible in proteins: α-helix, β-strand and P_{II}-helix [70]. In the folded population, α-helices and β-strands are abundant, whereas P_{II}-helices are rare. More specifically, isolated residues with P_{II} ϕ, ψ values are common in the non-α, non-β regions, accounting for approximately one-third of the remaining residues, but longer runs of consecutive residues with P_{II} ϕ, ψ-values are infrequent [90].

This finding can be rationalized by the fact that P_{II}-helices cannot participate in hydrogen bonds in globular proteins. Hydrogen bonds are eliminated because the spatial orientation of backbone donors and acceptors is incompatible with both intrasegment hydrogen bonding within P_{II}-helices and regular extra-segment hydrogen bonding between P_{II} helices and the three repetitive backbone structures. Upon folding, those backbone polar groups deprived of hydrogen-bonded solvent access can make compensatory hydrogen bonds in α-helices and strands of β-sheet, but not in P_{II}-helices.

Recent work by Creamer and coworkers focused renewed attention on P_{II} [21, 73, 90], raising the question of whether fluctuating P_{II} conformation might contribute substantially to the unfolded population in proteins [96]. Studies performed during the past few years lend support to this idea, as described next.

20.4.1.4 P_{II} in Unfolded Peptides and Proteins

The blocked peptide, *N*-acetylalanine-*N′*-methylamide, is a popular backbone model. Many groups have found P_{II} to be an energetically preferred conformation for this peptide in water [1, 26, 40, 41, 44, 69]. Does this finding hold for longer chains?

Again using alanine as a model, Pappu and Rose analyzed the conformational preferences of longer blocked polyalanyl chains, *N*-acetyl-Ala_n-*N′*-methylamide ($n \leq 7$) [65]. To capture nonspecific solvent effects, they minimized chain:chain interactions, mimicking the chain's expected behavior in good solvent. At physiological temperature, only three energy basins were needed to span ~75% of the population, and within each basin, the population of structures was homogeneous. Notably, the basin corresponding to P_{II} structure was dominant.

Pappu and Rose [65] used soft-sphere repulsion (the repulsive term in a Lennard-Jones potential) to calculate energy. More extensive testing using detailed force fields was performed by Sosnick and coworkers [104].

It is often assumed that the backbone is solvated uniformly in the unfolded state and that the energy of solvent stripping upon folding is not a significant consideration. This assumption follows directly from the random coil model, in which unfolded conformers are readily interconvertible. However, if unfolded state conformers exhibit conformational biases, it becomes important to question this assumption. Is solvation free energy conformation dependent?

A series of papers by Avbelj and Baldwin [4–6] offered a fresh perspective on this issue, motivated by an inconsistency between the measured energy of peptide hydrogen bond formation [81] and the corresponding energy derived from a simple thermodynamic cycle [8]. Specifically, their analysis uncovered a large enthalpy deficit (-7.6 kcal mol^{-1}) upon helix formation that could not be reconciled with data from typical model compounds, such as acetamide derivatives [6]. One or more terms had to be missing.

Avbelj and Baldwin's work prompted a re-examination of peptide solvation in proteins by a number of groups, including themselves [4–6]. Of particular interest are a series of unrelated simulations [4–6, 25, 35, 47, 57, 104], all of which reach a

common conclusion: water interacts preferentially with P_{II} peptides, imparting a previously unsuspected conformational bias.

In sum, both peptide:solvent interactions and peptide:peptide interactions [65] favor P_{II} conformers. In the former case, water is simply a better solvent for P_{II} than for other conformers, e.g., β-strands and α-helices. In the latter case, P_{II} affords the chain greater entropic freedom (i.e., more "wiggle room").

20.4.2 Questions from Experiment

Early NMR studies provided evidence for residual structure in the denatured state of both proteins [36, 61] and peptides excised from proteins [28]. However, the structured regions seen in proteins were not extensive. Furthermore, most isolated peptides lacked structure, and the few exceptions did not always retain the conformation adopted in the native protein [27].

Peptide studies tell a similar story. A prime example involves the assessment of autonomous stability in the α-helix. Early evidence indicated that the cooperative unit for stable helix formation is $\sim$100 residues [105], a length that exceeds the average protein helix ($\sim$12 residues) by almost an order of magnitude. Consequently, the prevailing view in the 1970s was that protein-sized helical peptides would be random coils in isolation. This view was reversed in the 1980s, after Bierzynski et al. [12], expanding upon earlier work by Brown and Klee [15], demonstrated helix formation in water at near-physiological temperature for residues 1–13 of ribonuclease, a cyanogen bromide cleavage product. This finding prompted a re-evaluation of helix propensities in peptides [53, 56, 62, 64] and motivated numerous biophysical studies of peptides [80]. Summarizing this large body of work, there is evidence for structure in some short peptides in aqueous solvent at physiological temperature, but it is marginal at best and, more often, undetectable altogether.

20.4.2.1 Residual Structure in Denatured Proteins and Peptides

The limited success of these early attempts to detect residual structure strengthened the conviction that denaturation abolishes structure and reinforced the notion that the unfolded state is a random coil. Consequently, the field was stunned when Shortle and Ackerman [85] demonstrated the persistence of native-like structure in staphylococcal nuclease under strongly denaturing conditions (8 M urea). Shortle and Ackerman's finding was based on evidence from residual dipolar couplings in oriented gels. However, their interpretation that these data provide evidence of global organization was questioned recently by Annila and coworkers [52]. The ultimate conclusions from such work are still unclear, but the perspective has definitely changed and many recent experiments now find evidence for substantial residual structure in the denatured state (e.g., [22, 34, 46, 76, 88, 102]).

In a similar vein, Shi et al. reanalyzed a blocked peptide containing seven consecutive alanine residues for the presence of residual structure [83]. This peptide

is too short to form a stable α-helix and should therefore be a random coil. Contrary to this expectation, the peptide is largely in P_{II} conformation, in agreement with predictions from theory [65]. While not all residues are expected to favor the P_{II} conformation [73], this result shows that the unfolded state is predominantly a single conformer, at least in the case of polyalanine.

20.4.3 The Reconciliation Problem

The measured radii of gyration, R_G, of denatured proteins have values [58] that are consistent with those expected for a random coil with excluded volume in good solvent (Section 20.3.2.2). Yet, experimental evidence in both proteins [85] and peptides [83] suggests the presence of residual structure in the unfolded population. How are these seemingly contradictory findings to be reconciled? Millett et al. refer to this as the reconciliation problem ([58], see their discussion, p. 257).

Paradox is often a prelude to perception. Equation (6), in its generality, necessarily neglects the chemical details of any particular polymer type. Accordingly, the resultant chain description is insensitive to short-range order, apart from the proportionality constant R_0, which is a function of the persistence length (Section 20.3.1). Sterically induced local order, encapsulated in R_0, is surely present in unfolded proteins [31, 66], but can it rationalize the apparent contradiction between random coil R_G values and global residual structure [85]? One possible explanation is that multiple regions of local structure dominate the ensemble average to such an extent that they are interpreted as global organization [52, 103].

The coil library may provide a useful clue to the resolution of this puzzle. The coil library is the collection of all nonrepetitive elements in proteins of known structure, that fraction of native structure which remains after α-helix and β-sheet are removed. Given that the library is composed of fragments extracted from solved structures, it is surely not "coil" in the polymer sense. However, the term "coil library" is intended to convey the hypothesis that such fragments do, in fact, represent the full collection of accessible chain conformers in unfolded proteins [87]. Taken to its logical conclusion, this hypothesis posits that the coil library is a collection of structured fragments in folded proteins and, at the same time, a collection of unstructured fragments in unfolded proteins. If so, this library, together with α-helix, β-strand, and P_{II} helix, represents an explicit enumeration of accessible conformers from which the unfolded ensemble might be reconstructed [5].

At this writing, the reconciliation problem remains an ongoing question. Regardless of the eventual outcome, this paradox appears to be moving the field in an informative direction.

20.4.4 Organization in the Unfolded State – the Entropic Conjecture

Are there general principles that lead to organization in the unfolded state? If accessible conformational space is vast and undifferentiated, the entropic cost of

populating the native basin exclusively will be large. However, if the unfolded state is largely restricted to a few basins, with nonuniform, sequence-dependent basin preferences, then entropy can function as a chain organizer.

Consider two thermodynamic basins, i and j. The Boltzmann-weighted ratio of their populations, n_i/n_j, is given by $(w_i/w_j)e^{-\beta\Delta U}$, where n_i and n_j designate the number of conformers in i and j, w_i and w_j are the degeneracies of state, β is the Boltzmann factor, and ΔU is the energy difference between the two basins. Both entropy and enthalpy contribute to this ratio. If w_i and w_j are conformational biases (i.e., the number of isoenergetic ways the chain can adopt conformations i and j), and w_i/w_j is the dominant term in the Boltzmann ratio, the entropy difference, $\Delta S_{conf} = R\ln(w_i/w_j)$, would promote organization in the unfolded population.

In particular, if P_{II} is a dominant conformation in polyalanyl peptides, then it is also likely to be favored in unfolded proteins, in which case the unfolded state is not as heterogeneous as previously believed. The usual estimate of about five accessible states per residue in an unfolded protein is based on a familiar argument: the free energy difference between the folded and unfolded populations, ΔG_{conf}, is a small difference between large value of ΔH_{conf} and $T\Delta S_{conf}$ [13, 14]. If $\Delta G_{conf} \cong -10$ kcal mol^{-1} (a typical value) and $\Delta H_{conf} \cong 100$ kcal mol^{-1}, then the counterbalancing $T\Delta S_{conf}$ is also $\sim$100 kcal mol^{-1}. Then $\Delta S_{conf} \cong 3.33$ entropy units per residue for a 100-residue protein at 300 K. Assuming $\Delta S_{conf} = R\ln W$, the number of states per residue, W, is 5.34.

However, instead of a reduction in the number of distinct states, this entropy loss on folding could result from a reduction in the degeneracy of a single state, providing the ϕ, ψ space of occupied regions in the unfolded population is further constricted upon folding. For example, a residue in P_{II} is within a room-temperature fluctuation of any sterically allowed ϕ, ψ value in the upper left quadrant of the dipeptide map ([57], table 1). Consequently, different ϕ, ψ values from these regions would be thermodynamically indistinguishable and therefore not distinct states at all. As a back-of-the-envelope approximation, consider a residue that can visit any allowed region of the upper left quadrant in the unfolded state. Upon folding, let this residue be constrained to lie within $\pm 30^\circ$ of ideal β-sheet ϕ, ψ values. The reduction in ϕ, ψ space would be a factor of 5.58, approximating the value attributed to distinct states. Similar, but less approximate, estimates can be obtained when the unfolded populations are Boltzmann weighted.

What physical factors might underwrite such entropy effects?

20.4.4.1 **Steric Restrictions beyond the Dipeptide**

It has long been believed that local steric restrictions do not extend beyond the dipeptide boundary [70], but, on re-analysis, this conviction requires revision [11, 66, 89] (see Section 20.4.1.1). In fact, systematic steric restrictions operate over chain regions of several adjacent residues, and they serve to promote organization in unfolded protein chains. Two recent lines of investigation focus on identifying the physical basis for longer range, sterically induced ordering.

In a series of remarkable papers, Banavar, Maritan and their colleagues show

that chain thickness alone imposes stringent, previously unrecognized restrictions on conformational space [7, 42, 55]. All the familiar secondary structure motifs emerge automatically when the protein is represented as a self-avoiding tube, coaxial with the main chain, and a single inequality is imposed on all triples of Cα atoms [7, 55]. The further addition of simple hydrogen bond and hydrophobic terms is sufficient to generate the common super-secondary structures [42]. These straightforward geometric considerations demonstrate that sequence-independent steric constraints predispose proteins toward their native repertoire of secondary and super-secondary structural motifs.

Investigating the atomic basis for longer range steric restrictions, Fitzkee and Rose found that a direct transition from an α-helix to a β-strand causes an unavoidable steric collision between backbone atoms [31]. Specifically, a nonnearest neighbor collision occurs between the carbonyl oxygens of an α-residue at position i ($O^{\alpha}{}_{i}$) and a β-residue at position i + 3 ($O^{\beta}{}_{i+3}$). This restriction also holds for the transition from α-helix to P_{II}. These simple steric constraints have pervasive organizational consequences for unfolded proteins because they eliminate all structural hybrids of the form . . . ααββ . . . and . . . αααP_{II} . . . , pushing the unfolded population toward pure segments of α, β, and P_{II} interconnected by irregular regions such as those found in the coil library.

20.5 Future Directions

The early analysis of steric restrictions in the alanyl dipeptide (more precisely, the compound Cα-CO-NH–CαHR–CO-NH-Cα, which has two degrees of backbone freedom like a dipeptide) by Ramachandran et al. [71] has become one of those rare times in biochemistry where theory is deemed sufficient to validate experiment [49]. The fact that the dipeptide map is based only on ''hard sphere'' repulsion alone led some to underestimate the generality of this work, but not Richards, who commented [72]:

> ***For chemically bonded atoms the distribution is not spherically symmetric nor are the properties of such atoms isotropic. In spite of all this, the use of the hard sphere model has a venerable history and an enviable record in explaining a variety of different observable properties. As applied specifically to proteins, the work of G. N. Ramachandran and his colleagues has provided much of our present thinking about permissible peptide chain conformations.***

The notion that repulsive interactions promote macromolecular organization is not limited to the alanyl dipeptide. Space-filling models [48], which represent each atom literally as a hard sphere, were central to Pauling's successful model of the α-helix [67] and have widespread application throughout chemistry. Much of

the theory of liquids is based on the organizing influence of repulsion interactions [19].

Despite such successes, the existence of sterically induced chain organization has had little influence on models of the unfolded state owing to the strongly held conviction that local steric restrictions extend no further than adjacent chain neighbors. Of course, long-range excluded volume effects do affect the population [18, 32], as reflected in the exponent of Eq. (6), but they are not thought to play any role in biasing unfolded proteins toward specific conformations. Given the finding of local steric restrictions beyond the dipeptide (Section 20.4.4.1), it is time to re-analyze the problem.

Re-analysis will involve at least three steps: (1) analysis of local steric restrictions beyond the dipeptide, (2) characterization of elements in the coil library, and (3) combination of the results from these two steps. To the extent that useful insights emerge from this prescription, the folding problem may not be as intractable as previously thought.

Acknowledgments

We thank Buzz Baldwin, Nicholas Fitzkee, Haipeng Gong, Nicholas Panasik, Kevin Plaxco, and Timothy Street for stimulating discussion and The Mathers Foundation for support.

References

1 Anderson, A. G., and Hermans, J. 1988. Microfolding: conformational probability map for the alanine dipeptide in water from molecular dynamics simulations. *Proteins* **3**, 262–265.

2 Ansari, A., Berendzen, J., Bowne, S. F., Frauenfelder, H., Iben, I. E., Sauke, T. B., Shyamsunder, E., and Young, R. D. 1985. Protein states and proteinquakes. *Proc. Natl Acad. Sci. USA* **82**, 5000–5004.

3 Aune, K. C., Salahuddin, A., Zarlengo, M. H., and Tanford, C. 1967. *J. Biol. Chem.* **242**, 4486–4489.

4 Avbelj, F. and Baldwin, R. L. 2002. Role of backbone solvation in determining thermodynamic beta propensities of the amino acids. *Proc. Natl Acad. Sci. USA* **99**, 1309–1313.

5 Avbelj, F. and Baldwin, R. L. 2003. Role of backbone solvation and electrostatics in generating preferred peptide backbone conformations: Distributions of phi. *Proc. Natl Acad. Sci. USA* **100**, 5742–5747.

6 Avbelj, F., Luo, P., and Baldwin, R. L. 2000. Energetics of the interaction between water and the helical peptide group and its role in determining helix propensities. *Proc. Natl Acad. Sci. USA* **97**, 10786–10791.

7 Banavar, J., Maritan, A., Micheletti, C., and Trovato, A. 2002. Geometry and physics of proteins. *Proteins* **47**, 315–322.

8 Baldwin, R. L. 2003. In search of the energetic role of peptide hydrogen bonds. *J. Biol. Chem.* **278**, 17581–17588.

9 Baldwin, R. L. and Rose, G. D. 1999a. Is protein folding hierarchic? I. Local structure and peptide folding. *Trends Biochem. Sci.* **24**, 26–33.

10 Baldwin, R. L. and Rose, G. D.

1999b. Is protein folding hierarchic? II. Folding intermediates and transition states. *Trends Biochem. Sci.* **24**, 77–83.

11 Baldwin, R. L. and Zimm, B. H. 2000. Are denatured proteins ever random coils? *Proc. Natl Acad. Sci. USA* **97**, 12391–12392.

12 Bierzynski, A., Kim, P. S., and Baldwin, R. L. 1982. A salt-bridge stabilizes the helix formed by isolated C-peptide of RNase A. *Proc. Natl Acad. Sci. USA* **79**, 2470–2474.

13 Brandts, J. F. 1964a. The thermodynamics of protein denaturation. I. The denaturation of chymotrypsinogen. *J. Am. Chem. Soc.* **86**, 4291–4301.

14 Brandts, J. F. 1964b. The thermodynamics of protein denaturation. II. A model of reversible denaturation and interpretations regarding the stability of chymotrypsinogen. *J. Am. Chem. Soc.* **86**, 4302–4314.

15 Brown, J. E. and Klee, W. A. 1971. Helix-coil transition of the isolated amino terminus of ribonuclease. *Biochemistry* **10**, 470–476.

16 Bryngelson, J. D., Onuchic, J. N., Socci, N. D., and Wolynes, P. G. 1995. Funnels, pathways and the energy landscape of protein folding-a synthesis. *Proteins Struct. Funct. Genet.* **21**, 167–195.

17 Cantor, C. R. and Schimmel, P. R. 1980. *Biophysical Chemistry.* Part III: *The Behavior of Biological Macromolecules.* Freeman, New York.

18 Chan, H. S. and Dill, K. A. 1991. Polymer principles in protein structure and stability. *Annu. Rev. Biophys. Chem.* **20**, 447–490.

19 Chandler, D., Weeks, J. D., and Andersen, H. C. 1983. The van der Waals picture of liquids, solids and phase transformations. *Science* **220**, 787–794.

20 Ciepiak, M. and Hoang, T. X. 2003. Universality classes in folding times of proteins. *Biophys. J.* **84**, 475–488.

21 Creamer, T. P. 1998. Left-handed polyproline II helix formation is (very) locally driven. *Proteins* **33**, 218–226.

22 Daggett, V., Li, A., Itzhaki, L. S., Otzen, D. E., and Fersht, A. R. 1996. Structure of the transition state for folding of a protein derived from experiment and simulation. *J. Mol. Biol.* **257**, 430–440.

23 Dill, K. A. and Chan, H. S. 1997. From Levinthal to pathways to funnels. *Nat. Struct. Biol.* **4**, 10–19.

24 Dill, K. A. and Shortle, D. 1991. Denatured states of proteins. *Annu. Rev. Biochem.* **60**, 795–825.

25 Doyle, R., Simons, K., Qian, H., and Baker, D. 1997. *Proteins Struct. Funct. Genet.* **29**, 282–291.

26 Drozdov, A. N., Grossfield, A., and Pappu, R. V. 2004. The role of solvent in determining conformational preferences of alanine dipeptide in water. *J. Am. Chem. Soc.* **126**, 2574–2581.

27 Dyson, H. J., Rance, M., Houghten, R. A., Lerner, R. A., and Wright, P. E. 1988. Folding of immunogenic peptide fragments of proteins in water solution. I. Sequence requirements for the formation of a reverse turn. *J. Mol. Biol.* **201**, 161–200.

28 Dyson, H. J., Sayre, J. R., Merutka, G., Shin, H. C., Lerner, R. A., and Wright, P. E. 1992. Folding of peptide fragments comprising the complete sequence of proteins. Models for initiation of protein folding II. Plastocyanin. *J. Mol. Biol.* **226**, 819–835.

29 Edsall, J. T. 1995. Hsien Wu and the first theory of protein denaturation (1931). In *Advances in Protein Chemistry* (eds D. S. Eisenberg, and F. M. Richards), pp. 1–26. Academic Press, San Diego.

30 Einstein, A. 1956. *Investigations on the Theory of Brownian Movement.* Dover Publications, New York.

31 Fitzkee, N. C. and Rose, G. D. 2004. Steric restrictions in protein folding: an α-helix cannot be followed by a contiguous β-strand. *Protein Sci.* **13**, 633–639.

32 Flory, P. J. 1953. *Principles of Polymer Chemistry.* Cornell University Press, New York.

33 Flory, P. J. 1969. *Statistical Mechanics of Chain Molecules.* Wiley, New York.

34 Garcia, P., Serrano, L., Durand, D., Rico, M., and Bruix, M. 2001. NMR and SAXS characterization of the denatured state of the chemotactic protein CheY: implications for protein folding initiation. *Protein Science* **10**, 1100–1112.

35 Garcia, A. E. 2004. Characterization of non-alpha helical conformations in Ala peptides. *Polymer* **45**, 669–676.

36 Garvey, E. P., Swank, J., and Matthews, C. R. 1989. A hydrophobic cluster forms early in the folding of dihydrofolate reductase. *Proteins Struct. Funct. Genet.* **6**, 259–266.

37 Ginsburg, A. and Carroll, W. R. 1965. Some specific ion effects on the conformation and thermal stability of ribonuclease. *Biochemistry* **4**, 2159–2174.

38 Go, N. 1984. The consistency principle in protein structure and pathways of folding. *Adv. Biophys.* **18**, 149–164.

39 Goldenberg, D. P. 2003. Computational simulation of the statistidal properties of unfolded proteins. *J. Mol. Biol.* **326**, 1615–1633.

40 Grant, J. A., Williams, R. L., and Scheraga, H. A. 1990. Ab initio self-consistent field and potential-dependent partial equalization of orbital electronegativity calculations of hydration properties of N-acetyl-N′-methyl-alanineamide. *Biopolymers* **30**, 929–949.

41 Han, W.-G., Jalkanen, K. J., Elstner, M., and Suhai, S. 1998. Theoretical study of aqueous N-acetyl-L-alanine N′-methylamide: structures and raman, VCD and ROA spectra. *J. Phys. Chem. B* **102**, 2587–2602.

42 Hoang, T. X., Trovato, A., Seno, F., Banavar, J., and Maritan, A. 2004. What determines the native state folds of proteins? submitted.

43 Itzhaki, L. S., Otzen, D. E., and Fersht, A. R. 1995. The structure of the transition state for folding of chymotrypsin inhibitor 2 analysed by protein engineering methods: evidence for a nucleation-condensation mechanism for protein folding. *J. Mol. Biol.* **254**, 260–288.

44 Jalkanen, K. J. and Suhai, S. 1996. N-Acetyl-L-Alanine N′-methylamide: a density functional analysis of the vibrational absorption and birational circular dichroism spectra. *Chem. Phys.* **208**, 81–116.

45 Kauzmann, W. 1959. Some factors in the interpretation of protein denaturation. *Adv. Protein Chem.* **14**, 1–63.

46 Kazmirski, S. L., Wong, K. B., Freund, S. M. V., Tan, Y. J., Fersht, A. R., and Daggett, V. 2001. Protein folding from a highly disordered denatured state: the folding pathway of chymotrypsin inhibitor 2 at atomic resolution. *Proc. Natl Acad. Sci. USA* **98**, 4349–4354.

47 Kentsis, A., Gindin, T., Mezei, M., and Osman, R. 2004. Unfolded state of polyalanine is a segmented polyproline II helix. Proteins **55**, 493–501.

48 Koltun, W. L. 1965. Precision space-filling atomic models. *Biopolymers* **3**, 665–679.

49 Laskowski, R. A., MacArthur, M. W., Moss, D. S., and Thornton, J. M. 1993. PROCHECK: a program to check the stereochemical quality of protein structures. *J. Appl. Cryst.* **26**, 283–291.

50 Lazaridis, T. and Karplus, M. 1997. *Science* **278**, 1928–1931.

51 Levinthal, C. 1969. How to fold graciously. Mossbauer spectroscopy in Biological Systems, Proceedings. *University of Illinois Bull.* **41**, 22–24.

52 Louhivuori, M., Paakkonen, K., Fredriksson, K., Permi, P., Lounila, J., and Annila, A. 2003. On the origin of residual dipolar couplings from denatured proteins. *J. Am. Chem. Soc.* **125**, 15647–15650.

53 Lyu, P. C., Liff, M. I., Marky, L. A., and Kallenbach, N. R. 1990. Side chain contributions to the stability of alpha-helical structure in peptides. *Science* **250**, 669–673.

54 Madison, V. and Schellman, J. A. 1970. Diamide model for the optical activity of collagen and polyproline I and II. *Biopolymers* **9**, 65–94.

55 Maritan, A., Micheletti, C., Trovato, A., and Banavar, J. 2000.

Optimal shapes of compact strings. *Nature* **406**, 287–290.

56 Merutka, G., Lipton, W., Shalongo, W., Park, S. H., and Stellwagen, E. 1990. Effect of central-residue replacements on the helical stability of a monomeric peptide. *Biochemistry* **29**, 7511–7515.

57 Mezei, M., Fleming, P. J., Srinivasan, R., and Rose, G. D. 2004. Polyproline II helix is the preferred conformation for unfolded polyalaine in water. *Proteins* **55**, 502–507.

58 Millett, I. S., Doniach, S., and Plaxco, K. W. 2002. Toward a taxonomy of the denatured state: small angle scattering studies of unfolded proteins. *Adv. Protein Chem.* **62**, 241–262.

59 Mirsky, A. E. and Pauling, L. 1936. On the structure of native, denatured, and coagulated proteins. *Proc. Natl Acad. Sci. USA* **22**, 439–447.

60 Munoz, V., Thompson, P. A., Hofrichter, J., and Eaton, W. A. 1997. *Nature* **390**, 196–199.

61 Neri, D., Billeter, M., Wider, G., and Wuthricht, K. 1992. NMR determination of residual structure in a urea-denatured protein, the 434-repressor. *Science* **257**, 1559–1563.

62 O'Neil, K. T. and DeGrado, W. F. 1990. A thermodynamic scale for the helix-forming tendencies of the commonly occurring amino acids. *Science* **250**, 646–651.

63 Ohkubo, Y. Z. and Brooks, C. L. 2003. Exploring Flory's isolated-pair hypothesis: statistical mechanics of helix-coil transitions in polyalanine and C-peptide from RNase A. *Proc. Natl Acad. Sci. USA* **100**, 13916–13921.

64 Padmanabhan, S., Marqusee, S., Ridgeway, T., Laue, T. M., and Baldwin, R. L. 1990. Relative helix-forming tendencies of nonpolar amino acids. *Nature* **344**, 268–270.

65 Pappu, R. V. and Rose, G. D. 2002. A simple model for polyproline II structure in unfolded states of alanine-based peptides. *Protein Sci.* **11**, 2437–2455.

66 Pappu, R. V., Srinivasan, R., and Rose, G. D. 2000. The flory isolated-pair hypothesis is not valid for polypeptide chains: implications for protein folding. *Proc. Natl Acad. Sci. USA* **97**, 12565–12570.

67 Pauling, L., Corey, R. B., and Branson, H. R. 1951. The structures of proteins: two hydrogen-bonded helical configurations of the polypeptide chain. *Proc. Natl Acad. Sci. USA* **37**, 205–210.

68 Plaxco, K. W. and Gross, M. 2001. Unfolded, yes, but random? Never! *Nat. Struct. Biol.* **8**, 659–660.

69 Poon, C.-D. and Samulski, E. T. 2000. Do bridging water molecules dictate the structure of a model dipeptide in aqueous solution? *J. Am. Chem. Soc.* **122**, 5642–5643.

70 Ramachandran, G. N. and Sasisekharan, V. 1968. Conformation of polypeptides and proteins. *Adv. Protein Chem.* **23**, 283–438.

71 Ramachandran, G. N., Ramakrishnan, C., and Sasisekharan, V. 1963. Stereochemistry of polypeptide chain configurations. *J. Mol. Biol.* **7**, 95–99.

72 Richards, F. M. 1977. Areas, volumes, packing, and protein structure. *Annu. Rev. Biophys. Bioeng.* **6**, 151–176.

73 Rucker, A. L., Pager, C. T., Campbell, M. N., Qualls, J. E., and Creamer, T. P. 2003. Host-guest scale of left-handed polyproline II helix formation. *Proteins* **53**, 68–75.

74 Sali, A., Shakhnovich, E., and Karplus, M. 1994a. Kinetics of protein folding – a lattice model study of the requirements for folding to the native state. *J. Mol. Biol.* **5**, 1614–1636.

75 Sali, A., Shakhnovich, E. I., and Karplus, M. 1994b. How does a protein fold? *Nature* **477**, 248–251.

76 Sanchez, I. E., and Kiefhaber, T. 2003. Origin of Unusual ϕ-values in protein folding: evidence against specific nucleation sites. *J. Mol. Biol.* **334**, 1077–1085.

77 Sanchez, I. E. and Kiefhaber, T. 2003. Origin of unusual ϕ-values in protein folding: evidence against specific nucleation sites. *J. Mol. Biol.* **334**, 1077–1085.

78 Schellman, J. A. 2002. Fifty years of solvent denaturation. *Biophys. Chem.* **96**, 91–101.

79 Schellman, J. A. and Schellman, C. G. 1964. In *The Proteins: Composition, Structure and Function*, 2nd edn, Vol 2, pp. 1–37. Academic Press, New York.

80 Scholtz, J. M. and Baldwin, R. L. 1992. The mechanism of alpha-helix formation by peptides. *Annu. Rev. Biophys. Biomol. Struct.* **21**, 95–118.

81 Scholtz, J. M., Marqusee, S., Baldwin, R. L., York, E. J., Stewart, J. M., Santoro, M., and Bolen, D. W. 1991. Calorimetric determination of the enthalpy change for the alpha-helix to coil transition of an alanine peptide in water. *Proc. Natl Acad. Sci. USA* **88**, 2854–2858.

82 Shastry, M. C. and Udgaonkar, J. B. 1995. The folding mechanism of barstar: evidence for multiple pathways and multiple intermediates. *J. Mol. Biol.* **247**, 1013–1027.

83 Shi, Z., Olson, C. A., Rose, G. D., Baldwin, R. L., and Kallenbach, N. R. 2002a. Polyproline II structure in a sequence of seven alanine residues. *Proc. Natl Acad. Sci. USA* **2002**, 9190–9195.

84 Shi, Z., Woody, R. W., and Kallenbach, N. R. 2002b. Is polyproline II a major backbone conformation in unfolded proteins? *Adv. Protein Chem.* **62**, 163–240.

85 Shortle, D. and Ackerman, M. 2001. Persistence of native-like topology in a denatured protein in 8 M urea. *Science* **293**, 487–489.

86 Simpson, R. B. and Kauzmann, W. 1953. The kinetics of protein denaturation. *J. Am. Chem. Soc.* **75**, 5139–5192.

87 Smith, L. J., Bolin, K. A., Schwalbe, H., MacArthur, M. W., Thornton, J. M., and Dobson, C. M. 1996. Analysis of main chain torsion angles in proteins: prediction of NMR coupling constants for native and random coil conformations. *J. Mol. Biol.* **255**, 494–506.

88 Sridevi, K., Lakshmikanth, G. S., Krishnamoorthy, G., and Udgaonkar, J. B. 2004. Increasing stability reduces conformational heterogeneity in a protein folding intermediate ensemble. *J. Mol. Biol.* **337**, 669–711.

89 Srinivasan, R. and Rose, G. D. 1999. A physical basis for protein secondary structure. *Proc. Natl Acad. Sci. USA* **96**, 14258–14263.

90 Stapley, B. J. and Creamer, T. P. 1999. A survery of left-handed polyproline II helices. *Protein Sci.* **8**, 587–595.

91 Tanford, C. 1968. Protein denaturation. *Adv. Protein Chem.* **23**, 121–282.

92 Tanford, C. 1970. Protein denaturation. Part C. Theoretical models for the mechanism of denaturation. *Adv. Protein Chem.* **24**, 1–95.

93 Tanford, C., Pain, R. H., and Otchin, N. S. 1966. Equilibrium and kinetics of the unfolding of lysozyme (muramidase) by guanidine hydrochloride. *J. Mol. Biol.* **15**, 489–504.

94 Tiana, G., Broglia, R. A., and Shakhnovich, E. I. 2000. Hiking in the energy landscape in sequence space: a bumpy road to good folders. *Proteins* **39**, 244–251.

95 Tiffany, M. L. and Krimm, S. 1968a. *Biopolymers* **6**, 1767–1770.

96 Tiffany, M. L. and Krimm, S. 1968b. New chain conformations of poly(glutamic acid) and polylysine. *Biopolymers* **6**, 1379–1382.

97 van Gunsteren, W. F., Bürgi, R., Peter, C., and Daura, X. 2001. The key to solving the protein-folding problem lies in an accurate description of the denatured state. *Angew. Chem. Int. Ed.* **40**, 351–355.

98 van Holde, K. E. 1971. *Physical Biochemistry.* Prentice-Hall, Englewood Cliffs, NJ.

99 van Holde, K. E., Johnson, W. C., and Ho, P. S. 1998. *Physical Biochemistry.* Prentice-Hall, Upper Saddle River, NJ.

100 Viguera, A. R., Serrano, L., and Wilmanns, M. 1996. Different folding transition states may result in the same native structure. *Nat. Struct. Biol.* **3**, 874–880.

101 Wu, H. 1931. Studies on denaturation of proteins. XIII. A theory of denaturation. *Chin. J. Physiol.* **V**, 321–344.

102 Yi, Q., Scalley-Kim, M. L., Alm, E. J., and Baker, D. 2000. NMR characterization of residual structure in the denatured state of protein L. *J. Mol. Biol.* **299**, 1341–1351.

103 Zagrovic, B., Snow, C. Khaliq, S., Shirts, M., and Pande, V. 2002. Native-like mean structure in the unfolded ensemble of small proteins. *J. Mol. Biol.* **323**, 153–164.

104 Zaman, M. H., Shen, M. Y., Berry, R. S., Freed, K. F., and Sosnick, T. R. 2003. Investigations into sequence and conformational dependence of backbone entropy, inter-basin dynamics and the Flory isolated-pair hypothesis for peptides. *J. Mol. Biol.* **331**, 693–711.

105 Zimm, B. H. and Bragg, J. K. 1959. Theory of the phase transition between helix and random coil in polypeptide chains. *J. Chem. Phys.* **31**, 526–535.

21
Conformation and Dynamics of Nonnative States of Proteins studied by NMR Spectroscopy

Julia Wirmer, Christian Schlörb, and Harald Schwalbe

21.1
Introduction

21.1.1
Structural Diversity of Polypeptide Chains

From a structural point of view, protein folding is one of the most fascinating aspects in structural biology. Protein folding proceeds from the disordered random coil polypeptide chain defined by its primary sequence to intermediates with increasing degree of conformational and dynamic order to the final native state of the protein (Figure 21.1). While the starting point of protein folding, probably best described as a statistical coil, but often called the random coil state of a protein, can be defined as a state in which few if any nonlocal interactions exist, the native state can be described by one predominant conformation around which only local fluctuations of low amplitude occur. Order exists and forms on various levels of the protein structure, the primary structure describing the conformational preferences of the amino acid residues differs from secondary structure elements, which are defined by the conformations adopted by consecutive residues to the final arrangement of secondary structure elements in the three-dimensional fold of the protein.

During folding, the polypeptide chain therefore adopts very different conformations and its interaction with the surrounding solvent changes considerably. This variability in conformational space of a polypeptide chain has become even more interesting with the observation of protein misfolding revealing that proteins can also adopt highly ordered, oligomeric states, so-called fibrillic states of proteins, in which residues adopt repetitive conformations very different to the native fold and in which hydrogen bonding is satisfied in an intermolecular fashion. In addition, the conformational equilibria between the various states of a protein are influenced by interactions with chaperones in the cell. The given sequence of a protein therefore can adopt a continuum of different conformational states and degrees of oligomerization, those states interconvert at different rates and therefore vary widely in persistency (Figure 21.1).

Protein Folding Handbook. Part I. Edited by J. Buchner and T. Kiefhaber

ISBN: 3-527-30784-2

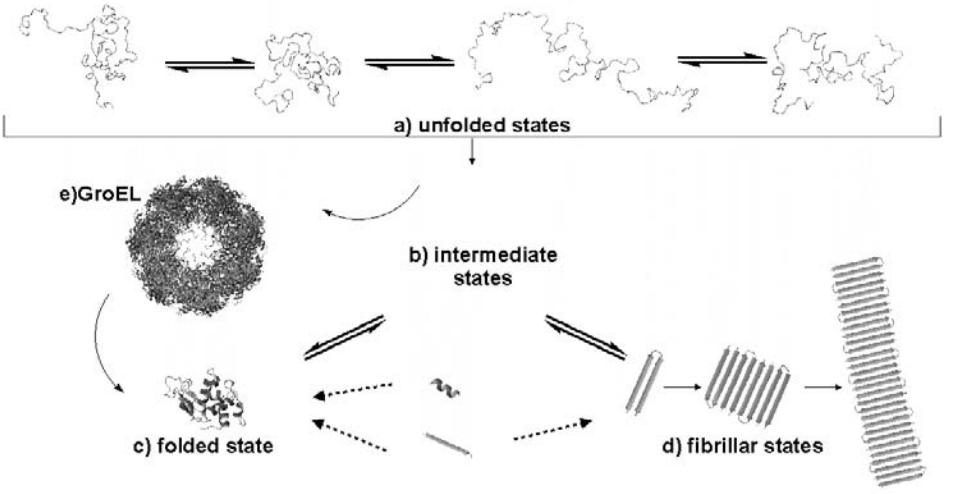

Fig. 21.1. The different conformations adopted by a polypeptide chain can range from the native, often monomeric state (c), in which a single conformation exists and which is build up from secondary structure elements and their specific arrangements, to the ensemble of conformers representing the random coil state of a protein (a). The individual members of this ensemble have widely different compaction, dynamics, local and nonlocal conformations. Protein folding preceeds via formation of folding intermediates (b) whose structure and dynamics may be modulated by protein-protein interactions with molecular chaperones such as GroEL (e) shown in the figure. At the other extreme of conformational states, proteins can aggregate and form oligomeric states called fibrils (d). Liquid and solid state NMR spectroscopy can provide detailed information on structure and dynamics in all of these states.

Spectroscopic techniques to study protein folding are reviewed in Chapter 2. NMR spectroscopy, applied to proteins both in their liquid and solid state, is intrinsically capable of characterizing the variety of conformations and dynamics associated with the polypeptide chain in different states with high precision. In contrast to the native state of proteins, many nonnative states of proteins are ensembles of interconverting conformers. Often, the averaging proceeds locally, e.g., by changes in torsion angles which are rapid (faster than microseconds) on the NMR time scale and lead to sharp NMR signals. In such cases, we will talk in the following of the ''random coil state'' of a protein. However, averaging can also involve the reorganization of preformed secondary structure elements which is considerably slower. In fact, from an NMR point of view, the observation of line broadening and the absence of detectable NMR signals indicative for a persistent tertiary fold serves as the definition of a ''molten globule state'' of a protein. NMR is also capable to study the kinetics of protein folding in real time as discussed in Chapter 16.

For nonnative states of proteins, the NMR observables do not directly define conformation and dynamics in these states. Rather, the experimental observables have to be interpreted in the light of models describing conformational averaging, in which the number of participating conformational states and the rate of their interconversion are the two most important parameters. Such models range from theoretical predictions of the properties of the polypeptide chain to extensive molecular

dynamics simulations. They are being developed to aid the interpretation of NMR parameters such as chemical shifts δ, spin–spin coupling constants J, homonuclear NOE data (NOEs), residual dipolar couplings (RDCs) and heteronuclear relaxation properties such as relaxation rates (^{15}N-R$_1$, ^{15}N-R$_2$) and heteronuclear NOEs ($\{^1$H$\}$-^{15}N-NOE).

21.1.2 Intrinsically Unstructured and Natively Unfolded Proteins

Nonnative states of proteins have also received attention recently because of the observation that an axiomatic linking of the function of a protein to persistent fold might not be general but a number of proteins have been identified that lack intrinsic globular structure in their normal functional form [1–3]. The expression ''intrinsically unstructured'' and ''natively unfolded'' are used synonymously, the latter being coined by Schweers et al. in 1994 in the context of structural studies of the protein tau [4]. Intrinsically unstructured proteins are extremely flexible, noncompact, and reveal little if any secondary structure under physiological conditions. In 2000, the list of natively unfolded protein comprised 100 entries [5] (see Table 21.1b). Natively unfolded proteins are implied in the development of a number of neurodegenerative diseases including Alzheimer's disease (deposition of amyloid-β, tau-protein, a-synuclein), Down's syndrome, and Parkinson disease to name a few (quoted after Ref. [5]). They are predicted to be ubiquituous in the proteome [6, 7] and algorithms available as a web-program (http://dis.embl.de/) have been developed to predict protein disorder [8]. According to the predictions, 35–51% of eukaryotic proteins have at least one long ($>$ 50 residues) disordered region and 11% of proteins in Swiss-Prot and between 6 and 17% of proteins encoded by various genomes are probably fully disordered (quoted from Ref. [6]). Proteins predicted to be intrinsically unstructured show low compositional complexity. These regions sometimes correspond to repetitive structural units in fibrillar proteins. Therefore, it seems likely that the unstructureness of the polypeptide chains in some states of a protein plays an important role in the development of fibrillar states and this further supports the importance for detailed structural and dynamic investigations of nonnative states of proteins. Chapter 8 in Part II is dedicated to the discussion of natively disordered proteins, and Chapter 33 in Part II discusses protein folding diseases.

It has also been noted by Gerstein that the average genomically encoded protein is significantly different in terms of size and amino acid composition from folded proteins in the PDB [9]. This difference would indicate that the structures deposited in the PDB are not random and in turn that they cannot be taken as representative for the entire structural diversity of polypeptide chains.

In this article, we discuss NMR investigations, primarily of nonnative states of proteins based on our investigations in the past using lysozyme and its mutants as well as α-lactalbumin and ubiquitin as model proteins. A number of excellent review articles have been published reporting on the topic of NMR investigations of nonnative states of proteins (see, for example, Refs [10–14]). In order to understand and determine unambiguously those parts of the polypeptide chain in which

residual structural elements are present, it is necessary to have a firm understanding of the NMR data to be expected for a random coil state of a protein that lacks any nonlocal structural elements and/or does not reveal sequence-specific differences in dynamics. Therefore, we interpret our data in the framework of a so-called random coil model (Section 21.4). According to this model, the random coil state is assumed to be a state in which there are no nonlocal interactions along the peptide chain, which is built up from the linear sequence of its repetition units, the amino acids. Different amino residues, embedded in their local sequence context, adopt different local conformations and their specific ϕ, ψ distributions have been extracted from residues in coil regions of native proteins to make theoretical predictions of NMR parameters for a random coil. According to this model, the dynamics of the polypeptide chain can be predicted using simple models treating the polypeptide as a branched or unbranched polypeptide chain. Comparisons of experimental NMR parameters with such predictions reveal regions in which residual conformational preferences and dynamic restrictions exist in the random coil state of a protein.

21.2 Prerequisites: NMR Resonance Assignment

For any detailed investigation of the conformation and dynamics of nonnative states of proteins at atomic resolution, the NMR resonances of the amino acids need to be assigned. For a long time, such investigation were considered impossible due to the very low chemical shift dispersion observed in ^{1}H-NMR experiments for nonnative states of proteins different to the native state (Figure 21.2).

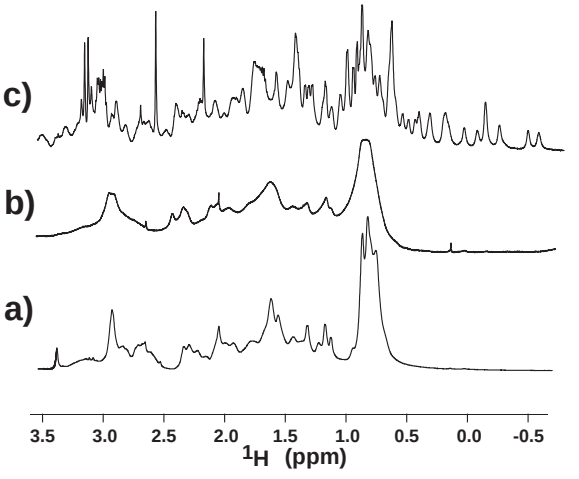

Fig. 21.2. One-dimensional ^{1}H-NMR experiments showing the differences in chemical shift dispersion and linewidth for different states accessible for the protein α-lactalbumin, a protein with 123 amino acid residues and four native disulfide bridges. They range from the random coil state (a) with sharp NMR resonance lines to the molten globule state (b) with extensive line broadening to the native state with well resolved peaks at least for some atomic groups (c).

In addition, while the random coil state of α-lactalbumin obtained by dissolving the protein in high concentrations of denaturant (8 M urea at pH 2) yields very sharp NMR resonances (Figure 21.2a), the molten globule state of α-lactalbumin at pH 2 reveals only an NMR spectra with very broad peaks (Figure 21.2b). The chemical shift dispersion in either of the two states is very limited and the signature of tertiary fold in the native state of the protein, visible in the appearance of upfield shifted methyl groups resonating at ppm values at or below 0.5 ppm is missing (Figure 21.2c).

One approach to overcome the substantial overlap problem observed for nonnative states of proteins was to dissect the protein of interest into smaller peptide fragments (see, for example, Refs [15–17]). These approaches also allowed delineation of those regions of the polypeptide chain that preserves local elements of structure.

Due to introduction of isotope labels and heteronuclear NMR experiments, the low chemical shift dispersion can be overcome in $^{1}H,^{15}N$ heteronuclear correlation experiments [18] and the modern sequential assignment procedures developed for native proteins by Bax and coworkers [19, 20] can be successfully applied also for the random coil state of proteins [21] (Figure 21.3). The addition of ^{13}C isotope labeling does, however, not provide additional resolution (Figure 21.4).

The surprising observation of relative high chemical shift resolution in the $^{1}H,^{15}N$ heteronuclear correlation can be predicted based on the analysis of chemi-

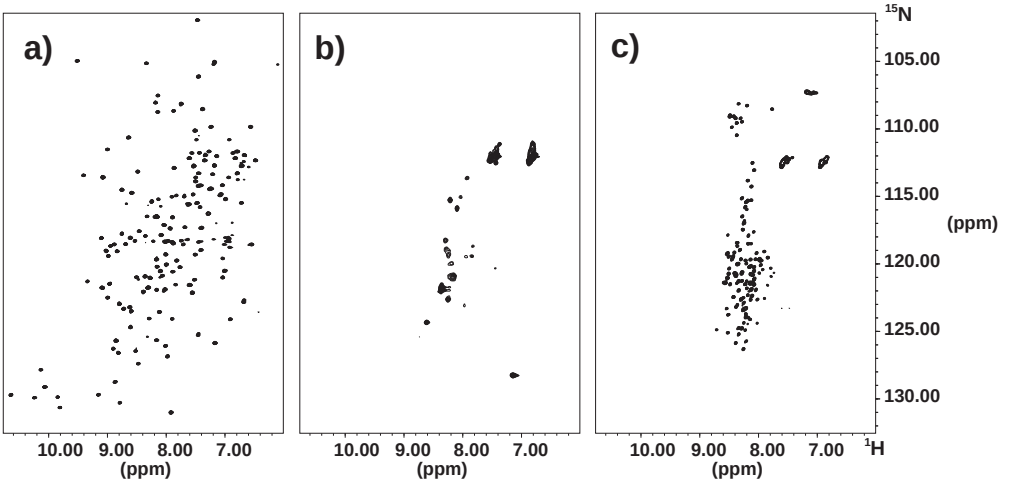

Fig. 21.3. Two-dimensional $^{1}H,^{15}N$-NMR correlation experiments showing the differences in chemical shift dispersion for different states accessible for the protein α-lactalbumin, a protein with 123 amino acid residues and four native disulfide bridges. For the random coil state of the protein (c), the resonances cluster in three regions in the spectra, largely reflecting the characteristic ^{15}N chemical shifts of the different types of amino acids when in unfolded conformations. For comparison, the similar spectrum for the native protein is also shown (a). At pH 2, the protein forms a molten globule state and the spectrum shows only very few peaks, while the other peaks are unobservable due to considerable line broadening (b).

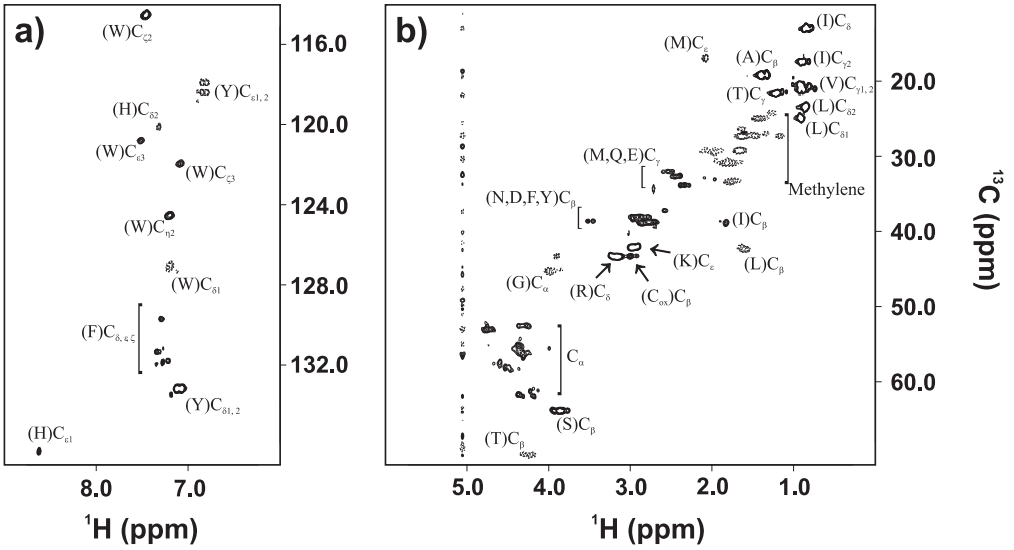

Fig. 21.4. Two-dimensional $^{1}H,^{13}C$-NMR correlation experiment of hen egg white lysozyme denatured in 8 M urea at pH 2. The chemical shift resolution in $^{1}H,^{13}C$ correlation is considerable lower than the $^{1}H,^{15}N$-NMR correlation experiment. a) Aromatic carbon region, and b) aliphatic carbon region. Distinct regions of ^{13}C resonances have been labeled with the one-letter amino acid code. The chemical shifts of the ^{13}C resonances are very similar to literature values for linear denatured hexapeptides [37].

Tab. 21.1a. Representive set of proteins that were investigated using heteronuclear NMR spectroscopy in their nonnative state.

Protein	*References*
α-Lactalbumin	39, 137, 138
Apomyoglobin	99, 139–143
Barnase	144–148
Beta(2)-microglobulin	149, 150
Bovine acyl-coenzyme A binding protein	151, 152
Bovine *β*-lactoglobulin	153–157
Chemotactic protein CheY	158
drkN SH3 domain	159–175
FK506 binding protein	21, 176
Glutaredoxin 3	177
Hen lysozyme	25, 42, 107, 126, 129, 178–186
HIV-1 protease tethered dimmer	187, 188
OmpX (outer membrane protein X)	189
Protein L	98
Reduced high-potential iron-sulfur protein	190
Ubiquitin	51, 138, 191–195

Tab. 21.1b. Representive set of natively unfolded proteins that were investigated using heteronuclear NMR spectroscopy in their nonnative state.

Protein	*References*
4E-binding proteins I and II	94
Anti-sigma factor FlgM	95
Antitermination protein N	96
CITED2 (CBP/p300-interacting transactivator with ED-rich tail)	97
Colicin translocation domain	98, 99
Cyclin-dependent kinase inhibitor $p21^{Waf1/Cip1/Sdi1}$	100
Dessication-related protein	101
eIF4G1, functional domain (393–490)	102
Engrailed homeodomain	103
Extracellular domain of beta-dystroglycan	104
Fibronectin-binding domain, D-type, *S. aureus*	105, 106
GCN4, DNA-binding domain	107
Heat shock transcription factor, N-terminal activation domain (*K. lactic* and *S. cerevisiae*)	108
IA3 (aspartic proteinase inhibitor)	109
Negative factor, NEF protein	110
Neutral zinc finger factor 1, two-domain fragment (487–606)	111
Nonhistone chromosomal protein HMG-14	112
Nonhistone chromosomal protein HMG-17	113
Nonhistone chromosomal protein HMG-H6	114
Nonhistone chromosomal protein HMG-T	112
N-terminal domain of p53	115
N-terminal regions of securin and cyclin B	116
Osteocalcin	117
PIR domain of Grb14	118
Prion protein N-terminal part	119, 120
Propeptide of subtilisin	121
Prothymosin α	122
Snc1, cytoplasmic domain	123
Staphylococcal nuclease (SNase), Δ131Δ fragment	58, 124–132
Synaptobrevin cytoplasmic domain	133
TAF_{II}-230_{11-77}, N-terminal region	134
β-Tubulin, 394–445 fragment	135

Tab. 21.1c. Representive examples of peptides studied in fibrillic states heteronuclear solid state NMR spectroscopy.

Protein	*References*
Alzheimer's amyloid peptids, β-amyloid	136–140
Transthyretin	141

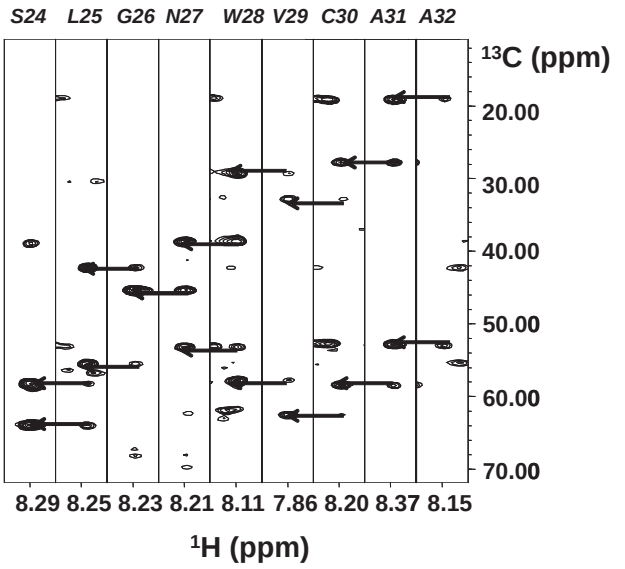

Fig. 21.5. (ω_1, ω_3) strips from the HNCACB experiment of cysteine reduced and methylated lysozyme with the N-terminal additional methionine, a nonnative state of lysozyme in H_2O and at pH 2, taken at the $^1H^N$ (ω_3) and ^{15}N (ω_1) frequencies of Ser24, Leu25, Gly26, Asn27, Trp28, Val29, Cys30, Ala31, and Ala32 (the additional methionine residue is labeled M_{-1} to keep the numbering of lysozyme). Intra- and interresidual correlation peaks are marked and clearly visible.

cal shift in protein structures [22] and from quantum chemical calculations [23]. Resonance assignment following this procedure have been reported for a number of different proteins as summarized in Table 21.1a. Table 21.1b gives an overview of natively unfolded proteins for which lack of structure has been identified by NMR spectroscopy. Table 21.1c summarizes solid state NMR investigations of fibrillar states of peptides.

Figure 21.5 shows the parts of three-dimensional spectra for hen egg white lysozyme for which sequential assignment is shown for a stretch of neighboring residues. The resonance assignment for random coil states of proteins with sharp resonance lines is straightforward provided the amino acid sequence is nonrepetitive.

21.3 NMR Parameters

In Section 21.3, the most important NMR parameters summarized in Table 21.2 will be introduced with an emphasis on the relevant aspects in the context of conformational averaging observed in nonnative states of proteins. It is important to stress here that in contrast to native proteins, the dependence of the measurable

Tab. 21.2. Overview of NMR parameters and their conformational dependence.

NMR parameter	*Conformational dependence*
Chemical shift δ (ppm)	Multiple torsion angles: $\phi, \varphi, \omega, \chi_1$
^{n}J couplings (Hz)	Single torsion angles via Karplus equations
Homonuclear NOEs (a.u.)	Distances, dependence on correlation time and motional properties
Heteronuclear relaxation (Hz)	Motional properties, dependence on τ_c, S^2, τ_e
Residual dipolar couplings (RDC) (Hz)	Overall shape, dynamics, S
H/D	exchangeable H^N
Diffusion	Radius of hydration (R_h)
Photo-CIDNP	Accessible Trp, Tyr, His

NMR parameters on conformation and dynamics for nonnative states of proteins is more complicated and requires additional models to predict the random coil NMR spectra. One successful approach to circumvent this problem is to investigate model peptides that should have no preferred conformation and define their properties such as chemical shifts, coupling constants, hydrogen exchange rates (Table 21.2) and such like as the ''random coil'' value. However, as discussed below, such an approach fails when one predicts NMR observables such as relaxation effects or residual dipolar couplings that show a pronounced dependence on the length of the polypeptide chain. These latter NMR parameters rely on anisotropic interactions and are different for segments of amino acids embedded in a short peptide or in a long polypeptide chain.

A different approach is to predict, using models from polymer theory and distinct torsion angle distributions, for example, the appearance of NMR spectra for the random coil state of a protein. These predictions provide a framework for the interpretation of NMR parameters such as NOEs and J coupling constants [24, 25] or residual dipolar couplings [26] (see Section 21.4).

21.3.1 Chemical Shifts δ

21.3.1.1 Conformational Dependence of Chemical Shifts

Chemical shifts δ depend on the chemical environment of the observed nuclei. Hence, the chemical shifts depend on how and to which degree (parts of) the polypeptide chains are folded. Generally, nonnative states of proteins show a considerably smaller chemical shift dispersion than proteins in their native states (see Figures 21.2a–c and 21.3a–c); NMR active nuclei (^{1}H, ^{13}C, ^{15}N) resonate close to or at their random coil chemical shift because of conformational averaging. For an ideal random coil polypeptide chain, NMR spectra are similar to the spectra of the mixture of the amino acids [27]. supporting the idea of the absence of any nonlocal interactions in the random coil state. The local amino acid sequence particularly affects the random coil chemical shifts of the $^{15}N^H$, $^1H^N$ and ^{13}CO resonances

[28]. Secondary and tertiary structures contribute to the observed chemical shifts and therefore can be investigated by analysis of the chemical shifts [29]. Deviations from random coil chemical shifts are also called secondary chemical shifts and are indicative for the content of residual structures in unfolded or partially folded proteins. An overall averaging over the deviations from random coil chemical shifts gives an impression of the extent of residual structure in denatured states of proteins.

Proper referencing of the chemical shifts to standard substances like DSS (2,2-dimethyl-2-silapentane-5-sulfonic acid) or TSP (3-(trimethylsilyl) propionate) is required for the comparison of experimental spectra to random coil chemical shifts from the literature [30, 31]. In general, the dispersion of the $^{15}N^{H}$, $^{1}H^{N}$, and ^{13}CO resonances in unfolded proteins is much greater than for the $^{13}C\alpha$, $^{13}C\beta$, $^{1}H\alpha$, and $^{1}H\beta$ resonances, reflecting the sensitivity of the former nuclei to the nature of the neighboring amino acids in the primary sequence of the protein [32]. Both $^{13}C\alpha$ and ^{13}CO chemical shifts are shifted downfield when they are in α-helical structures and upfield, when they are located in β-sheets, while $^{13}C\beta$ and $^{1}H\alpha$ resonances experience upfield shifts in α-helices and downfield shifts in β-structures [30, 31, 33].

So-called chemical shift index (CSI) calculations [33] can routinely be used to detect secondary structure elements in proteins. In this method, chemical shift deviations are normalized to 1, 0, and -1, depending on the extent and direction of the deviation, and then plotted against the residues of the protein sequence. The result of this is a topology plot of the protein from which one easily can spot α-helical structures and β-sheet regions, which differ in the direction of the secondary chemical shifts.

21.3.1.2 Interpretation of Chemical Shifts in the Presence of Conformational Averaging

In nonnative states of proteins we observe conformational averaging (e.g., between different rotameric states). Each rotameric state has a characteristic chemical shift which in a dynamic case will be averaged. However, the NMR signal is influenced by the averaging process both in terms of its resonance position and the observed linewidth (Figure 21.6).

In the case of fast conformational averaging (Figure 21.6c), the observed chemical shift is the population weighted average:

$$\delta^{\mathrm{obs}} = \sum_i p_i \delta^i \tag{1}$$

where δ^{obs} is the observed chemical shift, δ^i is the chemical shift in the ith conformation with weights p_i and $\sum_i p_i = 1$. The increase in linewidth at half height $\Delta\Gamma_{1/2}$ due to fast exchange between two site equally populated is given by:

$$\Delta\Gamma_{1/2} = \frac{\pi(\delta\nu)^2}{2k} \tag{2}$$

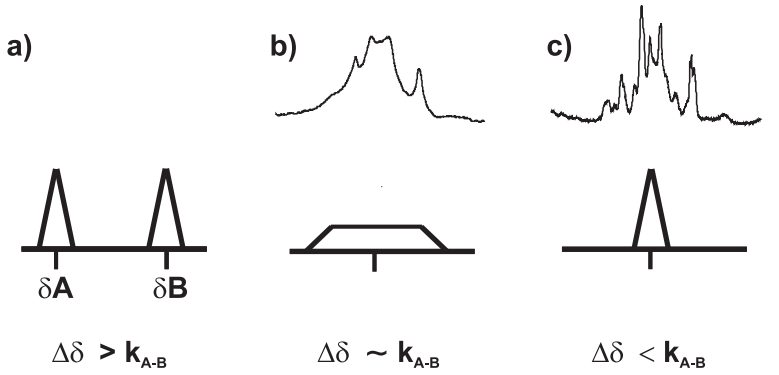

Fig. 21.6. Schematic picture indicating the appearance of NMR spectra for different chemical exchange regimes: a) Slow chemical exchange between conformers, e.g., in the nonnative (A) and native state of a protein (B). The height of the signals indicates the population between the two states, e.g., at a given denaturant concentration. b) Intermediate chemical exchange regime (molten globule state). c) Fast chemical exchange (random coil state).

where $\delta\nu = \nu_A - \nu_B$ and k is the rate of conformational exchange. For fast exchange and small chemical shift differences, a case typically encountered in the random coil conformation of a protein, NMR signals with very narrow linewidths are observed. Under the assumption of two-state fast folding kinetics, in which the unfolded state of a protein is in fast exchange with its folded state, the increase in linewidth (e.g., induced by subsequent addition of increasing amounts of urea starting from the folded state and thereby increasing the population of the unfolded state) can be analyzed to derive microsecond refolding kinetics for two-state folding [34, 35].

However, a detailed description of the random coil state of a protein cannot really be obtained from chemical shift measurement since the prediction of δ^i that is the conformational dependence of chemical shifts is not yet clearly established. It is therefore difficult to predict the chemical shifts for a random coil state of protein from a given distribution of conformations. Rather, reference values for random coil chemical shifts have been determined by measurement of so-called random coil peptides, first of the sequence GGXA [36] and then later of GGYXGG, with Y being either proline or glycine and X any of the 20 amino acids [37, 38].

The NMR spectrum becomes more difficult if the rate of interconversion approaches the differences in chemical shifts $\delta\nu$ (Figure 21.6b). In the case of intermediate conformational averaging between two equally populated sites, called intermediate exchange regime, one very broad line is observed. At the point of coalescance, the exchange rate k is given directly by:

$$k = \frac{|\delta\nu|}{\sqrt{8}} \tag{3}$$

where $\delta\nu = \nu_A - \nu_B$ and is the rate of conformational exchange. For intermediate exchange, a case associated with the molten globule state of a protein, the dramatic line broadening has made resonance assignment for a molten globule protein impossible so far (see Figures 21.2b and 21.3b). In case of unsymmetric exchange between multiple sites, the prediction of the conformations that participate in the chemical exchange is very difficult and always relies on limiting assumptions, such as fixing one or more of the conformations and the rate of exchange between those sites.

Recently, residues in α-lactalbumin have been identified that are involved in formation of a hydrophobic core undergoing slow conformational exchange and therefore forming a molten globule. Redfield et al. [39] started from the random coil state of the protein, stabilized in high concentrations of denaturants at pH 2, and for decreasing amounts of denaturants observed which residues would disappear first due to intermediate chemical exchange. Interestingly, the pattern of disappearance of resonance can be interpreted assuming a preformed core in the α-domain of the protein.

Under favorable conditions, NMR spectra can be recorded in which the folded and the unfolded state of a protein are in slow exchange; two sets of signals arising from either of the two states can be observed (Figure 21.6a). If exchange takes place on a time scale of hundreds of milliseconds, then exchange peaks between the two states can be observed in NOESY experiments [40], magnetization is transferred from one of the states to the other during the mixing time (of the order of 200–500 ms) of the NOESY experiment [41, 42]. These exchange peaks can be used to assign the spectrum of the unfolded state from known assignments in the folded state and exchange kinetics can be derived.

21.3.2 *J* Coupling Constants

21.3.2.1 Conformational Dependence of *J* Coupling Constants

Vicinal (^3J) spin–spin coupling constants can be used for conformational analysis in peptides and proteins. In general, ^3J coupling constants depend on the torsion angles between atoms three bonds apart and the relationship of the dependence of coupling constants on the respective dihedral angles is given by semi-empiric Karplus relations [43] (Table 21.3). Karplus relations are not single-valued, but instead give up to four dihedral angle values for a single coupling constant (Figure 21.7). Karplus parameters have been determined for most of the spin pairs relevant for conformational analysis in the polypeptide backbone and the amino acid side chains (Table 21.3). Coupling constants, especially the coupling constant $^3J(H^N,H_\alpha)$, can be used for the investigation of backbone conformations of partly folded or unfolded states of proteins [36, 44, 45], if the effect of conformational averaging is taken into account.

In addition, ^1J and ^2J coupling constants also contain information about torsion angles, however, their spread in values for different conformations is not as large as for the $^3J(H^N,H_\alpha)$ coupling constant [46–51].

Tab. 21.3. Overview of Karplus parametrization for different ^1J, ^2J, and ^3J coupling constants.

Coupling constant	*Karplus parameterization*	*References*
$^3J(\mathrm{H^N},\mathrm{H}_\alpha)$	$^3J = 6.51\cos^2(\phi - 60^\circ) - 1.76\cos(\phi - 60^\circ) + 1.60$	160
	$^3J = 6.40\cos^2(\phi - 60^\circ) - 1.40\cos(\phi - 60^\circ) + 1.90$	161
	$^3J = 6.60\cos^2(\phi - 60^\circ) - 1.30\cos(\phi - 60^\circ) + 1.50$	162
	$^3J = 7.90\cos^2(\phi - 60^\circ) - 1.05\cos(\phi - 60^\circ) + 0.65$	163
	$^3J = 6.64\cos^2(\phi - 60^\circ) - 1.43\cos(\phi - 60^\circ) + 1.86$	164
$^3J(\mathrm{H^N},\mathrm{C}')$	$^3J = 4.01\cos^2(\phi) + 1.09\cos(\phi) + 0.07$	165
	$^3J = 4.02\cos^2(\phi) + 1.12\cos(\phi) + 0.07$	164
$^3J(\mathrm{H^N},\mathrm{C}_\beta)$	$^3J = 4.70\cos^2(\phi + 60^\circ) - 1.50\cos(\phi + 60^\circ) - 0.20$	166
	$^3J = 2.78\cos^2(\phi + 60^\circ) - 0.37\cos(\phi + 60^\circ) + 0.03$	164
$^3J(\mathrm{H}_\alpha,\mathrm{C}')$	$^3J = 4.50\cos^2(\phi + 120^\circ) - 1.30\cos(\phi + 120^\circ) - 1.20$	166
	$^3J = 3.72\cos^2(\phi + 120^\circ) - 1.71\cos(\phi + 120^\circ) + 1.07$	167
	$^3J = 3.62\cos^2(\phi - 60^\circ) - 2.11\cos(\phi - 60^\circ) + 1.29$	164
$^3J(\mathrm{C}',\mathrm{C}_\beta)$	$^3J = 1.61\cos^2(\phi - 120^\circ) - 0.66\cos(\phi - 120^\circ) + 0.26$	168
	$^3J = 1.28\cos^2(\phi - 120^\circ) - 1.02\cos(\phi - 120^\circ) + 0.30$	169
	$^3J = 2.54\cos^2(\phi - 120^\circ) - 0.55\cos(\phi - 120^\circ) + 0.37$	167
$^3J(\mathrm{C}',\mathrm{C}')$	$^3J = 1.33\cos^2(\phi) - 0.88\cos(\phi) + 0.62$	170
	$^3J = 1.57\cos^2(\phi) - 1.07\cos(\phi) + 0.49$	170
$^1J(\mathrm{N_i},\mathrm{C}_{\alpha i})$	$^1J = 9.51 - 0.98\cos(\psi_i) + 1.70\cos^2(\psi_i)$	29
	$^1J = 8.65 - 1.21\cos(\psi_i) + 2.85\cos^2(\psi_i)$	171
$^2J(\mathrm{N_i},\mathrm{C}_{\alpha(i-1)})$	$^2J = 7.82 - 0.17\cos(\phi_{(i-1)}) - 0.64\cos^2(\phi_{(i-1)})$ $-1.39\cos(\psi_{(i-1)}) - 0.37\cos^2(\psi_{(i-1)})$	29
	$^2J = 7.85 - 1.52\cos(\psi_{(i-1)}) - 0.66\cos^2(\psi_{(i-1)})$	171

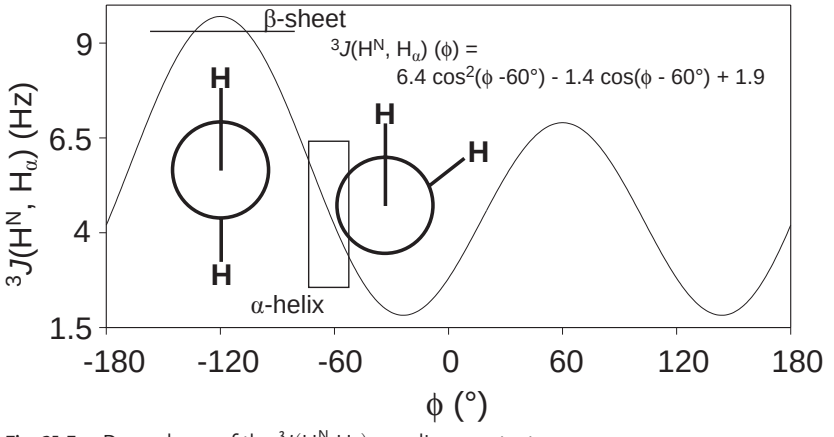

Fig. 21.7. Dependence of the $^3J(\mathrm{H^N},\mathrm{H}_\alpha)$ coupling constants on the backbone torsion angle ϕ using the parametrization by Vuister et al. (see Table 21.3).

Scalar couplings through H-bonds ($^{3h}J(N,C')$) provide information on the state of individual hydrogen bonds and therefore on the formation of α-helix [52]. This information is of particular interest for the investigation of folding states of proteins, because the helicity can be observed at atomic level. Thus, $^{3h}J(N,C')$ are valuable complements to chemical shift deviation data.

21.3.2.2 Interpretation of *J* Coupling Constants in the Presence of Conformational Averaging

In the case of fast conformational averaging, the observed scalar coupling constant is the population weighted average in close analogy to chemical shifts:

$$J^{\mathrm{obs}}(\alpha) = \sum_i p_{\mathrm{i}} J^{\mathrm{i}}(\alpha_{\mathrm{i}}) \tag{4}$$

where J^{obs} is the observed scalar coupling constant, J^{i} is the scalar coupling constant in the *i*th conformation with torsion angle α_{i} and weights p_{i} and $\sum_i p_{\mathrm{i}} = 1$. Two approaches have been developed to interpret the averaged scalar coupling constant. In one approach, random coil scalar coupling constants have been determined for random coil peptides GGXGG in close similarity with the reference chemical shift values [53].

Different to chemical shifts, the dependence of scalar coupling constants on the intervening torsion angle is well established (see Table 21.3) and therefore, coupling constants can be predicted using models for the distribution of torsion angle space in the random coil state of a protein (see Section 21.4).

Table 21.4 shows a comparison of coupling constants predicted from the random coil model and those measured for random coil peptide GGXGG in 6 M GdmCl.

21.3.3 Relaxation: Homonuclear NOEs

21.3.3.1 Distance Dependence of Homonuclear NOEs

NOE interactions between hydrogen atoms form the most important basis for the NMR structure determination (Figure 21.8). Distance information can be obtained through space-mediated transfers in NOESY experiments that reveal cross-peaks between two protons H1 and H2 that are closer than 5 Å together. The cross-relaxation rate between two protons that gives rise to observable cross-peaks in NOESY (ROESY) spectra is defined by the following equation:

$$\begin{aligned} \sigma^{\mathrm{NOE}}_{\mathrm{H1,H2}} &= \frac{d^2\tau_{\mathrm{c}}}{5}\left[-1 + \frac{6}{1+4\omega_0^2\tau_{\mathrm{c}}^2}\right] \\ \sigma^{\mathrm{ROE}}_{\mathrm{H1,H2}} &= \frac{d^2\tau_{\mathrm{c}}}{5}\left[2 + \frac{3}{1+\omega_0^2\tau_{\mathrm{c}}^2}\right] \end{aligned} \tag{5}$$

where ω_{H} is the Lamor frequencies of ^{1}H, $d = \mu_0 h\gamma_{\mathrm{H}}^2/(\sqrt{8}r^3_{\mathrm{H1,H2}}\pi^2)$ describes the

Tab. 21.4. Random coil $^3J(H^N,H_\alpha)$ coupling constants predicted on the basis of the random coil model (see Section 21.4) and measured experimentally. Values for $^3J(H^N,H_\alpha)^{pred.}$ are based on the distribution of ϕ angles in the protein database and represent an average over all the different adjacent amino acids, rather than for residues with adjacent glycines. Experimental coupling constants were measured using a GGXGG peptide in 6 M GdmCl at 20 °C, pH 5.0.

	$^3J(H^N,H_\alpha)^{pred.}$ (Hz)	$^3J(H^N,H_\alpha)^{exp.}$ (Hz)
Ala	6.1	6.1
Arg	6.9	7.2
Asn	7.7	7.4
Asp	7.8	7.2
Cys (ox)	7.7	n.d.
Cys (red)	7.3	6.8
Gln	7.1	7.1
Glu	6.7	6.8
His	7.8	7.2
Ile	7.1	7.6
Leu	6.8	7.1
Lys	7	7.1
Met	7.1	7.3
Phe	7.3	7.5
Ser	7	6.7
Thr	7.9	7.6
Trp	7	6.9
Tyr	7.8	7.3
Val	7.2	7.7

constant for dipolar interaction, μ_o is the permeability of the vacuum, h is Planck's constant, γ_H is the gyromagnetic ratio of nucleus i, and $r_{H1,H2}$ is the distance between H1 and H2.

In the following, we wish to discuss some of the assumptions and complications associated with the use of NOE information to derive structural information for nonnative and random coil states of proteins. In the native state of a protein, a

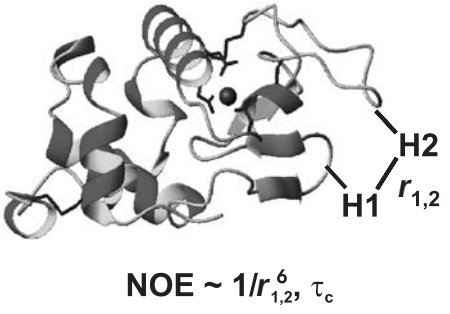

Fig. 21.8. The NOE interaction $\sigma^{NOE}_{H1,H2}$ between two protons H1 and H2 is the most important NMR parameter to determine structures of proteins.

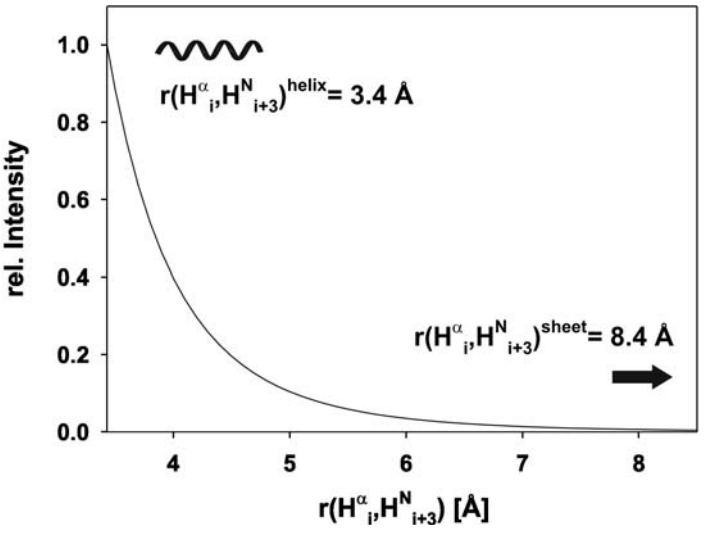

Fig. 21.9. Dependence of the cross-peak intensity $\sigma^{NOE}_{H1,H2}$ in NOESY spectra on the distance between protons H1 and H2. Characteristic secondary structure elements are indicated, the cross-peak for two protons 3.4 Å apart has arbitrarily been scaled to 1.

given cross-peak is interpreted as arising from a single conformation with fixed distance. It is further assumed that the overall rotational tumbling of a molecule is isotropic and can therefore be modeled by a single spectral density function that describes the distribution of motions in a molecule. Furthermore, additional local motions can to good approximation assumed to be absent. These local motions could modulate (decrease) the distance between protons H1 and H2. Under these assumptions, the observed intensity falls off with the inverse sixth power of the distance (Figure 21.9).

Spectral density function The spectral density function $J^{q}(\omega_q)$ is obtained by evaluating the correlation function of the spherical harmonics

$$J^{q}(\omega_q) = \int_0^{\infty} d\tau \overline{F^{(q)}(t)F^{(-q)}(t+\tau)} \exp(-i\omega_q\tau) \tag{6}$$

The bar indicates time average over *t*. *q* can assume values of 0, ±1, ±2. The correlation function describes the probability of a given internuclear vector to stay in a fixed orientation in dependence of the time τ. Due to rotational tumbling, the orientation is lost; for proteins of 15 kDa size, a typical time constant τ_c for this process is of the order of 5 ns. However, depending on the model of rotational reorientation (isotropic, axially symmetric, asymmetric), the spectral density function has

different forms. Different members of ensemble of conformers in the random coil state of a protein will have very different diffusion tensors, and therefore, the spectral density functions will not be identical for compact conformers compared to extended conformers. In the following, we discuss the isotropic case and the case of axial symmetry.

Spherical top molecules The spectral density function for isotropic rotational diffusion has been derived by Hubbard and coworkers [54–57]:

$$J^{q}(\omega_q) = \frac{2}{5}\left[\frac{6D}{(6D)^2 + \omega_q^2}\right] = \frac{1}{5}\left[\frac{2\tau_c}{1 + (\omega_q\tau_c)^2}\right] \tag{7}$$

where D denotes the diffusion constant, with $1/\tau_c = 6D$. The rotational diffusion constant is inversely proportional to the correlation time τ_c. The correlation time for brownian rotational diffusion can be measured by time-resolved fluorescence spectroscopy, light scattering, or NMR relaxation [58] and can be approximated for isotropic reorientation by the Stoke's-Einstein correlation: $\tau_c = \frac{4\pi\eta_w r_H^3}{3k_B T}$ in which η_w is the viscosity, r_H is the effective hydrodynamic radius of the protien, k_B is the Boltzmann constant, and T the temperature.

Axially symmetric top molecules For the case that $D_{xx} = D_{yy} = D_\perp$, one obtains the spectral density function of a symmetric top rotator ($D_{zz} = D_\parallel$) or of an axially symmetric top molecule whose rotational diffusion is defined by a second rank diffusion tensor with polar coordinates θ and ϕ:

$$\begin{aligned} J^{q}(\omega_q) &= \frac{1}{20}\{S_0^2 J^{q,0} + S_1^2 J^{q,1} + S_2^2 J^{q,2}\} \\ S_0^2 &= \langle(3\cos^2\theta - 1)\rangle\langle(3\cos^2\theta - 1)\rangle/4 \\ S_1^2 &= 3\langle(\sin\theta\cos\theta)(\cos\phi)\rangle^2 + \langle(\sin\theta\cos\theta)(\sin\phi)\rangle^2 \\ S_2^2 &= \frac{3}{4}\langle(\sin^2\theta)(\cos 2\phi)\rangle^2 + \langle(\sin^2\theta)(\sin 2\phi)\rangle^2 \end{aligned} \tag{8}$$

in which the reduced spectral density functions ($-2 \le m \le +2$)

$$J^{q,m} = \frac{2\tau_{c,m}}{1 + (\omega_q\tau_{c,m})^2} \tag{9}$$

have been used. The correlation times $\tau_{c,m}$ can be rewritten as diffusion constants $D_\parallel$ and $D_\perp$ according to

$$1/\tau_{c,m} = 6D_{\perp} + m^2(D_{\parallel} - D_{\perp}) \tag{10}$$

The analysis shows that of cross-peak intensities $\sigma^{NOE}_{H1,H2}$ will therefore be very different depending on the overall compactness of the conformer, ranging from nearly isotropic to highly extended and anisotropic shape, in the ensemble in the random coil state of a protein.

21.3.3.2 Interpretation of Homonuclear NOEs in the Presence of Conformational Averaging

In the ensemble of unfolded states, averaging around intervening torsion angles that connect the two protons of interest will lead to averaging of the distances. Local averaging of torsion angles will lead to modulation of the NOE signal in addition to the global reorientation of the molecule and the effect of local and global motions and the ratio of their characteristic time constants τ_e and τ_c, respectively, will influence the cross-peak intensities $\sigma^{NOE}_{H1,H2}$ in NOESY experiments. The formalism to deal with internal motion has been introduced for the analysis of heteronuclear two-spin systems such as C–H or N–H (see Section 21.3.4) and will be introduced for the treatment of a two-spin H–H system.

Internal motion *Derivation of spectral density functions by explicit calculation of the motion:* Internal motion can be incorporated into the spectral density either by the Lipari and Szabo [59, 60] approach or by explicit calculation of the motion from, for example, motional models of molecular dynamics trajectories. In the above given equations, the spectral densities are Fourier transformations of the rotational diffusive motion of the molecule with respect to the external magnetic field [61, 62].

Internal motions analyzed by Lipari-Szabo approach: The model-free or Lipari-Szabo approach for the analysis of relaxation rate aims at the provision of dynamic parameters describing the dynamic behavior of a two-spin system irrespective of any assumed motional model. This is desirable since the relaxation data does not contain any information on the nature of the motions that cause relaxation. The model-free formalism is the most widely applied one for the dynamic interpretation of relaxation data. In the simplest case (Figure 21.10a), these consist of the generalized order parameter S^2, which is a measure for the spatial restriction of the internal motion, and the effective correlation time τ_e defining the time scale of motion. Assuming isotropic diffusion, the spectral density function can then be expressed as follows:

$$J(\omega) = \frac{S^2\tau_c}{1+\omega^2\tau_c^2} + \frac{(1-S^2)\tau}{1+\omega^2\tau^2} \tag{11}$$

In Eq. (11), τ_c is the overall rotational correlation time of the molecule and $1/\tau = 1/\tau_c + 1/\tau_e$. In the absence of internal motion ($S^2 \sim 1$ and $\tau = \tau_c$), $J(\omega)$ simplifies to:

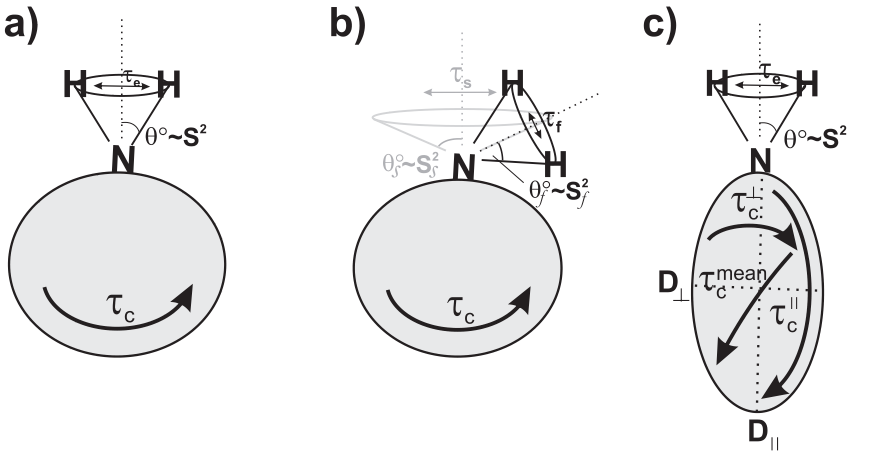

Fig. 21.10. Model-free parameters shown for a N–H spin system within a molecule that tumbles isotropically with the overall rotational correlation time τ_c. A) Simple model with the order parameter S^2 and the effective correlation time τ_e. The overall rotation is assumed to be isotropic. B) Two-time scale extended model with two S^2 parameters, S_S^2 and S_f^2 for slow and fast motions. C) like A but with anistropic overall rotation.

$$J(\omega) = \frac{\tau_c}{1 + \omega^2 \tau_c^2} \tag{12}$$

In cases where different fast motions take place, whose time scales differ by at least one order of magnitude, an extended model-free formalism has been developed with a separate S^2 for each motion, S_S^2 and S_f^2 (Figure 21.10b, Eq. (13)).

$$J(\omega) = \frac{S^2 \tau_c}{1 + \omega^2 \tau_c^2} + \frac{(S_f^2 - S^2)\tau}{1 + \omega^2 \tau^2} \tag{13}$$

In this two-time scale model it is assumed that the contribution of the faster of the two motions can be neglected, therefore, while it contributes to the overall S^2 since $S^2 = S_S^2 * S_f^2$, the term containing the fast effective correlation time τ_f is left out. The time scale of the slower internal motion τ_s is included in τ ($1/\tau = 1/\tau_c + 1/\tau_s$) similar to τ_e of the single-time scale model (it will therefore not be discriminated from τ_e in the following).

Figure 21.11 shows the dependence of the cross-peak intensity $\sigma_{H1,H2}^{NOE}$ in NOESY experiments on the overall correlation τ_c, the internal correlation time τ_e and the order parameter S^2 as defined in the single-time scale model. It can be seen that for global correlation time of 2 ns, an order parameter S^2 of 0.4, and an internal correlation time τ_e of 150 ps, $\sigma_{H1,H2}^{NOE}$ is scaled down from –0.36 in the absence of any internal motion ($S^2 = 1.0$) to -0.12. If one reduces τ_c to 1 ns, $\sigma_{H1,H2}^{NOE}$ is further reduced to -0.04. It is interesting to note that for longer internal correlation times τ_e, $\sigma_{H1,H2}^{NOE}$ increases again. The partition of τ_c and τ_e is difficult to assess by NMR. In the case, in which local and global motions cannot be entirely uncoupled and in

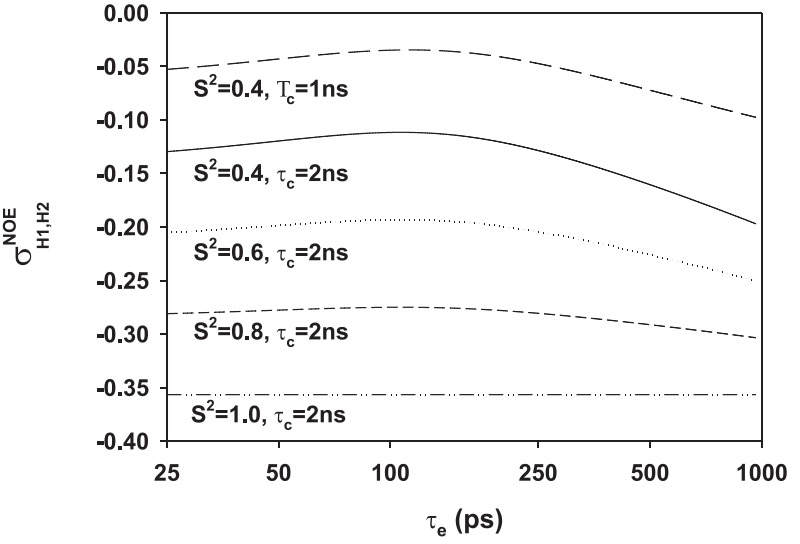

Fig. 21.11. Dependence of the cross-peak intensity $\sigma^{NOE}_{H1,H2}$ in NOESY spectra on the correlation time for local motions τ_e assuming different correlations times τ_2 for the global motion and different order parameters S^2.

which local motions have relative larger amplitudes, interpretation of $\sigma^{NOE}_{H1,H2}$ in terms of arising from an average distance is difficult. In addition, the correlation times for both internal and global motion may be affected in a different manner depending on the specific experimental conditions such as temperature and solvent viscosity; these effects make it difficult to argue that the absence of a specific cross-peak could be taken as evidence for specific conformation sample as is sometimes done in the literature.

Cooperativity in conformational sampling Different to coupling constants J that depend only on a single intervening torsion angle, the distances of atoms further remote is influenced by more than a single torsion and this leads to interesting questions regarding the analysis of cooperativity in sampling different conformations. In this discussion, cooperativity describes the influence of neighbouring residues and their (averaged) conformation on a given torsion angle distribution. Let us assume that the residues of a small peptide can adopt two conformations, α and β, both by 50% (Figure 21.12). Two extreme cases of cooperativity can be distinguished: In the cooperative case of conformational sampling, a residue $i+1$ assumes an $\alpha(\beta)$ conformation if residue i is in $\alpha(\beta)$; in the noncooperative case, a residue $i+1$ assumes either α or β conformation with 50% probability, if residue i is in $\alpha(\beta)$. In the noncooperative case, the eight possible conformations of a tripep-

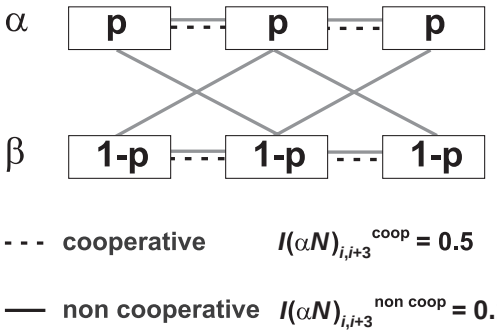

Fig. 21.12. Model of a consecutive stretch of three amino acid residues. For the sake of the argument, it is assumed that the residues can adopt only two different conformations, α and β. In the case of cooperative sampling of conformational space, which is indicated by the dashed lines, the intensity of the NOE cross-peak $I(\alpha, N)_{i,i+3}^{\text{coop}}$ is 50% of the cross-peak observed for a single static conformation. In the case of noncooperative conformational sampling, the intensity $I(\alpha, N)_{i,i+3}^{\text{non coop}}$ decreases to 17%, for which only two out of the eight possible conformation contribute (see Table 21.5).

tide $(\alpha\alpha\alpha, \beta\alpha\alpha, \alpha\beta\alpha, \beta\beta\alpha, \alpha\alpha\beta, \beta\alpha\beta, \alpha\beta\beta, \beta\beta\beta)$ are each sampled by 12.5%. Obviously, the J coupling constant in either of the two cases is the average $(J^{\alpha} + J^{\beta})/2$ and J couplings therefore do not differentiate between different degrees of cooperativity.

This is different for the measurement of an NOE, e.g., between a residue i and $i + 3$. In the cooperative case, there are two populations present $(\alpha\alpha\alpha, \beta\beta\beta)$, each by 50%. Let us assume that the $\alpha\alpha\alpha$ conformer represents a helical fragment and the $\beta\beta\beta$ conformer an extended fragment. Then, Figure 21.9 shows that no cross-peak can be observed for $\beta\beta\beta$ conformer. In the cooperative case, in which 50% of all molecules in the ensemble have an $\alpha\alpha\alpha$ conformation, the cross-peak intensity is 50% of the cross-peak intensity predicted for a helix (Table 21.5). In the noncooperative case, in which all eight conformations are equally populated, the cross-peak intensity drops to 0.17 and only two conformers $(\alpha\alpha\alpha, \beta\alpha\alpha)$ contribute to the cross-peak intensity.

21.3.4 Heteronuclear Relaxation (^{15}N R_1, R_2, hetNOE)

21.3.4.1 Correlation Time Dependence of Heteronuclear Relaxation Parameters

Heteronuclear relaxation rates (^{15}N-R_1, ^{15}N-R_2) and heteronuclear NOEs ($\{^1$H$\}$-^{15}N-NOE) are sensitive both to motions on a subnanosecond time scale and to slow conformational exchange in the millisecond time scale [63]. Motions that influence the NMR parameters are the overall rotational tumbling of a molecule and the local fluctuations (e.g., of an ***NH*** bond vector). The exact formula are given in Eq. (14a–c):

Tab. 21.5. Contribution to NOE cross-peak intensities from different conformations for two models: (i) cooperative sampling of conformational space defined by two different conformations, α and β, or (ii) noncooperative sampling of conformational space (see Figure 21.12).

Conformation of residues i + 1 to i + 3	*Cooperative sampling*		*Noncooperative sampling*	
	Population	*Cross-peak intensity (a.u.)*	*Population*	*Cross-peak intensity (a.u.)*
$\alpha\alpha\alpha$	50%	0.5	12.5%	0.124
$\beta\beta\beta$	50%	0	12.5%	[a]
$\alpha\alpha\beta$	–	–	12.5%	[a]
$\alpha\beta\alpha$	–	–	12.5%	[a]
$\beta\alpha\alpha$	–	–	12.5%	0.037
$\alpha\beta\beta$	–	–	12.5%	[a]
$\beta\alpha\beta$	–	–	12.5%	[a]
$\beta\beta\alpha$	–	–	12.5%	[a]

[a] All other conformations contribute 0.009 [a.u.] to the cross-peak intensity.

$$R_1 = \frac{d^2}{4}[J(\omega_H - \omega_N) + 3J(\omega_N) + 6J(\omega_H + \omega_N)] + c^2 J(\omega_N)$$

$$R_2 = \frac{d^2}{8}[4J(0) + J(\omega_H - \omega_N) + 3J(\omega_N) + 6J(\omega_H) + 6J(\omega_H + \omega_N)] + \frac{c^2}{6}[4J(0) + 3J(\omega_N)] + R_{ex} \qquad (14a\text{–}c)$$

$$\mathrm{NOE} = 1 + (d^2/4R_1)(\gamma_N/\gamma_H)[6J(\omega_H + \omega_N) - J(\omega_H + \omega_N)]$$

In this, ω_H and ω_N are the Lamor frequencies of ^1H and ^{15}N, respectively, $J(\omega)$ is the spectral density function at frequency ω; R_{ex} is the parameter accounting for conformational exchange contributions; $d = \mu_0 h \gamma_N \gamma_H / (8 r_{NH}^3 \pi^2)$ and $c = \omega_N \Delta\sigma_N / \sqrt{3}$ describe the dipolar and the chemical shift anisotropy (CSA) interaction, respectively. μ_o is the permeability of the vacuum; h is Planck's constant; γ_i is the gyromagnetic ratio of nucleus i; r_{NH} is the internuclear distance between N and H; $\Delta\sigma_N$ is the nitrogen CSA.

The dependence of the heteronuclear relaxation parameters on the overall rotational correlation time τ_c in the absence of internal motions and assuming isotropic tumbling is shown in Figure 21.13. While the longitudinal relaxation rate R_1 exhibits a maximum, R_2 increases monotonuously with τ_c. This difference arises from the dependence of R_2 but not of R_1 on a $J(0)$ term (see Eq. (14)), which is negligible at lower τ_c values but becomes more and more relaxation relevant for higher τ_c values. For macromolecules, τ_c usually lies right of the R_1 maximum and consequently small R_1 but large R_2 values are expected.

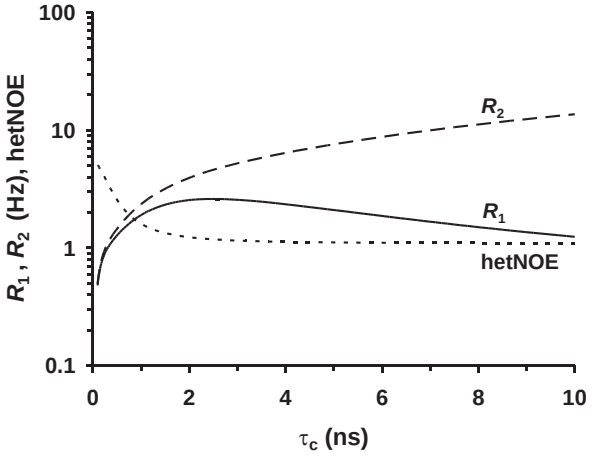

Fig. 21.13. Dependence of R_1, R_2 and the heteronuclear NOE (hetNOE) on τ_c. Calculations are based on the assumption of a rigid molecule tumbling isotropically.

21.3.4.2 **Dependence on Internal Motions of Heteronuclear Relaxation Parameters**

The relaxation rates are influenced by additional internal motions. In order to show the effect of such internal motions on the observed relaxation, Figure 21.14 shows the simulation of the transverse ^{15}N relaxation rates (^{15}N-R_2) as predicted using the Lipari-Szabo approach and a single-time scale model (Eq. (13)). For a given overall correlation time $\tau_c = 1$ ns, the relaxation rate decreases with increasing internal motion and order parameter. However, the use of the Lipari-Szabo

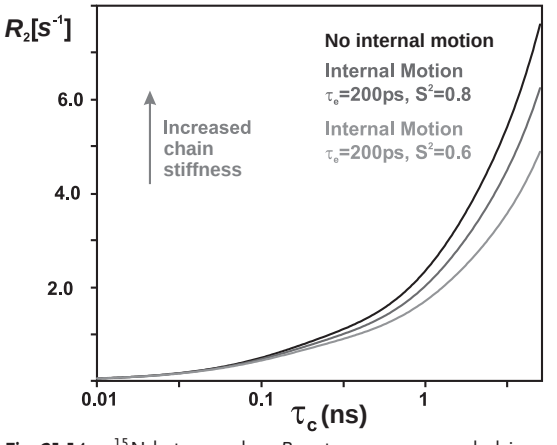

Fig. 21.14. ^{15}N heteronuclear R_2 rates as function of correlation time τ_c for global motions, τ_e for internal motions and the order parameters S^2. The appropriateness of the underlying model-free approach for the description of the dynamics in nonnative states of proteins is discussed in the text.

approach for random coil states of proteins is controversial, for a detailed discussion see, for example, Ref. [64]: the extraction of motional parameters using the Lipari-Szabo approach is based on two (single time scale model) or three (two time scale model) discrete correlation times that can be separated and are uncorrelated to the other motions. In other words, the approach assumes that the time scales of global and local motions can clearly be separated, an assumption questionable in the context of random coil states of proteins.

Alexandrescu and Shortle [65] have used a local model-free approach, according to which one global correlation time is fitted per residue. In the case of extensive averaging over a range of frequency in the nanosecond range, a continuous distribution of correlation times (and subsequently spectral density functions) can be introduced. One of such functions, the Cole-Cole distribution, has been used by Buevich and Baum to describe the relaxation behavior of the unfolded propeptide of subtilisin PPS [66]. An improved treatment of this problem has been proposed by Ochsenbein et al., in which a lorentzian distribution of correlation times (see Eq. (15)) is used to describe the underlying dynamics of the ensemble of conformers.

$$J(\omega) = \int_0^\infty F(\tau) J(\omega, \tau)\, \mathrm{d}\tau$$

$$F(\tau) = K \frac{\Delta}{\Delta^2 + (\tau - \tau_0)^2} \quad \text{for } 0 \le \tau \le \tau_{\max} \tag{15}$$

$$F(\tau) = 0 \quad \text{for } \tau \ge \tau_{\max}$$

In yet another approach, we have fitted the sequence dependence of relaxation rates to a simple two-parameter model, which assumes a common intrinsic relaxation rate for a given residue that depends on the viscosity of the solution, and a length dependence of the influence of neighboring residues on the relaxation properties of any member of the chain. Such simple approach fits the random coil behavior of the polypeptide chain but does not provide a deconvolution of the time scales of motion associated with the apparent relaxation behavior. However, the approach reliably predicts the sequence dependence of the relaxation rates in unbranched and disulfide bridge branched polypeptides based on a small number of parameters and is discussed in detail in Section 21.5.3.

21.3.5 Residual Dipolar Couplings

21.3.5.1 Conformational Dependence of Residual Dipolar Couplings

The measurement of residual dipolar couplings (RDCs), although early recognized as having potential [67], has only recently been reintroduced [68, 69] and is now routinely used as a means to obtain information on the orientation of bond vectors relative to an external alignment tensor, that is, NMR information on long-range orientation of individual bond vectors in a macromolecule. The introduction of residual dipolar couplings has considerably changed NMR structure determination

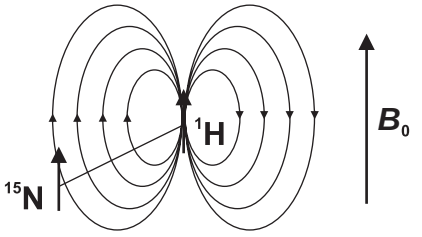

Fig. 21.15. A two-spin system of spin ^{1}H and ^{15}N connected by an internuclear vector r_{NH}. The ^{15}N nucleus exerts a dipolar field, which acts at the side of the ^{1}H nucleus. The magnetic moments of the nuclei are aligned parallel or antiparallel (not shown) relative to the static magnetic field B_o. The dipolar field of the ^{15}N nucleus can increase or decrease the static magnetic field active at the position of the ^{1}H nucleus depending on the orientation of the ***NH*** vector and the spin state of the proton (parallel or antiparallel to B_o).

for native proteins. A number of excellent review articles have been published [70–73]. Only recently have first measurements using RDCs in the case of nonnative states of proteins [74] been published.

In our description of the conformational dependence of RDCs, we follow a recent review article by Bax [73]: Dipolar couplings between NMR-active nuclei such as a spin N–H are caused by the magnetic dipole field exerted by the N nucleus at the site of nucleus H (Figure 21.14). In the following, we keep only the component of the magnetic dipole field that is parallel to the direction (the *z*-direction) of the magnetic field B_o. The dipole field exerted by the N nucleus will change the resonance frequency of the H nucleus. The dipolar coupling D^{NH} depends on the internuclear distance r_{NH} and on the orientation θ of the internuclear vector ***NH*** (bold, italics indicating the vector property) relative to B_o (Eq. (16)). For a fixed orientation of the vector, the dipolar field exerted by N can either increase or decrease the magnetic field of nucleus H, depending on whether the equally populated spin-states α and β of H are parallel or antiparallel relative to B_o.

$$D^{NH} = D^{NH}_{max}\langle(3\cos^2\theta - 1)/2\rangle \tag{16}$$

where θ is the angle between the internuclear vector ***NH*** and the magnetic field B_o, the angle brackets denote averaging over the ensemble of molecules, and

$$D^{NH}_{max} = -\mu_0(h/2\pi)\gamma_H\gamma_N/(4\pi^2 r^3_{NH}) \tag{17}$$

is the splitting observed for $\theta = 0$; the additional constants have the same meaning as explained for Eq. (14a–c).

In the case of isotropic rotational tumbling of a molecule in solution (Figure 21.16a), brownian motions average the magnetic dipole effects to zero, while in the solid state spectrum of a molecule, such dipolar couplings are not averaged and every nucleus couples with a large number of other nuclei, resulting in considerable line broadening.

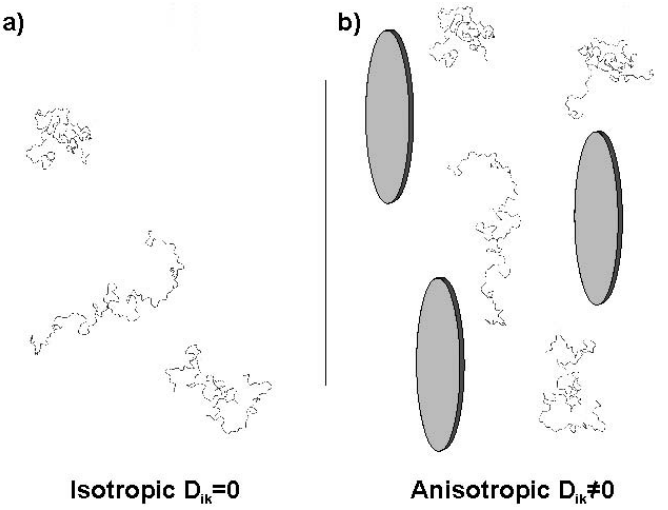

Fig. 21.16. a) Isotropic tumbling of a molecule leads to vanishing dipolar couplings. b) Introduction of non-isotropic medium leads to residual dipolar couplings (RDCs) in solution NMR. RDCs depend on the orientation of a given bond vector relative to an alignment tensor and provide information about the long-range order in high-resolution NMR studies.

However, there are now various methods that impart partial alignment to a dissolved molecule, Many of them are additives to the solution such as liquid crystalline media [75] and partial alignment is induced by steric and/or ionic interaction between the aligned medium and the dissolved macromolecule (Figure 21.16b). In the case of NMR investigations of nonnative states of proteins, the use of polyacrylamide gels that have been compressed in an anisotropic manner have been successful [76, 77].

Yet another different way of inducing alignment of a molecule is to use paramagnetic factors bound to the protein, either by using natural paramagnetic cofactors or metals [78, 79] or specifically designed binding sites for paramagnetic ions [80]. In contrast to external alignment media, alignment is not caused by intermolecular interactions but is rather a property of the molecule itself. This is advantageous in the case of nonnative states of proteins, since different interactions between the members of the ensemble of conformers representing these states and the aligning medium will lead to different extents of alignment for each member of the ensemble.

The aligning of the proteins has the effect that rotational tumbling is not isotropic, and not all orientations are equally likely to occur. The extent of difference in this tumbling can be expressed as an alignment tensor A. Its principal components A_{xx}, A_{yy}, and A_{zz} reflect the probabilities (along the x-, y-, and z-direction) for the diffusional motion relative to the external magnetic field B_o.

The dipolar coupling depends on the polar coordinates of the ***NH*** vector in the frame of the alignment tensor:

$$D^{NH}(\theta,\varphi) = 3/4 D^{NH}_{max}[(3\cos^2\theta - 1)A_{zz} + \sin^2\theta\cos 2\varphi(A_{xx} - A_{yy})] \quad (18)$$

Equation (18) can be rewritten as:

$$D^{NH}(\theta,\varphi) = D_a[(3\cos^2\theta - 1) + 3/2R\sin^2\theta\cos 2\varphi] \quad (19)$$

where $D_a = 3/4 D^{NH}_{max} A_{zz}$ is the magnitude of the dipolar coupling tensor and $R = 2/3(A_{xx} - A_{yy})/A_{zz}$ is the rhombicity.

In the context of the analysis of nonnative states based on residual dipolar couplings, it is of importance to discuss the ability to predict the dipolar couplings from a given conformation. In Eq. (19), the magnitude and rhombicity of the alignment tensor relative to the molecular frame need to be known. For a given conformation, this may be predicted on the basis of the molecular shape [81, 82]. However, best results have been obtained so far if the alignment mechanism is steric and due to the large number of members in the ensemble of structures, such approach is particularily difficult for nonnative states of proteins. A second approach is to obtain a tensor that fits the experimental data best in a linear fitting algorithm [83]. This approach, however, cannot be used to predict RDCs from theoretical models for the torsion angle distributions in nonnative states of proteins.

21.3.5.2 Interpretation of Residual Dipolar Couplings in the Presence of Conformational Averaging

Different NMR parameters are influenced by conformational averaging over different time scales. While relaxation data such as homonuclear NOEs or heteronuclear relaxation rates are sensitive to motions that are faster than the overall rotational correlation time, residual dipolar couplings are sensitive to motions on a considerable longer time scale. This observation has only recently be exploited to access the conformational dynamics of proteins in their native state using a combination of NMR experimental dipolar couplings measured in a number of different alignment media and predictions of dynamics from molecular dynamics calculations [84–86].

Louhivuori et al. [26] have calculated the effect of steric obstruction that an external alignment media can exert on a random coil polypeptide chain (i.e., a random flight chain). Such calculation consists of a model for the spatial distribution funcion for an ensemble of conformers and a treatment of the residual dipolar couplings.

The distribution of conformation of the Gaussian chain is different from the isotropic solution in that the aligning medium introduces a barrier to the free diffusion of the chain (Figure 21.17); the distribution function of the random flight chain in the presence of the aligning medium W^{obs} becomes obstructed and deviates from the distribution function W^{free} in isotropic solution. The effect of the aligning medium is also treated as a distribution function W^{bar}, yielding the equation:

$$W^{obs} = W^{free} - W^{bar} \quad (20)$$

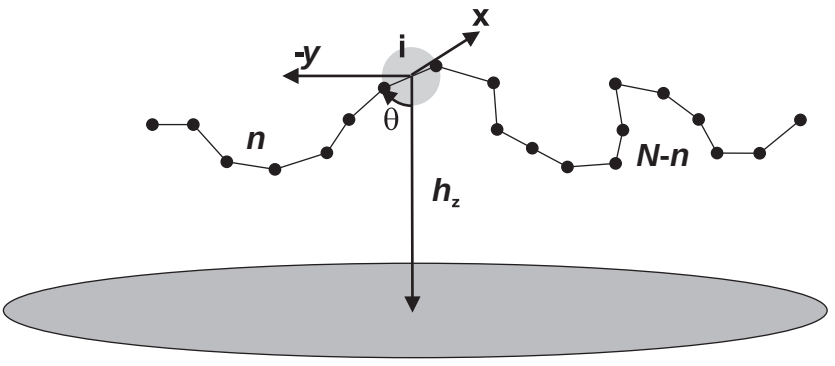

Fig. 21.17. Model for a random flight chain consisting of $N+1$ segment represented by dots and connected by straight lines. The chain tumble at distance h_z from a disk representing the aligning medium. At the locus i, placed at the origin of the molecular frame, the chain is partioned into two half chains containing n and $N-n$ segments. RDCs are functions of the average angle θ of i, the B_o field is parallel to the z-axis.

The random flight chain is composed of $N+1$ segments. For any given element of the chain i, there are n segments before i and $N-n$ segment after i. Therefore, the probability function contains two parts, W_n^{obs}, W_{N-n}^{obs}, and is given by:

$$\begin{aligned} W(z,h_z,c,n,N) &= \frac{1}{N}\{nW_n^{obs}(z,h_z,c,n)+(N-n)W_n^{obs}(z,h_z,c,N-n)\} \\ &= \frac{1}{N}\{n[W_n^{free}(z,c,n)-W_n^{bar}(z,h_z,c,n)] \\ &\quad +(N-n)[W_n^{free}(z,c,N-n)-W_n^{bar}(z,h_z,c,N-n)]\} \\ &= \frac{\sqrt{2n/\pi}}{N}\left\{\exp\left[-\frac{(2+1/2c)^2}{2n}\right]-\exp\left[-\frac{(2h_z-z+1/2c)^2}{2n}\right]\right\} \\ &\quad +\frac{\sqrt{2(N-n)/\pi}}{N}\left\{\exp\left[-\frac{(z-1/2c)^2}{2(N-n)}\right]\right. \\ &\quad \left.-\exp\left[-\frac{(2h_z-z-1/2c)^2}{2(N-n)}\right]\right\} \end{aligned} \tag{21}$$

where $c=\cos\theta$.

For any arbitrary pair of nuclei A and B in the segment i separated by the internuclear vector $\boldsymbol{r}_{AB}$, the vector $\boldsymbol{r}_{AB}$ will be at an angle α_{AB} with respect to the internal coordinate system of the seqment. The segment itself will be oriented at an angle θ with respect to the magnetic field B_o. The distribution W describing the averaging of the ith segment of the chain is a function of the position of each segment, each segment has its own averaged $\langle P_2\rangle$ polynomial. As a consequence, each segment

has its own alignment tensor A, which is axially symmetric due to the distribution functions for a random flight chain. The dipolar coupling D_{AB} is proportional to the axial component of the alignment tensor:

The average of $\cos^2 \theta$ contained in the expression of the dipolar coupling will be obtained by integration over all angles and space weighted by the distribution and normalized. The following observations can be made: For longer chains, $\langle P_2 \rangle$ will become smaller because the distributions of larger number of uncorrelated segments will become more spherical. Only polypeptide chains up to 100–200 residues will give rise to observable dipolar couplings. These observed residual dipolar couplings for a random flight chain are a consequence of the fact that such chain is restrained by the covalent structure of the chain, each segment is coupled and not free. The RDC originates from the individual loci along the chain, not from the whole chain average; each individual segment exhibits a nonvanishing $\langle P_2 \rangle$, it is time and ensemble averaged, but not averaged over all loci.

The treatment of residual dipolar couplings for random coil states of proteins is yet another example in which the prediction of what to expect for such state is of importance before deviations from random coil behavior can be interpreted with any vigor.

21.3.6 Diffusion

The dimensions of spherical proteins can be determined using diffusion NMR measurements since the hydrodynamic radius (R_h) of a protein is inversely proportional to its diffusion constant. Thus knowing the diffusion constant, R_h can be extracted using the Stokes-Einstein equation which requires the knowledge of the exact diffusion constant, temperature and viscosity of the solution. An easier approach for the determination of diffusion constants is by comparison to an internal probe with known hydrodynamic radius such as dioxane ($R_h = 2.12$ Å) [87]. Measurement of diffusion constants is usually done by PFG (pulse field gradient) NMR experiments performed with a PG-SLED (pulse gradient-simulated echo longitudinal encode-decode) sequence using bipolar gradient pulses for diffusion and varying the strength of the diffusion gradients between the experiments [88], the result of such experiments is shown in Figure 21.18: the signals decay with increasing strength of gradients, the decay rate is faster for the small molecule dioxane (b) than for the protein (a).

Empirical equations that relate the length of the polypeptide chain of isotropic native proteins to the hydrodynamic radius of a protein have been identified [87]. Thus, diffusion measurements are used to identify dimers or higher oligomers in native proteins (references 2, 3, 28 and 29 in Ref. [87]).

The situation is somewhat more complicated for nonnative proteins, since the ensemble of conformers in the denatured state can only be described as a distribution of polypeptides that have different hydrodynamic radii, each radius representing a group of conformations; this distribution cannot be determined experimentally, rather the average of the hydrodynamic radii present in a sample is observed.

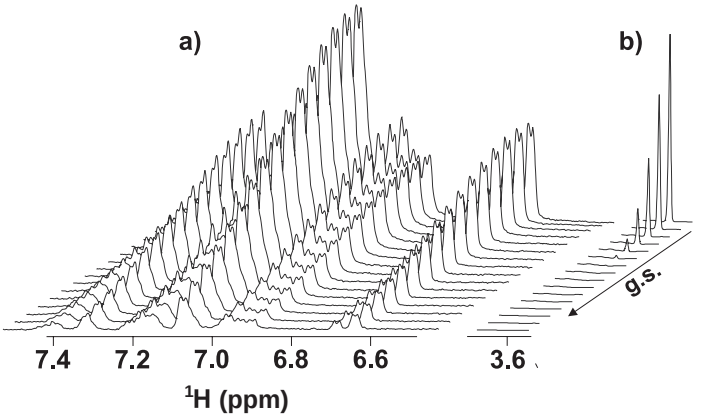

Fig. 21.18. Signal intensity in a ^{1}H 1D NMR spectrum as function of gradient strength (g.s.). a) lysozyme mutant W62G; b) dioxan.

Diffusion measurements have been used to identify urea unfolding of proteins (e.g., of lysozyme [89]) and to characterize different nonnative states of proteins such as BPTI [90] or α-lactalbumin [39]. The R_h of unfolded nondisulfide bridged proteins under highly denaturing conditions (high concentration of urea or GdmCl; extreme pH) can also be correlated to the length of the polypeptide chain [87].

21.3.7 Paramagnetic Spin Labels

Paramagnetic spin labels in proteins can be used to test long-range order or contacts. Spin labels such as nitroxide cause significant enhancement of relaxation rates of resonances that are within a distance of 15 Å away from the label [91, 92]. Spin labels can be attached to a number of residues containing reactive side chains such as Cys [93], His [91], or Lys [92]. Also the N-terminus of the protein can be used to attach a spin label [92]. Solvent-exposed residues especially in folded proteins have to be selected to prevent structure perturbations [94, 95], also paramagnetic metal ions such as Mn^{2+} or Gd^{3+} can be used if specific binding sites exist [96].

In folded proteins, distances can be extracted from the differential line broadening of the diamagnetic protein (reduction of the nitroxide with ascorbate to nitroxylamin) [94] to the paramagnetic protein [91, 92], whereas only a qualitative picture for nonnative states of proteins is gained, since they are composed of fluctuating conformations [97–99]. Using paramagnetic spin labels, long-range interactions were identified (e.g., in highly denatured myglobin) [99], in staphylococcal nuclease [97, 100], and in protein L [98]. Introduction of new binding sites for paramagnetic ions [80] and tagging those to nonnative states of proteins will allow detailed investigations using paramagnetic effects.

21.3.8
H/D Exchange

Hydrogen exchange methods can give insight into protein structure and dynamics by looking at the exchange of amide protons of the protein backbone with solvent protons. In general, protons that are involved in stable hydrogen bonds or are buried within the protein core are protected from exchange with the solvent. If either the buffer contains D_2O or the protein has been deuterated, the exchange of protons for deuterons or vice versa can be monitored by NMR. Hydrogen exchange techniques are valuable for the investigation of protein folding kinetics [101–104], folding intermediates, and unfolded states [105–107], since they can provide information on the degree and dynamics of secondary structure formation, which depends on the formation of stable hydrogen bonds. Hydrogen exchange is slow at low pH and faster at higher pH. In pulse labeling hydrogen exchange experiments [101], the process of folding or refolding could be investigated for some proteins. A typical approach of pulse-labeling hydrogen exchange is to let a deuterated protein initially refold for a short time (ms) (e.g., by diluting into D_2O refolding buffer) and give short pulses of protons at distinct times and high pH. This way, unprotected amide deuterons will exchange for protons and can be detected by 2D-NMR [108]. The reverse approach, namely refolding of nondeuterated protein in H_2O buffer and giving D_2O pulses, is also used [109–111]. The process of protein unfolding has been investigated in pulse-labeling hydrogen exchange NMR studies as well [112]. This topic is further described in Chapter 18.

21.3.9
Photo-CIDNP

Accessible aromatic side chains in proteins can be monitored using the photo-CIDNP (chemically induced dynamic nuclear polarization) NMR technique [113, 114]. The photo-CIDNP NMR technique relies on the temporary interaction of a photoexcited dye – mostly a flavin such as FMN (Figure 21.19) – with an aromatic amino acid side chain (Trp, Tyr, and His). Applying the photo-CIDNP technique to a protein results in signal enhancement as well as a better resolution in the aromatic region of the NMR spectrum (see Figure 21.19). Intensities of photo-CIDNP signals depend on (a) the polarization efficiency of a certain amino acid which is Trp $>$ Tyr $\gg$ His $\ggg$ Met and (b) the accessibility of the amino acid. Emissive photo-CIDNP signals are observed for Tyr residues, whereas the signals of Trp and His are absorptive – the sign of a signal therefore reports on the type of amino acid.

Using photo-CIDNP to achieve polarization enhancement is mostly seen in proton NMR spectroscopy – nevertheless higher enhancements are observed for ^{15}N nuclei [115]. One particular advantage of photo-CIDNP NMR for unfolded states is the better resolution due to the fact that only few residues are polarized. Using unlabeled protein, it is therefore often possible to assign peaks to the respective amino acid side chain and furthermore following changes in accessibility in differ-

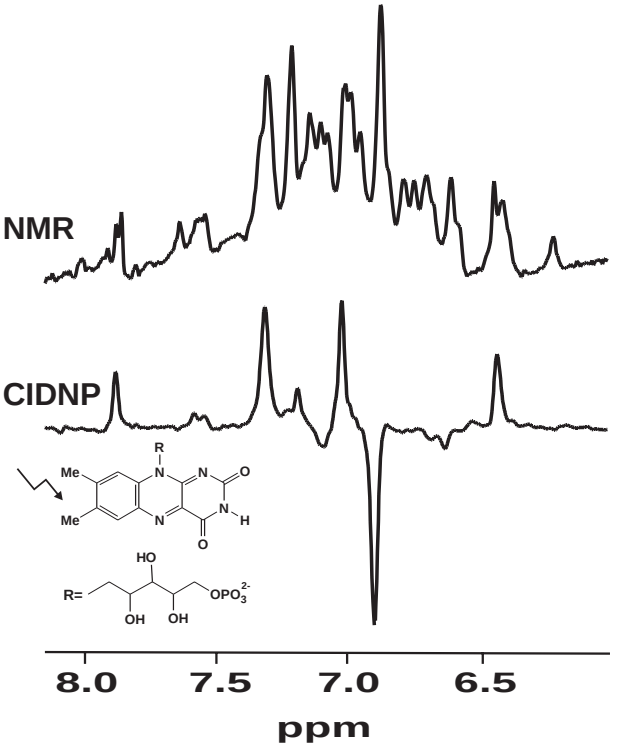

Fig. 21.19. 1D NMR and photo-CIDNP spectra of bovine α-lactalbumin. Photo-CIDNP is induced by irradiation of FMN (structure given at the lower left). Number of scans is 128 for the NMR spectrum and 1 for the CIDNP spectrum.

ent unfolded states [116]. Furthermore, photo-CIDNP NMR is being used in kinetic investigations of protein folding to monitor folding intermediates [117–119] – besides the better resolution since only few amino acids are polarized, better time resolution compared with normal NMR methods can be achieved due to the fact that the interscan delay depends only on the relaxation time of an electron (~10 ms). In addition, CIDNP experiment have been performed that transferred information on accessibilities in nonnative states of proteins onto the native protein using photo-CIDNP by polarizing the protein in the nonnative state, folding it rapidly, and observing polarized spins in the native state [120].

21.4
Model for the Random Coil State of a Protein

In a number of studies investigating nonnative states of lysozyme, α-lactalbumin, and ubiquitin, we have developed a model for the random coil state of a protein. The model assumes that the random coil state of a protein can be described using

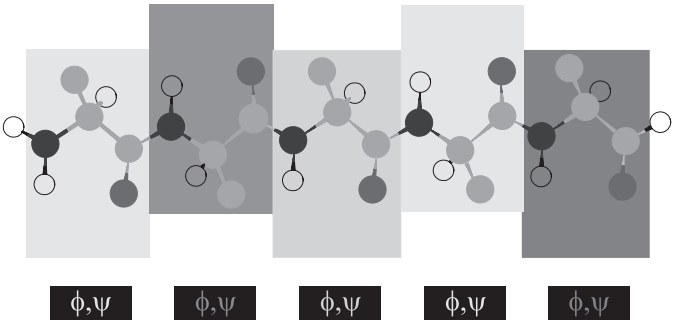

Fig. 21.20. The polypeptide chain consists of a chain of residues. Each residue has an intrinsic conformational preference even in the unfolded chain of protein. For a given distribution, NMR parameters such as *J* coupling constants and NOE can be predicted.

the notion that a polypeptide chain is a polymer consisting of 20 different amino acids. The conformational properties of the amino acids will depend on the nature of the side chain and therefore, amino acids exhibit distinct preferences in their sampling of conformational space described by the torsion angles ϕ, ψ (for the backbone conformation, depicted in Ramachandran plots) and correlated side-chain angles χ_n. Based on a conformational model for the distribution of torsion angle space, NMR parameters such as *J* coupling constants and, using some assumptions, NOEs can be predicted. G. Rose et al. further discuss the conformational properties of unfolded proteins in chapter 20.

Figure 21.21 shows the experimental ${}^3J(H^N H_\alpha)$ coupling constants in reduced and methylated lysozyme recorded in 8 M urea, pH 2. The measured coupling constants all fall in between the values predicted for either α-helical or β-strand secondary structure elements. However, the spread in the mesured values and the uneven distribution also calls for an interpretation of the data. Three models that do not invoke a residue-specific ϕ, ψ distribution could be envisioned to interpret the data: Model I would predict all ϕ-values $(-180^\circ < \phi < 180^\circ)$ to be equally likely, the averaged coupling constants would thus be predicted to be 5.3 Hz. Model II assumes an symmetric average between two conformations, namely 50% α-helical, 50% β-strand conformation. Model III assumes a distribution of ϕ-values as derived from the Ramachandran distribution found in all structure of proteins when averaged over all residues. Neither of the three models predicts the observed coupling constants well, especially the spread in couplings calls for a more detailed model including amino acid-specific sampling of the conformational space.

According to this random coil model, the random coil state of a polypeptide chain is presumed to be one in which there are no specific nonlocal interactions between residues [24, 25, 45, 121]. In such a state, individual residues will, however, have local conformational preferences and will sample the low energy ϕ, ψ conformations in the Ramachandran space. In the model, the ϕ, ψ populations for

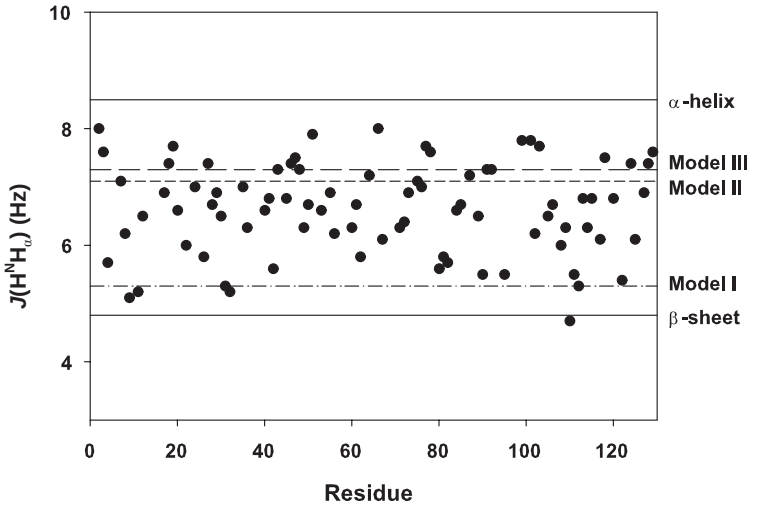

Fig. 21.21. $^3J(H^NH_\alpha)$ coupling constants in unfolded lysozyme (8 M urea, pH 2). Coupling constants expected for an α-helical and a β-sheet conformation are indicated as black lines. Models I–III indicate different averaging models that could be present in a random coil. Model I: all ϕ angles are equally likely (dashed-dotted line); model II: 50% α and 50% β-sheet conformation are populated (small dashed line); model III: populations are equally to the Ramachandran distribution (large dashed line).

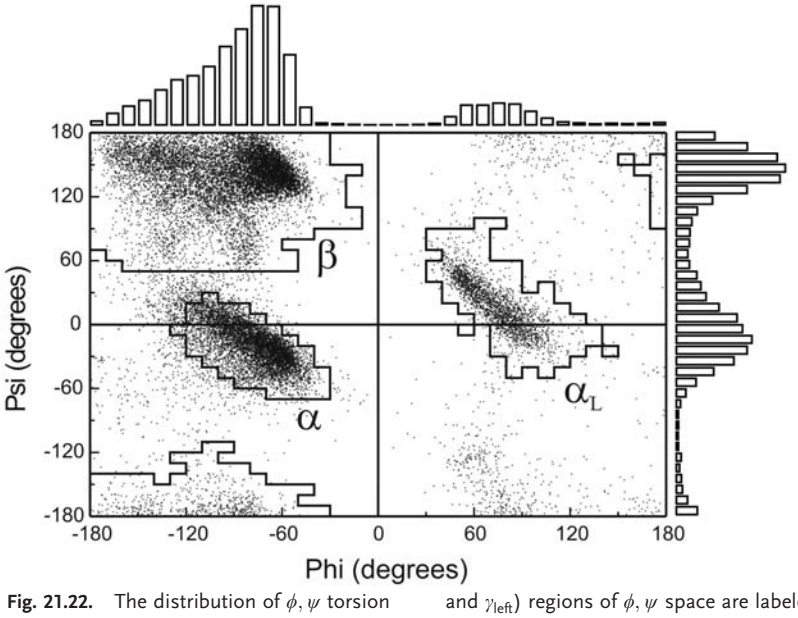

Fig. 21.22. The distribution of ϕ, ψ torsion angles for all amino acids not located in secondary structure elements in a database of 402 high-resolution crystal structures of native folded proteins. The α, β and α_L (combined α_{left} and γ_{left}) regions of ϕ, ψ space are labeled. Similar diagrams can be obtained with sufficient statistic for each amino acid individually.

residues in a random coil are derived from coil regions of 402 proteins from the protein data bank (Figure 21.22). It has been found that the distribution of ϕ, ψ torsion angles in the protein data bank resembles the experimental ϕ, ψ energy surface [24, 45, 122, 123], the effects of specific nonlocal interactions present in individual proteins are thus averaged out over the set of structures.

The amino acid-specific distribution obtained for each amino acid can also be used to calculate residue specific J coupling constants and also to calculate NOE intensities using a Monte-Carlo procedure and a simplified pentapeptide model. The pentapeptide model consists of explicit treatment of the backbone angles ϕ and ψ and a simplistic treatment of the side chains as a pseudoatom. Distributions of interproton distances can then be extracted from the conformational ensembles, and NOE intensities calculated assuming a two-spin approximation and r^{-6} averaging. Predicted values of NOE intensities converged with ensemble sizes of 10^5 conformers.

A different approach is chosen for the interpretation of dynamics in unfolded proteins. Backbone dynamics in proteins can be monitored by ^{15}N amide heteronuclear relaxation measurements. These heteronuclear relaxation measurements are sensitive to motions on a subnanosecond time scale and to slow conformational exchange in the millisecond time scale. Heteronuclear relaxation data unfolded proteins without disulfide bridges show only small variations over the sequence: Values approach a plateau at the middle of the protein while lower values are found at the termini of the sequence (Figure 21.23). This implies that the relaxation properties of a given amide are not influenced by its neighbor, but just by the fact that its part of the polypeptide chain. This relaxation behavior has been found for a number of unfolded proteins [21, 124] and in synthetic polymers [125] (see also Figure 21.35 for random coil state of ubiquitin). It was shown for atactic polystyrene that plateau values of R_1 relaxation rates remain constant for homopolymers between 10 kDa and 860 kDa. Individual segments of the long polymer chain therefore move independently in solutions – the apparent correlation time is therefore largely independent of the overall tumbling rate and only affected by segmental motions.

21.5
Nonnative States of Proteins: Examples from Lysozyme, α-Lactalbumin, and Ubiquitin

After the overview of NMR parameters that can measure aspects of conformation and dynamics of nonnative states of proteins, we wish to show the measurement of these NMR parameters primarily for one particular protein, lysozyme. Many of the experiments have been done together with Chris Dobson and former members of his group.

The native state of lysozyme consists of two domains, the α-domain, which spans from residue 1 to 35 and 85 to 129 and the β-domain that involves residues 36–84. Four disulfides bridges are present in the native structure; two of them in the α-domain of the protein, holding the N- and the C-termini together (C6–C127, C30–C115) one in the β-domain (C64–C80) and one between the domains (C76–C94).

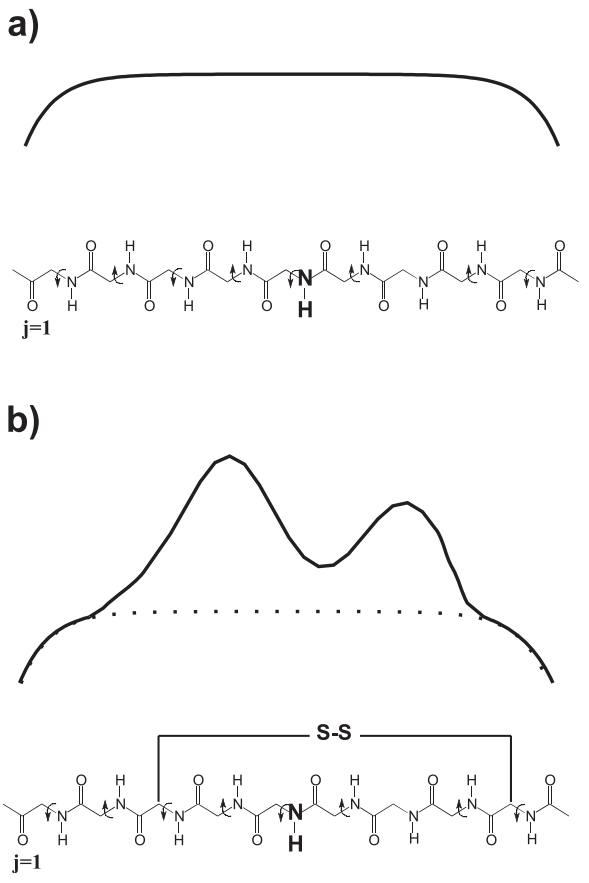

Fig. 21.23. Relaxation dynamics model for the random coil state. The relaxation properties of a given residue is influenced by the number of neighboring residues along the chain. For the interpretation of relaxation rates, one has to distinguish a) the unbranch polymer chain and b) the branched polymer chain, in which disulfide bridges cause additional cross-linking of the polypeptide chain and lead to increased relaxation rates.

Lysozyme has been studied under a range of denaturing conditions by NMR techniques [25, 42, 107, 126–129, 183, 253].

21.5.1 Backbone Conformation

21.5.1.1 Interpretation of Chemical Shifts

The measurement of chemical shifts is the most commonly used method to identify secondary structure in nonnative states of proteins. The most easily available chemical shifts are H^N, H^α, and ^{15}N amide chemical shifts as side products of the assignment of the protein backbone using ^{15}N-labeled protein. In addition, ^{13}C chemical shift assignment can be obtained and the interpretation of the data are

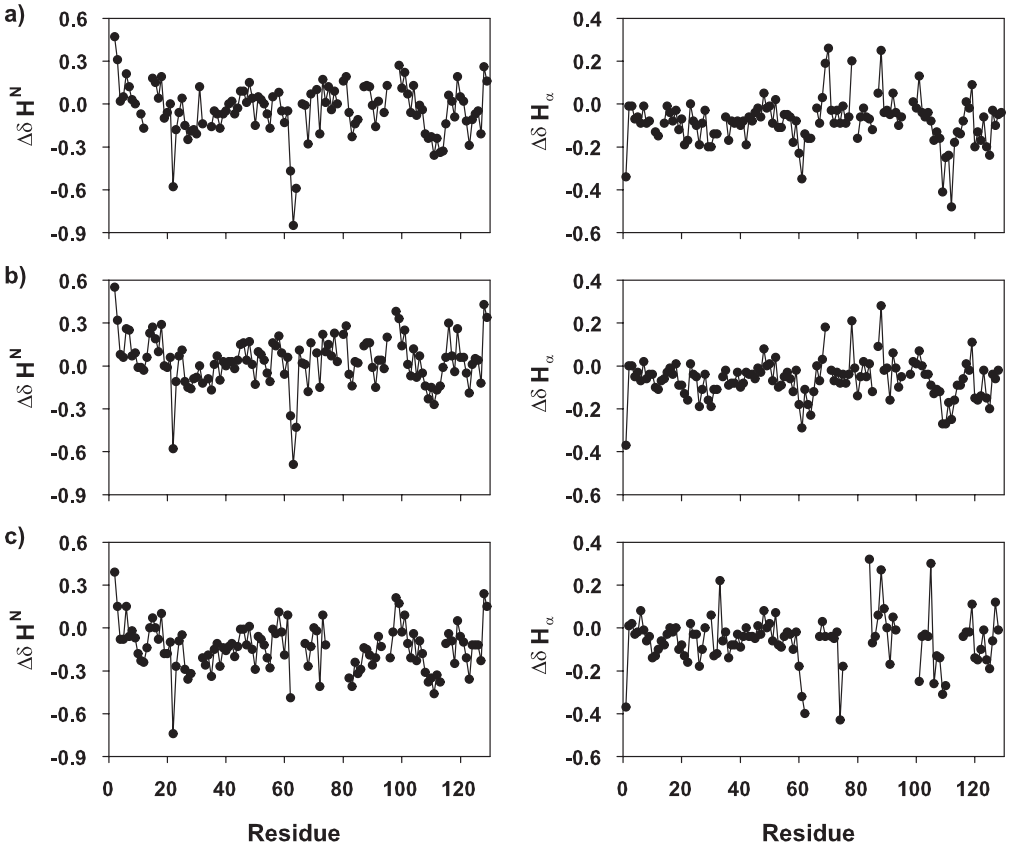

Fig. 21.24. Residual secondary structure in lysozyme as indicated by H^N and H_α chemical shifts pertubations ($\Delta\delta = \delta^{exp} - \delta^{rc}$) from random coil chemical shifts. a) Reduced and methylated hen lysozyme in water, pH 2, b) reduced and methylated hen lysozyme in 8 M urea, pH 2, and c) oxidized hen lysozyme in 8 M urea, pH 2.

shown in Figure 21.25. In the following section, it will be shown how these chemical shifts of random coil proteins can be used to (a) identify residual secondary structure (H^N and H^α) and to (b) investigate mean residue-specific properties of chemical shifts in unfolded states of proteins (^{15}N chemical shift).

H^N and H^α chemical shift perturbations ($\Delta\delta$) in unfolded variants of hen lysozyme from chemical shifts measured in short unstructured peptides are shown in Figure 21.24. The mean chemical shift pertubations are very close to the values measured in small unstructured peptides for all three variants. Figure 21.24a shows perturbations in a lysozyme variant in which all disulfide bridges have been reduced and subsequently methylated. This variant is unfolded at pH 2 in the presence and even in the absence of the denaturant urea. Large downfield deviations are found for Gly22 (H^N), for Val29 and Cys-S^{ME}30 (both H^α) around Trp62/Trp63 (R61 H^α; W62, W63 and C64 H^N), around Trp108/Trp111 (V109, R112 H^α; W111, N113, R114 H^N), and Trp123 indicating residual secondary struc-

ture. All these pertubations are found in aromatic patches of the protein, indicating that aromatic amino acids cluster and hereby form secondary structure elements, presumably to prevent contact with water. The cluster around Gly22 consists of the sequence Tyr-X-Gly-Tyr (where X can be any amino acid) and is also found to form a nonrandom cluster in BPTI [130–132]. Comparison of these chemical shift deviations to deviations of unfolded hen lysozyme in 8 M urea (oxidized and reduced) reveal that the formation of residual secundary structure around aromatic residues is a feature of the protein even detectable in 8 M urea.

Single point mutations of residues involved in patches of residual secondary structure in the unfolded state (A9G, W62G, W62Y, W111G, and W123G) do not change the pattern of chemical shift perturbations observed in methylated protein in water at pH 2 (see Figure 21.26) [253].

For an assessment of residue-specific properties of chemical shifts in random coil states of proteins, a data set of three proteins in 8 M urea at pH 2 was compared: human ubiquitin, reduced and methylated hen egg lysozyme and all-Ala α-lactalbumin [138]. As mentioned in Section 21.2, chemical shift dispersion in nonnative states of proteins is considerably smaller than in folded states of proteins, amide ^{15}N chemical shifts, however, display significant chemical shift dispersion and therefore have been analyzed as discussed below. Aromatic amino acids, cysteine, and methionine residues were excluded from the investigations because of the lack of experimental data and due to the fact that aromatic residues have been found to be involved in nonrandom structures in at least one of the three proteins.

Mean observed chemical shifts in native proteins of the BMRB (as of February 1999) are very close to the mean experimental ^{15}N chemical shifts in the three unfolded proteins ($R = 0.98$, see Figure 21.27). However, the spread of chemical shifts in the native state is very large, while there are only small variations in chemical shifts of the unfolded proteins.

21.5.1.2 Interpretation of NOEs

In contrast to the situation in the folded state of a protein, distances that can be observed by NOE measurements in nonnative states of proteins reflect an average of conformations with various distributions of ϕ, ψ, and χ_1 angles. Using the protein database (PDB), ϕ, ψ distributions of all amino acids can be generated. These distributions can be used as a model for a random coil in which no nonlocal interactions are present due to the fact that specific nonlocal interactions that are present in the individual proteins are averaged out over the ensemble of conformers contributing to the spectroscopic properties of the protein (see Section 21.4). Using this data set, interproton distance distributions can be extracted for the nonnative state of a protein. Table 21.6 shows statistics of interproton distance distributions. Effective interproton distances in the random coil state are given as $\langle r^{-6} \rangle^{-1/6}$ using the ϕ, ψ distributions of all proteins in the PDB.

Two features of the random coil state compared to the folded state of a protein are noticeable: (1) In contrast to the folded state of a protein, the distances αN $(i, i+1)$ and NN $(i, i+1)$ are short in every case, which reflects the averaged population of β and α conformations at the same time. (2) The effective αN $(i, i+2)$ dis-

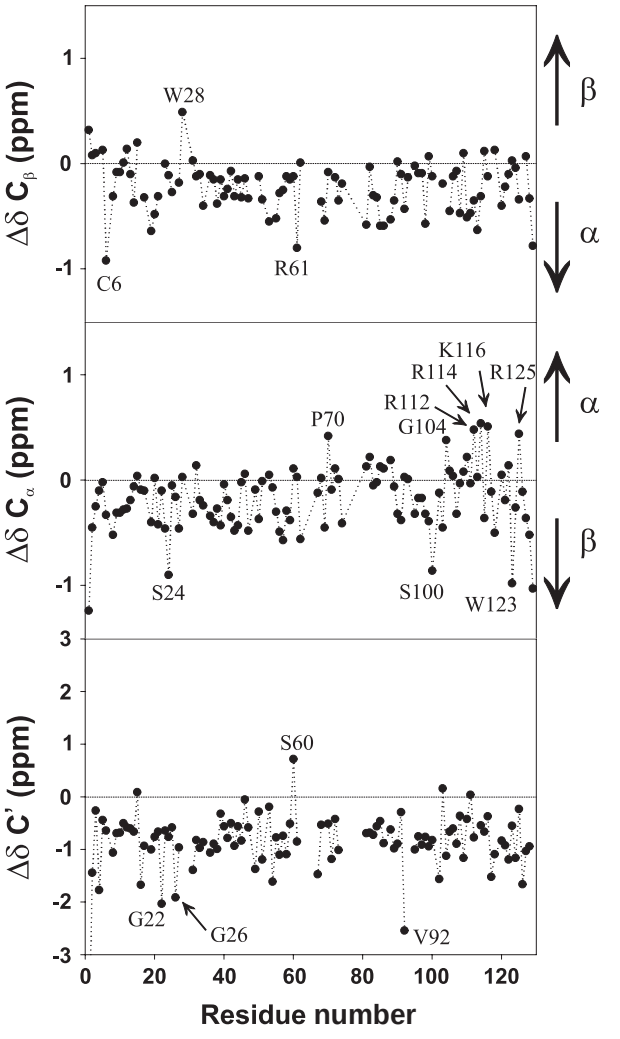

Fig. 21.25. Differences in $^{13}C'$, $^{13}C_\alpha$ and $^{13}C_\beta$ chemical shifts for lysozyme with its four disulfides intact denatured in 8 M urea from empirical values measured in short unstructured peptides ([37] $\Delta\delta = \delta^{exp} - \delta^{emp}$). ^{13}C chemical shifts in the present work are referenced indirectly to the internal standard TSP at pH 2 at 20 °C in 8 M urea. Mean secondary ^{13}C chemical shifts are (with standard deviations given in parentheses): $\langle\Delta\delta C_\alpha\rangle = -0.2$ (0.3) ppm, $\langle\Delta\delta C_\beta\rangle = -0.2$ (0.2) ppm, $\langle\Delta\delta C'\rangle = -0.9$ (0.6) ppm. Residues with $\Delta\delta \geq 0.38$ ppm, $\Delta\delta C_{\alpha,\beta} \leq -0.8$ ppm, and $\Delta\delta C' \leq -1.9$ ppm are labeled by one-letter amino acid code and residue number excluding terminal residues. Appropriate corrections for random coil shifts of Thr69 preceded by Pro70 were employed. Secondary chemical shifts for glutamate and aspartate residues have been omitted as the chemical shifts are affected by the protonation of the amino acid side chains at the low pH value of 2 used in this study. This is reflected by significant average deviations from random coil values for Asp, $\langle\Delta\delta C_\alpha\rangle = -1.6$ ppm, $\langle\Delta\delta C_\beta\rangle = -3.3$ ppm, $\langle\Delta\delta C'\rangle = -1.7$ ppm, and Glu, $\langle\Delta\delta C_\alpha\rangle = -1.3$ ppm, $\langle\Delta\delta C_\beta\rangle = -1.0$ ppm, $\langle\Delta\delta C'\rangle = -1.6$ ppm.

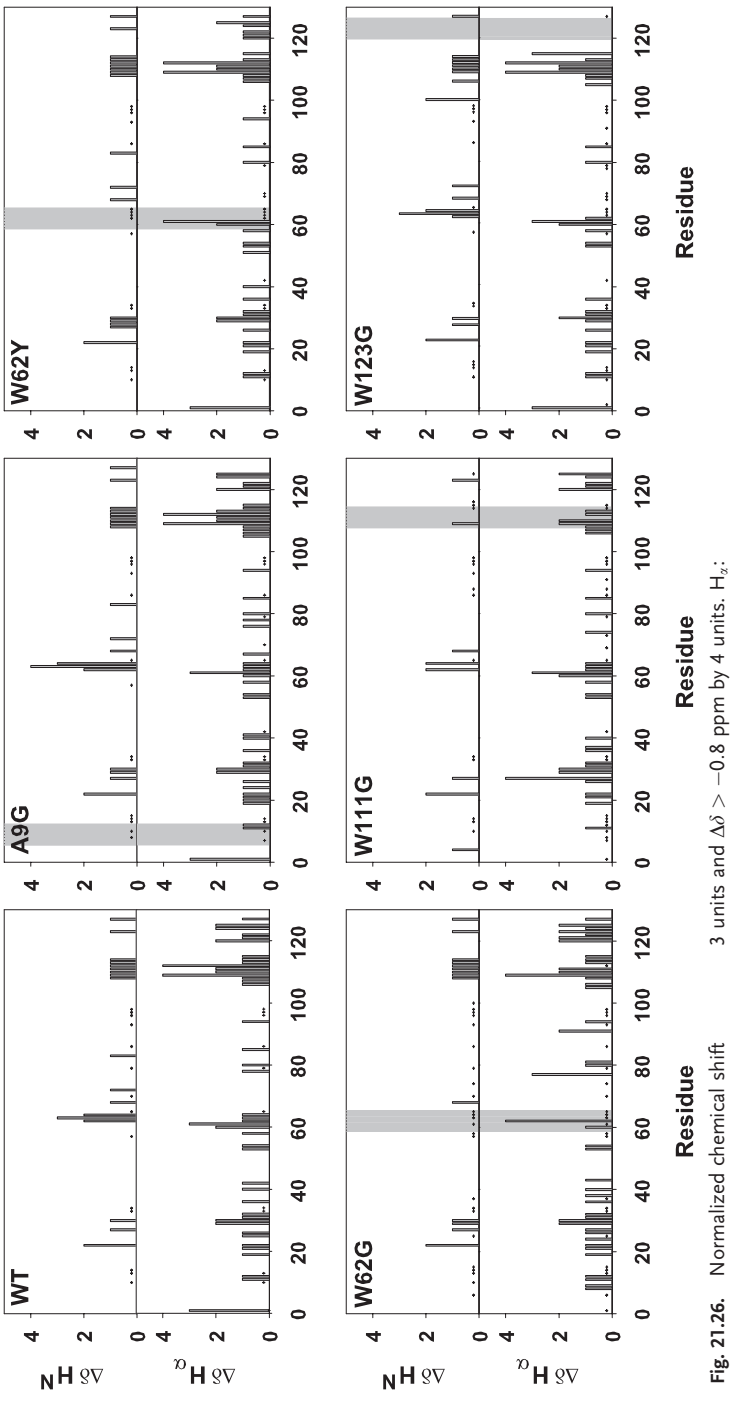

Fig. 21.26. Normalized chemical shift perturbations in methylated lysozyme single point mutants: A9G, W62G, W62Y, W111G and W123G. The following normalization scheme was applied: H^N: $\Delta\delta > -0.2$ ppm by 1 unit, $\Delta\delta > -0.4$ ppm by 2 units, $\Delta\delta > -0.6$ ppm by 3 units and $\Delta\delta > -0.8$ ppm by 4 units. H_α: $\Delta\delta > -0.1$ ppm by 1 unit, $\Delta\delta > -0.2$ ppm by 2 units, $\Delta\delta > -0.3$ ppm by 3 units, and $\Delta\delta > -0.4$ ppm by 4 units. Dots indicate missing assignments.

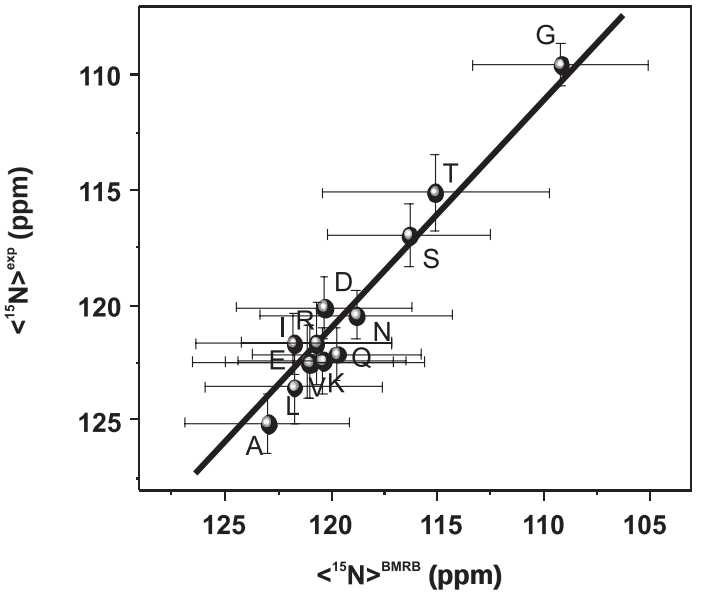

Fig. 21.27. Comparison of experimental ^{15}N chemical shifts in unfolded ubiquitin, hen lysozyme and all-Ala lactalbumin with chemical shifts in native proteins deposited in the databank for biomolecular NMR data (BMRB) (as of February 1999).

tance of 4.2 Å in the random coil state is shorter than in either of the secondary structure types. αN $(i, i+1)$, NN $(i, i+1)$, and αN $(i, i+2)$ as well as NN $(i, i+2)$, αN $(i, i+3)$, and NN $(i, i+3)$ distances have been predicted for hen lysozyme taking into account the amino acid sequence of hen lysozyme and using residue-specific ϕ, ψ distributions extracted from the PDB. The actual observability of NOE cross-peaks in the NOESY-HSQC of hen lysozyme (ox + red) in 8 M urea at pH 2 is dependent on the signal-to-noise ratio in the experiment and the effective correlation time of the protein, which could vary along the protein sequence (for the good signal-to-noise obtainable in the spectra of hen lysozyme, see Figure 21.28) [25].

Tab. 21.6. Comparison of the effective interproton distances in the ensemble of random coil conformers with interproton distances in regions of regular secondary structure. Effective interproton distances $\langle r-6\rangle^{-1/6}$ are given for an ensemble of random coil conformers generated using the ϕ, ψ torsion angle populations of all residues in the protein database.

Distance	*Random coil (Å)*	*α-helix (Å)*	*β-strand (Å)*
αN $(i, i+1)$	2.5	3.5	2.2
NN $(i, i+1)$	2.7	2.8	4.3
αN $(i, i+2)$	4.2	4.4	6.1
NN $(i, i+2)$	4.6	4.2	6.9

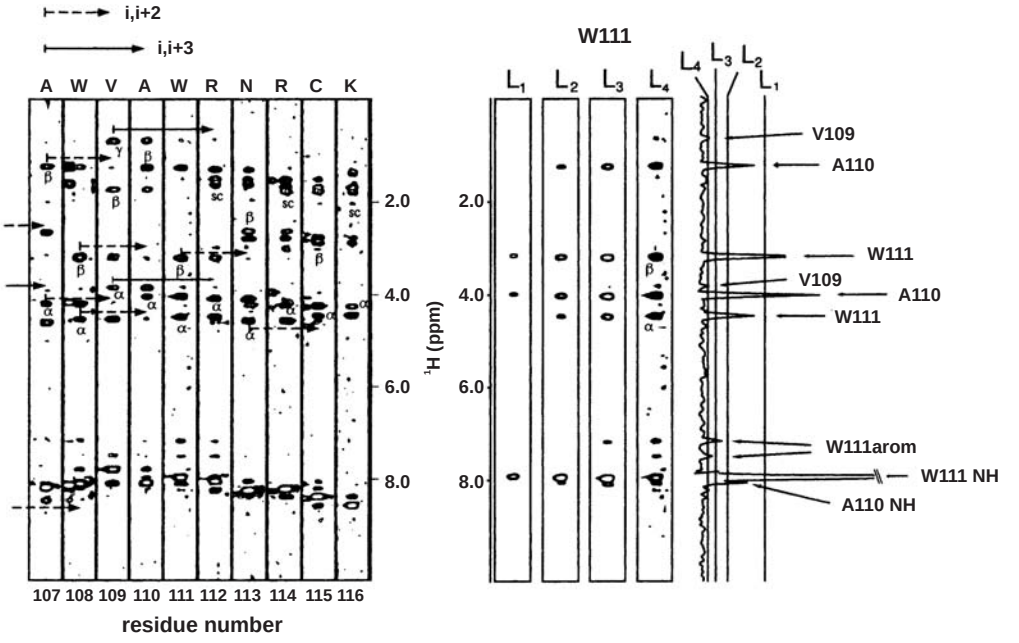

Fig. 21.28. Left: ^{1}H,^{1}H strips of residues 107–116 from a 3D NOESY spectrum of reduced and denatured lysozyme in 8 M urea at pH 2 (mixing time = 200 ms). Arrows indicated $(i, i+2)$ and $(i, i+3)$ cross-peaks as indicated. Right: ^{1}H,^{1}H strip of Trp111 is plotted at four different contour levels (= signal-to-noise levels), and 1D trace of Trp111. The different noise levels are indicated at the 1D trace, cross-peaks and the diagonal peak (Trp111 NH) are indicated.

The overall agreement between the predicted and experimental data from NOESY-HSQC spectra is remarkably good (Figure 21.29). αN $(i, i+1)$ and NN $(i, i+1)$ NOEs are predicted and observed throughout the protein sequence, furthermore 56 out of 82 predicted αN $(i, i+2)$ NOEs are seen while two of the αN $(i, i+2)$ NOEs are observed but not predicted. No correlation is observed between predicted and observed NN $(i, i+2)$ NOEs; while only 11 of the 27 predicted NN $(i, i+2)$ NOEs are observed, 10 NN $(i, i+2)$ cross-peaks are observed that are not predicted. A similarly poor correlation is observed for αN $(i, i+3)$ cross-peaks: two out of eight predicted NOEs are observed and seven NOEs are observed but not predicted. However, it is worth noting, that both the αN $(i, i+3)$ and the NN $(i, i+2)$ crosspeaks are predicted to be weak, and that the observability therefore depends very strongly on the signal-to-noise of the spectrum, which can vary locally. In summary, the considerable amount of predicted and observed NOEs in unfolded hen lysozyme, in particular αN $(i, i+1)$, NN $(i, i+1)$, and αN $(i, i+2)$ NOEs indicate that the averaged backbone conformation predicted from all proteins in the PDB describes the local preferences in lysozyme very well. It is important to note that this presence of NOEs is not a sign of persistent nonrandom structure

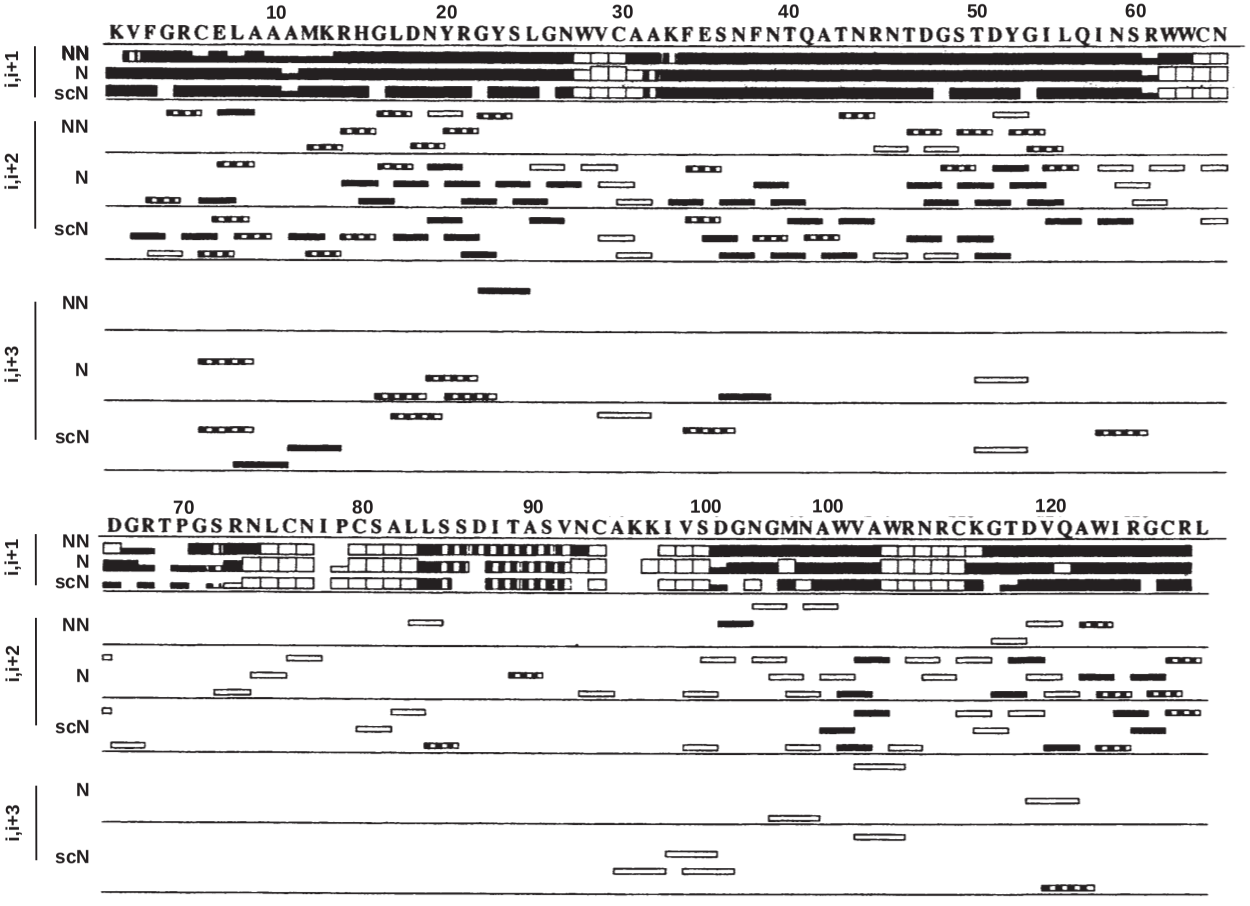

Fig. 21.29. Observed short- and medium-range NOEs in oxidized and reduced lysozyme (8 M urea, pH 2) from 3D NOESY-HSQC spectra (mixing time = 200 ms). Black bars are indicative for NOEs that are present in both states, whereas open bars indicated NOEs observed in the reduced state and dashed bars in the oxidized state only. NOEs to any side chain are summarized as scN NOEs.

in the unfolded state, but arises from statistical averaging of possible conformations in a random coil. This average is dominated by the shorter distances since the NOE is averaged as $\langle r^{-6} \rangle^{-1/6}$.

21.5.1.3 Interpretation of *J* Coupling Constants

A number of ^3J coupling constants (see Table 21.3) report on the torsion angle ϕ. $^3J(H^NH_\alpha)$, $^3J(C'C_\beta)$ and $^3J(C'C')$ have been measured in unfolded lysozyme (oxidized) in 8 M urea, pH 2 [183]. Moreover $^3J(H^NH_\alpha)$ coupling constants in unfolded ubiquitin and all-Ala lactalbumin (both in 8 M urea, pH 2) are available, to allow residue-specific analysis [138]. The experimental $^3J(H^NH_\alpha)$ coupling constants for all three proteins vary substantially along the protein sequence (see Figure 21.21 for reduced and methylated lysozyme in 8 M urea, pH 2, data for other proteins not shown), the values for a given amino acide type, however, typically cluster in small ranges. Figure 21.30 shows a comparison of experimental $^3J(H^NH_\alpha)$ coupling constants of the three proteins and predictions of $^3J(H^NH_\alpha)$ coupling constants using ϕ, ψ distributions from "coil" regions of 402 protein crystal structures and applying the Karplus parameterization shown in Table 21.3.

A fairly good correlation ($R = 0.85$) is observed for a complete data set including aromatic residues (not shown in Figure 21.30). The correlation improves if Glu and Asp residues that are protonated at pH 2 are excluded ($R = 0.89$). The best correlation, however, is observed if aromatics are left out as well ($R = 0.95$). Deviations of the coupling constants from mean values are similar for the predicted

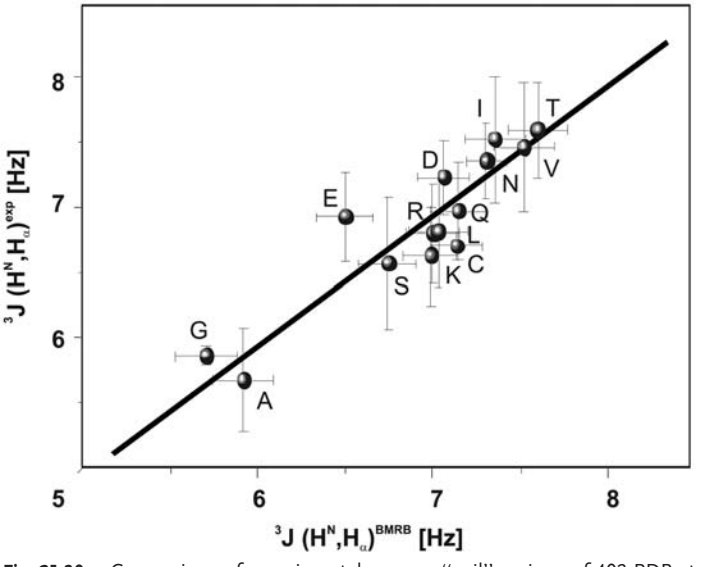

Fig. 21.30. Comparison of experimental $^3J(H^NH_\alpha)$ of unfolded ubiquitin, all-Ala α-lactalbumin, and lysozyme $^3J(H^NH_\alpha)^{exp}$ with $^3J(H^NH_\alpha)$ coupling constants predicted from "coil" regions of 402 PDB structures ($^3J(H^NH_\alpha)^{BMRB}$). Methionine, cysteine, and aromatic residues are left out due to the small amount of available data.

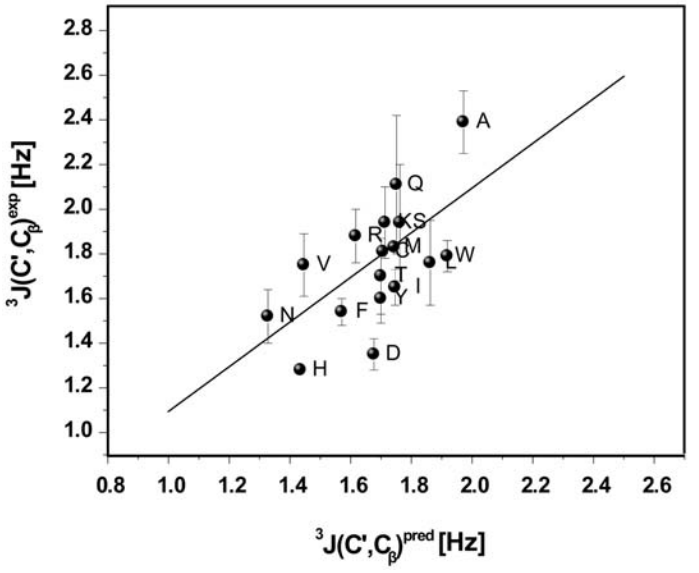

Fig. 21.31. Experimental versus predicted $^3J(C'C\beta)$ coupling constants using the coil model.

and the experimental coupling constants, reflecting the quality of the model used for the predictions. Investigations of the individual data sets (–Glu, –Asp and –aromatics) give rise to similar correlation coefficients ($R = 0.96$ for ubiquitin; $R = 0.94$ for lysozyme and $R = 0.90$ for all-Ala α-lactalbumin). These results indicate the independence of both the primary sequence and the native structure of the protein ubiquitin is composed of mainly β-sheets, while lysozyme and α-lactalbumin contain a significant number of α-helices in the native state.

The variation of $^3J(C'C_\beta)$ and $^3J(C'C')$ coupling constants is smaller than the variation in $^3J(H^NH_\alpha)$ coupling constants (Figure 21.31). The smallest variations are found in the $^3J(C'C')$ values, which range from 0.5 to 1 Hz. Nevertheless clustering of the experimental values is observable: values for eight Gly residues range from 0.5 to 0.7 Hz. A more detailed analysis of residue-specific properties of $^3J(C'C')$ coupling constants is not appropriate due to the small range of measured coupling constants.

Values of $^3J(C'C_\beta)$ in unfolded oxidized lysozyme range from 1.3 to 2.6 Hz. As observed for the $^3J(H^NH_\alpha)$ coupling constants, large variations along the sequence are found. These variations again cluster for different residue types. However a different trend is seen to that for the $^3J(H^NH_\alpha)$ coupling constants: the largest $^3J(C'C')$ are found for alanine residues, which have a high probability of being found in a conformation in the ϕ, ψ Ramachandran space, while the smaller values are found for residues with larger side chains such as histidine, asparagine, and valine residues. Figure 21.31 shows a correlation of experimental coupling constants with predicted coupling constants (Hz) from the coil theory. A correlation coefficient of $R = 0.63$ is observed for the complete data set (axis intercept = 0.07,

slope = 1), $R = 0.69$ (axis intercept = 0.0949, slope = 1) if Asp and Glu residues (that are protonated at pH 2 but not in the data sets used for the predictions) are left out.

The discussion thus far has focused on the determination of coupling constants that report on the backbone angle ϕ. Figure 21.32 shows a comparison of the prediction of $^3J(N^H,H_\alpha)$ coupling constants taking (a) all residues into account or (b)

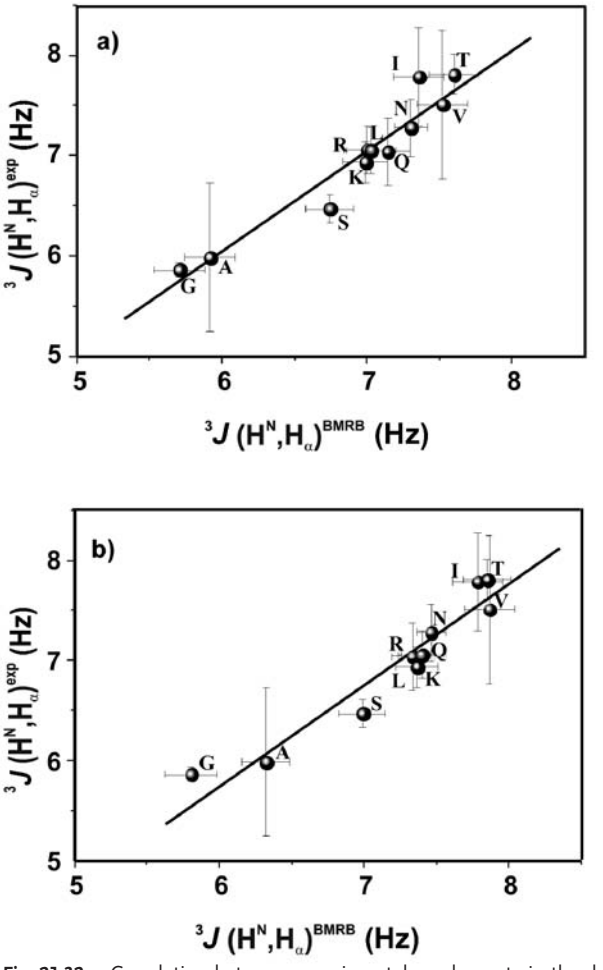

Fig. 21.32. Correlation between experimental $^3J(H^N,H_\alpha)$ averaged for a given residue type, e.g., all alanines in ubiquitin denatured in 8 M urea, pH 2, and $^3J(H^N,H_\alpha)$ coupling constants predicted for amino acids excluding aromatic amino acids and Asp and Glu residues. a) Comparison with predictions for residues that are not located in secondary structure elements in the database of native folded protein structures with ϕ, ψ torsion angles covering all regions of the Ramachandran diagram. b) Comparison with predictions for residues that are not located in secondary structure elements and that have positive ψ torsion angles only.

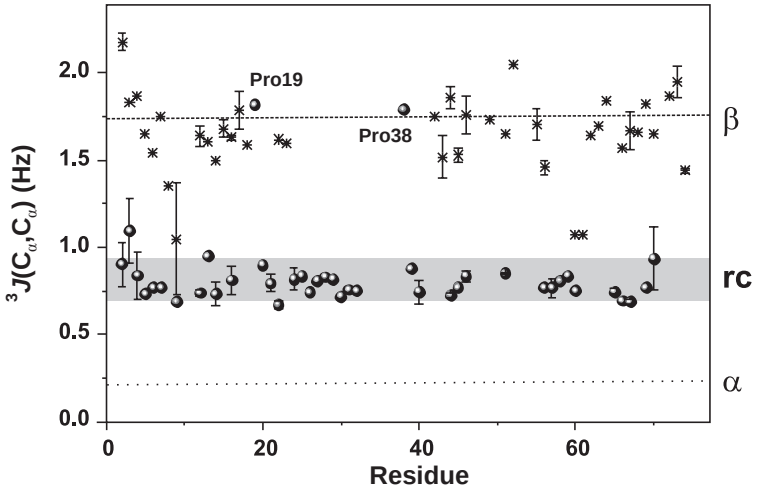

Fig. 21.33. $^3J(C_\alpha,C_\alpha)$ coupling constants in unfolded (dots) and folded (crosses) ubiquitin. Dashed line indicates expected coupling constants in a β-sheet, shaded area indicates expected values in a random coil (rc), and dotted line indicates values of coupling constants in the α-conformation.

only residues with positive ψ angle into account (compare Figure 21.22). A similar correlation ($R = 0.96$ in both cases) is observed showing that $^3J(N^H,H_\alpha)$ coupling constants cannot differentiate between a situation in which only extended conformations are being sampled (positive ψ values) and a situation in which the polypeptide chain samples both α- and β-regions of the Ramachandran space. The presence of experimental NOE contacts H^N_i, H^N_{i+1} and of $H_{\alpha i}$, H^N_{i+1} of similar intensity in nonnative states of proteins indicate that averaging involves sampling of positive and negative ψ torsion angles, which is compatible with predictions of our model. However, a quantitative analysis of populated rotamers from NOE intensities is difficult due to the r^{-6} averaging and complex dynamical properties that are potentially nonuniform along the denatured peptide chain.

$^3J(C_\alpha,C_\alpha)$ coupling constants can probe the conformation around the backbone angle ψ directly and are shown in Figure 21.33 for the random coil state and for the native state of ubiquitin [254]. The dependence of $^3J(C_\alpha,C_\alpha)$ on the angle ψ is unexpected and in contradiction to a simple Karplus-type dependence on the intervening torsion angle ω but was found for data obtained for native ubiquitin. The mean experimental coupling constants $^3J(C_\alpha,C_\alpha)$ for residues in β-sheet regions of native ubiquitin are 1.69 ± 0.1 Hz while coupling constants are too small to be observed in α-helical regions. In the random coil state of ubiquitin, $^3J(C_\alpha,C_\alpha)$ are larger than 0.7 Hz throughout the sequence, including residues 23–34 that are located in the α-helical region in the native state. The mean $^3J(C_\alpha,C_\alpha)$ coupling constant is 0.85 ± 0.2 Hz with a pairwise rmsd of 0.1 Hz for the 41 resonances that are sufficiently resolved to allow coupling constants to be determined. As an exception,

large $^3J(C_\alpha,C_\alpha)$ values are observed for Pro19 and Pro38. This might reflect a strong preference of prolines for ϕ,ψ torsion angles in the polyprolyl region of ϕ,ψ space ($\phi \sim -60°, \psi \sim +150°$) and potentially restricted ψ sampling.

The correlations found here confirm the previous conclusion based on the $^3J(H^N,H_\alpha)$ coupling constants, that the main-chain torsion angle populations in denatured lysozyme predominantly reflect the intrinsic ϕ,ψ preferences of the amino acids involved, and shows that coupling constant measurements can be used successfully to probe main-chain conformations in the nonnative state of a protein.

21.5.2 Side-chain Conformation

21.5.2.1 Interpretation of *J* Coupling Constants

According to the random coil model, the side-chain conformation in nonnative states of proteins has to be correlated with the type of amino acid and at least some degree of nonuniform sampling needs to be present between different amino acids. However, the measurement of such torsion angle distribution based on interpretation of NOE data is difficult due to spectral overlap and chemical shift analysis does not provide a detailed picture of the conformational averaging.

For the random coil state lysozyme, however, the measurement of $^3J(C',C_\gamma)$ and $^3J(N,C_\gamma)$ coupling constants has enabled side-chain χ_1 torsion angle populations to be probed in the random coil polypeptide chain [183]. Analysis of the coupling constant data has allowed the relative populations of the three staggered rotamers about χ_1 to be defined for 51 residues. Amino acids can broadly be divided into five classes which show differing side-chain conformational preferences in the random coil state (Figure 21.34).

The coupling constants were interpreted using a three-site jump model to describe qualitatively the χ_1 angle distributions (Pachler analysis). The analysis assumes, as a first approximation, that only the three staggered rotamers around the side-chain angle $\chi_1 = +60°, 180°, -60°$ have significant populations. It is assumed that there is rapid interconversion between these three rotamers so the observed coupling constants are a population weighted mean of the values expected for each of the three staggered rotamers (see Eqs (22a–c)):

$$
\begin{aligned}
&^3J_{exp}(N,C_\gamma) = p_{180°}\,{}^3J_{trans}(N,C_\gamma) + (1 - p_{180}) \cdot {}^3J_{gauche}(N,C_\gamma)\\
&^3J_{exp}(C',C_\gamma) = p_{-60°}\,{}^3J_{trans}(C',C_\gamma) + (1 - p_{-60}) \cdot {}^3J_{gauche}(C',C_\gamma) \qquad (22)\\
&p_{60} = 1 - p_{180} - p_{-60}
\end{aligned}
$$

Using Eqs (22a–c), the relative populations of the χ_1 conformers of 60°, −60°, and 180° have been calculated for each residue from the experimental $^3J(C',C_\gamma)$ and $^3J(N,C_\gamma)$ coupling constants. Analysis of the populations of the three staggered rotamers derived from the $^3J(C',C_\gamma)$ and $^3J(N,C_\gamma)$ coupling constants has enabled

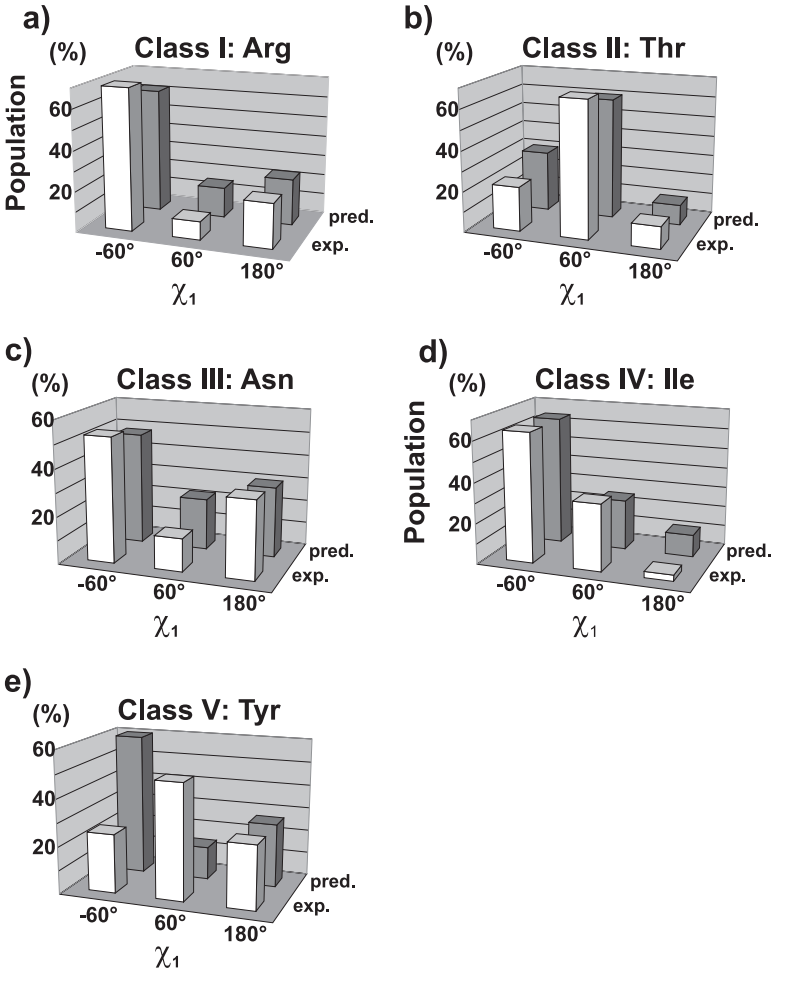

Fig. 21.34. Comparison of the mean percentage populations of the three staggered side chain χ_1 rotamers for different amino acids calculated from the experimental coupling constant data for lysozyme denatured in 8 M urea and predicted from the statistical model for a random coil. The aromatic residues are excluded from this comparison due to their anomalous behavior.

us to recognize several different classes of side-chain behavior (Figure 21.34). For residues with a long aliphatic side chain which is unbranched at C^{β} (Arg, Gln, Glu, Leu, Met; denoted class I), the -60° χ_1 rotamer is significantly favored (70–79% population) with a very low population ($< 10\%$) of the 60° χ_1 rotamer. In contrast for threonine (class II), it is the $+60^{\circ}$ χ_1 rotamer that is most highly populated (67%). For aspartate and asparagine (class III) the populations of the -60° χ_1 (53–55%) and 180° χ_1 rotamers (33–37%) are both significant while for isoleucine

(class IV) the -60° χ_1 rotamer is most populated (64%) with the lowest population for 180° χ_1 (3%). The behavior of the residues with aromatic side chains (class V) varies considerably with a range of populations being seen for a given type of aromatic side chain and different mean populations being observed for the various aromatic residues.

The behavior of the amino acid side chains observed experimentally in the random coil state of lysozyme has been compared with the predictions for a random coil from the statistical model. In particular the χ_1 populations derived from the experimental coupling constants have been compared with the χ_1 distributions in the PDB for residues that are not in recognized regions of secondary structure (COIL parameter set). The choice of this set of residues is important because the steric restraints of regular secondary structure elements can affect the χ_1 distributions significantly [122, 134, 135]. As the Pachler analysis does not consider the population of side-chain conformations other than those of the three staggered rotamers, we compare the relative proportions of χ_1 torsion angles falling within the ranges $\chi_1 = -60^\circ \pm 30^\circ$, $\chi_1 = +60^\circ \pm 30^\circ$ and $\chi_1 = 180^\circ \pm 30^\circ$ in the PDB with the analogous distributions calculated from the coupling constants. In general only a small number of residues in the database have χ_1 torsion angles that do not fall in the three ranges considered (e.g., 87 (5%) of the 1628 aspartate residues in the database). The PDB populations are listed in Table 21.7.

Many of the features of the side-chain populations derived from the experimental coupling constants are also clearly observed in the populations predicted for a random coil from the PDB. Examples of comparisons of the two sets of populations are shown in Figure 21.34. The PDB distributions predict that for all amino acids in a random coil, excluding serine, threonine, valine, isoleucine, cysteine, asparagine, and aspartic acid, the -60° χ_1 rotamer should have the highest population ($> 50\%$) and the $+60^\circ$ χ_1 rotamer the lowest population ($\leq 20\%$). The -60° χ_1 rotamer is most favored as it places the side chain in a position where the steric clash with the main chain is minimized while the $+60^\circ$ χ_1 rotamer is the most sterically restricted and therefore the least populated.

21.5.3 Backbone Dynamics

21.5.3.1 Interpretation of ^{15}N Relaxation Rates

Backbone dynamics in proteins can be monitored by ^{15}N amide heteronuclear relaxation measurements. These heteronuclear relaxation measurements are sensitive to motions on a subnanosecond time scale and to slow conformational exchange in the millisecond time scale. Figure 21.35 shows heteronuclear transverse relaxation rate of the random coil state of ubiquitin in 8 M urea at pH 2. The relaxation rates show only small variations over the sequence: Values approach a plateau at the middle of the protein while lower values are found at the termini of the sequence. This implies that the relaxation properties of a given amide are not influenced by its neighbor, but just by the fact that it is part of the polypeptide chain. The only exception from this behavior is Thr9 with considerable large relax-

Tab. 21.7. Predicted $^3J(C',C_\beta)$ and $^3J(C',C')$ coupling constants and populations of the three staggered side-chain χ_1 rotamers from the statistical model for a random coil. The coupling constant values and were calculated using the residues in all secondary structure elements (ALL) and for residues found neither in α nor β (COIL) in a database of 402 high-resolution crystal structures. The χ_1 populations were calculated using the COIL parameter set considering only the resides whose χ_1 torsion angles fall into 60% ranges centered about the distinct staggered rotamers ($\chi_1 = -60^\circ \pm 30^\circ$; $\chi_1 = 60^\circ \pm 30^\circ$ or $\chi_1 = 180^\circ \pm 30^\circ$). No side-chain populations are given for proline.

	Coupling constants (Hz)				***Relative χ_1 population (%)***		
	$^3J(C',C_\beta)$ ALL	$^3J(C',C_\beta)$ COIL	$^3J(C',C')$ ALL	$^3J(C',C')$ COIL	$\chi_1 - 60^\circ$ COIL	χ_1 60° COIL	χ_1 180° COIL
Ala	2.1	2.0	0.8	0.8	–	–	–
Asp	1.9	1.7	0.8	0.9	41	27	32
Asn	1.6	1.4	0.9	0.9	48	22	30
Arg	1.9	1.7	0.9	0.9	62	15	23
Cys	1.7	1.6	1.0	1.0	48	25	27
Gln	2.0	1.6	0.8	0.9	65	13	22
Glu	2.0	1.9	0.8	0.8	56	17	26
Gly	–	–	0.9	0.8	–	–	–
His	1.6	1.4	1.0	1.1	57	20	23
Ile	1.8	1.7	0.9	1.0	64	25	11
Leu	2.0	1.8	0.8	0.8	79	4	17
Lys	1.9	1.7	0.8	0.9	65	11	23
Met	1.9	1.7	0.8	0.9	65	11	23
Phe	1.7	1.6	1.0	1.0	62	13	25
Pro	2.4	2.4	0.5	0.5	–	–	–
Ser	1.8	1.7	1.0	1.0	31	46	23
Thr	1.7	1.6	1.0	1.0	30	60	10
Trp	1.8	1.7	0.9	0.9	52	17	31
Tyr	1.6	1.6	1.0	1.0	60	14	27
Val	1.7	1.6	1.0	1.0	26	9	64

ation rates. Besides that, the polypeptide chain of ubiquitin in 8 M urea, pH 2 does not exhibit any amino acid-specific variation of the heteronuclear relaxation rates. This relaxation behavior has also been found for a number of unfolded proteins [21, 124] and in synthetic polymers [125]. It was shown for atactic polystyrene that plateau values of R_1 relaxation rates remain constant for homopolymers between 10 kDa and 860 kDa. Individual segments of the long polymer chain therefore move independently in solutions – the apparent correlation time is therefore largely independent of the overall tumbling rate and only affected by segmental motions.

The relaxation rates for the random coil state of lysozyme are shown in Figure 21.36.

Using a model of segmental motions the relaxation properties can be described, assuming that relaxation contributions due to neighboring residues in a given

Tab. 21.8. Summary of the populations for χ_1 rotamers for denatured lysozyme calculated from the experimental coupling constants for the different classes of amino acids. The experimentally derived populations are mean values for each amino acid, the corresponding standard deviations being given in parentheses. Values for residues where the population of only one of the staggered rotamers could be defined have not been included when calculating the means (except of lysine). For isoleucine the populations listed are a mean of those calculated from coupling constants involving $C_{\gamma 1}$ and $C_{\gamma 2}$.

	Population (%) $\chi_1 = -60^\circ$	***Population (%)*** $\chi_1 = 60^\circ$	***Population (%)*** $\chi_1 = 180^\circ$
Class I: Long aliphatic side chains			
Arg	69.9 (4.1)	8.5 (9.7)	21.6 (11.9)
Gln	70.0 (1.6)	8.1 (1.6)	21.9 (2.7)
Glu	73.3 (0.3)	−1.7 (0.6)	28.5 (1.0)
Lys			35.1 (11.0)
Leu	74.3 (4.3)	−0.5 (2.8)	26.2 (4.7)
Met	78.5	−4.8	26.3
Class II: Side chains with OH at C_β			
Thr	22.1 (8.9)	66.8 (4.5)	11.1 (6.3)
Class III: Asx type residues			
Asn	52.5 (6.4)	14.4 (10.9)	33.1 (8.6)
Asp	55.4 (7.1)	7.4 (11.5)	37.2 (11.5)
Class IV: β-branched side chains			
Ile	63.7 (14.0)	33.2 (6.2)	3.1 (14.6)
Class V: Aromatic side chains			
His	55.5	13.4	31.1
Phe	45.3 (12.6)	23.0 (4.6)	31.7 (10.3)
Trp	24.0 (4.5)	20.9 (16.2)	55.1 (11.7)
Tyr	24.7 (6.5)	48.8 (9.1)	26.5 (15.4)

polypeptide chain decay exponentially as the distance from a given residue increases [25].

$$R_2^{\mathrm{rc}}(i) = R_{\mathrm{int}} \sum_{j=1}^{N} \mathrm{e}^{-(|i-j|/\lambda_0)} \tag{23}$$

A description of transverse relaxation rates (R_2 and $R_{1\rho}$) in reduced lysozyme (Figure 21.6d) using the segmental motion model (Eq. (23)) is shown in Figure 21.37 [25, 184]. R_2 relaxation rates and $R_{1\rho}$ relaxation rates are very similar, indicating the absence of significant chemical exchange contributions in the reduced and methylated protein. Deviations from relaxation rates predicted by the segmental motion model for a random coil are observed around Trp62/Trp63 and also near Trp108/Trp111 as well as around Trp123. Positive deviations from the segmental motions model indicate additional stiffness of the polypeptide chain, that is induced by interactions of the bulky side chains. A description of these deviations

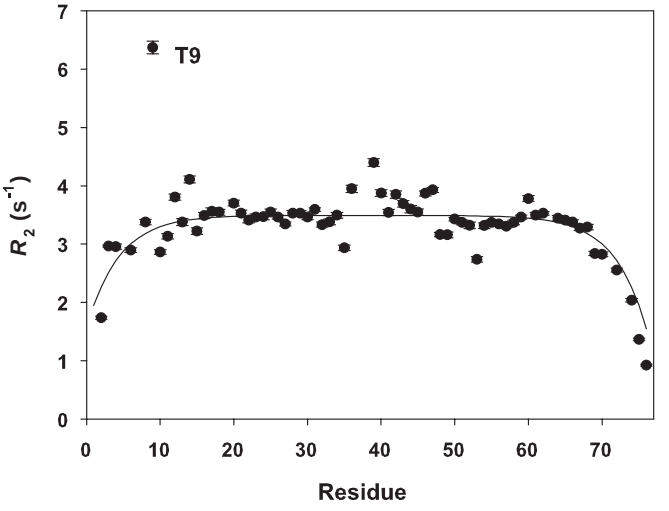

Fig. 21.35. Transverse relaxation rates of the random coil state of ubiquitin (8 M urea, pH 2) at 600 Hz. Fitting parameters for random coil predictions: $R_{int} = 0.4$, $\lambda = 4.35$.

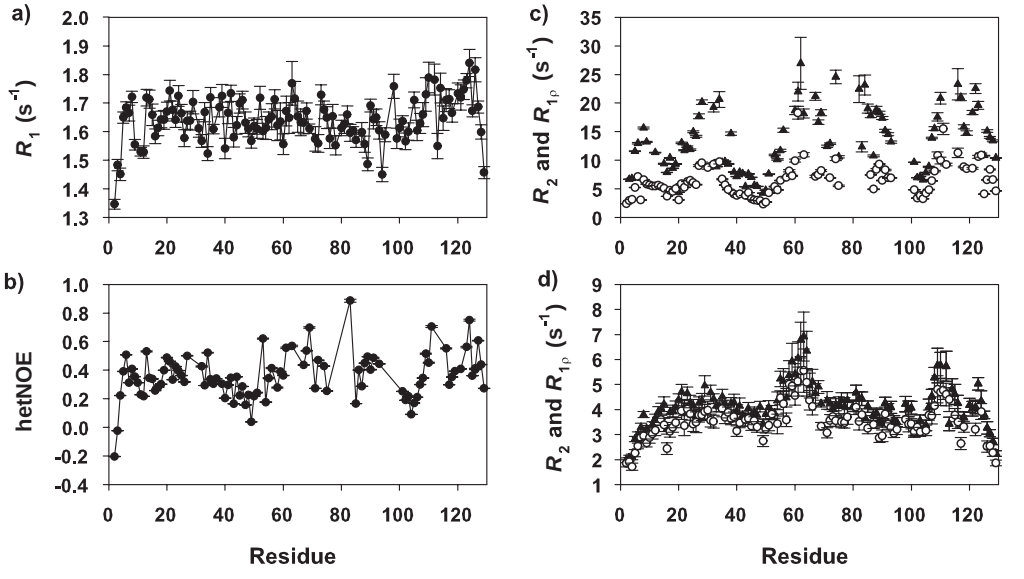

Fig. 21.36. Relaxation data of backbone amides of oxidized and reduced lysozyme in 8 M urea at pH 2. a) R_1 relaxation rates of reduced lysozyme, b) hetNOE of oxidized lysozyme, c) R_2 relaxation rates (filled triangles) and $R_{1\rho}$ relaxation rates (open circles) of oxidized lysozyme, and d) R_2 relaxation rates (filled triangles) and $R_{1\rho}$ relaxation rates (open circles) of reduced lysozyme.

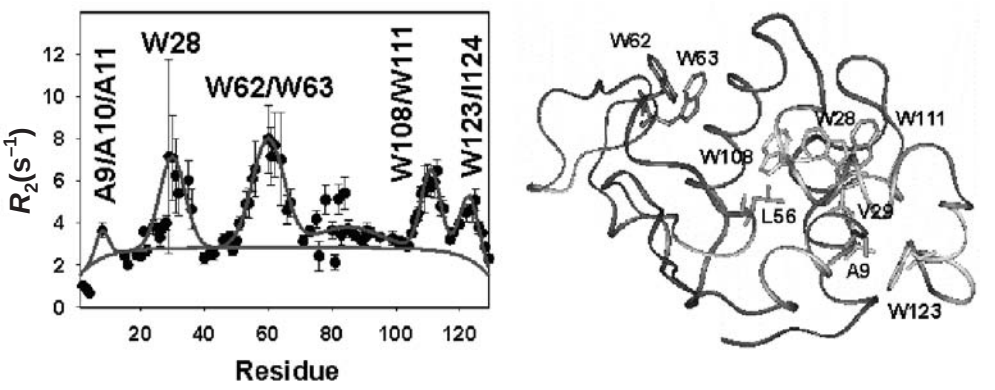

Fig. 21.37. a) ^{15}N R_2 in WT-S^{ME}. The experimental rates are shown as a scatterplot and the rates fitted by a model of segmental motion expected for a random coil with R_2^{rc} ($R_{int} = 0.2\ s^{-1}$ and $\lambda_0 = 7$) are shown as dashed lines. Translation of the relaxation data on the native structure of lysozyme is shown in b).

from the segmental motions model can be done introducing Gaussian clusters to the segmental motion model:

$$R_2^{exp}(i) = R_{int} \sum_{j=1}^{N} e^{-(|i-j|/\lambda_0)} + \sum_{cluster} R_{cluster} e^{-((i-x_{cluster})/2\lambda_{cluster})^2} \quad (24)$$

The clusters of restricted motions observed by relaxation measurements in reduced and methylated lysozyme correspond to the areas of residual secondary structure identified from chemical shift perturbations (see Figure 21.25). The dynamics of the unfolded peptide chain are also investigated in detail in Chapter 22.

The interpretation of R_2 and $R_{1\rho}$ relaxation rates in oxidized and therefore branched unfolded lysozyme is more complicated: not only residues that are near in sequence influence the relaxation properties of a given amide, but also residues that are near via disulfide bridges. A topological distance matrix, $\mathbf{dm}_{ij}$, which counts the shortest path from residue i to residue j, is used in which a disulfide bond counts the same as a peptide bond in connecting two residues (see Eq. (25)). R_2 and R_1 relaxation rates are clearly different, indicating exchange processes taking place around disulfide bridges. For a complete description of R_2 relaxation rates it is therefore necessary to include a term describing these exchange processes as shown in Eq. (25).

$$R_2^{exp}(i) = R_{int} \sum_{j=1}^{N} e^{-(dm_{ij}/\lambda_0)} + R_{exch} \sum_{k=1}^{N_{cys}} e^{-(|i-Cys_k|/\lambda_2)} \quad (25)$$

Due to the complexity of contributions to relaxation rates in branched systems further investigations concerning the nature of deviations from the segmental motion model have been performed using reduced and methylated variants of lysozyme

(i.e., unbranched polypeptide chains). Figure 21.37 shows R_2 relaxation rates measured in reduced and methylated lysozyme in water. Six hydrophobic clusters were identified in WT-S^{ME} using the extended segmental motion model (Eq. (24)). These clusters are centered at residues (1) L8, (2) C30, (3) S60, (4) S85, (5) W111, and (6) W123. The most prominent cluster, cluster 3 is found in the middle of the protein sequence which belongs to the β-domain in folded lysozyme. All other clusters (cluster 1, 2, 4, 5, and 6) are found in what is to be the α-domain in the folded state of the protein. While clusters 3, 5, and 6 are also observed in urea, cluster 2 which is near Trp28 is destroyed by the addition of urea. Furthermore the rather small clusters 1 and 4 cannot be identified in the presence of urea. The importance of weak interactions in protein folding is reviewed in Chapter 6.

Stabilization of these clusters can be tested by single point mutations in conjunction with relaxation measurements [184, 253]: Replacement of Trp62 in cluster 3 by glycine essentially abolishes not only its own cluster 3 but also clusters 1 through 4, and diminishes clusters 5 and 6 (as seen in Figure 21.38). The disruption of the clusters far away in sequence clearly indicates the presence of long-range interactions in WT-S^{ME}. Interestingly, clusters also seem to play an important role in refolding: hydrogen exchange measurements have shown that the α-domain of lysozyme folds a lot faster than the β-domain, with exception of residue W63, which becomes exchange-protected as quickly as the α-domain. An association of the region around W62/W63 with the α-domain as shown by relaxation measurements is therefore not only present in the unfolded state, but seems to be important for the folding nucleus of the protein.

In order to test whether this property of Trp62 to stabilize the folding nucleus is unique to tryptophan or may be more generally attributable to aromatic amino acids, the effect of replacing Trp62 by tyrosine is shown in Figure 21.38c. The W62Y mutation has a very minor effect on the relaxation properties of WT-S^{ME} compared with W62G-S^{ME}. This result suggests that aromatic residues play an important role in the stabilization of long-range interactions in unfolded states of lysozyme.

A9G-S^{ME} even more so displays WT-S^{ME} properties. There is not even an effect on its own cluster, cluster 1. The hydrophobic clusters remain of virtually identical size and position, indicating that Ala9 is not important for stabilizing the hydrophobic core.

In contrast, results of the replacement of tryptophan residues at positions 111 and 123 are very significant. When Trp111 (cluster 5) is replaced by glycine, the cluster in which the mutation is located disappears entirely, and cluster 6 also decreases significantly in intensity. Loss is also observed in the intensity of cluster 2 (surrounding Trp28) and a very small decrease in the intensity of cluster 3 (surrounding Trp62 and Trp63). Similarly, when Trp123 at the C-terminus (cluster 6) is changed to a glycine, the cluster around the mutation site essentially disappears, and the intensities of clusters 2, 3, and 5 are lessened. The effect of W123G replacement is less significant than that of W111G, as seen by the complete loss of cluster 5 in W111G-S^{ME} but not in W123G-S^{ME}. The largest changes in R_2 distribution as compared to WT-S^{ME} is observed with W62G-S^{ME}. W62G-S^{ME} on one,

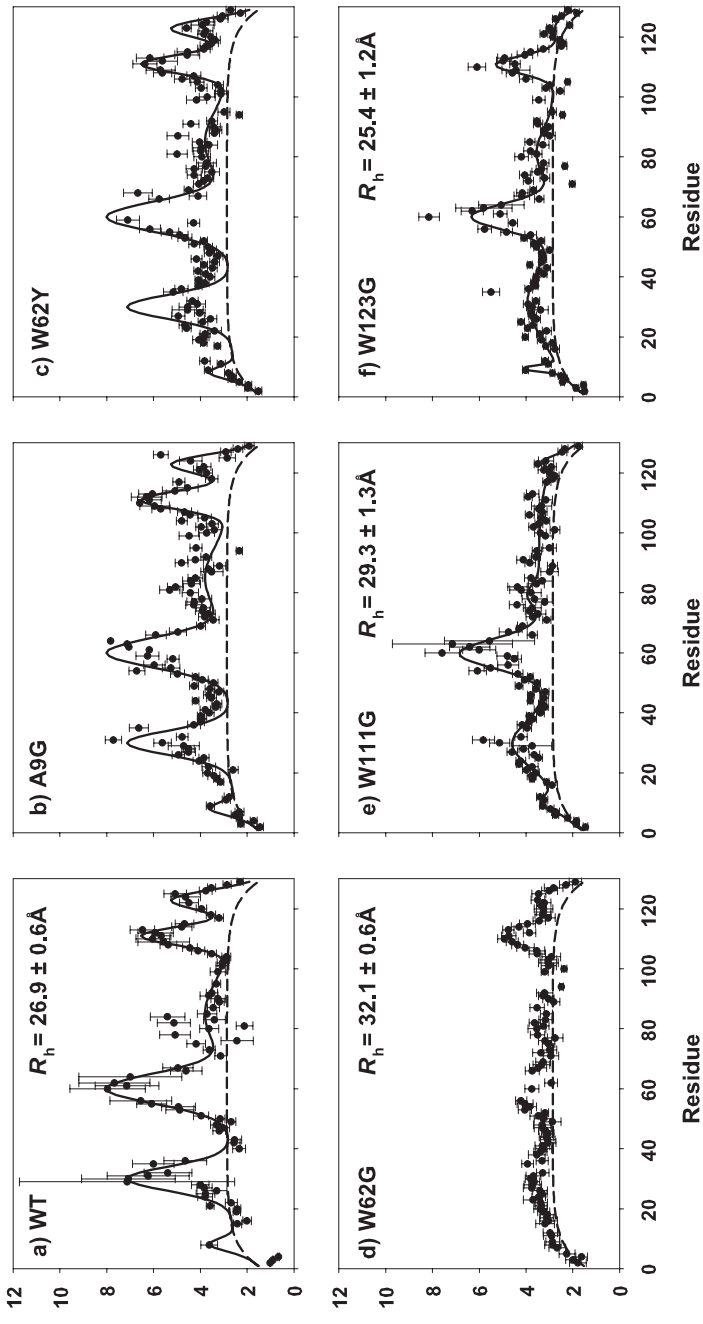

Fig. 21.38. ^{15}N R_2 in WT-S^{ME} and W62G-S^{ME}, W62Y-S^{ME}, A9G-S^{ME}, W111G-S^{ME}, and W123G-S^{ME} are shown in panels a–e, respectively. The experimental rates are shown as a scatter plot and the rates fitted by a model of segmental motion expected for a random coil with R_2^{rc} ($R_{int} = 0.2$ s^{-1} and $\lambda_0 = 7$) are shown as dashed lines; black lines show Gaussian fits for WT-S^{ME} (a,b,c) W111G-S^{ME} (e) and W123G-S^{ME} (f).

W111G-S^{ME} and W123G-S^{ME} on the other side appear complementary to each other: while the W62G mutation causes dramatic disruption of clusters 1–4, and to a lesser extent of clusters 5–6, the W111G and W123G replacements causing more disruption in clusters 2, 5, and 6 and more subtle changes in cluster 3.

21.6 Summary and Outlook

Here we summarize some of the findings from NMR investigations of nonnative states of proteins:

- The investigations show that NMR parameters can be predicted using models for the random coil state of a protein. The applied model treats the polypeptide chain as a (branched or unbranched) homopolymer for the prediction of anisotropic and global parameters such as relaxation rates or RDCs. On the other hand, for the prediction of local parameters, only explicit models such as the random coil model (Section 21.4) with amino acid-specific torsion angle distribution will allow correlation with experimental data such as *J*-couplings and NOEs, since the experiment is sensitive enough to detect small local differences in the conformational sampling. Second-order effects revealing the more detailed dependence on nearest neighbor effect will need a larger statistical database for their firm interpretation.
- Random coil states of proteins sample the ϕ, ψ and χ_1 conformational space according to distribution functions derived from the analysis of structures prevalent in all protein structures [24, 45, 122, 123]. The assumption that the distribution of ϕ, ψ torsion angles in the PDB resembles the experimental ϕ, ψ energy surface and that the effects of specific nonlocal interactions present in individual proteins are averaged out over the set of structures seems to be valid. More sophisticated approaches including molecular dynamics simulations of nonnative states of proteins will be of importance in the future to go beyond the current conformational and dynamic description of these states.
- On the basis of the delineation of the ''random coil'' behaviour, significant deviations identifying nonrandom structures in nonnative states can be found for a number of different proteins. These deviations include both nonrandom conformational preferences and differences from rapid dynamics that would interconvert the ensemble of states. The nonrandom structure can be shown to be stabilized both by local and global interactions and same of the global interactions trap the polypeptide chain into conformations not present in the native structure of the protein. In these investigations, combined mutational and NMR spectroscopic investigations have been particularly powerful tools in showing changes in overall compaction in these states. It is tempting to speculate that mutations do alter the energetics of the ensemble of states representing the unfolded states of a protein.

  Natively unfolded proteins form a significant part of the proteom and reveal

that the polypeptide chain may not necessarily adopt a globular, rigid fold to exert its function. Bioinformatic analysis suggests these states to be more abundant than initially assumed.

- At the same time, misfolded, yet highly regular fibrillar states of proteins are formed in many protein folding diseases. In light of these considerations, heteronuclear NMR spectroscopy seems to be the most versatile and powerful technique to characterize aspects of conformation and dynamics in all of these states of proteins. In all of these investigations, the clear definition of what to expect for a random coil protein will form a firm baseline to predict deviations in a reliable manner.

Acknowledgments

H.S. would like to acknowledge the fruitful and fascinating collaboration and discussions with C. M. Dobson, K. Fiebig, M. Buck, L. Smith, M. Hennig, W. Peti, S. Grimshaw, C. Redfield, J. Jones, S. Glaser, and C. Griesinger in characterizing nonnative states of proteins. The work in the group of H.S. has been carried out by a number of extremely creative and bright students, who we would like to thank: T. Kühn, E. Collins, J. Klein-Seethamaran, E. Duchardt, and K. Schlepckow. We would like to thank the DFG, the European Commission, the Fonds der Chemischen Industrie, the state of Hesse and the University of Frankfurt for financial Support.

References

1 Dyson, H. J. & Wright, P. E. (2002). Coupling of folding and binding for unstructured proteins. *Curr Opin Struct Biol* 12, 54–60.

2 Wright, P. E. & Dyson, H. J. (1999). Intrinsically unstructured proteins: re-assessing the protein structure-function paradigm. *J Mol Biol* 293, 321–331.

3 Uversky, V. N. (2002). What does it mean to be natively unfolded? *Eur J Biochem* 269, 2–12.

4 Schweers, O., Schonbrunn-Hanebeck, E., Marx, A. & Mandelkow, E. (1994). Structural studies of tau protein and Alzheimer paired helical filaments show no evidence for beta-structure. *J Biol Chem* 269, 24290–24297.

5 Uversky, V. N., Gillespie, J. R. & Fink, A. L. (2000). Why are "natively unfolded" proteins unstructured under physiologic conditions? *Proteins* 41, 415–427.

6 Tompa, P. (2002). Intrinsically unstructured proteins. *Trends Biochem Sci* 27, 527–533.

7 Uversky, V. N. (2002). Natively unfolded proteins: a point where biology waits for physics. *Protein Sci* 11, 739–756.

8 Linding, R., Jensen, L. J., Diella, F., Bork, P., Gibson, T. J. & Russell, R. B. (2003). Protein disorder prediction: implications for structural proteomics. *Structure (Camb)* 11, 1453–1459.

9 Gerstein, M. (1998). How representative are the known structures of the proteins in a complete genome? A comprehensive structural census. *Folding Des* 3, 497–512.

10 Dyson, H. J. & Wright, P. E. (2001).

Nuclear magnetic resonance methods for elucidation of structure and dynamics in disordered states. *Methods Enzymol* 339, 258–270.

11 Dobson, C. M. & Hore, P. J. (1998). Kinetic studies of protein folding using NMR spectroscopy. *Nat Struct Biol* 5 Suppl, 504–507.

12 Dyson, H. J. & Wright, P. E. (1996). Insights into protein folding from NMR. *Annu Rev Phys Chem* 47, 369–395.

13 Frieden, C., Hoeltzli, S. D. & Ropson, I. J. (1993). NMR and protein folding: equilibrium and stopped-flow studies. *Protein Sci* 2, 2007–2014.

14 Englander, S. W. & Mayne, L. (1992). Protein folding studied using hydrogen-exchange labeling and two-dimensional NMR. *Annu Rev Biophys Biomol Struct* 21, 243–265.

15 Dyson, H. J. & Wright, P. E. (1991). Defining solution conformations of small linear peptides. *Annu Rev Biophys Biophys Chem* 20, 519–538.

16 Dyson, H. J. & Wright, P. E. (1993). Peptide conformation and protein folding. *Curr Opin Struct Biol* 3, 60–65.

17 Case, D. A., Dyson, H. J. & Wright, P. E. (1994). Use of chemical shifts and coupling constants in nuclear magnetic resonance structural studies on peptides and proteins. *Methods Enzymol* 239, 392–416.

18 Neri, D., Billeter, M., Wider, G. & Wuthrich, K. (1992). NMR determination of residual structure in a urea-denatured protein, the 434-repressor. *Science* 257, 1559–1563.

19 Bax, A. & Grzesiek, S. (1993). Methodological Advances in Protein NMR. *Acc Chem Res* 26, 131–138.

20 Wittekind, M. & Mueller, L. (1993). HNCACB, a high-sensitivity 3D NMR experiment to correlate amide-proton and nitrogen resonances with the alpha- and beta-carbon resonances in proteins. *J Magn Reson Ser B* 101.

21 Logan, T. M., Theriault, Y. & Fesik, S. W. (1994). Structural characterization of the FK506 binding protein unfolded in urea and guanidine hydrochloride. *J Mol Biol* 236, 637–648.

22 Wishart, D. S. & Case, D. A. (2001). Use of chemical shifts in macromolecular structure determination. *Methods Enzymol* 338, 3–34.

23 Xu, X.-P. & Case, D. A. (2001). Automated prediction of 15N, 13Ca, 13Cβ and 13C′ chemical shifts in proteins using a density functional database. *J Biomol NMR* 21, 321–333.

24 Smith, L. J., Bolin, K. A., Schwalbe, H., MacArthur, M. W., Thornton, J. M. & Dobson, C. M. (1996). Analysis of main chain torsion angles in proteins: prediction of NMR coupling constants for native and random coil conformations. *J Mol Biol* 255, 494–506.

25 Schwalbe, H., Fiebig, K. M., Buck, M. et al. (1997). Structural and dynamical properties of a denatured protein. Heteronuclear 3D NMR experiments and theoretical simulations of lysozyme in 8 M urea. *Biochemistry* 36, 8977–8991.

26 Louhivuori, M., Paakkonen, K., Fredriksson, K., Permi, P., Lounila, J. & Annila, A. (2003). On the origin of residual dipolar couplings from denatured proteins. *J Am Chem Soc* 125, 15647–1550.

27 McDonald, C. A. & Phillips, D. C. (1969). Proton magnetic resonance spectra of proteins in random-coil configurations. *J. Am. Chem. Soc.* 91, 1513–1521.

28 Schwarzinger, S., Kroon, G. J., Foss, T. R., Chung, J., Wright, P. E. & Dyson, H. J. (2001). Sequence-dependent correction of random coil NMR chemical shifts. *J Am Chem Soc* 123, 2970–2978.

29 Wishart, D. S., Sykes, B. D. & Richards, F. M. (1991). Relationship between nuclear magnetic resonance chemical shift and protein secondary structure. *J Mol Biol* 222, 311–333.

30 Wishart, D. S. & Sykes, B. D. (1994). The ^{13}C chemical-shift index: a simple method for the identification of protein secondary structure using ^{13}C chemical-shift data. *J. Biomol. NMR* 4, 171–180.

31 Wishart, D. S. & Sykes, B. D. (1994). Chemical shifts as a tool for structure determination. *Methods Enzymol* 239, 363–392.

32 Yao, J., Dyson, H. J. & Wright, P. E. (1997). Chemical shift dispersion and secondary structure prediction in unfolded and partly folded proteins. *FEBS Lett* 419, 285–289.

33 Wishart, D. S., Sykes, B. D. & Richards, F. M. (1992). The chemical shift index: a fast and simple method for the assignment of protein secondary structure through NMR spectroscopy. *Biochemistry* 31, 1647–1651.

34 Burton, R. E., Huang, G. S., Daugherty, M. A., Fullbright, P. W. & Oas, T. G. (1996). Microsecond protein folding through a compact transition state. *J Mol Biol* 263, 311–322.

35 Sandstrom. (1982). *Dynamic NMR Spectroscopy*. Academic Press, London.

36 Bundi, A. & Wüthrich, K. (1979). ^{1}H NMR parameters of the common amino acid residues measured in aqueous solutions of the linear tetrapeptides H-Gly-Gly-X-L-Ala-OH. *Biopolymers* 18, 285–297.

37 Wishart, D. S., Bigam, C. G., Holm, A., Hodges, R. S. & Sykes, B. D. (1995). ^{1}H, ^{13}C and ^{15}N random coil NMR chemical shifts of the common amino acids. I. Investigations of nearest-neighbor effects. *J Biomol NMR* 5, 67–81.

38 Merutka, G., Dyson, H. J. & Wright, P. E. (1995). 'Random coil' 1H chemical shifts obtained as a function of temperature and trifluoroethanol concentration for the peptide series GGXGG. *J Biomol NMR* 5, 14–24.

39 Redfield, C., Schulman, B. A., Milhollen, M. A., Kim, P. S. & Dobson, C. M. (1999). Alpha-lactalbumin forms a compact molten globule in the absence of disulfide bonds. *Nature Struct Biol* 6, 948–952.

40 Jeener, J., Meier, B. H., Bachmann, P. & Ernst, R. R. (1979). Investigation of exchange processes by two-dimensional NMR spectroscopy. *J Chem Phys* 71, 4546–4553.

41 Dobson, C. M., Evans, P. A. & Williamson, K. L. (1984). Proton NMR studies of denatured lysozyme. *FEBS Lett* 168, 331–334.

42 Evans, P. A., Topping, K. D., Woolfson, D. N. & Dobson, C. M. (1991). Hydrophobic clustering in nonnative states of a protein: Interpretation of chemical shifts in NMR spectra of denatured states of lysozyme. *Proteins Struct Funct Genet* 9, 248–266.

43 Karplus, M. (1959). Contact electron-spin coupling of nuclear magnetic moments. *J Chem Phys* 30, 11–15.

44 Smith, L. J. (1996). Analysis of main chain torsion angles in proteins: prediction of NMR coupling constants for native and random coil conformations. *J Mol Biol* 255, 494–506.

45 Smith, L. J., Fiebig, K. M., Schwalbe, H. & Dobson, C. M. (1996). The concept of a random coil. Residual structure in peptides and denatured proteins. *Folding Des* 1, R95–106.

46 Juranic, N. & Macura, S. (2001). Correlations among 1JNC′ and h3JNC′ coupling constants in the hydrogen-bonding network of human ubiquitin. *J Am Chem Soc* 123, 4099–4100.

47 Mierke, D. F., Grdadolnik, S. G. & Kessler, H. (1992). Use of one-bond C alpha-H alpha coupling constants a restraints in MD simulations. *J Am Chem Soc* 114, 8283–8284.

48 Edison, A. S., Markley, J. L. & Weinhold, F. (1994). Calculations of one-, two- and three-bond nuclear spin-spin couplings in a model peptide and correlations with experimental data. *J Biomol NMR* 4, 519–542.

49 Edison, A. S., Weinhold, F., Westler, W. M. & Markley, J. L. (1994). Estimates of phi and psi torsion angles in proteins from one-, two- and three-bond nuclear spin-spin couplings: application to staphylococcal nuclease. *J Biomol NMR* 4, 543–551.

50 Delaglio, F., Torchia, D. A. & Bax,

A. (1991). Measurement of ^{15}N-^{13}C *J* couplings in staphylococcal nuclease. *J Biomol NMR* 1, 439–446.

51 Wirmer, J. & Schwalbe, H. (2002). Angular dependence of 1J(Ni,Cαi) and 2J(Ni,Cα(i-1)) coupling constants measured in J-modulated HSQCs. *J Biomol NMR* 23, 47–55.

52 Jaravine, Alexandrescu, A. T. & Grzesiek, S. (2001). Observation of the closing of individual hydrogen bonds during TFE-induced helix formation in a peptide. *Protein Sci* 10, 943–950.

53 Plaxco, K. W., Morton, C. J., Grimshaw, S. B. et al. (1997). The effects of guanidine hydrochloride on the 'random coil' conformations and NMR chemical shifts of the peptide series GGXGG. *J Biomol NMR* 10.

54 Hubbard, P. S. (1958). Nuclear magnetic relaxation of three and four spin molecules in a liquid. *Phys Rev* 109, 1153–1158.

55 Hubbard, P. S. (1969). Nonexponential relaxation of three-spin systems in nonspherical molecules. *J Chem Phys* 51, 1647–1651.

56 Hubbard, P. S. (1970). Nonexponential relaxation of rotating three-spin systems in molecules of a liquid. *J Chem Phys* 52, 563–568.

57 Kuhlmann, K. F. & Baldeschweiler, J. D. (1965). Analysis of the nuclear Overhauser effect in the difluoroethylenes. *J Chem Phys* 43, 572–593.

58 Cavanagh, J., Fairbrother, W. J., Palmer III, A. G. & Skelton, N. J. (1996). *Protein NMR Spectroscopy, Principles and Practice*. Academic Press, London.

59 Lipari, G. & Szabo, A. (1982). Model-free approach to the interpretation of nuclear magnetic-resonance relaxation in macromolecules. 2. Analysis of experimental results. *J Am Chem Soc* 104, 4559–4570.

60 Lipari, G. & Szabo, A. (1982). Model-free approach to the interpretation of nuclear magnetic-resonance relaxation in macromolecules. 1. Theory and range of validity. *J Am Chem Soc* 104, 4546–4559.

61 Brutscher, B., Skrynnikov, N. R., Bremi, T., Brüschweiler, R. & Ernst, R. R. (1998). Quantitative investigation of dipole–CSA cross-correlated relaxation by ZQ/DQ spectroscopy. *J Magn Reson* 130, 246–351.

62 Brüschweiler, R. & Case, D. A. (1994). Characterization of biomolecular structure and dynamics by NMR cross relaxation. *Prog NMR Spectrosc* 26, 27–58.

63 Wagner, G. (1993). NMR relaxation and protein mobility. *Curr Opin Struct Biol* 3, 748–754.

64 Ochsenbein, F., Neumann, J. M., Guittet, E. & van Heijenoort, C. (2002). Dynamical characterization of residual and nonnative structures in a partially folded protein by (15)N NMR relaxation using a model based on a distribution of correlation times. *Protein Sci* 11, 957–964.

65 Alexandrescu, A. T. & Shortle, D. (1994). Backbone dynamics of a highly disordered 131 residue fragment of staphylococcal nuclease. *J Mol Biol* 242, 527–546.

66 Buevich, A. V. & Baum, J. (1999). Dynamics of unfolded proteins: Incooporation of distributions of correlation times in the model free analysis of NMR relaxation data. *J Am Chem Soc* 121, 8671–8672.

67 Gayathri, C., Bothnerby, A. A., Van Zijl, P. C. M. & Maclean, C. (1982). Dipolar magnetic-field effects in NMR-spectra of liquids. *Chem Phys Lett* 87, 192–196.

68 Tjandra, N. & Bax, A. (1997). Direct measurement of distances and angles in biomolecules by NMR in a dilute liquid crystalline medium. *Science* 278, 1111–1114.

69 Tolman, J. R., Flanagan, J. M., Kennedy, M. A. & Prestegard, J. H. (1997). NMR evidence for slow collective motions in cyanometmyoglobin. *Nature Struct Biol* 4, 292–297.

70 Prestegard, J. H. & Kishore, A. I. (2001). Partial alignment of biomolecules: an aid to NMR characterization. *Curr Opin Chem Biol* 5, 584–590.

71 Tolman, J. R. (2001). Dipolar couplings as a probe of molecular dynamics and structure in solution. *Curr Opin Struct Biol* 11, 532–539.

72 Al-Hashimi, H. M. & Patel, D. J. (2002). Residual dipolar couplings: synergy between NMR and structural genomics. *J Biomol NMR* 22, 1–8.

73 Bax, A. (2003). Weak alignment offers new NMR opportunities to study protein structure and dynamics. *Protein Sci* 12, 1–16.

74 Shortle, D. & Ackerman, M. S. (2001). Persistence of native-like topology in a denatured protein in 8 M urea. *Science* 293, 487–489.

75 Gaemers, S. & Bax, A. (2001). Morphology of three lyotropic liquid crystalline biological NMR media studied by translational diffusion anisotropy. *J Am Chem Soc* 123, 12343–12352.

76 Sass, H. J., Musco, G., Stahl, S. J., Wingfield, P. T. & Grzesiek, S. (2000). Solution NMR of proteins within polyacrylamide gels: diffusional properties and residual alignment by mechanical stress or embedding of oriented purple membranes. *J Biomol NMR* 18, 303–309.

77 Tycko, R., Blanco, F. J. & Ishii, Y. (2000). Alignment of biopolymers in strained gels: A new way to create detectable dipole-dipole coupling in high-resolution biomolecular NMR. *J Am Chem Soc* 122, 9340–9341.

78 Banci, L., Bertini, I., Savellini, G. G. et al. (1997). Pseudocontact shifts as constraints for energy minimization and molecular dynamics calculations on solution structures of paramagnetic metalloproteins. *Proteins* 29, 68–76.

79 Barbieri, R., Bertini, I., Lee, Y. M., Luchinat, C. & Velders, A. H. (2002). Structure-independent cross-validation between residual dipolar couplings originating from internal and external orienting media. *J Biomol NMR* 22, 365–368.

80 Wohnert, J., Franz, K. J., Nitz, M., Imperiali, B. & Schwalbe, H. (2003). Protein alignment by a coexpressed lanthanide-binding tag for the measurement of residual dipolar couplings. *J Am Chem Soc* 125, 13338–13339.

81 Zweckstetter, M. & Bax, A. (2000). Prediction of sterically induced alignment in a dilute liquid crystalline phase: Aid to protein structure determination by NMR. *J Am Chem Soc* 122, 3791–3792.

82 Fernandes, M. X., Bernado, P., Pons, M. & Garcia de la Torre, J. (2001). An analytical solution to the problem of the orientation of rigid particles by planar obstacles. Application to membrane systems and to the calculation of dipolar couplings in protein NMR spectroscopy. *J Am Chem Soc* 123, 12037–12047.

83 Losonczi, J. A., Andrec, M., Fischer, M. W. F. & Prestegard, J. H. (1999). Order Matrix analysis of residual dipolar couplings using singular value decomposition. *J Magn Reson* 138, 334–342.

84 Meiler, J., Prompers, J. J., Peti, W., Griesinger, C. & Bruschweiler, R. (2001). Model-free approach to the dynamic interpretation of residual dipolar couplings in globular proteins. *J Am Chem Soc* 123, 6098–6107.

85 Tolman, J. R. (2002). A novel approach to the retrieval of structural and dynamic information from residual dipolar couplings using several oriented media in biomolecular NMR spectroscopy. *J Am Chem Soc* 124, 12020–12030.

86 Peti, W., Meiler, J., Bruschweiler, R. & Griesinger, C. (2002). Model-free analysis of protein backbone motion from residual dipolar couplings. *J Am Chem Soc* 124, 5822–5833.

87 Wilkins, D. K., Grimshaw, S. B., Receveur, V., Dobson, C. M., Jones, J. A. & Smith, L. J. (1999). Hydrodynamic radii of native and denatured proteins measured by pulse field gradient NMR techniques. *Biochemistry* 38, 16424–16431.

88 Wu, D., Chen, A. & Johnson Jr., C. S. (1995). An improved diffusion-ordered spectroscopy experiment incorporating bipolar-gradient pulses. *J Magn Reson A* 115, 260–264.

89 Jones, J. A., Wilkins, D. K., Smith, L. J. & Dobson, C. M. (1997). Characterisation of protein unfolding by NMR diffusion measurements. *J Biomol NMR* 10, 199–203.

90 Pan, H., Barany, G. & Woodward, C. (1997). Reduced BPTI is collapsed. A pulsed field gradient NMR study of unfolded and partially folded bovine pancreatic trypsin inhibitor. *Protein Sci* 6, 1985–1992.

91 Schmidt, P. G. & Kuntz, I. D. (1984). Distance measurements in spin-labeled lysozyme. *Biochemistry* 23, 4261–4266.

92 Kosen, P. A., Scheek, R. M., Naderi, H. et al. (1986). Two-dimensional 1H NMR of three spin-labeled derivatives of bovine pancreatic trypsin inhibitor. *Biochemistry* 25, 2356–2364.

93 Hubbell, W. L., McHaourab, H. S., Altenbach, C. & Lietzow, M. A. (1996). Watching proteins move using site-directed spin labeling. *Structure* 4, 779–783.

94 Matthews, B. W. (1995). Studies on protein stability with T4 lysozyme. *Adv Protein Chem* 46, 249–278.

95 McHaourab, H. S., Lietzow, M. A., Hideg, K. & Hubbell, W. L. (1996). Motion of spin-labeled side chains in T4 lysozyme. Correlation with protein structure and dynamics. *Biochemistry* 35, 7692–7704.

96 Lee, L. & Sykes, B. D. (1983). Use of lanthanide-induced nuclear magnetic resonance shifts for determination of protein structure in solution: EF calcium binding site of carp parvalbumin. *Biochemistry* 22, 4366–4373.

97 Gillespie, J. R. & Shortle, D. (1997). Characterization of long-range structure in the denatured state of staphylococcal nuclease. II. Distance restraints from paramagnetic relaxation and calculation of an ensemble of structures. *J Mol Biol* 268, 170–184.

98 Yi, Q., Scalley-Kim, M. L., Alm, E. J. & Baker, D. (2000). NMR characterization of residual structure in the denatured state of protein L. *J Mol Biol* 299, 1341–1351.

99 Lietzow, M. A., Jamin, M., Jane Dyson, H. J. & Wright, P. E. (2002). Mapping long-range contacts in a highly unfolded protein. *J Mol Biol* 322, 655–662.

100 Gillespie, J. R. & Shortle, D. (1997). Characterization of long-range structure in the denatured state of staphylococcal nuclease. I. Paramagnetic relaxation enhancement by nitroxide spin labels. *J Mol Biol* 268, 158–169.

101 Roder, H. & Wuthrich, K. (1986). Protein folding kinetics by combined use of rapid mixing techniques and NMR observation of individual amide protons. *Proteins* 1, 34–42.

102 Baldwin, R. (1993). Pulsed H/D-exchange studies of folding intermediates. *Curr Opin Struct Biol* 3, 84–91.

103 Miranker, A., Radford, S. E., Karplus, M. & Dobson, C. M. (1991). Demonstration by NMR of folding domains in lysozyme. *Nature* 349, 633–536.

104 Radford, S. E., Dobson, C. M. & Evans, P. A. (1992). The folding of hen lysozyme involves partially structured intermediates and multiple pathways. *Nature* 358, 302–307.

105 Roder, H., Wagner, G. & Wuthrich, K. (1985). Individual amide proton exchange rates in thermally unfolded basic pancreatic trypsin inhibitor. *Biochemistry* 24, 7407–7411.

106 Robertson, A. D. & Baldwin, R. L. (1991). Hydrogen exchange in thermally denatured ribonuclease A. *Biochemistry* 30, 9907–9914.

107 Buck, M., Radford, S. E. & Dobson, C. M. (1994). Amide hydrogen exchange in a highly denatured state. Hen egg-white lysozyme in urea. *J Mol Biol* 237, 247–254.

108 Jennings, P. A. & Wright, P. E. (1993). Formation of a molten globule intermediate early in the kinetic folding pathway of apomyoglobin. *Science* 262, 892–896.

109 Udgaonkar, J. B. & Baldwin, R. L. (1988). NMR evidence for an early framework intermediate on the

folding pathway of ribonuclease A. *Nature* 335, 694–699.

110 Udgaonkar, J. B. & Baldwin, R. L. (1990). Early folding intermediate of ribonuclease A. *Proc Natl Acad Sci USA* 87, 8197–8201.

111 Roder, H., Elove, G. A. & Englander, S. W. (1988). Structural characterization of folding intermediates in cytochrome c by H-exchange labelling and proton NMR. *Nature* 335, 700–704.

112 Juneja, J. & Udgaonkar, J. B. (2002). Characterization of the unfolding of ribonuclease a by a pulsed hydrogen exchange study: evidence for competing pathways for unfolding. *Biochemistry* 41, 2641–2654.

113 Kaptein, R. (1982). Photo-CIDNP studies of proteins. *Biol Magn Reson* 4, 145–191.

114 Hore, P. J. & Kaptein, R. (1993). Photo-CIDNP of biopolymers. *Prog NMR Spectr* 25, 345–402.

115 Lyon, C. E., Jones, J. A., Redfield, C., Dobson, C. M. & Hore, P. J. (1999). Two-dimensional 15N-1H photo-CIDNP as a surface probe of native and partially structured proteins. *J Am Chem Soc* 121, 6505–6506.

116 Broadhurst, R. W., Dobson, C. M., Hore, P. J., Radford, S. E. & Rees, M. L. (1991). A photochemically induced dynamic nuclear polarization study of denatured states of lysozyme. *Biochemistry* 30, 405–412.

117 Wirmer, J., Kühn, T. & Schwalbe, H. (2001). Millisecond time resolved photo-CIDNP NMR reveals a nonnative folding intermediate on the ion-induced pathway of bovine α-lactalbumin. *Ang Chem Int Ed* 40, 4248–4251.

118 Hore, P. J., Winder, S. L., Roberts, C. H. & Dobson, C. M. (1997). Stopped-flow photo-CIDNP observation of protein folding. *J Am Chem Soc* 119, 5049–5050.

119 Maeda, K., Lyon, C. E., Lopez, J. J., Cemazar, M., Dobson, C. M. & Hore, P. J. (2000). Improved photo-CIDNP methods for studying protein structure and folding. *J Biomol NMR* 16, 235–244.

120 Lyon, C. E., Suh, E. S., Dobson, C. M. & Hore, P. J. (2002). Probing the exposure of tyrosine and tryptophan residues in partially folded proteins and folding intermediates by CIDNP pulse-labeling. *J Am Chem Soc* 124, 13018–13024.

121 Fiebig, K. M., Schwalbe, H., Buck, M., Smith, L. J. & Dobson, C. M. (1996). Toward a description of the conformations of denatured states of proteins. Comparison of a random coil model with NMR measurements. *J Phys Chem* 100, 2661–2666.

122 Swindells, M. B., MacArthur, M. W. & Thornton, J. M. (1995). Intrinsic phi, psi propensities of amino acids, derived from the coil regions of known structures. *Nat Struct Biol* 2, 596–603.

123 Serrano, L. (1995). Comparison between the phi distribution of the amino acids in the protein database and NMR data indicates that amino acids have various phi propensities in the random coil conformation. *J Mol Biol* 254, 322–333.

124 Frank, M. K., Clore, G. M. & Gronenborn, A. M. (1995). Structural and dynamic characterization of the urea denatured state of the immunoglobulin binding domain of streptococcal protein G by multidimensional heteronuclear NMR spectroscopy. *Protein Sci* 4, 2605–2615.

125 Allerhand, A. & Hailstone, R. K. (1972). C-13 Fourier-transform nuclear magnetic-resonance. 10. Effect of molecular-weight on C-13 spin-lattice relaxation-times of polystyrene in solution. *J Chem Phys* 56, 3718.

126 Buck, M., Radford, S. E. & Dobson, C. M. (1993). A partially folded state of hen egg white lysozyme in trifluoroethanol: structural characterization and implications for protein folding. *Biochemistry* 32, 669–678.

127 Buck, M., Schwalbe, H. & Dobson, C. M. (1995). Characterization of conformational preferences in a partly folded protein by heteronuclear NMR spectroscopy: assignment and secondary structure analysis of hen egg-white lysozyme in trifluoro-

ethanol. *Biochemistry* 34, 13219–13232.

128 Buck, M., Boyd, J., Redfield, C. et al. (1995). Structural determinants of protein dynamics: analysis of 15N NMR relaxation measurements for main-chain and side-chain nuclei of hen egg white lysozyme. *Biochemistry* 34, 4041–4055.

129 Buck, M., Schwalbe, H. & Dobson, C. M. (1996). Main-chain dynamics of a partially folded protein: 15N NMR relaxation measurements of hen egg white lysozyme denatured in trifluoroethanol. *J Mol Biol* 257, 669–683.

130 Kemmink, J. & Creighton, T. E. (1993). Local conformations of peptides representing the entire sequence of bovine pancreatic trypsin inhibitor and their roles in folding. *J Mol Biol* 234, 861–878.

131 Kemmink, J. & Creighton, T. E. (1995). The physical properties of local interactions of tyrosine residues in peptides and unfolded proteins. *J Mol Biol* 245, 251–260.

132 Lumb, K. J. & Kim, P. S. (1994). Formation of a hydrophobic cluster in denatured bovine pancreatic trypsin inhibitor. *J Mol Biol* 236, 412–420.

133 Hennig, M., Bermel, W., Spencer, A., Dobson, C. M., Smith, L. J. & Schwalbe, H. (1999). Side-chain conformations in an unfolded protein: chi1 distributions in denatured hen lysozyme determined by heteronuclear 13C, 15N NMR spectroscopy. *J Mol Biol* 288, 705–723.

134 McGregor, M. J., Islam, S. A. & Sternberg, M. J. (1987). Analysis of the relationship between side-chain conformation and secondary structure in globular proteins. *J Mol Biol* 198, 295–310.

135 Dunbrack, R. L., Jr. & Karplus, M. (1993). Backbone-dependent rotamer library for proteins. Application to side-chain prediction. *J Mol Biol* 230, 543–574.

136 Shortle, D. R. (1996). Structural analysis of nonnative states of proteins by NMR methods. *Curr Opin Struct Biol* 6, 24–30.

137 Schulman, B. A., Kim, P. S., Dobson, C. M. & Redfield, C. (1997). A residue-specific NMR view of the non-cooperative unfolding of a molten globule. *Nat Struct Biol* 4, 630–634.

138 Peti, W., Smith, L. J., Redfield, C. & Schwalbe, H. (2001). Chemical shifts in denatured proteins: resonance assignments for denatured ubiquitin and comparisons with other denatured proteins. *J Biomol NMR* 19, 153–165.

139 Eliezer, D. & Wright, P. E. (1996). Is apomyoglobin a molten globule? Structural characterization by NMR. *J Mol Biol* 263, 531–538.

140 Eliezer, D., Jennings, P. A., Dyson, H. J. & Wright, P. E. (1997). Populating the equilibrium molten globule state of apomyoglobin under conditions suitable for structural characterization by NMR. *FEBS Lett* 417, 92–96.

141 Yao, J., Chung, J., Eliezer, D., Wright, P. E. & Dyson, H. J. (2001). NMR structural and dynamic characterization of the acid-unfolded state of apomyoglobin provides insights into the early events in protein folding. *Biochemistry* 40, 3561–3571.

142 Kitahara, R., Yamada, H., Akasaka, K. & Wright, P. E. (2002). High pressure NMR reveals that apomyoglobin is an equilibrium mixture from the native to the unfolded. *J Mol Biol* 320, 311–319.

143 Schwarzinger, S., Wright, P. E. & Dyson, H. J. (2002). Molecular hinges in protein folding: the urea-denatured state of apomyoglobin. *Biochemistry* 41, 12681–12686.

144 Arcus, V. L., Vuilleumier, S., Freund, S. M., Bycroft, M. & Fersht, A. R. (1994). Toward solving the folding pathway of barnase: the complete backbone 13C, 15N, and 1H NMR assignments of its pH-denatured state. *Proc Natl Acad Sci USA* 91, 9412–9416.

145 Arcus, V. L., Vuilleumier, S., Freund, S. M., Bycroft, M. & Fersht, A. R. (1995). A comparison of the pH, urea, and temperature-denatured states of barnase by

heteronuclear NMR: implications for the initiation of protein folding. *J Mol Biol* 254, 305–321.

146 Freund, S. M., Wong, K. B. & Fersht, A. R. (1996). Initiation sites of protein folding by NMR analysis. *Proc Natl Acad Sci USA* 93, 10600–10603.

147 Neira, J. L. & Fersht, A. R. (1996). An NMR study on the beta-hairpin region of barnase. *Folding Des* 1, 231–241.

148 Wong, K. B., Clarke, J., Bond, C. J. et al. (2000). Towards a complete description of the structural and dynamic properties of the denatured state of barnase and the role of residual structure in folding. *J Mol Biol* 296, 1257–1282.

149 Eakin, C. M., Knight, J. D., Morgan, C. J., Gelfand, M. A. & Miranker, A. D. (2002). Formation of a copper specific binding site in nonnative states of beta-2-microglobulin. *Biochemistry* 41, 10646–10656.

150 Katou, H., Kanno, T., Hoshino, M. et al. (2002). The role of disulfide bond in the amyloidogenic state of beta(2)-microglobulin studied by heteronuclear NMR. *Protein Sci* 11, 2218–2229.

151 Thomsen, J. K., Kragelund, B. B., Teilum, K., Knudsen, J. & Poulsen, F. M. (2002). Transient intermediary states with high and low folding probabilities in the apparent two-state folding equilibrium of ACBP at low pH. *J Mol Biol* 318, 805–814.

152 Lindorff-Larsen, K., Kristjansdottir, S., Teilum, K. et al. (2004). Determination of an ensemble of structures representing the denatured state of the bovine acyl-coenzyme a binding protein. *J Am Chem Soc* 126, 3291–3299.

153 Ragona, L., Pusteria, F., Zetta, L., Monaco, H. L. & Molinari, H. (1997). Identification of a conserved hydrophobic cluster in partially folded bovine beta-lactoglobulin at pH 2. *Folding Des* 2, 281–290.

154 Uhrinova, S., Uhrin, D., Denton, H., Smith, M., Sawyer, L. & Barlow, P. N. (1998). Complete assignment of 1H, 13C and 15N chemical shifts for bovine beta-lactoglobulin: secondary structure and topology of the native state is retained in a partially unfolded form. *J Biomol NMR* 12, 89–107.

155 Ragona, L., Fogolari, F., Romagnoli, S., Zetta, L., Maubois, J. L. & Molinari, H. (1999). Unfolding and refolding of bovine beta-lactoglobulin monitored by hydrogen exchange measurements. *J Mol Biol* 293, 953–969.

156 Katou, H., Hoshino, M., Kamikubo, H., Batt, C. A. & Goto, Y. (2001). Native-like beta-hairpin retained in the cold-denatured state of bovine beta-lactoglobulin. *J Mol Biol* 310, 471–484.

157 Kuwata, K., Li, H., Yamada, H., Batt, C. A., Goto, Y. & Akasaka, K. (2001). High pressure NMR reveals a variety of fluctuating conformers in beta-lactoglobulin. *J Mol Biol* 305, 1073–1083.

158 Garcia, P., Serrano, L., Durand, D., Rico, M. & Bruix, M. (2001). NMR and SAXS characterization of the denatured state of the chemotactic protein CheY: implications for protein folding initiation. *Protein Sci* 10, 1100–1112.

159 Zhang, O., Kay, L. E., Olivier, J. P. & Forman-Kay, J. D. (1994). Backbone 1H and 15N resonance assignments of the N-terminal SH3 domain of drk in folded and unfolded states using enhanced-sensitivity pulsed field gradient NMR techniques. *J Biomol NMR* 4, 845–858.

160 Zhang, O. & Forman-Kay, J. D. (1995). Structural characterization of folded and unfolded states of an SH3 domain in equilibrium in aqueous buffer. *Biochemistry* 34, 6784–6794.

161 Farrow, N. A., Zhang, O., Forman-Kay, J. D. & Kay, L. E. (1995). Comparison of the backbone dynamics of a folded and an unfolded SH3 domain existing in equilibrium in aqueous buffer. *Biochemistry* 34, 868–878.

162 Farrow, N. A., Zhang, O., Szabo, A., Torchia, D. A. & Kay, L. E. (1995). Spectral density function mapping

using 15N relaxation data exclusively. *J Biomol NMR* 6, 153–162.

163 Farrow, N. A., Zhang, O., Forman-Kay, J. D. & Kay, L. E. (1997). Characterization of the backbone dynamics of folded and denatured states of an SH3 domain. *Biochemistry* 36, 2390–2402.

164 Yang, D., Mok, Y. K., Forman-Kay, J. D., Farrow, N. A. & Kay, L. E. (1997). Contributions to protein entropy and heat capacity from bond vector motions measured by NMR spin relaxation. *J Mol Biol* 272, 790–804.

165 Zhang, O. & Forman-Kay, J. D. (1997). NMR studies of unfolded states of an SH3 domain in aqueous solution and denaturing conditions. *Biochemistry* 36, 3959–3970.

166 Zhang, O., Forman-Kay, J. D., Shortle, D. & Kay, L. E. (1997). Triple-resonance NOESY-based experiments with improved spectral resolution: applications to structural characterization of unfolded, partially folded and folded proteins. *J Biomol NMR* 9, 181–200.

167 Mok, Y. K., Kay, C. M., Kay, L. E. & Forman-Kay, J. (1999). NOE data demonstrating a compact unfolded state for an SH3 domain under non-denaturing conditions. *J Mol Biol* 289, 619–638.

168 Kortemme, T., Kelly, M. J., Kay, L. E., Forman-Kay, J. & Serrano, L. (2000). Similarities between the spectrin SH3 domain denatured state and its folding transition state. *J Mol Biol* 297, 1217–1229.

169 Choy, W. Y. & Forman-Kay, J. D. (2001). Calculation of ensembles of structures representing the unfolded state of an SH3 domain. *J Mol Biol* 308, 1011–1032.

170 Tollinger, M., Skrynnikov, N. R., Mulder, F. A., Forman-Kay, J. D. & Kay, L. E. (2001). Slow dynamics in folded and unfolded states of an SH3 domain. *J Am Chem Soc* 123, 11341–11352.

171 Mok, Y. K., Elisseeva, E. L., Davidson, A. R. & Forman-Kay, J. D. (2001). Dramatic stabilization of an SH3 domain by a single substitution: roles of the folded and unfolded states. *J Mol Biol* 307, 913–928.

172 Choy, W. Y., Mulder, F. A., Crowhurst, K. A. et al. (2002). Distribution of molecular size within an unfolded state ensemble using small-angle X-ray scattering and pulse field gradient NMR techniques. *J Mol Biol* 316, 101–112.

173 Crowhurst, K. A., Tollinger, M. & Forman-Kay, J. D. (2002). Cooperative interactions and a nonnative buried Trp in the unfolded state of an SH3 domain. *J Mol Biol* 322, 163–178.

174 Crowhurst, K. A. & Forman-Kay, J. D. (2003). Aromatic and methyl NOEs highlight hydrophobic clustering in the unfolded state of an SH3 domain. *Biochemistry* 42, 8687–8695.

175 Tollinger, M., Forman-Kay, J. D. & Kay, L. E. (2002). Measurement of side-chain carboxyl pK(a) values of glutamate and aspartate residues in an unfolded protein by multinuclear NMR spectroscopy. *J Am Chem Soc* 124, 5714–5717.

176 Logan, T. M., Olejniczak, E. T., Xu, R. X. & Fesik, S. W. (1993). A general method for assigning NMR spectra of denatured proteins using 3D HC(CO)NH-TOCSY triple resonance experiments. *J Biomol NMR* 3, 225–231.

177 Nordstrand, K., Ponstingl, H., Holmgren, A. & Otting, G. (1996). Resonance assignment and structural analysis of acid denatured E. coli [U-15N]-glutaredoxin 3: use of 3D 15N-HSQC-(TOCSY-NOESY)-15N-HSQC. *Eur Biophys J* 24, 179–184.

178 Radford, S. E., Woolfson, D. N., Martin, S. R., Lowe, G. & Dobson, C. M. (1991). A three-disulphide derivative of hen lysozyme. Structure, dynamics and stability. *Biochem J* 273(Pt 1), 211–217.

179 Radford, S. E., Buck, M., Topping, K. D., Dobson, C. M. & Evans, P. A. (1992). Hydrogen exchange in native and denatured states of hen egg-white lysozyme. *Proteins* 14, 237–248.

180 Roux, P., Delepierre, M., Goldberg, M. E. & Chaffotte, A. F. (1997). Kinetics of secondary structure

recovery during the refolding of reduced hen egg white lysozyme. *J Biol Chem* 272, 24843–24849.

181 Chung, E. W., Nettleton, E. J., Morgan, C. J. et al. (1997). Hydrogen exchange properties of proteins in native and denatured states monitored by mass spectrometry and NMR. *Protein Sci* 6, 1316–1324.

182 Buck, M. (1998). Trifluoroethanol and colleagues: cosolvents come of age. Recent studies with peptides and proteins. *Q Rev Biophys* 31, 297–355.

183 Hennig, M., Bermel, W., Dobson, C. M., Smith, L. J. & Schwalbe, H. (1999). Determination of side chain conformations in unfolded proteins: 1 Distribution for lysozyme by heteronuclear 13C,15N NMR spectroscopy. *J Mol Biol* 288, 705–723.

184 Klein-Seetharaman, J., Oikawa, M., Grimshaw, S. B. et al. (2002). Long-range interactions within a nonnative protein. *Science* 295, 1719–1722.

185 Baldwin, R. L. (2002). Making a network of hydrophobic clusters. *Science* 295, 1657–1658.

186 Noda, Y., Yokota, A., Horii, D. et al. (2002). NMR structural study of two-disulfide variant of hen lysozyme: 2SS[6–127, 30–115] – a disulfide intermediate with a partly unfolded structure. *Biochemistry* 41, 2130–2139.

187 Bhavesh, N. S., Panchal, S. C., Mittal, R. & Hosur, R. V. (2001). NMR identification of local structural preferences in HIV-1 protease tethered heterodimer in 6 M guanidine hydrochloride. *FEBS Lett* 509, 218–224.

188 Panchal, S. C., Bhavesh, N. S. & Hosur, R. V. (2001). Improved 3D triple resonance experiments, HNN and HN(C)N, for HN and 15N sequential correlations in (13C, 15N) labeled proteins: application to unfolded proteins. *J Biomol NMR* 20, 135–147.

189 Tafer, H., Hiller, S., Hilty, C., Fernandez, C. & Wuthrich, K. (2004). Nonrandom structure in the urea-unfolded Escherichia coli outer membrane protein X (OmpX). *Biochemistry* 43, 860–869.

190 Bentrop, D., Bertini, I., Iacoviello, R. et al. (1999). Structural and dynamical properties of a partially unfolded Fe4S4 protein: role of the cofactor in protein folding. *Biochemistry* 38, 4669–4680.

191 Harding, M. M., Williams, D. H. & Woolfson, D. N. (1991). Characterization of a partially denatured state of a protein by two-dimensional NMR: reduction of the hydrophobic interactions in ubiquitin. *Biochemistry* 30, 3120–3128.

192 Stockman, B. J., Euvrard, A. & Scahill, T. A. (1993). Heteronuclear three-dimensional NMR spectroscopy of a partially denatured protein: the A-state of human ubiquitin. *J Biomol NMR* 3, 285–296.

193 Nash, D. P. & Jonas, J. (1997). Structure of the pressure-assisted cold denatured state of ubiquitin. *Biochem Biophys Res Commun* 238, 289–291.

194 Permi, P. (2002). Intraresidual HNCA: an experiment for correlating only intraresidual backbone resonances. *J Biomol NMR* 23, 201–209.

195 Mizushima, T., Hirao, T., Yoshida, Y. et al. (2004). Structural basis of sugar-recognizing ubiquitin ligase. *Nat Struct Mol Biol* 11, 365–370.

196 Fletcher, C. M., McGuire, A. M., Gingras, A. C. et al. (1998). 4E binding proteins inhibit the translation factor eIF4E without folded structure. *Biochemistry* 37, 9–15.

197 Daughdrill, G. W., Hanely, L. J. & Dahlquist, F. W. (1998). The C-terminal half of the anti-sigma factor FlgM contains a dynamic equilibrium solution structure favoring helical conformations. *Biochemistry* 37, 1076–1082.

198 Mogridge, J., Legault, P., Li, J., Van Oene, M. D., Kay, L. E. & Greenblatt, J. (1998). Independent ligand-induced folding of the RNA-binding domain and two functionally distinct antitermination regions in the phage lambda N protein. *Mol Cell* 1, 265–275.

199 De Guzman, R. N., Martinez-Yamout, M. A., Dyson, H. J. & Wright, P. E. (2004). Interaction of

the TAZ1 domain of the CREB-binding protein with the activation domain of CITED2: regulation by competition between intrinsically unstructured ligands for non-identical binding sites. *J Biol Chem* 279, 3042–3049.

200 Collins, E. S., Whittaker, S. B., Tozawa, K. et al. (2002). Structural dynamics of the membrane translocation domain of colicin E9 and its interaction with TolB. *J Mol Biol* 318, 787–804.

201 Anderluh, G., Hong, Q., Boetzel, R. et al. (2003). Concerted folding and binding of a flexible colicin domain to its periplasmic receptor TolA. *J Biol Chem* 278, 21860–21868.

202 Kriwacki, R. W., Hengst, L., Tennant, L., Reed, S. I. & Wright, P. E. (1996). Structural studies of p21Waf1/Cip1/Sdi1 in the free and Cdk2-bound state: conformational disorder mediates binding diversity. *Proc Natl Acad Sci USA* 93, 11504–11509.

203 Lisse, T., Bartels, D., Kalbitzer, H. R. & Jaenicke, R. (1996). The recombinant dehydrin-like desiccation stress protein from the resurrection plant *Craterostigma plantagineum* displays no defined three-dimensional structure in its native state. *Biol Chem* 377, 555–561.

204 Hershey, P. E., McWhirter, S. M., Gross, J. D., Wagner, G., Alber, T. & Sachs, A. B. (1999). The Cap-binding protein eIF4E promotes folding of a functional domain of yeast translation initiation factor eIF4G1. *J Biol Chem* 274, 21297–21304.

205 Mayor, U., Grossmann, J. G., Foster, N. W., Freund, S. M. & Fersht, A. R. (2003). The denatured state of Engrailed Homeodomain under denaturing and native conditions. *J Mol Biol* 333, 977–991.

206 Bozzi, M., Bianchi, M., Sciandra, F. et al. (2003). Structural characterization by NMR of the natively unfolded extracellular domain of beta-dystroglycan: toward the identification of the binding epitope for alpha-dystroglycan. *Biochemistry* 42, 13717–13724.

207 Penkett, C. J., Redfield, C., Dodd, I. et al. (1997). NMR analysis of main-chain conformational preferences in an unfolded fibronectin-binding protein. *J Mol Biol* 274, 152–159.

208 Uversky, V. N., Gillespie, J. R., Millett, I. S. et al. (2000). Zn(2+)-mediated structure formation and compaction of the ''natively unfolded'' human prothymosin alpha. *Biochem Biophys Res Commun* 267, 663–668.

209 Weiss, M. A., Ellenberger, T., Wobbe, C. R., Lee, J. P., Harrison, S. C. & Struhl, K. (1990). Folding transition in the DNA-binding domain of GCN4 on specific binding to DNA. *Nature* 347, 575–578.

210 Cho, H. S., Liu, C. W., Damberger, F. F., Pelton, J. G., Nelson, H. C. & Wemmer, D. E. (1996). Yeast heat shock transcription factor N-terminal activation domains are unstructured as probed by heteronuclear NMR spectroscopy. *Protein Sci* 5, 262–269.

211 Green, T. B., Ganesh, O., Perry, K. et al. (2004). IA3, an aspartic proteinase inhibitor from Saccharomyces cerevisiae, is intrinsically unstructured in solution. *Biochemistry* 43, 4071–4081.

212 Geyer, M., Munte, C. E., Schorr, J., Kellner, R. & Kalbitzer, H. R. (1999). Structure of the anchor-domain of myristoylated and non-myristoylated HIV-1 Nef protein. *J Mol Biol* 289, 123–138.

213 Berkovits, H. J. & Berg, J. M. (1999). Metal and DNA binding properties of a two-domain fragment of neural zinc finger factor 1, a CCHC-type zinc binding protein. *Biochemistry* 38, 16826–16830.

214 Cary, P. D., King, D. S., Crane-Robinson, C. et al. (1980). Structural studies on two high-mobility-group proteins from calf thymus, HMG-14 and HMG-20 (ubiquitin), and their interaction with DNA. *Eur J Biochem* 112, 577–580.

215 Abercrombie, B. D., Kneale, G. G., Crane-Robinson, C. et al. (1978). Studies on the conformational

properties of the high-mobility-group chromosomal protein HMG 17 and its interaction with DNA. *Eur J Biochem* 84, 173–177.

216 Cary, P. D., Crane-Robinson, C., Bradbury, E. M. & Dixon, G. H. (1981). Structural studies of the non-histone chromosomal proteins HMG-T and H6 from trout testis. *Eur J Biochem* 119, 545–551.

217 Zeev-Ben-Mordehai, T., Rydberg, E. H., Solomon, A. et al. (2003). The intracellular domain of the *Drosophila* cholinesterase-like neural adhesion protein, gliotactin, is natively unfolded. *Proteins* 53, 758–767.

218 Cox, C. J., Dutta, K., Petri, E. T. et al. (2002). The regions of securin and cyclin B proteins recognized by the ubiquitination machinery are natively unfolded. *FEBS Lett* 527, 303–308.

219 Isbell, D. T., Du, S., Schroering, A. G., Colombo, G. & Shelling, J. G. (1993). Metal ion binding to dog osteocalcin studied by 1H NMR spectroscopy. *Biochemistry* 32, 11352–11362.

220 Moncoq, K., Broutin, I., Larue, V. et al. (2003). The PIR domain of Grb14 is an intrinsically unstructured protein: implication in insulin signaling. *FEBS Lett* 554, 240–246.

221 Donne, D. G., Viles, J. H., Groth, D. et al. (1997). Structure of the recombinant full-length hamster prion protein PrP(29–231): the N terminus is highly flexible. *Proc Natl Acad Sci USA* 94, 13452–13457.

222 Liu, A., Riek, R., Wider, G., von Schroetter, C., Zahn, R. & Wuthrich, K. (2000). NMR experiments for resonance assignments of 13C, 15N doubly-labeled flexible polypeptides: application to the human prion protein hPrP(23–230). *J Biomol NMR* 16, 127–138.

223 Buevich, A. V., Shinde, U. P., Inouye, M. & Baum, J. (2001). Backbone dynamics of the natively unfolded pro-peptide of subtilisin by heteronuclear NMR relaxation studies. *J Biomol NMR* 20, 233–249.

224 Gast, K., Damaschun, H., Eckert, K. et al. (1995). Prothymosin alpha: a biologically active protein with random coil conformation. *Biochemistry* 34, 13211–13218.

225 Fiebig, K. M., Rice, L. M., Pollock, E. & Brunger, A. T. (1999). Folding intermediates of SNARE complex assembly. *Nat Struct Biol* 6, 117–123.

226 Alexandrescu, A. T., Abeygunawardana, C. & Shortle, D. (1994). Structure and dynamics of a denatured 131-residue fragment of staphylococcal nuclease: a heteronuclear NMR study. *Biochemistry* 33, 1063–1072.

227 Alexandrescu, A. T., Jahnke, W., Wiltscheck, R. & Blommers, M. J. (1996). Accretion of structure in staphylococcal nuclease: an 15N NMR relaxation study. *J Mol Biol* 260, 570–587.

228 Ye, K. & Wang, J. (2001). Self-association reaction of denatured staphylococcal nuclease fragments characterized by heteronuclear NMR. *J Mol Biol* 307, 309–322.

229 Ackerman, M. S. & Shortle, D. (2002). Robustness of the long-range structure in denatured staphylococcal nuclease to changes in amino acid sequence. *Biochemistry* 41, 13791–13797.

230 Choy, W. Y. & Kay, L. E. (2003). Probing residual interactions in unfolded protein states using NMR spin relaxation techniques: an application to delta131delta. *J Am Chem Soc* 125, 11988–11992.

231 Choy, W. Y., Shortle, D. & Kay, L. E. (2003). Side chain dynamics in unfolded protein states: an NMR based 2H spin relaxation study of delta131delta. *J Am Chem Soc* 125, 1748–1758.

232 Hazzard, J., Sudhof, T. C. & Rizo, J. (1999). NMR analysis of the structure of synaptobrevin and of its interaction with syntaxin. *J Biomol NMR* 14, 203–207.

233 Liu, D., Ishima, R., Tong, K. I. et al. (1998). Solution structure of a TBP-TAF(II)230 complex: protein mimicry of the minor groove surface of the

TATA box unwound by TBP. *Cell* 94, 573–583.

234 Jimenez, M. A., Evangelio, J. A., Aranda, C. et al. (1999). Helicity of alpha(404–451) and beta(394–445) tubulin C-terminal recombinant peptides. *Protein Sci* 8, 788–799.

235 Spencer, R. G., Halverson, K. J., Auger, M., McDermott, A. E., Griffin, R. G. & Lansbury, P. T., Jr. (1991). An unusual peptide conformation may precipitate amyloid formation in Alzheimer's disease: application of solid-state NMR to the determination of protein secondary structure. *Biochemistry* 30, 10382–10387.

236 Benzinger, T. L., Gregory, D. M., Burkoth, T. S. et al. (2000). Two-dimensional structure of beta-amyloid(10–35) fibrils. *Biochemistry* 39, 3491–3499.

237 Antzutkin, O. N., Balbach, J. J., Leapman, R. D., Rizzo, N. W., Reed, J. & Tycko, R. (2000). Multiple quantum solid-state NMR indicates a parallel, not antiparallel, organization of beta-sheets in Alzheimer's beta-amyloid fibrils. *Proc Natl Acad Sci USA* 97, 13045–13050.

238 Balbach, J. J., Ishii, Y., Antzutkin, O. N. et al. (2000). Amyloid fibril formation by A beta 16–22, a seven-residue fragment of the Alzheimer's beta-amyloid peptide, and structural characterization by solid state NMR. *Biochemistry* 39, 13748–13759.

239 Petkova, A. T., Ishii, Y., Balbach, J. J. et al. (2002). A structural model for Alzheimer's beta-amyloid fibrils based on experimental constraints from solid state NMR. *Proc Natl Acad Sci USA* 99, 16742–16747.

240 Jaroniec, C. P., MacPhee, C. E., Astrof, N. S., Dobson, C. M. & Griffin, R. G. (2002). Molecular conformation of a peptide fragment of transthyretin in an amyloid fibril. *Proc Natl Acad Sci USA* 99, 16748–16753.

241 Vuister, G. W. & Bax, A. (1993). Quantitative J correlation: a new approach for measuring homonuclear three-bond J(HNH.alpha.) coupling constants in 15N-enriched proteins. *J Am Chem Soc* 115, 7772–7777.

242 Pardi, A., Billeter, M. & Wuthrich, K. (1984). Calibration of the angular dependence of the amide proton-C alpha proton coupling constants, 3JHN alpha, in a globular protein. Use of 3JHN alpha for identification of helical secondary structure. *J Mol Biol* 180, 741–751.

243 Ludvigsen, S., Andersen, K. V. & Poulsen, F. M. (1991). Accurate measurements of coupling constants from two-dimensional nuclear magnetic resonance spectra of proteins and determination of phi-angles. *J Mol Biol* 217, 731–736.

244 Schmidt, J. M., Blümel, M., Löhr, F. & Rüterjans, H. (1999). Self-consistent 3*J* coupling analysis for the joint calibration of Karplus coefficients and evaluation of torsion angles. *J Biomol NMR* 14, 1–12.

245 Wang, A. C. & Bax, A. (1996). Determination of the backbone dihedral angles in human ubiquitin from reparametrized empirical karplus equations. *J Am Chem Soc* 118, 2483–2494.

246 Wang, A. C. & Bax, A. (1995). Reparametrization of the Karplus relation for 3J(Hα-N) and 3J(HN-C′) in peptides from uniformly 13C/15N-enriched human ubiquitin. *J Am Chem Soc* 117, 1810–1813.

247 Bystrov, V. F. (1976). Spin-spin coupling and the conformational states of peptide systems. *Prog NMR Spectrosc* 10, 41–81.

248 Löhr, F., Blümel, M., Schmidt, J. M. & Rüterjans, H. (1997). Application of H(N)CA,CO-E.COSY experiments for calibrating the ϕ angular dependences of vicinal couplings J(C′i-1,Hiα), J(C′i-1,Ciβ) and J(C′i-1,C′i) in proteins.

249 Hu, J. S. & Bax, A. (1997). Determination of phi and chi1 angles in proteins from 13C–13C three-bond *J* couplings measured by three-dimensional heteronuclear NMR. How planar is the peptide bond? *J Am Chem Soc* 119.

250 Hu, J. S. & Bax, A. (1998).

Measurement of three-bond, 13C′–13C beta *J* couplings in human ubiquitin by a triple resonance, E. COSY-type NMR technique. *J Biomol NMR* 11, 199–203.

251 Hu, J. S. & Bax, A. (1996). Measurement of three-bond 13C–13C *J* couplings between carbonyl and carbonyl/carboxyl carbons in isotopically enriched proteins. *J Am Chem Soc* 118, 8170–8171.

252 Ding, K. & Gronenborn, A. M. (2004). Protein backbone (1)H(N)-(13)C(alpha) and (15)N-(13)C(alpha) residual dipolar and *J* couplings: new constraints for NMR structure determination. *J Am Chem Soc* 126, 6232–6233.

253 Wirmer, J., Schlörb, C., Klein-Scetharaman, J., Hirano, R., Veda, T., Imoto, T. & Schwalbe, H. (2004). Modulation of Compactness and Long-Range Interactions of Unfolded Lysozyme by Single Point Mutations. *Ang Chem Int Ed* 43, in press.

254 Peti, W., Hennig, M., Smith, L. J. & Schwalbe, H. (2002). NMR Spectroscopic Investigation of ψ Torsion Angle Distribution in Unfolded Ubiquitin from Analysis of $^3J(C_\alpha,C_\alpha)$ Coupling Constants and Cross-Correlated $\Gamma^{c}_{H^N N,C_\alpha H_\alpha}$ Relaxation Rates. *J Am Chem Soc* 122, 12017–12018.

22
Dynamics of Unfolded Polypeptide Chains

Beat Fierz and Thomas Kiefhaber

22.1
Introduction

During protein folding the polypeptide chain has to form specific side-chain and backbone interactions on its way to the native state. An important issue in protein folding is the rate at which a folding polypeptide chain can explore conformational space in its search for energetically favorable interactions. Conformational search within a polypeptide chain is limited by intrachain diffusion processes, i.e., by the rate at which two points along the chain can form an interaction. The knowledge of the rates of intrachain contact formation in polypeptide chains and their dependence on amino acid sequence and chain length is therefore essential for an understanding of the dynamics of the earliest steps in protein folding and for the characterization of the free energy barriers for protein folding reactions. In addition, intrachain diffusion provides an upper limit for the speed at which a protein can reach its native state just like free diffusion provides an upper limit for the rate constant of bimolecular reactions. Free diffusion of particles in solution was treated extensively almost 100 years ago by Einstein and von Smoluchowski [1–3] but until recently, only little was known about the absolute time scales of intrachain diffusion in polypeptides. Numerous theoretical studies have been made to investigate the process of intrachain diffusion in polymers [4–10]. These studies derived scaling laws for intrachain diffusion and made predictions on the kinetic behavior of the diffusion process but they were not able to give absolute numbers. This chapter will briefly introduce some theoretical concepts used to treat chain diffusion and then discuss experimental results on intrachain diffusion from different model systems.

22.2
Equilibrium Properties of Chain Molecules

Since chain dynamics strongly depend on the chain conformation we will briefly present some polymer models for chain conformations. This topic is discussed in

Protein Folding Handbook. Part I. Edited by J. Buchner and T. Kiefhaber

ISBN: 3-527-30784-2

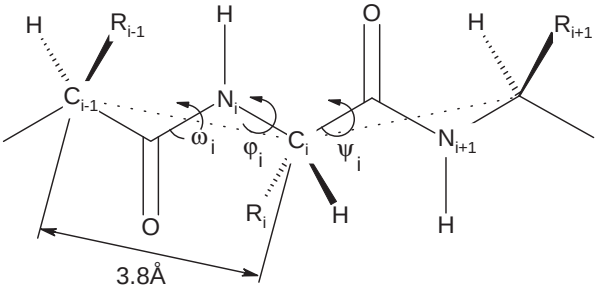

Fig. 22.1. Schematic representation of a polypeptide chain. The R_i denote the different amino acid side chains, the dashed lines denote the virtual chain segment. Adopted from Ref. [12].

more detail in Chapter 20 and in Refs [11–15]. The most simple description on an unfolded state of a protein is the idealized notion of a random coil. In a random coil no specific interactions between residues or more generally chain segments persist and a large conformational space is populated. Polypeptide chains are rather complex polymers as sketched in Figure 22.1. Usually simplified models are applied to calculate general properties of random coils.

22.2.1 The Freely Jointed Chain

The equilibrium properties of an ideal polymer can be described by a three-dimensional random walk. This hypothetical chain, the freely jointed chain, consists of n bonds of length l with equally probable angles at each joint. The chain is described by the $n+1$ position vectors of the joints (chain elements) $\mathbf{R_i}$ or the n bond vectors $\mathbf{r_i}$. The correlation of the bond vectors $\langle \mathbf{r_m} \cdot \mathbf{r_n} \rangle$ is zero for $n \neq m$ because of the independence of the bond vector direction. The average end-to-end distance $\langle r^2 \rangle$ for the freely jointed chain is given by

$$\langle r^2 \rangle = nl^2 \tag{1}$$

For such an ideal chain the end-to-end vectors are normally distributed. The often-used notion of a Gaussian chain, however, refers to a chain model with Gaussian distributed bond lengths. Thus the end-to-end vector distribution is also Gaussian and Eq. (1) holds. This chain model does not describe the local structure of a chain correctly but the global properties of long chains are modeled in a realistic way.

22.2.2 Chain Stiffness

In a chain with restricted angles between two neighboring segments the correlation between segments n, m is no longer zero for $n \neq m$ but asymptotically ap-

proaches zero with increasing distance. The chain is not as flexible as the freely jointed chain because every segment is influenced by its neighbors. This behavior can be described in terms of chain stiffness. The end-to-end distance for such a chain is larger than calculated from Eq. (1). Flory introduced the characteristic ratio (C_n) as a measure for the dimensions of a stiff chain compared to a freely jointed chain [12]

$$\langle r^2 \rangle = C_n n l^2 \tag{2}$$

For short chains C_n increases with chain length due to preferential chain propagation into one direction (see Figure 22.2). For long chains ($n \to \infty$) C_n reaches a constant limiting value (C_∞).

$$\langle r^2 \rangle = C_\infty n l^2 \tag{3}$$

In this limit $\langle r^2 \rangle$ grows proportional to n, like an ideal random-walk chain (see Eq. (1)). However, in a real chain $\langle r^2 \rangle$ increases by a factor of C_∞ more per segment compared with an ideal random-walk chain. The value of C_∞ gives the average number of consecutive chain segments that propagate in the same direction (''statistical segment''). Consequently, for an ideal Gaussian chain where there is no correlation between the bond vectors, the limiting characteristic ratio is 1 (see Eq. (1)). For real chains C_∞ is larger than 1 and larger values of C_∞ indicate stiffer chains.

Kuhn showed that for chains with limited flexibility and n bonds of length l an equivalent to the freely jointed chain can be defined introducing an hypothetical bond length b, the Kuhn length ($b > l$) [16, 17]. The Kuhn length is the length of chain segments that can move freely (i.e., without experiencing chain stiffness). The maximal length of the chain (r_{max}) is the same as for a freely jointed chain and thus $r_{max} = nl = n'b$ with $n' < n$. The Kuhn length b is defined as

$$b = \langle r^2 \rangle / r_{max} = C_\infty n l^2 / r_{max} = C_\infty l \tag{4}$$

Another widely used term is the persistence length l_p. It is a measure for the distance that an infinitely long chain continues in the same direction (i.e., is persistent). The Kuhn and the persistence lengths are connected by the simple relationship

$$b = 2 l_p \tag{5}$$

Both parameters are used as measures for chain stiffness.

22.2.3 Polypeptide Chains

Any real macromolecule like the polypeptide chain has defined segments which are connected by chemical bonds. Bond angles are constrained and the distribution

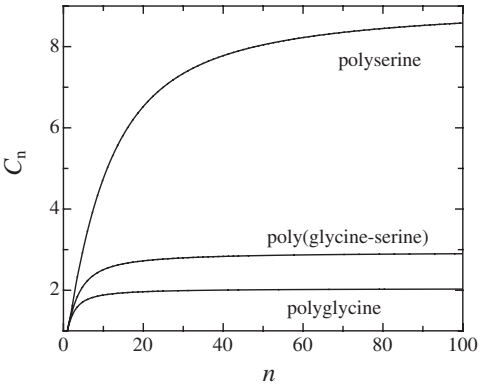

Fig. 22.2. Effect of chain length (n) on the characteristic ratio (C_n) for polyserine, polyglycine and a 50% mixture of serine and glycine. C_n was calculated using average transformation matrices given by Flory [12]. The transformation matrix for alanine was used to calculate the properties of serine.

of torsional angles is given by torsional potentials with several minima. In a peptide chain these torsional potentials are represented in conformational energy plots [18–21] or the Ramachandran map [22]. Flory and coworkers calculated statistical properties of various homopolypeptide chains [12, 18–21] based on the ϕ,ψ-angles from conformational energy plots. An average virtual bond length is defined from $C_{\alpha,i}$ to $C_{\alpha,i+1}$ and taken as 3.8 Å as shown in Figure 22.1 [12]. For polypeptide chains polyglycine represents the most flexible chain with $C_\infty = 2.2$ (see Figure 22.2) [12, 18, 19]. Poly-L-proline gives stiff chains with $C_\infty \approx 100$, due to the formation of a polyproline helix. For all other amino acids, C_∞ is between 8.5 and 9.5 [18]. These values correspond to persistence lengths around 19 Å for chains that do not contain glycine or proline and of 5.7 Å for poly-L-glycine [21]. It should be noted that these values apply for θ conditions, where the attractions between the chain segments (e.g., van der Waals or electrostatic interactions) compensate for the monomer–monomer repulsion due to excluded volume and the chain is apparently unperturbed. For details see Refs [11–15].

22.2.4 Excluded Volume Effects

In real (physical) chains two chain segments cannot occupy the same space. The excluded volume effect was first discussed by Kuhn [16] and leads to a non-ideal behavior of the chain. The chain dimensions increase as a result of the excluded volume, which leads to larger end-to-end distances. Flory obtained an approximate exponent for the chain dimensions including the contributions from the excluded volume effect by simple calculations [11].

$$\sqrt{\langle r^2 \rangle} \propto l \cdot n^{\nu}, \quad \nu = 0.59 \approx \text{or } 3/5 \tag{6}$$

This shows that the excluded volume effect is especially important for long chains. The excluded volume chain has been a subject of much research and is discussed in detail in the literature [13, 23–25] (see also Chapter 20).

For long real chains the end-to-end distribution function, $p(r)$, depends on the solvent conditions and on the temperature of the system if the intrachain interactions have enthalpic contributions. $p(r)$ for real chains can reasonably well be approximated by a skewed Gaussian function [26]

$$p(r) \propto 4\pi r^2 e^{-((r-r_0)/\sigma)^2} \tag{7}$$

where r is the end-to-end distance, σ is the half-width of the distribution and r_0 indicates the shift of the skewed Gaussian from the origin. Polypeptides in solution are complex molecules which may interact strongly with the solvent and with themselves enabling proteins to fold. The unfolded state of natural proteins was shown to contain both native and nonnative short-range and long-range interactions [27–39] (see Chapter 21). But many of the properties of GdmCl-unfolded proteins may be approximated by statistical chain models (see Section 22.4.2.4), although in some proteins specific intrachain interactions have also been found under strongly denaturing conditions [28, 39]. (see Chapter 21).

22.3 Theory of Polymer Dynamics

One of the major interests in polymer chemistry and biology is to elucidate the dynamic behavior of polymers in solution. Usually the dynamics of such molecules are complex and cannot be easily described by classical concepts. This is especially true for protein folding where the polypeptide chain not only moves freely in solution but also undergoes large cooperative structural transitions involving partially folded and native states. In the following we will give a short introduction to the theoretical concepts of polymer dynamics. More detailed information is given in Refs [8, 13, 23, 24].

22.3.1 The Langevin Equation

The energy surface on which a system moves is often complex with sequential and parallel events during the barrier crossing process (see Chapter 12.2). The motions of the system exhibit a diffusional character. The polymer chain in solution is immersed in solvent molecules which supply the energy for the movement by colliding with the polymer chain and at the same time dissipate this energy by exerting a frictional force on the molecule. The system can be described by the Langevin equation for Brownian motion if one assumes that the relaxation time scale for the solvent fluctuations is extremely short compared with the time scale of polymer motion [40]:

$$\ddot{\boldsymbol{x}} = -M^{-1}\frac{\partial U(x)}{\partial \boldsymbol{x}} - \gamma\dot{\boldsymbol{x}} + M^{-1}F_{\text{fluc}}(t) \tag{8}$$

where M is the particle mass, x is the reaction coordinate, $U(x)$ denotes the energy, and γ is a friction coefficient, which is determined by the interactions of the system with its environment and couples the system to the environment. It can be related to solvent viscosity in real solutions. $F_{\text{fluc}}(t)$ is the random force which represents the thermal motion of the environment. The random force is modeled by Gaussian white noise of zero mean and a δ correlation function

$$\langle F_{\text{fluc}}(t)\rangle = 0$$
$$\langle F_{\text{fluc}}(t)\cdot F_{\text{fluc}}(t')\rangle = 2k_{\text{B}}T\gamma M\delta(t-t') \tag{9}$$

22.3.2 Rouse Model and Zimm Model

For long unfolded polypeptide chains, the simplified models used in polymer theory should be applicable. The system, i.e., the peptide immersed in the solvent, encounters no large barriers and undergoes random conformational changes. The dynamic behavior of Gaussian chains can be described analytically using classical polymer theory. Models of a higher complexity are only accessible, however, by solving the equations numerically in computer simulations. Two models have been initially proposed to describe polymer dynamics in dilute solutions: the Rouse model [5] and the Zimm model [6]. In both models the polymer is treated as a set of beads connected by harmonic springs. The Langevin equation (Eq. (8)) is used to describe the brownian motion of the connected beads in the Rouse model. The frictional and activating force from the solvent independently acts on all beads. The movement of the chain is described as a set of n relaxation modes. These modes can be compared to the vibrational modes of a violin string. Each mode p is coupled to a relaxation time τ_{p} and involves the motion of a section of the chain with n/p monomers. The mode with the longest relaxation time describes the overall motion (rotational relaxation) of the polymer chain. All other modes represent internal motions.

Yet, the scaling laws obtained for Rouse chains are not consistent with experimental results [24]. When a chain segment moves through a viscous solvent it has to drag surrounding solvent molecules along. This creates a flow field around the particle. Surrounding monomers are additionally affected by this flow field. As a result, the motion of one chain segment influences the motion of all other segments by hydrodynamic interactions.

The resulting chain model including hydrodynamic interactions was put forward by Zimm [6]. This model also gives internal relaxation modes, but the hydrodynamic interactions lead to significant deviations from the Rouse model. The solvent viscosity influences the system in two ways. First, it affects the random force that delivers the energy and dissipates it at the same time (γ, in the Langevin equa-

tion). Secondly, viscosity changes the strength of the hydrodynamic interactions. Many studies have been performed to compare the predictions of Rouse model, the Zimm model, and more refined models to actual experiments [41]. The overall chain motions including hydrodynamic interactions agree well with experiment [24]. Measurements of dynamics in DNA molecules using time-resolved optical microscopy directly showed internal relaxation modes [42].

22.3.3 Dynamics of Loop Closure and the Szabo-Schulten-Schulten Theory

One particularly intensively treated dynamic event in polymer chains is the loop closure or end-to-end diffusion reaction. Organic chemists are interested in loop closure probabilities for the synthesis of cyclic compounds. Also in nucleic acids end-to-end diffusion is important during formation of cyclic DNA. The kinetics of such cyclization reactions critically depend on the rate of intrachain contact formation. A similar situation is encountered in protein folding, where residues have to come together and form specific non-covalent interactions. Jacobsen and Stockmayer [4] derived a scaling law for end-to-end ring closure probability as a function of the length of the polymer chain. The calculations were based entirely on entropic contributions and yielded

$$p_{\text{ring}} \propto n^{-3/2} \tag{10}$$

where p_{ring} denotes the probability of ring formation and n is the number of monomers in such a ring.

Szabo, Schulten, and Schulten [7] discussed the kinetics that can be expected from a diffusion controlled encounter of two groups attached to the ends of a Gaussian chain (SSS theory). They treated the loop closure reaction as an end-to-end diffusion of a polymer on a potential surface. It was shown that the kinetics of such a process can be approximated by an exponential decay of the probability $\Sigma(t)$ that the system has not reacted (i.e., has not made contact) at time t

$$\Sigma(t) \approx \Sigma_{\text{approx}}(t) = \mathrm{e}^{(-t/\tau)} \tag{11}$$

This approximation holds if the distribution of chain conformations is stationary throughout the reaction, i.e., the interchange of conformations is fast compared with the rate of reaction, and the probability of reaction is small, i.e., the reactive radius is small compared with the chain length. The time constant τ is the mean first passage time of this reaction and depends on the equilibrium end-to-end distribution of the polymer chain $p(x)$, on the diffusion constant D of the chain ends relative to one another and on the reactive boundary r_a, i.e., the distance which leads to contact between the two ends.

$$\tau = \frac{1}{D}\int_{r_a}^{\infty} p(x)^{-1}\left(\int_{x}^{\infty} p(y)\,\mathrm{d}y\right)^2 \mathrm{d}x \Big/ \int_{r_a}^{\infty} p(x)\,\mathrm{d}x \tag{12}$$

The mean first passage time of contact formation can be related to the root mean square end-to-end distance, r, by expanding Eq. (12):

$$\tau^{-1} = k_{\text{contact}} \propto D(\sqrt{\langle r^2 \rangle})^{-3} \tag{13}$$

With Eq. (1) this gives the well-known relationship [4]:

$$k_{\text{contact}} \propto n^{-3/2} \tag{14}$$

for an ideal chain. The effect of viscosity on the rate of reaction is included in the diffusion coefficient D, which is assumed to be inversely proportional to the solvent viscosity. Hydrodynamic interactions, the excluded volume effect and other non-idealities (e.g., a diffusion coefficient dependent on chain conformation) are not considered in these approximations and probably contribute to the dynamics and scaling laws in real systems.

22.4 Experimental Studies on the Dynamics in Unfolded Polypeptide Chains

22.4.1 Experimental Systems for the Study of Intrachain Diffusion

It is now widely accepted that the description of the unfolded state as a complete random coil where the polypeptide chain behaves like an ideal polymer is not accurate. Short stretches along the polypeptide chain behave in a highly non-ideal manner because of chain stiffness, solvent interactions, and excluded volume. In addition, there is evidence for residual short-range and long-range interactions in unfolded proteins in water and even at high concentrations of urea and GdmCl [27, 28, 34, 43, 44]. For the understanding of the dynamic properties of unfolded proteins it is therefore essential to compare scaling laws and absolute rate constants for chain diffusion in homopolymer models with the results from unfolded proteins or protein fragments. Suitable experimental systems to study intrachain diffusion should allow direct measurements of the kinetics of formation of van der Waals contacts between specific groups on a polypeptide chain. To obtain absolute rate constants, the applied method must be faster than chain diffusion and the detection reaction itself should be diffusion controlled (see Appendix).

In the following, we will describe various experimental systems that have been used to study the dynamics of intrachain diffusion. In Section 22.4.2 results from these studies will be discussed in more detail in terms of dynamic properties of unfolded polypeptide chains. A summary of the results is given in Tables 22.1 and 22.2.

22.4.1.1 Early Experimental Studies

Dynamics of synthetic polymers in various organic solvents have been studied for a long time by different means. End-to-end contact formation has been examined

Tab. 22.1. Comparison of end-to-end contact formation rate constants observed in different systems.

k_{app} (s^{-1})	Loop size (n)[a]	Method	Labels[b]	Sequence	Conditions	Reference
$3.3 \cdot 10^8$–$1.1 \cdot 10^8$	4–8, 50[c]	FRET	Dansyl/naphthalene	$(heGln)_n$[d]	Glycerol/TFE	48, 50[c]
$2.8 \cdot 10^4$	60	Bond formation	Heme/Met	Unfolded cytochrome *c*	5.4 GdmCl, 40 °C	52
$5 \cdot 10^7$–$1.2 \cdot 10^7$	3–9	TTET	Thioxanthone/NAla	$(Gly\text{-}Ser)_x$	EtOH	50
$9.1 \cdot 10^6$	10	Triplet quenching	Trp/Cys	$(Ala\text{-}Gly\text{-}Gln)_3$	H_2O, phosphate	59
$1.1 \cdot 10^7$	10	Triplet quenching	Trp/cystine	$(Ala\text{-}Gly\text{-}Gln)_3$	H_2O, phosphate	59
$1.7 \cdot 10^7$	10	Triplet quenching	Trp/lipoate	$(Ala\text{-}Gly\text{-}Gln)_3$	H_2O, phosphate	59
$6.2 \cdot 10^4$	10	Triplet quenching	Trp/lipoate	Pro_9	H_2O, phosphate	59
$2.4 \cdot 10^7$	10	Triplet quenching	Trp/lipoate	$(Ala)_2Arg(Ala)_4ArgAla$	H_2O, phosphate	59
$4.1 \cdot 10^7$–$1.1 \cdot 10^7$	1–21	Fluor. quenching	DBO/Trp	$(Gly\text{-}Ser)_x$	D_2O	65
$3.9 \cdot 10^7$–$1 \cdot 10^5$	7	Fluor. quenching	DBO/Trp	Xaa_6[e]	D_2O	66
$6.6 \cdot 10^6$	8	Single molecule fluor. quenching	MR121/Trp	Part of human p53	H_2O, PBS, 25 °C	67
$8.3 \cdot 10^6$	9	Single molecule fluor. quenching	MR121/Trp	Part of human p53	H_2O, PBS, 25 °C	67
$1.8 \cdot 10^8$–$6.5 \cdot 10^6$	3–57	TTET	Xanthone/NAla	$(Gly\text{-}Ser)_x$	H_2O, 22.5 °C	54
$8 \cdot 10^7$–$3.4 \cdot 10^7$	3–12	TTET	Xanthone/NAla	$(Ser)_x$	H_2O, 22.5 °C	54
$2.5 \cdot 10^8$–$2.0 \cdot 10^7$	4	TTET	Xanthone/NAla	Ser-Xaa-Ser[f]	H_2O, 22.5 °C	54
$4.0 \cdot 10^6$	15	Triplet quenching	Zn-porphyrin/Ru	Unfolded cytochrome c	5.4 M GdmCl, 22 °C	64
$2.0 \cdot 10^7$	17	TTET	Xanthone/NAla	Carp parvalbumin	H_2O, 22.5 °C	55

[a] *n* is the number of peptide bonds between the reacting groups.
[b] The structures of the labels are shown in Figure 22.3.
[c] Calculated in Ref. [50] from the diffusion coefficients and the donor–acceptor distances given in Ref. [48].
[d] heGln = (N^5-(2-hydroxyethyl-)-L-glutamine).
[e] $(Xaa)_6$ = homohexapeptides of 16 different amino acids. The highest (Gly_6) and lowest values (Pro_6) for the observed rate constants are given.
[f] Xaa = Gly, Ala, Ser, Gly, Arg, His, Ile, Pro. The highest (*cis* Pro) and lowest values (*trans* Pro) for the observed rate constants are given. See Figure 22.9.

Tab. 22.2. Comparison of end-to-end contact formation rates observed in different systems measured or extrapolated to $n \approx 10$.

k_{app} (s^{-1})	Loop size (n)	Method	Labels	Sequence	Conditions[b]	Reference
$1 \cdot 10^6$	10[a]	Bond formation	Heme/Met	Unfolded cytochrome *c*	5.4 GdmCl, 40 °C	52
$1.2 \cdot 10^7$	9	TTET	Thioxanthone/NAla	$(GS)_4$	EtOH	50
$9.1 \cdot 10^6$	10	Triplet quenching	Trp/Cys	$(AGQ)_3$	H_2O, phosphate buffer	59
$1.1 \cdot 10^7$	10	Triplet quenching	Trp/cystine	$(AGQ)_3$	H_2O, phosphate buffer	59
$1.7 \cdot 10^7$	10	Triplet quenching	Trp/lipoate	$(AGQ)_3$	H_2O, phosphate buffer	59
$3.1 \cdot 10^7$	9	Fluor. quenching	DBO/Trp	$(GS)_4$	D_2O	65
$8.3 \cdot 10^6$	9	Single molecule Fluor. quenching	MR121/Trp	Fragment from human p53	H_2O, PBS, 25 °C	67
$8.3 \cdot 10^7$	9	TTET	Xanthone/NAla	$(GS)_4$	H_2O, 22.5 °C	54
$4.1 \cdot 10^7$	10	TTET	Xanthone/NAla	$(Ser)_9$	H_2O, 22.5 °C	54
$1 \cdot 10^7$	10[a]	Triplet quenching	Zn-porphyrin/Ru	Unfolded cytochrome *c*	5.4 M GdmCl, 22 °C	64

[a] Extrapolated from larger loops to 10 amino acids, as the average loop size in proteins. It should be noted that extrapolations used the Jacobsen Stockmeyer or SSS theory scaling law ($k_c \sim n^{-1.5}$), which gives a slightly smaller length dependence than the experimentally determined scaling laws (cf. Figure 22.8). This would result in larger extrapolated values of k_c.

[b] solvent was H_2O unless indicated. The data measured in concentrated GdmCl solutions or EtOH were not corrected for solvent effects. This would lead to a significant increase in k_c (see Figure 22.10).

using phosphorescence quenching of benzophenone in long hydrocarbon polymers [45] and by excimer formation of pyrene groups attached to poly(ethylene glycols) [46]. The dynamics of unfolded polypeptide chains have first been studied using fluorescence resonance energy transfer (FRET) from an energy donor to an energy acceptor group. FRET was shown to be a powerful tool to determine donor–acceptor distances [47], but time-resolved FRET kinetics also contain major contributions from the diffusion of the two FRET probes relative to each other [48, 49]. The number of excited donor molecules ($N^*(r,t)$) with donor–acceptor distance r changes with time in the presence of an acceptor group. This can be described by a second-order partial differential equation for the reduced distance distribution, $\bar{N}(r,t)$, normalized to $N_0(r)$:

$$\frac{\partial \bar{N}(r,t)}{\partial t} = -\frac{1}{\tau}\left\{\left(1+\left(\frac{R_0}{r}\right)^6\right)\bar{N}(r,t)\right\} + \frac{1}{N_0(r)}\frac{\partial}{\partial r}\left\{N_0(r)D\frac{\partial \bar{N}(r,t)}{\partial r}\right\}$$

$$\text{with } \bar{N}(r,t) = \frac{N^*(r,t)}{N_0(r,t)} \tag{15}$$

where R_0 is the distance of 50% FRET efficiency, which is a property of the FRET labels, $N_0(r)$ denotes the equilibrium distribution of distances between donor and acceptor, and τ is the fluorescence lifetime of the donor. The first term (equilibrium term) on the right-hand side describes the change of donor excitation with time through spontaneous decay and nonradiative energy transfer. The second term (diffusion term) describes the replenishment of excited labels through brownian motion. This dynamic component of FRET was exploited to determine diffusion coefficients of segmental motion in short homopolypeptide chains (poly-N^5-(2-hydroxyethyl)-L-glutamine) in glycerol and trifluoroethanol mixtures [48, 49] (see Chapter 17). Naphthyl- and dansyl-groups were used as donor and acceptor, respectively (Figure 22.3A).

These studies allowed the first estimates of the time scale of chain diffusion processes in polypeptide chains. Converting the reported average diffusion constants reported by Haas and coworkers [48] into time constants ($\tau = 1/k$) for contact formation at van der Waals distance gives values between 9 and 3 ns for a donor–acceptor separation of between 4 and 8 peptide bonds, respectively [50]. The dynamic component of FRET is sensitive to motions around the Förster distance (R_0), which is around 22 Å for the dansyl–naphthyl pair used in these studies. It therefore remained unclear whether the same diffusion constants represent the dynamics for formation of van der Waals contact between two groups. In addition, analysis of the FRET data critically depends on the shape of the donor–acceptor distribution function, which had to be introduced in the data analysis and thus did not allow model-free analysis of the data. It was found that this distribution can be described most accurately by the skewed Gaussian function mentioned above [51]. It later turned out that the chain dynamics measured by FRET are significantly faster than rate constants for contact formation (see below), which might indicate a distance-dependent diffusion constant in unfolded polypeptide chains.

A

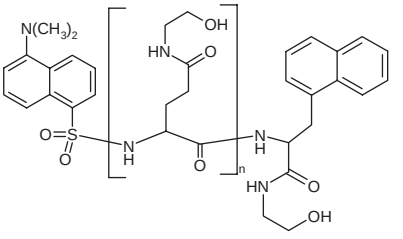

B

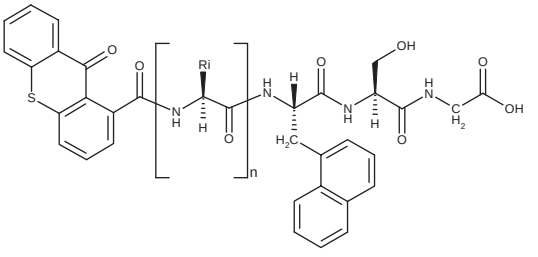

C

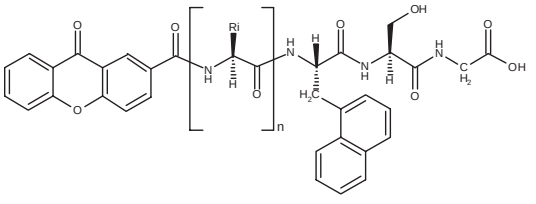

D

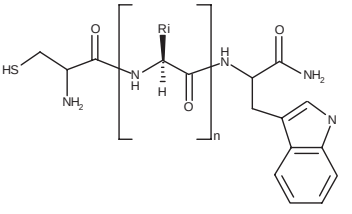

E

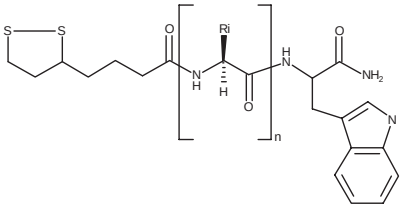

F

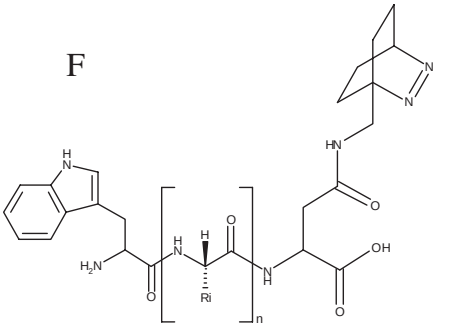

G

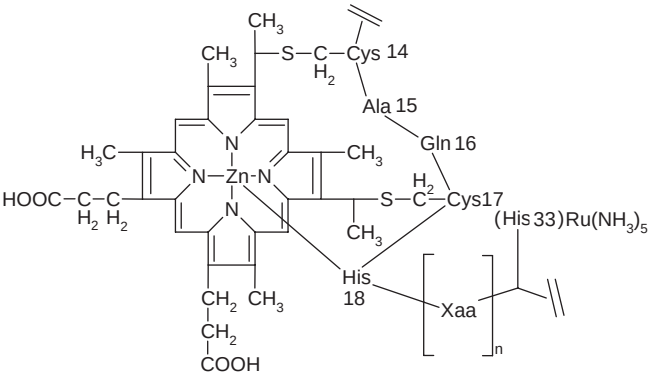

FRET was also used in several proteins to determine donor–acceptor distance distribution functions and diffusion coefficients (see Chapter 17).

Rates of intrachain diffusion have also been estimated from the rate constant for intramolecular bond formation in GdmCl-unfolded cytochrome *c* [52]. The reaction of a methionine with a heme group separated by 50–60 amino acids along the chain gave time constants around 35–40 μs. Extrapolating these data to shorter distances using SSS or Jacobsen-Stockmeyer theory ($k \sim n^{-1.5}$) gave an estimate of 1 μs for the time constant of contact formation at a distance of 10 peptide bonds, which was predicted to be the distance for the maximum rate of contact formation due to chain stiffness slowing down the diffusion process over shorter distances [53]. A problem with this experimental approach is that the recombination reaction of heme with methionine is not diffusion controlled. Thus, the chain dynamics allow a faster breakage of the heme–methionine contact than formation of the methionine–heme bond. Thus, not every contact was productive and the apparent rate constants obtained in these measurements were slower than the absolute rate constants measured with diffusion-controlled systems (see Experimental Protocols, Section 22.7).

22.4.1.2 Triplet Transfer and Triplet Quenching Studies

The early studies on intrachain diffusion did not yield absolute rate constants for contact formation, but they were important to trigger the development of more direct and model-free methods to study chain diffusion. Recently, several experimental systems using fast photochemical methods to directly monitor contact formation in model peptides and protein fragments have been introduced. Bieri et al. [50] and Krieger et al. [54, 55] used triplet–triplet transfer (TTET) between thioxanthone or xanthone derivatives and naphthalene (see Figure 22.3B,C) to directly measure rate constants for intrachain contact formation in synthetic polypeptide chains. A triplet donor and a triplet acceptor group are introduced at specific points in polypeptide chains. The donor is selectively excited by a laserflash and undergoes fast intersystem crossing into the triplet state (see Figure 22.4). Upon intrachain diffusion the triplet donor and triplet acceptor groups meet and the triplet state is transferred to the acceptor. Since TTET is a two electron exchange process (Dexter mechanism) it has a very strong distance dependence and usually requires

Fig. 22.3. Structures of different experimental systems used to measure intrachain contact formation. Results from these systems are summarized in Table 22.1. A) Dansyl and naphthyl-labeled poly-N^5-(2-hydroxyethyl)-L-glutamine used to determine diffusion constants by FRET [48]. B) Thioxanthone and naphthylalanine-labeled poly(Gly-Ser) peptides to measure contact formation by TTET [50]. C) Xanthone and naphthylalanine-labeled peptides to measure contact formation by TTET in various homopolymer chains and natural sequences with up to 57 amino acids between donor and acceptor [54, 55]. D,E) Tryptophan and cysteine or lipoate-labeled peptides to measure contact formation by Trp triplet quenching in various short peptide chains [59, 125, 126]. F) Short peptide chains ($n < 10$) for measuring DBO fluorescence quenching by tryptophan [65]. G) Quenching of Zn-porphyrin triplets by Ru-His complexes in unfolded cytochrome *c* [64].

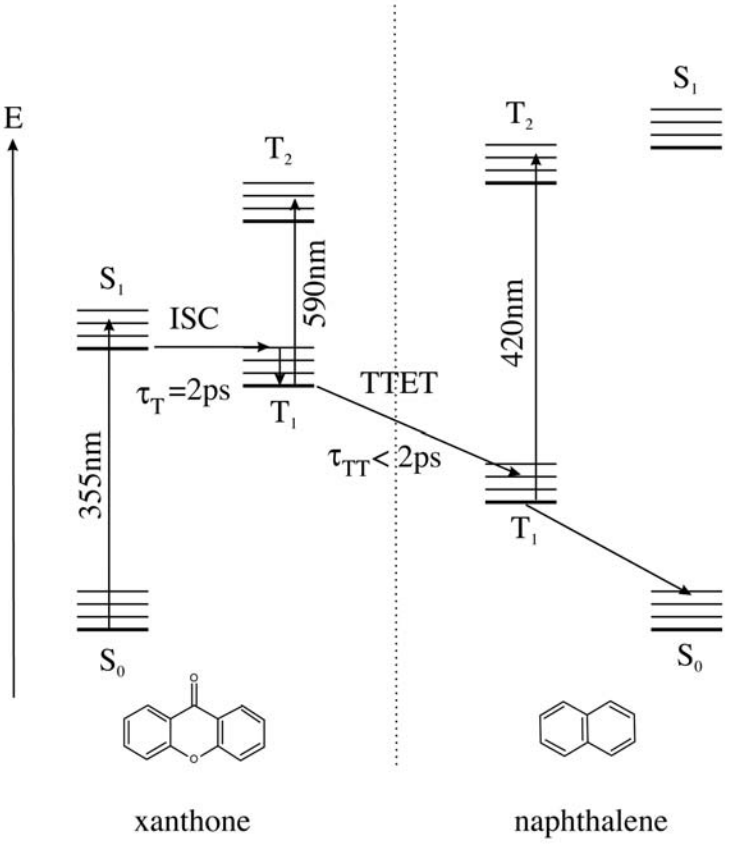

Fig. 22.4. Jablonski diagram for triplet–triplet energy transfer (TTET) from xanthone to naphthalene. Rate constants for triplet formation (k_T) and TTET (k_{TT}) were measured by laserflash photolysis using femtosecond pulses [56].

van der Waals contact to allow for electron transfer. This should be contrasted to FRET, which occurs through dipole–dipole interactions and thus allows energy transfer over larger distances (see above).

The triplet states of the labels have specific absorbance bands, which can easily be monitored to measure the decay of the donor triplet states and the concomitant increase of acceptor triplet states (Figure 22.5). The time constant for formation of xanthone triplet states is around 2 ps [56]. TTET between xanthone and naphthyl acetic acid is faster than 2 ps and has a bimolecular transfer rate constant of $4 \cdot 10^9$ M^{-1} s^{-1} [54, 56], which is the value expected for a diffusion-controlled reaction between small molecules in water (see Experimental Protocols, Section 22.7). Due to this fast photochemistry, TTET between xanthone and naphthalene allows measurements of absolute rate constants for diffusion processes slower than 10–20 ps (Figure 22.6 and Experimental Protocols, Section 22.7). The upper

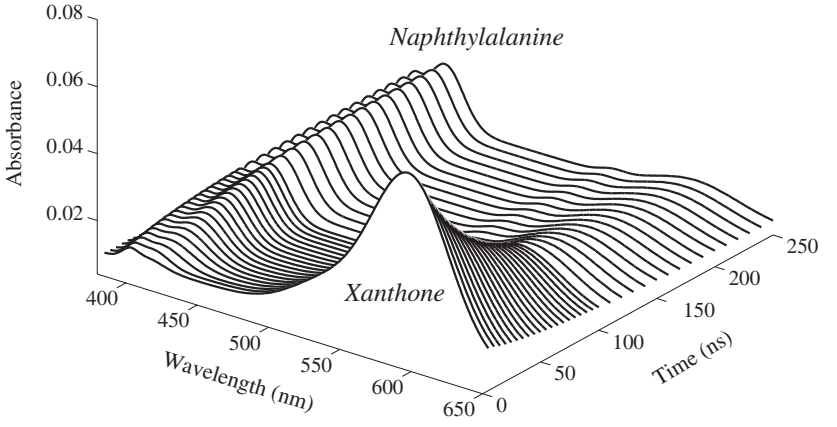

Fig. 22.5. Time-dependent change in the absorbance spectrum of a Xan-(Gly-Ser)$_{14}$-NAla-Ser-Gly peptide after a 4 ns laser flash at 355 nm. The decay in the intensity of the xanthone triplet absorbance band around 590 nm is accompanied by a corresponding increase in the naphthalene triplet absorbance band around 420 nm. Adapted from Ref. [54].

limit of the experimental time window accessible by TTET is set by the intrinsic lifetime of xanthone which is around 20–30 μs in water. Xanthone has a high quantum yield for intersystem crossing ($\phi_{ISC} = 0.99$, $\varepsilon \approx 4000\ M^{-1}\ cm^{-1}$) and the triplet state has a strong absorbance band with a maximum around 590 nm in water ($\varepsilon^{T}_{590} \approx 10\,000\ M^{-1}\ cm^{-1}$). This allows single-pulse measurements at rather low peptide concentrations (10–50 μM).

The low concentrations applied in the experiments also rule out contributions from intermolecular transfer reactions that would have half-times higher than 50 μs in this concentration range [50, 54]. Also contributions from through-bond transfer processes can be neglected, since this cannot occur over distances beyond eight bonds [57, 58] and even the shortest peptides used in TTET studies had donor and acceptor separated by 11 bonds.

Bieri et al. [50] initially used a derivate of thioxanthone as triplet donor and the nonnatural amino acid naphthylalanine (NAla) as triplet acceptor (see Figure 22.3B). Because of the sensitivity of the triplet energy of the donor on solvent polarity the measurements had to be carried out in ethanol. TTET detected single exponential kinetics in all peptides with time constants of 20 ns for the shortest loops in poly(glycine-serine)-based polypeptide chains [50]. The length dependence of contact formation in these peptides did not exhibit a maximum rate constant for transfer at $n = 10$, in contrast to the predicted behavior [53] (see Section 22.4.2.2). Based on these findings, the minimum time constant for intrachain contact formation was shown to be around 20 ns for short and flexible chains. The thioxanthone used in the initial experiments as triplet donor was later replaced by xanthone [54], which has a higher triplet energy than thioxanthone and thus allowed measurements in water (see Figure 22.3C). These results showed two- to threefold faster

rate constants for contact formation compared to the same peptides in ethanol [54], setting the time constant for intrachain diffusion in short flexible chains in water to 5–10 ns. The faster kinetics compared to the thioxanthone/NAla system could be attributed to the effect of ethanol [54] (see below).

A disadvantage of TTET from xanthone to NAla in its application to natural proteins is that Tyr, Trp, and Met interact with the xanthone triplet state either by TTET or by triplet quenching and thus should not be present in the studied polypeptide chains [55].

Lapidus et al. [59] used a related system to measure chain dynamics in short peptides. In this approach contact formation was measured by quenching of tryptophan triplet states by cysteine (see Figure 22.3D). Tryptophan can be selectively excited by a laserflash ($\phi_{ISC} = 0.18$, $\varepsilon_{266} \approx 3500\ M^{-1}\ cm^{-1}$, $\varepsilon^{T}_{460} \approx 5000\ M^{-1}\ cm^{-1}$) and its triplet decay can be monitored by absorbance spectroscopy [60]. The advantage of this system is that donor chromophore and quencher groups are naturally occurring amino acids, which can be introduced at any position in peptides and proteins. As in the case on TTET from xanthone to naphthalene some amino acids interfere with the measurements (e.g., Tyr, Met) since they interact with tryptophan triplets and should thus not be present in the studied polypeptide chains [61].

Major disadvantages of the Trp/Cys system are, (i) that the formation of tryptophan triplets is slow ($\tau = 3$ ns) [62], (ii) that triplet quenching is accompanied by the formation of S·radicals [59], and (iii) that the quenching process is not diffusion controlled [63]. These properties reduce the time window available for the kinetic measurements and do not allow direct and model-free analysis of the quenching time traces (see Experimental Protocols, Section 22.7). In addition, its low quantum yield makes the detection of the triplet states and the data analysis difficult, especially since the kinetics are obscured by radical absorbance bands. In addition to cysteine quenching, two other systems were presented by the same group [59] with cystine or the cyclic disulfide lipoate serving as quencher instead of cysteine (Figure 22.3E). The advantage of using lipoate is that the quenching kinetics are much closer to the diffusion limit. Thus, the rates measured with this system are generally faster. Still, all systems used for quenching of tryptophan triplets gave significantly slower kinetics of intrachain contact formation compared to TTET from xanthone to NAla in the same or in similar sequences (see Tables 22.1 and 22.2). This indicates that tryptophan triplet quenching does not allow measurements of chain dynamics on the absolute time scale [63].

Another recent experimental approach investigated intrachain contact formation in unfolded cytochrome *c* using electron transfer from a triplet excited Zn-porphyrine group to a Ru complex, which was bound to a specific histidine residue (His33; Figure 22.3G). Since electron transfer is fast and close to the diffusion limit these experiments should also yield absolute rate constants for chain diffusion. Contact formation in the 15-amino-acid loop from cytochrome *c* was observed with a time constant of 250 ns [64] in the presence of 5.4 M GdmCl. This is significantly faster than the dynamics in unfolded cytochrome *c* reported by Hagen et al. [52] under similar conditions. However, the dynamics measured by Chang et al. agree well with TTET measurements [50, 54, 55], when the kinetics are extrapolated from 5.4 M GdmCl to water (see below).

22.4.1.3 Fluorescence Quenching

Other approaches to measure contact formation applied quenching of long-lifetime fluorescence probes. Two studies used 2,3-diazabicyclo[2,2,2]oct-2-ene (DBO) as a fluorophore (see Figure 22.3F) [65, 66]. It has a lifetime of up to 1 μs and its excited singlet states can be quenched by tryptophan upon contact. The quenching rate of DBO by tryptophan lies close to the diffusion-controlled limit in water, yet the obtained rates are about a factor of 3 slower than the ones obtained with the xanthone/NAla system in the same peptides [54]. This suggests that the photochemistry of fluorescence quenching may not be faster than breakage of the van der Waals contact between DBO and Trp (see Figure 22.6 and Experimental Protocols, Section 22.7). Another disadvantage of this method is the rather short lifetime of the DBO excited state (< 1 μs), which limits the method to short peptides.

Recently, intrachain diffusion was measured using single molecule fluorescence quenching. Peptides were labeled with a fluorescent dye (MR121) which was quenched by tryptophan [67]. The quenching was reported to only occur efficiently via van der Waals contact. Contact formation between the labels resulted in fluorescence fluctuations, which were recorded by confocal fluorescence microscopy. The rate constants for contact formation were determined using time-correlated single-photon counting. The calculated rates are, however, significantly lower than those determined by more direct methods.

22.4.2 Experimental Results on Dynamic Properties of Unfolded Polypeptide Chains

The different systems presented above were applied to measure intrachain contact formation in a large variety of model peptides. The rates for contact formation have

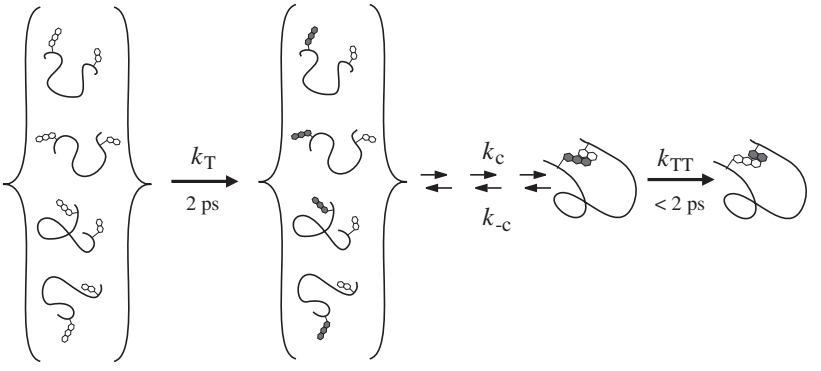

Fig. 22.6. Schematic representation of the triplet–triplet energy transfer (TTET) experiments. Triplet donor and acceptor groups are attached at specific positions on an unstructured polypeptide chain. Triplet states are produced in the donor group by a short laser flash and transferred to the acceptor upon encounter at van der Waals distance in a diffusion-controlled process. The experiments allow determination of the absolute rate constant for contact formation (k_c) in the ensemble of unfolded conformation, if formation of the triplet state (k_T) and the transfer process (k_{TT}) are much faster than chain dynamics ($k_T, k_{TT} \gg k_{-c}, k_c$; see Experimental Protocols, Section 22.7). The rate constants given for k_T and k_{TT} were taken from Ref. [56].

been found to vary depending on the method applied, on the sequence of the peptide and on the peptide length. Results from different groups are compared in Tables 22.1 and 22.2. The results reveal that TTET and electron transfer, which were shown to have fast photochemistry and diffusion-controlled transfer reactions, give virtually identical rate constants and have the fastest contact rates of all applied methods. These methods obviously allow the determination of absolute rate constants for contact formation. In the following, we will discuss results from experiments that used these methods to determine the effect of chain length, amino acid sequence and solvent properties on the rate constants of contact formation.

22.4.2.1 Kinetics of Intrachain Diffusion

All experiments applying TTET [50, 54] and electron transfer [64] to measure dynamics of unfolded polypeptide chains revealed single exponential kinetics on the ns time scale or slower (Figure 22.7). The only exception were short proline-containing peptides, where the kinetics of *cis* and *trans* Xaa-Pro peptide bonds could be resolved [54]. From the observation of single exponential kinetics several conclusions can be drawn. As observed by Szabo, Schulten, and Schulten [7] and pointed out by Zwanzig [68], single exponential kinetics indicate fast interconversion between the different conformations in the ensemble of unfolded states, thus allowing the chain to maintain the equilibrium distribution of the ensemble of conformations that has not made contact. Fast interconversion between individual chain conformations is in agreement with results on conformational relaxation processes in strained peptides, which were shown to occur in the picoseconds time scale [69, 70]. Secondly, the contact radius is small compared to the chain length, which leads to a small probability of contact formation in agreement with the observation that triplet–triplet transfer can only occur when the two labels are in van der Waals contact [7, 68]. A small fraction of chain conformations in equilibrium are predicted to have very short donor–acceptor distances [63] which might allow contact formation on the subnanosecond time scale. From the nanosecond TTET experiments it can be ruled out, however, that a significant fraction (> 5–10%) of chain molecules form donor–acceptor contacts on the subnanosecond time scale, even in the shortest peptides [54]. However, the dynamics of linear peptides in the subnanoseconds time region has not been investigated yet. The fast photochemistry of TTET between xanthone and naphthalene should allow the study of peptide dynamics on the picosecond time scale to detect small fraction of fast transfer processes.

22.4.2.2 Effect of Loop Size on the Dynamics in Flexible Polypeptide Chains

The scaling of the end-to-end diffusion with loop size was measured in TTET experiments by varying the number of amino acids between xanthone and naphthylalanine in two series of homopolypeptides. One series represented flexible polypeptide chains of Xan-$(Gly\text{-}Ser)_x$-NAla-Ser-Gly peptides with x varying from 1 to 28. These peptides allowed measurements of contact formation kinetics between two points on the chain separated by between 3 and 57 peptide bonds, which covers the range of side-chain contacts in small proteins. Figure 22.7 displays three repre-

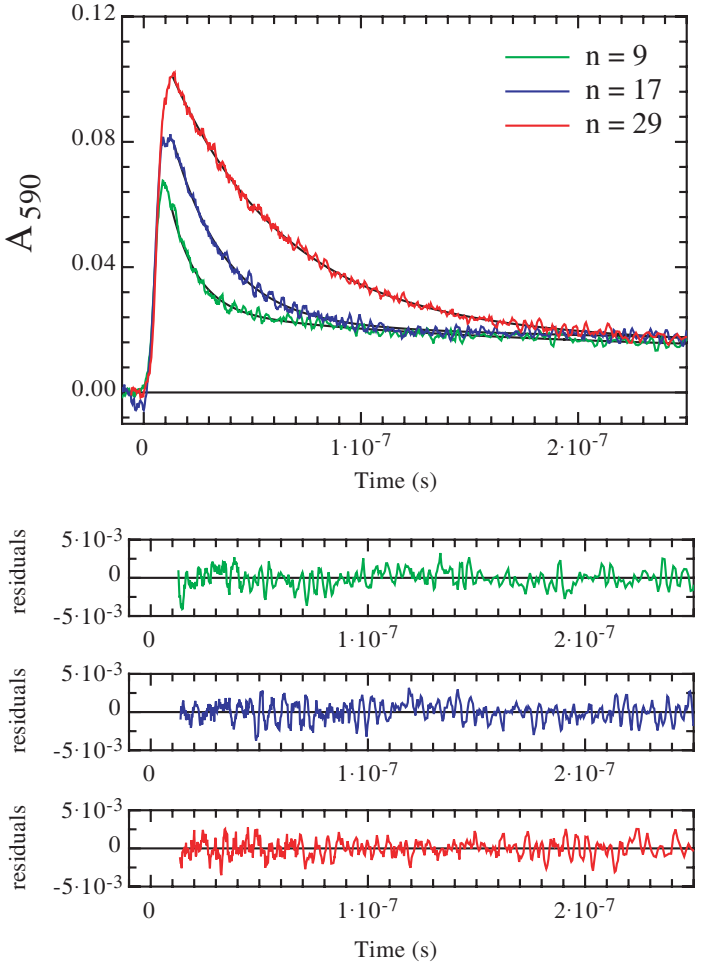

Fig. 22.7. Time course of formation and decay of xanthone triplets in peptides of the form Xan-(Gly-Ser)$_x$-NAla-Ser-Gly after a 4 ns laser flash at $t = 0$ measured by the change in absorbance of the xanthone triplets at 590 nm. Data for different numbers of peptide bonds (n) between donor and acceptor are displayed. Additionally, single exponential fits of the data and the corresponding residuals are shown. The fits gave time constants shown in Figure 22.8. Adapted from Ref. [54].

sentative TTET kinetics for peptides from this series. As mentioned above, single exponential kinetics for contact formation were observed for all peptides.

Figure 22.8 shows the effect of increasing loop size on the rate constant for contact formation. For long loops ($n > 20$) the rate of contact formation decreases with $n^{-1.7\pm0.1}$ (n is the number of peptide bonds between donor and acceptor). This indicates a stronger effect of loop size on the rate of contact formation than expected for purely entropy-controlled intrachain diffusion in ideal freely jointed Gaussian

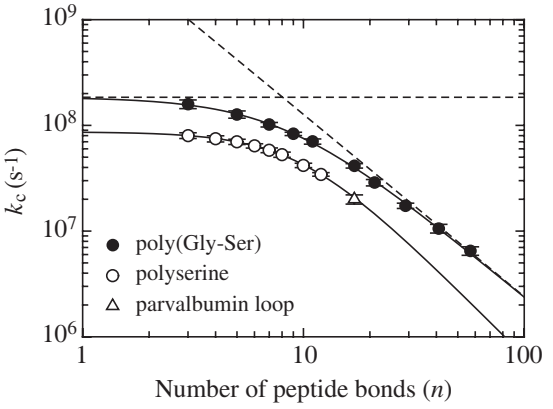

Fig. 22.8. Comparison of the rate constants (k_c) for end-to-end diffusion in poly(glycine-serine) (filled circles), polyserine (open circles) and a parvalbumin loop fragment 85–102 (triangles) measured by TTET between xanthone and naphthylalanine. The data were fitted to Eq. (16) and gave results of $k_a = (1.8 \pm 0.2) \cdot 10^8\ s^{-1}$, $k_b = (6.7 \pm 1.6) \cdot 10^9\ s^{-1}$ and $m = 1.72 \pm 0.08$ for the poly(glycine-serine) series and of $k_a = (8.7 \pm 0.8) \cdot 10^7\ s^{-1}$, $k_b = (1.0 \pm 0.8) \cdot 10^{10}\ s^{-1}$ and $m = 2.1 \pm 0.3$ for polyserine. The dashed lines indicate the limiting cases for dynamics for short chains ($k_c = k_a$) and long chains $k_c = k_b \cdot n^{-m}$). Data were taken from Refs [54, 55].

chains, which should scale with $k \sim n^{-1.5}$ (see above) [4, 7]. However, Flory already pointed out that excluded volume effects should significantly influence the chain dimensions [11]. Accounting for excluded volume effects in the end-to-end diffusion model of Szabo, Schulten, and Schulten [7] gives $k \sim n^{-1.8}$, which is nearly identical to the value found for the long poly(Gly-Ser) chains [54]. This indicates that the dimensions and the dynamics of unfolded polypeptide chains in water are significantly influenced by excluded volume effects, which is in agreement with recent results on conformational properties of polypeptides derived from simplified Ramachandran maps [25]. Additionally, hydrodynamic interactions and the presence of small enthalpic barriers, which were observed in the temperature dependence of intrachain diffusion might contribute to the length dependence (F. Krieger and T. Kiefhaber, unpublished).

The observed simple scaling law breaks down for $n < 20$ and contact formation becomes virtually independent of loop size for very short loops with a limiting value of $k_a = 1.8 \cdot 10^8\ s^{-1}$. As pointed out above, the limiting rate constant for contact formation in short loops is not due to limits of TTET (k_{TT} in Figure 22.6), since this process is faster than 2 ps. Obviously, the intrinsic dynamics of polypeptide chains are limited by different processes for motions over short and over long segments. This is in agreement with polymer theory, which suggests that the properties of short chains are strongly influenced by chain stiffness. This leads to a breakdown of theoretically derived scaling laws for ideal chains [12]. To compare the experimental results with predictions from polymer theory the effect of loop size on the rate constants for contact formation (Figure 22.8) can be compared to

the length dependence of the characteristic ratio (C_n; Figure 22.2). By comparison with polymer theory the limiting value for k_c for formation of short loops might be related to intrinsic chain stiffness, which causes the increase in C_n with chain length for short chains (see Section 22.2).

The 1:1 mixture of glycine and serine used in these experiments is expected to have a C_∞-value of about 3 and C_∞ should be reached for $n > 10$ (Figure 22.2) [21]. Figure 22.8 shows, however, that the poly(glycine-serine) chains behave like random chains only over distances longer than 20–30 amino acids, where $k_c \sim n^{-1.7}$. This indicates increased chain stiffness compared to the predicted value, which could be due to specific intrachain hydrogen bonds or van der Waals interactions and to excluded volume effects that restrict the number of chain conformations. This model is supported by the measurements of activation energies for the peptides of different length. Formation of long loops shows very low activation enthalpies whereas formation of short loops encounter significant energy barriers (F. Krieger and T. Kiefhaber, unpublished).

The complete effect of loop size on intrachain contact formation can be described by a model where length-dependent diffusional processes, which scale with $k = k_b \cdot n^{-m}$, limit the kinetics of formation of long loops. Contact formation reaches a limiting rate constant (k_a) when these diffusional motions become slower than length-independent short-range motions, which are probably governed by chain stiffness and steric effects. Accordingly, the effect of loop size on contact formation can be described by

$$k_c = \frac{1}{1/k_a + 1/(k_b \cdot n^{-m})} \tag{16}$$

The fit of the experimental results to Eq. (16) is shown in Figure 22.8 and gives a value of $k_a = (1.8 \pm 0.2) \cdot 10^8$ s^{-1}, $k_b = (6.7 \pm 1.6) \cdot 10^9$ s^{-1}, and $m = 1.72 \pm 0.08$ for poly(glycineserine), as discussed above.

22.4.2.3 Effect of Amino Acid Sequence on Chain Dynamics

Both theoretical considerations [18, 19, 21] (see Section 22.2) and experimental results from NMR measurements [71] show that polypeptide chains are especially flexible around glycyl residues. All amino acids except proline ($C_\infty > 100$) and glycine ($C_\infty = 2.2$) are predicted to have C_∞-values around 8.5–9.5 and C_∞ should be reached for intrachain distances longer than about 40–50 amino acids [18, 19, 21] (Figure 22.2). This indicates increased chain stiffness and longer root mean square end-to-end distances ($\sqrt{\langle r^2 \rangle_0}$) compared to the poly(glycine-serine) series (Figure 22.2). The effect of chain stiffness on peptide dynamics was tested in TTET experiments in polyserine chains [54]. Figure 22.8 compares the effect of loop size on intrachain diffusion in a series of Xan-$(Ser)_x$-NAla-Ser-Gly peptides with $x = 2$–11 ($n = 3$–12) to the behavior of poly(Gly-Ser) chains. Single exponential kinetics for contact formation were observed in all polyserine peptides. For short loops ($n < 5$) contact formation is virtually independent of loop size with a limiting value of $k_a = 8.7 \cdot 10^7$ s^{-1} (see Eq. (18)). This indicates that the local dynamics in polyser-

ine are about two- to threefold slower than in the poly(glycine-serine) peptides, which seems to be a small effect compared to the largely different properties expected for the stiffer polyserine chains (see Figure 22.2).

The decreased flexibility and the longer donor-acceptor distances in the polyserine chains are probably compensated by the decreased conformational space available for polyserine compared to poly(glycine-serine) peptides. [54] For longer polyserine chains contact formation slows down with increasing loop size. The effect of increasing loop size on the rates of contact formation seems to be slightly larger in polyserine compared to the poly(glycine-serine) series ($m = 2.1 \pm 0.3$; $k_b = (1.0 \pm 0.8) \cdot 10^{10}$ s^{-1}; see Eq. (16)). However, due to limitations in peptide synthesis it was not possible to obtain longer peptides, which would be required to get a more accurate scaling law for the polyserine peptides.

The kinetics of formation of short loops differ only by a factor of 2 for polyserine compared with poly(glycine-serine), arguing for only little effect of amino acid sequence on local chain dynamics (Figure 22.8). The effect of other amino acids on local chain dynamics was measured by performing TTET experiments on short host–guest peptides of the canonical sequence Xan-Ser-Xaa-Ser-NAla-Ser-Gly using the guest amino acids Xaa = Gly, Ser, Ala, Ile, His, Glu, Arg, and Pro [54]. Figure 22.9 shows that the amino acid side chain indeed has only little effect on the rates of contact formation. All amino acids except proline and glycine show very similar dynamics. Interestingly, there is a small but significant difference in rate between short side chains (Ala, Ser) and amino acids with longer side chains (Ile, Glu, Arg, His). Obviously, chains that extend beyond the C_β-atom slightly decrease the rates

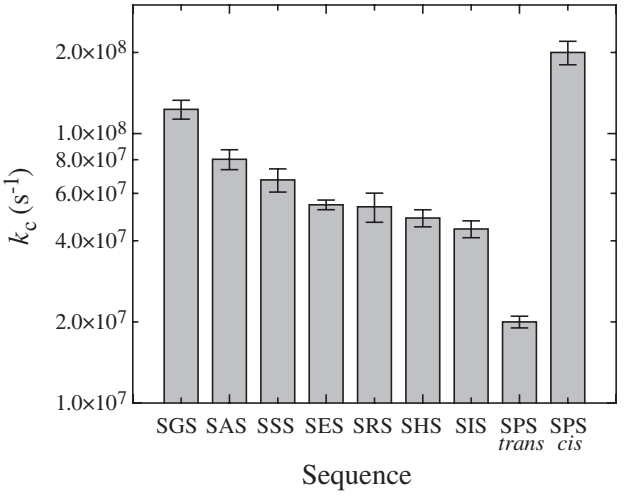

Fig. 22.9. Effect of amino acid sequence on local chain dynamics measured in host–guest peptides with the canonical sequence Xan-Ser-Xaa-Ser-NAla-Ser-Gly. The guest amino acid Xaa was varied and the rate constants for the different guest amino acids are displayed. Data taken from Ref. [54].

of local chain dynamics, whereas charges do not influence the dynamics. Glycyl and prolyl residues show significantly different dynamics compared with all other amino acids, as expected from their largely different conformational properties [19].

As shown before (Figure 22.8) glycine accelerates contact formation about two- to threefold compared with serine. Proline shows slower and more complex kinetics of contact formation with two rate constants of $k_1 = 2.5 \cdot 10^8$ s^{-1} and $k_2 = 2 \cdot 10^7$ s^{-1} and respective amplitudes of $A_1 = 20 \pm 5\%$ and $A_2 = 80 \pm 5\%$. This essentially reflects the *cis–trans* ratio at the Ser-Pro peptide bond in our host–guest peptide, which has a *cis* content of $16 \pm 2\%$ as determined by 1D ^{1}H-NMR spectroscopy using the method described by Reimer et al. [72]. Since the rate of *cis–trans* isomerization is slow ($\tau \sim 20$ s at 22 °C) there is no equilibration between the two isomers on the time scale of the TTET experiments. This allows the measurement of the dynamics of both the *trans* and the *cis* form. The results show that the two isomers significantly differ in their dynamic properties of $i, i+4$ contact formation and that the *cis*-prolyl isomer actually shows the fastest rate of local contact formation of all peptides (Figure 22.9).

22.4.2.4 Effect of the Solvent on Intrachain Diffusion

The dynamics of short poly(glycine-serine) peptides measured with the xanthone–naphthalene TTET pair in water [54] were about 3 times faster than the previously measured rates in the same peptides using the thioxanthone–naphthalene pair in EtOH [50], although both systems were shown to be diffusion-controlled. Figure 22.10 shows that this difference can be attributed to solvent effects [54]. $\ln k_c$ linearly decreases with increasing EtOH concentration in a Xan-(Gly-Ser)$_4$-NAla-Ser-Gly peptide (Figure 22.10A). EtOH is a better solvent for polypeptide chains than water and should thus lead to a more extended ensemble of unfolded states. This model was supported by measuring the effect of GdmCl and urea on the contact rates in aqueous solutions. Both denaturants show similar effects on intrachain diffusion as EtOH, with a linear decrease in $\ln k_c$ with increasing denaturant concentration. Interestingly, the change in $\ln k_c$ with denaturant concentration ($m_c = \partial \ln k_c / \partial$ [Denaturant]) is twofold higher for GdmCl compared with urea, which essentially corresponds to their relative strength in unfolding proteins [73] (see below). Similar m_c-values for EtOH, urea and GdmCl were observed in a Xan-(Ser)$_9$-NAla-Ser-Gly peptides. [54] The observed effect is significantly stronger than expected from the increased solvent viscosity in concentrated GdmCl and urea solutions [50, 74].

The effect of GdmCl and urea on the chain dynamics suggested that these cosolvents may significantly change the chain properties. This was supported by measurements of the effect of GdmCl on the distance dependence of intrachain contact formation. Figure 22.10B compares the effect of loop size on the kinetics of contact formation in the Xan-(Gly-Ser)$_n$-NAla-Ser-Gly series in 8 M GdmCl and water. At high denaturant concentrations the switch from the length-independent dynamics to the length-dependent regime occurs already for formation of shorter loops. This indicates decreased chain stiffness in 8 M GdmCl compared with

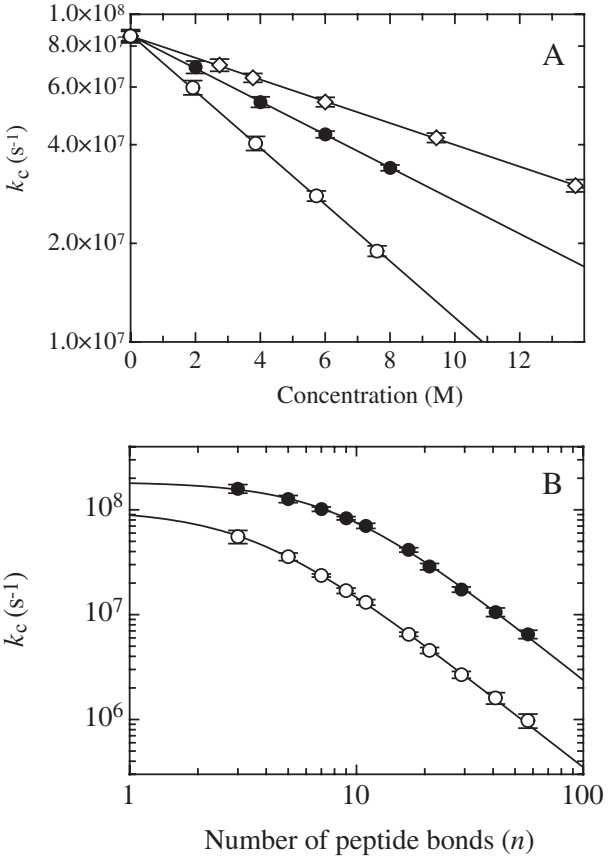

Fig. 22.10. A) Effect of various co-solvents on the dynamics of intrachain contact formation in a Xan-(Gly-Ser)$_4$-NAla-Ser-Gly peptide measured by TTET. Measurements were performed in aqueous solutions in the presence of ethanol (diamonds), urea (filled circles) and GdmCl (open circles). B) Effect of donor–acceptor distance (n) on the rate constant of contact formation in series of poly(Gly-Ser) peptides (cf. Figure 22.8). The rate constants for contact formation in water (filled circles) are compared with the values in 8 M GdmCl (open circles). Data taken from Ref. [54].

water, although the dynamics are significantly slowed down in the presence of GdmCl both for formation of short and long loops (Figure 22.10). For long peptides the effect of chain length on the rates of contact formation is similar in 8 M GdmCl and water with $k_c \sim n^{-1.8\pm0.1}$. These results revealed that denaturants like GdmCl and urea slow down local chain dynamics but lead to more flexible chains that behave like ideal polymers already at shorter donor–acceptor distances (Figure 22.10B). These seemingly contradicting findings can be rationalized based on the effect of denaturants on the conformational properties of polypeptide chains. Unlike water, solutions with high concentrations of denaturants represent good solvents for polypeptide chains. This reduces the strength of intramolecular in-

teractions like hydrogen bonds and van der Waals interactions relative to peptide–solvent interactions, which makes unstructured polypeptide chains more flexible and leads to a behavior expected for an unperturbed chain.

In agreement with this interpretation the effect of loop size on the rates of contact formation in 8 M GdmCl is close to the behavior of an unperturbed polypeptide chain predicted by Flory and coworkers [21] (see Figure 22.2). The decreased rate of contact formation at high denaturant concentrations can only in part be explained by an increased solvent viscosity. Additional effects like increased donor–acceptor distance, which is expected in good solvents compared to water and denaturant binding might also contribute to the decreased rate constants [74].

22.4.2.5 **Effect of Solvent Viscosity on Intrachain Diffusion**

Intrachain contact formation was shown to be strongly viscosity dependent as expected for a diffusional reaction. Viscosity effects on contact formation rates have been measured in TTET experiments on poly(Gly-Ser) peptides [50] (F. Krieger and T. Kiefhaber, unpublished). In all peptides a linear dependency of $\log k_c$ vs. $\log \eta$ was observed and the dependencies could be fitted with the empirical relationship

$$k = \frac{k_0}{\eta^{-\beta}} \tag{17}$$

with $\beta \leq 1$ (Figure 22.11). In the limit for long chains ($n > 15$) the rate of contact formation was found to be inversely proportional to the viscosity ($\beta = 1$) independent of the co-solvent used to alter the viscosity of the solution. In the limit for

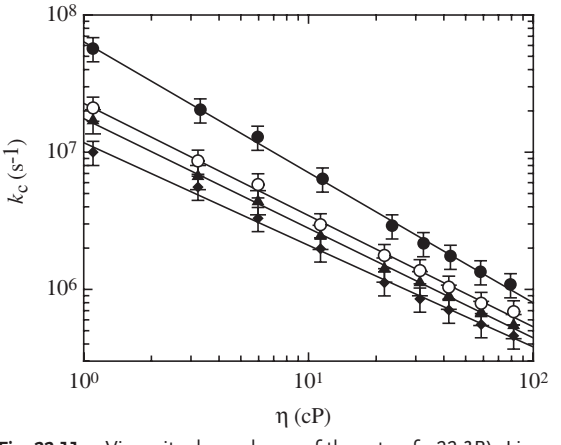

Fig. 22.11. Viscosity dependence of the rate of contact formation for poly(Gly-Ser)$_x$ peptides containing $x = 1$ (filled circles), 2 (open circles), 3 (filled triangles) and 4 (filled diamonds) glycine-serine pairs between thioxanthone and naphthylalanine (cf. Figure 22.3B). Linear fits of the double logarithmic plot of the data give slopes of -0.96 ± 0.05, -0.83 ± 0.05, -0.80 ± 0.05, and -0.81 ± 0.05, respectively. Experiments were carried out in ethanol/glycerol mixtures. Data were taken from Ref. [50].

short chains ($n < 10$), β was smaller than unity (0.8–0.9) [50]. This is not compatible with theoretical consideration which predict $\beta = 1$ as a result from Stokes law relating the solvent viscosity and the diffusion coefficient. β-values < 1 have also been observed for motions of simpler polymers in organic solvents [75–77] and for dynamics of native proteins [78–80].

Several origins have been proposed to explain such behavior like either position-dependent [81] or frequency-dependent [82, 83] friction coefficients. In addition, experiments on myoglobin [80] suggested that deviations from the Stokes law can also be caused by the structure of protein–solvent interfaces, which preferably contain water molecules and have the viscous co-solvent molecules preferentially excluded [84]. This results in a smaller microviscosity around the protein compared with bulk solvent. Additional experiments will be needed to identify the origin of fractional viscosity dependencies of dynamics in short chains.

22.4.2.6 End-to-end Diffusion vs. Intrachain Diffusion

When side-chain contacts are formed within a polypeptide chain during the folding process, the residues are commonly not located near the end of the polypeptide chain. Thus, the end-to-end contact formation experiments represent a rather specific and rare situation during the folding process. Based on the location of the contact sites, three categories of contact formation events in polymers can be distinguished (Figure 22.12). Type I corresponds to end-to-end contact formation. Type II corresponds to end-to-interior contacts and type III contacts are formed between two position remote from the chain ends. Measurements in long hydrocarbon chains yielded trends that cyclization rates are slowed down by additional groups at the ends of the chain [46] without yielding absolute magnitudes of the effects. The xanthone–NAla TTET system has proved to be suitable to perform such experiments in peptides. TTET experiments in type II and III systems have shown that k_c depends on the size of the additional tail (B. Fierz and T. Kiefhaber, unpublished). The strength of the effect is dependent on the nature of the sequence in the observed segment. In long and flexible chains between the labels (i.e., the long chain limit) the dependence on tail length is weaker than for short or stiff chains (the short chain limit).

Such behavior has been predicted by theory [85]. The observed effect should correlate with the surface of the additional amino acids on the ends, if solvent friction limits chain motions as suggested by the viscosity-dependence of the chain diffusion. However the chain movements should only be slowed down to a limiting value. In this limit, the segmental dynamics are independent on further extension of the chain. This limiting rate of innersegmental diffusion corresponds to the maximal rate at which specific side-chain contacts can be formed in the interior of a protein during folding.

22.4.2.7 Chain Diffusion in Natural Protein Sequences

Recently, contact formation rates have been measured in natural protein sequences from cytochrome *c* [64] and carp parvalbumin [55]. The results from these dynam-

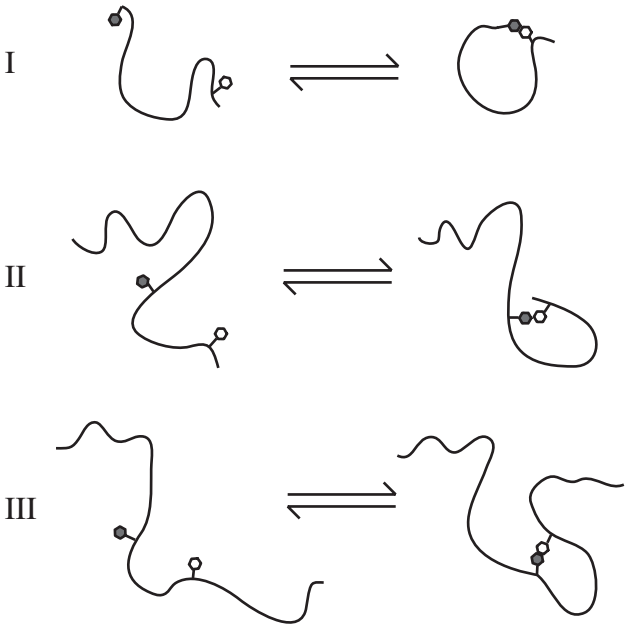

Fig. 22.12. Schematic representation of different types of contact formation in polymer chains. For details see text.

ics are in agreement with dynamics expected from the host–guest studies shown in Figure 22.9. The 18-amino-acid EF-loop of carp parvalbumin connects two α-helices and brings two phenylalanine residues into contact in the native protein, which were replaced by xanthone and naphthylalanine to measure TTET kinetics (Figure 22.13) [55]. The measured kinetics were single exponential (Figure 22.14) and the time constant for contact formation ($\tau = 50$ ns) was comparable to the dynamics for polyserine chains of the same length (Figure 22.8). The EF-loop contains several large amino acids like Ile, Val, and Leu but also four glycyl residues. Obviously, the effects of slower chain dynamics of bulkier side chains and faster dynamics around glycyl residues compensate, which leads to dynamics comparable to polyserine chains. These results indicate that polyserine is a good model to estimate the dynamics of glycine-containing loop sequences in proteins.

The Zn-porphyrine/Ru system was used to measure contact formation in cytochrome *c* unfolded in 5.4 M GdmCl [64]. The donor and quencher groups were separated by 15 amino acids (Figure 22.13) and contact formation was significantly slower ($\tau = 250$ ns) than for polyserine peptide chains of the same length. However, correcting for the effects of denaturant concentration (see Figure 22.10) and end-extensions (Section 22.4.2.6) on chain dynamics gives rate constants for the cytochrome *c* sequence which are comparable to the parvalbumin EF-loop in water.

A

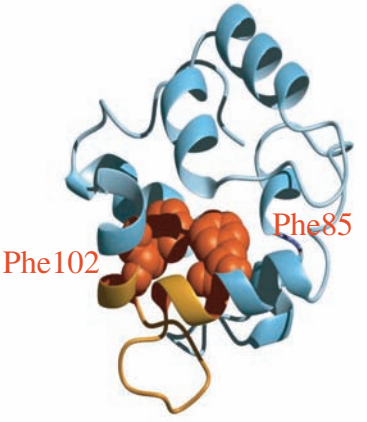

B

Residues 85-102 in carp parvalbumin:

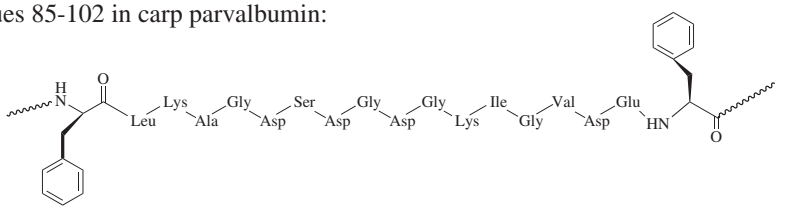

Chemically synthesized fragment with TTET labels:

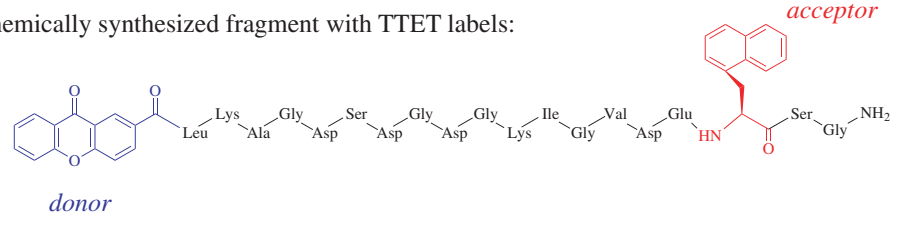

C

Residues 14-33 in horse heart cytochrome c with triplet quenching labels:

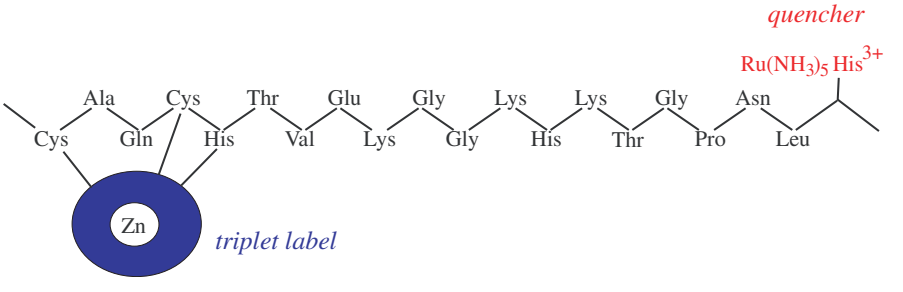

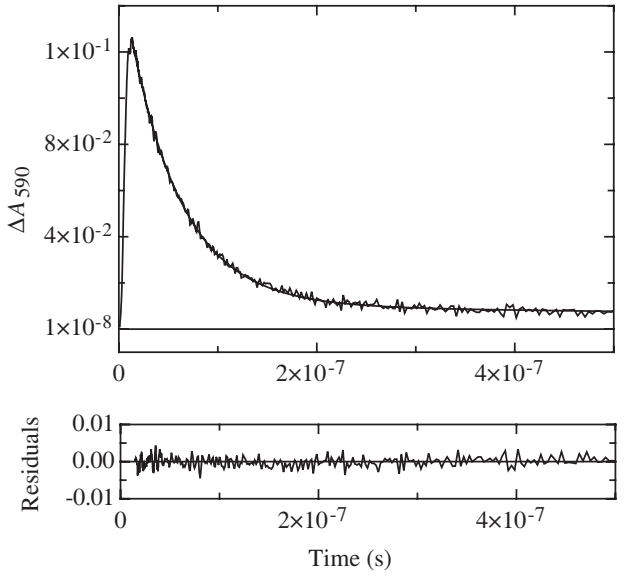

Fig. 22.14. Time course of formation and decay of xanthone triplets in parvalbumin loop fragment 85–102 after a 4 ns laser flash at $t = 0$. The change of xanthone triplet absorbance is measured at 590 nm. The dynamics of contact formation can be described by a single exponential with a time constant of 54 ± 3 ns. Data are taken from Ref. [55].

22.5 Implications for Protein Folding Kinetics

22.5.1 Rate of Contact Formation during the Earliest Steps in Protein Folding

The results on the time scales of intrachain diffusion in various unfolded polypeptide chains show that the amino acid sequence has only little effect on local dynamics of polypeptide chains. All amino acids show very similar rates of end-to-end diffusion with time constants between 12 and 20 ns for the formation of $i, i+4$

Fig. 22.13. A) Ribbon diagram of the structure of carp muscle β-parvalbumin [127]. Phe85 and Phe102 are shown as space-fill models. The phenylalanine residues have been replaced by the triplet donor and acceptor labels, xanthonic acid and naphthylalanine, respectively. The figure was prepared using the program MolMol [128] and the PDB file 4CPV [127]. B) Sequence of the carp muscle β-parvalbumin EF loop region (residues 85–102) and the synthesized fragment labeled with the two phenylalanine residues at position 85 and 102 replaced by donor (xanthone) and acceptor (naphthylalanine) groups for triplet–triplet energy transfer. C) Sequence from cytochrome *c* between the Zn-pophyrine group (excited triplet group) and the Ru-His complex used in triplet quenching experiments reported by Chang et al. [64].

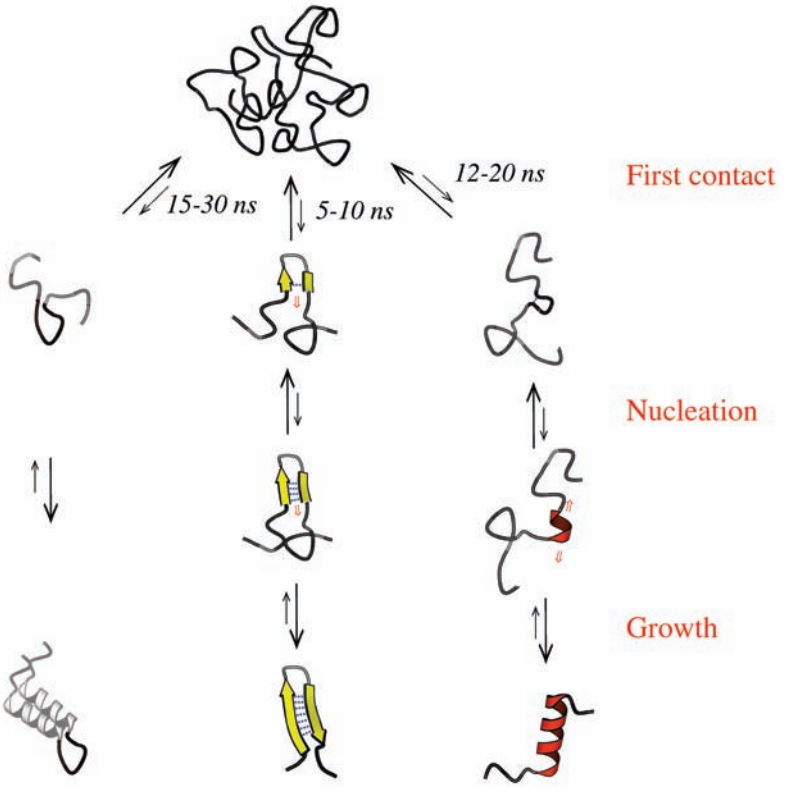

Fig. 22.15. Schematic representation of the time constants for the first steps in formation of loops, β-hairpins and α-helices during protein folding derived from the data measured by TTET in water. Adapted from Ref. [54].

contacts. Polypeptide chains are significantly more flexible around glycine ($\tau = 8$ ns) and stiffer around prolyl residues ($\tau = 50$ ns for the *trans* isomer). Presumably due to the shorter chain dimensions resulting from a *cis* peptide bond the rates of $i, i+4$ contact formation are fastest around the *cis* Ser-Pro bond ($\tau = 4$ ns). These results allow to set an upper limit for the rates of formation of the first productive local contacts during protein folding (Figure 22.15). They can directly be used to estimate the kinetics of loop formation, which are typically of the size of 6–10 amino acids [86]. The results suggest that loops can form with time constants of about 15 ns for glycine-rich loops and 30–40 ns for stiffer loops. β-hairpins, which are the most local structures in proteins, are often rich in glycine and proline [87]. Gly-Ser is actually one of the most frequent sequences found in hairpin loops. The results indicate that the time constants for the first steps in the formation of the tightest turns with $i, i+3$ contacts are around 5 ns for Gly and *cis* Xaa-Pro (Figures 22.8 and 22.9). In glycine- and proline-free turns these rates are slowed down to about 10–20 ns, depending on the amino acid sequence.

Formation of α-helices is most likely initiated by formation of a helical turn,

which involves formation of an $i, i+4$ interaction [88, 89]. Since helices are usually free of glycyl and prolyl residues the initiation cannot occur faster than in about 12–20 ns (Figures 22.8 and 22.9). It should be noted that these values do not represent time constants for nucleation of helices and hairpins (Figure 22.15), which most likely requires formation of more than one specific interaction and most likely encounters additional entropic and enthalpic barriers. The results on the rates of intrachain contact formation rather represent an upper limit for the dynamics of the earliest steps in secondary structure formation (i.e., $<$ for formation of the first contact during helix nucleation). They represent the prefactors (k_0) in the rate equation for secondary structure formation

$$k = k_0 \cdot e^{-\Delta G^{\circ\ddagger}/RT} \tag{18}$$

The measured contact rates thus allow us to calculate the height of the free energy barriers ($\Delta G^{\circ\ddagger}$) when they are compared to measured rate constants (k) for secondary structure formation. However, up to date no direct data on helix or hairpin formation in short model peptides are available. The dynamics of secondary structures were mainly studied by relaxation techniques like dielectric relaxation [90], ultrasonic absorbance [91], or temperature jump [92–94] starting from predominately folded structures (for a review see Ref. [95]). Since helix–coil and hairpin–coil transitions do not represent two-state systems, neither thermodynamically nor kinetically, the time constants for unfolding can not be directly related to rate constants of helix formation [96]. However, the observation of relaxation times around 1 μs for helix unfolding allowed the estimation of time constants for the growth steps of nucleated helices of about 1 to 10 ns, depending on the experimental system [90, 91, 93].

It may be argued that intrachain contacts in a polypeptide chain with a stronger bias towards folded structures can form faster than the observed dynamics in unstructured model polypeptide chains. However, weak interactions like van der Waals contacts between side chains and hydrogen bonds should dominate the early interactions during the folding process and the data on the dynamics of unfolded chains will provide a good model for the earliest events in folding. A stronger energy bias towards the native state will mainly increase the strength or the number of these interactions but not their dynamics of formation.

22.5.2
The Speed Limit of Protein Folding vs. the Pre-exponential Factor

Many small single domain proteins have been found to fold very fast, some of them even on the 10 to 100 μs time scale (for a review see Ref. [97]). These fast folding proteins include α-helical proteins like the monomeric λ-repressor [98, 99] or the engrailed homeodomain [100], β-proteins like cold shock protein of *Bacillus subtilis* or *B. cacodylicus* [101] or the WW-domains [102] and α,β-proteins like the single chain arc repressor [103]. There has been effort to design proteins that fold even faster [104, 105]. A folding time constant of 4.1 μs has been reported for a designed Trp-cage.

These very fast folding proteins sparked interest in finding the speed limit for protein folding, which is closely related to the speed limit of the fundamental steps of protein folding and thus also to the dynamics of the unfolded chain. The results on dynamics of contact formation in short peptides showed that no specific interactions between two points on the polypeptide chain can be formed faster than on the 5–10 ns time scale. Considering that dynamics are slowed down if the two groups are located in the interior of a long chain this time constant increases to about 50 ns. Formation of intrachain interactions represents the elementary step in the conformational search on the free energy landscape. Thus, the dynamics of this process set the absolute speed limit for the folding reaction. However, it will not necessarily represent the prefactor (k_0) for the folding process which represents the maximum rate for protein folding in the absence of free energy barriers ($\Delta G^{\circ\ddagger} = 0$, see Eq. (18)). It was shown that even fast apparent two-state folding proceeds through local minima and maxima on the free energy landscape [106, 107] and up to date it is unclear which processes contribute to the rate-limiting steps in protein folding (see Chapters 12.1, 12.2 and 14).

The transition state for folding seems to be native-like in topology but still partly solvated [108–111], Thus, both protein motions and dynamics of protein–solvent interactions in a native-like topology might contribute to the pre-exponential factor and k_0 will probably depend on the protein and on the location of the transition state along the reaction coordinate, which may change upon change in solvent conditions or mutation (see Section 5.3) [44, 106, 107].

22.5.3
Contributions of Chain Dynamics to Rate- and Equilibrium Constants for Protein Folding Reactions

As discussed above, the pre-exponential factor (k_0) for a protein folding reaction should contain major contributions from the rate of intrachain diffusion in an unfolded or partially folded polypeptide chain [112]. Thus, factors that influence intrachain diffusion, like denaturant concentration (Figure 22.10), will also affect the pre-exponential factor for folding. This will influence the observed folding rate constants and thus also the observed equilibrium constants [112]. A method that allows a quantitative description of reaction rates for processes in solution was developed by Kramers [113]. He considered a particle moving on an energy surface with two metastable states (e.g., native and unfolded protein) separated by a barrier (Figure 22.16). The motion of the particle is diffusional and can be described by the Langevin equation (Eq. (8)). The thermal motion of the solvent is modeled as the random force. Solving the diffusion equations, Kramers observed three different regimes which differ in the strength of interaction between system and environment. In the low friction limit the interactions are only weakly coupled. In this limit the rate of the barrier crossing reaction from the educt to the product state increases with increasing friction γ. In the intermediate friction limit the rate is independent on friction and the results from transition state theory and from Kramers' theory approach each other. In the high friction limit, which should cor-

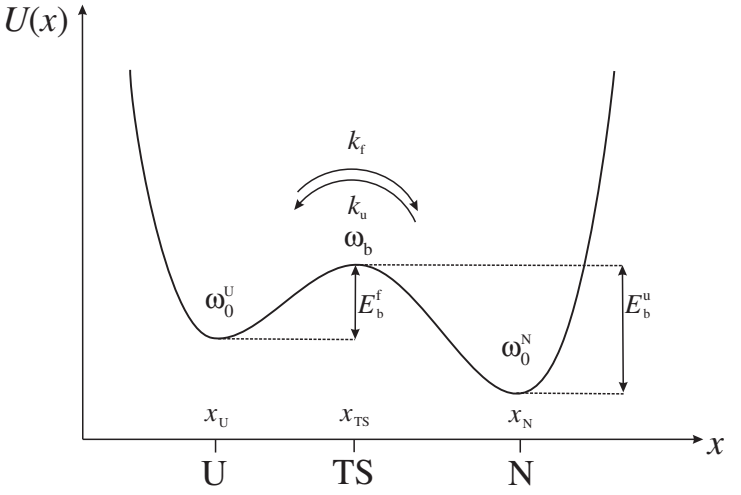

Fig. 22.16. Potential U(x) with two states N and U separated by an energy barriers. Escape from state U to N occurs via the rates k_f and k_u. E_b^f and E_b^u are the activation energies for the forward and back reaction. ω denotes the frequencies of phase point motion at the extremes of the potential. The drawing was adapted from Ref. [114].

respond to most reactions in solution and also to protein folding reactions, the rate of the reaction decreases when the friction is further increased. In this limit the equation for the rate as a function of friction, barrier height and temperature can be written as:

$$k = \frac{\omega_0 \omega_B}{2\pi\gamma} e^{(-E_b/kT)} \tag{19}$$

where ω stands for the frequency of motion of the particle in the starting well (ω_0) and on top of the barrier (ω_B). ω depends on the shape of the barrier and on the nature of the free energy surface [114]. By applying Stokes law this equation can then readily be expressed in terms of thermodynamic parameters and solvent viscosity.

$$k = \frac{C}{\eta(T)} \cdot \exp(-\Delta G^{\circ\ddagger}/RT) = k_0 \cdot \exp(-\Delta G^{\circ\ddagger}/RT) \tag{20}$$

It is not clear whether Kramers' approach in its simple form as described above is directly applicable to protein folding reactions, since it is difficult to measure the viscosity-dependence of folding and unfolding rate constants. The co-solvents used to modify solvent viscosity like glycerol, sucrose, or ethylene glycol generally stabilize the native state [84] and in part also the transition state of folding. This makes a quantification of the effect of solvent viscosity on protein folding rate constants difficult [115, 116].

The results from the viscosity dependence of end-to-end contact formation show that the rate constants in short peptides ($n < 10$) are not proportional to η^{-1} but rather to $\eta^{-0.8}$. This suggests that the presence of barriers in these peptides leads to a more complex behavior than expected from Eq. (20) and indicates that the frictional coefficient from Kramers' theory (γ, see. Eq. (19)) is not only determined by solvent viscosity for protein folding reactions.

Application of Kramers' theory to protein folding reactions shows the problems with quantitatively characterizing the barriers for protein folding. It is very difficult to determine pre-exponential factors for the folding and unfolding reaction, which are most likely different for each protein. Since the pre-exponential factors depend on the shape of the potential and on the dynamics in the individual wells (states), ω_0 will be different for the refolding reaction starting from unfolded protein (ω_0^{U}) and for the unfolding reaction starting from native protein (ω_0^{N}) and hence also the prefactors will be different for the forward and backward reactions. However, under all conditions Eq. (21) must be valid [117]:

$$K_{\mathrm{eq}} = \frac{k_{\mathrm{f}}}{k_{\mathrm{u}}} \tag{21}$$

Thus, the equilibrium constant (K_{eq}) contains contributions from the pre-exponential factors for folding (k_0^{f}) and unfolding (k_0^{u}) and from differences in $\Delta G^{\circ\ddagger}$, according to [112]

$$K_{\mathrm{eq}} = \frac{k_0^{\mathrm{f}} \cdot \mathrm{e}^{-\Delta G_{\mathrm{f}}^{\circ\ddagger}/RT}}{k_0^{\mathrm{u}} \cdot \mathrm{e}^{-\Delta G_{\mathrm{u}}^{\circ\ddagger}/RT}} \tag{22}$$

The contribution of differences in the prefactors for folding and unfolding to $\Delta G^{\circ}(= -RT \ln K_{\mathrm{eq}})$ are consequently [112]

$$\Delta G^{\circ} = \Delta G_{\mathrm{f}}^{\circ\ddagger} - \Delta G_{\mathrm{u}}^{\circ\ddagger} + \Delta G_{\mathrm{pref}}^{\circ}$$

$$\Delta G_{\mathrm{pref}}^{\circ} = RT \ln \frac{k_0^{\mathrm{u}}}{k_0^{\mathrm{f}}} \tag{23}$$

Differences in k_0 for folding and unfolding can thus significantly contribute to apparent protein folding barriers. A fivefold difference in k_0 would contribute 4 kJ mol^{-1} to the experimentally determined barrier height at 25 °C. Consequently, also changes in the dynamics of the unfolded state, which change the pre-exponential factor for the folding reaction by changing ω_0, will influence K_{eq}, even if the heights of the barriers are not changed. For many proteins significant residual structure in the unfolded state has been observed either directly by NMR [27, 28, 34, 43] or from the analysis of the denaturant dependence [44]. It was shown that this residual structure is sensitive to mutation, which can lead to significant changes in the solvent accessibility [44] and in the dynamics [39] of the unfolded state. This will lead to changes in k_0 for the folding reaction (k_0^{f}) by changing ω_0^{U} and will result in a change of the folding rate constant (k_{f}) and consequently also in the apparent free energy of activation, $\Delta G_{\mathrm{f}}^{\circ\ddagger}$(app) even if $\Delta G_{\mathrm{f}}^{\circ\ddagger}$ is

not affected by the mutations [112].

$$\Delta\Delta G_f^{\circ\ddagger}(\text{app}) = \Delta\Delta G_f^{\circ\ddagger} + RT \ln \frac{k_0^f(\text{wt})}{k_0^f(\text{mutant})} \quad (24)$$

As in the example above, a fivefold increase in k_0 of a mutant would apparently decrease $\Delta G_f^{\circ\ddagger}$ by 4 kJ mol^{-1}. This would have large effects on the interpretation of the results in terms of transition state structure (ϕ-value analysis, see Chapters 12.2 and 13), and might contribute to the large uncertainty in ϕ-value from mutants that lead to small changes in ΔG° [111].

Mutants that disrupt residual interactions in the unfolded state will most likely have only little effect on k_0 for unfolding (k_0^u), which should be determined by chain motions in the native state. Most native protein structures and transitions state structures were shown to be rather robust against mutations [44]. Thus, mutations which change the dynamics of unfolded proteins will result in an apparent change in ΔG°, in analogy to the effects discussed above (Eq. (24)).

Figure 22.10 shows that denaturants like urea and GdmCl significantly decrease the rate constants for intrachain diffusion (k_c). According to the considerations discussed above, this will also affect the denaturant dependence of the rate constants for protein folding (m_f-values with $m_f = \partial\Delta G_f^{\circ\ddagger}/\partial[\text{Denaturant}]$). Even if pre-equilibria involving unstable intermediates may dominate the early stages of folding, the observed denaturant dependence of intrachain diffusion will influence these steps by changing the forward rate constants of these equilibria. The m_c-values ($m_c = \partial(-RT \ln k_c)/\partial[\text{Denaturant}]$ for peptide dynamics vary only little with chain length and show values around 0.35 kJ mol^{-1} M^{-1} for urea and 0.50 kJ mol^{-1} M^{-1} for GdmCl [74]. Typical m_f-values for folding of the smallest fast folding proteins with chain length between 40 and 50 amino acids are around 1.0 kJ mol^{-1} M^{-1} for urea, indicating that up to 30% of the measured m_f-values may arise from contributions of chain dynamics. Larger two-state folders consisting of 70–100 amino acids typically show m_f-values around 3 kJ mol^{-1} M^{-1} for urea and 5 kJ mol^{-1} M^{-1} for GdmCl [107, 118], indicating that the denaturant dependence of chain dynamics constitutes up to 10% of the experimental m_f-values.

It is difficult to judge the effect of denaturants on the dynamics of the native state, which will influence the experimental m_u-values. However, it was observed that the effect of denaturants on chain dynamics is mainly based on increased chain dimensions (A. Möglich and T. Kiefhaber, unpublished results). This would argue for only little effects of denaturants on the internal dynamics of the native state and on the transition state structures, which were shown to be structurally robust against changes in denaturant concentration [44, 107, 111]. Thus, the m_u-values should have only little contributions from the effects of denaturants on chain dynamics.

Comparison of kinetic and equilibrium m-values ($m_{eq} = \partial\Delta G^\circ/\partial[\text{Denaturant}]$) is frequently used to characterize protein folding transition states according to the rate-equilibrium free energy relationship [44, 119, 120]:

$$\alpha_D = \frac{m_f}{m_{eq}} \quad (25)$$

α_D is interpreted as a measure for the solvent accessibility of the transition state. The contributions from chain dynamics to the m_f-values of small proteins lead to apparently higher α_D-values and thus to apparently less solvent exposed transition states. This might explain the commonly observed higher α_D-values compared to α_C-values ($\alpha_C = \frac{\Delta C_p^{\circ\ddagger}}{\Delta C_p^{\circ}}$), which are also believed to monitor the solvent accessibility of transition states [44, 120]. Temperature dependence of intrachain diffusion in unstructured peptides showed that this process is not associated with a measurable change in heat capacity (F. Krieger and T. Kiefhaber, unpublished results). This suggests that α_C-values give a more reliable picture of the solvent accessibility of the transition state than α_D-values.

This shows that changes in the dynamics of the unfolded state of a protein lead to changes in the prefactor for the folding reaction which has consequences for both the rate constant and the equilibrium constant of the folding reaction. In general, we cannot expect the pre-exponential factors to be independent of the solvent conditions such as denaturant concentration, temperature, and pressure. This will contribute to the experimentally determined *m*-values and the activation parameters ($\Delta H^{\circ\ddagger}, \Delta S^{\circ\ddagger}, \Delta V^{\circ\ddagger}$, and $\Delta C_p{}^{\ddagger}$) and to the equilibrium properties of the protein.

22.6 Conclusions and Outlook

Several experimental systems have been recently developed to measure rate constants for intrachain diffusion processes. Experimental studies on the dynamics of unfolded proteins have revealed single exponential kinetics for formation of specific intrachain interactions on the nanosecond time scale and have been able to elucidate scaling laws and sequence dependence of chain dynamics. It has further been shown that the results derived from homopolypeptide chains and host-guest studies are in agreement with dynamics of loop formation in short natural sequences. Further studies should aim at the investigation of the dynamics in full length unfolded proteins and in folding intermediates to obtain information on the special equilibrium and dynamic properties of free energy landscapes for protein folding reactions.

22.7 Experimental Protocols and Instrumentation

To measure absolute rate constants for contact formation several requirements have to be met by the experimental method and by the equipment for detection. The methods of choice to study contact formation are electron transfer or excited state quenching reactions. The main advantage of energy transfer systems is that they allow both the donor and the acceptor populations to be quantified during the experiment (see Figure 22.5).

22.7.1

Properties of the Electron Transfer Probes and Treatment of the Transfer Kinetics

The lifetime of excited states of the labels used in a specific system determine the time scale on which experiments can be performed. Triplet states are very long lived compared to fluorescence probes and thus allow studies in long chains and in unfolded proteins. Donor groups which undergo very fast intersystem crossing to the triplet state and which have a high quantum yield for intersystem crossing are well-suited. The xanthone derivatives used by Bieri et al. [50] and Krieger et al. [54, 55] form triplet states with a time constant of 2 ps and a quantum yield of 99% [56]. Tryptophan in contrast, which was used by Lapidus et al., has about 18% quantum yield [60] and forms triplet states with a time constant of 3 ns [62], which sets a limit to the fastest processes that can be monitored using tryptophan as a triplet donor. Triplet states usually have strong absorption bands that are easily observable. It is, however, important that the donor has an UV absorption band in a spectral region where no other part of the protein absorbs (i.e., >300 nm). This allows selective excitation of the donor. The requirements for the triplet acceptor are that the molecule should have lower triplet energy than the donor to enable exothermic TTET and it should not absorb light at the excitation wavelength of the donor. Additionally, no radicals should be formed at any time in the reaction, since they may damage the sample and their strong absorbance bands usually interfere with the measurements.

Further requirements of experimental systems which allow to measure the kinetics of contact formation on an absolute time scale are (i) that the process is very strongly distance dependent to allow transfer only at van der Waals distance between donor and acceptor and (ii) that the transfer reaction is faster than dissociation of the complex so that each van der Waals contact between the labels leads to transfer. The coupling of electron transfer to chain dynamics displayed in Figure 22.6 can be kinetically described by a three-state reaction if the excitation of the donor is fast compared to chain dynamics (k_c, k_{-c}) and electron transfer (k_{TT}).

$$\mathrm{O} \underset{k_{-c}}{\overset{k_c}{\rightleftharpoons}} \mathrm{C} \xrightarrow{k_{TT}} \mathrm{C}^* \tag{26}$$

O and C represent open chain conformations (no contact) and contact conformations of the chain, respectively. k_c and k_{-c} are apparent rate constant for contact formation and breakage, respectively. If the excited state quenching or transfer (k_{TT}) reaction is on the same time scale or slower than breaking of the contact (k_{-c}), the measured rate constants (λ_i) are functions of all microscopic rate constants.

$$\begin{aligned} \lambda_{1,2} &= \frac{B \pm \sqrt{B^2 - 4C}}{2} \\ B &= k_c + k_{-c} + k_{TT} \\ C &= k_c \cdot k_{TT} \end{aligned} \tag{27}$$

If the contact states have a much lower probability than the open conformations ($k_{-c} \gg k_c$) the kinetics will be single exponential and the observed rate constant corresponds to the smaller eigenvalue (λ_1) in Eq. (27). Since this is in agreement with experimental results we will only consider this scenario in the following. We can further simplify Eq. (27) if the time scales of electron transfer and chain dynamics are well separated. In the regime of fast electron transfer compared to chain dynamics ($k_{TT} \gg k_c, k_{-c}$) Eq. (27) can be approximated by

$$\lambda_1 = k_c \tag{28}$$

This is the desired case, since the observed kinetics directly reflect the dynamics of contact formation. In the regime of fast formation and breakage of the contact compared to electron transfer ($k_{TT} \ll k_c, k_{-c}$) Eq. (27) can be approximated by

$$\lambda_1 = \frac{k_c}{k_c + k_{-c}} \cdot k_{TT} \cong \frac{k_c}{k_{-c}} \cdot k_{TT} = K_c \cdot k_{TT} \tag{29}$$

where K_c reflects the ratio of contact conformations (C) over open chain conformations (O). In this limit the chain dynamics can not be measured but the fraction of closed conformations can be determined. It should be kept in mind that these simplifications only hold if the formation of excited states is fast compared to the following reactions. If the excitation is on the nanosecond time scale or slower, the solutions of the linear four-state model have to be used to analyze the kinetics [121, 122].

These considerations show that it is crucial to determine the rate constants for the photochemical processes in the applied system to be able to interpret the kinetic data. The photochemistry of the donor excitation and of the electron transfer process are usually characterized by investigating the isolated labels and the kinetics should be studied on the femtosecond to the nanosecond time scale to gain complete information on all photochemical processes in the system [56] (cf. Figure 22.6). To test whether each donor–acceptor contact leads to transfer it should be tested whether the reaction is diffusion controlled. This can be done by studying the bimolecular transfer process from the donor to acceptor groups and determine its rate constants, its temperature-dependence and its viscosity dependence (F. Krieger and T. Kiefhaber, in preparation). These tests will be described in detail in the following. The results showed, that both the xanthone/NAla system [54–56] and the porphyrin/Ru system [64] fulfill these requirements and thus allow measurements of absolute rate constant for contact formation. The Trp/Cys triplet quenching system, in contrast, is not diffusion controlled and gives significantly slower apparent contact rates than the diffusion-controlled systems [59, 63]. Also the DBO/Trp fluorescence quenching system does not seem to be completely diffusion controlled and might have slow electron transfer kinetics, since it gives significantly slower dynamics [65] compared to the xanthone/NAla system in the same peptides [54].

22.7.2 Test for Diffusion-controlled Reactions

22.7.2.1 Determination of Bimolecular Quenching or Transfer Rate Constants

To test whether an energy transfer or energy quenching pair has diffusion-controlled kinetics, the rate constant of energy transfer (k_q) should be measured using the free labels in solution under pseudo first-order conditions. In these experiments the concentration of the quencher or acceptor [Q] should be at least 10 times higher than the concentration of the donor to be in the pseudo first order regime. Since [Q] is approximately constant during the experiment, the apparent first-order rate constant (k) under pseudo first-order conditions is given by [123]

$$k = k_q \cdot [Q] \tag{30}$$

Thus, the bimolecular transfer constant (k_q) can be obtained by varying the quencher concentration [Q] and analyzing the data according to the Stern-Vollmer equation [124] (see Figure 22.17):

$$k = k_0 + k_q[Q] \tag{31}$$

Here, k_0 denotes the rate constant for triplet decay of the donor in absence of quencher (acceptor) and k the time constant in presence of the acceptor or quencher. For diffusion-controlled reactions of small molecules in water k_q is around $4–6 \cdot 10^9$ s^{-1}.

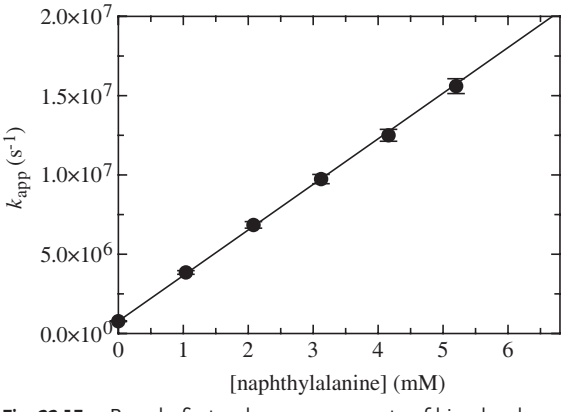

Fig. 22.17. Pseudo first-order measurements of bimolecular TTET from xanthonic acid to naphthylalanine in water. Xanthone concentration was 30 μM. The slope gives a bimolecular transfer constant (k_q) of $3 \cdot 10^9$ M^{-1} s^{-1} (see Eq. (31)). The data were discussed in Ref. [54].

22.7.2.2 Testing the Viscosity Dependence

For a diffusion-controlled reaction, k_q is inversely proportional to solvent viscosity ($k \sim 1/\eta$). The viscosity is usually varied by adding co-solvents like ethylene glycol or glycerol. To determine the final macroscopic viscosity instruments like the falling-ball viscosimeter or the Ubbelohde viscosimeter are used. The molecular size of the co-solvent used in a viscosity study is an important factor. The macroscopic viscosity of a glycerol/water mixture and a solution of polyethylene glycol might be the same, although the microscopic properties of these solutions are very different [80]. In the latter case the dissolved reactant molecules do only feel a fraction of the macroscopic viscosity. Thus it is advisable to use viscous co-solvents of small molecular weight. Glycerol/water mixtures have proven to be most useful because the viscosity can be varied from 1 cP (pure water) over three orders of magnitude by addition of glycerol. It is imperative to control the temperature when working with high concentrations of glycerol because the viscosity is strongly temperature dependent. Note that viscous co-solvents can interfere with the reaction that is studied.

In protein folding studies, the polyols used to vary the viscosity tend to stabilize the native state of proteins [84] making an analysis of the kinetic data difficult. However, for measurements of chain dynamics in unfolded polypeptide chains this effect should not interfere with the measurements as long as the co-solvents do not induce a structure. Specific effects of the polyols on chain conformations/dynamics can be tested by comparing the results from different co-solvents.

22.7.2.3 Determination of Activation Energy

Diffusion-controlled reactions typically have activation energies close to zero. The lack of an activation barrier in a diffusion controlled quenching reaction can be verified by determining the temperature dependence of k_q. The diffusion coefficients of the reactants are, however, temperature dependent, mainly through the effect of temperature on solvent viscosity according to the Stokes-Einstein equation.

$$D = \frac{k_B T}{6\pi r \eta} \tag{32}$$

After correcting for the change in viscosity of the solvent with temperature, the slope in an Arrhenius plot should not be higher than $k_B T$. As any photophysical reaction takes some time, diffusion control is only possible to a certain maximal concentration of quencher molecules. After that the photochemistry of the quenching or transfer process becomes rate limiting. This provides an upper limit of the rate constants that can be measured, even if the system is diffusion controlled at lower quencher concentrations. For the xanthone/naphthalene system TTET has been shown to occur faster than 2 ps and thus this system is suitable to obtain absolute time constants for all processes slower than 10–20 ps [56].

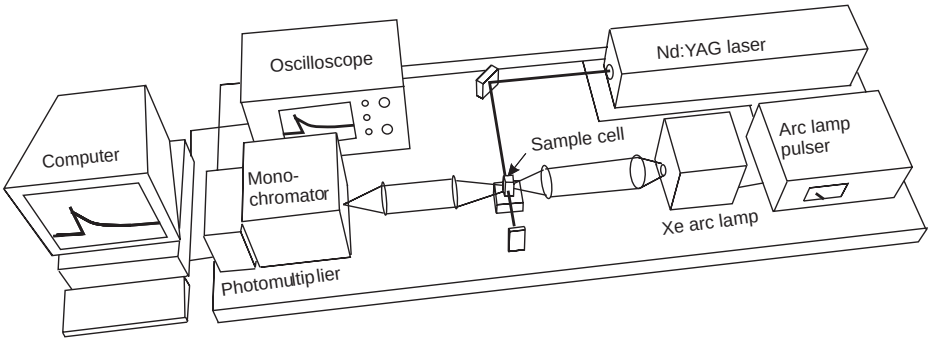

Fig. 22.18. Schematic representation of a laserflash set-up used to measure electron transfer reactions.

22.7.3 Instrumentation

The instrumentation required to perform experiments on contact formation kinetics consists of a high-energy light source to produce excited states and a detection mechanism (Figure 22.18). A pulsed laser is used to produce triplet donor states in TTET or triplet quenching experiments. The duration of the light pulse has to be very short (i.e., shorter than the time scale of the reaction of interest). Additionally, the excitation pulse has to provide enough energy to excite the major portion of the molecules in the sample to order to generate a large signal. A pulsed Nd:YAG laser with a pulse width of <5 ns and a pulse energy of $\sim$100 mJ is well-suited for these purposes. Transient UV absorption is used to detect the triplet states in TTET or triplet quenching experiments. A pulsed flash lamp generates enough light for the absorption measurements. The lamp intensity typically stays at a constant plateau value for several hundred microseconds, which is sufficient for TTET measurements. A monochromator is used to monitor single wavelengths. Transient spectra can be reconstructed from measurements at different wavelengths or by using a CCD camera.

Acknowledgments

We thank Annett Bachmann, Florian Krieger, Robert Kübler and Andreas Möglich for discussion and comments on the manuscript.

References

1 Einstein, A. (1906). Eine neue Bestimmung der Molekül-dimensionen. *Ann. d. Phys.* 19, 289–306.

2 von Smoluchowski, M. (1906). Zur kinetischen Theorie der Brownschen Molekularbewegung und der Suspensionen. *Ann. d. Phys.* 21, 756–780.

3 von Smoluchowski, M. (1916). Drei Vorträge über Diffusion, Brownsche Molekularbewegung und Koagulation von Kolloidteilchen. *Phys. Z.* 17, 557–571.

4 Jacobsen, H. & Stockmayer, W. H. (1950). Intramolecular reaction in polycondensations. I. The theory of linear systems. *J. Phys. Chem.* 18, 1600–1606.

5 Rouse, P. E. (1953). A theory of the linear viscoelastic properties of dilute solutions of coiling polymers. *J. Chem. Phys.* 21, 1272–1280.

6 Zimm, B. (1956). Dynamics of polymer molecules in dilute solutions: viscoelasticity, flow bifringence and dielectric loss. *J. Chem. Phys.* 24, 269–278.

7 Szabo, A., Schulten, K. & Schulten, Z. (1980). First passage time approach to diffussion controlled reactions. *J. Chem. Phys.* 72, 4350–4357.

8 de Gennes, P. G. (1985). Kinetics of collapse for a flexible coil. *J. Phys. Lett.* 46, L639–L642.

9 Fixman, M. (1987). Brownian dynamics of chain polymers. *Faraday Discuss. Chem. Soc.* 83, 199–211.

10 Thirumalai, D. (1995). From minimal models to real protein: time scales for protein folding kinetics. *J. Phys.* 5, 1457–1467.

11 Flory, P. J. (1953). *Principles of Polymer Chemistry.* Cornell University Press, Ithaca.

12 Flory, P. J. (1969). *Statistical Mechanics of Chain Molecules.* Hanser Publishers, Munich.

13 Yamakawa, H. (1971). *Modern Theory of Polymer Solutions.* Harper & Row, New York.

14 Doi, M. (1996). *Introduction to Polymer Science.* Oxford University Press, Oxford.

15 Rubinstein, M. & Colby, R. H. (2003). *Polymer Physics.* Oxford University Press, Oxford.

16 Kuhn, W. (1934). Über die Gestalt fadenförmiger Moleküle in Lösungen. *Kolloid-Z* 52, 269.

17 Kuhn, W. (1936). Beziehungen zwischen Molekülgrösse, statistischer Molekülgestalt und elastischen Eigenschaften hochpolymerer Stoffe. *Kolloid-Z* 76, 258.

18 Brant, D. A. & Flory, P. J. (1965). The configuration of random polypeptide chains. II. Theory. *J. Am. Chem. Soc.* 87, 2791–2800.

19 Schimmel, P. R. & Flory, P. J. (1967). Conformational energy and configurational statistics of poly-L-proline. *Proc. Natl Acad. Sci. USA* 58, 52–59.

20 Brant, D. A., Miller, W. G. & Flory, P. J. (1967). Conformational energy estimates for statistically coiling polypeptide chains. *J. Mol. Biol.* 23, 47–65.

21 Miller, W. G., Brant, D. A. & Flory, P. J. (1967). Random coil configurations of polypeptide chains. *J. Mol. Biol.* 23, 67–80.

22 Ramachandran, G. N. & Sasisekharan, V. (1968). Conformation of polypeptides and proteins. *Adv. Protein Chem.* 23, 283–437.

23 de Gennes, P. G. (1979). *Scaling Concepts in Polymer Physics.* Cornell University Press, Ithaca.

24 Doi, M. & Edwards, S. F. (1986). *The Theory of Polymer Dynamics.* Oxford University Press, Oxford.

25 Pappu, R. V., Srinavasan, R. & Rose, G. D. (2000). The Flory isolated-pair hypthesis is not valid for polypeptide chains: Implications for protein folding. *Proc. Natl Acad. Sci. USA* 97, 12565–12570.

26 Edwards, S. F. (1965). The statistical mechanics of polymers with excluded volume. *Proc. Phys. Soc.* 85, 613–624.

27 Evans, P. A., Topping, K. D., Woolfson, D. N. & Dobson, C. M. (1991). Hydrophobic clustering in nonnative states of a protein: interpretation of chemical shifts in NMR spectra of denatured states of lysozyme. *Proteins* 9, 248–266.

28 Neri, D., Billeter, M., Wider, G. & Wüthrich, K. (1992). NMR determination of residual structure in

a urea-denatured protein, the 434-repressor. *Science* 257, 1559–1563.

29 Logan, T. M., Theriault, Y. & Fesik, S. W. (1994). Structural characterization of the FK506 binding protein unfolded in urea and guanidine hydrochloride. *J. Mol. Biol.* 236, 637–648.

30 Smith, C. K., Bu, Z. M., Anderson, K. S., Sturtevant, J. M., Engelman, D. M. & Regan, L. (1996). Surface point mutations that significantly alter the structure and stability of a protein's denatured state. *Protein Sci.* 5, 2009–2019.

31 Sari, N., Alexander, P., Bryan, P. N. & Orban, J. (2000). Structure and dynamics of an acid-denatured protein G mutant. *Biochemistry* 39, 965–977.

32 Wong, K. B., Clarke, J., Bond, C. J. et al. (2000). Towards a complete description of the structural and dynamic properties of the denatured state of barnase and the role of residual structure in folding. *J. Mol. Biol.* 296, 1257–1282.

33 Teilum, K., Kragelund, B. B., Knudsen, J. & Poulsen, F. M. (2000). Formation of hydrogen bonds precedes the rate-limiting formation of persistent structure in the folding of ACBP. *J. Mol. Biol.* 301, 1307–1314.

34 Kortemme, T., Kelly, M. J., Kay, L. E., Forman-Kay, J. D. & Serrano, L. (2000). Similarities between the spectrin SH3 domain denatured state and its folding transition state. *J. Mol. Biol.* 297, 1217–1229.

35 Garcia, P., Serrano, L., Durand, D., Rico, M. & Bruix, M. (2001). NMR and SAXS characterization of the denatured state of the chemotactic protein CheY: implications for protein folding initiation. *Protein Sci.* 10, 1100–1112.

36 Choy, W. Y. & Forman-Kay, J. D. (2001). Calculation of ensembles of structures representing the unfolded state of an SH3 domain. *J. Mol. Biol.* 308, 1011–1032.

37 Kazmirski, S. L., Wong, K. B., Freund, S. M., Tan, Y. J., Fersht, A. R. & Daggett, V. (2001). Protein folding from a highly disordered denatured state: the folding pathway of chymotrypsin inhibitor 2 at atomic resolution. *Proc. Natl Acad. Sci. USA* 98, 4349–4354.

38 Yi, Q., Scalley-Kim, M. L., Alm, E. J. & Baker, D. (2000). NMR characterization of residual structure in the denatured state of protein L. *J. Mol. Biol.* 299, 1341–1351.

39 Klein-Seetharaman, J., Oikawa, M., Grimshaw, S. B., Wirmer, J., Duchardt, E., Ueda, T. et al. (2002). Long-range interactions within a nonnative protein. *Science* 295, 1719–1722.

40 Gardiner, C. W. (1985). *Handbook of Stochastic Methods.* Springer Verlag, Berlin, Heidelberg, New York.

41 Sakanishi, A. (1968). Dynamic viscoelastic properties of dilute polyisobutylene solutions. *J. Chem. Phys.* 48, 3850–3858.

42 Perkins, T. T., Quake, S. R., Smith, D. E. & Chu, S. (1994). Relaxation of a single DNA molecule observed by optical microscopy. *Science* 264, 822–826.

43 Dyson, H. J. & Wrigth, P. E. (2002). Insights into the structure and dynamics of unfolded proteins from nuclear magnetic resonance. *Adv. Protein Chem.* 62, 311–340.

44 Sánchez, I. E. & Kiefhaber, T. (2003). Hammond behavior versus ground state effects in protein folding: evidence for narrow free energy barriers and residual structure in unfolded states. *J. Mol. Biol.* 327, 867–884.

45 Mar, A. & Winnik, M. A. (1985). End-to-end cyclization of hydrocarbon chains: temperature effects on an intramolecular phosphorescence quenching reaction in solution. *J. Am. Chem. Soc.* 107, 5376–5382.

46 Lee, S. & Winnik, M. A. (1997). Cyclization rates for two points in the interior of a polymer chain. *Macromolecules* 30, 2633–2641.

47 Stryer, L. & Haugland, R. P. (1967). Energy transfer: a spectroscopic ruler. *Proc. Natl Acad. Sci. USA* 58, 719–726.

48 Haas, E., Katchalski-Katzir, E. & Steinberg, I. Z. (1978). Brownian

motion at the ends of oligopeptid chains as estimated by energy transfer between chain ends. *Biopolymers* 17, 11–31.

49 Beechem, J. M. & Haas, E. (1989). Simultaneous determination of intramolecular distance distributions and conformational dynamics by global analysis of energy transfer measurements. *Biophys J.* 55, 1225–1236.

50 Bieri, O., Wirz, J., Hellrung, B., Schutkowski, M., Drewello, M. & Kiefhaber, T. (1999). The speed limit for protein folding measured by triplet-triplet energy transfer. *Proc. Natl Acad. Sci. USA* 96, 9597–9601.

51 Haas, E., Wilchek, M., Katchalski-katzir, E. & Steinberg, I. Z. (1975). Distribution of end-to-end distances of oligopeptides in solution as estimated by energy-transfer. *Proc. Natl Acad. Sci. USA* 72, 1807–1811.

52 Hagen, S. J., Hofrichter, J., Szabo, A. & Eaton, W. A. (1996). Diffusion-limited contact formation in unfolded cytochrome c: Estimating the maximum rate of protein folding. *Proc. Natl Acad. Sci. USA* 93, 11615–11617.

53 Camacho, C. J. & Thirumalai, D. (1995). Theoretical predictions of folding pathways by using the proximity rule, with applications to bovine pancreatic inhibitor. *Proc. Natl Acad. Sci. USA* 92, 1277–1281.

54 Krieger, F., Fierz, B., Bieri, O., Drewello, M. & Kiefhaber, T. (2003). Dynamics of unfolded polypeptide chains as model for the earliest steps in protein folding. *J. Mol. Biol.* 332, 265–274.

55 Krieger, F., Fierz, B., Axthelm, F., Joder, K., Meyer, D. & Kiefhaber, T. (2004). Intrachain diffusion in a protein loop fragement from carp parvalbumin. *Chem. Phys.*, in press.

56 Satzger, H., Schmidt, B., Root, C. et al. (2004). Ultrafast quenching of the xanthone triplet by energy transfer: new insight into the intersystem crossing kinetics in press.

57 Closs, G. L., Johnson, M. D., Miller, J. R. & Piotrowiak, P. (1989). A connection between intramolecular long-range electron, hole and triplet energy transfer. *J. Am. Chem. Soc.* 111, 3751–3753.

58 Wagner, P. J. & Klán, P. (1999). Intramolecular triplet energy transfer in flexible molecules: electronic, dynamic, and structural aspects. *J. Am. Chem. Soc.* 121, 9626–9635.

59 Lapidus, L. J., Eaton, W. A. & Hofrichter, J. (2000). Measuring the rate of intramolecular contact formation in polypeptides. *Proc. Natl Acad. Sci. USA* 97, 7220–7225.

60 Volkert, W. A., Kuntz, R. R., Ghiron, C. A., Evans, R. F., Santus, R. & Bazin, M. (1977). Flash photolysis of tryptophan and *N*-acetyl-L-tryptophanamide; the effect of bromide on transient yields. *Photochem. Photobiol.* 26, 3–9.

61 Gonnelli, M. & Strambini, G. B. (1995). Phosphorescence lifetime of tryptophan in proteins. *Biochemistry* 34, 13847–13857.

62 Bent, D. V. & Hayon, E. (1975). Excited state chemistry of aromatic amino acids and related peptides: III. Tryptophan. *J. Am. Chem. Soc.* 97, 2612–2619.

63 Yeh, I. C. & Hummer, G. (2002). Peptide loop-closure kinetics from microsecond molecular dynamics simulations in explicit solvent. *J. Am. Chem. Soc.* 124, 6563–6568.

64 Chang, I.-J., Lee, J. C., Winkler, J. R. & Gray, H. B. (2003). The protein-folding speedlimit: Intrachain diffusion times set by electron-transfer rates in denatured $Ru(NH_3)_5$(His-33)-Zn-cytochrome c. *Proc. Natl Acad. Sci. USA* 100, 3838–3840.

65 Hudgins, R. R., Huang, F., Gramlich, G. & Nau, W. M. (2002). A fluorescence-based method for direct measurements of submicroscond intramolecular contact formation in biopolymers: an exploratory study with polypeptides. *J. Am. Chem. Soc.* 124, 556–564.

66 Huang, F. & Nau, W. M. (2003). A conformational flexibility scale for amino acids in peptides. *Angew. Chem. Int. Ed. Engl.* 42, 2269–2272.

67 Neuweiler, H., Schulz, A., Böhmer, M., Enderlein, J. & Sauer, M. (2003). Measurement of submicrosecond intramolecular contact formation in peptides at the single-molecule level. *J. Am. Chem. Soc.* 125, 5324–5330.

68 Zwanzig, R. (1997). Two-state models for protein folding. *Proc. Natl Acad. Sci. USA* 94, 148–150.

69 Spörlein, S., Carstens, H., Satzger, H. et al. (2002). Ultrafast spectroscopy reveals sub-nanosecond peptide conformational dynamics and validates molecular dynamics simulation. *Proc. Natl Acad. Sci. USA* 99, 7998–8002.

70 Bredenbeck, J., Helbing, J., Sieg, A. et al. (2003). Picosecond conformational transition and equilibration of a cyclic peptide. *Proc. Natl Acad. Sci. USA* 100, 6452–6457.

71 Schwalbe, H., Fiebig, K. M., Buck, M. et al. (1997). Structural and dynamical properties of a denatured protein. Heteronuclear 3D NMR experiments and theoretical simulations of lysozyme in 8 M urea. *Biochemistry* 36, 8977–8991.

72 Reimer, U., Scherer, G., Drewello, M., Kruber, S., Schutkowski, M. & Fischer, G. (1998). Side-chain effects on peptidyl-prolyl cis/trans isomerization. *J. Mol. Biol.* 279, 449–460.

73 Pace, C. N. (1986). Determination and analysis of urea and guanidine hydrochloride denaturation curves. *Methods Enzymol.* 131, 266–280.

74 Möglich, A., Krieger, F. & Kiefhaber, T. (2004). Molecular basis of the effect of urea and guanidinium chloride on the dynamics of unfolded proteins. submitted.

75 Zhu, W., Gisser, D. J. & Ediger, M. D. (1994). C-13 NMR measurements of polybutadiene local dynamics in dilute-solution – further evidence for non-Kramers behavior. *J. Polym. Sci. B Polym. Phys.* 32, 2251–2262.

76 Zhu, W. & Ediger, M. D. (1997). Viscosity dependence of polystyrene local dynamics in dilute solutions. *Macromolecules* 30, 1205–1210.

77 Tylianakis, E. I., Dais, P. & Heatley, F. (1997). Non-Kramers' behavior of the chain local dynamics of pvc in dilute solution. Carbon-13 NMR relaxation study. *J. Polym. Sci. B* 35, 317–329.

78 Beece, D., Eisenstein, L., Frauenfelder, H. et al. (1980). Solvent Viscosity and Protein Dynamics. *Biochemistry* 19, 5147–5157.

79 Yedgar, S., Tetreau, C., Gavish, B. & Lavalette, D. (1995). Viscosity dependence of O2 escape from respiratory proteins as a function of cosolvent molecular weight. *Biophys. J.* 68, 665–670.

80 Kleinert, T., Doster, W., Leyser, H., Petry, W., Schwarz, V. & Settles, M. (1998). Solvent composition and viscosity effects on the kinetics of CO binding to horse myoglobin. *Biochemistry* 37, 717–733.

81 Gavish, B. (1980). Position-dependent viscosity effects on rate coefficients. *Phys. Rev. Lett.* 44, 1160–1163.

82 Doster, W. (1983). Viscosity scaling and protein dynamics. *Biophys. Chem.* 17, 97–103.

83 Schlitter, J. (1988). Viscosity dependence of intramolecular activated processes. *Chem. Phys.* 120, 187–197.

84 Timasheff, S. N. (2002). Protein hydration, thermodynamic binding and preferential hydration. *Biochemistry* 41, 13473–13482.

85 Perico, A. & Beggiato, M. (1990). Intramolecular diffusion-controlled reactions in polymers in the optimized Rouse Zimm approach 1. The effects of chain stiffness, reactive site positions, and site numbers. *Macromolecules* 23, 797–803.

86 Leszcynski, J. F. & Rose, G. D. (1986). Loops in globular proteins: a novel category of secondary structure. *Science* 234, 849–855.

87 Wilmot, C. M. & Thornton, J. M. (1988). Analysis and prediction of the different types of β-turns in proteins. *J. Mol. Biol.* 203, 221–232.

88 Zimm, B. H. & Bragg, J. K. (1959). Theory of phase transition between helix and random coil in polypeptide chains. *J. Chem. Phys.* 31, 526–535.

89 Lifson, S. & Roig, A. (1961). On the

theory of helix-coil transitions in polypeptides. *J. Chem. Phys.* 34, 1963–1974.

90 Schwarz, G. & Seelig, J. (1968). Kinetic properties and the electric field effect of the helix-coil transition of poly(γ-benzyl L-glutamate) determined from dielectric relaxation measurements. *Biopolymers* 6. 1263–1277.

91 Gruenewald, B., Nicola, C. U., Lustig, A. & Schwarz, G. (1979). Kinetics of the helix-coil transition of a polypeptide with non-ionic side chain groups, derived from ultrasonic relaxation measurements. *Biophys. Chem.* 9, 137–147.

92 Williams, S., Causgrove, T. P., Gilmanshin, R. et al. (1996). Fast events in protein folding: helix melting and formation in a small peptide. *Biochemistry* 35, 691–697.

93 Thompson, P., Eaton, W. & Hofrichter, J. (1997). Laser temperature jump study of the helix-coil kinetics of an alanine peptide interpreted with a "kinetic zipper" model. *Biochemistry* 36, 9200–9210.

94 Munoz, V., Thompson, P., Hofrichter, J. & Eaton, W. (1997). Folding dynamics and mechanism of β-hairpin formation. *Nature* 390, 196–199.

95 Bieri, O. & Kiefhaber, T. (1999). Elementary steps in protein folding. *Biol. Chem.* 380, 923–929.

96 Schwarz, G. (1965). On the kinetics of the helix-coil transition of polypeptides in solution. *J. Mol. Biol.* 11, 64–77.

97 Kubelka, J., Hofrichter, J. & Eaton, W. A. (2004). The protein folding speed limit. *Curr. Opin. Struct. Biol.* 14, 76–88.

98 Huang, G. S. & Oas, T. G. (1995). Submillisecond folding of monomeric lambda repressor. *Proc. Natl Acad. Sci. USA* 92, 6878–6882.

99 Burton, R. E., Huang, G. S., Daugherty, M. A., Fullbright, P. W. & Oas, T. G. (1996). Microsecond protein folding through a compact transition state. *J. Mol. Biol.* 263, 311–322.

100 Mayor, U., Guydosh, N. R., Johnson, C. M. et al. (2003). The complete folding pathway of a protein from nanoseconds to microseconds. *Nature* 421, 863–867.

101 Perl, D., Welker, C., Schindler, T. et al. (1998). Conservation of rapid two-state folding in mesophilic, thermophilic and hyperthermophilic proteins. *Nat. Struct. Biol.* 5, 229–235.

102 Ferguson, N., Johnson, C. M., Macias, M., Oschkinat, H. & Fersht, A. R. (2001). Ultrafast folding of WW domains without structured aromatic clusters in the denatured state. *Proc. Natl Acad. Sci. USA* 98, 13002–13007.

103 Robinson, C. R. & Sauer, R. T. (1996). Equilibrium stability and submillisecond refolding of a designed single-chain arc repressor. *Biochemistry* 35, 13878–13884.

104 Neidigh, J. W., Fesinmeyer, R. M. & Andersen, N. H. (2002). Designing a 20-residue protein. *Nat. Struct. Biol.* 9, 425–430.

105 Qiu, L., Pabit, S. A., Roitberg, A. E. & Hagen, S. J. (2002). Smaller and faster: The 20-residue Trp-cage protein folds in 4 μs. *J. Am. Chem. Soc.* 124, 12952–12953.

106 Bachmann, A. & Kiefhaber, T. (2001). Apparent two-state tendamistat folding is a sequential process along a defined route. *J. Mol. Biol.* 306, 375–386.

107 Sánchez, I. E. & Kiefhaber, T. (2003). Evidence for sequential barriers and obligatory intermediates in apparent two-state protein folding. *J. Mol. Biol.* 325, 367–376.

108 Kuwajima, K., Mitani, M. & Sugai, S. (1989). Characterization of the critical state in protein folding. Effects of guanidine hydrochloride and specific Ca^{2+} binding on the folding kinetics of alpha-lactalbumin. *J. Mol. Biol.* 206, 547–561.

109 Makarov, D. E., Keller, C. A., Plaxco, K. W. & Metiu, H. (2002). How the folding rate constant of simple single-domain proteins depends on the number of native contacts. *Proc. Natl Acad. Sci. USA* 99, 3535–3539.

110 Makarov, D. E. & Plaxco, K. W. (2003). The topomer search model: A simple. quanitative theory of two-state protein folding kinetics. *Protein Sci.* 12, 17–26.

111 Sánchez, I. E. & Kiefhaber, T. (2003). Origin of unusual phi-values in protein folding: Evidence against specific nucleation sites. *J. Mol. Biol.* 334, 1077–1085.

112 Bieri, O. & Kiefhaber, T. (2000). Kinetic models in protein folding. In *Protein Folding: Frontiers in Molecular Biology*, 2nd edn (Pain, R., ed.), pp. 34–64. Oxford University Press, Oxford.

113 Kramers, H. A. (1940). Brownian motion in a field of force and the diffusion model of chemical reactions. *Physica* 4, 284–304.

114 Hänggi, P., Talkner, P. & Borkovec, M. (1990). Reaction-rate theory: fifty years after Kramers. *Rev. Mod. Phys.* 62, 251–341.

115 Jacob, M., Schindler, T., Balbach, J. & Schmid, F. X. (1997). Diffusion control in an elementary protein folding reaction. *Proc. Natl Acad. Sci. USA* 94, 5622–5627.

116 Plaxco, K. W. & Baker, D. (1998). Limited internal friction in the rate-limiting step of a two-state protein folding reaction. *Proc. Natl Acad. Sci. USA* 95, 13591–13596.

117 van't Hoff, J. H. (1884). *Etudes de dynamique.* Muller, Amsterdam.

118 Jackson, S. E. (1998). How do small single-domain proteins fold? *Folding Des.* 3, R81–R91.

119 Tanford, C. (1970). Protein denaturation. Part C. Theoretical models for the mechanism of denaturation. *Adv. Protein Chem.* 24, 1–95.

120 Sánchez, I. E. & Kiefhaber, T. (2003). Non-linear rate-equilibrium free energy relationships and Hammond behavior in protein folding. *Biophys. Chem.* 100, 397–407.

121 Szabo, Z. G. (1969). Kinetic characterization of complex reaction systems. In *Comprehensive Chemical Kinetics* (Bamford, C. H. & Tipper, C. F. H., eds), Vol. 2, pp. 1–80. 7 vols. Elsevier, Amsterdam.

122 Kiefhaber, T., Kohler, H. H. & Schmid, F. X. (1992). Kinetic coupling between protein folding and prolyl isomerization. I. Theoretical models. *J. Mol. Biol.* 224, 217–229.

123 Moore, J. W. & Pearson, R. G. (1981). *Kinetics and Mechanisms.*, John Wiley & Sons, New York.

124 Stern, O. & Volmer, M. (1919). Über die Abklingungszeit der Fluoreszenz. *Phys. Z.* 20, 183–188.

125 Lapidus, L. J., Eaton, W. A. & Hofrichter, J. (2001). Dynamics of intramolecular contact fromation in polypeptides: distance dependence of quenching rates in a room-temperature glass. *Phys. Rev. Lett.*, 258101-1–258101-4.

126 Lapidus, L. J., Steinbach, P. J., Eaton, W. A., Szabo, A. & Hofrichter, J. (2002). Effects of chain stiffness on the dynamics of loop formation in polypeptides. Appendix: Testing a 1-diensional diffusion model for peptide dynamics. *J. Phys. Chem. B* 106, 11628–11640.

127 Kumar, V. D., Lee, L. & Edwards, B. F. (1990). Refined crystal structure of calcium-liganded carp parvalbumin 4.25 at 1.5 Å resolution. *Biochemistry* 1404–1412.

128 Koradi, R., Billeter, M. & Wüthrich, K. (1996). MOLMOL: a program for display and analysis of macromolecular structures. *J. Mol. Graphics* 14, 51–55.

23
Equilibrium and Kinetically Observed Molten Globule States

Kosuke Maki, Kiyoto Kamagata, and Kunihiro Kuwajima

23.1
Introduction

The molten globule state has captured the attention of researchers studying the folding of globular proteins ever since it was proposed that this state is a general intermediate of protein folding [1–4]. Historically, the apparent incompatibility between the efficient folding of a protein into the native structure and the availability of an astronomically large number of different conformations, known as the Levinthal paradox [5], led to the premise that there must be specific pathways of folding, so that by restricting the protein molecule to these pathways, the polypeptide chain can reach its native structure efficiently. According to this view (the ''classical'' view), the folding occurs in a sequential manner with a series of intermediates populated along the specific pathway of folding (the sequential model of protein folding) [6–8]. Therefore, studies on protein folding were focused on detection and characterization of the specific folding intermediates of globular proteins. The discovery that the intermediates were formed during the kinetic folding of many globular proteins convinced the researchers of the significance of the intermediates in elucidating the mechanism of protein folding. The molten globule is the most typical of these folding intermediates, and has been regarded as a general intermediate of protein folding.

Nevertheless, recent theoretical studies of protein folding have shown that what is required for a protein to reach the unique native structure is not the presence of the specific pathway of folding, but just the presence of a small bias of the free-energy surface toward the native state in the multidimensional conformational hyperspace of the protein [9–11]. Therefore, according to this ''new'' view of protein folding, the Levinthal paradox is no longer a real paradox. It is obvious that the attempt to detect the folding intermediate to resolve the Levinthal paradox is now irrelevant, casting a fundamental doubt on the role of the molten globule state as a productive intermediate in protein folding [11, 12]. Apparently in support of this new perspective, kinetic folding of small, single-domain proteins with fewer than typically 100 amino acid residues has been shown to occur simply in a two-state manner without accumulation of the folding intermediates [13, 14]. Because the

Protein Folding Handbook. Part I. Edited by J. Buchner and T. Kiefhaber

ISBN: 3-527-30784-2

folding can take place without the intermediates, they are apparently not prerequisites for successful folding of these proteins. The molten globule state might not be obligatory, but rather produced by misfolding events or kinetic traps at local minima on the free-energy surface of the protein folding [3, 4, 15]. Therefore, whether folding intermediates such as the molten globule state are necessary for directing the folding reactions of globular proteins is still an open question, and there has been intense debate on this issue.

However, it is probably more appropriate to address the following question: Is the sequential model of protein folding truly in conflict with the simple two-state folding of small globular proteins, which has been shown to support the new view of protein folding? In spite of the argument in favor of the new perspective of folding, the experimental studies of the folding intermediates of various globular proteins have clearly demonstrated that the molten globule is a real productive folding intermediate in these proteins [16]. Therefore, there must be a more general model that can accommodate both the sequential and the simple two-state folding reactions of real globular proteins.

We have thus previously proposed a two-stage hierarchical model of protein folding [3, 4], in which the folding process of a protein is, in general, divided into at least two stages: stage I, formation of the molten globule state from the unfolded state; and stage II, formation of the native state from the molten globule, as shown in Scheme 23.1.

$$U \xrightarrow{I} I \xrightarrow{II} N$$

Scheme 23.1

The folding intermediates like the molten globule in this model are not to solve the Levinthal paradox, but they are present because the protein folding takes place in a hierarchical manner [17, 18], reflecting the hierarchy of three-dimensional structure of natural proteins. In this model, the interactions that stabilize the molten globule intermediate should be approximately consistent with the interactions that stabilize the native state. Whether or not the observed folding of a protein is a two-state or non-two-state (multistate) transition may depend on the stability of the intermediate (I) and/or the location of the rate-limiting step of folding. A main purpose of this review is thus to test this hypothesis on the basis of recent studies of various globular proteins.

In the present article, we thus first summarize the structural and thermodynamic properties of the molten globules at equilibrium, and then describe how the molten globule state has been identified as a productive intermediate in kinetic refolding reactions of globular proteins. We also describe our recent statistical analysis of the kinetic refolding data of globular proteins taken from the literature, which clearly demonstrates that the molecular mechanisms behind the non-two-state and two-state protein folding are essentially identical. Finally, practical aspects on the experimental study of the molten globule are presented.

23.2
Equilibrium Molten Globule State

23.2.1
Structural Characteristics of the Molten Globule State

The molten globule state was originally an equilibrium unfolding intermediate assumed by many globular proteins under mildly denaturing conditions [1, 19]. It is structurally characterized by (i) the presence of a substantial amount of secondary structure, (ii) the virtual absence of tertiary structure associated with tight packing of side-chains, (iii) the compact size of the protein molecule with a radius only 10–30% larger than that of the native state, (iv) the presence of a loosely packed hydrophobic core that increases the hydrophobic surface exposed to solvent, and (v) dynamic features of the structure that fluctuates in a time-scale longer than nanoseconds. Thus, in short, the molten globule is a compact globule with a "molten" side chain structure [20].

The mildly denaturing conditions in which we can observe the molten globule state at equilibrium include acid pH [1, 21, 22], moderate concentrations of denaturants [23–26], high temperatures [27, 28], low concentrations of alcohol and fluoroalcohol [29, 30], and high pressure [31–33]. It is, however, dependent on protein species whether the molten globule is stably populated under the conditions; the protein may be still in the native state or more extensively unfolded. Certain proteins extensively unfolded at acid pH are known to refold into the molten globule state in the presence of a stabilizing anion [34]. For ligand-binding proteins, the partial unfolding induced by removal of a tightly bound ligand can bring about the molten globule state [27, 35]. Chemical modification, site-directed mutation and covalent bond cleavage of a natural protein often lead to the molten globule-like partially unfolded state [36–40].

In conventional experimental studies, the molten globule state has been characterized by peptide and aromatic circular dichroism (CD) spectra that detect secondary and tertiary structures, respectively [1, 41], by hydrodynamic techniques that determine the molecular size of the protein [2, 42, 43], and by hydrophobic dye (1-anilinonaphthalene-8-sulfonate (ANS))-binding experiments that detect formation of a loose hydrophobic core accessible to solvent [44].

In addition to these conventional techniques, new experimental techniques, such as hydrogen/deuterium exchange NMR spectroscopy, NMR relaxation and heteronuclear secondary chemical shifts and nuclear Overhauser enhancement (NOE) measurements [45–53], solution small-angle X-ray scattering (SAXS) [54–57], and protein engineering techniques [38–40, 58–63], have been used successfully to further characterize the structure of the molten globule state in many globular proteins during the past decade. Use of these techniques has enabled us to describe the structure of the molten globule states more precisely, to at least the amino acid residue level, and to reveal more detailed characteristics of this state.

Studies using these new techniques have shown the structure of the molten globule state to be more heterogeneous than previously thought, that is, one por-

tion of the structure is more organized and native-like while the other portion is less organized [49, 51, 64–66]. The degree of structural organization and the stability of the molten globule state have both been found to be remarkably dependent on the species of protein conformer, there being a range of species possible within the basic molten globule characteristics of secondary structure, compactness and hydrophobic core. Although the classical concept of little or no persistent tertiary structure still often holds, it is not a universal requirement of the molten globule state.

23.2.2 Typical Examples of the Equilibrium Molten Globule State

Representative examples for showing the diversity of the structure of the molten globule state can be found in α-lactalbumin (α-LA) and Ca^{2+}-binding lysozymes from canine and equine milk [67–70] (Figure 23.1), which are homologous (123–130 amino acid residues). These proteins exhibit the equilibrium molten globule state at a moderate concentration of guanidinium chloride (GdmCl) as well as acidic pH [1, 23–26, 71–73]. The overall structures of the molten globule state of these proteins are similar; the α-helical domain (α-domain) composed of the A-, B-, C-, and D-helices, and the C-terminal 3_{10}-helix is more organized with the β-domain less organized as revealed by hydrogen/deuterium exchange and other techniques [22, 38–40, 47, 74–79]. Despite the similarity in overall structure, the lysozymes are substantially more native-like than α-LA. Significant ellipticity in the near-UV CD spectra and incomplete fluorescence quenching by acrylamide indicate the presence of an immobile tryptophan residue buried inside the molecule [22, 24, 25, 71, 80].

Apomyoglobin (apoMb), which is the apo-form of myoglobin, a 153-residue heme protein with eight helices (A–H) (Figure 23.2) [81], illustrates the diversity in the structure of the molten globule state [34, 82–84]. ApoMb forms a molten globule at pH 4 (the pH 4 intermediate or I_1) while the addition of a stabilizing anion (trichloroacetate (TCA), citrate, or sulfate) refolds the protein to form the second molten globule (I_2) [85, 86]. A similar compact molten globule is formed at acidic pH in the presence of chloride ion [34]. The structure of I_1 has been studied by hydrogen/deuterium exchange NMR as well as by other NMR techniques [45, 50, 66]. It has a compact subdomain consisting of the A-, G-, and H-helical regions as well as part of the B-helix region.

Cytochrome *c* (cyt *c*), which is a 104-residue globular protein with a covalently attached heme group surrounded by three α-helices (Figure 23.3) [87], forms a compact intermediate that has the molten globule characteristics [20]. The molten globule state stably populated at acidic pH in the presence of stabilizing anion from salt or acid is more structurally organized and more stable than the molten globule states of α-LA and apoMb [34, 88]. In contrast to the α-LA or apoMb molten globules that correspond to the early folding intermediates, the cyt *c* molten globule corresponds to a late-folding intermediate that is present after the rate-limiting step in the kinetic refolding [89, 90].

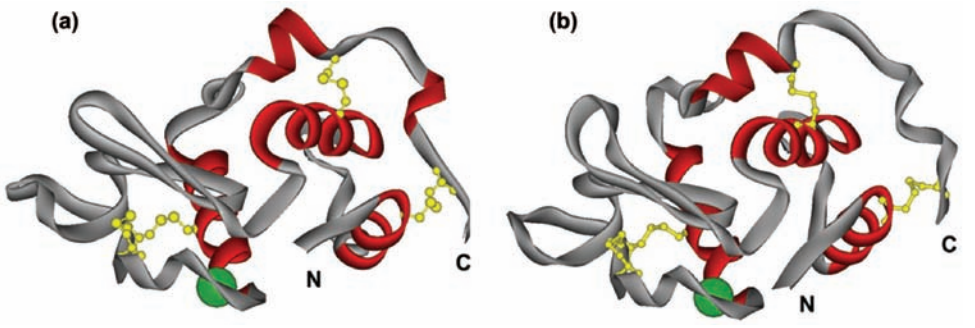

Fig. 23.1. X-ray crystallographic structure of a) human α-lactalbumin (PDB code: 1HML) and b) canine milk lysozyme (PDB code: 1EL1) drawn using DS Modeling. Helices formed in the molten globule state are in red. Four disulfide bonds are shown in yellow in ball-and-stick representation. One Ca^{2+} ion is bound to α-LA and the lysozyme, shown as a green ball.

23.2.3
Thermodynamic Properties of the Molten Globule State

The thermal unfolding of a native globular protein is a highly cooperative, first-order transition. The transition accompanies a large increase in enthalpy, which primarily arises from the disruption of the specific side chain packing interactions, namely, the van der Waals interactions of hydrophobic residues [91]. Because of the disruption of a large fraction of such specific interactions in the molten globule state, thermal unfolding from this state is always less cooperative than the unfold-

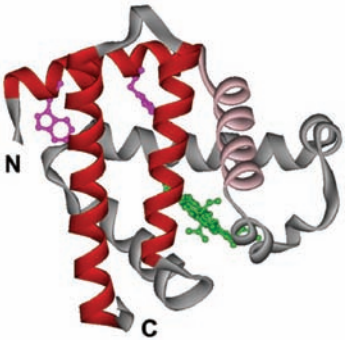

Fig. 23.2. X-ray crystallographic structure of sperm whale myoglobin in the holo form (PDB code: 1MBC) drawn using DS Modeling. The A-, G-, and H-helix regions, which are stably formed in the molten globule state, are in red. The B-helix region, which is partially formed in the structured molten globule state, is in pink. A bound heme and two tryptophan residues (Trp7 and Trp14) are shown in ball-and-stick representation. The heme is in green, and the two tryptophan residues are in purple.

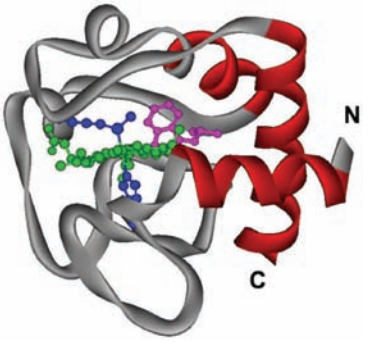

Fig. 23.3. X-ray crystallographic structure of horse cyt *c* (PDB code: 1HRC) drawn using DS Modeling. The N-terminal and C-terminal helices, and the 60s helix, which are stably formed in the molten globule state, are in red. His18, Trp59, Met80, and a bound heme are shown in ball-and-stick representation. His18 and Met80 are in blue, and Trp59 is in purple. Heme is in green.

ing from the native state. The best-characterized molten globules, such as the molten globule state of α-LA and the pH 4 intermediate of apoMb, do not apparently exhibit cooperative thermal transitions [2, 27, 92–94], so that the absence of the thermal transition was thought to be a characteristic of the molten globule state for some time.

However, it is now clear that the molten globules of certain proteins do exhibit a cooperative thermal unfolding transition with a significant increase in enthalpy [24, 28, 73, 95–97]. Thus, the apparent absence of cooperative thermal unfolding observed for the molten globules of α-LA and apoMb is due to their small enthalpy change. The unfolding transitions of the molten globules are apparently noncooperative for some proteins, but highly cooperative for others.

The most notable example of a cooperative thermal unfolding transition of a molten globule is displayed by equine and canine milk lysozymes [24, 28, 73, 97]. Although the overall structure of these molten globule states is very similar to that of the α-LA molten globule, the unfolding from these molten globules shows a cooperative heat absorption peak. The molten globules of cyt *c* and staphylococcal nuclease (SNase) also show cooperative thermal transitions [95, 96]. Therefore, it appears that the cooperative thermal unfolding of the molten globule state is more the rule than the exception.

The degree of cooperativity of the molten globule unfolding transition is, however, not only dependent on the protein species, but also, on the experimental conditions or the nature of amino acid replacements for a given protein [59, 90, 98–101]. The chloride-induced molten globule of apoMb at pH 2 shows a small but distinct heat absorption peak on thermal unfolding, and the TCA-induced molten globule is more stable and shows a still more cooperative unfolding transition [85, 99].

An important aspect concerning the variation in molten globule cooperativity is

the correlation between the intrinsic stability and the degree of cooperativity of the unfolding transition [101, 102]. The order of stability for the well-characterized molten globules for three proteins (α-LA, apoMb, and cyt *c*) is the same as the order of the cooperativity of the molten globule unfolding, that is, α-LA < apoMb < cyt *c* [23, 83, 86, 100, 103]. In apoMb, the molten globule state has been investigated for different mutants in different anion conditions, and there is again a good correlation between stability and cooperativity [101].

The correlation between the intrinsic stability and the degree of cooperativity of the molten globule state may reasonably be interpreted in terms of the two-stage hierarchical model of protein folding (see Scheme 23.1). In this model, the local interactions and nonspecific hydrophobic interactions that stabilize the molten globule state approximate, to a varying degree, the specific tertiary packing interactions that stabilize the native structure. Thus, the presence of specific native interactions further organizes structurally and stabilizes the molten globule state, and makes the unfolding transition more cooperative.

23.3
The Kinetically Observed Molten Globule State

23.3.1
Observation and Identification of the Molten Globule State in Kinetic Refolding

Various experimental techniques, including kinetic CD spectroscopy [41, 104–106], hydrogen/deuterium exchange pulse labeling combined with two-dimensional NMR spectroscopy [46], and stopped-flow SAXS [56, 57, 107], have been used to detect and characterize the kinetic folding intermediates in a number of globular proteins. These studies emphasize the close similarities between the equilibrium molten globule state and kinetic folding intermediates. Kinetic studies have further shown that similar intermediates commonly accumulate during refolding of other proteins whose equilibrium unfolding transitions are represented well by a two-state model. Here we describe how intermediates of protein folding have been identified experimentally as the molten globule states.

Pulsed peptide hydrogen/deuterium exchange combined with two-dimensional NMR and mass spectrometry has been used to characterize transient folding intermediates of several globular proteins, including cyt *c*, ribonuclease A, lysozyme, apoMb, and ribonuclease HI (RNase HI) [46, 74, 108–113]. The transient folding intermediate and the equilibrium molten globule state have both been characterized by hydrogen/deuterium exchange techniques. The two intermediates have been shown to be equivalent by comparison of their hydrogen/deuterium exchange profile in apoMb and RNase HI [109, 111, 113].

The folding intermediate of apoMb formed within 6 ms of refolding has protected protons in the A-, G-, and H-helices as well as in part of the B-helix and appears to be structurally the same as the pH 4 intermediate at equilibrium [109, 113–116]. The hydrogen/deuterium exchange combined with mass spectrometry

indicates that the folding intermediate is obligatory with a significant hydrogen-bonded secondary structure content [112].

The folding intermediate of RNase HI is formed within the dead time (12 ms) of the stopped-flow technique when the refolding starts from the unfolded state, and consists of a structural core region of the protein, namely helices A and D and β-strand 4. This kinetic intermediate resembles both the acid molten globule of the protein and sparsely populated, partially unfolded forms detected under native conditions [111]. Interactions formed in the intermediate persist in the transition and native states, suggesting that RNase HI folds through a hierarchical mechanism [117].

NMR spectroscopy can be applied in real-time to investigating the kinetics of folding and has been used to follow the refolding of bovine α-LA [74, 118, 119]. Although the dead time is approximately 1 s, the kinetics can be monitored directly by a series of one-dimensional NMR spectra and by a single two-dimensional (^{1}H-^{15}N HSQC) experiment, taking advantage of the slow refolding of apo-α-LA. The kinetics monitored by side-chain proton signals in the one-dimensional NMR spectra and by main-chain signals in the two-dmensional experiment are both coincident with those measured by CD and fluorescence [118, 119]. The one-dimensional NMR spectrum observed just after the dead time ($\sim$1 s) was very similar to that of the molten globule state, indicating the folding intermediate of α-LA is identical to the molten globule state [118]. Real-time NMR spectroscopy is a powerful technique, allowing the validity of a specific kinetic scheme to be tested, although it is applicable only for slow-folding proteins that have a rate constant less than $\sim$0.05 s^{-1}. The real-time NMR method is also applied to investigating the unfolding characteristics of interleukin-1β [120].

23.3.2
Kinetics of Formation of the Early Folding Intermediates

The folding intermediates of globular proteins have been observed and characterized as the burst-phase intermediate in most cases because they already accumulated during the dead time of typical stopped-flow instrumentations, which limited the kinetic folding measurements to a time resolution of a few milliseconds. However, recent development of new techniques, which have dead times much shorter than that of conventional stopped-flow instrumentations, allowed us to directly monitor the folding kinetics, including the formation of the molten globule, in submillisecond time region. These techniques include laser photochemically triggering method [121, 122], the temperature-jump method with electrical or laser triggering [123, 124], and the continuous-flow method [125–128].

The folding kinetics of apoMb from the cold-denatured state were monitored by the nanosecond laser temperature-jump method with fluorescence detection, and the subdomain assembly consisting of the A-, G-, and H-helices from the G-H loop and nascent A helix was observed in 5–20 μs after initiation of the folding [129]. CD and SAXS measurements of apoMb using the continuous-flow and stopped-flow techniques have revealed that significant compaction and helix forma-

tion occurs within ~300 μs after initiation of the pH-induced refolding, which is followed by the formation of an intermediate similar to the TCA-induced structured molten globule state of this protein [130].

The continuous-flow fluorescence measurements of cyt *c* revealed the accumulation of a series of intermediates [131]. The earliest intermediate (I_C, see Section 23.3.3) whose Trp fluorescence is fully quenched by the heme is formed with a time constant of ~65 μs, which is much shorter than a typical dead time (a few milliseconds) of the stopped-flow measurement [131]. In fact, this intermediate has been observed as the burst-phase intermediate when the stopped-flow method is used. The continuous-flow CD and SAXS measurements also revealed two intermediates along the sequential folding pathway of cyt *c* [132, 133]. The first intermediate was, however, observed as the burst-phase intermediate because the dead times of the measurements, 160–390 μs, were much longer than the time constant of formation of the first intermediate. The first intermediate is more compact than the unfolded state with ~20% helicity of the native state, and may correspond to the I_C intermediate. The second intermediate formed with a time constant of ~400 μs is further more compact with a radius of gyration ~30% larger than the native state with ~70% helicity of the native state, and hence its size is close to that of the molten globule state of this protein [132, 133]. The second intermediate may be more similar to the α-LA and apoMb molten globules that are known to be less structurally organized and less stable than the salt-induced cyt *c* molten globule (see Section 23.2.2).

23.3.3
Late Folding Intermediates and Structural Diversity

Although the molten globule states are formed in less than a few milliseconds as burst-phase intermediates, in many of the proteins shown above, the equilibrium molten globule states occasionally correspond to late-folding intermediates formed after the burst-phase and other early intermediates have accumulated. The late-folding intermediates, which are usually more structured than the burst-phase intermediates, often correspond to the structured molten globules formed by addition of stabilizing anions at equilibrium.

The best-studied example is the late-folding intermediate of cyt *c* [90, 134, 135]. Cyt *c* at neutral pH folds by a sequential mechanism, which involves three intermediates (I_C, I_{NC}, N*) as shown in Scheme 23.2 [89, 90, 108, 134].

$$U \rightarrow I_C \rightarrow I_{NC} \rightarrow N^* \rightarrow N$$

Scheme 23.2

I_C is the earliest intermediate characterized by the continuous-flow studies (see Section 23.3.2), and it was observed as the burst-phase intermediate by the stopped-flow method. I_{NC} is a more structured intermediate with tightly interacting N- and C-terminal α-helices, and this was characterized by pulsed hydrogen/

deuterium exchange and mutagenesis techniques [89, 108, 136]. The last intermediate, N*, is known to affect the kinetics of unfolding, but does not accumulate during refolding. It is structurally very close to the native state, but lacks the native Met80 heme ligand. Studies on the KCl-induced kinetic refolding of the protein from the acid-unfolded to the compact molten globule state suggest that the acid compact equilibrium molten globule state may correspond to N* [90].

Similarly, apoMb accumulates at least two intermediates, Ia and Ib, in the kinetic refolding, and the late intermediate, Ib, may correspond to the anion-induced, more structured, molten globule state observed at equilibrium [86]. These intermediates of apoMb may also correspond to the two folding intermediates detected by the continuous-flow experiments (see Section 23.3.2).

Apparently, there is a diversity of molten globule states in terms of where they accumulate along the folding pathway, and this is analogous to the diversity of the equilibrium molten globule state that depends on the protein species and the experimental conditions, as described in Section 23.2. When accumulation takes place at a late stage of refolding, it is more structured than the early intermediate and may correspond to the structured molten globule state observed at equilibrium.

23.3.4
Evidence for the On-pathway Folding Intermediate

The folding kinetics of certain globular proteins have been analyzed very carefully, and hence we can address the question of whether the molten globule intermediate formed during kinetic folding is a productive, on-pathway intermediate, or not. If the intermediate is productive, it must be placed between the fully unfolded and the native states along the folding pathway. Observation of a lag phase during the refolding is known to provide firm evidence that the intermediate is productive. Jennings and her coworkers have studied kinetic refolding of interleukin-1β by pulsed hydrogen/deuterium exchange mass spectrometric analysis, stopped-flow CD, and fluorescence. The transient folding intermediate accumulates with a time constant of 126 ms, and there is a lag phase in the production of the native state of at least 400 ms, clearly indicating that the intermediate is a productive on-pathway intermediate [137]. A similar lag phase has also been reported in SNase and dihydrofolate reductase (DHFR) [138–141], the refolding reactions of which have been characterized by tryptophan fluorescence and methotrexate (an inhibitor of DHFR) absorbance, respectively. In apoMb, two transient intermediates, Ia and Ib, accumulate during refolding from the acid-unfolded state, and the kinetics analyzed by interrupted refolding and interrupted unfolding experiments have been shown to be consistent with a linear folding pathway (U $\rightarrow$ Ia $\rightarrow$ Ib $\rightarrow$ N), in which both are productive on-pathway intermediates [86].

A detailed analysis of Im7 folding and unfolding by monitoring the whole fluorescence signal change using the continuous-flow and stopped-flow methods unambiguously revealed that the kinetic folding intermediate of this protein is an on-pathway, obligatory intermediate [142]. Similar quantitative analysis of the fold-

ing and unfolding reactions of several proteins, including the B1 domain of protein G, ubiquitin, cyt *c*, and interleukin-1β, indicates that the experimentally observed folding intermediates are on-pathway and obligatory [16, 143–146].

23.4 Two-stage Hierarchical Folding Funnel

Here, we consider the structural and energetic aspects of protein folding represented by the two-stage hierarchical model, and this together with the funnel representation of protein folding will give us a reasonable picture of the structural diversity of the molten globule state observed experimentally.

Structural changes and their associated energetic properties are different between the two stages in the two-stage hierarchical model of protein folding [3, 4]. In stage I, the protein molecule forms native-like secondary structure, tertiary fold and compact shape, lacking specific side-chain packing, thus acquiring the broad structural architecture of the native molecule. Local interactions that determine preference for secondary structure, and nonspecific hydrophobic interactions that determine the overall backbone topology and the compact shape are important in this stage. On the other hand, in stage II the specific side-chain packing is organized, and specific van der Waals contacts are dominant in this process. Furthermore, the structure formed in stage I may be similar to an expanded version of the structure formed in stage II, and the overall tertiary fold formed in stage I brings the appropriate side chains close in space to enable the specific native packing interaction between them to take place and stabilize the overall native-like tertiary fold.

Taking advantage of the funnel picture of protein folding, it is useful to describe the two-stage hierarchical folding model in terms of the folding funnel. The presence of the two stages indicates the presence of two corresponding folding funnels, I and II (Figure 23.4). The differences in the structural classes and energetics associated with the two stages are reflected in differences in shape between the two folding funnels. The compaction of protein, which occurs in stage I, results in a much larger decrease in the conformational entropy, suggesting that funnel I is much wider at its top than funnel II. The multiple specific tertiary packing interactions occurring in stage II are enthalpic in nature, and, because they are not always native-like, a previously formed interaction must often be broken to form a more stable set of interactions later in stage II. There must, therefore, be a number of enthalpic barriers along funnel II. Because the free-energy barrier is much more entropic in funnel I, the energy landscape must be much more rugged in funnel II.

The two-stage folding funnel provides a nice picture of why the experimentally observed molten globule states are structurally diverse. As described in Section 23.2, some molten globules have no observable tertiary structure, while others often contain native-like side-chain packing in a limited region of the molecule. The degree of structure in the molten globule state depends on where the largest

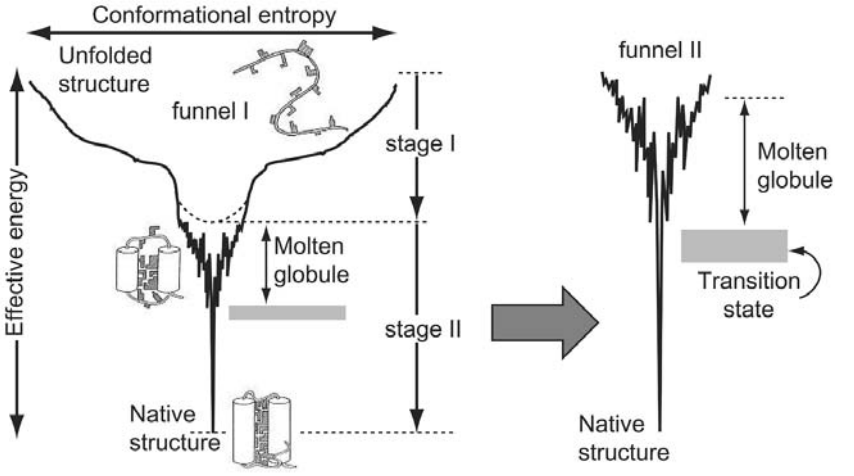

Fig. 23.4. A schematic representation of the hierarchical folding funnel. See the text for details.

energetic barrier is located along funnel II. When it is located at the top of funnel II, there will be no specific side-chain packing in the molten globule, but when close to the bottom, a number of the specific side-chain interactions may already be formed. In cases like apoMb, there may be two large energetic barriers along funnel II, resulting in accumulation of two structurally different molten globules.

23.5 Unification of the Folding Mechanism between Non-two-state and Two-state Proteins

Now we re-address the question raised at the beginning of this chapter, because a number of small globular proteins with fewer than 100 amino acid residues have been found to exhibit two-state folding without any accumulation of the intermediate [14]. These two-state proteins often correspond to a part (domain) of an entire protein molecule, and there are now more than 30 examples of the two-state proteins, including Src homology 3 domain [147–150], E9 colicin-binding immunity domain [151], cold shock protein B [152], N-terminal domain of λ repressor [153], IgG-binding domain of protein L [154], and chymotrypsin inhibitor 2 [155]. Apparently, the accumulation of the folding intermediate is not a prerequisite for the successful folding of these two-state proteins.

Questions thus arise. (i) Is the sequential model of protein folding truly in conflict with the simple two-state folding of small globular proteins? (ii) What is the role of the molten globule intermediate in protein folding if the successful folding takes place for the two-state proteins? (iii) What is a unified view of protein folding? Two possible answers to these questions are: (i) Protein folding is in principle a highly cooperative two-state transition, and any molten globule-like species observed at early stages of folding are not productive, but produced by kinetic trap-

ping and misfolding events; and (ii) non-two-state folding with the molten globule as a productive folding intermediate is more common in globular protein folding, and the two-state folding observed in the small proteins is rather a simplified version of the more common non-two-state folding. Which answer better represents real protein folding is crucial to our understanding of the mechanism of folding.

A recent paper by Kamagata et al. has shed light on this issue, and strongly suggested that the second answer is more appropriate in real globular proteins [156]. They have found that the rate constants for formation of the intermediate and the native state of non-two-state proteins both show essentially the same dependence on the native backbone structure as the rate constant of folding of two-state proteins. This indicates that the folding mechanisms behind the non-two-state and the two-state protein folding are essentially identical.

23.5.1 Statistical Analysis of the Folding Data of Non-two-state and Two-state Proteins

Kamagata et al. have collected the kinetic folding data of globular proteins from the literature, classified the proteins into non-two-state and two-state proteins, and investigated the relationships between the folding kinetics and the native three-dimensional structure of these proteins. Classification of the proteins as two-state folders was based on the criteria: (i) single-exponential refolding kinetics after exclusion of slow isomerization steps such as proline isomerization in the unfolded state, (ii) the absence of rollover behavior in the logarithmic folding rate constant as a function of denaturant concentration, and (iii) the agreement of unfolding parameters between the equilibrium and kinetic experiments. The proteins that did not satisfy these criteria might be non-two-state folders, but they also employed a more rigorous rule to identify non-two-state proteins; namely, the protein that showed the single-exponential refolding kinetics with the rollover behavior was classified as a non-two-state folder only if one of the following criteria was satisfied: (i) the presence of a burst-phase (i.e., missing amplitude) in the folding kinetics, and/or (ii) the accumulation of a well-characterized kinetic folding intermediate. Furthermore, only the proteins for which the kinetic folding mechanism had been determined clearly were used for the analysis, and the proteins with a heme group or disulfide bonds were excluded from the analysis. As a results, there were 16 natural proteins classified as the non-two-state folders; however, if we include proteins that satisfied only the condition of rollover behavior, additional five proteins could be included as well, resulting in 21 non-two-state folders. For 10 proteins among these 21 folders, the folding kinetics were multiphasic, and the rate constant for the formation of the folding intermediate was reported. On the other hand, there were 18 proteins that were classified as two-state folders.

Figure 23.5 shows the relationship between the rate constant (k_I) for formation of the folding intermediate and the parameter (the number of sequence-distant native pairs, Q_D) that represents the backbone topology of the native structure [157], and the relationship between the rate constant (k_N) for formation of the native state and Q_D, in the non-two-state proteins, and these relationships are compared with

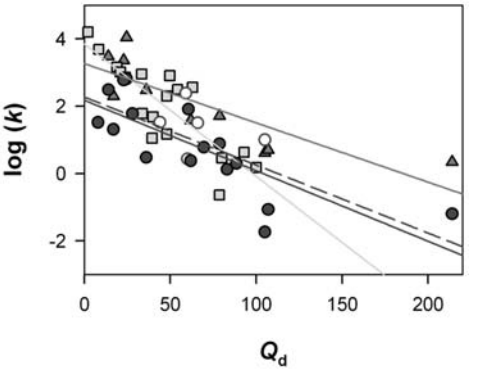

Fig. 23.5. A comparison of the folding rates of non-two-state and two-state folders. The logarithmic rate constants are plotted against the number of sequence-distant native pairs. Filled squares represent the folding of two-state folders. Filled triangles represent the formation of the intermediate of non-two-state folders. Filled circles and open circles represent the formation of the native state for the 16- and 21-protein data set, respectively, of non-two-state folders. The solid lines represent the best linear fit for the formation of the native state for 18 two-state folders, the intermediate for 10 non-two-state folders, and the native state for 16 non-two-state folders, respectively. The dashed line represents the best linear fit for the formation of the native state for 22 non-two-state folders [156].

the relationship between the folding rate constant (k_{UN}) and Q_D in the two-state proteins. It can be seen that all the rate constants (k_I, k_N, and k_{UN}) are significantly correlated with Q_D that is determined by the native backbone topology as given by:

$$Q_D = \sum_{i=2}^{L_p} \sum_{j=1}^{i-1} \Delta_{ij} \tag{1}$$

where i and j are the residues numbers of two contacting residues for which the Cα–Cα distance in space was within 6 Å in the PDB structure, and L_p is the total number of amino acid residues of a protein excluding the disordered terminal regions. $\Delta_{ij} = 1$ if $i - j > 12$, and otherwise $\Delta_{ij} = 0$. Similar correlations of these rate constants were also found with other structure-based parameters, the absolute contact order (ACO) [158] and cliquishness [159], but there were no significant correlations between the rate constants for the non-two-state proteins (k_I and k_N) and the relative contact order (RCO) [160], and this is in contrast with the significant correlation found between k_{UN} and RCO in the two-state proteins. The difference between the non-two-state and the two-state proteins with respect to the correlation with RCO was ascribed to a difference in the chain-length distribution between the two types of proteins. Because RCO is given by ACO/L_p, the correlations of the logarithmic rate constants with ACO and the chain length canceled each other out in the RCO for the non-two-state proteins that had a much wider distribution of L_p.

The significant correlations of both the logarithmic rate constants, $\log k_I$ and $\log k_N$, with Q_D (the correlation coefficient $r = -0.74 \sim -0.83$) in the non-two-state

proteins indicate that both the processes from the unfolded state (U) to the intermediate (I) and from I to the native state (N) are rate-limited by the process of forming a more native-like backbone topology. Protein molecules thus become progressively more native-like during the folding process from U to N via I, clearly demonstrating that the kinetic intermediate of refolding in the case of non-two-state proteins is a real, productive folding intermediate. Furthermore, both the value of log k_{UN} and its dependence on Q_D in the two-state proteins are very similar to those found in the plots of log k_I and log k_N versus Q_D for the non-two-state proteins (Figure 23.5). This clearly demonstrates that the mechanism of folding does not differ between the two classes of proteins. The non-two-state folding, with the accumulation of a productive folding intermediate, may be a more common mechanism of protein folding, and the two-state folding may be apparently a simplified version of the more common non-two-state folding.

23.5.2
A Unified Mechanism of Protein Folding: Hierarchy

The presence of the molten globule-like intermediate at an early stage of kinetic refolding, together with the productive nature of the intermediate, strongly suggests the two-stage hierarchical model shown earlier in this chapter (Scheme 23.1) as a general mechanism of protein folding. At this point, however, at least two questions arise. First, if the two-stage model is more general, why do certain small globular proteins exhibit two-state (i.e., single-stage) folding? Second, if stage II of Scheme 23.1 corresponds to the process of the specific tertiary packing of side chains from the molten globule to the native state, why does the k_N for non-two-state folders show essentially the same dependence on native backbone topology (i.e., Q_d) as k_I does (see Figure 23.5)?

As regards the first question as it relates to the two-state folders, there are two possible explanations. First, this effect could be due to the movement of the rate-limiting step from stage II in non-two-state folders to stage I in two-state folders. When the size of a protein decreases, it becomes easier to determine the specific conformation of side-chain packing due to the decrease in the number of specific interactions, thereby making the first stage, rather than the second stage, rate-limiting. Thus, this process would lead to the two-state kinetic behavior of the protein. On the other hand, a second explanation would ascribe the two-state behavior to the destabilization of the folding intermediate. When the intermediate is less stable than the unfolded state, a protein must undergo simple two-state folding without any accumulation of the intermediate. If the first explanation is applied to the two-state type of folding, the rate constant k_{UN} of the two-state protein may coincide with the rate constant k_I, at which the intermediate forms in the non-two-state protein. On the other hand, if the second explanation is applied, with the rate-limiting step remaining at stage II, then the rate constant k_{UN} of the two-state protein may coincide with the rate constant k_N, at which the native state for the non-two-state protein is formed. Figure 23.5 shows that the k_{UN} values for the two-state proteins coincide with the k_I values for the non-two-state proteins at Q_d

values of less than 25, suggesting the validity of the first explanation. However, when Q_d is larger than 25, the two-state k_{UN} shows variation in either the non-two-state k_I or k_N, or between the k_I and k_N, and hence both mechanisms given by the two explanations may play a role in the folding of two-state proteins.

However, it still remains unclear why the k_N for non-two-state folders shows essentially the same dependence on Q_d as does the k_I (Figure 23.5). This question may be even more difficult to answer than those discussed above; however, the known structural characteristics of the folding intermediates indicate that stage II includes the process of the specific tertiary packing of side chains. It is possible that this packing process is also dominated by the organization of the native backbone topology. Thus, the folding that occurs in stage II would again be correlated with the native backbone topology, but would take place in a concerted manner together with the tertiary packing of side chains and the organization of the backbone topology.

23.5.3
Hidden Folding Intermediates in Two-state Proteins

Although many small globular proteins fold fast and apparently in a two-state manner without detectable intermediates, it is now becoming increasingly clear that hidden meta-stable folding intermediate may exist along the folding pathway, but behind the rate-limiting transition state. Sanchez and Kiefhaber have shown that nonlinear activation free-energy relationships (i.e., nonlinear relationships of the logarithmic rate constant of folding or unfolding versus denaturant concentration) reported for 23 two-state proteins are caused by sequential folding pathways with consecutive distinct barriers and a few obligatory intermediate that are hidden from direct observation by the high free energies of the intermediates [161]. Bai has also suggested from native-state hydrogen/deuterium exchange data of a number of two-state proteins that partially folded intermediates may exist behind the rate-limiting transition state in these proteins and evade detection by conventional kinetic methods [162]. He proposed two types of the hidden intermediates: type I intermediates, more stable than the unfolded state but hidden behind the rate-limiting transition state located between the unfolded state and the intermediate, and type II intermediates that are less stable than the unfolded state. These are fully consistent with our explanation for the observation of the two-state folding proteins (see Section 23.5.2).

It is thus concluded that there is essentially no difference in mechanism between the non-two-state and the two-state protein folding, and the apparent two-state folding is merely a simplified version of more common non-two-state folding that accumulates obligatory folding intermediates. The major difference between the non-two-state and the two-state folding is the relative stability of the folding intermediates. In fact, non-two-state proteins also exhibit apparent two-state folding and unfolding kinetics under a solution condition where the intermediates are destabilized or by introduction of amino acid replacements that destabilize the intermediates [163].

23.6
Practical Aspects of the Experimental Study of Molten Globules

23.6.1
Observation of the Equilibrium Molten Globule State

As described in Section 23.2, certain proteins show equilibrium unfolding intermediates including the molten globule state, while the other proteins unfold without detectable intermediate. Therefore, when we analyze the experimentally observed unfolding transition of a protein, we must be careful about the possible presence or absence of the equilibrium unfolding intermediates. When there is no intermediate observed, we shall use a two-state model of the unfolding transition, and otherwise a model that involves the intermediates (see Section 23.6.1.2).

The unfolding transition curve of a protein can be obtained by measuring a physical parameter, which reflects the conformational states of the protein, as a function of denaturing perturbations such as denaturant (typically GdmCl or urea) concentration, pH and temperature [1, 23, 28]. The physical parameters often used are optical ones, such as absorption, CD and fluorescence. Here, we will describe a procedure widely used in the analysis of the protein unfolding transitions.

23.6.1.1 Two-state Unfolding Transition

Equilibrium unfolding transitions occurring without detectable intermediate states can be well approximated by the transition between only the two states [164], the native (N) and the fully unfolded (U) states as:

$$N \rightleftarrows U$$

This approximation of the unfolding transition is referred to as the two-state model.

When a denaturant-induced unfolding transition follows the two-state model, the observed value of a given physical parameter (optical absorbance, fluorescence, CD, etc.) $A(c)$ at denaturant concentrations c is given by:

$$A(c) = A_N \times f_N(c) + A_U \times f_U(c) = A_N \times f_N(c) + A_U \times (1 - f_N(c)) \quad (2)$$

where $f_N(c)$ and $f_U(c)$ ($f_N + f_U = 1$) are the fraction native and unfolded at denaturant concentration c, A_N and A_U are the ideal values of the parameter in the native and the unfolded states, respectively, and these are often obtained by linear extrapolations of the dependence of the parameter values on c from the pretransition (native) and the posttransition (unfolded) regions as $A_n = a_1 c + a_2$ and $A_U = a_3 c + a_4$, where a_i is constant. Because an equation essentially the same as Eq. (2) is obtained for the pH- and temperature-induced unfolding transitions, the description of the equilibrium unfolding transition shown below also applies to the pH- and temperature-induced unfolding transitions. Equation (2) is rewritten as:

$$f_N(c) = \frac{A(c) - A_U}{A_N - A_U} \quad (3)$$

This shows that a single observation probe can determine the fraction native and unfolded ($f_U = 1 - f_N$) in the two-state model.

Equation (3) indicates that the fraction native and unfolded calculated from the unfolding transition curves monitored by different probes should be superimposable to each other if the two-state approximation holds. This characteristic of the two-state unfolding transition is often used to distinguish between the two- and multistate unfolding transitions. Figure 23.6A shows an example of the two-state unfolding transition of hen egg white lysozyme [23].

The unfolding transitions approximated by the two-state model exhibit a specific point (for example, at a specific wavelength) in the spectra of the native and the

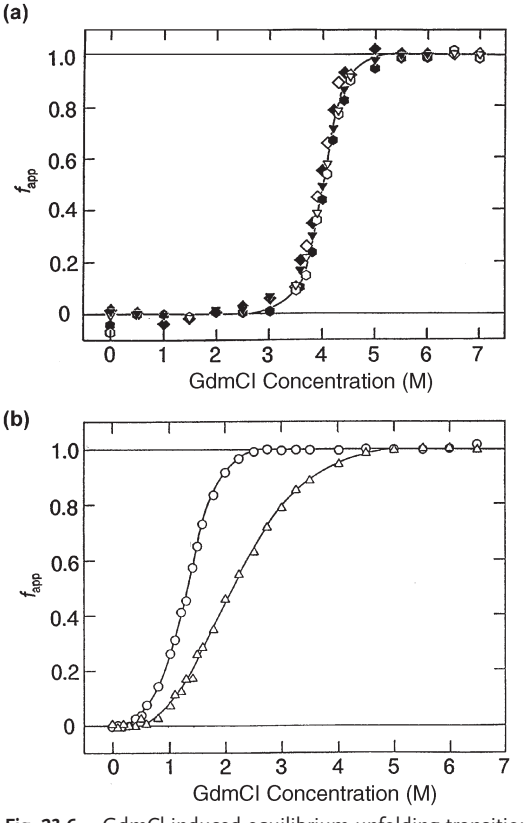

Fig. 23.6. GdmCl-induced equilibrium unfolding transition curves of a) hen egg white lysozyme and (b) α-lactalbumin monitored by CD spectra at a) 222 nm (inverted triangles), 255 nm (hexagons), and 289 nm (diamonds), and b) 222 nm (triangles) and 270 nm (circles) [23].

fully unfolded state, where these two states exhibit the identical value of the parameter used. If there exists such a point(s) in the spectra, all the spectra involved in the unfolding transition at different denaturant concentrations exhibit essentially the same value at that point with the condition that $a_1 \approx a_3 \approx 0$. This is readily evidenced by Eq. (2). Here we take an example of absorbance as an optical probe, and suppose that the absorbance spectra of the native and unfolded states exhibit the same value (A_λ) at a wavelength λ. According to the above assumption ($A_N = A_U = A_\lambda$), the absorbance value ($A(c)$) at λ should be essentially identical (A_λ) at any denaturant concentration [165].

Thus, the existence of these specific points (a single point in many cases), referred to as isosbestic and isodichroic points for absorbance and CD, respectively, lends support to the two-state unfolding transition whereas we have to think about a multistate unfolding transition in the absence of these kinds of points.

23.6.1.2 Multi-state (Three-state) Unfolding Transition

The three-state unfolding transition is a simple extension of the two-state unfolding transition in terms of an additional intermediate state that is stably populated at equilibrium. The unfolding equilibrium of the three-state model is described as:

$$N \rightleftarrows I \rightleftarrows U$$

where I is the equilibrium unfolding intermediate. The observed value of a given physical parameter $A(c)$ at denaturant concentrations c is thus given by

$$A(c) = A_N \times f_N(c) + A_I \times f_I(c) + A_U \times f_U(c) \tag{4}$$

where A_I is the ideal value of the parameter in the intermediate state, $f_I(c)$ is the fraction of the intermediate state at denaturant concentration c, and $f_N + f_I + f_U = 1$. When the intermediate is fully populated at an intermediate concentration of denaturant, we can experimentally determine A_I and extrapolate the values into regions where the intermediate is not stably populated. However, this is not always the case. For the molten globule intermediate, we can often assume that $A_I = A_N$ for the parameters that represent the native secondary structure and that $A_I = A_U$ for the parameters that represent the specific tertiary structure of side chains (see below). Although the two-state unfolding transition in principle requires only a single probe to determine the fraction native or unfolded, the three-state unfolding transition requires two independent probes when the two transitions, $N \rightleftarrows I$ and $I \rightleftarrows U$ are not separated from each other.

As described previously, the molten globule state has a native-like secondary structure with virtually no specific side-chain packing. Taking advantage of these properties of the molten globule state, CD spectroscopy in the far- and near-UV regions, which are sensitive to the backbone secondary structure and the asymmetry of the side chains in aromatic residues, respectively, is extremely useful because they can monitor individually these two properties specific for the molten globule state.

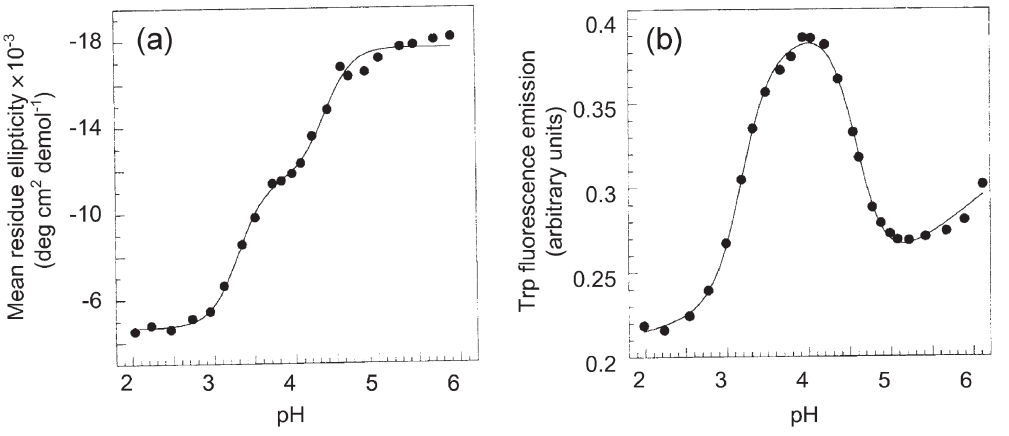

Fig. 23.7. pH-induced unfolding transition curves of apoMb monitored by a) CD at 222 nm and b) tryptophan fluorescence emission. From [84] with permission of Oxford University Press.

The equilibrium unfolding of α-LA monitored using CD spectroscopy in the far- and near-UV regions is an excellent example that clearly demonstrates that the molten globule is stably populated at equilibrium. The transition occurs at a lower denaturant concentration when monitored by the near-UV CD than when monitored by the far-UV CD (Figure 23.6b), and such noncoincidence of the apparent transition curves measured by the different probes is clear evidence that the molten globule intermediate accumulates between the two transition regions [23]. Accumulation of the molten globule state was also observed in the same manner in many other proteins, including canine and equine milk lysozymes [25, 80].

Another example demonstrating the population of the equilibrium unfolding intermediate is the observation of a two-step (or multi-step) unfolding transition measured by a single spectroscopic probe. A good example is the observation of the molten globule intermediate of apoMb at an intermediate pH (pH 4) in the pH-induced unfolding transition. Figure 23.7 shows the pH-induced unfolding transition curve of apoMb monitored by the far-UV CD and the intrinsic tryptophan fluorescence [84]. In contrast to the two-state unfolding transition curves that must have only a single-step transition, apoMb exhibits a two-step transition with a significant enhancement (more intense than the values in the native as well as the unfolded states) in the fluorescence and a plateau region in the far-UV CD at a modest acidic pH region around pH 4. These spectroscopic properties are consistent with population of the molten globule state at the intermediate pH as described in Section 23.2; it contains a portion of the native helical structure with two partially buried tryptophan residues that are located in the A-helix region and give rise to the enhancement of the fluorescence [45, 84].

The apparent difference in the behavior of the unfolding transition curves between α-LA and apoMb is, however, not essential. Because the α-LA molten globule

exhibits a substantial amount of the secondary structure with virtual lacking the specific side-chain packing, there is little change in the far- and the near-UV CD intensities on the N ⇄ I and I ⇄ U transitions, respectively, which results in non-coincident single-step unfolding transitions measured by these probes. On the other hand, the apoMb molten globule is sufficiently stable at the intermediate pH values, and exhibits the properties distinct from those in the native and the unfolded states, so that it emphasizes the population of the molten globule state in the unfolding transition curves.

23.6.2
Burst-phase Intermediate Accumulated during the Dead Time of Refolding Kinetics

For many globular proteins, a kinetic folding intermediate is accumulated at an early stage during the refolding from the fully unfolded state under a strongly native condition, and this accumulation of the intermediate often occurs within the dead time of the measurements. Figure 23.8 shows the kinetic trace of α-LA refolding monitored by CD in the far-UV region at 222 nm [106]. In the kinetic trace, a significant fraction of the CD change occurs within the dead time of the measure-

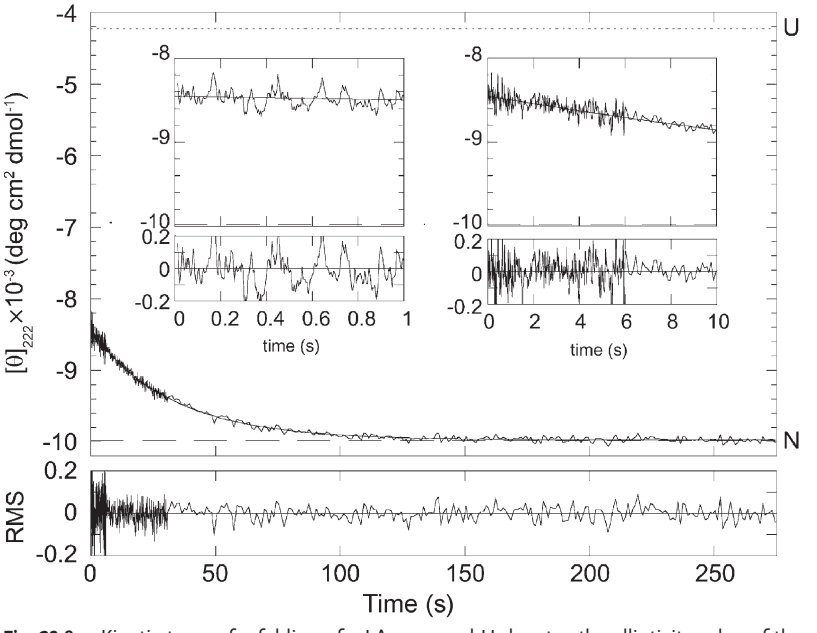

Fig. 23.8. Kinetic trace of refolding of α-LA monitored by CD at 222 nm. The refolding reaction was initiated by a GdmCl concentration jump from 5 M to 1 M. N denotes the ellipticity value of the native state, and U denotes the ellipticity value of the unfolded state at 1 M GdmCl obtained by linear extrapolation of the baseline for the unfolded state. From [106] with permission from Elsevier.

ments, indicating the transient accumulation of an intermediate state that has a substantial amount of the secondary structure.

The unresolved signal change (missing amplitude) occurring within the dead time of measurement in kinetic refolding experiments is referred to as the ''burst-phase'' change, and the corresponding intermediate is referred to as the ''burst-phase intermediate'' of refolding. Kinetic traces for the refolding reactions are fitted to a sum of exponential functions. If the significant structural formation occurs within the dead time during refolding, the value obtained by extrapolating the fitted kinetic refolding curve to zero time must be different from the expected value for the unfolded state that can be obtained by extrapolating the values of the unfolded state in the posttransition region of the equilibrium unfolding transition curve to the refolding condition. A more strict definition of the burst-phase change is, thus, a change from the expected value for the unfolded state to the zero-time extrapolated value of the fitted kinetic refolding curve. The burst-phase change results from at least one very fast phase unresolved in the observed kinetic trace, whose rate constant should be much larger than 1/(dead time).

The burst-phase change can be observed by using a variety of conformational probes, including CD, pulsed hydrogen/deuterium exchange, intrinsic and extrinsic fluorescence, and SAXS [57, 80, 104–106, 113, 166]. Among these, SAXS is useful in estimating the size and the overall shape of the burst-phase intermediate. Our previous SAXS measurements of α-LA have directly demonstrated that the burst-phase intermediate, accumulated within ~10 ms after the initiation of the refolding, has a radius of gyration very close to that of the equilibrium molten globule state (~10% larger than that of the native state) with a globular shape [57], lending support to the idea that the kinetic intermediate of α-LA is identical to the molten globule state.

Whether or not the burst-phase intermediate is observed in the kinetic refolding of a protein depends on the rate of formation of the intermediate and the dead time of measurement. For example, the fluorescence of cyt *c* is quenched by almost 80% of the total change expected on the refolding reaction within the dead time of stopped-flow measurement (a few milliseconds) while kinetic traces monitored by using continuous-flow fluorescence methods with a dead time of ~50 μs provides the total signal change expected [131].

23.6.3
Testing the Identity of the Molten Globule State with the Burst-Phase Intermediate

Measurements of the kinetic progress curves of refolding at various wavelengths will give us the CD spectrum of the intermediate state. Figure 23.9 shows the far- and near-UV CD spectra of α-LA burst-phase intermediate and they are compared with the equilibrium CD spectra of the protein [104]. The CD spectra of the burst-phase intermediate are similar to the equilibrium CD spectra of the molten globule state. These results further support the idea that the folding intermediate of α-LA is identical to the molten globule.

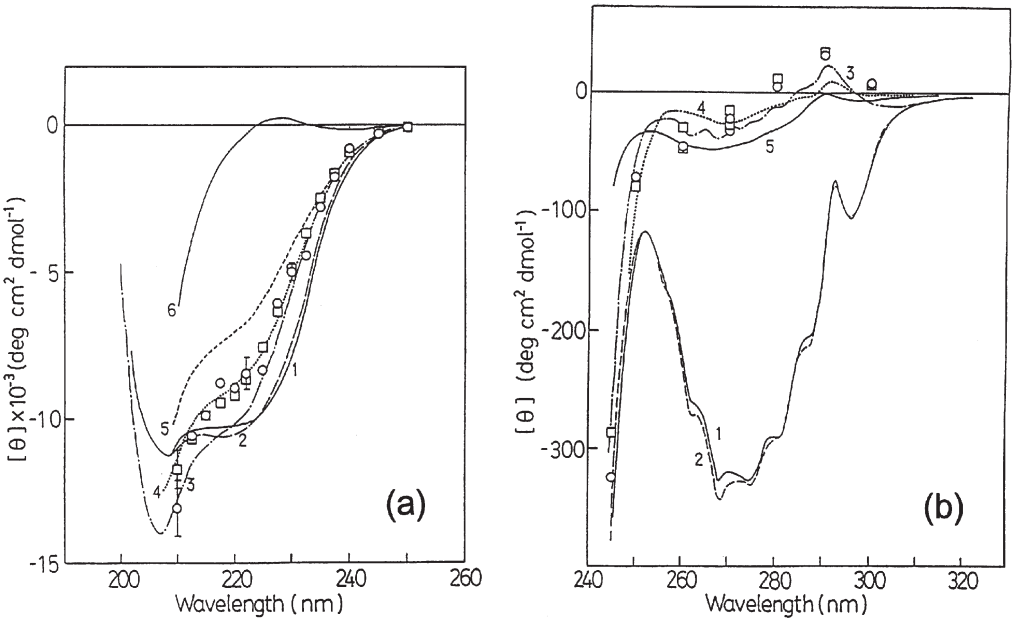

Fig. 23.9. CD spectra of the molten globule state of α-LA at pH 2.0 in the far- and near-UV regions compared with the CD spectra of the native and unfolded states. Open circles and squares show the CD values obtained by extrapolating to zero time of the refolding curves. 1 and 2, the native state of the holo and apo forms, respectively; 3, the molten globule state at pH 2.0; a) 4 and 5, the thermally unfolded states at 41 and 78 °C, respectively; 6, the unfolded state by GdmCl; b) 4, the thermally unfolded state at 62.5 °C; 5, the unfolded state by GdmCl. From [104] with permission from the American Chemical Society.

The formation of secondary structure in the burst-phase of refolding is a very rapid process occurring within a few milliseconds, so that the rapid pre-equilibrium between the unfolded and the intermediate states is established at a very early stage in the refolding reaction. The simplest example of the refolding reactions involving an on-pathway intermediate can be described as follows:

$$U \overset{\text{very rapid}}{\rightleftharpoons} I \xrightarrow{\text{slow}} N$$

where U, I, and N represent the unfolded, the intermediate, and the native states, respectively.

The unfolding transition curve of the intermediate state is obtained by measuring the refolding reactions at varying denaturant concentrations and by investigating the dependence of the burst-phase CD spectrum on the denaturant concentration. Comparison of the unfolding transitions of the molten globule state and the burst-phase provide an additional test for the identity of these two states in terms of stability. Figure 23.10 shows the unfolding transition curves of the burst-phase intermediate and the equilibrium molten globule state of α-LA measured by ellip-

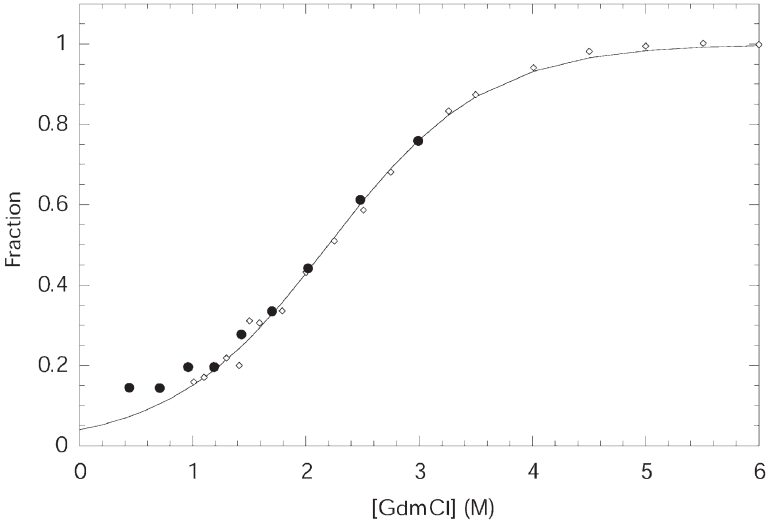

Fig. 23.10. The normalized unfolding transition curves of the burst-phase intermediate of α-LA (filled circles) compared with that of the equilibrium molten globule state at neutral pH (open diamonds). The solid line shows the theoretical curve assuming a two-state transition between the molten globule state and the unfolded state. From [106] with permission from Elsevier.

ticity at 222 nm [106]. The unfolding transition curve of the burst-phase intermediate is superimposable to the unfolding transition of the molten globule state that has been observed at equilibrium, indicating, again, that these two states of α-LA are identical to each other.

Although this method is powerful to compare the stability of the burst-phase intermediate with that of the molten globule, thermodynamic parameters of the burst-phase intermediate may not be able to be reliably obtained. As described in Section 23.2.3, the unfolding transitions of the molten globule state may not occur in a cooperative manner [58], which means that the two-state model may not apply to the transition between the unfolded state and the intermediates. Nevertheless, it is worth measuring these unfolding transitions for the purpose of comparing the molten globule and the burst-phase intermediate.

References

1 K. Kuwajima *Proteins* **1989**, *6*, 87–103.
2 O. B. Ptitsyn *Adv. Protein Chem.* **1995**, *47*, 83–229.
3 M. Arai, K. Kuwajima *Adv. Protein Chem.* **2000**, *53*, 209–282.
4 K. Kuwajima, M. Arai *Mechanisms of Protein Folding*, 2nd edn. Oxford University Press, Oxford, **2000**.
5 C. Levinthal *J. Chim. Phys.* **1968**, *65*, 44–45.
6 P. S. Kim, R. L. Baldwin *Annu. Rev. Biochem.* **1982**, *51*, 459–489.
7 P. S. Kim, R. L. Baldwin *Annu. Rev. Biochem.* **1990**, *59*, 631–660.
8 C. R. Matthews *Annu. Rev. Biochem.* **1993**, *62*, 653–683.

9 J. D. Bryngelson, J. N. Onuchic, N. D. Socci, P. G. Wolynes *Proteins* **1995**, *21*, 167–195.

10 K. A. Dill, S. Bromberg, K. Yue, K. M. Fiebig, D. P. Yee, P. D. Thomas, H. S. Chan *Protein Sci.* **1995**, *4*, 561–602.

11 K. A. Dill, H. S. Chan *Nat. Struct. Biol.* **1997**, *4*, 10–19.

12 A. M. Gutin, V. I. Abkevich, E. I. Shakhnovich *Biochemistry* **1995**, *34*, 3066–3076.

13 A. R. Fersht *Curr. Opin. Struct. Biol.* **1997**, *7*, 3–9.

14 S. E. Jackson *Fold. Des.* **1998**, *3*, R81–R91.

15 D. V. Laurents, R. L. Baldwin *Biophys. J.* **1998**, *75*, 428–434.

16 R. L. Baldwin *Fold. Des.* **1995**, *1*, R1–R8.

17 R. L. Baldwin, G. D. Rose *Trends Biochem. Sci.* **1999**, *24*, 26–33.

18 R. L. Baldwin, G. D. Rose *Trends Biochem. Sci.* **1999**, *24*, 77–83.

19 D. A. Dolgikh, L. V. Abaturov, I. A. Bolotina et al. *Eur. Biophys. J.* **1985**, *13*, 109–121.

20 M. Ohgushi, A. Wada *FEBS Lett.* **1983**, *164*, 21–24.

21 K. Kuwajima *FASEB J.* **1996**, *10*, 102–109.

22 L. A. Morozova-Roche, C. C. Arico-Muendel, D. T. Haynie, V. I. Emelyanenko, H. Van Dael, C. M. Dobson *J. Mol. Biol.* **1997**, *268*, 903–921.

23 M. Ikeguchi, K. Kuwajima, S. Sugai *J. Biochem. (Tokyo)* **1986**, *99*, 1191–1201.

24 H. Van Dael, P. Haezebrouck, L. Morozova, C. Arico-Muendel, C. M. Dobson *Biochemistry* **1993**, *32*, 11886–11894.

25 M. Mizuguchi, M. Arai, Y. Ke, K. Nitta, K. Kuwajima *J. Mol. Biol.* **1998**, *283*, 265–277.

26 M. Kikuchi, K. Kawano, K. Nitta *Protein Sci.* **1998**, *7*, 2150–2155.

27 K. Yutani, K. Ogasahara, K. Kuwajima *J. Mol. Biol.* **1992**, *228*, 347–350.

28 Y. V. Griko, E. Freire, G. Privalov, H. Van Dael, P. L. Privalov *J. Mol. Biol.* **1995**, *252*, 447–459.

29 V. E. Bychkova, A. E. Dujsekina, S. I. Klenin, E. I. Tiktopulo, V. N. Uversky, O. B. Ptitsyn *Biochemistry* **1996**, *35*, 6058–6063.

30 V. N. Uversky, N. V. Narizhneva, S. O. Kirschstein, S. Winter, G. Lober *Fold. Des.* **1997**, *2*, 163–172.

31 G. J. A. Vidugiris, C. A. Royer *Biophys. J.* **1998**, *75*, 463–470.

32 R. Kitahara, H. Yamada, K. Akasaka, P. E. Wright *J. Mol. Biol.* **2002**, *320*, 311–319.

33 M. W. Lassalle, H. Li, H. Yamada, K. Akasaka, C. Redfield *Protein Sci.* **2003**, *12*, 66–72.

34 Y. Goto, N. Takahashi, A. L. Fink *Biochemistry* **1990**, *29*, 3480–3488.

35 V. N. Uversky, V. P. Kutyshenko, N. Y. Protasova, V. V. Rogov, K. S. Vassilenko, A. T. Gudkov *Protein Sci.* **1996**, *5*, 1844–1851.

36 V. N. Uversky, V. V. Leontiev, A. T. Gudkov *Protein Eng.* **1992**, *5*, 781–783.

37 T. E. Creighton, J. J. Ewbank *Biochemistry* **1994**, *33*, 1534–1538.

38 S. J. Demarest, R. Fairman, D. P. Raleigh *J. Mol. Biol.* **1998**, *283*, 279–291.

39 S. J. Demarest, J. A. Boice, R. Fairman, D. P. Raleigh *J. Mol. Biol.* **1999**, *294*, 213–221.

40 P. Polverino de Laureto, D. Vinante, E. Scaramella, E. Frare, A. Fontana *Eur. J. Biochem.* **2001**, *268*, 4324–4333.

41 K. Kuwajima *Circular Dichroism and the Conformational Analysis of Biomolecules.* Plenum, New York, **1996**.

42 V. N. Uversky, O. B. Ptitsyn *Biochemistry* **1994**, *33*, 2782–2791.

43 K. Gast, H. Damaschun, R. Misselwitz, M. Mueller-Frohne, D. Zirwer, G. Damaschun *Eur. Biophys. J.* **1994**, *23*, 297–305.

44 G. V. Semisotnov, N. A. Rodionova, O. I. Razgulyaev, V. N. Uversky, A. F. Gripas, R. I. Gilmanshin *Biopolymers* **1991**, *31*, 119–128.

45 F. M. Hughson, P. E. Wright, R. L. Baldwin *Science* **1990**, *249*, 1544–1548.

46 R. L. Baldwin *Curr. Opin. Struct. Biol.* **1993**, *3*, 84–91.

47 B. A. Schulman, C. Redfield, Z. Y. Peng, C. M. Dobson, P. S. Kim *J. Mol. Biol.* **1995**, *253*, 651–657.
48 J. A. Jones, D. K. Wilkins, L. J. Smith, C. M. Dobson *J. Biomol. NMR* **1997**, *10*, 199–203.
49 B. A. Schulman, P. S. Kim, C. M. Dobson, C. Redfield *Nat. Struct. Biol.* **1997**, *4*, 630–634.
50 D. Eliezer, J. Yao, H. J. Dyson, P. E. Wright *Nat. Struct. Biol.* **1998**, *5*, 148–155.
51 C. Redfield, B. A. Schulman, M. A. Milhollen, P. S. Kim, C. M. Dobson *Nat. Struct. Biol.* **1999**, *6*, 948–952.
52 R. Wijesinha-Bettoni, C. M. Dobson, C. Redfield *J. Mol. Biol.* **2001**, *312*, 261–273.
53 S. Ramboarina, C. Redfield *J. Mol. Biol.* **2003**, *330*, 1177–1188.
54 D. Eliezer, P. A. Jennings, P. E. Wright, S. Doniach, K. O. Hodgson, H. Tsuruta *Science* **1995**, *270*, 487–488.
55 M. Kataoka, Y. Goto *Fold. Des.* **1996**, *1*, R107–R114.
56 M. Arai, T. Ikura, G. V. Semisotnov, H. Kihara, Y. Amemiya, K. Kuwajima *J. Mol. Biol.* **1998**, *275*, 149–162.
57 M. Arai, K. Ito, T. Inobe et al. *J. Mol. Biol.* **2002**, *321*, 121–132.
58 B. A. Schulman, P. S. Kim *Nat. Struct. Biol.* **1996**, *3*, 682–687.
59 J. L. Marmorino, M. Lehti, G. J. Pielak *J. Mol. Biol.* **1998**, *275*, 379–388.
60 L. C. Wu, P. S. Kim *J. Mol. Biol.* **1998**, *280*, 175–182.
61 J. Song, P. Bai, L. Luo, Z. Y. Peng *J. Mol. Biol.* **1998**, *280*, 167–174.
62 P. Bai, L. Luo, Z. Y. Peng *Biochemistry* **2000**, *39*, 372–380.
63 P. Bai, J. Song, L. Luo, Z. Y. Peng *Protein Sci.* **2001**, *10*, 55–62.
64 Z. Peng, P. S. Kim *Biochemistry* **1994**, *33*, 2136–2141.
65 L. C. Wu, Z. Peng, P. S. Kim *Nat. Struct. Biol.* **1995**, *2*, 281–286.
66 D. Eliezer, J. Chung, H. J. Dyson, P. E. Wright *Biochemistry* **2000**, *39*, 2894–2901.
67 H. Tsuge, H. Ago, M. Noma, K. Nitta, S. Sugai, M. Miyano *J. Biochem. (Tokyo)* **1992**, *111*, 141–143.
68 J. Ren, D. I. Stuart, K. R. Acharya *J. Biol. Chem.* **1993**, *268*, 19292–19298.
69 E. D. Chrysina, K. Brew, K. R. Acharya *J. Biol. Chem.* **2000**, *275*, 37021–37029.
70 T. Koshiba, M. Yao, Y. Kobashigawa et al. *Biochemistry* **2000**, *39*, 3248–3257.
71 K. Nitta, H. Tsuge, H. Iwamoto *Int. J. Pept. Protein Res.* **1993**, *41*, 118–123.
72 S. Sugai, M. Ikeguchi *Adv. Biophys.* **1994**, *30*, 37–84.
73 T. Koshiba, T. Hayashi, I. Miwako et al. *Protein Eng.* **1999**, *12*, 429–435.
74 V. Forge, R. T. Wijesinha, J. Balbach et al. *J. Mol. Biol.* **1999**, *288*, 673–688.
75 P. Haezebrouck, K. Noyelle, M. Joniau, H. Van Dael *J. Mol. Biol.* **1999**, *293*, 703–718.
76 M. Mizuguchi, K. Masaki, K. Nitta *J. Mol. Biol.* **1999**, *292*, 1137–1148.
77 M. Mizuguchi, K. Masaki, M. Demura, K. Nitta *J. Mol. Biol.* **2000**, *298*, 985–995.
78 Y. Kobashigawa, M. Demura, T. Koshiba, Y. Kumaki, K. Kuwajima, K. Nitta *Proteins* **2000**, *40*, 579–589.
79 M. Joniau, P. Haezebrouck, K. Noyelle, H. Van Dael *Proteins* **2001**, *44*, 1–11.
80 H. Van Dael, P. Haezebrouck, M. Joniau *Protein Sci.* **2003**, *12*, 609–619.
81 J. Kuriyan, S. Wilz, M. Karplus, G. A. Petsko *J. Mol. Biol.* **1986**, *192*, 133–154.
82 Y. V. Griko, P. L. Privalov, S. Y. Venyaminov, V. P. Kutyshenko *J. Mol. Biol.* **1988**, *202*, 127–138.
83 D. Barrick, R. L. Baldwin *Biochemistry* **1993**, *32*, 3790–3796.
84 P. E. Wright, R. L. Baldwin *Mechanisms of Protein Folding*, 2nd edn. Oxford University Press, Oxford, **2000**.
85 S. N. Loh, M. S. Kay, R. L. Baldwin *Proc. Natl Acad. Sci. USA* **1995**, *92*, 5446–5450.
86 M. Jamin, R. L. Baldwin *J. Mol. Biol.* **1998**, *276*, 491–504.
87 G. W. Bushnell, G. V. Louie, G. D. Brayer *J. Mol. Biol.* **1990**, *214*, 585–595.

88 M. F. Jeng, S. W. Englander, G. A. Elove, A. J. Wand, H. Roder *Biochemistry* **1990**, *29*, 10433–10437.

89 W. Colon, G. A. Eloeve, L. P. Wakem, F. Sherman, H. Roder *Biochemistry* **1996**, *35*, 5538–5549.

90 W. Colon, H. Roder *Nat. Struct. Biol.* **1996**, *3*, 1019–1025.

91 P. L. Privalov, S. J. Gill *Adv. Protein Chem.* **1988**, *39*, 191–234.

92 Y. V. Griko, E. Freire, P. L. Privalov *Biochemistry* **1994**, *33*, 1889–1899.

93 Y. V. Griko, P. L. Privalov *J. Mol. Biol.* **1994**, *235*, 1318–1325.

94 Y. V. Griko *J. Mol. Biol.* **2000**, *297*, 1259–1268.

95 S. Potekhin, W. Pfeil *Biophys. Chem.* **1989**, *34*, 55–62.

96 J. H. Carra, E. A. Anderson, P. L. Privalov *Protein Sci.* **1994**, *3*, 952–959.

97 T. Koshiba, Y. Kobashigawa, M. Demura, K. Nitta *Protein Eng.* **2001**, *14*, 967–974.

98 J. H. Carra, E. A. Anderson, P. L. Privalov *Biochemistry* **1994**, *33*, 10842–10850.

99 I. Nishii, M. Kataoka, Y. Goto *J. Mol. Biol.* **1995**, *250*, 223–238.

100 M. S. Kay, R. L. Baldwin *Nat. Struct. Biol.* **1996**, *3*, 439–445.

101 Y. Z. Luo, M. S. Kay, R. L. Baldwin *Nat. Struct. Biol.* **1997**, *4*, 925–930.

102 M. S. Kay, C. H. Ramos, R. L. Baldwin *Proc. Natl Acad. Sci. USA* **1999**, *96*, 2007–2012.

103 Y. Hagihara, Y. Tan, Y. Goto *J. Mol. Biol.* **1994**, *237*, 336–348.

104 K. Kuwajima, Y. Hiraoka, M. Ikeguchi, S. Sugai *Biochemistry* **1985**, *24*, 874–881.

105 M. Ikeguchi, K. Kuwajima, M. Mitani, S. Sugai *Biochemistry* **1986**, *25*, 6965–6972.

106 M. Arai, K. Kuwajima *Fold. Des.* **1996**, *1*, 275–287.

107 G. V. Semisotnov, H. Kihara, N. V. Kotova et al. *J. Mol. Biol.* **1996**, *262*, 559–574.

108 H. Roder, G. A. Eloeve, S. W. Englander *Nature* **1988**, *335*, 700–704.

109 P. A. Jennings, P. E. Wright *Science* **1993**, *262*, 892–896.

110 A. Miranker, C. V. Robinson, S. E. Radford, R. T. Aplin, C. M. Dobson *Science* **1993**, *262*, 896–900.

111 T. M. Raschke, S. Marqusee *Nat. Struct. Biol.* **1997**, *4*, 298–304.

112 V. Tsui, C. Garcia, S. Cavagnero, G. Siuzdak, H. J. Dyson, P. E. Wright *Protein Sci.* **1999**, *8*, 45–49.

113 C. Nishimura, H. J. Dyson, P. E. Wright *J. Mol. Biol.* **2002**, *322*, 483–489.

114 S. Cavagnero, H. J. Dyson, P. E. Wright *J. Mol. Biol.* **1999**, *285*, 269–282.

115 S. Cavagnero, C. Nishimura, S. Schwarzinger, H. J. Dyson, P. E. Wright *Biochemistry* **2001**, *40*, 14459–14467.

116 C. Nishimura, P. E. Wright, H. J. Dyson *J. Mol. Biol.* **2003**, *334*, 293–307.

117 T. M. Raschke, J. Kho, S. Marqusee *Nat. Struct. Biol.* **1999**, *6*, 825–831.

118 J. Balbach, V. Forge, N. A. van Nuland, S. L. Winder, P. J. Hore, C. M. Dobson *Nat. Struct. Biol.* **1995**, *2*, 865–870.

119 J. Balbach, V. Forge, W. S. Lau, N. A. J. Van Nuland, K. Brew, C. M. Dobson *Science* **1996**, *274*, 1161–1163.

120 M. Roy, P. A. Jennings *J. Mol. Biol.* **2003**, *328*, 693–703.

121 C. M. Jones, E. R. Henry, Y. Hu et al. *Proc. Natl Acad. Sci. USA* **1993**, *90*, 11860–11864.

122 T. Pascher, J. P. Chesick, J. R. Winkler, H. B. Gray *Science* **1996**, *271*, 1558–1560.

123 B. Nolting *Biochem. Biophys. Res. Commun.* **1996**, *227*, 903–908.

124 R. M. Ballew, J. Sabelko, M. Gruebele *Proc. Natl Acad. Sci. USA* **1996**, *93*, 5759–5764.

125 C. K. Chan, Y. Hu, S. Takahashi, D. L. Rousseau, W. A. Eaton, J. Hofrichter *Proc. Natl Acad. Sci. USA* **1997**, *94*, 1779–1784.

126 S. Takahashi, S. R. Yeh, T. K. Das, C. K. Chan, D. S. Gottfried, D. L. Rousseau *Nat. Struct. Biol.* **1997**, *4*, 44–50.

127 M. C. R. Shastry, S. D. Luck, H. Roder *Biophys. J.* **1998**, *74*, 2714–2721.

128 L. Pollack, M. W. Tate, N. C. Darnton et al. *Proc. Natl Acad. Sci. USA* **1999**, *96*, 10115–10117.

129 M. Gruebele *Annu. Rev. Phys. Chem.* **1999**, *50*, 485–516.

130 T. Uzawa, S. Akiyama, T. Kimura et al. *Proc. Natl Acad. Sci. USA* **2004**, *101*, 1171–1176.

131 M. C. R. Shastry, H. Roder *Nat. Struct. Biol.* **1998**, *5*, 385–392.

132 S. Akiyama, S. Takahashi, K. Ishimori, I. Morishima *Nat. Struct. Biol.* **2000**, *7*, 514–520.

133 S. Akiyama, S. Takahashi, T. Kimura et al. *Proc. Natl Acad. Sci. USA* **2002**, *99*, 1329–1334.

134 G. A. Eloeve, A. F. Chaffotte, H. Roder, M. E. Goldberg *Biochemistry* **1992**, *31*, 6876–6883.

135 H. Roder, W. Colon *Curr. Opin. Struct. Biol.* **1997**, *7*, 15–28.

136 J. M. Sauder, H. Roder *Fold. Des.* **1998**, *3*, 293–301.

137 D. K. Heidary, L. A. Gross, M. Roy, P. A. Jennings *Nat. Struct. Biol.* **1997**, *4*, 725–731.

138 W. F. Walkenhorst, S. M. Green, H. Roder *Biochemistry* **1997**, *36*, 5795–5805.

139 K. Maki, T. Ikura, T. Hayano, N. Takahashi, K. Kuwajima *Biochemistry* **1999**, *38*, 2213–2223.

140 K. Kamagata, Y. Sawano, M. Tanokura, K. Kuwajima *J. Mol. Biol.* **2003**, *332*, 1143–1153.

141 D. K. Heidary, J. C. O'Neill, M. Roy, P. A. Jennings *Proc. Natl Acad. Sci. USA* **2000**, *97*, 5866–5870.

142 A. P. Capaldi, M. C. Shastry, C. Kleanthous, H. Roder, S. E. Radford *Nat. Struct. Biol.* **2001**, *8*, 68–72.

143 S. Khorasanizadeh, I. D. Peters, H. Roder *Nat. Struct. Biol.* **1996**, *3*, 193–205.

144 S. H. Park, M. C. R. Shastry, H. Roder *Nat. Struct. Biol.* **1999**, *6*, 943–947.

145 J. M. Finke, P. A. Jennings *Biochemistry* **2002**, *41*, 15056–15067.

146 S. Gianni, C. Travaglini-Allocatelli, F. Cutruzzola, M. Brunori, M. C. Shastry, H. Roder *J. Mol. Biol.* **2003**, *330*, 1145–1152.

147 A. R. Viguera, J. C. Martinez, V. V. Filimonov, P. L. Mateo, L. Serrano *Biochemistry* **1994**, *33*, 2142–2150.

148 V. P. Grantcharova, D. Baker *Biochemistry* **1997**, *36*, 15685–15692.

149 J. I. Guijarro, C. J. Morton, K. W. Plaxco, I. D. Campbell, C. M. Dobson *J. Mol. Biol.* **1998**, *276*, 657–667.

150 K. W. Plaxco, J. I. Guijarro, C. J. Morton, M. Pitkeathly, I. D. Campbell, C. M. Dobson *Biochemistry* **1998**, *37*, 2529–2537.

151 N. Ferguson, A. P. Capaldi, R. James, C. Kleanthous, S. E. Radford *J. Mol. Biol.* **1999**, *286*, 1597–1608.

152 D. Perl, C. Welker, T. Schindler et al. *Nat. Struct. Biol.* **1998**, *5*, 229–235.

153 R. E. Burton, G. S. Huang, M. A. Daugherty, P. W. Fullbright, T. G. Oas *J. Mol. Biol.* **1996**, *263*, 311–322.

154 M. L. Scalley, Q. Yi, H. D. Gu, A. McCormack, I. I. I. Yates JR, D. Baker *Biochemistry* **1997**, *36*, 3373–3382.

155 S. E. Jackson, A. R. Fersht *Biochemistry* **1991**, *30*, 10428–10435.

156 K. Kamagata, M. Arai, K. Kuwajima *J. Mol. Biol.* **2004**, *339*, 951–965.

157 D. E. Makarov, K. W. Plaxco *Protein Sci.* **2003**, *12*, 17–26.

158 V. Grantcharova, E. J. Alm, D. Baker, A. L. Horwich *Curr. Opin. Struct. Biol.* **2001**, *11*, 70–82.

159 C. Micheletti *Proteins* **2003**, *51*, 74–84.

160 K. W. Plaxco, K. T. Simons, D. Baker *J. Mol. Biol.* **1998**, *277*, 985–994.

161 I. E. Sanchez, T. Kiefhaber *J. Mol. Biol.* **2003**, *325*, 367–376.

162 Y. Bai *Biochem. Biophys. Res. Commun.* **2003**, *305*, 785–788.

163 G. M. Spudich, E. J. Miller, S. Marqusee *J. Mol. Biol.* **2004**, *335*, 609–618.

164 C. Tanford *Adv. Protein Chem.* **1970**, *24*, 1–95.

165 C. D. Snow, H. Nguyen, V. S. Pande, M. Gruebele *Nature* **2002**, *420*, 102–106.

166 M. Engelhard, P. A. Evans *Protein Sci.* **1995**, *4*, 1553–1562.

24
Alcohol- and Salt-induced Partially Folded Intermediates

Daizo Hamada and Yuji Goto

24.1
Introduction

The structures and stabilities of proteins are perturbed by additives such as small organic and inorganic molecules. In this chapter, we discuss the effects of alcohols and salts on inducing partially folded intermediates of proteins. These co-solvents are expected to stabilize otherwise unstable folding intermediates. They can also reveal the conformational preference of the intermediate or unfolded states. This information is valuable for characterizing the structure and stability of the folding intermediates under physiological conditions in the absence of co-solvents. Since this chapter focuses on the effects on the intermediate and unfolded states among various effects on proteins, readers should refer to other reviews on the general effects of alcohols [1, 2] and salts [3–7] on proteins.

In the early 1960s, Tanford and coworkers performed pioneering studies about the effects of organic solvents on the conformational properties of proteins using optical rotatory dispersion (ORD) [3, 4, 8]. For example, the conformational transition of bovine ribonuclease A induced by the addition of 2-chloroethanol into aqueous solvent occurred in two distinct stages involving partial unfolding of the native structure followed by the formation of an α-helical structure. A similar conformational change was also observed for bovine β-lactoglobulin [3, 4] and diisopropylphosphoryl chymotrypsin [9]. Recently, circular dichroism (CD) spectroscopy has become more popular than ORD because of the simplicity in the interpretation of data. However, the results obtained by CD provide essentially the same information as can be obtained by ORD. Further information about the effects of alcohols can be analyzed even to atomic resolution by solution nuclear magnetic resonance (NMR) spectroscopy.

Alcohols are basically categorized as denaturants, as are guanidinium hydrochloride (GdmCl) or urea. Although GdmCl and urea induce random coil structures, alcohols tend to stabilize well-ordered conformations such as α-helical structures. According to the review by Tanford [3], Imahori and Doty first recognized that a high proportion of α-helical proteins form α-helical structures in 2-chloroethanol. Similar effects have been found for many other alcohols. Importantly, Herskovits and Mescanti [10] have reported that α_8-casein, a typical natively

Protein Folding Handbook. Part I. Edited by J. Buchner and T. Kiefhaber

ISBN: 3-527-30784-2

unfolded protein [11–14] is also converted into an α-helical structure in the presence of 2-chloroethanol or methanol. Although a significant number of α-helical structures are formed by alcohols, they are certainly not equivalent to the native conformation and are classified as denatured conformations, which lack the native protein's functions.

The properties of alcohols that induce the conformational change in proteins are also widely used for analyzing the intrinsic structural preference of proteins and peptides, particularly to analyze the kinetic intermediates accumulating at the early stages of folding. Although proteins assume significant levels of nonnative α-helical conformations at high concentrations of alcohols, several short peptides form β-turn or β-hairpin conformations according to the structural preference of the amino acid sequence [15–22]. The structures formed in alcohol/water solvent somehow mimic the properties of early intermediates in protein folding, since both structures are stabilized predominantly by local interactions which are formed between residues near each other in amino acid sequence (Figure 24.1) [23, 24]. Moreover, the molten globule state, a compact denatured state with a significant amount of native-like secondary structures but with fluctuating tertiary structures [25–29] (see Chapter 23), is sometimes observed during the alcohol-induced denaturation of several proteins under moderate concentrations of alcohols. Thus, alcohols have the potential to stabilize different types of partially folded structures of polypeptide chains depending on the alcohol species and concentration ranges used (Figure 24.2). It is noted that, in this chapter, our definition of the molten globule state is not as strict as the original proposal and can be also used for the compact denatured state with some native-like secondary structures.

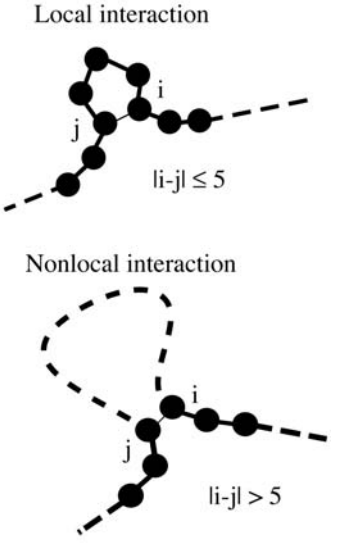

Fig. 24.1. Local (a) and nonlocal (b) interactions [23]. In the figure, circles represent each amino acid. The local interactions are formed between residues near each other in the amino acid sequence, whereas the nonlocal interactions are formed between residues apart each other in the sequence.

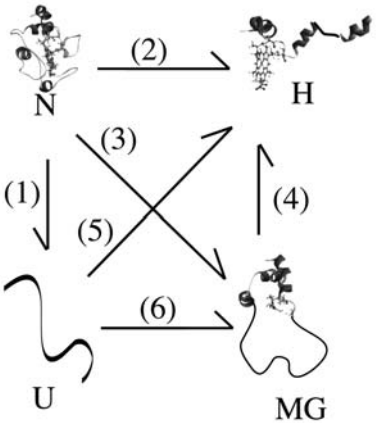

Fig. 24.2. Conformational transitions of proteins. N, native; U, fully unfolded; MG, molten globule; H, alcohol-induced helical states. Transitions by denaturants (GdmCl or urea) or at extreme pH (1), by strong helix inducers such as TFE or HFIP (2), by moderate concentrations of weak helix induces such as methanol or ethanol (3), by high concentrations of weak helix induces (4), by alcohols at extreme pH (5) and by anions at acidic pH (6) are represented schematically.

Salts have been used widely for various purposes in the preparation and characterization of proteins, including salt-induced precipitation (salting out), dissolution of proteins (salting in), and stabilizing or destabilizing protein structures [5–7] (see Chapter 3). Among them, denaturation of proteins by GdmCl is one of the most important applications of salt effects on proteins; we can understand the conformational stability of proteins on the basis of the salt-induced denaturation [1, 3, 4]. However, the findings that horse cytochrome *c* and several proteins form the molten globule intermediate in the presence of salts, as will be described in detail in this chapter, attracted much attention on the salt effects, suggesting that salts might be useful for specifically stabilizing the folding intermediates. Salt-stabilized molten globule states have been the target of extensive studies addressing the conformation and stability of the folding intermediates. In particular, characterization of the salt-dependent conformational changes of acid-denatured proteins have revealed a more clear view of the acid denaturation and effects of ions in modulating the conformations of the intermediate and unfolded states.

24.2
Alcohol-induced Intermediates of Proteins and Peptides

24.2.1
Formation of Secondary Structures by Alcohols

Alcohols promote the formation of ordered secondary structures in disordered polypeptide chains. The effectiveness of alcohols in inducing the conforma-

tional transition varies substantially (see below). Among various alcohols, 2,2,2-trifluoroethanol (TFE) is often used because of its relatively strong effects and low absorbance in the far-UV region, which makes far-UV CD measurements feasible. 1,1,1,3,3,3-hexafluoro-2-propanol (HFIP) has a higher potential than TFE to induce the alcohol-dependent effects, although the formation of alcohol clusters might complicate the interpretation of the alcohol effects (see below).

For many disordered peptides, α-helical structures are induced because they are stabilized by the most local interactions, but various peptides assume β-hairpin or β-turn structures in alcohol/water solvents [15–22]. Importantly, these secondary structures are all stabilized by local hydrogen bonds. The formation of β-sheet structures, which need a network of nonlocal hydrogen bonds, is not usually expected for short peptides unless the peptide molecules are associated into oligomeric structures or aggregates. Nevertheless, there are several examples of longer polypeptides or proteins, including tendamistat and leucocin A [30, 31], showing stabilization of β-sheet structures.

Thus, the exact types of secondary structures stabilized in alcohol/water solvent depend on the amino acid sequence. The intrinsic structural preference of each amino acid sequence is an important factor in determining the types of secondary structures in alcohol/water solvent [15–22, 30–39]. The ability of alcohols to induce the particular secondary structures is, therefore, useful to analyze the intrinsic conformational propensity of a short peptide with no appreciable ordered conformation in aqueous solution. The peptide conformation induced in alcohol/water solvent can be readily analyzed by conventional CD or solution NMR methods. These methods are also useful in detecting the structural properties of early intermediate of protein folding [32, 36, 39–42].

The same experimental system has been successfully applied to elucidate the conformational stabilities and properties of less structured de novo designed proteins in water solvent [19–20]. As is the case for short peptides, de novo proteins often fail to assume ordered conformations in water. In such a case, the addition of alcohol induces the formation of otherwise unstable secondary structures. By analyzing the alcohol-dependent transition, one can estimate the stability of the ordered conformation in water. Such an analysis is helpful to optimize the sequence of de novo proteins in order to create a rigid native-like structure even in the absence of alcohols. Furthermore, the structural properties of membrane proteins can be analyzed in alcohol/water solvent by solution NMR spectroscopy [43–46].

Interestingly, a high correlation was found between the α-helical content expected from secondary structure prediction based on amino acid sequence and the α-helical content estimated by CD in the presence of high concentrations of TFE [47, 48]. This observation supports the idea that the local interactions are dominant in the alcohol-induced protein conformations. Conventional secondary structure predictions consider mainly local interactions. A lesser correlation was found between the α-helical content in the native structure and that in the TFE state, indicating the role of nonlocal interactions for stabilizing the native structures. The α-helical content of the alcohol-induced state tends to be larger than that of the native state. Thus, the TFE-induced structures of polypeptide chains should contain a significant amount of nonnative α-helices.

24.2.2 Alcohol-induced Denaturation of Proteins

As described above, alcohols were originally used as denaturants. However, alcohols are not the first choice reagent for the analysis of protein stability since uncertainty exists in the thermodynamic interpretation of alcohol-induced states. Moreover, alcohols tend to induce nonspecific aggregates of proteins at neutral pH, probably because of the reduced electrostatic repulsion between protein molecules. Therefore, studies have often been performed under acidic conditions where the solubility of proteins in alcohol/water solvent increases.

Shiraki et al. [48] analyzed the effects of TFE on protein conformation using various types of proteins with different secondary structures. The transitions induced by TFE were monitored by far-UV CD. The transition curves obtained by plotting the ellipticity at 222 nm as a function of TFE concentration consisted of two phases. The initial transition was relatively cooperative showing an increase in α-helical content at a certain TFE concentration. At neutral pH, the concentration range of this transition was predominantly determined by the stability of native structure. On the other hand, at acidic pH $\sim$ 2, many proteins were unfolded in the absence of TFE. For most of these unfolded proteins at pH 2, the induction of α-helical structure was observed in the TFE concentrations of 10–20% (v/v). For proteins with a relatively low propensity toward α-helices, the α-helical content just after the first transition was low, but, in the second stage, it gradually increased with further increases in the TFE concentration. When the intrinsic α-helical propensity is high, the posttransitional increase in α-helical content was less obvious because the helical content achieved after the first cooperative transition is already high.

The transition curves observed, for example by the far-UV CD, can be simply analyzed by assuming a two-state mechanism between the native and alcohol-induced states (see chapter by Pace and Scholtz for details of two-state analysis). In most cases, this method works well, providing two parameters, namely $\Delta G(H_2O)$ (a free energy change between the native and TFE states) and the *m*-value (a measure of cooperativity of transition). The value of $\Delta G(H_2O)$ provided by a such treatment is often consistent with the value obtained from the analysis of GdmCl or urea unfolding curves [2]. This is rather surprising since the TFE denatured state with highly ordered secondary structures is unlikely to be thermodynamically equivalent to the GdmCl unfolded state. Unlike the native state, the denatured state consists of an ensemble of nonnative conformations. Thus, a conformation similar to the alcohol-induced state possibly pre-exists at a low level in such an ensemble of denatured structures even under the native conditions.

The TFE-induced states of several proteins, for example hen lysozyme and bovine β-lactoglobulin, have been well characterized by high-resolution heteronuclear NMR [49, 50]. The chemical shifts of NMR spectra for the TFE state show less dispersed signals compared to the native structures. Beside this, a number of nuclear Overhauser effects (NOEs) consistent with the presence of α-helices can be observed. Other information on the secondary structure, extracted from a chemical

shift index or coupling constants, also provides the evidence for the presence of α-helices. On the other hand, the backbone amide hydrogens are much less protected against hydrogen/deuterium exchange even though significant parts of the protein molecule are in an α-helical conformation. Thus, the secondary structures formed in the TFE state are mobile, and parts of polypeptide chain are rapidly interconverted to the extended configurations. In accordance with this, small-angle solution X-ray scattering indicated that the TFE-induced state of hen lysozyme possesses a chain-like character as is the case of fully unfolded structures in high concentrations of urea or GdmCl [51]. On the other hand, the radius of gyration of the TFE state was between the fully unfolded state and the compact native state. Taken together, the TFE state is considered to be an "open helical conformation" in which the α-helical rods are exposed to the solvent because of the absence of strong hydrophobic attraction between them, contrasting with the compact molten globule stabilized by salt. Similar results were obtained with the methanol-induced α-helical states of horse cytochrome *c* [52] and horse apomyoglobin [53].

24.2.3
Formation of Compact Molten Globule States

Although the alcohol-induced denaturation of proteins is often approximated by a two-state mechanism between the native and TFE-induced α-helical states, accumulation of the molten globule-like intermediate during the transition is sometimes observed in several proteins (Table 24.1) [52–67]. Generally speaking, the alcohols having less potential to induce α-helical structures seem to have a higher potential to induce a three-state transition with a molten globule intermediate. However, even an effective helix inducer such as TFE sometimes stabilizes the molten globule state, as has been shown for α-lactalbumin [60]. Interestingly, many such proteins are also known to form the molten globule states in the pres-

Tab. 24.1. Alcohol or salt-induced molten globule state under equilibrium conditions.

Protein	*Conditions*	*Reference*
Apomyoglobin	Salt at acidic pH	103
	Methanol at acidic pH	53
	HFIP at acid pH	67
β-Conglycinin	Ethanol at acidic pH	64
Cytochrome c	Salt at acidic pH	25, 112
	Methanol at acidic pH	54, 52, 57
	Glycerol at acidic pH	66, 59
	Polyol at acidic pH	61
Ervatamin C	Methanol at acidic pH	62
Retinol-binding protein	Methanol at acidic pH	55
β-Lactamase	Salt at acidic pH	102
α-Lactalbumin	TFE at acidic pH	60, 65
Lysozyme	3-Chloro-1,2-propanediol at acidic pH	63

ence of moderate concentrations of urea or GdmCl or by addition of salts in the acid-denatured state (Table 24.1).

The molten globule state is often found in the presence of moderate concentrations of alcohols. Higher concentrations of alcohols tend to stabilize the extended highly α-helical conformation as described above. The mechanism of how alcohols induce such a three-state transition with the molten globule intermediate is still ambiguous. A significant number of the native tertiary contacts between hydrophobic side chains are disrupted in the alcohol state. At the same time, the nonpolar environment introduced by alcohols forces the polypeptide chains to form nonnative α-helices. In the presence of moderate concentrations of alcohol, it is likely that such effects of alcohols are less obvious, so that some proteins remain in a compact denatured state with native-like secondary structures.

24.2.4 Example: β-Lactoglobulin

Alcohol can induce α-helical conformations even in proteins consisting of predominantly β-sheets. Most all-β proteins tend to show a less significant increase in α-helical content in alcohol/water solvents. An interesting example revealing a dramatic increase of α-helical content is bovine β-lactoglobulin. The native structure of β-lactoglobulin consists of nine antiparallel β-strands and a long α-helix at the C-terminal region (Figure 24.3A). Shiraki et al. [48] demonstrated that bovine β-lactoglobulin exhibits an extremely high α-helical content upon the addition of TFE (Figure 24.3B). Our systematic analysis of peptide fragments derived from the β-sheet regions of β-lactoglobulin demonstrated that the peptide fragments also have a high α-helical preference [36, 39]. As discussed above, the conformational propensity of peptide fragments in TFE/water solvent is thought to reproduce the situation of early intermediates formed during the refolding processes. Therefore, the intermediate with nonnative α-helical structures is assumed to be accumulated at the early folding stage of β-lactoglobulin. This was confirmed later by the study of folding kinetics using stopped-flow CD in the absence and presence of TFE [68–71].

Bovine β-lactoglobulin assumes a monomeric native state at pH 2, while it is dimeric at neutral pH. In addition, the presence of a free thiol group (Cys121) in addition to two disulfide bonds (Cys66-Cys16 and Cys106-Cys119) (Figure 24.3A) complicates the refolding experiments because of possible thiol/disulfide exchange reactions in the unfolded state [72]. Therefore, the refolding of β-lactoglobulin was initiated by diluting the unfolded protein in a high concentration of GdmCl at pH 2.0 into the refolding buffer at the same pH, and the folding kinetics were monitored by ellipticity measurements at 222 nm. Usually, the signal is expected to change from the unfolded baseline to the value of the native state (Figure 24.4). Contrary to expectation, the ellipticity at 222 nm exceeded the value of the native baseline at the burst phase and subsequently it slowly returned toward the native value. This suggested the transient formation of nonnative α-helices. Similar kinetic traces were monitored at various wavelengths to construct the far-UV CD

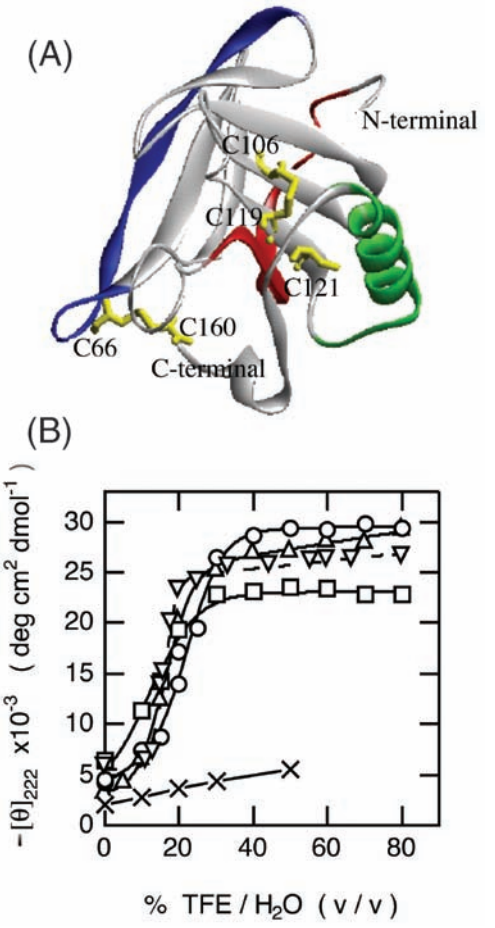

Fig. 24.3. Structure of native β-lactoglobulin (A) and the transitions of its peptide fragments by TFE (B). A) The positions of the fragments are represented by red (fragment 1), blue (fragment 2) and green (fragment 3). The cysteine residues are also shown by yellow. B) The transitions by fragment 1 (circle), fragment 2 (triangle) and fragment 3 (square) are shown. The transitions by intact β-lactoglobulin (reverse triangle) and I4 fragment from hen lysozyme (cross; taken from Ref. [32]) are also shown for comparison. Panel B reproduced from Ref. [36] with permission.

spectrum of the burst phase intermediate (Figure 24.4). The spectrum shows a clear minimum around 222 nm, confirming the presence of an increased amount of α-helical structure. The addition of 9.8% (v/v) TFE in the refolding buffer further increased the α-helical content of the burst phase intermediate, supporting the mechanism that the nonnative α-helices are formed at the early stage of the folding reaction of β-lactoglobulin.

A detailed analysis of the early intermediates of β-lactoglobulin was performed using ultra-rapid mixing techniques in conjunction with fluorescence detection

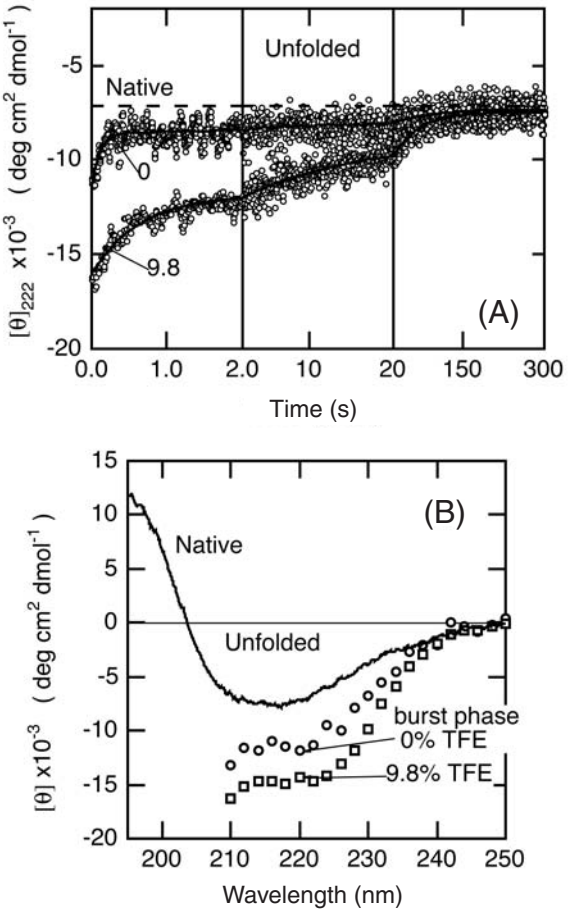

Fig. 24.4. Refolding kinetics of β-lactoglobulin in the presence and absence of TFE detected by stopped-flow CD. A) Time traces for refolding kinetics. The raw data are indicated by circles. The numbers refer to the final concentration of TFE in % (v/v). The ellipticities at 222 nm of the native and unfolded states are indicated by dashed and dotted lines, respectively. B) Far-UV CD spectra of the burst phase intermediate in the absence (circle) and presence (square) of 9.8% TFE. The CD spectra of the native and unfolded states are shown by solid and dotted lines, respectively. Reproduced from Ref. [69] with permission.

and hydrogen/deuterium exchange labeling probed by heteronuclear NMR [70, 71]. It has been shown that the βA-strand region is involved in the formation of nonnative α-helical structures (Figure 24.5). On the other hand, the data also suggested that, in the early intermediate, the native-like structure is also formed around the βG and βH-strands. This region corresponds to the hydrophobic core in the native structure, and both β-strands are linked by disulfide bonds between Cys106 and Cys119. These properties around the βG and βH strands are likely to

play an important role in the initial stage of the folding reaction of β-lactoglobulin [73]. On the other hand, the role of nonnative α-helices in the early intermediate state is still unknown. Indeed, the formation of such nonnative secondary structures might be less effective in terms of rapid folding since the structure should be disrupted at the later stage of folding. It is probable, however, that the formation of nonnative α-helical segments is useful for preventing intermolecular aggregation since the polypeptide chain becomes relatively compact. The folding mechanism of β-lactoglobulin is still intriguing to understand the interplay between the local and nonlocal interactions during protein folding, and moreover, to understand the α–β transition suggested from several biologically important processes [74, 75].

24.3 Mechanism of Alcohol-induced Conformational Change

Although alcohols are often used to probe the structural preferences of polypeptide chains, the detailed mechanism of how these co-solvents induce the conformational change of polypeptide chains is still debatable. The chemical properties of alcohols are relatively similar to detergents in a sense that the molecules consist of both hydrophobic (hydrocarbon or halogenated hydrocarbon) and hydrophilic (hydroxyl) groups. Possible mechanisms by which alcohols induce conformational changes in polypeptides, therefore, include (1) destabilizing intramolecular hydrophobic interactions and (2) promoting the formation of local backbone hydrogen bonds [23, 24, 76–79]. In alcohol/water solvents with low polarity or low dielectric constant, hydrophobic interactions stabilizing the native structure are weakened and instead the local hydrogen bonds are strengthened, resulting in denaturation and the simultaneous formation of an ''open helical conformation'' or ''open helical coil'', i.e., solvent-exposed helices.

In the case of nonhalogenated alcohols, the efficiency as a helix inducer linearly increases with an increase in the number of carbon atoms in an alcohol molecule [80, 81]. This confirms that the hydrophobic interactions play an important role in the alcohol effects. Although an alcohol is defined by the presence of hydroxyl (OH) group(s), the contribution of the OH group to the alcohol effects is negative. In other words, alcohol effects arise from the dissolved hydrophobic groups, and the OH group is important mainly for dissolving otherwise insoluble hydrocarbon groups into water. In this sense, halogenated alcohols might be expected to be poor alcohols in stabilizing α-helical structures in polypeptide chains, since the halogen atoms have a larger electronegativity than hydrogen atoms. In contrast, halogenated alcohols such as TFE and HFIP have higher potentials to induce the α-helical conformation than nonhalogenated alcohols. Systematic analysis of various halogenated alcohols indicated that the effect of fluoride is the lowest of the various halogens [80, 81]. Nevertheless, the low absorbance of fluoride in the far-UV region makes TFE and HFIP the most useful alcohols to examine the alcohol effects on proteins by CD.

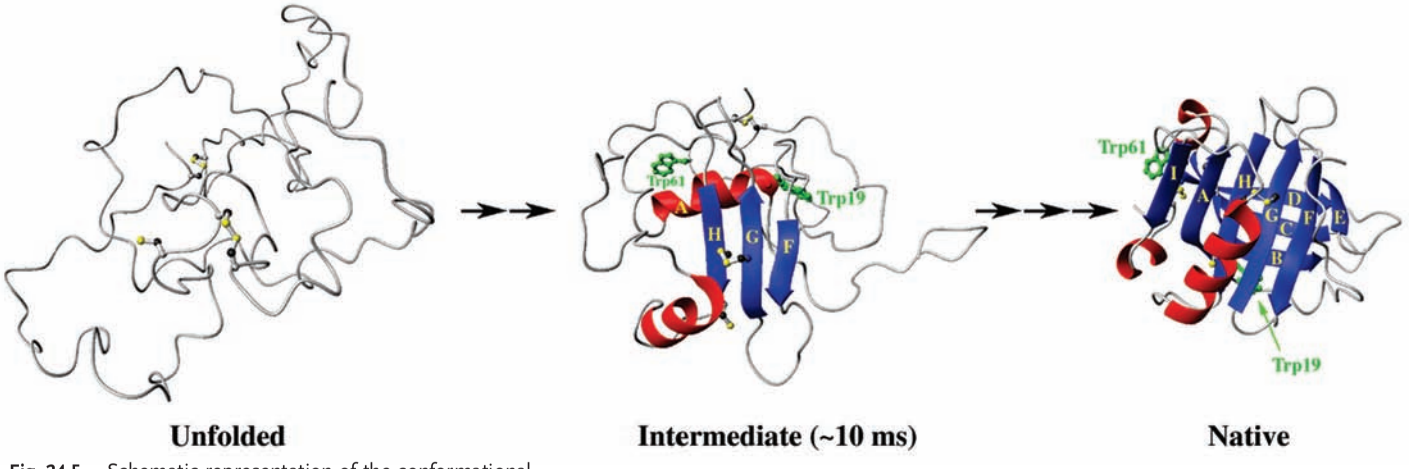

Fig. 24.5. Schematic representation of the conformational states encountered during folding of β-lactoglobulin, including the unfolded ensemble, a partially structured intermediate populated on the millisecond time scale and the native state. Reproduced from Ref. [71] with permission.

Importantly, studies with solution X-ray scattering provided the evidence that water/alcohol mixtures of some halogenated alcohols such as TFE or HFIP assume micelle-like clusters [82]. This suggests that the halogenated alcohols in fact have higher hydrophobicity than nonhalogenated ones, producing dynamically hydrophobic clusters of alcohols, which can interact effectively with protein molecules, thus enhancing the alcohol effects on proteins. In other words, the direct interactions between proteins and alcohol molecules by hydrophobic interactions play an important role in the alcohol effects on proteins.

From a systematic analysis of the alcohol-induced transitions of melittin, a basic and amphiphilic peptide of 26 amino acid residues present in honey bee venom, Hirota et al. [80, 81] indicated that the effects of each alcohol can be rationalized by the additive contribution from the hydrocarbon (CH), hydroxyl (OH), and halogen groups (F, Cl, and Br), providing the following equations for the *m*-value, a measure of the cooperativity for the alcohol-induced transition:

$$m = a\ \mathrm{ASA(CH)} + b\ \mathrm{ASA(OH)} + c\ \mathrm{ASA(F)} + d\ \mathrm{ASA(Cl)} + e\ \mathrm{ASA(Br)} \quad (1)$$

$$m = a\ [\mathrm{ASA(CH)}]^2 + b\ [\mathrm{ASA(OH)}]^2 + c\ [\mathrm{ASA(F)}]^2 + d\ [\mathrm{ASA(Cl)}]^2 + e\ [\mathrm{ASA(Br)}]^2 \quad (2)$$

where ASA(X) corresponds to the accessible surface area of each group X and the value of a, b, c, d, and e are the empirically determined proportionality coefficients which are summarized in Table 24.2. Equation (2) provides a better fit than Eq. (1) when the effects of TFE and HFIP are included. It is noted that the coefficient for the OH group is negative while others are positive. A similar relationship was observed for the alcohol-induced denaturation of β-lactoglobulin [83].

These results indicate the importance of the direct interaction between alcohols and polypeptide molecules. Accordingly, the results from NMR spectroscopy and molecular dynamics simulations suggested that TFE molecules preferentially bind to the backbone carbonyl oxygen group and minimize the solvent exposure of amide hydrogen groups, leading to the stabilization of intramolecular hydrogen bonds in a polypeptide chain [84–88].

These results, moreover, suggest that alcohols will be useful for dissolving protein aggregates stabilized by hydrophobic interactions. In fact, some alcohols such

Tab. 24.2. Fitting coefficients of the $m(\mathrm{ts})^a$ and $m(\mathrm{hc})^b$ values for Eqs (1) and (2).

	a	*b*	*c*	*d*	*e*
Two-state mechanism (m(TS))					
Eq. (1)	0.0251	−0.0197	0.0716	0.0558	0.0998
Eq. (2)	1.06×10^{-4}	-4.54×10^{-5}	3.83×10^{-4}	5.89×10^{-4}	1.34×10^{-3}
Helix/coil mechanism (m(HC))					
Eq. (1)	0.840	0.639	1.92	2.12	3.72
Eq. (2)	3.53×10^{-3}	1.41×10^{-3}	2.05×10^{-2}	1.12×10^{-2}	4.95×10^{-2}

Reproduced from table 3 of Ref. [81].

as TFE or HFIP are useful to dissolve aggregates formed during peptide synthesis. HFIP is often used to dissolve prion and Alzheimer's amyloid β-peptides which tend to form aggregates or amyloid fibrils [89–91]. On the other hand, these alcohols, in particular TFE, are known to induce well-ordered fibrillar architectures similar to the amyloid fibrils [92–95]. These observations are apparently inconsistent with each other and understanding of these contrasting phenomena will be of special importance to clarify the alcohol effects.

24.4 Effects of Alcohols on Folding Kinetics

The studies discussed above are mostly concerned with the behavior of polypeptide chains under equilibrium conditions. During protein folding, many different types of interactions including local hydrogen bonds play important roles. A simple question, therefore, arises: how do proteins behave during kinetic refolding in alcohol/water solvents? Interestingly, Lu et al. [96] first found that the folding kinetics of hen lysozyme is accelerated by the presence of low concentrations of TFE below 5.5% (v/v). In the presence of such a small amount of TFE, the protein is still able to fold into the native structure judging from several spectroscopic data including solution NMR. In addition, pulse-labeling studies suggested that the structural properties of folding intermediates of lysozyme are almost unaffected by the presence of TFE.

An extensive analysis using more than 10 proteins revealed that the acceleration of folding kinetics in the presence of a small amount of TFE is common to all of the proteins examined [97] (Figure 24.6). The logarithm of the refolding rate constant linearly increased with an increase in TFE concentration, but then decreased above a certain concentration of TFE. The concentration range that provides the maximum rate of folding depended on the protein species and other conditions such as pH or temperature. Interestingly, for proteins which fold by a two-state manner without accumulating observable intermediates (two-state proteins), the extent of acceleration by TFE correlates well with the amount of local backbone hydrogen bonds in the native structure (Figure 24.7). This behavior could be rationalized by the fact that TFE stabilizes the local hydrogen bonds in the polypeptide chains, thus forming α-helical or β-turn conformations.

On the other hand, for multi-state proteins which accumulate transient intermediates during the folding process, the acceleration of folding by the presence of TFE was always much less than that anticipated from the correlation found for the two-state proteins (Figure 24.7). The multi-state proteins often assume the molten globule intermediate at the burst phase just after the initiation of folding. According to stopped-flow CD or NMR pulse-labeling analysis, a significant amount of native-like secondary structures is formed in the molten globule intermediates. In such intermediates, the native-like local hydrogen bonds should be already formed. Since the rate-limiting step of folding of the multi-state protein is mainly associated with the rearrangement of partially folded subdomains, the number of local

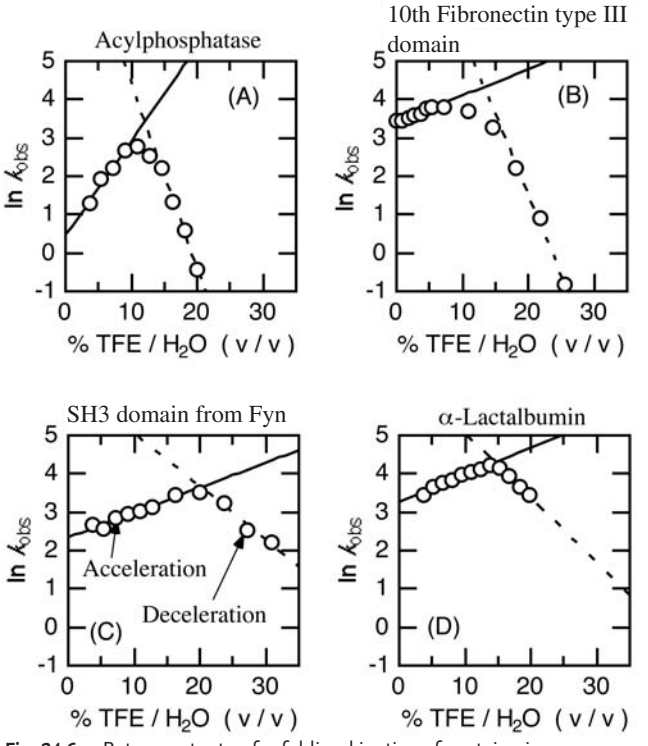

Fig. 24.6. Rate constants of refolding kinetics of proteins in the presence of TFE. Examples are shown for the cases of acylphosphatase (A), 10th type III domain from fibronectin (B), SH3 domain from human Fyn (C), and α-lactalbumin (D). Reproduced from Ref. [97] with permission.

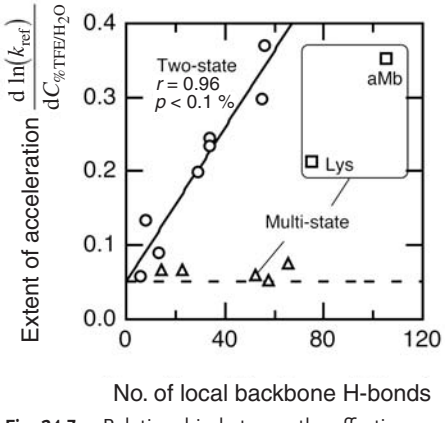

Fig. 24.7. Relationship between the effectiveness of TFE on the acceleration of protein folding and the number of local backbone hydrogen bonds in the native proteins. The data for two-state (circle) and multi-state proteins (triangle and square) are shown. Reproduced from Ref. [97] with permission.

hydrogen bonds which are formed during the rate-limiting step is less than the number in the native structure. The NMR pulse-labeling studies for several proteins have shown that the number of local hydrogen bonds formed in the intermediate states varies depending on proteins. Consistent with this, the acceleration of folding by TFE for multi-state proteins differs significantly even though the number of local hydrogen bonds in the native structure is similar, as is the case for lysozyme and α-lactalbumin.

In the case of acylphosphatase, a two-state protein, the refolding reaction observed by CD indicated that the absolute intensity at 222 nm for the burst phase intermediate increases upon addition of TFE (Figure 24.8), suggesting the formation of partially folded intermediates which do not accumulate in the absence of TFE [98]. The maximum rate of folding was obtained at the TFE concentration where the ellipticity at 222 nm for the burst phase intermediate is the same as that of the native protein. This observation is consistent with the conclusion drawn

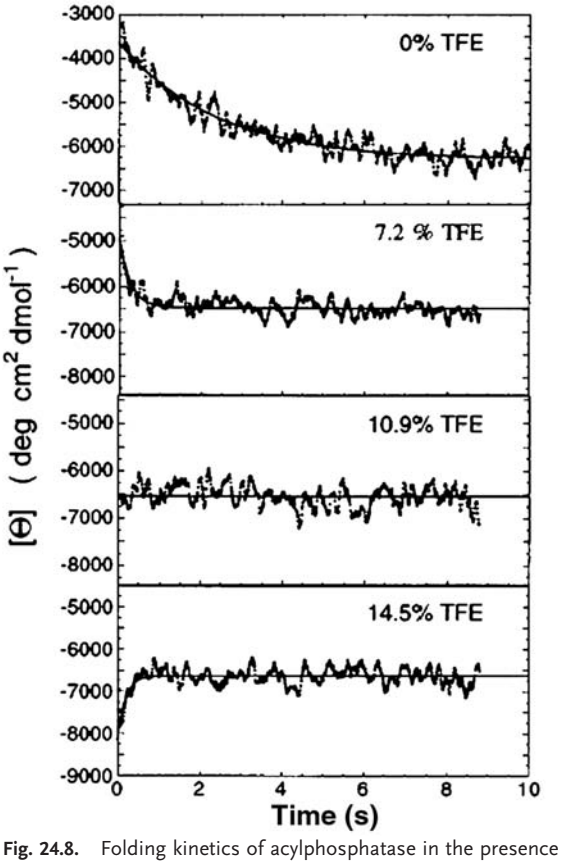

Fig. 24.8. Folding kinetics of acylphosphatase in the presence of TFE monitored by 222 nm far-UV CD. Reproduced from Ref. [98] with permission.

from the analysis of Hammond behavior and nonlinear activation free energy of the folding reaction [99, 100] (see opposing result by Yiu et al. [101]). The analysis indicates that the free energy barriers encountered by a folding polypeptide are generally narrow with robust maxima and that the change in the folding rate by the perturbation of folding landscape, for example, by mutations or changing conditions, is mainly due to the induction of folding intermediates for two-state proteins. Thus, the data suggest that the activation energy is decreased in the presence of TFE because of the decreased stability of the early intermediate relative to the transition state.

24.5 Salt-induced Formation of the Intermediate States

24.5.1 Acid-denatured Proteins

Acid-denatured proteins often assume an intermediate conformation. The most well-known example is the acidic molten globule state of α-lactalbumin [26–29] (see Chapter 23). However, the conformation of acid-denatured proteins depends on the protein species, and the nature of the acid-denatured state was ambiguous in comparison with the unfolded states induced by urea or GdmCl [4, 5] (see Chapter 8). The important results indicating the salt-dependent transition of the acid-denatured state came out with horse cytochrome *c* [25], followed by *Bacillus subtilis* β-lactamase [102] and horse apomyoglobin [103, 104]. These proteins are substantially unfolded at pH 2 in the absence of salt. The addition of a low concentration of salts induced an intermediate state with notable far-UV CD intensity, while the near-UV CD showed disordering (Figure 24.9). The salt-induced state is similar to the acidic molten globule state of α-lactalbumin [26–29]. In fact, the name of molten globule state was first used for the salt-stabilized acidic state of cytochrome *c* [25]. Similar observation with β-lactamase [102], apomyoglobin [103, 104], staphylococcal nuclease [105, 106], and other proteins established that the salt-dependent transition is common to various acid-denatured proteins.

The conformation of the acid-denatured state is determined by a balance of various factors stabilizing or destabilizing the folded state. The most important destabilizing force should be the charge repulsion between positive charges because most of the titratable groups are protonated at pH 2. Consistent with this, proteins with a high p*I* value (for example, cytochrome *c*) tend to be unfolded substantially. On the other hand, the driving forces for folding would be similar to those at neutral pH except that the electrostatic interactions are affected by pH. The addition of salts somehow shields the unfavorable charge repulsion, thus the folding forces come into play, although the distinct ionizations of the titratable groups prevent the formation of native structure.

The participation of hydrophobic interactions, although less than that of the native state, has been established by a series of studies using calorimetric analysis

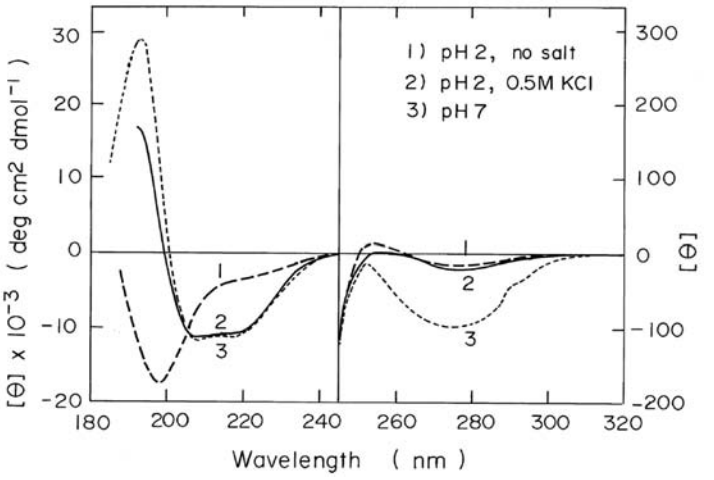

Fig. 24.9. Salt-dependent change of the CD spectrum of the acid-denatured *Bacillus cereus* β-lactamase at 20 °C. 1) The acid-unfolded state at pH 2.0 in the absence of salt; 2) the molten globule state at pH 2.0 in 0.5 M KCl; 3) the native state at pH 7.0. Reproduced from Ref. [102] with permission.

of the salt-stabilized intermediate states [107–111]. Nevertheless, the salt-induced transition itself does not reveal the detailed mechanism of the salt effects.

24.5.2
Acid-induced Unfolding and Refolding Transitions

In an attempt to fully acid-unfold proteins, an intriguing observation was made; increasing the concentration of HCl opposes the unfolding, and rather refolds the protein to the molten globule state [112] (Figure 24.10). The acid-stabilized state was essentially the same intermediate as stabilized by salts. Although the phenomenon was surprising at first, it is straightforward to understand the mechanism once the ionic strength effect is taken into account; decreasing the pH below 2 exponentially increases the concentration of anion as well as of protons by $[Cl^-] = [H^+] = 10^{-pH}$. This suggests that the apparent refolding phenomenon observed by increasing the HCl concentration is caused by the anion effect rather than the pH effects. Consistent with this idea, the acid-induced transition plotted against the concentration of HCl agreed well with that plotted against the concentration of NaCl or KCl [112] (Figure 24.11). By considering the ionic strength effect of HCl, the pH and salt-dependent phase diagram of acid-denatured proteins can be constructed [103, 104, 113] (Figure 24.12). It is important to recognize that decreasing pH increases the chloride concentration, thus producing the prohibited region in the phase. Consequently, decreasing the pH below 2 results in increasing ionic strength, causing the same effects as adding salt at pH 2.

The phase diagram is useful to understand the variation of acid denatured states among proteins. In the cases of horse cytochrome *c* [25, 113] and horse apomyo-

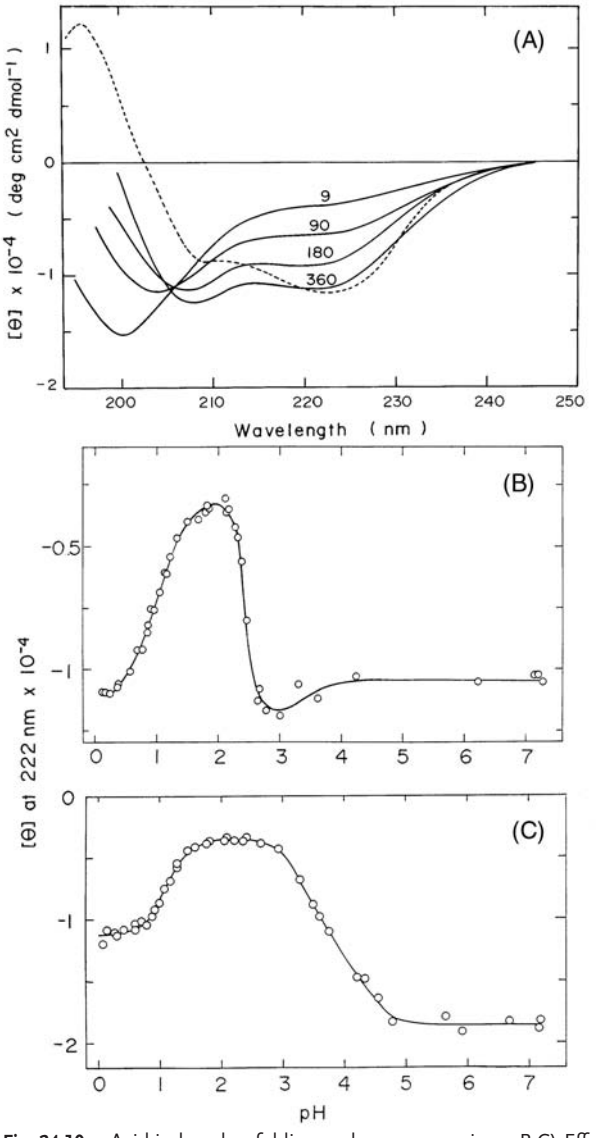

Fig. 24.10. Acid-induced unfolding and refolding transitions of cytochrome *c* and apomyolobin at 20 °C. A) Far-UV CD spectra of cytochrome *c* as a function of HCl concentration. The numbers refer to the HCl concentration in millimolar units. The spectrum of the native state (dotted line) is shown for comparison. B,C) Effects of increasing concentration of HCl on the ellipticity at 222 nm of cytochrome *c* (B) and apomyologobin (C). Upon decreasing pH by addition of HCl, the N (native) → U (acid-unfolded) → MG (molten globule) transition is observed. Reproduced from Ref. [111] with permission.

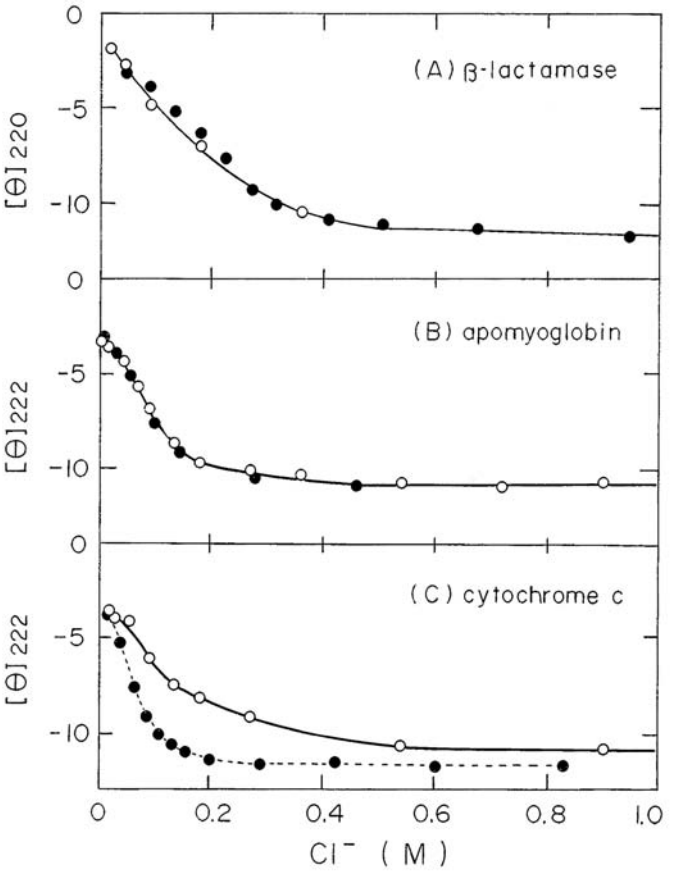

Fig. 24.11. Consistency between the HCl-induced (open circles) and KCl-induced (filled circles) transitions of acid-unfolded proteins as monitored by change in the far-UV CD. A) *Bacillus cereus* β-lactamase, B) horse apomyoglobin, C) horse cytochrome *c*. Reproduced from Ref. [111] with permission.

globin [103, 104], a clear boundary between the fully unfolded state and the molten globule state was observed. For the phase diagram of apomyoglobin, moreover, the unfolding intermediate was observed at moderately acidic pH regions. On the other hand, it is expected for a protein with less charge repulsion that the acid denaturation directly produces the molten globule intermediate without maximally unfolding the protein. This is considered to be the case for bovine α-lactalbumin. Cytochrome *c* species with various degrees of charge repulsion were prepared by acetylating lysine amino groups [107, 114]. The phase diagrams of these variously modifed cytochrome *c* species showed that the boundary between the fully unfolded state and the molten globule state depends on the charge repulsion: decreasing the net charge (that is, decreasing pH) decreases the concentration of salt

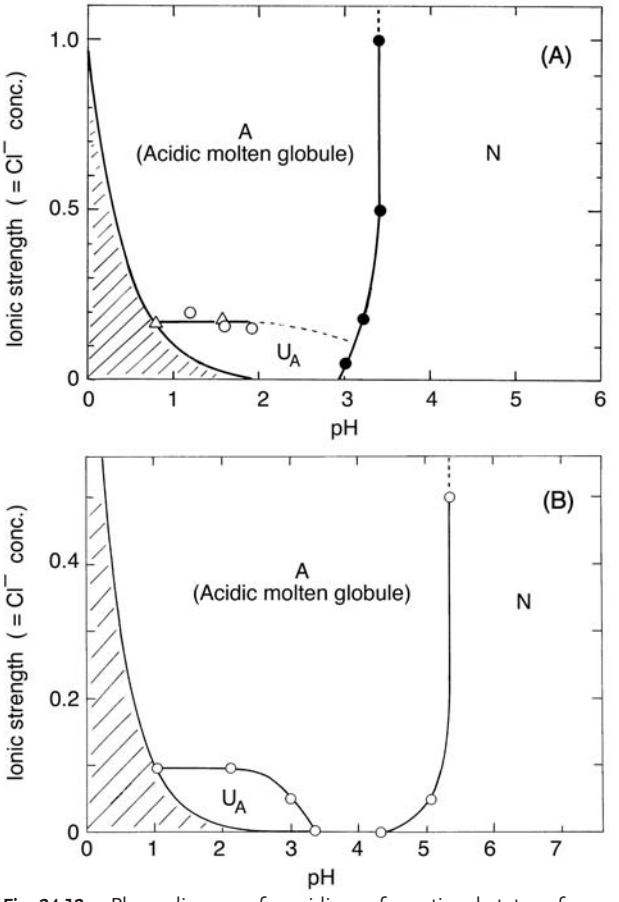

Fig. 24.12. Phase diagrams for acidic conformational states of horse cytochrome *c* (A) and horse apomyoglobin (B). Phase diagram for apomyoglobin reproduced from Ref. [102] with permission.

required to stabilize the molten globule state [113]. Thus, we can understand consistently the variation of acid denaturation among proteins.

An important implication is that to maximally unfold a protein by acid, pH 2 under the low salt conditions will be best. These conditions would also be optimal for dissolving proteins and peptides taking advantage of the net charge repulsion.

The role of charge repulsion and hydrophobic interactions were characterized by analyzing the salt-dependent transition of horse cytochrome *c* [107, 114]. Conformational transitions of variously acetylated cytochrome *c* derivatives, that is, modified cytochrome *c* species with different p*I* values, revealed that the net charge repulsion destabilizes the molten globule state by about 400 cal mol^{-1} per charge at 25 °C. In addition, thermal unfolding of these acytylated cytochrome *c* species verified the contribution of hydrophobic interactions in the stability of the molten glob-

ule state, which is about 30–40% of that of the native state [107]. The enthalpy change upon formation of the molten globule state and its temperature dependence were directly determined by isothermal titration calorimetry measurements of the salt-dependent conformational transition, which is consistent with the value determined by DSC measurements [110]. Similar measurements were performed with horse apomyoglobin [111].

24.6 Mechanism of Salt-induced Conformational Change

Although the importance of anions in shielding the charge repulsive forces is evident, anions can work in various ways [115]. (1) Salts can shield the charge repulsion through Debye-Hückel screening effects. (2) Some anions, such as sulfate, are well known to stabilize the native state, which has been interpreted in terms of the effects on water structure (that is, structure maker) consequently strengthening the hydrophobic interactions of proteins. (3) Anions can directly interact with positive charges on proteins to shield the charge repulsion. These three possibilities can be distinguished by examining the effects of various anion species [115].

Debye-Hückel effects are independent of anion species. It is known that the effects of anions in stabilizing protein structure follow the Hofmeister series [5, 6]. The representative series is:

$$\text{sulfate} > \text{phosphate} > \text{fluoride} > \text{chloride} > \text{bromide} > \text{iodide} > \text{perchlorate} > \text{thiocyanate} \quad (3)$$

Although the exact mechanism of stabilization or destabilization by these anions is unknown, the results are consistent with the idea that these salts affect the water structure. On the other hand, the affinity of a particular anion to an anion-exchange resin is called electroselectivity. The selectivity series of various anions depends critically on the structure of the resin and the solution conditions. However, the general trend of selectivity can be seen from the following examples [116, 117]:

$$\text{sulfite} > \text{sulfate} > \text{perchlorate} > \text{thiocyanate} > \text{iodide} > \text{nitrate} > \text{bromide} > \text{chloride} > \text{acetate} = \text{fluoride} \quad (4)$$

$$\text{perchlorate} > \text{iodide} > \text{trichloroacetate} = \text{thiocyante} > \text{nitrate} > \text{bromide} > \text{trifluoroacetate} > \text{chloride} > \text{acetate} > \text{fluoride} \quad (5)$$

The order of the Hofmeister series is distinct from that of electroselectivity. In particular, the orders of monovalent anions are opposite between the two. Moreover, the concentrations of salts to induce the Hofmeister effects are generally higher than those for anion binding (electroselectivity).

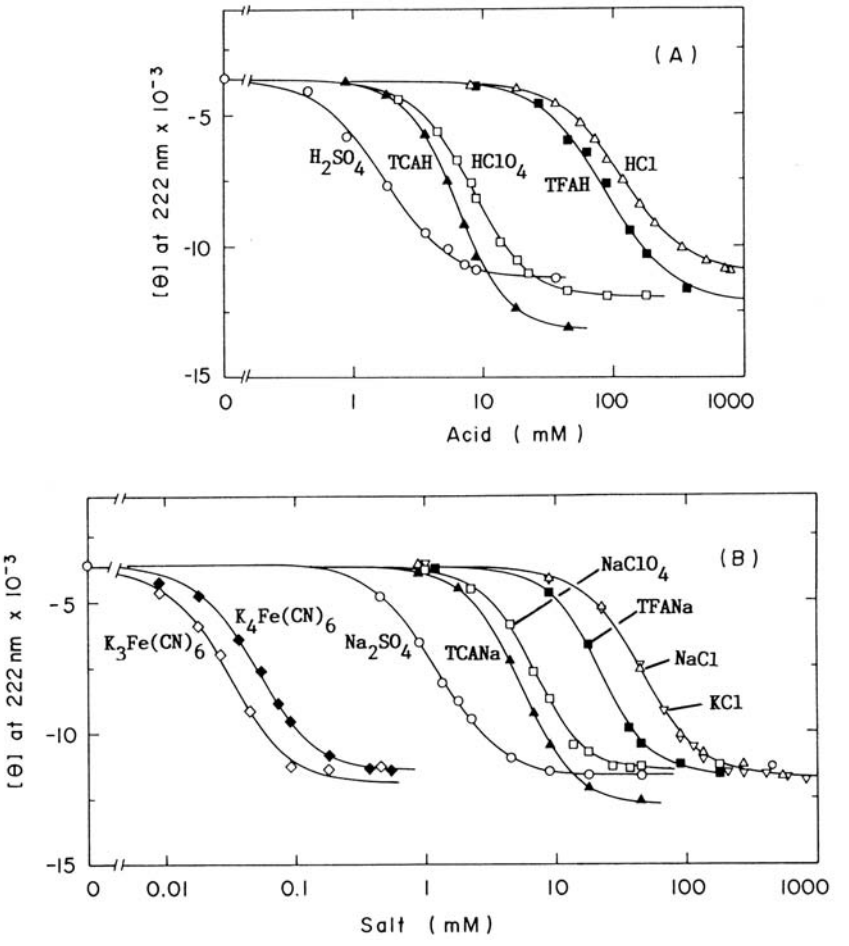

Fig. 24.13. Acid-induced (A) or salt-induced conformational transitions of horse cytochrome *c* in the presence of 18 mM HCl measured by the ellipticity at 222 nm at 20 °C. Reproduced from Ref. [114] with permission.

The effects of various salts on the acid-unfolded cytochrome *c* and apomyoglobin were examined [115] (Figure 24.13). Similar experiments with various acids were also performed, producing essentially the same results with respect to the order of anions:

$$\begin{aligned} &\text{ferricyanide} > \text{ferrocyanide} > \text{sulfate} > \text{trichloroacetate} > \text{thiocyanate} \\ &\quad > \text{perchlorate} > \text{iodide} > \text{nitrate} > \text{trifluoroacetate} \\ &\quad > \text{bromide} > \text{chloride} \end{aligned} \tag{6}$$

The results showed convincingly that the effects depend on anion species, and the order of effectiveness was consistent with the electroselectivity series (Eqs (4) and (5)). Anions with multiple charges show stronger potentials. Among the monovalent anions, chaotropic anions such as iodide or bromide show stronger effects while the effects of chloride are the weakest. These results demonstrate that the electrostatic attraction between the positively charged proteins and negatively charged anions causes the direct interactions between them, thus shielding the charge repulsion.

24.7 Generality of the Salt Effects

Although anion binding-induced stabilization of the intermediate state is often observed at acidic pH, it is likely that a similar interaction plays a role in determining the protein conformation under physiological pH when a protein is highly positively charged. The salt-dependent conformational transition has been known for many years for melittin. The conformational transition of melittin has been shown to be dependent on anion binding [118–120]. Moreover, the similar role of anion binding was also shown for another basic and amphiphilic bee venom peptide, mastoparan [121] and a designed amphiphilic peptide [122]. These results imply that the anion binding can control the conformational transition of some of natively unfolded proteins. Recently, a natively unfolded *Bacillus subtilis* ribonuclease P was shown to exhibit anion-dependent folding, indicating that the anion-dependent folding plays a role in the function of some proteins [123]. On the other hand, the role of cations in determining the conformation of proteins is less clear, although it is conceivable that the opposite situation takes place for negatively charged unfolded proteins and peptides.

Finally, it is useful to consider the effects of GdmCl in relation to the anion effects as described in this chapter. GdmCl is a salt made of a guanidinium cation and chloride. Hagihara et al. [124] observed intriguing GdmCl-dependent conformational transitions with the acid-unfolded horse cytochrome *c* and horse apomyoglobin (Figure 24.14). By the addition of low concentrations of GdmCl, the acid-unfolded proteins at first refolded to the molten globule intermediate before unfolding again at high GdmCl concentrations. Although the observation might be surprising, the interpretation is straightforward, as is the case of the acid-induced refolding. The first refolding by GdmCl is caused by the anion effect while subsequent unfolding is driven by the normal chaotropic effects of GdmCl. The similar refolding and unfolding transitions were observed for a designed amphiphilic peptide at neutral pH [122]. Moreover, the stabilizing effects of low concentrations of GdmCl may be common to several proteins under the physiological conditions [125]. Thus, when GdmCl is used, it is important to interpret the data taking into account the salt effects of GdmCl. It is also recommended to compare the results with the denaturation caused by urea, another popular denaturant.

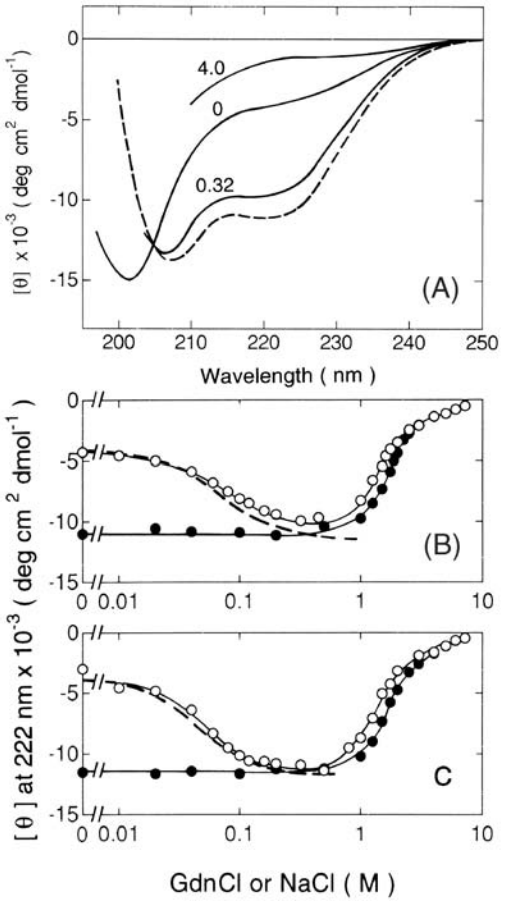

Fig. 24.14. GdmCl-induced refolding and unfolding transitions of acid-unfolded proteins. A) Far-UV CD spectra of horse apomyoglobin as a function of GdmCl concentration in 20 mM HCl (pH 1.8) at 20 °C. The numbers refer to the GdmCl concentration in molar units. The broken line shows the spectrum of the molten globule state stabilized by 0.4 M NaCl in 20 mM HCl. B,C) Conformational transitions of horse apomyoglobin (B) and horse cytochrome *c* (C) measured by the change in ellipticity at 222 nm. Open and filled circles indicate the GdmCl-induced transitions in the absence and presence of 0.4 M NaCl, respectively. Open squares show the reverse transition, in which proteins were initially unfolded in 4 M GdmCl. For comparison, NaCl-induced refolding transitions in the same buffer are shown by broken lines. Reproduced from Ref. [123] with permission.

24.8 Conclusion

Alcohols and salts affect the conformational stability of partially folded intermediate in various ways. The effects of alcohols are basically explained by destabiliza-

tion of intramolecular hydrophobic interactions and stabilization of the local hydrogen bonds, often resulting in the formation of the open helical conformation. The molten globule-like compact intermediate is occasionally observed at moderate concentrations of alcohols and, moreover, β-structures are stabilized for some peptides and proteins. Of particular interest is the formation of fibrillar architechtures similar to the amyloid fibrils in alcohol/water solvents. These results indicate that, although major effects of alcohols on protein and peptides are the same, the resultant conformation varies substantially depending on the balance of various forces, the details of which are still unknown. Salts can also stabilize the intermediates in several ways. Major effects of salts are Debye-Hückel screening effects, effects on water structure, resulting in the modulation of hydrophobic interactions, and counter ion binding. Among them, we discussed that the direct interactions of anions with positive charges on proteins play important roles in determining the structure and stability of partially folded intermediates. Understanding kinetic aspects of these alcohol and salt effects will further clarify the conformation and stability of the partially folded intermediates.

References

1 Lapanje, S. (1978) *Physicochemical Aspects of Protein Denaturation*. John Wiley & Sons, New York.
2 Buck, M. (1998) Trifluoroethanol and colleagues: co-solvents come of age. Recent studies with peptides and proteins. *Q. Rev. Biophys.* 31, 297–355.
3 Tanford, C. (1968) Protein denaturation. *Adv. Protein Chem.* 23, 121–282.
4 Tanford, C. (1970) Protein denaturation. *Adv. Protein Chem.* 24, 1–95.
5 von Hippel, P. H. and Schleich, T. (1969) *Biological Macromolecules* (Timasheff, S. and Fasman, G., Eds), Vol. II, pp. 417–574. Dekker, New York.
6 Collins, K. D. and Washabaugh, M. W. (1985) The Hofmeister effect and the behaviour of water at interfaces. *Q. Rev. Biophys.* 18, 323–422.
7 Timasheff, S. and Arakawa, T. (1989) Stabilization of protein structure by solvents. In *Protein Structure: A Practical Approach* (Creighton, T. E., Ed.), pp. 331–345. Oxford University Press, Oxford.
8 Weber, R. E. and Tanford, C. (1959) The conformation of ribonuclease at low pH in 2-chloroethanol and in 2-chloroethanol-water mixtures. *J. Am. Chem. Soc.* 81, 3255–3260.
9 Martin, C. J. and Bhatnagar, G. M. (1967) Unfolding reactions of proteins. II. Spectral and optical rotatory dispersion studies in urea, guanidinium chloride, and 2-chloroethanol. *Biochemistry* 6, 1638–1650.
10 Herskovits, T. T. and Mescanti, L. (1965) Conformation of proteins and polypeptides. II. Optical rotatory dispersion and conformation of the milk proteins and other proteins in organic solvents. *J. Biol. Chem.* 240, 639–644.
11 Dyson, H. J. and Wright, P. E. (2002) Coupling of folding and binding for unstructured proteins. *Curr. Opin. Struct. Biol.* 12, 54–60.
12 Tompa, P. (2002) Intrinsically unstructured proteins. *Trends Biochem. Sci.* 27, 527–533.
13 Uversky, V. N. (2002) Natively unfolded proteins: a point where biology waits for physics. *Protein Sci.* 11, 739–756.
14 Uversky, V. N. (2002) What does it mean to be natively unfolded? *Eur J. Biochem.* 269, 2–12.
15 Blanco, F. J., Jimenez, M. A.,

Pineda, A., Rico, M., Santoro, J., and Nieto, J. L. (1994) NMR solution structure of the isolated N-terminal fragment of protein-G B1 domain. Evidence of trifluoroethanol induced native-like β-hairpin formation. *Biochemistry* 33, 6004–6014.

16 Cann, J. R., Liu, X., Stewart, J. M., Gera, L., and Kotovych, G. (1994) A CD and an NMR study of multiple bradykinin conformations in aqueous trifluoroethanol solutions. *Biopolymers* 34, 869–878.

17 Vranken, W. F., Budesinsky, M., Fant, F., Boulez, K., and Borremans, F. A. (1995) The complete consensus V3 loop peptide of the envelope protein gp120 of HIV-1 shows pronounced helical character in solution. *FEBS Lett.* 374, 117–121.

18 Wang, J., Hodges, R. S., and Sykes, B. D. (1995) Effect of trifluoroethanol on the solution structure and flexibility of desmopressin: a two-dimensional NMR study. *Int. J. Pept. Protein Res.* 45, 471–481.

19 de Alba, E., Jimenez, M. A., Rico, M., and Nieto, J. L. (1996) Conformational investigation of designed short linear peptides able to fold into β-hairpin structures in aqueous solution. *Folding Des.* 1, 133–144.

20 Reiersen, H., Clarke, A. R., and Rees, A. R. (1998) Short elastin-like peptides exhibit the same temperature-induced structural transitions as elastin polymers: implications for protein engineering. *J. Mol. Biol.* 283, 255–264.

21 Bienkiewicz, E. A., Moon Woody, A., and Woody, R. W. (2000) Conformation of the RNA polymerase II C-terminal domain: circular dichroism of long and short fragments. *J. Mol. Biol.* 297, 119–133.

22 Ramirez-Alvarado, M., Blanco, F. J., and Serrano, L. (2001) Elongation of the BH8 β-hairpin peptide: electrostatic interactions in β-hairpin formation and stability. *Protein Sci.* 10, 1381–1392.

23 Dill, K. A. (1990) Dominant forces in protein folding. *Biochemistry* 29, 7133–7155.

24 Dill, K. A., Bromberg, S., Yue, K., Fiebig, K. M., Yee, D. P., Thomas, P. D., and Chan, H. S. (1995) Principles of protein folding: a perspective from simple exact models. *Protein Sci.* 4, 561–602.

25 Ohgushi, M. and Wada, A. (1983) 'Molten-globule state': a compact form of globular proteins with mobile side-chains. *FEBS Lett.* 164, 21–24.

26 Ptitsyn, O. B. (1991) How does protein synthesis give rise to the 3D-structure? *FEBS Lett.* 285, 176–181.

27 Ptitsyn, O. B. (1995) Molten globule and protein folding. *Adv. Protein Chem.* 47, 83–229.

28 Kuwajima, K. (1989) The molten globule state as a clue for understanding the folding and cooperativity of globular-protein structure. *Proteins* 6, 87–103.

29 Arai, M. and Kuwajima, K. (2000) Role of the molten globule state in protein folding. *Adv. Protein Chem.* 53, 209–282.

30 Fregeau-Gallagher, N. L., Sailer, M., Niemczura, W. P., Nakashima, T. T., Stiles, M. E., and Vederas, J. C. (1997) Three-dimensional structure of leucocin A in trifluoroethanol and dodecylphosphocholine micelles: spatial location of residues critical for biological activity in type IIa bacteriocins from lactic acid bacteria. *Biochemistry* 36, 15062–15072.

31 Schönbrunner, N., Wey, J., Engels, J., Georg, H., and Kiefhaber, T. (1996) Native-like β-structure in a trifluoroethanol-induced partially folded state of the all-beta-sheet protein tendamistat. *J. Mol. Biol.* 260, 432–445.

32 Segawa, S., Fukuno, T., Fujiwara, K., and Noda, Y. (1991) Local structures in unfolded lysozyme and correlation with secondary structures in the native conformation: helix-forming or -breaking propensity of peptide segments. *Biopolymers* 31, 497–509.

33 Sancho, J., Neira, J. L., and Fersht, A. R. (1992) An N-terminal fragment of barnase has residual helical struc-

ture similar to that in a refolding intermediate. *J. Mol. Biol.* 224, 749–758.

34 Dyson, H. J., Sayre, J. R., Merutka, G., Shin, H. C., Lerner, R. A., and Wright, P. E. (1992) Folding of peptide fragments comprising the complete sequence of proteins. Models for initiation of protein folding. II. Plastocyanin. *J. Mol. Biol.* 226, 819–835.

35 Dyson, H. J., Merutka, G., Waltho, J. P., Lerner, R. A., and Wright, P. E. (1992) Folding of peptide fragments comprising the complete sequence of proteins. Models for initiation of protein folding. I. Myohemerythrin. *J. Mol. Biol.* 226, 795–817.

36 Hamada, D., Kuroda, Y., Tanaka, T., and Goto, Y. (1995) High helical propensity of the peptide fragments derived from β-lactoglobulin, a predominantly β-sheet protein. *J. Mol. Biol.* 254, 737–746.

37 Yang, J. J., Buck, M., Pitkeathly, M., Kotik, M., Haynie, D. T., Dobson, C. M., and Radford, S. E. (1995) Conformational properties of four peptides spanning the sequence of hen lysozyme. *J. Mol. Biol.* 252, 483–491.

38 Bolin, K. A., Pitkeathly, M., Miranker, A., Smith, L. J., and Dobson, C. M. (1996) Insight into a random coil conformation and an isolated helix: structural and dynamical characterisation of the C-helix peptide from hen lysozyme. *J. Mol. Biol.* 261, 443–453.

39 Kuroda, Y., Hamada, D., Tanaka, T., and Goto, Y. (1996) High helicity of peptide fragments corresponding to β-strand regions of β-lactoglobulin observed by 2D-NMR spectroscopy. *Folding Des.* 1, 255–263.

40 Zitzewitz, J. A. and Matthews, C. R. (1991) Molecular dissection of the folding mechanism of the alpha subunit of tryptophan synthase: an amino-terminal autonomous folding unit controls several rate-limiting steps in the folding of a single domain protein. *Biochemistry* 38, 10205–10214.

41 Staley, J. P. and Kim, P. S. (1994) Formation of a native-like subdomain in a partially folded intermediate of bovine pancreatic trypsin inhibitor. *Protein Sci.* 3, 1822–1832.

42 Reymond, M. T., Merutka, G., Dyson, H. J., and Wright, P. E. (1997) Folding propensities of peptide fragments of myoglobin. *Protein Sci.* 6, 706–716.

43 Salinas, R. K., Shida, C. S., Pertinhez, T. A., Spisni, A., Nakaie, C. R., Paiva, A. C., and Schreier, S. (2002) Trifluoroethanol and binding to model membranes stabilize a predicted turn in a peptide corresponding to the first extracellular loop of the angiotensin II AT(1A) receptor. *Biopolymers* 65, 21–31.

44 Soulie, S., Neumann, J. M., Berthomieu, C., Moller, J. V., le Maire, M., and Forge, V. (1999) NMR conformational study of the sixth transmembrane segment of sarcoplasmic reticulum Ca^{2+}-ATPase. *Biochemistry* 38, 5813–5821.

45 Wray, V., Kinder, R., Federau, T., Henklein, P., Bechinger, B., and Schubert, U. (1999) Solution structure and orientation of the transmembrane anchor domain of the HIV-1-encoded virus protein U by high-resolution and solid-state NMR spectroscopy. *Biochemistry* 38, 5272–5282.

46 Taylor, R. M., Zakharov, S. D., Bernard Heymann, J., Girvin, M. E., and Cramer, W. A. (2000) Folded state of the integral membrane colicin E1 immunity protein in solvents of mixed polarity. *Biochemistry* 39, 12131–12139.

47 Luidens, M. K., Figge, J., Breese, K., and Vajda, S. (1996) Predicted and trifluoroethanol-induced α-helicity of polypeptides. *Biopolymers* 39, 367–376.

48 Shiraki, K., Nishikawa, K., and Goto, Y. (1995) Trifluoroethanol-induced stabilization of the α-helical structure of β-lactoglobulin: implication for non-hierarchical protein folding. *J. Mol. Biol.* 245, 180–194.

49 Buck, M., Schwalbe, H., and Dobson, C. M. (1995) Characterization of conformational preferences in a partly folded protein by heteronu-

clear NMR spectroscopy: assignment and secondary structure analysis of hen egg-white lysozyme in trifluoroethanol. *Biochemistry* 34, 13219–13232.

50 Kuwata, K., Hoshino, M., Era, S., Batt, C. A., and Goto, Y. (1998) $\alpha \rightarrow \beta$ transition of β-lactoglobulin as evidenced by heteronuclear NMR. *J. Mol. Biol.* 283, 731–739.

51 Hoshino, M., Hagihara, Y., Hamada, D., Kataoka, M., and Goto, Y. (1997) Trifluoroethanol-induced conformational transition of hen egg-white lysozyme studied by small-angle X-ray scattering. *FEBS Lett.* 416, 72–76.

52 Kamatari, Y. O., Konno, T., Kataoka, M., and Akasaka, K. (1996) The methanol-induced globular and expanded denatured states of cytochrome *c*: a study by CD, fluorescence, NMR and small-angle X-ray scattering. *J. Mol. Biol.* 259, 512–523.

53 Kamatari, Y. O., Ohji, S., Konno, T., Seki, Y., Soda, K., Kataoka, M., and Akasaka, K. (1999) The compact and expanded denatured conformations of apomyoglobin in the methanol-water solvent. *Protein Sci.* 8, 873–882.

54 Bychkova, V. E., Dujsekina, A. E., Klenin, S. I., Tiktopulo, E. I., Uversky, V. N., and Ptitsyn, O. B. (1996) Molten globule-like state of cytochrome *c* under conditions simulating those near the membrane surface. *Biochemistry* 35, 6058–6063.

55 Bychkova, V. E., Dujsekina, A. E., Fantuzzi, A., Ptitsyn, O. B., and Rossi, G. L. (1998) Release of retinol and denaturation of its plasma carrier, retinol-binding protein. *Folding Des.* 3, 285–291.

56 Uversky, V. N., Narizhneva, N. V., Kirschstein, S. O., Winter, S., and Lober, G. (1997) Conformational transitions provoked by organic solvents in β-lactoglobulin: can a molten globule like intermediate be induced by the decrease in dielectric constant? *Folding Des.* 2, 163–172.

57 Konno, T. (1998) Conformational diversity of acid-denatured cytochrome *c* studied by a matrix analysis of far-UV CD spectra. *Protein Sci.* 7, 975–982.

58 Konno, T., Iwashita, J., and Nagayama, K. (2000) Fluorinated alcohol, the third group of co-solvents that stabilize the molten globule state relative to a highly denatured state of cytochrome *c*. *Protein Sci.* 9, 564–569.

59 Santucci, R., Polizio, F., and Desideri, A. (1999) Formation of a molten-globule-like state of cytochrome *c* induced by high concentrations of glycerol. *Biochimie* 81, 745–751.

60 Gast, K., Zirwer, D., Muller-Frohne, M., and Damaschun, G. (1999) Trifluoroethanol-induced conformational transitions of proteins: insights gained from the difference between α-lactalbumin and ribonuclease A. *Protein Sci.* 8, 625–634.

61 Kamiyama, T., Sadahide, Y., Nogusa, Y., and Gekko, K. (1999) Polyol-induced molten globule of cytochrome *c*: an evidence for stabilization by hydrophobic interaction. *Biochim. Biophys. Acta* 1434, 44–57.

62 Sundd, M., Kundu, S., and Jagannadham, M. V. (2000) Alcohol-induced conformational transitions in ervatamin C. An α-helix to β-sheet switchover. *J. Protein Chem.* 19, 169–176.

63 Sasidhar, Y. U. and Prabha, C. R. (2000) Conformational features of reduced and disufide intact forms of hen egg white lysozyme in aqueous solution in presence of 3-chloro-1,2-propanediol and dioxane: implications for protein folding intermediates. *Indian J. Biochem. Biophys.* 37, 97–106.

64 Tsumura, K., Enatsu, M., Kuramori, K., Morita, S., Kugimiya, W., Kuwada, M., Shimura, Y., and Hasumi, H. (2001) Conformational change in a single molecular species, b3, of β-conglycinin in acidic ethanol solution. *Biosci. Biotechnol. Biochem.* 65, 292–297.

65 Polverino de Laureto, P., Frare, E., Gottardo, R., and Fontana, A. (2002) Molten globule of bovine α-lactalbumin at neutral pH induced by heat, trifluoroethanol, and oleic acid: a

comparative analysis by circular dichroism spectroscopy and limited proteolysis. *Proteins* 49, 385–397.

66 Bongiovanni, C., Sinibaldi, F., Ferri, T., and Santucci, R. (2002) Glycerol-induced formation of the molten globule from acid-denatured cytochrome *c*: implication for hierarchical folding. *J. Protein Chem.* 21, 35–41.

67 Sirangelo, I., Dal Piaz, F., Malmo, C., Casillo, M., Birolo, L., Pucci, P., Marino, G., and Irace, G. (2003) Hexafluoroisopropanol and acid destabilized forms of apomyoglobin exhibit structural differences. *Biochemistry* 42, 312–319.

68 Kuwajima, K., Yamaya, H., and Sugai, S. (1996) The burst-phase intermediate in the refolding of β-lactoglobulin studied by stopped-flow circular dichroism and absorption spectroscopy. *J. Mol. Biol.* 264, 806–822.

69 Hamada, D., Segawa, S., and Goto, Y. (1996) Non-native α-helical intermediate in the refolding of β-lactoglobulin, a predominantly β-sheet protein. *Nat. Struct. Biol.* 3, 868–873.

70 Forge, V., Hoshino, M., Kuwata, K., Arai, M., Kuwajima, K., Batt, C. A., and Goto, Y. (2000) Is Folding of β-lactoglobulin non-hierarchic? Intermediate with native-like β-sheet and non-native α-helix. *J. Mol. Biol.* 296, 1039–1051.

71 Kuwata, K., Shastry, R., Cheng, H., Hoshino, M., Batt, C. A., Goto, Y., and Roder, H. (2001) Structural and kinetic characterization of early folding events in β-lactoglobulin. *Nat. Struct. Biol.* 8, 151–155.

72 Yagi, M., Sakurai, K., Kalidas, C., Batt, C. A., and Goto, Y. (2003) Reversible unfolding of bovine β-lactoglobulin mutants without a free thiol group. *J. Biol. Chem.* 278, 47009–47015.

73 Katou, H., Hoshino, M., Batt, C. A., and Goto, Y. (2001) Native-like β-hairpin retained in the cold-denatured state of bovine β-lactoglobulin. *J. Mol. Biol.* 310, 471–484.

74 Prusiner, S. B. (1997) Prion diseases and the BSE crisis. *Science* 278, 245–251.

75 Jackson, G. S., Hosszu, L. L., Power, A., Hill, A. F., Kenney, J., Saibil, H., Craven, C. J., Waltho, J. P., Clarke, A. R., and Collinge, J. (1999) Reversible conversion of monomeric human prion protein between native and fibrilogenic conformations. *Science* 283, 1935–1937.

76 Thomas, P. D. and Dill, K. (1993) Local and nonlocal interactions in globular proteins and mechanisms of alcohol denaturation. *Protein Sci.* 2, 2050–2065.

77 Liu, Y. and Bolen, D. W. (1995) The peptide backbone plays a dominant role in protein stabilization by naturally occurring osmolytes. *Biochemistry* 34, 12884–12891.

78 Cammers-Goodwn, A., Allen, T. J., Oslick, S. L., McClure, K. F., Lee, J. H., and Kemp, D. S. (1996) Mechanism of stabilization of helical conformations of poplypeptides by water containing trifluoroethanol. *J. Am. Chem. Soc.* 118, 3082–3090.

79 Luo, P. and Baldwin, R. L. (1997) Mechanism of helix induction by trifluoroethanol: a framework for extrapolating the helix-forming properties of peptides from trifluoroethanol/water mixtures back to water. *Biochemistry* 36, 8413–8421.

80 Hirota, N., Mizuno, K., and Goto, Y. (1997) Cooperative α-helix formation of β-lactoglobulin and melittin induced by hexafluoroisopropanol. *Protein Sci.* 6, 416–421.

81 Hirota, N., Mizuno, K., and Goto, Y. (1998) Group additive contributions to the alcohol-induced α-helix formation of melittin: implication for the mechanism of the alcohol effects on proteins. *J. Mol. Biol.* 275, 365–378.

82 Hong, D.-P., Kuboi, R., Hoshino, M., and Goto, Y. (1999) Clustering of fluorine-substituted alcohols as a factor responsible for their marked effects on proteins and peptides. *J. Am. Chem. Soc.* 121, 8427–8433.

83 Hirota-Nakaoka, N. and Goto, Y. (1999) Alcohol-induced denaturation of β-lactoglobulin: a close correlation

to the alcohol-induced α-helix formation of melittin. *Bioorg. Med. Chem.* 7, 67–73.

84 Llinas, M. and Klein, M. P. (1975) Charge relay at the peptide bond. A proton magnetic resonance study of solvation effects on the amide electron density distribution. *J. Am. Chem. Soc.* 97, 4731–4737.

85 Brooks, C. L. and Nilsson, L. (1993) Promotion of helix formation in peptides dissolved in alcohol and water-alcohol mixtures. *J. Am. Chem. Soc.* 115, 11034–11035.

86 Guo, H. and Karplus, M. (1994) Solvent influence on the stability of the peptide hydrogen bond: a supramolecular cooperative effect. *J. Phys. Chem.* 98, 7104–7105.

87 Iovino, M., Falconi, M., Marcellini, A., and Desideri, A. (2001) Molecular dynamics simulation of the antimicrobial salivary peptide histatin-5 in water and in trifluoroethanol: a microscopic description of the water destructuring effect. *J. Pept. Res.* 58, 45–55.

88 Roccatano, D., Colombo, G., Fioroni, M., and Mark, A. E. (2002) Mechanism by which 2,2,2-trifluoroethanol/water mixtures stabilize secondary-structure formation in peptides: a molecular dynamics study. *Proc. Natl Acad. Sci. USA* 99, 12179–12184.

89 Barrow, C. J., Yasuda, A., Kenny, P. T., and Zagorski, M. G. (1992) Solution conformations and aggregational properties of synthetic amyloid β-peptides of Alzheimer's disease. Analysis of circular dichroism spectra. *J. Mol. Biol.* 225, 1075–1093.

90 Nilsson, M. R., Nguyen, L. L., and Raleigh, D. P. (2001) Synthesis and purification of amyloidogenic peptides. *Anal. Biochem.* 288, 76–82.

91 Hirota-Nakaoka, N., Hasegawa, K., Naiki, H., and Goto, Y. (2003) Dissolution of β2-microglobulin amyloid fibrils by dimethylsulfoxide. *J. Biochem.* 134, 159–164.

92 Ohnishi, S., Koide, A., and Koide, S. (2000) Solution conformation and amyloid-like fibril formation of a polar peptide derived from a β-hairpin in the OspA single-layer β-sheet. *J. Mol. Biol.* 301, 477–489.

93 Goda, S., Takano, K., Yamagata, Y., Maki, S., Namba, K., and Yutani, K. (2002) Elongation in a β-structure promotes amyloid-like fibril formation of human lysozyme. *J. Biochem.* 132, 655–661.

94 Zerovnik, E., Turk, V., and Waltho, J. P. (2002) Amyloid fibril formation by human stefin B: influence of the initial pH-induced intermediate state. *Biochem. Soc. Trans.* 30, 543–547.

95 Srisailam, S., Kumar, T. K., Rajalingam, D., Kathir, K. M., Sheu, H. S., Jan, F. J., Chao, P. C., and Yu, C. (2003) Amyloid-like fibril formation in an all β-barrel protein. Partially structured intermediate state(s) is a precursor for fibril formation. *J. Biol. Chem.* 278, 17701–17709.

96 Lu, H., Buck, M., Radford, S. E., and Dobson, C. M. (1997) Acceleration of the folding of hen lysozyme by trifluoroethanol. *J. Mol. Biol.* 265, 112–117.

97 Hamada, D., Chiti, F., Guijarro, J. I., Kataoka, M., Taddei, N., and Dobson, C. M. (2000) Evidence concerning rate-limiting steps in protein folding from the effects of trifluoroethanol. *Nat. Struct. Biol.* 7, 58–61.

98 Chiti, F., Taddei, N., Webster, P., Hamada, D., Fiaschi, T., Ramponi, G., and Dobson, C. M. (1999) Acceleration of the folding of acylphosphatase by stabilization of local secondary structure. *Nat. Struct. Biol.* 6, 380–387.

99 Sanchez, I. E. and Kiefhaber, T. (2003) Hammond behavior versus ground state effects in protein folding: evidence for narrow free energy barriers and residual structure in unfolded states. *J. Mol. Biol.* 327, 867–884.

100 Sanchez, I. E. and Kiefhaber, T. (2003) Non-linear rate-equilibrium free energy relationships and Hammond behavior in protein folding. *Biophys. Chem.* 100, 397–407.

101 Yiu, C. P., Mateu, M. G., and Fersht, A. R. (2000) Protein folding transition

states: elicitation of Hammond effects by 2,2,2-trifluoroethanol. *Chembiochemistry* 1, 49–55.

102 Goto, Y. and Fink, A. L. (1989) Conformational states of β-lactamase: molten-globule states at acidic and alkaline pH with high salt. *Biochemistry* 28, 945–952.

103 Goto, Y. and Fink, A. L. (1990) Phase diagram for acidic conformational states of apomyoglobin. *J. Mol. Biol.* 214, 803–805.

104 Goto, Y. and Fink, A. L. (1994) Acid-induced folding of heme proteins. *Methods Enzymol.* 232, 3–15.

105 Fink, A. L., Calciano, L. J., Goto, Y., Nishimura, M., and Swedberg, S. A. (1993) Characterization of the stable, acid-induced, molten globule-like state of staphylococcal nuclease. *Protein Sci.* 2, 1155–1160.

106 Fink, A. L., Calciano, L. J., Goto, Y., Kurotsu, T., and Palleros, D. R. (1994) Classification of acid denaturation of proteins: Intermediates and unfolded states. *Biochemistry* 33, 12504–12511.

107 Hagihara, Y., Tan, Y., and Goto, Y. (1994) Comparison of the conformational stability of the molten globule and native states of horse cytochrome *c*: effects of acetylation, heat, urea, and guanidine-hydrochloride. *J. Mol. Biol.* 237, 336–348.

108 Nishii, I., Kataoka, M., Tokunaga, F., and Goto, Y. (1994) Cold-denaturation of the molten globule states of apomyoglobin and a profile for protein folding. *Biochemistry* 33, 4903–4909.

109 Nishii, I., Kataoka, M., and Goto, Y. (1995) Thermodynamic stability of the molten globule states of apomyoglobin. *J. Mol. Biol.* 250, 223–238.

110 Hamada, D., Kidokoro, S., Fukada, H., Takahashi, K., and Goto, Y. (1994) Salt-induced formation of the molten globule state of cytochrome *c* studied by isothermal titration calorimetry. *Proc. Natl Acad. Sci. USA* 91, 10325–10329.

111 Hamada, D., Fukada, H., Takahashi, K., and Goto, Y. (1995) Salt-induced formation of the molten globule state of apomyoglobin studied by isothermal titration calorimetry. *Thermochim. Acta* 266, 385–400.

112 Goto, Y., Calciano, L. J., and Fink, A. L. (1990) Acid-induced folding of proteins. *Proc. Natl Acad. Sci. USA* 87, 573–577.

113 Goto, Y., Hagihara, Y., Hamada, D., Hoshino, M., and Nishii, I. (1993) Acid-induced unfolding and refolding transitions of cytochrome *c*: a three-state mechanism in H_2O and D_2O. *Biochemistry* 32, 11878–11885.

114 Goto, Y. and Nishikiori, S. (1991) Role of electrostatic repulsion in the acidic molten globule of cytochrome *c*. *J. Mol. Biol.* 222, 679–686.

115 Goto, Y., Takahashi, N., and Fink, A. L. (1990) Mechanism of acid-induced folding of proteins. *Biochemistry* 29, 3480–3488.

116 Gjerde, D. T., Schmuchler, G., and Fritz, J. S. (1980) Anion chromatography with low-conductivity eluents. II. *J. Choromatogr.* 187, 35–45.

117 Gregor, H. P., Belle, J., and Marcus, R. A. (1955) Studies on ion exchange resins. XIII. Selectivity coefficients of quaternary base anion-exchange resins toward univalent anions. *J. Am. Chem. Soc.* 77, 2713–2719.

118 Goto, Y. and Hagihara, Y. (1992) Mechanism of the conformational transition of melittin. *Biochemistry* 31, 732–738.

119 Hagihara, Y., Kataoka, M., Aimoto, S., and Goto, Y. (1992) Charge repulsion in the conformational stability of melittin. *Biochemistry* 31, 11908–11914.

120 Hagihara, Y., Oobatake, M., and Goto, Y. (1994) Thermal unfolding of tetrameric melittin: Comparison with the molten globule state of cytochrome *c*. *Protein Sci.* 3, 1418–1429.

121 Hoshino, M. and Goto, Y. (1994) Perchlorate-induced formation of the α-helical structure of mastoparan. *J. Biochem.* 116, 910–915.

122 Goto, Y. and Aimoto, S. (1991) Anion and pH-dependent conformational transition of an amphiphilic polypeptide. *J. Mol. Biol.* 218, 387–396.

123 Henkels, C. H., Kurz, J. C., Fierke, C. A., and Oas, T. G. (2001) Linked folding and anion binding of the *Bacillus subtilis* ribonuclease P protein. *Biochemistry* 40, 2777–2789.

124 Hagihara, Y., Aimoto, S., Fink, A. L., and Goto, Y. (1993) Guanidine hydrochloride-induced folding of proteins. *J. Mol. Biol.* 231, 180–184.

125 Santaro, M. M. and Bolen, D. W. (1992) A test of the linear extrapolation of unfolding free energy changes over an extended denaturant concentration range. *Biochemistry* 31, 4901–4907.

25
Prolyl Isomerization in Protein Folding

Franz Schmid

25.1
Introduction

Peptide bonds in proteins can occur in two isomeric states: *trans*, when the dihedral angle ω is 180°, and *cis*, when ω is 0°. For the bonds preceding residues other than proline (nonprolyl bonds[1]) the *trans* conformation is strongly favored energetically over *cis*, and therefore *cis* nonprolyl bonds are rare in folded proteins. Peptide bonds preceding proline (prolyl bonds) are frequently in the *cis* conformation. In this case the *trans* form is only slightly favored energetically over *cis*. *Cis* peptide bonds in native proteins complicate the folding process, because the incorrect *trans* forms predominate in the unfolded or nascent protein molecules, and because the *cis* $\rightleftharpoons$ *trans* isomerizations are intrinsically slow reactions. Incorrect prolyl isomers do not block the folding of a protein chain right at the beginning, but they strongly decelerate the overall folding process. This is clearly seen for small single-domain proteins. Many of them refold within milliseconds or even less when they contain correct prolyl isomers, but when incorrect isomers are present (typically *trans* isomers of bonds that are *cis* in the native state) folding is decelerated from milliseconds to the time range of several minutes.

Several strategies are useful for identifying proline-limited steps in a folding reaction. They include interrupted unfolding and refolding in double mixing experiments as well as the use of prolyl isomerases, which are enzymes that catalyze prolyl isomerizations (see Chapter 10 in Part II). The prolyl isomerases are ubiquitous proteins. They are found in all organisms, and in bacteria a prolyl isomerase

1) To facilitate reading I use the terms *cis* proline and *trans* proline for proline residues that are preceded by a *cis* or a *trans* peptide bond, respectively, in the *folded* protein. ''Native-like'' and ''incorrect, nonnative'' denote whether in an unfolded state a particular prolyl peptide bond shows the same conformation as in the native state or not. Further, I use the expression ''isomerization of Xaa'' for the isomerization of the peptide bond preceding Xaa. Peptide bonds preceding proline are referred to as ''prolyl bonds,'' those preceding residues other than proline as ''nonprolyl bonds.'' The folding reactions that involve Xaa-Pro isomerizations as rate-limiting steps are denoted ''proline-limited'' reactions.

Protein Folding Handbook. Part I. Edited by J. Buchner and T. Kiefhaber

ISBN: 3-527-30784-2

is associated with the ribosome. This enzyme, the trigger factor, accelerates proline-limited folding reactions particularly well and might in fact also catalyze prolyl isomerizations in the folding of nascent proteins. Prolyl isomerization in protein folding and its catalysis by prolyl isomerases are covered in a number of review articles [1–10].

25.2 Prolyl Peptide Bonds

In a peptide bond the distance between the carbonyl carbon and the nitrogen is 0.15 Å shorter than expected for a C–N single bond and both the C and the N atom show sp^2 hybridization [11], which indicates that the peptide bond has considerable double bond character. Peptide bonds are thus planar, and the flanking Cα atoms can be either in the *trans* or in the *cis* conformation (equivalent to dihedral angles ω of 180° and 0°, respectively). For peptide bonds preceding residues other than proline the *cis* state is strongly disfavored. Fischer and coworkers found *cis* contents between 0.11 and 0.48% for a number of nonprolyl peptide bonds in oligopeptides. The highest propensity to adopt the *cis* conformation was observed for a Tyr-Ala bond in a dipeptide [12].

In native, folded proteins nonprolyl *cis* peptide bonds are very rare [13–16]. Only 43 *cis* nonprolyl peptide bonds were found in a survey of 571 protein structures [16]. Interestingly carboxypeptidase A contains three of them [17].

For Xaa-Pro peptide bonds (''prolyl bonds'') the *cis* and *trans* conformations differ much less in energy because the Cα of Xaa is always arranged in *cis* with a C atom: either with the Cα or the Cδ of the proline (Figure 25.1). The *trans* isomer is thus favored only slightly over the *cis* isomer and in short peptides frequently *cis* contents of 10–30% are observed [18–21]. The *cis*/*trans* ratio depends on the properties of the flanking amino acids and on ionic or van der Waals interactions that are possible in one isomeric state, but not in the other.

In small, well-folded proteins the conformational state of each prolyl bond is usually clearly defined. It is either *cis* or *trans* in every molecule, depending on the structural framework imposed by the folded protein chain. About 5–7% of all prolyl peptide bonds in folded proteins are *cis* [13–16], and 43% of 1435 nonredundant protein structures in the Brookhaven Protein Database contain at least one *cis* proline [20]. Several proteins are heterogeneous and show *cis*/*trans* equilibria at

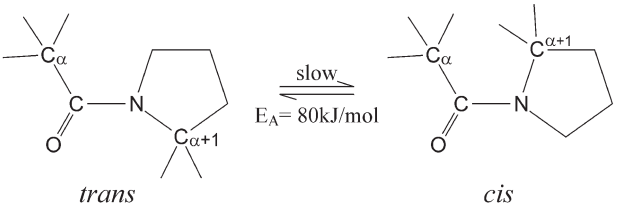

Fig. 25.1. Isomerization between the *cis* and *trans* forms of an Xaa-Pro peptide bond.

one or more prolyl bonds. Most of these heterogeneities were discovered by NMR spectroscopy. They will be discussed later (see Section 25.5).

The energy barrier between the *cis* and the *trans* form is enthalpic in nature. The average activation enthalpy is about 80 kJ mol^{-1} and the activation entropy is close to zero. Because of this high energy barrier prolyl isomerizations are intrinsically slow reactions with time constants that range between 10 and 100 s (at 25 °C). The absence of an activation entropy indicates that the surrounding solvent is not reorganized when the activated state of this intramolecular isomerization reaction is reached.

Secondary amide [22] and prolyl isomerizations are faster in nonpolar solvents than in water. This was traditionally explained by assuming that the transition state for isomerization is less polar than the ground state because the peptide bond is twisted and thus the resonance between the carbonyl group and the nitrogen is lost [23]. Eberhardt et al. [24] found, however, that the rate constant of prolyl isomerization in the dipeptide Ac-Gly-Pro-OCH_3 does not correlate with the dielectric constant of the solvent, but with its ability to donate a hydrogen bond to the carbonyl oxygen of the peptide.

The nitrogen of the amide bond can be protonated by very strong acids. This protonation abolishes the resonance between C=O and N of the prolyl bond. Thus, the partial double bond character is lost and the barrier to rotation is diminished. Prolyl isomerization is in fact well catalyzed by a solution of acetic acid in acetic anhydride [25] or by $\geq$7 M $HClO_4$ [26].

In summary, prolyl isomerization is slow because the resonance energy of the CN partial double bond must be overcome. The reaction is decelerated when the resonance is increased, such as in solvents that donate a hydrogen bond or a proton to the carbonyl oxygen. It is accelerated when the resonance is decreased, in particular by N protonation. The mechanism of nonenzymic prolyl isomerization is thoroughly discussed by Stein [23] and Fischer [21].

25.3
Prolyl Isomerizations as Rate-determining Steps of Protein Folding

25.3.1
The Discovery of Fast and Slow Refolding Species

In seminal work Garel and Baldwin [27] discovered that unfolded ribonuclease A (RNase A) consists of a heterogeneous mixture of molecules. They found fast-folding U_F molecules[2] that refolded in less than a second, and slow-folding U_S molecules that required several minutes to fold to completion. Similar U_F and U_S

2) Abbreviations used: U, I, N, the unfolded, the intermediate, and native state of a protein, respectively; U_F, U_S, fast- and slow-folding unfolded forms, I_N, native-like intermediate; τ and λ, apparent time constant and rate constant, respectively, of a reaction; k, microscopic rate constant.

species were later found in the folding of many other proteins [7, 28, 29]. In 1975, two years after the discovery by Garel and Baldwin, Brandts and coworkers [30] formulated the proline hypothesis and suggested that the U_F and U_S molecules differ in the *cis*/*trans* isomeric state of one or more Xaa-Pro peptide bonds.

In the native protein (N) usually each prolyl peptide bond is in a defined conformation, either *cis* or *trans*, depending on the constraints dictated by the ordered native structure. After unfolding ($N \rightarrow U_F$), however, these bonds become free to isomerize slowly as in short oligopeptides (in the $U_F \rightleftharpoons U_S^i$ reaction), as shown in Scheme 25.1.

$$N \xrightarrow[\text{fast}]{\text{unfolding}} U_F \underset{\text{slow}}{\overset{\text{Pro isomerization}}{\rightleftharpoons}} U_S^i$$

Scheme 25.1. Kinetic model for the coupling betweeen protein unfolding and prolyl isomerization.

The isomerizations thus create a mixture, which consists of a single unfolded species with correct prolyl isomers (U_F) and, depending on the number of prolines, one or more unfolded species with incorrrect prolyl isomers (U_S^i). The U_F molecules with the native-like prolyl isomers can refold directly in a fast reaction to the native conformation. The U_S^i molecules, however, refold slowly, because their refolding involves the re-isomerizations of the incorrect prolyl bonds.

25.3.2
Detection of Proline-limited Folding Processes

Proline-limited reactions in the unfolding and refolding of a protein can be identified and characterized in several ways.

1. *Rates and activation energies of refolding.* Circumstantial evidence for a proline-limited folding reaction is provided when its time constant is in the 10–100 s range (at 25 °C) and when its activation energy is about 80 kJ mol^{-1}. Conformational folding reactions can, however, show very similar kinetic properties, and therefore time constants and activation energies provide weak evidence for a proline-limited process.
2. *Properties of the refolding reactions.* The various U species that are populated at equilibrium in the unfolded protein give rise to parallel direct and proline-limited refolding reactions. The relative amplitudes of these refolding reactions should depend only on the relative populations of these U species. They should be independent of the final folding conditions and independent of the probe that was used to monitor refolding. The amplitudes of refolding should also be independent of the initial unfolding conditions, because the *cis*/*trans* equilibria at prolyl bonds are largely independent of the denaturant concentration, of temperature, and of the pH (unless the prolines are flanked by ionizable groups).

These criteria are valid only when direct folding is much faster than proline-limited folding and when partially folded intermediates with incorrect prolines do not accumulate during folding. U species with several incorrect prolines can enter alternative refolding routes, and the rank order of the re-isomerizations may change with the refolding conditions. Guidelines for the kinetic analysis of folding reactions that are coupled with prolyl isomerizations are given by Kiefhaber et al. [31, 32].

3. *Slow refolding assays (double jumps)*. Prolyl isomerizations in the unfolded form of a protein (after the $N \rightarrow U_F$ unfolding step, Scheme 25.1) can be measured by slow refolding assays. The $U_F \rightleftharpoons U_S$ isomerizations usually cannot be monitored directly by a spectroscopic probe. Rather, the amount of U_S formed after different times of unfolding is determined by slow refolding assays in "double jump" experiments [30, 33]. Samples are withdrawn from the unfolding solution at different time intervals after the initiation of unfolding; these samples are transferred to standard refolding conditions, and the amplitudes of the resulting slow refolding reactions, $U_S \rightarrow N$, are determined. These amplitudes are proportional to the concentrations of the U_S species present at the time when the sample was withdrawn for the assay, and their dependence on the time of unfolding reveals the kinetics of the $U_F \rightleftharpoons U_S$ reactions. An experimental protocol for double-jump experiments is given in Section 25.9 (Experimental Protocols). Slow refolding assays work very well when conditions can be found under which the conformational and the proline-limited events are well separated in both the unfolding step and in the subsequent refolding assay. It cannot be used when conformational folding ($U_F \rightarrow N$) in the second step shows a similar rate as the $U_F \rightleftharpoons U_S$ reactions. In this case the prolyl isomerizations couple with the $U_F \rightarrow N$ reaction in the refolding assay, and the amplitudes of refolding no longer reflect the concentration of the U_S molecules, as present at the time of sample transfer.
4. *Catalysis by prolyl isomerases*. Prolyl isomerases are excellent tools to identify proline-limited folding reactions. Since they catalyze only prolyl isomerizations (see Chapter 10 in Part II), the acceleration of a particular folding reaction by a prolyl isomerase provides compelling evidence that it involves a proline-limited step. Partial folding may render prolyl bonds inaccessible for a prolyl isomerase. Therefore a lack of catalysis does not strictly rule out prolyl isomerization as the rate-limiting step of a particular folding reaction. Several families of prolyl isomerases with different substrate specificities are available and can be used as tools in folding studies [3, 7, 8].
5. *Replacement of prolines by other residues*. Site-directed mutagenesis of proline residues is an apparently simple und straightforward means to detect proline-limited folding reactions and to identify the prolines that are involved in a particular folding reaction. The interpretation of the changes in the folding kinetics is usually straightforward when a *trans* prolyl bond of the wild-type protein is changed to a nonprolyl *trans* bond by the mutation, or when a *cis* prolyl bond is replaced by a "normal" nonprolyl *trans* bond. The protein stability and the rate of the direct folding reaction should not be changed strongly by the proline

substitution. For *cis* prolines such conditions are rarely met. Often, mutations of critical *cis* prolines are strongly destabilizing and the *cis* conformation of the respective bond is maintained even after the mutation to a residue other than proline. *Trans* → *cis* isomerizations at nonprolyl peptide bonds are also slow. An unchanged slow folding reaction after the replacement of a particular proline is therefore not sufficient evidence to exclude its isomerization as a possible rate-limiting reaction. It is necessary to analyze the unfolding and refolding kinetics after a proline replacement in detail, in order not to draw incorrect conclusions.

6. *Analysis of the folding kinetics by NMR spectroscopy.* Perhaps the best approach would be to follow the isomerization of a particular proline during folding directly by real-time NMR spectroscopy. The CαH resonance of the residue preceding the proline and the CδH resonance of proline are sensitive to the isomeric state of the prolyl bond and could be used to follow a prolyl isomerization directly in the course of a protein folding reaction. Unfortunately, these resonances are in a very crowded region of the NMR spectrum of a protein, and therefore, to the best of my knowledge, this approach has not yet been employed.

25.3.3
Proline-limited Folding Reactions

Proline-limited steps were found in the folding kinetics of many small single-domain proteins. The direct folding reactions of these proteins are usually fast (often in the time range of milliseconds) and therefore the proline-limited steps can easily be identified in unfolding and in refolding either directly or by double-mixing experiments, as described in Section 25.3.2 and in Section 25.9 (Experimental Protocols).

As expected, proline-limited reactions with large amplitudes are found for proteins with *cis* prolines, such as the immunoglobulin domains [34], thioredoxin [35], barstar [36], staphylococcal nuclease [37, 38], ubiquitin [39], plastocyanin [40], or pseudo-azurin [41]. In most of these cases partially folded intermediates accumulate in refolding before the final slow prolyl *trans* → *cis* isomerization.

Single-domain proteins with only *trans* prolines also show slow refolding reactions. Their amplitudes are usually small, because the *trans* isomer is favored in the unfolded molecules as well. Often, the amplitude of slow folding is smaller than expected from the number of *trans* prolines. This may originate from the fact that in unfolded polypeptides the *trans* form is more favored over *cis* than in short peptides and that some *trans* prolines are nonessential for folding. In addition, native-like intermediates may accumulate prior to re-isomerization, which also decreases the amplitudes of the slow folding reactions. Proteins with only *trans* prolines include cytochrome *c* [42], barnase [43], the chymotrypsin inhibitor CI2 [44], FKBP12 [45, 46], acylphosphatase [47], MerP [48] the immunity proteins Im7 and Im9 [49], the cell cycle protein p13suc1 [50], and the amylase inhibitor Tendamistat [51].

For large oligodomain or oligomeric proteins it is usually difficult to identify prolyl isomerizations in unfolding and refolding, chiefly because direct folding is often slow and not well separated from the proline-limited steps. As a consequence, the two reactions are strongly coupled, and the isomerizations cannot be followed easily by the double-mixing techniques. Nevertheless there are numerous examples for proline-limited steps in the folding of oligodomain and/or oligomeric proteins [52–55].

The immunoglobulins are heterotetramers that are composed of two light chains (with two domains each) and two heavy chains (with four domains each). The individual domains show a related fold (the "immunoglobulin fold") and typically contain a single *cis* proline. Its *trans* → *cis* isomerization determines the folding of the separate domains [34] and of the intact light chains [56]. In the folding of the F_{ab} fragment (which consists of four domain: two from the light chain and two from the heavy chain) proline isomerization can occur late in folding, after association [57]. In the folding of the isolated C_H3 domain, however, prolyl isomerization occurs before this domain associates to a homodimer [58].

The gene-3-protein in the coat of the phage fd is essential for its infectivity. Early in the infection of an *Escherichia coli* cell, the two N-terminal domains of the gene-3-protein (N2 and N1) interact successively with the F pilus and the TolA receptor. To expose the binding site for TolA the domains must disassemble, otherwise infection would be stopped. In refolding, the domains N1 and N2 fold rapidly, but the final domain assembly is unusually slow and shows a time constant of 6200 s (at 25 °C). It is controlled by the *trans* → *cis* isomerization of the Gln212-Pro213 bond in the hinge between the domains. The kinetic block of domain reassembly caused by this very slow isomerization at Pro213 could ensure that after the initial binding of N2 to the F pilus the domains disassemble and that this open state has a lifetime long enough for the N1 domain to approach and interact with TolA. Pro213 isomerization of the gene-3-protein might thus serve as a slow conformational switch during the infection process [59, 60].

Ure2 is a prion-like yeast protein with an unfolded N-terminal prion domain and a compactly folded C-terminal domain, which harbors a *cis* proline at position 166. Unfolded molecules with the native-like *cis* Pro166 fold and dimerize rapidly, whereas molecules with the incorrect *trans* isomer do not reach the native state within several hours [61]. Apparently, Pro166 isomerization decelerates productive folding so strongly that it can no longer compete with side reactions, such as aggregation.

A few important points should be considered when, in the folding of large proteins, the role of many *trans* prolines or of a mixture of *cis* and *trans* prolines is investigated.

1. Not all prolines are necessarily important for the folding kinetics.
2. The *trans* form is usually favored over the *cis*, and therefore *cis* → *trans* isomerizations show small amplitudes and are about 5–10 times faster than *trans* → *cis* isomerizations.

3. The prolyl isomerizations after unfolding are parallel reactions. As a consequence, the rate of U_S formation should increase with the number of prolines.
4. The rate of refolding, however, decreases with the number of incorrect prolines [62], because only the species with all prolines in the native-like isomeric state can complete folding.
5. For large proteins the direct refolding reaction is often rather slow and not well separated in rate from the proline-limited steps. As a consequence, the analysis by slow refolding assays becomes difficult.

Carbonic anhydrase provides a good example. It contains 15 *trans* and 2 *cis* prolines and after long-term denaturation virtually all molecules are in U_S states, i.e., they have nonnative prolines and refold slowly [63]. More than half of the U_S molecules form rapidly after unfolding in a reaction that is about tenfold faster than expected for a single prolyl isomerization [64]. This increase in rate is probably caused by the additive and independent isomerizations of the many *trans* prolines of this protein. The remainder of the slow-folding molecules is then created very slowly in a reaction that is probably caused by the *cis* $\rightleftharpoons$ *trans* isomerizations of one or both *cis* prolines. Short-term unfolding of carbonic anhydrase yields U_F molecules with correct prolines, but only a fraction of them can in fact refold rapidly, because molecules with incorrect isomers continue to form early in refolding, in competition with the direct refolding reaction, which is only marginally faster than the multiple *cis* $\rightleftharpoons$ *trans* isomerizations. Addition of cyclophilin had a peculiar effect on the refolding of the short-term denatured molecules. At the onset of the experiment this prolyl isomerase catalyzed *cis* $\rightleftharpoons$ *trans* isomerization in the unfolded molecules and thus increased the fraction of molecules that fold on slow proline-limited paths. These molecules, however, refolded more rapidly, because cyclophilin accelerated the proline-limited steps in their refolding [64]. A similar behavior was found for the single-chain Fv fragment of an antibody, which contains four *trans* and two *cis* prolines [65].

25.3.4
Interrelation between Prolyl Isomerization and Conformational Folding

When they initially suggested the proline hypothesis, Brandts and coworkers assumed that the nonnative prolyl isomers can block refolding right at its beginning [30], and that the slow $U_S \rightarrow U_F$ isomerization in the unfolded molecules is the first and rate-limiting step of folding. Since then many proline-limited folding reactions have been investigated (see Section 25.4), and it is clear now that conformational folding can start while some prolines are still in their nonnative states, and that partially folded intermediates can tolerate incorrect prolines. The final folding steps, however, require correct prolines and therefore they are limited in rate by the prolyl isomerizations [7, 29, 66, 67].

The extent of conformational folding that can occur prior to prolyl isomerization depends on the location of the nonnative prolyl bonds in the structure, on the

stability of partially folded intermediates and on the folding conditions. Generally, incorrect prolyl bonds in exposed or flexible chain regions will not interfere strongly with conformational folding, and solvent conditions that strongly stabilize folded proteins will also stabilize partially folded structure with incorrect isomers. Thus there is a close interdependence between conformational folding steps and prolyl isomerization. On the one hand the presence of incorrect isomers in the chain can decelerate its folding, and on the other hand rapid chain folding can affect the equilibrium and the kinetics of prolyl isomerization. The close interrelationship between structure formation and prolyl peptide bond isomerization is a key feature of slow folding steps and is of central importance for understanding the role of prolyl isomerases in these processes.

A simple $U_S \rightarrow U_F \rightarrow N$ refolding path is followed only under conditions where the fully folded protein is only marginally stable, such as at the onset of the equilibrium unfolding transition. Here a single incorrect kink in the protein backbone (as introduced by a nonnative prolyl bond) is sufficient to destabilize partially folded conformations.

25.4 Examples of Proline-limited Folding Reactions

25.4.1 Ribonuclease A

Bovine pancreatic RNase A played a central role in the elucidation of proline-limited folding reactions. This protein contains four prolines: Pro42 and Pro117 are *trans* and Pro93 and Pro114 are *cis* in the native protein. Both the proposal of the proline hypothesis and the first experimental evaluations are linked with RNase A. Garel and Baldwin [27] discovered the coexistence of U_F and U_S in unfolded RNase A, and Brandts and coworkers [30] developed the slow refolding assays to measure the $U_F \rightleftharpoons U_S$ equilibration in this protein. The quantitative analyses of the folding kinetics of RNase A in the thermal unfolding transition at pH 3 [68] and in the guanidinium chloride (GdmCl)-induced transition [69] demonstrated that they are in fact well described by a $U_S \rightleftharpoons U_F \rightleftharpoons N$ three-state mechanism. The $U_F \rightleftharpoons U_S$ reaction in unfolded RNase A was found to be independent of denaturants [70] and catalyzed by a strong acid [26], as expected for a proline-limited process.

The first partially folded intermediate with a nonnative prolyl isomer was also discovered in the refolding of RNase A [66, 67]. Under conditions that strongly favor the folded form, the major U_S species (called U_S^{II}) refolds to a native-like form I_N, an intermediate that is folded, as judged by amide circular dichroism and is already enzymatically active. This indicated for the first time that nonnative prolyl bonds do not necessarily block refolding, but that protein molecules with an incorrect prolyl bond could almost reach the native form. The final slow step of folding

($I_N \rightarrow N$) originates from the *trans* → *cis* isomerization of the Tyr92-Pro93 bond [71, 72]. It could be assigned before the advent of site-directed mutagenesis, because it is accompanied by a change in the fluorescence of Tyr92 [73].

The intermediate I_N is less stable and unfolds much faster than native RNase A. The interconversion between I_N and N could thus be measured by unfolding assays which exploited this strong difference between the unfolding rates of I_N and N. In these experiments refolding was interrupted after various times, samples were transferred to standard unfolding conditions and the amplitudes of the fast and slow unfolding reactions were determined as a function of the duration of refolding. These amplitudes reflected the time courses of I_N and N, respectively during folding [74]. Such interrupted folding experiments are excellent tools for discriminating native-like intermediates from the native protein and for following the time courses of these species in complex folding reactions. The method is so sensitive, because the native molecules are often separated from partially folded ones by a high activation barrier, and thus they differ strongly in the rate of unfolding. Section 25.9 gives a protocol for measuring silent slow prolyl isomerizations in largely folded intermediates by such unfolding assays.

The isomeric states of the four prolines in the various U species remained unclear for a long time. The kinetic analyses of the Baldwin, Brandts, and Schmid groups (for reviews see Refs [28, 75]) had indicated already that U_S is heterogeneous and consists of a minor U_S^{I} species and a major U_S^{II} species, which refolds via the native like intermediate I_N.

The Scheraga group re-evaluated the folding kinetics of RNase A, among others, by making many mutants with alterations at the four prolines (see Ref. [9] for a review). They found that the U_F species is heterogeneous as well [76], being composed of 5% of a very fast folding species U_{vf} and 13% of a fast-folding species U_f. U_{vf} and U_f differ in the isomeric state of Pro114. However, they fold with different rates only at low pH, where the conformational stability of RNase A is low. At neutral pH U_{vf} and U_f fold fast with indistinguishable rates. This is consistent with the original finding of 20% fast-folding U_F molecules [27], and it confirms the suggestion that Pro114 is nonessential for the folding of RNase A [66] under favorable conditions. Under unfavorable conditions, such as at low pH, or when an additional proline is incorrect (such as in the intermediate I_N with incorrect *trans* isomers at both Pro93 and Pro114), a *trans* Pro114 might in fact retard folding. Raines and coworkers replaced Pro114 by 5,5-dimethyl-L-proline, which stays almost exclusively in the native *cis* conformation. This mimic of a *cis* proline slightly accelerated the $U_S^{II} \rightarrow I_N$ reaction. The authors interpreted this to suggest that an incorrect *trans* Pro114 slightly decelerates the folding reaction of the U_S^{II} form of the wild-type protein [77]. Together all this suggests that Pro114 of RNase A is a conditional proline. It is unimportant for folding under favorable conditions, but retards folding slightly under unfavorable conditions.

U_S^{II} contains an incorrect *trans* Pro93. Comparative experiments with homologous RNases from various species [71, 78] and early directed mutagenesis work had already suggested a crucial role of Pro93 for the major folding reaction

$U_S^{II} \rightarrow I_N \rightarrow N$ [79]. The more recent results from the Scheraga group confirm this [9]. They also show that, after the Pro93Ala substitution, Tyr92 and Ala93 form a nonprolyl *cis* peptide bond in the folded form of P93A-RNase A [80].

The minor form U_S^I contains one or more incorrect prolines in addition to the incorrect *trans* Pro93 [71]. This destabilizes partially folded structure further and impairs the formation of intermediates such as I_N. Scheraga et al. have now found that U_S^I contains both an incorrect *trans* Pro93 and an incorrect *cis* Pro117 [9, 80–82]. According to their work, Pro42 is unimportant for folding.

25.4.2 Ribonuclease T1

RNase T1 from *Aspergillus oryzae* [83] is a small single-domain protein of 104 amino acids [83–86], which is not related structurally with RNase A. It contains two disulfide bonds (Cys2-Cys10 and Cys6-Cys103, two *trans* (Trp59-Pro60 and Ser72-Pro73) and two *cis* (Tyr38-Pro39 and Ser54-Pro55) prolyl bonds. RNase T1 is most stable near pH 5 and further stabilized when NaCl is added [87–89]. Importantly, in the absence of the disulfide bonds, RNase T1 can still fold to a native-like conformation when $\geq$1 M NaCl are present [87, 88, 90].

The equilibrium unfolding transition of RNase T1 is well described by a simple two-state model [91–94], but the unfolding and refolding kinetics are complex. Almost the entire folding of RNase T1 involves prolyl isomerizations [95, 96] both in the presence and in the absence of the two disulfide bonds [97, 98]. All observable phases in the unfolding and the refolding kinetics could be explained by contributions from the two *cis* prolines only [99–101]. RNase T1 is a good substrate for assaying prolyl isomerases [7, 8, 102].

The mechanism of unfolding is well explained by a model in which conformational unfolding ($N \rightarrow U_{55c}^{39c}$) is followed by the two *cis* $\rightleftharpoons$ *trans* isomerizations at Pro39 and Pro55 (Scheme 25.2). Both are *cis* in N and in U_{55c}^{39c}, but isomerize

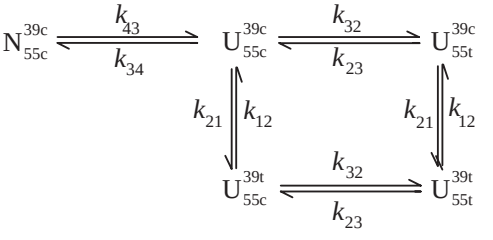

Scheme 25.2. Kinetic model for the unfolding and isomerization of RNase T1. This model is valid for unfolding only. The superscript and the subscript indicate the isomeric states of prolines 39 and 55, respectively, in the correct, native-like *cis* (c) and in the incorrect, nonnative *trans* (t) isomeric states. As an example, U_{55c}^{39t} is an unfolded species with Pro39 in the incorrect *trans* and Pro55 in the correct *cis* state. In the denatured protein the two isomerizations are independent of each other, therefore the scheme is symmetric with identical rate constants in the horizontal and vertical directions, respectively. At 25 °C and 6.0 M GdmCl, pH 1.6 $k_{43} = 0.49\ s^{-1}$, $k_{12} = 2.0 \times 10^{-3}\ s^{-1}$, $k_{21} = 22.6 \times 10^{-3}\ s^{-1}$, $k_{23} = 8.7 \times 10^{-3}\ s^{-1}$, $k_{32} = 50.5 \times 10^{-3}\ s^{-1}$ [103].

largely to the more favorable *trans* state in the unfolded protein. As a consequence, only 2–4% of all unfolded molecules remain in the U^{39c}_{55c} state with Pro39 and Pro55 in the correct *cis* state. U^{39t}_{55t}, the species with two incorrect isomers, predominates at equilibrium, and the two species with single incorrect isomers (U^{39t}_{55c} and U^{39c}_{55t}) are populated to 10–20% each.

Under strongly native conditions refolding is not a reversal of unfolding and cannot be explained solely with Scheme 25.2. Rather, refolding paths via intermediates originate from the different unfolded species (Scheme 25.3). The two slow-folding species with one incorrect prolyl isomer each (U^{39t}_{55c} and U^{39c}_{55t}) and the species with both prolines in the incorrect isomeric state (U^{39t}_{55t}) can regain rapidly most of their secondary structure in the milliseconds range (the $U_i \rightarrow I_i$ steps, Scheme 25.3) [104]. Subsequently, slow folding steps follow that involve the isomerizations of the incorrect prolyl isomers. A peculiar feature of the folding model in Scheme 25.3 is that the major unfolded species with two incorrect isomers (U^{39t}_{55t}) can enter two alternative folding pathways (the upper or the lower pathway in Scheme 25.3), depending upon which isomerization occurs first. The distribution of refolding molecules on these two pathways is determined by the relative rates of the *trans* → *cis* isomerizations of Pro39 and Pro55 at the stage of the intermediate I^{39t}_{55t}. The kinetic models in Schemes 25.2 and 25.3 were supported by experimental data on the slow folding of variants of RNase T1 where the *cis* prolines were replaced by other amino acids [99, 100, 105].

At equilibrium only 2–4% of all unfolded RNase T1 molecules have correct *cis* isomers at Pro39 and Pro55. Their fast direct refolding reaction ($U^{39c}_{55c} \rightarrow N^{39c}_{55c}$) could therefore not be measured initially.

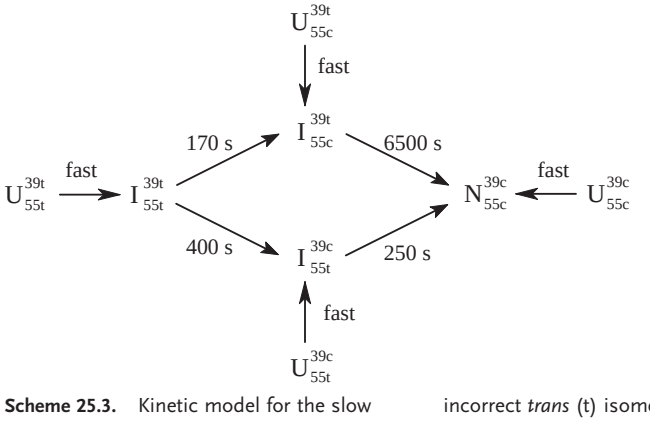

Scheme 25.3. Kinetic model for the slow refolding of RNase T1 under strongly native conditions. U stands for unfolded species, I for intermediates of refolding, and N is the native protein. The superscript and the subscript indicate the isomeric states of prolines 39 and 55, respectively, in the correct *cis* (c) and the incorrect *trans* (t) isomeric states. The rate constants given for the individual steps refer to folding conditions of 0.15 M GdmCl, pH 5.0, 10 °C [106]. The rate constant of the direct $U^{39c}_{55c} \rightarrow N^{39c}_{55c}$ reaction is 5.7 s^{-1} in 1.0 M GdmCl, pH 4.6, 25 °C [103].

Mayr et al. [103] exploited the sequential nature of unfolding ($N \rightarrow U_{55c}^{39c}$) and prolyl isomerizations (cf. Scheme 25.2) to characterize the direct $U_{55c}^{39c} \rightarrow N$ folding reaction. In the first step of a stopped-flow double-mixing experiment they produced U_{55c}^{39c} transiently at a high concentration under conditions, where the $N \rightarrow U_{55c}^{39c}$ unfolding reaction is much faster than the subsequent prolyl isomerizations and then measured its refolding in the second step. In addition, they varied the duration of the unfolding step and monitored the concentrations of all species of the wild-type protein in Scheme 25.2 as a function of time. Thus the rates of the individual prolyl isomerizations in the unfolded protein (cf. Scheme 25.2) could be determined.

The direct refolding reaction of RNase T1 with correct prolyl isomers shows a time constant of 175 ms (at 25 °C, pH 4.6) [103]. This reaction is almost unaffected by the proline substitutions. It depends nonlinearly on temperature with a maximum near 25 °C, which suggests that the activated state for this reaction resembles the native rather than the unfolded state in heat capacity. The folding of the species with single incorrect prolyl isomers ($U_{55c}^{39t} \rightarrow I_{55c}^{39t}$ and $U_{55t}^{39c} \rightarrow I_{55t}^{39c}$) was only about fivefold slower than direct folding and was also accompanied by a strong decrease in the apparent heat capacity.

Conformational folding and the re-isomerizations of the prolyl peptide bonds are thus tightly interrelated in the folding of RNase T1. As discussed above, rapid partial folding is possible in the presence of nonnative prolyl isomers [104, 106], but the final events of folding are coupled with the prolyl isomerizations and therefore very slow.

The partially folded structure in the intermediates affects the isomerization kinetics. In particular, the *trans* → *cis* isomerization at Pro39 (in the $I_{55c}^{39t} \rightarrow N$ step) is strongly decelerated by the folded structure in the intermediate I_{55c}^{39t} [106]. In the folding of pancreatic RNase A, however, prolyl isomerization is accelerated in the intermediate I_N [66, 67], and in the folding of dihydrofolate reductase an intramolecular catalysis of a prolyl isomerization was proposed to occur [107].

25.4.3
The Structure of a Folding Intermediate with an Incorrect Prolyl Isomer

In the S54G/P55N variant of RNase T1 [99] the *cis* Ser54-Pro55 prolyl bond is replaced by a *trans* Gly54-Asn55 peptide bond (Hinrichs et al., unpublished results). Thus a *cis* bond is abolished and the branched folding mechanism (Scheme 25.3) is strongly simplified to a sequential mechanism (Scheme 25.4). Only two unfolded species remain: 15% as a fast folding species with the native-like *cis* isomer of Pro39 (U^{39c}), and 85% as a slow folding species with the incorrect *trans* isomer of Pro39 (U^{39t}).

The U^{39t} molecules (Scheme 25.4) refold in two steps. First the intermediate I^{39t} is formed, which then converts to the native protein. This second step is limited in rate by the *trans* → *cis* isomerization of Pro39, which at 10 °C shows a time constant of about 8000 s. The I^{39t} intermediate is thus long-lived enough to obtain highly resolved structure information by kinetic NMR experiments [40, 108–110]

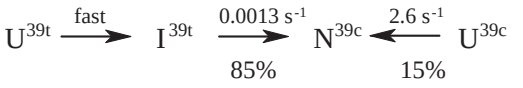

Scheme 25.4. Kinetic model for the slow refolding of S54G/P55N-RNase T1 under strongly native conditions. U stands for unfolded species, I for intermediates of refolding, and N is the native protein. The superscript indicates the isomeric state of proline 39 in the correct *cis* (c) and the incorrect *trans* (t) isomeric states. The rate constants given for the individual steps refer to folding conditions of 1.0 M GdmCl, pH 4.6, 25 °C.

and 2D-NOESY spectroscopy. Balbach et al. determined those protons in I^{39t} that are already surrounded by a native environment and thus show native distances to protons in close vicinity [111]. Surprisingly, amide protons in nonnative environments were found to be located not only close to the incorrect *trans* Tyr38-Pro39 bond in I^{39t}, but were spread throughout the entire protein. The destabilization caused by the incorrect *trans* Pro39 is thus not confined to the local environment of this proline, but involves several regions in the entire molecule.

25.5 Native-state Prolyl Isomerizations

Most prolyl peptide bonds in folded proteins show well defined conformations, being either in the *cis* or in the *trans* conformation. There are, however, a growing number of exceptions to this rule. High-resolution NMR spectroscopy, in particular, identified a series of prolines that are conformationally heterogeneous and exist as a mixture of *cis* and *trans* isomers in the folded state. Examples include staphylococcal nuclease [112], insulin [113], calbindin [114, 115], scorpion venom Lqh-8/6 [116], human interleukin-3 [117] and the TB6 domain of human fibrillin-1 [118, 119]. In folded staphylococcal nuclease *cis*/*trans* equilibria exist at Pro117 as well as at Pro47 [112, 120, 121], and the two equilibria seem to be independent of each other.

There are two strongly diverging, but not mutually exclusive, interpretations of these findings. The first is that conformationally heterogeneous proline residues occur in locally unfolded regions. They lack strong tertiary interactions, which would be necessary to stabilize one isomer over the other. Alternatively, heterogeneity at prolines might point to a functionally important *cis*/*trans* isomerization, which might be used as a slow molecular switch, for example, to regulate the function of the corresponding protein. Such switching functions, possibly modulated by prolyl isomerases, were suggested long time ago [122], but the evidence for proline switches remained circumstantial.

Evidence for a proline-dependent conformational switch was obtained for the SH2 domain of the tyrosine kinase Itk [123, 124]. Unlike other proteins with *cis* and *trans* prolyl conformers in the native state [115, 119, 125–127] the SH2 domain of Itk shows a pronounced change in structure upon *cis*/*trans* isomerization.

The *cis* and the *trans* forms of Itk-SH2 differ slightly in the affinity for the Itk-SH3 domain and for a phosphopeptide, which represent alternative substrates for the SH2 domain [128]. This conformational switch thus seems to modulate substrate recognition and can be regulated by the prolyl isomerase cyclophilin 18. A review of the proline switch in Itk and in other proteins is found in Ref. [10].

The prolyl isomerase, PIN1, catalyzes the isomerization of phosphoserine-proline bonds, and there is compelling evidence that PIN1 integrates phosphorylation-dependent and prolyl-isomerization-dependent switches for a wide range of signaling reactions [129] (see also Chapter 10 in Part II).

25.6 Nonprolyl Isomerizations in Protein Folding

For nonprolyl bonds the *trans* state is strongly favored over *cis*, and the *cis* content as measured for oligopeptides is far below 1% [12, 130]. A large amount of conformational energy is therefore required to lock such a bond in the *cis* state. A shift in the equilibrium from 0.2% to 99% *cis* requires a Gibbs free energy of 15 kJ mol^{-1}. Nevertheless *cis* nonprolyl bonds are found in folded proteins, but they are very rare, and presumably they are important for the function of a protein. In principle, a nonprolyl *cis* peptide bond would be well suited to construct a molecular switch in a protein that can be actuated only under a very strong load. A tight-binding ligand could, for example, supply a sufficient amount of free energy from its own binding to turn such a strong switch. A compilation of proteins with *cis* peptide bonds is found in Ref. [16]. Because the *trans* isomer is so strongly favored over the *cis*, *trans* → *cis* isomerizations at nonprolyl bonds during refolding must occur for such proteins in virtually all molecules.

The first evidence for a nonprolyl isomerization as a rate-determining step in protein folding was obtained for a variant of RNase T1. The replacement of one of the two *cis* prolines, *cis*-Pro39, of the wild-type protein by an alanine residue led to a variant with a *cis* nonprolyl peptide bond between Tyr38 and Ala39 [131]. This *cis* bond is located adjacent to His40, which is a catalytic residue. The Pro39Ala mutation reduced the stability of RNase T1 by about 20 kJ mol^{-1} and caused a major change in the folding mechanism. As shown in Scheme 25.5, the conformational unfolding of P39A-RNase T1 occurs first (in the $N \rightarrow U^{39c}_{55c}$ reaction) with a time constant of 20 ms. It leads to U^{39c}_{55c}, an unfolded form that has both Ala39 and

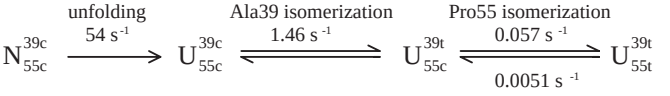

Scheme 25.5. Kinetic mechanism for the unfolding and isomerization of P39A-RNase T1. The superscript and the subscript indicate the isomeric states of Ala39 and Pro55, respectively, in the correct, native-like *cis* (c) and in the incorrect, nonnative *trans* (t) isomeric states. The rate constants refer to unfolding in 6.0 M GdmCl (pH 1.6) at 25 °C [96].

Pro55 still in the native-like *cis* conformation. Subsequently, the Tyr38-Ala39 bond isomerizes from *cis* to *trans* (in the $U^{39c}_{55c} \rightleftharpoons U^{39t}_{55c}$ step) in virtually all molecules. This nonprolyl isomerization ($\tau = 730$ ms) is about 60-fold faster than the corresponding prolyl isomerization (of the Tyr38-Pro39 bond) in wild-type RNase T1 [96]. It shows almost the same time constant as the *cis* → *trans* isomerization of the Tyr-Ala bond in the pentapeptide AAYAA ($\tau = 560$ ms [12]). In the unfolding the Tyr-Ala isomerization is then followed by the slow *cis* ⇌ *trans* equilibration at Pro55 ($\tau = 16$ s), which is still present in P39A-RNase T1.

Unfolded molecules in which the Tyr38-Ala39 bond was still in the native-like *cis* conformation (U^{39c}_{55c}) were produced in a stopped-flow double-mixing experiment by a short 100-ms unfolding pulse. They refolded rapidly to the native state with $\tau = 290$ ms (in 1.0 M GdmCl, pH 4.6, 25 °C). After the Ala39 *cis* → *trans* isomerization in the unfolded state, refolding is 1600-fold retarded and shows a time constant of 480 s. This slow refolding is limited in rate by the *trans* → *cis* reisomerization of the Tyr38-Ala39 bond. Under the same refolding conditions the *trans* → *cis* isomerization of the Tyr38-Pro39 bond in the wild-type protein is only twofold slower ($\tau = 1100$ s) [100, 105]. This comparison with the folding kinetics of wild-type RNase T1 indicates that the kinetics of Tyr38-Pro39 and of Tyr38-Ala39 isomerization differ predominantly in the rate of the *cis* → *trans*, rather than of the *trans* → *cis* reaction. The ratio of the rate constants for the *cis* → *trans* and the *trans* → *cis* reactions at the Tyr38-Ala39 bond gives an equilibrium constant of 0.0015, again in good agreement with the equilibrium constant of 0.0011 in the peptide AAYAA [12].

Very similar results were obtained later for the Pro93Ala mutation in RNase A [80, 132]. As in RNase T1, this mutation converted a *cis* Tyr-Pro bond into a *cis* Tyr-Ala bond and abolished the fast-folding reaction. The *cis* → *trans* isomerization of the Tyr-Ala bond in the unfolded protein occurred with $\tau = 1400$ ms at 15 °C [80], which agrees well with $\tau = 730$ ms, as measured for RNase T1 at 25 °C.

TEM-1 β-lactamase from *E. coli* contains a *cis* peptide bond between Glu166 and Pro167, in a large Ω loop near the active site. It is required for the catalytic activity of β-lactamase [133], and its *trans* → *cis* isomerization is a slow step in refolding [134–137]. Similar to Pro39 of RNase T1 the *cis* character of the 166–167 bond is retained when Pro167 of β-lactamase is replaced by a Thr residue, and the *trans* → *cis* isomerization of the Glu166-Thr167 peptide bond becomes rate limiting for the refolding of the P167T variant [135]. *Cis* peptide bonds between the residues equivalent to Glu166 and Pro167 of TEM-1 β-lactamase of *E. coli* are found in many β-lactamases, but interestingly, these *cis* peptide bonds are not always prolyl bonds. The β-lactamase PC1 from *Staphylococcus aureus* shows a *cis* Glu-Ile bond at this position [138].

In summary, the results obtained for RNase T1, RNase A and the β-lactamases show that the *trans* → *cis* isomerizations of nonprolyl peptide bonds are slow reactions (with time constants of several hundred seconds at 25 °C) and control the folding of proteins with nonprolyl *cis* peptide bonds. The *trans* → *cis* isomerizations of prolyl and nonprolyl bonds show similar rates, the reverse *cis* → *trans* isomerizations are 50–100 fold faster, however, for the nonprolyl peptide bonds.

Because the *trans* conformation is so strongly preferred, only one out of 500 or 1000 nonprolyl peptide bonds is in *cis* in an unfolded protein chain. Furthermore, it re-isomerizes to *trans* within less than a second when the protein folds at 25 °C. It is clear that such rare reactions are not easily identified in experimental folding kinetics.

First evidence for nonprolyl *cis* → *trans* isomerization in the refolding of a protein was obtained for a proline-free mutant of the small protein tendamistat [139]. Ninety-five per cent of all molecules of this protein fold rapidly with $\tau = 50$ ms, but 5% refold more slowly with $\tau = 400$ ms (at 25 °C). The slow-refolding molecules are created by isomerizations in the unfolded protein, most likely by the *cis* ⇌ *trans* isomerizations of nonprolyl peptide bonds. The fraction of molecules with incorrect *cis* nonprolyl isomers is small, because the correct *trans* isomer is favored so strongly over the *cis*.

25.7 Catalysis of Protein Folding by Prolyl Isomerases

Prolyl isomerases are ubiquitous enzymes that catalyze the *cis* ↔ *trans* isomerization of prolyl peptide bonds both in oligopeptides and during the folding of proteins. They are described in Chapter 10 in Part II. The first evidence for a catalysis of protein folding by a prolyl isomerase (porcine cytoplasmic cyclophilin 18, Cyp18) was obtained for the immunoglobulin light chain, porcine ribonuclease (RNase) and the S-protein fragment of bovine RNase A [140]. The slow refolding of RNase A could not be catalyzed, probably because the incorrect *trans* Tyr92-Pro93 is shielded from prolyl isomerases in the native-like intermediate I_N (cf. Section 25.5.1).

25.7.1 Prolyl Isomerases as Tools for Identifying Proline-limited Folding Steps

The prolyl isomerases, in particular Cyp18, are valuable tools to examine whether a slow folding reaction is rate-limited by a prolyl isomerization. A catalysis of proline-limited steps was observed in the folding of many proteins, including barnase [141], carbonic anhydrase [142, 143], β-lactamase (A. Lejeune, unpublished results), chymotrypsin inhibitor CI2 [44], yeast iso-2 cytochrome *c* [144, 145], the immunoglobulin light chain [57, 140], staphylococcal nuclease [146], and *trp* aporepressor [147]. *Cis* → *trans* and *trans* → *cis* isomerizations are catalyzed equally well in the folding of these proteins. In the maturation of the collagen triple helix prolyl and hydroxyprolyl isomerizations are rate-limiting steps, and this folding reaction is also accelerated by Cyp18 [148–150].

Proteins with incorrect prolyl isomers can start to fold before prolyl isomerization, and some of them reach a state that is native-like already. This often hinders prolyl isomerases in their access to the incorrect prolines and impairs catalysis of isomerization. The role of the accessibility of the prolines was studied for iso-2 cytochrome *c*. In aqueous buffer the folding of this protein is barely catalyzed by

cyclophilin. When, however, GdmCl is added in increasing, but still nondenaturing concentrations, catalysis is markedly improved, presumably because the denaturant destabilizes folding intermediates and thus improves the accessibility of the prolyl bonds [145].

In native RNase T1 *cis*-Pro55 is solvent exposed in the native protein and presumably also in folding intermediates, and therefore all prolyl isomerases catalyze the isomerization at Pro55 very well. *Cis*-Pro39 is buried in the native protein. Its *trans* → *cis* isomerization is only marginally accelerated, because rapid conformational folding hinders the access of the prolyl isomerases. Cyp18 from *E. coli* at a very high concentration (29 μM) was necessary to obtain a 300-fold acceleration of Pro39 isomerization in the refolding of 2.5 μM RNase T1 [151]. The catalysis at Pro39 is strongly improved when the formation of partially folded intermediates is suppressed by destabilizing mutations, or by breaking of the two disulfide bonds (as in the reduced and carboxymethylated RCM form of RNase T1) [152].

The reduced and carboxymethylated RCM form of the S54G/P55N variant (RCM-(-P55)RNase T1) is a particularly simple model protein for studying catalyzed protein folding, because it involves a single *trans* → *cis* isomerization only (at Pro39; Scheme 25.4) and because the access to this proline is not impaired by premature structure formation, as in the wild-type protein with intact disulfide bonds. The RCM form is unfolded in aqueous buffer but reversible folding to a native-like ordered conformation can be induced by adding 1 M NaCl [152]. Unfolding and refolding in the presence of prolyl isomerases can thus be studied in the absence of denaturants, simply by varying the NaCl concentration [90, 153–155]. This is important because several prolyl isomerases are sensitive to residual concentrations of denaturants, such as guanidinium chloride or urea.

Prolyl isomerases function in protein folding as enzymes. They catalyze *cis* ↔ *trans* isomerization in either direction and carry no information about the isomeric states of the prolyl peptide bonds in the protein substrates. This information is provided by the refolding protein itself. Molecules with native prolyl isomers refold rapidly and are thus no longer substrates for the isomerase. The prolyl isomerases are active in protein *unfolding* as well [152].

25.7.2 Specificity of Prolyl Isomerases

The catalytic function of the prolyl isomerases is restricted to prolyl bonds. They do not catalyze the isomerizations of "normal" nonprolyl peptide bonds. As outlined in Section 25.6, the folded form of the P39A variant of RNase T1 has a *cis* Tyr38-Ala39 bond, and the refolding of virtually all molecules is limited in rate by the very slow *trans* → *cis* re-isomerization of the Tyr38-Ala39 bond. This isomerization is not catalyzed by prolyl isomerases of the cyclophilin, FKBP, and parvulin families. It is also not catalyzed in the peptide Ala-Ala-Tyr-Ala-Ala [156].

Schiene-Fischer et al. discovered that DnaK, a chaperone of the Hsp70 family catalyzes the isomerization of nonprolyl bonds in oligopeptides and in the folding of the P39A variant of RNase T1. This new isomerase is described in Chapter 10 in Part II.

As folding enzymes, the prolyl isomerases can catalyze their own folding. The folding reactions of human cytosolic FKBP12 and of parvulin from *E. coli* are indeed autocatalytic processes [45, 155, 157].

25.7.3 The Trigger Factor

The trigger factor is a ubiquitous bacterial protein, which associates with the large subunit of the ribosome (see Chapter 13 in Part II). Originally it was thought to be involved in the export of secretory proteins [158, 159], but in 1995 Fischer and coworkers [160] discovered that the trigger factor is a prolyl isomerase. This enzymatic activity originates from the central FKBP domain, which encompasses residues 142 to 251. Indeed, a weak sequence homology had been noted between this region of the trigger factor and human FKBP12 [161].

Three domains have been identified in the trigger factor. The central FKBP domain harbors the prolyl isomerase activity of the trigger factor [162, 163] and the N-terminal domain (residues 1–118) mediates the interaction with the ribosome [164–168]. The function of the C-terminal domain is largely unknown. Its presence is required for the high activity of the trigger factor as a catalysts of protein folding [169, 170].

The trigger factor catalyzes the folding of RCM-RNase T1 very efficiently. The addition of as low as 2.5 nM trigger factor led to a doubling of the folding rate of this protein, and in the presence of 20 nM trigger factor this folding reaction is 14-fold accelerated. This remarkable catalytic efficiency of the trigger factor as a folding enzyme is reflected in a specificity constant k_{cat}/K_M of 1.1×10^6 M^{-1} s^{-1}. This is almost 100-fold higher than the respective value for human FKBP12 [170]. The K_M value is 0.7 μM, and the catalytic rate constant k_{cat}. is 1.3 s^{-1} [170]. For Cyp18 the catalysis of the *trans* ↔ *cis* prolyl isomerization in a tetrapeptide is characterized by K_M and k_{cat} values of 220 μM and 620 s^{-1}, respectively [64]. This comparison indicates that the high activity of the trigger factor as a folding catalyst does not originate from a high turnover number, but from a high affinity for the protein substrate.

Permanently unfolded proteins are strong, competitive inhibitors of trigger-factor-catalyzed folding. One of those, reduced and carboxymethylated bovine α-lactalbumin (RCM-La) inhibits the trigger factor of *Mycoplasma genitalium* with a K_I value of 50 nM. This binding of inhibitory proteins is independent of proline residues. Unfolded RCM-tendamistat (an α-amylase inhibitor with 74 residues) binds to the trigger factor with equal affinity in the presence and in the absence of its three proline residues [171]. The catalysis of folding of RCM-(-Pro55)-RNase T1 occurs at Pro39. The good inhibition by a nonfolding variant of RNase T1 that lacks Pro39 showed that this proline is dispensable for substrate binding [171]. The affinity of the trigger factor for short peptides is also independent of prolines [172]. The isolated FKBP domain is fully active as a prolyl isomerase towards a short tetrapeptide [162], but in protein folding its activity is about 800-fold reduced, and, moreover, this low residual activity of the FKBP domain alone is not inhibited by unfolded proteins, such as RCM-La [170]. The high enzymatic activity in protein

folding thus requires the intact trigger factor [169]. Together, these results suggest that the high-affinity binding site for unfolded proteins is probably distinct from the catalytic site of the trigger factor. It extends over several domains of the intact trigger factor or requires the interaction of these domains.

The good binding of the intact trigger factor to unfolded chain segments probably decelerates the dissociation of the protein substrate from the trigger factor, and the low k_{cat} value of 1.3 s^{-1} may reflect a change in the rate-limiting step from bond rotation (in tetrapeptide substrates) towards product dissociation (in protein substrates). In fact, an unfolded protein dissociates from the trigger factor with a rate constant of 5.8 s^{-1} [173], which is only fourfold higher than the k_{cat} for catalyzed folding. Since high-affinity binding to unfolded proteins is independent of prolines, it is likely that many binding events are nonproductive, because the reactive prolyl peptide bonds are not positioned correctly within the prolyl isomerase site. Indeed, a lowering of both K_M and k_{cat}, as observed for the intact trigger factor, points to nonproductive binding of a substrate to an enzyme [174].

The trigger factor thus seems to have properties of a folding enzyme and of a chaperone. The cooperation of both functions is required for its very high catalytic efficiency in protein folding. Indeed, trigger factor can function as a chaperone *in vitro* [175–177] and presumably also *in vivo* [178, 179]. A combination of the functions as a protein export factor and as a prolyl isomerase seems to be required in the secretion and maturation of a protease of the pathogenic bacterium *Streptococcus pyogenes* [180].

25.7.4
Catalysis of Prolyl Isomerization During de novo Protein Folding

The evidence for a catalysis of proline-limited folding steps during de novo protein folding in the cell remains circumstantial. Early evidence for a role of prolyl isomerization and of prolyl isomerases in cellular folding was provided by studies of collagen folding, which is limited in rate by successive prolyl isomerizations both in vitro and in vivo. Collagen maturation in chicken embryo fibroblasts is retarded by cyclosporin A, possibly by the inhibition of the cyclophilin-catalyzed folding in the endoplasmic reticulum [181]. A similar effect was found for the folding of luciferase in rabbit reticulocyte lysate [182].

Proteins that are targeted to the mitochondrial matrix must unfold outside the mitochondria, cross the two mitochondrial membranes and then refold in the matrix. In a synthetic precursor protein the presequence of subunit 9 of the *Neurospora crassa* F_1F_0-ATPase was linked to mouse cytosolic dihydrofolate reductase (Su9-DHFR) and used to investigate the function of cyclophilins as potential catalysts of protein folding in isolated mitochondria [183–185]. When measured by the resistance against proteinase K, the refolding of DHFR inside the mitochondria showed half-times of about 5 min and folding was about fivefold decelerated when the mitochondria had been preincubated with 2.5–5 μM CsA to inhibit the prolyl isomerase activity of mitochondrial cyclophilin. The refolding of DHFR was similarly retarded in mitochondria that were derived from mutants that lacked a functional mitochondrial cyclophilin. This suggests that the mitochondrial

cyclophilins acted as prolyl isomerases and thereby catalyzed protein folding in organello.

25.8 Concluding Remarks

Cis peptide bonds decelerate folding reactions, but nevertheless they occur frequently in folded proteins, mainly before proline and occasionally before other amino acid residues. *Cis* prolines are very well suited to introduce tight turns into proteins, but the structural consequences of *cis* peptide bonds cannot be the sole reason for their widespread occurrence. The coupling with prolyl isomerization is a simple means for increasing the energetic barriers of folding, and thus not only refolding but also unfolding would be decelerated. In such a way a native protein would be protected from sampling the unfolded state too frequently.

Nonprolyl *cis* peptide bonds are strongly destabilizing, because they introduce strain into the protein backbone. They are found preferentially near the active sites of enzymes where strained conformations might be important for the function.

In the overall folding process prolyl isomerizations and conformational steps are linked. Incorrect prolines decrease the stability of partially folded intermediates, and conformational folding can modulate the rate of prolyl isomerization.

Prolyl isomerizations are catalyzed by prolyl isomerases. Their functions reach far beyond the acceleration of de novo protein folding. In addition to the well-understood role in immunosuppression, prolyl isomerases modulate ion channels and transmembrane receptors, participate in hormone receptor complexes, are required for HIV-1 infectivity, and participate in the regulation of mitosis. The PIN1 protein discriminates between phosphorylated and unphosphorylated Ser/Thr-Pro sequences in its target proteins. Two principles of regulation are probably integrated at this point: phosphorylation and prolyl *cis*/*trans* isomerization.

Prolyl isomerization in folded proteins is thus well suited for switching between alternative states of a protein. The positions of the switch (*cis* and *trans*) can be determined by the binding of effectors, the rate of swichting can be modulated by prolyl isomerases. Some isomerases might be effector and isomerase at the same time. For such isomerases the distinction between binding and catalytic function, which has been discussed for a long time, may be inappropriate.

25.9 Experimental Protocols

25.9.1 Slow Refolding Assays ("Double Jumps") to Measure Prolyl Isomerizations in an Unfolded Protein

As shown in Scheme 25.1, the direct $N \rightarrow U_F$ unfolding reaction can be followed by one or more prolyl isomerizations ($U_F \rightleftharpoons U_S$) in the unfolded protein chains.

U_F and U_S are usually equally unfolded species and show similar physical properties. Therefore the kinetics of the $U_F \rightleftharpoons U_S$ equilibration reactions cannot be measured directly. Rather, the amount of U_S formed after different times of unfolding can be determined by slow refolding assays. Samples are withdrawn from the unfolding solution at different time intervals after the initiation of unfolding; these samples are transferred to standard refolding conditions, and the amplitude of the slow refolding reaction, $U_S \rightarrow N$, is determined. Refolding of the U_F species is usually complete within the time of manual mixing. The amplitude of the slow refolding reaction is proportional to the concentration of U_S which was present at the time when the sample was withdrawn for the assay. The dependence of these slow refolding amplitudes on the duration of unfolding yields the kinetics of the $U_F \rightleftharpoons U_S$ reaction. The measured rate constant λ is equal to the sum of the rate constants in the forward (k_{FS}) and the reverse (k_{SF}) directions, $\lambda = k_{FS} + k_{SF}$. When the equilibrium constant $K = [U_S]/[U_F] = k_{FS}/k_{SF}$ is known, the individual rate constants k_{FS} and k_{SF} can be derived.

25.9.1.1 Guidelines for the Design of Double Jump Experiments

Unfolding conditions Any unfolding conditions can be employed; for practical reasons, however, it is of advantage to select conditions (1) where the $N \rightarrow U_F$ unfolding step is rapid and (2) where the $U_F \rightleftharpoons U_S$ equilibration is slow. Under such conditions, $U_F \rightleftharpoons U_S$ can be studied without interference from the preceding unfolding step and manual sampling techniques can be used to perform the slow refolding assays. Usually it is best to perform the unfolding step at a high concentration of a strong denaturant, such as GdmCl, and at low temperature. The rate of conformational unfolding usually increases strongly with the denaturant concentration, and, because of the high activation enthalpy of proline isomerization, the $U_F \rightleftharpoons U_S$ reaction is strongly decelerated by decreasing the temperature. Consequently, the difference in rate between the two processes is highest in concentrated denaturant solutions and at low temperature. Often, the rate of conformational unfolding can be further enhanced by lowering the pH.

Refolding conditions The slow refolding assays are best carried out under conditions where (1) the $U_F \rightarrow N$ refolding reaction is complete within the time of manual mixing, and (2) the slow $U_S \rightarrow N$ reaction occurs in a single phase in a time range that is convenient for manual mixing experiments. This facilitates the accurate determination of the refolding amplitudes. After each refolding assay the actual protein concentration should be determined to correct for variations in the protein concentration in the individual assays. Usually the final absorbance or fluorescence reached after the refolding step is suitable for such a correction. As in the unfolding step, the rate of slow refolding can be fine-tuned by varying the concentration of denaturant, the temperature and the pH.

In cases where more than one U_S species is formed after unfolding, the individual rates of formation of these species can be measured when the refolding assays are carried out under conditions where the refolding of the various U_S species can be separated kinetically.

25.9.1.2 Formation of U_S Species after Unfolding of RNase A

I describe here a protocol that was used to follow the $U_F \rightleftharpoons U_S$ reaction in unfolded RNase A as an example. In these experiments the refolding assays were carried out under conditions where slow refolding is a single, monophasic reaction. Therefore, the refolding assays yielded the kinetics of overall formation of U_S species after unfolding. They did not discriminate between the different U_S species of RNase A (see Section 25.4.1).

Unfolding To initiate unfolding at time zero, 50 µL of native RNase A (1.5 mM in H_2O, 0 °C) is mixed with 250 µL of 6.0 M GdmCl solution in 0.1 M glycine, pH 2.0 at 0 °C. The resulting unfolding conditions are 0.25 mM RNase A in 5.0 M GdmCl, pH 2.0, 0 °C. Under these conditions the $N \rightarrow U_F$ unfolding step of RNase A is very rapid and complete before the onset of the $U_F \rightleftharpoons U_S$ equilibration. Thus the $U_F \rightleftharpoons U_S$ reaction can be measured in a convenient time range without interference from the preceding $N \rightarrow U_F$ unfolding step.

Refolding assays After different time intervals 70-µL samples are withdrawn from the unfolding solution and quickly diluted into 830 µL of the refolding buffer (1.2 M GdmCl in 0.1 M cacodylate, pH 6.2) in the spectrophotometer cell, which is kept at 25 °C. This gives final conditions of 1.5 M GdmCl, pH 6.0 and 25 °C. These conditions are chosen because slow refolding occurs in a single exponential phase in a time range, which is convenient for manual sampling techniques. The slow refolding reaction of U_S is monitored at 287 nm. At the end of each refolding assay the absorbance of the refolded sample is recorded at 277 nm to determine the actual concentration of RNase A in the assay.

Data treatment The refolding kinetics are analyzed. The time constant for refolding in the assay should be independent of the time of sampling, because the final folding conditions are the same in all assays. The amplitudes of refolding are corrected for variations in the protein concentration (if necessary) and plotted as a function of the time of unfolding. The increase in the refolding amplitude with the duration of unfolding yields the kinetics of the formation of the slow-folding species U_S.

25.9.2 Slow Unfolding Assays for Detecting and Measuring Prolyl Isomerizations in Refolding

Often protein molecules with incorrect prolyl isomers can fold to a conformation that appears native-like by spectroscopic properties or even by enzymatic activity. In such cases the re-isomerization of the incorrect prolines in the final step of folding is silent and cannot be followed by spectroscopic probes or by a functional assay.

To follow such silent isomerizations during refolding, a two-step assay is used. It measures the kinetics of the formation of fully folded protein molecules during a refolding reaction [33, 74]. This assay is based on the fact that native protein mole-

cules have passed beyond the highest activation barrier in their refolding and thus are separated from the unfolded state by this energy barrier. They unfold slowly when the conditions are switched to unfolding, because they must cross the high barrier again, now in the reverse direction. Partially folded molecules (such as those with incorrect prolyl isomers) have not yet passed the final transition state and unfold rapidly.

This translates into a double-mixing procedure. First, unfolded protein is mixed with refolding buffer to initiate refolding. Then, after variable time intervals, samples are withdrawn, transferred to standard unfolding conditions, and the amplitude of the subsequent slow unfolding reaction is determined. It is a direct measure for the amount of native molecules with correct prolyl isomers that had been present at the time when refolding was interrupted, and the increase of the amplitude of slow refolding with time gives the kinetics of formation of the native protein.

25.9.2.1 Practical Considerations

The unfolding assays are best carried out under conditions where the N → U unfolding reaction in the assay is monophasic and occurs in a time range that is convenient for manual mixing experiments. Thus the unfolding amplitudes can be determined with a high accuracy. Most proteins unfold in monoexponential reactions under strongly unfolding conditions, i.e., in the presence of a denaturant at high concentration. The rate of unfolding can be varied in a wide range by changes in the pH, the temperature and the denaturant concentration. As in the refolding assays (see above) the actual protein concentration should be determined to correct for variations in the protein concentration in the individual unfolding assays.

25.9.2.2 Kinetics of the Formation of Fully Folded IIHY-G3P* Molecules

Here I describe how this procedure was used to measure the time course of the *trans* → *cis* re-isomerization at Pro213 in the refolding of the gene-3-protein of the phage fd [59, 60]. This isomerization controls the domain docking in the final folding step of this protein. The unfolding assays were performed in 5.0 M GdmCl, pH 7.0 at 25 °C, conditions under which the gene-3-protein unfolds in a monoexponential reaction with a time constant of 25 s.

To follow the formation of native molecules, unfolded protein (50 μM in 5.0 M GdmCl) was first manually 10-fold diluted with buffer (in a test tube) to initiate refolding at 0.5 M GdmCl and then, after times of refolding between 1 and 540 min, samples were withdrawn and unfolded again at 5.0 M GdmCl by a manual 10-fold dilution with a GdmCl solution of 5.5 M in the fluorimeter cell. Unfolding was followed by the change in tyrosine fluorescence at 310 nm after excitation at 280 nm.

References

1 B. T. Nall, *Comments Mol. Cell. Biophys.* **1985**, *3*, 123–143.

2 S. F. Göthel, M. A. Marahiel, *Cell. Mol. Life Sci.* **1999**, *55*, 423–436.

3 G. Fischer, *Angew. Chem. Int. Ed.* **1994**, *33*, 1415–1436.
4 G. Fischer, F. X. Schmid, Peptidyl-prolyl cis/trans isomerases. In *Molecular Biology of Chaperones and Folding Catalysts* (B. Bukau, Ed.). Harwood Academic Publishers, New York, 1999, pp. 461–489.
5 F. X. Schmid, Catalysis of protein folding by prolyl isomerases. In *Molecular Chaperones in the Life Cycle of Proteins* (A. L. Fink and Y. Goto, Eds). Marcel Dekker, New York, 1998, pp. 361–389.
6 F. X. Schmid, *Adv. Protein Chem.* **2002**, *59*, 243–282.
7 F. X. Schmid, L. M. Mayr, M. Mücke, E. R. Schönbrunner, *Adv. Protein Chem.* **1993**, *44*, 25–66.
8 J. Balbach, F. X. Schmid, Prolyl isomerization and its catalysis in protein folding. In *Mechanisms of Protein Folding* (R. H. Pain, Ed.). Oxford University Press, Oxford. 2000, pp. 212–237.
9 W. J. Wedemeyer, E. Welker, H. A. Scheraga, *Biochemistry* **2002**, *41*, 14637–14644.
10 A. H. Andreotti, *Biochemistry* **2003**, *42*, 9515–9524.
11 G. E. Schulz, R. E. Schirmer, *Principles of Protein Structure*. Springer Verlag, New York, 1979.
12 G. Scherer, M. L. Kramer, M. Schutkowski, R. U. G. Fischer, *J. Am. Chem. Soc.* **1998**, *120*, 5568–5574.
13 D. E. Stewart, A. Sarkar, J. E. Wampler, *J. Mol. Biol.* **1990**, *214*, 253–260.
14 M. W. Macarthur, J. M. Thornton, *J. Mol. Biol.* **1991**, *218*, 397–412.
15 D. Pal, P. Chakrabarti, *J. Mol. Biol.* **1999**, *294*, 271–288.
16 A. Jabs, M. S. Weiss, R. Hilgenfeld, *J. Mol. Biol.* **1999**, *286*, 291–304.
17 D. C. Rees, M. Lewis, W. N. Lipscomb, *J. Mol. Biol.* **1983**, *168*, 367–387.
18 H. N. Cheng, F. A. Bovey, *Biopolymers* **1977**, *16*, 1465–1472.
19 C. Grathwohl, K. Wüthrich, *Biopolymers* **1981**, *20*, 2623–2633.
20 U. Reimer, G. Scherer, M. Drewello, S. Kruber, M. Schutkowski, G. Fischer, *J. Mol. Biol.* **1998**, *279*, 449–460.
21 G. Fischer, *Chem. Soc. Rev.* **2000**, *29*, 119–127.
22 T. Drakenberg, K.-I. Dahlqvist, S. Forsén, *J. Phys. Chem.* **1972**, *76*, 2178–2183.
23 R. L. Stein, *Adv. Protein Chem.* **1993**, *44*, 1–24.
24 E. S. Eberhardt, S. N. Loh, A. P. Hinck, R. T. Raines, *J. Am. Chem. Soc.* **1992**, *114*, 5437–5439.
25 I. Z. Steinberg, W. F. Harrington, A. Berger, M. Sela, E. Katchalski, *J. Am. Chem. Soc.* **1960**, *82*, 5263–5279.
26 F. X. Schmid, R. L. Baldwin, *Proc. Natl Acad. Sci. USA* **1978**, *75*, 4764–4768.
27 J. R. Garel, R. L. Baldwin, *Proc. Natl Acad. Sci. USA* **1973**, *70*, 3347–3351.
28 P. S. Kim, R. L. Baldwin, *Annu. Rev. Biochem.* **1982**, *51*, 459–489.
29 F. X. Schmid, Kinetics of unfolding and refolding of single-domain proteins. In *Protein Folding* (T. E. Creighton, Ed.). Freeman, New York, 1992, pp. 197–241.
30 J. F. Brandts, H. R. Halvorson, M. Brennan, *Biochemistry* **1975**, *14*, 4953–4963.
31 T. Kiefhaber, F. X. Schmid, *J. Mol. Biol.* **1992**, *224*, 231–240.
32 T. Kiefhaber, H. H. Kohler, F. X. Schmid, *J. Mol. Biol.* **1992**, *224*, 217–229.
33 F. X. Schmid, Fast-folding and slow-folding forms of unfolded proteins. In *Enzyme Structure Part l* (C. H. W. Hirs and S. N. Timasheff, Eds). Academic Press, New York, 1986, pp. 71–82.
34 Y. Goto, K. Hamaguchi, *J. Mol. Biol.* **1982**, *156*, 891–910.
35 R. F. Kelley, F. M. Richards, *Biochemistry* **1987**, *26*, 6765–6774.
36 R. Golbik, G. Fischer, A. R. Fersht, *Protein Sci.* **1999**, *8*, 1505–1514.
37 K. Maki, T. Ikura, T. Hayano, N. Takahashi, K. Kuwajima, *Biochemistry* **1999**, *38*, 2213–2223.
38 W. F. Walkenhorst, S. M. Green, H. Roder, *Biochemistry* **1997**, *36*, 5795–5805.
39 S. Khorasanizadeh, I. D. Peters,

T. R. Butt, H. Roder, *Biochemistry* **1993**, *32*, 7054–7063.
40 S. Koide, H. J. Dyson, P. E. Wright, *Biochemistry* **1993**, *32*, 12299–12310.
41 J. S. Reader, N. A. Van Nuland, G. S. Thompson, S. J. Ferguson, C. M. Dobson, S. E. Radford, *Protein Sci.* **2001**, *10*, 1216–1224.
42 M. M. Pierce, B. T. Nall, *J. Mol. Biol.* **2000**, *298*, 955–969.
43 A. R. Fersht, *FEBS Lett.* **1993**, *325*, 5–16.
44 S. E. Jackson, A. R. Fersht, *Biochemistry* **1991**, *30*, 10436–10443.
45 C. Scholz, T. Zarnt, G. Kern, K. Lang, H. Burtscher, G. Fischer, F. X. Schmid, *J. Biol. Chem.* **1996**, *271*, 12703–12707.
46 A. T. Russo, J. Rosgen, D. W. Bolen, *J. Mol. Biol.* **2003**, *330*, 851–866.
47 N. A. J. Van Nuland, F. Chiti, N. Taddei, G. Raugei, G. Ramponi, C. M. Dobson, *J. Mol. Biol.* **1998**, *283*, 883–891.
48 G. Aronsson, A. C. Brorsson, L. Sahlman, B. H. Jonsson, *FEBS Lett.* **1997**, *411*, 359–364.
49 N. Ferguson, A. P. Capaldi, R. James, C. Kleanthous, S. E. Radford, *J. Mol. Biol.* **1999**, *286*, 1597–1608.
50 F. Rousseau, J. W. Schymkowitz, M. Sanchez del Pino, L. S. Itzhaki, *J. Mol. Biol.* **1998**, *284*, 503–519.
51 G. Pappenberger, A. Bachmann, R. Muller, H. Aygun, J. W. Engels, T. Kiefhaber, *J. Mol. Biol.* **2003**, *326*, 235–246.
52 J. G. Bann, J. Pinkner, S. J. Hultgren, C. Frieden, *Proc. Natl Acad. Sci. USA* **2002**, *99*, 709–714.
53 T. F. Fu, E. S. Boja, M. K. Safo, V. Schirch, *J. Biol. Chem.* **2003**, *278*, 31088–31094.
54 W. J. Satumba, M. C. Mossing, *Biochemistry* **2002**, *41*, 14216–14224.
55 Y. Wu, C. R. Matthews, *J. Mol. Biol.* **2003**, *330*, 1131–1144.
56 M. Tsunenaga, Y. Goto, Y. Kawata, K. Hamaguchi, *Biochemistry* **1987**, *26*, 6044–6051.
57 H. Lilie, R. Rudolph, J. Buchner, *J. Mol. Biol.* **1995**, *248*, 190–201.
58 M. J. W. Thies, J. Mayer, J. G. Augustine, C. A. Frederick, H. Lilie, J. Buchner, *J. Mol. Biol.* **1999**, *293*, 67–79.
59 A. Martin, F. X. Schmid, *J. Mol. Biol.* **2003**, *329*, 599–610.
60 A. Martin, F. X. Schmid, *J. Mol. Biol.* **2003**, *331*, 1131–1140.
61 D. Galani, A. R. Fersht, S. Perrett, *J. Mol. Biol.* **2002**, *315*, 213–227.
62 T. E. Creighton, *J. Mol. Biol.* **1978**, *125*, 401–406.
63 C. Fransson, P. O. Freskgard, H. Herbertsson, A. Johansson, P. Jonasson, L. G. Martensson, M. Svensson, B. H. Jonsson, U. Carlsson, *FEBS Lett.* **1992**, *296*, 90–94.
64 D. Kern, G. Kern, G. Scherer, G. Fischer, T. Drakenberg, *Biochemistry* **1995**, *34*, 13594–13602.
65 M. Jäger, A. Plückthun, *FEBS Lett.* **1997**, *418*, 106–110.
66 F. X. Schmid, H. Blaschek, *Eur. J. Biochem.* **1981**, *114*, 111–117.
67 K. H. Cook, F. X. Schmid, R. L. Baldwin, *Proc. Natl Acad. Sci. USA* **1979**, *76*, 6157–6161.
68 P. J. Hagerman, R. L. Baldwin, *Biochemistry* **1976**, *15*, 1462–1473.
69 B. T. Nall, J.-R. Garel, R. L. Baldwin, *J. Mol. Biol.* **1978**, *118*, 317–330.
70 F. X. Schmid, R. L. Baldwin, *J. Mol. Biol.* **1979**, *133*, 285–287.
71 F. X. Schmid, R. Grafl, A. Wrba, J. J. Beintema, *Proc. Natl Acad. Sci. USA* **1986**, *83*, 872–876.
72 R. A. Sendak, D. M. Rothwarf, W. J. Wedemeyer, W. A. Houry, H. A. Scheraga, *Biochemistry* **1996**, *35*, 12978–12992.
73 A. Rehage, F. X. Schmid, *Biochemistry* **1982**, *21*, 1499–1505.
74 F. X. Schmid, *Biochemistry* **1983**, *22*, 4690–4696.
75 P. S. Kim, R. L. Baldwin, *Annu. Rev. Biochem.* **1990**, *59*, 631–660.
76 W. A. Houry, D. M. Rothwarf, H. A. Scheraga, *Biochemistry* **1994**, *33*, 2516–2530.
77 U. Arnold, M. P. Hinderaker, J. Koditz, R. Golbik, R. Ulbrich-Hofmann, R. T. Raines, *J. Am. Chem. Soc.* **2003**, *125*, 7500–7501.

78 H. Krebs, F. X. Schmid, R. Jaenicke, *J. Mol. Biol.* **1983**, *169*, 619–635.

79 D. A. Schultz, F. X. Schmid, R. L. Baldwin, *Protein Sci.* **1992**, *1*, 917–924.

80 R. W. Dodge, H. A. Scheraga, *Biochemistry* **1996**, *35*, 1548–1559.

81 W. A. Houry, H. A. Scheraga, *Biochemistry* **1996**, *35*, 11719–11733.

82 R. W. Dodge, J. H. Laity, D. M. Rothwarf, S. Shimotakahara, H. A. Scheraga, *J. Protein Chem.* **1994**, *13*, 409–421.

83 C. N. Pace, U. Heinemann, U. Hahn, W. Saenger, *Angew. Chem. Int. Ed. Engl.* **1991**, *30*, 343–360.

84 U. Heinemann, W. Saenger, *Nature* **1982**, *299*, 27–31.

85 U. Heinemann, U. Hahn, Structural and functional studies of ribonuclease t1. In *Protein–Nucleic Acid Interaction* (W. Saenger and U. Heinemann, Eds). Macmillan, London, 1989, pp. 111–141.

86 J. Martinez-Oyanedel, H.-W. Choe, U. Heinemann, W. Saenger, *J. Mol. Biol.* **1991**, *222*, 335–352.

87 M. Oobatake, S. Takahashi, T. Ooi, *J. Biochem.* **1979**, *86*, 55–63.

88 C. N. Pace, G. R. Grimsley, J. A. Thomson, B. J. Barnett, *J. Biol. Chem.* **1988**, *263*, 11820–11825.

89 L. M. Mayr, F. X. Schmid, *Biochemistry* **1993**, *32*, 7994–7998.

90 M. Mücke, F. X. Schmid, *Biochemistry* **1994**, *33*, 14608–14619.

91 C. N. Pace, D. V. Laurents, *Biochemistry* **1989**, *28*, 2520–2525.

92 T. Kiefhaber, F. X. Schmid, M. Renner, H.-J. Hinz, *Biochemistry* **1990**, *29*, 8250–8257.

93 C.-Q. Hu, J. M. Sturtevant, J. A. Thomson, R. E. Erickson, C. N. Pace, *Biochemistry* **1992**, *31*, 4876–4882.

94 Y. Yu, G. I. Makhatadze, C. N. Pace, P. L. Privalov, *Biochemistry* **1994**, *33*, 3312–3319.

95 T. Kiefhaber, R. Quaas, U. Hahn, F. X. Schmid, *Biochemistry* **1990**, *29*, 3053–3061.

96 C. Odefey, L. M. Mayr, F. X. Schmid, *J. Mol. Biol.* **1995**, *245*, 69–78.

97 C. N. Pace, T. E. Creighton, *J. Mol. Biol.* **1986**, *188*, 477–486.

98 C. Frech, F. X. Schmid, *J. Mol. Biol.* **1995**, *251*, 135–149.

99 T. Kiefhaber, H. P. Grunert, U. Hahn, F. X. Schmid, *Biochemistry* **1990**, *29*, 6475–6480.

100 L. M. Mayr, O. Landt, U. Hahn, F. X. Schmid, *J. Mol. Biol.* **1993**, *231*, 897–912.

101 T. Schindler, L. M. Mayr, O. Landt, U. Hahn, F. X. Schmid, *Eur. J. Biochem.* **1996**, *241*, 516–524.

102 F. X. Schmid, *Annu. Rev. Biophys. Biomol. Struct.* **1993**, *22*, 123–143.

103 L. M. Mayr, C. Odefey, M. Schutkowski, F. X. Schmid, *Biochemistry* **1996**, *35*, 5550–5561.

104 T. Kiefhaber, F. X. Schmid, K. Willaert, Y. Engelborghs, A. Chaffotte, *Protein Sci.* **1992**, *1*, 1162–1172.

105 L. M. Mayr, F. X. Schmid, *J. Mol. Biol.* **1993**, *231*, 913–926.

106 T. Kiefhaber, R. Quaas, U. Hahn, F. X. Schmid, *Biochemistry* **1990**, *29*, 3061–3070.

107 F. L. Texter, D. B. Spencer, R. Rosenstein, C. R. Matthews, *Biochemistry* **1992**, *31*, 5687–5691.

108 J. Balbach, V. Forge, N. A. J. van Nuland, S. L. Winder, P. J. Hore, C. M. Dobson, *Nat. Struct. Biol.* **1995**, *2*, 865–870.

109 S. D. Hoeltzli, C. Frieden, *Biochemistry* **1996**, *35*, 16843–16851.

110 J. Balbach, V. Forge, W. S. Lau, N. A. J. Vannuland, K. Brew, C. M. Dobson, *Science* **1996**, *274*, 1161–1163.

111 J. Balbach, V. Forge, W. S. Lau, N. A. J. van Nuland, K. Brew, C. M. Dobson, *Science* **1996**, *274*, 1161–1163.

112 P. A. Evans, C. M. Dobson, R. A. Kautz, G. Hatfull, R. O. Fox, *Nature*, **1987**, *329*, 266–268.

113 K. A. Higgins, D. J. Craik, J. G. Hall, P. R. Andrews, *Drug Design Delivery* **1988**, *3*, 159–170.

114 W. J. Chazin, J. Kördel, T. Drakenberg, E. Thulin, P. Brodin, T. Grundström, S. Forsén, *Proc.*

Natl Acad. Sci. USA **1989**, *86*, 2195–2198.

115 J. Kördel, S. Forsen, T. Drakenberg, W. J. Chazin, *Biochemistry* **1990**, *29*, 4400–4409.

116 E. Adjadj, V. Naudat, E. Quiniou, D. Wouters, P. Sautiere, C. T. Craescu, *Eur. J. Biochem.* **1997**, *246*, 218–227.

117 Y. Feng, W. F. Hood, R. W. Forgey, A. L. Abegg, M. H. Caparon, B. R. Thiele, R. M. Leimgruber, C. A. McWherter, *Protein Sci.* **1997**, *6*, 1777–1782.

118 X. Yuan, A. K. Downing, V. Knott, P. A. Handford, *EMBO J.* **1997**, *16*, 6659–6666.

119 X. Yuan, J. M. Werner, V. Knott, P. A. Handford, I. D. Campbell, K. Downing, *Protein Sci.* **1998**, *7*, 2127–2135.

120 S. N. Loh, C. W. Mcnemar, J. L. Markley, *Techn. Protein Chem.* **1991**, *II*, 275–282.

121 D. M. Truckses, J. R. Somoza, K. E. Prehoda, S. C. Miller, J. L. Markley, *Protein Sci.* **1996**, *5*, 1907–1916.

122 F. X. Schmid, K. Lang, T. Kiefhaber, S. Mayer, R. Schönbrunner, Prolyl isomerase. Its role in protein folding and speculations on its function in the cell. In *Conformations and Forces in Protein Folding* (B. T. Nall and K. A. Dill, Eds). AAAS, Washington, D.C. 1991.

123 R. J. Mallis, K. N. Brazin, D. B. Fulton, A. H. Andreotti, *Nat. Struct. Biol.* **2002**, *9*, 900–905.

124 K. N. Brazin, R. J. Mallis, D. B. Fulton, A. H. Andreotti, *Proc. Natl Acad. Sci. USA* **2002**, *99*, 1899–1904.

125 P. A. Evans, C. M. Dobson, R. A. Kautz, G. Hatfull, R. O. Fox, *Nature* **1987**, *329*, 266–268.

126 R. K. Gitti, B. M. Lee, J. Walker, M. F. Summers, S. Yoo, W. I. Sundquist, *Science* **1996**, *273*, 231–235.

127 T. A. Ramelot, L. K. Nicholson, *J. Mol. Biol.* **2001**, *307*, 871–884.

128 P. J. Breheny, A. Laederach, D. B. Fulton, A. H. Andreotti, *J. Am. Chem. Soc.* **2003**, *125*, 15706–15707.

129 M. B. Yaffe, M. Schutkowski, M. H. Shen, X. Z. Zhou, P. T. Stukenberg, J. U. Rahfeld, J. Xu, J. Kuang, M. W. Kirschner, G. Fischer, L. C. Cantley, K. P. Lu, *Science* **1997**, *278*, 1957–1960.

130 C. Schiene-Fischer, G. Fischer, *J. Am. Chem. Soc.* **2001**, *123*, 6227–6231.

131 L. M. Mayr, D. Willbold, P. Rösch, F. X. Schmid, *J. Mol. Biol.* **1994**, *240*, 288–293.

132 M. A. Pearson, P. A. Karplus, R. W. Dodge, J. H. Laity, H. A. Scheraga, *Protein Sci.* **1998**, *7*, 1255–1258.

133 N. C. Strynadka, H. Adachi, S. E. Jensen, K. Johns, A. Sielecki, C. Betzel, K. Sutoh, M. N. James, *Nature* **1992**, *359*, 700–705.

134 M. Vanhove, X. Raquet, J.-M. Frere, *Proteins Struct. Funct. Genet.* **1995**, *22*, 110–118.

135 M. Vanhove, X. Raquet, T. Palzkill, R. H. Pain, J. M. Frere, *Proteins Struct. Funct. Genet.* **1996**, *25*, 104–111.

136 M. Vanhove, A. Lejeune, R. H. Pain, *Cell Mol. Life Sci.* **1998**, *54*, 372–377.

137 M. Vanhove, A. Lejeune, G. Guillaume, R. Virden, R. H. Pain, F. X. Schmid, J. M. Frere, *Biochemistry* **1998**, *37*, 1941–1950.

138 O. Herzberg, *J. Mol. Biol.* **1991**, *217*, 701–719.

139 G. Pappenberger, H. Aygun, J. W. Engels, U. Reimer, G. Fischer, T. Kiefhaber, *Nat. Struct. Biol.* **2001**, *8*, 452–458.

140 K. Lang, F. X. Schmid, G. Fischer, *Nature* **1987**, *329*, 268–270.

141 A. Matouschek, J. T. Kellis, L. Serrano, M. Bycroft, A. R. Fersht, *Nature* **1990**, *346*, 440–445.

142 P. O. Freskgård, N. Bergenhem, B. H. Jonsson, M. Svensson, U. Carlsson, *Science* **1992**, *258*, 466–468.

143 G. Kern, D. Kern, F. X. Schmid, G. Fischer, *FEBS Lett.* **1994**, *348*, 145–148.

144 S. Veeraraghavan, B. T. Nall, *Biochemistry* **1994**, *33*, 687–692.

145 S. Veeraraghavan, S. Rodriguez-

Gdiharpour, C. MacKinnon, W. A. Mcgee, M. M. Pierce, B. T. Nall, *Biochemistry* **1995**, *34*, 12892–12902.
146 S. Veeraraghavan, B. T. Nall, A. L. Fink, *Biochemistry* **1997**, *36*, 15134–15139.
147 C. J. Mann, X. Shao, C. R. Matthews, *Biochemistry* **1995**, *34*, 14573–14580.
148 H. P. Bächinger, P. Bruckner, R. Timpl, D. J. Prockop, J. Engel, *Eur. J. Biochem.* **1980**, *106*, 619–632.
149 H.-P. Bächinger, *J. Biol. Chem.* **1987**, *262*, 17144–17148.
150 J. M. Davis, B. A. Boswell, H. P. Bächinger, *J. Biol. Chem.* **1989**, *264*, 8956–8962.
151 E. R. Schönbrunner, S. Mayer, M. Tropschug, G. Fischer, N. Takahashi, F. X. Schmid, *J. Biol. Chem.* **1991**, *266*, 3630–3635.
152 M. Mücke, F. X. Schmid, *Biochemistry* **1992**, *31*, 7848–7854.
153 M. Mücke, F. X. Schmid, *J. Mol. Biol.* **1994**, *239*, 713–725.
154 J.-U. Rahfeld, A. Schierhorn, K.-H. Mann, G. Fischer, *FEBS Lett.* **1994**b, *343*, 65–69.
155 C. Scholz, J. Rahfeld, G. Fischer, F. X. Schmid, *J. Mol. Biol.* **1997**, *273*, 752–762.
156 C. Scholz, G. Scherer, L. M. Mayr, T. Schindler, G. Fischer, F. X. Schmid, *Biol. Chem.* **1998**, *379*, 361–365.
157 S. Veeraraghavan, T. F. Holzman, B. T. Nall, *Biochemistry* **1996**, *35*, 10601–10607.
158 E. Crooke, W. Wickner, *Proc. Natl Acad. Sci. USA* **1987**, *84*, 5216–5220.
159 R. Lill, E. Crooke, B. Guthrie, W. Wickner, *Cell* **1988**, *54*, 1013–1018.
160 G. Stoller, K. P. Rücknagel, K. Nierhaus, F. X. Schmid, G. Fischer, J.-U. Rahfeld, *EMBO J.* **1995**, *14*, 4939–4948.
161 I. Callebaut, J. P. Mornon, *FEBS Lett.* **1995**, *374*, 211–215.
162 G. Stoller, T. Tradler, J.-U. Rücknagel, G. Fischer, *FEBS Lett.* **1996**, *384*, 117–122.
163 T. Hesterkamp, B. Bukau, *FEBS Lett.* **1996**, *385*, 67–71.
164 T. Hesterkamp, E. Deuerling, B. Bukau, *J. Biol. Chem.* **1997**, *272*, 21865–21871.
165 G. Kramer, T. Rauch, W. Rist, S. Vorderwulbecke, H. Patzelt, A. Schulze-Specking, N. Ban, E. Deuerling, B. Bukau, *Nature* **2002**, *419*, 171–174.
166 R. Maier, B. Eckert, C. Scholz, H. Lilie, F. X. Schmid, *J. Mol. Biol.* **2003**, *326*, 585–592.
167 G. Blaha, D. N. Wilson, G. Stoller, G. Fischer, R. Willumeit, K. H. Nierhaus, *J. Mol. Biol.* **2003**, *326*, 887–897.
168 O. Kristensen, M. Gajhede, *Structure* **2003**, *11*, 1547–1556.
169 T. Zarnt, T. Tradler, G. Stoller, C. Scholz, F. X. Schmid, G. Fischer, *J. Mol. Biol.* **1997**, *271*, 827–837.
170 C. Scholz, G. Stoller, T. Zarnt, G. Fischer, F. X. Schmid, *EMBO J.* **1997**, *16*, 54–58.
171 C. Scholz, M. Mücke, M. Rape, A. Pecht, A. Pahl, H. Bang, F. X. Schmid, *J. Mol. Biol.* **1998**, *277*, 723–732.
172 H. Patzelt, S. Rüdiger, D. Brehmer, G. Kramer, S. Vorderwulbecke, E. Schaffitzel, A. Waitz, T. Hesterkamp, L. Dong, J. Schneider-Mergener, B. Bukau, E. Deuerling, *Proc. Natl Acad. Sci. USA* **2001**, *98*, 14244–14249.
173 R. Maier, C. Scholz, F. X. Schmid, *J. Mol. Biol.* **2001**, *314*, 1181–1190.
174 A. Fersht, *Enzyme Structure and Mechanism*, 2nd edn. W.H. Freeman, New York, 1985.
175 K. Nishihara, M. Kanemori, H. Yanagi, T. Yura, *Appl. Environ. Microbiol.* **2000**, *66*, 884–889.
176 G. C. Huang, Z. Y. Li, J. M. Zhou, G. Fischer, *Protein Sci.* **2000**, *9*, 1254–1261.
177 Z. Y. Li, C. P. Liu, L. Q. Zhu, G. Z. Jing, J. M. Zhou, *FEBS Lett.* **2001**, *506*, 108–112.
178 S. A. Teter, W. A. Houry, D. Ang, T. Tradler, D. Rockabrand, G. Fischer, P. Blum, C. Georgopoulos, F. U. Hartl, *Cell* **1999**, *97*, 755–765.
179 E. Deuerling, A. Schulze-Specking, T. Tomoyasu, A. Mogk, B. Bukau, *Nature* **1999**, *400*, 693–696.

180 W. R. Lyon, M. G. Caparon, *J. Bacteriol.* **2003**, *185*, 3661–3667.
181 B. Steinmann, P. Bruckner, A. Supertifurga, *J. Biol. Chem.* **1991**, *266*, 1299–1303.
182 M. Kruse, M. Brunke, A. Escher, A. A. Szalay, M. Tropschug, R. Zimmermann, *J. Biol. Chem.* **1995**, *270*, 2588–2594.
183 J. Rassow, K. Mohrs, S. Koidl, I. B. Barthelmess, N. Pfanner, M. Tropschug, *Mol. Cell Biol.* **1995**, *15*, 2654–2662.
184 A. Matouschek, S. Rospert, K. Schmid, B. S. Glick, G. Schatz, *Proc. Natl Acad. Sci. USA* **1995**, *92*, 6319–6323.
185 O. von Ahsen, J. H. Lim, P. Caspers, F. Martin, H. J. Schönfeld, J. Rassow, N. Pfanner, *J. Mol. Biol.* **2000**, *297*, 809–818.

26
Folding and Disulfide Formation

Margherita Ruoppolo, Piero Pucci, and Gennaro Marino

26.1
Chemistry of the Disulfide Bond

The formation of a disulfide bond from two thiol groups is an electron-oxidation reaction that requires an oxidant. Protein thiol oxidation results from a thiol/disulfide exchange process that transfer equivalents from an external disulfide to the protein (Figure 26.1). The reaction occurs via direct attack of a nucleophilic thiolate anion on the most electron-deficient sulfur of the external disulfide bond. The rate constant for the reaction increases as the basicity of the attacking thiolate nucleophile (S_a) increases (pK_a increases) and as the basicity of the leaving thiolate (R_2S^-) decreases (pK_a decreases). The pK_a of the cysteine sulfhydryl group is generally in the range of 8–9; however this may vary considerably from protein to protein due to the effect of the local environment [1].

Protein disulfide formation in a redox buffer (e.g., low-molecular-weight disulfide and its corresponding thiol) is a reversible reaction that involves the formation of a mixed disulfide intermediate followed by an intramolecular attack in which a second cysteine thiol displaces the mixed disulfide to form the protein disulfide bond (Figure 26.1). Glutathione redox buffers are most commonly used in in vitro experiments since glutathione is present at high concentration in the endoplasmic reticulum [2–4]. Dithiothreitol is often used instead of linear reagents because it does not form long-lived mixed disulfides with protein thiols, thereby making oxidative folding studies easier to interpret because of the reduced number of possible intermediates in the experimental system [5]. However, it has to be taken in consideration that dithiothreitol is not physiological. During oxidative folding, the disulfide component of the redox buffer provides oxidizing equivalents for protein disulfide formation. The ability to form a disulfide will depend on the equilibrium and rate constants for the individual steps illustrated in Figure 26.1 and the concentrations and oxidation potential of the redox buffer [6]. A more oxidizing buffer will favor the formation of protein species with more and more disulfide bonds. At the same time, high concentrations of oxidant inhibit folding by formation of nonproductive intermediates which are too oxidized to fold correctly [2, 7].

The relevant intramolecular step for oxidative folding shown in Figure 26.1 heav-

Protein Folding Handbook. Part I. Edited by J. Buchner and T. Kiefhaber

ISBN: 3-527-30784-2

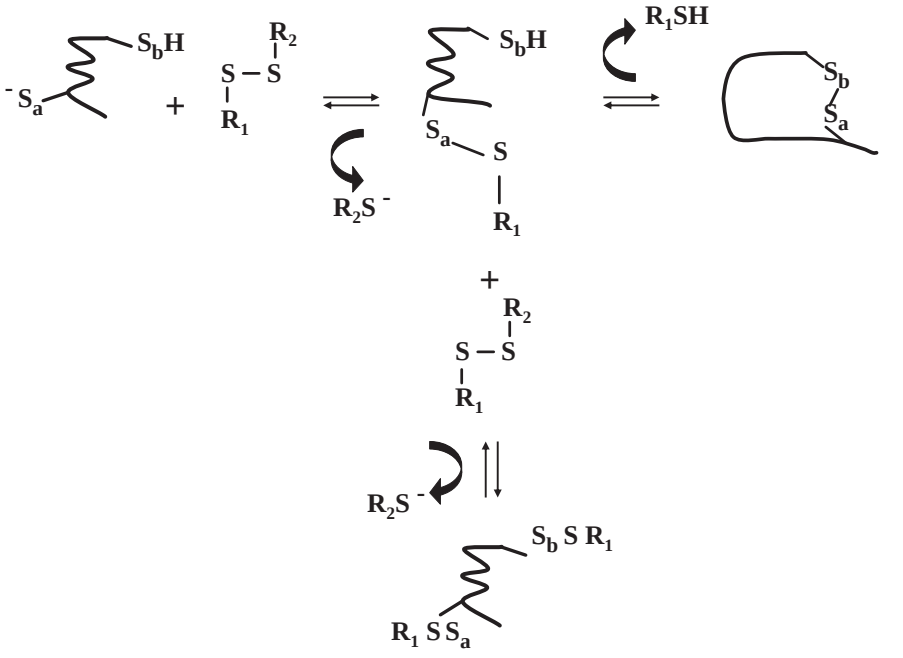

Fig. 26.1. Protein disulfide bond formation.

ily depends on the energetics of the protein conformational changes that bring the two cysteines into proximity to form the disulfide bond [8]. Among intermediates with the same number of intramolecular disulfide bonds, species with the most stable disulfides will have the highest equilibrium concentration regardless the redox buffer composition. The structures of intermediates that result in the formation of the most stable disulfide bond will be present at the highest concentration. Since interconversion among the intermediates with the same number of disulfide bonds constitute a rearrangements that does not involve the net use or production of oxidizing equivalents, the equilibrium distribution of the intermediates with the same number of disulfides will not be affected by the choice of the redox buffer or its composition but it will be an intrinsic property of the protein itself.

26.2 Trapping Protein Disulfides

The strategy of using disulfide bonds as probes to study the folding of disulfide-containing proteins was introduced and developed by Creighton and his group [8]. His pioneering work deserves credit and constitutes a milestone in the field of oxidative folding.

Disulfides present at any instant of time of folding can be trapped in a stable

form by simply blocking, rapidly and irreversibly, all thiol groups in the solution. The quenching reaction should be as rapid as possible to ensure that it faithfully traps the species present at the time of addition of the quenching reagent. Trapping with reagents like iodoacetamide or iodoacetic acid has the advantage of being irreversible, but the reaction has to be carried out in highly controlled experimental conditions to be effective. Once all free thiol groups are irreversibly blocked, the trapped species are indefinitely stable and may be then separated and characterized in details provided that disulfide shuffling is prevented.

Acidification also quenches disulfide bond formation, breakage, and rearrangement. Acidification is very rapid and is not prevented by steric accessibility, but it is reversible. There is then a possibility that separation methods used to separate the acidified species will induce disulfide rearrangements. Finally, acid-trapped species have the advantage that they can be isolated and then returned to the folding conditions, to define their kinetic roles.

The conformations that favor the formation of a particular disulfide bond are stabilized to the same extent by the presence of that specific disulfide bond in trapped intermediate. Because of this close relationship between the stability of disulfide bonds and the protein conformations that favored them, the procedures described above trap not only the disulfide bonds but also the conformations of the protein at that time of folding. Some aspects of the conformation of folding intermediates can then be deduced by identifying the cysteine residues that are involved in the disulfides present in the trapped intermediates.

Although the trapping reaction has the advantage to stabilize the folding intermediates, it has the disadvantage of altering the conformation of the intermediates because of the presence of the blocking groups on the cysteine residues not involved in disulfide bonds. Even intermediates trapped with acid have their free cysteine residues fully protonated, whereas the thiol groups should be at least partially ionized during folding process. Some studies were therefore addressed to prepare the analogs of the folding intermediates replacing the free cysteine residues with Ser or Ala by protein engineering methods [9–12]. These methods have the additional advantage that intermediates that do not accumulate to substantial levels and that they can be prepared in quantities sufficient for structural analysis.

26.3 Mass Spectrometric Analysis of Folding Intermediates

Mass spectrometry is used in protein folding studies to characterize the population of species formed on the folding pathway, and the disulfide bonds present at different times of the process [13, 14]. Figure 26.2 outlines the general strategy. Aliquots withdrawn at different times during the folding process are trapped by alkylation of the free thiol and analyzed by electrospray mass spectrometry (ESMS). The alkylation reaction increases the molecular mass of the intermediates by a fixed amount for each reacted free SH group. Intermediates containing different numbers of disulfide bonds can then be separated by mass, and their relative abundance in the sample can be determined. The nature and quantitative distribution

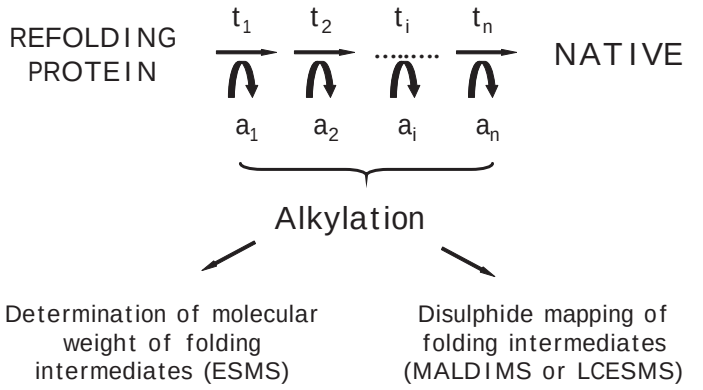

Fig. 26.2. General strategy for mass spectrometry analysis of folding intermediates.

of the disulfide bonded species present at a given time can be used to establish the folding pathway of the protein and to develop a kinetic analysis of the process. The method can also be used to determine the effect of folding catalysts on each step of the folding pathway. Any alteration in the relative distribution of the disulfide bonded species present at a given time due to the catalysts action, in fact, can be identified and quantitated [15].

It should be noted that the intermediates identified by the ESMS analysis are populations of molecular species characterized by the same number of disulfide bonds which may include nearly all possible disulfide bond isomeric species. Once the folding intermediates have been characterized by ESMS in terms of their content of disulfide bonds, a further step would consist in the structural assignment of the various disulfide bonds formed at different times in the entire process by matrix-assisted laser desorption ionization mass spectrometry (MALDIMS) or liquid chromatography ESMS. The experimental approach is based upon determination of the masses of disulfide-linked peptides of unfractionated or partially purified proteolytic digests of folding aliquots in mapping experiments [16, 17]. The folding intermediates should be cleaved at points between the potentially bridged cysteine residues under conditions known to minimize disulfide reduction and reshuffling, using aspecific enzymes or a combination of enzymes, in attempts to isolate any cysteine residue within an individual peptide. The disulfide mapping approach is then used to search for any S–S bonded peptides, which are characterized by their unique masses. The interpretation is then confirmed by performing reduction or EDMAN reactions followed by rerunning the MS spectrum [16].

26.4
Mechanism(s) of Oxidative Folding so Far – Early and Late Folding Steps

During the past three decades, the oxidative folding pathways of various small proteins containing disulfide bonds have been studied by identifying the nature of the intermediates that accumulate during their folding process [18–22]. At present,

no single oxidative folding scenario seems to distinctly emerge from these detailed studies. However some common principles have been highlighted. Disulfide folding pathways are not random: they converge to a limited number of intermediates that are more stables than others. The greater thermodynamic stability of some intermediate conformations can have kinetic consequences, as further folding from the stable conformations is favored. This is most clearly illustrated in the case of bovine pancreatic trypsin inhibitor (BPTI) [8], where early folding intermediates appear to be stabilized by strong native-like interactions. A pre-equilibrium occurs very quickly when the protein is placed under folding conditions; the nature of the pre-equilibrium mixture will only depend upon the final folding conditions. Any favorable conformations present in the pre-equilibrium need not to be present at detectable levels in the denatured state. Conversely, nonrandom conformations that might be present in the denatured state may have no relevance for folding. In the case of BPTI, the most stable partially folded conformations in the pre-equilibrium appear to involve interactions between elements of secondary structure, and there is a considerable evidence for the rapid formation of some elements of secondary structure during the folding of many proteins [8].

The rate-limiting step in disulfide folding occurs very late in the process before the acquisition of the native conformation [8, 15, 23, 24]. The highest free energy barrier separates the native conformation from all other intermediates. At late stages in ''structured'' intermediates, the existing disulfides are sequestered from the thiols of the protein and from the redox reagent, resulting in the slowing of the thiol-disulfide rearrangement reaction by several orders of magnitude (as compared to thiol-disulfide exchange in the ''unstructured'' intermediate at the early stages). As a result, ''structured'' species frequently accumulate during the folding process [23].

The rearrangements that take place in the slow steps of oxidative folding may constitute examples of the conformational rearrangements that take place during the rate-limiting steps in folding transitions not involving disulfide bonds. Such conformational rearrangements are the result of the cooperativiity of protein structure and the similarity of the overall folding transition state to the native conformation.

26.5
Emerging Concepts from Mass Spectrometric Studies

The study of oxidative folding carried out by our group indicated that in quasi-physiological conditions, the process occurs via reiteration of two sequential steps: (i) formation of a mixed disulfide with glutathione, and (ii) internal attack of a free SH group to form an intramolecular disulfide bond. This sequential pathway seems to be a general mechanism for single-domain disulfide-containing proteins as it has been observed in many different experimental conditions.

According to the above concepts, only a limited number of intermediates were detected in the folding mixture and isomerization between species with the same

number of disulfides was found to be only extensive at late stages of the process where slow conformational transitions become significant. Theoretically, the number of all the possible intermediates during the folding process should increase exponentially with the increase in the number of cysteine residues. In contrast, the number of the populations of intermediates increases linearly with the increase in the number of disulfide bonds. Within the frame of this general pathway, differences exist in the amount and accumulation rate of individual intermediates arising from the individual protein under investigation. When the folding pathways of RNase A and toxin α, both containing four disulfide bonds, are compared, some differences can be detected (see below). Species with two disulfide bonds predominate along the RNase A folding [15], while the intermediates containing three disulfides represent the most abundant species in the case of toxin α [15].

Data obtained using different proteins suggests the occurrence of a temporal hierarchy in the formation of disulfide bonds in oxidative folding, in which the sequential order of cysteine couplings greatly affect the rate of the total process. Even the order of formation of native disulfide bonds is in fact important to prevent the accumulation of nonproductive intermediates.

When the folding was carried out in the presence of protein disulfide isomerase (PDI), the folding pathway of reduced proteins was unchanged, but the relative distribution of the various populations of intermediates was altered. All the experiments suggest that PDI catalyzes: (1) formation of mixed disulfides with glutathione, (2) reduction of mixed disulfides, and (3) formation of intramolecular disulfide bonds. These results are not surprising considering the broad range of activities shown by PDI [4].

The oxidative folding pathway of some proteins investigated in our laboratory will be described in detail below.

26.5.1 Three-fingered Toxins

Snake toxins, which are short, all β-proteins, display a complex organization of disulfide bonds. Two S–S bonds connect consecutive cysteine residues (C43-C54, C55-C60) and two bonds intersect when bridging (C3-C24, C17-C41) to form a particular structure classified as ''disulfide β-cross'' [26] because cysteine residues tend to make a cross symbol when viewed along the length of the β-strands. The general organization of the polypeptide chain in snake toxins generates a trefoil structure termed the ''three-fingered fold'' (Figure 26.3). ''Three-fingered'' snake toxins act by blocking ion channels (neurotoxins), or enzymes such as acetylcholinesterase (fascicullin) or Na/K-ATPase and protein kinase C (cardiotoxins), in addition to less-defined targets.

We have shown that three-fingered snake toxins fold according to the general sequential mechanism described above [25, 27]. A single mutation located in an appropriate site of the neurotoxin structure is sufficient to substantially alter the rate of the sequential folding process of the protein and to deeply modify the proportion of intermediates that accumulate during the oxidative folding process. We

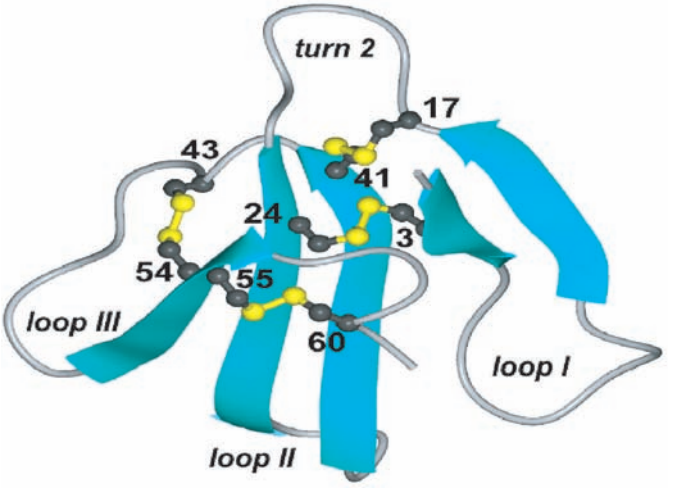

α LECHNQQSSQPPTTKTC-PGETNCYKKVWRDHRGTIIERGCGCPTVKPGIKLNCCTTDKCNN
α_{62} RICFNHQSSQPQTTKTCSPGESSCYNKQWSDFRGTIIQRGCGCPTVKPGIKLSCCESEVCNN
α_{60} LECHNQQSSQPPTTKTC-PG-TNCYKKVWRDHRGTIIERGCGCPTVKPGIKLNCCTTDKCNN
←-------loop I--------> <----------loop II----------> ←-------loop III--------->

Fig. 26.3. Structure of three-fingered toxin. Sequence alignment of neurotoxins and their variants used in our laboratory.

used three variants for which the length of a large turn, turn 2 (Figure 26.3), was increased from three (variant α60, sequence CPG) to four (toxin α, α61, sequence CPGE) and then to five (variant α62, sequence CSPGE) residues. The increase in the length of loop 2 greatly decreased the rate of the folding process. After 2 hours of incubation, about 90% of the variant α60 was folded, whereas no more than 70% of the 61 residues of toxin α and 20% of the variant α62 had reached the native state. Interestingly, three disulfide-containing intermediates were the predominant species in the folding of all variants but this population was markedly more abundant and persistent for the slowest-folding neurotoxin.

Two intermediates containing three disulfides were found to accumulate to detectable levels during early and late stages of neurotoxin α62 folding. Both intermediates consist of chemically homogeneous species containing three of the four native disulfide bonds and lacking the C43-C54 and the C17-C41 coupling, respectively. The des-[43–54] intermediate is the immediate precursor of the native species. Conversely, the des-[17–41] species is unable to form the fourth disulfide bond and has to rearrange into intermediates that can directly reach the native state. These isomerization reactions provide an explanation for the accumulation of three disulfide intermediates along the pathway, which caused the slow oxidative folding observed for neurotoxin α62.

The particular pathway adopted by neurotoxin α62 shares a number of common

features with that followed by BPTI, although the two proteins differ both in the number of disulfides and in their secondary structures. The main similarity is that no scrambled fully oxidized species occur as folding intermediates. In addition, all-but-one-disulfide-containing intermediates (i.e., intermediates containing three and two disulfides) exclusively possess native disulfide bonds [9, 28]. Finally, the native form for both the variant α62 and BPTI results from an intramolecular rearrangement within their respective all-but-one native disulfide populations, with one predominantly productive species, des-[43–54] for the variant α62 and C30-C51 and C5-C55 for BPTI [7]. However, formation of the native form from the productive species seems much faster in BPTI [7] than in neurotoxin α62. It is noteworthy that the folding pathway of variant α62 is much closer to that of BPTI than to those of other all-β disulfide-containing proteins, such as epidermal growth factor (EGF) [29]. In this case disulfide-scrambled isomers accumulate along the pathway and they have to rearrange before forming the native structure.

On more general grounds, the observation that only intermediates with native disulfide bonds accumulate strongly suggests that native disulfide bonds are dominant early in the folding, resulting in funnelling the conformations towards the native state.

26.5.2 RNase A

Bovine pancreatic ribonuclease A has been the model protein for folding studies [30–36] since the landmark discovery by Anfinsen [37] that the amino acid sequence provides all the information required for a protein to fold properly. RNase A contains four disulfide bonds (C26-C84, C40-C95, C65-C72, C58-C110), which are critical both to the function and stability of the native enzyme [38, 39]. The two disulfide bonds C26-C84 and C58-C110 that link a α-helix and a β-sheet in the protein core are the most important to conformational stability. On the other hand, the two disulfide bonds C40-C95 and C65-C72 that link surface loops greatly affect the catalytic activity because of their proximity to active site residues.

The folding of RNase A has been studied in many laboratories, and different mechanisms of folding have been proposed depending on the experimental conditions used. Initial folding studies performed by Creighton and coworkers [40–43] in the presence of reduced and oxidized glutathione suggested that the process proceeds through a single pathway, the rate-determining step being the formation of the C40-C95 disulfide bond.

Parallel studies were performed by Scheraga and coworkers in the presence of reduced and oxidized dithiothreitol [5, 23, 44–46]. These authors suggested that RNase A regenerates through two parallel pathways involving the formation of two native-like species containing three disulfide bonds. The main pathway produces a species lacking C40-C95, in line with former results [40–43], while a species lacking C65-C72 is produced in a minor regeneration pathway.

We showed that the folding of RNase A [15] proceeds throughout the sequential mechanism discussed above. The characterization of the population of one-

disulfide intermediates reveals the presence of only 12 disulfide-bonded species out of the expected 28. These results confirmed previous conclusions, that the formation of the S–S bonds during the folding of RNase A proceeds through a nonrandom mechanism [47] and is coupled to the formation of specific stabilizing structures that are either native or nonnative [8, 12, 23].

Mass spectrometry characterization revealed that in the early stages of the process: (1) the native C26-C84 pairing is absent; (2) disulfide bonds containing C26 are underrepresented; and (3) most of the nonnative disulfide bonds are formed by C110 [48].

The nonrandom coupling of cysteine residues is then biased in three respects: (1) towards the formation of short-range linkages; (2) towards the formation of native disulfides; and (3) towards the formation of disulfides involving cysteines located in the C-terminal rather than N-terminal portion of the molecule. While the first two of these trends are relatively easy to rationalize, the last one is more difficult to interpret. It could reflect more complete collapse of the C-terminal portion of the molecule, allowing easy disulfide interchange within a restricted volume or it could reflect formation of some stable structures around Cys26, which inhibit its interaction with other portions of the polypeptide chain.

The characterization of the population of one-disulfide intermediates produced in the presence of PDI reveals that the PDI-catalyzed refolding generates essentially the same disulfide bonds, and hence the same intermediates identified in the noncatalyzed reoxidation [48]. The similar distribution of isomeric species within the population of one-disulfide intermediates in the uncatalyzed and in the PDI-assisted process indicates that at the early stages of the folding, catalysis of the isomerization of disulfide bonds has no significant effect on the folding pathway. The observation that the population of one-disulfide intermediates is hardly affected by the presence of PDI further proves that thermodynamic control operates at this stage of RNase A refolding. Since nonnative disulfide bonds need to isomerize to produce native RNase A, PDI-dependent catalysis of the rearrangements of disulfide bonds is significant for the overall pathway at later stages of the refolding process. At that stage, the intermediates would already have acquired some tertiary structure and the key function of PDI is to catalyze disulfide rearrangements within kinetically trapped, structured folding intermediates as reported for the PDI-assisted refolding of BPTI [49].

The removal of the C65-C72 disulfide bond has no effect on the kinetics of folding of RNase A. The folding of the C65A/C72A mutant occurs in fact on the same time scale as the folding of wild-type protein [12]. Furthermore the individual native and nonnative disulfides appear at the same times during the folding processes of the mutant and the native protein (with the obvious exception of those involving the two absent cysteine residues). These results suggest that the folding processes of the wild-type and the mutant RNase A are driven by similar interatomic interactions without any great influence of the C65-C72 bond. Interestingly, the C65-C72 disulfide bond is the only disulfide bond that is not conserved throughout the RNase superfamily [50].

The C58A/C110A and C26A/C84A mutants fold much more slowly than the wild-type protein. A steady state is established between two- and three-disulfide

containing species in the folding processes of these two mutants, thus suggesting that the rate-limiting step might be the formation of the third disulfide bond. The assignments of disulfide bonds during the folding of the C58A/C110A and C26A/C84A mutants show that many nonnative disulfide bonds are still present in solution at late stages of the reaction, indicating that many scrambled molecular species have not yet completed the folding process. The formation of C58-C110 or C26-C84 disulfide bonds can function as a lock on the native structure, hampering the three-disulfide-containing species reshuffling in the folding of wild-type RNase A.

Finally, the identification of disulfide bonds formed during the folding of RNase A mutants showed that C110 is the most actively engaged cysteine residue in the formation of disulfide bonds, as occurred in the folding of the wild-type protein. C110 can then function as an internal catalyst able to promote reshuffling of disulfides in order to accelerate isomerization reactions in the regaining of the native state.

26.5.3 Antibody Fragments

Antibodies are multimeric proteins consisting of different domains characterized by two antiparallel β-sheets linked by an intradomain disulfide bond [51–53]. A characteristic feature of antibodies is that the intradomain disulfide bond, which connects residues far apart in the sequence, is completely buried in the core of the protein. Mechanistic studies on oxidative folding of immunoglobulins were previously carried out on antibody fragments and single antibody domains [54–59].

The analysis of immunoglobulin folding by our group was dissected by investigating the folding process of different portions of the antibody molecule. The elucidation of the folding pathway of the noncovalent homodimer formed by the C-terminal domain C_H3 containing a single intramolecular disulfide bond was the first step. We showed that folding, oxidation, and association of the immunoglobulin domain C_H3 requires a fine-tuned and well-coordinated interplay between structure formation to bring the cysteine residues into proximity and to shield the disulfide bond from the solvent and structural flexibility that is required for redox shuffling and rearrangements of structural elements [59].

Analysis of the folding of the Fc fragment constituted by C_H2 and C_H3 domains showed the presence of a kinetic trap during the process that impairs the formation of the second S–S bond from the species containing one intramolecular disulfide. The results indicated that the two domains present in the Fc fragment fold independently. A hierarchy of events exists in the overall process with the disulfide of the C_H3 domain forming faster than the C_H2 S–S bond. During the early stages of folding, the C_H3 domain attains a structure which is able to bring the two cysteines in the right orientation to form the first disulfide bond and to shield it from the solvent as happens for isolated C_H3 [59]. Conversely, the C_H2 domain seems to have a flexible conformation that prevents the formation of the second S–S bond. The rate-limiting step in the overall Fc folding process is then the coupling of

the two cysteines of the C_H2 domain. Consequently, spontaneous folding in the absence of folding helpers only occurs at a very slow rate. The addition of PDI catalyzes the process at various steps, promoting the formation of the C_H2 disulfide.

26.5.4 Human Nerve Growth Factor

Nerve growth factor (NGF), together with brain-derived neurotropic factor (BDNF), neurotrophin-3 (NT-3) and NT-4/5, belongs to the neurotrophin family of protein growth factors. Neurotrophins promote growth, survival, and plasticity of specific neuronal populations during developmental and adult life phases [60, 61]. NGF, BDNF, and other growth factors such as transforming growth factor (TGFβ2), bone morphogenetic protein 2 (BMP-2), and platelet-derived growth factor (PDGF) share characteristic tertiary and quaternary features: the proteins are homodimeric in their native and active conformations and have a typical tertiary fold, the cysteine knot. Our studies showed that the pro-region of recombinant human (rh)-NGF facilitates protein folding. Folding yields and kinetics of rh-pro-NGF were significantly enhanced when compared with the in vitro folding of mature rh-NGF. The characterization of the folding pathway of rh-pro-NGF indicates that structure formation is very efficient since a unique 3S species containing only the native disulfide bonds was detected at early time points of folding. The characterization of intermediates produced in the folding of mature rh-NGF revealed that the process is very slow with the formation of multiple unproductive intermediates containing nonnative cysteine couplings. Two out of the three native disulfide bonds formed after 1 hour, while the formation of the complete set of native disulfide bonds was reached only after 24 hours. Since denatured, mature rh-NGF is known to fold quantitatively as long as the cysteine knot is intact [62], it has been suggested that the pro-sequence assists the oxidative folding by possibly contributing to the formation of the cysteine knot. However, unlike BPTI, the pro-sequence of NGF does not contain a cysteine that could facilitate disulfide bond shuffling during folding of NGF [63].

A possible function of the pro-peptide may be that it acts as a specific scaffold during structure formation of the cysteine knot. Once the native disulfide bonds are formed, the characteristic β-sheet structure is built on and the two monomers can associate to form the rh-pro-NGF dimer. Alternatively, the pro-sequence of NGF could passively confer solubility to aggregation prone folding intermediates by shielding hydrophobic patches and thus enhancing folding yields.

26.6 Unanswered Questions

It is quite clear that many aspects of oxidative folding have been clarified so far. However some questions remain unsolved. An aspect that is still to be clarified

concerns how far the disulfide folding mechanism can be extrapolated to protein folding mechanisms in general. Some common aspects have been highlighted throughout the chapter. However oxidative folding shows peculiar features due to the fact that disulfide-containing proteins constitute a unique class of proteins. In our opinion, the main unanswered questions are related to the observation that some disulfide-containing proteins fold with high efficiency into their native structure while others do not. These aspects are intimately related to the role played in vivo by the multiple redox machineries that cooperate to make folding fast and efficient. These aspects are discussed in Chapters 9 and 19 in Part II.

26.7 Concluding Remarks

Practical considerations drawn from the study of oxidative folding are very important in the production of recombinant proteins with disulfide bonds, many of which are therapeutically useful. A systematic exploration of pH, salt concentration, effectors, cofactors, temperature, and protein concentrations has been made in order to define the best experimental conditions to achieve the highest yield of folded protein. However, fast and high-throughtput methods are still required to investigate optimal folding conditions. There is no doubt that mass spectrometry can be a very useful tool in these kinds of studies. Few solid conclusions have been reached that suggest widely applicable methods for folding denatured and reduced proteins [64]. Guidelines for the optimization of folding methods will be discussed in other chapters.

26.8 Experimental Protocols

26.8.1 How to Prepare Folding Solutions

1. Reduction and denaturation buffer: 0.1 M Tris–HCl, 1 mM EDTA containing 6 M guanidinium chloride, pH 8.5, stable at room temperature for up to 1 month.
2. Folding buffer: 0.1 M Tris–HCl, 1 mM EDTA, pH 7.5; stable at room temperature for up to 1 month.
3. Reduced glutathione stock solution: 50 mM reduced glutathione in folding buffer; prepare fresh daily.
4. Oxidized glutathione stock solution: 50 mM oxidized glutathione in folding buffer; prepare fresh daily.
5. Iodoacetamide (IAM) solution: 2.2 M iodoacetamide solution in folding buffer; prepare fresh daily. IAM is freshly dissolved in folding buffer at 65 °C and cooled to room temperature before use. During preparation of the reagents, the solutions should be protected from light to minimize iodine production, which is a very potent oxidizing agent for thiols.

26.8.2
How to Carry Out Folding Reactions

Preparation of reduced samples

1. Reduce protein with the reduction and denaturation buffer by incubation with reduced DTT (DTT mol/S–S mol = 50/1) for 2 h at 37 °C, under nitrogen atmosphere.
2. Add 0.2 vol of 1 M HCl.
3. Desalt the reaction mixture on a gel-filtration column equilibrated and eluted with 0.01 M HCl.
4. Recover the protein fraction, test for the SH content, lyophilize and store at −20 °C.

Folding reactions

1. Dissolve reduced proteins in 0.01 M HCl and then dilute into the folding buffer to the desired final concentration.
2. Add the desired amounts of GSH and GSSG stock solutions to initiate folding. The choice of the concentrations of reduced and oxidized glutathione depends on the protein under investigation and is based on conditions giving the highest yield of native protein at the end of the folding process. Adjust the pH of the solution to 7.5 with Tris–base and incubate at 25 °C under nitrogen atmosphere. In the case of antibody fragments start folding by diluting 100-fold the reduced and denatured protein in 0.1 M Tris–HCl (pH 8.0), 1 mM EDTA, containing 6 mM GSSG. Carry out the process at 4 °C.
3. Monitor the folding processes by removing 50–100 μL samples of the folding mixture at appropriate intervals.
4. Alkylate the protein samples as described below.
5. Purify from the excess of blocking reagent by rapid HPLC desalting.
6. Recover the protein fraction and lyophilize.
7. Alternatively, quench the folding by adding hydrochloric acid to a final concentration of 3% (experimentally determined pH ∼ 2).

Use of folding catalysts

1. Dissolve folding catalysts in folding buffer.
2. Preincubate for 10 min at 25 °C. Add this mixture to reduced proteins and continue the folding at 25 °C under nitrogen atmosphere, as described.

Alkylation of the folding aliquots

1. Add the folding aliquots (50–100 μL) to an equal volume of a 2.2 M iodoacetamide solution. Perform the alkylation for 30 s, in the dark, at room temperature, under nitrogen atmosphere as described [65].

2. Add 100 μL of 5% trifluoroacetic acid, vortex the aliquots, and store on ice prior loading on the HPLC for the desalting.

26.8.3
How to Choose the Best Mass Spectrometric Equipment for your Study

The determination of the molecular weight of intermediates containing a different numbers of disulfide bonds has to be carried out with a mass spectrometer equipped with an electrospray ion source. The analyzer can easily be a single quadrupole. You do not need very high mass resolution for this kind of analysis.

The assignment of disulfide bonds has to be carried out on the peptide mixtures by using a MALDI time-of-flight mass spectrometer. The instrument has to be a reflectron TOF. You need very high mass resolution for this kind of analysis.

26.8.4
How to Perform Electrospray (ES)MS Analysis

1. Perform mass-scale calibration by means of multiply charged ions from a separate injection of hen egg white lysozyme (average molecular mass 14 305.99 Da) or of horse heart myoglobin (average molecular mass 16 951.5 Da).
2. Dissolve the protein samples in a mixture of H_2O/CH_3CN (50/50) containing 1% acetic acid.
3. Inject the protein samples (10 μL) in concentrations ranging from 10 to 20 pmol μL^{-1} into the ion source via loop injection at a flow rate of 10 μL min^{-1}.
4. Record the spectra by scanning the quadrupole at 10 s per scan. Data are acquired and analyzed by the MassLynx software. Figure 26.4 shows, as an example, the deconvoluted ES spectra of the mixtures of species sampled at 1 min and 4 h from the folding mixture starting from reduced toxin α. The different populations of disulfide intermediates present were identified on the basis of their molecular mass. Each population of trapped intermediates is characterized by a different number of intramolecular disulfide bonds (indicated as *n*S), mixed disulfides with the exogenous glutathione (*n*G) and carboxyamidomethyl (CAM) groups. The number of CAM groups corresponds to the number of free thiols present in the folding intermediates and is therefore indicated as *n*H.

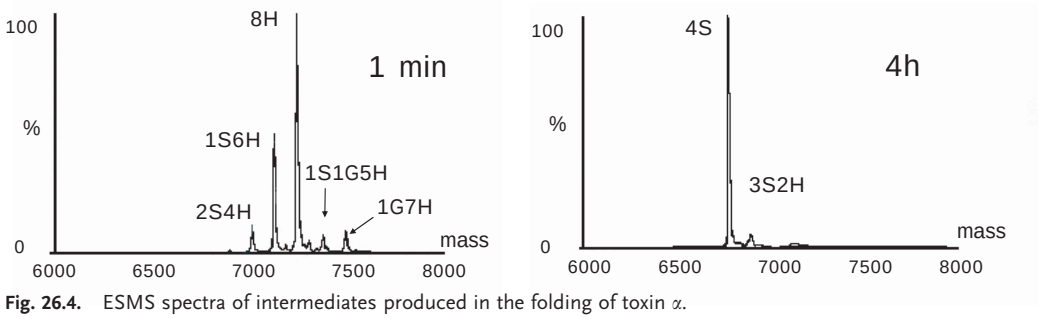

Fig. 26.4. ESMS spectra of intermediates produced in the folding of toxin α.

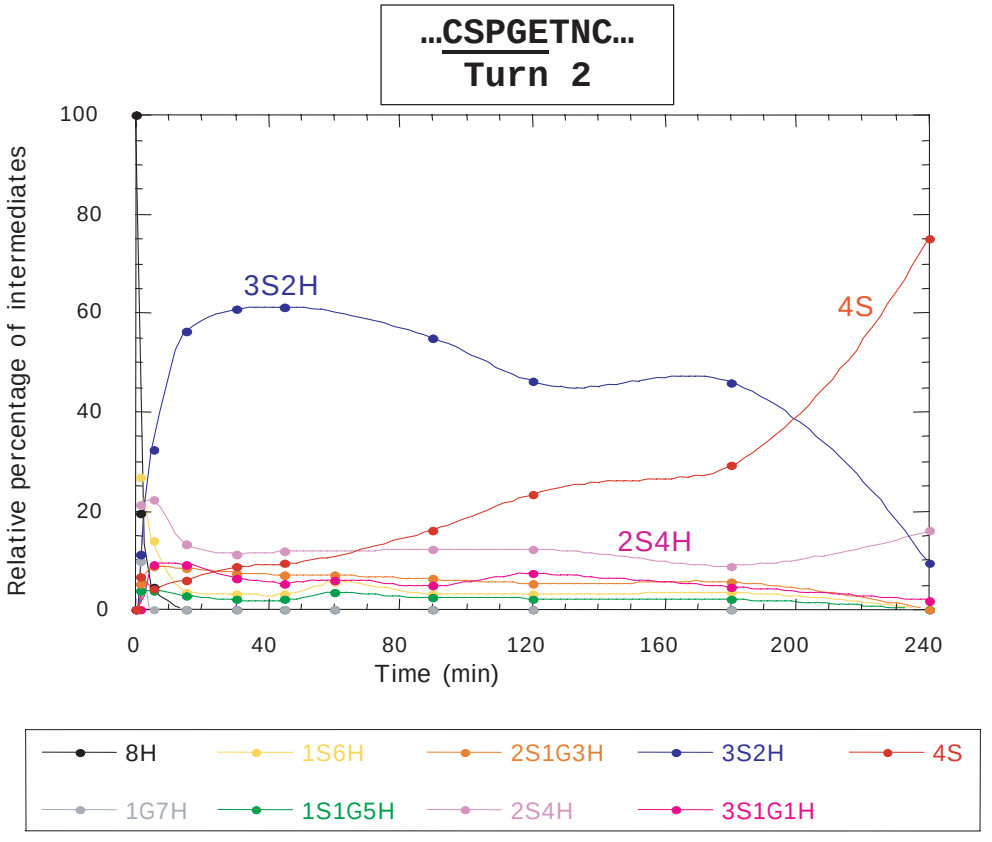

Fig. 26.5. Time course of folding of toxin α62.

Accurately quantify each population of intermediates by measuring the total ion current produced by each species provided that the different components are endowed with comparable ionization capabilities. Each set of folding data should be obtained as the mean of three independent folding experiments. The differences between folding experiments performed completely independently of each other should be about 5%. The time course of folding of toxin α62, plotted in Figure 26.5, shows that intermediates containing three disulfides are predominant from the beginning of the reaction up to about 200 min, when the relative concentration of the species 4S increases.

26.8.5

How to Perform Matrix-assisted Laser Desorption Ionization (MALDI) MS Analysis

1. Hydrolyze the protein samples withdrawn at different incubation times of folding.
2. Dissolve samples in 0.1% trifluoroacetic acid at 10 pmol/μL.
3. Apply 1 μL of sample to a sample slide and allow to air-dry.

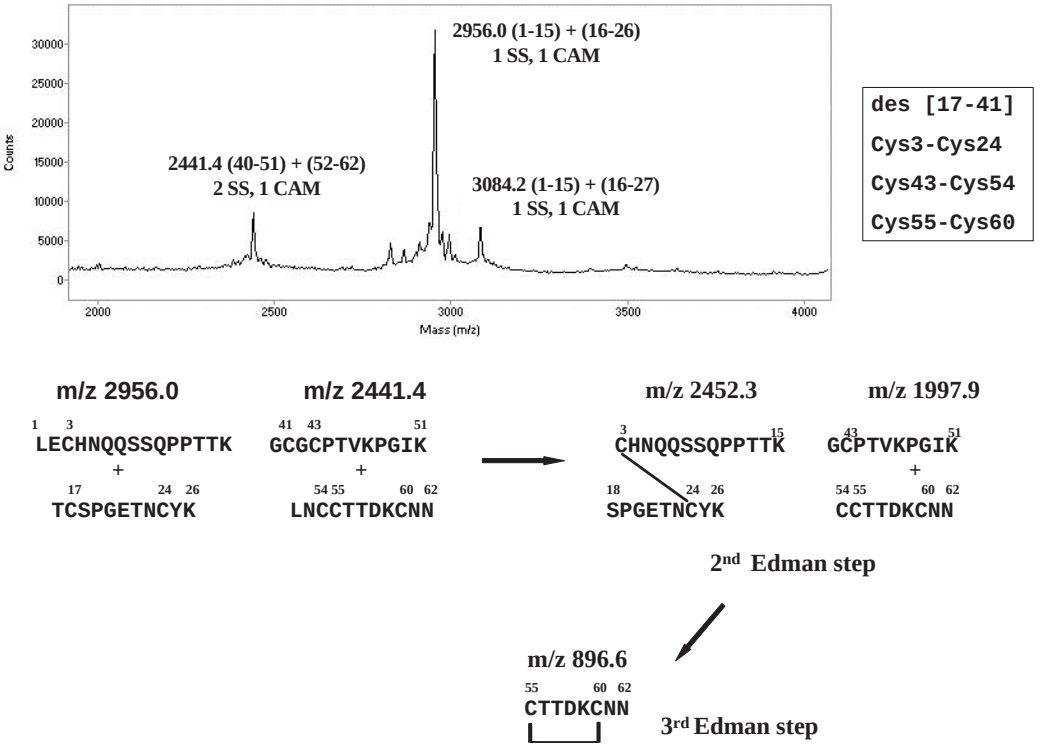

Fig. 26.6. Disulfide mapping of intermediates des-[17–41] accumulating in the folding of toxin α62.

4. Apply 1 μL of bovine insulin to the sample slide and allow to air-dry.
5. Apply 1 μL of α-cyano-4-hydroxycinnamic acid (10 mg mL^{-1}) in ethanol/acetonitrile/0.1% trifluoroacetic acid 1:1:1 (v:v:v) and allow to air-dry.
6. Collect spectra. Mass spectra are generated from the sum of 50 laser shots.
7. Calibrate the mass range using bovine insulin (average molecular mass 5734.6 Da) and a matrix peak (379.1 Da) as internal standards.

Figure 26.6 shows the MALDI mass spectrum of the tryptic mixtures of peptides derived by intermediate des-[17–41] accumulating in the folding of toxin α62. The Edman strategy adopted to assign the disulfide bonds present in the intermediate is also reported.

References

1 H. F. Gilbert (1994). The formation of native disulfide bonds, in *Mechanism of Protein Folding* (R. H. Pain eds), Oxford University Press, Oxford, pp 104–136.

2 C. Hwang, A. J. Sinskey and H. F. Lodish (1992). Oxidized redox state of glutathione in the endoplasmic reticulum. *Science* **257**, 1496–1502.

3 R. B. Freedman, H. C. Hawkins and

S. H. McLaughlin (1995). Protein disulfide isomerase. *Methods Enzymol* **251**, 387–406.

4 R. B. Freedman, P. Klappa and L. W. Ruddock (2002). Protein disulfide isomerases exploit synergy between catalytic and specific binding domains. *EMBO Rep* **3**, 136–140.

5 D. M. Rothwarf and H. A. Scheraga (1993). Regeneration of bovine pancreatic Ribonuclease A. 1. Steady-state distribution. *Biochemistry* **32**, 2671–2680.

6 H. F. Gilbert (1990). Molecular and cellular aspects of thiol-disulfide exchange. *Adv Enzymol* **63**, 69–75. 69–72.

7 J. S. Weissman and P. S. Kim (1991). Re-examination of the folding of BTPI: Predominance of native intermediates. *Science* **253**, 1386–1393.

8 T. E. Creighton (1992). Folding pathways determined using disulfide bonds, in *Protein Folding* (T. E. Creighton ed.), Freeman, New York, pp 301–352.

9 C. P. Van Mierlo, N. J. Darby, D. Neuhaus and T. E. Creighton (1991). Two-dimensional 1H nuclear magnetic resonance study of the (5–55) single-disulfide folding intermediate of bovine pancreatic trypsin inhibitor. *J Mol Biol* **222**, 373–390.

10 J. P. Staley and P. S. Kim (1992). Complete folding of bovine pancreatic trypsin inhibitor with only a single disulfide bond. *Proc Natl Acad Sci USA* **89**, 1519–1523.

11 T. A. Klink, K. J. Woycechowsky, K. M. Taylor and R. T. Raines (2000). Contribution of disulfide bonds to the conformational stability and catalytic activity of ribonuclease A. *Eur J Biochem* **267**, 566–572.

12 M. Ruoppolo, F. Vinci, T. A. Klink, R. T. Raines and G. Marino (2000). Contribution of individual disulfide bonds to the oxidative folding of ribonuclease A. *Biochemistry* **39**, 12033–12042.

13 M. Ruoppolo, R. B. Freedman, P. Pucci and G. Marino (1996). The glutathione dependent pathways of refolding of RNase T1 by oxidation and disulfide isomerization. Catalysis by protein disulfide isomerase. *Biochemistry* **35**, 13636–13646.

14 M. Ruoppolo, C. Torella, F. Kanda, G. Marino, M. Panico, P. Pucci and H. R. Morris (1996). Identification of disulfide bonds in the refolding of bovine pancreatic RNase A. *Folding Des* **1**, 381–390.

15 M. Ruoppolo, J. Lundstrom-Ljung, F. Talamo, P. Pucci and G. Marino (1997). Effect of Glutaredoxin and Protein Disulfide Isomerase on the glutathione-dependent folding of ribonuclease A. *Biochemistry* **36**, 12259–12267.

16 H. R. Morris and P. Pucci (1985). A new method for rapid assignment of S–S bridges in proteins. *Biochem Biophys Res Commun* **126**, 122–128.

17 H. R. Morris, P. Pucci, M. Panico and G. Marino. (1990). Protein folding/refolding analysis by mass spectrometry. *Biochem J* **268**, 803–806.

18 T. E. Creighton, N. J. Darby and J. Kemmink (1996). The roles of partly folded intermediates in protein folding. *FASEB J* **10**, 110–118.

19 N. W. Isaacs (1995). Cystine knots. *Curr Opin Struct Biol* **5**, 391–395.

20 R. S. Norton and P. K. Pallaghy (1998). The cystine knot structure of ion channel toxins and related polypeptides. *Toxicon* **36**, 1573–1583.

21 L. R. De Young, C. H. Schmelzer and L. E. Burton (1999). A common mechanism for recombinant human NGF, BDNF, NT-3, and murine NGF slow unfolding. *Protein Sci* **8**, 2513–2518.

22 R. J. Darling, R. W. Ruddon, F. Perini and E. Bedow (2000). Cystine knot mutations affect the folding of the glycoprotein hormone alpha-subunit. Differential secretion and assembly of partially folded intermediates. *J Biol Chem* **275**, 15413–15421.

23 M. Narayan, E. Welker, C. Wanjalla, G. Xu and H. A. Scheraga (2003). Shifting the competition between the intramolecular Reshuffling reaction and the direct oxidation reaction during the oxidative folding of

kinetically trapped disulfide-insecure intermediates. *Biochemistry* **42**, 10783–10789.

24 W. J. Wedemeyer, E. Welker, M. Narayan and H. A. Scheraga (2000). Disulfide bonds and protein folding. *Biochemistry* **39**, 4207–4216.

25 M. Ruoppolo, M. Moutiez, M. F. Mazzeo, P. Pucci, A. Menez, G. Marino and E. Quéméneur (1998). The length of a single turn controls the overall folding rate of ''three-fingered'' snake toxins. *Biochemistry* **37**, 16060–16068.

26 P. M. Harrison and M. J. E. Sternberg (1996). The disulfide beta-cross: from cystine geometry and clustering to classification of small disulfide-rich protein folds. *J Mol Biol* **264**, 603–623.

27 M. Ruoppolo, F. Talamo, P. Pucci, M. Moutiez, E. Quèmèneur, A. Mènez and G. Marino (2001). Slow folding of three-fingered toxins is associated with the accumulation of native disulfide-bonded intermediates. *Biochemistry* **40**, 15257–15266.

28 C. Eigenbrot, M. Randal and A. A. Kossiakoff (1990). Structural effects induced by removal of a disulfide-bridge: the X-ray structure of the C30A/C51A mutant of basic pancreatic trypsin inhibitor at 1.6 A. *Protein Eng* **3**, 591–598.

29 J. Y. Chang, L. Li and A. Bulychev (2000). The underlying mechanism for the diversity of disulfide folding pathways. *J Biol Chem* **275**, 8287–8289.

30 D. B. Wetlaufer and S. Ristow (1973). Acquisition of three-dimensional structure of proteins. *Annu Rev Biochem* **42**, 135–158.

31 D. B. Wetlaufer (1973). Nucleation, rapid folding and globular intra-chain regions in proteins. *Proc Natl Acad Sci USA* **70**, 697–701.

32 M. Karplus and D. C. Weaver (1976). Protein-folding dynamics *Nature (London)* **260**, 404–406.

33 R. T. Raines (1998). Ribonuclease A. *Chem Rev* **98**, 1045–1065.

34 J. R. Garel and R. L. Baldwin (1973). Both the fast and slow refolding reactions of ribonuclease A yield native enzyme. *Proc Natl Acad Sci USA* **70**, 3347–3351.

35 L. N. Lin and J. F. Brandts (1984). Involvement of prolines-114 and -117 in the slow refolding phase of ribonuclease A as determined by isomer-specific proteolysis. *Biochemistry* **23**, 5713–5723.

36 P. S. Kim and R. L. Baldwin (1982). Specific intermediates in the folding reactions of small proteins and the mechanism of protein folding. *Annu Rev Biochem* **51**, 459–489.

37 C. B. Anfinsen (1973). Principles that govern the folding of protein chains *Science* **181**, 223–230.

38 S. Shimotakahara, C. B. Rios, J. H. Laity, D. E. Zimmermann, H. A. Scheraga and G. T. Montelione (1997). NMR structural analysis of an analog of an intermediate formed in the rate-determining step of one pathway in the oxidative folding of bovine pancreatic ribonuclease A: automated analysis of 1H, 13C, and 15N resonance assignments for wild-type and [C65S, C72S] mutant forms. *Biochemistry* **36**, 6915–6929.

39 B. R. Kelemen, L. W. Schultz, R. Y. Sweeney and R. T. Raines (2000). Excavating an active site: the nucleobase specificity of ribonuclease A. *Biochemistry* **39**, 14487–14494.

40 T. E. Creighton (1979). Intermediates in the refolding of reduced ribonuclease A. *J Mol Biol* **129**, 411–431.

41 T. E. Creighton (1980). A three-disulfide intermediate in refolding of reduced Ribonuclease A with a folded conformation. *FEBS Lett* **118**, 283–288.

42 T. E. Creighton (1983). An empirical approach to protein conformation stability and flexibility. *Biopolymers* **22**, 49–60.

43 T. E. Creighton (1990). Protein folding. *Biochem J* **270**, 1–10.

44 D. M. Rothwarf and H. A. Scheraga (1993). Regeneration of bovine pancreatic Ribonuclease A. 2. Kinetics of regeneration. *Biochemistry* **32**, 2680–2690.

45 D. M. Rothwarf and H. A. Scheraga

(1993). Regeneration of bovine pancreatic Ribonuclease A. 3. Dependence on the nature of the redox reagent. *Biochemistry* **32**, 2690–2697.

46 D. M. Rothwarf and H. A. Scheraga (1993). Regeneration of bovine pancreatic ribonuclease A. 4. Temperature dependence of the regeneration rate. *Biochemistry* **32**, 2698–2706.

47 X. Xu, D. M. Rothwarf and H. A. Scheraga (1996). Non-random distribution of the one-disulfide intermediates in the regeneration of ribonuclease A. *Biochemistry* **35**, 6406.

48 F. Vinci, M. Ruoppolo, P. Pucci, R. B. Freedman and G. Marino (2000). Early intermediates in the PDI-assisted folding of ribonuclease A. *Protein Sci* **9**, 525–535.

49 J. S. Weissmann and P. S. Kim (1993). Efficient catalysis of disulfide bond rearrangements by protein disulfide isomerase. *Nature* **365**, 185–188.

50 J. J. Beintema, C. Schuller, M. Irie and A. Carsana (1988). Molecular evolution of the ribonuclease superfamily. *Progr Biophys Mol Biol* **51**, 165–192.

51 R. Huber, J. Deisenhofer, P. M. Colman, M. Matsushima and W. Palm (1976). Crystallographic structure studies of an IgG molecule and an Fc fragment. *Nature* **264**, 415–420.

52 J. Deisenhofer (1981). Crystallographic refinement and atomic models of a human Fc fragment and its complex with fragment B of protein A from *Staphylococcus aureus* at 2.9 and 2.8 Å resolution. *Biochemistry* **20**, 2361–2370.

53 J. G. Augustine, A. de La Calle, G. Knarr, J. Buchner and C. A. Frederick (2001). The crystal structure of the fab fragment of the monoclonal antibody MAK33. Implications for folding and interaction with the chaperone bip. *J Biol Chem* **276**, 3287–3294.

54 Y. Goto and Y. Tamaguchi (1979). The role of the intrachain disulfide bond in the conformation and stability of the constant fragment of the immuno-globulin light chain. *J Biochem* **86**, 1433–1441.

55 Y. Goto and Y. Tamaguchi (1982). Unfolding and refolding of the constant fragment of the immunoglobulin light chain. Kinetic role of the intrachain disulfide bond. *J Mol Biol* **156**, 911–926.

56 J. Buchner and R. Rudolph (1991). Renaturation, purification and characterization of recombinant Fab-fragments produced in *Escherichia coli*. *Bio/technology* **9**, 157–162.

57 H. Lilie, S. Mc Laughlin, R. Freedman and J. Buchner (1994). Influence of protein disulfide isomerase (PDI) on antibody folding in vitro. *J Biol Chem* **269**, 14290–14296.

58 M. J. W. Thies, J. Mayer, J. G. Augustine, C. A. Frederick, H. Lilie and J. Buchner (1999). Folding and association of the antibody domain C_H3: prolyl isomerization preceeds dimerization. *J Mol Biol* **293**, 67–79.

59 M. J. W. Thies, F. Talamo, M. Mayer, S. Bell, M. Ruoppolo, G. Marino and J. Buchner (2002). Folding and oxidation of the antibody domain C_H3. *J Mol Biol* **319**, 1267–1277.

60 Y. A. Barde (1990). The nerve growth factor family. *Prog Growth Factor Res* **2**, 237–248.

61 H. Thoenen (1995). Neurotrophins and neuronal plasticity. *Science* **270**, 593–598.

62 L. R. De Young, L. E. Burton, J. Liu, M. F. Powell, C. H. Schmelzer and N. J. Skelton (1996). RhNGF slow unfolding is not due to proline isomerization: possibility of a cystine knot loop-threading mechanism. *Protein Sci* **5**, 1554–1566.

63 J. S. Weissman and P. S. Kim (1992). The pro region of BPTI facilitates folding. *Cell* **71**, 841–851.

64 D. R. Thatcher and M. Hitchcock (1994). Protein folding in biotechnology in *Mechanism of Protein Folding* (R. H. Pain eds). Oxford University Press, Oxford, pp 229–261.

65 W. R. Gray (1993). Disulfide structures of highly bridged peptides: a new strategy for analysis. *Protein Sci* **2**, 1732–1748.

27
Concurrent Association and Folding of Small Oligomeric Proteins

Hans Rudolf Bosshard

27.1
Introduction

Our current understanding of protein folding has been mostly obtained through the study of monomeric, globular proteins. However, oligomeric proteins are probably more abundant in nature. There is strong evolutionary pressure for monomeric proteins to associate into oligomers [1]. Many results and conclusions acquired from the study of monomeric proteins can be applied to oligomeric proteins. For example, the stabilities of both monomeric and oligomeric proteins result from a delicate balance between opposing forces, the major contributors to stability being the hydrophobic effect, van der Waals interactions, and hydrogen bonds among polar residues [2–4]. In contrast to monomeric proteins, the stabilizing and destabilizing forces operate not only within single subunits but also between the subunits of an oligomeric protein; that means, both *intra*molecular and *inter*molecular forces contribute to stability. Nevertheless, there are no fundamental differences between the mechanisms of folding of monomeric and oligomeric proteins. For both types of proteins singular as well as multiple folding pathways are observed with no, a few, or many intermediates and sometimes with nonnative, dead-end products.

However, one difference is important: At least one step in the folding of an oligomeric protein must be concentration dependent. This is because the formation of an oligomeric protein includes folding *and* association; and folding and association are concurrent reactions. In some cases, folding and association can be studied as separate and virtually independent reactions, in others they are fully coupled into a single reaction step (''two-state'' mechanism or ''single-step'' mechanism), yet most often they can be distinguished but are not independent of each other. The degree of coupling between folding and association largely depends on the balance between the intra- and intermolecular forces that stabilize the oligomeric structure. If the isolated monomeric subunits are stabilized by strong intramolecular forces and the folded monomeric subunits themselves are thermodynamically stable folded structures, then folding and association are separate steps: formation of the oligomer corresponds to the association of preformed folded monomers. If the iso-

Protein Folding Handbook. Part I. Edited by J. Buchner and T. Kiefhaber

ISBN: 3-527-30784-2

lated monomeric subunits are unstable and stability is gained only by intermolecular forces within the oligomeric structure, then folding and association are intimately dependent on each other and are tightly coupled.

The concurrence of intra- and intermolecular reactions and the dependence of folding on concentration adds an extra level of complexity to folding. This is perhaps the main reason why our knowledge of the stability and folding of multisubunit proteins is still rudimentary and often of only a qualitative nature. Indeed, quantitative thermodynamic and kinetic analyses have been restricted to mainly dimeric proteins. Reliable quantitative thermodynamic and kinetic data on trimeric and higher order oligomeric structures are still scarce.

The present chapter focuses on the detailed, quantitative in vitro analysis of the thermodynamics and kinetics of folding of small dimeric proteins and protein motifs, with only brief and passing reference to trimeric and tetrameric structures. The emphasis is on concepts and methods. We do not present a comprehensive review of the assembly of dimeric proteins but select appropriate examples to illustrate experimental methods, concepts and principles. In vitro and in vivo folding and association of oligomeric and multimeric proteins has been reviewed before (see Refs [5–8]). In vivo folding and assembly of large, higher order multisubunit proteins is covered in Chapter 2 in Part II.

27.2 Experimental Methods Used to Follow the Folding of Oligomeric Proteins

In principle, the methods used in the study of monomeric proteins can be used to follow dissociation and unfolding of oligomeric proteins under equilibrium conditions and to measure the kinetics of folding, unfolding, and refolding. The main difference is in data analysis, which has to consider the association step that is lacking in monomeric proteins.

27.2.1 Equilibrium Methods

Chemical unfolding by urea or guanidinium chloride (GdmCl) is the most commonly used method to measure the fraction of folded and unfolded protein, respectively, and to calculate equilibrium constants. Free energies of unfolding at standard conditions, $\Delta G_U(H_2O)$, are obtained by linear extrapolation to zero denaturant as is done for monomeric proteins [9] (see Appendix: Section A2.2 and Chapter 3 for more details). Extrapolation is performed on any suitable signal change paralleling the denaturant-induced change of molecular state; examples are far-UV circular dichroism (CD) to follow secondary structure changes, or tryptophan fluorescence to monitor molecular packing density and polarity. In applying linear extrapolation one tacitly assumes that the effects of the denaturant on both unfolding and dissociation of the oligomeric protein are linear. This assumption is difficult to check. Extrapolating the same value of $\Delta G_U(H_2O)$ from urea and

GdmCl unfolding is a good indication of a linear denaturant dependence of dissociation and unfolding [10, 11].

Another popular equilibrium method is thermal unfolding. If the equilibrium between unfolded subunits and folded oligomer is reversible, the change with temperature of an appropriate spectroscopic signal such as fluorescence emission or CD can be used to determine the fraction of protein in the folded and unfolded states and, occasionally, also the fraction of intermediate states. The immediate result from the thermal melting curve of a protein is its midpoint temperature of unfolding, T_m. If the reversible unfolding of an oligomeric protein follows a two-state mechanism, half of the protein is unfolded and dissociated and half is folded and associated at T_m. (This does not apply to the midpoint T_m of a melting curve obtained by differential scanning calorimetry [12].) The melting curve provides the fraction of unfolded, monomeric protein, f_M, from which the equilibrium unfolding constant K_U and the free energy of unfolding $\Delta G_U = -RT \ln K_U$ is calculated. Note that in using K_U and ΔG_U, the folded, native state is the reference state.

From the temperature dependence of the equilibrium constants of unfolding, the van't Hoff enthalpy of the dissociation–unfolding transition at T_m can be calculated (see Appendix: Sections A2.3 and A2.4). From differential scanning calorimetry experiments the calorimetric enthalpy can be obtained, which is model independent and may differ from the van't Hoff enthalpy if the unfolding reaction is not two-state. Extrapolation of enthalpies and free energies to standard conditions (for example 25 °C) are based on the formalism of equilibrium thermodynamics (see Appendix: Section A2.5). Such extrapolation can be inaccurate if it extends over a large temperature range and the heat capacity change is not accurately known.

The fraction of protein in the oligomeric and monomeric state may also be obtained by following an appropriate signal after simple dilution. This approach is an added benefit of the concentration dependence of the monomer/oligomer equilibrium and can be used under benign buffer conditions, that is, in the absence of denaturant and at ambient temperature. If dissociation and unfolding are fully coupled, the dilution method yields the overall free energy of unfolding plus dissociation. However, if different free energies of unfolding are obtained from the dilution method and from chemical or thermal unfolding, this indicates that folding and association are not, or only partly, coupled. For example, a lower free energy of unfolding from dilution than from chemical unfolding is an indication for a folding intermediate that is populated under benign conditions but not in the presence of chemical denaturant. In other words, the oligomeric protein dissociates into (partly) folded subunits during dilution under benign conditions, yet it dissociates into unfolded subunits in the presence of a denaturant. The difference between $\Delta G_U(H_2O)$ from dilution and $\Delta G_U(H_2O)$ from chemical unfolding can then be ascribed to the unfolding free energy of the subunits.

Other methods to monitor the fraction of folded and unfolded oligomeric proteins under benign buffer conditions are sedimentation equilibrium analysis, gel-filtration chromatography, light-scattering analysis, and isothermal titration calorimetry. In the last method, the heat evolved or taken up when two (or more)

molecules interact with each other is measured and the reaction enthalpy is calculated from the integrated heat change. Isothermal titration calorimetry can only be applied to heterodimeric proteins whose subunits do not form homomeric structures. The procedure yields the change of the enthalpy, the Gibbs free energy and the subunit stoichiometry of the oligomeric structure [12–14].

It should be noted that all the methods based on dissociation under benign buffer conditions work only if the association between the subunits is relatively weak and association/dissociation occurs in the micromolar to nanomolar concentration range. If an oligomeric protein assembles at less than nanomolar concentration, spectroscopic signal changes and calorimetric heat changes may be too weak to monitor by dilution.

27.2.2 Kinetic Methods

The same kinetic methods used for monomeric proteins can be applied to study the time course of folding and association or unfolding and dissociation of oligomeric proteins. Time-resolved methods include conventional stopped-flow and quenched-flow techniques for the time range of milliseconds to seconds, and fast relaxation methods like temperature jump to follow more rapid reactions (see Chapter 14). Variation of the observation signal allows different aspects of the reaction to be investigated. For example, far-UV CD spectroscopy, pulse-labeling NMR and mass spectroscopy are used to follow secondary structure formation and formation of hydrogen bonds; intrinsic and extrinsic fluorescence measurements monitor molecular packing; fluorescence anisotropy and small angle X-ray estimate changes in molecule size; ligand binding reports the gain or loss of biological activity. (See Chapter 2 and Ref. [15] for spectroscopic methods used to study protein folding.)

As for monomeric proteins, unfolding and refolding is often studied by rapid dilution into denaturant and out of denaturant, respectively. This necessitates extrapolation to standard conditions in water. To avoid extrapolation, unfolding under benign buffer conditions may be studied from relaxation after a rapid change of temperature, pH or simply after rapid dilution (see Refs [16] and [17] and Appendix: Section A3). If an oligomeric protein is composed of different subunits, folding can be studied in a very direct way by rapid mixing of the different subunits. This means there is no need to first unfold the heterooligomeric protein and thereafter follow its refolding by returning to folding conditions.

The rates of dissociation of an oligomeric protein can also be measured by subunit exchange. To this end, the protein has to be labeled with a fluorescence tag or another appropriate marker. Folded protein with the marker is rapidly diluted with a large excess of folded protein lacking the marker. The change of the signal of the marker is then proportional to the rate of dissociation of the marked protein provided that reassociation is much more rapid than dissociation, which can be achieved by increasing the protein concentration [17, 18].

27.3
Dimeric Proteins

The simplest folding mechanism of a dimeric protein is a two-state or one-step reaction between two unfolded monomers M_u and the folded dimer D_f as described by Eq. (1).

$$2M_u \underset{k_u}{\overset{k_f}{\rightleftarrows}} D_f$$
$$K_d = \frac{k_u}{k_f} = \frac{[M_u]^2}{[D_f]} \tag{1}$$

Here and elsewhere, we use the notation M for monomer and D for dimer. The subscripts indicate unfolded and folded, respectively. For a monomeric protein both k_f and k_u are monomolecular rate constants (s^{-1}). In the case of a dimeric protein, k_f is a bimolecular rate constant ($M^{-1}\ s^{-1}$) and only k_u is unimolecular (s^{-1}). Square brackets indicate molar concentrations. Also, in contrast to a monomeric protein, the equilibrium dissociation constant K_d has the unit of a concentration. It is related to the thermodynamic parameters of unfolding by the well-known thermodynamic equation:

$$\Delta G_U = \Delta H_U - T\Delta S_U = -RT \ln K_d \tag{2}$$

Equation (1) says that the folding and association reactions are completely linked. In practice, this means that the association of the monomeric subunits and their folding to the native conformation of the final dimer cannot be experimentally separated. However, this does not exclude the fleeting existence of intermediates. Indeed, there are several instances where folding is thermodynamically two-state but kinetics reveal transitory intermediates (see the examples in Table 27.3). Hence, a more physically meaningful mechanism for the formation of a dimeric protein is described by Eq. (3).

$$2M_u \underset{k_{-1}}{\overset{k_1}{\rightleftarrows}} 2M_i \underset{k_{-2}}{\overset{k_2}{\rightleftarrows}} D_i \underset{k_{-3}}{\overset{k_3}{\rightleftarrows}} D_f$$
$$K_{d1} = \frac{[M_u]}{[M_i]} = \frac{k_{-1}}{k_1} \quad K_{d2} = \frac{[M_i]^2}{[D_i]} = \frac{k_{-2}}{k_2} \quad K_{d3} = \frac{[D_i]}{[D]} = \frac{k_{-3}}{k_3} \tag{3}$$

Here, monomeric and dimeric intermediates (subscript i) are at equilibrium with the unfolded monomer M_u and the folded dimer D_f, respectively. Intermediate M_i can be considered as an association-competent subset of conformational forms of the monomer, perhaps a set of partly folded monomers. Only M_i associates to the dimeric intermediate D_i, which then rearranges to the final folded dimer D_f. The first and third equilibria are unimolecular, the middle equilibrium is bimolecular. If the first equilibrium is far on the side of M_u and the last is far on the side of D_f, Eq. (3) simplifies to the one-step Eq. (1). In this case, only M_u and D_f are detected

under equilibrium conditions, but the kinetics of folding and unfolding may exhibit different phases indicative of transitory formation of intermediates.

27.3.1 Two-state Folding of Dimeric Proteins

Several dimeric proteins fold according to Eq. (1), exhibiting two-state transition between two unfolded monomers and a folded dimer. For monomeric proteins it has been shown that a two-state folding model is justified if the protein rapidly equilibrates between many unfolded conformations prior to complete folding [19]. By the same reasoning, two-state folding seems justified if intermediates M_i and D_i of Eq. (3) are ensembles of barely populated conformations at rapid equilibrium with M_u and D_f, respectively. One has to keep in mind that two-state folding is an operational concept: The sole observation of a folded dimer and an unfolded monomer under a given set of experimental conditions does not rule out the existence of folding intermediates. Table 27.1 lists operational criteria that typically apply to two-state folding. At least one of criteria i–iv referring to equilibrium experiments, and one of criteria v–vii referring to kinetic experiments, as well as criterion viii should be met to demonstrate two-state folding. The calorimetric and van't Hoff equality criterion ix is more difficult to test because thermal unfolding has to be over 90% reversible, which is not always the case.

The thermodynamic and kinetic formalism for two-state folding is relatively simple and has often been described (see the Appendix for details). As for monomeric proteins, the equilibrium dissociation constant K_d is obtained from the fraction of monomeric protein f_M, or the fraction of dimeric protein $f_D = 1 - f_M$. For a

Tab. 27.1. Criteria for two-state folding.

(i)	Equilibrium unfolding followed with different physical probes such as light absorption, fluorescence emission, circular dichroism yield superimposable curves
(ii)	Equilibrium measurements are dependent on protein concentration
(iii)	The change of the free energy of unfolding with denaturant concentration is linear
(iv)	The reciprocal midpoint temperature of unfolding ($1/T_m$) is linearly proportional to the logarithm of the total protein concentration
(v)	Refolding kinetics is concentration dependent, unfolding kinetics is concentration independent
(vi)	Kinetics of folding and unfolding exhibit single phases, and these account for the entire amplitude of the signal changes of folding and unfolding, respectively
(vii)	The change of the unfolding and refolding rate constants with denaturant is linear
(viii)	Equilibrium constants determined experimentally are the same within error as those calculated from the ratio of the association and dissociation rate constants
(ix)	The enthalpy change of the dimer to monomer transition obtained by van't Hoff analysis of thermal unfolding curves is the same within error as the calorimetrically measured enthalpy change

monomeric protein the equilibrium constant, defined as $K_d = f_M/(1 - f_M)$, is independent of the protein concentration. In contrast, to determine K_d of a dimeric protein, the protein concentration has to be known. Moreover, the relationship between K_d and concentration is different for homodimeric and heterodimer proteins, as shown by Eqs (4) and (5) (see also Appendix: Section A1).

$$K_d = \frac{2[P_t]f_M{}^2}{1 - f_M} \tag{4}$$

$$K_d = \frac{[P_t]f_M{}^2}{2(1 - f_M)} \tag{5}$$

In the above equations, $[P_t]$ is the total protein concentration expressed as the total monomer concentration: $[P_t] = [M] + 2[D]$. It is important to note that the protein concentration has to be accounted for in analyzing the thermodynamic and kinetic data. For example, the well-known linear extrapolation of chemical unfolding data to zero denaturant concentration has to consider protein concentration because ΔG_U is not zero at the transition midpoint of chemical unfolding (see Appendix: Section A2.2).

27.3.1.1 Examples of Dimeric Proteins Obeying Two-state Folding

Table 27.2 lists five representative examples of small dimeric proteins for which two-state folding has been demonstrated based on several of the criteria listed in Table 27.1. The Arc repressor of bacteriophage P22 is a small homodimeric protein composed of two 53 residue polypeptide chains [10]. Figure 27.1 shows that the fluorescence and CD changes induced by denaturant are superimposable (criterion i of Table 27.1). The position of the unfolding trace is dependent on protein concentration as predicted for a bimolecular reaction (criterion v of Table 27.1). The change of unfolding free energies with denaturant concentration is linear (criterion iii of Table 27.1) and extrapolation to water yields the same free energy of unfolding for both urea and GdmCl unfolding, supporting of the validity of the linear extrapolation approach for both the unfolding reaction and the dissociation of dimers into monomers.

Figure 27.2 shows the urea dependence of unfolding and refolding rates of the dimeric Arc repressor. The rate of refolding increases linearly when the denaturant concentration is lowered; the rate of unfolding increases linearly when the denaturant concentration increases (criterion vii). Refolding is concentration dependent, unfolding is concentration independent, and the single kinetic phases account for the entire amplitude of refolding and unfolding (criterion vi). Finally, the free energy of unfolding and dissociation extrapolated from equilibrium measurements and calculated from the ratio of the refolding and unfolding rate are very similar, as demanded by criterion viii. In the middle range of denaturant concentrations, both unfolding and refolding reactions have to be taken into account when analyzing the unfolding and refolding traces, respectively. The analysis was performed using Eq. (A29) [20]. Note that, unlike in the case of a monomeric protein, the

Tab. 27.2. Examples of dimeric proteins folding through a simple two-state mechanism: $2M_u \underset{k_u}{\overset{k_f}{\rightleftarrows}} D_f$.

Protein	*Equilibrium analysis*[a]	*Kinetic analysis*[a]	*Comments*
Arc repressor (homodimer)	$\Delta G_U = 40$ kJ mol^{-1}, $\Delta C_P = 6.7$ kJ M^{-1} K^{-1}, $\Delta H_U(54\ ^\circ C) = 297$ kJ M^{-1} [10]	$k_f = 9 \times 10^6$ M^{-1} s^{-1}, $k_u = 0.2$ s^{-1}, $\Delta G_U = 41$ kJ mol^{-1} [20]	Many native-like interactions in the dimeric transition state [21–23]
GCN4 leucine zipper (homodimer)	$\Delta G_U(5\ ^\circ C) = 39$ kJ mol^{-1} [72]	$k_f = 4 \times 10^5$ M^{-1} s^{-1}, $k_u = 3.3 \times 10^{-3}$ s^{-1}, $\Delta G_U(5\ ^\circ C) = 43$ kJ mol^{-1} [45]	Calorimetric analysis indicates two monomolecular pretransitions at 20 °C and 50 °C before the main bimolecular transition [26] Evidence for association-competent, partly helical monomer [48, 49]
Leucine zipper AB (heterodimer)	$\Delta G_U = 44$ kJ mol^{-1}, $\Delta C_P = 3$–4 kJ M^{-1} K^{-1}, $\Delta H_U(25\ ^\circ C) = 120$ kJ M^{-1} [27]	$k_f = 2 \times 10^7$ M^{-1} s^{-1}, $k_u = 0.2$ s^{-1}, $\Delta G_U = 46$ kJ mol^{-1} [28]	Folding, but not unfolding, is strongly dependent on ionic strength indicating electrostatically assisted association [28]
Nerve growth factor (homodimer)	$\Delta G_U = 81$ kJ mol^{-1} [11]		
Mannose-binding lectin (heterodimer)	$\Delta G_U = 55$ kJ mol^{-1}, $\Delta C_P = 13$ kJ M^{-1} K^{-1}, $\Delta H_U(66\ ^\circ C) = 728$ kJ M^{-1} [73]		ΔC_P-values from experiment and calculated from the buried subunit interface agree well

[a] Unless stated, thermodynamic and kinetic parameters refer to ambient temperature (20 to 25 °C).

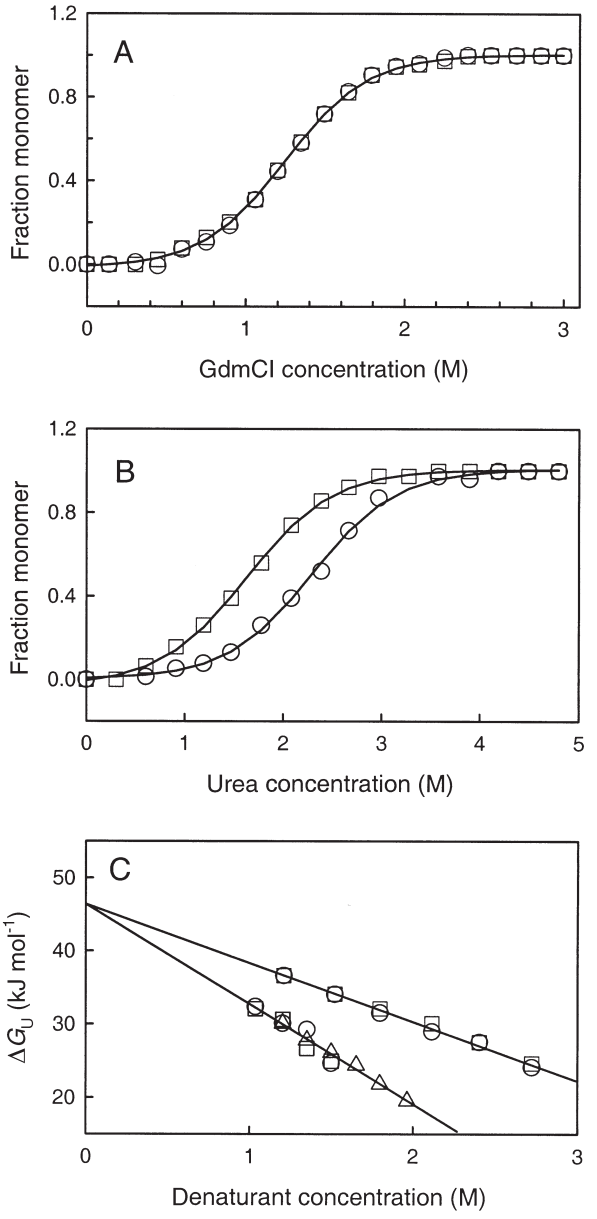

Fig. 27.1. Equilibrium unfolding of dimeric Arc repressor according to a two-state mechanism. A) Guanidinium chloride (GdmCl) denaturation curves monitored by fluorescence (squares) and CD (circles) are superimposable and the solid line is described by Eq. (4) for two-state folding. B) Urea denaturation is concentration dependent as predicted by Eq. (4). Experiments were performed with 1.6 μM (squares) and 16 μM (circles) total protein concentration. C) Free energies of unfolding measured with different total peptide concentrations (different symbols) are linearly dependent on GdmCl concentration (lower data) and urea concentration (upper data). Linear extrapolation of urea and GdmCl according to Eq. (A12) yields the same free energy of unfolding of $\Delta G_U(H_2O) = 46$ kJ mol^{-1}, supporting the validity of the linear extrapolation method. Figure adapted from Ref. [10] with permission.

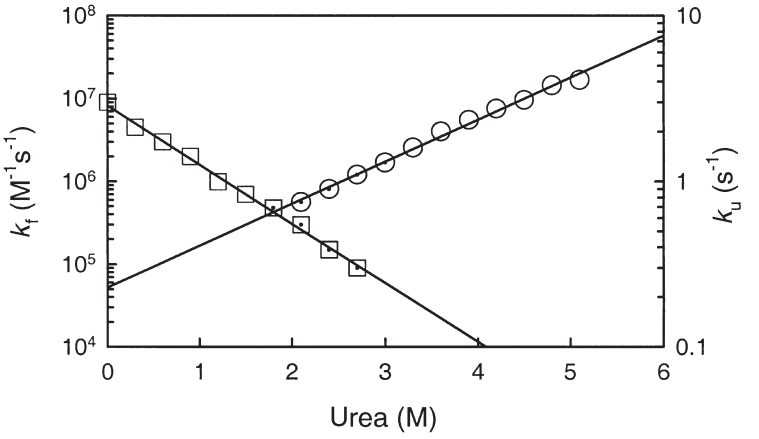

Fig. 27.2. Urea dependence of the rate constants of refolding (squares, left ordinate) and unfolding (circles, right ordinate) of Arc repressor. Empty symbols refer to data analysis neglecting unfolding (Eq. (A22)) or refolding (Eq. (A25)). Dotted symbols refer to data analysis including both unfolding and refolding as described by Eqs (A27) and (A29). Experiments were performed at pH 7.5 and 20 °C. Figure adapted from Ref. [20] with permission.

crossover point of the unfolding and refolding lines in Figure 27.2 do not yield the midpoint concentration of the denaturant at which $[M] = [D]/2$ and $\Delta G_U = 0$. This is because the refolding reaction and hence the midpoint of denaturation depends on the protein concentration.

Extrapolation of the folding rate constant of the Arc repressor to zero denaturant yields k_f of about 9×10^6 M^{-1} s^{-1}, which is about two orders of magnitude below the diffusion limit. Moreover, the folding rate is nearly independent of solvent viscosity. It seems that only a small fraction of collisions of unfolded monomers are productive, otherwise the rate should approach the diffusion limit and depend on solvent viscosity. This is supported by a dimeric transition state of folding exhibiting regions of native-like structure. In particular, there are native-like backbone interactions in the transition state of folding of the Arc repressor [21–23]. Mutating a cluster of buried charged residues forming a complex salt bridge network into hydrophobic residues speeds up folding, makes the folding rate viscosity dependent and brings the structure of the dimeric transition state closer to the unfolded state [24].

The leucine zipper domain of the yeast transcriptional activator protein GCN4 forms a coiled-coil structure in which two α-helices are wound around each other to form a superhelix [25]. This leucine zipper domain of GCN4 folds by a two-state mechanism. However, calorimetric analysis indicates two monomolecular pretransitions at 20 °C and 50 °C before the main concentration-dependent, bimolecular transition takes place [26]. Another coiled coil whose folding has been analyzed in much detail is the heterodimeric leucine zipper AB [27, 28]. This short, designed leucine zipper consists of two different 30 residue peptide chains whose sequences

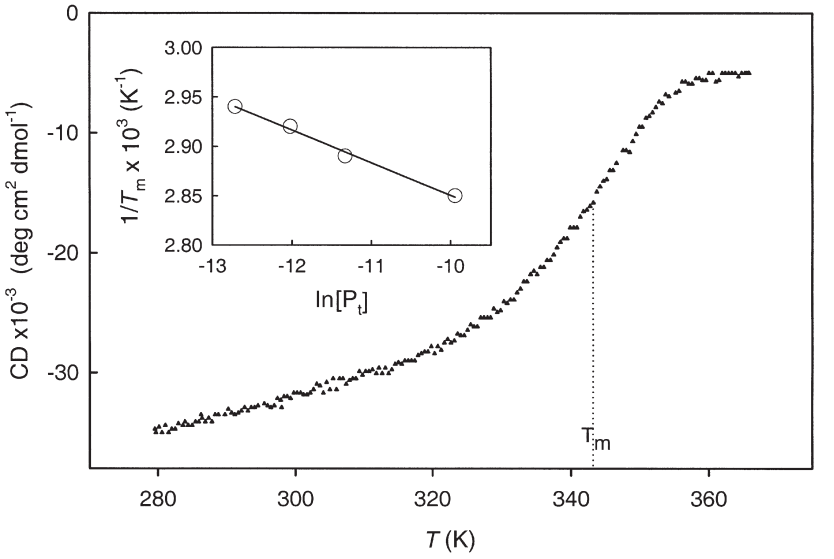

Fig. 27.3. Temperature-induced unfolding of the heterodimeric leucine zipper AB. The unfolding transition was monitored by the change in the CD signal at 222 nm. From $T_m = 343$ K and $[P_t] = 3.9 \times 10^{-5}$ M, the dissociation constant K_d of 1×10^{-5} M at T_m is calculated, corresponding to the free energy of unfolding of $\Delta G_U = 32.9$ kJ mol^{-1}. To calculate K_d at any temperature T, the pre- and post-transition slopes (thin lines) have to be taken into account. Figure adapted from Ref. [27] with permission.

are related to the GCN4 leucine zipper [25]. One chain is acidic (A-chain) and the other is basic (B-chain) so that inter-subunit electrostatic interactions are maximized [27, 29]. Figure 27.3 shows thermal unfolding of leucine zipper AB. The sigmoidal shape is described by Eq. (5) for two-state unfolding of a heterodimeric protein. The midpoint of the thermal transition yields the transition temperature T_m where half of the protein is dimeric and half is monomeric. The enthalpy of unfolding at T_m, $\Delta H_{U,m}$, is obtained from the data in Figure 27.3 by plotting ln K versus T according to the van't Hoff equation (Eq. (A14)). A further test for two-state unfolding is provided by a plot of $1/T_m$ against the logarithm of the total protein concentration, as shown in the inset of Figure 27.3 (Eq. (A18)).

To obtain the unfolding free energy, $\Delta G_U(T)$, at any temperature T, the data from the thermal unfolding curve of Figure 27.3 need to be extrapolated by the Gibbs-Helmholtz equation describing the change of ΔG_U with temperature.

$$\Delta G_U(T) = \Delta H_{U,m}\left(1 - \frac{T}{T_m}\right) + \Delta C_P\left[T - T_m - T\ln\left(\frac{T}{T_m}\right)\right] - RT\ln[K_d(T_m)] \quad (6)$$

The last term of Eq. (6) accounts for the concentration dependence of ΔG_U. This term is missing in the equation used for monomeric proteins. Figure 27.4 shows

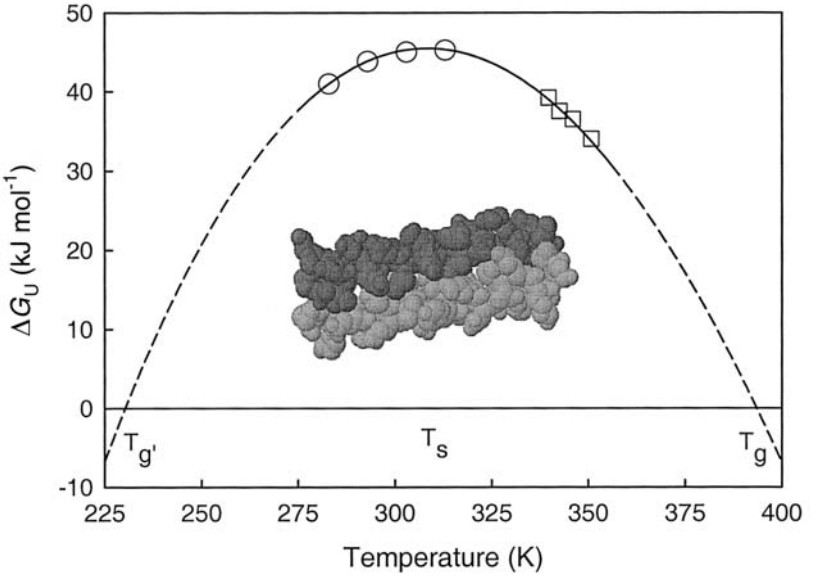

Fig. 27.4. Stability curve of the heterodimeric leucine zipper AB at pH 7.2 and 15 mM ionic strength. The curve was calculated by fitting experimental values of ΔG_U obtained by thermal unfolding (squares) and isothermal titration calorimetry (circles) with the help of Eq. (6). The maximum stability is at T_s = 36 °C, $\Delta G_U = 0$ is at $T_g = 120$ °C and $T_{g'} = -42$ °C. The solid line is a best fit in the range of the experimental data, the dashed line is the extrapolation to T_g and $T_{g'}$. Surface contour model of a leucine zipper is from 2ZTA.pdb. Figure adapted from Ref. [27] with permission.

the thermal stability curve of the heterodimeric leucine zipper AB. The curve was constructed using data sets from thermal unfolding in the range 340–350 K (T_m was varied with protein concentration) and from isothermal titration calorimetry performed between 283 and 313 K. Since neither peptide chain alone associates to a homodimer, the formation of the heterodimeric "AB-zipper" can be followed by titrating one chain to the other by isothermal titration calorimeter. The experiment yields the enthalpy and free energy changes of the coupled association and folding reaction [27]. In this way, the data from thermal unfolding can be complemented with thermodynamic data pertaining to a temperature range in which the folded protein dominates. The stability of the leucine zipper peaks at 309 K (36 °C) and decreases above and below this temperature. This is an example of cold denaturation visible already at ambient temperature. Extrapolation of the stability curve yields the temperatures of heat and cold denaturation, T_g and T'_g, at which $\Delta G_U = 0$.

The shape of the stability curve is governed by the heat capacity change, ΔC_P, of the unfolding reaction. ΔC_P of 4.3 kJ M^{-1} K^{-1} is obtained from a fit of the data in Figure 27.4 using Eq. (6). The positive value of ΔC_P implies that the unfolded monomeric peptide chains can take up more heat per degree K than the folded leucine zipper. The specific ΔC_P normalized per g of protein is 0.6 J g^{-1} K^{-1}. This is

of the same magnitude as the average specific ΔC_P for the unfolding of monomeric globular proteins [30] and points to similar types of inter- and intramolecular forces stabilizing dimeric and monomeric proteins. There have been many attempts to calculate ΔC_P from structural data based on the amount of polar and nonpolar surface buried at the interface of a dimeric protein [31, 32].

The kinetics of folding and unfolding of the leucine zipper AB are presented in Figure 27.5. This dimeric leucine zipper is characterized by several interheli-

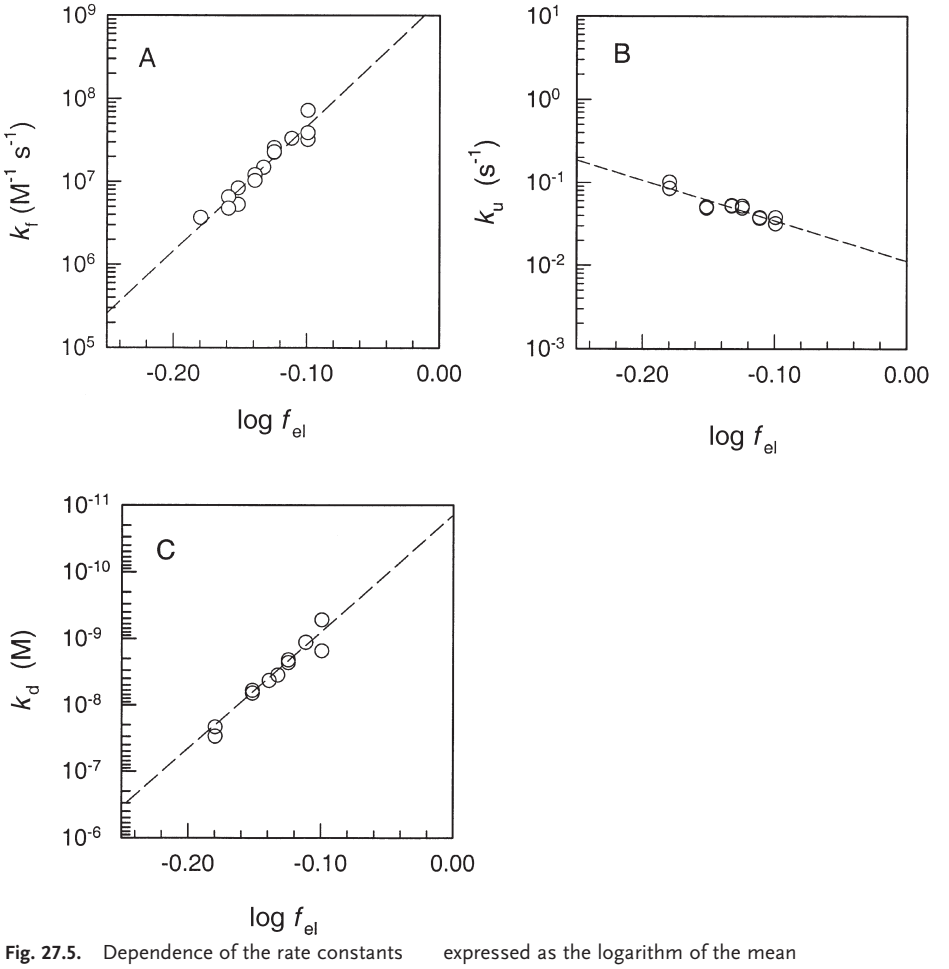

Fig. 27.5. Dependence of the rate constants and equilibrium dissociation constants of folding and association of the leucine zipper AB on ionic strength. A) Rate constant k_f of coupled association and folding. B) Rate constant k_u of coupled dissociation and unfolding. C) Equilibrium dissociation constant calculated as $K_d = k_u/k_f$. The ionic strength is expressed as the logarithm of the mean rational activity coefficient of NaCl [33]. Rate constants were determined under benign buffer conditions by rapid mixing of the unfolded peptide chains. Kinetic traces were analyzed with the help of Eq. (A29). Figure adapted from Ref. [28] with permission.

cal charge–charge interactions (salt bridges). Therefore, the rates of association/folding and dissociation/unfolding depend on ionic strength. The rate of association and folding decreases steeply when the ionic strength is raised (panel A) while dissociation and unfolding is only weakly ionic strength dependent (panel B). Consequently, the equilibrium constant is dominated by the ionic strength effect on the rate of folding (panel C). The strong decrease with ionic strength of the rate of folding could indicate a general effect on the free energy of activation of the folding and association reaction due to long-range electrostatic attraction between the oppositely charged, unfolded polypeptide chains [33]. A small effect of the ionic strength on the rate of unfolding and dissociation has been interpreted by the presence of native-like electrostatic interactions in the transition state of folding [34, 35]. However, in the case of several leucine zippers, interhelical salt bridges contribute negligibly to the stability of the coiled-coil structure, or even destabilize the folded dimer [36–39]. Therefore, the small ionic strength effect on the dissociation rate constant k_u confirms a minor role of electrostatic forces in stabilizing the folded structure [28].

The bimolecular rate constant of association and folding extrapolated to zero ionic strength is very large: $k_f = 9 \times 10^9\ M^{-1}\ s^{-1}$, larger than the rate of about $10^9\ M^{-1}\ s^{-1}$ estimated for the diffusion-limited association of two short, uncharged polypeptide chains [40–42]. The extremely large value of k_f in the absence of salt points to electrostatic acceleration of the association step as reported for other protein association reactions [33, 43]. Such very rapid association may indicate that the interaction is not much geometrically restricted. In other words, the transition state of folding of the leucine zipper is not well structured, which has been supported by kinetic transition state analysis [44].

The folding and association of leucine zipper AB as well as of other leucine zippers [45] are very tightly coupled and very rapid, yet there seems to be a transitory population of association-competent monomers preceding the actual association-folding reaction [$M_u \rightarrow M_i$ in Eq. (3)]. There is indirect evidenced for a small helix content in the association-competent conformation of the peptide chains forming a leucine zipper [46–49]. The impact of preformed helix on the rate of association and folding of a coiled coil has been manipulated by engineering a metal-binding site into the helix sequence to stabilize the helix conformation [50].

27.3.2
Folding of Dimeric Proteins through Intermediate States

As noted above, two-state folding is an operational concept since the lack of observable intermediates (or ensembles of intermediates) may have experimental reasons. Detection of intermediates depends on their stability as well as on the sensitivity and time resolution of thermodynamic and kinetic detection methods. Table 27.3 lists representative examples of dimeric proteins folding by a multistate mechanism, that means through at least one detectable intermediate. A good indication for a thermodynamic intermediate is the disparity between the free energy of unfolding determined by different methods. For example, the dimeric cAMP receptor

Tab. 27.3. Examples of dimeric proteins folding through intermediate states.

Protein	*Mechanism*	*Comments*[a]
cAMP receptor protein (CPR) (homodimer) [51]	$2M_u \rightarrow 2M_i \rightarrow D_f$	Thermodynamically stable monomeric intermediate. $\Delta G_U = 30$ kJ mol^{-1} for $D_f \rightarrow 2M_i$ and 50 kJ mol^{-1} for $2M_i \rightarrow 2M_u$. Equilibrium transition between folded dimer and monomeric intermediate from sedimentation equilibrium, overall unfolding and dissociation from unfolding by denaturant
Disulfoferredoxin (homodimer) [74]	$2M_u \rightarrow 2M_i \rightarrow D_f$	$\Delta G_U = 23$ kJ mol^{-1} for $D_f \rightarrow 2M_i$ and 50 kJ mol^{-1} for $2M_i \rightarrow 2M_u$
LC8, light chain of dynein (homodimer) [75]	$2M_u \rightarrow 2M_i \rightarrow D_f$	$G_U = 35$ kJ mol^{-1} for $D_f \rightarrow 2M_i$ and 62 kJ mol^{-1} for $2M_i \rightarrow 2M_u$
SecA dimeric bacterial ATPase (homodimer) [52]	$2M_u \rightarrow D_i \rightarrow D_f$	Plateau in denaturant unfolding curve indicates intermediate shown to be dimeric by sedimentation equilibrium. $\Delta G_U = 35$ kJ mol^{-1} for $D_f \rightarrow D_i$ and 59 kJ mol^{-1} for $D_i \rightarrow 2M_u$
Ketosteroid isomerase (homodimer) [53]	$2M_u \rightarrow 2M_i \rightarrow D_i \rightarrow D_f$	Two-state folding under equilibrium conditions with $\Delta G_U = 90$ kJ mol^{-1}. Four-state folding in kinetic analysis with $k = 60$ s^{-1} for $M_u \rightarrow M_i$, $k = 5.4 \times 10^4$ M^{-1} s^{-1} for $2M_i \rightarrow D_i$, $k = 0.017$ s^{-1} for $D_i \rightarrow D_f$
Glutathione transferase A1-1 (homodimer) [76, 77]	$2M_u \rightarrow 2M_i \rightarrow D_i \rightarrow D_i' \rightarrow D_f$	Under equilibrium conditions folding is two-state [77]. Folding through a monomeric and two dimeric intermediates; folding pathway complicated by proline *cis* → *trans* isomerization in M_u and M_i [76].
Trp repressor protein (TRP) (homodimer) [54, 58]	$2M_u \rightarrow 2M_i \rightarrow D_i \rightarrow D_f$	Rapid transition to two classes of association-competent monomers which associate in a combinatorial way to three different dimeric intermediates, and these rearrange in the rate-limiting step to the folded dimer [58]. Under equilibrium conditions, folding appears two state [54]
Bacterial luciferase (heterodimer) [59]	$M_{\alpha u} \rightarrow M_{\alpha i}$, $M_{\beta u} \rightarrow M_{\beta i}$ $M_{\alpha i} + M_{\beta i} \rightarrow D_i \rightarrow D_f$	Under equilibrium conditions folding is two state. Folding proceeds through monomeric and dimeric intermediates. The β-subunit can irreversibly form monomeric and dimeric dead-end species

[a] Unless stated, thermodynamic and kinetic parameters refer to ambient temperature (20–25 °C).

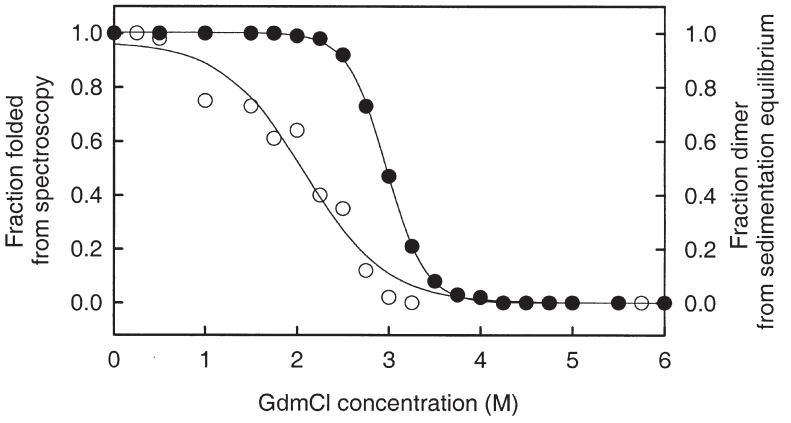

Fig. 27.6. Guanidinium chloride-induced unfolding of the homodimeric cAMP receptor protein (CPR) followed by different spectroscopic methods shows a sharp transition at 3 M GdmCl (filled circles, left ordinate). In contrast, the monomer/dimer ratio followed by sedimentation equilibrium analysis has a transition midpoint at 2 M GdmCl (empty circles, right ordinate). The latter midpoint is assigned to an equilibrium between folded dimer and (partly folded) monomeric intermediate. The midpoint at 3 M GdmCl is assigned to the equilibrium between the fully folded dimer and the fully unfolded monomers. Figure redrawn from Ref. [51] with permission.

protein (CRP) exhibits different unfolding curves depending on whether unfolding is observed by a spectroscopic probe or by sedimentation equilibrium analysis in the ultracentrifuge (Figure 27.6). The midpoint of the denaturant-induced unfolding curve obtained by measuring the monomer/dimer distribution in the ultracentrifuge is at 2 M GdmCl. However, the midpoint shifts to 3 M GdmCl when unfolding and dissociation is followed from the change of the far-UV CD spectrum, from fluorescence emission or from fluorescence anisotropy. The higher midpoint corresponds to unfolding and dissociation, the lower midpoint to dissociation alone, which does not significantly change the CD and fluorescence signals [51]. Thus, CRP folds through a thermodynamically stable monomeric intermediate. The overall free energy of unfolding and dissociation is $\Delta G_U = 80$ kJ mol^{-1}, that for dissociation alone (from ultracentrifugation) is $\Delta G_U = 30$ kJ mol^{-1}. The difference of 50 kJ mol^{-1} is the free energy of unfolding of the stable monomeric intermediate (Table 27.3).

The fourth protein in Table 27.3, dimeric bacterial enzyme SecA, folds through a thermodynamically stable dimeric intermediate, which appears as a plateau in the denaturant unfolding curve [52]. A larger amount of energy is necessary for the unfolding and dissociation reaction $D_i \rightarrow 2M_u$ than for unfolding of D_f into D_i, in accord with a thermodynamically stabilized dimeric intermediate. In the kinetics of folding, the monomolecular transition $D_i \rightarrow D_f$ is rate-determining since even at low protein concentration the bimolecular association $2M_u \rightarrow D_i$ is very rapid [52].

The first four proteins of Table 27.3 fold through thermodynamically stable intermediates. In many cases, however, the equilibrium distribution between folded dimer and unfolded monomer is well described by a two-state mechanism yet transitory intermediates are detectable in the kinetic analysis. Representative examples in Table 27.3 are the ketosteroid isomerase, the glutathione transferase A1-1 and the tryptophan repressor protein (TRP). Equilibrium analysis of all these proteins conforms to two-state folding and fulfills at least one of criteria i–iv but none of criteria v–viii listed in Table 27.1. Thus, dimeric ketosteroid isomerase is stabilized by $\Delta G_U = 90$ kJ mol^{-1} under equilibrium conditions [53]. However, the time course of unfolding exhibits three kinetic phases, a slow monomolecular phase $D_f \rightarrow D_i$, a bimolecular phase $D_i \rightarrow 2M_i$, and a rapid monomolecular phase $M_i \rightarrow M_u$. Thus, two additional states are seen in kinetics. One may say that the simple Eq. (1) applies to the enzyme at equilibrium yet the more realistic Eq. (3) to the time-dependent nonequilibrium situation of folding and unfolding.

Folding of TRP has been studied in much detail [54–58]. Matthews and coworkers have formulated the folding scheme shown in Figure 27.7 based on a large

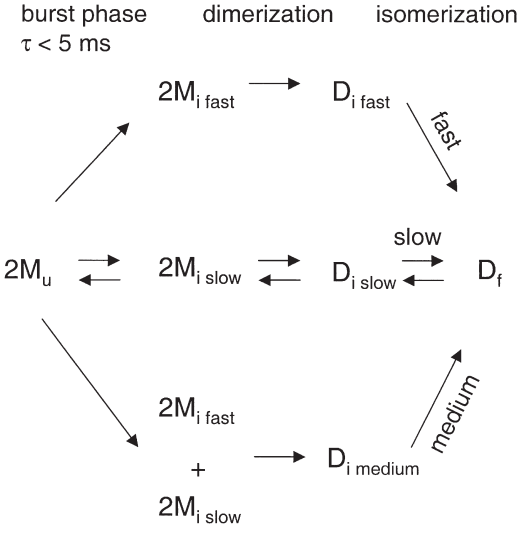

Fig. 27.7. Complex folding scheme for tryptophan repressor protein (TRP) from *Escherichia coli* through three "folding channels." Following the formation of two ensembles of partly folded monomeric intermediates, $M_{i\ fast}$ and $M_{i\ slow}$, folding to the dimer is controlled by three kinetic phases ("channels"). These are due to the association of two molecules of $M_{i\ fast}$ or $M_{i\ slow}$ or of $M_{i\ fast} + M_{i\ slow}$. "Fast," "slow," and "medium" refer to the rate of the final conformational rearrangement from the dimeric intermediate populations $D_{i\ fast}$, $D_{i\ slow}$, and $D_{i\ medium}$ to the unique folded dimer D_f. $D_{i\ slow}$ is a native-like intermediate and $D_{i\ fast}$ and $D_{i\ medium}$ are nonnative intermediates. Only the slow folding reaction through native-like intermediate $D_{i\ slow}$ is reversible. Figure adapted from Ref. [58] with permission.

series of kinetic experiments. In a burst phase following the removal of denaturant, unfolded monomeric TRP rearranges to two different ensembles of partly folded monomers, $M_{i\ fast}$ and $M_{i\ slow}$. These rapidly combine to the three dimeric intermediates $D_{i\ fast}$, $D_{i\ slow}$, and $D_{i\ medium}$. The unique folded dimer is formed in a fast, a medium, and a slow reaction from $D_{i\ fast}$, $D_{i\ medium}$, and $D_{i\ slow}$, respectively. The rate of this final unimolecular reaction exhibits very little dependence on denaturant concentration suggesting an isomerization reaction proceeding with no detectable change in solvent-accessible surface area. The structural basis for the three "folding channels" is the presence of two prefolded monomeric species that randomly associate in different pairwise combinations. The intermediates differ in their compactness. The fast and medium channels access the native structure through the most compact yet least native-like intermediates, $D_{i\ fast}$ and $D_{i\ medium}$, respectively. The slow channel, on the other hand, proceeds through a more "direct" folding route since the dimeric intermediate $D_{i\ slow}$ is native-like. Only this slow route is reversible. The example of TRP shows that the native structure can be accessed through alternative routes, that folding through nonnative states can accelerate folding, and that nonnative states need not lead into kinetic traps [58].

Kinetic traps have been detected in the folding of bacterial luciferase, the last example in Table 27.3. Figure 27.8 shows the complex folding scheme for this heterodimeric enzyme composed of an α- and a β-subunit. The unfolded monomeric subunits $M_{\alpha u}$ and $M_{\beta u}$ are converted to the monomeric intermediates $M_{\alpha i}$ and $M_{\beta i.}$, which associate to the heterodimeric intermediate D_i in a bimolecular reaction followed by the monomolecular rearrangement to the final folded dimer D_f. However, the β-subunit can enter into a dead-end trap as indicated by the irreversible reactions $M_{\beta i} \rightarrow M_{\beta x}$ and $2M_{\beta i} \rightarrow D_{\beta x}$ where $D_{\beta x}$ is a dead-end homodimer of the β-subunit [59].

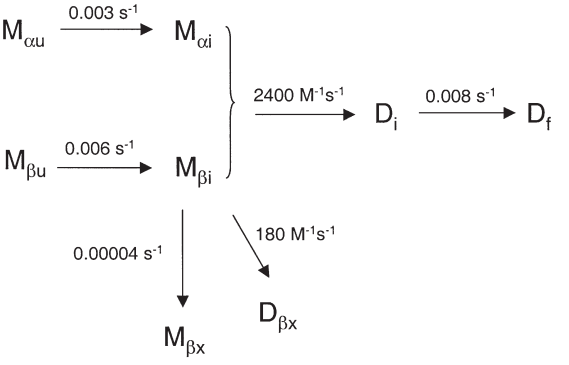

Fig. 27.8. Complex folding scheme for the heterodimeric bacterial luciferase composed of an α-subunit and a β-subunit. Folding proceeds through the monomeric intermediates $M_{\alpha i}$ and $M_{\beta i}$ and the dimeric intermediate D_i. Monomeric ($M_{\beta x}$) and dimeric ($D_{\beta x}$) dead-end species formed from the β-subunit intermediate $M_{\beta i}$ slow the folding and reduce the folding yield. Figure adapted from Ref. [59] with permission.

27.4
Trimeric and Tetrameric Proteins

We only briefly discuss a few examples of small trimeric and tetrameric proteins and refer to Chapter 2 in Part II presenting the folding and assembly in vivo of large, higher order multisubunit proteins. For statistical reasons, any reaction higher than second order is very slow. Therefore, simultaneous association of three polypeptide chains to a trimer is statistically unlikely, and simultaneous association of four chains to a tetramer is impossible. Thus, trimers (Tr) and tetramers (Te) are most likely to form by consecutive bimolecular reactions. For a trimer one can write:

$$3\mathrm{M} \underset{k_{-1}}{\overset{k_1}{\rightleftarrows}} \mathrm{D} + \mathrm{M} \underset{k_{-2}}{\overset{k_2}{\rightleftarrows}} \mathrm{Tr}$$

$$K_{\mathrm{d1}} = \frac{[\mathrm{M}]^2}{[\mathrm{D}]} = \frac{k_{-1}}{k_1} \quad K_{\mathrm{d2}} = \frac{[\mathrm{M}][\mathrm{D}]}{[\mathrm{Tr}]} = \frac{k_{-2}}{k_2} \quad \text{two-step folding of trimer} \tag{7}$$

Subscripts u, f, and i have been omitted in Eq. (7) to leave open the conformational state of the three species. Of course, there can be monomeric, dimeric, and trimeric intermediates, making the folding mechanism very complex.

Three-state or two-step folding described by Eq. (7) has been reported for the designed homotrimeric coiled-coil protein LZ16A composed of three 29-residue peptide chains [60]. In the range of 1–100 μM total protein concentration, monomer, dimer, and trimer are populated in a concentration-dependent equilibrium [61]. Figure 27.9 shows the decrease of the CD spectral minimum as a function of total protein concentration. The data are best fit by two equilibria with $K_{\mathrm{d1}} = 7.7 \times 10^{-7}$ M and $K_{\mathrm{d2}} = 2.9 \times 10^{-6}$ M, where K_{d1} refers to the monomer/dimer equilibrium and K_{d2} to the dimer/trimer equilibrium. $K_{\mathrm{d1}} < K_{\mathrm{d2}}$ means that the dimer is a stable intermediate dominating at lower protein concentration. For example, at 10 μM total protein concentration, there is 50% dimer, 35% trimer, and 15% monomer. From kinetic refolding experiments the four rate constants defined by Eq. (7) have been determined and were found to be in agreement with the equilibrium data (see the legend to Figure 27.9).

So it may seem surprising that a trimeric protein can apparently fold in a single-step reaction, which means by a two-state folding mechanism according to Eq. (8).

$$3\mathrm{M_u} \underset{k_{\mathrm{u}}}{\overset{k_{\mathrm{f}}}{\rightleftarrows}} \mathrm{Tr_f}, \quad K_{\mathrm{d}} = \frac{[\mathrm{M_u}]^3}{[\mathrm{Tr_f}]} = \frac{k_{\mathrm{u}}}{k_{\mathrm{f}}} \quad \text{one-step folding of trimer} \tag{8}$$

Here, k_{f} is a trimolecular association rate constant ($\mathrm{M^{-2}\ s^{-1}}$) and k_{u} is a monomolecular dissociation rate constant. One-step folding according to Eq. (8) occurs if the dimer (Eq. (7)) is very unstable and scarcely populated so that the first equilibrium of Eq. (7) is far on the side of the unfolded monomer and the second far on the side of the folded trimer. Under these conditions, trimer formation appears

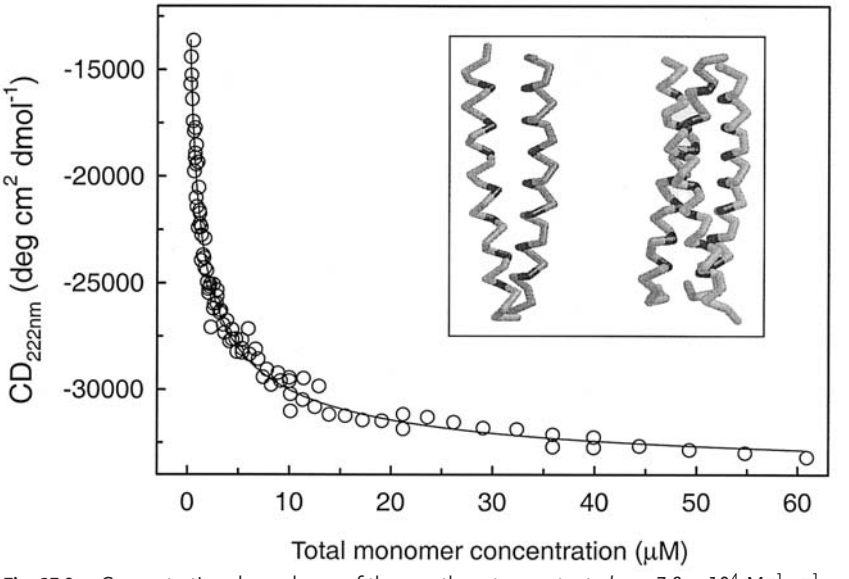

Fig. 27.9. Concentration dependence of the CD signal at 222 nm of the trimeric coiled coil LZ16A. The solid line is a best fit for a monomer–dimer–trimer equilibrium according to Eq. (7) with $K_{d1} = 7.7 \times 10^{-7}$ M and $K_{d2} = 2.9 \times 10^{-6}$ M. These values are in good agreement with the K_1 and K_2 calculated from the rate constants $k_1 = 7.8 \times 10^4$ M^{-1} s^{-1}, $k_{-1} = 1.5 \times 10^{-2}$ s^{-1}, $k_2 = 6.5 \times 10^5$ M^{-1} s^{-1}, and $k_{-2} = 1.1$ s^{-1}. Inset: backbone structure of dimer and trimer; ribbon models are from 2ZTA.pdb (dimer) and 1gcm.pdb (trimer). Figure adapted from Ref. [60] with permission.

two-state. It should be noted that $3M \rightarrow Tr$ can appear two-state despite the presence of a dimeric intermediate if $2M \rightarrow D$ is spectroscopically silent under the chosen detection conditions so that the entire spectral signal change is caused by $M + D \rightarrow Tr$ [60].

An example of a homotrimeric protein folding through only a single reaction step is the six-helix bundle at the core of the gp41 envelope protein of the human and simian immunodeficiency viruses [62]. The structure is shown in Figure 27.10 and is composed of three "hairpins" formed by two α-helices linked through a short peptide loop [63]. The trimer folds from three unfolded monomers in a single step according to Eq. (8). Equilibrium and kinetic data are in excellent agreement: $\Delta G_U(H_2O)$ determined by denaturant unfolding is 116 kJ mol^{-1}, and 114 kJ mol^{-1} when calculated from kinetic rate constants. The transition state of folding seems closer to the unfolded than the folded state. Only 20–40% of the surface buried in the folded trimer is already buried in the transition state of folding [62].

Formation of the catalytic trimer of aspartate transcarbamoylase is at the other extreme of possible folding mechanisms. Here, partly folded monomers are rapidly formed initially and thereafter rearrange in a slow step to association-competent monomers. These monomeric intermediates are thermodynamically stable. They

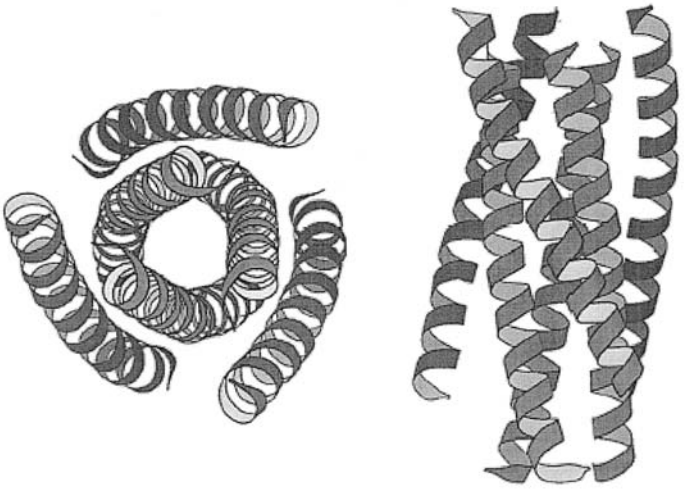

Fig. 27.10. Crystal structure of a six-helix bundle composed of three "hairpins." Each "hairpin" comprises two helices linked by a short loop; the loop is not visible in this crystal structure from Ref. [63]. Left: Axial view looking down the threefold axis of the helix bundle. Right: Lateral view. The trimer folds from unfolded monomers in a single step according to Eq. (8). $\Delta G_U(H_2O)$ determined by denaturant unfolding is 116 kJ mol^{-1}, and 114 kJ mol^{-1} when calculated from kinetic rate constants. The trimolecular rate constant of association is 1.3×10^{15} M^{-2} s^{-1} and the unimolecular rate constant of dissociation is 1.08×10^{-5} s^{-1} [62].

associate through at least two steps to the folded trimeric enzyme [64]. The folding scheme is $3M_u \rightarrow 3M_i \rightarrow\rightarrow Tr_f$.

Finally, we consider two tetrameric proteins: the C-terminal 30-residue domain of the tumor suppressor protein p53 [65] and a small bacterial dihydrofolate reductase composed of four 78-residue polypeptide chains [66]. The C-terminal p53 domain folds into a homotetramer in a thermodynamically fully reversible reaction. Interestingly, under equilibrium conditions, only folded tetramer and unfolded monomer are observed [67]. However, the time course of folding shows two consecutive bimolecular reactions with two kinetic, dimeric intermediates (Figure 27.11) [65]. Folding can be described as an association of dimers, in accord with the crystal structure, which has been likened to a dimer of dimers. The two intermediates shown in Figure 27.11 were deduced from extensive Φ-value analysis [65]. The first bimolecular association reaction is between highly unstructured monomers and can be described by a "nucleation-condensation" mechanism [68]. The first dimeric intermediate $D_{i,1}$ is formed through an early transition state that has little similarity to the native structural organization of the dimer. The second dimeric intermediate $D_{i,2}$ is highly structured and already includes most of the structural features of the native protein. The transition $D_{i,2} \rightarrow Te_f$ is an example of a "framework mechanism" in which stable preformed structural elements "diffuse and collide" [68].

A final example of a tetrameric protein is the bacterial R67 dihydrofolate reduc-

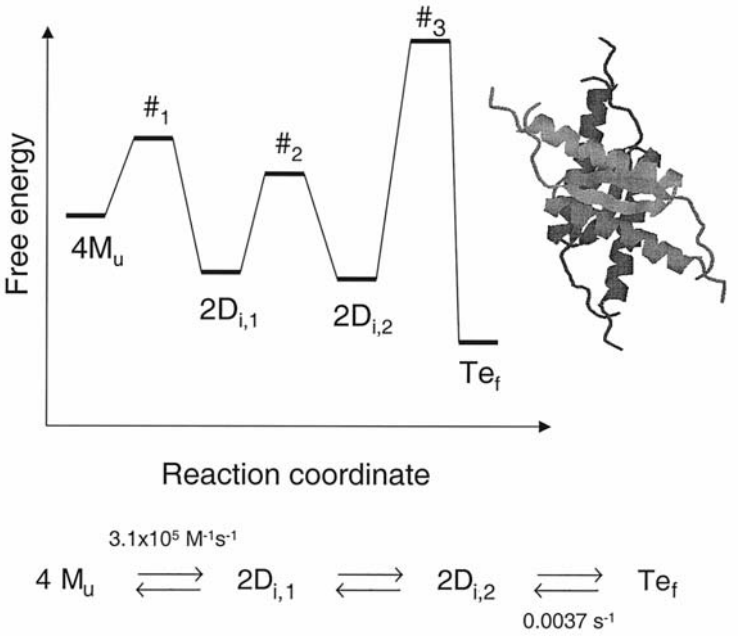

Fig. 27.11. Qualitative reaction coordinate diagram for the folding of the tetrameric protein domain from tumor suppressor p53. Under equilibrium conditions, only a single transition between unfolded monomer (M_u) and folded tetramer (Te_f) is seen [67]. Kinetic refolding and unfolding experiments show a single bimolecular association reaction and a single monomolecular dissociation reaction, which could be assigned as indicated [65]. Ribbon model of tetrameric C-terminal domain of tumor suppressor p53 from sak.pdb. See the text for a more detailed discussion. Figure adapted from Ref. [65] with permission.

tase [66]. Here, two monomeric intermediates (the formation of one being due to slow isomerization of peptidyl-proline bonds) precede dimer formation. Thereafter, two dimers associate to the folded tetramer. The folding reaction can be summarized as $4M_u \rightarrow 4M_{i,1} \rightarrow 4M_{i,2} \rightarrow 2D_i \rightarrow Te$.

27.5 Concluding Remarks

The mechanisms of folding of small oligomeric proteins is highly variable. At one extreme is the fully concerted association of unfolded monomers to folded dimers, trimers and even tetramers. Such folding without a thermodynamically stable intermediate is surprisingly frequent. Even in the case of the tetrameric p53 domain, whose folding proceeds through several kinetic folding intermediates among which the final dimeric intermediate is very native-like, none of the intermediates is sufficiently stable to be noticed at equilibrium. The reason for such scarcity of stable folding intermediates may be due, in part, to destabilizing nonpolar surface

exposed in the transitory intermediates. This surface becomes buried only in the final folded oligomer. Indeed, intermolecular or intersubunit forces dominate the stability of many oligomeric proteins. However, the interface between the subunits of the folded oligomeric proteins is highly variable. Shape complementarity between the contacting interfaces is a common feature and a main contributor to the specificity of intersubunit interactions. In a survey of 136 homodimeric proteins, a mixture of hydrophobic and intersubunit contacts was identified [69]. Small hydrophobic patches, polar interactions and water molecules are scattered over the intersubunit contact area in two-thirds of the proteins studied. Only in one-third of the dimers there was a single, large and contiguous hydrophobic core between the subunits. Though the hydrophobic effect plays an important role in subunit interactions, it seems to be less strong than that observed in the interior of monomeric proteins [70]. Only in a few cases, oligomerization conforms to the association of preformed stable subunits. The case of the trimeric coiled-coil LZ16A at equilibrium with a stable dimeric coiled coil is probably an exception.

From studies addressing the nature of the transition states of folding, it follows that the same principles deduced for monomeric proteins [71] apply also to oligomers. Folding of the subunits and their concurrent association to the oligomeric protein occurs by diffusion and collision of preformed structural frameworks (''framework model'') as well as by simultaneous nucleation and condensation. This is not surprising since the folded structure is always based on an extensive interplay of secondary and tertiary interactions in monomeric proteins and of secondary, tertiary, and quaternary interactions in oligomeric proteins. Because there is no intrinsic difference between tertiary and quaternary interactions there is no principal difference of folding between monomers and oligomers. The main difference is in the association step. Whereas the folding of a monomeric protein can be described by one or several consecutive or parallel monomolecular (single exponential) reactions, the folding of an oligomeric protein exhibits at least one concentration-dependent reaction step. On the one hand this feature complicates the thermodynamic and kinetic analysis. On the other hand the concentration dependence adds a useful variable to assist in the measurement of folding since the monomer/oligomer equilibrium can be studied by simple dilution under benign buffer conditions. Comparison of the data from dilution and from chemical or heat denaturation can give information about the contribution of intermolecular and intramolecular forces to the stability of the oligomeric protein. Also, determination of thermodynamic parameters such as the free energy of unfolding or the heat capacity change of unfolding is facilitated when the protein concentration can be adduced as an additional variable. Finally, in the case of heterooligomeric proteins, folding can be probed by simple mixing of the different subunits.

Appendix – Concurrent Association and Folding of Small Oligomeric Proteins

In this Appendix we have put together a set of equations for the analysis of thermodynamic and kinetic data of two-state folding. Many equations are equivalent to

those for the folding of monomeric proteins except for an additional term accounting for protein concentration. Derivation of equilibrium association constants for two-state folding of oligomeric systems and the relationship between equilibrium constants and the thermodynamic parameters $\Delta G, \Delta H$, and ΔS have been described in more detail by Marky and Breslauer [78]. The folded (native) state is taken as the reference state so that the thermodynamic parameters refer to the unfolding reaction ($\Delta G_U, \Delta H_U$, etc.). A special form of Eq. (A29) describing reversible two-state folding of a homodimer has been published by Milla and Sauer [20]. The method of deducing kinetic rate constants from the shift of a pre-existing equilibrium is briefly summarized (method of Bernasconi [16]).

The kinetic and equilibrium equations presented here are useful for the analysis of simple reaction steps, or steps that are kinetically or thermodynamically well separated. If the reaction steps are linked, numerical integration can be used to analyze kinetic and equilibrium data. There are good computer programs to aid kinetic analysis, some of the programs are freely available on the Web (for example DynaFit [79]). Depending on the scatter of experimental data, numerical fitting of linked reactions may result in large errors and distinguishing between different models can be very difficult.

Numbering of equations Equations appearing only in this Appendix have the prefix A. Other equations are numbered as in the main text.

Abbreviations M, monomer; D, dimer; N, *n*-mer; $[P_t]$, total protein concentration expressed as total concentration of monomer; f_M, fraction of free monomer defined as $[M]/[P_t]$. Subscripts; u, unfolded; i, intermediate; f, folded; m, midpoint; K_d, equilibrium dissociation constant ($= 1/K$).

A1
Equilibrium Constants for Two-state Folding

Association and dissociation of oligomeric proteins results in concentration-dependent equilibria. Expressions for the equilibrium constants of homooligomeric and heterooligomeric proteins are different.

A1.1 Homooligomeric Protein

For a homooligomeric protein, the equilibrium transition between n identical, unfolded monomeric subunits M and the folded n-meric protein N is described by

$$n\mathrm{M} \rightleftarrows \mathrm{N} \tag{A1}$$

The equilibrium dissociation constant K_d is defined as

$$K_d = \frac{[\mathrm{M}]^n}{[\mathrm{N}]} \tag{A2}$$

Defining the fraction of free monomeric subunits as

$$f_M = \frac{[M]}{[P_t]} \quad (0 \le f_M \le 1) \tag{A3}$$

we can write K_d as

$$K_d = \frac{n[P_t]^{n-1} {f_M}^n}{1 - f_M} \tag{A4}$$

where $[P_t] = [M] + n[N]$ is the total protein concentration expressed as total monomer concentration. At $f_M = 0.5$ we have

$$K_{d,f_M=0.5} = n([P_t]/2)^{n-1} \tag{A5}$$

A1.2 Heterooligomeric Protein

For a heterooligomeric protein, the equilibrium transition between n different, unfolded monomeric subunits $M_1, M_2 \ldots M_n$ and the folded n-meric protein N is described by

$$M_1 + M_2 + \cdots + M_n \rightleftarrows N \tag{A6}$$

The equilibrium dissociation constant K_d is defined as

$$K_d = \frac{[M_1][M_2] \ldots [M_n]}{[N]} \tag{A7}$$

The corresponding expression in terms of the fraction f_M of free monomeric subunits is

$$K_d = \frac{[P_t]^{n-1} {f_M}^n}{n^{n-1}(1 - f_M)} \tag{A8}$$

and at $f_M = 0.5$

$$K_{d,f_M=0.5} = \left(\frac{[P_t]}{2n}\right)^{n-1} \tag{A9}$$

In Eqs (A8) and (A9), $[P_t] = [M_1] + [M_2] + \cdots + [M_n] + n[N]$. The difference between Eqs (A4), (A5) and (A8), (A9) reflects the statistical difference between homooligomeric and heterooligomeric equilibria. Equations (4) and (5) of the main text correspond to Eqs (A4) and (A8), respectively.

A2 Calculation of Thermodynamic Parameters from Equilibrium Constants

A2.1 Basic Thermodynamic Relationships

The changes of free energy, enthalpy, and entropy are related by the well-known equation

$$\Delta G_U = \Delta H_U - T\Delta S_U = -RT \ln K_d \tag{2}$$

The superscript ° indicating standard conditions is omitted for simplicity. The van't Hoff enthalpy of unfolding is

$$\Delta H_U^{vH} = RT^2 \left(\frac{d \ln K_d}{dT} \right) \tag{A10}$$

The heat capacity change at constant pressure, ΔC_P, is defined by

$$\Delta C_P = \left(\frac{\partial \Delta H}{dT} \right)_P \tag{A11}$$

The calculation of thermodynamic parameters from equilibrium constants is based on Eqs (2), (A10), and (A11).

A2.2 Linear Extrapolation of Denaturant Unfolding Curves of Two-state Reaction

Linear extrapolation is performed by the same procedure as applied to denaturant unfolding of monomeric proteins, except that the concentration has to be taken into account. The linear extrapolation method is discussed in Chapter 3. Linear extrapolation of the free energy of two-state unfolding of homooligomeric and heterooligomeric proteins is described by

$$-RT \ln \left(\frac{n[P_t]^{n-1} f_M{}^n}{1 - f_M} \right) = \Delta G_U(H_2O) - m[\text{denaturant}] \quad \text{homooligomer} \tag{A12}$$

$$-RT \ln \left(\frac{[P_t]^{n-1} f_M{}^n}{n^{n-1}(1 - f_M)} \right) = \Delta G_U(H_2O) - m[\text{denaturant}] \quad \text{heterooligomer} \tag{A13}$$

The term on the left hand side of Eq. (A12) follows from Eqs (2) and (A4), that on the left hand side of Eq. (A13) from Eqs (2) and (A8). The slope m is the change of ΔG_U with denaturant concentration (J mol^{-1} M^{-1}).

A2.3 Calculation of the van't Hoff Enthalpy Change from Thermal Unfolding Data

From the change of K_d with T, the van't Hoff enthalpy is calculated according to Eq. (A10). In practice, one calculates ΔH_U^{vH} at T_m from a plot of ln K_d against $1/T$. With Eq. (2) one obtains the Arrhenius equation

$$\ln K_d = -\frac{\Delta H_{U,m}}{RT} + \frac{\Delta S_U}{R} \tag{A14}$$

where $\Delta H_{U,m}$ is the van't Hoff enthalpy at T_m. Only data points in a narrow interval around T_m should be used to calculate $\Delta H_{U,m}$ from the slope $\Delta H_{U,m}/R$ since Eq. (A14) neglects the change of the enthalpy with T (heat capacity change assumed to be zero).

A2.4 Calculation of the van't Hoff Enthalpy Change from the Concentration-dependence of T_m

Since association of an oligomeric protein is concentration dependent, T_m changes with concentration. Measuring T_m for varying $[P_t]$ is another way to calculate $\Delta H_{U,m}$. From Eqs (A5) and (A9) it follows that at T_m, K_d is described by

$$K_d(T_m) = n([P_t]/2)^{n-1} \quad \text{homooligomer} \tag{A15}$$

$$K_d(T_m) = ([P_t]/2n)^{n-1} \quad \text{heterooligomer} \tag{A16}$$

From Eqs (2), (A15), and (A16) one obtains after rearranging [78]:

$$\frac{1}{T_m} = \frac{(n-1)R}{\Delta H_m} \ln[P_t] + \frac{\Delta S - (n-1)R \ln 2 + R \ln n}{\Delta H_m} \quad \text{homooligomer} \tag{A17}$$

$$\frac{1}{T_m} = \frac{(n-1)R}{\Delta H_m} \ln[P_t] + \frac{\Delta S - (n-1)R \ln 2n}{\Delta H_m} \quad \text{heterooligomer} \tag{A18}$$

A2.5 Extrapolation of Thermodynamic Parameters to Different Temperatures: Gibbs-Helmholtz Equation

The calculation of the van't Hoff enthalpy described above refers to the transition temperature T_m. To obtain the thermodynamic parameters at any other temperature, the change of ΔH and ΔS with T has to be taken into account according to the Gibbs-Helmholtz equation:

$$\Delta G_U(T) = \Delta H_{U,m}\left(1 - \frac{T}{T_m}\right) + \Delta C_P\left[T - T_m - T \ln\left(\frac{T}{T_m}\right)\right] - RT \ln[K_d(T_m)] \tag{6}$$

The term $-RT \ln[K_d(T_m)]$ on the right hand side is necessary to account for the concentration dependence of ΔG_U. $K_d(T_m)$ corresponds to K_d at $f_M = 0.5$. Depending on the number of subunits and on whether the protein is a homo- or a heterooligomer, the appropriate form of K_d from Eq. (A5) or (A9) is inserted in Eq. (6). For example, the correction term for a homodimeric protein is $-RT \ln([P_t])$. The concentration-independent form of the Gibbs-Helmholtz equation is obtained by using the reference temperature T_g at which $\Delta G_U = 0$

$$\Delta G_U(T) = \Delta H(T_g)\left(1 - \frac{T}{T_g}\right) + \Delta C_P\left[T - T_g - T \ln\left(\frac{T}{T_g}\right)\right] \tag{A19}$$

A3
Kinetics of Reversible Two-state Folding and Unfolding: Integrated Rate Equations

The following integrated rate equations for two-state folding of a dimeric protein are used to calculate the folding rate constant k_f and the unfolding rate constant k_u from kinetic traces. Depending on experimental conditions, only folding (A3.1), only unfolding (A3.2), or both (A3.3) have to be taken into account.

A3.1 Two-state Folding of Dimeric Protein

$$2M \xrightarrow{k_f} D \tag{A20}$$

The time course of folding is given by

$$\frac{d[M]}{dt} = -k_f[M]^2 \tag{A21}$$

After integration, the time course of disappearance of the monomer fraction becomes

$$f_M(t) = \frac{[M_0]}{[P_t](k_f t + 1)} \tag{A22}$$

where $[M_0]$ is the initial monomer concentration at $t = 0$. $[M_0] = [P_t]$ if $[D] = 0$ at the beginning of the folding reaction. Equation (A22) is used to obtain k_f from a folding trace expressed as $f_M(t)$ if the unfolding reaction can be neglected (for example at low denaturant concentration).

A3.2 Two-state Unfolding of Dimeric Protein

$$D \xrightarrow{k_u} 2M \tag{A23}$$

The time course of unfolding is given by

$$\frac{d[D]}{dt} = -k_u[D] \tag{A24}$$

After integration, the time course of disappearance of the dimer fraction $f_D = 1 - f_M$ becomes

$$f_D(t) = \frac{2[D_0]}{[P_t]} \exp(-k_u t) \tag{A25}$$

where $[D_0]$ is the initial dimer concentration at $t = 0$. $[D_0] = [P_t]/2$ if $[M] = 0$ at $t = 0$. Equation (A25) is used to obtain k_u from an unfolding trace expressed as

$f_D(t) = 1 - f_M(t)$ if refolding can be neglected (for example at high denaturant concentration).

A3.3 Reversible Two-state Folding and Unfolding

A3.3.1 Homodimeric protein

$$2M \underset{k_u}{\overset{k_f}{\rightleftarrows}} D \tag{1}$$

The time course of disappearance of the monomer can be written as

$$\frac{d[M]}{dt} = -k_f[M]^2 + 2k_u[D] \tag{A26}$$

which can be recast into

$$\frac{d[M]}{a + b[M] + c[M]^2} = dt \tag{A27}$$

where

$$a = k_u[M_0], \quad b = -k_u, \quad c = -k_f \tag{A28}$$

After integration, the time course of disappearance of the monomer fraction is

$$f_M(t) = \frac{(b+s)(Z-1)}{[P_t]2c(1-Z)}$$
$$\text{where } Z = \left(\frac{2c[M_0] + b - s}{2c[M_0] + b + s}\right)\exp(st) \quad \text{and} \quad s = \sqrt{b^2 - 4ac} \tag{A29}$$

Equation (A29) is used to obtain k_f and k_u from a folding trace expressed as $f_M(t)$ under conditions where both folding and unfolding have to be taken into account (for example at intermediate denaturant concentration).

A3.3.2 Heterodimeric protein

$$M_1 + M_2 \underset{k_u}{\overset{k_f}{\rightleftarrows}} D \tag{A30}$$

The change of $[M_1]$ with time can be written as

$$\frac{d[M_1]}{dt} = -k_f[M_1][M_2] + k_u[D] \tag{A31}$$

The time course of disappearance of the fraction of M_1 or M_2 is again described by

Eq. (A27) except that the constants a, b, and c are different. If $[M_1] = [M_2]$, a, b, and c are

$$a = k_u[M_0]/2, \quad b = -k_u, \quad c = -k_f \tag{A32}$$

If $[M_1] \neq [M_2]$

$$a = k_u[M_{1,0}], \quad b = k_f([M_{1,0}] - [M_{2,0}]) - k_u, \quad c = -k_f \tag{A33}$$

or

$$a = k_u[M_{2,0}], \quad b = k_f([M_{2,0}] - [M_{1,0}]) - k_u, \quad c = -k_f \tag{A34}$$

Equation (A33) is valid for $f_{M1}(t)$ and (A34) for $f_{M2}(t)$; subscript 0 indicates concentration at $t = 0$.

A4

Kinetics of Reversible Two-state Folding: Relaxation after Disturbance of a Pre-existing Equilibrium (Method of Bernasconi)

Rate equations can be simplified if the reaction corresponds to a relaxation after a relatively small disturbance of the equilibrium. The procedure, pioneered by Bernasconi [16], allows rate constants to be obtained in those cases where there is no analytical solution of the differential rate equation. In practise, a pre-existing equi-

Tab. 27.4. Relaxation times for various reversible folding reactions.

Reaction	*Equation for relaxation time*[a]	
$2M \underset{k_u}{\overset{k_f}{\rightleftarrows}} D$	$\frac{1}{\tau} = 4k_f[\bar{M}] + k_u$	(A35)
$nM \underset{k_u}{\overset{k_f}{\rightleftarrows}} N$	$\frac{1}{\tau} = n^2 k_f[\bar{M}]^{n-1} + k_u$	(A36)
$M_1 + M_2 \underset{k_u}{\overset{k_f}{\rightleftarrows}} D$	$\frac{1}{\tau} = k_f([\bar{M}_1] + [\bar{M}_2]) + k_u$	(A37)
$2M \underset{k_{-1}}{\overset{k_1}{\rightleftarrows}} D_i \underset{k_{-2}}{\overset{k_2}{\rightleftarrows}} D$	$\tau_1 < \tau_2$: bimolecular association is faster than monomolecular rearrangement $\frac{1}{\tau_1} = 4k_1([\bar{M}]) + k_{-1}, \frac{1}{\tau_2} = \frac{4k_1k_2[\bar{M}]}{4k_1([M]) + k_{-1}} + k_{-2}$	(A38)
$2M \underset{k_{-1}}{\overset{k_1}{\rightleftarrows}} D_i \underset{k_{-2}}{\overset{k_2}{\rightleftarrows}} D$	$\tau_1 > \tau_2$: bimolecular association is slower than monomolecular rearrangement $\frac{1}{\tau_1} = k_1 + k_{-1}, \frac{1}{\tau_2} = 4k_1[\bar{M}] + \frac{k_{-1}k_{-2}}{k_2 + k_{-2}}$	(A39)

[a] Concentrations with overbars are equilibrium concentrations after relaxation to the new equilibrium.

librium between folded and unfolded protein is rapidly disturbed, for example by rapid dilution or rapid increase of temperature (T-jump), and the subsequent relaxation to the new equilibrium is observed. This relaxation is characterized by the relaxation time $\tau = 1/k_{app}$, where k_{app} (s^{-1}) is the apparent rate constant of the exponential decay to the new equilibrium. The number of relaxation times equals the number of reaction steps. Table 27.4 lists a few equations for different reversible folding reactions. They describe the relationship between the experimentally measured relaxation time τ and the individual rate constants of the reversible folding–unfolding reaction. The main difficulty with this procedure is that the equilibrium concentrations of the reactants at the new equilibrium, that is after relaxation, have to be known (concentrations with overbars in Table 27.4). These concentrations can be calculated if the equilibrium constants are known from independent experiments. Alternatively, a fitting procedure can be used in which initial estimates of the equilibrium constants are iteratively adapted until a best fit is obtained.

Acknowledgments

I thank Ilian Jelesarov and Daniel Marti for fruitful discussions and helpful comments on the manuscript. Work from my own laboratory has been supported in part by the Swiss National Science Foundation.

References

1 D. S. Godsell and A. J. Olson, *Trends Biochem. Sci.* **1993**, *18*, 65–68.
2 K. A. Dill, *Biochemistry* **1990**, *29*, 7133–7155.
3 W. Kauzmann, *Adv. Protein Chem.* **1959**, *14*, 1–63.
4 C. N. Pace, *Biochemistry* **2001**, *40*, 310–313.
5 R. Jaenicke and H. Lilie, *Adv. Protein Chem.* **2000**, 53.
6 K. E. Neet and D. E. Timm, *Protein Sci.* **1994**, *3*, 2167–2174.
7 R. Seckler, Assembly of multisubunit structures. In *Mechanisms of Protein Folding* (R. H. Pain, ed.), pp. 279–308. Oxford University Press, Oxford, 2000.
8 R. Jaenicke, *Biol. Chem.* **1998**, *379*, 237–43.
9 C. N. Pace, *Methods Enzymol.* **1986**, *131*, 266–280.
10 J. U. Bowie and R. T. Sauer, *Biochemistry* **1989**, *28*, 7139–7143.
11 D. E. Timm and K. E. Neet, *Protein Sci.* **1992**, *1*, 236–44.
12 I. Jelesarov and H. R. Bosshard, *J. Mol. Recogn.* **1999**, *12*, 13–18.
13 E. Freire, O. L. Mayorga and M. Straume, *Anal. Chem.* **1990**, *62*, 950A–959A.
14 T. Wiseman, S. Williston, J. F. Brandts and L.-N. Lin, *Anal. Biochem.* **1989**, *179*, 131–137.
15 K. W. Plaxco and C. M. Dobson, *Curr. Opin. Struct. Biol.* **1996**, *6*, 630–636.
16 C. F. Bernasconi, *Relaxation Kinetics*, 1st edn. Academic Press, New York, 1976.
17 H. Wendt, C. Berger, A. Baici, R. M. Thomas and H. R. Bosshard, *Biochemistry* **1995**, *34*, 4097–4107.
18 T. Jonsson, C. D. Waldburger and R. T. Sauer, *Biochemistry* **1996**, *35*, 4795–4802.
19 R. Zwanzig, *Proc. Natl Acad. Sci. USA* **1997**, *94*, 148–150.

20 M. E. Milla and R. T. Sauer, *Biochemistry* **1994**, *33*, 1125–1133.
21 T. Jonsson, C. D. Waldburger and R. T. Sauer, *Biochemistry* **1996**, *35*, 4795–4802.
22 A. K. Srivastava and R. T. Sauer, *Biochemistry* **2000**, *39*, 8308–8314.
23 M. E. Milla, B. M. Brown, C. D. Waldburger and R. T. Sauer, *Biochemistry* **1995**, *34*, 13914–13919.
24 C. D. Waldburger, T. Jonsson and R. T. Sauer, *Proc. Natl Acad. Sci. USA* **1996**, *93*, 2629–2634.
25 I. A. Hope and K. Struhl, *EMBO J.* **1987**, *6*, 2781–2784.
26 A. I. Dragan and P. L. Privalov, *J. Mol. Biol.* **2002**, *321*, 891–908.
27 I. Jelesarov and H. R. Bosshard, *J. Mol. Biol.* **1996**, *263*, 344–358.
28 H. Wendt, L. Leder, H. Härmä, I. Jelesarov, A. Baici and H. R. Bosshard, *Biochemistry* **1997**, *36*, 204–213.
29 E. K. O'Shea, K. J. Lumb and P. S. Kim, *Curr. Biol.* **1993**, *3*, 658–667.
30 P. L. Privalov and S. A. Potekhin, *Methods Enzymol.* **1986**, *131*, 4–51.
31 R. S. Spolar and M. T. Record, Jr., *Science* **1994**, *263*, 777–784.
32 G. I. Makhatadze and P. L. Privalov, *Adv. Protein Chem.* **1995**, *47*, 307–425.
33 G. Schreiber and A. R. Fersht, *Nature Struct. Biol.* **1996**, *3*, 427–431.
34 H. X. Zhou, *Biopolymers* **2001**, *59*, 427–433.
35 H. X. Zhou, *Protein Sci.* **2003**, *12*, 2379–2382.
36 H. R. Bosshard, D. N. Marti, and I. Jelesarov, *J. Mol. Recogn.* **2004**, *17*, 1–16.
37 K. J. Lumb and P. S. Kim, *Science* **1995**, *268*, 436–439.
38 P. Phelan, A. A. Gorfe, J. Jelesarov, D. N. Marti, J. Warwicker and H. R. Bosshard, *Biochemistry* **2002**, *41*, 2998–3008.
39 D. N. Marti and H. R. Bosshard, *J. Mol. Biol.* **2003**, *330*, 621–637.
40 C. C. Moser and P. L. Dutton, *Biochemistry* **1988**, *27*, 2450–2461.
41 E. Dürr, I. Jelesarov and H. R. Bosshard, *Biochemistry* **1999**, *38*, 870–880.
42 R. Koren and G. G. Hammes, *Biochemistry* **1976**, *15*, 1165–1171.
43 M. Vijayakumar, K. Y. Wong, G. Schreiber, A. R. Fersht, A. Szabo and H. X. Zhou, *J. Mol. Biol.* **1998**, *278*, 1015–1024.
44 H. R. Bosshard, E. Dürr, T. Hitz and I. Jelesarov, *Biochemistry* **2001**, *40*, 3544–3552.
45 J. A. Zitzewitz, O. Bilsel, J. B. Luo, B. E. Jones and C. R. Matthews, *Biochemistry* **1995**, *34*, 12812–12819.
46 R. A. Kammerer, T. Schulthess, R. Landwehr et al. *Proc. Natl Acad. Sci. USA* **1998**, *95*, 13419–13424.
47 J. K. Myers and T. G. Oas, *J. Mol. Biol.* **1999**, *289*, 205–209.
48 R. A. Kammerer, V. A. Jaravine, S. Frank et al. *J. Biol. Chem.* **2001**, *276*, 13685–13688.
49 J. A. Zitzewitz, B. Ibarra-Molero, D. R. Fishel, K. L. Terry and C. R. Matthews, *J. Mol. Biol.* **2000**, *296*, 1105–1116.
50 B. A. Krantz and T. R. Sosnick, *Nature Struct. Biol.* **2001**, *8*, 1042–7.
51 X. Cheng, M. L. Gonzalez and J. C. Lee, *Biochemistry* **1993**, *32*, 8130–9.
52 S. M. Doyle, E. H. Braswell and C. M. Teschke, *Biochemistry* **2000**, *39*, 11667–76.
53 D. H. Kim, D. S. Jang, G. H. Nam et al. *Biochemistry.* **2000**, *39*, 13084–92.
54 M. S. Gittelman and C. R. Matthews, *Biochemistry* **1990**, *29*, 7011–7020.
55 C. J. Mann, S. Xhao and C. R. Matthews, *Biochemistry* **1995**, *34*, 14573–14580.
56 L. M. Gloss and C. R. Matthews, *Biochemistry* **1997**, *36*, 5612–5623.
57 L. M. Gloss and C. R. Matthews, *Biochemistry* **1998**, *37*, 15990–15999.
58 L. M. Gloss, B. R. Simler and C. R. Matthews, *J. Mol. Biol.* **2001**, *312*, 1121–34.
59 A. C. Ciark, S. W. Raso, J. F. Sinclair, M. M. Ziegler, A. F. Chaffotte and T. O. Baldwin, *Biochemistry* **1997**, *36*, 1891–9.
60 E. Dürr and H. R. Bosshard, *Protein Sci.* **2000**, *9*, 1410–1415.
61 R. M. Thomas, H. Wendt, A. Zampieri and H. R. Bosshard, *Progr. Colloid. Polym. Sci.* **1995**, *99*, 24–30.

62 D. N. Marti, M. Lu, H. R. Bosshard and I. Jelesarov, *J. Mol. Biol.* **2004**, *336*, 1–8.

63 D. C. Chan, D. Fass, J. M. Berger and P. S. Kim, *Cell* **1997**, *89*, 263–273.

64 D. L. Burns and H. K. Schachman, *J. Biol. Chem.* **1982**, *257*, 8648–8654.

65 M. G. Mateu, M. M. S. Del Pino and A. R. Fersht, *Nature Struct. Biol.* **1999**, *6*, 191–198.

66 C. Bodenreider, N. Kellershohn, M. E. Goldberg and A. Mejean, *Biochemistry* **2002**, *41*, 14988–14999.

67 C. R. Johnson, P. E. Morin, C. H. Arrowsmith and E. Freire, *Biochemistry* **1995**, *34*, 5309–5316.

68 A. R. Fersht, *Curr. Opin. Struct. Biol.* **1997**, *7*, 3–9.

69 T. A. Larsen, A. J. Olson and D. S. Goodsell, *Structure* **1998**, *6*, 421–7.

70 C. J. Tsai, S. L. Lin, H. J. Wolfson and R. Nussinov, *Protein Sci.* **1997**, *6*, 53–64.

71 V. Daggett and A. R. Fersht, *Trends Biochem. Sci.* **2003**, *28*, 18–25.

72 K. S. Thompson, C. R. Vinson and E. Freire, *Biochemistry* **1993**, *32*, 5491–5496.

73 K. Bachhawat, M. Kapoor, T. K. Dam and A. Surolia, *Biochemistry* **2001**, *40*, 7291–300.

74 D. Apiyo, K. Jones, J. Guidry and P. Wittung-Stafshede, *Biochemistry* **2001**, *40*, 4940–4948.

75 E. Barbar, B. Kleinman, D. Imhoff, M. Li, T. S. Hays and M. Hare, *Biochemistry* **2001**, *40*, 1596–1605.

76 L. A. Wallace and H. W. Dirr, *Biochemistry* **1999**, *38*, 16686–16694.

77 L. A. Wallace, N. Sluis-Cremer and H. W. Dirr, *Biochemistry* **1998**, *37*, 5320–5328.

78 L. A. Marky and K. J. Breslauer, *Biopolymers* **1987**, *26*, 1601–1620.

79 P. Kuzmic, *Anal. Biochem.* **1996**, *237*, 260–273.

28
Folding of Membrane Proteins

Lukas K. Tamm and Heedeok Hong

28.1
Introduction

The major forces that govern the folding and thermodynamic stability of water-soluble proteins have been studied in significant detail for over half a century [1, 2]. Even though the reliable prediction of protein structure ab initio from amino acid sequence is still an elusive goal, a huge amount of information on the mechanisms by which soluble proteins fold into well-defined three-dimensional structures has been obtained over this long time period [3]. In marked contrast, our current knowledge on thermodynamic and mechanistic aspects of the folding of membrane proteins is several orders of magnitude less advanced than that of soluble proteins, although integral membrane proteins comprise about 30% of open reading frames in prokaryotic and eukaryotic organisms [4]. There are several reasons why the research on membrane protein folding lags far behind similar research on soluble proteins.

First, the first structure of a soluble protein (myoglobin) was solved in 1958, but the first membrane protein structure (photosynthetic reaction center) was only determined 27 years later in 1985. Even today, of the approximately 25 000 protein structures in the Protein Structure Databank (PDB), only about 140 (i.e., less than 0.6%) are structures of integral membrane proteins.

Second, membrane proteins are more difficult to express, purify, and handle in large batches than soluble proteins. They require the presence of nondenaturing detergents or lipid bilayers to maintain their native structure, which adds an additional layer of complexity to these systems compared with soluble protein systems. The requirement for detergents or membranes also explains why it is more difficult to crystallize membrane proteins or subject them to nuclear magnetic resonance (NMR) for high-resolution structural studies.

Third, it is very difficult to completely denature membrane proteins [5]. Solvent denaturation with urea or guanidinium chloride (GdmCl) is generally not applicable to membrane proteins because secondary structures that are buried in the membrane are often not accessible to these denaturants. Membrane proteins are also quite resistant to heat denaturation, and even if they can be (partially) dena-

Protein Folding Handbook. Part I. Edited by J. Buchner and T. Kiefhaber

ISBN: 3-527-30784-2

tured, they are prone to irreversible aggregation. These properties have not helped to make membrane proteins favorable targets for folding studies. However, as will be shown in this chapter, new and different techniques are being developed to study the folding of membrane proteins. If this is done with sufficient care, membrane proteins can be brought back "into the fold" and very useful and much needed information can be gathered on the molecular forces that determine their thermodynamic stability and mechanisms that lead to their native structures. Even though most helical membrane proteins are inserted into biological membranes by means of the translocon [6], knowledge of the energetics and kinetics of membrane protein structure formation are important from a basic science standpoint and for structure prediction and protein engineering of this still neglected class of proteins, which constitutes the largest fraction of all targets of currently available drugs.

To understand the folding of membrane proteins, we first need to understand the dynamic structure of the lipid bilayer (i.e., the "solvent") into which these proteins fold. Fluid lipid bilayers are highly dynamic, yet well-ordered two-dimensional arrays of two layers of lipids with their polar headgroups exposed towards water and their apolar fatty acyl chains shielded from water and facing the center of the bilayer. This structure [7, 8] is maintained almost entirely by the hydrophobic effect [9]. The hydrocarbon chains in the core of the bilayer are quite well ordered, but their order degrades towards the midplane of the bilayer. This region comprises a width of about 30 Å in a "typical" bilayer of dioleoylphosphatidylcholine. The two interfaces of the bilayer are chemically and structurally quite complex and comprise a width of about 15 Å each. These regions contain the phosphate and choline headgroups, the glycerol backbone and about 25 molecules of bound, but disordered water for each phosphatidylcholine (PC) headgroup. The lipids are free to diffuse laterally ($\sim$1 $\mu m^2\ s^{-1}$) and rotationally ($\sim$1 μs^{-1}), but basically do not flip-flop across the membrane.

The molecular packing of lipids in a fluid lipid bilayer is maintained mechanically by a combination of three types of opposing forces: lateral chain repulsions in the core region, headgroup repulsions, and surface tension at the polar–nonpolar interface [10]. These forces create a lateral pressure profile along the membrane normal that cannot be directly measured, but that has been calculated based on the known magnitudes of the relevant forces [11]. This packing and lateral pressure profile has profound consequences on the lipid hydrocarbon chain dynamics [12] and the folding of membrane proteins as will be summarized in later sections of this chapter. Therefore, the mechanical and dynamical properties as well as the chemical properties of membranes change dramatically as the composition of chemical groupings changes along the bilayer.

To dehydrate and bury a single peptide bond in the lipid bilayer is energetically unfavorable and costs 1.15 kcal mol^{-1} [13]. The energetic gain of folding a polypeptide into an internally hydrogen-bonded secondary structure in membranes is much smaller (i.e., of the order of -0.1 to -0.4 kcal per residue) [14–17]. This shows that partitioning of the bare backbone (e.g., polyglycine) into membranes is energetically unfavorable irrespective of whether the peptide is folded or not. Pro-

ductive membrane insertion of a polypeptide segment is only promoted if the segment contains a sufficiently large number of apolar side chains, which by virtue of their favorable partitioning can overcome the energy cost of transferring the peptide backbone into the membrane. As a rule of thumb, the equivalent of a minimum of five leucine substitutions are required to offset the unfavorable energy of trying to insert a 20-residue polyalanine helix (see below).

Forming intramolecular hydrogen bonds is moderately favorable at the interface and presumably quite favorable in the apolar core of the bilayer [18]. The energetic cost of opening a hydrogen bond in a membrane likely depends on the concentration of water or the probability of finding another hydrogen-bonding partner in that location. Since water and other hydrogen-bond acceptors are rare in membranes, one generally finds only fully hydrogen-bonded secondary structures in membrane proteins. Therefore, the predominant building blocks of membrane proteins are transmembrane (TM) helices and closed TM β-barrels. Other fully hydrogen-bonded secondary structures such as 3_{10}-helices and π-bulges are rare, but do occasionally occur in membrane proteins.

Since the α-helix and closed β-sheets are the main building blocks and since these two elementary secondary structures are rarely mixed in membrane proteins, we treat α-helical and β-barrel membrane proteins (for examples of two prototype membrane protein structures, see Figure 28.1) in separate sections of this chapter. These sections are preceded by a general section on the thermodynamics of side-chain partitioning, which applies to both classes of membrane proteins and which also forms the basis of membrane protein topology and structure prediction algorithms.

28.2
Thermodyamics of Residue Partitioning into Lipid Bilayers

The partitioning of apolar amino acid side chains into the membrane provides the major driving force for folding of α-helical and β-barrel membrane proteins. Folding of membrane proteins is always coupled to partitioning of the polypeptide from water into the membrane environment. A large number of hydropathy scales have been developed over the years. The different scales have been derived based on very different physical or statistical principles and, therefore, differ for different residues sometimes quite significantly. It is beyond the scope of this chapter to review the different scales that are in use. The only scales that are based on comprehensive partitioning measurements of peptides into membranes and membrane-mimetic environments are the two Wimley & White (WW) scales, namely the WW interface [19] and the WW octanol scale [13, 20].

The WW interface scale refers to partitioning into the interface region of phosphatidylcholine bilayers and the octanol scale refers to partitioning into octanol, which is thought to be a good mimetic of the core of the lipid bilayer. As has been demonstrated for the hydrophobic core of soluble proteins [21], the dielectric constant in the core of a lipid bilayer may be as high as 10 due to water penetration

(i.e., considerably larger than 2 in pure hydrocarbon and closer to that of wet octanol). Both scales are whole-residue scales, which means that they take into account the thermodynamic penalty of also partitioning the peptide backbone into the respective membrane locations. Based on these partition data, one may group the amino acid residues into three groups, namely those that do not favor membranes (Ala, Ser, Asn, Gly, Glu^-, Asp^-, Asp^0, Lys^+, Arg^+, His^+), those that favor the interface (Trp, Tyr, Cys, Thr, Gln, His^0, Glu^0), and those that favor the hydrocarbon core (Phe, Leu, Ile, Met, Val, Pro). Sliding a 19-residue window of summed WW hydropathy values over the amino acid sequences of membrane proteins and using the thermodynamic $\Delta G = 0$ cutoff predicts TM helices with high accuracy [13]. The residues that fall in the first and third group are not surprising. However, the residues that prefer the interface deserve a few comments. Statistical analyses and model studies of membrane proteins have indicated for quite some time that the aromatic residues Trp and Tyr residues have a strong preference for membrane interfaces [22] (see also Figure 28.1). It has been suggested that their bulkiness, aromaticity and slightly polar character are the major factors that determine their preferred location in the interface [23].

Hydrogen bonding is probably not important for this localization. The moderately polar residues in this group are not surprising. However, the uncharged form of glutamic acid interestingly is apolar enough to localize into the interface. The differential partitioning of glutamate depending on its charge state likely has profound consequences on the pK_a value of this residue at membrane surface because the pK_a is now coupled to partitioning. A manifestation of this shifted pK_a is seen, for example, when the binding and membrane penetration of the fusion peptide of influenza hemagglutinin is examined [16]. This peptide contains two Glu residues in its N-terminal portion. A shift of the pH from 7 to 5 is sufficient to bind the peptide more tightly and more deeply (i.e., deep enough to cause membrane fusion at pH 5, but not at pH 7).

28.3 Stability of β-Barrel Proteins

All β-barrel membrane proteins whose structures are known at high resolution are outer membrane proteins of gram-negative bacteria [24]. However, several mitochondrial and chloroplast outer membrane proteins, namely those that are part of the protein translocation machinery of these membranes also appear to be β-barrel membrane proteins [25, 26]. Bacterial outer membrane proteins are synthesized with an N-terminal signal sequence and their translocation through the inner membrane is mediated by the translocon consisting of the SecY/E/G complex with the assistance of the signal recognition particle and the SecA ATPase, which together constitute the prokaryotic protein export machinery [27]. Helical membrane proteins that reside in the inner membrane have contiguous stretches of about 20 hydrophobic residues that form TM helices, which presumably can exit the translocon laterally into the lipid bilayer [6]. The TM strands of outer mem-

brane proteins on the other hand are composed of alternating hydrophilic and hydrophobic residues [28]. Therefore, they lack the signal for lateral exit from the translocon into the inner membrane and become secreted into the periplasmic space, where they are presumably greeted by periplasmic chaperones such as Skp and SurA [29, 30]. Skp binds unfolded outer membrane proteins, prevents them from aggregation, but does not appear to accelerate their insertion into lipid model membranes (D. Rinehart, A. Arora, and L. Tamm, unpublished results).

The outer membrane proteins of gram-negative bacteria may be grouped into six families according to their functions [31]. Structures of members of each of these families have been solved by X-ray crystallography or NMR spectroscopy. The six families with representative solved structures are: (i) the general porins such as OmpF and PhoE [32, 33], (ii) passive sugar transporters such as LamB and ScrY [34, 35], (iii) active transporters of siderophores such as FepA, FecA, and FhuA [36–39] and of vitamin B_{12} such as BtuB [40], (iv) enzymes such as the phospholipase OmpLA [41], (v) defensive proteins such as OmpX [42], and (vi) structural proteins such OmpA [43]. All outer membrane proteins form β-barrels. The β-barrels of these proteins consist of even numbers of β-strands ranging from 8 to 22. The average length of the TM β-strands is 11 amino acid residues in trimeric porins and 13–14 residues in monomeric β-barrels. Since the strands are usually inclined at about 40° from the membrane normal, they span about 27–35 Å of the outer membrane, respectively.

Most outer membrane proteins have long extracellular loops and short periplamsic turns that alternatingly connect the TM β-strands in a meandering pattern. The loops exhibit the largest sequence variability within each outer membrane protein family [31]. The largest and smallest outer membrane proteins are monomeric, but others such as OmpLA are dimers and the porins are trimers of β-barrels.

Two general approaches have been taken to examine the thermodynamic stability of β-barrel membrane proteins: solvent denaturation by urea and guanidinium chloride and differential scanning calorimetry (DSC). In the following, we will discuss the thermodynamic stability of the simple monomeric β-barrel protein OmpA and then extend the discussion to complexities that arise by the presence of the central plug domain of FepA and FhuA and trimer formation in the case of porins. The most extensive thermodynamic stability studies have been carried out with the outer membrane protein A (OmpA) of *Escherichia coli*. OmpA is an abundant structural protein of the outer membrane of gram-negative bacteria. Its main function is to anchor the outer membrane to the peptidoglycan layer in the periplasmic space and thus to maintain the structural integrity of the outer cell envelope [44]. The 325-residue protein is a two-domain protein whose N-terminal 171 residues constitute an eight-stranded β-barrel membrane-anchoring domain and whose C-terminal 154 residues form the periplasmic domain that interacts with the peptidoglycan. The three-dimensional structure of the TM domain has been solved by X-ray crystallography [43] and, more recently, by solution NMR spectroscopy [45]. The structure resembles a reverse micelle with most polar residues facing the interior, where they form numerous hydrogen bonds and salt bridges, and the apolar residues facing the lipid bilayer [43]. Two girdles of aromatic side chains, trypto-

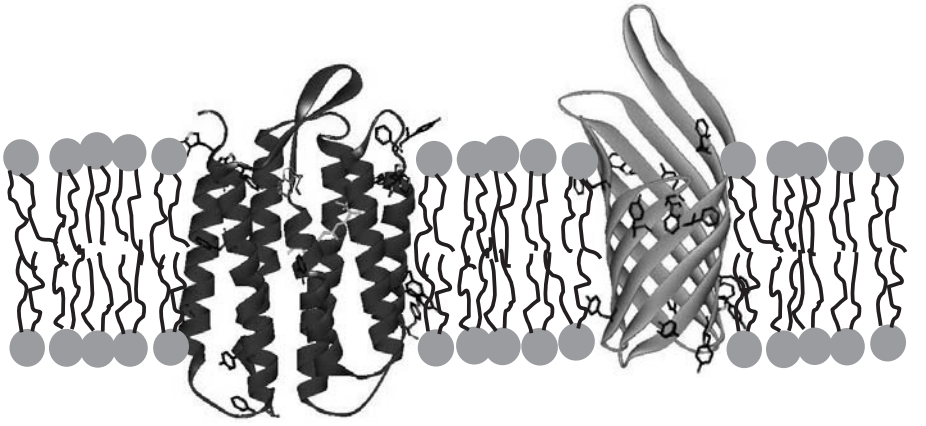

Fig. 28.1. Three-dimensional structures of representative α-helical and β-barrel membrane proteins. Left: Bacteriorhodopsin from *Halobacterium salinarium* (PDB code: 1C3W). Right: Transmembrane domain of OmpA (1QJP) from *Escherichia coli*. The aromatic side chains (Trp, Tyr, Phe) are concentrated at the bilayer–water interfaces as shown in both structures.

phans and tyrosines, delineate the rims of the barrel where they interact with the two membrane interfaces (Figure 28.1).

Extensive mutagenesis studies show that OmpA is quite robust against many mutations especially in the loop, turn, and lipid bilayer-facing regions [46]. OmpA can even be circularly permutated without impairing its assembly and function in outer membranes [47]. Dornmair et al. [48] showed that OmpA could be extracted from the outer membrane and denatured and solubilized in 6–8 M urea and that the protein spontaneously refolded into detergent micelles by rapid dilution of the denaturant. They subsequently showed that urea-unfolded OmpA can also be quantitatively refolded into preformed lipid bilayers by rapid dilution of urea [49].

Recently, we could achieve the complete and reversible refolding of OmpA in lipid bilayers [50]. The reaction was shown to be a coupled two-state membrane partition folding reaction with the unfolded state in urea being completely dissociated from the membrane and the folded state completely integrated into the membrane (Figure 28.2). This represents the first example of an integral membrane protein, for which the thermodynamic stability could be quantitatively accessed. To achieve this goal, a urea-induced equilibrium folding system was developed for OmpA. The system consisted of small unilamellar vesicles composed of 92.5 mol% phosphatidylcholine and 7.5 mol% phosphatidylglycerol in weakly basic (pH 7.0–10) and low ionic strength conditions. These conditions facilitate both the folding and unfolding reactions and dissociation of the unfolded form from the membrane surface. Folding of OmpA is monitored by tryptophan fluorescence or CD spectroscopy, or by sodium dodecylsulfate polyacrylamide gel electrophoresis (SDS-PAGE) (Figure 28.3).

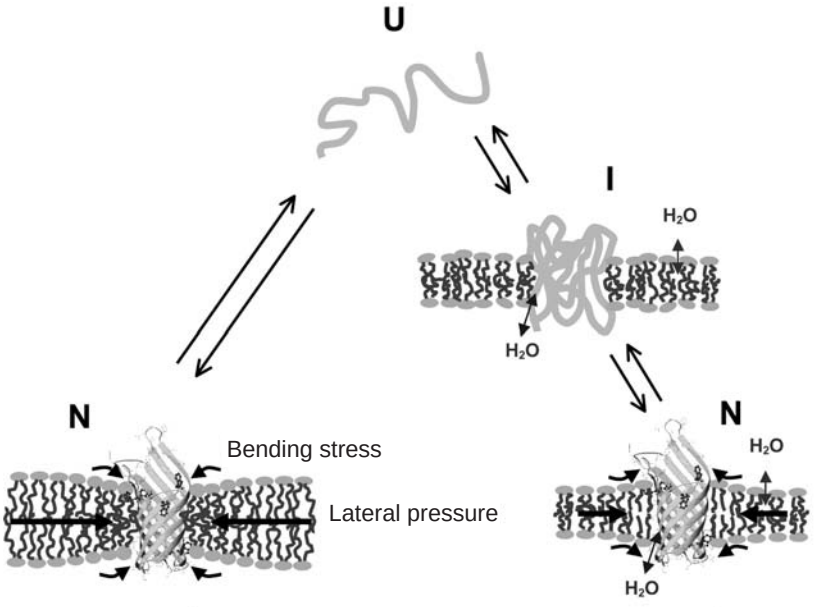

Fig. 28.2. Cartoon depicting the folding of OmpA into lipid bilayers. Left path: Folding into most bilayers is a thermodynamic two-state process. Right path: Folding into thin bilayers is multi-state (i.e., at least one equilibrium intermediate occurs). Bilayer forces acting on OmpA folding are indicated with arrows. The large black arrows indicate lateral bilayer pressure imparted on the lipid/protein interface in the hydrophobic core of the bilayer. Increasing this pressure increases the thermodynamic stability of the protein. The small black arrows indicate lipid deformation forces caused by hydrophobic mismatch between the protein and unstressed bilayers. These forces decrease the thermodynamic stability of the protein. Water molecules penetrate more easily into the hydrophobic core of thin bilayers (blue arrows) and stabilize equilibrium intermediates until, in very thin bilayers, complete unfolding is no longer observed. The unfolded state in urea is dissociated from the membrane. Adapted from Ref. [50].

Each of these techniques monitors a different aspect of the folding reaction. Trp fluorescence reports on the insertion of tryptophans into the lipid bilayer, far-UV CD on the formation secondary structure, and SDS-PAGE on the completion of the tertiary β-barrel structure. If samples are not boiled prior to loading onto the SDS gels, they run at an apparent molecular mass of 30 kDa if the protein is completely folded, but at 35 kDa if it is unfolded or incompletely folded.

This shift on SDS gels has proven to be a very useful assay for tertiary structure formation of OmpA and other outer membrane proteins [51]. Complete refolding as measured by the SDS-PAGE shift correlates with the reacquisition of the ion channel activity of OmpA [52]. Since unfolding/refolding curves as a function of denaturant concentration measured by three techniques that report on vastly different kinetic processes superimpose, it is very likely that folding/unfolding is a ther-

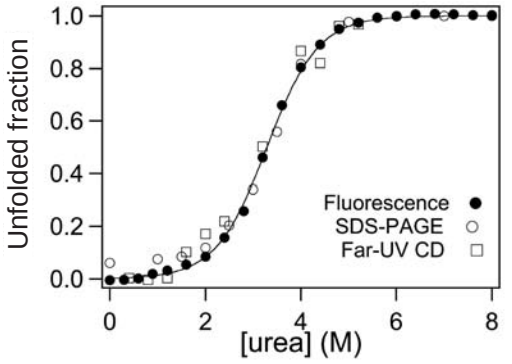

Fig. 28.3. Unfolded fraction of OmpA as a function of urea concentration obtained from the average fluorescence emission wavelength $\langle\lambda\rangle$, far-UV CD spectroscopy, and the SDS-PAGE shift assay. These measures of lipid binding, secondary structure, and tertiary structure, respectively, superimpose in equilibrium measurements although they develop at different times in kinetic experiments. Adapted from Ref. [50].

modynamic two-state process that can be analyzed using a two-state equilibrium folding model.

From such an analysis, Hong and Tamm [50] found a free energy of folding $\Delta G^{\circ}_{H2O} = -3.4$ kcal mol^{-1} and an m-value, which describes the cooperativity parameter of the folding/unfolding reaction, of $m = 1.1$. The rather small ΔG°_{H2O} of OmpA, which is of the same order of magnitude as that of water-soluble proteins, is perhaps surprising in view of the quite extreme heat resistance of this and other β-barrel membrane proteins. However, if one simply calculates the free energy of transfer of all residues that are transferred into the lipid bilayer with the augmented WW hydrophobicity scale, one finds that the net ΔG°_{H2O} amounts to only about -1 kcal mol^{-1}. This value may be further decreased by adding a few (negative) kcal mol^{-1} for folding, which would bring the prediction close to the experimentally determined value. The folding contribution may be the sum of contributions for secondary structure formation, estimated to be about 80×-0.2 kcal mol^{-1}, and on the order of 10 kcal mol^{-1} of entropy and other costs for packing polar residues in the core of the protein.

The take-home message from these measurements and theoretical considerations is that the overall stability of membrane proteins is not as large as one might have anticipated, but rather similar in magnitude to that of soluble proteins of similar size. As is true for soluble proteins, the thermodynamic stability of this and perhaps most membrane proteins is determined by the sum of many relatively large thermodynamic contributions that ultimately cancel to yield a relatively small net free energy of folding.

The study by Hong and Tamm [50] also examined the effect of lipid bilayer forces on the thermodynamic stability of OmpA. The effects of elastic lipid deformation due to a mismatch of the hydrophobic length of the protein compared with the bilayer thickness and due to curvature stress imposed by cone-shaped lipids

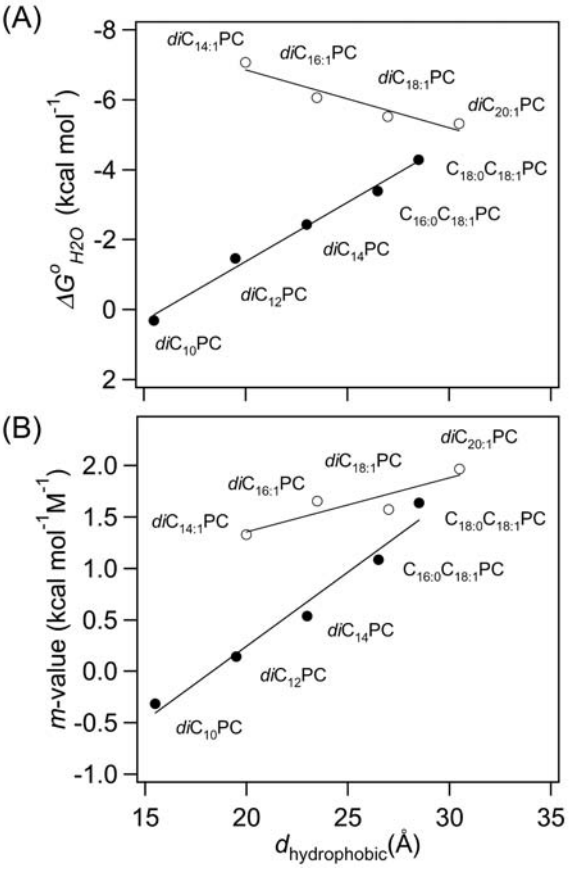

Fig. 28.4. Dependence of A) the free energy of folding ΔG°_{H2O} and B) the *m*-value reflecting the cooperativity of folding on the hydrophobic thickness of phosphatidylcholine bilayers. Filled circles: saturated acyl chain series with small lateral bilayer pressure. Open circles: double-unsaturated acyl chain series with increasing lateral bilayer pressure as hydrophobic thickness decreases. Adapted from Ref. [50].

were investigated. Increasing the thickness of the lipid bilayer increases the stability (i.e., decreases ΔG°_{H2O}) of OmpA. It also increases the cooperativity (*m*-value) of folding (Figure 28.4). The decrease in ΔG°_{H2O} is -0.34 kcal mol^{-1} per Å of increased bilayer thickness, which converts to -4 cal mol^{-1} per Å^2 of increased hydrophobic contact area. This is only about 20% of the standard value for the hydrophobic effect [9]. We conclude that elastic energy due to lipid deformation counteracts the energy gain that would be expected for a full development of the hydrophobic effect.

Including cone-shaped lipids with a smaller cross-sectional headgroup than acyl chain area increases the lateral pressure within lipid bilayers [53]. Increasing the lateral pressure in membranes by including lipids with increasing relative

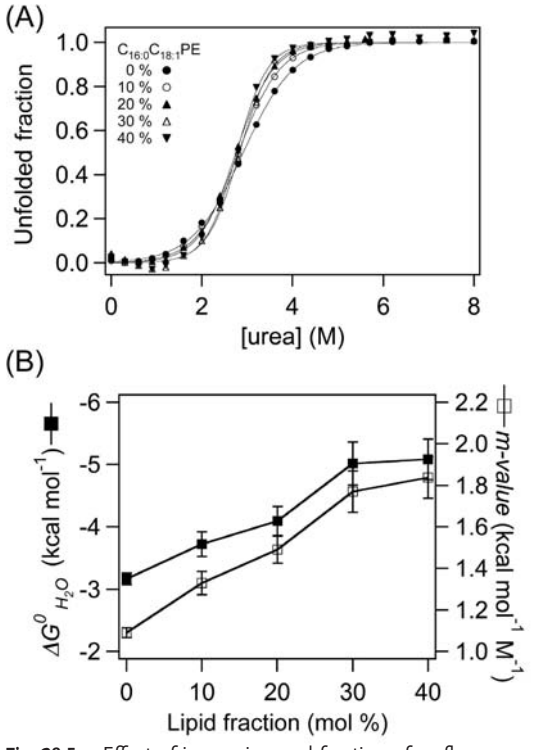

Fig. 28.5. Effect of increasing mol fraction of phosphatidylethanolamine ($C_{16:0}C_{18:1}$PE) in phosphatidylcholine ($C_{16:0}C_{18:1}$PC) bilayers on the thermodynamic stability of OmpA. A) Unfolding curves measured by Trp fluorescence. B) Dependence of ΔG°_{H2O} and *m*-value of OmpA folding on the cone-shaped and lateral pressure-inducing lipid $C_{16:0}C_{18:1}$PE. Adapted from Ref. [50].

amounts of *cis* double bonds in the hydrocarbon region increased the stability (i.e., decreased ΔG°_{H2O}) of OmpA from -3.4 to -7 kcal mol^{-1} and more negative values when phosphatidylethanolamines were included as cone-shape lipids (Figure 28.5). The *m*-value exhibited an increase that was correlated with the ΔG°_{H2O} decrease, in the case of bilayer thickening, but a decrease when the bilayer pressure was increased with *cis* double bonds. The various bilayer forces that act on OmpA and modulate its thermodynamic stability in membranes are illustrated in Figure 28.2.

Gram-negative bacteria possess active transport systems for the uptake of iron–siderophore complexes, vitamin B_{12}, and other essential nutrients. The systems consist of active ATP-requiring transporters in the inner membrane, the TonB linker protein that spans the periplasm, and a family of proteins called TonB-dependent transporters in the outer membrane. The TonB-dependent transporters share common structural features. They are monomeric 22-stranded β-barrels. The lumina of these large-diameter barrels are filled with a N-terminal

"cork" or "plug" domain with a globular mixed α-helix/β-structure. The plug domains are tightly inserted into the barrels and make extensive salt bridge and hydrogen bond contacts with the inner barrel wall. The mechanism of substrate transport through these transporters is presently not well understood.

A thermal denaturation study using DSC of FhuA demonstrated that the plug domain and the surrounding β-barrel are autonomous folding units [54]. In the absence of bound substrate (ferrichrome), a reversible transition centered at 65 °C was well separated from an irreversible transition centered at 74 °C. The binding of the substrate increased the lower transition temperature to 71 °C, while the higher transition temperature was not changed. Since the higher temperature transition was accompanied by a significant change of the CD signal at 198 nm and 215 nm, this transition was assigned to the denaturation of the β-barrel. The lower temperature transition was assigned to the denaturation of the plug domain and neighboring loops emerging from the β-barrel because antibodies targeting unfolded outer loops bound to FhuA only above the lower transition temperature of 65 °C. A deletion mutant (Δ21–128) that lacked the plug domain underwent a thermal denaturation at a lower temperature ($T_m = 62$ °C) than the wild-type protein, implying that the presence of the plug stabilizes the barrel structure.

The stability of FepA in Triton-X100 micelles was probed by solvent-induced denaturation and EPR spectroscopy [55, 56]. In these studies, FepA was functionally refolded from the denatured state by dialysing the denaturant in the presence of TX-100 micelles. When GdmCl- and urea-induced denaturation was monitored by site-directed spin-label EPR spectroscopy at an extracellular loop site, unfolding occurred in a sharp transition at 2.0 M GdmCl or 5.5 M urea, respectively. The free energies of unfolding were approximately 6 kcal mol^{-1} with both denaturants. The rate of unfolding of the substrate-bound protein was significantly smaller than that of the free protein. This confirms that the substrate has a stabilizing effect on FepA as has also been observed by DSC with FhuA. When residues pointing towards the center of the barrel were spin-labeled, their EPR spectra indicated completely mobile residues in 4 M GdmCl. However, residues facing the detergent were still quite immobilized at this GdmCl concentration. The authors argued that denatured FepA retained substantial residual hydrophobic interactions with the detergent micelle. This observation is reminiscent of residual hydrophobic interactions that have been observed in soluble proteins at high denaturant concentrations [57]. However, in these studies with FepA, the degree of denaturation was unfortunately not recorded by a global method such as CD spectroscopy and therefore, it is not clear whether the transition is two-state and whether fully denaturing conditions have been reached in this work.

Porins facilitate the general diffusion of polar solutes (< 400 Da) across the outer membranes of gram-negative bacteria. The porins are composed of 16-stranded β-barrels that assemble into rigid homotrimers whose trimer interfaces are formed by close van der Waals packing of nonpolar residues and aromatic ring stacking interactions [32, 33]. The lumen of each monomer is aqueous and surrounded by hydrophilic residues. An interesting structural and functional feature of the porins is that the long loop L3 folds back into the lumen of the channel where it engages

in a hydrophobic contact with a few residues inside the barrel. The loop forms a constriction in the channel and its acidic residues together with a cluster of basic residues on the opposite channel wall are thought to exert a transverse electric field across the channel opening. The shorter loop L2 forms a "latch" that reaches over from one subunit to a neighboring subunit and thereby further stabilizes inter-subunit interactions. Porins are extremely stable towards heat denaturation, protease digestion, and chemical denaturation with urea and GdmCl [31]. For example, extraction of OmpF from the *E. coli* outer membrane requires the heating of outer membranes in mixtures of isopropanol and 6 M GdmCl at 75 °C for more than 30 min [58]. The trimer structure itself is maintained up to 70 °C in 1% SDS [59].

A mutagenesis study combined with DSC and SDS-PAGE shift assays demonstrates that the inter-subunit salt bridge and hydrogen bonding interactions involving loop L2 contribute significantly to the trimer stability [59]. For example, mutations breaking the salt bridge between Glu71 and Arg100 decrease the trimer–monomer transition temperature from 72 to 47–60 °C and ΔH_{cal} from 430 to 200–350 kcal mol^{-1}. A similar behavior was observed when residues 69–77 of L2 were deleted. The energetic contribution of the nonpolar contact between neighboring barrel walls has not yet been investigated in porins, but would be interesting to examine and compare with lateral associations of interacting TM helices (see below).

28.4 Stability of Helical Membrane Proteins

In 1990, Popot and Engelman proposed a two-stage model for the folding of α-helical membrane proteins [60]. In the framework of this model, TM helices are thought to be independently folded units (stage I) that may laterally associate into TM helix bundles (stage II). The model was inspired by the finding of the same group that the seven-TM-helix protein bacteriorhodopsin (BR) can be split into helical fragments that would still integrate as TM helices and then laterally assemble into a seven-helix protein that was capable of binding to cofactor retinal just as the wild-type protein [61]. Since then, it has been realized that more stages are needed to describe the folding of helical proteins.

The interface is a membrane compartment that may be important in early stages of folding [62]. In addition, cofactors and polypeptide hinges and loops can be additional factors that sometimes play important roles in late stages of helical membrane protein folding [63]. Although the real world of membrane proteins is clearly more complex, the two-stage model has some merits because it is conceptually simple and because it appears to correctly describe the hierarchy of folding of at least a few simple membrane proteins. Therefore, we describe in this section how individual TM helices are established and then proceed in the following section with lateral helix associations and higher order structural principles of membrane protein folding.

As indicated above, open hydrogen bonds are energetically unfavorable in mem-

branes. Sequence segments with a sufficient number of apolar residues are driven into membranes by the hydrophobic effect where they fold into TM or interfacial α-helices. The thermodynamic gain of folding a 20-residue peptide into a TM helix is about -5 kcal mol^{-1}, if we take -0.25 kcal mol^{-1} as the per-residue increment of forming an helix in membranes [16]. Generally and in contrast to soluble protein α-helices, TM helices are quite rich in glycines. Prolines are also not uncommon in TM helices, where they often induce bends, but do not completely break the helix. Finally, serines, threonines, and cysteines are frequently interspersed into otherwise apolar TM sequences. These latter residues often form hydrogen bonds with backbone carbonyls and may therefore have a more apolar character in TM helices than in aqueous environments.

It is generally not possible to obtain interpretable results on the stability of helical integral membrane proteins from thermal denaturation studies because thermal denaturation of these proteins usually leads to irreversibly denatured states [5]. However, the thermodynamic stabilities of a few polytopic helical membrane proteins have been studied by partial denaturation with strong ionic detergents. Early refolding studies by Khorana and coworkers showed that BR could be quantitatively refolded by step-wise transfer from organic solvent to SDS to renaturing detergents or lipids [64, 65]. These protocols were later refined to measure the kinetics of refolding of BR upon transfer from the ionic detergent SDS into mixed lipid/detergent micelles [66, 67]. It should be kept in mind that although tertiary contacts are lost, most secondary structure is retained or perhaps even partially refolded in SDS. Therefore, the reactions observed with these protocols report only on the last stages of membrane protein folding. In 1997, Lau and Bowie developed a system to reversibly unfold native diacylglycerol kinase (DAGK) in *n*-decyl-β-maltoside (DM) micelles by the addition of SDS [68]. In these carefully controlled studies, the ratios of the denaturing and native structure-supporting detergents were systematically varied, so that reversibility of the partial unfolding reaction could be demonstrated. By analyzing their data with the two-state model of protein folding, these authors determined the stability of the three-helix TM domain of DAGK in DM relative to SDS to be -16 kcal mol^{-1}. This large (negative) value is somewhat surprising and indicates an extremely high thermodynamic stability of DAGK. A similar study has been carried out recently with BR [69].

28.5
Helix and Other Lateral Interactions in Membrane Proteins

The packing density and the hydrophobicity of amino acid residues involved in the intramolecular contact of α-helical membrane proteins are similar to those in the hydrophobic cores of water-soluble proteins. The basic principles of the hydrophobic organization of residues in water-soluble proteins appear to hold true also for membrane proteins. However, the energy gain of the hydrophobic effect has already been expended on inserting individual α-helices into membranes and cannot be a driving force for helix association. From comprehensive mutagenesis work

on the TM domain of glycophorin A [70] and later from genome-wide database searches [71], it has become clear that tight van der Waals contacts between complementary helix surfaces provide a strong driving force for lateral helix association in membranes. This force is perhaps best understood if one considers the possibility that lipids even in their fluid liquid-crystalline state do not conform as well to corrugated exposed helix interaction sites as the complementary helix binding partner. Lipids also gain entropy upon release from a helix surface into the bulk liquid-crystalline bilayer (''lipophobic effect''). Since thermodynamic driving forces are always determined by the energetic differences between two states, it is the unfavorable lipid solvation of corrugated helix surfaces that ultimately drives helix association.

Helices of membrane proteins are rarely oriented exactly perpendicular to the plane of the membrane. They are frequently tilted by about 20° from the membrane normal in structurally rugged membrane proteins [72] and by much larger angles in some recently solved structures of ion channels and complex transporters. TM helices interact with each other with left- or right-handed crossing angles [72, 73]. The specificity of helix interactions in membranes is thought to arise from complementary knob-in-the-hole van der Waals interactions. Glycines provide the holes and the β-branched side-chains of valine and isoleucine provide the most frequent knobs on the complementary surfaces. The generality of this interaction is supported by the frequent occurrence of GxxxG motifs in interacting TM segments [71]. The interaction energy of the helix dimer of the glycophorin A TM domain has been measured in C_8E_5 micelles by analytical ultracentrifugation and was found to be -9 kcal mol^{-1} [74]. Although this measurement offers a rare and important glimpse on the thermodynamics of TM helix–helix interactions, the value was determined in detergent micelles and may be different in lipid bilayers. Subsequent alanine scanning experiments indicated that mutation of Gly79 and Gly83 resulted in the largest energy penalty (1.5–3 kcal mol^{-1} relative to wild-type) for dimer formation of glycophorin [75]. The helix interaction ''knobs'' Leu75 and Ile76 also cost more than 1 kcal mol^{-1} in stabilization energy when replaced by alanines.

Another alanine scanning mutagenesis study examined the effect of all side chains of helix B of BR on the thermodynamic stability of helix interactions in this protein [69]. The most destabilizing mutations were Y57A (3.7 kcal mol^{-1} relative to wt) and T46A (2.2 kcal mol^{-1} relative to wt). These were followed by I45A, F42A, and K41A (1.9–1.6 kcal mol^{-1}). Apparently, very different types of side chains (polar, apolar, aromatic, charged) can cause large effects. These studies show that helix packing interactions may be more complex (and less predictable) than previously thought based on extrapolations from the glycophorin paradigm. A remarkable and important result from the Faham et al. [69] study is that each Å^2 of buried surface area yields about 26 cal mol^{-1} of stabilizing energy. This is about the same number as observed for the burying of residues in soluble proteins, which is usually thought to be driven by the hydrophobic effect. Since the hydrophobic effect is already consumed by inserting side chains into a hydrophobic environment (SDS micelle) and since polar residues essentially yield the same

number, the 26 cal mol^{-1} per $Å^2$, packing energy may be more universal than previously thought and may reflect van der Waals, hydrophobic, and lipophobic interactions. Alternatively, water may access helical surfaces in partially denaturing SDS micelles better than in native structure-supporting DMPC/CHAPSO micelles, in which case the result may still conform to the classical hydrophobic effect.

An additional mechanism of helix interaction is thought to arise from inter-helix hydrogen bonds. Side chain-to-side chain (Asn, Gln, Asp, Glu, His) hydrogen bonds have been introduced into engineered TM helical bundles and were found to stabilize homodimers and homotrimers [76–79]. Ser and Thr side chains were also examined in these host–guest model sequences, but were insufficient to support helix association. It has also been suggested that backbone Cα-H to backbone carbonyl hydrogen bonds might stabilize membrane proteins [80]. However, although such hydrogen bonds are observed quite frequently in crystal structures of membrane (and soluble) proteins, they may merely allow close packing and may not make significant energetic contributions to the association of neighboring helices as has been demonstrated for one such bond in BR [81]. Pore loops are found to intercalate into open angled helical membrane protein structures as exemplified by the KcsA potassium channel structure [82]. The loops are generally also fixed to the helical framework of the protein by side chain-to-side chain hydrogen bonds, namely a hydrogen bond from a loop Tyr to a neighboring helix Trp and Thr in the case of KcsA. Finally, many membrane protein structures contain cofactors and pigments that likely contribute significantly to the stability and interaction specificity of these structures. Intersubunit interactions that determine quaternary structures of membrane proteins generally follow the same helix packing rules as those determining their tertiary structures [83]. In case of BR, van der Waals packing between nonpolar surfaces, hydrogen bonding, and aromatic ring stacking of tyrosines in the bilayer interface all contribute to trimer formation.

28.6 The Membrane Interface as an Important Contributor to Membrane Protein Folding

In this and the following sections we turn to pathways and possible intermediates of membrane protein folding. Jacobs and White [84] proposed a three-step thermodynamic model of membrane protein folding based on structural and partitioning data of small hydrophobic peptides. In this model, the first three steps of membrane protein folding are thought include partitioning into the interface, folding in the interface, and translocation across the membrane to establish a TM helix. The model was later extended to a four-step model, which added helix–helix interactions as the fourth step [62]. The model is rather a thermodynamic concept than an actual pathway of folding of constitutive helical membrane proteins because their TM helices are inserted with the assistance of the translocon in biological membranes. However, the concept is relevant for the insertion of helical toxins into membranes, which occurs without the assistance of other proteins, and for the placement of interfacial helices into membranes. Separation of a partition and

folding step in the interface is probably also mostly semantic because in all observable reactions these two processes appear to be coupled. Nevertheless, to think of protein folding as a coupled process of two components is useful for separating the thermodynamic contributions of each component [14–16]. Partition–folding coupling was observed more than 20 years ago for toxic peptides [85], peptide hormones [86], signal peptides [87, 88], and membrane fusion peptides [89]. Beta-sheet forming proteins and peptides may also insert and fold in the membrane interface before they become completely inserted into and translocated across the membrane [90–93]. An example of the respective contributions of $\Delta G, \Delta H$, and ΔS to partitioning and folding of an α-helical fusion peptide in lipid bilayers is shown in Figure 28.6.

28.7 Membrane Toxins as Models for Helical Membrane Protein Insertion

There are several proteins that assume globular structures in solution, but upon interaction with a membrane receptor or at low pH insert into and sometimes translocate across membranes. Among them are several colicins, which are translocated across outer bacterial membranes via porins and subsequently inserted into the inner membrane where they form toxic pores. Other toxins such as diphtheria, tetanus, and botulinum toxins spontaneously insert their translocation domains into mammalian cell membranes and thereby permit the translocation of linked catalytic domains into the cells. Since these proteins form helical structures in solution and in membranes, they are good models to study the refolding of soluble helical proteins into membranes. The channel-forming colicins are perhaps in this regard the best-studied bacterial toxins. The structures of the soluble forms of the channel domains of several colicins are known [94]. They consist of a central hydrophobic helical hairpin that is surrounded by eight amphipathic helices.

Refolding at the membrane interface has been implicated in many models of colicin insertion into lipid bilayers. An early study found a molten globule intermediate at an early stage of colicin A insertion into membranes [95]. The helices were formed, but tertiary contacts were not. Subsequent fluorescence studies indicated that the helices of colicin E were located in the interface, but widely dispersed in this state [96, 97]. The central hydrophobic helical hairpin of colicin A appears to be more deeply inserted, but does not assume a complete TM topology [98]. How the voltage-gated ion channel is opened from this stage is still unclear. Apparently, long stretches of sequence translocate across the membrane upon the application of a membrane potential by a process that is still poorly understood structurally and mechanistically [99, 100].

The process of membrane insertion of the translocation domain of diphtheria toxin likely resembles that of the colicins. The structure of the soluble form features a hydrophobic helical hairpin similar to that of the colicins [101]. It is thought that this hairpin inserts first into the lipid bilayer. The membrane-bound protein can exist in two conformations with an either shallow or deeply inserted

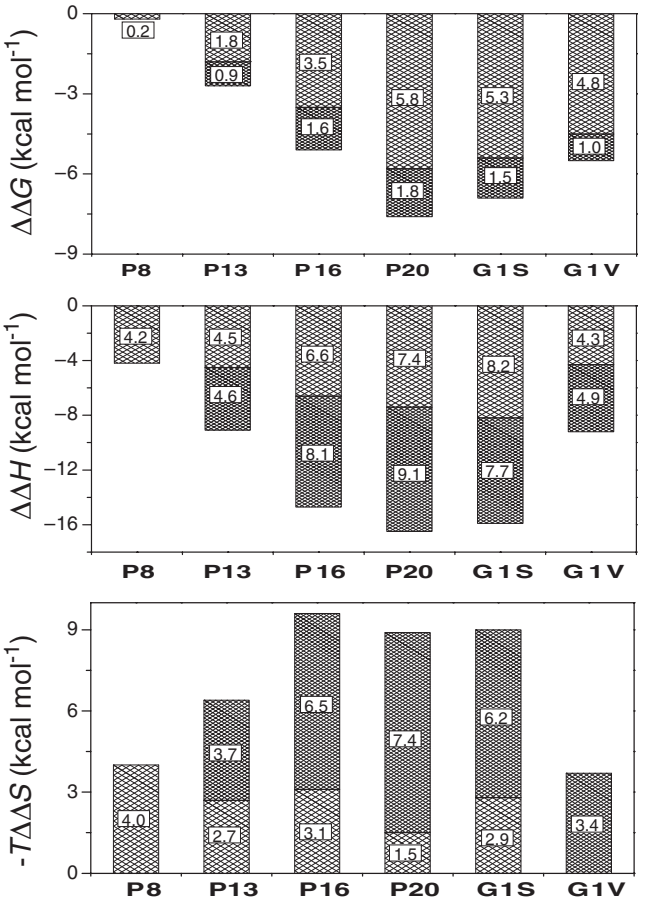

Fig. 28.6. Thermodynamics of partition-folding of the helical fusion peptide from influenza hemagglutinin. The lighter bars represent contributions from partitioning and the darker bars represent contributions from the coil → α-helix transition to ΔG, ΔH, and $T\Delta S$ upon peptide insertion into mixed phosphatidylcholine/phosphatidylglycerol bilayers. P8 through P20 are 8- to 20-residue peptides of the same sequence, and G1S and G1V are single amino acid mutations in position 1 of P20 that cause hemi-fusion or are defective in causing fusion, respectively. The numbers in the bars refer to the respective energies in kcal mol^{-1}. Adapted from Ref. [16].

helical hairpin [102]. Similar to the colicins, diphtheria toxin switches between two very different topologies in membranes and their relative populations depend on the applied membrane potential [103]. Again, the translocation mechanism is only poorly understood at the present time. However, despite many still unexplored details, the bacterial toxins appear to be an interesting class of facultative membrane proteins, from which we expect to learn a great deal about the mechanisms and energetics of refolding helical proteins in lipid bilayers.

28.8
Mechanisms of β-Barrel Membrane Protein Folding

The mechanism of folding and membrane insertion of the eight-stranded β-barrel protein OmpA has been studied by a number of kinetic experiments. The kinetics of folding into lipid bilayers composed of dimyristoylphosphatidylcholine in the fluid phase were found to be rather slow (i.e., on the order of many minutes at 30 °C) [104]. A more detailed kinetic study carried out with dioleoylphosphatidylcholine (DOPC) lipid bilayers in the 2–40 °C temperature range revealed three distinct kinetic phases [105]. The fastest phase detected by tryptophan (Trp) fluorescence changes had a time constant of 6 min and was rather independent of temperature. This phase was attributed to the initial binding of the unfolded protein to the bilayer surface. A second phase was strongly temperature dependent and had time constants in the 15 min to 3 h range (40–2 °C). The activation energy determined from an Arrhenius plot was 11 kcal mol^{-1}. This phase presumably corresponds to a deeper insertion, but not yet complete translocation of the β-strands in the lipid bilayer. The slowest phase was observed by the SDS gel-shift assay, which reports on the completion of the β-barrel. Complete folding in DOPC bilayers was only observed at temperatures greater than 30 °C, had a time constant of about 2 h, and took about 6 h to go to completion at 37 °C.

The translocation process of Trps of OmpA across the lipid bilayer was monitored by time-resolved Trp fluorescence quenching (TDFQ) [106]. In this technique, quenchers of Trp fluorescence are placed at different depths into the membrane and the time course of passage of Trps past these zones of quenchers is followed. When the technique was applied to single Trp mutants that were placed on different membrane-crossing β-hairpins, it was found that all four β-hairpins of OmpA crossed the membrane following the same time course (i.e., using a synchronized concerted mechanism of folding and insertion) [107]. This result is in accordance with the notion that interstrand hydrogen bonds and the barrel itself have to form while the protein translocates across the membrane. Again and very similar to the partition–folding coupling that was discussed in the context of helical membrane protein folding at membrane interfaces, we observe a folding–translocation coupling for this class of membrane proteins.

Thus the mechanism of β-barrel membrane protein folding in lipid bilayers is very different from the two (or more) stage models discussed above for helical membrane protein folding. The requirement that the barrel needs to be completely folded in order to translocate across the membrane probably also explains why the time constants of this process are so slow and the activation energies are so high. Folding and translocation of the barrel requires a large defect to be created in the membrane in order to insert a barrel of the size of OmpA. Moreover, the membrane provides a 100- to 1000-fold more viscous environment than water for folding and inserting membrane proteins.

In another kinetic study, the dependence of the rates of folding and insertion of OmpA on the bilayer thickness was examined [108]. As one might expect from the material properties of lipid bilayers, the folding and insertion rates increased sig-

nificantly as the bilayer thickness decreased. When the bilayers were sufficiently thin, folding of OmpA into large unilamellar vesicles was observed, whereas in average or thick bilayers complete folding and insertion occurs only in small unilamellar vesicles. Small vesicles are more strained and therefore exhibit more defects than large vesicles, which permits the quantitative refolding of OmpA in small, but not in large unilamellar vesicles if the hydrocarbon thickness of the bilayer is more than 20 Å (i.e., that of diC_{12}-phosphatidylcholine). Interestingly, the hydrophobic thickness of outer bacterial membranes is thought to be thinner than that of the inner membranes [109].

28.9 Experimental Protocols

28.9.1 SDS Gel Shift Assay for Heat-modifiable Membrane Proteins

The heat modifiability can be defined as a property of a protein whose electrophoretic mobility depends on the treatment of heat. It is characteristic for many bacterial outer membrane proteins [110]. For example, detergent-solubilized OmpA from *E. coli* migrates on SDS-polyacrylamide gels as a 30-kDa form without boiling, but as a 35-kDa form if boiled in SDS. Likewise, the iron transporter FepA shows an apparent molecular mass of 58 kDa if not boiled, but exhibits its actual molecular mass of 81 kDa after boiling [55]. The correlation between conformational states and electrophoretic mobilities on SDS-PAGE has been studied most extensively for unboiled samples OmpA. The 30-kDa form represents the membrane-inserted native state, which also exhibits a characteristic ion channel activity [45, 49, 52]. The 35-kDa form may represent a completely denatured state in the presence or absence of lipids [49–51], a misfolded state in the absence of lipid [111], a surface-adsorbed partially folded state [49, 90], or a kinetic intermediate at a stage before the complete insertion into membranes [105, 108].

28.9.1.1 Reversible Folding and Unfolding Protocol Using OmpA as an Example

1. Dilute OmpA in 8 M urea more than 100-fold into sonicated small unilamellar vesicles (SUV) composed of the desired lipids to give a final OmpA concentration of 12 μM and lipid-to-protein molar ratio of 800.
2. Incubate for 3 h at 37 °C for refolding.
3. Divide the refolded protein-lipid complex into 10 aliquots.
4. Add appropriate amounts of a freshly made 10 M urea and buffer (10 mM glycine, pH 10, 2 mM EDTA) solutions to the aliquots to reach a 2.5-fold dilution of OmpA and urea concentrations in the range of interest.
5. Incubate reactions overnight at 37 °C.
6. Terminate reactions by mixing the samples with an equal volume of 0.125 M Tris buffer, pH 6.8, 4% SDS, 20% glycerol, and 10% 2-mercaptoethanol at room temperature.

7. Without boiling, load equilibrated samples on 12.5% SDS polyacrylamide gels, run electrophoresis, and stain with Coomassie Blue.
8. Measure fractions folded and unfolded, F and U, by densitometry and fit to two-state equilibrium folding equation:

$$[\mathrm{U}] = \frac{([\mathrm{U}] + [\mathrm{F}])\ \exp(\{m[\mathrm{urea}] - \Delta G^{\circ}_{\mathrm{H2O}}\}/RT)}{1 + \exp(\{m[\mathrm{urea}] - \Delta G^{\circ}_{\mathrm{H2O}}\}/RT)} \quad (1)$$

The fit parameters are the free energy of unfolding, $\Delta G^{\circ}_{\mathrm{H2O}}$, and the *m*-value.

An example of a reversible unfolding/refolding reaction using this protocol is shown in Figure 28.7.

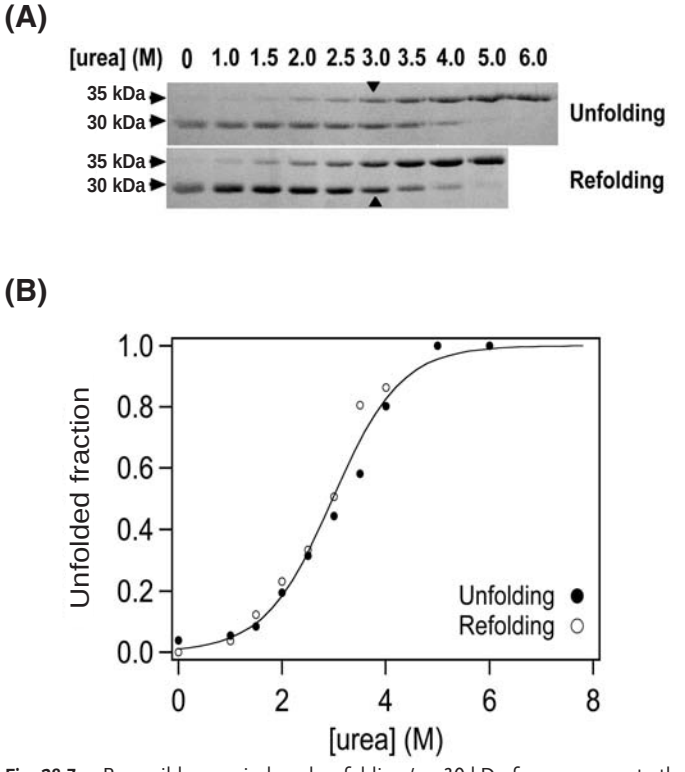

Fig. 28.7. Reversible urea-induced unfolding/refolding of OmpA in lipid bilayers composed of 92.5% phosphatidylcholine ($C_{16:0}C_{18:1}$PC) and 7.5% phosphatidylglycerol ($C_{16:0}C_{18:1}$PG) at pH 10 and 37 °C monitored by the SDS-PAGE shift assay. A) Unfolding (upper panel) and refolding (lower panel) of OmpA. The 30-kDa form represents the native state, and the 35-kDa form represents denatured states. B) Unfolded fractions as a function of urea concentration estimated from A. The data are fitted with the two-state equilibrium folding equation Eq. (1).

28.9.2

Tryptophan Fluorescence and Time-resolved Distance Determination by Tryptophan Fluorescence Quenching

Steady-state and time-resolved Trp fluorescence spectroscopy have been widely used to the study folding and stability of membrane proteins. The relatively large spectral shifts and fluorescence intensity changes of Trps as a result of changing local environments have made Trp fluorescence an excellent tool for such studies. Figure 28.8A shows typical fluorescence spectral changes of OmpA–lipid complexes equilibrated in various urea concentrations. The unfolding transition curves are constructed as a function of urea by parametrizing each spectrum to an average emission wavelength:

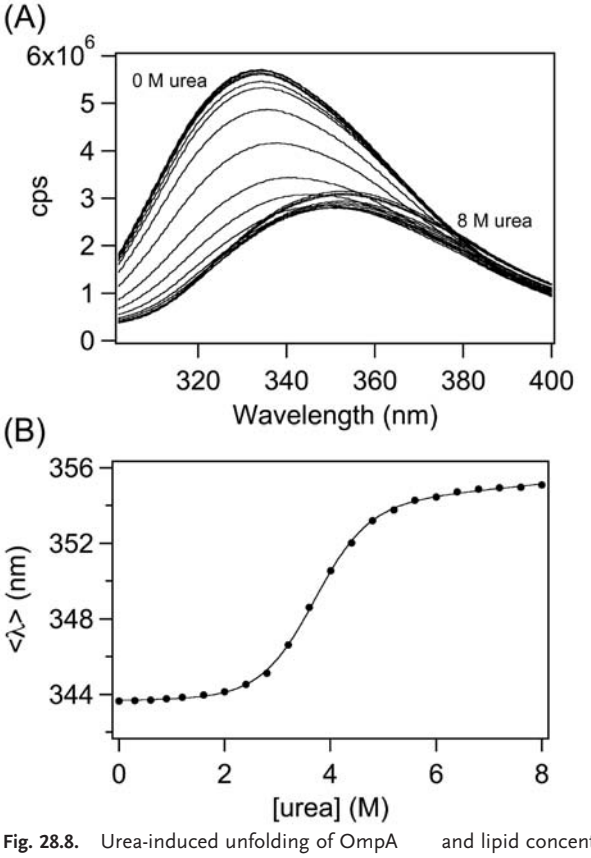

Fig. 28.8. Urea-induced unfolding of OmpA in lipid bilayers composed of 92.5% phosphatidylcholine ($C_{16:0}C_{18:1}$PC) and 7.5% phosphatidylglycerol ($C_{16:0}C_{18:1}$PG) at pH 10 and 37 °C monitored by Trp fluorescence. A) Fluorescence emission spectra of OmpA as a function of urea concentration. The protein and lipid concentrations were 1.2 μM and 10 mM, respectively, and the urea concentration ranged from 0 to 8 M (left to right). B) Unfolding transition monitored by the average emission wavelength $\langle\lambda\rangle$ (Eq. (2)) calculated from the spectra in A and fitted with the two-state equilibrium folding equation Eq. (3).

$$\langle\lambda\rangle = \frac{\sum_i (F_i\lambda_i)}{\sum_i (\lambda_i)} \tag{2}$$

and fitting the data to the two-state equilibrium folding equation:

$$\langle\lambda\rangle = \frac{\langle\lambda\rangle_F + \langle\lambda\rangle_U \frac{1}{Q_R} \exp[m([\text{denaturant}] - C_m)/RT]}{1 + \frac{1}{Q_R} \exp[m([\text{denaturant}] - C_m)/RT]} \tag{3}$$

Inclusion of the weighting factor $Q_R =$ (total fluorescence intensity in native state)/(total fluorescence intensity in denatured state) makes $\langle\lambda\rangle$ proportional to species concentrations and therefore permits $\langle\lambda\rangle$ to be taken as a measure of the fraction of folded protein [112]. The free energy of unfolding is calculated from the fitted denaturant concentration at the mid-point of the transition, C_m, and the m-value using $\Delta G^\circ_{H2O} = mC_m$. Figure 28.8B shows an example of equilibrium unfolding of OmpA measured by Trp fluorescence.

The degree of solvent exposure of Trp residues of membrane proteins and thus their degree of immersion in the lipid bilayer is often determined by the effect of polar (e.g., cesium, iodide, bromide, acrylamide) or nonpolar (e.g., molecular oxygen) quenchers on the fluorescence spectra. A more informative method to determine the depth of Trps in membranes involves the use of spin-labeled or brominated lipids as quenchers. Phospholipids selectively labeled with bromines or spin labels in various positions of the acyl chains are commercially available. Depths in membranes of specific Trps are often measured by using a whole set of these lipids and analyzing the resulting spectra with the ''parallax'' or ''distribution analysis'' methods [113]. These steady-state methods may be extended to measure the time dependence of Trp positions and more specifically the translocation of Trps across lipid bilayers during the folding of membrane proteins [106]. Reliable distances in membranes are obtained by the time-resolved distance determination by fluorescence quenching (TDFQ) technique because the positions and distributions of the bromines in the bilayer are known from X-ray diffraction studies [114].

28.9.2.1 TDFQ Protocol for Monitoring the Translocation of Tryptophans across Membranes

1. Mix solutions of DOPC and one each of DOPC plus 4,5-, 6,7-, 9,10-, and 11,12-diBrPC, respectively, at molar ratios of 7:3 (DOPC:m,n-diBrPC) in chloroform.
2. Dry the mixtures on the bottom of test tubes under a stream of nitrogen and further in a desiccator under a high vacuum overnight.
3. Disperse dried lipids in 1.0 mL buffer (10 mM glycine, pH 8.5, 1 mM EDTA, 150 mM NaCl) to a lipid concentration of 2 mg mL^{-1}.
4. Prepare SUVs by sonication of the lipid dispersions for 50 min using the microtip of a Branson ultrasonifier at 50% duty cycle in an ice/water bath.

5. Remove titanium dust by low-speed centrifugation (e.g., at 6000 rpm for 10 min on a tabletop centrifuge) and store vesicles at 4 °C overnight for equilibration.
6. Measure blank fluorescence emission spectra for each vesicle solution at 1 mM lipid concentration and at the controlled temperature of interest with instrument settings for Trp fluorescence (e.g., excitation at 290 nm with 2-nm slit; emission from 310 to 370 nm with 5-nm slit).
7. Add small volume of concentrated OmpA (stock is typically 20–50 mg mL^{-1}) in 8 M urea to give a final OmpA concentration of 1.4 μM and mix well.
8. Record fluorescence spectra with above settings every 2–5 min. (The first spectrum can be taken 30 s after mixing.) Repeat measurements for each of the five vesicle solutions.
9. Measure fluorescence intensities of smoothed spectra at 330 nm as a function of time and normalize values for each of the quenching vesicles to the corresponding values of vesicles without lipid quencher.
10. Fit normalized fluorescence intensities to the Gaussian distribution equation:

$$\frac{F(d_Q)}{F_0} = \exp\left\{-\frac{S}{\sigma\sqrt{2\pi}}\exp\left\{-\frac{1}{2}\left(\frac{d_Q - d_{Trp}}{\sigma}\right)^2\right\}\right\} \quad (4)$$

F_0 and $F(d_Q)$ are the fluorescence intensities in the absence and presence of a particular m,n-diBrPC quencher. d_Q are the known distances of the quenchers from the bilayer center, and d_{Trp} is the distance of the fluorophor from the center. The dispersion σ is a measure of the width of the distribution of the fluorophor in the membrane, which in turn depends on the sizes and thermal fluctuations of the fluorophors and quenchers. S is a function of the quenching efficiency and quencher concentration in the membrane. The fits yield d_{Trp}, σ, and S.
11. Plot d_{Trp} and σ as a function of time.

The accuracy of the distribution analysis could be improved if more than four membrane-bound quenchers at different depths in the membrane and/or a quencher attached to the polar lipid headgroup were used. Figure 28.9 shows two examples of Trp movements of OmpA into and across lipid bilayers, respectively, measured by TDFQ using four different bromine quenchers in the acyl chain region.

28.9.3 Circular Dichroism Spectroscopy

Circular dichroism (CD) refers to the differential absorption of the right- and left-handed circular polarized lights by a sample that exhibits molecular asymmetry. Far-UV CD spectroscopy has been used to characterize the secondary structures of

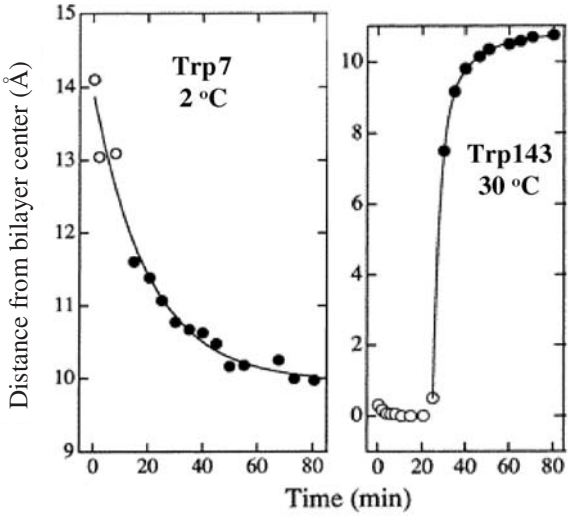

Fig. 28.9. Measurement of the translocation rate of single trypophans of OmpA into and across lipid bilayers composed of phosphatidylcholine ($diC_{18:1}PC$) by time-resolved fluorescence quenching (TDFQ). A) Time course of the movement of Trp7 of OmpA into lipid bilayer at 2 °C. This Trp stays on the *cis* side and does not cross the bilayer. B) Time course of the movement of Trp143 across the lipid bilayer at 30 °C. This Trp translocates across the bilayer with a time constant of 3.3 min at 30 °C. The solid lines are fits of the data to exponential functions. Adapted from Ref. [107].

proteins including membrane proteins because the differential amide absorptions of α-helices, β-sheets, turns, and random coils in the range between 180 and 250 nm yield characteristic CD signals that can be used to determine their secondary structure compositions. The CD spectra of α-helices exhibit minima at 208 and 222 nm. Beta-sheets show a weaker minimum at 216 nm. Both of these structures exhibit maxima just below 200 nm, but the spectra of random coils are negative in the entire accessible far-UV spectral range with a minimum just below 200 nm.

CD spectroscopy of membrane proteins is difficult because the proteo-liposomes, which are necessary for functional reconstitution of membrane proteins, are strong scatterers of UV light resulting in overwhelming spectral noise. Therefore, only SUVs, which are typically obtained by sonication and which are typically 30 nm in diameter, or protein–detergent mixed micelles are recommended for recording CD spectra of membrane proteins. Even with these samples, CD spectra cannot usually be recorded to below 200 nm, which limits the accuracy of secondary structure determinations. Good results can be obtained with 0.05-mm pathlength cells and protein concentrations of 0.5–1.0 mg mL^{-1} in buffers that do not absorb in the far UV. Relatively crude estimates of secondary structure content can be made from the spectral shapes in the 200–240 nm spectral region and using the follow-

ing rule of thumb values for 100% secondary structure: $\theta_{222} = -30\,000$ deg cm^2 dmol^{-1} for α-helix and $\theta_{216} = -15\,000$ deg cm^2 dmol^{-1} for β-sheet.

28.9.4 Fourier Transform Infrared Spectroscopy

Fourier transform infrared (FTIR) spectroscopy is a useful technique for determining the conformation and orientation of membrane proteins and lipids in lipid bilayers. The method has no light scattering artifacts and works well with turbid and even solid samples. Since the absorption bands of liquid water overlap with several bands that are of interest in protein and membrane spectroscopy, it is convenient to work in D_2O solutions. In conventional transmittance spectroscopy, the strong absorbances of residual H_2O and bulk D_2O are minimized by using high protein concentrations and measuring cells of short path lengths.

Another very convenient method for suppressing unwanted water signals is to record attenuated total reflection (ATR) FTIR spectra. In this method, the IR beam is reflected within an IR-transparent internal reflection element such as a germanium plate. An evanescent wave of the same frequency as the incoming IR light builds up at the germanium–water interface. The electric field of the evanescent wave decreases exponentially away from the interface with a characteristic decay length, d_p, which is on the order of a few hundred nanometers in typical applications. This wave probes with high sensitivity samples that are adsorbed at the germanium–water interface such as a reconstituted protein–lipid bilayer. Since absorptions from the bathing buffer solution are greatly suppressed in this surface-sensitive technique, small amounts of H_2O in D_2O are not a problem in ATR-FTIR spectroscopy. An additional advantage is that the orientation of membrane proteins and lipids in the bilayers can be obtained by using polarized light. Microgram quantities of membrane proteins in single supported bilayers are sufficient to record high quality spectra. Finally, buffer conditions can be varied in situ using a perfusable ATR measuring cell. A comprehensive description of ATR-FTIR spectroscopy on supported membranes has appeared [115].

The most widely used conformation-sensitive vibrational mode of proteins is the amide I′ band (1600–1700 cm^{-1}). The secondary structures of proteins are correlated with the amide I′ frequencies, which enables the assignment of the major secondary structure elements of proteins by spectral decomposition of this band (α-helix: 1648–1660 cm^{-1}; parallel and antiparallel β-sheet: 1625–1640 cm^{-1}; antiparallel β-sheet: 1675–1695 cm^{-1}; aggregated strands: 1610–1628 cm^{-1}; turns: 1660–1685 cm^{-1}; unordered structures: 1652–1660 cm^{-1} in H_2O and 1640–1648 cm^{-1} in D_2O). The peak corresponding to the α-helix is often not well resolved from nearby peaks of turns and unordered structures. However, β-sheet can usually be reliably assigned due to its distinctive components at about 1630 cm^{-1} and 1690 cm^{-1}.

The following bands of lipid vibrations are well separated from protein amide bands and are frequently analyzed in studies of protein–lipid interactions: sym-

metric and antisymmetric methylene stretches at 2850 cm^{-1} and 2920 cm^{-1}, respectively, and ester carbonyl stretch at 1730 cm^{-1}.

28.9.4.1 Protocol for Obtaining Conformation and Orientation of Membrane Proteins and Peptides by Polarized ATR-FTIR Spectroscopy

1. Fill liquid ATR cell containing germanium plate with D_2O buffer (e.g., 5 mM HEPES/10 mM MES pH 7.3, 135 mM NaCl) and record FTIR spectra at vertical and horizontal polarizations with a spectral resolution of 2 cm^{-1} to obtain reference spectra.
2. Deposit lipid monolayer on germanium plate by the Langmuir-Blogett technique at 32 mN m^{-1}.
3. Add proteoliposomes (typically about 0.5 mM lipid and 20 μg mL^{-1} protein in same H_2O buffer) to supported monolayer in assembled ATR cell and incubate with gentle shaking for 1 h. The proteoliposomes will fuse with the monolayer during this time and form a complete planar bilayer on the surface of the germanium plate.
4. Flush excess proteoliposomes out of measuring cell with 10 volumes of D_2O buffer. This step also exchanges H_2O for D_2O.
5. Incubate exchanged sample for 1 h at room temperature to equilibrate labile amide protons with deuteriums. This is done in the FTIR spectrometer and the spectrometer compartment is purged with dry air or nitrogen at the same time to remove water vapor.
6. Collect the sample spectra using the same experimental settings as reference spectra at vertical and horizontal polarizations.
7. Ratio sample and reference spectra and calculate absorption spectra.

The following steps describe a recipe to extract secondary structure information from complex (overlapped) amide I′ bands:

8. Calculate second-derivative spectra by differentiation with 11-point Savitsky-Golay smoothing. The minima in the second derivatives indicate possible component peaks.
9. Using only prominent and clearly identified component peaks as starting points, carry out spectral decomposition by least-squares fitting with Gaussian component line shapes. Use as few components as possible to reproduce the experimental line shape. Accept only fits that keep the Gaussian peak components centered close to the component frequencies that were identified in the second derivative spectra.
10. Integrate spectral components, assign to secondary structures, and calculate area fractions to indicate respective secondary structure fractions.

The following steps describe how to obtain orientations of secondary structure elements of proteins and orientations (order parameters) of lipid chemical groups:

11. Calculate ATR dichroic ratio for the amide I′ bands and symmetric or antisymmetric methylene stretching band intensities according to

$$R_{\text{amideI}}^{\text{ATR}} = \frac{\int A_{//}(\nu)\,\mathrm{d}\nu}{\int A_{\perp}(\nu)\,\mathrm{d}\nu} \tag{5}$$

and

$$R_{\text{Lipid}}^{\text{ATR}} = \frac{A_{//}(\nu)}{A_{\perp}(\nu)} \tag{6}$$

12. The order parameter is defined as

$$S_{\theta} = (3\langle\cos^2\theta\rangle - 1)/2 \tag{7}$$

where θ is the angle between the axis of rotational symmetry of an axially symmetric molecule (long axis of the lipid, α-helix, β-barrel, etc.) and the normal to the germanium plate and the angular brackets denote a time and space average over all angles in a given sample.

13. Calculate the order parameter for an amide I′ band component as:

$$S_{\text{amideI}} = \frac{E_{\text{x}}^2 - R_{\text{amideI}}^{\text{ATR}} E_{\text{y}}^2 + E_{\text{z}}^2}{E_{\text{x}}^2 - R_{\text{amideI}}^{\text{ATR}} E_{\text{y}}^2 - 2E_{\text{z}}^2} \tag{8}$$

where E_{x}, E_{y}, and E_{z} are the electric field amplitudes at the germanium–buffer interface. For a 45° germanium plate with a thin attached membrane in D_2O buffer $E_{\text{x}}^2 = 1.9691$, $E_{\text{y}}^2 = 2.2486$, and $E_{\text{z}}^2 = 1.8917$. For α-helices, where the angle between the amide I′ transition dipole moment and the helix axis is 39°, Eq. (8) transforms to

$$S_{\text{H}} = 2.46\frac{E_{\text{x}}^2 - R_{\text{amideI}}^{\text{ATR}} E_{\text{y}}^2 + E_{\text{z}}^2}{E_{\text{x}}^2 - R_{\text{amideI}}^{\text{ATR}} E_{\text{y}}^2 - 2E_{\text{z}}^2} \tag{9}$$

S_{H} is the order parameter that describes the helix orientation relative to the germanium plate and membrane normal. For β-sheets, there is no helical symmetry and Eq. (8) describes the order parameter of the transition dipole moment of the amide I′ band, which roughly coincides with the order parameter of the amide carbonyl bond orientations.

14. Lipid order parameters are obtained from the experimental dichroic ratios of the symmetric and/or antisymmetric methylene stretch vibrations:

$$S_{\text{L}} = -2\frac{E_{\text{x}}^2 - R_{\text{L}}^{\text{ATR}} E_{\text{y}}^2 + E_{\text{z}}^2}{E_{\text{x}}^2 - R_{\text{L}}^{\text{ATR}} E_{\text{y}}^2 - 2E_{\text{z}}^2} \tag{10}$$

Lipid order parameters should always be recorded along with those of embedded proteins because they provide essential controls of the bilayer quality.

Results on protein orientations are only meaningful if lipid orientations (to the germanium plate) are satisfactory.

Lipid-to-protein ratios in supported bilayers:

15. Use the following form of Beer-Lambert's law modified for polarized ATR spectroscopy to calculate the lipid/protein ratio in supported bilayers [116]:

$$L/P = 0.208(n_{\mathrm{res}} - 1)\frac{1 - S_{\mathrm{amideI}}}{1 + S_{\mathrm{L}}/2}\frac{\int_{2800}^{2980} A_{\perp}(\nu_{\mathrm{L}})\,\mathrm{d}\nu}{\int_{1600}^{1690} A_{\perp}(\nu_{\mathrm{amideI}})\,\mathrm{d}\nu} \tag{11}$$

where n_{res} is the number of residues in the polypeptide and ν_{L} and ν_{amideI} are the wavenumbers of the lipid methylene stretch and the protein amide I′ vibrations, respectively.

Acknowledgments

We thank members of the Tamm laboratory, past and present, for their contributions and many discussions. The work from our laboratory was supported by grants from the National Institutes of Health.

References

1 Dill, K. A. (1990). Dominant forces in protein folding. *Biochemistry* 29, 7133–7155.
2 Baldwin, R. L. (1999). Protein folding from 1962 to 1982. *Nature Struct. Biol.* 6, 814–817.
3 Fersht, A. (1999). *Structure and Mechanism in Protein Science*. Freeman, New York.
4 Wallin, E. & von Heijne, G. (1998). Genome-wide analysis of integral membrane proteins from eubacterial, archaean, and eukaryotic organisms. *Protein Sci.* 7, 1029–1038.
5 Haltia, T. & Freire, E. (1995). Forces and factors that contribute to the structural stability of membrane proteins. *Biochim. Biophys. Acta* 1228, 1–27.
6 Van den Berg, B., Clemons, W. M., Jr., Collinson, I., Kodis, Y., Hartman, E., Harrison, S. C. & Rapoport, T. A. (2004). X-ray structure of a protein-conducting channel. *Nature* 427, 37–44.
7 White, S. H. & Wiener, M. C. (1996). The liquid-crystallographic structure of fluid lipid bilayer membranes. In *Biological Membranes: A Molecular Perspective from Computation and Experiment* (Merz, K. M. & Roux, B., eds), pp. 127–144. Birkhauser, Boston.
8 Nagle, J. F. & Tristram-Nagle, S. (2000). Structure of lipid bilayers. *Biochim. Biophys. Acta* 1469, 159–195.
9 Tanford, C. (1980). *The Hydrophobic Effect*, 2nd edn. Wiley, New York.
10 Marsh, D. (1996). Lateral pressure in membranes. *Biochim. Biophys. Acta* 1286, 183–223.
11 Cantor, S. C. (1999). Lipid composition and the lateral pressure

profile in bilayers. *Biophys. J.* 76, 2625–2639.

12 Brown, M. F., Thurmond, R. L., Dodd, S. W., Otten, D. & Beyer, K. (2002). Elastic deformation of membrane bilayers probed by deuterium NMR relaxation. *J. Am. Chem. Soc.* 124, 8471–8484.

13 Jayasinghe, S., Hristova, K. & White, S. H. (2001). Energetics, stability, and prediction of transmembrane helices. *J. Mol. Biol.* 312, 927–934.

14 Ladokhin, A. S. & White, S. H. (1999). Folding of amphipathic α-helices on membranes: energetics of helix formation by melittin. *J. Mol. Biol.* 285, 1363–1369.

15 Wieprecht, T., Apostolov, O., Beyermann, M. & Seelig, J. (1999). Thermodynamics of the α-helix-coil transition of amphipathic peptides in a membrane environment: implications for the peptide-membrane binding equilibrium. *J. Mol. Biol.* 294, 785–794.

16 Li, Y., Han, X. & Tamm, L. K. (2003). Thermodynamics of fusion peptide-membrane interactions. *Biochemistry* 42, 7245–7251.

17 Wimley, W. C., Hristova, K., Ladokhin, A. S., Silvestro, L., Axelsen, P. H. & White, S. H. (1998). Folding of β-sheet membrane proteins: A hydrophobic hexapeptide model. *J. Mol. Biol.* 277, 1091–1110.

18 BenTal, N., Sitkoff, D., Topol, I. A., Yang, A.-S., Burt, S. K. & Honig, B. (1997). Free energy of amide hydrogen bond formation in vacuum, in water, and in liquid alkane solution. *J. Phys. Chem. B* 101, 450–457.

19 Wimley, W. C. & White, S. H. (1996). Experimentally determined hydrophobicity scale for proteins at membrane interfaces. *Nature Struct. Biol.* 3, 842–848.

20 Wimley, W. C., Creamer, T. P. & White, S. H. (1996). Solvation energies of amino acid side chains and backbone in a family of host-guest pentapeptides. *Biochemistry* 35, 5109–5124.

21 Dwyer, J. J., Gittis, A. G., Karp, D. A., Lattman, E. E., Spencer, D. S., Stites, W. E. & Garcia-Moreno, E. B. (2000). High apparent dielectric constants in the interior of a protein reflect water penetration. *Biophys. J.* 79, 1610–1620.

22 Killian, J. A. & von Heijne, G. (2000). How protein adapt to a membrane-water interface. *Trends Biochem. Sci.* 25, 429–434.

23 Yau, W.-M., Wimley, W. C., Gawrisch, K. & White, S. H. (1998). The preference of tryptophan for membrane interfaces. *Biochemistry* 37, 14713–14718.

24 Schulz, G. E. (2002). The structure of bacterial outer membrane proteins. *Biochim. Biophys. Acta* 1565, 308–317.

25 Gabriel, K., Buchanan, S. K. & Lithgow, T. (2001). The alpha and the beta: protein translocation across mitochondrial and plastid outer membranes. *Trends Biochem. Sci.* 26, 36–40.

26 Paschen, S. A., Waizenegger, T., Stan, T., Preuss, M., Cyrklaff, M., Hell, K., Rapaport, D. & Neupert, W. (2003). Evolutionary conservation of biogenesis of β-barrel membrane proteins. *Nature* 426, 862–866.

27 Danese, P. N. & Silhavy, T. J. (1998). Targeting and assembly of perplasmic and outer-membrane proteins in *Escherichia coli*. *Annu. Rev. Genet.* 32, 59–94.

28 Wimley, W. C. (2002). Toward genomic identification of β-barrel membrane proteins: Composition and architecture of known structures. *Protein Sci.* 11, 301–312.

29 Chen, R. & Henning, U. (1996). A periplasmic protein (Skp) of *Escherichia coli* selectively binds a class of outer membrane proteins. *Mol. Microbiol.* 19, 1287–1294.

30 Lazar, S. W. & Kolter, R. (1996). SurA assists the folding of *Escherichia coli* outer membrane proteins. *J. Bacteriol.* 178, 1770–1773.

31 Koebnik, R., Locher, K. P. & van Gelder, P. (2000). Structure and function of bacterial outer membrane proteins: barrels in a nutshell. *Mol. Microbiol.* 37, 239–253.

32 Cowan, S. W., Schirmer, T., Rummel, G., Steiert, M., Ghosh, R., Pauptit, R. A., Jansonius, J. N. & Rosenbusch, J. P. (1992). Crystal structures explain functional properties of two E. coli porins. *Nature* 358, 727–733.

33 Weiss, M. S., Abele, U., Weckesser, J., Welte, W., Schiltz, E. & Schulz, G. E. (1991). Molecular architecture and electrostatic properties of a bacterial porin. *Science* 254, 1627–1630.

34 Schirmer, T., Keller, T. A., Wang, Y. F. & Rosenbusch, J. P. (1995). Structural basis for sugar translocation through maltoporin channels in 3.1 A resolution. *Science* 267, 512–514.

35 Forst, D., Welte, W., Wacker, T. & Diederichs, K. (1998). Structure of the sucrose-specific porin ScrY from *Salmonella typhimurium* and its complex with sucrose. *Nature Struct. Biol.* 5, 37–46.

36 Ferguson, A. D., Hofmann, E., Coulton, J. W., Diederichs, K. & Welte, W. (1998). Siderophore-mediated iron transport: crystal structure of FhuA with bound lipopolysaccharide. *Science* 282, 2215–2220.

37 Locher, K. P., Rees, B., Koebnik, R., Mitschler, A., Moulinier, L. & Rosenbusch, J. P. (1998). Transmembrane signaling across the ligand-gated FhuA receptor: crystal structures of free and ferrichrome-bound states reveal allosteric changes. *Cell* 95, 771–778.

38 Buchanan, S. K., Smith, B. S., Venkatramani, L. et al. (1999). Crystal structure of the outer membrane active transporter FepA from *Escherichia coli*. *Nature Struct. Biol.* 6, 56–63.

39 Ferguson, A. D., Chakraborty, R., Smith, B. S., Esser, L., van der Helm, D. & Deisenhofer, J. (2002). Structural basis of gating by the outer membrane transporter FecA. *Science* 295, 1658–1659.

40 Chimento, D. P., Mohanty, A. K., Kadner, R. J. & Wiener, M. C. (2003). Substrate-induced transmembrane signaling in the cobalamin transporter BtuB. *Nature Struct. Biol.* 10, 394–401.

41 Snijder, J. J., Ubarretxena-Balandia, I., Blaauw, M. et al. (1999). Structural evidence for dimerization-regulated activation of an integral membrane protein phospholipase. *Nature* 401, 717–721.

42 Vogt, J. & Schulz, G. E. (1999). The structure of the outer membrane protein OmpX from *Escherichia coli* reveals possible mechanisms of virulence. *Structure* 7, 1301–1309.

43 Pautsch, A. & Schulz, G. E. (1998). Structure of the outer membrane protein A transmembrane domain. *Nature Struct. Biol.* 5, 1013–1017.

44 Sonntag, I., Schwarz, H., Hirota, Y. & Henning, U. (1978). Cell envelope and shape of *Escherichia coli*: multiple mutants missing the outer membrane lipoprotein and other major outer membrane proteins. *J. Bacteriol.* 136, 280–285.

45 Arora, A., Abildgaard, F., Bushweller, J. H. & Tamm, L. K. (2001). Structure of outer membrane protein A transmembrane domain by NMR spectroscopy. *Nature Struct. Biol.* 8, 334–338.

46 Koebnik, R. (1999). Membrane assembly of the *Escherichia coli* outer membrane protein OmpA: Exploring sequence constraints on transmembrane β-strands. *J. Mol. Biol.* 285, 1801–1810.

47 Koebnik, R. & Krämer, L. (1995). Membrane assembly of circularly permuted variants of the E. coli outer membrane protein OmpA. *J. Mol. Biol.* 250, 617–626.

48 Dornmair, K., Kiefer, H. & Jähnig, F. (1990). Refolding of an integral membrane protein. OmpA of *Escherichia coli*. *J. Biol. Chem.* 265, 18907–18911.

49 Surrey, T. & Jähnig, F. (1992). Refolding and oriented insertion of a membrane protein into a lipid bilayer. *Proc. Natl Acad. Sci. USA* 89, 7457–7461.

50 Hong, H. & Tamm, L. K. (2004). Elastic coupling of integral membrane

protein stability to lipid bilayer forces. *Proc. Natl Acad. Sci. USA* 101, 4065–4070.

51 Schweizer, M., Hindennach, I., Garten, W. & Henning, U. (1978). Major proteins of the *Escherichia coli* outer cell envelope membrane. Interaction of protein II with lipopolysaccharide. *Eur. J. Biochem.* 82, 211–217.

52 Arora, A., Rinehart, D., Szabo, G. & Tamm, L. K. (2000). Refolded outer membrane protein A of *Escherichia coli* forms ion channels with two conductance states in planar lipid bilayers. *J. Biol. Chem.* 275, 1594–1600.

53 Gruner, S. (1985). Intrinsic curvature hypothesis for biomembrane lipid composition: a role for nonbilayer lipids. *Proc. Natl Acad. Sci. USA* 82, 3665–3669.

54 Bonhivers, M., Desmadril, M., Moeck, G. S., Boulanger, P., Colomer-Pallas, A. & Letelier, L. (2001). Stability studies of FhuA, a two-domain outer membrane protein from *Escherichia coli*. *Biochemistry* 40, 2606–2613.

55 Klug, C. S., Su, W., Liu, J., Klebba, P. E. & Feix, J. B. (1995). Denaturant unfolding of the ferric enterobactin receptor and ligand-induced stabilization studied by site-directed spin labeling. *Biochemistry* 34, 14230–14236.

56 Klug, C. S. & Feix, J. B. (1998). Guanidine hydrochloride unfolding of a transmembrane β-strand in FepA using site-directed spin labeling. *Protein Sci.* 7, 1469–1476.

57 Ackerman, M. S. & Shortle, D. (2001). Persistence of native-like topology in a denatured protein in 8 M urea. *Science* 293, 487–489.

58 Surrey, T., Schmid, A. & Jähnig, F. (1996). Folding and membrane insertion of the trimeric β-barrel protein OmpF. *Biochemistry* 35, 2283–2288.

59 Phale, P. S., Phillippsen, A., Kiefhaber, T., Koebnik, R., Phale, V. P., Schirmer, T. & Rosenbusch, J. P. (1998). Stability of trimeric OmpF porin: The contributions of the latching loop L2. *Biochemistry* 37, 15663–15670.

60 Popot, J.-L. & Engelman, D. M. (1990). Membrane protein folding and oligomerization: the two-stage model. *Biochemistry* 29, 4031–4037.

61 Popot, J. L., Gerchman, S. E. & Engelman, D. M. (1987). Refolding of bacteriorhodopsin in lipid bilayers. A thermodynamically controlled two-stage process. *J. Mol. Biol.* 198, 655–676.

62 White, S. H. & Wimley, W. C. (1999). Membrane protein folding and stability: Physical principles. *Annu. Rev. Biophys. Biomol. Struct.* 28, 319–365.

63 Engelman, D. M., Chen, Y., Chin, C.-N. et al. (2003). Membrane protein folding: beyond the two stage model. *FEBS Lett.* 555, 122–125.

64 Huang, K. S., Bayley, H., Liao, M. J., London, E. & Khorana, H. G. (1981). Refolding of an integral membrane protein. Denaturation, renaturation, and reconstitution of intact bacteriorhodopsin and two proteolytic fragments. *J. Biol. Chem.* 256, 3802–3809.

65 London, E. & Khorana, H. G. (1982). Denaturation and renaturation of bacteriorhodopsin in detergents and lipid-detergent mixtures. *J. Biol. Chem.* 257, 7003–7011.

66 Booth, P. J., Flitsch, S. L., Stern, L. J., Greenhalgh, D. A., Kim, P. S. & Khorana, H. G. (1995). Intermediates in the folding of the membrane protein bacteriorhodopsin. *Nature Struct. Biol.* 2, 139–143.

67 Lu, H. & Booth, P. J. (2000). The final stages of folding of the membrane protein bacteriorhodopsin occur by kinetically indistinguishable parallel folding paths that are mediated by pH. *J. Mol. Biol.* 299, 233–243.

68 Lau, F. W. & Bowie, J. U. (1997). A method for assessing the stability of a membrane protein. *Biochemistry* 36, 5884–5892.

69 Faham, S., Yang, D., Bare, E., Yohannan, S., Whitelegge, J. P. &

Bowie, J. U. (2004). Side-chain contributions to membrane protein structure and stability. *J. Mol. Biol.* 335, 297–305.

70 Lemmon, M. A., Flanagan, J. M., Treutlein, H. R., Zhang, J. & Engelman, D. M. (1992). Sequence specificity in the dimerization of transmembrane alpha-helices. *Biochemistry* 31, 12719–12725.

71 Senes, A., Gerstein, M. & Engelman, D. M. (2000). Statistical analysis of amino acid patterns in transmembrane helices: the GxxxG motif occurs frequently and in association with beta-branched residues at neighboring positions. *J. Mol. Biol.* 296, 921–936.

72 Bowie, J. U. (1997). Helix packing in membrane proteins. *J. Mol. Biol.* 272, 780–789.

73 Popot, J. L. & Engelman, D. M. (2000). Helical membrane protein folding, stability, and evolution. *Annu. Rev. Biochem.* 69, 881–922.

74 Fleming, K. G., Ackerman, A. L. & Engelman, D. M. (1997). The effect of point mutations on the free energy of transmembrane alpha-helix dimerization. *J. Mol. Biol.* 272, 266–275.

75 Fleming, K. G. & Engelman, D. M. (2001). Specificity in transmembrane helix-helix interactions can define a hierarchy of stability for sequence variants. *Proc. Natl Acad. Sci. USA* 98, 14340–14344.

76 Zhou, F. X., Cocco, M. J., Russ, W. P., Brünger, A. T. & Engelman, D. M. (2000). Interhelical hydrogen bonding drives strong interactions in membrane proteins. *Nature Struct. Biol.* 7, 154–160.

77 Choma, C., Gratkowski, H., Lear, J. D. & DeGrado, W. F. (2000). Asparagine-mediated self-association of a model transmembrane helix. *Nature Struct. Biol.* 7, 161–166.

78 Gratkowski, H., Lear, J. D. & DeGrado, W. F. (2001). Polar side chains drive the association of model transmembrane peptides. *Proc. Natl Acad. Sci. USA* 98, 880–885.

79 Zhou, F. X., Merianos, H. J., Brünger, A. T. & Engelman, D. M. (2001). Polar residues drive association of polyleucine transmembrane helices. *Proc. Natl Acad. Sci. USA* 98, 2250–2255.

80 Senes, A., Ubarretxena-Belandia, I. & Engelman, D. M. (2001). The Calpha $-H\cdots O$ hydrogen bond: a determinant of stability and specificity in transmembrane helix interactions. *Proc. Natl Acad. Sci. USA* 98, 9056–9061.

81 Yohannan, S., Faham, S., Yang, D., Grosfeld, D., Chamberlain, A. K. & Bowie, J. U. (2004). A C(alpha)–$H\cdots O$ hydrogen bond in a membrane protein is not stabilizing. *J. Am. Chem. Soc.* 126, 2284–2285.

82 Doyle, D. A., Morais Cabral, J., Pfuetzner, R. A. et al. (1998). The structure of the potassium channel: molecular basis of K+ conduction and selectivity. *Science* 280, 69–77.

83 Stowell, M. H. B. & Rees, D. C. (1995). Structure and stability of membrane proteins. *Adv. Protein Chem.* 46, 279–311.

84 Jacobs, R. E. & White, S. H. (1989). The nature of the hydrophobic binding of small peptides at the bilayer interface: implications for the insertion of transbilayer helices. *Biochemistry* 28, 3421–3437.

85 Vogel, H. (1981). Incorporation of melittin into phosphatidylcholine bilayers. Study of binding and conformational changes. *FEBS Lett.* 134, 37–42.

86 Kaiser, E. T. & Kezdy, F. J. (1984). Amphiphilic secondary structure: design of peptide hormones. *Science* 223, 249–255.

87 Briggs, M. S., Cornell, D. G., Dluhy, R. A. & Gierasch, L. M. (1986). Conformations of signal peptides induced by lipids suggest initial steps in protein export. *Science* 233, 206–208.

88 Tamm, L. K. (1991). Membrane insertion and lateral mobility of synthetic amphiphilic signal peptides in lipid model membranes. *Biochim. Biophys. Acta* 1071, 123–148.

89 Lear, J. D. & DeGrado, W. F. (1987). Membrane binding and confor-

mational properties of peptides representing the NH_2 terminus of influenza HA-2. *J. Biol. Chem.* 262, 6500–6505.

90 Rodionova, N. A., Tatulian, S. A., Surrey, T., Jähnig, F. & Tamm, L. K. (1995). Characterization of two membrane-bound forms of OmpA. *Biochemistry* 34, 1921–1929.

91 Vecsey-Semjen, B., Lesieur, C., Mollby, R. & van der Goot, F. G. (1997). Conformational changes due to membrane binding and channel formation by staphylococcal alpha-toxin. *J. Biol. Chem.* 272, 5709–5717.

92 Terzi, E., Hölzemann, G. & Seelig, J. (1994). Reversible random coil-beta-sheet transition of the Alzheimer beta-amyloid fragment (25–35). *Biochemistry* 33, 1345–1350.

93 Bishop, C. M., Walkenhorst, W. F. & Wimley, W. C. (2001). Folding of beta-sheets in membranes: specificity and promiscuity in peptide model systems. *J. Mol. Biol.* 309, 975–988.

94 Zakharov, S. D. & Cramer, W. A. (2002). Colicin crystal structures: pathways and mechanisms for colicin insertion into membranes. *Biochim. Biophys. Acta* 1565, 333–346.

95 van der Goot, F. G., Gonzalez-Manas, J. M., Lakey, J. H. & Pattus, F. (1991). A "molten-globule" membrane-insertion intermediate of the pore-forming domain of colicin A. *Nature* 354, 408–410.

96 Zakharov, S. D., Lindeberg, M., Griko, Y. et al. (1998). Membrane-bound state of the colicin E1 channel domain as an extended two-dimensional helical array. *Proc. Natl Acad. Sci. USA* 95, 4282–4287.

97 Zakharov, S. D., Lindeberg, M. & Cramer, W. A. (1999). Kinetic description of structural changes linked to membrane import of the colicin E1 channel protein. *Biochemistry* 38, 11325–11332.

98 Lakey, J. H., Duche, D., Gonzalez-Manas, J. M., Baty, D. & Pattus, F. (1993). Fluorescence energy transfer distance measurements. The hydrophobic helical hairpin of colicin A in the membrane bound state. *J. Mol. Biol.* 230, 1055–1067.

99 Qiu, X. Q., Jakes, K. S., Kienker, P. K., Finkelstein, A. & Slatin, S. L. (1996). Major transmembrane movement associated with colicin Ia channel gating. *J. Gen. Physiol.* 107, 313–328.

100 Kienker, P. K., Qiu, X., Slatin, S. L., Finkelstein, A. & Jakes, K. S. (1997). Transmembrane insertion of the colicin Ia hydrophobic hairpin. *J. Membr. Biol.* 157, 27–37.

101 Weiss, M. S., Blanke, S. R., Collier, R. J. & Eisenberg, D. (1995). Structure of the isolated catalytic domain of diphtheria toxin. *Biochemistry* 34, 773–781.

102 Wang, Y., Malenbaum, S. E., Kachel, K., Zhan, H., Collier, R. J. & London, E. (1997). Identification of shallow and deep membrane-penetrating forms of diphtheria toxin T domain that are regulated by protein concentration and bilayer width. *J. Biol. Chem.* 272, 25091–25098.

103 Senzel, L., Gordon, M., Blaustein, R. O., Oh, K. J., Collier, R. J. & Finkelstein, A. (2000). Topography of diphtheria toxin's T domain in the open channel state. *J. Gen. Physiol.* 115, 421–434.

104 Surrey, T. & Jähnig, F. (1995). Kinetics of folding and membrane insertion of a β-barrel membrane protein. *J. Biol. Chem.* 270, 28199–28203.

105 Kleinschmidt, J. H. & Tamm, L. K. (1996). Folding intermediates of a beta-barrel membrane protein. Kinetic evidence for a multi-step membrane insertion mechanism. *Biochemistry* 35, 12993–13000.

106 Kleinschmidt, J. H. & Tamm, L. K. (1999). Time-resolved distance determination by tryptophan fluorescence quenching (TDFQ): Probing intermediates in membrane protein folding. *Biochemistry* 38, 4996–5005.

107 Kleinschmidt, J. H., den Blaauwen, T., Driessen, A. J. M. & Tamm, L. K. (1999). Outer membrane protein A of *Escherichia coli* inserts and folds

into lipid bilayers by a concerted mechanism. *Biochemistry* 38, 5006–5016.

108 Kleinschmidt, J. H. & Tamm, L. K. (2002). Secondary and tertiary structure formation of the beta-barrel membrane protein OmpA is synchronized and depends on membrane thickness. *J. Mol. Biol.* 324, 319–330.

109 Raetz, C. R. & Whitfield, C. (2002). Lipopolysaccharide endotoxins. *Annu. Rev. Biochem.* 71, 635–700.

110 Hindennach, I. & Henning, U. (1975). The major proteins of the *Escherichia coli* outer cell envelope membrane. Preparative isolation of all major membrane proteins. *Eur. J. Biochem.* 59, 207–213.

111 Kleinschmidt, J. H., Wiener, M. C. & Tamm, L. K. (1999). Outer membrane protein A of *E. coli* folds into detergent micelles, but not in the presence of monomeric detergent. *Protein Sci.* 8, 2065–2071.

112 Mann, C. J., Royer, C. A. & Matthews, C. R. (1993). Tryptophan replacements in the trp aporepressor from *Escherichia coli*: probing the equilibrium and kinetic folding models. *Protein Sci.* 2, 1853–1861.

113 London, E. & Ladokhin, A. S. (2002). Measuring the depth of amino acid residues in membrane-inserted peptides by fluorescence quenching. *Curr. Topics Membr.* 52, 89–115.

114 McIntosh, T. J. & Holloway, P. W. (1987). Determination of the depth of bromine atoms in bilayers formed from bromolipid probes. *Biochemistry* 26, 1783–1788.

115 Tamm, L. K. & Tatulian, S. A. (1997). Infrared spectroscopy of proteins and peptides in lipid bilayers. *Q. Rev. Biophys.* 30, 365–429.

116 Tamm, L. K. & Tatulian, S. A. (1993). Orientation of functional and nonfunctional PTS permease signal sequences in lipid bilayers. A polarized attenuated total reflection infrared study. *Biochemistry* 32, 7720–7726.

29
Protein Folding Catalysis by Pro-domains

Philip N. Bryan

29.1
Introduction

The activation of secreted proteases is tightly regulated by a variety of maturation mechanisms [1]. The zymogen form of some consists of a domain-sized extension attached to the N-terminus of the mature protease. Biosynthesis of these proteases involves the folding of the pro-protease followed by processing of the pro-domain from the folded protease. The biological imperative for tight regulation of protease activation creates a situation in which the protease domain must coevolve with the pro-domain. In many cases the mature protease does not have the capacity to fold independently of the pro-domain even though the mature protease appears to be a stable globular entity without obvious structural characteristics which would distinguish it from facile-folding proteins.

Some pro-domains will catalyze folding of the mature form of the protease even as a separate polypeptide chain. The bimolecular reaction is an intriguing case of complementation. The folded protease is stable in a practical sense. That is, the native conformation persists under favorable solvent conditions for many months. Yet, once denatured and returned to these same favorable conditions, it remains in an unfolded conformation for many months. When the isolated pro-domain is added to unfolded protein, however, folding of the two components into a stable complex occurs spontaneously. Examples of pro-domain mediated folding have been found in all four mechanistic families of proteases: serine proteases [2–7]; Aspartic proteases [8–10]; metalloproteases [11–15], and cysteine proteases [16].

For most well-studied proteins, sufficient information is contained within the protein sequence itself to guide the folding process without the requirement for additional factors. Thus the amino acid sequence of these proteins has evolved to encode both a stable native state and a folding pathway efficient enough to reach the native conformation on a biological time scale. The existence of high kinetic barriers to folding challenges many widely accepted ideas, namely thermodynamic determination of native structure and the sufficiency of thermodynamic stability to determine a pathway. Thus the evolution of pro-proteins as folding units appears to have created folding mechanisms which are outside the paradigm established from data on facile-folding proteins.

Protein Folding Handbook. Part I. Edited by J. Buchner and T. Kiefhaber

ISBN: 3-527-30784-2

This review will focus on what general inferences about protein folding can be made from pro-domain catalyzed folding. General questions include whether native protein conformation is always thermodynamically determined, what causes high kinetic barriers between unfolded and native states, and what do pro-domains do to reduce these kinetic barriers. The proteases that have provided the most mechanistic information on catalyzed folding are subtilisin (SBT) and α-lytic protease (ALP). Both are serine protease secreted from bacteria but are not evolutionarily related [17, 18]. Each has eukaryotic homologs. ALP is a structural homolog of chymotrypsin and trypsin and SBT is homologous in structure to prohormone convertases [19–21].

29.2
Bimolecular Folding Mechanisms

With regard to general questions about protein folding mechanisms, analysis of the bimolecular folding reaction has been particularly informative. Unlike unimolecular folding of pro-protease, which results in a metastable product, the product of bimolecular folding is a stable complex between the native protease and the folded pro-domain. The overall goal of many experiments on SBT and ALP has been to obtain a quantitative understanding of all steps in the bimolecular folding reaction. The mechanism of pro-domain-catalyzed folding is as follows:

$$\mathrm{P} + \mathrm{U} \underset{k_{-1}}{\overset{k_1}{\rightleftharpoons}} \mathrm{P\text{-}I} \underset{k_{-2}}{\overset{k_2}{\rightleftharpoons}} \mathrm{P\text{-}N} \underset{k_{\mathrm{on}}}{\overset{k_{\mathrm{off}}}{\rightleftharpoons}} \mathrm{N} + \mathrm{P}$$

where P is pro-domain, U is unfolded protease, N is native protease, P-I is a collision complex of a partially folded protease and pro-domain, P-N is the complex of native protease and pro-domain. To define mechanistically how the pro-domain participates in folding, it is necessary to measure the rates of all steps in the bimolecular folding reaction. It would also be useful to understand the structure of all populated species in this reaction. The approach has been to characterize the individual steps in the reaction and then use this information to understand the overall reaction.

29.3
Structures of Reactants and Products

29.3.1
Structure of Free SBT

Subtilisin BPN′ is the canonical member of the subtilisin family of proteases [22]. It is a heart-shaped protein consisting of a seven-stranded parallel β-sheet packed between two clusters of α-helices (Figure 29.1). Six α-helices are packed against one face of the central β-sheet and two α-helices are packed against the other [23–

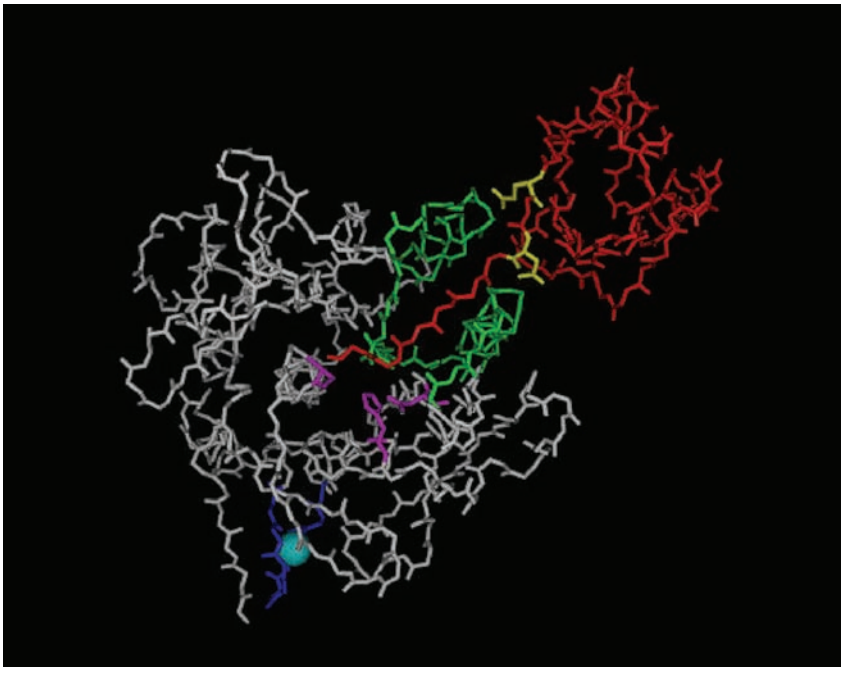

Fig. 29.1. Subtilisin (white) in complex with its pro-domain (red). Active-site triad is shown in violet; α-β-α structure to which pro-domain binds is shown in green; calcium at site A is light blue sphere; calcium-binding loop 75–83 is shown in dark blue. From 1SCJ in the Protein Data Bank [31].

25]. The catalytic triad is distributed as follows: The active-site Ser221 is on the N-terminal end of a long, central helix (helix F); Asp32 is on an interior strand of the β-sheet (β1); His64 is in the N-terminal end of the adjacent helix (helix C). Subtilisin contains a number of notable structural features which are highly conserved across the family. A *cis*-peptide bond occurs between Tyr167 and Pro168 and creates part of the substrate binding pocket. A rare left-handed cross-over occurs between strands β2 and β3. A loop of nine amino acids (75–83) interrupts the last turn of helix C [25]. The loop is part of the left-handed cross-over and forms the central part of a high affinity calcium-binding site (site A). Four carbonyl oxygen ligands to the calcium are provided by the loop (Figure 29.2). The other calcium ligands are a bidentate carboxylate (Asp41) which occurs on an ω-loop (36–45) and the side chain Gln2. Three hydrogen bonds link the N-terminal segment (1–4) to residues 78–82 in parallel-β arrangement. The 75–83 loop also has extensive interactions with a β-hairpin (202–219) so that the calcium ion is buried within the protein structure.

A second ion-binding site (site B) is located 32 Å from site A in a shallow crevice between two segments of polypeptide chain near the surface of the molecule. Evi-

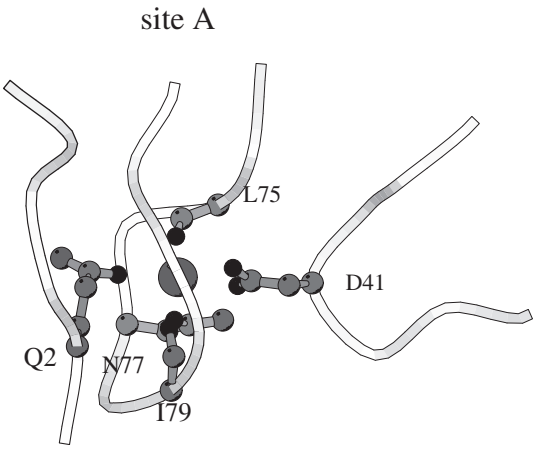

Fig. 29.2. Calcium site A of subtilisin. Ligands to calcium are labeled. From 1SUD in the Protein Data Bank [29].

dence that site B binds calcium comes from determining the occupancy of the site in a series of X-ray structures from crystals grown in 50 mM NaCl with calcium concentrations ranging from 1 to 40 mM [26]. In the absence of excess calcium, this locus was found to bind a sodium ion. The binding of these two ions appears to be mutually exclusive so that as the calcium concentration increases, the sodium ion is displaced, and a water molecule appears in its place directly coordinated to the bound calcium [26]. When calcium is bound, the coordination geometry of this site closely resembles a distorted pentagonal-bipyramid. Three of the ligands are derived from the protein and include the carbonyl oxygen atom of Glu195 and the two side-chain carboxylate oxygens of Asp197. Four water molecules complete the coordination sphere. When sodium is bound, its position is removed by 2.7 Å from that of calcium and the ligation pattern changes. The sodium ligands derived from the protein include a side-chain carboxylate oxygen of Asp197 and the carbonyl oxygen atoms of Gly169, Tyr171, Val174, and Glu195. Two water molecules complete the coordination sphere.

It is not understood how any of these structural features affect folding rate, except for the ion-binding sites. The architecture of site A is the major impediment to folding. Deleting amino acids 75–83 accelerates folding rate by at least 10^7-fold [27–29]. The X-ray structure of the deletion mutant has shown that except for the region of the deleted calcium-binding loop and N-terminal amino acids 1–4, the structure of the mutant and wild-type protein are remarkably similar (Figure 29.3). The structures of SBT with and without the deletion superimpose with an rms difference between 261 Cα positions of 0.17 Å with helix C exhibiting normal helical geometry over its entire length. The deletion also abolishes the calcium binding at site A. As will be discussed below, the formation of calcium site A appears to have a high activation barrier which may contribute to the inability of wild-type SBT to fold.

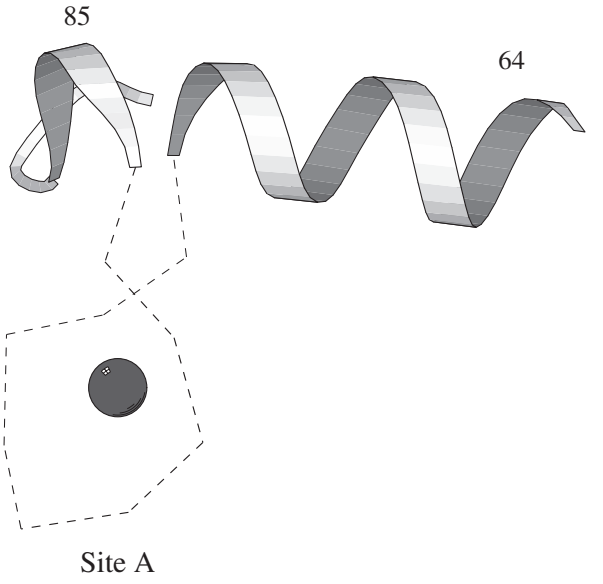

Fig. 29.3. Calcium-binding loop of subtilisin. Region of deletion (75–83) is shown by the dashed line. From 1SUC in the Protein Data Bank [29].

29.3.2 Structure of SBT/Pro-domain Complex

The structure of the native SBT is almost identical in free and complexed states. In the complex, the pro-domain is a single compact domain with an antiparallel four-stranded β-sheet and two three turn α-helices (Figure 29.1) [30, 31]. The β-sheet of the pro-domain packs tightly against the two parallel surface α-helices Asp and Glu (residues 104–116 and 133–144). The pro-domain residues Glu69 and Asp71 form helix caps for the N-termini of the two SBT helices. In another charge-dipole interaction, the carboxylate of Glu112 of SBT accepts H-bonds from the peptide nitrogens of pro residues 42, 43 and 44. The C-terminal residues 72–77 extend out from the central part of the pro-domain and bind in a substrate-like manner along SBT's active-site cleft. Residues Tyr77, Ala76, His75, and Ala74 of the pro-domain occupy subsites S1–S4 of SBT, respectively. If Tyr77 occupies the same position in unprocessed pro-SBT then residues 1–10 of mature SBT would be displaced from their native positions. This hypothetical conformer can be modeled by minor torsional reorganizations involving residues 1–10 with Ala1 and Gln2 of mature SBT occupying the S1′ and S2′ substrate sites. A major consequence for this ''active site'' conformer, is that the calcium site A cannot fully form until after processing because one of the calcium ligands (Gln2) cannot simultaneously bind in the S2′ subsite and bind to calcium in the A-site.

29.3.3
Structure of Free ALP

The overall fold of ALP is of the chymotrypsin type [17]. The fold is typified by the association of two similar domains each consisting of a six-stranded antiparallel β-barrel [32]. The active-site triad occurs in the interface between the domains with His57 and Asp102 in domain 1 and Ser221 in domain 2 (Figure 29.4). Numbering of ALP residues will be given according to the homologous position in chymotrysin. Proteases in this family typically contain multiple intradomain disulfide bonds and ALP contains three. One of these (137–159) is not found in the mammalian enzymes. The structural basis for the inability of ALP to fold independently is not apparent from its basic fold. The activation pathways of trypsin and chymotrypsin do not involve pro-domains but rather small N-terminal activation peptides. In fact active trypsin can be produced in *E. coli* from a gene lacking the hexapeptide activation region [33–35]. Hence the basic fold is not intrinsically problematic for folding. Unique structural features found in ALP and bacterial relatives with pro-domains include a high glycine content (16%) and the extended β-hairpin (167–179). Both features have been suggested as possible impediments to folding [36].

An additional feature which should be noted is a buried salt bridge between Arg138 and Asp194 (Figure 29.4). Asp194 is a key residue in zymogen activation of trypsinogen and chymotrypsinogen. The proteolytic event which creates the mature N-terminus (e.g., Ile16 in chymotrypsin) causes amino acids 189–194 to rearrange into the active conformation [1]. The rearrangement results from a salt bridge formed between the new N-terminus (Ile16) and Asp194. Thus a buried salt bridge occurs in both ALP and mammalian relatives but the burial of the salt bridge in trypsin and chymotrysin follows folding of the zymogen.

29.3.4
Structure of the ALP/Pro-domain Complex

The 166-amino-acid ALP pro-region wraps around the C-terminal half of mature ALP [37]. The contact interface is more than 4000 $Å^2$, almost four-times that of SBT and its pro-domain (Figure 29.4). Most of the contacts to ALP are made with the C-terminal half of the pro-domain (amino acids 65–166) [38], although both N- and C-terminal portions of the pro-domain are required for folding of ALP [39]. Amino acids 160–166 of the pro-domain are inserted like a substrate into the active site, reminiscent of the SBT complex. The edges of a three-stranded β-sheet in the C-terminal part of pro and a β-hairpin (167–179) of ALP abut and form a five-stranded β-sheet in the complex.

As with SBT, the C-terminus of the pro-domain binds tightly in the active site of ALP in the bimolecular complex [37] (Figure 29.4). Thus in the unprocessed molecule, the N-terminus of the active-site conformer would be displaced by 24 Å from

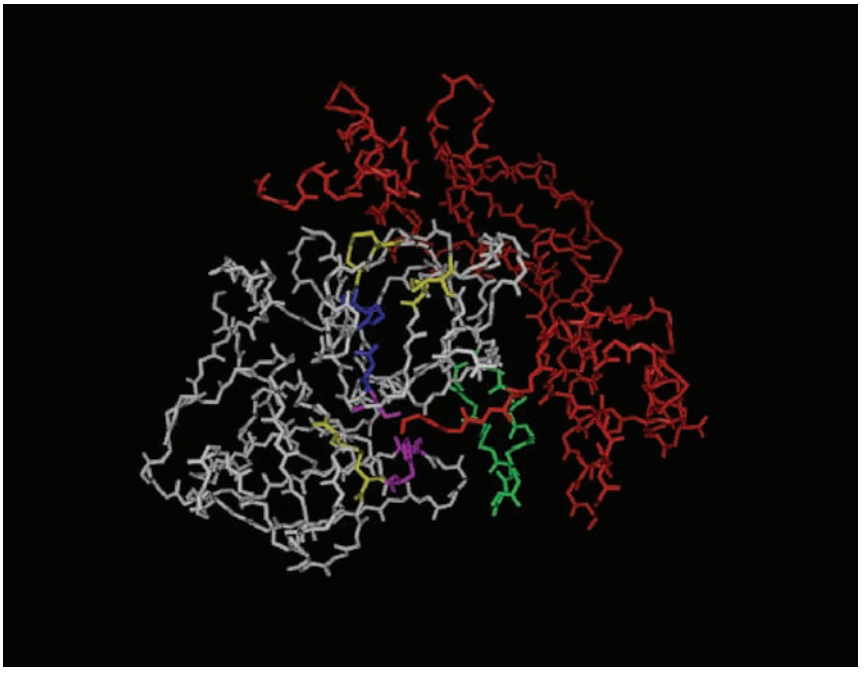

Fig. 29.4. Alpha-lytic protease (white) in complex with its pro-domain (red). Active-site triad is shown in violet; extended β-hairpin 167–179 is shown in green; buried salt bridge Asp194 and Arg138 is shown in dark blue; disulfide bridges are shown in yellow. From 2ALP in the Protein Data Bank [37].

its position in native ALP. Unlike SBT, ALP does not have the complications of metal binding, but it is possible that pro-domain binding organizes Asp194 so that it can form the buried salt bridge with Arg138.

There are some general features of the C-terminal half of the ALP pro-domain that are topologically similar to the SBT pro-domain [38]. Specifically, β-strands 2, 3, 4 and the α-helices connecting strands 1 to 3 and 2 to 4 in the SBT pro-domain have structural counterparts in the ALP pro-domain. Apart from the general similarity of the substrate-binding cleft interactions outlined above, however, there is little similarity in the interactions of pro-SBT and pro-ALP at their binding interfaces with the mature proteases.

ALP pro-domain has no similarity to the small activation peptides of its eukaryotic homologs trypsin and chymotrypsin [1]. The SBT pro-domain on the other hand has high structural homology to the pro-hormone convertase pro-domain, although little sequence similarity [40, 41]. Surprisingly, the SBT pro-domain also has the same basic fold as the pro-domains of eukaryotic carboxypeptidases [42, 43]. This is in spite of the lack of any structural similarity between the mature regions of SBT and the carboxypeptidases.

29.4
Stability of the Mature Protease

29.4.1
Stability of ALP

The most basic folding experiment is determining the free energy of the folding reaction. This is difficult with ALP and SBT because of the problem of establishing equilibrium under conditions in which the ratio of folded and unfolded states can be accurately measured. Denatured ALP diluted into native conditions rapidly collapses into a ensemble of conformations with an average hydrodynamic radius about midway between the native and guanidium chloride (GdmCl)-denatured forms and with almost the same amount of regular secondary structure as native ALP [44]. This collapsed state is stable for weeks at neutral pH without detectable conversion to the native state [44]. The free energy of a two-state reaction can sometimes be determined, however, by (1) measuring a folding rate at a standard state; (2) measuring unfolding rates as a function of denaturant; or (3) extrapolating the unfolding rate to the standard state. From the ratio of the rates of folding and unfolding at the standard state, the free energy of folding is determined. This was the approach taken with ALP [45]. To minimize the influence of autodigestion during the folding reaction, the measurements were made at pH 5.0. As the pH is decreased below the pK_a of the active-site histidine, the proteolytic activity of serine proteases decreases. A pH around 5 is commonly used as a compromise between low activity and preserving some conformational stability [46]. The refolding rate of ALP was determined by incubating denatured protein in native conditions and removing aliquots at intervals. The amount of active ALP was determined by measuring peptidase activity using a synthetic substrate. Over the course of days small but linear increases in activity were detected. Quantitation in the experiment is tricky because the accumulation of active ALP causes digestion of the unfolded protein, but the initial rate of the folding reaction is 6×10^{-12} s^{-1} at 25 °C. This was compared with the unfolding rate which was determined as a function of [GdmCl]. The rate of unfolding without GdmCl was estimated by linear extrapolation to be 1×10^{-7} s^{-1} at 25 °C. Since $\Delta G_{\text{unfolding}} = -RT \ln(k_{\text{unfolding}}/k_{\text{folding}})$ in a two-state system, the simplest interpretation of the unfolding and refolding rates would mean that $\Delta G_{\text{unfolding}}$ is about -6 kcal mol^{-1} at 25 °C.

Even given the uncertainties in determining the folding and unfolding rates, it is convincing that the unfolded state of ALP is more stable than the folded state at pH 5.0. The effect of pH 5.0 on the protonation of Asp194 also may bear consideration. If the formation of the buried salt bridge between Asp194 and Arg138 is involved in the transition state for folding, then partial protonation of Asp194 at pH 5.0 could destabilize its interaction with Arg138 and slow folding significantly.

The stability measurements on ALP were made with the three disulfide bonds intact in all forms, U, I and N. An unstrained disulfide cross-link should stabilize a protein by decreasing the entropic cost of folding. The loss of conformational en-

tropy in a polymer due to a cross-link has been estimated by calculating the probability that the ends of a polymer will simultaneously occur in the same volume element. According to statistical mechanics, the three disulfide bonds in ALP should destabilize the unfolded state by ~10 kcal mol^{-1} at 25 °C [47, 48]. Since the lifespan of a protease depends upon the kinetics rather than the thermodynamics of unfolding, however, disulfide bonds are a surprising feature. The effects of cross-links on the stability of the unfolded state would not generally be manifested in the activation energy of the unfolding reaction, because the transition states for unfolding reactions usually are compact, with a slightly larger heat capacity than the native state. In folding experiments on ALP, the disulfide bonds are present in both the I and N states of the protein and thus do not contribute to the thermodynamic measurements [45, 49].

29.4.2 Stability of Subtilisin

Ion binding has a dominant role in stabilizing SBT. The active-site mutant Ala221 of SBT can be unfolded at 25 °C by incubation in 30 mM Tris-HCl, pH 7.5, 0.1 mM EDTA. The rate of unfolding under these conditions is ~0.5 h [1]. (The S221A mutation reduces proteolytic activity of SBT by about 10^6-fold [50] and eliminates the problem of autoproteolysis during the unfolding process.) Addition of micromolar concentrations of free calcium or millimolar concentrations of sodium will reduce the unfolding rate to $>days^{-1}$. The role of calcium site A in the kinetic stability of SBT is well-documented [51]. SBT with the calcium site A occupied (e.g., 100 mM $CaCl_2$, 100 mM NaCl) unfolds 1000-times slower than the apo-form of SBT (e.g., 1 mM EDTA, 100 mM NaCl) [52] and the activation energy for calcium dissociation from the folded state is 23 kcal mol^{-1}. The binding parameters of calcium at site A have been determined previously by titration calorimetry: $\Delta H_{binding} = -11$ kcal mol^{-1} and $\Delta G_{binding} = -9.3$ kcal mol^{-1} at 25 °C [28]. Thus the binding of calcium is primarily enthalpically driven with only a small net loss in entropy ($\Delta S_{binding} = -6.7$ cal deg^{-1} mol^{-1}). This is surprising since transfer of calcium into water results in a loss of entropy of −60 cal deg^{-1} mol^{-1}. Therefore the freeing of water upon calcium binding to the protein will make a major contribution to the overall ΔS of the process. The gain in solvent entropy upon binding must be compensated for by a loss in entropy of the protein. Loop amino acids 75–83, N-terminal residues 1–5, the ω-loop (36–45) and the β-hairpin (202–219) have increased mobility when calcium is absent from the A-site [27].

Ion site B also influences stability but to a lesser extent. The K_d of site B for sodium is ~1 mM and 15 μM for calcium [52]. By binding at specific sites in the tertiary structure of subtilisin, cations contribute their binding energy to the stability of the native state and should have predictable effects on thermodynamic stability. If cation binding is exclusively to the native state then the contribution of cation binding to the free energy of unfolding would be:

$$\Delta G_{binding} = -RT \ln(1 + K_a\,[\text{cation}])$$

For example, the free energy of unfolding in 1 mM calcium would be increased by 5.5 kcal mol^{-1} due to the influence of binding at the A-site and an additional 2.5 kcal mol^{-1} due to site B, for a total of 8 kcal mol^{-1} per mM calcium (25 °C).

The distinction between thermodynamic and kinetic effects is blurred, however, by the observations of Eder and Fersht showing that a structured intermediate state of SBT can be induced by high salt (1 M KCl or 0.5 M $(NH_4)_2SO_4$) and calcium (1 mM) [53]. Ala221 SBT was denatured in 6 M HCl pH 1.8 and then either dialysed or diluted into refolding buffer around neutral pH. Upon return to native conditions in high salt (e.g., 1.0 M KCl) mature SBT slowly folds into a state reminiscent of the I-state of ALP: hydrodynamic radius intermediate between native and unfolded and a high percentage of secondary structure. Remarkably, the SBT intermediate state binds a stoichiometric amount of calcium with an affinity ≤ 1 μM. No conversion of the intermediate of the native form was detected in the absence of added pro-domain [54]. This experiment has a detection limit of ~1%, which would mean that uncatalyzed folding of mature Ala221 SBT occurs at a rate of $<10^{-8}$ s^{-1}.

If the salt-induced intermediate is part of the relevant folding landscape, this means that the net contribution of cation binding to the thermodynamics of unfolding would be much less than predicted based on exclusive binding to the native state. If high salt is avoided (e.g., $\leq$0.2 M KCl), however, unfolded SBT remains in a largely unstructured state, indicating the compact state may not be populated under more common folding conditions.

The most straightforward demonstration that mature SBT is thermodynamically stable in high salt was achieved by denaturing and renaturing SBT immobilized on agarose beads to prevent autodigestion [55]. Quantitative renaturation was achieved in 24 h in the presence of 2 M potassium salts, indicating that the folding rate under these conditions must be $>10^{-5}$ s^{-1}. The unfolding rate is not known under these conditions, but the $\Delta G_{unfolding}$ must be greater than 2 kcal mol^{-1} since recovery of native activity approaches 100%. This is surprising since Ala221 SBT in solution could not be renatured in high KCl. It should be noted, however, that SBT might be stabilized by immobilization.

Deleting the calcium A-loop creates a subtilisin that is thermodynamically stable at KCl concentrations above 10 mM. The folding rate of the deletion mutant is strongly ionic dependent [28]. In 30 mM Tris-HCl, pH 7.5 the mutant is not observed to fold. As NaCl or KCl is added, the folding rate increases with the log of the salt concentration. In 0.2 M KCl, pH 7.5, the mutant refolds to the native form in a single exponential process ($k_{fold} = 0.0027$ s^{-1}) [56] (Figure 29.5).

In summary, one can conclude that Ala221 SBT with the wild-type calcium loop is thermodynamically unstable at low ionic strength (e.g., 30 mM Tris-HCl pH 7.5, 0.1 M EDTA). Thermodynamic stability increases as calcium and monovalent salts are added but it is not certain under what ionic conditions the $\Delta G_{unfolding}$ exceeds zero because the folding and unfolding rates are so slow.

In spite of whether ALP or SBT is thermodynamically stable under a given set of conditions, their slow folding reactions are not due simply to instability of the folded state. If this were true folding could be thermodynamically driven by adding

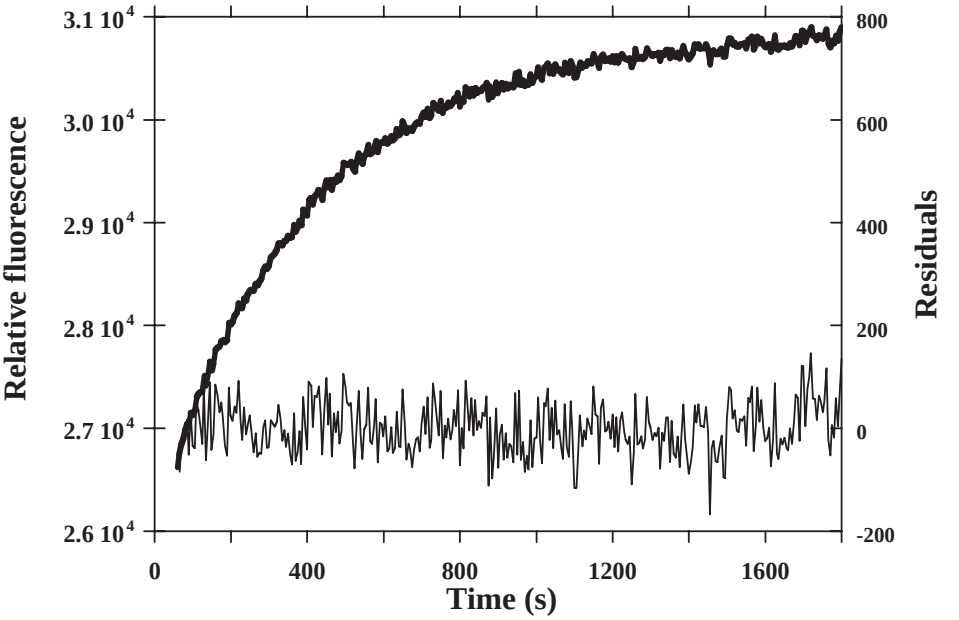

Fig. 29.5. Kinetics of refolding Ala221 Δ75–83 SBT. Refolding in 0.2 M KCl, 30 mM Tris-HCl, pH 7.5, and 25 °C is followed by the increase in tryptophan fluorescence. The curve plotted is the average of three experiments. The residuals after subtracting the data from a single exponential fit ($k = 0.0027\ s^{-1}$) are plotted on a five-times expanded scale.

a ligand which binds tightly and preferentially to the native state. For example, the streptomyces SBT inhibitor protein (SSI) has no detectable influence on the folding rate of SBT even though its binds to SBT more tightly than the pro-domain does [56]. Thus pro-domains must be capable of stablizing some structure in the folding pathway whose formation is limiting in its absence.

29.5
Analysis of Pro-domain Binding to the Folded Protease

$$\mathrm{P} + \mathrm{N} \underset{k_{\mathrm{off}}}{\overset{k_{\mathrm{on}}}{\longleftrightarrow}} \mathrm{P\text{-}N}$$

The SBT pro-domain is a competitive inhibitor of the active enzyme (K_i of 5.4×10^{-7}) [57]. Binding of ALP to its pro-domain is even tighter ($K_i \sim 10^{-10}$) [58]. The high affinity of the pro-domain for the native conformation suggests that its role in folding might be to stabilize native-like structures in the transition state for folding [59]. The details of the complementary interfaces between the respective pro-domains and proteases have been discussed above.

A feature of the isolated pro-domains which influences binding properties is independent stability. The ALP pro-domain is fully folded at 4 °C, independent of binding to ALP [60]. In contrast, the isolated SBT pro-domain is essentially unfolded at all temperatures [56], even though it is a compact globular structured in complex with SBT. This situation suggests that there is thermodynamic linkage between the SBT pro-domain stability and its binding affinity. This linkage can be established by examining the effects of mutations that do not directly affect contacts with the protease but that affect the stability of pro-domain. Although the stability of the isolated pro-domain is low, it has been measured by titration with stabilizing co-solvents and found to have a $\Delta G_{\text{unfolding}} \sim -2$ kcal mol^{-1} at 25 °C [61]. This propensity to fold can be altered by mutations. For example, the mutation I30T in the hydrophobic core of the SBT pro-domain weakens binding to SBT by ~100-fold [62].

A number of mutations have been described that increase the independent stability of the SBT pro-domain with concomitant increases in binding affinity to native SBT [63–67]. Sequentially introducing stabilizing mutations into the pro-domain shifted the equilibrium for independent folding from ~97% unfolded to >98% folded. As the independent stability of the pro-domain increases, the binding affinity for SBT increases concomitantly. The most stable pro-domain mutant bound about ~30-times more tightly than wild-type pro-domain [68]. Since these mutations were introduced in regions of the pro-domain that did not directly contact with SBT, their effects on binding to SBT were linked their to their stabilizing effects on the pro-domain. The linked equilibria for pro-domain folding and binding are:

$$\mathrm{P_u} \overset{K_f}{\leftrightarrow} \mathrm{P} + \mathrm{S} \overset{K_P}{\leftrightarrow} \mathrm{P\text{-}S}$$

where K_f is the equilibrium constant for folding the pro-domain and K_P is the association constant of folded pro-domain for SBT. The observed binding constant is expected to be: $K_{(P+Pu)} = [K_f/(1 + K_f)]K_P$. The data show that as the fraction of folded pro-domain approaches one, the observed association constant approaches its maximum, ~10^{10} M^{-1} [63].

The kinetics of the pro-domain binding to SBT also have been determined by measuring the rate of fluorescence change that occurs upon binding. If the reaction is carried out with a 10-fold or greater excess of P, then one observes a pseudo first-order kinetic process with a rate constant equal to $k_{on}[P] + k_{off}$. The k_{on} for binding the pro-domain to folded SBT is ~10^6 M^{-1} s^{-1} [69]. This value is fairly insensitive to mutations that change the stability of the pro-domain.

29.6 Analysis of Folding Steps

$$\mathrm{P} + \mathrm{U} \underset{k_{-1}}{\overset{k_1}{\rightleftarrows}} \mathrm{P\text{-}I} \underset{k_{-2}}{\overset{k_2}{\rightleftarrows}} \mathrm{P\text{-}N}$$

In the kinetic mechanism above, P is pro-domain, P-I is an initial complex between pro-domain and partially folded protease, and P-N is the folded complex of pro-domain and native protease. The reaction has been studied for both SBT and ALP as a function of [P]. Under similar conditions the catalyzed folding of SBT is much slower than that of ALP. For example, adding isolated pro-domain (5 μM) to unfolded Ala221 SBT (5 μM) results in only 50% recovery of the native complex after 8 days at 4 °C [53]. Under similar conditions ALP is expect to fold quantitatively within minutes [44]. At first glance this result suggests that the mechanisms of pro-domain catalyzed folding of ALP and SBT differ in some fundamental way. Closer examination reveals, however, that the mechanisms are more similar than they first appear.

Most of the difference in catalyzed folding rate can be explained by examination of the independent stabilities of the two pro-domains. Recall that the SBT pro-domain is largely unfolded at 25 °C ($\Delta G_{\text{unfolding}} = -2$ kcal mol^{-1}). In comparison, the ALP pro-domain is about 30–40% unfolded at 25 °C ($\Delta G_{\text{unfolding}} \sim 0.3$ kcal mol^{-1}) [60]. Further, the analysis of ALP folding usually is carried out at 4 °C, where its pro-domain is essentially fully folded. The affect of pro-domain stability on catalyzed folding can be seen by examining mutants of the SBT pro-domain which stabilize its independent folding. These mutants were selected based on examination of the X-ray structure of the pro-domain SBT complex and none of the mutations directly contact SBT. Using a fully folded pro-domain mutant (denoted proR9) the kinetics of the conversion of U + P to P-N were determined as a function of [P] ranging from 5 μM to 100 μM [69]. When the concentration of pro-domain is high relative to protease, the kinetics of a single turnover of folding are pseudo first order. The observed rate of folding can be explained by a rapid equilibrium model where k_{-1} is large relative to k_2. In this model, the equilibrium constant K_1 is equal to [P-I]/[U][P]. Since $[\text{P-I}]/[\text{P}_{\text{total}}] = \text{K}_1[\text{P}]/(1 + \text{K}_1[\text{P}])$, the observed rate of formation of P-N would be equal to

$$\{k_2 K_1[\text{P}]/(1 + K_1[\text{P}])\} + k_{-2}$$

At micromolar concentrations of pro-domain, the complex P-I reaches saturation and the reaction is limited by the folding of P-I to P-N. The rate of the isomerization step (k_2) is 0.1 min^{-1} for the folding Ala221 SBT and the stabilized pro-domain proR9 (Ruan and Bryan, unpublished). The kinetics of this reaction are unaffected by either calcium (≤ 100 mM) or EDTA (≤ 10 mM) even though these salts greatly affect the stability of the product.

For ALP folding the concentration dependence of the rate also follows a binding hyperbola, with $K_1 = 23$ μM [60]. The maximum rate of the reaction (k_2) is 0.03 s^{-1}. It appears from the plots that k_{-2} is very small compared with k_2.

Analysis of mutations of the ALP pro-domain indicate that interactions at or near the active site are involved in stabilizing the transition state between the initial complex and the native complex [49, 60]. In contrast these interactions have less effect on the stability of the initial complex (P-I). For example, successive deletions of the last four amino acids of the pro-domain decrease k_2 on average

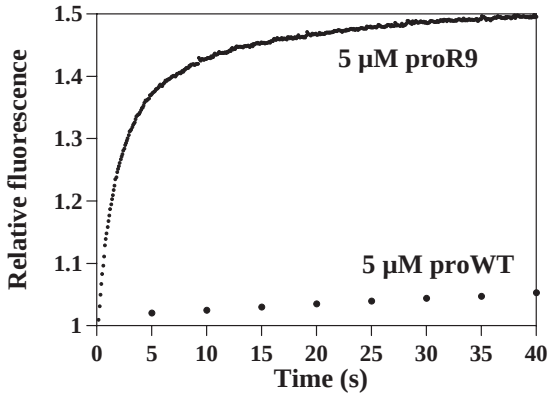

Fig. 29.6. Folding rate of Ala221, Δ75–83 SBT in the presence of the wild-type pro-domain and proR9. Pro-domain (5 μM) and 1 μM denatured SBT mutant were mixed in 5 mM KPO_4, 30 mM Tris pH 7.5 at 25 °C. The reaction was followed by the increase in tryptophan fluorescence which occurs upon folding of SBT into the pro-domain SBT complex.

>10-fold for each lost amino acid. Effects of K_1 are not detectable until three or more amino acids are deleted. Recall that these amino acids bind to ALP in a substrate-like manner (Figure 29.4). It is tempting to speculate that the reduction of k_2 is due to the diminished capacity of the deletion mutants to organize the 189–194 loop.

The catalyzed folding reaction of SBT has also been analyzed using an A221 mutant which lacks the calcium binding loop of site A and which folds more rapidly than wild-type SBT. Using wild-type pro-domain as catalyst, the rate of SBT folding increases linearly as a function of [P] ($[P] \leq 100$ μM) [56]. The absence of curvature in the plot implies that the formation of the initial complex, P-I, is the limiting step in the reaction up to $[P] = 100$ μM. These results indicated that initial association of wild-type pro-domain with Δ75–83 SBT is weak. As the pro-domain is stabilized, the folding reaction becomes faster and distinctly biphasic (Figure 29.6). The fast phase of the reaction corresponds to the second-order binding step (1×10^5 M^{-1} s^{-1}) and the slow phase to the isomerization step (0.15 s^{-1}). With the folded pro-domain proR9 the maximum isomerization rates for SBT and Δ75–83 SBT are similar (~0.1 s^{-1}).

It was possible to demonstrate that proline isomerization is rate limiting in folding Δ75–83 SBT. There are 13 proline residues in SBT. All but one (Pro168) exist as *trans* isomers in the native structure [25]. The peptide bond between proline and its preceding amino acid (Xaa-Pro bonds) exist as a mixture of *cis* and *trans* isomers in solution unless structural constraints, such as in folded proteins, stabilize one of the two isomers. In the absence of ordered structure, the *trans* isomer is favored slightly over the *cis* isomer. The isomerization *trans* ↔ *cis* is an intrinsically slow reaction with rates at 0.1–0.01 s^{-1} at 25 °C. Upon denaturation of SBT, the structural constraints are removed and the *trans* and *cis* isomers of all 13 prolyl peptide

bonds gradually come to equilibrium in the unfolded state, resulting in 2^{13} different proline isomer combinations. To study the catalyzed folding rate of SBT in the absence of prolyl peptide bond isomerization, folding kinetics were measured after a short denaturation time [70]. The Δ75–83 SBT mutant used in these studies can be denatured in acid in <1 s. The rapid denaturation time minimizes the amount of prolyl peptide bond isomerization occurring during the time require to unfold. In the absence of proline isomerization, the observed rate of folding increases as concentration of pro-domain increases, and follows a linear relationship with no intermediate detectable in the course of the reaction. This occurs because the formation of P-N from P-I is faster than the formation of initial collision complex P-I from P and U. The mechanism of folding reaction for denatured Δ75–83 SBT with native proline isomers is as follows:

$$\mathrm{P} + \mathrm{U} \underset{<0.05\ \mathrm{s}^{-1}}{\overset{9\times10^{4}\ \mathrm{M}^{-1}\ \mathrm{s}^{-1}}{\rightleftharpoons}} \mathrm{P\text{-}I} \underset{<0.01\ \mathrm{s}^{-1}}{\overset{>3\ \mathrm{s}^{-1}}{\rightleftharpoons}} \mathrm{P\text{-}N}$$

where U is denatured SBT with all prolyl peptide bond isomers the same as in the native structure. According to the mechanism proposed above, the pseudo first-order rate constant would reach its maximum when [P] is high enough that the value $k_1 \cdot [\mathrm{P}] > (k_2 + k_{-2})$. That point has not been reached at [P] = 20 μM. Thus, in the presence of an independently folded pro-domain mutant, the rate of SBT folding into a complex becomes typical of in vitro folding rates for many small globular proteins. That is, independent of proline isomerization, folding is largely complete within a few seconds [71].

In comparison, the rate of ALP folding plateaus at 0.03 s^{-1}, which is in the range of proline isomerization. ALP has three *trans* and one *cis* proline. It is not known how proline isomerization is involved in the kinetics of the P-I to P-N transition, however.

29.7 Why are Pro-domains Required for Folding?

The question remains as to why folding is so slow without the pro-domain. An efficient folding pathway implies that productive intermediates are significantly more stable than the surrounding landscape of unfolded conformations. Native state H-D exchange experiments for several proteins have shown that partially folded states exist with significantly lower energy than the globally unfolded state [72–74]. Native state H-D exchange experiments for ALP [75] and SBT (Sari et al., unpublished), show highly cooperative exchange behavior. Amides protons in all elements of secondary structure exchange with solvent deuterons at a rate in the range of $year^{-1}$. In ALP, there are 103 amide protons with protection factors $> 10^4$ and 31 amide proton with protection factor $> 10^9$. The most protected protons occur throughout both domains of ALP. In comparison, there are 131 protons in SBT with protection factors $\geq 10^5$. The 49 slowest exchangers have protection factors $\geq 10^9$. These strongly protected residues occur throughout the main structural elements of SBT, except for the short N-terminal α-helices, A and B, and

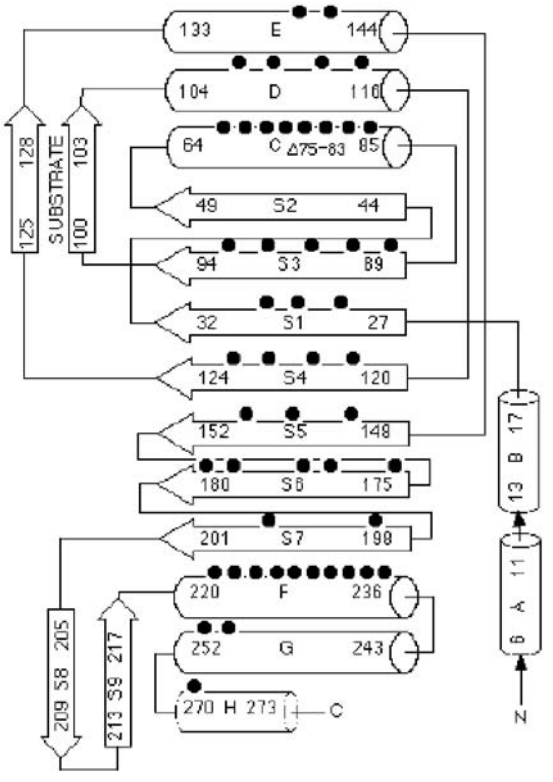

Fig. 29.7. Schematic representation of the subtilisin topology. The positions of the 49 slowest exchanging amide protons in SBT are shown by black dots. The slowest 49 exchanging protons reside throughout the central seven-stranded parallel β-sheet and in all the five major α-helical segments. Adapted from Siezen et al. [85].

strands, β8 and β9 (Figure 29.7). The large cooperative folding core may create a folding problem, because most of the tertiary structure must be acquired before a free energy well is encountered in conformational space. The enormous loss of conformational entropy before that energy well occurs would result in a large transition state barrier to folding [66, 75]. In this model, the transition state of uncatalyzed folding is of high energy because of its low conformational entropy. The prodomain decreases the entropic barrier by pushing the transition state back toward a less folded form of the proteinase. Thus much less conformational entropy is lost in the transition state. Once over the barrier, folding of P-I to P-N is rapid.

29.8
What is the Origin of High Cooperativity?

Formation of the calcium A-site may be responsible for the cooperative folding reaction of SBT. SBT is unstable in the absence of calcium and at low ionic strength.

Addition of calcium increases stability by 8 kcal mol^{-1} per mM but does accelerate the folding reaction to an observable level. The reason that the calcium does not affect folding rate may be that site A is not fully formed until considerable tertiary structure has accrued. The structure elements involved in forming the A-site are the N-terminus, the ω-loop, the 75–83 loop and the 202–219 β-hairpin. Thus calcium binding may not contribute to the stability of intermediately folded states but only to a substantially folded molecule. This situation creates a highly cooperative folding reaction. In addition, the burial of the charged calcium and the requirement for its desolvation prior to burial within the protein creates an additional kinetic barrier to folding. This suggestion is supported by the observation that the Δ75–83 mutant SBT folds $\geq 10^7$-times faster than SBT with the calcium A-site intact.

The origins of high cooperativity in ALP may also be related to a buried ionic interaction: the formation of the buried salt bridge between Arg138 and Asp194. Formation of a structurally homologous ionic interaction is involved in zymogen activation in trypsin and chymotrypsin.

Buried ionic interactions have been implicated previously in raising the activation barrier to folding because of unfavorable protein–solvent rearrangements. For example, replacing a buried salt bridge in ARC repressor dimer with a hydrophobic cluster has little effect on thermodynamic stability but increases the folding rate of the dimer by up to 1000-fold [76, 77]. Desolvating these charged residues in ALP may raise kinetic but not necessarily the thermodynamic barriers to unfolding.

29.9
How Does the Pro-domain Accelerate Folding?

The simplest model of catalyzed folding is one in which the pro-domain accelerates folding by stabilizing a substructure on the folding pathway which does not form frequently in the absence of pro-domain binding. Once the substructure forms, it acts as a folding nucleus with subsequent folding propagating into other regions. The nature of this substructure can be guessed at based on the structures of the folded complexes. In the bimolecular SBT complex, the pro-domain binds to an α–β–α structure (amino acids 100–144) which includes the parallel surface α-helices D and E. It also supplies caps to the N-termini of the two helices (Figure 29.1). In the intermediate P-I, the pro-domain may stabilize the α–β–α structure relative to other unfolded states. Subsequent folding may propagate from this folding nucleus into N- and C-terminal regions of SBT. In the absence of the pro-domain, the α–β–α structure may not have sufficient independent stability to initiate folding very frequently. It should be noted that unimolecular folding of proSBT may circumuvent the problem of calcium A-site formation. The covalent attachment of the pro-domain to SBT prevents the final folding of the calcium A-site region, until after the active site is sufficiently formed to cleave the pro-domain from the mature [30, 78].

In ALP, the pro-domain may stabilize the formation of a long β-hairpin (118–

130) in the C-terminal half of ALP [36, 37] but may also be involved in organizing the 189–194 loop through the interaction of the C-terminus of the pro-domain with the active-site Ser195.

29.10
Are High Kinetic Stability and Facile Folding Mutually Exclusive?

Broad specificity proteinases must be resistant to unfolding. Assuming that partially folded intermediates are good substrates for autolysis, the half-life of active protease would be determined by the equilibrium between the proteinase-resistant native state and the lowest energy, proteinase-labile intermediate [28, 36, 75, 79]. Thus to avoid autolysis, partially folded conformations must be of much higher energy than the native state so that excursions between the two states are rare. Since partially folded states with significant independent stability are important intermediates in the folding pathway of many proteins does resistance to partial unfolding cause proteins to be hard to fold? The answer appears to be not necessarily.

It has been possible artificially to evolved the facile-folding Δ75–83 SBT into a protease which is hyperstable and facile-folding [80, 81]. The initial deletion mutant is unfolds 100-times faster than wild type in 100 mM calcium, but deleting the loop creates the potential to use facile-folding structural solutions for stabilization. Four regions of subtilisin are directly affected by the deletion of the calcium loop: the N-terminal amino acids 1–5; the ω-loop amino acids 36–45; the α-helix amino acids 70–74; the β-ribbon amino acids 202–219. As a result the naturally occurring amino acids in these regions were not optimal for stability in the loop-deleted subtilisin. Residues in these regions were randomized and stabilizing mutations were selected in five iterations [80]. The final result was a mutant which unfolds 1000-times slower than wild-type SBT in 100 mM calcium [81] but, nevertheless, has an uncatalyzed folding rate of 0.02 s^{-1}. This protease can be expressed at high levels through its natural biosynthetic pathway in *Bacillus*, although obviously its long-term evolutionary fitness is unknown. The fact that facile folding and high kinetic stability are not mutually exclusive in the SBT fold suggests that the inability of wild-type SBT and ALP to fold without their pro-domains may be part of the mechanism to regulate the timing of protease activation. It is also possible that when evolution of the folding unit is uncoupled from the sequence of the mature enzyme that the facile folding of the mature enzyme is easily lost.

29.11
Experimental Protocols for Studying SBT Folding

29.11.1
Fermentation and Purification of Active Subtilisin

Subtilisin BPN′ and active mutants were expressed in *B. subtilis* in a 1.5-L New Brunswick fermenter at a level of ~500 mg L^{-1}. After fermentation 16 g of Tris–

base and 22 g of $CaCl_2$ (dihydrate) were added to ~1400 mL of broth. Cells and precipitate were pelleted into 250-mL bottles by centrifugation at 12 000 *g* for 30 min, 4 °C. Acetone (70% final volume) was added to the supernatant. The 70% acetone mixture was then centrifuged in 500-mL bottles at 12 000 *g* for 30 min, 4 °C. The pellet was resuspended in ~150 mL 20 mM HEPES, pH 7.0, 1 mM $CaCl_2$. Resuspended material was centrifuged at 12 000 *g* for 10 min, 4 °C to remove insoluble material. Using a vacuum funnel, the sample was passed over 150 g DE52, equilibrated in 20 mM HEPES, pH 7.0. The DE52 was washed twice with 150 mL 20 mM HEPES, 1 mM $CaCl_2$ buffer and the all washes pooled. Solid NH_4SO_4 was added to the sample to a final concentration of 1.8 M. Final purification was carried out using a 2 × 30 cm Poros HP 20 column on a Biocad Sprint. The sample was loaded and washed in 1.8 M NH_4SO_4, 20 mM HEPES, pH 7.0 and then eluted with a linear gradient (1.8–0 M NH_4SO_4 in 20 mM HEPES, pH 7.0). Subtilisin BPN′ eluted at a conductivity of 108 mS. Assays of peptidase activity were performed by monitoring the hydrolysis of sAAPF-pNA [82]. The [subtilisin] was determined using 1 mg mL^{-1} = 1.17 at 280 nm.

29.11.2
Fermentation and Purification of Facile-folding Ala221 Subtilisin from *E. coli*

Mutagenesis and protein expression of inactive Δ75–83 SBT mutants were performed using a vector called pJ1. Vector pJ1 is identical to pG5 [83] except that the *Cla*I site of pG5 has been removed. The SBT gene was inserted between *Nde*I and *Hin*dIII sites in the polycloning site of pJ1 and transformed into *E. coli* production strain BL21(DE3).

The transformed production strain BL21(DE3) was plated out on selection plates. Ten milliliters of 1LB broth (10 g of tryptone, 5 g of yeast extract, 10 g of NaCl L^{-1} media) supplemented with 100 μg mL^{-1} ampicillin was inoculated with 4–6 ampicillin-resistant colonies in a 250-mL baffled flask. The culture was grown at 37 °C, 300 rpm, until mid-log phase. This culture was used to inoculate 1.5 L of L Broth buffered with 2.3 g of KH_2PO_4, 12.5 g of K_2HPO_4 L^{-1} media supplemented with 100 μg mL^{-1} ampicillin. The culture was grown at 37 °C in a BioFlo Model C30 fermenter (New Brunswick Scientific Co., Edison, NJ, USA) until an A_{600} 1–1.2 was attained, upon which 1 mM IPTG was added to induce the production of T7 RNA polymerase that directs synthesis of target DNA message. Three hours after induction, the cells were harversted by centrifugation for 30 min at 4 °C, 10 000 rpm in a J2–21 centrifuge (Beckman Instruments, Fullerton, CA, USA) with a JA-14 rotor.

E. coli paste from a 1.5-L fermentation (~5 g) was resuspended in 50 mL lysis buffer (50 mM Tris-HCl pH 8.0/100 mM NaCl/1 mM EDTA) and PMSF was added to a final concentration of 1 mM and DNase I (in 40 mM Tris-HCl, 1 M $MgCl_2$) to 20 μg mL^{-1}. The cells were lysed by two passes through a French Press and additional DNase I was added to a final concentration of 25 μg mL^{-1}. Inclusion bodies containing mutant SBT were recovered by centrifugation at 10 000 *g*, 4 °C with a JA-17 rotor for 20 min in a Beckman J2-21 centrifuge. The resulting pellet was

washed three times by repeated resuspension in 60 mL of ice-cold 20 mM HEPES, pH 7.0, and centrifugation for 10 min at the same condition as above. The final pellet was then resuspended in 50 mL of ice-cold 20 mM HEPES, pH 7.0, containing 2 M urea, frozen on dry ice and allowed to thaw at room temperature to clarify the solution. If a precipitate formed, the volume was increased and the freeze/thaw cycle was repeated. The solution then was centrifuged for 10 min and the supernatant applied to a Productive DE cartridge (Metachem Technologies Inc., Torrance, CA, USA) equilibrated with 20 mM HEPES, pH 7.0/2 M urea. The cartridge was washed with 40 mL of cold 20 mM HEPES, pH 7.0/2 M urea. Flow through and wash fractions were combined and dialyzed 36–48 h at room temperature against 3.5 L of 100 mM KPi, pH 7.0 to fold the SBT.

An affinity agarose column was prepared by coupling the tetrapeptide A-L-A-L (Sigma, St. Louis, MO, USA) to Affi-Gel 10 (Bio-Rad, Hercules, CA, USA) following the manufacturer's protocol. The DE cartridge-purified protein was split and each half loaded onto a 4.5-mL column of A-L-A-L-agarose equilibrated with 20 mM HEPES, pH 7.0. The column was washed with 20 mL of 20 mM HEPES, pH 7.0/1 M NaCl followed by 10 mL of 20 mM HEPES, pH 7.0 and the protein was eluted with 50 mM of triethylamine, pH 11.1. Peak fractions (1 mL each) of the protein were immediately neutralized by the addition of 0.1 mL of 1 M KPi, pH 7.0 and pooled together, then dialyzed overnight against 3.5 L of 2 mM ammonium carbonate. Peak fractions were checked on SDS-polyacrymide (SDS-PAGE) gels (Novex Experimental Technoolgy, San Diego, CA, USA). The desired fractions were pooled and dialyzed against 2 mM ammonium bicarbonate, pH 7.0 at 4 °C. After lyophilization, the protein sample was stored at –20 °C.

29.11.3
Mutagenesis and Protein Expression of Pro-domain Mutants

The gene fragment encoding the 77-amino-acid pro-domain was cloned into vector pJ1. When superinfected with helper phage M13K07, the M13 origin enables the DNA replication in single-stranded form for mutagenesis and sequencing. Mutagenesis of the cloned pro-domain gene was performed according to the oligonucleotide-directed in vitro mutagenesis system, version 2, Sculptor system (Amersham International plc., Bucks, UK) or Kunkel dUTP incorporation method [84, 85]. *Escherichia coli* TG1 [K12, Δ(*lac-pro*), *sup*E, *thi*, *hsdD5*/F′traD36, *pro*A + B$^+$, *lacI*^{q}, *lacZ*ΔM15] was obtained from the oligonucleotide-directed in vitro mutagenesis system version 2 (Amersham International plc.). Competent *E. coli* TG1 cells were transformed with mutagenesis product and single-stranded phagemid DNA was then prepared from TG1 cells superinfected with helper phage, while double-stranded phagemid DNA was isolated using Wizard Plus Minipreps DNA Purification System. Phagemid DNA was sequenced as described in Sequenase Protocol (United States Biochemical, Cleveland, OH, USA), using either single-stranded or double-stranded phagemid DNA. Upon confirmation of the mutations, the mutant double-stranded phagemid DNA was used to transform the *E. coli* production strain BL21(DE3)[F$^-$, *hsdS*, *gal*] [86], BL21(DE3) cells contain

the bacteriophage T7 gene 10 which encodes the bacteriophage T7 RNA polymerase. Gene 10 is under the control of *lac* UV5 promoter, inducible by IPTG.

29.11.4 Purification of Pro-domain

Fermentation of of pro-domain was carried out in *E. coli* as described for SBT. Pro-domain was purified using a freeze-thaw method to release soluble protein from the cells [84]. *E. coli* paste from a 1.5-L fermentation (~5 g) was suspended in 10 mL of cold phosphate-buffered saline (PBS) and 20 mL water. PMSF was added to a final concentration of 1 mM, DNase I to 10 μg mL^{-1}, and the oxidized form of glutathione (100 mg in 1 mL total volume of 100 mM KPi, pH 7.0) to 1.6 mg mL^{-1}. The resuspension was frozen by submerging in a dry-ice/ethanol bath until it was completely frozen, and then thawed in a room temperature water bath. This cycle was repeated two additional times, with addition of 100 μL glutathione stock solution before each cycle. The final mixture was centrifuged at 4 °C for 10 min at 10 000 rpm in a J2-21 centrifuge (Beckman Instruments) with a JA-14 rotor. The supernatant containing the soluble protein was diluted four-fold with 20 mM HEPES, pH 7.0, and further purified as described [56]. The concentration of proR9 was determined by UV absorbance using 1 mg $mL^{-1} = A_{275}$ of 0.67.

29.11.5 Kinetics of Pro-domain Binding to Native SBT

The rate of binding of the pro-domain to folded SBT was monitored by fluorescence (excitation $\lambda = 300$ nm, emission λ, 340 nm cutoff filter) using a KinTek Stopped-Flow Model SF2001. The reaction was followed by the 1.2-fold increase in the tryptophan fluorescence of SBT upon its binding of the pro-domain [56]. Pro-domain solutions of 10–160 μM in 30 mM Tris-HCl, pH, 5 mM KPi, pH 7.5 were mixed with an equal volume of 2 μM subtilisin, 30 mM Tris-HCl, pH, 5 mM KPi, pH 7.5 in a single mixing step. Typically 10–15 kinetics traces were collected for each [P]. Final [SBT] was 1 μM and final [P] were 5–80 μM.

29.11.6 Kinetic Analysis of Pro-domain Facilitated Subtilisin Folding

29.11.6.1 Single Mixing

Refolding of subtilisin is accompanied by a 1.5-fold increase in the tryptophan fluorescence of subtilisin upon folding into its complex with the pro-domain. There are three tryptophan residues in the subtilisin mutants and none in pro-domain. Reaction kinetics were measured using a KinTek Stopped-Flow Model SF2001 (excitation $\lambda = 300$ nm, emission: 340 nm cutoff filter) as described [61]. A stock solution of subtilisin at a concentration of 100 μM in 100 mM KPi, pH 7.0 was pre-

pared for refolding studies. Subtilisin was denatured by diluting 20 μL of the stock solution into 1 mL of 50 mM HCl. The samples were neutralized by mixing the subtilisin and HCl solution into an equal volume of 60 mM Tris-base, pH 9.4, KPi and pro-domain in the KinTek Stopped-flow (final buffer concentrations were 30 mM Tris-HCl, pH, 5 mM KPi, pH 7.5). The final concentration of subtilisin was 1 μM, while the pro-domain concentration was varied from 5 to 20 μM. Typically 10–15 kinetics traces were collected for each [P].

29.11.6.2 **Double Jump: Renaturation–Denaturation**

The kinetics of the formation of the folded complex, PS, were determined by a double-jump renaturation-denaturation experiment. The KinTek Stopped Flow in the three syringe configuration was used to perform the two mixing steps. In the first mixing step, 3 μM subtilisin in 50 mM HCl is mixed with a variable concentration of pro-domain in 60 mM Tris-base and KPi. The resulting solution is 30 mM Tris-HCl, 5 mM KPi, pH 7.5. The final concentration of subtilisin was 1.5 μM, while the pro-domain concentration was varied from 5 to 20 μM after the first mixing step. Subtilisin and pro-domain are allowed to fold under native conditions in the delay line of the stopped-flow instrument for aging times ranging from 0.5 to 60 s. After the prescribed aging time the subtilisin/pro-domain solution is mixed 2:1 with 0.1 M H_3PO_4 to bring the pH to 2.3. Fluorescence data for the denaturation of folded complex was collected after the second mixing step. At each renaturation time point, the denaturation curve was fit to a single exponential decay curve. The amplitude of the decay curve was recorded as a function of refolding time to assess the amount of folded complex which had accumulated at each renaturation time. Typically 10–15 kinetics traces were collected for each renaturation time point.

29.11.6.3 **Double Jump: Denaturation–Renaturation**

A double jump denaturation–renaturation experiment was used to study the effect of denaturation time on the rates and amplitudes of the folding reaction. The KinTek Stopped Flow in the three syringe configuration was used to perform the two mixing steps. In the first mixing reaction 3 μM of subtilisin and 30 μM proR9 in 0.05 M KPi, pH 7.2 was denatured by mixing with an equal volume of 0.1 M phosphoric acid. The resulting solution has a pH of 2.15. The denaturation reaction was aged for varied lengths of time and then mixed with one-half volume of 0.15 M KPO_4, pH 12.0. The final conditions were 1 μM of sbt15 and 10 μM of proR9 in 0.1 M KPi, pH 7.2, at 25 °C. The folding process is then followed by fluorescence change.

A second double mixing denaturation–renaturation experiment was used to follow folding kinetics after 0.5 s of denaturation. The two mixing steps were performed using a BioLogic SFM-4 Q/S in the stopped flow mode. In the first step, 2 μM SBT in 10 mM KPi, pH 7.2 is mixed with an equal volume of 100 mM HCl. The resulting solution is 1 μM SBT, 50 mM HCl, 5 mM KPi, pH 2.1. After 0.5 s, the denatured SBT solution is mixed with an equal volume of 60 mM Tris-base, 5 mM KPi and variable amounts of proR9. The resulting solution is 0.5 μM SBT,

5–20 μM proR9, 30 mM Tris-HCl, 5 mM KPi, pH 7.5. The renaturation process is followed by fluorescence change.

29.11.6.4 Triple Jump: Denaturation–Renaturation–Denaturation

A triple mixing denaturation–renaturation–denaturation experiment to measure directly the accumulation of native complex after a denaturation time of 0.5 s. The three mixing steps were performed using a BioLogic SFM-4 Q/S in the stopped flow mode. In the first step, 5 μM SBT in 10 mM KPi, pH 7.2 is mixed with an equal volume of 100 mM HCl. The resulting solution is 2.5 μM SBT, 50 mM HCl, 5 mM KPi, pH 2.1. After 0.5 s, the denatured SBT solution is mixed with an equal volume of 60 mM Tris-base, 5 mM KPi and 10 μM proR9. The resulting solution is 1.25 μM SBT, 5 μM proR9, 30 mM Tris-HCl, 5 mM KPi, pH 7.5. SBT and proR9 are allowed to fold under native conditions in the delay line for aging times ranging from 0.5 to 60 s. After the prescribed aging time the SBT-proR9 solution is mixed 3:1 with 0.132 M H_3PO_4 to bring the pH to 2.3 and denature the folding reaction. At each renaturation time point, the denaturation curve was fit to a single exponential decay curve. The amplitude of the decay curve was recorded as a function of refolding time to assess the amount of folded complex which had accumulated at each renaturation time.

References

1 Khan, A. R. & James, M. N. (1998). Molecular mechanisms for the conversion of zymogens to active proteolytic enzymes. *Protein Sci* 7, 815–36.

2 Zhou, Y. & Lindberg, I. (1993). Purification and characterization of the prohormone convertase PC1(PC3). *J Biol Chem* 268, 5615–23.

3 Baier, K., Nicklisch, S., Maldener, I. & Lockau, W. (1996). Evidence for propeptide-assisted folding of the calcium-dependent protease of the cyanobacterium Anabaena. *Eur J Biochem* 241, 750–5.

4 Fabre, E., Nicaud, J. M., Lopez, M. C. & Gaillardin, C. (1991). Role of the proregion in the production and secretion of the *Yarrowia lipolytica* alkaline extracellular protease. *J Biol Chem* 266, 3782–90.

5 Fabre, E., Tharaud, C. & Gaillardin, C. (1992). Intracellular transit of a yeast protease is rescued by trans-complementation with its prodomain. *J Biol Chem* 267, 15049–55.

6 Chang, Y. C., Kadokura, H., Yoda, K. & Yamasaki, M. (1996). Secretion of active subtilisin YaB by a simultaneous expression of separate pre-pro and pre-mature polypeptides in *Bacillus subtilis*. *Biochem Biophys Res Commun* 219, 463–8.

7 Baardsnes, J., Sidhu, S., MacLeod, A., Elliott, J., Morden, D., Watson, J. & Borgford, T. (1998). *Streptomyces griseus* protease B: secretion correlates with the length of the propeptide. *J Bacteriol* 180, 3241–4.

8 van den Hazel, H. B., Kielland-Brandt, M. C. & Winther, J. R. (1993). The propeptide is required for in vivo formation of stable active yeast proteinase A and can function even when not covalently linked to the mature region. *J Biol Chem* 268, 18002–7.

9 Cawley, N. X., Olsen, V., Zhang, C. F., Chen, H. C., Tan, M. & Loh, Y. P. (1998). Activation and processing of non-anchored yapsin 1 (Yap3p). *J Biol Chem* 273, 584–91.

10 Fukuda, R., Horiuchi, H., Ohta, A. & Takagi, M. (1994). The prosequence of Rhizopus niveus aspartic proteinase-I supports correct folding and secretion of its mature part in Saccharomyces cerevisiae. *J Biol Chem* 269, 9556–61.

11 Nirasawa, S., Nakajima, Y., Zhang, Z. Z., Yoshida, M. & Hayashi, K. (1999). Intramolecular chaperone and inhibitor activities of a propeptide from a bacterial zinc aminopeptidase. *Biochem J* 341 (Pt 1), 25–31.

12 Marie-Claire, C., Ruffet, E., Beaumont, A. & Roques, B. P. (1999). The prosequence of thermolysin acts as an intramolecular chaperone when expressed in trans with the mature sequence in *Escherichia coli*. *J Mol Biol* 285, 1911–15.

13 Cao, J., Hymowitz, M., Conner, C., Bahou, W. F. & Zucker, S. (2000). The propeptide domain of membrane type 1-matrix metalloproteinase acts as an intramolecular chaperone when expressed in trans with the mature sequence in COS-1 cells. *J Biol Chem* 275, 29648–53.

14 Ventura, S., Villegas, V., Sterner, J., Larson, J., Vendrell, J., Hershberger, C. L. & Aviles, F. X. (1999). Mapping the pro-region of carboxypeptidase B by protein engineering. Cloning, overexpression, and mutagenesis of the porcine proenzyme. *J Biol Chem* 274, 19925–33.

15 Wetmore, D. R. & Hardman, K. D. (1996). Roles of the propeptide and metal ions in the folding and stability of the catalytic domain of stromelysin (matrix metalloproteinase 3). *Biochemistry* 35, 6549–58.

16 Yamamoto, Y., Watabe, S., Kageyama, T. & Takahashi, S. Y. (1999). Proregion of Bombyx mori cysteine proteinase functions as an intramolecular chaperone to promote proper folding of the mature enzyme. *Arch Insect Biochem Physiol* 42, 167–78.

17 James, M. N., Delbaere, L. T. & Brayer, G. D. (1978). Amino acid sequence alignment of bacterial and mammalian pancreatic serine proteases based on topological equivalences. *Can J Biochem* 56, 396–402.

18 Siezen, R. J. & Leunissen, J. A. (1997). Subtilases: the superfamily of subtilisin-like serine proteases. *Protein Sci* 6, 501–23.

19 Steiner, D., Smeekens, S. P., Ohagi, S. & Chan, S. J. (1992). The new enzymology of precursor processing endoproteases. *J. Mol. Biol.* 267, 23435–8.

20 Holyoak, T., Wilson, M. A., Fenn, T. D., Kettner, C. A., Petsko, G. A., Fuller, R. S. & Ringe, D. (2003). 2.4 A resolution crystal structure of the prototypical hormone-processing protease Kex2 in complex with an Ala-Lys-Arg boronic acid inhibitor. *Biochemistry* 42, 6709–18.

21 Henrich, S., Cameron, A., Bourenkov, G. P., Kiefersauer, R., Huber, R., Lindberg, I., Bode, W. & Than, M. E. (2003). The crystal structure of the proprotein processing proteinase furin explains its stringent specificity. *Nat Struct Biol* 10, 520–6.

22 Kraut, J. (1971). Subtilisin x-ray structure. In *The Enzymes* 3rd edn, Vol. 3, pp. 547–60. Academic, New York.

23 McPhalen, C. A., Schnebli, H. P. & James, M. N. (1985). Crystal and molecular structure of the inhibitor eglin from leeches in complex with subtilisin Carlsberg. *FEBS Lett* 188, 55–8.

24 McPhalen, C. A. & James, M. N. G. (1987). Crystal and molecular structure of the serine proteinase inhibitor CI-2 from barley seeds. *Biochemistry* 26, 261–9.

25 McPhalen, C. A. & James, M. N. G. (1988). Structural comparison of two serine proteinase–protein inhibitor complexes: Eglin-C-Subtilisin Carlsberg and CI-2-Subtilisin novo. *Biochemistry* 27, 6582–98.

26 Pantoliano, M. W., Whitlow, M., Wood, J. F. et al. (1988). The engineering of binding affinity at metal ion binding sites for the stabilization of proteins: Subtilisin as a test case. *Biochemistry* 27, 8311–17.

27 Gallagher, T. D., Bryan, P. & Gilliland, G. (1993). Calcium-free subtilisin by design. *Proteins Struct Funct Genetics* 16, 205–13.

28 Bryan, P., Alexander, P., Strausberg, S. et al. (1992). Energetics of folding subtilisin BPN′. *Biochemistry* 31, 4937–45.

29 Almog, O., Gallagher, T., Tordova, M., Hoskins, J., Bryan, P. & Gilliland, G. L. (1998). Crystal structure of calcium-independent subtilisin BPN′ with restored thermal stability folded without the pro-domain. *Proteins* 31, 21–32.

30 Gallagher, T. D., Gilliland, G., Wang, L. & Bryan, P. (1995). The prosegment-subtilisin BPN′ complex: crystal structure of a specific foldase. *Structure* 3, 907–14.

31 Jain, S. C., Shinde, U., Li, Y., Inouye, M. & Berman, H. M. (1998). The crystal structure of an autoprocessed Ser221Cys-subtilisin E-propeptide complex at 2.0 A resolution. *J Mol Biol* 284, 137–44.

32 Lesk, A. M. & Fordham, W. D. (1996). Conservation and variability in the structures of serine proteinases of the chymotrypsin family. *J Mol Biol* 258, 501–37.

33 Higaki, J. N., Evnin, L. B. & Craik, C. S. (1989). Introduction of a cysteine protease active site into trypsin. *Biochemistry* 28, 9256–63.

34 Vasquez, J. R., Evnin, L. B., Higaki, J. N. & Craik, C. S. (1989). An expression system for trypsin. *J Cell Biochem* 39, 265–76.

35 McGrath, M. E., Wilke, M. E., Higaki, J. N., Craik, C. S. & Fletterick, R. J. (1989). Crystal structures of two engineered thiol trypsins. *Biochemistry* 28, 9264–70.

36 Cunningham, E. L., Jaswal, S. S., Sohl, J. L. & Agard, D. A. (1999). Kinetic stability as a mechanism for protease longevity. *Proc Natl Acad Sci USA* 96, 11008–14.

37 Sauter, N. K., Mau, T., Rader, S. D. & Agard, D. A. (1998). Structure of alpha-lytic protease complexed with its pro region. *Nat Struct Biol* 5, 945–50.

38 Baker, D. (1998). Metastable states and folding free energy barriers. *Nat Struct Biol* 5, 1021–4.

39 Cunningham, E. L., Mau, T., Truhlar, S. M. & Agard, D. A. (2002). The Pro region N-terminal domain provides specific interactions required for catalysis of alpha-lytic protease folding. *Biochemistry* 41, 8860–7.

40 Tangrea, M. A., Alexander, P., Bryan, P. N., Eisenstein, E., Toedt, J. & Orban, J. (2001). Stability and global fold of the mouse prohormone convertase 1 pro-domain. *Biochemistry* 40, 5488–95.

41 Tangrea, M. A., Bryan, P. N., Sari, N. & Orban, J. (2002). Solution structure of the Pro-hormone convertase 1 pro-domain from *Mus musculus*. *J Mol Biol* 320, 801–12.

42 Guasch, A., Coll, M., Aviles, F. X. & Huber, R. (1992). Three-dimensional structure of porcine pancreatic procarboxypeptidase A. A comparison of the A and B zymogens and their determinants for inhibition and activation. *J Mol Biol* 224, 141–57.

43 Coll, M., Guasch, A., Aviles, F. X. & Huber, R. (1991). Three-dimensional structure of porcine procarboxypeptidase B: a structural basis of its inactivity. *EMBO J* 10, 1–9.

44 Baker, D., Sohl, J. L. & Agard, D. A. (1992). A protein-folding reaction under kinetic control. *Nature* 356, 263–5.

45 Sohl, J. L., Jaswal, S. S. & Agard, D. A. (1998). Unfolded conformations of alpha-lytic protease are more stable than its native state. *Nature* 395, 817–19.

46 Ottesen, M. & Svendsen, I. (1970). The subtilisins. *Methods Enzymol* 19, 199–215.

47 Poland, D. C. & Scheraga, H. A. (1965). Statistical mechanics of noncovalent bonds in polyamino acids. VIII. Covalent loops in proteins. *Biopolymers* 3, 379–99.

48 Pace, C. N., Grimsley, G. R., Thomson, J. A. & Barnett, B. J. (1988). Conformational stabilities and activity of ribonuclease T1 with zero,

one and two intact disulfide bonds. *J Biol Chem* 263, 11820–5.

49 Derman, A. I. & Agard, D. A. (2000). Two energetically disparate folding pathways of alpha-lytic protease share a single transition state. *Nat Struct Biol* 7, 394–7.

50 Carter, P. & Wells, J. A. (1988). Dissecting the catalytic triad of a serine protease. *Nature* 332, 564–8.

51 Voordouw, G., Milo, C. & Roche, R. S. (1976). Role of bound calcium in thermostable, proteolytic enzymes. Separation of intrinsic and calcium ion contributions to the kinetic thermal stability. *Biochemistry* 15, 3716–24.

52 Alexander, P. A., Ruan, B. & Bryan, P. N. (2001). Cation-dependent stability of subtilisin. *Biochemistry* 40, 10634–9.

53 Eder, J., Rheinnecker, M. & Fersht, A. R. (1993). Folding of subtilisin BPN′: Characterization of a folding intermediate. *Biochemistry* 32, 18–26.

54 Eder, J., Rheinnecker, M. & Fersht, A. R. (1993). Folding of subtilisin BPN′: role of the pro-sequence. *J Mol Biol* 233, 293–304.

55 Hayashi, T., Matsubara, M., Nohara, D., Kojima, S., Miura, K. & Sakai, T. (1994). Renaturation of the mature subtilisin BPN′ immobilized on agarose beads. *FEBS Lett* 350, 109–12.

56 Strausberg, S., Alexander, P., Wang, L., Schwarz, F. & Bryan, P. (1993). Catalysis of a protein folding reaction: Thermodynamic and kinetic analysis of subtilisin BPN′ interactions with its propeptide fragment. *Biochemistry* 32, 8112–19.

57 Ohta, Y., Hojo, H., Aimoto, S., Kobayashi, T., Zhu, X., Jordan, F. & Inouye, M. (1991). Pro-peptide as an intramolecular chaperone: renaturation of denatured subtilisin E with a synthetic pro-peptide [corrected]. *Mol Microbiol* 5, 1507–10.

58 Baker, D., Silen, J. L. & Agard, D. A. (1992). Protease pro region required for folding is a potent inhibitor of the mature enzyme. *Proteins* 12, 339–44.

59 Silen, J. L. & Agard, D. A. (1989). The alpha-lytic protease pro-region does not require a physical linkage to activate the protease domain in vivo. *Nature* 341, 462–4.

60 Peters, R. J., Shiau, A. K., Sohl, J. L. et al. (1998). Pro region C-terminus:protease active site interactions are critical in catalyzing the folding of alpha-lytic protease. *Biochemistry* 37, 12058–67.

61 Bryan, P., Wang, L., Hoskins, J. et al. (1995). Catalysis of a protein folding reaction: Mechanistic implications of the 2.0 Å structure of the subtilisin-prodomain complex. *Biochemistry* 34, 10310–18.

62 Li, Y., Hu, Z., Jordan, F. & Inouye, M. (1995). Functional analysis of the propeptide of subtilisin E as an intramolecular chaperone for protein folding. Refolding and inhibitory abilities of propeptide mutants. *J Biol Chem* 270, 25127–32.

63 Ruvinov, S., Wang, L., Ruan, B. et al. (1997). Engineering the independent folding of the subtilisin BPN′ prodomain: analysis of two-state folding vs. protein stability. *Biochemistry* 36, 10414–21.

64 Kojima, S., Minagawa, T. & Miura, K. (1997). The propeptide of subtilisin BPN′ as a temporary inhibitor and effect of an amino acid replacement on its inhibitory activity. *FEBS Lett* 411, 128–32.

65 Kojima, S., Minagawa, T. & Miura, K. (1998). Tertiary structure formation in the propeptide of subtilisin BPN′ by successive amino acid replacements and its close relation to function. *J Mol Biol* 277, 1007–13.

66 Ruan, B., Hoskins, J. & Bryan, P. N. (1999). Rapid folding of calcium-free subtilisin by a stabilized pro-domain mutant. *Biochemistry* 38, 8562–71.

67 Kojima, S., Yanai, H. & Miura, K. (2001). Accelerated refolding of subtilisin BPN′ by tertiary-structure-forming mutants of its propeptide. *J Biochem (Tokyo)* 130, 471–4.

68 Ruan, B., Hoskins, J., Wang, L. & Bryan, P. N. (1998). Stabilizing the subtilisin BPN′ pro-domain by phage display selection: how restrictive is the

amino acid code for maximum protein stability? *Protein Sci* 7, 2345–53.

69 Wang, L., Ruan, B., Ruvinov, S. & Bryan, P. N. (1998). Engineering the independent folding of the subtilisin BPN′ pro-domain: correlation of pro-domain stability with the rate of subtilisin folding. *Biochemistry* 37, 3165–71.

70 Ruan, B. (1998). Folding of subtilisin: Study of independent folding and pro-domain catalyzed folding. PhD Dissertation, University of Maryland, College Park.

71 Brandts, J. F., Halvorson, H. R. & Brennan, M. (1975). Consideration of the Possibility that the slow step in protein denaturation reactions is due to cis-trans isomerism of proline residues. *Biochemistry* 14, 4953–63.

72 Bai, Y., Sosnick, T. R., Mayne, L. & Englander, S. W. (1995). Protein folding intermediates: native-state hydrogen exchange. *Science* 269, 192–7.

73 Chamberlain, A. K., Handel, T. M. & Marqusee, S. (1996). Detection of rare partially folded molecules in equilibrium with the native conformation of RNaseH. *Nat Struct Biol* 3, 782–7.

74 Chung, E. W., Nettleton, E. J., Morgan, C. J. et al. (1997). Hydrogen exchange properties of proteins in native and denatured states monitored by mass spectrometry and NMR. *Protein Sci* 6, 1316–24.

75 Jaswal, S. S., Sohl, J. L., Davis, J. H. & Agard, D. A. (2002). Energetic landscape of alpha-lytic protease optimizes longevity through kinetic stability. *Nature* 415, 343–6.

76 Waldburger, C. D., Jonsson, T. & Sauer, R. T. (1996). Barriers to protein folding: formation of buried polar interactions is a slow step in acquisition of structure. *Proc Natl Acad Sci USA* 93, 2629–34.

77 Waldburger, C. D., Schildbach, J. F. & Sauer, R. T. (1995). Are buried salt bridges important for protein stability and conformational specificity? *Nat Struct Biol* 2, 122–8.

78 Yabuta, Y., Subbian, E., Takagi, H., Shinde, U. & Inouye, M. (2002). Folding pathway mediated by an intramolecular chaperone: dissecting conformational changes coincident with autoprocessing and the role of Ca^{2+} in subtilisin maturation. *J Biochem (Tokyo)* 131, 31–7.

79 Baker, D., Shiau, A. K. & Agard, D. A. (1993). The role of pro regions in protein folding. *Curr Opin Cell Biol* 5, 966–70.

80 Strausberg, S., Alexander, P., Gallagher, D. T., Gilliland, G., Barnett, B. L. & Bryan, P. (1995). Directed evolution of a subtilisin with calcium-independent stability. *Bio/technology* 13, 669–73.

81 Alexander, P. A., Ruan, B., Strausberg, S. L. & Bryan, P. N. (2001). Stabilizing mutations and calcium-dependent stability of subtilisin. *Biochemistry* 40, 10640–4.

82 DelMar, E., Largman, C., Brodrick, J. & Geokas, M. (1979). A sensitive new substrate for chymotrypsin. *Anal Biochem* 99, 316–20.

83 Alexander, P., Fahnestock, S., Lee, T., Orban, J. & Bryan, P. (1992). Thermodynamic analysis of the folding of the streptococcal protein G IgG-binding domains B1 and B2: why small proteins tend to have high denaturation temperatures. *Biochemistry* 31, 3597–603.

84 Kunkel, T. A. (1985). Rapid and efficient site-specific mutagenesis without phenotypic selection. *Proc Natl Acad Sci USA* 82, 488–92.

85 Kunkel, T. A., Sabatino, R. D. & Bambara, R. A. (1987). Exonucleolytic proofreading by calf thymus DNA polymerase delta. *Proc Natl Acad Sci USA* 84, 4865–9.

86 Studier, F. W. & Moffatt, B. A. (1986). Use of bacteriophage T7 RNA polymerase to direct selective high-level expression of cloned genes. *J Mol Biol* 189, 113–30.

30
The Thermodynamics and Kinetics of Collagen Folding

Hans Peter Bächinger and Jürgen Engel

30.1
Introduction

30.1.1
The Collagen Family

The human collagen family of proteins now consists of 27 types. The individual members are numbered with roman numerals. The family is subdivided in different classes: The fibrillar collagens (types I*, II, III, V*, XI*, XXIV, and XXVII), basement membrane collagens (type IV*), fibril-associated collagens with interrupted triple helices (FACIT collagens, types IX*, XII, XIV, XVI, XIX, XX and XXII), short chain collagens (types VIII* and X), anchoring fibril collagen (type VII), multiplexins (types XV and XVIII), membrane-associated collagens with interrupted triple helices (MACIT collagens, types XIII, XVII, XXIII, and XXV), and collagen type VI*. The types indicated by an asterisk are heterotrimers, consisting of two or three different polypeptide chains. All others consist of three identical chains or the chain composition is unknown. For type IV collagens six different polypeptide chains are known that form at least three distinct molecules and type V collagens contain three polypeptide chains in probably three molecules. The common feature of all collagens is the occurrence of triple helical domains with the repeated sequence -Gly-Xaa-Yaa- in the primary structure and the high content of proline and hydroxyproline residues. This sequence allows for the formation of a tertiary structure consisting of three polypeptide chains in a left-handed polyproline II helix. The three chains form a right-handed supercoiled triple helix, which is stabilized by hydrogen bonds. The glycine residues in every third position are packed tightly in the center of the triple helix. The residues in the Xaa and Yaa positions are exposed to the solvent and are often proline and hydroxyproline, respectively. All collagens are extracellular matrix proteins responsible for the architecture of connective tissues, such as bone, tendon, cartilage, skin, and basement membranes. Besides their structural roles, collagens interact with numerous other molecules and are crucial for development and homeostasis of connective tissue.

Protein Folding Handbook. Part I. Edited by J. Buchner and T. Kiefhaber

ISBN: 3-527-30784-2

30.1.2 Biosynthesis of Collagens

The biosynthesis of procollagens is now fairly well understood at least for the most abundant fibrillar collagens [1, 2]. The current hypothesis of fibrillar procollagen biosynthesis involves the following steps:

1. Translocation of the emerging N-terminal end of the pro-α-chains into the rER.
2. Soon after the synthesis of the N-terminal propeptide, this domain folds and forms intrachain disulfide bonds. HSP47, a collagen-specific heat shock protein, may specifically bind to the N-terminal propeptide, but additionally has binding sites along the helical portion of the molecule.
3. The synthesis continues and some of the proline residues become hydroxylated by prolyl 4-hydroxylase (EC 1.14.11.2) and prolyl 3-hydroxylase (EC 1.14.11.7). During the continued synthesis of the major helical sequences, some interactions with molecular chaperones take place to prevent premature triple helix formation. Some lysine residues are hydroxylated by lysyl hydroxylase (EC 1.14.11.4).
4. After completion of the synthesis of the C-terminal propeptide, this part of the molecule folds, forms intrachain disulfide bonds, and interacts directly or indirectly (with a docking molecule) with the lipid bilayer of the rER.
5. Selection and association of the correct chains occur by diffusion of the C-terminal propeptides attached to the rER membrane.
6. A nucleus for triple helix formation is formed that aligns the chains in the right order. This nucleus initiates triple helix formation and is between propeptides stabilized by interchain disulfide bonds being formed, a reaction probably catalyzed by protein disulfide isomerase (PDI). In mutations of the C-terminal propeptides, an association with GRP78/BiP is found, indicating a potential role for GRP78/BiP in the assembly of procollagen chains.
7. Hydroxylation of proline residues and some lysine residues continues and triple helix formation proceeds from the C-terminal end towards the N-terminal end. The fast propagation of the triple helix formation is followed by a slower folding determined by *cis* peptide bond isomerization at proline residues. These peptide bonds need to be isomerized into *trans* conformation to allow triple helix formation to continue. This step is catalyzed by peptidyl-prolyl *cis-trans* isomerases (PPIases).
8. After completion of the folding of the major helix, the N-terminal propeptides associate and form the small triple helix within this domain. Further modifications occur during the transport through the Golgi stack by cisternal maturation. The long-standing problem of how a 300-nm-long procollagen molecule is transported to the Golgi in 50-nm transport vesicles has recently been investigated [3, 4]. Procollagen traverses the Golgi stack without leaving the lumen of the cisternae, but rather is transported by cisternal maturation. Nothing is known about what proteins direct that process.

The rate of synthesis of procollagen chains was measured for type I and II collagen, and found to be 209 residues per minute [5, 6]. For a fibrillar procollagen mol-

ecule, the synthesis time then is about 7 min. The time for secretion was 30 min when analyzed in bone [7] and biphasic secretion kinetics with half-times of 14 and 115 min were found in fibroblasts [8].

30.1.3 The Triple Helical Domain in Collagens and Other Proteins

The length of the triple helix in fibrillar collagens is about 300 nm and consists of 330–340 Gly-Xaa-Yaa tripeptide units. These molecules can be described as semi-rigid rods, well suited for the formation of fibrils. The fibrils have an axial 67-nm periodicity, which results from electrostatic and hydrophobic sidechain interactions [9]. In other collagens, stretches of tripeptide units are interspersed by interruptions, making these molecules more flexible. A large variation in the length of triple helices can be found in nature, the shortest collagen described is 14 nm long (mini-collagen of hydra) and the longest one 2400 nm (cuticle collagen of annelids) [10]. Gly-Xaa-Yaa repeats that form triple helices are also found in a number of other proteins: complement protein C1q, lung surfactant proteins A and D, mannose-binding protein, macrophage scavenger receptors A (types I, II, and III) and MARCO, ectodysplasin-A, scavenger receptor with C-type lectin (SRCL), the ficolins (L, M and H), the asymmetric form of acetylcholinesterase, adiponectin, and hibernation proteins HP-20, 25, and 27.

30.1.4 N- and C-Propeptide, Telopeptides, Flanking Coiled-Coil Domains

All collagens are synthesized with noncollagenous domains. The fibrillar collagens contain an N-terminal propeptide, an N-terminal telopeptide, the major triple helix, a C-terminal telopeptide and a C-terminal propeptide. The propeptides prevent premature fibril formation within the cell and are cleaved by specific proteases within both the N- and C-terminal telopeptides. The C-terminal propeptide is responsible for chain selection and association. The N-terminal end of the C-terminal propeptide contains three to four heptad repeats indicative of a coiled-coil structure that might facilitate its trimerization and the nucleation of the triple helix [11]. After cleavage, the remaining telopeptides play important roles in the formation of fibrils. The telopeptides also contain the lysine residues for the formation of covalent cross-links between molecules. The N-terminal propeptide consists of a globular domain and a minor triple helix. The globular domain potentially interacts with growth factors. Coiled-coil domains are prevelant in nonfibrillar collagens as well. The transmembrane domain-containing molecules with triple helices show a preference for a coiled-coil domain at the N-terminal end of the ectodomain.

30.1.5 Why is the Folding of the Triple Helix of Interest?

Folding studies of collagens are of interest because of the unusual structure of the collagen triple helix, which is an obligatory trimer. The three chains have to com-

bine to the native state and do not have a defined structure if dissociated. Collagen belongs to the class of filamentous proteins and the mechanism of the folding process is distinctly different from folding pathways in globular proteins. Because of the repeating sequence and the uniform structure, wrong alignments of chains are likely and these are prevented by oligomerization domains.

There are also a number of practical aspects, which render folding studies interesting. Inherited and spontaneous mutations decrease triple helix stability and slow down the folding kinetics. Folding studies of wild-type and mutated collagens are needed for an understanding of theses diseases, which cause severe tissue disorders. The present review surveys the current knowledge of collagen folding. An earlier recent review on collagen folding is by Baum and Brodsky [12] and a useful general chapter on collagens was written by Bateman et al. [13].

30.2 Thermodynamics of Collagen Folding

30.2.1 Stability of the Triple Helix

The collagen molecules undergo a highly cooperative transition from a triple helix to an unfolded state upon heating. The temperature at the midpoint of this transition is termed T_m and is specific for different collagens from different species. Interestingly, the T_m of the collagens is around the body temperature of the organism from which it is isolated [14]. A linear correlation between the T_m and the number of imino acid residues was noticed early on [15]. Later, a better correlation was found between the T_m and the 4(*R*)-hydroxyproline content [16, 17]. Hydroxylation of proline residues is therefore important for the stability of the collagen triple helix and a summary of the posttranslational modifications of collagen molecules is needed. Further stabilization of the collagen molecules is achieved by the formation of supramolecular structures such as fibrils. In this review, we will only deal with individual collagen molecules in solution. The unfolding transition of triple helices occurs in a very narrow temperature interval, indicating a highly cooperative process. The T_m was found to be dependent on the rate of the increase in temperature and a hysteresis or apparent irreversibility is observed for the thermal transition of most extracted collagens. These difficulties in measuring such transition curves have led to the proposal that the collagen molecule is only kinetically stable [18, 19]. True equilibrium transition curves have been measured only recently for such collagens [14, 20]. From these measurements and from transition curves of short fragments of collagen or collagen-like synthetic peptides, it is now established that the collagen triple helix is a thermodynamically stable structure but establishment of equilibrium is slow. Synthetic collagen-like peptides have been extensively used in the characterization of the triple helical structure and its stability.

30.2.2
The Role of Posttranslational Modifications

Collagen molecules undergo extensive posttranslational modifications in the rough endoplasmic reticulum during biosynthesis (for a review see Refs [21, 22]). These enzymatic modifications occur on the nascent chains and require the collagen chains in an unfolded structure. Triple helical molecules are no longer substrates for these enzymes and it is thought that this regulates the stability of the triple helix. Three enzymes are involved in the hydroxylation of proline and lysine residues. Prolyl 4-hydroxylase (EC 1.14.11.2) hydroxylates proline residues in the Yaa position of collagens to form 4(*R*)-hydroxyproline [22]. Prolyl 3-hydroxylase (EC 1.14.11.7) can hydroxylate proline residues in the Xaa position to 3(*S*)-hydroxyproline, if the Yaa position is 4(*R*)-hydroxyproline. This modification occurs much less frequently in vertebrate collagens than the "obligatory" 4-hydroxylation. Certain lysine residues in collagen sequences are hydroxylated by lysine hydroxylase (EC 1.14.11.4) and *O*-linked oligosaccharides are attached. The carbohydrates were identified as 2-*O*-α-D-glucosyl-*O*-β-D-galactosylhydroxylysine and *O*-β-D-galactosylhydroxylysine. Hydroxylysine residues are also used for cross-linking of different collagen molecules in fibrils.

All these modifications affect the thermal stability of the collagen triple helix. When the stability of procollagen is investigated from cells that are incubated with α,α′-dipyridyl, an inhibitor of hydroxylases, the T_m was found to be about 15 °C lower than in the presence of hydroxylation. Such unhydroxylated procollagens are poorly secreted and tend to accumulate in the rough endoplasmic reticulum of the cell.

30.2.3
Energies Involved in the Stability of the Triple Helix

The enthalpy change of the coil ⇄ triple helix transition for collagens was determined to be $\Delta H^\circ - (15\text{–}18)$ kJ mol^{-1} tripeptide units [15]. The enthalpy change increases with increasing imino acid content. On a per residue basis, the change of negative enthalpy for structure formation of triple helices is significantly larger than that of globular proteins. The source of this large change in enthalpy is still controversial.

Another unique feature is the temperature independence of ΔH°. The specific heat of the reaction is zero within the error limits of the measurements [15]. Of the classical energies that determine protein stability, the electrostatic effect is the easiest to deal with in collagen. The stability of the collagen triple helix is only minimally affected by pH and salt concentrations, therefore electrostatic interactions can only play a minor role in the stability of the triple helix. The hydrophobic effect probably plays a role in stabilizing the triple helix, but its effect is not as dominant as in the stability of globular proteins. From the structure of the triple helix, it is evident that an interchain hydrogen bond between the NH group of glycine and the CO group of the amino acid in the Xaa position of a neighboring chain is pres-

ent. Hydrogen exchange studies indicate that two classes of hydrogen bonds exist. The first class consists of 1.0 ± 0.1 very slowly exchanging hydrogens per tripeptide unit and a second class of 0.7 ± 0.1 slowly exchanging hydrogens per tripeptide unit [166]. It is likely that the first class comprises the above-mentioned hydrogen bond. If the Xaa and Yaa positions are not occupied by proline residues, it was suggested that an additional interchain hydrogen bond can form between the carbonyl group of glycine and the amino group of the Xaa residue, probably involving one or two water molecules.

The particular effectiveness of 4(*R*)-hydroxyproline in stabilizing the triple helix has led to suggestions that it may form additional hydrogen bonds through an extended water structure [23]. This notion became weaker, when it was shown that 4(*R*)-fluoroproline formed more stable triple helices than 4(*R*)-hydroxyproline [24, 25]. The replacement of the hydroxyl group by fluorine has several effects. The inductive effect of the fluorine group influences the pucker of the pyrrolidine ring. This is a stereoelectronic effect as it depends on the configuration of the substituent. 4(*R*) substituents stabilize the Cγ-exo pucker, while 4(*S*) substituents stabilize the Cγ-endo pucker. The X-ray structure of $(\text{Pro-Pro-Gly})_{10}$ showed a preference of proline residues in the Xaa position in Cγ-endo pucker, while the Yaa position prolines preferred Cγ-exo puckering [26, 27]. This puckering influences the range of the main chain dihedral angles φ and ψ of proline, which are required for optimal packing in the triple helix. In addition, the trans/cis ratio of the peptide bond is influenced by the substituent [24]. Because all peptide bonds in the triple helix have to be trans, the helix is stabilized, if the amount of trans peptide bonds in the unfolded state is increased. None of these individual effects can fully explain the observed stability of the triple helix and it is difficult to quantitate the contribution of each of them.

A thermodynamic analysis of the triple coil $\rightleftarrows$ triple helix transition of fibrillar collagens shows that the calorimetric enthalpy and the van't Hoff enthalpy are significantly different [15]. The ratio of the van't Hoff enthalpy and the calorimetric enthalpy determines the cooperative length. For fibrillar collagens type I, II, and III a cooperative length of about 80–100 tripeptide units was determined [28]. This corresponds to about one-tenth of the total length of the triple helix. Therefore, the all-or-none model should be a good approximation for the shorter synthetic peptides. The cooperative length is an average parameter that applies to the whole triple helix and does not take into account the sequence variations that occur within a given molecule.

Because the rate of unfolding of the collagen triple helix is very slow in the transition region (see Section 30.3.4.4), great care must be given to the experimental rate of heating. Figures 30.1 and 30.2 show the dependence of the T_m of type III collagen as a function of the rate of heating. The T_m does not vary linearly with the heating rate and true equilibrium curves are only obtained by extrapolation of the heating rate to 0 (Figure 30.2). It should also be noted that most collagens show an irreversible denaturation curve, because the molecules were proteolytically cleaved and lack important domains for folding.

No equilibrium intermediates were observed during the unfolding transition for

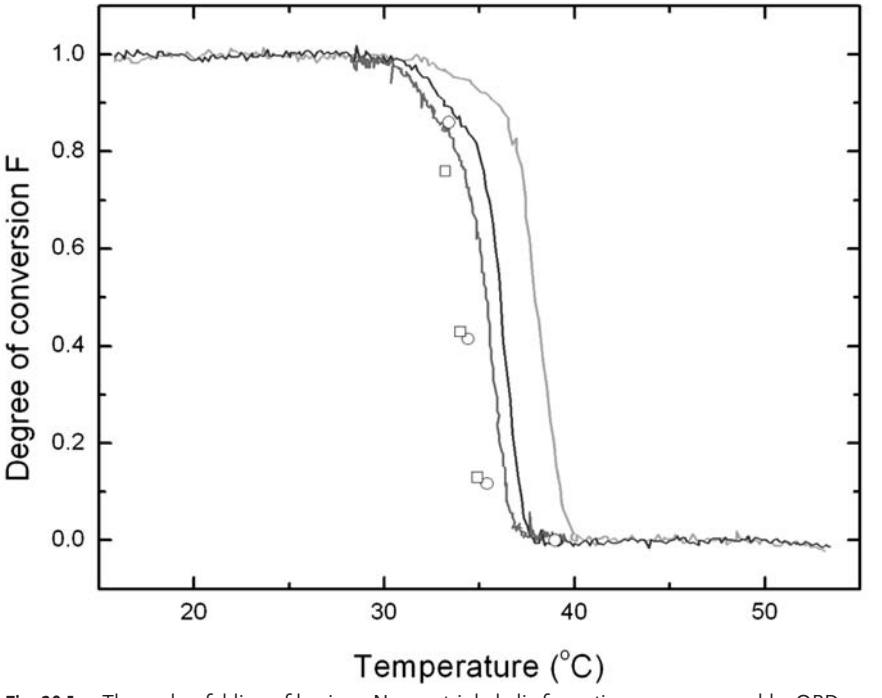

Fig. 30.1. Thermal unfolding of bovine pN type III collagen at different heating rates (thin line = 10 °C h^{-1}, thick line = 2 °C h^{-1}, and dashed line = 0.5 °C h^{-1}). The fraction of triple helix formation was measured by ORD at 365 nm. The endpoints of the unfolding (squares) and refolding (circles) kinetics at the indicated temperature are also shown.

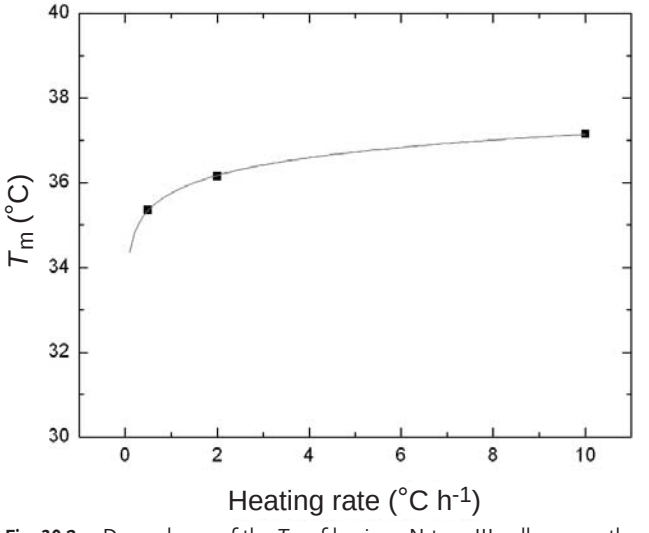

Fig. 30.2. Dependence of the T_m of bovine pN type III collagen on the rate of heating.

the triple helices of type I, II, and III collagen, despite the heterogeneity of the amino acid sequences along the triple helix. Several attempts have been made to calculate differences in stabilities of triple helical regions with the collagen triple helices. Sequence-dependent stabilities were calculated and these can explain the occurrence of unfolding intermediates in the transition of types V and XI collagen [29].

30.2.4 Model Peptides Forming the Collagen Triple Helix

30.2.4.1 Type of Peptides

Synthetic peptides containing Gly-Xaa-Yaa repeats have been used extensively to study the thermal stability and folding of the collagen triple helix. These peptides can be synthesized as either single chains or cross-linked peptides. The first peptides were synthesized by polycondensation of tri- or hexa-peptide units (for a review see Ref. [30]). This procedure resulted in a broad molecular weight distribution that was difficult to fractionate. The introduction of solid-phase methods allowed the synthesis of peptides with a defined chain length. In 1968 Sakakibara synthesized $(\text{Pro-Pro-Gly})_n$ with $n = 5, 10, 15$, and 20 [31]. Later, the oligomers of $(\text{Gly-Pro-Gly})_n$ $n = 1$–8 [32], $(\text{Gly-Pro-Pro})_n$ $n = 3$–7 [33], $(\text{Pro-4}(R)\text{Hyp-Gly})_n$ $n = 5$–10 [34], and $(\text{Pro-Pro-Gly})_n$ $n = 10, 12, 14$, and 15 [35] were synthesized. Sutoh and Noda introduced the concept of block copolymers, where two blocks of $(\text{Pro-Pro-Gly})_n$ $n = 5, 6$, or 7 were separated by a block of $(\text{Ala-Pro-Gly})_m$ $m = 5, 3$, and 1, respectively [35]. This concept was later extended to include all amino acids and called host-guest peptide system. The most studied host-guest system uses the sequence Ac-$(\text{Gly-Pro-4}(R)\text{Hyp})_3$-Gly-Xaa-Yaa-$(\text{Gly-Pro-4}(R)\text{Hyp})_4$-Gly-Gly-$NH_2$ [36], but other variations were also studied [37, 38].

Because the stability of collagen-like peptides is highly concentration dependent, covalently linked peptides were synthesized by various methods. Heidemann used propane tricarboxylate tris(pentachlorophenyl) and *N*-tris(6-amino hexanoyl)-lysyl-lysine as covalent bridging molecules for the three chains [39]. Other covalent linkers include Kemp triacid [40], a modified dilysine system [41], the sequence found at the C-terminal end of type III collagen Gly-Pro-Cys-Cys-Gly [42–46], and tris(2-aminoethyl)amine with succinic acid spacers [47]. Peptides with covalent cross-links at both ends were also synthesized [48]. The noncovalent obligatory trimer foldon [46], peptide amphiphiles [49–51], and the iron (II) complex of bipyridine [52] have also been used to study trimeric peptides.

Initially, all peptides were studied as homotrimers, but strategies were developed to synthesize heterotrimers. Fields proposed the dilysine system to synthesize heterotrimeric peptides of type IV collagen [41] and Moroder used a simplified cysteine bridge to synthesize the collagenase cleavage site of type I collagen [53].

30.2.4.2 The All-or-none Transition of Short Model Peptides

We will start with the triple helix $\rightleftarrows$ coil transition of single chains. The simplest mechanism for this transition can be written as follows [54]:

$$3C \overset{\beta s^x}{\rightleftharpoons} H_x \overset{s}{\rightleftharpoons} \cdots \overset{s}{\rightleftharpoons} H_i \overset{s}{\rightleftharpoons} \cdots \overset{s}{\rightleftharpoons} H_{3n-2} \tag{1}$$

where C is a coiled chain, H_i is a triple helical species with i tripeptide units in a triple helical conformation, β is the cooperativity parameter for the nucleation step, βs^x is the equilibrium constant for the step forming nucleus H_x, c_o is the total concentration of chains and s is the equilibrium constant for the addition of a tripeptide unit after nucleation. Because of the staggering of the chains, only $3n - 2$ tripeptide units can form hydrogen bonds in the triple helix and the complete triple helix is designated as H_{3n-2}. After nucleation, the triple helix is completed in propagation steps, which is the conversion of a coiled tripeptide unit adjacent to a triple helical tripeptide unit into a triple helical tripeptide unit. Since all these steps are essentially identical, the same equilibrium constant is applied to all of them. The process can be simplified if n is relatively small and $\beta {c_o}^2$ is less than 1. Under these conditions, the concentration of H_i becomes small compared with the concentrations of C and H_{3n-2}. The formation of the triple helix can then be approximated by an ''all-or-none'' reaction and the overall reaction can be described by an apparent equilibrium constant K.

$$K = \frac{[H_{3n-2}]}{[C]^3} = \beta s^{3n-2} = \frac{F}{3c_0^2(1-F)^3} \tag{2}$$

where F is the degree of helicity in terms of the fraction of chains or tripeptide units in the triple helical state and c_o the total molar concentration of chains, normally in mol tripeptide units l^{-1}.

$$F = \frac{3[H_{3n-2}]}{c_0} \tag{3}$$

From

$$\Delta G^\circ = -RT \ln K = \Delta H^\circ - T\Delta S^\circ \tag{4}$$

and from Eq. (2) it follows that at the midpoint of the transition ($F = 0.5$ and $T = T_m$),

$$T_m = \frac{\Delta H^\circ}{\Delta S^\circ + R \ln(0.75c_0^2)} \tag{5}$$

where ΔG° is the standard Gibbs free energy, ΔH° is the standard free enthalpy, and ΔS° is the standard entropy. It is important to note that the T_m is concentration dependant and stability values should only be compared at identical molar chain concentrations or concentrations which were corrected for concentration differences with Eq. (5).

ΔH° can be obtained from the slope of the transition curves. A first approximation of ΔH° can be obtained from the van't Hoff equation

$$\Delta H^\circ = 8RT_m^2\left(\frac{dF}{dT}\right)_{F=0.5} \tag{6}$$

It is much more accurate to obtain ΔH° by curve fitting of the entire transition curve with the equation

$$K = \exp\left[\frac{\Delta H^\circ}{RT}\left(\frac{T}{T_m} - 1\right) - \ln 0.75c_0^2\right] \tag{7}$$

which is obtained by solving Eq. (5) for ΔS° and substituting for ΔS° in Eq. (4). In this equation the specific heat c_p is assumed to be zero, as measured for several collagens by Privalov (see Section 30.2.3). In this regard, it is important to calculate F as a function of temperature. In the helical region and especially in the coiled region the circular dichroism (CD) signal shows a linear decrease with increasing temperature.

For a direct fit of F by K and c_o Eq. (2) is rewritten as the cubic equation:

$$F^3 - 3F^2 + bF - 1 = 0 \tag{8}$$

with:

$$b = \frac{9Kc_0^2 + 1}{3Kc_0^2} \tag{9}$$

By the method of Cardano [55] the real solution of this equation was obtained as:

$$F = u + v + 1 \tag{10}$$

with:

$$u = \sqrt[3]{-\frac{q}{2} + \sqrt{\left(\frac{q^2}{4} + \frac{p^3}{27}\right)}} \tag{11}$$

and:

$$v = \sqrt[3]{-\frac{q}{2} - \sqrt{\left(\frac{q^2}{4} + \frac{p^3}{27}\right)}} \tag{12}$$

in which $p = q = \dfrac{1}{3Kc_0^2}$.

When measuring CD the molar ellipticity is given by

$$[\Theta] = F([\Theta]_h - [\Theta]_c) + [\Theta]_c$$

where $[\Theta]_h$ and $[\Theta]_c$ are the ellipticities for the peptide in either the completely triple helical conformation or in the unfolded conformation. The linear temperature dependencies of $[\Theta]_h$ and $[\Theta]_c$ can be described by

$$[\Theta]_h = [\Theta]_{h,Tm} + p(T - T_m)$$

$$[\Theta]_c = [\Theta]_{c,Tm} + q(T - T_m)$$

Here the ellipticities at the midpoint temperature T_m are arbitrarily used as reference points. For a best fit of the transition curves, initially the T_m is kept constant and ΔH°, p and q are varied. After an initial fit, the T_m is then also varied.

For peptides that contain a cross-link, the triple helix $\rightleftarrows$ coil transition becomes concentration independent and the equations for the all-or-none model simplify to:

$$K = \frac{F}{1 - F}$$

then F becomes

$$F = \frac{K}{1 + K}$$

and

$$T_m = \frac{\Delta H^\circ}{\Delta S^\circ}.$$

The fitting procedure for the determination of the thermodynamic parameters is otherwise the same as for nonlinked chains. In all fitting procedures the temperature dependence of ΔH° was neglected since the heat capacity c_p was determined to be very small or zero [15].

30.2.4.3 Thermodynamic Parameters for Different Model Systems

The simplest way to study the stability of collagen-like peptides is to measure the thermal transition curve by circular dichroism. The temperature at the midpoint of the transition T_m is normally used as a comparison for the stability between different peptides. However, as shown above this value is dependent on the concentration of the peptide and the rate of heating, and only values either measured or corrected to the same concentration and heating rate should be compared. Heating rates above 10 °C h^{-1} lead to transition curves that are too steep, therefore an enthalpy change that is too large if evaluated by the van't Hoff equation, and to T_m values that are too high. The enthalpy change of the triple helix coil transition can be calculated by fitting of the transition curve with the van't Hoff equation (see Section 30.2.4.2) or measured directly by differential scanning calorimetry (DSC). Van't Hoff enthalpies are usually less accurate than calorimetric values and both methods suffer from uncertainties in baselines. Uncertainties in the thermody-

Tab. 30.1. Thermodynamic data of the triple helix–coil transition of model peptides in aqueous solution determined by circular dichroism ($\Delta H^\circ_{vH}, \Delta S^\circ$) and differential scanning calorimetry (ΔH°_{cal}). The values are expressed per mol of tripeptide units in a triple helix. The number of tripeptide units in the triple helix was calculated as $3n - 2$ for the peptide (Gly-Xaa-Yaa)$_n$.

Peptide	T_m (°C)	ΔH°_{vH} (kJ mol^{-1} tripeptide)	ΔS° (J mol^{-1} tripeptide K^{-1})	ΔH°_{cal} (kJ mol^{-1} tripeptide)	*Reference*
(Pro-Pro-Gly)$_{10}$	28	−10.6	−26.5		35
(Pro-Pro-Gly)$_{10}$	24.6	−7.91	−22.4	−7.68	54
(Pro-Pro-Gly)$_{10}$	25	−18.8	−58.6		159
(Pro-Pro-Gly)$_{10}$	34	−18.6	−60.9		112
(Pro-Pro-Gly)$_n$ $n = 10, 15, 20$		−8.2	−19.2		160
(Pro-Pro-Gly)$_n$ $n = 12, 14, 15$		−10.6	−26.5		35
(Pro-Pro-Gly)$_{10}$	32.6			−6.43	59
(Pro-4(*R*)Hyp-Gly)$_{10}$	57.3	−13.4	−36.4	−13.4	54
(Pro-4(*R*)Hyp-Gly)$_{10}$, pH 1	60.8	−23.6	−65.6		57
(Pro-4(*R*)Hyp-Gly)$_{10}$, pH 7	57.8	−23.3	−65.2		57
(Pro-4(*R*)Hyp-Gly)$_{10}$, pH 13	60.8	−25.1	−70.7		57
(Pro-4(*R*)Hyp-Gly)$_{10}$	60.0			−13.9	59
(Pro-4(*R*)Flp-Gly)$_{10}$	80	−17.1			112
(4(*S*)Flp-Pro-Gly)$_{10}$	58	−12.0			112
Ac-(Gly-4(*R*)Hyp-Thr)$_{10}$-NH$_2$	18	−27.1	−87.1	−27.5	98
Ac-(Gly-Pro-Thr(βGal)$_{10}$-NH$_2$	38.8	−14.0	−39.6		98
Ac-(Gly-4(*R*)Hyp-Thr(βGal)$_{10}$-NH$_2$	50.0	−11.1	−29.0		98
EK peptide,[a] pH 1	43.8	−27.4	−81.0		57
EK peptide,[a] pH 7	45.8	−26.3	−77.3		57
EK peptide,[a] pH 13	48.8	−22.6	−65.3		57
PTC((Pro-Ala-Gly)$_{12}$)$_3$[b]	12	−3.81	−13.3		161
PTC((Pro-Ala-Gly)$_{12}$)$_3$[c]	15	−3.63	−12.6		161
((Ala-Gly-Pro)$_9$)$_3$Lys-Lys	16.5	−7.32	−25.5		30
((Ala-Gly-Pro)$_{10}$)$_3$Lys-Lys	17.3	−6.69	−23.0		30
((Ala-Gly-Pro)$_{11}$)$_3$Lys-Lys	19.0	−6.65	−23.0		30
((Ala-Gly-Pro)$_{12}$)$_3$Lys-Lys	19.7	−7.28	−25.6		30
((Ala-Gly-Pro)$_{13}$)$_3$Lys-Lys	20.3	−5.69	−19.2		30
((Ala-Gly-Pro)$_{14}$)$_3$Lys-Lys	23.6	−5.31	−18.0		30
((Ala-Gly-Pro)$_{15}$)$_3$Lys-Lys	26.2	−5.36	−18.0		30
((Gly-Pro-Thr)$_{10}$-Gly-Pro-Cys-Cys)$_3$	13.8	−7.1	−41.5	−11.9	142
Ac-(Gly-Pro-4(*R*)Hyp)$_8$-Gly-Gly-NH$_2$	44.5	−16.0	−43.8		36
Ac-(Gly-Pro-4(*R*)Hyp)$_8$-Gly-Gly-NH$_2$	47.3	−19.8		−9.77[d]	58
T1-892	22.9	−15.6	−48.1		96
T1-892(O24A)	18.9	−18.7	−59.7		96
T1-892(P26A)	20.4	−18.3	−57.9		96
HT(I)[e] A	9	−18.6	−55.1		53
HT(I) B	33	−16.6	−47.6		53
HT(I) C	33	−14.7	−41.2		53
HT(I) D	41	−15.6	−43.8		53
HT(IV)[f] A	42	−4.49		−15.2	56
HT(IV) B	30	−4.30		−14.3	56
HT Ac-(Gly-Pro-4(*R*)Hyp)$_5$-Cys[g]	56.3	−15.8	−48.0	−15.5	44

Tab. 30.1. *(continued)*

Peptide	T_m *(°C)*	ΔH°_{vH} *(kJ mol^{-1} tripeptide)*	ΔS° *(J mol^{-1} tripeptide K^{-1})*	ΔH°_{cal} *(kJ mol^{-1} tripeptide)*	*Reference*
(Ac-(Pro-4(*R*)Hyp-Gly)$_5$ Pro-Cys-Cys-Gly-Gly-Gly-NH_2)$_3$	68	−13.8	−40.4	−15.5	45
(Ac-Cys-Cys-Gly-(Pro-4(*R*)Hyp-Gly)$_5$-Gly-Gly-Gly-NH_2)$_3$	58.4	−10.1	−30.5	−14.5	45
GPP*(8)[h]	62.5	−3.39	−10.1		162
PP*G(8)	50.7	−3.73	−11.5	−4.25	162
PP*G(7)	44.4	−3.4	−10.7		162
PP*G(6)	39.4	−5.85	−18.7		162
MG[i]	16.6	−25.1	−81.3		163
((Gly-Pro-Pro)$_{10}$-Gly-Pro-Cys-Cys)$_3$	82				165
((Gly-Pro-Pro)$_{10}$)$_3$–foldon	66			−10.7	46
	70				165

[a] The EK peptide is (Pro-4(*R*)Hyp-Gly)$_4$-Glu-Lys-Gly-(Pro-4(*R*)Hyp-Gly)$_5$.
[b] Peptide with a parallel chain arrangement.
[c] Peptide with an antiparallel chain arrangement.
[d] Calorimetric data from Ref. [59].
[e] Heterotrimeric type I collagen peptide containing the collagenase cleavage site.
[f] Heterotrimeric type IV collagen peptide containing the $\alpha 1\beta 1$ integrin binding site.
[g] Heterotrimeric (Gly-Pro-4(*R*)Hyp)$_5$ with cysteine bridge.
[h] Dilysine bridged peptide with a collagen type III sequence and a Gly-Pro-4(*R*)Hyp clamp at the N-terminus.
[i] Synthetic α1-CB2.
Flp, fluoroproline.

namic data also arise from the facts that the transition curves monitored by CD are measured at a much lower concentration than the calorimetric measurements and that the concentration dependence is unknown in many studies. All measurements of single-chain peptides include the uncertainty of misaligned chains and errors in the fitting procedures. Data from different sources are summarized in Tables 30.1 and 30.2. In view of the many sources of error it is highly recommended to consult the individual publications in order to gain information on reliability.

For the reasons mentioned above, the published thermodynamic data for the triple helix coil transitions of synthetic peptides vary significantly. The commercially available peptides (Pro-Pro-Gly)$_{10}$ and (Pro-4(*R*)Hyp-Gly)$_{10}$ have been measured in several laboratories. The van't Hoff enthalpy change varies from −7.91 to −18.8 kJ mol^{-1} tripeptide units for (Pro-Pro-Gly)$_{10}$ and from −13.4 to −25.25 kJ mol^{-1} tripeptide units for (Pro-4(*R*)Hyp-Gly)$_{10}$. The published values for the calorimetric enthalpies of these peptides are more consistent.

Tab. 30.2. Thermodynamic data of the triple helix formation of host-guest peptides in PBS determined by circular dichroism ($\Delta H^{\circ}_{vH}, \Delta S^{\circ}$) and differential scanning calorimetry (ΔH°_{cal}). The values are expressed per mol of triple helix.

Peptide	T_m (°C)	ΔH°_{vH} (kJ mol^{-1})	ΔS° (J mol^{-1} K^{-1})	ΔH°_{cal} (kJ mol^{-1})	*Reference*
HG[a] Gly-Pro-4(*R*)Flp	43.7			−204	59
HG Gly-4(*R*)Hyp-Pro	43.0			−204	59
HG Gly-4(*R*)Hyp-4(*R*)Hyp	47.3			−217	59
HG Gly-Pro-Pro	45.5			−213	59
HG Gly-Ala-4(*R*)Hyp	39.9	−423.7	−1214		36
HG Gly-Ala-4(*R*)Hyp	41.7	−480			58
HG Gly-Leu-4(*R*)Hyp	39.0	−437.5	−1256		36
HG Gly-Phe-4(*R*)Hyp	33.5	−514.1	−1549		36
HG Gly-Pro-Ala	38.3	−358.0	−1005		36
HG Gly-Pro-Ala	40.9	−502			58
HG Gly-Pro-Leu	32.7	−514.6	−1549		36
HG Gly-Pro-Leu	31.7	−514			58
HG Gly-Pro-Phe	28.3	−557.3	−1717		36
HG Gly-Pro-Arg	47.2	−610	−1100		62
HG Gly-Pro-Arg pH 2.7	45.5	−560	−1300		62
HG Gly-Pro-Arg pH 12.2	43.1	−390	−1100		62
HG Gly-Pro-Met	42.6	−436			58
HG Gly-Pro-Ile	41.5	−559			58
HG Gly-Pro-Gln	41.3	−559			58
HG Gly-Pro-Val	40.0	−481			58
HG Gly-Pro-Glu	39.7	−630	−1900		62
HG Gly-Pro-Glu pH 2.7	41.9	−570	−1700		62
HG Gly-Pro-Glu	38.5	−640	−1900		62
HG Gly-Pro-Thr	39.7	−647			58
HG Gly-Pro-Cys	37.7	−471			58
HG Gly-Pro-Lys	36.8	−400	−1200		62
HG Gly-Pro-Lys pH 2.7	37.1	−430	−1300		62
HG Gly-Pro-Lys pH 12.2	38.8	−440	−1300		62
HG Gly-Pro-His	35.7	−497			58
HG Gly-Pro-Ser	35.0	−435			58
HG Gly-Pro-Asp	34.0	−776			58
HG Gly-Pro-Asp	30.1	−550	−2000		62
HG Gly-Pro-Asp pH 2.7	33.1	−590	−1800		62
HG Gly-Pro-Asp pH 12.2	30.1	−770	−1700		62
HG Gly-Pro-Gly	32.7	−665			58
HG Gly-Pro-Asn	30.3	−640			58
HG Gly-Pro-Tyr	30.2	−657			58
HG Gly-Pro-Trp	26.1	−670			58
HG Gly-Glu-4(*R*)Hyp	42.9	−590	−1800		62
HG Gly-Glu-4(*R*)Hyp pH 2.7	39.7	−470	−1400		62
HG Gly-Glu-4(*R*)Hyp pH 12.2	40.9	−670	−2000		62
HG Gly-Lys-4(*R*)Hyp	41.5	−540	−1600		62
HG Gly-Lys-4(*R*)Hyp pH 2.7	40.4	−510	−1500		62
HG Gly-Lys-4(*R*)Hyp pH 12.2	38.3	−530	−1600		62

Tab. 30.2. *(continued)*

Peptide	T_m (°C)	ΔH°_{vH} (kJ mol^{-1})	ΔS° (J mol^{-1} K^{-1})	ΔH°_{cal} (kJ mol^{-1})	*Reference*
HG Gly-Arg-4(*R*)Hyp	40.6	−520	−1500		62
HG Gly-Arg-4(*R*)Hyp pH 2.7	39.4	−470	−1400		62
HG Gly-Arg-4(*R*)Hyp pH 12.2	38.0	−510	−1500		62
HG Gly-Gln-4(*R*)Hyp	40.4	−565			58
HG Gly-Asp-4(*R*)Hyp	40.1	−520	−1500		62
HG Gly-Asp-4(*R*)Hyp pH 2.7	37.6	−540	−1600		62
HG Gly-Asp-4(*R*)Hyp pH 12.2	38.0	−560	−1600		62
HG Gly-Val-4(*R*)Hyp	38.9	−518			58
HG Gly-Met-4(*R*)Hyp	38.6	−452			58
HG Gly-Ile-4(*R*)Hyp	38.4	−624			58
HG Gly-Asn-4(*R*)Hyp	38.3	−502			58
HG Gly-Ser-4(*R*)Hyp	38.0	−506			58
HG Gly-His-4(*R*)Hyp	36.5	−580			58
HG Gly-Thr-4(*R*)Hyp	36.2	−506			58
HG Gly-Cys-4(*R*)Hyp	36.1	−423			58
HG Gly-Tyr-4(*R*)Hyp	34.3	−629			58
HG Gly-Gly-4(*R*)Hyp	33.2	−575			58
HG Gly-Trp-4(*R*)Hyp	31.9	−593			58
HG Gly-Asp-Lys pH 2.7	26.5	−600	−1000		62
HG Gly-Asp-Lys	30.9	−520	−1600		62
HG Gly-Asp-Lys pH 12.2	29.9	−490	−1500		62
HG Gly-Asp-Arg pH 2.7	33.4	−550	−1700		62
HG Gly-Asp-Arg	37.1	−580	−1700		62
HG Gly-Asp-Arg pH 12.2	34.4	−460	−1300		62
HG Gly-Glu-Lys pH 2.7	29.5	−490	−1500		62
HG Gly-Glu-Lys	35.0	−590	−1800		62
HG Gly-Glu-Lys pH 12.2	33.1	−530	−1600		62
HG Gly-Glu-Arg pH 2.7	37.3	−530	−1600		62
HG Gly-Glu-Arg	40.4	−520	−1500		62
HG Gly-Glu-Arg pH 12.2	39.1	−510	−1500		62
HG Gly-Ala-Ala	29.3	−450	−1400		62
HG Gly-Lys-Asp pH 2.7	30.5	−770	−2400		62
HG Gly-Lys-Asp	35.8	−720	−2200		62
HG Gly-Lys-Asp pH 12.2	30.2	−720	−2300		62
HG Gly-Arg-Asp pH 2.7	28.8	−720	−2300		62
HG Gly-Arg-Asp	35.0	−720	−2200		62
HG Gly-Arg-Asp pH 12.2	31.9	−630	−1900		62
HG Gly-Lys-Glu pH 2.7	36.5	−620	−1900		62
HG Gly-Lys-Glu	35.3	−630	−1900		62
HG Gly-Lys-Glu pH 12.2	31.6	−680	−2100		62
HG Gly-Arg-Glu pH 2.7	35.0	−630	−1900		62
HG Gly-Arg-Glu	33.8	−680	−2100		62
HG Gly-Arg-Glu pH 12.2	32.2	−710	−2200		62
HG Gly-Gly-Phe	19.7	−647	−2093		61
HG Gly-Gly-Leu	23.9	−578	−1800		61
HG Gly-Gly-Ala	25.0	−559	−1758		61

Tab. 30.2. *(continued)*

Peptide	T_m (°C)	ΔH°_{vH} (kJ mol^{-1})	ΔS° (J mol^{-1} K^{-1})	ΔH°_{cal} (kJ mol^{-1})	*Reference*
HG Gly-Ala-Leu	27.8	−574	−1758		36
HG Gly-Phe-Ala	23.4	−593	−1884		36
HG Gly-Ala-Phe	20.7	−637	−2051		36

[a] HG refers to the host–guest peptides with the structure Ac(Pro-4(*R*)Hyp-Gly)$_3$-Gly-Xaa-Yaa-(Pro-4(*R*)Hyp-Gly)$_4$-Gly-Gly-NH$_2$. The tripeptide sequence given after HG corresponds to Gly-Xaa-Yaa. The peptides were measured in PBS, pH 7, unless indicated otherwise. Flp, fluoroproline.

Generally, the triple helix ⇄ coil transitions of short peptides can be described by the all-or-none model discussed in the previous section. Most peptides for which calorimetric data are available show that the ratio of the van't Hoff enthalpy and the calorimetric enthalpy is close to 1, indicating that the all-or-none mechanism is a good approximation, which is expected for peptides smaller than the cooperative length. However, exceptions have been reported, especially in heterotrimeric peptides [56].

Figure 30.3 shows the triple helix coil transition of Ac-(Gly-Pro-4(*R*)Hyp)$_{10}$-NH$_2$ measured by CD in water. The heating/cooling rate was 10 °C h^{-1} and the unfolding and refolding curves are shown for three different concentrations.

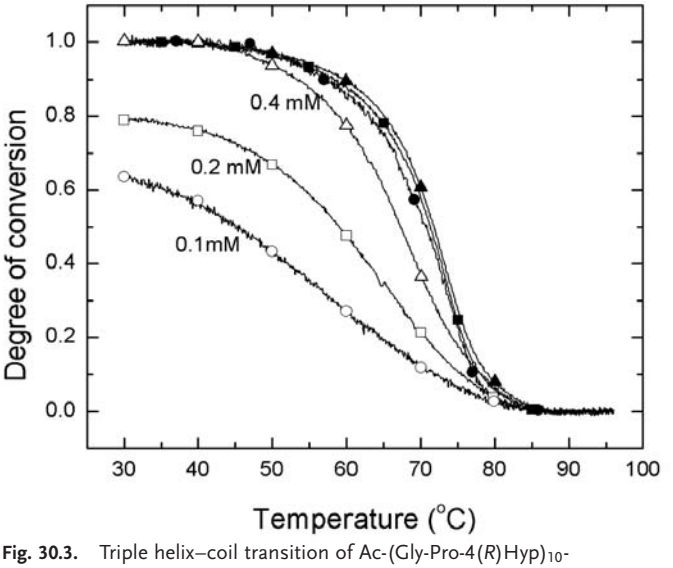

Fig. 30.3. Triple helix–coil transition of Ac-(Gly-Pro-4(*R*)Hyp)$_{10}$-NH$_2$ in water. The transition was monitored by circular dichroism at 225 nm. Closed symbols are for heating and open symbols for cooling, The heating/cooling rate was 10 °C h^{-1}.

The experimental data can be described by the all-or-none model (Mizuno and Bächinger, unpublished). The T_m increases with increasing concentration, but a concentration-dependent hysteresis is observed during refolding (see Section 30.3.4.4).

The studies with synthetic model peptides confirm the stabilizing role of 4(*R*)Hyp in the Yaa position of the triple helix. The influence of 4(*S*)Hyp, 3(*S*)Hyp, 4(*S*)Flp, and 4(*R*)Flp on the stability of the triple helix is entirely based on measurements with synthetic peptides (see Section 30.2.4.7).

The peptides in the host–guest system carry no charges at the ends and the values for the enthalpy and entropy changes are measured over a $(Gly\text{-}Pro\text{-}4(R)Hyp)_7$ background. The stability of $(Pro\text{-}4(R)Hyp\text{-}Gly)_{10}$ was shown to be pH dependent. At acidic and basic pH the peptide carries charges at only one end and is more stable than at neutral pH, where charges are present at both ends [57]. The peptides have the general sequence $Ac\text{-}(Gly\text{-}Pro\text{-}4(R)Hyp)_3\text{-}Gly\text{-}Xaa\text{-}Yaa\text{-}(Gly\text{-}Pro\text{-}4(R)Hyp)_4\text{-}Gly\text{-}Gly\text{-}NH_2$. The thermodynamic data for the guest peptides can be used to predict the stability of triple helices with any sequence [58, 59]. The limitations of this approach are discussed in Section 30.2.4.4. Table 30.2 lists the thermodynamic parameters determined for the host–guest peptides. In contrast to other synthetic peptides and CNBr peptides of type I collagen [60], where the enthalpy change increases with an increasing amount of imino acids, the Gly-Pro-4(*R*)Hyp containing host peptide has one of the lowest enthalpy change observed. The host–guest studies clearly show that hydrophobic residues do not play a major role in the stabilization of the triple helix, rather they perform important tasks in the assembly of collagen molecules into fibrils [36]. Gly-Gly containing peptides show a strong influence in destabilizing the triple helix, which may play an important role in specific functions by modulating the local triple helical stability [61]. These studies also clarify the dependence of the triple helical stability on the identity, position and ionization state of charged residues [62].

30.2.4.4 **Contribution of Different Tripeptide Units to Stability**

The high content of imino acids in collagens suggests a crucial role in the stabilization of the triple helix. Indeed, the most stable natural tripeptide unit is Gly-Pro-4(*R*)Hyp. Heidemann's group used statistical data [63], and published studies of stabilities of synthetic peptides [30, 64, 65] to derive four classes of the most common tripeptide units found in collagens. The first class of tripeptide units, the collagen-typical tripeptides, consists of Gly-Pro-Hyp, Gly-Pro-Ala, Gly-Ala-Hyp, Gly-Glu-Hyp, Gly-Glu-Arg, and Gly-Pro-Lys. The second class consists of tripeptide units often found in clusters with the collagen-typical tripeptides and includes Gly-Leu-Hyp, Gly-Pro-Ser, Gly-Phe-Hyp, Gly-Ala-Ala, Gly-Ala-Arg, Gly-Glu-Hyp, Gly-Asp-Ala, and Gly-Pro-Gln. The third class consists of tripeptide units that do not occur in the collagen-typical clusters and includes Gly-Glu-Ala, Gly-Ala-Lys, Gly-Asp-Arg, Gly-Ala-Asp, Gly-Pro-Ile, Gly-Arg-Hyp, Gly-Glu-Thr, and Gly-Ser-Hyp. The fourth class includes all the rest of the tripeptide units, which do not occur often enough for the statistical analysis.

A sequence-dependent stability profile along the triple helix was generated by assigning numerical values to the classes derived by Heidemann, using a sliding

average to simulate cooperativity [66]. While empirical, this method was able to qualitatively explain the occurrence of unfolding intermediates in the triple helix of type V and XI collagens. In contrast to other fibrillar collagens, collagens type V and XI show unfolding intermediates in the triple helix coil transition [29]. A comparison of the sequence-dependent stability profiles indicates that type V and XI collagens lack a very stable region at the N-terminal end of the triple helix, that is present in other fibrillar collagens. The N-terminal region of the triple helix unfolds at lower temperatures in collagen types V and XI, and this leads to stable unfolding intermediates, that consist of the more C-terminal regions of the triple helix.

Brodsky's group used a host–guest system to quantitate the influence of naturally occurring tripeptide units to the triple helical stability [36, 58, 59, 61, 62, 67, 68, 69, 70]. The host–guest peptide system Ac-(Gly-Pro-Hyp)$_3$-Gly-Xaa-Yaa-(Gly-Pro-Hyp)$_4$-Gly-Gly-NH_2 is used to study the influence of the Xaa and Yaa residues on the thermal stability of the triple helix. While there are over 400 possible combinations of host–guest peptides, only about 80 appear with a significant frequency in known collagen sequences and only 24 tripeptides have a frequency of higher than 1% [71]. These peptides can be divided into three groups: the Gly-Xaa-Hyp group, the Gly-Pro-Yaa group, and the Gly-Xaa-Yaa group. Not surprisingly, the most stable of the 20 peptides of group 1 is Gly-Pro-Hyp, followed by Gly-Glu-Hyp and Gly-Ala-Hyp. The T_m values range from 47.3 °C for Gly-Pro-Hyp to 31.9 °C for Gly-Trp-Hyp. For group 2, the most stable of the 20 peptides is again Gly-Pro-Hyp, followed by Gly-Pro-Arg and Gly-Pro-Met. The T_m values range from 47.3 °C for Gly-Pro-Hyp to 26.1 °C for Gly-Pro-Trp. A reasonable correlation was found between the observed stabilities and the frequencies of occurrence in fibrillar collagen sequences [58]. Forty-one peptides of group 3 that contained no imino acids were synthesized and their stabilities measured [69]. Theoretical calculations, assuming no interaction between the Xaa and Yaa residues, allow the prediction of the stability of all 361 possible peptides. Sixteen of the 41 peptides show a reasonable agreement between the predicted and the measured stability ($\Delta T_m \leq 2$ °C). Seven peptides had a lower T_m than predicted and 18 had a higher T_m, most likely indicating side-chain interactions in the triple helix. These studies should now allow the prediction of the thermal stability of the triple helix in any Gly-Xaa-Yaa sequence. Unfortunately, this is not the case. The tripeptide units Gly-Hyp-Pro and Gly-3Hyp-Hyp show T_m values in the host-guest system that are comparable to Gly-Pro-Hyp, but neither forms a triple helix as a homopolymer [72]. A similar result was also obtained for the guest tripeptide unit Gly-Pro-fluoroproline [59]. The conclusion one has to draw is that these stabilities are dominated by the very stable tripeptide units at either end of the guest tripeptide unit, and that this system has little predictive power for the stability of Gly-Xaa-Yaa in homopolymers.

30.2.4.5 **Crystal and NMR Structures of Triple Helices**

The molecular structure of the triple helix was first derived from diffraction patterns of collagen fibrils [74, 75]. These models and data on the diffraction of tail tendon [76] showed a 10/3 symmetry (3.33 residues per turn). The first structure of

the synthetic model peptide $(Pro\text{-}Pro\text{-}Gly)_{10}$ showed a 7/2 symmetry, giving rise to 3.5 residues per turn [77]. In 1994, a true single crystal was grown from a peptide that consisted of 10 repeats of Pro-Hyp-Gly with a single substitution of a glycine residue by an alanine in the middle [78]. This peptide was a triple helical molecule with a length of 87 Å and a diameter of 10 Å. The structure was solved to 1.9 Å and was consistent with the general parameters derived from the fiber diffraction model, but showed a 7/2 symmetry. It was hypothesized that imino acid-rich peptides have a 7/2 symmetry, but imino acid-poor regions adopt a 10/3 helix [78]. This was later confirmed with a synthetic peptide that contained an imino acid poor region [79, 80]. The structure also confirmed the expected hydrogen bond between the GlyNH and C=O of the proline in the Xaa position. In addition, an extensive water network forms hydrogen bonds with all available carbonyl and hydroxyl groups [23, 81].

The structure of the peptides $(Pro\text{-}Pro\text{-}Gly)_{10}$ [82, 83] and $(Pro\text{-}Hyp\text{-}Gly)_{10}$ [84] was also determined. The structure of $(Pro\text{-}Pro\text{-}Gly)_{10}$ obtained from crystals grown in microgravity, which diffracted up to a resolution of 1.3 Å, showed a preferential distribution of proline backbone and side-chain conformations, depending on the position [85, 26]. Proline residues in the Xaa position exhibit an average main chain torsion angle of -75° and a positive side-chain χ_1 (down puckering), while proline residues in the Yaa position were characterized by a significantly smaller main-chain torsion angle of -60° and a negative χ_1 (up puckering). These results were used to explain the stabilizing effect of hydroxyproline in the Yaa position, because hydroxyproline has a strong preference for up puckering. It also would explain the destabilizing effect of 4(*R*)-hydroxyproline in the Xaa position (see also Section 30.2.4.7).

The structure of $(Gly\text{-}Pro\text{-}Pro)_{10}$ was also solved in the context of the attached oligomerization domain foldon [86].

NMR studies with synthetic model peptides of the triple helix are difficult because of overlapping resonances of the repetitive sequence and by peak broadening from the shape [87–89]. Isotopic labeling was used to observe specific residues using heteronuclear NMR techniques. Hydrogen exchange studies were used to show that the NH groups of glycine exchanged faster in the imino acid-poor region of a synthetic peptide compared with the Gly-Pro-Hyp region [87]. The NH of threonine and the NH of glycine showed a very slow exchange with deuterium in the galactosyl-containing peptide $Ac\text{-}(Gly\text{-}Pro\text{-}Thr(\beta\text{-}Gal))_{10}\text{-}NH_2$ [90]. Heteronuclear NMR was used to monitor the folding kinetics of the triple helix [91, 92]. The hydration of the triple helix was also studied by NMR [93]. The hydration shell was found to be kinetically labile with upper limits for water molecule residence times in the nanosecond to subnanosecond range.

30.2.4.6 Conformation of the Randomly Coiled Chains

Little attention has been paid to the conformation of the unfolded chains in considering the stability of the collagen triple helix. Because the stability is determined by the free energy difference of the unfolded and the folded state, changes in the unfolded state can also contribute to the stability of the triple helix. The triple helix

requires all peptide bonds to be in the trans conformation, so changes in the *cis* to *trans* ratio of peptide bonds in the unfolded state have a direct influence on the stability (see Section 30.2.4.8). Another example comes from studies with synthetic peptides, in which galactosyl threonine was incorporated [94]. The deep-sea hydrothermal vent worm *Riftia pachyptila* has a cuticle collagen that has a very low content of proline and hydroxyproline residues, but a high T_m of 37 °C [95, 42]. The Yaa position of the triple helical sequence in this cuticle collagen is frequently occupied by threonine. Threonines in the Yaa position were frequently galactosylated with one to three galactosyl units. The peptide Ac-(Gly-Pro-Thr)$_{10}$-NH_2 was unable to form a triple helix, whereas the galactosylated version Ac-(Gly-Pro-Thr(β-Gal))$_{10}$-NH_2 showed a T_m of 39 °C [94]. The stabilizing effect of galactosyl threonine has been explained by the occlusion of water molecules and by hydrogen bonding [90]. Additionally, galactosylation of the threonine residues also restricts the available conformations in the unfolded state. The end-to-end distance, determined by fluorescence energy transfer, is increased in the peptide Dabcyl-(Gly-Pro-Thr(β-Gal))$_5$-Gly-EDANS when compared with the peptide Dabcyl-(Gly-Pro-Thr)$_5$-Gly-EDANS (Bächinger, unpublished). However, it is difficult to quantitate the contribution of these different effects to the overall stability of the triple helix.

The importance of the restriction of imino acids in the unfolded state for the efficient folding of the triple helix has recently been described [96].

30.2.4.7 Model Studies with Isomers of Hydroxyproline and Fluoroproline

As mentioned before, it was recognized early on that hydroxproline played a crucial role in the stabilization of the triple helix. Synthetic peptides were used to establish that only 4(*R*)-hydroxyproline stabilized the triple helical structure. 4(*S*)-Hydroxyproline in the peptides (4(*S*)Hyp-Pro-Gly)$_{10}$ and (Pro-4(*S*)Hyp-Gly)$_{10}$ prevented the formation of a triple helix [97]. It was also shown that 4(*R*)-hydroxyproline in the Xaa position prevented triple helix formation in the peptide (4(*R*)Hyp-Pro-Gly)$_{10}$ [70]. Recent studies show that 4(*R*)-hydroxyproline in the Xaa position can lead to an increase in the stability of the triple helix, when the Yaa position is not proline. The peptide Ac-(Gly-Pro-Thr)$_{10}$-NH_2 does not form a triple helix in aqueous solution, but when the proline is hydroxylated the peptide Ac-(Gly-4(*R*)Hyp-Thr)$_{10}$-NH_2 does form a stable triple helix [98]. Further studies of peptides with 4(*R*)-hydroxyproline in the Xaa position showed that valine, but not serine or allo-threonine are able to form stable triple helical peptides, indicating that both the methyl group and the hydroxyl group of threonine, as well as the stereo configuration are important for the stability [73]. It was hypothesized that the methyl group shields the interchain hydrogen bond between the glycine and the Xaa residue from solvent and that the hydroxyl group of threonine and hydroxyproline can form a direct or water-mediated hydrogen bond. In addition, the peptide Ac-(Gly-4(*R*)Hyp-4(*R*)Hyp)$_{10}$-NH_2 has a T_m that is similar to the that of Ac-(Gly-Pro-4(*R*)Hyp)$_{10}$-NH_2 (Mizuno *et al.*, in press).

A small number of 3(*S*)-hydroxyproline residues are present in most collagens in the Xaa position. The occurrence of 3(*S*)Hyp is much less frequent than that of 4(*R*)Hyp in the total amino acid content of collagens. In basement membrane collagens, fractions range from 1 [99] to 15 residues per 1000 residues [100]. 3(*S*)-

Hydroxyproline is also found in other types of collagens, such as type I [100], type V [101, 102], type X [103], and interstitial and cuticle collagens of annelids [105]. The only reported sequences containing 3(*S*)Hyp are in Gly-3(*S*)Hyp-4(*R*)Hyp tripeptide units. Synthetic peptides with 3(*S*)Hyp in a host–guest system decrease the stability of the triple helix in either the Xaa or the Yaa position [38]. A more severe decrease was observed for 3(*S*)Hyp in the Yaa position. It was concluded that the inductive effect of the 3-hydroxyl group of 3(*S*)Hyp decreases the strength of the GlyNH $\cdots$ OC3(*S*)Hyp hydrogen bond, when 3(*S*)Hyp is in the Xaa position, and that, when 3(*S*)Hyp is in the Yaa position, the pyrrolidine ring pucker leads to inappropriate mainchain dihedral angles and steric clashes [38]. When the influence of 3(*S*)Hyp was studied in homopolymers, the peptide Ac-(Gly-Pro-3(*S*)Hyp)$_{10}$-NH_2 did not form a triple helix [104]. Surprisingly, the peptide Ac-(Gly-3(*S*)Hyp-4(*R*)Hyp)$_{10}$-NH_2 was also unable to form a triple helix as a homopolymer. Even when foldon was attached to (Gly-3(*S*)Hyp-4(*R*)Hyp)$_{10}$, no triple helix formation was observed, ruling out a kinetic difficulty for this peptide to form such a structure [104].

While fluoroproline was used in biosynthetic experiments in the sixties [105, 106, 107], its importance to the stability of the triple helix was established by incorporating 4(*R*)-fluoroproline (4(*R*)Flp) into collagen model peptides [25]. Raines and coworkers showed that the substitution of 4(*R*)Hyp by 4(*R*)Flp in the peptide (Gly-Pro-4(*R*)Hyp)$_{10}$ leads to a significant increase in the stability of the triple helix. The authors initially cited an ''unappreciated inductive effect'' as the reason for this increase in stability, but more importantly, this result showed that an electron withdrawing substituent in the 4(*R*) position of proline can stabilize the triple helix without an extended network of water molecules [108]. Since this initial discovery, the inductive effect has been characterized in great detail [109, 110, 111]. The *gauche* effect determines the proline ring puckering (up puckering, Cγ-exo) and therefore predetermines the main-chain dihedral angles. In addition, the *trans* to *cis* ratio of the peptide bond preceeding 4(*R*)Flp increases. Both of these effects increase the stability of the triple helix. Peptides with 4(*R*)Flp in the Xaa position do not form a triple helix [112, 113]. Peptides with 4(*S*)Flp in the Yaa position also do not form a triple helix [44, 110]. In contrast to the peptide (4(*S*)Hyp-Pro-Gly)$_{10}$, which does not form a triple helix, the peptides (4(*S*)Flp-Pro-Gly)$_n$ form a stable triple helix ($n = 7$ [113]; $n = 10$ [112]). This is an unexpected result, because the *trans* to *cis* ratio of the peptide bond is decreased by 4(*S*)Flp. On the other hand, the preorganization of the ring puckering should promote triple helix formation. Why then do peptides with 4(*S*)Hyp in the Xaa position not form a triple helix? It was hypothesized that unfavorable steric interactions occur with 4(*S*)Hyp that are absent with 4(*S*)Flp [113].

The substitution of 4(*R*)Hyp by 4(*R*)-aminoproline in the peptide (Gly-Pro-4(*R*)Hyp)$_6$ also increases the stability of the triple helix. The extent of this increase in stability was strongly pH dependent [114].

30.2.4.8 *Cis* $\rightleftarrows$ *trans* Equilibria of Peptide Bonds

The peptide bond shows partial double bond character, as indicated by a shorter distance between the carbonyl carbon and the nitrogen than expected for a single

C–N bond. Consequently, the peptide bond is planar and the flanking Cα atoms can be either in *trans* ($\omega = 180°$) or *cis* ($\omega = 0°$) conformation. For peptide bonds preceding residues other than proline, only a small fraction (0.11–0.48%) was found to be in the *cis* conformation [115]. Peptide bonds preceding proline are much more frequently in the *cis* conformation, because the energy difference between the two conformations is rather small. *Cis* contents from 10 to 30% were found in short unstructured peptides [116, 117]. The activation energy for the *cis-trans* isomerization is high (80 kJ mol^{-1}) and the rate of isomerization is slow (see Section 30.3.2.4).

The collagen triple helix can accommodate only *trans* peptide bonds, so the ratio of *cis* to *trans* peptide bonds in the unfolded state has a direct influence on the stability of the triple helix. As mentioned above, the stereoelectronic effect of 4-substituents of proline residues influences the *cis*/*trans* ratio of the peptide bond preceding proline. It was proposed that the conformational stability of the triple helix relies on the change in the *cis*/*trans* ratio [110, 118]. These authors measured the $K_{cis/trans}$ for a number of 4-substituted proline residues. Table 30.3 summerizes these results.

There is indeed a good correlation of the observed *cis*/*trans* ratios and the thermal stability of homopolymers containing these residues in the Yaa position. However, a quantitation of this effect can be calculated [119]. The observed stability differences in the homopolymeric peptides $(Pro\text{-}Pro\text{-}Gly)_{10}$ and $(Pro\text{-}4(R)Hyp\text{-}Gly)_{10}$ are too large to be accounted for solely by the change in the *cis*/*trans* ratio of peptide bonds in the unfolded state (Bächinger, unpublished).

30.2.4.9 Interpretations of Stabilities on a Molecular Level

At present it is not possible to derive and quantitate all individual contributions that lead to the stability of the triple helix. It seems likely that a number of small

Tab. 30.3. $K_{cis/trans}$ in model compounds and unfolded type I collagen measured by NMR.

Compound	$K_{cis/trans}$	*Reference*
Ac-4(*S*)Hyp-OMe	0.37	Bächinger and Peyton, unpublished
Ac-Pro-OMe	0.16	
Ac-4(*R*)Hyp-OMe	0.12	
Ac-Pro-OMe	0.217	118
Ac-4(*R*)Hyp-OMe	0.164	
Ac-4(*R*)Flp-OMe	0.149	
Ac-4(*S*)Flp-OMe	0.4	
Ac-4(*S*)Hyp-OMe	0.417	110
Unfolded type I collagen		
X-Pro	0.19	164
X-Hyp	0.087	

Ac, acetyl; OMe, methyl ester; Flp, fluoroproline; Hyp, hydroxyproline.

contributions from the unfolded and folded state lead ultimately to the stable triple helix.

30.3 Kinetics of Triple Helix Formation

30.3.1 Properties of Collagen Triple Helices that Influence Kinetics

The complexity of the kinetics largely depends on the length of the triple helix to be formed. For short collagens and for short model peptides an all-or-none mechanism is a good approximation. The kinetics of systems with up to 45 tripeptide units per molecule (15 units per chain) have been successfully treated using this approximation [35, 120, 121]. Triple helices of most collagens are however much longer (1000–7200 amino acids) and the extent of cooperativity in triple helix formation is not sufficient for all-or-none transitions in systems of this size. The cooperative length of the triple helix in interstitial collagens with about 1000 tripeptide units was estimated to be about 100 tripeptide units from equilibrium studies [28]. This value was determined for the main triple helix of collagens I, II, and III and may apply to other collagens only in a first approximation because of sequence variations. The value is however consistent with the experimentally observed all-or-none nature of transitions with less than 45 tripeptide units. As expected the kinetics of long triple helices are more complex than those of short naturally occurring or designed model systems.

A second feature that largely influences the kinetics is the presence or absence of a cross-link between the three chains in a collagen molecule. As described in the Introduction most collagens contain nucleation domains (also called registration or oligomerization domains), which are located N-terminal or C-terminal of the triple helical domain. As explained in the first part of this review these domains serve to register the three chains at a side at which triple helix formation is nucleated. They are also involved in the selection of different chains in cases in which the collagen is a heterotrimer. The presence of trimerizing noncollagenous domains (designated as NC-domains or N-propeptides and C-propeptides) was found to be essential for proper folding of the triple helical domain. In addition, many collagen triple helical domains contain disulfide cross-links between their chains. The best-studied example is collagen III in which a disulfide knot of six cysteines (two per chain) connects the three chains at the C-terminus. During the physiological folding process, formation of this knot is most likely dependent on earlier noncovalent interactions between the adjacent NC-domains. After its formation it serves as an ideal registration and nucleation site, thus replacing the action of the NC-domain [122].

We shall first deal with the kinetics of folding from noncross-linked single chains and then turn to collagen triple helices, which are trimerized by either the disulfide knot of collagen III or by NC1-domains with strong trimerization poten-

tial. Natural proteins or fragment but also designed collagen-like proteins were employed in these studies.

30.3.2 Folding of Triple Helices from Single Chains

30.3.2.1 Early Work

Historically, all work on collagen folding started with single chains for the simple reason that before about 1980 only collagens from which the NC-domains were removed were available. Key publications of this time are by Piez and Carrillo [123] and Harrington and Rao [124]. In fact, the knowledge about N- and C-terminal NC-domains (frequently named N- and C-propeptides) and their importance developed only at this time and later. Before 1980, some work was also performed with cross-linked collagen chains derived from gelatin [125]. In contrast to the specific links leading to trimers, these chains were more statistically linked by nonreducible cross-links to dimers and higher oligomers.

An intriguing feature of early work in which collagens were refolded from their unfolded denatured chains was the observation that only a small fraction of native trimeric molecules was recovered. This fraction was very small at low temperatures and became higher at refolding temperatures close to the melting temperature [126]. Reaction orders varied between 1 and 2 depending on conditions and the time courses were difficult to interpret by a unique kinetic mechanism. Data indicated formation of products in which collagen triple helices with wrong alignment between the chains were formed. Annealing of these unstable products to native correctly aligned molecules was found to be very slow (for a review see Ref. [127]).

An early breakthrough in the kinetics of collagen triple helix formation from noncross-linked chains was achieved in studies with a short fragment chain of collagen I α1-CB2 [120]. An advantage of this system is its small size (12 tripeptide units per chain, 36 in the triple helix). A reaction order close to 3 was found for α1-CB2 and equilibrium transition curves indicated that the transition was of the all-or-none type with only unfolded chains and triple helices in equilibrium. Because of the relatively low stability of the triple helix formed by α1-CB2 it was difficult to reach a completely folded state at low temperatures. Furthermore, the fragment was isolated from a natural source and was available in small amounts only. Perhaps for these reasons no kinetic constant was derived and measurements of the concentration dependence were performed in a small interval only.

30.3.2.2 Concentration Dependence of the Folding of $(PPG)_{10}$ and $(POG)_{10}$

An extended study on the folding of short chains was performed with the synthetic model peptides $(PPG)_{10}$ and $(POG)_{10}$ [121]. Solutions were first heated to 60 °C ($(PPG)_{10}$) or 70 °C ($(POG)_{10}$) for 5 min to achieve complete unfolding. Time courses of refolding were recorded after fast cooling to 7 °C, at which the triple helix is completely folded according to equilibrium measurements. Kinetics of refolding was found to be extremely concentration dependent as expected for recombination of three chains (Figure 30.4).

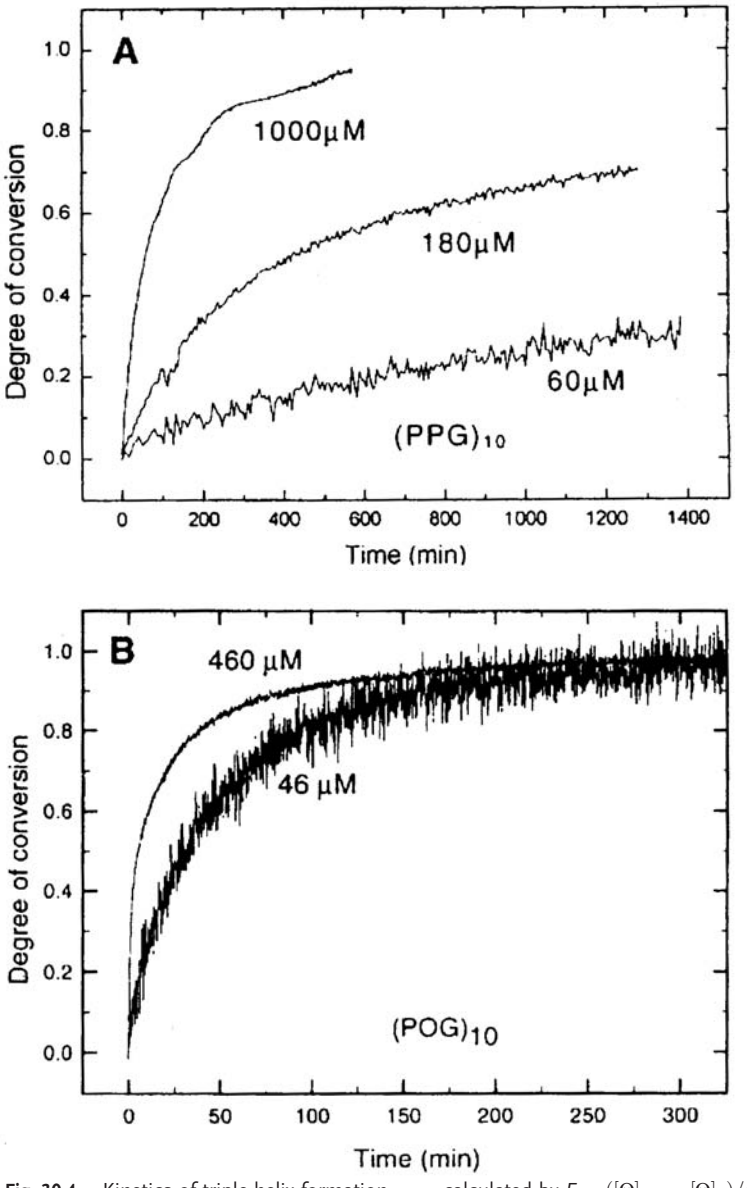

Fig. 30.4. Kinetics of triple helix formation of A) (ProProGly)$_{10}$ ((PPG)$_{10}$)) and B) (ProHypGly)$_{10}$ ((POG)$_{10}$)) at different peptide concentrations. The conversion was monitored at 7 °C after a temperature jump (dead time 2 min) from 60 °C in (A) and 70 °C in (B), temperatures at which the peptides are fully unfolded. The degree of conversion F was calculated by $F = ([\Theta]_{225} - [\Theta]_u)/([\Theta]_f - [\Theta]_u)$, where $[\Theta]_f$ and $[\Theta]_u$ are the ellipticities of the unfolded and folded state. The time courses for 60, 180, and 1000 μM concentrations of (PPG)$_{10}$ demonstrate a high dependence of the folding rate on concentration. For (POG)$_{10}$ the concentration dependence is much smaller and the rates are higher.

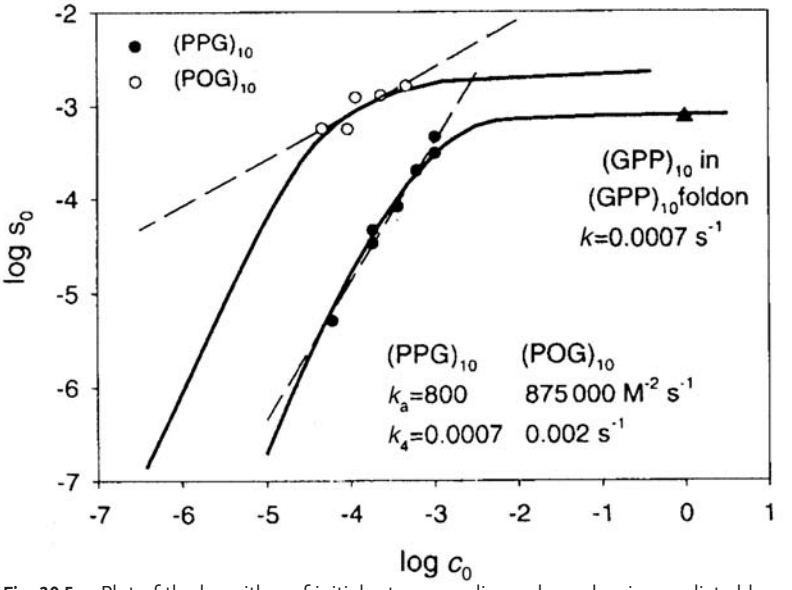

Fig. 30.5. Plot of the logarithm of initial rate of triple helix formation $s_o = (dF/dt)_{t=0}$ as a function of the logarithm of total chain concentration c_o for $(ProProGly)_{10}$ and $(ProHypGly)_{10}$. Broken lines show the best linear fits according to Eq. (2) with the apparent reaction orders of $n = 2.5$ and 1.5 for $(ProProGly)_{10}$ and $(ProHypGly)_{10}$, respectively. Continuous curves show better fits with nonlinear dependencies predicted by mechanism 13. The triangular point indicates the rate constant for $(ProProGly)_{10}$ in $(GlyProPro)_{10}$–foldon. This point was placed at a peptide concentration of 1 M ($\log c_o = 0$), which is the estimated intrinsic chain concentration at the junction of the $(GlyProPro)_{10}$ and foldon domain in $(GlyProPro)_{10}$–foldon.

Satisfactory fits of the time courses with theoretical integrated equations for even reaction orders could not be achieved, but fits with reaction orders of 2 were better than for 1 or 3. In agreement with similar observation with host–guest peptides [128], the data suggested that the reaction order changed with the progress of the kinetics. Therefore, initial slopes s_o were determined by careful extrapolations of the initial phases of the time courses (Figure 30.5).

Plotting $\log s_o$ as a function of $\log c_o$ yielded reaction orders that were 3 at very low concentrations but dropped with increasing concentration. Here c_o is the total concentration of single chains. Interestingly the concentration dependence of s_o for single chains of $(PPG)_{10}$ converged to the value measured for the first-order folding of the peptide cross-linked by foldon or the Cys-knot (see $(GPP)_{10}$–foldon and $(GPP)_{10}$–Cys_2 below).

Activation energies were determined from the temperature dependence of the folding kinetics of $(PPG)_{10}$ and $(POG)_{10}$. Values were much lower than for the cross-linked polypeptides (Table 30.4).

Tab. 30.4. Rate constants and activation energies of triple helix formation from single chains and trimerized chains at 20 °C.

Protein	k_a (M^{-2} s^{-1})	k_4 (s^{-1})	E_a (kJ mol^{-1})
$(ProProGly)_{10}$	900[a]	–	7
$(ProHypGly)_{10}$	about 10^6*	–	8
$(GlyProPro)_{10}$–foldon	0.00197	54.5	
$(GlyProPro)_{10}$–Cys_2	0.00033	52.5	

[a] Experimental values at 7 °C were 800 s^{-1} and 875 000 s^{-1}, respectively.

30.3.2.3 Model Mechanism of the Folding Kinetics

The following mechanism was proposed to explain the high reaction order and its concentration dependence

$$\begin{array}{l} C \\ + \\ 2C \underset{k_2}{\overset{k_1}{\rightleftarrows}} D^* \xrightarrow{k_3} H^* \xrightarrow{k_4} H \end{array} \qquad (13)$$

A schematic view of mechanism 13 is presented in Figure 30.6.

In this mechanism a very unstable dimeric nucleus D^* is in fast pre-equilibrium with monomers. Clearly a simultaneous collision of three particles in solution phase is an extremely infrequent event and a direct formation of a triple helical nu-

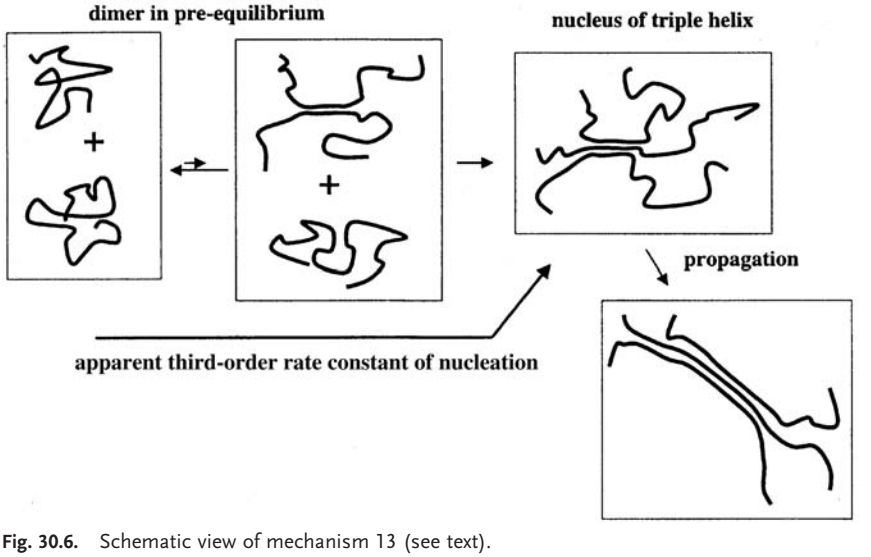

Fig. 30.6. Schematic view of mechanism 13 (see text).

cleus H^* can therefore be excluded. D^* forms in a bimolecular reaction and H^* is formed from it by combination with a third chain.

$$d[D^*]/dt = k_1[C]^2 - k_2[D^*] - k_3[D^*][C] = 0 \quad (14)$$

D^* is present only in very small amounts and therefore a steady state equilibrium ($d[D^*]/dt = 0$) is achieved shortly after the start of the reaction. Furthermore, dissociation into monomers is much faster than formation of H^* ($k_2 \gg k_3$ [C]) and the last term in Eq. (14) can be neglected. It follows that

$$k_1[C]^2 - k_2[D^*] = 0 \quad \text{or} \quad [D^*]/[C]^2 = k_1/k_2 = K \quad (15)$$

The rate of forming H^* (neglecting the decay term $- k_4[H^*]$) is

$$d[H^*]/dt = k_3[D^*][C] = Kk_3[C]^3 = k_a[C]^3 \quad (16)$$

It follows that the apparent third order rate constant k_a is the product of the equilibrium constant K and a true second-order rate constant k_3.

It is safe to assume that the nuclei D^* and H^* do not significantly contribute to the CD signal. This assumption is justified by the high instability and lack of triple helical structure of D^* and a very short segment of H^* (compared with the final length of H), which acts as a nucleus. Mechanism 13 predicts two limiting cases in which either nucleation or propagation is rate limiting.

At very low concentrations formation of H^* is the rate-limiting step and the rate of triple helix formation d[H]/dt equals the rate of nucleus formation as predicted by Eq. (16). In this case, the rate of helix propagation is faster than the rate of nucleation $k_4[H^*] \gg k_a[C]^3$. The experimentally observed degree of conversion F is related to [H] by $F = 3[H]/[C_0]$ in which $[C_0]$ is the total concentration of chains. Consequently the initial rate

$$(dF/dt)_{t=0} = 3k_a[C_0]^2 \quad (17)$$

At sufficiently high concentration nucleation will be faster than propagation and $[H^*] = (1/3)[C_0]$ after an initial phase. Propagation will then be the rate-limiting step of a first-order reaction

$$(dF/dt)_{t=0} = k_4[C_0] \quad (18)$$

Theoretical curves were calculated for mechanism 13 also for intermediate situations by numerical integration [121] and these curves are included in Figure 30.5. The dependencies were calculated with $k_a = 800$ and 875 000 M^{-2} s^{-1} and $k_4 = 0.0007$ s^{-1} and 0.002 s^{-1} for $(PPG)_{10}$ and $(POG)_{10}$, respectively. It can be seen that limiting case 1 is nearly reached for $(PPG)_{10}$, whose reaction order is 2.8–3 in the lowest concentration range. The average reaction order for all data

was 2.5 and as mentioned an extrapolation to high concentration of 1 M is consistent with the rate constant $k_4 = 0.0007\ s^{-1}$ determined for $(GPP)_{10}$ in $(GPP)_{10}$–foldon. Folding of $(POG)_{10}$ has an average reaction order of 1.5 and the initial rate plateaus at higher concentrations. It should be mentioned that experimental determinations of reaction orders are possible only in a rather narrow concentration interval, which is defined by the sensitivity of the CD spectrometer and the solubility of the model peptides.

30.3.2.4 Rate Constants of Nucleation and Propagation

The rate constants derived by mechanism 13 are summarized in Table 30.4. The apparent third-order rate constant k_a reflects the finding of the three chains and the nucleation process. According to the model mechanism 13 this includes formation of a dimeric precursor and the first short trimeric helical nucleus. The model is certainly oversimplified and in reality, chains may meet at many sites. Because of the repetitive sequence of the model peptides, precursors and nuclei will be of comparable stability if nucleated at different sites. The apparent rate constant k_a can therefore not be assigned to a single event. It should be noted that wrong nucleations and mismatching would also happen in natural collagens with their long repetitive sequences. This is probably the reason why special noncollagenous nucleation domains have been invented as registration domains.

Interestingly k_a differs by a factor of 1000 between $(PPG)_{10}$ and $(POG)_{10}$. A faster kinetics is expected in the presence of 4-hydroxyprolines in the Y-position because of its stabilizing action (see Section 30.2.4.3). The large effect of hydroxyprolines on the rate of nucleation may be based in a stabilization of the precursor dimer (increase of K) or in an increase of the rate of addition of the third chain (increase of k_3). Activation energies for k_a are much lower than for the rate constant of propagation (Table 30.4). It should be recalled that k_a is the product of an equilibrium constant with a negative temperature dependence and a true kinetic constant, which always increases with increasing temperature. The small activation energy is therefore most likely caused by a compensation of these opposing effects in a similar way as observed for other kinetics with pre-equilibria [129].

Propagation rate constants of $(PPG)_{10}$ and $(POG)_{10}$ differ only by a factor of 6 and are in fair agreement with the values found for the cross-linked trimerized peptides (Table 30.4). It is a long accepted fact that the rate-limiting events in propagation of collagen triple helices are the *cis–trans* isomerization steps of peptide bond preceding prolines or hydroxyprolines [122, 130, 131]. In unfolded chains, a certain fraction of peptide bonds is in *cis* configuration at equilibrium. In the triple helix, only the *trans* configuration can be accommodated. In other prolines containing proteins, *cis–trans* isomerization is also a slow rate-determining step. In collagens, this effect is particularly prominent because of their unusually high content of prolines and hydroxyprolines. *Cis–trans* isomerization steps process an unusually high activation energy, which originates from the need to uncouple the π-electron system of the semi-double bond during the transition from *cis* to *trans*. Rate constants of *cis–trans* isomerization and their activation energies are dependent on amino acids adjacent to prolines [117], but these changes are in a rather

narrow range and differences of no more than a factor of 10 in rate constants are expected.

An additional feature that may influence the kinetics is the equilibrium ratio of *cis* to *trans*, which again depends to some extent on the amino acid side chains preceding prolines or hydroxyprolines [117]. The approximate value for the equilibrium constant $K_{\text{cis-trans}}$ is 0.2 for the peptide bond between glycine and prolines. A rate constant $k_{\text{cis-trans}} = 0.003\ \text{s}^{-1}$ at 20 °C was determined for the isomerization of this bond in short peptides [116, 117]. Furthermore, variations of the prolines and hydroxyprolines content in the sequence will lead to differences in the number of *cis–trans* isomerization steps required for folding of a collagen segment. The last point does not apply to the comparison of $(\text{PPG})_{10}$ and $(\text{POG})_{10}$, but is relevant for the folding of natural collagens.

30.3.2.5 Host–guest Peptides and an Alternative Kinetics Model

Numerous studies have been performed with collagen-like model peptides of the design $(\text{GPO})_3\text{GXY}(\text{GPO})_4\text{GG}$. Here a guest tripetide is housed between stable hydroxyprolines containing host segments. Peptides of this type were mainly employed for studies of relative stability of guest tripetides with different residues in the X and Y position (see equilibrium part of this review). Kinetic studies were performed comparing guests GPO and GPP [128] in the host. A single GPP interrupting the GPO sequence is not expected to influence the nucleation rate by a large factor. Indeed the rate for the GPP containing peptide was only by a factor of 1.3 slower than that of $(\text{GPO})_8\text{GG}$. Apparently, the kinetic data as well as the equilibrium stabilities are mainly determined by the host regions (see equilibrium part). Time courses of refolding could not be fitted with even reactions orders and measurements of concentration dependencies were restricted to two concentrations. A third-order rate constant about $20\,000\ \text{M}^{-2}\ \text{s}^{-1}$ at 15 °C was derived.

The kinetics of another designed peptide T1-892Y with $(\text{GPO})_4$ at the C-terminus was investigated in greater detail [132]. The N-terminal part of this peptide AcG-PAGPAGPVGPAGARGPA was derived from collagen I. Data were fitted by a mechanism

$$3\text{C}_{cis} \underset{k_{\text{tc}}}{\overset{k_{\text{ct}}}{\rightleftarrows}} 3\quad \text{C}_{trans} \underset{k_{\text{fr}}}{\overset{k_{\text{rf}}}{\rightleftarrows}} \text{H}$$

in which k_{ct} and k_{tc} are the rate constants of *cis–trans* isomerization and k_{rf} and k_{fr} are the rate constants of folding of residues in *trans* conformation. To improve the fits the mechanism was expanded by a branching reaction at C_{trans}. Fitting results supported a nucleation domain composed mainly of the $(\text{GPO})_4$ moiety, which must be in *trans* form before the monomer is competent to initiate triple helix formation. Contrary to the highly positive activation energy of *cis–trans* isomerization, a negative activation energy was found, which was explained by a fast pre-equilibrium. Contrary to mechanism 13 the mechanism does not contain a dimer precursor and assumes a third-order reaction at any concentration in contrast to experimental findings with other model peptides.

N-terminal triple helix (fragment Col1-3)

Human $(GXY)_{10}$ GSOGPOGICESCPT
Mouse $(GXY)_{10}$ GPOGSOGICESCPT
Bovine $(GXY)_{10}$ GSOGPOGICESCPT

Central triple helix

Human $(GXY)_{340}$ GPOGAOGPCCGG
Mouse $(GXY)_{340}$ GPOGAOGPCCGG
Bovine $(GXY)_{339}$ GPOGAOGPCCGA

Fig. 30.7. Sequences of the short N-terminal and the central triple helix in collagen III. In major parts of the GXY repeats, the residues in the X and Y positions are not indicated. Hydroxyprolines residues (O) were only defined by amino acid sequencing of bovine collagen III. In the other sequences proposed by cDNA sequencing, proline residues in the Y position are probably also hydroxylated, and are indicated by O.

The folding of the designed peptide T1-892 was also investigated by NMR spectroscopy [12, 92]. By this technique *cis–trans* isomerization steps of Gly-Pro and Pro-Hyp bonds were monitored. The study identified individual residues involved in *cis–trans* isomerization as the rate-limiting step in triple helix propagation. Interestingly, the authors were able to define the direction of growth. It started in the $(Gly\text{-}Pro\text{-}Hyp)_4$ part of the peptide, which was defined as a nucleation domain. This finding was incorporated in the above mechanism [132]. Furthermore, a zipper-like folding (see below) was confirmed by the NMR study.

30.3.3
Triple Helix Formation from Linked Chains

Pioneering kinetic work was performed with the short N-terminal and the long central triple helical domains of collagen III, which consists of three identical chains [122, 130, 131]. Both domains are terminated by a disulfide knot. Sequences from three species are compared in Figure 30.7 with the N-terminal parts of the triple helices schematically indicated by GXY repeats [133]. It should be recalled that prolines in Y-positions are hydroxylated to hydroxyproline probably in all chains (Figure 30.7).

Note that the cysteine-containing sequences are different in the two domains. It was however established by molar mass determinations that the three chains are interlinked to trimers in both cases. The three-dimensional structure of the disulfide knots has not been solved yet but two likely models were proposed for the knot terminating the central helix [45, 131].

30.3.3.1 The Short N-terminal Triple Helix of Collagen III in Fragment Col1–3

Fragment Col1–3 consists of the N-terminal propeptide, the short triple helix and a noncollagenous telopeptide. Trimerization by the knot led to an increase in thermal stability and the fragment melts reversibly in an all-or-none type transition

with a midpoint temperature of 53 °C. It refolded in a first-order reaction with a rate constant of 8×10^{-3} s^{-1}, indicating *cis–trans* isomerization to be the rate-determining step. The value matches the later measured values for the propagation rate constants of other systems (Table 30.4). Values are not expected to be identical, because of differences of amino acid composition in the different systems. As a control for the function of the disulfide knot, refolding of Col1–3 was also studied after reductive cleavage. Kinetics was extremely slow and concentration dependent and the transition temperature of the product dropped to 35 °C.

A closer look at the refolding kinetics of Col1–3 trimerized by the disulfide knot revealed that kinetics proceeds in two phases [130]. In experiments with a dead time of 25 s the fast phase remained unresolved. The amplitude of the fast phase was about 50% of the total and rather temperature independent. The amplitude was significantly increased when refolding was started from a nonequilibrium state of the unfolded molecule in which less *cis*-peptide bonds were present than in the equilibrium state. The nonequilibrium state was achieved by refolding from chains, which were unfolded so quickly that most of the *trans* configuration present in the native triple helix was maintained. Experiments closely followed the double jump experiments [134] designed for similar experiments with ribonuclease S. Data are quantitatively analyzed by the zipper model of folding, which will be presented after discussing the kinetic data of the central triple helical domain.

30.3.3.2 Folding of the Central Long Triple Helix of Collagen III

For the central long triple helix the C-terminal propeptide provides a noncovalent link between the chains in the nonprocessed state but even after its removal the chains remain linked by the disulfide knot. The refolding kinetics of this trimerized, purely triple helical domain has been studied in great detail [28, 122]. Contrary to the refolding from noncross-linked chains, the unfolding–refolding process was completely reversible and end-products of refolding at 25 °C were identical to the native molecules as judged by their melting profiles, molecular weights, and sedimentation behavior. Mismatched structures of low stability were formed only at temperatures <15 °C.

The growth of the triple helix was found to proceed from the disulfide knot at the C-terminus at a rather uniform rate in a zipper-like fashion. This was most clearly shown by experiments in which the appearance and disappearance of folding intermediates was monitored directly (Figure 30.8).

The proteolytic assay is based on the ability of the collagen triple helix to resist trypsin digestion whereas the unfolded chains are readily degraded to small fragments [135]. Applying this method it was clearly shown that the folding intermediates all included the disulfide knot. Intermediates with short native triple helices are found at the start of the folding process. They decay and are replaced by longer fragments and finally native molecules with triple helices of full length are formed. In Figure 30.8 this is shown for the chains liberated by disulfide cleavage after digestion by trypsin. Gels were also run under nonreducing conditions [122]. In this

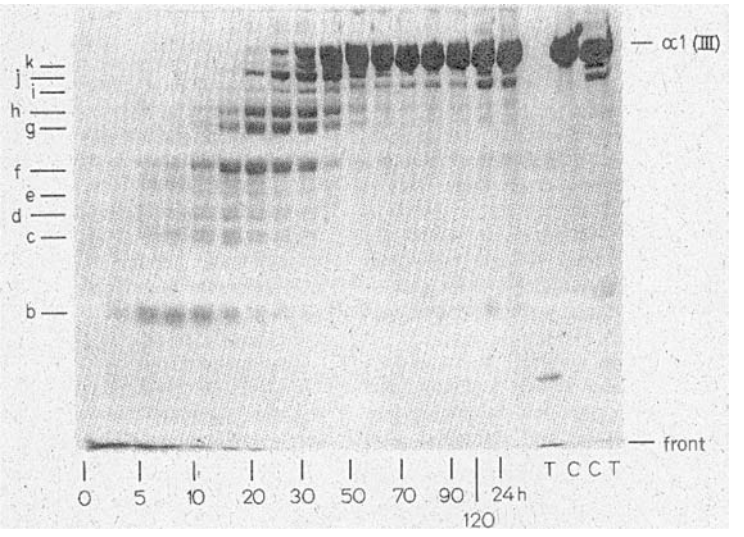

Fig. 30.8. Dodecyl sulfate slab gel electrophoresis of chain fragments which were protected against trypsin digestion by refolding. Type III collagen was denatured at 45 °C for 20 min and renatured at 25 °C for the time interval indicated. After incubation with trypsin at 20 °C for 2 min, sodium dodecyl sulfate was added and the sample was run on 10% polyacrylamide gel under reducing conditions. Eleven trypsin-resistant chain fragments designated by the letters a–k can be clearly distinguished. For comparison, native untreated collagen (C), native trypsin-treated collagen (CT) and trypsin (T) were also run.

case intermediates are not as well resolved because of their three times larger size but the same conclusions can be drawn. Furthermore, identical results were obtained with pN-collagen III, demonstrating that the N-terminal propeptides are not involved in the folding process.

For the zipper-like folding from the C-terminus zero-order kinetics is expected for a large initial fraction of the conversion (see next section). This behavior was experimentally observed for time courses followed by CD (Figure 30.9) [122].

Comparing the kinetics of the long central triple helix with those of the Col1–3 domain and the so-called one-quarter fragment obtained by selective proteolytic cleavage [136], a direct proportionality of the half-times to chain length was observed (Figure 30.9). This observation provides strong additional support to the zipper-like folding.

From the temperature dependence of refolding, activation energies of 85 kJ mol^{-1} were derived for the folding of the central triple helical domains, supporting that the propagation of the zipper is rate limited by *cis–trans* isomerization steps [130]. With the help of a model mechanism, it was concluded that on average, 30 amino acid residues occur in uninterrupted stretches without *cis* peptide bonds. They convert in a fast reaction after each isomerization step. The average rate constant of the isomerization steps was found to be 0.015 s^{-1} at 20 °C.

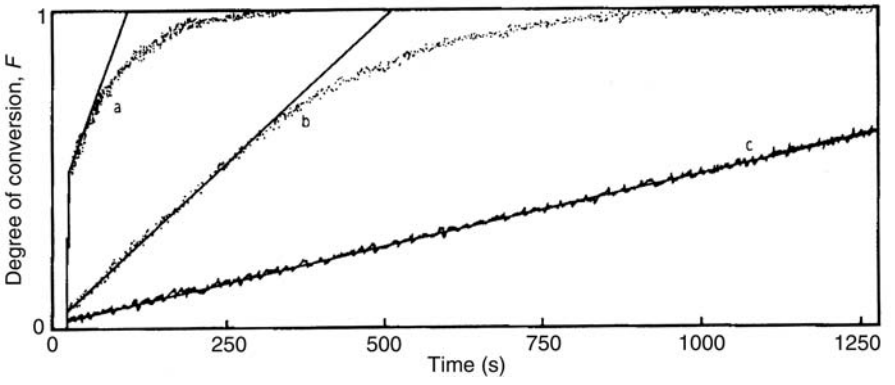

Fig. 30.9. Comparison of the folding kinetics of type III pN-collagen, the quarter fragment of type III collagen, and peptide Col1–3. Refolding of the collagen (c), the quarter fragment (b), and Col1–3 (a) were measured by circular dichroism. The straight lines represent the initial rates.

30.3.3.3 **The Zipper Model**

The model for the zipper-like folding of collagen triple helices is shown in Figure 30.10.

Here the disulfide knot is called h_0 and tripeptide units in correct helical conformation are called h. In the coiled state tripeptide units (v) with all peptide bonds in *trans* configuration are distinguished from units (w) which contain a *cis* peptide

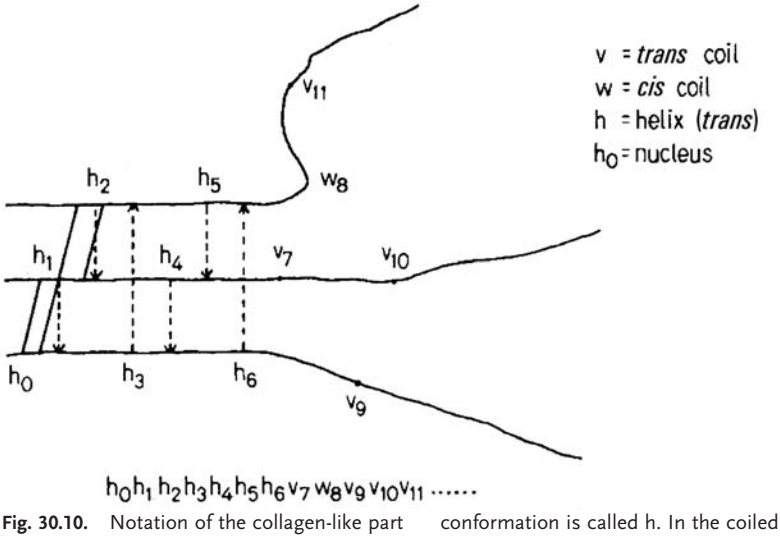

Fig. 30.10. Notation of the collagen-like part of Col1–3 as a linear sequence of letters. The three disulfide bridges are called h_0 and a tripeptide unit while the correct helical conformation is called h. In the coiled state, tripeptide units (v) with all peptide bonds in the *trans* configuration are distinguished from units (w) that contain a *cis* peptide bond.

bond. Tripeptide units are numbered in the way triple helix formation is believed to occur in a sequential way: to an already formed triple helix a tripeptide unit of chain A is added, followed by addition of the closest unit from chain B and then from C. A, B, and C are the designations for the three different chains in collagens. Each addition of a tripeptide unit is defined as a propagation step.

With the above notation, any state during folding can be written as a linear sequence of letters h, v, and w. For example, the partially folded state of Figure 30.10 reads $h_0$hhhhhhvwvvv ..., with h_0 acting as a permanent nucleus. It was shown by designed models for the triple helix (see following sections) that nucleation is mainly achieved by enforcement of a close neighborhood of residues near to the disulfide knot. The local concentration near the disulfide knot is close to 1 M as estimated from the model of the disulfide knot [131] and from the stability of $(GPP)_{10}$–foldon (see equilibrium part). The studies with designed proteins demonstrated that the disulfide knot may be replaced by any other trimerizing agent without affecting the nucleation potential. It should also be recalled that the disulfide knot (or other trimerizing cross-links) serve the important function of keeping the chains in the correct register and preventing misalignments.

Only the stretch of uninterrupted v units, which starts from h_0 and is terminated by the first w, can convert to the triple helix without *cis–trans* isomerization. Under conditions in which back reactions can be neglected, the relative amplitude of the fast phase (δA_f) or slow phase (δA_s) becomes

$$\left(\frac{\delta A_f}{\delta A_0}\right)_{max} = 1 - \left(\frac{\delta A_s}{\delta A_0}\right) = \frac{\langle i_v \rangle}{n} \tag{19}$$

with

$$\langle i_v \rangle = \sum_{i=1}^{n-1} i p_v^i p_w + n p_v^n = \frac{p_v(1 - p_v^n)}{1 - p_v} \tag{20}$$

Here δA_0 is the total change, $\langle i_v \rangle$ is the average length of uninterrupted v units, and n is the total number of tripeptide units in the triple helix. The probabilities of v and w states, p_v and p_w, are related by the equilibrium constant $K = [v]/[w]$ of *trans* to *cis* isomerization.

$$p_v = \frac{K}{1 + K} \tag{21}$$

It can be shown for large n that $\langle i_V \rangle$ may be approximated by K. For peptide Col1–3 with $n = 43$ (Figure 30.9) the relative amplitude of the fast phase was 0.5 and a value of $K = 25$–30 is derived. Note that this equilibrium constant is an average over regions of variable proline and hydroxyproline content and is much larger than the equilibrium constant for the isomerization of a single X-Pro or X-Hyp bond. Assuming that K is identical for the central triple helix ($n = 1026$) and the

quarter fragment ($n = 248$) the relative amplitude is predicted to be inversely proportional to n. This is exactly fulfilled by the experimental data shown in Figure 30.9.

After the initial fast phase, helix propagation will proceed with a rate determined by the rate constant of *cis–trans* isomerization k. Each isomerization step will liberate $(1 + K)$ v segments and the initial rate of the change in degree of helicity F will be

$$\left(\frac{dF}{dt}\right)_{t=0} = k\frac{(1+K)}{n} = k_{app} \tag{22}$$

From kinetic experiments, (Figure 30.9) it was only possible to determine the apparent rate constant k_{app} from the initial rates of the curves. Assuming a rate constant of $k = 0.015\ s^{-1}$ as measured for the isomerization of a Gly-Pro bond [137], other data in [116, 117, 130] follow $K = 30$ in close agreement with the value obtained from the amplitude of the fast phase. This implies that on average about every thirtieth tripeptide unit in the coiled chains of collagen III contains a *cis* peptide bond. This value fits well with qualitative estimates from the distribution of proline and hydroxyproline residues.

It was also possible to derive the time course of the entire slow phase (Figure 30.11).

The probability of finding i w segments in a molecule of n coiled segments is given by a binominal distribution with the probabilities for *trans* and *cis* segments defined in Eq. (14)

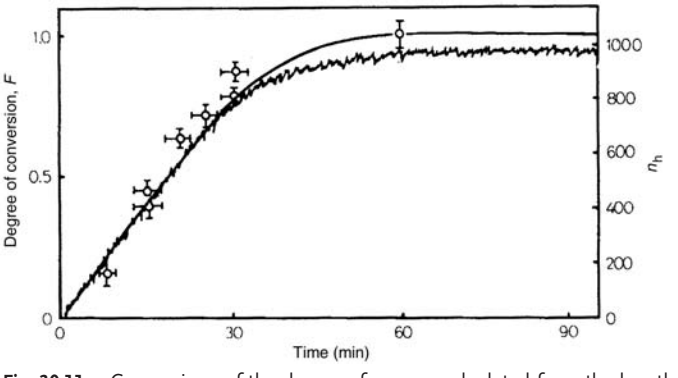

Fig. 30.11. Comparison of the degree of conversion F and length of the chains in triple helical conformation n_h during refolding of type III pN collagen at 25 °C. The experimental curve for the recovery of F with time at 25 °C was taken from Figure 30.9. It is compared with the number of residues in helical conformation n_h (open circles), which was calculated from the length of the trypsin-restistant fragments of Figure 30.8. The experimental time dependencies of n_h and F are compared with theoretical refolding kinetics (drawn-out curve). This was calculated by Eqs (24) and (28) with $k = 0.015\ s^{-1}$ and $K = 30$.

$$\hat{p}_{\mathrm{i}}^{n} = \binom{n}{i} p_{\mathrm{v}}^{n-i} p_{\mathrm{w}}^{i} \tag{23}$$

We consider a species that initially contains i w segments and that converts to a fully helical molecule without w segments. Whenever the growing helix reaches a w segment a *cis* → *trans* isomerization at the h–w junction will lead to a continuation of helix growth and to a species with one w segment less. A *cis* ↔ *trans* isomerization will also occur at other places of the molecule. Since these steps are not coupled to the irreversible helix formation, they are reversible and on average, the same number of w segments will be formed and destroyed. These steps will therefore not contribute to the reaction of interest. As noted above, the rate of helix formation is constant as long as all species contain at least one w segment. This certainly holds true in the beginning of the reaction since $\hat{p}_0^{1018}$ in the binominal distribution (Eq. (23)) is essentially zero. In the later phase of the reaction, however, fully helical species with no h–w junctions will be formed which no longer contribute to the reaction. The approximation $[\mathrm{hw}] \approx c_{\mathrm{P}}$ in Eq. (22) is no longer valid and $f_{\mathrm{hw}} = [\mathrm{hw}]/c_{\mathrm{P}}$ must be calculated as a function of time. Equation (22) becomes

$$\frac{\mathrm{d}F}{\mathrm{d}t} = \frac{k(1+K)}{n} f_{\mathrm{hw}}(t) \tag{24}$$

In order to calculate f_{hw}, the species that initially contains i w segments is designated M_1, the species that is derived from it by disappearance of one w segment M_2, etc. The formation of the final product with no w segments, M_{i+1}, will require i sequential steps which all proceed with the rate constant of *cis* → *trans* isomerization k:

$$\begin{array}{ccccccccc} \mathrm{M}_1 & \xrightarrow{k} & \mathrm{M}_2 & \xrightarrow{k} & \cdots & \xrightarrow{k} & \mathrm{M}_{\mathrm{r}} & \xrightarrow{k} \cdots \xrightarrow{k} & \mathrm{M}_{i+1} \\ i & & i-1 & & i-r+1 & & & & 0 \end{array} \tag{25}$$

$i, i-1, i-r+1$ and 0 indicate the number of w segments in the species.

The rate equations are

$$\frac{\mathrm{d}f_1}{\mathrm{d}t} = -kf_1 \tag{26a}$$

$$\frac{\mathrm{d}f_r}{\mathrm{d}t} = -kf_r + kf_{r-1} \tag{26b}$$

$$\frac{\mathrm{d}f_{r+1}}{\mathrm{d}t} = -kf_{r+1} + kf_r \tag{26c}$$

with $1 < r < i+1$.

Here $f_1, f_2 \ldots f_r, f_{r+1} \ldots f_{i+1}$ are the fractions of species in reaction (25). A fraction is defined by $f_r = c_r/c_1^0$ where c_1^0 is the initial concentration of M_1. To find a solution of this set of first-order linear differential equations we introduce

$$f_r = \Phi(t)e^{-kt} \quad \text{and} \quad f_{r+1} = \Psi(t)e^{-kt}$$

it follows that

$$\frac{df_{r+1}}{dt} = -kf_{r+1} + \frac{d\Psi}{dt}e^{-kt}$$

and with Eq. (26c)

$$\frac{d\Psi}{dt} = k\Phi(t)$$

The initial conditions at $t = 0$ are $f_1^0 = 1$ and all other $f_r = 0$. Integration of the first differential Eq. (26a) with this conditions yields

$$f_1 = e^{-kt} \quad \text{and} \quad \Phi(t) = 1$$

It follows that

$$\Psi(t) = kt \quad \text{and} \quad f_2 = kte^{-kt}$$

Stepwise application of this scheme to $r = 3, 4, \ldots r$ yields the general solution

$$f_r = \frac{(kt)^{r-1}}{(r-1)!}e^{-kt} \tag{27}$$

In order to obtain the fraction of molecules which contain at least one w segment we have to take the sum of f_r from $r = 1$ to $r = i$. Since these are fractions of the species present in the initial distribution we have to multiply each sum over f_r by corresponding $\hat{p}_i^n$ and to take the sum over this distribution in order to obtain the total fraction of species with at least one w segment and with one h–w junction

$$f_{hw} = \sum_{i=0}^{i=n} \hat{p}_i^n \sum_{r=1}^{r=i} \frac{(kt)^{r-1}}{(r-1)!}e^{-kt} \tag{28}$$

The rate of helix formation can now be calculated by Eqs (24) and (28) and the time dependence of F can be obtained by numerical integration of Eq. (24) into which f_{hw} Eq. (28) was substituted. A good fit to the experimental time course was obtained with the parameters $k = 0.015\ s^{-1}$ and $K = 30$ (see Figure 30.11).

30.3.4 Designed Collagen Models with Chains Connected by a Disulfide Knot or by Trimerizing Domains

Natural collagens contain triple helices whose chemical and physical properties are different at different positions of the helix. This property originates from variations of residues in X and Y positions. As described in the equilibrium part stabilities largely depend on the nature of X and Y in short peptides and differences may also result in long triple helices although cooperative influences of neighboring segments may reduce the effect.

Kinetic measurements of designed model proteins with GPP-, GPO-, or other collagen-like repeats, avoid complication caused by sequence heterogeneity. In addition, it is possible to study the influences of cross-linking in a quantitative way. Two methods of cross-linking were applied. In the first one, two Cys residues were added to the ends of the chains either by peptide synthesis or by fusion of the disulfide knot of type III collagen by recombinant technology. The chains were then joined by controlled oxidative coupling. In the second method, noncollagenous domains were fused to either the N- or C-terminus of the model peptide.

30.3.4.1 Disulfide-linked Model Peptides

Cys repeats that differ from those found at the ends of the central helix of collagen III and were different in different chains were placed at the C-termini of model peptides by elaborate peptide chemistry [138]. This strategy was primarily followed to design substrates for matrix metalloproteases (MMPs) and for integrins, which are both structure dependent and recognize triple helices composed of all three chains. The model collagens designed in his way refolded reversibly with first-order kinetics [138]. If reduced they lacked the potential to reform intact triple helices upon reoxidation in the presence of glutathione (L. Moroder, personal communication). Reoxidation was successful, however, when the disulfide sequence GPPGPCCGG of collagen III was used, proving the potential of this sequence for spontaneous formation of a disulfide knot [44–46].

In particular $(GPP)_{10}GPCCGG$ (abbreviated $(GPP)_{10}–Cys_2$) was expressed recombinantly and converted to a trimer in triple helical conformation by reoxidation in the presence of 9 mM oxidized and 0.9 mM reduced glutathione [121]. Data on the stabilization of the $(GPP)_{10}$ triple helix by the cross-link have been reported in the equilibrium part of this review. The kinetics of refolding was monitored after cooling from 70 °C to temperatures between 7 and 35 °C in the presence of 2.5 M GdmCl. The denaturant was added to shift the transition region to a more accessible region, since in plain buffer $(GPP)_{10}–Cys_2$ melts at 90 °C. Kinetics proceeded in a fast, experimentally unresolved phase and a dominant slow phase, which was of first order and concentration independent over a broad range of peptide concentrations. Measurements were performed by CD at the ''collagen CD signal'' at 221 nm. A large temperature dependence of the CD signal pointed to nonconformation-dependent signal change, which was also kinetically unresolved and subtracted from the time course. The measured first-order kinetic

constants are included in Table 30.1 for comparison with the apparent third-order constants for the free uncross-linked chains. For reasons discussed in Ref. [121] activation energies (Table 30.4) were somewhat lower than measured for the *cis–trans* isomerzation of dipeptides [116, 117]. There is no doubt that the slow phase of the refolding reflects the propagation step, whose rate is determined by *cis–trans* isomerization of peptide bonds. The rate constants for the isomerization of individual prolines containing bonds in $(GPP)_{10}$–Cys_2 are unknown and it should be recalled that the overall rate constants are composites of these values.

30.3.4.2 Model Peptides Linked by a Foldon Domain

The foldon domain of T4 phage fibritin consists of three chains with 29 amino acid residues each and forms an obligatory trimer of high stability [46, 86]. Foldon domains were fused to the $(GPP)_{10}$ chains via a GS-linker and the chains were trimerized very efficiently. Care was taken not to unfold the foldon domain in all kinetic measurements performed with $(GPP)_{10}$–foldon. All data therefore correspond to the $(GPP)_{10}$ domains interlinked by an intact foldon trimer.

Results obtained with $(GPP)_{10}$–foldon were very similar to the results obtained with $(GPP)_{10}$–Cys_2 (Table 30.4). The identity of results shows that nucleation of the collagen triple helix is primarily determined by the trimerization at one end and that it does not matter which trimerization domain is applied. It is concluded that a domain like foldon, which was designed to nucleate the folding of fibritin to a trimeric coiled-coil structure, has the same function as the collagen-specific disulfide knot and probably also all other C- or N-terminal propeptide domains of natural collagens. The argument is supported by the observation that propeptide domains differ largely in structure (see Introduction) but do all form trimers.

30.3.4.3 Collagen Triple Helix Formation can be Nucleated at either End

As mentioned earlier, propeptides and disulfide bonds, which are believed to nucleate triple helix folding, are located at the C-terminus of most natural collagens. Exceptions are the membrane-spanning collagens XIII, XVII, XXIII, and XXV, which contain coiled-coil domains at the N-terminal side of the triple helix [139]. Three-stranded coiled-coil domains frequently act as oligomerization domains in extracellular membrane (ECM) proteins [140] and mutation data suggested that the coiled-coil domains nucleate triple helix formation in collagen XIII [141].

In this context, it was of interest to learn whether the kinetics of triple helix formation may be different for nucleation at the N- or C-terminal end. The problem was approached by a comparison of model peptides $(GlyProPro)_{10}$, which were either linked to trimers at the N- or C-terminus [165]. Linkage was either achieved by fusion with a short segment containing the disulfide knot of collagen III or by attachment of the foldon domains. In both cases a stabilization of the triple helix after cross-linking was observed, which was however somewhat less pronounced in the case of N-terminal attachment compared with C-terminal fusion. This difference may be explained by energy differences in the contact regions between the oligomerization domains and the triple helix. In the crystal structure of

$(GlyProPro)_n$–foldon [86] several bad contacts were observed in the contact region between the triple helix and the foldon domain. It was concluded that unfavorable enthalpic interactions may in part counteract the entropic stabilization by cross-linking. The structure of foldon–$(GlyProPro)_n$ was not solved yet but different and probably more unfavorable interactions are anticipated in its contact region. It was also noticed that the insertion of Gly-Ser spacers between the oligomerzation domain and the triple helix is essential. Most importantly, however, the kinetics of triple helix formation was identical for all four model systems $(GlyProPro)_n$–foldon, foldon–$(GlyProPro)_n$, $(GlyProPro)_n$–Cys_2 and Cys_2–$(GlyProPro)_n$. Also, the activation energies of folding were identical for all four peptides. Rate constants of folding were about 10^{-3} s^{-1} at 20 °C and the activation energy was 50 kJ mol^{-1} [165]. In summary, triple helix formation proceeds with closely similar rates in both directions. For the alignment of strands and nucleation of triple helical folding, oligomerization domains are needed but these may be placed at both ends of the triple helix. Their more frequent occurrence at the C-end is not explained by an easier folding from this side.

30.3.4.4 Hysteresis of Triple Helix Formation

As mentioned in Section 30.2.3, thermal unfolding and refolding of the triple helix is highly rate dependent in the transition region. Consequently, transition curves recorded by heating and by cooling form a hysteresis loop (see Figure 30.1). Hysteresis is very prominent for long natural collagens like collagen III and is also observed under isothermal conditions when unfolding is induced by increasing the concentration of guanidine hydrochloride [28]. In the case of collagen III with an intact disulfide knot at the C-terminus, correct and complete refolding of native molecules is achieved at temperatures 10 or more degrees below the transition temperature (or 0.5 M below the GdmCl midpoint concentration) after short incubation times of a few hours. In these cases, true hysteresis, in which equilibrium values are not reached even after very long waiting times, is limited to the range near the transition temperature. As mentioned in Section 30.3.2.1 and other parts of this review, unlinked single chains refold to misaligned structures at low temperatures. In these cases, an apparent hysteresis is observed, when monitoring CD or other parameters. The nature of this apparent hysteresis is very different from the true hysteresis because refolding products differ from the native parent molecules.

It was noticed that hysteresis was less prominent for short collagen triple helices like the one-quarter fragment of collagen III [28]. More recently, it was found that hysteresis loops are clearly observable also for short model peptides as long as the heating and cooling rates are not too slow. The major difference between native long triple helices and short model peptides is apparently the time dependence. For long triple helices the loops persist even at very slow scan rates whereas for short triple helices equilibrium is achieved more quickly.

For the model systems with linked chains, a simple kinetic hysteresis mechanism is proposed (Boudko, Bächinger, and Engel, in preparation). In the transition region the reciprocal apparent rate constant is

$$k_{\mathrm{app}}^{-1} = \frac{1}{k_{\mathrm{f}} + k_{\mathrm{u}}} \tag{29}$$

in which k_{f} and k_{u} are the rate constants of folding and unfolding, respectively. Rate constant k_{f} is dependent on temperature according to the Arrhenius relation with the high activation energy $E_{\mathrm{a,f}}$ of *cis–trans* isomerization (see Section 30.3.3). The temperature dependence of k_{u} is much lower and its activation energy $E_{\mathrm{a,v}}$ can be calculated from $E_{\mathrm{a,f}}$ and the enthalpy of the reaction by $E_{\mathrm{a,v}} = E_{\mathrm{a,f}} - \Delta H^{\circ}$. A satisfactory fit of the experimentally observed change of helicity F during heating or cooling is obtained when the rate law

$$\frac{\mathrm{d}F}{\mathrm{d}t} = k_{\mathrm{f}}(1 - F) - k_{\mathrm{u}}F \tag{30}$$

is integrated with the starting conditions (1) $F = 1$ at $t = 0$ for heating and (2) $F = 0$ at $t = 0$ for cooling. Case 1 yields the time course

$$F = \frac{K}{1 + K} + \frac{1}{1 + K}\mathrm{e}^{-k_{\mathrm{app}}t} \tag{31}$$

and case 2

$$F = \frac{K}{1 + K}(1 - \mathrm{e}^{-k_{\mathrm{app}}t}) \tag{32}$$

with $K = k_{\mathrm{f}}/k_{\mathrm{u}}$. The hysteresis loops can be constructed by calculation of F after different times at different temperatures. Obviously for infinite times t the equilibrium curve $F = K/(1 + K)$ is obtained.

The mechanism of hysteresis for long triple helices of natural collagens is clearly more complicated. They do not fold in an all-or-none reaction like the short proteins as demonstrated by a cooperative length that is about 1/10 of the length of the molecule [28]. A possible mechanism was proposed in Ref. [142].

30.3.5
Influence of *cis–trans* Isomerase and Chaperones

Catalysis of the folding of many proline-containing proteins was discovered shortly after the discovery of the kidney enzyme peptidyl-prolyl *cis-trans* isomerase (PPIase) [143]. Three protein families are now known to have PPIase activities: the cyclophilins, the FK506 binding proteins (FKBP) and the parvulins. In vitro experiments showed that cyclophilin has an accelerating effect on the folding of collagen III [144], but the factor was only close to 2. A similar effect was also found for collagen IV [145]. The action of PPIase on collagen was substantiated by the finding that cyclosporin A [146] and to a lesser extent FK506 [147] slows triple helix forma-

tion in vivo. FKBP65 had only a small effect on the rate of refolding on type III collagen [148]. PPIases are widely distributed and the *Escherichia coli* variant was also investigated with collagen [149]. It was speculated that the relatively small accelerations may originate from the use of enzymes that are not specific for collagen. A PPIase with an acceleration factor of 100 or more as observed for other proteins has not yet been observed. Such an enzyme may, however, be a necessity for animals living in a cold environment at which *cis–trans* isomerization is very slow, because of its high activation energy.

Numerous other helper proteins have been identified in the context of collagens (for reviews see Refs [150, 151, 152]). A collagen-specific chaperone is HSP47, whose physiological importance is manifested by a severe phenotype of transgenic mice lacking HSP47 [153]. Several very different mechanisms of action were discussed for HSP47, but with the exception of a specific binding to collagen, molecular explanations remain to be explored.

30.3.6
Mutations in Collagen Triple Helices Affect Proper Folding

Mutations in collagen genes cause a number of severe inherited diseases [154, 155]. The best-studied collagen-related genetic disease is osteogenesis imperfecta (brittle bone disease). Point mutations at different positions of the triple helix lead to improperly folded and instable triple helices, disturbed fiber formation, and severe pathological changes of the collagen matrix. Mutations near the C-terminus tend to be more severe than similar mutations near the N-terminus. In view of the steric need of small glycine residues in every third position (see Section 30.1.4), mutations of glycines to residues with larger side chains are particularly disturbing and cause large decreases of transition temperatures. In some cases, even kinks were visualized in such mutated collagens [156]. A delayed triple helix formation of mutant collagen from patients with osteogenesis imperfecta was observed [157]. Hydroxylation of prolines only occurs in the unfolded state and consequently the extent of hydroxylation and other posttranlational modifications was much increased in the mutated collagens, apparently at the N-terminal side of the mutation. Recently model peptides were studied with sequence irregularities designed after important natural mutations [158]. With this approach, it is hoped to gain deeper explanations of how a single-point mutation in the triple helix may cause a global pathological condition.

References

1 Mayne, R. & Burgeson, R. E. (1987). *Structure and Function of Collagen Types*. Academic Press, Orlando, Fl.

2 Olsen, B. R. (1991). Collagen biosynthesis. In: *Cell Biology of the Extracellular Matrix* (Hay, E. D., ed.). Plenum Press, New York, pp. 177–212.

3 Mironov, A. A., Weidman, P. & Luini, A. (1997). Variations on the

intracellular transport theme: maturing cisternae and trafficking tubules. *J Cell Biol* **138**, 481–4.

4 Bonfanti, L., Mironov, A. A., Jr., Martinez-Menarguez, J. A. et al. (1998). Procollagen traverses the Golgi stack without leaving the lumen of cisternae: evidence for cisternal maturation. *Cell* **95**, 993–1003.

5 Vuust, J. & Piez, K. A. (1972). A kinetic study of collagen biosynthesis. *J Biol Chem* **247**, 856–62.

6 Miller, E. J., Woodall, D. L. & Vail, M. S. (1973). Biosynthesis of cartilage collagen. Use of pulse labeling to order the cyanogen bromide peptides in the alpha L(II) chain. *J Biol Chem* **248**, 1666–71.

7 Morris, N. P., Fessler, L. I., Weinstock, A. & Fessler, J. H. (1975). Procollagen assembly and secretion in embryonic chick bone. *J Biol Chem* **250**, 5719–26.

8 Kao, W. W., Berg, R. A. & Prockop, D. J. (1977). Kinetics for the secretion of procollagen by freshly isolated tendon cells. *J Biol Chem* **252**, 8391–7.

9 Bateman, J. F., Lamande, S. R. & Ramshaw, J. A. M. (1996). Collagen superfamily. In: *Extracellular Matrix* (Comper, W. D., ed.). Harwood Academic Publishers, Amsterdam, pp. 27–67.

10 Engel, J. (1997). Versatile collagens in invertebrates. *Science* **277**, 1785–6.

11 McAlinden, A., Smith, T. A., Sandell, L. J., Ficheux, D., Parry, D. A. & Hulmes, D. J. (2003). Alpha-helical coiled-coil oligomerization domains are almost ubiquitous in the collagen superfamily. *J Biol Chem.* **278**, 42200–7.

12 Baum, J. & Brodsky, B. (2000) Case study 2: Folding of the collagen triple-helix and its naturally occuring mutants. In: *Frontiers in Molecular Biology: Mechanisms of Protein Folding*, 2nd edn (Pain, R. H., ed.). Oxford University Press, Oxford.

13 Bateman, J. F., Lamande, R. & Ramshaw, J. A. M. (1996) Collagen superfamily. In: *Extracellular Matrix*, Vol. 2 (Comper, W. D., ed.). Harwood Academic Publishers, Amsterdam, pp. 22–67.

14 Leikina, E., Mertts, M. V., Kuznetsova, N. & Leikin, S. (2002). Type I collagen is thermally unstable at body temperature. *Proc Natl Acad Sci USA* **99**, 1314–18.

15 Privalov, P. L. (1982). Stability of proteins. Proteins which do not present a single cooperative system. *Adv Protein Chem* **35**, 1–104.

16 Burjanadze, T. V. (1979). Hydroxyproline content and location in relation to collagen thermal stability. *Biopolymers* **18**, 931–8.

17 Burjanadze, T. V. & Veis, A. (1997). A thermodynamic analysis of the contribution of hydroxyproline to the structural stability of the collagen triple helix. *Connect Tissue Res* **36**, 347–65.

18 Miles, C. A., Wardale, R. J., Birch, H. L. & Bailey, A. J. (1994). Differential scanning calorimetric studies of superficial digital flexor tendon degeneration in the horse. *Equine Vet J* **26**, 291–6.

19 Miles, C. A., Burjanadze, T. V. & Bailey, A. J. (1995). The kinetics of the thermal denaturation of collagen in unrestrained rat tail tendon determined by differential scanning calorimetry. *J Mol Biol* **245**, 437–46.

20 Bächinger, H. P. & Engel, J. (2001). Thermodynamic vs. kinetic stability of collagen triple helices. *Matrix Biol* **20**, 267–9.

21 Kivirikko, K. I. (1998). Collagen biosynthesis: a mini-review cluster. *Matrix Biol* **16**, 355–6.

22 Kivirikko, K. I. & Myllyharju, J. (1998). Prolyl 4-hydroxylases and their protein disulfide isomerase subunit. *Matrix Biol* **16**, 357–68.

23 Bella, J., Brodsky, B. & Berman, H. M. (1995). Hydration structure of a collagen peptide. *Structure* **3**, 893–906.

24 Panasik, N., Jr., Eberhardt, E. S., Edison, A. S., Powell, D. R. & Raines, R. T. (1994). Inductive effects on the structure of proline residues. *Int J Pept Protein Res* **44**, 262–9.

25 Holmgren, S. K., Taylor, K. M., Bretscher, L. E. & Raines, R. T.

(1998). Code for collagen's stability deciphered [letter]. *Nature* **392**, 666–7.

26 Vitagliano, L., Berisio, R., Mastrangelo, A., Mazzarella, L. & Zagari, A. (2001). Preferred proline puckerings in cis and trans peptide groups: implications for collagen stability. *Protein Sci* **10**, 2627–32.

27 Vitagliano, L., Berisio, R., Mazzarella, L. & Zagari, A. (2001). Structural bases of collagen stabilization induced by proline hydroxylation. *Biopolymers* **58**, 459–64.

28 Davis, J. M. & Bächinger, H. P. (1993). Hysteresis in the triple helix-coil transition of type III collagen. *J Biol Chem* **268**, 25965–72.

29 Morris, N. P., Watt, S. L., Davis, J. M. & Bächinger, H. P. (1990). Unfolding intermediates in the triple helix to coil transition of bovine type XI collagen and human type V collagens alpha 1(2) alpha 2 and alpha 1 alpha 2 alpha 3. *J Biol Chem* **265**, 10081–7.

30 Heidemann, E. & Roth, W. (1982). Synthesis and Investigation of collagen model peptides. *Adv Polym Sci* 43, 144–203.

31 Sakakibara, S., Kishida, Y., Kikuchi, Y., Sakai, R. & Kkiuchi, K. (1968). Synthesis of poly-(L-prolyl-L-prolylglycyl) of defined molecular weights. *Bull Chem Soc Japan* **41**, 1273–80.

32 Rothe, M., Theyson, R., Steffen, K. D. et al. (1970). Synthesis and conformation of collagen models. *Angew Chem Int Ed Engl* **9**, 535.

33 Weber, R. W. & Nitschmann, H. (1978). Der Einfluss der O-Acetylierung auf das konformative Verhalten des Kollagen-Modellpeptides $(L\text{-Pro-L-Hyp-Gly})_{10}$ und von Gelatine. *Helv Chim Acta* **61**, 701–8.

34 Sakakibara, S., Inouye, K., Shudo, K., Kishida, Y., Kobayashi, Y. & Prockop, D. J. (1973). Synthesis of (Pro-Hyp-Gly) n of defined molecular weights. Evidence for the stabilization of collagen triple helix by hydroxypyroline. *Biochim Biophys Acta* **303**, 198–202.

35 Suto, K. & Noda, H. (1974). Conformational change of the triple-helical structure. IV. Kinetics of the helix-folding of (Pro-Pro-Gly)n (n equals 10, 12, and 15). *Biopolymers* **13**, 2477–88.

36 Shah, N. K., Ramshaw, J. A., Kirkpatrick, A., Shah, C. & Brodsky, B. (1996). A host-guest set of triple-helical peptides: stability of Gly-X-Y triplets containing common nonpolar residues. *Biochemistry* **35**, 10262–8.

37 Kwak, J., Jefferson, E. A., Bhumralkar, M. & Goodman, M. (1999). Triple helical stabilities of guest-host collagen mimetic structures. *Bioorg Med Chem* **7**, 153–60.

38 Jenkins, C. L., Bretscher, L. E., Guzei, I. A. & Raines, R. T. (2003). Effect of 3-hydroxyproline residues on collagen stability. *J Am Chem Soc* **125**, 6422–7.

39 Heidemann, E., Neiss, H. G., Khodadadeh, K., Heymer, G., Sheikh, E. M. & Saygin, O. (1977). Structural studies of collagen-like sequential polypeptides. *Polymer* **18**, 420–4.

40 Feng, Y., Melacini, G., Taulane, J. P. & Goodman, M. (1996). Collagen-based structures containing the peptoid residue N-isobutylglycine (Nleu): synthesis and biophysical studies of Gly-Pro-Nleu sequences by circular dichroism, ultraviolet absorbance, and optical rotation. *Biopolymers* **39**, 859–72.

41 Fields, C. G., Lovdahl, C. M., Miles, A. J., Hagen, V. L. & Fields, G. B. (1993). Solid-phase synthesis and stability of triple-helical peptides incorporating native collagen sequences. *Biopolymers* **33**, 1695–707.

42 Mann, K., Mechling, D. E., Bächinger, H. P., Eckerskorn, C., Gaill, F. & Timpl, R. (1996). Glycosylated threonine but not 4-hydroxyproline dominates the triple helix stabilizing positions in the sequence of a hydrothermal vent worm cuticle collagen. *J Mol Biol* **261**, 255–66.

43 Mechling, D. E. & Bächinger, H. P. (2000). The collagen-like peptide (GER)15GPCCG forms pH-dependent covalently linked triple helical trimers. *J Biol Chem* **275**, 14532–6.

44 Barth, D., Musiol, H. J., Schutt, M. et al. (2003). The role of cystine knots in collagen folding and stability, Part I. Conformational properties of (Pro-Hyp-Gly)5 and (Pro-(4S)-FPro-Gly)5 model trimers with an artificial cystine knot. *Chemistry* **9**, 3692–702.

45 Barth, D., Kyrieleis, O., Frank, S., Renner, C. & Moroder, L. (2003). The role of cystine knots in collagen folding and stability, Part II. Conformational properties of (Pro-Hyp-Gly)n model trimers with N- and C-terminal collagen type III cystine knots. *Chemistry* **9**, 3703–14.

46 Frank, S., Kammerer, R. A., Mechling, D. et al. (2001). Stabilization of short collagen-like triple helices by protein engineering. *J Mol Biol* **308**, 1081–9.

47 Kwak, J., De Capua, A., Locardi, E. & Goodman, M. (2002). TREN (Tris(2-aminoethyl)amine): an effective scaffold for the assembly of triple helical collagen mimetic structures. *J Am Chem Soc* **124**, 14085–91.

48 Tanaka, Y., Suzuki, K. & Tanaka, T. (1998). Synthesis and stabilization of amino and carboxy terminal constrained collagenous peptides. *J Pept Res* **51**, 413–19.

49 Yu, Y. C., Berndt, P., Tirrell, M. & Fields, G. B. (1996). Self-assembling amphiphiles for the construction of protein molecular architecture. *J Am Chem Soc* **118**, 12515–20.

50 Yu, Y. C., Tirrell, M. & Fields, G. B. (1998). *J Am Chem Soc* **120**, 9979–87.

51 Yu, Y. C., Roontga, V., Daragan, V. A., Mayo, K. H., Tirrell, M. & Fields, G. B. (1999). Structure and dynamics of peptide-amphiphiles incorporating triple-helical proteinlike molecular architecture. *Biochemistry* **38**, 1659–68.

52 Koide, T., Yuguchi, M., Kawakita, M. & Konno, H. (2002). Metal-assisted stabilization and probing of collagenous triple helices. *J Am Chem Soc* **124**, 9388–9.

53 Ottl, J., Musiol, H. J. & Moroder, L. (1999). Heterotrimeric collagen peptides containing functional epitopes. Synthesis of single-stranded collagen type I peptides related to the collagenase cleavage site. *J Pept Sci* **5**, 103–10.

54 Engel, J., Chen, H. T., Prockop, D. J. & Klump, H. (1977). The triple helix in equilibrium with coil conversion of collagen-like polytripeptides in aqueous and nonaqueous solvents. Comparison of the thermodynamic parameters and the binding of water to (L-Pro-L-Pro-Gly)n and (L-Pro-L-Hyp-Gly)n. *Biopolymers* **16**, 601–22.

55 Bartsch, H.-J. (1982). *Taschenbuch mathematischer Formeln*. Verlag Harri Deutsch, Thun, p. 66.

56 Sacca, B., Renner, C. & Moroder, L. (2002). The chain register in heterotrimeric collagen peptides affects triple helix stability and folding kinetics. *J Mol Biol* **324**, 309–18.

57 Venugopal, M. G., Ramshaw, J. A., Braswell, E., Zhu, D. & Brodsky, B. (1994). Electrostatic interactions in collagen-like triple-helical peptides. *Biochemistry* **33**, 7948–56.

58 Persikov, A. V., Ramshaw, J. A., Kirkpatrick, A. & Brodsky, B. (2000). Amino acid propensities for the collagen triple-helix. *Biochemistry* **39**, 14960–7.

59 Persikov, A. V., Ramshaw, J. A., Kirkpatrick, A. & Brodsky, B. (2003). Triple-helix propensity of hydroxyproline and fluoroproline: comparison of host-guest and repeating tripeptide collagen models. *J Am Chem Soc* **125**, 11500–1.

60 Saygin, O. & Heidemann, E. (1978). The triple helix-coil transition of cyanogen-bromide peptides of the alphal-chain of the calf-skin collagen. *Biopolymers* **17**, 511–22.

61 Shah, N. K., Sharma, M., Kirkpatrick, A., Ramshaw, J. A. & Brodsky, B. (1997). Gly-Gly-containing triplets of low stability adjacent to a type III collagen epitope. *Biochemistry* **36**, 5878–83.

62 Chan, V. C., Ramshaw, J. A., Kirkpatrick, A., Beck, K. & Brodsky, B. (1997). Positional preferences of ionizable residues in Gly-X-Y triplets of the collagen triple-helix. *J Biol Chem* **272**, 31441–6.

63 Dölz, R. & Heidemann, E. (1986). Influence of different tripeptides on the stability of the collagen triple helix. I. Analysis of the collagen sequence and identification of typical tripeptides. *Biopolymers* **25**, 1069–80.

64 Germann, H. P. & Heidemann, E. (1988). A synthetic model of collagen: an experimental investigation of the triple-helix stability. *Biopolymers* **27**, 157–63.

65 Thakur, S., Vadolas, D., Germann, H. P. & Heidemann, E. (1986). Influence of different tripeptides on the stability of the collagen triple helix. II. An experimental approach with appropriate variations of a trimer model oligotripeptide. *Biopolymers* **25**, 1081–6.

66 Bächinger, H. P. & Davis, J. M. (1991). Sequence specific thermal stability of the collagen triple helix. *Int J Biol Macromol* **13**, 152–6.

67 Yang, W., Chan, V. C., Kirkpatrick, A., Ramshaw, J. A. & Brodsky, B. (1997). Gly-Pro-Arg confers stability similar to Gly-Pro-Hyp in the collagen triple-helix of host-guest peptides. *J Biol Chem* **272**, 28837–40.

68 Yang, W., Battineni, M. L. & Brodsky, B. (1997). Amino acid sequence environment modulates the disruption by osteogenesis imperfecta glycine substitutions in collagen-like peptides. *Biochemistry* **36**, 6930–5.

69 Persikov, A. V., Ramshaw, J. A., Kirkpatrick, A. & Brodsky, B. (2002). Peptide investigations of pairwise interactions in the collagen triple-helix. *J Mol Biol* **316**, 385–94.

70 Persikov, A. V. & Brodsky, B. (2002). Unstable molecules form stable tissues. *Proc Natl Acad Sci USA* **99**, 1101–3.

71 Ramshaw, J. A., Shah, N. K. & Brodsky, B. (1998). Gly-X-Y tripeptide frequencies in collagen: a context for host-guest triple-helical peptides. *J Struct Biol* **122**, 86–91.

72 Inouye, K., Kobayashi, Y., Kyogoku, Y., Kishida, Y., Sakakibara, S. & Prockop, D. J. (1982). Synthesis and physical properties of (hydroxyproline-proline- glycine)10: hydroxyproline in the X-position decreases the melting temperature of the collagen triple helix. *Arch Biochem Biophys* **219**, 198–203.

73 Mizuno, K., Hayashi, T. & Bächinger, H. P. (2003). Hydroxylation-induced stabilization of the collagen triple helix: Further characterization of peptides with 4(R)-hydroxyproline in the Xaa position. *J Biol Chem* **278**, 32373–9.

74 Ramachandran, G. N. & Kartha, G. (1955). Structure of collagen. *Nature* **176**, 593–5.

75 Rich, A. & Crick, F. H. (1955). The structure of collagen. *Nature* **176**, 915–16.

76 Fraser, R. D., MacRae, T. P. & Suzuki, E. (1979). Chain conformation in the collagen molecule. *J Mol Biol* **129**, 463–81.

77 Okuyama, K., Arnott, S., Takayanagi, M. & Kakudo, M. (1981). Crystal and molecular structure of a collagen-like polypeptide (Pro-Pro-Gly)10. *J Mol Biol* **152**, 427–43.

78 Bella, J., Eaton, M., Brodsky, B. & Berman, H. M. (1994). Crystal and molecular structure of a collagen-like peptide at 1.9 Å resolution. *Science* **266**, 75–81.

79 Kramer, R. Z., Bella, J., Mayville, P., Brodsky, B. & Berman, H. M. (1999). Sequence dependent conformational variations of collagen triple-helical structure. *Nat Struct Biol* **6**, 454–7.

80 Kramer, R. Z., Bella, J., Brodsky, B. & Berman, H. M. (2001). The crystal and molecular structure of a collagen-like peptide with a biologically relevant sequence. *J Mol Biol* **311**, 131–47.

81 Bella, J., Brodsky, B. & Berman, H. M. (1996). Disrupted collagen architecture in the crystal structure of a triple-helical peptide with a

Gly → Ala substitution. *Connect Tissue Res* **35**, 401–6.

82 Kramer, R. Z., Vitagliano, L., Bella, J. et al. (1998). X-ray crystallographic determination of a collagen-like peptide with the repeating sequence (Pro-Pro-Gly). *J Mol Biol* **280**, 623–38.

83 Nagarajan, V., Kamitori, S. & Okuyama, K. (1998). Crystal structure analysis of collagen model peptide (Pro-pro-Gly)10. *J Biochem (Tokyo)* **124**, 1117–23.

84 Nagarajan, V., Kamitori, S. & Okuyama, K. (1999). Structure analysis of a collagen-model peptide with a (Pro-Hyp-Gly) sequence repeat. *J Biochem (Tokyo)* **125**, 310–18.

85 Berisio, R., Vitagliano, L., Mazzarella, L. & Zagari, A. (2002). Crystal structure of the collagen triple helix model [(Pro-Pro-Gly)(10)](3). *Protein Sci* **11**, 262–70.

86 Stetefeld, J., Frank, S., Jenny, M. et al. (2003). Collagen stabilization at atomic level: crystal structure of designed $(GlyProPro)_{10}$–foldon. *Structure (Camb)* **11**, 339–46.

87 Fan, P., Li, M. H., Brodsky, B. & Baum, J. (1993). Backbone dynamics of (Pro-Hyp-Gly)10 and a designed collagen-like triple-helical peptide by 15N NMR relaxation and hydrogen-exchange measurements. *Biochemistry* **32**, 13299–309.

88 Li, M. H., Fan, P., Brodsky, B. & Baum, J. (1993). Two-dimensional NMR assignments and conformation of (Pro-Hyp-Gly)10 and a designed collagen triple-helical peptide. *Biochemistry* **32**, 7377–87.

89 Melacini, G., Feng, Y. & Goodman, M. (1996) Acetyl-terminated and template-assembled collagen-based polypeptides composed of Gly-Pro-Hyp sequences. 3. Conformational analysis by ^{1}H-NMR and molecular modeling studies. *J Am Chem Soc* 118, 10359–64.

90 Bann, J. G., Bächinger, H. P. & Peyton, D. H. (2003). Role of carbohydrate in stabilizing the triple-helix in a model for a deep-sea hydrothermal vent worm collagen. *Biochemistry* **42**, 4042–8.

91 Liu, X., Siegel, D. L., Fan, P., Brodsky, B. & Baum, J. (1996). Direct NMR measurement of folding kinetics of a trimeric peptide. *Biochemistry* **35**, 4306–13.

92 Buevich, A. V., Dai, Q. H., Liu, X., Brodsky, B. & Baum, J. (2000). Site-specific NMR monitoring of cis-trans isomerization in the folding of the proline-rich collagen triple helix. *Biochemistry* **39**, 4299–308.

93 Melacini, G., Bonvin, A. M., Goodman, M., Boelens, R. & Kaptein, R. (2000). Hydration dynamics of the collagen triple helix by NMR. *J Mol Biol* **300**, 1041–9.

94 Bann, J. G., Peyton, D. H. & Bächinger, H. P. (2000). Sweet is stable: glycosylation stabilizes collagen. *FEBS Lett* **473**, 237–40.

95 Gaill, F., Mann, K., Wiedemann, H., Engel, J. & Timpl, R. (1995). Structural comparison of cuticle and interstitial collagens from annelids living in shallow sea-water and at deep-sea hydrothermal vents. *J Mol Biol* **246**, 284–94.

96 Xu, Y., Hyde, T., Wang, X., Bhate, M., Brodsky, B. & Baum, J. (2003). NMR and CD spectroscopy show that imino acid restriction of the unfolded state leads to efficient folding. *Biochemistry* **42**, 8696–703.

97 Inouye, K., Sakakibara, S. & Prockop, D. J. (1976). Effects of the stereo-configuration of the hydroxyl group in 4- hydroxyproline on the triple-helical structures formed by homogenous peptides resembling collagen. *Biochim Biophys Acta* **420**, 133–41.

98 Bann, J. G. & Bächinger, H. P. (2000). Glycosylation/hydroxylation-induced stabilization of the collagen triple helix. 4-trans-hydroxyproline in the Xaa position can stabilize the triple helix. *J Biol Chem* **275**, 24466–9.

99 Kresina, T. F. & Miller, E. J. (1979). Isolation and characterization of basement membrane collagen from human placental tissue. Evidence for the presence of two genetically distinct collagen chains. *Biochemistry* **18**, 3089–97.

100 Kefalides, N. A. (1973). Structure and biosynthesis of basement membranes. *Int Rev Connect Tissue Res* **6**, 63–104.

101 Burgeson, R. E., El Adli, F. A., Kaitila, II & Hollister, D. W. (1976). Fetal membrane collagens: identification of two new collagen alpha chains. *Proc Natl Acad Sci USA* **73**, 2579–83.

102 Rhodes, R. K. & Miller, E. J. (1978). Physicochemical characterization and molecular organization of the collagen A and B chains. *Biochemistry* **17**, 3442–8.

103 Bos, K. J., Rucklidge, G. J., Dunbar, B. & Robins, S. P. (1999). Primary structure of the helical domain of porcine collagen X. *Matrix Biol* **18**, 149–53.

104 Mizuno, K., Hayashi, T., Peyton, D. H. & Bächinger, H. P. (2004) The peptides acetyl-(Gly-3(S)Hyp-4(R)Hyp)$_{10}$-NH_2 and acetyl-(Gly-Pro-3(S)Hyp)$_{10}$-NH_2 do not form a collagen triple helix. *J Biol Chem* **279**, 282–7.

105 Bakerman, S., Martin, R. L., Burgstahler, A. W. & Hayden, J. W. (1966). In vitro studies with fluoroprolines. *Nature* **212**, 849–50.

106 Takeuchi, T. & Prockop, D. J. (1969). Biosynthesis of abnormal collagens with amino acid analogues. I. Incorporation of L-azetidine-2-carboxylic acid and cis-4-fluoro-L-proline into protocollagen and collagen. *Biochim Biophys Acta* **175**, 142–55.

107 Takeuchi, T., Rosenbloom, J. & Prockop, D. J. (1969). Biosynthesis of abnormal collagens with amino acid analogues. II. Inability of cartilage cells to extrude collagen polypeptides containing L-azetidine-2-carboxylic acid or cis-4-fluoro-L-proline. *Biochim Biophys Acta* **175**, 156–64.

108 Engel, J. & Prockop, D. J. (1998). Does bound water contribute to the stability of collagen? [letter]. *Matrix Biol* **17**, 679–80.

109 Holmgren, S. K., Bretscher, L. E., Taylor, K. M. & Raines, R. T. (1999). A hyperstable collagen mimic. *Chem Biol* **6**, 63–70.

110 Bretscher, L. E., Jenkins, C. L., Taylor, K. M., DeRider, M. L. & Raines, R. T. (2001). Conformational stability of collagen relies on a stereoelectronic effect. *J Am Chem Soc* **123**, 777–8.

111 Jenkins, C. L. & Raines, R. T. (2002). Insights on the conformational stability of collagen. *Nat Prod Rep* **19**, 49–59.

112 Doi, M., Nishi, Y., Uchiyama, S., Nishiuchi, Y., Nakazawa, T., Ohkubo, T. & Kobayashi, Y. (2003). Characterization of collagen model peptides containing 4-fluoroproline; (4(S)-fluoroproline-pro-gly)10 forms a triple helix, but (4(R)-fluoroproline-pro-gly)10 does not. *J Am Chem Soc* **125**, 9922–3.

113 Hodges, J. A. & Raines, R. T. (2003). Stereoelectronic effects on collagen stability: the dichotomy of 4-fluoroproline diastereomers. *J Am Chem Soc* **125**, 9262–3.

114 Babu, I. R. & Ganesh, K. N. (2001). Enhanced triple helix stability of collagen peptides with 4R-aminoprolyl (Amp) residues: relative roles of electrostatic and hydrogen bonding effects. *J Am Chem Soc* **123**, 2079–80.

115 Scherer, G., Kramer, M. L., Schutkowski, M. U. R. & Fischer, G. (1998). Barriers to rotaion of secondary amide peptide bonds. *J Am Chem Soc* **120**, 5568–74.

116 Gratwohl, C. & Wüthrich, K. (1976). The X-Pro peptide bond as an NMR probe for conformational studies of flexible linear peptides. *Biopolymers* **15**, 2025–41.

117 Reimer, U., Scherer, G., Drewello, M., Kruber, S., Schutkowski, M. & Fischer, G. (1998). Side-chain effects on peptidyl-prolyl cis/trans isomerisation. *J Mol Biol* **279**, 449–60.

118 Raines, R. T., Bretscher, L. E., Holmgren, S. K. & Taylor, K. M. (1999). The stereoelectronic basis of collagen stability. In: *Peptides for the New Millennium: Proceedings of the 16th American Peptide Symposium* (Fields, G. B., Tam, J. P., & Barany, G., eds). Kluwer Academic, Norwell, MA.

119 Kiefhaber, T., Köhler, H. H. & Schmid, F. X. (1992). Kinetic coupling between protein folding and prolyl isomerization. I. Theoretical models. *J Mol Biol* **224**, 217–29.

120 Piez, K. A. & Sherman, M. R. (1970). Equilibrium and kinetic studies of the helix-coil transition in alpha 1-CB2, a small peptide from collagen. *Biochemistry* **9**, 4134–40.

121 Boudko, S., Frank, S., Kammerer, R. A. et al. (2002). Nucleation and propagation of the collagen triple helix in single-chain and trimerized peptides: transition from third to first order kinetics. *J Mol Biol* **317**, 459–70.

122 Bächinger, H. P., Bruckner, P., Timpl, R., Prockop, D. J. & Engel, J. (1980). Folding mechanism of the triple helix in type-III collagen and type-III pN-collagen. Role of disulfide bridges and peptide bond isomerization. *Eur J Biochem* **106**, 619–32.

123 Piez, K. A. & Carrillo, A. L. (1964). Helix formation by single- and double-chain gelatins from rat skin collagen. *Biochemistry* **155**, 908–14.

124 Harrington, W. F. & Rao, N. V. (1970). Collagen structure in solution. I. Kinetics of helix regeneration in single-chain gelatins. *Biochemistry* **9**, 3714–24.

125 Yuan, L. & Veis, A. (1973). The characteristics of the intermediates in collagen-fold formation. *Biophys Chem* **1**, 117–24.

126 Kühn, K., Engel, J., Zimmermann, B. & Grassmann, W. (1964). Renaturation of soluble collagen. III. Reorganization of native collagen molecules from completely separated units. *Arch Biochem Biophys* **105**, 387–403.

127 Engel, J. (1987). Folding and unfolding of collagen triple helices. In: *Advances in Meat Research*, Vol 4. Van Nostrand Reinhold, New York, pp. 145–58.

128 Ackerman, M. S., Bhate, M., Shenoy, N., Beck, K., Ramshaw, J. A. & Brodsky, B. (1999). Sequence dependence of the folding of collagen-like peptides. Single amino acids affect the rate of triple-helix nucleation. *J Biol Chem* **274**, 7668–73.

129 Pörschke, D. & Eigen, M. (1971). Co-operative non-enzymic base recognition. 3. Kinetics of the helix-coil transition of the oligoribouridylic–oligoriboadenylic acid system and of oligoriboadenylic acid alone at acidic pH. *J Mol Biol* **62**, 361–81.

130 Bächinger, H. P., Bruckner, P., Timpl, R. & Engel, J. (1978). The role of cis-trans isomerization of peptide bonds in the coil ⇌ triple helix conversion of collagen. *Eur J Biochem* **90**, 605–13.

131 Bruckner, P., Bächinger, H. P., Timpl, R. & Engel, J. (1978). Three conformationally distinct domains in the amino-terminal segment of type III procollagen and its rapid triple helix leads to and comes from coil transition. *Eur J Biochem* **90**, 595–603.

132 Xu, Y., Bhate, M. & Brodsky, B. (2002). Characterization of the nucleation step and folding of a collagen triple-helix peptide. *Biochemistry* **41**, 8143–51.

133 Brandt, A., Gianville, R. W., Hörlein, D., Bruckner, P., Timpl, R., Fietzek, P. P. & Kuhn, K. (1984). Complete amino acid sequence of the N-terminal extension of calf skin type III procollagen. *Biochem J* **219**, 625–34.

134 Brandts, J. F., Halvorson, H. R. & Brennan, M. (1975). Consideration of the Possibility that the slow step in protein denaturation reactions is due to cis-trans isomerism of proline residues. *Biochemistry* **14**, 4953–63.

135 Bruckner, P. & Prockop, D. J. (1981). Proteolytic enzymes as probes for the triple-helical conformation of procollagen. *Anal Biochem* **110**, 360–8.

136 Gross, J. & Bruschi, A. B. (1971). The pattern of collagen degradation in cultured tadpole tissues. *Dev Biol* **26**, 36–41.

137 Cheng, H. N. & Bovey, F. A. (1977). Cis-trans equilibrium and kinetic studies of acetyl-L-proline and glycyl-L-proline. *Biopolymers* **16**, 1465–72.

138 Fiori, S., Sacca, B. & Moroder, L. (2002). Structural properties of a

collagenous heterotrimer that mimics the collagenase cleavage site of collagen type I. *J Mol Biol* **319**, 1235–42.

139 Franzke, C. W., Tasanen, K., Schumann, H. & Bruckner-Tuderman, L. (2003). Collagenous transmembrane proteins: collagen XVII as a prototype. *Matrix Biol* **22**, 299–309.

140 Engel, J. & Kammerer, R. A. (2000). What are oligomerization domains good for? *Matrix Biol* **19**, 283–8.

141 Snellman, A., Tu, H., Vaisanen, T., Kvist, A. P., Huhtala, P. & Pihlajaniemi, T. (2000). A short sequence in the N-terminal region is required for the trimerization of type XIII collagen and is conserved in other collagenous transmembrane proteins. *EMBO J* **19**, 5051–9.

142 Engel, J. & Bächinger, H. P. (2000). Cooperative equilibrium transitions coupled with a slow annealing step explain the sharpness and hysteresis of collagen folding. *Matrix Biol* **19**, 235–44.

143 Lang, K., Schmid, F. X. & Fischer, G. (1987). Catalysis of protein folding by prolyl isomerase. *Nature* **329**, 268–70.

144 Bächinger, H. P. (1987). The influence of peptidyl-prolyl cis-trans isomerase on the in vitro folding of type III collagen. *J Biol Chem* **262**, 17144–8.

145 Davis, J. M., Boswell, B. A. & Bächinger, H. P. (1989). Thermal stability and folding of type IV procollagen and effect of peptidyl-prolyl cis-trans-isomerase on the folding of the triple helix. *J Biol Chem* **264**, 8956–62.

146 Steinmann, B., Bruckner, P. & Superti-Furga, A. (1991). Cyclosporin A slows collagen triple-helix formation in vivo: indirect evidence for a physiologic role of peptidyl-prolyl cis-trans-isomerase. *J Biol Chem* **266**, 1299–303.

147 Bächinger, H. P., Morris, N. P. & Davis, J. M. (1993). Thermal stability and folding of the collagen triple helix and the effects of mutations in osteogenesis imperfecta on the triple helix of type I collagen. *Am J Med Genet* **45**, 152–62.

148 Zeng, B., MacDonald, J. R., Bann, J. G., Beck, K., Gambee, J. E., Boswell, B. A. & Bächinger, H. P. (1998). Chicken FK506-binding protein, FKBP65, a member of the FKBP family of peptidylprolyl cis-trans isomerases, is only partially inhibited by FK506. *Biochem J* **330**, 109–14.

149 Compton, L. A., Davis, J. M., Macdonald, J. R. & Bächinger, H. P. (1992). Structural and functional characterization of Escherichia coli peptidyl-prolyl cis-trans isomerases. *Eur J Biochem* **206**, 927–34.

150 Lamande, S. R. & Bateman, J. F. (1999). Procollagen folding and assembly: the role of endoplasmic reticulum enzymes and molecular chaperones. *Semin Cell Dev Biol* **10**, 455–64.

151 Hendershot, L. M. & Bulleid, N. J. (2000). Protein-specific chaperones: the role of hsp47 begins to gel. *Curr Biol* **10**, R912–15.

152 Tasab, M., Batten, M. R. & Bulleid, N. J. (2000). Hsp47: a molecular chaperone that interacts with and stabilizes correctly-folded procollagen. *EMBO J* **19**, 2204–11.

153 Nagai, N., Hosokawa, M., Itohara, S. et al. (2000). Embryonic lethality of molecular chaperone hsp47 knockout mice is associated with defects in collagen biosynthesis. *J Cell Biol* **150**, 1499–506.

154 Kuivaniemi, H., Tromp, G. & Prockop, D. J. (1991). Mutations in collagen genes: causes of rare and some common diseases in humans. *FASEB J* **5**, 2052–60.

155 Uitto, J. & Lichtenstein, J. R. (1976). Defects in the biochemistry of collagen in diseases of connective tissue. *J Invest Dermatol* **66**, 59–79.

156 Engel, J. & Prockop, D. J. (1991). The zipper-like folding of collagen triple helices and the effects of mutations that disrupt the zipper. *Annu Rev Biophys Biophys Chem* **20**, 137–52.

157 Raghunath, M., Bruckner, P. &

Steinmann, B. (1994). Delayed triple helix formation of mutant collagen from patients with osteogenesis imperfecta. *J Mol Biol* **236**, 940–9.

158 Baum, J. & Brodsky, B. (1999). Folding of peptide models of collagen and misfolding in disease. *Curr Opin Struct Biol* **9**, 122–8.

159 Gough, C. A. & Bhatnagar, R. S. (1999). Differential stability of the triple helix of (Pro-Pro-Gly)10 in H2O and D2O: thermodynamic and structural explanations. *J Biomol Struct Dyn* **17**, 481–91.

160 Go, N. & Suezaki, Y. (1973). Letter: Analysis of the helix-coil transition in (Pro-Pro-Gly)n by the all-or-none model. *Biopolymers* **12**, 1927–30.

161 Greiche, Y. & Heidemann, E. (1979). Collagen model peptides with antiparallel structure. *Biopolymers* **18**, 2359–61.

162 Henkel, W., Vogl, T., Echner, H. et al. (1999). Synthesis and folding of native collagen III model peptides. *Biochemistry* **38**, 13610–22.

163 Consonni, R., Zetta, L., Longhi, R., Toma, L., Zanaboni, G. & Tenni, R. (2000). Conformational analysis and stability of collagen peptides by CD and by 1H- and 13C-NMR spectrocopies. *Biopolymers* **53**, 99–111.

164 Sarkar, S. K., Young, P. E., Sullivan, C. E. & Torchia, D. A. (1984). Detection of cis and trans X-Pro peptide bonds in proteins by 13C NMR: application to collagen. *Proc Natl Acad Sci USA* **81**, 4800–3.

165 Frank, S., Boudko, S., Mizuno, K. et al. (2003). Collagen triple helix formation can be unchecked at either end. *J Biol Chem* **278**, 7747–50.

166 Privalov, P. L., Tiktopulo, E. I. & Tischenko, V. M. (1979). Stability and mobility of the collagen structure. *J Mol Biol* **15**, 203–216.

31
Unfolding Induced by Mechanical Force

Jane Clarke and Phil M. Williams

31.1
Introduction

Force spectroscopy has, as yet, been used in very few protein folding laboratories. One has to ask why this is so. There are several possible explanations. First, until relatively recently, only specialized instrumental laboratories had the technical expertise to build instruments. This has been overcome with the advent of commercially available instruments that are relatively simple to use, menu driven, and in one case, where the programming software (Igor) can be adapted for the investigators' convenience – facilitating data collection, collation and analysis. Second, preparing a protein sample is time consuming. With current molecular biology techniques it is possible to clone and express many single domain mutant proteins in the matter of a couple of weeks. But despite the development of versatile cloning systems, the cloning of a polyprotein substrate can take months (and this has to be repeated for each mutant protein you wish to analyze), and after this, a number of simple-to-express, single domain proteins have turned out to be insoluble as polyproteins. Third, the data are complex and time consuming to collect and analyze. Ironically many repeats of the single molecule experiments are required to collect enough data to analyze, and even the very best data can be noisy and are intrinsically unsatisfactory for those of us who are used to collecting many kinetic data points with exquisite accuracy. Worse still, the investigator has to select which data to analyze and which to discard – an anathema to careful experimentalists. Fourth, the data cannot be analyzed by fitting to a simple model, rather a Monte-Carlo or analytical approach has to be used to extract kinetic data.

So, why bother with these experiments? First, there is a biological imperative. It is increasingly apparent that many proteins experience significant force in vivo. In fact, response to mechanical stress has been implicated in a number of signaling pathways. This means that proteins have evolved to resist unfolding when subject to an external force. It has been shown in at least one case that the barrier to unfolding under mechanical stress is not that investigated by traditional unfolding experiments. Only dynamic force experiments can reveal these details of the protein folding landscape. Second, there is an interesting structural biology problem

Protein Folding Handbook. Part I. Edited by J. Buchner and T. Kiefhaber

ISBN: 3-527-30784-2

of comparison. Why are certain protein folds stronger than others? How does sequence variation affect mechanical stability? Can the effect of mutation be predicted? How are domains assembled in some of the large multidomain natural load-bearing proteins? Finally, forced unfolding experiments can easily be directly compared with computer simulations. The reaction coordinate (N–C length) is known and measurable.

In this chapter we first describe the experiments and summarize the theoretical background for the analysis of these experiments. We describe how the analysis is performed and what kinetic parameters can be obtained and the confidence limits of these parameters. (We are concentrating on atomic force spectroscopy, as techniques that exploit lower loading rates, such as optical tweezers, have yet to be used on single protein domains and the instrumentation is more complex.) We then show how complementary techniques can be used to help our understanding of the data obtained. We end with a case study of a single protein, illustrating how combination of a number of techniques has enabled the forced unfolding mechanism to be examined in detail.

31.2 Experimental Basics

31.2.1 Instrumentation

A number of commercial instruments are available for use in protein folding laboratories. Figure 31.1 shows the basic components of such instruments. The principle components are a stage, to which is attached the protein substrate, a microfabricated cantilever, and a piezoelectric positioner which adjusts the relative position of the cantilever and stage with subnanometer accuracy.

The protein sample is placed onto the stage. In most experimental studies published to date the protein substrate is a long, multimodular molecule. This may be either a natural multimodular protein, such as a portion of a long extracellular matrix or muscle protein or an engineered construct of multiple repeats of single domains (see Section 31.2.2). Attachment of the protein to the stage may be achieved by specific attachment, for example a gold-sulfur linkage with cysteines at the terminus of the protein, or by nonspecific adsorption onto a glass surface. The protein and cantilever are surrounded by solvent, either as a droplet or in an enclosed cell.

Likewise, attachment to the cantilever is generally through nonspecific adsorption to the surface, although cantilevers can be modified to allow specific attachment. The commercial cantilevers used are usually made of silicon nitride, and are ~20–300 μm in length. The key component is an unsharpened tip (radius ~ 50 nm) to which the protein adsorbs. (Sharper tips are available, but this larger, blunter tip gives a better surface for adsorption of the protein.) Cantilevers used in protein unfolding experiments typically have spring constants in the range 10–

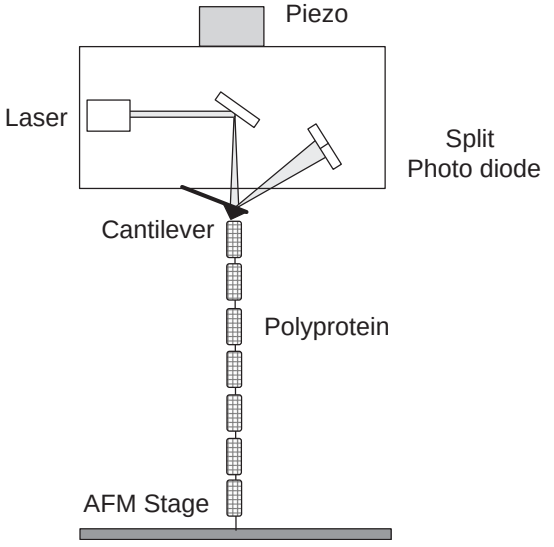

Fig. 31.1. Diagram of an atomic force microscope. The protein molecule is deposited onto the stage and adsorbed to the microfabricated silicon nitride cantilever. The deflection of the cantilever is used to determine the force exerted upon the protein, once the spring constant of the cantilever is known. The separation between stage and cantilever is controlled by the piezo which is capable of repeated cycles of extension and retraction. The photodiode measures the laser light reflected off the back of the cantilever. The deflection of the cantilever is determined from the difference in the output voltages from the two halves.

100 pN nm^{-1}. The actual spring constant has to be measured at the start of each experiment, using methods that are integrated into the software of the commercial instruments. The backs of the cantilevers are reflective and the position of the cantilever is determined by use of a laser reflected onto a split photodiode. Following calibration of the instrument to determine the relationship between photodiode output and bending of the cantilever, the force applied on the protein is determined directly from the deflection of the cantilever. A piezoelectric positioner adjusts the separation of the cantilever tip and the surface.

31.2.2 Sample Preparation

As a tool for protein folding, fragments of large, natural multidomain proteins such as the giant muscle protein titin [1], or the cytoskeleton protein spectrin [2], are of limited use, as they do not report on the unfolding of specific protein domains. Although a few experiments have been reported where a single protein domain has been suspended between tip and stage (see, for example, Ref. [3]), most experiments have used large "polyproteins" which have multiple repeats of a single protein domain cloned in tandem. These large polyproteins have the advantage

of holding the protein at a significant distance from the surface before unfolding occurs, so that tip/surface or protein/surface interactions are minimized.

A number of approaches for constructing such repeats have been reported [4–6], but the most versatile are those that use different restriction enzyme sites at the start and end of each domain. One such system is available on request from our laboratory [6]. The first protein to be multimerized in this way was titin I27. It has a poly-His tag at the N-terminus to facilitate affinity purification, and two cysteines at the C-terminus to attach the protein to an AFM stage by a gold-sulfur linkage. This protein can be produced in large amounts as a soluble polyprotein in *Escherichia coli*. The protein can be used after a one-step purification, but we tend to get better results following a second, size exclusion step. I27 is a very versatile protein – it has proved to be a useful ''handle'' for attaching other proteins, which may not polymerize so easily or where only a single domain of a protein of interest is required [7, 8]. In these circumstances it acts as an internal control.

A few studies have used novel methods to produce multimodular proteins. Yang et al. exploited crystal packing in T4 lysozyme [9]. Cysteines were engineered at contact points and the polyprotein was formed in the crystal. In studies to investigate the effect of attachment point on the effect of force on a protein Fernandez and coworkers used the only known natural polyprotein ubiquitin, linked either via the N- and C-terminus or via specific surface lysine–C-terminus linkages [10]. Brockwell et al. used an elegant, novel lipoic acid–lysine linkage to study the same problem in the protein E2Lip3 [8].

When working with multidomain constructs it is important to know whether the protein is folded in, and how far its properties are changed by, inclusion in a polyprotein. Again, I27 is a ''model'' protein in this respect; it has the same thermodynamic stability and the same kinetic properties in the polyprotein as does an isolated domain [4]. However, the same is not true of all proteins. Some are stabilized and some destabilized by inclusion in the protein. Remarkably, although traditional equilibrium denaturation and stopped flow kinetic experiments can be performed as easily on the polyprotein as on small individual domains these simple controls are very rarely carried out. We have also been able to show that NMR experiments can be easily undertaken on three-module constructs, so structural integrity can also be verified [7].

31.2.3 Collecting Data

Although there are recent reports of constant force experiments (see, for example, Ref. [11]), most experiments reported to date have used a ramp of force induced by retracting the piezo at constant speed. The cantilever is lowered to the surface repeatedly, picking a protein molecule up at random. Since this is a blind ''fishing'' step the experimentalist has little control over whether a protein is picked up and no control over the position on the polyprotein where the protein is attached to the cantilever tip. If the protein is adsorbed at too high a concentration onto the sub-

strate then more than one protein molecule is likely to be attached to the tip. Such traces have to be discarded, as they cannot be interpreted. If the protein is too dilute there will be too few pick-ups. It is estimated that where one approach in 10 picks up a protein we can be confident that most data will be from a single molecule [12]. The concentration of protein that results in such a success rate has to be determined empirically.

The tip is retracted at constant speed and when a protein molecule is picked up a force trace is observed. A large number of such traces have to be collected at a number of pulling speeds. The range of experimentally useful pulling speeds allowed by the commercial instruments currently available is on the order of 10 nm s^{-1} to 10 000 nm s^{-1} but in practice, most useful data are collected in the pulling speed range of ~300 to ~3000 nm s^{-1}. Instrumental drift is a problem at low pulling speeds and at very high pulling speeds, viscous drag and cantilever response time introduce error.

31.2.4
Anatomy of a Force Trace

A ''typical'' force trace is shown and described in Figure 31.2. At the start of the trace there is usually a peak of unpredictable height that reflects tip:surface interactions, deadsorption of the protein from the surface and other nonspecific effects (see arrow on Figure 31.2a). As the cantilever retracts force is applied to the protein. As the force increases unfolded parts of the chain are stretched. At some force one of the protein domains will unfold and this results in a sharp drop in the force trace. The trace does not drop to the baseline, however, as the entropic elasticity of the unfolded protein maintains a force on the cantilever. The force increases again until another domain unfolds, resulting in the signature saw-tooth pattern. The base of subsequent peaks is higher that that of the preceding peak. The spacing between the peaks is regular, reflecting the all-or-none nature of the unfolding events, so that a number of traces can be overlaid. Finally the cantilever is retracted so far that the protein becomes detached. A final ''pull off'' peak is observed, typically much higher than all preceding peaks and the trace returns to the baseline.

31.2.5
Detecting Intermediates in a Force Trace

If the protein domains unfold without populating intermediates the trace should be simple with a single unfolding event per domain, and the unfolded protein should extend as a featureless smooth curve, fitting to a simple model of an elastic polymer (see Section 31.3.4). However, intermediates have been detected in a few forced unfolding experiments by careful examination of forced unfolding data. The intermediates have been detected either by the presence of two consecutive unfolding events per domain (e.g., Ref. [13]), or from the presence of a ''hump'' in the unfolding traces [14] (described in more detail in Section 31.7).

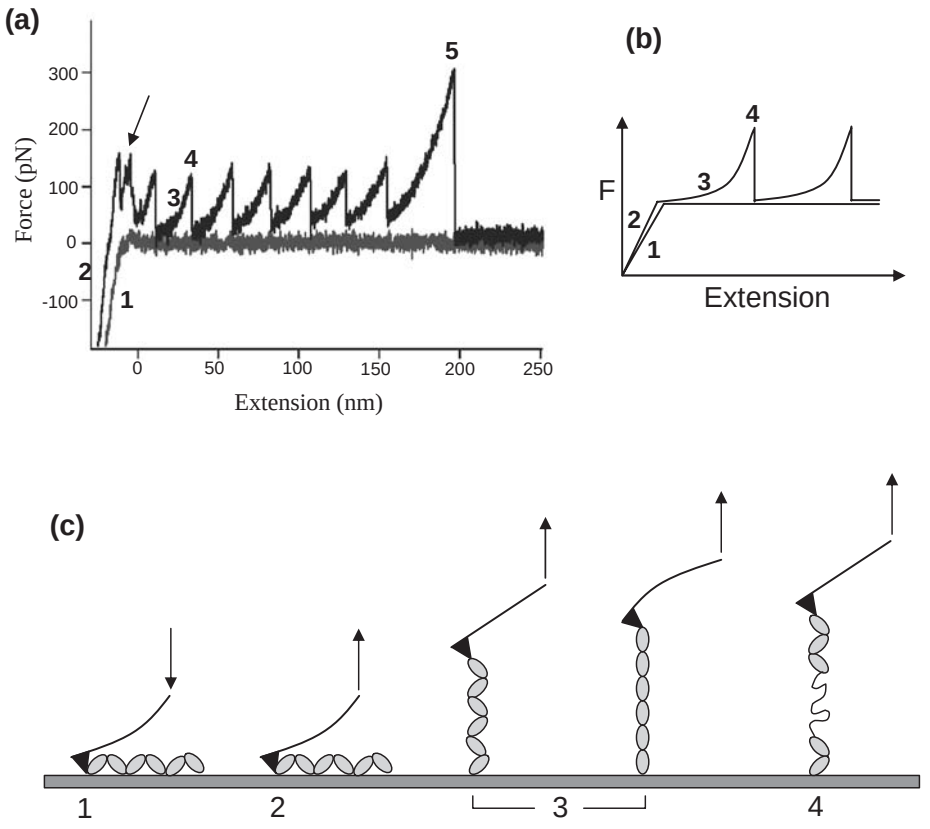

Fig. 31.2. Anatomy of a force trace. Force trace (a) and diagram (b) showing the response of the cantilever during different phases of the AFM approach-retraction cycle. The cartoon in (c) describes the response of the protein and cantilever during the different phases shown in (a). 1) Tip makes contact with surface and is deflected. 2) Protein adsorbs to the cantilever tip. 3) Tip is retracted at a fixed pulling speed from the surface. An entropic restoring force of the protein is generated when it is extended. The cantilever deflects in response to this force. 4) A domain unfolds and extends. The system relaxes. The arrow in (a) shows non-specific adsorption between the tip and/or the protein and the surface.

31.2.6
Analyzing the Force Trace

The unfolding forces can be determined by analysis of the force traces, however, one of the most difficult features of forced protein unfolding experiments is that one has to choose which traces to analyze. As described above, most approach–retract cycles result in no protein being attached to the cantilever at all. Furthermore, a number of the traces where a protein is attached may have large peaks of ''noise'' at the start of the trace, possibly because the protein was attached to other (possibly unfolded) protein molecules on the surface or there may be more than one molecule attached to the cantilever. It is an essential assumption of all the

analysis that the data are collected from a single molecule attached to the tip. It is therefore essential that consistent and rational criteria are applied in choosing which peaks to analyze. This has been discussed elsewhere and a set of criteria have been proposed [15]:

1. Force peaks must be equally spaced and the distance between them must be consistent with the expected contour length of the protein.
2. The trace must include three or more peaks, the last of which is assumed to be the detachment of the protein from the AFM tip.
3. The base of each successive peak should be higher than base of the previous peak.
4. The approach and retraction baselines should overlay, indicating that there was no drift during the course of the pulling experiment.
5. The final baseline should be straight, indicating complete relaxation of the cantilever.

We find that analyzing the trace from the right, at the pull-off peak, towards the left, until the base of the peak touches the baseline, gives us most consistent analysis between investigators and from day to day. Note that all peaks must be counted. The temptation to discard peaks that meet all other criteria on the basis that they are ''too high'' or ''too low'' must be resisted – these will not contribute to analysis of the modal forces.

To determine the height of a peak, the full-length final baseline should be fitted to a line and the height of the peak above this line determined. This allows for drift in the instrument to be accounted for. Once these peak heights have been collected, the modal unfolding force can be determined (see Section 31.3.7).

We have found that it is important to collect data with different cantilevers and on different days to minimize error. We estimate that it is necessary to collect at least three full data sets, where each data set contains at least 40–50 force peaks at each pulling speed [15]. A full range of pulling speeds should be used to minimize errors in analysis. However, for some proteins we have found that we need to collect significantly more data to get reliable estimates of the modal unfolding force.

31.3
Analysis of Force Data

31.3.1
Basic Theory behind Dynamic Force Spectroscopy

In a fluid environment molecular structural transformations, such as those of protein unfolding, are driven by Brownian thermal excitation [16]. It is this agitation by the solvent that ''kicks'' a protein over transition states and provides the activation energy necessary for folding and unfolding. Brownian dynamics therefore sets

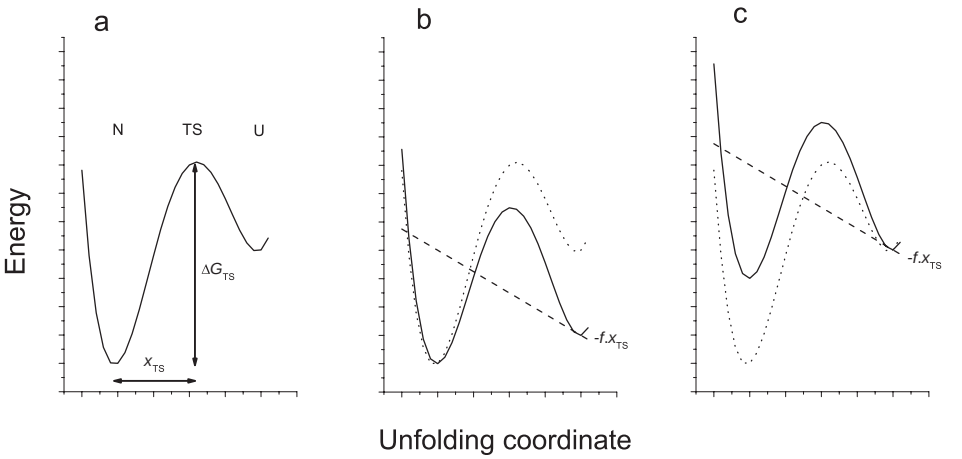

Fig. 31.3. Unfolding energy landscape and the effect of force. a) The rate of unfolding from N is dictated by the magnitude of the free energy relative to the transition state ΔG_{TS} and the shape of the energy potential (encompassed in Eq. (1) as ω_N and ω_{TS}). b) A force f acts on the potential to drop the transition state relative to the native state by the product of the force and the displacement, x_{TS}, of the transition state. Here, force can be considered as having a stabilizing effect on the transition and denatured states. c) Force can be considered as having a destabilizing effect on the native state and unfolding transition states. The effect of force on the unfolding kinetics in (b) and (c) is the same.

the time scale for motions in condensed liquids, which commences at the nanosecond for small ligands and slows with increased molecular size. As shown by Kramers in the 1940s [17], the rate of thermally activated escape from an unfolding potential energy well (Figure 31.3a) can be written as

$$v_o = \left(\frac{(\omega_N \omega_{TS})^{1/2}}{2\pi\zeta}\right) \exp\left(-\frac{\Delta G_{TS}}{k_B T}\right) \quad (1)$$

where ζ is the frictional coefficient of movement (viscous damping), ω_N and ω_{TS} are the curvatures of the energy potential at the native (N) and transition state (TS) respectively and ΔG_{TS} is the relative energy of TS. Although little is known of the exponential prefactor, one does not require its value to measure kinetics. However, conversion from rates to activation energies is not possible without this.

As shown in Figure 31.3b, force has several effects on an energy landscape. Under a persistent force the landscape is "tilted" in the direction at which the force is applied, and this both lowers and shifts the transition state maximum relative to the potential well of the folded, native state. Alternatively, one can consider force as stabilizing the protein's unfolded state and destabilizing the transition state and the folded state more so (Figure 31.3c). Either way, the net effect on the kinetics is the same. Under an external force potential, therefore, the unfolding rate is increased as force (f) lowers the energy of the unfolding transition state relative to

the native state. The amount that the transition state energy has been lowered by is the product of the force applied and the displacement of the state in the direction of force (x_{TS}), and we can re-write Eq. (1) to show this effect:

$$v_u(f) = h\left(\frac{fx_{TS}}{k_B T}\right)\left(\frac{(\omega_N \omega_{TS})^{1/2}}{2\pi\zeta}\right)\exp\left(-\frac{(\Delta G_{TS} - fx_{TS})}{k_B T}\right) \quad (2)$$

where $h(\ )$ describes the movement of the transition state under force [18]. Since the dominant effect of force is the lowering of the transition state, $h(\ )$ can usually be ignored, which gives the rate equation

$$v_u(f) = v_o \exp\left(\frac{fx_{TS}}{k_B T}\right) = v_o \exp\left(\frac{f}{f_\beta}\right) \quad (3)$$

where v_o is the unfolding rate over this TS barrier in the absence of force. Importantly this equation introduces f_β ($= k_B T/x_{TS}$), the *force scale*, commonly used in dynamic force spectroscopy and x_{TS} (or x_u as it is usually referred to in protein unfolding studies) representing the displacement between N and TS. At room temperature, thermal energy $k_B T$ is 4.11×10^{-21} J and over the nanometer length scale of proteins is equal to forces of only a few piconewtons (4.11 pN nm). The catalytic effect of a 100 pN force over this nanometer distance is equivalent to over 14 kcal mol^{-1} (1 kcal mol^{-1} = 6.9 pN nm).

31.3.2 The Ramp of Force Experiment

Virtually all experiments of protein unfolding measured by the atomic force microscope are of the kind where force is increased in time and the maximum force that the protein can withstand recorded. The tip is approached to the surface, protein adheres to the tip, and the tip is then withdrawn from the surface at a constant velocity. The simplest case to consider is where force increases steadily with time and the loading rate on the protein, $r_f = df/dt$, is constant. As we show later, this is usually not true for these experiments but this first approximation provides the introduction to dynamic force spectroscopy. The rate at which force increases is the product of the stiffness of the system (in this first approximation the this is the stiffness of the cantilever alone) and the speed at which the cantilever is withdrawn. Lever stiffness κ_c is of the order of 10–100 pN nm^{-1}, and retract rates v_r can vary from around 10 nm s^{-1} to approaching 10 000 nm s^{-1} (thermal drift and operator patience limiting the low speed and hydrodynamic drag restricting high speeds). AFM loading rates can theoretically range, therefore, between 100 and 1 000 000 pN s^{-1}, although practically achieving more than two to three orders of loading rate is problematic.

As an illustration, we consider the effect of increasing force on a transition state located $x_u = 0.5$ nm along the projection of force. Since at room temperature thermal energy, $k_B T$, is 4.11 pN nm at a loading rate of 1 000 000 pN s^{-1} it takes nearly

10 μs ($k_B T/x_u.r_f = 4.11/0.5/1\,000\,000$) to drop the barrier by 1 $k_B T$. On the time scale of a thermal attempt frequency (see above), therefore, force and the landscape are quasi-static. Experiments of strength adopting a ramp of force can thus normally be considered as a series of many tests under an equally large set of different forces. However, were the rate at which energy is added to the transition state by force ($x_u.r_f/k_B T$) to be comparable to, or exceed, the kinetic prefactor then the dynamics would deviate from that described here.

As unfolding is a kinetic process driven by random fluctuations one must make many measurements to sample the process. In this respect, the measurement of the behavior of a single molecule many times is identical to the measurement of an ensemble of molecules all at once. We can consider each measurement as a sample of this population, the numbers in which follow a simple rate equation. Commencing with all folded proteins, the fraction of the population that are folded under force decays in time as

$$\frac{dS}{dt} = -\nu_u(t)S(t) + \nu_f(t)[1 - S(t)] \tag{4}$$

where $\nu_u(t)$ is the rate at which unfolding occurs at time t, and $\nu_f(t)$ is the rate of refolding. Since time and force are related through the loading rate r_f, Eq. (4) can be written for an increasing force as

$$\frac{dS}{df} = \frac{1}{r_f}\{-\nu_u(f)S(f) + \nu_f(f)[1 - S(f)]\} \tag{5}$$

Until now, we have ignored the refolding term. In fact, since force causes an exponential decrease in folding in the same manner in which it exponentiates unfolding, at forces above a few 10 s of piconewtons refolding can safely be neglected. The master rate equation is simply

$$\frac{dS}{df} = \frac{1}{r_f}\{-\nu_u(f)S(f)\} \tag{6}$$

This can be integrated to reveal the probability distribution of folded states, as

$$S(f) = \frac{1}{r_f}\exp\left(-\int_0^f (\nu_u(g)/r_f)\,dg\right) \tag{7}$$

Equation (7) gives the fraction of the ensemble (the probability) that remain folded as the force increases from 0 to f. The probability that a protein will unfold at this force is the product of this, the survivability to force f, and the unfolding rate at this force. The probability of unfolding at f is therefore the product

$$p(f) = \frac{1}{r_f}\nu_u(f)\exp\left(-\int_0^f (\nu_u(g)/r_f)\,dg\right) \tag{8}$$

substituting for v_u (Eq. (3)) this can be written as

$$p(f) = \left(\frac{1}{r_f} v_o \exp\left(\frac{f}{f_\beta}\right)\right) \exp\left(-\int_0^f \frac{1}{r_f} v_o \exp\left(\frac{g}{f_\beta}\right) dg\right) \tag{9}$$

The integral of an exponential is unchanged, so taking the limits of force the integral can be solved as

$$p(f) = \left(\frac{1}{r_f} v_o \exp\left(\frac{f}{f_\beta}\right)\right) \exp\left(\frac{1}{r_f}\left(f_\beta v_o - f_\beta v_o \exp\left(\frac{f}{f_\beta}\right)\right)\right) \tag{10}$$

A series of tests of strength using a ramp of force at a constant loading rate will form a distribution given by Eqs (8), (9), and (10). There is not a single force at which a protein will unfold. The most probable unfolding force is that where this distribution is at a maximum, and therefore has a zero gradient. This value is found by finding the force where the first derivative is zero. To solve this, we rely on the property that we can scale the distribution and not affect the location of the maximum, and a useful scaling is the natural logarithm. The logarithm of Eq. (10), expanded for clarity, is

$$\ln[p(f)] = \ln[v_o] + \ln\left[\exp\left(\frac{f}{f_\beta}\right)\right] - \ln[r_f] + \ln\left[\exp\left(\frac{1}{r_f}\left(f_\beta v_o - f_\beta v_o \exp\left(\frac{f}{f_\beta}\right)\right)\right)\right] \tag{11}$$

The logarithms of the exponentials cancel, so

$$\ln[p(f)] = \ln[v_o] + \left(\frac{f}{f_\beta}\right) - \ln[r_f] + \frac{1}{r_f}\left(f_\beta v_o - f_\beta v_o \exp\left(\frac{f}{f_\beta}\right)\right) \tag{12}$$

The maximum of this distribution at the most probable unfolding force is found by differentiation with respect to force. The terms that do not depend of force disappear, leaving the maximum as

$$\partial \ln[p(f)] = \left[\frac{1}{f_\beta} - v_o \exp\left(\frac{f}{f_\beta}\right) \Big/ r_f\right]_{f=f^*} = 0 \tag{13}$$

31.3.3 The Golden Equation of DFS

Using Eq. (13) we can find the most probable unfolding force f^* (see Ref. [18])

$$f^* = f_\beta[\ln(r_f) - \ln(f_\beta v_o)] = \frac{k_B T}{x_u} \ln\left[\frac{r_f x_u}{k_B T v_0}\right] \tag{14}$$

Equation (14), the "golden equation" of DFS, has been derived from numerous assumptions (single transition state, stationary in location under force, linear force

loading, $x_u.r_f/k_BT \ll 1/t_D$, etc.) but shows elegantly the features of DFS. A plot of f^* against the logarithm of the loading rate has slope f_β, revealing the location (x_u) of the transition state along the force axis. Similar to the *m*-value of chemical unfolding measurements, f_β is the susceptibility of the unfolding kinetics to force. But here this value has a direct physical relationship to geometric coordinates and structure (x_u). Further, the plot cuts the loading rate axis, where f^* is zero, when $r_f = f_\beta v_o$. Since f_β is known one can determine through this extrapolation the force-free unfolding rate across the transition state (v_o).

Equation 14 is derived for the most probable rupture force; the mode of the distribution. The equation does not hold true for the mean force. In fact, the mean of the force distribution (Eq. (8)) is complex to find, involving exponential integrals with no exact solution. Thus it is important to find the mode of the distribution of forces measured and analyze these, and not their mean. Additionally, the mode of the distribution is less affected by outlying forces from nonspecific tip/sample interactions, multiple unfolding events and instrumental noise. As a rule-of-thumb, however, at high forces the mean unfolding force can be crudely approximated by [12]:

$$\bar{f} \sim f_\beta[\ln(r_f) - \ln(f_\beta v_o) - 0.6] \tag{15}$$

and with force scales f_β for proteins approaching 20 pN, mean forces are 10 pN or so lower than the modes.

31.3.4 Nonlinear Loading

The approximation used above, that the stiffness of the system is dominated by the cantilever, is not valid for most protein unfolding measurements. Typically, tandem repeats of the protein are stressed and multiple copies are unfolded in series revealing the characteristic saw-toothed force extension curve. In this arrangement, the mechanical stiffness of the protein polymer may well be less than the cantilever. The stiffness of the system κ_s, with two springs stressed in series (the cantilever with stiffness κ_c and molecular system κ_m) is

$$\frac{1}{\kappa_s} = \frac{1}{\kappa_c} + \frac{1}{\kappa_m} \tag{16}$$

Clearly the molecule has to be stiffer than the lever ($\kappa_m > \kappa_c$) for the approximation that lever stiffness dominates loading. With soft levers of 10 pN nm^{-1} or so this can be true. However, the saw-tooth pattern measured in the AFM experiments derives from the stretching of the unfolded polypeptide chain after each repeat has unfolded. This means that force loading is not constant during protein unfolding experiments. This has two consequences. First data have to be represented as unfolding force vs. retract velocity (v_r) and second, we need to consider the mechanical stiffness of such random-coil polypeptide chains.

31.3.4.1 The Worm-line Chain (WLC)

The WLC is a convenient description of the mechanical properties of a random coil of amino acids, an unfolded protein. The configurational space accessible to a long polymer is considerable and when free in solution the end-to-end distance fluctuates. When this distance is constrained, such as being tethered between an AFM tip and a sample surface, configurational space has been lost and thus the entropy of the system has been reduced. The force required to maintain an extension is a function of this loss in entropy. The polymer behaves as an entropic spring.

The stiffness of an entropic spring is a function of the contour length of the molecule, L, and a persistence length, b. This is the length corresponding to a bending energy of one $k_B T$. It is generally agreed that a value of ≈ 0.4 nm for the persistence length fit the experimental measurements of proteins well. Under low extensions x (where $x \ll L$), the spring is Hookian and exerts a force of [19]:

$$f_{\mathrm{WLC}}(x) \approx \frac{k_B T}{b}\frac{x}{L} \tag{17}$$

As the extension approaches the contour length (the asymptote as the molecule is inextensible), force increases anharmonically as

$$f_{\mathrm{WLC}}(x) \approx \frac{k_B T}{b}\left(1-\frac{x}{L}\right)^{-2} \tag{18}$$

A convenient equation to show the behaviour of a WLC over all extensions, and one that matches that seen in AFM experiments, is an interpolation between Eqs (17) and (18), as

$$f_{\mathrm{WLC}}(x) \approx \frac{k_B T}{b}\left(\frac{1}{4\left(1-\frac{x}{L}\right)^2}-\frac{1}{4}+\frac{x}{L}\right) \tag{19}$$

A polymer exerts a force of 150 pN (a typical titin I27 unfolding force) when the chain is extended to around 90% of its contour length. The stiffness of the chain $\kappa_{\mathrm{WLC}}(f)$ at this extension is approximately 10 pN nm^{-1}, and for all but the softest of AFM cantilevers it is the polymer that dominates the loading rate (Eq. (16)). So instead of a steady loading rate, r_f depends on the force and increases nonlinearly in time as $r_f = v_r \kappa_{\mathrm{WLC}}(f)$. Substitution of this loading rate term into Eq. (9) and subsequent solving for f^* gives a good approximation of the unfolding kinetics under WLC polymer loading, as [20]:

$$\begin{aligned} f^* &\approx f_\beta\left[\ln\left(\frac{v_r}{v_\beta}\right)+\ln\left(\frac{f^*}{f_\beta}-\frac{3}{2}\right)+\frac{1}{2}\ln\left(\frac{f^*}{f_\beta}\right)\right] \\ v_\beta &= \frac{L v_o}{4}\left(\frac{x_u}{b}\right)^{1/2} \end{aligned} \tag{20}$$

Equation (20) is transcendental (the force term f^* is expressed in terms of f^*) and therefore can be awkward to solve. Methods to fit this equation to data are explained below. A simpler, although less accurate method of fitting to experimental data is to use the each force value to find the stiffness of the system at the point of unfolding, and then multiply this by the retract velocity v_r to give a loading rate (this is only an estimate as the force distributions are no longer described fully by Eqs (8), (9), and (10) since the loading rate increases during cantilever retraction). The stiffness of the protein chain ($b = 0.4$ nm, $k_B T = 4.11$ pN nm) is approximately

$$\kappa_{WLC}(f) \approx 4\frac{k_B T}{bL}\left(\frac{bf}{k_B T}\right)^{3/2} \tag{21}$$

The rate of loading at the point of unfolding can be estimated, therefore, by calculating the stiffness of the unfolded protein at the unfolding force (Eq. (21)), determining the stiffness of the system (Eq. (16)) and multiplying this by the retract velocity v_r. The modal unfolding force can then be plotted against this loading rate estimate and Eq. (14) used to find a reasonable estimate of the force-free unfolding rate and transition state displacement.

31.3.5 Experiments under Constant Force

An attractive method to remove the problems of the nonlinear loading induced by the dynamics of the polymer is to measure the lifetime of the protein under a constant force [11]. Instrumentally, such an experiment requires the incorporation of a feedback system that modulates the cantilever position to maintain a constant deflection, and hence constant force.

The time for which a protein can withstand a constant force is the reciprocal of its unfolding rate

$$t_u(f) = \frac{1}{v_o}\exp\left(-\frac{f}{f_\beta}\right) \tag{22}$$

The constant force experiment has the advantage that it should be independent of the system dynamics, such as the nonlinear loading rate introduced by the polymer stiffness, but suffers from two shortcomings. First, analysis assumes that force is kept constant and that the force-feedback system can respond faster than the unfolding rate of the protein under the force applied. Fortunately, this is often the case. However, a greater limitation of this class of experimentation is that control of force relates to exponential changes in lifetime, as seen in Eq. (22). Therefore, as force is lowered, the experiment lasts for exponentially increasing periods of time. Conversely, at high forces, it becomes increasingly difficult to determine lifetime with the necessary accuracy. The advantage of the ramp of force measurement is

that the force is a direct measurement of lifetime since these are related through the loading rate. However, since the ramp of force measurement is a continuous collection of constant force measurements, these two regimes can be considered identical. The experiment of constant loading rate can be considered as the ideal and relatively simple technological developments are required to realize this methodology. The potential of the constant force experiment is to measure the kinetics of unfolding under high forces. To measure this, however, requires the ability to apply the force instantaneously (through the use of magnetism or electrostatic attraction for instance) and measure the diminishing lifetime with increasing temporal resolution. Current AFM technology, depending on peizo displacement and at best having kilohertz temporal resolution, is incapable of exploiting this potential.

31.3.6
Effect of Tandem Repeats on Kinetics

The use of tandem repeats of proteins in forced unfolding experiments is beneficial for several reasons as previously discussed; including providing a characteristic signature for a single molecule, extension of the unfolding event away from any interactions of the surface, and increased number of data points per trace. But the presence of multiple proteins affects the unfolding kinetics, and this must be accounted for [19].

For a chain of identical tandem repeats there is no specific order in which they will unfold under force as none is more likely to unfold before another. For a chain of N folded proteins, the probability that any one protein will unfold is N-times higher than the probability of failure of the protein on its own. So the unfolding rate of the first event is N-times the unfolding rate of the constituent protein. For the second event, the number of units that may unfold is $N-1$, and the unfolding rate for this is $N-1$ times one, and so on [21]. The effective unfolding rate of the chain decreases for each peak n of N seen in the experiment, as

$$v_{\mathrm{u}}(f,n,N) = (N-n-1)v_{\mathrm{o}} \exp\left(\frac{f}{f_\beta}\right) \tag{23}$$

In addition to the unfolding rate decreasing with the event number, the loading rate also decreases as the length of unfolded protein increases with each event. The drop in unfolding rate leads to an increase in the force, whilst the drop in loading rate causes a competing decrease in force. Between the first and second event the fractional change in rate is small (from Nv_{o} to $(N-1)v_{\mathrm{o}}$) whereas the loading rate changes considerably as the unfolded polymer has increased considerably in length (Eq. (21)). The forces drop over the first events. Conversely, between the second-to-last and last event the unfolding rate halves whereas the fractional change in polymer length is small. The forces increase towards the last events. On average, the net effect is a decrease and then increase in the average rupture force for event number [22].

To analyze accurately the unfolding forces for tandem repeats requires knowledge of the length of repeat being pulled, which can change from test to test, and analysis of individual events based on the each total length, i.e., the 1st, 2nd, and 3rd events of pulls of three repeats, the 1st, 2nd, 3rd, and 4th of pulls of four repeats, etc. A useful observation is that the sixth event in a chain of eight repeats behaves similarly to the mode of all measurements [23]. Fortunately, the effect of changing unfolding rate and polymer length with event number shift the most probable rupture force by only 20 pN or so, and so this effect is usually ignored in all protein folding studies. Titin I27 has been studied in different laboratories using polyproteins with 12, 8, and 5 repeats and the results are essentially the same [4, 5, 24].

31.3.7 Determining the Modal Force

To analyze the kinetics of unfolding using force spectroscopy requires measurement of the full distribution of forces (lifetimes), since unfolding is random. In the inevitable presence of noise, this requires many (several hundred) measurements at each speed. To determine the mode of the distribution (remembering the issues discussed above with the mean) usually requires resorting to a graphics program, binning the data into arbitrary sized bins, and plotting the resulting histogram.

A useful alternative that does not require the use of bins is to estimate a continuous spectrum of forces [25]. Each force measured is assumed to be subject to noise, and assumed to be Gaussian. The largest sources of noise in the force data are from thermal fluctuations of the cantilever, limited sampling rate and hydrodynamic drag. Whilst drag effects are limited by restricting retract velocities to below a few microns per second, and sampling rates are increasing with every new generation of force microscope, thermal noise cannot be easily overcome. The thermal fluctuation of the lever is related to its spring constant κ_c, given as

$$\langle \sigma \rangle = \sqrt{\frac{k_B T}{\kappa_c}} \tag{24}$$

and a cantilever of typical stiffness (30 pN nm^{-1}) fluctuates around 0.3 nm, showing that the standard deviation of the force noise for these soft levers is over 10 pN. The force noise for an AFM is typically between 10 and 20 pN, and we can assume that each force measured is drawn from a Gaussian 10 or 20 pN wide. The sum of all these Gaussians, centered on each force recorded, is calculated and the mode force, where the sum is greatest, found. It is often worthwhile seeing how this estimate of the mode depends on the level of noise chosen, which ideally should be invariant.

The distribution of forces for unfolding over a single transition state has a well-defined form given by Eq. (10). Since the full distribution of forces at a particular rate of loading is given by the two parameters measured, the unfolding rate ν_o and

the transition state location x_u, the distribution serves to validate the experimental measurements. Having found the mode, the histogram of recorded forces (and not the artificial Gaussian sum used above) should be plotted and the distribution predicted using Eq. (10) overlaid.

31.3.8 Comparing Behavior

Dynamic force spectroscopy reveals uniquely the presence of multiple transition states, their locations along a reaction coordinate, and the rate at which they are crossed. As shown in Eq. (1), conversion of these rates to a free energy requires knowledge of the exponential prefactor. However, the ratio of two rates does reveal the difference in free energy between the transition states assuming a constant prefactor, as

$$\begin{aligned} \nu_1 &= \frac{1}{t_D}\exp\left(-\frac{\Delta G_{TS1}}{k_B T}\right) \\ \nu_2 &= \frac{1}{t_D}\exp\left(-\frac{\Delta G_{TS2}}{k_B T}\right) \\ \frac{\nu_1}{\nu_2} &= \exp\left(\frac{\Delta G_{TS2} - \Delta G_{TS1}}{k_B T}\right) \end{aligned} \tag{25}$$

An assumption of the constant prefactor is one of the difficulties in application of Eq. (25). This is a concern when one is comparing mutant proteins with wild-type. Where the transition state being probed is the same, deformed by a point mutation for example, then this assumption is reasonable. But with such a mutation it is still not assured that the same transition state from the same point along the unfolding coordinate is being probed. Good examples are some of the single point mutants of titin I27 studied by AFM [23, 26]. Many proline mutants, and even conservative mutants such as V86A, have been shown to cause a change in the ground state from which unfolding is measured [23]. Whilst it is believed that the same transition state is being studied, the folded state from which the protein unfolds is different (wild type unfolds from an intermediate whereas the mutants unfold from the native state). Therefore, the ratio of unfolding rates extrapolated from these measurements of the mutant behavior to the wild type does not represent the change in kinetic stability caused by the mutation.

31.3.9 Fitting the Data

The data need to be analyzed to extract the two parameters requires, x_u and the unfolding rate at 0 force ν_o. Probably the most obvious method to predict the be-

havior of a system under load is to perform a "Monte-Carlo" simulation [27]. Here, small intervals of time are sampled and the events that could occur within these windows are chosen at random. Commencing at time $t = 0$, the force on the system is determined by the position of the cantilever ($x = v_r t$) and the mechanical properties of the system (Eq. (19)). This force is used to calculate the probability of an unfolding event within the window of time, as the product of the time slice Δt and Eq. (23). This probability is sampled at random by its comparison to a uniform random number. If the event is chosen (i.e., the random number selected is not more than the probability) then the unfolding event has occurred, this domain is deemed to have unfolded and the length of the unfolded polymer increased by the length of the polypeptide chain forming the domain. Next, the cantilever is moved back by a distance equal to the product of the retract velocity and the time-step, the new force calculated and the process of random sampling continued until all the domains have unfolded.

Monte-Carlo simulations such as these provide full force versus extension traces as they represent a reasonably accurate simulation of the experiment (Figure 31.4). However, for this very reason, the simulation must be repeated many times to sample the stochastic nature of unfolding. Furthermore, whilst capable of predicting a distribution of unfolding forces for given values of ν_o and x_u, it is not simple to fit these values to experimental results.

An alternative method of obtaining the full distribution of unfolding forces is to integrate the Master rate equations (for example Eq. (5)) across an increasing force [28]. Unfortunately, the fact that the probability of unfolding increases exponentially in force whilst the probability of surviving to each force decreases exponentially, the equations are so-called stiff, and can be difficult to integrate numerically.

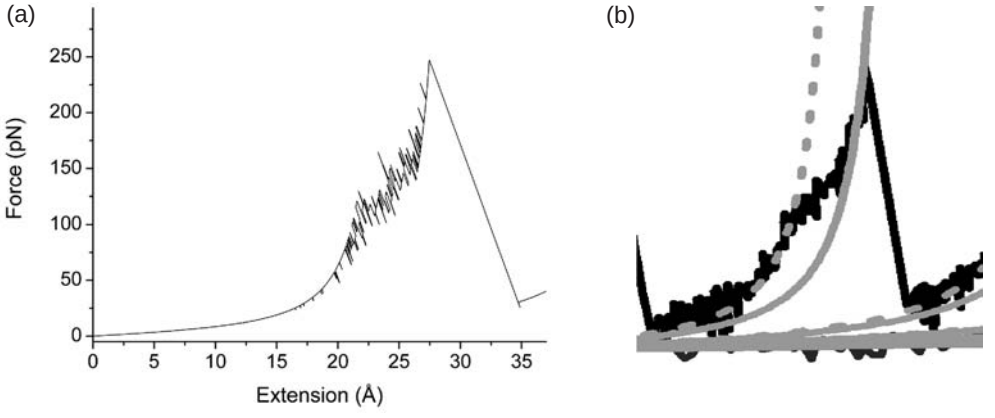

Fig. 31.4. Monte-Carlo simulations. Monte-Carlo simulations (a) of the AFM experiment reveal the full force vs. distance trace of the experiment (b). By incorporating details of refolding and unfolding rate constants and unfolding intermediates fine detail, such as the presence of the force plateau around 100 pN attributed to the population of the force-stabilized unfolding intermediate of I27, can be resolved.

We find the semi-implicit extrapolation method of the Bulirsch-Stoer integration procedure to be the most suitable [23, 29]. Such numerical solutions provide the full unfolding force distribution, an extremely valuable cross-check of the experiment [19]. They do not, however, provide any insight of the individual force vs. extension curve.

Fitting requires predicting the unfolding forces for a set of trial parameters (x_u and ν_o) with each measured value at the rates explored, calculating a difference (commonly as the sum of the squares), and changing the trial parameters until this difference is as small as possible. There are many methods available to perform such minimizations, and a useful method is the simplex minimization procedure. Simplex minimization can be slow, but does not require the use of derivatives that are difficult to compute. A good discussion of simplex minimization is given by Press et al. [29]. Simply, in the n parameter space of the fit ($n = 2$ for a single transition state, x_u and ν_o) the best result is enclosed by a simplex, a shape of $n + 1$ vertices. For example, all possible values of x_u and ν_o can be plotted on a graph, the abscissa representing all the x_u values and the ordinate the ν_o values. The smallest simplex that can be drawn at any point on the graph is a triangle ($n + 1 = 3$). Simplex minimization starts with the simplex occupying an arbitrary region of the parameter space, and then walks the simplex through space depending on a series of rules. The rules can include contracting the shape towards the vertex with the best fit, moving the best fitting vertex away from the worst, etc. Minimization is terminated when all the vertices lie close in space and in value. Again, see Press et al. for a much clearer explanation of this and other minimization and optimization methods [29].

A final note is in the assessment of the goodness of fit and the magnitude of errors. A useful method here, again explained in detail by Press et al. is the bootstrap Monte-Carlo method [29]. Having obtained a fit between the measured and the predicted force data, the goodness of the fit can be estimated by the replacement method. The original data is subsampled and padded with copies. About $1/e$ of the data is removed and these points replaced by remaining values. The total number of forces in the set, therefore, remains the same. The x_u and ν_o parameters are then fitted to this subset of data, and this procedure repeated many times. The variance in the results of these fittings equals the variance in the original fit. Finally, when measuring and reporting variances in ν_o it is important to remember that this value is not linear but exponential, and variances of $\log(\nu_o)$ and not ν_o should be used. For this reason rates are often reported as exponents, as $2 \times 10^{-4 \pm 1.1}$ s^{-1} for example. Since small uncertainties in the experimentally determined x_u lead to large differences in ν_o the errors can be large [15, 30].

31.4 Use of Complementary Techniques

Two complementary techniques have been exploited increasingly in the study of protein folding mechanisms – protein engineering Φ-value analysis and computer

simulation. Both these techniques can also be exploited in the study of forced unfolding mechanisms.

31.4.1 Protein Engineering

One of the best ways to determine the regions of the protein structure involved in the resistance of a protein domain to force is to make site-specific mutants and to investigate the response of these mutants to force. However, unless we combine force spectroscopy with biophysical data, any information gained is purely qualitative. If mutations in two different regions of the protein have different effects on force it is not possible to say that one region is more structured in the transition state than the other unless the effect of the protein on the stability of the native state has been quantified.

Fortunately, the analysis of mutant proteins as a means of investigating protein folding (and unfolding) mechanisms is well established [31]. Essentially, the effect of the mutation on the stability of the protein and on the stability of the transition state for unfolding is compared:

$$\Phi = \frac{\Delta\Delta G_{\mathrm{D-TS}}}{\Delta\Delta G_{\mathrm{D-N}}} = 1 - \frac{\Delta\Delta G_{\mathrm{TS-N}}}{\Delta\Delta G_{\mathrm{D-N}}} \tag{26}$$

where $\Delta\Delta G_{\mathrm{D-N}}$ is the change in free energy on mutation (determined from equilibrium denaturation experiments) and $\Delta\Delta G_{\mathrm{D-TS}}$ and $\Delta\Delta G_{\mathrm{TS-N}}$ are changes in free energy of the transition state (TS), relative to the denatured (D) and native (N) states, respectively, determined from ratios of folding and unfolding rate constants:

$$\Delta\Delta G_{\mathrm{D-TS}} = RT \ln\left(\frac{k_{\mathrm{f}}^{\mathrm{wt}}}{k_{\mathrm{f}}^{\mathrm{mut}}}\right) \quad \text{and} \quad \Delta\Delta G_{\ddagger\mathrm{-N}} = -RT \ln\left(\frac{k_{\mathrm{u}}^{\mathrm{wt}}}{k_{\mathrm{u}}^{\mathrm{mut}}}\right) \tag{27}$$

where k_{f} and k_{u} are the folding and unfolding rate constants, and the superscripts wt and mut refer to the rate constants for wild-type and mutant proteins, respectively.

We have shown that this Φ-value analysis can be applied to force experiments, however, they are somewhat more complex, due to the nature of the data collected [30].

31.4.1.1 Choosing Mutants

The assumptions inherent in Φ-value analysis have been clearly described [32]. The three most important criteria are:

1. The mutations should not alter the structure of the native state significantly: To this end, the mutations should be conservative, nondisruptive mutations. They should not distort the structure or add new interactions. The most suitable mutations are simple deletion mutants such as Ile to Val or Val to Ala.

2. The mutations should not alter the stability of the denatured state significantly, or at least the effect on D should be significantly less than on N. For this reason mutations of or to Pro or Gly should be avoided where possible, as should mutants that change the polar/nonpolar nature of the sidechain.
3. The change in stability ($\Delta\Delta G_{D-N}$) should be significant. Where $\Delta\Delta G_{D-N}$ is small Φ cannot be determined with confidence. In AFM experiments this is particularly important since there is much more error in the experimental data. We do not choose to analyze mutants with a $\Delta\Delta G_{D-N} < 2$ kcal mol^{-1}. Where the effect of mutation is less than this it is unlikely that differences between wild type and mutant can be quantified with any confidence.

31.4.1.2 Determining $\Delta\Delta G_{D-N}$

The effect of the mutation on the stability of the native, starting state, relative to the unfolding state has to be determined from equilibrium denaturation experiments. This can be undertaken on either single domains of the protein, where ΔG_{D-N} has been shown to be unaffected by inclusion in a polyprotein, or by equilibrium investigations of the mutant polyprotein itself. Of course, the denatured state in the forced unfolding experiments is not the same as that measured in the equilibrium unfolding studies. One has to make the reasonable assumption that the effect of the mutation in the compact denatured state ensemble will be the same as the effect of the mutation on the stretched denatured state, or that, at least, the difference is significantly less than the effect on the native state. This is most likely to be true where the mutation is conservative. In some conventional kinetic investigations a ΔG has been determined by the ratio of the folding and unfolding rate constants. This cannot be applied to forced unfolding experiments, however. It has been shown to be possible to determine a folding rate constant for some proteins when the force is (very nearly) reduced to zero, but the protein still held on the tip[4]. However, the principle that $\Delta G_{D-N} = RT \ln\left(\frac{k_f}{k_u}\right)$, applies only where the folding and unfolding reaction are the reverse of each other, i.e., where the same transition state is being explored. Since it is most unlikely that unfolding in the presence of a directional force will be the reverse of folding in the absence of such a force (and it has been shown that this is not the case for at least one protein) measurements of ΔG from the rate constants derived in AFM experiments is not possible. A final important corollary, however, is that if under force the protein adopts an alternative native state, N^F (or unfolding intermediate, I) that is significantly different in structure to N, then this analysis will not hold.

31.4.1.3 Determining $\Delta\Delta G_{TS-N}$

In principle $\Delta\Delta G_{TS-N}$ can be determined from forced unfolding experiments simply by directly comparing the unfolding rate in the absence of force (ν_o, also termed k_f^0) determined from the experimental data. However, as described above, these values are highly sensitive to small changes in the slope of the force vs. log ν_r plot. Again, principles well established in protein folding experiments can be applied. This situation is akin to differences in $\Delta\Delta G_{TS-N}$ determined directly

from experimental measurements and those extrapolated to 0 M denaturant: small changes in the slope can lead to large errors in v_o. We have shown that where the slope is the same within error, i.e., where x_u can be assumed to be the same for wild-type and mutant proteins a number of methods can be used to determine $\Delta\Delta G_{TS-N}$.

1. Analyze the data for wild type and mutant as described above (Section 31.3.9) but assuming a mean, fixed x_u.
2. Fit the force spectra to a fixed mean slope and then compare the pulling speeds (v_r) of wild type (wt) and mutant (mut) at a fixed force in the range of the experimental data:

$$\Delta\Delta G_{TS-N} = -RT \ln\left(\frac{{v_r}^{wt}}{{v_r}^{mut}}\right) \tag{28}$$

3. Fit the force spectra (F vs. ln v_r) to a fixed mean slope (m) and then compare the unfolding force at a fixed pulling speed in the range of the experimental data:

$$\Delta\Delta G_{TS-N} = RT(F^{wt} - F^{mut})/m \tag{29}$$

We have shown that all three methods give the same Φ-value [30].

It is important to note that Φ-value analysis only applies where the unfolding transition that is being measured is the same in wt and mutant proteins. If a mutation changes the folding behaviour so that a different barrier is being explored then this method cannot be used. As an indication of this, the x_u should always be the same for wt and mutant proteins.

31.4.1.4 Interpreting the Φ-values

- $\Phi = 1$: If the mutation is in a region of the protein that is fully structured in the transition state then the mutation will destabilize the transition state to the same extent as the native state. Thus the free energy difference between N and TS will remain the same ($\Delta\Delta G_{TS-N} = 0$) and the force required to unfold the protein will remain the same. In this case $\Phi = 1$.
- $\Phi = 0$: If the mutation is in a region that is fully unstructured in the transition state, then the mutation will have no effect on the stability of TS, while destabilizing N. Thus the difference in free energy between N and TS will be reduced by the same amount as N ($\Delta\Delta G_{TS-N} = \Delta\Delta G_{D-N}$). The unfolding force will be lowered in a manner that can be predicted using Eq. (29).
- $0 < \Phi < 1$: If the mutation is in a region that is partially structured in TS then the unfolding force will be lowered, but not as significantly as might be predicted from $\Delta\Delta G_{D-N}$. Formally, in traditional protein engineering studies, partial Φ-values can be interpreted in a number of ways. A Φ-value of 0.5, for instance, could indicate that half the free energy of the residue was lost in TS, or it could

mean that the protein unfolded by two pathways, one where the Φ-value was 1 and a second where Φ was 0. In these single molecule experiments, however, these two possibilities can be distinguished. If there are two different pathways then the forced unfolding should show a bi-modal distribution of forces. This has not been seen to date, and so the simpler interpretation of partial loss of contacts can be made.

Given the nature of the AFM experiment the error on Φ is larger than that from traditional unfolding experiments. It is probably not possible to say more than that a region is ''fully, or almost fully structured'' (Φ close to 1), ''fully or almost fully unstructured'' (Φ close to 0) or ''partly structured'' (Φ less than 1 but more than 0). This is one reason why mutants being studied should be significantly less stable than wild type, to allow Φ-values to be assigned with confidence. In traditional Φ-value analysis Φ-values are considered to be too prone to error if $\Delta\Delta G_{D-N} < 0.75$ kcal mol^{-1} (it has recently suggested that this limit should be set significantly higher). We suggest that for mechanical Φ-value analysis $\Delta\Delta G_{D-N}$ should be as large as possible and at least >1.5 kcal mol^{-1}.

31.4.2 Computer Simulation

Since even the most detailed protein engineering experiment can only provide ''snapshots'' of the unfolding process, simulations are important to understand the effect of force at the atomistic level. Mechanical unfolding experiments are apparently ideal for comparison with simulation. Unlike addition of temperature or denaturant, the perturbation is directional, suggesting that the reaction coordinate (N–C distance) is comparable in simulation and experiment. Furthermore, it is easy to identify in a forced unfolding trajectory, both metastable unfolding intermediates and the position of the transition state barrier. The problem of time scale is, however, just as difficult in simulations of forced unfolding as it is for other unfolding simulations. To increase the rate of unfolding the system has to be perturbed using conditions that are far from experiment. In simulations of thermal unfolding this requires the use of very high temperatures in a simulation. In forced unfolding simulations the rate of application of force (the loading rate) is significantly higher in simulation than experiment. Since theory suggests that different barriers to unfolding will be exposed at different loading rates, it is not possible to assume that the same barrier will be investigated in theory and experiment. Thus it is important that simulation be bench-marked by experiment.

A number of increasingly computationally expensive techniques have been applied to the study of mechanical unfolding and where these can be directly compared to experiment, the simulations seem to perform well. Lattice and off-lattice simulations have been used to describe the effect of force, and other perturbants (denaturant, temperature) on energy landscapes (e.g., [33–36]). The phase diagrams suggest that interesting data may be obtained if force is applied at higher temperatures and/or in the presence of denaturant. Steered molecular dynamics

simulations, with and without explicit solvent, have been successful in reproducing a number of experimental features. They have also been successful in describing the order of unfolding events in titin I27 (e.g., [37, 38]). The hierarchy of unfolding of different protein domains has been predicted [39]. Simulations have observed unfolding intermediates in experimental systems where they have later been detected in experiment [13, 14, 37, 40, 41]. (But again, a note of caution is required. In only one case has the intermediate been shown to have experimental properties consistent with the intermediate observed in the simulations [14, 24]. In the other cases, the correct experiments have not yet been performed.) Finally, simulations have been successful in predicting the effect of mutation on the unfolding force [42]. Where simulation and experiment agree, the simulations can be used to understand details of the transitions between experimentally observable states.

Recent advances have reduced the unfolding forces observed in simulations to within an order of magnitude of those observed in experiment. Perhaps the most exciting phase is before us. Unlike previous studies in the field of protein folding where simulations have lagged behind experiment, the opposite is true of simulations of mechanical unfolding experiment. There are far more protein unfolding simulations in the literature than detailed experimental analyzes. The good simulation papers suggest experiments to be done.

31.5 Titin I27: A Case Study

31.5.1 The Protein System

Only one protein has, at the time of writing, been investigated in depth. This study shows how a combination of force spectroscopy, biophysical techniques, protein engineering, and simulation can be used to describe the mechanical unfolding of a single protein in detail. Titin I27 was the first protein made into a polyprotein and thus, the first where domain-specific force characteristics were elucidated [4]. It is one of the most mechanically stable proteins yet studied and remains a paradigm for forced unfolding experiments. The studies described here represent the work of a number of different experimental and theoretical groups.

To understand these experiments the structure of the protein has to be considered [43]. Titin I27 has an I-type immunoglobulin (Ig) fold. It has a beta sandwich structure, with the first sheet comprised of antiparallel strands A, B, E, and D and the second of antiparallel strands C, F, and G with, importantly, the A′ strand running parallel to strand G. In the polyprotein, the N and C termini (A and G strands) are connected by two-residue linkers (encoded by the restriction sites used in the cloning process). The N- and C-termini are found at opposite ends of the protein (Figure 31.5).

The first experiments revealed that the v_o was $\sim 10^{-4}$ s^{-1} and the $x_u \sim 3$ Å [4]. Since the unfolding rate was close to that observed in standard stopped-flow experi-

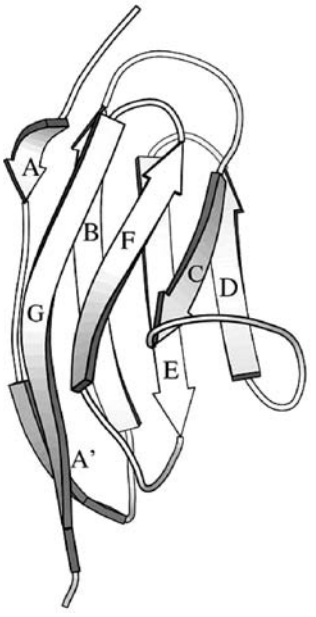

Fig. 31.5. Structure of titin I27. I27 has a beta-sandwich structure with the hydrophobic core enclosed by two antiparallel beta sheets. The strands are labeled A–G. A runs antiparallel to strand B, and A′ runs parallel to strand G.

ments it was suggested that the transition state for unfolding under force was the same as that observed in the absence of force. This idea, however, did not hold for long [5, 24].

31.5.2 The Unfolding Intermediate

The first step observed in the simulations of forced unfolding of I27 was the detachment of the A-strand, to form a metastable unfolding intermediate, which lived longer than the native state in the simulation conditions [37, 40]. Careful examination of the experimental force traces revealed the presence of a ''hump'' in the AFM traces, at around 100 pN, which was attributed to a lengthening due to the detachment of the A-strand in all the domains of the polyprotein [14]. A mutant that disrupted the hydrogen bonding between the A- and B-strands did not show these ''humps.''

Thus, apparently, at forces around 100 pN, the native state becomes less stable than this intermediate, I. If this explanation were correct, then the observed unfolding force reflects the unfolding of this intermediate, and not the denatured state. Studies of an I27 polyprotein with a conservative mutation V4 to A in the A-strand confirmed this explanation [24]. This mutation destabilized the native state

of the protein by ~2.5 kcal mol^{-1}, yet had no effect of the unfolding force, consistent with the intermediate hypothesis, since, if the A-strand is detached in I the V4A mutant would simply lead to I being populated at lower forces as N is destabilized, but I is not. Thus, the experiment and theory agree and the first process, N → I, in the unfolding pathway can be understood, and the unfolding rate constant at 0 force, ν_o, and the unfolding distance, x_u, can be assigned to the unfolding of this intermediate. In a traditional protein folding study of I27, no such folding intermediate is observed [44]. A model of this intermediate (I27 with the A-strand deleted) was purified, shown to be stable and, by NMR spectroscopy, to be structurally very similar to the native state. In MD simulations this intermediate had all the properties of the intermediate induced by force [24].

31.5.3 The Transition State

Possibly the most important state along the unfolding pathway is the transition state, the barrier to forced unfolding. Proteins that can withstand significant force have a free energy barrier to unfolding that remains significant under applied force. In order to probe the nature of this barrier protein engineering Φ-value analysis was undertaken [30]. Mutations were made in the A′, B, C′, E, F, and G strands. Most of these mutations, although strongly destabilizing, had no effect on the unfolding force, i.e., had a Φ-value of 1 (Figure 31.6) [42]. Only mutations in the A′ and G strand lowered the unfolding force. The effect of the mutation in the A′-strand (V13A) was to lower the unfolding force by ~25 pN without changing the x_u giving a Φ-value of ~0.5. The mutation in the G-strand (V86A) changed the slope of the force spectrum (Figure 31.6) so that a Φ-value could not be determined (see Section 31.3.8). Since mechanical Φ-values are much harder to determine than in traditional protein engineering studies (the molecular biology is more laborious, the data are harder to collect, and the $\Delta\Delta G_{D-N}$ of each mutant must be significantly larger than traditionally) only eight mutants were made. This can give only a general picture of the transition state. However, on the contrary, the transition state in MD simulations of forced unfolding experiments is easier to identify than in high temperature simulations of unfolding. The transition state is represented by the structures just at the point where extension proceeds rapidly to a fully unfolded structure. Direct comparison was made between the experimental Φ-values and the Φ-values determined from the simulations. The agreement was very good. This means that the structure of the transition state can be directly inferred from the simulation [42].

The transition state structure is essentially the same as the native structure except in the region of the A, A′, and G strands (Figure 31.7). The A-strand is, of course, completely detached, as it is in I. The hydrogen bonding and side-chain interactions between the A′ and G strands are lost, as are interactions between the A′-strand and the E–F loop and between the G-strand and the A′–B loop. Other interactions of the A′ and G strands with the rest of the protein are, however, maintained in this structure. The mechanical strength of the I27 domain lies in the

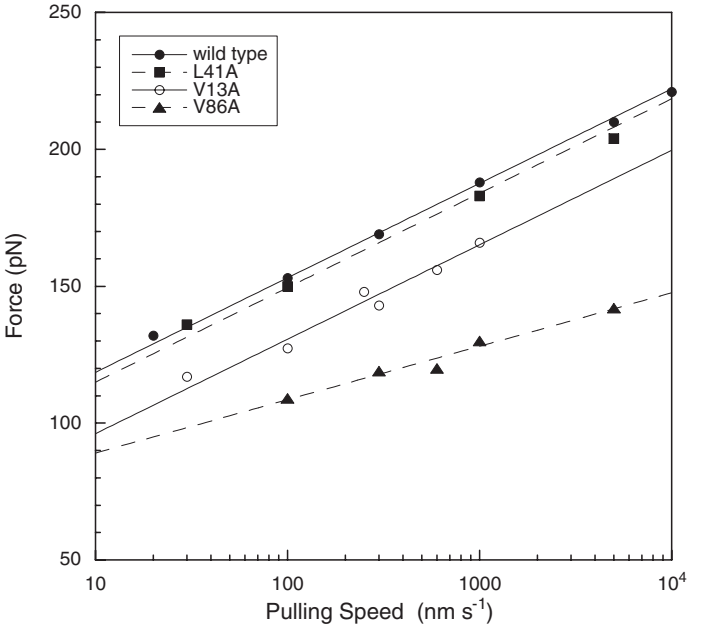

Fig. 31.6. Force spectra of titin I27. Most mutants (such as L41A) have no effect on the unfolding force, nor on the dependence of the unfolding force on the retract speed. V13A lowers the unfolding force but does not affect the pulling speed dependence. V86A both lowers the unfolding force and changes the dependence of the unfolding force on the puling speed. The slope of the force spectrum is $f_\beta \kappa_s = k_B T \kappa_s / x_u$ (i.e., the decrerase in slope for the mutant V86A reflects an increase in x_u).

strength of interactions between the A′ and G strands, and in the strength of interactions of these strands with other regions of the protein. (A mutant I27 studied elsewhere had shown that a substitution that made contacts in the BC loop, also lowered the unfolding force, consistent with these results [5].) Importantly, these experiments show that the interactions of the side chains contribute significantly to mechanical strength, and it is not just the hydrogen bonding pattern that determines mechanical strength, as had been suggested in some theoretical studies [38]. Whether it is simply packing interactions, or a more complex effect of shielding of the hydrogen bonds from attack by solvent has yet to be determined. This side chain dependence does, however, seem to be at the root of the relative mechanical stability of different I-band domains of titin [45, 46].

31.5.4
The Relationship Between the Native and Transition States

Thus far theory and experiment had elucidated the structure of the principle states along the pathway and the relative height of the barrier between I and TS (corresponding to $v_o \sim 10^{-4}$ s^{-1}) and the distance between I and TS ($x_u \approx 3$ Å). However,

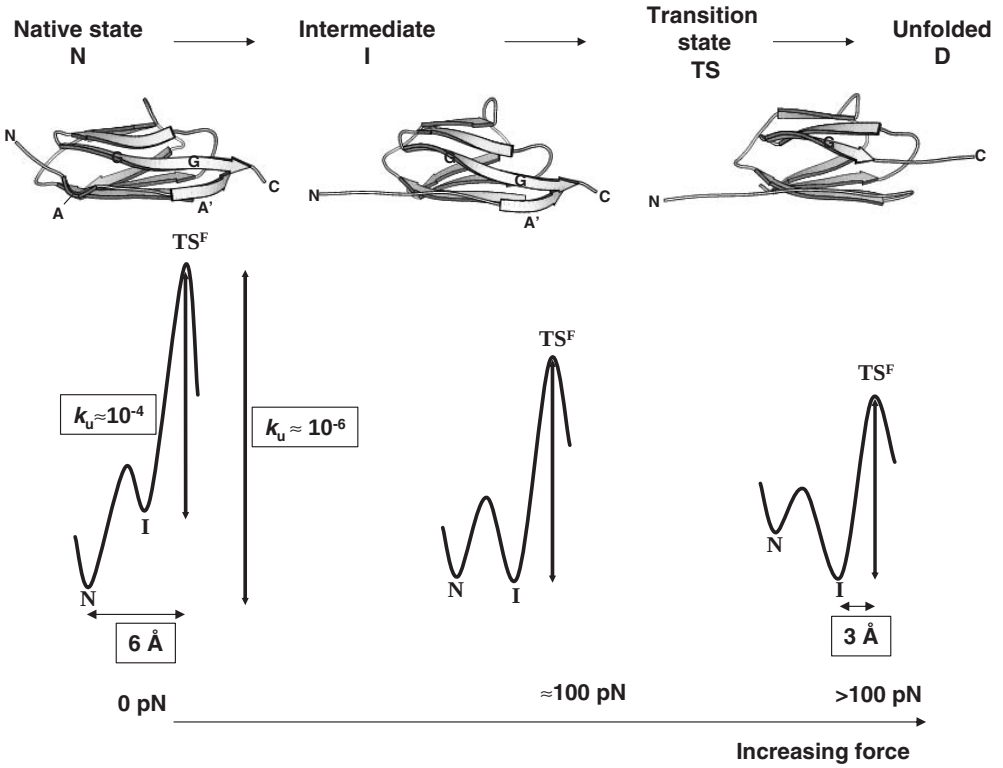

Fig. 31.7. The unfolding of TI I27 in the presence of force. Experiment and simulation combined have allowed the structure of the important states on the forced unfolding pathway to be elucidated. The effect of force on the unfolding landscape and the height and relative position of the energy barriers and the intermediate have been determined. Structures Courtesy of E. Paci.

the relative height of the barrier between N and TS and the distance between these two states was unknown. It is not possible, using AFM, to collect data at pulling speeds low enough to unfold the protein at forces below 100 pN, i.e., when I is not yet populated. However, here again mutant studies were instructive. One of the mutants (V86A) changed the slope of the force spectrum ($x_u \approx 6$ Å) [23]. The same behavior had been seen in a separate study for mutants with prolines inserted into the A′-strand [26]. The anomalous result was that these highly destabilized mutants had, apparently a lower unfolding rate at 0 force (ν_o) than wild type. The simplest explanation is that these mutations lowered the stability of I and/or lowered the TS energy to such an extent that the protein unfolded directly from N before I was populated. In this case, ν_o is the unfolding rate directly from N and x_u is the unfolding distance from N to the transition state. By using this as a model and modeling the data for wild type and mutants it was possible to estimate the rate constant between N and TS at 0 force for wild-type I27 ($\nu_o \approx 10^{-6}$ s^{-1}) [23].

31.5.5
The Energy Landscape under Force

Using all these results a pathway for the forced unfolding of titin I27 could be constructed (Figure 31.7). It is was also possible to compare the transition state in the absence of force (TS^0, as determined by traditional Φ-value analysis) with that observed in the force experiments (TS^F). The height of the energy barrier between N and TS^0 ($\nu_o = 5 \times 10^{-4}$ s^{-1}) is >3 kcal mol^{-1} lower than that between N and TS^F ($\nu_o = 10^{-6}$ s^{-1}). There is also a difference in structure. TS^F is more structured, with higher Φ-values than TS^0. However, the region of the protein that is responsible for mechanical stability (the region that breaks at the transition state) is apparently the same as the region that unfolds early in the denaturant induced unfolding studies, the A′ and G strands. When force is applied to the protein energy landscape, the unfolding pathway changes, and the protein unfolds along a pathway occupied by a high-energy barrier, TS^F, that resists unfolding.

31.6
Conclusions – the Future

Forced unfolding of proteins is in its infancy as a technique for studying proteins. Much of the work that has been done has been to demonstrate the power of atomic force microscopy as a tool. However, now forced unfolding is moving beyond a descriptive science towards analysis of the molecular effect of force on protein structure, stability, and unfolding landscapes. The use in the study of proteins that experience force in vivo is obvious. However, it can also be used, combined with simulation, to test our understanding of the molecular forces responsible for protein folding. How, for example, does a protein molecule respond to force applied in different directions? Can we explain the relationship between protein topology and mechanical strength? Altering the solvent conditions (e.g., temperature, pH, salt) may be used to determine the relative importance of different intramolecular forces. We can also look forward to the development of systems allowing proteins to be attached to the beads of optical tweezers, or the biomolecular force probe so that far lower loading rates, probably closer to those experienced in vivo, can be applied. As yet, the single molecule nature of the unfolding process has yet to be exploited, although rare events (misfolding and cooperative unfolding) have been observed [47, 48]. There are moves to combine single molecule fluorescence with single molecule force measurements. We would expect to see significant advances in the field in the next decade.

References

1 Rief, M., Gautel, M., Oesterhelt, F., Fernandez, J. M. & Gaub, H. E. (1997). Reversible unfolding of individual titin immunoglobulin

domains by AFM. *Science* 276, 1109–1112.

2 Rief, M., Pascual, J., Saraste, M. & Gaub, H. E. (1999). Single molecule force spectroscopy of spectrin repeats: Low unfolding forces in helix bundles. *J. Mol. Biol.* 286, 553–561.

3 Wang, T. & Ikai, A. (1999). Protein stretching III: Force-extension curves of tethered bovine carbonic anhydrase B to the silicon substrate under native, intermediate and denaturing conditions. *Jpn. J. Appl. Phys. 1* 38, 3912–3917.

4 Carrion-Vazquez, M., Oberhauser, A. F., Fowler, S. B., Marszalek, P. E., Broedel, S. E., Clarke, J. & Fernandez, J. M. (1999). Mechanical and chemical unfolding of a single protein: A comparison. *Proc. Natl Acad. Sci. USA* 96, 3694–3699.

5 Brockwell, D. J., Beddard, G. S., Clarkson, J. et al. (2002). The effect of core destabilization on the mechanical resistance of I27. *Biophys. J.* 83, 458–472.

6 Steward, A., Toca-Herrera, J. L. & Clarke, J. (2002). Versatile cloning system for construction of multimeric proteins for use in atomic force microscopy. *Protein Sci.* 11, 2179–2183.

7 Best, R. B., Li, B., Steward, A., Daggett, V. & Clarke, J. (2001). Can non-mechanical proteins withstand force? Stretching barnase by atomic force microscopy and molecular dynamics simulation. *Biophys. J.* 81, 2344–2356.

8 Brockwell, D. J., Paci, E., Zinober, R. C. et al. (2003). Pulling geometry defines the mechanical resistance of a beta-sheet protein. *Nat. Struct. Biol.* 10, 731–737.

9 Yang, G., Cecconi, C., Baase, W. A. et al. (2000). Solid-state synthesis and mechanical unfolding of polymers of T4 lysozyme. *Proc. Natl Acad. Sci. USA* 97, 139–144.

10 Carrion-Vazquez, M., Li, H. B., Lu, H., Marszalek, P. E., Oberhauser, A. F. & Fernandez, J. M. (2003). The mechanical stability of ubiquitin is linkage dependent. *Nat. Struct. Biol.* 10, 738–743.

11 Oberhauser, A. F., Hansma, P. K., Carrion-Vazquez, M. & Fernandez, J. M. (2001). Stepwise unfolding of titin under force-clamp atomic force microscopy. *Proc. Natl Acad. Sci. USA* 98, 468–472.

12 Williams, P. M. (2003). Analytical descriptions of dynamic force spectroscopy: Behaviour of multiple connections. *Anal. Chim. Acta.* 479, 107–115.

13 Lenne, P. F., Raae, A. J., Altmann, S. M., Saraste, M. & Horber, J. K. H. (2000). States and transitions during forced unfolding of a single spectrin repeat. *FEBS Lett.* 476, 124–128.

14 Marszalek, P. E., Lu, H., Li, H. B., Carrion-Vazquez, M., Oberhauser, A. F., Schulten, K. & Fernandez, J. M. (1999). Mechanical unfolding intermediates in titin modules. *Nature* 402, 100–103.

15 Best, R. B., Brockwell, D. J., Toca-Herrera, J. L. et al. (2003). Force mode atomic force microscopy as a tool for protein folding studies. *Anal. Chim. Acta.* 479.

16 Evans, E. (2001). Probing the relation between force lifetime and chemistry in single molecular bonds. *Annu. Rev. Biophys. Biomol. Struct.* 30, 105–128.

17 Hanggi, P., Talkner, P. & Borkovec, M. (1990). Reaction-rate theory – 50 Years after Kramers. *Rev. Mod. Phys.* 62, 251–341.

18 Evans, E. & Ritchie, K. (1997). Dynamic strength of molecular adhesion bonds. *Biophys. J.* 72, 1541–1555.

19 Evans, E. & Williams, P. M. (2002). Dynamic force spectroscopy: I. Single bonds. In *Les Houches Session LXXV. Physics of bio-molecules and cells* (Flyvbjerg, H., Jülicher, F., Ormos, P., & David, F., Eds), pp. 145–186. Berlin: Springer-Verlag.

20 Evans, E. & Richie, K. (1999). Strength of a weak bond connecting flexible polymer chains. *Biophys. J.* 76, 2439–2447.

21 Patel, A. B., Allen, S., Davies, M. C., Roberts, C. J., Tendler, S. J. B. & Williams, P. M. (2004). Influence of architecture on the kinetic stability of

molecular assemblies. *J. Am. Chem. Soc.* 126, 1318–1319.

22 Zinober, R. C., Brockwell, D. J., Beddard, G. S. et al. (2002). Mechanically unfolding proteins: the effect of unfolding history and the supramolecular scaffold. *Protein Sci.* 22, 2759–2765.

23 Williams, P. M., Fowler, S. B., Best, R. B. et al. (2003). Hidden complexity in the mechanical properties of titin. *Nature* 422, 446–449.

24 Fowler, S. B., Best, R. B., Toca-Herrera, J. L. et al. (2002). Mechanical unfolding of a titin Ig domain: (1) Structure of unfolding intermediate revealed by combining molecular dynamic simulations, NMR and protein engineering. *J. Mol. Biol.* 322, 841–849.

25 Williams, P. M. A method to analyze bond rupture and protein unfolding forces. Manuscript submitted.

26 Li, H. B., Carrion-Vazquez, M., Oberhauser, A. F., Marszalek, P. E. & Fernandez, J. M. (2000). Point mutations alter the mechanical stability of immunoglobulin modules. *Nat. Struct. Biol.* 7, 1117–1120.

27 Rief, M., Fernandez, J. M. & Gaub, H. E. (1998). Elastically coupled two-level systems as a model for biopolymer extensibility. *Phys. Rev. Lett.* 81, 4764–4767.

28 Williams, P. M. & Evans, E. (2002). Dynamic force spectroscopy: II. Multiple bonds. In *Les Houches Session LXXV. Physics of bio-molecules and cells* (Flyvbjerg, H., Jülicher, F., Ormos, P., & David, F., Eds), pp. 187–204. Berlin: Springer-Verlag.

29 Press, W. H., Teukolsky, S. A., Vetterling, W. T. & Flannery, B. P. (1992). *Numerical recipes in C.* Cambridge: Cambridge University Press.

30 Best, R. B., Fowler, S. B., Toca-Herrera, J. L. & Clarke, J. (2002). A simple method for probing the mechanical unfolding pathway of proteins in detail. *Proc. Natl Acad. Sci. USA* 99, 12143–12148.

31 Fersht, A. R. (1998). *Structure and Mechanism in Protein Science: a Guide to Enzyme Catalysis and Protein Folding.* New York: W.H. Freeman.

32 Fersht, A. R., Matouschek, A. & Serrano, L. (1992). The folding of an enzyme. I. Theory of protein engineering analysis of stability and pathway of protein folding. *J. Mol. Biol.* 224, 771–782.

33 Klimov, D. K. & Thirumalai, D. (1999). Stretching single-domain proteins: Phase diagram and kinetics of force induced folding. *Proc. Natl Acad. Sci. USA* 96, 6166–6170.

34 Klimov, D. K. & Thirumalai, D. (2000). Native topology determines force induced unfolding pathways in globular proteins. *Proc. Natl Acad. Sci. USA* 97, 7254–7259.

35 Klimov, D. K. & Thirumalai, D. (2001). Lattice model studies of force-induced unfolding of proteins. *J. Phys. Chem. B* 105, 6648–6654.

36 Cieplak, M., Hoang, T. X. & Robbins, M. O. (2001). Thermal unfolding and mechanical unfolding oathways of protein secondary structures. *Proteins* 49, 104–113.

37 Lu, H., Isralewitz, B., Krammer, A., Vogel, V. & Schulten, K. (1998). Unfolding of titin immunoglobulin domains by steered molecular dynamics simulation. *Biophys. J.* 75, 662–671.

38 Lu, H. & Schulten, K. (2000). The key event in force-induced unfolding of titin's immunoglobulin domains. *Biophys. J.* 79, 51–65.

39 Craig, D., Gao, M., Schulten, K. & Vogel, V. (2004). Tuning the mechanical stability of fibronectin type III modules through sequence variations. *Structure* 12, 21–30.

40 Lu, H. & Schulten, K. (1999). Steered molecular dynamics simulation of conformational changes of immunoglobulin domain I27 interpret atomic force microscopy observations. *Chem. Phys.* 247, 141–153.

41 Paci, E. & Karplus, M. (2000). Unfolding proteins by external forces and temperature: The importance of topology and energetics. *Proc. Natl Acad. Sci. USA* 97, 6521–6526.

42 Best, R. B., Fowler, S. B., Toca-Herrera, J. L., Steward, A., Paci, E. & Clarke, J. (2003). Mechanical unfolding of a titin Ig domain: (2) Structure of transition state revealed by combining AFM, protein engineering and molecular dynamics simulations. *J. Mol. Biol.* 330, 867–877.

43 Pfuhl, M. & Pastore, A. (1995). Tertiary structure of an immunoglobulin-like domain from the giant muscle protein titin: a new member of the I set. *Structure* 3, 391–401.

44 Fowler, S. B. & Clarke, J. (2001). Mapping the folding pathway of an immunoglobulin domain: Structural detail from phi value analysis and movement of the transition state. *Structure* 9, 355–366.

45 Li, H., Oberhauser, A. F., Fowler, S. B., Clarke, J. & Fernandez, J. M. (2000). Atomic force microscopy reveals the mechanical design of a modular protein. *Proc. Natl Acad. Sci. USA* 92, 6527–6531.

46 Li, H. B., Linke, W. A., Oberhauser, A. F. et al. (2002). Reverse engineering of the giant muscle protein titin. *Nature*, 998–1002.

47 Oberhauser, A. F., Marszalek, P. E., Carrion-Vazquez, M. & Fernandez, J. M. (1999). Single protein misfolding events captured by atomic force microscopy. *Nat. Struct. Biol.* 6, 1025–1028.

48 Law, R., Carl, P., Harper, S., Dalhaimer, P., Speicher, D. W. & Discher, D. E. (2003). Cooperativity in forced unfolding of tandem spectrin repeats. *Biophys. J.* 84, 533–544.

32
Molecular Dynamics Simulations to Study Protein Folding and Unfolding

Amedeo Caflisch and Emanuele Paci

32.1
Introduction

Proteins in solution fold in time scales ranging from microseconds to seconds. A computational approach to folding that should work, in principle, is to use an atom-based model for the potential energy (force field) and to solve the time-discretized Newton equation of motion (molecular dynamics, MD [1]) from a denatured conformer to the native state in the presence of the appropriate solvent. With the available simulation protocols and computing power, such a trajectory would require approximately 10–100 years for a 100-residue protein where the experimental transition to the folded state takes place in about 1 ms. Hence, there is a clear problem related to time scales and sampling (statistical error). On the other hand, we think that current force fields, even in their most detailed and sophisticated versions, i.e., explicit water and accurate treatment of long-range electrostatic effects, are not accurate enough (systematic error) to be able to fold a protein on a computer. In other words, even if one could use a computer 100 times faster than the currently fastest processor to eliminate the time scale problem, most proteins would not fold to the native structure because of the large systematic error and the marginal stability of the folded state typically ranging from 5 to 15 kcal mol^{-1}. Interestingly, only designed peptides of about 20 residues have been folded by MD simulations (see Section 32.2.1) using mainly approximative models of the solvent (see Section 32.3.4). Alternatively, protein unfolding which is a simpler process than folding (e.g., the unfolding rate shows Arrhenius-like temperature dependence whereas folding does not because of the importance of entropy, see Section 32.2.1.2) can be simulated on shorter time scales (1–100 ns) at high temperature or by using a suitable perturbation.

MD simulations can provide the ultimate detail concerning individual atom motion as a function of time. Hence, future improvements in force fields and simulation protocols will allow specific questions about the folding of proteins to be addressed. The understanding at the atomic level of detail is important for a complicated reaction like protein folding and cannot easily be obtained by experiments. Yet, experimental approaches and results are essential in validating the force fields

Protein Folding Handbook. Part I. Edited by J. Buchner and T. Kiefhaber

ISBN: 3-527-30784-2

and simulation methods: comparison between simulation and experimental data is *conditio sine qua non* to validate the simulation results and very helpful for improving force fields.

This chapter cannot be comprehensive. Results obtained by using atom-based force fields and MD are presented whereas lattice models [2] as well as off-lattice coarse-grained models (e.g., one interaction center per residue) [3] are not mentioned because of size limitations. It is important to note that the impact of MD simulations of folding and unfolding is increasing thanks to faster computers, more efficient sampling techniques, and more accurate force fields as witnessed by several review articles [1, 4] and books [5–7].

32.2 Molecular Dynamics Simulations of Peptides and Proteins

32.2.1 Folding of Structured Peptides

Several comprehensive review articles on MD simulations of structured peptides have appeared recently [8–10]. Here, we first focus on simulation results obtained in our research group and then discuss the Trp-cage, a model system that has been investigated by others.

32.2.1.1 Reversible Folding and Free Energy Surfaces

***β*-Sheets** The reversible folding of two designed 20-residue sequences, beta3s and ^{D}PG, having the same three-stranded antiparallel *β*-sheet topology was simulated [11, 12] with an implicit model of the solvent based on the accessible surface area [13]. The solution conformation of beta3s (TWIQNGSTKWYQNGSTKIYT) has been studied by NMR [14]. Nuclear Overhauser enhancement spectroscopy (NOE) and chemical shift data indicate that at 10 °C beta3s populates a single structured form, the expected three-stranded antiparallel *β*-sheet conformation with turns at Gly6-Ser7 and Gly14-Ser15, (Figure 32.1) in equilibrium with the denatured state. The *β*-sheet population is 13–31% based on NOE intensities and 30–55% based on the chemical shift data [14]. Furthermore, beta3s was shown to be monomeric in aqueous solution by equilibrium sedimentation and NMR dilution experiments [14].

^{D}PG is a designed amino acid sequence (Ace-VFITS^{D}PGKTYTEV^{D}PG-Orn-KILQ-NH), where ^{D}P are D-prolines and Orn stands for ornithine. Circular dichroism and chemical shift data have provided evidence that ^{D}PG adopts the expected three-stranded antiparallel *β*-sheet conformation at 24 °C in aqueous solution [15]. Moreover, ^{D}PG was shown to be monomeric by equilibrium sedimentation. Although the percentage of *β*-sheet population was not estimated, NOE distance restraints indicate that both hairpins are highly populated at 24 °C.

In the MD simulations at 300 K (started from conformations obtained by spon-

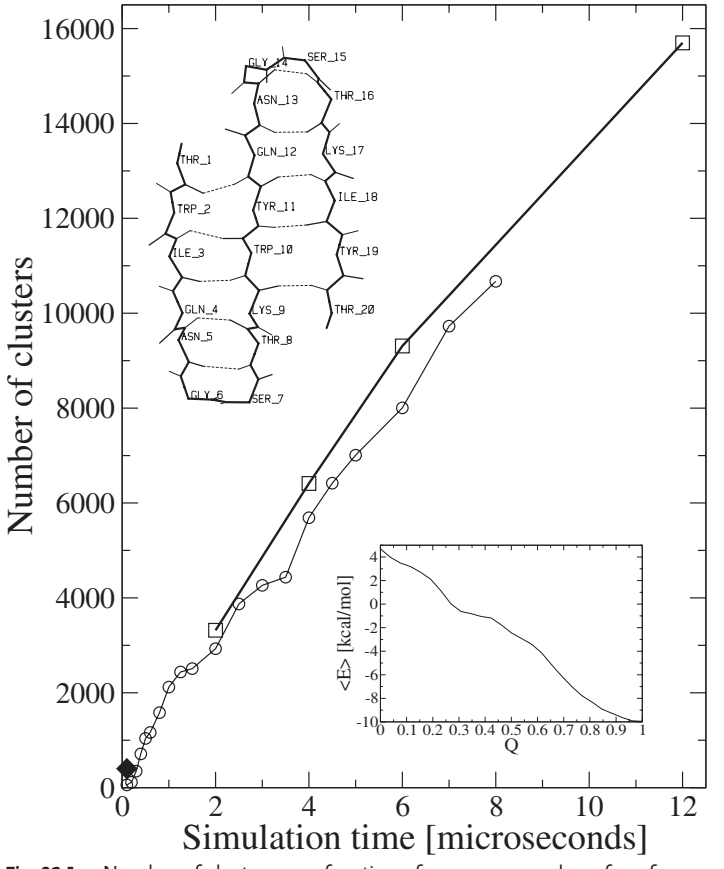

Fig. 32.1. Number of clusters as a function of time. The "leader" clustering procedure was used with a total of 120 000 snapshots saved every 0.1 ns (thick line and square symbols). The clustering algorithm which uses the Cα RMSD values between all pairs of structures was used only for the first 8 μs (80 000 snapshots) because of the computational requirements (thin line and circles). The diamond in the bottom left corner shows the average number of conformers sampled during the folding time which is defined as the average time interval between successive unfolding and refolding events. The insets show a backbone representation of the folded state of beta3s with main chain hydrogen bonds in dashed lines, and the average effective energy as a function of the fraction of native contacts Q which are defined in [11]. Figure from Ref. [33].

taneous folding at 360 K) both peptides satisfy most of the NOE distance restraints (3/26 and 4/44 upper distance violations for beta3s and ^{D}PG, respectively). At a temperature value of 360 K which is above the melting temperature of the model (330 K), a statistically significant sampling of the conformational space was obtained by means of around 50 folding and unfolding events for each peptide [11, 12]. Average effective energy and free energy landscape are similar for both peptides, despite the sequence dissimilarity. Since the average effective energy has a downhill profile at the melting temperature and above it, the free energy barriers

are a consequence of the entropic loss involved in the formation of a β-hairpin which represents two-thirds of the chain. The free energy surface of the β-sheet peptides is completely different from the one of a helical peptide of 31 residues, $Y(MEARA)_6$ (see below). For the helical peptide, the folding free energy barrier corresponds to the helix nucleation step, and is much closer to the fully unfolded state than for the β-sheet peptides. This indicates that the native topology determines to a large extent the free energy surface and folding mechanism. On the other hand, the ^{D}PG peptide has a statistically predominant folding pathway with a sequence of events which is the inverse of the one of the most frequent pathway for the beta3s peptide. Hence, the amino acid sequence and specific interactions between different side chains determine the most probable folding route [12].

It is interesting to compare with experimental results on two-state proteins. Despite a sequence identity of only 15%, the 57-residue IgG-binding domains of protein G and protein L have the same native topology. Their folded state is symmetric and consists mainly of two β-hairpins connected such that the resulting four-stranded β-sheet is antiparallel apart from the two central strands which are parallel [16]. The ϕ value analysis (see Section 32.2.3 for a definition of ϕ value) of protein L and protein G indicates that for proteins with symmetric native structure more than one folding pathway may be consistent with the native state topology and the selected route depends on the sequence [16]. Our MD simulation results for the two antiparallel three-stranded β-sheet peptides (whose sequence identity is also 15%) go beyond the experimental findings for protein G and L. The MD trajectories demonstrate the existence of more than one folding pathway for each peptide sequence [12]. Interestingly, Jane Clarke and collaborators [17] have recently provided experimental evidence for two different unfolding pathways using the anomalous kinetic behavior of the 27th immunoglobulin domain (β-sandwich) of the human cardiac muscle protein titin. They have interpreted the upward curvature in the denaturant-dependent unfolding kinetics as due to changes in the flux between transition states on parallel pathways. In the conclusion of their article [17] they leave open the question "whether what is unusual is not the existence of parallel pathways, but the fact that they can be experimentally detected and resolved."

α-Helices Richardson et al. [18] have analyzed the structure and stability of the synthetic peptide $Y(MEARA)_6$ by circular dichroism (CD) and differential scanning calorimetry (DSC). This repetitive sequence was "extracted" from a 60-amino-acid domain of the human CstF-64 polyadenylation factor which contains 12 nearly identical repeats of the consensus motif MEAR(A/G). The CD and DSC data were insensitive to concentration indicating that $Y(MEARA)_6$ is monomeric in solution at concentrations up to 2 mM. The far-UV CD spectrum indicates that the peptide has a helical content of about 65% at 1 °C. The DSC profiles were used to determine an enthalpy difference for helix formation of 0.8 kcal mol^{-1} per amino acid. The length of $Y(MEARA)_6$ makes it difficult to study helix formation by MD simulations with explicit water molecules. Therefore, multiple MD runs were performed with the same implicit solvation model used for the β-sheet peptides [13].

The simulation results indicate that the synthetic peptide $Y(MEARA)_6$ assumes a mainly α-helical structure with a nonnegligible content of π-helix [149]. This is not inconsistent with the currently available experimental evidence [18]. A significant π-helical content was found previously by explicit solvent molecular dynamics simulations of the peptides $(AAQAA)_3$ and $(AAKAA)_3$ [19], which provides further evidence that the π-helical content of $Y(MEARA)_6$ is not an artifact of the approximations inherent to the solvation model.

An exponential decay of the unfolded population is common to both $Y(MEARA)_6$ [149] and the 20-residue three-stranded antiparallel β-sheet [14] previously investigated by MD at the same temperature (360 K) [11]. The free energy surfaces of $Y(MEARA)_6$ and the antiparallel β-sheet peptide differ mainly in the height and location of the folding barrier, which in $Y(MEARA)_6$ is much lower and closer to the fully unfolded state. The main difference between the two types of secondary structure formation consists of the presence of multiple pathways in the α-helix and only two predominant pathways in the three-stranded β-sheet. The helix can nucleate everywhere, with a preference for the C-terminal third of the sequence in $Y(MEARA)_6$. Furthermore, two concomitant nucleation sites far apart in the sequence are possible. Folding of the three-stranded antiparallel β-sheet peptide beta3s started with the formation of most of the side chain contacts and hydrogen bonds between strands 2 and 3, followed by the 1–2 interstrand contacts. The inverse sequence of events, i.e., first formation of 1–2 and then 2–3 contacts was also observed, but less frequently [11].

The free energy barrier seems to have an important entropic component in both helical peptides and antiparallel β-sheets. In an α-helix, it originates from constraining the backbone conformation of three consecutive amino acids before the first helical hydrogen bond can form, while in the antiparallel β-sheet it is due to the constraining of a β-hairpin onto which a third strand can coalesce [11]. Therefore, the folding of the two most common types of secondary structure seems to have similarities (a mainly entropic nucleation barrier and an exponential folding rate) as well as important differences (location of the barrier and multiple vs. two pathways). The similarities are in accord with a plethora of experimental and theoretical evidence [20] while the differences might be a consequence of the fact that $Y(MEARA)_6$ has about 7–9 helical turns whereas the three-stranded antiparallel β-sheet consists of only two ''minimal blocks'', i.e., two β-hairpins.

32.2.1.2 Non-Arrhenius Temperature Dependence of the Folding Rate

Small molecule reactions show an Arrhenius-like temperature dependence, i.e., faster rates at higher temperatures. Protein folding is a complex reaction involving many degrees of freedom; the folding rate is Arrhenius-like at physiological temperatures, but deviates from Arrhenius behavior at higher temperatures [20].

To quantitatively investigate the kinetics of folding, MD simulations of two model peptides, Ace-$(AAQAA)_3$-$NHCH_3$ (α-helical stable structure) and Ace-$V_5{}^DPGV_5$-NH_2 (β-hairpin), were performed using the same implicit solvation model [13]. Folding and unfolding at different temperature values were studied by 862 simulations for a total of 4 μs [21]. Different starting conformations (folded

and random) were used to obtain a statistically significant sampling of conformational space at each temperature value. An important feature of the folding of both peptides is the negative activation enthalpy at high temperatures. The rate constant for folding initially increases with temperature, goes through a maximum at about T_m, and then decreases [21]. The non-Arrhenius behavior of the folding rate is in accord with experimental data on two mainly alanine α-helical peptides [22, 23], a β-hairpin [24], CI2, and barnase [25], lysozyme [26, 27], and lattice simulation results [28–30]. It has been proposed that the non-Arrhenius profile of the folding rate originates from the temperature dependence of the hydrophobic interaction [31, 32]. The MD simulation results show that a non-Arrhenius behavior can arise at high values of the temperature in a model where all the interactions are temperature independent. This has been found also in lattice simulations [28, 29]. The curvature of the folding rate at high temperature may be a property of a reaction dominated by enthalpy at low temperatures and entropy at high temperatures [30]. The non-Arrhenius behavior for a system where the interactions do not depend on the temperature might be a simple consequence of the temperature dependence of the accessible configuration space. At low temperatures, an increase in temperature makes it easier to jump over the energy barriers, which are rate limiting. However, at very high temperatures, a larger portion of the configuration space becomes accessible, which results in a slowing down of the folding process.

32.2.1.3 Denatured State and Levinthal Paradox

The size of the accessible conformational space and how it depends on the number of residues is not easy to estimate. To investigate the complexity of the denatured state four molecular dynamics runs of beta3s were performed at the melting temperature of the model (330 K) for a total simulation time of 12.6 μs [33]. The simulation length is about two orders of magnitude longer than the average folding or unfolding time (about 85 ns each), which are similar because at the melting temperature the folded and unfolded states are equally populated. The peptide is within 2.5 Å Cα root mean square deviation (RMSD) from the folded conformation about 48% of the time. Figure 32.1 shows the results of a cluster analysis based on Cα RMSD. There are more than 15 000 conformers (cluster centers) and it is evident that a plateau has not been reached within the 12.6 μs of simulation time. However, the number of significantly populated clusters (see Ref. [12] for a detailed description) converges already within 2 μs. Hence, the simulation-length dependence of the total number of clusters is dominated by the small ones. At each simulation interval between an unfolding event and the successive refolding event additional conformations are sampled. More than 90% of the unfolded state conformations are in small clusters (each containing less than 0.1% of the saved snapshots) and the total number of small clusters does not reach a plateau within 12.6 μs. Note that there is also a monotonic growth with simulation time of the number of snapshots in the folded-state cluster. After 12.6 μs (and also within each of the four trajectories) the system has sampled an equilibrium of folded and unfolded states despite a large part of the denatured state ensemble has not yet been explored. In fact, the average folding time converges to a value around 85 ns which

shows that the length of each simulation is much larger than the relaxation time of the slowest conformational change. Interestingly, in the average folding time of about 85 ns beta3s visits less than 400 clusters (diamond in Figure 32.1). This is only a small fraction of the total amount of conformers in the denatured state. It is possible to reconcile the fast folding with the large conformational space by analyzing the effective energy, which includes all of the contributions to the free energy except for the configurational entropy of the protein [11, 34]. Fast folding of beta3s is consistent with the monotonically decreasing profile of the effective energy (inset in Figure 32.1). Despite the large number of conformers in the denatured state ensemble, the protein chain efficiently finds its way to the folded state because native-like interactions are on average more stable than nonnative ones.

In conclusion, the unfolded state ensemble at the melting temperature is a large collection of conformers differing among each other, in agreement with previous high temperature molecular dynamics simulations [8, 35]. The energy "bias" which makes fast folding possible does not imply that the unfolded state ensemble is made up of a small number of statistically relevant conformations. The simulations provide further evidence that the number of denatured state conformations is orders of magnitudes larger than the conformers sampled during a folding event. This result also suggests that measurements which imply an average over the unfolded state do not necessarily provide information on the folding mechanism.

32.2.1.4 **Folding Events of Trp-cage**

Very small proteins are ideal systems to validate force fields and simulation methodology. Neidigh et al. [36] have truncated and mutated a marginally stable 39-residue natural sequence thereby designing a 20-residue peptide, the Trp-cage, that is more than 95% folded in aqueous solution at 280 K. The stability of the Trp-cage is due to the packing of a Trp side chain within three Pro rings and a Tyr side chain. Moreover, the C-terminal half contains four Pro residues which dramatically restrict the conformational space, i.e., entropy, of the unfolded state [36, 37].

Four MD studies have appeared in the 12 months following the publication of the Trp-cage structure [38–41]. All of the simulations were started from the completely extended conformation and used different versions of the AMBER force field and the generalized Born continuum electrostatic solvation model [42]. Two simulations were run with conventional constant temperature MD at 300 K [40] and 325 K [38], a third study used replica exchange MD with a range of temperatures from 250 K to 630 K [41], and in the fourth paper distributed computing simulations at 300 K with full water viscosity were reported [39].

An important problem of the three constant temperature studies is that the Trp-cage seems to fold to a very deep free energy minimum and no unfolding events have been observed [38–40]. Moreover, only one folding event is presented by Simmerling et al. [38] and Chowdhury et al. [40]. The poor statistics does not allow to draw any conclusions on free energy landscapes or on the folding mechanism of the Trp-cage.

Another potential problem is the discrepancy between the most stable state

sampled by MD and the NMR conformers. Only in two of the four MD studies NOE distance restraints were measured along the trajectories and about 20% were found to be violated [40, 41]. Moreover, as explicitly stated by the authors, the native state sampled by distributed computing contains a π-helix (instead of the α-helix) and the Trp is not packed correctly in the core [39]. These discrepancies are significant because the Trp-cage has a very small core and a rather rigid C-terminal segment.

32.2.2 Unfolding Simulations of Proteins

32.2.2.1 High-temperature Simulations

Since the early work of Daggett and Levitt [43] and Caflisch and Karplus [44], several other high-temperature simulation studies have been concerned with exploring protein unfolding pathways. Several comprehensive review articles exist on this simulation protocol [45] which has been widely used since. Recent MD simulations at temperatures of 100 °C and 225 °C of a three-helix bundle 61-residue protein, the engrailed homeodomain (En-HD), by Daggett and coworkers [46, 47] have been used to analyze a folding intermediate at atomic level of detail. The unfolding half-life of the En-HD at 100 °C has been extrapolated to be about 7.5 ns, a time scale that can be accessed by MD simulations with explicit water molecules.

Also, unfolding simulations in the presence of explicit urea molecules have shown that the protein (barnase) remains stable at 300 K but unfolds partially at moderately high temperature (360 K) [48]. The results suggested a mechanism for urea induced unfolding due to the interaction of urea with both polar and nonpolar groups of the protein.

32.2.2.2 Biased Unfolding

Because of the limitations on simulation times and height of the barriers to conformational transitions in proteins, a number of methods, alternative to the use of high, nonphysical temperatures, have been proposed to accelerate such transitions by the introduction of an external time-dependent perturbation [49–54]. The perturbation induce the reaction of interest in a reasonable amount of time (the strength of the perturbation is inversely proportional to the available computer time). These methods have been used for studying not only protein unfolding at native or realistic denaturing conditions, but also large conformational changes between known relevant conformers [51]. Their goal is to generate pathways which are realistic, in spite of the several orders of magnitude reduction in the time required for the conformational change. They are not alternatives to methods to compute free energy profiles along defined pathways. The external perturbation is usually applied to a function of the coordinates which is assumed to vary monotonically as the protein goes from the native to the nonnative state of interest. For certain perturbations the unfolding pathways obtained have been shown to depend on the nature of the perturbation and the choice of the reaction coordinate [52];

this is even more the case when the perturbation is strong and the reaction is induced too quickly for the system to relax along the pathway.

A perturbation which is particularly "gentle" since it exploits the intrinsic thermal fluctuations of the system and produces the acceleration by selecting the fluctuations that correspond to the motion along the reaction coordinate has also been used to unfold proteins [55, 56]. This perturbation has been employed, in particular, to expand α-lactalbumin by increasing its radius of gyration starting from the native state, and generate a large number of low-energy conformers that differ in terms of their root mean square deviation, for a given radius of gyration. The resulting structures were relaxed by unbiased simulations and used as models of the molten globule (see Chapter 23) and more unfolded denatured states of α-lactalbumin based on measured radii of gyration obtained from nuclear magnetic resonance experiments [57]. The ensemble of compact nonnative structures agree in their overall properties with experimental data available for the α-lactalbumin molten globule, showing that the native-like fold of the α-domain is preserved and that a considerable proportion of the antiparallel β-sheet in the β-domain is present. This indicated that the lack of hydrogen exchange protection found experimentally for the β-domain [58] is due to rearrangement of the β-sheet involving transient populations of nonnative β-structures in agreement with more recent infrared spectroscopy measurements [59]. The simulations also provide details concerning the ensemble of structures that contribute as the molten globule unfolds and shows, in accord with experimental data [60], that the unfolding is not cooperative, i.e., the various structural elements do not unfold simultaneously.

32.2.2.3 **Forced Unfolding**

Unfolding by stretching proteins individually has become routinely mainly thanks to the advent of the atomic force microscopy technology [61]. This peculiar way of unfolding proteins opened new perspectives on protein folding studies. Experiments are usually performed on engineered homopolyproteins, and the I27 domain from titin has become the reference system for this type of studies. Experiments measure force-extension profiles, and show typical "saw-tooth" profiles, where peaks are due to the sudden unfolding of individual domains, sequentially in time, causing a drop in the recorded force. These profiles are generally interpreted assuming that the unfolding event is determined by a single barrier which is decreased by the external force. For a detailed description of the experimental techniques and of the most recent results on forced unfolding of single molecules (by atomic force microscopy and optical tweezers) see Chapter 31.

To provide a structural interpretation of the typical saw-tooth-like spectra measured in single molecule stretching experiments, various simulation techniques have been proposed, where detailed all-atom models of proteins are stretched by pulling two atoms apart [62, 63], differing mainly in the way the solvent is treated.

In some cases simulation can effectively explain the force patterns measured (see Ref. [64] for a review). For all the proteins experimentally unfolded by pulling, only a simple saw-tooth pattern has been recorded related to the sudden unfolding

when the protein was pulled beyond a certain length, i.e., a simple two-state behavior. Simulations showed a more complex behavior [63] with possible intermediates on the forced unfolding pathways for certain proteins.[1]

Simulation has been used [65] to compare forced unfolding of two protein classes (all-β-sandwich proteins and all-α-helix bundle proteins). In particular, simulations suggested that different proteins should show a significantly different forced unfolding behavior, both within a protein class and for the different classes and dramatic differences between the unfolding induced by high temperature and by external pulling forces. The result was shown to be correlated to the type of perturbation, the folding topologies, the nature of the secondary and tertiary interactions and the relative stability of the various structural elements [65]. Improvements in the AFM technique combined with protein engineering methods have now confirmed (see Chapter 31) that chemical (or thermal) and forced unfolding occur through different pathways and that forced unfolding is related to crossing of a free energy barrier which might not be unique, but might change with force magnitude or upon specific mutations [66].

It should be borne in mind, however, that the forced unfolding of proteins is a nonequilibrium phenomenon strongly dependent on the pulling speed, and, since time scales in simulations and experiments are very different, the respective pathways need not to be the same. Recently, through a combination of experimental analysis and molecular dynamics simulations it has been shown that, in the case of mechanical unfolding, pathways might effectively be the same in a large range of pulling speeds or forces [67, 68], thus providing another demonstration of the robustness of the energy landscape (i.e., the funnel-like shape of the free energy surface sculpted by evolution is not affected by the application of even strong perturbations [69, 70]). In two recent papers [71, 72] it has been shown that proteins resist differently when pulled in different directions. In both cases the experiments have been complemented with simulations, with either explicit or implicit solvents. In both cases the behavior observed experimentally is qualitatively reproduced. This fact strongly suggests, although does not prove it, that in this particular case the forced unfolding mechanisms explored in the simulations is the same as that which determines the experimentally measured force.

Difference between solvation models is discussed in detail in Section 32.3.4 in the context of forced unfolding simulations, the disadvantage of an explicit solvation model [62, 72, 73] relative to an implicit [63, 65, 67, 68, 71] is not only that of being much slower, but also to provide an environment which relaxes slowly relative to the fast unraveling of the protein under force. Moreover, properly hydrating with explicit water a partially extended protein requires a large quantity of water, thus requiring a very large amount of CPU time for a single simulation. Implicit solvent models, on the other hand, allow unfolding to be performed at much lower

1) The presence of "late" intermediates on the forced unfolding pathway was first observed [63] in the 10th domain of fibronectin type III from fibronectin (FNfn3). A more complex pattern than equally spaced peaks in the force extension profile was predicted to arise from the presence of a kinetically metastable state. Most recent experimental results (J. Fernandez, personal communication) confirm the behavior predicted by the simulation.

forces (or pulling speeds) and multiple simulations to be used to study the dependence of the results on the initial conditions and/or on the applied force.

32.2.3 Determination of the Transition State Ensemble

The understanding of the folding mechanism has crucially advanced since the development of a method which provide information on the transition state [74] (see Chapter 13). The method allows the structure of the transition state at the level of single residue to be probed by measuring the change in folding and unfolding rates upon mutations. The method provides a so-called ϕ-value for each of the mutated residues which is a measure of the formation of native structure around the residue: a ϕ-value of 1 suggests that the residue is in a native environment at the transition state while a ϕ-value of 0 can be interpreted as a loss of the interactions of the residue at the transition state. Fractional ϕ-values are more difficult to interpret, but have been shown to arise from weakened interactions [75] and not from a mixture of species, some with fully formed and some with fully broken interaction.

As we discussed in Section 32.2.2.1, the use of high temperature makes it possible to observe the unfolding of a protein by MD on a time scale which can be simulated on current computers. Valerie Daggett and collaborators [76] first had the idea of performing a very high-temperature simulation and looking for a sudden change in the structure of the protein along the trajectory, indicating the escape from the native minimum of the free energy surface. The collections of structures around the ''jump'' were assumed to constitute a sample of the putative transition state. Assuming that the experimental ϕ-values correspond in microscopic terms to fraction of native contacts, they found a good agreement between calculated and experimental values. This approach was initially applied to the protein CI2, a small two-state proteins which has been probably the most thoroughly studied by experimental ϕ-value analysis; it has been subsequently improved and extended to the study of several proteins for which experimental ϕ-values were available (see Ref. [77] for review and other references).

Another related method has been used recently [78] to unfold a protein by high-temperature simulation (srcSH3 in the specific case) and determine a putative transition state by looking for conformations where the difference between calculated and experimental ϕ-values was smallest.

Both methods presented above have the advantage of providing structures extracted from an unfolding trajectory and thus the fast refolding or complete unfolding from these structures (a property of transition states) has been reported [78, 79]. But both approaches only provide few transition state structures, because a long simulation is required to generate each member of the transition state ensemble, while the transition state can be a quite broad ensemble for some proteins [80].

In a recent development, it has been shown that the amount of information that can be obtained from experimental measurements can be expanded further by

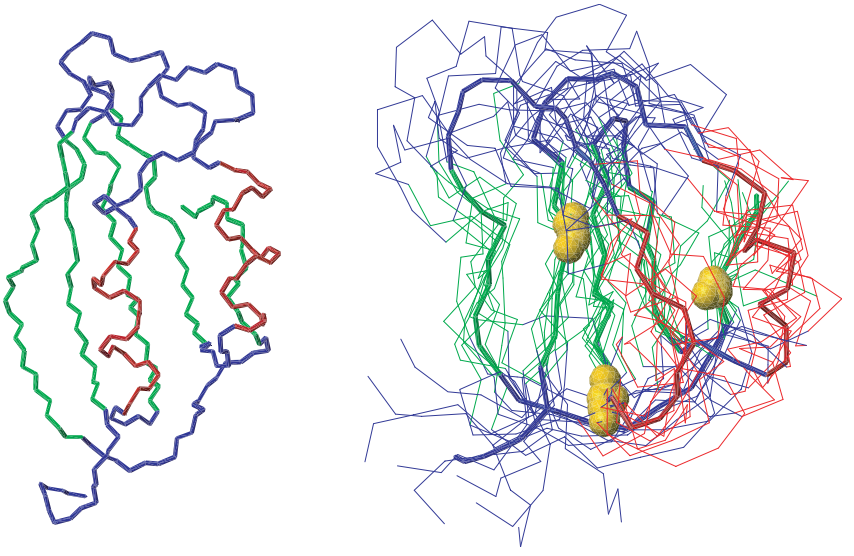

Fig. 32.2. Comparison between the native state structure (left) and the most representative structures of the transition state ensemble of AcP, determined by all-atom molecular dynamics simulations [82]. Native secondary structure elements are show in color (the two α-helices are plotted in red and the β-sheet in green). The three key residues for folding are shown as gold spheres [81, 82]. Figure from Ref. [69].

using the data to build up phenomenological energy functions to bias computer generated trajectories. With this approach (see Section 32.3.2 for a more detailed description of the technique), conformations compatible with experimental data are determined directly during the simulations [81, 82], rather than being obtained from filtering procedures such as those discussed above [78]. The incorporation of experimental data into the energy function creates a minimum in correspondence of the state observed experimentally and therefore allows for a very efficient sampling of conformational space. The transition state for folding of acylphosphatase (see Figure 32.2) was determined in this way [81, 82], showing that the network of interactions that stabilize the transition state is established when a few key residues form their native-like arrangement.

Based on this computational technique, a general approach in which theory and experiments are combined in an iterative manner to provide a detailed description of the transition state ensemble has been recently proposed [83]. In the first iteration, a coarse-grained determination of the transition state ensemble (TSE) is carried out by using a limited set of experimental ϕ-values as constraints in a molecular dynamics simulation. The resulting model of the TSE is used to determine the additional residues whose ϕ-value measurement would provide the most information for refining the TSE. Successive iterations with an increasing number of ϕ-value measurements are carried out until no further changes in the properties of the TSE are detected or there are no additional residues whose ϕ-values can be

measured. The method can be also used to find key residues for folding (i.e., those that are most important for the formation of the TSE).

The study of the transition state represents probably the most interesting example of how experiment and molecular dynamics simulations complement each other in understanding and visualizing the folding mechanisms in terms of relevant structures involved. Simulations are performed with approximate force fields and unfolding induced using artificial means (such as high temperature or other perturbations). At this stage in the development of MD simulations, the experiment provides evidence that what is observed in silico is consistent with what happens in vitro. On the other hand, and particularly in the case in which the full ensemble of conformations compatible with the experimental results is generated [82, 83], the simulation suggests further mutations to increase the resolution of the picture of the transition state, and allows detailed hypothesis of the mechanisms, such as the identity and structure of the residues involved in the folding nucleus [150].

32.3 MD Techniques and Protocols

32.3.1 Techniques to Improve Sampling

A thorough sampling of the relevant conformations is required to accurately describe the thermodynamics and kinetics of protein folding. Since the energetic and entropic barriers are higher than the thermal energy at physiological temperature, standard MD techniques often fail to adequately sample the conformational space. As already mentioned in this chapter, even for a small protein it is currently not yet feasible to simulate reversible folding with a high-resolution approach (e.g., MD simulations with an all-atom model). The practical difficulties in performing such brute force simulations have led to several types of computational approaches and/or approximative models to study protein folding. An interesting approach is to unfold starting from the native structure [84–86] but detailed comparison with experiments [47] is mandatory to make sure that the high-temperature sampling does not introduce artifacts. In addition, a number of approaches to enhance sampling of phase space have been introduced [87, 88]. They are based on adaptive umbrella sampling [89], generalized ensembles (e.g., entropic sampling, multicanonical methods, replica exchange methods) [90], modified Hamiltonians [91–93], multiple time steps [94], or combinations thereof.

32.3.1.1 Replica Exchange Molecular Dynamics

Replica exchange is an efficient way to simulate complex systems at low temperature and is the simplest and most general form of simulated tempering [95]. Sugita and Okamoto have been the first to extend the original formulation of replica exchange into an MD-based version (REMD), testing it on the pentapeptide Met-

enkephalin in vacuo [96]. The basic idea of REMD is to simulate different copies (replicas) of the system at the same time but at different temperatures values.

We recently applied a REMD protocol to implicit solvent simulations of a 20-residue three-stranded antiparallel β-sheet peptide (beta3s) [97]. Each replica evolves independently by MD and every 1000 MD steps (2 ps), states i, j with neighbor temperatures are swapped (by velocity rescaling) with a probability $w_{ij} = \exp(-\Delta)$ [96], where $\Delta \equiv (\beta_i - \beta_j)(E_j - E_i)$, $\beta = 1/kT$ and E is the potential energy. During the 1000 MD steps the Berendsen thermostat [98] is used to keep the temperature close to a given value. This rather tight coupling and the length of each MD segment (2 ps) allow the kinetic and potential energy of the system to relax. High temperature simulation segments facilitate the crossing of the energy barriers while the low-temperature ones explore in detail the conformations present in the minimum energy basins. The result of this swapping between different temperatures is that high-temperature replicas help the low-temperature ones to jump across the energy barriers of the system. In the beta3s study eight replicas were used with temperatures between 275 and 465 K [97].

The higher the number of degrees of freedom in the system the more replicas should be used. It is not clear how many replicas should be used if a peptide or protein is simulated with explicit water. The transition probability between two temperatures depends on the overlap of the energy histograms. The histograms' width depends on $1/\sqrt{N}$ (where N is the size of the system). Hence, the number of replicas required to cover a given temperature range increases with the size. Moreover, in order to have a random walk in temperature space (and then a random walk in energy space which enhances the sampling), all the temperature exchanges should occur with the same probability. This probability should be at least of 20–30%. To optimize the efficiency of the method, one should find the best compromise between the number of replicas to be used, the temperature space to cover and the acceptance ratios for temperature exchanges. In the literature there is no clear indication about the selection of temperatures and empirical methods are usually applied (weak point of the method). The choice of the boundary temperatures depends on the system under study. The highest temperature has to be chosen in order to overcome the highest energy barriers (probably higher in explicit water) separating different basins; the lowest temperature to investigate the details of the different basins.

Sanbonmatsu and Garcia have applied REMD to investigate the structure of Met-enkephalin in explicit water [99] and the α-helical stabilization by the arginine side chain which was found to originate from the shielding of main-chain hydrogen bonds [100]. Furthermore, the energy landscape of the C-terminal β-hairpin of protein G in explicit water has been investigated by REMD [101, 102]. Recently, a multiplexed approach with multiple replicas for each temperature level has been applied to large-scale distributed computing of the folding of a 23-residue miniprotein [103]. Starting from a completely extended chain, conformations close to the NMR structures were reached in about 100 trajectories (out of a total of 4000) but no evidence of reversible folding (i.e., several folding and unfolding events in the same trajectory) was presented [103].

32.3.1.2 Methods Based on Path Sampling

A very promising computational method, called transition path sampling (reviewed in Ref. [104]) has been recently used [105] to study the folding of a β-hairpin in explicit solvent. The method allows in principle the study of rare events (such as protein folding) without requiring knowledge of the mechanisms, reaction coordinates, and transition states. Transition path sampling focuses on the sampling not of conformations but of trajectories linking two conformations or regions (possibly basins of attraction) in the conformational space. Other methods focus on building ensemble of paths connecting states; the stochastic path approach [106] and the reaction path method [107] have been also used to study the folding of peptides and small proteins in explicit solvent. The stochastic path ensemble and the reaction path methods introduce a bias in the computed trajectories but allow the exploration of long time scales. All the methods mentioned above are promising but rely on the choice of a somewhat arbitrary initial unfolded conformation beside the final native one.

32.3.2 MD with Restraints

A method to generate structures belonging to the TSE ensemble discussed in Section 32.2.3 consists in performing molecular dynamics simulations restrained with a pseudo-energy function based on the set of experimental ϕ-values. The ϕ-values are interpreted as the fraction of native contacts present in the structures that contribute to the TSE. With this restraint the TSE becomes the most stable state on the potential energy surface rather than being an unstable region, as it is for the true energy function of the protein. This procedure is conceptually related to that used to generate native state structures compatible with measurements from nuclear magnetic resonance (NMR) experiments, in that pseudo-energy terms involving experimental restraints are added to the protein force field [108, 109]. The main difference is that an approach is required to sample a broad state compatible with some experimental restraints, rather than a method to search for an essentially unique native structure.

The method is based on molecular dynamics simulations using an all-atom model of the protein [110, 111] and an implicit model for the solvent [112] with an additional term in the energy function:

$$\rho = \frac{1}{N_\phi} \sum_{i \in E} (\phi_i - \phi_i^{\exp})^2 \tag{1}$$

where E is the list of the N_ϕ available experimental ϕ-values, $\phi_i^{\exp}$. The ϕ_i-value of amino acid i in the conformation at time t is defined as

$$\phi_i(t) = \frac{N_i(t)}{N_i^{\text{nat}}} \tag{2}$$

where $N_i(t)$ is the number of native contacts of i at time t and N_i^{nat} the number of native contacts of i in the native state.

Molecular dynamics simulations are then performed to sample all the possible structures compatible with the restraints. The structures thus generated are not necessarily at the transition state for folding for the potential used. They provide instead a structural model of the experimental transition state, including all possible structures compatible with the restraints derived from the experiment. The experimental information provided by the ϕ-values might not be enough to restrain the sampling to meaningful structures (e.g., when only few mutations have been performed). In such circumstance, other experimentally measured quantities, such as the m-value, which is related to the solvent accessible surface, must be used to restrain the sampling or to a posteriori select meaningful structures.

This type of computational approach relies on the assumption implicit in Eq. (2). This consists in approximating a ϕ-value, measured as a ratio of free energy variations upon mutation, as a ratio of side-chain contacts. A definition based on side-chains is appropriate since experimental ϕ-values are primarily a measure of the loss of side-chain contacts at the transition state, relative to the native state. Although simply counting contacts, rather than calculating their energies, is a crude approximation [113], it has been shown that there is a good correlation between loss of stability and loss of side-chain contacts within about 6 Å on mutation [114]. Also, Shea et al. [115] have found in their model calculations that this approximation for estimating ϕ-values from structures is a good one under certain conditions. A more detailed relation between experimental ϕ-values and atomic contacts could in principle be established by using the energies of the all-atom contacts made by the side chain of the mutated amino acid.

The same approach can be extended to generate the structures corresponding to other unfolded or intermediate states as the site-specific information provided by the experiment is steadily increasing (see Chapters 20 and 21).

32.3.3 Distributed Computing Approach

As mentioned in the introduction, the problem of simulating the folding process of any sequence from a random conformation is mainly a problem of potentials and computer time. Duan and Kollman [116] have showed that a huge effort in parallelizing (on a medium-scale, 256 processors) an MD code and exploiting for several months a several million dollars computer (a Cray T3E) could lead to the simulation of 1 μs of the small protein villin headpiece. Even approaching the typical experimental folding times (which is, however, larger than 1 ms for most proteins), a statistical characterization of the folding process is still impossible in the foreseeable future.

Developing a large-scale parallelization method seems the most viable approach, as the cost of fast CPUs decreases steadily and their performances approach those of much more expensive mainframes. Time being sequential, MD codes are not massively parallelizable in an efficient way. A good scaling is usually obtained for

large systems with explicit water and a relatively small number of processors (between 2 and 100, depending on the program and the problem studied). One approach has been proposed that allows the scalability of a MD simulation to be pushed to the level of being able to use efficiently a network of heterogeneous and loosely connected computer [117]. The approach (called distributed computing) exploits the stochastic nature of the folding process. In general protein folding involves the crossing of free energy barriers. The approach is most easily understood assuming that the proteins have a single barrier and a single exponential kinetic (which is the case for a large number of small proteins [118]). The probability that a protein is folded after a time t is $P(t) = 1 - \exp(-kt)$, where k is the folding rate. Thus, for short times, and considering M proteins or independent simulations, the probability of observing a folding event is Mkt. So, if M is large, there is a sizable probability of observing a folding event on simulations much shorter than the time constant of the folding process [119]. The folding rate could then in principle be estimated by running M independent simulations (starting from the completely extended conformation with different random velocities) for a time t and counting the number N of simulations which end up in the folded state as $k = N/(Mt)$. Simulations have been reported where the folding rate estimated in this way (assuming that partial refolding counts as folding) is in good agreement with the experimental one (see, for example, Ref. [39]).

However, it has been argued [120] that even for simple two-state proteins, folding has a series of early conformational steps that lead to lag phases at the beginning of the kinetics. Their presence can bias short simulations toward selecting minor pathways that have fewer or faster lag steps and so miss the major folding pathways. This fact has been clearly observed by comparing equilibrium and fast folding trajectories simulations [121] for a 20-residue three-stranded antiparallel β-sheet peptide (beta3s). It was found that the folding rate is estimated correctly by the distributed computing approach when trajectories longer than a fraction of the equilibrium folding time are considered; in the case of the 20-residue peptide studied within the frictionless implicit solvation model used for the simulations, this time is about 1% of the average folding time at equilibrium. However, careful analysis of the folding trajectories showed that the fastest folding events occur through high-energy pathways, which are unlikely under equilibrium conditions (see Section 32.2.1.1). Along these very fast folding pathways the peptide does not relax within the equilibrium denatured state which is stabilized by the transient presence of both native and nonnative interactions. Instead, collapse and formation of native interactions coincides and, unlike at equilibrium, the formation of the two β-hairpins is nearly simultaneous.

These results demonstrate that the ability to predict the folding rate does not imply that the folding mechanisms are correctly characterized: the fast folding events occur through a pathway that is very unlikely at equilibrium. However, extending the time scale of the short simulations to 10% of the equilibrium folding time, the folding mechanism of the fast folding events becomes almost indistinguishable from equilibrium folding events. It must be stressed that this result is not general but concerns the specific peptide studied; the explicit presence of sol-

vent molecule (and the consequent friction), might decrease the differences between equilibrium and shortest folding events. Unfortunately, this kind of validation of the distributed computing approach is not possible for a generic protein in a realistic solvent, as equilibrium simulations are not feasible.

An alternative method to use many processors simultaneously to access time scales relevant in the folding process by MD simulations has recently been proposed by Settanni et al. [122]. The method is based on parallel MD simulations that are started from the denatured state; trajectories are periodically interrupted, and are restarted only if they approach the transition (or some other target) state. In other words, the method choses trajectories along which a cost function decreases. The effectiveness of such an approach was shown by determining the transition state for folding an SH3 domain using as cost function the deviation between experimental and computed ϕ-values (Eq. (1) in Section 32.3.2). The method can efficiently use a large number of computers simultaneously because simulations are loosely coupled (i.e., only the comparison between final conformations, needed periodically to choose which trajectory to restart, involve communications between CPUs). This method can also be extended to complex nondifferentiable cost functions.

32.3.4
Implicit Solvent Models versus Explicit Water

Incorporating solvent effects in MD and Monte-Carlo simulations is of key importance in quantitatively understanding the chemical and physical properties of biomolecular processes. Accurate electrostatic energies of proteins in an aqueous environment are needed in order to discriminate between native and nonnative conformations. An exact evaluation of electrostatic energies considers the interactions among all possible solute–solute, solute–solvent, and solvent–solvent pairs of charges. However, this is computationally expensive for macromolecules. Continuum dielectric approximations offer a more tractable approach [123–127]. The essential concept in continuum models is to represent the solvent by a high dielectric medium, which eliminates the solvent degrees of freedom, and to describe the macromolecule as a region with a low dielectric constant and a spatial charge distribution. The Poisson equation provides an exact description of such a system. The increase in computation speed for a finite difference solution of the Poisson equation [128–131] with respect to an explicit treatment of the solvent is remarkable but still not enough for effective utilization in computer simulations of macromolecules. The generalized Born (GB) model was introduced to facilitate an efficient evaluation of continuum electrostatic energies [42]. It provides accurate energetics and the most efficient implementations are between five and ten times slower than in vacuo simulations [132–134]. The essential element of the GB approach is the calculation of an effective Born radius for each atom in the system which is a measure of how deeply the atom is buried inside the protein. This information is combined in a heuristic way to obtain a correction to the Coulomb law for each atom pair [42]. For the integration of energy density, necessary to obtain the effective Born radii, both numerical [42, 132, 135] and analytical [134, 136, 137]

implementations exist. The former are more accurate but slower than the latter [135]. Moreover, analytical derivatives that are required for MD simulations are not given by numerical implementations.

For efficiency reasons empirical dielectric screening functions are the most common choice in MD simulations with implicit solvent. One kind of solvation model is based on the use of a dielectric function that depends linearly on the distance r between two charges ($\varepsilon(r) = \alpha r$) [138, 139] or has a sigmoidal shape [140, 141]. Although very fast, these options suffer from their inability to discriminate between buried and solvent exposed regions of a macromolecule and are therefore rather inaccurate. A distance and exposure dependent dielectric function has been proposed [142]. Recently, an approach based on the distribution of solute atomic volumes around pairs of charges in a macromolecule has been proposed to calculate the effective dielectric function of proteins in aqueous solution [143].

The simulation results presented in Section 32.2.1 were obtained using an implicit solvent model based on a fast analytical approximation of the solvent accessible surface (SAS) [13] and the CHARMM force field [110]. The former drastically reduces the computational cost with respect to an explicit solvent simulation. The SAS model is based on the approximation proposed by Lazaridis and Karplus [112] for dielectric shielding due to the solvent, and the surface area model for the hydrophobic effect introduced by Eisenberg and McLachlan [144]. Electrostatic screening effects are approximated by a distance-dependent dielectric function and a set of partial charges with neutralized ionic groups [112]. An approximate analytical expression [145] is employed to calculate the SAS because an exact analytical or numerical computation of the SAS is too slow to compete with simulations in explicit solvent. The SAS model is based on the assumptions that most of the solvation energy arises from the first water shell around the protein [144] and that two atomic solvation parameters are sufficient to describe these effects at a qualitative level of accuracy. Within these assumptions, the SAS energy term approximates the solute–solvent interactions (i.e., it should account for the energy of cavity formation, solute–solvent dispersion interactions, and the direct (or Born) solvation of polar groups). The two atomic solvation parameters were optimized by performing 1 ns MD simulations at 300 K on six small proteins [13]. It is important to underline that the structured peptides discussed in Section 32.2.1 were not used for the calibration of the SAS atomic solvation parameters. The SAS model is a good approximation for investigating the folded and denatured state (large ensemble of conformers) of structured peptides. Its limitations, in particular for highly charged peptides and large proteins, have been discussed [13].

The most detailed and physically sound approaches (e.g., explicit solvent and particle mesh Ewald treatment of the long-range electrostatic interactions [146]) are still approximations and might introduces artifacts (see, for example, Ref. [147]). All solvation models, even those computationally most expensive, are approximations and their range of validity is difficult to explore. It is likely that most proteins will unfold fast relative to the experimental time scale if one could afford long (e.g., 100 ns) explicit water MD simulations even at room temperature. Some evidence of this instability has been recently published [148].

32.4 Conclusion

It is a very exciting time for studying protein folding using multidisciplinary approaches rooted in physics, chemistry, and computer science. The time scale gap between folding in vitro and in silico is being continuously reduced and this will bring interesting surprises. We expect an increasing role of MD simulations in the elucidation of protein folding thanks to further improvements in force fields and solvation models.

References

1 Karplus, M. & McCammon, J. A. (2002). Molecular dynamics simulations of biomolecules. *Nature Struct. Biol.* **9**, 646–652.

2 Dill, K. A. & Chan, H. S. (1997). From Levinthal to pathways to funnels. *Nature Struct. Biol.* **4**, 10–19.

3 Mirny, L. & Shakhnovich, E. (2001). Protein folding theory: From lattice to all-atom models. *Annu. Rev. Biophys. Biomol. Struct.* **30**, 361–396.

4 Daggett, V. & Fersht, A. R. (2003). Is there a unifying mechanism for protein folding? *Trends Biochem. Sci.* **28**, 18–25.

5 Creighton, T. E. (1992). *Protein Folding*. W. H. Freeman & Co., New York.

6 Merz Jr, K. M. & LeGrand, S. M. (1994). *The Protein Folding Problem and Tertiary Structure Prediction*. Birkhäuser, Boston.

7 Pain, R. H., ed. (2000). *Mechanisms of Protein Folding*. Oxford University Press, Oxford.

8 Shea, J. E. & Brooks III, C. L. (2001). From folding theories to folding proteins: A review and assessment of simulation studies of protein folding and unfolding. *Annu. Rev. Phys. Chem.* **52**, 499–535.

9 Galzitskaya, O. V., Higo, J. & Finkelstein, A. V. (2002). α-helix and β-hairpin folding from experiment, analytical theory and molecular dynamics simulations. *Curr. Protein Pept. Sci.* **3**, 191–200.

10 Gnanakaran, S., Nymeyer, H., Portman, J., Sanbonmatsu, K. Y. & Garcia, A. E. (2003). Peptide folding simulations. *Curr. Opin. Struct. Biol.* **13**, 168–174.

11 Ferrara, P. & Caflisch, A. (2000). Folding simulations of a three-stranded antiparallel β-sheet peptide. *Proc. Natl Acad. Sci. USA* **97**, 10780–10785.

12 Ferrara, P. & Caflisch, A. (2001). Native topology or specific interactions: What is more important for protein folding? *J. Mol. Biol.* **306**, 837–850.

13 Ferrara, P., Apostolakis, J. & Caflisch, A. (2002). Evaluation of a fast implicit solvent model for molecular dynamics simulations. *Proteins* **46**, 24–33.

14 de Alba, E., Santoro, J., Rico, M. & Jimenez, M. A. (1999). De novo design of a monomeric three-stranded antiparallel β-sheet. *Protein Sci.* **8**, 854–865.

15 Schenck, H. L. & Gellman, S. H. (1998). Use of a designed triple-stranded antiparallel β-sheet to probe β-sheet cooperativity in aqueous solution. *J. Am. Chem. Soc.* **120**, 4869–4870.

16 McCallister, E. L., Alm, E. & Baker, D. (2000). Critical role of β-hairpin formation in protein G folding. *Nature Struct. Biol.* **7**, 669–673.

17 Wright, C. F., Lindorff-Larsen, K., Randles, L. G. & Clarke, J. (2003). Parallel protein-unfolding pathways

revealed and mapped. *Nature Struct. Biol.* **10**, 658–662.

18 Richardson, J. M., McMahon, K. W., MacDonald, C. C. & Makhatadze, G. I. (1999). MEARA sequence repeat of human CstF-64 polyadenylation factor is helical in solution. A spectroscopic and calorimetric study. *Biochemistry* **38**, 12869–12875.

19 Shirley, W. A. & Brooks III, C. L. (1997). Curious structure in ''canonical'' alanine-based peptides. *Proteins* **28**, 59–71.

20 Karplus, M. (2000). Aspects of protein reaction dynamics: Deviations from simple behavior. *J. Phys. Chem. B* **104**, 11–27.

21 Ferrara, P., Apostolakis, J. & Caflisch, A. (2000). Thermodynamics and kinetics of folding of two model peptides investigated by molecular dynamics simulations. *J. Phys. Chem. B* **104**, 5000–5010.

22 Clarke, D. T., Doig, A. J., Stapley, B. J. & Jones, G. R. (1999). The α-helix folds on the millisecond time scale. *Proc. Natl Acad. Sci. USA* **96**, 7232–7237.

23 Lednev, I. K., Karnoup, A. S., Sparrow, M. C. & Asher, S. A. (1999). α-Helix peptide folding and unfolding activation barriers: A nanosecond UV resonance raman study. *J. Am. Chem. Soc.* **121**, 8074–8086.

24 Muñoz, V., Thompson, P. A., Hofrichter, J. & Eaton, W. A. (1997). Folding dynamics and mechanism of β-hairpin formation. *Nature* **390**, 196–199.

25 Oliveberg, M., Tan, Y. J. & Fersht, A. R. (1995). Negative activation enthalpies in the kinetics of protein folding. *Proc. Natl Acad. Sci. USA* **92**, 8926–8929.

26 Segawa, S. & Sugihara, M. (1984). Characterization of the transition state of lysozyme unfolding. I. Effect. *Biopolymers* **23**, 2473–2488.

27 Matagne, A., Jamin, M., Chung, E. W., Robinson, C. V., Radford, S. E. & Dobson, C. M. (2000). Thermal unfolding of an intermediate is associated with non-Arrhenius kinetics in the folding of hen lysozyme. *J. Mol. Biol.* **297**, 193–210.

28 Karplus, M., Caflisch, A., Sali, A. & Shakhnovich, E. (1995). Protein dynamics: From the native to the unfolded state and back again. In *Modelling of Biomolecular Structures and Mechanisms* (Pullman, A., Jortner, J. & Pullman, B., eds), pp. 69–84, Kluwer Academic, Dordrecht, The Netherlands.

29 Karplus, M. (1997). The Levinthal paradox: Yesterday and today. *Folding Des.* **2**, S69–S75.

30 Dobson, C. M., Sali, A. & Karplus, M. (1998). Protein folding: A perspective from theory and experiment. *Angew. Chem. Int. Ed.* **37**, 868–893.

31 Scalley, M. L. & Baker, D. (1997). Protein folding kinetics exhibit an Arrhenius temperature dependence when corrected for the temperature dependence of protein stability. *Proc. Natl Acad. Sci. USA* **94**, 10636–10640.

32 Chan, H. S. & Dill, K. A. (1998). Protein folding in the landscape perspective: Chevron plots and non-Arrhenius kinetics. *Proteins* **30**, 2–33.

33 Cavalli, A., Haberthür, U., Paci, E. & Caflisch, A. (2003). Fast protein folding on downhill energy landscape. *Protein Sci.* **12**, 1801–1803.

34 Dinner, A. R., Sali, A., Smith, L. J., Dobson, C. M. & Karplus, M. (2000). Understanding protein folding via free-energy surfaces from theory and experiment. *Trends Biochem. Sci.* **25**, 331–339.

35 Wong, K. B., Clarke, J., Bond, C. J. et al. (2000). Towards a complete description of the structural and dynamic properties of the denatured state of barnase and the role of residual structure in folding. *J. Mol. Biol.* **296**, 1257–1282.

36 Neidigh, J. W., Fesinmeyer, R. M. & Andersen, N. H. (2002). Designing a 20-residue protein. *Nature Struct. Biol.* **9**, 425–430.

37 Gellman, S. H. & Woolfson, D. N. (2002). Mini-proteins Trp the light

fantastic. *Nature Struct. Biol.* **9**, 408–410.

38 Simmerling, C., Strockbine, B. & Roitberg, A. E. (2002). All-atom structure prediction and folding simulations of a stable protein. *J. Am. Chem. Soc.* **124**, 11258–11259.

39 Snow, C. D., Zagrovic, B. & Pande, V. S. (2002). The Trp cage: Folding kinetics and unfolded state topology via molecular dynamics simulations. *J. Am. Chem. Soc.* **124**, 14548–14549.

40 Chowdhury, S., Lee, M. C., Xiong, G. & Duan, Y. (2003). Ab initio folding simulation of the Trp-cage mini-protein approaches NMR resolution. *J. Mol. Biol.* **327**, 711–717.

41 Pitera, J. W. & Swope, W. (2003). Understanding folding and design: replica-exchange simulations of "Trp-cage" miniproteins. *Proc. Natl Acad. Sci. USA* **100**, 7587–7592.

42 Still, W. C., Tempczyk, A., Hawley, R. C. & Hendrickson, T. (1990). Semianalytical treatment of solvation for molecular mechanics and dynamics. *J. Am. Chem. Soc.* **112**, 6127–6129.

43 Daggett, V. & Levitt, M. (1993). Protein unfolding pathways explored through molecular dynamics simulations. *J. Mol. Biol.* **232**, 600–619.

44 Caflisch, A. & Karplus, M. (1994). Molecular dynamics simulation of protein denaturation: Solvation of the hydrophobic cores and secondary structure of barnase. *Proc. Natl Acad. Sci. USA* **91**, 1746–1750.

45 Daggett, V. & Fersht, A. (2003). Opinion: The present view of the mechanism of protein folding. *Nature Rev. Mol. Cell Biol.* **4**, 497–502.

46 Mayor, U., Johnson, C. M., Daggett, V. & Fersht, A. R. (2000). Protein folding and unfolding in microseconds to nanoseconds by experiment and simulation. *Proc. Natl Acad. Sci. USA* **97**, 13518–13522.

47 Mayor, U., Guydosh, N. R., Johnson, C. M. et al. (2003). The complete folding pathway of a protein from nanoseconds to microseconds. *Nature* **421**, 863–867.

48 Caflisch, A. & Karplus, M. (1999). Structural details of urea binding to barnase: A molecular dynamics analysis. *Structure* **7**, 477–488.

49 Hao, M.-H., Pincus, M. R., Rachovsky, S. & Scheraga, H. A. (1993). Unfolding and refolding of the native structure of bovine pancreatic trypsin inhibitor studied by computer simulations. *Biochemistry* **32**, 9614–9631.

50 Harvey, S. C. & Gabb, H. A. (1993). Conformational transition using molecular dynamics with minimum biasing. *Biopolymers* **33**, 1167–1172.

51 Schlitter, J., Engels, M., Kruger, P., Jacoby, E. & Wollmer, A. (1993). Targeted molecular dynamics simulation of conformational change. Application to the TR transition in insulin. *Mol. Simulations* **10**, 291–308.

52 Hünenberger, P. H., Mark, A. E. & van Gunsteren, W. F. (1995). Computational approaches to study protein unfolding: Hen egg white lysozyme as a case study. *Proteins* **21**, 196–213.

53 Ferrara, P., Apostolakis, J. & Caflisch, A. (2000). Computer simulations of protein folding by targeted molecular dynamics. *Proteins* **39**, 252–260.

54 Ferrara, P., Apostolakis, J. & Caflisch, A. (2000). Targeted molecular dynamics simulations of protein unfolding. *J. Phys. Chem. B* **104**, 4511–4518.

55 Paci, E., Smith, L. J., Dobson, C. M. & Karplus, M. (2001). Exploration of partially unfolded states of human α-lactalbumin by molecular dynamics simulation. *J. Mol. Biol.* **306**, 329–347.

56 Marchi, M. & Ballone, P. (1999). Adiabatic bias mlecular dynamics: A method to navigate the conformational space of complex molecular systems. *J. Chem. Phys.* **110**, 3697–3702.

57 Wilkins, D. K., Grimshaw, S. B., Receveur, V., Dobson, C. M., Jones, J. A. & Smith, L. J. (1999). Hydrodynamic radii of native and denatured proteins measured by pulse NMR techniques. *Biochemistry* **38**, 16424–16431.

58 Kuwajima, K. (1996). The molten globule state of α-lactalbumin. *FASEB J.* **10**, 102–109.

59 Troullier, A., Reinstädler, D., Dupont, Y., Naumann, D. & Forge, V. (2000). Transient nonnative secondary structures during the refolding of α-lactalbumin by infrared spectroscopy. *Nature Struct. Biol.* **7**, 78–86.

60 Schulman, B., Kim, P. S., Dobson, C. M. & Redfield, C. (1997). A residue-specific NMR view of the non-cooperative unfolding of a molten globule. *Nature Struct. Biol.* **4**, 630–634.

61 Rief, M., Gautel, M., Oesterhelt, F., Fernandez, J. M. & Gaub, H. E. (1997). Reversible unfolding of individual titin immunoglobulin domains by AFM. *Science* **276**, 1109–1112.

62 Lu, H., Isralewitz, B., Krammer, A., Vogel, V. & Schulten, K. (1998). Unfolding of titin immunoglobulin domains by steered molecular dynamics simulation. *Biophys. J.* **75**, 662–671.

63 Paci, E. & Karplus, M. (1999). Forced unfolding of fibronectin type 3 modules: An analysis by biased molecular dynamics simulations. *J. Mol. Biol.* **288**, 441–459.

64 Isralewitz, B., Gao, M. & Schulten, K. (2001). Steered molecular dynamics and mechanical functions of proteins. *Curr. Opin. Struct. Biol.* **11**, 224–230.

65 Paci, E. & Karplus, M. (2000). Unfolding proteins by external forces and high temperatures: The importance of topology and energetics. *Proc. Natl Acad. Sci. USA* **97**, 6521–6526.

66 Williams, P. M., Fowler, S. B., Best, R. B. et al. (2003). Hidden complexity in the mechanical properties of titin. *Nature* **422**, 446–449.

67 Fowler, S., Best, R. B., Toca-Herrera, J. L. et al. (2002). Mechanical unfolding of a titin Ig domain: Structure of unfolding intermediate revealed by combining AFM, molecular dynamics simulations, NMR and protein engineering. *J. Mol. Biol.* **322**, 841–849.

68 Best, R. B., Fowler, S., Toca-Herrera, J. L., Steward, A., Paci, E. & Clarke, J. (2003). Mechanical unfolding of a titin Ig domain: Structure of transition state revealed by combining atomic force microscopy, protein engineering and molecular dynamics simulations. *J. Mol. Biol.* **330**, 867–877.

69 Vendruscolo, M. & Paci, E. (2003). Protein folding: Bringing theory and experiment closer together. *Curr. Opin. Struct. Biol.* **13**, 82–87.

70 Vendruscolo, M., Paci, E., Karplus, M. & Dobson, C. M. (2003). Structures and relative free energies of partially folded states of proteins. *Proc. Natl Acad. Sci. USA* **100**, 14817–14821.

71 Brockwell, D. J., Paci, E., Zinober, R. C. et al. (2003). Pulling geometry defines the mechanical resistance of a β-sheet protein. *Nature Struct. Biol.* **10**, 731–737.

72 Carrion-Vazquez, M., Li, H., Lu, H., Marszalek, P. E., Oberhauser, A. F. & Fernandez, J. M. (2003). The mechanical stability of ubiquitin is linkage dependent. *Nature Struct. Biol.* **10**, 738–743.

73 Lu, H. & Schulten, K. (2000). The key event in force-induced unfolding of titin's immunoglobulin domains. *Biophys. J.* **79**, 51–65.

74 Fersht, A. R., Matouschek, A. & Serrano, L. (1992). The folding of an enzyme. I. Theory of protein engineering analysis of stability and pathway of protein folding. *J. Mol. Biol.* **224**, 771–782.

75 Fersht, A. R., Itzhaki, L. S., elMasry, N. F., Matthews, J. M. & Otzen, D. E. (1994). Single versus parallel pathways of protein folding and fractional structure in the transition state. *Proc. Natl Acad. Sci. USA* **91**, 10426–10429.

76 Li, A. & Daggett, V. (1994). Characterization of the transition state of protein unfolding by use of molecular dynamics: Chymotrypsin inhibitor 2. *Proc. Natl Acad. Sci. USA* **91**, 10430–10434.

77 Daggett, V. (2002). Molecular dynamics simulations of the protein

unfolding/folding reaction. *Acc. Chem. Res.* **35**, 422–429.

78 Gsponer, J. & Caflisch, A. (2002). Molecular dynamics simulations of protein folding from the transition state. *Proc. Natl Acad. Sci. USA* **99**, 6719–6724.

79 DeJong, D., Riley, R., Alonso, D. O. & Daggett, V. (2002). Probing the energy landscape of protein folding/unfolding transition states. *J. Mol. Biol.* **319**, 229–242.

80 Fersht, A. R. (1999). *Structure and Mechanism in Protein Science: A Guide to Enzyme Catalysis and Protein Folding.* W. H. Freeman & Co., New York.

81 Vendruscolo, M., Paci, E., Dobson, C. M. & Karplus, M. (2001). Three key residues form a critical contact network in a protein folding transition state. *Nature* **409**, 641–645.

82 Paci, E., Vendruscolo, M., Dobson, C. M. & Karplus, M. (2002). Determination of a transition state at atomic resolution from protein engineering data. *J. Mol. Biol.* **324**, 151–163.

83 Paci, E., Clarke, J., Steward, A., Vendruscolo, M. & Karplus, M. (2003). Self-consistent determination of the transition state for protein folding. Application to a fibronectin type III domain. *Proc. Natl Acad. Sci. USA* **100**, 394–399.

84 Daggett, V. & Levitt, M. (1993). Realistic simulations of native-protein dynamics in solution and beyond. *Annu. Rev. Biophys. Biomol. Struct.* **22**, 353–380.

85 Caflisch, A. & Karplus, M. (1995). Acid and thermal denaturation of barnase investigated by molecular dynamics simulations. *J. Mol. Biol.* **252**, 672–708.

86 Lazaridis, T. & Karplus, M. (1997). "New View" of protein folding reconciled with the old through multiple unfolding simulations. *Science* **278**, 1928–1931.

87 Frenkel, D. & Smit, B. (1996). *Understanding Molecular Simulation*, 2nd edition, Academic Press, London.

88 Berne, B. J. & Straub, J. E. (1997). Novel methods of sampling phase space in the simulation of biological systems. *Curr. Opin. Struct. Biol.* **7**, 181–189.

89 Bartels, C. & Karplus, M. (1997). Multidimensional adaptive umbrella sampling: Applications to main chain and side chain peptide conformations. *J. Comput. Chem.* **18**, 140–1462.

90 Mitsutake, A., Sugita, Y. & Okamoto, Y. (2001). Generalized-ensemble algorithms for molecular simulations of biopolymers. *Biopolymers* **60**, 96–123.

91 Wu, X. & Wang, S. (1998). Self-guided molecular dynamics simulation for efficient conformational search. *J. Phys. Chem. B* **102**, 7238–7250.

92 Apostolakis, J., Ferrara, P. & Caflisch, A. (1999). Calculation of conformational transitions and barriers in solvated systems: Application to the alanine dipeptide in water. *J. Chem. Phys.* **110**, 2099–2108.

93 Andricioaei, I., Dinner, A. R. & Karplus, M. (2003). Self-guided enhanced sampling methods for thermodynamic averages. *J. Chem. Phys.* **118**, 1074–1084.

94 Schlick, T., Barth, E. & Mandziuk, M. (1997). Biomolecular dynamics at long timesteps: bridging the time-scale gap between simulation and experimentation. *Annu. Rev. Biophys. Biomol. Struct.* **26**, 181–222.

95 Marinari, E. & Parisi, G. (1992). Simulated tempering: A new Monte Carlo scheme. *Europhys. Lett.* **19**, 451–458.

96 Sugita, Y. & Okamoto, Y. (1999). Replica-exchange molecular dynamics method for protein folding. *Chem. Phys. Lett.* **314**, 141–151.

97 Rao, F. & Caflisch, A. (2003). Replica exchange molecular dynamics simulations of reversible folding. *J. Chem. Phys.* **119**, 4035–4042.

98 Berendsen, H. J. C., Postma, J. P. M., van Gunsteren, W. F., DiNola, A. & Haak, J. R. (1984). Molecular dynamics with coupling to an external bath. *J. Chem. Phys.* **81**, 3684–3690.

99 Sanbonmatsu, K. Y. & Garcia, A. E. (2002). Structure of Met-enkephalin in

explicit aqueous solution using replica exchange molecular dynamics. *Proteins* **46**, 225–234.

100 Garcia, A. E. & Sanbonmatsu, K. Y. (2002). Alpha-helical stabilization by side chain shielding of backbone hydrogen bonds. *Proc. Natl Acad. Sci. USA* **99**, 2782–2787.

101 García, A. E. & Sanbonmatsu, K. Y. (2001). Exploring the energy landscape of a hairpin in explicit solvent. *Proteins* **42**, 345–354.

102 Zhou, R., Berne, B. J. & Germain, R. (2001). The free energy landscape for β hairpin folding in explicit water. *Proc. Natl Acad. Sci. USA* **98**, 14931–14936.

103 Rhee, Y. M. & Pande, V. S. (2003). Multiplexed-replica exchange molecular dynamics method for protein folding simulation. *Biophys. J.* **84**, 775–786.

104 Bolhuis, P. G., Chandler, D., Dellago, C. & Geissler, P. L. (2002). Transition path sampling: Throwing ropes over rough mountain passes, in the dark. *Annu. Rev. Phys. Chem*, **53**, 291–318.

105 Bolhuis, P. G. (2003). Transition-path sampling of β-hairpin folding. *Proc. Natl Acad. Sci. USA* **100**, 12129–12134.

106 Elber, R., Meller, J. & Olender, R. (1999). Stochastic path approach to compute atomically detailed trajectories: Application to the folding of C peptide. *J. Phys. Chem. B*, **103**, 899–911.

107 Eastman, P., Gronbech-Jensen, N. & Doniach, S. (2001). Simulation of protein folding by reaction path annealing. *J. Chem. Phys.* **114**, 3823–3841.

108 Wüthrich, K. (1989). Protein structure determination in solution by nuclear magnetic resonance spectroscopy. *Science* **243**, 45–50.

109 Clore, G. M. & Schwieters, C. D. (2002). Theoretical and computational advances in biomolecular NMR spectroscopy. *Curr. Opin. Struct. Biol.* **12**, 146–153.

110 Brooks, B. R., Bruccoleri, R. E., Olafson, B. D., States, D. J., Swaminathan, S. & Karplus, M. (1983). CHARMM: A program for macromolecular energy, minimization and dynamics calculations. *J. Comput. Chem.* **4**, 187–217.

111 Neria, E., Fischer, S. & Karplus, M. (1996). Simulation of activation free energies in molecular dynamics system. *J. Chem. Phys.* **105**, 1902–1921.

112 Lazaridis, T. & Karplus, M. (1999). Effective energy function for protein dynamics and thermodynamics. *Proteins* **35**, 133–152.

113 Paci, E., Vendruscolo, M. & Karplus, M. (2002). Native and nonnative interactions along protein folding and unfolding pathways. *Proteins* **47**, 379–392.

114 Cota, E., Hamill, S. J., Fowler, S. B. & Clarke, J. (2000). Two proteins with the same structure respond very differently to mutation: The role of plasticity in protein stability. *J. Mol. Biol.* **302**, 713–725.

115 Shea, J.-E., Onuchic, J. N. & Brooks III, C. L. (1999). Exploring the origins of topological frustration: Design of a minimally frustrated model of fragment B of protein A. *Proc. Natl Acad. Sci. USA* **96**, 12512–12517.

116 Duan, Y. & Kollman, P. A. (1998). Pathways to a protein folding intermediate observed in a 1-microsecond simulation in aqueous solution. *Science* **282**, 740–744.

117 Shirts, M. & Pande, V. (2000). COMPUTING: Screen savers of the world unite! *Science* **290**, 1903–1904.

118 Jackson, S. E. (1998). How do small single-domain proteins fold? *Folding Des.* **3**, R81–R91.

119 Pande, V. S., Baker, I., Chapman, J. et al. (2003). Atomistic protein folding simulations on the submillisecond time scale using worldwide distributed computing. *Biopolymers* **68**, 91–109.

120 Fersht, A. R. (2002). On the simulation of protein folding by short time scale molecular dynamics and distributed computing. *Proc. Natl Acad. Sci. USA* **99**, 14122–14125.

121 Paci, E., Cavalli, A., Vendruscolo, M. & Caflisch, A. (2003). Analysis of

the distributed computing approach applied to the folding of a small β peptide. *Proc. Natl Acad. Sci. USA* **100**, 8217–8222.

122 Settanni, G., Gsponer, J. & Caflisch, A. (2004). Formation of the folding nucleus of an SH3 domain investigated by loosely coupled molecular dynamics simulations. *Biophys. J.* **86**, 1691–1701.

123 Roux, B. & Simonson, T. (1999). Implicit solvent models. *Biophys. Chem.* **78**, 1–20.

124 Gilson, M. K. (1995). Theory of electrostatic interactions in macromolecules. *Curr. Opin. Struct. Biol.* **5**, 216–223.

125 Tomasi, J. & Persico, M. (1994). Molecular interactions in solution: An overview of methods based on continuous distributions of the solvent. *Chem. Rev.* **94**, 2027–2094.

126 Cramer, C. J. & Truhlar, D. G. (1999). Implicit solvation models: Equilibria, structure, spectra, and dynamics. *Chem. Rev.* **99**, 2161–2200.

127 Orozco, M. & Luque, F. J. (2000). Theoretical methods for the description of the solvent effect in biomolecular systems. *Chem. Rev.* **100**, 4187–4226.

128 Warwicker, J. & Watson, H. C. (1982). Calculation of the electric potential in the active site cleft due to α-helix dipoles. *J. Mol. Biol.* **157**, 671–679.

129 Gilson, M. K. & Honig, B. H. (1988). Energetics of charge-charge interactions in proteins. *Proteins* **3**, 32–52.

130 Bashford, D. & Karplus, M. (1990). pKa's of ionizable groups in proteins: Atomic detail from a continuum electrostatic model. *Biochemistry* **29**, 10219–10225.

131 Davis, M. E., Madura, J. D., Luty, B. A. & McCammon, J. A. (1991). Electrostatics and diffusion of molecules in solution – simulations with the University-of-Houston-brownian dynamics program. *Comput. Phys. Comm.* **62**, 187–197.

132 Scarsi, M., Apostolakis, J. & Caflisch, A. (1997). Continuum electrostatic energies of macromolecules in aqueous solutions. *J. Phys. Chem. B* **101**, 8098–8106.

133 Bashford, D. & Case, D. A. (2000). Generalized Born models of macromolecular solvation effects. *Annu. Rev. Phys. Chem.* **51**, 129–152.

134 Lee, M. S., Feig, M., Salsbury, F. R. & Brooks III, C. L. (2003). New analytic approximation to the standard molecular volume definition and its application to generalized Born calculations. *J. Comput. Chem.* **24**, 1348–1356.

135 Lee, M. S., Salsbury, F. R. & Brooks III, C. L. (2002). Novel generalized Born methods. *J. Chem. Phys.* **116**, 10606–10614.

136 Qiu, D., Shenkin, P. S., Hollinger, F. P. & Still, W. C. (1997). The GB/SA continuum model for solvation. A fast analytical method for the calculation of approximate Born radii. *J. Phys. Chem. A* **101**, 3005–3014.

137 Dominy, B. N. & Brooks III, C. L. (1999). Development of a generalized Born model parametrization for proteins and nucleic acids. *J. Phys. Chem. B* **103**, 3765–3773.

138 Warshel, A. & Levitt, M. (1976). Theoretical studies of enzymic reactions: dielectric, electrostatic and steric stabilization of the carbonium ion in the reaction of lysozyme. *J. Mol. Biol.* **103**, 227–249.

139 Gelin, B. R. & Karplus, M. (1979). Side-chain torsional potentials: effect of dipeptide, protein, and solvent environment. *Biochemistry* **18**, 1256–1268.

140 Mehler, E. L. (1990). Comparison of dielectric response models for simulating electrostatic effects in proteins. *Protein Eng.* **3**, 415–417.

141 Wang, L., Hingerty, B. E., Srinivasan, A. R., Olson, W. K. & Broyde, S. (2002). Accurate representation of B-DNA double helical structure with implicit solvent and counterions. *Biophys. J.* **83**, 382–406.

142 Mallik, B., Masunov, A. & Lazaridis, T. (2002). Distance and exposure dependent effective dielectric

function. *J. Comput. Chem.* **23**, 1090–1099.

143 Haberthür, U., Majeux, N., Werner, P. & Caflisch, A. (2003). Efficient evaluation of the effective dielectric function of a macromolecule in aqueous solution. *J. Comput. Chem.* **24**, 1936–1949.

144 Eisenberg, D. & McLachlan, A. D. (1986). Solvation energy in protein folding and binding. *Nature* **319**, 199–203.

145 Hasel, W., Hendrickson, T. F. & Still, W. C. (1988). A rapid approximation to the solvent accessible surface areas of atoms. *Tetrahedron Comput. Methodol.* **1**, 103–116.

146 Darden, T. A., York, D. M. & Pedersen, L. (1993). Particle mesh Ewald: An N log(N) method for computing Ewald sums. *J. Chem. Phys.* **98**, 10089–10092.

147 Weber, W., Hunenberger, P. H. & McCammon, J. A. (2000). Molecular dynamics simulations of a polyalanine octapeptide under Ewald boundary conditions: Influence of artificial periodicity on peptide conformation. *J. Phys. Chem. B* **104**, 3668–3675.

148 Fan, H. & Mark, A. E. (2003). Relative stability of protein structures determined by X-ray crystallography or NMR spectroscopy: a molecular dynamics simulation study. *Proteins* **53**, 111–120.

149 Hiltpold, A., Ferrara, P., Gsponer, J. & Caflisch, A. (2000). Free energy surface of the helical peptide Y(MEARA)6. *J. Phys. Chem. B* **104**, 10080–10086.

150 Lindorff-Larsen, K., Vendruscolo, M., Paci, E. & Dobson, C. M. (2004). Transition states for protein folding have native topologies despite high structural variability. *Nature Struct. Mol. Biol* **11**, 443–449.

33
Molecular Dynamics Simulations of Proteins and Peptides: Problems, Achievements, and Perspectives

Paul Tavan, Heiko Carstens, and Gerald Mathias

33.1
Introduction

When viewed from the standpoint of theoretical physics, proteins are extremely complex materials. They are inhomogeneous, non-isotropic, and exhibit dynamic processes covering many spatial and temporal scales (instead of only one or two), that is, they do not offer any of the nice features that make other materials readily accessible to simplified or coarse-grained descriptions. Therefore, theoretical approaches towards protein and peptide dynamics have to be based on microscopic descriptions. Here, atomistic molecular dynamics (MD) simulations, which are based on molecular mechanics (MM) force fields, currently represent the standard [1]. It should be noted, however, that these MM methods represent a first level of coarse graining, because they try to account for the electronic degrees of freedom mediating the interactions between the atoms by simplified parametric descriptions coded into standard MM force fields (for a recent review see Ponder and Case [2]).

In this article we want to address the question, to what extent can MM-MD simulations currently or in the near future contribute to the understanding of protein folding? Although simulations have been published (for a review see Ref. [3]) that allegedly describe folding processes of peptides or small proteins, there are also serious arguments (e.g., in Ref. [2]) that the available MM force fields may not be accurate enough for qualitatively correct descriptions. This would imply that the published simulations, instead of providing a ''virtual reality'' of folding processes, actually represent ''real artifacts.'' Thus, it is worthwhile addressing the issue of accuracy.

Because there are many excellent textbooks and review articles on MD simulation methods for liquids [4] and proteins (Ref. [2] and references therein), there is no point in duplicating this material. Instead, we have chosen to outline our own perspective of the issue, which has been and still is guiding our longstanding efforts to develop and improve the required computational methods. We start with a sketch of the basic physics of protein structure and dynamics. This sketch will

Protein Folding Handbook. Part I. Edited by J. Buchner and T. Kiefhaber

ISBN: 3-527-30784-2

serve to identify key challenges that have to be mastered by any attempt aiming at a theoretical description of these complicated processes.

33.2
Basic Physics of Protein Structure and Dynamics

The molecular machinery of life, designed by Darwinian selection in the process of evolution, essentially consists of proteins. Like all machines, these nano-machines are composed of rigid parts that define a specific three-dimensional structure and flexible parts that enable the particular functional dynamics for which the respective protein has been designed. Because proteins are polymer molecules, ''flexibility'' here implies a liquid state, like the one found in polymer melts. Therefore, under physiological thermodynamic conditions, proteins are generally found in a mixed state close to the melting transition between the solid and liquid phases.

The solid ''secondary'' substructures of proteins, for example the α-helices and β-sheets, are shaped by attractive interactions between strong electric dipoles, which are attached to the locally stiff and planar peptide groups within the polypeptide chains (Figure 33.1 illustrates the dipole–dipole interactions within a β-sheet). Here, the specific sequence of amino acid residues selects the respective secondary structures or, alternatively, precludes the formation of such rigid structures by inducing a local melting of the backbone into a flexible loop or random coil. There-

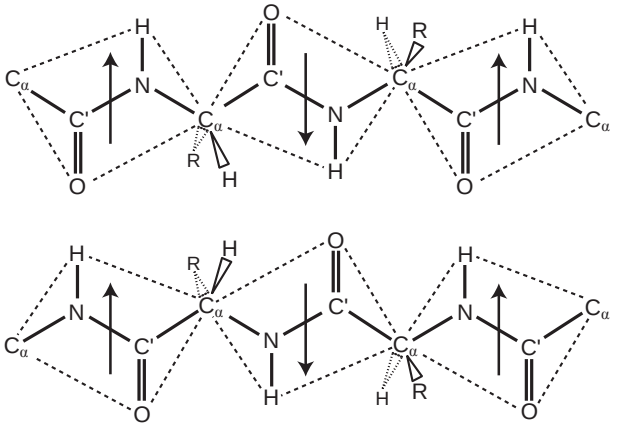

Fig. 33.1. Organization of the dipole–dipole interactions within a β-sheet. As explained by the resonance structures shown in Figure 33.3, the peptide groups form rigid platelets (indicated by the dashed lines) and exhibit strong electric dipole moments (arrows). Such dipoles attract each other, if their arrangement is parallel and axial ($\rightarrow\rightarrow$) or antiparallel and equatorial ($\uparrow\downarrow$). The structural stability of β-sheets is caused by a dipolar organization integrating both arrangements in an optimized fashion. Here, in contrast to α-helices, which exclusively exhibit the ($\rightarrow\rightarrow$)-arrangement, the local dipoles do not add up to a macroscopic dipole.

fore, the specific combination and three-dimensional organization of solid and liquid building blocks into the complex structure and dynamics characteristic for proteins is predetermined by their amino acid sequence.

Considering the thermodynamic state, proteins resemble a mixture of ice and liquid water, which, likewise, is characterized by a competition between enthalpic dipolar binding interactions attempting to generate solid order and temperature-driven entropic unbinding interactions attempting to generate liquid disorder. Nevertheless, there is a distinct difference concerning the complexity of the system: whereas a water–ice mixture homogeneously consists of only one molecular species, proteins are made up of a specific sequence of at least the 20 different residues coded in the genes, not counting all the additional cofactors, which also contribute to the complexity of protein structure and dynamics.

33.2.1 Protein Electrostatics

When attempts are made at a theoretical description, a first difficulty becomes apparent here. The dipole–dipole interactions (commonly called hydrogen bonds), which provide the main contribution to the folding of the polypeptide chains into specific three-dimensional structures, provide binding energies not much larger than the thermal energy $k_B T$ and it is only the combination of many different dipole–dipole interactions that generates the stability of a specific structure. Therefore, the precise description of the many weak electrostatic interactions within a protein is of key importance, since these interactions determine whether particular solid structures are formed or not. This instance is only a specific manifestation of the general fact that electrostatic interactions are dominant in shaping protein structure and dynamics [5]. In contrast, the weaker van der Waals interactions are less important as they are nonspecifically acting between all chemically nonbonded atoms in a similar way.

To obtain a quantitative estimate, consider a hypothetical protein with $N = 100$ residues, whose native conformation lies the typical energy value of $\Delta E = 20$ kJ mol^{-1} below either a compact misfolded conformation or the huge variety of unfolded ones. Then the acceptable error per residue allowing us still to identify the correct conformation is approximately $\Delta E/N^{1/2}$ or 2 kJ mol^{-1} (see Ref. [2] and references therein), where the errors are assumed to be randomly distributed. Systematic errors in the description of the electrostatics will reduce the acceptable error down to $\Delta E/N$ or 0.2 kJ mol^{-1}. Thus, great care has to be taken in the description of intraprotein electrostatics if one wants to generate a ''virtual reality.'' Its quantitatively correct description constitutes the first key problem for theoretical approaches.

33.2.2 Relaxation Times and Spatial Scales

Besides the strong variations of the physicochemical (predominantly electrostatic) properties among the residues, there is a second important difference between a

water–ice equilibrium and a protein, which adds to the indicated complexity. In liquid water the molecules are free to move individually, which confines the relaxation time of water in response to an external perturbation (e.g., to a change of the electric field) to the scale of a few picoseconds. Furthermore, in pure water at room temperature spatially ordered structures are found only up to a distance of about 1.5 nm from a given water molecule; beyond this distance water starts to behave like a dielectric continuum [6]. In contrast, in a protein the motions of the molecular components are strongly constrained by the polymeric connectivity and by solid substructures. These constraints lead to relaxation times that are larger than those in liquid water by up to 12 orders of magnitude or more.

Motions that change the conformation of a protein proceed through thermally activated rotations around the covalent single bonds linking the Cα atoms to the adjacent peptide groups of the backbone. At room temperature such rotations take at least a few 10–100 ps, which is why a protein can start to statistically sample its available conformational space only at time scales above 1 ns. Here, the number of atoms involved in a conformational transition defines a spatial scale and the time required for this transition increases rapidly with the size of the spatial scale. Up to now it is not yet clear whether the resulting time scales of conformational transitions represent a well-ordered hierarchy, within which distinct time scales can be associated to specific processes, or a continuum extending from nanoseconds to seconds. Whereas the former alternative would immediately suggest coarse-grained approaches to protein dynamics, the latter would make them difficult to construct. But whichever of these alternative pictures may be true, the vastly different temporal and spatial scales of molecular motions in proteins generate the second key problem for theoretical descriptions by simulation techniques.

33.2.3 Solvent Environment

Up to this point we have looked at the problem of describing the native structure and dynamics of proteins as if they could be understood as isolated objects. Assuming this hypothesis we have identified two key problems with which any attempt of a realistic description is confronted. The first is posed by the high accuracy required for the modeling of the electrostatics within a protein and the second by the huge span of time scales that have to be covered. But the issue is even more complicated, since proteins cannot be isolated from their surroundings.

Proteins acquire their native structure and functional dynamics solely within their physiological environment, which in the case of soluble proteins is characterized by certain ranges of temperature, pressure, pH, and concentrations of ions and of other molecular components within the aqueous solvent. Although these ranges may vary from protein to protein, there are specific physiological ranges for each of them. Therefore, any attempt to provide a quantitative description for the dynamic processes of protein folding and function has to properly include the environment at its physiological thermodynamic state.

33.2.4 Water

The key component of the environment is liquid water, whose adequate representation in computer simulations represents a challenge on its own (see Ref. [7] for a critical review and Ref. [6] for recent results). A water molecule is nearly spherical and very small (approximately the size of an oxygen atom), it carries large electrical dipole and quadrupole moments, and is strongly polarizable by electric fields generated, for example, by other water molecules, ions, or polar groups in its surroundings.

The large dipole moment causes the unusually large dielectric constant of 78, by which liquid water scales down electrostatic interactions. For proteins and peptides this dielectric mean-field property of water is important, because they are usually polyvalent ions and therefore generate a reaction field by polarization of the aqueous environment, which modifies the electrostatic interactions within the protein. The proper description of these very long-ranged effects thus represents the first problem specifically posed by MD simulations of protein–solvent systems.

The sizable quadrupole moment of the water molecule shapes the detailed structures of the hydration shells of solute molecules and, in particular, also those of proteins. If, as suggested by Brooks [8], water molecules actively support secondary structure formation, for example, by bridging nascent β-sheets, then an accurate modeling of the quadrupole moment is required for the understanding of the detailed folding pathways.

The strong electronic polarizability of the water molecules poses yet another challenge. As illustrated by the computational result in Figure 33.2, due to polar-

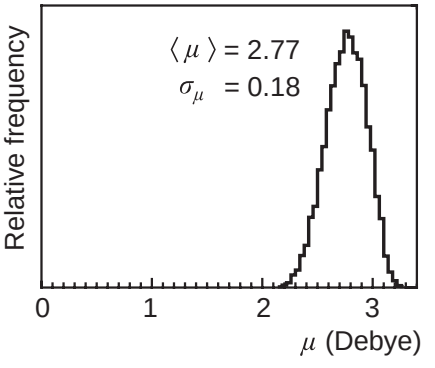

Fig. 33.2. Distribution of the dipole moment of a water molecule dissolved in pure water as obtained from a hybrid MD simulation combining density functional theory (DFT) for the given water molecule with an MM description of the aqueous environment. The DFT description of an isolated water molecule yields a dipole moment of 1.92 D, which is very close to the experimental value of 1.85 D. Thus, the induced dipole moment determined by the calculations is 0.85 D, that is about 40% of the gas-phase value. In liquid water the fluctuations of the dipole moment generated by the electronic polarization are 6.5% as measured by $\sigma_\mu/\langle\mu\rangle$. For technical details and explanations see Ref. [9].

ization the dipole moment increases from a value of 1.85 D for a water molecule isolated in the gas-phase to a value of about 2.6–3.0 D in the liquid phase [7, 9, 10]. Correspondingly the dipole moment of a water molecule will sizably change when it moves from a hydration shell of an ion through bulk water towards a nonpolar surface of a protein.

33.2.5 Polarizability of the Peptide Groups and of Other Protein Components

The polarization-induced changes of the dipole moments of the water molecules sketched above are important in the hydrophobic interactions [11], which are commonly believed to provide a key driving force in protein folding (see Ref. [12] for a discussion). Here, particularly the dipole–induced-dipole interactions, for example, between ordered hydration shells and nonpolar surfaces, are expected to provide large contributions. Therefore, not only the electronic polarizability of the water molecules, but also that of the various protein components has to be included for a quantitative description of the hydrophobic effect.

Furthermore, the electronic polarizability of the components can stabilize local structures in proteins. For instance, about 50% of the binding energy between a positive charge and an aromatic ring is due to polarization (as shown in Ref. [2] for the representative example of potassium bound to benzene). Particularly the polarizability of the peptide groups can be expected to decide about the relative stabilities of the secondary structure motifs in proteins. This claim is proven by the following simple argument:

We have stated further above (and illustrated in Figure 33.1 for the case of a β-sheet) that the dipole–dipole interactions within a protein, particularly those between the peptide groups of the backbone, shape the secondary structures of proteins. The peptide groups, in addition to exhibiting strong dipole moments, are highly polarizable as one can deduce from the resonance structures depicted in Figure 33.3. In response to the electric field generated by the dipole moments of neighboring peptide groups, with which a peptide group interacts in a given secondary structure motif (cf. Figure 33.1), an induced dipole moment will be added to the static dipole moment of the given group, and will correspondingly strengthen or weaken its dipole–dipole interactions (H-bonds). Here, the size and direction of the induced dipole moment will be determined by the spatial distribution and orientation of the neighboring dipoles and partial charges, that is, predominantly by the surrounding secondary structure.

As is also apparent from Figure 33.3, the electronic polarization will concomitantly change the force constants and equilibrium lengths of the chemical bonds (O=C–N–H) within the peptide groups. This effect is apparent in the vibrational spectra of proteins, which are dominated by the normal modes of the peptide groups giving rise to so-called amide bands. The shape of these broad bands is a signature of the differences in polarization experienced by the various peptide groups and, therefore, can be used for an approximate determination of secondary

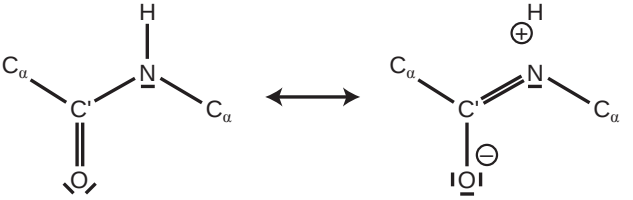

Fig. 33.3. π-electron resonance structures of a peptide group explaining its strong dipole moment and polarizability. An external electric field can modify the relative weights, by which these resonance structures contribute to the electronic wave function. Correspondingly, it will sizably change the dipole moment and the force constants.

structure content (see Ref. [13] for further information). Peaks of the so-called amide-I band, for instance, which belongs to the C=O stretching vibrations of the backbone, are found in the spectral range between 1620 and 1700 cm^{-1}, indicating that the polarization can change the associated C=O force constants by 5%. Conversely, (i) the fact that the large and specific frequency shifts of the amide modes can indicate the secondary structure environment of the corresponding peptide groups, and (ii) the resonance argument in Figure 33.3 uniquely demonstrate that the electronic polarization will entail sizably different strengths ($\geq$5%) of the dipolar interactions (''H-bonds'') within the various secondary structure motifs. This proves our above conjecture that the electronic polarizability provides a differential contribution to the relative stabilities of secondary structure motifs.

As a result, theoretical descriptions of protein dynamics have to include the electronic polarizability. In addition to this general insight, the above considerations have led us also to quantitative estimates as to how much the polarizability contributes to the electrostatics. We found numbers ranging between 50% (charge on top of an aromatic ring) and 5% (peptide groups in different secondary structure motifs). These contributions systematically and differentially change the electrostatic interactions within protein–solvent systems and do not represent random variations. This instance is obvious if one compares the interaction of a dipolar group with a charged and a nonpolar group, respectively. Furthermore, it has been demonstrated above for the dipolar interactions within secondary structure motifs. Below we will refer to the thus established 5% lower bound of the polarizability contribution to protein electrostatics for purposes of accuracy estimates.

Finally, we would like to add that enzymatic catalysis in proteins, which is a prominent feature of these materials, is essentially an effect of polarizability. Here, a substrate is noncovalently attached in a specific orientation to a binding pocket and a highly structured electric field, which is generated by a particular arrangement of charged, polar and nonpolar residues, exerts a polarizing strain on its charge distribution such that a particular chemical bond either breaks or is formed. This example underlines the decisive contribution of the electronic polarizability to protein structure, dynamics and function.

33.3
State of the Art

By considering the basic physics of protein–solvent systems we have identified key challenges that have to be met by MD-based theoretical descriptions of protein and peptide dynamics. The majority of these problems are posed by (i) the complex electrostatics in such systems and comprise (a) the long range of these interactions, (b) their shielding by the surrounding solvent, and (c) their local variability, which is caused by differential electronic polarization in these inhomogeneous and nonisotropic materials. Further challenges derive from the need (ii) to properly account for the thermodynamic conditions and (iii) to cover the relevant time scales.

During the past 25 years, since the first MD simulation of a protein was reported [14], the true complexities of the challenge have become more and more apparent. By now some of the problems have been solved, whereas others are still awaiting a solution. Quite naïvely, the first MD simulation dealt with a protein embedded in vacuum. However, the importance of the aqueous environment and the correct choice of the thermodynamic conditions soon became apparent [15, 16].

33.3.1
Control of Thermodynamic Conditions

In the theory of liquids and long before the history of protein simulations began, MD simulation systems representing a well-defined thermodynamic ensemble had been set up by filling periodic boxes with MM models of the material of interest (cf. the first simulation of liquid water by Rahman and Stillinger [17]). Whereas the temperature (or internal energy) is trivially accessible in any MD approach, up to now the pressure (or volume) can be controlled solely (cf. Mathias et al. [18] for a discussion) through the use of periodic boundary conditions (PBCs). This control can be executed safely and poses no problems.

33.3.2
Long-range Electrostatics

PBCs generate an unbounded simulation system of finite size with the topology of a three-dimensional torus. Therefore, they create the problem of artificial self-interactions whenever the interactions among the simulated particles are long ranged as is the case for electrostatics. To avoid such self-interactions one has to follow the minimum image convention (MIC), which dictates that all interactions beyond the MIC-distance $R_{\mathrm{MIC}} = L/2$ should be neglected, where L is the size of the periodic simulation box [4]. On the other hand, a corresponding truncation of the long-ranged electrostatic interactions in the so-called straight-cutoff (SC) approach leads to serious structural and energetic artifacts, even if the simulated system consists solely of pure water [18–20]. For solutions of polyvalent ions, like proteins or nucleic acids, the SC-artifacts become even worse.

Nevertheless, up to about a decade ago MD simulations of pure water and protein–solvent systems used to apply the SC approach with small cutoff distances $R_C \approx 1$ nm (i.e., $R_C \ll R_{MIC}$) mainly for computational reasons: In an N-particle system the number of long-range interactions scales like N^2 and, therefore, seems to imply an intractable computational effort. However, in the sequel, the unacceptably large errors connected with this crude approximation forced investigators to ignore the MIC and to apply lattice sum (LS) methods [21–23] to the computation of the long-range electrostatics. LS methods take advantage of the periodicity of the simulated system and can evaluate the correspondingly periodic electrostatic potential at a computational effort scaling with $N \log N$. On the other hand, the neglect of the MIC now introduces periodicity artifacts into the description of nonperiodic systems such as liquids and proteins in solution [24]. However, for large simulation systems with $L > 6$ nm in the case of pure water and $L \gg 2d$ in the case of a solvated protein of diameter d, the periodicity artifacts should become negligible or small, respectively [6, 18].

Today, we can even give absolute error bounds for the accuracy of the electrostatics computation in MD simulations. This is due to the recent development of a new algorithmic approach, which avoids the use of a periodic potential and, nevertheless, provides an accurate and computationally efficient alternative to the LS methods [18]. Therefore, it allows us to estimate, for example, the size of the LS artifacts and, in combination with LS results, to actually measure the SC errors. Because a comparably accurate alternative to LS had been lacking before, such accuracy measurements had been impossible. Figure 33.4 sketches the basic concept of this recent multiple-scale approach, which combines toroidal boundary conditions with a reaction field correction (TBC/RF).

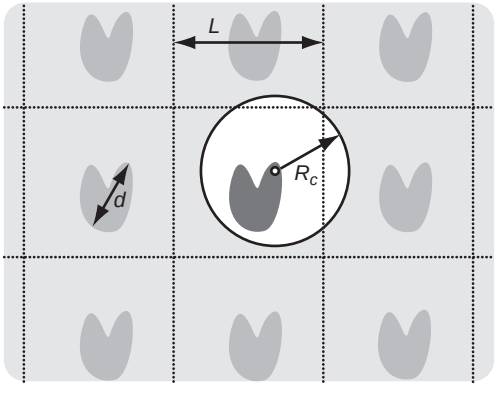

Fig. 33.4. Concept of the TBC/RF approach to the computation of long-range electrostatics in MD simulations of proteins in solution [18]. Each atom of the periodic simulation system of size L containing a protein of diameter d in solution is surrounded by a sphere of radius $R_C = R_{MIC} = L/2$. The polarization of the dielectric outside of that sphere generates a reaction field acting on the central charge, whose interactions with the charges within the sphere are rapidly calculated by fast, hierarchical, and structure-adapted multipole expansions. Here, the applied SAMM algorithm [25, 26] scales linearly with N.

To provide an example for such error bounds, we consider the PBC/LS, TBC/RF, and SC simulations on large water systems ($L = 8$–12 nm, $N = 34\,000$–$120\,000$), which have been executed with two different programs (GROMACS [27], EGOMMII [28]) under otherwise identical conditions (see Refs [6, 18]). The enthalpies of vaporization ΔH per water molecule calculated by PBC/LS and TBC/RF showed relative deviations of at most 3/1000, that is 0.1 kJ mol^{-1}. This deviation is smaller by a factor of 2 than the acceptable systematic error per residue estimated in Section 33.1.1 and by a factor of 20 below the acceptable random error. In contrast, the ΔH value calculated by SC using a cutoff radius $R_C \approx 4$ nm (system size $L = 8$ nm) deviated by 1.2 kJ mol^{-1} from the PBC/LS and TBC/RF values, which is larger by a factor of 6 than the acceptable systematic error introduced in Section 33.1.1.

This example quantitatively proves that SC simulations grossly miss the accuracy required for protein structure prediction in purely dipolar systems, whereas here the two other methods are acceptable. For solutions containing ions and particularly proteins similar comparisons of PBC/LS and TBC/RF treatments will soon provide clues as to which measures can be used to avoid computational artifacts and to achieve the required accuracy in these more complicated cases. As a result, the longstanding problem of how the long-range electrostatics of protein–solvent systems can be treated in MD simulations with sufficient accuracy and manageable computational effort will find a final answer in the near future. Furthermore, we can safely state that the remaining accuracy problems connected with long-range electrostatics computation are much smaller than those associated with the MM force fields to which we will now turn our attention.

33.3.3 Polarizability

As shown in Sections 33.1.4–33.1.5, many components of a protein–solvent system exhibit a significant electronic polarizability and, therefore, their electrostatic signatures, as measured by their multipole moments, will strongly vary with their position within these complex and inhomogeneous systems. In spite of the decisive part played by the electronic polarizability in protein structure, dynamics, and function, all available MM force fields still use static partial charges to model the electrostatic properties of the molecules (see, however, the ongoing development reported by Kaminski et al. [29]). Thus, they try to account for the electronic polarizability in a mean field fashion, which is invalid in inhomogeneous and nonisotropic materials. The examples discussed in Sections 33.1.4–33.1.5 suggest a lower bound of 5% for the size of the relative errors, which the neglect of polarization introduces into the description of the electrostatics.

To convert this relative error into an absolute number, we have conducted a sample TBC/RF simulation for bovine pancreatic trypsin inhibitor (BPTI) [30] in water at a temperature of 300 K and a pressure of 1 bar using the set-up described in Ref. [31]. Here, a periodic simulation box of 8 nm side length, filled with 17 329 rigid TIP3P water molecules [32] (cf. Figure 33.5) and a CHARMM22 model [33] of BPTI ($N_{res} = 58$ amino acid residues), was equilibrated for 1 ns. We took this equi-

librated system as the starting point for a 100 ps simulation and evaluated the average total electrostatic energy $E_{e,tot}$ of the protein atoms. Less than 1% of all electrostatic interactions between the protein charges occur within a given residue. Due to the so-called 1–3 exclusion commonly used in MM force fields [33] they act at comparable distances like the interactions with charges residing at neighboring residues or solvent molecules. Therefore, we estimate the intra-residue contribution to $E_{e,tot}$ to be sizably smaller than at most 20% of $E_{e,tot}$. As a result, the expression

$$E_{e,res} \approx 0.8 \times E_{e,tot}/N_{res}$$

should represent a lower limit for the average electrostatic energy $E_{e,res}$ per residue. Inserting the computed number, we find $E_{e,res} \approx 160$ kJ Mol^{-1}. With the 5% lower bound for the systematic error, which is expected to be caused by the neglect of polarizability, we thus find a lower limit to the ''polarizability error'' of 8 kJ mol^{-1} per residue. This polarizability error is by a factor 4 larger than the acceptable random error and exceeds the acceptable systematic error, which should be more relevant here, by a factor of 40.

Therefore, the neglect of the electronic polarizability is the key drawback of the available MM force fields and, up to now, prevents quantitative MD descriptions of protein structure. Furthermore, it is the reason why the parameterization of such force fields is confronted with insurmountable difficulties. As outlined in Section 33.1.5, the electronic polarizability of the peptide groups provides a differential contribution to the relative stabilities of secondary structure motifs. As a result, the common nonpolarizable MM force fields can either describe the stability of α-helices or that of β-sheets at an acceptable accuracy, but never both. Correspondingly and as illustrated in Ponder and Case [2] by sample simulations, such force fields either favor α-helical structures (e.g., AMBER ff94 [34]) or β-sheets (e.g., OPLS-AA [35]), or else fail concerning intermediate structures (e.g., CHARMM22 [33]).

33.3.4 Higher Multipole Moments of the Molecular Components

For computational reasons, MM force fields apply the partial charge approximation, according to which the charge distribution within the molecular components of a simulation system is modeled by charges located at the positions of the nuclei. Although this approximation should be sufficiently accurate in most instances (if the problem of the missing polarizability is put aside), it will cause problems concerning the description of local structures, whenever ''electron lone pairs'' occur at oxygen atoms [29]. Important examples for this chemical motif are the peptide C=O groups (cf. Figure 33.3) and the water molecule. At the small oxygen atoms the lone pairs cause large higher multipole moments, whose directional signature cannot be properly represented within the partial charge approximation. Although the electric field generated by these multipole moments rapidly decays beyond the

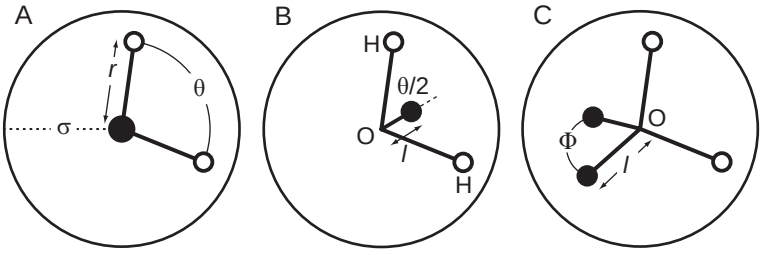

Fig. 33.5. Geometries of three different nonpolarizable MM models for water. Black circles indicate the positions of negative and open circles those of the positive partial charges. The large circle indicates the van der Waals radius. A) TIP3P, B) TIP4P (both Jorgensen et al. [33]), C) TIP5P [36].

first shell of neighboring atoms, it steers the directions of the H-bonds within that shell and, thus, shapes the corresponding local structures. The consequences of this subtle effect are yet to be explored for proteins. For water, however, whose experimental and theoretical characterization has always been and still is at a much higher stage than that of proteins, the importance of this effect is well known.

33.3.5 MM Models of Water

In an excellent review, Guillot [7] has recently given "a reappraisal of what we have learnt during three decades of computer simulations on water." Within the partial charge approximation, MM models of water comprise three charges at the positions of its three atoms ("three point models"). By symmetry and neutrality of the molecule, in this case three parameters (one charge, bond angle, and bond length) suffice to specify the charge distribution (cf. Figure 33.5A). However, these simple three-point models, which are commonly used in MD simulations of protein–water systems, do not correctly account for the higher multipole moments and, therefore, miss essential features of the correlation functions in pure water (see, for example, Ref. [6]). Because of this defect and of the missing polarizability, they cannot be expected to provide an adequate description of the hydration shell structures surrounding proteins.

For an improved description of the higher multipole moments, four- and five-point models have been suggested positioning partial charges away from the positions of the nuclei. Figure 33.5 compares the geometries of correspondingly extended models with that of a simple three-point model. In addition, a series of polarizable models using "fluctuating charges" or inducible dipoles have been proposed. Guillot gives an impressive table listing about 50 different MM models of water and, subsequently, classifies the performance of these models concerning the reproduction of experimentally established properties in simulations. Although Guillot mainly discusses pure water, he also shortly comments on the topic of transferability, which is the unsolved problem of how to construct an MM water

model performing equally well for all kinds of solute molecules. Summarizing his review he arrives at the conclusion that "one has a taste of incompletion, if one considers that not a single water model available in the literature is able to reproduce with a great accuracy all the water properties. Despite many efforts to improve this situation very few significant progress can be asserted." In his view this is due to "the extreme complexity of the water force field in the details, and their influence on the macroscopic properties of the condensed phase." Nevertheless, being a committed scientist he does not suggest that we should quit attempts at an MM description but instead adds several suggestions as to how one should account for the polarizability and for other details in a better way.

33.3.6 Complexity of Protein–Solvent Systems and Consequences for MM-MD

The state of the MM-MD descriptions of pure water sketched above is sobering when one turns to protein–solvent systems, whose complexity exceeds that of pure water by orders of magnitude. This enormous increase of complexity is caused only in part by the much larger spatial and temporal scales characterizing protein dynamics (cf. Section 33.1.2). More important is the combinatorial complexity, which is posed by the fact that one has to parameterize the interactions between a large variety of chemically different components (water, peptide groups, amino acid residues, ions, etc.) into a single effective energy function in a balanced way. If already in the case of a one-component liquid like water subtle details of the MM models determine the macroscopic properties, a difficulty which, up to now, has prevented the construction of a model capable of explaining all known properties, then one may ask whether the MM approach will ever live up to its promises concerning proteins at all. This critical question gains support by our above estimate concerning the size of the errors introduced by the neglect of the electronic polarizability characteristic for the common force fields. Our conservative estimate suggests that nowadays not even a single and most basic property of soluble proteins, namely their structure, can be reliably predicted by extended MM-MD simulations.

33.3.7 What about Successes of MD Methods?

However, this disastrous result on the accuracy of current MM-MD simulations does not imply that their results are always completely wrong. Instead it may sometimes happen that numbers computed by MD for certain observables surprisingly agree with experimental data within a few per cent. Examples are the peptide simulations presented by Daura et al. [37], which have shown a mixture of peptide conformations compatible with NMR data, the simulation of AFM experiments on the rupture force required to pull a biotin substrate out of its binding pocket in streptavidin [38], or the simulation of the light-induced relaxation dynamics in small cyclic peptides [39] (see Section 33.3 for a more detailed discussion of this

example). In such cases, the apparent "success" of an MD simulation may be due (i) to the choice of an observable that happens to be extremely stable with respect to the sizable inaccuracies of the MM force field, or (ii) to the fortunate cancellation of many different errors [40]. Therefore, one cannot readily conclude from such favorable examples that the MD approach towards biomolecular dynamics has "come of age" [41]. Instead, one must expect that observables computed by unrestricted MD simulations differ either quantitatively from experimental data by 10–50% or are qualitatively wrong.

Furthermore, the deficiencies of the MM force fields do not imply that results of MD simulations that are restricted by experimental data are wrong. On the contrary, this type of simulation [42] has led to the greatest success of the MD method and is largely responsible for its widespread application on proteins. In this experimentally restricted MD approach the chemical expertise that is coded into the various parameters of the MM force field (providing standard values for the bond lengths, bond angles, dihedral angles, for the elasticity of these internal coordinates etc.) is combined with a large set of experimental constraints (e.g., from X-ray diffraction or more-dimensional NMR). Shortly after their suggestion in 1987, the corresponding MD-based "annealing simulations" have become the standard tool in the computation of protein and peptide structures from X-ray and NMR data and have acquired a key role in structural biology, because they have enabled the automation of protein structure refinement. In this context, the deficiencies of the MM force fields play a minor role as they are largely corrected by the experimental constraints. Note that the protein electrostatics and its shielding by the solvent are usually ignored in these experimentally restricted simulations, because here one neither wants nor has to deal with the associated complexities.

Finally, another type of restricted MD simulation also does not suffer too much from the deficiencies of the MM force fields. These are the so-called QM/MM hybrid methods, in which a small fragment of a simulation system is treated by quantum mechanics (QM) and the large remainder by MM (the basic concepts of this approach were described in a seminal paper by Warshel and Levitt in 1976 [43]). Here, the attention is restricted to the properties of the QM fragment, which are calculated as exactly as possible by numerical solution of the electronic Schrödinger equation. The electronic polarization of the QM fragment is obtained by importing the electric field generated by the MM environment as an external perturbation into the QM Hamiltonian. If this perturbation changes a certain property of the QM fragment by 10%, then even 10% errors in the external field calculated by MM will entail only errors of 1% in the QM result.

To provide an example we consider the vibrational spectra of molecules. Due to the development [44, 45] and widespread accessibility [46] of density functional theory (DFT) highly accurate computations of intramolecular force fields and of associated gas-phase vibrational spectra have become feasible at a moderate computational effort. On average, the spectral positions of the computed lines deviate by only about 1.5% from the observations, which is sufficient for a safe assignment of observed bands to normal modes [47, 48]. Note that calculated molecular structures are more exact by orders of magnitude than the spectra, because the molecu-

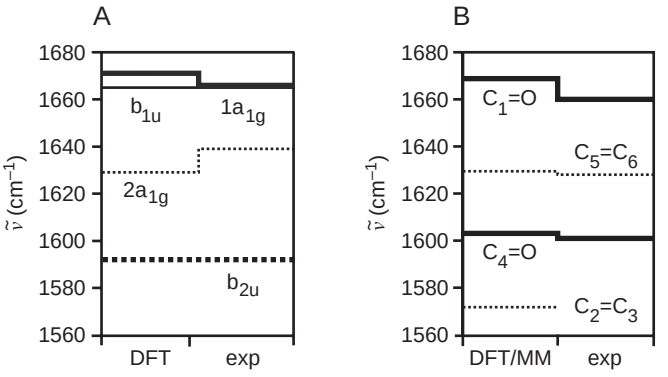

Fig. 33.6. Comparison of DFT (A) and DFT/MM (B) computations with experimental data for the vibrational spectra of the C=O (solid lines) and C=C (dashed lines) modes of quinone molecules in the gas-phase and in a protein, respectively. The DFT results pertain to *p*-benzoquinone [48] and the DFT/MM results to the ubiquinone Q_A in the reaction center of *Rb. sphaeroides* [49]. Both computational results agree very well with the observations. In particular, the DFT/MM treatment correctly predicts the sizable 60 cm^{-1} red shift of one of the C=O modes, which is caused by the protein environment through electrostatic polarization of the quinone.

lar structure is much less sensitive to inaccuracies of the QM treatment than the intramolecular force field.

In condensed phase, the computation of vibrational spectra [49, 50] has recently been enabled by the development of a DFT/MM hybrid method [9]. The perturbation argument given further above entails the expectation that DFT/MM can describe condensed-phase vibrational spectra at an accuracy comparable to the one previously achieved by DFT for the gas-phase spectra. This expectation is confirmed by the results shown in Figure 33.6 and by the infrared spectra of *p*-bezoquinone on water, which have been calculated from a QM/MM hybrid MD trajectory [50]. Thus, although the common nonpolarizable MM force fields are not accurate enough for unrestricted MD simulations of biomolecules, they are valuable in more restricted settings.

33.3.8
Accessible Time Scales and Accuracy Issues

Concerning MM-MD simulations of protein or peptide folding, the insufficient accuracy of MM force fields has the following consequence: If we had computer power enough to simulate the folding dynamics of a small protein or peptide in solution for milliseconds or seconds starting from a random coil conformation, we would have to expect at a high probability that the conformation predicted by the simulation has nothing to do with the native conformation, that is, represents a ''real artifact.''

In this respect it is, in a sense, fortunate that computational limitations have previously restricted MM-MD simulations of protein–solvent systems to the time scale of a few nanoseconds. Because simulations usually start from a structure determined by X-ray crystallography or by more-dimensional NMR, and because in proteins small-scale conformational transitions only begin to occur at this time scale, the actual metastability of a MM-MD protein model is likely to become apparent only in much more extended simulations than in the ones that are currently feasible. At the accessible nanosecond time scale, the large-scale and slow relaxation processes changing a metastable structure are simply "frozen out," and protein simulations are strongly restricted by the accessible time scales. Structural stabilities observed in short-time simulations are due to this restriction and cannot be attributed to the particular quality of the force field. Nevertheless, the apparent stability of protein structures even in grossly erroneous MM-MD simulations (like in those applying the SC truncation to the long-range electrostatics) may have led scientists to believe in the validity of MD results. For the field of MD simulations on protein dynamics this was fortunate, because it has created a certain public acceptance (cf. e.g., Ref. [41]) and has attracted researchers. On the other hand it was also quite unfortunate, because the urgent necessity to improve the MD methods to meet the challenges outlined in Section 33.1 remained an issue of concern only in a small community of methods developers.

However, the speed of computation has been increasing by a factor of 2 each year during the past decades and, according to the plans of the computer industry, will continue to exhibit this type of exponential growth within the coming decade. For the available MM force fields this progress would imply that MD simulations spanning about 0.5 ms become feasible, because the current technology already allows series of MD simulations spanning 10 ns each for protein–solvent systems comprising 10^4–10^5 atoms. Therefore, the deficiencies of the current MM force fields are becoming increasingly apparent in unrestricted long-time simulations through changes of supposedly stable protein or peptide conformations. This experience will drive the efforts to construct better force fields, which must be more accurate by at least one order of magnitude, although such an improvement necessarily will imply a larger computational effort and, therefore, will impede the tractability of large proteins at extended time scales. Here, the accurate and computationally efficient inclusion of the electronic polarizability will be of key importance.

33.3.9
Continuum Solvent Models

The above discussion on the accessible time scales was based on the assumption that a microscopic model of the aqueous environment is employed to account for the important solvent–protein interactions. This approach represents the state of the art and, at the same time, an obstacle in accessing more extended time scales, because in the corresponding simulation systems 90% of the atoms must belong to the solvent (for an explanation see Section 33.2.2 and Mathias et al. [18]). Thus, one simulates mainly a liquid solvent slightly polluted by protein atoms, and most

of the computer time is spent on the calculation of the forces acting on the solvent molecules.

It is tempting to get rid of this enormous computational effort by applying so-called implicit solvent models. Here, one tries to replace the microscopic modeling of the solvent by mean field representations of its interactions with the solute protein, which are mainly the electrostatic free energy of solvation and the hydrophobic effect caused by the solvent. The hydrophobic effect is usually included by an energy term proportional to the surface of the solute. Much more complicated is the computation of the electrostatic free energy of solvation. Here one has to find solutions to the electrostatics problem of an irregularly shaped cavity filled with point charges (the solute) and embedded in a dielectric and possibly ionic continuum (the solvent). Standard numerical methods to solve the corresponding Poisson and Poisson-Boltzmann equations are much too expensive to be used in MD simulations and have many other drawbacks (see Egwolf and Tavan [31] for a discussion).

To circumvent the problem of actually having to solve a partial differential equation (PDE) at each MD time step, the so-called generalized Born methods (GB) have been suggested (for a review see Bashford and Case [51]). GB methods introduce screening functions that are supposed to describe the solvent-induced shielding of the electrostatic interactions within the solute and are empirically parameterized using sets of sample molecules. The required parameters then add to the combinatorial complexity of the force field parameterization.

The GB approximation enables the computation of impressive MD trajectories covering several hundred microseconds [52]. However, not surprisingly, the resulting free energy landscapes drastically differ from those obtained with explicit solvent [53, 54]. Thus, the GB methods apparently oversimplify the complicated electrostatics problem for the sake of computational efficiency and, therefore, fail in structure prediction.

A physically correct method to compute the free energy of solvation and, in particular, the forces on the solute atoms in implicit solvent MD simulations has recently been developed by Egwolf and Tavan [31, 55]. In this analytical ''one-parameter'' approach the reaction field arising from the polarization of the implicit solvent continuum is represented by Gaussian dipole densities localized at the atoms of the solute. These dipole densities are determined by a set of coupled equations, which can be solved numerically by a self-consistent iterative procedure. The required computational effort is comparable to that of introducing the electronic polarizability into MM force fields. This effort is by many orders of magnitude smaller than that of standard numerical methods for the solution of PDEs.

The resulting reaction field forces agree very well with those of explicit solvent simulations, and the solvation free energies match closely those obtained by the standard numerical methods [31]. However, this progress is only a first step towards MD simulations with implicit solvent. For its use in MD, one has to correct the violations of the reaction principle resulting from the reaction field forces. In addition, the surface term covering the hydrophobic forces has to be parameterized in order to match the free energy landscapes found in explicit solvent simulations.

33.3.10
Are there Further Problems beyond Electrostatics and Structure Prediction?

Up to this point, our analysis has been focused on the complex electrostatics in protein–solvent systems and the accuracy problems that are caused by the electrostatics in the construction and numerical solution of MM-MD models. In this discussion we have taken the task of protein structure prediction as our yardstick to judge the accuracy of the available force fields and computational techniques. If MD is supposed to provide a contribution to protein folding or to the related problem of structure-based drug design, this yardstick is certainly relevant. However, there are many more possible fields of application for MD simulation than just these two. Each of them has its own accuracy requirements pertaining to different parts of the force field, as has been illustrated by the various examples of restricted MD-based methods given in Section 33.2.7.

If MD is taken seriously as a method for generating a virtual reality of the conformational dynamics that enables, for instance, energy-driven processes of protein function, then additional aspects of the MM force fields become relevant. Because this conformational dynamics involves torsions around chemical bonds and requires evasive actions to circumvent steric hindrances in these strongly constrained macromolecules, the potential functions mapping the mechanical elasticity and flexibility must be adequately represented for correct descriptions of the kinetics. Here, these so-called ''bonded'' potential functions must be balanced with the van der Waals potentials of the various atoms and with the modeling of the electrostatics. To illustrate the delicate dependence of simulation descriptions on these details of the force field parameterization, we will now return to one of the examples mentioned in Section 33.2.7.

33.4
Conformational Dynamics of a Light-switchable Model Peptide

An important obstacle impeding the improvement of MM force fields is the lack of sufficiently specific and detailed experimental data on the conformational dynamics in proteins and peptides. Structural methods like X-ray or NMR render only information on the equilibrium fluctuations or on the equilibrium conformational ensemble, respectively. In X-ray, a structurally and temporally resolved monitoring of relaxation processes may become accessible through the Laue technique, but this approach is still in its infancy. On the other hand, time-resolved spectroscopic methods for the visible and infrared spectral regions are well-established and, with the recent development of two-dimensional correlation techniques [56], promising perspectives are opening up.

To become useful for the evaluation of MM force fields, these techniques must be applied to small peptide–solvent systems of strongly restricted complexity, because, otherwise, the multitude of the many weak interactions characteristic for large proteins in solution prevents the unique identification of force field deficien-

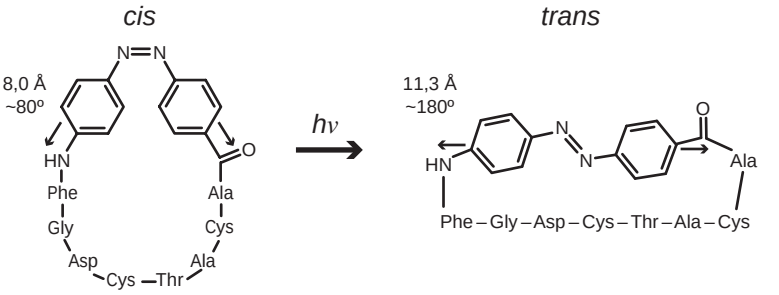

Fig. 33.7. Chemical structures of a small cyclic peptide (cAPB) and scheme of the light-induced photoisomerization, which changes the isomeric state of the azobenzene dye integrated into the backbone of the peptide from *cis* to *trans*. The isomerization widens the angle of the stiff linkage between the chromophore and the peptide from about 80° to 180° and elongates the chromophore by 3.3 Å. The strain exerted by the chromophore after photoisomerization forces the peptide to relax from an ensemble of helical and loop-like conformations into a stretched β-sheet (see Figure 33.9 for structural details).

cies. Furthermore, the dynamical processes monitored spectroscopically should proceed rapidly on the time scale of at most nanoseconds, because this time scale is already accessible to MD simulations.

Adopting this view, Spörlein et al. [39] have recently presented an integrated approach towards the understanding of peptide conformational dynamics, in which femtosecond time-resolved spectroscopy on model peptides with built-in light switches has been combined with MD simulation of the light-triggered motions. It has been applied to monitor the light-induced relaxation dynamics occurring on subnanosecond time scales in a peptide that was backbone-cyclized with an azobenzene derivative as optical switch and spectroscopic probe.

Figure 33.7 depicts the chemical structure of this molecule (cAPB) and schematically indicates the changes of geometry that are induced by the photoisomerization of the azobenzene dye. The femtosecond spectra [39] allows us to clearly distinguish and characterize the subpicosecond photoisomerization of the chromophore, the subsequent dissipation of vibrational energy and the subnanosecond conformational relaxation of the peptide. It was interesting to see to what extent these processes can be described by MM-MD simulation.

33.4.1 Computational Methods

To enable the MD simulation of the photochemical *cis–trans* isomerization of the chromophore and of the resulting peptide relaxations, an MM model potential has been constructed (see Refs [39] and [57] for details), which drives the chromophore along an inversion coordinate at one of the central nitrogen atoms from *cis* to *trans* and, concomitantly, deposits the energy of 260 kJ mol^{-1}, which is equal to that of the absorbed photon, into the cAPB molecule. This approach serves to

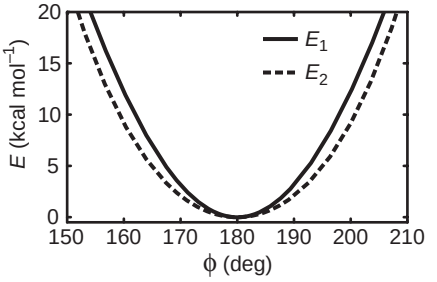

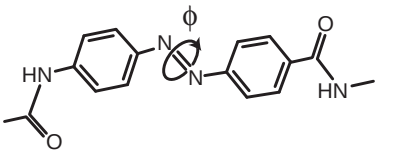

Fig. 33.8. Two different MM potentials obtained from fits to DFT potential curves for the torsion of the chromophore around the central N=N double bond by a dihedral angle Φ [57]. The stiff potential E_1 results from a fit of a cosine to the DFT potential curve in the vicinity of the *trans*-configuration ($\Phi = 180°$) and the softer potential E_2 from a fit of a Fourier expansion aiming at an improved description of the DFT potential curve in a wider range of torsion angles $\Phi \in [70°, 300°]$.

model the photoexcitation of the dye, its relaxation on the excited-state surface, and its ballistic crossing back to the potential energy surface of the electronic ground state through a conical intersection. To describe the subsequent dissipation of the absorbed energy into the solvent and the relaxation of the peptide from the initial *cis*-ensemble of conformations to the target *trans*-conformation, MM parameters for the chromophore, the peptide and the surrounding solvent were required.

Apart from a slight modification [57], the peptide parameters were adopted from the CHARMM22 force field [33]. Like in the experimental set-up, dimethyl-sulfoxid (DMSO) was used as the solvent. For this purpose an all-atom, fully flexible DMSO model was designed by DFT/MM techniques [9], was characterized by TBC/RF-MD simulations, and was compared with other MM models known in the literature [57]. Likewise, the MM parameters of the chromophore were determined by series of DFT calculations. Figure 33.8 illustrates the subtle differences that may result from such a procedure of MM parameter calculation, taking the stiffness of the central N=N bond with respect to torsions as a typical example. The stiffer potential E_1 has been employed in Spörlein et al. [39] and the consequences of choosing the slightly softer potential E_2 will be discussed further below.

A larger number of MD simulations, each spanning 1–10 ns (some even up to 40 ns), have been carried out to characterize the equilibrium conformational ensembles in the *cis* and *trans* states as well as the kinetics and pathways of their photo-induced conversion [57]. The simulation system was periodic, shaped as a rhombic dodecahedron (inner diameter of 54 Å), and was initially filled with 960 DMSO molecules. The best 10 NMR solutions [58] for the structure of the cAPB peptide were taken as starting structures for the simulations of the photoisomerization. They were placed into the simulation system, overlapping DMSO molecules were removed, and the solvent was allowed to adjust in a 100 ps MD simulation at 300 K to the presence of the rigid peptide. Then the geometry restraints initially imposed on the peptide were slowly removed during 50 ps, the system was equilibrated for another 100 ps at 300 K and 1 bar, it was heated to 500 K for

50 ps, and cooled within 200 ps to 300 K. In this way 10 different starting structures were obtained for the 1 ns simulations of the *cis–trans* isomerization, which was initiated by suddenly turning on the model potential driving the inversion reaction. To obtain estimates for the equilibrium conformational ensembles in the *cis* and *trans* states, 10 ns MD simulations were carried out at 500 K starting from the best NMR structures modified by the equilibration procedure outlined above. At this elevated temperature a large number of conformational transitions occur in the peptide during the simulated 10 ns. In all simulations the TBC/RF approach (cf. Section 33.2.2) was used with a dielectric constant of 45.8 modeling the DMSO continuum at large distances (for further details see Ref. [57]).

Due to the lack of space, the methods applied for the statistical analysis of the simulation data cannot be presented in detail here. Instead a few remarks must suffice: The 10 ns trajectories at 500 K have been analyzed by a new clustering tool, which is based on the computation of an analytical model of the configuration space density sampled by the simulation. The model is a Gaussian mixture [59], enables the construction of the free energy landscape and allows the identification of a hierarchy of conformational substates. The associated minima of the free energy are then characterized by prototypical conformations [57]. Concerning the characterization of the photo-induced relaxation dynamics, we will restrict our analysis to the temporal evolution of the total energy left in the cAPB molecule after photoisomerization and will omit structural aspects.

33.4.2 Results and Discussion

Figure 33.9 shows the prototypical conformations of *cis*- and *trans*-cAPB in DMSO at 500 K and 1 bar, which have been obtained from the 10 ns simulations by the procedures sketched in the preceding section. Whereas *cis*-cAPB exhibits a series

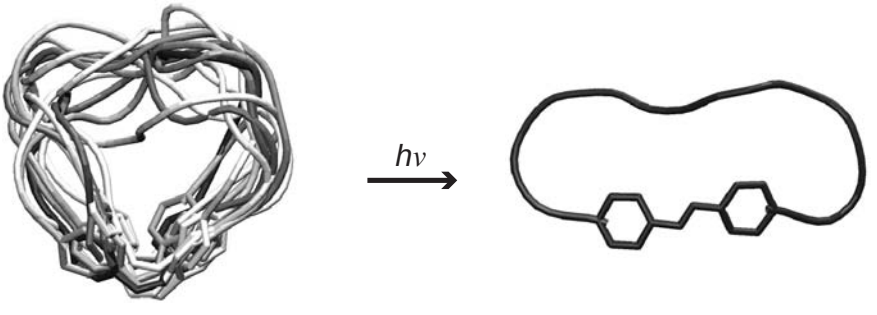

Fig. 33.9. Conformational ensembles in the *cis* and *trans* states of the cAPB peptide as obtained from 10 ns simulations at 500 K. Each backbone structure represents a different local minimum of the free energy landscape. The gray-scale indicates the depth of the respective minimum. Whereas there is only one such minimum in *trans*, there are many in *cis* (see Ref. [57] for details).

of different conformations, which are dynamically related by thermal flips around the dihedral angles at the Cα atoms of the backbone, there is only a single *trans*-cAPB conformer. Although the depicted conformers derive from high-temperature simulations, they are compatible [57] with the NOE-restraints observed by NMR [58]. This agreement may not be taken as a big surprise, because the conformational flexibility of peptide is sizably restricted by the strong covalent linkages within the cyclic structure. Apparently, in the given case these restrictions suffice to compensate those inaccuracies of the force field, which involve weaker dipolar interactions or the neglect of the electronic polarizability.

Figure 33.9 illustrates the process that is driven by the photoisomerization. The photons are absorbed by an ensemble of *cis*-conformers, and the geometry change of the chromophore forces the peptide backbone to relax through flips around the bonds at the Cα atoms towards the *trans*-conformation. In this conformation, the structure of the peptide is that of a β-sheet, up to turns at the covalent linkage with the chromophore. Therefore, the process may be considered as protein folding "en miniature."

As far as the photo-induced relaxation dynamics is concerned, Figure 33.10 illustrates a surprising and, as we will argue below, also somewhat frustrating result, reported previously in Ref. [39]. The kinetics of energy relaxation calculated by MD for the *cis–trans* photoisomerization of cAPB agrees nearly perfectly with that of a corresponding spectroscopic observable! As far as the match within the first picosecond is concerned, this agreement simply reflects the careful design of the MM model potential driving the ballistic photoisomerization and, therefore, is what one should expect, if the assumption of an inversion reaction is correct.

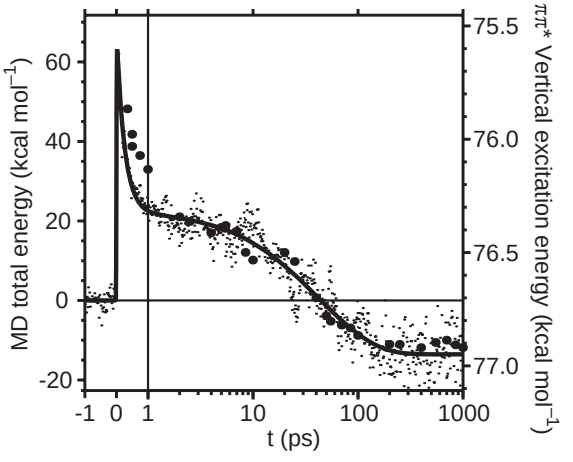

Fig. 33.10. Comparison of the energy relaxation kinetics following *cis–trans* isomerization as observed by femtosecond spectroscopy (black dots, monitoring the spectral position of the main absorption band) and as calculated by MD (black pixels and fit to the MD trajectories, monitoring the total energy of the cAPB molecule) on a linear-logarithmic time scale [39].

From a global fit of all spectroscopic data, covering a wide spectral range, four time constants have been obtained for the relaxation processes, and the analysis of the spectra has allowed to assign elementary processes to these kinetics [39]. Thus, according to spectroscopy, the ballistic isomerization proceeds within 230 fs, a second relaxation channel from the excited state surface to the electronic ground state (not included in the MM model by construction) takes 3 ps, the dissipation of heat from the chromophore into the solvent and the peptide chain proceeds within 15 ps, and a 50 ps kinetics is assigned to conformational transitions in the peptide. As shown in Ref. [60] further conformational transitions in the peptide occur above the time scale of 1 ns until the relaxation process is complete.

The limited statistics of the MD data shown in Figure 33.10 allows us to determine two time constants within the first nanosecond. These time constants are 280 fs for the isomerization of the chromophore and 45 ps for the conformational relaxation of the peptide form the *cis*-ensemble towards the *trans*-conformation. The corresponding two-exponential decay is depicted by the solid fit curve in Figure 33.10. Due to the proximity of the cooling kinetics (15 ps) to that of the conformational dynamics (50 ps) these processes cannot be distinguished in the MD data on cAPB. According to the simulations, after 1 ns the *trans*-conformation has not yet been reached in most trajectories. Thus, within the first nanosecond the relaxation kinetics of the simulated ensemble quantitatively agrees with the observations to the extent, to which the limited MD statistics allows the identification of kinetic constants.

Further above we have stated that this result has been somewhat frustrating for us. Representing the theory group that had been involved in the design of the model system and of its experimental characterization from the very beginning about a decade ago, we had hoped that our integrated approach [39] would provide hints as to how one has to improve the MD methods and MM force fields. This hope had been a key driving force in the original set-up of this interdisciplinary approach. Instead, the results have merely validated our MD methods, raising the question whether (i) the integrated approach is sensitive enough to the details of the MM force field or (ii) our skepticism with respect to the quality of MD descriptions is justified.

To check these questions we have conducted a series of simulations in which certain details of the applied MM force fields were changed one by one [57]. From the huge pile of results collected in this way we have selected a typical example which provides enough evidence to answer both questions. In this example we have changed a single model potential of the MM force field, that is, we have replaced the stiff torsion potential E_1 by the slightly weaker potential E_2 (see Figure 33.8 for plots of these function and Section 33.3.1 for further explanation). One can expect that this potential is important for transmitting the mechanical strain from the chromophore to the peptide after *cis–trans* isomerization. If it is stiff (E_1), then the strain is strong and the relaxation should be fast, and if it is weaker (E_2) the relaxation should become slowed down.

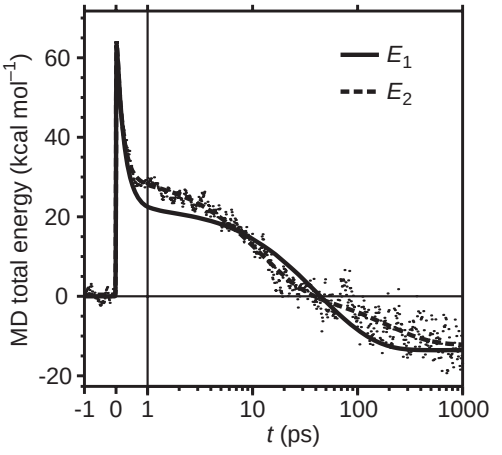

Fig. 33.11. Comparison of the energy relaxation kinetics calculated by MD for two slightly different force fields: The original model potential E_1 is replaced by E_2 (cf. Figure 33.8). The fit curve belonging to E_1 has been taken from Figure 33.10. The dashed fit curve to the 10 MD trajectories (pixels) calculated with E_2 exhibits three kinetic constants. Besides showing a 190 fs ballistic isomerization (exp: 230 fs), it separates an 11 ps heat dissipation (exp: 15 ps) from a 190 ps conformational relaxation (exp: 50 ps).

The above expectation is confirmed by the MD results for the softer potential E_2 shown in Figure 33.11 and by the kinetic data listed in the associated caption. In the case of E_2, the prolonged time scale (190 ps) of the conformational relaxation, which is caused by the slightly softer spring, has enabled us to additionally identify the kinetics of heat dissipation (11 ps) in the data. The results demonstrate that a small change of a single model potential can change the kinetic time constant calculated for the conformational relaxation from 45 ps to 190 ps, that is, by a factor of 4.

This example answers the two questions voiced above, because it provides evidence that (i) our integrated approach is sensitive enough to detect small changes in a force field and (ii) that our skepticism with respect to the quality of MM force fields is well-justified. The latter is apparent from the fact that both fit procedures for obtaining a torsion potential from DFT calculations, the one that has led to E_1, and the one yielding E_2, represent a priori valid choices. It was actually a matter of luck that we happened to choose the right one for the first few simulations published in Ref. [39]. As we now definitely know [57], only a series of further lucky choices in the force field used for our original simulations enabled the surprisingly perfect match. On the other hand, the perfect match obtained in our first attempt to describes the light-induced relaxation in the cAPB peptide also demonstrates that, in principle, MD simulations can give quantitative descriptions. In this sense it gives credit to the method and justifies further efforts aiming at the improvement of the force fields and the extension of time scales.

Summary

As of today, MM force fields are not yet accurate enough to enable a reliable prediction of protein and peptide structures by MD simulation. Here the key deficiency is the neglect of the electronic polarizability in the MM force fields. However, MM-MD is valid in restricted settings, for instance, when complemented by experimental constraints, when applied to systems of reduced complexity, or in the restricted context of QM/MM hybrid calculations. In particular, the development of the DFT/MM methods has generated key tools that are required for the improvement of the MM force fields, because they allow highly accurate computations of intramolecular force fields of molecules polarized by a condensed phase environment. The latter has been demonstrated by computations of IR spectra in condensed phase, whose accurate description critically depends on the quality of the computed force field. For the validation of future MM force fields more specific experimental characterizations of the materials are necessary. Thus, the improvement of the computational methods has to rely on close cooperation between scientists working in experimental and theoretical biophysics, chemistry, biochemistry, and beyond.

Acknowledgments

Financial support by the Volkswagen-Stiftung (Project I/73 224) and by the Deutsche Forschungsgemeinschaft (SFB533/C1) is gratefully acknowledged. The authors would like to thank W. Zinth, F. Siebert, L. Moroder, C. Renner, and J. Wachtveitl for fruitful discussions.

References

1 M. Karplus, J. A. McCammon, *Nature Struct. Biol.* **2002**, *9*, 646–652.
2 J. W. Ponder, D. A. Case, *Adv. Protein Chem.* **2003**, *66*, 27–85.
3 S. Gnanakaran et al., *Current Opinion in Struct. Biol.* **2003**, *13*, 168–174.
4 M. P. Allen, D. J. Tildesley, *Computer Simulations of Liquids*. Clarendon, Oxford, 1987.
5 A. Warshel, S. T. Russel, *Q. Rev. Biophys.* **1984**, *17*, 283–422.
6 G. Mathias, P. Tavan, *J. Chem. Phys.* **2004**, *120*, 4393–4403.
7 B. Guillot, *J. Mol. Liquids* **2002**, *101*, 219–260.
8 C. L. Brooks, *Acc. Chem. Res.* **2002**, *35*, 447–454.
9 M. Eichinger, P. Tavan, J. Hutter, M. Parrinello, *J. Chem. Phys.* **1999**, *110*, 10452–10467.
10 K. Laasonen, M. Sprik, M. Parrinello, R. Car, *J. Chem. Phys.* **1993**, *99*, 9080–9089.
11 C. Tanford, *The Hydrophobic Effect: Formation of Micelles and Biological Membranes*. Wiley, New York, 1980.
12 P. L. Privalov, in *Protein Folding*, Ed: T. E. Creighton, Freeman, New York, 1992.
13 F. Siebert, *Meth. Enzymol.* **1995**, *246*, 501–526.
14 J. A. McCammon, B. R. Gelin, M. Karplus, *Nature* **1977**, *267*, 585–590.
15 W. F. van Gunsteren, H. J. C.

Berendsen, *J. Mol. Biol.* **1984**, *176*, 559–564.
16 M. Levitt, R. Sharon, *Proc. Natl Acad. Sci. USA* **1988**, *85*, 7557–7561.
17 A. Rahman, F. H. Stillinger, *J. Chem. Phys.* **1971**, *55*, 3336–3359.
18 G. Mathias, B. Egwolf, M. Nonella, P. Tavan, *J. Chem. Phys.* **2003**, *118*, 10847–10860.
19 I. G. Tironi, R. Sperb, P. E. Smith, W. F. van Gunsteren, *J. Chem. Phys.* **1995**, *102*, 5451–5459.
20 P. H. Hünenberger, W. F. van Gunsteren, *J. Chem. Phys.* **1998**, *108*, 6117–6134.
21 T. A. Darden, D. York, L. Pedersen, *J. Chem. Phys.* **1993**, *98*, 10089–10092.
22 U. Essmann et al., *J. Chem. Phys.* **1995**, *103*, *8577–8593*.
23 B. A. Luty, I. G. Tironi, W. F. van Gunsteren, *J. Chem. Phys.* **1995**, *103*, 3014–3021.
24 P. H. Hünenberger, J. A. McCammon, *Biophys. Chem.* **1999**, *78*, 69–88.
25 C. Niedermeier, P. Tavan, *J. Chem. Phys.* **1994**, *101*, 734–748.
26 C. Niedermeier, P. Tavan, *Mol. Simul.* **1996**, *17*, 57–66.
27 E. Lindahl, B. Hess, D. van der Spoel, *J. Mol. Mod.* **2001**, *7*, 306–317.
28 G. Mathias et al., *EGO-MMII Users Guide*. Lehrstuhl für BioMolekulare Optik, LMU München, Oettingenstrasse 67, D-80538 München, unpublished.
29 G. A. Kaminski et al., *J. Comput. Chem.* **2002**, *23*, 1515–1531.
30 M. Marquart et al., *Acta Crystallogr. Sec.* **1983**, *39*, 480–490.
31 B. Egwolf, P. Tavan, *J. Chem. Phys.* **2003**, *118*, 2039–2056.
32 L. Jorgensen et al., *J. Chem. Phys.* **1983**, *79*, 926–935.
33 A. D. MacKerell et al., *J. Phys. Chem. B* **1998**, *102*, 3586–3616.
34 W. D. Cornell et al., *J. Am. Chem. Soc.* **1995**, *115*, 9620–9631.
35 G. A. Kaminski, R. A. Friesner, J. Tirado-Rives, W. L. Jorgensen, *J. Phys. Chem. B* **2001**, *105*, 6474–6487.
36 M. W. Mahoney, W. L. Jorgensen, *J. Chem. Phys.* **2000**, *112*, 8910–8922.
37 X. Daura et al., *J. Am. Chem. Soc.* **2001**, *123*, 2393–2404.
38 H. Grubmüller, B. Heymann, P. Tavan, *Science* **1996**, *271*, 997–999.
39 S. Spörlein et al., *Proc. Natl Acad. Sci. USA* **2002**, *99*, 7998–8002.
40 W. F. van Gunsteren, A. E. Mark, *J. Chem. Phys.* **1998**, *108*, 6109–6116.
41 H. J. C. Berendsen, *Science* **1996**, *271*, 954–955.
42 A. T. Brünger et al., *Science* **1987**, *235*, 1049–1053.
43 A. Warshel and M. Levitt, *J. Mol. Biol* **1976**, *103*, 227–249.
44 P. Hohenberg, W. Kohn, *Phys. Rev B* **1964**, *136*, 864–870.
45 W. Kohn, L. J. Sham, *Phys. Rev. A* **1965**, *140*, 1133–1138.
46 M. J. Frisch et al., *Gaussian98*, Gaussian, Inc., Pittsburgh PA, 1998.
47 J. Neugebauer, B. A. Hess, *J. Chem. Phys.* **2003**, *118*, 7215–7225.
48 M. Nonella, P. Tavan, *Chem. Phys.* **1995**, *199*, 19–32.
49 M. Nonella, G. Mathias, M. Eichinger, P. Tavan, *J. Phys. Chem. B* **2003**, *107*, 316–322.
50 M. Nonella, G. Mathias, P. Tavan, *J. Phys. Chem. A* **2003**, *107*, 8638–8647.
51 D. Bashford, D. A. Case, *Annu. Rev. Phys. Chem.* **2000**, *51*, 129–152.
52 C. D. Snow, N. Nguyen, V. S. Pande, M. Gruebele, *Nature* **2002**, *420*, 102–106.
53 R. H. Zhou, B. J. Berne, *Proc. Natl Acad. Sci. USA* **2002**, *99*, 12777–12782.
54 H. Nymeyer, A. E. Garcia, *Proc. Natl Acad. Sci. USA* **2003**, *100*, 13934–13939.
55 B. Egwolf, P. Tavan, *J. Chem. Phys.* **2004**, *120*, 2056–2068.
56 S. Woutersen, P. Hamm, *J. Phys. Chem. B* **2000**, *104*, 11316–11320.
57 H. Carstens, Dissertation, Ludwig-Maximilians-Universität München, 2004.
58 C. Renner et al., *Biopolymers* **2000**, *54*, 489–500.
59 M. Kloppenburg, P. Tavan, *Phys. Rev. E* **1997**, *55*, 2089–2092.
60 S. Spörlein, Dissertation, Ludwig-Maximilians-Universität München, 2001.

Part II

1
Paradigm Changes from "Unboiling an Egg" to "Synthesizing a Rabbit"

Rainer Jaenicke

1.1
Protein Structure, Stability, and Self-organization

Max Perutz, in reviewing Anson and Mirsky's discovery [1–3] that hemoglobin fully recovers its functional properties after reversible acid denaturation, felt that "making a protein alive again is as impossible as inventing the *perpetuum mobile*"; this was in 1940 [4]. As we know today from 75 years practice since his first experiments, Anson (Figure 1.1) was right, despite Kailin's protest that "boiling an egg does not denature its protein, it kills it!" [5]: proteins do have the capacity to spontaneously and autonomously organize their three-dimensional structure. At Anson's time this was a model, because the antivitalist creed that the composition of proteins is revealed by analytical chemistry and their behavior, by physical chemistry (which in the last analysis depends on their structure [6]) was no more than a guiding principle for chemists interested in biological material [7]. Svedberg had just published the determination of the molecular weight of the first protein, equine hemoglobin, making use of his newly developed analytical ultracentrifuge [8]. With this data, it became clear that proteins are monodisperse entities with well-defined molecular masses. To determine the detailed 3D structure of hemoglobin at atomic resolution still took more than a generation [9]. Thus, the first folding experiments were based on the assumption that an isolated homogeneous component of mammalian blood, obtained by fractional crystallization, not only had the intrinsic property of self-organization but also allowed one to quantify its physiological activity in vivo in terms of cooperative ligand binding, allostery, Bohr effect etc., following the reductionist's creed and methodology. With this paradigm in mind, the alchemy of protein folding addressed a wide range of fundamental biological problems, tacitly assuming that the results of in vitro studies are biologically relevant. As sometimes happens, a few results of this bold hypothesis turned out to be practicable in various ways, so that, in the long run, the scope switched from pure physical to biological chemistry. After a generation or two, research and development in biotechnology shifted the dimensions of in vitro folding experiments from microliter pipettes and Eppendorf vials to pipelines and 5–10-m^3 tanks, nowadays used in the production of pharmaceutically or technologically im-

Protein Folding Handbook. Part II. Edited by J. Buchner and T. Kiefhaber

ISBN: 3-527-30784-2

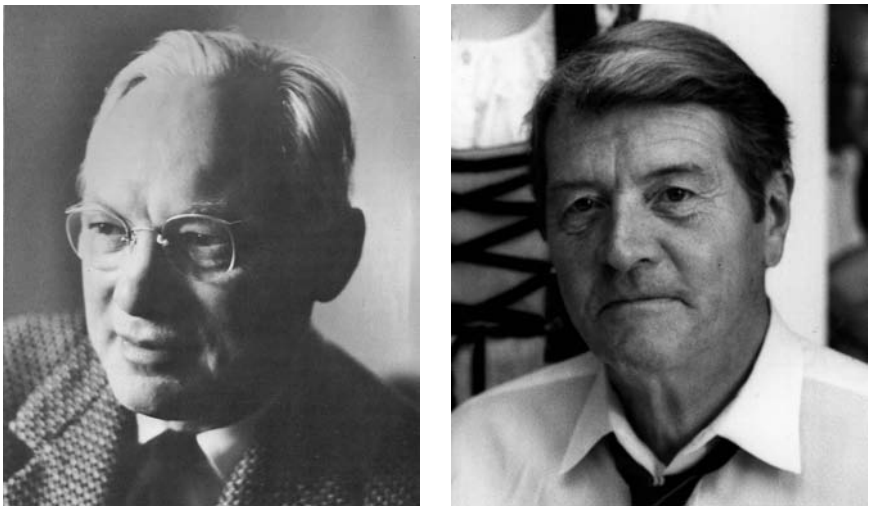

Fig. 1.1. Pioneers in the early days of protein folding: left, M. L. (''Tim'') Anson (1901–1968), right, Chris B. Anfinsen (1916–1995).

portant proteins. Frequently the final products are modified in one way or the other to alter their long-term stability, their specificity, or other properties.

In this context, Anfinsen's (Figure 1.1) classical experiments influenced the philosophy of his followers right from the beginning by the fact that he started from *reduced* ribonuclease A (RNaseA) rather than the natural enzyme with its cystine cross-bridges intact. In spite of the chemical modification, the reshuffling process led to the correctly cross-linked native state, thus proving that all the information required for folding and stabilizing the native three-dimensional conformation of proteins is encoded in their amino acid sequence [10]. Extending this conclusion to the entire structural hierarchy of proteins, it was postulated that the primary structure directs not only the formation of multiple noncovalent (''weak'') and covalent (''strong'') bonds within a single polypeptide chain but also the interactions between the subunits of oligomeric proteins, driving the sequential folding-association reaction and stabilizing the final tertiary and quaternary structure.

In distinguishing between weak and strong interactions, it is important to note that globular proteins in their natural aqueous environment show only marginal Gibbs free energies of stabilization. With numerical data on the order of 50 kJ mol^{-1}, they are the equivalent of a small number of hydrogen bonds or hydrophobic interactions, or perhaps just one or two ion pairs. This holds despite the fact that thousands of atoms may be involved in large numbers of attractive and repulsive interactions, in total adding up to molecular energies a million times larger than the above average value [11]. The reason for this apparent discrepancy is that proteins are *multifunctional*: they need to fold, they serve specific modes of action, and they provide amino acid pools in both catabolic and anabolic processes.

With this in mind, the point is that, given one single device, it is impossible to simultaneously *maximize* the efficiency of all these ''functions''; nature has to compromise, and since stability, biological activity, and turnover all require a certain degree of flexibility, stability (equivalent to rigidity) cannot win.

Recent advances in our understanding of the different types of weak interactions involved in the self-organization and stabilization of proteins were derived from theoretical studies on the one hand ([12–15], cf. R. L. Baldwin, Vol. I/1) and from the analysis of complete genomes of phylogenetically related mesophiles and (hyper-)thermophiles, as well as systematic mutant studies, on the other [16–18]. Apart from the latter ''quasi-Linnaean approach,'' protein engineering provides us with a wealth of alternatives to crosscheck the genomix results [19–23]; in combining and applying these approaches to technologically relevant systems, increases in thermal stability of up to 50 °C have been accomplished [24]. In contrast to such success stories, Kauzmann's catalog of weak intermolecular interactions [25] has not changed since 1959, and a 2004 ''balance sheet of ΔG_{stab} contributions to folding'' would be as tentative or postdictive as J. L. Finney and N. C. Pace's classical attempts to predict ΔG_{stab} for RNase and lysozyme in 1982 and 1996 [26, 27]. What has become clear in recent years is that increases in overall packing density, helicity, and proline content (i.e., destabilization of the unfolded state) and improved formation of networks of H-bonds and ion-pairs are important increments of protein stabilization. In the long-standing controversy regarding the prevalence of the various contributions, evidently all components are significant. In the case of hydrophobic interactions, entropic (water-release) *and* enthalpic (London-van der Waals) effects seem to be equally important [28, 29]. That hydrogen bonding and ion pairs are essential is now generally accepted [27, 30, 31]; surprisingly, recent evidence seems to indicate that polar-group burial also makes a positive contribution to the free energy of stabilization [32].

As has been mentioned, the balance of the attractive and repulsive forces yields only marginal free energies of stabilization. They may be affected by mutations or changes in the solvent, the latter often highly significant due to their effect on the unfolding *kinetics*. The reason is that by adding specific ions or other ligands, the free energy of activation ($\Delta G^{\neq}_{stab}$) of the N → U transition, i.e., the free-energy difference between the native and the transition states, may be drastically increased. The resulting ''kinetic stabilization'' has been shown to be essential for the extrinsic stabilization or longevity of the native state as well as for the folding competence of conjugated and ultrastable proteins [16, 33, 34].

From the thermodynamic point of view, protein folding is a hierarchical process, driven by the accumulation of increments of free energy from local interactions among neighboring residues, secondary structural elements, domains, and subunits (Scheme 1.1). Domains represent independent folding units. Correspondingly, the folding kinetics divide into the collapse of subdomains and domains and their merging to form the compact tertiary fold. Establishing the particular steps allows the folding pathway for a given protein to be elucidated. In proceeding to oligomeric proteins, docking of structured monomers is the final step. In agreement with this mechanism, in vitro experiments have shown that the overall fold-

Structural levels: primary → secondary/supersecondary → tertiary → quaternary structure
Interactions: short-range and long-range (= short-range through-chain and through-space) [11, 12, 42]
Folding pathway: next-neighbor interactions → collapsed unfolded state and/or molten globule state [43, 44] → docking of domains [45, 46] → assembly [47, 48]
Intermediates: kernels/molten globule → folded/unfolded subdomains and domains → native-like structured monomers → stepwise assembly, e.g., nM → n/2 M_2 → n/4 M_4 for a tetramer
Off-pathway reactions: misfolding, domain swapping, misassembly, aggregation [34, 36–40]

Scheme 1.1. Hierarchy of protein folding and association

ing and association reaction can be quantified by a consecutive uni-bimolecular kinetic scheme. In a first folding step, the subunits need to expose specific interfaces to recognize the correct partners; then, after complementary docking sites have been formed, association to well-defined oligomers can occur in a concentration-dependent fashion. Their affinity depends on the same types of weak interactions that participate in the stabilization of the monomeric entities. No wonder that intra- and intermolecular interactions can replace each other, causing misassembly and subsequent aggregation rather than proper quaternary structure formation. At high subunit concentrations, when folding becomes rate-limiting and association becomes diffusion-controlled, aggregation is expected to become predominant. In fact, early refolding studies (focusing on the structure-function relationship of oligomeric proteins) proved that reactivation yielded optimum curves, confirming the consecutive mechanism with aggregation as a competing side reaction [35–37] (Figure 1.2). Later, when "inclusion bodies" were identified as typical byproducts of protein overexpression in vivo, it became clear that the sequential folding/association mechanism (including the kinetic partitioning between the two processes) also holds for the nascent protein when it leaves the ribosome. It took 10 more years to fully appreciate that evolution took care of the problem by providing folding catalysts and heat shock proteins as chaperones [41]. Evidently, they shift the kinetic partitioning between assembly and aggregation toward the native state. So far, the detailed co-translational and post-translational processes *in the cell* have withstood a sound kinetic and structural analysis.

1.2 Autonomous and Assisted Folding and Association

The contributions to the present volume deal with the above side reactions in the self-organization of proteins as well as the helper proteins involved in either avoidance of misfolding or the catalysis of rate-determining steps along the folding pathway. Reading the seminal papers, and having in mind the procedures that were applied in early protein denaturation-renaturation experiments, it becomes clear that the pioneers in the field were aware of the possible role of accessory components long before they were discovered: *templates* assisting the nascent polypeptide chain

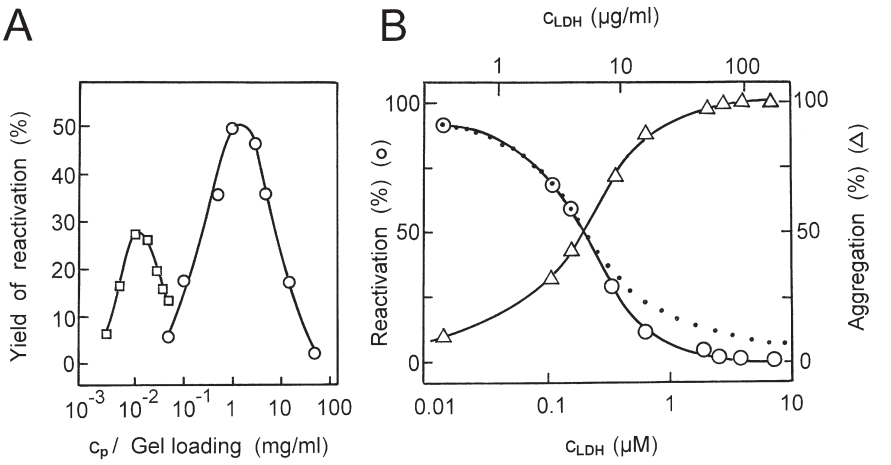

Fig. 1.2. Kinetic competition between folding and aggregation. (A) Effect of protein concentration on the renaturation of α-glucosidase after urea denaturation, illustrating the partitioning between "renativation" and aggregation. Denaturation in 8 M urea, 10 mM K-phosphate pH 7.7, 1 h incubation at 20 °C; reactivation in 10 mM Na-phosphate pH 7.6, 10 °C, 30 mM NaCl, and 8% ethylene glycol, measured after ≥24 h renaturation. (□) refers to wild-type α-glucosidase and (○) to the fusion protein containing a C-terminal hexa-arginine tail, which allows the stabilization of the enzyme on heparin-Sepharose. The yield of reactivation is expressed as a percentage of the activity of the corresponding native enzyme (data from Ref. [38]). (B) With increasing protein concentration, the yield of reactivation of lactate dehydrogenase after acid denaturation in 0.1 M H_3PO_4, pH 2, and subsequent renaturation in phosphate buffer pH 7.0 decreases (○) and aggregation increases (△) in a complementary way [37]. As indicated by the dotted line, to a first approximation, the kinetic competition can be modeled by Eq. (5), i.e., by sequential unimolecular folding ($k_1 = 0.01\ s^{-1}$) and (diffusion-controlled) bimolecular aggregation ($k_2 = 10^5\ M^{-1}\ s^{-1}$), with molar concentrations based on a subunit molecular mass of 35 kDa [39].

on its pathway toward the native conformation, or *shuffling enzymes* and *foldases* as catalysts were postulated or even isolated early in the game [49, 50]. However, they were ignored for the simple reason that there seemed to be no real need for helpers, because the spontaneous reaction was autonomous and fast enough to proceed without accessory components. It took more than two decades to change the paradigm from Cohn and Edsall's purely physicochemical approach [7] to considerations comparing optimal in vitro conditions with the situation in the cell [51, 52]. That catalysts or chaperones might be biologically significant was suggested by three observations (Figure 1.3). First, experiments with mouse microsomes depleted of Anfinsen's "shuffling enzyme" proved *protein disulfide isomerase* (PDI) to be essential for protein folding in the endoplasmic reticulum (ER) [55]. Second, the unexpected bimodal N ↔ I ↔ U kinetics of the two-state N ↔ U equilibrium transition of ribonuclease (RNaseA) and its physicochemical characteristics suggested proline isomerization to be involved in protein folding [56, 57]; in fact, the enzyme *peptidyl-prolyl cis-trans isomerase* (PPI) was found to catalyze rate-limiting steps on the folding pathway of proteins [58–60]. Third, increasing numbers of

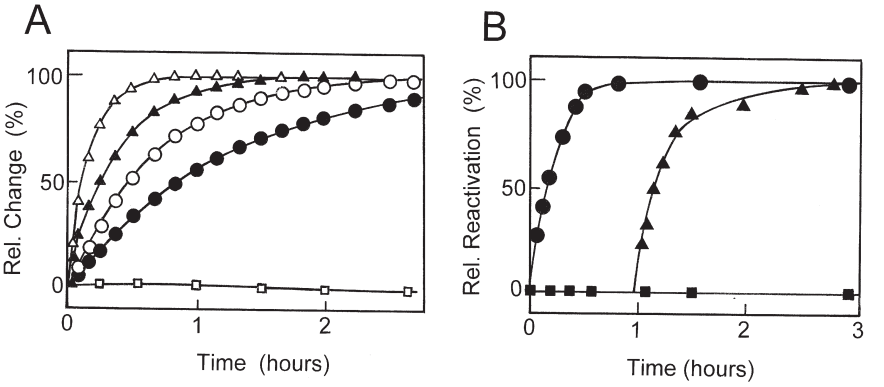

Fig. 1.3. Folding catalysts and chaperones. (A) Acceleration of the oxidative refolding of ribonuclease T1 by PPI and PDI, monitored by tryptophan fluorescence at 320 nm: 2.5 μM RNaseT1 in 0.1 M Tris-HCl pH 7.8, 0.2 M guanidinium chloride, 4 mM reduced/0.4 mM oxidized glutathione, 25 °C. Re-oxidation in the absence of PPI and PDI (●), in the presence of 1.4 μM PPI (○), in the presence of 1.6 μM PDI (▲), in the presence of 1.4 μM PPI plus 1.6 μM PDI (△), and in the presence of 10 mM dithioerythritol (to block disulfide bond formation) (□); the slight decrease in the latter signal is caused by aggregation of the reduced and unfolded protein. Curves calculated for single first-order reactions with time constants $\tau = 4300$ s (●), 2270 s (○), 1500 s (▲), and 650 s (△) [53]. (B) Reactivation of citrate synthase (CS) after preceding denaturation in 6 M guanidinium chloride in the presence of GroEL without GroES and ATP (■), with GroES and ATP (●), and with GroES and ATP added after 55 min (▲). Parallel light-scattering measurements show that in the absence of the components of the GroE system, CS forms inactive aggregates [54].

stress-response proteins (Hsps) were found to be ubiquitous and by no means restricted to heat stress; evidently, they played a role as *molecular chaperones*, i.e., they mediated or promoted correct protein folding by transiently interacting with the nascent polypeptide or with the protein at an early stage of the folding process, without becoming components of its final functional state [61] (see the respective chapters 4, 5, 14–16, 20–24, 31, 32). Evidently, this definition also holds for helper or scaffold proteins that are known to aid the genetically determined *morphopoiesis* of complex assembly systems such as phage [34].

The given examples stand for the end of an era that might be called the heroic age of protein chemistry, with names such as M. Calvin, E. J. Cohn, J. T. Edsall, G. Embden, H. A. Krebs, K. U. Linderstrøm-Lang, F. Lipmann, F. Lynen, O. Meyerhoff, A. Szent-Györgyi, H. Theorell, and O. Warburg, to mention just a few. They developed the methodology to purify proteins by fractionation and to systematically search for their respective biological activities. In proceeding from the inventory of the relevant molecules and the elucidation of their structures, they identified the molecular partners, measuring the rate and equilibrium constants for each reaction. As the next steps, the molecules were localized in the various compartments of live cells, physiological tests for the participation in specific cellular processes

were developed, and mathematical models for understanding the system's behavior were formulated. Crowning the reductionist approach, the data were finally put together, ending up with the sequences and cycles of reactions that constitute the awesome networks of metabolic pathways and information transfer, including their regulation and energetics.

Faced with these Herculean efforts on the one hand, and the pressure in present-day paper production on the other, we reach the latest paradigm change: from the reductionist detail to the simplistic concept that by replacing the atomic complexity of molecules with the information pool encoded in genomes, proteomes and their corollaries at the metabolic, regulatory, and developmental levels might help to solve the riddle of life just by simplifying proteins and their interactions to spheres, squares, triangles, and arrows (as symbols for interactions).[1]

In the minds of some of the above "heroes," this change started long before the *-omix* age: in 1948, at the end of his lectures on *The Nature of Life*, the alternative to mere speculation or getting your hands dirty with experiments led Albert Szent-Györgyi to ironically promise his audience that next time he would pull a synthetic rabbit out of his pocket [64].

In the present context of protein folding vs. protein misfolding, it seems appropriate to start with a critical discussion of the physicochemical principles of self-organization, with special emphasis on the kinetic competition of folding and aggregation that led nature to evolve folding catalysts and chaperones. Combining the structural hierarchy of proteins with the processes involved in folding and association (cf. Scheme 1.1), it has been shown that commonly small (single-domain) proteins can fold without helpers, in many cases undergoing fully reversible equilibrium transitions without significant amounts of intermediates. In contrast, large (multi-domain) proteins and subunit assemblies, owing to the above-mentioned kinetic competition of intra- and intermolecular interactions in the processes of folding and association, require careful optimization to reach high yields; at high protein levels and in the absence of accessory proteins, off-pathway reactions take over (cf. Figure 1.2B) [46–48, 61].

To the uninitiated, the above hierarchical scheme might suggest that the self-organization of proteins necessarily occurs along a compulsory pathway with well-separated consecutive steps, in contrast to the alternative random-search hypothesis, which favors the idea that a jigsaw puzzle might be a more appropriate way to model protein folding [65]. When inspecting available kinetic data, it becomes clear that there is a wide variance of mechanisms that suggest "energy landscapes" rather than simple two-dimensional energy profiles as adequate pictographs to illustrate folding paths [13, 66–68] (Figure 1.4). Relevant experimental facts include

1 For a critical discussion of the dominating role of the "pictorial molecular paradigm" in the biosciences and its philosophical implications, including the question as to whether chemical formulae and graphical representations of biopolymers such as proteins are objective representations of reality, see Refs. [62, 63].

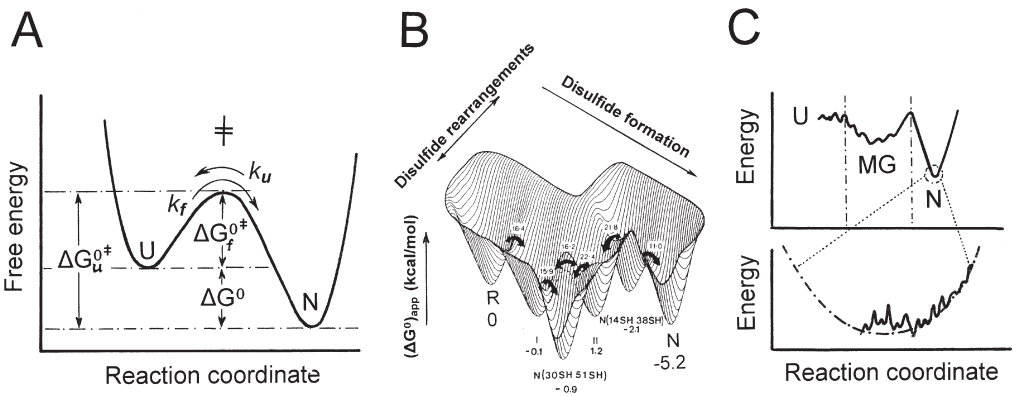

Fig. 1.4. Free-energy profiles and energy landscapes for protein folding and unfolding. (A) Relationships between the free energies of activation for folding ($\Delta G^{0\ddagger}{}_f$), and unfolding ($\Delta G^{0\ddagger}{}_u$) and of the equilibrium free energy (ΔG^0), using conventional transition-state theory. (B) "Energy-landscape" presentation describing the oxidative in vitro folding pathway of basic pancreatic trypsin inhibitor (BPTI) according to Creighton [68, 69]. The apparent free energies (in kcal mol^{-1}) are given for the fully reduced (R), intermediate (I and II), and folded (N) forms of the protein and for the transition states of the *SH* → *SS* reshuffling reaction. The reaction coordinate is represented by the three-dimensional downhill sequence of arrows. The species *I* and *II* include the one- and two-disulfide intermediates; $N_{(14SH,38SH)}$ and $N_{(30SH\text{-}51SH)}$ are native-like intermediates [34]. (C) Hypothetical conformational energy plot illustrating local energy minima and barriers along a possible protein-folding pathway. The lower "rugged potential" depicts the vicinity of the native state [13].

the following. (1) Folding as a cooperative process rarely allows true intermediates to be accumulated to a level suitable for a detailed characterization; this finding does not exclude ordered pathways but just requires a proper choice of conditions to optimize the population of intermediates. (2) For methodological reasons, the analysis of next-neighbor interactions in the folding process is prone to "in vitro artifacts," because anomalous intermediates may be populated (see the classical studies devoted to the folding pathway of basic pancreatic trypsin inhibitor [69] and to the early events in the flash-induced folding of cytochrome *c* [70, 71]). (3) For lysozyme, it has been shown that folding in fact follows multiple pathways [72]. (4) Finally, in the case of bacterial luciferase, it appears that the kinetic competition of folding and association of the $\alpha\beta$-heterodimer constitute a trap on the folding path that guides the individual subunits to the energy minimum of the active dimer [73]. Taken together, these and other examples seem to indicate that individual proteins show individual folding characteristics, an observation that also holds for the stability and stabilization of proteins. Evidently, any generalization in the world of proteins has its limitations, so that firm statements regarding "the in vitro/in vivo issue" or the wealth of expressions for "different types of molten globules" or the distinction between "short-range and long-range intermolecular forces" should either be ignored or at least taken with a grain of salt.

1.3
Native, Intermediate, and Denatured States

Before entering today's jungle of protein folding, with its roots deep in the solid ground of topology, thermodynamics, molecular dynamics, and kinetics from the microsecond to the minutes, hours, or days time range [74] (cf. Vol. I) and its youngest branches in present-day mainstream biotechnology and molecular medicine, it seems appropriate to briefly remind the reader what the starting points look like and what kind of problems motivated the aborigines to settle in the woods before the age of genomics, protein design, and folding diseases. The challenging questions were as follows. Is there a correlation between the 1D information at the level of the gene and the 3D structure of the correspondding protein? What does denaturation of proteins mean? What do the native and denatured states imply with respect to the folding mechanism of proteins? What are the best denaturation-renaturation conditions with minimal side reactions, and which criteria are best suited to characterize the authentic (native) state? What are the limits of in vitro protein folding and reconstitution, with respect to size, compartmentation, and structural complexity? Here are just a few short answers that might help in setting the frame for the crucial questions concerning the ''folding pathology'' in vitro and in vivo.

Owing to the large size of protein molecules and the unresolved problem of how to summarize the weak attractive and repulsive interatomic forces in a unique potential function, theorists have been unsuccessful in the a priori solution of the protein-folding code that would allow one to translate amino acid sequences into their corresponding three-dimensional structures. Considering the present-day output of solved X-ray and NMR structures *per anno* and the promise of developing high-throughput techniques, ''cracking the protein folding code'' has evidently lost its former challenging priority. The reason for this is simply that in order to understand the physical and functional properties of a protein at the atomic level or to acquire insight into the mechanistic details of enzyme catalysis, a resolution of <2 Å is required. This level of accuracy cannot be accomplished by any predictive approach [75].

The question of whether the physical state of a protein obtained either from the crystalline state or at high protein concentration in dilute buffer is related to or indistinguishable from its functional state in vivo has been extensively discussed since Kendrew, Perutz, and Phillips came up with their first 3D structures. Hardly any scientific result has ever been challenged to this extent; the final answer has been fundamentally positive [76], with one important limitation. Owing to their marginal stability in solution, any protein undergoes steady $N \leftrightarrow U$ transitions between the native and unfolded states. Under physiological conditions, the less-structured state is unstable and the protein reassumes its native configuration. Thus, proteins in their native functional state are dynamic systems exhibiting a high degree of local flexibility; ligand binding, allosteric transitions, and catalytic mechanisms depend on the interconversion of multiple states. The detailed quantitative understanding must necessarily take into account the structures of these

alternative states and the energetics of their interconversion. The structural fluctuations are on the order of 2 Å on a picosecond timescale. In the case of myoglobin, they allow the funneling of O_2 to the heme group in terms of "functionally important motions" [77, 78]. Whether structural heterogeneity is determined by thermal fluctuations or represents well-populated conformational substates (defined by high activation barriers beyond the thermal energy) is still under debate (Figure 1.4C). Attempts to characterize the physical and chemical properties of single molecules seem to support the second alternative [79, 80].

The term protein denaturation is essentially vague, because proteins do not unfold to a simple reference state [47, 81]. Instead, various modes of denaturation lead to different denatured states, each of them consisting of an astronomically large ensemble of different conformations but closely similar energy. Their common denominator is that they are solvated to a higher extent than the native state. Considering the amount of hydrophobic residues present in most soluble proteins, water is a poor solvent. Structure formation in the cytosol or in aqueous buffers is driven by this very fact. Making use of heteropolymers with approximately equal amounts of polar and nonpolar residues, nature allows solvation to balance by exposing hydrophilic groups to the aqueous solvent, while at the same time minimizing the hydrophobic surface. Solubilization of the inner core by denaturants leads to unfolding; however, it is obvious from the above balance of hydrophobic and hydrophilic amino acids that complete solvation cannot be accomplished. For this reason it is doubtful whether a polypeptide chain will ever be "fully randomized." Evidence from Tanford's observation that the intrinsic viscosity of denatured proteins obeyed Einstein's equation for spherical particles was weak from the beginning [82]. Even for the nascent protein in the process of translation, the conformational space is expected to be limited, because of the space-filling properties of the nascent polypeptide and its side chains, which do not allow all φ/ψ angles in the Ramachandran plot to be occupied [83]. From the practical point of view, it is important to keep in mind that the extent of unfolding of globular proteins depends not only on the denaturant but also on the physical conditions of the solvent. For the chaotrope, concentration and environmental parameters such as pH and temperature are trivial; however, specific stabilizing ligands or kinetic barriers may be essential as well [34, 84–86]. When analyzing the mechanisms of evolutionary adaptation to the wide variety of extreme physical conditions in nature, it becomes clear that extremophiles took advantage of the specific differences in protein stability [16, 33].

The fact that U is conformationally heterogeneous gives rise to multiple folding reactions in going from the unfolded to the native state. Partially folded intermediates (I) are to be expected as transients in the individual folding reactions. To find out whether intermediates are populated and what their physical properties are, it is mandatory to use different probes to follow folding and to vary the conditions for comparison. The above-mentioned bimodal $N \leftrightarrow I \leftrightarrow U$ folding kinetics of RNaseA [57–60] exemplified a well-established three-state system, with populated *cis-trans* proline isomers as structural intermediates; Figure 1.5 shows stopped-flow NMR spectra of dihydrofolate reductase from *E. coli* to illustrate the structural de-

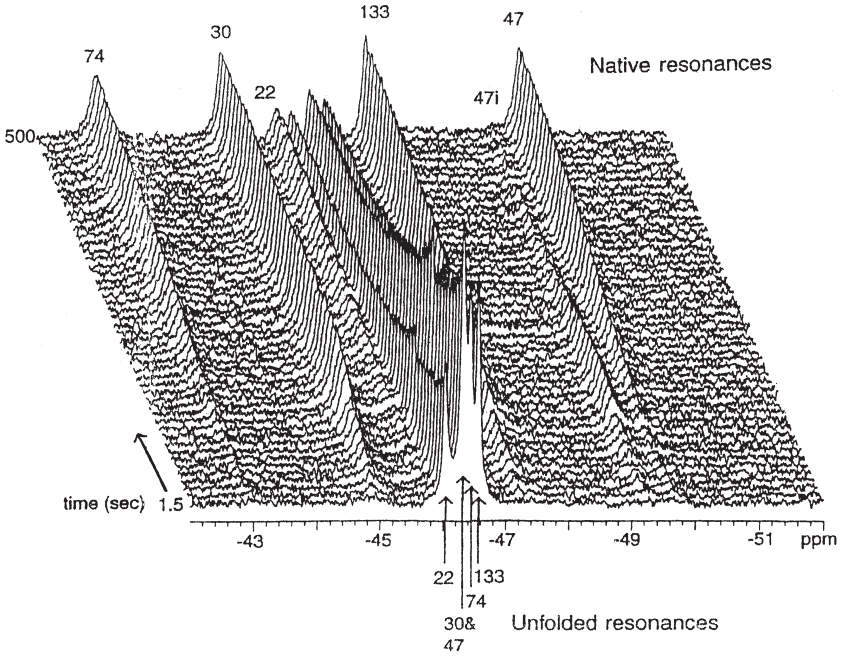

Fig. 1.5. Protein-folding kinetics studied by NMR spectroscopy. Stopped-flow ^{19}F NMR of the refolding of 6-^{19}F-tryptophan-labeled dihydrofolate reductase following dilution from 5.5 M to 2.75 M urea at 5 °C in the presence of 4 mM $NADP^+$. Each spectrum represents the sum of 41 separate rapid dilution experiments. The kinetics and chemical shifts suggest the formation of an intermediate that is unable to bind NAD^+ strongly, having a native-like side chain environment in the regions around Trp 30, 47, and 133 and little if any native side chain environment around Trp 22 and 74. The resonance labeled 47i is that of Trp47 in the intermediate [87].

tail and the time resolution for a specific system [87]. For further details, see Refs. [88, 89].

1.4 Folding and Merging of Domains – Association of Subunits

Domains as compact substructures within protein molecules show the typical characteristics of small globular proteins. There have been many definitions using either the visual inspection of crystal structures or surface area calculations, topological distance considerations, sequence homology at the protein level, or the intron-exon organization at the level of the gene. Among all these definitions [90], the one that is most relevant in connection with the folding and assembly of large proteins refers to the observation that domain proteins "fold by parts," i.e., their constituent parts fold and unfold independently as individual entities in a stepwise fashion [91] (Figure 1.6). This holds not only in vitro but also in the cell, where the

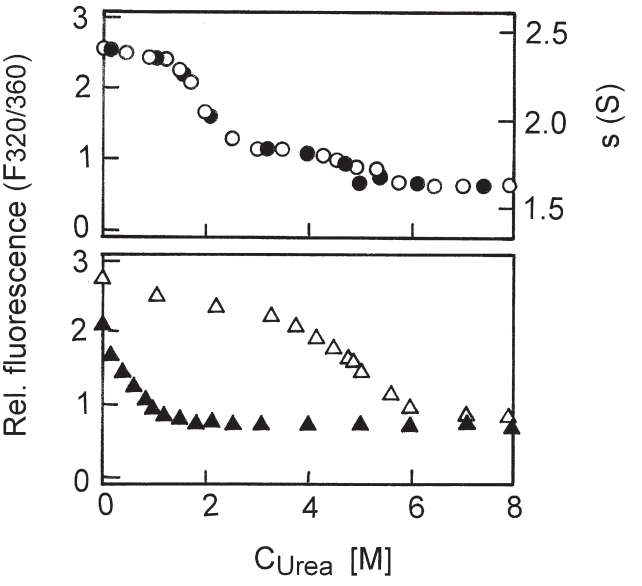

Fig. 1.6. "Folding-by-parts" of γB-crystallin, a prototype two-domain protein. Urea-dependent denaturation-renaturation of γB in 0.1 M NaCl/HCl, pH 2, 20 °C, monitored by intrinsic fluorescence (○) and sedimentation analysis (●). Upper frame: Denaturation equilibrium transition of the natural two-domain protein. Lower frame: Denaturation profiles of the recombinant isolated N-terminal (△) and C-terminal (▲) domains. The difference in ΔG^0_{stab} originates from the difference in net charge z between the two domains: at pH 2, z for the N- and C-terminal domains amounts to 13 and 16, respectively. Approaching the isoelectric point, the difference vanishes [90, 91].

sequential formation of cystine bridges within the single domains of antibody chains has been shown to occur as a co-translational process [51]. Oligomeric proteins share essential properties with domain proteins: in both cases, evolution allowed proteins to acquire the capacity (1) to create new functions by the cooperation of two or more entities, e.g., by forming shared active centers or by allowing allosteric regulation; (2) to become multifunctional, as in the case of multi-enzyme complexes; (3) to improve the intrinsic stability by increasing the state of association [16, 92]; and (4) to enhance the rate of self-organization by synchronous folding and association of medium-sized subunits instead of covalently linked giant proteins. At this point, considering the in vivo situation, the rate enhancement by synchronous nucleation at multiple sites protects the nascent polypeptide chain from proteases; additional advantages are the elimination of misfolded chains from the assembly process on the one hand and the swapping of domains on the other [34, 46].[2]

2 Keeping in mind that many "typical domain proteins" have non-contiguous domains, such evolutionary "advantages" have to be taken with a grain of salt.

Evidently, for some large substrates, domains are the only way to tackle the problem of binding, activating, and releasing the substrate. The classical example to illustrate this combinatorial playground of evolution is the NAD-dependent dehydrogenases, with the Rossmann fold as coenzyme-binding domain and the wide variety of different substrate-binding domains determining the redox specificity of the various enzymes [93]. The key to our understanding of multi-domain proteins is multifunctionality as the common denominator of regulated networks such as the basal membrane, the blood-clotting system, and the non-ribosomal synthesis of peptide and polyketide antibiotics [90]. It is obvious that evolution has gained an enormous combinatorial potential by domain shuffling.

Regarding their folding and association mechanism, multi-domain and multi-subunit systems have been modeled as the sum of their constituent parts plus contributions attributable to their mutual interactions. This approach sounds trivial and easily accomplishable, but it is not, for the simple reason that both folding and assembly may involve multiple-intermediate species differing in either their local conformation or their state of association. Thus, in most cases the two-state model does not hold. Only under "strongly native conditions," i.e., far away from the denaturation transition, can the denaturation-renaturation reaction be approximated by the two-state equation,

$$N \Leftrightarrow U \tag{1}$$

leaving first-order folding as the only significant process. For modular proteins, this may be attributed to the last folding step connected with the docking of the domains; for multimeric proteins, it represents the formation of the "structured monomers" with the correct complementary interfaces required for the specific recognition of subunits. In proceeding from structured monomers to the native quaternary structure, *subunit association* represents a bimolecular reaction that adds concentration-dependent steps to the first-order folding processes. If biological function (as the criterion of the native state) requires the cooperation of domains, domain pairing is expected to be essential in acquiring catalytic activity. Taking NAD-dependent monomeric octopine dehydrogenase as an example, it has been shown that at high solvent viscosity, *domain pairing* becomes rate-limiting; as one would predict from the Stokes-Einstein model of rotational and translational diffusion of rigid bodies, at high viscosity (in the presence of glycerol, sucrose, or polyethylene glycol) reactivation of the enzyme after preceding denaturation is slowed down [34, 89, 90, 94]. Thus, the overall folding kinetics for a two-domain protein may be determined by the folding and pairing of the domains according to,

$$U \xrightarrow{k_{D1}} I \xrightarrow{k_{D2}} N' \xrightarrow{k_{pairing}} N \tag{2}$$

with k_{D1}, k_{D2}, and $k_{pairing}$ as rate constants for the folding of the individual domains and their pairing. In cases in which proline isomerization or other slow reactions participate in the overall mechanism, these steps will lead to kinetic schemes of even higher complexity [94].

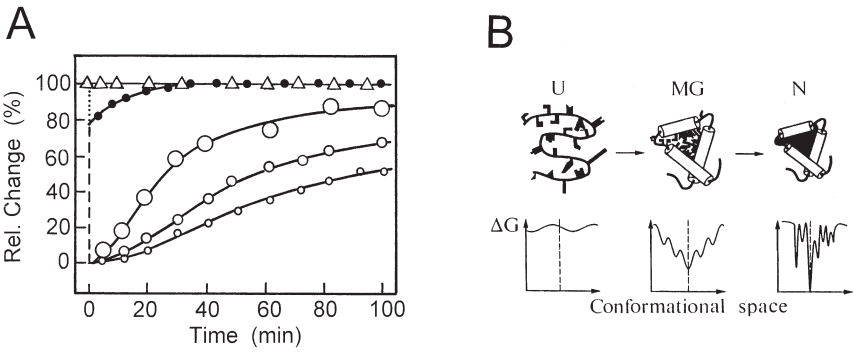

Fig. 1.7. Hierarchical folding of proteins as a multi-step reaction involving the collapse of the unstructured polypeptide and subsequent shuffling (and eventual assembly) of a "molten globule" intermediate. (A) Folding-association pathway of invertase from *Saccharomyces cerevisiae*: changes in circular dichroism (△), fluorescence (●), and enzymatic activity (open circles) allow us to monitor the sequential formation of (1) α-helices, (2) the correct environment of aromatic side chains, and (3) the correct, "native" tertiary (and quaternary) structure. In the case of yeast invertase, catalytic activity requires the dimeric quaternary structure; thus, reactivation is concentration-dependent: ◯, ○, and ○ refer to decreasing subunit concentrations (68, 17, and 8.5 nM) during reactivation. The co-translational glycosylation of the enzyme does not affect the folding/association mechanism [48, 95]. (B) Two-step model for sequential protein folding. The hypothetical structures of a protein in the unfolded (U), molten globule (MG), and native states (N) are shown with the free-energy landscapes at different stages of structure formation [96].

If intermediates on the folding pathway still expose significant hydrophobic surface area, interchain and intrachain interactions may compete, leading to either association (quaternary structure formation) or irregular aggregation. Since association requires complementary surfaces in the periphery of the subunits, folding and association must be consecutive reactions obeying a uni-bimolecular kinetic scheme [34]. In oligomeric systems, the steps preceding subunit assembly are the same as in domain proteins. The overall mechanism consists again of three stages (Figure 1.7): (1) the formation of elements of secondary and super-secondary structure, (2) their collapse to subdomains and domains, ending up with "structured monomers," and (3) association to form the correct stoichiometry and geometry of the native quaternary structure (cf. Scheme 1.1). Evidently, the collision complex of the structured monomers may still undergo intramolecular rearrangements before reaching the state of maximum packing density and minimum hydrophobic surface area; on the other hand, it may be trapped in side reactions of misfolding and/or misassembly, resulting in aggregates or inclusion bodies [47]. Thus, the uni-bimolecular folding-association mechanism may involve further rate-limiting, first-order steps belonging to slow shuffling processes at the level of the native-like assembly or higher-order reactions, attributable to the kinetic competition between correct reconstitution and misassembly. The latter has been observed (and neglected) from the very beginning of protein chemistry. It was considered an irk-

some, unavoidable annoyance that you just had to live with. When I started my own projects in physical biochemistry 40 years ago, my primary interests were the intermolecular forces involved in heat aggregation and the question of how protein denaturation and aggregation are correlated [97]. In asking these basic questions, I was in good company [98, 99]; however, in contrast to protein aggregates, the *interpretation of protein denaturation* and the question *which factors are responsible for protein stability* have turned out to be insoluble to this day. The formal kinetic treatment is obvious: in the simplest case of a dimer, the overall sequential reaction obeys either uni-bi-molecular or uni-bi-uni-molecular kinetics according to:

$$2\ M_u \xrightarrow{k_1} 2\ M_i \xrightarrow{k_2} N \quad \text{or} \quad 2\ M_u \xrightarrow{k_1} 2\ M_i \xrightarrow{k_2} (M_i)_2 \xrightarrow{k_1'} N \tag{3}$$

In the case of aggregation competing with reconstitution, ''kinetic partitioning'' between the sequential folding-association reaction and (higher than second-order) misassembly will occur (see section 1.5):

$$\begin{array}{ccccccc} (m+n+2)M_u & \xrightarrow{k_1} & (n+2)M_i & \xrightarrow{k_1'} & 2M' & \xrightarrow{k_2} & M'_2 \xrightarrow{k_1''} N \\ \downarrow{\scriptstyle k_{>2}} & & \downarrow{\scriptstyle k_{>2}} & & & & \\ (M_u)_m & & (M_i)_n & & & & \end{array} \tag{4}$$

In Eqs. (3) and (4), k_1 and $k_2, k_{>2}$ are first- and second or higher-order rate constants; M_u, M_i, and M' are the monomers in the unfolded, intermediate, and ''structured'' states, respectively, and N is the native dimer. Higher oligomers have been shown to obey the same kinetic scheme because commonly there is only one rate-limiting assembly step in going from the structured monomer to the native oligomer (Figure 1.8).

An enormous repertoire of methods has been devised to analyze the single steps along the paths of folding, association, and aggregation. By applying intrinsic and extrinsic spectral characteristics, flash photolysis, H-D exchange, chemical cross-linking, light-scattering and other kinetic techniques, sequential folding steps have been resolved on the timescale down to microseconds and below. In all these approaches, possible artifacts due to the interference of intra- and intermolecular interactions have to be carefully excluded. Considering these precautions, different methods have been shown to be in excellent agreement, corroborating the above sequential folding-association mechanisms. In the case of combined folding-association reactions, obviously, the alternative of which of the consecutive or competing reactions is rate-limiting depends not only on protein concentration but also on the specific properties of the system. For example, in the case of tetrameric lactate dehydrogenase, the reactivation kinetics after acid denaturation and maximum randomization in 6 M guanidinium chloride differ drastically: acid denaturation starts from a partially active ''structured monomer,'' leaving the association reaction as the rate-determining step, whereas reactivation from the inactive unfolded polypeptide chain follows the sequential uni-bimolecular folding-association mechanism [34, 101]. As expected from the above ''kinetic partitioning'' between proper

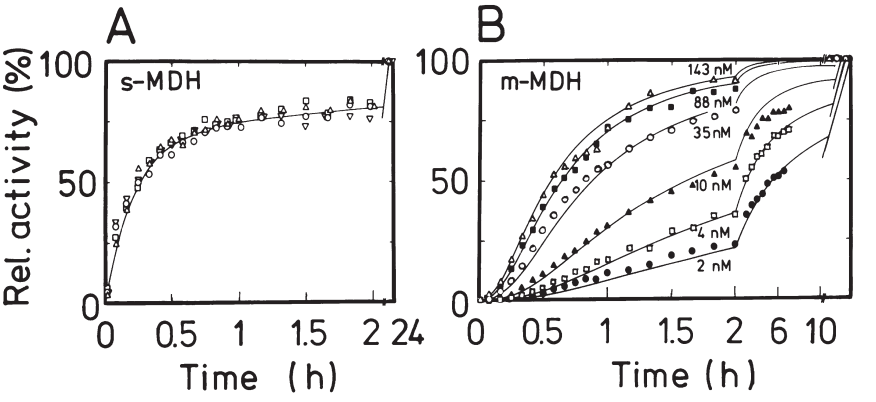

Fig. 1.8. Alternative mechanisms of the sequential folding and association of a dimeric protein: a case study on cytoplasmic (s-MDH) and mitochondrial malate dehydrogenase (m-MDH). (A) Reconstitution kinetics of s-MDH in 0.2 M phosphate buffer pH 7.6 after denaturation in 6 M guanidinium chloride in the concentration range between 1 and 13 μg mL^{-1}. The process is governed by rate-determining folding, yielding structured monomers that (in a subsequent diffusion-controlled step) form the active dimer [34]. (B) Reconstitution kinetics of m-MDH after denaturation in 1 M glycine/H_3PO_4, pH 2.3; renaturation as in (A), at 0.07 (●), 0.14 (□), 0.35 (▲), 1.2 (○), 3.1 (■), and 5.0 (△) μg mL^{-1}. Curves calculated according to Eq. (3), with $k_1 = 6.5 \times 10^{-4}$ s^{-1} and $k_2 = 3 \times 10^4$ M^{-1} s^{-1} (20 °C) [97]. Varying the mode of denaturation (low pH, high guanidinium chloride, urea) or adding the coenzyme (NAD^+) has no effect on the renaturation mechanism [100].

folding and misassembly (cf. "aggregation" in Figure 1.2), association generally contributes as a rate-determining step only below the concentration limit at which the production of structured monomers becomes rate-limiting. If a slow folding reaction at the level of the monomer determines the overall reaction, and association is diffusion-controlled, no concentration dependence can be detected in spite of the bimolecular step; the same holds if an assembly undergoes slow intramolecular rearrangements to finally reach the native state after slow reshuffling [51].

Coming back to the "kinetic partitioning," three questions are of interest: (1) what is the committed step in aggregate formation, (2) when is the "structured monomer" committed to end up as the native protein, and (3) what is known about the structure of aggregates and their constituent polypeptide chains? Regarding the first two points, commitment to aggregation was shown to be a fast reaction, whereas the kinetics of the commitment to renaturation follows precisely the slow kinetics of overall reactivation. This means that early collapsed conformers are much more sensitive to aggregation than later species; after a certain intermediate state has been formed, slow shuffling leads "one way" to the native state. Only the native state is fully protected from misassembly [47, 102]. Concerning the structure of aggregates, electron microscopy and circular dichroism showed that wrong subunit interactions give rise to irregular networks with a broad distribution of highly structured particles at least 10 times the size of the native proteins. At high concentrations, (e.g., at the cellular levels of recombinant pro-

teins giving rise to inclusion bodies), they may form gel-like phases, which in the early days of protein downstream processing were appropriately named "refractile bodies." They resemble the native protein in certain spectral properties, as far as turbidity allows such conclusions [37, 103].

1.5 Limits of Reconstitution

The assumption that "unboiling the egg," after preceding deactivation, randomization, and coagulation (or whatever Max Perutz might have associated with "boiling"), leads to the unrestrained recovery of proteins to their "initial native state" has been accepted as a working hypothesis since Anson and Mirsky's days [1]. In 1944, when the first review on protein denaturation was published, the authors came to the conclusion that "... certain proteins are capable of reverting from the denatured insoluble state to a soluble form which resembles the parent native protein in one or more properties [while] other proteins appear to be incapable of this conversion" [104]. Thirty years later, when the author used this argument, Harold Scheraga's reply was "you didn't try long enough."[3] In the meanwhile, the situation had shifted from the playground of two lonely researchers at the Princeton Institute for Animal and Plant Pathology to a topologically and functionally important hot issue, called the protein-folding problem [105]. To give an example, the question at which state of association on the folding-association pathway an oligomeric enzyme gains enzymatic or regulatory properties required optimal reversibility of both dissociation-reassociation and deactivation-reactivation. Optimization was pure alchemy, blended with some insight into standard denaturation mechanisms and the physicochemical basis of protein stability. There were at least five variables, and the initial and final products had to be carefully compared using all available physical and biochemical characteristics [106]. Proving the native state the proper way, i.e., by X-ray analysis, was the only thing we were unable to do; later we found out that the commercial "crystallized enzyme" we had started out with had been purified using a routine denaturation-renaturation cycle.

As mentioned earlier (cf. section 1.3), different denaturants yield different denatured states. Commonly, maximum yields of renaturation are obtained after "complete randomization" (e.g., at high guanidinium chloride concentration), under essentially irreversible conditions. Exceedingly low protein levels are necessary to minimize aggregation. To escape this highly uneconomical requirement, i.e., to increase the steady-state concentration of the refolding protein at low levels of aggregation-competent intermediates, recycling, pulse dilution, and immobilization techniques were devised [84]. False intermediates, trapped under strongly native

3 Twenty years later, his suggestion might have been "try molecular chaperones or any other accessory protein," because there *are* proteins that have resisted renaturation to this day.

conditions, may be destabilized at optimally chosen residual denaturant conditions or in the presence of 0.5–1.0 M arginine; the rationale behind these unexpectedly efficient recipes is that under strongly native conditions, weakly destabilizing agents help the kinetically trapped aggregation-competent intermediates and aggregates to overcome the activation barrier between the aggregated state and the global energy minimum of the renatured protein [47, 84].

There is no doubt that in general proteins do undergo reversible unfolding and that under optimal conditions the product of renaturation is indistinguishable from the native starting material [34]. As has been shown, side reactions may compete with full recovery. They can be minimized by carefully optimizing the denaturation-renaturation conditions: oxidation by properly adjusting the pH and the redox state of the solvent, proteolysis by adding inhibitors, misassembly by reducing the protein level below the critical concentration of aggregate formation, etc. In asking what the limits of in vitro protein folding and reconstitution are regarding size, structural complexity, and compartmentation in the cell, evolution may teach us how the observed high efficiency of protein self-organization is correlated with the basic architecture of proteins and their genes. In this context, the following questions have been addressed. (1) How is the domain structure of large polypeptide chains correlated with the codon usage and the organization of their corresponding genes? (2) Is there a correlation between the occurrence of domains and the state of association of polypeptides that would clearly support the domain-swapping hypothesis? (3) Does intrinsic form determination of the subunits govern the self-assembly of multimeric proteins? (4) At which level of complexity are assembly structures such as ribosomes or phage and virus particles determined by extrinsic morphopoietic factors or vectorial transcriptional programs? (5) Subunit exchange in oligomeric proteins requires highly homologous subunit interfaces; here the question arises, how can the reciprocity be analyzed to understand the occurrence of homo- and hetero-oligomeric quaternary structures? (6) Finally, is the specific compartmentation of isoenzymes within the cell correlated with specific folding-association mechanisms? The results have been summarized in a number of reviews [33, 34, 46, 51, 90, 106].

In the present context, a few comments may suffice. Domains have been shown to fold as independent entities that, in certain cases, may give rise to large assemblies [34, 47]. Intrinsic form determination holds not only for high-molecular-weight assemblies of a single macromolecular species (e.g., apoferritin, TMV protein, and coats of other viruses) but also for heteromultimeric systems (such as multi-enzyme complexes) [34, 107, 108]. In the case of highly complex multicomponent systems, nature either provides *scaffold proteins* or "aids assembly" by the sequential co-transcriptional supply of protein components. Mimicking this *genetically determined morphopoiesis*, successful in vitro reconstitution was accomplished by sequentially adding "primary," "secondary," "tertiary," etc., components on the one hand and by optimizing the solvent conditions on the other [34, 108, 109]. That nature makes use of the limited specificity of subunit contacts became clear when the five isoenzymes of lactate dehydrogenase were discovered in the 1960s. The general question of how specific the recognition of complementary protein

surfaces is in oligomeric proteins is highly significant because, in the cell, nascent polypeptide chains fold in the presence of high levels of other proteins, including chains coded by the same gene but not synchronized in their translation. Thus, the problem arises whether and to what extent chimeric assemblies of structurally related proteins might occur, either as intermediates or final products. In using two dimeric NAD-dependent dehydrogenases (lactate dehydrogenase from *Limulus* and malate dehydrogenase from pig mitochondria), the result of careful denaturation-renaturation experiments was negative: both the time course and concentration dependence, as well as the yield of reactivation in the absence and in the presence of the prospective hybridization partner, remained unaltered. Similarly, equilibrium experiments did not indicate any exchange of subunits [110]. Similar experiments, using mitochondrial and cytoplasmic malate dehydrogenase, showed that the two isoenzymes could be easily synchronized with respect to their folding and reactivation kinetics; however, their dimerization mechanism differs widely, so that hybrid formation again does not occur [100, 111, R. Jaenicke, unpublished results]. The conclusion that no hybrids are formed is by no means trivial from the perspective of the present-day results of protein engineering, with circular permutants of domains, fragmentation of polypeptides into their (hypothetical) functional modules, and similar acrobatics in our daily routine.

1.6
In Vitro Denaturation-Renaturation vs. Folding in Vivo

In the last chapter I tried to summarize certain limits where the physicochemist's optimism that biological morphogenesis is just a variant of abiotic self-organization might be wrong. At this point it is amusing to meet respectable biologists who, faced with the "in vitro/in vivo issue," happily welcome Aristotle again, assuming that in the crowded cell the vitalistic doctrine is better than Descartes' radicalism. Having in mind that in vivo folding is part of the cellular process of protein biosynthesis and subsequent compartmentation, undoubtedly, there are significant differences between the co- and post-translational structure formation on the one hand, and optimally controlled reconstitution processes involving mature proteins in vitro on the other. There are two questions: are these differences relevant, and can we combine available fragmentary evidence from in vitro translation data with in vivo data on other cell-biological events related to self-organization, growth, and differentiation? In his excellent review on protein folding in the cell, Freedman [112] related the paradigm change from Anfinsen's dogma "one sequence → one 3D structure" to the "Anfinsen-cage" concept in chaperon research to two experimental observations: (1) the formation of misfolded recombinant proteins in microbial host cells and (2) the fate of translation products and their ultimate functional intra- or extracellular location. The wish to understand protein folding in the context of the wide variety of co- and posttranslational processes clearly emphasized that in vitro refolding studies on isolated unfolded proteins provide an incomplete model for describing protein folding in the

cell. In the context of the above observations, two examples may be taken to prove that the model studies do provide essential background against which the cellular events can be understood. One deals with the attempt to gain direct insight into the detailed kinetic mechanism of the folding and assembly of the tailspike endorhamnosidase from *Salmonella* bacteriophage P22 in vitro and in the cell. Making use of temperature-sensitive mutants, spectral and pulse-labeling experiments showed that in both sets of experiments the rate-limiting folding intermediates are formed at identical rates [47] (Figure 1.9). In the other example, it was shown that misfolding and subsequent inclusion-body formation at high levels of recombinant

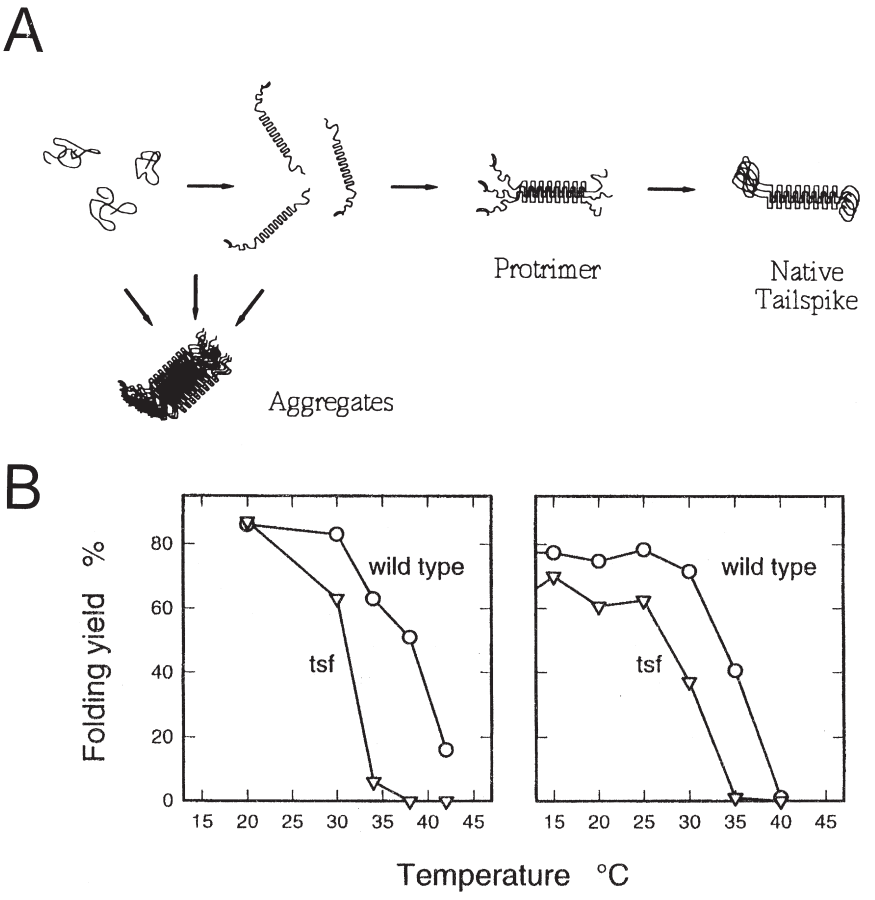

Fig. 1.9. In vitro and in vivo folding and assembly of the trimeric tailspike endorhamnosidase (Tsp) of *Salmonella* bacteriophage P22, making use of the temperature-sensitive folding and aggregation of folding intermediates. (A) Schematic representation of the folding/assembly/aggregation pathways. (B) Folding yields of wild-type and mutant Tsp upon biosynthesis in vivo on the one hand (left), and dilution from denaturant in vitro (right) on the other. The similarity of the data shows that the in vitro reconstitution applies to the situation in the living cell [113, 114].

proteins can be quantitatively described by kinetic partitioning between one rate-determining folding step (k_1) and parallel diffusion-controlled aggregation (k_2), in accordance with Eq. (4) in the simplified form

$$N \overset{k_1}{\leftarrow} U/M_u \overset{k_2}{\rightarrow} A \tag{5}$$

(cf. Figure 1.2B) [39].

The observation that overexpression often leads to the deposition of recombinant proteins in the host cell may favor the idea that under normal physiological conditions in vivo, structure formation yields exclusively native protein. This assumption is incorrect because, in the eukaryotic cell, trafficking through the ER and the Golgi and subsequent quality control may reduce the yield considerably [115]. Thus, in mechanistic terms, refolding does not differ significantly from in vivo folding. The same holds for the directionality of translation in the cell, which, on first sight, seems to be fundamentally different from the integral folding of the complete polypeptide chain in renaturation experiments. Here, due to the involvement of chaperone proteins in the initial folding events, structure formation in vivo does not necessarily occur co-translationally in a vectorial fashion. Furthermore, circular permuted proteins and protein fragments have been shown to fold into stable, functional conformers, indicating that multiple folding pathways exist (altogether leading to the same 3D structure) and that the original N-terminus is not required for the folding process. In this context, inverting the direction of either protein biosynthesis (by Merrifield synthesis) or protein folding (by immobilization) has been shown to end up with the native functional protein: with Merrifield synthesis, one may argue that the synthesis from the C- to the N-terminal end includes coupling-uncoupling and protection-deprotection reactions under nonnative conditions, but the final product is still in its native state [116]. In order to promote the direction of folding in either the natural (N → C) or the inverse (C → N) direction, immobilization of standard proteins at their N- or C-termini (by histidine or arginine tags, combined with ion-exchange chromatography) was applied. In both cases, denaturation-renaturation cycles have shown that the products were the same, independent of the free end of the polypeptide chain [38].[4]

In the present context, the above *one sequence → one 3D structure* dogma is incomplete without stressing the importance of the solvent environment. In contrast to the alchemy of solvent variations that have been worked out in order to optimize the downstream processing of recombinant proteins, evolutionary adaptation has fixed the protein inventory of mesophiles and extremophiles to specific cellular solvent conditions. Making use of the expression of recombinant extremophile proteins in mesophilic hosts, limits can be defined about how far physical variables may be varied without interfering with the ''foldability'' of guest proteins. It is evident that early intermediates on the folding path are most accessible toward delete-

4 An additional spin-off of this approach was that immobilization allowed the kinetic partitioning to be shifted from *A* to *N* (cf. Eq. (5)): the tagged proteins showed not only significantly increased yields of reactivation but also enhanced intrinsic stabilities.

rious solvent effects. Thus, if the native structure can be reached either after recombinant expression or after refolding in vitro, intermediates and subunits must be stable under the respective conditions. Considering temperature, it turns out that alterations in the folding conditions often have surprisingly little effect. A drastic example is the expression of active enzymes from hyperthermophilic bacteria in *Escherichia coli*, in which the temperature difference ΔT_{opt} between the host and the guest may amount to >60 °C. Here, it has been shown that denaturation-renaturation experiments at up to 100 °C yield the fully active protein, indistinguishable from its initial native state, proving that all folding-association intermediates must be stable over the whole temperature range [16]. When comparing homologous proteins from mesophiles and thermophiles, it is interesting to note that thermophilic proteins are often kinetically stabilized, showing drastically decreased unfolding rates but unchanged folding kinetics [18], no doubt highly advantageous considering short-term exposure to lethal temperatures in hydrothermal vents on the one hand, and kinetic competition of protein folding and proteolytic degradation on the other.

Little is known about the effects of the other extreme physical parameters on protein folding. Because the cytosolic pH is close to neutrality, even in the case of extreme acidophiles and alkalophiles, standard in vitro conditions are close to those in the cell. Halophilic proteins seem to require salt, not only as stabilizing agent but also for folding and assembly [117]. For non-halophilic proteins, the ionic strength is not as critical, apart from general Hofmeister effects that may be used to optimize the in vitro folding conditions. Regarding possible effects of high hydrostatic pressure on cellular processes, it is obvious that the adaptive effort to cope with the biologically relevant extremes of pressure (<120 MPa) can be ignored in comparison to the adaptation to low temperature prevailing in the deep sea [118]. Finally, viscosity should be considered because of macromolecular crowding in the cytosol. As has been mentioned, glycerol, sucrose, and other carbohydrates have been used to simulate frictional effects on domain pairing. In connection with protein folding, information is scarce, especially because polyols not only increase the viscosity of the solvent but also enhance the stability of the solute owing to excluded-volume effects and preferential solvation; there is no way to alter viscosity alone.

1.7 Perspectives

As we have witnessed, interest in the protein-folding problem started from the sensational resurrection of denatured proteins in Tim Anson's hands, long before the first 3D structure of a globular protein was elucidated. After self-organization had become an accepted fact, experimental studies were centered mainly on the investigation of the mechanisms of folding and association of model proteins in terms of the complete description of the unfolded (nascent) and final (native) states, including all accessible intermediates along the U → N transition. The main obstacle

in reaching this goal was the elusive nature of the folding protein, especially the question of whether folding is in fact a sequential reaction with well-populated intermediates or a multiple-pathway process, as in the case of a jigsaw puzzle [119]. What was important at this point was the observation that model peptides as well as separate protein fragments and domains were able to form ordered structures, supporting the idea that local structures and modules may serve as ''seeds'' in the folding process. That such nuclei did not necessarily adopt the same conformation in unrelated protein structures was no argument against their significance as intermediates. Specific ligands such as metal ions were found to be essential as guides along the folding path; interestingly, in cases like these, estimated cellular levels were found to be close to the optimum concentration in in vitro refolding experiments [34].

Regarding folding in the cell, in the early days it was tacitly assumed that the in vitro mechanism could be directly transferred to describe the folding and association of the nascent polypeptide as the final step of translation. Obvious discrepancies were clear from the beginning; for example, ''unscrambling'' of ribonuclease took unreasonably long, in vitro reactivation at standard cellular protein levels ended up with aggregates rather than active material, certain proteins were found to be inaccessible to ''renativation,'' etc. The discovery of a whole spectrum of folding catalysts and molecular chaperones resolved most of these challenges because they were clearly correlated with the three established rate-limiting steps in the overall folding reaction: PDI with disulfide shuffling, PPI with proline isomerization, and molecular chaperones with the kinetic partitioning between folding and aggregation. Based on mutant studies and on the fact that under normal physiological conditions several percent of the cellular proteins are molecular chaperones, there could hardly be any doubt that all three classes of proteins were physiologically essential. As a matter of fact, complementing the in vitro experiments with the accessory components allowed the in vitro results to mimic the reality in the cell.

No new biophysical principles emerged from all these studies; on the contrary, the better the mechanisms of folding catalysts and molecular chaperones were understood, the more it became clear that the basic principles of catalysis, allosteric regulation, and compartmentation hold also in the cellular environment. In spite of that, attempts at quantifying protein folding in vivo in physicochemical terms failed because the cytosol represents a *complex macromolecular multicomponent system under crowding conditions*, the full description of which still goes beyond the presently available repertoire of experimental methods. As in other ''real systems'' such as the real gas or concentrated simple electrolytes, the quantitative treatment of the non-ideality of highly charged polyelectrolytes in aqueous multicomponent systems is still beyond the reach of a sound theoretical treatment.

Twenty-five years ago, at the end of the first International Conference on Protein Folding in Regensburg, Cyrus Chothia quoted Johannes Kepler's treatise *On the Six-cornered Snowflake* as the first ''theory of biological structures.'' In his essay Kepler argued that a material's structure arises from its intrinsic properties and that in biological structures it is important to consider the structure-function rela-

tionship [120]. In this context, focusing on protein folding, at the 1979 conference attempts were made to combine the intrinsic physical and chemical properties of proteins and the laws of kinetics and thermodynamics in order to predict how they determine the structure and activity. At that time, ''simple protein molecules'' such as basic pancreatic trypsin inhibitor, ribonuclease, and lactate dehydrogenase were discussed as adequate models, the argument being that the central problem at all levels of biological structure is to understand how the intrinsic entropy of its various constituents is overcome to form particular stable structures in a finite time and how the physical and chemical properties of the materials determine the way in which they function. Cyrus, the theoretician, ended by vaguely announcing that ''the next time we meet in Regensburg we shall talk about more biological systems such as the red cell membrane or coated vesicles'' [121]. I do not have to explain why this second conference never materialized. Now, after a quarter of a century, two former Regensburg graduate students are keeping Cyrus' promise, figuring as editors of the present volume. In fact, this volume covers the state of the art, from the principles, dynamics, and mechanisms of protein stability, protein design, and structure prediction to the function and regulation of chaperones and research and development in the fields of engineering protein folding and stability and refolding technology, an amazing horizon having in mind the first steps in protein folding in the dark age of biocolloidology, when the chemical establishment still considered proteins to be loose aggregates of smaller entities, unflinchingly opposing the term *macromolecule*.

Acknowledgements

This perspectives article is dedicated to my teachers, Camille Montfort, Hans Kautsky, Joachim Stauff, and Max A. Lauffer, and to my students, Rainer Rudolph and Franz Schmid, who taught me more than I was able to teach them.

References

1 M. L. Anson, A. E. Mirsky, On some general properties of proteins. *J. gen. Physiol.* **1925**, *9*, 169–179.
2 M. L. Anson, A. E. Mirsky, The equilibria between native and denatured hemoglobin in salicylate solutions and the theoretical consequences of the equilibrium between native and denatured protein. *J. gen Physiol.* **1934**, *7*, 399–408.
3 M. L. Anson, Protein denaturation and the properties of protein groups. *Adv. Protein Chem.* **1945**, *2*, 361–386.
4 M. F. Perutz, Unboiling an egg. Discovery **1940**, March, reprinted in [5] p. 14.
5 M. F. Perutz, Chairman's Introduction. In: Protein Folding (R. Jaenicke, Ed.) Elsevier/North-Holland Biomed. Press, Amsterdam, New York **1980**, 13.
6 E. J. Cohn, The physical chemistry of the proteins. *Physiol. Rev.* **1925**, *5*, 349–437.
7 C. Tanford, Cohn and Edsall: Physical chemistry conclusively supports a protein model. *Biophys. Chem.* **2003**, *100*, 81–90.

8 T. Svedberg, R. Fåhraeus, A new method for the determination of the molecular weight of the proteins. *J. Amer. Chem. Soc.* **1926**, *48*, 430–438.

9 M. F. Perutz, M. G. Rossmann, A. F. Cullis, H. Muirhead, G. Will, A. C. T. North, Structure of haemoglobin: A three-dimensional Fourier synthesis at 5.5 Å resolution obtained by X-ray analysis. *Nature* **1960**, *185*, 416–422.

10 C. B. Anfinsen, The limited digestion of ribonuclease with pepsin. *J. Biol. Chem.* **1956**, *221*, 405–412.

11 R. L. Baldwin, D. Eisenberg, Protein stability. In Protein Engineering (D. L. Oxender, C. F. Fox, Eds.) A. R. Liss, New York **1987**, 127–148.

12 K. A. Dill, Dominant forces in protein folding. *Biochemistry* **1990**, *29*, 7133–7155.

13 M. Karplus, E. Shakhnovich, Protein folding: Theoretical studies of thermodynamics and dynamics. In: Protein Folding (T. E. Creighton, Ed.) W. H. Freeman, New York, **1992**, 127–195.

14 A. Fersht, Forces between molecules, and binding energies. In: Structure and Mechanism in Protein Science, W. H. Freeman, New York, **1999**, 324–348.

15 T. Lazaridis, M. Karplus, Thermodynamics of protein folding. *Biophys. Chem.* **2003**, *100*, 367–395.

16 R. Jaenicke, R. Sterner, Life at high temperature. In: The Prokaryotes, 3rd Ed. (M. Dworkin et al., Eds.) An Evolving Electronic Resource, Latest Update Release 3.9, Springer-New York **2002**, 1–56.

17 R. Jaenicke, G. Böhm, Stabilization of proteins: What extremophiles teach us about protein stability. *Curr. Opin. Struct. Biol.* **1998**, *8*, 738–748.

18 D. Perl, C. Welker, T. Schindler, M. A. Marahiel, R. Jaenicke, F. X. Schmid, Rapid two-state folding is conserved in cold-shock proteins from mesophiles, thermophiles and hyperthermophiles. *Nature Struct. Biol.* **1998**, *5*, 229–235.

19 D. Perl, U. Müller, U. Heinemann, F. X. Schmid, Two exposed amino acid residues confer thermostability on a cold shock protein. *Nature Struct. Biol.* **2000**, *7*, 380–383.

20 F. H. Arnold (Ed.) Evolutionary Protein Design, *Adv. Protein Chem.* **2001**, Vol. 55.

21 P. L. Wintrode, F. H. Arnold, Temperature adaptation of enzymes: Lessons from laboratory evolution. *Adv. Protein Chem.* **2001**, *55*, 161–226.

22 W. P. C. Stemmer, Rapid evolution of a protein in vitro by DNA shuffling. *Nature* **1994**, *370*, 389–391.

23 M. Lehmann, C. Loch, A. Middendorf, D. Studer, S. F. Lassen, L. Pasamontes, A. P. van Loon, M. Wyss, The consensus concept for thermostability of proteins: Further proof of concept. *Protein Eng.* **2002**, 403–411.

24 N. Declerck, M. Machius, P. Joyet, G. Wiegand, R. Huber, C. Gaillardin, Hyperthermostabilization of *Bacillus licheniformis* α-amylase and modulation of its stability over a 50 degrees C temperature range. *Protein Eng.* **2003**, *16*, 287–293.

25 W. Kauzmann, Some factors in the interpretation of protein denaturation. *Adv. Protein Chem.* **1959**, *14*, 1–63.

26 J. L. Finney, Solvent effects in biomolecular processes. In: Biophysics of Water (F. Franks, S. Mathias, Eds.), J. Wiley & Sons Chichester **1982**, 55–58.

27 N. C. Pace, B. A. Shirley, M. McNutt, K. Gajiwala, Forces contributing to the conformational stability of proteins. *FASEB J.* **1996**, *10*, 75–83.

28 G. I. Makhatadze, P. L. Privalov, Hydration effects in protein unfolding. *Biophys. Chem.* **1994**, *51*, 291–309.

29 G. I. Makhatadze, P. L. Privalov, Energetics of protein structure. *Adv. Protein Chem.* **1995**, *47*, 307–425.

30 R. L. Baldwin, John Schellman and his scientific work. *Biophys. Chem.* **2002**, *101–102*, 9–13.

31 M. F. Perutz, H. Raidt, Stereochemical basis of heat stability in bacterial ferredoxins and in hemoglobin A2. *Nature* **1975**, *255*, 256–259.

32 C. N. Pace, Polar group burial contributes more to protein stability

than non-polar group burial. *Biochemistry* **2001**, *40*, 310–313.

33 R. Jaenicke, C. Slingsby, Eye lens crystallins and their bacterial homologs. *Crit. Rev. Biochem. Mol. Biol.* **2001**, *36*, 435–499.

34 R. Jaenicke, Folding and association of proteins. *Progr. Biophys. Mol. Biol.* **1987**, *49*, 117–237.

35 R. Jaenicke, Reassociation and reactivation of LDH from the unfolded subunits. *Eur. J. Biochem.* **1974**, *46*, 149–155.

36 G. Orsini, M. E. Goldberg, The renaturation of reduced chymotrypsinogen A in GdmCl: Refolding vs. aggregation. *J. Biol. Chem.* **1978**, *253*, 3453–3458.

37 G. Zettlmeissl, R. Rudolph, R. Jaenicke, Reconstitution of LDH: Non-covalent aggregation vs. reactivation. I. Physical properties and kinetics of aggregation. *Biochemistry* **1979**, *18*, 5567–5571.

38a G. Stempfer, B. Höll-Neugebauer, E. Kopetzki, R. Rudolph, Improved refolding of an immobilized fusion protein. *Nature Biotechnol.* **1996**, *14*, 329–334.

38b G. Stempfer, B. Höll-Neugebauer, R. Rudolph, A fusion protein designed for non-covalent immobilization: Stability, enzymatic activity and use in an enzyme reactor. *Nature Biotechnol.* **1996**, *14*, 481–484.

39 T. Kiefhaber, R. Rudolph, H.-H. Kohler, J. Buchner, Protein aggregation in vitro and in vivo: A quantitative model of the kinetic competition between folding and aggregation. *Bio/Technology* **1991**, *9*, 825–829.

40 E. De Bernardez Clark, E. Schwarz, R. Rudolph, Inhibition of aggregation side reactions during in vitro protein folding. *Meth. Enzymol.* **1999**, *309*, 217–236.

41 R. I. Morimoto, A. Tissières, C. Georgopoulos, The stress response: Function of the proteins, and perspectives. *Cold Spring Harbor Monograph Ser.* **1990**, 19, 1–36.

42 K. P. Murphy, Non-covalent forces important to the conformational stability of protein structures. In: Protein Stability and Folding (B. A. Shirley, Ed.), *Meth. Mol. Biol.* Vol. 40, Humana Press, Totowa **1995**, 1–34.

43 O. B. Ptitsyn, Molten globule and protein folding. *Adv. Protein Chem.* **1995**, *49*, 83–229.

44 M. Arai, K. Kuwajima, Role of the molten globule state in protein folding. *Adv. Protein Chem.* **2000**, *53*, 209–282.

45 J. Janin, S. J. Wodak, Structural domains in proteins and the role in the dynamics of protein function. *Progr. Biophys. Mol. Biol.* **1983**, *42*, 21–78.

46 M. P. Schlunegger, M. J. Bennett, D. Eisenberg, Oligomer formation by three-dimensional domain swapping: A model for protein assembly and misassembly. *Adv. Protein Chem.* **1997**, *50*, 61–122.

47 R. Jaenicke, R. Seckler, Protein misassembly in vitro. *Adv. Protein Chem.* **1997**, *50*, 1–59.

48 R. Jaenicke, H. Lilie, Folding and association of oligomeric and multimeric proteins. *Adv. Protein Chem.* **2000**, *53*, 329–401.

49 R. F. Goldberger, C. J. Epstein, C. B. Anfinsen, Acceleration of reactivation of reduced bovine pancreatic ribonuclease by a microsomal system from rat liver. *J. Biol. Chem.* **1963**, *238*, 628–635.

50 P. Venetianer, F. B. Straub, The enzymic reactivation of reduced ribonuclease. *Biochem. Biophys. Acta* **1963**, *67*, 166–168.

51 R. Jaenicke, Protein folding and association: Significance of in vitro studies for self-organization and targeting in the cell. *Curr. Topics Cellular Regulation* **1996**, *34*, 209–314.

52 R. Jaenicke, Protein self-organization in vitro and in vivo: Partitioning between physical biochemistry and cell biology. *Biol. Chem.* **1998**, *379*, 237–243.

53 E. R. Schönbrunner, F. X. Schmid, Peptidyl-prolyl *cis-trans* isomerase improves the efficiency of protein disulfide isomerase as a catalyst of protein folding. *Proc. Natl. Acad. Sci. USA* **1992**, *89*, 4510–4513.

54 J. Buchner, M. Schmidt, M. Fuchs, R. Jaenicke, R. Rudolph, F. X. Schmid, T. Kiefhaber, GroE facilitates refolding of citrate synthase by suppressing aggregation. *Biochemistry* **1991**, *30*, 1586–1591.

55 R. B. Freedman, Protein disulfide isomerase: multiple roles in the modification of nascent secretory proteins. *Cell* **1989**, *57*, 1069–1072.

56 J. F. Brandts, H. R. Halvorson, M. Brennan, Consideration of the possibility that the slow step in protein denaturation reactions is due to *cis-trans* isomerism of protein residues. *Biochemistry* **1975**, *14*, 4953–4963.

57 F. X. Schmid, R. L. Baldwin, Acid catalysis of the formation of the slow-folding species of RNaseA: Evidence that the reaction is proline isomerization. *Proc. Natl. Acad. Sci. USA* **1978**, *75*, 4764–4768.

58 G. Fischer, H. Bang, The refolding of urea denatured RNaseA is catalyzed by peptidyl-prolyl *cis-trans* isomerase. *Biochim. Biophys. Acta* **1985**, *828*, 39–42.

59 K. Lang, F. X. Schmid, G. Fischer, Catalysis of protein folding by prolyl isomerase. *Nature* **1987**, *329*, 268–270.

60 T. Kiefhaber, H. P. Grunert, U. Hahn, F. X. Schmid, Replacement of a *cis* proline simplifies the mechanism of RNase T1 folding. *Biochemistry* **1990**, *29*, 6475–6480.

61 R. J. Ellis, S. M. van der Vies, Molecular chaperones. *Annu. Rev. Biochem.* **1991**, *60*, 321–347.

62 R. Rorty, Philosophy and the Mirror of Nature. Princeton Univ. Press, Princeton, **1979**.

63 P.-L. Luisi, R. M. Thomas, The pictorial molecular paradigm: Pictorial communication in the chemical and biological sciences. *Naturwissenschaften* **1990**, *77*, 67–74.

64 A. Szent-Györgyi, The Nature of Life, **1948**, Academic Press, New York.

65 S. C. Harrison, R. Durbin, Is there a single pathway for the folding of a polypeptide chain? *Proc. Natl. Acad. Sci. USA* **1985**, *82*, 4028–4030.

66 K. A. Dill, S. Bromberg, K. Yue, K. M. Fiebig, D. P. Yee, P. D. Thomas, H. S. Chan, Principles of protein folding: A perspective from simple exact models. *Protein Sci.* **1995**, *4*, 561–602.

67 L. A. Mirny, V. Abkevich, E. I. Shakhnovich, Universality and diversity of the protein folding scenario: A comprehensive analysis with the aid of a lattic model. *Folding and Design* **1996**, *1*, 103–116.

68 J. N. Onuchic, Z. Luthey-Schulten, P. G. Wolynes, Theory of protein folding: The energy landscape perspective. *Annu. Rev. Phys. Chem.* **1997**, *48*, 545–600.

69 T. E. Creighton, Protein folding coupled to disulphide-bond formation. In: Mechanisms of Protein Folding, 2nd Ed. (R. H. Pain, Ed.) Oxford University Press, Oxford **2000**, 250–278.

70 S. J. Hagen, J. Hofrichter, A. Szabo, W. A. Eaton, Diffusion-limited contact formation in unfolded cytochrome c: Estimating the maximum rate of protein folding. *Proc. Natl. Acad. Sci. USA* **1996**, *93*, 11615–11617.

71 W. A. Eaton, V. Munoz, S. J. Hagen, G. S. Jas, L. J. Lapidus, E. R. Henry, J. Hofrichter, Fast kinetics and mechanism in protein folding. *Annu. Rev. Biophys. Biomol. Str.* **2000**, *29*, 327–359.

72 S. E. Radford, C. M. Dobson, P. A. Evans, The folding of hen lysozyme involves partially structured intermediates and multiple pathways. *Nature* **1992**, *358*, 302–307.

73 J. F. Sinclair, M. M. Ziegler, T. O. Baldwin, Kinetic partitioning during protein folding yields multiple native states. *Nature Struct. Biol.* **1994**, *1*, 320–326.

74 O. Bieri, T. Kiefhaber, Elementary processes in protein folding. *Biol. Chem.* **1999**, *380*, 923–929.

75 E. E. Eaton (Ed.), 4th Meeting on the CASP, Proteins: Structure, Function and Genetics, **2001**, *45*, *S5*, 1–199.

76 J. A. Rupley, The comparison of protein structure in crystal and in solutions. In: Structure and Stability of Biological Macromolecules (S. N.

Timasheff, G. D. Fasman, Eds.) Marcel Dekker, New York **1965**, 291–352.

77 H. Frauenfelder, H. Hartmann, M. Karplus, I. D. Kuntz, J. Kuriyan, F. Parak, G. A., Petsko, D. Ringe, R. F. Tilton, Jr., M. L. Connolly, N. Max, Thermal expansion of a protein. *Biochemistry* **1987**, *26*, 254–261.

78 P. A. Rejto, S. T. Freer, Protein conformational substates from X-ray crystallography. *Progr. Biophys. Mol. Biol*. **1996**, *66*, 167–196.

79 Q. Xue, E. S. Yeung, Difference in the chemical reactivity of individual molecules of an enzyme. *Nature* **1995**, *373*, 681–683.

80 B. Schuler, E. A. Lipman, W. A. Eaton, Probing the free energy surface for protein folding with single-molecule fluorescence spectroscopy. *Nature* **2002**, *419*, 743–747.

81 G. D. Rose (Ed.), Unfolded Proteins. *Adv. Protein Chem*. **2002**, Vol. 62.

82 C. Tanford, Protein denaturation: Characterization of the denatured state and the transition from the native to denatured state. *Adv. Protein Chem*. **1968**, *23*, 121–282; Theoretical models for the mechanism of denaturation, *ibid*. **1970**, *24*, 1–95.

83 C. Branden, J. Tooze, Building blocks of protein structures. In: Introduction to Protein Structure, 2nd Ed. Garland Publ., New York, **1998**, 8–12.

84 R. Rudolph, G. Böhm, H. Lilie, R. Jaenicke, in: Protein function: A practical approach (T. E. Creighton, Ed.) 2nd Ed., IRL Press, Oxford, **1997**, 57–99.

85 T. Dams, R. Jaenicke, Stability and folding of DHFR from the hyperthermophilic bacterium *Thermotoga maritima*. *Biochemistry* **1999**, *38*, 9169–9178.

86 M. Kretschmar, E.-M. Mayr, R. Jaenicke, Kinetic and thermodynamic stabilization of the $\beta\gamma$-crystallin homolog spherulin 3a from *Physarum polycephalum* by Ca^{2+}. *J. Mol. Biol*. **1999**, *289*, 701–705.

87 S. D. Hoeltzli, C. Frieden, Refolding of 6^{19}F tryptophan labelled *Escherichia coli* DHFR in the presence of ligand: A stopped-flow NMR spectroscopy study. *Biochemistry* **1998**, *37*, 387–398.

88 F. X. Schmid, Kinetics of unfolding and refolding of single-domain proteins. In: Protein Folding (T. E. Creighton, Ed.) Freeman, New York, **1992**, 197–241.

89 O. Bieri, T. Kiefhaber, Kinetic models in protein folding. In: Mechanisms of Protein Folding, 2nd Ed. (R. H. Pain, Ed.) Oxford University Press, Oxford **2000**, 34–64.

90 R. Jaenicke, Folding and stability of domain proteins. *Progr. Biophys. Mol. Biol*. **1999**, *71*, 155–241.

91 R. Rudolph, R. Siebendritt, G. Nesslauer, A. K. Sharma, R. Jaenicke, Folding of an all-β-protein: Independent domain folding in γII crystallin from calf eye lens. *Proc. Natl. Acad. Sci. USA* **1990**, *87*, 4625–4629.

92 R. Jaenicke, Protein folding: Local structures, domains, subunits and assemblies. *Biochemistry* **1991**, *30*, 3147–3161.

93 M. G. Rossmann, P. Argos, Protein folding. *Annu. Rev. Biochem*. **1981**, *50*, 497–532.

94 J.-R. Garel, Folding of large proteins: Multidomain and multisubunit proteins. In: Protein Folding (T. E. Creighton, Ed.) W. H. Freeman, New York, **1992**, 405–454.

95 G. Kern, D. Kern, R. Jaenicke, R. Seckler, Kinetics of folding and association of differently glycosylated variants of invertase from *Saccharomyces cerevisiae*. *Protein Sci*. **1993**, *2*, 1862–1868.

96 L. C. Wu, P. L. Kim, A specific hydrophobic core in the α-lactalbumin molten globule. *J. Mol. Biol*. **1998**, *280*, 175–182.

97 R. Jaenicke, Intermolecular forces in the process of heat aggregation of globular proteins and the correlation between aggregation and denaturation. *J. Polymer Sci*., **1967**, *16*, 2143–2160.

98 L. Pauling, Aggregation of proteins. *Disc. Faraday Soc*., **1953**, *13*, 170–176.

99 J. D. Bernal, Structural arrangements of macromolecules. *Disc. Faraday Soc.*, **1958**, *25*, 7–18.

100 R. Jaenicke, R. Rudolph, I. Heider, Quaternary structure, subunit activity and in vitro association of porcine mitochondrial malate dehydrogenase. *Biochemistry* **1979**, *18*, 1217–1223.

101 R. Rudolph, I. Heider, E. Westhof, R. Jaenicke, Mechanism of refolding and reactivation of LDH after dissociation in various solvent media. *Biochemistry* **1977**, *16*, 3384–3390.

102 M. E. Goldberg, R. Rudolph, R. Jaenicke, A kinetic study of the competition between renaturation and aggregation during the refolding of denatured-reduced egg-white lysozyme. *Biochemistry* **1991**, *30*, 2790–2797.

103 G. A. Bowden, A. M. Paredes, G. Georgiou, Structure and morphology of protein inclusion bodies in *Escherichia coli*. *Biotechnology* **1991**, *9*, 725–730.

104 H. Neurath, J. P. Greenstein, F. W. Putnam, J. O. Erickson, The chemistry of protein denaturation. *Chem. Reviews* **1944**, *34*, 157–265.

105 R. Jaenicke (Ed.), Protein Folding, Elsevier/North-Holland Biomed. Press, Amsterdam, New York, **1980**.

106 R. Jaenicke, R. Rudolph, Refolding and association of oligomeric proteins. *Meth. Enzymol.* 1986, *131*, 218–250.

107 M. Gerl, R. Jaenicke, J. M. A. Smith, P. M. Harrison, Selfassembly of apoferritin from horse spleen after reversible chemical modification with 2.3-dimethylmaleic anhydride. *Biochemistry* **1988**, *27*, 4089–4096.

108 G. E. W. Wolstenholme, M. O'Connor (Eds.), Principles of Biomolecular Organization, Ciba Foundation Symp. 1965, Churchill Ltd., London **1966**.

109 K. H. Nierhaus, Assembly of the prokaryotic ribosome. In: Protein Synthesis and Ribosome Structure (K. H. Nierhaus, D. Wilson, Eds.), Wiley-VCH, Weinheim, **2004**.

110 M. Gerl, R. Rudolph, R. Jaenicke, Mechanism and specificity of reconstitution of dimeric lactate dehydrogenase from *Limulus polyphemus*. *Biol. Chem. Hoppe-Seyler* **1985**, *366*, 447–454.

111 R. Rudolph, I. Fuchs, R. Jaenicke, Reassociation of dimeric c-MDH is determined by slow and very fast folding reactions. *Biochemistry* **1986**, *25*, 1662–1667.

112 R. B. Freedman, Protein folding in the cell. In: Protein Folding (T. E. Creighton, Ed.) Freeman, New York, **1992**, 455–539.

113 M. Danner, R. Seckler, Mechanism of phage P22 tailspike protein folding mutations. *Protein Sci.* **1993**, *2*, 1869–1881.

114 M. Danner, A. Fuchs, S. Miller, R. Seckler, Folding and assembly of phage p22 tailspike endorhamnosidase lacking the N-terminal, head-binding domain. *Eur. J. Biochem.* **1993**, *215*, 653–661.

115 A. Helenius, T. Marquart, I. Braakman, The endoplasmic reticulum as a protein-folding compartment. *Trends Cell Biol.* **1992**, *2*, 227–231.

116 B. M. Merrifield, Life During a Golden Age of Peptide Chemistry: The Concept and Development of Solid-phase Peptide Synthesis. ACS, Washington, **1993**.

117 K. Hecht, R. Jaenicke, Malate dehydrogenase from the extreme halophilic archaebacterium *Halobacterium marismortui*: Reconstitution of the enzyme after denaturation and dissociation in various denaturants. *Biochemistry* **1989**, *28*, 4979–4985.

118 M. Gross, R. Jaenicke, Proteins under pressure: The influence of high hydrostatic pressure on structure, function and assembly of proteins and protein complexes. *Eur. J. Biochem.* **1994**, *221*, 617–630.

119 R. L. Baldwin, The nature of protein folding pathways. *J. Biomol. NMR* **1995**, *5*, 103–109.

120 J. Kepler, *STRENA, Seu De Nive Sexangula*, G. Tampach, Francofurti a.M., **1611**.

121 C. Chothia, Closing remarks. In: R. Jaenicke (Ed.) Protein Folding Elsevier/North-Holland Biomed. Pess, Amsterdam, New York, **1980**, 583–585.

2
Folding and Association of Multi-domain and Oligomeric Proteins

Hauke Lilie and Robert Seckler

2.1
Introduction

Folding and association of nascent or refolding polypeptide chains are spontaneous and autonomous processes. All information required for the formation of the native three-dimensional structure of a given protein or protein complex is encoded in the amino acid sequence. The structure of a protein is the result of an optimum partitioning of the nonpolar and polar parts of the polypeptide chain between regions of high and low dielectric constant in the solvent environment [1]. In aqueous solution this leads to a minimization of hydrophobic surface area. This basic principle governs both structure formation of monomeric proteins and association of subunits of oligomeric proteins.

In many cases the biological activity of proteins depends on their association state. The association can result in homo- or hetero-oligomers that may be either stable or only transiently formed during their specific functional cycle. The Protein Data Bank (pdb) of protein structures contains more than 2000 oligomeric structures, the largest of which comprise virus shells, and homomeric or heteromeric protein complexes containing more than 20 subunits, such as ferritin (24 identical subunits, [2]), the chaperonin complex GroEL/ES (21 subunits $\alpha 14\beta 7$, [3]), and dihydrolipoyl acetyltransferase (60 subunits, [4]).

For quite a number of multi-domain and even oligomeric proteins, folding and assembly pathways as well as their thermodynamic stabilities and dissociation constants have been determined. This chapter deals with the general principles of structure formation and stabilization of multi-domain and oligomeric proteins and the experimental approaches to analyze these reactions. Some closely related topics, which are not part of this chapter, are summarized in other chapters of this book. These comprise virus assembly (Chapter 5), collagen folding in vitro (Chapter 21 in Part I) and in vivo (Chapter 26), formation of protein fibrils (Chapters 31–36), and the catalysis of rate-limiting steps of folding such as peptide bond isomerization (Chapter 27) or disulfide bond formation (Chapter 29).

Protein Folding Handbook. Part II. Edited by J. Buchner and T. Kiefhaber

ISBN: 3-527-30784-2

2.2
Folding of Multi-domain Proteins

2.2.1
Domain Architecture

Domains are compact substructures within protein molecules. There are different definitions of "domain" based on analysis of the three-dimensional structure of the respective protein, the autonomous folding units of a protein, and functions such as cofactor binding or resistance to proteolysis. Interestingly, in a number of cases the boundaries of protein domains correlate with intron-exon boundaries on the genetic level [5, 6]. This suggests that exon shuffling (and thus domain shuffling) is an important mechanism in generating functional diversity during evolution of multi-domain proteins [1].

A hierarchical classification of domain structures (CATH) has been proposed, using as parameters the *secondary structure composition* (C for class), the *gross arrangement of secondary structure* (A for architecture), the *sequential connectivities* (T for topology), and the *structural and functional similarity* (H for homology) [7–9]. By this procedure 27 000 known domain structures can be grouped into 1800 sequence families, 700 fold groups, 245 superfamilies, and about 30 different architectures (Figure 2.1, see p. 36/37) of a total of three major classes (all-α, α/β, all-β).

Based on the three-dimensional structure and structure acquisition of proteins, domains are considered as cooperative units in the folding process. In this concept, the individual domains of a multi-domain protein can be considered simply as small, one-domain proteins that fold to a native-like structure independently of the remaining part of the protein. This holds for both in vitro folding and co-translational folding. The latter has been shown for the folding and assembly of nascent antibody chains [10]. Based on this kind of vectorial mechanism with well-defined assembly modules, large polypeptide chains speed up folding by many orders of magnitude. At the same time, possible wrong long-range interactions that would lead to an incorrectly folded protein are minimized.

Methods used to investigate the structure formation process of multi-domain proteins are the same as for simple model proteins and will not be discussed here. The most important techniques are listed in Table 2.1. A detailed description of some of these methods can be found in several chapters of Volume I of this handbook.

Detailed analyses on the structure, thermodynamic stability, and folding of multi-domain proteins have been performed, e.g., for γB-crystallin, lysozyme, α-lactalbumin, the light chain of antibodies, and many other proteins [11, 12]. From these studies it can be concluded that in most cases the domains fold independently kinetically and that they are thermodynamically stable entities. The complete refolding, however, often requires an additional kinetic phase involving intramolecular domain association. If the interaction sites of the domains are very

Tab. 2.1. Experimental approaches to study folding of domain proteins.

Assay	*Methods*	*Information*
Spectroscopy	Circular dichroism (CD)	
	In the far UV region	secondary structure information
	In the near UV region	environment of aromatic side chains
	Fluorescence	tertiary and quaternary structure
	NMR (combined with H/D exchange) and 2D-NMR	changes of the environment of single amino acids
Function	Enzymatic activity and/or ligand binding	monitoring the native state (sometimes can be active as well)
Stability	Limited proteolysis or denaturant	only folded domains or the native state might be resistant to proteolytic degradation or increased denaturant concentration

large, then domain-domain interactions may contribute significantly to the stability of the respective domains, and thus the isolated domains are thermodynamically unstable on their own. In such cases the folding and structure of the partner domain represent an essential template for structure formation of the other domain [13, 14].

One might suggest that proteins with very similar structure should show similar folding characteristics. This, however, is not the case. An intriguing example is the comparison of hen egg white lysozyme (HEWL) and α-lactalbumin. Both proteins with a molecular mass of approximately $Mr = 14\,400$ are structurally almost identical, containing an α-helical and a β-sheet domain. However, both their denaturant-induced equilibrium transitions and their folding characteristics are quite different. HEWL shows an equilibrium transition according to a classical two-state model (cf. Chapter 3 in Part I), i.e., only the native and the completely denatured state of the protein are populated in the transition region. In contrast, α-lactalbumin shows a three-state unfolding transition (in the absence of Ca^{2+} ions) according to the model $N \leftrightarrow I \leftrightarrow U$, where N is the native state, I is a partially structured folding intermediate, and U is the completely denatured protein [15]. The equilibrium intermediate I retains the α-helical domain, whereas the β-sheet domain is denatured. This same kind of intermediate can also be observed during the refolding kinetics of α-lactalbumin. It has been used as a model structure for the definition of the molten globule, a type of intermediate often observed in the folding of proteins (cf. Chapter 13 in Part I). Under strong refolding conditions (low residual concentration of denaturant), HEWL also folds via intermediates, which, however, do not resemble a classical molten globule [16]. Furthermore, in the case of HEWL, the intermediate is not obligatory; the protein can fold directly from the denatured to the native state. Due to kinetic competition, a fraction of the denatured molecules folds to an intermediate state, which subsequently undergoes a structural conversion to the native state [17].

2.2.2 γ-Crystallin as a Model for a Two-domain Protein

γ-Crystallin as an eye-lens protein of vertebrates belongs to a superfamily of β-sheeted proteins with a Greek key topology. It is a two-domain protein of a molecular mass of 21 kDa. The two domains, connected by a short peptide linker, are highly homologous (cf. Figure 2.5). γ-Crystallin is extremely stable, retaining its native structure at pH 1–10 or in 7 M urea at neutral pH [18]. The denaturant-induced equilibrium transition at neutral pH yields a broad transition and a partially irreversible denaturation. At acidic pH, however, the overall denaturation process splits into two transitions, both of which are fully reversible [18–20]. Making use of sedimentation analysis, intrinsic protein fluorescence, and circular dichroism, the urea-dependent equilibrium unfolding at pH 2 can be quantitatively described by a three-state transition $N \leftrightarrow I \leftrightarrow U$, with the intermediate populated at 2–4 M urea (Figure 2.2).

The kinetic data on folding and unfolding of γ-crystallin fit well to the biphasic equilibrium transition. Below 3 M urea, the denaturation kinetic is monophasic, representing the reaction N → I. At higher urea concentrations, the unfolding reaction becomes biphasic, the faster reaction corresponding to the structural conversion N → I and the slower one to I → U. Similar effects are observed for the refolding: at 3 M urea, the folding reaction is monophasic (U → I), while under strongly native conditions both reactions U → I and I → N can be observed. On the other hand, when starting either denaturation or refolding from the intermediate state, the respective kinetics are monophasic. Summarizing the dependence of the rate constants (or relaxation times) of folding and unfolding on the urea concentration, two separate V-shaped profiles (chevron plot) are obtained (Figure 2.2). The respective reactions correspond to structural transition of N → I, I → N, U → I, and I → U.

Structural interpretation of these data, however, is difficult. It is not possible to assign any of the equilibrium transitions and kinetic reactions to a certain domain of this two-domain protein. In order to correlate the mechanism with the specific structural properties of γ-crystallin, the recombinantly produced, isolated domains were investigated [19]. Both the C-terminal and the N-terminal domains have been shown to be monomeric in their isolated states as well as if simultaneously incubated even at very high protein concentrations. The thermodynamic stability and folding and unfolding reactions of the isolated N-terminal domain of γ-crystallin resemble those of the intermediate I of the full-length protein [18, 19], indicating that the intermediate I consists of a native-like structured N-terminal and a completely unfolded C-terminal domain. The isolated C-terminal domain, however, is much less stable than it is in the context of the whole protein (Figure 2.3). In fact, even in denaturant-free buffer, a significant fraction of the isolated C-terminal domain is unfolded.

The difference in the stability of the C-terminal domain in its isolated form and in the context of the full-length protein implies a significant contribution of the do-

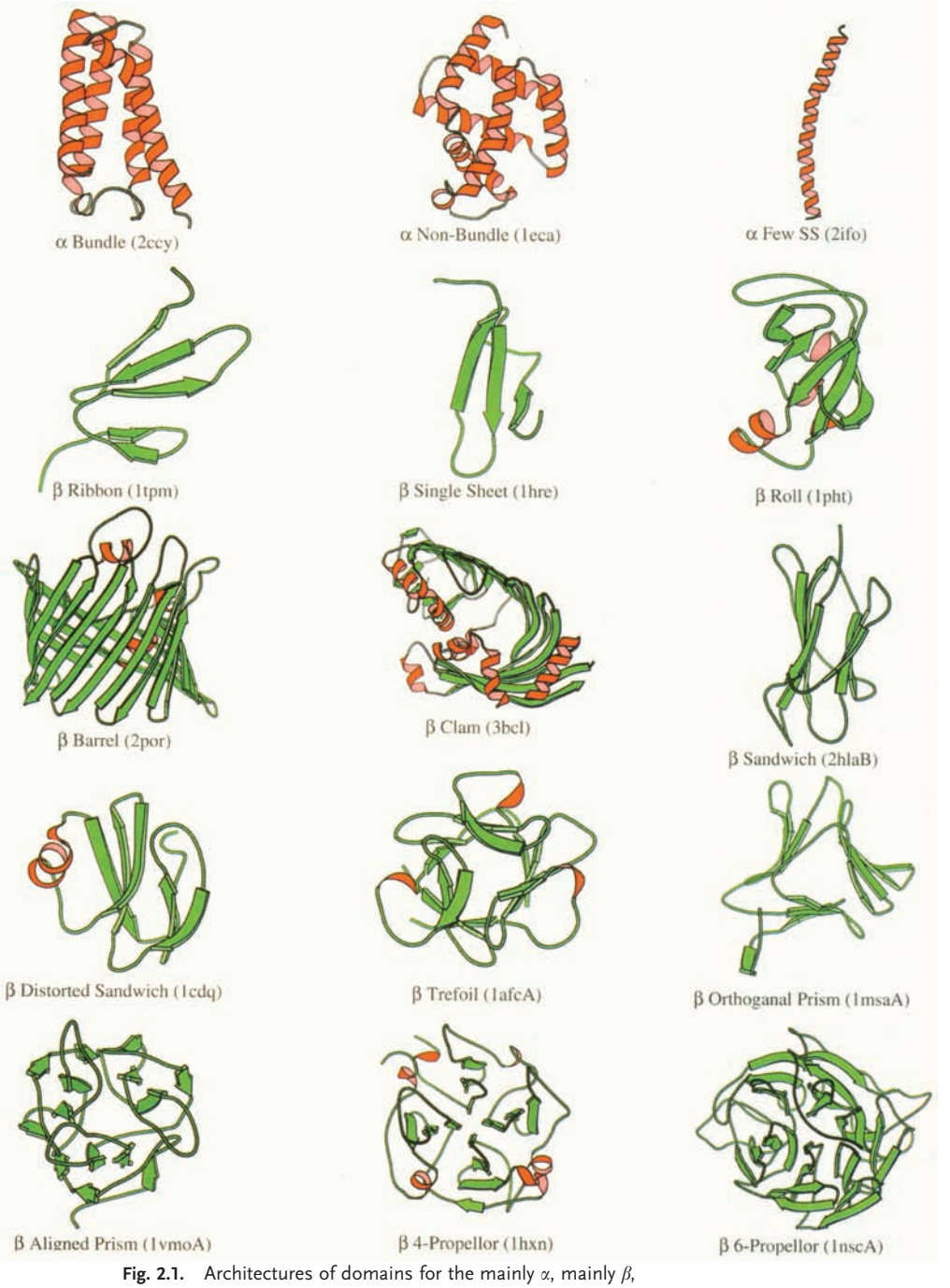

Fig. 2.1. Architectures of domains for the mainly α, mainly β, and $\alpha\beta$ classes of the CATH database [7–9].

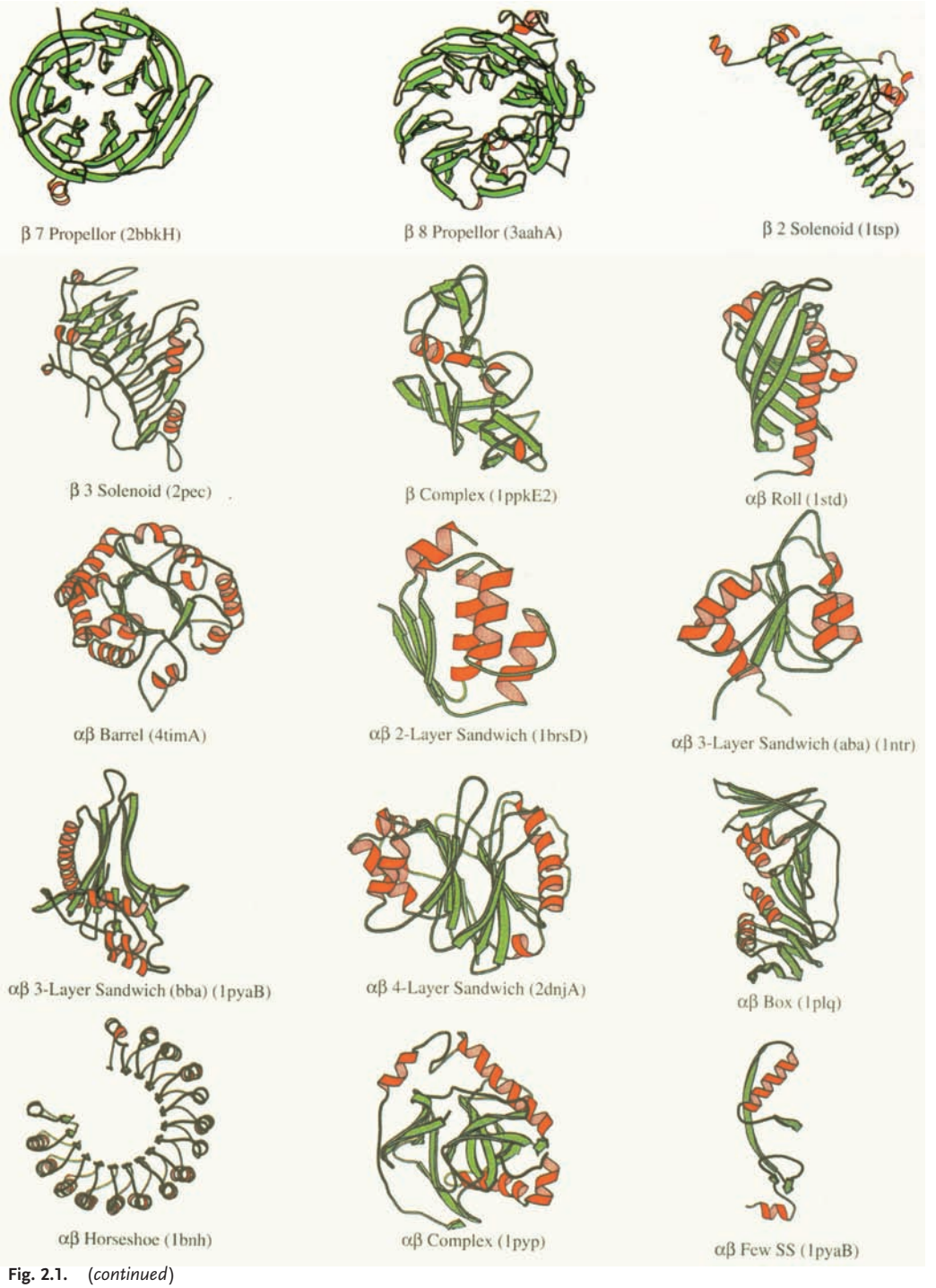

Fig. 2.1. (*continued*)

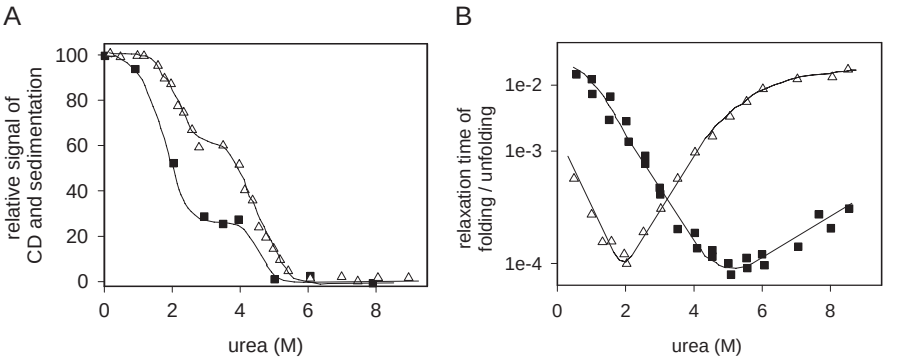

Fig. 2.2. Stability and folding of γ-crystallin (adapted from Ref. [18]). (A) Urea-induced equilibrium transition of γ-crystallin. The protein at a concentration of 0.2 mg mL^{-1} in 10 mM HCl (pH 2), 0.1 M NaCl was incubated at different urea concentrations. Subsequently, the samples were analyzed using CD (△) and sedimentation (s20,w: ■). (B) Kinetics of folding/unfolding of γ-crystallin (△,■) measured by fluorescence and HPLC gel filtration. The relaxation times of the kinetics are plotted against the urea concentration used for folding/unfolding.

main interactions (ΔG_{int}) to the overall free energy of stabilization (ΔG_{γ}), in addition to the sum of the intrinsic stabilities of the isolated domains ($\Delta G_{\mathrm{N}}, \Delta G_{\mathrm{C}}$):

$$\Delta G_{\gamma} = \Delta G_{\mathrm{N}} + \Delta G_{\mathrm{C}} + \Delta G_{\mathrm{int}}$$

Under the given conditions (pH 2) the stability ΔG_{C} amounts to only -4.7 kJ mol^{-1}, whereas the ΔG_{int} is -16 kJ mol^{-1}. Thus, at low pH the C-terminal do-

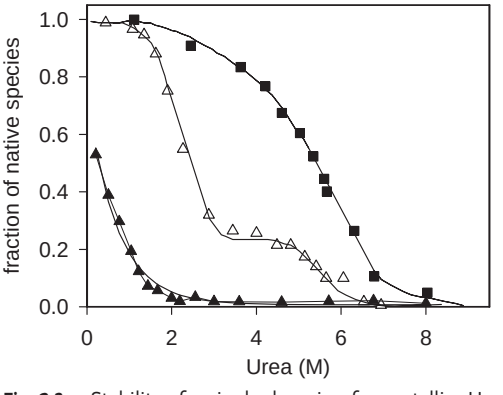

Fig. 2.3. Stability of a single domain of γ-crystallin. Urea-induced equilibrium transition of γ-crystallin and its single domains measured in 10 mM HCl pH 2, 0.1 M NaCl. Complete γ-crystallin (△), the isolated N-terminal domain (■), and the isolated C-terminal domain (▲).

main of γ-crystallin is mainly stabilized by an intramolecular association with the N-terminal domain. This intramolecular interface is characterized by a well-defined hydrophobic core of Phe 56, Val 132, Leu 145, and Val 170. If Phe 56 of the N-terminal domain is replaced by either Ala, thus creating a cavity in the hydrophobic core, or Asp, placing a non-saturated charge in the contact site, the C-terminal domain is considerably destabilized, again emphasizing the importance of the interaction free energy of stabilization (ΔG_{int}) in stabilizing the structure of the C-terminal domain of γ-crystallin.

2.2.3 The Giant Protein Titin

Titin is a protein located in the sarcomere of vertebrate striated muscle cells. A single molecule of titin spans half the sarcomere from the Z-disc to the M-line, extending about 1 μm in length (Figure 2.4). The protein consists mostly of several hundred copies of β-sheet domains of the immunoglobulin type and of fibronectin type III (Fn3); the molecular mass ranges from 3 MDa to 4 MDa, depending on the source of titin. The function of titin varies along the sarcomere. In the M-line it forms an integral part of the protein meshwork, while in the A-band it probably regulates the assembly of the thick filaments and might be involved in the inter-filament interaction of myosin and the actin/nebulin thin filament [21, 22]. In the I-band, titin serves as an elastic connection between the Z-disc and the thick filaments. It is hypothesized that these elastic properties depend on partial unfolding/refolding of titin during muscle tension.

In order to obtain insight into the molecular properties of this giant protein, single immunoglobulin and Fn3 domains as well as tandem repeats of these two domains have been cloned and biophysically analyzed. The individual domains vary considerably in sequence. Using fluorescence and circular dichroism as probes in equilibrium unfolding experiments, the thermodynamic stability of a variety of these domains was determined to be in the range of 8.6–42 kJ mol^{-1} [23]. Similarly, the rates of chemical unfolding of individual domains vary by almost six orders of magnitude [23]. It has been speculated that this dramatic variation in folding behavior is important in ensuring independent folding of domains in the multi-domain protein titin.

Site-directed mutagenesis of each position in a protein together with a detailed analysis of the folding and unfolding kinetics of these mutants permit the structural mapping of the transition state of folding (θ-value analysis, cf. Chapter 2 in Part I). Such an analysis for the titin domain I27 reveals that the transition state of folding is highly structured and remarkably native-like regarding its solvent accessibility. Only a small region close to the N-terminal region of the domain remains completely unfolded.

How do the molecular properties of the single domains of titin correlate with the function of the whole molecule? Titin is involved in muscle tension and elasticity and thus is subjected to mechanical forces. The elasticity of a protein can be measured by atomic force microscopy (AFM) [22]. To this end, the protein is fixed at

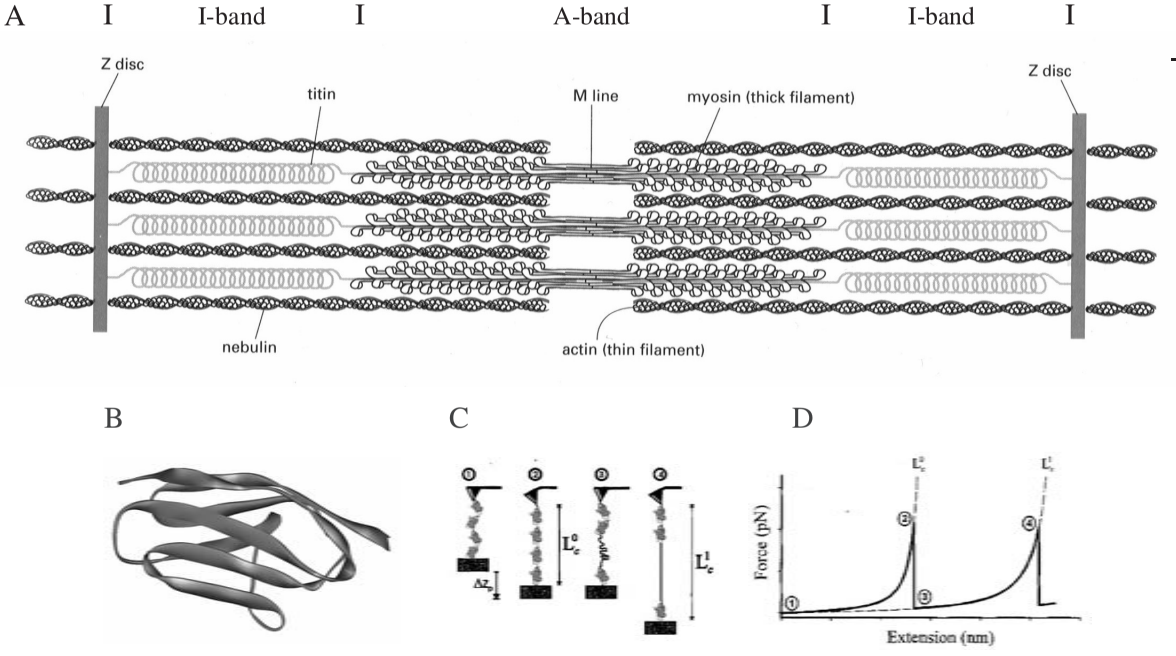

Fig. 2.4. (A) Schematic representation of a sarcomere of striated muscle. (B–D) Single-molecule AFM measurements of an engineered polyprotein of the titin domain I27. (B) Structure of the I27 Ig-like domain. (C, D) Schematic representation of the sequence of events during the stretching of I27 multi-domain protein. Stretching the ends of the polyprotein with an atomic force microscope sequentially unfolds the protein modules, generating a saw-tooth pattern in the force-extension relationship that reveals the mechanical characteristics of the protein. (1) An anchored multi-domain protein composed of four I27 domains. The protein is relaxed. (2) Stretching this protein requires a force that is measured as a deflection of the cantilever. (3) The applied force triggers unfolding of a domain, increasing the contour length of the protein and relaxing the cantilever back to its resting position. (4) Further stretching removes the slack and brings the protein to its new contour length Lc 1.

one end on a surface and at the other end on the tip of a so-called cantilever (Figure 2.4). Moving the cantilever slowly and on an Angstrom scale from the surface and thus continuously increasing the mechanical force leads to a stretching of the fixed protein. The resistance of the protein to this stretching results in a bending of the cantilever that is optically detected. At some point a protein domain unfolds, the resistance is partially released, and the cantilever returns to its starting position. This procedure is repeated as often as domains are located between the static surface and the cantilever. The experimental result is a sawtooth-shaped curve, in which the width of a single sawtooth reflects the difference in length of the folded and unfolded domains (28 nm for the titin domain I27) and the height of the peak corresponds to the mechanical force necessary for domain unfolding (Figure 2.4). The immunoglobulin domain I27 of titin unfolds at 210 pN, and the Fn3 domain I28 unfolds at ca. 260 pN. However, the hetero-oligomer $(I27–I28)_4$ is slightly stabilized, hence the mechanical force to denature the domain I28 in this construct increases to 306 pN [24]. Such a stabilization of the Fn3 domain I28 in the context of the neighboring I27 domain was also observed using chemical denaturation methods [25]. Comparison of the chemically induced unfolding and the mechanically induced unfolding reveals similar mechanisms of denaturation. The forced unfolding starts with the detachment of the N-terminal β-strand from the otherwise stable β-sheet. This N-terminal β-strand is not structured in the transition state of chemical denaturation. Site-directed mutagenesis studies show that the region important for kinetic stability is very similar in both cases, although there are also significant differences in the forced and chemically induced unfolding transition states [26, 27].

Presently, it seems that chemical and mechanical denaturation processes are related, at least for proteins evolved to respond to mechanical stress. However, in the case of barnase, a globular two-domain protein, mechanically and chemically induced unfolding seem to proceed quite differently on the structural level [28].

2.3
Folding and Association of Oligomeric Proteins

2.3.1
Why Oligomers?

Oligomers consist of noncovalently associated subunits of identical origin (homo-oligomers) or different origin (hetero-oligomers). Two or more monomers form dimers, trimers, tetramers, etc. Higher oligomers may possess topological units (e.g., the dodecameric aspartate transcarbamylase (ATCase) from *E. coli* consists of two catalytic trimers and three regulatory dimers). Tetramers of glyceraldehyde-3-phosphate dehydrogenase and yeast pyruvate decarboxylase are formed as dimers of dimers. Compared to other tetramerization pathways such as the addition of monomers to dimers or trimers, the specific topology of a tetramer as a dimer of

dimers leads to kinetics of association that seem to be less prone to competition with off-pathway reactions of nonnative assemblies or accumulation of association intermediates [29].

The advantage of oligomeric proteins compared to their non-associated monomeric counterparts may be found on the functional, structural, and genetic levels. Oligomerization permits an allosteric regulation of enzyme activity. In multienzyme complexes, the catalytic efficiency of the overall process may be significantly increased. This would especially be the case if labile intermediates were channeled from one active site to the other. These functional advantages, however, can be conferred not only by oligomeric structures but also by large multi-domain proteins. Indeed, a few such very large multi-domain proteins consisting of more than 10 000 amino acids are known [30]. There is no fundamental structural or functional distinction between domains and subunits. The eukaryotic fatty acid synthase contains the whole assembly line of fatty acid synthesis [31, 32]; similarly, many non-ribosomal peptides are synthesized by very large proteins (e.g., the cyclosporin synthetase, in which all the different enzyme functions are located in one polypeptide chain) [33]. However, these very large multi-domain proteins are rare: most large protein structures are formed by association of subunits. Oligomerization of small gene products is by far more economical; this is quite obvious in the case of viruses, where a small protein, and thus a small gene, is sufficient for building up a large virus capsid of the size of several megadaltons. Furthermore, errors occurring during protein synthesis can be eliminated more easily in the case of oligomeric structures. Another possible advantage of oligomeric protein complexes versus large multi-domain proteins may result from differences in folding. It has been shown that domains in the context of a larger polypeptide chain fold more slowly than the same domain in its isolated state [34–36]. This difference may result from nonnative long-range interactions with other parts of the polypeptide chain and/or diffusional limitations of a long polypeptide during folding. In the case of the central domain of bacteriophage P22 tail spike protein, the folding of this β-helix domain is accelerated about twofold upon removal of the N-terminal, structurally unrelated domain. This slightly accelerated folding increases the yield of folding significantly both in vitro and in vivo [36, 37].

2.3.2 Inter-subunit Interfaces

The increasing number of high-resolution crystal structures of oligomeric proteins and protein complexes available in the Protein Data Bank allows a statistical analysis of the properties of interfaces of subunits and domains [38–41]. The majority of the subunit interfaces have a surface of 1000–3000 $Å^2$. The major part of this surface is usually hydrophobic, conveying the stability of interaction; polar interactions, including hydrogen bonding and ionic interactions, as well as surface complementarity serve as specificity factors of interaction [43, 44]. In fact, the molecular properties of the interface of stably associated subunits regarding the distribution of hydrophobic versus polar residues are very similar to that of the

hydrophobic core of proteins and, conversely, very different from that of the solvent-accessible surface. In contrast to the interfaces responsible for stable subunit association, the contact sites of proteins that interact only transiently with other proteins are less hydrophobic [41].

A qualitative analysis of 136 subunit interfaces of homodimeric proteins [45] showed that about 30% are characterized by a well-defined hydrophobic core, surrounded by polar interactions [45, 46]. However, the majority of interfaces consist of multiple small, hydrophobic patches interspersed by hydrogen bonds and polar interactions [45].

Such large differences in interface structure might correspond to differences in interface stability and in folding and assembly mechanisms, as proposed by Nussinov and coworkers [40, 47]. This is illustrated by the tetrameric yeast pyruvate decarboxylase (PDC). The topology of PDC is reminiscent of a dimer of dimers. The interface between the dimers that form the tetramer is largely polar, and the tetramer spontaneously dissociates to dimers upon dilution. The dissociation constant of this dimer-tetramer equilibrium is 8.1 μM [48]. The interface between the monomers, however, is strongly hydrophobic; the dimer does not dissociate into monomers just by dilution of the protein. Only in the presence of 2–3 M urea can folded monomers be populated [48]. Unfortunately, there are only very few cases where thermodynamic, kinetic, and crystallographic data of a certain protein can be combined in order to assess these questions. Recent studies suggest that, in a given interface, a few amino acids may play a dominant role in determining the free energy of stabilization of the interaction. These residues are called hot spots of the binding surface [46].

Whereas in most cases the association of proteins is mediated by globular, native-like structured domains, a growing number of protein-protein interactions have been discovered in which one of the partners is unstructured in its isolated state. These natively unstructured proteins can be grouped into two classes, one with random coil structures and the other with a pre-molten globule structure [13]. Only upon association with their targets do these proteins develop an ordered and biologically active structure. Examples are several ribosomal proteins that transform to a rigid well-folded conformation only in the presence of the ribosomal RNA [49, 50]. In the case of cyclin-dependent kinase inhibitor p21, the N-terminal fragment lacks stable secondary and tertiary structure in the free solution state. However, when bound to its target, Cdk 2, it adopts a well-ordered conformation [51].

Besides the usual subunit interaction via globular domains, there is also another major type of protein-protein interaction mediated by special helical structures: the so-called coiled coils [52]. A detailed description of this interaction that may lead to dimers, trimers, or tetramers, depending on the sequence of the coiled coils, can be found in Chapter 18 in part I.

Furthermore, completely artificially designed peptides have been described, conferring heterodimerization of proteins fused to them. These peptides are based on only a stretch of eight charged amino acids and an additional cysteine. Two of these peptides containing complementary charged side chains associate with each

other due to their polyionic interaction; subsequently, the cysteines can form a disulfide bond, thus stabilizing the heterodimerization [53–55].

2.3.3 Domain Swapping

As pointed out by Bennett et al. [56–58], the gradual accumulation of random mutations on the surface of a monomeric protein that are required to create a suitable subunit interface and stabilize a dimer cannot be accomplished within a biologically feasible time. At least in some cases the evolution of domains offers a key to understanding the mechanism to proceed from monomers to dimers. Starting from a two-domain monomer, domain swapping permits the transition from monomers to dimers (or any other association state) simply by switching from an inter-domain to an inter-subunit interaction. In this scheme, the interface that is almost impossible to create by random mutagenesis in evolution is available a priori. Based on the already-existing interaction site, additional mutations might then stabilize the domain-swapped dimer compared to the monomer (Figure 2.5).

The concept of domain swapping may be illustrated by $\beta\gamma$-crystallins. $\beta\gamma$-crystallins are members of the superfamily of β-sheeted proteins containing the Greek key motif. γ-crystallin is monomeric even at extremely high protein concentrations, whereas β-crystallin forms dimers or higher oligomers. Both show highly homologous two-domain structures. Comparison of the structures of γ- and β-crystallins suggests that the β dimers are the product of domain swapping and association of a γ ancestor (Figure 2.5). This hypothesis is supported by the fact that 60% of the interface residues of the N- and C-terminal domains of γ-crystallin are identical or highly conserved compared to those of the N- and C-terminal domains of the two subunits of β-crystallin [59].

Domain swapping does not correlate necessarily with structural domains. Instead, the swapped portion can vary from a large globular domain, as described for $\beta\gamma$-crystallins, to a structural element as short as a single helix or β-strand. In fact, of the ca. 40 structurally characterized cases of domain-swapped proteins, most swapped domains are either at the N- or C-terminus and are diverse in their primary and secondary structure [60]. Hsp33, for example, forms a dimer in which a C-terminal arm of one monomer consisting of two α-helices wraps around a second monomer [61, 62]. This C-terminal arm is connected to the remaining part of the protein by a putatively flexible hinge region. The chaperone-active dimer is in equilibrium with a less active or even inactive monomer ($K_D = 0.6$ μM, [63]). A detailed structural and functional analysis of Hsp33 is presented in Chapter 21. Unfortunately, the structure of the Hsp33 monomer is not known. Thus, at present it is only speculation that in the monomeric structure the C-terminal arm folds back on the monomer.

Higher association states of domain-swapped proteins are found in several virus capsids, in which capsomers swap β-strands, or pathologic aggregates in the case of α1-antitrypsin [64].

Although domain swapping is an intriguing concept in understanding evolution

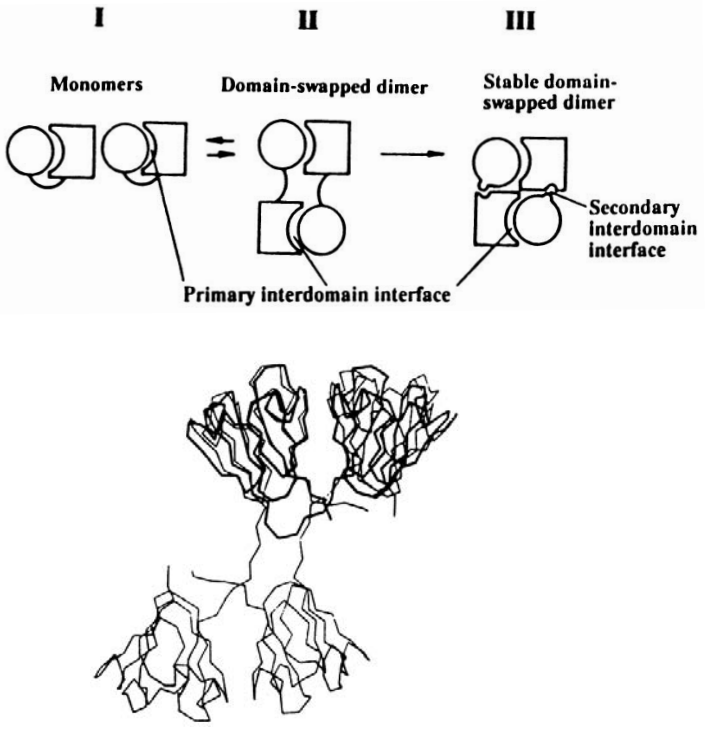

Fig. 2.5. Domain swapping. (A) The monomer (I) with its primary inter-domain interface may participate in interchain interactions, generating domain-swapped dimmers (II). Stabilizing mutations in the linker region allow stable dimers (III) to be formed [56]. (B) β-crystallin dimer (thin line) as potential product of swapped domains of γ-crystallin (thick line) (adapted from Ref. [11]).

of protein dimerization and oligomerization, it can be applied only in a limited number of cases. It cannot explain hetero-oligomerization of subunits encoded by widely differing genes as these subunits do not share a common inter-domain interface or different parallel routes of dimerization, as shown for bovine seminal ribonuclease, which exists in both a domain-swapped and a non-swapped dimeric form [65, 66].

2.3.4 Stability of Oligomeric Proteins

The laws of thermodynamics require that association equilibria be shifted towards the dissociated state at low protein concentrations. Indeed, for several oligomers it has been shown that the dissociation constants of dimerization are in the nanomolar to micromolar range, and thus the dissociation can be achieved directly by dilu-

tion experiments. Examples are phosphofructokinase [67], dimeric Arc repressor [68], Hsp33 [63], and yeast hexokinase [69, 70]. In some cases this association equilibrium is functionally and physiologically relevant. Dimeric Hsp33 is active as a molecular chaperone, whereas the monomeric form is less active or non-active [63, 71]. The K_D describing the monomer-dimer equilibrium is in the range of the physiological concentration of Hsp33 in *E. coli* [63]. In the case of yeast hexokinase, the monomeric state of the protein is less active than the dimeric form. Interestingly, the dimerization is favored in the presence of the substrate glucose [69].

Most oligomeric proteins, however, dissociate only at concentrations too low to observe dissociation by mere dilution [1]. This finding suggests that subunit interactions account for a large fraction of the conformational stability of oligomeric proteins; sub-nanomolar dissociation equilibrium constants for dimerization correspond to standard free energy changes of >50 kJ mol^{-1}. In such cases, dissociation is achievable only by denaturation. Whereas the denaturant-induced equilibrium transition of denaturation of monomeric proteins is independent of the protein concentration, the midpoint of transition of oligomeric proteins varies with protein concentration. In the simplest case of a reversibly denaturing dimeric protein, this transition can be ascribed to the reaction $N_2 \leftrightarrow 2U$. The linear extrapolation method, used for analysis of the transition (cf. Chapter 3 in Part I), yields a straight line with a slope depending on the protein concentration used (Figure 2.6). These lines describing the denaturation transition at different protein concentrations will

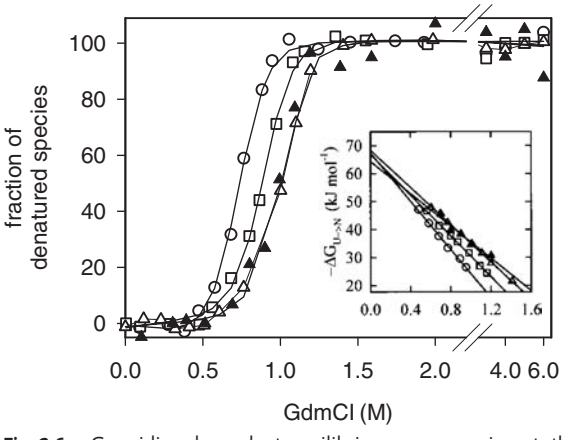

Fig. 2.6. Guanidine-dependent equilibrium transitions of the dimeric antibody domain CH3. Samples were incubated for six days at 20 °C in 0.1 M Tris-HCl (pH 8.0) and varying GdmCl concentrations. For the fluorescence measurements the excitation wavelength was set to 280 nm and emission was analyzed at 355 nm. The CH3 dimer concentrations were 0.2 μM (open circles), 1.6 μM (open squares), and 4.1 μM (open triangles). For the CD experiment, the ellipticity was recorded at 213 nm (filled triangles) at a protein concentration of 4.1 μM. All measurements were carried out at 20 °C. Inset: From the transitions, the stability ΔG could be calculated at the respective GdmCl concentrations. These ΔG values were plotted against the respective GdmCl concentration and linear extrapolated to 0 M GdmCl [42].

intersect the y-axis at the same value that corresponds to the stability of the dimeric native state in the absence of denaturant [72].

Oligomeric states often are not only thermodynamically stable but also kinetically stabilized, i.e., the activation energy of dissociation under native conditions is very high. Dissociation rates in denaturant-free buffer have been estimated by extrapolation to be as low as 10^{-14} s^{-1} [73].

2.3.5 Methods Probing Folding/Association

The reconstitution of oligomeric proteins comprises folding of subunits and their association. Therefore, all methods suited to analyze folding of proteins and domains can be applied to oligomeric proteins as well (cf. Table 2.1). In the following section, only methods that detect association reactions are discussed. In using these methods, one should be very careful, because these techniques do not always distinguish between specific association and unspecific aggregation. The latter, however, will often be found to compete with proper refolding and association.

2.3.5.1 Chemical Cross-linking

Highly reactive bifunctional chemicals can be used to covalently cross-link subunits of an oligomeric structure with each other. In the case that cross-linking proceeds much faster than oligomerization, it is possible to get time-resolved information of the association reaction by cross-linking aliquots of the reaction at different time points. The amount of cross-linked oligomers can subsequently be analyzed on SDS-PAGE. Glutaraldehyde has been shown to be ideally suited as a cross-linker for several reasons. It forms a Schiff base with lysine side chains, which are usually located on the surface of a folded subunit. The reaction is very fast and efficient. It is not dependent on a specific distance between two lysine residues because glutaraldehyde exists in differently polymerized forms in aqueous solutions; therefore, the distance between the two reactive aldehyde groups of glutaraldehyde varies with its polymerization state. For a given protein, the glutaraldehyde concentration, reaction time, temperature, and protein concentration need to be optimized in order to guarantee that non-associated subunits are not cross-linked artificially. A protocol for glutaraldehyde cross-linking is given in the Appendix.

2.3.5.2 Analytical Gel Filtration Chromatography

Gel filtration is a standard technique to determine the molecular mass of proteins. Using it for kinetic analyses of association, however, poses problems. Gel filtration is a comparatively slow method; the time resolution of kinetic measurement will therefore be low. The protein analyzed will be diluted on the column, thus shifting a possible association equilibrium towards the dissociated species. Only if the dissociation of the oligomer is much slower than the time it takes to carry out the gel-filtration chromatography will significant results be obtained (the rate of dissociation might be slowed down by cooling the column). Gel-filtration chromatography

has been used successfully to characterize, among others, the reconstitution of β-galactosidase [74], P22 tail spike protein [75], and an antibody Fab fragment [76].

2.3.5.3 Scattering Methods

Light scattering, small-angle X-ray scattering, and neutron scattering provide information on particle size and shape. They can be used online without the necessity of taking aliquots during reconstitution for analysis. However, scattering methods need high protein concentrations (small-angle X-ray and neutron scattering, several milligrams per milliliter; light scattering, depending on the size of the oligomer, not less than 0.1 mg mL^{-1}). At these high protein concentrations, unspecific aggregation is often favored over correct reconstitution. Light scattering has been used predominantly to monitor formation of large assemblies such as viruses or protein filaments. More often it is used as a method to follow aggregation [77, 78].

2.3.5.4 Fluorescence Resonance Energy Transfer

Fluorescence resonance energy transfer (FRET) can be measured if the emission spectrum of a fluorophore overlaps with the absorption spectrum of another fluorophore. Then the energy of the excited donor fluorophore will not be emitted as fluorescence but will be transferred to the acceptor fluorophore. In this setup, the donor fluorophore will be excited and the fluorescence of the acceptor is measured. The transfer efficiency is inversely proportional to the sixth power of the distance between the two fluorophores, thus permitting measurement of distances within proteins [79] and monitoring of protein complex formation [80]. FRET measurements have to be carefully controlled. The fluorescence dyes that are coupled to the respective subunits are bulky hydrophobic chromophores and might induce association or aggregation of the coupled proteins artificially.

The FRET technique has become increasingly important to study protein-protein interaction in the cellular context. To this end, the proteins in question are fused to different variants of the green fluorescent protein, e.g., BFP and GFP. If these fusion proteins associate in vivo, FRET can be observed and quantified by fluorescence microscopy.

2.3.5.5 Hybrid Formation

The concentration of unassembled subunits can be measured by their ability to form hybrid oligomers. Originally, the technique used a large excess of chemically modified or isoenzyme subunits added after varied reconstitution time to trap unassembled subunits [81–84]. Problems such as slow folding of added subunits and preferential formation of homo-oligomers are associated with this approach. More-reliable data may be obtained with naturally occurring or site-directed mutant proteins with altered net charge but unaffected folding and association kinetics [37, 75, 85]. The technique may be illustrated using the trimeric tail spike protein from phage P22. Wild-type and mutant tail spikes with altered charge were separately denatured by urea at pH 3. Subsequently, both proteins were diluted separately into neutral buffer to remove the denaturants and start refolding. After dif-

ferent times, aliquots from both solutions were mixed, reconstitution of native trimers was allowed to reach completion, and the differently charged hybrids and homo-oligomers were separated by electrophoresis [75]. In samples mixed early during renaturation, wild-type homotrimers, hybrids, and mutant homotrimers formed at the statistically expected ratio of 1:2:2:1, whereas in samples mixed late, only homo-oligomers were detected. The half-time of assembly can be estimated from the amount of hybrid present in samples mixed at intermediate renaturation times.

It should be noted that hybrid formation measures only stably associated protomers; those in rapid exchange between loosely associated oligomers will be equivalent to free subunits.

2.3.6 Kinetics of Folding and Association

2.3.6.1 General Considerations

The reconstitution of oligomeric proteins from the denatured state generally constitutes a series of uni- and bimolecular steps. For a dimeric protein, reconstitution involves the following steps (neglecting possible off-pathway side reactions):

$$2U \rightarrow 2M \rightarrow M_2 \rightarrow N_2$$

where U is the denatured state. M represents a folded monomer, M_2 a nonnative dimer, and N_2 the native dimer. The folding reactions preceding subunit assembly are identical to those of single-domain or multi-domain proteins. They consist of a hydrophobic collapse, formation of secondary structure, and the merging of domains, leading to association-competent monomers. As in the case of monomeric proteins, these reactions may occur as sequential or parallel reactions on multiple pathways [86, 87]. All these reactions follow first-order kinetics and do not depend on protein concentration. In contrast, the association of subunits ($2M \rightarrow M_2$) is a bimolecular and therefore probably a second-order reaction. Subsequently, the dimer may need to undergo further unimolecular rearrangements to reach the final native state ($M_2 \rightarrow N_2$).

The assembly of larger oligomers can be described accordingly as a series of multiple uni- and bimolecular steps. The assembly of a homotrimer is expected to proceed via a dimeric intermediate:

$$3M \leftrightarrow M_2 + M \rightarrow M_3$$

In this reaction scheme, the first association resulting in a dimer, in which only one of two interfaces is buried, is considered a fast equilibrium. This first association step is unfavorable and the dimeric intermediate is not populated in equilibrium. The second association step will pull this equilibrium towards the native trimeric state. In this concept, the overall process follows apparent third-order kinetics [84].

A tetramer may be envisioned as a dimer of dimers. Thus, the scheme for this reaction is just an extension of that shown for a dimeric protein [1, 88]:

$$4U \rightarrow 4M \rightarrow 2M'_2 \rightarrow 2M_2 \rightarrow M_4 \rightarrow N_4$$

In the case of multimers such as fibrillary proteins or virus capsids, the simplest model comprises a stepwise addition of monomers to the growing chain:

$$2A \leftrightarrow A_2, A_2 + A \leftrightarrow A_3, A_3 + A \leftrightarrow A_4, \ldots$$

In this scheme the equilibrium constants of association may be all identical. However, the first steps of multimerization are often thermodynamically disfavored, i.e., the equilibrium is on the side of the non-associated species. Only after reaching a certain size of the oligomer structure does further addition of monomers to this nucleus become thermodynamically favorable. This would lead to an overall assembly process characterized by a nucleation/polymerization reaction.

2.3.6.2 **Reconstitution Intermediates**

Because the half-time of association is concentration-dependent, the nature of the rate-limiting step of reconstitution of oligomeric proteins may change with protein concentration [1]. At high protein concentrations, the formation of association-competent subunits is rate-limiting; at low protein concentrations, dimerization is rate-limiting, and the overall reaction follows second-order kinetics. Under these conditions, highly structured, association-competent subunits often are populated kinetically during refolding/assembly.

Such intermediates can be observed spectroscopically. In general, secondary structure as monitored by far-UV circular dichroism is formed quickly upon folding/association. Furthermore, the secondary structural content of the folded subunits does not change significantly upon subsequent association. Thus, the change in CD signal follows first-order kinetics, reaching the signal of the native protein as subunit folding is completed. In contrast, if reconstitution is analyzed by reactivation, i.e., regain of enzyme activity, no reactivation is observed during subunit folding provided that the non-associated subunits do not possess enzyme activity by themselves. The folding of the subunits results in a lag-phase in regain of activity; reactivation occurs upon association. Thus, the overall reactivation is described by a uni-bimolecular process that follows a sigmoidal time course, with the lag-phase determined by first-order subunit folding (Figure 2.7) [89].

Another method often used to analyze protein folding is fluorescence. However, whereas circular dichroism monitors secondary structure formation almost exclusively on the subunit level and, in most cases, enzymatic activity corresponds to the native state after assembly, fluorescence may detect both subunit folding and association, depending on the localization of the fluorophores in the quaternary structure. Therefore, the interpretation of fluorescence data might be more difficult. On the other hand it allows the detection of the association process even if the protein is enzymatically inactive.

In some cases the folded but non-associated subunit already shows ligand bind-

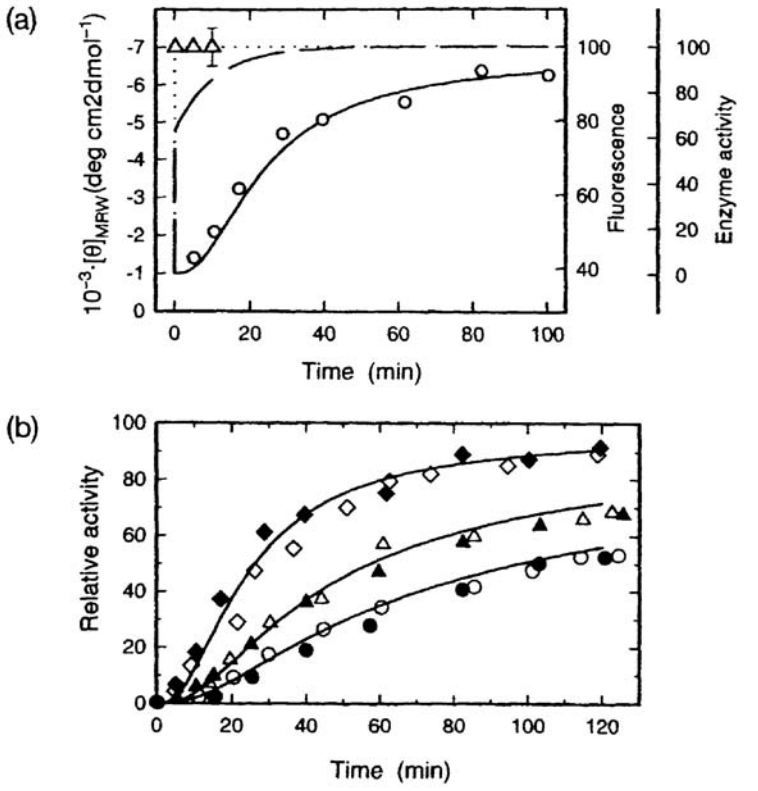

Fig. 2.7. Folding and association pathway of yeast invertase. (a) Changes in circular dichroism (open triangles), fluorescence emission (broken line), and enzymatic activity (open circles) occur with very different kinetics during the reconstitution of homodimeric yeast invertase. (b) The first-order folding rate obtained from the fluorescence change can be used to fit a sequential uni-bimolecular mode to the reactivation data obtained at different protein concentrations (full lines). Subunit concentrations were 8.5 nM (circles), 17 nM (triangles), and 68 nM (diamonds) [89].

ing or partial enzyme activity. Examples are mammalian aldolases [90], lactate dehydrogenase [91], the P22 tail spike protein [92], and yeast hexokinases [69, 70].

Monomeric folding intermediates of oligomeric proteins often possess large interfaces for subunit association. This subunit interaction is quite similar to the domain-domain interactions in multi-domain proteins. As shown before for γ-crystallin, the association can contribute substantially to the overall stability of the subunits. Thus, it is not surprising that folded subunits usually are not detectable as equilibrium unfolding intermediates if the native protein is subjected to high temperature or chemical denaturants [1, 88]. Structured monomers of lactate dehydrogenase have been obtained at low pH in the presence of the stabilizing salt sodium sulfate [93–95]. Another possibility to obtain stably folded monomeric subunits is based on protein engineering, as has been demonstrated for triose phos-

phate isomerase [96, 97], tetrameric human aldolase [98], and P22 tail spike protein [92]. In all these cases the engineered monomeric form retained some enzyme activity, but, as expected, the variants were strongly destabilized compared to the oligomeric wild-type form.

2.3.6.3 Rates of Association

The maximum rate of association of two molecules is determined by their random diffusional collision. For a common protein domain, this limit is about 10^9 M^{-1} s^{-1} [99]. Indeed, this limit is reached in the binding of chaperones to their substrate proteins. Chaperones recognize a wide variety of substrate proteins mainly by hydrophobic interactions. Since these interactions do not need a pre-orientation of chaperone and substrate, most of the diffusional collisions result in complex formation. However, this is quite different for the specific association of folded subunits. Here, the pre-formed interfaces require an exact rotational alignment for association, and this reduces the diffusion-controlled rate by several orders of magnitude. Brownian dynamics simulations estimate the rate of association of model proteins to be 10^6 M^{-1} s^{-1} [100]. Most second-order rate constants determined experimentally are even smaller (Table 2.2). There are, however, two examples published—the core domain of trp repressor and the arc repressor—that show faster dimerization than expected (Table 2.2) [101, 102]. In both cases folding is tightly coupled to association; the association-competent monomers are only partially structured.

2.3.6.4 Homo- Versus Heterodimerization

The molecular interaction of subunits in oligomers can be considered as specific as the formation of the hydrophobic core of a protein. The structure of a protein or subunit determines the kinetic and thermodynamic characteristics of its interaction with other molecules. Therefore, a competition between homo- and heterodimerization is expected only if the different subunits of the oligomer are highly homologous.

Tab. 2.2. Rates of association of some oligomeric proteins.

Protein	*Subunit mass (kDa)*	*Reaction*	*k (M^{-1} s^{-1})*	*Reference*
Triosephosphate isomerase	27	2M → D	3×10^5	1
Malate dehydrogenase (mitochondrial)	33	2M → D	3×10^4	1
Invertase	76	2M → D	1×10^4	89
β-Galactosidase	116	2M → D	4×10^3	74
Alcohol dehydrogenase (liver)	40	2M → D	2×10^3	1
Phosphoglycerate mutase	27	2M → D	6×10^3	103
		2D → T	3×0^4	103
Lactate dehydrogenase	36	2D → T	2×10^4	1
Arc repressor	62	2M → D	1×10^7	102
Trp aporepressor	12	2M → D	3×10^8	101

The most prominent example of such a competition is the reconstitution of heterodimeric bacterial luciferase from *Vibrio harveyi*. The two subunits consisting of a $(\beta\alpha)_8$ barrel are structurally homologous and probably result from gene duplication [104]. The association is mediated by two helices from each subunit forming a four-helix bundle at the contact site [105, 106]. The reconstitution of luciferase from the urea-denatured state is fully reversible. It comprises as rate-limiting steps the folding of the subunits on the monomeric level, the association of the subunits to an inactive heterodimer (at low protein concentrations), and a conformational rearrangement on the dimeric level leading to the native state [107–110]. As shown by far-UV circular dichroism, the inactive dimer seems to be incompletely folded.

Whereas the reconstitution of luciferase is quantitative if the subunits are refolded together, refolding of the subunits separately with a subsequent assembly does not lead to active heterodimer [107, 111]. In a detailed study, it could be shown that active heterodimeric luciferase can be assembled upon folding of the β-subunit in the presence of the pre-folded α-subunit, but not vice versa [73]. In the absence of the α-subunit, the β-subunit forms a homodimer that is almost as stable thermodynamically as the heterodimer. Furthermore, the β_2 homodimer is kinetically very stable, and under native conditions the dissociation does not occur on a biological or experimental timescale [73].

Upon reconstitution, the association of the β_2 homodimer and the $\alpha\beta$ heterodimer compete with each other. The almost exclusive formation of the heterodimer is due to the kinetics of association: the rate of heterodimerization is more than tenfold higher than that of the β_2 homodimerization. The structures of the homo- and heterodimer are almost identical regarding the contacts within the interfaces; most of the inter-subunit hydrogen bonds and water-mediated contacts are conserved between the two dimers [105, 106]. Thus, from the structural point of view, there is no obvious explanation for the different association kinetics of homo- and heterodimeric luciferase.

Mammalian lactate dehydrogenase (LDH) may serve as another example of the competition of homo- and hetero-oligomerization. LDH is a tetrameric protein that exists in two homomeric variants: in skeletal muscle (LDH-M_4) and in the heart (LDH-H_4). If these two isoforms are reconstituted together from the denatured monomers, the product is not only the two homomeric tetramers M_4 and H_4 but also all types of hybrids. Even more surprising, the distribution of all the variants fits to a statistical process, e.g., the ratio of M_4, M_3H_1, M_2H_2, M_1H_3, and H_4 is 1:4:6:4:1 [1, 94]. The beauty of this system is that it can be used to analyze the two different association steps upon reconstitution; at different time points of the reconstitution of LDH-M_4, an excess of LDH-H subunits can be added to the reaction. From the ratios of the hybrids reconstituted after addition of LDH-H subunits to the refolding LDH-M, the amount of monomeric, dimeric, and tetrameric M-subunits can be calculated [94].

Distinguishing homo- from hetero-oligomers is not always a simple matter, because in order to obtain competition of homo- and hetero-oligomerization, the subunits have to be highly homologous. The different hybrids of LDH could be separated by native electrophoresis, and in the case of luciferase the two subunits show

different pI values, allowing a separation of the different subunits by ion-exchange chromatography [109]. Furthermore, enzymatic activity or varying stability of the different species may be used to distinguish between homo- and hetero-oligomers.

2.4 Renaturation versus Aggregation

Folding and association of multi-domain and oligomeric proteins are complex processes involving partially structured folding intermediates. These processes can be accompanied by nonspecific side reactions leading to aggregation. The molecular basis for aggregation is that intermediates in refolding/reassembly may engage in wrong intermolecular rather than in correct intramolecular or assembly interactions. Thus, aggregation is at least a second-order or even higher-order reaction, depending strongly on the concentration of folding intermediates [112, 113]. Therefore, the kinetic partitioning between folding and aggregation favors aggregation at high protein concentrations. In contrast, at low protein concentrations, folding dominates over aggregation (Figure 2.8).

Using reduced lysozyme as a model system, it could be shown that commitment to aggregation is a fast reaction preceding the commitment to renaturation; early folding intermediates were especially prone to aggregation [114]. After a certain intermediate state is reached, slow conformational changes lead exclusively to the native state (Scheme 2.1 [114]).

As shown by circular dichroism and Fourier transform infrared spectroscopy (FTIR), aggregated proteins possess a high content of secondary structure and probably of native-like structured protein domains [115, 116].

Aggregation is not an artifact of in vitro refolding; the same phenomenon occurs in vivo. It is especially obvious in the case of inclusion body formation upon high-level expression of recombinant proteins in microorganisms and the accumulation of fibrillary aggregates in human diseases [115–118]. Cells have developed a set of chaperones and folding catalysts to deal with aggregation. These two protein classes are discussed in detail in several chapters of this book.

2.5 Case Studies on Protein Folding and Association

2.5.1 Antibody Fragments

Antibodies are hetero-oligomeric proteins consisting of two light chains and two heavy chains. These four polypeptides are covalently linked by several disulfide bonds. The light chain consists of two domains and the heavy chain of four domains, with each domain adopting a typical immunoglobulin-like topology of a two-sheeted β structure. Folding of these domains has been shown to be a highly

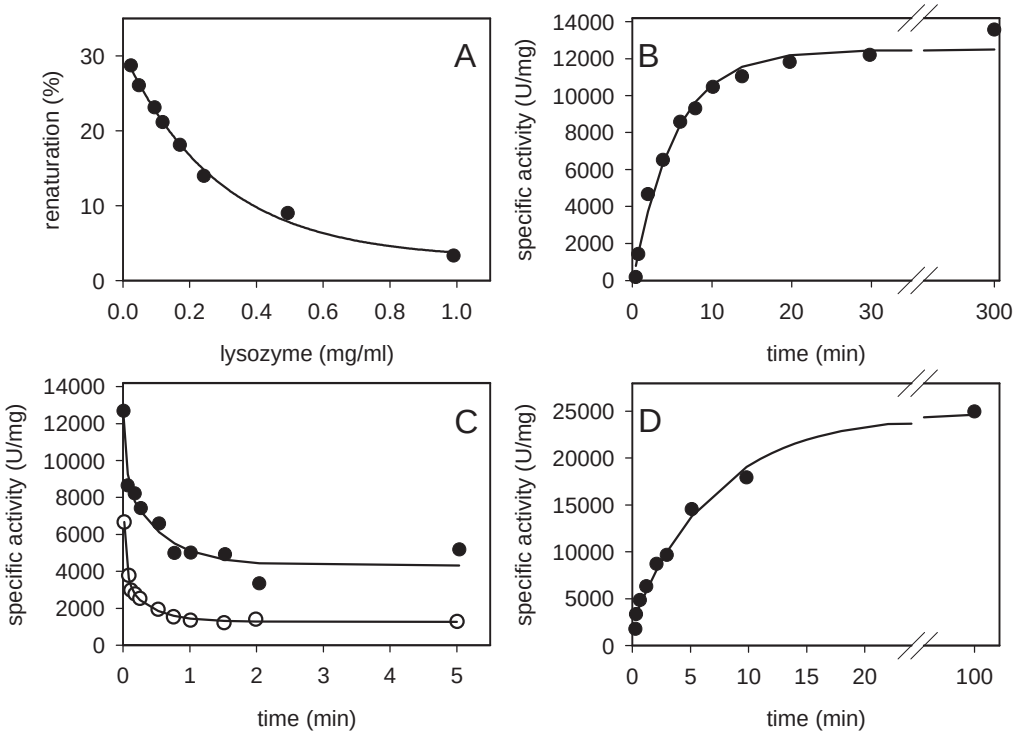

Fig. 2.8. Folding and aggregation of reduced lysozyme. (A) Yield of enzymatic activity as a function of turkey lysozyme concentration during oxidative refolding. (B) Kinetics of reactivation of turkey lysozyme. (C) Kinetics of commitment of aggregation of denatured and reduced lysozyme. Starting protein concentration for renaturation was 0.185 mg mL^{-1} (●) and 0.74 mg mL^{-1} (○). At different time points of renaturation, the samples were further diluted 10-fold and incubated overnight. (D) Kinetics of commitment of renaturation. Renaturation was performed with denatured and reduced turkey lysozyme. At different time points, a high concentration of denatured and reduced hen lysozyme was added. After completion of renaturation, the activity of turkey lysozyme was determined (adapted from Ref. [114]).

cooperative and reversible process involving an intermediate with already native-like secondary structure [119, 120].

The two antibody domains of the light chain (κ-type) and the C_H1 and C_H3 domain of the heavy chain (γ1-type) contain conserved *cis*-prolines. In the denatured

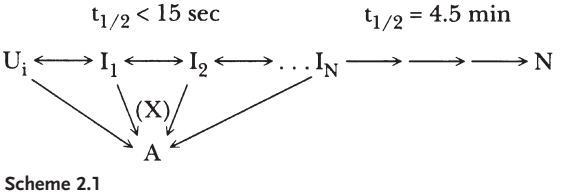

Scheme 2.1

state (depending on the denaturation time) equilibration between the *cis* and *trans* configuration occurs. Since the two configurations are separated by a high-energy barrier, re-isomerization is a slow process. This is reflected by an additional slow folding phase observed during refolding [119] that can be accelerated by prolyl isomerases [121, 122]. As soon as immunoglobulin domains are covalently linked, as in the case of the immunoglobulin light chain, which is composed of two domains, an additional slow folding phase is detected that may be due to interactions of the individual domains [120]. An additional level of complexity is observed in the case of the antibody Fab fragment, which consists of the light chain and the two N-terminal domains of the heavy chains, the Fd fragment (Figure 2.9). The two polypeptide chains associate noncovalently via contact sites between both the variable domains and the constant domains of each chain. Precise assembly of the two

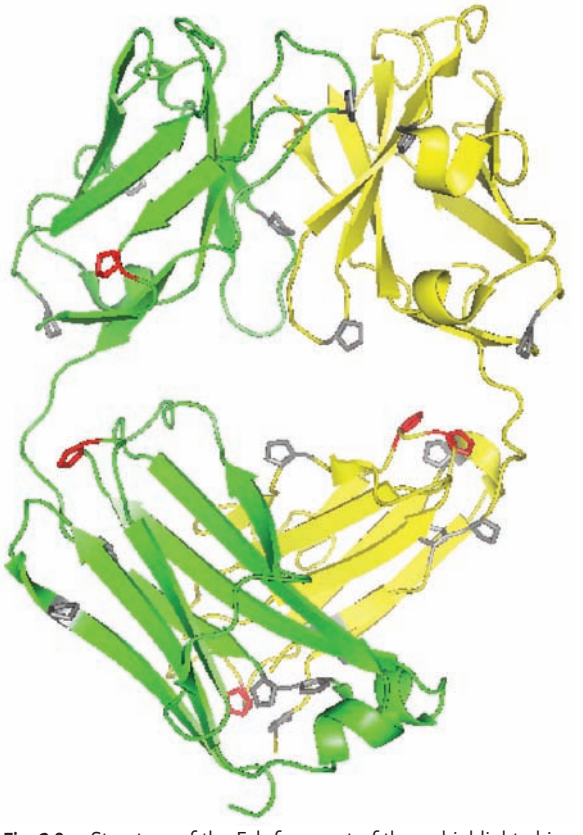

Fig. 2.9. Structure of the Fab fragment of the monoclonal antibody MAK33 (κ/IgG1) (pdb: 1FHE5, [123]). The light chain and the Fd chain are colored in green and yellow, respectively. Proline residues in *trans* configuration are highlighted in gray, those in *cis* configuration in red. The intermolecular disulfide bond connecting the C-terminus of the two chains is not resolved in the structure.

chains is required for antigen-binding activity [124, 125]. Furthermore, a disulfide bond connects the C-terminal domains of both chains covalently.

Despite this molecular complexity, the regain of antigen-binding activity of a Fab fragment, measured by ELISA, follows simple first-order kinetics [76, 122]. Spectroscopic analyses, however, reveal a complex folding behavior, which is expected for a multi-domain protein. The Fab fragment contains 22 prolyl residues, five of them in the *cis* configuration in the native state. Hence, upon refolding all these prolines need to isomerize to their native peptide bond configuration; this reaction dominates the overall folding process. Consequently, as described for the single-antibody domains, the folding of the Fab fragment can be catalyzed by peptidyl-prolyl-*cis*/*trans* isomerases [122]. A detailed description of peptidyl-prolyl-*cis*/*trans* isomerases and their effect on protein folding is given in Chapter 27 of this book.

If the disulfide between the two chains of the Fab fragment is deleted (with the remaining intra-domain disulfides still intact), then the reconstitution comprises both folding of the four domains and association of the two subunits. In this case, the regain of antigen-binding activity follows a sigmoidal time course (Figure 2.10). The kinetics of reconstitution does not depend on protein concentration, indicating that the association of the subunits is not rate-limiting [76]. Instead, the reconstitution process can be described by a serial first-order reaction with one of the phases identical to the proline-determined refolding of the disulfide-bonded Fab described before ($k = 0.04$ min^{-1}, Scheme 2.2). The other phase describes the slow formation of an association-competent state of the light chain.

It is known that structure formation of the two domains of the light chain is a fast process compared to the overall folding/reconstitution of the whole Fab frag-

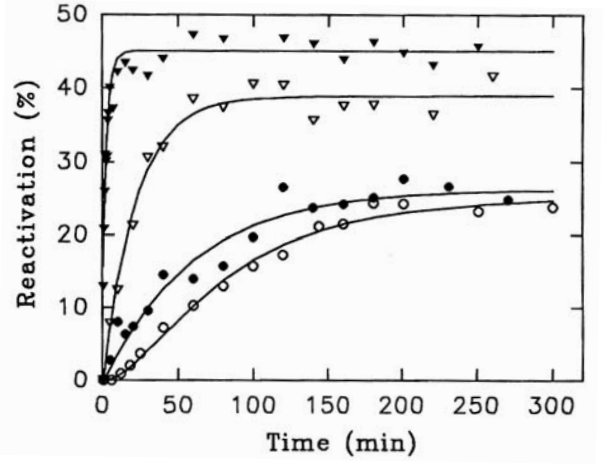

Fig. 2.10. Folding of Fab, not containing the C-terminal disulfide bond between the two chains. Refolding was achieved by diluting the denatured protein into 0.1 M Tris, pH 8, either starting from a long-term denatured protein in the absence (○) or presence (▽) of a fivefold molar excess of native light chain or starting from short-term denatured protein in the absence (●) or presence (▼) of a fivefold molar excess of native light chain. The data were fitted to a single first-order or a serial first-order reaction [76].

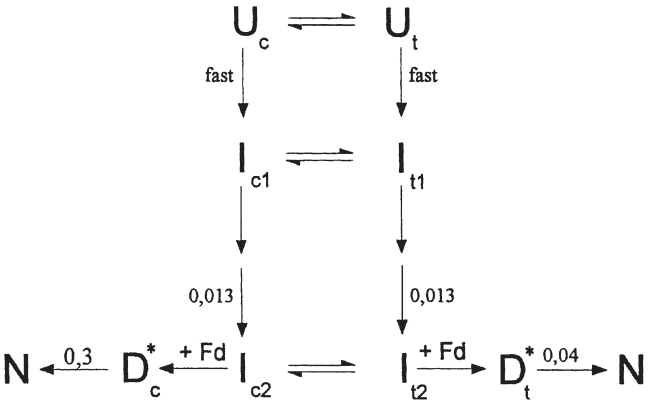

Scheme 2.2. Folding/reconstitution of the non-disulfide-bonded Fab fragment. *U* and *N* donate the denatured and the native state of the Fab fragment. *Fd* marks the position at which the association of light chain and Fd along the reconstitution pathway takes place. *D* describes an intermediate of associated light chain and Fd fragment, and *I* represents non-associated folding intermediates. The subscribed *c* and *t* reflect the *cis* and *trans* configuration of the rate-limiting proline peptide bond, respectively. The values given at two of the arrows indicate the rate constants (min^{-1}) of the respective reactions (adapted from Ref. [76]).

ment, even though folding of the light chain itself is limited by prolyl isomerization [121]. If the prolyl isomerization is catalyzed (or excluded from the folding/assembly reaction by short-term denaturation), the time course of reconstitution of the Fab fragment switches from a sigmoidal to a monophasic first-order kinetic; prolyl isomerization is not rate-limiting anymore. The yield of reconstitution does not change. The yield is determined by aggregation of the Fd fragment. Because peptidyl-prolyl-*cis*/*trans* isomerases catalyze the rate-limiting step occurring after subunit association of the Fab fragment, they do not effect the kinetic competition of off-pathway aggregation and productive reconstitution.

The situation changes if the Fab reconstitution is performed in the presence of an excess of native light chain. Under these conditions, the rate-limiting step before subunit association vanishes, and the regain of Fab activity becomes identical to the prolyl isomerization-determined folding of the Fab fragment, in which the two chains are disulfide-linked. This shows that (1) the rate-limiting step of reconstitution on the monomeric level is the folding of the light chain, presumably corresponding to a specific intramolecular pairing of the two folded domains [120], and (2) the rate-limiting prolyl isomerization on the level of the already associated subunits occurs in the Fd part of the Fab fragment (Scheme 2.2).

The folding/reconstitution of the disulfide-bonded and the non-disulfide-bonded Fab fragment comprise domain folding and domain interactions that are identical on the molecular level; however, in one case the domain pairing occurs intramolecularly, in the other case intermolecularly. The rate-limiting folding of the light chain can be observed only for the non-disulfide-bonded Fab fragment, clearly in-

dicating that in the disulfide-bonded form the folding of the light chain is intramolecularly chaperoned by the nearby Fd part of the Fab fragment. On the other hand, the reconstitution of the non-disulfide-bonded Fab shows that the isomerization of at least one prolyl residue of the Fd part obligatorily occurs only after subunit association. Thus, only the association with the folded light chain provides the structural information for the isomerization state of the respective proline in the Fd part. This is an intriguing example of how folding and association of subunits are interrelated.

Whereas in the case of the Fab fragment the association of the two polypeptides precedes prolyl isomerization, it is different for the antibody domain C_H3. The isolated C_H3 domain forms a dimer. Under conditions where prolyl isomerization does not contribute to the folding kinetics, formation of the β-sandwich structure is a slow process, even compared to other antibody domains, while the subsequent association of the folded monomers is fast. After long-term denaturation, the majority of the unfolded C_H3 molecules reach the native state in two serial reactions involving the re-isomerization of one proline bond to the *cis*-configuration. The folded species with the wrong isomer accumulates as a monomeric intermediate; the proline isomerization is a prerequisite for dimerization of the C_H3 domain [42].

2.5.2 Trimeric Tail spike Protein of Bacteriophage P22

The tail spike protein (TSP) of bacteriophage P22 from *Salmonella typhimurium* has been a paradigm in studying protein folding and association in vivo since Jonathan King's early attempts to solve the problem of phage morphogenesis by genetic methods [126–130]. The beauty of both the system and the approach is that it has provided insight not only into the principles of protein self-organization in the cytoplasm but also into the mechanisms of misfolding, aggregation, and inclusion body formation [85, 115, 131–134]. It has been shown that in vitro reconstitution is clearly related to the situation in the living cell [115, 132].

The tail spike is a multifunctional trimeric protein composed of identical 72-kDa polypeptide chains, attached to the viral capsid by their 108-residue N-terminal domain. Six of these trimers assemble onto the virus head to form the tail, completing the infectious phase of the phage. In the absence of heads, tail spikes accumulate as soluble protein in the bacterial cytosol. Their assembly and the competing formation of inclusion bodies at high temperature have been studied in detail using temperature-sensitive (*ts*) mutants. In this connection, the assembly of viable phage was used as an in vitro assay for proper folding. Other means to follow the folding and assembly pathway of TSP, in addition to spectroscopic and hydrodynamic techniques, are its endorhamnosidase activity (directed toward the *O*-antigen of the host), its reactivity with monoclonal antibodies, and the thermal stability and detergent-resistance of the mature protein.

Crystal structures of wild-type TSP and mutant variants of the protein have been determined at high resolution [135, 136]. The major part of the trimer represents a

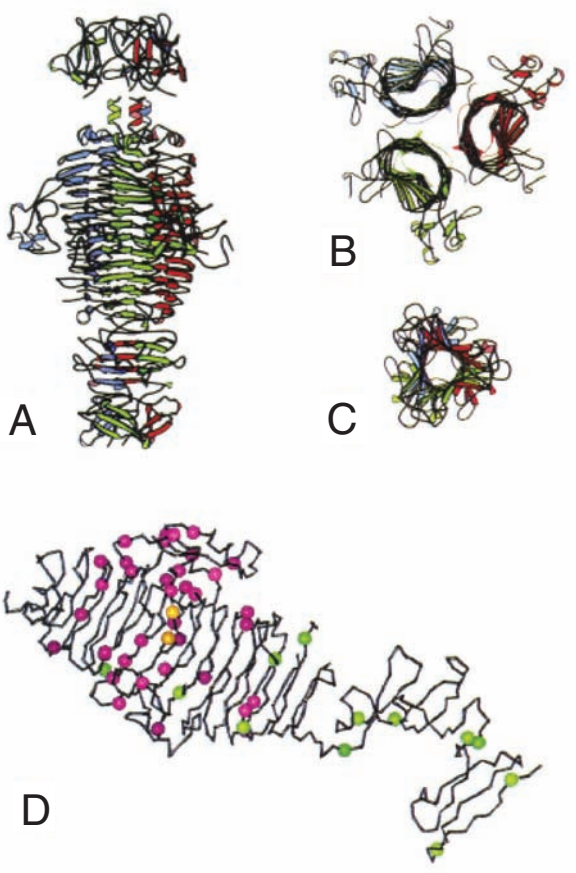

Fig. 2.11. Structure of the tail spike protein (TSP) from *Salmonella* bacteriophage P22. (A) TSP trimer assembled from the structures of the N-terminal (above) and C-terminal (below) fragments [136]. (B) Section through the parallel β-helix in the central domain of the trimer. (C) Section through the C-terminal domain where the subunits form mixed β-sheets. (D) Single TSP subunit with sites of *tsf* mutations in the main body and in the "dorsal fin" (red), sites of global suppressors of the *tsf* phenotype in the central part of the β-helix (yellow), and sites of lethal mutations (green) [134, 135].

perfect right-handed parallel beta-helix; the side-by-side association of the single polypeptide chains is illustrated in Figure 2.11. Evidently, this part of the molecule can fold separately in the subunits, whereas the interdigitated C-terminal part (Figure 2.11) can be formed only after subunit association.

The native TSP trimer in the absence of denaturants is stable up to temperatures well above 80 °C. However, there are numerous point mutations that prevent phage proliferation at the much lower temperature of 40 °C. Interestingly, the *ts* mutations do not affect protein synthesis, and the mutant proteins are perfectly

stable and biologically active at 40 °C, once synthesized and assembled at lower temperature. However, after expression at the restrictive temperature, they are inactive and react with antibodies specific for the denatured protein. Thus, they have been coined "temperature-sensitive for folding" mutants (*tsf*). A second class of mutants represents global intragenic suppressors (*su*) of the *tsf* phenotype, showing an increase in the yield of correctly folded and assembled TSP at high temperature at the expense of ligand-binding affinity or thermal stability of the native state [131, 132, 137]. Figure 2.11 shows that all these mutations are located in the parallel beta-helix domain and the associated "dorsal fin domain" of the fishlike structure. From the point of view of the folding mechanism, this means that these parts of the polypeptide chain must acquire a native-like conformation at an early stage of the folding pathway [133, 135, 138].

The mechanism shown in Scheme 2.3 describes the folding and association of TSP, starting from the unfolded (or nascent) polypeptide chains (U):

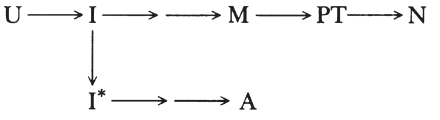

Scheme 2.3

I represents a loosely folded conformation exhibiting native-like secondary and tertiary structure, but it is still quite thermolabile and susceptible to misfolding ($I \rightarrow I^*$) and subsequent irreversible aggregation ($I^* \rightarrow A$); this pathway is preferred at high temperature. At low temperature, polypeptide chains end up in the native trimer (*N*) via the "structured monomer" (*M*). Folding mutations affect the thermal stability of the intermediate (*tsf* mutations destabilizing and *tsf* suppressor mutations stabilizing *I*), thus altering the partitioning between the two pathways. In *M*, the β-helix is preformed in a native-like conformation [92, 133, 138]. Subunit assembly then leads to the incompletely folded, metastable "protrimer" (PT) in which the polypeptides are stably associated but still incompletely folded (i.e., prone to proteolysis and SDS denaturation) [139]. Because PT formation is independent of protein concentration, a unimolecular isomerization reaction must be rate-limiting [85]. The "maturation" of the trimer, in which the protein acquires the high thermal stability and SDS resistance of the native protein, is associated with a high activation energy and occurs with identical rates both in vitro and in vivo [37, 139]. Thus, the reconstitution from unfolded polypeptide chains may be considered a valid model for the self-assembly of the tail spike part of the phage in its host, supporting the conclusion that neither codon frequencies nor co-translational reactions can play a significant role in this part of the phage morphogenesis.

The folding and assembly of TSP confirm the general observation that misfolding and irreversible aggregation are intimately related in the sense that at high pro-

tein concentrations, kinetic competition of folding and association occurs. In the case of TSP, decreasing the stability of an on-pathway intermediate by mutation or high temperature leads to accumulation of less-structured or misfolded conformations that aggregate at a faster rate.

As TSP has been the paradigm for folding studies in vitro and in vivo, this might be the right place to consider briefly the significance of chaperones on the above reconstitution reactions. Incompletely folded TSP chains can be trapped on the *E. coli* chaperonin GroEL in the absence of ATP. However, even an excess of GroEL/GroES increases the yield of TSP reconstitution only marginally at temperatures higher than 30 °C [140]. Overexpression of the chaperone system in *Salmonella* does not suppress *tsf* mutations [141, 142]. On recombinant expression in *E. coli*, TSP mutants impaired in folding or assembly are proteolyzed more rapidly when GroE is simultaneously overexpressed, thereby preventing aggregation of TSP in inclusion bodies [134]. The irreversible aggregation reaction itself has been studied by initiating refolding at intermediate denaturant concentrations at which a large fraction of refolding proteins can be induced to aggregate at low temperature [93, 115, 132, 143, 144]. The misassembly process can be described as a nucleated linear polymerization reaction involving partially folded or misfolded rather than fully unfolded polypeptide chains. It is specific so that TSP does not form mixed aggregates with other proteins (e.g., P22 coat protein), in agreement with the observation that overexpression or heterologous expression of proteins in bacteria commonly leads to inclusion bodies consisting of a single or very few polypeptide species [145].

2.6 Experimental Protocols

Protocol 1: Monitoring Aggregation by Light Scattering

1. Place a stirrable cuvette with the appropriate renaturation buffer in a fluorometer or photometer and adjust the temperature.
2. Set the excitation and emission wavelength to 500 nm. At this wavelength neither protein nor buffer shows any spectroscopic signal. Therefore, any signal observed results from scattering of the light by particles such as aggregates. Start a time-dependent measurement of the light-scattering signal until a stable base line is reached.
3. Dilute the denatured protein to an appropriate protein concentration (e.g., 10–100 μg mL^{-1}) into the renaturation buffer under vigorous stirring and follow the kinetics of aggregation by light scattering. Depending on the folding kinetics of the respective protein, the aggregation can occur on a minute or hour time range.
4. Aggregation can be minimized by variation of the protein concentration, temperature, buffer components and pH, and addition of solubilizing chemicals such as molar concentrations of arginine [113].

Protocol 2: Cross-linking by Glutaraldehyde

1. Dialyze the native protein against a suitable buffer, which should not contain reactive amino groups (e.g., Tris is not suitable).
2. Incubate the protein at concentrations between 5 and 100 μg mL^{-1} with 100 mM glutaraldehyde at room temperature for 2 min. Depending on the amount of cross-linking, the concentration of glutaraldehyde, the temperature, and the time can be varied.
3. Further cross-linking is blocked by addition of 200 mM $NaBH_4$ in 0.1 M NaOH.
4. The cross-linking product is analyzed by SDS-PAGE. The samples at low protein concentration have to be precipitated before. Add 0.01 volume 10% Na-desoxycholate (dissolved in slightly alkaline buffer). Subsequently, add 0.01 volume of 85% phosphoric acid. Incubate for 15 min at room temperature. Harvest the precipitate by centrifugation and resolubilize the pellet in Laemmli buffer.
5. For reconstitution experiments, choose the protein concentration at which the cross-linking is quantitative without formation of any higher molecular mass products (unspecific cross-linking).
6. Initiate reconstitution by diluting the denatured protein into the refolding buffer at the respective protein concentration.
7. Take aliquots at different time points of reconstitution and cross-link the protein as described before.
8. The bands of monomeric and oligomeric species can be quantified by densitometry of Coomassie-stained gels. (Band intensities of silver-stained gels are proportional to the amount of loaded protein only over a very narrow range and are only rarely suited for quantitative analysis.)

Protocol 3: Determination of the Dissociation Constant of a Homodimer by Analytical Ultracentrifugation

1. Dialyze the protein extensively against an appropriate buffer. If the analytical ultracentrifuge is equipped with an absorbance unit, the buffer should not absorb strongly at the detection wavelengths (230 nm and 280 nm). The buffer should contain at least 50 mM salt.
2. Dilute the protein with dialysis buffer to concentrations between 10 and 1000 μg mL^{-1}. Using an eight-hole rotor and six-channel center pieces, 21 samples (150 μL each) can be measured simultaneously.
3. Choose an appropriate rotor speed. Sedimentation equilibrium is reached when the radial distribution of the protein no longer changes over time (identical scans over a time span of 5 h). Depending on the sample volume and the size of the protein, this may take 24–72 h. Ideally, at equilibrium the protein should be completely depleted from the meniscus of the solution. The sedimentation equilibrium can be run at temperatures between 4 °C and 40 °C.
4. Measure the radial distribution of the protein at different wavelength (usually 280 nm and 230 nm).

5. Calculate the apparent molecular mass *Mr* from the equilibrium profile. This can be done using the standard software provided with the ultracentrifuge. A manual method would be the analysis of the slope of a plot of ln *A* versus r^2 according to Eq. (1)

$$Mr = (\mathrm{d} \ln A/\mathrm{d}r^2) \times 2RT/(1 - v\rho)\omega^2 \quad (1)$$

with *A* being the absorbance, *r* the distance to the center of the rotor, *v* the partial specific volume of the protein, ρ the density of the solvent, and ω the angular velocity. The partial specific volume of the protein can be calculated from its amino acid composition [146].

6. If a monomer-dimer equilibrium exits in the respective concentration range, the apparent molecular mass *Mr* will vary with the protein concentration. A semilogarithmic plot of log cp (in molar units) against *Mr* results in a sigmoidal curve. The dissociation constant K_D can be calculated by fitting the data to the following equations:

$$Mr(\mathrm{app}) = ((c_M{}^*M) + c_D{}^*D))/(c_M + c_D) \quad (2)$$

where c_M and c_D are the concentrations of the monomeric and dimeric forms, respectively. *M* and *D* represent the molecular mass of the monomer and dimer. c_D can be expressed as a function of c_M and the dissociation constant, K_D (Eq. (3)):

$$c_D = {c_M}^2/K_D \quad (3)$$

c_M is a function of the total protein concentration c_{total} according to Eq. (4):

$$c_M = -0.5^*K_D/2 + [(0.5^*K_D/2)^2 + 0.5^*K_D{}^*c_{total}]^{0.5} \quad (4)$$

Protocol 4: Thermodynamic Stability of Dimers

The interaction of subunits often contributes significantly to the overall stability of a protein. In some cases, dissociation of the subunits leads to complete denaturation of the protein. Under these conditions, the stability of the oligomeric protein can be inferred from a denaturant-induced transition curve (cf. Chapter 3 in Part I). The analysis of such data, however, is slightly different from that of monomeric proteins.

1. Prepare stock solutions of the native protein, the denatured protein (e.g., in 6 M GdmCl or 10 M urea), and the denaturation buffer (either GdmCl or urea; for preparation of denaturation buffer, compare Chapter 3 in Part I).
2. Dilute the protein into different concentrations of denaturant and allow the solutions to equilibrate. Depending on the protein, this may take only a few hours or several days. Usually a transition curve should consist of 20–30 different denaturant concentrations. To assay the reversibility of the process, the tran-

sition has to be set up starting from both the native and the denatured protein, respectively.

3. Measure the transition at different protein concentrations (e.g., 10–100 μg mL^{-1}) and using different methods (e.g., enzyme activity, fluorescence, CD). Only if the transition is reversible and the different methods yield the same transition curve (at a given protein concentration) can the data be analyzed according to a two-state model. (A reversible transition with different transition curves measured by different methods can be analyzed by a three-state model [15].) The higher the protein concentration, the more the transition midpoint is shifted to higher denaturant concentrations.
4. Calculate the equilibrium constant K_U for each data point within the transitions. K_U is defined as:

$$K_U = [D^2]/[N] = 2P_t[f^2{}_d/(1 - f_d)] \quad (5)$$

In this equation, P_t corresponds to the total monomer concentration of the protein and f_d to the fraction of denatured protein.

5. Calculate the free energy of stabilization ΔG at the different denaturant concentrations from the equilibrium constants using the equation

$$\Delta G = -RT \ln K_U \quad (6)$$

6. Obtain $\Delta G_{U\rightarrow N}$ in the absence of denaturant by linear extrapolation of the data to 0 M denaturant. If the two-state analysis is valid, the linear extrapolation of the ΔG values of transitions measured at different protein concentrations should intersect the y-axis at the same point (compare Figure 2.6).

References

1 Jaenicke, R. (1987). Folding and association of proteins. *Prog. Biophys. Mol. Biol.*, 49, 117–237.

2 Lawson, D. M., Artymiuk, P. J., Yewdall, S. J., Smith, I. M., Livingstone, I. C., Treffry, A., Luzzago, A., Levi, S., Arosio, P., Cesareni et al. (1991). Solving the structure of human H ferritin by genetically engineering intermolecular crystal contacts. *Nature*, 349, 541–544.

3 Xu, Z., Horwich, A. L. & Sigler, P. B. (1997). The crystal structure of the asymmetric GroEL-GroES-(ADP)7 chaperonin complex. *Nature*, 388, 741–750.

4 Izard, T., Aevarsson A., Allen, M. D., Westphal, A. H., Perham, R. N., de Kok, A. & Hol, W. G. (1999). Principles of quasi-equivalence and euclidean geometry govern the assembly of cubic and dodecahedral cores of pyruvate dehydrogenase complexes. *Proc. Natl Acad. Sci. USA*, 96, 1240–1245.

5 Gilbert, W. (1978). Why genes in pieces? *Nature*, 271, 501.

6 Gilbert, W. (1985). Genes-in-pieces revisited. *Science*, 228, 823–824.

7 Orengo, C. A., Michie, A. D., Jones, S., Jones, D. T., Swindells, M. B. & Thornton, J. M. (1997). CATH – a hierarchic classification of protein domain structures. *Structure*, 5, 1093–1108.

8 Thornton, J. M., Orengo, C. A., Todd, A. E. & Pearl, F. M. (1999). Protein folds, functions and evolution. *J. Mol. Biol.*, 293, 333–342.

9 Orengo, C. A., Bray, J. E., Buchan, D. W., Harrison, A., Lee, D., Pearl, F. M., Sillitoe, I., Todd, A. E. & Thornton, J. M. (2002). The CATH protein family database: a resource for structural and functional annotation of genomes. *Proteomics*, 2, 11–21.

10 Bergman, L. W. & Kuehl, M. W. (1979). Formation of intermolecular disulfide bonds on nascent immunoglobulin polypeptides. *J. Biol. Chem.*, 254, 5690–5694.

11 Jaenicke, R. (1999) Stability and folding of domain proteins. *Prog. Biophys. Mol. Biol.*, 71, 155–241.

12 Kuwajima, Y. (1989). The molten globule state as a clue for understanding the folding and cooperativity of globular-protein structure. *Proteins*, 6, 87–103.

13 Uversky, V. N. (2002). Natively unfolded proteins: A point where biology waits for physics. *Prot. Science*, 11, 739–756.

14 Namba, K. (2001). Roles of partly unfolded conformations in macromolecular self-assembly. *Genes to Cells*, 6, 1–12.

15 Ikeguchi, M., Kuwajima, K. & Sugai, S. (1986). Ca2+-induced alteration in the unfolding behavior of alpha-lactalbumin. *J. Biochem.*, 99, 1191–1201.

16 Segel, D. J., Bachmann, A., Hofrichter, J., Hodgson, K. O., Doniach, S. & Kiefhaber, T. (1999). Characterization of transient intermediates in lysozyme folding with time-resolved small-angle X-ray scattering. *J. Mol. Biol.*, 288, 489–499.

17 Wildegger, G. & Kiefhaber, T. (1997). Three-state model for lysozyme folding: triangular folding mechanism with an energetically trapped intermediate. *J. Mol. Biol.*, 270, 294–304.

18 Rudolph, R., Siebendritt, R., Nesslauer, G., Sharma, A. K. & Jaenicke, R. (1990). Folding of an all-beta protein: independent domain folding in gamma II-crystallin from calf eye lens. *Proc. Natl Acad. Sci. USA*, 88, 2854–2858.

19 Mayr, E. M., Jaenicke, R. & Glockshuber, R. (1997). The domains in gamma B-crystallin: identical fold-different stabilities. *J. Mol. Biol.*, 269, 260–269.

20 Palme, S., Slingsby, C. & Jaenicke, R. (1997). Mutational analysis of hydrophobic domain interactions in gamma B-crystallin from bovine eye lens. *Protein Sci.*, 6, 1529–1536.

21 Guiterrez-Cruz, G., Van Heerden, A. H. & Wang, K. (2001). Modular motif, structural folds and affinity profiles of the PEVK segment of the human fetal skeletal muscle titin. *J. Biol. Chem.*, 276, 7442–7449.

22 Smith, D. A. & Redford, S. (2000). Protein folding: Pulling back the frontiers. *Current Biol.*, 10, 662–664.

23 Head, J. G., Houmeida, A., Knight, P. J., Clarke, A. R., Trinick, J. & Brady, R. L. (2001). Stability and folding rates of domains spanning the large A-band super-repeat of titin. *Biophys. J.*, 81, 1570–1579.

24 Li, H., Oberhauser, A. F., Fowler, S. B., Clarke, J. & Fernandez, J. M. (2000). Atomic force microscopy reveals the mechanical design of a modular protein. *Proc. Natl Acad. Sci. USA*, 97, 6527–6531.

25 Politou, A. S., Gautel, M., Improta, M., Vangelista, L. & Pastore, A. (1996). The elastic I band region of titin is assembled in a ''modular'' fashion by weakly interacting Ig-like domains. *J. Mol. Biol.*, 255, 604–616.

26 Fowler, S. B. & Clarke, J. (2001). Mapping the folding pathway of an immunoglobulin domain: structural detail from Phi value analysis and movement of the transition state. *Structure*, 9, 355–366.

27 Best, R. B., Fowler, S. B., Herrera, J. L., Steward, A., Paci, E. & Clarke, J. (2003). Mechanical unfolding of a titin Ig domain: structure of the transition state revealed by combining atomic force microscopy, protein engineering and molecular dynamics simulations. *J. Mol. Biol.*, 330, 867–877.

28 Best, B., Li, B., Steward, A., Daggett, V. & Clarke, J. (2001). Can non-mechanical proteins withstand force? Stretching barnase by atomic force microscopy and molrcular dynamics simlation. *Biophys. J.*, 81, 2344–2356.

29 Powers, E. T. & Powers, D. L. (2004). A perspective of mechanisms of protein tetramer formation. *Biophys. J.*, 85, 3587–3599.

30 Seckler, R. (2000). Assembly of multi-subunit strucutres. In: Mechanisms of Protein Folding, Ed.: R. H. Pain, 2nd ed., Oxford Press, pp. 279–308.

31 Branden, C.-I. and Tooze, J. (1999). Introduction to protein structure, (2nd edn). Garland, New York, p. 410.

32 Smith, S. (1994). The animal fatty add synthase: one gene, one polypeptide, seven enzymes. *FASEB J.*, 8, 1248–1259.

33 Weber, G., Schorgendorfer, K., Schneider-Scherzer, E. & Leitner, E. (1994). The peptide synthetase catalyzing cyclosporin production in Tolypocladium niveum is encoded by a giant 45.8-kilobase open reading frame. *Curr. Genet.*, 26, 120–125.

34 Dautry-Varsat, A. & Garel, J. R. (1978). Refolding of a bifunctional enzyme and its monofunctional fragment. *Proc. Natl Acad. Sci. USA*, 75, 5979–5982.

35 Creighton, T. E. (1992). Proteins: structures and molecular properties, (2nd edn). W. H. Freeman, New York, p. 309–325.

36 Miller, S., Schuler, B. & Seckler, R. (1998). Phage P22 tailspike protein: removal of head binding domain unmasks effects of folding mutations on native-state thermal stability. *Prot. Sci.*, 7, 2223–2232.

37 Danner, M., Fuchs, A., Miller, S. and Seckler, R. (1993). Folding and assembly of phage P22 tailspike endo-rhamnosidase lacking the N-terminal, head-binding domain. *Eur. J. Biochem.*, 215, 653–661.

38 Jones, S. & Thornton, J. M. (1997). Analysis of protein-protein interaction sites using surface patches. *J. Mol. Biol.*, 272, 121–132.

39 Tsai, C. J., Lin, S. L., Wolfson, H. J. & Nussinov, R. (1997). Studies of protein-protein interfaces: a statistical analysis of the hydrophobic effect. *Protein Sci.*, 6, 53–64.

40 Tsai, C. J., Xu, D. & Nussinov, R. (1997). Structural motifs at protein-protein interfaces: protein cores versus two-state and three-state model complexes. *Prot. Sci.*, 6, 1793–1805.

41 Le Conte, L., Chothia, C. & Ianin, J. (1999). The atomic structure of protein-protein recognition sites. *J. Mol. Biol.*, 285, 2177–2198.

42 Thies, M., Mayer, S., Augustine, J. G., Frederick, C. A., Lilie, H. & Buchner, J. (1999). Folding and association of the antibody domain C_H3: Prolyl isomerization preceeds dimerization. *J. Mol. Biol.*, 293, 67–79.

43 Chothia, C. and Janin, J. (1975). Principles of protein-protein recognition. *Nature*, 256, 705–708.

44 Dill, K. A. (1990). Dominant forces in protein folding. *Biochemistry*, 29, 7133–7155.

45 Larsen, T. A., Olson, A. J. & Goodsell, D. S. (1998). Morphology of protein-protein interfaces. *Structure*, 6, 421–427.

46 DeLano, W. L. (2002). Unravelling hot spots in the binding interface: progress and challenges. *Curr. Opin. Struct. Biol.*, 12, 14–20.

47 Xu, D., Tsai, C. J. & Nussinov, R. (1998). Mechanism and evolution of protein dimerization. *Protein Sci.*, 7, 533–544.

48 Killenberg-Jabs, M., Jabs, A., Lilie, H., Golbik, R. & Hubner, G. (2001). Active oligomeric states of pyruvate decarboxylase and their functional characterization. *Eur. J. Biochem.*, 268, 1698–1704.

49 Venyaminov, S. Yu., Gudkov, A. T., Gogia, Z. V. & Tumanova, L .G. (1981). Absorption and cicular dichroism spectra of individual proteins from Escherichia coli ribosomes. Pushkino, Russia.

50 Yusupov, M. M., Yusupova, G. Z., Baucom, A., Lieberman, K., Earnest, T. N., Cate, J. H. & Noller, H. F. (2001). *Science*, 292, 883–896.

51 Kriwacki, R. W., Hengst, L., Tennant, L., Reed, S. I. & Wright, P. E. (1996). Structural studies of p21 in the free and Cdk2-bound state: Conformational disorder mediates binding diversity. *Prog. Natl Acad. Sci. USA*, 93, 11504–11509.

52 Yu, Y. B. (2002). Coiled coils: stability, specificity, and drug delivery potential. *Adv. Drug Deliv. Rev.*, 54, 1113–1129.

53 Richter, S., Stubenrauch, K., Lilie, H. & Rudolph, R. (2001). Polyionic fusion peptides function as specific dimerization motifs. *Prot. Engineering*, 14, 775–783.

54 Stubenrauch, K., Gleiter, S., Brinkmann, U., Rudolph, R. & Lilie, H. (2001). Tumor cell specific targeting and gene transfer by recombinant polyoma virus like particle/antibody conjugates. *Biochem. J.*, 356, 867–873.

55 Kleinschmidt, M., Rudolph, R. & Lilie, H. (2003). Design of a modular immunotoxin connected by polyionic adapter peptides. *J. Mol. Biol.*, 327, 445–452.

56 Bennett, M. J., Choe, S. & Eisenberg, D. (1994). Domain swapping: entangling alliances between proteins. *Proc. Natl Acad. Sci. USA*, 91, 3127–3131.

57 Bennett, M. J., Schlunegger, M. P. & Eisenberg, D. (1995). 3D domain swapping: a mechanism for oligomer assembly. *Protein Sci.*, 4, 2455–2468.

58 Schlunegger, M. P., Bennett, M. J. & Eisenberg, D. (1997). Oligomer formation by 3D domain swapping: a model for protein assembly and misassembly. *Adv. Protein Chem.*, 50, 61–122.

59 Bax, B., Lapatto, R., Nalini, V., Driessen, H., Lindley, P. V., Mahadevan, D., Blundell, T. L. & Slingsby, C. (1990). X-ray analysis of beta B2-crystallin and evolution of oligomeric lens proteins. *Nature*, 347, 776–779.

60 Liu, Y. & Eisenberg, D. (2202). 3D domain swapping: As domains continue to swap. *Prot. Science*, 11, 1285–1299.

61 Vijayalakshmi, J., Mukhergee, M. K., Graumann, J., Jakob, U. & Saper, M. A. (2001). The 2.2 A crystal structure of Hsp33: A heat shock protein with a redox-regulated chaperone activity. *Structure*, 9, 367–375.

62 Kim, S. J., Jeong, D. G., Chi, S. W., Lee, J. S. & Rya, S. E. (2001). Crystal structure of proteolytic fragments of the redox-sensitive Hsp33 with constitutive chaperone activity. *Nat. Struct. Biol.*, 8, 459–466.

63 Graumann, J., Lilie, H., Tang, X., Tucker, K. A., Hoffmann, J., Janakiraman, V., Saper, M., Bardwell, J. C. A. & Jakob, U. (2001). Activation of the redox regulated chaperone Hsp33 – a two step mechanism. *Structure*, 9, 377–387.

64 Lomas, D. A., Evans, D. L., Finch, J. T. & Carrell, R. W. (1992). The mechanism of Z alpha 1-antitrypsin accumulation in the liver. *Nature*, 357, 541–542.

65 D'Alessio, G. (1995). Oligomer evolution in action? *Nat. Struct. Biol.*, 2, 11–13.

66 Piccoli, R., Tamburrini, M., Piccialli, G., Di Donato, A., Parente, A. & D'Alessio, G. (1992). The dual-mode quaternary structure of seminal RNase. *Proc. Natl Acad. Sci. USA*, 89, 1870–1874.

67 Kono, N., Uyeda, K. & Oliver, R. M. (1973). Chicken liver phosphofructokinase. I. Crystallization and physicochemical properties. *J. Biol. Chem.*, 248, 8592–8602.

68 Bowie, J. U. & Sauer, R. T. (1989). Equilibrium dissociation and unfolding of the Arc repressor dimer. *Biochemistry*, 28, 7139–7143.

69 Golbik, R., Naumann, M., Otto, A., Müller, E.-C., Behlke, J., Reuter, R., Hübner, G. & Kriegel, T. M. (2001). Regulation of phosphotransferase activity of hexokinase 2 from Saccharomyces cerevisiae by modification at serine-14. *Biochemistry*, 40, 1083–1090.

70 Baer, D., Golbik, R., Huebner, G., Lilie, H., Mueller, E. C., Naumann, M., Otto, A., Reuter, R., Breunig, K. D. & Kriegel, T. M. (2003). The unique hexokinase of Kluyveromyces lactis: Isolation, molecular characteri-

zation and evaluation of a role in glucose signaling. *J. Biol. Chem.*, 278, 39280–39286.

71 Hoffmann, J. H., Linke, K., Graf, P. C., Lilie, H. & Jakob, U. (2004). Identification of a redox regulated chaperone network. *EMBO J.*, 23, 160–168.

72 Neet, K. E. & Timm, D. E. (1994). Conformational stability of dimeric proteins: quantitative studies by equilibrium denaturation. *Protein Sci.*, 3, 2167–2174.

73 Sinclair, J. F., Ziegler, M. M. & Baldwin, T. O. (1994). Kinetic partitioning during protein folding yields multiple native states. *Nature Struct. Biol.*, 1, 320–326.

74 Nichtl, A., Buchner, J., Jaenicke, R., Rudolph, R. & Scheibel, T. (1998). Folding and association of beta-galactosidase. *J. Mol. Biol.*, 282, 1083–1091.

75 Fuchs, A., Seiderer, C. & Seckler, R. (1991). In vitro folding pathway of phage P22 tailspike protein. *Biochemistry*, 30, 6598–6604.

76 Lilie, H., Rudolph, R. & Buchner, J. (1995). Association of antibody chains at different stages of folding; Prolyl isomerization occurs after formation of quaternary structure. *J. Mol. Biol.*, 248, 190–201.

77 Cleland, J. L. & Wang, D. I. (1990). Refolding and aggregation of bovine carbonic anhydrase B: quasi-elastic light scattering analysis. *Biochemistry*, 29, 11072–11078.

78 Buchner, J., Grallert, H. & Jakob, U. (1998). Analysis of chaperone function using citrate synthase as nonnative substrate protein. *Methods Enzymol.*, 290, 323–338.

79 Stryer, L. (1978) Fluorescence energy transfer as a spectroscopic ruler. *Annu. Rev. Biochem.*, 47, 819–846.

80 Hassiepen, U., Federwisch, M., Mulders, T., Lenz, v. J., Gattner, H. G., Kruger, P. & Wollmer, A. (1998). Analysis of protein self-association at constant concentration by fluorescence-energy transfer. *Eur. J. Biochem.*, 255, 580–587.

81 Tenenbaum-Bayer, H. & Levitzki, A. (1976). The refolding of lactate dehydrogenase subunits and their assembly to the functional tetrarner. *Biochim. Biophys. Acta*, 445, 261–279.

82 Cardenas, J. M., Hubbard, D. R. and Anderson, s. (1977). Subunit structure and hybrid formation of bovine pyruvate kinases. *Biochemistry*, 16, 191.

83 Grossman, S. H., Pyle, J. & Steiner, R. J. (1981). Kinetic evidence for active monomers during the reassembly of denatured creatine kinase. *Biochemistry*, 20, 6122–6128.

84 Burns, D. L. & Schachman, H. K. (1982). Assembly of the catalytic trimers of aspartate transcarbamoylase from folded monomers. *J. BioI. Chem.*, 257, 8638–8647.

85 Danner, M. & Seckler, R. (1993). Mechanism of phage P22 tailspike protein folding mutations. *Protein Sci.*, 2, 1869–1881.

86 Weissman, J. S. (1995). All roads lead to Rome? The multiple pathways of protein folding. *Chem. Biol.*, 2, 255–260.

87 Dill, K. A. & Chan, H. S. (1997). From Levinthal to pathways to funnels. *Nat. Struct. Biol.*, 4, 10–19.

88 Jaenicke, R. & Lilie, H. (2000). Folding and association of oligomeric and multimeric proteins. *Adv. Prot. Chem.*, 53, 329–401.

89 Kern, G., Kern, D., Jaenicke, R. & Seckler, R. (1993). Kinetics of folding and association of differently glycosylated variants of invertase from Saccharomyces cerevisiae. *Prot. Science*, 2, 1862–1867.

90 Rudolph, R., Westhof, E. & Jaenicke, R. (1977). Kinetic analysis of the reactivation of rabbit muscle aldolase after denaturation with guanidine-HCl. *FEBS Lett.*, 73, 204–206.

91 Opitz, U., Rudolph, R., Jaenicke, R., Ericsson, L. & Neurath, H. (1987). Proteolytic dimers of porcine muscle lactate dehydrogenase: characterization, folding, and reconstitution of the truncated and nicked polypeptide chain. *Biochemistry*, 26, 1399–13406.

92 Miller, S., Schuler, B. & Seckler,

R. (1998). A reversibly unfolding fragment of P22 tailspike protein with native structure: the isolated beta-helix domain. *Biochemistry*, 37, 9160–9168.

93 Jaenicke, R. & Rudolph, R. (1986). Refolding and association of oligomeric proteins. *Methods Enzymol.*, 131, 218–250.

94 Hermann, R., Rudolph, R. & Jaenicke, R. (1982). The use of subunit hybridization to monitor the reassociation of porcine lactate dehydrogenase after acid dissociation. *Hoppe Seylers Z. Physiol. Chem.*, 363, 1259–1265.

95 Geri, M., Rudolph, R. & Jaenicke, R. (1985). Mechanism and specificity of reconstitution of dimeric lactate dehydrogenase from Limulus polyphemus. *Biol. Chem. Hoppe Seyler*, 366, 447–454.

96 Borchert, T. V., Abagyan, R., Jaenicke, R. & Wierenga, R. K. (1994). Design, creation, and characterization of a stable, monomeric triosephosphate isomerase. *Proc. Natl Acad. Sci. USA*, 91, 1515–1518.

97 Schliebs, W., Thanki, N., Jaenicke, R. & Wierenga, R. K. (1997). A double mutation at the tip of the dimer interface loop of triosephosphate isomerase generates active monomers with reduced stability. *Biochemistry*, 36, 9655–9662.

98 Beernink, P. T. & Tolan, D. R. (1996). Disruption of the aldolase A tetramer into catalytically active monomers. *Proc. Natl Acad. Sci. USA*, 93, 5374–5379.

99 Koren, R. & Hammes, G. G. (1976). A kinetic study of protein-protein interactions. *Biochemistry*, 15, 1165–1171.

100 Northrup, S. H. & Erickson, H. P. (1992). Kinetics of protein-protein association explained by Brownian dynamics computer simulation. *Proc. Natl Acad. Sci. USA*, 89, 3338–3342.

101 Gloss, L. M. & Matthews, C. R. (1998). Mechanism of folding of the dimeric core domain of Escherichia coli trp repressor: a nearly diffusion-limited reaction leads to the formation of an on-pathway dimeric intermediate. *Biochemistry*, 37, 15990–15998.

102 Milla, M. E. & Sauer, R. T. (1994). P22 Arc repressor: folding kinetics of a single-domain, dimeric protein. *Biochemistry*, 33, 1125–1131.

103 Herrmann, R., Rudolph, R., Jaenicke, R., Price, N. C. & Scobbie, A. (1983). The reconstitution of denatured phosphoglycerate mutase. *J. Biol. Chem.*, 258, 11014–11019.

104 Fisher, A. J., Raushel, F. M., Baldwin, T. O. & Rayment, I. (1995). Three-dimensional structure of bacterial luciferase from Vibrio harveyi at 2.4 A resolution. *Biochemistry*, 34, 6581–6586.

105 Thoden, J. B., Holden, H. M., Fisher, A. J., Sinclair, J. F., Wesenberg, G., Baldwin, T. O. & Rayment, I. (1997). Structure of the beta 2 homodimer of bacterial Iuciferase from Vibrio harveyi: X-ray analysis of a kinetic protein folding trap. *Protein Sci.*, 6, 13–23.

106 Tanner, J. J., Miller, M. D., Wilson, K. S., Tu, S. C. & Krause, K. L. (1997). Structure of bacterial luciferase beta 2 homodimer: implications for flavin binding. *Biochemistry*, 36, 665–672.

107 Waddle, J. J., Johnston, T. C. & Baldwin, T. O. (1987). Polypeptide folding and dimerization in bacterial-luciferase occur by a concerted mechanism in vivo. *Biochemistry*, 26, 4917–4921.

108 Ziegler, M. M., Goldberg, M. E., Chaffotte, A. F. & Baldwin, T. O. (1993). Refolding of luciferase subunits from urea and assembly of the active heterodimer. Evidence for folding intermediates that precede and follow the dimerization step on the pathway to the active form of the enzyme. *J. Biol. Chem.*, 268, 10760–10765.

109 Baldwin, T. O., Ziegler, M. M., Chaffotte, A. F. & Goldberg, M. E. (1993). Contribution of folding steps involving the individual subunits of bacterial luciferase to the assembly of the active heterodimeric enzyme. *J. Biol. Chem.*, 268, 10766–10772.

110 Clark, A. C., Sinclair, J. F. & Baldwin, T. O. (1993). Folding of

bacterial luciferase involves a non-native heterodimeric intermediate in equilibrium with the native enzyme and the unfolded subunits. *J. Biol. Chem.*, 268, 10773–10779.

111 Sinclair, J. F., Waddle, J. J., Waddill, E. F. & Baldwin, T. O. (1993). Purified native subunits of bacterial luciferase are active in the bioluminescence reaction but fail to assemble into the alpha beta structure. *Biochemistry*, 32, 5036–5044.

112 Zettlmeissl, G., Rudolph, R. & Jaenicke, R. (1979). Reconstitution of lactic dehydrogenase. Noncovalent aggregation vs. reactivation. 1. Physical properties and kinetics of aggregation. *Biochemistry*, 18, 5567–5571.

113 De Bernadez Clark, E., Schwarz, E. & Rudolph, R. (1999). Inhibition of Aggregation Side Reactions during in vitro Protein Folding. *Methods in Enzymology*, 309, 217–236.

114 Goldberg, M. E., Rudolph, R. & Jaenicke, R. (1991). A kinetic study of the competition between renaturation and aggregation during the refolding of denatured-reduced egg white lysozyme. *Biochemistry*, 30, 2790–2797.

115 Jaenicke, R. & Seckler, R. (1997). Protein misassembly in vitro. *Adv. Protein Chem.*, 50, 1–59.

116 Wetzel, R. (1997). Domain stability in immunoglobulin light chain deposition disorders. *Adv. Protein Chem.*, 50, 183–242.

117 Sunde, M. & Blake, C. (1997). The structure of amyloid fibrils by electron microscopy and X-ray diffraction. *Adv. Protein Chem.*, 50, 123–159.

118 Kiefhaber, T., Rudolph, R., Kohler, H. H. & Buchner, J. (1991). Protein aggregation in vitro and in vivo: a quantitative model of the kinetic competition between folding and aggregation. *Biotechnology (N.Y.)*, 9, 825–829.

119 Goto, Y. & Hamaguchi, K. (1982). Unfolding and refolding of the constant fragment of the immunoglobulin light chain. *J. Mol. Biol.*, 156, 891–910.

120 Tsunenaga, M., Goto, Y., Kawata, Y. & Hamaguchi, K. (1987). Unfolding and refolding of a type kappa immunoglobulin light chain and its variable and constant fragments. *Biochemistry*, 26, 6044–6051.

121 Lang, K., Schmid, F. X. & Fischer, G. (1987). Catalysis of protein folding by prolyl isomerase. *Nature*, 329, 268–270.

122 Lilie, H., Lang, K., Rudolph, R. & Buchner, J. (1993). Prolyl isomerases catalyze antibody folding in vitro. *Prot. Sci.*, 2, 1490–1496.

123 Augustine, J. G., de La Calle, A., Knarr, G., Buchner, J. & Frederick, C. A. (2001). The crystal structure of the fab fragment of the monoclonal antibody MAK33. Implications for folding and interaction with the chaperone bip. *J. Biol. Chem.*, 276, 3287–3294.

124 Padlan, E. A., Cohen, G. H. & Davies, D. R. (1986). Antibody Fab assembly: the interface residues between C_H1 and C_L. *Mol. Immunol.*, 23, 951–960.

125 Chothia, C., Novotny, Y., Bruccoleri, R. & Karplus, M. (1985). Domain association in immunoglobulin molecules. The packing of variable domains. *J. Mol. Biol.*, 186, 651–663.

126 Smith, D. H., Berget, P. B. & King, J. (1980). Temperature-sensitive mutants blocked in the folding or subunit assembly of the bacteriophage P22 tail-spike protein. I. Fine-structure mapping. *Genetics*, 96, 331–352.

127 Goldenberg, D. P. & King, J. (1981). Temperature-sensitive mutants blocked in the folding or subunit of the bacteriophage P22 tail spike protein. II. Active mutant proteins matured at 30 degrees C. *J. Mol. Biol.*, 145, 633–651.

128 Smith, D. H. & King, J. (1981). Temperature-sensitive mutants blocked in the folding or subunit assembly of the bacteriophage P22 tail spike protein. III. Intensive polypeptide chains synthesized at 39 degrees C. *J. Mol. Biol.*, 145, 653–676.

129 King, J. and Yu, M. H. (1986). Mutational analysis of protein folding

pathways: the P22 tailspike endorhamnosidase. *Methods Enzymol.*, 131, 250–266.

130 Betts, S. & King, J. (1999). There's a right way and a wrong way: in vivo and in vitro folding, misfolding and subunit assembly of the P22 tailspike. *Structure Fold. Des.*, 7, 131–139.

131 Mitraki, A., Fane, B., Haase Pettingell, C., Sturtevant, J. & King, J. (1991). Global suppression of protein folding defects and inclusion body formation. *Science*, 253, 54–58.

132 Mitraki, A., Danner, M., King, J. & Seckler, R. (1993). Temperature-sensitive mutations and second-site suppressor substitutions affect folding of the P22 tailspike protein in vitro. *J. Biol. Chem.*, 268, 20071–20075.

133 Schuler, B. & Seckler, R. (1998). P22 tailspike folding mutants revisited: effects on the thermodynamic stability of the isolated beta-helix domain. *J. Mol. Biol.*, 281, 227–234.

134 Seckler, R. (1998). Folding and function of repetitive structure in the homotrimeric phage P22 tailspike protein. *J. Struct. Biol.*, 122, 216–222.

135 Steinbacher, S., Seckler, R., Miller, S., Steipe, B., Huber, R. & Reinemer, P. (1994). Crystal structure of P22 tailspike protein: interdigitated subunits in a thermostable trimer. *Science*, 265, 383–386.

136 Steinbacher, S., Miller, S., Baxa, U., Budisa, N., Weintraub, A., Seckler, R. & Huber, R. (1997). Phage P22 tailspike protein: crystal structure of the head-binding domain at 2.3 A, fully refined structure of the endorhamnosidase at 1.56 A resolution, and the molecular basis of O-antigen recognition and cleavage. *J. Mol. Biol.*, 267, 865–880.

137 Baxa, U., Steinbacher, S., Weintraub, A., Huber, R. & Seckler, R. (1999). Mutations improving the folding of phage P22 tailspike protein affect its receptor binding activity. *J. Mol. Biol.*, 293, 693–701.

138 Beissinger, M., Lee, S. C., Steinbacher, S., Reinemer, P., Huber, R., Yu, M. H. & Seckler, R. (1995). Mutations that stabilize folding intermediates of phage P22 tailspike protein: folding in vivo and in vitro, stability, and structural context. *J. Mol. Biol.*, 249, 185–194.

139 Goldenberg, D. & King, J. (1982). Trimeric intermediate in the in vivo folding and subunit assembly of the tail spike endorhamnosidase of bacteriophage P22. *Proc. Natl Acad. Sci. USA*, 79, 3403–3407.

140 Brunschier, R., Danner, M. & Seckler, R. (1993). Interactions of phage P22 tailspike protein with GroE molecular chaperones during refolding in vitro. *J. Biol. Chem.*, 268, 2767–2772.

141 Gordon, C. L., Sather, S. K., Casjens, S. & King, J. (1994). Selective in vivo rescue by GroEL/ES of thermolabile folding intermediates to phage P22 structural proteins. *J. Biol. Chem.*, 269, 27941–27951.

142 Sather, S. K. & King, J. (1994). Intracellular trapping of a cytoplasmic folding intermediate of the phage P22 tailspike using iodoacetamide. *J. Biol. Chem.*, 269, 25268–25276.

143 Speed, M. A., Wang, D. I. & King, J. (1995). Multimeric intermediates in the pathway to the aggregated inclusion body state for P22 tailspike polypeptide chains. *Protein Sci.*, 4, 900–908.

144 Speed, M. A., Morshead, T., Wang, D. I. & King, J. (1997). Conformation of P22 tailspike folding and aggregation intermediates probed by monoclonal antibodies. *Protein Sci.*, 6, 99–108.

145 Speed, M. A., Wang, D. I. & King, J. (1996). Specific aggregation of partially folded polypeptide chains: the molecular basis of inclusion body composition. *Nat. Biotechnol.*, 14, 1283–1287.

146 Durchschlag, H. (1986). Specific volumes of biological macromolecules and some other molecules of biological interest. In: Thermodynamic data for biochemistry and biotechnology, ed.: H.-J. Hinz, Springer Verlag, Heidelberg, pp. 45–127.

3
Studying Protein Folding in Vivo

I. Marije Liscaljet, Bertrand Kleizen, and Ineke Braakman

3.1
Introduction

To be biologically active, proteins must fold into their three-dimensional, native structure. Christian Anfinsen and others showed decades ago that all information required for a protein to attain this three-dimensional structure resides in its primary sequence [1]. Irrespective of whether a protein folds in an intact cell, in vivo, or in a test tube, in vitro, essentially the same end product is obtained. Yet, many differences exist between the two. While in vivo folding starts co-translationally [2, 3], in vitro (re)folding starts from the complete protein molecule. The folding environment is different as well: in vivo proteins are folded in an extremely crowded environment [4–6], containing hundreds of milligrams of protein per milliliter, in contrast to in vitro folding where the protein is purified and folds in a diluted system. In vitro, folding often is inefficient under biological conditions such as physiological temperatures, with a large fraction of the protein misfolding and precipitating. In vivo, proteins are assisted during folding, and because of chaperones and folding enzymes [7–9], the folding process is more efficient and results in less aggregation than in vitro [10]. In vitro folding can take place in milliseconds, proteins can be studied directly at the molecular level, and there are no barriers such as membranes between experimenter and the folding proteins. Success rate is highest with relatively small, single-domain proteins, whereas especially mammalian proteins usually are large, consisting of more than one domain. Although in vitro folding experiments provide information on molecular details of the folding process, in vivo studies are essential for a complete view on protein folding. This chapter will discuss how protein folding in a cell can be studied and manipulated, with a slight focus on the endoplasmic reticulum.

3.2
General Features in Folding Proteins Amenable to in Vivo Study

In contrast to in vitro protein folding, protein folding in vivo can be studied only via indirect methods. Instead of direct measurements on the protein itself, the fold-

Protein Folding Handbook. Part II. Edited by J. Buchner and T. Kiefhaber

ISBN: 3-527-30784-2

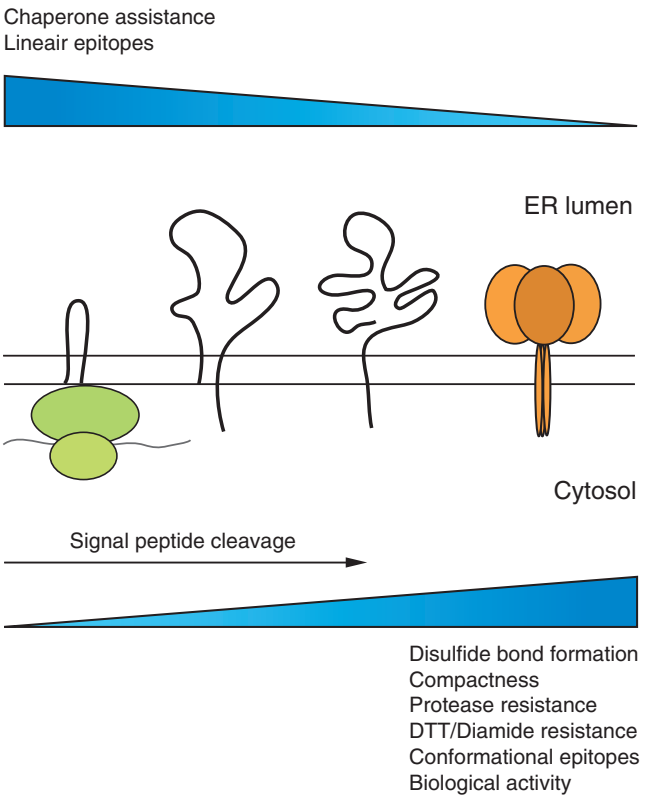

Fig. 3.1. Studying protein folding in the ER. Newly synthesized proteins that are folding in the ER lose and gain various features, which can be used to determine their folding status; examples are given in this figure. Folding starts on the nascent chain and continues after chain termination, during or after which the protein may oligomerize.

ing status of a protein can be followed through changes in shape, associations with other proteins, co- and posttranslational modifications, and its compartmental location (Figure 3.1). During in vivo folding, proteins are not purified but are part of the cell "soup." So far the best way to follow folding of a small population of newly synthesized proteins in a cell is by labeling them with ^{35}S-labeled cysteine and/or -methionine. In this way, changes in a small, synchronized protein population can be followed with time.

A pulse-chase experiment (Figure 3.2) in intact cells is an assay in which kinetics and characteristics of sequential steps are determined in vivo. Newly synthesized proteins are labeled with radioactive amino acids for a very short pulse time, because folding starts during synthesis and one would ideally follow folding from the very first folding intermediates. Labeled proteins are "chased" by incubation with unlabeled amino acids. After different times of chase, cells and supernatants can be collected and cooled on ice, and free cysteines are blocked with an alkylating

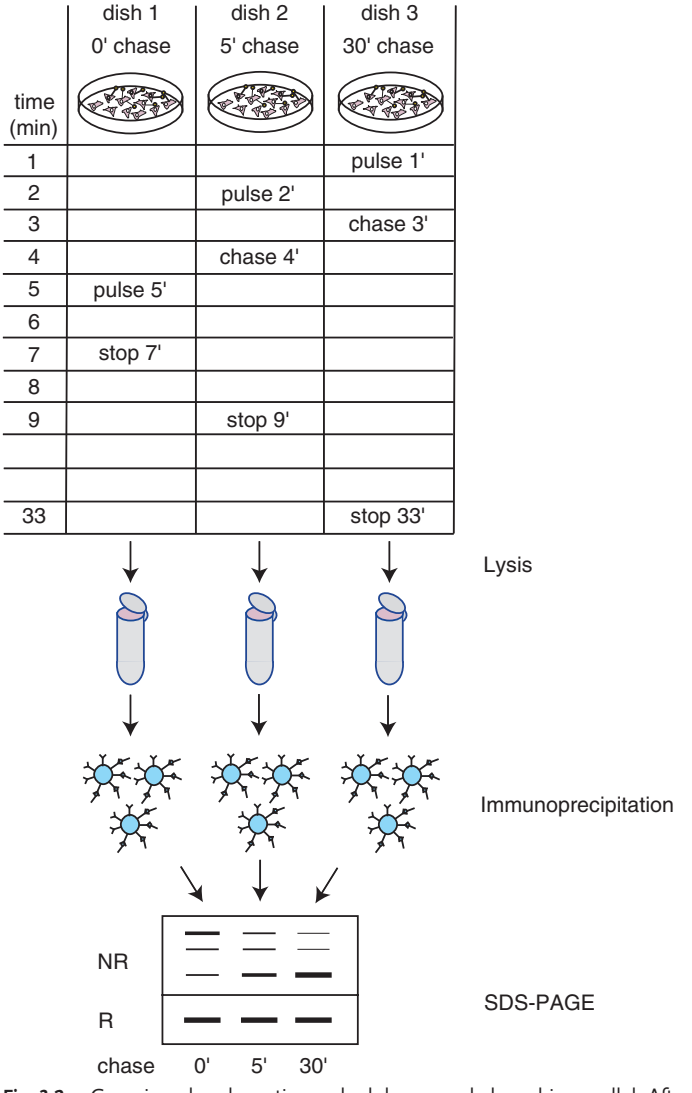

Fig. 3.2. Generic pulse-chase time schedule. To study folding and disulfide bond formation of a newly synthesized protein in the ER, adherent cells expressing the protein of interest are pulse labeled for a short period and chased with unlabeled amino acids; one dish is needed per time point. The experimental design is such that dishes can be pulse labeled and chased in parallel. After different times of chase, free cysteines are blocked with an alkylating agent and cells are lysed in a detergent-containing buffer. The protein is isolated using immunoprecipitation, and samples are analyzed using non-reducing (NR) and reducing (R) SDS-PAGE to visualize disulfide bond formation and changes in molecular weight.

agent. Cells are lysed in a detergent-containing buffer and the protein under study is isolated by immunoprecipitation. Samples can be analyzed by various types of gel electrophoresis, including native gels suitable for detection of complexes, and reducing and non-reducing SDS-PAGE to detect folding intermediates with a variable set of disulfide bonds (see the Appendix and [11]). Other changing features of folding proteins, such as their compactness or resistance to proteolytic digestion, can be determined with this pulse-chase assay as well.

Other labeling assays that can be used to study protein folding include the pulse-chase assay in suspension cells, microsomes, or semi-permeabilized cell systems [12] in which mRNA is translated in vitro in the presence of a source of ER membranes (see Chapter 18) and the recently developed in vitro chase assay in which a protein is translated in vivo and chased in a detergent lysate (Maggioni et al., manuscript submitted). These assays will be discussed in the Appendix.

3.2.1 Increasing Compactness

One of the general features of a protein during folding is its increasing compactness. During the folding process of a soluble protein, all hydrophobic side chains will strive to be buried inside the molecule and all hydrophilic ones to be exposed on the outside; hydrogen bonds are formed within the protein and between exposed residues and water. Electrostatic, van der Waals, and hydrophobic interactions play a major role during the folding process, and disulfide bridges will form within the protein when conformation and environmental conditions allow. The end product of the folding process will be the native conformation of the protein, which is assumed to be the most compact, energy-favorable form. To study the increase in compactness of proteins, non-denaturing gel electrophoresis can be used. The formation of oligomers, protein complexes, and transient protein-protein interactions can be detected on a native gel as well as by sucrose velocity gradient centrifugation. To monitor disulfide bond formation within or between polypeptide chains, non-reducing denaturing gel electrophoresis (SDS-PAGE) [13] is an effective technique. In the assays described in this chapter, the folding process of a (disulfide bond containing glyco)protein can be followed kinetically.

3.2.2 Decreasing Accessibility to Different Reagents

Due to the increasing compactness of a protein on its folding pathway, it will become less accessible to various reagents including proteases. Changes in protein conformation usually result in decreased sensitivity to protease digestion, since potential cleavage sites are buried inside the protein during the folding process. To limit the appearance of protease-specific bands, a range of proteases should be used optimally, some of which cleave frequently in a protein. Examples of the latter are proteinase K, TPCK-trypsin, and TLCK-chymotrypsin. Limited proteolysis was first used to identify domains in immunoglobulin [14] and is a very powerful tool.

The target protein is exposed to a protease, and in a time course the generation of stable products, i.e. protected inaccessible domains, can be monitored. To identify these domains, the digestion pattern of full-length protein can be compared to that of expressed isolated fragments of the protein, or domain-specific antibodies can be used to identify protease-resistant fragments.

Other reagents that can be used to obtain more information about the folding status of a protein include diazenedicarboxylic acid *bis*(*N*,*N*-dimethylamide) (diamide) and 4,4′-dithiodipyridine (4-DPS) [15, 16]. Diamide is an oxidant that, when added to the chase medium, will over-oxidize all compartments in the cell, resulting in oxidation of all cellular thiols, including those in proteins and glutathione. Since only proteins with free sulfhydryl groups are sensitive to diamide treatment, in the secretory pathway, only folding intermediates will oxidize, as most mature folded proteins have disulfide bonds. If treated and non-treated proteins are analyzed by non-reducing SDS-PAGE, folding intermediates and the native protein can be discriminated [17–19] (Braakman and Helenius, in preparation).

Like diamide, reducing agents such as dithiothreitol (DTT) or 2-mercaptoethanol (2ME) can be used in a pulse-chase assay to determine the folding status of a protein. The influenza virus hemagglutinin (HA) [20, 21] and other proteins with disulfide bonds [22, 23] undergo a conversion from DTT sensitivity to DTT resistance during their conformational maturation in the ER. In combination with conformation-sensitive and epitope-specific antibodies, DTT sensitivity is very useful in determining the folding hierarchy in a protein.

3.2.3
Changes in Conformation

During folding, domains are formed within a protein, coinciding with changes in conformation. Antigenic epitopes become exposed, are masked, or form because distant parts of the polypeptide chain start to interact. Conformational changes can be followed by probing the folding protein with conformation-sensitive antibodies. Contrary to general belief, completely conformation-sensitive antibodies are rare. Polyclonal as well as monoclonal antibodies generally recognize a limited conformation range of a protein, depending on how the antigen used to produce the antibody was obtained. Protein bands cut out of SDS-PA gels, when injected into rabbits, yield antibodies that work well in Western blotting (against SDS-denatured antigen) but that often fail to work in immunofluorescence, EM, or immunoprecipitation, which are conditions that allow proteins to remain more or less native. Antibodies generated against native, properly folded and assembled antigens often fail to interact with folding intermediates or SDS-denatured protein. Antibodies against peptides often fail to bind protein, because the peptide is not representative of the protein conformation or the peptide is not exposed in the complete protein. Therefore, an antibody needs to be characterized before it becomes a powerful tool in protein-folding studies.

Another assay that can be used concerns biological function of the folding pro-

tein: this includes binding to ligands and other proteins or an increase in enzymatic activity. To test, for instance, whether the protein can bind its receptor, the receptor may be coupled to Sepharose beads, which can be used in a precipitation assay to isolate the desired protein, or, alternatively, interaction can be tested in an ELISA-like assay.

3.2.4 Assistance During Folding

All information required for a protein to attain its final three-dimensional structure resides in its primary sequence [1]. However, complex proteins need the assistance of molecular chaperones and folding enzymes to reach their native structure efficiently without formation of (large) aggregates. Molecular chaperones interact with nonnative states of proteins; they are important during folding of newly synthesized polypeptides where they facilitate rate-limiting steps, stabilize unfolded proteins, and prevent unwanted intra- and interchain interactions, which could lead to aggregation [24–26]. Classical chaperones in the ER, such as BiP [27], recognize exposed hydrophobic patches [28, 29], while calnexin and calreticulin recognize monoglucosylated glycan chains on proteins in the ER [30]. BiP is a member of the Hsp70 family; ATP binding and hydrolysis are crucial for the cycle of binding and release of substrate [31, 32]. The preference for binding of either BiP or calnexin/calreticulin is thought to depend on the position of the first N-linked glycan in the polypeptide chain [33]. When *N*-glycans are present in the first ~50 amino acids, a protein in general will associate with calnexin and calreticulin first, whereas proteins with *N*-glycans downstream in the sequence may bind BiP or other chaperones first. Other observations, however, suggest that calnexin/calreticulin may interact with non-glycosylated proteins as well [34, 35]. As a rule, a protein's association with molecular chaperones will decrease its folding rate but increase folding efficiency and thereby yield.

The ER in addition possesses a wealth of enzymes that assist proteins during folding. Protein disulfide isomerase (PDI) (56 kDa) [36] is a member of the thioredoxin superfamily that acts catalytically in both the formation and reduction of disulfide bonds, and hence in disulfide bond rearrangements. Another PDI family member is ERp57, which facilitates disulfide bond formation in newly synthesized proteins [37] and works in a complex with either calnexin or calreticulin [38]. A different class of enzymes comprises the peptidyl-prolyl isomerases (PPIases) [39], which catalyze *cis*/*trans* isomerization of peptide bonds N-terminally to proline residues [40] and thereby increase folding rates [41]. The ribosome attaches amino acids in the *trans* conformation, which requires an isomerization step for all *cis* prolines in the final folded structure. PPIases belong to three structurally diverse families: the cyclophilins (inhibited by cyclosporin A [CsA]), the FK506-binding proteins (inhibited by FK506 and rapamycin), and the parvulins. They reside in the cytoplasm as well as in various eukaryotic organelles including the ER. In 1991 Steinmann et al. [42] and Lodish and Kong [43] showed that the folding of procollagen I and transferrin is slowed down by CsA due to inhibition of cyclophilin.

Folding proteins can be assisted by chaperones and folding enzymes from differ-

ent compartments. If a protein is soluble, only the chaperones and folding enzymes that are located in the same compartment as the protein will assist folding. Membrane-bound or membrane-spanning proteins, however, will have domains in different compartments. For example, both P-glycoprotein and the cystic fibrosis transmembrane conductance regulator (CFTR) are multiple-membrane-spanning proteins that are members of the ABC transporter family. For both P-glycoprotein and CFTR, approximately 10–15% of the protein is located in the ER lumen and ER membrane, whereas the bulk is located in the cytosol. The only ER chaperone that interacts with these membrane proteins is calnexin [44, 45]. On the cytosolic side, the most abundant chaperone Hsp70 assists in folding these proteins [46, 47]. Interestingly, when folding attempts fail, Hsp70 also promotes proteasomal degradation of misfolded CFTR by targeting the E3 ubiquitin ligase CHIP to this protein [48]. Cytosolic Hsp90 also has been demonstrated to be involved in degrading CFTR [49]. Since both ER and cytosolic chaperones impose a quality control on this type of membrane protein, it will be of great interest to investigate how events at the two sides of a membrane are communicated and coordinated.

To study a possible interaction of a substrate protein with folding enzymes and chaperones, co-immunoprecipitations (see protocols) can be done using antibodies against folding factors; if interactions are too weak or too transient, chemical cross-linkers may stabilize the complex during analysis. To examine the role of a particular chaperone on the folding of a substrate protein, one may examine the effect of its increased or decreased expression in the cell or its presence or absence in a folding assay. To test whether an ATP-dependent chaperone is involved, ATP can be depleted from cells. Section 3.4 will address these and other conditions that may affect the folding process.

3.3
Location-specific Features in Protein Folding

3.3.1
Translocation and Signal Peptide Cleavage

One location-specific feature of protein folding is its potential coupling to translocation into an organelle and subsequent signal peptide cleavage. Proteins that are targeted to mitochondria, chloroplasts, and the ER normally carry a signal peptide at their N-terminus.

Mitochondria have two membranes: the inner membrane, which encloses the matrix space, and the outer membrane, which is in contact with the cytosol. The majority of mitochondrial proteins are encoded in the cell nucleus and need to be imported from the cytosol via the macromolecular Tim/Tom complex into the mitochondrial matrix, the mitochondrial inner membrane, or the intermembrane space [50].

Chloroplasts are chlorophyll-containing, double membrane-bounded organelles that are present in all higher plants. They possess the same compartments and membranes as mitochondria but have an extra subcompartment, the thylakoid

space, which is surrounded by the thylakoid membrane. Like mitochondria, proteins are posttranslationally imported via the Tic/Toc complex [51].

Proteins that need to be imported into the ER lumen of eukaryotes are translocated from the cytosol through the translocon. Co-translational translocation is signal recognition particle (SRP)-dependent [52]. SRP binds to the signal sequence on the nascent chain, the ribosome/nascent polypeptide/SRP complex docks onto the SRP receptor at the ER membrane, and via multiple steps, the protein is translocated into the ER lumen. Oligosaccharyl transferase (OST) attaches glycans to the nascent chains, and in most proteins the signal peptide is cleaved off co-translationally by the signal peptidase present in the membrane with its active site in the lumen of the ER. Up to now, only few exceptions have been reported in which signal peptide removal is (at least partially) posttranslational, all of them viral glycoproteins [53, 54]. Posttranslational translocation is SRP-independent; this type of translocation needs additional factors to associate with the translocon complex.

Proteolytic cleavage events in mitochondria, chloroplasts, and the ER can be followed by mobility changes of the protein in reducing SDS-PAGE. If the signal peptide of a certain protein is cleaved off, the protein will have an increased electrophoretic mobility. Signal peptide cleavage in nascent chains is not detectable in a one-dimension gel, but it can be followed in two-dimensional SDS-PAGE, where the protein sample is digested with an SDS-resistant protease between the first and second dimension [55].

To test which population of full-length folding intermediates has lost its signal sequence in the ER (when cleavage is posttranslational), the process can be correlated to disulfide bond formation by using another two-dimensional SDS-PAGE system [56]. Samples are run non-reduced in the first dimension (horizontal) and subsequently are reduced in the second dimension (vertical). In this gel all proteins lacking disulfides will run on the diagonal. If a protein has intrachain disulfide bonds, it will run faster in the first (nonreducing) dimension than in the second (reducing) dimension and thus will end up above the diagonal. Proteins that form interchain disulfide-linked complexes will run below the diagonal. Antibodies against the signal peptide itself or antibodies that recognize the N-terminus of the protein after, but not before, cleavage can be used to monitor the process of signal peptide cleavage more directly [57]. Translocation of proteins in a cell-free translation organellar system can be demonstrated by protease-resistance. A newly synthesized protein that is not translocated yet will be degraded by (membrane-impermeable) proteases added to the membranes but will be protected from digestion once translocated.

3.3.2 Glycosylation

Glycan moieties on proteins are essential for folding, sorting, and targeting of glycoproteins through the secretory pathway to various cellular compartments. N-linked glycans affect local conformation of the polypeptide chain they are attached to; increase local solubility of proteins, thereby preventing aggregation; are impor-

tant for the interaction with the two lectin chaperones in the ER, calnexin and calreticulin; and are important for targeting misfolded proteins for degradation. Hence, for most glycoproteins, their N-linked glycans are indispensable for proper folding.

The glycosylation process starts at the cytosolic side of the ER, where monosaccharides are added to the lipid intermediate dolichol phosphate up to $Man_5GlcNac_2$-PP-Dol. This precursor is translocated to the lumenal side, where it is elongated to $Glc_3Man_9GlcNAc_2$-PP-Dol. The oligosaccharyl transferase then transfers the 14-mer to an asparagine residue in the consensus sequence N-X-S/T of a nascent polypeptide chain, wherein X is any amino acid except proline [58]. Glucosidase I (GI, a membrane-bound enzyme) removes the first glucose and glucosidase II (GII, a soluble enzyme), the second and third. Monoglucosylated oligosaccharides associate with the ER-resident lectins calnexin (membrane-bound) and calreticulin (soluble), which are in a complex with ERp57 [38]. When GII cleaves the last glucose, the protein is released from calnexin/calreticulin and, if correctly folded, can leave the ER. UDP-Glc:glycoprotein glucosyltransferase (GT), a soluble ER protein of 160 kDa, is a sensor of glycoprotein conformation and reglucosylates glycans close to un- or misfolded amino acid stretches [59–61]. By reglucosylating the protein, it becomes a ligand again for calnexin/calreticulin and therefore a substrate for this quality-control cycle [9]. Two ER mannosidases can remove one or two mannoses in the ER before the protein is transported to the Golgi, where further oligosaccharide processing proceeds and proteins can be *O*-linked glycosylated. Alternatively, a permanently misfolded protein may be targeted for degradation from the ER through glycan recognition (see Section 3.3.4).

The enzyme endoglycosidase H (Endo H) often is used to monitor the movement of newly synthesized glycoproteins from the ER to the Golgi complex. Glycans on proteins remain sensitive to digestion by Endo H as long as they are in the ER and in early regions of the Golgi, but they become resistant beyond. Endo H digestion after the immunoprecipitation of a glycoprotein allows conclusions to be made on the protein's location. If a protein is highly heterogeneously glycosylated, e.g., HIV envelope, which has ~30 N-linked glycans, Endo H can also be used after the immunoprecipitation to increase mobility of folding intermediates in the ER and to bring about a collapse of smeary bands into one sharp band in a gel, which enables identification and quantitation. The enzyme PNGase F in principle removes all glycans, irrespective of composition, and theoretically is the better deglycosylation enzyme. Its activity changes the glycosylated asparagine into an aspartic acid, however, which in some proteins decreases mobility, increases fuzziness of bands, and may confuse the pattern. The enzyme of choice needs to be determined for every protein one studies. To gather more information on how glycosylation affects protein folding, glycosylation site mutants and enzymes involved in glycosylation can be used (see Section 3.4).

3.3.3
Disulfide Bond Formation in the ER

The lumen of the ER supports a relatively oxidizing environment that facilitates the formation of disulfide bonds in folding proteins. Disulfide bonds are thought

to stabilize proteins during and after folding, but this is an oversimplification of their role. In the cytosol the ratio between reduced glutathione (GSH) and oxidized glutathione (GSSG) is ~60:1, while in the ER this ratio is 3:1 [62]. Glutathione is the major redox buffer in the ER. Therefore, glutathione was thought for a long time to be responsible for generating and maintaining the redox potential in the ER. This view changed with the identification of the FAD-binding [63] ER oxidoreductase 1 (Ero1p) in *Saccharomyces cerevisiae* [64, 65] and its homologues Ero1α and Ero1β in more complex eukaryotes [66, 67]. Disulfide-linked complexes between Ero1p and PDI have been captured in yeast as well as mammalian cells. In addition, disulfide-linked complexes were found between PDI and a newly synthesized secretory protein [68]. Ero1 transfers disulfides to (or rather, electrons from) substrate proteins via protein disulfide isomerase (PDI). Other oxidoreductases, such as Erv proteins [69] and PDI homologues, play a role as well [70].

Formation of disulfide bonds in a folding protein can be followed through a pulse-chase assay. In combination with an immunoprecipitation and reducing and non-reducing SDS-PAGE, the formation of disulfides can be monitored (see the Appendix and [11]). To study which enzymes are involved during disulfide bond formation and isomerization, co-immunoprecipitations can be performed with different antibodies against folding enzymes with or without prior cross-linking. Furthermore, the folding enzyme concentration can be changed, as is described below.

If the studied protein contains disulfide bonds, an alkylating agent must always be added to the stop solution and lysis buffer of the pulse-chase assay to block free sulfhydryl groups [71, 72]. This will prevent formation of (additional) disulfide bonds in the protein after cell lysis. Three commonly used blocking agents are iodoacetamide (IAM), iodoacetic acid (IAC), and *N*-ethyl maleimide (NEM). IAM and IAC bind relatively slowly, but irreversibly. IAC is negatively charged, which decreases mobility of proteins it is attached to. NEM is smaller than IAM and IAC; it binds fast but is under certain conditions partially reversible. It is therefore less suitable when prolonged incubation periods at 37 °C are required. Since all alkylating agents have different characteristics, the alkylation protocol may be optimized for each individual protein.

3.3.4 Degradation

In the ER, a stringent quality-control system operates that discriminates between correctly folded proteins, misfolded proteins, and unassembled protein subunits. This prevents misfolded proteins from leaving the ER, where they can cause harm to the cell or even to the complete organism. The ER-associated degradation (ERAD) pathway ensures ubiquitin-mediated degradation of ER-associated misfolded proteins [73]. Trimming of the α1,2-linked mannose of the middle branch by mannosidase I to $Man_8GlcNac_2$ uncovers a degradation signal [74, 75]. EDEM (ER degradation-enhancing α-mannosidase-like protein) functions in the ERAD pathway by accepting terminally misfolded glycoproteins from calnexin [76, 77]. The substrate is retro-translocated into the cytosol, where proteins are deglycosylated, ubiquiti-

nated, and then degraded by the 26S proteasome [73]. Post-ER quality-control systems exist as well: proteins can be transported to the Golgi or the plasma membrane before they are degraded, most often by vacuolar/lysosomal proteases.

Proteins can be degraded after synthesis as well as during their translation, which is undetectable in a pulse-chase assay. The net result is a lower amount of labeled protein, which can be visualized only through the use of a proteasome inhibitor during the pulse labeling. If the total signal of labeled protein at the end of the pulse is higher in the presence than in the absence of the inhibitor, cotranslational degradation apparently does happen in the control situation. Degradation *after* translation can be followed on gel, because the total protein signal will decrease during the chase. Proteasome inhibitors and lysosomal enzyme inhibitors can be added to prove degradation and identify the site of breakdown. A useful system to study protein folding without degradation is an in vitro translation system in the absence or presence of a membrane source, the latter ranging from enriched organelles to digitonin-permeabilized cells. The hemin present in the reticulocyte lysate inhibits proteasomal activity.

3.3.5
Transport from ER to Golgi and Plasma Membrane

Different methods can be used to monitor transport of a protein out of the ER to the Golgi complex or the plasma membrane. Endo H resistance is a good tool to monitor the movement of newly synthesized glycoproteins from ER (sensitive to digestion by Endo H) to Golgi (resistant to Endo H). Resistance of newly synthesized proteins to reduction by DTT (or oxidation by diamide) can be used to determine the folding status of a protein. If a protein is transported very rapidly from ER to Golgi, which then coincides with rapid and massive changes in electrophoretic mobility, such as *O*-glycosylation [78] or *N*-glycan modification [79], and one wants to trap the protein in the ER, in vitro translation in the presence of microsomes or semi-intact cells [12] can be used, since these systems lack ER-to-Golgi transport.

Cell surface arrival of proteins can be shown using protease digestion on intact cells, biotinylation of intact cells, or indirect immunofluorescence on fixed cells. Indirect immunofluorescence allows detection of possible locations of a protein in the cell, but this steady-state method does not allow any conclusion on precursor-product status, or on kinetics of processes. To follow a traveling protein with time throughout a living cell, it may be fused to a fluorescent marker protein such as GFP. For this purpose, the protein population needs to be synchronized by for example release from a protein synthesis block (cycloheximide incubation and removal) [80], a disulfide-bond formation block (DTT incubation and removal) [20], or use of a conditional mutant of either the protein under study or a transport protein such as the Sec mutants often used in *S. cerevisiae* [81]. Receptor or ligand binding can be tested biochemically, either in the cell lysate or on intact cells, after the protein's arrival on the plasma membrane, and when the studies concern a soluble protein, protein secretion can be measured by collecting the chase medium.

3.4 How to Manipulate Protein Folding

3.4.1 Pharmacological Intervention (Low-molecular-weight Reagents)

To study the role of folding factors in vivo, their activity needs to be manipulated. Drugs act fast and do not allow time for genetic adaptation of cells, but they may not inhibit to 100% and may exhibit pleiotropic effects. Genetic changes of cells circumvent this lack of specificity. One particular folding factor can be changed, but compensatory regulation processes may completely change the protein composition of the cell. With these limitations in mind, both high- and low-molecular-weight manipulations can increase our understanding of protein folding in cells.

3.4.1.1 Reducing and Oxidizing Agents

Reducing and oxidizing agents not only are useful to determine the conformation of a folding protein (as discussed in Section 3.2), but also they can be used as a tool to manipulate protein folding. If separation of protein translation and protein folding is desired, for example, to study protein folding in the absence of ATP or to determine whether co-translational disulfide bond formation is needed for a certain protein to fold, a reducing agent such as DTT can be added to the pulse medium to prevent disulfide bond formation during protein synthesis. Furthermore, reducing and oxidizing agents can be added to the chase medium to determine the effect of reduction/oxidation on protein folding and (posttranslational) signal peptide cleavage.

3.4.1.2 Calcium Depletion

In addition to its role in protein folding, the ER has an important role in calcium signaling and in sequestering calcium from the cytosol. The ER contains many calcium-binding proteins, which have a large capacity for calcium and help keep the cellular internal calcium concentration constant. The first identified calcium-binding protein was calsequestrin in the sarcoplasmic reticulum of striated muscle [82]. Its C-terminal domain binds calcium with low affinity but with high capacity. The calcium level in the ER is important not only for signaling but also for proteins traveling through the ER. During folding they are assisted by calcium-binding molecular chaperones such as BiP (Grp78), Grp94 (endoplasmin), and the lectins calnexin and calreticulin. When the level of calcium in the ER drops, some of the newly synthesized proteins misfold and aggregate [83]. To study the effect of calcium on protein folding, calcium in the cell can be depleted using various chemicals. A23187 is a divalent cation ionophore [84] that can be added to calcium-free starvation, pulse, and chase media. Thapsigargin is a potent cell permeable, IP3-independent, intracellular calcium releaser, as it efficiently inhibits all members of the Ca-ATPase family of calcium pumps, which pump calcium into the ER [85, 86]. Calcium chelators such as BAPTA, EDTA, and EGTA can be used as well to study the effect of calcium (and calcium-binding chaperones) on protein folding.

3.4.1.3 ATP Depletion

ATP is a common currency of energy in all cells, and its presence is needed for various reactions and processes, including protein folding [87]. The ER contains many chaperones such as BiP, the lumenal Hsp70 of the ER, which has an N-terminal ATP-binding domain and a C-terminal peptide-binding domain and whose activities are tightly coupled. In the Hsp70 family of chaperones, association and dissociation with the substrate protein are controlled by ATP binding and hydrolysis. To test the effect of ATP(-dependent chaperones) on protein folding, ATP generation can be blocked. 2-Deoxy-glucose inhibits glycolysis and, thereby, anaerobic ATP generation. It can be added to glucose-free cell culture medium and has been shown to be effective in pulse chase experiments [87]. Because 2-deoxy-glucose in some studies was shown to inhibit glycosylation [88], the incubation time and concentration need to be determined carefully. Sodium azide and the uncoupling protonophore carbonyl cyanide 3-chlorophenylhydrazone (CCCP) [89] poison mitochondria, and thus inhibit aerobic ATP generation. Inhibition of both glycolysis and oxidative phosphorylation by combination treatment usually depletes ATP effectively from living cells [87]. After depletion, ATP levels in the cell lysates can be measured, e.g., with a luciferase-luciferin assay in a scintillation counter or luminometer [21, 90].

3.4.1.4 Cross-linking

Chemical cross-linkers are useful for multiple purposes in protein science, such as the stabilization of protein-chaperone complexes. There are two prominent groups of cross-linkers: homobifunctional cross-linking reagents, which have two identical reactive groups, and heterobifunctional cross-linking reagents, in which the reactive groups are chemically distinct. Further variation is present in spacer arm length, cleavability, or membrane permeability, and cross-linkers may react chemically or photochemically upon UV illumination. Whereas membrane-permeable cross-linkers are suitable for cross-linking in the cell, membrane-impermeable reagents are useful for cross-linking at the cell surface and in cell lysates. Cross-linkers with shorter spacer arms (4–8 Å) often are used for intramolecular cross-linking, and reagents with longer spacers are favored for intermolecular cross-linking. The most frequently used cross-linkers at the moment are DSP (dithio-*bis*-succinimidylpropionate), a water-insoluble, homobifunctional *N*-hydroxysuccimide ester with a spacer arm length of 12 Å, which is thiol-cleavable and primary amine reactive and is used in many applications [91], and BMH (*bis*-maleimidohexane), a water insoluble, homobifunctional, non-cleavable cross-linker with a spacer arm length of 16 Å, which is reactive towards sulfhydryl groups and is also used in many applications [92, 93]. Since there is a wide variety in characteristics and potential applications of cross-linkers, it is desirable to compare different cross-linkers before protein-folding studies are performed.

3.4.1.5 Glycosylation Inhibitors

Inhibitors that prevent glycan synthesis or modify the carbohydrate portion of the glycoprotein are useful to determine function of the glycan or change fate of a pro-

tein. A wide variety in glycosylation inhibitors exists (see also chapter 17), each blocking a specific step in glycosylation. Tunicamycin, for instance, was isolated from *Streptomyces lysosuperificus* in the early 1970s [94]; it inhibits transfer of *N*-acetylglucosamine to dolichol phosphate, thereby completely blocking N-linked glycosylation, which most often causes misfolding of glycoproteins. The misfolding of many proteins in the ER can lead to upregulation of classical chaperones and folding-facilitating proteins through a so-called unfolded protein response (UPR) [95].

Other than complete inhibition by tunicamycin, which can trigger the UPR, more subtle inhibitors can be used, e.g., castanospermine. This is a plant alkaloid that was isolated from the seeds of the Australian tree *Castanospermum australe*, which inhibits glucosidase I and II. An example of a glucosidase I-specific inhibitor is australine, whereas deoxynojirimycin inhibits glucosidase II better than glucosidase I. Glucosidase I and II inhibitors can be useful in preventing association of the folding protein with the molecular chaperones calnexin and calreticulin, which bind only to monoglucosylated proteins. If a prolonged association with calnexin or calreticulin is desired, a glucosidase II inhibitor can be added during the chase period in a pulse-chase assay. This prevents cleavage of the last glucose, such that the glycoprotein will remain bound to the lectins calnexin and calreticulin. If a mannosidase I inhibitor such as kifunensine is added during the pulse chase, degradation of misfolded glycoproteins can be prevented.

Glycosylation inhibitors are useful reagents in determining the role of oligosaccharides during protein folding, but because they often do not inhibit 100% and because some inhibitors can have an effect on protein synthesis, it is very important to always include the proper controls when they are used in experiments.

3.4.2 Genetic Modifications (High-molecular-weight Manipulations)

3.4.2.1 Substrate Protein Mutants

To study the effect of certain amino acids or modifications on the folding pattern of a protein, various mutations can be made in the cDNA encoding the protein. To investigate the effect of glycosylation on a protein, *N*-glycosylation consensus sequences can be removed or created by site-directed mutagenesis. Mutations of choice are the exchange of Asn for Gln or the downstream Ser or Thr for Ala; to exclude the effect of an amino acid change rather than of a lacking glycan, both strategies can be used and compared. This allows study of the role of every individual glycosylation site for proper folding, alone or in combination. Additional glycosylation sites can be generated to study the effect of hyperglycosylation. The addition of glycosylation consensus sequences is also used to determine the topology of a protein [96]; interpretation of such data needs care, however, because a glycan may change the topology or fate of a protein.

The role of a specific disulfide bond for protein folding can be studied by changing the cysteines into another residue using site-directed mutagenesis. By creating single-cysteine and double (-cystine) mutations, the effect of removal of a complete

disulfide bond on protein folding can be compared to the removal of a single cysteine, hence the presence of an odd number of cysteines. Cysteines are best changed into alanines, because they leave "only" a small gap in the protein structure, i.e., where the thiol atom resided. Although serines are thought to resemble cysteines more closely than alanines, their higher hydrophilicity and their hydrogen atoms may cause problems when incorporated into the tightly packed core of a protein. Methionines and valines in some instances are better replacements for cysteines, but they may be too large in other sites. To be certain that the result reflects the removal of a disulfide bond rather than the change of an amino acid in the sequence, it is wise to substitute cysteine for more than one other amino acid and compare the effects.

Many other mutants can be thought of. The signal peptide of a protein can be modified to determine which residues are responsible for signal peptide cleavage, and the cleavage site can be changed to determine the effect of timing and cleavage on folding. In addition, the original signal sequence can be replaced completely by the signal sequence of another protein, and folding kinetics and secretion can be studied, as was done for HIV envelope [53]. To determine sequence and hierarchy of domain folding within a protein, and to determine whether domains fold independently of each other, single domains can be expressed, and C-terminal and N-terminal truncation mutants can be studied.

When protein mutations result in clinical phenotypes, as in many inherited diseases, it is interesting to focus on those mutations that result in folding defects.

3.4.2.2 **Changing the Concentration or Activity of Folding Enzymes and Chaperones**

To determine the effect of molecular chaperones and folding enzymes on the folding of a protein, the protein can be overexpressed by infection/transfection. Cells can be transiently transfected using a plasmid encoding the protein of interest behind an appropriate promoter. High expression can be achieved using virus-based expression systems; one example is the recombinant vaccinia virus expressing T7 polymerase in combination with a plasmid containing the protein of interest behind the T7 promoter. Stable, overexpressing cell lines can be used as well; one example is the Dorner cell lines [97], which overexpress a particular ER chaperone, such as PDI, BiP, or Grp94.

Because of the redundancy of many chaperones and folding enzymes, overexpression of a folding factor may not lead to a desired effect. Lowering expression or activity may be more successful. In cases where molecular details of the activity of a folding factor are known, dominant-negative mutants have been generated: the "trap" mutants of chaperones such as GroEL [98] and BiP [99] and active-site mutants of enzymes such as Ero [66]. Many cell lines exist in which a particular folding factor is absent or incapacitated. Examples are the CHO-derived Lec cell lines [100], which include the glucosidase I-negative Lec23 cells [101]. Other examples are the BW 5147 mouse lymphoma-derived PhaR2.7 cell line, which is glucosidase II-deficient (because of which the lectins calnexin and calreticulin cannot bind to their substrates anymore) [102], and the human T lymphoblastoid cell

line CEM.NKR [103], which is resistant to natural killer cells (NK cells) and has no calnexin.

The most dramatic effect can be expected when a folding factor is completely absent. In various organisms such as yeast, genes can be deleted. In mammalian cell lines, this is still a procedure with little success. Alternatives are cell lines derived from knockout animals, which are becoming increasingly available. In other organisms or cell lines, depletion of a gene is the maximum reachable. Gene expression can be suppressed by siRNA, which was first discovered in the nematode worm *C. elegans*; this animal is capable of sequence-specific gene silencing in response to double-stranded RNA (dsRNA) [104]. The technology has been adapted for use in mammalian cells, and an increasing number of siRNA constructs and libraries are becoming available, which makes siRNA a powerful tool to study how chaperones and folding enzymes influence protein folding.

3.5 Experimental Protocols

3.5.1 Protein-labeling Protocols

3.5.1.1 Basic Protocol Pulse Chase: Adherent Cells

In vivo, conformational changes during folding, disulfide bond formation, signal peptide cleavage, other proteolytic processing steps, glycosylation and glycan modifications, transport to other compartments, and some aspects of biological activity all can be studied in intact suspension cells or in adherent cells growing in monolayers in tissue culture dishes [11]. The adherent cells are easiest to use because they allow multiple wash steps in a short period of time, which are needed for short pulse and chase times or for studies requiring frequent changes of media with very different composition. When cells do not adhere or when low volumes of media are desirable (e.g., when expensive additives are needed), most of the analyses can be done in suspension, as described in the alternate protocol. Prepare the cells expressing the protein of choice in 35- or 60-mm dishes. For each time point, at least one dish is needed; the protocol is written for 60-mm dishes. On the day of the pulse chase, the cell monolayer needs to be almost confluent (80–90%).

Prepare all solutions needed. Also prepare a pulse-chase scheme on which all steps in the procedure (pulse, chase, stop) are noted. We use a 1-min scheme, meaning that every minute one action (pulse, chase, or stop) is performed. If aspiration is fast (which depends on the vacuum system used) and the experimenter is experienced, 30-s intervals become possible.

1. Prepare the pulse-chase setup, which includes a water bath at the desired temperature, with tube racks and 1–2 mm water above them, which can be maintained at this temperature. *Make sure the water level is just above the racks, such*

that the bottom of a tissue culture dish is completely in contact with the water but dishes are not floating when they are without cover.

2. Wash the cells with 2 mL wash buffer and add 2 mL starvation medium. Incubate for 15–40 min. at 37 °C in the presence of 5% CO_2.
3. Place the dishes on the rack in the water bath. *Make sure there are no air bubbles below the dishes.*
4. After 15 min pre-incubation with starvation medium, start the first pulse labeling. The staggering schedule (Figure 3.2) should allow labeling of the last dish within ~40 min of the start of starvation. Pulse label the cells one dish at a time: aspirate depletion medium, add 400 µL labeling medium at time 0 s. to the center of the dish, swirl gently, and incubate for the desired labeling time on the water bath. For pulse times longer than 15 min, a larger volume and incubation (on a rocker) in a 37 °C incubator in the presence of 5% CO_2 is recommended. *The pulse time optimally is equal to or shorter than the synthesis time of the protein under study (an average of 4–5 amino acid residues per second). Labeling time should be long enough to detect the protein.*
5. Add 2 mL chase medium at precisely the end of the pulse (i.e., at time 2′0″ if a 2-min pulse is aimed for). Swirl gently to mix; the labeling stops immediately upon addition of chase medium. Aspirate this mix of labeling and chase medium and add another 2 mL of chase medium. For short chases: incubate on the water bath. For chases longer than 30 min, incubate dishes in the incubator. For 0′ chase: add 2 mL chase medium at precisely the end of the pulse. Swirl gently to mix. Aspirate chase medium, place the dish immediately on ice, and add 2 mL of ice-cold stop buffer. *This is best achieved by putting an aluminum plate on top of an ice pan full of ice, with a wet paper towel on top to allow optimal contact between the plastic of the cell culture dish and the ice-cold surface.*
6. Stop the chase: aspirate chase medium at precisely the endpoint of the chase time, place the dish on the aluminum plate on ice, and immediately add 2 mL of ice-cold stop buffer. *If the studied protein will be secreted, collect the chase medium and use it for immunoprecipitation.*
7. Just before lysis: wash the cells again with 2 mL ice-cold stop buffer.
8. Aspirate the dish as dry as possible without letting cells warm up and add 600 µL ice-cold lysis buffer.
9. Scrape the cell lysate and nuclei off the dish with a cell scraper and transfer the lysate to a microcentrifuge tube.
10. Centrifuge lysates at 16 000 *g* at 4 °C for 10 min to spin down the nuclei. Use the supernatant directly for immunoprecipitations or transfer the supernatant to a new microcentrifuge tube, snap freeze, and store at −80 °C.

Buffers for the Pulse Chase

Wash buffer: Hank's Balanced Salt Solution (Invitrogen) or PBS with calcium and magnesium. Keep at 37 °C.

Starvation medium: cysteine- and methionine-free tissue culture medium (ICN) supplemented with 10 mM Na-HEPES (pH 7.4). Keep at 37 °C.

Pulse medium: cysteine- and methionine-free medium containing 10 mM Na-HEPES (pH 7.4), 125 μCi ^{35}S-cysteine/methionine per milliliter. Keep at 37 °C. *To manipulate protein folding, chemicals such as glycosylation inhibitors, proteasome inhibitors, and DTT can be added to the pulse medium.*

Chase medium: complete tissue culture medium for the appropriate cell line (also a 1/1 mix with serum-free medium is possible) supplemented with 10 mM Na-HEPES (pH 7.4), 5 mM cysteine, and 5 mM methionine. Keep at 37 °C. *If protein-folding kinetics is to be studied, 1 mM cycloheximide needs to be added to the chase medium to stop elongation of unfinished nascent chains; without it, the amount of labeled full-length protein may increase during the chase, even though incorporation of ^{35}S label is stopped completely. To manipulate protein folding, chemicals such as glycosylation inhibitors, proteasome inhibitors, DTT, diamide, or cross-linkers can be added to the chase medium, or ATP can be depleted.*

Stop buffer: Hank's Balanced Salt Solution (Invitrogen) or PBS with calcium and magnesium, supplemented with 20 mM alkylating agent (IAC, IAM, or NEM). Keep at 0 °C. *See Section 3.3.3.*

Lysis buffer: PBS (pH 7.4) or similar salt-containing buffer, containing 0.5% Triton X-100, 1 mM EDTA, 20 mM alkylating agent, 1 mM PMSF, and 10 μg μL^{-1} each of chymostatin, leupeptin, antipain, and pepstatin. Keep at 0 °C. *Add PMSF to the lysis buffer just before lysis. PMSF is highly unstable in water and has a half-life of only a few hours on ice. Different proteins may need the use of different protease inhibitors. The combination in the protocol is an empirically determined one that works well for proteins used in our lab. Salt concentration should be isotonic to prevent nuclei from disrupting. When noncovalent interactions are studied, other detergents may work better. Examples include CHAPS, octyl glucoside, or digitonin. When the protein associates with detergent-resistant membranes, the use of Triton X-100 and CHAPS should be avoided. Octyl glucoside is one of the detergents that will solubilize all membranes.*

Postponed Posttranslational Folding To separate translation from the folding process, e.g., to study the effect of factors that would affect translation, such as ATP depletion, oxidative folding can be postponed until after synthesis by addition of a reducing agent to the pulse medium [20]. This will prevent disulfide bond formation during the pulse. When the reducing agent is removed after the pulse, disulfide bond formation and folding can proceed. For various proteins, oxidative folding can be postponed until after synthesis without it creating a problem for folding.

1. Add DTT to the pulse medium to a concentration of 5–10 mM and pre-incubate for 5 min with DTT before the pulse. *The DTT concentration needs to be titrated for each protein, but usually 5 mM should be sufficient. Since labeling efficiency might decrease in DTT, labeling time may need to be increased. DTT may affect cellular ATP levels during long incubations, depending on the cell line. Therefore, a comparison with co-translational folding always needs to be made and ATP levels need to be measured.*

DTT Resistance When proteins fold and become more compact, this is usually reflected by resistance to reduction by DTT in vivo. Influenza hemagglutinin, for example, acquires DTT resistance when it is a completely oxidized monomer that is trimerization-competent but not yet a trimer [21].

1. Label the protein (see pulse-chase protocol) and chase for different times.
2. After the chase: perform in a parallel dish with the same chase time an additional chase of 5 min with 5 mM DTT. Compare this sample with the sample in which the protein is chased without DTT.

Diamide Resistance

1. Label the protein (see pulse-chase protocol) and chase for different times.
2. After the chase: perform in a parallel dish with the same chase time an additional chase of 5 min with 5 mM diamide. Compare this sample with the sample in which the protein is chased without diamide.

3.5.1.2 Pulse Chase in Suspension Cells

When cells do not adhere properly or when small volumes are desired, cells can be pulse labeled in solution. In this assay the different chase samples can be collected from one tube. Wash steps after the pulse and chase are not included, because the centrifugation steps would take too much time. Prior to starting the experiment it is necessary to determine:

- the minimum volume for incubating the cells during the pulse (x µL), (*This is cell line dependent.*)
- the number of chase points (y), and
- the desired sample volume (z). We used, for example, $x = 300$ µL, $y = 3$, and $z = 500$ µL.

1. Transfer suspension cells to a sterile 50-mL tube with cap. We used, for example, $\sim 10^6$ cells per time point.
2. Pellet cells at 500 g for 4 min at RT. Resuspend cells in $2y$ mL depletion medium and pellet cells again. Resuspend cells in $2y$ mL depletion medium. Incubate cells for 15 min at 37 °C in a CO_2 incubator.
3. Pellet cells at 500 g for 4 min at RT. Resuspend cells in x µL depletion medium, change to appropriate tube if necessary, and place in a water bath at 37 °C or the desired temperature for the experiment.
4. Add 50–100 µCi ^{35}S-labeled methionine and cysteine per time point and mix gently to start the pulse. Incubate for the pulse period.
5. Add $\geq yz$ µL chase medium. The total volume should be slightly more than $y \times z$ µL to allow for fluid loss due to evaporation during the experiment. Mix by gently pipetting up and down.
6. Immediately take the first sample (z µL). Transfer to microcentrifuge tube with pre-prepared z µL 2× concentrated lysis buffer on ice, mix well, and keep on ice.

7. After every chase interval, collect a sample and add to 2× concentrated lysis buffer on ice, mix well, and keep on ice.
8. Spin the lysates at 16 000 *g* for 10 min at 4 °C to pellet the nuclei. The post-nuclear lysate can be directly used for immunoprecipitations or transferred to a new microcentrifuge tube, snap frozen, and stored at −80 °C.

Semi-permeabilized Cell System (see Chapter 18) In vitro translation in the presence of semi-permeabilized cells [12] is a method with a complexity between the pulse-chase assay and the in vitro chase assay, since there is only one membrane between the protein and the experimenter, whereas there are two in the pulse-chase assay and none during the second part of the in vitro chase assay.

In the semi-permeabilized cell system, cells are treated with the detergent digitonin, which selectively permeabilizes the plasma membrane, leaving cellular organelles such as ER and Golgi complex intact. These semi-permeabilized cells (SP cells) are added to an in vitro translation system, where they act as a source of ER membranes. Only the mRNA of the protein of interest is present, which precludes the need for immunoprecipitations. This assay is especially useful when there are no antibodies available against the protein under study, for protease resistance studies, or when only the ER form of a protein is under study and ER-to-Golgi transport is undesirable.

In Vitro Chase Assay In the in vitro chase assay (Maggioni et al., manuscript submitted), a protein is pulse labeled/translated in vivo and chased in a detergent lysate. Since there are no membranes during the chase period, the direct environment of the folding protein can be manipulated. For example, ATP levels in the detergent lysate can be depleted, and chaperones and organellar cell fractions can be added.

After point 4 of the basic pulse-chase protocol (now using 10-cm dishes):

For the in vitro assay 10-cm dishes are used instead of 6-cm dishes. Therefore, all buffer volumes used in steps 1–4 of the basic pulse-chase protocol need to be multiplied by 2–2.5.

1. Wash cells twice with 4 mL ice-cold HBSS wash buffer, aspirate the buffer, and immediately lyse with 1.8 mL ice-cold lysis buffer without alkylating agent.
2. Scrape the cell lysate and nuclei off the dish with a cell scraper, transfer lysates to a microcentrifuge tube, and immediately take out 1/6 of the lysate and add NEM to this sample to a concentration of 20 mM (0 min sample in the in vitro chase assay).
3. Spin cell lysates for 10 min at 16 000 *g* at 4 °C to pellet nuclei. Transfer post-nuclear cell lysate to a new tube. The supernatant of the lysate without NEM is used in the rest of the in vitro chase assay.

After transfer to a new tube, add 5 mM GSSG and transfer the tube immediately to a water bath at 30 °C.

4. After different times of in vitro chase, take 300 μL of the lysate and transfer it

into a new tube that contains NEM to a final concentration of 20 mM and immediately incubate on ice.
5. Use the supernatant directly for immunoprecipitations or snap freeze and store at −80 °C.

3.5.2 (Co)-immunoprecipitation and Accessory Protocols

3.5.2.1 Immunoprecipitation

1. Mix 50 µL of washed protein A-Sepharose beads and the optimal amount of antibody and shake in a shaker for 60 min at 4 °C. *Optimize the incubation time for each antibody. The optimal amount of antibody is the amount that precipitates all, or at least the maximum amount, of antigen from the solution. This needs to be tested for each antibody-antigen combination by re-incubation of the supernatant from the beads-antibody-antigen incubation (see step 3 below) with antibody and beads. If the antibody has a low affinity for protein A, protein G-Sepharose beads or a bridging antibody between the primary antibody and the protein A beads, such as a goat or rabbit anti-mouse Ig, can be used. Instead of Sepharose beads, heat-killed and fixed* S. aureus *cells can be used to immobilize the antibody. Because these cells are more difficult to resuspend than Sepharose beads, spin conditions should be 5 min at 1500* g *rather than 1 min at max speed. Resuspension time will be longer and should be added to the wash time.*
2. Add 100 µL to 600 µL post-nuclear cell lysate and couple in the head-over-head rotator for at least 30 min (depending on the antibody) at 4 °C. *Test for each antibody the minimum incubation time needed (between 30 min and overnight). With one lysate, different immunoprecipitations (such as one with an antibody that recognizes all forms of the protein, a conformation-sensitive antibody, or a co-immunoprecipitation) can be done to obtain as much information as possible on the folding protein.*
3. Pellet beads by spinning 1 min at RT max, aspirate the supernatant, and use it for re-precipitation to test whether the antibody precipitated all antigen molecules in the solution (see step 1 above). Add 1 mL washing buffer and shake for at least 5 min in a shaker at RT. Repeat this washing procedure once. *Test different wash buffers with different concentrations of SDS, other detergents, combinations thereof, and salt. Also test different wash times and wash temperatures. It is not necessary to wash more than twice. Rather than increase the number of washes, conditions of the two washes should be changed. If this does not give the desired result, pre-clearing of the detergent cell lysate is the method of choice (see calnexin protocol).*
4. Pellet beads and aspirate supernatant. Add 20 µL TE to the beads, vortex to resuspend the beads, and add 20 µL 2× concentrated sample buffer and vortex again. *If an Endo H digestion is performed, add here the Endo H buffer instead of the TE. It is important to resuspend in TE before adding SDS, because addition of SDS to a pellet may induce or increase aggregation.*

5. Heat samples for 5 min at 95 °C, vortex when still hot, and pellet the beads. The supernatant is the non-reduced sample.
6. To make a reduced sample, transfer 18 µL supernatant to a new tube to which a defined drop of DTT solution has been added (final DTT concentration should be 20 mM) and vortex. Heat samples for 5 min at 95 °C. Centrifuge shortly to spin down the condensation fluid. The samples are now ready to be loaded onto an SDS-PA gel. *Addition of DTT to the bottom of the tube allows one to check whether DTT actually has been added to the sample. Re-oxidation during electrophoresis, which happens if proteins have many cysteines, is prevented by adding an excess alkylating agent, such as 100 mM NEM, to all samples before loading.*

Buffers for Immunoprecipitation

Protein A-Sepharose beads: 10% protein A-Sepharose beads in PBS or the same buffer in which the cells were lysed in, supplemented with 1/10 of the concentration of the same detergent used in the lysis buffer and 0.25% BSA. *The beads are washed twice in this solution to remove the buffer in which the Sepharose was stored. When using* S. aureus *cells, washing should be done twice as well, in the same centrifuge that will be used for the immunoprecipitation, to ensure that the same-sized particles will be pelleted during all washes.*

Wash buffer: PBS, pH 7.4, containing 0.5% Triton X-100 or 150 mM NaCl (representing some of the mildest conditions) or another buffer (such as a harsher one with SDS).

TE buffer: 10 mM Tris-HCl, pH 6.8, 1 mM EDTA.

2× concentrated sample buffer: 400 mM Tris-HCl, pH 6.8, 6% (w/v) SDS, 20% glycerol, 2 mM EDTA, 0.04% (w/v) bromophenol blue.

5× concentrated sample buffer: 1 M Tris-HCl, pH 6.8, 7.5% (w/v) SDS, 50% glycerol, 5 mM EDTA, 0.08% (w/v) bromophenol blue.

3.5.2.2 Co-precipitation with Calnexin ([30]; adapted from Ou et al. [105])

After step 7 from the pulse chase:

1. Aspirate the dish as dry as possible and add 600 µL ice-cold lysis buffer (2% CHAPS in 50 mM Na-HEPES pH 7.6 and 200 mM NaCl. *Do not add EDTA to the lysis buffer, since calcium is needed for the interaction.*
2. Scrape the cell lysate and nuclei from the dish and transfer into a microcentrifuge tube.
3. Use around 200 µL of the lysate for the co-immunoprecipitation and use a parallel amount for an immunoprecipitation using an antibody that recognizes all antigen that is present.
4. Add 0.1 mL of a 10% suspension of heat-killed and fixed *S. aureus* cells to the lysate to reduce background and rotate or shake for 30–60 min at 4 °C.

5. Pellet the fixed *S. aureus* and nuclei at max speed to remove the smallest particles and use the supernatant for the immunoprecipitation.
6. Couple the antibody to the protein A-Sepharose beads for 30 min at 4 °C in a shaker.
7. Add the pre-cleared lysate.
8. Couple at 4 °C for 1–16 h, depending on the antibody.
9. Pellet the beads by centrifugating for 2 min at 8000 *g*.
10. Wash twice with 0.5% CHAPS in 50 mM Na-HEPES pH 7.6, containing 200 mM NaCl.
11. After the last wash: continue the immunoprecipitation protocol at step 4.

3.5.2.3 **Co-immunoprecipitation with Other Chaperones**

The calnexin co-immunoprecipitation protocol can be used as a basic protocol when the interaction of a protein with another chaperone is to be studied. Since each protein-chaperone interaction is different, protocols should be optimized for each new co-immunoprecipitation. To stabilize the interaction of the molecular chaperone BiP with its substrate, adding an ATP-depleting agent to the lysis buffer is recommended, to lock the ATP cycle of the chaperone. When interactions with calcium-binding chaperones are studied, calcium chelators such as EDTA should be omitted from the lysis buffer.

3.5.2.4 **Protease Resistance**

Limited proteolysis can be used to investigate the conformation of proteins. However, most investigators often perform limited proteolysis on purified protein, which will represent only the steady-state conformation. To obtain more dynamic information on how proteins acquire their conformation during the folding process, one can combine in vivo pulse-chase analysis and immunoprecipitation, as described earlier in this chapter, with limited proteolysis. Important considerations should be made before using this technique. First, methionines and cysteines within the protein should be evenly distributed. Second, a highly specific antibody is needed to immunoprecipitate the protein of interest. Third, a mild denaturing buffer should be used for cell lysis and immunoprecipitation to prevent large conformational changes of the protein. For most proteins in our lab, we use MNT (20 mM MES, 100 mM NaCl, 30 mM Tris-HCl, pH 7.4) containing 0.5% Triton X-100 as a mild lysis buffer. It is important to omit protease inhibitors and EDTA during cell lysis. Therefore, perform the immunoprecipitation as shortly as possible to prevent protein degradation.

After the last wash of the immunoprecipitation protocol (step 3):

(Note: one protease concentration tested in a proteolysis experiment is one immunoprecipitation.)

1. Pellet the antigen-antibody-bead complexes and aspirate all wash buffer.

2. Add 10 μL MNT + 0.5% Triton X-100 to the beads and resuspend gently.
3. Add 1 μL protease from a 10× stock. Resuspend by vortexing and incubate for *exactly* 15 min on ice. Use a protease titration range (for example, 0.25, 1, 5, 25, 100, or 500 μg mL^{-1} final concentration) to investigate protease susceptibility of each protein. TPCK-trypsin, TLCK-chymotrypsin, proteinase K, and endoproteinase Glu-C V8 are suitable proteases (Sigma) for these studies.
4. After incubation, inhibit the protease by first adding 1 μL PMSF (phenylmethylsulfonyl fluoride) from a 10× stock before adding 10 μL 2× sample buffer. TPCK-trypsin is specifically inhibited by adding a fivefold excess of soybean trypsin inhibitor.
5. Heating the sample for 5 min at 95 °C will completely inactivate the protease.
6. Analyze the radio-labeled proteolytic pattern on a 12–15% SDS-PA gel and expose to film or phosphor screen.

3.5.2.5 **Endo H Resistance**

After the last wash of the immunoprecipitation protocol (step 3):

1. Pellet beads and aspirate all wash buffer from the protein A-Sepharose beads.
2. Add 15 μL 0.2% SDS in 100 mM sodium acetate, pH 5.5, and heat for 5 min at 95 °C to denature the protein.
3. Cool and add 15 μL 100-mM sodium acetate, pH 5.5, containing 2% Triton X-100 and protease inhibitors: 10 μg μL^{-1} each of chymostatin, leupeptin, antipain, and pepstatin and 1 mM PMSF. Add 0.0025 U Endo H (Roche).
4. Mix and incubate for 1.5–2 h at 37 °C. *Optimize incubation time for each protein.*
5. Spin down the fluid and add 7.5 μL 5× sample buffer and mix.
6. Heat for 5 min to 95 °C.
7. Spin down. At this moment a reducing sample can be prepared (see immunoprecipitation protocol).

3.5.2.6 **Cell Surface Expression Tested by Protease**

Arrival of a protein that followed the secretory pathway at the plasma membrane can be biochemically monitored. At the cell surface, the protein is accessible to various reagents, such as antibodies, proteases, and biotinylation agents. Below is a typical protocol for cell surface detection by proteases.

1. Wash the cells twice with 2 mL stop buffer.
2. Add 0.5 mL PBS containing 100 μg mL^{-1} trypsin or another protease and 2 mM $CaCl_2$ (if the protease needs calcium) at 4 °C to the cells.
3. Incubate for 30 min on ice. *At this step surface accessible protein either will be completely digested, or it will be cleaved specifically into a limited number of fragments.*
4. Collect fluid from cells and add 100 μg mL^{-1} soybean trypsin inhibitor, 1 mM PMSF, and 10 μg mL^{-1} each of chymostatin, leupeptin, antipain, and pepstatin (final concentrations).
5. Add to the cells 0.5 mL of 100 μg mL^{-1} soybean trypsin inhibitor, 1 mM PMSF,

and 10 μg mL^{-1} each of chymostatin, leupeptin, antipain, and pepstatin (final concentrations). Incubate on ice and repeat the incubation. *It is essential to properly inhibit the protease, because it will otherwise digest internal protein upon lysis.*

6. Lyse the cells in 600 μL lysis buffer and continue with the pulse-chase protocol at step 9. *The comparison between untreated and treated cells will show how much of the protein of interest disappeared because of the proteolysis, or the treated sample will contain a mixture of undigested (internal) and digested protein (cell surface–localized).*

3.5.3 SDS-PAGE [13]

1. Prepare 0.75-mm thick polyacrylamide separating and stacking gels. *The acrylamide percentage depends on the molecular weight of the studied protein and should position the protein just below the middle of the gel to allow maximal separation of different forms of the protein.*
2. Load 8 μL of each sample (and 3 μL of the total lysates on a separate gel to check labeling efficiency). Not using the outer lanes of the gel, load 1× sample buffer in the outside as well as empty lanes to prevent "smiling" of the bands. *When reduced and non-reduced samples are loaded in adjacent lanes in SDS-PAGE, DTT can diffuse into the non-reduced lanes. Either one or two lanes should be left open between the two samples, or an excess quencher should be added to all samples (including the non-reduced ones) just before loading. We frequently use 100 mM N-ethylmaleimide (final concentration in the sample) for this purpose.*
3. Run each gel at max speed at constant current (25 mA per gel for Hoefer minigels) until the dye front is at the bottom of the gel. *Maximum speed without overheating limits lateral diffusion and guarantees sharper bands.*
4. Stain the gel with Coomassie brilliant blue for 5 min and destain to visualize antibody bands.
5. Neutralize gels for 1–3 × 5 min. *If incubated too long in the absence of acid, bands will become diffuse. A minimum time of neutralization is needed to prevent precipitation of salicylic acid, if gels are too acidic.*
6. Treat gels with enhancer solution for 15 min. *Do not incubate longer than 15 min to prevent non-specific signal.*
7. Dry gels at 80 °C on 0.4-mm Schleicher & Schuell filter paper.
8. Expose to film at −80 °C or to a phosphor-imaging screen.

Solutions for SDS-PAGE

Coomassie stain: 0.25% (w/v) Coomassie brilliant blue in destain

Destain: 30% (v/v) methanol and 10% (v/v) acetic acid in H_2O

Neutralizer: 30% (v/v) methanol in PBS

Enhancer: 1.5 M sodium salicylate in 30% (v/v) methanol in H_2O

Various types of native gels can be used to study the conformation of proteins, oligomerization, aggregation, and the interactions between different proteins. The mobility depends on both the protein's charge and its hydrodynamic size. Blue native gels [106] are often are used for membrane proteins.

Two-dimensional SDS-PAGE

1. Load samples on a tube gel and run, or run on a slab gel with pre-stained markers on either side of the lane. *The first dimension can be a native gel or a non-reducing SDS-PA gel, an IEF gel, or virtually any other kind.*
2. Extract tube gel from capillary, or cut the lane of interest out of the first dimension slab gel.
3. Boil the tube or strip for 10 min in reducing sample buffer.
4. Place the tube or strip on an SDS-polyacrylamide slab gel.
5. A reduced sample can be run in a separate lane close to the edge of the slab gel.
6. Run in the second dimension as a regular slab gel.

Acknowledgements

We thank Claudia Maggioni for sharing the in vitro chase assay protocol and for assistance with the figures, and we thank other members of the Braakman lab, especially Ari Ora, Aafke Land, and Nicole Hafkemeijer, for critical reading of the manuscript.

References

1 Anfinsen, C. B. (1973). Principles that govern the folding of protein chains. *Science* **181**, 223–230.
2 Bergman, L. W. & Kuehl, W. M. (1979). Formation of an intrachain disulfide bond on nascent immunoglobulin light chains. *J Biol Chem* **254**, 8869–8876.
3 Chen, W., Helenius, J., Braakman, I. & Helenius, A. (1995). Cotranslational folding and calnexin binding during glycoprotein synthesis. *Proc Natl Acad Sci USA* **92**, 6229–6233.
4 Fulton, A. B. (1982). How crowded is the cytoplasm? *Cell* **30**, 345–347.
5 Minton, A. P. (1983). The effect of volume occupancy upon the thermodynamic activity of proteins: some biochemical consequences. *Mol Cell Biochem* **55**, 119–140.
6 Ellis, R. J. (2001). Macromolecular crowding: obvious but underappreciated. *Trends Biochem Sci* **26**, 597–604.
7 Hammond, C. & Helenius, A. (1995). Quality control in the secretory pathway. *Curr Opin Cell Biol* **7**, 523–529.
8 Hartl, F. U. & Hayer-Hartl, M. (2002). Molecular chaperones in the cytosol: from nascent chain to folded protein. *Science* **295**, 1852–1858.
9 Ellgaard, L. & Helenius, A. (2003). Quality control in the endoplasmic reticulum. *Nat Rev Mol Cell Biol* **4**, 181–191.
10 Gething, M. J. & Sambrook, J. (1992). Protein folding in the cell. *Nature* **355**, 33–45.
11 Braakman, I., Hoover-Litty, H.,

Wagner, K. R. & Helenius, A. (1991). Folding of influenza hemagglutinin in the endoplasmic reticulum. *J Cell Biol* **114**, 401–411.

12 Wilson, R., Allen, A. J., Oliver, J., Brookman, J. L., High, S. & Bulleid, N. J. (1995). The translocation, folding, assembly and redox-dependent degradation of secretory and membrane proteins in semi-permeabilized mammalian cells. *Biochem J* **307**, 679–687.

13 Laemmli, U. K. (1970). Cleavage of structural proteins during the assembly of the head of bacteriophage T4. *Nature* **227**, 680–685.

14 Porter, R. R. (1959). The hydrolysis of rabbit y-globulin and antibodies with crystalline papain. *Biochem J* **73**, 119–126.

15 Grassetti, D. R. & Murray, J. F., Jr. (1967). Determination of sulfhydryl groups with 2,2′- or 4,4′-dithiodipyridine. *Arch Biochem Biophys* **119**, 41–49.

16 Ostergaard, H., Henriksen, A., Hansen, F. G. & Winther, J. R. (2001). Shedding light on disulfide bond formation: engineering a redox switch in green fluorescent protein. *EMBO J* **20**, 5853–5862.

17 Kosower, E. M. & Kosower, N. S. (1969). Lest I forget thee, glutathione. *Nature* **224**, 117–120.

18 Kosower, N. S. & Kosower, E. M. (1995). Diamide: an oxidant probe for thiols. *Methods Enzymol* **251**, 123–133.

19 Tortorella, D., Story, C. M., Huppa, J. B., Wiertz, E. J., Jones, T. R., Bacik, I., Bennink, J. R., Yewdell, J. W. & Ploegh, H. L. (1998). Dislocation of type I membrane proteins from the ER to the cytosol is sensitive to changes in redox potential. *J Cell Biol* **142**, 365–376.

20 Braakman, I., Helenius, J. & Helenius, A. (1992). Manipulating disulfide bond formation and protein folding in the endoplasmic reticulum. *EMBO J* **11**, 1717–1722.

21 Tatu, U., Braakman, I. & Helenius, A. (1993). Membrane glycoprotein folding, oligomerization and intracellular transport: effects of dithiothreitol in living cells. *EMBO J* **12**, 2151–2157.

22 de Silva, A., Braakman, I. & Helenius, A. (1993). Posttranslational folding of vesicular stomatitis virus G protein in the ER: involvement of noncovalent and covalent complexes. *J Cell Biol* **120**, 647–655.

23 Lodish, H. F., Kong, N. & Wikstrom, L. (1992). Calcium is required for folding of newly made subunits of the asialoglycoprotein receptor within the endoplasmic reticulum. *J Biol Chem* **267**, 12753–12760.

24 Ellis, R. J. (1990). The molecular chaperone concept. *Semin Cell Biol* **1**, 1–9.

25 Hartl, F. U. & Martin, J. (1995). Molecular chaperones in cellular protein folding. *Curr Opin Struct Biol* **5**, 92–102.

26 Jaenicke, R. & Lilie, H. (2000). Folding and association of oligomeric and multimeric proteins. *Adv Protein Chem* **53**, 329–401.

27 Haas, I. G. & Wabl, M. (1983). Immunoglobulin heavy chain binding protein. *Nature* **306**, 387–389.

28 Flynn, G. C., Pohl, J., Flocco, M. T. & Rothman, J. E. (1991). Peptide-binding specificity of the molecular chaperone BiP. *Nature* **353**, 726–730.

29 Blond-Elguindi, S., Cwirla, S. E., Dower, W. J., Lipshutz, R. J., Sprang, S. R., Sambrook, J. F. & Gething, M. J. (1993). Affinity panning of a library of peptides displayed on bacteriophages reveals the binding specificity of BiP. *Cell* **75**, 717–728.

30 Hammond, C., Braakman, I. & Helenius, A. (1994). Role of N-linked oligosaccharide recognition, glucose trimming, and calnexin in glycoprotein folding and quality control. *Proc Natl Acad Sci USA* **91**, 913–917.

31 Kassenbrock, C. K. & Kelly, R. B. (1989). Interaction of heavy chain binding protein (BiP/GRP78) with adenine nucleotides. *EMBO J* **8**, 1461–1467.

32 Wei, J. & Hendershot, L. M. (1995).

Characterization of the nucleotide binding properties and ATPase activity of recombinant hamster BiP purified from bacteria. *J Biol Chem* **270**, 26670–26676.

33 Molinari, M. & Helenius, A. (2000). Chaperone selection during glycoprotein translocation into the endoplasmic reticulum. *Science* **288**, 331–333.

34 Swanton, E., High, S. & Woodman, P. (2003). Role of calnexin in the glycan-independent quality control of proteolipid protein. *EMBO J* **22**, 2948–2958.

35 Ihara, Y., Cohen-Doyle, M. F., Saito, Y. & Williams, D. B. (1999). Calnexin discriminates between protein conformational states and functions as a molecular chaperone in vitro. *Mol Cell* **4**, 331–341.

36 Bulleid, N. J. & Freedman, R. B. (1988). Defective co-translational formation of disulphide bonds in protein disulphide-isomerase-deficient microsomes. *Nature* **335**, 649–651.

37 Molinari, M. & Helenius, A. (1999). Glycoproteins form mixed disulphides with oxidoreductases during folding in living cells. *Nature* **402**, 90–93.

38 Oliver, J. D., van der Wal, F. J., Bulleid, N. J. & High, S. (1997). Interaction of the thiol-dependent reductase ERp57 with nascent glycoproteins. *Science* **275**, 86–88.

39 Fischer, G., Bang, H. & Mech, C. (1984). [Determination of enzymatic catalysis for the cis-trans-isomerization of peptide binding in proline-containing peptides]. *Biomed Biochim Acta* **43**, 1101–1111.

40 Schmid, F. X., Mayr, L. M., Mucke, M. & Schonbrunner, E. R. (1993). Prolyl isomerases: role in protein folding. *Adv Protein Chem* **44**, 25–66.

41 Lang, K., Schmid, F. X. & Fischer, G. (1987). Catalysis of protein folding by prolyl isomerase. *Nature* **329**, 268–270.

42 Steinmann, B., Bruckner, P. & Superti-Furga, A. (1991). Cyclosporin A slows collagen triple-helix formation in vivo: indirect evidence for a physiologic role of peptidyl-prolyl cis-trans-isomerase. *J Biol Chem* **266**, 1299–1303.

43 Lodish, H. F. & Kong, N. (1991). Cyclosporin A inhibits an initial step in folding of transferrin within the endoplasmic reticulum. *J Biol Chem* **266**, 14835–14838.

44 Loo, T. W. & Clarke, D. M. (1994). Prolonged association of temperature-sensitive mutants of human P-glycoprotein with calnexin during biogenesis. *J Biol Chem* **269**, 28683–28689.

45 Pind, S., Riordan, J. R. & Williams, D. B. (1994). Participation of the endoplasmic reticulum chaperone calnexin (p88, IP90) in the biogenesis of the cystic fibrosis transmembrane conductance regulator. *J Biol Chem* **269**, 12784–12788.

46 Loo, T. W. & Clarke, D. M. (1995). P-glycoprotein. Associations between domains and between domains and molecular chaperones. *J Biol Chem* **270**, 21839–21844.

47 Yang, Y., Janich, S., Cohn, J. A. & Wilson, J. M. (1993). The common variant of cystic fibrosis transmembrane conductance regulator is recognized by hsp70 and degraded in a pre-Golgi nonlysosomal compartment. *Proc Natl Acad Sci USA* **90**, 9480–9484.

48 Meacham, G. C., Patterson, C., Zhang, W., Younger, J. M. & Cyr, D. M. (2001). The Hsc70 co-chaperone CHIP targets immature CFTR for proteasomal degradation. *Nat Cell Biol* **3**, 100–105.

49 Loo, M. A., Jensen, T. J., Cui, L., Hou, Y., Chang, X. B. & Riordan, J. R. (1998). Perturbation of Hsp90 interaction with nascent CFTR prevents its maturation and accelerates its degradation by the proteasome. *EMBO J* **17**, 6879–6887.

50 Truscott, K. N., Brandner, K. & Pfanner, N. (2003). Mechanisms of protein import into mitochondria. *Curr Biol* **13**, R326–337.

51 Soll, J. (2002). Protein import into

chloroplasts. *Curr Opin Plant Biol* **5**, 529–535.

52 Walter, P. & Blobel, G. (1980). Purification of a membrane-associated protein complex required for protein translocation across the endoplasmic reticulum. *Proc Natl Acad Sci USA* **77**, 7112–7116.

53 Li, Y., Luo, L., Thomas, D. Y. & Kang, C. Y. (1994). Control of expression, glycosylation, and secretion of HIV-1 gp120 by homologous and heterologous signal sequences. *Virology* **204**, 266–278.

54 Rehm, A., Stern, P., Ploegh, H. L. & Tortorella, D. (2001). Signal peptide cleavage of a type I membrane protein, HCMV US11, is dependent on its membrane anchor. *EMBO J* **20**, 1573–1582.

55 Josefsson, L. G. & Randall, L. L. (1983). Analysis of cotranslational proteolytic processing of nascent chains using two-dimensional gel electrophoresis. *Methods Enzymol* **97**, 77–85.

56 Land, A., Zonneveld, D. & Braakman, I. (2003). Folding of HIV-1 envelope glycoprotein involves extensive isomerization of disulfide bonds and conformation-dependent leader peptide cleavage. *FASEB J* **17**, 1058–1067.

57 Li, Y., Bergeron, J. J., Luo, L., Ou, W. J., Thomas, D. Y. & Kang, C. Y. (1996). Effects of inefficient cleavage of the signal sequence of HIV-1 gp 120 on its association with calnexin, folding, and intracellular transport. *Proc Natl Acad Sci USA* **93**, 9606–9611.

58 Gavel, Y. & von Heijne, G. (1990). Sequence differences between glycosylated and non-glycosylated Asn-X-Thr/Ser acceptor sites: implications for protein engineering. *Protein Eng* **3**, 433–442.

59 Sousa, M. C., Ferrero-Garcia, M. A. & Parodi, A. J. (1992). Recognition of the oligosaccharide and protein moieties of glycoproteins by the UDP-Glc:glycoprotein glucosyltransferase. *Biochemistry* **31**, 97–105.

60 Trombetta, S. E. & Parodi, A. J. (1992). Purification to apparent homogeneity and partial characterization of rat liver UDP-glucose:glycoprotein glucosyltransferase. *J Biol Chem* **267**, 9236–9240.

61 Ritter, C. & Helenius, A. (2000). Recognition of local glycoprotein misfolding by the ER folding sensor UDP-glucose:glycoprotein glucosyltransferase. *Nat Struct Biol* **7**, 278–280.

62 Hwang, C., Sinskey, A. J. & Lodish, H. F. (1992). Oxidized redox state of glutathione in the endoplasmic reticulum. *Science* **257**, 1496–1502.

63 Tu, B. P., Ho-Schleyer, S. C., Travers, K. J. & Weissman, J. S. (2000). Biochemical basis of oxidative protein folding in the endoplasmic reticulum. *Science* **290**, 1571–4.

64 Frand, A. R. & Kaiser, C. A. (1998). The ERO1 gene of yeast is required for oxidation of protein dithiols in the endoplasmic reticulum. *Mol Cell* **1**, 161–170.

65 Pollard, M. G., Travers, K. J. & Weissman, J. S. (1998). Ero1p: a novel and ubiquitous protein with an essential role in oxidative protein folding in the endoplasmic reticulum. *Mol Cell* **1**, 171–182.

66 Cabibbo, A., Pagani, M., Fabbri, M., Rocchi, M., Farmery, M. R., Bulleid, N. J. & Sitia, R. (2000). ERO1-L, a human protein that favors disulfide bond formation in the endoplasmic reticulum. *J Biol Chem* **275**, 4827–4833.

67 Pagani, M., Fabbri, M., Benedetti, C., Fassio, A., Pilati, S., Bulleid, N. J., Cabibbo, A. & Sitia, R. (2000). Endoplasmic reticulum oxidoreductin 1-lbeta (ERO1-Lbeta), a human gene induced in the course of the unfolded protein response. *J Biol Chem* **275**, 23685–23692.

68 Frand, A. R. & Kaiser, C. A. (1999). Ero1p oxidizes protein disulfide isomerase in a pathway for disulfide bond formation in the endoplasmic reticulum. *Mol Cell* **4**, 469–477.

69 Sevier, C. S., Cuozzo, J. W., Vala, A., Aslund, F. & Kaiser, C. A. (2001). A flavoprotein oxidase defines a new endoplasmic reticulum pathway for biosynthetic disulphide bond formation. *Nat Cell Biol* **3**, 874–882.

70 Tu, B. P. & Weissman, J. S. (2004). Oxidative protein folding in eukaryotes: mechanisms and consequences. *J Cell Biol* **164**, 341–346.

71 Creighton, T. E. (1978). Experimental studies of protein folding and unfolding. *Prog Biophys Mol Biol* **33**, 231–297.

72 Creighton, T. E. (1990). Disulphide bonds between cysteine residues. In *Protein structure. A practical approach*. (Creighton, T. E., ed.), pp. 155–168. IRL Press, Oxford.

73 Sommer, T. & Wolf, D. H. (1997). Endoplasmic reticulum degradation: reverse protein flow of no return. *FASEB J* **11**, 1227–1233.

74 Hosokawa, N., Wada, I., Hasegawa, K., Yorihuzi, T., Tremblay, L. O., Herscovics, A. & Nagata, K. (2001). A novel ER alpha-mannosidase-like protein accelerates ER-associated degradation. *EMBO Rep* **2**, 415–422.

75 Jakob, C. A., Bodmer, D., Spirig, U., Battig, P., Marcil, A., Dignard, D., Bergeron, J. J., Thomas, D. Y. & Aebi, M. (2001). Htm1p, a mannosidase-like protein, is involved in glycoprotein degradation in yeast. *EMBO Rep* **2**, 423–430.

76 Oda, Y., Hosokawa, N., Wada, I. & Nagata, K. (2003). EDEM as an acceptor of terminally misfolded glycoproteins released from calnexin. *Science* **299**, 1394–1397.

77 Molinari, M., Calanca, V., Galli, C., Lucca, P. & Paganetti, P. (2003). Role of EDEM in the release of misfolded glycoproteins from the calnexin cycle. *Science* **299**, 1397–1400.

78 Cummings, R. D., Kornfeld, S., Schneider, W. J., Hobgood, K. K., Tolleshaug, H., Brown, M. S. & Goldstein, J. L. (1983). Biosynthesis of N- and O-linked oligosaccharides of the low density lipoprotein receptor. *J Biol Chem* **258**, 15261–15273.

79 Leonard, C. K., Spellman, M. W., Riddle, L., Harris, R. J., Thomas, J. N. & Gregory, T. J. (1990). Assignment of intrachain disulfide bonds and characterization of potential glycosylation sites of the type 1 recombinant human immunodeficiency virus envelope glycoprotein (gp120) expressed in Chinese hamster ovary cells. *J Biol Chem* **265**, 10373–10382.

80 Pelletier, L., Jokitalo, E. and Warren, G. (2000). The effect of Golgi depletion on exocytic transport. *Nature Cell Biology* **2**, 840–846.

81 Stevens, T., Esmon, B. & Schekman, R. (1982). Early stages in the yeast secretory pathway are required for transport of carboxypeptidase Y to the vacuole. *Cell* **30**, 439–448.

82 Campbell, K. P., MacLennan, D. H., Jorgensen, A. O. & Mintzer, M. C. (1983). Purification and characterization of calsequestrin from canine cardiac sarcoplasmic reticulum and identification of the 53,000 dalton glycoprotein. *J Biol Chem* **258**, 1197–1204.

83 Lodish, H. F. & Kong, N. (1990). Perturbation of cellular calcium blocks exit of secretory proteins from the rough endoplasmic reticulum. *J Biol Chem* **265**, 10893–10899.

84 Klenk, H. D., Garten, W. & Rott, R. (1984). Inhibition of proteolytic cleavage of the hemagglutinin of influenza virus by the calcium-specific ionophore A23187. *EMBO J* **3**, 2911–2915.

85 Thastrup, O., Cullen, P. J., Drobak, B. K., Hanley, M. R. & Dawson, A. P. (1990). Thapsigargin, a tumor promoter, discharges intracellular Ca2+ stores by specific inhibition of the endoplasmic reticulum Ca2(+)-ATPase. *Proc Natl Acad Sci USA* **87**, 2466–2470.

86 Lytton, J., Westlin, M. & Hanley, M. R. (1991). Thapsigargin inhibits the sarcoplasmic or endoplasmic reticulum Ca-ATPase family of calcium pumps. *J Biol Chem* **266**, 17067–17071.

87 Braakman, I., Helenius, J. & Helenius, A. (1992). Role of ATP and disulphide bonds during protein folding in the endoplasmic reticulum. *Nature* **356**, 260–262.

88 Datema, R. & Schwarz, R. T. (1979). Interference with glycosylation of glycoproteins. Inhibition of formation of lipid-linked oligosaccharides in vivo. *Biochem J* **184**, 113–123.

89 Dorner, A. J., Wasley, L. C. & Kaufman, R. J. (1990). Protein dissociation from GRP78 and secretion are blocked by depletion of cellular ATP levels. *Proc Natl Acad Sci USA* **87**, 7429–7432.

90 Lundin, A. & Thore, A. (1975). Analytical information obtainable by evaluation of the time course of firefly bioluminescence in the assay of ATP. *Anal Biochem* **66**, 47–63.

91 Joshi, S. & Burrows, R. (1990). ATP synthase complex from bovine heart mitochondria. Subunit arrangement as revealed by nearest neighbor analysis and susceptibility to trypsin. *J Biol Chem* **265**, 14518–14525.

92 Chen, L. L., Rosa, J. J., Turner, S. & Pepinsky, R. B. (1991). Production of multimeric forms of CD4 through a sugar-based cross-linking strategy. *J Biol Chem* **266**, 18237–18243.

93 Oliver, J. D., Roderick, H. L., Llewellyn, D. H. & High, S. (1999). ERp57 functions as a subunit of specific complexes formed with the ER lectins calreticulin and calnexin. *Mol Biol Cell* **10**, 2573–2582.

94 Takatsuki, A., Arima, K. & Tamura, G. (1971). Tunicamycin, a new antibiotic. I. Isolation and characterization of tunicamycin. *J Antibiot (Tokyo)* **24**, 215–223.

95 Patil, C. & Walter, P. (2001). Intracellular signaling from the endoplasmic reticulum to the nucleus: the unfolded protein response in yeast and mammals. *Curr Opin Cell Biol* **13**, 349–355.

96 Chang, X. B., Hou, Y. X., Jensen, T. J. & Riordan, J. R. (1994). Mapping of cystic fibrosis transmembrane conductance regulator membrane topology by glycosylation site insertion. *J Biol Chem* **269**, 18572–18575.

97 Dorner, A. J., Wasley, L. C., Raney, P., Haugejorden, S., Green, M. & Kaufman, R. J. (1990). The stress response in Chinese hamster ovary cells. Regulation of ERp72 and protein disulfide isomerase expression and secretion. *J Biol Chem* **265**, 22029–22034.

98 Rye, H. S., Burston, S. G., Fenton, W. A., Beechem, J. M., Xu, Z., Sigler, P. B. & Horwich, A. L. (1997). Distinct actions of cis and trans ATP within the double ring of the chaperonin GroEL. *Nature* **388**, 792–798.

99 Hendershot, L., Wei, J., Gaut, J., Melnick, J., Aviel, S. & Argon, Y. (1996). Inhibition of immunoglobulin folding and secretion by dominant negative BiP ATPase mutants. *Proc Natl Acad Sci USA* **93**, 5269–5274.

100 Stanley, P., Sallustio, S., Krag, S. S. & Dunn, B. (1990). Lectin-resistant CHO cells: selection of seven new mutants resistant to ricin. *Somat Cell Mol Genet* **16**, 211–223.

101 Ray, M. K., Yang, J., Sundaram, S. & Stanley, P. (1991). A novel glycosylation phenotype expressed by Lec23, a Chinese hamster ovary mutant deficient in alpha-glucosidase I. *J Biol Chem* **266**, 22818–22825.

102 Reitman, M. L., Trowbridge, I. S. & Kornfeld, S. (1982). A lectin-resistant mouse lymphoma cell line is deficient in glucosidase II, a glycoprotein-processing enzyme. *J Biol Chem* **257**, 10357–10363.

103 Howell, D. N., Andreotti, P. E., Dawson, J. R. & Cresswell, P. (1985). Natural killing target antigens as inducers of interferon: studies with an immunoselected, natural killing-resistant human T lymphoblastoid cell line. *J Immunol* **134**, 971–976.

104 Fire, A., Xu, S., Montgomery, M. K., Kostas, S. A., Driver, S. E. & Mello, C. C. (1998). Potent and specific

genetic interference by double-stranded RNA in Caenorhabditis elegans. *Nature* **391**, 806–811.

105 Ou, W. J., Cameron, P. H., Thomas, D. Y. & Bergeron, J. J. (1993). Association of folding intermediates of glycoproteins with calnexin during protein maturation. *Nature* **364**, 771–776.

106 Schagger, H. & von Jagow, G. (1991). Blue native electrophoresis for isolation of membrane protein complexes in enzymatically active form. *Anal Biochem* **199**, 223–231.

4
Characterization of ATPase Cycles of Molecular Chaperones by Fluorescence and Transient Kinetic Methods

Sandra Schlee and Jochen Reinstein

4.1
Introduction

4.1.1
Characterization of ATPase Cycles of Energy-transducing Systems

ATP has long been known to be involved in many important cellular processes such as energy transduction in molecular motors, ion transport and signal transmission, topological processing of nucleic acids and the fidelity of protein synthesis. In spite of the diverse functions of ATPases, their mechanism includes some universal steps: the specific recognition and binding of the nucleotide, a conformational change induced by nucleotide binding, phosphoryl transfer (chemical reaction), adjustment of the conformation to the product state, and the release of products, which is accompanied by the regeneration of the initial state of the enzyme.

Although ATPases in principle employ the same reaction steps, they have to cope with entirely different tasks. Therefore, the consequence of a single reaction step on a molecular level depends on the respective system. The ATP state of DnaK, for example, represents a form that rapidly traps and releases potential substrate proteins [1, 2]. In the context of molecular motor proteins, ATP binding causes the forward movement of conventional kinesin (power stroke), but ATP binding to myosin, on the other hand, leads to dissociation of myosin from actin and is accompanied by the recovery stroke of its lever arm [3].

With some exceptions, an exact definition of the coupling between ATP hydrolysis and enzymatic action is still missing for many of the systems. History has revealed repeatedly that mechanisms remain a matter of speculation until equilibrium constants and reaction rates of all relevant intermediates (functional states) have been identified. In addition, the stability of enzyme-bound nucleotide as well as the velocity of product release represent molecular timers that are carefully regulated by accessory proteins in many ATPases. Determination of kinetics and measurements of force and motion of single molecules are therefore essential for a comprehensive understanding of the respective enzymatic mechanism.

Protein Folding Handbook. Part II. Edited by J. Buchner and T. Kiefhaber

ISBN: 3-527-30784-2

This review summarizes various aspects of fluorescent nucleotide analogues that were used to determine the ATPase cycles of the molecular chaperones DnaK, Hsp90, and ClpB and their regulation by accessory co-chaperones. Experimental protocols and conceptual considerations regarding nucleotide-binding and ATPase reactions of these chaperone systems can be found in the Section 4.3 of this review. The particular details of roles and properties of DnaK/Hsc70 or Hsp90 are not described here since they are well covered by other chapters in this volume.

4.1.2 The Use of Fluorescent Nucleotide Analogues

4.1.2.1 Fluorescent Modifications of Nucleotides

Numerous ATP analogues have been synthesized to report on the action of ATP in biosystems by means of a spectroscopic signal (absorption, fluorescence, and EPR and NMR probes) [4, 5]. Since a comprehensive intrinsic tryptophan fluorescence signal for nucleotide binding is rarely available, the use of fluorescent nucleotide analogues to study nucleotide-binding proteins prevails. Fluorescent nucleotide analogues combine the localization to a defined position with the inherent high sensitivity of the method: fluorophores with high quantum yields (i.e., >0.1) can be readily detected at submicromolar concentrations. Fluorescence can provide information about the size of proteins and structural features of the nucleotide-binding site and allows quantification of the kinetic and equilibrium constants describing the system. The intrinsic fluorescence of the common nucleotides, at ambient temperatures and neutral pH, is far too low (quantum yields on the order of 10^{-4}) to be of general use in the investigation of nucleotide-binding proteins, especially since the furthest reaching absorption maxima of nucleotides are near 260 nm, which overlaps with intrinsic protein absorption. To improve the utility of nucleotides as fluorescent probes, modifications have been introduced to different positions of the nucleotide moiety: the adenosine ring, the ribose groups, and the phosphate moiety [4].

Among the most conservative changes is the substitution of an adenosine with a fluorescent formycin or aminopurine ring (Figure 4.1). These analogues have been used to study the ATPase kinetics of $(Na^+ + K^+)$-ATPase and myosin [6–8]. It was shown that C8-MABA-ADP, with a substitution in the 8 position of adenine, was a useful probe for the nucleotide-binding site of the molecular chaperone DnaK [9–11]. However, one limitation is that the substitutions tend to stabilize the base in the unusual *syn* conformation rather than in the extended *anti* conformation of unmodified nucleotides. As a consequence, binding parameters, specifically kinetic constants, may be altered.

Another fluorescent analogue, etheno-ATP (ε-ATP), includes the addition of an aromatic ring to the adenine moiety [12]. This modification and the addition of different aromatic rings result in bulky fluorophores that are not readily tolerated by many nucleotide-binding sites.

Modifications that do not alter the purine ring systems offer an alternative approach to fluorescent nucleotide analogues. For example, an ATP analogue with

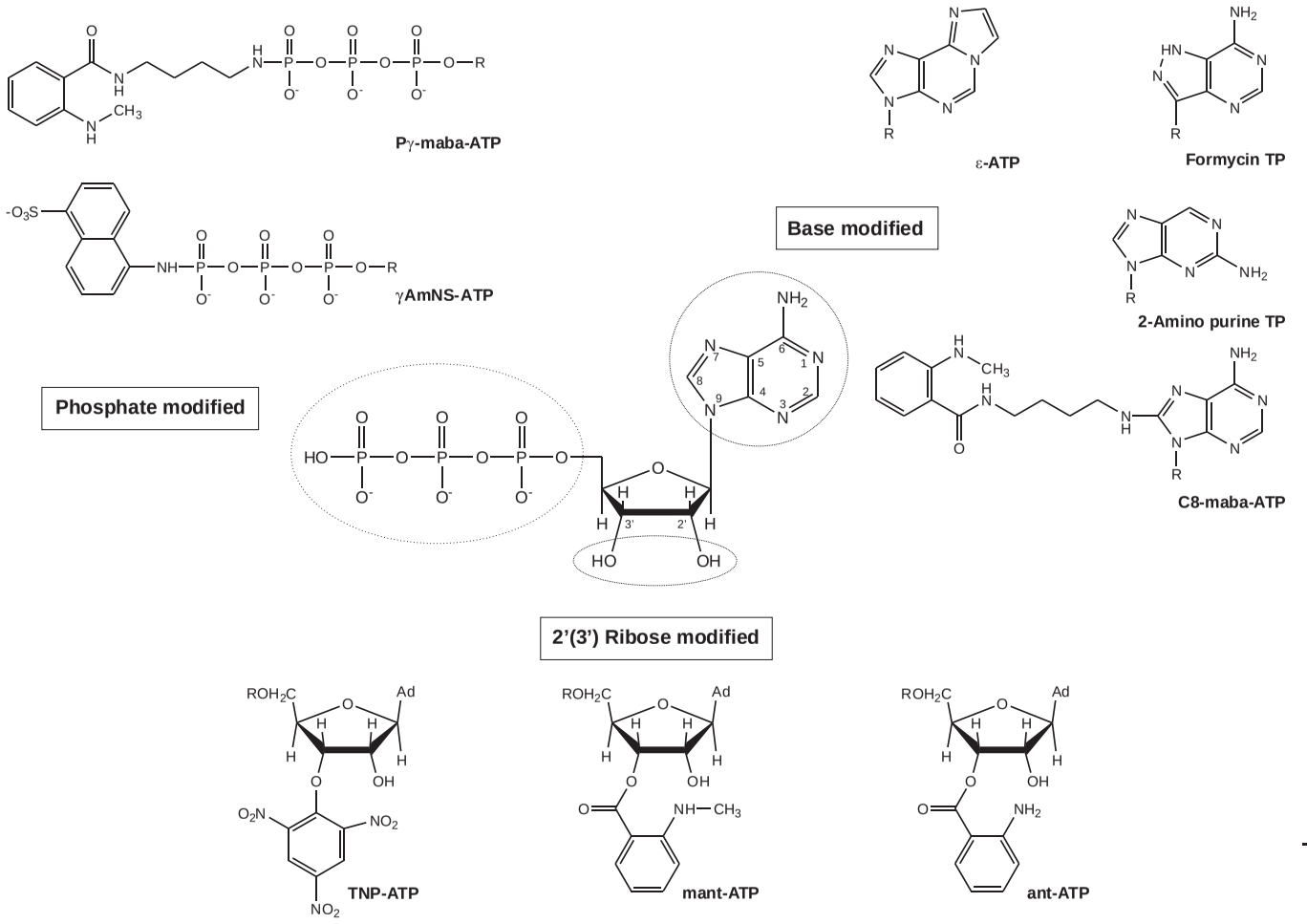

Fig. 4.1. Fluorescent nucleotide analogues. The structures of fluorescent nucleotide derivatives mentioned in the text are shown and derivatives are grouped according to the position of modifications.

altered phosphoryl structure, namely, adenosine-5′-triphospho-γ-1-(5-sulfonicacid)-naphtylamine (γAmNS-ATP), which is a good substrate for *E.coli* RNA polymerase, has been described [13]. By coupling a fluorescent *N*-methylanthraniloyl-group to the phosphate moiety of nucleotides via a butyl linker, nucleotide analogues were obtained that allow the direct determination of binding constants. (P_γ)MABA-ATP (adenosine-5′-triphospho-γ-(*N*′-methylanthraniloyl-aminobutyl)-phosphoamidate) was used for the kinetic characterization of the ATPase cycle of the molecular chaperone Hsp90 [14]. The fluorescent CDP analogue (P_β)MABA-CDP proved to be a specific probe for the NMP-binding site of UMP/CMP kinase [15].

In many cases modification of the ribose moiety of nucleotides offers a satisfactory approach in that the resultant analogues closely mimic the behavior of their parent nucleotides. The advantage of such ribose modification can be understood by examination of the structures of nucleoside 5′-triphosphatases such as p21ras [16], in which case the 2′,3′-hydroxyl groups of the nucleotide project out of the binding domain.

Among the first ribose-modified nucleotides was 2′,3′-O-(2,4,6-trinitrocyclohexadienylidene) adenosine 5′-triphosphate (TNP-ATP), introduced by Hiratsuka and Uchida [17]. Ribose-modified analogues used extensively in studies of nucleoside 5′-triphosphatases are the 2′(3′)-*O*-anthraniloyl (Ant) and 2′(3′)-*O*-methylanthraniloyl (MANT) derivatives of adenine [18–20]. The motivations for this choice of fluorophores were their relatively small size, which implies that perturbation of binding properties would be minimal, and the fact that the fluorescence properties of these probes are environmentally sensitive. MANT-ADP has been applied, among others, to investigate the ATPase cycle of ClpB [21, 22].

It has to be kept in mind that one complication of derivatizing the ribose hydroxyls is that a mixture of 2′ and 3′ isomers will be generated, which may differ in their fluorescent and binding capacities. One way to avoid the complication of mixed isomers is to use nucleotide derivatives based on 2′ deoxyribose.

4.1.2.2 How to Find a Suitable Analogue for a Specific Protein

ATP-utilizing systems vary enormously in their specificity, with the consequence that what acts as a good analogue in one case may be a very poor probe in another case. Without structural information about the nucleotide-protein complex, it is very difficult to accurately predict the effectiveness of a fluorescent nucleotide analogue in a novel biological system. To facilitate the screening of potential candidates, use can be made of the binding of ATPases to ATP-agarose. ATP- and ADP-agaroses are available with their ATP moiety coupled chemically to the N6 or C8 position of the adenine ring or the ribose hydroxyls via linkers of variable length (Table 4.1). If binding of an ATPase to a specific kind of ATP-agarose is observed, chances are high that fluorescent nucleotide analogues, modified at the according position, represent specific probes for the respective protein.

A good indicator for the suitability of a fluorescent derivative as substrate for a specific system is the accordance of the binding parameters (K_d, k_{on}, k_{off}) [23] and kinetic parameters (e.g., K_m, V_{max}) of the ATPase reaction of the fluorescent derivative and the unmodified nucleotide. In addition, the modified nucleotide should support the enzymatic activity of a protein equally to the unmodified nucleotide.

Tab. 4.1. Commercially available AXP matrices for affinity chromatography with ATPases.

Matrix	*Nucleotide*	*Matrix attachment*	*Matrix spacer*
Agarose	5′ATP/ADP/AMP	N6	11 atoms
Agarose	5′AMP	N6	8 atoms
Agarose	5′ATP/AMP	C8	9 atoms
Agarose	5′ATP/AMP	Ribose hydroxyl	11 atoms
Agarose	5′ATP	Ribose hydroxyl	22 atoms
Agarose	2′AMP	C8	9 atoms
Agarose	2′5′ADP	N6	8 atoms
Agarose	3′5′ADP	N6	8 atoms
Sepharose	2′5′ADP	N6	8 atoms
Sepharose	5′AMP	N6	8 atoms

4.2 Characterization of ATPase Cycles of Molecular Chaperones

4.2.1 Biased View

The following description of the ATPase cycles of DnaK, Hsp90, and ClpB systems certainly does not claim to give a comprehensive overview of the many roles and aspects of these chaperones. For this purpose, other excellent reviews in this book and outside, as mentioned in the individual chapters, should be referred to. We are also aware that the selection of results and methods here is highly biased towards fluorescence, nucleotide analogues, and related methods, but we feel that the reader may benefit more from a description of the various aspects of these techniques than from a (bound-to-fail) attempt to cover all conceivable approaches.

4.2.2 The ATPase Cycle of DnaK

The ATPase cycles of DnaK and its eukaryotic ortholog Hsc70 are well characterized from a variety of methods at this point. Comprehensive overviews may be found in this volume and in other reviews (e.g., Refs. [24–27]).

Where applicable, references to particular aspects concerning ATPase activity or nucleotide binding are covered in Section 4.3.

4.2.3 The ATPase Cycle of the Chaperone Hsp90

Hsp90 has a central role in communicating numerous folding as well as other processes in the cell [28–32]. Despite great interest in its molecular mechanism, the involvement of ATP in its function remained a matter of debate for an extended time period. It was reported by Csermely and co-workers that Hsp90 has an ATP-

binding site and autophosphorylation activity that is dependent on catalytic Mg^{2+} and stimulated by Ca^{2+} [33]. ATP-binding studies showed similar dependencies on these cations and were based on affinity labeling with azido-ATP and the ability of Hsp90 to bind to ATP-agarose.

Apparent ATPase activity of Hsp90 was also reported by other groups [34, 35], but considering the low enzymatic activity involved, it was questionable whether the activities observed were not the consequences of minor impurities, e.g., protein kinases that constitute one of the substrates for Hsp90 and may be dragged along the purification process.

Further studies observed the dependence of circular dichroism and Fourier infrared spectra of Hsp90 as a function of ATP concentration. Here ATP was shown to increase the content of β-plated sheet structures and increased interchain interactions. Also, a decrease in intrinsic tryptophan fluorescence and susceptibility to tryptic digestion were seen in the presence of ATP [36]. The conditions necessary to achieve these observed effects, however, still raised some concerns about specific binding of ATP to Hsp90. In a comparative study of highly purified Hsp90 with Hsc70 [37], Hsp90 failed to show any significant binding to immobilized ATP (ATP-agarose) or three different fluorescent nucleotide analogues, namely, 2′(3′)-*O*-(*N*-methylanthraniloyl)-adenosine 5′-diphosphate (MANT-ADP), N^8-(4-*N*′-methylanthraniloylaminobutyl)-8-aminoadenosine 5′-diphosphate (MABA-ADP), or 1,N^6-ethenoadenosine diphosphate (see also Figure 4.1). A subsequent reinvestigation with electron paramagnetic resonance (EPR) spectroscopy and spin-labeled nucleotide analogues, however, detected weak binding of ATP ($K_d = 400$ μM) [38]. This weak binding of ATP remained enigmatic, however, since even BSA is capable of binding ATP with this affinity, again as determined by EPR [39]. This should not mean that weak binding of substrates in general has to be regarded with distrust, but usually weak binding goes hand in hand with high activity, whereas the ATPase activity of Hsp90 was not identified to be particularly high.

A major breakthrough concerning this question arrived with the X-ray structure of the N-terminal domain of Hsp90 in complex with ADP and Mg^{2+} [40]. This important structure showed that ADP and ATP bind in the same binding pocket as the antitumor drug geldanamycin [41], suggesting that geldanamycin acts by blocking nucleotide binding and not in direct competition with protein substrates.

The nucleotide binds to Hsp90 in a peculiar mode with a kinked phosphate chain. The ribose and base are not readily accessible, explaining why fluorescent nucleotide analogues with modifications at the ribose or base could not bind [42]. Based on previous experience with modifications at the terminal phosphate groups [15], fluorescent analogues of ADP and ATP were synthesized. Binding of these new compounds, namely, adenosinediphospho-β-(*N*′-methylanthraniloylaminobutyl)-phosphoramidate and adenosinetriphospho-γ-(*N*′-methylanthraniloylaminobutyl)-phosphoramidate (see also Table 4.1), to Hsp90 results in enhancement of MANT fluorescence. Although it is usually desirable that modified fluorescent nucleotide analogues behave as closely to their ''native'' siblings as possible, with Hsp90 it turned out that this is fortunately not the case. Here the fluorescent analogues bind much more tightly (K_d of 20 μM for Hsp90) than the unmodified nu-

cleotide, with K_d around 500 μM [14]. This fortunate fact allowed us to determine many individual steps of the ATPase cycle of Hsp90 with stopped-flow and other methods. Once the basic properties of P(γ)-MABA-ATP binding were determined, they served as a diagnostic tool to help clarify the role of individual residues or domains [43, 44] and, similarly to studies concerning DnaK and its nucleotide-exchange factor GrpE, the effect of regulating co-chaperones such as Sti1 on the catalytic cycle [45, 46].

4.2.4 The ATPase Cycle of the Chaperone ClpB

4.2.4.1 ClpB, an Oligomeric ATPase With Two AAA Modules Per Protomer

The molecular chaperone ClpB belongs to the AAA superfamily of proteins that couple ATP binding and hydrolysis to the disruption of protein-protein interaction and the remodeling of protein complexes in an extraordinary variety of biological circumstances (for reviews, see Refs. [47, 48]). AAA proteins contain at least one ATPase module consisting of two physical domains with conserved sequence motifs (Walker A, Walker B, sensor-1) [49] and form ring-shaped oligomers. The conformation of the oligomer and in some cases oligomerization itself are controlled by the bound nucleotide [50, 51].

In contrast to the related proteins ClpA and ClpX, which unfold soluble protein substrates for proteolysis, ClpB and its *S. cerevisiae* homologue Hsp104 act directly on protein aggregates to return them to the soluble state [52–54]. Recovery of active proteins from the aggregated state by ClpB requires the assistance of the DnaK-DnaJ chaperone system [52, 55–57].

The molecular details of the mechanism linking ATP binding and hydrolysis to the disruption of interactions in protein aggregates remain largely undefined. In the case of ClpB, which comprises two nucleotide-binding domains (NBD), clarification of this mechanism is a particularly difficult problem. On the one hand, one has to obtain site-specific information regarding the contribution of each NBD to the activity (catalysis and binding), but, on the other hand, one has to consider that these properties are regulated by the activity of the other site. In addition, the accumulation of ATP-binding sites within the ClpB oligomer is suggestive of complex allosteric behavior, in which inter-ring communications might contribute to complexity.

4.2.4.2 Nucleotide-binding Properties of NBD1 and NBD2

To provide an initial, general sense of the nucleotide-binding properties of the two NBDs, the fluorescent nucleotide analogue MANT-ADP was titrated with increasing amounts of ClpB from *T. thermophilus* [21, 22]. The same experiment was executed with ClpB mutants (ClpB(K204Q), ClpB(K601Q)), which were selectively inactivated at one NBD by substituting a conserved lysine residue within the Walker A consensus sequence. As these conserved lysine residues interact directly with the β- and γ-phosphates of bound nucleotides, the introduction of an uncharged amino acid at this position impairs nucleotide binding. The fluorescence of MANT-ADP

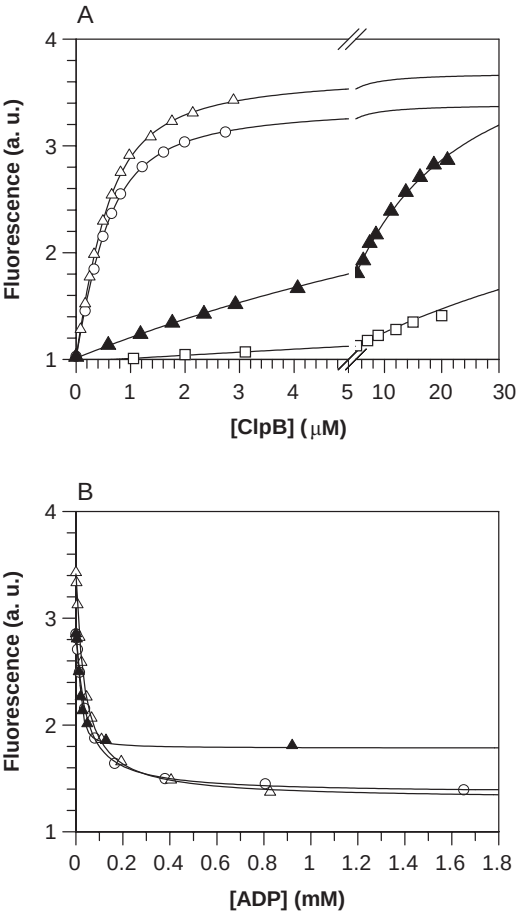

Fig. 4.2. Equilibrium titration experiments with $ClpB_{Tth}$ and MANT-ADP. (A) 0.5 μM MANT-ADP was titrated with $ClpB_{Tth}$(wt) (○), $ClpB_{Tth}$(K204Q) (△), $ClpB_{Tth}$(K601Q) (▲), and the double mutant $ClpB_{Tth}$(K204Q/K601Q) (□) at 25 °C. The excitation wavelength was 360 nm and emission was detected at 440 nm. Data were fitted according to the quadratic equation assuming a 1:1 binding stoichiometry. A K_d of 0.2 μM (±0.02) was observed for $ClpB_{Tth}$(wt) and $ClpB_{Tth}$(K204Q) and a K_d of 15.9 μM (±1.0) was observed for $ClpB_{Tth}$(K601Q). (B) Displacement titration. A preformed $ClpB_{Tth}$*MANT-ADP complex was titrated with ADP ($T = 25$ °C, $\lambda_{ex} = 360$ nm, $\lambda_{em} = 440$ nm). Fitting the curves to a cubic equation yields K_d values of 1.5 μM (±0.08) for $ClpB_{Tth}$(wt) (○), of 2.8 μM (±0.09) for $ClpB_{Tth}$(K204Q) (△), and of 2.3 μM (±0.8) for $ClpB_{Tth}$(K601Q) (▲).

changes in response to binding at both NBDs, and for both ClpB(wt) and the NBD mutants, a saturable increase in fluorescence was observed (Figure 4.2A). Fitting the data to the quadratic binding equation (see Section 4.3) yielded a K_d of 0.2 μM for ClpB(K204Q) and of 16 μM for ClpB(K601Q), indicating that the NBD2 represents a high-affinity and the NBD1 a low-affinity binding site. As the binding affinities differ by two orders of magnitude, MANT-ADP binding to the high-affinity

site of ClpB(wt) masks binding to the low-affinity site. Active site titrations with MANT-ADP and ClpB(K204Q) showed that data are best described by a stoichiometry of 1:2 (one molecule of MANT-ADP binds to a dimer of ClpB), whereas binding to the low-affinity binding site NBD1 follows a 1:1 stoichiometry.

Determination of the affinities for ADP and ATP was based on displacement titrations with a preformed MANT-ADP–ClpB complex and the corresponding nonfluorescent nucleotides (Figure 4.2B). According to the K_d values obtained by fitting this data to the cubic equation (see Section 4.3), ATP binds with a ca. 10-fold lower affinity compared to ADP. (ATP hydrolysis might tamper with the apparent K_d calculated from displacement titrations with ATP. As ATPase activity especially of the NBD mutants is very low, this effect could be neglected.) Surprisingly, the displacement titrations did not confirm the assignment of the NBDs as low- and high-affinity binding sites. With regard to the displacement titrations, both NBDs bind nucleotides with approximately the same affinity (K_d (ADP) ≈ 2 μM; K_d (ATP) ≈ 30 μM).

In contrast to ClpB from *E.coli*, which is capable of hexamerization only in the presence of ATP [51, 58], $ClpB_{Tth}$ forms a hexamer in the absence of nucleotides and in the presence of ATP. ADP binding to $ClpB_{Tth}$ triggers dissociation of high-order oligomers and formation of dimers. Gel-filtration studies with $ClpB_{Tth}$(wt) and the NBD mutants indicated that ADP binding to the NBD1 is responsible for ClpB dissociation [21]. As the bound nucleotide determines the oligomeric state of ClpB, according to the rules of thermodynamics, the oligomeric state should influence nucleotide affinity. To investigate this, the ClpB concentration was kept constant during the fluorescence equilibrium titration with increasing amounts of MANT-ADP (Figure 4.3A). This experiment was repeated with ClpB concentrations ranging from 0.5 μM to 50 μM, thereby covering different distributions of oligomers. Analysis of the obtained data showed that the affinity of the NBD2 to MANT-ADP indeed depends on the oligomeric state of $ClpB_{Tth}$ (Figure 4.3B). The ClpB dimer represents the high-affinity state, while high-order oligomers bind with decreased affinity.

In the case of the chaperone ClpB, application of the fluorescent MANT nucleotide in combination with mutants partially deficient in nucleotide binding has some drawbacks. In the first place MANT-ATP does not meet the requirements of an ATP analogue. The rate of hydrolysis is 100-fold slower compared to ATP, and binding of MANT-ATP triggers oligomer dissociation in contrast to ATP, which stabilizes high-order oligomers. In addition, affinities for MANT-ADP and the unmodified nucleotide differ by a factor of 10, indicating altered kinetic parameters of the modified nucleotide. Notably, these effects are distinct from another technical problem: that of mutations in one active site, such as the K204Q mutation in the Walker A motif of $ClpB_{Tth}$ NBD1, which affects properties of the second site by altering the oligomeric state of the protein.

Because of such problems, we suggest that the site-specific modification of ClpB to introduce fluorescent reporter groups into the NBDs is more suitable to obtain information regarding the properties of each module. A single tryptophan substitution (Y819W) in the C-terminal domain of NBD2 of Hsp104, which has no other

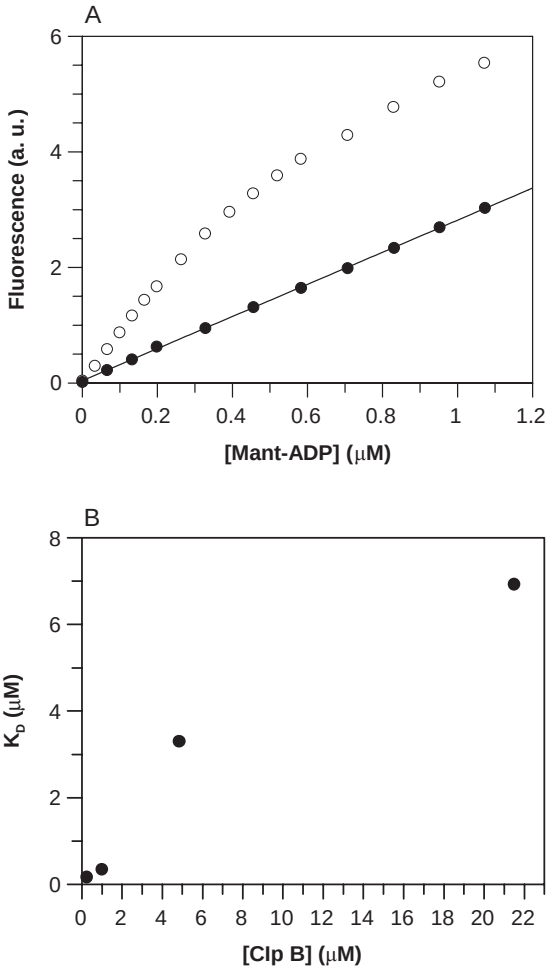

Fig. 4.3. Reverse equilibrium titration of $ClpB_{Tth}$. (A) 0.5 μM $ClpB_{Tth}$(wt) (○) or buffer (●) was titrated with MANT-ADP at 25 °C (λ_{ex} = 360 nm, λ_{em} = 440 nm). The titration curve was corrected for the contribution of the free fluorophore and fitted to a quadratic equation. (B) The plot shows the observed K_d dependent on the ClpB concentration applied in the titra-tion experiment.

tryptophan residues, could be used as an intrinsic fluorescent probe of binding to this site [59]. Site-specific labeling with IANBD of ClpB mutants, carrying Cys substitutions within the NBDs, also proved to be a practical method (S. Schlee and J. Reinstein, unpuplished data).

4.2.4.3 Cooperativity of ATP Hydrolysis and Interdomain Communication

Since ClpB is a hexamer with two binding sites per monomer, the ATP hydrolysis reaction is likely to be regulated at both the homotypic (between identical sites on

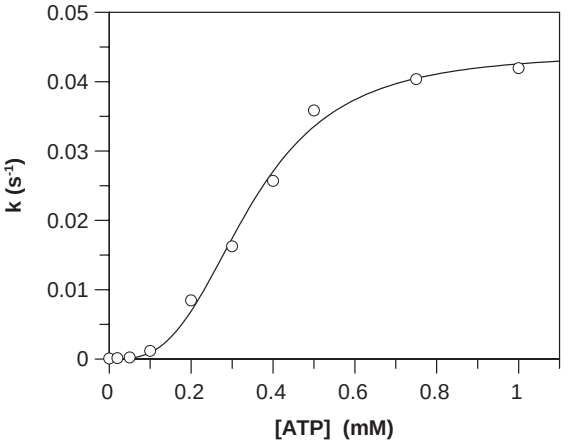

Fig. 4.4. Steady-state kinetic analysis of ATP hydrolysis by $ClpB_{Tth}$. The turnover rate k was determined in a coupled colorimetric assay by incubating 5 μM $ClpB_{Tth}$ with various amounts of Mg-ATP at 25 °C. A fit of the sigmoidal curve with the Hill equation (see "Coupled Enzymatic Assay") yields $n = 3.0$, $k_{cat} = 0.044$ s^{-1}, and $K_m = 0.34$ mM.

different subunits) and heterotypic (between NBD1 and NBD2) levels. Quantitative understanding of the catalytic properties of both ATPase domains is complicated by the fact that effects of mutations on the ATPase activity studied to date are not consistent for different ClpB/Hsp104 proteins [58, 60, 61]. Indeed, measurements of ATP hydrolysis, determined in a coupled colorimetric assay with $ClpB_{Tth}$ [21] or by quantifying released P_i in the case of Hsp104/Hsp78 [61, 62], identified positive cooperativity (Figure 4.4). Mutations in both Walker A motifs of $ClpB_{Tth}$ caused a complete loss of cooperativity and a 100-fold reduction of the ATPase activity. However single-turnover experiments show that both NBDs retain a basal ATPase activity [21]. Remarkably, formation of mixed oligomers, consisting of subunits from ClpB(wt) and the Walker A mutants, leads to a decrease in the ATPase activity, indicating that cooperative effects are based on inter-ring interactions.

A very detailed characterization of the properties of the two AAA modules of Hsp104 could be attained by using [γ-^{32}P]ATP in combination with quantification of a molybdate–inorganic phosphate complex [59]. Analysis of the kinetics of ATP hydrolysis of NBD1 and NBD2 shows that one site (NBD1) is a low-affinity site with a relatively high turnover ($K_m1 = 170$ μM, $k_{cat}1 = 76$ min^{-1}) and that the second site is characterized by a much higher affinity and a 300-fold slower turnover ($K_m2 = 4.7$ μM, $k_{cat}2 = 0.27$ min^{-1}). Both sites show positive cooperativity, with Hill coefficients of 2.3 and 1.6 for the low- and high-affinity sites, respectively. Using mutations in the AAA sensor-1 motif of NBD1 and NBD2 that reduce the rate of ATP hydrolysis without affecting nucleotide binding, Lindquist and coworkers probed the communication between both sites [63]. Impairing ATP hydrolysis of the NBD2 significantly alters the steady-state kinetic behavior of NBD1. Thus, Hsp104 exhibits allosteric communication between the two sites in addition to homotypic cooperativity at both NBD1 and NBD2.

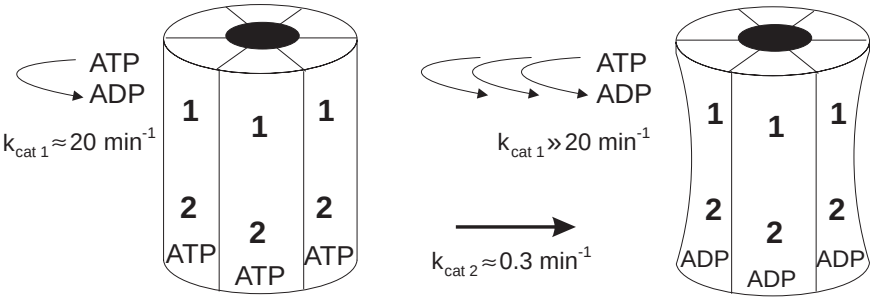

Fig. 4.5. Model for regulation of ATP hydrolysis at Hsp104 NBD1 by the hydrolysis cycle at NBD2 (adapted from Hattendorf et al. [63]). When ATP is bound to NBD2, hydrolysis at NBD1 is relatively slow. Upon ATP hydrolysis at NBD2, a presumed conformational change occurs, resulting in a state in which the rate at NBD1 is elevated.

Interpretation of this data led up to a model predicting that ATP hydrolysis at Hsp104 NBD1 is regulated by the nucleotide-bound state of NBD2 (Figure 4.5). Verification of this model will require transient kinetic measurement of the rate constants associated with ATP binding, ATP hydrolysis, and ADP release at NBD2. Because the oligomeric state stabilized by the bound nucleotide and the effect of mutations within the NBDs were not consistent for ClpB analogues from different organisms, it remains to be clarified whether this model can be generalized or is valid only for Hsp104. In addition, to gain a comprehension of the mechanism linking ATP binding and hydrolysis to the chaperone function of ClpB, the influence of substrates and chaperone cofactors on the ATPase cycle of ClpB has to be defined.

4.3 Experimental Protocols

4.3.1 Synthesis of Fluorescent Nucleotide Analogues

4.3.1.1 Synthesis and Characterization of (P_β)MABA-ADP and (P_γ)MABA-ATP

Synthesis of *N*-(4′-aminobutyl)-2-(methylamino)-benzoylamide *N*-(4′-aminobutyl)-2-(methylamino)-benzoylamide (referred to as tetralinker) was synthesized as follows. To 16.5 g (188 mmol) of 1,4-diaminobutane, 1.66 g (9.38 mmol) of *N*-methylisatoic anhydride was added in small portions. After 4 h of boiling under reflux, the diamine was distilled under vacuum, and the residual (1.86 g, 90%) was dissolved in CH_2Cl_2/MeOH/Et_3N (49:49:2). Chromatography over silica gel 60 (70–230 mesh; Merck, Germany) in the above solvent yielded 1.30 g (63% relative to *N*-methylisatoic acid) of tetralinker with $R_f = 0.14$ (silica gel; CH_2Cl_2/MeOH/Et_3N [49:49:2]) and a melting point of 90–91 °C.

^{1}H-NMR (DMSO-d_6, 500 MHz): $\delta = 1.57$ (m; 4H, $(CH_2)_2$), $\delta = 2.68$ (m; 4H, $(NCH_2)_2$), $\delta = 2.88$ (d; 3H, aryl-NCH_3), $\delta = 3.33$ (t; 2H, alkyl-NH_2), $\delta = 6.73$ (d; 1H, aryl-3-H), $\delta = 6.66$ (m; 1H, aryl-4-H), $\delta = 7.39$ (m; 1H, aryl-5-H), $\delta = 7.65$ (d; 1H, aryl-6-H), $\delta = 7.78$ (t; 1H, OCNH), $\delta = 8.45$ (q; 1H, aryl-NH).

Synthesis of (P_β)MABA-ADP [15] The water-soluble *N*-ethyl-*N*′-(3-dimethylaminopropyl)-carbodiimide (EDC) was used to condense the synthesized tetralinker with the β-phosphate of ADP to give adeninediphospho-β-(*N*′-methylanthraniloylaminobutyl)-phosphoramidate (referred to as (P_β)MABA-ADP) (Figure 4.6). 100 mg (450 μmol) of tetralinker, 19.1 mg (100 μmol) of EDC, and 100 mg (234 μmol) of ADP were dissolved in 1.0 mL 100-mM MES/NaOH pH 6.7 and heated to 50 °C for 35 min. The crude product was purified by HPLC (Waters, Massachusetts, USA) on a semi-preparative reversed-phase C_{18} column (ODS Hypersil Reversed Phase C-18, 5 μm, 120 Å, 250 × 8 mm; Bischoff, Germany) in 0.1 M TEA/HOAc, 25% MeCN with absorption at 260 nm and 350 nm and fluorescence at 430 nm after excitation at 350 nm to identify the product that elutes between ADP and free tetralinker. (P_β)MABA-ADP–containing fractions were pooled, the solvent was distilled under vacuum, and the pure product was lyophilized. The final yield was 31% (relative to ADP) of (P_β)MABA-ADP; the integrity of (P_β)MABA-ADP was proved by ESI-MS and NMR.

^{1}H-NMR (D_2O, 500 MHz; TSP): $\delta = 1.29$ (t; 18H; CH_3; $(CH_3CH_2)_3NH^+$-counter-ion); 1.93 (m; 4H; $(CH_2)_2$); 2.78 (s; 3H; aryl-NCH_3); 2.91 (m; 4H; $N(CH)_2$); 3.21 (q; 12H; CH_2; $(CH_3CH_2)_3NH^+$-counter-ion); 3.74 (m; 1H; 4′-H); 4.23 (m; 2H; 5′-H); 4.37 (m; 1H; 3′-H); 4.49 (m; 1H; 2′-H); 6.08 (d; 1H; 1′-H); 6.72 (m; 1H; aryl-4-H); 6.79 (d; 1H; aryl-6-H); 7.30 (d; 1H; aryl-3-H); 7.37 (m; 1H; aryl-5-H); 8.16 (s; 1H; H-2); 8.47 (s; 1H; H-8).

^{31}P-NMR (D_2O; 500 MHz, PO_4^{3-}): $\delta = -1.24$ (d; α-phosphate); -11.29 (d; β-phosphate).

ESI-MS (negative ion mode): 629.1 g·mol^{-1}, 629.4 g·mol^{-1} were expected.

The extinction coefficient of (P_β)MABA-ADP was determined by comparison of the absorption at 325 nm of (P_β)MABA-ADP and that of the cleaved material. At this wavelength, only the tetralinker contributes to the absorption spectrum. The extinction coefficient of the tetralinker was determined to be 2700 M^{-1} cm^{-1} from a solution of known concentration. Cleavage of (P_β)MABA-ADP is complete after heating the compound for 15 min to 60 °C in 0.1 M HCl according to HPLC analysis. After neutralization, the absorption at 325 nm was unchanged, and the extinction coefficient of (P_β)MABA-ADP is therefore $\varepsilon_{325} = 2700$ M^{-1} cm^{-1}.

Synthesis of (P_γ)MABA-ATP EDC was used to condense the tetralinker with the γ-phosphate of ATP to give adenine triphospho-γ-(*N*′-methylanthraniloylaminobutyl)-phosphoramidate (referred to as (P_γ)MABA-ATP). The synthesis was carried out as described for (P_β)MABA-ADP with 100 mg ATP instead of ADP.

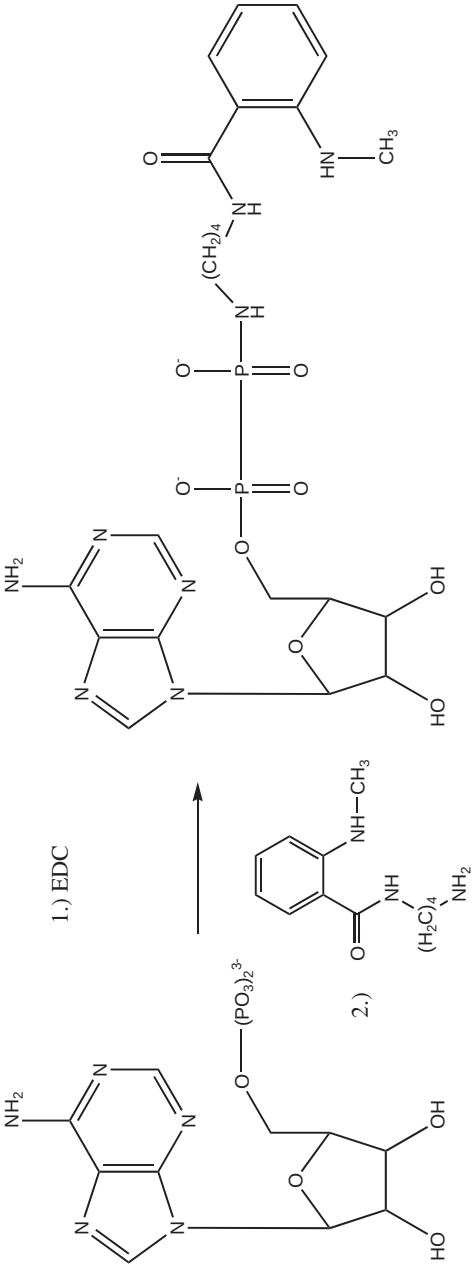

Fig. 4.6. Synthesis of P(β)MABA-ADP. Condensation of ADP with *N*-(4'-aminobutyl)-2-(methylamino)benzoylamide.

^{1}H-NMR (D_2O, 500 MHz; TSP): $\delta = 1.29$ (t; 27H; CH_3; $(CH_3CH_2)_3NH^+$-gegenion); 1.92 (m; 4H; $(CH_2)_2$); 2.78 (s; 3H; aryl-NCH_3); 2.91 (m; 4H; $N(CH)_2$); 3.21 (q; 18H; CH_2; $(CH_3CH_2)_3NH^+$-gegenion); 3.78 (m; 1H; 4′-H); 4.26 (m; 2H; 5′-H); 4.38 (m; 1H; 3′-H); 4.53 (m; 1H; 2′-H); 6.08 (d; 1H; 1′-H); 6.71 (m; 1H; aryl-4-H); 6.78 (d; 1H; aryl-6-H); 7.31 (d; 1H; aryl-3-H); 7.35 (m; 1H; aryl-5-H); 8.16 (s; 1H; H-2); 8.45 (s; 1H; H-8).

^{31}P-NMR (D_2O; 500 MHz, PO_4^{3-}): $\delta = -2.83$ (d; α-phosphate); -13.35 (d; γ-phosphate); -24.73 (t; β-phosphate).

ESI-MS (negative ion mode): 709.1 g·mol^{-1}, 708.4 g·mol^{-1} were expected.

4.3.1.2 Synthesis and Characterization of N8-MABA Nucleotides

Synthesis of MABA-AMP [11] The fluorophores N^8-(4-N'-methylanthraniloyl-aminobutyl)-8-aminoadenosine 5′-tri- and diphosphate (MABA-ATP and MABA-ADP) were synthesized in a four-step reaction. The starting material was AMP that was converted to N8-(4-aminobutyl)-8-aminoadenosine 5′-phosphate (ABA-AMP) [64]. ABA-AMP (50 µmol) was dissolved in 1 mL 0.5-M sodium carbonate (pH 9–10), and 600 µL of 200-mM succinimidyl-*N*-methylanthranylate (SMANT, Molecular Probes) in DMF was added. The mixture was agitated vigorously and left at 50 °C for about 4 h. To quench unreacted SMANT, 1.3 mL of concentrated ammonia (final concentration 8 M) was added, and after 30 min the reaction mixture was diluted with 60 mL water at 4 °C. To remove byproducts, the solution was applied to the quaternary anion-exchange resin QAE Sephadex A 25 (2.2 × 13 cm, Pharmacia). After a wash with water, the column was eluted with a linear gradient to 0.3 M triethyl ammonium bicarbonate (TEAB), pH 7.5. The effluent was monitored by UV absorbance at 260 nm; the product elutes between 0.2 M and 0.25 M TEAB in a single peak. The fractions estimated to contain pure MABA-AMP were pooled and lyophilized three times from water.

Purity of the product was analyzed by reverse phase HPLC with a C_{18} column (ODS-Hypersil, 5 µM, 250 × 4.6 mm) and detection at 280 nm. The sample was eluted with 20% (v/v) acetonitrile in 50 mM potassium phosphate, pH 7.0, over 20 min at 2 mL min^{-1}. A single major peak was observed after 12 min.

The final concentration was determined by UV absorbance with $\varepsilon_{280} = 18\,000$ M^{-1} cm^{-1} at pH 7.5. The molar extinction coefficient was obtained from MABA-ATP by enzymatic ATP determination with hexokinase and glucose-6-phosphate-dehydrogenase [65]. The yield of MABA-AMP from ABA-AMP was ca. 50%.

Synthesis of MABA-ATP MABA-AMP (31 µmol) was dissolved in 0.6 mL water, and 0.23 mL (1 mol) tributylamine was added. The solution was concentrated under reduced pressure and the viscous residue was dried by repeated addition and evaporation of anhydrous pyridine (5 × 0.5 mL) followed by anhydrous DMF (3 × 0.3 mL). The anhydrous tributyl ammonium salt of MABA-AMP was dissolved in 0.5 mL DMF, and 24 mg (0.15 mmol) N,N'-carbonyldiimidazole (CDI) was added. The mixture was agitated vigorously for 20 min and left overnight at

room temperature in a desiccator. In order to hydrolyze excess CDI, 7.5 μL methanol was added, and after 30 min the mixture was concentrated to dryness at 40 °C under reduced pressure. The imidazolide was dissolved in 0.3 mL DMF and stored under anhydrous conditions.

Pyrophosphoric acid (26.7 mg; 0.3 mmol) and 142 μL (0.6 mmol) tributylamine were dissolved in methanol, evaporated, and then evaporated three times with 0.5 mL pyridine and an additional 10 μL tributylamine (0.04 mmol). The precipitate was dissolved in 0.3 mL dry dimethyl formamide (DMF) and added to the imidazolide solution; after shaking vigorously for 30 min, the reaction mixture was left in a desiccator at room temperature for 1–2 days. The precipitate of imidazolium phosphate that formed during the reaction was removed by centrifugation and extracted three times with 0.5 mL DMF. The combined extracts were added to an equal volume of methanol, and the resulting solution was concentrated at 40 °C. The residue was dissolved in 50% (v/v) aqueous ethanol (20 mL) and applied to a QAE Sephadex A25 column (see above).

After washing with 100 mL of 50% (v/v) aqueous ethanol, the sample was eluted with a linear gradient to 1 M TEAB, pH 7.5. The eluent was monitored by UV absorbance at 260 nm. Three major peaks were observed: the first peak at about 0.25 M TEAB was unreacted MABA-AMP, the second at 0.4 M TEAB was MABA-ADP (presumably from phosphoric acid in the pyrophosphoric acid), and the last at 0.6 M TEAB contained MABA-ATP. These fractions were pooled and lyophilized three times from water. Purity was determined by reverse-phase HPLC as described for MABA-AMP. A single major peak was observed at 5 min. The final concentration was determined by enzymatic ATP determination [65]. The UV absorption properties are the same as for MABA-AMP. The yield of MABA-ATP was ca. 27%.

MABA-ADP can be prepared with tributyl-ammonium phosphate instead of the tributyl-ammonium pyrophosphate in the reaction sequence described above.

^{1}H-NMR of MABA-ATP (D_2O, 360 MHz) pH 7.0, 24 °C. The chemical shifts are relative to an external tetramethylsilane standard.

$\delta = 7.98$ (s; 1H; H-2); 7.27 (t; 1H; CH3″) ^3J (7.63 Hz); 7.15 (d; 1H; CH5″) ^3J (7.83 Hz); 6.68 (d; 1H; CH2″) ^3J (8.41 Hz); 6.50 (t; 1H; CH4″) ^3J (7.46 Hz); 5.96 (d; 1H; 1′-H) $^3J1'2'$ (7.8 Hz); 4.65 (t; 1H; 2′-H) $^3J2'3'$ (6.74 Hz); 4.44 (m; 1H; 3′-H); 4.35 (s; 1H; 4′-H); 4.18 (m; 2H; 5′5″-H); 3.55 (m; 2H, $(CH_2)_4$); 3.38 (m; 2H; $(CH_2)_1$); 2.72 (s; 3H; Ph-N-CH_3); 1.79 (m, 2H, $(CH_2)_2$); 1.72 (m; 2H; $(CH_2)_3$); plus counterion (triethylammonium) peaks.

4.3.1.3 Synthesis of MANT Nucleotides

Synthesis of MANT-ADP and MANT-ATP [18] The nucleotide (0.5 mmol ADP, ATP) was dissolved in 7 mL water at 38 °C. The pH was adjusted to 9.6 with NaOH. To this solution a crystalline preparation of methylisatoic anhydride (2.5 mmol) was added in small portions with continuous stirring. The pH was maintained at 9.6 by titration with 2 N NaOH for 2 h. The reaction mixture was cooled and washed three times with 10 mL chloroform; the derivative remains in the

aqueous phase. The reaction products can be monitored by TLC on silica gel. On a silica gel plate developed in 1-propanol/NH_4OH/water (6:3:1, v/v, containing 0.5 g L^{-1} of EDTA), the R_f values behave as follows: unmodified nucleotides < fluorescent nucleotides (R_f (MANT-ADP): 0.44, R_f (MANT-ATP): 0.21) < *N*-methylanthranilic acid. The fluorescent analogue can be identified under an ultraviolet lamp (366 nm) by its brilliant blue fluorescence, while *N*-methylanthranilic acid shows violet fluorescence.

The reaction mixture was then diluted to a volume of 100 mL and the pH adjusted to 7.5 with 1 M acetic acid. To remove byproducts, the solution was applied to the anion-exchange resin Q-Sepharose FF (3.0 × 25 cm, Pharmacia). After a wash with 50 mM triethyl ammonium bicarbonate (TEAB), pH 7.5 at a flow rate of 5 mL min^{-1}, the column was eluted with a linear gradient to 0.7 M TEAB. The effluent was monitored by UV absorbance at 260 nm and 366 nm; the fluorescent nucleotide analogues elute after the unreacted nucleotide and the fluorescent byproduct between 0.6 and 0.7 M TEAB in a single peak. MANT nucleotide-containing fractions were identified by TLC and the absorption profiles. Fractions were pooled, the solvent was distilled under vacuum, the residual was dissolved in methanol, and the pure product was lyophilized.

Purity of the product was analyzed by reverse-phase HPLC with a C_{18} column (ODS-Hypersil, 5 μM 250 × 4.6 mm, Bischoff). The column was developed with a linear gradient to 50% (v/v) acetonitrile in 50 mM potassium phosphate, pH 6.5, over 20 min at 1.5 mL min^{-1} and elution products were monitored by absorption at 280 nm and fluorescence (excitation, 360 nm; emission, 440 nm). MANT-ADP elutes as a single peak after 12.5 min, while MANT-ATP elutes after 11.7 min.

The final concentration of MANT nucleotides was determined by UV absorbance with $\varepsilon_{255} = 23\,300\ M^{-1}\ cm^{-1}$ at pH 8.0. The yield of MANT nucleotide amounts to ~50%. MANT nucleotides exist in solution as an equilibrium mixture of both the 2′ and 3′ isomers (60% 3′ isomer), which are in slow base-catalyzed exchange ($t_{1/2} \sim 10$ min, pH 7.5, 25 °C).

4.3.2
Preparation of Nucleotides and Proteins

4.3.2.1 Assessment of Quality of Nucleotide Stock Solution

It is important that fluorescent nucleotide analogues be fully characterized in terms of structure and purity. The latter should demonstrate the absence of unmodified nucleotides or non-nucleotide fluorescent species that could seriously affect binding studies. Checks on purity are most easily achieved by high-performance liquid chromatography (HPLC).

Unmodified Nucleotides In our experience, commercially available ATP contains a background level of ADP (typically 1–4%). Impurities in nucleotide stock solutions give rise to artifacts when determining rate constants of the ATPase cycle. Therefore, we advise controlling the purity of nucleotide stock solutions by HPLC analysis. The purity of ATP and ADP solutions can be analyzed by reverse-phase HPLC

Tab. 4.2. HPLC program for purity control of P-MABA nucleotides.

Time (min)	*Flow rate (mL min^{-1})*	*A (%)*	*B (%)*
Start	2	70	30
7	2	70	30
7.1	2	0	100
12	2	0	100
12.1	2	70	30
20	2	70	30

with a C_{18} column (ODS-Hypersil, 5 μM, 250 × 4.6 mm, Bischoff) and detection at 254 nm. The sample (usually 20 μL of a 10-μM solution) was eluted with 50 mM potassium phosphate (pH 6.8) over 10 min at 1.5 mL min^{-1}. Nucleotides elute as single peaks with retention times of 3.5 min (ATP), 4.1 min (ADP), and 5.0 min (AMP) at room temperature.

P(β)MABA-ADP and P(γ)MABA-ATP Purity of the phosphate-modified nucleotide analogues P(β)MABA-ADP and P(γ)MABA-ATP was determined by reverse-phase HPLC with a C_{18} column (ODS-Hypersil, 5 μM 250 × 8 mm, Bischoff) and monitoring UV absorption at 254 nm and 325 nm and fluorescence (excitation, 335 nm; emission, 440 nm). The sample was eluted with a step gradient at 2 mL min^{-1} (see Table 4.2) (buffer A: 100 mM triethylammonium acetate pH 7.0; buffer B: 100 mM triethylammonium acetate pH 7.0, 70% acetonitrile). Peaks were observed after 3.8 min (ADP, ATP), 5.7 min (P(γ)MABA-ATP), and 7.6 min (P(β)MABA-ADP).

N8-MABA-ADP and N8-MABA-ATP Purity of nucleotides modified at the N8 position was analyzed by reverse-phase HPLC with a C_{18} column (ODS-Hypersil, 5 μM, 250 × 4.6 mm) and detection at 280 nm [11]. The sample was eluted with 20% (v/v) acetonitrile in 50 mM potassium phosphate, pH 7.0, over 20 min at 2 mL min^{-1}. Peaks were observed after 5.3 min (N8-MABA-ATP), 9.1 min (N8-MABA-ADP), and 12.0 min (N8-MABA-AMP).

MANT-ADP and MANT-ATP The purity of MANT nucleotides can be examined by reverse-phase HPLC with a C_{18} column (ODS-Hypersil, 5 μM, 250 × 4.6 mm), and the effluent is monitored by measuring UV absorbance at 254 nm as well as fluorescence (excitation, 360; emission 440). The column was eluted with a linear gradient to 50% acetonitrile in 50 mM potassium phosphate (pH 6.5) at 1.5 mL min^{-1} (see Table 4.3). MANT-nucleotides elute as double peaks (2′ and 3′ derivatives) with retention times of 13.7 min (MANT-ATP) and 14.5 min (MANT-ADP).

4.3.2.2 Determination of the Nucleotide Content of Proteins

For the investigation of nucleotide-binding capacities of chaperones, the proteins had to be prepared in a nucleotide-free state. To determine the nucleotide content of a protein preparation, 16 μL of a 100-μM protein solution was mixed with 4 μL

Tab. 4.3. HPLC program for purity control of MANT nucleotides.

Time (min)	*Flow rate (mL min^{-1})*	*A (%)*	*B (%)*
0	1.5	100	0
2.0	1.5	100	0
22.0	1.5	0	100
23.0	1.5	100	0
30.0	1.5	100	0

50% (w/v) trichloroacetic acid and incubated for 10 min on ice. The precipitated protein was removed by centrifugation. 10 µL of the supernatant was neutralized with 20 µL of a 2-M solution of potassium acetate. The sample was diluted 1:10 in 50 mM potassium phosphate (pH 6.8) and 20 µL of this solution was analyzed by HPLC (see "Assessment of Quality of Nucleotide Stock Solution" for HPLC conditions). By comparing the integrated peaks with calibration peaks corresponding to nucleotide stock solutions of known concentrations, the nucleotide content of the probe can be calculated.

4.3.2.3 Nucleotide Depletion Methods

Preparation of nucleotide-free chaperones is crucial for the determination of nucleotide-binding kinetics. The nucleotide depletion method applied to a specific chaperone depends on the nucleotide affinity. To prepare ClpB, whose nucleotide affinity is comparatively low (micromolar range), in a nucleotide-free form, it is sufficient to remove Mg^{2+} before a gel-filtration step and thus weaken the binding of nucleotides [21]. Nucleotide depletion of DnaK, which binds nucleotides with dissociation constants in the nanomolar range [66], requires more thorough procedures, which are listed below.

K^+ and Mg^{2+} Depletion As two K^+ and one Mg^{2+} coordinate the bound nucleotide in the ATPase site of DnaK [67], removal of these ions should decrease nucleotide affinity. Therefore, the nucleotide depletion procedure included extensive dialysis over 2–3 days against a buffer containing 1 mM EDTA in the absence of K^+ and Mg^{2+} ions followed by size-exclusion chromatography [68]. A shortcoming of this method is that at high protein concentrations the dissociation of a very small percentage of the bound nucleotide provides enough free nucleotide to prevent further dissociation. When reducing the enzyme concentration to facilitate the dialysis of the bound nucleotide, protein denaturation occurs easily [69].

Exchange Against Low-affinity Nucleotide Analogues Nucleotide removal from DnaK preparations was accomplished by competing off bound nucleotide with excess AMP-PNP or AMP, followed by dialysis to remove less tightly bound AMP-PNP or AMP [68–70]. Nucleotide exchange can be accelerated by addition of catalytic amounts of GrpE to the sample. As for the K^+ and Mg^{2+} depletion procedure, extensive dialysis (72 h) is indispensable. Therefore, the procedure is not suitable

with regard to aggregation-prone proteins. The final purification step is again a size-exclusion chromatography.

Incubation With Alkaline Phosphatase Entirely nucleotide-free $DnaK_{Tth}$ was obtained after treatment with 3–4 U alkaline phosphatase (Boehringer, Mannheim) for 4–6 h in a buffer without K^+ and Mg^{2+} and simultaneous removal of AMP by dialysis. Alkaline phosphatase was removed by a further gel-filtration step [9].

4.3.3 Steady-state ATPase Assays

Observing the ATPase reaction under steady-state conditions implies that the rate of reaction is constant for a relatively long period of time and that multiple turnovers take place. This is the case when the ATP concentration exceeds the chaperone concentration substantially and, ideally, the ATP concentration does not change during the experiment. This could be achieved by using an ATP-regenerating system. Steady-state ATPase assays allow determination of the enzymatic parameters K_m and V_{max}; however, it is not possible to define individual steps and rate constants of the ATPase mechanism. Procedures for determining the steady-state ATPase activity of chaperones are listed below.

4.3.3.1 Coupled Enzymatic Assay

In a colorimetric assay, the hydrolysis of ATP is coupled to the oxidation of NADH by using the enzymes pyruvate kinase and lactate dehydrogenase (Figure 4.7). Because NADH but not NAD^+ absorbs at 340 nm, ATP hydrolysis can be monitored by a decrease in A_{340} [71]. The steady-state ATPase rate of $ClpB_{Tth}$ has been investigated by the coupled enzymatic assay [21].

The assay is carried out in microtiter plates or plastic cuvettes. Measurements are initiated by the addition of an appropriate amount of chaperones (5 μM ClpB) to various concentrations of Mg*ATP and 20 μg mL^{-1} lactate dehydrogenase, 50 μg mL^{-1} pyruvate kinase in 50 mM Tris/HCl (pH 7.5), 100 mM KCl, 5 mM $MgCl_2$, 2 mM EDTA, 2 mM DTE, 0.4 mM PEP, 0.4 mM NADH. The ATP turnover rate in the presence of various ATP concentrations is calculated as follows:

$$k = \Delta A_{340}/(\varepsilon_{NADH} \cdot d \cdot c_p) \quad (1)$$

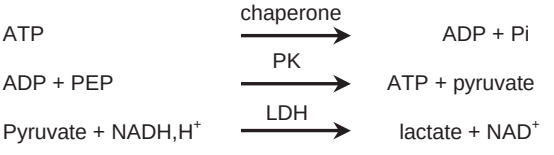

Fig. 4.7. The coupled colorimetric assay. ADP produced by the hydrolysis of ATP reacts with PEP (phosphoenolpyruvate) to form pyruvate in a reaction catalyzed by the PK (pyruvate kinase), whereby ATP is regenerated. Pyruvate is reduced to lactate by the LDH (lactate dehydrogenase), while NADH is oxidized. The decrease of the NADH absorption at 340 nm is a measure for hydrolytic activity.

k: ATP turnover rate in s^{-1}
ΔA_{340}: change of A_{340} in absorption units per s
ε_{NADH}: extinction coefficient of NADH $\varepsilon_{340} = 6220\ M^{-1}\ cm^{-1}$
d: path length in cm
c_p: protein concentration (M)

The k_{cat} and K_m of the ATPase reaction can be determined by plotting the ATP turnover rate k against the ATP concentration and by fitting the obtained curve to the Michaelis-Menten equation (Eq. (2)). If allosteric effects play a role in ATP hydrolysis, the Michaelis-Menten equation should be expanded by introducing the Hill coefficient n (Eq. (3)) (Figure 4.4).

$$k = k_{cat} \cdot S/(K_M + S) \quad (2)$$

$$k = k_{cat} \cdot S^n/(K_M{}' + S^n) \quad (3)$$

k: ATP turnover rate (s^{-1}) at specific ATP concentration
k_{cat}: maximal ATP turnover rate (s^{-1})
S: ATP concentration (M)
K_M: Michaelis-Menten constant (M)
n: Hill coefficient

4.3.3.2 Assays Based on [α-^{32}P]-ATP and TLC

The use of radioactive-labeled ATP facilitates quantification of hydrolytic products. Assays of this kind have been used extensively to characterize the ATPase activity of $DnaK_{Eco}$ [70, 72–75]. Exemplary reaction mixtures (75 µL) contained 50 µg mL^{-1} BSA, 1 nM DnaK, 3 µCi mL^{-1} of [α-^{32}P]ATP or [γ-^{32}P]ATP (1 nM), and 2–80 nM unlabeled ATP in buffer (40 mM HEPES/KOH, pH 7.6, 11 mM magnesium acetate, 200 mM potassium glutamate) [70]. DnaK was pre-incubated at the indicated reaction temperature for 5 min, and hydrolysis reactions were initiated with the addition of ATP. Samples from the reaction mixture (≥ 6 per reaction) were quenched at various times by adding 8 µL of the reaction mixture to 2 µL of 1-N HCl and placing the samples on ice. Each sample (2 µL) was spotted on polyethylenimine cellulase TLC sheets, which were developed in 1 M formic acid, 0.5 M LiCl. The fraction of nucleotide present as ADP could be determined using a phosphorimager system, or spots were cut out and the radioactivity was quantified by liquid scintillation counting. Hydrolysis of ATP should not exceed ~15%, as formed ADP competes with ATP and decreases the hydrolytic rate.

At each concentration of ATP, v_0 was determined from a linear regression analysis. K_M and k_{cat} were determined by fitting a plot of (v_0/[DnaK]) against the concentration of ATP to the Michaelis-Menten equation.

4.3.3.3 Assays Based on Released P_i

Quantification of the P_i released during ATP hydrolysis represents a sensitive measure [76]. A modified method allowed the evaluation of cooperative effects in the

ATPase reaction of Hsp104 [63]. All measurements were performed in 20 mM HEPES pH 7.5, 20 mM NaCl, and 10 mM $MgCl_2$. Hydrolysis reactions were initiated by mixing 12.5 μL of an Hsp104 solution (final concentration 200 nM) and 12.5 μL of an ATP solution containing 10 μCi of [γ-^{32}P]ATP and 1–1000 μM ATP. At varying times reactions were stopped by addition of 175 μL of 1 M $HClO_4$ and 1 mM Na_3PO_4. Ammonium molybdate was added (400 μL of 20 mM) and the molybdate–inorganic phosphate complex was extracted by addition of 400 μL of isopropyl acetate followed by vortexing. The cold P_i is present as carrier and facilitates extraction of the molybdate-phosphate complex into the organic phase.

The amounts of radioactivity in the organic phase and in the aqueous phase were determined by scintillation counting and used to determine the percentage of ATP hydrolysis. After subtraction of free phosphate in a blank reaction, the initial reaction rate was calculated. Plots of the initial reaction rates versus ATP concentration were fitted to a sum of two independent cooperative kinetic transitions [63].

Another possible way to monitor P_i release in real time is the application of the fluorescent reporter PBP-MDCC (A197C mutant of phosphate-binding protein from *E. coli* with attached *N*-[2-(1-maleimidyl)ethyl]-7-(diethylamino)coumarin-3-carboxamide) [77].

4.3.4 Single-turnover ATPase Assays

For measurements of single-turnover ATPase activity, the chaperone has to be present in excess over ATP, so that saturation of the chaperone is achieved (depends on K_d!) and only one turnover of ATP takes place. Conversion of ATP to ADP as a function of time is described by a first-order exponential equation ($y = A \cdot e^{-kt}$).

Typically, ATP and the chaperone are mixed, the reaction is stopped at various times by addition of a quencher, and the fraction of nucleotide present as ADP is determined. As a rule of thumb, the reaction can be analyzed by ''hand mixing'' procedures if $t_{1/2}$ (ATP) > 10 s; faster ATPase rates have to be determined by quenched-flow procedures. If product release (ADP or P_i) is rate-limiting in the ATPase cycle, the rate constant determined under single-turnover conditions exceeds the one observed under steady-state conditions.

4.3.4.1 Manual Mixing Procedures

Reaction mixtures and reactions are essentially identical to those described for measurement of steady-state ATPase activity, except that the protein concentration exceeds ATP concentration and ATP hydrolysis is followed to completion. A protocol used for determining the single-turnover ATPase activity of $ClpB_{Tth}$ is given in ref. [21].

The reaction was started by adding 150 μM ClpB to 75 μM ATP in 50 mM Tris/HCl (pH 7.5), 5 mM $MgCl_2$, 2 mM EDTA, 2 mM DTE, 100 mM KCl. After incubation for appropriate periods (0, 10, 20, 30, . . . , 120 min), 4 μL samples were drawn and the protein was precipitated by addition of 2 μL of 1-M $HClO_4$. After vortexing,

the mixture was incubated for 5 min on ice, and 40 μL of 2-M potassium acetate was added for neutralization. After centrifugation, 20 μL of the supernatant was analyzed with reverse-phase HPLC on a C_{18} column (ODS-Hypersil, 5 μM 250 × 4.6 mm, Bischoff) and detection at 254 nm (for conditions, see 4.3.2.1 "Unmodified Nucleotides"). The relative amounts of ATP and ADP present in each sample were calculated by integrating peaks corresponding to ADP and ATP from the elution profile.

The single-turnover ATPase activity of DnaK has been characterized with radioactive [α-^{32}P]ATP [70, 78] and [γ-^{32}P]ATP [9] using procedures similar to those described for steady-state measurements.

4.3.4.2 Quenched Flow

$DnaJ_{Eco}$ is capable of stimulating the single-turnover ATPase activity of $DnaK_{Eco}$ ≥ 200-fold [78]. As the stimulated ATP-hydrolysis occurred too rapidly to measure by hand, it was monitored using a rapid quench-flow apparatus [79, 80]. Proteins and [α-^{32}P]ATP were loaded into separate 1-mL syringes that were used to fill the 15-μL sample loops. The drive syringes were pushed at a constant velocity, mixing the sample solutions in a 1:1 ratio. The reactions were automatically quenched after a defined reaction time (0.05–120 s) with 80 μL of a 0.3 N HCl solution present in a separate drive syringe [80]. To evaluate the influence of DnaJ on the ATPase activity of DnaK, equal volumes of ATP (8 μM) and nucleotide-free DnaK (9.6 μM) were pre-incubated for 10 s before 1:1 mixing with various concentrations of DnaJ in a quenched-flow apparatus. The reaction was quenched after 0.5 s with perchloric acid [79]. The ATP/ADP ratio in every sample is determined as described for steady-state measurements by HPLC analysis or, in the case of radioactive ATP, with TLC.

4.3.5 Nucleotide-binding Measurements

Techniques used to obtain equilibrium-binding constants (K_a and K_d) are manifold, and methods range from analytical ultracentrifugation to surface plasmon resonance and fluorescence titrations. Hereafter, the methods frequently used to characterize binding equilibria of nucleotides and chaperones are described.

4.3.5.1 Isothermal Titration Calorimetry

In isothermal titration calorimetry (ITC), the heat of interaction between two molecules is used to define the binding process. A syringe containing a "ligand", e.g., the nucleotide, is titrated into a cell containing a solution of the "macromolecule", mostly a protein. As the two elements interact, heat is released or absorbed in direct proportion to the amount of binding that occurs. When the macromolecule in the cell becomes saturated with added ligand, the heat signal diminishes until only the background heat of dilution is observed. The area underneath each injection peak is equal to the total heat released for that injection. When this is plotted against the molar ratio of ligand added to macromolecule in the cell, a complete

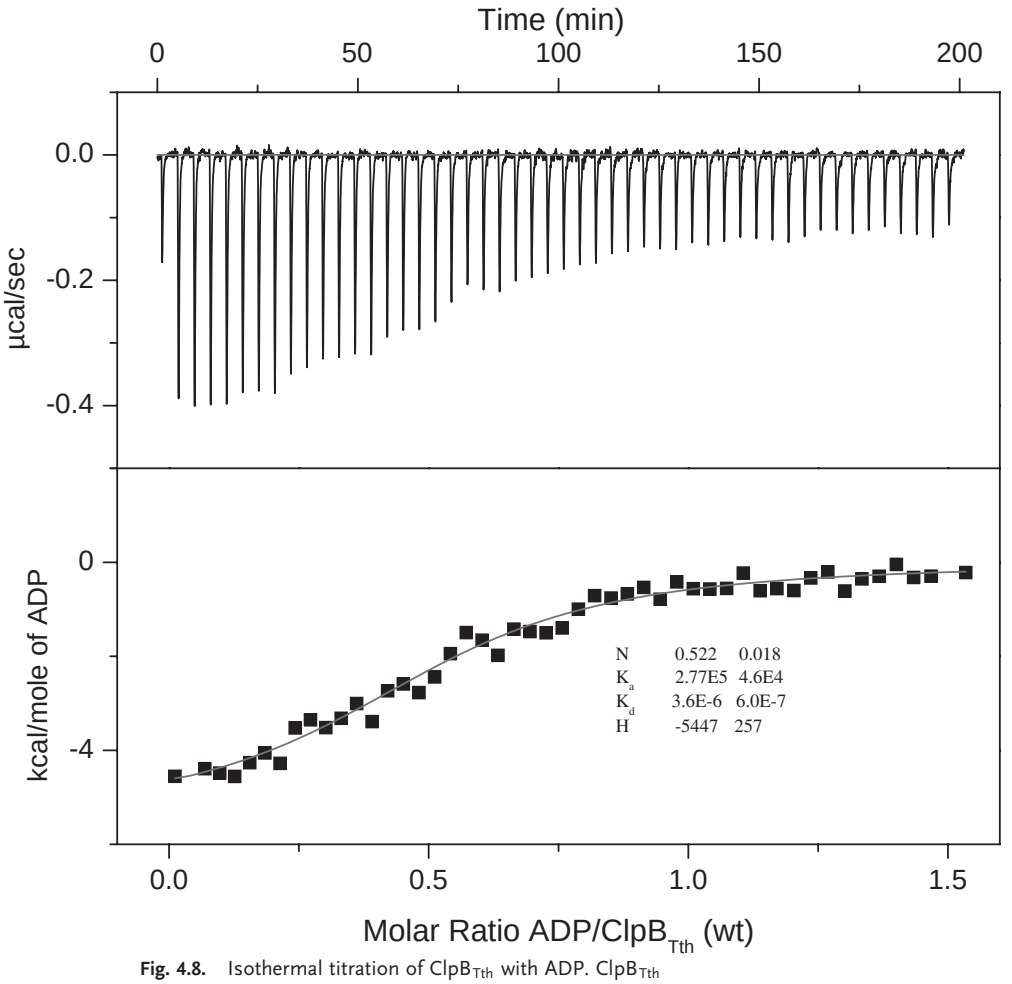

Fig. 4.8. Isothermal titration of $ClpB_{Tth}$ with ADP. $ClpB_{Tth}$ (40 µM) was titrated with 300 µM ADP at 25 °C in an isothermal titration calorimeter in 7-µL steps until saturation was achieved.

binding isotherm for the interaction is obtained (Figure 4.8). ITC measurements yield an entire set of experimental parameters for the binding process, including binding affinity (K_a or K_d), binding stoichiometry (n), heat (ΔH), and heat capacity (ΔCp). ITC measurements were used to identify the ATP-binding site of Hsp90 [81]. The protocol cited below was used for equilibrium studies of the DnaK-GrpE-ADP system from *T. thermophilus* [82].

A solution of 10 µM $DnaK_{Tth}$ in the presence or absence of 42 µM $GrpE_{Tth}$ in 25 mM HEPES-NaOH (pH 7.5), 100 mM KCl, 5 mM $MgCl_2$ (cell volume 1.3 mL), was titrated with 142 µM MABA-ADP in 6-µL steps until saturation was achieved. In the same way, a solution of 11 µM $DnaK_{Tth}$ or $DnaK_{Tth}$ pre-incubated with 20 µM

MABA-ADP was titrated with a solution of 162 μM $GrpE_{Tth}$ in 7-μL steps until saturation. Solutions were incubated for 5 h before measurements to allow for completion of the binary $DnaK_{Tth}$-$GrpE_{Tth}$ or $DnaK_{Tth}$–MABA-ADP complex formation. Data were analyzed by Eq. (4) using the program Microcal Origin for ITC to give the enthalpy, stoichiometry of binding, and association constant.

$$Q = \frac{n \cdot [E] \cdot \Delta H_B \cdot V}{2} \cdot \left(1 + \frac{[L]}{n \cdot [E]} + \frac{1}{n \cdot K_A \cdot [E]} - \sqrt{\left(1 + \frac{[L]}{n \cdot [E]} + \frac{1}{n \cdot K_A \cdot [E]} \right)^2 - \frac{4 \cdot [L]}{n \cdot [E]}} \right) \quad (4)$$

Q: heat in J
$[E]$: total concentration of the protein in M
$[L]$: total concentration of the ligand in M
V: volume of cell in liters
ΔH_B: molar enthalpy of the binding reaction in J mol^{-1}
n: number of active binding sites on the protein
K_A: association equilibrium constant in M^{-1}

4.3.5.2 Equilibrium Dialysis

Nucleotide-binding properties of Hsp70s have been studied extensively by equilibrium dialysis [66, 69]. In any mixture of the ligand and macromolecule, it is difficult to distinguish between bound and free ligand. If, however, the free ligand can be dialyzed through a membrane, until its concentration across the membrane is at equilibrium, free ligand concentration can be measured.

A typical experiment proceeds as follows [66]: [^{14}C]ATP or [^{14}C]ADP together with a regenerating system (creatine kinase/creatine phosphate for ATP, glucose/hexokinase for ADP) were added to both sides of the membrane, while nucleotide-free Hsp70 was added to only one side of the membrane at the beginning of the experiment. Then the dialysis chambers were put in a 4 °C cold room for 24 h with gentle agitation. The nucleotide contents on each side of the membrane were quantified by scintillation counting at the end of the dialysis and yielded the concentration of the free-nucleotide and total nucleotide concentration. Data obtained from several experiments and with varying initial concentrations of ligand can provide the association constant and stoichiometry of the binding reaction.

4.3.5.3 Filter Binding

Apparent rates of association and dissociation of nucleotides with Hsc70 as well as equilibrium dissociation constants were established by filter-binding experiments [83]. To determine the equilibrium-binding constant for MgADP-protein complexes, protein at concentrations from 20 nM to 2.56 μM was incubated with 1 nM [α-^{32}P]ADP at 25 °C. The solution was then filtered and the K_d and the filter efficiency E were determined by a least-squares fit of the equation

$$\theta = \frac{[\text{protein}]}{[\text{protein}] + K_D} E \tag{5}$$

to the data on the fraction of background-corrected counts retained on the filter ($\theta = (C - C_B)/(C_T - C_B)$, where C is the total counts retained on the filter, C_B is the background counts retained when ATP is filtered without protein, and C_T is the total input counts) as a function of protein concentration.

4.3.5.4 Equilibrium Fluorescence Titration

There are two possible situations that can be exploited to study protein-ligand interaction by fluorescence [84]. Either the fluorescence of the protein changes on binding, or the fluorescence of the nucleotide ligand is altered. In general control of temperature and solution conditions is important in binding studies. The fluorescence of most fluorophores, as well as association constants, is sensitive to temperature. Also, care should be taken to control pH during a titration (check pH of nucleotide stock solution!). Dust particles should be removed from both ligand and protein solutions by Millipore filtration or by centrifugation, and buffers should be degassed thoroughly. It is necessary to have accurate values for the total concentrations of ligand ($[L]_0$) and enzyme ($[E]_0$), which may be the greatest limitation for the determination of accurate values of K_d.

Intrinsic Tryptophan Fluorescence When changes in the fluorescence of a protein are observed, the fluorophore may be one or more of the intrinsic tryptophan residues, because emission from this amino acid usually dominates the fluorescence of proteins. The λ_{max} of tryptophan emission ranges from 308 nm for deeply buried tryptophans, to 350 nm for solvent-exposed residues in unfolded proteins. Therefore, not only changes of the amplitude but also shifts of the emission maximum can be exploited as signal. Another advantage of using tryptophan fluorescence is that no chemical modification of either protein or ligand is needed.

The binding of a ligand to a protein may directly affect the fluorescence of a tryptophan residue by acting as a quencher (i.e., by a collisional or energy-transfer mechanism), as seen for ATP quenching the tryptophan fluorescence in human Hsp90 [81, 85], or by physically interacting with the fluorophore and thereby changing the polarity of its environment and/or its accessibility to solvent. Alternatively, a ligand may bind at a site that is remote from the tryptophan residue and may induce a change in conformation of the protein that alters the microenvironment of the tryptophan. These changes in microenvironment may result either in enhancement or quenching of fluorescence or in shifts in the spectrum to the red or blue. Such a fluorescent probe was reported for the NBD2 of Hsp104 [59], where a single tryptophan substitution (Y819W) in the C-terminal domain of NBD2 served as a probe for nucleotide binding.

Tryptophan fluorescence is measured with λ_{ex} between 290 nm and 295 nm and λ_{em} between 310 nm and 350 nm. For equilibrium fluorescence titrations, the applied concentration of the protein should be far below the K_d of the interaction. Nucleotide is added in sequential increments from highly concentrated stock solu-

tion (1–50 mM) until saturation of fluorescence emission is obtained. Fluorescence is corrected for dilution from nucleotide addition, and fluorescence is plotted as a function of nucleotide concentration. Data are usually fit to the quadratic equation (see 4.3.6.1 "Quadratic Equation" below).

Fluorescent Nucleotide Analogues The choice of the fluorescent probe depends on its ability to replace the native nucleotide (Is the modified nucleotide hydrolyzed? Does it bind like the unmodified nucleotide?) and its environmental sensitivity and thus the amplitude of the signal [5]. In addition, binding specificity should be probed before application. The presence of hydrophobic groups in the fluorescent nucleotide analogues presents the possibility that they may bind to proteins at sites other than the nucleotide-binding site. The occurrence of such nonspecific binding can be determined by carrying out the relevant experiment in the presence of a large excess of the physiological nucleotide, which should not give rise to changes in the fluorescent signal. Usually MANT nucleotides show little or no nonspecific binding to ATPases.

With regard to chaperones, examples for equilibrium fluorescence titrations with fluorescent nucleotide analogues are found in Ref. [21] (MANT-ADP and $ClpB_{Tth}$), Ref. [11] (N8-MABA-ADP and $DnaK_{Eco}$), and Ref. [14] (($P\gamma$)-MABA-ATP and yeast Hsp90). In a standard procedure, the fluorescent nucleotide is placed in a cuvette (0.5 μM in standard fluorescence buffer: 50 mM Tris/HCl (pH 7.5), 100 mM KCl, 5 mM $MgCl_2$, 2 mM EDTA, 2 mM DTE), aliquots of the chaperone solution are added (with mixing), and the signal after a brief period of time is measured (correcting the signal for dilution of the fluorescent species and for the inner-filter effect). Curves are fitted according to the quadratic equation (see below). MANT fluorescence is measured with λ_{ex} at 360 nm and λ_{em} at 440 nm. For a tightly binding system, one must be concerned that equilibrium is reached after each addition of reactant. Association is often limited only by diffusion, but dissociation rate constants are much smaller. In such a case, measurements can also be made with a series of prepared solutions, covering various ratios of protein and nucleotide. An example of a fluorescence-binding study is presented in Figure 4.2A.

Active Site Titration In order to perform proper analyses of ligand-binding data and to evaluate enzymatic mechanisms, it is desirable to know with which stoichiometry binding partners interact. For this purpose, a straightforward approach exists that can be performed with various methods; it is described here for the case of fluorescent nucleotide–protein interaction [86]. It is important to note that some constraints apply for successful application of this technique. Firstly, the initial concentration of the signaling ligand, in this case the fluorescent nucleotide, should be well above the estimated K_d (say 5-fold or, even better, 10-fold) such that addition of protein results in nearly complete binding until all nucleotide is bound (saturated). Secondly, the concentrations of the binding partners should be determined accurately, which is straightforward in the case of nucleotides since they are usually pure and have a well-defined extinction coefficient. In the case of protein, this could be more problematic since most common methods to deter-

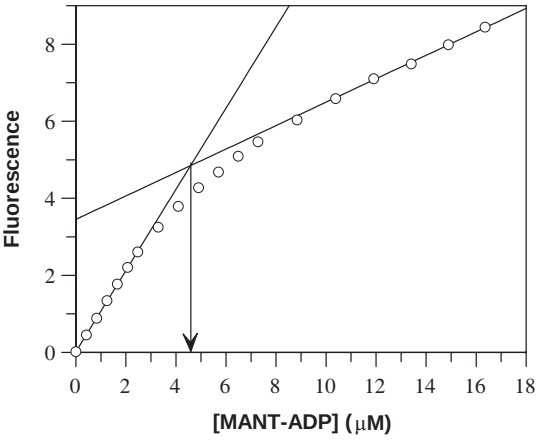

Fig. 4.9. Active site titration of $ClpB_{Tth}$(trunc) with MANT-ADP. Concentration of ClpB(trunc), a shortened ClpB variant lacking the NBD1, at start was 10 μM (measured according to Ref. [106]), and initial volume was 600 μL. Interpolation of the two phases gives an intersection at [MANT-ADP] = 4.8 μM. The volume-corrected concentration of ClpB(trunc) at this point is 9.8 μM. This indicates that one ClpB-dimer is able to bind one molecule of MANT-ADP.

mine protein concentration can deviate for certain proteins. Once these two prerequisites are met, the actual experiment/analysis is quite simple. Protein is added to the ligand in small steps, usually corresponding to concentration increases that amount to 1/20th of the initial ligand concentration until an appreciable saturation of the fluorescence signal is obtained. Now the protein may be added in larger steps until (after volume correction) no further change of signal is observed. The two resulting phases of this titration, initial nearly linear increase and saturation, are extrapolated by hand with linear slopes. The point of intersection then determines at which concentration of added protein the ligand is saturated and as such the stoichiometry of the binding isotherm.

An example for such an experiment is given in Figure 4.9, where MANT-ADP was titrated to $ClpB_{Tth}$(trunc), a shortened ClpB variant lacking a functional NBD1. Interpolation of the two phases gives an intersection at [MANT-ADP] = 4.8 μM, while the volume-corrected concentration of ClpB(trunc) at this point is 9.8 μM. This indicates that one molecule of MANT-ADP is bound per ClpB dimer. Adding $ClpB_{Tth}$(trunc) to MANT-ADP under similar conditions also results in a biphasic curve, where the slope of the second phase is close to zero. The intersection also points to a 2:1 stoichiometry (ClpB(trunc):MANT-ADP).

4.3.5.5 **Competition Experiments**

The affinities of the unmodified nucleotides ADP or ATP for DnaK or ClpB were determined by competition experiments [11, 21, 87]. Therefore, a preformed complex out of the chaperone and the fluorescent nucleotide was titrated with the unmodified nucleotide, and the decrease of the fluorescence signal caused by the displacement of the fluorophore by the non-fluorescent nucleotide was used together

with the known K_d for the fluorescent nucleotide to obtain the affinity (see Figure 4.2B). The general mathematical description of this system is the solution of a cubic equation (see "Cubic Equation" below) [88]. This complete analysis is specifically required if the affinities of the two ligands are very high such that the corresponding K_d values are much lower than the initial concentration of the substance to be titrated.

4.3.6 Analytical Solutions of Equilibrium Systems

4.3.6.1 Quadratic Equation

$[A]$, $[B]$, and $[C]$ are the free concentrations of the compounds A, B, and C.
$[A_o]$, $[B_o]$, and $[C_o]$ are the total concentrations of the compounds A, B, and C.
$[AB]$ and $[AC]$ are complex concentrations of the complexes of A and B or A and C, respectively (e.g., with A being the protein and B a binding ligand).

$$A + B \underset{Kd_{AB}}{\rightleftharpoons} AB$$

Scheme 4.1

Many kinetic experiments require that the concentration of a ligand-protein complex be calculated as a function of any defined concentration of the two substances and a given dissociation constant Kd_{AB}. For a 1:1 stoichiometry (one ligand binds to one binding site of a protein), the dissociation constant is defined as:

$$Kd_{AB} = \frac{[A][B]}{[AB]} \tag{6}$$

Equations of mass conservation:

$$[A_o] = [A] + [AB] \qquad [B_o] = [B] + [AB] \tag{7), (8}$$

Inserting Eqs. (7) and (8) into Eq. (6) gives

$$\begin{aligned} Kd_{AB} &= \frac{[A][B]}{[AB]} \\ &= \frac{([A_o] - [AB])([B_o] - [AB])}{[AB]} \\ &= \frac{[A_o][B_o] - [AB][B_o] - [AB][A_o] + [AB]^2}{[AB]} \\ &\equiv [AB]^2 - [AB]([A_o] + [B_o] + Kd_{AB}) + [A_o][B_o] = 0 \end{aligned} \tag{9}$$

A quadratic equation usually gives two solutions, but here only one is biochemically meaningful, and the final solution to calculate the concentration of the complex AB as a function of the total concentrations of A and B and a given dissociation constant Kd_{AB} therefore is:

$$[AB] = \frac{[A_o] + [B_o] + Kd_{AB}}{2} - \sqrt{\left(\frac{[A_o] + [B_o] + Kd_{AB}}{2}\right)^2 - [A_o][B_o]} \tag{10}$$

The measured quantity is usually the increase/decrease of the fluorescence emission ΔF in every titration step. This quantity is proportional to the binding ratio $[AB]/[B_0]$ and ΔF_{max}, the maximal emission change observed when all the ligand B is bound to the protein (saturation conditions).

$$\Delta F = \Delta F_{max} \cdot \frac{[AB]}{[B_0]} \tag{11}$$

The observed total fluorescence F in every titration step is composed out of the fluorescence of the free ligand F_0 and the change in fluorescence ΔF. Substituting $[AB]$ with Eq. (10) yields an equation for the observed total fluorescence:

$$F = F_0 + \Delta F_{max} \cdot \frac{\frac{[A_0] + [B_0] + Kd_{AB}}{2} - \sqrt{\left(\frac{[A_0] + [B_0] + Kd_{AB}}{2}\right)^2 - [A_0][B_0]}}{B_0} \tag{12}$$

4.3.6.2 Cubic Equation

If two ligands compete for one binding site, as it is the case for displacement titrations with a fluorescent and a non-fluorescent nucleotide, and a 1:1 binding stoichiometry holds, the cubic equation may be applied.

A kinetic system where the ligands B and C compete for binding to A is described in Scheme 4.2.

$$\mathrm{A} + \mathrm{B} \underset{Kd_{AB}}{\rightleftharpoons} \mathrm{AB} \qquad \mathrm{A} + \mathrm{C} \underset{Kd_{AC}}{\rightleftharpoons} \mathrm{AC}$$

Scheme 4.2

The dissociation constants Kd_{AB} and Kd_{AC} are defined as follows:

$$Kd_{AB} = \frac{[A][B]}{[AB]}; \quad Kd_{AC} = \frac{[A][C]}{[AC]} \tag{13), (14}$$

The corresponding mass conservation gives:

$$[A_o] = [A] + [AB] + [AC]$$
$$[B_o] = [B] + [AB] \qquad (15), (16), (17)$$
$$[C_o] = [C] + [AC]$$

If the total concentrations of B and C are much higher than that of A, then the observed dissociation constant of the AC complex, $Kd_{AC}(\text{obs})$, is defined by the simple relationship:

$$Kd_{AC}(obs) = Kd_{AC}\left(1 + \frac{[B]}{Kd_{AB}}\right) \approx Kd_{AC}\left(1 + \frac{B_o}{Kd_{AB}}\right)$$

If the total concentrations of B and C are close to that of A, however, the assumption that $[C] \approx [C_o]$ and $[B] \approx [B_o]$ no longer holds. The deviation from a simple hyperbolic binding is most evident if $[A_o] \gg Kd_{AB}$ and Kd_{AC}.

The general solution of the system in Scheme 4.2 is the solution of a cubic equation. This solution is not based on any assumptions with respect to the relationship of $[A_0]$, $[B_0]$, and $[C_0]$ to Kd_{AB} and Kd_{AC}.

Insert Eqs. (16) and (17) into Eq. (15):

$$[A_o] = [A] + ([B_o] - [B]) + ([C_o] - [C]) \qquad (18)$$

Insert Eq. (13) into Eq. (16) and solve for $[B]$

$$[B] = \frac{[B_o]}{1 + \frac{[A]}{Kd_{AB}}} \qquad (19)$$

Insert Eq. (14) into Eq. (17) and solve for $[C]$.

$$[C] = \frac{[C_o]}{1 + \frac{[A]}{Kd_{AC}}} \qquad (20)$$

Now insert Eqs. (19) and (20) into Eq. (18)

$$[A_o] = [A] + \left([B_o] - \frac{[B_o]}{1 + \frac{[A]}{Kd_{AB}}}\right) + \left([C_o] - \frac{[C_o]}{1 + \frac{[A]}{Kd_{AC}}}\right) \qquad (21)$$

$[A]$ has to be replaced by $[AB]$ since we want to calculate the concentration of the complex $[AB]$. Insert Eq. (19) into Eq. (18) and solve for $[A]$:

$$[AB] = \frac{[A]\dfrac{[B_o]}{1+\dfrac{[A]}{Kd_{AB}}}}{Kd_{AB}}$$

rearrange,

$$[A] = [AB]\frac{Kd_{AB}}{\left(\dfrac{[B_o]}{1+\dfrac{[A]}{Kd_{AB}}}\right)}$$

and finally

$$[A] = -\frac{[AB]Kd_{AB}}{[AB]-[B_o]} \tag{22}$$

Now insert Eq. (22) into Eq. (21)

$$[A_o] = -\frac{[AB]Kd_{AB}}{[AB]-[B_o]} + \left([B_o] - \frac{[B_o]}{1+\dfrac{-\dfrac{[AB]Kd_{AB}}{[AB]-[B_o]}}{Kd_{AB}}}\right) + \left([C_o] - \frac{[C_o]}{1+\dfrac{-\dfrac{[AB]Kd_{AB}}{[AB]-[B_o]}}{Kd_{AC}}}\right) \tag{23}$$

This equation now implicitly expresses $[AB]$ as a function of total concentrations of the three compounds and the two dissociation constants. Now we have to rearrange (factorize for $[AB]$) all terms to get the following cubic equation.

The general form of a cubic equation is:

$$[AB]^3 + a_1[AB]^2 + a_2[AB] + a_3 = 0 \tag{24}$$

and we find the corresponding coefficients to be

$$a_o = Kd_{AB} - Kd_{AC} \tag{25}$$

$$a_1 = \frac{[A_o](Kd_{AC} - Kd_{AB}) + [B_o](2Kd_{AC} - Kd_{AB}) + [C_o]Kd_{AB} - Kd_{AB}{}^2 + Kd_{AB}Kd_{AC}}{a_o} \tag{26}$$

$$a_2 = \frac{[A_o][B_o](Kd_{AB} - 2Kd_{AC}) - [B_o]^2 Kd_{AC} - [B_o]Kd_{AB}([C_o] + Kd_{AC})}{a_o} \tag{27}$$

$$a_3 = \frac{[A_o][B_o]^2 Kd_{AC}}{a_o} \tag{28}$$

The general solution of the cubic equation Eq. (24) may be obtained as described [89].

$$Q \equiv \frac{{a_1}^2 - 3a_2}{9}; \quad R \equiv \frac{2{a_1}^3 - 9a_1a_2 + 27a_3}{54} \tag{29}$$

if $Q^3 - R^2 \geq 0$, then there are three solutions to the cubic equation:

$$\Theta = \arccos\left(\frac{R}{\sqrt{Q}^3}\right)$$

$$[AB]_1 = -2\sqrt{Q}\cos\left(\frac{\Theta}{3}\right) - \frac{a_1}{3}$$

$$[AB]_2 = -2\sqrt{Q}\cos\left(\frac{\Theta + 2\pi}{3}\right) - \frac{a_1}{3}$$

$$[AB]_3 = -2\sqrt{Q}\cos\left(\frac{\Theta + 4\pi}{3}\right) - \frac{a_1}{3}$$

However, only one out of the three solutions given above is meaningful and has to be selected.

The automatic selection is a bit tricky, but once it is implemented it works pretty well. Imagine there is no substance C present; then a quadratic solution would be sufficient to calculate the concentration of the complex $[AB]$. We can still apply the cubic solution since it is valid for any arbitrary situation. If we now compare the solutions from the quadratic equation with the three solutions of the cubic equation, we realize that only one of those three solutions is correct. Now we know which of the three solutions to use. It turns out that this will still hold even if $[C_0]$ is not zero.

A more comprehensive treatment of this problem revealed that it is always the first solution $[AB]_1$ that represents the physically meaningful solution [90].

If $R^2 - Q^3 > 0$, then there is only one solution:

$$[AB] = -sign(R)\left[\sqrt[3]{\sqrt{R^2 - Q^3} + |R|} + \frac{Q}{\sqrt[3]{\sqrt{R^2 - Q^3} + |R|}}\right] - \frac{a_1}{3}$$

This case rarely occurs with the usual values of concentrations and dissociation constants all being positive.

This approach to analyzing competition experiments is complicated and often unnecessary, but experimental constraints do not always allow choosing conditions such that a simple analysis is possible. The choice of appropriate experimental conditions, in conjunction with the complete analysis as described above, also allows gathering information about binding stoichiometries in a competition experiment.

4.3.6.3 Iterative Solutions

Four-component System as an Example: Newton-Raphson Root Search

$A + C \rightleftharpoons AC;\ A + D \rightleftharpoons AD;\ B + C \rightleftharpoons BC;\ B + D \rightleftharpoons BD$

Scheme 4.3

In the examples given above, we searched for analytical solutions that allowed us to define the desired complex concentrations as a function of total concentrations and K_d values. The order of the corresponding equation was directly related to the number of different ligands present. It was a quadratic equation (order 2) for two compounds and a cubic equation (order 3) for three compounds. In principle we could also obtain an analytical solution for a four-component system since the resulting quadric equation would still be solvable. We will avoid this hassle and instead use an iterative method that searches for the roots of a coupled equilibrium system. This method is known as the Newton-Raphson algorithm to find roots in systems of nonlinear equations and is also used by most commercial software packages (e.g., Scientist). It should be noted that these computer programs solve implicit equilibrium systems with this numerical method even with simple two-component systems.

An early practical example of a four-component system was the competition of Mg^{2+} and Ca^{2+} for the metal chelators ATP and EDTA or EGTA in muscle research [91]. Solutions for multi-species equilibria are also regaining attention in chaperone research due to the multi-enzyme–multi-ligand complexes involved. The effects of the DnaK nucleotide-exchange factor GrpE as measured with fluorescent nucleotide in competition with its unlabeled form, e.g., constitute a quaternary system [10, 82, 92], with

$$A \equiv Ca^{2+};\quad B \equiv Mg^{2+};\quad C \equiv EGTA;\quad D \equiv ATP \tag{30}$$

Definition of equilibrium constants:

$$Kd_{AC} = \frac{[A][C]}{[AC]};\quad Kd_{AD} = \frac{[A][D]}{[AD]} \tag{31), (32}$$

$$Kd_{BC} = \frac{[B][C]}{[BC]};\quad Kd_{BD} = \frac{[B][D]}{[BD]} \tag{33), (34}$$

Conservation equations:

$$\begin{aligned}[A_o] &= [A] + [AC] + [AD]\\ [B_o] &= [B] + [BC] + [BD]\\ [C_o] &= [C] + [AC] + [BC]\\ [D_o] &= [D] + [AD] + [BD]\end{aligned} \tag{35)–(38}$$

Rearrangement of Eqs. (35)–(38) and insertion into Eqs. (31)–(34) gives:

$$
\begin{aligned}
&[A] + \frac{[A][C]}{Kd_{AC}} + \frac{[A][D]}{Kd_{AD}} - [A_o] = 0\\
&[B] + \frac{[B][C]}{Kd_{BC}} + \frac{[B][D]}{Kd_{BD}} - [B_o] = 0\\
&[C] + \frac{[B][C]}{Kd_{BC}} + \frac{[A][C]}{Kd_{AC}} - [C_o] = 0\\
&[D] + \frac{[A][D]}{Kd_{AD}} + \frac{[B][D]}{Kd_{BD}} - [D_o] = 0
\end{aligned}
\qquad (39)–(42)
$$

Eqs. (39)–(42) describe the system of equations that has to be solved. One step that is necessary to get the Newton-Raphson (NR) algorithm to work is to generate a matrix of partial derivatives where the species that are iterated (x) are freely selectable. For example:

- If the total concentrations are given, calculate free concentrations and concentrations of complexes.
- If free concentrations are fixed, calculate total concentrations and concentration of complexes.
- If complex concentrations are given, calculate free and total concentrations.

General case:

$$
\begin{bmatrix}
\frac{\partial y_1}{\partial x_1} & \cdots & \cdots & \frac{\partial y_1}{\partial x_4}\\
\cdot & \cdots & \cdots & \cdot\\
\cdot & \cdots & \cdots & \cdot\\
\frac{\partial y_4}{\partial x_1} & \cdots & \cdots & \frac{\partial y_4}{\partial x_4}
\end{bmatrix}
$$

Let us assume that we define the total concentrations and want to calculate the free concentrations; then the matrix of partial derivatives would read:

$$
\begin{bmatrix}
\frac{\partial\left([A] + \frac{[A][C]}{Kd_{AC}} + \frac{[A][D]}{Kd_{AD}} - [A_o]\right)}{\partial[A]} & \cdots & \cdots & \frac{\partial\left([A] + \frac{[A][C]}{Kd_{AC}} + \frac{[A][D]}{Kd_{AD}} - [A_o]\right)}{\partial[D]}\\
\frac{\partial\left([B] + \frac{[B][C]}{Kd_{BC}} + \frac{[B][D]}{Kd_{BD}} - [B_o]\right)}{\partial[A]} & \cdots & \cdots & \frac{\partial\left([B] + \frac{[B][C]}{Kd_{BC}} + \frac{[B][D]}{Kd_{BD}} - [B_o]\right)}{\partial[D]}\\
\frac{\partial\left([C] + \frac{[B][C]}{Kd_{BC}} + \frac{[A][C]}{Kd_{AC}} - [C_o]\right)}{\partial[A]} & \cdots & \cdots & \frac{\partial\left([C] + \frac{[B][C]}{Kd_{BC}} + \frac{[A][C]}{Kd_{AC}} - [C_o]\right)}{\partial[D]}\\
\frac{\partial\left([D] + \frac{[A][D]}{Kd_{AD}} + \frac{[B][D]}{Kd_{BD}} - [D_o]\right)}{\partial[A]} & \cdots & \cdots & \frac{\partial\left([D] + \frac{[A][D]}{Kd_{AD}} + \frac{[B][D]}{Kd_{BD}} - [D_o]\right)}{\partial[D]}
\end{bmatrix}
\qquad (43)
$$

The result is the following matrix:

$$\begin{bmatrix} 1+\frac{[C]}{Kd_{AC}}+\frac{[D]}{Kd_{AD}} & 0 & \frac{[A]}{Kd_{AC}} & \frac{[A]}{Kd_{AD}} \\ 0 & 1+\frac{[C]}{Kd_{BC}}+\frac{[D]}{Kd_{BD}} & \frac{[B]}{Kd_{BC}} & \frac{[B]}{Kd_{BD}} \\ \frac{[C]}{Kd_{AC}} & \frac{[C]}{Kd_{BC}} & 1+\frac{[B]}{Kd_{BC}}+\frac{[A]}{Kd_{AC}} & 0 \\ \frac{[D]}{Kd_{AD}} & \frac{[D]}{Kd_{BD}} & 0 & 1+\frac{[A]}{Kd_{AD}}+\frac{[B]}{Kd_{BD}} \end{bmatrix} \tag{44}$$

Why do we need this matrix of partial derivatives (see Ref. [89] p. 306)?

If $\vec{x}$ is the vector of all x_i, then each function f_i may be extended in a Taylor series around $\vec{x}$.

$$f_i(\vec{x}+\delta\vec{x}) = f_i(\vec{x}) + \sum_{j=1}^{N} \frac{\partial f_i}{\partial x_j}\delta x_j + O(\delta\vec{x}^2) \tag{45}$$

A system of linear equations for the correction factors $\delta\vec{x}$ is obtained if $\delta\vec{x}^2$ and all higher-order terms are neglected. All equations could thus be optimized simultaneously:

$$\sum_{j=1}^{N} \alpha_{ij}\delta x_j = \beta_i \quad \text{where } \alpha_{ij} \equiv \frac{\partial f_i}{\partial x_j} \text{ and } \beta_i = -f_i \tag{46}$$

α thus represents the matrix of partial derivatives. Since we reduced our problem to a system of linear equations, it may be solved by any standard numerical technique like partial pivoting or lower/upper triangular (LU) decomposition. This proceeds iteratively and usually needs some 2 to 10 iterations to converge; the computer simulates the approach to equilibrium!

Trial runs indicated that the numerical calculations became very unstable when the matrix of partial derivatives was generated by the approximation of finite differences, e.g.,

$$\frac{\partial f_i}{\partial x_j} \cong \frac{f_i(x+\Delta x_j)}{f_i(x)} \tag{47}$$

The partial derivatives thus have to be generated analytically.

If the free concentrations of the complexes are defined and the corresponding total concentrations should be calculated, then the matrix of partial derivatives is:

$$\begin{bmatrix} \frac{\partial\left([A]+\frac{[A][C]}{Kd_{AC}}+\frac{[A][D]}{Kd_{AD}}-[A_o]\right)}{\partial[A_o]} & \cdots & \cdots & \frac{\partial\left([A]+\frac{[A][C]}{Kd_{AC}}+\frac{[A][D]}{Kd_{AD}}-[A_o]\right)}{\partial[D_o]} \\ \frac{\partial\left([B]+\frac{[B][C]}{Kd_{BC}}+\frac{[B][D]}{Kd_{BD}}-[B_o]\right)}{\partial[A_o]} & \cdots & \cdots & \frac{\partial\left([B]+\frac{[B][C]}{Kd_{BC}}+\frac{[B][D]}{Kd_{BD}}-[B_o]\right)}{\partial[D_o]} \\ \frac{\partial\left([C]+\frac{[B][C]}{Kd_{BC}}+\frac{[A][C]}{Kd_{AC}}-[C_o]\right)}{\partial[A_o]} & \cdots & \cdots & \frac{\partial\left([C]+\frac{[B][C]}{Kd_{BC}}+\frac{[A][C]}{Kd_{AC}}-[C_o]\right)}{\partial[D_o]} \\ \frac{\partial\left([D]+\frac{[A][D]}{Kd_{AD}}+\frac{[B][D]}{Kd_{BD}}-[D_o]\right)}{\partial[A_o]} & \cdots & \cdots & \frac{\partial\left([D]+\frac{[A][D]}{Kd_{AD}}+\frac{[B][D]}{Kd_{BD}}-[D_o]\right)}{\partial[D_o]} \end{bmatrix}$$

which is as simple as:

$$\begin{bmatrix} -1 & 0 & 0 & 0 \\ 0 & -1 & 0 & 0 \\ 0 & 0 & -1 & 0 \\ 0 & 0 & 0 & -1 \end{bmatrix}$$

All the examples presented above concern calculations of the same type: free concentrations, total concentrations, or complex concentrations. The question is now whether there is a way to calculate mixed species. It is obvious that the choice of species that may be defined or calculated is limited to a certain extent. For example, if the total amount of A_o and the complex concentration is specified, then the concentration of A_f cannot be specified since it has to be varied to give the AC desired. In this case, the system would be overdetermined. There could also be cases where the system is underdetermined; then the solution will not be unique or the system will not converge.

4.3.7 Time-resolved Binding Measurements

4.3.7.1 Introduction

Mechanistic questions and kinetic models are closely related, since a kinetic model is usually derived from hypotheses of the enzyme's mechanism. The model is then scrutinized by other appropriate kinetic measurements that should ideally be designed to falsify – not "prove" – the model. The link between the model and experimental data is provided by the equations that are obtained by solving the differential system determined by the model. Although it is becoming more popular to use computer programs that avoid the hassle of analytical solutions (through numerical integration), it is often still more instructive to use these solutions, and some examples of the most often needed types are shown below.

Differential equations systems could be solved in principle by three major methods: Laplace transformation, matrix method, and substitution method. Because a proper introduction to these mathematical approaches, as well as experimental methods to obtain relevant transient kinetic data, would go far beyond the scope of this chapter, the reader is kindly asked to refer to the following major references that provide fundamental and thorough introductions and overviews.

1) Laplace transformation: Refs. [93, 94]
2) Substitution: Ref. [94]
3) Matrix method: Ref. [95]

A ''cookbook'' that provides solutions to many systems [96] is unfortunately no longer commercially available but could be found in some libraries.

4.3.7.2 One-step Irreversible Process

A well-known example for one-step irreversible processes is radioactive decay of isotopes.

The according kinetic model represents the simplest scheme available:

$$A \xrightarrow{k} B$$

Under certain boundary conditions, this scheme can also be applied to enzymatic reactions, e.g., single-step hydrolysis of ATP where either ATP binding is not rate-limiting and saturating or the reaction is initiated with pre-bound ATP (e.g., by addition of catalytic Mg^{2+}). Another example is the displacement of fluorescently labeled, pre-bound nucleotide by an excess of unlabeled ligand (usually also nucleotide) to measure directly the rate constant for dissociation [10, 11, 97].

If the initial concentration of B at $t = 0$ (B_o) is 0, then the differential equations for that system read:

$$\frac{d[A]}{dt} = -k[A] \qquad \text{(D1)}$$

$$\frac{d[B]}{dt} = k[A] \qquad \text{(D2)}$$

Converted to Laplace space (please refer to literature above for information on how to set up equations)

$$sa = -ka + a_0 \qquad \text{(L1)}$$

$$sb = ka \qquad \text{(L2)}$$

and solved for a and b, respectively:

$$a = \frac{a_0}{s+k}$$

$$b = \frac{ka}{s} = \frac{ka_0}{s(s+k)} \qquad \text{(S1), (S2)}$$

Looking in the table for the back transformation and setting k equal to α gives

$$\mathrm{L}^{-1}\left(\frac{const}{s(s+\alpha)}\right) = \frac{const}{\alpha}(1 - e^{-\alpha t})$$

and

$$\mathrm{L}^{-1}\left(\frac{const}{s+\alpha}\right) = e^{-\alpha t}.$$

Therefore, $[A](t) = [A_0] \cdot e^{-kt}$ and $[B](t) = [A_0](1 - e^{-kt})$.

4.3.7.3 One-step Reversible Process

First-order reversible processes are routinely encountered in protein folding and are discussed here in great detail. Related to that are structural changes that may be induced by ligands or other factors, e.g., light, pH, or temperature among others.

Model:

$$A \underset{k_{-1}}{\overset{k_1}{\rightleftharpoons}} B$$

$$\frac{d[A]}{dt} = -k_1[A] + k_{-1}[B]$$

$$\frac{d[B]}{dt} = k_1[A] - k_{-1}[B] \qquad \text{(D1), (D2)}$$

$$sa - a_0 = -k_1 a + k_{-1} b$$

$$sb = k_1 a + k_{-1} b \qquad \text{(L1), (L2)}$$

$$\Rightarrow a = \frac{a_0 + k_{-1} b}{s + k_1} \qquad \text{(S1)}$$

Inserting S1 into L2 and factorizing for b gives

$$b = \frac{k_1 a_o}{(s+k_1)\left(s + k_{-1} - \dfrac{k_1 k_{-1}}{s+k_1}\right)} = \frac{k_1 a_o}{s(s + k_1 + k_{-1})}$$

with $k_1 + k_{-1} \equiv \alpha$.

The transform table gives as the back transformation of

$$\mathrm{L}^{-1}\frac{const}{s(s+\alpha)} = \frac{const}{\alpha}(1-e^{-\alpha t}) \tag{S2}$$

and hence $B(t) = \dfrac{k_1[A_0]}{k_1+k_{-1}}(1-e^{-(k_1+k_{-1})\cdot t})$.

4.3.7.4 Reversible Second Order Reduced to Pseudo-first Order

Reversible second-order processes are mostly observed in simple ligand-binding processes where the binding of ligand does not induce further structural changes.

The corresponding model reads

$$\mathrm{A} + \mathrm{B} \underset{k_{-1}}{\overset{k_{+1}}{\rightleftharpoons}} \mathrm{C}$$

with an according set of differential equations

$$\begin{aligned}
\frac{d[A]}{dt} &= -k_{+1}[A][B] + k_{-1}[C] \\
\frac{d[B]}{dt} &= -k_{+1}[A][B] + k_{-1}[C] \qquad \text{(D1)–(D3)} \\
\frac{d[C]}{dt} &= k_{+1}[A][B] - k_{-1}[C]
\end{aligned}$$

If the boundary conditions are such that $B_o \gg A_o$ (that is, the species B at $t = 0$ is in excess) and $C_o = 0$, then the reaction becomes pseudo-first order since the concentration of B does not change significantly over time, $B(t) \approx B_o$. The set of (approximated) differential equations then is:

$$\begin{aligned}
\frac{d[A]}{dt} &\cong -k_{+1}[A][B_o] + k_{-1}[C] \\
\frac{d[B]}{dt} &\cong 0 \qquad \text{(D4)–(D6)} \\
\frac{d[C]}{dt} &\cong k_{+1}[A][B_o] - k_{-1}[C]
\end{aligned}$$

The equations in Laplace space are:

$$\begin{aligned}
sa - a_o &\cong -k_{+1}ab_o + k_{-1}c \\
sc &\cong k_{+1}ab_o - k_{-1}c
\end{aligned} \qquad \text{(L1), (L3)}$$

Solve for a

$$a \cong \frac{a_o + k_{-1}c}{s + k_{+1}b_0} \tag{S1}$$

Insert S1 into L3 and solve for c:

$$c \cong \frac{a_o b_o k_{+1}}{s(s + b_o k_{+1} + k_{-1})} \tag{S2}$$

In the tables we find the transformation back to real space

$$\mathrm{L}^{-1}\left(\frac{1}{s(s+\alpha)}\right) = \frac{1}{\alpha}(1 - e^{-\alpha t}) \quad \text{with } \alpha = b_0 k_{+1} + k_{-1}$$

and therefore the solution is:

$$[C](t) \cong \frac{A_o B_o k_{+1}}{B_o k_{+1} + k_{-1}}(1 - e^{-(B_o k_{+1} + k_{-1})t})$$

Note that the amplitude is also an approximation, but in practice a three- to four-fold excess of B_o should be sufficient. To answer how close this approximation is to the real solution, we perform an exemplary calculation.

Assume: $\mathrm{A}_0 = 1\ \mu\mathrm{M}$; $\mathrm{B}_0 = 10\ \mu\mathrm{M}$; $k_{+1} = 1\ \mu\mathrm{M}^{-1}\cdot\mathrm{s}^{-1}$; $k_{-1} = 1\ \mathrm{s}^{-1} \Rightarrow K_\mathrm{d} = 1\ \mu\mathrm{M}$

The approximation according to the kinetic solution is:

$$[C](t = \text{infinity}) = \frac{1 \cdot 10 \cdot 1}{10 \cdot 1 + 1} = \frac{10}{11} = 0.909\ \mu\mathrm{M}$$

The exact solution as calculated with the quadratic binding equation is:

$$\frac{1 + 1 + 10}{2} - \sqrt{\left(-\frac{1 + 1 + 10}{2}\right)^2 - 10 \cdot 1} = 0.90098\ \mu\mathrm{M}$$

We can conclude that the approximation of the amplitude is sufficiently good under these conditions.

If $B_0 = 2\ \mu\mathrm{M}$, i.e., if the excess of ligand is just twofold over A_0, then the kinetic "solution" gives an amplitude of $\frac{1 \cdot 2 \cdot 1}{2 \cdot 1 + 1} = \frac{2}{3} = 0.666$ in comparison to the exact quadratic equation, which gives $2 - \sqrt{4 - 2} = 0.5857$ as a value for the final complex concentration after equilibration. This shows that, even being far from pseudo-first-order conditions, the amplitude derived under these conditions is still

a fair approximation. We should be aware, however, that the shape of the time trace will be substantially different and thus large errors will be introduced for the resulting rate constant after a fitting procedure, including large visible systematic deviations that are clearly visible with a residual plot [95].

One should also note here that in general, without the assumption that one ligand is in excess, binding systems are rarely solvable – as are many other nonlinear systems.

4.3.7.5 Two Simultaneous Irreversible Pathways – Partitioning

Partitioning experiments are very useful and often are the only accessible way to obtain information about particular kinetic systems. One example where this technique was used successfully is in the case of Hsp90. Here a complex of radioactive ATP with Hsp90 was chased off with an excess of unlabeled ATP, and the yield of hydrolyzed, radioactive ADP compared to the yield without chase showed commitment to hydrolysis since the enzyme goes through a complete round of hydrolysis before the chase takes affect [14].

A complete treatment of this method follows the model in Scheme 4.4:

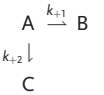

Scheme 4.4

Again, the differential equation system (DES) is generated by summing up all steps that lead away from a certain species with the steps that lead to it.

$$\frac{d[A]}{dt} = -(k_1 + k_2)[A]$$

$$\frac{d[B]}{dt} = k_1[A] \qquad \text{(D1)–(D3)}$$

$$\frac{d[C]}{dt} = k_2[A]$$

Again, in Laplace space, we replace d/dt with the symbol s. Any species N that is not initially zero (at time 0, start of the reaction) gets the additional integration term n_o.

$$sa - a_o = -(k_1 + k_2)a$$

$$sb = k_1 a \qquad \text{(L1)–(L3)}$$

$$sc = k_2 a$$

Solving the resulting linear system in Laplace space:

Solve L1 for a to give S1

$$a = \frac{a_o}{s + k_1 + k_2} \tag{S1}$$

Now insert S1 into L2 and solve for b

$$sb = k_1 \frac{a_o}{s + k_1 + k_2} \Rightarrow b = \frac{k_1 a_o}{s(s + k_1 + k_2)} \tag{S2}$$

The table of Laplace back transformations tells us that the back transformation to real space (L^{-1}) of our system is:

$$L^{-1} \frac{1}{s(s + \alpha)} = \frac{1}{\alpha}(1 - e^{-\alpha t})$$

so that:

$$[B](t) = [A_o] \frac{k_1}{k_1 + k_2}(1 - e^{-(k_1 + k_2)t}) \tag{S3}$$

and accordingly:

$$\begin{aligned} [A](t) &= [A_o]\left(1 - \frac{k_1}{k_1 + k_2}(1 - e^{-(k_1 + k_2)t})\right) \\ [C](t) &= [A_o] \frac{k_2}{k_1 + k_2}(1 - e^{-(k_1 + k_2)t}) \end{aligned} \tag{S3), (S4}$$

The observed rate constant of $k_1 + k_2$ as well as the observed amplitude of $k_1/(k_1 + k_2)$ for the formation of B gives independent information about the rate constants and may be used to obtain k_1 and k_2 from one simple time trace. The example shown in Figure 4.10 demonstrates that for the same $k_{obs} = k_1 + k_2 = 10 + 1 = 11\ s^{-1}$, the different amplitudes allow us to unequivocally assign the individual rate constants. The same holds for equal amplitudes: now the observed rate constants allow us to assign the individual rate constants.

Some useful relationships are

$$k_{obs} = k_1 + k_2$$

$$B_{obs} = A_o \frac{k_1}{k_1 + k_2}$$

$$k_1 = \frac{A_{obs}}{A_o} k_{obs}$$

$$k_2 = k_{obs} - k_1$$

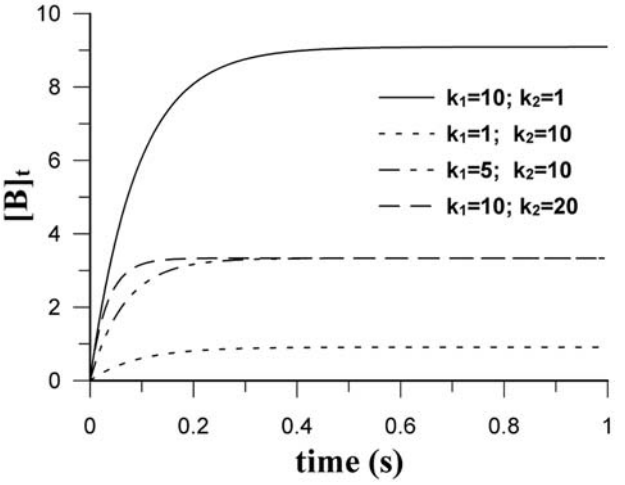

Fig. 4.10. Simulation for time traces according to partitioning scheme.

4.3.7.6 **Two-step Consecutive (Sequential) Reaction**

The following model

$$A \overset{k_1}{\rightarrow} B \overset{k_2}{\rightarrow} C$$

provides a simplified version of two-step irreversible mechanisms that can be applied under certain conditions e.g., binding of ATP (treated as a single step since a conformational change following initial encounter [to give complex A] is rate-limiting) followed by irreversible hydrolysis [79, 80]. In these literature examples, it was important to first generate a hydrolysis-competent DnaK-ATP state that could then be ''chased'' by ATPase-stimulating DnaJ in a second mixing reaction. The experiments therefore had to be designed to allow for complete ATP binding, including the conformational change it induces, without appreciable hydrolysis occurring before the DnaJ ''chase''. The amount of the ''reaction'' intermediate B (DnaK-ATP complex in the closed and DnaJ stimulation-competent conformation) thus had to be maximized prior to addition of DnaJ.

The **differential equation system** that describes this kinetic system is:

$$\frac{d[A]}{dt} = -k_1[A]$$

$$\frac{d[B]}{dt} = k_1[A] - k_2[B] \qquad \text{(D1)–(D3)}$$

$$\frac{d[C]}{dt} = k_2[B]$$

This system is transformed forward into Laplace space to give the following **linear equation system**: boundary conditions: $A(t = 0, A_0)$ and $B_0, C_0 = 0$

$$\begin{aligned} sa - a_o &= -k_1 a \\ sb &= -k_1 a - k_2 b \\ sc &= k_2 b \end{aligned} \qquad \text{(L1)–(L3)}$$

To solve for c, we first solve for a to give:

$$a = \frac{a_o}{s + k_1} \qquad \text{(S1)}$$

Then insert this expression into L2 and solve for b:

$$b = \frac{k_1 a_o}{s + k_1} \cdot \frac{1}{s + k_2} \qquad \text{(S2)}$$

Finally, insert this expression into L3 and solve for c:

$$c = \frac{k_2}{s} \cdot \frac{k_1 a_o}{s + k_1} \cdot \frac{1}{s + k_2} \qquad \text{(S3)}$$

Looking in the table of Laplace back transformations gives us:

$$\mathrm{L}^{-1}\left(\frac{1}{s(s + \alpha_1)(s + \alpha_2)}\right) = \frac{1}{\alpha_1 \alpha_2}\left(1 + \frac{1}{\alpha_1 - \alpha_2}(\alpha_2 e^{-\alpha_1 t} - \alpha_1 e^{-\alpha_2 t})\right)$$

so that transforming back to real space gives:

$$[C](t) = [A_o]\left(1 + \frac{1}{k_1 - k_2}(k_2 e^{-k_1 t} - k_1 e^{-k_2 t})\right)$$

In summary, if the boundary conditions are chosen such that $A_0 \neq 0$, $B_0, C_0 = 0$, then the solutions are:

$$[A](t) = [A_o] e^{-k_1 t}$$

$$[B](t) = [A_o] \frac{k_1}{k_2 - k_1}(e^{-k_1 t} - e^{-k_2 t})$$

$$[C](t) = [A_o]\left(1 + \frac{1}{k_1 - k_2}(k_2 e^{-k_1 t} - k_1 e^{-k_2 t})\right)$$

Common questions that appear (e.g., in double-mixing or time-resolved structural

measurements) are what the maximum of $[B]$ is that can be obtained and at which time this is reached.

$$\frac{d[B]}{dt} = 0 = \frac{d\left([A_o]\frac{k_1}{k_2 - k_1}(e^{-k_1 t} - e^{-k_2 t})\right)}{dt}$$

$$= [A_o]\frac{k_1}{k_2 - k_1}(-k_1 e^{-k_1 t_{B\max}} + k_2 e^{-k_2 t_{B\max}})$$

$$t_{B\max} = \frac{\ln \frac{k_2}{k_1}}{k_2 - k_1}$$

Accordingly, the maximal amount of the intermediate B formed is:

$$[B](t_{B\max}) = [A_o]\frac{k_1}{k_2 - k_1}(e^{-k_1 t_{B\max}} - e^{-k_2 t_{B\max}})$$

A plot of the maximal relative yield of the intermediate B as a function of the individual rate constants is simulated and shown in Figure 4.11. Additionally, a similar plot for the time when this maximum is reached is shown in Figure 4.12.

4.3.7.7 Two-step Binding Reactions

The following system represents a reversible two-step binding process that already results in substantial complexity of the according equations. This description was kindly provided by Roger S. Goody and was only slightly adjusted in minor parts.

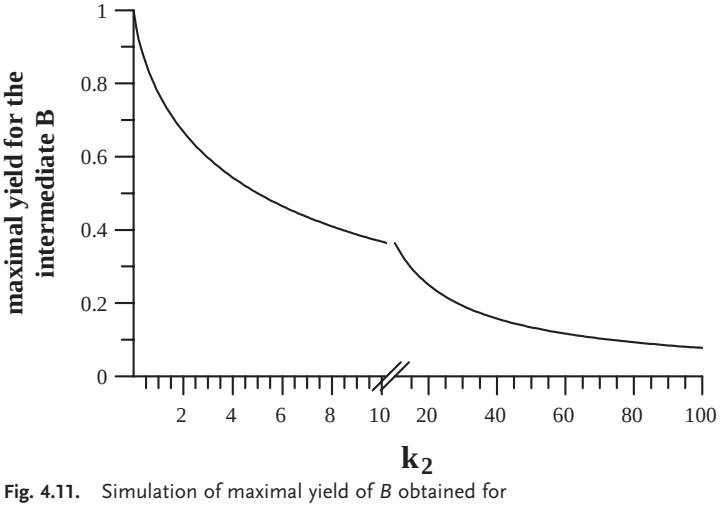

Fig. 4.11. Simulation of maximal yield of *B* obtained for different ratios of k_1 (10) and k_2 of a consecutive reaction ($A \xrightarrow{k_1} B \xrightarrow{k_2} C$).

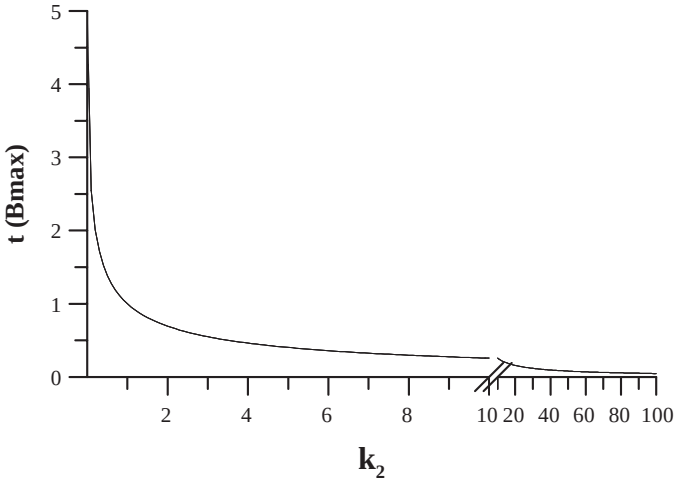

Fig. 4.12. Plot of time point where maximal yield of *B* is reached in consecutive reaction ($k_1 = 10$, k_2 as indicated on x-axis).

For an even advanced treatment, which is necessary for two-step binding mechanisms including competition, the reader is referred to Refs. [98, 99] and to some related "classics" that are concerned mostly with muscle research [100–104].

These mechanisms occur when, e.g., a fluorescent nucleotide serves as an established monitor for a two-step binding process, but of interest are the properties of the unmodified analogue that may also bind in two steps. An approach that uses numerical integration was also described for binding/competition of N^8-(4-*N'*-methylanthraniloylaminobutyl)-8-aminoadenosine 5'-diphosphate and ADP to DnaK from *Thermus thermophilus* [9].

Many binding interactions occur in two or more steps. How do we recognize this and what are the consequences? Two types of mechanism have often been observed. In principle, two different mechanisms are possible: initial "weak" binding followed by an isomerization reaction

$$E + L \rightleftharpoons EL \rightleftharpoons E^*L \qquad \text{(Case 1)}$$

or pre-binding isomerization of one of the components

$$E \rightleftharpoons E^* + L \rightleftharpoons E^*L \qquad \text{(Case 2)}$$

with the asterisk indicating a conformational change.

This problem was also discussed comprehensively for possible two-state binding mechanisms when ATP binding to Hsc70 was analyzed for the first time with stopped-flow measurements using the intrinsic single-tryptophan signal [105].

To derive the according kinetic equations in the most general fashion, we use the following model:

$$A \underset{k_{-1}}{\overset{k_1}{\rightleftharpoons}} B \underset{k_{-2}}{\overset{k_{+2}}{\rightleftharpoons}} C$$

$$\frac{dc}{dt} = k_{+2}b - k_{-2}c = k_{+2}(a_0 - a - c) - k_{-2}c$$

$$\frac{da}{dt} = -k_{+1}a + k_{-1}b = -k_{+1}(a_0 - b - c) + k_{-1}b$$

$$b = \frac{dc}{dt} \cdot \frac{1}{k_{+2}} + \frac{k_{-2}c}{k_{+2}}$$

$$\frac{da}{dt} = -\left(a_0 - \frac{dc}{dt} \cdot \frac{1}{k_{+2}} - \frac{k_{-2}c}{k_{+2}} - c\right)k_{+1} + \frac{dc}{dt} \cdot \frac{k_{-1}}{k_{+2}} + \frac{k_{-1}k_{-2}c}{k_{+2}}$$

$$\frac{d^2c}{dt^2} = -k_{+2}\frac{da}{dt} - k_{+2}\frac{dc}{dt} - k_{-2}\frac{dc}{dt}$$

$$= -k_{+2}\left[-a_o k_{+1} + \frac{dc}{dt} \cdot \frac{k_{+1}}{k_{+2}} + k_{+1}c\frac{k_{-2}}{k_{+2}} - ck_{+1} + \frac{dc}{dt} \cdot \frac{k_{-1}}{k_{+2}} + \frac{k_{-1}k_{-2}c}{k_{+2}}\right]$$

$$- k_{+2}\frac{dc}{dt} - k_{-2}\frac{dc}{dt}$$

$$\frac{d^2c}{dt} + \frac{dc}{dt}[k_{+1} + k_{-1} + k_{+2} + k_{-2}] + c[k_{+1}k_{-1} + k_{+2}k_{+1} + k_{-1}k_{-2}] = k_{+2}k_{+1}a_0$$

$$\lambda_1, \lambda_2 = \frac{-[k_{+1} + k_{-1} + k_{+2} + k_{-2}] \pm \sqrt{[k_{+1} + k_{-1} + k_{+2} + k_{-2}]^2 - 4[k_{+1}k_{-2} + k_{+2}k_{+1} + k_{-1}k_{-2}]}}{2}$$

For the case $1(E + L \rightleftharpoons EL \rightleftharpoons E^*L)$ and assuming that $l_0 \gg e_0$, the expression k_{+1} is replaced by $k_{+1}l_o$, or briefly $k_{+1}{}'$, to indicate that the product of k_{+1} and l_o is virtually constant under these conditions:

$$\lambda_1\lambda_2 = \frac{-[k_{+1}{}' + k_{-1} + k_{+2} + k_{-2}] \pm \sqrt{[k_{+1}{}' + k_{-1} + k_{+2}]^2 - 4[k_{+1}{}'k_{-2} + k_{+2}k_{+1}{}' + k_{-1}k_{-2}]}}{2}$$

In the general case, this means complex kinetic behavior, with both solutions (λ_1 and λ_2) of the differential equation contributing to the transient observed. However, under certain conditions, simpler behavior is seen.

Examples are:

1. If k_{-1} is much larger than k_{+2} and k_{-2}, the second term under the square root bracket will always be much smaller than the first, and we can use the first two terms of the binomial expansion as a good approximation.

We can also simplify the first term by removing k_{+2} and k_{-2}.

[Binomial expansion of $a(a-b)^n = a^n - \frac{na^{n-1}b}{1}\ldots$]
Thus,

$$\lambda_1, \lambda_2 = -\frac{[k_{+1}{}' + k_{-1}] \pm \left[[k_{+1}{}' + k_{-1}] - \frac{1}{2}\cdot 4\frac{[k_{+1}{}'k_{-2} + k_{+2}k_{+1}{}' + k_{-1}k_{-2}]}{[k_{+1}{}' + k_{-1}]}\right]}{2}$$

$$\approx [k_{+1}{}' + k_{-1}] \tag{48}$$

or

$$\frac{k_{+1}{}'k_{-2} + k_2k_{+1}{}' + k_{-1}k_{-2}}{k_{+1}{}' + k_{-1}}$$

Note: The solutions of the equation are actually all negative, but the sign will be dropped at this point (terms in the solution are of the form $Ae^{-\lambda t}$).

$$k_{\text{obs}} = \frac{k_{-2}(k_{+1}{}' + k_{-1}) + k_2k_{+1}{}'}{k_{+1}{}' + k_{-1}}$$

$$= k_{-2} + \frac{k_2k_{+1}{}'}{k_{+1}{}' + k_{-1}}$$

$$= k_{-2} + \frac{k_2}{1 + \frac{k_{-1}}{k_{+1}{}'}} = k_{-2} + \frac{k_2}{1 + \frac{K_d{}'}{l_o}}$$

where K_d' is the dissociation constant for the first step. This behavior is shown in Figure 4.13 and was, e.g., observed for the binding of ATP to DnaK [11].

2. If k_{-1} is much smaller than k_{+2} and k_{-2}, we have the following situation when $k_{+1}{}'$ is also small (i.e., at low $l = l_o$):

$$\lambda_{1,2} = \frac{-[k_{+2} + k_{-2}] \pm \sqrt{[k_{+2} + k_{-2}]^2 - 4[k_{+1}lk_{-2} + k_{+2}k_{+1}l + k_{-1}k_{+2}]}}{2} \tag{49}$$

Again, under the conditions chosen, the second term under the square root sign is small compared to the first and to a first approximation

$$\lambda_{1,2} = [k_{+2} + k_{-2}] \quad \text{or} \quad \frac{k_{+1}lk_{-2} + k_{+2}k_{+1}l + k_{-1}k_{+2}}{k_{+2} + k_{-2}} \tag{50}$$

large and of small amplitude if E^*L gives the signal.

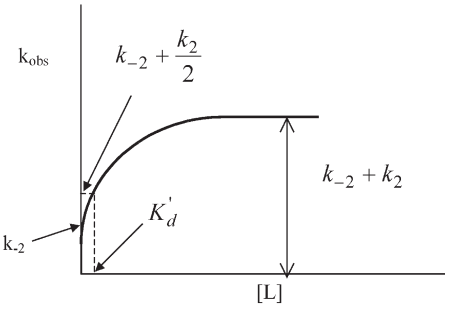

Fig. 4.13. Dependence of observed rate constant for large k_{-1} (fast first step).

The second solution simplifies to

$$k_{+1}l + \frac{k_{-1}k_{+2}}{k_{+2} + k_{-2}} \tag{51}$$

$$k_{+1}l + \frac{k_{-1}}{1 + \frac{k_{-2}}{k_{+2}}} = k_{+1}l + \frac{k_{-1}}{1 + \frac{1}{K_2}} = k_{obs} \tag{52}$$

A corresponding plot is shown in Figure 4.14.

At intermediate concentrations of L (when $k_{+1} \approx k_{+2}l + k_{-2}$), this system will show a lag phase in the kinetics of production of E^*L (comparable to the simple case of $A \rightarrow B \rightarrow C$ when the rate constants are of similar magnitude).

At concentrations at which $k_{+1}l$ is much greater than all the other rate constants, k_{obs} simplifies to:

$$k_{obs} = k_{+2} + k_{-2} \tag{53}$$

(i.e., the rate constant for production of E^*L can never be greater than the sum of k_{+2} and k_{-2}. This essentially simplifies the system to be analogous to the situation discussed previously for the rate of equilibration of A ⇄ B).

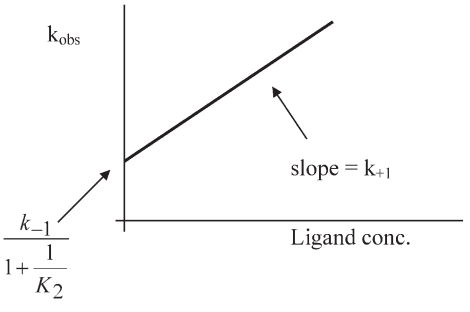

Fig. 4.14. Dependence of k_{obs} on ligand concentration for fast second step in two-step binding mechanism.

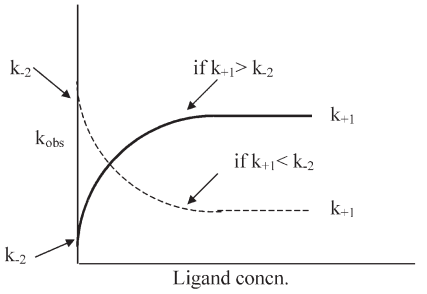

Fig. 4.15. Pre-isomerization dependence of k_{obs} on ligand concentration for large k_{-1}.

In the second possible two-step binding mechanism, a pre-binding isomerization occurs:

$$E \rightleftharpoons E^* + L \rightleftharpoons E^*L$$

In this case, k_{+2} in Eq. (49) is replaced with $k_{+2}l$:

$$\lambda_{1,2} = \frac{-[k_{+1} + k + k_{+2}l + k_{-2}] \pm \sqrt{[k_{+1} + k_{-1} + k_{+2}l + k_{-2}]^2 - 4[k_{+1}k_{-2} + k_{+2}l + k_{-1}k_{-2}]}}{2} \tag{54}$$

If E is mainly in the form without a star in the absence of the ligand, then k_{-1} must be much larger than k_{+1}.

If we also assume that $k_{-1} \gg k_{-2}$, the equation simplifies to:

$$\lambda_{1,2} = \frac{-[k_{-1} + k_{+2}l] \pm \sqrt{[k_{+1} + k_{+2}l]^2 - 4[k_{+2}lk_{+1} + k_{-1}k_{-2}]}}{2} \tag{55}$$

Again, the second term under the square root sign is much smaller than the first, so that:

$$\lambda_{1,2} = [k_{-1} + k_{+2}l] \pm [k_{-1} + k_{+2}] - \frac{1}{2} \cdot \frac{4[k_{+2}lk_{+1} + k_{-1}k_{-2}]}{[k_{-1} + k_{+2}l]}$$

$$= [k_{-1} + k_{+2}l] \quad \text{(always large and of small amplitude)}$$

or

$$\frac{k_{+2}lk_{+1} + k_{-1}k_{-2}}{k_{-1} + k_{+2}l} = \frac{k_{+1}}{1 + \dfrac{k_{-1}}{k_{+2}l}} + \frac{k_{-2}}{1 + \dfrac{k_{+2}l}{k_{-1}}}$$

$$k_{obs} = \frac{k_{+1}}{1 + \dfrac{k_{-1}}{k_{+2}l}} + \frac{k_{-2}}{1 + \dfrac{k_{+2}l}{k_{-1}}}$$

The first term tends to 0 as l tends to 0 and to k_{+1} as l tends to ∞. The second term tends to k_{-2} as l tends to 0 and to 0 as l tends to ∞. The corresponding plot is shown in Fig. 4.15.

References

1 Buchberger, A., Theyssen, H., Schröder, H., McCarty, J. S., Virgallita, G., Milkereit, P., Reinstein, J., & Bukau, B. (1995). Nucleotide-induced conformational Changes in the ATPase and Substrate Binding Domains of the DnaK Chaperone Provide Evidence for Interdomain Communication. *J. Biol. Chem.* **270**, 16903–16910.

2 McCarty, J. S., Buchberger, A., Reinstein, J., & Bukau, B. (1995). The Role of ATP in the Functional Cycle of the DnaK Chaperone System. *J. Mol. Biol.* **249**, 126–137.

3 Vale, R. D. & Milligan, R. A. (2000). The way things move: looking under the hood of molecular motor proteins. *Science* **288**, 88–95.

4 Bagshaw, C. R. (2001). ATP analogues at a glance. *J. Cell Sci.* **114**, 459–460.

5 Jameson, D. M. & Eccleston, J. F. (1997). Fluorescent nucleotide analogues: synthesis and applications. *Methods Enzymol.* **278**, 363–390.

6 Cross, R. A., Jackson, A. P., Citi, S., Kendrick-Jones, J., & Bagshaw, C. R. (1988). Active site trapping of nucleotide by smooth and non-muscle myosins. *J. Mol. Biol.* **203**, 173–181.

7 Karlish, S. J., Yates, D. W., & Glynn, I. M. (1978). Conformational transitions between Na+-bound and K+-bound forms of (Na+ + K+)-ATPase, studied with formycin nucleotides. *Biochim. Biophys. Acta* **525**, 252–264.

8 White, D. C., Zimmerman, R. W., & Trentham, D. R. (1986). The ATPase kinetics of insect fibrillar flight muscle myosin subfragment-1. *J. Muscle Res. Cell Motil.* **7**, 179–192.

9 Klostermeier, D., Seidel, R., & Reinstein, J. (1998). Functional Properties of the Molecular Chaperone DnaK from *Thermus thermophilus*. *J. Mol. Biol.* **279**, 841–853.

10 Packschies, L., Theyssen, H., Buchberger, A., Bukau, B., Goody, R. S., & Reinstein, J. (1997). GrpE Accelerates Nucleotide Exchange of the Molecular Chaperone DnaK with an Associative Displacement Mechanism. *Biochemistry* **36**, 3417–3422.

11 Theyssen, H., Schuster, H.-P., Packschies, L., Bukau, B., & Reinstein, J. (1996). The Second Step of ATP Binding to DnaK Induces Peptide Release. *J. Mol. Biol.* **263**, 657–670.

12 Leonard, N. J. (1993). Etheno-bridged nucleotides in enzyme reactions and protein binding. *Chemtracts Biochem. Mol. Biol.* **4**, 251–284.

13 Yarbrough, L. R., Schlageck, J. G., & Baughman, M. (1979). Synthesis and properties of fluorescent nucleotide substrates for DNA-dependent RNA polymerases. *J. Biol. Chem.* **254**, 12069–12073.

14 Weikl, T., Muschler, P., Richter, K., Veit, T., Reinstein, J., & Buchner, J. (2000). C-terminal regions of hsp90 are important for trapping the nucleotide during the ATPase cycle. *J. Mol. Biol.* **303**, 583–592.

15 Rudolph, M. G., Veit, T. J. H., & Reinstein, J. (1999). The novel fluorescent CDP-analogue (P_b)MABA-CDP is a specific probe for the NMP binding site of UMP/CMP-kinase. *Protein Science* **8**, 2697–2704.

16 Scheidig, A. J., Franken, S. M., Corrie, J. E. T., Reid, G. P., Wittinghofer, A., Pai, E. F., & Goody, R. S. (1995). X-ray crystal-structure analysis of the catalytic domain of the oncogene product p21(h-ras) complexed with caged gtp and mant dgppnhp. *J. Mol. Biol.* **253**, 132–150.

17 Hiratsuka, T. & Uchida, K. (1973). Preparation and properties of 2′(or

3′)-O-(2,4,6-trinitrophenyl) adenosine 5′-triphosphate, an analogue of adenosine triphosphate. *Biochim. Biophys. Acta* **320**, 635–647.

18 Hiratsuka, T. (1983). New ribose-modified fluorescent analogues of adenine and guanine nucleotides available as substrates for various enzymes. *Biochim. Biophys. Acta* **734**, 496–508.

19 Moore, K. J. M. & Lohman, T. M. (1994). Kinetic Mechanism of Adenine Nucleotide Binding to and Hydrolysis by the *Escherichia coli* Rep Monomer. 1. Use of Fluorescent Nucleotide Analogues. *Biochemistry* **33**, 14550–14564.

20 Woodward, S. K., Eccleston, J. F., & Geeves, M. A. (1991). Kinetics of the interaction of 2′(3′)-O-(N-methylanthraniloyl)-ATP with myosin subfragment 1 and actomyosin subfragment 1: characterization of two acto-S1-ADP complexes. *Biochemistry* **30**, 422–430.

21 Schlee, S., Groemping, Y., Herde, P., Seidel, R., & Reinstein, J. (2001). The Chaperone Function of ClpB from *Thermus thermophilus* Depends on Allosteric Interactions of its Two ATP-binding Sites. *J. Mol. Biol.* **306**, 889–899.

22 Watanabe, Y. Y., Motohashi, K., & Yoshida, M. (2002). Roles of the Two ATP Binding Sites of ClpB from *Thermus thermophilus*. *J. Biol. Chem.* **277**, 5804–5809.

23 Bujalowski, W. & Jezewska, M. J. (2000). Kinetic mechanism of nucleotide cofactor binding to Escherichia coli replicative helicase DnaB protein. stopped-flow kinetic studies using fluorescent, ribose-, and base-modified nucleotide analogues. *Biochemistry* **39**, 2106–2122.

24 Witt, S. N. & Slepenkov, S. V. (1999). Unraveling the Kinetic Mechanism of the 70-kDa Molecular Chaperones Using Fluorescence Spectroscopic Methods. *Journal of Fluorescence* **9**, 281–293.

25 Buchberger, A., Reinstein, J., & Bukau, B. (1999) in *Molecular Chaperones and Folding Catalysts: Regulation, Cellular Functions and Mechanisms* (Bukau, B., Ed.) pp 573–635, Harwood Academic Publishers, Amsterdam.

26 Bukau, B. & Horwich, A. L. (1998). The hsp70 and hsp60 chaperone machines. *Cell* **92**, 351–366.

27 Schlee, S. & Reinstein, J. (2002). The DnaK/ClpB chaperone system from Thermus thermophilus. *Cellular and Molecular Life Sciences* **59**, 1598–1606.

28 Pearl, L. H. & Prodromou, C. (2002). Structure, function, and mechanism of the Hsp90 molecular chaperone. *Adv. Protein Chem.* **59**, 157–186.

29 Richter, K. & Buchner, J. (2001). Hsp90: chaperoning signal transduction. *J. Cell Physiol* **188**, 281–290.

30 Mayer, M. P. & Bukau, B. (1999). Molecular chaperones: the busy life of Hsp90. *Curr. Biol.* **9**, R322–R325.

31 Buchner, J. (1999). Hsp90 & Co. – a holding for folding. *Trends Biochem. Sci.* **24**, 136–141.

32 Pratt, W. B. & Toft, D. O. (2003). Regulation of signaling protein function and trafficking by the hsp90/hsp70-based chaperone machinery. *Exp. Biol. Med. (Maywood.)* **228**, 111–133.

33 Csermely, P. & Kahn, C. R. (1991). The 90-kDa heat shock protein (hsp-90) possesses an ATP binding site and autophosphorylating activity. *J. Biol. Chem.* **266**, 4943–4950.

34 Nadeau, K., Das, A., & Walsh, C. T. (1993). Hsp90 chaperonins possess ATPase activity and bind heat shock transcription factors and peptidyl prolyl isomerases. *J. Biol. Chem.* **268**, 1479–1487.

35 Nadeau, K., Sullivan, M. A., Bradley, M., Engman, D. M., & Walsh, C. T. (1992). 83-kilodalton heat shock proteins of trypanosomes are potent peptide-stimulated ATPases. *Protein Sci.* **1**, 970–979.

36 Csermely, P., Kajtar, J., Hollosi, M., Jalsovszky, G., Holly, S., Khan, C. R., Gergely, P., Söti, C., Mihaly, K., & Somogyi, J. (1993). ATP Induces a Conformational Change of the 90-kDa Heat Shock Protein (hsp90). *J. Biol. Chem.* **268**, 1901–1907.

37 Jakob, U., Scheibel, T., Bose, S., Reinstein, J., & Buchner, J. (1996). Assessment of the ATP Binding Properties of Hsp90. *J. Biol. Chem.* **271**, 10035–10041.

38 Scheibel, T., Neuhofen, S., Weikl, T., Mayr, C., Reinstein, J., Vogel, P. D., & Buchner, J. (1997). ATP-binding Properties of Human Hsp90. *J. Biol. Chem.* **272**, 18608–18613.

39 Bauer, M., Baumann, J., & Trommer, W. E. (1992). ATP binding to bovine serum albumin. *FEBS Lett.* **313**, 288–290.

40 Prodromou, C., Roe, S. M., O'Brien, R., Ladbury, J. E., Piper, P. W., & Pearl, L. H. (1997). Identification and Structural Characterization of the ATP/ADP-Binding Site in the HSP90 Molecular Chaperone. *Cell* **90**, 65–75.

41 Stebbins, C. E., Russo, A. A., Schneider, C., Rosen, N., Hartl, F. U., & Pavletich, N. P. (1997). Crystal structure of an Hsp90-geldanamycin complex: targeting of a protein chaperone by an antitumor agent. *Cell* **89**, 239–250.

42 Buchner, J. (1996). Supervising the fold: functional principles of molecular chaperones. *FASEB Journal* **10**, 10–19.

43 Wegele, H., Muschler, P., Bunck, M., Reinstein, J., & Buchner, J. (2003). Dissection of the contribution of individual domains to the ATPase mechanism of Hsp90. *J. Biol. Chem.* **78**, 39303–39310.

44 Richter, K., Reinstein, J., & Buchner, J. (2002). N-terminal residues regulate the catalytic efficiency of the Hsp90 ATPase cycle. *J. Biol. Chem.* **277**, 44905–44910.

45 Richter, K., Muschler, P., Hainzl, O., Reinstein, J., & Buchner, J. (2003). Sti1 Is a Non-competitive Inhibitor of the Hsp90 ATPase. Binding prevents the N-terminal dimerization reaction during the ATPase cycle. *J. Biol. Chem.* **278**, 10328–10333.

46 Wegele, H., Haslbeck, M., Reinstein, J., & Buchner, J. (2003). Sti1 Is a Novel Activator of the Ssa Proteins. *J. Biol. Chem.* **278**, 25970–25976.

47 Vale, R. D. (2000). AAA proteins. Lords of the ring. *J. Cell Biol.* **150**, F13–F19.

48 Ogura, T. & Wilkinson, A. J. (2001). AAA+ superfamily ATPases: common structure–diverse function. *Genes Cells* **6**, 575–597.

49 Neuwald, A. F., Aravind, L., Spouge, J. L., & Koonin, E. V. (1999). AAA+: A class of chaperone-like ATPases associated with the assembly, operation, and disassembly of protein complexes. *Genome Res.* **9**, 27–43.

50 Parsell, D. A., Kowal, A. S., & Lindquist, S. (1994). *Saccharomyces cerevisiae* Hsp104 Protein: Purification and characterization of ATP-induced structural changes. *J. Biol. Chem.* **269**, 4480–4487.

51 Zolkiewski, M., Kessel, M., Ginsburg, A., & Maurizi, M. R. (1999). Nucleotide-dependent oligomerization of ClpB from *Escherichia coli*. *Protein Sci.* **8**, 1899–1903.

52 Glover, J. R. & Lindquist, S. (1998). Hsp104, Hsp70, and Hsp40: A Novel Chaperone System that Rescues Previously Aggregated Proteins. *Cell* **94**, 73–82.

53 Motohashi, K., Watanabe, Y., Yohda, M., & Yoshida, M. (1999). Heat-inactivated proteins are rescued by the DnaK·J-GrpE set and ClpB chaperones. *Proc. Natl. Acad. Sci. U.S.A.* **96**, 7184–7189.

54 Parsell, D. A., Kowal, A. S., Singer, M. A., & Lindquist, S. (1994). Protein disaggregation mediated by heat-shock protein Hsp104. *Nature* **372**, 475–478.

55 Goloubinoff, P., Mogk, A., Zvi, A. P., Tomoyasu, T., & Bukau, B. (1999). Sequential mechanism of solubilization and refolding of stable protein aggregates by a bichaperone network. *Proc. Natl. Acad. Sci. U.S.A.* **96**, 13732–13737.

56 Mogk, A., Tomoyasu, T., Goloubinoff, P., Rüdiger, S., Röder, D., Langen, H., & Bukau, B. (1999). Identification of thermolabile *Escherichia coli* proteins: prevention

and reversion of aggregation by DnaK and ClpB. *EMBO J.* **18**, 6934–6949.

57 Zolkiewski, M. (1999). ClpB Cooperates with DnaK, DnaJ, and GrpE in Suppressing Protein Aggregation: A NOVEL MULTI-CHAPERONE SYSTEM FROM *ESCHERICHIA COLI*. *J. Biol. Chem.* **274**, 28083–28086.

58 Mogk, A., Schlieker, C., Strub, C., Rist, W., Weibezahn, J., & Bukau, B. (2003). Roles of individual domains and conserved motifs of the AAA+ chaperone ClpB in oligomerization, ATP hydrolysis, and chaperone activity. *J. Biol. Chem.* **278**, 17615–17624.

59 Hattendorf, D. A. & Lindquist, S. L. (2002). Analysis of the AAA sensor-2 motif in the C-terminal ATPase domain of Hsp104 with a site-specific fluorescent probe of nucleotide binding. *Proc. Natl. Acad. Sci. U.S.A.*

60 Kim, K. I., Woo, K. M., Seong, I. S., Lee, Z.-W., Baek, S. H., & Chung, C. H. (1998). Mutational analysis of the two ATP-binding sites in ClpB, a heat shock protein with protein-activated ATPase activity in *Escherichia coli*. *Biochem. J.* **333**, 671–676.

61 Schirmer, E. C., Queitsch, C., Kowal, A. S., Parsell, D. A., & Lindquist, S. (1998). The ATPase activity of Hsp104, effects of environmental conditions and mutations [published erratum appears in *J Biol Chem* 1998 Jul 31; 273(31):19922]. *J. Biol. Chem.* **273**, 15546–15552.

62 Krzewska, J., Konopa, G., & Liberek, K. (2001). Importance of Two ATP-binding Sites for Oligomerization, ATPase Activity and Chaperone Function of Mitochondrial Hsp78 Protein. *J. Mol. Biol.* **314**, 901–910.

63 Hattendorf, D. A. & Lindquist, S. L. (2002). Cooperative kinetics of both Hsp104 ATPase domains and interdomain communication revealed by AAA sensor-1 mutants. *EMBO J.* **21**, 12–21.

64 Barker, R., Trayer, I. P., & Hill, R. L. (1974). Nucleoside Phosphates Attached to Agarose. *Methods Enzymol.* **34B**, 479–491.

65 Lambrecht, W. & Trautschold, I. (1974) in *Methoden der enzymatischen Analyse II* (Anonymouspp 2151–2160, Verlag Chemie, Weinheim.

66 Gao, B., Emoto, Y., Greene, L., & Eisenberg, E. (1993). Nucleotide Binding Properties of Bovine Brain Uncoating ATPase. *J. Biol. Chem.* **268**, 8507–8513.

67 Wilbanks, S. M. & McKay, D. B. (1995). How Potassium Affects the Activity of the Molecular Chaperone Hsc70: II. POTASSIUM BINDS SPECIFICALLY IN THE ATPase ACTIVE SITE. *J. Biol. Chem.* **270**, 2251–2257.

68 Feifel, B., Sandmeier, E., Schönfeld, H.-J., & Christen, P. (1996). Potassium ions and the molecular-chaperone activity of DnaK. *Eur. J. Biochem.* **237**, 318–321.

69 Gao, B., Greene, L., & Eisenberg, E. (1994). Characterization of Nucleotide-Free Uncoating ATPase and Its Binding to ATP, ADP, and ATP Analogues. *Biochemistry* **33**, 2048–2054.

70 Russell, R., Jordan, R., & McMacken, R. (1998). Kinetic Characterization of the ATPase Cycle of the DnaK Molecular Chaperone. *Biochemistry* **37**, 596–607.

71 Adam, H. (1962) in *Methoden der enzymatischen Analyse* (Bergmeyer, H. U., Ed.) pp 573–577, Verlag Chemie, Weinheim.

72 Buchberger, A., Valencia, A., McMacken, R., Sander, C., & Bukau, B. (1994). The chaperone function of DnaK requires the coupling of ATPase activity with substrate binding through residue E171. *EMBO J.* **13**, 1687–1695.

73 Liberek, K., Marszalek, J., Ang, D., Georgopoulos, C., & Zylicz, M. (1991). *Escherichia coli* DnaJ and GrpE heat shock proteins jointly stimulate ATPase activity of DnaK. *Proc. Natl. Acad. Sci. U.S.A.* **88**, 2874–2878.

74 McCarty, J. S. & Walker, G. C. (1991). DnaK as a thermometer: Threonine-199 is site of autophosphorylation and is critical for ATPase activity. *Proc. Natl. Acad. Sci. U.S.A.* **88**, 9513–9517.

75 O'Brien, M. C. & McKay, D. B. (1995). How Potassium Affects the Activity of the Molecular Chaperone Hsc70: I. POTASSIUM IS REQUIRED FOR OPTIMAL ATPase ACTIVITY. *J. Biol. Chem.* **270**, 2247–2250.

76 Chock, S. P., Chock, P. B., & Eisenberg, E. (1979). The mechanism of the skeletal muscle myosin ATPase. II. Relationship between the fluorescence enhancement induced by ATP and the initial Pi burst. *J. Biol. Chem.* **254**, 3236–3243.

77 Brune, M., Hunter, J. L., Corrie, J. E. T., & Webb, M. R. (1994). Direct, Real-Time Measurement of Rapid Inorganic Phosphate Release Using a Novel Fluorescent Probe and Its Application to Actomyosin Subfragment 1 ATPase. *Biochemistry* **33**, 8262–8271.

78 Karzai, A. W. & McMacken, R. (1996). A bipartite signaling mechanism involved in DnaJ-mediated activation of the *Escherichia coli* DnaK protein. *J. Biol. Chem.* **271**, 11236–11246.

79 Laufen, T., Mayer, M. P., Beisel, C., Klostermeier, D., Mogk, A., Reinstein, J., & Bukau, B. (1999). Mechanism of regulation of Hsp70 chaperones by DnaJ cochaperones. *Proc. Natl. Acad. Sci. U.S.A* **96**, 5452–5457.

80 Russell, R., Karzai, A. W., Mehl, A. F., & McMacken, R. (1999). DnaJ Dramatically Stimulates ATP Hydrolysis by DnaK: Insight into Targeting of Hsp70 Proteins to Polypeptide Substrates. *Biochemistry* **38**, 4165–4176.

81 Garnier, C., Lafitte, D., Tsvetkov, P. O., Barbier, P., Leclerc-Devin, J., Millot, J. M., Briand, C., Makarov, A. A., Catelli, M. G., & Peyrot, V. (2002). Binding of ATP to heat shock protein 90: evidence for an ATP-binding site in the C-terminal domain. *J. Biol. Chem.* **277**, 12208–12214.

82 Groemping, Y., Klostermeier, D., Herrmann, C., Veit, T., Seidel, R., & Reinstein, J. (2001). Regulation of ATPase and Chaperone Cycle of DnaK from *Thermus thermophilus* by the Nucleotide Exchange Factor GrpE. *J. Mol. Biol.* **305**, 1173–1183.

83 Ha, J.-H. & McKay, D. B. (1994). ATPase Kinetics of Recombinant Bovine 70 kDa Heat Shock Cognate Protein and Its Amino-Terminal ATPase Domain. *Biochemistry* **33**, 14625–14635.

84 Eftink, M. R. (1997). Fluorescence Methods for Studying Equilibrium Macromolecule-Ligand Interactions. *Methods Enzymol.* **278**, 221–257.

85 Bartha, B. B., Ajtai, K., Toft, D. O., & Burghardt, T. P. (1998). ATP sensitive tryptophans of hsp90. *Biophys. Chem.* **72**, 313–321.

86 Reinstein, J., Vetter, I. R., Schlichting, I., Rösch, P., Wittinghofer, A., & Goody, R. S. (1990). Fluorescence and NMR Investigations on the Ligand Binding Properties of Adenylate Kinases. *Biochemistry* **29**, 7440–7450.

87 Klostermeier, D., Seidel, R., & Reinstein, J. (1999). The Functional Cycle and Regulation of the *Thermus thermophilus* DnaK Chaperone System. *J. Mol. Biol.* **287**, 511–525.

88 Thrall, S. H., Reinstein, J., Wöhrl, B. M., & Goody, R. S. (1996). Evaluation of human immunodeficiency virus type 1 reverse transcriptase primer tRNA binding by fluorescence spectroscopy: specificity and comparison to primer/template binding. *Biochemistry* **35**, 4609–4618.

89 Press, W. H., Flannery, B. P., Teukolsky, S. A., & Vetterling, W. T. (1989) in *Numerical recipes in Pascal; The art of scientific computing*, Cambridge University Press, Cambridge, USA.

90 Wang, Z. X. (1995). An exact mathematical expression for describing competitive binding of two different ligands to a protein molecule. *FEBS Lett.* **360**, 111–114.

91 Fabiato, A. & Fabiato, F. (1987). Multiligand program and constants. *Eur. J. Biochem.* **162**, 357–363.

92 Brehmer, D., Rüdiger, S., Gassler, C. S., Klostermeier, D., Packschies, L., Reinstein, J., Mayer, M. P., &

Bukau, B. (2001). Tuning of chaperone activity of Hsp70 proteins by modulation of nucleotide exchange. *Nat. Struct. Biol.* **8**, 427–432.

93 Steinfeld, J. I., Francisco, J. S., & Hase, W. L. (1989) in *Chemical Kinetics and Dynamics*, Prentice-Hall, Inc., New Jersey 07632.

94 Roberts, D. V. (1977) in *Enzyme kinetics*, Cambridge University Press, Cambridge.

95 Gutfreund, H. (1995) in *Kinetics for the Life Sciences: Receptors, transmitters and catalysts*, University Press, Cambridge.

96 Bernasconi, C. F. (1976) in *Relaxation kinetics*, AcademicPress, New York.

97 Schlee, S., Beinker, P., Akhrymuk, A., & Reinstein, J. (2004). A chaperone network for the resolubilization of protein aggregates: direct interaction of ClpB and DnaK. *J. Mol. Biol.* **336**, 275–285.

98 Wu, X., Gutfreund, H., & Chock, P. B. (1992). Kinetic Method for Differentiating Mechanisms for Ligand Exchange Reactions: Application To Test for Substrate Channeling in Glycolysis. *Biochemistry* **31**, 2123–2128.

99 Johnson, K. A. (2003) in *Kinetic Analysis of Macromolecules*, Oxford University Press.

100 Bagshaw, C. R., Eccleston, J. F., Eckstein, F., Goody, R. S., Gutfreund, H., & Trentham, D. R. (1974). The Magnesium Ion-Dependent Adenosine Triphosphatase of Myosin: Two-Step processes of adenosine triphospahte association and adenosine dophosphate dissociation. *Biochem. J.* **141**, 351–364.

101 Nowak, E., Strzelecka-Golaszewska, H., & Goody, R. S. (1988). Kinetics of Nucleotide and Metal Ion Interaction with G-Actin. *Biochemistry* **27**, 1785–1792.

102 Geeves, M. A., Branson, J. P., & Attwood, P. V. (1995). Kinetics of nucleotide binding to pyruvate carboxylase. *Biochemistry* **34**, 11846–11854.

103 Trentham, D. R., Eccleston, J. F., & Bagshaw, C. R. (1976). Kinetic analysis of ATPase mechanisms. *Q. Rev. Biophys.* **9**, 217–281.

104 Eccleston, J. F. & Trentham, D. R. (1979). Magnesium ion dependent rabbit skeletal muscle myosin guanosine and thioguanosine triphosphatase mechanism and a novel guanosine diphosphatase reaction. *Biochemistry* **18**, 2896–2904.

105 Ha, J.-H. & McKay, D. B. (1995). Kinetics of Nucleotide-Induced Changes in the Tryptophan Fluorescence of the Molecular Chaperone Hsc70 and Its Subfragments Suggest the ATP-Induced Conformational Change Follows Initial ATP Binding. *Biochemistry* **34**, 11635–11644.

106 Ehresmann, B., Imbault, P., & Weil, J. H. (1973). Spectrophotometric Determination of Protein Concentration in Cell Extracts Containing tRNA's and rRNA's. *Anal. Biochem.* **54**, 454–463.

5
Analysis of Chaperone Function in Vitro

Johannes Buchner and Stefan Walter

5.1
Introduction

The intention of this chapter is to provide a manual of how to identify a protein as a molecular chaperone and to carry out the experiments required for its basic characterization.

Originally, the term *molecular chaperone* had been coined by Laskey to describe the role of nucleoplasmin in the association of histones (1, 2). Later, the concept was extended to heat shock proteins by John Ellis (3, 4). He also invented the term ''chaperonin'' for GroE (Hsp60) and related proteins. Over the years, *molecular chaperone* has acquired additional meanings, some of which represent useful extensions of the original definition, whereas others, such as ''chemical chaperones'', may cause some confusion. In the first section of this chapter, we will discuss the distinct features of a molecular chaperone. We will then describe the types of reactions that can be facilitated by molecular chaperones in general and present some important functional aspects. The theoretical section concludes with a discussion of the principal assays that can be used to investigate chaperone function in vitro. In the second part of this chapter, we provide selected protocols to measure and characterize chaperone function.

Molecular chaperones are a functionally related family of proteins assisting conformational changes in proteins without becoming part of the final structure of the client protein [5–9]. Originally, the focus of the concept was on the correct association of proteins and the prevention of unspecific aggregation of polypeptide chains during protein folding. Interestingly, all major chaperones belong to the class of heat shock or stress proteins, i.e., they are synthesized in response to stress situations such as elevated temperatures. Under these conditions, proteins tend to aggregate in vivo. This was demonstrated for *E. coli* strains lacking the heat shock response [10]. In these bacteria, elevated temperature caused the accumulation of proteins in large insoluble aggregates, which resemble the so-called inclusion bodies sometimes obtained upon overexpression of recombinant proteins [11]. These experiments showed that under stress there is a strong influence of molecular chaperones on protein homeostasis. However, this seems to hold true also for physiological conditions: many molecular chaperones have homologues that are

Protein Folding Handbook. Part II. Edited by J. Buchner and T. Kiefhaber

ISBN: 3-527-30784-2

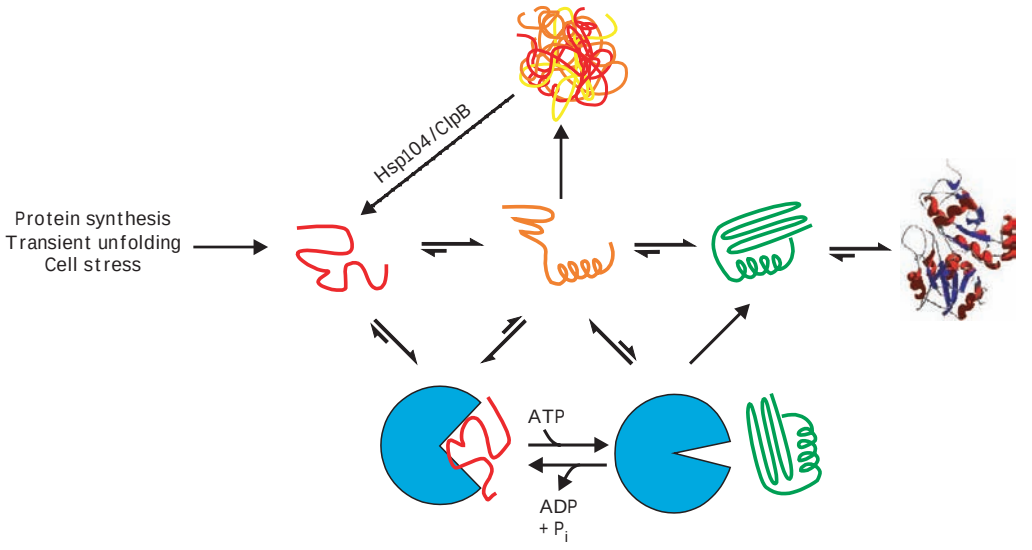

Fig. 5.1. Model for assisted protein folding by molecular chaperones. Several processes generate unfolded polypeptide chains (red), which can fold via partially structured intermediates (orange, green) to the native, biologically active state (right). Depending on the conditions and the nature of the polypeptide, a significant fraction of the molecules may form aggregates (top). The yield of cellular protein folding is significantly improved by the action of general molecular chaperones (bottom, blue). They bind to nonnative polypeptides and thus prevent their aggregation. Further, they may alter the conformation of the bound polypeptide so that once it dissociates, it is less prone to aggregation. Often, release is triggered by a change in the nucleotide state of the chaperone or by ATP hydrolysis. Recently, it was shown that some chaperones of the Hsp100 class such as ClpB and Hsp104 are able to reverse aggregation (top).

constitutively expressed [12], and some of them are essential for viability [13, 14]. This finding suggests that these helper proteins are of general importance for the folding and assembly of newly synthesized polypeptide chains. Furthermore, the observation of strong aggregation of overexpressed proteins under otherwise physiological conditions is consistent with the notion of a balance between protein synthesis/folding and chaperone expression, which has been developed through evolution and can be modulated only within a certain range.

At first glance, the concept outlined above is in conflict with the paradigm of autonomous, spontaneous protein folding established by Anfinsen and many others [15, 16]. The apparent contradiction is that if the acquisition of the unique three-dimensional structure of a protein is governed by its amino acid sequence and the resulting interactions between amino acid side chains, there should be no need for molecular chaperones (Figure 5.1). However, additional factors have to be taken into account. The most important is the possibility of unspecific intermolecular interactions during the folding process of proteins [17, 18]. This reaction depends on the concentration of unfolded or partially folded polypeptide chains and their folding kinetics. Thus, either conditions under which proteins fold slowly or high concentrations of folding proteins will favor aggregation [19]. In consequence, the fraction of molecules reaching the native state will decrease. The basic function of molecular chaperones is to counteract this nonproductive side reaction and thereby

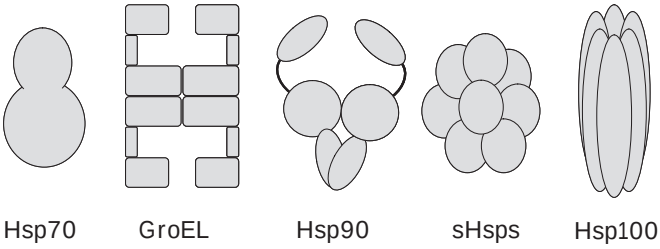

Fig. 5.2. Classes of general molecular chaperones. From left to right: Hsp70 is a monomeric chaperone consisting of an ATPase domain and a peptide-binding domain. The bacterial chaperone GroEL forms two rings comprised of seven subunits each. In the cross-section shown here, two subunits of each ring are depicted. Interactions between the subunits are mediated by the equatorial domains in the center of the molecule, which also contain the ATPase site. The dimeric Hsp90 chaperone consists of three domains. While the C-terminal domains are responsible for dimerization, the N-terminal domains bind and hydrolyze ATP. The small Hsps form large oligomeric structures that contain 24–32 identical subunits. They are the only general chaperones without ATPase function. Chaperones of the Hsp100 class form ring-shaped homohexamers. Each subunit contains two similar, but not identical, ATPase sites.

increase the efficiency of folding (Figure 5.1). Molecular chaperones do not provide steric information for the folding process and thus do not violate the concept of autonomous folding. (The information for folding is encoded solely in the amino acid sequence.) Rather, molecular chaperones assist the spontaneous folding of proteins. Interestingly, the principal possibility of assisted folding had already been hypothesized by Anfinsen in 1963 [20].

It is difficult to assess what fraction of the cellular proteome depends on molecular chaperones to reach its active conformation. But clearly not all newly synthesized proteins need their assistance. While for the chaperone role model GroE (see Chapter 20) it was shown that 40% of the *E. coli* proteins can be influenced in their folding [21], in the cell only about 10–15% may need this assistance under physiological conditions [22, 23]. Similar values were reported for other chaperones [24, 25]. Under conditions where proteins are destabilized (such as heat shock), the requirement for chaperone assistance is clearly increased.

There are only a few classes of general molecular chaperones (Figure 5.2) that have to take care of a large number of different proteins, implying that chaperones have to be promiscuous in their interaction with nonnative proteins, i.e., they must be able to recognize and handle a large variety of different proteins. With the exception of small Hsps, all of them possess an intrinsic ATPase activity (Table 5.1). ATP-dependent structural changes in molecular chaperones are essential for the conformational processing of client proteins. While some basic functional features seem to be conserved between different classes of chaperones, the structure and mode of action are completely different among individual chaperones.

5.2
Basic Functional Principles of Molecular Chaperones

The classification of an enzyme is usually based on the type of reaction it catalyzes and the substrate(s) it turns over. In the field of protein folding and molecular

Tab. 5.1. Properties of general chaperones.

	Hsp60	*Hsp70*	*Hsp90*	*Hsp100*	*sHsp*
Representatives	GroEL (eubacteria) CCT/TRiC (eukaryotes)	DnaK (*E. coli*) Ssa1 (*S. cerevisiae*) Hsp72 (higher eukaryotes)	HtpG (*E. coli*) Hsp82 (*S. cerevisiae*) Hsp90 (human)	Hsp104 (*S. cerevisiae*) ClpB (bacteria) ClpA (bacteria)	Hsp16.5 (*M. jannashii*) Hsp26 (*S. cerevisiae*) α-crystallin
Structure: PDB accession number	1AON (GroEL) [40] 1A6D (thermosome) [125]	1DKZ (DnaK peptide-binding domain) [33] 1S3X(Hsp72 ATPase domain) [150]	1AM1 (Hsp82 ATPase domain) [126] 1HK7 (Hsp82 middle domain) [127]	1QVR (ClpB *T. thermophilus*) [128]	1SHS (Hsp16.5) [129] 1GME (Hsp16.9) [151]
Molecular mass of the monomer (kDa)	57 (GroEL) 57–60 (human CCT-α)	69 (DnaK) 72 (human Hsp72)	81 (Hsp82) 85 (human Hsp90α)	102 (Hsp104) 96 (ClpB) 84 (ClpA)	16.5 (Hsp16.5) 24 (Hsp26) 20 (bovine α-crystallin)
Co-chaperones	GroES (*E. coli*) Prefoldin (human)	Hsp40 GrpE (*E. coli*) Hop/Sti1	Hop/Sti1 p23/Sba1 Cdc37	Hsp70/Hsp40 (Hsp104) DnaK/DnaJ/GrpE (ClpB)	Not known
Quaternary structure	Homo 14mer (GroEL) Hetero 16mer (archaea/eukaryotes)	Monomer[1]	Dimer	Dynamic hexamer	Dynamic 24mer (Hsp26) 32mer (α-crystallin)
ATPases per subunit	1	1	1	2[2]	–
ATPase rate per subunit (min^{-1})	3 (GroEL) [67] 1–7 (bovine CCT) [130]	0.02–0.04 (DnaK) [131] 0.04 (Ssa1) [132]	1.0 (Hsp82) [54] 0.05 (Hsp90) [60]	70 (Hsp104) [93] 10–30 (ClpB) [133]	–
T_M (°C)	67 (GroEL) [134]	50 (Ssa1)[3]	62 (Hsp82)[3]	48 (Hsp104)[3]	75 (Hsp26) [135]

[1] Can form oligomers in the absence of ATP.
[2] Some Hsp100s contain only one ATPase/monomer.
[3] Unpublished data from our labs.

chaperones, applying this concept is rather difficult for three reasons. First, though we currently lack a detailed understanding of the mechanisms of protein folding, especially in the context of a living cell, we know it is a rather complex process involving multiple pathways, intermediates, and potential side reactions. As a consequence, molecular chaperones can interfere with and assist protein folding in many different ways, and in most cases our knowledge of how chaperones influence protein folding on a molecular level is very limited. A second problem arises from the heterogeneity of the substrates. As already mentioned, the in vivo substrates of most chaperones are not known in detail. However, it is clear that they include a substantial fraction of the proteome. Finally, it is very difficult to assess which conformational state(s) of these client proteins interact with a certain chaperone. In classic enzymology, reaction intermediates can often be trapped by changing the solvent conditions or temperature. Due to their low intrinsic stability, this is in general not possible for nonnative proteins. Here, a change in solvent conditions will almost always result in a change in the conformational state of the client protein. Under ''folding'' conditions, the nonnative protein will continue to ''react'' until a final state (e.g., native structure or aggregate) is reached. Therefore, great care must be taken when the structure of these intermediates is studied. Otherwise, the result will most likely not reflect the conformation of the protein at the time the sample was taken [26–29].

In the following sections, we present key features that many chaperones have in common and that we consider as the functionally most relevant.

5.2.1 Recognition of Nonnative Proteins

The most fascinating trait of a molecular chaperone is its ability to discriminate between the folded and nonnative states of a protein. It would be deleterious for the cell if chaperones would bind to native proteins or fail to recognize the accumulation of the nonnative protein species. Thus, the promiscuous general chaperones have to use a property for recognition and binding that is common to all nonnative proteins. This is the exposure of hydrophobic amino acid side chains, the hallmark of unfolded or partially folded protein structures. In the unfolded state, extended stretches of polypeptide chains containing hydrophobic residues can be recognized by chaperones. This is well documented for proteins of the Hsp70 family [30, 31]. In partially folded proteins, these residues are often clustered in areas that are part of a domain/subunit interface in the folded protein, and they will become buried in subsequent folding/association events. These regions can thus be utilized by molecular chaperones to identify potential client polypeptides, i.e., to distinguish a nonnative conformation from a native protein. The respective binding site of the chaperone usually contains a number of hydrophobic residues that interact with the substrate [32, 33]. The low specificity of hydrophobic interactions is the basis for the substrate promiscuity of molecular chaperones. Since the extended exposure of hydrophobic surfaces in an unfolded or partially folded state is an important determinant for its probability to aggregate, the shielding of these surfaces upon binding to a chaperone is a very efficient means to prevent aggregation.

Besides hydrophobicity, a polypeptide may have to meet additional requirements in order to bind to a chaperone. It was shown for GroEL that negative charges on the substrate significantly weaken interaction with the chaperone due to electrostatic repulsion [34]. In the case of DnaK (Hsp70), the preferred substrate is a stretch of hydrophobic residues flanked by basic amino acids [35, 36]. Another important aspect that can influence the affinity of a polypeptide towards a chaperone is its conformational plasticity. Due to their promiscuity, chaperones cannot provide an optimal binding surface for each of their client proteins. Consequently, the polypeptide, and to some extent the chaperone itself, may have to adjust its conformation to establish tight binding [37]. Because this process requires a certain degree of flexibility, it may serve as a second checkpoint to discriminate between native and nonnative conformations.

An important consequence of the unspecific recognition of exposed hydrophobic residues is that chaperones will not bind just one specific nonnative conformation of a protein. In contrast, it has to be assumed that all conformations exhibiting a certain degree of hydrophobicity will be recognized. In the case of GroE, the conformations that are stably bound range from completely unfolded to a native-like dimer [38, 39].

The sites of interaction with nonnative proteins are known for Hsp70 and GroEL. In the crystal structure of the protein-binding domain of DnaK (Hsp70) in complex with a short peptide [33], the peptide adopts an extended conformation and the hydrophobic side chains of the peptide make contact with the binding groove, but there are also polar interactions between Hsp70 and the peptide backbone. In the case of GroEL, the analysis of numerous point mutations together with the crystal structure indicated that the nonnative protein binds to hydrophobic residues of the apical domains, which are located on the top of the inner rim of the GroEL cylinder [32, 40]. This conclusion was confirmed several years later by the X-ray structure of a GroEL-peptide complex [41, 42]. Detailed descriptions of the substrate-binding sites and their properties can be found in the chapters dedicated to the respective molecular chaperones.

A notable exception from the theme of hydrophobic binding motifs is chaperones involved in the unfolding of proteins. Many of their client proteins adopt a fully folded conformation and thus do not expose hydrophobic surfaces. At the same time, an unambiguous signal is required to tell the chaperone which protein should be unfolded for subsequent degradation. Evolution has solved this problem by attaching specific tags, such as ubiquitin [43, 44] or the ssrA peptide [45], to these proteins, which serve as recognition sites for the respective degradation systems [46]. Little is known about the structure/sequence motifs recognized by chaperones involved in disaggregation, such as ClpB or Hsp104, as it has proved difficult to obtain stable chaperone-substrate complexes in these cases.

5.2.2
Induction of Conformational Changes in the Substrate

Prevention of aggregation by (transient) binding of partially folded proteins clearly is an important part of chaperone function in vivo. But in a number of cases, this

"buffering capacity" appears not to be the primary task. This is especially true for the ATP-consuming chaperones. An increasing amount of evidence suggests that the energy provided by ATP hydrolysis is used to induce conformational changes in the bound polypeptide. For the ClpA chaperone, Horwich and coworkers demonstrated that it can actively unfold ssrA-tagged, native GFP [47]. In this case, ATP hydrolysis is required to overcome the free energy of folding. In the case of the Hsp90 system, an immature conformation of a bound steroid hormone receptor (a client protein) is converted into a conformation that is capable of binding the hormone ligand [48, 49]. ATP binding and hydrolysis are essential for this process, as they seem to control the association of the chaperone with its various cofactors [50] (see also Chapter 23). During the whole sequence of reactions, the receptor is assumed to remain bound to the Hsp90 chaperone.

For the general chaperones, we know that conformational changes occur in the chaperone upon both ATP binding and hydrolysis [51–54]. However, much less is known about how and to what extent these changes result in conformational rearrangements in substrate proteins associated with the chaperone. As mentioned above, this is mainly because the species involved are often only transiently populated and very labile and thus are not easily susceptible to methods of structure determination. Also, the bound target protein may represent an ensemble of conformations [39].

Two mechanisms can be envisaged as to how a chaperone causes a structural change in a client protein. In both cases, a conformational change in the chaperone is induced by the binding of a ligand (ATP or a cofactor) or by ATP hydrolysis. This in turn results in a change in the nature/geometry of the substrate-binding site that weakens the interaction with the bound polypeptide. As the system ligand/chaperone tends to assume a state of minimum free energy, the substrate has two choices: (1) it may undergo structural rearrangements to adopt a conformation that has a higher affinity towards the binding site or (2) it may start to fold. Both processes will lower the free energy of the system, but in the first case the energy drop primarily results from interactions between chaperone and substrate, whereas in the second case it results solely from interactions within the client polypeptide. Although these rearrangements are driven by thermodynamics, kinetics may be important as well in defining whether binding or folding dominates for a given polypeptide conformation [55–57].

An alternative to this "passive" model is that the conformational change in the chaperone generates a "power stroke" that is used to perform work on the substrate, e.g., by moving apart two sections of the bound protein. If the substrate is a single polypeptide, this could result in a forced unfolding reaction [58]. If the substrate is an oligomeric species, e.g., a small aggregate, the power stroke may cause its dissociation into individual molecules. This "active" mechanism requires that the substrate remains associated with the chaperone during the conformational switch, which is not required in the first model. After the power stroke, the substrate will probably undergo a series of conformational relaxation reactions.

For both models, the concept of general chaperones requires that the conformational change in the substrate be encoded by its amino acid sequence rather than

being forced onto the substrate by the chaperone. The chaperone merely enables the polypeptide to use its inherent folding information.

5.2.3 Energy Consumption and Regulation of Chaperone Function

Most of the general chaperones require ATP to carry out their task (Table 5.1). Examples of ATP-hydrolyzing chaperones are GroEL; the Hsp104/ClpB proteins, which participate in the dissociation of protein aggregates; Hsp90; and Hp70, which is involved in a large variety of reactions ranging from the general folding of nascent polypeptide chains to specific functions. As stated above, the cycle of ATP binding and hydrolysis drives an iterative sequence of conformational changes in the chaperone, which may induce structural rearrangements in a bound polypeptide or trigger binding/release of client proteins and co-chaperones. In contrast to the conformational changes that occur within both the chaperone and a bound substrate protein, the ATPase activity of molecular chaperones is experimentally very easily accessible. Because of its crucial functional importance, ATP turnover is usually modulated by both the substrate and helper chaperones.

Stimulation of ATP hydrolysis in the presence of unfolded proteins or peptides has been observed, e.g., for Hsp70, Hsp90, and Hsp104 [30, 59–61]. Apparently, the binding of the substrate induces a conformational change in these chaperones that results in a state with a higher intrinsic ATPase activity. This ''activation on demand'' may serve as a means to reduce the energy consumption by the empty chaperones. In contrast, ATP hydrolysis by GroEL is only marginally affected by the presence of protein substrates.

A well-characterized example of the regulation of ATP hydrolysis by co-chaperones is the DnaK system of *E. coli* (see Chapter 15). The ATPase cycle, and thus the cycle of substrate binding and release, is governed by two potential rate-limiting steps: the hydrolysis reaction and the subsequent exchange of ADP by ATP [62]. Both steps can be accelerated by specific cofactors, namely DnaJ and GrpE [59, 63, 64]. The rates of nucleotide exchange and hydrolysis determine how fast a substrate is processed and how long it is on average associated with the ADP and ATP states of DnaK, respectively.

While Hsp70 is subject mainly to positive regulation, other chaperone systems appear to include negative regulators as well. Hsp90, which plays an essential role in the activation of many regulatory proteins such as hormone receptors and kinases, is controlled by a large number of cofactors (see Chapter 23). Two of these co-chaperones, p23 and Hop/Sti1, were found to decrease the ATPase activity by stabilizing specific conformational states of Hsp90 [50, 65]. Intriguingly, Hop/Sti1 from *S. cerevisiae* seems to have a dual regulatory function: besides its inhibitory effect on Hsp90, Sti1 was also shown to be a very potent activator of Hsp70 [66]. Another example of a negative regulator is GroES, which reduces the ATP hydrolysis of its partner protein GroEL to 10–50% depending on the conditions used [67, 68]. The role of GroES in the functional cycle of the GroE chaperone, however, goes far beyond its modulation of ATP turnover, as it is essential for the encapsu-

lation of a polypeptide in the folding compartment of the GroE particle (see Chapter 20). The example of GroES is instructive, as it demonstrates that regulation of ATP turnover may not be the most important function of a cofactor. Nevertheless, the combination of experimental simplicity and functional relevance makes the ATPase of a general chaperone a preferred choice for mechanistic studies.

Some chaperones are regulated by temperature. Hsp26, a small heat shock protein from *S. cerevisiae*, has no chaperone activity at 30 °C, the physiologic temperature for yeast. At this temperature, Hsp26 forms hollow spherical particles consisting of 24 subunits [69]. Under heat stress, e.g., at 42 °C, these large complexes dissociate into dimers that exhibit chaperone activity and bind to nonnative polypeptides. Another interesting example of temperature regulation is the hexameric chaperone/protease degP of the *E. coli* periplasm [70]. At low temperature the protein acts as a chaperone, whereas at elevated temperature it possesses proteolytic activity (see Chapter 28). The regulatory switch is thought to involve the reorientation of inhibitory domains, which block access to the active site of the protease at low temperature [71]. Interestingly, switching can also be achieved by the addition of certain peptides.

A further variation of the scheme of activating chaperones by stress conditions is the regulation of Hsp33. Here, oxidative stress leads to the formation of disulfide bonds within the chaperone and its subsequent dimerization, which is a prerequisite for efficient substrate binding [72] (see also Chapter 19).

5.3 Limits and Extensions of the Chaperone Concept

The term chaperone and the underlying concept are attractive. Therefore, it is not surprising that the term itself has been proved to be rather promiscuous, as it is increasingly used for different proteins and even non-proteinaceous molecules. In its most basic interpretation, it has been applied to all proteins that have an effect on the aggregation of another protein or that influence the yield of correct folding. Most of these proteins have hydrophobic patches on their surface and thus, irrespective of their biological function, will associate with nonnative proteins. However, to qualify for a molecular chaperone, additional requirements should be met. This includes the defined stoichiometry of the binding reaction and the regulated release of the bound polypeptide (e.g., triggered by binding of ATP).

An extension of the term chaperone are the so-called intramolecular chaperones. These are regions of proteins that are required for their productive folding without being part of the mature protein because they are cleaved off after folding is complete. Well-investigated examples include the pro-regions of subtilisin E and α-lytic protease [73, 74]. The variation of the chaperone concept is that an intramolecular chaperone is specific for one protein and is covalently attached to its target. Furthermore, these chaperones act only once: after completing their job, they are cleaved off and degraded. These properties do not agree with the basic definition of a chaperone.

Chemical chaperone is a term that has become fashionable in recent years. It refers to small molecules (not proteins or peptides) that are added to refolding reac-

tions to increase the efficiency of protein folding in vitro. For instance, the folding yields for many enzymes can be improved by adding a substrate to the refolding buffer [75–77]. These compounds are thought to stabilize critical folding intermediates by binding to the active site, thereby enhancing folding. Besides these rather specific ligands, a number of substances, the most prominent of them being Tris and arginine, were found to promote the yield of folding in many cases when present in large excess over the folding proteins (see Chapter 38). In contrast to molecular chaperones, both chemical chaperones and intramolecular chaperones cannot be regulated in their activity.

5.3.1 Co-chaperones

For many chaperones, cofactors/co-chaperones exist that seem to directly influence the function of the chaperone. Some of them are essential constituents of their respective chaperone system, while others only improve its efficiency. Often, the role of cofactors is not limited to the regulation of the ATPase function but involves the recognition of nonnative proteins. These proteins thus have features of a chaperone. The DnaJ/Hsp40 co-chaperones seem to bind unfolded proteins and transfer them to Hsp70 [62, 78]. At the same time, as mentioned above, binding of DnaJ/Hsp40 stimulates ATP hydrolysis by Hsp70. Far more complex is the situation for the Hsp90 system. Here a plethora of cofactors exist, many of which seem to be able to recognize and bind nonnative proteins as demonstrated by in vitro chaperone assays [79, 80]. There is good reason to assume that they exert this function also within the Hsp90 chaperone complex, i.e., they interact with the substrate when it is associated with Hsp90.

The term co-chaperone implies that the function of these proteins is restricted to the context of their respective chaperones. However, recent evidence suggests that this may not be true in all cases. One example is the Hsp90 co-chaperone p23, which clearly has a distinct function in the Hsp90 system but also seems to be able to disassemble transcription factor complexes bound to DNA [81]. Similarly, Cdc37 was reported to exhibit an autonomous chaperone function [82].

It is important to remember that while in vitro chaperone assays can be used to detect chaperone properties in a cofactor, their functional relevance in the context of a chaperone complex has to be addressed in subsequent experiments.

5.3.2 Specific Chaperones

In addition to the general chaperones, a number of proteins exist for which the basic definition of chaperone function applies. However, these chaperones are dedicated to one or a few target proteins. In these cases, recognition is highly specific and does not necessarily involve hydrophobic interactions. An example for this class of chaperones is Hsp47, a resident protein of the endoplasmic reticulum that is a dedicated folding factor for collagen [83]. It interacts with immature collagen, is required for its correct folding and association, and is not part of the final collagen trimer. Thus, all the criteria for a molecular chaperone are fulfilled. Colla-

gen release is not triggered by ATP hydrolysis but by changes in the pH upon transit from the ER to the Golgi [84, 85].

Another well-studied example is the pili assembly proteins of gram-negative bacteria (see Chapter 29). Here, unassembled pili subunits are bound by specific chaperones that prevent their premature association in the periplasmic space. These chaperones bind very specifically and can be considered as surrogate subunits.

5.4 Working with Molecular Chaperones

5.4.1 Natural versus Artificial Substrate Proteins

An important point in studying molecular chaperones is the choice of substrate protein. Section 5.6 of this chapter will describe several of the most commonly used chaperone substrate proteins in detail. For many of them it is clear that they do not represent authentic in vivo substrates for the chaperone studied. The question is whether this poses a limitation on the validity of the results obtained with these proteins.

For the promiscuous general chaperones and co-chaperones, the interaction with the substrate protein is relatively unspecific. As a consequence, any unfolded protein can be regarded as a bona fide substrate. Interestingly, almost all mechanistic studies on GroE have been performed with ''artificial'' substrate proteins. Using a standard set of model substrates has a number of important advantages: (1) they are commercially available at a fairly low cost, (2) they are very well characterized in their folding and aggregation properties, and (3) they allow a direct comparison among chaperones to assess functional differences (Table 5.2). Moreover, they likely reflect the spectrum of polypeptides that chaperones may encounter in the cell. The situation is different for chaperones with high substrate specificity. Here, assays with model substrate proteins may allow analysis of certain aspects of their mechanisms. However, it is desirable to use authentic substrate proteins whenever possible.

5.4.2 Stability of Chaperones

There seems to be a common misconception that chaperones are exceptionally stable proteins because they are active under conditions, such as heat shock, that lead to the unfolding of many proteins. However, it has to be considered that the heat shock response is able to protect organisms only a few degrees above their optimum growth temperature. In general, there is no selection pressure on any intracellular protein to be stable above the maximum temperature tolerated by the host. As outlined above, many chaperones are functionally important under both physiological and stress conditions, i.e., they have to be active over a broad temperature range. From a mechanistic point of view, flexibility and conformational changes are of exceptional importance for molecular chaperones since they have to interact

Tab. 5.2. Protein substrates for molecular chaperones.

	Organism	*Molecular mass (kDa)*	*$A_{280\ nm}$ (1 mg mL^{-1}, 1 cm)*	*Commercially available*	*Activity assay available*	*General handling*	*Remarks*	*References*
Alpha-glucosidase	*S. cerevisiae*	68	2.61	Yes	Yes	Good		115, 136
Alpha-lactalbumin	*Bos taurus*	14	1.7	Yes	Yes, but awkward	Very good	Permanently unfolded derivate (RCMLA)	137, 138
Citrate synthase	*Sus scrofa*	2 × 49	1.56	Yes	Yes (expensive)	Good	Model substrate	87, 107, 139
Luciferase	*Photinus pyralis*	60.7	0.59	Yes	Yes (expensive)	Very poor	Very sensitive	140–143
Insulin	*Bos taurus*	5.8	1.06	Yes	No	Good	Useful only for aggregation assays	114, 115, 144
Malate dehydrogenase	*Sus scrofa*	2 × 33	0.2	Yes	Yes	Good	Model substrate	99, 145
Maltose binding protein	*E. coli*	40.7	1.6	No	No (but change in Trp fluorescence upon folding)	Good	Spontaneous folding is decelerated by chaperones	55, 146
Rhodanese	*Bos taurus*	33	1.8	Yes	Yes (toxic)	Good	Model substrate	56, 97, 147
Rubisco	*R. rubrum*	2 × 50.5	1.11	No	Yes, but uses $^{14}CO_2$	Good	First substrate ever used for in vitro assays	139, 148, 149

with a large variety of substrate proteins. For the reasons given, it is therefore plausible that chaperones cannot be extremely stable and rigid proteins (Table 5.1). This imposes certain restrictions on the design of in vitro chaperone assays (see experimental Section).

5.5 Assays to Assess and Characterize Chaperone Function

The first in vitro assays for a molecular chaperone using purified components were presented by Lorimer and coworkers in 1989 [86]. They analyzed and dissected the function of the two components of the GroE system (GroEL and GroES) using unfolded bacterial Rubisco as a substrate protein. The methods employed included activity assays to monitor the refolding to the native state, CD spectroscopy to analyze the conformation of the nonnative substrate protein at the beginning of the reaction, and native PAGE to demonstrate a direct physical interaction between the chaperone and Rubisco. This landmark paper became a role model for numerous studies to follow. Among other things, it showed that artificially denatured proteins can serve as substrates for molecular chaperones and that they can be refolded in a strictly ATP-dependent manner. In many cases, the increase in the yield of refolded protein is due to the suppression of aggregation during refolding. This was first shown for GroE using light scattering [87].

5.5.1 Generating Nonnative Conformations of Proteins

To produce the nonnative conformation of a substrate protein, all the conditions and substances known to denature proteins can be employed. Chaotropic compounds such as guanidinium chloride (GdmCl) and urea are used if a completely unfolded state of the substrate protein is desirable. This is referred to as ''chemical unfolding.'' In these cases, the substrate protein is diluted from a high concentration of denaturant into a solution containing the chaperone. Note that for most chaperone substrates there is competition between binding to the chaperone, folding, and aggregation. Alternatively, the test protein can be unfolded at elevated temperature. In this case, the unfolded protein cannot be stored because aggregation starts shortly after the temperature increase. In assays that employ thermally unfolded model substrates, the chaperone is therefore added before the heating step. Unfolding of proteins can also be achieved at low pH (acid denaturation) or, in the case of disulfide-containing polypeptides, by reduction.

5.5.2 Aggregation Assays

Since the prevention of aggregation is one of the key biological functions of general chaperones, this test can be considered an ''activity assay.'' In the simplest case, a temperature-labile protein, such as citrate synthase, is incubated at a tem-

perature at which it starts to unfold. The subsequent aggregation process can be monitored by the extent of light scattering shown by the sample, preferably in a fluorescence spectrometer or a regular UV/VIS photometer. In the presence of a chaperone, a decrease in the scattering signal at the end of the reaction should be observed. When an excess of chaperone is used, aggregation may be suppressed completely.

However, one should be cautious not to over-interpret results obtained from aggregation experiments. The intrinsic problem with aggregation is that, as a stochastic process, it is of limited reproducibility. Moreover, it is notoriously sensitive to small changes in conditions. Therefore, it is essential to include appropriate controls. Further, it yields only qualitative data: during the time course of aggregation, there is a concomitant increase in the number of aggregates as well as in the size of the aggregates. The contribution of the two processes will be different at different time points during the kinetics. Lastly, some proteins may suppress the aggregation of a test substrate without being chaperones.

5.5.3
Detection of Complexes Between Chaperone and Substrate

Many chaperones form remarkably stable complexes with unfolded polypeptides [48, 88, 89]. As described above, complex formation is due mainly to hydrophobic interactions between the binding site on the molecular chaperone and hydrophobic patches on the surface of the substrate protein.

To obtain complexes of chaperones with nonnative proteins, a concentrated solution of a chemically unfolded test protein is added to the chaperone. Alternatively, a mixture of a thermolabile protein and a chaperone is incubated at an elevated temperature. Depending on their stability, the complexes can be identified by several methods. Usually, unbound substrate is first separated from the complexes by size-exclusion chromatography, native PAGE, centrifugation, or other methods. The presence of the test substrate in the purified complexes is then shown on SDS-PAGE gels or by immunological methods if an antibody against the substrate is available. Alternatively, the test protein can be tagged for detection with, e.g., biotin or labeled with a fluorescent marker. Labile chaperone-substrate complexes must be trapped by either chemical- or photo-cross-linking before further analyses can be carried out. An extension of this type of experiment is the identification of complexes between a chaperone and its cofactors [90] (see also Chapter 23).

5.5.4
Refolding of Denatured Substrates

This type of assay is more complex than the ones described above because (1) it requires some knowledge about the mechanism of substrate release and (2) successful refolding may depend on the presence of (co-)chaperones or other factors. The most convenient refolding assays use test substrates whose enzymatic activity can be measured without interference from the chaperone. The use of classical spectroscopic probes for folding such as fluorescence or far-UV CD may be difficult

because of the high background signal from the chaperone and (if present) ATP. However, some chaperones such as GroEL, GroES, and Hsp104 lack intrinsic tryptophans, and in these cases one may use fluorescence to directly monitor changes in the structure of Trp-containing test proteins.

The general procedure for a refolding assay is as follows. First, a complex between the chaperone and the test substrate is formed (see Section 5.5.3). Usually, it is not necessary to remove molecules that have not bound to the chaperone. Afterwards, substrate release and refolding are triggered by adding the appropriate components, e.g., GroES and ATP in the case of GroEL. At various time points, aliquots are withdrawn from the sample and the enzyme activity is determined.

5.5.5
ATPase Activity and Effect of Substrate and Cofactors

Many general chaperones have an intrinsic ATPase activity, though their rates of hydrolysis can differ significantly (Table 5.1). ATP hydrolysis by a chaperone can be measured using several assay systems (see Section 5.6). Once the basal ATPase activity has been determined, the effect of substrates and cofactors in various combinations can be tested. Concerning the substrate, a polypeptide is preferred that adopts a stable, nonnative conformation. Otherwise, its conformation and thus its effect on ATP hydrolysis may change during the experiment. Alternatively, a small peptide may be used.

A more extensive characterization of the ATPase may include the determination of enzymatic parameters such as K_M or k_{cat}, in both the absence and the presence of effectors (see Chapter 4). However, one should be aware that in the case of oligomeric chaperones, a detailed analysis can be very challenging due to homotropic and heterotropic allosteric effects [91].

5.6
Experimental Protocols

5.6.1
General Considerations

5.6.1.1 Analysis of Chaperone Stability

When setting out to analyze the function of molecular chaperones, it is highly recommended to determine the intrinsic stability of the chaperone as a first step. This enables the experimenter to choose the appropriate reaction conditions for the chaperone assays. The conformational stability against urea or GdmCl should be measured using the protocols provided in the first volume of this book (see Chapter 3 in Part I). In the case of ATP-dependent chaperones, the GdmCl- or urea-induced unfolding transitions may be recorded in the presence and absence of ATP to determine whether the ligand has an effect on protein stability. In addition to the conventional assays for determining protein stability, for molecular

chaperones it is useful to specifically determine the stability against thermal unfolding because assays at heat shock temperatures are convenient. CD spectroscopy is frequently used to monitor changes in the secondary structure with increasing temperature.

5.6.1.2 Generation of Nonnative Proteins

Because most substrates are stable proteins at ambient temperature, they have to be unfolded prior to complex formation. This can be achieved by chemical denaturation, thermal unfolding, or – in the case of some disulfide-containing proteins – reduction. Each of these methods has its own merits but may not be applicable for a certain combination of substrate and chaperone. Chemical unfolding is a very reproducible method to generate unfolded protein substrates, and the product can usually be stored for several hours. However, one has to be aware that urea slowly decomposes into cyanate, which is reactive and can covalently modify amino acid side chains [92]. Further, it has been shown for both Hsp104 and GroE that GdmCl can severely interfere with chaperone function [93, 94]. To keep the residual concentration of denaturant in the chaperone assay below 0.1 M (urea) and 0.05 M (GdmCl), respectively, one should use fairly concentrated stock solutions of unfolded polypeptide.

Unfolding substrates at elevated temperature mimics conditions of heat shock and thus could be considered the most physiologic method to generate unfolded polypeptides. Also, there are no problems arising from the addition of problematic chemicals. The main disadvantage is that thermally unfolded proteins cannot be stored, as they will start to aggregate quickly. Thus, the thermal inactivation has to take place in the presence of chaperone. This implies that the chaperone itself has to be stable under the conditions used to unfold the substrate. Also, the reproducibility is not as high as when chemical denaturation is used. In the case of proteins that contain disulfide bonds, these can be broken by the addition of reducing agents such as glutathione or DTT. This may destabilize the protein enough so that it will unfold either spontaneously or at mildly denaturing conditions. As for the previous procedures, it should be verified that the chaperone is not compromised by the reducing agent. While reducing conditions may not be a problem for cytosolic chaperones, proteins operating in a more oxidative environment such as the ER or the periplasm may not tolerate low redox potentials.

5.6.1.3 Model Substrates for Chaperone Assays

Numerous proteins have been used as substrates to investigate assisted protein folding. Due to features such as availability, ease of handling and detection, and general suitability as chaperone substrates, some of these proteins were repeatedly used and eventually became model substrates. In the following sections, we will briefly describe the most important ones. Additionally, Table 5.2 includes a number of less commonly used substrates along with selected references.

Rhodanese (Bovine Liver) Rhodanese from liver mitochondria is a small (33 kDa) monomeric enzyme that catalyzes sulfur transfer reactions [95]. It is commercially

available from several sources, but batches may differ in the degree of purity. The structure of rhodanese has been determined [96]. The reactivation of rhodanese is dependent on chaperones [97], although spontaneous refolding has been observed in the presence of lauryl maltoside, β-mercaptoethanol, and thiosulfate [75]. Rhodanese has been extensively used over the years to study assisted protein folding. One disadvantage of rhodanese is that the activity assay uses the toxic compound KCN.

Mitochondrial Malate Dehydrogenase MDH (Porcine Heart) Malate dehydrogenase is an enzyme of the mitochondrial Krebs cycle. The enzyme from *Sus scrofa* consists of two subunits of ~33 kDa each and is commercially available. Its reactivation is highly dependent on the assistance of chaperones, although spontaneous refolding occurs in the presence of high phosphate concentrations [98, 99]. The crystal structure of MDH has been solved [100]. This model substrate was extensively used to investigate the mechanism of GroEL [29, 101]. MDH can be unfolded with both urea and GdmCl. Moreover, it starts to unfold (and aggregate) at ~45 °C in Tris buffer at pH 8 [102]. MDH has been shown to form stable complexes with a number of chaperones, including sHsps (Hsp18.1) and GroEL. In addition, aggregated MDH has been used to study the disaggregation properties of the chaperone ClpB [103]. Finally, the regaining of MDH activity during refolding is easy to monitor (see Chapter 20).

Mitochondrial Citrate Synthase CS (Porcine Heart) Citrate synthase, a mitochondrial enzyme like MDH, is a homodimeric protein of two 49-kDa subunits. It is commercially available, and its crystal structure is solved at a resolution of 2.7 Å [104]. Spontaneous reactivation after denaturation by urea or GdmCl is possible only at low protein concentrations [87]. Folding of CS can be assisted by GroE in vitro and in *E. coli* [87, 105]. A convenient enzymatic assay exists that can be used to monitor the regaining of activity [106, 107].

CS is temperature-sensitive and starts to unfold above ~40 °C. Because of its low stability, CS is the substrate of choice to measure temperature-induced aggregation and its suppression by molecular chaperones. Thermal aggregation is preceded by the loss of enzymatic activity. Several molecular chaperones have been tested for their influence on the thermal aggregation and inactivation of CS [87, 107–109].

Reduced Carboxymethylated Alpha-lactalbumin RCMLA (Bovine Milk) The disadvantage of all substrates mentioned so far is that once the unfolded protein is added to the chaperone solution, its conformation is no longer defined. As a consequence, these types of substrates are not suited to carry out equilibrium studies, e.g., to determine binding constants. For these purposes, one requires a permanently unfolded polypeptide that does not aggregate. Reduced, carboxymethylated alpha-lactalbumin has been successfully employed in this context [110, 111]. It was also used as a competitive inhibitor for the binding of other nonnative proteins [112]. Its only drawback is that it is not very hydrophobic, and the resulting chaperone complexes are often rather labile.

Alpha-lactalbumin is a small protein (14.2 kDa) from bovine milk and can be purchased from a number of suppliers. Its conformational stability is highly dependent on the presence of the four disulfide bridges. To obtain a permanently unfolded version of lactalbumin, the disulfides first have to be disrupted by DTT in the presence of GdmCl (Protocol 1). This unfolded conformation can be maintained by irreversible alkylation of the eight cysteine residues with iodoacetic acid. Compared with unmodified lactalbumin, this derivative carries eight additional negative charges that increase its solubility but may interfere with the binding to certain chaperones. An alternative form can be obtained by using iodoacetamide in the alkylation step. The resulting derivative carries no additional charges but is prone to aggregation at high concentration.

Protocol 1: Preparation of RCMLA

1. Dissolve 5.6 mg alpha-lactalbumin in 305 µL 200 mM Tris/HCl pH 8.7, 7 M GdmCl, 2 mM EDTA, 20 mM DTT, and incubate for 90 min at room temperature.
2. Add 60 µL of 0.6 M iodoacetic acid in 200 mM Tris/HCl pH 7.5 (check pH!) under dark room conditions and incubate for 10 min.
3. Stop the reaction by adding 100 µL of 0.5 M reduced glutathione in 200 mM Tris/HCl pH 7.5.
4. The derivatized protein is purified via a Sephadex G25 desalting column equilibrated with 200 mM Tris/HCl pH 7.5.

5.6.2 Suppression of Aggregation

The simplest type of activity test for a chaperone determines its capability to prevent the aggregation of a model substrate. An unfolded conformation of the test substrate is first prepared. Then the aggregation of this protein is measured, in both the presence and the absence of the potential chaperone. A number of controls have to be carried out to verify that the chaperone does not aggregate itself and that the buffer in which the chaperone is stored does not change aggregation. The process of aggregation is usually monitored by the increase in light scattering. For detection, a thermostated photometer or fluorescence spectrometer is required. Aggregates can be monitored at wavelengths between 320 nm and 500 nm (no interference from aromatic residues) depending on the size of the aggregates. The scattering intensity increases with decreasing wavelengths. Since there is no linear relationship between the extent of aggregation and the light-scattering signal, we advise against using a percent scale when plotting aggregation data.

Protocol 2, in which the aggregation of CS at 43 °C is measured, can be performed only for chaperones that are stable at this temperature. If this is not the case, chemical denaturants have to be used to destabilize the protein whose aggregation will be monitored. Two different approaches can be applied. In the cases of insulin (Protocol 3) and alpha-lactalbumin (Protocol 4), aggregation can be induced

by the addition of a reducing agent such as DTT. The B chain of reduced insulin will start to aggregate within minutes at room temperature [113]. For lactalbumin, efficient aggregation requires reduction at higher temperatures. Additionally, aggregation can be induced by diluting a concentrated solution of an unfolded test protein, e.g., in GdmCl or urea, into buffer without denaturant. In the absence of chaperones, the polypeptide will aggregate. This process can be enhanced by increasing the temperature.

As a rule of thumb, complete suppression of aggregation requires that the amount of chaperone – or, more precisely, the concentration of protein-binding sites – be at least as high as that of the aggregating polypeptide. Thus, chaperones act stoichiometrically and not catalytically. As some of the assays, especially the ones using insulin and alpha-lactalbumin, require a high concentration of the test protein, the consumption of chaperone can be considerable. Secondly, the interaction between the chaperone and the polypeptide has to be tight (see Figure 5.3, left panel). Otherwise, the irreversible process of aggregation will eventually pull all polypeptide molecules from the chaperone. In this case, a deceleration of the aggregation process may be observed in the presence of the chaperone, while the final amplitude remains unchanged (Figure 5.3, middle panel).

It may be worthwhile to check whether the test protein is indeed associated with the chaperone at the end of the aggregation assay by employing one of the methods described in the following section. If a refolding assay for the test protein is available, one can also examine whether the protein can be recovered from the chaperone complexes by transferring the sample to refolding conditions, e.g., by lowering the temperature (see Protocol 7). Finally, one should note that a positive result from an aggregation assay alone is not sufficient to classify the protein under investigation as a molecular chaperone.

Protocol 2: Thermal Aggregation of Citrate Synthase The major advantage of this assay is that it requires only small amounts of chaperone. However, the chaperone must withstand a temperature of 43 °C for at least 1 h (Figure 5.3). Tris and a number of salts such as KCl have been observed to stabilize CS and should be avoided.

1. Prepare a stock solution of 65 μM CS (monomers) in 50 mM Tris/HCl pH 8, 2 mM EDTA (if an ammonium sulfate suspension is used, the protein has to be extensively dialyzed first).
2. Remove aggregates by centrifugation at 12 000 *g* in a bench-top centrifuge.
3. Assay buffer: 50 mM HEPES/KOH pH 7.5, 150 mM KCl, 10 mM $MgCl_2$ (the buffer must be degassed and filtered through a 0.2-μm membrane before use).
4. Add 2494 μL assay buffer to a 1 × 1 cm fluorescence cuvette equipped with a stirring bar.
5. Incubate the cuvette for >5 min at 43 °C in a thermostated fluorescence spectrometer.
6. To start aggregation, add 6 μL CS solution and follow the increase in light scattering for 60 min (set both excitation and emission to 360 nm; adjust the slits to obtain a good signal/noise ratio).

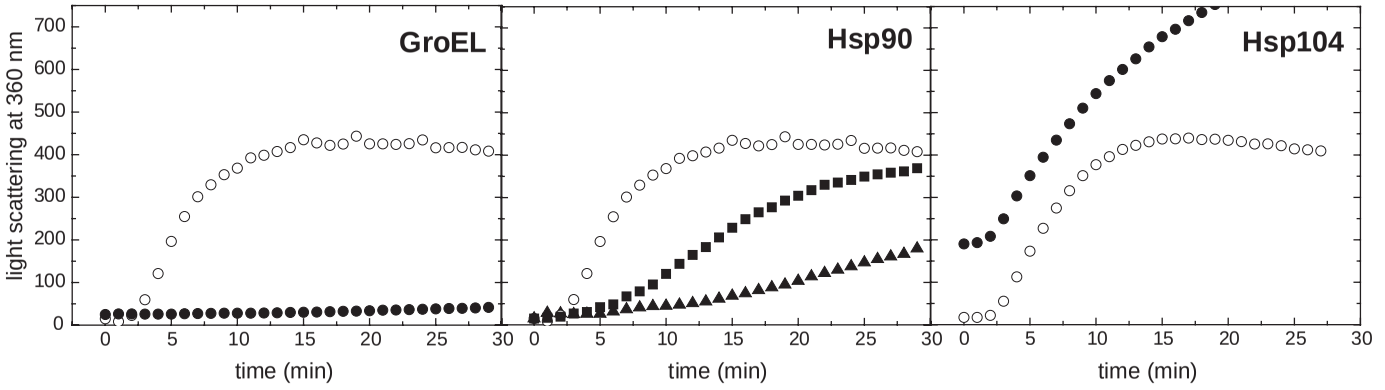

Fig. 5.3. Aggregation assays for three chaperones using citrate synthase as a test substrate. The aggregation of 0.15 μM citrate synthase (○) at 43 °C was followed by light scattering at 360 nm in a fluorescence spectrometer. (Left) In the presence of 0.2 μM GroEL (●), complete suppression of aggregation is observed. (Middle) Unlike GroEL, Hsp90 (0.1 μM ■ and 0.2 μM ▲) decreases the rate but not the extent of aggregation, indicating a transient interaction with CS. (Right) In contrast, 0.2 μM Hsp104 (●) is not able to suppress the aggregation of citrate synthase. In comparison to the reaction in the absence of the chaperone, the extent of aggregation is even increased since Hsp104 is not stable at this temperature.

7. Start a new experiment in which some of the buffer in the sample cuvette is replaced by a stock solution of your chaperone before the addition of CS; use the following chaperone concentrations: 0.1, 0.2, and 0.5 μM (the final concentration of CS in the cuvette is 0.15 μM).
8. To test the influence of the buffer in which the chaperone is stored, carry out a set of control experiments in which the chaperone is replaced by equal volumes of this buffer.
9. If an absorbance photometer is used, concentrations may have to be increased. Set the wavelength to 360 nm.

Protocol 3: Aggregation of Insulin B Chain In the presence of DTT, the three disulfide bridges within the insulin molecule are broken, and the two chains dissociate. While the A chain remains soluble, the B chain will readily start to aggregate [113, 114]. This process can be suppressed by molecular chaperones. A major disadvantage of this assay is that it consumes substantial amounts of chaperone, of which a highly concentrated stock solution is needed. The assay can be performed at different temperatures [69] and salt concentrations, but note that the extent of aggregation is very sensitive to changes in pH.

1. Dissolve 4.06 mg insulin (bovine pancreas) in 1 mL 10 mM sodium phosphate buffer pH 7 (if the protein does not dissolve, add concentrated HCl until the solution is clear, then add 10 M NaOH and adjust the pH to ∼7).
2. Keep the stock solution (∼ 700 μM) on ice.
3. Assay buffer: 50 mM Tris/HCl pH 8, 2 mM EDTA.
4. To a 120-μL UV cuvette, add 110 μL of assay buffer and 10 μL of insulin (the small sample volume minimizes chaperone consumption, but larger cuvettes may be used as well).
5. Incubate the cuvette for >5 min at 25 °C in a thermostated photometer.
6. Start the aggregation by adding 20 μL of 0.35 M DTT in assay buffer.
7. Follow the aggregation by measuring the extinction at 400 nm.
8. Start a new experiment in which some of the buffer in the sample cuvette is replaced by a stock solution of your chaperone before the addition of insulin; use the following chaperone concentrations: 25, 50, and 100 μM (the final concentration of insulin in the cuvette is 50 μM).
9. To test the influence of the buffer in which the chaperone is stored, carry out a set of control experiments in which the chaperone is replaced by equal volumes of this buffer.

Protocol 4: Aggregation of Alpha-lactalbumin The conformational stability of alpha-lactalbumin is highly dependent on the presence of the four disulfide bridges and the bound Ca^{2+}. Thus, the addition of a reducing agent such as DTT in the presence of EDTA causes the protein to unfold and aggregate [114]. This process is quite slow at 25 °C but can be significantly accelerated by raising the temperature. The best results are obtained between 25 °C and 45 °C.

1. Assay buffer: 50 mM sodium phosphate pH 7.0, 0.2 M NaCl, 2 mM EDTA.
2. 300 μM alpha-lactalbumin (bovine) in assay buffer. (Note: Aggregation is significantly inhibited by Tris and HEPES. It is therefore recommended to dialyze the chaperone against the assay buffer.)
3. Add 100 μL buffer and 20 μL alpha-lactalbumin to a 120-μL UV cuvette (the small sample volume minimizes chaperone consumption, but larger cuvettes may be used as well).
4. Incubate the cuvette for >5 min at the chosen temperature (25–45 °C) in a thermostated photometer.
5. Start the reaction with 20 μL of 0.35 M DTT in assay buffer and follow the aggregation by measuring the extinction at 500 nm.
6. Start a new experiment in which some of the buffer in the sample cuvette is replaced by a stock solution of your chaperone before the addition of alpha-lactalbumin; use the following chaperone concentrations: 25, 50, and 100 μM (the final concentration of lactalbumin in the cuvette is 43 μM).
7. To test the influence of the buffer in which the chaperone is stored, carry out a set of control experiments in which the chaperone is replaced by equal volumes of this buffer.

The kinetics of the aggregation reaction depends on the DTT concentration and is considerably faster at higher temperature. At 25 °C, complete aggregation may take several hours.

5.6.3
Complex Formation between Chaperones and Polypeptide Substrates

For the preparation of complexes with a nonnative polypeptide, an unfolded test substrate must be generated first. As mentioned in ''Generation of Nonnative Proteins'' above, it is very important to verify that the chaperone under investigation is compatible with the selected methods of protein denaturation.

Protocol 5: Preparation of Chaperone-Substrate Complexes Using Urea-denatured MDH

1. Remove stabilizing agents such as glycerol or $(NH_4)_2SO_4$ by dialysis or by passage through a desalting column (buffer: 50 mM Tris/HCl pH 7.5, 2 mM DTT); the concentration of MDH monomers after this step should be at least 150 μM (5 mg mL^{-1}).
2. To 3 μL of mMDH (150 μM), add 6 μL of 9 M urea, 50 mM Tris/HCl pH 7.5, 10 mM DTT; allow the protein to unfold for 30 min at 25 °C.
3. Prepare a solution of your chaperone (1 μM) in 198 μL 50 mM Tris/HCl pH 7.5, 10 mM DTT, 50 mM KCl and incubate at 25 °C for 5 min.
4. Add 2 μL of unfolded MDH, mix rapidly, and incubate for 15 min.
5. Spin down the sample in a bench-top centrifuge (12 000 *g*) to remove aggregated MDH.

Protocol 6: Formation of Complexes Between GroEL and Thermally Denatured CS

1. Prepare a stock solution of 65 μM CS (monomers) in 50 mM Tris/HCl pH 8, 2 mM EDTA (if an ammonium sulfate suspension is used, the protein has to be extensively dialyzed first).
2. Remove aggregates by centrifugation at 12 000 *g* in a bench-top centrifuge.
3. Aliquots are prepared, frozen in liquid nitrogen, and stored at −20 °C; once thawed, the aliquots should be used up.
4. Prepare a solution of your chaperone (1 μM) in 197 μL 50 mM HEPES/KOH pH 7.5, 50 mM KCl and incubate at 43 °C for 5 min.
5. Add 3 μL of CS and incubate for additional 30 min.
6. Remove aggregates by centrifugation at 12 000 *g* in a bench-top centrifuge.

Some applications may require concentrations of chaperone-CS complexes higher than 1 μM, as given in the protocol. This can be achieved by increasing the concentration of both CS and chaperone in the mixture. However, there may be a significant loss of CS due to aggregation.

Once the complexes between the polypeptide and the chaperone have been prepared, their composition can be examined by various methods. If binding is strong, analytical size-exclusion chromatography can be used in combination with a UV or fluorescence detection unit. In addition, the substrate polypeptide may be modified to carry a fluorescent label (Figure 5.4). This allows the direct analysis of different components in one peak. Otherwise, the elution profile may be analyzed with SDS-PAGE [115]. If complexes are only transient, as in the case of Hsp104 or Hsp70-ATP, chemical cross-linking with glutaraldehyde in combination with SDS-PAGE can be used. Other methods that have been successfully used to demonstrate physical interaction include immunoprecipitation [66], native PAGE [86, 90], and analytical ultracentrifugation [116].

5.6.4 Identification of Chaperone-binding Sites

The identification of binding sites for chaperones in a given substrate is an important issue in the context of characterizing a molecular chaperone. The experimental approaches that have been developed to address this kind of problem are rather advanced, and thus we will give only a brief outline.

For chaperones known to bind to extended peptide sequences such as the Hsp70 family members, early studies used phage display to analyze the interaction with the chaperone [117, 118]. The analysis of this large dataset of binding and non-binding peptides led to an algorithm for the prediction of BiP-binding sites in the primary sequences of proteins. The predictive power of this program was found to be about 50% for binding sequences as tested by a survey of synthetic peptides [119].

A related approach is to screen for chaperone-binding sites in proteins using sets

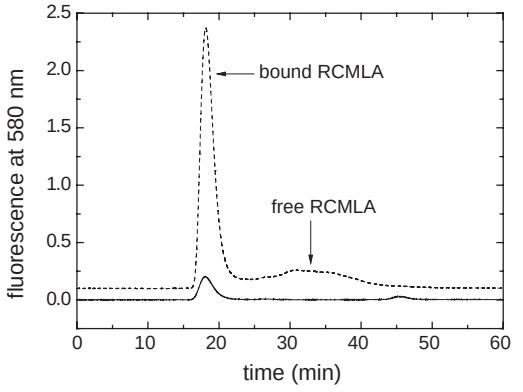

Fig. 5.4. Size-exclusion chromatography of a complex between GroEL and RCMLA (dashed line). Complexes were formed by incubating 3 μM RCMLA (labeled with tetramethylrhodamin) with 2 μM $GroEL_{14}$ for 5 min at 30 °C in 50 mM HEPES/KOH pH 7.5, 150 mM KCl, 10 mM $MgCl_2$. 100 μL of this mixture was applied to a Superdex-200 HR 10/30 column equilibrated in the same buffer. Complexes were detected by following the fluorescence of the labeled substrate. In a control experiment, GroEL alone was injected (solid line). Note that the position of the GroEL peak at 18 min is not significantly shifted upon binding of RCMLA, as the apparent molecular mass increases only marginally from ~800 kDa to ~820 kDa.

of overlapping synthetic peptides that represent the entire primary structure of the respective proteins. The peptides are immobilized on filters. This allows a correlation between sequence and signals. Binding is usually detected by antibodies against the respective chaperone in a Western blot–like manner. This technique has been successfully applied for several chaperones and target proteins [120, 121].

A caveat is that these approaches will provide information on all potential binding sites in a protein. Which of these will actually be used in vivo may depend on the kinetics of folding or on the degree of unfolding under stress conditions, similar to *N*-glycosylation sites in proteins. Moreover, this technique is unable to detect binding sites that are formed by residues distant in sequence but close in space, e.g., in a partially folded intermediate. Thus, its value may be restricted to identifying binding sites for chaperones such as Hsp70, which are known to bind consecutive stretches of amino acids.

Identifying the binding site(s) for nonnative proteins in chaperones is even more challenging. Here, chemical cross-linking of chaperone-substrate complexes and subsequent analysis of the site of interaction by protease digestion and mass spectrometry is the method of choice. Mutational analyses using deletion fragments to identify protein-binding sites should be considered with great caution because they have repeatedly yielded false or contradictory results. However, after a potential binding site has been identified biochemically, site-specific mutagenesis of residues in the respective region may be employed to further corroborate the result.

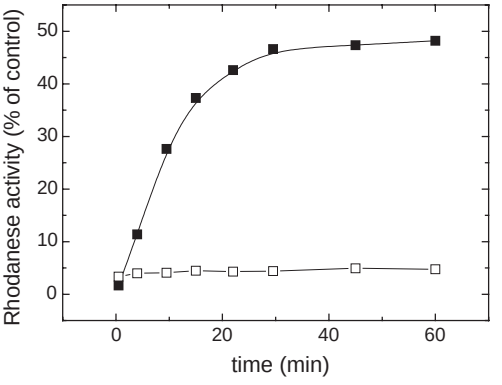

Fig. 5.5. GroE-assisted reactivation of rhodanese. Urea-denatured rhodanese (0.5 μM) was refolded in the presence of 1 μM GroEL/2 μM GroES/2 mM ATP (■) or in the absence of chaperones (□). At the indicated time points, aliquots were withdrawn from the refolding reaction, and the rhodanese activity was determined as described in Protocol 7.

5.6.5
Chaperone-mediated Refolding of Test Proteins

Usually, refolding is carried out by diluting a solution of a nonnative test enzyme, e.g., unfolded in 6 M GdmCl, into a buffer that contains the chaperone under investigation. At various time points, aliquots are withdrawn and the enzyme activity of the test protein is determined (Figure 5.5). In a control experiment, the assay is carried out with the native test enzyme instead of the unfolded protein. Concentrations, pre-incubation times, buffer conditions, etc., should be identical to the ones used in the refolding experiment. If a denaturant was used to prepare the unfolded test protein, an amount of denaturant equivalent to its residual concentration in the refolding assay should be added. This experiment yields the 100% value for the activity of the substrate, as it accounts for any changes in the enzyme activity that are due to its incubation in the refolding solution. In a further control experiment, one has to determine to what extent the enzyme refolds spontaneously. This is simply done by carrying out the refolding experiment in the absence of the chaperone but under otherwise unchanged conditions. Again, it is essential to include all additional factors such as ATP in this control, as they may stabilize or destabilize the enzyme and thus influence spontaneous refolding. Furthermore, an additional control reaction should include substantial amounts of a non-chaperone protein such as BSA, e.g., a fivefold excess over the substrate protein, to account for unspecific protein effects on refolding.

For many test proteins, spontaneous refolding can be quite efficient at certain conditions, e.g., at low protein concentration or temperature or in the presence of stabilizing reagents. To identify potential chaperones, refolding experiments should be carried out under stringent conditions where no refolding occurs in the absence of chaperones. As already mentioned, efficient refolding by the chaperone

may require further components such as ATP, cofactors, or other chaperones. Therefore, some knowledge about the chaperone under investigation has to be acquired beforehand. Once the conditions for successful reactivation of a substrate have been established, parameters such as the type or concentration of cofactors can be varied to obtain further insight into the mechanism of the chaperone.

Protocol 7: GroE-assisted Refolding of Rhodanese

Unfolding of Rhodanese

In this protocol urea is used to denature rhodanese, but 6 M GdmCl will work as well. Depending on your rhodanese stock, the protein solution may have to be concentrated by ultrafiltration prior to unfolding.

1. Remove stabilizing agents such as glycerol or $(NH_4)_2SO_4$ by dialysis or by using a desalting column (buffer: 50 mM Tris/HCl, 2 mM DTT); the concentration of rhodanese after this step should be at least 300 μM (10 mg mL^{-1}).
2. To 3.3 μL of rhodanese (300 μM), add 17 μL of 10 M urea, 50 mM Tris/HCl pH 7.5, 10 mM DTT; allow the protein to unfold for 60 min at 25 °C.

Refolding of Rhodanese by the GroE System

The concentration of rhodanese in the refolding reaction is 0.5 μM. A twofold excess of GroEL and GroES is used (Figure 5.5).

1. Prepare a solution of 1 μM $GroEL_{14}$ and 2 μM $GroES_7$ in 50 mM Tris/HCl pH 7.5, 1 mM DTT, 50 mM KCl, 10 mM $MgCl_2$, 20 mM $Na_2S_2O_3$.
2. Add 2.5 μL of unfolded rhodanese, mix rapidly, and incubate at 25 °C for 5 min.
3. Start reactivation by adding 1 mM ATP (total volume of refolding reaction: ~250 μL).
4. Withdraw aliquots of 24 μL every 4 min and measure rhodanese activity (see next section).

Note that in the refolding assay 20 mM $S_2O_3^{2-}$ is present to stabilize refolded rhodanese. To determine the extent of spontaneous refolding, conduct a control experiment without GroEL.

Enzyme Assay for Rhodanese

The enzyme test is based on a sulfur transfer reaction catalyzed by rhodanese [95]. Sulfur atoms of the substrate thiosulfate are passed onto cyanide anions, generating SCN^-. The reaction is stopped at timed intervals with a solution of iron(III)-nitrate. The concentration of the resulting red complex $[Fe(SCN)_3]$ is determined by measuring the absorbance of the samples at $\lambda = 470$ nm using a standard spectrophotometer.

EDTA is important to complex magnesia ions. This blocks the ATPase activity of residual chaperones. Otherwise, refolding would continue during the activity assay.

Caution: KCN is toxic. Work under a fume hood and wear gloves at all times.

1. Premix: 9% (v/v) formaldehyde.
2. Staining solution: 16% (w/v) $Fe(NO_3)_3$, 1 M HNO_3.
3. Prepare the number of activity tests tubes you will require (one for every time point of the refolding kinetics): 24 µL KH_2PO_4 (1 M), 12 µL EDTA (0.5 M, pH 9), 30 µL $Na_2S_2O_3$ (1 M), 30 µL KCN (1 M), 480 µL H_2O, total volume 576 µL each.
4. For each activity test tube, prepare six disposable cuvettes with 575 µL of premix solution.
5. Incubate test tubes at 25 °C.
6. Start the activity test by adding 24 µL of rhodanese-containing solution from the refolding reaction to the test tube. The final conditions of the activity tests are: 25 °C, 40 mM KH_2PO_4, 10 mM EDTA, 30 mM $S_2O_3^{2-}$, 30 mM CN^-, 20 nM rhodanese (from refolding reaction), total volume = 600 µL.
7. Every 2 min, withdraw 90 µL from the activity test tube and add it to the premix solution in the cuvette.
8. Quench sample with 325 µL staining solution and mix rapidly.
9. Measure the absorbance at 470 nm (the orange color is stable for at least 2 h).
10. Blank: cuvette with premix solution.
11. Draw a straight line by plotting absorbance at 470 nm vs. time.
12. Use slope $dA_{470\,nm}/dt$ to calculate enzymatic activity.

5.6.6 ATPase Activity

Several assay systems have been developed to monitor ATP hydrolysis. The most sensitive technique uses either α-[^{32}P]-ATP or γ-[^{32}P]-ATP. Upon hydrolysis, either radioactive phosphate or ADP is released and can be detected and quantified [122]. Another method uses the dye malachite green to determine the amount of phosphate produced by hydrolysis of ATP [123]. A more elegant approach employs a coupled enzyme system [124]. In the first step, pyruvate kinase regenerates ATP from ADP and phosphoenol pyruvate. This reaction also produces pyruvate, which is reduced in a second step catalyzed by lactate dehydrogenase under the consumption of NADH, a reaction that can be followed at 340 nm in a spectrometer. Detailed information on the experimental design and evaluation of ATPase experiments is provided in Chapter 4 of this volume.

Acknowledgments

We would like to thank V. Grimminger, B. Bösl, and K. Ruth for contributing to this chapter and M. Haslbeck and H. Wegele for critically reading the manuscript. Work in the authors' labs was supported by grants from the DFG to J.B. and S.W. and by grants from the Fonds der Chemischen Industrie to J.B.

References

1 Earnshaw, W. C., Honda, B. M., Laskey, R. A., & Thomas, J. O. (1980). Assembly of nucleosomes: the reaction involving *X. laevis* nucleoplasmin. *Cell* **21**, 373–383.

2 Dingwall, C. & Laskey, R. A. (1990). Nucleoplasmin: the archetypal molecular chaperone. *Semin. Cell Biol.* **1**, 11–17.

3 Ellis, R. J. & Hemmingsen, S. M. (1989). Molecular chaperones: proteins essential for the biogenesis of some macromolecular structures. *Trends Biochem. Sci.* **14**, 339–342.

4 Ellis, R. J. & van der Vies, S. M. (1991). Molecular chaperones. *Annu. Rev. Biochem.* **60**, 321–347.

5 Gething, M. J. & Sambrook, J. (1992). Protein folding in the cell. *Nature* **355**, 33–45.

6 Hartl, F. U. (1996). Molecular chaperones in cellular protein folding. *Nature* **381**, 571–579.

7 Bukau, B. & Horwich, A. L. (1998). The Hsp70 and Hsp60 chaperone machines. *Cell* **92**, 351–366.

8 Hartl, F. U. & Hayer-Hartl, M. (2002). Molecular chaperones in the cytosol: from nascent chain to folded protein. *Science* **295**, 1852–1858.

9 Walter, S. & Buchner, J. (2002). Molecular chaperones–cellular machines for protein folding. *Angew. Chem. Int. Ed Engl.* **41**, 1098–1113.

10 Gragerov, A. I., Martin, E. S., Krupenko, M. A., Kashlev, M. V., & Nikiforov, V. G. (1991). Protein aggregation and inclusion body formation in *Escherichia coli* rpoH mutant defective in heat shock protein induction. *FEBS Lett.* **291**, 222–224.

11 Schoemaker, J. M., Brasnett, A. H., & Marston, F. A. (1985). Examination of calf prochymosin accumulation in *Escherichia coli*: disulphide linkages are a structural component of prochymosin-containing inclusion bodies. *EMBO J.* **4**, 775–780.

12 Ingolia, T. D. & Craig, E. A. (1982). Drosophila gene related to the major heat shock-induced gene is transcribed at normal temperatures and not induced by heat shock. *Proc. Natl. Acad. Sci. U.S.A* **79**, 525–529.

13 Fayet, O., Ziegelhoffer, T., & Georgopoulos, C. (1989). The groES and groEL heat shock gene products of *Escherichia coli* are essential for bacterial growth at all temperatures. *J. Bacteriol.* **171**, 1379–1385.

14 Borkovich, K. A., Farrelly, F. W., Finkelstein, D. B., Taulien, J., & Lindquist, S. (1989). hsp82 is an essential protein that is required in higher concentrations for growth of cells at higher temperatures. *Mol. Cell Biol.* **9**, 3919–3930.

15 Anfinsen, C. B., Haber, E., Sela, M., & White, F. H. (1961). The kinetics of formation of native ribonuclease during oxidation of the reduced polypetide chain. *Proc. Natl. Acad. Sci. U.S.A.* **47**, 1309–1314.

16 Anfinsen, C. B. (1973). Principles that govern the folding of protein chains. *Science* **181**, 223–230.

17 Jaenicke, R. (1987). Folding and association of proteins. *Prog. Biophys. Mol. Biol.* **49**, 117–237.

18 Seckler, R. & Jaenicke, R. (1992). Protein folding and protein refolding. *FASEB J.* **6**, 2545–2552.

19 Kiefhaber, T., Rudolph, R., Kohler, H. H., & Buchner, J. (1991). Protein aggregation in vitro and in vivo: a quantitative model of the kinetic competition between folding and aggregation. *Biotechnology* **9**, 825–829.

20 Epstein, C. J., Goldberger, R. F., & Anfinsen, C. B. (1963). Genetic Control of Tertiary Protein Structure: Studies with Model Systems. *Cold Spring Harbor Symp. Quant. Biol.* **28**, 439–449.

21 Viitanen, P. V., Gatenby, A. A., & Lorimer, G. H. (1992). Purified chaperonin 60 (groEL) interacts with the nonnative states of a multitude of *Escherichia coli* proteins. *Protein Sci.* **1**, 363–369.

22 Horwich, A. L., Low, K. B., Fenton, W. A., Hirshfield, I. N., & Furtak, K. (1993). Folding in vivo of bacterial

cytoplasmic proteins: role of GroEL. *Cell* **74**, 909–917.

23 Houry, W. A., Frishman, D., Eckerskorn, C., Lottspeich, F., & Hartl, F. U. (1999). Identification of in vivo substrates of the chaperonin GroEL. *Nature* **402**, 147–154.

24 Teter, S. A., Houry, W. A., Ang, D., Tradler, T., Rockabrand, D., Fischer, G., Blum, P., Georgopoulos, C., & Hartl, F. U. (1999). Polypeptide flux through bacterial Hsp70: DnaK cooperates with trigger factor in chaperoning nascent chains. *Cell* **97**, 755–765.

25 Haslbeck, M., Braun, N., Stromer, T., Richter, B., Model, N., Weinkauf, S., & Buchner, J. (2004). Hsp42 is the general small heat shock protein in the cytosol of *Saccharomyces cerevisiae*. *EMBO J.* **23**, 638–649.

26 Robinson, C. V., Gross, M., Eyles, S. J., Ewbank, J. J., Mayhew, M., Hartl, F. U., Dobson, C. M., & Radford, S. E. (1994). Conformation of GroEL-bound alpha-lactalbumin probed by mass spectrometry. *Nature* **372**, 646–651.

27 Zahn, R., Perrett, S., & Fersht, A. R. (1996). Conformational states bound by the molecular chaperones GroEL and secB: a hidden unfolding (annealing) activity. *J. Mol. Biol.* **261**, 43–61.

28 Goldberg, M. S., Zhang, J., Sondek, S., Matthews, C. R., Fox, R. O., & Horwich, A. L. (1997). Native-like structure of a protein-folding intermediate bound to the chaperonin GroEL. *Proc. Natl. Acad. Sci. U.S.A* **94**, 1080–1085.

29 Chen, J., Walter, S., Horwich, A. L., & Smith, D. L. (2001). Folding of malate dehydrogenase inside the GroEL-GroES cavity. *Nat. Struct. Biol.* **8**, 721–728.

30 Flynn, G. C., Pohl, J., Flocco, M. T., & Rothman, J. E. (1991). Peptide-binding specificity of the molecular chaperone BiP. *Nature* **353**, 726–730.

31 Landry, S. J., Jordan, R., McMacken, R., & Gierasch, L. M. (1992). Different conformations for the same polypeptide bound to chaperones DnaK and GroEL. *Nature* **355**, 455–457.

32 Fenton, W. A., Kashi, Y., Furtak, K., & Horwich, A. L. (1994). Residues in chaperonin GroEL required for polypeptide binding and release. *Nature* **371**, 614–619.

33 Zhu, X., Zhao, X., Burkholder, W. F., Gragerov, A., Ogata, C. M., Gottesman, M. E., & Hendrickson, W. A. (1996). Structural analysis of substrate binding by the molecular chaperone DnaK. *Science* **272**, 1606–1614.

34 Katsumata, K., Okazaki, A., Tsurupa, G. P., & Kuwajima, K. (1996). Dominant forces in the recognition of a transient folding intermediate of alpha-lactalbumin by GroEL. *J. Mol. Biol.* **264**, 643–649.

35 Gragerov, A., Zeng, L., Zhao, X., Burkholder, W., & Gottesman, M. E. (1994). Specificity of DnaK-peptide binding. *J. Mol. Biol.* **235**, 848–854.

36 Crouy-Chanel, A., Kohiyama, M., & Richarme, G. (1996). Specificity of DnaK for arginine/lysine and effect of DnaJ on the amino acid specificity of DnaK. *J. Biol. Chem.* **271**, 15486–15490.

37 Wang, Z., Feng, H., Landry, S. J., Maxwell, J., & Gierasch, L. M. (1999). Basis of substrate binding by the chaperonin GroEL. *Biochemistry* **38**, 12537–12546.

38 Gervasoni, P., Staudenmann, W., James, P., Gehrig, P., & Pluckthun, A. (1996). beta-Lactamase binds to GroEL in a conformation highly protected against hydrogen/deuterium exchange. *Proc. Natl. Acad. Sci. U.S.A* **93**, 12189–12194.

39 Lilie, H. & Buchner, J. (1995). Interaction of GroEL with a highly structured folding intermediate: iterative binding cycles do not involve unfolding. *Proc. Natl. Acad. Sci. U.S.A* **92**, 8100–8104.

40 Braig, K., Otwinowski, Z., Hegde, R., Boisvert, D. C., Joachimiak, A., Horwich, A. L., & Sigler, P. B. (1994). The crystal structure of the

bacterial chaperonin GroEL at 2.8 Å. *Nature* **371**, 578–586.

41 Buckle, A. M., Zahn, R., & Fersht, A. R. (1997). A structural model for GroEL-polypeptide recognition. *Proc. Natl. Acad. Sci. U.S.A* **94**, 3571–3575.

42 Chen, L. & Sigler, P. B. (1999). The crystal structure of a GroEL/peptide complex: plasticity as a basis for substrate diversity. *Cell* **99**, 757–768.

43 Chin, D. T., Kuehl, L., & Rechsteiner, M. (1982). Conjugation of ubiquitin to denatured hemoglobin is proportional to the rate of hemoglobin degradation in HeLa cells. *Proc. Natl. Acad. Sci. U.S.A* **79**, 5857–5861.

44 Parag, H. A., Raboy, B., & Kulka, R. G. (1987). Effect of heat shock on protein degradation in mammalian cells: involvement of the ubiquitin system. *EMBO J.* **6**, 55–61.

45 Karzai, A. W., Roche, E. D., & Sauer, R. T. (2000). The SsrA-SmpB system for protein tagging, directed degradation and ribosome rescue. *Nat. Struct. Biol.* **7**, 449–455.

46 van Nocker, S., Deveraux, Q., Rechsteiner, M., & Vierstra, R. D. (1996). *Arabidopsis* MBP1 gene encodes a conserved ubiquitin recognition component of the 26S proteasome. *Proc. Natl. Acad. Sci. U.S.A* **93**, 856–860.

47 Weber-Ban, E. U., Reid, B. G., Miranker, A. D., & Horwich, A. L. (1999). Global unfolding of a substrate protein by the Hsp100 chaperone ClpA. *Nature* **401**, 90–93.

48 Pratt, W. B. & Toft, D. O. (1997). Steroid receptor interactions with heat shock protein and immunophilin chaperones. *Endocr. Rev.* **18**, 306–360.

49 Pratt, W. B. & Toft, D. O. (2003). Regulation of signalling protein function and trafficking by the hsp90/hsp70-based chaperone machinery. *Exp. Biol. Med.* **228**, 111–133.

50 Richter, K., Muschler, P., Hainzl, O., Reinstein, J., & Buchner, J. (2003). Sti1 is a non-competitive inhibitor of the Hsp90 ATPase. Binding prevents the N-terminal dimerization reaction during the atpase cycle. *J. Biol. Chem.* **278**, 10328–10333.

51 Liberek, K., Skowyra, D., Zylicz, M., Johnson, C., & Georgopoulos, C. (1991). The Escherichia coli DnaK chaperone, the 70-kDa heat shock protein eukaryotic equivalent, changes conformation upon ATP hydrolysis, thus triggering its dissociation from a bound target protein. *J. Biol. Chem.* **266**, 14491–14496.

52 Xu, Z., Horwich, A. L., & Sigler, P. B. (1997). The crystal structure of the asymmetric GroEL-GroES-$(ADP)_7$ chaperonin complex. *Nature* **388**, 741–750.

53 Ranson, N. A., Farr, G. W., Roseman, A. M., Gowen, B., Fenton, W. A., Horwich, A. L., & Saibil, H. R. (2001). ATP-bound states of GroEL captured by cryo-electron microscopy. *Cell* **107**, 869–879.

54 Richter, K., Muschler, P., Hainzl, O., & Buchner, J. (2001). Coordinated ATP hydrolysis by the Hsp90 dimer. *J. Biol. Chem.* **276**, 33689–33696.

55 Hardy, S. J. & Randall, L. L. (1991). A kinetic partitioning model of selective binding of nonnative proteins by the bacterial chaperone SecB. *Science* **251**, 439–443.

56 Weissman, J. S., Kashi, Y., Fenton, W. A., & Horwich, A. L. (1994). GroEL-mediated protein folding proceeds by multiple rounds of binding and release of nonnative forms. *Cell* **78**, 693–702.

57 Frieden, C. & Clark, A. C. (1997). Protein folding: how the mechanism of GroEL action is defined by kinetics. *Proc. Natl. Acad. Sci. U.S.A* **94**, 5535–5538.

58 Shtilerman, M., Lorimer, G. H., & Englander, S. W. (1999). Chaperonin function: folding by forced unfolding. *Science* **284**, 822–825.

59 Jordan, R. & McMacken, R. (1995). Modulation of the ATPase activity of the molecular chaperone DnaK by peptides and the DnaJ and GrpE heat shock proteins. *J. Biol. Chem.* **270**, 4563–4569.

60 McLaughlin, S. H., Smith, H. W., & Jackson, S. E. (2002). Stimulation of

the weak ATPase activity of human hsp90 by a client protein. *J. Mol. Biol.* **315**, 787–798.

61 Cashikar, A. G., Schirmer, E. C., Hattendorf, D. A., Glover, J. R., Ramakrishnan, M. S., Ware, D. M., & Lindquist, S. L. (2002). Defining a pathway of communication from the C-terminal peptide binding domain to the N-terminal ATPase domain in a AAA protein. *Mol. Cell* **9**, 751–760.

62 Gamer, J., Multhaup, G., Tomoyasu, T., McCarty, J. S., Rudiger, S., Schonfeld, H. J., Schirra, C., Bujard, H., & Bukau, B. (1996). A cycle of binding and release of the DnaK, DnaJ and GrpE chaperones regulates activity of the *Escherichia coli* heat shock transcription factor sigma32. *EMBO J.* **15**, 607–617.

63 Liberek, K., Marszalek, J., Ang, D., Georgopoulos, C., & Zylicz, M. (1991). *Escherichia coli* DnaJ and GrpE heat shock proteins jointly stimulate ATPase activity of DnaK. *Proc. Natl. Acad. Sci. U.S.A* **88**, 2874–2878.

64 Packschies, L., Theyssen, H., Buchberger, A., Bukau, B., Goody, R. S., & Reinstein, J. (1997). GrpE accelerates nucleotide exchange of the molecular chaperone DnaK with an associative displacement mechanism. *Biochemistry* **36**, 3417–3422.

65 Sullivan, W. P., Owen, B. A., & Toft, D. O. (2002). The influence of ATP and p23 on the conformation of hsp90. *J. Biol. Chem.* **277**, 45942–45948.

66 Wegele, H., Haslbeck, M., Reinstein, J., & Buchner, J. (2003). Sti1 is a novel activator of the Ssa proteins. *J. Biol. Chem.* **278**, 25970–25976.

67 Gray, T. E. & Fersht, A. R. (1991). Cooperativity in ATP hydrolysis by GroEL is increased by GroES. *FEBS Lett.* **292**, 254–258.

68 Todd, M. J., Viitanen, P. V., & Lorimer, G. H. (1994). Dynamics of the chaperonin ATPase cycle: implications for facilitated protein folding. *Science* **265**, 659–666.

69 Haslbeck, M., Walke, S., Stromer, T., Ehrnsperger, M., White, H. E., Chen, S., Saibil, H. R., & Buchner, J. (1999). Hsp26: a temperature-regulated chaperone. *EMBO J.* **18**, 6744–6751.

70 Spiess, C., Beil, A., & Ehrmann, M. (1999). A temperature-dependent switch from chaperone to protease in a widely conserved heat shock protein. *Cell* **97**, 339–347.

71 Krojer, T., Garrido-Franco, M., Huber, R., Ehrmann, M., & Clausen, T. (2002). Crystal structure of DegP (HtrA). reveals a new protease-chaperone machine. *Nature* **416**, 455–459.

72 Jakob, U., Muse, W., Eser, M., & Bardwell, J. C. (1999). Chaperone activity with a redox switch. *Cell* **96**, 341–352.

73 Kobayashi, T. & Inouye, M. (1992). Functional analysis of the intramolecular chaperone. Mutational hot spots in the subtilisin pro-peptide and a second-site suppressor mutation within the subtilisin molecule. *J. Mol. Biol.* **226**, 931–933.

74 Jaswal, S. S., Sohl, J. L., Davis, J. H., & Agard, D. A. (2002). Energetic landscape of alpha-lytic protease optimizes longevity through kinetic stability. *Nature* **415**, 343–346.

75 Mendoza, J. A., Rogers, E., Lorimer, G. H., & Horowitz, P. M. (1991). Unassisted refolding of urea unfolded rhodanese. *J. Biol. Chem.* **266**, 13587–13591.

76 Zhi, W., Landry, S. J., Gierasch, L. M., & Srere, P. A. (1992). Renaturation of citrate synthase: influence of denaturant and folding assistants. *Protein Sci.* **1**, 522–529.

77 Aghajanian, S., Walsh, T. P., & Engel, P. C. (1999). Specificity of coenzyme analogues and fragments in promoting or impeding the refolding of clostridial glutamate dehydrogenase. *Protein Sci.* **8**, 866–872.

78 Szabo, A., Korszun, R., Hartl, F. U., & Flanagan, J. (1996). A zinc finger-like domain of the molecular chaperone DnaJ is involved in binding to denatured protein substrates. *EMBO J.* **15**, 408–417.

79 Bose, S., Weikl, T., Bugl, H., &

Buchner, J. (1996). Chaperone function of Hsp90-associated proteins. *Science* **274**, 1715–1717.

80 Freeman, B. C., Toft, D. O., & Morimoto, R. I. (1996). Molecular chaperone machines: chaperone activities of the cyclophilin Cyp-40 and the steroid aporeceptor-associated protein p23. *Science* **274**, 1718–1720.

81 Freeman, B. C. & Yamamoto, K. R. (2002). Disassembly of transcriptional regulatory complexes by molecular chaperones. *Science* **296**, 2232–2235.

82 Kimura, Y., Rutherford, S. L., Miyata, Y., Yahara, I., Freeman, B. C., Yue, L., Morimoto, R. I., & Lindquist, S. (1997). Cdc37 is a molecular chaperone with specific functions in signal transduction. *Genes Dev.* **11**, 1775–1785.

83 Nagata, K. (1996). Hsp47: a collagen-specific molecular chaperone. *Trends Biochem. Sci.* **21**, 22–26.

84 Saga, S., Nagata, K., Chen, W. T., & Yamada, K. M. (1987). pH-dependent function, purification, & intracellular location of a major collagen-binding glycoprotein. *J. Cell Biol.* **105**, 517–527.

85 Natsume, T., Koide, T., Yokota, S., Hirayoshi, K., & Nagata, K. (1994). Interactions between collagen-binding stress protein HSP47 and collagen. Analysis of kinetic parameters by surface plasmon resonance biosensor. *J. Biol. Chem.* **269**, 31224–31228.

86 Goloubinoff, P., Christeller, J. T., Gatenby, A. A., & Lorimer, G. H. (1989). Reconstitution of active dimeric ribulose bisphosphate carboxylase from an unfolded state depends on two chaperonin proteins and Mg-ATP. *Nature* **342**, 884–889.

87 Buchner, J., Schmidt, M., Fuchs, M., Jaenicke, R., Rudolph, R., Schmid, F. X., & Kiefhaber, T. (1991). GroE facilitates refolding of citrate synthase by suppressing aggregation. *Biochemistry* **30**, 1586–1591.

88 Sigler, P. B., Xu, Z., Rye, H. S., Burston, S. G., Fenton, W. A., & Horwich, A. L. (1998). Structure and function in GroEL-mediated protein folding. *Annu. Rev. Biochem.* **67**, 581–608.

89 Ehrnsperger, M., Hergersberg, C., Wienhues, U., Nichtl, A., & Buchner, J. (1998). Stabilization of proteins and peptides in diagnostic immunological assays by the molecular chaperone Hsp25. *Anal. Biochem.* **259**, 218–225.

90 Langer, T., Pfeifer, G., Martin, J., Baumeister, W., & Hartl, F. U. (1992). Chaperonin-mediated protein folding: GroES binds to one end of the GroEL cylinder, which accommodates the protein substrate within its central cavity. *EMBO J.* **11**, 4757–4765.

91 Horovitz, A., Fridmann, Y., Kafri, G., & Yifrach, O. (2001). Review: allostery in chaperonins. *J. Struct. Biol.* **135**, 104–114.

92 Stark, G. R. (1965). Reactions of cyanate with functional groups of proteins. 3. Reactions with amino and carboxyl groups. *Biochemistry* **4**, 1030–1036.

93 Grimminger, V., Richter, K., Imhof, A., Buchner, J., & Walter, S. (2004). The prion curing agent guanidinium chloride specifically inhibits ATP hydrolysis by Hsp104. *J. Biol. Chem.* **279**, 7378–7383.

94 Todd, M. J. & Lorimer, G. H. (1995). Stability of the asymmetric Escherichia coli chaperonin complex. Guanidine chloride causes rapid dissociation. *J. Biol. Chem.* **270**, 5388–5394.

95 Sörbo, B. H. (1953). Crystalline Rhodanese: The Enzyme Catalyzed Reaction. *Acta Chem. Scand.* **7**, 1137–1145.

96 Ploegman, J. H., Drent, G., Kalk, K. H., & Hol, W. G. (1978). Structure of bovine liver rhodanese. I. Structure determination at 2.5 Å resolution and a comparison of the conformation and sequence of its two domains. *J. Mol. Biol.* **123**, 557–594.

97 Mendoza, J. A., Rogers, E., Lorimer, G. H., & Horowitz, P. M. (1991). Chaperonins facilitate the in vitro folding of monomeric mitochondrial rhodanese. *J. Biol. Chem.* **266**, 13044–13049.

98 Jaenicke, R., Rudolph, R., & Heider, I. (1979). Quaternary structure, subunit activity, & in vitro association of porcine mitochondrial malic dehydrogenase. *Biochemistry* **18**, 1217–1223.

99 Staniforth, R. A., Cortes, A., Burston, S. G., Atkinson, T., Holbrook, J. J., & Clarke, A. R. (1994). The stability and hydrophobicity of cytosolic and mitochondrial malate dehydrogenases and their relation to chaperonin-assisted folding. *FEBS Lett.* **344**, 129–135.

100 Roderick, S. L. & Banaszak, L. J. (1986). The three-dimensional structure of porcine heart mitochondrial malate dehydrogenase at 3.0-Å resolution. *J. Biol. Chem.* **261**, 9461–9464.

101 Ranson, N. A., Dunster, N. J., Burston, S. G., & Clarke, A. R. (1995). Chaperonins can catalyse the reversal of early aggregation steps when a protein misfolds. *J. Mol. Biol.* **250**, 581–586.

102 Lee, G. J., Roseman, A. M., Saibil, H. R., & Vierling, E. (1997). A small heat shock protein stably binds heat-denatured model substrates and can maintain a substrate in a folding-competent state. *EMBO J.* **16**, 659–671.

103 Goloubinoff, P., Mogk, A., Zvi, A. P., Tomoyasu, T., & Bukau, B. (1999). Sequential mechanism of solubilization and refolding of stable protein aggregates by a bichaperone network. *Proc. Natl. Acad. Sci. U.S.A* **96**, 13732–13737.

104 Remington, S., Wiegand, G., & Huber, R. (1982). Crystallographic refinement and atomic models of two different forms of citrate synthase at 2.7 and 1.7 Å resolution. *J. Mol. Biol.* **158**, 111–152.

105 Haslbeck, M., Schuster, I., & Grallert, H. (2003). GroE-dependent expression and purification of pig heart mitochondrial citrate synthase in Escherichia coli. *J. Chromatogr. B Analyt. Technol. Biomed. Life Sci.* **786**, 127–136.

106 Srere, P. A., Brazil, H., & Gonen, L. (1963). Citrate synthase assay in tissue homogenates. *Acta Chem. Scand.* **17**, 129–134.

107 Buchner, J., Grallert, H., & Jakob, U. (1998). Analysis of chaperone function using citrate synthase as nonnative substrate protein. *Methods Enzymol.* **290**, 323–338.

108 Wiech, H., Buchner, J., Zimmermann, R., & Jakob, U. (1992). Hsp90 chaperones protein folding in vitro. *Nature* **358**, 169–170.

109 Shao, F., Bader, M. W., Jakob, U., & Bardwell, J. C. (2000). DsbG, a protein disulfide isomerase with chaperone activity. *J. Biol. Chem.* **275**, 13349–13352.

110 Cyr, D. M., Lu, X., & Douglas, M. G. (1992). Regulation of Hsp70 function by a eukaryotic DnaJ homolog. *J. Biol. Chem.* **267**, 20927–20931.

111 Panse, V. G., Swaminathan, C. P., Surolia, A., & Varadarajan, R. (2000). Thermodynamics of substrate binding to the chaperone SecB. *Biochemistry* **39**, 2420–2427.

112 Scholz, C., Stoller, G., Zarnt, T., Fischer, G., & Schmid, F. X. (1997). Cooperation of enzymatic and chaperone functions of trigger factor in the catalysis of protein folding. *EMBO J.* **16**, 54–58.

113 Sanger, F. (1949). Fractionation of oxidized insulin. *Biochem. J.* **44**, 126–128.

114 Horwitz, J., Huang, Q. L., Ding, L., & Bova, M. P. (1998). Lens alpha-crystallin: chaperone-like properties. *Methods Enzymol.* **290**, 365–383.

115 Stromer, T., Ehrnsperger, M., Gaestel, M., & Buchner, J. (2003). Analysis of the interaction of small heat shock proteins with unfolding proteins. *J. Biol. Chem.* **278**, 18015–18021.

116 Schonfeld, H. J. & Behlke, J. (1998). Molecular chaperones and their interactions investigated by analytical ultracentrifugation and other methodologies. *Methods Enzymol.* **290**, 269–296.

117 Blond-Elguindi, S., Cwirla, S. E., Dower, W. J., Lipshutz, R. J., Sprang, S. R., Sambrook, J. F., & Gething, M. J. (1993). Affinity

panning of a library of peptides displayed on bacteriophages reveals the binding specificity of BiP. *Cell* **75**, 717–728.

118 Fourie, A. M., Sambrook, J. F., & Gething, M. J. (1994). Common and divergent peptide binding specificities of hsp70 molecular chaperones. *J. Biol. Chem.* **269**, 30470–30478.

119 Knarr, G., Gething, M. J., Modrow, S., & Buchner, J. (1995). BiP binding sequences in antibodies. *J. Biol. Chem.* **270**, 27589–27594.

120 Rudiger, S., Germeroth, L., Schneider-Mergener, J., & Bukau, B. (1997). Substrate specificity of the DnaK chaperone determined by screening cellulose-bound peptide libraries. *EMBO J.* **16**, 1501–1507.

121 Rudiger, S., Schneider-Mergener, J., & Bukau, B. (2001). Its substrate specificity characterizes the DnaJ co-chaperone as a scanning factor for the DnaK chaperone. *EMBO J.* **20**, 1042–1050.

122 Kornberg, A., Scott, J. F., & Bertsch, L. L. (1978). ATP utilization by rep protein in the catalytic separation of DNA strands at a replicating fork. *J. Biol. Chem.* **253**, 3298–3304.

123 Lanzetta, P. A., Alvarez, L. J., Reinach, P. S., & Candia, O. A. (1979). An improved assay for nanomole amounts of inorganic phosphate. *Anal. Biochem.* **100**, 95–97.

124 Norby, J. G. (1988). Coupled assay of Na^+,K^+-ATPase activity. *Methods Enzymol.* **156**, 116–119.

125 Ditzel, L., Lowe, J., Stock, D., Stetter, K. O., Huber, H., Huber, R., & Steinbacher, S. (1998). Crystal structure of the thermosome, the archaeal chaperonin and homolog of CCT. *Cell* **93**, 125–138.

126 Prodromou, C., Roe, S. M., O'Brien, R., Ladbury, J. E., Piper, P. W., & Pearl, L. H. (1997). Identification and structural characterization of the ATP/ADP-binding site in the Hsp90 molecular chaperone. *Cell* **90**, 65–75.

127 Meyer, P., Prodromou, C., Hu, B., Vaughan, C., Roe, S. M., Panaretou, B., Piper, P. W., & Pearl, L. H. (2003). Structural and functional analysis of the middle segment of hsp90: implications for ATP hydrolysis and client protein and cochaperone interactions. *Mol. Cell* **11**, 647–658.

128 Lee, S., Sowa, M. E., Watanabe, Y. H., Sigler, P. B., Chiu, W., Yoshida, M., & Tsai, F. T. (2003). The structure of ClpB: a molecular chaperone that rescues proteins from an aggregated state. *Cell* **115**, 229–240.

129 Kim, K. K., Kim, R., & Kim, S. H. (1998). Crystal structure of a small heat-shock protein. *Nature* **394**, 595–599.

130 Melki, R., Rommelaere, H., Leguy, R., Vandekerckhove, J., & Ampe, C. (1996). Cofactor A is a molecular chaperone required for beta-tubulin folding: functional and structural characterization. *Biochemistry* **35**, 10422–10435.

131 Russell, R., Jordan, R., & McMacken, R. (1998). Kinetic characterization of the ATPase cycle of the DnaK molecular chaperone. *Biochemistry* **37**, 596–607.

132 Lopez-Buesa, P., Pfund, C., & Craig, E. A. (1998). The biochemical properties of the ATPase activity of a 70-kDa heat shock protein (Hsp70) are governed by the C-terminal domains. *Proc. Natl. Acad. Sci. U.S.A* **95**, 15253–15258.

133 Barnett, M. E., Zolkiewska, A., & Zolkiewski, M. (2000). Structure and activity of ClpB from *Escherichia coli*. Role of the amino-and-carboxyl-terminal domains. *J. Biol. Chem.* **275**, 37565–37571.

134 Surin, A. K., Kotova, N. V., Kashparov, I. A., Marchenkov, V. V., Marchenkova, S. Y., & Semisotnov, G. V. (1997). Ligands regulate GroEL thermostability. *FEBS Lett.* **405**, 260–262.

135 Stromer, T., Fischer, E., Richter, K., Haslbeck, M., & Buchner, J. (2004). Analysis of the regulation of the molecular chaperone Hsp26 by temperature-induced dissociation: the N-terminal domain is important for oligomer assembly and the binding of unfolding proteins. *J. Biol. Chem.* **279**, 11222–11228.

136 Holl-Neugebauer, B., Rudolph, R., Schmidt, M., & Buchner, J. (1991). Reconstitution of a heat shock effect in vitro: influence of GroE on the thermal aggregation of alpha-glucosidase from yeast. *Biochemistry* **30**, 11609–11614.

137 Hayer-Hartl, M. K., Ewbank, J. J., Creighton, T. E., & Hartl, F. U. (1994). Conformational specificity of the chaperonin GroEL for the compact folding intermediates of alpha-lactalbumin. *EMBO J.* **13**, 3192–3202.

138 Lindner, R. A., Kapur, A., & Carver, J. A. (1997). The interaction of the molecular chaperone, alpha-crystallin, with molten globule states of bovine alpha-lactalbumin. *J. Biol. Chem.* **272**, 27722–27729.

139 Schmidt, M., Buchner, J., Todd, M. J., Lorimer, G. H., & Viitanen, P. V. (1994). On the role of groES in the chaperonin-assisted folding reaction. Three case studies. *J. Biol. Chem.* **269**, 10304–10311.

140 Schroder, H., Langer, T., Hartl, F. U., & Bukau, B. (1993). DnaK, DnaJ and GrpE form a cellular chaperone machinery capable of repairing heat-induced protein damage. *EMBO J.* **12**, 4137–4144.

141 Buchberger, A., Schroder, H., Hesterkamp, T., Schonfeld, H. J., & Bukau, B. (1996). Substrate shuttling between the DnaK and GroEL systems indicates a chaperone network promoting protein folding. *J. Mol. Biol.* **261**, 328–333.

142 Zolkiewski, M. (1999). ClpB cooperates with DnaK, DnaJ, & GrpE in suppressing protein aggregation. A novel multi-chaperone system from *Escherichia coli*. *J. Biol. Chem.* **274**, 28083–28086.

143 Dumitru, G. L., Groemping, Y., Klostermeier, D., Restle, T., Deuerling, E., & Reinstein, J. (2004). DafA Cycles Between the DnaK Chaperone System and Translational Machinery. *J. Mol. Biol.* **339**, 1179–1189.

144 Farahbakhsh, Z. T., Huang, Q. L., Ding, L. L., Altenbach, C., Steinhoff, H. J., Horwitz, J., & Hubbell, W. L. (1995). Interaction of alpha-crystallin with spin-labeled peptides. *Biochemistry* **34**, 509–516.

145 Miller, A. D., Maghlaoui, K., Albanese, G., Kleinjan, D. A., & Smith, C. (1993). *Escherichia coli* chaperonins cpn60 (groEL) and cpn10 (groES) do not catalyse the refolding of mitochondrial malate dehydrogenase. *Biochem. J.* **291**, 139–144.

146 Sparrer, H., Lilie, H., & Buchner, J. (1996). Dynamics of the GroEL-protein complex: effects of nucleotides and folding mutants. *J. Mol. Biol.* **258**, 74–87.

147 Hayer-Hartl, M. K., Weber, F., & Hartl, F. U. (1996). Mechanism of chaperonin action: GroES binding and release can drive GroEL-mediated protein folding in the absence of ATP hydrolysis. *EMBO J.* **15**, 6111–6121.

148 Viitanen, P. V., Lubben, T. H., Reed, J., Goloubinoff, P., O'Keefe, D. P., & Lorimer, G. H. (1990). Chaperonin-facilitated refolding of ribulosebisphosphate carboxylase and ATP hydrolysis by chaperonin 60 (groEL) are K^+ dependent. *Biochemistry* **29**, 5665–5671.

149 Rye, H. S., Burston, S. G., Fenton, W. A., Beechem, J. M., Xu, Z., Sigler, P. B., & Horwich, A. L. (1997). Distinct actions of *cis* and *trans* ATP within the double ring of the chaperonin GroEL. *Nature* **388**, 792–798.

150 Sriram, M., Osipiuk, J., Freeman, B., Morimoto, R., & Joachimiak, A. (1997). Human Hsp70 molecular chaperone binds two calcium ions within the ATPase domain. *Structure* **5**, 403–414.

151 van Montfort, R. L., Basha, E., Friedrich, K. L., Slingsby, C., & Vierling, E. (2001). Crystal structure and assembly of a eukaryotic small heat shock protein. *Nat. Struct. Biol.* **8**, 1025–1030.

6
Physical Methods for Studies of Fiber Formation and Structure

Thomas Scheibel and Louise Serpell

6.1
Introduction

Elucidating protein fiber assembly and analyzing the acquired regular fibrous structures have engaged the interest of scientists from different disciplines for a long time. The complexity of the problem, together with the paucity of interpretable data, has generated a large volume of literature concerned with speculations about possible assembly mechanisms and structural conformations.

Fibrous proteins are essential building blocks of life, providing a scaffold for our cells, both intracellularly and extracellularly. However, despite nearly a century of research of the assembly mechanisms and structures of fibrous protein, we have only recently begun to get insights. In the last 10 years, atomic models for some of the most important fibrous proteins have been proposed. We are increasingly knowledgeable about how fibrous proteins form and how they function (for example, the interaction of actin and myosin to produce muscular movement). Development of methods specific to the study of fibrous proteins has enabled these investigations, since fibrous proteins are generally insoluble and often heterogeneous in length, and therefore methods used for examining the structure of globular proteins cannot be used.

In this chapter, an overview of some commonly used methods to examine the assembly and structure of fibrous proteins is given. However, additional methods can be suitable to analyze fibrous proteins. Among the methods not discussed are solid-state NMR (ssNMR), near-field scanning optical microscopy (NSOM), scanning transmission electron microscopy (STEM), and light microscopy, for all of which reviews can be found elsewhere. Other complementary methods, specific for the particular protein, include cross-linking studies and antibody-binding epitope studies. These are valuable techniques that can help us to interpret structural data and contribute to the understanding of the assembly pathway, but due to space limitations they can not be discussed in this chapter.

Protein Folding Handbook. Part II. Edited by J. Buchner and T. Kiefhaber

ISBN: 3-527-30784-2

6.2
Overview: Protein Fibers Formed in Vivo

6.2.1
Amyloid Fibers

The term "amyloid" describes extracellular, fibrillar protein deposits associated with disease in humans. The deposits accumulate in various tissue types and are defined by their tinctorial and morphological properties [1]. Although the involved proteins are distinct with respect to amino acid sequence and function, the fibrils formed by different amyloidogenic proteins are structured similarly. This observation is remarkable since the soluble native forms of these proteins vary considerably: some proteins are large, some are small, and some are largely α-helical (see chapter 9 in Part I) while some are largely β-sheet (see chapter 10 in Part I). Some are intact in the fibrous form, while others are at least partially degraded. Some are cross-linked with disulfide bonds and some are not. Amyloid fibers are unusually stable and unbranched, range from 6 to 12 nm in diameter, and specifically bind the dye Congo red (CR), showing an apple-green birefringence in polarized light [2, 3]. Amyloid fibers are also rich in β-sheet structure and produce a characteristic "cross-β" X-ray diffraction pattern, consistent with a model in which stacked β-sheets form parallel to the fiber axis with individual β-strands perpendicular to the fiber axis [1, 4]. Diseases characterized by amyloids are referred to as amyloidoses (see chapters 33, 36, 37); these diseases are slow in onset and degenerative and can be found not only in humans but also in most mammals. Some of the amyloidoses are familial, while some are associated with medical treatment (e.g., hemodialysis) or infection (prion diseases), and some are sporadic (e.g., most forms of Alzheimer's disease). Certain diseases, such as the amyloidoses associated with the protein transthyretin, can be found in both sporadic and familial forms. In addition to diseases with extracellular deposits, there are others, notably Parkinson's and Huntington's disease, that appear to involve very similar aggregates, which are intracellular, and these diseases are therefore not included in the strict definition of amyloidoses [5, 6].

Amyloidogenic proteins are not found only in mammals. Studies of *Saccharomyces cerevisiae* have resulted in the discovery of proteins that have properties related to those of mammalian prions [7, 8] (see chapters 34, 35). These yeast prions have been found to convert in vitro into ordered aggregates with all the characteristics of amyloid fibers [9]. Also, amyloidogenic peptides are found in egg envelopes (chorions) of invertebrates. More than 95% of the chorion's dry mass consists of proteins that have remarkable mechanical and chemical properties that protect the oocyte and the developing embryo from a wide range of environmental hazards. About 200 proteins have been detected and classified into two major classes, A and B. Interestingly, within the chorion, protein fibrils can be detected with characteristics of amyloid fibrils. These features include a high proportion of intermolecular β-sheet, positive staining and green birefringence with CR, and detection of long, unbranched fibrils with a diameter of 4–6 nm [10, 11].

6.2.2 Silks

Arthropods produce a great variety of silks that are used in the fabrication of structures outside of the body of the animal. Silks are typically fibrous filaments or threads with diameters ranging from a few hundred nanometers to 50 μm. Insects and spiders use their silks for lifelines, nests, traps, and cocoons. Characteristically, the silk is produced in specialized glands and stored in a fluid state in the lumen of the gland. As the fluid passes through the spinning duct, a rapid transformation to the solid state takes place and the silk becomes water-insoluble [12–15]. However, some of the materials that are called silks are not produced by silk glands in the traditional sense but by extrusions of the guts, e.g., in antlions, lacewings, and many beetles [16].

The major components of traditional silks are fibrous proteins, which in the final insoluble state have a high content of regular secondary structure. Wide variations in composition and structure have been found among different silks. Therefore, the classification of silks is often based on the predominant form of regular secondary structure in the final product as determined by X-ray diffraction studies. Silks are classified as beta silks (which are rich in β-sheets; see Section 6.3.1.3), alpha silks (which resemble the X-ray diffraction pattern obtained from α-keratin and which have a much lower content of Gly and a much higher content of charged residues than any other silk; see Section 6.3.2.4), Gly-rich silks (which form a polyglycine II-like structure), and collagen-like silks (which resemble the X-ray diffraction pattern given by collagen; see Section 6.3.2.1). While silks from the class of Arachnida (spiders) are generally β-silks, in the class of Insecta all four classes of silk can be found, e.g., β-silks in the family of Bombycidae (moths, includes *Bombyx mori*, whose caterpillar is the silkworm), α-silks in the family of Apidae (bees), Gly-rich silks in the family of Blennocampinae (subspecies of sawflies), and collagen-like silks in the family of Nematinae (subspecies of sawflies) [15, 17–20]. In contrast, silks from extrusions of the guts do not form traditional silk filaments or threads; rather, they are hardened fibrous feces.

6.2.3 Collagens

Collagens are a family of highly characteristic fibrous proteins found in all multicellular animals (see chapter 30 in Part I). In combination with elastin (see Section 6.2.8), mucopolysaccharides, and mineral salts, collagens form the connective tissue responsible for the structural integrity of the animal body. The characteristic feature of a typical collagen molecule is its long, stiff, triple-stranded helical structure, in which three collagen polypeptide chains, called α-chains, are wound around each other in a rope-like superhelix (see Section 6.3.2.1). The polypeptide chains in collagens have a distinctive conformation that is intimately related to their structural function [21–25]. All collagen polypeptides have a similar primary structure, in which every third amino acid is Gly (Gly-Xaa-Yaa)$_n$ with a predominance of Pro residues at position Xaa and Yaa. Many of the Pro residues, as well

as occurring Lys residues at the position Yaa, are hydroxylated as a posttranslational modification. The repeating sequence of the collagen chain is the reason for the three-dimensional structure of collagens, which has a slightly twisted, left-handed, threefold helical conformation like that of poly(Pro) II and poly(Gly) II and entirely different from that of an α-helix [25–27]. Collagen polypeptide chains typically have about 1000 residues, but considerable variation occurs in certain types. Polypeptide chains of 1000 residues produce a collagen triple helix 1.4 nm in diameter and 300 nm in length. In vivo the triple helix of collagens is assembled correctly because the polypeptide chains are synthesized with non-helical, globular extensions of just over 100 residues at the amino-terminal and 300 residues at the carboxy-terminal ends. The carboxy-terminal extensions associate specifically and serve to align the three polypeptide chains and to nucleate assembly of the triple helix. Next, collagens aggregate side by side into microfibrils, which are thin in diameter (10–300 nm) and hundreds of micrometers long. The collagen fibrils often aggregate further into larger, cable-like bundles with several micrometers in diameter [21–23, 27].

The main types of collagen found in connective tissue are types I, II, III, V, and XI, with type I being the principal collagen of skin and bone and by far the most common. These are the fibrillar collagens and have the rope-like structure. Types IX and XII are called fibril-associated collagens, as they decorate the surface of collagen fibrils. They are thought to link these fibrils to one another and to other components of the extracellular matrix. Types IV and VII are network-forming collagens. Type IV molecules assemble into a felt-like sheet or meshwork that constitutes a major part of mature basal lamina, while type VII molecules form dimers that assemble into specialized structures called anchoring fibrils, which help to attach the basal lamina of multi-layered epithelia to the underlying connective tissue [21–23]. In some metazoans, collagens of ectodermal origin are used to construct materials outside the confines of the living organism [28, 29]. Gooseberry sawfly silk [30], selachian egg capsules [31], worm cuticle collagens [32, 33], spongin [34], and mussel byssus are a few examples of such exoskeletal collagenous materials. These threads were dubbed "collagenous" on the basis of fiber X-ray diffraction [35, 36], hydroxyproline content [37], amino acid composition [38, 39], and shrinkage temperatures [40]. The primary structure of collagenous proteins found in the mussel byssus threads, however, encodes unprecedented natural block copolymers with three major domain types: a central collagen domain, flanking elastic or stiff domains, and histidine-rich terminal domains. The elastic domains have sequence motifs that strongly resemble those of elastin (see Section 6.2.8), and the stiff domains closely resemble amorphous glycine-rich regions of spider silks (see Section 6.2.2) [41, 42].

6.2.4
Actin, Myosin, and Tropomyosin Filaments

All eukaryotic species contain actin, which is the most abundant protein in many eukaryotic cells. Actin filaments (F actin) can form both stable and labile structures

in cells. Stable actin filaments are a crucial component of the contractile apparatus of muscle cells in so-called myofibrils (see below). Many cell movements, however, depend on labile structures constructed from actin filaments. Actin filaments are about 8 nm wide and consist of a tight helix of uniformly oriented actin molecules also known as globular actin (G actin). Like a microtubule (see Section 6.2.7), an actin filament is a polar structure with two structurally different ends. The so-called minus end is relatively inert and slow growing, while the so-called plus end is faster growing [43, 44]. Some lower eukaryotes, such as yeasts, have only one actin gene encoding a single protein. All higher eukaryotes have several isoforms encoded by a family of actin genes. At least six types of actin are present in mammalian tissue, which fall into three classes depending on their isoelectric point: α actins are found in various types of muscle, whereas β and γ actins are the principal constituents of non-muscle cells. Although there are subtle differences in the properties of different forms of actin, the amino acid sequences have been highly conserved in evolution and all assemble into filaments in vitro. Polymerization of actin in vitro requires ATP as well as both monovalent and divalent cations, such as K^+ and Mg^{2+}. ATP hydrolysis weakens the bonds in the polymer (F actin) and thereby promotes depolymerization [43].

Myofibrils are cylindrical structures 1–2 μm in diameter, which in addition to thin filaments formed by actin contain thick filaments made of muscle isoforms of myosin II. Muscle myosin has two heads with ATPase and motor activity and a long, rod-like tail. A myosin II molecule is composed of two identical heavy chains, each of which is complexed to a pair of light chains. The amino-terminal portion of the heavy chain forms the motor-domain head, while the carboxy-terminal half of the heavy chain forms an extended α-helix. Two heavy chains associate by twisting their α-helical tail domains together into a coiled coil to form a stable dimer that has two heads and a single rod-like tail [45–47]. A major role of the rod-like tail is to allow the molecules to polymerize into bipolar filaments. Myosin II filaments play an important role in muscle contraction, drive membrane furrowing during cell division, and generate tension in stress fibers.

Tropomyosins are a group of proteins that bind to the sides of actin filaments and (together with troponins) regulate the interaction of the filaments with myosin in response to Ca^{2+}. They are parallel, α-helical, coiled-coil dimers. Vertebrates typically express approximately 20 different tropomyosins from alternative splicing from about four tropomyosin genes [48]. Tropomyosins exist as both homodimers and heterodimers held together by a series of salt bridges and hydrophobic interactions. They may also interact through their amino and carboxyl termini in solution (especially in low-ionic-strength buffers). There are two major groups of tropomyosin, the high- and low-molecular-weight tropomyosins. The former type exists primarily in muscle tissues (cardiac, smooth, and skeletal), whereas non-muscle tissues express both high- and low-molecular-weight tropomyosins. Tropomyosins bind cooperatively to actin filaments [49–51], probably because there is end-to-end binding of the tropomyosin molecules, but possibly also because tropomyosin restricts the movement of the filament, causing the filament repeat distance to be made more regular [52]. The binding of tropomyosin to actin is strongly

Mg^{2+}-dependent [49]. High-molecular-weight tropomyosins consist most often of 284 amino acids and bind seven actin monomers, while the low-molecular-weight tropomyosins consist of about 245–250 amino acids and span six actins.

The thick filaments of invertebrate muscles contain, in addition to myosin, the protein paramyosin, a rod-like, coiled-coil molecule similar to myosin [53]. Paramyosin filaments play an important part in certain molluscan and annelid muscles because they allow these muscles to maintain tension for prolonged periods without a large expenditure of energy.

6.2.5 Intermediate Filaments/Nuclear Lamina

Intermediate filaments are tough, durable, 10-nm wide protein fibers found in the cytoplasm of most, but not all, animal cells, particularly in cells that are subject to mechanical stress [54]. Unlike actin and tubulin, which are globular proteins, monomeric intermediate filament proteins are highly elongated, with an amino-terminal head, a carboxy-terminal tail, and a central rod domain. The central rod domain consists of an extended α-helical region containing long tandem repeats of a distinct amino acid sequence motif called heptad repeats. These repeats promote the formation of coiled-coil dimers between two parallel α-helices. Next, two of the coiled-coil dimers associate in an antiparallel manner to form a tetrameric subunit. The antiparallel arrangement of dimers implies that the tetramer and the intermediate filaments formed thereof are non-polarized structures. This distinguishes intermediate filaments from microtubules (see Section 6.2.7) and actin filaments (see Section 6.2.4), which are polarized and whose functions depend on this polarity [55–58].

The cytoplasmic intermediate filaments in vertebrate cells can be grouped into three classes: keratin filaments, vimentin/vimentin-related filaments, and neurofilaments. By far the most diverse family of these proteins is the family of α-keratins, with more than 20 distinct proteins in epithelia and over eight more so-called hard keratins in nails and hair. The α-keratins are evolutionarily distinct from β-keratins found in bird feathers, which have an entirely different structure and will not be further discussed in this context. Based on their amino acid sequence, α-keratins can be subdivided into type I (acidic) and type II (neutral/basic) keratins, which always form heterodimers of type I and type II but never homodimers [59]. Unlike keratins, the class of vimentin and vimentin-related proteins (e.g., desmin, peripherin) can form homopolymers [60]. In contrast to the first two classes of intermediate filaments, the third one, neurofilaments, is found uniquely in nerve cells, wherein they extend along the length of an axon and form its primary cytoskeletal component [61].

The nuclear lamina is a meshwork of intermediate filaments that lines the inside surface of the inner nuclear membrane in eukaryotic cells. In mammalian cells the nuclear lamina is composed of lamins, which are homologous to other intermediate filament proteins but differ from them in several ways. Lamins have a longer central rod domain, contain a nuclear localization signal, and assemble into a

two-dimensional, sheet-like lattice, which is unusually dynamic. This lattice rapidly disassembles at the start of mitosis and reassembles at the end of mitosis [61, 62].

6.2.6 Fibrinogen/Fibrin

Fibrinogen is a soluble blood plasma protein, which during the process of clotting is modified to give a derived product termed fibrin. Fibrinogen is a multifunctional adhesive protein involved in a number of important physiological and pathological processes. Its multifunctional character is connected with its complex multidomain structure. Fibrinogen consists of two identical subunits, each of which is formed by three nonidentical polypeptide chains, Aα, Bβ, and γ, all of which are linked by disulfide bonds and assemble into a highly complex structure [63–65]. Conversion of fibrinogen into fibrin takes place under the influence of the enzyme thrombin. The proteolysis results in spontaneous polymerization of fibrin and formation of an insoluble clot that prevents the loss of blood upon vascular injury. This clot serves as a provisional matrix in subsequent tissue repair. The polymerization of fibrin is a multi-step process. First, two stranded protofibrils are generated, which associate with each other laterally to produce thicker fibrils. The fibrils branch to form the fibrin clot, which is subsequently stabilized by the formation of intermolecular cross-linkages [66]. Fibrinogen is a rather inert protein, but after conversion fibrin interacts with different proteins, such as tissue-type plasminogen activator, fibronectin, and some cell receptors, and participates in different physiologically important processes, including fibrinolysis, inflammation, angiogenesis, and wound healing [67–69].

6.2.7 Microtubules

Microtubules are stiff polymers formed from molecules of tubulin. Microtubules extend throughout the cytoplasm and govern the location of membrane-bounded organelles and other cell components. Particles can use the microtubules as tracks, and motor proteins, such as kinesin and dynein, can move, e.g., organelles along the microtubules [70, 71]. The protein building blocks of microtubules, tubulins, are heterodimers consisting of two closely related and tightly linked globular polypeptides, α-tubulin and β-tubulin. In mammals there are at least six forms of α-tubulin and a similar number of forms of β-tubulin. The different tubulins are very similar and copolymerize into mixed microtubules in vitro, although they can have distinct cellular locations. A microtubule can be regarded as a cylindrical structure with a 25-nm diameter, which is built from 13 linear protofilaments, each composed of alternating α- and β-tubulin subunits and bundled in parallel to form the cylinder. Since the 13 protofilaments are aligned in parallel with the same polarity, the microtubule itself is a polar structure and it is possible to distinguish both ends [71–74]. Microtubules reflect dynamic protein polymers that can polymerize and depolymerize depending on their biological function. Tubulin will polymerize into

microtubules in vitro, as long as Mg^{2+} and GTP are present, by addition of free tubulin to the free end of the microtubule. Hydrolysis of the bound GTP takes place after assembly and weakens the bonds that hold the microtubule together. Without stabilization by cellular factors capping the free ends, microtubules become extremely unstable and disassemble [73, 75].

6.2.8 Elastic Fibers

The proteins elastin, fibrillin, and resilin occur in the highly elastic structures found in vertebrates and insects, which are at least five times more extensible than a rubber band of the same cross-sectional area. Elastin is a highly hydrophobic protein that, like collagen, is unusually rich in Pro and Gly residues, but unlike collagen it is not glycosylated and contains little hydroxyproline and no hydroxylysine. Elastin molecules are secreted into the extracellular space and assemble into elastic fibers close to the plasma membrane. After secretion, the elastin molecules become highly cross-linked between Lys residues to generate an extensive network of fibers and sheets. In its native form, elastin is devoid of regular secondary structure [76–79].

The elastic fibers are not composed solely of elastin, but the elastin core is covered with microfibrils that are composed of several glycoproteins including the large glycoprotein fibrillin [80, 81]. Microfibrils play an important part in the assembly of elastic fibers. They appear before elastin in developing tissues and seem to form a scaffold on which the secreted elastin molecules are deposited. As the elastin is deposited, the microfibrils become displaced to the periphery of the growing fiber [81].

Elastin and resilin are not known to be evolutionarily related, but their functions are similar. Resilin forms the major component in several structures in insects possessing rubber-like properties. Similar to elastin, the polypeptide chains are three-dimensionally cross-linked and are devoid of regular secondary structure. The amino acid composition of resilin resembles that of elastin insofar as the Gly content is high, but otherwise there is little sequence homology between these two proteins [19, 79, 82].

6.2.9 Flagella and Pili

Prokaryotes and archaea use a wide variety of structures to facilitate motility, most of which include fibrillar proteins. The best studied of all prokaryotic motility structures is the bacterial flagellum, which is composed of over 20 different proteins. The bacterial flagellum is a rotary structure driven from a motor at the base and a protein fiber acting as a propeller. The propeller consists of three major substructures: a filament, a hook, and a basal body. The filament is a tubular structure composed of 11 protofilaments about 20 nm in diameter, and the protofilaments are typically built by a single protein called flagellin. Less commonly, the filament

is composed of several different flagellins [83–85]. Strikingly, monomeric flagellin does not polymerize under physiological conditions. The amino- and carboxy-terminal regions of flagellin monomers are known to be intrinsically unfolded, which prevents flagellin from assembling into a nucleus for polymerization [86, 87]. Flagellin assembly is regulated through a combination of transcriptional, translational, and posttranslational regulatory mechanisms too complex to be explained in detail in this chapter. Only the unusual filament growth should be mentioned, since individual flagellin monomers are added to the growing polymer not at the base closest to the cell surface, but at the distal tip furthest from the cell, probably by passing through the hollow interior of the tubule [85, 88].

Motility is also conferred by flagella in the domain archaea, yet these structures and the sequences of the involved proteins bear little similarity to their bacterial counterparts. Rather, archaeal flagella demonstrate sequence similarity to another bacterial motility apparatus named pili. Both types of proteins have extremely hydrophobic amino acids over the first 50 amino acids and, in contrast to bacterial flagellin, are made as preproteins with short, positively charged leader peptides that are cleaved by leader peptidases. In archaea multiple flagellins are found that form a filament with a diameter of approximately 12 nm [89, 90].

Pili are responsible for various types of flagellar-independent motility, such as twitching motility in prokaryotes, and they are formed of pilins (see chapter 29). The outer diameter of a pilus fiber is about 6 nm, and, unlike in bacterial flagellum, there is no large channel in the center of the fiber. Therefore, pili grow by adding monomers at the base closest to the cell surface. The amino terminus of pilin forms α-helices, which compose the core of the pilus fiber. The outside of the pilus fiber is made of β-sheets packed against the core and an extended carboxy-terminal tail [90–92].

6.2.10
Filamentary Structures in Rod-like Viruses

Filamentous phages comprise a family of simple viruses that have only about 10 genes and grow in gram-negative bacteria. Different biological strains have been isolated, all of which have a similar virion structure and life cycle. The most prominent filamentous phage is bacteriophage fd (M13), which infects *E. coli*. The wild-type virion is a flexible rod about 6 nm in diameter and 800–2000 nm in length. Several thousand identical α-helical proteins form a helical array around a single-stranded circular DNA molecule at the core. It is assumed that the protein subunits forming the helical array pre-assemble within the membrane of the host into ribbons with the same inter-subunit interactions as in the virion. A ribbon grows by addition of newly synthesized protein subunits at one end, and at the same time the other end of a ribbon twists out of the membrane and merges into the assembling virion [93–95].

Some proteins of plant viruses, such as the tobacco mosaic virus (TMV), also form self-assembled macromolecules. The virion of TMV is a rigid rod (18×300 nm) consisting of 2130 identical virion coat protein (CP) subunits stacked in a he-

lix around a single strand of plus-sense RNA. Depending upon solution conditions, TMV CP forms three general classes of aggregates, the 4S or A protein composed of a mixture of low-ordered monomers, dimers, and trimers; the 20S disk or helix composed of approximately 38 subunits; and an extended virion-like rod. Under cellular conditions, the 20S helix makes up the predominant CP aggregate [96–99]. In the absence of RNA, the structure within the central hole of the 20S filament is disordered, but upon RNA binding structural ordering occurs, which locks the nucleoprotein complex into a virion-like helix and allows assembly to proceed [100]. Virion elongation occurs in both the 5′ and 3′ directions of the RNA. Assembly in the 5′ direction occurs rapidly and is consistent with the addition of 20S aggregates to the growing nucleoprotein rod. Assembly in the 3′ direction occurs considerably slower and is thought to involve the addition of 4S particles [97, 99].

6.2.11
Protein Fibers Used by Viruses and Bacteriophages to Bind to Their Hosts

Certain viruses and bacteriophages use fibrous proteins to bind to their host receptors. Examples are adenovirus, reovirus, and the T-even bacteriophages, such as bacteriophage T4. The fibers of adenovirus, reovirus, and T4 share common structural features: they are slim and elongated trimers with asymmetric morphologies, and the proteins consist of an amino-terminal part that binds to the viral capsid, a thin shaft, and a globular carboxy-terminal domain that attaches to a cell receptor. Strikingly, the fibers formed of these proteins are resistant to proteases, heat, and, under certain conditions, sodium dodecyl sulfate (SDS) [101]. The assembly of the tail spike from *Salmonella* phage P22 is the most extensively studied model system and has allowed detailed study of in vitro and in vivo folding pathways in light of structural information [102].

6.3
Overview: Fiber Structures

Structural elucidation of fibrous proteins is nontrivial and often involves the use of several structural techniques combined to derive a model structure. Structural studies have often involved X-ray crystallography from single crystals of monomeric or complexed proteins to elucidate the structure of fibrous protein subunits. Electron microscopy with helical image reconstruction and X-ray fiber diffraction have then been used to examine the structure of the fiber, and, where possible, modeling of a crystal structure has been matched with the electron microscopy maps or X-ray diffraction data. Protein fiber structures that have been extensively studied include natural proteins such as actin, tubulin, collagen, intermediate filaments, silk, myosin, and tropomyosin as well as misfolded protein fibers such as amyloid, paired helical filaments, and serpin polymers. In this section, a few selected examples will be discussed.

6.3.1 Study of the Structure of β-sheet-containing Proteins

6.3.1.1 Amyloid

Amyloid fibrils extracted from tissue are extremely difficult to study due to contaminants and the degree of order within the fibrils themselves. For this reason, structural studies of amyloid fibrils have concentrated on examining the structure of amyloid formed in vitro from various peptides with homology to known amyloid-forming proteins. It was clear from the early work of Eanes and Glenner [2] that amyloid fibrils resembled cross-β silk (see Section 6.3.1.3), in that the fiber diffraction pattern gave the cross-β diffraction signals. This means that the diffraction pattern consists of two major diffraction signals at 4.7 Å and around 10 Å, on perpendicular axes, that correspond to the spacing between hydrogen-bonded β-strands and the intersheet distance, respectively. Models of amyloid fibrils have been built using X-ray diffraction data [1, 103–106], solid-state NMR data [107–109], and electron microscopy [110, 111]. Many of these models have a common core structure in which the β-strands run perpendicular to the fiber axis and are hydrogen-bonded along the length of the fiber. Whether the amyloid fibrils are composed of parallel or antiparallel β-sheets may vary depending on the composite protein. X-ray diffraction and FTIR data from various amyloid fibrils have suggested an antiparallel β-sheet arrangement for some amyloid fibrils formed from short peptides [105]. Solid-state NMR data from full-length Aβ peptides appear to be consistent with a parallel arrangement [108]. Alternative models of amyloid fibril core structure involving β-helical structure have been suggested [112, 113]. The mature amyloid fibril is thought to be composed of several protofilaments; evidence for this comes from electron microscopy [111, 114] and atomic force microscopy data [115].

6.3.1.2 Paired Helical Filaments

Paired helical filaments (PHFs) are found deposited in disease and are composed of the microtubule-associated protein Tau [116]. PHFs are found in neurofibrillary tangles (NFT) in Alzheimer's disease brains as well as in a group of neurodegenerative diseases collectively known as the tauopathies. Electron microscopy structural work on PHFs has revealed that the filaments are composed of two strands twisted around one another, giving the characteristic appearance [117]. Straight filaments (SF) have also been isolated and are thought to be composed of the same building blocks. Calculated cross-sectional views showed that C-shaped subunits make up each strand for both PHFs and SFs [117]. More recently, X-ray and electron diffraction from synthetic and isolated PHFs have revealed a cross-β structural arrangement, similar to that shown for amyloid [118], indicating that the core structure of PHFs may share the generic amyloid-like structure.

6.3.1.3 β-Silks

All silk fibroins appear to contain crystalline regions or regions of long-range order, interspersed with short-range-ordered, non-crystalline regions [14]. Silks spun by

different organisms vary in the arrangement, proportions, and length of the crystalline and non-crystalline regions. Generally, β-pleated sheets are packed into tight crystalline arrays with spacer regions of more loosely associated β-sheets, α-helices, and/or β-spirals [14]. X-ray fiber diffraction has been used extensively to examine the structure of silks made by different spiders and insects [14]. The crystalline domains of *Bombyx mori* fibroin silk are composed of repeating glycine-alanine residues and form an antiparallel arrangement of β-pleated strands that run parallel to the fiber axis. For this structural arrangement, a model was proposed by Marsh, Corey, and Pauling [119], in which the intersheet distance is about 5.3 Å, which accommodates the small side chains. A recent refinement of the model [120] showed that the methyl groups of the alanine residues alternately point to either side of the sheet structure along the hydrogen-bonding direction, so that the structure consists of two antipolar, antiparallel β-sheet structures. Major ampullate (dragline) silk from the spider *Nephila clavipes* has been examined by X-ray diffraction and solid-state NMR, and, again, the silk structure is dominated by β-strands aligned parallel to the fiber axis [121]. Tussah silk, which is the silk of the caterpillar of the moth *Antherea mylitta*, also has an antiparallel arrangement of β-strands parallel to the fiber axis and gives an X-ray diffraction pattern similar to that of *Bombyx mori* silk, although some significant differences are observed. These differences are thought to arise from different modes of sheet packing due to the high polyalanine content of Tussah silk [19].

Cross-β silk was identified in the egg stalk of the green lacewing fly, *Chrysopa flava* [122]. The X-ray diffraction pattern was examined in detail and found to arise from an arrangement where the β-strands run orthogonal to the fiber axis and hydrogen bonding extends between the strands forming a β-sheet that runs the length of the fiber. A model was proposed by Geddes et al. [4] in which the β-pleated strand folded back on to itself to form antiparallel β-sheet ribbons. The length of the β-strands was about 25 Å, giving the ribbon a width of 25 Å. Several ribbons then stacked together in the crystallite. This model has been used as the basis of the amyloid core structure (see Section 6.3.1.1).

6.3.1.4 β-Sheet-containing Viral Fibers

Adenovirus fiber shaft, P22 tail spike, and bacteriophage T4 short and long fibers are known to be predominantly β-sheet-structured [101]. The shaft regions of the adenovirus and bacteriophage T4 fibers contain repeating sequences, indicating that they might fold into regular, repeating structures. The adenovirus type-2 fiber shaft has been shown to fold into a novel triple β-spiral. The crystal structure of a four-repeat fragment was solved and showed that each repeat folded into an extended β-strand that runs parallel to the fiber axis [123]. Each β-strand is followed by a sharp β-turn enabled by the positioning of a proline or glycine residue, and the turn is then followed by another β-strand, which runs backward at an angle of about 45° to the fiber shaft axis. This fold results in an elongated molecule with β-strands spiraling around the fiber axis. A model of the fiber shaft suggests a diameter of around 15–22 Å and a length of around 300 Å. This fold is also thought to be included in other viral fiber structures (e.g., reovirus structure).

Several proteins have been shown to fold into a parallel β-helix, including pectate lyase [124] and the bacteriophage P22 tail spike [125]. These have right-handed, single-chain helices that have a bean-shaped cross-section, and the β-strands run perpendicular to the long axis. Left-handed β-helices (e.g., UDP *N*-acetylglucosamine acyltransferase) have a triangular cross-section, as each turn of the helix is made up of three β-strands, connected by short linkers [126]. A triple β-helix fold has been identified in part of the short-tail fiber of bacteriophage T4, gp12. It has a triangular cross-section and is made up of three intertwined chains [127]. The β-strands are again perpendicular to the long axis. This arrangement has also been identified in a region of P22 tail spike, and a similar fold has been found in bacteriophage T4 protein gp5. The arrangement forms the needle used by T4 to puncture host cell membranes [128]. Very recently, the structure of the T4 baseplate-tail complex was determined to 12 Å by cryo-electron microscopy, and this has enabled the known crystal structures to be fitted into the cryo-electron microscopy map to build up a full structure of the T4 tail tube and the arrangement of proteins at the baseplate [129].

6.3.2 α-Helix-containing Protein Fibers

6.3.2.1 Collagen

The structure of the collagen superfamily has been studied for over 50 years. Collagen has a complex supramolecular structure, involving the interaction of different molecules giving different functions. It has a characteristic periodic structure, forming many levels of association [130]. The primary structure consists of a repeating motif, Gly-Xaa-Yaa, interspersed by more variable regions. The secondary structure involves the central domain of collagen α-chain folding into a tight, right-handed helix with an axial residue-to-residue distance determined by the spacing of the Pro residues (Xaa) and hydroxyprolines (Yaa). This arrangement results in a Gly residue row following a slightly left-handed helix winding around the coil, and this is responsible for the packing to form the tertiary structure, a triple helix, where the Glys are buried inside the supercoiled molecules [130]. Depending on the collagen type, the triple helices may be comprised of differing collagen chains or of three identical chains [130]. The triple helix is a long, rod-like molecule around 1.5 nm wide. Recently, the crystal structure of the collagen triple helix formed synthetically from $[(\text{Pro-Pro-Gly})_{10}]_3$ peptide was solved to a resolution of 1.3 Å [25] (Figure 6.1). The triple helix undergoes fibrillogenesis to form supramolecular structures. Non-helical ends that do not contain the Gly-Xaa-Yaa sequence are known as the telopeptides. Many models of the molecular packing have been presented (summarized in Ref. [130]). The most recent model of type I collagen appears to fit data from X-ray diffraction, electron microscopy, and cross-linking studies [130]. The proposed model is a one-dimensional, staggered, left-handed microfibril. The packing allows for interconnections between the microfibrils via the telopeptides [131]. This model was deduced by careful testing of several models to compare calculated and observed X-ray diffraction data [132].

Fig. 6.1. Collagen triple helix model: the crystal structure of $[(\text{Pro-Pro-Gly})_{10}]_3$ (PDB: 1K6F.pdb) [25]. The three chains of the collagen-like peptide are represented as space-filling models and a ribbon model.

6.3.2.2 **Tropomyosin**

Tropomyosin molecules are arranged within the thin filament of muscle bound to actin filaments (see below). The molecules are two-chain, α-helical, coiled-coil proteins around 400 Å in length that link end to end to form continuous strands. The crystal structure of full-length tropomyosin was solved from low-resolution X-ray diffraction data with a contribution from electron microscopy, revealing a pitch of around 140 Å [133, 134].

6.3.2.3 **Intermediate Filaments**

Knowledge of the structural detail of the intermediate filament (IF) is incomplete at present. However, the primary sequence of the central rod domain of the cytoplasmic IF proteins (cytokeratin 18, cytokeratin 8, vimentin, neurofilament L protein, and nuclear laminin), reveals the heptad repeat characteristic of coiled-coil structures [58]. Coiled coils were first identified by X-ray diffraction from oriented α-keratin in hair and quill [135]. A model for the structure of vimentin has been proposed, using crystallographic structure of short fragments of conserved regions of vimentin [136]. The structure reveals the four coiled-coil regions interspersed with linker regions. The dimers assemble to form tetramers, which then associate

into rod-like filaments (about 60 nm long and 16 nm in diameter), known as unit-length filaments (ULFs). Finally, the ULFs anneal longitudinally to form extended filaments [58]. These mature filaments undergo some internal rearrangement that results in the final diameter being 11 nm. The arrangement and association of the dimers has been examined using cross-linking studies as well as analysis of X-ray fiber diffraction patterns and electron micrographs [58]. From these studies it has been proposed that two oppositely oriented, left-handed coiled coils may wind around one another to form a left-handed super helix with a pitch of around 140–180 Å. Cryo-electron microscopy and X-ray diffraction from hard α-keratin have suggested that the IFs have a low density core with a diameter of around 3 nm. It has been suggested that the ULFs may be a circular assembly of tetramers arranged as a hollow cylinder. Upon compaction, when the ULFs anneal into an extended filament, the lateral packing of the dimers alters and four dimers form octameric protofilaments that pack more densely, resulting in a much narrower hollow center [58].

6.3.3 Protein Polymers Consisting of a Mixture of Secondary Structure

6.3.3.1 Tubulin

The structure of microtubules has been studied using cryo-electron microscopy, electron diffraction, and X-ray crystallography. The structure of a bacterial homologue of tubulin called FtsZ has also been solved using X-ray diffraction [137], and synthetic polymers of FtsZ have been studied by electron microscopy and image reconstruction [138]. Tubulin exists as $\alpha\beta$ heterodimers that polymerize into protofilaments that make up the microtubule. The crystal structure of tubulin heterodimers was solved by electron crystallography [139] from two-dimension crys-

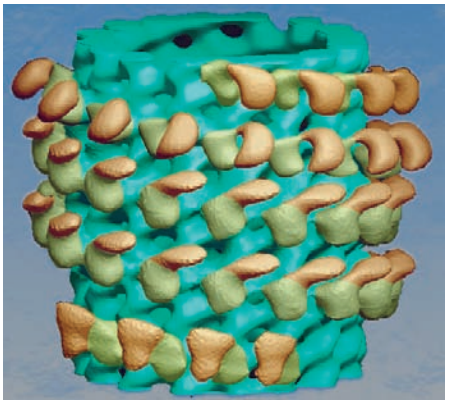

Fig. 6.2. Structure of the microtubule from electron microscopy image reconstruction. The microtubule is shown in green with directly bound kinesin heads in yellow and tethered heads of kinesin dimers in orange. Thanks to Linda A. Amos, LMB, Cambridge for the donation of this figure.

tals of zinc-induced tubulin sheets in ice, and the structural interpretation was supported by the X-ray crystal structure of FtsZ [137]. Each monomer is a compact ellipsoid made up of three domains, an amino terminal nucleotide-binding domain, a smaller second domain, and a helical carboxy terminal domain [140]. The tubulin heterodimers polymerize in a polar fashion to make longitudinal protofilaments that in turn bundle to form the microtubule. The dimer structure was docked into 20-Å maps from cryo-electron microscopy of microtubules, creating a near-atomic model of the microtubule [140]. This model revealed that the carboxy terminal helices form a crest on the outside of the protofilaments and that the long loops define the microtubule lumen [140]. The microtubule is polar, with plus and minus ends, and the structure showed that the exchangeable nucleotide bound to β-tubulin was exposed at the plus end of the microtubule, whereas the proposed catalytic residue in α-tubulin was exposed at the minus end.

Cryo-electron microscopy and helical image reconstruction techniques have proved particularly powerful in examining the arrangement and interaction of motor proteins bound to microtubules [141]. Three-dimensional maps of microtubules decorated with motor domains or kinesin in different nucleotide states could be compared to naturally occurring microtubules (Figure 6.2, see p. 211) [141].

6.3.3.2 Actin and Myosin Filaments

The structure of actin filaments has been extensively studied using X-ray diffraction and electron microscopy [142]. Early work by Hanson and Lowry [143] revealed the basic geometry of F-actin by negative stain electron microscopy. Major advances were made when the crystal structure of actin was solved in complex with DNase I [144]. Since then, a more detailed picture of the structure of the actin filament has been built up [145, 146] by positioning the atomic resolution crystal structure against X-ray diffraction data. The filament is composed of actin monomers arranged in a left-handed helix with 13 monomers per six turns. The pitch is about 59 Å and the separation between monomers is about 27.5 Å. Two strands of actin monomers slowly twist around one another, with a cross-over repeat of 360–380 Å. Tropomyosin chains bind along the actin filament in the grooves between the two actin strands. Each tropomyosin has a troponin complex bound, and the positioning of the troponin marks a 385-Å repeat along the axis of the actin filaments.

X-ray fiber diffraction has been utilized to examine changes in the structure of muscle fibers in order to try to understand the mechanism of muscle contraction [147]. Muscular force is produced when myosin filaments interact with actin filaments by an ATP-dependent process. Time-resolved, low-angle diffraction patterns from muscle in various states can be taken and the positions and intensities of signal can be compared [147] to allow conclusions to be made about the movement of various components of the muscle fibers.

Myosin filaments make up the thick filaments of striated muscle and the structure has also been examined using X-ray diffraction and electron microscopy. Modeling of the arrangement of the myosin heads from X-ray and electron microscopy data have been performed, but the arrangement of the heads has been inconclu-

sive. Four arrangements of the heads are possible, whereby the heads may be parallel or antiparallel. In each case the two heads may lie on the same helical track in a compact arrangement or on neighboring tracks in a splayed arrangement [148]. Recent work on electron microscopy data from filaments of the spider *Brachypelma smithi* (tarantula) [149] tested the four possible arrangements by fitting the crystal structure of myosin heads [150] into the map generated from electron microscopy of negatively stained thick filaments. A good fit was obtained when the myosin heads were arranged antiparallel and packed on the same helical ridge.

6.4 Methods to Study Fiber Assembly

6.4.1 Circular Dichroism Measurements for Monitoring Structural Changes Upon Fiber Assembly

6.4.1.1 Theory of CD

Circular dichroism (CD) is a phenomenon that gives information about the unequal absorption of left- and right-handed circularly polarized light by optically active molecules in solution [151–154] (see chapter 2 in Part I). CD signals are observed in the same spectral regions as the absorption bands of a particular compound, if the respective chromophores or the molecular environment of the compound are asymmetric. CD signals of proteins occur mainly in two spectral regions. The far-UV or amide region (170–250 nm) is dominated by contributions of the peptide bonds, whereas CD signals in the near-UV region (250–320 nm) originate from aromatic amino acids. In addition, disulfide bonds give rise to minor CD signals around 250 nm. The two main spectral regions give different kinds of information about protein structure.

CD signals in the amide region contain information about the peptide bonds and the secondary structure of a protein and are frequently employed to monitor changes in secondary structure in the course of structural transitions [155–157]. Since many fiber-forming proteins undergo certain conformational changes upon fiber assembly (e.g., from an intrinsically unfolded state to a β-sheet-rich fiber as seen in some amyloid-forming proteins; see Figure 6.3), far-UV CD measurements can be used to monitor the kinetics of fiber assembly.

CD signals in the near-UV region are observed when aromatic side chains are immobilized in a folded protein and thus transferred to an asymmetric environment. Since Tyr and Phe residues yield in very small near-UV CD signals, only Trp residues lead to utilizable near-UV CD spectra. The CD signal of aromatic residues is very small in the absence of ordered structure (e.g., in short peptides) and therefore serves as a good tool for monitoring fiber assembly of peptides (in case Trp residues are present). The magnitude as well as the wavelengths of the aromatic CD signals cannot be predicted, since they depend on the structural and electronic environment of the immobilized chromophores. Therefore, the individ-

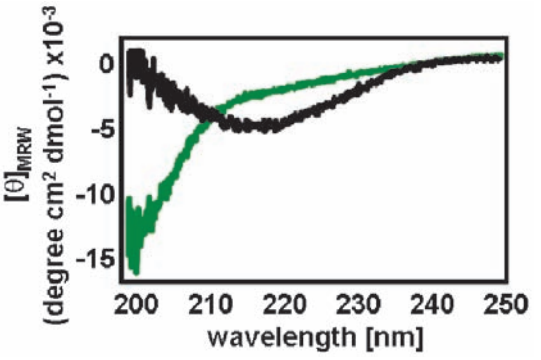

Fig. 6.3. Far-UV CD spectra of the yeast prion protein Sup35p-NM [9]. The green line represents the spectrum of soluble protein that depicts a random coil conformation. The black line represents the spectrum of protein after fiber assembly, which reflects a β-sheet-rich conformation.

ual peaks in the complex near-UV CD spectrum of a protein usually cannot be assigned to transitions in the vicinity of specific amino acid side chains. However, the near-UV CD spectrum represents a highly sensitive criterion for the structural state of a protein. It can thus be used as a fingerprint for either conformational state, the soluble and the fibrous one [156, 157].

6.4.1.2 Experimental Guide to Measure CD Spectra and Structural Transition Kinetics

Preferably only fused quartz cuvettes that display high transparency below 200 nm and are not birefringent should be used. Their quality can be examined by recording the CD of the thoroughly cleaned empty cuvettes, which should coincide with the instruments' baseline in the absence of the cell. Deviations occur if the cell is birefringent or, more likely, if traces of impurities, such as residual proteins, cover the glass surface. The contribution of buffers and salts to the total absorbance of the sample should be as small as possible. This poses severe restrictions on the choice of solvents for CD measurements, particularly in the far-UV region. Therefore, absorbance values for salts and buffers have to be determined in the far-UV region prior to the measurement. Common denaturants such as urea and guanidinium chloride absorb strongly in the far-UV region, which restricts their use to wavelengths above 210 nm. Only highly purified salts and denaturants should be used to avoid interference from absorbing contaminants. Oxygen absorbs light below 200 nm, which makes it necessary to degas solvents for measurements in this region prior to the CD measurement. The cell compartment and the optics of the instrument should be purged with nitrogen [152, 156].

The following considerations are important for an optimal choice of protein concentration: path length and solvent condition. A good signal-to-noise ratio is achieved when the absorbance is around 1.0, but in general it should stay below 2.0. The magnitude of the CD depends on the protein concentration, and therefore

its contribution to the total optical density of the sample should be as high as possible. This implies that the absorbance of the solvent should be as small as possible. Absorbance spectra of the samples prior to the CD experiment should be recorded to determine the protein concentration necessary for the calculation of the molar CD and to select the optimal conditions for the CD measurement. Most buffers are transparent in the near-UV region, and path lengths of 1 cm or more can be selected in this spectral region. For measurements in the far-UV region, short path lengths (0.2–0.01 cm) and increased protein concentrations should be employed to minimize the contributions of the solvent to the total absorbance. As a rule, 0.1-cm cells can be used for the spectral region down to 200 nm. For measurements extending below 200 nm, 0.01-cm cells are advisable. Solutions to be employed for CD measurements should be filtered or centrifuged to remove dust or other solid suspended particles. The presence of light scattering in CD measurements leads to artifacts that result in anomalous, red-shifted spectra. Since light scattering increases during assembly of protein fibers, this point has to be taken into consideration before evaluating the received data. When protein samples are exposed to UV light around 220 nm for an extended time, as is frequently the case when measuring far-UV CD spectra or conformational transition kinetics, photochemical damage can occur. It is advisable to examine some functional or structural properties of the protein under investigation after long-term CD measurements [152, 155, 156].

6.4.2 Intrinsic Fluorescence Measurements to Analyze Structural Changes

6.4.2.1 Theory of Protein Fluorescence

Fluorescence emission is observed when, after excitation, an electron returns from the first excited state back to the ground state (see chapter 2 in Part I). As the lifetime of the excited state is long, a broad range of interactions or perturbations can influence this state and thereby the emission spectrum. Fluorescence is thus an excellent probe to investigate conformational changes of proteins and fiber assembly [158–162].

The fluorescence of proteins originates from Phe, Tyr, and Trp residues, which show the following absorbance and fluorescence properties in water at neutral pH: Trp $\lambda_{max}(abs) = 280$ nm, $\varepsilon_{max}(abs) = 5600\ M^{-1}cm^{-1}$, $\lambda_{max}(fluor) = 355$ nm; Tyr $\lambda_{max}(abs) = 275$ nm, $\varepsilon_{max}(abs) = 1400\ M^{-1}cm^{-1}$, $\lambda_{max}(fluor) = 304$ nm; Phe $\lambda_{max}(abs) = 258$ nm, $\varepsilon_{max}(abs) = 200\ M^{-1}cm^{-1}$, $\lambda_{max}(fluor) = 282$ nm. In proteins that contain all three aromatic amino acids, fluorescence is usually dominated by the contribution of the Trp residues because both their absorbance at the wavelength of excitation and their quantum yield of emission are considerably higher than the respective values for Tyr and Phe residues. Phe fluorescence is typically not observed in native proteins due to its low intensity. The other factor in fluorescence is energy transfer between residues. Therefore, Phe fluorescence is also not observed because its emission is efficiently quenched by energy transfer to the other two aromatic amino acids. In proteins that contain both Tyr and Trp resi-

dues, fluorescence of Tyr is barely detectable due to the strong emission of Trp, due to wavelength shifts of Trp emission towards the wavelength of Tyr emission, and due to non-radiative energy transfer from Tyr to Trp residues in compactly folded proteins.

Changes in protein conformation very often lead to large changes in fluorescence emission, since fluorescence of aromatic amino acids depends on their environmental conditions. In Trp-containing proteins, both shifts in emission wavelength and changes in intensity can generally be observed upon conformational changes. In hydrophobic environments, such as in the interior of a folded protein or protein fibers, Trp emission occurs at lower wavelengths than in aqueous ones. The fluorescence of Trp residues can be investigated selectively by excitation at wavelengths greater than 295 nm. Due to the red shift and the increased intensity of the absorbance spectrum of Trp residues, when compared with that of Tyr residues, protein absorbance above 295 nm originates almost exclusively from Trp residues. Unlike absorbance, the changes in fluorescence upon folding can be very large, which makes intrinsic Trp fluorescence useful as a sensitive probe for conformational changes of proteins upon fiber assembly and in analyzing the kinetics thereof.

The fluorescence maximum of Tyr residues remains around 303 nm irrespective of its molecular environment. Therefore, conformational changes of proteins are accompanied by changes in the Tyr emission intensity, but not in the wavelength of emission, which makes Tyr fluorescence a less sensitive tool for studying conformational changes in comparison to Trp fluorescence [159, 160, 163, 164].

6.4.2.2 **Experimental Guide to Measure Trp Fluorescence**

Emission is usually observed at a right angle to the excitation beam. Therefore, fluorescence cuvettes are manufactured with polished surfaces on all four sides. Quartz cells are required for work in the UV region. Fluorescence is an extremely sensitive technique, so it is mandatory to avoid contamination of cuvettes and glassware with fluorescent substances. Deionized and quartz-distilled water should be used, and plastic containers that may leach out fluorescent additives should be avoided. Also, laboratory detergents usually contain strongly fluorescing substances. Fluorometer cells should be cleaned with 50% nitric acid. If detergents are used for cleansing, extensive rinsing with distilled water is required.

Any solvent can be used for fluorescent measurements, provided that it does not absorb in the spectral regions of the excitation and emission of the fluorophore to be examined, which implies that the buffers or solvent additives should not absorb or fluoresce at wavelengths greater than 250 nm. Because of the high sensitivity of fluorescence measurements, impurities and dust have to be avoided entirely. A single dust particle moving slowly through the light beam can cause severe distortions of the signal due to light scattering. It is helpful to stir the sample solution continuously during the fluorescence measurement, using tiny magnetic stirring bars placed at the bottom of the cuvette. However, in the case of fiber assembly kinetics, extreme care has to be taken that stirring does not influence the assembly/aggregation process. Magnetic stirrers that fit underneath the cuvette in the sample

compartment of the instrument and cuvettes with specially designed bottoms for magnetic bars are commercially available.

Protein emission spectra are broad and without detectable fine structure. Changes upon structural transitions frequently involve the entire fluorescence spectrum. Therefore, a variety of wavelengths and wide emission slits can be used to follow conformational changes of proteins. The fluorescence intensity generally decreases with increasing temperature. This decrease is substantial, with Tyr emission decreasing $\geq 1\%$ per degree increase in temperature and an even more pronounced temperature dependence of Trp fluorescence. In contrast, there is no linear relationship between fluorophore concentration and emission intensity. The actual form of the concentration dependence varies with the optical geometry of the fluorometer and the cell. The nonlinearity is caused by inner filter optical effects. Between the entrance window of the cells and the volume element of the sample, from which fluorescence emission is collected, the exciting light is attenuated by absorbance of the protein and the solvent. In strongly absorbing samples (i.e., at high protein concentrations), the emission intensity is actually decreased, as almost the entire incident light is absorbed before it can reach the center of the cuvette [158, 159, 161]. Since growing fibers are large enough to scatter light, light scattering as measured in the spectrofluorometer can be used as an analytic tool to investigate fiber assembly kinetics (see Section 6.4.5).

6.4.3 Covalent Fluorescent Labeling to Determine Structural Changes of Proteins with Environmentally Sensitive Fluorophores

6.4.3.1 Theory on Environmental Sensitivity of Fluorophores

Fluorescence spectra and fluorescence quantum yields are generally more dependent on the environment than are absorption spectra and extinction coefficients. For example, coupling a single fluorescein label to a protein reduces its quantum yield by approximately 60%, but decreases its extinction coefficient by only approximately 10%. Interactions between two adjacent fluorophores or between a fluorophore and other species in the surrounding environment can produce environment-sensitive fluorescence. The most common environmental influences on fluorescence properties are fluorophore-fluorophore interactions, solvent polarity, proximity and concentrations of quenching species, and pH of the aqueous medium. Environmental influences on fluorescence by quenching are the result of a bimolecular process that reduces the fluorescence quantum yield without changing the fluorescence emission spectrum. Fluorescence resonance energy transfer (FRET) is a strongly distance-dependent, excited-state interaction in which emission of one fluorophore is coupled to the excitation of another. Some excited fluorophores interact to form excimers, which are excited-state dimers that exhibit altered emission spectra [159, 165].

Several chemical groups in side chains of amino acids can be used to covalently cross-link fluorophores. Among the most important are amine and thiol groups. Amine-reactive groups are widely used to prepare protein and peptide bioconju-

gates for immunochemistry, fluorescence in situ hybridization, cell tracing, receptor labeling, and fluorescent analogue cytochemistry. In contrast, thiol-reactive dyes are principally used to prepare fluorescent proteins and peptides for probing biological structure, function, and interactions. Since the thiol functional group can be labeled with high selectivity, thiol modification is often employed to estimate both inter- and intramolecular distances using FRET. In proteins, thiol groups (also called mercaptans or sulfhydryls) are present in Cys residues. The thiol-reactive functional groups are primarily alkylating reagents including iodoacetamides, maleimides, benzylic halides, and bromomethyl ketones. Among the dyes that are particularly sensitive to environmental and conformational changes are benzoxadiazole, naphthalene, and pyrene derivatives [166]. When protein conjugates of these dyes are denatured or undergo a change in conformation, a decrease in fluorescence intensity and a shift in emission to longer wavelengths are often observed. The use of covalently linked fluorophores recently allowed the investigation of the degradation, aggregation, and fiber assembly kinetics of Aβ peptides and of the amyloid-forming NM-region of the yeast prion protein Sup35 [167–169]. These reports indicate the power of covalently attached fluorophores in determining fiber assembly mechanisms.

In addition to the broadly applicable dyes discussed above, some fluorophores are specifically crafted to label actin (e.g., phallotoxins) or tubulin, but these fluorophores are not further discussed in the context of this chapter [166].

6.4.3.2 Experimental Guide to Labeling Proteins With Fluorophores

We will focus in this section on binding of reagents that can be coupled to thiol groups on proteins or peptides to give thioether-coupled products. Most of the commercially available fluorophores react rapidly at near-neutral pH and usually can be coupled to thiol groups selectively in the presence of amine groups. Haloalkyl reagents (primarily iodoacetamides) are among the most frequently used reagents for thiol modification. In most proteins, the site of reaction is at Cys residues that either are intrinsically present or result from reduction of cystines. In addition, Met residues can sometimes react with haloalkyl reagents. Maleimides are similar to iodoacetamides in their application as reagents for thiol modification. However, they are more thiol-selective than iodoacetamides, since they do not react with His or Met residues.

For labeling in general, the protein should be dissolved in a suitable buffer at 50–100 μM at pH 8.0–8.5 (10–100 mM tris-(hydroxymethyl)-aminomethane [Tris] or *N*-(2-hydroxyethyl)-piperazine-*N*′-2-ethansulfonic acid [HEPES]) at room temperature. In this pH range, the protein thiol groups are sufficiently nucleophilic that they react almost exclusively with the reagent in the presence of the more numerous protein amines, which are protonated and relatively unreactive. Reduction of disulfide bonds in the protein is best carried out at this stage. A 10-fold molar excess of a reducing agent, such as 1,4-dithiothreit (DTT) or tris-(2-carboxyethyl) phosphine (TCEP), is usually sufficient. If DTT is used, then dialysis is required to remove the excess DTT prior to introducing the reactive dye. It is not necessary to remove excess TCEP during conjugation with iodoacetamides, haloalkyl deriva-

tives, or maleimides. It is advised to carry out thiol modifications in an oxygen-free environment, because thiols can be oxidized to disulfides, especially when the protein has been treated with DTT prior to thiol modification. A 10- to 20-mM stock solution of the reactive dye in a suitable solvent should be prepared immediately prior to use, and all stock solutions have to be protected from light as much as possible. Sufficient protein-modification reagent is added to give approximately 10–20 moles of reagent for each mole of protein. The reaction should proceed for 2 h at room temperature or overnight at 4 °C. For haloalkyl reactive dyes and to a lesser extent maleimides, it is essential to protect the reaction mixture from light as much as possible. Upon completion of the reaction with the protein, an excess of glutathione, mercaptoethanol, or other soluble low-molecular-weight thiols can be added to consume excess thiol-reactive reagent. The conjugate should be separated on a gel-filtration column, such as a Sephadex G-25 column or equivalent matrix, or by extensive dialysis to remove non-protein-bound dye. It is important to calculate the degree of labeling by determining both protein concentration and concentration of label (through the fluorophore-specific absorption) (for an overview, see Ref. [170]).

After successfully labeling the protein, the fluorescence emission of the dye can be monitored upon fiber assembly. In case the reagent was linked at a site that changes its conformation upon fiber assembly, kinetics thereof can be monitored. Commonly used dyes for such investigations are 6-acryloyl-2-dimethylaminonaphthalene (acrylodan) and *N*,*N*′-dimethyl-*N*-(iodoacetyl)-*N*′-(7-nitrobenz-2-oxa-1,3-diazol-4-yl) ethylene diamine (IANBD amide).

6.4.4 1-Anilino-8-Naphthalensulfonate (ANS) Binding to Investigate Fiber Assembly

6.4.4.1 Theory on Using ANS Fluorescence for Detecting Conformational Changes in Proteins

Fluorescent dyes can be used to investigate conformational changes of proteins without the necessity of conjugation. Some substances, such as the *N*-benzyl derivatives of 3-chloro-6-methoxy-9 aminoacridine and amino naphthalene sulfonic acids, do not fluoresce in aqueous solution but are highly fluorescent when adsorbed onto proteins, with the intensity of fluorescence depending on the structural state of the protein [171, 172]. Such fluorescent dyes exist in a soluble nonplanar form, in which the radiative transition is forbidden. The adsorbed dye, on the other hand, exists in a planar configuration, in which the transition is allowed [173]. 1-Anilino-8-naphthalensulfonate (ANS) is the most commonly used fluorescent dye for analyzing conformational changes of proteins. ANS is brilliantly fluorescent in solvents such as isopropanol, but it shows practically no fluorescence in water. ANS can bind to nonpolar (hydrophobic) sites in proteins through its anilinonaphthalene group and therefore reflects an excellent tool to investigate the unfolding of a protein, in which usually tightly packed hydrophobic patches become surface-exposed. However, ANS binding to proteins also depends on proteins' cationic charge and solution pH, since the ANS sulfonate group is also involved in the

ANS-protein interaction [174, 175]. Importantly, the dependence of ANS binding on electrostatic interaction between the sulfonate group and protein cationic groups does not require preexisting hydrophobic sites on or in the protein to start the binding reaction. Moreover, ANS fluorescence is quenched by water, so fluorescence is profoundly affected if a change in protein hydration or ANS accessibility to water occurs during binding [176]. Therefore, ANS can be used not only to monitor protein unfolding but also to analyze structural changes upon fiber assembly.

6.4.4.2 Experimental Guide to Using ANS for Monitoring Protein Fiber Assembly

ANS has been used to study the partially folded states of globular proteins as well as the binding pockets of a number of carrier proteins and enzymes. ANS has also been used to characterize fibrillar forms of proteins, such as fibronectin, islet amyloid polypeptide, or infectious isoforms of the prion protein PrP [177–180]. After binding to fibers, ANS can show an increased fluorescence and a blue shift of its fluorescence maxima. Protein concentrations should be in the range of 0.5–20 μM and ANS should be added in a 10- to 100-fold excess. The concentration of ANS can be determined by using a molar extinction coefficient of 6.8×10^3 M^{-1} cm^{-1} at 370 nm in methanol [181]. In a 1-cm cell the fluorescence inner-filter effect (see Section 6.4.2.2) becomes significant at ~30 μM ANS. Therefore, correction factors have to be used for the fluorescence of ANS when its total concentration exceeds 10 μM. The magnitude of the inner-filter effect must be experimentally determined for each instrument and whenever the instrumental configuration is altered. The magnitude of the correction depends on the wavelength range and the path length, but not on slit-width or sample turbidity for most of the instruments [182].

To determine whether ANS binds to the fibrous protein, but not to the soluble counterpart, fluorescence emission spectra should be recorded from 400–650 nm with an excitation wavelength of 380 nm. After measuring ANS fluorescence spectra before and after fiber assembly, it can be determined whether ANS serves as a tool for investigating fiber assembly of the chosen protein. Extreme care has to be taken in determining whether ANS fluorescence changes are based solely on fiber formation or whether ANS is also able to bind non-fibrous assembly intermediates. If ANS binding is specific to the fibrous form of the protein, the wavelength with maximal fluorescence differences before and after assembly can be used to monitor fiber assembly kinetics.

6.4.5 Light Scattering to Monitor Particle Growth

Hydrodynamic studies can be carried out to obtain qualitative descriptions of the shape and dimensions of macromolecules and to gain precise information on molecular geometry [183] (see chapter 19 in Part I). The interpretation of hydrodynamic measurements is always based on an assumption that the real molecule must be presented by a particle of simpler shape, characterized by a small number of geometric parameters that can be determined experimentally. As a result, the choice of an inadequate model may result in incorrect interpretation.

6.4.5.1 Theory of Classical Light Scattering

Classical light scattering is an absolute method for the determination of the molar mass of intact macromolecules, and it is particularly suited for studying large macromolecular assemblies, up to a maximum of 50×10^6 M_r. Beyond this maximum, the theory of classical light scattering, known as the ''Rayleigh-Gans-Debye'' approximation, is not valuable. Classical light scattering is the total, or time-integrated, intensity of light scattered by a macromolecular solution compared with the incident intensity for a range of concentrations and/or angles. The intensity of light scattered by a protein solution is measured as a function of angle with a light-scattering photometer. If the macromolecule solution is heterogeneous, as it is usually the case for fiber assembly reactions, M_r will be a weight-average molar mass M_w, which makes it difficult to determine precise fiber assembly kinetics [184, 185]. However, in combination with field-flow fractionation (FFF) (see Section 6.4.6), classical light scattering serves as a powerful tool to investigate the growth of protein fibers. The combination of classical light scattering with FFF is realized by using multi-angle laser light-scattering photometers (MALS). In addition, it is necessary to have a concentration detector, which is usually a highly sensitive differential refractometer equipped with a flow cell. Taken together, FFF-MALS is most valuable for the analysis of heterogeneous and polydispersed protein mixtures (see Section 6.4.6) [186–188].

6.4.5.2 Theory of Dynamic Light Scattering

The principle of dynamic light scattering (DLS) experiments is based on the high intensity, monochromaticity, collimation, and coherence of laser light. The primary parameter that comes from DLS measurements is the translational diffusion coefficient D. In DLS measurements, laser light is directed into a thermostated protein solution, and the intensity is recorded at either a single angle (90°) or multiple angles using a photomultiplier/photodetector. The intensities recorded will fluctuate with time, caused by Brownian diffusive motions of the macromolecules. This movement causes a ''Doppler'' type of wavelength broadening of the otherwise monochromatic light incident on the protein molecules. Interference with light at these wavelengths causes a fluctuation in intensity, which depends on the mobility of the protein molecules. An autocorrelator evaluates this fluctuation by a normalized intensity autocorrelation function as a function of delay time. The decay of the correlation, averaged over longer time intervals, can then be used to obtain the value of D [185]. To obtain molar mass information from the value of D, a calibration of log D versus log M_r is produced, based on globular protein standards. The logarithmic plot of the normalized autocorrelation decay is a straight line for homodispersed solutions, but will tend to curve for solutions with assembling protein fibers. The spread of diffusion coefficients is indicated by a parameter known as the polydispersity factor, which can be evaluated by computer programs. DLS is particularly valuable for the investigation of changes in macromolecular systems, when the time-scale of changes is minutes or hours and not seconds or shorter, which makes it valuable for the investigation of fiber assembly [184, 189–192].

6.4.5.3 Experimental Guide to Analyzing Fiber Assembly Using DLS

Solutions have to be as free as possible from dust and supramolecular aggregates. This requirement is met by filtering all solutions with filters of appropriate size (0.1–0.45 μm). An optimal protein concentration is 2 mg mL^{-1} for a 30-kDa protein, with proportionally lower concentrations for larger proteins. The diffusion coefficient is a sensitive function of temperature and the viscosity of the solvent in DLS measurements. Therefore, measurement and calibration have to be made at the same temperature and solvent viscosity conditions. The diffusion coefficient measured at a single concentration is an apparent one (D_{app}) because of non-ideality effects (finite volume and charge). These effects become vanishingly small as the concentration approaches zero. Importantly, for non-globular proteins (such as growing fibers) a multi-angle instrument has to be used [185].

6.4.6 Field-flow Fractionation to Monitor Particle Growth

6.4.6.1 Theory of FFF

Field-flow fractionation (FFF) is a one-phase chromatography in which high-resolution separation is achieved within a very thin flow against which a perpendicular force field is applied. This technique will be described in more detail, but it has to be mentioned that other types of fields are also used. In the cross-field technique, the flow and sample are confined within a channel consisting of two plates that are separated by a spacer foil with a typical thickness of 100–500 μm. The upper channel plate is impermeable, while the bottom channel plate is permeable and is made of a porous frit. An ultrafiltration membrane covers the bottom plate to prevent the sample from penetrating the channel. Within the flow channel, a parabolic flow profile is created due to the laminar flow of the liquid: the stream moves slower closer to the boundary edges than it does at the center of the channel flow. When the perpendicular force field is applied to the flowing, laminar stream, the analytes are driven towards the boundary layer of the channel, the so-called accumulation wall. Diffusion associated with Brownian motion in turn creates a counteracting motion. Smaller particles, which have higher diffusion rates, tend to reach an equilibrium position farther away from the accumulation wall. Thus, the velocity gradient flowing inside the channel separates different sizes of particles. Smaller particles move much more rapidly than larger particles due to their higher diffusion coefficients, which results in smaller particles eluting before larger ones. This is exactly the opposite of a size-exclusion chromatography separation, in which large molecules elute first.

With FFF separation there is no column media to interact with the samples. Even for very high-molar-mass polymers, such as protein fibers, no shearing forces are applied. The entire separation is gentle, rapid, and non-destructive, without a stationary phase that may interact, degrade, or alter the sample [193–196]. The knowledge of the actual molecular shape is of great importance for analyzing proteins using FFF. Regular and simple geometrical shapes with well-defined bound-

ary surfaces are formed by just a few macromolecules. In contrast, most dissolved macromolecules, especially protein fibers, have to be described in terms of an asymmetrical, expanded and inhomogeneous coil. Considering the complex nature of protein fiber conformations, two parameters are important: the root-mean-square radius and the hydrodynamic radius of the macromolecule. Although a theory predicts the hydrodynamic size of eluting species as a function of elution time, absolute determination of size without reference to standards, assumptions about the conformation of the particles, etc., can be obtained only by combination of FFF with multi-angle light-scattering (MALS) detectors (see Section 6.4.3) [186–188]. FFF in combination with MALS allows separation of protein fibers of different sizes and therefore serves as a tool to monitor assembly and elongation of protein fibers.

6.4.6.2 Experimental Guide to Using FFF for Monitoring Fiber Assembly

FFF reflects a unique tool for analyzing fiber assembly, since it is independent of sample impurities and sample composition. The amount of sample injected can vary widely (0.5–500 μg) because sample size has a negligible effect on the separation efficiency, as long as it is sufficiently large to yield a good detector response and sufficiently small to avoid overloading (a few micrograms is usually a suitable amount for injection). Unlike for other techniques described in this chapter, no general experimental guidelines can be provided, since the flexible operation of FFF has to be adapted for specific needs. For the two most important parameters, cross-flow and channel flow, the optimum flow rates have to be adjusted specifically for each protein investigated. At fixed flow rates, retention time significantly increases with increasing molar mass, accompanied by a growth in bandwidth. At low flow rates, separation power is sacrificed unnecessarily and rather narrow peaks are obtained. At high flow rates, detectability decreases due to increasing dilution [196–198].

6.4.7 Fiber Growth-rate Analysis Using Surface Plasmon Resonance

6.4.7.1 Theory of SPR

Surface plasmon resonance (SPR) is an optical technique that is a valuable tool for investigating biological interactions. SPR offers real-time in situ analysis of dynamic surface events and thus is, for instance, capable of defining rates of fiber growth. When light traveling through an optically dense medium (e.g., glass) reaches an interface between this medium and a medium of a lower optical density (e.g., air), a phenomenon of total internal reflection back into the dense medium occurs [199]. Although the incident light is totally internally reflected, a component of this light, the evanescent wave, penetrates the interface into the less dense medium to a distance of one wavelength [200]. In SPR measurements a monochromatic, polarized light source is used, and the interface between the two optically dense media is coated with a thin metal film (less than one wavelength of light

thick). The choice of metal used is critical, since the metal must exhibit free electron behavior. Suitable metals include silver, gold, copper, and aluminum. Silver and gold are the most commonly used, since silver provides a sharp SPR resonance peak and gold is highly stable [201]. The evanescent wave of the incoming light is able to couple with the free oscillating electrons (plasmons) in the metal film at a specific angle of incidence, and thus the plasmon resonance is resonantly excited. This causes energy from the incident light to be lost to the metal film, resulting in a reduction in the intensity of reflected light, which can be detected by a two-dimensional array of photodiodes or charge-coupled detectors. Therefore, if the refractive index directly above the metal surface changes by the adsorption of a protein layer, a change in the angle of incidence required to excite a surface plasmon will occur [202]. By monitoring the angle at which resonance occurs during an adsorption process with respect to time, an SPR adsorption profile can be obtained. The difference between the initial and the final SPR angle gives an indication of the extent of adsorption, and the positive gradient of the SPR adsorption curve determines the rate of adsorption, allowing analysis of, e.g., assembly kinetics of a growing protein fiber.

6.4.7.2 Experimental Guide to Using SPR for Fiber-growth Analysis

One of the most important parameters for SPR measurements is the surface where the molecules interact. The commercial availability of sensor chips with robust and reproducible surfaces makes SPR convenient to use. The most commonly used surface is carboxymethyl dextran (CMD) bound to a gold substrate. CMD is covalently bound to the sensor chip surface via carboxyl moieties of dextran. Functional groups on the ligand that can be used for coupling proteins include NH_2, SH, CHO, and COOH. CMD sensor chips can be regenerated by selective dissociation of the bound protein from the covalently immobilized ligand. Other commercially available sensor chips have: surfaces made of dextran matrices with a low degree of carboxylation (providing fewer negative charges), shorter carboxymethylated dextran matrices (valuable for large protein assemblies), chips with coupled nitrilotriacetic acid (designed to bind histidine-tagged molecules), chips with pre-immobilized streptavidin (for capturing biotinylated ligands), and plain gold surfaces (no dextran or hydrophobic coating), which provides the freedom to design customized surface chemistry such as self-assembled monolayers (SAM) [203]. The specific coupling chemistry has to be selected for each experiment individually. In the case of fiber growth kinetics, it is necessary to couple initiating molecules, which could be seeds, nuclei, or monomeric protein, in a manner that polymerization is not sterically hindered. This implies some fundamental knowledge on the polymerization process of the protein to be investigated. Experimental design and data processing dramatically influence the quality of SPR-derived data. However, when properly utilized, SPR can be a powerful tool for determining kinetic and equilibrium constants of molecular interactions [204]. After kinetic analysis of fiber assembly, the SPR chips can be microscopically investigated by atomic force microscopy (AFM) to obtain additional morphological insights into the assembled protein fibers (see Sections 6.4.8 and 6.5.5) [205].

6.4.8 Single-fiber Growth Imaging Using Atomic Force Microscopy

6.4.8.1 Theory of Atomic Force Microscopy

Atomic force microscopy (AFM) measures the height of a solid probe over a specimen surface. AFM has been developed as a tool for imaging biological specimens and dynamic measurements of biological interactions. AFMs operate by measuring attractive or repulsive forces between a tip and a sample, with the force between the sample and the tip causing the cantilever to bend. The magnitude of this force depends on the distance between the tip and the sample and on the chemical and mechanical properties (i.e., stiffness) of the sample. Deflection of a laser beam focused onto the end of the cantilever detects the bending of the cantilever. Since the sample is mounted on top of a ceramic piezoelectric crystal (piezo), a feedback loop between the laser detector and the piezo controls the vertical movement of the sample. Depending on the AFM design, scanners are used to translate either the sample under the cantilever or the cantilever over the sample. By scanning in either way, the local height of the sample is measured. Three-dimensional topographical maps of the surface are then constructed by plotting the local sample height versus horizontal probe tip position [206]. AFM can achieve a resolution of 10 pm and, unlike electron microscopes, can image samples in air and under liquids, thereby allowing the imaging of hydrated specimens [207, 208]. This feature can be used to monitor fiber growth as previously shown for amyloid fibril formation [115, 209–211].

In its repulsive ''contact'' mode, the instrument lightly touches a tip at the end of a leaf spring or ''cantilever'' to the sample. As a raster scan drags the tip over the sample, a detection apparatus measures the vertical deflection of the cantilever, which indicates the local sample height. Thus, in contact mode the AFM measures hard-sphere repulsion forces between the tip and sample. In tapping mode, the cantilever oscillates at its resonant frequency (often hundreds of kilohertz) and is positioned above the surface, so that it taps the surface for only a very small fraction of its oscillation period. The very short time over which this contact occurs means that lateral forces are dramatically reduced as the tip scans over the surface. Tapping mode is commonly used for poorly immobilized or soft samples. Thus, in both modes the surface topography of the biological specimen is recorded and its elevations and depressions can be accurately monitored [207, 208, 212].

6.4.8.2 Experimental Guide for Using AFM to Investigate Fiber Growth

Experiments should be carried out in tapping mode in liquid using a fluid cell, since this mode allows for higher-resolution liquid imaging than does the contact mode. The proteins should be dissolved in low-salt buffers (it is best to avoid any salts) such as 10 mM Tris/HCl or 5 mM potassium phosphate. Protein concentrations should be around 50 $\mu g\ mL^{-1}$ to obtain high-quality images. Also, atomically flat surfaces should be used to immobilize the assembling proteins. Mica is a commonly used surface material for protein attachment and fibril growth. Since slight drifts during repeated scans can occur in experiments that take several hours, com-

mon points easily visible on the surface should be chosen as a reference (such as protein aggregates or other impurities). The use of short, narrow-legged silicon nitride cantilevers (nominal spring constant 0.032 N/m) is emphasized. The best imaging results can be obtained using a tapping frequency in the range of 9 to 10 kHz. Typical scan rates are between 1 and 2 Hz, with drive amplitudes in the range of 150 to 300 mV [115, 210].

6.4.9 Dyes Specific for Detecting Amyloid Fibers

6.4.9.1 Theory on Congo Red and Thioflavin T Binding to Amyloid

Congo red (CR) is a diazo dye that binds relatively specifically to many amyloid proteins [213, 214]. The absorbance spectrum of CR changes upon binding to amyloid (Figure 6.4). Binding interactions of CR and the concomitant spectral shift depend on the structure of the amyloid, specifically the β-sheet conformation [215]. Protein fibers, which lack or contain only a minor proportion of β-sheet secondary structure, do not stain with CR. However, β-sheet secondary structure is not sufficient for CR binding, since no soluble β-sheet-rich globular protein is known to bind CR. It is suggested that CR binding occurs through a combination of both hydrophobic and electrostatic interactions [216]. The spectral shift upon binding might be caused by the stacking of several CR molecules in a defined manner along the amyloid fibers. Importantly, CR is a well-established inhibitor of fibril formation for several proteins, such as Aβ, amylin, prions, and insulin, and therefore it cannot be used to monitor fiber assembly in real time [216]. The mechanism of assembly inhibition is so far unsolved, but it could be shown that CR in addition to fibrous protein binds to native or partially unfolded conformational states and stabilizes them, which might prevent fiber formation. However, binding to the non-fibrous proteins does not lead to any spectral shift. Although binding of

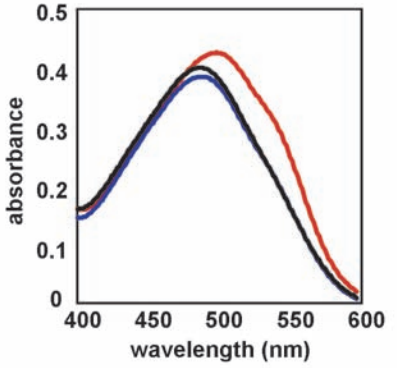

Fig. 6.4. Absorption spectra of CR in buffer (without protein) (black line), of CR in the presence of soluble yeast Sup35p-NM (blue line), and of CR in the presence of amyloid fibers assembled with Sup35p-NM (red line).

CR to amyloid fibers formed by Aβ peptides and insulin was highly specific and could be quantified [214], the fact that CR also binds to native, partially unfolded conformations of several proteins indicates that it must be used with caution as a diagnostic test for the presence of amyloid fibrils in vitro.

The benzothiazoles thioflavin S and thioflavin T (ThT) are other classical amyloid stains that bind specifically to β-sheet-rich fibers but not to monomeric or oligomeric intermediates [217, 218]. ThT proved to be particularly attractive because of a substantial hypochromic shift of the excitation maximum of the bound dye from 336 to 450 nm, permitting selective excitation of the bound species. ThT fluoresces only when it is bound to many but not all amyloid fibrils and fibrillar β-sheet species [218]. The binding reaction is rapid (completed within 30 s) and is sensitive enough to avoid significant contributions from light scattering. The advantage of ThT over CR is that ThT does not inhibit fiber assembly and can therefore also be used as a dye for real-time fiber growth, although it is important to investigate in each particular case whether ThT stimulates assembly kinetics or stabilizes the fibers [219].

6.4.9.2 Experimental Guide to Detecting Amyloid Fibers with CR and Thioflavin Binding

In a typical CR binding assay, CR binding can be quantified by a specific spectral shift. The classic CR birefringence used for histochemistry is only a qualitative technique that cannot be used for quantification. For spectral shift analysis, the amyloid fibrils should be dissolved in phosphate buffer, mixed with a solution of CR in phosphate buffer to yield a final CR concentration of 2–20 μM and incubated for 10 min, since an absorption maximum is reached after 10 min of incubation time [214]. The ratio of CR (in micromolar) to amyloid fibrils (in micrograms per milliliter, determined by the total concentration of soluble protein) should not fall below 1:5. Therefore, the total protein concentration should not exceed 100 μg μL^{-1}. The absorbance of control samples containing only CR (without protein) and only protein fibrils (without CR) should be monitored at 540 nm and 477 nm, respectively. Calculating the zeroed (to the controls) absorbances of the amyloid fibrils incubated with CR at 540 nm and 477 nm with the formula $(A_{540}/25295) - (A_{477}/46306)$ leads to the moles CR bound per liter. From this, the moles CR bound per mole protein can be calculated.

For ThT binding experiments, a stock solution of ThT is prepared at a concentration of 1 mM in double-distilled water and stored at 4 °C protected from light to prevent quenching until it is used. For high-throughput measurements, ThT fluorescence can be determined in 96-microwell plates using a fluorescence plate reader 20 μM ThT is added. To the protein fiber solutions to be incubated in 96-microwell polystyrene plates with flat bottoms. A sample volume of 200 μL is added to each well. Five replicates corresponding to five wells are measured for each sample to minimize the well-to-well variation. The plates should be covered by ELAS septum sheets and incubated without agitation or shaking. Fluorescence measurements should be performed every 30 min (excitation at 450 nm, emission at 482 nm). The read time for each well is 1 s, and the total read time for the whole

plate is approximately 3 min. Protein fiber adsorption to the plates has to be investigated by incubating protein fiber solutions in the plate for 10 min at 37 °C with stirring and by determining the protein concentration before and after incubation by measuring the UV absorbance.

Alternatively, fibril formation can be performed in glass vials. Ten-microliter aliquots are withdrawn from the glass vials and added directly to a fluorescence cuvette (1-cm path length semi-micro quartz cuvette) containing 1 mL of a ThT mixture (5 μM ThT, 50 mM Tris buffer, and 100 mM NaCl pH 7.5). Emission spectra are recorded immediately after addition of the aliquots to the ThT mixture from 470 nm to 560 nm (excitation at 450 nm). For each sample, the signal can be obtained as the ThT intensity at 482 nm, from which a blank measurement recorded prior to addition of protein to the ThT solution is subtracted.

6.5 Methods to Study Fiber Morphology and Structure

6.5.1 Scanning Electron Microscopy for Examining the Low-resolution Morphology of a Fiber Specimen

6.5.1.1 Theory of SEM

Scanning electron microscopy (SEM) involves the electron beam being passed over a conductive surface in a series of parallel lines, in a manner similar to that used in television imaging. Electrons leave the source and are focused onto the surface of a specimen as a very fine point. The probing electron beam penetrates only less than a few microns into the specimen and the electrons interact with the specimen surface, inducing a variety of radiations. Each leaves the specimen in a variety of directions and can be counted by a detector and displayed. The direction is not important; only the number of photons or electrons leaving the spot on the sample needs to be measured. The probing beam is moved to an adjacent spot on the specimen and the information is output to the display. This continues rapidly across the specimen, each point being amplified and magnified to form the image [220]. The type of information collected depends on the particular radiation being used as the information signal. The types of radiation utilized include visible light, X-rays, backscattered-electron current, and induced-specimen current [220]. Most commonly, secondary electrons emitted by the interaction of the beam are collected by a detector and the three-dimensional topographic image is built up. This technique, known as emissive mode, is commonly used for large specimens to examine morphological details. Coating the specimen in a conductive layer, usually gold coating, improves the specimen image, since the lower the atomic number of the specimen, the better the emission of secondary electrons [221]. The technique has been used extensively for the observation of silk fibers' overall morphology. In general, however, the range of resolution (typically 100 nm to 1 mm) is lower than is required for examination of most protein fibers but is ideally suited for topographic

imaging. SEM allows a large depth of field compared to the optical microscope, permitting the visualization of rough surfaces in focus across the whole specimen. In addition, the contrast within scanning micrographs provides a three-dimensional effect when the specimen is tilted with respect to the electron beam.

6.5.1.2 Experimental Guide to Examining Fibers by SEM

SEM gives information only about the external surface of the specimen. Usually, the specimen requires fixation and dehydration. Fixation is commonly performed using osmium tetroxide or formaldehyde-glutaraldehyde as a fixative, depending on the nature of the material being examined. Dehydration is usually carried out by passing the specimen though a graded series of alcohol. Freeze-drying may be used to remove water from a specimen, and this is best achieved by freeze-drying from a nonpolar solvent rather than from water (e.g., amyl acetate can be substituted for water). After freeze-drying, the specimen is warmed to room temperature before air is re-admitted to the vacuum chamber to prevent rehydration. The specimen is often coated with a thin layer of carbon to maintain the dried state and finally coated with a layer of heavy metal. Possibly, dehydration and coating may be performed within the same vacuum chamber. Critical point drying is also a method used for dehydration of some specimens. This involves replacing the water within a specimen first by a dehydrating agent, such as ethyl alcohol, followed by an intermediate liquid (e.g., amyl acetate) and a transitional liquid (e.g., carbon dioxide). This transitional liquid will be removed from the specimen at a ''critical point'' of temperature and pressure, when it becomes converted to a gas. Air drying is used less often due to the surface tension effects causing distortion in the specimen, but it is occasionally used for certain specimens.

In order to improve the electrical potential of the specimen surface, specimens are coated with a thin layer of conducting materials, since the dehydrated biological specimen usually conducts poorly and may also build up beam-induced charge, which results in artifacts. Usually, a specimen will be coated with a thin layer of carbon, followed by an outer layer of a heavy metal, commonly gold. The thin layer of gold is applied by vacuum evaporation from a tungsten filament.

The method of data collection will depend considerably upon the type of specimen [220]. In general, for biological specimens, it is thought that the acceleration should be kept low (10 kV) to reduce damage. The current should also be kept low, while enabling the collection of a relatively noise-free image. Astigmatism (i.e., a different direction focus at different points) is a very common limitation to resolution and therefore should be prevented as much as possible by maintaining the microscope to a high standard and corrected during data collection. Selection of the final aperture depends on the magnification and the depth of focus required. A large aperture (200 micron) is appropriate for high-resolution work, whereas at low magnification, depth of focus may be the prime requirement and therefore a small final aperture may be used (50 micron). It may prove useful to image the specimen at different tilts to examine different angles of the material. Data recording can be on film or, more commonly, on CCD camera. The images may then be examined in detail (Figure 6.5).

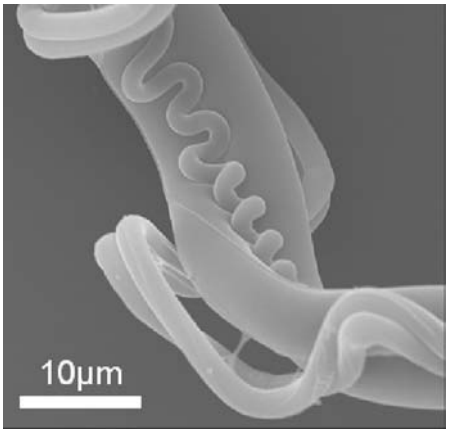

Fig. 6.5. SEM of major and minor ampullate silks collected from the garden cross spider *Araneus diadematus*.

6.5.2 Transmission Electron Microscopy for Examining Fiber Morphology and Structure

6.5.2.1 Theory of TEM

Electron micrographs represent a projection of the density distribution of the specimen onto a plane [222]. Therefore, an electron microscope image may contain sufficient information to generate the three-dimensional structure of an object. Transmission electron microscopy (TEM) is commonly used for examination of macromolecular protein assemblies, from single particles, such as viruses, to fibers, such as microtubules. Materials for TEM must be specially prepared to a thickness that allows electrons to transmit through the sample in a manner similar to how light is transmitted through materials in conventional optical microscopy. Since the wavelength of electrons is much smaller than that of light, the optimal resolution attainable for TEM images is many orders of magnitude better than that of a light microscope. This means that TEMs can reveal the finest details of internal structure – in some cases as small as individual atoms. The energy of the electrons in the TEM determines the relative degree of penetration of electrons in a specific sample or, alternatively, influences the thickness of material from which useful information may be obtained. Conventional electron microscopes tend to be run at 80–200 kV. The electron dose must be kept low to reduce radiation damage to the biological specimen. Thus, the contrast from a micrograph of biological specimens can be very poor, and therefore negative staining is required to visualize the sample. The negative stains are composed of heavy metals (such as uranyl acetate) that scatter the electrons and are electron-opaque, which results in a dark image of the stain deposited around a protein molecule or fiber.

The image visualized within the electron microscope is two-dimensional. Image reconstruction techniques can be applied to produce three-dimensional images by

single-particle averaging for globular molecules or by helical image reconstruction for fibers. Further analysis of electron micrographs is useful to exceed what is possible by visual interpretation to overcome problems such as signal detection in the presence of noise and interpretation of phase contrast images. For further discussion on analysis of images, see Section 6.5.3 on cryo-electron microscopy.

6.5.2.2 Experimental Guide to Examining Fiber Samples by TEM

The way in which the sample is prepared can vary depending on the stability of the specimen. The sample must be dehydrated since it is viewed in a vacuum. In some cases the sample is fixed prior to preparing microscope grids. The grids used for TEM can consist of a layer of plastic, such as Formvar or Pioloform, overlaid with carbon or simply a thin carbon film. The grids may be purchased ready-made or can be made to the user's specifications. Detailed procedures for making electron microscope grids can be found in Ref. [223]. Improved contrast and resolution can be obtained by using a thin-layer support, and this is best achieved by making carbon support films on mica that are then transferred to the grid. Alternatively, the carbon can be evaporated onto grids covered with a plastic film. The plastic film can then either be dissolved, leaving the thin carbon film, or left in place, resulting in more robust grids but a higher background upon imaging of a specimen.

Negative Staining for Imaging Fibrous Proteins As previously mentioned, it is usually necessary to provide contrast for visualization of a biological specimen by negative staining. These are usually heavy metal salts such as uranyl acetate, potassium phosphotungstate and ammonium molybdate. Detailed considerations of the advantages of different stains and choice of concentration are summarized in Ref. [223]. Uranyl salts give the greatest amplitude contrast but have slightly larger microcrystallinity/granularity after drying than some other negative stains, whereas potassium phosphotungstate gives fine granularity but lower image contrast [223]. Spreading agents may be a useful part of preparation of some samples. Surfactants such as *n*-octyl-*β*-glucopyranoside can be used to evenly disperse the molecules. The spreading agent can be added to the biological sample or to the negative stain. However, glow-discharge treatment of the microscope grid may be sufficient to allow even spread of the sample.

The staining procedure varies considerably among different researchers. However, the simplest technique involves the placement of droplets ($\sim$20 μL) of the specimen, several of filtered water and stain in a row, onto parafilm. The grid can then be placed facedown on each droplet in turn and for a specified amount of time. Alternatively, droplets ($\sim$4 μL) may be placed onto an upturned grid and blotted away using filter paper before the next droplet is placed on the grid.

Metal Shadowing for Enhanced Contrast of Fibrous Proteins The contrast provided by negative-stain techniques may be inadequate for visualization of rod-shaped particles, and metal shadowing may increase the contrast [224], allowing better imaging of the morphological features. Metal shadowing may be unidirectional or rotary. The protein to be examined must be in a solution of glycerol (50% v/v) and

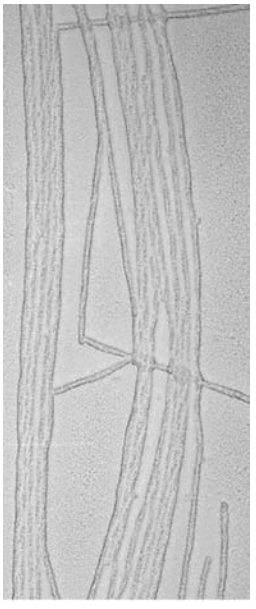

Fig. 6.6. Platinum carbon shadowing micrographs of wild-type alpha-synuclein fibrils (assembled as previously described [250]).

then be sprayed onto a piece of freshly cleaved mica and dried. The protein-covered mica is coated with platinum or another heavy metal (such as tantalum/tungsten) by evaporation and then coated with a layer of carbon. The metal/carbon replicas are then floated off onto cleaned grids and finally examined under the electron microscope. Contact prints of the micrographs provide the best images for further analysis (Figure 6.6). Details of this procedure can be found in Ref. [224].

6.5.3 Cryo-electron Microscopy for Examination of the Structure of Fibrous Proteins

6.5.3.1 Theory of Cryo-electron Microscopy

Cryo-electron microscopy allows the imaging of samples in a hydrated state encased in a thin layer of ice. No stain is required and contrast is produced by the density difference between the molecule and the vitreous (non-crystalline) ice. The samples benefit from the fact that they are not flattened by gravity, are unstained, and can be viewed at near-physiological conditions (i.e., hydrated). High-resolution data can be collected from samples at liquid nitrogen temperatures using low-dose techniques, which minimize radiation damage to the sample. Cryo-electron micrographs usually show a low signal-to-noise ratio due to the low dose of electrons, the lack of stain, and the use of small defocuses. Therefore, cryo-electron micrographs benefit from additional analysis such as Fourier filtering and

image-reconstruction techniques. High-resolution structures (to 6 Å) have been elucidated by single-particle analysis from cryo-electron micrographs of large protein molecules. Helical image reconstruction from electron micrographs can allow the elucidation of fibrous structures.

6.5.3.2 Experimental Guide to Preparing Proteins for Cryo-electron Microscopy

Cryo-electron microscopy grid preparation involves a certain amount of development to find the ideal conditions for examination of a particular protein sample. Grids are made from a holey carbon film, and the size of the holes and thickness of the carbon should be optimized for the protein molecule's size, as the thickness of the ice layer in which the protein is encased should be ideal for the size of the protein. The thickness of the ice within a carbon hole will depend on the diameter of the holes, the thickness of the carbon, and the treatment of the grid during freezing. Often, grids are glow-discharged to spread out the water layer, resulting in thinner ice, or amylamine is used to increase the thickness. Finally, the technique used for grid blotting before the sample is flash-frozen will affect the ice thickness. Holey carbon grids can be purchased or made by a procedure similar to that for making carbon films for negative-stain electron microscope grids [223]. The concentration of the fiber sample should be optimized for cryo-electron microscopy first by negative-stain EM. Ideally, the concentration should be such that several fibers are found in the scope of a micrograph but that they rarely cross over. A droplet of the fiber sample is then placed onto the optimally prepared holey carbon grids, blotted, and plunged into liquid ethane cooled by liquid nitrogen. If the procedure is carried out correctly, the grid will be covered in a thin layer of vitreous ice. The grid should be stored in liquid nitrogen until required.

Transfer to the cryo-stage specimen holder for the electron microscope must be performed at low humidity and at a temperature lower than −160 °C to prevent ice accumulation on the grid and to preserve the vitreous water. Specialized equipment to transfer the grid to the electron microscope specimen holder is available (Oxford Instruments, Gatan). The cryo-TEM must also have low vapor content; this is achieved by a liquid nitrogen pre-cooled anti-contaminator system to maintain the vitreous ice. The temperature of the specimen should then be maintained at less than −125 °C to prevent transformation of the vitreous water to crystalline cubic ice. The appearance of crystalline ice may not be visible in the microscope but can be observed as diffraction spots upon electron diffraction. Usually, cryo-electron micrographs will be collected at various defocuses in order to collect a full dataset. This is because at each defocus the contrast transfer function will pass through zero, giving rings of uncollected data in the power spectrum.

6.5.3.3 Structural Analysis from Electron Micrographs

Data collection for revealing images of protein fibers may include systematically tilting the specimen to produce a series of images with different projections of the material. However, it may be possible to reconstruct the structure of a helical molecule using only a single image, since the high symmetry of a helical fiber allows observation of many views simultaneously [225]. In order to analyze the micro-

graph images, they must be digitized (some electron microscopes have fitted CCD cameras, thus avoiding this step). Ideally, a fiber image will be scanned such that the fiber is vertical in order to avoid interpolation resulting in loss of data at the later stages. Examination of images can be carried out using a suitable program such as Ximdisp [226]. Regions of fiber images may be selected and must be boxed and floated. This involves masking off all density not belonging to the particle and surrounding the particle box to reduce the density step at the edge of the box [227]. Fiber images may benefit from Fourier filtering and/or background subtraction. The fibers may be straightened by a number of established techniques [228]. If necessary, the image may be interpolated. Interactive Fourier transforms are calculated to look for repeating features with the fiber. If a diffraction pattern is observed, then further analysis may be carried out on the fiber image using helical image reconstruction [227, 229, 230]. The determination of the position and tilt of the helix axis must first be performed, followed by indexing of the layer line spot positions. The indexing is tested and phases are measured, allowing a reconstruction to be carried out [227, 229, 230]. This results in a three-dimensional density function for the object. This methodology can be followed in detail [222, 229].

6.5.4 Atomic Force Microscopy for Examining the Structure and Morphology of Fibrous Proteins

6.5.4.1 Experimental Guide for Using AFM to Monitor Fiber Morphology

Minimal sample preparation is necessary for visualizing amyloid fibers by atomic force microscopy (AFM) [231]. A clean, uncontaminated solution of the sample can be placed onto freshly cleaved mica, glass, or other suitable smooth support. The substrate should be thoroughly cleaned with an excess of buffer (salt-free is best) or water. In order to get good contrast and to reduce mechanical damage of the soft biological materials, the samples can be stabilized by adding covalent cross-linking agents or certain cations that are able to link the constituents of the sample to each other or to the substrate. Cooling can also stiffen the sample to reduce sample disruption and damage.

Tapping mode is most commonly used for imaging relatively soft biomolecules. The force generated between the sample and tip depends on the amplitude of free oscillation and the set point amplitude [232]. The observed amplitude of oscillation is maintained by adjusting the vertical position of the sample. The strength of tapping must be optimized for a particular sample, since tapping too hard will reduce image resolution and quality due to damage to the tip or protein. Tapping too softly might cause adhesive forces between the sample and cantilever tip, resulting in damping of oscillation and causing spurious height data for the sample [232]. Once these conditions are optimized, image data may be collected. Visual representations of the data are often generated by assigning a color or brightness to the relative height in the image. This will enable clear images of the fiber in question to be observed above the background smooth surface (Figure 6.7). Height measurements may be taken from the data, but width cannot be measured accurately due

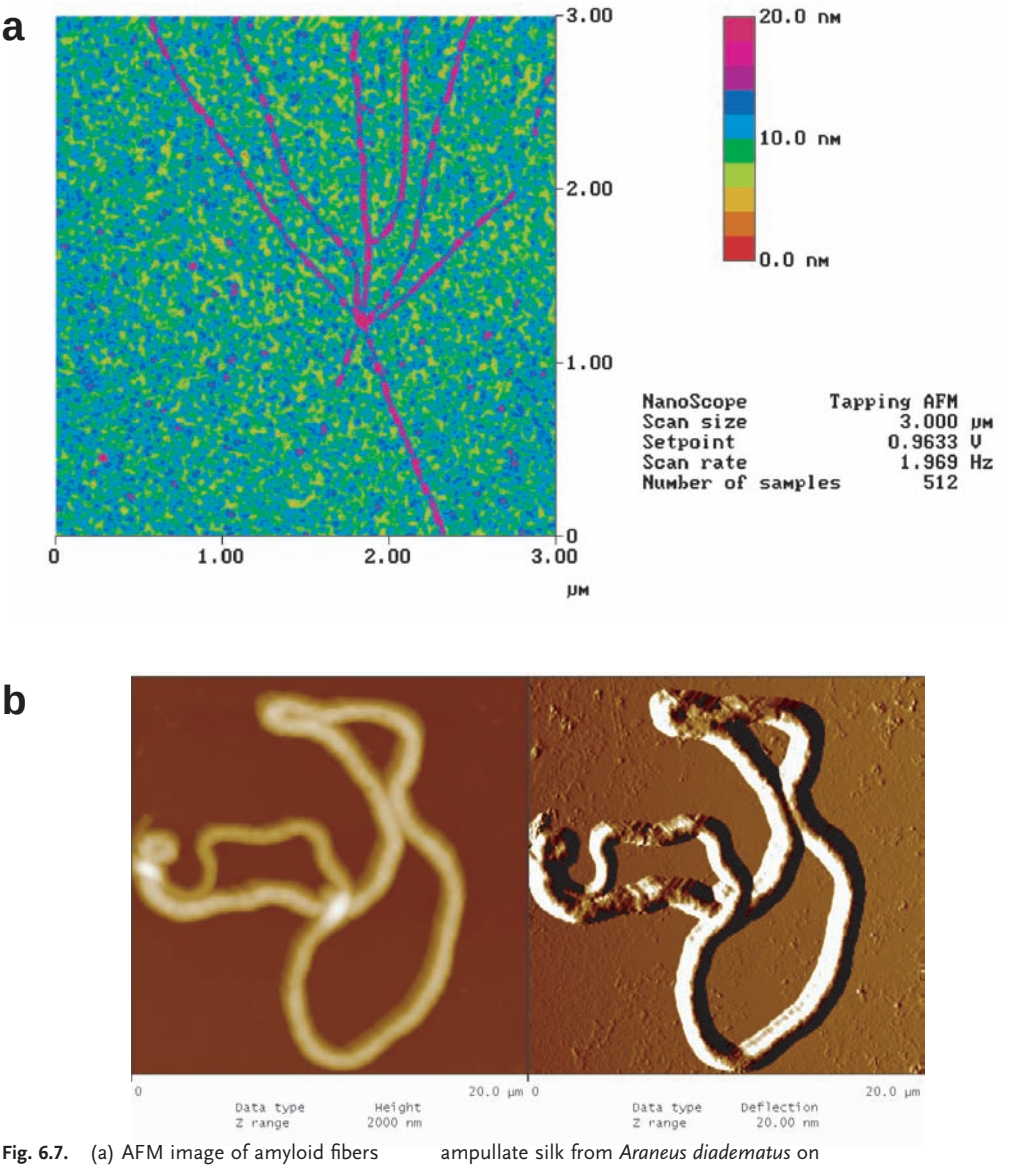

Fig. 6.7. (a) AFM image of amyloid fibers assembled with biotinylated yeast Sup35p-NM on streptavidin scanned in contact mode [251]. The scale bar gives the color code for the height information. (b) AFM images of major ampullate silk from *Araneus diadematus* on mica scanned in tapping mode. The left image reflects the sample height above the surface, and the right image depicts the tip deflection.

to the shape and size of the tip. Of course, height measurements taken from specimens in air may be affected by dehydration of the specimen, by the effect of gravity, or by the force of the cantilever compressing soft protein. However, morphological features may be clearly observed.

6.5.5 Use of X-ray Diffraction for Examining the Structure of Fibrous Proteins

6.5.5.1 Theory of X-Ray Fiber Diffraction

X-ray diffraction involves the use of proteins in an ordered arrangement. The amount of information that can be obtained is directly related to the degree of order within the diffracting object. The most ordered arrangement will be in a crystal where each identical protein molecule is arranged periodically on a three-dimensional lattice. Diffraction from crystals results in a pattern comprised of sharp spots. However, fibrous proteins usually do not crystallize due to their size, insolubility, or heterogeneity. Fibrous proteins form partly ordered structures, and standard methods of crystal structure analysis are not applicable to fibers due to the degree of disorder and number of overlapping reflections. However, X-ray fiber diffraction can be performed. Details concerning the theory of X-ray fiber diffraction may be found in Ref. [19]. For a single, isolated chain molecule, the crystalline lattice extends in only one dimension, parallel to the axis of the fiber (z-direction). The scattering appears on layer lines, and the layer planes have a separation of the reciprocal of the periodic repeat along the fiber axis. Since a single-chain molecule has no periodicity in the x- and y-directions, the scatter is a continuous function. In practice, however, a fiber specimen is composed of several chain molecules with rotational averaging. The molecules may be axial in register but arranged at all possible azimuthal orientations. These molecules are related to one another, but not by a crystallographic lattice. Therefore, a collection of chain molecules gives the scattering effect for the isolated molecules plus the effects caused by the orientation of the molecules and the packing, size, and mutual disposition of ordered regions.

Fibers are cylindrically symmetrical, so each reflection is spread out into a disk and intercepts the Ewald sphere at two symmetrical points. This means that the diffraction pattern is symmetrical. On the fiber diffraction diagram, the direction parallel to the fiber axis is known as the meridian and the perpendicular direction is the equator. Fibers are crystalline along the fiber axis and this produces strong, sharp reflections on the meridian. The degree of disorientation of the fibers relative to one another will produce more or less arcing of reflections. The appearance of diffraction arcs depends on the arrangement of crystallites (microstructure) within the material, known as the texture. Individual fibers may be aligned relative to one another, thus reducing disorientation and reducing the spread of the arcs. A sample in which the fibers have not been aligned at all will produce a diffraction pattern where the reflections appear as rings, much like a powder diffraction pattern. X-ray diffraction from a partially aligned specimen will allow distinction between the meridional and equatorial reflections. Even further orientation of the fiber within the specimen may produce a series of lines of intensity known as layer lines, running perpendicular to the meridian of the pattern. The intensities on closely spaced layer lines may overlap. In fact, it is rare to find non-overlapping reflections. If the fiber is mounted with the fiber axis normal to the X-ray beam, the diffraction pattern will be symmetrical above and below the equator (Figure 6.8).

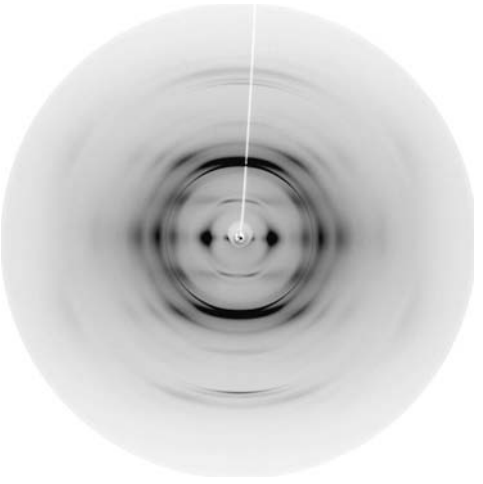

Fig. 6.8. X-ray fiber diffraction from amyloid fibrils from a short peptide homologous to the central region of Aβ peptide showing the cross-β diffraction pattern.

However, there will be regions of reciprocal space for which no data is recorded. By tilting the specimen, additional data can be collected.

6.5.5.2 Experimental Guide to X-Ray Fiber Diffraction

Sample Preparation Fibers in general are weakly diffracting, and therefore specimen preparation is particularly important. The specimen should be of an optimum size and thickness to fill the beam. Otherwise background scatter may obscure weak reflections. The amount of information that can be obtained from an X-ray fiber diffractogram is closely associated with the degree of alignment. Some fibrous proteins occur naturally in a highly oriented form (e.g., keratin and collagen). Often regions of orientation are quite limited, and therefore it can be useful to use a microfocus X-ray beam for data collection. Orientation may be improved by physical manipulation or by chemical treatment. For example, the orientation of *Chrysopa* egg stalk silk fiber orientation was increased by stretching in water or urea [4]. Preparation of oriented films and fibers from soluble fibrous proteins has involved a number of procedures that include stretching, rolling, casting films, drawing fibers from precipitate, shearing, magnetic alignment, centrifugation, and capillary flow. Long-chain molecules can be drawn from the solution in a manner similar to that used for making diffraction samples of DNA. Samples that cannot be pulled into long fibers may be aligned by hanging a drop between two wax-plugged capillary tubes arranged 1–2 mm apart [1]. Casting flat sheets is often used as a method for aligning polymers [233–235], and this can be achieved by placing a high concentration of a fiber solution on a suitable surface and allowing the solution to dry to form a thin film that can be removed from the surface (such

as Teflon). The film will show alignment of the fibers in the direction parallel to the film surface but no alignment in the perpendicular direction. Further improvement to alignment of fiber bundles or films may be achieved by annealing in high humidity. Some fibrous protein specimens are diamagnetically anisotropic [236] and may benefit from magnetic alignment [105, 237, 238]. The effect of the magnetic field on a single molecule is small, and therefore it is necessary to embed the molecules in a liquid crystal so that the molecules act together and to use a high-energy magnet [239]. The alignment can be fixed in the specimen by slow drying while the specimen is still in the magnetic field.

Data Collection Since fibrous proteins are often weak scatterers, long exposure times may be needed. Cameras specially designed for the particular qualities of the specimen may be helpful. The arrangement of the apparatus will depend on whether a high- or low-angle diffraction is being collected. The use of a helium chamber and an evacuated camera can be helpful to reduce air scatter as well as to allow the humidity around the specimen to be controlled if required. In the past, the recording of diffraction data was performed using photographic film. This allowed the placement of several films in the detector to record a range of intensities. However, it is now more common to use detectors used for crystallography, such as a MarResearch image plate or CCD cameras. If film has been used, then the diffraction image must be digitized and converted to an appropriate format for data analysis.

Data Analysis There are a number of fiber diffraction processing programs available to facilitate processing of fiber diffraction data. CCP13 [240] is a collection of programs designed to analyze high-quality diffraction patterns. FIT2D (www.esrf.fr/computing/expg/subgroups/data_analysis/FIT2D) can be used to analyze one- and two-dimensional datasets. The CCP4 suite [241] is intended for protein crystallography, but many of its components such as ipdisp and Mosflm can be utilized for examining the diffraction pattern. The data from the detector must be converted into a format compatible with the other programs in the chain. Examples of such programs are XCONV (CCP13) [147], marcvt (www.marresearch.com/software.htm) and Denzo [242]. The diffraction image must be carefully centered to avoid a systematic error while measuring spot locations. Mosflm allows this to be done by manually moving the image with respect to a series of overlaid concentric circles. XFIX (CCP13) allows the user to find the center of the pattern and to calibrate the specimen to film distance. One may also wish to correct for the shape of the image plate and determine the sample's tilt and rotation [243]. Background subtraction is often beneficial to correct for detector fog, white radiation, and X-ray scattering from air, camera components, the sample holder, and amorphous material in the specimen such as solvent and disordered polymer [244, 245]. The positions of the reflection can then be assessed. An initial survey can be carried out by noting spot locations and resolutions. This is straightforward in Mosflm, since the resolutions are calculated by clicking on spot maxima using a zoomed image. Re-

solution calculation can also be done by hand using an approximation to Bragg's law. This is the result of the product of the wavelength of the X-rays and the distance between the sample and the image plate, divided by the distance of the diffraction spot from the center of the diffraction pattern. For high-quality diffraction patterns containing diffraction peaks on layer lines, the CCP13 suite of programs allows the user to quadrant-average the diffraction pattern given the calculated tilt/rotation of the image. This image can then be processed further to include background subtraction and modeling of the position, size, shape, and intensity of the reflections.

Model Building An X-ray diffraction pattern from an unknown structure cannot directly lead to a structure since only amplitudes, but not phases, can be measured from the diffractogram. One method of solving this phase problem is by trial and error, so that from consideration of the diffraction pattern, symmetry, and chemical composition, a model is built and refined until a calculated diffraction can be generated that is similar to the observed [239]. A final model will predict the observed diffraction pattern so well that the possibility of the existence of another model that also predicts the diffraction pattern is virtually eliminated. Fibers by their nature are highly symmetrical and consist of repeating units, which reduces the number of possibilities for arrangement. Structural information about the subunits may already be available, either from crystal structures of individual monomers or from other biophysical techniques that indicate a secondary or tertiary structure. A molecular structure may be modeled using software such as LALS [246] or Cerius2 (http://www.accelrys.com/cerius2/cerius248/), which then allows the calculation of a simulated diffractogram to compare with the empirical data. Fxplor (www.molbio.vanderbilt.edu/fiber/software.html) is an extension of X-Plor, a program useful for atomic model refinement.

6.5.6 Fourier Transformed Infrared Spectroscopy

6.5.6.1 Theory of FTIR

Fourier transformed infrared spectroscopy (FTIR) has been used to gain information about the conformation of fibrous proteins. Proteins yield three major infrared bands of interest that arise from the peptide backbone. These are the amide I absorption at 1600–1700 cm^{-1}, arising from the C=O stretch; the amide II absorption at 1500–1600 cm^{-1}, arising from the N–H deformation; and the amide III absorption at 1200–1350 cm^{-1}. A N–H stretch also absorbs at about 3300 cm^{-1} [247]. The presence of hydrogen bonding within the sample shifts the energies of the peptide variations, therefore allowing the determination of the presence of α-helical and β-sheet conformations in theory. However, this is complicated in practice due to coupling between individual peptide vibrations, which leads to splitting of the bands into a series of bands. The symmetry of α-helical fibers leads to a distinctive set of bands upon aggregation from the monomer [247, 248], whereas

the spectra observed from the formation of all-β-sheet protein fibers are more subtle [248]. Observed and calculated infrared spectra from α-helix and antiparallel and parallel β-structures can be found in Ref. [247].

6.5.6.2 Experimental Guide to Determining Protein Conformation by FTIR

FTIR data collection is complicated by the fact that the bending vibrations H–O–H from water are near 1640 cm^{-1}, which can obscure the amide I band. This problem can be overcome by examination of the protein in the solid state, when little water is present, or by exchanging the hydrogen for deuterium. The D–O–D bending vibration is shifted to 1220 cm^{-1}, but care must be taken to fully exchange the H for D, since partial exchange will result in bands in the amide I region [248]. However, for examining the structure of *ex vivo* samples of fibrous proteins, exchange of deuterium may not be possible, and in order to overcome this, the signal-to-noise resolution of the data must be high. For solution samples, the use of a short path length (4–10 μm) and high protein concentration (1–50 mg mL^{-1}) should reduce the water absorbance relative to the protein signal at 1640 cm^{-1} [248]. To minimize scattering, samples may be prepared in dry state in KBr pellets by combining oven-dried KBr with the protein. The sample is then kept under vacuum and pressed (5–10 kbar) using a Carver press to form a thin, translucent pellet. This pellet can then be transferred to the transmission holder and a spectrum can be collected [248]. The spectrum is then compared with the spectrum collected from a KBr-only pellet. However, this harsh method may cause denaturation of the protein.

Alternative methods include attenuated total reflectance (ATR) FTIR, diffuse reflectance FTIR, and transmission-mode FTIR from a thin film. For ATR-FTIR, the sample is placed on a surface composed of a material of high refractive index, which is known as the internal reflection element (IRE) and is often composed of germanium or zinc selenide. The beam penetrates to the boundary between the IRE and the sample and is not transmitted through the sample. This makes this method ideal for examining fibrous proteins, and the method may be used for samples prepared as a thin film or suspension [249]. For ATR experiments, the maximum amount of light throughput is required and the amount of water vapor is reduced (by purging the system with dry nitrogen or dry air) to increase the sensitivity. Oberg et al. [249] recommend the use of out-of-compartment, horizontal, trapezoid-shaped IREs. To prepare a sample for ATR-FTIR, thin films can be prepared of the fibrous protein using a solution (50–100 μL of 0.5–1.0 mg mL^{-1}) or suspension placed onto the IRE and dried using nitrogen gas. The thin films are partly hydrated, maintaining the protein structure. Further, the limited-depth penetration of the ATR method reduces the contribution of water to the spectra [248]. Lyophilized proteins may also be spread onto the IRE for collection of spectra from powdered proteins. Alternatively, the diffuse reflectance (DRIFT) method can be used for dry samples [248]. In contrast to the ATR method, in transmission-mode FTIR, the beam passes directly through the sample [248]. High protein concentrations (2–60 mg mL^{-1}) and small path lengths (less than 10 μm) are required, although for a D_2O sample, lower protein concentrations and longer path lengths

(25–50 μm) may be used. Thin films can be prepared by drying the protein suspension or solution onto thin silver chloride disks.

Data analysis of FTIR spectra involves some expertise. Water or buffer subtraction must be performed before analysis of the spectrum. The conformation of the polypeptide chain has a signature in the amide I band. However, the bands may overlap, making interpretation difficult. This can be tackled in two ways. One approach is resolution enhancement methods or deconvolution to decrease the widths of the infrared bands and to allow determination of the overlapping components. A second approach is to use pattern-recognition methods for which software packages are available (e.g., GRAMS, Galactic Corp.).

6.6 Concluding Remarks

In the present chapter, fiber-forming proteins and methods to determine their fiber assembly and fiber morphology have been described. There is a wide variation among fibrous proteins with regard to the content of regular secondary structure. Fibers of proteins such as collagen and tropomyosin with highly elongated molecules tend to have a high content of regular secondary structure (generally greater than 90%). In contrast, fibers of globular proteins, such as actin, feather keratin, and flagellin, generally have much lower contents of regular structure (often less than 50%). In another group of proteins, comprising elastin, resilin, and the matrix proteins of mammalian keratins, the content of regular secondary structure is very small. In these cases the protein fibers are cross-linked and have rubber-like elastic properties.

So far, any attempt to correlate sequence with structure and function in fibrous proteins is highly speculative. Therefore, from a given sequence it cannot be concluded whether a protein forms fibers or not. However, the structure-function relation based on sequence data is the aim of many biologists, chemists, physicists, and material scientists. One main conformation-determining factor in fibrous proteins appears to be regions with repeating sequences. The simplest examples of repeating sequences are found among the silks, which have, for instance, runs of Gly_n. The corresponding sections of the chains adopt conformations that appear to be identical to those observed in synthetic homopolypeptides. Four other conformation-determining factors in fibrous proteins are interactions involving side chains, interactions between apolar side chains, hydrogen bond formation, and the content and distribution of Gly and Pro residues.

Aggregation studies on amyloids, collagens, myofibrils, and silks illustrate the capacity of fibrous proteins for self-assembly into filaments and other organized aggregates. The mode of aggregation is generally found to be sensitive to changes in pH, ionic strength, and the presence of other solutes, indicating that the assembly process depends upon a fine balance among various types of weak secondary bonding. Packing considerations are also clearly involved, but in the case of assembly in aqueous environment, these will be less important than in a solvent-free

crystalline phase. Several features of the self-assembly process in vivo are still not well understood, such as nucleation and termination of fiber formation. For termination of fiber formation, two possibilities can be envisaged: the assembly process could be intrinsically self-limiting, with the information residing in the individual protein molecules, or the size of the aggregate is potentially unlimited, but regulation of size is achieved through some external agency.

The future aim in investigating fibrillar proteins is to understand the kinetics of fiber assembly (which will be a basis for controlling fiber assembly) and to gain more insights into fibrous structure to learn about sequence-structure relationships. Such knowledge will be a basis for elucidating the relevance of assembly processes in cellular development, cellular structure, and cellular stability; for assessing fundamental influences leading to protein-folding diseases; and for developing products through material science.

Acknowledgements

T.S. is supported by the Deutsche Forschungsgemeinschaft (SFB 563 A9); SCHF 603/4-1, the Fonds der Chemischen Industrie, and the Leonhard-Lorenz-Stiftung. L.S. is funded by a Welcome Trust Research Career Development fellowship. The authors would like to thank Linda Amos for the donation of Figure 6.2, Bettina Richter for technical assistance, and Daniel Hümmerich, Sumner Makin, and Thusnelda Stromer for critical reading of the manuscript.

References

1 Sunde, M. & Blake, C. (1997). The structure of amyloid fibrils by electron microscopy and X-ray diffraction. *Adv. Protein Chem.* **50**, 123–159.
2 Eanes, E. D. & Glenner, G. G. (1968). X-ray diffraction studies on amyloid filaments. *J. Histochem. Cytochem.* **16**, 673–677.
3 Teplow, D. B. (1998). Structural and kinetic features of amyloid beta-protein fibrillogenesis. *Amyloid* **5**, 121–142.
4 Geddes, A. J., Parker, K. D., Atkins, E. D. & Beighton, E. (1968). "Cross-beta" conformation in proteins. *J. Mol. Biol.* **32**, 343–358.
5 Rochet, J. C. & Lansbury, P. T. (2000). Amyloid fibrillogenesis: themes and variations. *Curr. Opin. Struct. Biol.* **10**, 60–68.
6 Dobson, C. M. (2001). The structural basis of protein folding and its links with human disease. *Philos. Trans. R. Soc. Lond. B Biol. Sci.* **356**, 133–145.
7 Lindquist, S. (1997). Mad cows meet psi-chotic yeast: the expansion of the prion hypothesis. *Cell* **89**, 495–498.
8 Wickner, R. B., Edskes, H. K., Maddelein, M. L., Taylor, K. L. & Moriyama, H. (1999). Prions of yeast and fungi. Proteins as genetic material. *J. Biol. Chem.* **274**, 555–558.
9 Scheibel, T. (2002). [PSI]-chotic yeasts: protein-only inheritance of a yeast prion. in *Recent Research in Molecular Microbiology* **1** (ed. Pandalai, S. G.), Hindustan Publ. Corp., Delhi, 71–89.
10 Iconomidou, V. A., Vriend, G. & Hamodrakas, S. J. (2000). Amyloids protect the silkmoth oocyte and embryo. *FEBS Lett.* **479**, 141–145.

11 Podrabsky, J. E., Carpenter, J. F. & Hand, S. C. (2001). Survival of water stress in annual fish embryos: dehydration avoidance and egg envelope amyloid fibers. *Am. J. Physiol. Regul. Integr. Comp. Physiol.* **280**, R123–131.

12 Guhrs, K. H., Weisshart, K. & Grosse, F. (2000). Lessons from nature – protein fibers. *J. Biotechnol.* **74**, 121–134.

13 Knight, D. P. & Vollrath, F. (2001). Comparison of the spinning of selachian egg case ply sheets and orb web spider dragline filaments. *Biomacromolecules* **2**, 323–334.

14 Craig, C. L. & Riekel, C. (2002). Comparative architecture of silks, fibrous proteins and their encoding genes in insects and spiders. *Comp. Biochem. Physiol. B Biochem. Mol. Biol.* **133**, 493–507.

15 Valluzzi, R., Winkler, S., Wilson, D. & Kaplan, D. L. (2002). Silk: molecular organization and control of assembly. *Philos. Trans. R. Soc. Lond. B Biol. Sci.* **357**, 165–167.

16 Vollrath, F. (1999). Biology of spider silk. *Int. J. Biol. Macromol.* **24**, 81–88.

17 Warwicker, J. O. (1960). Comparative studies of fibroins II. The crystal structures of various fibroins. *J. Mol. Biol.* **2**, 350–362.

18 Rudall, K. M. & Kenchington, W. (1971). Arthropod silks: The problem of fibrous proteins in animal tissues. *Annu. Rev. Entomol.* **16**, 73–96.

19 Fraser, R. D. & MacRae, T. P. (1973) in *Conformation in fibrous proteins and related synthetic polypeptides* (eds. Horecker, B., Kaplan, N. O., Marmur, J. & Scheraga, H. A.) Academic Press London, 293–343.

20 Vollrath, F. (2000). Strength and structure of spiders' silks. *J. Biotechnol.* **74**, 67–83.

21 Burgeson, R. E. (1988). New collagens, new concepts. *Annu. Rev. Cell Biol.* **4**, 551–577.

22 van der Rest, M. & Garrone, R. (1991). Collagen family of proteins. *FASEB J.* **5**, 2814–2823.

23 Mayne, R. & Brewton, R. G. (1993). New members of the collagen superfamily. *Curr. Opin. Cell Biol.* **5**, 883–890.

24 Fratzl, P., Misof, K., Zizak, I., Rapp, G., Amenitsch, H. & Bernstorff, S. (1998). Fibrillar structure and mechanical properties of collagen. *J. Struct. Biol.* **122**, 119–122.

25 Berisio, R., Vitagliano, L., Mazzarella, L. & Zagari, A. (2002). Recent progress on collagen triple helix structure, stability and assembly. *Protein Pept. Lett.* **9**, 107–116.

26 Creighton, T. E. (1993) in *Proteins – structures and molecular properties* W. H. Freeman New York, 193–198.

27 Brodsky, B. & Ramshaw, J. A. (1997). The collagen triple-helix structure. *Matrix Biol.* **15**, 545–554.

28 Gross, J. (1963). Comparative biochemistry of collagen. *Comp. Biochem.* **5**, 307–345.

29 Adams, E. (1978). Invertebrate collagens. *Science* **202**, 591–598.

30 Spiro, R. G., Lucas, F. & Rudall, K. M. (1971). Glycosylation of hydroxylysine in collagens. *Nat. New Biol.* **231**, 54–55.

31 Knight, D. P., Feng, D., Stewart, M. & King, E. (1993). Changes in the macromolecular organization in collagen assemblies during secretion in the nidamental gland and formation of the egg capsule wall in the dogfish *Scyliorhinus canicula*. *Phil. Trans. R. Soc. Lond. B* **341**, 419–436.

32 Kramer, J. M., Cox, G. N. & Hirsch, D. (1992). Comparisons of the complete sequences of two collagen genes from *Caenorhabditis elegans*. *Cell* **30**, 599–606.

33 Mann, K., Gaill, F. & Timpl, R. (1992). Amino acid sequence and cell adhesion activity of fibril-forming collagen from the tube worm *Riftia pachyptila* living at deep sea hydrothermal vents. *Eur. J. Biochem.* **210**, 839–847.

34 Garrone, R. (1978). Phylogenesis of connective tissue. In *Frontiers of matrix biology Vol. 5* (ed. Robert, L.) Karger Basel, 1–250.

35 Mercer, E. H. (1952). Observations on the molecular structure of byssus

fibers. *Austr. J. Mar. Freshwater Res.* **3**, 199–204.

36 Rudall, K. M. (1955). The distribution of collagen and chitin. *Symp. Soc. Exp. Biol.* **9**, 49–71.

37 Melnick, S. C. (1958). Occurrence of collagen in the phylum Mollusca. *Nature* **181**, 1483.

38 DeVore, D. P., Engebretson, G. H., Schactele, C. F. & Sauk, J. J. (1984). Identification of collagen from byssus threads produced by the sea mussel *Mytilus edulis*. *Comp. Biochem. Physiol.* 77B, 529–531.

39 Benedict, C. V. & Waite, J. H. (1986). Location and analysis of byssal structural proteins. *J. Morphol.* **189**, 261–270.

40 Pikkarainen, J., Rantanen, J., Vastamaki, M., Lapiaho, K., Kari, A. & Kulonen, E. (1968). On collagens of invertebrates with special reference to *Mytilus edulis*. *Eur. J. Biochem.* **4**, 555–560.

41 Qin, X. X. & Waite, J. H. (1995). Exotic collagen gradients in the byssus of the mussel Mytilus edulis. *J. Exp. Biol.* **198**, 633–644.

42 Coyne, K. J., Qin, X. X. & Waite, J. H. (1997). Extensible collagen in mussel byssus: a natural block copolymer. *Science* **277**, 1830–1832.

43 Carlier, M. F. (1991). Actin: protein structure and filament dynamics. *J. Biol. Chem.* **266**, 1–4; Kabsch, W. & Vandekerckhove, J. (1992). Structure and function of actin. *Annu. Rev. Biophys. Biomol. Struct.* **21**, 49–76.

44 Janmey, P. A., Shah, J. V., Tang, J. X. & Stossel, T. P. (2001). Actin filament networks. *Results Probl. Cell. Differ.* **32**, 181–199.

45 Cheney, R. E., Riley, M. A. & Mooseker, M. S. (1993). Phylogenetic analysis of the myosin superfamily. *Cell Motil. Cytoskeleton* **24**, 215–223.

46 Titus, M. A. (1993). Myosins. *Curr. Opin. Cell. Biol.* **5**, 77–81.

47 Berg, J. S., Powell, B. C. & Cheney, R. E. (2001). A millennial myosin census. *Mol. Biol. Cell.* **12**, 780–794.

48 Perry, S. V. (2001). Vertebrate tropomyosin: distribution, properties and function. *J. Muscle Res. Cell Motil.* **22**, 5–49.

49 Wegner, A. (1979). Equilibrium of the actin-tropomyosin interaction. *J. Mol. Biol.* **131**, 839–853.

50 Yang, Y.-Z., Korn, E. D. & Eisenberg, E. (1979). Cooperative binding of tropomyosin to muscle and *Acanthamoeba* actin. *J. Biol. Chem.* **254**, 7137–7140.

51 Zot, A. S. & Potter, J. D. (1987) Structural aspects of troponin-tropomyosin regulation of skeletal muscle contraction. *Ann. Rev. Biophys. Biophys. Chem.* **16**, 535–539.

52 Stokes, D. L. & DeRosier D. J. (1987). The variable twist of actin and its modulation by actin-binding proteins. *J. Cell Biol.* **104**, 1005–1017.

53 Pante, N. (1994). Paramyosin polarity in the thick filament of molluscan smooth muscles. *J. Struct. Biol.* **113**, 148–163.

54 Albers, K. & Fuchs, E. (1992). The molecular biology of intermediate filament proteins. *Int. Rev. Cytol.* **134**, 243–279.

55 Chou, Y. H., Bischoff, J. R., Beach, D. & Goldman, R. D. (1990). Intermediate filament reorganization during mitosis is mediated by p34cdc2 phosphorylation of vimentin. *Cell* **62**, 1063–1071.

56 Stewart, M. (1993). Intermediate filament structure and assembly. *Curr. Opin. Cell Biol.* **5**, 3–11.

57 Herrmann, H. & Aebi, U. (2000). Intermediate filaments and their associates: multi-talented structural elements specifying cytoarchitecture and cytodynamics. *Curr. Opin. Cell Biol.* **12**, 79–90.

58 Strelkov, S. V., Herrmann, H. & Aebi, U. (2003). Molecular architecture of intermediate filaments. *Bioessays* **25**, 243–251.

59 Coulombe, P. A. (1993). The cellular and molecular biology of keratins: beginning a new era. *Curr. Opin. Cell Biol.* **5**, 17–29.

60 Garrod, D. R. (1993). Desmosomes and hemidesmosomes. *Curr. Opin. Cell Biol.* **5**, 30–40.

61 Nigg, E. A. (1992). Assembly and cell

cycle dynamics of the nuclear lamina. *Semin. Cell Biol.* **3**, 245–253.

62 Rzepecki, R. (2002) The nuclear lamins and the nuclear envelope. *Cell. Mol. Biol. Lett.* **7**, 1019–1035.

63 Privalov, P. L. & Medved, L. V. (1982). Domains in the fibrinogen molecule. *J. Mol. Biol.* **159**, 665–683.

64 Doolittle, R. F. (1984). Fibrinogen and fibrin. *Annu. Rev. Biochem.* **53**, 195–229.

65 Medved, L. V., Litvinovich, S., Ugarova, T., Matsuka, Y. & Ingham, K. (1997). Domain structure and functional activity of the recombinant human fibrinogen gamma-module (gamma148–411). *Biochemistry* **36**, 4685–4693.

66 Budzynski, A. Z. (1986). Fibrinogen and fibrin: biochemistry and pathophysiology. *Crit. Rev. Oncol. Hematol.* **6**, 97–146.

67 Mosher, D. F. & Johnson, R. B. (1983). Specificity of fibronectin–fibrin cross-linking. *Ann. N.Y. Acad. Sci.* **408**, 583–594.

68 Varadi, A. & Patthy, L. (1983). Location of plasminogen-binding sites in human fibrin(ogen). *Biochemistry* **22**, 2440–2446.

69 Bach, T. L., Barsigian, C., Yaen, C. H. & Martinez, J. (1998). Endothelial cell VE-cadherin functions as a receptor for the beta15–42 sequence of fibrin. *J. Biol. Chem.* **273**, 30719–30728.

70 Skoufias, D. A. & Scholey, J. M. (1993). Cytoplasmic microtubule-based motor proteins. *Curr. Opin. Cell. Biol.* **5**, 95–104.

71 Mandelkow, E. & Mandelkow, E. M. (1995). Microtubules and microtubule-associated proteins. *Curr. Opin. Cell. Biol.* **7**, 72–81.

72 Amos, L. A. & Baker, T. S. (1979). The three-dimensional structure of tubulin protofilaments. *Nature* **279**, 607–612.

73 Nogales, E. (2001). Structural insight into microtubule function. *Annu. Rev. Biophys. Biomol. Struct.* **30**, 397–420.

74 Job, D., Valiron, O. & Oakley, B. (2003). Microtubule nucleation. *Curr. Opin. Cell. Biol.* **15**, 111–117.

75 Mandelkow, E. M. & Mandelkow, E. (1992). Microtubule oscillations. *Cell. Motil. Cytoskeleton* **22**, 235–244.

76 Gosline, J. M. (1976). The physical properties of elastic tissue. *Int. Rev. Connect Tissue Res.* **7**, 211–249.

77 Ellis, G. E. & Packer, K. J. (1976). Nuclear spin-relaxation studies of hydrated elastin. *Biopolymers* **15**, 813–832.

78 Urry, D. W. (1988). Entropic elastic processes in protein mechanisms. II. Simple (passive) and coupled (active) development of elastic forces. *J. Protein Chem.* **7**, 1–34.

79 Tatham, A. S. & Shewry, P. R. (2002). Comparative structures and properties of elastic proteins. *Philos. Trans. R. Soc. Lond. B Biol. Sci.* **357**, 229–234.

80 Cleary, E. G., & Gibson, M. A. (1983). Elastin-associated microfibrils and microfibrillar proteins. *Int. Rev. Connect Tissue Res.* **10**, 97–209.

81 Vaughan, L., Mendler, M., Huber, S., Bruckner, P., Winterhalter, K. H., Irwin, M. I. & Mayne, R. (1988). D-periodic distribution of collagen type IX along cartilage fibrils. *J. Cell Biol.* **106**, 991–997.

82 Ardell, D. H. & Andersen, S. O. (2001). Tentative identification of a resilin gene in Drosophila melanogaster. *Insect. Biochem. Mol. Biol.* **31**, 965–970.

83 Morgan, D. G., Owen, C., Melanson, L. A. & DeRosier, D. J. (1995). Structure of bacterial flagellar filaments at 11 A resolution: packing of the alpha-helices. *J. Mol. Biol.* **249**, 88–110.

84 Mimori, Y., Yamashita, I., Murata, K., Fujiyoshi, Y., Yonekura, K., Toyoshima, C. & Namba, K. (1995). The structure of the R-type straight flagellar filament of Salmonella at 9 A resolution by electron cryomicroscopy. *J. Mol. Biol.* **249**, 69–87.

85 Aldridge, P. & Hughes, K. T. (2002). Regulation of flagellar assembly. *Curr. Opin. Microbiol.* **5**, 160–165.

86 Vondervisztt, F., Kanto, S., Aizawa, S. & Namba, K. (1989). Terminal

regions of flagellin are disordered in solution. *J. Mol. Biol.* **209**, 127–133.

87 Namba, K., Yamashita, I. & Vondervisztt, F. (1989). Structure of the core and central channel of bacterial flagella. *Nature* **342**, 648–654.

88 Yonekura, K., Maki-Yonekura, S. & Namba, K. (2002). Growth mechanism of the bacterial flagellar filament. *Res. Microbiol.* **153**, 191–197.

89 Thomas, N. A., Bardy, S. L. & Jarrell, K. F. (2001). The archaeal flagellum: a different kind of prokaryotic motility structure. *FEMS Microbiol. Rev.* **25**, 147–174.

90 Bardy, S. L., Ng, S. Y. & Jarrell, K. F. (2003). Prokaryotic motility structures. *Microbiology* **149**, 295–304.

91 Forest, K. T. & Tainer, J. A. (1997). Type-4 pilus-structure: outside to inside and top to bottom – a mini-review. *Gene* **192**, 165–169.

92 Wall, D. & Kaiser, D. (1999). Type IV pili and cell motility. *Mol. Microbiol.* **32**, 1–10.

93 Marvin, D. A. & Wachtel, E. J. (1976). Structure and assembly of filamentous bacterial viruses. *Philos. Trans. R. Soc. Lond. B Biol. Sci.* **276**, 81–98.

94 Marvin, D. A. (1998). Filamentous phage structure, infection and assembly. *Curr. Opin. Struct. Biol.* **8**, 150–158.

95 Pederson, D. M., Welsh, L. C., Marvin, D. A., Sampson, M., Perham, R. N., Yu, M. & Slater, M. R. (2001). The protein capsid of filamentous bacteriophage PH75 from Thermus thermophilus. *J. Mol. Biol.* **309**, 401–421.

96 Durham, A. C., Finch, J. T. & Klug, A. (1971). States of aggregation of tobacco mosaic virus protein. *Nat. New Biol.* **1971**, *229*, 37–42.

97 Schuster, T. M., Scheele, R. B., Adams, M. L., Shire, S. J., Steckert, J. J. & Potschka, M. (1980). Studies on the mechanism of assembly of tobacco mosaic virus. *Biophys. J.* **32**, 313–329.

98 Diaz-Avalos, R. & Caspar, D. L. (1998). Structure of the stacked disk aggregate of tobacco mosaic virus protein. *Biophys. J.* **74**, 595–603.

99 Culver, J. N. (2002). Tobacco mosaic virus assembly and disassembly: determinants in pathogenicity and resistance. *Annu. Rev. Phytopathol.* **40**, 287–308.

100 Butler, P. J. (1984). The current picture of the structure and assembly of tobacco mosaic virus. *J. Gen. Virol.* **65**, 253–279.

101 Mitraki, A., Miller, S. & van Raaij, M. J. (2002). Review: conformation and folding of novel beta-structural elements in viral fiber proteins: the triple beta-spiral and triple beta-helix. *J. Struct. Biol.* **137**, 236–247.

102 Betts, S. & King, J. (1999). There's a right way and a wrong way: in vivo and in vitro folding, misfolding and subunit assembly of the P22 tailspike. *Structure Fold. Des.* **7**, R131–139.

103 Inouye, H., Fraser, P. & Kirschner, D. (1993). Structure of β-Crystallite Assemblies by Alzheimer β Amyloid Protein Analogues: Analysis by X-Ray Diffraction. *Biophys. J.* **64**, 502–519.

104 Blake, C. & Serpell, L. (1996). Synchrotron X-ray studies suggest that the core of the transthyretin amyloid fibril is a continuous b-helix. *Structure* **4**, 989–998.

105 Sikorski, P., Atkins, E. D. T. & Serpell, L. C. (2003). Structure and textures of fibrous crystals of the Abeta(11–25) fragment from Alzheimer's Abeta amyloid protein. *Structure* **11**, 1–20.

106 Malinchik, S., Inouye, H., Szumowski, K. & Kirschner, D. (1998). Structural analysis of Alzheimer's b(1–40) amyloid: protofilament assembly of tubular fibrils. *Biophys. J.* **74**, 537–545.

107 Griffiths, J. M., Ashburn, T. T., Auger, M., Costa, P. R., Griffin, R. G. & Lansbury, P. T. (1995). Rotational resonance solid state NMR elucidates a structural model of pancreatic amyloid. *J. Am. Chem. Soc.* **117**, 3539–3546.

108 Balbach, J. J., Petkova, A. T., Oyler, N. A., Antzukin, O. N., Gordon, D. J., Meredith, S. C. & Tycko, R.

(2002). Supramolecular structure in full-length Alzheimer's b-amyloid fibrils: evidence for parallel b-sheet organisation from solid state nuclear magnetic resonance. *Biophys. J.* **83**, 1205–1216.

109 Benzinger, T. L. S., Gregory, D. M., Burkoth, T. S., Miller-Auer, H., Lynn, D. G., Botto, R. E. & Meredith, S. C. (2000). Two-dimensional structure of b-amyloid (10–35) fibrils. *Biochemistry* **39**, 3491–3499.

110 Serpell, L. & Smith, J. (2000). Direct visualisation of the beta-sheet structure of synthetic Alzheimer's amyloid. *J. Mol. Biol.* **299**, 225–231.

111 Jimenez, J. L., Guijarro, J. I., Orlova, E., Zurdo, J., Dobson, C., Sunde, M. & Saibil, H. (1999). Cryo-electron microscopy structure of an SH3 amyloid fibril and model of the molecular packing. *EMBO J.* **18**, 815–821.

112 Lazo, N. & Downing, D. (1998). Amyloid fibrils may be assembled from b-helical protofibrils. *Biochemistry* **37**, 1731–1735.

113 Perutz, M. F., Finch, J. T., Berriman, J. & Lesk, A. (2002). Amyloid fibers are water-filled nanotubes. *Proc Natl Acad Sci USA* **99**, 5591–5595.

114 Serpell, L., Sunde, M., Benson, M., Tennent, G., Pepys, M. & Fraser, P. (2000). The protofilament substructure of amyloid fibrils. *J Mol Biol.* **300**, 1033–1039.

115 Goldsbury, C., Kistler, J., Aebi, U., Arvinte, T. & Cooper, G. J. (1999) Watching amyloid fibrils grow by time-lapse atomic force microscopy. *J. Mol. Biol.* **285**, 33–39.

116 Crowther, R. (1993). TAU Protein and Paired Helical Filaments of Alzheimers Disease. *Curr. Opin. Struct. Biol.* **3**, 202–206.

117 Crowther, R. (1991). Structural Aspects of Pathology in Alzheimers Disease. *Biochim. Biophys. Acta* **1096**, 1–9.

118 Berriman, J., Serpell, L. C., Oberg, K. A., Fink, A. L., Goedert, M. & Crowther, R. A. (2003). Tau filaments from human brain and from in vitro assembly of recombinant protein show cross-beta structure. *Proc. Natl. Acad. Sci. USA* **100**, 9034–9038.

119 Marsh, R. E., Corey, R. B. & Pauling, L. (1955). An investigation of the structure of silk fibroin. *Biochim. Biophys. Acta* **16**, 1–34.

120 Takahashi, Y., Gehoh, M. & Yuzuriha, K. (1999). Structure refinement and diffuse streak scattering of silk (Bombyx mori). *Int. J. Biol. Macromol.* **24**, 127–138.

121 Parkhe, A. D., Seeley, S. K., Gardner, K., Thompson, L. & Lewis, R. V. (1997). Structural studies of spider silk proteins in the fiber. *J. Mol. Recognit.* **10**, 1–6.

122 Parker, K. & Rudall, K. (1957). The silk of the egg-stalk of the green lacewing fly. *Nature* **179**, 905–907.

123 van Raaij, M. J., Mitraki, A., Lavigne, G. & Cusack, S. (1999). A triple b-spiral in the adenovirus fiber shaft reveals a new structural motif for a fibrous protein. *Nature* **401**, 935–938.

124 Yoder, M., Keen, N. & Jurnak, F. (1993). New domain motif – the structure of pectate lyase-C, a secreted plant virulence factor. *Science* **260**, 1503–1506.

125 Steinbacher, S., Seckler, R., Miller, D., Steipe, B., Huber, R. & Reinemer, P. (1994). Crystal-structure of P22 tailspike protein – interdigitated subunits in a thermostable trimer. *Science* **265**, 383–386.

126 Raetz, C. & Roderick, S. (1995). A left-handed parallel b-helix in the structure of UDP-N- Acetylglucosamine acyltransferase. *Science* **270**, 997–1000.

127 van Raaij, M. J., Schoehn, G., Jaquinod, M., Ashman, K., Burda, M. R. & Miller, S. (2001). Crystal structure of a heat- and protease-stable part of the bacteriophage t4 short tail fiber. *J. Mol. Biol.* **314**, 1137–1146.

128 Kanamaru, S., Leiman, P. G., Kostyuchenko, V. A., Chipman, P. R., Mesyanzhinov, V. V., Arisaka, F. & Rossman, M. G. (2002). The structure of the bacteriophage T4 cell-puncturing device. *Nature* **415**, 553–557.

129 Kostyuchenko, V. A., Leiman, P. G., Chipman, P. R., Kanamaru, S., van Raaij, M. J., Arisaka, F., Mesyanzhinov, V. V. & Rossman, M. G. (2003). Three-dimensional structure of the bacteriophage T4 baseplate. *Nat. Struct. Biol.* **10**, 688–693.

130 Ottani, V., Martini, D., Franchi, M., Ruggeri, A. & Raspanti, M. (2002). Hierarchical structures in fibrillar collagens. *Micron* **33**, 587–596.

131 Wess, T. J., Hammersley, A. P., Wess, L. & Miller, A. (1998). A consensus model for molecular packing of type I collagen. *J. Struct. Biol.* **122**, 92–100.

132 Wess, T. J., Hammersley, A. P., Wess, L. & Miller, A. (1995). Type I Collagen packing conformation of the triclinic unit cell. *J. Mol. Biol.* **248**, 487–493.

133 Phillips, G. N., Fillers, J. P. & Cohen, C. (1986). Tropomyosin crystal structure and muscle regulation. *J. Mol. Biol.* **192**, 111–131.

134 Whitby, F. G., Kent, H., Stewart, F., Stewart, M., Xie, X., Hatch, V., Cohen, C. & Phillips, G. N. (1992). Structure of tropomyosin at 9 Angstroms resolution. *J. Mol. Biol.* **227**, 441–452.

135 Crick, F. H. C. (1952). Is alpha-keratin a coiled coil. *Nature* **170**, 882–883.

136 Strelkov, S. V., Herrman, H., Geisler, N., Wedig, T., Zimbelmann, R., Aebi, U. & Burkhard, P. (2002). Conserved segments 1A and 2B of the intermediate filament dimer: their atomic structures and role in filament assembly. *EMBO J.* **21**, 1255–1266.

137 Lowe, J. & Amos, L. A. (1998). Crystal structure of the bacterial cell-division protein FtsZ. *Nature* **391**, 203–206.

138 Lowe, J. & Amos, L. A. (1999). Tubulin-like protofilaments in Ca2+ induced FtsZ sheets. *EMBO J.* **18**, 2364–2371.

139 Nogales, E., Wolf, S. & Downing, K. H. (1998). Structure of the alpha-beta tubulin dimer by electron crystallography. *Nature* **391**, 199–203.

140 Nogales, E., Whittaker, M., Milligan, R. A. & Downing, K. H. (1999). High-resolution model of the microtubule. *Cell* **96**, 79–88.

141 Hirose, K., Amos, W. B., Lockhart, A., Cross, R. A. & Amos, L. A. (1997). Three-dimensional cryo-electron microscopy of 16-protofilament microtubules: structure, polarity and interaction with motor proteins. *J. Struct. Biol.* **118**, 140–148.

142 Squire, J. & Morris, E. (1998). A new look at thin filament regulation in vertebrate skeletal muscle. *FASEB J.* **12**, 761–771.

143 Hanson, E. J. & Lowry, J. (1963). The structure of F-actin and of actin filaments isolated from muscle. *J. Mol. Biol.* **6**, 48–60.

144 Kabsch, W., Mannherz, H. G., Suck, D., Pai, E. F. & Holmes, K. C. (1990). Atomic structure of the actin filament. *Nature* **347**, 44–49.

145 Holmes, K., Popp, D., Gerhard, W. & Kabsch, W. (1990). Atomic Model of the Actin Filament. *Nature* **347**, 44–49.

146 Lorenz, M., Poole, K., Popp, D., Rosenbaum, G. & Holmes, K. (1995). An Atomic Model of the Unregulated Thin Filament Obtained by X-ray Fiber Diffraction on Oriented Actin-Tropomyosin Gels. *J. Mol. Biol.* **246**, 108–119.

147 Squire, J. M., Knupp, C., Al-Khayat, H. A. & Harford, J. J. (2003). Millisecond time-resolved low-angle X-ray fiber diffraction: a powerful high-sensitivity technique for modelling real-time movements in biological macromolecular assemblies. *Fib. Diff. Rev.* **11**, 28–35.

148 Morris, E., Squire, J. & Fuller, G. (1991). The 4-Stranded Helical Arrangement of Myosin Heads on Insect (Lethocerus) Flight Muscle Thick Filaments. *J. Struct. Biol.* **107**, 237–249.

149 Padron, R., Alamo, L., Murgich, J. & Craig, R. (1998). Towards an atomic model of the thick filaments of muscle. *J. Mol. Biol.* **275**, 35–41.

150 Rayment, I., Rypniewski, W., Schmidt-Base, K., Smith, R.,

Tomcheck, D., Benning, M., Winkelmann, D., Wesenberg, G. & Holden, H. (1993). 3D-Structure of Myosin Subfragment-1: A Molecular Motor. *Science* **261**, 50–57.

151 Adler, A. J., Greenfield, N. J. & Fasman, G.D. (1973). Circular dichroism and optical rotatory dispersion of proteins and polypeptides. *Methods Enzymol.* **27**, 675–735.

152 Johnson, W. C. (1990). Protein secondary structure and circular dichroism: a practical guide. *Proteins* **7**, 205–214.

153 Kuwajima, K. (1995). Circular dichroism. *Methods Mol. Biol.* **40**, 115–135.

154 Woody, R. W. (1995). Circular dichroism. *Methods Enzymol.* **246**, 34–71.

155 Bloemendal, M. & Johnson, W. C. (1995). Structural information on proteins from circular dichroism spectroscopy possibilities and limitations. *Pharm. Biotechnol.* **7**, 65–100.

156 Greenfield, N. J. (1996). Methods to estimate the conformation of proteins and polypeptides from circular dichroism data. *Anal. Biochem.* **235**, 1–10.

157 Kelly, S. M. & Price, N. C. (2000). The use of circular dichroism in the investigation of protein structure and function. *Curr. Protein Pept. Sci.* **1**, 349–384.

158 Penzer, G. R. (1980) in *An introduction to spectroscopy for biochemists* (ed. Brown, S. B.) Academic Press London, 70–114.

159 Royer, C. A. (1995). Fluorescence spectroscopy. *Methods Mol. Biol.* **40**, 65–89M.

160 Roy, S. & Bhattacharyya, B. (1995). Fluorescence spectroscopic studies of proteins. *Subcell. Biochem.* **24**, 101–114.

161 Schmid, F. X. (1997) in *Protein structure – a practical approach* (ed. Creighton, T. E.) Oxford University Press, 261–298.

162 McLaughlin, M. L. & Barkley, M. D. (1997). Time-resolved fluorescence of constrained tryptophan derivatives: implications for protein fluorescence. *Methods. Enzymol.* **278**, 190–202.

163 Beechem, J. M. & Brand, L. (1985). Time-resolved fluorescence of proteins. *Annu. Rev. Biochem.* **54**, 43–71.

164 Papp, S. & Vanderkooi, J. M. (1989). Tryptophan phosphorescence at room temperature as a tool to study protein structure and dynamics. *Photochem. Photobiol.* **49**, 775–784.

165 Mathies, R. A., Peck, K. & Stryer, L. (1990). Optimization of high-sensitivity fluorescence detection. *Anal. Chem.* **62**, 1786–1791.

166 Haugland, R. P. (1996) in *Handbook of fluorescent probes and research chemicals* (ed. Spence, M. T. Z.) Molecular Probes Inc.

167 Gorman, P. M., Yip, C. M., Fraser, P. E. & Chakrabartty, A. (2003). Alternate aggregation pathways of the Alzheimer beta-amyloid peptide: Abeta association kinetics at endosomal pH. *J. Mol. Biol.* **325**, 743–757.

168 Leissring, M. A., Lu, A., Condron, M. M., Teplow, D. B., Stein, R. L., Farris, W. & Selkoe, D. J. (2003). Kinetics of amyloid beta-protein degradation determined by novel fluorescence- and fluorescence polarization-based assays. *J. Biol. Chem.* **278**, 37314–37320.

169 Scheibel, T., Bloom, J. & Lindquist, S. L. The elongation of yeast prion fibers involves separable steps of association and conversion. *Proc. Natl. Acad. Sci. USA*, **101**, 2287–2292.

170 Hermanson, G. (1996) in *Bioconjugate techniques* Academic Press London.

171 Udenfriend, S. (1962) in *Fluorescence assay in biology and medicine* (eds. Horecker, B., Kaplan, N. O., Marmur, J. & Scheraga, H. A.) Academic Press London, 223–229.

172 Slavik, I. (1982). Anilinonaphthalene sulfonate as a probe of membrane composition and function. *Biochim. Biophys. Acta* **694**, 1–25.

173 Förster, T. (1951) in *Fluoreszenz organischer Verbindungen*, Vandenhoeck and Ruprecht Göttingen.

174 Matulis, D. & Lovrien, R. (1998). 1-Anilino-8-naphthalene sulfonate anion-protein binding depends primarily on ion pair formation. *Biophys. J.* **72**, 422–429.

175 Matulis, D., Baumann, C. G., Bloomfield, V. A. & Lovrien, R. (1999). 1-anilino-8-naphthalene sulfonate as a protein conformational tightening agent. *Biopolymers* **49**, 451–458.

176 Kirk, W., Kurian, E. & Prendergast, F. (1996). Affinity of fatty acid for (r)rat intestinal fatty acid binding protein: further examination. *Biophys. J.* **70**, 69–83.

177 Safar, J., Roller, P. P., Gajdusek, D. C. & Gibbs, C. J. (1984). Scrapie amyloid (prion) protein has the conformational characteristics of an aggregated molten globule folding intermediate. *Biochemistry* **33**, 8375–8383.

178 Litvinovich, S. V., Brew, S. A., Aota, S., Akiyama, S. K., Haudenschild, C. & Ingham, K. C. (1998). Formation of amyloid-like fibrils by self-association of a partially unfolded fibronectin type III module. *J. Mol. Biol.* **280**, 245–258.

179 Kayed, R., Bernhagen, J., Greenfield, N., Sweimeh, K., Brunner, H., Voelter, W. & Kapurniotu, A. (1999). Conformational transitions of islet amyloid polypeptide (IAPP) in amyloid formation in vitro. *J. Mol. Biol.* **287**, 781–796.

180 Baskakov, I. V., Legname, G., Baldwin, M. A., Prusiner, S. B. & Cohen, F. E. (2002). Pathway complexity of prion protein assembly into amyloid. *J. Biol. Chem.* **277**, 21140–21148.

181 Mann, C. J. & Matthews, C. R. (1993). Structure and stability of an early folding intermediate of Escherichia coli trp aporepressor measured by far-UV stopped-flow circular dichroism and 8-anilino-1-naphthalene sulfonate binding. *Biochemistry* **32**, 5282–5290.

182 Subbarao, N. K. & MacDonald, R. C. (1993). Experimental method to correct fluorescence intensities for the inner filter effect. *Analyst* **118**, 913–916.

183 Benoit, H., Freund, L. & Spach, G. (1967) in: *Poly-α-amino acids* (ed. Fasman, G. D.) Marcel Dekker Inc. New York, 105–155.

184 Shen, C. L., Scott, G. L., Merchant, F. & Murphy, R. M. (1993). Light scattering analysis of fibril growth from the amino-terminal fragment beta(1–28) of beta-amyloid peptide. *Biophys. J.* **65**, 2383–2395.

185 Harding, S. E. (1997) in *Protein structure – a practical approach* (ed. Creighton, T. E.) Oxford University Press, 219–251.

186 Wyatt, P. J. (1991). Combined differential light scattering with various liquid chromatography separation techniques. *Biochem. Soc. Trans.* **19**, 485.

187 Roessner, D. & Kulicke, W. M. (1994). On-line coupling of flow field-flow fractionation and multi-angle laser light scattering *J. Chromatogr.* **687**, 249–258.

188 Wyatt, P. J. & Villalpando, D. (1997). High-Precision Measurement of Submicrometer Particle Size Distributions. *Langmuir* **13**, 3913–3914.

189 Harding, S. E. (1986). Applications of light scattering in microbiology. *Biotechnol. Appl. Biochem.* **8**, 489–509.

190 Walsh, D. M., Lomakin, A., Benedek, G. B., Condron, M. M. & Teplow, D. B. (1997). Amyloid beta-protein fibrillogenesis. Detection of a protofibrillar intermediate. *J. Biol. Chem.* **272**, 22364–22372.

191 Tseng, Y., Fedorov, E., McCaffery, J. M., Almo, S. C. & Wirtz, D. (2001). Micromechanics and ultrastructure of actin filament networks crosslinked by human fascin: a comparison with alpha-actinin. *J. Mol. Biol.* **310**, 351–366.

192 Kita, R., Takahashi, A., Kaibara, M. & Kubota, K. (2002). Formation of fibrin gel in fibrinogen-thrombin system: static and dynamic light scattering study. *Biomacromolecules* **3**, 1013–1020.

193 Giddings, J. C., Yang, F. J. & Myers, M. N. (1977). Flow field-flow fractionation as a methodology for protein separation and characterization. *Anal. Biochem.* **81**, 394–407.

194 Wahlund, K. G. & Giddings, J. C. (1987). Properties of an asymmetrical

flow field-flow fractionation channel having one permeable wall. *Anal. Chem.* **59**, 1332–1339.

195 Giddings, J. C. (1989). Field-flow fractionation of macromolecules. *J. Chromatogr.* **470**, 327–335.

196 Liu, M. K., Li, P. & Giddings, J. C. (1993). Rapid protein separation and diffusion coefficient measurement by frit inlet flow field-flow fractionation. *Protein Sci.* **2**, 1520–1531.

197 Nilsson, M., Birnbaum, S. & Wahlund, K. G. (1996). Determination of relative amounts of ribosome and subunits in Escherichia coli using asymmetrical flow field-flow fractionation. *J. Biochem. Biophys. Methods* **33**, 9–23.

198 Adolphi, U. & Kulicke, W. M. (1997). Coil dimensions and conformation of macromolecules in aqueous media from flow field-flow fractionation/multi-angle laser light scattering illustrated by studies on pullulan. *Polymer* **38**, 1513–1519.

199 Kretchmann, E. (1971). The determination of the optical constants of metals by excitation of surface plasmons. *Z. Phys.* **241**, 313–324.

200 Fagerstam, L. G., Frostell-Karlsson, A., Karlsson, R., Persson, B. & Ronnberg, I. (1992). Biospecific interaction analysis using surface plasmon resonance detection applied to kinetic, binding site and concentration analysis. *J. Chromatogr.* **597**, 397–410.

201 De Bruijn, H. E., Kooyman, R. P. & Greve, J. (1992). Choice of metal and wavelength for SPR sensors: some considerations. *Appl. Opt.* **31**, 440–442.

202 Green, R. J., Frazier, R. A., Shakesheff, K. M., Davies, M. C., Roberts, C. J. & Tendler, S. J. (2000). Surface plasmon resonance analysis of dynamic biological interactions with biomaterials. *Biomaterials* **21**, 1823–1835.

203 Rich, R. L. & Myszka, D. G. (2000). Advances in surface plasmon resonance biosensor analysis. *Curr. Opin. Biotechnol.* **11**, 54–61.

204 Myszka, D. G., Wood, S. J., Biere, A. L. (1999) Analysis of fibril elongation using surface plasmon resonance biosensors. *Methods Enzymol.* **309**, 386–402.

205 Vikinge, T. P., Hansson, K. M., Benesch, J., Johansen, K., Ranby, M., Lindahl, T. L., Liedberg, B., Lundstom, I. & Tengvall, P. (2000). Blood plasma coagulation studied by surface plasmon resonance. *J. Biomed. Opt.* **5**, 51–55.

206 Binnig, G., Quate, C. F. & Gerber, C. (1986). Atomic force microscope. *Phys. Rev. Lett.* **56**, 930–933.

207 Stolz, M., Stoffler, D., Aebi, U. & Goldsbury, C. (2000). Monitoring biomolecular interactions by time-lapse atomic force microscopy. *J. Struct. Biol.* **131**, 171–180.

208 Yang, Y., Wang, H. & Erie, D. A. (2003). Quantitative characterization of biomolecular assemblies and interactions using atomic force microscopy. *Methods* **29**, 175–187.

209 Harper, J. D., Lieber, C. M. & Lansbury, P. T. (1997). Atomic force microscopic imaging of seeded fibril formation and fibril branching by the Alzheimer's disease amyloid-beta protein. *Chem. Biol.* **4**, 951–959.

210 Blackley, H. K., Sanders, G. H., Davies, M. C., Roberts, C. J., Tendler, S. J. & Wilkinson, M. J. (2000). In-situ atomic force microscopy study of beta-amyloid fibrillization. *J. Mol. Biol.* **298**, 833–840.

211 DePace, A. H., Weissman, J. S. (2002). Origins and kinetic consequences of diversity in Sup35 yeast prion fibers. *Nat. Struct. Biol.* **9**, 389–396.

212 da Silva, L. P. (2002). Atomic force microscopy and proteins. *Protein Pept. Lett.* **9**, 117–126.

213 Puchtler, H. & Sweat, F. (1965). Congo red as a stain for fluorescence microscopy of amyloid. *J. Histochem. Cytochem.* **13**, 693–694.

214 Klunk, W. E., Jacob, R. F. & Mason, R. P. (1999). Quantifying amyloid by congo red spectral shift assay. *Methods Enzymol.* **309**, 285–305.

215 DeLellis, R. A., Glenner, G. G. & Ram, J. S. (1968). Histochemical observations on amyloid with

reference to polarization microscopy. *J. Histochem. Cytochem.* **16**, 663–665.

216 Khurana, R., Uversky, V. N., Nielsen, L. & Fink, A. L. (2001). Is Congo red an amyloid-specific dye? *J. Biol. Chem.* **276**, 22715–22721.

217 Naiki, H., Higuchi, K., Hosokawa, M., Takeda, T. (1989). Fluorometric determination of amyloid fibrils in vitro using the fluorescent dye, thioflavin T1. *Anal. Biochem.* **177**, 244–249.

218 LeVine, H. (1997). Stopped-flow kinetics reveal multiple phases of thioflavin T binding to Alzheimer beta (1–40) amyloid fibrils. *Biochem. Biophys.* **342**, 306–316.

219 Ban, T., Hamada, D., Hasegawa, K., Naiki, H. & Goto, Y. (2003). Direct observation of amyloid fibril growth monitored by thioflavin T fluorescence. *J. Biol. Chem.* **278**, 16462–16465.

220 Hayes, T. L. (1973). Scanning electron microscope techniques in biology. In *Advanced Techniques in Biological Electron Microscopy* (ed. Koehler, J. K.). Springer-Verlag, Berlin, Heidelberg, New York.

221 Echlin, P. (1971). The application of SEM to biological research. *Phil. Trans. Soc. Lond. B* **261**, 51–59.

222 DeRosier, D. J. & Moore, P. B. (1970). Reconstruction of three-dimensional images from electron micrographs of structures with helical symmetry. *J. Mol. Biol.* **52**, 355–369.

223 Harris, J. R. (1997). *Negative staining and cryoelectron microscopy.* Royal Microscopical Society, Microscopy handbook series, Bios scientific publishers limited, Oxford.

224 Glenney, J. R. (1987). Rotary metal shadowing for visualizing rod-shaped proteins. In *Electron microscopy in molecular biology* (eds. Sommerville, J. & Scheer, U.), IRL press, Oxford, Washington DC, 167–178.

225 DeRosier, D. J. & Klug, A. (1968). Reconstruction of three-dimensional structures from electron micrographs. *Nature* **217**, 130–134.

226 Smith, J. M. (1999). XIMDISP – A visualization tool to aid in structure determination from electron micrograph images. *J. Struct. Biol.* **125**, 223–228.

227 Crowther, R. A., Henderson, R. & Smith, J. (1996). MRC Image processing programs. *J. Struct. Biol.* **116**, 9–16.

228 Egelman, E. H. (1986). An algorithm for straightening images of curved filamentous structures. *Ultramicroscopy* **19**, 367–373.

229 Stewart, M. (1988). Computer image processing of electron micrographs of biological structures with helical symmetry. *J. Electron microscopy technique* **9**, 325–358.

230 Frank, J. (1973). Computer Processing of Electron Micrographs. In *Advanced Techniques in Biological Electron Microscopy* (ed. Koehler, J. K.). Springer-Verlag, Berlin, Heidelberg, New York.

231 Stine, W. B., Snyder, S. W., Ladror, U. S., Wade, W. S., Miller, M. F., Perun, T. J., Holzman, T. F. & Krafft, G. A. (1996) The nanometer-scale structure of amyloid-beta visualized by atomic force microscopy. *J. Protein Chem.* **15**, 193–203.

232 Ding, T. T. & Harper, J. D. (1999). Analysis of amyloid-beta assemblies using tapping mode atomic force microscopy under ambient conditions. In *Methods in Enzymology: Amyloid, prions and other protein aggregates* (ed. Wetzel, R.) Academic press New York, **309**, 510–525.

233 Sikorski, P. & Atkins, E. D. T. (2001). The three-dimensional structure of monodisperse 5-amide nylon 6 crystals in the lambda phase. *Macromolecules* **34**, 4788–4794.

234 Krejchi, M. T., Cooper, S. J., Deguchi, Y., Atkins, E. D. T., Fournier, M. J., Mason, T. L. & Tirrell, D. A. (1997). Crystal structures of chain-folded antiparallel beta-sheet assemblies from sequence-designed periodic polypeptides. *Macromolecules* **17**, 5012–5024.

235 Fandrich, M. & Dobson, C. (2002). The behaviour of polyamino acids reveals an inverse side-chain effect in amyloid structure formation. *EMBO Journal* **21**, 5682–5690.

236 Worcester, D. (1978). Structural Origins of Diamagnetic Anisotropy in Proteins. *Proc. Natl. Acad. Sci. USA* **75**, 5475–5477.

237 Torbet, J., Freyssinet, J.-M. & Hudry-Clergron, G. (1981). Oriented Fibrin Gels Formed by Polymerization in Strong Magnetic Fields. *Nature* **289**, 91–93.

238 Torbet, J. & Dickens, M. J. (1984). Orientation of skeletal muscle actin in strong magnetic field. *FEBS Lett.* **173**, 403–406.

239 Marvin, D. A. & Nave, C. (1982). X-ray fiber diffraction. In *Structural molecular biology* (eds. Davies, D. B., Srenger, W. & Danyluk, S. S.). Plenum Publishing corporation.

240 Squire, J., Al-Khayat, H., Arnott, S., Crawshaw, J., Denny, R., Diakun, G., Dover, D., Forsyth, T., He, A., Knupp, C., Mant, G., Rajkumar, G., Rodman, M., Shotton, M. & Windle, A. (2003). New CCP13 software and the strategy behind further developments: stripping and modelling of fiber diffraction data. *Fiber diffraction review* **11**, 13–19.

241 CCP4. (1994). The CCP4 Suite Programs for Crystallography. *Acta Cryst.* **D50**, 760–763.

242 Otwinowski, Z. & Minor, W. (1997). Processing of X-ray diffraction data collected in oscillation mode. In *Methods in Enzymology* (eds. Carter, C. W. & Sweet, R. M.) Academic press New York, **276**, 307–326.

243 Fraser, R. D. B., Macrae, T. P., Miller, A. & Rowlands, R. J. (1976). Digital Processing of Fiber Diffraction Patterns. *J. Appl. Cryst.* **9**, 81–94.

244 Millane, R. P. & Arnott, S. (1985). Background subtraction in X-ray fiber diffraction patterns. *J. Appl. Cryst.* **18**, 419–423.

245 Ivanova, M. I. & Makowski, L. (1998). Iterative low-pass filtering for estimation of the background in fiber diffraction patterns. *Acta Cryst. A* **54**, 626–631.

246 Okada, K., Noguchi, K., Okuyama, K. & Arnott, S. (2003). WinLALS for a linked-atom least squares refinement program for helical polymers on Windows PCs. *Computational Biology and Chemistry* **3**, 265–285.

247 Cantor, C. R. & Schimmel, P. R. (1980). In *Biophysical Chemistry. Part II: Techniques for the study of biological structure and function*. W. H. Freeman and company New York.

248 Seshadri, S., Khurana, R. & Fink, A. L. (1999). Fourier transform infrared spectroscopy in analysis of protein deposits. In *Methods in Enzymology: Amyloid, prions and other protein aggregates* (ed. Wetzel, R.) Academic press New York, **309**, 559–576.

249 Oberg, K. A. & Fink, A. L. (1998). A new attenuated total reflectance Fourier transform infrared spectroscopy method for the study of proteins in solution. *Anal. Biochem.* **256**, 92–106.

250 Serpell, L. C., Berriman, J., Jakes, R., Goedert, M. & Crowther, R. A. (2000). Fiber diffraction of synthetic a-synuclein filaments shows amyloid-like cross-b conformation. *Proc. Natl. Acad. Sci. USA* **97**, 4897–4902.

251 Scheibel, T., Kowal, A., Bloom, J. & Lindquist, S. (2001). Bi-directional amyloid fiber growth for a yeast prion determinant. *Curr. Biol.* **11**, 366–369.

7
Protein Unfolding in the Cell

Prakash Koodathingal, Neil E. Jaffe, and Andreas Matouschek

7.1
Introduction

Regulated protein unfolding is a key step in biological processes such as translocation across membranes and degradation by ATP-dependent proteases (Figure 7.1). Most cellular proteins are encoded within the nucleus and subsequently imported into different organelles such as mitochondria, chloroplasts, microsomes, and peroxisomes. The dimensions of protein import channels in many of these compartments are such that native proteins simply do not fit through them. In the case of ATP-dependent proteases, the unfolding requirement is imposed by the sequestration of the proteolytic active sites deep inside the protease structure. Access to this site is controlled by the narrow opening at the entrance of the degradation channel. Unfolding is catalyzed during translocation across membranes and degradation by ATP-dependent proteases. The mechanisms of catalyzed unfolding in these processes resemble each other and differ from global unfolding processes induced by chaotropic agents. In this chapter, we will discuss findings that led to the current understanding of unfolding observed in cell.

7.2
Protein Translocation Across Membranes

7.2.1
Compartmentalization and Unfolding

The eukaryotic cytoplasm is divided into several functionally distinct compartments or organelles. Most proteins are synthesized in the cytosol and then have to be imported into compartments. In order for proteins to fit through import channels, unfolding is required. The best-understood example of a compartment that requires unfolding for protein transport is the mitochondria [1–3]. Mitochondria are surrounded by two well-defined membranes. The protein import channel across the outer mitochondrial membrane is rigid and has a diameter of approxi-

Protein Folding Handbook. Part II. Edited by J. Buchner and T. Kiefhaber

ISBN: 3-527-30784-2

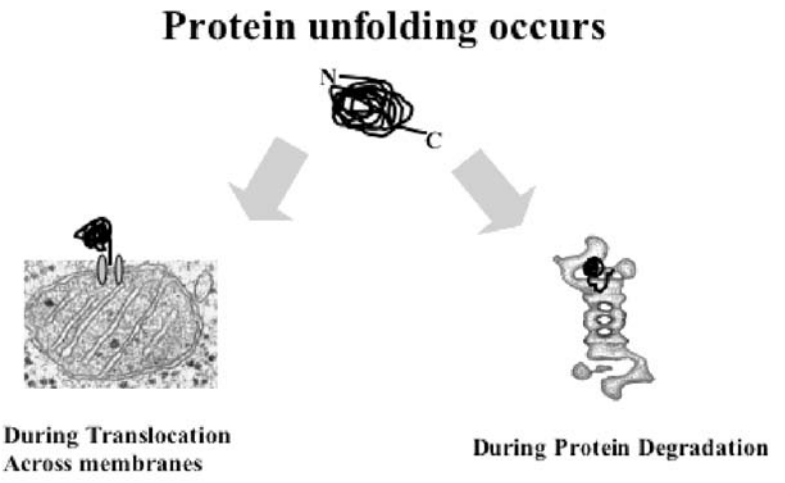

Fig. 7.1. Protein unfolding occurs during translocation across some membranes (left) and during degradation by ATP-dependent proteases (right).

mately 24 Å [4–6]. The channel across the inner membrane is flexible, but its maximum diameter is smaller than that of the outer-membrane channel [6–8]. The majority of mitochondrial proteins are synthesized in the cytosol as preproteins with positively charged N-terminal targeting signals [9]. After synthesis, preproteins are localized to the mitochondria.

Several lines of evidence indicate that most precursor proteins are not in their native conformation during translocation across the mitochondrial matrix. First, import of mouse dihydrofolate reductase (DHFR) is blocked when its unfolding is inhibited by the tightly binding ligand methotrexate [10]. Second, studies using *Neurospora crassa* mitochondria at a low temperature identified a translocation intermediate during the import of F_1-ATPase β-subunit and cytochrome c_1 precursors [11]. This intermediate appeared to span both mitochondrial membranes, which is a conformation that is possible only when the precursor protein is at least partially unfolded. Third, attaching oxidized BPTI (containing three intramolecular disulfide bridges) to the C-terminus of mouse DHFR prevented the import of the DHFR moiety completely inside the mitochondria [12]. Finally, a study using barnase mutants showed that a single disulfide bridge in a precursor protein slowed import [7]. It is now widely accepted that proteins are in a fully unfolded conformation during import.

The next question is when and where preproteins are unfolded. One possibility could be that proteins never fold before import. However, it is thought that multidomain proteins fold co-translationally in eukaryotes [13]. The N-terminal domain of nascent polypeptide chains folds before the synthesis of the C-terminal domain is complete [13, 14]. In vitro studies using three model proteins demonstrated that pre-sequences of differing lengths do not affect the stability or folding and unfold-

ing kinetics of the mature proteins [15–17]. Two in vivo experiments show that precursor proteins can be in the native conformation prior to import. Studies in *S. cerevisiae* showed that a hybrid protein consisting of the amino-terminal third of cytochrome b_2 followed by the DHFR domain accumulates outside the mitochondrial matrix as a translocation intermediate in the presence of the substrate analogue aminopterin [18]. This shows that the DHFR domain was completely translated and folded before translocation across the membrane. Similarly, precursors containing the tightly folded heme-binding domain could be completely imported into mitochondria only when the pre-sequence could actively engage the mitochondrial unfolding machinery [19], suggesting that an authentic mitochondrial protein folds in the cytosol.

A subset of precursors, such as subunits of larger complexes or integral membrane proteins, is unable to fold in the cytosol and interact with chaperones [20, 21]. These precursors require ATP outside the mitochondrial matrix for import. The requirement for cytosolic ATP can be negated by denaturing the precursors with urea [21]. Thus, cytosolic chaperones can facilitate import of precursors that are unable to fold in the cytosol (precursors prone to aggregation). Although cytosolic chaperones affect import of some proteins, it is well documented that purified mitochondria can import chemically pure folded precursor proteins [10, 22].

7.2.2 Mitochondria Actively Unfold Precursor Proteins

Mitochondria can import folded precursor proteins much faster than the spontaneous unfolding measured in free solution [22, 23]. In other words, mitochondria actively unfold proteins during import. Two models can explain the nature of the unfolding activity during translocation into mitochondria. One possibility is that the mitochondrial membrane surface destabilizes importing proteins. For example, it has been shown that lipid vesicles induce the partially unfolded molten-globule state observed in diphtheria toxin [24–28]. However, the mitochondrial membrane surface does not appear to affect the stability of importing proteins. This question has been studied extensively using artificial precursor proteins composed of barnase. Barnase is a small ribonuclease that is bound by its stabilizing ligand barstar. Mutations had the same effect on the stability of barnase at the import site on the mitochondria and in free solution [29]. In addition, the dissociation constant of the barnase-barstar complex at the mitochondrial surface coincides with that in free solution [29].

It appears that mitochondria can accelerate unfolding of at least some precursor proteins by changing their unfolding pathway (Figure 7.2, see p. 258). Experiments that measured the effect of mutations on the unfolding rate and stability of barnase showed that the spontaneous unfolding pathway of barnase begins with a specific sub-domain (formed by the second and third α-helices and some loops packed against the edge of a β-sheet) and follows with the rest of the protein (the N-terminal α-helix and the five-stranded β-sheet located at the C-terminus). The catalyzed unfolding pathway during mitochondrial import is different: the mitochondrial im-

port machinery begins unfolding by unraveling the N-terminal α-helix and then processively unravels the protein to its C-terminus [15]. Thus, mitochondria unfold this precursor protein by unraveling it from its targeting signal [15]. Additional evidence for this model comes from the observation that some model substrates that are stabilized against spontaneous unfolding are not stabilized during unfolding by the mitochondrial translocase [15]. However, stabilizing other proteins can completely prevent their import, and, therefore, mitochondrial unfolding machinery relies on the structure of the precursor protein near the targeting signal.

7.2.3 The Protein Import Machinery of Mitochondria

Import of precursor proteins into the mitochondrial matrix is catalyzed by the translocation machinery of the outer and inner mitochondrial membranes (Figure 7.3). In the outer membrane, components of the TOM complex (translocase of the outer mitochondrial membrane) recognize and translocate precursors. The TOM complex of *N. crassa* and yeast is composed of at least eight proteins [1, 30]. In the inner membrane, two separate TIM complexes (translocase of the inner mitochondrial membrane) are required for import, one for proteins destined for the inner membrane and one for proteins destined for the matrix and inter-membrane space. The structures and roles of the TOM and TIM complexes are discussed in chapter 30.

Import into the mitochondrial matrix requires both an electrochemical gradient across the inner membrane and the action of the Hsp70 homologue found in the mitochondrial matrix (mHsp70). mHsp70 is required for the matrix import of all mitochondrial proteins [31–33] and interacts directly with translocating precursors. The TIM complex recruits mHsp70 to the import site and facilitates the stepwise movement of the polypeptide across the translocation pore [34, 35]. The electrical potential across the inner membrane was found to act on pre-sequences of precursor proteins before they interact with the mHsp70 physically [36], and the potential is required for import of all proteins into the matrix [37, 38]. Respiring yeast mitochondria maintain an electrical potential of approximately 150 mV across the inner membrane, which is positive at the outer surface and negative at the inner surface. The electrical potential performs two main functions in precursor unfolding and import. First, it enhances the dimerization of Tim23, a component of the import channel, presumably to augment the interaction between the targeting signal and the import channel. Second, it unfolds precursor proteins. Reducing the electrical potential with an uncoupler of respiration reduces the import rate of precursors whose targeting sequence reaches mitochondrial inner membranes [39]. The slower import rate is due to a reduced unfolding activity. Experiments in which the charges of the mitochondrial targeting sequences are changed by mutating the sequence suggest that the potential acts directly on the charged targeting sequence [39]. Precursors with targeting sequences of approximately 50 amino acids or more can interact with mHsp70 while the mature domain is still folded at the mitochondrial surface. For these precursors the membrane potential is required

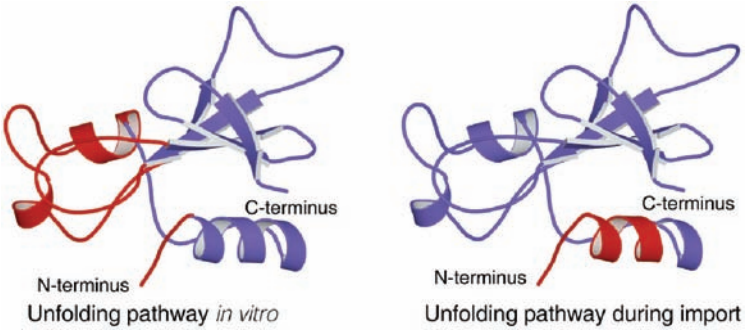

Fig. 7.2. Unfolding pathways of barnase. Structure of barnase, color-coded according to the order in which structure is lost (left) during spontaneous global unfolding in vitro and (right) during import into mitochondria. The parts of the structure shown in red unfold early, whereas those shown in blue unfold late. Figure reproduced from Ref. [15] with permission.

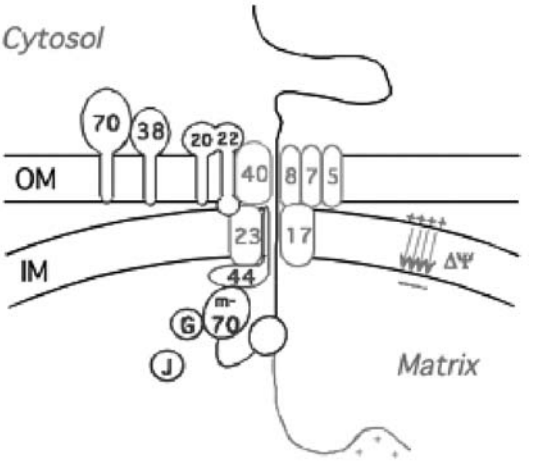

Fig. 7.3. The mitochondrial protein import machinery. Proteins in the outer/inner membrane are called Tom/Tim, followed by the number indicated in the figure. The number reflects their approximate molecular weight. During import, precursor proteins first interact with the Tom20 and Tom22 receptors through their targeting sequence. The Tom70 receptor binds precursors associated with cytosolic chaperones. Targeting sequences insert into the Tom40 channel and pass through the Tom23 complex into the matrix. Import into the matrix always requires an electrical potential across the inner membrane and the ATP-dependent action of mHsp70. mHsp70 is found bound to the import machinery through Tim44 and free in the matrix. Precursors begin to interact with mHsp70 while they are still associated with the import channels. G, J: mGrpE, Mdj1, two co-chaperones of Hsp70; IM/OM: inner/outer membrane; m-70: mHsp70. Figure reproduced from Ref. [40] with permission.

only for the insertion of the targeting sequence in to the import channel. Unfolding can be induced by mHsp70 in the absence of an electrical potential. The actual length of natural targeting sequences is uncertain. However, databases indicate that the mean cleavage site is at amino acid position 31. This suggests that most targeting signals are too short to interact with mHsp70 before they unfold [40].

7.2.4 Specificity of Unfolding

The susceptibility to unfolding by the mitochondrial import machinery depends on the structure of the preprotein near the targeting signal. When a collection of random peptides were attached to the N-terminus of subunit IV of cytochrome oxidase (COX IV), approximately a quarter of these constructs were imported into mitochondria [41]. In addition, there have been some reports that the mature domain affects import efficiency [42, 43]. Indeed, when proteins of different stabilities and folds are attached to the same targeting sequence, the import efficiencies of these constructs vary considerably, with precursors that are more difficult to unfold importing less efficiently [15, 23, 44, 45]. Together, these results suggest that the susceptibility of the mature domain of precursor proteins to unfolding contributes to the specificity of protein import into mitochondria.

7.2.5 Protein Import into Other Cellular Compartments

Unfolding may also play an important role in protein import into ER and chloroplasts. Chloroplasts are surrounded by two membranes and are divided into two compartments, the stroma and the thylakoids. Most chloroplast proteins are imported posttranslationally from the cytosol and, presumably, some precursors will fold before translocation. However, in the case of chloroplast protein import, it is not clear whether unfolding is always required. For example, one study indicates that chloroplast membranes can import small folded proteins [46]. On the other hand, import is blocked when large proteins or protein complexes are stabilized against unfolding [47–50]. Within the chloroplast, translocation of proteins from stroma into thylakoids occurs through two different machineries that seem to impose different steric requirements on the transporting proteins. One subset of proteins uses the ATP-dependent Sec system [51], while other proteins are transported by a mechanism that does not require ATP but is instead dependent on the pH gradient across the thylakoidal membrane [51]. The Sec-related pathway requires protein unfolding, whereas the ΔpH-dependent pathway tolerates folded proteins.

Protein translocation into the endoplasmic reticulum generally does not require unfolding because it occurs mostly co-translationally. However, at least in *S. cerevisiae*, there are examples of posttranslational translocation, and it is possible that some of these precursor proteins fold in the cytosol. The internal diameter of the translocon complex is 20–40 Å at its narrowest point, and experiments suggest that several proteins have to be in an unfolded conformation to fit through the translo-

cation channel [9, 52]. Together these findings suggest that protein unfolding may play a role in the import of a subset of ER-associated proteins. The ER import machinery resembles those of mitochondria and chloroplasts in that an Hsp70 homologue is located at the exit of the protein import channel [53].

Protein unfolding may also play a key role in ER retro-translocation of misfolded or unassembled polypeptides back into the cytoplasm for degradation [54–56]. Misfolded or unassembled polypeptides inside the ER are directed to proteasome-mediated degradation in the cytoplasm in a process called ER-associated degradation (ERAD) [54, 56]. During this process, the polypeptide chain may be translocated backwards into the cytoplasm by a pulling force generated by cytoplasmic chaperones such as CDC48/p97/VCP, by proteins involved in the ubiquitination process, or by the proteasome itself [55, 57–59].

7.3 Protein Unfolding and Degradation by ATP-dependent Proteases

Protein unfolding and degradation by ATP-dependent proteases is a key step in many biological processes, including signal transduction, cell cycle control, DNA transcription, DNA repair, angiogenesis, and apoptosis. In eukaryotic cells, the majority of regulated protein degradation is mediated by the ubiquitin-proteasome pathway [60]. The proteasome also removes proteins that are misfolded as a result of mutations and various stresses. In prokaryotes, similar functions are performed by functional analogues of the proteasome such as ClpAP, ClpXP, Lon, and FtsH (on the membrane) and HslUV (ClpYQ) proteases [60–63]. Unfolding processes driven by ATP-dependent proteases and by the mitochondrial import machinery exhibit several similarities. Both processes involve the hydrolysis of ATP, and unfolding is coupled to the movement of the extended polypeptide chain through a narrow channel. We will now examine protein unfolding by ATP-dependent proteases and draw generalizations about protein unfolding in the cell.

7.3.1 Structural Considerations of Unfoldases Associated With Degradation

ATP-dependent proteases share similar overall structures [60, 61, 63–67]. The 26S eukaryotic proteasome is a 2-MDa structure composed of two structurally and functionally separated subunits: a catalytic subunit, called the 20S core particle, and the ATPase subunit, called the 19S regulatory particle [60, 64]. The core particle is composed of four stacked heptameric rings, two of which consist of α-subunits and two of β-subunits. The two β-rings are stacked together at the core of the proteasome and contain the active sites for proteolysis. One ring of α-subunits flanks the β-rings on each side. Together, the α- and β-rings form a cylindrical structure that is flanked on each side by the regulatory subunit. The 19S cap, which has a molecular weight of 700 kDa, contains 18 different subunits that rec-

ognize ubiquitinated proteins and present the substrate proteins to the proteolytic core in an ATP-dependent manner [60, 61].

Substrate proteins are targeted to the proteasome by the covalent attachment of multiple ubiquitin chains to their surface-exposed lysine residues [68]. A cascade of reactions, catalyzed by ubiquitin-activating enzyme (E1), ubiquitin-conjugating enzymes (E2), and ubiquitin ligases (E3), forms isopeptide linkages between the C-terminus of the ubiquitin moieties and the ε-amino group of lysine residues on the acceptor protein. Successive rounds of ubiquitination result in the formation of polyubiquitin chains, and at least four ubiquitins are required for efficient targeting [69]. The polyubiquitin chains are recognized by the S5a subunit of the 19S cap of the 26S proteasome [70]. However, at least one protein (ornithine decarboxylase [71]) has been identified that is targeted to the proteasome without ubiquitin modification. In addition, the 19S regulatory cap can interact with misfolded or natively unfolded intermediates in an ubiquitin-independent manner [72].

Other ATP-dependent proteases, such as ClpAP and ClpXP, share structural similarities to the 26S proteasome (Figure 7.4). ClpAP and ClpXP are elongated cylindrical complexes composed of hexameric ATPase single rings (ClpA and ClpX), juxtaposed to a proteolytic component of two stacked heptameric rings (ClpP) [60, 61, 63, 65, 66]. The active sites of proteolysis in the Clp proteases are located on the inside of the ClpP ring. Lon and the HflB proteases, unlike other ATP-dependent proteases, are homo-oligomeric complexes. However, they share the overall cylindrical structure of other proteases, with the active sites buried deep inside the central cavity [61, 62, 67].

Substrates of prokaryotic ATP-dependent proteases are recognized through their targeting tags, which are mostly N- or C-terminal extensions of varying length. The sequences of these targeting signals often show some homology, but definitive consensus sequences for these targeting signals are still being determined and may be specific to the various proteases. Interestingly, there are cases where specific targeting signals can specify more than one ATP-dependent protease. For example, substrates tagged with the ssrA peptide are targeted to ClpAP, ClpXP, and HflB [73–75]. Yet ClpAP, ClpXP, and HflB can also possess specific substrate preferences [62, 76, 77]. Specificity is often conferred by adaptor proteins, which bind substrates and deliver them in a *trans*-targeting mechanism to the protease [78].

7.3.2
Unfolding Is Required for Degradation by ATP-dependent Proteases

A requirement for unfolding for degradation is imposed by the sequestration of the proteolytic active sites deep inside the protease structure. Access to these active sites is possible only through a narrow channel that runs along the long axis of the cylindrical particle [63, 79]. The entrance to the degradation channel of the proteasome is also blocked by the N-termini of the α-subunits at the small end of the cylindrical particle [79]. The requirement for unfolding during proteasome degradation is demonstrated experimentally by biochemical studies where stabilizing the folded state of the substrate protein, DHFR, prevented its degradation [80].

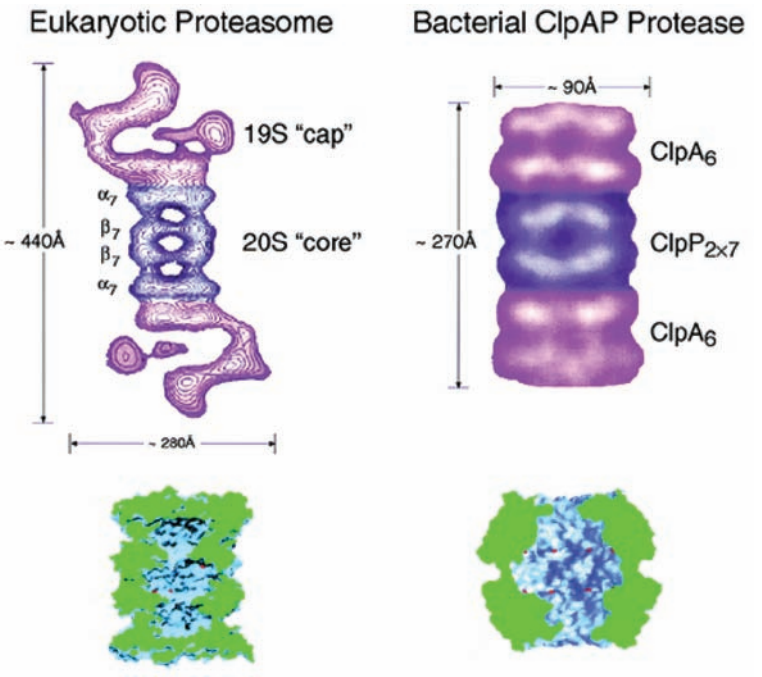

Fig. 7.4. Structures of the proteasome and ClpAP. Top left: Structure of the eukaryotic proteasome holo-enzyme from *Xenopus laevis* as determined by electron microscopy; the core particle is shown in blue, and the ATPase caps are in pink. Bottom left: Medial sections of the proteasome core particles from yeast as determined by crystallography; active sites of proteolysis are indicated by red dots, and the slice surface is shown in green. Top right: Structure of the ClpAP holo-enzyme as determined by electron microscopy. Bottom right: Structure of the ClpP particle, the proteolytic core of ClpAP, as determined by crystallography. Figure reproduced from Ref. [62] with permission.

7.3.3
The Role of ATP and Models of Protein Unfolding

Degradation by ATP-dependent proteases requires ATP, which serves to power the unfolding and translocation of the polypeptide chain from the outer surface of the protease to the proteolytic sites deep inside the cylindrical structure [61, 63, 65, 81, 82] (Figure 7.5). Additionally, ATP is required for the cooperative association of the cap structures at both ends of the catalytic cylinder [81, 82]. Not only ATP binding but also ATP hydrolysis is required for proteolysis to occur [81, 82], and there is a direct relationship between the amount of ATP hydrolyzed by ClpXP and the length and stability of the substrate [83]. The exact mechanism by which ATP binding and ATP hydrolysis induce unfolding has not yet been elucidated. Two general models have emerged for the mechanism of ATP-driven unfolding and translocation of substrate proteins into the proteolytic chamber. The first model proposes that ATP drives the translocation of the substrate's polypeptide chain from the

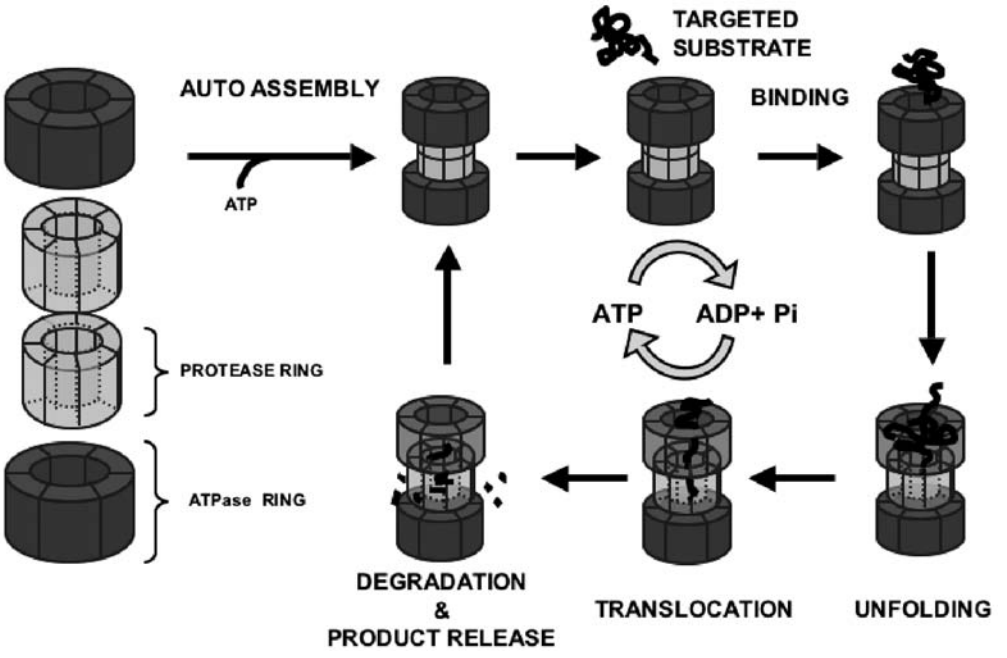

Fig. 7.5. The process of protein unfolding and degradation by ATP-dependent proteases. ATP binding and hydrolysis are required for the assembly of a functional ATP-dependent protease. Targeted substrates for degradation bind noncovalently to the ATPase particle. Repeated cycles of ATP binding and hydrolysis drive unfolding of the substrate within the ATPase component. The unfolded polypeptide chain is fed into the proteolytic chamber in a process called translocation. Subsequently, the polypeptide reaches the active sites of proteolysis, where it is rapidly degraded and released. The assembled ATP-dependent protease can unfold and degrade several substrates before disassembly.

substrate-binding site at the ends of the cylindrical protease particle to the proteolytic chamber where degradation occurs. The translocation would result in a pulling force on the native polypeptide, which could help to collapse the structure of the substrate [83, 84, 85]. An alternative model proposes that unfolding is not coupled to translocation into the proteolytic compartment [86]. Instead, unfolding occurs on the surface of the ATPase ring, where ATP binding and hydrolysis cause the substrate-binding domains to undergo concerted conformational changes that exert mechanical strain on the bound protein and result in unfolding. The proposed role of ATP in this model draws parallels to the role of ATP in the action of the molecular chaperone GroEL [87–89].

7.3.4
Proteins Are Unfolded Sequentially and Processively

ATP-dependent proteases degrade their substrates by sequentially unraveling them from the degradation signal [84, 85]. Sequential degradation was demonstrated us-

ing multi-domain proteins consisting of barnase and DHFR. Experiments showed that stabilizing the domain closer to the degradation tag by tightly binding ligands protected the downstream domain from proteolysis. The sequential degradation of substrates by ClpAP was also demonstrated by FRET experiments [85]. In these experiments the energy donor was attached to the protease subunits of ClpAP and a fluorescence acceptor was attached to either the N-terminus or the C-terminus of substrate proteins [85]. Kinetic analysis of ATP-triggered reactions showed that the probe near the degradation signal interacted with the protease probe before the probe farther away from the degradation signal did, reflecting a directional translocation of substrates from ClpA to ClpP. In addition, biochemical and electron microscopy experiments demonstrated the sequential interaction of substrate proteins first with the ATPase subunits and then with the protease subunits of ClpAP and ClpXP [90–92].

7.3.5
The Influence of Substrate Structure on the Degradation Process

The local structure of the protein near the degradation tag determines the ability of the protein to be degraded [83, 84]. This is best exemplified by studies with circular permutants of DHFR where the original N- and C-termini are connected by a short series of glycine residues and the structure is disrupted to create new termini [93]. The resulting proteins have almost identical structure and enzymatic activities [84, 93] and differ primarily in the location of the signals. However, these circular permutants showed substantially different susceptibilities towards unfolding and degradation by ATP-dependent proteases [84]. In these studies, susceptibility to unfolding correlated with the local structure adjacent to the targeting signal, not with the stability against spontaneous global unfolding. When the degradation signal leads into a stretch of polypeptide chain that forms an α-helix or a surface loop, the proteins were unfolded and degraded efficiently. Substrates were more difficult to unfold and degrade when the degradation signal led into an internal β-strand [84].

7.3.6
Unfolding by Pulling

The susceptibility to unfolding correlates with neither the global thermodynamic stability nor the kinetic stability determined by in vitro experiments [94]. In a study using titin, it was found that only mutations near the degradation signal influence unfolding by ClpXP [83]. Mutations elsewhere have no effect. These studies, together with experiments demonstrating the sequential unfolding and degradation of proteins, suggest that ATP-dependent proteases catalyze unfolding by altering the unfolding pathway of their substrates, just as mitochondria unfold proteins [83, 84].

Although it is clear that unfolding occurs as the polypeptide chain is translocated

into the proteolytic chamber, the mechanics of force exertion are still under investigation. In unfolding during both translocation and the degradation process, the unraveling mechanism is more reminiscent of unfolding by atomic force microscopy than of unfolding by chemical denaturants or heat. The spontaneous unfolding pathway of proteins by chaotropic agents follows a global mechanism. When unfolded by AFM, substrate proteins are unfolded by pulling mechanically on the polypeptide chain [95–99]. However, the processes of protein unfolding during AFM experiments and during protein degradation and translocation are not identical [79, 100]. During AFM experiments, a mechanical force is applied continuously from both ends of the polypeptide chain until the protein unfolds. This resembles a stretching force. In unfolding mediated by ATP-dependent proteases and mitochondrial import machinery, a force would be applied by pulling the substrate against the sterically restrictive entrance of the translocation channel. In addition, studies on ClpXP-mediated protein unfolding and degradation suggest that the unfolding force is applied iteratively on the substrates, possibly by tugging at them repeatedly [83].

7.3.7 Specificity of Degradation

The fact that the susceptibility to degradation depends on the local structure near the degradation tag may contribute to the specificity of degradation. This particular mechanism may have several physiological consequences. First, it allows the proteases to degrade specific subunits of a multi-protein complex without affecting other components. For example, the proteasome specifically degrades the cell-cycle inhibitor Sic1 while it is associated with the yeast cyclin-cyclin-dependent kinase (CDK) complex to release active CDK [101]. Second, the observation that β-structures are difficult to unfold is important in the context of diseases that are characterized by the accumulation of large intracellular protein aggregates, such as Parkinson's and Huntington's diseases [102, 103]. Protein aggregates are found associated with ubiquitin and components of the proteasome, suggesting that the cell tries to degrade the aggregates but is unable to do so. The aggregates associated with amyloid diseases are characterized by the accumulation of long fibers with extensive β-sheet character [104–106]. Third, in multi-domain proteins, differences in susceptibility to unfolding of individual domains will influence the end product of the degradation reaction and may provide a mechanism for processing proteins by partial degradation. Experimental evidence suggests that this mechanism explains the activation of NFκB, which plays a central role in the regulation of immune and inflammatory responses in mammals [84, 107]. The p105 precursor of the p50 subunit of NF-kappa B is processed by proteasome-mediated degradation. The proteasome degrades the domain at the C-terminus of p105 and spares the N-terminal p50 domain. Processing by a partial degradation mechanism may occur elsewhere in the cell. For example, the transcription factors cubitus interruptus in *Drosophila* [108] and Spt23 and Mga2 in yeast [109] are activated by partial proteasome processing.

7.4 Conclusions

Regulated protein unfolding is a critical step in several processes in the cell, including translocation across membranes and degradation by ATP-dependent proteases.

Translocases and ATP-dependent proteases catalyze unfolding using machineries driven by ATP. These machineries denature proteins and translocate their polypeptide chains across the barrier. In both of these processes, the proteins unravel sequentially and processively as the machinery pulls the polypeptide chain at one end, resulting in a cooperative collapse of the protein. As a consequence, the susceptibility of a protein to unfolding depends on its local structure as well as on its overall stability.

7.5 Experimental Protocols

7.5.1 Size of Import Channels in the Outer and Inner Membranes of Mitochondria

The diameters of the import channels in the outer and inner membranes of purified yeast mitochondria are measured by using precursor proteins in which the C-termini are cross-linked to rigid compounds of specific dimensions [6]. The effects of these modifications on translocation across the outer and inner mitochondrial membranes are then determined.

Radioactive precursor proteins are synthesized by in vitro transcription and translation in a rabbit reticulocyte lysate supplemented with [^{35}S] methionine (Promega). Ribosomes and their associated incompletely translated polypeptide chains are removed by centrifugation at 150 000 *g* for 15 min. Precursor proteins are then partially purified by precipitation with 50% (v/v) saturated ammonium sulfate for at least 30 min on ice, pelleted by centrifugation at 20 800 *g* for 15 min, and resuspended in import buffer (50 mM HEPES-KOH, pH 7.4, 50 mM KCl, 10 mM $MgCl_2$, 2 mM KH_2PO_4, 5 mM unlabeled methionine, 1 mg mL^{-1} fatty acid-free BSA). Size probes (Monomaleimido-Nanogold and Monomaleimido-Undecagold) are then attached to barnase precursors containing a single cysteine residue at their C-termini. After incubation for 2 h at room temperature, modified precursors are used directly in the import experiments. To assess the diameter of the inner-membrane protein import pore, the outer membrane of mitochondria is ruptured by hypo-osmotic shock before the import experiments.

7.5.2 Structure of Precursor Proteins During Import into Mitochondria

The structure of precursor proteins during translocation into mitochondria is determined by looking into the import kinetics of a series of precursors. These precursors have a β-sheet where two, three, four, or five of the strands are chemically

cross-linked by disulfide bridges. Because mitochondria have no mechanism for reducing disulfides at their surface, this modification makes it impossible for the import machinery to separate the cross-linked strands.

Radioactive precursor proteins are synthesized by in vitro transcription and translation in rabbit reticulocyte lysate. To induce disulfide bridge formation between cysteine residues, precursors are oxidized with 10 mM $K_3Fe(CN)_6$ for 2 min at room temperature before precipitation with ammonium sulfate. To test for disulfide bridge formation, unrelated cysteine residues are modified with 4-acetamido-4′-maleididylstilbene-2,2′ disulfonic acid (stilbene disulfonate maleimide [SDSM]) and detected through a change in mobility of the modified proteins in SDS-PAGE.

7.5.3
Import of Barnase Mutants

Determining the import characteristics of a series of barnase mutants allows understanding of the pathway of unfolding of this substrate during import. Unfolding of barnase in free solution follows a defined pathway, with the sub-domain formed by the second and third α-helices and several loops packing against the edges of the β-sheet unfolding before the remaining portion of the protein. In contrast, import-driven unfolding begins at the N-terminus of the protein; therefore, mutations that destabilize this part of the protein accelerate the unfolding. Additionally, stabilizing the N-terminal portion by cross-linking to the rest of the protein slows down the import rate. To lock the N-terminus, residues 5 and 78 are mutated to cysteines and a disulfide bridge is induced by oxidation with 10 mM $K_3Fe(CN)_6$. Import experiments are then performed. The stability of cross-linked precursors under import conditions is assessed by proteinase K digestion. After incubation of the substrate with proteinase K at 35°C, the protease is inhibited with 1 mM phenylmethylsulfonyl fluoride and the sample is analyzed by SDS-PAGE and electronic autoradiography.

The role of mitochondrial membrane potential in precursor unfolding and import is tested by measuring the effect of CCCP (cyanide *m*-chlorophenylhydrazone), an uncoupler of respiration, on the import rates of precursor proteins. Reducing the membrane potential with CCCP leads to a progressive reduction in the initial import rates of a barnase precursor whose rate of import is limited by the unfolding step. For titrating the protonophore CCCP, 0.4 mM NADH and different amounts of CCCP are added to 0.4 mg mL^{-1} mitochondria in import mix. Oligomycin (5 g mL^{-1}) is added to prevent the reverse action of F_oF_1-ATPase to generate membrane potential. The import mix is incubated at 25°C for 10 min. Import experiments are then performed.

7.5.4
Protein Degradation by ATP-dependent Proteases

Proteins to be degraded by proteasome are targeted by the covalent attachment of ubiquitin; one mechanism by which ubiquitination can occur is the N-end rule

pathway. Ubiquitination occurs on two lysine residues in a 40-amino-acid extension at the N-terminus of the substrate proteins. This system can be used to target model proteins to proteasome in reticulocyte lysate [80, 84]. Substrate translated in vitro is added to ATP-depleted reticulocyte lysate supplemented with 1 mM DTT and is incubated for 20 min at 25°C to allow cleavage of the substrate protein. Ubiquitination and degradation are initiated by addition of ATP and an ATP-regenerating system (0.5 mM ATP, 10 mM creatine phosphate, 0.1 mg mL^{-1} creatine phosphokinase; final concentrations) and incubation is continued at 25 °C. At designated time points, aliquots are transferred to ice-cold 5% trichloroacetic acid (TCA), and the TCA-insoluble fractions are analyzed by SDS-PAGE and quantified by electronic autoradiography.

Proteins are targeted to prokaryotic proteases by the attachment of specific degradation signals to the N- or C-terminus of the polypeptide chain. A typical degradation experiment is performed in a total of 120 μL degradation buffer (50 mM Tris-HCl pH 8.0, 100 mM KCl, 0.02% Triton X-100, 20 mM $MgCl_2$). Substrate protein is added to 100 μL prewarmed degradation buffer containing 4 mM ATP, 1 mM DTT, 20 mM creatine phosphate, 0.1 mg mL^{-1} creatine kinase, and appropriate concentration of the protease.

7.5.5
Use of Multi-domain Substrates

The clever use of multi-domain substrates in degradation experiments helps to analyze the mechanism of action of different unfoldases associated with various cellular proteases. Stabilizing individual domains against unfolding by ligand binding helps to prevent the unfolding and degradation of domains away from the degradation signal. A fusion protein consisting of the degradation tag followed first by DHFR and then by barnase is fully degraded by different proteases in both the presence and absence of the barnase ligand barstar. However, when DHFR is stabilized by a ligand, neither DHFR nor barnase is degraded. Thus, the DHFR domain protects the downstream barnase from degradation. Similarly, in a construct that consists of the degradation tag followed by barnase and then DHFR, the fusion protein is fully degraded in the presence or absence of the barnase ligand. However, in this construct, stabilizing DHFR no longer protects barnase from degradation. This mechanism implies that in multi-domain proteins, the protease would unravel domains sequentially from the degradation tag.

7.5.6
Studies Using Circular Permutants

The observation that different ATP-dependent proteases degrade multi-domain proteins sequentially suggests that the structure adjacent to the degradation tag influences its susceptibility to unfold. The use of circular permutants helps to determine which aspect of the substrate structure is easily unraveled by the protease. In circular permutants, the original N- and C-termini are connected by a linker, and the structure is interrupted to produce new N- and C-termini. The resulting pro-

teins have almost identical structures and similar enzymatic activities, differing only in the location of the N- and C-termini within their structure [93]. In the easily digested proteins, the degradation signals lead directly into α-helices or surface loops, whereas in the structures that can be too stable to be degraded, the degradation tags are attached to β-strands. These findings implicate that the local structure near the degradation signal strongly influences the ability of a protein to be degraded by an ATP-dependent protease.

References

1 Neupert, W. (1997). Protein import into mitochondria. *Annu. Rev. Biochem.* **66**, 863–917.

2 Pfanner, N., Craig, E. A. and Honlinger, A. (1997). Mitochondrial preproteins translocase. *Annu Rev Cell Dev Biol.* **13**, 25–51.

3 Neupert, W., Hartl, F. U., Craig, E. A. and Pfanner, N. (1990). How do polypeptides cross the mitochondrial membranes? *Cell*, **63**, 447–450.

4 Kunkele, K. P., Heins, S., Dembowski, M., Nargang, F. E., Benz, R., Thieffry, M., Walz, J., Lill, R., Nussberger, S. and Neupert, W. (1998). The preprotein translocation channel of the outer membrane of mitochondria. *Cell*, **93**, 1009–1019.

5 Hill, K., Model, K., Ryan, M. T., Dietmeier, K., Martin, F., Wagner, R. and Pfanner, N. (1998). Tom40 forms the hydrophilic channel of the mitochondrial import pore for preproteins. *Nature*, **395**, 516–521.

6 Schwartz, M. P. and Matouschek, A. (1999). The dimensions of the protein import channels in the outer and inner mitochondrial membranes. *Proc. Natl. Acad. Sci. USA*, **96**, 13086.

7 Schwartz, M. P., Huang, S. and Matouschek, A. (1999). The structure of precursor proteins during import into mitochondria. *J. Biol. Chem.* **274**, 12759–12764.

8 Truscott, K. N., Kovermann, P., Geissler, A., Merlin, A., Meijer, M., Driessen, A. J., Rassow, J., Pfanner, N. and Wagner, R. (2001). A presequence- and voltage-sensitive channel of the mitochondrial preprotein translocase formed by Tim23. *Nat. Struct. Biol.* **8**, 1074–1082.

9 Zheng, N. and Gierasch, L. M. (1996). Signal sequences: the same yet different. *Cell*, **86**, 849–852.

10 Eilers, M. and Schatz, G. (1986). Binding of a specific ligand inhibits import of a purified precursor protein into mitochondria. *Nature*, **322**, 228–232.

11 Schleyer, M. and Neupert, W. (1985). Transport of proteins into mitochondria: Translocational intermediates spanning contact sites between outer and inner membranes. *Cell*, **43**, 339–350.

12 Vestweber, D. and Schatz, G. (1988). A chimeric mitochondrial precursor protein with internal disulfide bridges blocks import of authentic precursors into mitochondria and allows quantification of import sites. *J. Cell Biol.* **107**, 2037–2043.

13 Netzer, W. and Hartl, F. (1997). Recombination of protein domains facilitated by co-translational folding in eukaryotes. *Nature*, **388**, 343–349.

14 Lin, L., DeMartino, G. N. and Greene, W. C. (1998). Cotranslational biogenesis of NF-κB p50 by the 26S proteasome. *Cell*, **92**, 819–828.

15 Huang, S., Ratliff, K. S., Schwartz, M. P., Spenner, J. M. and Matouschek, A. (1999). Mitochondria unfold precursor proteins by unraveling them from their N-termini. *Nat. Struct. Biol.* **6**, 1132–1138.

16 Endo, T. and Schatz, G. (1988). Latent membrane perturbation activity of a mitochondrial precursor protein is exposed by unfolding. *EMBO. J.* **7**, 1153–1158.

17 Mattingly, Jr., J. R., Iriarte, A. and Martinez-Carrion, M. (1993).

Structural features which control folding of homologous proteins in cell-free translation systems. The effect of a mitochondrial-targeting presequence on aspartate aminotransferase. *J. Biol. Chem.* **268**, 26320–26327.

18 Wienhues, U., Becker, K., Schleyer, M., Guiard, B., Tropschug, M., Horwich, A. L., Pfanner, N. and Neupert, W. (1991). Protein folding causes an arrest of preprotein translocation into mitochondria in vivo. *J. Cell Biol.* **115**, 1601–1609.

19 Bomer, U., Meijer, M., Guiard, B., Dietmeier, K., Pfanner, N. and Rassow, J. (1997). The sorting route of cytochrome b_2 branches from the general mitochondrial import pathway at the preprotein translocase of the inner membrane. *J. Biol. Chem.* **272**, 30439–30446.

20 Mihara, K. and Omura, T. (1996). Cytoplasmic chaperones in precursor targeting to mitochondria: the role of MSF and hsp70. *Trends. Cell. Biol.* **6**, 104–108.

21 Wachter, C., Schatz, G. and Glick, B. S. (1994). Protein import into mitochondria: the requirement for external ATP is precursor-specific whereas intramitochondrial ATP is universally needed for translocation into the matrix. *Mol. Biol. Cell*, **5**, 465–474.

22 Lim, J. H., Martin, F., Guiard, B., Pfanner, N. and Voos, W. (2001). The mitochondrial Hsp70-dependent import system actively unfolds preproteins and shortens the lag phase of translocation. *EMBO J.* **20**, 941–950.

23 Matouschek, A., Azem, A., Ratliff, K., Glick, B. S., Schmid, K. and Schatz, G. (2000). Active unfolding of precursor proteins during mitochondrial protein import. *EMBO J.* **16**, 6727–6736.

24 Muga, A., Mantsch, H. H. and Surewicz, W. K. (1991). Membrane binding induces destabilization of cytochrome *c* structure. *Biochemistry* **30**, 7219–7224.

25 van der Goot, F. G., Gonzalez-Manas, J. M., Lakey, J. H. and Pattus, F. (1991). A 'molten-globule' membrane insertion intermediate of the pore-forming domain of colicin A. *Nature (London)*, **354**, 408–410.

26 de Jongh, H. H., Killian, J. A. and de Kruijff, B. (1992). A water-lipid interface induces a highly dynamic folded state in apocytochrome *c* and cytochrome *c*, which may represent a common folding intermediate. *Biochemistry.* **31**, 1636–1643.

27 Bychkova, V. E., Dujsekina, A. E., Klenin, S. I., Tiktopulo, E. I., Uversky, V. N. and Ptitsyn, O. B. (1996). Molten globule-like state of cytochrome c under conditions simulating those near the membrane surface. *Biochemistry*, **35**, 6058–6063.

28 Ren, J., Kachel, K., Kim, H., Malenbaum, S. E., Collier, R. J. and London, E. (1999). Interaction of diphtheria toxin T domain with molten globule-like proteins and its implications for translocation. *Science*, **284**, 955–957.

29 Huang, S., Murphy, S. and Matouschek, A. (2000). Effect of the protein import machinery at the mitochondrial surface on precursor stability. *Proc. Natl. Acad. Sci. USA*, **97**, 12991–12996.

30 Schneider, H. C., Berthold, J., Bauer, M. F., Dietmeier, K. and Guiard, B. (1994). Mitochondrial Hsp70/MIM44 complex facilitates protein import. *Nature*, **371**, 768–774.

31 Kang, P. L., Ostermann, J., Shilling, J., Neupert, W., Craig, E. A. and Pfanner, N. (1990). Requirement for hsp70 in the mitochondrial matrix for translocation and folding of precursor proteins. *Nature*, **348**, 137–143.

32 Gambill, B. D., Voos, W., Kang, P. J., Miao, B., Langer, T., Craig, E. A. and Pfanner, N. (1993). A dual role for mitochondrial heat shock protein 70 in membrane translocation of preproteins. *J. Cell Biol.* **123**, 109–117.

33 Kronidou, N. G., Oppliger, W., Bolliger, L., Hannavy, K. and Glick, B. S. (1994). Dynamic interaction between Isp45 and mitochondrial

hsp70 in the protein import system of the yeast mitochondrial inner membrane. *Proc. Natl. Acad. Sci. USA*, **91**, 12818–12822.

34 Hartl, F. U. (1996). Molecular chaperones in cellular protein folding. *Nature*, **381**, 571–579.

35 Cyr, D. M., Langer, T. and Douglas, M. G. (1994). A matrix ATP requirement for presequence translocation across the inner membrane of mitochondria. *Trends Biochem. Sci.* **19**, 176–181.

36 Martin, J., Mahlke, K. and Pfanner, N. (1991) Role of an energized inner membrane in mitochondrial protein import: $\Delta\varphi$ drives the movement of pre-sequences. *J. Biol. Chem.* **266**, 18051–18057.

37 Schleyer, M., Schmidt, B. and Neupert, W. (1982). Requirement of a membrane potential for the post-translational transfer of proteins into mitochondria. *Eur. J. Biochem.* **125**, 109–116.

38 Gasser, S. M., Daum, G. and Schatz, G. (1982). Import of proteins into mitochondria. Energy-dependent uptake of precursors by isolated mitochondria. *J. Biol. Chem.* **257**, 13034–13041.

39 Huang, S., Ratliff, K. S. and Matouschek, A. (2002). Protein unfolding by the mitochondrial membrane potential. *Nature Struct. Biol.* **9(4)**, 301–307.

40 Matouschek, A. (2003). Protein unfolding – an important process in vivo? *Curr. Opin. Struct. Biol.* **13(1)**, 98–109.

41 Lemire, B. D., Fankhauser, C., Baker, A. and Schatz, G. (1989). The mitochondrial targeting function of randomly generated peptide sequences correlates with predicted helical amphiphilicity. *J. Biol. Chem.* **264**, 20206–20215.

42 Van Steeg, H., Oudshoorn, P., Van Hell, B., Polman, J. E. and Grivell, L. A. (1986). Targeting efficiency of a mitochondrial pre-sequence is dependent on the passenger protein. *EMBO J.* **5**, 3643–3650.

43 Verner, K. and Lemire, B. D. (1989). Tight folding of a passenger protein can interfere with the targeting function of a mitochondrial pre-sequence. *EMBO J.* **8**, 1491–1495.

44 Vestweber, D. and Schatz, G. (1988). Point mutations destabilizing a precursor protein enhance its post-translational import into mitochondria. *EMBO J.* **7**, 1147–1151.

45 Eilers, M., Hwang, S. and Schatz, G. (1988). Unfolding and refolding of a purified precursor protein during import into isolated mitochondria. *EMBO J.* **7**, 1139–1145.

46 Clark, S. A. and Theg, S. M. (1997). A folded protein can be transported across the chloroplast envelope and thylakoid membranes. *Mol. Biol. Cell*, **8**, 923–934.

47 Guera, A., America, T., van Waas, M. and Weisbeek, P. J. (1993). A strong protein unfolding activity is associated with the binding of precursor chloroplast proteins to chloroplast envelopes. *Plant Mol. Biol.* **23**, 309–324.

48 America, T., Hageman, J., Guera, A., Rook, F., Archer, K., Keegstra, K. and Weisbeek, P. (1994). Methotrexate does not block import of a DHFR fusion protein into chloroplasts. *Plant Mol. Biol.* **24**, 283–294.

49 Wu, C., Seibert, F. S. and Ko, K. (1994). Identification of chloroplast proteins in close physical proximity to a partially translocated chimeric precursor protein. *J. Biol. Chem.* **269**, 32264–32271.

50 della-Cioppa, G. and Kishore, G. (1988). Import of precursor protein is inhibited by the herbicide Glyphosate. *EMBO. J.* **7**, 1299–1305.

51 Endo, T., Kawakami, M., Goto, A., America, T., Weisbeek, P. and Nakai, M. (1994). Chloroplast protein import. Chloroplast envelopes and thylakoids have different abilities to unfold proteins. *Eur. J. Biochem.* **225**, 403–409.

52 Muller, G. and Zimmermann, R. (1988). Import of honeybee pre-promelittin into the endoplasmic reticulum: energy requirements for

membrane insertion. *EMBO J.* **7**, 639–648.

53 Schatz, G. and Dobberstein, B. (1996). Common principles of protein translocation across membranes. *Science*, **271**, 1519–1526.

54 Johnson, A. E. and Haigh, N. G. (2000). The ER translocon and retrotranslocon: is the shift into reverse manual or automatic? *Cell*, **102**, 709–712.

55 Brodsky, J. L., Hamamoto, S., Feldheim, D., Schekman, R. (1993). Reconstitution of protein translocation from solubilized yeast membranes reveals topologically distinct roles for BiP and cytosolic Hsc70. *J. Cell Biol.* **120**, 95–102.

56 Plemper, R. K. and Wolf, D. H. (1999). Retrograde protein translocation: ERADication of secretory proteins in health and disease. *Trends Biochem. Sci.* **24**, 266–270.

57 Haigh, N. G. and Johnson, A. E. (2002). A new role for BiP: closing the aqueous translocon pore during protein integration into the ER membrane. *J Cell Biol.* **156**, 261–270.

58 Hamman, B. D., Hendershot, L. M. and Johnson, A. E. (1998). BiP maintains the permeability barrier of the ER membrane by sealing the lumenal end of the translocation pore before and early in translocation. *Cell*, **92**, 747–758.

59 Ooi, C. E. and Weiss, J. (1992). Bidirectional movement of a nascent polypeptide across microsomal membranes reveals requirements for vectorial translocation of proteins. *Cell*, **71**, 87–96.

60 Wickner, S., Maurizi, M. R. and Gottesman, S. (1999). Posttranslational quality control: folding, refolding, and degrading proteins. *Science*, **286**, 1888–1893.

61 Lupas, A., Flanagan, J. M., Tamura, T. and Baumeister, W. (1997). Self-compartmentalizing proteases. *Trends Biochem. Sci.* **22**, 399–404.

62 Larsen, C. N. and Finley, D. (1997). Protein translocation channels in the proteasome and other proteases. *Cell*, **91**, 431–434.

63 Wang, J., Hartling, J. A. and Flanagan, J. M. (1997). The structure of ClpP at 2.3 A resolution suggests a model for ATP-dependent proteolysis. *Cell*, **91(4)**, 447–456.

64 Lowe, J., Stock, D., Jap, B., Zwickl, P., Baumeister, W. and Huber, R. (1995). Crystal structure of the 20S proteasome from the archaeon T. acidophilum at 3.4 A resolution. *Science*, **268(5210)**, 533–9.

65 Grimaud, R., Kessel, M., Beuron, F., Steven, A. C. and Maurizi, M. R. (1998). Enzymatic and structural similarities between the Escherichia coli ATP-dependent proteases, ClpXP and ClpAP. *J Biol Chem*, **273(20)**, 12476–81.

66 Wang, J., Hartling, J. A. and Flanagan, J. M. (1998). Crystal structure determination of Escherichia coli ClpP starting from an EM-derived mask. *J. Struct Biol.* **124(2–3)**, 151–63.

67 Sousa, M. C., Trame, C. B., Tsuruta, H., Wilbanks, S. M., Reddy, V. S., McKay, D. B. (2000). Crystal and solution structures of an HslUV protease-chaperone complex. *Cell*, **103(4)**, 633–43.

68 Ciechanover, A. (1998). The ubiquitin-proteasome pathway: on protein death and cell life. *EMBO J.* **17**, 7151–7160.

69 Thrower, J. S., Hoffman, L., Rechsteiner, M., Pickart, C. M. (2000). Recognition of the polyubiquitin proteolytic signal. *EMBO. J.* **19(1)**, 94–102.

70 Lam, Y. A., Lawson, T. G., Velayutham, M., Zweier, J. L. and Pickart, C. M. (2002). A proteasomal ATPase subunit recognizes the polyubiquitin degradation signal. *Nature*, **416**, pp. 763–766.

71 Zhang, M., Pickart, C. and Coffino, P. (2003). Determinants of proteasome recognition of ornithine decarboxylase, a ubiquitin-independent substrate. *EMBO. J.* **22(7)**, 1488–1496.

72 Braun, B. C. et al. (1999). The base of the proteasome regulatory particle exhibits chaperone-like activity. *Nature Cell Biol.* **1**, 221–226.

73 Keiler, K. C., Waller, P. R. and

Sauer, R. T. (1996). Role of a peptide tagging system in degradation of proteins synthesized from damaged messenger RNA. *Science*, **16;271**, (5251):990–3.

74 Smith, C. K., Baker, T. A. and Sauer, R. T. (1999). Lon and Clp family proteases and chaperones share homologous substrate-recognition domains. *Proc. Natl. Acad. Sci. USA*, **8;96(12)**, 6678–82.

75 Herman, C., Thevenet, D., Bouloc, P., Walker, G. C. and D'Ari, R. (1998). Degradation of carboxy-terminal-tagged cytoplasmic proteins by the Escherichia coli protease HflB (FtsH). *Genes Dev.* **1;12(9)**:1348–55.

76 Hoskins, J. R., Singh, S. K., Maurizi, M. R. and Wickner, S. (2000). Protein binding and unfolding by the chaperone ClpA and degradation by the protease ClpAP. *Proc. Natl. Acad. Sci. USA*, **97**, 8892–8897.

77 Herman, C., Prakash, S., Lu, C. Z., Matouschek, A. and Gross, C. A. (2003). Lack of a Robust Unfoldase Activity Confers a Unique Level of Substrate Specificity to the Universal AAA Protease FtsH. *Mol. Cell*, **11(3)**, 659–669.

78 Dougan, D. A., Mogk, A., Zeth, K., Turgay, K. and Bukau, B. (2002). AAA+ proteins and substrate recognition, it all depends on their partner in crime. *FEBS Lett.* **529**, 6–10.

79 Groll, M., Ditzel, L., Lowe, J., Stock, D., Bochtler, M., Bartunik, H. D., Huber, R. (1997). Structure of the 20S proteasome from yeast at 2.4 Å resolution. *Nature*, **386**, 463–471.

80 Johnston, J. A., Johnson, E. S., Waller, P. R. H. and Varshavsky, A. (1995). Methotrexate inhibits proteolysis of dihydrofolate reductase by the N-end rule pathway. *J. Biol. Chem.* **270**, 8172–8178.

81 Maurizi, M. R., Singh, S. K., Thompson, M. W., Kessel, M. and Ginsburg, A. (1998). Molecular properties of ClpAP protease of Escherichia coli: ATP-dependent association of ClpA and ClpP. *Biochemistry*, **37(21)**, 7778–7786.

82 Singh, S. K., Guo, F. and Maurizi, M. R. (1999). ClpA and ClpP Remain Associated during Multiple Rounds of ATP-Dependent Protein Degradation by ClpAP Protease. *Biochemistry*, **38**, 14906–14915.

83 Kenniston, J. A., Baker, T. A., Fernandez, J. M., Sauer, R. T. (2003). Linkage between ATP Consumption and Mechanical Unfolding during Protein Processing Reactions of an AAA+ Degradation Machine. *Cell*, **114**, 511–520.

84 Lee, C., Schwartz, M. P., Prakash, S., Iwakura, M. and Matouschek, A. (2001). ATP-dependent proteases degrade their substrates by processively unraveling them from the degradation signal. *Mol. Cell*, **7**, 627–637.

85 Reid, B., G. Fenton, W. A., Horwich, A. L., Weber-Ban, E. U. (2001). ClpA mediates directional translocation of the substrate proteins into the ClpP protease. *Proc. Natl. Acad. Sci. USA*, **98(7)**, 3768–3772.

86 Navon, A. and Goldberg, A. L. (2001). Proteins are unfolded on the surface of the ATPase ring before transport into the proteasome. *Mol. Cell*, **8**, 1339–1349.

87 Saibil, H. R., Horwich, A. L. and Fenton, W. A. (2001). Allostery and protein substrate conformational change during GroEL/GroES-mediated protein folding. *Adv Protein Chem*, **59**, 45–72.

88 Roseman, A. M., Chen, S., White, H., Braig, K. and Saibil, H. R. (1996). The chaperonin ATPase cycle: mechanism of allosteric switching and movements of substrate-binding domains in GroEL. *Cell*, **87(2)**: p. 241–51.

89 Ranson, N. A., Farr, G. W., Roseman, A. M., Gowen, B., Fenton, W. A., Horwich, A. L. and Saibil, H. R. (2001). ATP-bound states of GroEL captured by cryo-electron microscopy. *Cell*, **107(7)**, 869–79.

90 Kim, Y. I., Burton, R. E., Burton, B. M., Sauer, R. T. and Baker, T. A. (2000). Dynamics of substrate denaturation and translocation by the

ClpXP degradation machine. *Mol. Cell*, **5**, 639–648.

91 Hoskins, J. R., Singh, S. K., Maurizi, M. R. and Wickner, S. (2000). Protein binding and unfolding by the chaperone ClpA and degradation by the protease ClpAP. *Proc. Natl. Acad. Sci. USA*, **97**, 8892–8897.

92 Singh, S. K., Grimaud, R., Hoskins, J. R., Wickner, S. and Maurizi, M. R. (2000). Unfolding and internalization of proteins by the ATP-dependent proteases ClpXP and ClpAP. *Proc. Natl. Acad. Sci. USA*, **97**, 8898–8903.

93 Iwakura, M., Nakamura, T., Yamane, C., Maki, K. (2000). Systematic circular permutation of an entire protein reveals essential folding elements. *Nature Struct. Biol.* **7(7)**, 680–585.

94 Burton, R. E., Siddiqui, S. M., Kim, Y. I., Baker, T. A. and Sauer, R. T. (2001). Effects of protein stability and structure on substrate processing by the ClpXP unfolding and degradation machine. *EMBO J.* **20(12)**, 3092–3100.

95 Kellermayer, M. S. Z., Smith, S. B., Granzier, H. L. & Bustamante, C. (1997). Folding-Unfolding Transitions in Single Titin Molecules Characterized with Laser Tweezers. *Science*, **276**, 1112–1116.

96 Rief, M., Gautel, M., Oesterhelt, F., Fernandez, J. M. & Gaub, H. E. (1997). Reversible Unfolding of Individual Titin Immunoglobulin Domains by AFM. *Science*, **276**, 1109–1112.

97 Kellermayer, M. S., Bustamante, C. & Granzier, H. L. (2003). Mechanics and structure of titin oligomers explored with atomic force microscopy. *Biochim. Biophys. Acta*. **1604**, 105–114.

98 Brockwell, D. J., Paci, E., Zinober, R. C., Beddard, G. S., Olmsted, P. D., Smith, D. A., Perham, R. N. & Radford, S. E. (2003). Pulling geometry defines the mechanical resistance of a β-sheet protein. *Nat. Struct. Biol.* **10(9)**, 731–737.

99 Carrion-Vazquez, M., Li, H., Lu, H., Marszalek, P. E., Oberhauser, A. F. & Fernandez, J. M. (2003). The mechanical stability of ubiquitin is linkage dependent. *Nat. Struct. Biol.* **10(9)**, 738–743.

100 Matouschek, A. and Bustamante, C. (2003). Finding a proteins Achilles heel. *Nat. Struct. Biol.* 2003, **13(1)**, 98–109.

101 Verma, R., McDonald, H., Yates, III. J. R. and Deshaies, R. J. (2001). Selective degradation of ubiquitinated Sic1 by purified 26S proteasome yields active S phase cyclin-Cdk. *Mol. Cell*, **8**, 439–448.

102 Sherman, M. Y. and Goldberg, A. L. (2001). Cellular defenses against unfolded proteins: a cell biologist thinks about neurodegenerative diseases. *Neuron*. **29**, 15–32.

103 Rochet, J. C. and Lansbury, Jr., P. T. (2000). Amyloid fibrillogenesis: themes and variations. *Curr. Opin. Struct. Biol.* **10**, 60–68.

104 Sunde, M. and Blake, C. (1997). The structure of amyloid fibrils by electron microscopy and X-ray diffraction. *Adv. Protein Chem.* **50**, 123–159.

105 Jimenez, J. L., Nettleton, E. J., Bouchard, M., Robinson, C. V., Dobson, C. M. and Saibil, H. R. (2002). The protofilament structure of insulin amyloid fibrils. *Proc. Natl. Acad. Sci. USA*, **99**, 9196–9201.

106 Jimenez, J. L., Guijarro, J. I., Orlova, E., Zurdo, J., Dobson, C. M., Sunde, M. and Saibil, H. R. (1999). Cryo-electron microscopy structure of an SH3 amyloid fibril and model of the molecular packing. *EMBO J.* **18**, 815–821.

107 Perkins, N. D. (2000). The Rel/NF-κB family: friend and foe. *Trends Biochem. Sci.* **25**, 434–440.

108 Jiang, J. and Struhl, G. (1998). Regulation of the Hedgehog and Wingless signaling pathways by the F-box/WD40-repeat protein Slimb. *Nature*, **391**, 493–496.

109 Hoppe, T., Matuschewski, K., Rape, M., Schlenker, S., Ulrich, H. D. and Jentsch, S. (2000). Activation of a membrane-bound transcription factor by regulated ubiquitin/proteasome-dependent processing. *Cell*, **102**, 577–586.

8
Natively Disordered Proteins

Gary W. Daughdrill, Gary J. Pielak, Vladimir N. Uversky, Marc S. Cortese, and A. Keith Dunker

8.1
Introduction

To understand natively disordered proteins, it is first important to introduce the structure-function paradigm, which dominates modern protein science. We then discuss the terminology used to describe natively disordered proteins and present a well-documented example of a functionally disordered protein. Finally, we compare the standard structure-function paradigm with structure-function relationships for natively disordered proteins and, from this comparison, suggest an alternative for relating sequence, structure, and function.

8.1.1
The Protein Structure-Function Paradigm

The structure-function paradigm states that the amino acid sequence of a protein determines its 3-D structure and that the function requires the prior formation of this 3-D structure. This view was deeply engrained in protein science long before the 3-D structure of a protein was first glimpsed almost 50 years ago. In 1893 Emil Fischer developed the ''lock-and-key'' hypothesis from his studies on different types of similar enzymes, one of which could hydrolyze α- but not β-glycosidic bonds and another of which could hydrolyze β- but not α-glycosidic bonds [1]. By 1930 it had become clear that globular proteins lose their native biological activity (i.e., they become denatured) when solution conditions are altered by adding heat or solutes. Anson and Mirsky showed in 1925 that denatured hemoglobin could be coaxed back to its native state by changing solution conditions [2]. This reversibility is key because it means that the native protein and the denatured protein can be treated as separate thermodynamic states. Most importantly, this treatment leads directly to the idea that a protein's function is determined by the *definite structure* of the native state. In short, the structure is known to exist because it is destroyed by denaturation. Wu stated as much in 1931, but his work was probably unknown outside China, even though his papers were published in English [3]. The West

Protein Folding Handbook. Part II. Edited by J. Buchner and T. Kiefhaber

ISBN: 3-527-30784-2

had to wait until 1936, when Mirsky and Pauling published their review of protein denaturation [4].

Anfinsen and colleagues used the enzyme ribonuclease to solidify these ideas. Their work led in 1957 to the "thermodynamic hypothesis." Anfinsen wrote [5], "This hypothesis states that the three-dimensional structure of a native protein in its normal physiological milieu is the one in which the Gibbs free energy of the whole system is lowest: that is, the native conformation is determined by the totality of interatomic interactions and hence by the amino acid sequence, in a given environment." Merrifield and colleagues then performed an elegant experiment that drove home the idea; they synthesized ribonuclease in the test tube from the amino acid sequence [6]. Their experiments provided direct evidence that the amino acid sequence determines all other higher-order structure, function, and stability.

As mentioned above, the observation that denaturation is reversible allows the application of equilibrium thermodynamics. It was soon realized that many small globular proteins exist in only two states, the native state or the denatured state. That is, each protein molecule is either completely in the native state or completely in the denatured state. Such two-state behavior leads directly to expressions for the equilibrium constant, K_D, and free energy, ΔG_D, of denaturation:

$$K_D = [D]/[N] \tag{1}$$

$$\Delta G_D = -RT \ln(K_D) \tag{2}$$

where R is the gas constant, T is the absolute temperature, and $[N]$ and $[D]$ represent the concentrations of the native and denatured states, respectively (see chapters 2 and 3 in Part I).

The definition of K_D, Eq. (1), is straightforward, but quantifying K_D is more difficult than defining it. The difficulty arises because K_D usually cannot be quantified at the conditions of interest, i.e., at room temperature in buffered solutions near physiological pH. Specifically, most biophysical techniques can only sensitively measure K_D between values of about 10 and 0.1, but the overwhelmming majority ($> 99.9\%$) of two-state globular protein molecules are in the native state at the conditions of interest. The difficulty can be overcome by extrapolation. Increasing the temperature or adding solutes such as urea or guanidinium chloride pushes K_D into the quantifiable region. Plots of $-RT \ln(K_D)$ versus temperature or solute concentration are then extrapolated back to the unperturbed condition to give ΔG_D at the conditions of interest. Many such studies indicate that small globular proteins have a stability of between about 1 and 10 kcal mol^{-1} at room temperature near neutral pH. We introduced this formal definition of stability so that later we can discuss the idea that the higher-order structure within some intrinsically disordered proteins is simply unstable.

What exactly is higher-order structure? Pauling showed that the protein chain was organized in definite local structures, helices and sheets [7], but it was unclear how these structures interact to form the native state. Because the conceptual accessibility of physical representations is greater than that of thermodynamics, the advent of X-ray crystallography strongly reinforced the sequence-structure-function

paradigm. In 1960, Kendrew and Perutz used X-ray crystallography to reveal the intricate, atomic-level structures of myoglobin [8] and hemoglobin [9], effectively locking in the sequence-to-structure paradigm. The paradigm took on the aura of revealed truth when Phillips solved the first structure of an enzyme, lysozyme, in 1965 [10]. The position of the bound inhibitor revealed the structure of the active site, making it clear that the precise location of the amino acid side chains is what facilitates catalysis.

Given all this evidence, it appeared that the case was closed: the native state of every protein possesses a definite and stable three-dimensional structure, and this structure is required for biological function. But even early on there were worrying observations. Sometimes loops were missing from high-resolution structures, and these loops were known to be required for function [11, 12]. Nuclear magnetic resonance spectroscopy also showed that some proteins with known biological functions did not possess stable, defined structure in solution [13].

Perhaps the most important difference to bear in mind when relating the sequence-structure-function paradigm to intrinsically disordered proteins is the difference between a structural state and a thermodynamic state. The native state of a globular protein is *both* a structural state and thermodynamic state, but the disordered (and denatured) state is *only* a thermodynamic state. That is, all the molecules in a sample of the native state of a globular protein have nearly the same structure, and this structure is what is lost upon denaturation. On the other hand, the denatured state consists of a broad ensemble of molecules – each having a different conformation. Therefore, averaged quantities have different meanings for native and disordered states. For a native globular protein, an averaged quantity, such as the CD signal (see Section 8.2.4), gives information about each molecule in the sample because nearly all the molecules are in the same structural state. For a denatured or disordered protein, an averaged quantity contains information about the ensemble, and this information may or may not be applicable to individual molecules in the sample.

8.1.2
Natively Disordered Proteins

Many proteins carry out function by means of regions that lack specific 3-D structure, existing instead as ensembles of flexible, unorganized molecules. In some cases the proteins are flexible ensembles along their entire lengths, while in other cases only localized regions lack organized structure. Still other proteins contain regions of disorder without ascribed functions, but functions might be associated with these regions at a later date. Whether the lack of specific 3-D structure occurs wholly or in part, such proteins do not fit the standard paradigm that 3-D structure is a prerequisite to function.

Various terms have been used to describe proteins or their regions that fail to form specific 3-D structure, including: flexible [14], mobile [15], partially folded [16], rheomorphic [400], natively denatured [17], natively unfolded [18], intrinsically unstructured [19], and intrinsically disordered [20].

None of these terms or combinations is completely appropriate. ''Flexible,'' ''mo-

bile,'' and ''partially folded'' have the longest histories and most extensive use; however, all three of these terms are used in a variety of ways, including many that are not associated with proteins that exist as structural ensembles under apparently native conditions. For example, ordered regions with high B factors are often called flexible or mobile. ''Partially folded'' is often used to describe transient intermediates involved in protein folding. With regard to the term ''natively,'' it is difficult to know whether a protein is in its native state. Even when under apparently physiological conditions, a protein might fail to acquire a specific 3-D structure due to the absence of a critical ligand or because the crowded conditions inside the cell are needed to promote folding. Because of such uncertainties, ''intrinsically'' is often chosen over ''natively.'' Unfolded and denatured are often used interchangeably, so the oxymoron ''natively denatured'' has a certain appeal but has not gained significant usage. ''Unfolded'' and ''unstructured'' both imply lack of backbone organization, but natively disordered proteins often have regions of secondary structure, sometimes transient and sometimes persistent. There are even examples of apparently native proteins with functional regions that resemble molten globules [21]; the molten globule contains persistent secondary structure but lacks specific tertiary structures, having instead regions of non-rigid side chain packing that leads to mobile secondary structure units [22, 23, 32] (see chapters 23 and 24 in Part I). Rheomorphic, which means ''flowing structure'' [400], provides an interesting alternative to random coil, but again would not indicate native molten globules. Since ''disordered'' encompasses both extended and molten globular forms, this descriptor has some advantage, but the widespread use of ''disorder'' in association with human diseases complicates computer searches and gives a negative impression.

Here we use ''natively disordered,'' which has been infrequently used if at all, mainly to distinguish this work from previous manuscripts on this topic. Developing a standardized vocabulary in this field would be of great benefit. We propose ''collapsed disorder'' for proteins and domains that exist under physiological conditions primarily as molten globules and ''extended disorder'' for proteins and regions that exist under physiological conditions primarily as random coil.

A significant body of work suggests that the unfolded state is not a true random coil but instead possesses substantial amounts of an extended form that resembles the polyproline II helix [24–26] as well as other local conformations that resemble the native state (see chapter 20 in Part I). For this reason, extended disorder may be a preferable term to random coil, but the latter term continues to have widespread usage; therefore, for convenience, we will continue to use this term here – with the understanding that by the term random coil we do not mean the true random coil defined by the polymer chemist.

It is useful to introduce the topic of natively disordered proteins with a specific, very clear example. Calcineurin (Figure 8.1A) makes a persuasive case for the existence and importance of native disorder [27–29]. This protein contains a catalytic A subunit and a B subunit with 35% sequence identity to calmodulin. The A subunit is a serine-threonine phosphatase that becomes activated upon association with the Ca^{2+}-calmodulin complex. Thus, calcineurin, which is widespread among the eukaryotes, connects the very important signaling systems based on Ca^{2+} levels and

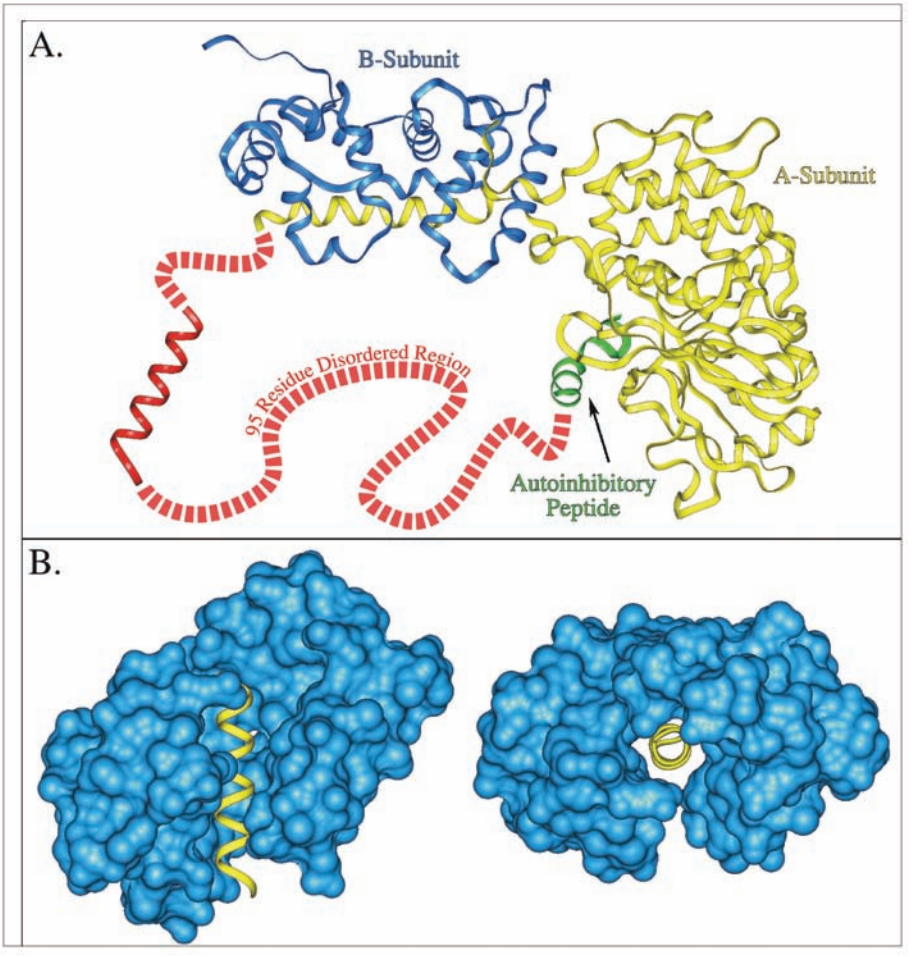

Fig. 8.1. (A) 3-D structure of calcineurin, showing the A subunit (yellow), the B subunit (blue), the autoinhibitory peptide (green), and the location of a 95-residue disordered region (red). The calmodulin-binding site (red helix) is located within the disordered region. (B) Side and top views of calmodulin (blue) binding a target helix (yellow). Note that the calmodulin molecule surrounds the target helix when bound.

phosphorylation/dephosphorylation. When Ca^{2+}-calmodulin binds to its target helix within calcineurin, the autoinhibitory peptide becomes displaced from its association with the active site, and by this means the phosphatase activity is turned on. Since Ca^{2+}-calmodulin wraps around its target helix (Figure 8.1B), this helix must lack tertiary contacts and therefore lies in a disordered region. The disordered character of the region surrounding the target helix in calcineurin has been shown by its sensitivity to trypsin digestion [27, 28] and by the missing electron density of over 95 consecutive residues in the crystal structure [29]. In this example, these lines of evidence combine to support the importance of intrinsic disorder for biological function.

8.1.3 A New Protein Structure-Function Paradigm

The standard view is that amino acid sequence codes for 3-D structure and that 3-D structure is a necessary prerequisite for protein function. In contrast, not only calcineurin but also many additional proteins, as we have shown elsewhere [30, 31], are natively disordered or contain natively disordered regions. For such proteins or protein regions, lack of specific 3-D structures contributes importantly to their functions. Here we explore the distinctions between the standard and our alternative view of protein structure-function relationships.

The standard structure-function paradigm as discussed above arose initially from the study of enzymes. The original lock-and-key proposal [1] was based on distinctive substrate recognition by a pair of enzymes. In the approximately 110 years since this initial proposal, studies of enzyme catalysis have continuously reinforced this view.

While more than 20 proposals have been made to explain enzyme catalysis [33], it has become accepted that the most profitable way to think about the problem is in terms of transition-state stabilization [34]. That is, as first suggested by Polanyi [35] and later by Pauling [36], for an enzyme to carry out catalysis, it must bind more tightly to the transition state than to the ground state. This tighter binding lowers the transition-state energy and accelerates the reaction rate [34–36]. Transition states are derived from ground states by very slight movements of atoms (typically half the length or so of a chemical bond). Attempts to understand the mechanistic details of how an enzyme can bind more tightly to the transition state have occupied a number of protein chemists and theoreticians, and this is not completely clear in every aspect even today [37], with some researchers arguing that electrostatic contributions provide the dominant effects [38] (see chapter 7 in Part I) and others emphasizing the importance of entropic effects [39] or other contributions [40]. Despite these uncertainties, there seems to be universal agreement that tighter binding to the transition state depends on an accurate prior positioning of the key residues in the enzyme. This prior positioning requires a well-organized protein 3-D structure. Thus, in short, the evolution of ordered structure in proteins was likely reinforced by or resulted directly from the importance of enzyme catalysis.

For not only the calcineurin example given above but also for most of the natively disordered proteins we have studied [30, 31], the function of the disorder is for signaling, regulation, or control. Compared to order, disorder has several clear advantages for such functions. When disordered regions bind to signaling partners, the free energy required to bring about the disorder-to-order transition takes away from the interfacial, contact free energy, with the net result that a highly specific interaction can be combined with a low net free energy of association [20, 41, 77]. High specificity coupled with low affinity seems to be a useful pair of properties for a signaling interaction so that the signaling interaction is reversible. It would appear to be more difficult to evolve a highly specific yet weak interaction between two ordered structures. In addition, a disordered protein can readily bind to multiple partners by changing shape to associate with different targets [20, 42,

43]. Multiple interactions are now being commonly documented, and proteins having 20 or more partners are being described. In protein interaction or signaling networks, proteins with multiple partners are often called hubs. We previously suggested that the ability to interact with multiple partners may depend on regions of native disorder [44], but so far we have investigated only a limited number of examples. Whether hub proteins utilize regions of native disorder to enable their binding diversity is an important question for proteins of this class.

Given the above information, we propose a new protein structure-function paradigm. Simply put, we propose a two-pathway paradigm, with sequence ➛ 3-D structure ➛ function for catalysis and sequence ➛ native disorder ➛ function for signaling and regulation.

8.2
Methods Used to Characterize Natively Disordered Proteins

8.2.1
NMR Spectroscopy

Intrinsically disordered proteins have dynamic structures that interconvert on a number of timescales. Nuclear magnetic resonance spectroscopy can detect this molecular motion as well as any transient secondary or tertiary structure that is present. Several reviews have focused on the use of NMR to characterize the structure and dynamics of intrinsically disordered proteins [45–49]. There is also a rich body of literature reviewing the use of NMR to characterize the structure and dynamics of nonnative states of globular proteins [50–55] (see chapters 18 and 21 in Part I). Due to the high activation barrier for studying the structure and dynamics of intrinsically disordered proteins, much of the work reviewed here was performed on nonnative states of globular proteins. Fortunately, these nonnative states have many similarities to intrinsically disordered proteins. The barrier to studying intrinsically disordered proteins seems to prevail regardless of their functional relevance and the abundance of NMR techniques available to characterize their structure and dynamics. This barrier is based on an entrenched attitude of most protein chemists regarding the relationship between protein structure and function. For example, when graduate students present an HSQC spectrum of an intrinsically disordered protein displaying limited ^{1}H chemical shift dispersion and narrow resonance line shape to their advisor, they are likely to be ridiculed for making an error during the purification of the protein. This attitude prevails despite more than a decade of overwhelming evidence that intrinsic protein disorder exists and can be essential for function. It is time to move beyond the limited view that defined 3-D structure is a requirement for protein function and to acknowledge the growing body of evidence that natively disordered proteins exist and have functions.

In this report, a systematic approach for using NMR to investigate the structure, dynamics, and function of intrinsically disordered proteins will be suggested based on a subset of NMR experiments. Our objective is to develop a comprehensive pic-

ture of the structure and dynamics of intrinsically disordered proteins. This objective is most easily accomplished by unifying the different types of NMR data collected on intrinsically disordered proteins while avoiding the pitfall described in the following quotation from a classic paper on NMR and protein disorder [56]: "[U]ntil the amount of structural information provided by NMR methods increases by several orders of magnitude, descriptions of non-native structure will probably consist of simple lists of estimates of fractional population of secondary-structure segments and of side-chain interactions."

It is interesting that the author of this quote has provided one of the most complete descriptions of the structure and dynamics of an unfolded protein, a fragment of staphylococcal nuclease referred to as Δ131Δ [56–64].

The most complete description of the structure and dynamics of intrinsically disordered proteins would include the population and structure of the different members of the rapidly interconverting ensemble along with the rate of interconversion between unique structures. Some of these parameters can be estimated from NMR chemical shifts and resonance line shape measurements [48, 50, 51, 65–67]. Because liquid-state NMR detects the ensemble average, chemical shifts can be treated as macroscopic equilibrium constants for secondary structure formation [50, 51]. This information can be combined with measurements of hydrodynamic radii, using pulsed field gradient methods, to place limits on the conformational space that is being explored, which ultimately facilitates structure calculation of ensemble members [68–70]. Of course, it remains unclear how many discrete states are represented in the resonance line shape measurements, which presents the fundamental limitation of current NMR practice and theory to provide a more detailed description of the ensemble members. Many consider this problem insoluble, given the large number of possible conformations, even for a small polypeptide. However, there is ample evidence that intrinsically disordered proteins do not explore all of these conformations. Further, several systems have been characterized where resonance line shape measurements were deconvoluted to provide information about the number of ensemble members or to characterize the interconversion rate between conformations [71–73, 397].

8.2.1.1 Chemical Shifts Measure the Presence of Transient Secondary Structure

Resonance assignments are the first step in characterizing the structure and dynamics of any protein using NMR. Resonance assignments specify the atomic identity of unique frequencies observed in the spectrum. These frequencies are generally normalized to some standard and are reported in parts per million as the chemical shift. Chemical shift measurements for $^{1}H_{\alpha}$, $^{13}C_{\alpha}$, $^{13}C_{\beta}$, and $^{13}C(O)$ nuclei are sensitive to $\phi\Psi$ dihedral angles and deviate systematically from random coil values for helical and beta conformations [65, 67, 74, 75]. The deviations are diagnostic for the presence of secondary structure, regardless of stability, as long as the interconversion rate is fast and the deviation from the random coil chemical shift value is greater than the spectral resolution. For stably folded proteins, the chemical shift measurement of $^{1}H_{\alpha}$, $^{13}C_{\alpha}$, $^{13}C_{\beta}$, and $^{13}C(O)$ nuclei provide a picture of secondary structure that represents a lower limit on the equilibrium con-

stant for folding from the unfolded state [50]. The extension of this relationship to intrinsically disordered proteins makes the same two-state assumption. In this case, the fraction of helix or strand present can be determined by comparing the chemical shift value observed in an intrinsically disordered protein to the value expected in a stably folded protein [50, 51]. These data combined with knowledge of the Stokes radius can be used to restrict the available conformations in a structure calculation. This assumption is in agreement with a recent analysis of the effective hydrodynamic radius of protein molecules in a variety of conformationnal states [76]. In fact, based on the analysis of 180 proteins in different conformational states, it has been shown that the overall protein dimension could be predicted based on the chain length, i.e., the protein molecular weight, with an accuracy of 10%. Furthermore, it has been emphasized that the incorporation of biophysical constraints, which can be rationalized based on conventional biophysical measurements, might lead to considerable improvement in structure simulation procedures. Clearly, the size and shape of the bounding volume used for structure simulations play a crucial role in determining the efficiency and accuracy of any algorithm. The incorporation of a size/shape constraint derived from experimental data might lead to considerable improvement of simulation procedures [76].

In a study of an intrinsically disordered negative regulator of flagellar synthesis, FlgM, chemical shift deviations from random coil values were observed for $^{13}C_{\alpha}$, $^{13}C_{\beta}$, and $^{13}C(O)$ nuclei [77]. Similar deviations were not observed for $^{1}H_{\alpha}$ nuclei, and this may be a general property of intrinsically disordered proteins. For FlgM, the chemical shift deviations indicated the presence of helical structure in the C-terminal half of the protein and a more extended flexible structure in the N-terminal half. Two regions with significant helical structure were identified, containing residues 60–73 and 83–90. Additional NMR and genetic studies demonstrated that these two helical regions were necessary for interactions with the sigma factor. The chemical shift deviations observed for FlgM exhibited a characteristic variation where the central portion of the helix had a larger helical chemical shift difference than the edges. To test whether the helical structure based on chemical shifts represented an ensemble of nonrandom conformations, the $^{13}C_{\alpha}$ chemical shifts were measured in the presence of increasing concentrations of the chemical denaturant urea. As the concentration of urea was increased, the $^{13}C_{\alpha}$ chemical shifts moved toward the random coil value in a manner characteristic of a non-cooperative unfolding transition.

In a study of the basic leucine zipper transcription factor GCN4, transient helical structure was observed in the basic region based on chemical shift deviations from random coil values for $^{13}C_{\alpha}$, $^{13}C_{\beta}$, and $^{13}C(O)$ nuclei [78]. The temperature dependence of the three chemical shifts was also monitored. For the folded leucine zipper region, a small dependence between chemical shift and temperature was observed. Conversely, the unfolded basic region showed large changes in $^{13}C_{\alpha}$, $^{13}C_{\beta}$, and $^{13}C(O)$ chemical shifts when the temperature was changed [78]. The dynamic behavior of the basic region and rapidly interconverting structures are responsible for the temperature dependence of the chemical shifts [45]. In contrast, the temperature dependence of the chemical shifts in the folded leucine zipper

was small, and this behavior is generally observed for both folded and random coil regions.

8.2.1.2 Pulsed Field Gradient Methods to Measure Translational Diffusion

Another easily applied NMR method is measurement of the translational diffusion coefficient, *D*, using pulsed field gradients (PFG) [68–70]. This approach relies on the fact that a protein molecule undergoing translational diffusion will differentially sense a gradient of signal designed to destroy any acquired magnetization. An array of gradient strength or time can be used to calculate *D* [69]. Knowledge of *D* can be used to calculate the hydrodynamic radius. The hydrodynamic radius can then be compared to the expected value based on molecular weight to determine whether the protein is compact and globular or extended and flexible. Empirical relationships were recently established between the hydrodynamic radius determined using PFG translational diffusion measurements and the number of residues in the polypeptide chain for native folded proteins and highly denatured states [68]. This study provided evidence for significant coupling between local and global features of the conformational ensembles adopted by disordered polypeptides. As expected, the hydrodynamic radius of the polypeptide was dependent on the level of persistent secondary structure or the presence of hydrophobic clusters.

8.2.1.3 NMR Relaxation and Protein Flexibility

NMR relaxation is the premier method to investigate protein flexibility [45, 47, 56, 57, 79]. It is the first-order decay of an inductive signal back to equilibrium with the applied field. In particular, ''The relaxation mechanism for the NH spin system arises from the local time-varying magnetic fields generated at the ^{1}H and ^{15}N nuclei due to global tumbling and internal mobility of the various N–H bond vectors'' [80:2676].

This means relaxation of the NH spin system is sensitive to both local and global motion. Measuring the longitudinal relaxation rate, R_1, the transverse relaxation rate, R_2, and the heteronuclear Overhauser effect between the amide proton and its attached nitrogen, NH-NOE, is useful for describing the internal dynamics and molecular motions associated with proteins and typically measurable for every amide N–H pair in proteins less than 40 kDa [79–83].

In particular, the NH-NOE experiment provides a fast, powerful, and easy-to-interpret diagnostic tool for the presence of intrinsic protein disorder. The sign of the NH-NOE resonance is sensitive to the rotational correlation time and is positive for N–H bond vectors with a long rotational correlation time ($>$ 1–10 ns) and negative for N–H bond vectors with a short rotational correlation time ($<$ 0.1–1 ns). The NH-NOE experiment can be performed on any uniformly ^{15}N-labeled protein sample that can be concentrated without aggregation to between 0.1 and 1.0 mM. The relatively short rotational correlation time observed for intrinsically disordered proteins results in sharp, narrow lines in the NMR spectrum. Because of this property, the NH-NOE experiment can be used to detect intrinsic disorder in proteins up to 200 kDa [84].

We argue that the NH-NOE experiment is such a valuable diagnostic tool for the

presence of intrinsic protein disorder that it should be incorporated into all screening protocols developed for structural genomics. It is generally a waste of time and resources to directly pursue crystallization of proteins that are intrinsically disordered. Crystallization meets with limited success for proteins containing intrinsically disordered regions. This is because the presence of structural interconversions for intrinsically disordered proteins prohibits the formation of an isomorphous lattice, unless there are one or a few stable, low-energy conformations that can be populated. During screening, proteins determined to have intrinsically disordered regions can be marked for further NMR analysis. On a technical note, a range of relaxation and saturation delays should be used when measuring the NH-NOE values in intrinsically disordered proteins [85].

Some of the most valuable contributions to understanding the structure and dynamics of intrinsically disordered proteins have come from using R_1, R_2, and NH-NOE data to model molecular motion or to solve the spectral density function. The two most successful models for relaxation data analysis are the so called ''model-free'' approach of Lipari and Szabo [86, 87] and reduced spectral density mapping introduced by Peng and Wagner [80, 88].

8.2.1.4 Using the Model-free Analysis of Relaxation Data to Estimate Internal Mobility and Rotational Correlation Time

In the interpretation of ^{15}N relaxation data, it is assumed that the relaxation properties are governed solely by the ^{1}H-^{15}N dipolar coupling and the chemical shift anisotropy [89]. Using these assumptions, a spherical molecule with an overall correlation time, τ_m, and an effective correlation time for fast internal motions, τ_e, will have a spectral density function of the following form [86, 87]:

$$J(\omega) = \frac{2}{5}\left\{\frac{S^2\tau_m}{(1+(\omega\tau_m)^2)} + \frac{(1+S^2)\tau}{(1+(\omega\tau)^2)}\right\} \tag{3}$$

where $1/\tau = 1/\tau_m + 1/\tau_e$ and S^2 is the square of the generalized order parameter describing the amplitude of internal motions. The overall correlation time, τ_m, is determined based on an assumption of isotropic Brownian motion. For a folded protein of known structure, the diffusion tensor can be incorporated into the model to compensate for anisotropic motions [90–92]. It is unclear how valid the assumption of isotropic rotation is for intrinsically disordered proteins. It is assumed that anisotropic structures will populate the conformational ensemble of an intrinsically disordered protein. This is in the absence of little direct evidence on the subject. It has been suggested that the effects of rapid interconversion between more isotropic structures will tend to smooth out static anisotropy and result in an isotropic average conformation [57].

Regardless of the analytical limitations, the model-free analysis of several natively disordered proteins has provided to be a useful qualitative picture of the heterogeneity in rotational diffusion that is observed for these systems [58, 77, 93–95]. Some general trends are observed: (1) correlation times are greater than

those calculated based on polymer theory, and (2) transient secondary structure tends to induce rotational correlations.

Changes in S^2 have been used to estimate changes in conformational entropy due to changes in ns-ps bond vector motions during protein folding and for intrinsically disordered protein folding that is coupled to binding [45, 63, 77, 96, 97]. In aqueous buffer and near neutral pH, the N-terminal SH3 domain of the *Drosophila* signal transduction protein Drk is in equilibrium between a folded, ordered structure and an unfolded, disordered ensemble. The unfolded ensemble is stabilized by 2 M guanidine hydrochloride and the folded structure is stabilized by 0.4 M sodium sulfate. Order parameters were determined for both the unfolded and folded Drk SH3 domains. The unfolded ensemble had an average S^2 value of 0.41 ± 0.10 and the folded structure had an average S^2 value of 0.84 ± 0.05. Based on the difference in S^2 between the unfolded and folded structures, the average conformational entropy change per residue was estimated to be 12 J $(\text{molK})^{-1}$. This approach does not address additional entropy contributions from slower motional processes or the release of solvent. Interestingly, the estimate of 12 J $(\text{molK})^{-1}$ is similar to the average total conformational entropy change per residue estimated from other techniques ($\sim$14 J $(\text{molK})^{-1}$ [96]. Another study has also suggested that changes in order parameters provide a reliable estimate of the total conformational entropy changes that occur during protein folding [63].

8.2.1.5 Using Reduced Spectral Density Mapping to Assess the Amplitude and Frequencies of Intramolecular Motion

The Stokes-Einstein equation defines a correlation time for rotational diffusion of a spherical particle:

$$\tau_c = \frac{\eta V_{sph}}{T k_B} \tag{4}$$

In Eq. (4), this rotational correlation time, τ_c, depends directly on the volume of the sphere (V_{sph}) and the solution viscosity (η) and inversely on the temperature (T). The spectral density function, $J(\omega)$, describes the frequency spectrum of rotational motions of the N–H bond vector relative to the external magnetic field and is derived from the Fourier transform of the spherical harmonics describing the rotational motions [80]. For isotropic Brownian motion, $J(\omega)$ is related to τ_c in a frequency-dependent manner:

$$J(\omega) = \frac{2}{5} \frac{\tau_c}{1 + \omega^2 \tau_c^2} \tag{5}$$

Reduced spectral density mapping uses the conveniently measured ^{15}N R_1, R_2, and NH-NOE to estimate the magnitude of the spectral density function at 0, ^{1}H, and ^{15}N angular frequencies. According to Eq. (5), $J(\omega)$ at 0 frequency is equal to $2/5\ \tau_c$. This relationship represents an upper limit on $J(0)$, which is usually reduced by fast internal motions such as local anisotropic N–H bond vector fluctuations. It is also important to note that chemical exchange that is in the microsec-

ond to millisecond range contributes positively to $J(0)$ but that this effect can be attenuated by measuring R_2 under spin-lock conditions [80].

Reduced spectral density mapping is a robust approach for analyzing intrinsic disorder because it does not depend on having a model of the molecular motions under investigation. Several groups have characterized intrinsic protein disorder using reduced spectral density mapping, providing new insights into protein dynamics [77, 78, 80, 94, 98–101]. In one of these studies, reduced spectral density mapping was used to help demonstrate that the intrinsically disordered anti-sigma factor, FlgM, contained two disordered domains [77]. One domain, representing the N-terminal half of the protein, was characterized by fast internal motions and small $J(0)$ values. The second domain, representing the C-terminal half of the protein, was characterized by larger $J(0)$ values, representing correlated rotational motions induced by transient helical structure. NMR was also used to help demonstrate that the C-terminal half of FlgM contained the sigma factor–binding domain, and it was proposed that the transient helical structure was stabilized by binding to the sigma factor. However, more recent NMR studies of FlgM showed that this structure appears to be stabilized in the cell due to molecular crowding, which would reduce the role of conformational entropy on the thermodynamics of the FlgM/sigma factor interaction [102].

In another study, a temperature-dependent analysis of the reduced spectral density map was performed on the GCN4 bZip DNA-binding domain [78]. In the absence of DNA, GCN4 exists as a dimer formed through a coiled-coil C-terminal domain and a disordered N-terminal DNA-binding domain. This disordered DNA-binding domain becomes structured when DNA is added [54]. In the GCN4 study, the reduced spectral density map was evaluated at three temperatures; 290 K, 300 K, and 310 K. $J(0)$ values increased in a manner consistent with changes in solvent viscosity induced by increasing temperature. When $J(0)$ was normalized for changes in solvent viscosity, values for the C-terminal dimerization domain and the intrinsically disordered N-terminal DNA-binding domain were identical within experimental error. This behavior suggested that the correlated rotational motion of the folded leucine zipper had the dominant influence on the solution-state backbone dynamics of the basic leucine zipper of GCN4. A recently completed study monitored the temperature dependence of the reduced spectral density map for a partially folded fragment of thioredoxin [401]. Unlike GCN4, the thioredoxin fragment does not contain a stably folded domain. In this study, normalizing $J(0)$ for changes in solvent viscosity induced a trend in the data, with $J(0)$ increasing with increasing temperature. In the absence of chemical exchange, these data suggest that we are monitoring an increase in the hydrodynamic volume of the fragment (G. W. Daughdrill, unpublished data).

8.2.1.6 Characterization of the Dynamic Structures of Natively Disordered Proteins Using NMR

In 1994 Alexandrescu and Shortle described the first complete NMR relaxation analysis of a partially folded protein under non-denaturing conditions [57, 58]. It was a fragment of staphylococcal nuclease referred to as Δ131Δ. For the ma-

jority of Δ131Δ residues, their experimental data was best described by a modified "model-free" formalism that included contributions from internal motions on intermediate and fast timescales and slow overall tumbling. They observed that the generalized order parameter S^2 correlated with sequence hydrophobicity and the fractional populations of three alpha helices in the protein. In a more recent study, residual dipolar couplings were measured for native staphylococcal nuclease and Δ131Δ [60–63]. Native-like dipolar couplings were observed in Δ131Δ, even in high concentrations of denaturant.

An extensive NMR dataset was used to identify an ensemble of three-dimensional structures for the N-terminal SH3 domain of the *Drosophila* signal transduction protein Drk, with properly assigned population weights [103, 104]. This was accomplished by calculating multiple unfolding trajectories of the protein using the solution structure of the folded state as a starting point. Of course this approach is limited to proteins that have a compact rigid conformation. However, the ability to integrate multiple types of data describing the structural and dynamic properties of disordered proteins is pertinent to this discussion. Population weights of the structures calculated from the unfolding trajectories were assigned by optimizing their fit to experimental data based on minimizing pseudo energy terms defined for each type of experimental constraint. This work marks the first time that NOE, J-coupling, chemical shifts, translational diffusion coefficients, and tryptophan solvent-accessible surface area data were used in combination to estimate ensemble members. As seen with many other studies of the structure and dynamics of intrinsically disordered proteins, the unfolded ensemble for this domain was significantly more compact than a theoretical random coil (see chapter 20 in Part I).

8.2.2 X-ray Crystallography

Wholly disordered proteins would not be expected to crystallize and thus could not be studied by X-ray crystallography. On the other hand, proteins consisting of both ordered and disordered regions can form crystals, with the ordered parts forming the crystal and the disordered regions occupying spaces between the ordered parts. Regions of disorder vary in location from one molecule to the next and therefore fail to scatter X-rays coherently. The lack of coherent scattering leads to missing electron density.

A given protein crystal is made up of identical repeating unit cells, where each unit cell contains one to several protein molecules depending on the symmetry of the crystal. Each atom, j, in the protein occupies a particular position, xj, yj, and zj. It is convenient to express the positions as dimensionless coordinates that are fractions of the lengths of the unit cell, yielding Xj, Yj, and Zj as the indicators of the position of atom j. The result of an X-ray diffraction experiment is a 3-D grid of spots that are indexed by three integers, h, k, and l. The positions of the spots are determined by the crystal lattice. The intensities of the spots are determined by both the symmetries in the crystal and the positions of the atoms in the molecule. Specifically, each spot has an intensity that is the square of the magnitude of the

structure factor, $F(h,k,l)$, which is given by the following equation:

$$F_{(h,k,l)} = \sum_{j=1}^{atoms} f_{(j)} \exp[2\pi \cdot i(hX_j + kY_j + lZ_j)] \quad (6)$$

where h, k, and l are the indices of the spots in the diffraction pattern, $f_{(j)}$ is the scattering power of atom j (dependent on the square of the number of electrons in the atom), i is the square root of -1, and X_j, Y_j, and Z_j are the coordinates of atom j given as fractions of the unit cell dimensions as mentioned above.

Each $F_{(h,k,l)}$ has both a magnitude and a phase. The magnitude of $F_{(h,k,l)}$ is determined by the square root of the intensity of each spot in the diffraction pattern. For wavelets from two different spots, the phase is the shift in the peak values and is 0 degrees for two wavelets that are exactly in phase (constructive interference) and 180 degrees for two wavelets that are totally out of phase (which leads to destructive interference). The phase for two arbitrary wavelets can be found to be any value between 0 and 360 degrees. Thus, given a structure, both the magnitude and phase of each $F_{(h,k,l)}$ can be calculated by carrying out the summation in Eq. (6) over all of the atoms in the structure. Taking the Fourier transform of Eq. (6) gives:

$$\rho_{(x,y,z)} = \frac{1}{V} \sum_h \sum_k \sum_l F_{(h,k,l)} \exp[-2\pi \cdot i(hx + ky + lz)] \quad (7)$$

where $\rho_{(x,y,z)}$ is the electron density of the protein at x, y, and z and V is the volume of the unit cell (the other terms have been defined above).

Thus, to determine a structural model of the given protein, one merely has to carry out the summation of Eq. (7) and then fit the resulting electron density map with a set of atoms that correspond to the connected set of residues in the structure. To carry out this triple-vector sum, it is necessary to know both the magnitude and the phase of each $F_{(h,k,l)}$. While the magnitude is obtainable simply as the square root of the intensity of the spot, the phase information is lost during data collection because the time of arrival of the peak of each wavelet relative to those of the others cannot be recorded with current technologies. The loss of this critical information is commonly called the phase problem.

Three main methods have been developed to find the missing phase information for each structure factor, $F_{(h,k,l)}$. Each of these methods has advantages and disadvantages.

The earliest successful approach for proteins was to add heavy atoms. Since scattering power depends on the number of electrons squared, even a small number of heavy atoms can perturb the diffraction values enough to allow the determination of the phase values. The mathematical details are fairly involved, but for this approach to work, the positions of the heavy atoms must be determined by comparing the phase intensities with and without the heavy atoms. In addition, the addition of the heavy atoms cannot significantly perturb the structure of the protein. With regard to this second point, the protein structure with and without the heavy atom must be isomorphous. Thus, this approach is called isomorphous replace-

ment, and at least two such heavy atom replacements must be made to determine each phase value.

A second approach is to use multiple X-ray wavelengths that traverse the absorption edge of a selected heavy atom. The change in scattering over the absorption edge becomes substantial, which enables the phases to be determined. This approach is called multi-wavelength anomalous dispersion, or MAD. For protein structure determination by this approach, it is common to introduce selenium in the form of selenomethionine. This is a convenient atom that has an absorption edge at an appropriate wavelength value, and often (but not always) substitution of methionine with selenomethionine does not significantly affect the structure or activity of the protein of interest.

Finally, if the structure of a closely related protein is already known, it is often possible to use the phases from the related protein with the intensities from the protein of interest to generate the initial model structure. This approach is called molecular replacement. Often the homologous structure is not similar enough, so the phases are too inaccurate to give a reasonable starting structure. A second major difficulty is determining the correct orientation of the known structure relative to that of the unknown so that the phases can be correctly associated with the intensities. Since a very large number of possible orientations exist, a complex search of the possibilities needs to be developed. Evolutionary algorithms have recently been found to be useful for this task [105].

Structure determination by X-ray crystallography typically involves not only straightforward calculation and equation solving (as indicated above) but also significant modeling and simulation. Once the phase problem has been solved by experiment, an electron density map is generated by the calculations described in Eq. (7). However, there are important technical difficulties in solving the phases, so the phase values usually contain large errors and the resulting electron density map contains many mistakes. To give an example of the difficulty, it is unclear whether the heavy atom derivatives are truly isomorphous; even small protein movements upon heavy atom binding can lead to significant errors in the estimation of the phases. Modeling is then used to fit the amino acid sequence into the error-containing electron density map. The structural model that emerges is typically adjusted by dynamics and simulation to improve bond lengths, bond angles, and inter-atom contacts. The model is then used to calculate improved phases and the whole process is reiterated until the structure no longer changes in successive cycles.

In the overall process of protein crystallography, there are no clear-cut rules for dealing with regions of low intensity or missing electron density. Some crystallographers are more aggressive than others in attempting to fit (or model) such low-density or missing regions. This variability means that missing coordinates in the Protein Data Bank (PDB) have not been assigned by uniform standards, which in turn leads to variability in the assignment of disorder. All of this is compounded by the imperfections (packing defects) in real crystals, which can additionally contribute to the absence of electron density.

Crystallographers have classified regions of missing electron density as being

either static or dynamic [106, 107]. Static disorder is trapped into different conformations by the crystallization process, while dynamic disorder is mobile. A dynamically disordered region could potentially freeze into a single preferred position upon cooling, while static disorder would be fixed regardless of temperature. By collecting data and determining structures at a variety of temperatures, dynamic disorder sometimes becomes frozen and thus distinguished from static disorder [108].

From our point of view, more important than static or dynamic is whether the region of missing electron density has a single set of coordinates along the backbone or whether the region exists as an ensemble of structures. A missing region with one set of coordinates could be trapped in different positions by the crystal lattice (statically disordered) or could be moving as a rigid body (dynamically disorder). In either case, the wobbly domain [20] is not an ensemble of structures, i.e., is not natively disordered, but rather is an ordered region that adopts different positions due to a flexible hinge.

Given the difficulties in ascribing disorder to regions of missing electron density or to missing coordinates in the PDB, it is useful to use a second method, such as NMR or protease sensitivity, to confirm that a missing region is due to intrinsic disorder rather than some other cause. While such confirmation has been carried out for a substantial number of proteins [20], the importance of disorder has not been generally recognized, so such confirmation is not routine.

Despite the uncertainties described above, missing electron density provides a useful sampling of native disorder in proteins. To estimate the frequency of such regions, a representative set of proteins was studied for residues with missing coordinates [109]. The representative set, called PDB_Select_25, was constructed by first grouping the PDB into subsets of proteins with greater than 25% sequence identity and then choosing the highest-quality structure from each subset [110]. Out of 1223 chains with 239 527 residues, only 391 chains, or 32%, displayed no residues with missing backbone atoms (Table 8.1). Thus, 68% of the

Tab. 8.1. Disorder in PDB_Select_25*.

Parameter	*Number*	*Percentage*
Total chains	1223	
Chains with no disorder	391	32
Chains with disorder	832	68
Disordered regions	1168	
Disordered regions/disordered chains	1.4	
Disordered regions > 30 residues in length	68	5.8
Total residues	239 527	
Disordered residues	12 138	5.1
Residues in disordered regions > 30	3710	1.5

* Data extracted from PDB as of 10/1/2001.

non-redundant proteins contained some residues that lacked electron density. The 832 chains with missing electron density contained 1168 distinct regions of disorder, corresponding to ∼1.4 such regions/chain. These 1168 disordered regions contained 12 138 disordered residues, or ∼10 residues/disordered region on average. While most of the disordered regions are short, a few are quite long: 68 of the disordered regions are greater than 30 residues in length. Overall, the residues with missing coordinates are about 5% of the total.

A substantial fraction of the disorder-containing proteins in PDB are fragments rather than whole proteins. Since disordered regions tend to inhibit crystallization, they are often separated from ordered domains by genetic engineering or protease digestion prior to crystallization attempts. In either case, longer regions of disorder become shortened, presumably leading to improved probability of obtaining protein crystals. Given that wholly disordered proteins do not crystallize, and given that the proteins in PDB often contain truncated disordered regions or are ordered fragments that have been separated from flanking regions of disorder, it is clear that the PDB substantially underrepresents the amount of protein disorder in nature.

To further understand the distribution of order and disorder in crystallized proteins, we carried out a comparison between the PDB and the Swiss-Prot databases. Swiss-Prot provides an easy mechanism to extract information about various proteins [111], so this comparison allows a convenient means to study disorder across the different kingdoms. The overall results of this comparison are given in Table 8.2. Of 4175 exact sequence matches between proteins in PDB_Select_25 and Swiss-Prot, 2258 were from eukaryotes, 1490 were from bacteria, 170 were from archaea, and 257 were from viruses. Proteins with no disorder or only short disorder were estimated by considering proteins for which at least 95% of the primary structure was represented as observed coordinates in the PDB structures. The number and percentage of proteins in each set for these mostly ordered proteins were 428 (19%) for eukaryotes, 594 (40%) for bacteria, 82 (48%) for archaea, and 42 (16%) for viruses. Proteins with substantial regions of disorder were estimated by considering proteins for which the crystal structure contained less than half of the entire sequence. The number and percentage of proteins in each set for these proteins likely to contain substantial amounts of disorder were 713 (32%) for eu-

Tab. 8.2. Comparison of disorder between the PDB_Select_25 and Swiss-Prot databases.

	Number listed in both databases	*Proteins with ≥90% assigned coordinates*		*Proteins with ≤50% assigned coordinates*	
		Number	*Percentage*	*Number*	*Percentage*
Eukaryotes	2258	428	19	713	32
Bacteria	1490	594	40	97	6.5
Archaea	170	82	48	4	2.3
Viruses	257	42	16	123	48

karyotes, 97 (6.5%) for bacteria, 4 (2.3%) for archaea, and 123 (48%) for viruses. These data suggest that both eukaryotes and viruses are likely to have proteins with large regions of disorder flanking fragmentary regions of ordered, crystallizable domains.

8.2.3 Small Angle X-ray Diffraction and Hydrodynamic Measurements

Both small-angle X-ray scattering (SAXS) and hydrodynamic methods such as gel-exclusion chromatography or dynamic light scattering (see chapter 19 in Part I) have been used to estimate the sizes of protein molecules in solution. Analytical ultracentrifugation is another method for determining the molecular weight and the hydrodynamic and thermodynamic properties of a protein [112]. The observed size of a given protein can then be compared with the size of a globular protein of the same mass. As expected, by these methods molten globules have overall sizes similar to those of the globular proteins of the same mass, whereas random coil forms are considerably extended and thus have a significantly larger size than their globular counterparts. Natively disordered proteins and globular proteins can be compared using several features of these techniques.

With regard to SAXS, one approach is to plot the normalized $I(S)S^2$ versus S, where I is the scattering intensity at a given scattering angle and S is the given scattering angle. This method emphasizes changes in the signal at higher scattering angles, which in turn strongly depends on the dimensions of the scattering molecule. The resulting graph, called a Kratky plot [113–115], readily distinguishes random coil proteins from globular structures. That is, globular proteins give parabolas, with scattering intensity increasing and then dropping sharply due to the reduced scattering intensity at large angles. On the other hand, random coil forms give monotonically increasing curves. Importantly, the natively disordered proteins with extended disorder are characterized by low (coil-like) intramolecular packing density, reflected by the absence of a maximum on their Kratky plots [116–122]. This statement is illustrated by Figure 8.2, which compares the Kratky plots of five natively disordered proteins with those of two rigid globular proteins. One can see that the Kratky plots of natively disordered proteins do not exhibit maxima. Maxima on Kratky plots are typical of the folded conformations of globular proteins such as staphylococcal nuclease. In other words, the absence of a maximum indicates the lack of a tightly packed core under physiological conditions in vitro [123].

A second SAXS approach is to compare the radius of gyration, R_g, with that from a globular protein of the same size. The R_g value is estimated from the Guinier approximation [124]:

$$I(S) = I(0)\exp\left(-\frac{S^2 \cdot R_g^2}{3}\right) \tag{8}$$

where $I(S)$ is the scattering intensity at angle S. The value of R_g can then be deter-

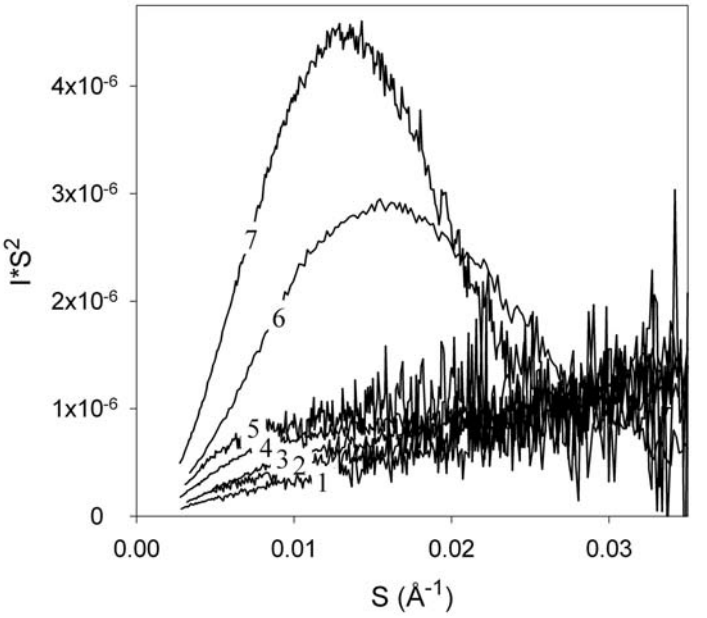

Fig. 8.2. Kratky plots of SAXS data for natively disordered α-synuclein (1), β-synuclein (2), prothymosin α (3), caldesmon 636–771 fragment (4), and core histones (5). The Kratky plots of native globular staphylococcal nuclease (6) and hexameric insulin (7) are shown for comparison.

mined from plots of $\ln[I(S)]$ versus S^2. As tabulated by Millet, Doniach, and Plaxco [125], the radii of gyration of proteins unfolded by low pH, methanol, urea, or guanidinium chloride are typically 1.5–2.5 times larger than the radii of gyration of the same proteins in their native globular states. Note, however, that denaturation does not always result in complete conversion to extended coil formation: some structure may persist [126, 127].

SAXS can also be used to estimate the maximum dimension of the protein. The distance distribution function $P(r)$ can be estimated by Fourier inversion of the scattering intensity, $I(S)$ [128, 129], where $P(r)$ is the probability of finding a dimension of length r. A plot of $P(r)$ versus r yields the maximum dimension in the limit as $P(r)$ goes to zero. The observed maximal dimension can then be compared with those observed for globular and random coil forms of various proteins [130, 131].

A fourth method is to compare hydrodynamic volumes. Globular proteins differ significantly from fully or partly unstructured proteins in their hydrodynamic properties. For both native, globular proteins and fully denatured proteins, empirical relationships have been determined between the Stoke's radius, *Rs*, and the number of residues in the chain [68, 132, 133]. These relationships in turn provide estimates of the overall hydrodynamic sizes compared to the respective controls.

Two common methods for estimating the Stoke's radius are gel-exclusion chromatography and dynamic light scattering. In the former, the mobility of the protein of interest is compared to the mobilities of a collection of protein standards [132, 133]. In the latter, the translational diffusion coefficient is estimated and the Stoke's radius is calculated from the Stoke's-Einstein equation.

For a given Stoke's radius, *Rs*, the hydrodynamic volume is given by:

$$Vh = \left(\frac{4}{3}\right)\pi(Rs)^3 \tag{9}$$

where the Stoke's radius of a given protein can be estimated by comparison to known standards using gel-exclusion chromatography. Alternatively, the Stoke's radius can also be estimated from diffusion values estimated by dynamic light-scattering measurements as described previously [68].

Plots of the logarithm of the hydrodynamic volume versus number of residues yield distinct straight lines for three different classes of reference proteins: (1) native, globular proteins, (2) molten globules, and (3) proteins unfolded by guanidinium chloride [123, 134]. As expected, the molten globule forms are just slightly larger than their ordered, globular counterparts, while the unfolded proteins exhibit significantly larger hydrodynamic volumes.

This conclusion is illustrated by Figure 8.3, which compares the $\log(R_S)$ versus $\log(M)$ curves for natively disordered proteins with those of native, molten globule, pre-molten globule, and guanidinium chloride-unfolded globular proteins [123]. Additionally, Figure 8.3 shows that the $\log(R_S)$ versus $\log(M)$ dependencies for different conformations of globular proteins can be described by the following set of straight lines:

$$\log(R_S^N) = -(0.204 \pm 0.023) + (0.357 \pm 0.005) \cdot \log(M) \tag{10}$$

$$\log(R_S^{MG}) = -(0.053 \pm 0.094) + (0.334 \pm 0.021) \cdot \log(M) \tag{11}$$

$$\log(R_S^{PMG}) = -(0.210 \pm 0.180) + (0.392 \pm 0.041) \cdot \log(M) \tag{12}$$

$$\log(R_S^{U\text{-}GdmCl}) = -(0.723 \pm 0.033) + (0.543 \pm 0.007) \cdot \log(M) \tag{13}$$

where N, MG, PMG, and U-GdmCl correspond to the native, molten globule, pre-molten globule, and guanidinium chloride-unfolded globular proteins, respectively.

For the non-molten globular natively disordered proteins, their $\log(R_S)$ versus $\log(M)$ dependence may be divided in two groups: natively disordered proteins behaving as random coils in poor solvent (denoted as NU-coil in Eq. (14)) and essentially more compact proteins, which are similar to pre-molten globules with respect to their hydrodynamic characteristics (denoted as NU-PMG in Eq. (15)) [123, 135]:

$$\log(R_S^{NU\text{-}coil}) = -(0.551 \pm 0.032) + (0.493 \pm 0.008) \cdot \log(M) \tag{14}$$

$$\log(R_S^{NU\text{-}PMG}) = -(0.239 \pm 0.055) + (0.403 \pm 0.012) \cdot \log(M) \tag{15}$$

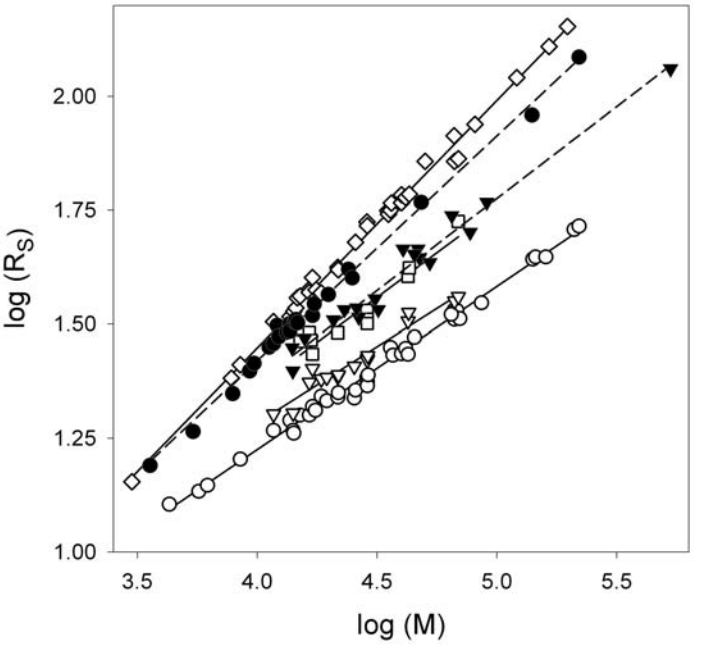

Fig. 8.3. Dependencies of the hydrodynamic dimensions, R_S, on protein molecular mass, *M*, for native globaular (open circles), molten globule (open triangles), pre-molten globule (open squares), 6 M guanidinium chloride-unfolded conformational states of globular proteins (open diamonds), natively disordered proteins with coil-like (black circles) and pre-molten globule-like (black inverse triangles) properties [123].

Non-molten globular, natively disordered proteins might be expected to contain subregions of various lengths, each having differing degrees of partial folding. If this were indeed the case, plots of the logarithm of the hydrodynamic volumes versus residue numbers for a set of such natively disordered proteins would give a scatter plot having values randomly located between the lines specified by the extensively unfolded and the molten globular reference forms. Instead of this expectation, two distinct types of natively disordered proteins were observed [123]. One type closely resembles the reference proteins that were extensively unfolded by guanidinium chloride. The other type gives a log volume versus residue line between that of the fully extended protein molecules and that of the molten globules. The line for this second type is nearly superimposable [123] with a previously described denaturation intermediate called the pre-molten globule [136].

The finding of two distinct classes of extended disorder – random coil-like and pre-molten globule-like – is difficult to understand. Polymers in good solvents tend to be collapsed but still unstructured. Uversky (2002) suggested that sequence differences could be responsible for whether a natively disordered protein behaves more like a random coil or more like a pre-molten globule; however, a clear se-

quence distinction between the two classes has not been found [123, 135]. But even if a sequence distinction is found, it remains difficult to understand the origin of this partition into two distinct classes. For example, if a hybrid protein were created, with one half being random coil-like and one-half being pre-molten globule-like, would its hydrodynamic properties lie between those of the two classes? Why haven't such chimeras been found in nature? Perhaps the simple explanation is that not enough natively disordered proteins have been characterized. But if a wide variety of natively disordered proteins have not been found in the current sampling, even though such proteins do exist, what is leading to the partition observed so far? This question deserves further study.

8.2.4 Circular Dichroism Spectropolarimetry

Circular dichroism (CD) measures the difference in the absorbance of left versus right circularly polarized light and is therefore sensitive to the chirality of the environment [137]. There are two types of UV-absorbing chromophores in proteins: side chains of aromatic amino acid residues and peptide bonds [137, 138]. CD spectra in the near-ultraviolet region (250–350 nm), also known as the aromatic region, reflect the symmetry of the aromatic amino acid environment and, consequently, characterize the protein tertiary structure. Proteins with rigid tertiary structure are typically characterized by intense near-UV CD spectra, with unique fine structure, which reflect the unique asymmetric environment of individual aromatic residues. Thus, natively disordered proteins are easily detected since they are characterized by low-intensity, near-UV CD spectra of low complexity. The far-UV region of a protein's absorbance spectrum (190–240 nm) is dominated by the electronic absorbance from peptide bonds. The far-UV CD spectrum provides quantifiable information about the secondary structure of a protein because each category of secondary structure (e.g., α-helix, β-sheet) has a different effect on the chiral environment of the peptide bond. Because the timescale for electronic absorbance ($\sim 10^{-12}$ seconds) is so much shorter than that of folding or unfolding reactions (at least $\sim 10^{-6}$ seconds), CD provides information about the weighted average structure of all the peptide bonds in the beam.

CD provides different information about native globular versus denatured or disordered proteins. In a native globular protein, the weighted average can be applied to each molecule because nearly all the molecules are in the native state and each molecule of the native state has a similar structure. For instance, if the CD data indicate that 30% of the peptide bonds in a sample of a 100-residue native globular protein are in the α-helical conformation and 70% are in the β-sheet conformation, then 30 peptide bonds in each protein molecule are helical and the other 70 are sheet. Furthermore, it is the same 30 and 70 in each molecule. For a denatured or disordered protein, the CD spectrum provides information about the ensemble of conformations, and the information will not be generally applicable to any single molecule. For instance, changing the above example to a disordered protein, we

can say that 30% of the peptide bonds in the sample are helical and 70% are sheet, but with only these data in hand, nothing can be inferred about the structure of an individual molecule – neither the helix and sheet percentage nor the location of those structures along the chain.

A good correlation exists between the relative decrease in hydrodynamic volume and the increase in secondary structure content. This correlation was shown for a set of 41 proteins that had been evaluated by both far-UV CD and hydrodynamic methods [139]. Study of the equilibrium unfolding of these globular proteins revealed that the Stokes radii (R_S) and secondary structure of native and partially folded intermediates were closely correlated. Results of this analysis are presented in Figure 8.4 as the dependence of $(R_S^U/R_S)^3$ versus $[\theta]_{222}/[\theta]_{222}^U$, which represent relative compactness and relative content of ordered secondary structure, respectively. Significantly, Figure 8.4 illustrates that data for both classes of conformations (native globular and partially folded intermediates) are accurately described by a single dependence (correlation coefficient, $r^2 = 0.97$) [139]:

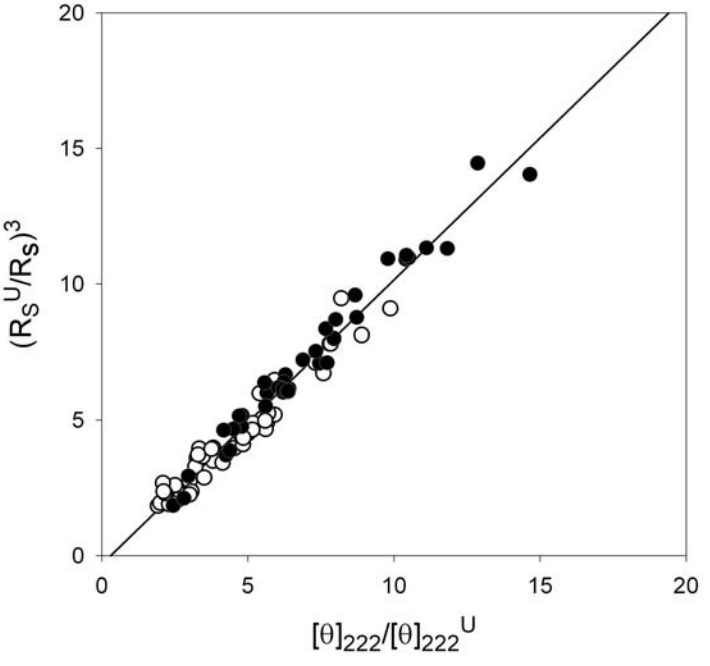

Fig. 8.4. Correlation between the degree of compactness and the amount of ordered secondary structure for native globular proteins (filled circles) and their partially folded intermediates (open circles). The degree of compactness, $(R_S^U/R_S)^3$, was calculated for different conformational states as the decrease in hydrodynamic volume relative to the volume of the unfolded conformation, while the amount of ordered secondary structure, $[\theta]_{222}/[\theta]_{222}^U$, was calculated from far-UV CD spectra as the increase in negative ellipticity at 222 nm relative to the unfolded conformation. The data used to plot these dependencies are taken from Uversky [139].

$$\left(\frac{R_S^U}{R_S}\right)^3 = (1.047 \pm 0.010) \cdot \left(\frac{[\theta]_{222}}{[\theta]_{222}^U}\right) - (0.31 \pm 0.12) \quad (16)$$

This correlation means that the degree of compactness and the amount of ordered secondary structure are conjugate parameters. In other words, there is no compact equilibrium intermediate lacking secondary structure or any highly ordered but non-compact species among the proteins analyzed. Therefore, hydrophobic collapse and secondary structure formation occur simultaneously rather than as two subsequent independent processes. This conclusion generalizes earlier observations made for several individual proteins including DnaK [140], apomyoglobin [141], and staphylococcal nuclease [142].

Tiffany and Krimm noted over 35 years ago that CD spectra of reversibly denatured proteins resemble that of a left-handed polyproline II helix [143]. It was only recently, however, that Creamer revisited these data and put them on a more sound footing with studies of non-proline model peptides [144, 145]. Polyproline helices made from non-proline residues have a negative CD band at 195 nm and positive band at 218 nm. These wavelengths are shorter than those of true polyproline helices, (205 nm and 228 nm, respectively) because of the different absorption maxima for primary and secondary amides. Inspection of the literature shows that many intrinsically disordered proteins exhibit a negative feature near 195 nm, with near-zero ellipticity near 218 nm [17, 18, 146–149], and some exhibit both the negative and the positive features [150, 151]. The interpretation of CD spectra in terms of polyproline II helix content remains controversial for several reasons. First, it is not yet clear what the difference is between the CD spectrum of a random coil and the CD spectrum of a polyproline II helix. Second, there is not yet a way to quantify the amount of polyproline II helix.

The conclusion is clear: many intrinsically disordered proteins resemble reversibly denatured proteins and may exist, on average, in a polyproline II helix. However, some of these proteins exhibit small amounts of other secondary structures [77]. Sometimes [102, 152–157], but not always [148, 158], secondary structure can be induced by molecular crowding and ''structure-inducing'' co-solutes.

8.2.5
Infrared and Raman Spectroscopy

Infrared (IR) spectra are the result of intramolecular movements (bond stretching, change of angles between bonds along with other complicated types of motion) of various functional groups (e.g., methyl, carbonyl, amide, etc.) [159]. The merits of spectral analysis in the IR region originate from the fact that the modes of vibration for each group are sensitive to changes in chemical structure, molecular conformation, and environment. In the case of proteins and polypeptides, two infrared bands that are connected with vibrational transitions in the peptide backbone and reflect the normal oscillations of simple atom groups are of the most interest. These bands correspond to the stretching of N–H and C=O bonds (amide I band) and the deformation of N–H bonds (amide II band). The amide I and amide

II bands are characterized by frequencies within the ranges of 1600–1700 cm^{-1} and 1500–1600 cm^{-1}, respectively [159–161]. The position of the bands changes due to the formation of hydrogen bonds. Thus, analysis of IR spectra allows determination of the relative content of α-helical, β-, and irregular structure in proteins by monitoring the intensity of the bands within the amide I and amide II regions.

The main advantage of using IR spectroscopy to determine the secondary structure of protein is that this method is based on a simple physical phenomenon, the change of vibrational frequency of atoms upon the formation of hydrogen bonds. Thus, it is possible to calculate the parameters of normal vibrations of the main asymmetrical units forming secondary structure and to compare these calculated values with experimental data. Calculations of normal vibrational parameters for α-helices and β-sheets were done by Miyazawa [162]. Further, Chirgadze et al. have shown that there is a good correlation between the calculated and experimental data for the amide I and amide II bands [159, 161]. Thus, such calculations may serve as a rational basis for the interpretation of polypeptide and protein IR spectra (Figure 8.5). The application of IR spectroscopy to evaluate protein secondary structure is based on the following assumptions about protein structure: (1) protein consists of a limited set of different types of secondary structure (α-helix, parallel and antiparallel β-structures, β-turns, and irregular structure), (2) the IR spectra of protein is a simple sum of the spectra of these structures taken with the

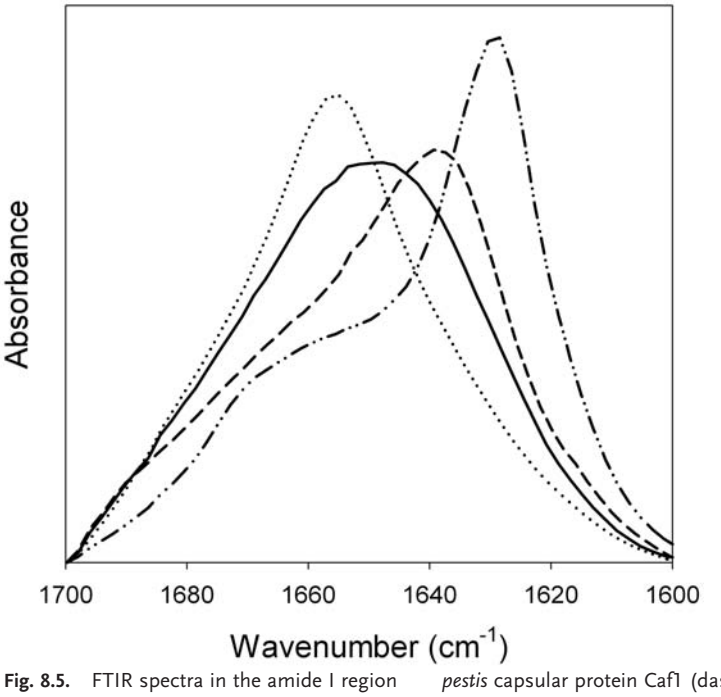

Fig. 8.5. FTIR spectra in the amide I region measured for the natively disordered α-synuclein (solid line), α-helical human α-fetoprotein (dotted line), β-structural *Yersinia pestis* capsular protein Caf1 (dashed line), and α-synuclein amyloid fibril with cross-β-structure (dash-dot-dotted line). Spectra are normalized to have same area.

weights corresponding to their content in the protein, and (3) the spectral characteristics of secondary structure are the same for all proteins and for all the structural elements of one type in the protein. The finding that Fourier transform infrared spectroscopy (FTIR) exhibited a high sensitivity to the conformational state of macromolecules resulted in numerous studies where this approach was used to analyze protein molecular structure (including a number of natively disordered proteins) and to investigate the processes of protein denaturation and renaturation.

Raman is complementary to IR, depending on inelastic light scattering rather than absorption to obtain vibrational information, and is further complementary to IR in emphasizing vibrations lacking changes in dipole moments. Raman spectroscopy has long been used for the analysis of protein structure and protein conformational changes [398]. Recently, specialized Raman methods, namely surface enhanced resonance Raman [399] and Raman optical activity [400], have demonstrated significant usefulness for the characterization of natively disordered proteins.

FTIR also provides a means of keeping track of conformational changes in proteins. These are followed by monitoring the changes in the frequencies of the IR bands that result from deuteration (substitution of hydrogen atoms by deuterium) of the molecule [159]. Since it is usually known which band belongs to which functional group (carbonyl, oxy-, or amino group), one can identify the exchangeable groups by observing the changes in band position as a result of deuteration. The rate of deuteration depends on the accessibility of a given group to the solvent that, in turn, varies according to changes in conformation. Thus, by tracking the changes in the deuterium-exchange rates for different solvent compositions and other environmental parameters, one can obtain information about the resultant conformational changes within a given protein.

8.2.6 Fluorescence Methods

8.2.6.1 Intrinsic Fluorescence of Proteins

Proteins contain only three residues with intrinsic fluorescence. These chromophores form the following series: tryptophan > tyrosine > phenylalanine according to their quantum yield. The fluorescence of tryptophan is most commonly used for analysis of proteins since the quantum yield of phenylalanine fluorescence is extremely low and tyrosine fluorescence is strongly quenched in the majority of cases. Quenching of tyrosine fluorescence can be due to ionization, proximity to amide or carboxyl groups, the energy transfer to tryptophan [163]. Application of intrinsic fluorescence to the study of protein conformational analysis relies on the fact that the parameters of tryptophan emission (intensity and wavelength of maximal fluorescence) depend essentially on environmental factors, including solvent polarity, pH, and the presence or absence of quenchers [163]. For example, a completely solvated tryptophan residue (e.g., free tryptophan in water or tryptophan in an unfolded polypeptide chain) has a maximum fluorescence in the vicinity of 350 nm, whereas embedding this chromophore into the nonpolar interior of a compact globular protein results in a characteristic blue shift of its fluorescence maximum (Stokes shift) by as much as 30–40 nm [163–165]. This

means that λ_{max} of tryptophan fluorescence contains some basic information about whether the protein is compact under the experimental conditions. For this reason, the analysis of intrinsic protein fluorescence is frequently used to study protein structure and conformational change.

8.2.6.2 Dynamic Quenching of Fluorescence

Additional information about the accessibility of protein chromophores to solvent (and thus on relative compactness of a protein molecule) can be obtained from the analysis of dynamic quenching of intrinsic fluorescence by small molecules. Fluorescence quenching data are frequently analyzed using the general form of the Stern-Volmer equation [166]:

$$\frac{I_0}{I} = (1 + K_{SV}[Q])e^{V[Q]} \tag{17}$$

where I_0 and I are the fluorescence intensities in the absence and presence of quencher, K_{SV} is the dynamic quenching constant, V is a static quenching constant, and $[Q]$ is the quencher concentration.

To some extent, the information obtained from dynamic quenching of intrinsic fluorescence is similar to that obtained from studies of deuterium exchange (see Section 8.2.8 and chapter 18 in Part I), since it reflects the accessibility of defined protein groups to the solvent. However, in distinction from the deuterium exchange, this method can be used to evaluate the amplitude and timescale of dynamic processes by using quenchers of different size, polarity, and charge. In one example, it has been shown that the rate of diffusion of oxygen (which is one of the smallest and most efficient quenchers of intrinsic protein fluorescence) within a protein molecule is only two to four times slower than in an aqueous solution [167, 168]. Furthermore, oxygen was shown to affect even those tryptophan residues that, according to X-ray structural analysis, should not be accessible to the solvent. These observations clearly demonstrated the presence of substantial structural fluctuations in proteins on the nanosecond timescale [167, 168].

Acrylamide is one of the most widely used quenchers of intrinsic protein fluorescence [169, 170]. Acrylamide, like oxygen, is a neutral quencher but has a much larger molecular size. This size difference results in a dramatic decrease in the rate of protein fluorescence quenching over that of oxygen [170, 171]. This decrease is due to the inaccessibility of the globular protein interior to the acrylamide molecule. Thus, acrylamide actively quenches only the intrinsic fluorescence of solvent-exposed residues. As applied to conformational analysis, acrylamide quenching was shown to decrease by two orders of magnitude as unstructured polypeptide chains transitioned to globular structure [170, 171]. Importantly, the degree of shielding of tryptophan residues by the intramolecular environment of the molten globule state was shown to be close to that determined for the native globular proteins, whereas the accessibility of tryptophans to acrylamide in the pre-molten globule state was closer to that in the unfolded polypeptide chain [142]. The fluorescence quenching by acrylamide of the single tryptophan residue in the beta 2 subunit of tryptophan synthase was used to verify the presence of a

conformational transition induced by interaction with the cofactor pyridoxal 5′-phosphate [172].

Simultaneous application of quenchers of different size, polarity, and charge (oxygen, nitrite, methyl vinyl ketone, nitrate, acrylate, acrylamide, acetone, methyl ethyl ketone, succinimide, etc.) could be more informative since it may yield information not only about protein dynamics but also about peculiarities of the local environment of chromophores. Information on the local environment of chromophores can also be retrieved from simple quenching experiments. In an example of simultaneous application of multiple quenchers, the heterogeneous fluorescence of yeast 3-phosphoglycerate kinase was resolved into two approximately equal components, one that was accessible and one that was inaccessible to the quencher succinimide [173]. The fluorescence of the inaccessible component was shown to be blue-shifted, and it exhibited a heterogeneous fluorescence decay that had steady-state acrylamide quenching properties and a temperature dependence typical of a single tryptophan in a buried environment. This component was assigned to the buried tryptophan W333. The presence of succinimide greatly simplified the fluorescence, allowing the buried tryptophan to be studied with little interference from the exposed tryptophan [173].

8.2.6.3 Fluorescence Polarization and Anisotropy

Useful information about the mobility and aggregation state of macromolecules in solution can be obtained from analysis of fluorescence polarization or anisotropy. If the excitation beam is polarized and passed through a protein solution, fluorescence will be depolarized or remain partially polarized. The degree of fluorescence depolarization results from the following factors that characterize the structural state of the protein molecules: (1) mobility of the chromophores (strongly dependent on the viscosity of their environment) and (2) energy transfer between similar chromophores [163, 165, 174–178]. Furthermore, the relaxation times of tryptophan residues determined from polarized luminescence data are a reliable indicator of the compactness of the polypeptide chain. For example, it has been noted that the retention of intact disulfide bonds in the unfolded state often results in a nonessential decrease of intrinsic fluorescence polarization, whereas reduction of the disulfide bonds leads to a dramatic decrease in the luminescence polarization to values that are approximately equal for all proteins [177, 178]. The relaxation times of tryptophan residues determined by fluorescence polarization for α-lactalbumin [23, 179] and bovine carbonic anhydrase B [180] showed a high degree of protein compactness in both the native and the molten globule states.

8.2.6.4 Fluorescence Resonance Energy Transfer

Along with intrinsic protein fluorescence, the fluorescence of extrinsic chromophore groups is widely used in conformational studies. Extrinsic chromophores are divided into covalently attached labels and noncovalently interacting probes. Fluorescence labels are indispensable tools in studies of energy transfer between two chromophores. The essence of the phenomenon is that in the interaction of oscillators at small distances the electromagnetic field of the excited (donor) oscillator can induce oscillation in the non-excited (acceptor) oscillator [163, 165, 181]

(see chapter 17 in Part I). It should be noted that the transfer of excitation energy between the donor and the acceptor originates only upon the fulfillment of several conditions: (1) the absorption (excitation) spectrum of the acceptor overlaps with the emission (luminescence) spectrum of the donor (an essential prerequisite for resonance), (2) spatial proximity of the donor and the acceptor (within a few dozen angstroms), (3) a sufficiently high quantum yield of the donor, and (4) a favorable spatial orientation of the donor and acceptor. The biggest advantage, and hence the attractiveness, of fluorescence resonance energy transfer (FRET) is that it can be used as a molecular ruler to measure distances between the donor and acceptor. According to Förster, the efficiency of energy transfer, E, from the excited donor, D, to the non-excited acceptor, A, located from the D at a distance R_{DA} is determined by the equation [181]

$$E = \frac{1}{1 + \left(\frac{R_{DA}}{R_o}\right)^6} \tag{18}$$

where R_o is the characteristic donor-acceptor distance, so-called Förster distance, which has a characteristic value for any given donor-acceptor pair given by the equation [181]

$$R_o^6 = \frac{9000 \ln 10}{128\pi^5 N} \frac{\langle k^2 \rangle \phi_D}{n^4} \int_0^\infty F_D(\lambda)\varepsilon_A(\lambda)\lambda^4 \, d\lambda \tag{19}$$

where the parameter ϕ_D is the fluorescence quantum yield of the donor in the absence of the acceptor, n is the refractive index of the medium, N is the Avogadro's number, λ is the wavelength, $F_D(\lambda)$ is the fluorescence spectrum of the donor with the total area normalized to unity, and $\varepsilon_A(\lambda)$ is the molar extinction coefficient of the acceptor. These parameters are obtained directly from independent experiments. Finally, $\langle k^2 \rangle$ represents the effect of the relative orientations of the donor and acceptor transition dipoles on the energy transfer efficiency. For a particular donor-acceptor orientation, this parameter is given as

$$k = (\cos \alpha - 3 \cos \beta \cos \gamma) \tag{20}$$

where α is the angle between the transition moments of the donor and the acceptor and β and γ are the angles between the donor and acceptor transition moments and the donor-acceptor vector, respectively. Experimentally, the efficiency of direct energy transfer, E, is calculated as the relative loss of donor fluorescence due to the interaction with the acceptor [163, 181]:

$$E = 1 - \frac{\phi_{D,A}}{\phi_D} \tag{21}$$

where ϕ_D and $\phi_{D,A}$ are the fluorescence quantum yields of the donor in the absence and the presence of acceptor, respectively.

For FRET experiments, one typically uses the intrinsic chromophores (tyrosines or tryptophans) as donors and covalently attached chromophores (such as dansyl) as acceptors. According to Eq. (18), the efficiency of energy transfer is proportional to the inverse sixth power of the distance between donor and acceptor. Obviously, structural changes within a protein molecule might be accompanied by changes in this distance, giving rise to the considerable changes in energy transfer. FRET has been used to show that the urea-induced unfolding of proteins is accompanied by a considerable increase in hydrodynamic dimensions. This expansion resulted in a significant decrease in the efficiency of energy transfer from the aromatic amino acids within the protein (donor) to the covalently attached dansyl (acceptor).

An elegant approach based on the unique spectroscopic properties of nitrated tyrosine (which has maximal absorbance at ~350 nm, does not emit light, and serves as an acceptor for tryptophan) has been recently elaborated [182–187]. For these experiments tyrosine residues are modified by reaction with tetranitromethane to convert them to a nitro form, Tyr(NO_2). The extent of decrease of tryptophan fluorescence in the presence of Tyr(NO_2) provides a measure of average distance (R_{DA}) between these residues. This approach has been applied to study the 3-D structure of apomyoglobin in different conformational states [187]. These conformations included the native, molten globule, and unfolded conformations. The A-helix of horse myoglobin contains Trp7 and Trp14, the G-helix contains Tyr103, and the H-helix contains Tyr146. Both tyrosine residues can be converted successively into the nitro form [186]. Comparison of tryptophan fluorescence in unmodified and modified apomyoglobin permits the evaluation of the distances from tryptophan residues to individual tyrosine residues (i.e., the distances between identified points on the protein). Employing this energy transfer method to a variety of nonnative forms of horse apomyoglobin revealed that the helical complex formed by the A-, G-, and H-helices exists in both the molten globule and premolten globule states [187].

8.2.6.5 **ANS Fluorescence**

Hydrophobic fluorescent probes can be used to detect the hydrophobic regions of protein molecules exposed to the solvent. Hydrophobic fluorescent probes characteristically exhibit intense fluorescence upon interaction with protein and low fluorescence intensity in aqueous solutions. One such probe that is frequently used for studying the structural properties of protein molecules is 8-anilino-1-naphthalene sulfonate (ANS) [188–190]. Interest in this probe reached its peak after it was shown that there was a predominant interaction of ANS with the equilibrium and kinetic folding intermediates in comparison with the native and completely unfolded states of globular proteins [180, 190–193]. The interaction of ANS with protein molecules in the molten globular state is accompanied by a pronounced blue shift of maximal fluorescence and a significant increase of the probe fluorescence intensity, making the latter property a useful tool for the detection of partially folded intermediates in the process of protein folding (Figure 8.6A). Furthermore, the interaction of ANS with protein is also accompanied by a change in the fluorescence lifetime [192, 193]. Fluorescence decay of free ANS is well described by the

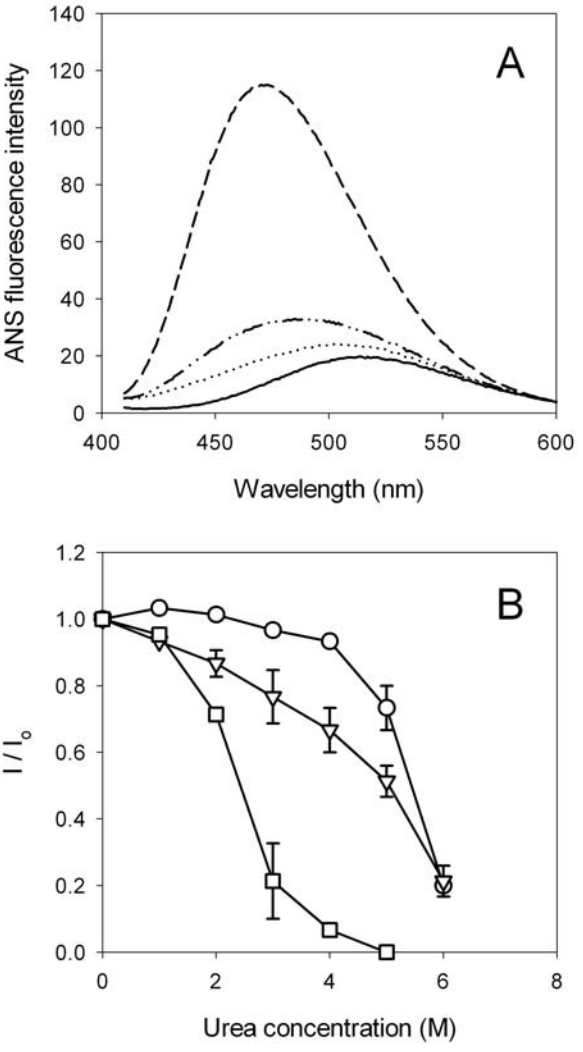

Fig. 8.6. ANS interaction with proteins. (A) ANS fluorescence spectra measured for free dye (solid line) and in the presence of natively disordered coil-like α-synuclein (dotted line), natively disordered pre-molten globule-like caldesmon 636–771 fragment (dash-dot-dotted line), and molten globule state of α-lactalbumin (dashed line). The native molten globular domain of clusterin has an ANS spectrum comparable with that of the molten globular state of α-lactalbumin (see text). (B) Dependence of the ANS fluorescence intensity on urea concentration measured for a series of rigid globular proteins capable of ANS binding: bovine serum albumin (circles), apomyoglobin, pH 7.5 (squares), and hexokinase (inverse triangles).

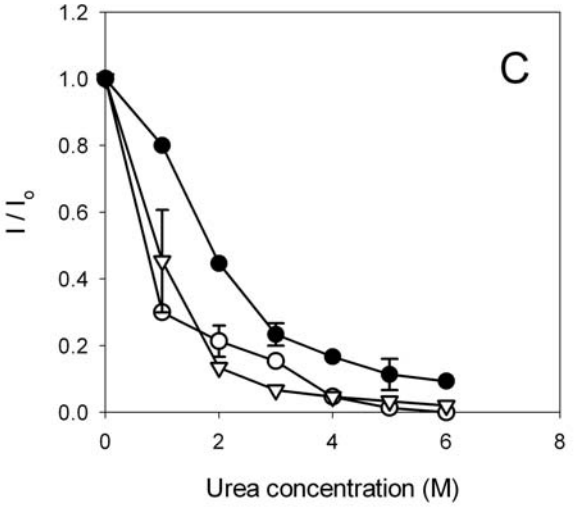

Fig. 8.6. (C) Dependence of the ANS fluorescence intensity on urea concentration measured for a series of molten globular proteins: apomyoglobin, pH 2.0 (open circles), α-lactalbumin, pH 2.0 (open inverse triangles), and clusterin, a protein with a native molten globular domain (black circles).

monoexponential law. However, in the case of formation of complexes between ANS and proteins, fluorescence decay has a more complex dependence. In fact, analysis of the ANS fluorescence lifetimes of a number of proteins revealed that there are at least two types of ANS-protein complexes. The complexes of the first type are characterized by a fluorescence lifetime ranging from 1 to 5 ns. In this type, the probe molecules are bound to the surface hydrophobic clusters of the protein and remain relatively accessible to the solvent. Complexes of the second type are characterized by a fluorescence lifetime of 10 to 17 ns, with the probe molecules embedding themselves inside the protein molecule and therefore being poorly accessible to the solvent [192]. The interaction of ANS with both molten globules and pre-molten globules of different proteins exhibits fluorescence lifetimes characteristic of the second type, with molten globules reacting more strongly than pre-molten globules [134]. Furthermore, an increased affinity for ANS was shown to be a characteristic property of several natively disordered proteins.

Some native globular proteins also possess significant affinity to ANS [188–190]. However, ordered proteins unfold cooperatively, whereas the unfolding of molten globular forms are typically much less cooperative [194]. It has been found that urea titration of ANS fluorescence could be used to distinguish between the binding of ANS to the hydrophobic pocket of an ordered protein and the binding of ANS to a molten globule. This experimental approach has been successfully applied in studies of clusterin. Results like those in Figure 8.6B indicate that this protein likely contains a molten globule-like domain in its native state [21]. This con-

clusion follows from the comparison of denaturation profiles of clusterin with those for rigid and molten globular forms of a globular protein (Figure 8.6C).

An alternative method is based on comparing Stern-Volmer quenching curves for a polar quencher, acrylamide, with the quenching curves for a nonpolar quencher, trichloroethanol (TCE). The essence of this method is based on the following reasoning. If the hydrophobic groups surrounding a chromophore are rigidly packed, then both acrylamide and TCE are excluded from the potential contact with chromophore and therefore exhibit little quenching. On the other hand, if the hydrophobic groups surrounding the chromophore are loosely packed and dynamic, then the hydrophilic quencher, acrylamide, is still excluded and continues to show little quenching. However, the hydrophobic quencher, TCE, partitions into the hydrophobic region surrounding the chromophore, leading to quenching that is much stronger than if the chromophores were completely exposed on the protein surface. These concepts were proved during the characterization of three different forms of fd phage. The fluorescence emission maxima and intensities for the tryptophans in all three forms are nearly identical, suggesting that all of the environments had very similar overall polarities. For the fd filament there was a very little difference in the quenching by TCE or acrylamide, suggesting that the indole rings were in tightly packed environments. On the other hand, for the two contracted forms, quenching by TCE was much stronger than quenching by acrylamide. Furthermore, the quenching of the contracted forms by TCE was shown to be even stronger than the quenching of a free indole ring in water. This result was interpreted as indicating that the residues surrounding the tryptophans in the contracted forms of fd phage were likely to be highly dynamic (similar to the inside of an SDS micelle), thus leading to accumulation of TCE and therefore increased quenching [195]. We believe that this approach has useful features that provided additional insights into the molten globular state.

8.2.7 Conformational Stability

Intrinsic disorder may be detected by the analysis of protein conformational stability. For example, the presence or absence of a cooperative transition in a calorimetric melting curve is a simple and convenient criterion that indicates the presence or absence of a rigid tertiary structure [196–198] (see chapter 4 in Part I). Furthermore, the response of a protein to denaturing conditions may be used to discriminate between collapsed (molten globule-like) and extended intrinsic disorder (coil-like and pre-molten globule-like conformations). In fact, the increase in temperature and changes in pH (as well as the increase in urea or guanidinium chloride concentration) will induce relatively cooperative loss of the residual ordered structure in molten globule-like disordered proteins, whereas temperature and pH will bring formation of residual structure in native coils and native pre-molten globules (see sections 8.2.7.1 and 8.2.7.2). Furthermore, the steepness of urea- or guanidinium chloride-induced unfolding curves depends strongly on whether a given protein has a rigid tertiary structure (i.e., is a native globular protein) or is already

denatured and exists as a molten globule [194, 199]. To perform this type of analysis, the values of $\Delta\nu^{eff}$ (the difference in the number of denaturant molecules ''bound'' to one protein molecule in each of the two states) should be determined. This quantity should be compared to the $\Delta\nu^{eff}_{N\rightarrow U}$ and $\Delta\nu^{eff}_{MG\rightarrow U}$ values corresponding to the native-to-coil and molten globule-to-coil transitions in globular protein of that given molecular mass [194].

8.2.7.1 Effect of Temperature on Proteins with Extended Disorder

It has been pointed out that at low temperatures, natively disordered proteins with extended disorder show far-UV CD spectra typical of an unfolded polypeptide chain (see Section 8.2.4). However, as the temperature increases, the spectrum changes, consistent with temperature-induced formation of secondary structure [123, 135]. In fact, such behavior was observed for natively disordered proteins such as α-synuclein [119], the phosphodiesterase γ-subunit [200], the caldesmon 636–771 fragment [121], the extracellular domain of the nerve growth factor receptor [201] and α_s-casein [202]. Thus, an increase in temperature can induce the partial folding of natively disordered proteins, rather than the unfolding typical of globular proteins. The effects of elevated temperatures may be attributed to increased strength of the hydrophobic interaction at higher temperatures, leading to a stronger hydrophobic driving force for folding.

8.2.7.2 Effect of pH on Proteins with Extended Disorder

Several natively disordered proteins with extended disorder, including α-synuclein [119], prothymosin α [116], pig calpastatin domain I [203], histidine rich protein II [204], naturally occurring human peptide LL-37 [205], and several other proteins, show intriguing dependence of their structural parameters on pH. In fact, these proteins possess low structural complexity at neutral pH but have significant residual structure under conditions of extreme pH. These observations show that a decrease (or increase) in pH induces partial folding of natively disordered proteins due to the minimization of their large net charge present at neutral pH, thereby decreasing charge/charge intramolecular repulsion and permitting hydrophobic-driven collapse to partially folded conformations.

8.2.8 Mass Spectrometry-based High-resolution Hydrogen-Deuterium Exchange

To obtain high-resolution structural information using X-ray crystallography, it is necessary to produce crystals. This can be impossible for proteins with substantial amounts of intrinsic disorder. High-resolution structural information can also be provided by NMR, but this technique is limited by protein size and the need for high concentrations of protein. Mass spectrometry-based high-resolution hydrogen-deuterium exchange (MSHDX) shows promise in becoming a third source of high-resolution structural information.

Monitoring the exchange rate between main chain amides and solvent hydrogens as a method to study the structure of proteins has seen increased usage over

the past 40 years [206]. Hydrogen-deuterium exchange (HDX) rates are dependent on thermodynamics and dynamic behavior and thus yield information regarding the structural stability of the protein under study. The study of HDX as applied to proteins was initiated by Kaj Linderstrøm-Lang in the 1950s as a method to investigate Pauling's newly postulated α-helix and β-sheet secondary structures [207]. The two-step model of HDX is described as [208]

$$C^H \underset{k_{cl}}{\overset{k_{op}}{\rightleftharpoons}} O^H \underset{k_{ch}}{\overset{k_{ch}}{\rightleftharpoons}} O^D \underset{k_{op}}{\overset{k_{cl}}{\rightleftharpoons}} C^D \tag{22}$$

where H and D denote protonated and deuterated forms, respectively, of the "closed" or C (non-exchanging) and "open" or O (exchanging) conformations; k_{op} is the rate constant for the conformational change that exposes the hydrogen; k_{ch} is the rate constant for the chemical exchange reaction; and k_{cl} is the rate constant for the return to the closed conformation.

The fundamental equation for the observed exchange rate formulated by Linderstrøm-Lang still applies:

$$k_{ex} = \left(\frac{k_{op} \cdot k_{ch}}{k_{cl} + k_{op}}\right) \tag{23}$$

The EX2 HDX mechanism, where $k_{cl} \gg k_{ch}$, describes most proteins at or below neutral pH. In this case, k_{ex} can be found using the following equation:

$$k_{ex} = \left(\frac{k_{op} \cdot k_{ch}}{k_{cl}}\right) = K_{op} \cdot k_{ch} \tag{24}$$

where K_{op} is the unfolding equilibrium constant that is also equal to the ratio of the observed rate (k_{ex}) to that of a random coil amide (k_{ch}).

HDX rates for random coil amides (k_{ch}), which depend on pH, primary sequence, and temperature, can be obtained from studies of peptide behavior [209]. The ratio of the observed rate of exchange (k_{ex}) to that of a random coil (k_{ch}) relates to the free energy of unfolding by the following equation:

$$\Delta G_{op} = -RT \ln\left(\frac{k_{ex}}{k_{ch}}\right) = -RT \ln(K_{op}) \tag{25}$$

Eq. (25) shows that there is a logarithmic correlation between the exchange rate and the conformation stability, i.e., the faster the exchange rate, the less stable the folded state. Being initially developed to study protein folding on a global scale, this formalism could also be used to analyze the intrinsic dynamic behavior of proteins and, most attractively, to quantify the stability of localized regions within protein molecules.

Hydrogen bonding, accessibility to the protein surface, and flexibility of the immediate and adjacent regions affect the HDX rate. The combined contribution of these structural and dynamic factors is termed the "protection factor," which has

been observed to vary by as much as 10^8-fold [210]. Based on these observations, it has been suggested that each amide hydrogen in the polypeptide can be viewed as a sensor of the thermodynamic stability of localized regions within the protein structure [211]. HDX can yield data to single-amide resolution.

In the 1960s, HDX rates were determined using tritium incorporation, size-exclusion chromatography, and liquid scintillation counting [212]. Structural resolution remained a limitation of this procedure. Improvements in resolution were facilitated by separating fragments using HPLC and analysis of tritium or deuterium incorporation using mass spectrometric methods [212–214, 405]. Recent improvements in automation, consisting of solid-phase proteolysis, automated liquid handling and sample preparation, online ESI MS, and specialized data reduction software, have enhanced throughput and sequence coverage of MSHDX [211]. As high as six-amide resolution has been achieved [211]. The use of multiple proteases to generate more overlaps in the peptide map can be used to increase the resolution even further.

Crystallization success rates can be improved by detecting and excluding sequences coding for unstructured regions when designing recombinant expression constructs. As part of a structural genomics effort, 24 proteins from *Thermotoga maritima* were analyzed using MSHDX to detect unstructured regions [215]. Prior to HDX analysis, parameters affecting fragmentation were optimized to maximize the number of fragments available for analysis. These conditions included denaturant concentration, protease type, and duration of incubation. As a prerequisite for MSHDX analysis, the ability to generate complete fragment maps using SYQUEST (Thermo Finnigan, San Jose, CA) and DXMS data reduction software was tested for each protein. Satisfactory fragment maps were generated for 21 of the 24 proteins. Next, labeling conditions were optimized for discrimination of fast-exchanging amide protons. In this procedure, the proteins were subjected to proteolysis prior to exchange and HDX analysis. An exchange duration of 10 s was determined to be sufficient to allow differentiation between deuterated freely solvated and non-deuterated inaccessible amides. MSHDX analysis detected regions of rapidly changing amides that were greater than 10% of total protein length in five of the proteins. From these five, MSHDX analysis led to the construction of deletion mutants for two recalcitrant proteins. Proteins produced from these two deletion mutants were subsequently crystallized, and their structures solved [215].

8.2.9
Protease Sensitivity

Numerous enzymes, including trypsin, pepsin and carboxypeptidase, catalyze the hydrolysis of peptide bonds, including trypsin, pepsin, carboxy peptidase, etc. Those that cleave at specific sites within protein chains have long been used to probe protein structure. In the 1920s Wu and others showed that native (ordered) proteins are typically much more resistant to protease digestion than are denatured (disordered) forms [216]. These early indications were substantiated over the next

~20 years [217]. Increasing the stability of a protein, e.g., by ligand or substrate binding, in turn often leads to reduced digestion rates [218].

In essentially all biochemistry textbooks, the structure of proteins is described as a hierarchy. The amino acid sequence is the primary structure; the local folding of the backbone into helices, sheets, turns, etc. is the secondary structure; and the overall arrangement and interactions of the secondary structural elements make up the tertiary structure. Many details of this hierarchy were determined from the first protein 3-D structure [16], but the original proposal for the primary-secondary-tertiary hierarchy was based on differential protease digestion rates over the three types of structure [217].

While acknowledging that flexible protein regions are easy targets for proteolysis, some researchers argued that the surface exposure of susceptible amino acids in appropriate conformations could provide important sites for accelerated digestion rates [219]. Indeed, proteins that inhibit proteases, such as soybean trypsin inhibitor [220], have local regions of 3-D structure that fit the active sites and bind irreversibly to their target proteases. Despite the examples provided by the inhibitors, susceptible surface digestion sites in ordered proteins are not very common [221, 222]. Despite the paucity of examples, the importance of surface exposure rather than flexibility or disorder seems to have become widely accepted as the main feature determining protease sensitivity.

In the well-studied protease trypsin, most of the lysine and arginine target residues are located on protein surfaces, but, as mentioned above, very few of these are actually sites of digestion when located in regions of organized structure. Starting with a few protein examples having specific surface-accessible digestion sites, attempts were made to use molecular simulation methods to dock the backbones of susceptible residues into the active site of trypsin. These studies suggested the need to unfold more than 10 residues to fit each target residue's backbone into trypsin's active site [223]. Indeed, recent studies show that backbone hydrogen bonds are protected from water by being surrounded or wrapped with hydrophobic side chains from nearby residues, with essentially every ordered residue being well wrapped [224]. Backbone hydrogen bond wrapping and binding the backbone deep within trypsin's active site are mutually exclusive, and so the requirement for local unfolding (unwrapping) is easily understood.

Direct support for the importance of local unfolding has been provided by comparison of the digestion rates of myoglobin and apomyoglobin [225]. Myoglobin is digested very slowly by several different proteases. Removal of the heme leads to local unfolding of the F-helix. This disordered loop becomes the site of very rapid digestion by several different proteases including trypsin. The trypsin digestion rate following the order-to-disorder transition of the F-helix is at least five orders of magnitude faster.

Many fully ordered proteins, such as the myoglobin example given above, are digested by proteases without observable intermediates of significant size. That is, if digestion progress were followed using PAGE, myoglobin would be seen to disappear and small fragments would appear, but mid-sized intermediates would not be observed. In contrast, digestion of the F-helix in apomyoglobin leads to two rela-

tively stable mid-sized fragments. The likely cause of the lack of observable mid-sized intermediates for fully ordered proteins is that digestion proceeds at multiple sites within the ordered regions of the protein. Access to these sites is mediated by transient unfolding events within ordered regions that allow initial digestion events. These initial cuts perturb the local structure and inhibit refolding. The sum of these changes leads to the exposure of multiple protease sites, which are rapidly cleaved in a random order. Additional transient unfolding events elsewhere in the structure lead to the same outcome. Thus the regions of the protein where structure has been disturbed become rapidly digested into a multitude of different-sized intermediate fragments without the accumulation of an observable quantity of any particular mid-sized intermediate [225].

Molten globules have also been probed by protease digestion [226]. Protease digestion of molten globules leads rapidly to multiple mid-sized fragments; upon further digestion, the intermediates convert to smaller-sized fragments consistent with nearly complete digestion. The transient stability of several mid-sized intermediates suggests that molten globules have multiple regions of high flexibility that are easy to digest interspersed with stabler structured regions that are resistant to digestion.

At this time we have not found published, systematic studies of fully unfolded, natively disordered proteins. One would expect such proteins to undergo digestion in a random fashion with all of the target residues equally accessible to digestion and with only sequence-dependent effects to modulate the digestion rates at the various sites. If this general picture were true, then proteolytic digestion would lead to rapid conversion of the primary protein into small fragments, without significant amounts of transient, mid-sized intermediates. Highly disordered proteins such as $p21^{Waf1/Cip1/Sdi1}$ [402, 403] and cytochrome *c* [404] undergo digestion to small fragments without any observable intermediates, as suggested here. The digestion patterns of extensively unfolded proteins likely resemble those of fully folded proteins: both evidently lack the accumulation of mid-sized intermediates. However, the two types of proteins can be distinguished by their vastly different digestion rates: extensively unfolded proteins would be expected to be digested at least 10^5 times faster than fully folded forms.

8.2.10
Prediction from Sequence

Amino acid sequence codes for protein 3-D structure [5]. Since native disorder can be viewed as a type of structure, we wanted to test whether the amino acid compositions of disordered regions differed from the compositions of ordered regions and, if so, whether the types of enrichments and depletions gave insight into the disorder. Thus, we studied amino acid compositions of collections of both ordered and natively disordered protein regions longer than 30 amino acids. We chose such long regions to lessen the chance that non-local interactions would complicate our analysis.

Natively disordered sequences characterized by X-ray diffraction, NMR spectros-

copy, and CD spectroscopy all contain similar amino acid compositions, and these are very different from the compositions of the ordered parts of proteins in PDB. For example, compared to the ordered proteins, natively disordered proteins contain (on average) 50% less W, 40% less F, 50% less isoleucine, 40% less Y, and 25% or so less C, V, and L, but 30% more K, 40% more E, 40% more P, and 25% more S, Q, and R [31]. Thus, natively disordered proteins and regions are substantially enriched in typically hydrophilic residues found on protein surfaces and significantly depleted of hydrophobic, especially aromatic, residues found in protein interiors. These data help to explain why natively disordered proteins fail to form persistent, well-organized 3-D structure.

Because ordered and disordered proteins contain significantly different amino acid compositions, it is possible to construct order/disorder predictors that use amino acid sequence data as inputs. By now, several researchers have published predictors of order and disorder [13, 30, 109, 227–233]. The first predictor, developed by R. J. P. Williams, separated just two natively disordered proteins from a small set of ordered proteins by noting the abnormally high charge/hydrophobic ratio for the two natively disordered proteins. This paper is significant as being the first indication that natively disordered proteins have amino acid compositions that differ substantially from those of proteins with 3-D structure. The predictor by Uversky et al. [227] also utilizes the relative abundance of charged and hydrophobic groups, but on a much larger set of proteins. Most of the other predictors [30, 109, 229–233] utilize neural networks.

Predicting order and disorder was included in the most recent cycle of the Critical Assessment of Protein Structure Prediction (CASP) [234]. While the summary publication contained papers from two sets of researchers [109, 233], several additional groups participated. All of the groups achieved similar levels of accuracy [234]. Furthermore, prediction accuracies were on the order of 90% or so for regions of order and 75–80% for regions of intrinsic disorder. These values are significantly above what could be expected by chance. The predictability of native disorder from sequence further supports the conjecture that natively disordered proteins and regions lack specific 3-D structures as a result of their amino acid sequences. That is, amino acid sequence codes for both order and disorder.

8.2.11 Advantage of Multiple Methods

Given the limitations of the various physical methods, it is useful if natively disordered proteins are characterized by multiple methods. Each approach gives a slightly different view, with better understanding arising from the synthesis of the different perspectives (see chapter 2 in Part I).

A significant difficulty with long disordered regions identified by X-ray diffraction is that the missing coordinates could indicate either native disorder or a wobbly domain that moves as a folded, ordered, rigid body. Thus, it is especially useful if X-ray-indicated disorder is confirmed by additional methods. The X-ray-indicated regions of disorder in calcineurin [29, 235], clotting factor Xa [236–238], histone H5 (C. Crane-Robinson, personal communication) [239–241], and topoisomerase

II (J. M. Berger, personal communication) [242–244] were all confirmed by limited proteolysis. The X-ray-indicated regions of disorder in Bcl-X_L [245–248], the gene 3 protein (g3p) of filamentous phage [249–251], and the negative factor of HIV1 (Nef) [252–255] were all confirmed by NMR spectroscopy. Given the importance of natively disordered regions, it would be helpful if disordered regions indicated by X-ray were routinely subjected to further study by an alternative method.

To illustrate the advantages of combining X-ray and NMR analysis, a hypothetical example is given here. Suppose an X-ray structure reveals that a protein has a short N-terminal disordered region, a central region composed of an ordered region flanked by two disordered segments, and a long C-terminal disordered region. Figure 8.7 shows the expected $^{15}N\{^1H\}$-NOE spectra for two different possibilities. Figure 8.7A shows the expected result if all three regions of missing electron density are truly disordered with very little secondary structure: in this case all three regions of missing electron density give negative values, indicating unfolded, peptide-like motions for these segments. In Figure 8.7B, the C-terminal region shows a short region of disorder followed by a large region of order; this would be consistent with an ordered but wobbly domain that would lead to missing electron density in the X-ray structure.

The nucleoprotein N of the measles virus contains more than 100 disordered residues at its C-terminus, a region called Ntail. The disordered character of Ntail was first identified by prediction and was confirmed by Ntail's hypersensitivity to protease digestion and by its NMR and CD spectra [256]. Predictions on the N proteins of related Paramyxoviridae indicate that the Ntail regions, which have hypervariable sequences, are all predicted to be natively disordered [257]. Cloning, expressing, and isolation of the Ntail region have enabled multiple studies of this region. The native disorder of this region by now has been confirmed by CD spectroscopy, SAXS, and dynamic light scattering (for the determination of *Rs*) [257]. The Ntail is apparently of the pre-molten globule type. Furthermore, although natively disordered and separated from the remainder of the molecule, Ntail retains its biological function of binding to a protein partner [258].

8.3
Do Natively Disordered Proteins Exist Inside Cells?

8.3.1
Evolution of Ordered and Disordered Proteins Is Fundamentally Different

8.3.1.1 The Evolution of Natively Disordered Proteins

Low-resolution structural models of novel proteins can be generated based on sequence similarity and evolutionary relationships to proteins with known structures [259–265]. This process assumes that the proteins being compared adopt compact rigid structures. Natively disordered proteins have important biological functions, and analysis of genome sequence data has revealed that proteins with intrinsically disordered segments longer than 50 amino acids are common in nature [20, 30, 266–271]. The lack of biophysical data characterizing the partially collapsed dy-

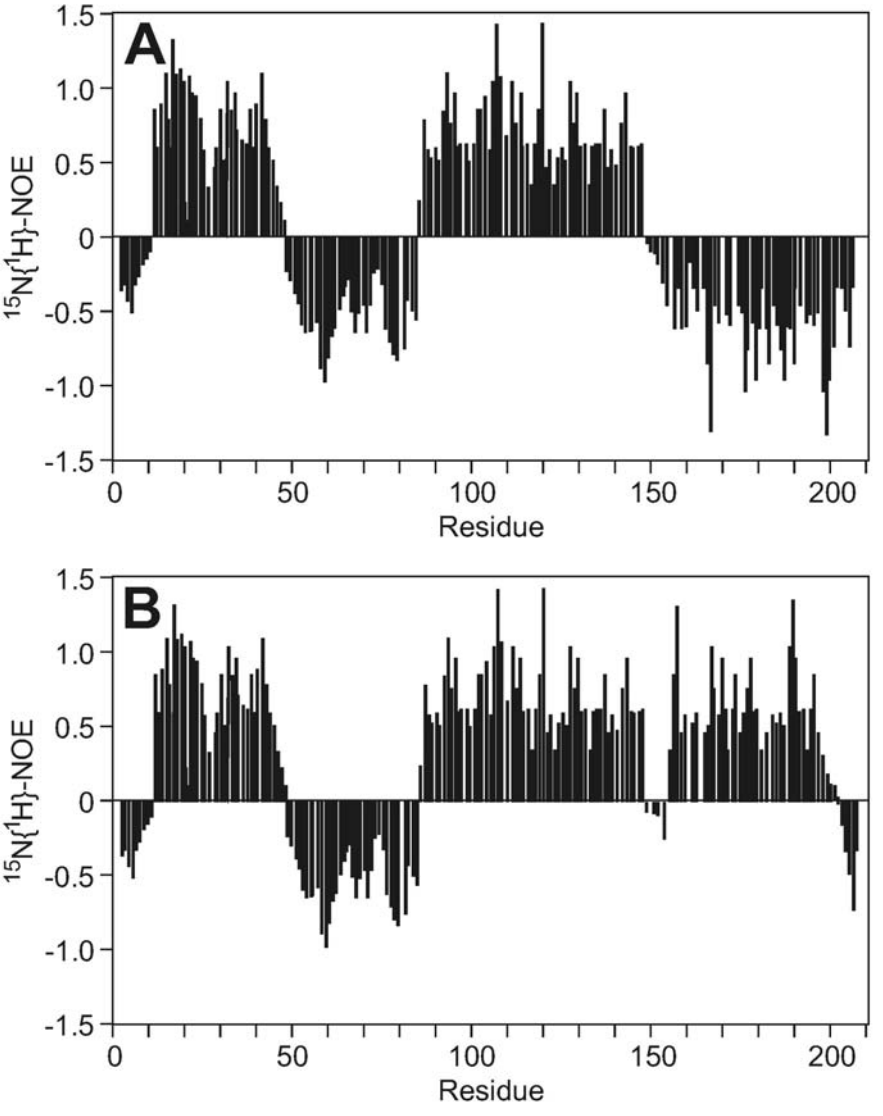

Fig. 8.7. Idealized steady-state heteronuclear $^{15}N\{^1H\}$-NOE for the backbone amides of the hypothetical protein discussed in the text. The domain profile of this protein based on the X-ray crystal structure is: short disordered N-terminal region/ordered region/disordered region/ordered region/long disordered C-terminal region. (A) $^{15}N\{^1H\}$-NOE that is in agreement with X-ray-determined structure; all regions of missing electron density in the X-ray crystal structure have negative values. (B) $^{15}N\{^1H\}$-NOE indicating that the C-terminal domain is a wobbly domain (a structured domain attached via a short, flexible linker) and is not totally disordered as determined by X-ray crystallography.

namic structures of natively disordered proteins limits our ability to predict their existence based on sequence data. It also limits our understanding of how the sequences of such regions specify function, the presence or absence of residual structure, and degree of flexibility.

The evolution of globular protein structures depends on the maintenance of a nonpolar interior and a polar exterior to promote collapse and folding through the hydrophobic effect [261]. This is achieved by the placement and distribution of nonpolar amino acids so that those making favorable nonpolar contacts in the folded structure will be far apart in the linear sequence (so-called long-range interactions). Therefore, the evolution of globular protein structure is partly dependent on selection for this property. In addition to the hydrophobic effect, desolvation of backbone hydrogen bonds appears to be of similar importance [224].

The evolution of intrinsically disordered protein structure seems to depend on selection for other properties. Natively disordered proteins with extended disorder do not form globular structures and therefore do not have a requirement to maintain long-range interactions such as those required by globular proteins. This creates a potential for these sequences to accumulate more variation and to generate more sequence divergence than globular proteins (see Section 8.3.1.2). For globular proteins, the selection for structural motifs is apparent by sequence and structural comparison of evolutionarily related protein structures. In an attempt to develop evolutionary relationships for intrinsically disordered proteins, the Daughdrill lab is currently investigating the structure, dynamics, and function of a conserved flexible linker from the 70-kDa subunit of replication protein A (RPA70). The flexible linker for human RPA70 is ~70 residues long [269, 272]. For the handful of sequenced RPA70 homologues, the similarity among linker sequences varies significantly, going from 43% sequence identity between *Homo sapiens* and *Xenopus laevis* to no significant similarity between *Homo sapiens* and *Saccharomyces cerevisiae*. It is unclear which selective processes have resulted in the observed sequence variations among RPA70 linkers. It is also unclear how the observed sequence variation affects the structure and function of the linkers. If natural selection works to preserve flexible structures, then one would expect that the linkers from different species have evolved to the same level of flexibility although adopting different sequences. By testing this hypothesis, we will begin understanding the rules governing the evolution of natively disordered protein sequences.

8.3.1.2 **Adaptive Evolution and Protein Flexibility**

The ability to align multiple sequences and reconstruct phylogenies based on sequence data is essential to understanding molecular evolution. The development of reliable algorithms that can align multiple sequences and reconstruct phylogenies is encumbered by the presence of highly divergent segments within otherwise obviously related sequences [259, 260, 273, 274]. This problem appears to be especially acute for totally disordered proteins and disordered protein domains. We hypothesize that intrinsically disordered regions will have a higher rate of evolution than compact rigid structures because their rate of evolution is not constrained by the requirement to maintain long-range interactions. Genetic distance measure-

ments of the RPA70 homologues lend support to this hypothesis and suggest that the linker has evolved at a rate 1.5 to 5 times faster than the rest of RPA70 [275]. This study tested the evolutionary rate heterogeneity between intrinsically disordered regions and ordered regions of proteins by estimating the pairwise genetic distances among the ordered and disordered regions of 26 protein families that have at least one member with a region of disorder of 30 or more consecutive residues that has been characterized by X-ray crystallography or NMR. For five of the protein families, there were no significant differences in pairwise genetic distances between ordered and disordered sequences. Disordered regions evolved more rapidly than ordered regions for 19 of the 26 families. The known functions for some of these disordered regions were diverse, including flexible linkers and binding sites for protein, DNA, or RNA. The functions of other disordered regions were unknown. For the two remaining families, the disordered regions evolved significantly more slowly than the ordered regions. The functions of these more slowly evolving disordered regions included sites for DNA binding. According to the authors, much more work is needed to understand the underlying causes of the variability in the evolutionary rates of intrinsically ordered and disordered proteins. Figure 8.8 illustrates the point, showing the contrast between the protein sequence alignment for the flexible linker and a fragment of the ssDNA binding domain from eight RPA70 homologues. Because of the known functional consequences of linker deletion in RPA70 [272, 276–279], we are interested in how the level of functional selection for flexible regions is related to their evolutionary rates. As is observed for folded proteins, most likely this relationship depends on the function under selection [259–261, 273]. However, because the substitution rate for flexible regions can be uncoupled from the maintenance of long-range interactions, the exact dependence between the rate of evolution and functional selection should differ significantly from that observed for folded proteins. Experiments planned to test the functional consequences of swapping divergent flexible linkers between species will begin to address this subject.

8.3.1.3 Phylogeny Reconstruction and Protein Structure

We are interested in developing reliable algorithms that can align multiple sequences and reconstruct phylogenies for highly divergent sequences. We hypothesize that flexible linkers and other disordered protein domains will often be highly divergent. Recent efforts at phylogeny reconstruction using models that incorporate the effects of secondary structure and solvent accessibility on amino acid substitution rate and type have yielded significantly improved maximum likelihood scores [280–282]. These models depend on an empirically determined three-dimensional structure for at least one member in a homologous family and incorporate four classes of secondary structure (helix, sheet, turn, and coil) as well as two solvent accessibility classes (buried and exposed). In particular, the inclusion of a flexible secondary structure class (coil) is necessary to model the evolution of natively disordered protein domains. The coil category was based on relatively short regions (≤ 5 residues) whose ends are constrained by the compact globular part of the protein. For proteins with longer flexible regions, the current model must be adapted

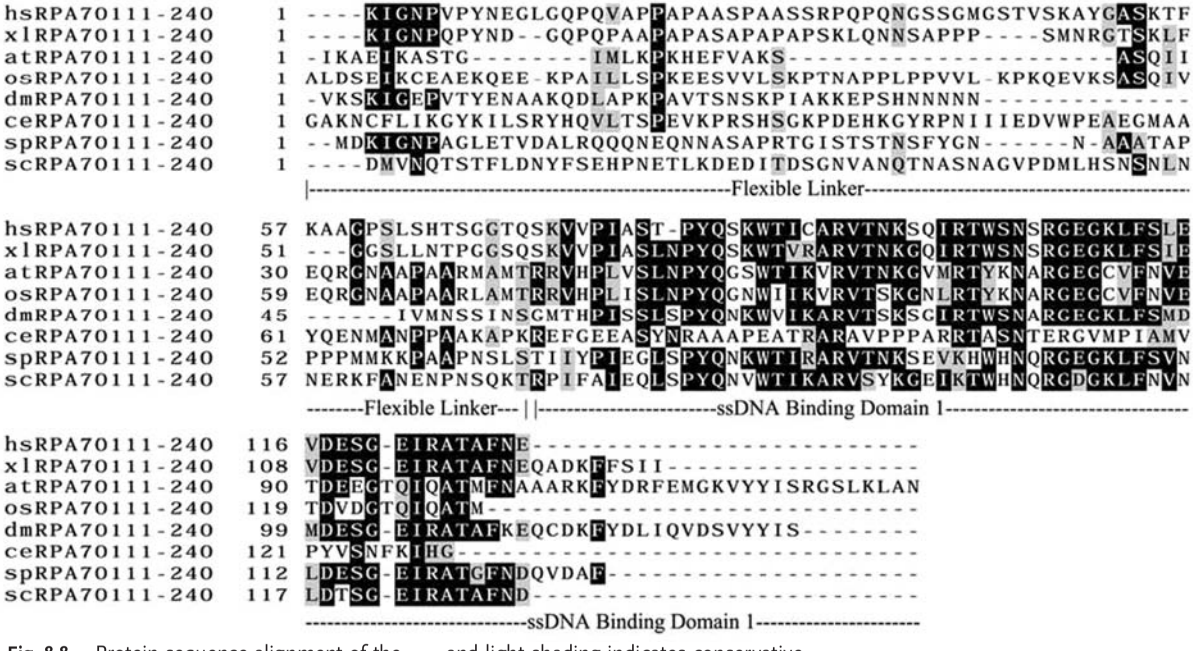

Fig. 8.8. Protein sequence alignment of the RPA70 flexible linker and a fragment of the first ssDNA-binding domain from *Homo sapiens* (hs), *Xenopus laevis* (xl), *Arabidopsis thaliana* (at), *Oriza sativa* (os), *Drosophila melanogaster* (dm), *Caenorhabditis elegans* (ce), *Saccharomyces pombe* (sp), and *Saccharomyces cerevisiae* (sc). Dark shading indicates identity, and light shading indicates conservative substitutions. The alignment was performed using Clustal 1.8 for residues 111–240 of all eight sequences. The alignment shows the stark contrast in the level of sequence similarities between the ssDNA-binding domain and the flexible linker regions.

to incorporate structural classes that are based on the presence of residual secondary structure and the degree of flexibility estimated from NMR relaxation measurements.

Another important feature of protein evolution is the pattern of amino acid substitutions observed over time. For ordered proteins, the change of an amino acid into one of a similar chemical type is commonly observed, whereas the change to a chemically dissimilar one is rare. For example, isoleucine to leucine, aspartate to glutamate, and arginine to lysine are all commonly observed in related ordered proteins, while tryptophan to glycine, lysine to aspartate, and leucine to serine are all uncommon changes, especially for buried residues.

Patterns of amino acid substitutions are readily observed in substitution matrices used to assign values to various possible sequence alignments. These scoring matrices are constructed by first assembling a set of aligned sequences, typically with low rates of change in pairs of sequences so that there is confidence in the alignments. Given such a set of high-confidence alignments, the frequencies of the various amino acid substitutions are then calculated and used to build a scoring matrix. Important and commonly used scoring matrices are the PAM [283] and the Blossum [284] series.

To improve alignments of disordered regions, a scoring matrix for disordered regions was developed [285]. First, homologous groups of disordered proteins were aligned by standard protocols using the Blossum 62 scoring matrix. From this set of aligned sequences, a new scoring matrix was calculated and then realignment was carried out with this new scoring matrix. As compared to the first alignment, the new alignment was improved as estimated by a reduction in the sizes and number of gaps in the pairwise alignments. The new set of alignments was then used to develop a new scoring matrix, and a new set of alignments was generated. These steps were repeated in an iterative manner until little or no change was observed in successive sets of alignments and in successive scoring matrices.

The resulting scoring matrix for disordered regions showed significant differences from the Blossum 62 or PAM 250 scoring matrices [286]. Glycine/tryptophan, serine/glutamate, and alanine/lysine substitutions, for example, were much more common in aligned regions of native disorder as compared to aligned regions of ordered proteins. Since natively disordered regions lack specific structure and the accompanying specific amino acid interactions, substitutions of disparate amino acids are not so strongly inhibited by the need to conserve structure. Thus the commonness of such disparate substitutions in natively disordered regions is readily understood.

The commonly observed higher rates of amino acid change [287] and the distinctive pattern of amino acid substitutions [286] both strongly support the notion that native disorder exists inside the cell.

8.3.2
Direct Measurement by NMR

The inside of cells are extremely crowded, and proteins themselves do most of the crowding since they occupy 40% of a cell's volume and achieve concentrations of

greater than 500 g L^{-1} [288–290]. Despite the crowded nature of the cell's interior, almost all proteins are studied outside cells and in dilute solutions, i.e., total solute concentrations of less than 1 g L^{-1}. It is also clear that macromolecular and small-molecule crowding can increase protein stability [291–293]. Could some disordered proteins be artifacts of the way proteins are studied? Are some just unstable proteins that unfold in dilute solution? A recent study by Dedmon et al. [102] on a protein called FlgM shows that the answer to the question is yes and no. Some disordered proteins probably have structure in cells while others do not.

Bacteria use rotating flagella to move through liquids [294, 295]. The protein FlgM is part of the system controlling flagellar synthesis. It binds the transcription factor σ^{28}, arresting transcription of the genes encoding the late flagellar proteins. Transcription can resume when FlgM leaves the cell, most probably via extrusion through the partially assembled flagellum.

Free FlgM is mostly disordered in dilute solution, but NMR studies in dilute solution indicate that the C-terminal half of FlgM becomes structured on binding σ^{28}, as is shown by the disappearance of cross-peaks from residues in the C-terminal half of FlgM in the FlgM-σ^{28} complex [77, 267]. One signature of protein structure can be the absence of cross-peaks in ^{1}H-^{15}N HSQC NMR spectra because of conformational exchange [296–298]. The disappearance of cross-peaks results from chemical exchange between a disordered and more ordered form. Specifically, cross-peaks broaden until they are undetectable when the rate of chemical exchange between states is about the same as the difference in the resonance frequencies of the nuclei undergoing exchange. The bipartite behavior of FlgM (i.e., disappearance of cross-peaks from the C-terminal half with retention of cross-peaks from the N-terminal half) provides a valuable built-in control for studying the response of FlgM to different solution conditions.

How do these observations about the ability of FlgM to gain structure on binding its partner relate to what might happen in cells? Until recently, all protein NMR was performed in vitro on purified protein samples in dilute solution. Two years ago, Dötsch and colleagues showed the feasibility of obtaining the spectra of ^{15}N-labeled proteins inside living *Escherichia coli* cells [299–301]. Overexpression is key to the success of in-cell NMR. The protein of interest must contain a large proportion of the ^{15}N in the sample so that the spectrum of the overexpressed protein can be observed on top of signals arising from other ^{15}N-enriched proteins in the cell, which contribute to a uniform background.

^{15}N-enriched FlgM was found to give excellent in-cell NMR data [102]. About half the cross-peaks disappear in cells. Most importantly, the cross-peaks that disappear are the same ones that disappear on σ^{28} binding in simple buffered solution, and the cross-peaks that persist are the same ones that persist on σ^{28} binding. These data suggest that FlgM gains structure all by itself under the crowded conditions found in the cell, but it is important to rule out alternative explanations. There is a homologue of *S. typhimurium* σ^{28} in *E. coli*, but there is not enough of the homologue present in *E. coli* (i.e., FlgM is overexpressed, the σ^{28} homologue is not) for σ^{28}-FlgM binding to explain the results. Furthermore, the same behavior is observed in vitro – in the complete absence of σ^{28} – when intracellular crowding was mimicked by using 450 g L^{-1} glucose, 400 g L^{-1} bovine serum albumin, or

450 g L^{-1} ovalbumin. The lack of cross-peaks from the C-terminal half of the protein is not caused by degradation, because the FlgM can be isolated intact at the end of the in-cell experiment. The gain of structure in cells does not seem to be an artifact of FlgM overexpression because the total protein concentration is independent of FlgM expression. Two observations show that the presence or absence of cross-peaks is not simply a matter of viscosity. First, cross-peaks from the N-terminal half of FlgM are present under all conditions tested even though the relative viscosities of the solutions differ dramatically. Second, the absence of cross-peaks does not correlate with increased viscosity. Taken together, these data strongly suggest that even in the absence of its binding partner, the C-terminal portion of FlgM gains structure in cells and in crowded in vitro conditions.

Does this observation about the C-terminal part of FlgM mean that all intrinsically disordered proteins will gain structure under crowded conditions? No. First, the N-terminal part of FlgM remains disordered under crowded conditions both inside and outside the cell. Second, the same observation has been made for another protein under crowded conditions in vitro [302]. Third, as discussed below, several functions of disordered proteins require the absence of stable structure. Perhaps the N-terminal half of FlgM gains structure only upon binding some yet unknown molecule, or maybe it needs to remain disordered to ensure its exit from the cell. It is also important to note, however, that crowding can induce compaction even when it does not introduce structure [158].

In summary, some, but certainly not all, so-called natively disordered proteins will gain structure in cells. In terms of the equilibrium thermodynamics of protein stability (Eqs. (1) and (2)), these proteins are best considered as simply very unstable. This instability may be essential for function, e.g., allowing rapid degradation or facilitating exit from the cell. And, finally, it is important to consider this discussion in terms of Anfinsen's thermodynamic hypothesis. Specifically the last four words of his statement [5]: "the native conformation is determined by the totality of inter-atomic interactions and hence by the amino acid sequence, *in a given environment*."

8.4 Functional Repertoire

8.4.1 Molecular Recognition

8.4.1.1 The Coupling of Folding and Binding

Molecular recognition is an essential requirement for life. Protein/protein, protein/nucleic acid, and protein/ligand interactions initiate and regulate most cellular processes. Many natively disordered proteins can fold upon binding to other proteins or DNA. The loss of conformational entropy that occurs during folding can influence the kinetics and thermodynamics of binding [78, 267, 303–305]. The most appealing model for the coupling of folding and binding proposes an initial encounter complex that forms nonspecifically while the protein is still unfolded

[303]. The release of solvent will provide a favorable entropic contribution to the binding. The extent of this favourable effect depends on the amount of hydrophobic burial that occurs during the formation of the nonspecific encounter complex. This encounter complex will undergo a sequential selection to achieve a specific complex. Sequential selection is achieved by consecutive structural interconversions that increase the surface complementarity. A subsequent increase in surface complementarity leads to a stabler complex. Of course, this model does not address the possibility that folding to a single structure does not occur but rather the bound structure is dynamic and the overall stability is governed by a collection of competing interactions.

8.4.1.2 Structural Plasticity for the Purpose of Functional Plasticity

There is increasing evidence that multiple binding modes can be accommodated in protein/ligand, protein/protein, and protein/DNA interactions [306–311]. In some cases, different segments of a single polypeptide can be used for recognition of different substrates. In other cases a single protein surface can accommodate the coupled binding and folding of multiple polypeptide sequences into different structures. For instance, the phosphotyrosine-binding domain of the cell fate determinant Numb can recognize peptides that differ in both primary and secondary structure by engaging various amounts of the binding surface [308].

The importance of structural plasticity in molecular recognition is made more concrete by considering a specific example: the activation of calcineurin (CaN) by calmodulin (CaM). The calcium-dependent binding of CaM to CaN brings about exposure of CaN's serine-threonine phosphatase active site by displacement of the autoinhibitory peptide and thereby turns on the phosphatase activity (Figure 8.1). This interaction forms a bridge between phosphorylation-dephosphorylation-based signaling and calcium-based signaling. The CaN-CaM interaction plays important roles in a wide variety of eukaryotic cells. For example, dephosphorylation of Nfat by Ca^{2+}-CaM-activated CaN leads to killer T cell proliferation and foreign tissue rejection [312]; blockage of CaN activation by complexation with FK506-FK-binding protein leads to suppression of the rejection [313].

The intrinsic disorder (plasticity) of CaM-binding domains enables them to bind to a wide variety of target sequences [314, 315]. The four EF hands of CaM undergo disorder-to-order transitions upon Ca^{2+} binding [316]. The two domains of CaM are connected by a helix in the crystal, but NMR shows the central region to be melted in solution, thus providing a flexible hinge that enables CaM to wrap around its target helix [317]. On the CaN side, intrinsic disorder flanks the CaM target and thus provides space for CaM to wrap around its target helix [235]. Indeed, before the CaN disordered region was revealed to be missing electron density in its X-ray crystal structure, trypsin digestion had already indicated disorder in CaN's CaM-binding region [318, 319]. Similar trypsin digestion analyses show that many CaM-binding sites are within disordered regions.

8.4.1.3 Systems Where Disorder Increases Upon Binding

Two studies have shown that disorder can increase upon binding to hydrophobic ligands and proteins [320, 321]. Increased protein backbone conformational en-

tropy was observed for the mouse major urinary protein (MUP-I) upon binding the hydrophobic mouse pheromone 2-*sec*-butyl-4,5-dihydrothiazole [320]. ^{15}N relaxation measurements of free and pheromone-bound MUP-I were fitted using the Lipari-Szabo model-free approach [86, 87]. Order parameter differences were observed between free and bound MUP-I that were consistent with an increase in the conformational entropy. Out of 162 MUP-I residues, 68 showed significant reductions in S^2 upon pheromone binding. The changes were distributed throughout the β-barrel structure of MUP-I, with a particular prevalence in a helical turn proposed to form a ligand entry gate at one end of the binding cavity. The authors called into question assumptions that the protein backbone becomes more restricted upon ligand binding.

Increased side chain entropy facilitates effector binding to the signal transduction protein Cdc42Hs [321]. Cdc42Hs is a member of the Ras superfamily of GTP-binding proteins that displays a wide range of side chain flexibility. Methyl axis order parameters ranged from 0.3 ± 0.1 (highly disordered) in regions near the effector-binding site to 0.9 ± 0.1 in some helices. Upon effector binding, the majority of methyl groups showed a significant reduction in their order parameters, indicating increased entropy. Many of the methyl groups that showed increased disorder were not part of the effector-binding interface. The authors propose that increased methyl dynamics balance entropy losses as the largely unstructured effector peptide folds into an ordered structure upon binding.

Actually, there is an entire class of proteins for which ligand binding may be accompanied by destabilization of the native state [306, 307]. For example, the introduction of a Ca^{2+}-binding amino acid sequence did not affect the structure or stability of the T4 lysozyme in the absence of calcium. However, in the presence of this cation, the stability of the mutant protein was detectably less than that of wild-type T4 lysozyme. This instability suggests that the binding of Ca^{2+} might be accompanied by considerable conformational changes in the modified loop that lead to destabilization of the protein [322]. Similar effects have been described for the calcium-binding N-domain fragments of *Paramecium* calmodulin [323], rat calmodulin [324], and isolated domains of troponin C [325].

Similarly, the tertiary structure of calreticulin, a 46.8-kDa chaperone involved in the conformational maturation of glycoproteins in the lumen and endoplasmic reticulum, was distorted by Zn^{2+} binding, which resulted in a concomitant decrease in the conformational stability of this protein [326]. The zinc-induced structural perturbations and destabilization are characteristic of several calcium-binding proteins, including α-lactalbumin, parvalbumin, and recoverin [307].

Of special note are some biomedical implications of the observed destabilization upon binding. For example, β2-microglobulin is able to bind Cu^{2+}. The binding is accompanied by a significant destabilization of the protein, suggesting that the ion has a higher affinity for the unfolded form [327]. β2-microglobulin is a 12-kDa polypeptide that is necessary for the cell surface expression of the class I major histocompatibility complex (MHC). Turnover of MHC results in release of soluble β2-microglobulin, followed by its catabolism in the kidney. In patients suffering from kidney disease treated by dialysis, β2-microglobulin forms amyloid deposits

principally in the joints, resulting in a variety of arthropathies. Importantly, the zinc-induced destabilization of the β2-microglobulin native structure was implicated as the driving force of this amyloidosis [327].

8.4.2 Assembly/Disassembly

Protein crystallographers are often frustrated in attempts to ply their trade because disordered N- and C-termini prevent crystallization. The idea that such sequences have been retained by nature to frustrate crystallographers, although enticing, is probably invalid since the termini have been around longer than crystallographers. Instead, disordered termini are often conserved to facilitate assembly and disassembly of complex objects, such as viruses.

The main idea of disorder-assisted assembly is that sequences from several different proteins are required for the disordered termini to fold into a defined structure that stabilizes the assembly. In some instances, only one player is disordered, while in others disordered chains must interact to gain structure. Disorder-assisted assembly accomplishes two beneficial goals. First, it ensures assembly only when all the players are in their correct positions. Second, it prevents aggregation of individual components. For example, the N-terminal 20 residues of porcine muscle lactate dehydrogenase form a disordered tail in the monomer that is essential for tetramerization [328]. Namba has reviewed several of these systems, including examples from the assembly of tobacco mosaic virus, bacterial flagella, icosahedral viruses, and DNA/RNA complexes [329].

8.4.3 Highly Entropic Chains

These are the elite of protein disorder – proteins, whole or in part, that function only when disordered. Terms such as ''entropic bristles,'' ''entropic springs,'' and ''entropic clocks'' have been used to describe these systems, but these terms can be misleading because all matter, except for perfect crystals at 0 Kelvin, has nonzero entropy values.

Hoh set down the main concept in his contribution about entropic bristle domains [330]. Disordered regions functioning as entropic bristles within a binding site will block binding until the bristle is modified. The modification causes the disordered region to move to one side of the binding site. Members of this class can be recognized by the effects of deletion. That is, removal of the bristle should lead to permanent activation [330]. The C-terminal region of p53 has been shown to function as an entropic bristle domain of this type [330, 331]. Bristles can also act as springs when two sets of disordered proteins are brought into contact with each other. The interactions of neurofilaments may be controlled in this way [332–334].

An extended unfolded region is important for the timed inactivation of some

voltage-gated potassium channels [335]. The extended disordered region functions as one component of an entropic clock. Charge migrations within the tetrameric pore proteins are associated with the majority of state changes of voltage-gated K^+ ion channels [336]. However, the timing of the inactivation step is determined by the time it takes for a mobile domain to find and block the channel. The movement of the mobile domain is restricted by a tether composed of ~60 disordered residues (Figure 8.9). The timing of channel inactivation is a function of the length of the disordered tether [337]. Since ion channels serve to modulate the excitability of nerve cells, their malfunction can have substantial impact on human health.

One further example of entropic disordered region function is length adjustment within the muscle protein [338]. Please note, however, that for each of the three

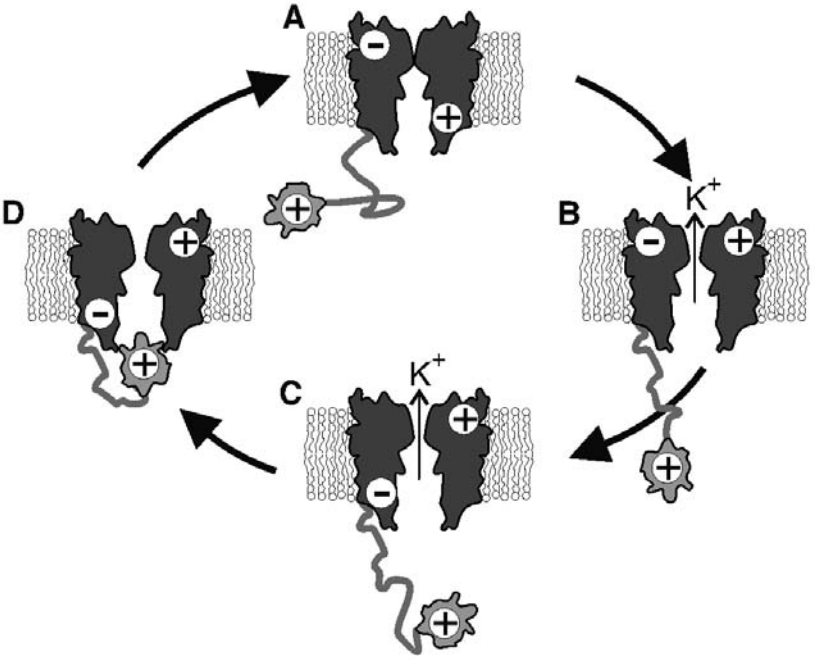

Fig. 8.9. Example of an entropic clock. Simplified model of a Shaker-type voltage-gated K^+ ion channel (dark grey) with a "ball-and-chain" timing mechanism. The ball-and-chain is comprised of an inactivation, or ball, domain (light grey) that is tethered to the pore assembly by a disordered chain of ~60 residues. For simplicity, only four of the proposed 10 states are shown [336]. The cytoplasmic side of the assembly is oriented downward. (A) Closed state prior to membrane depolarization. Note that conformational changes in the pore have sealed the channel and that a positive charge on the cytoplasmic side of the pore assembly excludes binding of the ball domain. (B) Open state following membrane depolarization. (C) After depolarization, the cytoplasmic side of the pore opening assumes a negative charge that facilitates interaction with the positively charged ball domain. (D) Inactivation of the channel occurs when the ball domain occludes the pore. The transition from (C) to (D) does not involve charge migration and can be modeled as a random walk of the ball domain towards the pore opening. (Portions of the figure are based on Antz et al. [396]).

examples described above, there are counter examples from related systems or proteins where the region either is absent or is replaced by a globular domain.

8.4.4 Protein Modification

As discussed above, protease digestion occurs preferentially in unfolded regions of proteins. The need to protect backbone hydrogen bonds in folded structure [224] and the need for extensive contacts with the backbone residues to bring about hydrolysis [222] are mutually exclusive. This can explain the observations that there is a very strong preference for protease-sensitive regions to be located in disordered regions [339, 340]. It is much less clear whether protein modification involving side chains would occur preferentially in ordered or disordered regions.

In a study of the functions associated with more than 100 long disordered regions, many were found to contain sites of protein modification [30, 31]. These modifications included phosphorylation, acetylation, fatty acylation, methylation, glycosylation, ubiquitination, and ADP ribosylation. These observations suggest the possibility that protein modifications commonly occur in regions of disorder.

Phosphorylation by the kinases and dephosphorylation by the phosphatases provide an extremely important signaling system for eukaryotic cells, with an estimate that up to one-third of eukaryotic proteins are phosphorylated [341]. As mentioned above, many sites of protein phosphorylation were found to be in regions structurally characterized as natively disordered [30, 31]. Thus, further study of the relationship between phosphorylation and disorder seems appropriate.

Several lines of evidence support the view that protein phosphorylation in eukaryotic cells occurs primarily in regions of disorder: (1) despite the very high interest in phosphorylation, very few structures in PDB exist for both the unphosphorylated and phosphorylated forms of the same protein [342, 343] (a possible explanation is that the prevalence of disorder in proteins that become phosphorylated tends to inhibit their crystallization [343, 344]); (2) nine structures of eukaryotic kinase substrates in their unphosphorylated forms show that the residues of the phosphorylation site have extended, irregular conformation that are consistent with disordered structure [343]; (3) the structures of substrate or inhibitor polypeptides indicate that the residues corresponding to the sites of phosphorylation are within segments that lack secondary structure and that are held in place not only by side chain burial but also by backbone hydrogen bonds to the surrounding kinase side chains [345–350] (just as for protease digestion, this is a strong indicator that the substrate must be locally unfolded before binding to its enzyme partner); (4) in a database of more than 1500 well-characterized sites of phosphorylation and a larger number of sites that are not phosphorylated, the residues flanking the sites of phosphorylation are substantially and systematically enriched in the same amino acids that promote protein disorder and are depleted in the amino acids that promote protein order [343]; (5) the sequence complexity distribution of the residues flanking phosphorylation sites matches almost exactly the complexity distribution obtained for a collection of experimentally characterized re-

gions of disorder, while the complexity distribution of the residues flanking non-phosphorylation sites matches almost exactly the complexity distribution obtained for a collection of ordered proteins. In addition, there is a high correspondence between the prediction of disorder and the occurrence of phosphorylation and, conversely, the prediction of order and the lack of phosphorylation (unpublished observations). This is expected from the amino acid compositions of the residues flanking phosphorylation and non-phosphorylation sites. A new predictor of phosphorylation exhibited small but significant improvement if predictions of order and disorder were added [343]. These observations support the suggestion that sites of protein phosphorylation occur preferentially in regions of native disorder.

Data support the suggestion that protease digestion and phosphorylation both occur preferentially within regions of disorder. Also, several other types of protein modification, such as acetylation, fatty acid acylation, ubiquitination, and methylation, have also been observed to occur in regions of intrinsic disorder [30, 31]. From these findings, it is tempting to suggest that sites of protein modification in eukaryotic cells universally exhibit a preference for natively disordered regions.

What might be the basis of a preference for locating sites of modification within regions of native disorder? For all of the examples discussed above, the modifying enzyme has to bind to and modify similar sites in a wide variety of proteins. If all the regions flanking these sites are disordered before binding to the modifying enzyme, it is easy to understand how a single enzyme could bind to and modify a wide variety of protein targets. If instead all of these regions bind as ordered structures, then there is the complicating feature that the proteins being regulated by the modification must all adopt the same local structure at the site of modification. This imposes significant constraints on the site of modification. The structural simplification that arises from locating the sites of modification within regions of disorder is herein proposed to be an important principle. Elsewhere we point out that a particular advantage of disorder for regulatory and signaling regions is that changes such as protein modification lead to large-scale disorder-to-order structural transitions: such large-scale structural changes are not subtle and so could be an advantage for signaling and regulation as compared to the much smaller changes that would be expected from the decoration of an ordered protein structure (see Section 8.1.3).

8.5 Importance of Disorder for Protein Folding

Interest in the unfolded protein state has increased markedly in recent years. A major motivation has been to better understand the structural transitions that occur as a protein acquires 3-D structure, both from the point of view of the mechanism of folding and from the point of view of the energetics. A major effort has been to connect structural models of the unfolded polypeptide chain with experimental data supporting the given model. The overall sizes of guanidinium chloride-denatured proteins fit the values expected for random coils when excluded

volume effects were taken into account [351]. For a true random coil, the Φ and Ψ angles of a given dipeptide are independent of the angles of the dipeptides before and after. This is often called the Flory isolated-pair hypothesis [352]. Both experiments and calculations call the isolated-pair hypothesis into question [353]. For example, using primarily repulsive terms, Pappu et al. [354] computed the effects of steric clash (or excluded volume) on blocked polyalanines of various lengths. Contrary to Flory's isolated hypothesis, they found that excluded volume effects were sufficient to lead to preferred backbone conformations, with the polyproline II helix being among the most preferred. Representing unfolded proteins as polymer chain models, which have the advantage of simplifications that result from ignoring most atomic details, is proving useful for modeling experimental data pertaining to protein stability, folding, and interactions [355].

While there has been substantial emphasis on the study of unfolded proteins as precursors to 3-D structures, as briefly described above, to our knowledge there has been no systematic discussion or studies of how natively disordered regions affect protein 3-D structure and folding kinetics. Here we will consider several possibilities, each of which is a simple hypothesis that has not yet been tested by experiment. These hypotheses form the basis for experiments into the effects of native disorder on protein structure and folding.

First, a well-known example with ample experimental support is provided. Trypsinogen folds into a stable 3-D structure, but compared to trypsin, the folding is incomplete and the protein is inactive. Trypsinogen's folding does involve the formation of the crucial catalytic triad, and yet trypsinogen remains inactive evidently because the binding pocket for the substrate lysine or arginine fails to form completely, e.g., remains natively disordered [12, 356]. Thus, trypsinogen, the precursor to trypsin, remains inactive and thus does not harm the interior of the cell. The folding into active trypsin is inhibited by a short region of native disorder at the amino terminus; this region is completely missing in the electron density map of trypsinogen [357]. Once trypsinogen has been exported from the cell, this disordered region is cleaved by trypsin. The amino terminus changes from a highly charged moiety into a hydrophobic terminus of isoleucine followed by valine (IV). In the absence of the natively disordered, charged extension, this IV terminus becomes capable of binding into a particular site elsewhere in the structure. This binding of the IV moieties brings about a disorder-to-order transition of trypsin's binding pocket, now enabling the protein to bind arginine or lysine and thereby converting inactive trypsinogen into active trypsin [358]. Even in the absence of the cleavage, high levels of an IV dipeptide can stimulate the protease activity of uncleaved trypsinogen by binding into the site used by the IV terminus [12]. We speculate that proteolytic removal of a natively disordered region may be a common mechanism for regulating protein folding and function, but we have not yet searched systematically for other examples.

While trypsinogen provides an example of a protein for which a region of native disorder inhibits protein folding, we speculate that there are proteins for which regions of native disorder promote protein folding. Suppose, for example, that a protein contained a short, highly charged region of native disorder and a folded do-

main with an opposite charge of significant magnitude. From various analyses suggesting that a high net charge can lead to a natively unfolded protein [123, 227, 359], the region of oppositely charged disorder might be essential for overall charge balance and, if so, would be required for protein folding. A simple experiment is proposed here: (1) identify example proteins in the PDB with short, highly charged tails and oppositely charged, folded domains; (2) determine which domains are likely not to fold without their oppositely charged tail by means of the net charge versus hydropathy plot [227]; (3) remove the charged tail by proteolysis or genetic engineering; and (4) compare the folding rate of the shorter protein with that of the full-length protein. The prediction is that, if located in the unfolded region of the net charge hydropathy plot, the shorter protein would fail to fold or would require higher ionic strength to fold as compared to the full-length protein.

Various theoretical analyses on protein folding have suggested relationships among the size, stability, and topology of a protein fold and the rate and mechanism by which the fold is achieved. The characterization of the folding of a large number of simple, single-domain proteins enabled detailed studies to test the various models and assertions regarding the mechanism of protein folding. The simple proteins in this set are characterized by having single domains; by the lack of prosthetic groups, disulfide bonds, and *cis* proline residues; and by two-state refolding kinetics. Despite the simplicity of this set, more than a million-fold variation in refolding rates was observed. A remarkable finding was that the statistically significant correlations among the folding rate, the transition state placement, and the relative contact order are observed, where the transition state placement is an estimate of the fraction of the burial of the hydrophobic surface area in the transition state as compared to the native state, and where the relative contact order is the length-normalized sequence separation between contacting residues in the native state [360]. A number of alternative empirical measures of topology were later shown to correlate about equally well with folding rates as does the relative contact order, including local secondary structure content [406], the number of sequence-distant contacts per residue [361], the fraction of contacts that are distant in the sequence [362], and the total contact distance [363]. The quality of these alternative measures supports the conjecture that contact order predicts rates, not because it is directly related to the mechanism of folding, but rather because it is related to an alternative physical parameter of importance [364].

Attempts to reconcile the observed relationship between contact order or other measures of topology and folding rates has led to the topomer search model [365], which was based substantially on similar prior models [366, 367]. Simply put, the topomer search model stipulates that the rate-limiting step in protein folding is the search for an unfolded conformation with the correct overall topology. The unfolded form with the correct topology then rapidly folds into the native state [364].

Assuming for the sake of discussion the basic correctness of the topomer search model, the expected effects of native disorder can be readily described. First let us consider natively disordered regions at the amino or carboxy terminus that do not affect the overall protein stability and that do not stabilize misfolded intermediates.

Such natively disordered regions would be expected to have very small effects on the folding rates. On the other hand, natively disordered internal loops would be expected to slow the rate of folding in a length-dependent manner. Indeed, a systematic study of the folding rates of simple, two-state proteins with natively disordered loops of varying lengths could provide a useful test of the topomer search model.

The relationship between the log of the folding rates of simple two-state proteins and the contact order value exhibits an r^2 value of about 0.8, suggesting that this measure captures in excess of 3/4 of the variance in the logarithms of the reported folding rates [364]. The topomer search model, which evidently captures the dependence of protein folding on the contact order, ignores variation in foldability along the sequence. On the other hand, predictors of order and disorder capture local sequence tendencies for order or disorder. Such a local tendency for disorder could be overridden by non-local interactions in the final native structure, and so a local tendency for disorder could be important for a folded protein even if the native structure does not exhibit actual disorder. We wonder whether there is any relationship between protein folding rates and variations in order/disorder tendencies along an amino acid sequence. That is, we wonder whether the 1/4 variability in the logarithms of the folding rate that is not captured by relative contact order could be related to differences in the amounts or in the organization of disorder tendencies along the amino acid sequences. Local regions with high tendencies for disorder could, for example, lead to very non-uniform polymer chain models by local alterations in the stiffness or persistence length; locating such anomalies at topologically critical sites could greatly speed up or slow down protein folding rates. These ideas could be tested both computationally and experimentally.

8.6 Experimental Protocols

In this section we include several protocols for NMR spectroscopy, X-ray crystallography, and circular dichroism spectropolarimetry. We focus on these methods because they are traditionally the most frequently used techniques to characterize native disorder in proteins. Protocols for small angle X-ray diffraction, hydrodynamic measurement, fluorescence methods, conformational stability, mass spectrometry-based high-resolution hydrogen-deuterium exchange, protease sensitivity, and prediction from sequence are available from the references cited in the above methods section.

8.6.1 NMR Spectroscopy

8.6.1.1 General Requirements

The following methods assume that the experimenter has access to a high field digital nuclear magnetic resonance spectrometer and a soluble, homogeneous pro-

tein sample at a concentration of ~1 mM. These methods also assume that the incorporation of an NMR-active isotope such as ^{15}N and/or ^{13}C is possible.

8.6.1.2 Measuring Transient Secondary Structure in Secondary Chemical Shifts

Resonance assignments are the first step in the analysis of protein structure using NMR. A convenient outcome of these measurements is the determination of protein secondary structure. The C_α, C_β, and C' chemical shifts are the most sensitive to phi and psi angles. To measure these chemical shifts, sensitivity-enhanced HNCACB and HNCO experiments can be performed on uniformly ^{15}N- and ^{13}C-labeled protein samples [368–370]. An appropriate digital resolution for the HNCACB and HNCO experiments is 9.8 Hz/pt in ^{1}H with 512 complex points, 47.1 Hz/pt in ^{13}C with 128 complex points, and, 34.4 Hz/pt in ^{15}N with 32 complex points. After transformation of the data, it is essential to apply the appropriate referencing before comparing the protein chemical shifts to random coil standards [67].

8.6.1.3 Measuring the Translational Diffusion Coefficient Using Pulsed Field Gradient Diffusion Experiments

Pulsed field gradient diffusion measurements can be made using a variation of the water-sLED sequence developed by Altieri et al. 1995 [69]. Collect data at an appropriate field strength, temperature, sweep width, gradient pulse width, and delay time. The amplitude of the gradient pulses should be varied from ~1–31 gauss cm^{-1} in increments of 2 gauss cm^{-1}. However, this range will vary depending on the protein and typically must be determined empirically. It is also possible to perform the experiment by varying the length of the gradient pulses and holding the magnitude constant [371]. The NMR data must be processed so that resonance intensity measurements can be made. An entire region of the spectrum can be integrated, or individual resolved resonances can be measured. Resonance assignments are not necessary, the experiment can be performed on an unlabeled sample, and it is probably best to integrate the resonances of non-labile nuclei. Data should be collected over at least a four-fold reduction in signal. Resonance intensity measurements should be normalized, averaged, and fit to the function relating the normalized resonance intensity, A, to the translational diffusion coefficient, D:

$$A = \exp(-Dg^2\delta^2\gamma^2(\Delta - \delta/3)) \tag{26}$$

where g and δ are, respectively, the magnitude and duration of the gradient pulses, Δ is the time between gradient pulses, and γ is the gyromagnetic ratio of the observed nucleus [372]. Nonlinear least-squares regression of a decaying exponential function onto the data can be used to extract D. It is useful to combine these measurements with another technique such as sedimentation to obtain information about the shape of the protein.

8.6.1.4 Relaxation Experiments

For ^{15}N relaxation experiments the spin-lattice relaxation rates (R_1), spin-spin relaxation rates (R_2), and ^{1}H-^{15}N NOEs can be measured by inverse-detected two-

dimensional NMR methods [81]. Spin-lattice relaxation rates are typically determined by collecting 8–12 two-dimensional spectra using relaxation delays from 10–1500 ms. Spin-spin relaxation rates can determined by collecting 8–12 two-dimensional spectra using spin-echo delays of 10–300 ms. Peak heights from each series of relaxation experiments are then fitted to a single decaying exponential. To measure the ^{1}H-^{15}N NOEs, one spectrum is acquired with a 3-s mixing time for the NOE to buildup and another spectrum is acquired with a 3-s recycle delay for a reference. It is often necessary to optimize this delay, as intrinsically disordered proteins and longer delays will attenuate larger-than-predicted negative NHNOE values for highly dynamic regions of the protein [85]. For all experiments, water suppression can be achieved by using pulsed field gradients. Uncertainties in measured peak heights are usually estimated from baseline noise level and, with good tuning and shimming, are typically less than 1% of the peak heights from the first R_1 and R_2 delay points.

8.6.1.5 Relaxation Data Analysis Using Reduced Spectral Density Mapping

Relaxation data are typically analyzed using the reduced spectral density mapping approach [80, 88, 373, 374]. The ^{15}N chemical shift anisotropy and the dipolar coupling between the amide ^{15}N nucleus and the attached proton have the greatest influence on the ^{15}N nuclear relaxation [89]:

$$R_1 = \left(\frac{d^2}{4}\right)[3J(\omega_N) + 6J(\omega_H + \omega_N) + J(\omega_H - \omega_N)] + c^2 J(\omega_N) \tag{27}$$

$$R_2 = \left(\frac{d^2}{8}\right)[4J(0) + 3J(\omega_N) + 3J(\omega_H + \omega_N) + 6J(\omega_H) + J(\omega_H - \omega_N)] + \left(\frac{c^2}{6}\right)[J(0) + 6J(\omega_N)] + R_{ex} \tag{28}$$

$$NOE = 1 + \left(\frac{d^2}{4R_1}\right)\left(\frac{\gamma_H}{\gamma_N}\right)[6J(\omega_H + \omega_N) - J(\omega_H - \omega_N)] \tag{29}$$

where $d = \left(\frac{\mu_0 h \gamma_H \gamma_N}{8\pi^2}\right)\langle r_{NH}^{-3}\rangle$ and $c = \frac{\omega_N \Delta\sigma}{\sqrt{3}}$, μ_0 is the permeability of free space, h is Planck's constant, γ_H and γ_N are the gyromagnetic ratios of ^{1}H and ^{15}N, respectively, r_{NH} is the amide bond length (1.02 Å), $\Delta\sigma$ is the chemical shift anisotropy (−160 ppm), and R_{ex} is the chemical exchange contribution to R_2. $J(\omega)$ is the power spectral density function defining the reorientation of the N–H bond vector by stochastic (global) and intramolecular motions. Reduced spectral density mapping uses an average value of $J(\omega_H)$ for the linear combinations of $J(\omega_H + \omega_N), J(\omega_H)$, and $J(\omega_H - \omega_N)$ leading to values of $J(0), J(\omega_N)$, and $J(\omega_H)$ that are given by:

$$\sigma_{NH} = R_1(NOE - 1)\frac{\gamma_N}{\gamma_H} \tag{30}$$

$$J(\omega_H) = \frac{4\sigma_{NH}}{5d^2} \tag{31}$$

$$J(\omega_N) = \frac{[4R_1 - 5\sigma_{NH}]}{[3d^2 + 4c^2]} \tag{32}$$

$$J(0) = \frac{[6R_2 - 3R_1 - 2.72\sigma_{NH}]}{[3d^2 + 4c^2]} \tag{33}$$

This approach estimates the magnitude of the spectral density function at the given frequencies, making no assumptions about the form of the spectral density function or about the molecular behavior giving rise to the relaxation.

8.6.1.6 In-cell NMR

Although a potentially powerful technique, there are few published studies involving in-cell NMR [102, 299–301, 375]. Therefore, the suggestions here will have to be quite general. Most of the following suggestions are distilled from publications by Volker Dötsch's group, and a few are from the Pielak laboratory.

Most importantly, protein expression is, at present, more of an art than a science; the suitability of each protein expression system (i.e., inducer concentration, induction time, cell density at induction) must be determined empirically. Although yeast and insect cells have been tried, the technique currently works best for proteins expressed in *E. coli*. Overexpression of the protein to be studied in ^{15}N- or ^{13}C-enriched media is essential. Overexpression is operationally defined as the ability to isolate greater than 10 mg of pure protein from 1 L of saturated culture, using the same media and conditions that will be used for the in-cell NMR experiment. It is best to check expression using unenriched media first. The HSQC experiment works well for in-cell NMR. It is important to know what the ''background'' spectrum looks like when the experiment fails. Background spectra contain cross-peaks from metabolites that become enriched in ^{15}N. That is, a spectrum without protein overexpression (i.e., untransformed cells) should be collected. It can often take as long as 15 h to obtain a spectrum with a conventional probe. Using a cryoprobe can dramatically decrease this time. When the experiment is over, it is important to perform dilution and plating experiments to show that the cells are still alive and that the protein of interest has remained inside the cells. Gentle centrifugation of the NMR sample followed by SDS-PAGE analysis of both the supernatant and the pellet is the best way to show that the protein was overexpressed and did not leave the cells.

8.6.2 X-ray Crystallography

Determination of protein structure by X-ray crystallography has become almost routine once crystals are obtained. Many excellent books and papers provide the details of protein structure determination by X-ray crystallography. Two books that emphasize practical experimental approaches are by Stout and Jensen [376] and by McRee [377]. In this section, we will concentrate on how to obtain crystals in the face of native disorder.

The presence of large regions of disorder can block attempts to crystallize pro-

teins. Failure to obtain crystals is the single greatest experimental problem in X-ray crystallography. Here, we present calsequestrin as a case study illustrating the successful crystallization of a natively disordered protein.

Calsequestrin is a calcium-storage protein located within the sarcoplasmic reticulum that binds 40–50 calcium ions with ~1 mM affinity. Calsequestrin is a highly acidic protein with many of its acidic residues located in clusters. The physiochemical properties of purified calsequestrin as revealed by tryptophan fluorescence [378–381], circular dichroism [378, 380–383], Raman spectroscopy [380, 384], NMR [380], and proteolytic digestion [381, 384, 385] indicated that calsequestrin was mostly unfolded at low ionic strength. As ionic strength was increased, folding into a compact structure was observed. This structure can be induced by calcium as well as by other ions such as Na^+, Zn^{2+}, Sr^{2+}, Tb^{2+}, K^+, and H^+. The high Ca^{2+}-binding capacity of calsequestrin was believed to require the formation of aggregates, thus transitioning from a soluble disordered form to a solid crystalline form [381, 386, 387]. However, crystallization attempts in the presence of Ca^{2+} resulted in needle-like crystals. These liner polymeric forms were also observed in vivo, suggesting that this was the physiologically relevant form of the complex [388]. These narrow crystals were unsuitable for structure determination but did demonstrate that crystallization of calsequestrin was possible. The facts that calsequestrin adopted structure in the presence of mono- and divalent cations other than calcium and that these forms were not observed to aggregate and precipitate as the needle-like crystals did suggested that alternate crystal forms could be possible.

The following hypothesis was formed: the growth of needle-like crystals of calsequestrin is a two-step process [389]. The first step was the induction of structure by high ionic strength. The second was the calcium-specific cross-bridging of individual calsequestrin molecules by means of the unneutralized charges remaining after initial nonspecific binding of ions by the monomers. This cross-bridging could account for growth in a single direction, thereby producing the needles. To test this hypothesis, crystallization in the absence of Ca^{2+} was attempted [389, 390].

Calsequestrin was purified from the skeletal muscle of New Zealand white rabbits as previously described [381]. Approximately 500 initial crystallization experiments were conducted using the hanging-drop vapor-diffusion method [391] with an incomplete factorial approach [392] to cover a wide range of conditions. Each condition was tested in a volume of 1 μL containing 5–10 μg of calsequestrin. Conditions with high monovalent cation concentrations were emphasized, along with a range of 16 different precipitation reagents. Good-sized non-needle crystals were obtained when 2-methyl-2,4 pentane diol (MPD) was used as the precipitating reagent. The best crystals were grown from a solution containing 10% (v/v) MPD, 0.1 M sodium citrate, 0.05 M sodium cacodylate, pH 6.5, and 5 mg mL^{-1} calsequestrin. The nominal initial Na^+ concentration was 0.35 M. The rectangular crystals formed within one week and grew to $0.2 \times 0.2 \times 0.8$ mm by the second week. Structure determination details can be found elsewhere [389, 390].

Surprisingly, the resulting structure of calsequestrin exhibited three identical domains, each with a thioredoxin protein fold. The three domains interact to form a disk-like shape with an approximate radius of 32 Å and a thickness of 35 Å. No

clues to this three-domain structure were obtained from sequence analysis [393, 394]. Rather, analysis pointed towards a globular N-terminal domain and a C-terminal disordered region [381]. Even in hindsight, no significant similarities among the three similar domains could be deduced from the sequence.

A common approach to disordered regions in proteins is to remove the coding regions for the disordered parts from the recombinant expression constructs so that these regions do not prevent the protein from crystallizing [344]. In the case of calsequestrin, the fact that structure could be induced in the disordered protein by increasing cation concentration led to attempts at crystallization under non-intuitive conditions. The result was the elucidation of an interesting and important structure.

8.6.3 Circular Dichroism Spectropolarimetry

There is an excellent book on protein circular dichroism that contains several sections on the collection and interpretation of spectra [137]. As discussed above (see Section 8.2.4), the interpretation of spectra from disordered proteins remains controversial. However, the two most important experimental concepts are well agreed upon.

First, collect data as far into the ultraviolet region as possible. The far-UV region, from 260 nm to 190 nm, contains a great deal of information about secondary structure. With a powerful UV source (which often means a new lamp) and a well-behaved sample, data can be obtained down to wavelengths below 190 nm. Second, only the electronic transitions of the protein being studied should contribute to the absorbance. Any extrinsic absorbance degrades the instrument's ability to detect the small differences between left and right circularly polarized light absorbed by the protein under study.

The two most common sources of unwanted absorbance are light scattering and buffer/co-solute absorbance. The protein must not aggregate to such an extent that the sample scatters light. It is important to pass every sample through a 0.2-micron filter prior to data acquisition. A common mistake is to use a buffer that absorbs in the ultraviolet region. Histidine is a common buffer because it is used to elute His-tagged proteins from Ni^{2+}-affinity columns, but at the concentrations used for elution, the histidine contributes to an excessive amount of ultraviolet absorbance. Tris is also a poor choice. Phosphate and acetate are more useful buffers, at least in terms of absorbance. Absorbance can also be a problem when collecting spectra at high co-solute (e.g., sugars, urea, etc.) concentrations.

The best way to proceed is to collect a spectrum of filtered water or buffer and then compare this spectrum to that of the solution. After choosing appropriate solution conditions, there is no better protocol for preparing the sample than thorough dialysis followed by filtration. The reference solution is then made from a filtered sample of the solution from outside the dialysis bag.

CD analysis is especially sensitive to error due to misestimation of protein concentration. It is important that extreme care be taken during concentration deter-

mination. Additionally, we prefer the method of Gill and von Hippel [395] rather than any of the popular colorimetric assays. This method is based on the calculation of a molar extinction coefficient based on the amino acid content of the protein under study and is typically accurate to $\pm 5\%$.

Acknowledgements

A.K.D. and M.S.C. are supported by NIH grant R01 LM 007688 (Indiana University School of Medicine). A.K.D. is additionally supported by NIH grants R43 CA099053, R43 CA 097629, R43 CA 097568, and R43 GM 066412 (Molecular Kinetics, Inc.). G.J.P. thanks the NSF and NIH for support and Trevor Creamer for helpful discussions. G.W.D. is supported by NIH grant P20 RR 16448 from the COBRE Program of the National Center for Research Resources.

References

1 Fisher, E. (1894). Einfluss der configuration auf die wirkung den enzyme. *Ber. Dtsch. Chem. Ges.* **27**, 2985–2993.
2 Anson, M. L. & Mirsky, A. E. (1925). On some general properties of proteins. *J. Gen. Physiol.* **9**, 169–179.
3 Edsall, J. T. (1995). Hsien Wu and the first theory of protein denaturation (1931). *Adv. Protein Chem.* **46**, 1–5.
4 Mirsky, A. E. & Pauling, L. (1936). On the structure of native, denatured and coagulated proteins. *Proc. Natl. Acad. Sci. U.S.A.* **22**, 439–447.
5 Anfinsen, C. B. (1973). Principles that govern the folding of protein chains. *Science* **181**, 223–230.
6 Gutte, B. & Merrifield, R. B. (1969). The total synthesis of an enzyme with ribonuclease A activity. *J. Am. Chem. Soc.* **91**, 501–2.
7 Pauling, L., Corey, R. B. & Branson, R. H. (1951). The structure of proteins: two hydrogen-bonded configurations of the polypeptide chain. *Proc. Natl. Acad. Sci. U.S.A.* **37**, 205–210.
8 Kendrew, J. C., Dickerson, R. E. & Strandberg, B. E. (1960). Structure of myoglobin: a three-dimensional Fourier synthesis at 2 Å resolution. *Nature* **206**, 757–763.
9 Perutz, M. F., Rossmann, M. P., Cullis, A. F., Muirhead, H., Will, G. & North, A. C. (1960). Structure of haemoglobin: a three-dimensional Fourier synthesis at 5.5 Å resolution, obtained by X-ray analysis. *Nature* **185**, 416–422.
10 Blake, C. C., Koenig, D. F., Mair, G. A., North, A. C., Phillips, D. C. & Sarma, V. R. (1965). Structure of hen egg-white lysozyme. A three-dimensional Fourier synthesis at 2 Ångstrøm resolution. *Nature* **206**, 757–761.
11 Bloomer, A. C., Champness, J. N., Bricogne, G., Staden, R. & Klug, A. (1978). Protein disk of tobacco mosiac virus at 2.8 Å resolution showing the interactions within and between subunits. *Nature* **276**, 362–368.
12 Bode, W., Schwager, P. & Huber, R. (1978). The transition of bovine trypsinogen to a trypsin-like state upon strong ligand binding. The refined crystal structures of the bovine trypsinogen-pancreatic trypsin inhibitor complex and of its ternary complex with Ile-Val at 1.9 Å resolution. *J. Mol. Biol.* **118**, 99–112.
13 Williams, R. J. (1978). The conformational mobility of proteins and its

functional significance. *Biochem. Soc. Trans.* **6**, 1123–1126.

14 Pullen, R. A., Jenkins, J. A., Tickle, I. J., Wood, S. P. & Blundell, T. L. (1975). The relation of polypeptide hormone structure and flexibility to receptor binding: the relevance of X-ray studies on insulins, glucagon and human placental lactogen. *Mol. Cell. Biochem.* **8**, 5–20.

15 Cary, P. D., Moss, T. & Bradbury, E. M. (1978). High-resolution proton-magnetic-resonance studies of chromatin core particles. *Eur. J. Biochem.* **89**, 475–82.

16 Linderstrøm-Lang, K. U. & Schellman, J. A. (1959). Protein structure and enzyme activity. In *The Enzymes* (Boyer, P. D., Lardy, H. & Myrback, K., eds.), Vol. 1, pp. 443–510. Academic Press, New York.

17 Schweers, O., Schönbrunn-Hanebeck, E., Marx, A. & Mandelkow, E. (1994). Structural studies of tau protein and Alzheimer paired helical filaments show no evidence for *β*-structure. *J. Biol. Chem.* **269**, 24290–24297.

18 Weinreb, P. H., Zhen, W., Poon, A. W., Conway, K. A. & Lansbury, P. T., Jr. (1996). NACP, a protein implicated in Alzheimer's disease and learning, is natively unfolded. *Biochemistry* **35**, 13709–13715.

19 Wright, P. E. & Dyson, H. J. (1999). Intrinsically unstructured proteins: re-assessing the protein structure-function paradigm. *J. Mol. Biol.* **293**, 321–331.

20 Dunker, A. K., Lawson, J. D., Brown, C. J., Williams, R. M., Romero, P., Oh, J. S., Oldfield, C. J., Campen, A. M., Ratliff, C. M., Hipps, K. W., Ausio, J., Nissen, M. S., Reeves, R., Kang, C., Kissinger, C. R., Bailey, R. W., Griswold, M. D., Chiu, W., Garner, E. C. & Obradovic, Z. (2001). Intrinsically disordered protein. *J. Mol. Graph. Model.* **19**, 26–59.

21 Bailey, R. W., Dunker, A. K., Brown, C. J., Garner, E. C. & Griswold, M. D. (2001). Clusterin: a binding protein with a molten globule-like region. *Biochemistry* **40**, 11828–11840.

22 Kuwajima, K. (1989). The molten globule state as a clue for understanding the folding and cooperativity of globular-protein structure. *Proteins* **6**, 87–103.

23 Dolgikh, D. A., Gilmanshin, R. I., Brazhnikov, E. V., Bychkova, V. E., Semisotnov, G. V., Venyaminov, S. & Ptitsyn, O. B. (1981). Alpha-lactalbumin: compact state with fluctuating tertiary structure? *FEBS Lett.* **136**, 311–315.

24 Tiffany, M. L. & Krimm, S. (1968). New chain conformations of poly(glutamic acid) and polylysine. *Biopolymers* **6**, 1379–82.

25 Shi, Z., Woody, R. W. & Kallenbach, N. R. (2002). Is polyproline II a major backbone conformation in unfolded proteins? *Adv Protein Chem* **62**, 163–240.

26 Creamer, T. P. & Campbell, M. N. (2002). Determinants of the polyproline II helix from modeling studies. *Adv. Protein Chem.* **62**, 263–82.

27 Klee, C. B., Crouch, T. H. & Krinks, M. H. (1979). Calcineurin: a calcium- and calmodulin-binding protein of the nervous system. *Proc. Natl. Acad. Sci. U.S.A.* **76**, 6270–6273.

28 Klee, C. B., Draetta, G. F. & Hubbard, M. J. (1988). Calcineurin. *Adv. Enzymol. Relat. Areas Mol. Biol.* **61**, 149–200.

29 Kissinger, C. R., Parge, H. E., Knighton, D. R., Lewis, C. T., Pelletier, L. A., Tempczyk, A., Kalish, V. J., Tucker, K. D., Showalter, R. E., Moomaw, E. W., Gastinel, L. N., Habuka, N., Chen, X., Maldanado, F., Barker, J. E., Bacquet, R. & Villafranca, J. E. (1995). Crystal structures of human calcineurin and the human FKBP12-FK506-calcineurin complex. *Nature* **378**, 641–644.

30 Dunker, A. K., Brown, C. J., Lawson, J. D., Iakoucheva, L. M. & Obradovic, Z. (2002). Intrinsic disorder and protein function. *Biochemistry* **41**, 6573–82.

31 Dunker, A. K., Brown, C. J. & Obradovic, Z. (2002). Identification and functions of usefully disordered proteins. *Adv. Protein Chem.* **62**, 25–49.

32 Ptitsyn, O. (1995). Molten globule and protein folding. *Adv. Protein Chem.* **47**, 83–229.

33 Page, M. I. (1987). Enzyme Mechanisms. In *Enzyme Mechanisms* (Page, M. I. & Williams, A., eds.), pp. 1–13. Royal Society of Chemistry, London.

34 Kraut, J. (1988). How do enzymes work? *Science* **242**, 533–40.

35 Polanyhi, M. (1921). Über Adsorptionskatalyse. *Zeitschrift für Electrochemie* **27**, 142–150.

36 Pauling, L. (1946). Molecular architecture and biological reactions. *Chemical Engineering News* **24**, 1375–1377.

37 Borman, S. (2004). Much ado about enzyme mechanisms. *Chemical and Engineering News* **82**, 35–39.

38 Warshel, A. (1998). Electrostatic origin of the catalytic power of enzymes and the role of preorganized active sites. *J Biol Chem* **273**, 27035–27038.

39 Bruice, T. C. & Benkovic, S. J. (2000). Chemical basis for enzyme catalysis. *Biochemistry* **39**, 6267–74.

40 Hur, S. & Bruice, T. C. (2003). Just a near attack conformer for catalysis (chorismate to prephenate rearrangements in water, antibody, enzymes, and their mutants). *J Am Chem Soc* **125**, 10540–2.

41 Schulz, G. E. (1979). Nucleotide Binding Proteins. In *Molecular Mechanism of Biological Recognition* (Balaban, M., ed.), pp. 79–94. Elsevier/North-Holland Biomedical Press, New York.

42 Karush, F. (1950). Heterogeneity of the binding sites of bovine serum albumin. *J. Am. Chem. Soc.* **72**, 2705–2713.

43 Kriwacki, R. W., Hengst, L., Tennant, L., Reed, S. I. & Wright, P. E. (1996). Structural studies of $p21^{Waf1/Cip1/Sdi1}$ in the free and Cdk2-bound state: conformational disorder mediates binding diversity. *Proc. Natl. Acad. Sci. U.S.A.* **93**, 11504–11509.

44 Dunker, A. K. & Obradovic, Z. (2001). The protein trinity – linking function and disorder. *Nat. Biotechnol.* **19**, 805–806.

45 Bracken, C. (2001). NMR spin relaxation methods for characterization of disorder and folding in proteins. *J. Mol. Graph. Model.* **19**, 3–12.

46 Dyson, H. J. & Wright, P. E. (1998). Equilibrium NMR studies of unfolded and partially folded proteins. *Nat. Struct. Biol.* **5 Suppl**, 499–503.

47 Dyson, H. J. & Wright, P. E. (2001). Nuclear magnetic resonance methods for elucidation of structure and dynamics in disordered states. *Methods Enzymol.* **339**, 258–270.

48 Dyson, H. J. & Wright, P. E. (2002). Insights into the structure and dynamics of unfolded proteins from nuclear magnetic resonance. *Adv. Protein Chem.* **62**, 311–40.

49 Barbar, E. (1999). NMR characterization of partially folded and unfolded conformational ensembles of proteins. *Biopolymers* **51**, 191–207.

50 Yao, J., Chung, J., Eliezer, D., Wright, P. E. & Dyson, H. J. (2001). NMR structural and dynamic characterization of the acid-unfolded state of apomyoglobin provides insights into the early events in protein folding. *Biochemistry* **40**, 3561–71.

51 Eliezer, D., Yao, J., Dyson, H. J. & Wright, P. E. (1998). Structural and dynamic characterization of partially folded states of apomyoglobin and implications for protein folding. *Nat. Struct. Biol.* **5**, 148–155.

52 Arcus, V. L., Vuilleumier, S., Freund, S. M., Bycroft, M. & Fersht, A. R. (1994). Toward solving the folding pathway of barnase: the complete backbone 13C, 15N, and 1H NMR assignments of its pH-denatured state. *Proc. Natl. Acad. Sci. U.S.A.* **91**, 9412–6.

53 Arcus, V. L., Vuilleumier, S., Freund, S. M., Bycroft, M. & Fersht, A. R. (1995). A comparison of the pH, urea, and temperature-denatured states of barnase by heteronuclear NMR: implications for the initiation of protein folding. *J. Mol. Biol.* **254**, 305–21.

54 Weiss, M. A., Ellenberger, T., Wobbe, C. R., Lee, J. P., Harrison, S. C. & Struhl, K. (1990). Folding transition in the DNA-binding domain

of GCN4 on specific binding to DNA. *Nature* **347**, 575–578.

55 Dobson, C. & Hore, P. (1998). Kinetic studies of protein folding using NMR spectroscopy. *Nat. Struct. Biol.* **5**, 504–507.

56 Shortle, D. R. (1996). Structural analysis of non-native states of proteins by NMR methods. *Curr. Opin. Struct. Biol.* **6**, 24–30.

57 Alexandrescu, A. T. & Shortle, D. (1994). Backbone dynamics of a highly disordered 131 residue fragment of staphylococcal nuclease. *J. Mol. Biol.* **242**, 527–46.

58 Alexandrescu, A. T., Abeygunawardana, C. & Shortle, D. (1994). Structure and dynamics of a denatured 131-residue fragment of staphylococcal nuclease: a heteronuclear NMR study. *Biochemistry* **33**, 1063–1072.

59 Gillespie, J. R. & Shortle, D. (1997). Characterization of long-range structure in the denatured state of staphylococcal nuclease. II. Distance restraints from paramagnetic relaxation and calculation of an ensemble of structures. *J. Mol. Biol.* **268**, 170–84.

60 Gillespie, J. R. & Shortle, D. (1997a). Characterization of long-range structure in the denatured state of *staphylococcal* nuclease. I. Paramagnetic relaxation enhancement by nitroxide spin labels. *J. Mol. Biol.* **268**, 158–169.

61 Shortle, D. & Ackerman, M. S. (2001). Persistence of native-like topology in a denatured protein in 8 M urea. *Science* **293**, 487–9.

62 Sinclair, J. F. & Shortle, D. (1999). Analysis of long-range interactions in a model denatured state of staphylococcal nuclease based on correlated changes in backbone dynamics. *Protein Sci.* **8**, 991–1000.

63 Wrabl, J., Shortle, D. & Woolf, T. (2000). Correlation between changes in nuclear magnetic resonance order parameters and conformational entropy: molecular dynamics simulations of native and denatured staphylococcal nuclease. *Proteins* **38**, 123–133.

64 Wrabl, J. O. & Shortle, D. (1996). Perturbations of the denatured state ensemble: modeling their effects on protein stability and folding kinetics. *Protein Sci.* **5**, 2343–52.

65 Wishart, D. S., Sykes, B. D. & Richards, F. M. (1992). The chemical shift index: a fast and simple method for the assignment of protein secondary structure through NMR spectroscopy. *Biochemistry* **31**, 1647–51.

66 Wishart, D. S. & Sykes, B. D. (1994). The 13C chemical-shift index: a simple method for the identification of protein secondary structure using 13C chemical-shift data. *J. Biomol. NMR* **4**, 171–80.

67 Wishart, D. S. & Sykes, B. D. (1994). Chemical shifts as a tool for structure determination. *Methods Enzymol.* **239**, 363–92.

68 Wilkins, D. K., Grimshaw, S. B., Receveur, V., Dobson, C. M., Jones, J. A. & Smith, L. J. (1999). Hydrodynamic radii of native and denatured proteins measured by pulse field gradient NMR techniques. *Biochemistry* **38**, 16424–31.

69 Altieri, A. S., Hinton, D. P. & Byrd, R. A. (1995). Association of biomolecular systems via pulsed field gradient NMR self-diffusion measurements. *J. Am. Chem. Soc.* **117**, 7566–67.

70 Pan, H., Barany, G. & Woodward, C. (1997). Reduced BPTI is collapsed. A pulsed field gradient NMR study of unfolded and partially folded bovine pancreatic trypsin inhibitor. *Protein Sci.* **6**, 1985–92.

71 Davis, D. G., Perlman, M. E. & London, R. E. (1994). Direct measurements of the dissociation-rate constant for inhibitor-enzyme complexes via the T1 rho and T2 (CPMG) methods. *J. Magn. Reson. B* **104**, 266–75.

72 Farrow, N. A., Zhang, O., Forman-Kay, J. D. & Kay, L. E. (1994). A heteronuclear correlation experiment for simultaneous determination of 15N longitudinal decay and chemical exchange rates of systems in slow equilibrium. *J. Biomol. NMR* **4**, 727–34.

73 Feeney, J., Batchelor, J. G., Albrand, J. P. & Roberts, G. C. K. (1979). Effects of intermediate

exchange processes on the estimation of equilibrium-constants by NMR. *J. Magn. Reson.* **33**, 519–529.

74 Spera, S. & Bax, A. (1991). Empirical correlation between protein backbone conformation and C-alpha and C-beta C-13 nuclear-magnetic-resonance chemical-shifts. *J. Am. Chem. Soc.* **113**, 5490–5492.

75 Wishart, D. S., Sykes, B. D. & Richards, F. M. (1991). Relationship between nuclear magnetic resonance chemical shift and protein secondary structure. *J. Mol. Biol.* **222**, 311–33.

76 Tcherkasskaya, O., Davidson, E. A. & Uversky, V. N. (2003). Biophysical constraints for protein structure prediction. *J. Proteome Res.* **2**, 37–42.

77 Daughdrill, G. W., Hanely, L. J. & Dahlquist, F. W. (1998). The C-terminal half of the anti-sigma factor FlgM contains a dynamic equilibrium solution structure favoring helical conformations. *Biochemistry* **37**, 1076–1082.

78 Bracken, C., Carr, P. A., Cavanagh, J. & Palmer, A. G., 3rd. (1999). Temperature dependence of intramolecular dynamics of the basic leucine zipper of GCN4: implications for the entropy of association with DNA. *J. Mol. Biol.* **285**, 2133–2146.

79 Palmer, A. G., 3rd. (1993). Dynamic properties of proteins from NMR spectroscopy. *Curr. Opin. Biotechnol.* **4**, 385–91.

80 Lefevre, J. F., Dayie, K. T., Peng, J. W. & Wagner, G. (1996). Internal mobility in the partially folded DNA binding and dimerization domains of GAL4: NMR analysis of the N–H spectral density functions. *Biochemistry* **35**, 2674–86.

81 Kay, L. E., Torchia, D. A. & Bax, A. (1989). Backbone dynamics of proteins as studied by 15N inverse detected heteronuclear NMR spectroscopy: application to staphylococcal nuclease. *Biochemistry* **28**, 8972–9.

82 Skelton, N. J., Palmer, A. G., Akke, M., Kordel, J., Rance, M. & Chazin, W. J. (1993). Practical aspects of 2-dimensional proton-detected N-15 spin relaxation measurements. *J. Magn. Reson. B* **102**, 253–264.

83 Kordel, J., Skelton, N. J., Akke, M., Palmer, A. G. & Chazin, W. J. (1992). Backbone dynamics of calcium-loaded calbindin D9k studied by 2-dimensional proton-detected N15 NMR spectroscopy. *Biochemistry* **31**, 4856–4866.

84 McEvoy, M. M., de la Cruz, A. F. & Dahlquist, F. W. (1997). Large modular proteins by NMR. *Nat. Struct. Biol.* **4**, 9.

85 Renner, C., Schleicher, M., Moroder, L. & Holak, T. A. (2002). Practical aspects of the 2D N-15-{H-1}-NOE experiment. *J. Biomol. NMR* **23**, 23–33.

86 Lipari, G. & Szabo, A. (1982). Model-Free Approach to the Interpretation of Nuclear Magnetic-Resonance Relaxation in Macromolecules .1. Theory and Range of Validity. *J. Am. Chem. Soc.* **104**, 4546–4559.

87 Lipari, G. & Szabo, A. (1982). Model-Free Approach to the Interpretation of Nuclear Magnetic-Resonance Relaxation in Macromolecules .2. Analysis of Experimental Results. *J. Am. Chem. Soc.* **104**, 4559–4570.

88 Peng, J. W. & Wagner, G. (1992). Mapping of the spectral densities of N–H bond motions in eglin c using heteronuclear relaxation experiments. *Biochemistry* **31**, 8571–86.

89 Abragam, A. (1961). *The principles of nuclear magnetism.* The International series of monographs on physics, Clarendon Press, Oxford.

90 Bruschweiler, R., Liao, X. & Wright, P. E. (1995). Long-range motional restrictions in a multi-domain zinc-finger protein from anisotropic tumbling. *Science* **268**, 886–9.

91 Tjandra, N., Feller, S. E., Pastor, R. W. & Bax, A. (1995). Rotational diffusion anisotropy of human ubiquitin from N-15 NMR relaxation. *J. Am. Chem. Soc.* **117**, 12562–12566.

92 Lee, L. K., Rance, M., Chazin, W. J. & Palmer, A. G. (1997). Rotational diffusion anisotropy of proteins from simultaneous analysis of N-15 and C-13(alpha) nuclear spin relaxation. *J. Biomol. NMR* **9**, 287–298.

93 Buck, M., Schwalbe, H. & Dobson,

C. M. (1996). Main-chain dynamics of a partially folded protein: 15N NMR relaxation measurements of hen egg white lysozyme denatured in trifluoroethanol. *J. Mol. Biol.* **257**, 669–83.

94 Buevich, A. V., Shinde, U. P., Inouye, M. & Baum, J. (2001). Backbone dynamics of the natively unfolded pro-peptide of subtilisin by heteronuclear NMR relaxation studies. *J. Biomol. NMR* **20**, 233–249.

95 Farrow, N. A., Zhang, O., Muhandiram, R., Formankay, J. D. & Kay, L. E. (1995). A comparative-study of the backbone dynamics of the folded and unfolded forms of an SH3 domain. *J. Cell. Biochem.*, 44–44.

96 Yang, D. & Kay, L. E. (1996). Contributions to conformational entropy arising from bond vector fluctuations measured from NMR-derived order parameters: application to protein folding. *J. Mol. Biol.* **263**, 369–82.

97 Yang, D., Mok, Y. K., Forman-Kay, J. D., Farrow, N. A. & Kay, L. E. (1997). Contributions to protein entropy and heat capacity from bond vector motions measured by NMR spin relaxation. *J. Mol. Biol.* **272**, 790–804.

98 Viles, J. H., Donne, D., Kroon, G., Prusiner, S. B., Cohen, F. E., Dyson, H. J. & Wright, P. E. (2001). Local structural plasticity of the prion protein. Analysis of NMR relaxation dynamics. *Biochemistry* **40**, 2743–53.

99 Landry, S. J., Steede, N. K. & Maskos, K. (1997). Temperature dependence of backbone dynamics in loops of human mitochondrial heat shock protein 10. *Biochemistry* **36**, 10975–86.

100 Bhattacharya, S., Falzone, C. J. & Lecomte, J. T. (1999). Backbone dynamics of apocytochrome b5 in its native, partially folded state. *Biochemistry* **38**, 2577–89.

101 Campbell, A. P., Spyracopoulos, L., Irvin, R. T. & Sykes, B. D. (2000). Backbone dynamics of a bacterially expressed peptide from the receptor binding domain of *Pseudomonas aeruginosa* pilin strain PAK from heteronuclear 1H-15N NMR spectroscopy. *J. Biomol. NMR* **17**, 239–55.

102 Dedmon, M. M., Patel, C. N., Young, G. B. & Pielak, G. J. (2002). FlgM gains structure in living cells. *Proc. Natl. Acad. Sci. U.S.A.* **99**, 12681–12684.

103 Choy, W. Y., Mulder, F. A., Crowhurst, K. A., Muhandiram, D. R., Millett, I. S., Doniach, S., Forman-Kay, J. D. & Kay, L. E. (2002). Distribution of molecular size within an unfolded state ensemble using small-angle X-ray scattering and pulse field gradient NMR techniques. *J. Mol. Biol.* **316**, 101–12.

104 Choy, W. Y. & Forman-Kay, J. D. (2001). Calculation of ensembles of structures representing the unfolded state of an SH3 domain. *J. Mol. Biol.* **308**, 1011–1032.

105 Kissinger, C. R., Gehlhaar, D. K., Smith, B. A. & Bouzida, D. (2001). Molecular replacement by evolutionary search. *Acta. Crystallogr. D Biol. Crystallogr.* **57**, 1474–9.

106 Huber, R. (1987). Flexibility and rigidity, requirements for the function of proteins and protein pigment complexes. Eleventh Keilin memorial lecture. *Biochem. Soc. Trans.* **15**, 1009–20.

107 Huber, R. & Bennett, W. S., Jr. (1983). Functional significance of flexibility in proteins. *Biopolymers* **22**, 261–279.

108 Douzou, P. & Petsko, G. A. (1984). Proteins at work: "stop-action" pictures at subzero temperatures. *Adv. Protein Chem.* **36**, 245–361.

109 Obradovic, Z., Peng, K., Vucetic, S., Radivojac, P., Brown, C. J. & Dunker, A. K. (2003). Predicting intrinsic disorder from amino acid sequence. *Proteins* **53**, 566–572.

110 Hobohm, U. & Sander, C. (1994). Enlarged representative set of protein structures. *Protein Sci.* **3**, 522–524.

111 Bairoch, A. & Apweiler, R. (2000). The SWISS-PROT protein sequence database and its supplement TrEMBL in 2000. *Nucleic Acids Res.* **28**, 45–48.

112 Schachman, H. K. (1959). *Ultracentrifugation in Biochemistry*, Academic Press, New York.

113 Glatter, O. & Kratky, O. (1982). *Small Angle X-ray Scattering*, Academic Press, London, England.

114 Doniach, S., Bascle, J., Garel, T. & Orland, H. (1995). Partially folded states of proteins: characterization by X-ray scattering. *J. Mol. Biol.* **254**, 960–7.

115 Kataoka, M. & Goto, Y. (1996). X-ray solution scattering studies of protein folding. *Fold. Des.* **1**, R107–14.

116 Uversky, V. N., Gillespie, J. R., Millett, I. S., Khodyakova, A. V., Vasiliev, A. M., Chernovskaya, T. V., Vasilenko, R. N., Kozlovskaya, G. D., Dolgikh, D. A., Fink, A. L., Doniach, S. & Abramov, V. M. (1999). Natively unfolded human prothymosin alpha adopts partially folded collapsed conformation at acidic pH. *Biochemistry* **38**, 15009–16.

117 Uversky, V. N., Gillespie, J. R., Millett, I. S., Khodyakova, A. V., Vasilenko, R. N., Vasiliev, A. M., Rodionov, I. L., Kozlovskaya, G. D., Dolgikh, D. A., Fink, A. L., Doniach, S., Permyakov, E. A. & Abramov, V. M. (2000). Zn(2+)-mediated structure formation and compaction of the "natively unfolded" human prothymosin alpha. *Biochem. Biophys. Res. Commun.* **267**, 663–668.

118 Li, J., Uversky, V. N. & Fink, A. L. (2001). Effect of familial Parkinson's disease point mutations A30P and A53T on the structural properties, aggregation, and fibrillation of human alpha-synuclein. *Biochemistry* **40**, 11604–13.

119 Uversky, V. N., Li, J. & Fink, A. L. (2001). Evidence for a partially folded intermediate in alpha-synuclein fibril formation. *J. Biol. Chem.* **276**, 10737–10744.

120 Uversky, V. N., Li, J., Souillac, P., Jakes, R., Goedert, M. & Fink, A. L. (2002). Biophysical properties of the synucleins and their propensities to fibrillate: inhibition of alpha-synuclein assembly by beta- and gamma-synucleins. *J. Biol. Chem.* **25**, 25.

121 Permyakov, S. E., Millett, I. S., Doniach, S., Permyakov, E. A. & Uversky, V. N. (2003). Natively unfolded C-terminal domain of caldesmon remains substantially unstructured after the effective binding to calmodulin. *Proteins* **53**, 855–62.

122 Munishkina, L. A., Fink, A. L. & Uversky, V. N. (In press). Formation of amyloid fibrils from the core histones in vitro. *J. Mol. Biol.*

123 Uversky, V. N. (2002). What does it mean to be natively unfolded? *Eur. J. Biochem.* **269**, 2–12.

124 Guinier, A. & Fournet, G. (1955). *Small-angle scattering of X-rays*, John Wiley & Sons.

125 Millett, I. S., Doniach, S. & Plaxco, K. W. (2002). Toward a taxonomy of the denatured state: small angle scattering studies of unfolded proteins. *Adv. Protein Chem.* **62**, 241–62.

126 Jaenicke, R. & Seckler, R. (1997). Protein misassembly in vitro. *Adv. Protein Chem.* **50**, 1–59.

127 Rose, G. D. (2002). *Unfolded Proteins.* Advances in Protein Chemistry (F. M., R., S., E. D. & J., K., Eds.), 62, Academic Press, New York.

128 Severgun, D. I. (1992). Determination of the regularization parameter in indirect-transform methods using perceptual criteria. *J. Appl. Cryst.* **25**, 495–503.

129 Bergmann, A., Orthaber, D., Scherf, G. & Glatter, O. (2000). Improvement of SAXS measurements on Kratky slit systems by Göbel mirrors and imaging-plate detectors. *J. Appl. Cryst.* **33**, 869–875.

130 Panick, G., Malessa, R., Winter, R., Rapp, G., Frye, K. J. & Royer, C. A. (1998). Structural characterization of the pressure-denatured state and unfolding/refolding kinetics of staphylococcal nuclease by synchrotron small-angle X-ray scattering and Fourier-transform infrared spectroscopy. *J. Mol. Biol.* **275**, 389–402.

131 Pérez, J., Vachette, P., Russo, D., Desmadril, M. & Durand, D. (2001). Heat-induced unfolding of neocarzinostatin, a small all-beta protein investigated by small-angle X-ray scattering. *J. Mol. Biol.* **308**, 721–43.

132 Uversky, V. N. (1993). Use of fast protein size-exclusion liquid chromatography to study the unfolding of proteins which denature through the molten globule. *Biochemistry* **32**, 13288–13298.

133 Uversky, V. N. (1994). Gel-permeation

chromatography as a unique instrument for quantitative and qualitative analysis of protein denaturation and unfolding. *Int. J. Bio-Chromatography* **1**, 103–114.

134 Uversky, V. N. (2003). Protein folding revisited. A polypeptide chain at the folding – misfolding – no-folding crossroads: Which way to go? *Cell. Mol. Life Sci.*

135 Uversky, V. N. (2002). Natively unfolded proteins: a point where biology waits for physics. *Protein Sci.* **11**, 739–756.

136 Uversky, V. N. & Ptitsyn, O. B. (1996). Further evidence on the equilibrium "pre-molten globule state": four-state guanidinium chloride-induced unfolding of carbonic anhydrase B at low temperature. *J. Mol. Biol.* **255**, 215–28.

137 Fasman, G. D. (1996). *Circular Dichroism and the Conformational Analysis of Biomolecules*, Plenem Press, New York.

138 Adler, A. J., Greenfield, N. J. & Fasman, G. D. (1973). Circular dichroism and optical rotatory dispersion of proteins and polypeptides. *Methods Enzymol.* **27**, 675–735.

139 Uversky, V. N. & Fink, A. L. (2002). The chicken-egg scenario of protein folding revisited. *FEBS Lett.* **515**, 79–83.

140 Palleros, D. R., Reid, K. L., McCarty, J. S., Walker, G. C. & Fink, A. L. (1992). DnaK, hsp73, and their molten globules. Two different ways heat shock proteins respond to heat. *J. Biol. Chem.* **267**, 5279–85.

141 Fink, A. L., Oberg, K. A. & Seshadri, S. (1998). Discrete intermediates versus molten globule models for protein folding: characterization of partially folded intermediates of apomyoglobin. *Fold. Des.* **3**, 19–25.

142 Uversky, V. N., Karnoup, A. S., Segel, D. J., Seshadri, S., Doniach, S. & Fink, A. L. (1998). Anion-induced folding of *Staphylococcal* nuclease: characterization of multiple equilibrium partially folded intermediates. *J. Mol. Biol.* **278**, 879–894.

143 Krimm, S. & Tiffany, M. L. (1974). The circular dichroism spectrum and structure of unordered polypeptides and proteins. *Israeli J. of Chem.* **12**, 189–200.

144 Kelly, M. A., Chellgren, B. W., Rucker, A. L., Troutman, J. M., Fried, M. G., Miller, A. F. & Creamer, T. P. (2001). Host-guest study of left-handed polyproline II helix formation. *Biochemistry* **40**, 14376–83.

145 Rucker, A. L. & Creamer, T. P. (2002). Polyproline II helical structure in protein unfolded states: lysine peptides revisited. *Protein Sci.* **11**, 980–5.

146 House-Pompeo, K., Xu, Y., Joh, D., Speziale, P. & Hook, M. (1996). Conformational changes in the binding MSCRAMMs are induced by ligand binding. *J. Biol. Chem.* **271**, 1379–1384.

147 Gast, K., Damaschun, H., Eckert, K., Schulze-Forster, K., Maurer, H. R., Müller-Frohne, M., Zirwer, D., Czarnecki, J. & Damaschun, G. (1995). Prothymosin alpha: a biologically active protein with random coil conformation. *Biochemistry* **34**, 13211–13218.

148 Flaugh, S. L. & Lumb, K. J. (2001). Effects of macromolecular crowding on the intrinscially disordered proteins c-Fos and p27(Kip 1). *Biomacromolecules* **2**, 538–540.

149 Denning, D. P., Patel, S. S., Uversky, V., Fink, A. L. & Rexach, M. (2003). Disorder in the nuclear pore complex: the FG repeat regions of nucleoporins are natively unfolded. *Proc. Natl. Acad. Sci. U.S.A.* **100**, 2450–2455.

150 Bothner, B., Aubin, Y. & Kriwacki, R. W. (2003). Peptides derived from two dynamically disordered proteins self-assemble into amyloid-like fibrils. *J. Am. Chem. Soc.* **125**, 3200–1.

151 Mackay, J. P., Matthews, J. M., Winefield, R. D., Mackay, L. G., Haverkamp, R. G. & Templeton, M. D. (2001). The hydrophobin EAS is largely unstructured in solution and functions by forming amyloid-like structures. *Structure (Camb)* **9**, 83–91.

152 Baskakov, I. & Bolen, D. W. (1998). Forcing thermodynamically unfolded proteins to fold. *J. Biol. Chem.* **273**, 4831–4834.

153 Qu, Y., Bolen, C. L. & Bolen, D. W. (1998). Osmolyte-driven contraction of a random coil protein. *Proc. Natl. Acad. Sci. U.S.A.* **95**, 9268–9273.

154 Baskakov, I. V., Kumar, R., Srinivasan, G., Ji, Y. S., Bolen, D. W. & Thompson, E. B. (1999). Trimethylamine N-oxide-induced cooperative folding of an intrinsically unfolded transcription-activating fragment of human glucocorticoid receptor. *J. Biol. Chem.* **274**, 10693–10696.

155 Qu, Y. & Bolen, D. W. (2002). Efficacy of macromolecular crowding in forcing proteins to fold. *Biophys. Chem.* **101–102**, 155–65.

156 Davis-Searles, P. R., Morar, A. S., Saunders, A. J., Erie, D. A. & Pielak, G. J. (1998). Sugar-induced molten-globule model. *Biochemistry* **37**, 17048–17053.

157 Saunders, A. J., Davis-Searles, P. R., Allen, D. L., Pielak, G. J. & Erie, D. A. (2000). Osmolyte-induced changes in protein conformational equilibria. *Biopolymers* **53**, 293–307.

158 Morar, A. S., Olteanu, A., Young, G. B. & Pielak, G. J. (2001). Solvent-induced collapse of alpha-synuclein and acid-denatured cytochrome c. *Protein Sci.* **10**, 2195–2199.

159 Chirgadze, Y. N., Shestopalov, B. V. & Venyaminov, S. Y. (1973). Intensities and other spectral parameters of infrared amide bands of polypeptides in the beta- and random forms. *Biopolymers* **12**, 1337–51.

160 Susi, H., Timasheff, S. N. & Stevens, L. (1967). Infrared spectra and protein conformations in aqueous solutions. I. The amide I band in H2O and D2O solutions. *J. Biol. Chem.* **242**, 5460–6.

161 Chirgadze, Y. N. & Brazhnikov, E. V. (1974). Intensities and other spectral parameters of infrared amide bands of polypeptides in the alpha-helical form. *Biopolymers* **13**, 1701–12.

162 Miyazawa, T. & Blout, E. R. (1961). The Infrared Spectra of Polypeptides in Various Conformations: Amide I and II Bands. *J. Am. Chem. Soc.* **83**, 712–719.

163 Lackowicz, J. (1999). *Principals of Fluorescence Spectroscopy*, Kluwer Academic/Plenum Publishers, New York.

164 Stryer, L. (1968). Fluorescence spectroscopy of proteins. *Science* **162**, 526–33.

165 Permyakov, E. A. (1993). *Luminescence spectroscopy of proteins*, CRC Press, London.

166 Eftink, M. R. & Ghiron, C. A. (1981). Fluorescence quenching studies with proteins. *Anal. Biochem.* **114**, 199–227.

167 Lakowicz, J. R. & Weber, G. (1973). Quenching of fluorescence by oxygen. A probe for structural fluctuations in macromolecules. *Biochemistry* **12**, 4161–70.

168 Lakowicz, J. R. & Weber, G. (1973). Quenching of protein fluorescence by oxygen. Detection of structural fluctuations in proteins on the nanosecond timescale. *Biochemistry* **12**, 4171–9.

169 Eftink, M. R. & Ghiron, C. A. (1976). Exposure of tryptophanyl residues in proteins. Quantitative determination by fluorescence quenching studies. *Biochemistry* **15**, 672–80.

170 Eftink, M. R. & Ghiron, C. A. (1975). Dynamics of a protein matrix revealed by fluorescence quenching. *Proc. Natl. Acad. Sci. U.S.A.* **72**, 3290–4.

171 Eftink, M. R. & Ghiron, C. A. (1977). Exposure of tryptophanyl residues and protein dynamics. *Biochemistry* **16**, 5546–51.

172 Chaffotte, A. F. & Goldberg, M. E. (1984). Fluorescence-quenching studies on a conformational transition within a domain of the beta 2 subunit of *Escherichia coli* tryptophan synthase. *Eur. J. Biochem.* **139**, 47–50.

173 Varley, P. G., Dryden, D. T. & Pain, R. H. (1991). Resolution of the fluorescence of the buried tryptophan in yeast 3-phosphoglycerate kinase using succinimide. *Biochim. Biophys. Acta.* **1077**, 19–24.

174 Weber, G. (1952). Polarization of the

fluorescence of macromolecules. II. Fluorescent conjugates of ovalbumin and bovine serum albumin. *Biochem. J.* **51**, 155–67.

175 Weber, G. (1952). Polarization of the fluorescence of macromolecules. I. Theory and experimental method. *Biochem. J.* **51**, 145–55.

176 Weber, G. (1953). Rotational Brownian motion and polarization of the fluorescence of solutions. *Adv. Protein Chem.* **8**, 415–59.

177 Weber, G. (1960). Fluorescence-polarization spectrum and electronic-energy transfer in proteins. *Biochem. J.* **75**, 345–52.

178 Semisotnov, G. V., Zikherman, K. K., Kasatkin, S. B., Ptitsyn, O. B. & V., A. E. (1981). Polarized luminescence and mobility of tryptophan residues in polypeptide chains. *Biopolymers* **20**, 2287–2309.

179 Dolgikh, D. A., Abaturov, L. V., Bolotina, I. A., Brazhnikov, E. V., Bychkova, V. E., Gilmanshin, R. I., Lebedev Yu, O., Semisotnov, G. V., Tiktopulo, E. I., Ptitsyn, O. B. & et al. (1985). Compact state of a protein molecule with pronounced small-scale mobility: bovine alpha-lactalbumin. *Eur. Biophys. J.* **13**, 109–21.

180 Rodionova, N. A., Semisotnov, G. V., Kutyshenko, V. P., Uverskii, V. N. & Bolotina, I. A. (1989). [Staged equilibrium of carbonic anhydrase unfolding in strong denaturants]. *Mol Biol (Mosk)* **23**, 683–92.

181 Förster, T. (1948). Intermolecular energy migration and fluorescence. *Ann. Physik.* **2**, 55–75.

182 Lundblad, R. L. (1991). *Chemical reagents for protein modification*, CRC Press, Boca Raton.

183 Rischel, C. & Poulsen, F. M. (1995). Modification of a specific tyrosine enables tracing of the end-to-end distance during apomyoglobin folding. *FEBS Lett.* **374**, 105–9.

184 Uversky, V. N. & Fink, A. L. (1999). Do protein molecules have a native-like topology in the pre-molten globule state? *Biochemistry (Mosc)* **64**, 552–5.

185 Tcherkasskaya, O. & Ptitsyn, O. B. (1999). Molten globule versus variety of intermediates: influence of anions on pH-denatured apomyoglobin. *FEBS Lett.* **455**, 325–31.

186 Tcherkasskaya, O. & Ptitsyn, O. B. (1999). Direct energy transfer to study the 3D structure of non-native proteins: AGH complex in molten globule state of apomyoglobin. *Protein Eng.* **12**, 485–90.

187 Tcherkasskaya, O. & Uversky, V. N. (2001). Denatured collapsed states in protein folding: example of apomyoglobin. *Proteins* **44**, 244–254.

188 Stryer, L. (1965). The interaction of a naphthalene dye with apomyoglobin and apohemoglobin. A fluorescent probe of non-polar binding sites. *J. Mol. Biol.* **13**, 482–495.

189 Turner, D. C. & Brand, L. (1968). Quantitative estimation of protein binding site polarity. Fluorescence of N-arylaminonaphthalenesulfonates. *Biochemistry* **7**, 3381–90.

190 Semisotnov, G. V., Rodionova, N. A., Razgulyaev, O. I., Uversky, V. N., Gripas, A. F. & Gilmanshin, R. I. (1991). Study of the "molten globule" intermediate state in protein folding by a hydrophobic fluorescent probe. *Biopolymers* **31**, 119–128.

191 Semisotnov, G. V., Rodionova, N. A., Kutyshenko, V. P., Ebert, B., Blanck, J. & Ptitsyn, O. B. (1987). Sequential mechanism of refolding of carbonic anhydrase B. *FEBS Lett.* **224**, 9–13.

192 Uversky, V. N., Winter, S. & Lober, G. (1996). Use of fluorescence decay times of 8-ANS-protein complexes to study the conformational transitions in proteins which unfold through the molten globule state. *Biophys. Chem.* **60**, 79–88.

193 Uversky, V. N., Winter, S. & Lober, G. (1998). Self-association of 8-anilino-1-naphthalene-sulfonate molecules: spectroscopic characterization and application to the investigation of protein folding. *Biochim. Biophys. Acta.* **1388**, 133–142.

194 Uversky, V. N. & Ptitsyn, O. B. (1996). All-or-none solvent-induced transitions between native, molten

globule and unfolded states in globular proteins. *Fold. & Des.* **1**, 117–122.

195 Roberts, L. M. & Dunker, A. K. (1993). Structural changes accompanying chloroform-induced contraction of the filamentous phage fd. *Biochemistry* **32**, 10479–10488.

196 Privalov, P. L. (1979). Stability of proteins: small globular proteins. *Adv. Protein. Chem.* **33**, 167–241.

197 Ptitsyn, O. (1995). Molten globule and protein folding. *Adv. Protein Chem.* **47**, 83–229.

198 Uversky, V. N. (1999). A multiparametric approach to studies of self-organization of globular proteins. *Biochemistry (Mosc)* **64**, 250–266.

199 Ptitsyn, O. B. & Uversky, V. N. (1994). The molten globule is a third thermodynamical state of protein molecules. *FEBS Lett.* **341**, 15–18.

200 Uversky, V. N., Permyakov, S. E., Zagranichny, V. E., Rodionov, I. L., Fink, A. L., Cherskaya, A. M., Wasserman, L. A. & Permyakov, E. A. (2002). Effect of zinc and temperature on the conformation of the gamma subunit of retinal phosphodiesterase: a natively unfolded protein. *J. Proteome Res.* **1**, 149–159.

201 Timm, D. E., Vissavajjhala, P., Ross, A. H. & Neet, K. E. (1992). Spectroscopic and chemical studies of the interaction between nerve growth factor (NGF) and the extracellular domain of the low affinity NGF receptor. *Protein Sci.* **1**, 1023–31.

202 Kim, T. D., Ryu, H. J., Cho, H. I., Yang, C. H. & Kim, J. (2000). Thermal behavior of proteins: heat-resistant proteins and their heat-induced secondary structural changes. *Biochemistry* **39**, 14839–46.

203 Konno, T., Tanaka, N., Kataoka, M., Takano, E. & Maki, M. (1997). A circular dichroism study of preferential hydration and alcohol effects on a denatured protein, pig calpastatin domain I. *Biochim. Biophys. Acta.* **1342**, 73–82.

204 Lynn, A., Chandra, S., Malhotra, P. & Chauhan, V. S. (1999). Heme binding and polymerization by *Plasmodium falciparum* histidine rich protein II: influence of pH on activity and conformation. *FEBS Lett.* **459**, 267–71.

205 Johansson, J., Gudmundsson, G. H., Rottenberg, M. E., Berndt, K. D. & Agerberth, B. (1998). Conformation-dependent antibacterial activity of the naturally occurring human peptide LL-37. *J. Biol. Chem.* **273**, 3718–3724.

206 Englander, S. W. & Krishna, M. M. (2001). Hydrogen exchange. *Nat. Struct. Biol.* **8**, 741–2.

207 Linderstrøm-Lang, K. (1955). Deuterium exchange between peptides and water. *Chem. Soc. (London) Spec. Publ.* **2**, 1–20.

208 Hvidt, A. & Nielsen, S. O. (1966). Hydrogen exchange in proteins. *Adv. Protein Chem.* **21**, 287–386.

209 Bai, Y., Milne, J. S., Mayne, L. & Englander, S. W. (1993). Primary structure effects on peptide group hydrogen exchange. *Proteins* **17**, 75–86.

210 Hamuro, Y., Coales, S. J., Southern, M. R., Nemeth-Cawley, J. F., Stranz, D. D. & Griffin, P. R. (2003). Rapid analysis of protein structure and dynamics by hydrogen/deuterium exchange mass spectrometry. *J Biomol Tech* **14**, 171–82.

211 Hamuro, Y., Coales, S. J., Southern, M. R., Nemeth-Cawley, J. F., Stranz, D. D. & Griffin, P. R. (2003). Rapid analysis of protein structure and dynamics by hydrogen/deuterium exchange mass spectrometry. *J. Biomol. Tech.* **14**, 171–82.

212 Englander, J. J., Rogero, J. R. & Englander, S. W. (1985). Protein hydrogen exchange studied by the fragment separation method. *Anal. Biochem.* **147**, 234–44.

213 Rosa, J. J. & Richards, F. M. (1979). An experimental procedure for increasing the structural resolution of chemical hydrogen-exchange measurements on proteins: application to ribonuclease S peptide. *J. Mol. Biol.* **133**, 399–416.

214 Zhang, Z. & Smith, D. L. (1996). Thermal-induced unfolding domains in aldolase identified by amide

hydrogen exchange and mass spectrometry. *Protein Sci* **5**, 1282–9.

215 Pantazatos, D., Kim, J. S., Klock, H. E., Stevens, R. C., Wilson, I. A., Lesley, S. A. & Woods, V. L., Jr. (2004). Rapid refinement of crystallographic protein construct definition employing enhanced hydrogen/deuterium exchange MS. *Proc. Natl. Acad. Sci. U.S.A.* **101**, 751–6.

216 Wu, H. (1931). Studies on denaturation of proteins XIII A theory of denaturation. *Chin. J. Physiol.* **1**, 219–234.

217 Linderstrøm-Lang, K. (1952). Structure and enzymatic break-down of proteins. *Lane Medical Lectures* **6**, 117–126.

218 Markus, G. (1965). Protein substrate conformation and proteolysis. *Proc. Natl. Acad. Sci. U.S.A.* **54**, 253–258.

219 Wright, H. T. (1977). Secondary and conformational specificities of trypsin and chymotrypsin. *Eur. J. Biochem.* **73**, 567–578.

220 Sweet, R. M., Wright, H. T., Janin, J., Chothia, C. H. & Blow, D. M. (1974). Crystal structure of the complex of porcine trypsin with soybean trypsin inhibitor (Kunitz) at 2.6-A resolution. *Biochemistry* **13**, 4212–4228.

221 Hubbard, S. J., Campbell, S. F. & Thornton, J. M. (1991). Molecular recognition. Conformational analysis of limited proteolytic sites and serine proteinase protein inhibitors. *J. Mol. Biol.* **220**, 507–530.

222 Hubbard, S. J., Beynon, R. J. & Thornton, J. M. (1998). Assessment of conformational parameters as predictors of limited proteolytic sites in native protein structures. *Protein Eng.* **11**, 349–359.

223 Hubbard, S. J., Eisenmenger, F. & Thornton, J. M. (1994). Modeling studies of the change in conformation required for cleavage of limited proteolytic sites. *Protein Sci.* **3**, 757–768.

224 Fernandez, A. & Scheraga, H. A. (2003). Insufficiently dehydrated hydrogen bonds as determinants of protein interactions. *Proc. Natl. Acad. Sci. U.S.A.* **100**, 113–8.

225 Fontana, A., de Laureto, P. P., de Filippis, V., Scaramella, E. & Zambonin, M. (1997). Probing the partly folded states of proteins by limited proteolysis. *Fold. Des.* **2**, R17–R26.

226 Fontana, A., Zambonin, M., Polverino de Laureto, P., De Filippis, V., Clementi, A. & Scaramella, E. (1997). Probing the conformational state of apomyoglobin by limited proteolysis. *J. Mol. Biol.* **266**, 223–230.

227 Uversky, V. N., Gillespie, J. R. & Fink, A. L. (2000). Why are "natively unfolded" proteins unstructured under physiologic conditions? *Proteins* **41**, 415–27.

228 Williams, R. J. (1978). Energy states of proteins, enzymes and membranes. *Proc. R. Soc. Lond. B Biol. Sci.* **200**, 353–389.

229 Linding, R., Russell, R. B., Neduva, V. & Gibson, T. J. (2003). GlobPlot: Exploring protein sequences for globularity and disorder. *Nucleic Acids Res.* **31**, 3701–8.

230 Linding, R., Jensen, L. J., Diella, F., Bork, P., Gibson, T. J. & Russell, R. B. (2003). Protein disorder prediction: implications for structural proteomics. *Structure (Camb)* **11**, 1453–1459.

231 Romero, P., Obradovic, Z. & Dunker, A. K. (1997). Sequence data analysis for long disordered regions prediction in the calcineurin family. *Genome Inform. Ser. Workshop Genome Inform.* **8**, 110–124.

232 Romero, P., Obradovic, Z., Li, X., Garner, E. C., Brown, C. J. & Dunker, A. K. (2001). Sequence complexity of disordered protein. *Proteins* **42**, 38–48.

233 Jones, D. T. & Ward, J. (2003). Prediction of disordered regions in proteins from position specific score matrices. *Proteins* **53**, 573–578.

234 Melamud, E. & Moult, J. (2003). Evaluation of disorder predictions in CASP5. *Proteins* **53 Suppl 6**, 561–5.

235 Yang, S. A. & Klee, C. B. (2000). Low affinity Ca2+-binding sites of calcineurin B mediate conformational changes in calcineurin A. *Biochemistry* **39**, 16147–16154.

236 Brandstetter, H., Bauer, M., Huber, R., Lollar, P. & Bode, W. (1995). X-ray structure of clotting factor IXa: active site and module structure related to Xase activity and hemophilia B. *Proc. Natl. Acad. Sci. U.S.A.* **92**, 9796–9800.

237 Brandstetter, H., Kuhne, A., Bode, W., Huber, R., von der Saal, W., Wirthensohn, K. & Engh, R. A. (1996). X-ray structure of active site-inhibited clotting factor Xa. Implications for drug design and substrate recognition. *J. Biol. Chem.* **271**, 29988–29992.

238 Padmanabhan, K., Padmanabhan, K. P., Tulinsky, A., Park, C. H., Bode, W., Huber, R., Blankenship, D. T., Cardin, A. D. & Kisiel, W. (1993). Structure of human des(1–45) factor Xa at 2.2 A resolution. *J. Mol. Biol.* **232**, 947–966.

239 Aviles, F. J., Chapman, G. E., Kneale, G. G., Crane-Robinson, C. & Bradbury, E. M. (1978). The conformation of histone H5. Isolation and characterisation of the globular segment. *Eur. J. Biochem.* **88**, 363–371.

240 Ramakrishnan, V., Finch, J. T., Graziano, V., Lee, P. L. & Sweet, R. M. (1993). Crystal structure of globular domain of histone H5 and its implications for nucleosome binding. *Nature* **362**, 219–223.

241 Graziano, V., Gerchman, S. E., Wonacott, A. J., Sweet, R. M., Wells, J. R., White, S. W. & Ramakrishnan, V. (1990). Crystallization of the globular domain of histone H5. *J. Mol. Biol.* **212**, 253–257.

242 Shaiu, W. L., Hu, T. & Hsieh, T. S. (1999). The hydrophilic, protease-sensitive terminal domains of eucaryotic DNA topoisomerases have essential intracellular functions. *Pac. Symp. Biocomput.* **4**, 578–589.

243 Berger, J. M., Gamblin, S. J., Harrison, S. C. & Wang, J. C. (1996). Structure and mechanism of DNA topoisomerase II. *Nature* **379**, 225–232.

244 Caron, P. R., Watt, P. & Wang, J. C. (1994). The C-terminal domain of Saccharomyces cerevisiae DNA topoisomerase II. *Mol. Cell. Biol.* **14**, 3197–3207.

245 Muchmore, S. W., Sattler, M., Liang, H., Meadows, R. P., Harlan, J. E., Yoon, H. S., Nettesheim, D., Chang, B. S., Thompson, C. B., Wong, S. L., Ng, S. L. & Fesik, S. W. (1996). X-ray and NMR structure of human Bcl-x_L, an inhibitor of programmed cell death. *Nature* **381**, 335–341.

246 Yamamoto, K., Ichijo, H. & Korsmeyer, S. J. (1999). BCL-2 is phosphorylated and inactivated by an ASK1/Jun N-terminal protein kinase pathway normally activated at G(2)/M. *Mol. Cell. Biol.* **19**, 8469–8478.

247 Cheng, E. H., Kirsch, D. G., Clem, R. J., Ravi, R., Kastan, M. B., Bedi, A., Ueno, K. & Hardwick, J. M. (1997). Conversion of Bcl-2 to a Bax-like death effector by caspases. *Science* **278**, 1966–1968.

248 Chang, B. S., Minn, A. J., Muchmore, S. W., Fesik, S. W. & Thompson, C. B. (1997). Identification of a novel regulatory domain in Bcl-X(L) and Bcl-2. *EMBO J.* **16**, 968–977.

249 Holliger, P., Riechmann, L. & Williams, R. L. (1999). Crystal structure of the two N-terminal domains of g3p from filamentous phage fd at 1.9 A: evidence for conformational lability. *J. Mol. Biol.* **288**, 649–657.

250 Holliger, P. & Riechmann, L. (1997). A conserved infection pathway for filamentous bacteriophages is suggested by the structure of the membrane penetration domain of the minor coat protein g3p from phage fd. *Structure* **5**, 265–275.

251 Nilsson, N., Malmborg, A. C. & Borrebaeck, C. A. (2000). The phage infection process: a functional role for the distal linker region of bacteriophage protein 3. *J. Virol.* **74**, 4229–4235.

252 Lee, C. H., Saksela, K., Mirza, U. A., Chait, B. T. & Kuriyan, J. (1996). Crystal structure of the conserved core of HIV-1 Nef complexed with a Src family SH3 domain. *Cell* **85**, 931–942.

253 Arold, S., Franken, P., Strub, M. P., Hoh, F., Benichou, S., Benarous, R. & Dumas, C. (1997). The crystal structure of HIV-1 Nef protein bound to the Fyn kinase SH3 domain suggests a role for this complex in altered T cell receptor signaling. *Structure* **5**, 1361–1372.

254 Geyer, M., Munte, C. E., Schorr, J., Kellner, R. & Kalbitzer, H. R. (1999). Structure of the anchor-domain of myristoylated and non-myristoylated HIV-1 Nef protein. *J. Mol. Biol.* **289**, 123–138.

255 Arold, S. T. & Baur, A. S. (2001). Dynamic Nef and Nef dynamics: how structure could explain the complex activities of this small HIV protein. *Trends Biochem. Sci.* **26**, 356–363.

256 Karlin, D., Longhi, S., Receveur, V. & Canard, B. (2002). The N-terminal domain of the phosphoprotein of *morbilliviruses* belongs to the natively unfolded class of proteins. *Virology* **296**, 251–262.

257 Karlin, D., Ferron, F., Canard, B. & Longhi, S. (2003). Structural disorder and modular organization in Paramyxovirinae N and P. *J. Gen. Virol.* **84**, 3239–52.

258 Longhi, S., Receveur-Brechot, V., Karlin, D., Johansson, K., Darbon, H., Bhella, D., Yeo, R., Finet, S. & Canard, B. (2003). The C-terminal domain of the measles virus nucleoprotein is intrinsically disordered and folds upon binding the C-terminal moiety of the phosphoprotein. *J. Biol. Chem.* **278**, 18638.

259 Lesk, A. M., Levitt, M. & Chothia, C. (1986). Alignment of the amino acid sequences of distantly related proteins using variable gap penalties. *Protein Eng.* **1**, 77–8.

260 Lesk, A. M. & Chothia, C. (1980). How different amino acid sequences determine similar protein structures: the structure and evolutionary dynamics of the globins. *J. Mol. Biol.* **136**, 225–70.

261 Chothia, C. & Lesk, A. M. (1987). The evolution of protein structures. *Cold Spring Harb. Symp. Quant. Biol.* **52**, 399–405.

262 Harrison, R. W., Chatterjee, D. & Weber, I. T. (1995). Analysis of six protein structures predicted by comparative modeling techniques. *Proteins* **23**, 463–71.

263 Skolnick, J. & Fetrow, J. S. (2000). From genes to protein structure and function: novel applications of computational approaches in the genomic era. *Trends Biotechnol.* **18**, 34–9.

264 Skolnick, J., Fetrow, J. S. & Kolinski, A. (2000). Structural genomics and its importance for gene function analysis. *Nat. Biotechnol.* **18**, 283–287.

265 Thornton, J. M., Orengo, C. A., Todd, A. E. & Pearl, F. M. (1999). Protein folds, functions and evolution. *J. Mol. Biol.* **293**, 333–42.

266 Dunker, A. K., Obradovic, Z., Romero, P., Garner, E. C. & Brown, C. J. (2000). Intrinsic protein disorder in complete genomes. *Genome Inform. Ser. Workshop Genome Inform.* **11**, 161–171.

267 Daughdrill, G. W., Chadsey, M. S., Karlinsey, J. E., Hughes, K. T. & Dahlquist, F. W. (1997). The C-terminal half of the anti-sigma factor, FlgM, becomes structured when bound to its target, sigma 28. *Nat. Struct. Biol.* **4**, 285–291.

268 Donne, D. G., Viles, J. H., Groth, D., Mehlhorn, I., James, T. L., Cohen, F. E., Prusiner, S. B., Wright, P. E. & Dyson, H. J. (1997). Structure of the recombinant full-length hamster prion protein PrP(29–231): the N terminus is highly flexible. *Proc. Natl. Acad. Sci. U.S.A.* **94**, 13452–13457.

269 Jacobs, D. M., Lipton, A. S., Isern, N. G., Daughdrill, G. W., Lowry, D. F., Gomes, X. & Wold, M. S. (1999). Human replication protein A: global fold of the N-terminal RPA-70 domain reveals a basic cleft and flexible C-terminal linker. *J. Biomol. NMR* **14**, 321–331.

270 Lee, H., Mok, K. H., Muhandiram, R., Park, K. H., Suk, J. E., Kim, D. H., Chang, J., Sung, Y. C., Choi, K. Y. & Han, K. H. (2000). Local structural elements in the mostly

unstructured transcriptional activation domain of human p53. *J. Biol. Chem.* **275**, 29426–29432.

271 Tompa, P. (2002). Intrinsically unstructured proteins. *Trends Biochem. Sci.* **27**, 527–33.

272 Daughdrill, G. W., Ackerman, J., Isern, N. G., Botuyan, M. V., Arrowsmith, C., Wold, M. S. & Lowry, D. F. (2001). The weak interdomain coupling observed in the 70 kDa subunit of human replication protein A is unaffected by ssDNA binding. *Nucleic Acids Res.* **29**, 3270–3276.

273 Chothia, C. & Lesk, A. M. (1986). The relation between the divergence of sequence and structure in proteins. *EMBO J.* **5**, 823–826.

274 Phillips, A., Janies, D. & Wheeler, W. (2000). Multiple sequence alignment in phylogenetic analysis. *Mol. Phylogenet. Evol.* **16**, 317–30.

275 Brown, C. J., Takayama, S., Campen, A. M., Vise, P., Marshall, T., Oldfield, C. J., Williams, C. J. & Dunker, A. K. (2002). Evolutionary rate heterogeneity in proteins with long disordered regions. *J. Mol. Evol.* **55**, 104–110.

276 Shen, J. C., Lao, Y., Kamath-Loeb, A., Wold, M. S. & Loeb, L. A. (2003). The N-terminal domain of the large subunit of human replication protein A binds to Werner syndrome protein and stimulates helicase activity. *Mech. Ageing. Dev.* **124**, 921–30.

277 Longhese, M. P., Plevani, P. & Lucchini, G. (1994). Replication factor A is required in vivo for DNA replication, repair, and recombination. *Mol. Cell. Biol.* **14**, 7884–90.

278 Umezu, K., Sugawara, N., Chen, C., Haber, J. E. & Kolodner, R. D. (1998). Genetic analysis of yeast RPA1 reveals its multiple functions in DNA metabolism. *Genetics* **148**, 989–1005.

279 Wold, M. S. (1997). Replication protein A: a heterotrimeric, single-stranded DNA-binding protein required for eukaryotic DNA metabolism. *Annu. Rev. Biochem.* **66**, 61–92.

280 Goldman, N., Thorne, J. L. & Jones, D. T. (1998). Assessing the impact of secondary structure and solvent accessibility on protein evolution. *Genetics* **149**, 445–58.

281 Lio, P., Goldman, N., Thorne, J. L. & Jones, D. T. (1998). PASSML: combining evolutionary inference and protein secondary structure prediction. *Bioinformatics* **14**, 726–33.

282 Thorne, J. L., Goldman, N. & Jones, D. T. (1996). Combining protein evolution and secondary structure. *Mol. Biol. Evol.* **13**, 666–73.

283 Dayhoff, M. O., Schwartz, R. M. & Orcutt, B. C. (1978). A model of evolutionary change in proteins. *Atlas of Protein Sequence and Structure* **5**, 345–352.

284 Henikoff, S. & Henikoff, J. G. (1992). Amino acid substitution matrices from protein blocks. *Proc. Natl. Acad. Sci. U.S.A.* **89**, 10915–9.

285 Radivojac, P., Obradovic, Z., Brown, C. J. & Dunker, A. K. (2002). Improving sequence alignments for intrinsically disordered proteins. *Pac. Symp. Biocomput.* **7**, 589–600.

286 Radivojac, P., Obradovic, Z., Brown, C. J. & Dunker, A. K. (2002). *Pac. Symp. Biocomput.*

287 Brown, C. J., Takayama, S., Campen, A. M., Vise, P., Marshall, T. W., Oldfield, C. J., Williams, C. J. & Dunker, A. K. (2002). Evolutionary rate heterogeneity in proteins with long disordered regions. *J. Mol. Evol.* **55**, 104–10.

288 Luby-Phelps, K. (2000). Cytoarchitecture and physical properties of cytoplasm: volume, viscosity, diffusion, intracellular surface area. *Int. Rev. Cytol.* **192**, 189–221.

289 Zimmerman, S. B. & Minton, A. P. (1993). Macromolecular crowding: biochemical, biophysical and physiological consequences. *Annu. Rev. Biophys. Biomol. Struct.* **22**, 27–65.

290 Fulton, A. B. (1982). How crowded is the cytoplasm? *Cell* **30**, 345–347.

291 Davis-Searles, P. R., Saunders, A. J., Erie, D. A., Winzor, D. J. & Pielak, G. J. (2001). Interpreting the effects of small uncharged solutes on protein-folding equilibria. *Annu. Rev. Biophys. Biomol. Struct.* **30**, 271–306.

292 Minton, A. P. (2001). The influence of macromolecular crowding and macromolecular confinement on biochemical reactions in physiological media. *J. Biol. Chem.* **276**, 10577–80.

293 Sasahara, K., McPhie, P. & Minton, A. P. (2003). Effect of dextran on protein stability and conformation attributed to macromolecular crowding. *J. Mol. Biol.* **326**, 1227–37.

294 Elston, T. C. & Oster, G. (1997). Protein turbines. I: The bacterial flagellar motor. *Biophys. J.* **73**, 703–21.

295 Hughes, K. T., Gillen, K. L., Semon, M. J. & Karlinsey, J. E. (1993). Sensing structural intermediates in bacterial flagellar assembly by export of a negative regulator. *Science* **262**, 1277–80.

296 Schulman, B. A., Kim, P. S., Dobson, C. M. & Redfield, C. (1997). A residue-specific NMR view of the non-cooperative unfolding of a molten globule. *Nat. Struct. Biol.* **4**, 630–634.

297 Redfield, C., Schulman, B. A., Milhollen, M. A., Kim, P. S. & Dobson, C. M. (1999). Alpha-lactalbumin forms a compact molten globule in the absence of disulfide bonds. *Nat. Struct. Biol.* **6**, 948–52.

298 McParland, V. J., Kalverda, A. P., Homans, S. W. & Radford, S. E. (2002). Structural properties of an amyloid precursor of beta(2)-microglobulin. *Nat. Struct. Biol.* **9**, 326–331.

299 Shimba, N., Serber, Z., Ledwidge, R., Miller, S. M., Craik, C. S. & Dötsch, V. (2003). Quantitative identification of the protonation state of histidines in vitro and in vivo. *Biochemistry* **42**, 9227–34.

300 Serber, Z. & Dötsch, V. (2001). In-cell NMR spectroscopy. *Biochemistry* **40**, 14317–23.

301 Serber, Z., Ledwidge, R., Miller, S. M. & Dötsch, V. (2001). Evaluation of parameters critical to observing proteins inside living *Escherichia coli* by in-cell NMR spectroscopy. *J. Am. Chem. Soc.* **123**, 8895–901.

302 Honnappa, S., Cutting, B., Jahnke, W., Seelig, J. & Steinmetz, M. O. (2003). Thermodynamics of the Op18/stathmin-tubulin interaction. *J. Biol. Chem.* **278**, 38926–34.

303 Demchenko, A. P. (2001). Recognition between flexible protein molecules: induced and assisted folding. *J. Mol. Recognit.* **14**, 42–61.

304 Dyson, H. J. & Wright, P. E. (2002). Coupling of folding and binding for unstructured proteins. *Curr. Opin. Struct. Biol.* **12**, 54–60.

305 Spolar, R. S. & Record, M. T., Jr. (1994). Coupling of local folding to site-specific binding of proteins to DNA. *Science* **263**, 777–84.

306 Uversky, V. N. & Narizhneva, N. V. (1998). Effect of natural ligands on the structural properties and conformational stability of proteins. *Biochemistry (Mosc)* **63**, 420–33.

307 Uversky, V. N. (2003). A rigidifying union: The role of ligands in protein structure and stability. In *Recent Research Developments in Biophysics & Biochemistry* (Pandalai, S. G., ed.), Vol. 3, pp. 711–745. Transworld Research Network, Kerala, India.

308 Zwahlen, C., Li, S. C., Kay, L. E., Pawson, T. & Forman-Kay, J. D. (2000). Multiple modes of peptide recognition by the PTB domain of the cell fate determinant Numb. *EMBO J.* **19**, 1505–15.

309 Li, S. C., Zwahlen, C., Vincent, S. J., McGlade, C. J., Kay, L. E., Pawson, T. & Forman-Kay, J. D. (1998). Structure of a Numb PTB domain-peptide complex suggests a basis for diverse binding specificity. *Nat. Struct. Biol.* **5**, 1075–83.

310 Jen-Jacobson, L., Engler, L. E. & Jacobson, L. A. (2000). Structural and thermodynamic strategies for site-specific DNA binding proteins. *Structure Fold. Des.* **8**, 1015–23.

311 Wester, M. R., Johnson, E. F., Marques-Soares, C., Dansette, P. M., Mansuy, D. & Stout, C. D. (2003). Structure of a substrate complex of mammalian cytochrome P450 2C5 at 2.3 A resolution: evidence for multiple substrate binding modes. *Biochemistry* **42**, 6370–9.

312 Furuke, K., Shiraishi, M.,

Mostowski, H. S. & Bloom, E. T. (1999). Fas ligand induction in human NK cells is regulated by redox through a calcineurin-nuclear factors of activated T cell-dependent pathway. *J. Immunol.* **162**, 1988–93.

313 Liu, J., Farmer, J. D., Jr., Lane, W. S., Friedman, J., Weissman, I. & Schreiber, S. L. (1991). Calcineurin is a common target of cyclophilin-cyclosporin A and FKBP-FK506 complexes. *Cell* **66**, 807–815.

314 O'Day, D. H. (2003). CaMBOT: profiling and characterizing calmodulin-binding proteins. *Cell Signal.* **15**, 347–54.

315 Zhang, L. & Lu, Y. T. (2003). Calmodulin-binding protein kinases in plants. *Trends Plant Sci.* **8**, 123–7.

316 Urbauer, J. L., Short, J. H., Dow, L. K. & Wand, A. J. (1995). Structural analysis of a novel interaction by calmodulin: high-affinity binding of a peptide in the absence of calcium. *Biochemistry* **34**, 8099–8109.

317 Sandak, B., Wolfson, H. J. & Nussinov, R. (1998). Flexible docking allowing induced fit in proteins: insights from an open to closed conformational isomers. *Proteins* **32**, 159–74.

318 Yang, S. A. & Klee, C. (2002). Study of calcineurin structure by limited proteolysis. *Methods Mol. Biol.* **172**, 317–34.

319 Manalan, A. S. & Klee, C. B. (1983). Activation of calcineurin by limited proteolysis. *Proc. Natl. Acad. Sci. U.S.A.* **80**, 4291–4295.

320 Zidek, L., Novotny, M. V. & Stone, M. J. (1999). Increased protein backbone conformational entropy upon hydrophobic ligand binding. *Nat. Struct. Biol.* **6**, 1118–21.

321 Loh, A. P., Pawley, N., Nicholson, L. K. & Oswald, R. E. (2001). An increase in side chain entropy facilitates effector binding: NMR characterization of the side chain methyl group dynamics in Cdc42Hs. *Biochemistry* **40**, 4590–600.

322 Leontiev, V. V., Uversky, V. N., Permyakov, E. A. & Murzin, A. G. (1993). Introduction of Ca(2+)-binding amino-acid sequence into the T4 lysozyme. *Biochim. Biophys. Acta.* **1162**, 84–8.

323 VanScyoc, W. S. & Shea, M. A. (2001). Phenylalanine fluorescence studies of calcium binding to N-domain fragments of Paramecium calmodulin mutants show increased calcium affinity correlates with increased disorder. *Protein Sci.* **10**, 1758–68.

324 Sorensen, B. R. & Shea, M. A. (1998). Interactions between domains of apo calmodulin alter calcium binding and stability. *Biochemistry* **37**, 4244–53.

325 Fredricksen, R. S. & Swenson, C. A. (1996). Relationship between stability and function for isolated domains of troponin C. *Biochemistry* **35**, 14012–26.

326 Li, Z., Stafford, W. F. & Bouvier, M. (2001). The metal ion binding properties of calreticulin modulate its conformational flexibility and thermal stability. *Biochemistry* **40**, 11193–201.

327 Eakin, C. M., Knight, J. D., Morgan, C. J., Gelfand, M. A. & Miranker, A. D. (2002). Formation of a copper specific binding site in non-native states of beta-2-microglobulin. *Biochemistry* **41**, 10646–10656.

328 Opitz, U., Rudolph, R., Jaenicke, R., Ericsson, L. & Neurath, H. (1987). Proteolytic dimers of porcine muscle lactate dehydrogenase: characterization, folding, and reconstitution of the truncated and nicked polypeptide chain. *Biochemistry* **26**, 1399–406.

329 Namba, K. (2001). Roles of partly unfolded conformations in macromolecular self-assembly. *Genes Cells* **6**, 1–12.

330 Hoh, J. H. (1998). Functional protein domains from the thermally driven motion of polypeptide chains: a proposal. *Proteins* **32**, 223–228.

331 Hupp, T. R., Meek, D. W., Midgley, C. A. & Lane, D. P. (1992). Regulation of the specific DNA binding function of p53. *Cell* **71**, 875–86.

332 Brown, H. G. & Hoh, J. H. (1997). Entropic exclusion by neurofilament sidearms: a mechanism for maintaining interfilament spacing. *Biochemistry* **36**, 15035–15040.

333 Kumar, S., Yin, X., Trapp, B. D., Hoh, J. H. & Paulaitis, M. E. (2002). Relating interactions between neurofilaments to the structure of axonal neurofilament distributions through polymer brush models. *Biophys. J.* **82**, 2360–2372.

334 Kumar, S., Yin, X., Trapp, B. D., Paulaitis, M. E. & Hoh, J. H. (2002). Role of long-range repulsive forces in organizing axonal neurofilament distributions: evidence from mice deficient in myelin-associated glycoprotein. *J. Neurosci. Res.* **68**, 681–690.

335 Wissmann, R., Baukrowitz, T., Kalbacher, H., Kalbitzer, H. R., Ruppersberg, J. P., Pongs, O., Antz, C. & Fakler, B. (1999). NMR structure and functional characteristics of the hydrophilic N terminus of the potassium channel beta-subunit Kvbeta1.1. *J. Biol. Chem.* **274**, 35521–35525.

336 Armstrong, C. M. & Bezanilla, F. (1977). Inactivation of the sodium channel. II. Gating current experiments. *J. Gen. Physiol.* **70**, 567–590.

337 Hoshi, T., Zagotta, W. N. & Aldrich, R. W. (1990). Biophysical and molecular mechanisms of *Shaker* potassium channel inactivation. *Science* **250**, 533–538.

338 Helmes, M., Trombitas, K., Centner, T., Kellermayer, M., Labeit, S., Linke, W. A. & Granzier, H. (1999). Mechanically driven contour-length adjustment in rat cardiac titin's unique N2B sequence. *Circ. Res.* **84**, 1339–1352.

339 Fontana, A., Fassina, G., Vita, C., Dalzoppo, D., Zamai, M. & Zambonin, M. (1986). Correlation between sites of limited proteolysis and segmental mobility in thermolysin. *Biochemistry* **25**, 1847–1851.

340 Fontana, A., de Laureto, P. P., de Filippis, V., Scaramella, L. & Zambonin, M. (1999). Limited proteolysis in the study of protein conformation. In *Proteolytic Enzymes: Tool and Targets*, pp. 257–284, Springer Verlag.

341 Marks, F. (1996). *Protein Phosphorylation*, VCH Weinheim, New York, Basel, Cambridge, Tokyo.

342 Johnson, L. N. & Lewis, R. J. (2001). Structural basis for control by phosphorylation. *Chem. Rev.* **101**, 2209–2242.

343 Iakoucheva, L. M., Radivojac, P., Brown, C. J., O'Connor, T. R., Sikes, J. G., Obradovic, Z. & Dunker, A. K. (2004). The importance of intrinsic disorder for protein phosphorylation. *Nucleic Acids Res.* **32**, 1037–49.

344 Kwong, P. D., Wyatt, R., Desjardins, E., Robinson, J., Culp, J. S., Hellmig, B. D., Sweet, R. W., Sodroski, J. & Hendrickson, W. A. (1999). Probability analysis of variational crystallization and its application to gp120, the exterior envelope glycoprotein of type 1 human immunodeficiency virus (HIV-1). *J. Biol. Chem.* **274**, 4115–23.

345 Bossemeyer, D., Engh, R. A., Kinzel, V., Ponstingl, H. & Huber, R. (1993). Phosphotransferase and substrate binding mechanism of the cAMP-dependent protein kinase catalytic subunit from porcine heart as deduced from the 2.0 A structure of the complex with Mn^{2+} adenylyl imidodiphosphate and inhibitor peptide PKI(5–24). *EMBO J.* **12**, 849–59.

346 Narayana, N., Cox, S., Shaltiel, S., Taylor, S. S. & Xuong, N. (1997). Crystal structure of a polyhistidine-tagged recombinant catalytic subunit of cAMP-dependent protein kinase complexed with the peptide inhibitor PKI(5–24) and adenosine. *Biochemistry* **36**, 4438–4448.

347 Lowe, E. D., Noble, M. E., Skamnaki, V. T., Oikonomakos, N. G., Owen, D. J. & Johnson, L. N. (1997). The crystal structure of a phosphorylase kinase peptide substrate complex: kinase substrate recognition. *Embo. J.* **16**, 6646–6658.

348 ter Haar, E., Coll, J. T., Austen, D. A., Hsiao, H. M., Swenson, L. & Jain, J. (2001). Structure of GSK3beta reveals a primed phosphorylation mechanism. *Nat. Struct. Biol.* **8**, 593–596.

349 Hubbard, S. R. (1997). Crystal structure of the activated insulin receptor tyrosine kinase in complex with peptide substrate and ATP analog. *Embo. J.* **16**, 5572–5581.

350 McDonald, I. K. & Thornton, J. M. (1994). Satisfying hydrogen bonding potential in proteins. *J. Mol. Biol.* **238**, 777–793.

351 Tanford, C. (1968). Protein denaturation. *Adv. Protein Chem.* **23**, 121–282.

352 Flory, P. J. (1969). *Statistical Mechanics of Chain Molecules*, John wiley.

353 Baldwin, R. L. (2002). A new perspective on unfolded proteins. *Adv Protein Chem* **62**, 361–7.

354 Pappu, R. V., Srinivasan, R. & Rose, G. D. (2000). The Flory isolated-pair hypothesis is not valid for polypeptide chains: implications for protein folding. *Proc. Natl. Acad. Sci. U.S.A.* **97**, 12565–12570.

355 Zhou, H. X. (2004). Polymer models of protein stability, folding, and interactions. *Biochemistry* **43**, 2141–54.

356 Huber, R. (1979). Conformational flexibility in protein molecules. *Nature* **280**, 538–539.

357 Kossiakoff, A. A., Chambers, J. L., Kay, L. M. & Stroud, R. M. (1977). Structure of bovine trypsinogen at 1.9 A resolution. *Biochemistry* **16**, 654–664.

358 Bennett, W. S. & Huber, R. (1984). Structural and functional aspects of domain motions in proteins. *Crit. Rev. Biochem.* **15**, 291–384.

359 Romero, P., Obradovic, Z., Li, X., Garner, E. C., Brown, C. J. & Dunker, A. K. (2001). Sequence complexity and disordered protein. *Proteins: Structure, Function, Genetics* **42**, 38–49.

360 Plaxco, K. W., Simons, K. T. & Baker, D. (1998). Contact order, transition state placement and the refolding rates of single domain proteins. *J Mol Biol* **277**, 985–94.

361 Gromiha, M. M. & Selvaraj, S. (2001). Comparison between long-range interactions and contact order in determining the folding rate of two-state proteins: application of long-range order to folding rate prediction. *J Mol Biol* **310**, 27–32.

362 Mirny, L. & Shakhnovich, E. (2001). Protein folding theory: from lattice to all-atom models. *Annu Rev Biophys Biomol Struct* **30**, 361–96.

363 Zhou, H. & Zhou, Y. (2002). Folding rate prediction using total contact distance. *Biophys J* **82**, 458–63.

364 Makarov, D. E. & Plaxco, K. W. (2003). The topomer search model: A simple, quantitative theory of two-state protein folding kinetics. *Protein Sci* **12**, 17–26.

365 Makarov, D. E., Keller, C. A., Plaxco, K. W. & Metiu, H. (2002). How the folding rate constant of simple, single-domain proteins depends on the number of native contacts. *Proc Natl Acad Sci USA* **99**, 3535–9.

366 Debe, D. A. & Goddard, W. A., 3rd. (1999). First principles prediction of protein folding rates. *J Mol Biol* **294**, 619–25.

367 Debe, D. A., Carlson, M. J. & Goddard, W. A., 3rd. (1999). The topomer-sampling model of protein folding. *Proc Natl Acad Sci USA* **96**, 2596–601.

368 Kay, L. E., Keifer, P. & Saarinen, T. (1992). Pure absorption gradient enhanced heteronuclear single quantum correlation spectroscopy with improved sensitivity. *J. Am. Chem. Soc.* **114**, 10663.

369 Muhandiram, D. R. & Kay, L. E. (1994). Gradient-enhanced triple-resonance three-dimensional NMR experiments with improved sensitivity. *J. of Magn. Reson. B* **3**, 203–216.

370 Wittekind, M. & Mueller, L. (1993). HNCACB, a high-sensitivity 3D NMR experiment to correlate amide-proton and nitrogen resonances with the alpha- and beta-carbon resonances in proteins. *J. of Magn. Reson. B* **2**, 201–205.

371 Dingley, A. J., Mackay, J. P., Chapman, B. E., Morris, M. B., Kuchel, P. W., Hambly, B. D. & King, G. F. (1995). Measuring protein self-association using pulsed-field-

gradient NMR spectroscopy: application to myosin light chain 2. *J. Biomol. NMR* **6**, 321–8.

372 Stejskal, E. O. & Tanner, J. E. (1965). Spin diffusion measurements spin echoes in the presence of a time dependent field gradient. *J. Chem. Phys.* **42**, 288–292.

373 Peng, J. W. & Wagner, G. (1995). Frequency spectrum of NH bonds in eglin c from spectral density mapping at multiple fields. *Biochemistry* **34**, 16733–52.

374 Farrow, N. A., Zhang, O. W., Szabo, A., Torchia, D. A. & Kay, L. E. (1995). Spectral density-function mapping using N-15 relaxation data exclusively. *J. Biomol. NMR* **6**, 153–162.

375 Planson, A. G., Guijarro, J. I., Goldberg, M. E. & Chaffotte, A. F. (2003). Assistance of maltose binding protein to the in vivo folding of the disulfide-rich C-terminal fragment from Plasmodium falciparum merozoite surface protein 1 expressed in *Escherichia coli*. *Biochemistry* **42**, 13202–11.

376 Stout, G. H. & Jensen, L. H. (1989). *X-Ray Structure Determination: A Practical Guide*, Wiley-Interscience, New York.

377 McRee, D. E. (1997). *Practical Protein Crystallography.* 2nd edit, Academic Press, New York.

378 Ikemoto, N., Nagy, B., Bhatnagar, G. M. & Gergely, J. (1974). Studies on a metal-binding protein of the sarcoplasmic reticulum. *J. Biol. Chem.* **249**, 2357–65.

379 Ostvald, T. V., MacLennon, D. H. & Dorrington, K. J. (1974). Effects of Cation Binding on the Conformation of Calsequestrin and the High Affinity Calcium-binding Protein of Sarcoplasmic Reticulum. *J. Biol. Chem.* **249**, 567–5871.

380 Aaron, B. M., Oikawa, K., Reithmeier, R. A. & Sykes, B. D. (1984). Characterization of skeletal muscle calsequestrin by 1H NMR spectroscopy. *J. Biol. Chem.* **259**, 11876–11881.

381 He, Z., Dunker, A. K., Wesson, C. R. & Trumble, W. R. (1993). Ca(2+)-induced folding and aggregation of skeletal muscle sarcoplasmic reticulum calsequestrin. The involvement of the trifluoperazine-binding site. *J. Biol. Chem.* **268**, 24635–24641.

382 Ikemoto, N., Bhatnagar, G. M., Nagy, B. & Gergely, J. (1972). Interaction of divalent cations with the 55,000-dalton protein component of the sarcoplasmic reticulum. Studies of fluorescence and circular dichroism. *J. Biol. Chem.* **247**, 7835–7.

383 Cozens, B. & Reithmeier, R. A. (1984). Size and shape of rabbit skeletal muscle calsequestrin. *J. Biol. Chem.* **259**, 6248–6252.

384 Ohnishi, M. & Reithmeier, R. A. (1987). Fragmentation of rabbit skeletal muscle calsequestrin: spectral and ion binding properties of the carboxyl-terminal region. *Biochemistry* **26**, 7458–65.

385 Mitchell, R. D., Simmerman, H. K. & Jones, L. R. (1988). Ca2+ binding effects on protein conformation and protein interactions of canine cardiac calsequestrin. *J Biol. Chem.* **263**, 1376–81.

386 Williams, R. W. & Beeler, T. J. (1986). Secondary structure of calsequestrin in solutions and in crystals as determined by Raman spectroscopy. *J. Biol. Chem.* **261**, 12408–12413.

387 Maurer, A., Tanaka, M., Ozawa, T. & Fleischer, S. (1985). Purification and crystallization of the calcium binding protein of sarcoplasmic reticulum from skeletal muscle. *Proc. Natl. Acad. Sci. U.S.A.* **82**, 4036–40.

388 Franzini-Armstrong, C., Kenney, L. J. & Varriano-Marston, E. (1987). The structure of calsequestrin in triads of vertebrate skeletal muscle: a deep-etch study. *J. Cell Biol.* **105**, 49–56.

389 Kang, C. H., Trumble, W. R. & Dunker, A. K. (2001). Crystallization and structure-function of calsequestrin. In *Calcium Binding Protein Protocols: volume 1 reviews and case studies* (Vogel, H. J., ed.), Vol. 172, pp. 281–294. Humana Press, Totowa, New Jersey.

390 Wang, S., Trumble, W. R., Liao, H., Wesson, C. R., Dunker, A. K. & Kang, C. H. (1998). Crystal structure of calsequestrin from rabbit skeletal muscle sarcoplasmic reticulum. *Nat. Struct. Biol.* **5**, 476–483.

391 McPherson, A. (1990). Current approaches to macromolecular crystallization. *Eur. J. Biochem.* **189**, 1–23.

392 Jancarik, J. & Kim, S.-H. (1991). Sparse matrix sampling: a screening method for crystallization of proteins. *J. Appl. Cryst.* **24**, 409–411.

393 Fliegel, L., Ohnishi, M., Carpenter, M. R., Khanna, V. K., Reithmeier, R. A. F. & MacLennan, D. H. (1987). Amino acid sequence of rabbit fast-twitch skeletal muscle calsequestrin deduced from cDNA and peptide sequencing. *Proc. Natl. Acad. Sci. U.S.A.* **84**, 1167–1171.

394 Scott, B. T., Simmerman, H. K., Collins, J. H., Nadal-Ginard, B. & Jones, L. R. (1988). Complete amino acid sequence of canine cardiac calsequestrin deduced by cDNA cloning. *J Biol. Chem.* **263**, 8958–64.

395 Gill, S. C. & von Hippel, P. H. (1989). Calculation of protein extinction coefficients from amino acid sequence data. *Anal Biochem* **182**, 319–26.

396 Antz, C., Geyer, M., Fakler, B., Schott, M. K., Guy, H. R., Frank, R., Ruppersberg, J. P. & Kalbitzer, H. R. (1997). NMR structure of inactivation gates from mammalian voltage-dependent potassium channels. *Nature* **385**, 272–275.

397 Korzhnev, D. M., Salvatella, X., Vendruscolo, M., Di Nardo, A. A., Davidson, A. R., Dobson, C. M. & Kay, L. E. (2004). Low-populated folding intermediates of Fyn SH3 characterized by relaxation dispersion NMR. *Nature* **430**, 586–590.

398 Spiro, T. G., Gaber, B. P. (1977). Laser Raman scattering as a probe of protein structure. *Annu. Rev. Biochem.* **46**, 553–572.

399 Maiti, N. C., Apetri, M. M., Zagorski, M. G., Carey, P. R. & Anderson, V. E. (2004). Raman spectroscopic characterization of secondary structure in natively unfolded proteins: alpha-synuclein. *J. Am. Chem. Soc.* **126**, 2399–2408.

400 Syme, C. D., Blanch, E. W., Holt, C., Jakes, R., Goedert, M., Hecht, L. & Barron, L. D. (2002). A Raman optical activity study of rheomorphism in caseins, synucleins and tau. New insight into the structure and behaviour of natively unfolded proteins. *Eur. J. Biochem.* **269**, 148–156.

401 Daughdrill, G. W., Vise, P. D., Zhou, H., Yang, X., Yu, W. F., Tasayco, M. L. & Lowry, D. F. (2004). Reduced spectral density mapping of a partially folded fragment of E. coli thioredoxin. *J. Biomol. Struct. Dyn.* **21**, 663–670.

402 Kriwacki, R. W., Hengst, L., Tennant, L., Reed, S. I. & Wright, P. E. (1996). Structural studies of p21Waf1/Cip1/Sdi1 in the free and Cdk2-bound state: conformational disorder mediates binding diversity. *Proc. Natl. Acad. Sci. U.S.A.* **93**, 11504–11509.

403 Kriwacki, R. W., Wu, J., Tennant, J., Wright, P. E. & Siuzdak, G. (1997). Probing protein structure using biochemical and biophysical methods. Proteolysis, matrix-assisted laser desorption/ionization mass spectrometry, high-performance liquid chromatography and size-exclusion chromatography of p21Waf1/Cip1/Sdi1. *J. Chromatogr. A* **777**, 23–30.

404 Sadqi, M., Hernandez, F., Pan, U., Perez, M., Schaeberle, M. D., Avila, J. & Munoz, V. (2002). Alpha-helix structure in Alzheimer's disease aggregates of tau-protein. *Biochemistry* **41**, 7150–7155.

405 Ghaemmaghami, S., Fitzgerald, M. C. & Oas, T. G. (2000). A quantitative, high-throughput screen for protein stability. *Proc. Natl. Acad. Sci. USA* **97**, 8296–8301.

406 Gong, H., Isom, D. G., Srinivasan, R. & Rose, G. D. (2003). Local secondary structure content predicts folding rates for simple, two-state proteins. *J. Mol. Biol.* **327**, 1149–1154.

9
The Catalysis of Disulfide Bond Formation in Prokaryotes

Jean-Francois Collet and James C. Bardwell

9.1
Introduction

Oxidation of two cysteine residues leads to the formation of a disulfide bond and the concomitant release of two electrons. The formation of disulfide bonds is a required step in the folding pathway of many secreted proteins. It takes place in the eukaryotic endoplasmic reticulum or in the bacterial periplasm. In contrast, this oxidation reaction is harmful to most cytoplasmic proteins and may lead to protein misfolding and aggregation. Both eukaryotic and prokaryotic cells possess mechanisms to ensure that cytoplasmic cysteines are kept reduced. These mechanisms involve enzymes of the thioredoxin and glutaredoxin systems.

This review will focus on disulfide bond formation in bacteria, taking *Escherichia coli* as a model. In the first two sections we will discuss disulfide bond formation and isomerization in the periplasm. In the third section, we will present some of the techniques that have been used to study thiol-disulfide chemistry.

9.2
Disulfide Bond Formation in the *E. coli* Periplasm

9.2.1
A Small Bond, a Big Effect

In both eukaryotes and prokaryotes, structural disulfide bonds are found in extracytoplasmic proteins. The presence of a covalent bond between two cysteine residues confers a higher stability to these proteins and is often required for their correct folding. One striking example of the importance of disulfide bonds for the correct folding of secreted proteins is the *E. coli* flagellar protein FlgI, a component of the bacterial flagellum. The folding of FlgI requires a disulfide bond. When this disulfide is not introduced in FlgI, FlgI cannot be properly folded and a functional flagellum cannot be assembled [1]. This results in the complete loss of motility as shown in Figure 9.1.

Protein Folding Handbook. Part II. Edited by J. Buchner and T. Kiefhaber

ISBN: 3-527-30784-2

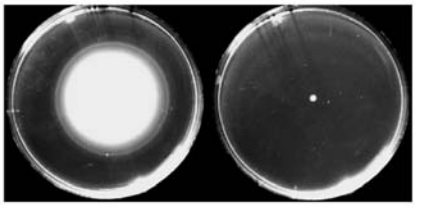

Fig. 9.1. The correct folding of the flagellum component FlgI requires a disulfide bond.

9.2.2 Disulfide Bond Formation Is a Catalyzed Process

Disulfide bonds can be formed spontaneously by molecular oxygen according to the following equation:

$$2\ \text{R-SH} + 1/2\ O_2 \rightarrow \text{RS-SR} + H_2O$$

However, this reaction is very slow, occurring on the hour timescale in vitro. Such reaction times are unrealistic in vivo, where proteins are synthesized and folded within minutes. This discrepancy led Anfinsen in the early 1960s to postulate the existence of catalysts of disulfide bond formation. In 1964, he discovered the first catalyst for disulfide bond formation, the eukaryotic protein disulfide isomerase (PDI). PDI is a multi-domain enzyme that is active in the eukaryotic endoplasmic reticulum. The eukaryotic disulfide formation pathway has been recently reviewed by Sevier and Kaiser and will not be discussed here [2].

In *E. coli*, disulfide bonds are introduced exclusively in the periplasm. The enzymes responsible are members of the Dsb (disulfide bond) protein family: DsbA and DsbB, which are involved in disulfide bond formation, and DsbC, DsbG, and DsbD, which are involved in disulfide bond isomerization.

9.2.3 DsbA, a Protein-folding Catalyst

DsbA is a 21-kDa soluble protein that is required for disulfide bond formation in the *E. coli* periplasm. In agreement with the central role of this protein in the oxi-

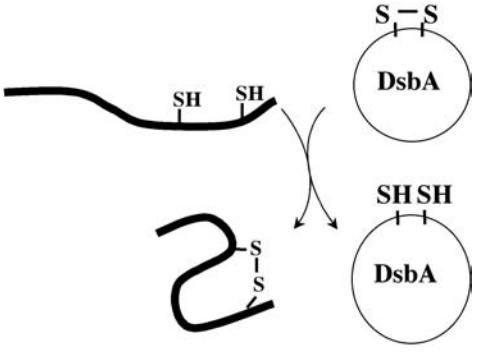

Fig. 9.2. Disulfide bond transfer from DsbA to the target protein. Oxidized DsbA is very unstable and reacts rapidly with unfolded proteins entering the periplasm. The disulfide bond is transferred onto the target protein and DsbA is reduced.

dative protein-folding pathways, *dsbA*$^-$ strains exhibit pleiotropic phenotypes [3]. For instance, *dsbA*$^-$ mutants are hypersensitive to benzylpenicillin, dithiothreitol, and metals [4, 5]. They show reduced levels of several secreted proteins such as the outer-membrane OmpA and alkaline phosphatase [3].

Like many other oxidoreductases, DsbA has a thioredoxin-like fold and a catalytic CXXC motif. In agreement with DsbA acting as a thiol-oxidase, the CXXC motif is found to be predominantly oxidized in vivo [6]. Biochemical and biophysical studies have shown that the disulfide bond present in DsbA is very unstable [7] and can be rapidly transferred to newly translocated proteins (Figure 9.2).

With a redox potential around −120 mV [7], DsbA is the second most oxidizing protein after DsbB (see below). The oxidizing power of DsbA originates from the low pK_a of Cys30, the first cysteine of the CXXC motif [8]. This residue has a pK_a of ≈3, which is much more acidic than the usual pK_a of cysteine residues (≈9). Due to its low pK_a value, Cys30 is in the thiolate-anion state at physiological pH. Structural studies have shown that this thiolate anion, which is highly accessible in the folded protein, is stabilized by electrostatic interactions [9]. The most important electrostatic interactions take place between Cys30 and the third residue of the CXXC motif, His32. Mutations of this single His32 residue increase the stability of the oxidized protein, thereby decreasing the redox potential of DsbA and the reactivity of the enzyme [10]. The stabilization of the thiolate anion is a key characteristic of DsbA, as it drives the reaction towards the reduction of DsbA and the transfer of the disulfide bond to the folding protein.

In addition to the thioredoxin-like domain, DsbA contains a second compactly folded helical domain [9]. This domain covers the CXXC active site and contains several residues that form a hydrophobic patch. This patch, together with a long and relatively deep groove running in the thioredoxin domain below the active site, is likely to interact in a hydrophobic manner with unfolded protein substrates

[11]. Such hydrophobic interactions have indeed been reported to take place. Using NMR, Couprie et al. showed that DsbA binds a model peptide in a hydrophobic way [12]. In a mixed disulfide between DsbA and the substrate protein Rnase T1, the conformational stability of Rnase T1 is decreased by 5 kJ mol^{-1} and the conformational stability of DsbA is increased by 5 kJ mol^{-1}, suggesting that DsbA interacts with the unfolded protein by preferential noncovalent interactions [13]. Proteolysis experiments also showed that oxidized DsbA is more flexible than reduced DsbA. This flexibility might help the oxidized protein to establish interactions with different partner proteins by accommodating the peptide-binding groove to various substrates. On the other hand, the increased rigidity of the reduced form could facilitate the release of oxidized products [14].

9.2.4
How is DsbA Re-oxidized?

After the transfer of the disulfide bond to target proteins, DsbA is reduced and therefore incapable of donating a disulfide bond. The protein responsible for the re-oxidation of DsbA is an inner-membrane protein called DsbB [4, 15]. Mutants lacking DsbB accumulate DsbA in the reduced state and exhibit the same pleiotropic phenotypes as *dsbA*$^-$ mutants, indicating that DsbA and DsbB are on the same pathway [15]. This was confirmed in vitro when we purified DsbB to homogeneity and showed that it is able to catalytically oxidize DsbA in the presence of molecular oxygen [16].

DsbB is a 21-kDa protein that is predicted to have four transmembrane segments and two loops protruding into the periplasm. Each of these periplasmic domains contains a conserved pair of cysteine residues: Cys41 and Cys44 in domain 1 and Cys104 and Cys130 in domain 2. These cysteines can undergo oxidation-reduction cycles. They are essential for activity, as removal of any one of these cysteines causes the accumulation of reduced DsbA [17–19]. The first pair of cysteine residues (Cys41–Cys44) is present in a CXXC motif, a motif that is often found in thioredoxin-like folds. However, the first periplasmic loop of DsbB contains no other recognizable similarity to thioredoxin, and because it is predicted to be only ≈17 residues long, it is far too short to contain a thioredoxin fold.

9.2.5
From Where Does the Oxidative Power of DsbB Originate?

In vivo data obtained by Kobayashi et al. suggested that DsbB is recycled by the electron transport chain [20]. We confirmed this hypothesis by successfully reconstituting the complete disulfide bond formation system in vitro [16, 21]. Using purified components, we showed that electrons flow from DsbB to ubiquinone, then onto cytochrome oxidases *bd* and *bo*, and finally to molecular oxygen. Under anaerobic conditions, electrons are transferred from DsbB to menaquinone then to fumarate or nitrate reductase (see Figure 9.3).

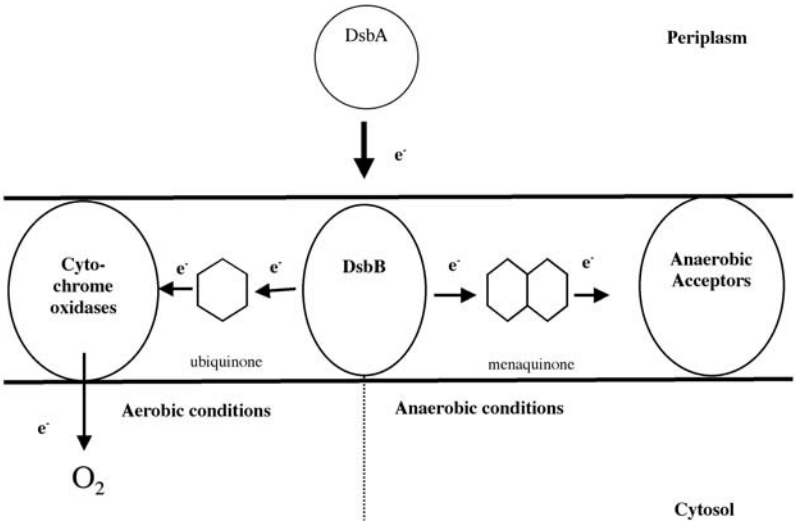

Fig. 9.3. Oxidation pathway in the disulfide periplasm. Reduced proteins are oxidized by DsbA. DsbA is re-oxidized by the inner-membrane protein DsbB. Under aerobic conditions, DsbB is re-oxidized by molecular oxygen in a ubiquinone- and cytochrome oxidase-dependent reaction. Under anaerobic conditions, electrons flow to menaquinone and then to alternative terminal acceptors.

DsbB is a key element of the disulfide bond formation pathway, as it uses the oxidizing power of quinones to generate disulfides de novo [22]. This is a novel catalytic activity that seems to be the major source of disulfide bonds in prokaryotes. We showed that purified DsbB contains a single, highly specific quinone-binding site and has a K_M of 2 μM for quinones [22]. The quinone-binding domain of DsbB seems to be in close proximity to residues 91–97 of the protein [23]. This segment is in the second periplasmic domain of DsbB, in a loop connecting transmembrane helices 3 and 4. Another residue, R48, is also likely to be involved in quinone binding. R48 mutants exhibit a major defect in catalyzing disulfide bond formation in vivo [24]. We purified some of these DsbB mutant proteins and showed that the R48H mutant has a K_M value for quinones that is seven times greater than that of wild-type DsbB, indicating that R48 is involved in quinone binding [24].

9.2.6 How Are Disulfide Bonds Transferred From DsbB to DsbA?

An interesting question is how disulfide bonds are transferred from DsbB to DsbA. Under aerobic conditions, the CXXC motif of DsbB is very difficult to reduce with dithiothreitol when quinones are present in the preparation [25]. This is one of the major arguments in favor of a direct oxidation of Cys41 and Cys44 by quinones.

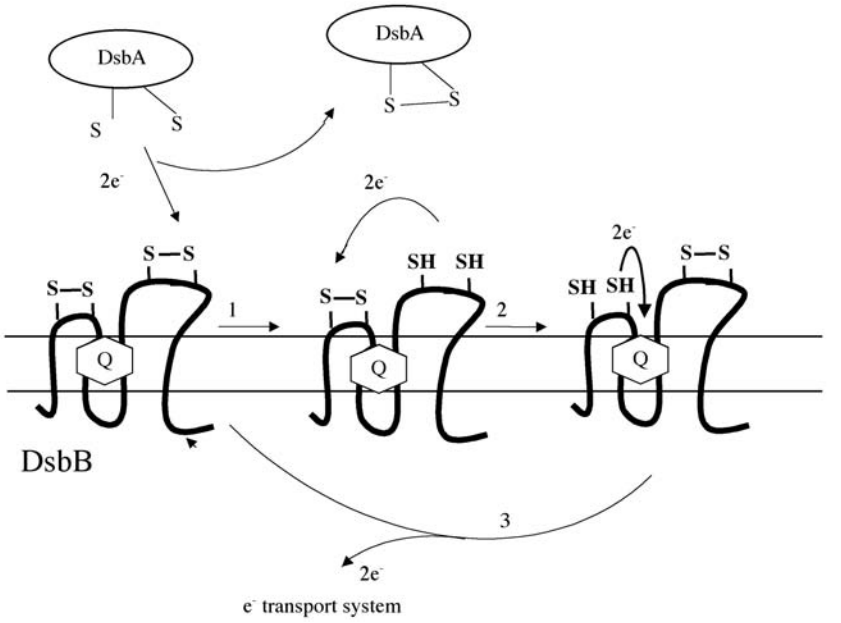

Fig. 9.4. DsbB transfers electrons by a succession of thiol-disulfide exchange reactions. Step 1: a disulfide bond is transferred from the C-terminal cysteine residues of DsbB (Cys104 and Cys130) to DsbA. Cys104 and Cys130 are reduced and DsbA is oxidized. Step 2: a disulfide bond is transferred from the N-terminal cysteine residues of DsbB (Cys41 and Cys44) to the C-terminal cysteine residues. Cys104–Cys130 are oxidized and Cys41–Cys44 are reduced. Step 3: Cys41 and Cys44 are re-oxidized by quinone reduction. Electrons are transferred to the electron transport system.

Then, according to a model first proposed by Ito and coworkers [18, 19, 26], the generated disulfide bond is transferred to the cysteine pair Cys104–Cys130 and then onto DsbA (Figure 9.4). Indeed, a mixed disulfide between Cys30 of DsbA and Cys104 of DsbB has been isolated [18]. This model has been a matter of controversy, and results obtained recently by us and two other labs do not entirely agree with it [26–28]. However, in a paper published recently, Glockshuber and coworkers reported strong arguments in favor of the proposed original mechanism [29]. They showed that Cys104–Cys130 of a quinone-depleted DsbB can indeed directly transfer a disulfide to DsbA and is then re-oxidized by the Cys41–Cys44 disulfide bond. They determined the redox potential of Cys41–Cys44 and Cys104–Cys130 disulfide bonds of DsbB to be −69 mV and −186 mV, respectively. This high redox potential of the Cys41–Cys44 disulfide bond provides strong support for the above-mentioned model, because this redox potential lies between that of ubiquinone (+100 mV) and that of DsbA. This redox potential makes the Cys41–Cys44 disulfide bond the most oxidizing disulfide ever identified in proteins.

The redox potential of Cys104–Cys130 is about 40 mV more negative than the

redox potential of DsbA, but the very oxidizing Cys41–Cys44 disulfide bond could provide the thermodynamic driving force that allows the energetically uphill oxidation of DsbA by the Cys104–Cys130 disulfide in DsbB to occur.

9.2.7
How Can DsbB Generate Disulfide by Quinone Reduction?

Another very intriguing and still unanswered question is, how can DsbB form disulfide bonds by reducing quinone molecules? We recently showed that purified DsbB has a purple color, presumably due to the presence of a quinhydrone, a purple charge-transfer complex consisting of a hydroquinone and a quinone in a stacked conformation [30]. This finding suggested that the DsbB mechanism involves two quinone molecules. According to our model, one of these quinones is very tightly bound to DsbB, whereas the other one is exchangeable. The resident quinone would be directly involved in disulfide bond formation and would undergo oxidation-reduction cycles: it would be reduced during the generation of a disulfide bond and then re-oxidized by an exchangeable quinone derived from the oxidized quinones pool (see Figure 9.5).

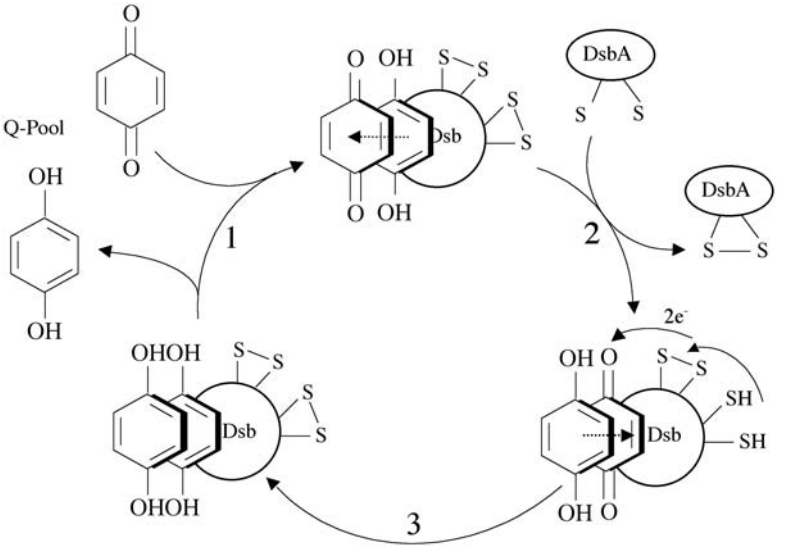

Fig. 9.5. Model for the quinone reductase activity of DsbB. The quinone reductase activity of DsbB involves two quinone molecules: a tightly bound quinone and an exchangeable quinone. The two quinones are initially reduced. Step 1: the reduced exchangeable quinone is replaced by an oxidized quinone derived from the quinone pool. A purple quinhydrone-like charge-transfer complex is formed between the reduced and the oxidized quinone molecules. Step 2: Electrons are transferred from DsbA to the C-terminal disulfide in DsbB. Then, electrons are transferred to the N-terminal disulfide of DsbB. Step 3: the N-terminal cysteine residues reduce the resident quinone. The two reduced quinone molecules do not form a stable complex, and the transient quinone is exchanged with an oxidized one.

9.3
Disulfide Bond Isomerization

9.3.1
The Protein Disulfide Isomerases DsbC and DsbG

The powerful oxidant DsbA can introduce nonnative disulfide bonds into proteins with more than two cysteines. It is important to quickly resolve these incorrect disulfides and thus prevent the accumulation of misfolded proteins. Cells therefore contain a "disulfide correction system," which, in *E. coli*, involves the two protein disulfide isomerases DsbC and DsbG. The proteins are homologous (≈30% amino acid identity) and share many common properties. They seem to differ, however, in their substrate specificity. We showed, for instance, that RNAse I and MepA, which contain eight and six conserved cysteines, respectively, are substrates for DsbC but not for DsbG [31].

DsbC and DsbG are dimeric proteins with a thioredoxin-like domain and a CXXC active site motif. In contrast to DsbA, the two cysteine residues of these motifs are kept reduced in the periplasm [32]. This allows the proteins to reduce nonnative disulfides and to isomerize them to the correct form. According to the proposed mechanism for DsbC and DsbG action (Figure 9.6), the first cysteine res-

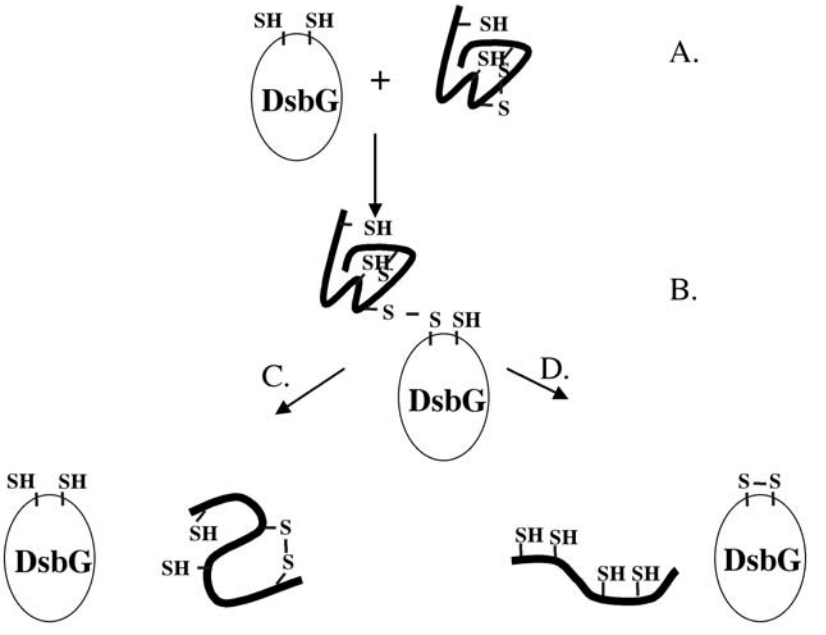

Fig. 9.6. Disulfide bond isomerization by DsbG. (A) Reduced DsbG reacts with a nonnative disulfide. (B) A mixed disulfide is formed between DsbG and the target protein. The mixed disulfide is resolved either by attack of another cysteine of the substrate (C) or by attack of the second cysteine of DsbG (D).

idue attacks a nonnative disulfide bond in the substrate protein, leading to the formation of a mixed disulfide. This mixed disulfide can then be resolved either by the attack of the second active site cysteine of the isomerase or by attack of a third cysteine of the target protein. In the first case, the nonnative disulfide in the substrate protein is reduced and the isomerase is released in the oxidized state. In the second case, alternative disulfide bonds form in the substrate protein and the isomerase is released in the reduced state.

DsbC and DsbG have been shown to be able to correct nonnative disulfide bonds both in vitro and in vivo. They have been found to assist in the refolding of eukaryotic recombinant proteins expressed in *E. coli*, such as bovine pancreatic trypsin inhibitor (three disulfide bonds), RNAse A (four disulfide bonds), and mouse urokinase (12 disulfide bonds) [22, 33–35]. We have recently shown that DsbC is required to fold at least two native *E. coli* proteins, RNAse I (four disulfides) and MepA (six conserved cysteines) [31]. Curiously, so far in vivo substrates of DsbG are restricted to eukaryotic proteins expressed in *E. coli*, and its physiological substrates are still unknown. It seems likely that DsbG has a very limited substrate specificity, which makes the identification rather difficult. Alternatively, it is conceivable that DsbG has an in vivo function that is not related to its ability to act on disulfide bonds. Further work is needed to further characterize the function and substrate specificity of DsbC and DsbG. This should help us to understand why *E. coli* has evolved two homologous protein disulfide isomerases.

9.3.2 Dimerization of DsbC and DsbG Is Important for Isomerase and Chaperone Activity

An important feature of DsbC and DsbG is the presence of a dimerization domain at the amino-terminus of the protein [36]. Although no catalytically active cysteine residues are present in this domain, this region is important for the isomerase activity of DsbC. This was suggested by limited proteolysis experiments performed on DsbC, which showed that monomeric DsbC lacking the amino-terminal domain is inactive as an isomerase and cannot catalyze the formation of correct disulfide bonds in proteins such as RNase A and bovine pancreatic trypsin inhibitor [36]. In particular, this amino-terminal domain is thought to be important for peptide binding. This was suggested by the crystal structure of DsbC, which showed that DsbC is a V-shaped dimer, with each monomer forming one arm of the V [37]. The dimerization domains form an extended cleft in the DsbC structure. The surface of this cleft is predominantly composed of hydrophobic residues, which are predicted to bind misfolded substrates. These hydrophobic interactions are proposed to stabilize the complex formed between DsbC and the target protein until the target protein reaches a more stable conformation. Depending on the redox state of the CXXC motif, the hydrophobic cleft switches between an open and a closed conformation [38]. This allows DsbC to adapt to the size and shape of the substrate proteins. In addition to the isomerase activity, both DsbC and DsbG have been reported to have a chaperone activity. DsbC can assist in the refolding of lysozyme and promotes the in vitro reactivation of denatured D-glyceraldehyde-3-phosphate dehydrogenase [39]. DsbG is able to prevent the aggregation of citrate

synthase and luciferase in vitro [40]. Dimerization seems to be required for this activity, as truncated DsbC variants that lack the dimerization domain have no chaperone activity [36]. Furthermore, addition of the DsbC amino-terminal domain to DsbA or thioredoxin, two oxidoreductases that do not exhibit chaperone activity, causes their dimerization and confers some chaperone activity [41]. The formation of similar V-shaped dimers with a hydrophobic cleft by these hybrid proteins is likely to be the cause of this new activity.

9.3.3
Dimerization Protects from DsbB Oxidation

If DsbB were able to oxidize the active-site cysteines of DsbC and DsbG, the proteins would no longer be able to act as disulfide isomerases. However, we and others have found that DsbB is unable to oxidize DsbC and DsbG either in vivo or in vitro [22, 32, 35, 42]. The observed dimerization of DsbC and DsbG appears to be the molecular basis for this discrimination, as disruption of the dimer interface produces a monomeric DsbC protein that is now oxidized by DsbB both in vivo and in vitro and that can substitute for DsbA in the cell [43].

9.3.4
Import of Electrons from the Cytoplasm: DsbD

In order to stay reduced and active in the oxidizing environment of the periplasm, DsbC and DsbG have to be kept reduced. This reduction of DsbC and DsbG depends on the protein DsbD (Figure 9.7). DsbD is an inner-membrane protein of 59 kDa. It is composed of three domains (Figure 9.7): a periplasmic amino-terminal domain (α), a central membranous domain with eight transmembrane segments (β), and a periplasmic carboxy-terminal domain with a thioredoxin-like fold (γ). Each of these domains harbors a conserved pair of cysteine residues. These six conserved cysteine residues are important for DsbD activity, as removal of any one of them leads to the accumulation of oxidized DsbC and DsbG in the *E. coli* periplasm [44, 45].

Rietsche et al. showed that the cytoplasmic thioredoxin system is the source of reducing equivalents that keep DsbD reduced [32, 34]. The thioredoxin system, which consists of thioredoxin (TrxA), thioredoxin reductase (TrxB), and NADPH, is responsible for maintaining cytoplasmic proteins in a reduced state. Thus, the function of DsbD is to transfer electrons across the inner membrane, using the cytoplasmic pool of NADPH as a source of electrons.

The mechanism by which DsbD transfers electrons across the membrane is still unclear. In vivo and in vitro experiments suggest that electrons are transferred via a cascade of disulfide bond exchange reactions. According to the current model [46], the first step is the reduction of the two conserved cysteine residues within the transmembrane β domain by cytoplasmic TrxA. Then, electrons are successively transferred to the γ and α domains and finally onto DsbC or DsbG. Most of the steps that have been proposed by this model are well characterized, especially the reactions taking place in the cytoplasm and in the periplasm. The isolation of a

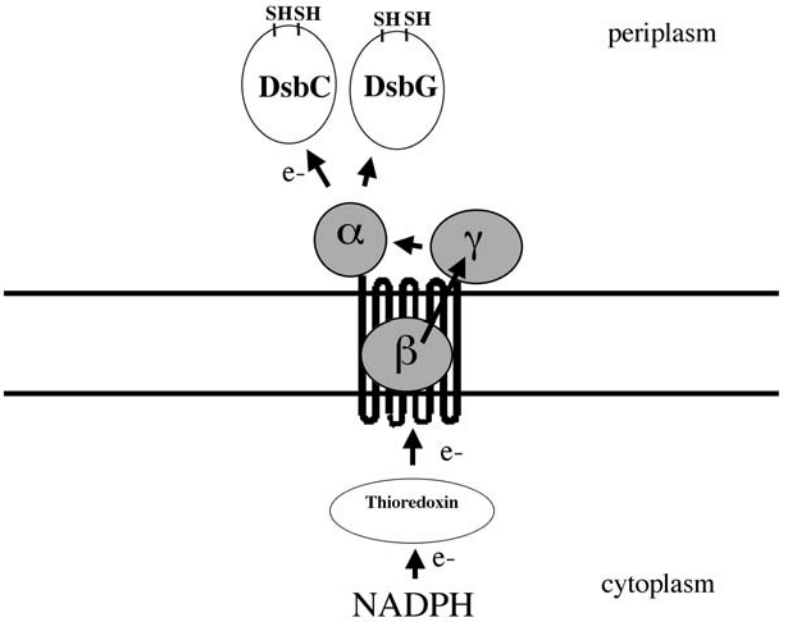

Fig. 9.7. Disulfide bond isomerization pathway in the periplasm. DsbC and DsbG are kept reduced by DsbD. DsbD is kept reduced by the thioredoxin system in the cytoplasm. The proposed direction for the electron flow is shown by the arrows.

mixed disulfide between TrxA and one of the conserved cysteines of the β domain is an argument in favor of a direct interaction between TrxA and the β domain [46]. Using purified components, we showed that electrons flow from the cysteines of the γ domain to the α domain and then to DsbC or DsbG [47]. This was further confirmed by the determination of the redox potential of the cysteine residues in the γ domain (-241 mV) and in the α domain (-229 mV). These lie midway between the redox potential of thioredoxin (-270 mV) and that of DsbC (-134 mV) [47]. The fact that the cysteine residues of the γ domain are more reducing than the cysteine residues of the α domain is consistent with the reaction being thermodynamically driven.

The structure of the γ domain has been determined, and residues that might be important for the interaction with the α domain have been identified [48]. The interaction between the α domain and DsbC or DsbG is also well characterized. In vitro, cysteines of the α domain can efficiently reduce DsbC and DsbG with a K_M of 5 μM, and the structure of a complex between the α domain and DsbC has been solved [38].

The membranous part of the DsbD reaction is still obscure. Removal of the β domain leads to the accumulation of oxidized γ and α domains, which is a strong argument that the β domain is required to transfer electrons to the periplasmic domains [46]. However, *how* electrons are transferred from the β domain to the γ domain is still unclear. Is it by pure disulfide exchange? Is a cofactor, such as a quinone, required as with DsbB? So far, there is no evidence that the cysteine residues

of the β domain interact directly with the cysteine residues of the γ domain, and attempts to isolate mixed disulfides between the two domains have been unsuccessful. Moreover, according to a recent report, both cysteine residues of the β domain are on the cytoplasmic side of the membrane [49]. If this is the case, how can they reduce the cysteines of the γ domain, which are in the periplasm? We purified the β domain and showed that it can transfer electrons from TrxA to the cysteines of the γ domain in vitro [47]. However, the small amount of pure β domain that we were able to produce and the relatively low activity of the preparation prevented us from either proving or ruling out the presence of a cofactor. The important question of how electrons are transferred across the membrane is still unanswered and further work, such as crystallization studies and biochemical characterization of the β domain, is required.

9.3.5 Conclusions

Before the discovery of DsbA in 1991, it was thought that disulfide bond formation in the periplasm was an uncatalyzed process. Since the discovery of this enzyme, much work has been done and most of the important steps in the pathways of disulfide bond formation and isomerization in the *E. coli* periplasm have been unraveled. However, some very interesting questions remain unanswered. These mainly concern the mechanism of action of the two membrane proteins of the Dsb protein family, DsbB and DsbD. DsbB generates disulfides de novo via quinone reduction. More work is required to establish exactly how it performs this key reaction, which appears to be the source of the vast majority of disulfides in *E. coli*. DsbD acts to transport disulfides across the membrane, but how it does so is almost entirely unclear. Characterization of the membranous domain of DsbD will help us to understand how DsbD solves this unique problem. There are many examples of proteins involved in the transport of metals, sugars, or even complex polypeptides across the membranes, and some of these proteins are very well characterized. In contrast, DsbD and its homologues are the only proteins known to transport disulfides, and their mechanism is still obscure. It is not surprising that these two membrane proteins are the least understood of the family of Dsb proteins, as membrane proteins are traditionally difficult to work with. However, both DsbB and DsbD can be purified in large amounts, so further biochemical progress is likely.

9.4 Experimental Protocols

9.4.1 Oxidation-reduction of a Protein Sample

The common way to reduce or oxidize a protein is to incubate the protein with reduced dithiothreitol (DTT) or oxidized glutathione (GSSG), respectively. Then, the excess redox agents are removed by gel filtration or dialysis.

Procedure

1. Incubate the protein with DTT or GSSG for 30 min at 30 °C. DTT and GSSG concentrations are chosen so that they are in large excess compared to the protein. Typical DTT and GSSG concentrations vary between 10 and 20 mM, whereas protein concentrations are usually in the micromolar range. It is often overlooked that the pH for the incubation should be alkaline (8.0–9.0), as most thiols have pK_a values in this range. Thiol disulfide exchange reactions are dependent on the presence of a thiolate ion attacking a disulfide. Thus, reactions are decreased about 10-fold with each pH unit below the pK_a of the relevant thiol.
2. After the oxidation/reduction reaction, the protein is separated from excess DTT and GSSG by dialysis or gel filtration on Sephadex G25 columns. If using prepacked NAP5 or PD10 columns (Amersham), it is important to choose an elution volume allowing a complete separation of the protein from the small redox molecules.

9.4.2
Determination of the Free Thiol Content of a Protein

A simple method to determine whether the cysteine residues present in a protein are reduced or oxidized is to perform an Ellman assay. This assay relies on the reaction between dithionitrobenzoate (DTNB) and reduced thiols (Figure 9.8).

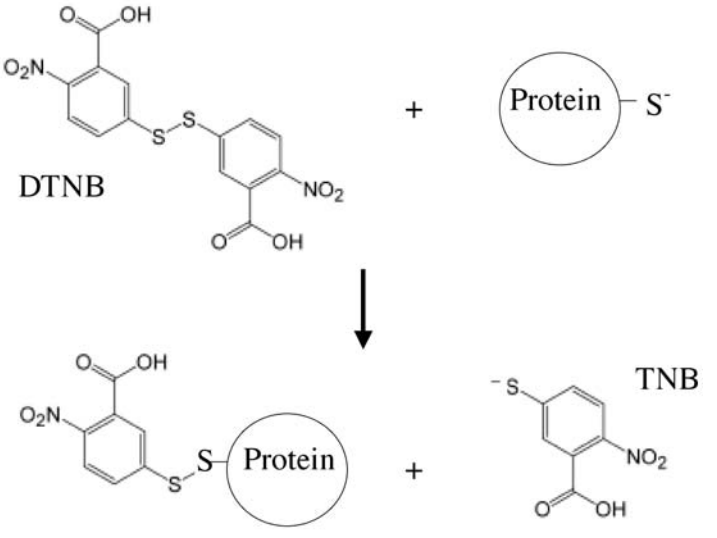

Fig. 9.8. Ellman assay for free thiols. Reaction of DTNB with thiols releases thionitrobenzoate (TNB), which absorbs at 412 nm.

The released TNB anion absorbs at 412 nm ($\varepsilon = 13\,700\ M^{-1}$ or $14\,150\ M^{-1}$ with or without 6 M guanidinium chloride, respectively), which allows the determination of the concentration of reduced cysteine residues in the protein sample.

Procedure

1. Prepare a 3-mM DNTB solution in 100 mM phosphate buffer, pH 7.4. Keep in the dark at 4 °C.
2. Prepare the protein in 100 mM phosphate buffer, pH 7.4, containing 6 M guanidinium chloride and 100 mM EDTA. Guanidinium is used to denature the protein, which increases the accessibility of all thiol groups to DTNB. Choose a protein concentration high enough to allow detection of all free thiols (absorbance of 1 μM TNB anion = 0.0137 unit). Prepare a reference sample without the protein.
3. Measure the absorbance at 412 nm of both the reference and the protein samples.
4. Add 50 μL of the DTNB solution to 1 mL of each sample.
5. Follow the increase in absorbance at 412 nm until it stops increasing.
6. Subtract the absorbance of the reference sample from the absorbance of the protein sample and calculate the molar concentration of free thiols present in the protein using the absorption coefficient (ε). This methodology performed in the absence of denaturants can also allow one to measure the accessibility and reactivity of thiol groups [50].

9.4.3 Separation by HPLC

Reverse-phase HPLC has been used to separate the reduced and oxidized forms of several redox proteins such as TrxA, DsbA, or the periplasmic domains of DsbD [47, 51]. First, the thiol-disulfide exchange reactions are stopped by acidification and the samples are loaded onto a hydrophobic HPLC column. Then, elution conditions are optimized to allow the separation of the oxidized form from the reduced form. The absorbance at 280 nm (aromatic residues) or 214 nm (peptide bond) is recorded and the respective amounts of both forms are determined by integration of the chromatogram.

The time-consuming part of this technique is the optimization of the elution conditions, as it often varies from protein to protein. It is often necessary to experiment with different column types (C4, C8, or C18 columns), to vary the elution buffer's composition, or to vary the type of elution (gradient or isocratic). Once appropriate elution conditions are found, separation of the two redox forms of a protein by HPLC is an accurate, sensitive, fast, and reliable technique. We describe below the conditions that we used to separate oxidized and reduced forms of the γ and α domains of DsbD.

Procedure

1. Add 25 μL of 1% H_3PO_4 to 25 μL of a 50 μM protein sample.
2. Add 50 μL of 50% acetonitrile in 0.1% trifluoroacetic acid (TFA).
3. Load 80 μL on a C18 column (for instance, a Phenomenex Primesphere, 250 × 4.60 mm).

A. Separation of the redox forms of the γ domain was performed using a linear aqueous 39–51% acetonitrile gradient in 0.1% trifluoroacetic acid over 25 min at a flow rate of 1 mL min^{-1}.

B. The oxidized and reduced forms of the α domain were separated using an isocratic elution with 15% methanol and 28% acetonitrile in 0.1% trifluoroacetic acid over 20 min at a flow rate of 0.5 mL min^{-1} [47].

9.4.4 Tryptophan Fluorescence

Protein tryptophan fluorescence is sensitive to changes in the environment of the chromophore residue. Formation of a disulfide bond between two cysteine residues that are in proximity to a tryptophan usually quenches its fluorescence signal. For instance, the fluorescence signal of DsbA is reduced by more than threefold upon disulfide bond formation. This can be used to determine the redox state of the protein of interest. For example, the catalytic oxidation reaction of DsbA by DsbB was characterized by following the fluorescence signal of DsbA [16].

Procedure

1. Prepare a protein solution (≈1–3 μM) in a quartz cuvette. Use sodium phosphate as a buffer, pH 7.0. The fluorescence signal decreases with increasing temperature, so the buffer solution should be equilibrated at the desired temperature.
2. Use 278 nm as the excitation wavelength and record the emission signal between 300 and 400 nm. The peak of the signal should be around 350 nm.

9.4.5 Assay of Disulfide Oxidase Activity

The ability of a protein to form disulfide bonds can be assayed by hirudin folding experiments [52]. Hirudin is a 65-residue protein, purified from the medicinal leech, with three disulfide bonds in the native state. It is a well-characterized substrate for DsbA. The stoichiometric reaction between oxidized DsbA and reduced hirudin is characterized by a rapid random oxidation of hirudin by DsbA. Then, reduced DsbA, formed in the course of hirudin oxidation, catalyzes the slow iso-

merization of the nonnative disulfide bonds to form native hirudin. The formation of native hirudin can be analyzed by reverse-phase HPLC.

Procedure

1. Mix completely reduced and unfolded hirudin (≈25 μM) with three molar equivalents of oxidized DsbA in 100 mM sodium phosphate pH 7.0, 0.2 M KCl, and 1 mM EDTA.
2. Incubate at 25 °C. At different times, take 50-μL aliquots and quench disulfide exchange reactions by addition of 50 μL formic acid (final pH < 2).
3. Separate the hirudin folding intermediates at 55 °C on a C18 reversed-phase HPLC column using a gradient from 20% to 24% (v/v) acetonitrile in 0.1% (v/v) trifluoroacetic acid at a flow rate of 0.5 mL min^{-1}.

References

1 Dailey, F. E. & Berg, H. C. (1993). Mutants in disulfide bond formation that disrupt flagellar assembly in Escherichia coli. *Proc Natl Acad Sci USA* **90**, 1043–7.

2 Sevier, C. S. & Kaiser, C. A. (2002). Formation and transfer of disulphide bonds in living cells. *Nat Rev Mol Cell Biol* **3**, 836–47.

3 Bardwell, J. C., McGovern, K. & Beckwith, J. (1991). Identification of a protein required for disulfide bond formation in vivo. *Cell* **67**, 581–9.

4 Missiakas, D., Georgopoulos, C. & Raina, S. (1993). Identification and characterization of the Escherichia coli gene dsbB, whose product is involved in the formation of disulfide bonds in vivo. *Proc Natl Acad Sci USA* **90**, 7084–8.

5 Stafford, S. J., Humphreys, D. P. & Lund, P. A. (1999). Mutations in dsbA and dsbB, but not dsbC, lead to an enhanced sensitivity of Escherichia coli to Hg2+ and Cd2+. *FEMS Microbiol Lett* **174**, 179–84.

6 Kishigami, S., Akiyama, Y. & Ito, K. (1995). Redox states of DsbA in the periplasm of Escherichia coli. *FEBS Lett* **364**, 55–8.

7 Zapun, A., Bardwell, J. C. & Creighton, T. E. (1993). The reactive and destabilizing disulfide bond of DsbA, a protein required for protein disulfide bond formation in vivo. *Biochemistry* **32**, 5083–92.

8 Grauschopf, U., Winther, J. R., Korber, P., Zander, T., Dallinger, P. & Bardwell, J. C. (1995). Why is DsbA such an oxidizing disulfide catalyst? *Cell* **83**, 947–55.

9 Martin, J. L., Bardwell, J. C. & Kuriyan, J. (1993). Crystal structure of the DsbA protein required for disulphide bond formation in vivo. *Nature* **365**, 464–8.

10 Guddat, L. W., Bardwell, J. C., Glockshuber, R., Huber-Wunderlich, M., Zander, T. & Martin, J. L. (1997). Structural analysis of three His32 mutants of DsbA: support for an electrostatic role of His32 in DsbA stability. *Protein Sci* **6**, 1893–900.

11 Guddat, L. W., Bardwell, J. C., Zander, T. & Martin, J. L. (1997). The uncharged surface features surrounding the active site of Escherichia coli DsbA are conserved and are implicated in peptide binding. *Protein Sci* **6**, 1148–56.

12 Couprie, J., Vinci, F., Dugave, C., Qu inverted question markem inverted question markeneur, E. & Moutiez, M. (2000). Investigation of the DsbA mechanism through the

synthesis and analysis of an irreversible enzyme-ligand complex. *Biochemistry* **39**, 6732–42.

13 Frech, C., Wunderlich, M., Glockshuber, R. & Schmid, F. X. (1996). Preferential binding of an unfolded protein to DsbA. *EMBO J* **15**, 392–98.

14 Vinci, F., Couprie, J., Pucci, P., Quemeneur, E. & Moutiez, M. (2002). Description of the topographical changes associated to the different stages of the DsbA catalytic cycle. *Protein Sci* **11**, 1600–12.

15 Bardwell, J. C., Lee, J. O., Jander, G., Martin, N., Belin, D. & Beckwith, J. (1993). A pathway for disulfide bond formation in vivo. *Proc Natl Acad Sci USA* **90**, 1038–42.

16 Bader, M., Muse, W., Zander, T. & Bardwell, J. (1998). Reconstitution of a protein disulfide catalytic system. *J Biol Chem* **273**, 10302–7.

17 Guilhot, C., Jander, G., Martin, N. L. & Beckwith, J. (1995). Evidence that the pathway of disulfide bond formation in Escherichia coli involves interactions between the cysteines of DsbB and DsbA. *Proc Natl Acad Sci USA* **92**, 9895–9.

18 Kishigami, S., Kanaya, E., Kikuchi, M. & Ito, K. (1995). DsbA-DsbB interaction through their active site cysteines. Evidence from an odd cysteine mutant of DsbA. *J Biol Chem* **270**, 17072–4.

19 Kishigami, S. & Ito, K. (1996). Roles of cysteine residues of DsbB in its activity to reoxidize DsbA, the protein disulphide bond catalyst of Escherichia coli. *Genes Cells* **1**, 201–8.

20 Kobayashi, T., Kishigami, S., Sone, M., Inokuchi, H., Mogi, T. & Ito, K. (1997). Respiratory chain is required to maintain oxidized states of the DsbA-DsbB disulfide bond formation system in aerobically growing Escherichia coli cells. *Proc Natl Acad Sci USA* **94**, 11857–62.

21 Bader, M., Muse, W., Ballou, D. P., Gassner, C. & Bardwell, J. C. (1999). Oxidative protein folding is driven by the electron transport system. *Cell* **98**, 217–27.

22 Bader, M. W., Xie, T., Yu, C. A. & Bardwell, J. C. (2000). Disulfide bonds are generated by quinone reduction. *J Biol Chem* **275**, 26082–8.

23 Xie, T., Yu, L., Bader, M. W., Bardwell, J. C. & Yu, C. A. (2002). Identification of the ubiquinone-binding domain in the disulfide catalyst disulfide bond protein B. *J Biol Chem* **277**, 1649–52.

24 Kadokura, H., Bader, M., Tian, H., Bardwell, J. C. & Beckwith, J. (2000). Roles of a conserved arginine residue of DsbB in linking protein disulfide-bond-formation pathway to the respiratory chain of Escherichia coli. *Proc Natl Acad Sci USA* **97**, 10884–9.

25 Kobayashi, T. & Ito, K. (1999). Respiratory chain strongly oxidizes the CXXC motif of DsbB in the Escherichia coli disulfide bond formation pathway. *EMBO J* **18**, 1192–8.

26 Inaba, K. & Ito, K. (2002). Paradoxical redox properties of DsbB and DsbA in the protein disulfide-introducing reaction cascade. *EMBO J* **21**, 2646–54.

27 Regeimbal, J. & Bardwell, J. C. (2002). DsbB catalyzes disulfide bond formation de novo. *J Biol Chem* **277**, 32706–13.

28 Kadokura, H. & Beckwith, J. (2002). Four cysteines of the membrane protein DsbB act in concert to oxidize its substrate DsbA. *EMBO J* **21**, 2354–63.

29 Grauschopf, U., Fritz, A. & Glockshuber, R. (2003). Mechanism of the electron transfer catalyst DsbB from Escherichia coli. *EMBO J* **22**, 3503–13.

30 Regeimbal, J., Gleiter, S., Trumpower, B. L., Yu, C. A., Diwakar, M., Ballou, D. P. & Bardwell, J. C. (2003). Disulfide bond formation involves a quinhydrone-type charge-transfer complex. *Proc Natl Acad Sci USA* **100**, 13779–84.

31 Hiniker, A. & Bardwell, J. C. (2004). In vivo substrate specificity of periplasmic disulfide oxidoreductases. *J Biol Chem* **279**, 12967–73.

32 Rietsch, A., Bessette, P., Georgiou, G. & Beckwith, J. (1997). Reduction of the periplasmic disulfide bond isomerase, DsbC, occurs by passage of electrons from cytoplasmic thioredoxin. *J Bacteriol* **179**, 6602–8.

33 Zapun, A., Missiakas, D., Raina, S. & Creighton, T. E. (1995). Structural and functional characterization of DsbC, a protein involved in disulfide bond formation in Escherichia coli. *Biochemistry* **34**, 5075–89.

34 Rietsch, A., Belin, D., Martin, N. & Beckwith, J. (1996). An in vivo pathway for disulfide bond isomerization in Escherichia coli. *Proc Natl Acad Sci USA* **93**, 13048–53.

35 Bessette, P. H., Cotto, J. J., Gilbert, H. F. & Georgiou, G. (1999). In vivo and in vitro function of the Escherichia coli periplasmic cysteine oxidoreductase DsbG. *J Biol Chem* **274**, 7784–92.

36 Sun, X. X. & Wang, C. C. (2000). The N-terminal sequence (residues 1–65) is essential for dimerization, activities, and peptide binding of Escherichia coli DsbC. *J Biol Chem* **275**, 22743–9.

37 McCarthy, A. A., Haebel, P. W., Torronen, A., Rybin, V., Baker, E. N. & Metcalf, P. (2000). Crystal structure of the protein disulfide bond isomerase, DsbC, from Escherichia coli. *Nat Struct Biol* **7**, 196–9.

38 Haebel, P. W., Goldstone, D., Katzen, F., Beckwith, J. & Metcalf, P. (2002). The disulfide bond isomerase DsbC is activated by an immunoglobulin-fold thiol oxidoreductase: crystal structure of the DsbC-DsbDalpha complex. *EMBO J* **21**, 4774–84.

39 Chen, J., Song, J. L., Zhang, S., Wang, Y., Cui, D. F. & Wang, C. C. (1999). Chaperone activity of DsbC. *J Biol Chem* **274**, 19601–5.

40 Shao, F., Bader, M. W., Jakob, U. & Bardwell, J. C. (2000). DsbG, a protein disulfide isomerase with chaperone activity. *J Biol Chem* **275**, 13349–52.

41 Zhao, Z., Peng, Y., Hao, S. F., Zeng, Z. H. & Wang, C. C. (2003). Dimerization by domain hybridization bestows chaperone and isomerase activities. *J Biol Chem* **278**, 43292–8.

42 Joly, J. C. & Swartz, J. R. (1997). In vitro and in vivo redox states of the Escherichia coli periplasmic oxidoreductases DsbA and DsbC. *Biochemistry* **36**, 10067–72.

43 Bader, M. W., Hiniker, A., Regeimbal, J., Goldstone, D., Haebel, P. W., Riemer, J., Metcalf, P. & Bardwell, J. C. (2001). Turning a disulfide isomerase into an oxidase: DsbC mutants that imitate DsbA. *EMBO J* **20**, 1555–62.

44 Stewart, E. J., Katzen, F. & Beckwith, J. (1999). Six conserved cysteines of the membrane protein DsbD are required for the transfer of electrons from the cytoplasm to the periplasm of Escherichia coli. *EMBO J* **18**, 5963–71.

45 Chung, J., Chen, T. & Missiakas, D. (2000). Transfer of electrons across the cytoplasmic membrane by DsbD, a membrane protein involved in thiol-disulphide exchange and protein folding in the bacterial periplasm. *Mol Microbiol* **35**, 1099–109.

46 Katzen, F. & Beckwith, J. (2000). Transmembrane electron transfer by the membrane protein DsbD occurs via a disulfide bond cascade. *Cell* **103**, 769–79.

47 Collet, J. F., Riemer, J., Bader, M. W. & Bardwell, J. C. (2002). Reconstitution of a disulfide isomerization system. *J Biol Chem* **277**, 26886–92.

48 Kim, J. H., Kim, S. J., Jeong, D. G., Son, J. H. & Ryu, S. E. (2003). Crystal structure of DsbDgamma reveals the mechanism of redox potential shift and substrate specificity(1). *FEBS Lett* **543**, 164–9.

49 Katzen, F. & Beckwith, J. (2003). Role and location of the unusual redox-active cysteines in the hydrophobic domain of the transmembrane electron transporter DsbD. *Proc Natl Acad Sci USA* **100**, 10471–6.

50 Wunderlich, M., Otto, A., Maskos, K., Mucke, M., Seckler, R. & Glockshuber, R. (1995). Efficient

catalysis of disulfide formation during protein folding with a single active-site cysteine. *J Mol Biol* **247**, 28–33.

51 Aslund, F., Berndt, K. D. & Holmgren, A. (1997). Redox potentials of glutaredoxins and other thiol-disulfide oxidoreductases of the thioredoxin superfamily determined by direct protein-protein redox equilibria. *J Biol Chem* **272**, 30780–6.

52 Wunderlich, M., Otto, A., Seckler, R. & Glockshuber, R. (1993). Bacterial protein disulfide isomerase: efficient catalysis of oxidative protein folding at acidic pH. *Biochemistry* **32**, 12251–6.

10
Catalysis of Peptidyl-prolyl *cis*/*trans* Isomerization by Enzymes

Gunter Fischer

10.1
Introduction

The proper function of proteins within living cells depends on how those macromolecules adopt a unique three-dimensional structure and on how spatial-temporal control underlies the mechanism of protein folding in vivo. The numerous contact points formed and released in the course of protein folding are based on countless rotational movements. Most rotations of covalent bonds have proven to be intrinsically very fast and do not need further rate acceleration by either external factors or intramolecular assistance. Potentially, external influences on rotational rates could be mediated by a wide variety of physical and chemical means such as enzyme catalysis, catalysis by low-molecular-mass compounds, heat, mechanical forces, and supportive microenvironments. Acid-base catalysis, torsional strain, and proximity and field effects are major forces with the potential to act in intramolecular assistance. Submillisecond burst phase signals measured in the kinetics of protein-folding experiments and triplet-triplet energy transfer rates measured for side chain contacts of oligopeptides have been widely interpreted in terms of the fast formation of collapsed folding intermediates and secondary structures formation, both involving countless conformational interconversions [1–3]. Thus, in the evolutionary history, attempts to invent mechanisms of rate acceleration for the formation of collapsed polypeptides by accessory molecules appeared to be futile. However, in contrast to the information provided by its graphical representation, a protein backbone possesses a considerable degree of rigidity that exists independently of the three-dimensional fold. Despite the formal single-bond, fast-rotation nature of its covalent linkages, the repeating unit of the polypeptide backbone suffers from at least one slow bond rotation. It is the high rotational barrier of the carbon-nitrogen linkage of the peptide bond (angle ω) that casts serious doubt on the validity of the structure-based treatment of a polypeptide chain as an array of single-bond units. Considering the influences on the dynamics of biochemical reactions such as protein folding/restructuring and protein-ligand/protein-protein interactions, the electronic structure of the C–N bond is best described as a partial double bond. Under this classical view, the peptide bond ex-

Protein Folding Handbook. Part II. Edited by J. Buchner and T. Kiefhaber

ISBN: 3-527-30784-2

hibits characteristic features of *E-Z* geometrical isomerism: the existence of chemically and physically distinct *cis*/*trans* isomers, a high barrier to rotation, and a distinct chemistry of the *cis*/*trans* interconversion [4, 5]. By virtue of having two thermodynamically stable chain arrangements of different chemical reactivity separated by an energetic barrier, peptide bond *cis*/*trans* isomerization resembles a molecular switch. Switching is manifested in the form of directed mechanical movement of the polypeptide chain. This fact is best illustrated by analysis of the protein crystal structure database for homologous proteins with a different isomeric state of a certain prolyl residue. A subset of structures has been created that has a particular proline residue either in the *cis* or the *trans* isomeric state for similar proteins [6]. Structural alignment of matched pairs of isomeric proteins generates three classes with respect to position-specific distribution of Cα-atom displacements around the isomeric proline imide bond. Besides small bidirectional chain displacements, there is a class of 12 protein pairs in which the structural changes are unidirectional relative to the isomerizing bond. The magnitude of the isomer-specific distance effect exceeds 3.0 ± 2.0 Å at sequence positions remote from the prolyl bond. Interestingly, the magnitude of the intramolecular isomer-specific Cα atom displacements reveals a lever-arm amplification of distance effects because there is only a *cis*-specific chain contraction of 0.8 Å for the Cα atoms directly involved in the prolyl bond. A type of directed oscillating movement within the backbone in its native conformation, if a fast kinetic step precedes it, offers a structural basis for the explanation of the isomer-specific control of the bioactivity. The findings indicate that cellular folding catalysts may provide a previously unrecognized level of control for the biological activity of the equilibrium-folding pathway of native proteins, which exists independently of the de novo folding pathway.

Chemically, peptide bond *cis*/*trans* isomerization is reminiscent of other important biological events, such as the retinal-mediated photocycle, carotenoids in antioxidant processes, and phytochrome-based reactions, which, like retinal-based, display isomerization-linked geometrical distortions that are transmitted to amino acid residues of their respective binding protein [7]. Whereas visible light absorption gives rise to the very fast *cis*/*trans* isomerization-mediated photocycle of the protein-bound 11-*cis*-retinal chromophore, which finally results in the formation of a G-protein-interacting state of rhodopsin, the rate of peptide bond *cis*/*trans* isomerization is naturally insensitive to irradiation at wavelengths > 220 nm [8]. Thus, light irradiation is also unable to decrease the double-bond character of the bonds determining protein backbone rigidity, with the consequent lack of directed atomic displacements as well as structural "backbone liquification" or facilitating torsional movements by "lubrication." However, specific peptide bond *cis*/*trans* isomerases have evolved to trigger a similar type of structural response and, thereby, to have a specific contribution to lowering of the high rotational barrier of peptide bonds [9, 10]. Unlike photochemical triggering, where a very slow dark reaction at the carbon-carbon double bond after switching off the light is to occur, enzyme-catalyzed peptide *cis*/*trans* isomerizations tend to be both fast and reversible under most conditions.

It should be noted that the peptide bond *cis*/*trans* isomerases identified up to

now could not shift a *cis*/*trans* equilibrium but could accelerate re-equilibration after transient chemical or physical perturbbations. Except for enzyme concentrations much larger than substrate concentrations, where the Michaelis complexes of the substrate and the product will confer an individual isomer ratio, peptide bond *cis*/*trans* isomerases must be considered simple catalysts in bioreactions. Obviously, enzymatic coupling to an energy-consuming process would allow generating a permanent non-equilibrium composition of *cis*/*trans* isomers free in solution. Such multifunctional peptide bond *cis*/*trans* isomerases have not yet been found but are likely to exist as isolated enzymes or hetero-oligomeric complexes.

From the point of view of biological importance, when a polypeptide binds to a native protein, the resulting complex forms a global ensemble that must seek its own minimum free-energy fold. Consequently, the rules underlying the process of de novo protein folding do not change, in principle, for chain rearrangements induced in native proteins during ligand association, enzyme catalysis, and other reactions. Since peptide bond *cis*/*trans* isomers are frequently found to exist in a dynamic equilibrium in the context of a native fold, the data collected for the isomerization process in the refolding of denatured proteins are principally applicable for the analysis of native-state *cis*/*trans* isomerizations. Most importantly, native-state isomers might exhibit significant differences in their biological activity [6, 11–13]. In an approach to understanding the nature of catalyzed *cis*/*trans* isomerizations in cells, two major effects have to be assumed: (1) accelerated re-equilibration of a transiently perturbed *cis*/*trans* isomer ratio and (2) enhanced conformational dynamics in the presence of a catalyst in an already equilibrated mixture of *cis*/*trans* isomers. The increase in the rate of re-equilibration brought about by the catalyst according to effect (1) requires a fast-equilibrium, perturbing-type reaction prior to the *cis*/*trans* isomerization in order for isomer-specific reaction control to occur. In contrast, effect (2) permanently enables a small segment of the polypeptide backbone to escape the steric restrictions imposed by the partial double-bond character of the C–N linkage. Concomitantly, the position of the substrate chain oscillates in a directed manner with a frequency determined by k_{cat} values of the reversible enzyme reaction. Because of dynamic coupling within the enzyme-substrate or enzyme-product complexes, specific amino acid residues of the enzyme might oscillate with the same frequency [14].

10.2
Peptidyl-prolyl *cis*/*trans* Isomerization

Proline is the only one of the 20 canonical amino acids that is involved in the formation of an imidic peptide bond at its N-terminal tail because the peptide bond nitrogen is in an *N*-alkylated state (Figure 10.1). Essential features of the peptidyl-prolyl peptide bond and the peptidyl-prolyl bond's *cis*/*trans* isomerization, which we subsequently refer to as prolyl bond and prolyl isomerization, respectively, are dynamics and unique conformational constraints. Among all peptide bonds, prolyl bonds should be afforded special attention regarding conformational polymor-

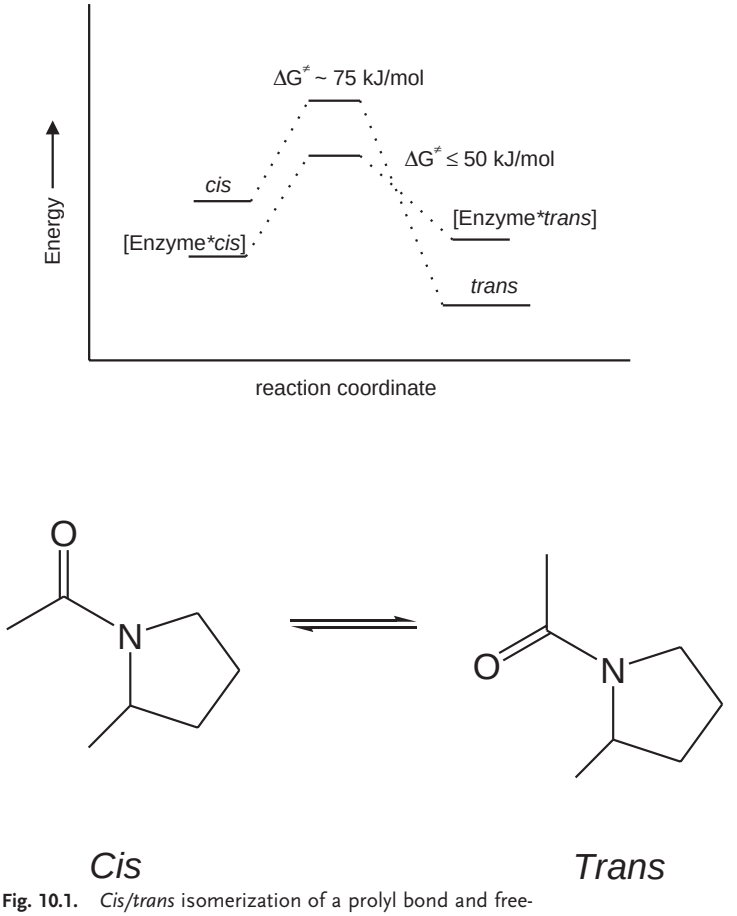

Fig. 10.1. *Cis/trans* isomerization of a prolyl bond and free-energy profiles of the spontaneous and enzyme-catalyzed reactions.

phism of proline-containing polypeptides. Regardless of their sequential context, the *cis* and *trans* prolyl conformers in unstructured or partially structured polypeptide chains exhibit energetic differences that tend to be small, thus leading to a comparable level of isomers in solution. The slow rate of *cis*/*trans* interconversion obtained in refolding studies plays a significant role in determining the uniqueness of prolyl isomerization because just one covalent bond serves to control an enormous body of structural changes from the seconds time range of slow folding steps in small globular proteins [15] to the hours time range for the zipper-like mechanism of the triple-helix formation of collagen [16, 17] or protein-protein associations [18]. The classical experiment conducted by Brandts et al. led us to realize that a prolyl isomerization is also involved in protein denaturation [19]. The experimental data reveal that the relatively few examples of functional coupling between protein folding and prolyl isomerization are seemingly at odds with the

large number of proline residues in proteins. According to the marked differences of the *cis*/*trans* isomer ratios between the unfolded and the folded states, every proline residue might cause slow folding events unless intramolecular assistance greatly enhances the isomerization rate. This ambiguity is of more than theoretical interest since the whole body of slowly isomerizing prolyl bonds can be seen as a potential molecular basis of metastable states of proteins and classed as potential targets for enzyme catalysis. Obviously, the existence of non-rate-limiting prolyl isomerizations must take into account the potential impact of intramolecular catalysis by amino acid side chains and steric strain in polypeptides, but only a few examples have been identified [20, 21]. An alternative explanation has been to suggest that the prolyl isomerization is silent in common folding probes. This case is easily conceivable, but nevertheless, it is likely that formation of bioactivity might be affected in many cases [22–24].

In principle, peptides or proteins with *n* proline residues can form 2^n isomers unless structural constraints (such as the three-dimensional fold of proteins) stabilize one isomer strongly relative to the others. While being a highly abundant motif in proteins, a polyproline stretch tends to be a conformationally uniform segment but is largely undefined in its isomerization dynamics [25, 26]. For example, all theoretically predicted *cis*/*trans* isomers could be identified by ^{1}H-NMR spectroscopy for the octapeptide Ile-Phe-Pro-Pro-Val-Pro-Gly-Pro-Gly, which is derived from the prolactin receptor [27]. Counter to the expectations drawn from statistics, a decreasing fractional isomer probability among the 16 isomeric forms does not correlate with a decreasing number of *trans* peptide bonds in the respective isomer. In many cases among prolyl isomers presented to other proteins for interactions to occur, some isomers might lack productive binding. In fact, proteins have evolved highly efficient means of selecting a particular structure among an ensemble of conformers of ligands.

Consequently, isomer-specific enzymes and transporters, such as proteases [28], protein phosphatases [29], proline-directed protein kinases [30], and the peptide transporter Pept1 [31], that favor molecules with *trans* prolyl bonds at critical positions discriminating the coexisting *cis* isomer have been found. However, bioactivity is not stringently linked with chains with all-*trans* peptide bond conformations. In several cases the optimal receptor-ligand interaction requires appropriately positioned *cis* prolyl bonds [32–35].

Since bioactivity of polypeptides exhibits specificity for the slowly interconverting prolyl isomers, enzymes have evolved (1) to accelerate the interconversion of the isomers and (2) to establish a new level of conformational control.

In the years following the discovery of the first peptidyl-prolyl *cis*/*trans* isomerase (PPIase) in pig kidney in 1984, three different families of PPIases have been characterized, which now collectively form the enzyme class EC 5.2.1.8 [9, 28, 36]. In humans, the families of FK506-binding proteins (FKBPs) and cyclophilins have many members, whereas the human genome probably restricts the total number of the parvulins to not more than two members (Figure 10.2). Sequence similarity of the catalytic domains forms the signature of family membership. Across families, the catalytic domains are unrelated to each other in their amino acid se-

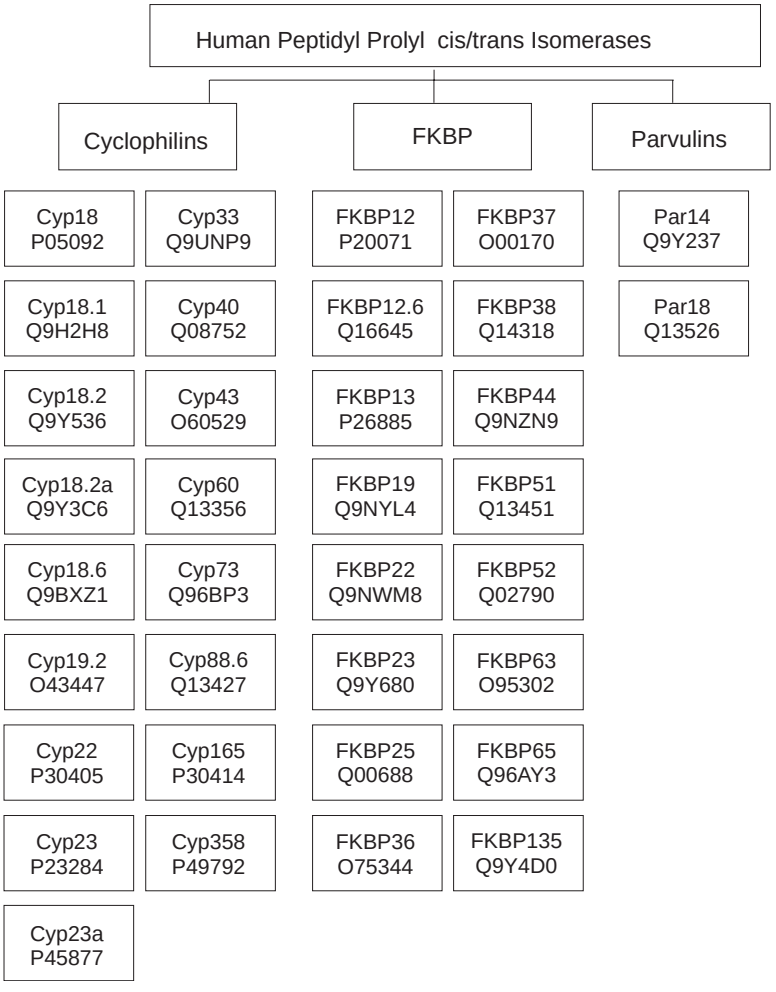

Fig. 10.2. Presently known peptidyl-prolyl *cis/trans* isomerase in humans classified according to amino acid sequence-based similarities. The individual enzymes have been identified by the SWISS-Prot/TREMBL accession numbers.

quences, confer distinct substrate specificities, and prove to be binders for different types of inhibitors. In their three-dimensional structures, parvulins appeared to be closely related to FKBPs in that, by comparison, a FKBP superfold could be extracted [37]. Family members of the ubiquitous enzyme class of PPIases are found in abundance in virtually all organisms and subcellular compartments. Within families, the amino acid sequences are highly conserved phylogenetically. Organisms simultaneously express paralogs within the families that encompass one or more PPIase domains complemented with other functional polypeptide segments.

Except for targeting motifs and metal-ion-binding polypeptide stretches, the functional interplay between the supplementing domains of the larger PPIases and the catalytic domain(s) is still unclear.

Since some prototypic PPIases are proven drug targets either by blockage of the active site or by utilizing the PPIase as a presenter protein of the drug [38], knowledge about functional consequences of the supplementary domains in the multidomain-like PPIases is urgently needed.

Recently, the secondary amide peptide bond *cis*/*trans* isomerases (abbreviated APIases) were added to the class of peptide bond *cis*/*trans* isomerases, indicating that an expanded set of polypeptide substrates is potentially sensitive to biocatalysis of a conformational interconversion in the cell. This enzyme activity is discussed in chapter 11.

10.3 Monitoring Peptidyl-prolyl *cis*/*trans* Isomerase Activity

The chemical and physical principles described for the detection of isomer-specific reactions and native-state isomerizations of prolyl bond-containing oligopeptide chains apply, in general, to all PPIase assays. In all cases, the rate enhancement in the presence of the PPIase quantitatively reflects the enzyme activity. As a monomolecular reaction, the spontaneous *cis*/*trans* isomerization conforms to first-order kinetics with a specific rate constant k_o (s^{-1}) that is independent of the substrate concentration. With some exceptions, the isomer ratio cannot be extracted from the data of the spectrometric PPIase assays, but NMR-based methods can be utilized.

Under favorable conditions, where the concentration of the active PPIase is much smaller than the total substrate concentration and the total substrate concentration is much smaller than the K_m value, Eq. (1) provides a quantitative estimate of enzyme catalysis. Such conditions also include first-order kinetics of the PPIase-catalyzed progress curves.

$$k_{cat}/K_m = (k_{ob} - k_o)/E_o \quad (1)$$

The k_{cat}/K_m (L $mol^{-1}s^{-1}$) value is the specificity constant for the enzymatic catalysis of the interconversion of the *cis*/*trans* isomers of the substrate, k_{ob} (s^{-1}) is the first-order rate constant of the catalyzed interconversion, k_o (s^{-1}) is the first-order rate constant of the spontaneous *cis*/*trans* interconversion, and E_o (mol L^{-1}) is the concentration of active enzyme molecules. However, active-site titration methods cannot be employed for PPIases except for cyclophilins. Cyclosporin A proved to be useful for fluorescence-based active-site titration of those cyclophilins with a tryptophan residue corresponding to position 121 of Cyp18 [39]. Detailed inspection of the catalyzed reaction will reveal the specific meaning of the k_{cat}/K_m value: either that the reversible *cis*/*trans* interconversion determines this constant or that there is a direct coupling to an irreversible process, with preceding *trans* to *cis* or *cis*

to *trans* interconversions, that plays a role in determining the available enzymatic parameters. The presence of PPIases with high affinity for a substrate ($K_M \ll [S]$) is indicated by deviations of the experimental data from strict first-order kinetics in the initial phase of the progress curve for the catalyzed interconversion.

Several assays make use of the transient production of pure *cis* or *trans* isomers or at least of an isomer ratio different from that expected based on the steady-state reaction conditions. A comparison between the PPIase assays revealed that the higher the deviation from the equilibrium ratio of isomers, the higher the signal-to-noise ratio of the assay.

Rate enhancement measurements usually require monitoring of reaction kinetics over an extended period of time. It is vital to reliable activity measurements that kinetic traces be followed over at least three half-times of the reaction. Use of the assays as endpoint-determination methods has not yet been established.

Assaying PPIases with protein substrates has proven to be more difficult. Three-dimensional protein structures derived from crystals reveal a defined isomeric state for every prolyl peptide bond being in either *cis* or *trans* conformation, with the majority of prolyl bonds in *trans* form [6, 40]. In some cases the crystallization process was found to be a crucial determinant of the conformational state of prolyl bonds in the sample [6]. The seeming homogeneity results only partially from isomer-specific stabilization effects by intramolecular long-range interactions or isomer-specific crystal lattice sampling. When probed by NMR spectroscopy in solution, many proteinaceous prolyl bonds show conformational polymorphism, where the isomeric proteins interconvert in a reversible reaction. Typically, these native-state isomerizations exhibit a wide range of isomer ratio values. The rate of the spontaneous interconversion of isomers is usually found to be slow on the NMR time-scale. Due to a considerable isomer-specific dispersion of proton signals adjacent to the isomeric bond, dynamic ^{1}H-NMR methods provide powerful tools for locating isomerizing peptide bonds in polypeptides. Rate constants of interconversion are also available from this probe, but NMR methods are limited to rather high substrate concentrations. Dynamic NMR methods generally do not require prior chemical perturbation of isomer composition by chemical means. Instead, transferred magnetization to isomers is detected. However, one-dimensional ^{1}H-NMR spectroscopy also has been used in combination with classical solvent-jump techniques when subsequent monitoring of the time course of an isomer-specific signal intensity is to occur [41].

^{19}F nuclei in labeled amino acids can also serve as a probe, as was shown for a PPIase-catalyzed isomerization reaction in a derivative of the tissue hormone bradykinin [42].

Based on the combination of dynamic ^{1}H-NMR spectroscopy and conformational polymorphism of proteins, PPIase activity can be easily determined if the number of isomerizing prolyl bonds is limited (preferably to one or two prolyl bonds) and the isomer ratio does not deviate much from unity. Because one-dimensional ^{1}H-NMR experiments reveal slow dynamics in spontaneous prolyl isomerization, line broadening is not significant for the *cis* and *trans* signals. However, in the presence of PPIases, signals experience line broadening and coales-

cence [43] that can be quantified by comparison with simulated line shapes based on quantum-mechanical density matrix formalism [44, 45]. The two-dimensional NOESY experiments are more sensitive to catalytically enhanced interconversion rates than are one-dimensional NMR techniques. Exchange cross-peak intensity at different mixing times gives access to the rate constants of interconversion [46, 47].

Isomer-specific proteolysis has been widely employed to assay PPIase activity with oligopeptide substrates. This robust method can be considered as the standard test for routine determination of enzyme activity for all families of PPIases in their pure state as well as in crude cell extracts and biological fluids [9, 48]. The assay is based on the fact that a linear oligopeptide containing a single prolyl bond usually consists of a mixture of two slowly interconverting conformers, the *cis* and the *trans* prolyl isomers, in solution. Depending on the nature of the amino acid flanking the proline residue of substrates in the -Xaa-Pro-Ala- moiety, the percentage of *cis* conformer is in the range of 6% to 38% in aqueous solutions [41].

Slow re-equilibration after rapid disturbance of the conformational equilibrium is a common feature of most prolyl isomerizations. Proteases such as chymotrypsin, various elastases, trypsin, subtilisin, clostripain, and others liberate 4-nitroaniline from -Pro-Yaa-4-nitroanilides (typically, Yaa = Phe, Tyr, Leu, Arg, Lys, Val, Ala) only if a *trans* prolyl bond exists in the penultimate amino acid position from the scissile linkage. Isomer-specific hydrolysis by a protease can serve as a chemical means of displaycing the isomer distribution in a very efficient manner, resulting in a transient population of about 100% *cis* isomer. A protease has not yet been detected that discriminates to the isomer level, hydrolyzing substrates with a *cis* prolyl bond exclusively. To ensure rapid cleavage of the entire population of the *trans* isomeric substrate, the protease concentration is set at a high value. The k_{cat} value of the proteolytic reaction determines the limiting cleavage rate at very high protease concentrations and defines an upper limit estimate of isomerization rates accessible to this assay. Thus, after consumption of the entire population of the *trans* isomer using this strong proteolytic pulse, the *cis* isomer of the peptide is left over. Such a reaction cannot continue to completeness, which is defined by consumption of the total amount of substrate, unless a parallel reaction couples. The coupled reaction is the first-order *cis* to *trans* interconversion, which precedes the rapid proteolytic consumption of the *trans* isomer formed during the conformational interconversion as a rate-limiting step after the initial phase of the reaction. Biphasic kinetics can be monitored under these conditions, where the PPIase-mediated rate acceleration will reside in the slow phase of the reaction (Figure 10.3). It is clear that only a small fraction of the total absorbance of a protease-coupled reaction can be utilized for assaying PPIases. Due to the distinctive characteristics of the protease-coupled assay, the part of absorbance released in the dead time of mixing at 390 nm contributes to the unwanted background signal. Substitution of 4-nitroaniline by fluorogenic leaving groups or the use of intramolecularly quenched fluorescent protease substrates allows for fluorescence-based protease-coupled PPIase assays [49, 50]. The signal-to-noise ratio of this modified assay also suffers the limitations of UV/Vis detection.

Deficits of the protease-coupled assay such as proteolytic degradation of PPIases

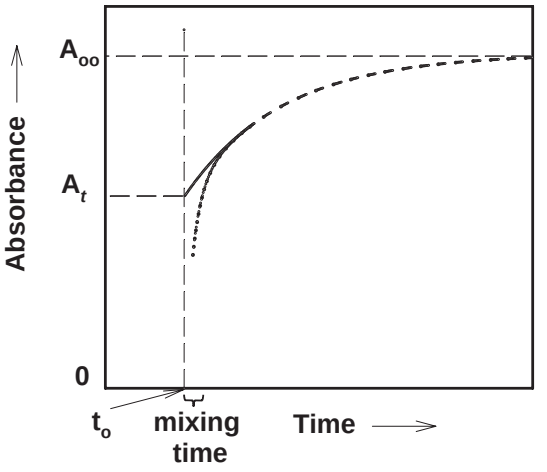

Fig. 10.3. First-order progress curve of a typical proteolytic PPIase assay. Zero-time t_o is taken at the time point of injection of the assay peptide. The time period required for sample mixing is depicted on the time axis. By extrapolation, the time zero intercept value A_t and the absorbance at infinite reaction time A_{oo} become available, the difference of which gives an estimate of the *cis/trans* ratio if it is set relative to the amplitude of absorbance of the very rapid kinetic phase visible at zero time.

and substrates are partially avoided by carefully selecting the helper protease. However, most PPIases may have evolved to accelerate *cis/trans* interconversions at or near the *cis/trans* equilibrium of a cellular substrate [44]. The protease-coupled assay utilizes reaction conditions that necessarily lead to a quasi-irreversible isomerization under non-equilibrium conditions. In contrast, small physical perturbations of a *cis/trans* equilibrium can serve to realize PPIase assays under more natural conditions

Provided that isomer-specific differences of UV/Vis spectra, NMR signals, fluorescence quenching, or chemical properties (pK_a values) exist, the time courses of re-equilibration of prolyl isomers may provide a signal that is determined in rate by the sum of the first-order rate constants for the *cis* to *trans* and *trans* to *cis* interconversion. Transient deviations from the actual equilibrium conditions have been achieved mainly by pH and solvent jumps [51–53].

Given the experimental fact that signal amplitudes arising from solvent perturbations are usually very small, improvement in signal quality of the assays is expected to be associated with covalent modifications that serve as a means for potentially increasing the *cis/trans* isomer ratio. By intramolecular disulfide bridging, 2-aminobenzoyl-Cys-Phe-Pro-Ala-Cys-Ala-4-nitroanilide or 2-aminobenzoyl-Cys-Phe-Pro-Ala-Cys-3-nitro-tyrosineamide experienced about 100% *cis* isomer for the Phe-Pro moiety, which declined after disulfide ring reduction to an open-chain *cis* isomer level of about 10% [54]. In the presence of high concentrations of reductive agent, such as dithiothreitol or tris-(2-carboxyethyl)-phosphine, ring opening is

a rapid reaction followed by the slow equilibration of the Phe-Pro moiety. Efficient fluorescence quenching of the 2-aminobenzoyl residue by the 4-nitroanilide moiety requires the *cis* conformation. Thus, subsequent to the reductive pulse, the time course of the fluorescence increase corresponds to the *cis*/*trans* interconversion in the open-chain peptide that is able to reveal the presence of a PPIase [55]. Fortunately, most substrates and enzymes are not susceptible to interference from the reductive agents.

Quite early in the development of PPIase assays, it was noted that slow kinetic phases of refolding of chemically denatured RNases are sensitive to PPIase catalysis [56–58]. The reaction progress curves may in turn serve as a tool for assaying PPIase activity. For this to occur, the PPIase must recognize partially folded intermediates that result in limited access to the catalyzable prolyl bond. Both wild-type ribonuclease T1 (abbreviated wtRNaseT1) and its site-directed mutagenized protein variants turned out to be especially suitable substrates for peptide bond *cis*/*trans* isomerases.

Two prolyl bonds of RNase T1 (Tyr38-Pro39 and Ser54-Pro55) adopt the *cis* conformation in the native state but display a diminished *cis* population in the unfolded state. Thus, the *trans* to *cis* isomerization is a quasi-irreversible process because the reverse isomerization is disfavored under strongly native refolding conditions. The refolding kinetics can be probed by fluorescence, CD, UV/Vis, and real-time NMR spectroscopy and the regain of enzymatic activity [58–60]. Recently, time-resolved FTIR-difference spectroscopy has also been applied successfully for the spontaneous reaction [61]. A complete kinetic folding model has been established by unfolding-refolding double mixing experiments [62, 63]. If RNase T1 is denatured and reduced and the cysteine side chains are carboxmethylated, it is still able to adopt an active, native-like conformation, but only if high ionic strength applies. Thus, instead of utilizing denaturing agents or extreme thermal conditions, variable concentrations of NaCl allow for shuttling between native and unfolding conditions. In general, the PPIase activity does not reflect significant interference with the shuttling conditions. Using the remarkable features of RNaseT1, this refolding reaction is the established standard assay for PPIase catalysis on proteinaceous substrates in the refolding and unfolding directions [64].

Tendamistat provides an example where PPIase catalysis of native-state prolyl isomerization can be probed by fluorescence spectroscopy using double-jump techniques. In interrupted refolding experiments, a very slow folding reaction, with an amplitude of about 12%, was detected that is still present, although at a reduced level of amplitude, in the native state. It indicates conformational heterogeneity at the proline positions 7 and 9. Catalysis by cyclophilin identifies this very slow reaction as a limiting prolyl isomerization. The very low *cis*/*trans* ratio of about 0.02 for these prolyl bonds suggests that the native-state isomerization would probably escape detection by NMR spectroscopy [65].

Accelerated recovery of enzyme activity can be used to identify and quantitate PPIase catalysis on prolyl bond-limited refolding phases that are spectroscopically silent. Monitoring the time-resolved appearance of native muscle acyl phosphatase exemplifies this approach [22].

10.4
Prototypical Peptidyl-prolyl *cis/trans* Isomerases

10.4.1
General Considerations

This chapter addresses some fundamental principles underlying the biochemical functions of PPIases based on the discussion of prototypical enzymes. Prototypical PPIases are monomerically active enzymes ranging in size from 92 to 177 amino acids, which, per definition, do not contain any targeting signal or supplementary domain. Functional and structural studies have been performed mostly for the prototypical enzymes, whereas present knowledge of the enzymatic properties of multidomain PPIases is rather limited.

Four different molecular mechanisms can be hypothesized to define the biochemical basis of the physiological effects known to be exerted by the members of the three families of PPIases: (1) the catalysis of prolyl isomerization, (2) a holding function for unfolded polypeptides, (3) a presenter-protein function for physiological ligands, and (4) a proline-directed binding function for other proteins. The underlying reactions might control, either in isolation or collectively, the physiological role of prototypical and domain-complemented enzymes. A general consensus has not yet been reached to which extent the biochemical principles above contribute to the generation of physiological signals by PPIases [36].

In vitro experiments frequently reveal that peptide bond *cis/trans* isomerases encompassing more domains than just the catalytic module are able to prevent chain aggregation in typical chaperone assays [66–69]. Proline residues are not essential for sequestration of the polypeptide chain. However, polypeptide sequestration by PPIases is due to the presence of an extended stretch of catalytic subsites, also termed secondary binding sites. Classically, many polypeptide-utilizing enzymes form extensive contacts both in the active site and through secondary binding sites. All these interacting sites are closely linked to the activation of the catalytic machinery, but they will not give rise to physiological functions independent of the catalyzed reaction. More specifically, the properties of maintaining and catalyzing unfolded chains are not mutually exclusive. Therefore, although an important determinant of catalysis, the holding function plays an auxiliary role in contributing to the physiological effects of PPIases [36].

Immunosuppressive PPIase inhibitors produce a multitude of effects in transplantation medicine, reflecting the causal relationship between physiological effects and the multifunctional nature of the biochemical platform of PPIases [70–72]. The molecular mechanism underlying immunosuppression mediated by PPIase inhibitors was found to be associated with a gain of function in the form of drug activation by PPIase/inhibitor complex formation. This example unequivocally demonstrates the importance of drug target control by presenter molecules (according to the biochemical principle 3). Consequently, the most prominent effect of the Cyp18 and FKBP inhibitors CsA and FK506, respectively, i.e., the prevention of clonal expansion after antigenic stimulation of T cells, has been dis-

cussed exclusively in terms of this presenter-protein strategy. The active complex is targeted to the inhibition of the protein phosphatase calcineurin. Structurally the PPIase/drug complex was thought to present a composite surface, which is next to active-site residues of the PPIase, to other cytosolic binding partners, whereas no independent role could be elucidated for the simultaneously occurring blockage of the catalytic machinery of the PPIase [73]. Care must be taken, however, when interpreting the drug-mediated immunosuppression as a model for physiological PPIase function in humans, as the microbial drugs do not belong to the normal constituents of mammalian cells. The fact of the matter is that an authentic polypeptide ligand utilizing the presenter-protein function of a PPIase has not yet been identified, thus challenging the view of a presenter-protein function of PPIases in normal cell life. Moreover, gain of function appears to be released in a few special cases, such as the Cyp18/cyclosporin A complex. When substituted in the 3 position, cyclosporin derivatives inhibit calcineurin on their own but are inactive in the Cyp18/drug complexes. Of the most important structural parameters, only the ring conformation of the cyclosporins proved to be a decisive feature [74].

Only recently has attention turned to the role of inhibiting the catalytic function of PPIases for the interpretation of drug effects under physiological and pathophysiological conditions [75–78]. Small cell-permeable effectors represent in principle powerful tools for identification of functional links between catalyzed prolyl isomerization and physiological processes in living cells. Most attempts to unravel physiological functions of PPIases in vivo have been done by this pharmacological approach. In particular, the immunosuppressants cyclosporin A (CsA), FK506, and rapamycin, as well as their non-immunosuppressive derivatives, have been proposed as biochemical markers, which may provide results useful for dissecting functions in vivo. These compounds are competitive inhibitors of many cyclophilins or FKBPs present in human tissues, but to a different extent. There are only a few inhibitors available for the enzymes of the parvulin family [53, 79, 80]. A long-standing aspiration of researchers in the field has been the design and synthesis of inhibitors capable of selectively inhibiting closely related PPIase paralogs, but success is still limited at this stage.

Among all known enzymes, PPIases exhibit a unique reaction profile with a large number of potentially reactive sites in a polypeptide substrate and a low degree of electronic differences between substrate and product. Regarding a microscopic description, the minimal kinetic mechanism of the enzyme-catalyzed prolyl isomerization of protein and peptide substrates operates on the basis of three chemical transitions. Accordingly, the two Michaelis complexes, the *trans* and *cis* isomers in their enzyme-bound state, are able to interconvert to each other with or without forming a non-Michaelis complex-like intermediate. In the simplest case, the catalytic rate enhancement is due to enzyme-mediated stabilization of the partially rotated state of the prolyl bond. However, the limited access to transition-state analogue inhibitors and the minimal activities of catalytic antibodies generated against surrogates of twisted peptide bonds [81, 82] do not support an exclusive role of noncovalent transition-state stabilization for catalysis. Large inverse solvent deuterium isotope effects (J. Fanghänel and G. Fischer, in preparation),

the pH dependence of k_{cat}/K_m values [83, 84], and the results of site-directed mutagenesis [85–87] point to the involvement of distinct catalytic groups in the mechanism of rate enhancement. Therefore, it is likely that the desolvation, the twisted transition-state stabilization, and the acid-base catalysis are acting in combination rather than as isolated routes to enzymatic catalysis [88]. It appears likely that only physiological substrates correctly recruiting the complete ensemble of secondary binding sites provided by the PPIase are able to make the catalytic machinery fully active [84].

PPIases have been shown to exhibit pronounced subsite recruitment, supporting the presence of many enzyme–substrate-contacting sites in the transition state of catalysis, but for most PPIases knowledge remains limited and fragmentary. In the reported cases, this secondary specificity contributes much to efficient catalysis [9, 53]. With a few exceptions, the parent five-membered proline ring represents a major determinant of catalytic specificity [89]. The active sites of some eukaryotic members of the parvulin family impose considerable constraints on substrate selection. The marked preference for substrates containing the (PO_3H_2)Thr-Pro-/(PO_3H_2)Ser-Pro-moiety illustrate a unique ability of several parvulins to isomerize polypeptides targeted by the large superfamily of proline-directed protein kinases, including cyclin-dependent and mitogen-activated protein kinases [90–92]. As a common property of PPIases, stereospecificity causes detrimental effects on catalysis when D-amino acid substitution in the P1 and P1′ positions is to occur [93].

10.4.2 Prototypic Cyclophilins

Prototypic cyclophilins consist of a single catalytic domain with no N-terminal and C-terminal extensions bearing a discrete biochemical function. Their amino acid sequences are highly conserved from yeast to humans, with a smaller degree of conservation across prokaryotic taxa [94]. Currently, this group of cyclophilins comprises six members in human cells, with polypeptide chains of 160–177 amino acids long whose biochemical functions have been at least partially characterized. Many additional prototypic cyclophilins can be derived from the complete human genome, but their protein expression must await characterization. Cytosolic Cyp18 (CypA) is the most abundant constitutively expressed cyclophilin in the cytosol of mammal cells. Unexpectedly, Cyp18 can be extracellularly secreted in response to inflammatory stimuli [95] and is recognized by the chemotaxis cell-surface receptor CD147 only if the Cyp18 active site is functional [96]. Other members are the nuclearly localized Cyp19.2 (CypH, USA-Cyp, Snu-Cyp, Cyp20) [97]; the cancer-related Cyp18.1a (COAS2-Cyp) [98]; the two splicing variants of the gene *PPIL3*, Cyp18.6 and Cyp18.1 (CypJ) [99]; and Cyp18.2a (CypZ) [100]. Among the best-characterized prototypic cyclophilins, Cyp19.2 is biochemically dissected along with resolved crystal structures [101–103].

Cyp18 represents a thermally and chemically rather stable protein that contains a well-defined PPIase active site, a hidden catalytic triad typical of serine proteases [104], and a poorly defined second peptide ligand-binding site [105]. The calcium/

magnesium-dependent nuclease activity reported for cyclophilins [106, 107] is not a property of the native Cyp18 structure but might result from a nuclease contamination of Cyp18 preparations [108].

The binding partner of U4/U6-60K and hPrp18, the splicosomal Cyp19.2, contains two well-defined protein-protein interaction sites: the PPIase site and an oppositely located peptide-binding site. Both sites are believed to act in conjunction [102].

The Cyp18 concentration approaches high levels in the brain but is also remarkable in other tissues and cells, as could be exemplified by the measurement of 5–10 $\mu g/mg^{-1}$ total protein in kidney tubules and endothelial cells [109–111].

In contrast to FKBP12, Cyp18 is rather promiscuous toward substrates of a series of -Xaa-Pro- with comparable k_{cat}/K_m values for tetrapeptides, while the Xaa position varied within the natural amino acids [112, 113]. Specificity constants approach high values of about $>10^7$ M^{-1} s^{-1}, implying a nearly diffusion-controlled bimolecular reaction, and the energy barrier of Cyp18-catalyzed isomerization is almost entirely determined by the activation entropy.

General acid catalysis by Arg55 has been argued to be the major driving force of catalyzed isomerization for Cyp18 [85, 114]. Another critical residue in hydrogen bonding distance to the rotating prolyl bond is His126, but its specific function has not yet been explored. Kinetic secondary deuterium isotope effects for substrates with an H/D exchange at the Cα position of the amino acid preceding proline are found to be similar between the spontaneous and the Cyp18-catalyzed reaction. The occurrence of a tetrahedral intermediate on the catalytic pathway is ruled out by the isotope effect $k_H/k_D > 1$ for these substrates [83]. However, a detailed picture of Cyp18 catalysis has not yet begun to emerge.

Most strikingly, all genes encoding cyclophilins could be deleted without seriously affecting viability of *Saccharomyces cerevisiae* [115]. Similarly, disruption of both copies of the mouse gene encoding for Cyp18 indicates the nonessential character of this protein [116]. On the other hand, mutations of the Cpa1 and Cpa2 proteins alone, the Cyp18 homologues in *Cryptococcus neoformans*, conferred dramatic phenotypes in that cell growth, mating, virulence, and cyclosporin A toxicity were affected. Cpa1/Cpa2 double mutants exhibited severe synthetic defects in growth and virulence [117].

Cyp18 itself has pronounced biochemical and physiological effects on living cells. When Cyp18 is secreted by vascular smooth muscle cell in response to oxidative stress, it mediates typical effects of reactive oxygen species: the activation of extracellular signal-regulated kinase (ERK1/2) and stimulation of cell growth [118]. Whole-cell experiments assaying the phosphorylation status of extracellular signal-regulated protein kinases in the presence of a panel of wild-type Cyp18 and Cyp18 variants served to display possible enzymatically controlled initiation of downstream signaling events. The extracellular part of the multifunctional transmembrane glycoprotein CD147 (basigin) is considered to be the docking site of Cyp18 [95]. Whereas externally added wild-type Cyp18 fully enhances the level of ERK phosphorylation in CHO.CD147 cells, but not in CHO cells lacking induced CD147 expression, Cyp18 variants are effective only according to their level of re-

sidual PPIase activity. Site-directed mutagenesis of the CD147 extracellular domain revealed that the Asp179-Pro180 segment was the Cyp18-directed substrate region. Neutrophil chemotaxis, a downstream signaling effect of CD147 stimulation by Cyp18, is also dependent on the intact Asp179-Pro180 recognition segment [96]. Another topic concerns the intracellularly localized fraction of Cyp18 that controls the functional expression of homo-oligomeric α7 neuronal nicotinic and type 3 serotonin receptors in a manner dependent on its PPIase activity in *Xenopus laevis* oocytes [119].

An antisense deoxynucleotide effectively reduced Cyp18 expression in a rat neuroblastoma cell line and provided the first indication that this enzyme participates in the activation of the caspase cascade in neuronal cells [120].

Functional analysis revealed that overexpression of Cyp18 inhibited prolactin-induced Rac activation, while simultaneously prolonging Jak2 phosphorylation. This effect indicates that Cyp18 might be involved in the various prolactin receptor-mediated signaling pathways [121].

Cyp18 physically interacts with many protein ligands in cells, some of which may involve substantial chain reorganization during functional interaction affecting their bioactivity. If ligand binding is strong enough, as realized by the retinoblastoma gene product RB, it can interfere with the blockage of CsA-mediated NF-AT dephosphorylation if the Cyp18 concentration is limiting [122]. Direct evidence for the functional role of Cyp18 has come from signals associated with oxidative stress. In particular, stimulation of the ligand activity was found to occur when Cyp18 binds to the thiol-specific antioxidant protein Aop1 [123]. The familial amyotrophic lateral sclerosis (FALS)-associated mutant Cu/Zn superoxide dismutase-l (SOD) induces apoptosis of neuronal cells in culture associated with high levels of reactive oxygen species. An increased protein turnover might result from altered cellular free radical balance that requires an increased level of folding-supportive enzymes. Thus, the apoptosis-enhancing effect of cyclosporin A and FK506, as well as non-immunosuppressive analogues of cyclosporin A, in PC12 cells infected with the AdV-SOD Val148Gly- and SOD Ala4Val variants might result from the increased need for PPIase activity in this oxidative stress situation. The importance of enzymatic activity in mutant SOD-mediated apoptosis was supported by experiments showing that overexpressed wild-type Cyp18, but not Cyp18 Arg55Ala variant with a reduced catalytic activity of about 0.1% of the wild-type enzyme, protected cells from death after SOD Val148Gly expression [124].

Interleukin-2 tyrosine kinase catalytic activity is inhibited according to Cyp18 PPIase activity level. NMR structural studies combined with mutational analysis show that a proline-dependent conformational switch within the Itk SH2 domain regulates substrate recognition and mediates regulatory interactions with the active site of the PPIase. Cyp18 and Itk form a stable complex in Jurkat T cells that is disrupted by treatment with cyclosporin A [125].

Despite the fact that the Cyp18 gene is regarded as a housekeeping gene, the regulated expression of Cyp18 mRNA in the brain points to stress control of expression [126]. Many Cyp18 homologues are subject to stress regulation [127–129]. Similarly, proteome analyses detected upregulation of Cyp18 in the higher

passages of fetal skin cells and downregulation in the fibroblasts of older adults [130, 131]. A proteome-based analysis of potential mitogens to human bone marrow stromal cells secreted by PC3 cancer cells identified Cyp18 [132]. Both the prototypic COAS-Cyp and Cyp18 belong to the highly overexpressed proteins in human tumors [98, 133, 134]. Secretion of prototypic cyclophilins appears to be involved in host cell defense against parasitic invasions, because a *Toxoplasma gondii* Cyp18 homologue induces IL-12 production in dendritic cells via chemokine receptor signaling [135]. In other parasites, Cyp18 inactivation causes anti-parasite effects [136].

Cyclophilins and FKBPs have frequently been found to be involved in protein trafficking. Yeast Cyp17 (Cpr1p) was identified as the protein that is required for fructose-1,6-bisphosphatase import into intermediate transport vesicles. Mutants lacking Cpr1p were defective in this import function, but addition of the purified Cyp17 restored import function in the ΔCpr1p mutants [137].

The three-dimensional structure of human Cyp18 revealed an eight-stranded, antiparallel β-barrel capped by two short helices, with the active-site groove located on one side of the barrel. Many three-dimensional structures of Cyp18 exist either in the free state or in complex with a variety of inhibitors and oligopeptide substrates, and the structure of a ternary complex of Cyp18/CsA/calcineurin has also been resolved [138–140]. Generally, the Cyp18 fold does not change much in response to ligand binding.

Complexes of Cyp18 with physiological ligands have been realized for human Cyp18 bound to HIV-1 capsid protein fragments [141, 142]. HIV-1 replication requires capsid protein-mediated host cell Cyp18 packaging [143]. The binding portion of the capsid protein fragments extend over nine residues, at least, with a Gly89-Pro90-Ile91 moiety bound to the primary catalytic site of Cyp18. As already discussed above, such extended ground-state binding sites may have the potential to sequester unfolded polypeptide chains, thus realizing the properties of a holding chaperone. The reaction conditions, however, determine whether Cyp18 is able to prevent aggregation [144] or remains refractory to unfolded chains [145]. In response to their additional domains, larger cyclophilins frequently exhibit chaperone-like function. The mobility of the binding loop of the capsid protein fragments causes native-state isomers to exist in the unbound state. Cyp18 effectively exerts control on the dynamics of native-state prolyl isomerization by increasing the isomerization rate [146, 147]. It can be hypothesized that the Cyp18/capsid protein interaction protects HIV-1 from the host cell restriction factor Ref-1 by a catalyzed distortion of a capsid protein segment representing the Ref-1 docking site [148].

A Cyp18-mediated rate enhancement has been established as a standard probe for the identification of prolyl-bond-limited steps in refolding [149–154]. This enzyme is also a major component of the mixture of folding helper proteins of the oxidative refolding chromatography used, for example, for "empty" MHC class I-like molecules to assemble at physiological temperatures in the absence of ligand [155–157].

Cyp18 constitutes a common target protein for the immunosuppressants cyclo-

sporin A and sanglifehrin, which both inhibit the enzyme by binding to the deep hydrophobic pocket of the PPIase active site [158–161].

Besides cyclosporin A and its derivatives, only a few other Cyp18 inhibitors have been reported, but at a reduced level of inhibitory potency [162–164]. To date the Cyp18/cyclosporin A complex forms a sole example among the Cyp18/inhibitor complexes in that complex formation results in a gain of function that is exclusively targeted to the Ser/Thr protein phosphatase calcineurin [71].

10.4.3 Prototypic FK506-binding Proteins

The FK506-binding proteins (FKBPs) are a family of PPIases in which the prototypic enzymes have been found to bind to and become inhibited by the peptidomacrolides FK506 and rapamycin. The group of prototypic FKBPs is much smaller than those of Cyp18 because FKBP12, FKBP12.6, and a third, uncharacterized FKBP12 encoded on human chromosome 6 are the only members. FKBP12 differs from FKBP12 in 16 out of 107 amino acids. The genomes of lower eukaryotes, eubacteria, and archaea encode homologues that have, in some cases, a bulge insertion in the flap region of FKBP12, conferring holding chaperone properties to the prototypic enzymes [165]. The property is most easily explained with largely extended catalytic subsites required for optimal recognition of the cellular substrates in these organisms.

In the catalytic modules of FKBPs, in view of the sequence similarity among members of the FKBP family, affinity to FK506 is less well conserved [87]. As was already found for cyclophilins, sequence variations at the positions that are crucial for binding the inhibitors and enzyme activity are relatively small. The human members of the FKBP family are depicted in Figure 10.2.

The concentration of FKBP12 in T cells is extraordinarily high for an enzyme (about 20 μM) [28]. Furthermore, there is an increased level of FKBP12 in neurons situated in areas of degeneration [166].

Mimicking the intrinsically high concentrations of authentic FKBP12 in the male reproductive tract, recombinant FKBP12 enhances the curvilinear velocity of immature sperm, suggesting a role for FKBP12 in motility initiation [167]. FKBP12 also possesses chemotactic effects on neutrophils unless the active site is blocked by FK506 [168].

Native FKBP12 contains seven *trans*-prolyl peptide bonds, and the *cis* to *trans* isomerizations of some or all of them constitute the slow, rate-limiting event in folding. Its refolding process from a chemically denatured state constituted the first example of an autocatalytic formation of a native protein from kinetically trapped species with nonnative proline isomers [169, 170].

Knowledge of FKBP12 and FKBP12.6 structures either alone or complexed with ligands exists, but the structure of an FKBP12/oligopeptide substrate complex is still missing [171]. Thus, the FK506-binding site was taken to represent the catalytic site. A docking procedure to FKBP12 was used for a potential substrate: the

proline-rich prolactin receptor-derived octapeptide. When bound to FKBP12, the docked peptide reveals a type I β-turn conformation and many hydrophobic contacting sites [172]. The major structural elements surrounding the hydrophobic catalytic cleft are a concave five-stranded antiparallel β-sheet, wrapping around a short alpha-helix, and a large flap region. In most preferred substrates, hydrophobic side chains are positioned toward the N-terminus of the reactive prolyl bond [83]. Unlike Cyp18 and Par10, however, k_{cat}/K_m values of FKBP12 do not achieve the diffusion-controlled limit. Both PPIase activity and FK506 inhibition proved to be similar for FKBP12.6 and FKBP12 [173]. Consequently, steady-state catalytic data of prototypic FKBPs suggest an unassisted conformational twist mechanism with rate enhancement due in part to desolvation of the peptide bond at the active site [88, 174].

Comparison of the effects of point mutations on k_{cat}/K_m values for tetrapeptide substrates revealed catalytically important side chains of FKBP12 [86]. Several FKBP12 variants (Tyr82Phe, Trp59Ala, and Asp37Val) experienced marked reduction (about 10-fold) in the specificity constant k_{cat}/K_m, with the k_{cat} value being the most severely affected parameter. None of the point mutations confers complete catalytic inactivity to the enzyme variants.

In comparison to Cyp18, FKBP12 confers a more diverse gain of function because the FKBP12/FK506 complex inhibits the protein phosphatase calcineurin, but the structurally related FKBP12/rapamycin complex inactivates the human target of rapamycin (mTOR) protein, a cell-cycle-specific protein kinase known to be involved in signaling pathways that promote protein synthesis and cell growth [175]. The downstream events that follow the inactivation of TOR result in the blockage of cell-cycle progression at the juncture of the G1 and S phases.

Besides the natural products FK506 and rapamycin and their derivatives, many other inhibitors of several totally unrelated substance classes have been developed, indicating a highly promiscuous binding affinity of the active site of FKBP12 [176–178]. That is, a rather limited number of contacting sites suffice to account for specificity and affinity. The dissociation constants for the FKBP12 complexes of dimethyl sulfoxide and 5-diethylamino-2-pentanone of 20 mM and 500 μM, respectively, highlight the unique ligand-affinity pattern of the FKBP12 catalytic cleft [179].

Most potent compounds are derived from α-ketoamides, from which the potent neuroactive inhibitor GPI 1046 (3-(3-pyridyl)-1-propyl (2S)-1-(3,3-dimethyl-1,2-dioxopentyl)-2-pyrrolidinecarboxylate) was derived [180–183]. Displacement of enzyme-bound water molecules upon inhibitor binding is a major driving force for the tight binding of α-ketoamides to the active site [184].

Some FKBPs, notably FKBP12, have defined roles in regulating ion channels, protein transport, or cell signaling. Using cells from FKBP12-deficient ($FKBP12^{(-/-)}$) mice, cell-cycle arrest in the G(1) phase could be detected. These cells can be rescued by FKBP12 transfection [185]. The transgenic mice do not show abnormal development of skeletal muscle but have severe dilated cardiomyopathy and ventricular septal defects that mimic a human congenital heart disorder [186]. In contrast, disruption of the FKBP12.6 gene in mice results in cardiac

hypertrophy in male mice, but not in females. However, female FKBP12.6$^{(-/-)}$ mice treated with an estrogen receptor antagonist develop cardiac hypertrophy similar to that of male mice [187].

Physically interacting proteins of FKBP12 and FKBP12.6 include the intracellular calcium release channels [188, 189], the type II TGF-β receptor [190], the EGF receptor [191], the HMG-box proteins 1 and 2 [192], aspartokinase [193], FAP48, a fragment of the glomuvenous malformation-related glomulin [194, 195], and the transcription factor YY1 [196]. An interacting protein similar to FAP48, the FAP48 homologue FIP37, has been found for the prototypic plant FKBP12 in *Arabidopsis thaliana* [197].

Two transmembrane receptor protein kinases have been shown to be downregulated in their activating phosphorylation in the presence of FKBP12. FKBP12 can affect TGF-β signaling by preventing Ser/Thr phosphorylation of the type I TGF-β receptor by the type II TGF-β receptor via binding to a Leu-Pro motif of the type I TGF-β receptor [190]. Type I TGF-β receptor affinity for FKBP12 is abolished for a receptor molecule phosphorylated on the GS box. The modulation of the EGF receptor signaling by FKBP12 is directed against the tyrosine autophosphorylation of the cytoplasmic domain of the receptor [191]. FK506 and rapamycin abolish the FKBP12 effect to the same extent in EGF receptor-rich A431 fibroblasts, leading to an increase in cell growth. In both cases, by impeding the activation of receptors in the absence of native ligands, FKBP12 may provide a safeguard against leaky signaling, resulting in a basal level of receptor phosphorylation. In cell signaling, the function of prototypic FKBPs emerges as catalysts affecting the rate of decay of metastable states of receptor proteins (C. Schiene-Fischer, in preparation).

The sarco(endo)plasmic reticulum, the main Ca^{2+} storage compartment, contains two different families of Ca^{2+} release channels: the ryanodine receptors (RyR) and the inositol 1,4,5-trisphosphate receptors (IP_3R), both of which share affinity binding to prototypic FKBPs.

Mammalian tissues express three large, high-conductance ryanodine receptors known as skeletal muscle (RyR1), cardiac muscle (RyR2), and brain (RyR3). They are able to control dynamically the level of intracellular Ca^{2+} by releasing Ca^{2+} from the intracellular sarco(endo)plasmic reticulum.

The skeletal muscle ryanodine receptor (RyR1) can be isolated as a hetero-oligomer containing FKBP12 whereas the cardiac ryanodine receptor (RyR2) selectively associates with FKBP12.6. However, RyR2 isolated from many vertebrates contains both FKBP12 and FKBP12.6 [198]. The structural response to mutation suggests that considerable hydrophobicity of tryptophan 59 (which is a phenylalanine in FKBP12.6) contributes to the specificity of binding between FKBP12 isoforms and ryanodine receptors. More specifically, the triple mutant (Gln31Glu/Asn32Asp/Phe59Trp) of FKBP12.6 was found to lack selective binding to RyR2, comparable to that of FKBP12. In complementary studies, mutations of FKBP12 to the three critical amino acids of FKBP12.6 conferred selective binding to RyR2 [199].

The 4:1 molar ratio of FKBP12/tetrameric RyR indicates the stoichiometric binding of one FKBP12 molecule to one RyR subunit. The heterocomplex dissociation

by titration with FK506 reveals that the interaction involves the active site of FKBP12.

The prototypic FKBPs are regulatory constituents of the RyR that can dramatically affect RyR function, e.g., by overexpression [200] or deletion [186, 200]. For example, when FKB12 is bound to RyR1, it inhibits the channel by stabilizing its closed state. Taking a more detailed view, FKBP12 deficiency causes longer mean open times and greater open probability in cardiac myocytes of the ryanodine receptor when compared with reference cells. Generally, the Ca^{2+} leak rate increases considerably [187]. Marks et al. reported that the FKBP12 Phe36Tyr variant is still able to bind but not to modulate RyR channeling, pointing to a crucial role of the unperturbed enzyme activity of FKBP12 [201].

In a canine model of pacing-induced heart failure, the ratio of FKBP12.6 per failing RyR2 is significantly decreased. A conformational change was suggested for RyR2 chains concomitant with abnormal Ca^{2+} leak of the channel [202].

Ca^{2+} stores of the endoplasmic reticulum become superfilled after co-expression of FKBP12.6, but not of FKBP12, in CHOhRyR2 cells. The effects of FKBP12.6 on hRyR2-mediated intracellular Ca^{2+} handling could be antagonized using the FKBP inhibitor rapamycin [203].

10.4.4
Prototypic Parvulins

The parvulins represent the most recently discovered PPIase family [204, 205]. The most typical parvulin known to date is the *E. coli* Par10, a monomerically active enzyme comprising 92 amino acids in its mature form. Parvulin sequences are characterized by two conserved histidine motifs (three to five amino acids in each segment), which are separated by a stretch of about 70–85 amino acids containing a few other conserved residues. There is no sequence similarity to either cyclophilins or FKBPs. In various plants, a parvulin member corresponds to the prototypical form (it is 117–119 amino acids in length) because it does not show an N-terminal or C-terminal extension when compared to Par10 [47, 91, 206]. The difference of Par10 in chain length is due to a single polypeptide segment of 23 amino acids inserted in the N-terminal half of the protein that adopt a loop conformation in the $\alpha 1/\beta 1$ region [207]. In two other eukaryotic parvulins, functional domains complement N-terminally the catalytic domain, a DNA-binding domain, and a (PO_3H_2)Ser/Thr-directed type IV WW domain in Par14 and Pin1, respectively. So far, the existence of only these two genes encoding parvulin proteins has been described in the human genome, i.e., they have a low frequency compared with both Cyp and FKBP sequences (Figure 10.2). Originally, an activity-based screening approach for cytosolic extracts identified Par10, and it was not shown to be a predicted ORF of the *E. coli* genome. Besides plants, no other organism was reported to possess a prototypic parvulin. However, the concept of ORF identification is confounded by several factors. The procedure may permit small proteins to escape detection due to their size falling below some arbitrary researcher-defined minimum cutoff, or there may be an inability to precisely define a promoter or translational

start [208]. Thus, future identification of new prototypic enzymes is predicted. Many larger parvulins have been characterized in prokaryotes.

It is of interest that Par10 is as active as Cyp18 toward oligopeptide substrates but that proteins are catalyzed less efficiently. When compared to Cyp18, Par10 was found to have a much narrower substrate specificity at the position preceding proline (measured by k_{cat}/K_m), a finding reminiscent of FKBP12 [204]. However, unlike other PPIase families, the parvulins exhibit an extraordinary pattern of substrate specificity across the family members, ranging from the positively charged arginine side chain to the double-negative phosphoserine (phosphothreonine) side chain for Par14 and plant Par13 or Pin1, respectively.

Like FKBP12, Par10 accelerates its own refolding in an autocatalytic fashion, and the rate of refolding increases 10-fold when the concentration of parvulin is increased from 0.5 to 3.0 μM [209]. In larger parvulins, such as *E. coli* SurA, two parvulin-like domains exist, one of which, by itself, is devoid of PPIase activity [210]. The enzymatically active parvulin-like domain protrudes out from the core domain about 25–30 Å in the three-dimensional structure, implicating an isolated action onto substrates [211]. The three-dimensional structure of Par10 is not yet published, but sequence similarity suggests a common structural pattern shared by human Par14, Pin1, the active domain of SurA, and *Arabidopsis thaliana* Par13. Analyses of the tertiary structures of the parvulins revealed the existence of an FKBP-like superfold that is also found for the *E. coli* GreA transcript cleavage factor of 17.6 kDa [37]. When measuring 2D-^{1}H-^{15}N HSQC NMR spectra of human Par14 in the presence of a substrate, site-directed chemical shift changes in the protein were identified [212]. Hydrophobic amino acids in positions Met90, Val91, and Phe94 have been identified to be substrate-sensitive residues that match those of the active site of Pin1 [213]. However, the basic cluster of two neighboring arginines and a lysine, which collectively determine the -(PO_3H_2)Ser/Thr-Pro- directed substrate specificity of Pin1 and plant Par13, is absent in Par10 and Par14.

The putative biological functions of human Pin1, which has highly conserved homologues in eukaryotes, are best considered in the context of the manifold of known phosphoprotein targets [214]. Cellular processes include cell cycle progression, transcriptional regulation, cell proliferation and differentiation, DNA damage response, p53 functions, Alzheimer's disease, and other tauopathies. On these Pin1 topics, excellent comprehensive reviews have been compiled recently [24, 214, 215].

Although plant prototypic parvulins lack the type IV WW domain, they are able to rescue the lethal mitotic phenotype of a temperature-sensitive mutation in the Pin1 homologue ESS1/PTF1 gene in *Saccharomyces* [91, 206]. Plant Par13 proteins are expressed in high abundance, predominantly in rapidly dividing cells. Expression of apple Par13 is tightly associated with cell division during both apple fruit development in vivo and cell cultures in vitro.

An oxidative stress phenotype could be observed for *E. coli* Par10 deletion strains. The results of complementation experiments with several Par10 variants suggest a correlation between residual enzyme activity and the capability to rescue protein

most strongly associated with the putative Par10 function (B. Hernandez-Alavarez, unpublished results).

10.5 Concluding Remarks

Elucidation of the molecular mechanisms active in conformational regulation of bioactivity as applied in catalytic fashion to polypeptide chains of various folding states by peptide bond *cis/trans* isomerases is an emerging research field. Regarding safety of conformational control, the high-resistance on/off switch of a prolyl bond offers unique advantages over other conformational rearrangements within the polypeptide backbone. Thus, the topic extends from de novo protein folding to allosteric control and protein metastability and includes processes that govern the spatial-temporal control of bioactivity in cell life. Research should make use of highly multidisciplinary approaches involving physicochemical techniques and bioorganic chemistry as well as molecular and cell biology. Fundamental probes characterizing prolyl isomerizations in larger polypeptide chains are complicated, are in part insufficiently developed, and suffer from severe limitations regarding sensitivity and selectivity. Advances in current detection methods on the one-bond level of conformational couplings for proteins in vivo will be of essence if the molecular aspect of regulation is to be explored. Experiments combining gene deletion with variant enzyme gene transfection and the small-molecule approach with monofunctional PPIase inhibitors must be supplemented with new techniques allowing the externally controlled switching of a peptide bond conformation.

10.6 Experimental Protocols

10.6.1 PPIase Assays: Materials

Pancreatic α-chymotrypsin, subtilisin Carlsberg type VIII, pancreatic elastase, and trypsin are available from a number of vendors. In the substrate, the position succeeding proline determines the type of protease required: α-chymotrypsin for -Pro-Phe(Tyr)-, trypsin and clostripain for Pro-Lys(Arg)-, and pancreatic elastase for Pro-Val-. Because defined reaction conditions are essential, determination of the active protease concentration is required using an appropriate method for the respective enzyme [216]. Stock solutions of the protease (typically 40 mg mL^{-1} active enzyme solutions) are prepared in assay buffer subsequent to the addition of a small amount of 1-mM HCl to improve dissolution and can be stored at 0 °C for several days.

Typical PPIase substrates such as succinyl-Ala-Ala-Pro-Phe-4-nitroanilide and succinyl-Ala-Leu-Pro-Phe-4-nitroanilide can be purchased from Bachem (Heidelberg, Germany). The purity of the substrate peptides should be checked by HPLC at 330 nm because the clear separation of the kinetic phases of the assay stringently relates to the absence of chromogenic impurities in the substrates. Stock solutions are prepared in analytical grade DMSO mixtures or 0.2–0.5 M LiCl dissolved in anhydrous trifluoroethanol. Typically, a sample of 25 mg peptide is dissolved in 1 mL DMSO for the stock solution. Human PPIases, such as Cyp18 and FKBP12, and *E. coli* Par10 can be easily prepared recombinantly in *E. coli* by standard procedures or are present as a mixture of many PPIases in most cytosolic extracts of tissues and cells. Except for human Pin1 [90], PPIase mixtures may be difficult to differentiate based solely on a panel of different substrates. HEPES buffer is degassed prior to use.

10.6.2
PPIase Assays: Equipment

Measurements can be performed by monitoring the UV/Vis absorbance of released 4-nitroaniline at 390 nm ($\varepsilon = 11\,800$ mM cm^{-2} on a Hewlett-Packard 8452 diode array spectrophotometer (Hewlett Packard, USA) equipped with a thermostated cell holder and a stirring device within the sample cell ($d = 1$ cm, silica cell). The reference wavelength is set to 510 nm. Constant temperature of 10 °C is maintained within the cell by water circulated from a Cryostat Haake D8 (Haake-Fisons, Germany). The Sigma-Plot Scientific Graphing System Vers. 8.0 (SPSS Science, USA) is used for data analysis. The possibility of monitoring of the reaction kinetics over three or more half-times of the reaction is the necessary precondition to reliable PPIase assays.

10.6.3
Assaying Procedure: Protease-coupled Spectrophotometric Assay

The example given here is for the chymotrypsin-coupled Cyp18 assay [217]. HEPES buffer 0.035 M, pH 7.8 (1.19 mL) and 10 μL of the stock solution of pancreatic α-chymotrypsin are preincubated at 10 °C in the cell holder for 5 min. In a typical PPIase assay, recombinant human Cyp18 is added to a final concentration of 2–5 nM. In our hand-mixing experiment, too-high isomerization rates at high PPIase concentrations result in datasets that are incompatible with the fitting procedure of the first-order calculations. Assays in the absence of a PPIase yield rate constants that characterize the spontaneous rates of prolyl isomerization of substrates. Continuous stirring is necessary during the assay. After the solution has reached thermal equilibrium, the reaction is initiated by the addition of 2 μL of the stock solution of the succinyl-Ala-Ala-Pro-Phe-4-nitroanilide, and time-absorbance readings are stored. After the reaction is finished, the data list is transferred to the first-order routine of the Sigma-Plot program for calculating the first-order rate constant and the amplitude of the slow kinetic phase. Prior to calcu-

lation, sample-mixing-corrupted data points (the first 5–15 s after reaction start) are removed from the data table by visual inspection (Figure 10.2).

A considerable improvement of the signal-to-noise ratio of the assay is achieved with the peptide dissolved in 0.2 M LiCl/trifluoroethanol [218]. Due to an increase in the equilibrium population of the *cis* isomer from about 5% to about 50%, the amplitude of the kinetic phase of the *cis* to *trans* isomerization increases in a similar manner. The residual water content in the TFE/LiCl/peptide mixture determines the percentage of *cis* isomer.

10.6.4 Assaying Procedure: Protease-free Spectrophotometric Assay

For assaying prolyl isomerization with the protease-free method, progress curves are recorded, applying the experimental conditions already described above, with the exception that a protease is omitted from the assay mixture, and a different detection wavelength [51]. The slight difference of 600 mM^{-1} cm^{-2} of the UV/Vis absorption coefficients at 330 nm between the *cis* and the *trans* isomer of many standard peptide 4-nitroanilide substrates (or other ring-substituted peptide anilides) is utilized. At 330 nm a time-dependent decrease of absorbance is recorded subsequent to a rapid 88-fold dilution from a dry stock solution of succinyl-Ala-Ala-Pro-Phe-4-nitroanilide in 0.47 M LiCl/trifluoroethanol into 1.2 mL of 0.0035-M HEPES buffer, pH 7.8. The readout of time-absorbance data pairs provides the basis for the calculation of first-order rate constants according to the procedure described above.

Besides a nanomolar concentration of Cyp18, the final reaction mixture should contain bovine serum albumin (1 μM) to avoid absorption of the PPIase to the surface of the silica cell. The first-order rate constant for approach to *cis*/*trans* equilibrium equals $k_{obs} = k_{cis\ to\ trans} + k_{trans\ to\ cis}$.

References

1 Eaton, W. A., Munoz, V., Hagen, S. J., Jas, G. S., Lapidus, L. J., Henry, E. R. & Hofrichter, J. (2000). Fast kinetics and mechanisms in protein folding. *Annu. Rev. Biophys. Biomol. Struct* **29**, 327–359.

2 Bieri, O., Wirz, J., Hellrung, B., Schutkowski, M., Drewello, M. & Kiefhaber, T. (1999). The speed limit for protein folding measured by triplet-triplet energy transfer. *Proc. Natl. Acad. Sci. USA* **96**, 9597–9601.

3 Krieger, F., Fierz, B., Bieri, O., Drewello, M. & Kiefhaber, T. (2003). Dynamics of unfolded polypeptide chains as model for the earliest steps in protein folding. *J. Mol. Biol.* **332**, 265–274.

4 Dugave, C. & Demange, L. (2003). *Cis*/*trans* isomerization of organic molecules and biomolecules: implications and applications. *Chem. Rev.* **103**, 2475–2532.

5 Fischer, G. (2000). Chemical aspects of peptide bond isomerization. *Chem. Soc. Rev.* **29**, 119–127.

6 Reimer, U. & Fischer, G. (2002). Local structural changes caused by peptidyl-prolyl *cis*/*trans* isomerization

in the native state of proteins. *Biophys. Chem.* **96**, 203–212.

7 Neutze, R., Pebay Peyroula, E., Edman, K., Royant, A., Navarro, J. & Landau, E, M. (2002). Bacteriorhodopsin: a high-resolution structural view of vectorial proton transport. *Biochim. Biophys. Acta* **1565**, 144–167.

8 Song, S. H., Asher, S. A., Krimm, S. & Shaw, K. D. (1991). Ultraviolet resonance raman studies of *trans*-peptides and *cis*-peptides – photochemical consequences of the twisted pi-star excited state. *J. Am. Chem. Soc.* **113**, 1155–1163.

9 Fischer, G., Bang, H. & Mech, C. (1984). Determination of enzymatic catalysis for the *cis*/*trans* isomerization of peptide bonds in proline-containing peptides. *Biomed. Biochim. Acta* **43**, 1101–1111.

10 Schiene-Fischer, C., Habazettl, J., Schmid, F. X. & Fischer, G. (2002). The hsp70 chaperone DnaK is a secondary amide peptide bond *cis*/*trans* isomerase. *Nat. Struct Bio.l* **9**, 419–424.

11 Andreotti, A. H. (2003). Native state proline isomerization. *Biochemistry* **42**, 9515–9524.

12 Stukenberg, P. T., Kirschner, M. W. (2001). Pin1 acts catalytically to promote a conformational change in Cdc25. *Mo.l Cell* **7**, 1071–1083.

13 Ng, K. K. S. & Weis, W. I. (1998). Coupling of prolyl peptide bond isomerization and Ca^{2+} binding in a C-type mannose-binding protein. *Biochemistry* **37**, 17977–17989.

14 Eisenmesser, E. Z., Bosco, D. A., Akke, M. & Kern, D. (2002). Enzyme dynamics during catalysis. *Science* **295**, 1520–1523.

15 Schmid, F. X. (1992). The mechanism of protein folding. *Curr. Opin. Struct. Biol.* **2**, 21–25.

16 Bächinger, H. P. (1987). The influence of peptidyl-prolyl *cis*/*trans* isomerase on the in vitro folding of type III collagen. *J. Biol. Chem.* **262**, 17144–17148.

17 Steinmann, B., Bruckner, P. & Superti Furga, A. (1991). Cyclosporin A slows collagen triple-helix formation in vivo: indirect evidence for a physiologic role of peptidyl-prolyl *cis*/*trans*-isomerase. *J. Biol. Chem.* **266**, 1299–1303.

18 Thies, M. J. W., Mayer, J., Augustine, J. G., Frederick, C. A., Lilie, H. & Buchner, J. (1999). Folding and association of the antibody domain C(H)3: Prolyl isomerization preceeds dimerization. *J. Mol. Biol.* **293**, 67–79.

19 Brandts, J. F., Halvorson, H. R. & Brennan, M. (1975). Consideration of the possibility that the slow step in protein denaturation reactions is due to *cis*/*trans* isomerism of proline residues. *Biochemistry* **14**, 4953–4963.

20 Reimer, U., Elmokdad, N., Schutkowski, M. & Fischer, G. (1997). Intramolecular assistance of *cis*/*trans* isomerization of the histidine-proline moiety. *Biochemistry* **36**, 13802–13808.

21 Texter, F. L., Spencer, D. B., Rosenstein, R. & Matthews, C. R. (1992) Intramolecular Catalysis of a Proline Isomerization Reaction in the Folding of Dihydrofolate Reductase. *Biochemistry* **31**, 5687–5691.

22 Chiti, F., Taddei, N., Giannoni, E., van Nuland, N. A. J., Ramponi, G. & Dobson, C. M. (1999). Development of enzymatic activity during protein folding – Detection of a spectroscopically silent native-like intermediate of muscle acylphosphatase. *J. Biol. Chem.* **274**, 20151–20158.

23 Yan, S. Z., Beeler, J. A., Chen, Y. B., Shelton, R. K. & Tang, W. J. (2001). The regulation of type 7 adenylyl cyclase by its C1b region and Escherichia coli peptidylprolyl isomerase, SlyD. *J. Biol. Chem.* **276**, 8500–8506.

24 Lu, K. P., Liou, Y. C. & Vincent, I. (2003). Proline-directed phosphorylation and isomerization in mitotic regulation and in Alzheimer's Disease. *Bioessays* **25**, 174–181.

25 Reiersen, H. & Rees, A. R. (2001). The hunchback and its neighbours: proline as an environmental modulator. *Trends Biochem. Sci.* **26**, 679–684.

26 Creamer, T. P. & Campbell, M. N. (2002). Determinants of the poly-

proline II helix from modeling studies. *Adv. Prot. Chem.* **62**, 263–282.

27 Oneal, K. D., Chari, M. V., Mcdonald, C. H., Cook, R. G., Yulee, L. Y., Morrisett, J. D. & Shearer, W. T. (1996). Multiple *cis*/*trans* conformers of the prolactin receptor proline-rich motif (prm) peptide detected by reverse-phase HPLC, CD and NMR spectroscopy. *Biochem. J.* **315**, 833–844.

28 Fischer, G. (1994). Peptidyl-prolyl *cis*/*trans* isomerases and their effectors. *Angew. Chem. Intern. Ed. Engl.* **33**, 1415–1436.

29 Zhou, X. Z., Kops, O., Werner, A., Lu, P. J., Shen, M. H., Stoller, G., Küllertz, G., Stark, M., Fischer, G. & Lu, K. P. (2000). Pin1-dependent prolyl isomerization regulates dephosphorylation of Cdc25C and tau proteins. *Mol. Cell* **6**, 873–883.

30 Weiwad, M., Küllertz, G., Schutkowski, M. & Fischer, G. (2000). Evidence that the substrate backbone conformation is critical to phosphorylation by p42 MAP kinase. *FEBS Lett.* **478**, 39–42.

31 Brandsch, M., Thunecke, F., Küllertz, G., Schutkowski, M., Fischer, G. & Neubert, K. (1998). Evidence for the absolute conformational specificity of the intestinal H^+/peptide symporter, PEPT1. *J. Biol. Chem.* **273**, 3861–3864.

32 Feng, Y. Q., Hood, W. F., Forgey, R. W., Abegg, A. L., Caparon, M. H., Thiele, B. R., Leimgruber, R. M. & Mcwherter, C. A. (1997). Multiple conformations of a human interleukin-3 variant. *Protein. Sci.* **6**, 1777–1782.

33 Keller, M., Boissard, C., Patiny, L., Chung, N. N., Lemieux, C., Mutter, M. & Schiller, P. W. (2001). Pseudoproline-containing analogues of morphiceptin and endomorphin-2: Evidence for a *cis* Tyr-Pro amide bond in the bioactive conformation. *J. Med. Chem.* **44**, 3896–3903.

34 Nielsen, K. J., Watson, M., Adams, D. J., Hammarstrom, A. K., Gage, P. W., Hill, J. M., Craik, D. J., Thomas, L., Adams, D., Alewood, P. F. & Lewis, R. J. (2002). Solution structure of mu-conotoxin PIIIA, a preferential inhibitor of persistent tetrodotoxin-sensitive sodium channels. *J. Biol. Chem.* **277**, 27247–27255.

35 Brauer, A. B. E., Domingo, G. J., Cooke, R. M., Matthews, S. J. & Leatherbarrow, R. J. (2002). A conserved *cis* peptide bond is necessary for the activity of Bowman-Birk inhibitor protein. *Biochemistry* **41**, 10608–10615.

36 Fischer, G. & Aumüller, T. (2003). Regulation of peptide bond *cis*/*trans* isomerization by enzyme catalysis and its implication in physiological processes. *Rev. Physiol Biochem. Pharmacol.* **148**, 105–150.

37 Sekerina, E., Rahfeld, J. U., Müller, J., Fanghänel, J., Rascher, C., Fischer, G. & Bayer, P. (2000). NMR solution structure of hPar14 reveals similarity to the peptidyl-prolyl *cis*/*trans* isomerase domain of the mitotic regulator hPin1 but indicates a different functionality of the protein. *J. Mol. Biol.* **301**, 1003–1017.

38 Schreiber, S. L., Liu, J., Albers, M. W., Rosen, M. K., Standaert, R. F., Wandless, T. J., Somers, P. K. (1992). Molecular recognition of immunophilins and immunophilin-ligand complexes. *Tetrahedron* **48**, 2545–2558.

39 Husi, H. & Zurini, M. G. M. (1994). Comparative binding studies of cyclophilins to cyclosporin A and derivatives by fluorescence measurements. *Anal. Biochem.* **222**, 251–255.

40 MacArthur, M. W. & Thornton, J. M. (1991). Influence of proline residues on protein conformation. *J. Mol. Biol.* **218**, 397–412.

41 Reimer, U., Scherer, G., Drewello, M., Kruber, S., Schutkowski, M. & Fischer, G. (1998). Side-chain effects on peptidyl-prolyl *cis*/*trans* isomerization. *J. Mol. Biol.* **279**, 449–460.

42 London, R. E., Davis, D. G., Vavrek, R. J., Stewart, J. M. & Handschumacher, R. E. (1990). Bradykinin and its Gly6 analogue are substrates of cyclophilin: a fluorine-19 magnetiza-

tion transfer study. *Biochemistry* **29**, 10298–10302.

43 Hübner, D., Drakenberg, T., Forsen, S. & Fischer, G. (1991). Peptidyl-prolyl *cis/trans* isomerase activity as studied by dynamic proton NMR spectroscopy. *FEBS Lett.* **284**, 79–81.

44 Kern, D., Kern, G., Scherer, G., Fischer, G. & Drakenberg, T. (1995). Kinetic analysis of cyclophilin-catalyzed prolyl *cis/trans* isomerization by dynamic NMR spectroscopy. *Biochemistry* **34**, 13594–13602.

45 Videen, J. S., Stamnes, M. A., Hsu, V. L. & Goodman, M. (1994). Thermodynamics of cyclophilin catalyzed peptidyl-prolyl isomerization by NMR spectroscopy. *Biopolymers* **34**, 171–175.

46 Baine, P. (1986). Comparison of rate constants determined by two-dimensional NMR spectroscopy with rate constants determined by other NMR techniques. *Magn. Res. Chem.* **24**, 304–307.

47 Landrieu, I., De Veylder, L., Fruchart, J. S., Odaert, B., Casteels, P., Portetelle, D., Van Montagu, M., Inze, D. & Lippens, G. (2000). The Arabidopsis thaliana PIN1At gene encodes a single-domain phosphorylation-dependent peptidyl-prolyl *cis/trans* isomerase. *J. Biol. Chem.* **275**, 10577–10581.

48 Küllertz, G., Luthe, S. & Fischer, G. (1998). Semiautomated microtiter plate assay for monitoring peptidyl-prolyl *cis/trans* isomerase activity in normal and pathological human sera. *Clin. Chem.* **44**, 502–508.

49 Garel, J. R. (1980). Evidence for involvement of proline *cis/trans* isomerization in the slow unfolding reaction of RNase A. *Proc. Natl Acad. Sci. USA* **77**, 795–798.

50 Gracia-Echeverria, C., Kofron, J. L., Kuzmic, P., Kishore, V. & Rich, D. H. (1992). Continuous fluorimetric direct (uncoupled) assay for peptidyl-prolyl *cis/trans*-isomerases. *J. Am. Chem. Soc.* **114**, 2758–2759.

51 Janowski, B., Wollner, S., Schutkowski, M. & Fischer, G. (1997). A protease-free assay for peptidyl-prolyl *cis/trans* isomerases using standard peptide substrates. *Anal. Biochem.* **252**, 299–307.

52 Gracia-Echeverria, C., Kofron, J. L., Kuzmic, P. & Rich, D. H. (1993) A continuous spectrophotometric direct assay for peptidyl-prolyl *cis/trans*-isomerases. *Biochem. Biophys. Res. Commun.* **191**, 70–75.

53 Zhang, Y. X., Füssel, S., Reimer, U., Schutkowski, M. & Fischer, G. (2002). Substrate-based design of reversible Pin1 inhibitors. *Biochemistry* **41**, 11868–11877.

54 Weisshoff, H., Frost, K., Brandt, W., Henklein, P., Mugge, C. & Frommel, C. (1995). Novel disulfide-constrained pentapeptides as models for beta-VIa turns in proteins. *FEBS Lett.* **372**, 203–209.

55 Fischer, G., Schutkowski, M., & Küllertz, G. (2001) Peptidic substrates for directly assaying enzyme activities. Patent DE 100 23743 A1.

56 Lin, L. N., Hasumi, H. & Brandts, J. F. (1988). Catalysis of proline isomerization during protein-folding reactions. *Biochim. Biophys. Acta* **956**, 256–266.

57 Lang, K., Schmid, F. X. & Fischer, G. (1987). Catalysis of protein folding by prolyl isomerase. *Nature* **329**, 268–270.

58 Kiefhaber, T., Quaas, R., Hahn, U. & Schmid, F. X. (1990). Folding of ribonuclease T1. 2. Kinetic models for the folding and unfolding reactions. *Biochemistry* **29**, 3061–70.

59 Kiefhaber, T., Quaas, R., Hahn, U. & Schmid, F. X. (1990). Folding of ribonuclease T1. 1. Existence of multiple unfolded states created by proline isomerization. *Biochemistry* **29**, 3053–61.

60 Balbach, J., Steegborn, C., Schindler, T. & Schmid, F. X. (1999). A protein folding intermediate of ribonuclease T-1 characterized at high resolution by 1D and 2D real-time NMR spectroscopy. *J. Mol. Biol.* **285**, 829–842.

61 Moritz, R., Reinstadler, D., Fabian,

H. & Naumann, D. (2002). Time-resolved FTIR difference spectroscopy as tool for investigating refolding reactions of ribonuclease T1 synchronized with *trans* to *cis* prolyl isomerization. *Biopolymers* **67**, 145–155.

62 Kiefhaber, T. & Schmid, F. X. (1992). Kinetic coupling between protein folding and prolyl isomerization. 2. folding of ribonuclease-A and ribonuclease-T1. *J. Mol. Biol.* **224**, 231–240.

63 Mayr, L. M., Odefey, C., Schutkowski, M. & Schmid, F. X. (1996). Kinetic analysis of the unfolding and refolding of ribonuclease Tl by a stopped-flow double-mixing technique. *Biochemistry* **35**, 5550–5561.

64 Mücke, M. & Schmid, F. X. (1992). Enzymatic catalysis of prolyl isomerization in an unfolding protein. *Biochemistry* **31**, 7848–7854.

65 Pappenberger, G., Bachmann, A., Muller, R., Aygun, H., Engels, J. W. & Kiefhaber, T. (2003). Kinetic mechanism and catalysis of a native-state prolyl isomerization reaction. *J. Mol. Biol.* **326**, 235–246.

66 Bose, S., Weikl, T., Bugl, H. & Buchner, J. (1996). Chaperone function of hsp90-associated proteins. *Science* **274**, 1715–1717.

67 Freeman, B. C., Toft, D. O. & Morimoto, R. I. (1996). Molecular chaperone machines – chaperone activities of the cyclophilin cyp-40 and the steroid aporeceptor-associated protein p23. *Science* **274**, 1718–1720.

68 Scholz, C., Stoller, G., Zarnt, T., Fischer, G. & Schmid, F. X. (1997). Cooperation of enzymatic and chaperone functions of trigger factor in the catalysis of protein folding. *EMBO J.* **16**, 54–58.

69 Schaffitzel, E., Rüdiger, S., Bukau, B. & Deuerling, E. (2001). Functional dissection of Trigger factor and DnaK: Interactions with nascent polypeptides and thermally denatured proteins. *Biol. Chem.* **382**, 1235–1243.

70 Schreier, M. H., Baumann, G. & Zenke, G. (1993). Inhibition of T-cell signaling pathways by immunophilin drug complexes – are side effects inherent to immunosuppressive properties. *Transplant. Proc.* **25**, 502–507.

71 Schreiber, S. L., Albers, M. W. & Brown, E. J. (1993). The cell cycle, signal transduction, and immunophilin ligand complexes. *Acc. Chem. Res.* **26**, 412–420.

72 Hamilton, G. S. & Steiner, J. P. (1998). Immunophilins: Beyond immunosuppression. *J. Med. Chem.* **41**, 5119–5143.

73 Vogel, K. W., Briesewitz, R., Wandless, T. J. & Crabtree, G. R. (2001). Calcineurin inhibitors and the generalization of the presenting protein strategy. *Adv. Protein Chem.* **56**, 253–291.

74 Baumgrass, R., Zhang, Y., Erdmann, F., Thiel, A., Radbruch, A., Weiwad, M. & Fischer, G. (2004). Substitution in position 3 of cyclosporin A abolishes the cyclophilin-mediated gain-of-function mechanism but not immunosuppression. *J. Biol. Chem.*, in press.

75 Steiner, J. P., Hamilton, G. S., Ross, D. T., Valentine, H. L., Guo, H. Z., Connolly, M. A., Liang, S., Ramsey, C., Li, J. H. J., Huang, W., Howorth, P., Soni, R., Fuller, M., Sauer, H., Nowotnik, A. C. & Suzdak, P. D. (1997). Neurotrophic immunophilin ligands stimulate structural and functional recovery in neurodegenerative animal models. *Proc. Natl. Acad. Sci. USA* **94**, 2019–2024.

76 Bartz, S. R., Hohenwalter, E., Hu, M. K., Rich, D. H. & Malkovsky, M. (1995). Inhibition of human immunodeficiency virus replication by non-immunosuppressive analogs of cyclosporin A. *Proc. Natl. Acad. Sci. USA* **92**, 5381–5385.

77 Christner, C., Herdegen, T. & Fischer, G. (2001). FKBP ligands as novel therapeutics for neurological disorders. *Mini Rev. Med. Chem.* **1**, 377–397.

78 Waldmeier, P. C., Feldtrauer, J. J., Qian, T. & Lemasters, J. J. (2002). Inhibition of the mitochondrial permeability transition by the

nonimmunosuppressive cyclosporin derivative NIM811. *Mol. Pharmacol.* **62**, 22–29.

79 Uchida, T., Takamiya, M., Takahashi, M., Miyashita, H., Ikeda, H., Terada, T., Matsuo, Y., Shirouzu, M., Yokoyama, S., Fujimori, F. & Hunter, T. (2003). Pin1 and Par14 peptidyl-prolyl isomerase inhibitors block cell proliferation. *Chem. Biol.* **10**, 15–24.

80 Hennig, L., Christner, C., Kipping, M., Schelbert, B., Rücknagel, K. P., Grabley, S., Küllertz, G. & Fischer, G. (1998). Selective inactivation of parvulin-like peptidyl-prolyl *cis/trans* isomerases by juglone. *Biochemistry* **37**, 5953–5960.

81 Yli-Kauhaluoma, J. T., Ashley, J. A., Lo, C. H. L., Coakley, J., Wirsching, P. & Janda, K. D. (1996). Catalytic antibodies with peptidyl-prolyl *cis/trans* isomerase activity. *J. Am. Chem. Soc.* **118**, 5496–5497.

82 Ma, L. F., Hsieh-Wilson, L. C. & Schultz, P. G. (1998). Antibody catalysis of peptidyl-prolyl *cis/trans* isomerization in the folding of RNase T1. *Proc. Natl. Acad. Sci. USA* **95**, 7251–7256.

83 Stein, R. L. (1993). Mechanism of enzymic and non-enzymic prolyl *cis/trans* isomerization. *Adv. Protein Chem.* **44**, 1–24.

84 Schutkowski, M., Bernhardt, A., Zhou, X. Z., Shen, M. H., Reimer, U., Rahfeld, J. U., Lu, K. P. & Fischer, G. (1998). Role of phosphorylation in determining the backbone dynamics of the serine/threonine-proline motif and Pin1 substrate. *Biochemistry* **37**, 5566–5575.

85 Zydowsky, L. D., Etzkorn, F. A., Chang, H. Y., Ferguson, S. B., Stolz, L. A., Ho, S. I. & Walsh, C. T. (1992). Active site mutants of human cyclophilin-a separate peptidyl-prolyl isomerase activity from cyclosporin-A binding and calcineurin inhibition. *Protein Sci.* **1**, 1092–1099.

86 Decenzo, M. T., Park, S. T., Jarrett, B. P., Aldape, R. A., Futer, O., Murcko, M. A. & Livingston, D. J. (1996). FK506-binding protein mutational analysis – defining the active-site residue contributions to catalysis and the stability of ligand complexes. *Protein Eng.* **9**, 173–180.

87 Tradler, T., Stoller, G., Rucknagel, K. P., Schierhorn, A., Rahfeld, J. U. & Fischer, G. (1997). Comparative mutational analysis of peptidyl-prolyl *cis/trans* isomerases – active sites of *Escherichia coli* trigger factor and human FKBP12. *FEBS Lett.* **407**, 184–190.

88 Kramer, M. L. & Fischer, G. (1997). FKBP-like catalysis of peptidyl-prolyl bond isomerization by micelles and membranes. *Biopolymers* **42**, 49–60.

89 Kern, D., Schutkowski, M. & Drakenberg, T. (1997). Rotational barriers of *cis/trans* isomerization of proline analogues and their catalysis by cyclophilin. *J. Am. Chem. Soc.* **119**, 8403–8408.

90 Yaffe, M. B., Schutkowski, M., Shen, M. H., Zhou, X. Z., Stukenberg, P. T., Rahfeld, J. U., Xu, J., Kuang, J., Kirschner, M. W., Fischer, G., Cantley, L. C. & Lu, K. P. (1997). Sequence-specific and phosphorylation-dependent proline isomerization – a potential mitotic regulatory mechanism. *Science* **278**, 1957–1960.

91 Metzner, M., Stoller, G., Rucknagel, K. P., Lu, K. P., Fischer, G., Luckner, M. & Küllertz, G. (2001). Functional replacement of the essential ESS1 in yeast by the plant parvulin DlPar13. *J. Biol. Chem.* **276**, 13524–13529.

92 Lu, K. P., Liou, Y. C. & Zhou, X. Z. (2002). Pinning down proline-directed phosphorylation signaling. *Trends Cell Biol.* **12**, 164–172.

93 Schiene, C., Reimer, U., Schutkowski, M. & Fischer, G. (1998). Mapping the stereospecificity of peptidyl-prolyl *cis/trans* isomerases. *FEBS Lett.* **432**, 202–206.

94 Galat, A. (2003). Peptidylprolyl *cis/trans* isomerases (immunophilins): biological diversity-targets-functions. *Curr. Top. Med. Chem.* **3**, 1315–1347.

95 Bukrinsky, M. I. (2002). Cyclophilins: unexpected messengers in inter-

cellular communications. *Trends Immunol.* **23**, 323–325.

96 Yurchenko, V., Zybarth, G., O'Connor, M., Dai, W. W., Franchin, G., Hao, T., Guo, H. M., Hung, H. C., Toole, B., Gallay, P., Sherry, B. & Bukrinsky, M. (2002). Active site residues of cyclophilin A are crucial for its signaling activity via CD147. *J. Biol. Chem.* **277**, 22959–22965.

97 Horowitz, D. S., Kobayashi, R. & Krainer, A. R. (1997). A new cyclophilin and the human homologues of yeast prp3 and prp4 form a complex associated with U4/U6 snRNPs. *RNA* **3**, 1374–1387.

98 Meza-Zepeda, L. A., Forus, A., Lygren, B., Dahlberg, A. B., Godager, L. H., South, A. P., Marenholz, I., Lioumi, M., Florenes, V. A., Maelandsmo, G. M., Serra, M., Mischke, D., Nizetic, D., Ragoussis, J., Tarkkanen, M., Nesland, J. M., Knuutila, S. & Myklebost, O. (2002). Positional cloning identifies a novel cyclophilin as a candidate amplified oncogene in 1q21. *Oncogene* **21**, 2261–2269.

99 Zhou, Z., Ying, K., Dai, J., Tang, R., Wang, W., Huang, Y., Zhao, W., Xie, Y. & Mao, Y. (2001). Molecular cloning and characterization of a novel peptidylprolyl isomerase (cyclophilin)-like gene (PPIL3) from human fetal brain. *Cytogenet. Cell Genet.* **92**, 231–236.

100 Ozaki, K., Fujiwara, T., Kawai, A., Shimizu, F., Takami, S., Okuno, S., Takeda, S., Shimada, Y., Nagata, W., Watanabe, T., Takaichi, A., Takahashi, E., Nakamura, Y. & Shin, S. (1996). Cloning, expression and chromosomal mapping of a novel cyclophilin-related gene (PPIL1) from human fetal brain. *Cytogenet. Cell Genet.* **72**, 242–245.

101 Horowitz, D. S., Lee, E. J., Mabon, S. A. & Misteli, T. (2002). A cyclophilin functions in pre-mRNA splicing. *EMBO J.* **21**, 470–480.

102 Reidt, U., Wahl, M. C., Fasshauer, D., Horowitz, D. S., Luhrmann, R. & Ficner, R. (2003). Crystal structure of a complex between human spliceosomal cyclophilin H and a U4/U6 snRNP-60K peptide. *J. Mol. Biol.* **331**, 45–56.

103 Reidt, U., Reuter, K., Achsel, T., Ingelfinger, D., Luhrmann, R. & Ficner, R. (2000). Crystal structure of the human U4/U6 small nuclear ribonucleoprotein particle-specific SnuCyp-20, a nuclear cyclophilin. *J. Biol. Chem.* **275**, 7439–7442.

104 Wallace, A. C., Laskowski, R. A. & Thornton, J. M. (1996). Derivation of 3D coordinate templates for searching structural databases: application to Ser-His-Asp catalytic triads in the serine proteinases and lipases. *Protein Sci.* **5**, 1001–1013.

105 Demange, L., Moutiez, M., Vaudry, K. & Dugave, C. (2001). Interaction of human cyclophilin hCyp-18 with short peptides suggests the existence of two functionally independent subsites. *FEBS Lett.* **505**, 191–195.

106 Montague, J. W., Hughes, F. M. & Cidlowski, J. A. (1997). Native recombinant cyclophilins A, B, and C degrade DNA independently of peptidylprolyl *cis/trans*-isomerase activity – potential roles of cyclophilins in apoptosis. *J. Biol. Chem.* **272**, 6677–6684.

107 Nicieza, R. G., Huergo, J., Connolly, B. A. & Sanchez, J. (1999). Purification, characterization, and role of nucleases and serine proteases in *Streptomyces* differentiation – Analogies with the biochemical processes described in late steps of eukaryotic apoptosis. *J. Biol. Chem.* **274**, 20366–20375.

108 Schmidt, B., Tradler, T., Rahfeld, J. U., Ludwig, B., Jain, B., Mann, K., Rücknagel, K. P., Janowski, B., Schierhorn, A., Küllertz, G., Hacker, J. & Fischer, G. (1996). A cyclophilin-like peptidyl-prolyl *cis/trans* isomerase from *Legionella pneumophila* – characterization, molecular cloning and overexpression. *Mol. Microbiol.* **21**, 1147–1160.

109 Ryffel, B., Foxwell, B. M., Gee, A., Greiner, B., Woerly, G. & Mihatsch, M. J. (1988). Cyclosporine

– relationship of side effects to mode of action. *Transplantation* **46**, 90S–96S.

110 Goldner, F. M. & Patrick, J. W. (1996). Neuronal localization of the cyclophilin a protein in the adult rat brain. *J. Comp. Neurol.* **372**, 283–293.

111 Arckens, L., Van der Gucht, E., Van den Bergh, G., Massie, A., Leysen, I., Vandenbussche, E., Eysel, U. T., Huybrechts, R. & Vandesande, F. (2003). Differential display implicates cyclophilin A in adult cortical plasticity. *Eur. J. Neurosci.* **18**, 61–75.

112 Bergsma, D. J., Eder, C., Gross, M., Kersten, H., Sylvester, D., Appelbaum, E., Cusimano, D., Livi, G. P., McLaughlin, M. M., Kasyan, K., Porter, T. G., Silverman, C., Dunnington, D., Hand, A. Pritchett, W. P., Bossard, M. J. Brandt, M. & Levy, M. A. (1991). The cyclophilin multigene family of peptidyl-prolyl isomerases. Characterization of three separate human isoforms. *J. Biol. Chem.* **266**, 23204–23214.

113 Harrison, R. K. & Stein, R. L. (1992). Mechanistic studies of enzymic and nonenzymic prolyl *cis/trans* isomerization. *J. Am. Chem. Soc.* **114**, 3464–3471.

114 Howard, B. R., Vajdos, F. F., Li, S., Sundquist, W. I. & Hill, C. P. (2003). Structural insights into the catalytic mechanism of cyclophilin A. *Nat. Struct. Biol.* **10**, 475–481.

115 Dolinski, K., Muir, S., Cardenas, M. & Heitman, J. (1997). All cyclophilins and FK506 binding proteins are, individually and collectively, dispensable for viability *in Saccharomyces cerevisiae*. *Proc. Natl. Acad. Sci. USA* **94**, 13093–13098.

116 Colgan, J., Asmal, M. & Luban, J. (2000). Isolation, characterization and targeted disruption of mouse Ppia: Cyclophilin A is not essential for mammalian cell viability. *Genomics* **68**, 167–178.

117 Wang, P., Cardenas, M. E., Cox, C. M., Perfect, J. R. & Heitman, J. (2001). Two cyclophilin A homologs with shared and distinct functions important for growth and virulence of *Cryptococcus neoformans*. *EMBO Rep.* **2**, 511–518.

118 Jin, Z. G., Melaragno, M. G., Liao, D. F., Yan, C., Haendeler, J., Suh, Y. A., Lambeth, J. D. & Berk, B. C. (2000). Cyclophilin A is a secreted growth factor induced by oxidative stress. *Circ. Res.* **87**, 789–796.

119 Helekar, S. A. & Patrick, J. (1997). Peptidyl-prolyl *cis/trans* isomerase activity of cyclophilin a in functional homo-oligomeric receptor expression. *Proc. Natl. Acad. Sci. USA* **94**, 5432–5437.

120 Capano, M., Virji, S. & Crompton, M. (2002). Cyclophilin-A is involved in excitotoxin-induced caspase activation in rat neuronal B50 cells. *Biochem. J.* **363**, 29–36.

121 Syed, F., Rycyzyn, M. A., Westgate, L. & Clevenger, C. V. (2003). A novel and functional interaction between cyclophilin A and prolactin receptor. *Endocrine* **20**, 83–89.

122 Cui, Y., Mirkia, K., Fu, Y. H. F., Zhu, L., Yokoyama, K. K. & Chiu, R. (2002). Interaction of the retinoblastoma gene product, RB, with cyclophilin A negatively affects cyclosporin-inhibited NFAT signaling. *J. Cell. Biochem.* **86**, 630–641.

123 Jaschke, A., Mi, H. F. & Tropschug, M. (1998). Human T cell cyclophilin18 binds to thiol-specific antioxidant protein AOP1 and stimulates its activity. *J. Mol. Biol.* **277**, 763–769.

124 Lee, J. P., Palfrey, H. C., Bindokas, V. P., Ghadge, G. D., Ma, L., Miller, R. J. & Roos, R. P. (1999). The role of immunophilins in mutant superoxide dismutase-1-linked familial amyotrophic lateral sclerosis. *Proc. Natl. Acad. Sci. USA* **96**, 3251–3256.

125 Brazin, K. N., Mallis, R. J., Fulton, D. B. & Andreotti, A. H. (2002). Regulation of the tyrosine kinase Itk by the peptidyl-prolyl isomerase cyclophilin A. *Proc. Natl. Acad. Sci. USA* **99**, 1899–1904.

126 Porter, R. H., Burnet, P. W., Eastwood, S. L. & Harrison, P. J. (1996). Contrasting effects of electroconvulsive shock on mRNAs encoding the high affinity kainate receptor sub-

units (KA1 and KA2) and cyclophilin in the rat. *Brain Res.* **710**, 97–102.

127 Sykes, K., Gething, M. J. & Sambrook, J. (1993). Proline isomerases function during heat shock. *Proc. Natl. Acad. Sci. USA* **90**, 5853–5857.

128 Küllertz, G., Liebau, A., Rücknagel, P., Schierhorn, W., Dietrich, B., Fischer, G. & Luckner, M. (1999). Stress-induced expression of cyclophilins in proembryonic masses of *Digitalis lanata* does not protect against freezing thawing stress. *Planta* **208**, 599–605.

129 Andreeva, L., Heads, R. & Green, C. J. (1999). Cyclophilins and their possible role in the stress response. *Int. J. Exp. Pathol.* **80**, 305–315.

130 Vuadens, F., Crettaz, D., Scelatta, C., Servis, C., Quadroni, M., Bienvenut, W. V., Schneider, P., Hohlfeld, P., Applegate, L. A. & Tissot, J. D. (2003). Plasticity of protein expression during culture of fetal skin cells. *Electrophoresis* **24**, 1281–1291.

131 Boraldi, F., Bini, L., Liberatori, S., Armini, A., Pallini, V., Tiozzo, R., Pasquali-Ronchetti, I. & Quaglino, D. (2003). Proteome analysis of dermal fibroblasts cultured in vitro from human healthy subjects of different ages. *Proteomics* **3**, 917–929.

132 Andersen, H., Jensen, O. N. & Eriksen, E. F. (2003). A proteome study of secreted prostatic factors affecting osteoblastic activity: identification and characterisation of cyclophilin A. *Eur. J. Cancer* **39**, 989–995.

133 Campa, M. J., Wang, M. Z., Howard, B., Fitzgerald, M. C. & Patz, E. F. (2003). Protein expression profiling identifies macrophage migration inhibitory factor and cyclophilin A as potential molecular targets in non-small cell lung cancer. *Cancer Res.* **63**, 1652–1656.

134 Lim, S. O., Park, S. J., Kim, W., Park, S. G., Kim, H. J., Kim, Y. I., Sohn, T. S., Noh, J. H. & Jung, G. (2002). Proteome analysis of hepatocellular carcinoma. *Biochem. Biophys. Res. Commun.* **291**, 1031–1037.

135 Alberti, J., Valenzuela, J. G., Carruthers, V. B., Hieny, S., Andersen, J., Charest, H., Sousa, C. R. E., Fairlamb, A., Ribeiro, J. M. & Sher, A. (2003). Molecular mimicry of a CCR5 binding-domain in the microbial activation of dendritic cells. *Nat. Immunol.* **4**, 485–490.

136 Dutta, M., Delhi, P., Sinha, K. M., Banerjee, R. & Datta, A. K. (2001). Lack of abundance of cytoplasmic cyclosporin A-binding protein renders free-living *Leishmania donovani* resistant to cyclosporin A. *J. Biol. Chem.* **276**, 19294–19300.

137 Brown, C. R., Cui, D. Y., Hung, G. G. C. & Chiang, H. L. (2001). Cyclophilin a mediates Vid22p function in the import of fructose-1,6-bisphosphatase into vid vesicles. *J. Biol. Chem.* **276**, 48017–48026.

138 Taylor, P., Husi, H., Kontopidis, G. & Walkinshaw, M. D. (1997). Structures of cyclophilin-ligand complexe. *Prog. Biophys. Mol. Biol.* **67**, 155–181.

139 Huai, Q., Kim, H. Y., Liu, Y. D., Zhao, Y. D., Mondragon, A., Liu, J. O. & Ke, H. M. (2002). Crystal structure of calcineurin-cyclophilin-cyclosporin shows common but distinct recognition of immunophilin-drug complexes. *Proc. Natl. Acad. Sci. USA* **99**, 12037–12042.

140 Jin, L. & Harrison, S. C. (2002). Crystal structure of human calcineurin complexed with cyclosporin A and human cyclophilin. *Proc. Natl. Acad. Sci. USA* **99**, 13522–13526.

141 Gamble, T. R., Vajdos, F. F., Yoo, S. H., Worthylake, D. K., Houseweart, M., Sundquist, W. I. & Hill, C. P. (1996). Crystal structure of human cyclophilin A bound to the amino-terminal domain of HIV-1 capsid. *Cell* **87**, 1285–1294.

142 Zhao, Y. D., Chen, Y. Q., Schutkowski, M., Fischer, G. & Ke, H. M. (1997). Cyclophilin A complexed with a fragment of HIV-1 gag protein – insights into HIV-1 infectious activity. *Structure* **5**, 139–146.

143 Franke, E. K., Yuan, H. E. H. & Luban, J. (1994). Specific incorpora-

tion of cyclophilin A into HIV-1 virions. *Nature* **371**, 359–362.

144 Ou, W. B., Luo, W., Park, Y. D. & Zhou, H. M. (2001). Chaperone-like activity of peptidyl-prolyl *cis/trans* isomerase during creatine kinase refolding. *Protein Sci.* **10**, 2346–2353.

145 Kern, G., Kern, D., Schmid, F. X. & Fischer, G. (1995). A kinetic analysis of the folding of human carbonic anhydrase II and its catalysis by cyclophilin. *J. Biol. Chem.* **270**, 740–745.

146 Bosco, D. A., Eisenmesser, E. Z., Pochapsky, S., Sundquist, W. I. & Kern, D. (2002). Catalysis of *cis/trans* isomerization in native HIV-1 capsid by human cyclophilin A. *Proc. Natl. Acad. Sci. USA* **99**, 5247–5252.

147 Reimer, U., Drewello, M., Jakob, M., Fischer, G. & Schutkowski, M. (1997). Conformational state of a 25-mer peptide from the cyclophilin-binding loop of the HIV type 1 capsid protein. *Biochem. J.* **326**, 181–185.

148 Towers, G. J., Hatziioannou, T., Cowan, S., Goff, S. P., Luban, J. & Bieniasz, P. D. (2003). Cyclophilin A modulates the sensitivity of HIV-1 to host restriction factors. *Nat. Med.* **9**, 1138–1143.

149 Schmid, F. X. (2002). Prolyl isomerases. *Adv. Prot. Chem.* **59**, 243–282.

150 Chiti, F., Mangione, P., Andreola, A., Giorgetti, S., Stefani, M., Dobson, C. M., Bellotti, V. & Taddei, N. (2001). Detection of two partially structured species in the folding process of the amyloidogenic protein beta 2-microglobulin. *J. Mol. Biol.* **307**, 379–391.

151 Golbik, R., Fischer, G. & Fersht, A. R. (1999). Folding of barstar C40A/C82A/P27A and catalysis of the peptidyl-prolyl *cis/trans* isomerization by human cytosolic cyclophilin (Cyp18). *Protein Sci.* **8**, 1505–1514.

152 Veeraraghavan, S., Nall, B. T. & Fink, A. L. (1997). Effect of prolyl isomerase on the folding reactions of staphylococcal nuclease. *Biochemistry* **36**, 15134–15139.

153 Reader, J. S., Van Nuland, N. A. J., Thompson, G. S., Ferguson, S. J., Dobson, C. M. & Radford, S. E. (2001). A partially folded intermediate species of the beta-sheet protein apo-pseudoazurin is trapped during proline-limited folding. *Protein Sci.* **10**, 1216–1224.

154 Martin, A. & Schmid, F. X. (2003). A proline switch controls folding and domain interactions in the gene-3-protein of the filamentous phage fd. *J. Mol. Biol.* **331**, 1131–1140.

155 Altamirano, M. M., Garcia, C., Possani, L. D. & Fersht, A. R. (1999). Oxidative refolding chromatography: folding of the scorpion toxin Cn5. *Nature Biotechnol.* **17**, 187–191.

156 Altamirano, M. M., Woolfson, A., Donda, A., Shamshiev, A., Briseno-Roa, L., Foster, N. W., Veprintsev, D. B., De Libero, G., Fersht, A. R. & Milstein, C. (2001). Ligand-independent assembly of recombinant human CD1 by using oxidative refolding chromatography. *Proc. Natl. Acad. Sci. USA* **98**, 3288–3293.

157 Karadimitris, A., Gadola, S., Altamirano, M., Brown, D., Woolfson, A., Klenerman, P., Chen, J. L., Koezuka, Y., Roberts, I. A. G., Price, D. A., Dusheiko, G., Milstein, C., Fersht, A., Luzzatto, L. & Cerundolo, V. (2001). Human CD1d-glycolipid tetramers generated by in vitro oxidative refolding chromatography. *Proc. Natl. Acad. Sci. USA* **98**, 3294–3298.

158 Schutkowski, M., Wöllner, S. & Fischer, G. (1995). Inhibition of peptidyl-prolyl *cis/trans* isomerase activity by substrate analog structures: Thioxo tetrapeptide-4-nitroanilides. *Biochemistry* **34**, 13016–13026.

159 Sanglier, J. J., Quesniaux, V., Fehr, T., Hofmann, H., Mahnke, M., Memmert, K., Schuler, W., Zenke, G., Gschwind, L., Maurer, C. & Schilling, W. (1999). Sanglifehrins A, B, C and D, novel cyclophilin-binding compounds isolated from *Streptomyces* sp A92-308110-I. Taxonomy, fermentation, isolation and biological activity. *J. Antibiot.* **52**, 466–473.

160 Sedrani, R., Kallen, J., Cabrejas, L. M. M., Papageorgiou, C. D., Senia, F., Rohrbach, S., Wagner, D., Thai, B., Eme, A. M. J., France, J., Oberer, L., Rihs, G., Zenke, G. & Wagner, J. (2003). Sanglifehrin-cyclophilin interaction: Degradation work, synthetic macrocyclic analogues, X-ray crystal structure, and binding data. *J. Am. Chem. Soc.* **125**, 3849–3859.

161 Zhang, L. H. & Liu, J. O. (2001). Sanglifehrin A, a novel cyclophilin-binding immunosuppressant, inhibits IL-2-dependent T cell proliferation at the G(1) phase of the cell cycle. *J. Immunol.* **166**, 5611–5618.

162 Wu, Y. Q., Belyakov, S., Choi, C., Limburg, D., Thomas, B. E., Vaal, M., Wei, L., Wilkinson, D. E., Holmes, A., Fuller, M., McCormick, J., Connolly, M., Moeller, T., Steiner, J. & Hamilton, G. S. (2003). Synthesis and biological evaluation of non-peptidic cyclophilin ligands. *J. Med. Chem.* **46**, 1112–1115.

163 Demange, L., Moutiez, M. & Dugave, C. (2002). Synthesis and evaluation of Gly psi(PO2R-N)pro-containing pseudopeptides as novel inhibitors of the human cyclophilin hCyp-18. *J. Med. Chem.* **45**, 3928–3933.

164 Wang, H. C., Kim, K., Bakhtiar, R. & Germanas, J. P. (2001). Structure-activity studies of ground- and transition-state analogue inhibitors of cyclophilin. *J. Med. Chem.* **44**, 2593–2600.

165 Maruyama, T. & Furutani, M. (2000). Archaeal peptidyl-prolyl *cis/trans* isomerases (PPIases). *Front. Biosci.* **5**, D821–D836.

166 Avramut, M. & Achim, C. L. (2002). Immunophilins and their ligands: insights into survival and growth of human neurons. *Physiol. Behav.* **77**, 463–468.

167 Walensky, L. D., Dawson, T. M., Steiner, J. P., Sabatini, D. M., Suarez, J. D., Klinefelter, G. R. & Snyder, S. H. (1998). The 12 kD FK506 binding protein FKBP12 is released in the male reproductive tract and stimulates sperm motility. *Mol. Med.* **4**, 502–514.

168 Leiva, M. C. & Lyttle, C. R. (1992). Leukocyte chemotactic activity of FKBP and inhibition by FK506. *Biochem. Biophys. Res. Commun.* **186**, 1178–1183.

169 Veeraraghavan, S., Holzman, T. F. & Nall, B. T. (1996). Autocatalyzed protein folding. *Biochemistry* **35**, 10601–10607.

170 Scholz, C., Zarnt, T., Kern, G., Lang, K., Burtscher, H., Fischer, G. & Schmid, F. X. (1996). Autocatalytic folding of the folding catalyst FKBP12. *J. Biol. Chem.* **271**, 12703–12707.

171 Deivanayagam, C. C. S., Carson, M., Thotakura, A., Narayana, S. V. L. & Chodavarapu, R. S. (2000). Structure of FKBP12.6 in complex with rapamycin. *Acta Crystallogr. D Biol. Crystallogr.* **56**, 266–271.

172 Soman, K. V., Hanks, B. A., Tien, H., Chari, M. V., Oneal, K. D. & Morrisett, J. D. (1997). Template-based docking of a prolactin receptor proline-rich motif octapeptide to FKBP12 – Implications for cytokine receptor signaling. *Protein Sci.* **6**, 999–1008.

173 Lam, E., Martin, M. M., Timerman, A. P., Sabers, C., Fleischer, S., Lukas, T., Abraham, R. T., Okeefe, S. J., Oneill, E. A. & Wiederrecht, G. J. (1995). A novel FK506 binding protein can mediate the immunosuppressive effects of FK506 and is associated with the cardiac ryanodine receptor. *J. Biol. Chem.* **270**, 26511–26522.

174 Park, S. T., Aldape, R. A., Futer, O., DeCenzo, M. T. & Livingston, D. J. (1992). PPIase catalysis by human FK506-binding protein proceeds through a conformational twist mechanism. *J. Biol. Chem.* **267**, 3316–3324.

175 Kirken, R. A. & Wang, Y. L. (2003). Molecular actions of sirolimus: Sirolimus and mTor. *Transplant. Proc.* **35**, 227S–230S.

176 Yang, W., Rozamus, L. W., Narula, S., Rollins, C. T., Yuan, R., Andrade, L. J., Ram, M. K., Phillips, T. B., van Schravendijk, M. R., Dalgarno, D., Clackson, T. & Holt,

D. A. (2000). Investigating protein-ligand interactions with a mutant FKBP possessing a designed specificity pocket. *J. Med. Chem.* **43**, 1135–1142.

177 Christner, C., Wyrwa, R., Marsch, S., Küllertz, G., Thiericke, R., Grabley, S., Schumann, D. & Fischer, G. (1999). Synthesis and cytotoxic evaluation of cycloheximide derivatives as potential inhibitors of FKBP12 with neuroregenerative properties. *J. Med. Chem.* **42**, 3615–3622.

178 Dragovich, P. S., Barker, J. E., French, J., Imbacuan, M., Kalish, V. J., Kissinger, C. R., Knighton, D. R., Lewis, C. T., Moomaw, E. W., Parge, H. E. & Pelletier, L. A. (1996). Structure-based design of novel, urea-containing FKBP12 inhibitors. *J. Med. Chem.* **39**, 1872–1884.

179 Burkhard, P., Taylor, P. & Walkinshaw, M. D. (2000). X-ray structures of small ligand-FKBP complexes provide an estimate for hydrophobic interaction energies. *J. Mol. Biol.* **295**, 953–962.

180 Wei, L., Wu, Y. Q., Wilkinson, D. E., Chen, Y., Soni, R., Scott, C., Ross, D. T., Guo, H., Howorth, P., Valentine, H., Liang, S., Spicer, D., Fuller, M., Steiner, J. & Hamilton, G. S. (2002). Solid-phase synthesis of FKBP12 inhibitors: N-sulfonyl and N-carbamoylprolyl/pipecolyl amides. *Bioorg. Med. Chem. Lett.* **12**, 1429–1433.

181 Hamilton, G. S., Huang, W., Connolly, M. A., Ross, D. T., Guo, H., Valentine, H. L., Suzdak, P. D. & Steiner, J. P. (1997). FKBP12-binding domain analogues of FK506 are potent, nonimmunosuppressive neurotrophic agents in vitro and promote recovery in a mouse model of Parkinsons-disease. *Bioorg. Med. Chem. Lett.* **7**, 1785–1790.

182 Yamashita, D. S., Oh, H. J., Yen, H. K., Bossard, M. J., Brandt, M., Levy, M. A., Newmantarr, T., Badger, A., Luengo, J. I. & Holt, D. A. (1994). Design, synthesis and evaluation of dual domain FKBP ligands. *Bioorg. Med. Chem. Lett.* **4**, 325–328.

183 Holt, D. A., Luengo, J. I., Yamashita, D. S., Oh, H. J., Konialian, A. L., Yen, H. K., Rozamus, L. W., Brandt, M., Bossard, M. J., Levy, M. A., Eggleston, D. S., Liang, J., Schultz, L. W., Stout, T. J. & Clardy, J. (1993). Design, synthesis, and kinetic evaluation of high-affinity FKBP ligands and the X-ray crystal structures of their complexes with FKBP12. *J. Am. Chem. Soc.* **115**, 9925–9938.

184 Connelly, P. R., Aldape, R. A., Bruzzese, F. J., Chambers, S. P., Fitzgibbon, M. J., Fleming, M. A., Itoh, S., Livingston, D. J., Navia, M. A., Thomson, J. A. & Wilson, K. P. (1994). Enthalpy of hydrogen bond formation in a protein-ligand binding reaction. *Proc. Natl. Acad. Sci. USA* **91**, 1964–1968.

185 Aghdasi, B., Ye, K. Q., Resnick, A., Huang, A., Ha, H. C., Guo, X., Dawson, T. M., Dawson, V. L. & Snyder, S. H. (2001). FKBP12, the 12-kDa FK506-binding protein, is a physiologic regulator of the cell cycle. *Proc. Natl. Acad. Sci. USA* **98**, 2425–2430.

186 Shou, W. N., Aghdasi, B., Armstrong, D. L., Guo, Q. X., Bao, S. D., Charng, M. J., Mathews, L. M., Schneider, M. D., Hamilton, S. L. & Matzuk, M. M. (1998). Cardiac defects and altered ryanodine receptor function in mice lacking FKBP12. *Nature* **391**, 489–492.

187 Xin, H. B., Senbonmatsu, T., Cheng, D. S., Wang, Y. X., Copello, J. A., Ji, G. J., Collier, M. L., Deng, K. Y., Jeyakumar, L. H., Magnuson, M. A., Inagami, T., Kotlikoff, M. I. & Fleischer, S. (2002). Oestrogen protects FKBP12.6 null mice from cardiac hypertrophy. *Nature* **416**, 334–337.

188 Dargan, S. L., Lea, E. J. A. & Dawson, A. P. (2002). Modulation of type-1 Ins(1,4,5)P-3 receptor channels by the FK506-binding protein, FKBP12. *Biochem. J.* **361**, 401–407.

189 Marks, A. R. (2002). Ryanodine receptors, FKBP12, and heart failure. *Front. Biosci.* **7**, D970–D977.

190 Chen, Y. G., Liu, F. & Massague, J. (1997). Mechanism of TBF-beta receptor inhibition by FKBP12. *EMBO J.* **16**, 3866–3876.

191 Lopezilasaca, M., Schiene, C., Küllertz, G., Tradler, T., Fischer, G. & Wetzker, R. (1998). Effects of FK506-binding protein 12 and FK506 on autophosphorylation of epidermal growth factor receptor. *J. Biol. Chem.* **273**, 9430–9434.

192 Dolinski, K. J. & Heitman, J. (1999). Hmo1p, a high mobility group 1/2 homolog, genetically and physically interacts with the yeast FKBP12 prolyl isomerase. *Genetics* **151**, 935–944.

193 Alarcon, C. M. & Heitman, J. (1997). FKBP12 physically and functionally interacts with aspartokinase in *Saccharomyces cerevisiae*. *Mol. Cell. Biol.* **17**, 5968–5975.

194 Chambraud, B., Radanyi, C., Camonis, J. H., Shazand, K., Rajkowski, K. & Baulieu, E. E. (1996). FAP48, a new protein that forms specific complexes both immunophilins FKBP59 and FKBP12 – prevention by the immunosuppressant drugs FK506 and rapamycin. *J. Biol. Chem.* **271**, 32923–32929.

195 Brouillard, P., Boon, L. M., Mulliken, J. B., Enjolras, O., Ghassibe, M., Warman, M. L., Tan, O. T., Olsen, B. R. & Vikkula, M. (2002). Mutations in a novel factor, glomulin, are responsible for glomuvenous malformations ("glomangiomas"). *Am. J. Hum. Genet.* **70**, 866–874.

196 Yang, W. M., Inouye, C. J. & Seto, E. (1995). Cyclophilin A and FKBP12 interact with YY1 and alter its transcriptional activity. *J. Biol. Chem.* **270**, 15187–15193.

197 Faure, J. D., Gingerich, D. & Howell, S. H. (1998). An *Arabidopsis* immunophilin, atFKBP12, binds to atFIP37 (FKBP interacting protein) in an interaction that is disrupted by FK506. *Plant J.* **15**, 783–789.

198 Jeyakumar, L. H., Ballester, L., Cheng, D. S., McIntyre, J. O., Chang, P., Olivey, H. E., Rollins-Smith, L., Barnett, J. V., Murray, K., Xin, H. B. & Fleischer, S. (2001). FKBP binding characteristics of cardiac microsomes from diverse vertebrates. *Biochem. Biophys. Res. Commun.* **281**, 979–986.

199 Xin, H. B., Rogers, K., Qi, Y., Kanematsu, T. & Fleischer, S. (1999). Three amino acid residues determine selective binding of FK506-binding protein 12.6 to the cardiac ryanodine receptor. *J. Biol. Chem.* **274**, 15315–15319.

200 Prestle, J., Janssen, P. M. L., Janssen, A. P., Zeitz, O., Lehnart, S. E., Bruce, L., Smith, G. L. & Hasenfuss, G. (2001). Overexpression of FK506-Binding protein FKBP12.6 in cardiomyocytes reduces ryanodine receptor-mediated Ca^{2+} leak from the sarcoplasmic reticulum and increases contractility. *Circ. Res.* **88**, 188–194.

201 Gaburjakova, M., Gaburjakova, J., Reiken, S., Huang, F., Marx, S. O., Rosemblit, N. & Marks, A. R. (2001). FKBP12 binding modulates ryanodine receptor channel gating. *J. Biol. Chem.* **276**, 16931–16935.

202 Yano, M., Ono, K., Ohkusa, T., Suetsugu, M., Kohno, M., Hisaoka, T., Kobayashi, S., Hisamatsu, Y., Yamamoto, T., Noguchi, N., Takasawa, S., Okamoto, H. & Matsuzaki, M. (2000). Altered stoichiometry of FKBP12.6 versus ryanodine receptor as a cause of abnormal Ca^{2+} leak through ryanodine receptor in heart failure. *Circulation* **102**, 2131–2136.

203 George, C. H., Sorathia, R., Bertrand, B. M. A. & Lai, F. A. (2003). In situ modulation of the human cardiac ryanodine receptor (hRyR2) by FKBP12.6. *Biochem. J.* **370**, 579–589.

204 Rahfeld, J. U., Schierhorn, A., Mann, K. & Fischer, G. (1994). A novel peptidyl-prolyl *cis/trans* isomerase from *Escherichia coli*. *FEBS Lett.* **343**, 65–69.

205 Rahfeld, J. U., Rücknagel, K. P., Schelbert, B., Ludwig, B., Hacker, J., Mann, K. & Fischer, G. (1994). Confirmation of the existence of a third family among peptidyl-prolyl

cis/trans isomerases – Amino acid sequence and recombinant production of parvulin. *FEBS Lett.* **352**, 180–184.

206 Yao, J. L., Kops, O., Lu, P. J. & Lu, K. P. (2001). Functional conservation of phosphorylation-specific prolyl isomerases in plants. *J. Biol. Chem.* **276**, 13517–13523.

207 Landrieu, I., Wieruszeski, J. M., Wintjens, R., Inze, D. & Lippens, G. (2002). Solution structure of the single-domain prolyl *cis/trans* isomerase PIN1At from *Arabidopsis thaliana*. *J. Mol. Biol.* **320**, 321–332.

208 Ray, W. C., Munson, R. S, & Daniels, C. J. (2001). Tricross: using dot-plots in sequence-id space to detect uncataloged intergenic features. *Bioinformatics* **17**, 1105–1112.

209 Scholz, C., Rahfeld, J., Fischer, G. & Schmid, F. X. (1997). Catalysis of protein folding by parvulin. *J. Mol. Biol.* **273**, 752–762.

210 Rouviere, P. E. & Gross, C. A. (1996). SurA, a periplasmic protein with peptidyl-prolyl isomerase activity, participates in the assembly of outer membrane porins. *Genes Dev.* **10**, 3170–3182.

211 Bitto, E. & McKay, D. B. (2002). Crystallographic structure of SurA, a molecular chaperone that facilitates folding of outer membrane porins. *Structure* **10**, 1489–1498.

212 Terada, T., Shirouzu, M., Fukumori, Y., Fujimori, F., Ito, Y., Kigawa, T., Yokoyama, S. & Uchida, T. (2001). Solution structure of the human parvulin-like peptidyl-prolyl *cis/trans* isomerase, hPar14. *J. Mol. Biol.* **305**, 917–926.

213 Ranganathan, R., Lu, K. P., Hunter, T. & Noel, J. P. (1997). Structural and functional analysis of the mitotic rotamase Pin1 suggests substrate recognition is phosphorylation dependent. *Cell* **89**, 875–886.

214 Ryo, A., Liou, Y. C., Lu, K. P. & Wulf, G. (2003). Prolyl isomerase Pin1: a catalyst for oncogenesis and a potential therapeutic target in cancer. *J. Cell Sci.* **116**, 773–783.

215 Maleszka, R., Lupas, A., Hanes, S. D. & Miklos, G. L. G. (1997). The dodo gene family encodes a novel protein involved in signal transduction and protein folding. *Gene* **203**, 89–93.

216 Hsia, C, Y., Ganshaw, G., Paech, C. & Murray, C, J. (1996) Active-site titration of serine proteases using a fluoride ion selective electrode and sulfonyl fluoride inhibitors. *Anal. Biochem.* **242**, 221–227.

217 Fischer, G., Wittmann Liebold, B., Lang, K.; Kiefhaber, T. & Schmid, F. X. (1989). Cyclophilin and peptidyl-prolyl *cis/trans* isomerase are probably identical proteins. *Nature* **337**, 476–478.

218 Kofron, J. L., Kuzmic, P., Kishore, V., Colon Bonilla, E. & Rich, D. H. (1991). Determination of kinetic constants for peptidyl-prolyl *cis/trans* isomerases by an improved spectrophotometric assay. *Biochemistry* **30**, 6127–6134.

11
Secondary Amide Peptide Bond *cis*/*trans* Isomerization in Polypeptide Backbone Restructuring: Implications for Catalysis

Cordelia Schiene-Fischer and Christian Lücke

11.1
Introduction

As a recurring element in the polypeptide backbone, peptide bonds occur at a high molar concentration in cells and tissues. The ability of the nitrogen lone electron pair to delocalize over the entire secondary amide moiety results in planarity and enhanced barriers to rotation of the C–N bond. The resonance stabilization of the planar moiety causes restrictions in the number of energy minima with respect to the torsional movements characterized by the dihedral angle ω. The *cis* conformation ($\omega \approx 0^\circ$) is separated from the *trans* conformation ($\omega \approx 180^\circ$) by a rotational barrier much higher than that found for neighboring covalent bonds [1]. Analyses of protein dynamics have revealed the significance of the rigidity of the peptide bond, which is flanked on either side by mobile single bonds forming a crucial folding unit of proteins.

Peptidyl-prolyl *cis*/*trans* isomerases (PPIases) have evolved to accelerate the interconversion between the *cis* and *trans* conformation, but catalysis is restricted to the imidic bond that is formed at the N-terminal side of prolyl residues [2]. The Hsp70 protein DnaK was identified as the first member of the novel enzyme class of secondary amide peptide bond *cis*/*trans* isomerases (APIases), which selectively accelerate the *cis*/*trans* isomerization of secondary amide peptide bonds formed by 19 out of the 20 gene-coded amino acids [3]. In contrast to prolyl bonds, these peptide linkages occur in *cis* conformation for only a minor fraction of oligopeptide molecules in solution. The close proximity of two neighboring Cα atoms in the *cis* conformation has been associated with the low percentage of the secondary amide *cis* peptide bonds, as steric strain is released in the *trans* isomer. Due to a large number of well-defined intramolecular contacts under native conditions, proteins usually exhibit each peptide bond in a defined conformational state, either *cis* or *trans*, unless the peculiarity of the tertiary structure favors native-state isomerization [4]. In a non-redundant set of 571 proteins, 5.2% of the prolyl bonds are in *cis* conformation, whereas only 0.03% secondary amide *cis* peptide bonds are found [5].

Surprisingly, the free-energy difference of the rotational barriers between imidic bonds and secondary amide peptide bonds is rather small. $\Delta\Delta G^{\neq}$ amounts to 5–

Protein Folding Handbook. Part II. Edited by J. Buchner and T. Kiefhaber

ISBN: 3-527-30784-2

10 kJ mol^{-1} in structurally related oligopeptides at 25 °C, with the higher barriers found for the prolyl bonds [6–8]. In both cases, the low spontaneous rate of *cis*/*trans* isomerization indicates the potential importance of these interconversions as rate-limiting steps in protein backbone rearrangements. Hence, an enzymatic acceleration of this isomerization may be required to avoid accumulation of folding intermediates susceptible to aggregation.

Critical steps in protein folding include rotations about peptide bonds. Thus, frequent occurrence of slow kinetic folding phases with high activation enthalpies $\Delta H^{\neq}$ suggests that prolyl bond *cis*/*trans* isomerization may be of considerable significance [9–12]. Similarly, secondary amide *cis* peptide bonds in the native state have been found to cause slow steps in the folding kinetics for virtually all molecules of the proteins involved [13, 14]. Generally, secondary amide peptide bonds in *cis* conformation may be more common in native proteins than usually suspected, as their existence may be overlooked by the refinement algorithms [15]. These bonds often occur at positions critical to biological function. Some locations were found to be close to active sites, and others correspond to reactive linkages [16–20]. It has been hypothesized that the sterically constrained geometry associated with *cis* peptide bonds is able to provide potential energy to molecular reactions [18]. However, supporting experimental evidence is still lacking.

Most importantly, the directed bond rotation involved in the mechanism of *cis*/*trans* interconversion might represent a general feature of folding proteins since the barrier to rotation restricts the backbone mobility of a narrow region of the folding chain. The rotational frequency is determined by the sum of the "*cis* to *trans*" and the "*trans* to *cis*" rate constants in the unfolded and partially folded chains. Thus, a high *cis*/*trans* ratio in the native state, usually assumed as being critical for the contribution of *cis* secondary amide peptide bonds in refolding, is not considered essential [21, 22].

11.2 Monitoring Secondary Amide Peptide Bond *cis*/*trans* Isomerization

Detection of secondary amide peptide bond *cis*/*trans* isomerization in oligopeptides is usually hampered by the small amount of *cis* isomer in equilibrium and the half-time of re-equilibration of about 1 s at 25 °C. By using dynamic NMR spectroscopy, *cis*/*trans* isomerization rates of peptide bonds in the unperturbed equilibrium can be detected in water under neutral conditions, provided that the respective isomers display NMR signals at sufficiently different chemical shift values. The spontaneous interconversion of the peptide bond conformers proved to be slow on the NMR timescale. Analyses of proline-free oligopeptides (-Ala-Tyr/Phe-Ala-) showed two well-separated β-methyl proton resonances for alanyl residues located next to an aromatic amino acid, indicating conformational heterogeneity. In fact, the aromatic ring current shifts the methyl signal of the *cis* isomer upfield ($|\Delta\delta| \approx$

0.5 ppm) into an empty region of the ^{1}H spectrum. Exchange cross-peaks in two-dimensional nuclear Overhauser enhancement and exchange spectroscopy (NOESY) spectra between the minor and major alanine methyl signals are direct evidence for the existence of interconverting conformers (see the Section 11.6). High-resolution NMR techniques such as magnetization transfer experiments, line-shape analysis, and exchange spectroscopy can be utilized for the quantification of this kind of conformational dynamics [6].

Spectral differences in the UV region between the *cis* and *trans* isomers have been reported for the zwitterionic dipeptide Gly-Gly. This difference is greatest at 216 nm but exhibits an optimal signal-to-noise ratio at 220 nm. It can be utilized to study the kinetics of the *cis*/*trans* isomerization directly. The re-equilibration of the Gly-Gly isomers after pH jump from pH 2.0 to 7.5 is a first-order reaction and can be monitored with a stopped-flow spectrophotometer at 220 nm. The reverse signal, monitored for a pH jump from pH 7.5 to 2.0, demonstrated the reversibility of the spectral changes. The pH-jump technique can also be used for dipeptides consisting of residues other than glycine. It is thus useful to search for enzymes that catalyze the *cis*/*trans* isomerization of secondary amide peptide bonds. The reaction can be monitored even in the presence of crude protein extracts [7].

The O/S one-atom substitution of the carbonyl oxygen (C=O to C=S) in secondary amide peptide bonds results in isosteric peptide bonds. The $\pi \rightarrow \pi^*$(C=S) thioxo amide UV absorption is red-shifted relative to the $\pi \rightarrow \pi^*$(C=O) absorption. In zwitterionic thioxo peptide bonds (denoted as -ψ[CS-NH]-), the spectral difference between the *cis* and *trans* isomers is especially large. In addition, a light pulse will allow controlled triggering of the *cis*/*trans* isomerization. Large spectroscopic changes can be observed upon irradiation at 254 nm or laser irradiation at 337 nm, which is based on the absorption resulting from the $n \rightarrow \pi^*$ excitation of the thioxo carbonyl group. A large increase of the *cis* isomer content in the photostationary state, as recorded by NMR spectroscopy and capillary electrophoresis, and a slow thermal re-equilibration rate characterize the O to S substitution in a peptide unit. Thus, irradiation of a thioxo peptide bond provides a predictable conformational switch for a narrow segment of a polypeptide chain [43].

For thioxo dipeptides, the kinetics of the *cis*/*trans* isomerization can also be studied at 290 nm by alteration of the ionization state through pH jump. For proteins with a *cis* peptide bond in the native state, secondary amide peptide bond *cis*/*trans* isomerizations could be characterized both in the unfolded state and during refolding. The *trans* to *cis* isomerization could be measured directly by intrinsic fluorescence changes, which reflect the rate of slow folding [13, 14]. The kinetic parameters of the *cis* to *trans* isomerization after unfolding could be measured in double-mixing experiments (unfolding followed by refolding), since unfolded molecules that still contain the *cis* isomer refold rapidly [13]. The *cis*/*trans* equilibration in the unfolded form of a protein with all-*trans* peptide bonds in the native form after conformational unfolding was demonstrated for a proline-free tendamistat variant by the appearance of a slow refolding phase [21]. Again, double mixing (unfolding followed by refolding) was used in these experiments.

11.3 Kinetics and Thermodynamics of Secondary Amide Peptide Bond *cis/trans* Isomerization

Simple *N*-alkyl-substituted secondary amides such as *N*-methylformamide and *N*-methylacetamide have often been used as models to study the conformational characteristics of the peptide backbone. Equilibrium constants for the *cis*/*trans* isomerization determined by NMR methods agree with molecular mechanics calculations and Monte Carlo simulations that point to a rather low percentage of the *cis* isomer [23]. *N*-methylformamide exists as *cis* isomer to the extent of 8% in D_2O and 10.3% in $CDCl_3$. In *N*-methylacetamide, which more closely resembles a peptide unit, a free-energy difference of about 10.5 kJ mol^{-1} between the *trans* and *cis* isomers – corresponding to 1.5% *cis* isomer at equilibrium – has been detected in D_2O. Nonpolar solvents do not cause a significant alteration [24].

In the dipeptide Ala-Tyr, the *cis* content depends on the protonation states of the amino and carboxyl groups. The maximal *cis* fraction of 0.41% occurs in the zwitterionic state of the molecule, decreasing below the pK_a of the carboxyl group and above the pK_a of the amino group. The pH dependence of the *cis* content suggests that oppositely charged groups close to the isomerizing bond lead to enhanced *cis* populations. ^{13}C-NMR spectra revealed a *cis* population of 1.0% for the zwitterionic form of Gly-Gly. This value agrees with the estimate of 0.5% *cis* Gly-Gly detected in UV resonance Raman experiments [25].

Elongation of the peptide at both ends decreases the *cis* content of the central peptide bond by favoring the *trans* isomer with about 3 kJ mol^{-1}. The *cis* populations of the Ala2-Tyr3 and Tyr3-Ala4 bonds of the pentapeptide Ala-Ala-Tyr-Ala-Ala have been determined to be 0.14% and 0.11%, respectively [6]. These values approach the value of 0.1% *cis* Ala-Ala, as estimated by conformational energy calculations for the center of a peptide segment containing three peptide bonds [26]. Despite this rather low probability of *cis* isomers, the existence of at least one *cis* peptide bond fluctuating in an unstructured polypeptide chain of 1000 amino acid residues has to be considered.

Because the fraction of the *cis* isomer is so small, little is known about the isomerization kinetics. Rotational barriers of $\Delta G^{\neq} = 79$ kJ mol^{-1} (*cis* to *trans*) and $\Delta G^{\neq} = 89$ kJ mol^{-1} (*trans* to *cis*) have been determined for *N*-methylacetamide by NMR line-shape analysis of the *N*-methyl signals at 60 °C in water [27].

Peptide bond isomerization is a unimolecular process characterized by a first-order rate constant $k_{obs} = k_{cis\ to\ trans} + k_{trans\ to\ cis}$ for the reversible reaction. The equilibration of secondary amide peptide bonds, with rate constants of about 0.5 s^{-1} at 25 °C, is almost entirely determined by $k_{cis\ to\ trans}$, because the *cis* to *trans* isomerization is at least two orders of magnitude faster than the reverse reaction.

For Gly-Gly, an isomerization rate lower than 1.5 s^{-1} at 45 °C was estimated by ^{1}H-NMR. In support of this approximation, rate constants of about 0.3 s^{-1} at 25 °C were determined by directly monitoring the kinetics of the *cis*/*trans* isomerization of zwitterionic Gly-Gly following a pH jump. The Eyring activation enthalpy $\Delta H^{\neq}$ of 72 kJ mol^{-1} is in good agreement with the lower limit of 65 kJ mol^{-1} esti-

mated from line broadening in ^{1}H-NMR spectra. For Ala-Tyr the rate constants were determined to be $k_{cis\ to\ trans} = 0.57\ s^{-1}$ and $k_{trans\ to\ cis} = 2.4 \times 10^{-3}\ s^{-1}$ by NMR magnetization transfer experiments. As exemplified by Ala-Phe, $k_{cis\ to\ trans}$ is pH-independent between pH 4.5 and pH 8.6 [6, 7]. The activation enthalpies $\Delta H^{\neq}$ of the *cis*/*trans* isomerization of secondary amide peptide bonds are in a range typical of imidic peptide bond isomerizations [8]. Increasing the peptide chain length led to an increase of the isomerization rate and to a decrease of $\Delta H^{\neq}$ for the central peptide bonds.

Experimental data for the kinetics of *cis*/*trans* isomerization in entire proteins were mainly derived from protein variants, in which (1) a *cis* prolyl bond was replaced by a secondary amide bond and (2) the *cis* conformation was retained in the native state. This substitution usually results in structural destabilization of about 8–21 kJ mol^{-1} in comparison to the wild-type proteins, as reported for the carbonic anhydrase Pro202Ala variant [28], the bovine pancreatic ribonuclease A Pro93Ala variant [29, 30], the ribonuclease T_1 Pro39Ala variant [31, 32], and the TEM-1 β-lactamase Pro167Thr variant [14]. This effect was attributed to the unfavorable *cis*/*trans* ratio of the secondary amide peptide bonds in the unfolded state.

The rate constant $k_{cis\ to\ trans}$ of the Tyr92-Ala93 bond of the ribonuclease A Pro93Ala variant in the unfolded state was found to be 0.702 s^{-1} at 15 °C [33]. For the ribonuclease T_1 Pro39Ala variant with the *cis* Tyr38-Ala39 bond in the native state, rate constants for the *cis* to *trans* isomerization of 0.9–1.4 s^{-1}, depending on the GdmCl concentration present in the unfolding reaction, were detected in the unfolded protein by double-mixing experiments at 25 °C. The *trans* to *cis* isomerization of the Tyr38-Ala39 bond leads to a slow refolding phase in a partially structured folding intermediate. It is characterized by a rate constant of 4×10^{-3} s^{-1} at 25 °C [13]. During the refolding of the TEM-1 β-lactamase Pro167Thr variant, the *cis* Glu166-Thr167 bond is formed with a rate constant between 1×10^{-3} and 4×10^{-3} s^{-1} [14]. These *trans* to *cis* isomerization rates resemble those obtained for the oligopeptides, although the *cis*/*trans* ratio differs considerably between these folded proteins and the unstructured peptide chains. Evidently, the *trans* to *cis* isomerization rates do not provide a kinetic basis for the stability of the *cis* conformer in the native states of the ribonuclease T_1 and β-lactamase variants. A large part of the thermodynamic stability of the *cis* conformation has to originate from a considerable deceleration of the *cis* to *trans* isomerization in native proteins.

For the folding of proteins such as *Escherichia coli* dehydrofolate reductase [34] and staphylococcal nuclease [35], kinetic complications were encountered that have been discussed assuming conformational heterogeneity of the secondary amide peptide bonds.

Experimental proof for this hypothesis came from refolding data of a proline-free variant of the α-amylase inhibitor tendamistat. A fraction of the tendamistat variant molecules, with a tryptophan fluorescence amplitude of 5%, folds in a reaction assigned to the *cis* to *trans* isomerization of secondary amide peptide bonds. The activation energy of 51 kJ mol^{-1} and the reaction enthalpy of −29 kJ mol^{-1} are both in agreement with data obtained for oligopeptides. Interestingly, the denaturation of proline-free tendamistat in LiCl/trifluoroethanol leads, dependent on the

LiCl concentration, to a linear increase of the slow refolding fraction of the molecules. Lithium chloride in anhydrous trifluoroethanol, which has already been shown to increase the *cis* content of prolyl bonds [36], evidently is able to increase the *cis* content of secondary amide peptide bonds as well. The *cis* population of the Ala-Tyr bond of Ala-Ala-Tyr in LiCl/trifluoroethanol was determined to be 0.5% compared to 0.19% in aqueous solution. These data support the assumption that the conformational heterogeneity of secondary amide peptide bonds in the unfolded state of the protein is the cause for the slow refolding phase, which can also be found in the refolding of wild-type tendamistat [21].

The observed complex folding kinetics may originate from either a particular secondary amide peptide bond exhibiting an increased propensity for the *cis* conformation in the unfolded state or a certain level of *cis* isomer at any position of the peptide chain. A secondary amide peptide bond isomerization occurring randomly throughout the unfolded chain has already been suggested as a distinct reaction during refolding of proteins lacking secondary amide *cis* peptide bonds in the native state [37, 38]. Generally, the higher number of peptide bonds of larger proteins includes a statistical advantage in favor of a higher number of fluctuating *cis* peptide bonds in the whole polypeptide chain. For larger proteins this effect might cause more complex folding kinetics.

11.4 Principles of DnaK Catalysis

Cis/*trans* isomerization of peptide bonds has proved to be slow on the timescale of biorecognition involving polypeptides. A general possibility to accelerate peptide bond *cis*/*trans* isomerization in cells is enzyme catalysis. Indeed, the chaperone DnaK displays *cis*/*trans* isomerase activity toward secondary amide peptide bonds, but not towards prolyl bonds, and thus represents a novel class of enzymes that have been termed secondary amide peptide bond *cis*/*trans* isomerases (APIases) [3]. DnaK accelerates Ala-Ala dipeptide *cis*/*trans* isomerization, and the time courses are in accordance with the minimal model of an enzymatically catalyzed reversible reaction with a k_{cat}/K_M value of $3.5 \times 10^5\ M^{-1}\ s^{-1}$. The K_M and k_{cat} values are estimated at 8 mM and $3 \times 10^3\ s^{-1}$ (at 25 °C), respectively. Dose-dependent inhibition of the APIase activity of DnaK in the presence of the heptapeptide NRLLLTG or the undecapeptide RPKPQQFFGLM-NH_2 (substance P), which are known to be DnaK ligands, indicates that the catalysis occurs at or near the peptide-binding groove.

The APIase activity exhibits both regio- and stereoselectivity. DnaK catalysis displays subsite specificity for the C-terminal residue of the isomerizing peptide bond in a series of Ala-Xaa dipeptides. The best substrates were the dipeptides with Xaa = Met, Ala, and Ser, followed by Ala-Glu and Ala-Leu. Ile, Gly, and Lys in the position Xaa formed less-efficient substrates, whereas isomerizations in Asp, Tyr, Thr, Asn, Phe, Arg, Val, Gln, and Pro derivatives could not be catalyzed. Interestingly, the nature of the preferred subsites for catalysis flanking the reactive bond

is at variance with the hydrophobic core affinity sites, as concluded from a library of 13mer peptides [39]. Both studies survey different properties of DnaK. According to the enzyme transition-state complementarity, the k_{cat}/K_M values describe transition-state affinities. The affinity to matrix-bound peptides of a peptide library, on the other hand, may reveal ground-state binding, which is characterized by the microscopic dissociation constant K_s. Only leucine is a preferred residue for both properties, K_s and k_{cat}/K_M. The high relevance of steric features for catalysis can be inferred from the detrimental consequences of the C_β-branched hydrophobic residues Val, Ile, and Thr. The lack of catalysis of prolyl bonds is probably due to *N*-alkylation. Obviously, the APIase activity is an intrinsic property of the DnaK chain, closely resembling PPIase activity in its mechanistic consequences. Neither hydrolysis of ATP nor the presence of accessory proteins is imperative to the elementary step of catalysis of *cis*/*trans* isomerization. However, a functional overlap between APIase and PPIase substrate specificity has been excluded. Analysis of DnaK in PPIase assays displayed no PPIase activity, and for PPIases of different families such as human Cyp18, human FKBP12, and *Escherichia coli* Par10, no APIase activity was detected in the dipeptide assay [3].

As mentioned above, two-dimensional ^{1}H-NMR NOESY spectroscopy is the most sensitive NMR method for determining the dynamics of the conformational interconversion of peptide bonds neighboring aromatic amino acids. At 5 °C, the *cis*/*trans* isomerization rates of the Ala2-Tyr3 and the Tyr3-Ala4 bond of the pentapeptide Ala-Ala-Tyr-Ala-Ala become sufficiently slow to suppress the exchange cross-peaks. In the presence of 20 μM DnaK, however, the Ala2-Tyr3 exchange cross-peak reappears at this temperature, indicating a DnaK-mediated dynamic exchange between the *cis* and *trans* isomers (Figure 11.1). This DnaK-mediated acceleration of the *cis*/*trans* isomerization found for the Ala2-Tyr3 bond represents a lower limit due to the very high substrate concentration of 25 mM required for NMR measurements. Moreover, in addition to the two bonds that flank the tyrosine residue and can be monitored by NMR in their isomeric states, the substrate contains two additional peptide bonds that compete for the catalytic site of the enzyme. Usually, DnaK complemented with ATP, as well as its co-chaperones DnaJ and GrpE, is needed to perform successful protein renaturation experiments. The observed NOESY cross-peak intensities in the presence of the complete DnaK/DnaJ/GrpE/ATP system are similar for the Ala2-Tyr3 bond, but considerably larger for the Tyr3-Ala4 linkage, in comparison to the presence of DnaK alone. These data suggest an extension of the range of productive enzyme-substrate interactions by the complete chaperone mixture, leading to a more promiscuous enzyme specificity.

DnaK also catalyzes *cis*/*trans* isomerization in a partially folded protein. It accelerates the *trans* to *cis* isomerization of the Tyr38-Ala39 bond in the refolding of the ribonuclease T_1 Pro39Ala variant under conditions where partial folding precedes Tyr-Ala *trans* to *cis* isomerization.

The interrelation between APIase function and chaperone activity was examined in the DnaK/GrpE/DnaJ-assisted refolding of GdmCl-denatured firefly luciferase. In a series of peptide ligands of DnaK, APIase inhibition parallels the inhibi-

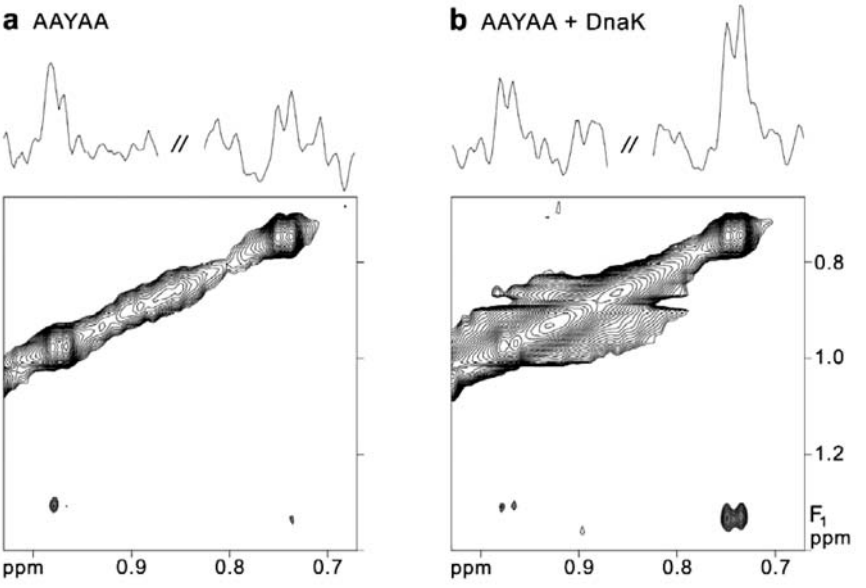

Fig. 11.1. *cis*-Alanine methyl region in the NOESY spectra of Ala-Ala-Tyr-Ala-Ala at 5 °C. The one-dimensional traces above the two-dimensional plots are taken along F_2 at the F_1 position of the correlated *trans* signals. (a) Peptide alone: the exchange cross-peaks at 0.74 ppm and 0.97 ppm in F_2 are assigned to the *cis*/*trans* isomerization of the Ala2-Tyr3 and the Tyr3-Ala4 peptide bond, respectively. (b) Peptide in the presence of 20 μM DnaK.

tion of chaperoning activity. This finding can be interpreted as an indication of a direct catalytic effect in the refolding of denatured proteins, since functional coupling of both folding probes is obvious. Remarkably, DnaK caused a concentration-dependent increase in the refolding yield and a concentration-independent lag phase in the refolding kinetics of luciferase. These data suggest the rapid formation of enzymatically inactive folding intermediates of luciferase, which are all captured in a metastable kinetic trap before they can reach their native conformation. The structure of most folding intermediates favors formation of aggregates. Absence of DnaK/GrpE/DnaJ/ATP is associated with a very slow rate of appearance of native luciferase via a productive folding intermediate, and only a very small fraction refolds productively. To describe the general features of the APIase-assisted refolding accelerated formation of a productive folding intermediate from aggregation-prone intermediates suffices to obtain increasing refolding yields [40].

Peptide bond *cis*/*trans* isomerases transiently initiate decreased torsional stiffness for a certain part of the polypeptide chain, while leaving other chain segments less flexible. As a consequence, these enzymes may mediate the reversal of local kinetic traps that can be detrimental to productive folding (Figure 11.2). DnaK may catalyze the isomerization at a large part of the secondary amide peptide bonds of a protein. However, it is not possible at present to assess the precise number of DnaK-catalyzable bond rotations. A single turnover of a substrate will affect

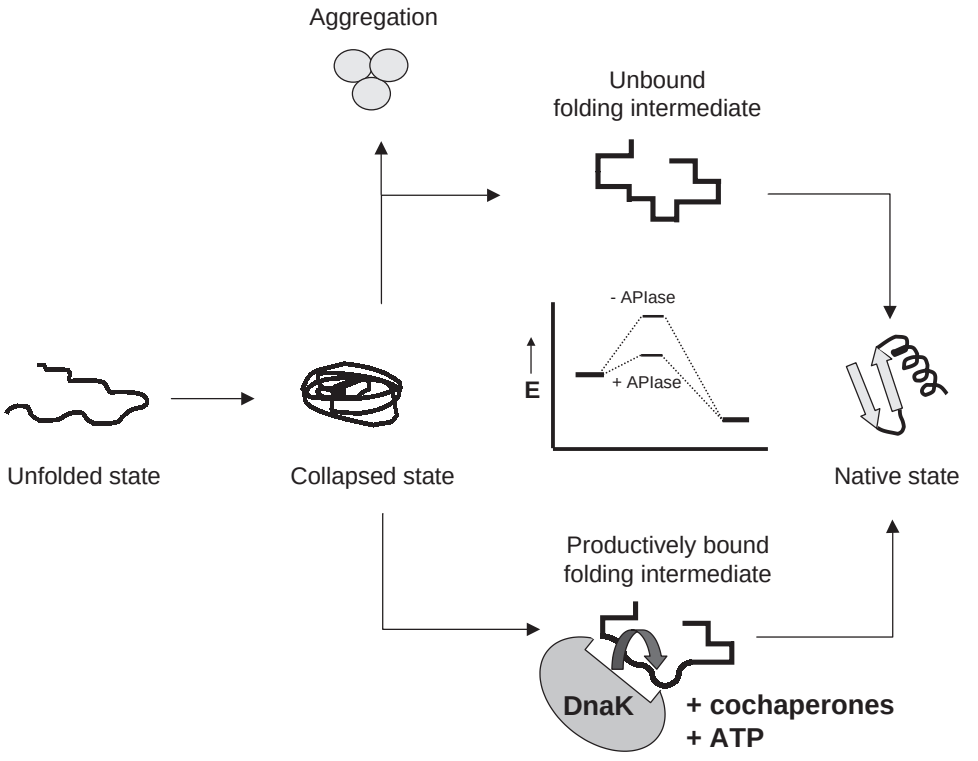

Fig. 11.2. Schematic model of the action of peptide bond *cis*/*trans* isomerases during refolding of a denatured protein. The action of DnaK involves scanning of the polypeptide chain by multiple attacks on peptide bonds. Thus, the torsional stiffness of a certain part of the polypeptide chain is decreased in a reaction intermediate. The function of ATP is to mediate release of the polypeptide chain in its folding-competent conformation from DnaK.

only a small polypeptide segment. Large k_{cat} values form the precondition for rapid scanning of peptide bonds throughout the entire polypeptide chain. Hence, a new catalytic function was proposed for DnaK: kinetic proofreading, which has been discussed previously for chaperone action [41], targets certain bonds in a specific context of amino acid residues. This catalytic process of bond rotation transiently abolishes the steric restrictions associated with the electronic structure of the peptide bond.

11.5 Concluding Remarks

Novel assays for the analysis of the *cis*/*trans* isomerization of secondary amide peptide bonds allowed the identification of DnaK as the first member of the enzyme

class of APIases. APIases strongly resemble PPIases in that they confer a loss of rotational restrictions, but at different positions in the polypeptide backbone. The major difference between these two enzyme classes lies in the nature of the targeted peptide bond. PPIases are specific to imidic linkages that are formed by the imino acid proline. In contrast, the Hsp70 protein DnaK catalyzes the isomerization at the much larger contingent of secondary amide peptide bonds. Based on the above-described results, we assume that in response to the APIase activity of DnaK, the high internal rotational barrier of a particular secondary amide peptide bond in a multiply bound polypeptide substrate will be decreased. As a consequence, a highly mobile structural unit that is confined by an extended, rigid backbone on both sides of the catalyzed bond will be generated. The resulting higher backbone flexibility may impede the formation of incorrect folds. A remaining challenge will be to analyze folding intermediates of proteins susceptible to APIase activity. Future studies are likely to involve the search for additional members of the APIase family, the identification of their catalytic mechanisms, and the search for specific inhibitors of these enzymes.

11.6 Experimental Protocols

11.6.1 Stopped-flow Measurements of Peptide Bond *cis/trans* Isomerization

Peptides can be purchased from Bachem (Heidelberg, Germany). Measurements are performed with a stopped-flow spectrophotometer (Applied Photophysics, Leatherhead, UK). The path length of the observation chamber should be 2 mm. For measurement of the peptide bond *cis/trans* isomerization of dipeptides, the peptides are dissolved in 50 mM sodium phosphate buffer at the appropriate pH (pH 2.0 for the pH jump to pH 7.5, where the zwitterionic form exists) to obtain a stock solution of 20–200 mM. The required pH is adjusted with dilute NaOH or phosphoric acid. Small differences in the final concentrations of the peptide may result from the pH adjustment but are unimportant for the assay.

The reaction is started by a 26-fold dilution of the peptides into 50 mM sodium phosphate buffer at the appropriate pH (pH 7.5 for the pH jump to the zwitterionic form or pH 2.0 for the reverse jump). (Examination of the resulting pH is highly recommended.) The time course of the reaction is monitored at 220 nm and 25 °C for 10 s. The time traces should be averages of at least five measurements. Data analysis is performed by single-exponential nonlinear regression using, e.g., the SigmaPlot scientific graphing system Version 8.0 (Jandel Corp., USA) to yield first-order rate constants $k_{c/t}$ of the *cis/trans* isomerizations.

To assay APIase activity of proteins, jumps from pH 2.0 to pH 7.5 are performed with the dipeptides as described above. Either protein fractions or pure proteins are added to the dilution buffer (12.5 mM Tris·HCl pH 8.0, 50 mM KCl, 11 mM $MgCl_2$) stored in the 2.5-mL syringe. To reduce the total absorbance at 220 nm,

the dipeptides are dissolved in water to obtain a concentration of 50 mM. The required pH of 2.0 is adjusted with dilute HCl. Check in controls that the final pH 7.5 is achieved.

11.6.2 Two-dimensional ^{1}H-NMR Exchange Experiments

The homonuclear, two-dimensional NOESY experiment provides a very sensitive method to detect the chemical exchange that occurs during peptide bond isomerization. The NOESY exchange cross-peaks observed between the *cis* and *trans* isomer forms are very low in intensity and can thus be clearly observed only in spectral regions that are devoid of other signals. In the case of the pentapeptide Ala-Ala-Tyr-Ala-Ala (25 mM in 12.5 mM Tris·HCl pH 7.1, 50 mM KCl, 11 mM $MgCl_2$, 90% H_2O/10% D_2O), the methyl proton resonance of Ala2 is considerably shifted upfield when the Ala2-Tyr3 peptide bond takes on the *cis* conformation, due to the ring-current effect of the neighboring Tyr3 side chain. Subsequently, the NOESY exchange cross-peak that represents the *cis*/*trans* interconversion appears at a resonance frequency where no other peaks occur in the spectrum of this peptide. This allows monitoring of the *cis*/*trans* isomerization rate under various conditions, even in the presence of substoichiometric amounts of DnaK or other proteins. To distinguish the DnaK-mediated isomer exchange from the spontaneous *cis*/*trans* interconversion of the pentapeptide at 20 °C, all spectra have to be collected at low temperature (5 °C), where the latter effect is too slow on the NMR timescale (300–410 ms mixing time) for the corresponding NOESY exchange cross-peaks to be observed.

Therefore, the magnetization transfer between the Ala2 methyl proton resonances of the *cis* and *trans* isomer forms directly reflects the isomerization rate [42]. In the NOESY experiment, this chemical exchange takes place almost exclusively during the mixing period, since the evolution time of the two-dimensional experiment is comparatively short relative to the mixing time (τ_m). Assuming that the rate constant (k) and the longitudinal relaxation rate (R_1) remain approximately the same in both isomer forms of the peptide, the exchange signal intensity at a constant τ_m is proportional to $(x_b - x_b{}^2)$, where x_b represents the mole fraction of the *cis* component. Hence, the signal intensity (I_{ab}) of the NOESY exchange cross-peak between the *trans* (a) and the *cis* (b) isomer form shows a parabolic dependence on the *cis* mole fraction, whereby $I_{ab} = f(x_b)$ lies very close to the inflection point at $x_b \sim 0.15\%$. At this rather low *cis* content (0.15% of a 25-mM pentapeptide concentration equals a 37.5-μM *cis* population), the addition of 20 μM DnaK could cause a maximal increase to $x_b = 0.23\%$, if the enzyme were to raise the *cis* content at a 1:1 molar ratio. This would induce a change in I_{ab} of less than 0.5%. The experimentally observed intensity enhancement effects, however, are considerably higher, indicating an enzymatic increase of the isomerization rate.

All NMR experiments should be performed with a high-field magnet for better spectral resolution, such as a Bruker DRX500 spectrometer (operating at a proton frequency of 500.13 MHz) that is equipped with a 5-mm triple-resonance (^{1}H, ^{13}C,

^{15}N) probe with Z-gradient capability. Data acquisition and processing are achieved with special computer software (e.g., XWINNMR 2.5, Bruker, Germany). For spectra calibration, proton chemical shifts are usually referenced relative to internal DSS in the sample. All spectra should be recorded in a phase-sensitive mode, with time-proportional phase incrementation of the initial pulse and quadrature detection in both dimensions. The carrier is placed in the center of the spectrum on the water resonance for suppression of the solvent signal. Suppression of the water signal can be achieved by presaturation during the relaxation delay and with a WATERGATE pulse sequence after the mixing period. The NOESY experiments should be collected at 5 °C with a mixing time of 330 ms and a relaxation delay of 1.45 s. For optimal resolution, the time-domain data should consist of at least $512(t_1) \times 3072(t_2)$ complex points at a spectral width of 11 ppm (i.e., 5482.5 Hz) in both dimensions. Prior to Fourier transformation, the time-domain data can be zero-filled to 1024 and 4096 points in the t_1 and t_2 dimensions, respectively, and multiplied by a 90°-shifted squared sine-bell window function. Baseline correction needs to be performed in ω_2 from 1.76–1.51 ppm and from 1.06–0.56 ppm prior to peak integration with the program SPARKY (http://www.cgl.ucsf.edu/home/sparky).

During the course of the enzymatic catalysis reaction, NOESY exchange cross-peaks associated with the *cis* and *trans* isomer forms of the Ala2-Tyr3 and Tyr3-Ala4 bonds can be observed for the methyl groups of Ala2 ($\omega_1 = 1.33$ ppm, $\omega_2 = 0.74$ ppm) and Ala4 ($\omega_1 = 1.31$ ppm, $\omega_2 = 0.97$ ppm), whereby the resonances of the *cis* forms are shifted upfield in both cases. In order to provide a reliable intensity reference relative to the total peptide concentration, all signal intensities can be normalized to the NOESY exchange cross-peak between the two ^{13}C satellites of the Ala1 methyl group ($\omega_1 = 1.31$ ppm, $\omega_2 = 1.57$ ppm) after baseline correction has been performed.

References

1 Fischer, G. (2000). Chemical aspects of peptide bond isomerisation. *Chem. Soc. Rev.*, **29**, 119–127.

2 Fischer, G. (1994). Peptidyl-prolyl *cis/trans* isomerases and their effectors. *Angew. Chem. Int. Ed. Engl.*, **33**, 1415–1436.

3 Schiene-Fischer, C., Habazettl, J., Schmid, F. X. & Fischer, G. (2002). The hsp70 chaperone DnaK is a secondary amide peptide bond *cis-trans* isomerase. *Nat. Struct. Biol.*, **9**, 419–424.

4 Andreotti, A. H. (2003). Native state proline isomerization: an intrinsic molecular switch. *Biochemistry*, **42**, 9515–9524.

5 Jabs, A., Weiss, M. S. & Hilgenfeld, R. (1999). Non-proline *cis* peptide bonds in proteins. *J. Mol. Biol.*, **286**, 291–304.

6 Scherer, G., Kramer, M. L., Schutkowski, M., Reimer, U. & Fischer, G. (1998). Barriers to rotation of secondary amide peptide bonds. *J. Am. Chem. Soc.*, **120**, 5568–5574.

7 Schiene-Fischer, C. & Fischer, G. (2001). Direct measurement indicates a slow *cis/trans* isomerization at the secondary amide peptide bond of glycylglycine. *J. Am. Chem. Soc.*, **123**, 6227–6231.

8 Stein, R. L. (1993). Mechanism of

enzymic and non-enzymic prolyl *cis*/*trans* isomerization. *Adv. Protein Chem.*, **44**, 1–24.

9 Lin, L. N. & Brandts, J. F. (1984). Involvement of prolines-114 and -117 in the slow refolding phase of ribonuclease A as determined by isomer-specific proteolysis. *Biochemistry*, **223**, 5713–5723.

10 Schmid, F. X., Grafl, R., Wrba, A. & Beintema, J. J. (1986). Role of proline peptide bond isomerization in unfolding and refolding of ribonuclease. *Proc. Natl. Acad. Sci. USA*, **83**, 872–876.

11 Semisotnov, G. V., Uversky, V. N., Sokolovsky, I. V., Gutin, A. M, Razgulyaev, O. I. & Rodionova, N. A. (1990). Two slow stages in refolding of bovine carbonic anhydrase B are due to proline isomerization. *J. Mol. Biol.*, **213**, 561–568.

12 Thies, M. J. W., Mayer, J., Augustine, J. G., Frederick, C. A., Lilie, H. & Buchner, J. (1999). Folding and association of the antibody domain C_H3: Prolyl isomerization preceeds dimerization. *J. Mol. Biol.*, **293**, 67–79.

13 Odefey, C., Mayr, L. M. & Schmid, F. X. (1995). Non-prolyl *cis-trans* peptide bond isomerization as a rate-determining step in protein unfolding and refolding. *J. Mol. Biol.*, **245**, 69–78.

14 Vanhove, M., Raquet, X., Palzkill, T., Pain, R. H. & Frere, J. M. (1996). The rate-limiting step in the folding of the *cis*-Pro167Thr mutant of TEM-1 β-lactamase is the *trans* to *cis* isomerization of a non-proline peptide bond. *Proteins: Struct. Funct. Genet.*, **25**, 104–111.

15 Weiss, M. S., Jabs, A. & Hilgenfeld, R. (1998) Peptide bonds revisited. *Nat. Struct. Biol.*, **5**, 676.

16 Bouckaert, J., Loris, R., Poortmans, F. & Wyns, L. (1995). Crystallographic structure of metal-free concanavalin A at 2.5 angstrom resolution. *Proteins: Struct. Funct. Genet.*, **23**, 510–524.

17 Bouckaert, J., Dewallef, Y., Poortmans, F., Wyns, L. & Loris, R. (2000). The structural features of concanavalin A governing non-proline peptide isomerization. *J. Biol. Chem.*, **275**, 19778–19787.

18 Stoddard, B. L. & Pietrokovski, S. (1998). Breaking up is hard to do. *Nat. Struct. Biol.*, **5**, 3–5.

19 Heroux, A., White, E. L., Ross, L. J., Davis, R. L. & Borhani, D. W. (1999). Crystal structure of *Toxoplasma gondii* hypoxanthine-guanine phosphoribosyltransferase with XMP, pyrophosphate, and two Mg^{2+} ions bound: Insights into the catalytic mechanism. *Biochemistry*, **38**, 14495–14506.

20 Banerjee, S., Shigematsu, N., Pannell, L. K., Ruvinov, S., Orban, J., Schwarz, F. & Herzberg, O. (1997) Probing the non-proline *cis* peptide bond in β-lactamase from *Staphylococcus aureus* PC1 by the replacement Asn136 → Ala, *Biochemistry*, **36**, 10857–10866.

21 Pappenberger, G., Aygun, H., Engels, J. W., Reimer, U., Fischer, G. & Kiefhaber, T. (2001). Nonprolyl *cis* peptide bonds in unfolded proteins cause complex folding kinetics. *Nat. Struct. Biol.*, **8**, 452–458.

22 Eyles, S. J. (2001). Proline not the only culprit? *Nat. Struct. Biol.*, **8**, 380–381.

23 Jorgensen, W. L. & Gao, J. (1988). *Cis*/*trans* energy difference for the peptide bond in the gas phase and in aqueous solution. *J. Am. Chem. Soc.*, **110**, 4212–4216.

24 Radzicka, A., Pedersen, L. & Wolfenden, R. (1988). Influences of solvent water on protein folding: free energies of solvation of *cis* and *trans* peptides are nearly identical. *Biochemistry*, **27**, 4538–4541.

25 Li, P. S., Chen, X. G., Shulin, E. & Asher, S. A. (1997). UV resonance Raman ground and excited state studies of amide and peptide isomerization dynamics. *J. Am. Chem. Soc.*, **119**, 1116–1120.

26 Ramachandran, G. N. & Mitra, A. K. (1976). An explanation for the rare occurrence of *cis* peptide units in proteins and polypeptides. *J. Mol. Biol.*, **107**, 85–92.

27 Drakenberg, T. & Forsen, S. (1971).

The barrier to internal rotation in monosubstituted amides. *J. Chem. Soc. D: Chem. Commun.*, 1404–1405.

28 Tweedy, N. B., Nair, S. K., Paterno, S. A., Fierke, C. A. & Christianson, D. W. (1993). Structure and energetics of a non-proline *cis*-peptidyl linkage in a proline-202 → alanine carbonic anhydrase-II variant. *Biochemistry*, **32**, 10944–10949.

29 Schultz, D. A. & Baldwin, R. L. (1992). *Cis* proline mutants of ribonuclease-A.I. Thermal stability. *Protein Sci.*, **1**, 910–916.

30 Pearson, M. A., Karplus, P. A., Dodge, R. W., Laity, J. H. & Scheraga, H. A. (1998). Crystal structures of two mutants that have implications for the folding of bovine pancreatic ribonuclease A. *Protein Sci.*, **7**, 1255–1258.

31 Mayr, L. M., Landt, O., Hahn, U. & Schmid, F. X. (1993). Stability and folding kinetics of ribonuclease T_1 are strongly altered by the replacement of *cis*-proline 39 with alanine. *J. Mol. Biol.*, **231**, 897–912.

32 Mayr, L. M., Willbold, D., Rösch, P. & Schmid, F. X. (1994). Generation of a non-prolyl *cis* peptide bond in ribonuclease T_1. *J. Mol. Biol.*, **240**, 288–293.

33 Dodge, R. W. & Scheraga, H. A. (1996). Folding and unfolding kinetics of the proline-to-alanine mutants of bovine pancreatic ribonuclease A. *Biochemistry*, **35**, 1548–1559.

34 Jennings, P. A., Finn, B. E., Jones, B. E. & Matthews, C. R. (1993). A reexamination of the folding mechanism of dihydrofolate reductase from *Escherichia coli*: verification and refinement of a four-channel model. *Biochemistry*, **32**, 3783–3789.

35 Maki, K., Ikura, T., Hayano, T., Takahashi, N. & Kuwajima, K. (1999). Effects of proline mutations on the folding of staphylococcal nuclease. *Biochemistry*, **38**, 2213–2223.

36 Kofron, J. L., Kuzmic, P., Kishore, V., Colon-Bonilla, E. & Rich, D. H. (1991). Determination of kinetic constants for peptidyl prolyl *cis-trans* isomerases by an improved spectrophotometric assay. *Biochemistry*, **30**, 6127–6134.

37 Udgaonkar, J. B. & Baldwin, R. L. (1990). Early folding intermediate of ribonuclease A. *Proc. Natl. Acad. Sci. USA*, **87**, 8197–8201.

38 Walkenhorst, W. F., Green, S. M. & Roder, H. (1997). Kinetic evidence for folding and unfolding intermediates in staphylococcal nuclease. *Biochemistry*, **36**, 5795–5805.

39 Mayer, M. P., Rüdiger, S. & Bukau, B. (2000). Molecular basis for interactions of the DnaK chaperone with substrates. *Biol. Chem.*, **381**, 877–885.

40 Schiene-Fischer, C., Habazettl, J., Tradler, T. & Fischer, G. (2002). Evaluation of similarities in the *cis/trans* isomerase function of trigger factor and DnaK. *Biol. Chem.*, **383**, 1865–1873.

41 Gulukota, K. & Wolynes, P. G. (1994). Statistical mechanics of kinetic proofreading in protein folding *in vivo*. *Proc. Natl. Acad. Sci. USA*, **91**, 9292–9296.

42 Baine, P. (1986). Comparison of rate constants determined by two-dimensional NMR spectroscopy with rate constants determined by other NMR techniques. *Magn. Reson. Chem.*, **24**, 304–307.

43 Zhao, J., Wildemann, D., Jakob, M., Vargas, C. & Schiene-Fischer, C. (2003). Direct photomodulation of peptide backbone conformations. *Chem. Commun.*, 2810–2811.

12
Ribosome-associated Proteins Acting on Newly Synthesized Polypeptide Chains

Sabine Rospert, Matthias Gautschi, Magdalena Rakwalska, and Uta Raue

12.1
Introduction

Translation of the genetic message into a polypeptide is carried out by ribosomes. Eukaryotic ribosomes are macromolecular structures of about 4000 kDa consisting of two-thirds RNA and one-third protein [1–3]. The structures of the 30S subunit of the eubacterium *Thermus thermophilus* [4] and the 50S subunit of the archaebacterium *Haloarcula marismortui* [5] and of the eubacterium *Deinococcus radiodurans* [6] have been solved by X-ray crystallography. Although the core of the ribosome is conserved in all organisms, eukaryotes contain an additional rRNA molecule plus 20–30 more ribosomal proteins than do prokaryotes. So far neither the 60S nor the 40S eukaryotic ribosomal subunits are available in atomic detail. Our current understanding of the eukaryotic ribosome comes from a combination of cryo-electron microscopy, crystallography data on individual components, and homology modeling based on the prokaryotic ribosome [7–10].

The key event in polypeptide synthesis is the catalysis of peptide bond formation. The peptidyl transferase (PT) center is located on the large ribosomal subunit and is composed of RNA (23S rRNA) [5, 11]. A mechanism of catalysis was proposed based on the arrangement of RNA elements in the active site and their interactions with an intermediate-state analogue [11]. The newly formed polypeptide leaves the ribosome through a tunnel. First observed in the mid-1980s, the tunnel was assumed to be a passive path to exit the ribosome [12, 13]. The crystal structure of the *H. marismortui* 50S subunit revealed that the tunnel from the site of peptide synthesis to its exit is about 10 nm in length and between 1 and 2 nm in width. The tunnel can accommodate a polypeptide chain of approximately 40 amino acids [5, 11] and is formed by RNA and protein (23S rRNA, L4, L22, L39e: *H. marismortui* nomenclature; compare Table 12.1). Its surface is largely hydrophilic and includes exposed hydrogen-bonding groups from bases, phosphates, and polar amino acids. It has been suggested that this results in a Teflon-like tunnel surface, similar to the chaperonin GroEL [14] in its non-binding conformation [11]. However, recent findings suggest that the tunnel may very well interact with the nascent polypeptide chain and play a rather active role in regulating translation

Protein Folding Handbook. Part II. Edited by J. Buchner and T. Kiefhaber

ISBN: 3-527-30784-2

Tab. 12.1. Yeast ribosomal proteins with homology to ribosomal proteins of *Haloarcula marismortui* localized in close proximity to the polypeptide tunnel exit [5, 6, 11]. The name of the yeast homologue is given according to the Rp nomenclature [156].

Family of ribosomal proteins	*H. marismortui*	*E. coli*	*S. cerevisiae*	*Phenotype of the deletion in* S. cerevisiae	*Attachment site for ribosome-associated proteins*
Ribosomal proteins close to the exit of the polypeptide tunnel					
L24	L24	L24	Rpl26a/b	Δrpl26a: viable Δrpl26b: viable [157]	
L22	L22	L22	Rpl17a/b	Δrpl17a: lethal Δrpl17b: viable [157]	
L23	L23	L23	Rpl25	Δrpl25: lethal [158]	Binding site for TF [46] and SRP [51] in *E. coli*. Binding site for eukaryotic SRP [36]
L29	L29	L29	Rpl35a/b	Δrpl35a: viable Δrpl35b: viable [70, 157]	Binding site for eukaryotic SRP [36]
L19e	L19	–	Rpl19a/b	Δrpl19a: viable Δrpl19b: viable Δrpl19aΔrpl19b: lethal [157, 159]	
L39e	L39e	–	Rpl39	Δrpl39: viable [160]	
L31e	L31e	–	Rpl31a/b	Δrpl31a: viable Δrpl31b: viable [157]	
Ribosomal proteins lining the exit tunnel					
L4e/L4p	L4	L4	Rpl4a/b	Δrpl4a: viable Δrpl4b: viable [161]	
L22	L22	L22	Rpl17a/b	Compare above	
L39e	L39e	–	Rpl39	Compare above	

events downstream of polypeptide bond formation. An example for such an active regulatory role of the ribosomal tunnel came from mechanistic studies on co-translational translocation into the mammalian endoplasmic reticulum (ER). Specific nascent polypeptides harbored within the ribosomal tunnel have been shown to induce structural changes in the ER translocon upon ribosome binding [15, 16]. This finding suggests that a polypeptide is able to affect the process of membrane translocation from within the tunnel. Recently, a number of studies have suggested sequence-specific interactions between the exit tunnel and nascent peptides [17]. Thus, the original idea of a passive tunnel seems to be no longer valid. Significant interaction of the tunnel surface with newly synthesized polypeptides raises the question of what drives translocation of the polypeptide.

Besides the main tunnel, there might be several additional routes for a polypeptide to leave the ribosome [18]. It has been suggested that the translation state of

the ribosome influences the tunnel (system) via communication between the small and large ribosomal subunits [18]. The basis of this idea is that it might be important to hold the polypeptide chain in a defined position during peptide bond synthesis. Subsequently, opening of the tunnel would allow movement of the polypeptide and provide space for the next amino acid to be added. Indeed, the diameter of the tunnel entrance of a translating ribosome has been found to be significantly larger than that of a non-translating ribosome.

The tunnel exit is surrounded by a number of ribosomal proteins that are thought to provide the binding sites for additional proteins affecting the newly synthesized polypeptide chain upon exit from the tunnel (Figure 12.1 and Table 12.1). These ribosome-associated proteins are thought to serve a variety of functions; however, their exact cellular roles are only poorly understood. One subgroup of proteins is localized so closely to the nascent polypeptide chain that they can be covalently linked by cross-linking reagents. Some belong to the classical chaperone families of Hsp70 and Hsp40 homologues [19], while others have enzymatic functions and covalently modify nascent polypeptides [20]. Still others lack homologues in other compartments of the cell, and their role in protein biogenesis is currently

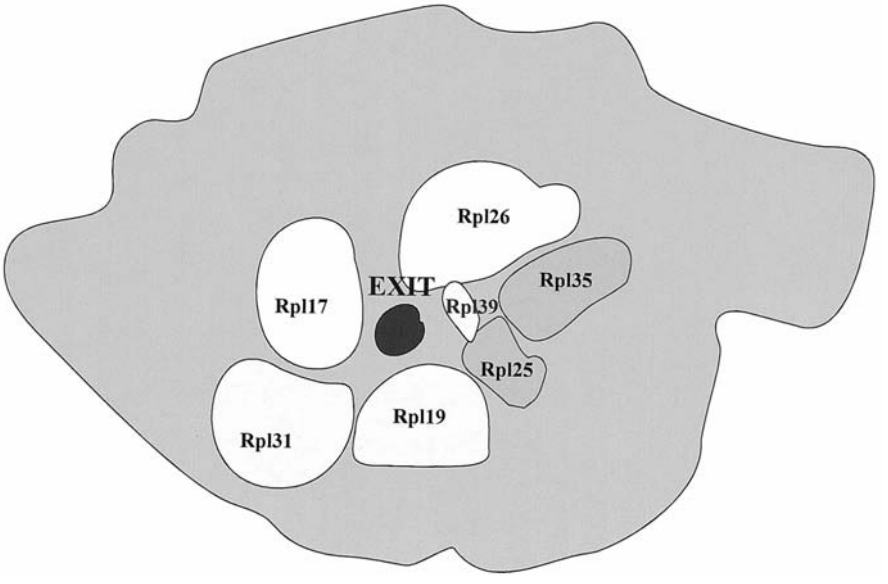

Fig. 12.1. Potential arrangement of yeast ribosomal proteins in close proximity to the polypeptide exit tunnel. The model is based on the crystal structure of the large ribosomal subunit of the archaebacterium *Haloarcula marismortui* [5, 11]. Archaebacterial ribosomes share a high degree of similarity with eukaryotic ribosomes. The mammalian homologues of Rpl25 and Rpl35 have been identified as the binding sites for SRP [36]. The eubacterial L23 (yeast homologue of Rpl25) was identified as the binding site for trigger factor and bacterial SRP [46, 51]. Proteins present in only archaebacteria and eukaryotes are lightly shaded (compare also Table 12.1).

Tab. 12.2. Major ribosome-associated proteins and complexes in yeast (in alphabetical order).

	Subunits (protein family)	*Interaction with the ribosome via:*	*Direct binding to the nascent polypeptide chain*	*Selected references*
NAC (Nascent polypeptide-associated complex)	α NAC = Egd2p β_1 NAC = Egd1p β_2 NAC = Btt1p	β NAC	α NAC β NAC	21, 29, 154, 162
NatA (N^{α}-acetyl-transferase A)	Nat1p Ard1p Nat5p	Nat1p	Nat1p	31, 132, 138, 139
RAC (Ribosome-associated complex)	Zuotin (Hsp40) Ssz1p (Hsp70)	Zuotin	–	63, 71, 87, 107
Ssb1p Ssb2p	– (Hsp70)	Ssb1/2p	Ssb1/2p	62, 66, 87
SRP (Signal recognition particle)	Srp72p Srp68p Sec65p Srp54p Srp21p Srp14p scR1 (RNA)	Srp54p Srp14p + part of scR1 (Alu-domain)	Srp54p	23, 24, 36, 163–165

unclear [21]. This review focuses on our current knowledge of ribosome-associated proteins affecting nascent polypeptides in the eukaryote *Saccharomyces cerevisiae* (Table 12.2) and the eubacterium *Escherichia coli*.

12.2 Signal Recognition Particle, Nascent Polypeptide–associated Complex, and Trigger Factor

12.2.1 Signal Recognition Particle

The function of signal recognition particle (SRP) is specific for a subgroup of newly synthesized proteins and is conserved throughout all kingdoms of life [22]. In eukaryotes, SRP acts on nascent polypeptide chains, which are either secreted or integrated into the membrane of the endoplasmic reticulum, and connects their translation with translocation. Eukaryotic SRP is a multi-protein complex containing an RNA molecule. In yeast, SRP is not essential; however, cells lacking functional SRP grow only very poorly and show severe translocation defects [23]. In prokaryotes, SRP-dependent export is responsible for the translocation of the majority of proteins targeted to the membrane and periplasmic space. Its structure is less complex than that of its eukaryotic counterpart. *E. coli* SRP consists of only

the protein Ffh and a 4.5S RNA molecule [22, 24, 25]. In both eukaryotes and prokaryotes, SRP recognizes N-terminally localized signal sequences co-translationally. Signal sequences share no specific consensus on the amino acid level but display common structural properties: they possess the capability to adopt an α-helical conformation, plus they contain a central hydrophobic core [24, 25]. In eukaryotes, binding of SRP to nascent polypeptides leads to a translational arrest (Figure 12.2B) and is required for the productive interaction of the complex, consisting of ribosome and nascent chain (RNC), with the translocation machinery [22].

12.2.2
An Interplay between Eukaryotic SRP and Nascent Polypeptide–associated Complex?

Nascent polypeptide–associated complex (NAC) is a heterodimeric complex present in all eukaryotic cells [21]. In eubacteria, NAC homologues have not been detected thus far. Several studies based on cross-linking approaches indicate that both subunits of NAC are located in close proximity to ribosome-bound nascent polypeptide chains [26–31]. These cross-link experiments suggest that NAC does not display pronounced sequence specificity but ubiquitously binds to nascent polypeptide chains. In the mammalian system, NAC cross-links have been detected to nascent polypeptide chains as short as 17 amino acids in length [26, 32]. In yeast, the minimal length of the nascent polypeptide chain forming a cross-link to NAC has been determined to be 40–50 amino acids [31]. Based on the structure of the ribosomal tunnel (compare Section 12.1); [11], the nascent polypeptide chain is predicted to exit the ribosome at a length of approximately 40 amino acids. In yeast, NAC would thus bind just after the polypeptide emerges from the ribosome. After termination of translation, NAC does not stably interact with newly synthesized polypeptides. Binding to proteins after release from the ribosome has not been detected so far [26, 28].

It has been suggested that SRP and NAC compete for the same binding site on the ribosome [33, 34]. This competition might facilitate SRP's sampling of nascent polypeptide chains for signal sequences, which is achieved by binding and release of SRP from the ribosome during the elongation process. NAC might increase the rate at which SRP dissociates from RNCs lacking signals. However, it is presently unknown exactly how NAC influences SRP's function [33, 35]. Recently it was shown that the Srp54p subunit of SRP is positioned close to ribosomal proteins L23a (corresponding to Rpl25 in yeast) and L35 (corresponding to Rpl35a/b in yeast) at the exit site of the mammalian ribosome [36] (Figure 12.1). Upon binding of SRP to its receptor in the ER membrane, Srp54p is repositioned and loses contact with L23a [36].

12.2.3
Interplay between Bacterial SRP and Trigger Factor?

Trigger factor (TF) is a protein found in eubacteria; homologues in eukaryotes have so far not been detected. TF was initially described as a ribosome-bound protein

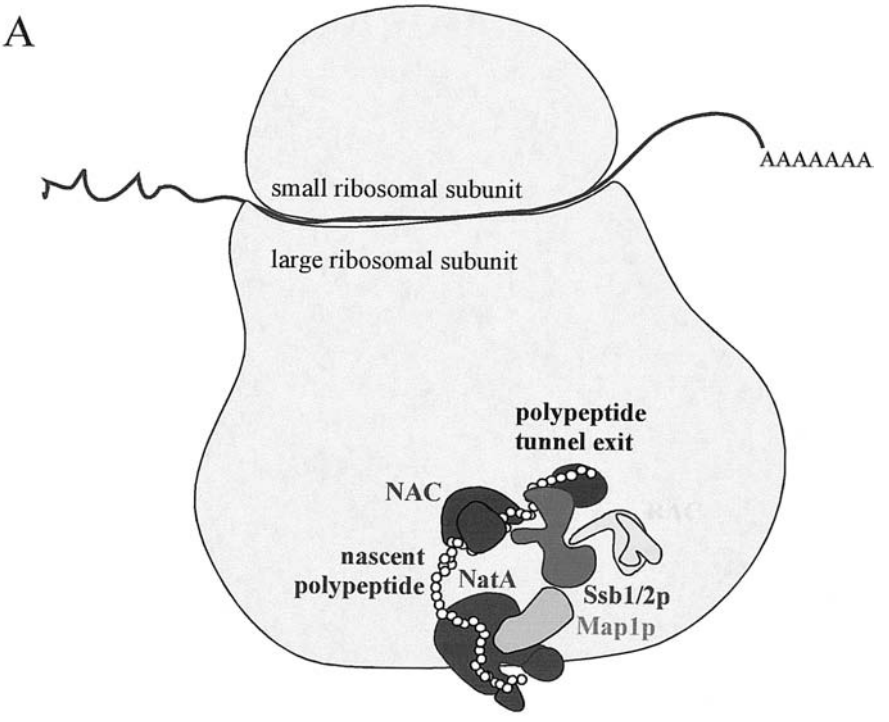

Fig. 12.2. Hypothetical arrangement of ribosome-associated proteins at the yeast polypeptide tunnel exit. (A) Ribosome-bound factors that bind to nascent polypeptide chains in a sequence-independent manner. NAC (nascent polypeptide–associated complex), the Hsp70 homologue Ssb1/2p, and the N^{α}-acetyltransferase NatA interact with nascent polypeptide chains independent of their amino acid sequence. NAC and Ssb1/2p require a minimal polypeptide length of 40–50 amino acids [31]. Binding of NAC and Ssb1/2p precedes binding of Nat1p, which is in close proximity only to nascent polypeptide chains longer than 70 amino acids [31]. Whether NAC, Ssb1/2p, and NatA simultaneously bind to one and the same ribosome (as suggested here) or independently to different molecules is currently unknown. The chaperone complex RAC and the methionine aminopeptidase Map1p bind to translating ribosomes; however, direct binding to the nascent polypeptide has so far not been observed. RAC functionally interacts with Ssb1/2p and potentially binds in its close proximity. The binding site for Map1p should enable the protein to act prior to NatA, which N^{α}-acetylates residues generated by Map1p (for details, compare text).

involved in protein export [37, 38]. Later TF was shown to possess peptidyl-prolyl isomerase activity and to localize in close proximity to a variety of nascent polypeptide chains [39–41]. TF is dispensable under normal growth conditions, and its deletion causes only a mild phenotype [42–44].

TF binds to the large ribosomal subunit [38, 45]. Recently it was shown that L23 (homologue of yeast Rpl25, Table 12.1), a ribosomal protein in close proximity to the exit tunnel, serves as the attachment site [46]. TF binds to both the ribosome and unfolded substrate proteins with an affinity in the sub- to low-micromolar range [38, 47–50]. However, the dynamics of interaction differ significantly. While

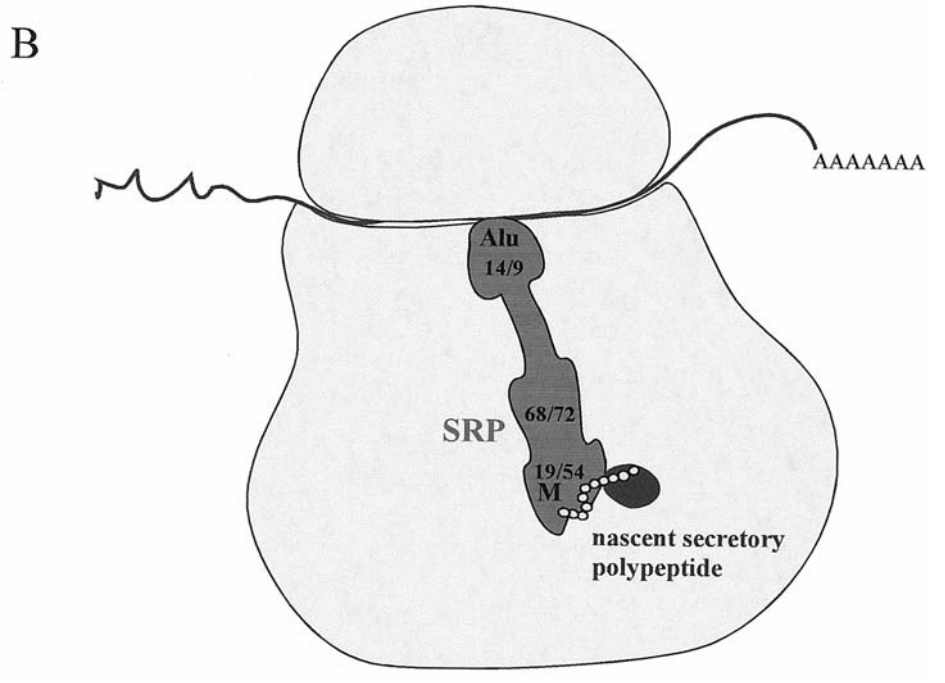

Fig. 12.2. (B) Signal recognition particle (SRP) binds to secretory nascent polypeptides. SRP binds through the M-domain of Srp54p to signal peptides of membrane or secretory proteins. This causes a transient arrest of translation, possibly through the interaction of the Alu-domain with the A-site of the peptidyl-transferase center (discussed in Ref. [155]). The numbers indicate the position of the mammalian SRP subunits on the RNA molecule (for recent reviews on structural details, see Refs. [25, 155]). Whether secretory proteins interact simultaneously with SRP plus one or more of the sequence-independent nascent-chain-binding factors shown in (A) is currently unknown (compare also Table 12.2).

the TF-ribosome complex is stable for about 30 s (2 μM concentration of TF and ribosome, 20 °C), binding to unfolded proteins is very transient (100 ms at 15 °C) [47]. As the binding sites for the ribosome and the nascent polypeptide chain reside in distinct domains, their differences in kinetic properties might enable TF to scan a growing polypeptide chain while at the same time remaining bound to the ribosome.

Like TF, SRP was localized in close proximity to ribosomal protein L23 with a cross-linking approach. In contrast to eukaryotic SRP, no cross-link to L29 (homologue of yeast Rpl35a/b, Table 12.1) was detected [51] (Table 12.1). The cross-linking pattern between L23 and SRP was unchanged in the presence of the SRP receptor FtsY; however, it was modified by the presence of a nascent signal peptide. No contacts to other ribosomal proteins were found. Given the fact that L23 exposes only a small surface at the exit of the tunnel [6], it seems unlikely that TF and SRP can bind simultaneously. Rather, they might alternate in transient binding to the ribosome until a nascent polypeptide chain emerges [52]. Upon recogni-

tion of the nascent polypeptide, binding of either SRP or TF might be stabilized. Alternatively, the ribosome may sense the nature of the nascent peptide already within its exit tunnel [15, 53–55]. In this scenario, the ribosome might actively recruit SRP or TF to polypeptides. L23 clearly plays a central role in the fate of the newly synthesized polypeptide chain.

12.2.4 Functional Redundancy: TF and the Bacterial Hsp70 Homologue DnaK

By transient association with short peptide segments, Hsp70 chaperones assist a large variety of processes, such as protein translocation, folding, and degradation (compare also below) [56]. The bacterial Hsp70 homologue DnaK is not itself directly bound to the ribosome; however, a fraction of DnaK in the cell is associated with nascent polypeptides. In *E. coli* the simultaneous deletion of both TF and DnaK is lethal and leads to the aggregation of a number of newly synthesized proteins [43, 44]. This synthetic effect suggests that TF and DnaK have overlapping functions and assist in the folding of newly synthesized polypeptides. How these structurally very different proteins cope with the newly synthesized polypeptide chain is currently only poorly understood. It is clear, however, that DnaK does not directly become associated with the ribosome in the absence of TF [57]. Recently it was shown that *Bacillus subtilis* can survive in the absence of DnaK and TF, suggesting that yet another factor can functionally complement for Dnak and TF [58].

12.3 Chaperones Bound to the Eukaryotic Ribosome: Hsp70 and Hsp40 Systems

The family of weak ATPases termed Hsp70s (70-kDa heat shock proteins) have three domains: a highly conserved N-terminal ATPase domain, a less well-conserved peptide-binding domain, and a C-terminal variable domain [56, 59, 60]. Hsp70s assist in a variety of processes in all kingdoms of life. Most importantly, they are involved in protein folding, translocation of proteins across cellular membranes, cooperation with the protein degradation machinery, and in the assembly of oligomeric complexes [56, 61]. The common principle that enables Hsp70s such broad functionality is their ability to interact with a variety of short, hydrophobic peptide segments exposed in partly folded or unfolded proteins. The interaction of Hsp70s with their substrates is regulated by an ATPase cycle controlling its affinity for peptide segments. Yeast contains a number of different Hsp70 subfamilies in the cytosol. Two subfamilies, Ssb and Ssz, are ribosome-associated [62, 63] (Figure 12.2). Published data are inconsistent regarding ribosome association of the essential Ssa subfamily (consisting of Ssa1, Ssa2, Ssa3, and Ssa4) ([64–66]; compare Section 12.3.1).

A number of co-chaperones modulate Hsp70s' function and tailor them for specific cellular processes [56, 61]. The best-studied group of Hsp70 co-chaperones are the Hsp40 homologues [56, 67–69]. Yeast contains more than 20 different Hsp40s,

all containing a common domain of approximately 80 amino acids, the so-called J-domain. Two of the yeast Hsp40s have been localized on the ribosome: Sis1p and zuotin [70, 71]. The primary function of Hsp40s is to mediate ATP hydrolysis–dependent interaction of peptide segments with the peptide-binding domain of Hsp70. The J-domain is essential for this regulation and stimulates the rate of ATP hydrolysis by interacting with the ATPase domain of Hsp70s. In addition, some Hsp40s can associate with substrate proteins and transfer them to the Hsp70 partner. The mechanism of this transfer reaction is not very well understood [56, 68].

12.3.1
Sis1p and Ssa1p: an Hsp70/Hsp40 System Involved in Translation Initiation?

Sis1p is an essential Hsp40 homologue localized in the cytosol of yeast [72]. Initial experiments suggested that Sis1p was mainly bound to the small ribosomal subunit. This binding was less stable than that of other ribosome-bound chaperones and was strongly decreased at salt concentrations higher than 50 mM KCl [70]. Later it was shown that a small fraction of Sis1p is associated with polysomes even at concentrations as high as 500 mM KCl [64]. It is currently unclear how these different pools of Sis1p might relate to each other. Using a temperature-sensitive variant of Sis1p (*sis1*-Δ85), it was shown that loss of function leads to a decrease in polysomes and to the accumulation of 80S ribosomes. Consistent with these data, it was suggested that Sis1p function is required for the initiation of translation [70, 73]. Interestingly, temperature sensitivity of *sis1*-Δ85 can be suppressed by deletion of either *RPL39* or *RPL35*, two proteins of the large ribosomal subunit localized close to the exit of the polypeptide tunnel [70] (Table 12.1). The unusual genetic interaction between *SIS1* and *RPL39* connects the proteins to *PAB1*, encoding poly(A)-binding protein. Deletion of *RPL39* suppresses not only temperature sensitivity of *sis1*-Δ85 but also the otherwise lethal deletion of *PAB1* [74]. Pab1p binds to the poly(A)-tail of mRNA, plays a role in mRNA stabilization, and is also essential for efficient translation initiation [75, 76]. Therefore, Pab1p and Sis1p may functionally interact in translation initiation. This cooperation also seems to involve Ssa1p, a chaperone of the Hsp70 class. Ssa1p is present mainly in the soluble fraction of the cytosol and is involved in a multitude of different processes [77–81]. Like Sis1p, and also Pab1p, a small fraction of Ssa1p might be bound to polysomes in a salt-resistant manner [64]. However, in another study Ssa1p did not behave like a polysome-associated protein [65]. Two additional findings support the notion that Sis1p may act as a co-chaperone for Ssa1p. Firstly, Sis1p can stimulate the ATPase activity of Ssa1p and facilitate the refolding of denatured protein together with Ssa1p in vitro [82]. Secondly, Sis1p interacts with the C-terminal 15-amino-acid residues of Ssa1p and might be involved in the transfer of substrate proteins to Ssa1p [64, 83]. However, cross-link products indicating direct interaction of Ssa1p with nascent polypeptide chains have not been observed so far [66]. Future studies will have to clarify the role of Sis1p and Ssa1p during translation.

12.3.2 Ssb1/2p, an Hsp70 Homologue Distributed Between Ribosomes and Cytosol

The two members of the Ssb family of Hsp70 homologues, Ssb1p and Ssb2p, differ by only four amino acids and localize to the cytosol of yeast [84]. Single deletion of the respective genes does not result in a phenotype. However, cells expressing neither Ssb1p nor Ssb2p (Δ*ssb1*Δ*ssb2*) display strong growth defects. The optimal growth temperature is shifted from 30 °C to 37 °C, and Δ*ssb1*Δ*ssb2* strains are cold-sensitive [85]. In addition, Δ*ssb1*Δ*ssb2* strains are hypersensitive towards a number of antibiotics affecting the translational apparatus, among them, the aminoglycoside antibiotics paromomycin, hygromycin B, and G418, which increase the error rate during translation [62, 86].

Approximately 50% of Ssb1p and Ssb2p (Ssb1/2p) is associated with ribosomes [62, 63, 66]. Ssb1/2p binds both translating and non-translating ribosomes, but the salt sensitivity of the Ssb1/2p-ribosome interaction suggests two different binding modes (Table 12.3). Ssb1/2p binding to non-translating ribosomes is salt-sensitive.

Tab. 12.3. Salt sensitivity of the binding of major ribosome-bound proteins. Polysome binding was determined using sucrose-density gradients. Binding to translating ribosomes in vitro was demonstrated by cross-linking. The experimental conditions used in the different studies vary considerably. However, salt-resistant binding is always defined to be stable at concentrations of at least 500 mM salt. A question mark indicates either that salt sensitivity has not been determined or that results are inconsistent.

Eukaryotic ribosome-bound factors	*Polysome (translating ribosomes)*	*80S ribosomes (empty ribosomes)*	*References*
Ssb1/2p	+	+	66
	Salt resistant	Salt sensitive	63, 65, 87, 88
SRP	+	+	33, 166, 167
	Salt resistant	Salt sensitive	
RAC (zuotin)	+	+	63, 71
	Salt sensitive	Salt sensitive	
NAC	+	+	29, 31, 63, 168
	Salt sensitive	Salt sensitive	
NatA	+	+	31
	Salt sensitive	Salt sensitive	
Map1p	+	+	137
	?	?	
Sis1p	+	(+)	64, 70
	?	?	
Eukaryotic ribosome-bound factors	*Polysome (translating ribosomes)*	*70S ribosomes (empty ribosomes)*	*References*
Trigger factor	+	+	41
	Salt resistant	Salt sensitive	
SRP	+	+	51, 169
	?	?	

When the ribosome is involved in translation, binding of Ssb1/2p becomes salt-resistant [62, 66]. Ssb1/2p interacts directly with ribosome-associated polypeptides, suggesting that it is localized close to the exit of the ribosomal tunnel [31, 66, 87] (Figure 12.2). The ability to bind the nascent polypeptide chain is a prerequisite for the formation of the salt-resistant complex between Ssb1/2p and the ribosome [88]. Salt-resistant binding, however, is most likely not achieved exclusively via interaction of Ssb1/2p with the nascent polypeptide. Without the context of the ribosome, binding of Ssb1/2p to polypeptide chains has not been observed so far [88], suggesting that this interaction is not stable enough to resist at high salt concentrations. Conformational changes between empty and translating ribosomes, possibly induced by Ssb1/2p interaction with the nascent polypeptide chain, might contribute to the different binding modes [66]. Expression of Ssb1/2p is regulated like a core component of the ribosome [89], which is in agreement with its close relation to the translational process. Whether Ssb1/2p cycles between a ribosomal-bound and a soluble pool and whether this dual localization reflects distinct functions of this chaperone remains to be determined.

12.3.3 Function of Ssb1/2p in Degradation and Protein Folding

In eukaryotic cells, the vast majority of proteins in the cytosol and nucleus are degraded via the proteasome-ubiquitin pathway [90]. *SSB1* was isolated as a multicopy suppressor of a temperature-sensitive growth phenotype observed in a yeast strain carrying a mutation in one of the proteasome subunits. Later it was found that high levels of Sis1p lead to suppression of temperature sensitivity in the proteasome mutant and that co-overexpression of Ssb1/2p and Sis1p showed an even stronger effect [91, 92]. The findings suggest that Ssb1/2p and Sis1p together facilitate the degradation of proteins, possibly mediating the transfer of damaged proteins to the proteasome. In vitro, however, there is so far no evidence for a typical Hsp70-Hsp40-type interaction between Ssb1/2p and Sis1p [82, 93]. High levels of Ssb1/2p have also been reported to suppress a temperature-sensitive mutant displaying defects in vesicular transport [94] and a mutant with a defect in the mitochondrial import machinery [95]. Possibly, Ssb1/2p also aids the degradation of precursor proteins that fail to reach the correct destination in these mutant strains. Alternatively, high levels of Ssb1/2p might indirectly affect protein trafficking by enhancing folding or stability of factors required for the respective transport processes.

Evidence for a classical chaperone function of Ssb1/2p in protein folding comes from a study on the chaperone TRiC [96]. TRiC cooperates with GimC and assists in the folding of a subset of aggregation-sensitive polypeptides [96–98]. The function of TRiC is essential, whereas GimC function is dispensable for the life of yeast [97, 99, 100]. However, simultaneous loss of GimC and Ssb1/2p results in synthetic lethality, suggesting that GimC and Ssb1/2p are able to functionally replace each other in assisting in the folding of a subset of TRiC substrate proteins [96].

So far, no mammalian Hsp70 family member has been found to be in direct as-

sociation with the ribosome. In higher eukaryotes, a number of cytosolic proteins are assisted by the cytosolic Hsp70 homologues and TRiC in co-translational folding (reviewed in Refs. [101, 102]). While TRiC might interact with the ribosome directly [103], the mammalian Hsp70 homologues studied so far seem to be attached to the ribosome–nascent chain complex via the nascent polypeptide chain only.

12.3.4
Zuotin and Ssz1p: a Stable Chaperone Complex Bound to the Yeast Ribosome

The Hsp40 homologue zuotin was found in 1998 to be a ribosome-associated protein [71]. Later it was discovered that the bulk of zuotin forms a stable complex with the Hsp70 homologue Ssz1p. The complex, termed RAC (ribosome-associated complex), is a stable dimer and is almost entirely associated with ribosomes [63]. A stable complex between an Hsp70 and an Hsp40 homologue is unusual but is not without precedence. *Thermus thermophilus* DnaK (Hsp70) and DnaJ (Hsp40) form a stable 3:3 complex that contains an additional three subunits of the 8-kDa protein Daf [104, 105]. How Ssz1p and zuotin stably interact is currently unknown. Deletion analysis of zuotin revealed that the very N-terminus up to the J-domain results in a nonfunctional protein that is still able to associate with the ribosome [71]. This N-terminus, which bears no homology to any other known J-protein, is a good candidate domain for binding to Ssz1p. Stable binding of RAC to the ribosome is mediated via the zuotin subunit: in the absence of zuotin, Ssz1p is not associated with the ribosome, while zuotin remains ribosome-associated in the absence of Ssz1p [63].

12.3.5
A Functional Chaperone Triad Consisting of Ssb1/2p, Ssz1p, and Zuotin

Deletion of either *zuo1* or *ssb1/2* results in slow growth, cold sensitivity, sensitivity towards aminoglycosides, and high osmolarity. This genetic interaction, in combination with the finding that both chaperones bind to the ribosome, strongly suggests that Ssb1/2p and zuotin have a common function [71]. Later it turned out that Ssz1p and zuotin not only form the stable RAC complex but also that deletion of *ssz1* as well as simultaneous deletion of *ssz1zuo1ssb1/2* leads to the same set of growth defects [63, 87, 106]. Overexpression of zuotin or Ssb1/2p can partially suppress the growth defect caused by deletion of *ssz1*, while overexpression of Ssz1p cannot support growth of Δ*zuo1* or Δ*ssb1/2* strains. The combination of data suggests that Ssz1p, while not obligatory for Ssb1/2p and zuotin's common function, is involved in the same cellular process [87, 106].

How RAC and Ssb1/2p work together is so far only poorly understood. In vitro studies of the purified proteins will be required to better understand their interaction on a molecular level. The first insights on how they might cooperate have come from cross-linking experiments. So far, cross-link products to neither of the RAC subunits have been detected. In contrast, Ssb1/2p can be cross-linked to a va-

riety of nascent polypeptide chains in vitro, suggesting that it interacts with many, possibly all, newly synthesized polypeptide chains on their way through the ribosomal tunnel [66, 87]. As outlined above, high-salt treatment of ribosome–nascent chain complexes does not release Ssb1/2p but rather other factors such as RAC. Unexpectedly, on such high-salt-treated complexes, nascent polypeptide chains and Ssb1/2p no longer form cross-link products. However, cross-linking of the nascent polypeptide chain to Ssb1/2p can be restored by re-addition of purified RAC [87]. This finding suggests that RAC is required for the efficient binding of Ssb1/2p to the nascent polypeptide chain (Figure 12.3). This function of RAC depends on an intact J-domain, suggesting that zuotin acts as a J-partner for the Hsp70 Ssb1/2p while being simultaneously bound to another Hsp70, namely, Ssz1p. Interestingly, the presence of Ssz1p is required for efficient cross-linking to Ssb1/2p. Possibly the nascent polypeptide chain initially binds to Ssz1p and is subsequently

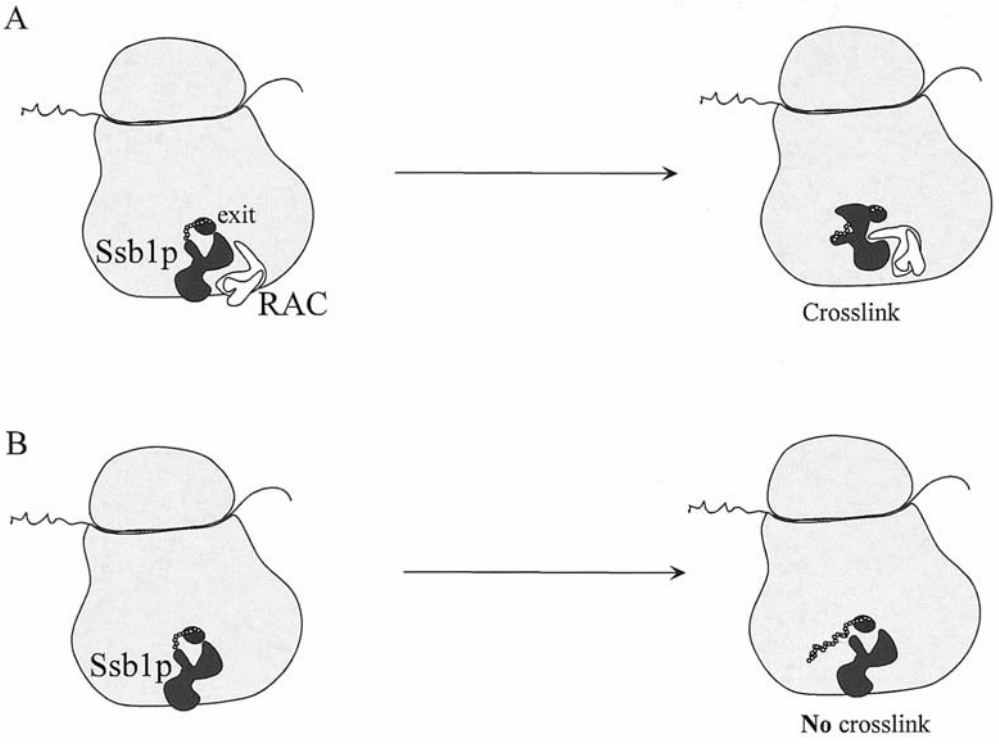

Fig. 12.3. Efficient cross-linking of Ssb1/2p depends on functional RAC. Ssb1/2p and RAC (zuotin + Ssz1p) are associated with translating ribosomes. (A) When the nascent polypeptide chain reaches a length of approximately 45 amino acids, it can be cross-linked to the Hsp70 homologue Ssb1/2p. (B) If RAC is absent from the ribosome–nascent chain complex, zuotin carries an inactivating mutation in its J-domain, or, if Ssz1p is missing, the cross-link is no longer formed, suggesting that RAC influences nascent polypeptide binding of Ssb1/2p [87] (for details, compare text).

transferred to Ssb1/2p. Fast transfer of the nascent polypeptide chain from Ssz1p to the more tightly binding Ssb1/2p might account for the lack of a direct cross-link to Ssz1p. However, sequential binding of the nascent polypeptide chain to Ssz1p and Ssb1/2p seems to be unessential for functionality of the chaperone triad. Lack of the unusually short peptide-binding domain of Ssz1p does not result in the same phenotype as observed for the deletion [106]. It is possible that Ssz1p modulates zuotin's ability to act as a partner chaperone for Ssb1/2p. Alternatively, Ssz1p might interact only with a specific, possibly small, subset of nascent polypeptide chains. Ssz1p, originally named Pdr13p, was identified as a posttranslational regulator of the transcription factor Pdr1p [107]. Whether Pdr1p or a subset of newly synthesized polypeptides directly interacts with Ssz1p and whether Ssz1p's function is influenced by zuotin's J-domain await further investigation.

Various speculations have been made on the in vivo role of ribosome-bound Ssb1/2p: folding of ribosome-bound nascent polypeptide chains, maintaining nascent polypeptide chains in an unfolded yet folding-competent state, preventing the nascent polypeptide chain from slipping backwards into the ribosome, facilitating movement of the chain through the exit tunnel or away from the ribosome, clearance of aggregated proteins from the ribosome. However, experimental evidence is scarce. Ssb1/2p cooperates with TRiC in posttranslational completion of protein folding and has a partly overlapping function with the TRiC co-chaperone GimC ([96] and compare above). It should be pointed out that this is most likely not a function of the Ssb1/2p/RAC system. While the lack of Ssb1/2p is lethal in the absence of GimC, the lack of zuotin is not [96]. This strongly suggests that soluble, and not ribosome-associated, Ssb1/2p assists in protein folding by TriC, possibly in combination with an as yet unidentified cytosolic Hsp40 homologue.

12.3.6
Effects of Ribosome-bound Chaperones on the Yeast Prion [*PSI*$^+$]

The prion-forming proteins of yeast are members of a larger class of Gln/Asn-rich proteins. Yeast prions are replicated by a protein-only mechanism resulting in a dominant, non-Mendelian mode of inheritance. The best-characterized yeast prion is [*PSI*$^+$], the polymerized form of the translation termination factor Sup35p with properties characteristic of prion proteins. The formation of [*PSI*$^+$] results in depletion of functional Sup35p and leads to a defect in translation termination that manifests itself by an increase in stop codon read-through [108–111].

Chaperones are thought to play an important role in prion biogenesis. In particular, the cytosolic chaperone Hsp104 has been implicated in yeast prion propagation [109, 112]. [*PSI*$^+$], for example, can be cured by either overproduction or inactivation of Hsp104 [113]. Hsp104, a homohexameric ATPase of the AAA protein family, functions in solubilization and refolding of aggregated proteins [114–117]. This ability provides the explanation for [*PSI*$^+$] being cured by excess Hsp104: Hsp104 overproduction leads to the release of Sup35p from [*PSI*$^+$] aggregates [118, 119]. The reason for the failure to inherit [*PSI*$^+$] in the absence of Hsp104 is most likely connected to the lack of smaller prion seeds, required for the trans-

mission of [PSI^+] to daughter cells. However, other models have been proposed ([120] and references therein).

In addition to Hsp104, a number of cytosolic chaperones have been implicated in yeast prion propagation, among them, the partially ribosome-associated chaperones Ssb1/2p, Ssa1p, and Sis1p. The reported effects are variable, suggesting the action of complex chaperone networks and variations between different prion strains [121, 122]. The effects are only poorly understood on a mechanistic level. High levels of Ssa have been reported to protect [PSI^+] from being cured by an excess of Hsp104 [123]. In contrast, other studies have reported curing of [PSI^+] due to overexpression of Ssa1p [124, 125]. Ssb1/2p increases, while lack of Ssb1/2p prevents [PSI^+] curing by excess of Hsp104 [126, 127]. High levels of Ssa or Ssb1/2p might either prevent formation of misfolded Sup35p intermediates, which serve as the seeds for [PSI^+], or stimulate degradation of such seeds. High levels of the Hsp40 homologues Ydj1p, Sis1p, Sti1p, and Apj1p have also been shown to influence prion propagation [124]. Sis1p might exert its function in combination with Ssa or Ssb (compare above). Sis1p is also necessary for the propagation of [RNQ^+], another prion of yeast. As Ydj1p cannot substitute for this function of Sis1p, Hsp40s might provide specificity to the prion curing effects of Hsp70 homologues [128, 129]. Sti1p functionally interacts with Ssa and might cooperate with Ssa in prion curing [130, 131]. So far, Apj1p has been only poorly characterized, and its Hsp70 partner has not been found.

12.4 Enzymes Acting on Nascent Polypeptide Chains

Two co-translational modifications, cleavage of N-terminal methionine residues and N^{α}-terminal acetylation, are by far the most common protein modifications in eukaryotes [20, 132]. N-terminal methionine is cleaved from nascent polypeptide chains of prokaryotic and eukaryotic proteins when the residue following the initial methionine is small and uncharged. N^{α}-terminal acetylation predominantly occurs in eukaryotic cells. Most frequently modified are serine and alanine N^{α}-termini, and these residues along with methionine, glycine, and threonine account for more than 95% of the N-terminally acetylated residues [20].

12.4.1 Methionine Aminopeptidases

Methionine aminopeptidase (MetAP) catalyzes the removal of the initiator methionine from nascent polypeptides. In yeast, there are two homologous MetAPs, Map1p and Map2p. Their combined activities are essential, but their relative intracellular roles are unclear [133, 134]. The efficiency with which specific N-terminal amino acids become exposed in nascent polypeptides by the action of Map1p and Map2p correlates very well with the stability of the generated proteins according to the N-end rule [135]. As an example, methionine in front of alanine, serine, and

Tab. 12.4. Yeast N^{α}-acetyltransferases. NatA, NatB, NatC, and Nat4p differ in substrate specificity and subunit composition but all contain at least one catalytic subunit homologous to the GNAT family of acetyltransferases [132, 144]. For details, compare text.

	Large non-catalytic subunit	*Catalytic subunit (GNAT)*	*Auxiliary subunit*	*References*
NatA	Nat1p (98 kDa)	Ard1p (27 kDa)	Nat5p (20 kDa) (GNAT homologue, possibly catalytically active)	31, 138
NatB	Mdm20p (92 kDa)	Nat3p (23 kDa)		142, 143
NatC	Mak10p (84 kDa)	Mak3p (20 kDa) Nat4p (32 kDa)	Mak31p (10 kDa)	170 147

threonine is cleaved very efficiently, and the resulting polypeptides display high stability. On the other hand, methionine is not efficiently cleaved in front of, e.g., lysine, arginine, or glutamate. These N-terminal residues, which would destabilize the generated protein, are not commonly generated co-translationally [135, 136]. Consistent with its co-translational mode of action, it was recently demonstrated that Map1p is associated with polysomes [137] (Figure 12.2). Map2p has so far not been localized.

12.4.2 *N*$^{\alpha}$-acetyltransferases

Three N^{α}-terminal acetyltransferase complexes termed NatA, NatB, and NatC have been identified in yeast [31, 138–143]. They differ in substrate specificity and subunit composition, but all contain at least one catalytic subunit homologous to the GNAT family of acetyltransferases [132, 144] (Table 12.4). All three NATs contain a large subunit that does not possess catalytic activity but is required for activity of the catalytic subunits in vivo. Analogous to the large, multiple tetratrico peptide repeats (TPR) containing subunits of NatA, they might anchor the catalytic subunits to the ribosome and facilitate interaction with the nascent polypeptide substrate [31, 145, 146]. Recently Nat4, a novel catalytic subunit, has been found to specifically N^{α}-acetylate histone H4 and H2A [147]. No potential ''anchor'' for Nat4 has been found so far.

NatA is the major N^{α}-terminal acetyltransferase in yeast, responsible for the acetylation of serine, alanine, threonine, and glycine [140, 148, 149]. NatA contains three subunits: Ard1p, the catalytically active GNAT subunit; Nat5p, a GNAT homologue for which catalytic activity has not yet been demonstrated; and the TPR domain protein Nat1p [31, 146] (Table 12.4). In accordance with its co-translational mode of action, NatA is quantitatively bound to ribosomes [31] (Figure 12.2). Binding is mediated by Nat1p, which not only anchors Ard1p and Nat5p to the ribosome but also is in close proximity to a variety of nascent polypeptide chains [31].

The lack of N^{α}-terminal acetylation does not cause a general defect in the stability or folding of the affected proteins [20]. In agreement with this observation, N^{α}-acetyltransferases are not essential for the life of yeast. However, Δ*nat1* and Δ*ard1* strains display temperature sensitivity plus some specific phenotypes, such as reduced sporulation efficiency, failure to enter G_0 under specific conditions, and defects in silencing of the silent mating-type loci [31, 139, 140, 150, 151]. The pleiotropic phenotypes are thought to reflect functional defects of various target proteins lacking proper acetylation at their N-terminus. So far there are surprisingly few examples demonstrating the biological importance of N^{α}-terminal protein acetylation [20]. For NatA no clear-cut example has been described. One of the few well-documented examples has been reported for Mak3p, the catalytic subunit of NatC. N^{α}-acetylation by Mak3p is essential for the coat protein assembly of the L-A double-stranded RNA virus in yeast [141, 152].

Ssb1/2p can partially suppress temperature sensitivity and the silencing defect caused by the lack of NatA [31]. It seems unlikely that high levels of Ssb1/2p would restore N^{α}-acetylation of NatA substrates. Suppression of both temperature sensitivity and the silencing defect suggests that Ssb1/2p is able to complement a general function of NatA. Whether Ssb1/2p can partially substitute for Nat1p function on the ribosome or whether it suppresses defects caused by specific proteins that lack N^{α}-terminal acetylation awaits further investigation.

12.5
A Complex Arrangement at the Yeast Ribosomal Tunnel Exit

Of all the nascent polypeptide chain-binding proteins discussed in this chapter, SRP is exceptional in that it interacts with nascent polypeptides bearing a signal sequence and its in vivo role precisely correlates with this specificity: SRP functions in the co-translational translocation of signal sequence bearing preproteins (compare above). The role of the other factors is less well defined; most likely they are multi-functional, as reflected by their ability to bind to a variety of nascent polypeptide chains. However, yeast Ssb1/2p and *E. coli* TF share an important characteristic with SRP. Consistent with a functional interaction rather than coincidental proximity, their mode of binding to empty ribosomes and ribosome-nascent polypeptide chain complexes differs. SRP, Ssb1/2p, and TF bind much more stably to ribosomes when simultaneously interacting with a nascent polypeptide chain [33, 41, 54, 66, 87] (Table 12.3). NAC and NatA also interact with the ribosome and have been found in close proximity to a variety of nascent polypeptide chains by cross-linking approaches [29, 31]. However, significant stabilization of ribosome association by nascent polypeptide chain binding has not been observed for NAC or NatA (Table 12.3). Whether proximity of NAC and NatA to nascent polypeptide chains indicates binding or rather reflects co-localization has not yet firmly been established [21, 31].

The presence of various factors at the yeast ribosomal tunnel exit implies a highly ordered arrangement and sequence of binding and release events. To date

nothing is known about how proteins are arranged at the yeast exit site and to which ribosomal proteins or portions of the rRNA they bind. The first evidence for an ordered sequence of events comes from a comparison of the nascent polypeptide length required for the in vitro generation of cross-link products. Srp54p interacts with nascent secretory polypeptides of 60–70 amino acids in length [153]. Recently it has been found that longer nascent polypeptide chains also can interact with SRP [54]. Ssb1/2p and NAC can be cross-linked to nascent polypeptides – including secretory nascent polypeptides – from a minimal length of 45 amino acids, and NatA ultimately attaches to nascent polypeptides longer than 70 amino acids [31] (Figure 12.2). These results suggest that the emerging polypeptide first passes Ssb1/2p and NAC, possibly interacting with one or both. Whether NatA (and possibly other enzymes) acts on the very N-terminus while Ssb1/2p and/or NAC are still in close proximity to the nascent polypeptide is not known. Also, the interplay between SRP and the other factors on secretory nascent chains is far from being fully understood. Future studies should establish the arrangement of these factors and how they dynamically interact with the ribosome and the nascent polypeptide to perform their function.

12.6 Experimental Protocols

12.6.1 Purification of Ribosome-associated Protein Complexes from Yeast

Here we describe the protocols for the purification of wild-type NAC and RAC (Table 12.5), two abundant, ribosome-associated, heterodimeric complexes from *Saccharomyces cerevisiae*. Starting material for the purification is the pool of ribosome-associated proteins that can be released from ribosomes by high-salt treatment. The original purification of the proteins was followed using a functional assay that has been described elsewhere [63, 154]. In this protocol the first purification step is followed by Western blotting (Figure 12.4A). Later steps can be fol-

Tab. 12.5. Properties of NAC and RAC.

Complex	*Oligomeric state*	*Gene/protein MWM, pI*	*References*
NAC (Nascent polypeptide-associated complex)	Heterodimeric (Analytical ultracentrifugation)	*EGD2* α-NAC 18.6 kDa, pI 4.7 *EGD1* β-NAC 16.8 kDa, pI 6.3	29, 154, 162
RAC (Ribosome-associated complex)	Heterodimeric (Analytical ultracentrifugation)	*SSZ1* Ssz1p 58 kDa, pI 4.8 *ZUO1* zuotin 49 kDa, pI 8.4	63

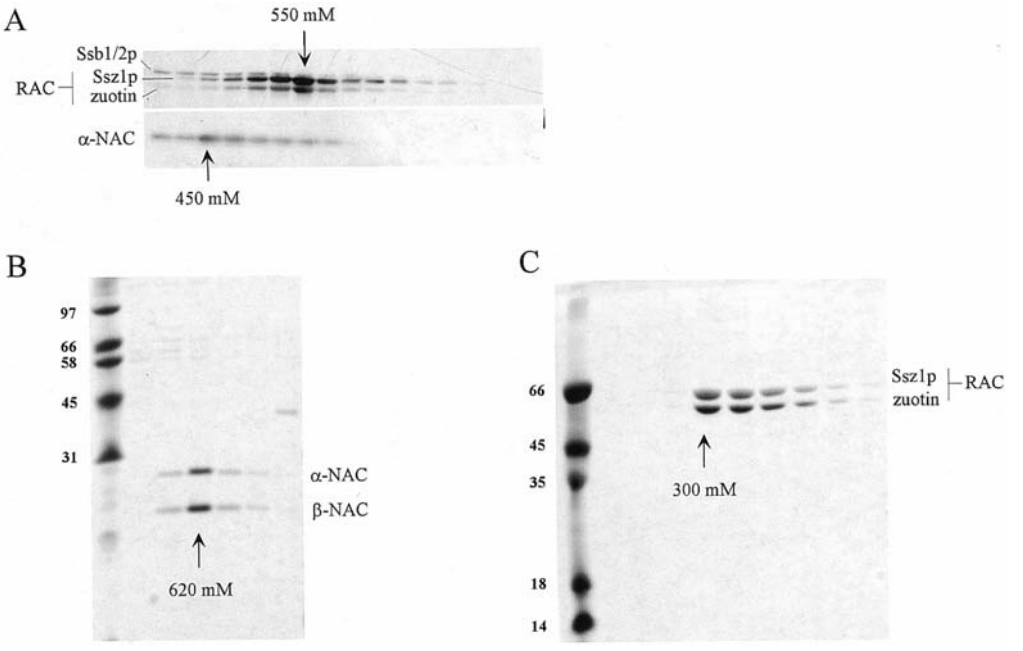

Fig. 12.4. Purification of NAC and RAC. (A) Fractions of a ribosomal salt-wash generated on ResourceQ were analyzed by Western blotting using antibodies directed against Ssb1/2p, Ssz1p, zuotin, and α-NAC. The bulk of Ssb1/2p elutes at lower K-acetate concentrations and is not shown. Note that the different intensities of the signals for Ssz1p and zuotin are caused by the different affinities of the respective antibodies. β-NAC co-elutes with α-NAC and was not analyzed in this experiment. (B) and (C) show coomassie-stained gels of the peak fractions after purification of NAC on MonoQ (B) and after purification of RAC on MonoS (C). Concentrations of K-acetate in the peak fraction of the respective proteins are given. For details, compare Appendix.

lowed by coomassie staining. Initial isolation of ribosomes, which carry the bulk of RAC and NAC, followed by high-salt release of the proteins from ribosomes provides an efficient first purification step. The purified protein complexes are able to rebind to high-salt-washed ribosomes and are functionally active [63, 87, 154].

12.6.2
Growth of Yeast and Preparation of Ribosome-associated Proteins by High-salt Treatment of Ribosomes

An initial overnight culture of wild-type yeast is used to inoculate 10 L of YPD (1% yeast extract, 2% peptone, 2% dextrose). Cells are grown in 5-L flasks, each containing 2 L of medium, to midlog phase ($OD_{600} \sim 2.0$) at 30 °C. Under these conditions wild-type yeast strains display a doubling time of approximately 1.5 h.

Cells are harvested by centrifugation for 5 min at 2700 *g*, resuspended in 300 mL

ice-cold water, and transferred to pre-weight tubes. The cells are recollected for 5 min, the supernatant is discarded, and the mass of the cell pellet is determined.

The cell pellet is resuspended carefully in 200 mL sorbitol buffer (1.4 M sorbitol, 50 mM potassium phosphate pH 7.4, 10 mM DTT), and 2.5 mg zymolyase (20T) per gram cell pellet is added. In order to generate spheroplasts, cells are incubated in the presence of zymolyase for 30–40 min in a 30 °C water bath at 120 rpm.

Spheroplasts are collected by centrifugation for 5 min at 2700 *g* and are washed three times by resuspension and centrifugation with a total volume of 0.9 L sorbitol buffer (1.4 M sorbitol, 50 mM potassium phosphate pH 7.4, 5 mM DTT). After washing, spheroplasts are resuspended in 50–100 mL lysis buffer (20 mM HEPES-KOH, pH 7.4, 100 mM K-acetate, pH 7.4, 5 mM Mg-acetate, 1 mM PMSF, 1.25 μg mL^{-1} leupeptin, 0.75 μg mL^{-1} antipain, 0.25 μg mL^{-1} chymotrypsin and elastinol, 5 μg mL^{-1} pepstatin) and broken in an all-glass Dounce homogenizer (pestle-tube clearance 60 μm) with at least 20 strokes. The suspension is cleared by centrifugation for 15 min at 27 000 *g*.

The cleared supernatant is transferred to ultracentrifugation tubes and centrifuged for 30 min at 80 000 *g*. The resulting supernatant contains most of the ribosomes and the soluble cytosolic proteins and is referred to as cytosol.

In order to isolate low-salt-washed ribosomes (ribosomes and polysomes containing salt-sensitive associated proteins), the cytosol is centrifuged for 1.5–2 h at 200 000 *g*. The resulting supernatant (post-ribosomal supernatant) is discarded and the ribosomal pellet is resuspended in high-salt buffer (20 mM HEPES-KOH, pH 7.4, 720 mM K-acetate, 5 mM Mg-acetate, 1 mM PMSF) in a Dounce homogenizer with a Teflon piston. Resuspended ribosomes are collected by centrifugation for 1.5–2 h at 200 000 *g*. The resulting pellet contains high-salt-washed ribosomes, and the supernatant contains the proteins released from the ribosomes by high-salt treatment (ribosomal salt-wash) and is used for the purification of RAC and NAC.

12.6.3 Purification of NAC and RAC

The ribosomal salt-wash is diluted with six volumes of 40 mM HEPES-KOH, pH 7.4, and is subsequently loaded onto a ResourceQ (6 mL) anion-exchange column (Amersham-Pharmacia). Bound proteins are eluted with a linear 30–80 mL (100–800 mM) K-acetate gradient in 40 mM HEPES-KOH, pH 7.4. NAC is eluted at 450 mM K-acetate and RAC is eluted at 550 mM K-acetate (Figure 12.4A). Peak fractions enriched in NAC or RAC, respectively, are pooled and are used for further purification of the proteins.

The pooled fractions are diluted with 40 mM HEPES-KOH, pH 7.4, to a final concentration of 100 mM K-acetate and are loaded separately onto a MonoQ (1 mL) anion-exchange column (Amersham Pharmacia). In each case bound proteins are eluted with a linear 25–60 mL (100–1200 mM) K-acetate gradient in 40 mM HEPES-KOH pH 7.4. NAC is eluted at 620 mM and RAC at 850 M K-acetate. On MonoQ, NAC and RAC are present in two clearly separated peaks. As estimated on

coomassie gels, NAC is enriched to more than 80% in the peak fractions (Figure 12.4B). NAC-containing fractions can be pooled, diluted with one volume of 40 mM HEPES-KOH pH 7.4, and concentrated in a Centricon-30 device (Millipore, Bedford, MA). Frozen in small aliquots and stored at −80 °C, the protein is stable for at least 1 year.

RAC can be further purified by cation-exchange chromatography. For this purpose RAC is diluted with six volumes of 100 mM MES, pH 6.5, and loaded onto a MonoS (1 mL) column (Amersham Pharmacia). Bound RAC is eluted with a linear 25-mL (150–600 mM) K-acetate gradient in 40 mM MES, pH 6.5. RAC is eluted at 300 mM K-acetate and is enriched to more than 95% in the peak fractions (Figure 12.4C). RAC-containing fractions are stored at −80 °C. Note that RAC at pH 6.5 cannot be concentrated to a protein concentration of higher than 1 mg mL^{-1} because of aggregation. If higher concentrations are required, the pH of the solution should be previously adjusted to pH 7.4.

References

1 Green, R. & Noller, H. F. (1997). Ribosomes and translation. *Annu. Rev. Biochem.* 66, 679–716.

2 Maguire, B. A. & Zimmermann, R. A. (2001). The ribosome in focus. *Cell* 104, 813–816.

3 Ramakrishnan, V. (2002). Ribosome structure and the mechanism of translation. *Cell* 108, 557–572.

4 Wimberly, B. T., Brodersen, D. E., Clemons, W. M., Jr., Morgan-Warren, R. J., Carter, A. P., Vonrhein, C., Hartsch, T. & Ramakrishnan, V. (2000). Structure of the 30S ribosomal subunit. *Nature* 407, 327–339.

5 Ban, N., Nissen, P., Hansen, J., Moore, P. B. & Steitz, T. A. (2000). The complete atomic structure of the large ribosomal subunit at 2.4 A resolution. *Science* 289, 905–920.

6 Harms, J., Schluenzen, F., Zarivach, R., Bashan, A., Gat, S., Agmon, I., Bartels, H., Franceschi, F. & Yonath, A. (2001). High resolution structure of the large ribosomal subunit from a mesophilic eubacterium. *Cell* 107, 679–688.

7 Morgan, D. G., Menetret, J. F., Radermacher, M., Neuhof, A., Akey, I. V., Rapoport, T. A. & Akey, C. W. (2000). A comparison of the yeast and rabbit 80S ribosome reveals the topology of the nascent chain exit tunnel, inter-subunit bridges and mammalian rRNA expansion segments. *J. Mol. Biol.* 301, 301–321.

8 Agrawal, R. K. & Frank, J. (1999). Structural studies of the translational apparatus. *Curr. Opin. Struct. Biol.* 9, 215–21.

9 Stark, H. (2002). Three-dimensional electron cryomicroscopy of ribosomes. *Curr. Protein Pept. Sci.* 3, 79–91.

10 Doudna, J. A. & Rath, V. L. (2002). Structure and function of the eukaryotic ribosome: the next frontier. *Cell* 109, 153–156.

11 Nissen, P., Hansen, J., Ban, N., Moore, P. B. & Steitz, T. A. (2000). The structural basis of ribosome activity in peptide bond synthesis. *Science* 289, 920–930.

12 Milligan, R. A. & Unwin, P. N. (1986). Location of exit channel for nascent protein in 80S ribosome. *Nature* 319, 693–695.

13 Yonath, A., Leonard, K. R. & Wittmann, H. G. (1987). A tunnel in the large ribosomal subunit revealed by three-dimensional image reconstruction. *Science* 236, 813–816.

14 Xu, Z., Horwich, A. L. & Sigler, P. B. (1997). The crystal structure of the

asymmetric GroEL-GroES-(ADP)7 chaperonin complex. *Nature* 388, 741–750.

15 Liao, S., Lin, J., Do, H. & Johnson, A. E. (1997). Both lumenal and cytosolic gating of the aqueous ER translocon pore are regulated from inside the ribosome during membrane protein integration. *Cell* 90, 31–41.

16 Siegel, V. (1997). Recognition of a transmembrane domain: another role for the ribosome? *Cell* 90, 5–8.

17 Tenson, T. & Ehrenberg, M. (2002). Regulatory nascent peptides in the ribosomal tunnel. *Cell* 108, 591–594.

18 Gabashvili, I. S., Gregory, S. T., Valle, M., Grassucci, R., Worbs, M., Wahl, M. C., Dahlberg, A. E. & Frank, J. (2001). The polypeptide tunnel system in the ribosome and its gating in erythromycin resistance mutants of L4 and L22. *Mol. Cell* 8, 181–188.

19 Craig, E. A., Eisenman, H. C. & Hundley, H. A. (2003). Ribosome-tethered molecular chaperones: the first line of defense against protein misfolding? *Curr. Opin. Microbiol.* 6, 157–162.

20 Polevoda, B. & Sherman, F. (2000). Nalpha-terminal acetylation of eukaryotic proteins. *J. Biol. Chem.* 275, 36479–36482.

21 Rospert, S., Dubaquié, Y. & Gautschi, M. (2002). Nascent-polypeptide-associated complex. *Cell. Mol. Life Sci.* 59, 1632–1639.

22 Koch, H. G., Moser, M. & Müller, M. (2003). Signal recognition particle-dependent protein targeting, universal to all kingdoms of life. *Rev. Physiol. Biochem. Pharmacol.* 146, 55–94.

23 Hann, B. C. & Walter, P. (1991). The signal recognition particle in S. cerevisiae. *Cell* 67, 131–144.

24 Keenan, R. J., Freymann, D. M., Stroud, R. M. & Walter, P. (2001). The signal recognition particle. *Annu. Rev. Biochem.* 70, 755–775.

25 Nagai, K., Oubridge, C., Kuglstatter, A., Menichelli, E., Isel, C. & Jovine, L. (2003). Structure, function and evolution of the signal recognition particle. *Embo J.* 22, 3479–3485.

26 Wiedmann, B., Sakai, H., Davis, T. A. & Wiedmann, M. (1994). A protein complex required for signal-sequence-specific sorting and translocation. *Nature* 370, 434–440.

27 Raden, D. & Gilmore, R. (1998). Signal recognition particle-dependent targeting of ribosomes to the rough endoplasmic reticulum in the absence and presence of the nascent polypeptide-associated complex. *Mol. Biol. Cell* 9, 117–130.

28 Plath, K. & Rapoport, T. A. (2000). Spontaneous release of cytosolic proteins from posttranslational substrates before their transport into the endoplasmic reticulum. *J. Cell Biol.* 151, 167–178.

29 Reimann, B., Bradsher, J., Franke, J., Hartmann, E., Wiedmann, M., Prehn, S. & Wiedmann, B. (1999). Initial characterization of the nascent polypeptide-associated complex in yeast. *Yeast* 15, 397–407.

30 Beatrix, B., Sakai, H. & Wiedmann, M. (2000). The alpha and beta subunit of the nascent polypeptide-associated complex have distinct functions. *J. Biol. Chem.* 275, 37838–37845.

31 Gautschi, M., Just, S., Mun, A., Ross, S., Rücknagel, P., Dubaquié, Y., Ehrenhofer-Murray, A. & Rospert, S. (2003). The yeast N^{α}-acetyltransferase NatA is quantitatively anchored to the ribosome and interacts with nascent polypeptides. *Mol. Cell. Biol.* 23, 7403–7414.

32 Wang, S., Sakai, H. & Wiedmann, M. (1995). NAC covers ribosome-associated nascent chains thereby forming a protective environment for regions of nascent chains just emerging from the peptidyl transferase center. *J. Cell. Biol.* 130, 519–528.

33 Powers, T. & Walter, P. (1996). The nascent polypeptide-associated complex modulates interactions between the signal recognition particle and the ribosome. *Curr. Biol.* 6, 331–338.

34 Möller, I., Jung, M., Beatrix, B., Levy, R., Kreibich, G., Zimmermann, R., Wiedmann, M. & Lauring, B.

(1998). A general mechanism for regulation of access to the translocon: competition for a membrane attachment site on ribosomes. *Proc. Natl. Acad. Sci. USA* 95, 13425–13430.

35 Ogg, S. C. & Walter, P. (1995). SRP samples nascent chains for the presence of signal sequences by interacting with ribosomes at a discrete step during translation elongation. *Cell* 81, 1075–1084.

36 Pool, M. R., Stumm, J., Fulga, T. A., Sinning, I. & Dobberstein, B. (2002). Distinct modes of signal recognition particle interaction with the ribosome. *Science* 297, 1345–1348.

37 Crooke, E. & Wickner, W. (1987). Trigger factor: a soluble protein that folds pro-OmpA into a membrane-assembly-competent form. *Proc. Natl. Acad. Sci. USA* 84, 5216–5220.

38 Lill, R., Crooke, E., Guthrie, B. & Wickner, W. (1988). The "trigger factor cycle" includes ribosomes, presecretory proteins, and the plasma membrane. *Cell* 54, 1013–1018.

39 Stoller, G., Rücknagel, K. P., Nierhaus, K. H., Schmid, F. X., Fischer, G. & Rahfeld, J. U. (1995). A ribosome-associated peptidyl-prolyl cis/trans isomerase identified as the trigger factor. *Embo J.* 14, 4939–4948.

40 Valent, Q. A., Kendall, D. A., High, S., Kusters, R., Oudega, B. & Luirink, J. (1995). Early events in preprotein recognition in E. coli: interaction of SRP and trigger factor with nascent polypeptides. *Embo J.* 14, 5494–505.

41 Hesterkamp, T., Hauser, S., Lutcke, H. & Bukau, B. (1996). Escherichia coli trigger factor is a prolyl isomerase that associates with nascent polypeptide chains. *Proc. Natl. Acad. Sci. USA* 93, 4437–4441.

42 Gothel, S. F., Scholz, C., Schmid, F. X. & Marahiel, M. A. (1998). Cyclophilin and trigger factor from Bacillus subtilis catalyze in vitro protein folding and are necessary for viability under starvation conditions. *Biochemistry* 37, 13392–13399.

43 Teter, S. A., Houry, W. A., Ang, D., Tradler, T., Rockabrand, D., Fischer, G., Blum, P., Georgopoulos, C. & Hartl, F. U. (1999). Polypeptide flux through bacterial Hsp70: DnaK cooperates with trigger factor in chaperoning nascent chains. *Cell* 97, 755–765.

44 Deuerling, E., Schulze-Specking, A., Tomoyasu, T., Mogk, A. & Bukau, B. (1999). Trigger factor and DnaK cooperate in folding of newly synthesized proteins. *Nature* 400, 693–696.

45 Kristensen, O. & Gajhede, M. (2003). Chaperone Binding at the Ribosomal Exit Tunnel. *Structure* 11, 1547–1556.

46 Kramer, G., Rauch, T., Rist, W., Vorderwulbecke, S., Patzelt, H., Schulze-Specking, A., Ban, N., Deuerling, E. & Bukau, B. (2002). L23 protein functions as a chaperone docking site on the ribosome. *Nature* 419, 171–174.

47 Maier, R., Eckert, B., Scholz, C., Lilie, H. & Schmid, F. X. (2003). Interaction of trigger factor with the ribosome. *J. Mol. Biol.* 326, 585–592.

48 Scholz, C., Stoller, G., Zarnt, T., Fischer, G. & Schmid, F. X. (1997). Cooperation of enzymatic and chaperone functions of trigger factor in the catalysis of protein folding. *Embo J.* 16, 54–58.

49 Maier, R., Scholz, C. & Schmid, F. X. (2001). Dynamic association of trigger factor with protein substrates. *J. Mol. Biol.* 314, 1181–1190.

50 Scholz, C., Mücke, M., Rape, M., Pecht, A., Pahl, A., Bang, H. & Schmid, F. X. (1998). Recognition of protein substrates by the prolyl isomerase trigger factor is independent of proline residues. *J. Mol. Biol.* 277, 723–732.

51 Gu, S. Q., Peske, F., Wieden, H. J., Rodnina, M. V. & Wintermeyer, W. (2003). The signal recognition particle binds to protein L23 at the peptide exit of the Escherichia coli ribosome. *Rna* 9, 566–573.

52 Ullers, R. S., Houben, E. N., Raine, A., ten Hagen-Jongman, C. M., Ehrenberg, M., Brunner, J., Oudega, B., Harms, N. & Luirink, J.

(2003). Interplay of signal recognition particle and trigger factor at L23 near the nascent chain exit site on the Escherichia coli ribosome. *J. Cell Biol.* 161, 679–684.

53 Nakatogawa, H. & Ito, K. (2002). The ribosomal exit tunnel functions as a discriminating gate. *Cell* 108, 629–636.

54 Flanagan, J. J., Chen, J. C., Miao, Y., Shao, Y., Lin, J., Bock, P. E. & Johnson, A. E. (2003). Signal recognition particle binds to ribosome-bound signal sequences with fluorescence-detected subnanomolar affinity that does not diminish as the nascent chain lengthens. *J. Biol. Chem.* 278, 18628–18637.

55 Gong, F. & Yanofsky, C. (2002). Instruction of translating ribosome by nascent peptide. *Science* 297, 1864–1867.

56 Mayer, M. P., Brehmer, D., Gässler, C. S. & Bukau, B. (2002). Hsp70 chaperone machines. *Adv. Protein Chem.* 59, 1–44.

57 Kramer, G., Ramachandiran, V., Horowitz, P. M. & Hardesty, B. (2002). The molecular chaperone DnaK is not recruited to translating ribosomes that lack trigger factor. *Arch. Biochem. Biophys.* 403, 63–70.

58 Reyes, D. Y. & Yoshikawa, H. (2002). DnaK chaperone machine and trigger factor are only partially required for normal growth of Bacillus subtilis. *Biosci. Biotechnol. Biochem.* 66, 1583–1586.

59 Flaherty, K. M., DeLuca-Flaherty, C. & McKay, D. B. (1990). Three-dimensional structure of the ATPase fragment of a 70K heat-shock cognate protein. *Nature* 346, 623–628.

60 Wang, T.-F., Chang, J.-H. & Wang, C. (1993). Identification of the peptide binding domain of hsc70. 18-kilodalton fragment located immediately after ATPase domain is sufficient for high affinity binding. *J. Biol. Chem.* 268, 26049–26051.

61 Walter, S. & Buchner, J. (2002). Molecular chaperones–cellular machines for protein folding. *Angew. Chem. Int. Ed. Engl.* 41, 1098–1113.

62 Nelson, R. J., Ziegelhoffer, T., Nicolet, C., Werner-Washburne, M. & Craig, E. A. (1992). The translation machinery and 70 kd heat shock protein cooperate in protein synthesis. *Cell* 71, 97–105.

63 Gautschi, M., Lilie, H., Fünfschilling, U., Mun, A., Ross, S., Lithgow, T., Rücknagel, P. & Rospert, S. (2001). RAC, a stable ribosome-associated complex in yeast formed by the DnaK-DnaJ homologs Ssz1p and zuotin. *Proc. Natl. Acad. Sci. USA* 98, 3762–3767.

64 Horton, L. E., James, P., Craig, E. A. & Hensold, J. O. (2001). The yeast hsp70 homologue Ssa is required for translation and interacts with Sis1 and Pab1 on translating ribosomes. *J. Biol. Chem.* 276, 14426–14433.

65 James, P., Pfund, C. & Craig, E. A. (1997). Functional specificity among Hsp70 molecular chaperones. *Science* 275, 387–389.

66 Pfund, C., Lopez-Hoyo, N., Ziegelhoffer, T., Schilke, B. A., Lopez-Buesa, P., Walter, W. A., Wiedmann, M. & Craig, E. A. (1998). The molecular chaperone Ssb from Saccharomyces cerevisiae is a component of the ribosome-nascent chain complex. *Embo J.* 17, 3981–3989.

67 Ryan, M. T. & Pfanner, N. (2001). Hsp70 proteins in protein translocation. *Adv. Protein Chem.* 59, 223–242.

68 Bukau, B. & Horwich, A. L. (1998). The Hsp70 and Hsp60 chaperone machines. *Cell* 92, 351–366.

69 Kelley, W. L. (1998). The J-domain family and the recruitment of chaperone power. *Trends Biochem. Sci.* 23, 222–227.

70 Zhong, T. & Arndt, K. T. (1993). The yeast SIS1 protein, a DnaJ homolog, is required for the initiation of translation. *Cell* 73, 1175–1186.

71 Yan, W., Schilke, B., Pfund, C., Walter, W., Kim, S. & Craig, E. A. (1998). Zuotin, a ribosome-associated DnaJ molecular chaperone. *Embo J.* 17, 4809–4817.

72 Luke, M. M., Sutton, A. & Arndt, K. T. (1991). Characterization of SIS1, a Saccharomyces cerevisiae homologue

of bacterial dnaJ proteins. *J. Cell Biol.* 114, 623–638.

73 Salmon, D., Montero-Lomeli, M. & Goldenberg, S. (2001). A DnaJ-like protein homologous to the yeast co-chaperone Sis1 (TcJ6p) is involved in initiation of translation in Trypanosoma cruzi. *J. Biol. Chem.* 276, 43970–43979.

74 Sachs, A. B. & Davis, R. W. (1989). The poly(A) binding protein is required for poly(A) shortening and 60S ribosomal subunit-dependent translation initiation. *Cell* 58, 857–867.

75 Wilusz, C. J., Wormington, M. & Peltz, S. W. (2001). The cap-to-tail guide to mRNA turnover. *Nat. Rev. Mol. Cell. Biol.* 2, 237–246.

76 Preiss, T. & Hentze, M. W. (1999). From factors to mechanisms: translation and translational control in eukaryotes. *Curr. Opin. Genet. Dev.* 9, 515–521.

77 Bush, G. L. & Meyer, D. I. (1996). The refolding activity of the yeast heat shock proteins Ssa1 and Ssa2 defines their role in protein translocation. *J. Cell Biol.* 135, 1229–1237.

78 Duttagupta, R., Vasudevan, S., Wilusz, C. J. & Peltz, S. W. (2003). A yeast homologue of Hsp70, Ssa1p, regulates turnover of the MFA2 transcript through its AU-rich 3′ untranslated region. *Mol. Cell. Biol.* 23, 2623–2632.

79 Geymonat, M., Wang, L., Garreau, H. & Jacquet, M. (1998). Ssa1p chaperone interacts with the guanine nucleotide exchange factor of ras Cdc25p and controls the cAMP pathway in Saccharomyces cerevisiae. *Mol. Microbiol.* 30, 855–864.

80 Kim, S., Schilke, B., Craig, E. A. & Horwich, A. L. (1998). Folding in vivo of a newly translated yeast cytosolic enzyme is mediated by the SSA class of cytosolic yeast Hsp70 proteins. *Proc. Natl. Acad. Sci. USA* 95, 12860–12865.

81 Liu, Y., Liang, S. & Tartakoff, A. M. (1996). Heat shock disassembles the nucleolus and inhibits nuclear protein import and poly(A)+ RNA export. *Embo J.* 15, 6750–6757.

82 Lu, Z. & Cyr, D. M. (1998). Protein folding activity of Hsp70 is modified differentially by the hsp40 co-chaperones Sis1 and Ydj1. *J. Biol. Chem.* 273, 27824–27830.

83 Qian, X., Hou, W., Zhengang, L. & Sha, B. (2002). Direct interactions between molecular chaperones heat-shock protein (Hsp)70 and Hsp40: yeast Hsp70 Ssa1 binds the extreme C-terminal region of yeast Hsp40 Sis1. *Biochem. J.* 361, 27–34.

84 Shulga, N., James, P., Craig, E. A. & Goldfarb, D. S. (1999). A nuclear export signal prevents Saccharomyces cerevisiae Hsp70 Ssb1p from stimulating nuclear localization signal-directed nuclear transport. *J. Biol. Chem.* 274, 16501–16507.

85 Craig, E. A. & Jacobsen, K. (1985). Mutations in cognate genes of Saccharomyces cerevisiae hsp70 result in reduced growth rates at low temperatures. *Mol. Cell. Biol.* 5, 3517–3524.

86 Ogle, J. M., Carter, A. P. & Ramakrishnan, V. (2003). Insights into the decoding mechanism from recent ribosome structures. *Trends Biochem. Sci.* 28, 259–266.

87 Gautschi, M., Mun, A., Ross, S. & Rospert, S. (2002). A functional chaperone triad on the yeast ribosome. *Proc. Natl. Acad. Sci. USA* 99, 4209–4214.

88 Pfund, C., Huang, P., Lopez-Hoyo, N. & Craig, E. A. (2001). Divergent functional properties of the ribosome-associated molecular chaperone Ssb compared with other Hsp70s. *Mol. Biol. Cell* 12, 3773–3782.

89 Lopez, N., Halladay, J., Walter, W. & Craig, E. A. (1999). SSB, encoding a ribosome-associated chaperone, is coordinately regulated with ribosomal protein genes. *J. Bacteriol.* 181, 3136–3143.

90 Hochstrasser, M., Johnson, P. R., Arendt, C. S., Amerik, A., Swaminathan, S., Swanson, R., Li, S. J., Laney, J., Pals-Rylaarsdam, R., Nowak, J. & Connerly, P. L. (1999). The Saccharomyces cerevisiae ubiquitin-proteasome system. *Philos.*

Trans. R. Soc. Lond. B Biol. Sci. 354, 1513–1522.

91 Ohba, M. (1997). Modulation of intracellular protein degradation by SSB1-SIS1 chaperon system in yeast S. cerevisiae. *FEBS Lett.* 409, 307–311.

92 Ohba, M. (1994). A 70-kDa heat shock cognate protein suppresses the defects caused by a proteasome mutation in Saccharomyces cerevisiae. *FEBS Lett.* 351, 263–266.

93 Lopez-Buesa, P., Pfund, C. & Craig, E. A. (1998). The biochemical properties of the ATPase activity of a 70-kDa heat shock protein (Hsp70) are governed by the C-terminal domains. *Proc. Natl. Acad. Sci. USA* 95, 15253–15258.

94 Kosodo, Y., Imai, K., Hirata, A., Noda, Y., Takatsuki, A., Adachi, H. & Yoda, K. (2001). Multicopy suppressors of the sly1 temperature-sensitive mutation in the ER-Golgi vesicular transport in Saccharomyces cerevisiae. *Yeast* 18, 1003–1014.

95 Dunn, C. D. & Jensen, R. E. (2003). Suppression of a defect in mitochondrial protein import identifies cytosolic proteins required for viability of yeast cells lacking mitochondrial DNA. *Genetics* 165, 35–45.

96 Siegers, K., Bolter, B., Schwarz, J. P., Bottcher, U. M., Guha, S. & Hartl, F. U. (2003). TRiC/CCT cooperates with different upstream chaperones in the folding of distinct protein classes. *Embo J.* 22, 5230–5240.

97 Siegers, K., Waldmann, T., Leroux, M. R., Grein, K., Shevchenko, A., Schiebel, E. & Hartl, F. U. (1999). Compartmentation of protein folding in vivo: sequestration of non-native polypeptide by the chaperonin-GimC system. *EMBO Journal* 18, 75–84.

98 Hansen, W. J., Cowan, N. J. & Welch, W. J. (1999). Prefoldin-nascent chain complexes in the folding of cytoskeletal proteins. *J. Cell Biol.* 145, 265–277.

99 Stoldt, V., Rademacher, F., Kehren, V., Ernst, J. F., Pearce, D. A. & Sherman, F. (1996). Review: the Cct eukaryotic chaperonin subunits of Saccharomyces cerevisiae and other yeasts. *Yeast* 12, 523–529.

100 Geissler, S., Siegers, K. & Schiebel, E. (1998). A novel protein complex promoting formation of functional alpha- and gamma-tubulin. *Embo J.* 17, 952–966.

101 Hartl, F. U. & Hayer-Hartl, M. (2002). Molecular chaperones in the cytosol: from nascent chain to folded protein. *Science* 295, 1852–1858.

102 Frydman, J. (2001). Folding of newly translated proteins in vivo: The Role of molecular chaperones. *Annu. Rev. Biochem.* 70, 603–647.

103 McCallum, C. D., Do, H., Johnson, A. E. & Frydman, J. (2000). The interaction of the chaperonin tailless complex polypeptide 1 (TCP1) ring complex (TRiC) with ribosome-bound nascent chains examined using photo-cross-linking. *J. Cell Biol.* 149, 591–602.

104 Motohashi, K., Yohda, M., Endo, I. & Yoshida, M. (1996). A novel factor required for the assembly of the DnaK and DnaJ chaperones of Thermus thermophilus. *J. Biol. Chem.* 271, 17343–17348.

105 Schlee, S. & Reinstein, J. (2002). The DnaK/ClpB chaperone system from Thermus thermophilus. *Cell. Mol. Life Sci.* 59, 1598–1606.

106 Hundley, H., Eisenman, H., Walter, W., Evans, T., Hotokezaka, Y., Wiedmann, M. & Craig, E. (2002). The in vivo function of the ribosome-associated Hsp70, Ssz1, does not require its putative peptide-binding domain. *Proc. Natl. Acad. Sci. USA* 99, 4203–4208.

107 Hallstrom, T. C., Katzmann, D. J., Torres, R. J., Sharp, W. J. & Moye-Rowley, W. S. (1998). Regulation of transcription factor Pdr1p function by an Hsp70 protein in Saccharomyces cerevisiae. *Mol. Cell. Biol.* 18, 1147–1155.

108 Lindquist, S., Krobitsch, S., Li, L. & Sondheimer, N. (2001). Investigating protein conformation-based inheritance and disease in yeast. *Philos. Trans. R. Soc. Lond. B Biol. Sci.* 356, 169–76.

109 Tuite, M. F. & Lindquist, S. L. (1996). Maintenance and inheritance of yeast prions. *Trends Genet*. 12, 467–471.

110 Osherovich, L. Z. & Weissman, J. S. (2002). The utility of prions. *Dev. Cell* 2, 143–151.

111 Tuite, M. F. (2000). Yeast prions and their prion-forming domain. *Cell* 100, 289–92.

112 Wickner, R. B., Taylor, K. L., Edskes, H. K., Maddelein, M. L., Moriyama, H. & Roberts, B. T. (2000). Prions of yeast as heritable amyloidoses. *J. Struct. Biol*. 130, 310–322.

113 Chernoff, Y. O., Lindquist, S. L., Ono, B., Inge-Vechtomov, S. G. & Liebman, S. W. (1995). Role of the chaperone protein Hsp104 in propagation of the yeast prion-like factor [psi+]. *Science* 268, 880–884.

114 Schirmer, E. C., Glover, J. R., Singer, M. A. & Lindquist, S. (1996). HSP100/Clp proteins: a common mechanism explains diverse functions. *Trends Biochem. Sci*. 21, 289–296.

115 Parsell, D. A., Sanchez, Y., Stitzel, J. D. & Lindquist, S. (1991). Hsp104 is a highly conserved protein with two essential nucleotide-binding sites. *Nature* 353, 270–3.

116 Sanchez, Y., Taulien, J., Borkovich, K. A. & Lindquist, S. (1992). Hsp104 is required for tolerance to many forms of stress. *Embo J*. 11, 2357–2364.

117 Glover, J. R. & Lindquist, S. (1998). Hsp104, Hsp70, and Hsp40: a novel chaperone system that rescues previously aggregated proteins. *Cell* 94, 73–82.

118 Patino, M. M., Liu, J. J., Glover, J. R. & Lindquist, S. (1996). Support for the prion hypothesis for inheritance of a phenotypic trait in yeast. *Science* 273, 622–6.

119 Paushkin, S. V., Kushnirov, V. V., Smirnov, V. N. & Ter-Avanesyan, M. D. (1996). Propagation of the yeast prion-like [psi+] determinant is mediated by oligomerization of the SUP35-encoded polypeptide chain release factor. *Embo J*. 15, 3127–3134.

120 Wegrzyn, R. D., Bapat, K., Newnam, G. P., Zink, A. D. & Chernoff, Y. O. (2001). Mechanism of prion loss after Hsp104 inactivation in yeast. *Mol. Cell. Biol*. 21, 4656–4669.

121 Uptain, S. M., Sawicki, G. J., Caughey, B., Lindquist, S., Chien, P. & Weissman, J. S. (2001). Strains of [PSI(+)] are distinguished by their efficiencies of prion-mediated conformational conversion conformational diversity in a yeast prion dictates its seeding specificity. *Embo J*. 20, 6236–6245.

122 True, H. L. & Lindquist, S. L. (2000). A yeast prion provides a mechanism for genetic variation and phenotypic diversity. *Nature* 407, 477–483.

123 Newnam, G. P., Wegrzyn, R. D., Lindquist, S. L. & Chernoff, Y. O. (1999). Antagonistic interactions between yeast chaperones Hsp104 and Hsp70 in prion curing. *Mol. Cell. Biol*. 19, 1325–1333.

124 Kryndushkin, D. S., Smirnov, V. N., Ter-Avanesyan, M. D. & Kushnirov, V. V. (2002). Increased expression of Hsp40 chaperones, transcriptional factors, and ribosomal protein Rpp0 can cure yeast prions. *J. Biol. Chem*. 277, 23702–23708.

125 Kushnirov, V. V., Kryndushkin, D. S., Boguta, M., Smirnov, V. N. & Ter-Avanesyan, M. D. (2000). Chaperones that cure yeast artificial [PSI+] and their prion-specific effects. *Curr. Biol*. 10, 1443–1446.

126 Chernoff, Y. O., Newnam, G. P., Kumar, J., Allen, K. & Zink, A. D. (1999). Evidence for a protein mutator in yeast: role of the Hsp70-related chaperone ssb in formation, stability, and toxicity of the [PSI] prion. *Mol. Cell. Biol*. 19, 8103–8112.

127 Chacinska, A., Szczesniak, B., Kochneva-Pervukhova, N. V., Kushnirov, V. V., Ter-Avanesyan, M. D. & Boguta, M. (2001). Ssb1 chaperone is a [PSI+] prion-curing factor. *Curr. Genet*. 39, 62–7.

128 Sondheimer, N., Lopez, N., Craig, E. A. & Lindquist, S. (2001). The role of Sis1 in the maintenance of the [RNQ+] prion. *Embo J*. 20, 2435–42.

129 Lopez, N., Aron, R. & Craig, E. A. (2003). Specificity of Class II Hsp40 Sis1 in Maintenance of Yeast Prion [RNQ(+)]. *Mol. Biol. Cell* 14, 1172–1181.

130 Chang, H. C., Nathan, D. F. & Lindquist, S. (1997). In vivo analysis of the Hsp90 cochaperone Sti1 (p60). *Mol. Cell. Biol.* 17, 318–3125.

131 Wegele, H., Haslbeck, M., Reinstein, J. & Buchner, J. (2003). Sti1 is a novel activator of the Ssa proteins. *J. Biol. Chem.* 278, 25970–25976.

132 Polevoda, B. & Sherman, F. (2003). N-terminal acetyltransferases and sequence requirements for N-terminal acetylation of eukaryotic proteins. *J. Mol. Biol.* 325, 595–622.

133 Li, X. & Chang, Y. H. (1995). Amino-terminal protein processing in Saccharomyces cerevisiae is an essential function that requires two distinct methionine aminopeptidases. *Proc. Natl. Acad. Sci. USA* 92, 12357–12361.

134 Dummitt, B., Micka, W. S. & Chang, Y. H. (2003). N-terminal methionine removal and methionine metabolism in Saccharomyces cerevisiae. *J. Cell Biochem.* 89, 964–974.

135 Gonda, D. K., Bachmair, A., Wunning, I., Tobias, J. W., Lane, W. S. & Varshavsky, A. (1989). Universality and structure of the N-end rule. *J. Biol. Chem.* 264, 16700–16712.

136 Moerschell, R. P., Hosokawa, Y., Tsunasawa, S. & Sherman, F. (1990). The specificities of yeast methionine aminopeptidase and acetylation of amino-terminal methionine in vivo. Processing of altered iso-1-cytochromes c created by oligonucleotide transformation. *J. Biol. Chem.* 265, 19638–19643.

137 Vetro, J. A. & Chang, Y. H. (2002). Yeast methionine aminopeptidase type 1 is ribosome-associated and requires its N-terminal zinc finger domain for normal function in vivo. *J. Cell Biochem.* 85, 678–688.

138 Park, E. C. & Szostak, J. W. (1992). ARD1 and NAT1 proteins form a complex that has N-terminal acetyltransferase activity. *Embo J.* 11, 2087–2093.

139 Mullen, J. R., Kayne, P. S., Moerschell, R. P., Tsunasawa, S., Gribskov, M., Colavito-Shepanski, M., Grunstein, M., Sherman, F. & Sternglanz, R. (1989). Identification and characterization of genes and mutants for an N-terminal acetyltransferase from yeast. *Embo J.* 8, 2067–2075.

140 Polevoda, B., Norbeck, J., Takakura, H., Blomberg, A. & Sherman, F. (1999). Identification and specificities of N-terminal acetyltransferases from Saccharomyces cerevisiae. *Embo J.* 18, 6155–6168.

141 Tercero, J. C. & Wickner, R. B. (1992). MAK3 encodes an N-acetyltransferase whose modification of the L-A gag NH2 terminus is necessary for virus particle assembly. *J. Biol. Chem.* 267, 20277–20281.

142 Polevoda, B., Cardillo, T. S., Doyle, T. C., Bedi, G. S. & Sherman, F. (2003). Nat3p and Mdm20p are required for function of yeast NatB Nalpha-terminal acetyltransferase and of actin and tropomyosin. *J. Biol. Chem.* 3, 3.

143 Singer, J. M. & Shaw, J. M. (2003). Mdm20 protein functions with Nat3 protein to acetylate Tpm1 protein and regulate tropomyosin-actin interactions in budding yeast. *Proc. Natl. Acad. Sci. USA* 100, 7644–9.

144 Neuwald, A. F. & Landsman, D. (1997). GCN5-related histone N-acetyltransferases belong to a diverse superfamily that includes the yeast SPT10 protein. *Trends Biochem. Sci.* 22, 154–155.

145 Blatch, G. L. & Lassle, M. (1999). The tetratricopeptide repeat: a structural motif mediating protein-protein interactions. *Bioessays* 21, 932–939.

146 Polevoda, B. & Sherman, F. (2003). Composition and function of the eukaryotic N-terminal acetyltransferase subunits. *Biochem. Biophys. Res. Commun.* 308, 1–11.

147 Song, O. K., Wang, X., Waterborg,

J. H. & Sternglanz, R. (2003). An Nalpha-acetyltransferase responsible for acetylation of the N-terminal residues of histones H4 and H2A. *J. Biol. Chem.* 278, 38109–38112.

148 Takakura, H., Tsunasawa, S., Miyagi, M. & Warner, J. R. (1992). NH2-terminal acetylation of ribosomal proteins of Saccharomyces cerevisiae. *J. Biol. Chem.* 267, 5442–5445.

149 Arnold, R. J., Polevoda, B., Reilly, J. P. & Sherman, F. (1999). The action of N-terminal acetyltransferases on yeast ribosomal proteins. *J. Biol. Chem.* 274, 37035–37040.

150 Whiteway, M., Freedman, R., Van Arsdell, S., Szostak, J. W. & Thorner, J. (1987). The yeast ARD1 gene product is required for repression of cryptic mating-type information at the HML locus. *Mol. Cell. Biol.* 7, 3713–3722.

151 Whiteway, M. & Szostak, J. W. (1985). The ARD1 gene of yeast functions in the switch between the mitotic cell cycle and alternative developmental pathways. *Cell* 43, 483–492.

152 Tercero, J. C., Dinman, J. D. & Wickner, R. B. (1993). Yeast MAK3 N-acetyltransferase recognizes the N-terminal four amino acids of the major coat protein (gag) of the L-A double-stranded RNA virus. *J. Bacteriol.* 175, 3192–3194.

153 Kurzchalia, T. V., Wiedmann, M., Girshovich, A. S., Bochkareva, E. S., Bielka, H. & Rapoport, T. A. (1986). The signal sequence of nascent preprolactin interacts with the 54K polypeptide of the signal recognition particle. *Nature* 320, 634–636.

154 Fünfschilling, U. & Rospert, S. (1999). Nascent Polypeptide-associated Complex Stimulates Protein Import into Yeast Mitochondria. *Mol. Biol. Cell.* 10, 3289–3299.

155 Wild, K., Weichenrieder, O., Strub, K., Sinning, I. & Cusack, S. (2002). Towards the structure of the mammalian signal recognition particle. *Curr. Opin. Struct. Biol.* 12, 72–81.

156 Planta, R. J. & Mager, W. H. (1998). The list of cytoplasmic ribosomal proteins of Saccharomyces cerevisiae. *Yeast* 14, 471–477.

157 Winzeler, E. A., Shoemaker, D. D., Astromoff, A., Liang, H., Anderson, K., Andre, B., Bangham, R., Benito, R., Boeke, J. D., Bussey, H., Chu, A. M., Connelly, C., Davis, K., Dietrich, F., Dow, S. W., El Bakkoury, M., Foury, F., Friend, S. H., Gentalen, E., Giaever, G., Hegemann, J. H., Jones, T., Laub, M., Liao, H., Davis, R. W. & et al. (1999). Functional characterization of the S. cerevisiae genome by gene deletion and parallel analysis. *Science* 285, 901–906.

158 Rutgers, C. A., Schaap, P. J., van't Riet, J., Woldringh, C. L. & Raue, H. A. (1990). In vivo and in vitro analysis of structure-function relationships in ribosomal protein L25 from Saccharomyces cerevisiae. *Biochim. Biophys. Acta* 1050, 74–79.

159 Song, J. M., Cheung, E. & Rabinowitz, J. C. (1996). Organization and characterization of the two yeast ribosomal protein YL19 genes. *Curr. Genet.* 30, 273–278.

160 Sachs, A. B. & Davis, R. W. (1990). Translation initiation and ribosomal biogenesis: involvement of a putative rRNA helicase and RPL46. *Science* 247, 1077–1079.

161 Lucioli, A., Presutti, C., Ciafre, S., Caffarelli, E., Fragapane, P. & Bozzoni, I. (1988). Gene dosage alteration of L2 ribosomal protein genes in Saccharomyces cerevisiae: effects on ribosome synthesis. *Mol. Cell. Biol.* 8, 4792–4798.

162 George, R., Beddoe, T., Landl, K. & Lithgow, T. (1998). The yeast nascent polypeptide-associated complex initiates protein targeting to mitochondria in vivo. *Proc. Natl. Acad. Sci. USA* 95, 2296–2301.

163 Brown, J. D., Hann, B. C., Medzihradszky, K. F., Niwa, M., Burlingame, A. L. & Walter, P. (1994). Subunits of the Saccharomyces cerevisiae signal recognition particle required for its functional expression. *Embo J.* 13, 4390–4400.

164 Mason, N., Ciufo, L. F. & Brown,

J. D. (2000). Elongation arrest is a physiologically important function of signal recognition particle. *Embo J.* 19, 4164–4174.

165 Willer, M., Jermy, A. J., Steel, G. J., Garside, H. J., Carter, S. & Stirling, C. J. (2003). An in vitro assay using overexpressed yeast SRP demonstrates that cotranslational translocation is dependent upon the J-domain of Sec63p. *Biochemistry* 42, 7171–7177.

166 Zopf, D., Bernstein, H. D., Johnson, A. E. & Walter, P. (1990). The methionine-rich domain of the 54 kd protein subunit of the signal recognition particle contains an RNA binding site and can be crosslinked to a signal sequence. *Embo J.* 9, 4511–4517.

167 High, S. & Dobberstein, B. (1991). The signal sequence interacts with the methionine-rich domain of the 54-kD protein of signal recognition particle. *J. Cell Biol.* 113, 229–233.

168 George, R., Walsh, P., Beddoe, T. & Lithgow, T. (2002). The nascent polypeptide-associated complex (NAC) promotes interaction of ribosomes with the mitochondrial surface in vivo. *FEBS Lett.* 516, 213–216.

169 Valent, Q. A., de Gier, J. W., von Heijne, G., Kendall, D. A., ten Hagen-Jongman, C. M., Oudega, B. & Luirink, J. (1997). Nascent membrane and presecretory proteins synthesized in Escherichia coli associate with signal recognition particle and trigger factor. *Mol. Microbiol.* 25, 53–64.

170 Polevoda, B. & Sherman, F. (2001). NatC Nalpha-terminal acetyltransferase of yeast contains three subunits, Mak3p, Mak10p, and Mak31p. *J. Biol. Chem.* 276, 20154–20159.

13
The Role of Trigger Factor in Folding of Newly Synthesized Proteins

Elke Deuerling, Thomas Rauch, Holger Patzelt, and Bernd Bukau

13.1
Introduction

The efficient folding of newly synthesized proteins in vivo requires the assistance of molecular chaperones [1, 2]. Well established is the role of cytosolic chaperones in protein folding, which mainly act posttranslationally, e.g., the *E. coli* chaperones DnaK and GroEL with their respective DnaJ/GrpE and GroES co-chaperones (see also Chapters 14 and 20). During the past few years, however, the discovery of ribosome-associated chaperones that associate with nascent polypeptides as soon as they emerge from the ribosomal exit tunnel has shed new light on the process of de novo protein folding and has expanded the repertoire of chaperones forming a functional network to support productive protein folding in vivo. The coupling of protein biosynthesis with protein folding via ribosome-associated chaperones seems to be an evolutionarily conserved principle that exists in all organisms even though many different types of chaperones are involved (see also Chapter 12). So far *E. coli* trigger factor is the best studied of these chaperones. In this chapter we will summarize the current knowledge about the in vivo role of trigger factor in protein folding, we will describe in detail the structure-function relationship of trigger factor, and we will put emphasis on biochemical methods used to analyze trigger factor in vitro.

13.2
In Vivo Function of Trigger Factor

13.2.1
Discovery

Trigger factor was first identified in 1987 by W. Wickner and coworkers as a factor triggering the translocation-competent conformation of pro-outer-membrane protein A (proOmpA) for its import into membrane vesicles [3]. Trigger factor was shown to be an abundant cellular protein that associates in a 1:1 stoichiometry

Protein Folding Handbook. Part II. Edited by J. Buchner and T. Kiefhaber

ISBN: 3-527-30784-2

with 70S ribosomes via the large ribosomal subunit [4]. These results were initially interpreted to indicate a secretion-specific chaperone function for trigger factor during the shuttling of secretory precursor proteins. However, it was shown thereafter that *E. coli* cells depleted of trigger factor did not show any secretion defects [5].

Years later, trigger factor was simultaneously rediscovered by three groups who investigated different processes related to protein folding in vivo [6–8]. A search by G. Fischer and coworkers for a ribosome-associated peptidyl-prolyl *cis*/*trans* isomerase (PPIase) led to the identification of trigger factor [6]. Purified trigger factor catalyzed the prolyl-peptide bond isomerization in tetrapeptides and in refolding RNase T1. J. Luirink and coworkers used an in vitro translation system to investigate the interactions of the signal recognition particle (SRP) with a variety of nascent polypeptides by chemical cross-linking [8]. Besides cross-links of nascent chains to SRP, they found that trigger factor efficiently cross-links to nascent chains of preprolactin and other secretory substrates. When searching for *E. coli* chaperones that associate with nascent *β*-galactosidase produced in an in vitro transcription/translation system, B. Bukau and colleagues discovered that ribosome-associated trigger factor interacts with both cytosolic and secretory nascent polypeptides during protein biosynthesis [7]. The association of trigger factor with the ribosome proved to be sensitive to the translational state of the ribosome, as the release of the nascent polypeptides by puromycin caused dissociation of trigger factor from the ribosome. It was therefore proposed that trigger factor is a folding catalyst acting co-translationally during the biogenesis of proteins on ribosomes [6, 7, 9].

13.2.2 Trigger Factor Cooperates With the DnaK Chaperone in the Folding of Newly Synthesized Cytosolic Proteins

The deletion of the trigger factor gene *tig* in *E. coli* results neither in defects in growth at temperatures between 15 °C and 42 °C nor in protein folding [10, 11]. A similar finding was made when the *dnaK* gene, encoding the major Hsp70 protein in *E. coli*, was deleted. Δ*dnaK* cells are viable between 15 °C and 37 °C and have only mild protein-folding defects of newly synthesized proteins [10–13]. Δ*dnaK* cells are, however, not viable at temperatures above 37 °C, probably because DnaK is essential to prevent misfolding at elevated temperatures and to repair heat-damaged proteins. Genetic evidence clarified why the loss of trigger factor or DnaK has no phenotype at permissive temperature and no consequence on the de novo folding of proteins. The simultaneous deletion of the *tig* and *dnaK* gene leads to synthetic lethality at 30 °C and above [10, 11]. Thus, either trigger factor or DnaK is sufficient for cell viability at permissive temperatures, but the loss of both leads to cell death, indicating that these two chaperones cooperate in the folding of newly synthesized polypeptides. A physical interaction between DnaK and newly synthesized proteins was demonstrated by co-immunoprecipitation experi-

ments [10, 11]. In wild-type *E. coli* cells about 5–18% of newly synthesized proteins interact transiently with DnaK. This level increased two- to threefold (26–36%) in the absence of trigger factor, indicating that upon the loss of trigger factor, the cells make more intensive use of the DnaK chaperone [10, 11]. A fraction of these proteins is in *statu nascendi*, indicating that DnaK interacts co- and posttranslationally. Moreover, it was shown that deletion of the *tig* gene induces the heat shock response in *E. coli*, thereby leading to a compensatory increase in the steady-state levels of chaperones including DnaK [14]. Thus, DnaK may serve as a potent backup system in the absence of trigger factor.

13.2.3
In Vivo Substrates of Trigger Factor and DnaK

The depletion of DnaK in the absence of trigger factor leads to the aggregation of cytosolic proteins in *E. coli*. The isolation of aggregated cytosolic proteins from *E. coli* cells is achieved by a centrifugation step after cell lysis and repetitive washing steps of the pellet containing aggregates with NP40 to remove membrane contaminations [15]. Through two-dimensional SDS-PAGE more than 340 aggregated protein species in DnaK-deficient Δ*tig* cells could be detected (Figure 13.1A) [14]. Quantitative comparison of total cellular proteins with aggregated proteins in these cells revealed that approximately 10% of the total cellular cytosolic proteins are aggregation-prone at 37 °C, a condition at which growth of these chaperone-deficient cells was not yet impaired. In contrast, only about 1% of the cytosolic proteins aggregated in DnaK-depleted tig^+ cells [14]. Although the total amount of aggregated proteins differed significantly in DnaK-depleted tig^+ and tig^- cells, the aggregation-prone protein species in these cells were similar. This finding suggests that trigger factor and DnaK share overlapping substrate pools. In cells lacking only trigger factor, no protein aggregates could be detected [10]. Proteins that are misfolded in Δ*tig* cells are likely to be rescued by the DnaK system, since the protein level of DnaK is elevated about two- to three-fold in these cells.

The aggregated protein species found in cells lacking trigger factor and DnaK range in their molecular weights from 16 kDa up to 167 kDa, whereby large-sized multi-domain proteins ($>$ 60 kDa) are enriched. It is unclear which features of large-sized proteins render them vulnerable to misfolding and aggregation during de novo folding. Unfolded conformers of large proteins expose statistically more hydrophobic surface patches than do small proteins and as a consequence may have a greater chance of undergoing intra- and intermolecular aggregation. Furthermore, hydrophobic interdomain surfaces may become exposed and thus may nucleate aggregation during co- and posttranslational folding. Finally, large-sized proteins may fold more slowly to the native state, which increases the timeframe during which aggregation of folding intermediates may occur.

Ninety-four different aggregated proteins isolated from DnaK-depleted Δ*tig* cells have been identified by mass spectrometry [14], including many essential proteins such as the elongation factor EF-Tu and the RNA-polymerase subunit RpoB, which

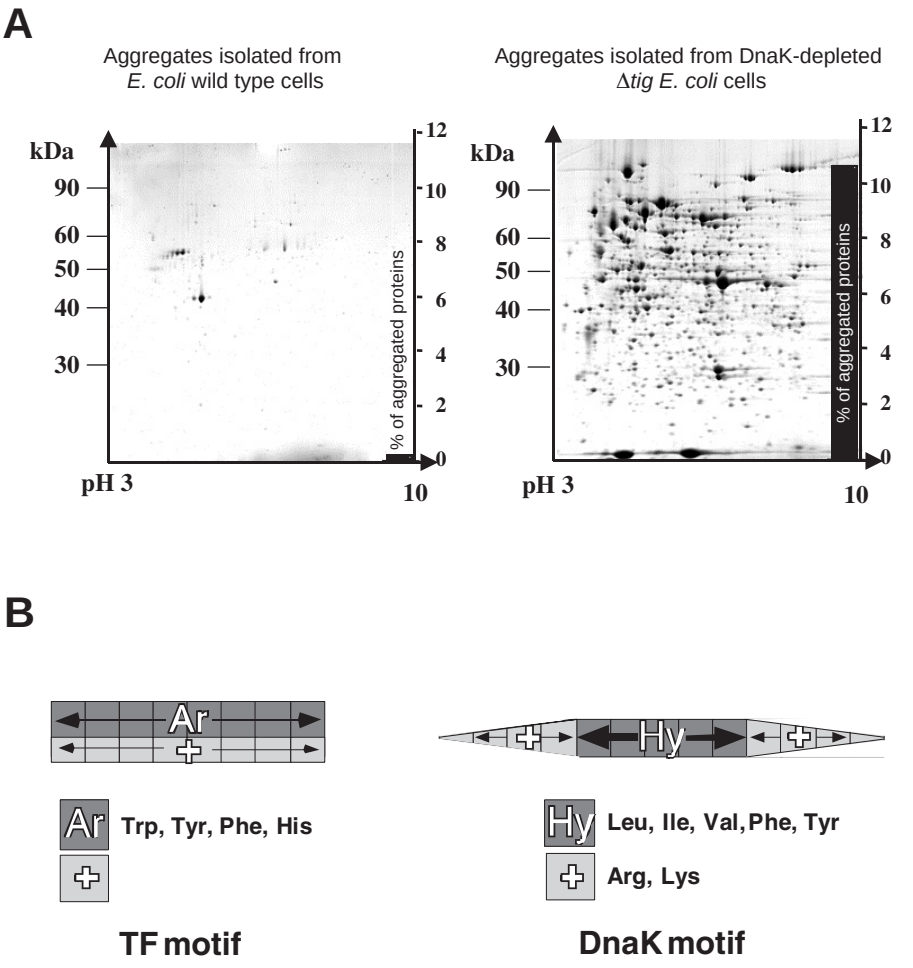

Fig. 13.1. Trigger factor and DnaK substrates. (A) Aggregated cytosolic proteins (isolated from cells grown at 37 °C in LB) were separated by 2D gel electrophoresis and Coomassie stained. Data were taken with permission from Ref. [14]. (B) Trigger factor and DnaK overlap in their binding specificities. The recognition motifs of both chaperones are shown schematically. TF and DnaK data were taken with permission from Ref. [17].

could explain the synthetic lethality of Δ*tig*Δ*dnaK* mutant cells. The identified proteins are involved in a large variety of cellular processes, including transcription, translation, and metabolism. They do not show any common features regarding pI, specific secondary structural elements, or content of prolines, which could depend on the PPIase activity of trigger factor. Interestingly, 70% of the identified proteins were also identified as thermolabile proteins that aggregate in Δ*dnaK* cells under heat shock conditions at 45 °C [16].

13.2.4 Substrate Specificity of Trigger Factor

Since trigger factor and DnaK work by completely different mechanisms, it was unclear how they were able to support folding of the same protein pool in the cytosol. The mapping of potential binding sites of trigger factor and DnaK in natural substrate proteins using cellulose-bound peptide libraries (for protocol, see Chapter 15) revealed that DnaK and trigger factor share a high overlap (77%) in binding peptides [14]. This finding is consistent with the overlapping features of the substrate-binding motifs of both chaperones (Figure 13.1B) [17].

Trigger factor binds to peptides enriched in aromatic and basic amino acids, whereas peptides with acidic amino acids are disfavored [17]. The trigger factor binding motif consists of eight amino acids whereby the positioning of basic and aromatic residues within this motif seems not to be crucial for binding (Figure 13.1B). Interestingly, prolyl residues do not contribute to the binding of trigger factor to peptides [17]. Moreover, trigger factor binds to the protein substrate RNase T1 independently of prolyl residues [18]. These results were unexpected since trigger factor is a PPIase and catalyzes the *cis*/*trans* isomerization of peptidyl-prolyl peptide bonds in peptides and protein substrates [6, 7]. The prolyl-independent substrate recognition and the PPIase activity involve the same substrate-binding pocket in the PPIase domain of trigger factor (see Section 13.3.1), suggesting that trigger factor scans nascent polypeptide chains for stretches of aromatic and basic amino acids and may isomerize peptidyl-prolyl peptide bonds within these stretches when present. However, since the majority of binding peptides (55%) do not even contain a proline [17], the isomerization reaction may not be the major activity of trigger factor when interacting with nascent polypeptide chains. Mapping of the potential trigger factor binding sites (identified by peptide library screening) within the three-dimensional structures of the substrate proteins does not reveal any enrichment within specific secondary structure elements or clustering of binding sites near the N- or C-terminus of proteins or within or outside of signal sequences. On average, trigger factor binding sites appear every 32 amino acids in a protein and are mostly localized in the interior of the native protein structures.

A related but not identical binding motif is recognized by DnaK. This chaperone recognizes a short stretch of five amino acid residues with hydrophobic character, among which leucine is especially favored (Figure 13.1B; see also Chapter 15). This hydrophobic core is flanked by positively charged amino acids, whereas negative charges are excluded [19, 20]. Trigger factor and DnaK thus both prefer to interact with hydrophobic and positively charged stretches in proteins [17, 21]. This overlap in binding specificity might be required so that both chaperones, despite their different mechanisms of action, can protect similar hydrophobic stretches in unfolded protein species and therefore promote folding of the same substrate pool.

While investigating the interaction of trigger factor and DnaK with nascent polypeptides in an in vitro transcription/translation system (see protocols, Section 13.5), it was shown that trigger factor and DnaK compete for cross-linking to a

shared binding site in a short nascent polypeptide chain of proOmpA [14]. DnaK, however, is not efficiently cross-linked to this chain in the presence of trigger factor. This is in agreement with data showing that two to three times more newly synthesized proteins associate with DnaK in the absence of trigger factor [10, 11]. Chaperone interaction with nascent polypeptides is therefore likely to follow a hierarchical order imposed by the positioning of trigger factor adjacent to the polypeptide exit tunnel on the large ribosomal subunit (see Section 13.3.4) [22, 32].

13.3
Structure–Function Analysis of Trigger Factor

13.3.1
Domain Structure and Conservation

E. coli trigger factor consists of 432 amino acids with a molecular weight of 48 kDa. To date, no high-resolution structure of the full-length trigger factor protein is available. Limited proteolysis of full-length trigger factor with proteases revealed a compactly folded, protease-resistant domain spanning residues 145–247 (Figure 13.2A). This domain has homology to the FK506-binding protein (FKBP) type of PPIases (see also Chapter 10) [6, 7, 23]. The main structural element of trigger factor's PPIase domain is a five-stranded, antiparallel β-sheet. Recently, the NMR structure of the PPIase domain of the *Mycoplasma genitalium* trigger factor was solved and it confirmed the FKBP-like fold of this domain [24]. An alignment of the PPIase domains of trigger factor homologues from different bacteria with human FKPB12 shows that the six aromatic key residues forming the FKBP12 substrate-binding pocket are conserved within the trigger factor family (Figure 13.2C). In contrast to other FKBP-like proteins, trigger factor cannot bind the PPIase inhibitor drug FK506. This is due to structural differences in the binding pocket that narrow the active site thereby causing steric clashes with FK506 [24]. Besides its catalytic activity, the PPIase domain mediates the binding specificity of trigger factor [17]. It was shown that the isolated PPIase domain displays a similar binding pattern towards membrane-coupled peptides and hence a binding specificity similar to full-length trigger factor. The structural features of the PPIase domain are compatible with the determined binding specificity of trigger factor for peptides that are enriched in aromatic and basic residues. The ring of aromatic side chains is located within a groove (Figure 13.2C) that is surrounded by negatively charged amino acids. While the aromatic amino acid residues could mediate hydrophobic interactions with aromatic amino acids enriched in peptides that are bound by trigger factor, the negative charges could explain the preference of trigger factor for basic amino acids within the substrate. However, a 10-fold higher concentration of the PPIase domain had to be used to obtain binding signals on peptide libraries with comparable intensity as compared to full-length trigger factor [17]. This finding indicates a role of the flanking domains of trigger factor in substrate binding, e.g., by forming additional contacts to the backbone of the substrate or by modulating the conformation of the PPIase domain. This hypothesis is sup-

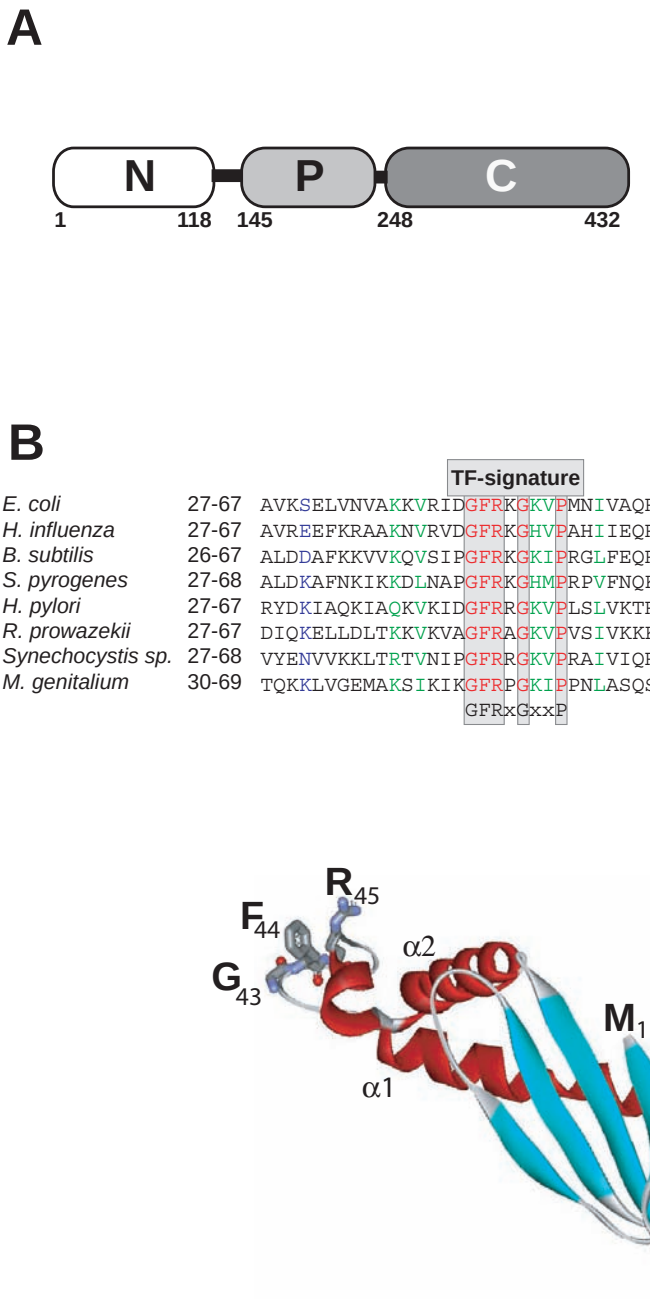

Fig. 13.2. Structure-function relationship of *E. coli* trigger factor. (A) Domain organization of *E. coli* trigger factor. (B) Alignment of the conserved region within the N-terminal trigger factor domain from different bacteria. The conserved TF signature is highlighted (top). Crystal structure of N-terminal domain in ribbon representation based on Kristensen et al. [28] (bottom).

C

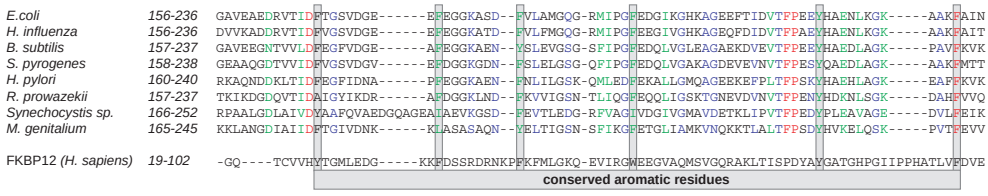
E.coli 156-236 GAVEAEDRVTIDFIGSVDGE------EPEGGKASD--FVLAMGQG-RMIPGFEDGIKGHKAGEEFTIDVTFPEEYHAENLKGK-----AAKFAIN
H. influenza 156-236 DVVKADDRVTIDFVGSVDGE------EPEGGKATD--FVLFMGQG-RMIPGFEEGIVGHKAGEQFDIDVTFPAEYHAENLKGK-----AAKFAIT
B. subtilis 157-237 GAVEEGNTVVLDFEGFVDGE------APEGGKAEN--YSLEVGSG-SFIPGFEDQLVGLEAGAEKDVEVTFPEEYHAEDLAGK-----PAVFKVK
S. pyrogenes 158-238 GEAAQGDTVVIDFVGSVDGV------EPDGGKGDN--FSLELGSG-QFIPGFEDQLVGAKAGDEVEVNVTFPESYQAEDLAGK-----AAKFMTT
H. pylori 160-240 RKAQNDDKLTIDFEGFIDNA------PPEGGKAEN--FNLILGSK-QMLEDFEKALLGMQAGEEKEFPLTFPSKYHAEHLAGK-----EAFFKVK
R. prowazekii 157-237 TKIKDGDQVTIDAIGYIKDR------APDGGKLND--FKVVIGSN-TLIQGFEQQLIGSKTGNEVDVNVTFPENYHDKNLSGK-----DAHFVVQ
Synechocystis sp. 166-252 RPAALGDLAIVDYAAFQVAEDGQAGEAIAEVKGSD--FEVTLEDG-RFVAGIVDGIVGMAVDETKLIPVTFPEDYPLEAVAGE-----DVLFEIK
M. genitalium 165-245 KKLANGDIAIIDFEGIVDNK------KLASASAQN--YELTIGSN-SFIKGFETGLIAMKVNQKKTLALTFPSDYHVKELQSK-----PVTFEVV
FKBP12 (H. sapiens) 19-102 -GQ----TCVVHYTGMLEDG-----KKFDSSRDRNKPFKFMLGKQ-EVIRGWEEGVAQMSVGQRAKLTISPDYAYGATGHPGIIPPHATLVFDVE
conserved aromatic residues

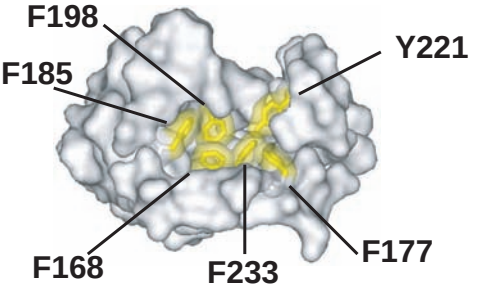
F198
Y221
F185
F168
F233
F177

D

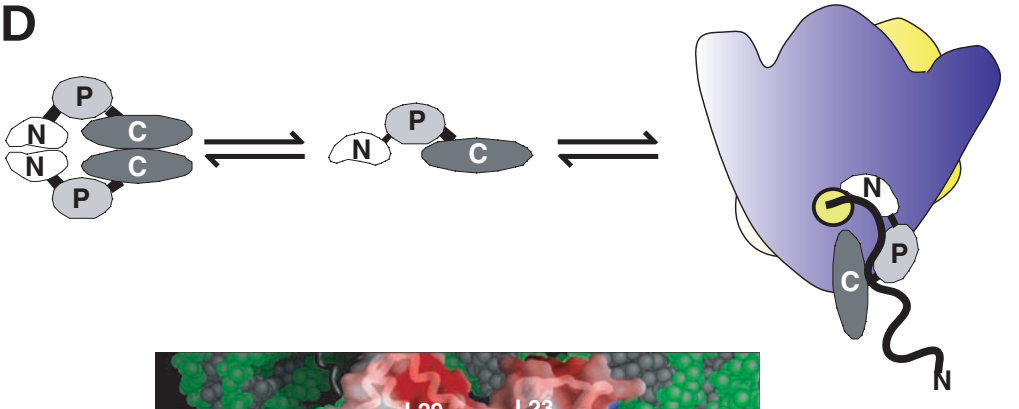
P
N
C
N
C
P
P
N
C
N
P
C
N

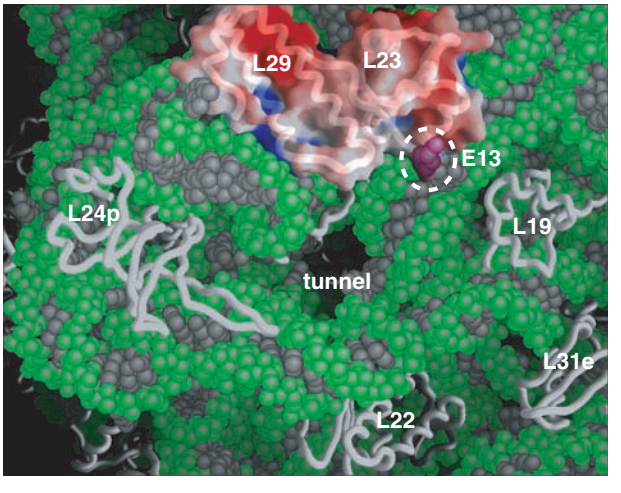
L29
L23
E13
L24p
L19
tunnel
L31e
L22

ported by the finding that the PPIase domain alone cannot efficiently promote peptidyl-prolyl isomerization-limited folding of the model protein RNase T1 [25, 26].

The N-terminal part of trigger factor (amino acids 1–144) forms another structural and functional module (Figure 13.2A,B) that is necessary and sufficient for the specific binding of trigger factor to ribosomes [27]. The N-terminus contains a compactly folded domain comprising the first 118 amino acids that mediates binding of trigger factor to the ribosome. Sequence alignments of several trigger factor homologues revealed a highly conserved GFRXGXXP motif termed TF-signature within this domain (Figure 13.2B) [22]. Evidence that the TF signature is involved in the binding to ribosomes came from mutational analysis. Introduction of three alanine residues at positions 44–46 (FRK, see Figure 13.2B) within the *E. coli* TF signature results in a strong ribosome-binding deficiency. The crystal structure of the N-terminal domain was recently solved and supports the biochemical data [28]. This domain consists of a four-stranded, antiparallel β-sheet flanked by two long α-helices (Figure 13.2B). Importantly, both helices are linked via a connecting loop that forms a protruding tip. This twisted loop contains the TF signature and shows high structural flexibility (Figure 13.2B) [28]. The molecular details of the interaction of this TF-signature loop with the ribosome remain to be determined.

The function of the C-terminal domain, which constitutes nearly half of the trigger factor protein, is unknown. This domain is poorly conserved among trigger factor proteins and no homology to any other protein is known [29]. For *E. coli* trigger factor it has been shown that the high affinity of trigger factor for unfolded RNaseT1 is severely decreased in the absence of the C-terminal domain [26], indicating that this domain itself participates in substrate binding or modulates the substrate interactions of the other domains.

So far trigger factor has been found in prokaryotes but not in the cytoplasm of eukaryotic cells [1] or archaea [30]. A potential eukaryotic trigger factor homologue is found in *Arabidopsis thaliana*, where it is most likely targeted to the chloroplast. The *A. thaliana* trigger factor has a predicted mass of 65 kDa and displays a total identity of 21% and similarity of 42% to *E. coli* trigger factor. Fragments of at least

Fig. 13.2. (C) Alignment of the trigger factor PPIase domains from different bacteria with the human FKBP12 homologue; conserved aromatic residues are highlighted (top); homology modeling of trigger factor's PPIase domain based on the yeast FKBP12 structure using INSIGHT II. The stick representation shows the conserved aromatic residues of the FKBP-like binding pocket (yellow), numbered by their position in full-length *E. coli* trigger factor. Data were taken with permission from Ref. [17]. (D) Model of trigger factor's three-state equilibrium. Trigger factor is monomeric when associated with the ribosome. The conformation might differ from the conformation of monomeric non-ribosome-associated trigger factor. In solution, TF follows a monomer-dimer equilibrium. The magnification of the ribosome (bottom) shows a space-filling model of the ribosomal polypeptide exit region of the 50S subunit from *H. marismortui*. L23/L29 are shown in a surface charge distribution illustration (GRASP) [57]. The surface-exposed E13 (corresponding to E18 in *E. coli*) involved in the interaction with trigger factor is shown in purple and circled. Other proteins at the exit are visible by their Cα traces. Data were taken with permission from Refs. [31] and [22].

four additional putative trigger factor homologues exist in barley (*Hordeum vulgare*), sugar beet (*Beta vulgaris*), wheat (*Triticum aestivum*), and an insect herbivory (*Medicago truncatula*). These potential trigger factor homologues are 50–65% identical to the *A. thaliana* protein and include the signature motif GFRPxxxxP that is very similar to their bacterial homologues (Figure 13.2B). A potential targeting sequence and the fact that, when compared to eubacterial trigger factor homologues, the *A. thaliana* protein shows the highest similarity to the trigger factor of the cyanobacterium *Synechocystis* spp. argue for a localization in chloroplasts.

It remains elusive why trigger factor is conserved in plant chloroplasts but not in mitochondria. Mitochondria have a much lower protein synthesis activity than chloroplasts, which may render the presence of a ribosome-associated chaperone unnecessary. Alternatively, mitochondria may have evolved a different chaperone system that acts as a functional equivalent of trigger factor.

13.3.2 Quaternary Structure

Experiments using size-exclusion chromatography, glutaraldehyde cross-linking (see protocols, Section 13.5), and ultracentrifugation show that non-ribosome-associated trigger factor is in a monomer-dimer equilbrium with a dissociation constant of dimeric trigger factor of approximately 18 μM [31]. Cross-linked dimeric trigger factor species were observed only in the absence of ribosomes, whereas only monomeric trigger factor was discovered in association with the ribosome, indicating that trigger factor is a monomer when attached to ribosomes. Consistent with this finding is that under saturating conditions trigger factor binds ribosomes in an apparent 1:1 stoichiometry [4, 7, 31]. Opposing results were obtained from a study based on calculations from neutron-scattering experiments with trigger factor–ribosome complexes, suggesting that trigger factor may bind to the ribosome as a homodimer [32]. Association of trigger factor with ribosomes can be monitored by the incubation of purified components and subsequent isolation of trigger factor–ribosome complexes by sucrose cushion centrifugation and analysis of the pellet by SDS-PAGE (see Section 13.5). Quantitative analysis of the binding data revealed a dissociation constant for the trigger factor–ribosome complex of approximately 1 μM [31, 33].

Glutaraldehyde cross-linking using recombinant trigger factor fragments (see Section 13.5) demonstrates that the N-terminal and C-terminal domains individually form cross-linking products corresponding to dimeric species, whereas no oligomeric species was detected for the isolated PPIase domain. In contrast to the full-length protein, however, much higher concentrations of the fragments were necessary to observe efficient cross-linking, which indicates that in the full-length protein, contacts between the N- and C-terminal domains of the monomers contribute to dimerization. Taken together, trigger factor exists in three states: the non-ribosome dimer and monomer states, which are in fast equilibrium, and the

ribosome-associated monomer state. Based on the determined dissociation constants for the trigger factor dimer and the trigger factor–ribosome complex together with the already known in vivo concentrations of trigger factor (50 μM) [11] and ribosomes (20 μM) [4], 39% of the cellular trigger factor is a free dimer, 26% a free monomer, and 35% is associated with ribosomes as monomer. Furthermore, about 90% of all ribosomes in the *E. coli* cytosol are found in association with trigger factor [31]. The in vivo function of the trigger factor dimer formation remains elusive. The dimeric trigger factor species might be a storage form, in which the protease-sensitive ribosome attachment site of trigger factor is protected. It was observed earlier that trigger factor's N-terminal domain is cleaved by endogenous proteases within the TF signature [22]. The fast monomer/dimer equilibrium would then ensure a permanent presence of functional monomeric trigger factor and saturation of ribosomes with trigger factor in the cell. Alternatively, non-ribosome-associated trigger factor might fulfill a yet unknown cellular function as a dimeric species in vivo.

13.3.3
PPIase and Chaperone Activity of Trigger Factor

Trigger factor carries out at least two activities. In vitro, both activities have been characterized. Trigger factor catalyzes the peptidyl-prolyl isomerization of chromogenic tetrapeptides [6, 7] and the peptidyl-prolyl isomerization-limited refolding of the model substrate RNase T1 [6]. The high catalytic efficiency of trigger factor towards the protein substrate results from its tight binding to protein substrates with a K_D of approximately 0.7 μM [25]. In contrast, the affinity of trigger factor for peptides is orders of magnitude lower (K_D of approximately 120 μM) [17, 24]. Moreover, trigger factor acts as a typical chaperone in vitro. It binds to unfolded proteins including denatured RNaseT1, D-glyceraldehyde-3-phosphate dehydrogenase (GAPDH), lysozyme, and bovine carbonic anhydrase [25, 34, 35] and prevents aggregation of these unfolded proteins upon dilution from the denaturant. Furthermore, it was shown that trigger factor supports the refolding of chemically denatured GAPDH in vitro [34] (see also Section 13.5). A recent study addressed the question of whether the activity of trigger factor as a ribosome-associated folding factor relies on both its chaperone and its PPIase activity [36]. The trigger factor mutant protein TF F198A, carrying a point mutation in its PPIase domain, fully retained its chaperone activity but lacked the catalytic PPIase function in vitro. Expression of the TF F198A-encoding gene complemented the synthetic lethality of Δ*tig*Δ*dnaK* cells and prevented global protein misfolding at temperatures between 20 °C and 34 °C in these cells. This indicates that the PPIase activity is not essential for the function of trigger factor in folding of newly synthesized proteins at permissive temperature.

It is possible that the PPIase function of trigger factor might be required under specific conditions or for specific substrates. In *Bacillus subtilis* the simultaneous

deletion of the *tig* gene and the *ppiB* gene encoding for the second cytosolic PPIase in *Bacillus* inhibits growth under starvation conditions in minimal media lacking certain amino acids [37]. It is, however, unclear whether this phenotype relates to trigger factor's PPIase or chaperone function. Fischer and colleagues reported on the trigger factor mutant protein F233Y, which has reduced PPIase activity towards peptides [38]. When the F233Y mutant was used to complement a Δ*tig* strain, a reduced survival rate on plates after storage for 25 days at 6 °C was observed compared to wild-type trigger factor [39]. This might suggest an involvement of trigger factor in cell viability at very low temperatures. However, the interpretation of this finding is difficult since 6 °C is below the physiological growth temperature of *E. coli*. Very recently, it was reported that the maturation of the extracellular protease SpeB of *Streptococcus pyogenes* is influenced by the PPIase activity of its trigger factor [40]. However, a database search revealed that no SpeB homologue exists in *E. coli* [36].

13.3.4 Importance of Ribosome Association

The atomic structures of the large (50S) and small (30S) ribosomal subunits of bacterial and archaeal ribosomes were recently solved [41–45]. The structure of the *Haloarcula marismortui* large ribosomal subunit revealed a tunnel approx. 100 Å in length with an average diameter of 15 Å, through which the nascent polypeptide extends while still connected to the tRNA in the peptidyl-transferase center [42, 46]. The tunnel is long enough to accommodate a 30- to 35-amino-acid segment of a growing polypeptide chain [47] and it is, in principle, wide enough to allow a peptide to acquire a helical structure [46]. The tunnel exit, where the nascent polypeptide emerges, is surrounded by a protein ring of at least five ribosomal proteins including L32, L22, L24, L29, and L23 (Figure 13.2D). Through use of the engineered trigger factor mutant TF-D42C with a UV-activatable cross-linker located directly adjacent to the TF signature, trigger factor was cross-linked to the neighboring ribosomal proteins L23 and L29 of the large ribosomal subunit (Figure 13.2D; see also protocols, Section 13.5) By using neutron-scattering experiments, Nierhaus and coworkers confirmed that trigger factor is located near the ribosomal proteins L23 and L29 [32]. Analyses of *E. coli* strains carrying mutations in ribosomal protein genes provided evidence that trigger factor binds to L23 but does not associate with L29. Binding of trigger factor occurs via the conserved residue Glu18 of L23, and mutational alteration of Glu18 resulted in a strong binding deficiency for trigger factor [22] (Figure 13.2D). The association of trigger factor with L23 is crucial for its association with nascent polypeptides and its in vivo function as a chaperone for newly synthesized proteins. This was demonstrated by using an in vitro transcription/translation system (see protocols), where employing L23 mutant ribosomes leads to a drastic reduction of the cross-linking efficiency of trigger factor towards nascent polypeptides compared to wild-type ribosomes. *E. coli* strains carrying L23 mutant ribosomes showed conditional lethality at 34 °C in the ab-

sence of the cooperating DnaK chaperone [22], providing evidence that the interaction with L23 is essential for the chaperone function of trigger factor in vivo. Ribosomal protein L23 thus plays a key role in linking two fundamental cellular events: translation and chaperone-assisted protein folding. Interestingly, the signal recognition particle (SRP), which is important for the export of proteins, was also found to cross-link to L23 in both prokaryotes and eukaryotes [48–50]. The ribosomal exit site thus provides a platform that recruits proteins needed to control the early interactions of nascent polypeptide chains. It is not clear how the different partners in such a system could bind without steric conflict and in a coordinated fashion. Recent data suggest that trigger factor and SRP compete for the binding to L23 [49], which raises the question of how the activities of these proteins at the ribosome can be coordinated.

The association of trigger factor with the ribosomal exit site and the nascent polypeptide chains raises interesting questions regarding the dynamic nature of these interactions. So far the kinetics of the interactions of trigger factor with ribosomes and substrates has been investigated exclusively by using purified components and vacant ribosomes. Fluorescently labeled trigger factor was used to investigate its interaction with vacant ribosomes. The affinity of trigger factor to these ribosomes is rather low and is similar to its affinity for unfolded protein substrates (K_D of both is approximately 1 μM) [25, 33, 51]. The association and dissociation of trigger factor with vacant ribosomes are rather slow processes, with an average lifetime of the complex of about 20 s at 20 °C [33]. In contrast, the substrate binding is highly dynamic, with an estimated lifetime of a trigger factor–substrate complex of about 100 ms [51]. The difference in the dynamics might be relevant for trigger factor's function. In principle, the long lifetime of the trigger factor–ribosome complex would allow the chaperone to remain bound while a complete protein or at least a protein domain is synthesized. Since the interaction with the polypeptide substrate is much faster, several cycles of substrate binding and release may occur during this timeframe. However, the most relevant parameters, the association and dissociation rates of the trigger factor complex with translating ribosomes and nascent chains, have not been determined so far. These rates may differ significantly from those mentioned above when, e.g., ongoing translation causes structural changes at the ribosomal docking site for trigger factor, thereby affecting the affinity for trigger factor. In addition the binding of trigger factor to ribosomes and nascent chains could be allosterically coupled.

13.4 Models of the Trigger Factor Mechanism

How does trigger factor promote the folding of newly synthesized proteins? To account for the folding activity of trigger factor, two alternative working models are conceivable (Figure 13.3): the "looping model," where trigger factor remains ribosome-associated while scanning the nascent polypeptides, or the "cycling model,"

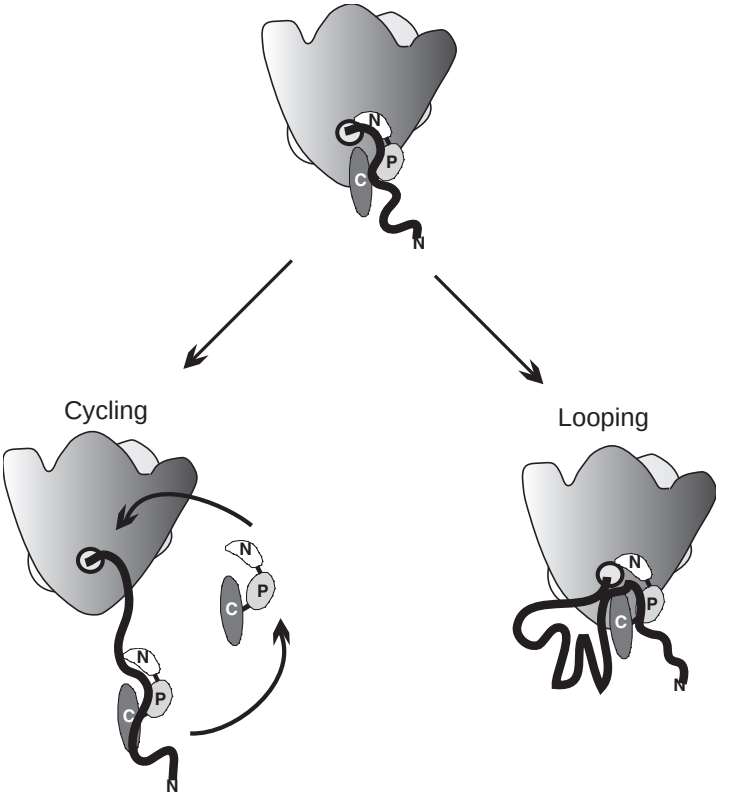

Fig. 13.3. Model of the folding of newly synthesized proteins in *E. coli*. Ribosome-associated trigger factor associates with all nascent polypeptides emerging from the ribosomal exit tunnel. The mechanism of trigger factor action is unclear. Two models are conceivable: the cycling model and the looping model (see text for detail). Beyond the interaction of newly synthesized proteins with trigger factor, at least a subset of proteins needs further chaperoning by DnaK and GroEL to reach the native conformation (not depicted here).

where trigger factor escorts the nascent chain as it moves away from the exit site. The cycling model predicts that binding of trigger factor to a nascent polypeptide substrate causes the release of trigger factor from the ribosome and its transient co-migration with the nascent chain (Figure 13.3). After dissociation from its substrate, trigger factor may rebind to the same or another ribosome and start a new round of substrate interaction. Such a mechanism has two possible consequences. First, trigger factor may protect the growing polypeptide from premature and possibly incorrect folding by allowing a longer stretch of amino acids, i.e., a folding domain, to emerge from the ribosomal tunnel before folding starts upon trigger factor dissociation. Second, trigger factor may spatially separate the ribosome

from the folding process and thereby avoid potential clashes of folding intermediates with the ribosomal surface. Interestingly, it was shown recently that nascent polypeptides cross-link to the ribosomal protein L23 in the absence of trigger factor [52, 53], a finding that indicates a shielding function of the chaperone. The two- to threefold molar excess of trigger factor over ribosomes in *E. coli* and the high frequency of trigger factor binding sites in protein sequences (every 30–40 residues) [17] are in agreement with the demands of the cycling model. As soon as trigger factor dissociates from the ribosome binding site together with its bound nascent chain, a second trigger factor molecule can immediately occupy the ribosome for the next nascent chain interaction.

The looping model predicts that trigger factor stays bound to the ribosome during its interaction with the nascent peptide. This would create a ternary complex in which the nascent chain is tethered to the translating ribosome via trigger factor. Due to the ongoing synthesis, this would result in a ''looping out'' of the nascent polypeptide and, as proposed in this model, prevent folding of the looped-out polypeptide stretch. The dissociation of trigger factor from the nascent chain, preferably after a folding domain has emerged, will then allow the folding of the domain as a discrete entity. Dissociation of trigger factor may be triggered by several possible mechanisms. First, trigger factor may dissociate with a rate governed solely by its substrate- and ribosome-binding properties. Second, the folding process may generate a mechanical force that ''strips'' trigger factor from the polypeptide chain. Third, trigger factor dissociation may be controlled by a mechanism that couples the folding process to the translation process. Accordingly, the translation status of the ribosome determines the dissociation rates of trigger factor–substrate and trigger factor–ribosome complexes.

In summary, the mechanism of trigger factor in assisting the folding of nascent polypeptide chains is elusive and can be understood only by detailed kinetic analysis of the involved interactions. A molecular understanding of the trigger factor function would be propelled by the availability of an atomic structure of trigger factor in association with ribosomes.

13.5 Experimental Protocols

13.5.1 Trigger Factor Purification

Trigger factor carrying a C-terminal hexa-histidine tag shows properties identical to wild-type trigger factor. Therefore, all trigger factor variants and fragments are purified as hexa-histidine-tagged versions, which can be overexpressed and purified in large quantities by the following two-step purification protocol. We recommend conducting the entire purification (starting with cell lysis) within one day since the

trigger factor protein is prone to proteolysis during the purification procedure, especially within the surface-exposed TF signature motif.

Cell Growth Conditions, Overexpression, and Cell Lysis *E. coli* cells carrying the *tig* gene on a pDS56 vector [27] and either a chromosomal or plasmid-encoded *lacIq* gene are grown at 30 °C in Luria broth (LB), supplemented with 100 μg mL^{-1} ampicillin for plasmid selection, to an OD_{600} of 0.6. Induction of trigger factor expression is then started by addition of 500 μM IPTG. Two hours later, cells are harvested, shock-frozen in liquid nitrogen, and stored at −20 °C. One and a half liters of culture can yield up to 100 mg of trigger factor protein.

The cell pellet is thawed and resuspended in 25 mL ice-cold French press buffer (50 mM Tris/HCl pH 7.5, 20 mM imidazole pH 7.5, 200 mM NaCl, 1 mM EDTA) supplemented with either 1 mM PMSF or Complete protease inhibitor according to the manufacturer (EDTA-free, Roche). Cells are lysed with a French press two times at 8000 psi pressure. Cell debris is separated from the soluble fraction by centrifugation at 20 000 *g* for 30 min.

Step 1: Ni-NTA Purification The Ni/NTA purification is done as a batch purification. Six to eight milliliters of Ni-NTA agarose (QIAGEN) is equilibrated with five volumes of cold French press buffer in a suction filter. The supernatant from the centrifugation step is supplemented with 10 mM $MgCl_2$ (to complex free EDTA), and this solution is incubated with the equilibrated Ni-NTA agarose on ice for 15 min with gentle stirring. The solution is then passed through the suction filter. The agarose is washed with at least half a liter of ice-cold washing buffer (50 mM Tris/HCl pH 7.5, 20 mM imidazole pH 7.5, 500 mM NaCl). Next, the salt concentration is reduced by the application of five volumes of ice-cold low-salt buffer (50 mM Tris/HCl pH 7.5, 20 mM imidazole pH 7.5, 25 mM NaCl). The protein is then eluted from the Ni-NTA agarose with three volumes of cold elution buffer (50 mM Tris/HCl pH 7.5, 250 mM imidazole pH 7.5, 25 mM NaCl).

Step 2: Anion-exchange Chromatography Since the Ni-NTA elution buffer contains low salt, the Ni-NTA eluate can be directly applied to an anion-exchange column (e.g., ResourceQ6, Pharmacia) at 4 °C and eluted with a salt gradient (low-salt buffer [50 mM Tris/HCl pH 7.5, 25 mM NaCl, 1 mM EDTA] to high-salt buffer [50 mM Tris/HCl pH 7.5, 1 M NaCl, 1 mM EDTA]). Under these conditions, trigger factor elutes at 150 mM NaCl (15% high-salt buffer). Time of elution of trigger factor fragments or mutants may vary. Trigger factor-containing fractions from the anion-exchange chromatography step are analyzed by SDS-PAGE, pooled, and dialyzed against 2 L of storage buffer (20 mM Tris/HCl pH 7.5, 100 mM NaCl, 1 mM EDTA) overnight at 4 °C. Typically, one purification yields about 6–12 mL of a 4–8 mg mL^{-1} trigger factor solution.

13.5.2
GAPDH Trigger Factor Activity Assay

The chaperone activity of trigger factor can be monitored by following the aggregation or refolding of chemically denatured glyceraldehyde-3-phosphate dehydrogenase (GAPDH) in the presence of trigger factor [34].

Prevention of Unfolded GAPDH Aggregation Equal amounts of freshly prepared GAPDH solution in GAPDH buffer (250 μM GAPDH, Sigma G-2267, in 0.1 M Ca phosphate pH 7.5, 1 mM EDTA, 5 mM DTT) and denaturation buffer (6 M GdnHCl, 5 mM DTT) are mixed and kept for 1 min at 4 °C. Denatured GAPDH is diluted to a final concentration of 2.5 μM into the GAPDH buffer containing trigger factor. Immediately after dilution, aggregation of GAPDH is measured in a spectrofluorometer as an increase in light scattering at 620 nm. In the absence of any additional factor, GAPDH aggregation is complete within 10 min. The addition of stoichiometric amounts of trigger factor suppresses GAPDH aggregation completely and no increase in light scattering is observed during this time period [34].

GAPDH Refolding Assay GAPDH is denatured by mixing equal amounts of GAPDH solution and denaturation buffer (see above) for 1 min at 4 °C. The denatured GAPDH protein is diluted to a final concentration of 2.5 μM into cold GAPDH buffer containing trigger factor at a concentration of 2.5 μM. The solution is incubated for 30 min at 4 °C and is then shifted to room temperature, where GAPDH refolding starts. Within 3–4 h, aliquots are taken from the solution and GAPDH activity is measured as follows. Final concentrations of 0.67 mM glyceraldehyde-3-phosphate (GAP, Sigma G-5251) and 0.67 mM β-nicotinamide adenine dinucleotide (NAD, Sigma N-0632) are premixed in GAPDH buffer. An aliquot from the GAPDH/trigger factor solution is diluted 1:5 into the mixture and absorption at 340 nm is measured immediately in a photometer. After 4–5 min, the reaction is complete. The rate constants of the reactions are determined by a single-exponential fit of the absorption data. GAPDH activity is best represented as the percentage of non-denatured GAPDH activity, i.e., by dividing the measured rate constant by the rate constant determined for the same amount of non-denatured GAPDH enzyme.

13.5.3
Modular Cell-free *E. coli* Transcription/Translation System

The in vitro transcription/translation system allows the synthesis of any target protein in vitro based on a plasmid-encoded target gene transcribed from a T7 promoter. The basic principle of this system is outlined in Figure 13.4. For the generation of a homogenous population of arrested nascent polypeptides, an antisense oligonucleotide and RNaseH are added to produce an mRNA lacking the stop

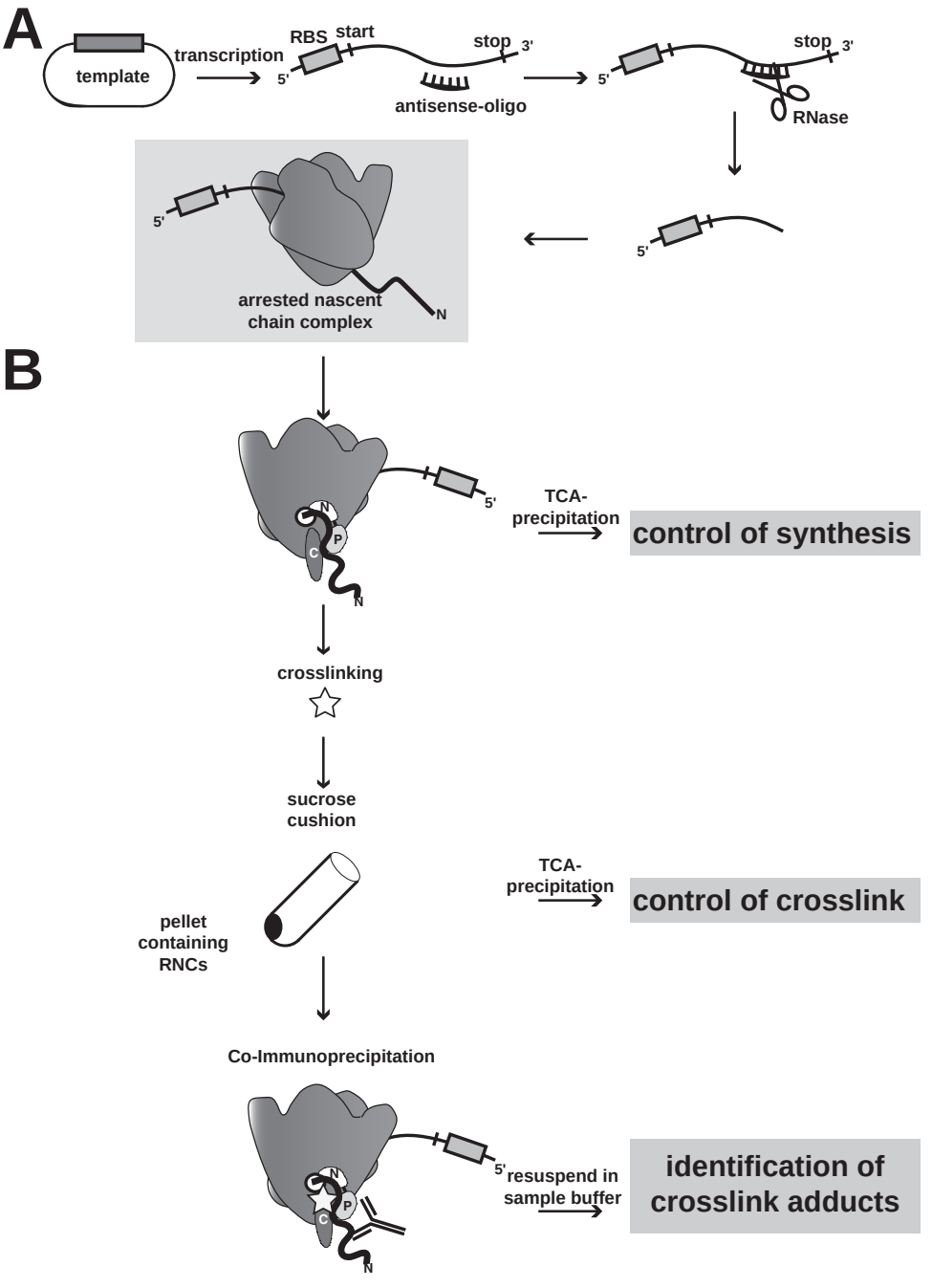

Fig. 13.4. Schematic outline of the in vitro transcription/translation system. (A) Generation of stalled ribosomes by truncation of the mRNA transcript. (B) Chemical cross-linking between radioactively labeled arrested nascent chains and trigger factor and subsequently co-immunoprecipitation.

codon. The addition of a chemical cross-linker allows subsequent monitoring of the interaction of arrested ^{35}S-radio-labeled nascent polypeptides with trigger factor.

The transcription/translation system consists of a subfraction of *E. coli* lysate, termed "translation-active fraction," and high-salt-washed ribosomes. The system is derived from Δ*tig* cells and thus allows for the addition of trigger factor or, if appropriate, of other chaperones. The modular setup makes it easy to test mutant ribosomes or chaperones using the same translation-active fraction. All components can be mixed on ice, and the in vitro transcription/translation reaction is initiated by the addition of ^{35}S-methionine and a shift to 37 °C.

Preparation of the components for in vitro translation essentially follows the protocol described by Zubay [54] with slight modifications. The preparation of components is carried out in three steps:

1. cell culturing and preparation of the S30 extract,
2. isolation of the S150 extract and ribosomes, and
3. separation of the extract by sucrose density centrifugation.

The *E. coli* wild-type strain MC4100, or the derived strain MC4100Δ*tig*, is used as a source for the extracts. To prevent RNase contamination, glassware and centrifuge tubes should be washed with DEPC water. In addition, all buffers should be freshly prepared with the same water and supplemented with proteinase inhibitors (PMSF or Complete EDTA-free, Roche).

Cell Culturing and Preparation of the S30 Extract A 100-mL preculture is grown overnight in LB at 37 °C. Both preculture and main culture are grown in the absence of antibiotics to acquire fully active ribosomes. In the MC4100Δ*tig* strain an integrated kanamycin-resistance cassette replaces the *tig* gene and is stable even in the absence of selective pressure [10].

The preculture is diluted into S30 medium to an OD_{600} of 0.08 and the culture is grown at 37 °C to an OD_{600} of 1.2. Two liters of culture should be grown in a 5-L flask for optimal aeration growth. At the desired OD_{600} cultures are cooled on ice and centrifuged (JA-10 rotor, 6000 *g*, 15 min, 4 °C) and the cell pellets are resuspended in S30 buffer (1 mL of buffer per 1 g of cell pellet). Cells are lysed using a French press equipped with a 40-mL pressure chamber at 8000 psi. Cells are lysed twice and 1 μL of DTT (1 M) is added per 10 mL of lysate. The cell lysates are then centrifuged (30 000 *g*, 4 °C, 30 min) and the resulting supernatant is the S30 extract. The extract can be used immediately or frozen in liquid nitrogen and stored at −80 °C. (S30 medium (per liter): 5.6 g KH_2PO_4, 28.9 g K_2HPO_4, 10 g yeast extract, 1% glucose, pH 7.4; S30 buffer: 50 mM triethanolamine-OAc (pH 8.0), 50 mM KOAc, 15 mM $Mg(OAc)_2$, 1 mM DTT, 0.5 mM PMSF.)

Isolation of the S150 Extract and Ribosomes The S30 extract is centrifuged in a Ti 50 rotor at 150 000 *g* at 4 °C for 3 h to separate ribosomes and membrane fragments from soluble cytosolic proteins. Two-milliliter aliquots of the supernatant

(the S150 extract) can be frozen in liquid nitrogen and stored at −80 °C. The yield of S150 extract from 4 L of culture was about 16 mL in the case of MC4100 (48 g L^{-1}).

The remaining pellet is used for ribosome isolation. These pellets are usually overlayed with a yellow viscous layer containing membrane and cellular debris. This layer can be removed by washing the pellet briefly with RL buffer. The clear pellet is suspended overnight in 5 mL RL buffer. The suspended ribosomes are again centrifuged (20 min, 30 000 *g*, 4 °C) and the remainder of the cell debris is found in the pellet. The supernatant of this centrifugation step containing the ribosomes is diluted in RL buffer to a final volume of 20 mL and the final KOAc concentration is adjusted to 1 M. This ribosome-containing fraction is loaded onto a 40-mL 20% sucrose cushion in high-salt buffer and is centrifuged at 150 000 *g* at 4 °C for 4 h (in a Ti 45 rotor). The resulting ribosomal pellet is suspended in ribosome-buffer and the concentration is determined by measuring the absorption at 260 nm. Absorption of 1.0 equals the ribosome concentration of 23 pmol mL^{-1} or 23 nM. The A_{260}/A_{280} ratio should be ∼2. Ribosomes were aliquoted, frozen in liquid nitrogen, and stored at −80 °C.

RL buffer:	50 mM triethanolamine-OAc (pH 8.0)
	100 mM KOAc
	6 mM $Mg(OAc)_2$
	4 mM β-mercaptoethanol
Sucrose cushions:	20% (w/v) sucrose in high-salt buffer
High-salt buffer:	50 mM triethanolamine-OAc (pH 8.0)
	1 M KOAc
	6 mM $Mg(OAc)_2$
	4 mM β-mercaptoethanol
Ribosome buffer:	50 mM triethanolamine-OAc (pH 8.0)
	50 mM KOAc
	6 mM $Mg(OAc)_2$
	4 mM β-mercaptoethanol

Isolation of the Translation-active Fraction from the S150 Extract To obtain a concentrated and efficient translation-active fraction, the S150 extract is separated on a preformed sucrose gradient [55, 56]. To prepare the gradients, 13-mL centrifuge tubes are filled with 6 mL 10% sucrose solution and afterwards 6 mL of the 30% sucrose solution is slowly injected with a syringe below the 10% layer. Linear gradients are subsequently generated by the "Gradient Master" (Life Technologies), which rotates the tilted tubes until the gradients are formed. The tubes containing the sucrose gradient are then cooled at 4 °C for 1 h. Six-hundred-fifty microliters of the S150 extract is loaded onto each gradient and the centrifugation is carried out (in a SW41 rotor) at 39 000 rpm at 4 °C for 19 h. After the sedimentation equilibrium is reached, the centrifuge is stopped (without braking to prevent mixing of the gradients). The bottoms of the tubes are punctured with a needle and the gra-

dients are fractionated while recording the UV absorption at 280 nm. Twenty-one fractions of 600 µL can be collected per gradient. The recorded absorption data allows comparison of the gradients and comparable fractions can be pooled. The fractions can be frozen in liquid nitrogen and stored at −80 °C. Because not every fraction is sufficiently active for the in vitro transcription/translation system, each fraction is tested for its ability to transcribe and translate a target gene, and active fractions are pooled. The end concentration of the MC4100 extract should be roughly 5.4 g L^{-1}. Five hundred microliter aliquots of the concentrated and active fractions are frozen in liquid nitrogen and stored at −80 °C.

Sucrose solutions: 10% or 30% (w/v) sucrose
50 mM HEPES/KOH (pH 7.5)
50 mM KOAc (pH 7.5)
5 mM $Mg(OAc)_2$
1 mM DTT
0.5 mM PMSF

The in Vitro Transcription/Translation Reaction Several additional components (cofactor mix) must be added to the purified ribosomes and translation-active fraction to generate the active transcription/translation system. The final volume of one reaction is 25 µL. The coding DNA template (under control of a T7 promotor) and T7 RNA polymerase were added on ice. Addition of [^{35}S]-methionine and a shift of the samples to 37 °C start the transcription/translation reaction. The produced mRNA is translated in the presence of [^{35}S]-methionine to synthesize a radioactively labeled protein or nascent chain.

Cofactor mix:

Co-factor	Final concentration
PEG	3.2% (w/v)
19-amino-acid mix (no methionine)	0.1 mM each
DTT	2 mM
Nucleotide mix, pH 7.5	2.5 mM ATP
	0.5 mM (CTP, UTP, GTP)
Phosphoenol-pyruvate	5 mM
Putrescine	8 mM
Creatine phosphate	8 mM
Creatine phosphokinase	40 µg mL^{-1}

10× compensation buffer:

	Final concentration
HEPES (pH 7.5)	310 mM
KOAc (pH 7.5)	540 mM
$Mg(OAc)_2$	89 mM
Spermidine	8 mM
H_2O (DEPC)	Adjust volume

The final transcription/translation reaction (25 μL) is composed of the following components (use DEPC water to adjust the volume to 25 μL):

	Concentration	Amount (μL)	Final concentration
Translation-active fraction		4.0–6.0	
Ribosomes	5 μM	1.0	100 nM
Template DNA		1.0	
T7 RNA polymerase	20 U	0.5	0.4 U μL^{-1}
Cofactor mix		6.25	
[^{35}S]-methionine	15 μCi μL^{-1}	0.5	0.3 μCi (0.3 μM)
Compensation buffer (10×)		2.5	

The optimal concentration of the template DNA was individually determined for each product and it varied between 50 and 200 ng μL^{-1}. The ideal ion and buffer concentration was determined to be 40 mM HEPES (pH 7.5), 70 mM KOAc (pH 7.5), 10 mM $Mg(OAc)_2$, and 0.8 mM spermidine. The ion and buffer concentration is adjusted using the 10× compensation buffer, taking into account the buffer content of ribosomes (50 mM triethanolamine-OAc, 50 mM KOAc, 6 mM $Mg(OAc)_2$), the translation-active fraction (50 mM HEPES, 50 mM KOAc, 5 mM $Mg(OAc)_2$), and proteins added that contain additional buffers and salts. Proteins added to the system should be dialyzed against translation buffer (50 mM HEPES, 50 mM KOAc, 5 mM $Mg(OAc)_2$) prior to use.

For a given experiment, components that are identical to each reaction (except the [^{35}S]-methionine) are mixed into a master mix, and this mix is kept on ice. Aliquots of the master mix can be added to the different samples with varying DNA templates or protein components. The [^{35}S]-methionine is added last and the samples are mixed well using a pipette. Shifting the samples from ice to 37 °C starts the reaction, and the samples are incubated for 45 min. After this time, cooling the samples on ice and addition of 3.2 μL chloramphenicol solution (25 mg mL^{-1} in ethanol) stop the transcription/translation reaction.

The transcription/translation efficiency is determined by TCA precipitation of all proteins and subsequent separation by SDS-PAGE and detection of radioactively labeled chains by autoradiography. One volume of 10% TCA is added to the desired sample, and the proteins are precipitated for at least 30 min on ice. Precipitated proteins are collected by centrifugation (16 000 *g*, 4 °C, 10 min) and are resuspended in 25 μL alkaline sample buffer (pH 9), denatured for 5 min at 99 °C, and used for SDS-PAGE. In addition, the translation efficiency can be determined using a scintillation counter to measure the amount of [^{35}S]-methionine incorporated into the newly synthesized protein.

Synthesis of Arrested Ribosome–Nascent Chain Complexes (RNCs) Translation can be arrested in the *statu nascendi* if translation is carried out from an mRNA lacking a stop codon. In vitro such an mRNA can be generated by addition of an oligonucleotide that anneals with the mRNA and subsequent digestion with RNaseH,

which cleaves the DNA-mRNA hybrid upstream of the stop codon (Figure 13.4). The translating ribosomes stop at the end of the mRNA and cannot proceed. The *E. coli* ssrA system has the potential to release the arrested ribosomes; therefore, an anti-*ssrA* oligonucleotide can be added to the reaction that targets and inactivates the 10Sa RNA of the *E. coli ssrA* machinery.

The optimal concentration of template DNA, oligonucleotides, RnaseH, and anti-*ssrA* oligonucleotides must be determined by titration for each nascent chain. In addition to the components described above, one 25-μL reaction contains the following additives (example):

	Final concentration
Oligonucleotide	0.5–2 ng[1]
RNaseH	0.04 U
Anti-*ssrA* oligonucleotide (5′-ttaagctgctaaagcgtagttttcgtcgtttgcgacta-3′)	0.12 μg

[1]Optimal concentration of the oligonucleotides must be determined for each nascent chain.

TCA		10% in ddH_2O
Alkaline SDS sample buffer:	Solution 1:	0.2 M Tris-Base
		0.02 M EDTA pH 8.0
	Solution 2:	8.3% SDS
		83.3 mM Tris-Base
		29.2% glycerol
		0.03% bromphenol blue

The sample buffer is made by mixing solution 1:solution 2:water in the ratio 5:4:1.

Cross-linking of Trigger Factor to Nascent Polypeptides The interaction of proteins (like chaperones) with nascent chains can be studied using cross-linking experiments, which employ different chemical nonspecific cross-linking agents (DSS, EDC) to create a covalent bond between the nascent chain and the protein of interest. For a cross-linking experiment, the sample reaction can be scaled up 10-fold (i.e., 250 μL transcription/translation reaction). One volume of the reaction (i.e., 25 μL) is used to assess the efficiency of the transcription/translation reaction, two volumes are used to assess efficiency of cross-linking, and the remaining seven volumes are used for co-immunoprecipitation analysis (see below). Samples are loaded immediately on a gel for comparison.

Cross-linking With DSS Disuccinimidyl suberate (DSS, Pierce #21555) is a highly mobile NHS ester that preferentially reacts with amines. Therefore, the protein buffers should not contain any primary amines (e.g., Tris). HEPES is used as buffer since it is also compatible with the transcription/translation system. After

stopping the transcription/translation reaction, 2.5 μL of DSS (25 mM in DMSO) are added per 25-μL reaction, and cross-linking is performed for 30 min at RT. To quench the free DSS, Tris/HCl (pH 7.5) is added to a final concentration of 50 mM and quenching is carried out for 15 min at RT. The quenched cross-linking reaction can then be precipitated with TCA and analyzed by SDS-PAGE and autoradiography, or it can be centrifuged through a 20% sucrose cushion to collect ribosomal pellets plus cross-linking partners for further analysis.

Cross-linking With EDC EDC (1-ethyl-3-(3-dimethylaminopropyl); Pierce #22980) is a carbodiimide that couples carboxyl and amino groups via an amide bond. HEPES should be used once again for EDC cross-linking steps. A transcription/translation reaction (25 μL) is supplemented with 5 μL EDC (480 mM freshly prepared with ddH_2O). After cross-linking at 30 °C for 30 min, free EDC is quenched by adding 1/10 volume of quench buffer and incubating samples on ice for 15 min.

EDC:	480 mM in ddH_2O
Quench buffer:	1 M glycine
	100 mM $NaHCO_3$
	100 mM β-mercaptoethanol, pH 8.5

Isolation of RNCs After the transcription/translation reaction and cross-linking, the samples are centrifuged (16 000 *g*, 5 min, 4 °C) to remove potential protein aggregates generated during the procedure from the solution. To isolate RNCs the supernatants are subsequently loaded onto chilled sucrose cushions (cushions should be 2–3× volume of the loaded sample), and the samples are centrifuged in either a TLA-100 or a TLA-100.2 rotor, depending on the volume, at 75 000 rpm at 4 °C for 90 min. The supernatant is rapidly removed after the centrifugation and the clear ribosomal pellet can be resuspended in either 100 μL of ribosome buffer (plus 0.3 mg mL^{-1} chloramphenicol and Complete EDTA-free, Roche) for co-immunoprecipitation or in sample buffer for immediate analysis by SDS-PAGE.

Ribosome buffer:	50 mM triethanolamine-OAc (pH 8.0)
	100 mM KOAc
	15 mM $Mg(OAc)_2$
	1 mM DTT
Sucrose cushion:	20% sucrose
	50 mM HEPES/KOH (pH 7.5)
	100 mM KOAc (pH 7.5)
	10 mM $Mg(OAc)_2$
	4 mM β-mercaptoethanol
	0.3 mg mL^{-1} chloramphenicol

Co-immunoprecipitation of the Cross-linking Products Co-immunoprecipitation of the cross-linking products under denaturating conditions is carried out at 4 °C with antibodies directed against the target protein, e.g., trigger factor. The ribosomal pellet from at least seven reactions (175 µL of the original transcription/translation reaction) is used for immunoprecipitation. The suspended pellet is mixed with 50 µL protein A Sepharose suspension (0.125 g mL^{-1} equilibrated with RIPA buffer) and 5 µL (depending on the quality of the antibody) of antibody; the mixture is diluted with RIPA buffer to a final volume of 1 mL. The binding is allowed to proceed for at least 1 h at 4 °C with constant mixing. The protein A Sepharose with the bound antibody-protein complexes is pelleted (1600 *g*, 4 °C, 1 min) and washed twice with 1 mL RIPA buffer and once with 1 mL PBS. Finally, the pellet is resuspended in 30 µL of sample buffer and denatured at 100 °C prior to SDS-PAGE analysis.

Protein A Sepharose CL-4 B: 0.125 mg mL^{-1} equilibrated with RIPA buffer

RIPA buffer:	150 mM NaCl
	50 mM Tris/HCl (pH 7.5)
	0.5 mM EDTA
	1% NP40
	0.5% Doc
	0.1% SDS
PBS:	137 mM NaCl
	2.7 mM KCl
	10 mM Na_2HPO_4
	2 mM KH_2PO_4
	pH 7.4

13.5.4

Isolation of Ribosomes and Add-back Experiments

High-salt-washed ribosomes can be purified from Δ*tig E. coli* strains and used for in vitro rebinding assays with purified trigger factor. The purification protocol is identical to the one described above for the transcription/translation system, except that LB medium can be used for the main culture and that the sucrose cushion centrifugation can be repeated, to yield very pure ribosomes. For cross-linking experiments with trigger factor D42C-BPIA (see below), a HEPES-ribosome buffer can be used to suspend the ribosomes. This prevents quenching of the cross-linker by Tris.

HEPES-ribosome buffer:	25 mM HEPES pH 7.5
	6 mM $MgCl_2$
	30 mM NH_4Cl

Binding Trigger Factor to Ribosomes in Vitro Purified trigger factor can be rebound to high-salt-washed ribosomes in vitro and the bound protein can be separated

from soluble trigger factor by sucrose cushion centrifugation. After the centrifugation, the ribosomes and bound proteins are found in the pellet, while soluble proteins remain in the supernatant.

In a typical binding experiment, 6 μM trigger factor is added to 2 μM ribosomes and the final volume is adjusted to 60 μL using one of the ribosome buffers described above. To allow trigger factor to bind to the ribosomes, the sample is incubated at 30 °C for 30 min, and the reaction mixture is then layered on top of a 120-μL 20% sucrose cushion prepared with ribosome-buffer. The volume of the cushion should be 3× volume of the sample. Samples are centrifuged for 70 min at 75 000 rpm and 4 °C in a TLA-100 rotor.

Eighty microliters of the resulting supernatant is mixed with 20 μL of 5× SDS sample buffer, and the rest of the supernatant is removed. The clear ribosomal pellet is suspended in 50 μL 1× SDS sample-buffer. After denaturing the samples at 100 °C for 5 min, 30 μL of the supernatant and 15 μL of the pellet are used for SDS-PAGE. A typical gel depicting the rebinding of trigger factor to *E. coli* ribosomes is shown in Figure 13.5.

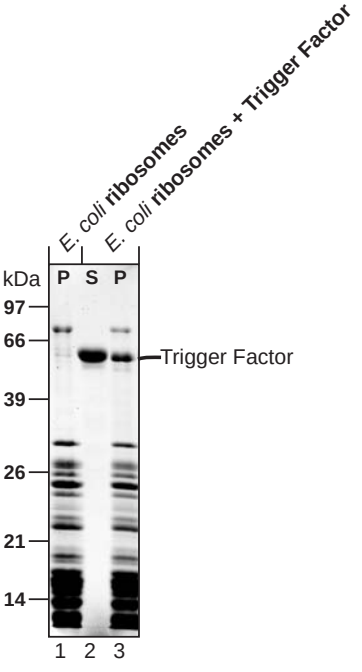

Fig. 13.5. Rebinding of purified trigger factor to ribosomes. Two micromoles of purified ribosomes were incubated with 6 μM trigger factor under physiological salt conditions. Ribosome–trigger factor complexes were purified by sucrose cushion centrifugation. Ribosomal pellets (P) and supernatants (S) were analyzed by SDS-PAGE and Coomassie staining.

13.5.5
Cross-linking Techniques

Labeling TF-D42C Protein With BPIA The TF-D42C mutant of trigger factor is purified from MC4100Δ*tig* cells as described above. To reduce the protein, 500 μL (3–4 mg mL^{-1}) is mixed with 50 μL of immobilized TCEP disulfide reducing gel (Pierce #77712) and the sample is incubated at RT for 10 min with gentle shaking. The immobilized TCEP can be removed by centrifugation and transfer of the protein-containing supernatant into a new tube (twice).

One micromole of the chemical cross-linker BPIA (4-(2-iodoacetamido)benzophenone; Molecular Probes) is added to the protein and the sample is incubated at 30 °C for 30 min. The BPIA should be protected against extensive light exposure during the entire process. Addition of 2 μL *β*-mercaptoethanol (14.4 M) and cooling on ice stop the labeling process, and the labeling efficiency can be checked by mass spectrometry. The labeled protein is dialyzed against the cross-linking buffer and is frozen in liquid nitrogen and stored at −80 °C.

Cross-linking buffer: 25 mM HEPES pH 7.5
50 mM NaCl

Cross-linking TF-D42C BPIA to Ribosomes in Vitro The TF-D42C BPIA protein (6 μM) is incubated with ribosomes (2 μM) as described above. After incubating the sample for 30 min at 30 °C (in the dark), the tubes are placed on ice, are opened, and are UV irradiated using a UV lamp at 365 nm for 10 min. The cross-linked samples can then be analyzed as described above, and the bands corresponding to cross-linking adducts can be cut out of the gel for analysis by mass spectrometry.

Cross-linking Trigger Factor With Glutaraldehyde Trigger factor dimers can be cross-linked using the nonspecific cross-linker glutaraldehyde. Different concentrations of trigger factor protein are incubated for 15 min at 30 °C in a glutaraldehyde buffer with varying NaCl concentrations. Cross-linking is initiated by addition of 0.1% glutaraldehyde (Sigma) and is stopped after 10 min by adding 100 mM Tris pH 7.5 for 10 min at RT. Soluble proteins are precipitated by mixing the samples with one volume 10% TCA and incubating for 60 min on ice. After centrifugation (16 000 *g*, 4 °C, 10 min), the pellet is analyzed by SDS-PAGE.

Glutaraldehyde buffer: 20 mM HEPES pH 7.5
100 mM–2 M NaCl
1 mM EDTA

References

1 B. Bukau, E. Deuerling, C. Pfund, and E. A. Craig. Getting newly synthesized proteins into shape. *Cell* **2000**, *101*, 119–122.

2 F. U. Hartl, and M. Hayer-Hartl. Molecular chaperones in the cytosol: from nascent chain to folded protein. *Science* **2002**, *295*, 1852–1858.

3 E. Crooke, and W. Wickner. Trigger factor: a soluble protein that folds pro-OmpA into a membrane-assembly competent form. *Proc. Natl. Acad. Sci. USA* **1987**, *84*, 5216–5220.

4 R. Lill, E. Crooke, B. Guthrie, and W. Wickner. The "Trigger factor cycle" includes ribosomes, presecretory proteins and the plasma membrane. *Cell* **1988**, *54*, 1013–1018.

5 B. Guthrie, and W. Wickner. Trigger factor depletion or overproduction causes defective cell division but does not block protein export. *J. Bacteriol.* **1990**, *172*, 5555–5562.

6 G. Stoller, K. P. Ruecknagel, K. H. Nierhaus, F. X. Schmid, G. Fischer, and J.-U. Rahfeld. A ribosome-associated peptidyl-prolyl *cis*/*trans* isomerase identified as the trigger factor. *EMBO J.* **1995**, *14*, 4939–4948.

7 T. Hesterkamp, S. Hauser, H. Lütcke, and B. Bukau. *Escherichia coli* trigger factor is a prolyl isomerase that associates with nascent polypeptide chains. *Proc. Natl. Acad. Sci. USA* **1996**, *93*, 4437–4441.

8 Q. A. Valent, D. A. Kendall, S. High, R. Kusters, B. Oudega, and J. Luirink. Early events in preprotein recognition in *E. coli*: interaction of SRP and trigger factor with nascent polypeptides. *EMBO J.* **1995**, *14*, 5494–5505.

9 B. Bukau, T. Hesterkamp, and J. Luirink. Growing up in a dangerous enviroment: a network of multiple targeting and folding pathways for nascent polypetides in the cytosol. *Trends Cell Biol.* **1996**, *6*, 480–486.

10 E. Deuerling, A. Schulze-Specking, T. Tomoyasu, A. Mogk, and B. Bukau. Trigger factor and DnaK cooperate in folding of newly synthesized proteins. *Nature* **1999**, *400*, 693–696.

11 S. A. Teter, W. A. Houry, D. Ang, T. Tradler, D. Rockabrand, G. Fischer, P. Blum, C. Georgopoulos, and F. U. Hartl. Polypeptide flux through bacterial Hsp70: DnaK cooperates with Trigger Factor in chaperoning nascent chains. *Cell* **1999**, *97*, 755–765.

12 B. Bukau, and G. C. Walker. Cellular Defects caused by deletion of the *Escherichia coli dnaK* gene indicates roles for heat shock protein in normal metabolism. *J. Bact.* **1989**, *171*, 2337–2346.

13 T. Hesterkamp, and B. Bukau. Role of the DnaK and HscA homologs of Hsp70 chaperones in protein folding in *E. coli*. *EMBO J.* **1998**, *17*, 4818–4828.

14 E. Deuerling, H. Patzelt, S. Vorderwülbecke, et al. Trigger Factor and DnaK possess overlapping substrate pools and binding specificities. *Mol. Microbiol.* **2003**, *47*, 1317–1328.

15 T. Tomoyasu, A. Mogk, H. Langen, P. Goloubinoff, and B. Bukau. Genetic dissection of the roles of chaperones and proteases in protein folding and degradation in the Escherichia coli cytosol. *Mol Microbiol* **2001**, *40*, 397–413.

16 A. Mogk, T. Tomoyasu, P. Goloubinoff, S. Rüdiger, D. Röder, H. Langen, and B. Bukau. Identification of thermolabile *E. coli* proteins: prevention and reversion of aggregation by DnaK and ClpB. *EMBO J.* **1999**, *18*, 6934–6949.

17 H. Patzelt, S. Rudiger, D. Brehmer, et al. Binding specificity of Escherichia coli trigger factor. *Proc Natl Acad Sci USA* **2001**, *98*, 14244–14249.

18 C. Scholz, M. Mücke, M. Rape, A. Pecht, A. Pahl, H. Bang, and F. X. Schmid. Recognition of protein substrates by the prolyl isomerase trigger factor is independent of proline residues. *J. Mol. Biol.* **1998**, *277*, 723–732.

19 S. Rüdiger, L. Germeroth, J. Schneider-Mergener, and B. Bukau. Substrate specificity of the

DnaK chaperone determined by screening cellulose-bound peptide libraries. *EMBO J*. **1997**, *16*, 1501–1507.

20 X. Zhu, X. Zhao, W. F. Burkholder, A. Gragerov, C. M. Ogata, M. Gottesman, and W. A. Hendrickson. Structural analysis of substrate binding by the molecular chaperone DnaK. *Science* **1996**, *272*, 1606–1614.

21 S. Rüdiger, A. Buchberger, and B. Bukau. Interaction of Hsp70 chaperones with substrates. *Nat Struct Biol*. **1997**, *4*, 342–349.

22 G. Kramer, T. Rauch, W. Rist, S. Vorderwülbecke, H. Patzelt, A. Schulze-Specking, N. Ban, E. Deuerling, and B. Bukau. L23 protein functions as a chaperone docking site on the ribosome. *Nature* **2002**, *419*, 171–174.

23 I. Callebaut, and J. P. Mornon. Trigger factor, one of the Escherichia coli chaperone proteins, is an original member of the FKBP family. *FEBS Lett* **1995**, *374*, 211–215.

24 M. Vogtherr, D. M. Jacobs, T. N. Parac, M. Maurer, A. Pahl, K. Saxena, H. Ruterjans, C. Griesinger, and K. M. Fiebig. NMR solution structure and dynamics of the peptidyl-prolyl cis-trans isomerase domain of the trigger factor from Mycoplasma genitalium compared to FK506-binding protein. *J Mol Biol* **2002**, *318*, 1097–1115.

25 C. Scholz, G. Stoller, T. Zarnt, G. Fischer, and F. X. Schmid. Cooperation of enzymatic and chaperone functions of trigger factor in the catalysis of protein folding. *EMBO J*. **1997**, *16*, 54–58.

26 T. Zarnt, T. Tradler, G. Stoller, C. Scholz, F. X. Schmid, and G. Fischer. Modular Structure of the Trigger Factor Required for High Activity in Protein Folding. *J. Mol. Biol*. **1997**, *271*, 827–837.

27 T. Hesterkamp, E. Deuerling, and B. Bukau. The amino-terminal 118 amino acids of *Escherichia coli* trigger factor constitute a domain that is necessary and sufficient for binding to ribosomes. *J. Biol. Chem*. **1997**, *272*, 21865–21871.

28 O. Kristensen, and M. Gajhede. Chaperone binding at the ribosomal exit tunnel. *Structure (Camb)* **2003**, *11*, 1547–1556.

29 T. Hesterkamp, and B. Bukau. Identification of the prolyl isomerase domain of *Escherichia coli* trigger factor. *FEBS Letters* **1996**, *385*, 67–71.

30 A. J. L. Macario, M. Lange, B. K. Ahring, and E. Conway de Macario. Stress genes and proteins in the Archaea. *Microbiol. Mol. Biol. Rev.* **1999**, *63*, 923–967.

31 H. Patzelt, G. Kramer, T. Rauch, H. J. Schönfeld, B. Bukau, and E. Deuerling. Three-Sate Equilibrium of *Escherichi coli* Trigger Factor. *Biol. Chem*. **2002**, *383*, 1611–1619.

32 G. Blaha, D. N. Wilson, G. Stoller, G. Fischer, R. Willumeit, and K. H. Nierhaus. Localization of the trigger factor binding site on the ribosomal 50S subunit. *J Mol Biol* **2003**, *326*, 887–897.

33 R. Maier, B. Eckert, C. Scholz, H. Lilie, and F. X. Schmid. Interaction of trigger factor with the ribosome. *J Mol Biol* **2003**, *326*, 585–592.

34 G. C. Huang, Z. Y. Li, J. M. Zhou, and G. Fischer. Assisted folding of D-glyceraldehyde-3-phosphate dehydrogenase by trigger factor. *Protein Sci* **2000**, *9*, 1254–1261.

35 C. P. Liu, and J. M. Zhou. Trigger factor-assisted folding of bovine carbonic anhydrase II. *Biochem Biophys Res Commun* **2004**, *313*, 509–515.

36 G. Kramer, H. Patzelt, T. Rauch, T. A. Kurz, S. Vorderwülbecke, B. Bukau, and E. Deuerling. Trigger Factor's peptidyl-prolyl cis/trans isomerase activity is not essential for the folding of cytosolic proteins in Escherichia coli. *J. Biol. Chem*. **2004**, *in press*.

37 S. F. Göthel, C. Scholz, F. X. Schmid, and M. A. Marahiel. Cyclophilin and Trigger Factor from *Bacillus subtilis* Catalyze in Vitro

Protein Folding and are Necessary for Viability under Starvation Conditions. *Biochemistry* **1998**, *37*, 13392–13399.

38 T. Tradler, G. Stoller, K. P. Rücknagel, A. Schierhorn, J.-U. Rahfeld, and G. Fischer. Comparative mutational analysis of peptidyl prolyl *cis/trans* isomerases: active sites of *Escherichia coli* trigger factor and human FKBP12. *FEBS Letters* **1997**, *407*, 184–190.

39 C. Schiene-Fischer, J. Habazettl, T. Tradler, and G. Fischer. Evaluation of similarities in the cis/trans isomerase function of trigger factor and DnaK. *Biol Chem* **2002**, *383*, 1865–1873.

40 W. R. Lyon, and M. G. Caparon. Trigger factor-mediated prolyl isomerization influences maturation of the Streptococcus pyogenes cysteine protease. *J Bacteriol* **2003**, *185*, 3661–3667.

41 N. Ban, P. Nissen, J. Hansen, M. Capel, P. B. Moore, and T. A. Steitz. Placement of protein and RNA structures into a 5 Å-resolution map of the 50S ribosomal subunit. *Nature* **1999**, *400*, 841–847.

42 N. Ban, P. Nissen, J. Hansen, P. B. Moore, and T. A. Steitz. The complete atomic structure of the large ribosomal subunit at 2.4 Å resolution. *Science* **2000**, *289*, 905–920.

43 J. Harms, F. Schluenzen, R. Zarivach, A. Bashan, S. Gat, I. Agmon, H. Bartels, F. Franceschi, and A. Yonath. High resolution structure of the large ribosomal subunit from a mesophilic eubacterium. *Cell* **2001**, *107*, 679–688.

44 F. Schluenzen, A. Tocilj, R. Zarivach, et al. Structure of functionally activated small ribosomal subunit at 3.3 angstroms resolution. *Cell* **2000**, *102*, 615–623.

45 B. T. Wimberly, D. E. Brodersen, W. M. Clemons, Jr., R. J. Morgan-Warren, A. P. Carter, C. Vonrhein, T. Hartsch, and V. Ramakrishnan. Structure of the 30S ribosomal subunit. *Nature* **2000**, *407*, 327–339.

46 P. Nissen, J. Hansen, N. Ban, P. B. Moore, and T. A. Steitz. The structural basis of ribosome activity in peptide bond synthesis. *Science* **2000**, *289*, 920–930.

47 B. Hardesty, and G. Kramer. Folding of a nascent peptide on the ribosome. *Prog Nucleic Acid Res Mol Biol* **2001**, *66*, 41–66.

48 M. R. Pool, J. Stumm, T. A. Fulga, I. Sinning, and B. Dobberstein. Distinct modes of signal recognition particle interaction with the ribosome. *Science* **2002**, *297*, 1345–1348.

49 R. S. Ullers, E. N. Houben, A. Raine, C. M. ten Hagen-Jongman, M. Ehrenberg, J. Brunner, B. Oudega, N. Harms, and J. Luirink. Interplay of signal recognition particle and trigger factor at L23 near the nascent chain exit site on the Escherichia coli ribosome. *J Cell Biol* **2003**, *161*, 679–684.

50 S. Q. Gu, F. Peske, H. J. Wieden, M. V. Rodnina, and W. Wintermeyer. The signal recognition particle binds to protein L23 at the peptide exit of the Escherichia coli ribosome. *Rna* **2003**, *9*, 566–573.

51 R. Maier, C. Scholz, and F. X. Schmid. Dynamic association of trigger factor with protein substrates. *J Mol Biol* **2001**, *314*, 1181–1190.

52 G. Eisner, H. G. Koch, K. Beck, J. Brunner, and M. Muller. Ligand crowding at a nascent signal sequence. *J Cell Biol* **2003**, *163*, 35–44.

53 R. S. Ullers, E. N. G. Houben, A. Raine, C. M. Ten Hagen-Jongman, M. Ehrenberg, J. Brunner, B. Oudega, N. Harms, and J. Luirink. Interplay of SRP and Trigger Factor at L23 near the nascent chain exit site on the *E. coli* ribosome. *J. Mol. Biol.* **2003**, *in press*.

54 G. Zubay. In vitro synthesis of protein in microbial systems. *Annu. Rev. Genet.* **1973**, *7*, 267–287.

55 E. Schaffitzel, S. Rüdiger, B. Bukau, and E. Deuerling. Functional dissection of Trigger Factor and DnaK: Interactions with nascent polypeptides and thermally denatured proteins.

Biological Chemistry **2001**, *382*, 1235–1243.

56 M. Behrmann, H.-G. Koch, T. Hengelage, B. Wieseler, H. K. Hoffschulte, and M. Müller. Requirements for the translocation of elongation-arrested, ribosome-associated OmpA across the plasma membrane of *Escherichia coli*. *J. Biol. Chem.* **1998**, *273*, 13898–13904.

57 A. Nicholls, R. Bharadwaj, and B. Honig. Grasp – Graphical representation and analysis of surface properties. *Biophys. J.* **1993**, *64*, A166–A166.

14
Cellular Functions of Hsp70 Chaperones

Elizabeth A. Craig and Peggy Huang

14.1
Introduction

Hsp70s are ubiquitous molecular chaperones that function in a wide variety of physiological processses, including protein folding, protein translocation across membranes, and assembly/disassembly of multimeric protein complexes. Hsp70s rarely, if ever, function alone, but rather with J-protein (also known as Hsp40 or DnaJ-like protein) partners. All eukaryotic, and the vast majority of prokaryotic, genomes encode Hsp70 and J-proteins. Most, in fact, encode multiple Hsp70 and J-proteins, indicative of the evolution of Hsp70s/J-proteins such that they function in a variety of cellular processes. For example, the yeast genome encodes 14 Hsp70s (Figure 14.1), while the mouse genome encodes at least 12; the number of J-proteins is even more numerous, with the yeast and mouse genomes encoding approximately 20 and 23, respectively [1]. The larger number of J-proteins likely reflects the fact that a single Hsp70 can function with more than one J-protein, driving the function of an Hsp70 in a particular cellular role. In fact, in some cases, J-proteins act as specificity factors, modulating the activity of Hsp70s or delivering specific substrates to them.

This proliferation of Hsp70 and J-protein genes reflects the divergence in their biological functions, the subject of this chapter. In most cases, the basic biochemical properties of Hsp70s and J-proteins utilized when carrying out their functions are the same. Diverse cellular roles result from harnessing these basic biochemical properties in different ways. For example, by tethering a chaperone to a particular cellular location or substrate protein, or by evolving the substrate specificity of these chaperones, they are optimized to function in a particular cellular function.

The general structure of Hsp70s has been conserved [2, 3]: a highly conserved N-terminal ATPase domain, followed by a less conserved domain having a cleft in which hydrophobic peptides can bind, and a variable C-terminal 10-kDa region. ATP binding and hydrolysis in the N-terminus regulate the interaction of the C-terminus with unfolded polypeptides, with ATP hydrolysis stabilizing the interaction. J-proteins transiently interact with the ATPase domain of ATP-bound Hsp70 via their highly conserved J-domains and stimulate its ATPase activity, thus facili-

Protein Folding Handbook. Part II. Edited by J. Buchner and T. Kiefhaber

ISBN: 3-527-30784-2

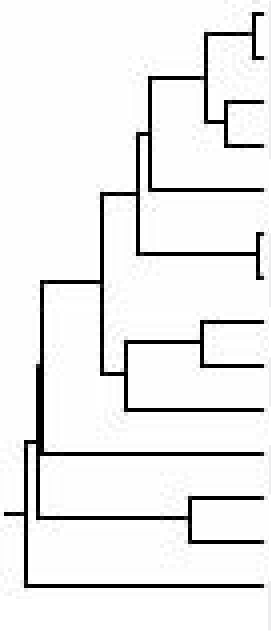

Name	Cellular Compartment	Tethered/Soluble	Functions	J-Protein Partners
Ssa1 Ssa2 Ssa3 Ssa4	Cytosol /Nucleus	Soluble (Ribosome-associated /Tethered to ER/Mito membrane)	Assist folding and prevent aggregation; assist translocation into ER and Mito; translation initiation; clathrin uncoating	Ydj1, Sis1, Swa2(auxilin)
Kar2	ER	Tethered to translocon complex /Soluble	Protein translocation, folding, assembly, quality control, UPR	Sec63, Scj1, Jem1
Ssb1 Ssb2	Cytosol	Tethered to ribosomes	Folding of ribosome-bound nascent chains	Zuo1
Ecm10	Mito	Soluble	?	?
Ssc1	Mito	Tethered to translocon /Soluble	Protein translocation and folding	Pam18, Mdj1
Ssq1	Mito	Soluble	Fe/S cluster insertion	Jac1
Ssz1	Cytosol	Tethered to ribosomes	Folding of nascent chains on ribosomes, PDR	?
Sse1 Sse2	Cytosol /(Nucleus)	Soluble	Folding and working with Hsp90	?
Lhs1	ER	Soluble	Protein translocation, folding, UPR	?

Fig. 14.1. Phylogenetic tree of Hsp70 proteins from the yeast *Saccharomyces cerevisiae*. Subcellular locations, functions, and J-protein partners are indicated for each Hsp70 family. The tree was created using MegAlign software from DNASTAR (Madison, WI) with the clustal method. See text for references regarding evidence for information on particular genes and their functions. Locations or functions that should be considered tentative assignments are in parentheses.

tating the chaperone cycle. Some J-proteins themselves are also able to bind polypeptide substrates, delivering them to Hsp70s. In addition to J-proteins, some Hsp70s also require nucleotide releasing factors to facilitate the exchange of ADP from ATP [2, 3]. For a more thorough discussion of Hsp70 and/or J-protein function, see Chapters 15 and 16.

In this chapter, we first focus on Hsp70/J-proteins' role in the folding of newly synthesized proteins and the recovery of proteins partially denatured by stress, a function carried out by the abundant soluble Hsp70/J-proteins found in all major cellular compartments. Secondly, we discuss Hsp70s/J-proteins, tethered to specific sites within the cell, that are involved in the early stages of protein folding and translocation across membranes. Thirdly, we discuss examples in which Hsp70/J-proteins function in specific cellular processes where folded proteins, rather than unfolded polypeptides, serve as substrates for Hsp70s/J-proteins. In such cases, specific effects on protein conformation, disassembly of multimeric protein complexes, and/or regulation of activity are the typical effects of chaperone action. At the end of the chapter, we discuss two examples in which a member of the yeast Hsp70 family has evolved a function distinct from that of a chaperone, raising the possibility that during evolution some such proteins have been usurped to play other, perhaps regulatory, roles.

14.2
"Soluble" Hsp70s/J-proteins Function in General Protein Folding

The "classic" notion of an Hsp70 is an abundant, likely stress-inducible, soluble protein that primarily facilitates the refolding of proteins partially denatured by stress or the folding of newly synthesized proteins. Such Hsp70s are ubiquitous in the cytosol of eubacteria, eukarya, and some archaea, as well as in the matrix of mitochondria and the lumen of the endoplasmic reticulum (ER).

14.2.1
The Soluble Hsp70 of *E. coli*, DnaK

The *E. coli* Hsp70 DnaK is an abundant protein even under optimal growth conditions, making up about 1% of cellular protein. It is also inducible when cells encounter a stress, such as a rapid temperature increase, at which point it can become 3% of cellular protein, making it the most abundant cellular chaperone [4]. DnaK works with its J-protein partner DnaJ and its nucleotide releasing factor GrpE to perform chaperone functions in the cell (see Chapter 15 for more discussion). The evidence that the DnaK system is critical for preventing the aggregation of cellular proteins upon heat stress and for assisting in the refolding of denatured proteins is incontrovertible [5–10]. At high temperatures, 15–25% of cytosolic proteins, comprising 150–200 different species of polypeptides, aggregate after a temperature upshift of cells lacking DnaK [4, 11].

DnaK also plays a role in the folding of newly synthesized proteins, but that

function is not unique to DnaK and can be performed by other chaperones, particularly the ribosome-associated chaperone trigger factor (for more discussion about trigger factor, see Chapter 13). Cells lacking either DnaK or trigger factor are viable and little or no protein aggregation is seen [12, 13]. But a double mutant is inviable; upon depletion of trigger factor in cells lacking DnaK, a dramatic increase in aggregation of more than 40 proteins was observed prior to cell death [12, 13]. Experiments using pulse-labeling of newly synthesized proteins to track the flux of newly synthesized proteins through DnaK revealed that between 5% and 18% of newly made proteins, mainly polypeptides larger than 30 kDa, could be immunoprecipitated with DnaK-specific antibodies in wild-type cells [12]. But, in the absence of trigger factor, this number increased two- to threefold, up to as much as 36% [13]. Together these results suggest that DnaK acts as a chaperone for newly synthesized chains but that function can be taken over by other chaperones, particularly trigger factor, in DnaK's absence. In turn, DnaK is able to take over some of the chaperone activities of trigger factor in its absence. Such overlaps in chaperone function likely are common and reflect a general plasticity of the chaperone networks.

14.2.2 Soluble Hsp70s of Major Eukaryotic Cellular Compartments

14.2.2.1 Eukaryotic Cytosol

While the data for eukaryotic cells is less extensive than that available for *E. coli*, Hsp70s, working with J-protein co-chaperones, are thought to be important for protein folding in the cytosol of eukaryotes as well. In yeast the major cytosolic family of Hsp70s, the Ssa's, is most closely related to the abundant cytosolic Hsp70s of mammalian cells, Hsc70 and Hsp70. Ssa's are thought to participate in ''bulk'' protein folding in the cytosol, mainly in cooperation with the J-protein Ydj1. Perhaps the most compelling evidence that Ssa proteins are involved in protein folding in the cytosol is the fact that yeast cells carrying a temperature-sensitive *SSA* mutant accumulate newly synthesized ornithine transcarbamylase in a misfolded, but soluble, form after shift to the non-permissive temperature [14].

In mammalian tissue culture cells, Hsc70 has also been implicated in bulk folding of newly synthesized proteins. It has been found to interact with ~20% of newly synthesized polypeptides [15, 16]. In addition, overexpression of human Hsp70 and the J-protein Hdj2 enhances refolding of heat-inactivated luciferase in vivo [17]. Interestingly, in several eukaryotic model systems for protein aggregation, including overexpression of disease-related proteins such as huntingtin and ataxin, Hsp70s and J-proteins have been found to co-localize with such proteins and/or overexpression of the chaperones have been found to decreases their aggregations (reviewed in Ref. [3], also see Chapters 36 and 37 for more discussion).

While in many cases Hsp70s, along with their co-chaperone J-protein, are thought to function alone in protein folding, there are many indications that they also function cooperatively with other chaperone systems to assist posttranslational protein folding. In particular, Hsp70s are thought to function with the Hsp90 sys-

tem, interacting with Hsp90 client proteins prior to interacting with Hsp90 itself [18]. In yeast both the Ssa and the Sse classes of Hsp70s have been implicated in such cooperation [19, 20]. These issues are described in detail in Chapter 23.

14.2.2.2 Matrix of Mitochondria

As perhaps expected of an organelle evolved from eubacteria, the major Hsp70 and its J-protein partner in the mitochondrial matrix (called Ssc1 and Mdj1, respectively, in yeast) are more closely related to the bacterial Hsp70 DnaK and its J-protein partner DnaJ than to other Hsp70s of the same species. A nucleotide release factor, related to *E. coli* GrpE, called Mge1 completes the prokaryotic-type chaperone triad of mitochondria. This chaperone triad is involved in the folding of proteins synthesized on cytosolic ribosomes and imported into the matrix [21–24] as well as of proteins encoded by mitochondrial DNA and translated on mitochondrial ribosomes [23, 25]. Ssc1 also has a second role: a portion of Ssc1 is tethered to the mitochondrial inner membrane and is critical for the process of protein translocation across membranes.

14.2.2.3 Lumen of the Endoplasmic Reticulum

Approximately 30% of the proteins synthesized on cytosolic ribosomes are translocated into ER, where posttranslational modification, folding, and assembly take place. These include secreted and cell-surface proteins as well as resident proteins of the endocytic and exocytic organelles. Hsp70s in the ER interact with these newly translocated proteins, assisting in their folding and assembly and preventing their aggregation. BiP (also known as GRP78) in mammalian cells and its yeast homologue, Kar2, are the best-studied ER lumenal Hsp70s that have been shown to interact with a number of secretory pathway proteins to promote their folding and assembly [26–28] (see also Chapter 16). BiP/Kar2 have also been found to play a role in retaining proteins in the ER that do not mature properly and in directing them to back across the ER membrane to be degraded by the proteasome, a process known as ER quality control (reviewed in Refs. [29–31]). In addition, the interaction between unfolded proteins and BiP/Kar2 has been shown to serve as a sensor for ER stress [32]. Working with ER-membrane-associated J-proteins (Sec63 and Mtj1), BiP/Kar2 are also involved in the early step of protein translocation into ER (see Sections 14.3.1 and 14.3.2 for more discussion).

In addition to Kar2, a second Hsp70, Lhs1 (also known as Ssi1 or Cer1), has also been found to function in the lumen of the ER in yeast. Unlike *KAR2*, *LHS1* is not an essential gene and is not induced by heat shock. However, Δ*lhs1* strains are cold-sensitive for growth and accumulate precursor forms of several secretory proteins [33, 34]. Lhs1 is thus believed to play important roles in protein translocation into the ER. Increased ER protein aggregation and degradation after heat stress have also been found in strains lacking Lhs1, suggesting a role in the refolding of denatured proteins in the ER as well [35]. Genetic analysis also strongly imply that it plays a role in unfolded protein response (UPR) in the ER [34, 36]. A number of genetic interactions have been reported between Lhs1 and Kar2 [33, 34, 37], indicating a complex relationship between these two Hsp70s. Recently, Steel et al.

reported that the ATPase activities of Kar2 and Lhs1 are coupled and coordinately regulated. It was shown that Lhs1 stimulates Kar2's ATPase activity by serving as a nucleotide exchange factor, which could be a novel function of Hsp70s [38]. Because the mammalian homologues of Kar2 and Lhs1, BiP and GRP170, both bind to unfolded immunoglobulin chains [39, 40], their chaperone functions might be coupled in vivo by this coordinated regulation.

14.3 "Tethered" Hsp70s/J-proteins: Roles in Protein Folding on the Ribosome and in Protein Translocation

Examples of Hsp70s that are targeted to particular positions within the cell have been known for some time. Of these, the best-studied is the tethering of organellar Hsp70s to the import channel, where they play critical roles in the import of proteins from the cytosol into both the ER and mitochondria. In these cases, Hsp70 binding to unfolded proteins provides a driving force for the import process by favoring vectorial movement of the translocating polypeptide into the organelle, preventing movement back towards the cytosol. In other cases, chaperones tethered to their site of action appear to play a role similar to that of soluble chaperones, but their targeting places them in very close proximity to their protein substrate. One such example is the ribosome-associated Hsp70/J-protein pair Ssb/Zuo1 of yeast, discussed in Section 14.3.2.

14.3.1 Membrane-tethered Hsp70/J-protein

Translocation across both the endoplasmic reticulum membrane and the mitochondrial inner membrane requires passage through channels whose narrow width demands that proteins be substantially unfolded. In both cases, organellar Hsp70s tethered to the translocation channel play a significant role in protein translocation into the ER lumen and the mitochondrial matrix. In the ER, Hsp70 is important for both SRP-dependent co-translational and posttranslational translocation [41, 42]. In mitochondria, Hsp70 is particularly important for translocation of proteins that are tightly folded [43] and thus need to be unfolded before translocation.

In the ER of yeast, Sec63, a polytopic membrane J-protein with a substantial cytosolic domain and a lumenal J-domain, is thought to tether the lumenal Hsp70 Kar2 to the channel, as well as to stimulate its ATPase activity [44]. In mitochondria, the roles of tether and J-protein are separated into (or at least shared by) two proteins, the tether being Tim44 [45–47] and the J-protein being Pam18 [48–50]. Both are associated with the import channel. Tim44 is a peripheral membrane protein, while Pam18 is an integral membrane protein with an N-terminal domain extending into the intermembrane space and a J-domain extending into the matrix.

Pam18 stimulates the ATPase activity of Ssc1; Tim44 does not, but also does not interfere with stimulation by Pam18.

While the exact mechanism of Hsp70 function at the channel remains controversial, there is no debate over the idea that Hsp70 makes use of the same basic biochemical properties utilized in other chaperone activities such as protein folding and binding of short hydrophobic peptide segments, which are regulated by ATP binding and hydrolysis, which in turn is modulated by J-proteins [51–53]. This binding drives vectorial movement of the polypeptide chain by sterically blocking movement back through the narrow channel. Minimally, the act of tethering to the channel allows an extremely high local concentration at the channel. It has also been argued that Hsp70 exerts a force upon the incoming chain, making use of an ATP-dependent conformational change to ''pull'' it into the organelle. Proof of such an unprecedented activity for an Hsp70 awaits more sophisticated biophysical experiments than have been carried out to date.

Interestingly, however, there is evidence for an additional and unusual role for Hsp70 at the translocon in the ER membrane: gating the channel [54]. The lumenal Hsp70 is responsible for sealing the translocon pore, thereby maintaining the permeability barrier of a non-translocating pore. Mechanistically, how this occurs and which domains of Hsp70 are involved have not been established.

Hsp70s and J-proteins also play a role in protein import into organelles from the cytosolic side. There are multiple reports, both in vivo and in vitro and in both yeast and mammalian cells, that indicate that soluble cytosolic chaperones facilitate translocation, presumably by preventing the premature folding of precursor proteins [51]. While soluble cytosolic chaperones play significant roles in this process, it is intriguing that the J-protein Ydj1 is farnesylated [55] and a portion is found to be associated with the membrane. Whether this association is important for aiding translocation is not clear. However, an intriguing means of targeting chaperone-associated proteins to mitochondria has been reported by Young et al. [56]. Tom70 is an outer mitochondrial membrane receptor for proteins with internal mitochondrial targeting signals that are present in certain mitochondrial proteins such as membrane carrier proteins of the inner membrane. Tom70 is also a tetratrico peptide repeat (TPR) domain-containing protein. The TPR domain of Tom70 interacts with the C-terminus of Hsp70, targeting it to the mitochondria and thus facilitating the interaction of Tom70 with the targeting signal of the protein. Thus, Tom70 serves to target cytosolic Hsp70 (and Hsp90 in mammalian cells), carrying its cargo to the mitochondrial outer membrane.

14.3.2
Ribosome-associated Hsp70/J-proteins

One can imagine more than one possible function for molecular chaperones associated with ribosomes. Three examples are discussed below. While none of them has been thoroughly mechanistically defined, they represent three ways that chaperones may function in protein translation and folding of newly synthesized polypeptides: directly interacting with the nascent chain, modulating protein translocation across membranes, and in the process of translation itself.

The advantage of tethering molecular chaperones near the exit site of the ribosome in terms of protein folding is perhaps the easiest to envision. As protein translation occurs in a vectorial fashion, a newly synthesized polypeptide emerging from the ribosome cannot fold until the entire domain is synthesized. Being exposed to the crowded cellular environment, ribosome-bound nascent chains are thus prone to misfolding and/or aggregation. In the yeast *S. cerevisiae*, two types of Hsp70s (Ssb and Ssz1) and one type of J-protein (Zuo1) have been found to nearly quantitatively associate with ribosomes, with Ssz1 and Zuo1 forming a surprisingly stable heterodimer known as RAC (ribosome-associated complex) [57–59]. The ribosome association of Ssb and RAC is believed to situate them in close proximity to nascent chains, thus facilitating their chaperone functions. Actually, Ssb is believed to bind to the ribosome near the polypeptide exit tunnel since it can be cross-linked to short ribosome-bound nascent chains with a length only slightly longer than that required to span the ribosome exit tunnel [60]. It has been shown that Ssb and Zuo1 bind ribosomes independently, whereas Ssz1 associates with ribosome via its interaction with Zuo1 [59].

Genetic analysis has implied that Ssb, Zuo1, and Ssz1 function together in the same biological pathway, as any combinatory deletions of the three cause the same phenotypes [60, 61]. A chaperone system containing two Hsp70s and one J-protein such as this had not been observed before. How do they function together to chaperone nascent chains on ribosomes? Current evidence suggests that this chaperone triad is actually a variation of the classic Hsp70/J-protein pair, in which the J-protein's role is played by RAC, the Zuo1-Ssz1 complex. Ssb is believed to be the main Hsp70 chaperone interacting with ribosome-bound nascent chains, since it can be cross-linked to nascent chains of between 54 and 152 amino acids [60, 62] and its peptide-binding domain has been shown to be important for its in vivo function [63]. In contrast, Ssz1, the other Hsp70 in this system, has not been observed to interact with nascent chains, and its entire putative peptide-binding domain is dispensable [60].

However, compelling evidence has shown the importance of Ssz1 in working with Zuo1 to assist Ssb's function, as Ssb's cross-link to nascent chain depends on the presence of a functional RAC [61]. In addition, Zuo1 carrying an alteration in its J-domain, even though bound to Ssz1, could not restore the cross-link by Ssb, indicating that Zuo1 is the J-protein partner for Ssb [61]. Collectively, it has been proposed that Ssz1 functions as a cofactor/regulator of Zuo1, modifying the ability of Zuo1 to stimulate Ssb's chaperone activity [60]. This model is supported by the recent finding that Ssb's ATPase activity can be stimulated by Zuo1 only when it is in complex with Ssz1 (P. Huang, personal communication). Genetic analysis also suggests more central roles for Ssb and Zuo1 than for Ssz1, since overexpression of Zuo1 or Ssb can partially compensate for the absence of Ssz1, but Ssz1 overexpression cannot compensate for the lack of either Zuo1 or Ssb [61]. It seems that Ssz1 has evolved to function differently from classic Hsp70s (see Section 14.6.1 for more discussion).

It should be noted that only around half of the total Ssb proteins are found to be ribosome-associated, whereas all of Zuo1 and Ssz1 are found on the ribosomes [57–59]. This suggests that Ssb might play additional roles in the cytosol or that it

could move along with the elongating nascent chains to facilitate their folding. It was recently proposed that Ssb might cooperate with the yeast chaperonin system (TriC; for further detail, see Chapters 21 and 22) in the cytosol to fold a specific class of substrates containing WD domains [64].

A ribosome-associated J-protein, Mtj1p, from dog pancreas microsomes has recently been identified and characterized [65]. Mtj1p is thought to function very differently from Zuo1. It is an ER membrane protein having a single transmembrane domain; its J-domain, which extends into the ER lumen, interacts with the ER lumenal Hsp70 BiP. The large cytosolic domain of Mtj1p interacts with translating and non-translating ribosomes at low ionic strength, up to 200 mM KCl. Using truncation constructs, the ribosome-interacting region of Mtj1p was mapped to a highly charged N-terminal region (amino acids 176–194) in its cytosolic domain. Intriguingly, the interaction of Mtj1p with the ribosome appears to affect translation. Translation of a number of proteins in reticulocyte lysates is dramatically decreased when either Mtj1p's cytosolic domain or a peptide derived from its ribosome-interacting region is present. It has been proposed that Mtj1p acts during co-translational protein transport into ER to recruit both the ribosome and BiP to the translocon complex. In the process, it could help to modulate translation and facilitate any number of aspects of the translocation process, including: facilitating the handover of nascent polypeptides from the signal recognition particle (SRP) to the translocon complex, transmitting signals from the ribosome to BiP, or regulating lumenal gating of the translocon [65].

Ribosome association has also been observed for a portion of yeast Hsp70 Ssa and one of its J-protein partners, Sis1 [66, 67]. However, the exact nature of their ribosome association has not been established. The data indicate that Ssa interacts with Sis1 and poly(A)-binding protein (Pab1) via its C-terminal 10-kDa domain [66, 68, 69], and its interaction with Sis1 and Pab1 occurs preferentially on translating ribosomes [66]. Supporting a meaningful role for Sis1 on ribosomes, genetic interactions have been reported between mutations in genes encoding ribosomal subunit proteins and mutations in *SIS1* [66, 67]. A dramatic decrease in interaction between Pab1 and the translation initiation factor, eIF4G, has also been observed in strains carrying a temperature-sensitive allele of *SSA* growing at non-permissive temperature [66]. Collectively, the data suggest that Ssa and Sis1 may function in translation initiation on yeast ribosomes, possibly via interaction with Pab1. For further discussion of ribosome-associated chaperones see Chapter 12.

14.4 Modulating of Protein Conformation by Hsp70s/J-proteins

Although the examples are limited, Hsp70 and J-proteins have evolved in some instances to interact with proteins that are fully, or nearly fully, folded. In this manner, chaperones function in specific, and very diverse, cellular functions, including the biogenesis of Fe/S proteins, regulation of the heat shock response, and regulation of initiation of DNA replication. In some cases an abundant chaperone that functions in generic protein folding, interacting with many unfolded protein sub-

strates, will also interact with one or a few specific folded proteins. The interaction of DnaK with the heat shock transcription factor σ^{32} and the function of mammalian Hsc70 in clathrin uncoating are such examples. In other cases, such as the biogenesis of Fe/S centers, Hsp70 and J-proteins have evolved to work in a single, specific function.

14.4.1 Assembly of Fe/S Centers

Although in vitro Fe/S clusters can be formed in proteins directly from elemental iron and sulfur, in vivo this task falls to highly conserved and complex assembly systems. Central to this system is a scaffold protein onto which a cluster is assembled and then transferred to a recipient protein [70, 71]. The scaffold, called Isu in eukaryotes and IscU in prokaryotes, is a substrate protein for a specialized Hsp70:J-protein pair (Ssq1:Jac1 in eukaryotes and Hsc66:Hsc20 in prokaryotes) [72, 73]. IscU/Isu proteins are small, highly conserved proteins, with the mammalian and bacterial proteins having about 70% amino acid identity. One of the stretches (LPPVK) of complete identity among the proteins from diverse organisms contains the binding site for the specialized Hsp70. The binding site for the J-protein has been elusive; the site may not be a continuous stretch of amino acids and thus is technically more difficult to define. In both eukaryotes and prokaryotes, the J-protein and the Hsp70 of this pair are very specialized. In fact, there is no evidence of the existence of substrate proteins in addition to the Fe/S cluster scaffold protein.

This J-protein:Hsp70 pair plays a very important role in assembly of Fe/S clusters, an essential cellular process [71, 74]. Bacteria have redundant systems for Fe/S cluster assembly, so the lack of Hsc66:Hsc20 has a fairly modest effect on the activity of Fe/S-containing enzymes in the cell [75]. However, *JAC1* is essential in most yeast strain backgrounds, and cells lacking Ssq1 have greatly reduced Fe/S-containing enzyme activity. Based on the extensive data available concerning Hsp70:J-protein function, it would be logical to propose that the chaperones alter the conformation of the scaffold proteins to facilitate either the assembly of the cluster or its transfer to a recipient protein. Recent results from the Lill laboratory [76], utilizing the labeling of Isu with radioactive iron, suggest that the chaperones may function in aiding cluster transfer. Strains depleted of Ssq1 or Jac1 accumulated higher than normal amounts of iron associated with Isu, while those having a decreased amount of proteins known to be needed for assembly of the cluster, such as the sulfur-transfer protein Nfs1, had lower levels. But, the mechanistic role of chaperones in the process remains to be clarified.

While it is clear that these chaperones involved in Fe/S cluster assembly are quite specialized, it is not so clear whether the abundant "generic" chaperones of the same cellular compartment can carry out this role as well. The data from bacteria suggest that the generic DnaK/DnaJ/GrpE system functions completely separately from the Hsc66/Hsc20 system [77]. But in yeast it appears that there is at least some functional overlap between the systems. Overexpression of the abun-

dant Hsp70 of the mitochondrial matrix Ssc1, which also functions in protein translocation and folding of many matrix proteins, can substantially suppress the effects of the absence of Ssq1 [78]. Also, Ssq1 and Ssc1 appear to share the nucleotide release factor Mge1 [73]. Interestingly, it is not clear whether mammalian mitochondria have a specialized Hsp70 for Fe/S assembly, as no obvious homologue of Ssq1 has been found in these genomes. However, a homologue of Jac1 does exist. Perhaps in mammalian cells the major Hsp70, which is involved in protein translocation and general protein folding, also fulfils the role of facilitating Fe/S cluster assembly, using the Jac1 homologue as its alternative J-protein partner.

14.4.2 Uncoating of Clathrin-coated Vesicles

Regulated dynamic interaction among plasma membranes and cellular membrane compartments is accomplished by transport vesicles. Budding and fusion of vesicles require a series of assembly and disassembly cycles of the coat protein complex that provide the mechanical support for membrane bending and cargo selection. Hsc70, the constitutive form of Hsp70, has been known to play important roles in uncoating of clathrin-coated vesicles (CCVs), the major class of transport vesicles involved in endocytosis and synaptic transmission (for review, see Ref. [79]).

Hsc70, the major cytosolic Hsp70 of mammalian cells, promotes the disassembly of clathrin coats by binding to clathrin in an ATP-dependent manner, thereby releasing monomeric clathrin triskelia and other coat proteins from CCVs [80–82]. Like other members of the Hsp70 family, Hsc70 works with a J-protein partner in this process. The specialized type of J-protein involved is called auxilin, a name that encompasses brain-specific auxilin 1 and the ubiquitously expressed auxilin 2 (also called G-cyclin-associated kinase, or GAK) [83–88]. It is believed that auxilin binds to clathrin first and then recruits Hsc70 to CCVs via its J-domain, which then stimulates ATP hydrolysis and clathrin binding to Hsc70, resulting in release of clathrin monomers from CCVs [89–91].

Auxilin homologues have been identified in several species, including yeast, *C. elegans*, and mammals; they all contain a clathrin-binding domain and a C-terminal J-domain [87, 89, 90, 92–94]. Recent studies indicate that, as expected, the J-domain is important for interaction with Hsc70 [95] but that it also has features different from previously studied J-domains [96]. The structure of the bovine auxilin J-domain has been solved and was found to contain an extra N-terminal helix and a long loop inserted between helices I and II in addition to conserved J-domain features. Surface plasmon resonance analysis of auxilin mutants reveals that several positively charged residues in the long loop are also important for Hsc70 binding.

Recently, the results of a flurry of in vivo studies, including RNA interference in nematode cells [90] and dominant-negative interference experiments in mammalian cells [97], suggest that Hsc70s and auxilin play a more general role in clathrin dynamics than just uncoating of CCVs. Auxilin is released from CCVs during uncoating, but Hsc70 remains associated with free clathrin, possibly performing

additional functions such as preventing clathrin-spontaneous polymerization or priming it for membrane recruitment by adaptor complex [98]. In addition, inactivation of auxilin in yeast also results in a phenotype similar to cells lacking clathrin [93].

Besides their functions with clathrin, Hsc70 and auxilin have recently been found to have unanticipated roles in other stages of vesicle transport. For example, Newmyer et al. [99] found that Hsc70 and auxilin can interact with GTP-bound dynamin, a protein well-known for its importance in vesicle formation. Two domains in auxilin were identified as being involved in dynamin binding; overexpression of these domains in vivo inhibited endocytosis without changing the dynamics or distribution of clathrin. It is thus suggested that Hsc70 and auxilin also participate in the early step of CCV formation [99]. In addition, Hsc70 has been suggested to play a role in neurotransmitter exocytosis. Mutations in Hsc70-4, a major cytosolic Hsp70 of *Drosophila*, were found to impair nerve-evoked neurotransmitter release in vivo. Genetic analysis suggested that Hsc70-4 might cooperate with cysteine string protein, a specialized J-protein on the membrane of secretary vesicles, to increase the Ca^{2+} sensitivity of neurotransmitter release upon vesicle fusion [100]. Additionally, a block in exocytosis has also been observed in squid synapses expressing dominant-interfering Hsc70 mutant proteins [95]. However, the critical protein substrates of Hsc70 during exocytosis are not yet known.

14.4.3
Regulation of the Heat Shock Response

While there are indications that Hsp70s play a role in regulation of the heat shock response in a variety of organisms, this role is by far best understood in bacteria. The heat shock response in *E. coli* is transcriptionally controlled by the heat shock promoter-specific transcription factor σ^{32}, a subunit of RNA polymerase (reviewed in Refs. [101, 102]). Upon heat shock, the level and activity of σ^{32} are rapidly increased due to the altered translatability of the σ^{32} gene (*rpoH*) and elevated stability of σ^{32} protein. The shutoff of the response results from the reversal of these effects, a decrease in the level and activity of σ^{32}. The *E. coli* Hsp70 system, DnaK/DnaJ/GrpE, has been found to regulate the heat shock response by directly associating with σ^{32} and modulating its degradation by proteases.

In non-heat-shocked cells, σ^{32} has an extremely short half-life of less than 1 minute. After heat shock, the half-life rapidly increases to, and remains at, eightfold, until the shutoff phase of the heat shock response begins [103, 104]. Several proteases are involved in σ^{32} degradation, including Lon (la), ClpAP and HslVU, and, most significantly, the ATP-dependent metalloprotease FtsH (previously known as HflB) [105–108]. The DnaK chaperone system was first implicated in the regulation of the heat shock response because strains carrying mutations in any one of the genes encoding components of the DnaK/DnaJ/GrpE system showed elevated expression of heat shock-inducible genes [109]. Later it was proposed that the DnaK and co-chaperones present σ^{32} to the proteases, thus negatively regulating the stability of σ^{32}. This model provides an attractive mechanism that links the level of σ^{32} to the level of unfolded proteins, the stress sensed by the DnaK chaper-

one system. Upon heat shock, less DnaK and DnaJ would be available for σ^{32} association and degradation, since more substrates (e.g., unfolded proteins) are competing for binding to the chaperones, resulting in the increased stability of σ^{32} [110]. This model predicts that the actual levels of the DnaK system proteins directly affect the heat shock response, which has been proven to be the case [111].

A significant amount of work has been done to understand the interaction between the DnaK system and σ^{32}, but exactly how the DnaK system modulates the degradation of σ^{32} by FtsH remains unclear. It has been reported that when binding to RNA polymerase, σ^{32} is resistant to FtsH-mediated degradation [111]. It is thus possible that the DnaK system affects the stability of σ^{32} by preventing its binding to the RNA polymerase, hence indirectly increasing the chance of σ^{32} degradation by FtsH. However, it has been shown that a mutant version of σ^{32} that cannot bind to RNA polymerase, but interacts normally with DnaK/DnaJ/GrpE, has a normal stability in the cells lacking DnaK or cells lacking both DnaJ and the DnaJ homologue ClbA [112], suggesting a more active role of the DnaK system in promoting the degradation of σ^{32}. It was recently reported that the in vitro interaction between DnaK and σ^{32} is highly temperature-sensitive, possibly due to a destabilized structural element in σ^{32} at elevated temperature [113], thus providing another way of regulating the stability of σ^{32} by the DnaK system.

The actual regions of σ^{32} that interact with DnaK and DnaJ, and thus are involved in regulation, remain elusive. In vitro, DnaK and the co-chaperone DnaJ bind independently to free σ^{32}, and it has been proposed that σ^{32} interacts similarly to any other substrate, with σ^{32} binding/release controlled by the ATP hydrolysis cycle [114]. Screening of a σ^{32}-derived peptide library for chaperone binding sites revealed two binding sites in the highly conserved RpoH box in σ^{32}, between residues 133 and 140 [115, 116]. Peptides corresponding to this region bind to DnaK and can be degraded by FtsH in vitro. However, introduction of alterations within these regions in the full-length σ^{32} protein did not affect DnaK binding in vitro or its degradation in vivo and in vitro [117]. Instead, these mutants of σ^{32} show decreased affinity for RNA polymerase and reduced transcriptional activity. It is thus still unclear whether the RpoH box in σ^{32} is directly involved in DnaK binding in vivo.

In addition to the turnover of σ^{32}, the DnaK system has also been suggested to modulate the activity of σ^{32} directly, since overexpression of DnaK and DnaJ in a Δ*ftsH* strain leads to reduced activity of σ^{32}, while the level of σ^{32} remains unchanged [108]. This type of modulation has also been reported in *Agrobacterium tumefaciens*, in which RpoH, the σ^{32} homologue, is normally quite stable and a change of the level of DnaK and DnaJ specifically changes the activity of RpoH [118]. However, little is known about how the activity of σ^{32} or RpoH is altered by the DnaK system.

14.4.4
Regulation of Activity of DNA Replication-initiator Proteins

Many plasmid-encoded DNA initiator proteins exist as monomers and dimers in equilibrium. Monomers activate initiation of DNA replication by binding to

specific DNA-binding sites around the origin of replication, whereas dimers are inactive due to altered DNA-binding specificities. The role of the Hsp70 chaperone machinery in regulating the activity of DNA replication initiators was first demonstrated by the work of Wickner et al. [119–122] in the *E. coli* system of RepA, the replication-initiator protein of plasmid P1, motivated by earlier in vivo observations that mutations in *dnaK*, *dnaJ*, or *grpE* resulted in plasmid P1 instability [123]. The DnaK/DnaJ/GrpE chaperone machinery altered the equilibrium between dimer and monomer, destabilizing dimeric RepA in vitro and rendering it more active in origin binding [119, 120–122]. How DnaK/DnaJ/GrpE interacts with the folded RepA dimer and promotes its monomerization is still not fully understood. Both DnaJ and DnaK bind to a RepA dimer, but at different sites [119, 124]. It was proposed that DnaJ tags the RepA dimer for recognition by DnaK, which then stimulates the monomerization of RepA in an ATP-dependent reaction [121].

The DnaK chaperone system has also been shown to assist the monomerization of other replication initiation proteins, including RepA of plasmid P7 [122] and TrfA of RK2 plasmid [125]. Konieczny et al. [125] reported that ClpB, the Clp/Hsp100 family, cooperates with the DnaK chaperone system to convert TrfA dimers into active monomers. The activation of TrfA seems to be specific for bacterial chaperones (ClpB, DnaK, DnaJ, and GrpE) since the corresponding yeast mitochondrial homologues (Hsp78, Ssc1, Mdj1, and Mge1) did not activate TrfA in an in vitro system reconstituted with purified components.

Recent identification of similarities between RepA and the origin-recognition complex (ORC) subunit from eukaryotes and archaea raises the question as to whether Hsp70s play a more general role in DNA replication. Giraldo et al. [126] found that the C-terminal domain of ScOrc4p, a subunit of *S. cerevisiae* ORC, shares sequence and potential structural similarity with the N-terminal domain of RepA, including a common winged-helix domain and a leucine-zipper dimerization motif. Furthermore, they found that ScOrc4p can interact with yeast Hsp70 both in vivo and in cell lysates, although it is not clear with which Hsp70 it interacts [126]. Collectively, these results suggest Hsp70's role in regulating the assembly of active ORC in eukaryotes, possibly through a mechanism involving disassembly of ORC subunits.

In addition to monomerization of initiators for DNA replication, Hsp70/J-protein systems have long been known to play important roles in the assembly and activation of viral DNA replicative machinery in both prokaryotes and eukaryotes (see review in Ref. [127]). In the case of bacteriophage λ replication in *E. coli*, it was proposed that DnaJ interacts with DnaB-λP-λO-DNA complex and facilitates recognition by DnaK, which then stimulates DnaB helicase activity by catalyzing the release of λP from the initiation complex [120, 128–130]. In mammalian cells, Hsp70 and J-protein have also been found to enhance the origin binding of UL9, the origin-binding protein of herpes simplex virus type 1 [131]. In addition, hTid-1, a human homologue of DnaJ, was found to associate with UL9 and promote the multimer formation from dimeric UL9 [132]. The DNA binding and activity of helicase E1 from human papilloma virus is also promoted by human Hsp70 and J-protein [133, 134]. In summary, mounting evidence suggests that

Hsp70/J-protein systems interact with folded initiator proteins and play regulatory roles in DNA replication.

14.5 Cases of a Single Hsp70 Functioning With Multiple J-Proteins

The previous sections discuss many physiological roles of Hsp70s and their partner J-proteins (Figure 14.1). In some of the cases discussed, specific functions depend upon a functional specificity inherent in the Hsp70 itself. The Hsp70 evolved in Fe/S cluster biogenesis and the one evolved to bind to ribosomes, and to be regulated like ribosomal proteins, are examples of such specialized Hsp70s. Although dispersed in different sections of this chapter, there are also multiple examples of a single Hsp70 functioning with different J-proteins in very different physiological roles. Examples exist in mitochondria, the ER, and the cytosol of eukaryotes.

In mitochondria, the abundant Hsp70 Ssc1 is one such example. A portion of Ssc1 is tethered to the membrane and functions in translocation of proteins into the matrix with the membrane J-protein Pam18 [48–50]. The remainder of Ssc1 is soluble and functions with the soluble J-protein Mdj1 in the folding of imported and mitochondrially encoded proteins [21, 24]. In the ER, the predominant Hsp70, Kar2/BiP, functions with several J-proteins. Analogous to the case in the mitochondria, a portion of Kar2 is tethered to the translocon and acts with the integral membrane J-protein Sec63 in protein translocation. As a soluble protein in the lumen, it has the J-protein partners Scj1 and Jem1.

Multiple examples exist in the cytosol as well. The best-studied example in mammalian systems is the involvement of Hsc70 not only in protein folding and translocation into mitochondria but also in vesicle transport. In the former process, Hsc70 works with J-proteins Hdj1 and Hdj2, among others; in vesicle transport it works with auxilin and cysteine-string proteins (described in Section 14.4.2).

Similar examples exist in the yeast cytosol, where the Ssa class of Hsp70s has multiple J-protein partners, including Ydj1, Sis1, and Swa2 (yeast auxilin). Ydj1 and Sis1 are particularly interesting examples, in that the J-proteins show extensive similarity beyond their J-domains but are functionally distinct, in the sense that the functions of the essential Sis1 cannot be carried out by Ydj1. Interestingly, this functional specificity has been conserved, as the mammalian homologue of Sis1, Hdj1, can rescue a Δ*sis1* strain, but the homologue of Ydj1, Hdj2, cannot [135, 136]. The biochemical basis of this functional difference has yet to be defined.

14.6 Hsp70s/J-proteins – When an Hsp70 Maybe Isn't Really a Chaperone

As we learn more about the complex workings of cells, the idea has emerged that genes have been duplicated and evolved to serve additional functions. Such evolu-

tion includes the examples described above, as Hsp70 and J-proteins have evolved to serve specialized functions utilizing their inherent ability to interact with hydrophobic sequences in proteins in their peptide-binding clefts. However, examples have also been found in which Hsp70s have evolved to carry out functions that are no longer dependent on their ability to interact with substrate proteins. Below we discuss two examples in which an Hsp70 forms a heterodimer with another protein, perhaps serving a regulatory role.

14.6.1 The Ribosome-associated "Hsp70" Ssz1

Ssz1 (previously known as Pdr13) from *S. cerevisiae* is an example of a protein with sequence similarity to Hsp70s that clearly functions in ways not expected of an Hsp70 chaperone. Ssz1 is typically classified as an Hsp70 because it contains a conserved N-terminal ATPase domain that shares around 35% sequence identity with ATPase domains of Hsp70s across species and because its size of 60 kDa is close to that expected of an Hsp70. However, Ssz1's C-terminal region has little sequence similarity with known Hsp70s, rendering its overall sequence similarity to Hsp70s only 20–25%.

Ssz1's cellular properties also differ significantly from those of well-studied Hsp70s. First, although Ssz1 interacts with a J-protein, the ribosome-associated Zuo1, the complex, called the ribosome-associated complex (RAC), is surprisingly stable [59]. Typically, Hsp70–J-protein interactions are quite transient, while the RAC subunits cannot be separated without denaturation. But most compelling is the fact that Ssz1's C-terminal putative peptide-binding domain is not required for its in vivo function. The C-terminal truncated Ssz1, having only the ATPase domain, fully rescues the phenotypes of a Δ*ssz1* strain [60]. Up to now, there is no evidence to indicate that Ssz1 interacts with nascent chains or has any chaperone activity.

However, there is every indication that Ssz1 has an important in vivo role working with Zuo1, but as a component required for Zuo1's ability to act as the J-protein partner of the ribosome-associated Hsp70 Ssb. Both Ssz1 and Zuo1 are required for Ssb cross-link to nascent chains on the ribosomes [61]. Genetic analysis also suggests that Ssz1, Zuo1, and Ssb work in the same biological pathway, as the phenotypes of any single mutant are the same as cells lacking all three [60, 61]. Therefore, it has been proposed that Ssz1 functions as a modulator of Zuo1, priming it to interact with Ssb in chaperoning newly synthesized polypeptides on the ribosomes [60, 61] (see Section 14.3.2 on ribosome-associated Hsp70s). Consistent with this idea, Zuo1 stimulates Ssb's ATPase activity only when it is in complex with Ssz1, supporting the idea that Ssz1 functions as a modulator of a J-protein (P. Huang, personal communication).

The only other known in vivo activity of Ssz1 is its role in pleiotropic drug resistance (PDR), the resistance to multiple drugs with unrelated structures or modes of action [137]. PDR occurs because cells increase the efflux of drugs, primarily be-

cause of the increase in activity of the transcription factor Pdr1, which acts on a number of genes, including those encoding ABC transporters, which are responsible for drug efflux. Actually, Ssz1 (previously known as Pdr13) was first isolated from a genetic screen for genes that, when overexpressed from a multicopy plasmid, increased PDR in a Pdr1-dependent fashion [137]. Ssz1's activation of PDR is independent of Zuo1 or Ssb and does not require its C-terminal putative peptide-binding domain (H. Eisenman, personal communication). Although it remains an enigma as to how Ssz1 mediates Pdr1-dependent transcription, its ability to do so without its putative peptide-binding domain indicates that it does not act as a chaperone in this role.

14.6.2 Mitochondrial Hsp70 as the Regulatory Subunit of an Endonuclease

The major mitochondrial Hsp70, Ssc1, from *S. cerevisiae* serves as another example of an Hsp70 that carries out a function other than that of a conventional chaperone. Ssc1 forms a stable heterodimer with the endonuclease *Sce*I [138]. *Sce*I functions as a multisite-specific endonuclease in yeast mitochondria, where it cleaves more than 30 sites on mitochondrial DNA to induce homologous recombination upon zygote formation [139]. Ssc1 not only increased the thermostability and endonuclease activity of *Sce*I but also broadened its sequence specificity, as in the absence of Ssc1, *Sce*I is a unisite-specific endonuclease [140].

Although the mechanism by which Ssc1 alters the substrate specificity of *Sce*I is not thoroughly understood, progress has been made in understanding the interaction between Ssc1 and *Sce*I. The interaction between Ssc1 and *Sce*I is more stable in the presence of ADP than in the presence of ATP or in the absence of nucleotides [140]. *Sce*I was found to interact with Ssc1's ATPase domain; in addition, interaction of full-length Ssc1 could not be competed away by an excess of an unfolded protein substrate. Thus, *Sce*I is not a substrate of Ssc1 but rather a protein partner. However, only when full-length Ssc1 is complexed with *Sce*I does it confer multisite-specific endonuclease activity. It remains unclear whether Ssc1's ATPase activity plays any role in regulating *Sce*I's activity and specificity. However, no J-proteins seem to be required for Ssc1's effect on endonuclease activity, as in vitro reconstituted *Sce*I/Ssc1 heterodimers can recapitulate the multisite-specific endonuclease activity observed in mitochondrial extracts.

A similar function of mitochondrial Hsp70 in regulating endonuclease specificity has been found in another yeast strain, *Saccharomyces uvarum*. *Suv*I, the ortholog of the *Sce*I in *S. uvarum*, is a mitochondrial endonuclease that forms a stable heterodimer with the homologue of Ssc1, called mtHsp70, resulting in a change from a unisite-specific to a multisite-specific endonuclease [141]. In the absence of mtHsp70, *Suv*I and *Sce*I have the same unisite sequence specificity but show different multisite specificities upon binding to mtHsp70. These findings suggest that mtHsp70 can regulate the variety of sites cleaved by regulating the sequence specificity of endonucleases.

14.7
Emerging Concepts and Unanswered Questions

This chapter attempts to summarize the explosion of information and to outline emerging themes regarding the variety of functions of Hsp70s and J-proteins in the cell. Elegant biochemical experiments carried out over the past 15 years have established the basic biochemical parameters of the Hsp70:J-protein partnership and serve as the foundation for understanding the in vivo function of the myriad of individual J-protein:Hsp70 pairs that function in the cell. Clearly, much work remains, and certainly many surprises await us.

References

1 Ohtsuka, K. & Hata, M. (2000). Mammalian HSP40/DNAJ homologues: cloning of novel cDNAs and a proposal for their classification and nomenclature. *Cell Stress Chaperones* 5, 98–112.

2 Bukau, B. & Horwich, A. L. (1998). The Hsp70 and Hsp60 chaperone machines. *Cell* 92, 351–366.

3 Hartl, F. & Hayer-Hartl, M. (2002). Molecular chaperones in the cytosol: from nascent chain to folded protein. *Science* 295, 1852–8.

4 Hesterkamp, T. & Bukau, B. (1998). Role of the DnaK and HscA homologues of Hsp70 chaperones in protein folding in *E. coli*. *EMBO J* 17, 4818–4828.

5 Gaitanaris, G. A., Papavassiliou, A. G., Rubock, P., Silverstein, S. J. & Gottesman, M. E. (1990). Renaturation of denatured lambda repressor requires heat shock proteins. *Cell* 61, 1013–20.

6 Skowyra, D., Georgopoulos, C. & Zylicz, M. (1990). The *E. coli dnak* gene product, the hsp70 homologue, can reactivate heat-inactivated RNA polymerase in an ATP hydrolysis-dependent manner. *Cell* 62, 939–944.

7 Langer, T., Lu, C., Echols, H., Flanagan, J., Hayer, M. K. & Hartl, F. U. (1992). Successive action of DnaK, DnaJ, and GroEL along the pathway of chaperone-mediated protein folding. *Nature* 356, 683–689.

8 Schroder, H., Langer, T., Hartl, F.-U. & Bukau, B. (1993). DnaK, DnaJ and GrpE form a cellular chaperone machinery capable of repairing heat-induced protein damage. *EMBO Journal* 12, 4137–4144.

9 Ziemienowicz, A., Skowyra, D., Zeilstra-Ryalls, J., Fayet, O., Georgopoulos, C. & Zylicz, M. (1993). Both the Escherichia coli chaperone systems, GroEL/GroES and DnaK/DnaJ/GrpE, can reactivate heat-treated RNA polymerase. Different mechanisms for the same activity. *Journal of Biological Chemistry* 268, 25425–25431.

10 Szabo, A., Langer, T., Schroder, H., Flanagan, J., Bukau, B. & Hartl, F. U. (1994). The ATP hydrolysis-dependent reaction cycle of the Escherichia coli Hsp70 system DnaK, DnaJ, and GrpE. *Proc Natl Acad Sci USA* 91, 10345–9.

11 Mogk, A., Tomoyasu, T., Goloubinoff, P., Fudiger, S., Roder, D., Langen, H. & Bukau, B. (1999). Identification of thermolabile *Escherichia coli* proteins: prevention and reversion of aggregation by DnaK and ClpB. *EMBO J* 18, 6934–6949.

12 Teter, S. A., Houry, W. A., Ang, D., Tradler, T., Rockabrand, D., Fischer, G., Blum, P., Georgopoulus, C. & Hartl, F. U. (1999). Polypeptide Flux through Bacterial Hsp70: DnaK Cooperates with Trigger

Factor in Chaperoning Nascent Chains. *Cell* 97, 755–765.

13 Deuerling, E., Schulze-Specking, A., Tomoyasu, T., Mogk, A. & Bukau, B. (1999). Trigger factor and DnaK cooperate in folding of newly synthesized proteins. *Nature* 400, 693–696.

14 Kim, S., Schilke, B., Craig, E. & Horwich, A. (1998). Folding in vivo of a newly translated yeast cytosolic enzyme is mediated by the SSA class of cytosolic yeast Hsp70 proteins. *Proc Natl Acad Sci USA* 95, 12860–12865.

15 Thulasiraman, V., Yang, C.-F. & Frydman, J. (1999). In vivo newly translated polypeptides are sequestered in a protected folding environment. *EMBO J* 18, 85–95.

16 Eggers, D. K., Welch, W. J. & Hansen, W. J. (1997). Complexes between Nascent Polypeptides and Their Molecular Chaperones in the Cytosol of Mammalian Cells. *Molecular Biology of the Cell* 8, 1559–1573.

17 Michels, A. A., Kanon, B., Konings, A. W., Ohtsuka, K., Bensaude, O. & Kampinga, H. H. (1997). Hsp70 and Hsp40 chaperone activities in the cytoplasm and the nucleus of mammalian cells. *J Biol Chem* 272, 33283–9.

18 Pratt, W. B. & Toft, D. O. (2003). Regulation of signaling protein function and trafficking by the hsp90/hsp70-based chaperone machinery. *Exp Biol Med* 228, 111–133.

19 Chang, H. C. & Lindquist, S. (1994). Conservation of Hsp90 macromolecular complexes in Saccharomyces cerevisiae. *J Biol Chem* 269, 24983–8.

20 Liu, X. D., Morano, K. A. & Thiele, D. J. (1999). The yeast Hsp110 family member, Sse1, is an Hsp90 cochaperone. *J Biol Chem* 274, 26654–60.

21 Kang, P. J., Ostermann, J., Shilling, J., Neupert, W., Craig, E. A. & Pfanner, N. (1990). Requirement for hsp70 in the mitochondrial matrix for translocation and folding of precursor proteins. *Nature* 348, 137–143.

22 Westermann, B., Prip-Buus, C., Neupert, W. & Schwarz, E. (1995). The role of the GrpE homologue, Mge1p, in mediating protein import and protein folding in mitochondria. *EMBO J* 13, 1998–2006.

23 Westermann, B., Gaume, B., Herrmann, J. M., Neupert, W. & Schwarz, E. (1996). Role of the mitochondrial DnaJ homologue Mdj1p as a chaperone for mitochondrially synthesized and imported proteins. *Mol Cell Biol* 16, 7063–7071.

24 Liu, Q., Krzewska, J., Liberek, K. & Craig, E. A. (2001). Mitochondrial Hsp70 Ssc1: role in protein folding. *J. Biol. Chem.* 276, 6112–8.

25 Hermann, J., Stuart, R., Craig, E. & Neupert, W. (1994). Mitochondrial heat shock protein 70, a molcular chaperone for proteins encoded by mitochondrial DNA. *J. Cell Biol.* 127, 893–902.

26 Haas, I. G. & Wabl, M. (1983). Immunoglobulin heavy chain binding protein. *Nature* 306, 387–9.

27 Simons, J. F., Ferro-Novick, S., Rose, M. D. & Helenius, A. (1995). BiP/Kar2p serves as a molecular chaperone during carboxypeptidase Y folding in yeast. *J Cell Biol* 130, 41–49.

28 Hendershot, L., Wei, J., Gaut, J., Melnick, J., Aviel, S. & Argon, Y. (1996). Inhibition of immunoglobulin folding and secretion by dominant negative BiP ATPase mutants. *Proc Natl Acad Sci USA* 93, 5269–74.

29 Ellgaard, L. & Helenius, A. (2001). ER quality control: towards an understanding at the molecular level. *Curr Opin Cell Biol* 13, 431–7.

30 Brodsky, J. L., Werner, E. D., Dubas, M. E., Goeckeler, J. L., Kruse, K. B. & McCracken, A. A. (1999). The requirement for molecular chaperones during endoplasmic reticulum-associated protein degradation demonstrates that protein export and import are mechanistically distinct. *J Biol Chem* 274, 3453–60.

31 Plemper, R. K., Bohmler, S., Bordallo, J., Sommer, T. & Wolf, D. H. (1997). Mutant analysis links

the translocon and BiP to retrograde protein transport for ER degradation. *Nature* 388, 891–5.

32 Bertolotti, A., Zhang, Y., Hendershot, L. M., Harding, H. P. & Ron, D. (2000). Dynamic interaction of BiP and ER stress transducers in the unfolded-protein response. *Nat Cell Biol* 2, 326–32.

33 Baxter, B. K., James, P., Evans, T. & Craig, E. A. (1996). *SSI1* encodes a novel Hsp70 of the *Saccharomyces cerevisiae* endoplasmic reticulum. *Mol. Cell Biol.* 16, 6444–6456.

34 Craven, R. A., Egerton, M. & Stirling, C. J. (1996). A novel Hsp70 of the yeast ER lumen is required for the efficient translocation of a number of protein precursors. *EMBO J.* 15, 2640–2650.

35 Saris, N., Holkeri, H., Craven, R. A., Stirling, C. J. & Makarow, M. (1997). The Hsp70 homologue Lhs1p is involved in a novel function of the yeast endoplasmic reticulum, refolding and stabilization of heat-denatured protein aggregates. *J Cell Biol* 137, 813–824.

36 Tyson, J. R. & Stirling, C. J. (2000). LHS1 and SIL1 provide a lumenal function that is essential for protein translocation into the endoplasmic reticulum. *EMBO J* 19, 6440–52.

37 Hamilton, T. G. & Flynn, G. C. (1996). Cer1p, a novel Hsp70-related protein required for posttranslational endoplasmic reticulum translocation in yeast. *J Biol Chem* 271, 30610–3.

38 Steel, G. J., Fullerton, D. M., Tyson, J. R. & Stirling, C. J. (2004). Coordinated Activation of Hsp70 Chaperones. *Science* 303, 98–101.

39 Lin, H. Y., Masso-Welch, P., Di, Y. P., Cai, J. W., Shen, J. W. & Subjeck, J. R. (1993). The 170-kDa glucose-regulated stress protein is an endoplasmic reticulum protein that binds immunoglobulin. *Mol Biol Cell* 4, 1109–19.

40 Meunier, L., Usherwood, Y. K., Chung, K. T. & Hendershot, L. M. (2002). A subset of chaperones and folding enzymes form multiprotein complexes in endoplasmic reticulum to bind nascent proteins. *Mol Biol Cell* 13, 4456–69.

41 Panzner, S., Dreier, L., Hartmann, E., Kostka, S. & Rapoport, T. A. (1995). Posttranslational protein transport in yeast reconstituted with a purified complex of Sec proteins and Kar2p. *Cell* 81, 561–570.

42 Young, B. P., Craven, R. A., Reid, P. J., Willer, M. & Stirling, C. J. (2001). Sec63p and Kar2p are required for the translocation of SRP-dependent precursors into the yeast endoplasmic reticulum in vivo. *EMBO J* 20, 262–271.

43 Voisine, C., Craig, E. A., Zufall, N., von Ahsen, O., Pfanner, N. & Voos, W. (1999). The protein import motor of mitochondria: unfolding and trapping of preproteins are distinct and separable functions of matrix Hsp70. *Cell* 97, 565–574.

44 Corsi, A. K. & Schekman, R. (1997). The lumenal domain of Sec63p stimulates the ATPase activity of BiP and mediates BiP recruitment to the translocon in *Saccharomyces cerevisiae*. *J Cell Biol* 137, 1483–1493.

45 Schneider, H.-C., Berthold, J., Bauer, M. F., Dietmeier, K., Guiard, B., Brunner, M. & Neupert, W. (1994). Mitochondrial Hsp70/MIM44 complex facilitates protein import. *Nature* 371, 768–774.

46 Rassow, J., Maarse, A., Krainer, E., Kubrich, M., Muller, H., Meijer, M., Craig, E. & Pfanner, N. (1994). Mitochondrial protein import: biochemical and genetic evidence for interaction of matrix Hsp70 and the inner membrane protein Mim44. *J. Cell Biol.* 127, 1547–1556.

47 Liu, Q., D'Silva, P., Walter, W., Marszalek, J. & Craig, E. A. (2003). Regulated cycling of mitochondrial Hsp70 at the protein import channel. *Science* 300, 139–41.

48 D'Silva, P. D., Schilke, B., Walter, W., Andrew, A. & Craig, E. A. (2003). J protein cochaperone of the mitochondrial inner membrane required for protein import into the mitochondrial matrix. *Proc Natl Acad Sci USA* 100, 13839–44.

49 Mokranjac, D., Sichting, M., Neupert, W. & Hell, K. (2003). Tim14, a novel key component of the import motor of the Tim23 protein translocase of mitochondria. *EMBO J* 22, 4945–4956.

50 Truscott, K. N., Voos, W., Frazier, A. E., Lind, M., Li, Y., Geissler, A., Dudek, J., Muller, H., Sickmann, A., Meyer, H. E., Meisinger, C., Guiard, B., Rehling, P. & Pfanner, N. (2003). A J-protein is an essential subunit of the presequence translocase-associated protein import motor of mitochondria. *J Cell Biol* 163, 707–13.

51 Fewell, S. W., Travers, K. J., Weissman, J. S. & Brodsky, J. L. (2001). The action of molecular chaperones in the early secretory pathway. *Ann. Rev. Gen.* 35, 149–191.

52 Neupert, W. & Brunner, M. (2002). The protein import motor of mitochondria. *Nat Rev Mol Cell Biol* 8, 555–565.

53 Matouschek, A., Pfanner, N. & Voos, W. (2000). Protein unfolding by mitochondria. The Hsp70 import motor. *EMBO Rep* 5, 404–410.

54 Hamman, B. D., Henderschot, L. M. & Johnson, A. E. (1998). BiP maintains the permeability barrier of the ER membrane by sealing the lumenal end of the translocon pore before and early in translocation. *Cell* 92, 747–758.

55 Caplan, A. J., Tsai, J., Casey, P. J. & Douglas, M. G. (1992). Farnesylation of YDJ1p is required for function at elevated growth temperatures in *S. cerevisiae*. *J Biol Chem* 267, 18890–18895.

56 Young, J. C., Hoogenraad, N. J. & Hartl, F.-U. (2003). Molecular Chaperones Hsp90 and Hsp70 Deliver Proteins to the Mitochondrial Import Receptor Tom70. *Cell* 112, 41–50.

57 Nelson, R. J., Ziegelhoffer, T., Nicolet, C., Werner-Washburne, M. & Craig, E. A. (1992). The translation machinery and seventy kilodalton heat shock protein cooperate in protein synthesis. *Cell* 71, 97–105.

58 Yan, W., Schilke, B., Pfund, C., Walter, W., Kim, S. & Craig, E. A. (1998). Zuotin, a ribosome-associated DnaJ molecular chaperone. *EMBO J* 17, 4809–4817.

59 Gautschi, M., Lilie, H., Funfschilling, U., Mun, A., Ross, S., Lithgow, T., Rucknagel, P. & Rospert, S. (2001). RAC, a stable ribosome-associated complex in yeast formed by the DnaK-DnaJ homologues Ssz1p and zuotin. *Proc Natl Acad Sci USA* 98, 3762–7.

60 Hundley, H., Eisenman, H., Walter, W., Evans, T., Hotokezaka, Y., Wiedmann, M. & Craig, E. (2002). The in vivo function of the ribosome-associated Hsp70, Ssz1, does not require its putative peptide-binding domain. *Proc Natl Acad Sci USA* 99, 4203–8.

61 Gautschi, M., Mun, A., Ross, S. & Rospert, S. (2002). A functional chaperone triad on the yeast ribosome. *Proc Natl Acad Sci USA* 99, 4209–14.

62 Pfund, C., Lopez-Hoyo, N., Ziegelhoffer, T., Schilke, B. A., Lopez-Buesa, P., Walter, W. A., Wiedmann, M. & Craig, E. A. (1998). The Molecular Chaperone *SSB* from *S. cerevisiae* is a Component of the Ribosome-Nascent Chain Complex. *EMBO Journal* 17, 3981–3989.

63 Pfund, C., Huang, P., Lopez-Hoyo, N. & Craig, E. (2001). Divergent functional properties of the ribosome-associated molecular chaperone Ssb compared to other Hsp70s. *Mol. Biol. Cell* 12, 3773–3782.

64 Siegers, K., Bölter, B., Schwarz, J. P., Böttcher, U., Guha, S. & Hartl, F.-U. (2003). TRiC/CCT cooperates with different upstream chaperones in the folding of distinct protein classes. *EMBO J* 22, 5230–5240.

65 Dudek, J., Volkmer, J., Bies, C., Guth, S., Muller, A., Lerner, M., Feick, P., Schafer, K. H., Morgenstern, E., Hennessy, F., Blatch, G. L., Janoscheck, K., Heim, N., Scholtes, P., Frien, M., Nastainczyk, W. & Zimmermann, R. (2002). A novel type of co-chaperone mediates transmembrane recruitment of DnaK-

like chaperones to ribosomes. *EMBO J* 21, 2958–67.

66 Horton, L. E., James, P., Craig, E. A. & Hensold, J. O. (2001). The yeast hsp70 homologue Ssa is required for translation and interacts with Sis1 and Pab1 on translating ribosomes. *J Biol Chem* 276, 14426–33.

67 Zhong, T. & Arndt, K. T. (1993). The yeast *SIS1* protein, a DnaJ homologue, is required for initiation of translation. *Cell* 73, 1175–1186.

68 Qian, X., Li, Z. & Sha, B. (2001). Cloning, expression, purification and preliminary X-ray crystallographic studies of yeast Hsp40 Sis1 complexed with Hsp70 Ssa1 C-terminal lid domain. *Acta Crystallogr D Biol Crystallogr* 57, 748–50.

69 Qian, X., Hou, W., Zhengang, L. & Sha, B. (2002). Direct interactions between molecular chaperones heat-shock protein (Hsp) 70 and Hsp40: yeast Hsp70 Ssa1 binds the extreme C-terminal region of yeast Hsp40 Sis1. *Biochem J* 361, 27–34.

70 Frazzon, J. & Dean, D. R. (2003). Formation of iron-sulfur clusters in bacteria: an emerging field in bioinorganic chemistry. *Current Opinion in Chemical Biology* 7, 166–173.

71 Lill, R. & Kispal, G. (2000). Maturation of cellular Fe–S proteins: an essential function of mitochondria. *Trends in Biochemical Sciences* 25, 352–356.

72 Hoff, K. G., Ta, D. T., L., T. T., Silberg, J. J. & Vickery, L. E. (2002). Hsc66 substrate specificity is directed toward a discrete region of the iron-sulfur cluster template protein IscU. *J Biol Chem* 277, 27353–27359.

73 Dutkiewicz, R., Schilke, B., Knieszner, H., Walter, W., Craig, E. A. & Marszalek, J. (2003). Ssq1, a mitochondrial Hsp70 involved in iron-sulfur (Fe/S) center biogenesis: Similarities to and differences from its bacterial counterparts. *J Biol Chem* 278, 29719–29727.

74 Craig, E. A. & Marszalek, J. (2002). A specialized mitochondrial molecular chaperone system: a role in formation of Fe/S centers. *Cell Mol Life Sci*. 59, 1658–65.

75 Schwartz, C. J., Djaman, O., Imlay, J. A. & Kiley, P. J. (2000). The cysteine desulferase, IscS, has a major role in in vivo Fe–S cluster formation in *Escherichia coli*. *Proc Natl Acad Sci USA* 97, 9009–9014.

76 Muhlenhoff, U., Gerber, J., Richhardt, N. & Lill, R. (2003). Components involved in assembly and dislocation of iron-sulfur clusters on the scaffold protein Isu1p. *EMBO J*. 22, 4815–25.

77 Silberg, J. J., Hoff, K. G. & Vickery, L. E. (1998). The Hsc66-Hsc20 chaperone system in Escherichia coli: chaperone activity and interactions with the DnaK-DnaJ-grpE system. *J Bacteriol* 180, 6617–24.

78 Voisine, C., Schilke, B., Ohlson, M., Beinert, H., Marszalek, J. & Craig, E. A. (2000). Role of the mitochondrial Hsp70s, Ssc1 and Ssq1, in the maturation of Yfh1. *Molecular and Cellular Biology* 10, 3677–3684.

79 Cremona, O. (2001). Live stripping of clathrin-coated vesicles. *Dev Cell* 1, 592–4.

80 Schlossman, D. M., Schmid, S. L., Braell, W. A. & Rothman, J. E. (1984). An enzyme that removes clathrin coats: purification of an uncoating ATPase. *J Cell Biol* 99, 723–33.

81 Barouch, W., Prasad, K., Greene, L. E. & Eisenberg, E. (1994). ATPase activity associated with the uncoating of clathrin baskets by Hsp70. *J Biol Chem* 269, 28563–8.

82 Hannan, L. A., Newmyer, S. L. & Schmid, S. L. (1998). ATP- and cytosol-dependent release of adaptor proteins from clathrin-coated vesicles: A dual role for Hsc70. *Mol Biol Cell* 9, 2217–29.

83 Ahle, S. & Ungewickell, E. (1990). Auxilin, a newly identified clathrin-associated protein in coated vesicles from bovine brain. *J Cell Biol* 111, 19–29.

84 Ungewickell, E., Ungewickell, H., Holstein, S. E., Lindner, R., Prasad, K., Barouch, W., Martin, B.,

Greene, L. E. & Eisenberg, E. (1995). Role of auxilin in uncoating clathrin-coated vesicles. *Nature* 378, 632–5.

85 Kanaoka, Y., Kimura, S. H., Okazaki, I., Ikeda, M. & Nojima, H. (1997). GAK: a cyclin G associated kinase contains a tensin/auxilin-like domain. *FEBS Lett* 402, 73–80.

86 Kimura, S. H., Tsuruga, H., Yabuta, N., Endo, Y. & Nojima, H. (1997). Structure, expression, and chromosomal localization of human GAK. *Genomics* 44, 179–87.

87 Greener, T., Zhao, X., Nojima, H., Eisenberg, E. & Greene, L. E. (2000). Role of cyclin G-associated kinase in uncoating clathrin-coated vesicles from non-neuronal cells. *J Biol Chem* 275, 1365–70.

88 Umeda, A., Meyerholz, A. & Ungewickell, E. (2000). Identification of the universal cofactor (auxilin 2) in clathrin coat dissociation. *Eur J Cell Biol* 79, 336–42.

89 Pishvaee, B., Costaguta, G., Yeung, B. G., Ryazantsev, S., Greener, T., Greene, L. E., Eisenberg, E., McCaffery, J. M. & Payne, G. S. (2000). A yeast DNA J protein required for uncoating of clathrin-coated vesicles in vivo. *Nat Cell Biol* 2, 958–63.

90 Greener, T., Grant, B., Zhang, Y., Wu, X., Greene, L. E., Hirsh, D. & Eisenberg, E. (2001). Caenorhabditis elegans auxilin: a J-domain protein essential for clathrin-mediated endocytosis in vivo. *Nat Cell Biol* 3, 215–9.

91 Zhao, X., Greener, T., Al-Hasani, H., Cushman, S. W., Eisenberg, E. & Greene, L. E. (2001). Expression of auxilin or AP180 inhibits endocytosis by mislocalizing clathrin: evidence for formation of nascent pits containing AP1 or AP2 but not clathrin. *J Cell Sci* 114, 353–65.

92 Holstein, S. E., Ungewickell, H. & Ungewickell, E. (1996). Mechanism of clathrin basket dissociation: separate functions of protein domains of the DnaJ homologue auxilin. *J Cell Biol* 135, 925–37.

93 Gall, W. E., Higginbotham, M. A., Chen, C., Ingram, M. F., Cyr, D. M. & Graham, T. R. (2000). The auxilin-like phosphoprotein Swa2p is required for clathrin function in yeast. *Curr Biol* 10, 1349–58.

94 Lemmon, S. K. (2001). Clathrin uncoating: Auxilin comes to life. *Curr Biol* 11, R49–52.

95 Morgan, J. R., Prasad, K., Jin, S., Augustine, G. J. & Lafer, E. M. (2001). Uncoating of clathrin-coated vesicles in presynaptic terminals: roles for Hsc70 and auxilin. *Neuron* 32, 289–300.

96 Jiang, J., Taylor, A. B., Prasad, K., Ishikawa-Brush, Y., Hart, P. J., Lafer, E. M. & Sousa, R. (2003). Structure-function analysis of the auxilin J-domain reveals an extended Hsc70 interaction interface. *Biochemistry* 42, 5748–53.

97 Newmyer, S. L. & Schmid, S. L. (2001). Dominant-interfering Hsc70 mutants disrupt multiple stages of the clathrin-coated vesicle cycle in vivo. *J Cell Biol* 152, 607–20.

98 Jiang, R., Gao, B., Prasad, K., Greene, L. E. & Eisenberg, E. (2000). Hsc70 chaperones clathrin and primes it to interact with vesicle membranes. *J Biol Chem* 275, 8439–47.

99 Newmyer, S. L., Christensen, A. & Sever, S. (2003). Auxilin-dynamin interactions link the uncoating ATPase chaperone machinery with vesicle formation. *Dev Cell* 4, 929–40.

100 Bronk, P., Wenniger, J. J., Dawson-Scully, K., Guo, X., Hong, S., Atwood, H. L. & Zinsmaier, K. E. (2001). Drosophila Hsc70-4 is critical for neurotransmitter exocytosis in vivo. *Neuron* 30, 475–88.

101 Arsene, F., Tomoyasu, T. & Bukau, B. (2000). The heat shock response of Escherichia coli. *Int J Food Microbiol* 55, 3–9.

102 Lund, P. A. (2001). Regulation of expression of molecular chaperones. In *Moleuclar Chaperones in the Cell*, pp. 235–256. Oxford University Press Inc., New York.

103 Straus, D. B., Walter, W. A. & Gross, C. A. (1989). The activity of sigma 32 is reduced under conditions

of excess heat shock protein production in Escherichia coli. *Genes Dev* 3, 2003–10.

104 Morita, M. T., Kanemori, M., Yanagi, H. & Yura, T. (2000). Dynamic interplay between antagonistic pathways controlling the sigma 32 level in Escherichia coli. *Proc Natl Acad Sci USA* 97, 5860–5.

105 Herman, C., Thevenet, D., D'Ari, R. & Bouloc, P. (1995). Degradation of sigma 32, the heat shock regulator in Escherichia coli, is governed by HflB. *Proc Natl Acad Sci USA* 92, 3516–20.

106 Tomoyasu, T., Gamer, J., Bukau, B., Kanemori, M., Mori, H., Rutman, A. J., Oppenheim, A. B., Yura, T., Yamanaka, K., Niki, H. et al. (1995). Escherichia coli FtsH is a membrane-bound, ATP-dependent protease which degrades the heat-shock transcription factor sigma 32. *EMBO J* 14, 2551–60.

107 Kanemori, M., Nishihara, K., Yanagi, H. & Yura, T. (1997). Synergistic roles of HslVU and other ATP-dependent proteases in controlling in vivo turnover of sigma32 and abnormal proteins in Escherichia coli. *J Bacteriol* 179, 7219–25.

108 Tatsuta, T., Tomoyasu, T., Bukau, B., Kitagawa, M., Mori, H., Karata, K. & Ogura, T. (1998). Heat shock regulation in the ftsH null mutant of Escherichia coli: dissection of stability and activity control mechanisms of sigma32 in vivo. *Mol Microbiol* 30, 583–93.

109 Straus, D., Walter, W. & Gross, C. A. (1990). DnaK, DnaJ, and GrpE heat shock proteins negatively regulate heat shock gene expression by controlling the synthesis and stability of sigma 32. *Genes Dev* 4, 2202–9.

110 Bukau, B. (1993). Regulation of the Escherichia coli heat-shock response. *Mol Microbiol* 9, 671–80.

111 Tomoyasu, T., Ogura, T., Tatsuta, T. & Bukau, B. (1998). Levels of DnaK and DnaJ provide tight control of heat shock gene expression and protein repair in Escherichia coli. *Mol Microbiol* 30, 567–81.

112 Tatsuta, T., Joob, D. M., Calendar, R., Akiyama, Y. & Ogura, T. (2000). Evidence for an active role of the DnaK chaperone system in the degradation of sigma(32). *FEBS Lett* 478, 271–5.

113 Chattopadhyay, R. & Roy, S. (2002). DnaK-sigma 32 interaction is temperature-dependent. Implication for the mechanism of heat shock response. *J Biol Chem* 277, 33641–7.

114 Laufen, T., Mayer, M. P., Beisel, C., Klostermeier, D., Mogk, A., Reinstein, J. & Bukau, B. (1999). Mechanism of regulation of hsp70 chaperones by DnaJ cochaperones. *Proc Natl Acad Sci USA* 96, 5452–7.

115 Nakahigashi, K., Yanagi, H. & Yura, T. (1995). Isolation and sequence analysis of rpoH genes encoding sigma 32 homologues from gram negative bacteria: conserved mRNA and protein segments for heat shock regulation. *Nucleic Acids Res* 23, 4383–90.

116 McCarty, J. S., Rudiger, S., Schonfeld, H. J., Schneider-Mergener, J., Nakahigashi, K., Yura, T. & Bukau, B. (1996). Regulatory region C of the E. coli heat shock transcription factor, sigma32, constitutes a DnaK binding site and is conserved among eubacteria. *J Mol Biol* 256, 829–37.

117 Arsene, F., Tomoyasu, T., Mogk, A., Schirra, C., Schulze-Specking, A. & Bukau, B. (1999). Role of region C in regulation of the heat shock gene-specific sigma factor of Escherichia coli, sigma32. *J Bacteriol* 181, 3552–61.

118 Nakahigashi, K., Yanagi, H. & Yura, T. (2001). DnaK chaperone-mediated control of activity of a sigma(32) homologue (RpoH) plays a major role in the heat shock response of Agrobacterium tumefaciens. *J Bacteriol* 183, 5302–10.

119 Wickner, S. H. (1990). Three Escherichia coli heat shock proteins are required for P1 plasmid DNA replication: formation of an active complex between E. coli DnaJ protein and the P1 initiator protein. *Proc Natl Acad Sci USA* 87, 2690–4.

120 Wickner, S., Hoskins, J. & McKenney, K. (1991). Function of DnaJ and

DnaK as chaperones in origin-specific DNA binding by RepA. *Nature* 350, 165–7.

121 Wickner, S., Hoskins, J. & McKenney, K. (1991). Monomerization of RepA dimers by heat shock proteins activates binding to DNA replication origin. *Proc Natl Acad Sci USA* 88, 7903–7.

122 Wickner, S., Skowyra, D., Hoskins, J. & McKenney, K. (1992). DnaJ, DnaK, and GrpE heat shock proteins are required in oriP1 DNA replication solely at the RepA monomerization step. *Proc Natl Acad Sci USA* 89, 10345–9.

123 Tilly, K. & Yarmolinsky, M. (1989). Participation of Escherichia coli heat shock proteins DnaJ, DnaK, and GrpE in P1 plasmid replication. *J Bacteriol* 171, 6025–9.

124 Kim, S. Y., Sharma, S., Hoskins, J. R. & Wickner, S. (2002). Interaction of the DnaK and DnaJ chaperone system with a native substrate, P1 RepA. *J Biol Chem* 277, 44778–83.

125 Konieczny, I. & Liberek, K. (2002). Cooperative action of Escherichia coli ClpB protein and DnaK chaperone in the activation of a replication initiation protein. *J Biol Chem* 277, 18483–8.

126 Giraldo, R. & Diaz-Orejas, R. (2001). Similarities between the DNA replication initiators of Gram-negative bacteria plasmids (RepA) and eukaryotes (Orc4p)/archaea (Cdc6p). *Proc Natl Acad Sci USA* 98, 4938–43.

127 Sullivan, C. S. & Pipas, J. M. (2001). The virus-chaperone connection. *Virology* 287, 1–8.

128 Alfano, C. & McMacken, R. (1989). Heat shock protein-mediated disassembly of nucleoprotein structures is required for the initiation of bacteriophage lambda DNA replication. *J Biol Chem* 264, 10709–18.

129 Liberek, K., Osipiuk, J., Zylicz, M., Ang, D., Skorko, J. & Georgopoulos, C. (1990). Physical interactions between bacteriophage and Escherichia coli proteins required for initiation of lambda DNA replication. *J Biol Chem* 265, 3022–9.

130 Zylicz, M., Ang, D., Liberek, K. & Georgopoulos, C. (1989). Initiation of lambda DNA replication with purified host- and bacteriophage-encoded proteins: the role of the dnaK, dnaJ and grpE heat shock proteins. *EMBO J* 8, 1601–8.

131 Tanguy Le Gac, N. & Boehmer, P. E. (2002). Activation of the herpes simplex virus type-1 origin-binding protein (UL9) by heat shock proteins. *J Biol Chem* 277, 5660–6.

132 Eom, C. Y. & Lehman, I. R. (2002). The human DnaJ protein, hTid-1, enhances binding of a multimer of the herpes simplex virus type 1 UL9 protein to oris, an origin of viral DNA replication. *Proc Natl Acad Sci USA* 99, 1894–8.

133 Liu, J. S., Kuo, S. R., Makhov, A. M., Cyr, D. M., Griffith, J. D., Broker, T. R. & Chow, L. T. (1998). Human Hsp70 and Hsp40 chaperone proteins facilitate human papillomavirus-11 E1 protein binding to the origin and stimulate cell-free DNA replication. *J Biol Chem* 273, 30704–12.

134 Lin, B. Y., Makhov, A. M., Griffith, J. D., Broker, T. R. & Chow, L. T. (2002). Chaperone proteins abrogate inhibition of the human papillomavirus (HPV) E1 replicative helicase by the HPV E2 protein. *Mol Cell Biol* 22, 6592–604.

135 Marchler, G. & Wu, C. (2001). Modulation of Drosophila heat shock transcription factor activity by the molecular chaperone DROJ1. *EMBO J* 20, 499–509.

136 Lopez, N., Aron, R. & Craig, E. A. (2003). Specificity of Class II Hsp40 Sis1 in Maintenance of Yeast Prion [RNQ(+)]. *Mol Biol Cell* 14, 1172–81.

137 Hallstrom, T. C., Katzmann, D. J., Torres, R. J., Sharp, W. J. & Moye-Rowley, W. S. (1998). Regulation of transcription factor Pdr1p function by an Hsp70 protein in Saccharomyces cerevisiae. *Mol Cell Biol* 18, 1147–55.

138 Morishima, N., Nakagawa, K., Yamamoto, E. & Shibata, T. (1990). A subunit of yeast site-specific endonuclease SceI is a mitochondrial

version of the 70-kDa heat shock protein. *J Biol Chem* 265, 15189–97.

139 Shibata, T., Nakagawa, K. & Morishima, N. (1995). Multi-site-specific endonucleases and the initiation of homologous genetic recombination in yeast. *Adv Biophys* 31, 77–91.

140 Mizumura, H., Shibata, T. & Morishima, N. (1999). Stable association of 70-kDa heat shock protein induces latent multisite specificity of a unisite-specific endonuclease in yeast mitochondria. *J Biol Chem* 274, 25682–90.

141 Mizumura, H., Shibata, T. & Morishima, N. (2002). Association of HSP70 with endonucleases allows the expression of otherwise silent mutations. *FEBS Lett* 522, 177–82.

15
Regulation of Hsp70 Chaperones by Co-chaperones

Matthias P. Mayer and Bernd Bukau

15.1
Introduction

The 70-kDa heat shock proteins (Hsp70s) are central components of the chaperone network that assists and controls numerous protein folding processes inside the cell. As part of their quality-control functions, Hsp70s are involved in refolding of stress-denatured proteins. They continuously survey the folding status of cellular proteins and bind to misfolded proteins to prevent their aggregation or, in conjunction with Hsp100 proteins, to disaggregate already-aggregated proteins. Since these functions are especially important under stress conditions, in most organisms at least one Hsp70 encoding gene is under heat stress control. In addition to the quality-control functions, Hsp70 are built-in components of cellular pathways. They are involved in the folding of newly synthesized proteins in the cytosol as well as in the translocation into and the folding within organelles. Hsp70s assist in assembly and disassembly of oligomeric protein structures, for example, the clathrin coat, and they are involved in signal transduction and cell cycle progression by controlling the stability and activity of regulatory proteins such as receptors, protein kinases, and transcription factors. To no other class of chaperones has such a plethora of functions been attributed. Hsp70 proteins are consequently abundant and constitutive cellular components that are, at least in eukaryotic organisms, essential for viability under all conditions. For more details on Hsp70 functions see chapters 14 and 36.

The interaction of Hsp70 proteins with their substrates has features that contribute to their versatility. First, their interaction with substrate proteins is restricted to a short peptide stretch within the substrate polypeptide and is therefore independent of the size and overall structure of the substrate protein. Second, the interaction with substrates is transient and is controlled in a nucleotide-dependent manner. Third, Hsp70 chaperones are influenced by a number of co-chaperones, which regulate binding to substrates and the lifetime of the Hsp70-substrate complex and thereby specify Hsp70-substrate interactions. Finally, Hsp70s cooperate with chaperones of other classes, for example, Hsp90 and Hsp100, to accomplish spe-

Protein Folding Handbook. Part II. Edited by J. Buchner and T. Kiefhaber

ISBN: 3-527-30784-2

cific tasks such as control of regulatory proteins and disaggregation of protein aggregates.

In this chapter we will briefly describe the Hsp70 structure and the functional cycle of Hsp70s, but we focus mainly on the control of Hsp70 function by co-chaperones. Special emphasis will be given to the description of biochemical and biophysical methods used for the analysis of Hsp70 functions.

15.2 Hsp70 Proteins

15.2.1 Structure and Conservation

Hsp70 proteins are composed of an N-terminal ATPase domain of ca. 45 kDa, a substrate-binding domain of ca. 15 kDa, and a C-terminal domain of ca. 10 kDa, the function of which is not completely clear. The ATPase domain, which is structurally homologous to actin, hexokinase, and glycerokinase [1–3], is built of two subdomains (I and II) that are linked to each other via two crossed α-helices. The two subdomains form a deep cleft between each other, at the bottom of which nucleotide is bound in complex with one Mg^{2+} and two K^{+} ions (Figure 15.1A).

The substrate-binding domain is made up of a sandwich of two twisted β-sheets with four antiparallel strands each. The substrate-binding pocket, which seems to be tailored for a large hydrophobic residue, preferably leucine, is formed by the upward-bent strands 1 and 2 together with the upward-protruding connecting loops $L_{1,2}$ and $L_{3,4}$. These loops are stabilized by a second layer of loops ($L_{4,5}$ and $L_{5,6}$) and the two α-helices A and B. The distal part of helix B is connected to the outer loops by hydrogen bonds and a salt bridge, thereby forming the so-called latch that is in part responsible for the tight binding to substrates when no nucleotide or ADP is bound to the ATPase domain (Figure 15.1A).

The Hsp70 family of proteins is highly conserved throughout evolution, with around 50% sequence identity between bacteria and human. The overall homology is highest in the ATPase domain and decreases continuously towards the C-terminus. Parallel to this orthologous conservation, a radiative adaptation has taken place, creating paralogs with significantly lower sequence identity; for example, the sequence identity between *Escherichia coli* HscC and *E. coli* DnaK is around 27%. In addition, more distant relatives are found in eukaryotic cells: the Hsp110 and Hsp170 chaperones. Homology between the Hsp70 family and the Hsp110 and Hsp170 proteins is comparatively high (up to 40% sequence identity) in the ATPase domain, and homology modeling yields a very similar structure. Overall sequence identity in the part that is C-terminal to the ATPase domain is much lower and is scattered over a large portion of this domain, which together with secondary structure predictions suggests a homologous three-dimensional structure. It therefore could function as a substrate-binding domain [4]. A biochemical deletion

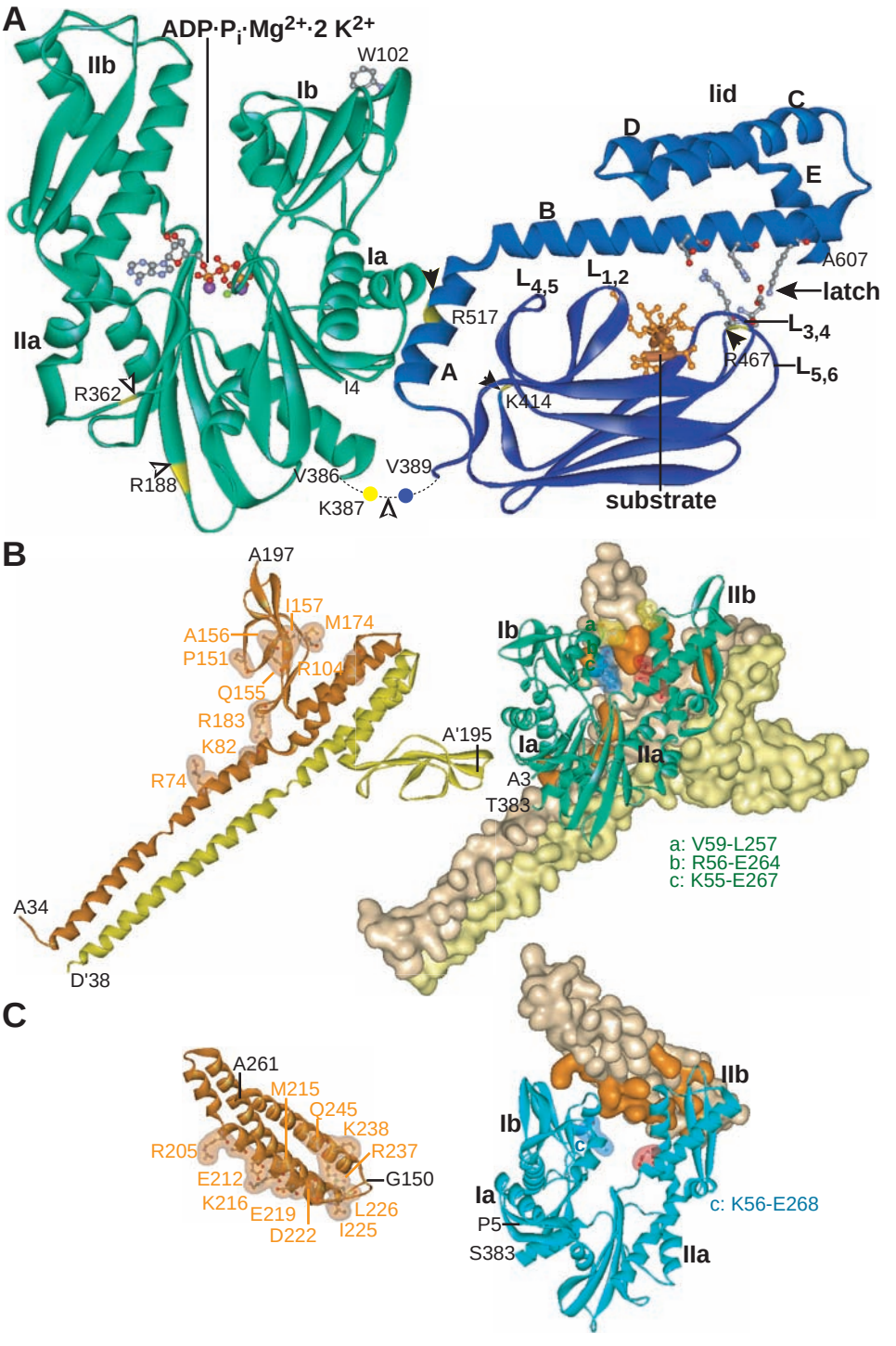
A
ADP·P$_i$·Mg^{2+}·2 K^{2+}
IIb
W102
Ib
lid
C
D
E
B
Ia
L$_{4,5}$
L$_{1,2}$
A607
latch
L$_{3,4}$
R517
IIa
R467
L$_{5,6}$
A
R362
I4
K414
R188
V386
V389
K387
substrate
B
A197
I157
M174
A156
P151
R104
Q155
R183
K82
R74
A'195
A3
T383
A34
D'38
a: V59-L257
b: R56-E264
c: K55-E267
C
A261
M215
Q245
K238
R205
R237
E212
G150
K216
E219
L226
D222
I225
P5
S383
c: K56-E268

analysis suggests that this part of the Hsp110 proteins indeed has a substrate-binding function [5]. The Hsp110 and Hsp170 proteins have characteristic insertions of unknown function within their substrate-binding domain. On the other end of the scale, there are Hsp70 homologues with a much-reduced C-terminal domain, including the yeast protein Ssz1 and the STCH protein of higher eukaryotes [6–9].

15.2.2 ATPase Cycle

The basic principles of the Hsp70 ATPase cycle have been elucidated using mainly *E. coli* DnaK, human Hsc70, and hamster BiP as model proteins. Therefore, we will first describe the ATPase cycle for *E. coli* DnaK and will subsequently discuss some variations found in other Hsp70 proteins (Figure 15.2). In the ATP-bound state DnaK has a low affinity for substrates but high substrate association and dissociation rate constants. In contrast, in the ADP-bound state the affinity for substrates is high but substrate association and dissociation rates are low [10–12]. Genetic and biochemical data clearly demonstrate that ATP hydrolysis is essential for DnaK's chaperone function in vitro and in vivo. However, the intrinsic ATP hydrolysis rate of DnaK is very low (ca. 6×10^{-4} s^{-1}; [13–16]) and is considered much

Fig. 15.1. Structure of the ATPase domain and substrate-binding domain of Hsp70 and of nucleotide-exchange factors. (A) (Left) Ribbon model of the ATPase domain of DnaK modeled onto the crystal structure of bovine Hsc70 in complex with Mg^{2+}·ADP·P_i, and two K^+ ions (1BUP; SWISS-MODEL [116, 216–218]). Indicated are first and last residues, the unique tryptophan (W102), and the trypsin cleavage sites (yellow). (Right) Ribbon model of the substrate-binding domain of DnaK in complex with a substrate peptide (orange) (1DKX) [93]. Indicated are the substrate-enclosing loops $L_{1,2}$ to $L_{5,6}$, helices A–E, and the lid. The latch-forming residues are shown as ball-and-stick models. The two missing amino acids between the C-terminus of the ATPase domain and the N-terminus of the substrate-binding domain are represented by a dashed line and two dots. The trypsin cleavage sites are marked in yellow. Filled arrowheads indicate residues that are more accessible for trypsin cleavage in the ATP-bound state, and open arrowheads indicate residues that become protected from trypsin cleavage in the ATP-bound state. (B) (Left) Ribbon representation of the asymmetric GrpE dimer from the co-crystal structure of GrpE with the ATPase domain of DnaK (1DKG) [110]. The DnaK-interacting residues are shown in ball-and-stick representation and are enveloped in the solvent-accessible surface. (Right) Surface representation of the GrpE dimer in complex with the ATPase domain of DnaK in ribbon representation. Indicated in orange are the DnaK-interacting parts of GrpE. The hydrophobic patches and the two pairs of charged residues that bridge the nucleotide-binding cleft in the closed conformation are shown in ball-and-stick and surface representation and are marked with the letters a–c. (C) (Left) Ribbon representation of the Bag domain of Bag-1 from the co-crystal structure of the Bag domain with the ATPase domain of bovine Hsc70 (3HSC) [120]. The Hsc70-interacting residues are shown in ball-and-stick representation and are enveloped in the solvent-accessible surface. (Right) Surface representation of the Bag domain in complex with the ATPase domain of Hsc70 in ribbon representation. Indicated in orange are the Hsc70-interacting parts of the Bag domain. The pair of charged residues that bridge the nucleotide-binding cleft in the closed conformation are shown in ball-and-stick and surface representation and marked with the letter c.

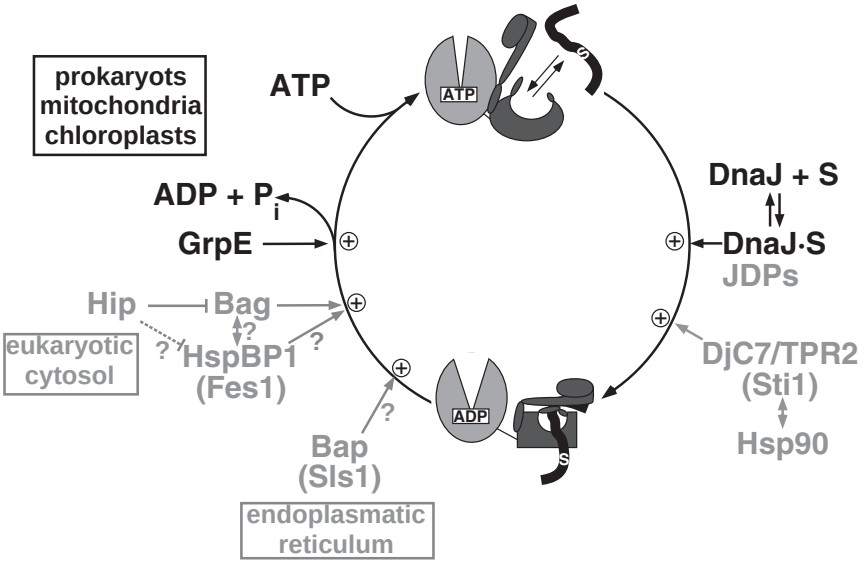

Fig. 15.2. Functional cycle of Hsp70 chaperones. In black is shown the basal cycle as described in Section 15.2.2 for *E. coli* DnaK and in gray are shown variations of the cycle found in eukaryotes. Protein names for mammalian cells are given with yeast homologues and analogues, respectively, in parenthesis.

too low to be of any physiological relevance. Similar basal ATPase rates, in the range of 3×10^{-4} s^{-1} to 1.5×10^{-2} s^{-1}, have been reported for all Hsp70s so far investigated [17–23]. This intrinsic ATPase rate, however, is stimulated by substrates by a factor of 2 to 10 and by the DnaJ co-chaperone by a factor of 5 at physiological concentrations (see Section 15.3) [13, 23, 24]. If both DnaJ and substrate are present at the same time, the ATP hydrolysis rate is stimulated synergistically several thousand-fold [25–29]. From these data it was concluded that substrates associate primarily to DnaK·ATP with high association rates and are subsequently trapped by the substrate and DnaJ-induced ATP hydrolysis, which leads to the transition from the low-affinity to the high-affinity state [25–27, 30, 31]. The ADP dissociation rate is approximately one order of magnitude greater than substrate dissociation rates in the high-affinity state. Under physiological conditions, i.e., high ATP concentrations, ADP will dissociate and ATP will rebind to DnaK, triggering the transition to the low-affinity state prior to substrate release. Nucleotide exchange therefore determines the lifetime of the DnaK-substrate complex. For DnaK, ADP dissociation is accelerated by the nucleotide-exchange factor GrpE several thousand-fold [24, 32]. ATP binds to the nucleotide-free DnaK with high association rates (1.2×10^5 M^{-1} s^{-1}; [33, 34]) and high affinity (1 nM; [34]), leading to the transition to the low-affinity state of DnaK and substrate release. The cycle then restarts with association of a new substrate. Under optimal refolding conditions for the model substrate luciferase (with 80 nM luciferase, 800 nM DnaK, 160 nM

DnaJ, and 400 nM GrpE), one cycle takes about 1 s. Since reactivation of 50% of the luciferase molecules takes about 5 min, many cycles are on average necessary to achieve refolding.

Although the basic scheme of the ATPase cycle seems to be conserved, a number of variations of this theme have been observed within the Hsp70 family. First, nucleotide dissociation rates vary dramatically between Hsp70 proteins. Human Hsc70 and *E. coli* HscA have a 20- and 700-fold higher dissociation rate, respectively, as compared to DnaK [35]. The structural reason for these differences was found in two salt bridges and an exposed loop in the ATPase domain and was used to classify the Hsp70 proteins in three subfamilies, the DnaK-type, the Hsc70-type, and the HscA-type Hsp70 chaperones [35].

Second, variations have also been found in the difference between the high- and low-affinity states for substrates, which for DnaK is a factor of 400–2500 in substrate dissociation rate constants (k_{diss}) and 10–20 in substrate dissociation equilibrium constants (K_d). For example, for the *E. coli* Hsp70 homologue HscC, identical K_d values were measured for the HscC-peptide complex in both nucleotide states. The measured value was thereby similar to the K_d of the corresponding DnaK-peptide complex in the ADP state. However, k_{diss} was stimulated 20-fold by ATP, meaning that dissociation and association rates change to the same extent in response to ATP binding [19]. Therefore, the affinity of HscC for substrates is affected not by ATP but by the turnover rate.

15.2.3 Structural Investigations

ATP binding and hydrolysis in Hsp70 proteins are coupled to conformational changes, not only within the ATPase domain but also within the substrate-binding domain. As described above, ATP binding to the ATPase domain leads to the transition of the high-affinity state of the substrate-binding domain to the low-affinity state, while ATP hydrolysis causes the reverse transformation. Since crystallization of a full-length Hsp70 protein has failed so far and since all available structures from ATPase domain and substrate-binding domain represent the high-affinity state, a number of different techniques have been employed to probe nucleotide-induced conformational changes, including partial proteolysis by trypsin, tryptophan fluorescence, Fourier transform infrared spectroscopy, small angle X-ray scattering, and, most recently, amide hydrogen exchange [36–42] (C. Graf, W. Rist, B. Bukau, and M. P. Mayer, unpublished results).

Comparison of tryptic digestion patterns of the nucleotide-free, ADP-, and ATP-bound states of *E. coli* DnaK revealed that digestion sites within the ATPase domain (R188, R362) and the region connecting the ATPase domain with the substrate-binding domain, the so-called linker region (K387), become less accessible upon ATP binding, while sites within the substrate-binding domain (K414, R467, R517) become more accessible (Figure 15.1A). These observations demonstrate that ATP binding leads to a tighter conformational packing of the ATPase domain and to a more open conformation of the substrate-binding domain [39].

The digestion pattern of eukaryotic Hsp70s (e.g., hamster BiP and yeast Ssa1) also shows characteristic changes upon ATP binding. The ATP-dependent appearance of a 60-kDa fragment, which contains the entire ATPase domain and part of the substrate-binding domain, indicates a stabilization of the ATPase domain and a decrease in accessibility of the linker region [40, 41, 43]. On the basis of these results, it was suggested that the ATPase domain and the substrate-binding domain are more tightly linked in the ATP state than in the ADP or nucleotide-free states. Such a close-up of the ATPase domain and substrate-binding domain was also indicated by small angle X-ray scattering data [42]. Upon ATP binding the radius of gyration R_g decreased by 3.6 Å, and the pair distribution function $P(r)$ (as defined in Ref. [42]) showed a shift from an elongated molecule in the presence of ADP to a more compact shape in the presence of ATP. These data, however, relate only to a truncated version of the Hsp70 protein, the 60-kDa fragment, because small angle X-ray scattering data of full-length Hsp70 cannot easily be interpreted due to the tendency for self-assembly into heterogeneous oligomers.

Tryptophan fluorescence was also used to monitor nucleotide-dependent conformational changes in Hsp70 proteins [33, 36, 39, 44]. *E. coli* DnaK has a single tryptophan in the ATPase domain (position 102) (Figure 15.1A). Upon binding of ATP – but not AMP, ADP, ADP + inorganic phosphate or non-hydrolyzable ATP analogues (AMPPCP, AMPPNP, ATPγS) – the maximum of fluorescence shifts by 3–4 nm towards shorter wavelength (blue shift) and decreases by about 15% [33, 36, 39]. Quench and blue shift are almost entirely due to conformational changes in the substrate-binding domain and to movement of both domains relative to each other, since the isolated ATPase domain does not show any blue shift and shows a quench of only about 5% [39]. Measurements of the fluorescence lifetime and quenching of the fluorescence with polar quenchers indicate that accessibility of the tryptophan is drastically reduced upon ATP binding [45]. Due to the observed ATP-dependent quench, tryptophan fluorescence was used to determine the kinetics of ATP binding and hydrolysis in *E. coli* DnaK [46, 47] and bovine Hsc70 [44].

15.2.4 Interactions With Substrates

On the one hand, Hsp70 chaperones interact promiscuously with virtually all unfolded proteins but generally do not bind their native counterparts. On the other hand, they recognize certain folded proteins with high specificity. Therefore, an important question is how Hsp70s can combine in their substrate specificity both seemingly contradictory properties. A number of different approaches have been used to elucidate the substrate specificity of Hsp70s. One approach used the f1 phage peptide display library method, selecting high-affinity binding phages out of a library of phages exposing a stretch of 6–12 residues with random sequence [48, 49]. The advantage of this method is that a significant part, although not all, of the theoretical possible sequence space can be accessed (with a stretch of nine residues, the complexity of the library would have to be at least 4^{27} ($\approx 10^{16}$), equal to 100 L phage lysate with a titer of 10^{11} pfu mL^{-1}). The drawback of this method

is that the number of clones, which have to be sequenced to elucidate the binding motif, increases exponentially with the degenerateness of the binding motif. In one study a phage library of 6×10^9 clones was incubated with immobilized DnaK, unbound phages were washed away, and bound phages were eluted by addition of ATP. Forty-eight clones out of the selected pool, and, for comparison, 44 clones out of the original pool, were sequenced. DnaK was found to prefer positively charged and hydrophobic residues, whereby the hydrophobic residues are more favorable in a central position within the peptide and negatively charged amino acids are disfavored [49]. Using the same phage display technique, it was found for the Hsp70 homologue of the endoplasmic reticulum, BiP, that binding peptides are enriched in aromatic and hydrophobic amino acids in alternating positions, suggesting binding of the substrates to BiP in an extended conformation [48]. Another approach screened synthetic peptides, scanning the sequence of a natural Hsp70 substrate for binding to Hsp70 and for ability to stimulate Hsp70's ATPase activity [50–52]. In this way the potential binding sites of Hsp70 within the tested protein sequence could be identified, but no general motif was derived.

The most extensive analysis of the substrate specificity of an Hsp70 protein used a library of cellulose-bound 13mer peptides scanning the sequences of natural proteins with an overlap of 10 amino acids [53]. Although this method, due to the limited number of peptides ($<$ 5000 in the case of Ref. [53]), does not allow one to exhaust the theoretically possible sequences, it provides a relatively large basis for a statistical analysis. In addition, the use of protein sequences guarantees that the tested peptides represent biologically relevant sequences. The peptides are attached over a β-alanine linker via their C-terminus to the cellulose membrane. The Hsp70 protein (0.1–1 μM) is incubated with the cellulose membrane at room temperature. The membranes are washed and bound proteins are transferred by fractionated electroblotting onto PVDF membranes for immunodetection using a visualization method with a high dynamic range, such as chemifluorescence (ECF™, Amersham Bioscience). Quantification of all spots results in values that correspond to the affinity of the peptides for the Hsp70 protein tested, revealing directly the potential binding sites of Hsp70 in the protein, the sequence of which was used in the peptide library. To elucidate the binding motif, a statistical analysis of a sufficient number of peptides has to be performed. First, the contribution of each amino acid to the binding affinity can be determined by comparing the relative abundance of each residue in high-affinity peptides with the average occurrence in the library (compare Ref. [19]). Second, since protein sequences are scanned with 13mer peptides and an overlap of 10 residues, in general, three or four peptides in a row show significant affinity to the Hsp70 protein. These peptides can therefore be aligned, and the overlapping part corresponds to the region that most likely is bound in the substrate-binding pocket of the Hsp70. The aligned regions can be rooted at a position where a residue is found that contributes most to binding affinity, and the preference for neighboring amino acids can be analyzed. Using this method on a library with more than 4000 peptides, the binding motif for DnaK was elucidated. It consists of a core of five amino acids enriched in hydrophobic residues, flanked on both sides by a region where positively charged residues are

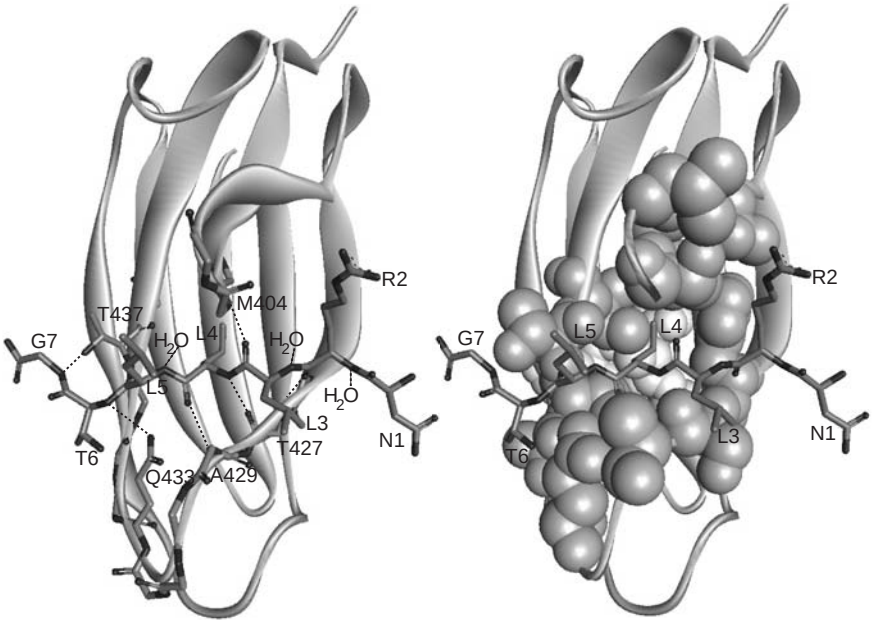

Fig. 15.3. DnaK-substrate interactions. The left panel shows the hydrogen bonding between the substrate-binding domain of DnaK and the backbone of the co-crystallized substrate peptide (NRLLLTG). The substrate is given in stick representation and the substrate-binding domain without α-helices is shown as a ribbon model with the interacting backbone and side chain residues (Q433, T437) in stick representation. Hydrogen bonds are indicated as dashed lines. Two of the seven hydrogen bonds between DnaK and the substrate are not, or are only barely, visible (R2:O to DnaK-T427:N; L5:O to DnaK-T437:N). The right panel emphasizes the hydrophobic interaction between the substrate-binding domain of DnaK and the side chains of the substrate peptide. The hydrophobic cleft with the deep pocket for the central substrate side chain (L4) is clearly visible. For clarity, methionine 404, which arches over the substrate backbone, is left out.

preferred. This binding motif is fully consistent with the crystal structure of the substrate-binding domain of DnaK in complex with a substrate peptide (Figure 15.3).

Two problems can occur in such an analysis. First, the size of the library could be too small to elucidate the binding motif or to determine whether rare (e.g., Met, Trp) or highly abundant (e.g., Leu) residues contribute to binding affinity. Second, since natural sequences are used, some residues may not be randomly distributed. For example, in the library of 557 peptides used for the analysis of the binding specificity of *E. coli* HscC, isoleucine was significantly more frequent in negatively charged peptides than in positively charged peptides. This was even more prominent when peptides were analyzed that contained two or more isoleucines. The case for methionine was similar. Since HscC was strongly biased against negatively charged amino acids, isoleucine and methionine were found with a lower frequency in HscC binding peptides than in the average of the library. From this find-

ing, however, it cannot be concluded that the presence of isoleucine or methionine in a peptide disfavors binding of HscC. In contrast, glycine was much more abundant in positively charged peptides than in negatively charged peptides. Since positively charged residues are strongly favored by HscC, it should be expected that glycine is enriched in peptides with high affinity for HscC. The result that glycine was not enriched in HscC-binding peptides, therefore, has to be interpreted such that the presence of glycine in a peptide is not favorable for binding to HscC.

The binding motif of DnaK is frequent in protein sequences. In the native state these sites are generally buried in the hydrophobic core of the protein. This explains the promiscuous binding of DnaK to unfolded polypeptides. Comparison of the binding preferences of DnaK with *E. coli* HscA and HscC revealed that substrate specificity can vary substantially within the Hsp70 family, probably as a manifestation of adaptive specialization [19, 54] (unpublished data). The structural reason for these differences is found in the substrate-binding cavity, in particular in the arch-forming amino acids that, in contrast to the other substrate-contacting residues, show a significantly lower degree of evolutionary conservation [55].

To understand the chaperone activity of Hsp70 proteins it is necessary not only to know the binding specificity but also to analyze the kinetics of association and dissociation of substrates. These parameters were investigated for peptide substrates using fluorescence intensity/anisotropy and surface plasmon resonance spectroscopy [10–12, 27, 56–60]. For *E. coli* DnaK, a number of different peptides labeled at N- or C-terminal cysteines with fluorescent dyes such as 2-(4′-(iodoacetamido)anilino) naphthalene-6-sulfonic acid (IAANS; Molecular Probes) or 6-acryloyl-2-dimethylaminonaphthalene (acrylodan; Molecular Probes) gave a significant change in fluorescence emission upon binding that was used to determine association and dissociation rate constants and the dissociation equilibrium constant to DnaK in the ADP and ATP states [10, 11, 58]. Such changes in fluorescence emission, however, were not observed when these peptides were incubated with C-terminally truncated DnaK variants [11, 61], *E. coli* HscA, or human Hsc70 (unpublished results), despite the fact that the peptides bound with high affinity to these Hsp70 proteins. More recently a 5-dimethylaminonaphthalene-1-sulfonyl (dansyl) modified peptide was found to be suitable for fluorescence intensity measurements with human Hsc70, giving a much improved signal-to-noise ratio [62]. Together these findings show that Hsp70 proteins differ with respect to the interaction with fluorescent labels attached to binding peptides. As an alternative approach, the association and dissociation rates can be determined by fluorescence anisotropy as shown for human Hsc70 and a fluorescein-labeled peptide [60].

The affinity of DnaK in the nucleotide-free or ADP-bound state for peptide substrates varies dramatically, with K_d values between 50 nM and >100 μM [57]. In the ATP state the K_d values are around 10- to 20-fold higher. When the K_d value for the DnaK-peptide complexes in the ATP state was blotted against the corresponding K_d value in the ADP state, a linear relationship was observed [11]. This was interpreted such that peptides bind to the substrate-binding domain of DnaK in the ADP and ATP states in a similar way. The alteration of affinity of DnaK for peptides with the nucleotide bound to the ATPase domain was illustrated by mea-

surements of the association and dissociation rates. While the association rates of peptides increased by up to two orders of magnitude upon ATP binding to the ATPase domain, the dissociation rates changed by up to three orders of magnitude [10, 11, 58]. This led to the model that in the ATP state the substrate-binding domain is in an open conformation, where association and dissociation of substrates occur with high rates. In the ADP state, in contrast, the substrate-binding domain is in a closed conformation, where binding and release of substrates are slow. The elucidation of the crystal structure of the substrate-binding domain of DnaK in complex with a substrate peptide made clear that a closed conformation as found in the crystal structure would not allow association or dissociation of the substrate. In this conformation the substrate is completely enclosed by the substrate-binding cavity, with seven hydrogen bonds to the backbone of the substrate peptide and numerous hydrophobic contacts to side chains of the substrate. However, since association and dissociation of substrates do occur even when DnaK is in the ADP-state, it was concluded that both the open and closed conformations of the substrate-binding domain exist in the ADP state with continuous interconversion [11]. This hypothesis is supported by measurements of the association rates of peptides to DnaK in the ADP state, which followed biphasic kinetics indicating a two-step process, the first being limited by the opening rate of the substrate-binding domain [59]. Similarly, it was hypothesized that in the ATP state the substrate-binding domain is not always in the open conformation but also cycles between the open and closed states, only with a much higher frequency than in the ADP state [11]. This hypothesis was based on the findings that the association rates of peptides to DnaK·ATP are three orders of magnitude lower than expected from a diffusion-controlled process.

Surface plasmon resonance spectroscopy was also used to determine binding affinities to substrates. Peptides or proteins were thereby immobilized via a thiol-linkage through a cysteine residue or by chemical cross-linking using EDC/NHS, and the flow cell was perfused with the Hsp70 protein (yeast Kar2 and *E. coli* DnaK) at increasing concentrations [27, 56]. This method allowed determination of the dissociation equilibrium constants. The association and dissociation rate constants, however, could not be determined due to the complexity of the observed kinetics, which was probably due to oligomerization of the Hsp70 protein (for a detailed discussion, see Section 15.3.3).

15.3 J-domain Protein Family

15.3.1 Structure and Conservation

The J-domain proteins (JDP) (Hsp40s, DnaJ proteins) comprise a large family of multi-domain proteins that are characterized by a highly conserved stretch of 70 amino acids referred to as the J-domain [63–65]. The prototype for this family,

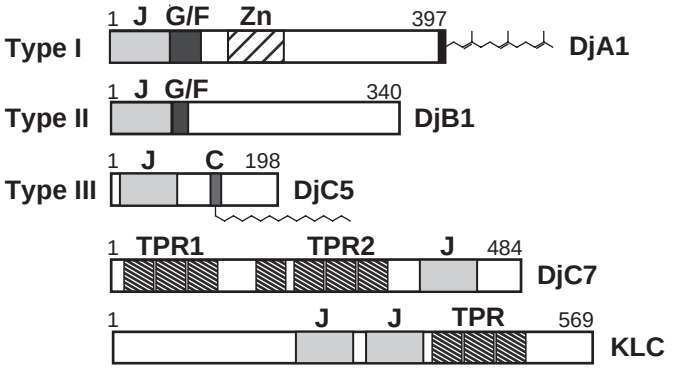

Fig. 15.4. Domain structure of J-domain proteins. For type I and type II JDPs, the human proteins DjA1/Hdj2 and DjB1/Hdj1 are given as examples, and for type III JDPs, the human proteins DjC5/cyteine string protein, DjC7/TPR2, and kinesin light chain (KLC1) are given as examples. For DjA1 and DjC5, farnesylation of the C-terminal CaaX-box and palmitoylation of the cysteine string (C), respectively, are indicated.

the *E. coli* protein DnaJ, has, in addition to its N-terminal J-domain, a glycine/phenylalanine-rich region (G/F), a Zn^{2+}-binding domain, and a C-terminal β-sheet domain. According to the degree of homology to DnaJ, the JDP family is divided into three subfamilies. The type I JDPs share significant homology to all four domains of DnaJ. The type II JDPs show homology to the C-terminal domain of DnaJ and generally contain a G/F-rich region, but do not have a Zn^{2+}-binding domain. The type III JDPs have only the J-domain in common with DnaJ (Figure 15.4). A unifying nomenclature for all mammalian JDPs was proposed by Ohtsuka and Hata [66], consisting of the acronym Dj for DnaJ-like protein, followed by the letter A, B, or C, for type I, II, or III, and a number. Type I and type II JDPs always have their J-domain at the N-terminus, while in type III JDPs the J-domain can be at any position. Type III JDPs can have a large variety of additional domains and protein motifs, including transmembrane anchors (e.g., *E. coli* DjlA, human DjC9/hSec63, yeast mitochondrial Pam18), tetratricopeptide repeat (TPR) motifs (e.g., mouse DjC2/Zrf1/Mida1, human DjC3/hp58, and DjC7/hTpr2), and cysteine-rich domains (mammalian DjC5/cysteine string protein) (Figure 15.4). A number of JDPs of all three types contain at their C-terminus a CaaX box (C, cysteine; a, aliphatic amino acid; X, any amino acid) as farnesylation signal (e.g., yeast Ydj1, mammalian DjA1/Hdj-2, mammalian DjC11/Mdg1). The farnesylation signals found in JDPs are usually not optimal, and the farnesylation ratio in vivo is usually well below 100%. However, a removal of the farnesylation signal in yeast Ydj1 leads to a temperature-sensitive phenotype, indicating its importance [67]. The number of JDPs per organism has increased dramatically in the course of evolution. Genome sequencing revealed that in *E. coli* six homologues exist, in *S. cerevisiae*, 19; in *Caenorhabditis elegans*, 29; in *Drosophila melanogaster*, 38; in humans, 44; and in *Arabidopsis thaliana*, 94 [68].

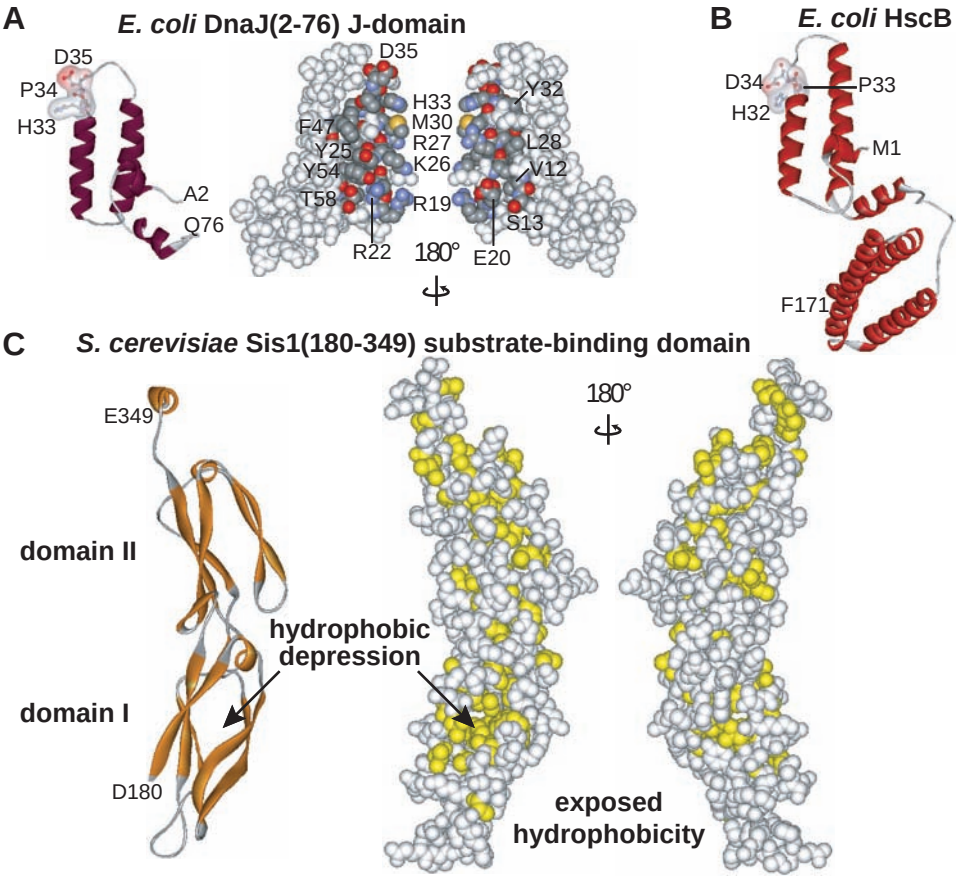

Fig. 15.5. Structures of J-domain proteins. (A) NMR structure of the J-domain of *E. coli* DnaK (2–76) (1XBL) [70]. Left, ribbon model with the invariable HPD motif indicated in ball-and-stick and surface representation. Middle and right, two faces of the J-domain in space-filling representation with the DnaK-interacting residues as elucidated by chemical shift perturbation and line broadening in NMR experiments in atomic colors. Not labeled are residues of the hydrophobic core. (B) Ribbon model of the crystal structure of *E. coli* HscB (1FPO) [82]. (C) Ribbon (left) and space-filling (right) models of the crystal structure of the substrate-binding domain of *S. cerevisiae* Sis1 (residues 180–349) (1C3G) [75]. Indicated is the hydrophobic depression that was proposed to be the substrate-binding site. Hydrophobic residues are shown in yellow.

Structural information is available for the J-domains of *E. coli* DnaJ, human DjB1/Hdj-1, bovine auxilin, polyomavirus T-antigen [69–73], the Zn^{2+}-binding domain of *E. coli* DnaJ (residues 121–209; [74]), the C-terminal domain of yeast Sis1 (residues 171–352) [75], and the Zn^{2+}-binding domain plus C-terminal domain of yeast Ydj1, which has a high homology to the C-terminal domain of DnaJ [76] (Figure 15.5, see p. 528/529). All structures are unique to DnaJ proteins and have not been found in other structures listed in databases.

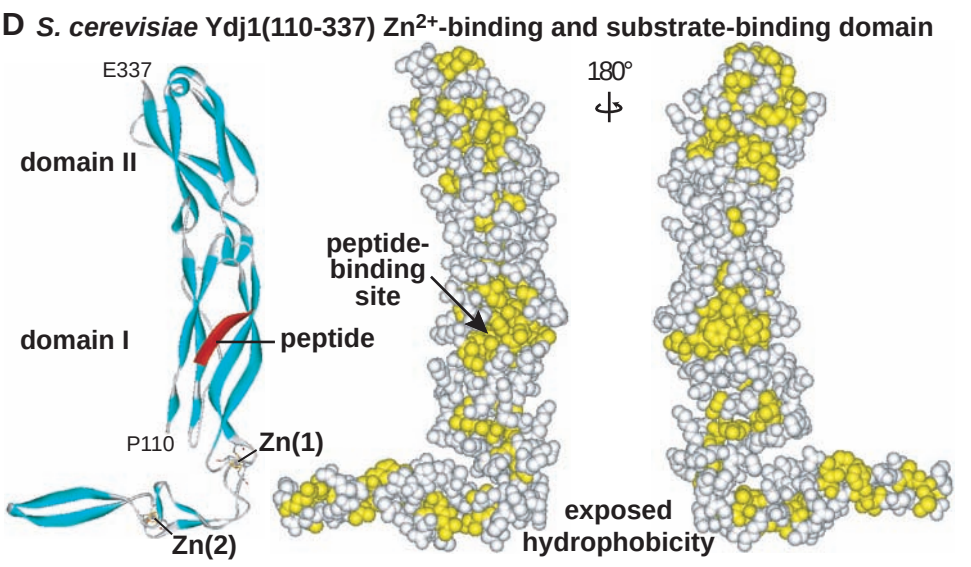

Fig. 15.5. (D) Ribbon (left) and space-filling (right) models of the crystal structure of the substrate-binding domain of *S. cerevisiae* Ydj1 (residues 110–337) (1NLT) [76]. The co-crystallized peptide is shown in red. Hydrophobic residues are shown in yellow.

The J-domain is essential for the JDP function to stimulate the ATPase activity of Hsp70 proteins [13, 24–27, 77, 78] (Figure 15.5A). It consists of four helices. Helices II and III form an antiparallel helical coiled-coil. Helix I runs from the end of helix III to the middle of helix II, approximately parallel to the plane formed by helices II and III. Helix IV starts near the C-terminal end of helix III on the same side of the coiled-coil as helix I, but it is oriented approximately perpendicular to the plane of the helices II and III. Helices I through III form a hydrophobic core between them. The loop connecting helices II and III is of variable length and contains the highly conserved and functionally essential histidine–proline–aspartic acid (HPD) motif. The surface of the J-domain is mainly positively charged due to a number of conserved basic residues, in particular in helix II.

The Zn^{2+}-binding domain consists of a segment of 76 amino acids characterized by four repeats of the motif C-X-X-C-X-G-X-G [79]. NMR spectroscopy revealed a V-shaped extended hairpin topology consisting of three pairs of antiparallel β-strands separated by the two Zn^{2+}-binding sites [74]. Due to this topology, the N- and C-termini are on the same side of the structure, and the first and the last C-X-X-C-X-G-X-G motif of the sequence form the first Zn^{2+}-binding site, while the two middle C-X-X-C-X-G-X-G motifs form the second Zn^{2+}-binding site. Removal of the Zn^{2+} ions causes unfolding of the structure, demonstrating the importance of the Zn^{2+} ions for the structural stability of the domain. The functional role of the Zn^{2+}-binding domain remains obscure.

Most structural information on how a JDP may bind substrates comes from the 2.7-Å crystal structures of the C-terminal substrate-binding domain (residues 171–

352) of the type II homologue, Sis1 of *S. cerevisiae* [75], and the Zn^{2+}-binding and C-terminal domains (102–350) of the type I homologue, Ydj1 of *S. cerevisiae* [76]. The Sis1 substrate-binding domain consists of two highly similar domains, each formed by a sandwich of two β-sheets and a short α-helix (Figure 15.5C). The C-terminus of the second domain extends into a short α-helix, which is involved in the dimerization of Sis1 in the crystals. Although Sis1 and other DnaJ homologues form dimers and higher-order oligomers in solution, it is not clear whether a dimer is the active form. The structure of the Sis1 fragment did not reveal an obvious substrate-binding cavity. However, the authors proposed a small hydrophobic depression in domain I as peptide-binding site for two reasons. First, the analogous hydrophobic depression in domain II is occupied by the aromatic side chain of a phenylalanine residue. Second, in the crystal packing the side chain of a proline residue from an adjacent Sis1 molecule was inserted into this hydrophobic depression [75]. Alteration of hydrophobic residues within this pocket affected the ability of Sis1 to bind substrates in vitro [80].

The Ydj1 structure is L-shaped and consists of three domains, whereby domains I and II are superimposable to the structure of Sis1 and the Zn^{2+}-binding domain is very similar to the NMR structure of the DnaJ Zn^{2+}-binding domain [76] (Figure 15.5D). Ydj1 was crystallized with the peptide GWLYEIS, which was bound in a small hydrophobic groove in domain I of Ydj1. This location is homologous to the hydrophobic depression in Sis1 that was proposed to serve as substrate-binding site. The peptide was bound in an extended conformation, forming an antiparallel β-strand to strand 2 of domain I of Ydj1. The central Leu of the peptide is completely buried in a hydrophobic pocket, while the aromatic side chains of the peptide do not make contact with Ydj1 in the crystal structure. The apparent strong contribution of hydrogen bonds to the backbone of the peptide and the missing contacts of the aromatic residues are difficult to reconcile with the substrate-binding specificity of the type I homologue *E. coli* DnaJ ([81]; discussed below in Section 15.3.3). Although the Ydj1 fragment was crystallized as a monomer, the authors argue that in vivo it forms a dimer similar to Sis1. The reason for the monomer structure was suggested to be due to an alteration of Phe335, the homologous residue of which in Sis1 is involved in dimerization. This Phe335 to Asp alteration was introduced because the authors could not obtain suitable crystals of the wild-type Ydj1 fragment.

The crystal structure of the *E. coli* type III protein HscB represents the only full-length structure of a JDP (Figure 15.5B). The N-terminal J-domain, which is very similar to the J-domain structures solved by NMR despite the very limited degree of sequence identity, is connected to a C-terminal three-helix bundle by a flexible linker [82]. The structure did not convey any idea of where and how HscB might interact with substrates.

15.3.2
Interaction With Hsp70s

The physical interaction of full-length JDP with Hsp70s was first investigated by size-exclusion chromatography and an ELISA assay using *E. coli* DnaJ and *E. coli*

DnaK as model proteins [83]. With these assays a complex between the two proteins could be detected only when ATP was present. Mutational alteration of the HPD motif in the J-domain completely abolished the interaction, indicating that the J-domain is involved. C-terminal truncation of DnaJ also reduced the interaction significantly, suggesting that the C-terminal domains also participate in the interaction [78, 84]. A more detailed analysis using surface plasmon resonance spectroscopy with immobilized DnaJ demonstrated that the thus observed interactions are very similar if not identical to the DnaJ-mediated interaction of Hsp70 proteins with substrates [56, 85]. This conclusion is based on the findings that the interaction depends on DnaJ-stimulated ATP hydrolysis, an intact inter-domain communication between ATPase and the substrate-binding domain of DnaK, and a high-affinity interaction with the substrate-binding cavity of DnaK. Interactions of the J-domain alone with full-length DnaK, as well as interactions of full-length DnaJ with the ATPase domain of DnaK, could not be detected by this method. The DnaJ interaction with the substrate-binding domain of DnaK was further investigated using a photoactivatable heterobifunctional cross-linker attached to cysteines in close proximity to the substrate-binding cavity of DnaK [26]. This approach demonstrated that DnaJ could be cross-linked to DnaK in a nucleotide-modulated manner. This cross-link was abolished in the presence of a good DnaK-binding peptide but not in the presence of a peptide that binds only to DnaJ and not to DnaK. These results indicate that DnaJ binds to DnaK in close proximity to, if not within the substrate-binding cavity of, DnaK [26]. The physiological significance of this interaction is still unclear. It was proposed that this interaction is an intermediate during the transfer of substrates from DnaJ to DnaK [85]. Investigations using the J-domain of the SV40 large T-antigen revealed that Hsp70 proteins bind to and stabilize almost all proteins to which a J-domain is added [86]. In this reaction, multiple Hsp70 molecules were observed to bind to the same protein. Similar results were obtained when the J-domain of DnaJ was fused to biotin carrier protein and the J-domain of Sec63 was fused to glutathione-S-transferase [85, 87]. The J-domain may therefore signify to Hsp70 proteins the close proximity of a substrate, whereby Hsp70 binds to DnaJ itself if DnaJ has no substrate bound.

The interaction site of the J-domain of DnaJ within DnaK was identified by two distinct approaches. The *dnaK*-R167H mutant was isolated as an allele-specific extragenic suppressor of the *dnaJ*-D35N mutant allele [88]. Independently, the crystal structure of the ATPase domain of Hsc70 was searched for highly conserved surface-exposed residues that are in close proximity to the nucleotide-binding cleft. The identified residues were exchanged by alanine-scanning mutagenesis and the interaction with DnaJ was analyzed. All thus identified residues are localized within a conserved channel in the ATPase domain [89].

To study the physical interaction of the J-domain with Hsp70 on the J-domain site, NMR was employed with ^{15}N-labeled J-domain of *E. coli* DnaJ and either full-length DnaK or the ATPase domain of DnaK [90]. Residues that are directly involved in the interaction, or indirectly affected through a conformational change during binding, were hereby revealed by quenching of the NMR signal and by chemical shift perturbation upon addition of DnaK (Figure 15.5A). Most affected by the interaction are residues in helix II and the loop between helices II and III

containing the HPD motif. This study also showed that the interaction of the J-domain with the ATPase domain is very weak (K_d 10–30 μM), explaining why the interaction was not detected by surface plasmon resonance spectroscopy. More recently, using a combination of NMR and isothermal titration calorimetry with wild-type and mutant J-domains and the DnaK ATPase domain, Landry showed that the interaction between the J-domain and the ATPase domain indeed is mainly of an electrostatic nature [91].

The functional importance of conserved residues of the J-domain was also investigated by alanine-scanning mutagenesis of the J-domain of *E. coli* DnaJ. The functionality of the mutant proteins was tested in vivo by complementation of the temperature-sensitive phenotype and the inability to support plaque formation of the bacteriophage λ of a Δ*dnaJ* Δ*cbpA* strain [92]. In addition to the HPD motif, three residues in helices II (Y25, K26) and III (F47) were found to be essential for DnaJ function (Figure 15.5A).

15.3.3 Interactions with Substrates

The additional domains in JDPs in general serve as protein-protein interaction domains, or they localize the JDP to a defined structure within the cell. Type I and type II and some of the type III JDPs can interact promiscuously with many different unfolded proteins, and many of them are able to prevent aggregation of these substrates. How the type I protein *E. coli* DnaJ recognizes its substrates was addressed by the peptide library approach, as described above for DnaK (see Section 15.2.4) [81]. The binding motif is slightly longer as compared to DnaK and consists of a core of eight amino acids enriched in large, hydrophobic, especially aromatic residues, and the charge of the peptide is not as important as in the case of DnaK. Therefore, like DnaK, DnaJ recognizes stretches of hydrophobic residues that in native structures are usually found in the interior hydrophobic core, explaining its promiscuous binding to many unfolded proteins. Due to these similarities in the recognition motif, about 70% of all good DnaK-binding peptides also have a significant affinity to DnaJ and vice versa. Only a minority of peptides with affinity to one of the two chaperones are not recognized by the other. Interestingly, when DnaK and DnaJ were compared in their binding affinities to D-amino acids, clear differences became apparent. DnaK's affinity to peptides was abolished in the D-stereoisomers even when the side chain conformation was conserved. This demonstrates that for DnaK interactions with the substrate backbone are essential, consistent with the crystal structure, which shows a number of hydrogen bonds between DnaK and the substrate backbone [93] (Figure 15.3). In contrast to this result, DnaJ was completely insensitive to the stereochemistry of the peptide bond, indicating that contacts to the substrate backbone do not contribute significantly to the binding strength and that the side chains are the only determinants for affinity. Similar observations were made by Christen and coworkers using D-amino acids containing peptides in solution [94]. It was therefore proposed that DnaJ and type I JDP in general are scanning factors that search the surface of proteins for large hydrophobic areas [81]. Assuming that Ydj1 binds to substrates in a way similar to DnaJ,

these results do not seem to fit to the proposed substrate-binding pocket of Ydj1. As discussed above, in this structure interactions between the substrate backbone and Ydj1 were particularly important and only the hydrophobic side chain of the central leucine seems to contribute to binding stability.

Earlier publications also suggested that other parts of the type I JDP could contribute to substrate binding. In particular, the Zn^{2+}-binding domain was proposed to be important in vitro and in vivo [95, 96], although it could not be ruled out that the mutant DnaJ proteins used in these studies were structurally defective. A recent study by Jakob and coworkers clearly showed that the first Zn^{2+}-binding center is important for substrate binding, as measured by testing the prevention of aggregation of chemically denatured luciferase by DnaJ [97]. Despite the loss of ability to bind to substrates, the mutant missing the first Zn^{2+}-binding center was functional in refolding assays in vitro and complemented the temperature-sensitive growth phenotype of Δ*dnaJ* cells. In contrast, the second Zn^{2+}-binding center was essential for DnaJ function in vitro and in vivo, but it did not contribute to substrate binding. A contribution of the Zn^{2+}-binding domain to the interaction of type I JDPs with substrates was also suggested by recent domain-swap experiments [98].

Interestingly, the affinity of DnaJ for protein substrates is much higher (K_d in the low nanomolar range) than for peptide substrates (K_d in the micromolar range) [94, 99]. These findings are consistent with more than one binding site within the same DnaJ protein, as well as with an oligomerization of DnaJ and cooperative binding of a substrate molecule by several DnaJ proteins within the oligomer. The C-terminal part of Sis1 was crystallized as dimer, and for Ydj1, Sha and coworkers also suggest that the dimer is in the natural state [76]. Analytical ultracentrifugation experiments had demonstrated earlier that DnaJ also exists in an oligomeric state including dimers and high-order oligomers [100]. Dimerization of DnaJ might be important to give DnaJ more specificity. Since many proteins expose hydrophobic patches on their surface even in the native state, a single binding site for DnaJ might be found quite frequently. If DnaJ, however, needs two binding sites at a certain distance from each other, the accidental binding of a native protein is less likely.

Most type III JDPs show exclusive association with a single substrate or a small set of specific substrates; for example, the JDP auxilin interacts only with clathrin, and the JDP kinesin light chain interacts only with kinesin heavy chain. Alternatively, type III proteins are localized to a specific structure in the cell, which allows them to target their Hsp70 partner proteins to thereby pre-selected targets. Thus, Zuo1 is bound to the ribosome [101], Sec63 is bound to the Sec61 protein transport channel of the endoplasmatic reticulum [102], Pam18 is tethered to the Tim23 presequence translocase of the inner mitochondrial membrane [103–105], and cysteine string proteins are located in the membrane of secretory vesicles through multiple palmitoylation of their cysteines [106, 107]. At least in the first two cases, the J-domain is thereby positioned at a location where Hsp70 substrates appear. The function of the cysteine string proteins at the secretory vesicles is not yet elucidated.

The functional importance of this close proximity between Hsp70 substrate and

J-domain was demonstrated by surface plasmon resonance spectroscopy, where a substrate (peptide or protein) and a J-domain were immobilized either separately or together on the same chip and the interaction with Hsp70 was measured [27, 56]. While the interaction of the Hsp70 with the J-domain was not detectable and with the substrate in the absence of the J-domain was very weak, a strong binding of Hsp70 to the substrate was detected when both the substrate and the J-domain were co-immobilized. This interaction was strictly dependent on the presence of ATP and the ability of Hsp70 to hydrolyze ATP. These data demonstrate that the J-domain increases the apparent affinity of Hsp70s for substrates by allowing the association of Hsp70 to the substrate in the ATP state with a high rate but slowing down the dissociation by timely stimulation of ATP hydrolysis. This increase in apparent affinity was also demonstrated by the use of a fusion construct consisting of the J-domain of DnaJ and a peptide substrate of DnaK [108].

15.4 Nucleotide Exchange Factors

15.4.1 GrpE: Structure and Interaction with DnaK

GrpE has a molecular weight of 22 kDa and forms a stable dimer in solution [109]. The X-ray structure of GrpE in complex with the ATPase domain of DnaK was solved to 2.8-Å resolution [110] (Figure 15.1B). The GrpE mutant protein used for crystallization was truncated, missing the first 33 residues, and in addition had the Gly122-to-Asp exchange of the GrpE280 mutant protein [111, 112]. The N-terminus of the truncated GrpE monomer constitutes an α-helix with the remarkable length of 100 Å. Both helices of the GrpE dimer lie in the same plane and interact tightly without forming a classical coiled-coil. The N-terminal helix is connected via a rather unstructured loop to two additional short α-helices and a small β-sheet domain composed of six short β-strands. In addition to the N-terminal helix, the dimer interface is formed by the two short helices of each monomer, which together build up a four-helix bundle. In the crystal structure GrpE forms an asymmetric and bent dimer whereby only one GrpE monomer contacts the ATPase domain of DnaK through five major contact sites, including an exposed loop identified biochemically to be essential for stable GrpE-DnaK interaction [113]. The bent structure of the GrpE dimer prevents it from interacting with two DnaK molecules at the same time, consistent with the $GrpE_2$:DnaK stoichiometry of the complex identified in solution [109] (Figure 15.1B).

GrpE binds to the ADP-bound and nucleotide-free states of DnaK with high affinity ($K_d = 1$ nM). Addition of ATP leads to the dissociation of the complex [109, 114, 115]. As described above, the superposition of the structure of the nucleotide-free ATPase domain of DnaK in complex with GrpE with the structure of the ADP + P_i-bound ATPase domain of Hsc70 [116] shows that subdomain IIB in DnaK is rotated outwards by 14°, thereby opening up the nucleotide-binding cleft.

This rotation displaces residues Ser274, Lys270, and Glu267 of DnaK by 2–3 Å. The corresponding amino acids in Hsc70 are involved in the coordination of the adenine and the ribose rings of the bound ADP. Furthermore, residues that constitute hydrophobic patches and the upper of two salt bridges (E264-R56) spanning the nucleotide-binding cleft interact with GrpE [110]. The right panel of Figure 15.1B shows how GrpE loosens the inter-subdomain interface in the nucleotide-binding cleft by interfering with the hydrophobic contact and the salt bridges.

The mechanism by which GrpE accelerates the nucleotide release thus seems to rely on an active opening of the nucleotide-binding cleft. Furthermore, GrpE stabilizes the open conformation of the nucleotide-binding pocket, which facilitates the rapid binding of ATP to the nucleotide-free state of DnaK [32]. In addition, it has been proposed that the long N-terminal α-helices together with the missing residues of the N-terminus reach to the substrate-binding domain, thereby influencing substrate binding and release [110]. Experimental evidence for such an acceleration of substrate release by GrpE has also been reported [110, 117, 118]. However, an intensive investigation of the release kinetics of peptide and protein substrates could not confirm this possibility [219].

15.4.2 Nucleotide Exchange Reaction

Several methods have been employed to measure nucleotide exchange. One method employs radio-labeled nucleotides. The Hsp70 protein is pre-incubated with the radio-labeled nucleotide, before unlabelled nucleotide is added at time point 0. At different time points thereafter, Hsp70-bound and -free nucleotide are separated either by binding to nitrocellulose filters or by rapid gel filtration over a Nick-column (Amersham Bioscience), and both fractions are quantified by scintillation counting or thin-layer chromatography and phosphoimaging [20, 119]. However, this method is limited to relatively slow reactions. Since the basal nucleotide exchange rates vary between Hsp70 proteins up to 700-fold, it is not applicable for all members of the family. In particular, the exchange reaction that is stimulated by nucleotide exchange factors cannot be determined precisely by this method. An alternative method employs the fluorescent nucleotide analogue N^8-(4-*N'*-methylanthraniloylaminobutyl)-ADP/ATP (MABA-ADP/MABA-ATP), which allows the use of stopped-flow instrumentation as first described by Reinstein and coworkers [33]. The association of MABA-ADP and MABA-ATP is thereby determined by rapidly mixing the fluorescent nucleotide (0.5 μM) with the Hsp70 protein (0.5–10 μM) and following the fluorescence at 420 nm with 350-nm excitation wavelength. The dissociation rates for MABA-ADP are determined by pre-incubating the nucleotide (0.5 μM) with an equal amount of Hsp70 protein and subsequent mixing with an excess of unlabeled ADP (1 mM). For determination of the ATP dissociation rate, a double-mixing procedure has to be used to avoid ATP hydrolysis before the measurement of the release. MABA-ATP is mixed with nucleotide-free Hsp70 for 0.5–2 s and subsequently mixed with an excess of unlabeled ATP. Since ATP

release is slow, the ATP hydrolysis during the dissociation reaction has to be taken into account when calculating the ATP dissociation rates from the fluorescence traces.

15.4.3 Bag Family: Structure and Interaction With Hsp70

Like JDPs the members of the Bag family are multi-domain proteins that have in common a conserved domain of approximately 120 residues, the so-called Bag domain, which is essential for the interaction with Hsp70 proteins. The Bag domain consists of a three-helix bundle that interacts with domains IB and IIB of the ATPase domain of Hsc70 [120, 121] (Figure 15.1C). The structure of the ATPase domain of Hsc70 when in complex with the Bag domain is very similar to the structure of the ATPase domain of DnaK when in complex with GrpE, showing a 14° outward rotation of subdomain IIB and thereby opening the nucleotide-binding cleft (Figure 15.1.B). Nevertheless, biochemical evidence suggests a different mechanism by which the Bag domain achieves such an opening [62]. While GrpE accelerated the dissociation of ADP in the absence and presence of inorganic phosphate (P_i), as well as the dissociation of ATP with the same efficacy, in the presence of P_i, a higher concentration of Bag-1 was necessary to stimulate ADP release than in the absence of P_i, and ATP dissociation was not stimulated under the conditions tested. These data were interpreted such that the ATPase domain of Hsp70s is in equilibrium between two conformations, an open conformation with subdomain IIB rotated outward and a closed conformation. The frequency of transition between the two conformations would depend on the nucleotide bound, with ATP $<$ ADP $\cdot$ P_i $<$ ADP $<$ nucleotide-free. GrpE seems to be able to interact with the closed conformation and actively open the nucleotide-binding cleft, whereas Bag-1 appears to interact only with the open conformation and, by stabilizing it, catalyzes nucleotide exchange in a more passive way. In favor of such different mechanisms is the fact that GrpE interacts with the ATPase domain more extensively than does Bag-1. In addition, the transition of the GrpE dimer from a symmetric form in solution to the asymmetric form when bound to DnaK may provide the necessary opening force.

In addition to the Bag domain, other domains are found within Bag proteins, including an ubiquitin-like domain (Bag-1, Bag-6) and the WW domain (Bag-3), which mediates protein-protein interactions (Figure 15.6). Therefore, Bag proteins seem to differ from the GrpE-type nucleotide exchange factors by their ability to associate with ligands other than Hsp70 proteins. Although not shown experimentally, it is generally assumed that Bag proteins use this ability to connect the nucleotide dissociation–dependent delivery of Hsp70 bound cargo with cellular processes. These cellular processes seem to be highly diverse, since Bag homologues have been implicated by genetic two-hybrid screens [122] and co-immunoprecipitation [123, 124] in signal transduction processes related to cellular stress responses, including apoptosis, proliferation, and development. Bag proteins have been found in complexes with the antiapoptotic Bcl-2, the protein kinase Raf, the transcription

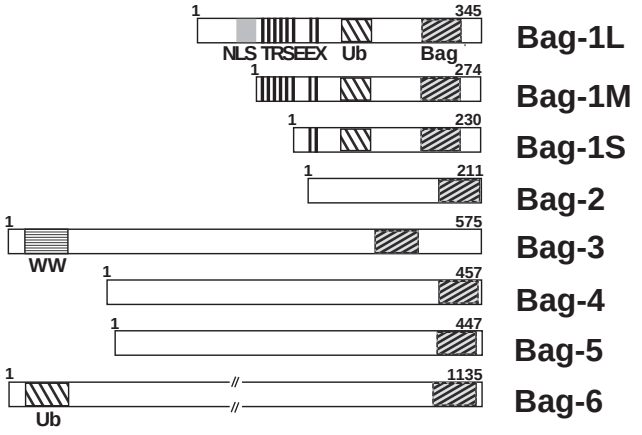

Fig. 15.6. Domain structure of Bag proteins. The following abbreviations for the different domains were used: NLS, nuclear localization sequence; TRSEEX, Thr-Arg-Ser-Glu-Glu-Xaa repeat motif; Ub, ubiquitin-like domain; Bag, Bag homology region; WW, Trp-Trp-domain.

factor c-Jun, the receptors for vitamin D, androgen, and glucocorticoid [122–128], and the proteasome [129].

The family of Bag proteins is composed of the homologues Bag-1, Bag-2, Bag-3 (CAIR/BIS), Bag-4 (SODD), Bag-5, and Bag-6 (BAT3/Scythe) [130], most of which have been identified by two-hybrid screens and genome mining of human cDNA libraries [131, 132] (Figure 15.6). All homologues per definition contain a Bag domain but otherwise show a high degree of difference in their domain composition. For example, four of these homologues do not code for any of the other domains found in Bag-1 (Figure 15.6). Bag-1 is produced in the cell as four translation initiation variants, Bag-1L (50 kDa), Bag-1M (46 kDa), Bag-1p33 (33 kDa), and Bag-1S (29 kDa) [133] (Figure 15.6). Bag-1M is identical to Rap46, a protein found in the cytosol of higher eukaryotes [119, 122, 124]. The N-terminal segment, which exists only in Bag-1L, is rich in basic amino acids that have been implicated in DNA binding. Bag-1L is indeed found mainly in the nucleus [134]. More recently, DNA-binding was attributed to the KKKTRRR sequence present in Bag-1L and at the beginning of Bag-1M [135]. This study showed that Bag-1M is also found in the nucleus and is able to bind to DNA unspecifically. The positively charged region and the interaction with Hsc70 were both necessary for the downregulation of the transcriptional activity of glucocorticoid receptor. The second region, present in Bag-1L and Bag-1M, contains a stretch of six TRSEEX repeats (threonine, arginine, serine, glutamic acid, glutamic acid, any amino acid; TRS not identical in all repeats). It has been suggested that these repeats stimulate transcriptional processes in an unspecific fashion in analogy to an acidic activation domain [136]. However, there is also evidence that these TRSEE repeats are involved in downregulation of the tran-

scriptional activity of the glucocorticoid receptor [137]. Common to all four Bag-1 variants is an ubiquitin-like domain that was proposed to mediate the interaction of Bag-1 with the proteasome. Such interaction has been demonstrated by co-immunoprecipitation experiments [129]. It is tempting to speculate that the association of Bag-1M with the proteasome allows it to dissociate substrates from a complex with Hsp70 for degradation by the proteasome. Such a role would directly link the Hsp70 activity to proteolysis. Alternatively, Bag-1 may act as an anti-targeting factor that prevents Hsp70 from binding to substrates of the proteasome, since this may interfere with the degradation process.

Whatever the functions of Bag proteins are in the above cellular processes, it is clear from the work of several laboratories that Bag proteins are not strictly essential for the chaperone activity of Hsp70 proteins in the folding of nonnative proteins [62, 127, 131, 138–141]. This is in sharp contrast to the essential role for GrpE in the chaperone cycle of DnaK. On the contrary, Bag proteins, in particular Bag-1M (see below), have been proposed to act as negative regulators of the Hsp70 and Hsc70 homologues in a more general sense. This proposal was first based on studies revealing that Bag-1 at a variety of concentrations inhibits the chaperone activity of Hsp70 and Hsc70 in the folding of denatured luciferase and β-galactosidase in vitro and in vivo [127, 138, 140, 141]. However, at physiological concentrations of inorganic phosphate (which slows down the nucleotide dissociation from Hsc70 and Hsp70 by 5- to 10-fold), Bag-1 at low concentrations stimulates slightly (by up to 1.3-fold) the luciferase refolding activity of Hsp70 or Hsc70 with DjB1/Hdj-1 or DjA1/Hdj-2 in vitro [62]. Since the cellular concentration of Bag-1 is rather low (3% of the Hsc70 concentration [142]), it might be that the inhibitory effects of Bag-1, observed in vitro in the absence of P_i and in vivo when Bag-1 is overproduced, are restricted to special environmental and metabolic conditions of the cell. An attractive hypothesis is that in the cell, most Bag proteins are associated with their protein partners and exert their regulatory role only locally.

15.4.4 Relevance of Regulated Nucleotide Exchange for Hsp70s

Meanwhile, a number of proteins have been proposed to act as nucleotide-exchange factors for different Hsp70s on the basis of stimulated steady-state ATPase activity in the presence of a J-domain protein and by measuring nucleotide release using the gel-filtration assay as described above. Sls1 (synthetic lethal with 7S RNA mutation) and Bap (BiP-associated protein) were suggested as nucleotide-exchange factors for the yeast endoplasmatic reticulum Hsp70, Kar2, and the mammalian endoplasmic reticulum Hsp70, BiP, respectively [143, 144]. Both proteins share a limited homology with each other and with the cytoplasmic proteins Fes1 and HspBP1, which were proposed to be nucleotide-exchange factors for the yeast cytosolic Hsp70, Ssa1, and the human Hsc70 (see Table 15.1) [145, 146]. Consequently, HspBP1 would be a second type of nucleotide-exchange factor for Hsc70 in addition to the Bag proteins. Although final proof of the nucleotide exchange function of these proteins is still missing, it seems that the regulation of nucleotide ex-

Tab. 15.1. Specificity and activity of known and proposed nucleotide-exchange factors.

	E. coli			*S. cerevisiae*					*Mammalian*			*References*
	DnaK	*HscA*	*HscC*	*Ssa1*	*Ssb1*	*Kar2*	*Ssc1*	*Ssq1*	*Hsc70*	*Hsp70*	*BiP*	
GrpE/Mge1[a]	+++[b]	−−−	−−				++	++	−−−	−−−		24, 32, 35, 211–213
Bag	−−−	−−−							+++	+++		35, 62, 119, 138
HspBP1				+=					+=	+=		146, 214
Fes1				+=		−						146
Sls1				(+)		++						143, 146, 215
Bap											++	144

[a] Mge1, mitochondrial GrpE homologue.
[b] The first position indicates the physical interaction, the second position, the stimulation of the ATPase activity in conjunction with a JDP, and the third position, the determination of the stimulated dissociation rate constant.
+, interacting/stimulating; −, not interacting/no effect; (+), weak interaction; =, inhibiting; no entry, physical or functional interaction has not been reported.

change is quite common and that the number of Hsp70 proteins, for which no nucleotide-exchange factors have been found, grows thinner.

One Hsp70 homologue that is independent of an exchange factor is *E. coli* HscA (Hsc66). This homologue does not interact with GrpE, the only nucleotide-exchange factor for Hsp70s so far discovered in *E. coli*. However, the basal nucleotide-exchange rate of HscA is 700-fold higher than the rate of DnaK, which is almost as high as the exchange rate of DnaK when fully stimulated by GrpE [35]. The molecular reason for this difference was found in two salt bridges and a hydrophobic patch that span the nucleotide-binding cleft in DnaK but are absent in HscA [35]. It is therefore clear that the architecture of the ATPase domain of Hsp70 proteins allows the adjustment of the nucleotide-exchange rate to different tasks. The question of why nucleotide-exchange factors are needed arises, to which there are three possible answers. First, nucleotide exchange could be regulated in a spatial manner. This seems to be the case for the mammalian Hsp70s, where the Bag-family proteins are located at different places in the cell and accelerate nucleotide exchange more locally. Second, nucleotide exchange could be regulated in a timely manner. The concentration or the activity of the nucleotide-exchange factor could be adjusted to the needs in response to internal or external signals. This seems to be the case for *E. coli* GrpE, which was shown to unfold reversibly during mild to severe heat shock and to become inactive. Since nucleotide exchange is rate-limiting for substrate release in the presence of ATP and in particular at physiological concentrations of P_i, the lifetime of the Hsp70-substrate complex is prolonged during heat shock conditions, where refolding into the native state is less likely

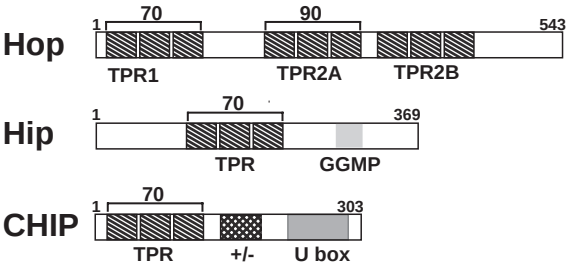

Fig. 15.7. Domain structure of the TPR motifs containing Hsp70 co-chaperones Hip, Hop, and Chip. The following abbreviations for the different domains were used: TPR, tetratricopeptide repeat; GGMP, Gly-Gly-Met-Pro repeat motif; +/−, charged region; U box, U box motif of E3 ubiquitin ligases; 70, interaction site for Hsp70/Hsc70; 90, interaction site for Hsp90.

[147–151]. Similar results were obtained for *Thermus thermophilus* GrpE [149]. Third, nucleotide exchange could be regulated in response to the bound substrate. Due to individual folding characteristics, different substrates may need to interact with Hsp70 proteins for different lengths of time. A nucleotide-exchange factor that also interacts with the substrate could then regulate the nucleotide exchange according to the needs of the substrate. There is, however, no evidence so far for such a mechanism.

15.5 TPR Motifs Containing Co-chaperones of Hsp70

TPR domains consist of 34 amino acid repeats forming a twisted helix-loop-helix motif. A minimum of three repeats form the TPR protein-protein interaction domain (Figures 15.7 and 15.8). In general, TPR domain proteins can act as scaffold and targeting factors [152]. In addition to the above-mentioned type III JDPs such as DjC3/hp58 and DjC7/hTPR2, a number of other Hsp70-interacting proteins also contain TPR repeats. Most of them bind with their TPR domain to the EEVD motif present at the C-termini of most eukaryotic cytosolic Hsp70 and Hsp90 proteins. Some of the TPR domains are more promiscuous, allowing binding to both Hsp70 and Hsp90 (e.g., Chip, Tom70), while others are highly selective (e.g., the TPR domains of Hop). The TPR domain, however, can also bind to a different part of the Hsp70 protein, as is the case with Hip (see below). A scaffold function was proposed for the proteins Hop and SGT, the first assembling the complex of Hsp70 and Hsp90 with a substrate, and the second binding Hsc70 and cysteine string proteins to the secretory vesicles [153, 154]. A targeting function was found for Tom70 [155, 156]. TPR domain–containing interaction partners of Hsp70 proteins also bring new functionalities to the chaperone machinery and can act as regulatory co-chaperones.

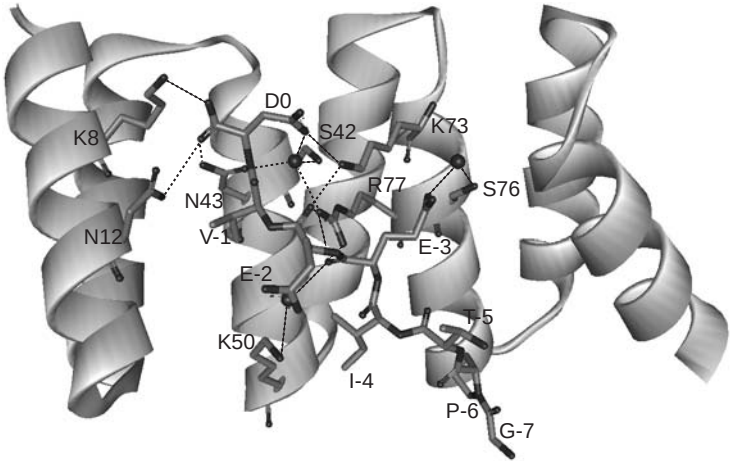

Fig. 15.8. Interaction of the TPR domain with the C-terminus of Hsp70. The TPR1 domain of Hop is shown as ribbon model with the Hsp70-interacting residues in stick representation and numbered consecutively. The co-crystallized peptide (GPTIEEVD) representing the highly conserved C-terminus of eukaryotic cytosolic Hsp70s is shown in stick representation and numbered in the reverse sense starting at the C-terminus with D0. Hydrogen bonds are indicated as dashed lines.

15.5.1 Hip

The 48-kDa Hsc70-interacting protein (Hip, p48) was found twice independently, first in a two-hybrid screen using the ATPase domain of human Hsc70 as bait [157, 158] and subsequently by co-immuno precipitation as a transient component of the progesterone receptor activation complex [159]. This protein consists of an N-terminal oligomerization domain, an acidic domain, three TPR motifs important for interaction with Hsp70, a series of degenerate GGMP repeats, and a C-terminal region similar to the Sti1/Hop/p60 protein [159, 160]. In *A. thaliana* two homologues of Hip are found, one of which does not contain the GGMP repeats and the C-terminal region but instead has a thioredoxin-like domain with protein disulfide reductase activity [161, 162].

Although the native Hip protein elutes from a size-exclusion column at a volume similar to a globular protein with four to five times its molecular weight, analytical ultracentrifugation clearly demonstrated that Hip is a dimer in solution [163]. Hip was proposed to inhibit nucleotide release from Hsc70 [119]; however, close scrutiny of nucleotide exchange of human Hsc70 using the fluorescent ADP analogue MABA-ADP did not support this hypothesis (unpublished results). Hip was also shown to interact with the unfolded protein, reduced carboxymethylated α-lactalbumin, and to prevent the aggregation of denatured proteins [163, 164]. However, the physiological significance of these observations is still obscure.

The cellular function of Hip is not clear. In vitro and in vivo experiments suggest that it opposes the negative effect of Bag proteins on the Hsc70-substrate complex

[165, 166]. By competing with Bag for binding to the ATPase domain of Hsc70, Hip prevents accelerated ADP dissociation and thereby slows down the ATP-mediated substrate release. Three cellular processes have been described where Hip seems to be involved: (1) the activation of nuclear receptors, (2) the translocation of proteins across the lysosomal membrane, and (3) the internalization of G-protein-coupled receptors [159, 167, 168]. In all three processes Hip seems to contribute to the efficient binding of Hsc70 to its substrates, which would be consistent with its role to counteract the effects of Bag proteins. These observations taken together support the notion that the co-chaperones Hip and Bag fine-tune the Hsp70 chaperone machinery for certain substrates or at specific locations.

15.5.2 Hop

The 60-kDa Hsp70-Hsp90 organizing protein (Hop/Sti1/p60) has been identified in a genetic screen for proteins involved in the regulation of the heat shock response in yeast [169] and was subsequently found to be a component of the progesterone receptor complex [170]. The Hop protein is characterized by three TPR domains with three TPR motifs each and it forms a dimer in solution. The TPR domains bind to the EEVD motif present at the C-termini of most eukaryotic cytosolic Hsp70s and Hsp90s. The recent elucidation of the crystal structures of two TPR domains of Hop, in complex with a peptide containing the EEVD motifs of Hsp70 and Hsp90, respectively, and biochemical data show that these motifs allow specific binding to the TPR domains [171–173].

A Hop protein preparation from rabbit reticulocyte lysate was shown to stimulate the ATPase and chaperone activity of Hsp70 in vitro. This stimulation was proposed to result from Hop's acceleration of ADP release and ATP binding [174] and the thereby accelerated substrate release. However, the ATP association rate and ADP and substrate dissociation rates in the presence of Hop were not determined, and it was therefore not clear how Hsp70 chaperone function was enhanced by Hop. More recently, it was shown that the yeast homologue Sti1 stimulates the steady-state ATPase activity of its cognate Hsp70 protein, Ssa1, up to 200-fold even in the absence of a J-domain protein [175]. This stimulation could not be explained with an acceleration of the nucleotide exchange since γ-phosphate cleavage was rate-limiting under the conditions tested. Sti1 therefore acted in these experiments like a JDP. In the same study the mammalian homologue Hop had no effect on the ATPase activity of its cognate Hsp70 protein, and the question was put forward whether the yeast and mammalian Hsp70/Hsp90 systems act through a similar mechanism. However, a recent study on DjC7/hTPR2 showed that this protein is similar to Sti1 in yeast, stimulating the ATPase activity of Hsp70 with its J-domain and interacting with Hsp70 and Hsp90 with its TPR domains [176].

Hop is an important, although not strictly essential, component of the Hsp70-Hsp90 chaperone machinery that activates nuclear receptors, protein kinases, and other regulatory proteins [177–180]. In contrast to its action on Hsp70, Hop inhibits the ATPase activity of Hsp90, thereby holding it in an open conformation, ready

to bind to substrates [181, 182]. Thus, Hop coordinates the action of Hsp70 and Hsp90 during the activation of client proteins. For more detail on Hop, see Chapter 23.

15.5.3 Chip

The 35-kDa C-terminus of Hsc70-interacting protein (Chip) consists of an N-terminal TPR motif domain, a region with a high number of positively and negatively charged residues (mixed charge region), and a C-terminal RING-finger-type E3 ubiquitin-protein isopeptide ligase motif, a so-called U box [183, 184]. Based on these criteria, Chip proteins can be identified in a variety of eukaryotic organisms ranging from *C. elegans* to man. *A. thaliana* Chip shows a significant degree of identity to only the U box of human Chip. In contrast, the homology of this protein to the TPR motifs of human Chip is very weak, and it does not contain a mixed charge region. It nevertheless seems to function as a bona fide Chip protein [185]. No Chip homologues exist in *S. cerevisiae* or *Schizosaccharomyces pombe*. Chip dimerizes through its middle domain, which is predicted to form a coiled-coil, and dimerization is essential for its function [186].

The N-terminal TPR motifs are involved in the interaction of Chip with the C-terminal EEVD domain of Hsp70 and Hsp90, whereby Chip competes with other TPR domain proteins such as Hop and immunophilins. Chip inhibits the in vitro chaperone activity of Hsc70 and Hsp70, as measured by preventing the aggregation of denatured rhodanese and refolding of denatured luciferase. Chip inhibits the ATPase activity of Hsc70 without influencing ADP dissociation [184]. How Chip acts on ATPase activity and whether this inhibitory activity is responsible for the effects of Chip on the chaperone activity of Hsc70 and Hsp70 are unclear.

Chip was recently identified as an E3 ubiquitin-protein isopeptide ligase by several laboratories based on the criteria of (1) self-ubiquitination; (2) ubiquitination of several native substrates, including Hsp70, Raf-1 kinase, and unidentified proteins of a bacterial extract, and denatured substrate proteins such as heat-denatured luciferase; and (3) a physical and/or functional interaction of Chip with E2 enzymes such as UbcH5A that act specifically in the degradation of misfolded and aberrant proteins [187–190]. It is therefore believed that Chip takes part in the triage decision by ubiquitin-tagging of hopelessly misfolded proteins for degradation by the proteasome [191, 192]. In vivo and in vitro, increasing concentrations of Chip induce the ubiquitination of Hsc70 and Hsp90 substrates, including the glucocorticoid receptor, the dioxin receptor, the cystic fibrosis transmembrane conductance regulator (CFTR), and the receptor tyrosine kinase Erb2, and promote their degradation by the proteasome [193–197]. Chip also promoted the ubiquitination and degradation of a misfolded mutant form of αB-crystalline, suggesting a general function in the clearance of aberrant proteins and thereby slowing down the accumulation of large aggregates [198]. In addition, Chip was able to polyubiquitinate Bag-1 in vivo and in vitro without influencing the half-life of Bag-1 [199]. This ubiquitination was proposed to enhance the affinity of Bag-1 to the protea-

some. Chip therefore not only shares with Bag-1 the potential to connect the activity of Hsp70 chaperones with proteolysis but also seems to act synergistically with Bag-1.

There is, however, also evidence for a seemingly degradation-independent function of Chip. The trafficking of the endothelial NO synthase to the plasmalemma was influenced by overexpression of Chip, and the activity of the NO synthase was thereby downregulated. In contrast, the half-life of the NO synthase was not decreased by Chip [200]. The heat shock factor HSF1 was found to be activated by the interaction with Chip and translocated into the nucleus in complex with Chip and Hsp70 to activate transcription of heat shock genes [201]. Chip may therefore have more functions to be discovered, and ubiquitination by Chip may not always doom to degradation as has been shown for other E3 ubiquitin ligases.

15.6 Concluding Remarks

In the course of evolution, the Hsp70 chaperone machinery has adapted to a large variety of protein-folding tasks by (1) variation of the Hsp70 protein itself, (2) cooperation with the modular J-domain proteins that are ideally suited as targeting factors due to the large variety of protein-protein interaction domains, and (3) an increasing number of auxiliary co-chaperones that fine-tune the action of the Hsp70-J-domain protein team or link it to other chaperones such as Hsp90. As novel co-chaperones for the Hsp70 chaperones are found, novel protein-folding tasks for the Hsp70 folding machine may be discovered.

15.7 Experimental Protocols

All purification steps are performed on ice or at 4 °C. In particular, ammonium sulfate precipitation is carried out on ice as described in Ref. [202], using fine powdered ammonium sulfate. For buffer changes, samples are generally dialyzed overnight against 100 sample volumes of the respective buffer. Purified proteins are aliquoted, quick frozen in liquid N_2, and stored at −80 °C.

15.7.1 Hsp70s

Many of the classical Hsp70 proteins can be purified by a combination of anion-exchange chromatography and affinity chromatography over an ATP-agarose column [203, 204], as described in the following for the *E. coli* homologue DnaK. DnaK-overproducing cells are lysed in 50 mM TRIS/HCl pH 7.6, 18 mM Spermidin, 10 mM $(NH_4)_2SO_4$, 5 mM EDTA, 5 mM DTT, 10% sucrose, 1 mM phenylmethylsulfonyl fluoride using a French press or sonication. After clarifying centrifuga-

tions (20 min, 30 000 *g*; 2 h, 100 000 *g*), the cell extract is subjected to a differential ammonium sulfate precipitation (30% and 60% saturation). The second DnaK-containing ammonium sulfate pellet is resuspended in buffer A (25 mM HEPES/KOH pH 7.6, 50 mM KCl, 5 mM $MgCl_2$, 10 mM β-mercaptoethanol, 1 mM EDTA), dialyzed overnight against buffer A, and applied to anion-exchange chromatography over a DEAE Sepharose column equilibrated in the same buffer. DnaK is eluted using a linear KCl gradient of 0–500 mM. The DnaK-containing fractions are pooled and incubated in a batch procedure with an appropriate amount of ATP-agarose (ATP linked over C8; 1 mL per 10 mg DnaK, swollen in water, washed in 10 bed volumes of buffer A, 10 bed volumes of buffer B, and again 10 bed volumes of buffer A) rotating end over end at 4 °C for 30 min. The slurry is poured into a plastic, disposable 10-mL column (BioRad), and unspecific contaminants are removed with subsequent washes of five column volumes buffer A and five column volumes buffer A plus 1 M KCl and re-equilibrated to buffer A. For the elution of DnaK, the ATP-agarose is gently resuspended in the column in one column volume buffer A plus ATP (5 mM) and incubated at 4 °C for 45 min. After collecting the eluate, the column is eluted with a second column volume of ATP-containing buffer A. To remove bound substrates, the pooled and concentrated DnaK-containing fractions of the ATP-agarose are further purified by size-exclusion chromatography in the presence of ATP (1 mM) and finally concentrated by chromatography over a strong anion-exchange column (e.g., resource Q; Amersham Bioscience). Alternative purification methods for DnaK, not including an ATP-agarose step, have also been used successfully [33].

The protocol described here works well for many Hsp70 proteins from overproducing sources, whereas for some proteins the salt concentrations of the anion-exchange chromatography have to be adjusted. The protocol can even be adapted to the purification from sources with a natural Hsp70 content (e.g., Ref. [205]). However, not all Hsp70 proteins can be purified by this protocol because the affinity for nucleotide varies substantially between the different Hsp70s; consequently, not all Hsp70s bind tightly enough to ATP-agarose (see, e.g., Refs. [19, 35, 206]). Purification of Hsp70 proteins using a tag (e.g., His_6-tag) is not advisable because tags on both ends influence the ATPase activity and interaction with co-chaperones.

15.7.2
J-Domain Proteins

E. coli DnaJ can be purified by taking advantage of its high isoelectric point (pI $\approx$ 8) using chromatography on a cation-exchange resin and hydroxyapatite [100, 207]. One of the major obstacles in DnaJ purification is the hydrophobicity of the protein and its tendency to aggregate and to associate with membranes. To overcome these obstacles, urea (2 M) and the detergent Brij 58 (0.6%) is used.

DnaJ-overproducing *E. coli* cells, resuspended in lysis buffer (50 mM TRIS/HCl, pH 8, 10 mM DTT, 0.6% (w/v) Brij 58, 1 mM phenylmethylsulfonyl fluoride, 0.8 mg mL^{-1} lysozyme), are lysed using a French press or sonication, and cell debris is removed by centrifugation (20 min, 30 000 *g*; 2 h, 100 000 *g*). The supernatant is

diluted by addition of one volume of buffer A (50 mM sodium phosphate buffer pH 7, 5 mM DTT, 1 mM EDTA, 0.1% (w/v) Brij 58), and DnaJ is precipitated by addition of $(NH_4)_2SO_4$ to a final concentration of 65%. The ammonium sulfate pellet is dissolved in buffer B (50 mM sodium phosphate buffer pH 7, 5 mM DTT, 1 mM EDTA, 0.1% (w/v) Brij 58, 2 M urea) and dialyzed against buffer B. DnaJ is loaded onto an equilibrated strong cation-exchange column (e.g., Poros SP20, Applied Biosystems), washed with buffer B, and eluted with a linear gradient of 0–666 mM KCl (15 column volumes). DnaJ-containing fractions are pooled and dialyzed against buffer C (50 mM TRIS/HCl, pH 7.5, 2 M urea, 0.1% (w/v) Brij 58, 5 mM DTT, 50 mM KCl). The dialyzed sample is loaded onto a Bio-Gel HT hydroxyapatite column equilibrated in buffer C and washed with one column volume buffer C + 1 M KCl and two column volumes buffer C. DnaJ is eluted with a linear gradient of one column volume 0–50% buffer D (50 mM TRIS/HCl, pH 7.5, 2 M urea, 0.1% (w/v) Brij 58, 5 mM DTT, 50 mM KCl, 600 mM KH_2PO_4) and two column volumes of 50% buffer D. The DnaJ-containing fractions are pooled and dialyzed against buffer E (50 mM TRIS/HCl, pH 7.7, 100 mM KCl). This protocol works equally well for the human J-domain proteins DjB1/Hdj-1 and DjA1/Hdj-2 [62].

The J-domain of DnaJ can be purified according to a protocol from Karzai and McMacken [25]. The cleared extract from a J-domain-overproducing *E. coli* strain in buffer A (50 mM HEPES/NaOH pH 7.6, 2 mM DTT, 1 M NaCl, 2 mM $MgCl_2$) is subjected to ammonium sulfate precipitation by addition of solid ammonium sulfate to 75% saturation and centrifugation (1 h, 30 000 *g*). The J-domain-containing supernatant is dialyzed extensively against buffer B (50 mM HEPES/NaOH, pH 7.6, 2 mM DTT, 25 mM NaCl, 10% glycerol), applied onto an equilibrated cation-exchange column, washed with buffer B, and eluted with a linear gradient of 0.025–0.7 M NaCl in buffer B. The J-domain-containing fractions are applied to a Bio-Gel HT hydroxyapatite column equilibrated in buffer C (50 mM potassium phosphate buffer pH 6.8, 2 mM DTT, 0.15 M KCl, 10% glycerol), washed with buffer C, and eluted with a linear gradient of 0.05–0.5 M potassium phosphate in buffer C. The purified J-domain is dialyzed against buffer D (25 mM HEPES/KOH, pH 7.6, 100 mM KCl, 2 mM DTT).

15.7.3 GrpE

GrpE can be purified by affinity chromatography on a DnaK column [114] or, alternatively, by a combination of anion-exchange chromatography, hydroxyapatite chromatography, and size-exclusion chromatography [109]. In the first protocol cells of the *E. coli* strain C600 dnaK103 [208] are resuspended in 5 mL per gram cell paste buffer A (50 mM TRIS/HCl pH 8, 0.06 μg mL^{-1} spermidine, 6.6 mM EDTA, 6.6 mM DTT, 200 mM ammonium sulfate, 10% sucrose, 1 mM phenylmethylsulfonyl fluoride)and lysed using a French press or sonication, and cell debris is removed by centrifugation (30 min 100 000 *g*). Ammonium sulfate is added to the supernatant to a final concentration of 0.35 g mL^{-1}. The GrpE-containing precipitate is

resuspended in 2 mL buffer B (25 mM HEPES/KOH pH 8, 1 mM EDTA, 10 mM 2-mercaptoethanol, 10% glycerol) and dialyzed against three times 1 L of buffer B. The dialyzed sample is diluted with buffer B to a final volume of 20 mL and applied to a 20-mL equilibrated DnaK column previously prepared by cross-linking purified DnaK to an activated chromatographic material (e.g., Affi-Gel 10; BioRad) according to the manufacturer's recommendations. The column is washed successively with 200 mL of 50-mM KCl in buffer B, 70 mL of 0.5-M KCl in buffer B, and 70 mL of 2-M KCl in buffer B. The column is re-equilibrated with 100 mL of 50-mM KCl in buffer B, followed by elution of GrpE with 50 mL of 50-mM KCl, 20 mM $MgCl_2$, and 10 mM ATP in buffer B (pH adjusted to 7.6). The GrpE fraction is dialyzed three times against 2 L buffer C (25 mM HEPES/KOH pH 8, 50 mM KCl, 0.1 mM EDTA, 10 mM 2-mercaptoethanol, 20% glycerol). The number and duration of final dialysis steps are particularly important to remove all traces of ATP.

In the second protocol GrpE is purified from overproducing cells of a ΔdnaK strain (e.g., BB1553) [209]. The cell pellet is resuspended in lysis buffer (50 mM TRIS/HCl, pH 7.5, 100 mM KCl, 2 mM DTT, 3 mM EDTA, 1 mM phenylmethylsulfonyl fluoride) at 5 mL per gram cell paste, the cells are lysed, and cell debris is removed by centrifugation (20 min, 30 000 *g*; 90 min, 100 000 *g*). Ammonium sulfate is added to the supernatant to a final concentration of 0.35 g mL^{-1}, and the precipitate is dissolved in buffer A (50 mM TRIS/HCl, pH 7.5, 100 mM KCl, 1 mM DTT, 1 mM EDTA, 10% glycerol) and dialyzed twice against buffer A. The dialyzed sample is applied onto a DEAE-Sepharose column equilibrated with buffer A, and GrpE is eluted with a linear gradient of one column volume 0–30% buffer B (50 mM TRIS/HCl, pH 7.5, 1 M KCl, 1 mM DTT, 1 mM EDTA, 10% glycerol). The pooled GrpE-containing fractions are dialyzed against buffer C (10 mM potassium phosphate buffer, pH 6.8, 1 mM DTT, 10% glycerol), applied to an equilibrated Bio-Gel HT hydroxyapatite column, and eluted by stepwise increase of the phosphate concentration (4%, 8%, 15%, 20%, and 100% buffer D; 0.5 M potassium phosphate buffer, pH 6.8, 1 mM DTT, 10% glycerol). The pooled GrpE-containing fractions are applied to a Superdex 200 gel-filtration column equilibrated in buffer A and afterwards are concentrated on a strong anion-exchange column (e.g., Resource Q, Amersham Bioscience) using a steep gradient of buffer B. The GrpE fraction is dialyzed against buffer E (25 mM HEPES/KOH pH 8, 50 mM KCl, 0.1 mM EDTA, 10 mM 2-mercaptoethanol, 20% glycerol). If GrpE is purified from a wild-type *E. coli* strain, co-purifying DnaK can be removed by extensive washing of the Bio-Gel HT hydroxyapatite-bound GrpE with buffer C containing 10 mM ATP before stepwise elution. In addition, the size-exclusion chromatography is carried out in the presence of 1 mM ATP.

15.7.4 Bag-1

Bag-1 is purified by a combination of anion exchange, hydroxyapatite, and size-exclusion chromatography according to a published protocol [62]. The Bag-1-over-

producing *E. coli* cells are lysed in lysis buffer (50 mM TRIS/HCl pH 7.6, 18 mM spermidine, 100 mM $(NH_4)_2SO_4$, 5 mM EDTA, 5 mM DTT, 10% sucrose, 1 mM phenylmethylsulfonyl fluoride) using a French press or sonication, and cell debris is removed by centrifugation (20 min, 30 000 *g*; 2 h, 100 000 *g*). The supernatant is subjected to a fractionated ammonium sulfate precipitation on ice by adding first 226 g L^{-1}, removing the precipitated proteins by centrifugation and then adding again 187 g L^{-1} to the supernatant to reach a final ammonium sulfate concentration of 70% saturation. The Bag-1-containing precipitate is resuspended in buffer A (20 mM MOPS/KOH pH 7.2, 50 mM KCl, 1 mM EDTA, 1 mM 2-mercaptoethanol), dialyzed extensively against buffer A, and applied to an anion-exchange chromatography column (DEAE-Sepharose) equilibrated in buffer A. The column is washed with four column volumes of buffer A and Bag-1 is eluted with a linear gradient of 50–500 mM KCl over 10 column volumes. The Bag-1-containing fractions are pooled, dialyzed against buffer B (50 mM potassium phosphate buffer, pH 7, 1 mM 2-mercaptoethanol), and applied onto an equilibrated Bio-Gel HT hydroxyapatite (BioRad) column. The column is washed with buffer B, Bag-1 is eluted using a linear gradient of 50–500 mM potassium phosphate in buffer B over five column volumes, and the Bag-1-containing fractions are dialyzed against buffer C (20 mM MOPS/KOH pH 7.2, 20 mM KCl, 0.5 mM EDTA, 1 mM 2-mercaptoethanol). Contaminating ATPases are removed by incubation of the dialyzed Bag-1 sample with 0.5 mL ATP-agarose (swollen and equilibrated as described above in Section 15.7.1) rotating end over end at 4 °C for 30 min. The agarose is pelleted and the supernatant is transferred to a new tube. Bag-1 is precipitated by addition of ammonium sulfate to a final concentration of 80%, and the precipitate is resuspended in a minimal volume of buffer C and applied to size-exclusion chromatography on a Superdex 200 column (Amersham Bioscience). The Bag-1-containing fractions are concentrated by chromatography on a strong anion-exchange column (MonoQ HR5/5; Amersham Bioscience) and eluted with a linear gradient of 100–500 mM KCl over 10 column volumes. Bag-1 is dialyzed against buffer C.

15.7.5
Hip

Hip is purified by a combination of anion-exchange, hydroxyapatite, and size-exclusion chromatography following a modified protocol by Höhfeld and Jentsch [119]. The Hip-overproducing *E. coli* cells are lysed in lysis buffer (50 mM TRIS/HCl pH 7.6, 18 mM spermidine, 100 mM $(NH_4)_2SO_4$, 5 mM EDTA, 5 mM DTT, 10% sucrose, 1 mM phenylmethylsulfonyl fluoride) using a French press or sonication, and cell debris is removed by centrifugation (20 min, 30 000 *g*; 2 h, 100 000 *g*). Ammonium sulfate is added to the supernatant to a final concentration of 0.29 g mL^{-1} (50% saturation), and the Hip-containing precipitate is dissolved in buffer A (20 mM MOPS/KOH pH 7.2, 50 mM KCl, 1 mM EDTA, 1 mM 2-mercaptoethanol), dialyzed extensively against buffer A, and applied to an anion-exchange chromatography column (DEAE-Sepharose) equilibrated in buffer A. The column is washed with four column volumes of buffer A and Hip is eluted with a linear gra-

dient of 50–500 mM KCl over 10 column volumes. The Hip-containing fractions are pooled, dialyzed against buffer B (50 mM potassium phosphate buffer, pH 7, 1 mM 2-mercaptoethanol), and applied onto an equilibrated Bio-Gel HT hydroxyapatite (BioRad) column. The column is washed with buffer B, Hip is eluted using a linear gradient of 50–500 mM potassium phosphate buffer over five column volumes, and the Hip-containing fractions are pooled and precipitated by addition of ammonium sulfate to a final concentration of 80%. The precipitate is resuspended in a minimal volume of buffer C (20 mM MOPS/KOH pH 7.2, 20 mM KCl, 0.5 mM EDTA, 1 mM 2-mercaptoethanol) and applied to size-exclusion chromatography on a Superdex 200 column (Amersham Bioscience) equilibrated in the same buffer. The Hip-containing fractions are concentrated by chromatography on a strong anion-exchange column (MonoQ HR5/5; Amersham Bioscience) and eluted with a linear gradient of 100–1000 mM KCl over 10 column volumes. The purified Hip is dialyzed against buffer C.

15.7.6 Hop

Hop is purified according to a protocol by Buchner and coworkers [210] using anion-exchange chromatography, hydroxyapatite, and size-exclusion chromatography. The cell pellet from a human Hop-overproducing *E. coli* strain is resuspended in 3 mL of 10 mM TRIS/HCl, pH 7.5 per gram of wet cell pellet containing 1 mM phenylmethylsulfonyl fluoride, *p*-aminobenzoic acid (PABA 520 μg mL^{-1}), and pepstatin A (1 μg mL^{-1}) as protease inhibitors. The cells are lysed and the suspension is clarified by centrifugation at 40 000 *g* for 60 min at 4 °C. The supernatant is loaded onto a 40-mL Q-Sepharose column (Amersham Bioscience) equilibrated with lysis buffer. Bound protein is eluted from the column with a linear gradient of 0–15 M NaCl over 10 column volumes. Hop elutes around 0.13 M NaCl. Hop-containing fractions are pooled and concentrated by ultrafiltration. The concentrate is dialyzed overnight against 10 mM potassium phosphate buffer, pH 7.5. The Hop pool is then loaded onto a pre-equilibrated 2-mL FPLC hydroxyapatite column (BioRad) and eluted with a linear potassium phosphate buffer gradient ranging from 10 to 300 mM over 15 column volumes (pH 7.5). Hop elutes between 80 and 220 mM phosphate. The Hop-containing fractions are pooled, concentrated as described above, and loaded onto a 120-mL Superdex 200 preparative-grade gel-filtration column (Amersham Bioscience) equilibrated with two column volumes of 10 mM TRIS/HCl, pH 7.5, 400 mM NaCl. Hop-containing fractions are pooled, concentrated as described above to 5 mg mL^{-1}, and finally dialyzed against 40 mM HEPES-KOH, pH 7.5.

15.7.7 Chip

Wild-type untagged human Chip is purified from overproducing *E. coli* cells using three steps: anion-exchange, cation-exchange, and size-exclusion chromatography according to a published protocol [186]. The cell pellet from the Chip-producing

E. coli strain is resuspended in buffer A (50 mM HEPES, pH 7.0, 50 mM KCl, 5 mM DTT, 10% glycerol, 1 mM phenylmethylsulfonyl fluoride) containing 0.4 mg mL^{-1} lysozyme, lysed by sonification, and clarified by ultracentrifugation at 100 000 *g* for 1 h. The supernatant is precipitated by addition of ammonium sulfate to a final saturation of 40%. The pellet is resuspended in buffer A, dialyzed against the same buffer, and loaded onto a DEAE-Sepharose column (Sigma) that is equilibrated with the same buffer. The column is washed with two column volumes of buffer A, and bound proteins are eluted with a linear gradient from 0% to 100% buffer B (50 mM HEPES/KOH, pH 7.0, 1 M KCl, 5 mM DTT, 10% glycerol, 1 mM phenylmethylsulfonyl fluoride) over two column volumes. Chip-containing fractions are pooled and dialyzed against buffer A and loaded onto an SP Sepharose column (Amersham Bioscience). The column is washed with two column volumes of buffer A, and bound proteins are eluted with a linear gradient of 0–100% buffer B over five column volumes. The peak fractions are pooled, concentrated, and applied to a Superdex 200 high-load gel-filtration column (Amersham Biosciences) equilibrated with buffer A. Highly pure Chip-containing fractions are pooled, frozen in liquid nitrogen, and stored at −80 °C.

References

1 R. J. Fletterick, D. J. Bates, and T. A. Steitz. The structure of a yeast hexokinase monomer and its complexes with substrates at 2.7-A resolution. *Proc. Natl. Acad. Sci. USA* **1975**, *72*, 38–42.

2 W. Kabsch, H. G. Mannherz, D. Suck, E. F. Pai, and K. C. Holmes. Atomic structure of the actin:DNase I complex. *Nature* **1990**, *347*, 37–44.

3 J. H. Hurley, H. R. Faber, D. Worthylake, N. D. Meadow, S. Roseman, D. W. Pettigrew, and S. J. Remington. Structure of the regulatory complex of *E. coli* IIIGlc with glycerol kinase. *Science* **1993**, *259*, 673–677.

4 D. P. Easton, Y. Kaneko, and J. R. Subjeck. The Hsp110 and Grp170 stress proteins: newly recognized relatives of the Hsp70s. *Cell Stress & Chaperones* **2000**, *5*, 276–290.

5 H. J. Oh, D. Easton, M. Murawski, Y. Kaneko, and J. R. Subjeck. The chaperoning activity of hsp110. Identification of functional domains by use of targeted deletions. *J. Biol. Chem.* **1999**, *274*, 15712–15718.

6 M. Gautschi, H. Lilie, U. Fünfschilling, A. Mun, S. Ross, T. Lithgow, P. Rucknagel, and S. Rospert. RAC, a stable ribosome-associated complex in yeast formed by the DnaK-DnaJ homologs Ssz1p and zuotin. *Proc. Natl. Acad. Sci. USA* **2001**, *98*, 3762–3767.

7 H. Hundley, H. Eisenman, W. Walter, T. Evans, Y. Hotokezaka, M. Wiedmann, and E. Craig. The in vivo function of the ribosome-associated Hsp70, Ssz1, does not require its putative peptide-binding domain. *Proc Natl Acad Sci USA* **2002**, *99*, 4203–4208.

8 G. A. Otterson, G. C. Flynn, R. A. Kratzke, A. Coxon, P. G. Johnston, and F. J. Kaye. Stch encodes the 'ATPase core' of a microsomal stress 70 protein. *Embo J* **1994**, *13*, 1216–1225.

9 G. A. Otterson, and F. J. Kaye. A 'core ATPase', Hsp70-like structure is conserved in human, rat, and C. elegans STCH proteins. *Gene* **1997**, *199*, 287–292.

10 D. Schmid, A. Baici, H. Gehring,

and P. Christen. Kinetics of molecular chaperone action. *Science* **1994**, *263*, 971–973.

11 M. P. Mayer, H. Schröder, S. Rüdiger, K. Paal, T. Laufen, and B. Bukau. Multistep mechanism of substrate binding determines chaperone activity of Hsp70. *Nature Struct. Biol.* **2000**, *7*, 586–593.

12 S. M. Gisler, E. V. Pierpaoli, and P. Christen. Catapult Mechanism Renders the Chaperone Action of Hsp70 Unidirectional. *J. Mol. Biol.* **1998**, *279*, 833–840.

13 J. S. McCarty, A. Buchberger, J. Reinstein, and B. Bukau. The role of ATP in the functional cycle of the DnaK chaperone system. *J. Mol. Biol.* **1995**, *249*, 126–137.

14 M. Zylicz, J. H. LeBowitz, R. McMacken, and C. Georgopoulos. The dnaK protein of *Escherichia coli* possesses an ATPase and autophosphorylating activity and is essential in an in vitro DNA replication system. *Proc. Natl. Acad. Sci. USA* **1983**, *80*, 6431–6435.

15 R. Jordan, and R. McMacken. Modulation of the ATPase activity of the molecular chaperone DnaK by peptides and the DnaJ and GrpE heat shock proteins. *J. Biol. Chem.* **1995**, *270*, 4563–4569.

16 D. R. Palleros, K. L. Reid, L. Shi, W. J. Welch, and A. L. Fink. ATP-induced protein-Hsp70 complex dissociation requires K^+ but not ATP hydrolysis. *Nature* **1993**, *365*, 664–666.

17 J.-H. Ha, E. R. Johnson, D. B. McKay, M. C. Sousa, S. Takeda, and S. M. Wilbanks. Structure and mechanism of Hsp70 proteins. In *Molecular Chaperones and Folding Catalysts. Regulation, Cellular Function and Mechanism* (B. Bukau, ed), pp. 573–607, Harwood Academic Publishers, Amsterdam, **1999**.

18 J. J. Silberg, and L. E. Vickery. Kinetic characterization of the ATPase cycle of the molecular chaperone Hsc66 from *Escherichia coli*. *J. Biol. Chem.* **2000**, *275*, 7779–7786.

19 C. Kluck, H. Pazelt, P. Genevaux, D. Brehmer, W. Rist, J. Schneider-Mergener, B. Bukau, and M. P. Mayer. Structure-function analysis of HscC, the *Escherichia coli* member of a novel subfamily of specialized Hsp70 chaperones. *J. Biol. Chem.* **2002**, *277*, 41060–41069.

20 J.-H. Ha, and D. B. McKay. ATPase kinetics of recombinant bovine 70 kDa heat shock cognate protein and its amino-terminal ATPase domain. *Biochemistry* **1994**, *33*, 14625–14635.

21 P. Lopez-Buesa, C. Pfund, and E. A. Craig. The biochemical properties of the ATPase activity of a 70-kDa heat shock protein (Hsp70) are governed by the C-terminal domains. *Proc. Natl. Acad. Sci. USA* **1998**, *95*, 15253–15258.

22 D. Klostermeier, R. Seidel, and J. Reinstein. The functional cycle and regulation of the *Thermus thermophilus* DnaK chaperone system. *J. Mol. Biol.* **1999**, *287*, 511–525.

23 G. C. Flynn, T. G. Chappell, and J. E. Rothman. Peptide binding and release by proteins implicated as catalysts of protein assembly. *Science* **1989**, *245*, 385–390.

24 K. Liberek, J. Marszalek, D. Ang, C. Georgopoulos, and M. Zylicz. *Escherichia coli* DnaJ and GrpE heat shock proteins jointly stimulate ATPase activity of DnaK. *Proc. Natl. Acad. Sci. USA* **1991**, *88*, 2874–2878.

25 A. W. Karzai, and R. McMacken. A bipartite signaling mechanism involved in DnaJ-mediated activation of the *Escherichia coli* DnaK protein. *J. Biol. Chem.* **1996**, *271*, 11236–11246.

26 T. Laufen, M. P. Mayer, C. Beisel, D. Klostermeier, J. Reinstein, and B. Bukau. Mechanism of regulation of Hsp70 chaperones by DnaJ co-chaperones. *Proc. Natl. Acad. Sci. USA* **1999**, *96*, 5452–5457.

27 B. Misselwitz, O. Staeck, and T. A. Rapoport. J proteins catalytically activate Hsp70 molecules to trap a wide range of peptide sequences. *Mol Cell* **1998**, *2*, 593–603.

28 K. G. Hoff, J. J. Silberg, and L. E. Vickery. Interaction of the iron-sulfur cluster assembly protein IscU with the Hsc66/Hsc20 molecular chaperone

system of *Escherichia coli*. *Proc. Natl. Acad. Sci. USA* **2000**, *97*, 7790–7795.

29 W. Barouch, K. Prasad, L. Greene, and E. Eisenberg. Auxilin-induced interaction of the molecular chaperone Hsc70 with clathrin baskets. *Biochemistry* **1997**, *36*, 4303–4308.

30 B. Bukau, and A. L. Horwich. The Hsp70 and Hsp60 chaperone machines. *Cell* **1998**, *92*, 351–366.

31 A. Szabo, T. Langer, H. Schröder, J. Flanagan, B. Bukau, and F. U. Hartl. The ATP hydrolysis-dependent reaction cycle of the *Escherichia coli* Hsp70 system-DnaK, DnaJ and GrpE. *Proc. Natl. Acad. Sci. USA* **1994**, *91*, 10345–10349.

32 L. Packschies, H. Theyssen, A. Buchberger, B. Bukau, R. S. Goody, and J. Reinstein. GrpE accelerates nucleotide exchange of the molecular chaperone DnaK with an associative displacement mechanism. *Biochemistry* **1997**, *36*, 3417–3422.

33 H. Theyssen, H.-P. Schuster, B. Bukau, and J. Reinstein. The second step of ATP binding to DnaK induces peptide release. *J. Mol. Biol.* **1996**, *263*, 657–670.

34 R. Russell, R. Jordan, and R. McMacken. Kinetic Characterization of the ATPase Cycle of the DnaK Molecular Chaperone. *Biochemistry* **1998**, *37*, 596–607.

35 D. Brehmer, S. Rüdiger, C. S. Gässler, D. Klostermeier, L. Packschies, J. Reinstein, M. P. Mayer, and B. Bukau. Tuning of chaperone activity of Hsp70 proteins by modulation of nucleotide exchange. *Nat Struct Biol.* **2001**, *8*, 427–432.

36 D. R. Palleros, K. L. Reid, J. S. McCarty, G. C. Walker, and A. L. Fink. DnaK, hsp73, and their molten globules. Two different ways heat shock proteins respond to heat. *J. Biol. Chem.* **1992**, *267*, 5279–5285.

37 B. Banecki, M. Zylicz, E. Bertoli, and F. Tanfani. Structural and functional relationships in DnaK and DnaK756 heat-shock proteins from *Escherichia coli*. *J. Biol. Chem.* **1992**, *267*, 25051–25058.

38 K. Liberek, D. Skowyra, M. Zylicz, C. Johnson, and C. Georgopoulos. The *Escherichia coli* DnaK chaperone, the 70-kDa heat shock protein eukaryotic equivalent, changes conformation upon ATP hydrolysis, thus triggering its dissociation from a bound target protein. *J. Biol. Chem.* **1991**, *266*, 14491–14496.

39 A. Buchberger, H. Theyssen, H. Schröder, J. S. McCarty, G. Virgallita, P. Milkereit, J. Reinstein, and B. Bukau. Nucleotide-induced conformational changes in the ATPase and substrate binding domains of the DnaK chaperone provide evidence for interdomain communication. *J. Biol. Chem.* **1995**, *270*, 16903–16910.

40 J. Wei, J. R. Gaut, and L. M. Hendershot. in vitro Dissociation of BiP-Peptide Complexes Requires a Conformational Change in BiP after ATP Binding but Does Not Require ATP Hydrolysis. *J. Biol. Chem.* **1995**, *270*, 26677–26682.

41 J. Wei, and L. M. Hendershot. Characterization of the Nucleotide Binding Properties and ATPase Activity of Recombinant Hamster BiP Purified from Bacteria. *J. Biol. Chem.* **1995**, *270*, 26670–26676.

42 S. M. Wilbanks, L. Chen, H. Tsuruta, K. O. Hodgson, and D. B. McKay. Solution small-angle X-ray scattering study of the molecular chaperone hsc70 and its subfragments. *Biochem.* **1995**, *34*, 12095–12106.

43 K. L. Fung, L. Hilgenberg, N. M. Wang, and W. J. Chirico. Conformations of the Nucleotide and Polypeptide Binding Domains of a Cytosolic Hsp70 Molecular Chaperone Are Coupled. *J. Biol. Chem.* **1996**, *271*, 21559–21565.

44 J.-H. Ha, and D. B. McKay. Kinetics of Nucleotide-Induced Changes in the Tryptophane Fluorescence of the Molecular Chaperone Hsc70 and Its Subfragments Suggest the ATP-Induced Conformational Change Follows Initial ATP Binding. *Biochemistry* **1995**, *34*, 11635–11644.

45 F. Moro, V. Fernandez, and A. Muga. Interdomain interaction through helices A and B of DnaK peptide binding domain. *FEBS Lett* **2003**, *533*, 119–123.

46 B. Banecki, and M. Zylicz. Real Time Kinetics of the DnaK/DnaJ/GrpE Molecular Chaperone Machine Action. *J. Biol. Chem.* **1996**, *271*, 6137–6143.

47 S. V. Slepenkov, and S. N. Witt. Kinetics of the Reactions of the *Escherichia coli* Molecular Chaperone DnaK with ATP: Evidence that a Three-Step Reaction Precedes ATP Hydrolysis. *Biochemistry* **1998**, *37*, 1015–1024.

48 S. Blond-Elguindi, S. E. Cwirla, W. J. Dower, R. J. Lipshutz, S. R. Sprang, J. F. Sambrook, and M.-J. H. Gething. Affinity panning of a library of peptides displayed on bacteriophages reveals the binding specificity of BiP. *Cell* **1993**, *75*, 717–728.

49 A. Gragerov, L. Zeng, X. Zhao, W. Burkholder, and M. E. Gottesman. Specificity of DnaK-peptide binding. *J. Mol. Biol.* **1994**, *235*, 848–854.

50 A. M. Fourie, J. F. Sambrook, and M. J. Gething. Common and divergent peptide binding specificities of Hsp70 molecular chaperones. *J. Biol. Chem.* **1994**, *269*, 30470–30478.

51 A. M. Fourie, T. R. Hupp, D. P. Lane, B. C. Sang, M. S. Barbosa, J. F. Sambrook, and M. J. Gething. HSP70 binding sites in the tumor suppressor protein p53. *J Biol Chem* **1997**, *272*, 19471–19479.

52 G. Knarr, M. J. Gething, S. Modrow, and J. Buchner. BiP binding sequences in antibodies. *J Biol Chem* **1995**, *270*, 27589–27594.

53 S. Rüdiger, L. Germeroth, J. Schneider-Mergener, and B. Bukau. Substrate specificity of the DnaK chaperone determined by screening cellulose-bound peptide libraries. *EMBO J.* **1997**, *16*, 1501–1507.

54 K. G. Hoff, D. T. Ta, T. L. Tapley, J. J. Silberg, and L. E. Vickery. Hsc66 substrate specificity is directed toward a discrete region of the iron-sulfur cluster template protein IscU. *J Biol Chem* **2002**, *277*, 27353–27359.

55 S. Rüdiger, M. P. Mayer, J. Schneider-Mergener, and B. Bukau. Modulation of the specificity of the Hsp70 chaperone DnaK by altering a hydrophobic arch. *J. Mol. Biol.* **2000**, *304*, 245–251.

56 M. P. Mayer, T. Laufen, K. Paal, J. S. McCarty, and B. Bukau. Investigation of the interaction between DnaK and DnaJ by surface plasmon resonance spectroscopy. *J. Mol. Biol.* **1999**, *289*, 1131–1144.

57 J. S. McCarty, S. Rüdiger, H.-J. Schönfeld, J. Schneider-Mergener, K. Nakahigashi, T. Yura, and B. Bukau. Regulatory region C of the *E. coli* heat shock transcription factor, σ^{32}, constitutes a DnaK binding site and is conserved among eubacteria. *J. Mol. Biol.* **1996**, *256*, 829–837.

58 E. V. Pierpaoli, E. Sandmeier, A. Baici, H.-J. Schönfeld, S. Gisler, and P. Christen. The power stroke of the DnaK/DnaJ/GrpE molecular chaperone system. *J. Mol. Biol.* **1997**, *269*, 757–768.

59 E. V. Pierpaoli, S. M. Gisler, and P. Christen. Sequence-specific rates of interaction of target peptides with the molecular chaperones DnaK and DnaJ. *Biochemistry* **1998**, *37*, 16741–16748.

60 S. Takeda, and D. B. McKay. Kinetics of Peptide Binding to the Bovine 70 kDa Heat Shock Cognate Protein, a Molecular Chaperone. *Biochemistry* **1996**, *35*, 4636–4644.

61 M. Pellecchia, D. L. Montgomery, S. Y. Stevens, C. W. Vander Kooi, H. Feng, L. M. Gierasch, and E. R. P. Zuiderweg. Structural insights into substrate binding by the molecular chaperone DnaK. *Nat Struct Biol.* **2000**, *7*, 298–303.

62 C. S. Gässler, T. Wiederkehr, D. Brehmer, B. Bukau, and M. P. Mayer. Bag-1M accelerates nucleotide release for human Hsc70 and Hsp70 and can act concentration-dependent as positive and negative cofactor. *J Biol Chem* **2001**, *276*, 32538–32544.

63 M. l. E. Cheetham, and A. J. Caplan.

Structure, function and evolution of DnaJ: conservation and adaptation of chaperone function. *Cell Stress Chap.* **1998**, *3*, 28–36.

64 W. L. Kelley. The J-domain family and the recruitment of chaperone power. *Trends Biochem Sci* **1998**, *23*, 222–227.

65 T. Laufen, U. Zuber, A. Buchberger, and B. Bukau. DnaJ proteins. In *Molecular chaperones in proteins: Structure, function, and mode of action* (A. L. Fink, and Y. Goto, eds), pp. 241–274, Marcel Dekker, New York, **1998**.

66 K. Ohtsuka, and M. Hata. Mammalian HSP40/DNAJ homologs: cloning of novel cDNAs and a proposal for their classification and nomenclature. *Cell Stress & Chaperones* **2000**, *5*, 98–112.

67 A. J. Caplan, J. Tsai, P. J. Casey, and M. G. Douglas. Farnesylation of YDJ1p is required for function at elevated growth temperatures in Saccharomyces cerevisiae. *J. Biol. Chem.* **1992**, *267*, 18890–18895.

68 J. C. Venter, M. D. Adams, E. W. Myers, et al. The sequence of the human genome. *Science* **2001**, *291*, 1304–1351.

69 J. Jiang, A. B. Taylor, K. Prasad, Y. Ishikawa-Brush, P. J. Hart, E. M. Lafer, and R. Sousa. Structure-function analysis of the auxilin J-domain reveals an extended Hsc70 interaction interface. *Biochemistry* **2003**, *42*, 5748–5753.

70 M. Pellecchia, T. Szyperski, D. Wall, C. Georgopoulos, and K. Wüthrich. NMR structure of the J-domain and the Gly/Phe-rich region of the *Escherichia coli* DnaJ chaperone. *J. Mol. Biol.* **1996**, *260*, 236–250.

71 Y. Q. Qian, D. Patel, F. U. Hartl, and D. J. McColl. Nuclear magnetic resonance solution structure of the human Hsp40 (HDJ-1) J-domain. *J. Mol. Biol.* **1996**, *260*, 224–235.

72 T. Szyperski, M. Pellecchia, D. Wall, C. Georgopoulos, and K. Wüthrich. NMR structure determination of the *Escherichia coli* DnaJ molelcular chaperone: secondary structure and backbone fold of the N-terminal region (residues 2–108) containing the highly conserved J domain. *Proc. Natl. Acad. Sci. USA* **1994**, *91*, 11343–11347.

73 M. V. Berjanskii, M. I. Riley, A. Xie, V. Semenchenko, W. R. Folk, and S. R. Van Doren. NMR structure of the N-terminal J domain of murine polyomavirus T antigens. Implications for DnaJ-like domains and for mutations of T antigens. *J. Biol. Chem.* **2000**, *275*, 36094–36103.

74 M. Martinez-Yamout, G. B. Legge, O. Zhang, P. E. Wright, and H. J. Dyson. Solution structure of the cysteine-rich domain of the *Escherichia coli* chaperone protein DnaJ. *J. Mol. Biol.* **2000**, *300*, 805–818.

75 B. Sha, S. Lee, and D. M. Cyr. The crystal structure of the peptide-binding fragment from the yeast Hsp40 protein Sis1. *Structure* **2000**, *15*, 799–807.

76 J. Li, X. Qian, and B. Sha. The crystal structure of the yeast Hsp40 Ydj1 complexed with its peptide substrate. *Structure (Camb)* **2003**, *11*, 1475–1483.

77 R. Russell, A. Wali Karzai, A. F. Mehl, and R. McMacken. DnaJ dramatically stimulates ATP hydrolysis by DnaK: Insight into targeting of Hsp70 proteins to polypeptide substrates. *Biochemistry* **1999**, *38*, 4165–4176.

78 D. Wall, M. Zylicz, and C. Georgopoulos. The NH_2-terminal 108 amino acids of the *Escherichia coli* DnaJ protein stimulate the ATPase activity of DnaK and are sufficient for λ replication. *J. Biol. Chem.* **1994**, *269*, 5446–5451.

79 J. C. Bardwell, K. Tilly, E. Craig, J. King, M. Zylicz, and C. Georgopoulos. The nucleotide sequence of the Escherichia coli K12 dnaJ+ gene. A gene that encodes a heat shock protein. *J. Biol. Chem.* **1986**, *261*, 1782–1785.

80 S. Lee, C. Y. Fan, J. M. Younger, H. Ren, and D. M. Cyr. Identification of essential residues in the type II Hsp40 Sis1 that function in polypeptide

binding. *J Biol Chem* **2002**, *277*, 21675–21682.

81 S. Rüdiger, J. Schneider-Mergener, and B. Bukau. Its substrate specificity characterizes the DnaJ chaperone as scanning factor for the DnaK chaperone. *EMBO J*. **2001**, *20*, 1–9.

82 J. R. Cupp-Vickery, and L. E. Vickery. Crystal structure of Hsc20, a J-type Co-chaperone from Escherichia coli. *J Mol Biol* **2000**, *304*, 835–845.

83 A. Wawrzynów, and M. Zylicz. Divergent effects of ATP on the binding of the DnaK and DnaJ chaperones to each other, or to their various native and denatured protein substrates. *J. Biol. Chem*. **1995**, *270*, 19300–19306.

84 D. Wall, M. Zylicz, and C. Georgopoulos. The conserved G/F motif of the DnaJ chaperone is necessary for the activation of the substrate binding properties of the DnaK chaperone. *J. Biol. Chem*. **1995**, *270*, 2139–2144.

85 W.-C. Suh, C. Z. Lu, and C. A. Gross. Structural features required for the interaction of the Hsp70 molecular chaperone DnaK with its cochaperone DnaJ. *J. Biol. Chem*. **1999**, *274*, 30534–30539.

86 R. Schirmbeck, M. Kwissa, N. Fissolo, S. Elkholy, P. Riedl, and J. Reimann. Priming polyvalent immunity by DNA vaccines expressing chimeric antigens with a stress protein-capturing, viral J-domain. *Faseb J* **2002**, *16*, 1108–1110.

87 B. Misselwitz, O. Staeck, K. E. S. Matlack, and T. A. Rapoport. Interaction of BiP with the J-domain of the Sec63p component of the endoplasmic reticulum protein translocation complex. *J. Biol. Chem*. **1999**, *274*, 20110–20115.

88 W.-C. Suh, W. F. Burkholder, C. Z. Lu, X. Zhao, M. E. Gottesman, and C. A. Gross. Interactions of the Hsp70 Molecular Chaperone, DnaK, with its Cochaperone DnaJ. *Proc. Natl. Acad. Sci. USA* **1998**, *95*, 15223–15228.

89 C. S. Gässler, A. Buchberger, T. Laufen, M. P. Mayer, H. Schröder, A. Valencia, and B. Bukau. Mutations in the DnaK chaperone affecting interaction with the DnaJ co-chaperone. *Proc. Natl. Acad. Sci. USA* **1998**, *95*, 15229–15234.

90 M. K. Greene, K. Maskos, and S. J. Landry. Role of the J-domain in the cooperation of Hsp40 with Hsp70. *Proc. Nat. Acad. Sci. USA* **1998**, *95*, 6108–6113.

91 S. J. Landry. Structure and Energetics of an Allele-Specific Genetic Interaction between dnaJ and dnaK: Correlation of Nuclear Magnetic Resonance Chemical Shift Perturbations in the J-Domain of Hsp40/DnaJ with Binding Affinity for the ATPase Domain of Hsp70/DnaK. *Biochemistry* **2003**, *42*, 4926–4936.

92 P. Genevaux, F. Schwager, C. Georgopoulos, and W. L. Kelley. Scanning mutagenesis identifies amino acid residues essential for the in vivo activity of the Escherichia coli DnaJ (Hsp40) J-domain. *Genetics* **2002**, *162*, 1045–1053.

93 X. Zhu, X. Zhao, W. F. Burkholder, A. Gragerov, C. M. Ogata, M. Gottesman, and W. A. Hendrickson. Structural analysis of substrate binding by the molecular chaperone DnaK. *Science* **1996**, *272*, 1606–1614.

94 B. Feifel, H.-J. Schönfeld, and P. Christen. D-peptide ligands for the co-chaperone DnaJ. *J. Biol. Chem*. **1998**, *273*, 11999–12002.

95 B. Banecki, K. Liberek, D. Wall, A. Wawrzynów, C. Georgopoulos, E. Bertoli, F. Tanfani, and M. Zylicz. Structure-function analysis of the zinc finger region of the DnaJ molecular chaperone. *J. Biol. Chem*. **1996**, *271*, 14840–14848.

96 A. Szabo, R. Korzun, F. U. Hartl, and J. Flanagan. A zinc finger-like domain of the molecular chaperone DnaJ is involved in binding to denatured protein substrates. *EMBO J*. **1996**, *15*, 408–417.

97 K. Linke, T. Wolfram, J. Bussemer, and U. Jakob. The roles of the two zinc binding sites in DnaJ. *J Biol Chem* **2003**, *278*, 44457–44466.

98 C. Y. Fan, S. Lee, H. Y. Ren, and D. M. Cyr. Exchangeable chaperone modules contribute to specification of Type I and Type II Hsp40 cellular function. *Mol Biol Cell* **2004**, *15*, 761–773.

99 J. Gamer, G. Multhaup, T. Tomoyasu, J. S. McCarty, S. Rudiger, H. J. Schonfeld, C. Schirra, H. Bujard, and B. Bukau. A cycle of binding and release of the DnaK, DnaJ and GrpE chaperones regulates activity of the Escherichia coli heat shock transcription factor sigma32. *Embo J* **1996**, *15*, 607–617.

100 H.-J. Schönfeld, D. Schmidt, and M. Zulauf. Investigation of the molecular chaperone DnaJ by analytical ultracentrifugation. *Progr Colloid Polym Sci* **1995**, *99*, 7–10.

101 W. Yan, B. Schilke, C. Pfund, W. Walter, S. Kim, and E. A. Craig. Zuotin, a ribosome-associated DnaJ molecular chaperone. *EMBO J*. **1998**, *17*, 4809–4817.

102 D. Feldheim, J. Rothblatt, and R. Schekman. Topology and functional domains of Sec63p, an endoplasmic reticulum membrane protein required for secretory protein translocation. *Mol Cell Biol*. **1992**, *12*, 3288–3296.

103 K. N. Truscott, W. Voos, A. E. Frazier, et al. A J-protein is an essential subunit of the presequence translocase-associated protein import motor of mitochondria. *J. Cell Biol*. **2003**, *163*, 707–713.

104 D. Mokranjac, M. Sichting, W. Neupert, and K. Hell. Tim14, a novel key component of the import motor of the TIM23 protein translocase of mitochondria. *Embo J* **2003**, *22*, 4945–4956.

105 P. D. D'Silva, B. Schilke, W. Walter, A. Andrew, and E. A. Craig. J protein cochaperone of the mitochondrial inner membrane required for protein import into the mitochondrial matrix. *Proc Natl Acad Sci USA* **2003**, *100*, 13839–13844.

106 G. J. Evans, A. Morgan, and R. D. Burgoyne. Tying everything together: the multiple roles of cysteine string protein (CSP) in regulated exocytosis. *Traffic* **2003**, *4*, 653–659.

107 L. H. Chamberlain, and R. D. Burgoyne. Cysteine-string protein: the chaperone at the synapse. *J Neurochem* **2000**, *74*, 1781–1789.

108 P. Wittung-Stafshede, J. Guidry, B. E. Horne, and S. J. Landry. The J-domain of Hsp40 couples ATP hydrolysis to substrate capture in Hsp70. *Biochemistry* **2003**, *42*, 4937–4944.

109 H.-J. Schönfeld, D. Schmidt, H. Schröder, and B. Bukau. The DnaK chaperone system of *Escherichia coli*: quaternary structures and interactions of the DnaK and GrpE components. *J. Biol. Chem*. **1995**, *270*, 2183–2189.

110 C. J. Harrison, M. Hayer-Hartl, M. Di Liberto, F.-U. Hartl, and J. Kuriyan. Crystal structure of the nucleotide exchange factor GrpE bound to the ATPase domain of the molecular chaperone DnaK. *Science* **1997**, *276*, 431–435.

111 D. Ang, G. N. Chandrasekhar, M. Zylicz, and C. Georgopoulos. Escherichia coli grpE gene codes for heat shock protein B25.3, essential for both lambda DNA replication at all temperatures and host growth at high temperature. *J. Bacteriol*. **1986**, *167*, 25–29.

112 B. Wu, D. Ang, M. Snavely, and C. Georgopoulos. Isolation and Characterization of Point Mutations in the *Escherichia coli grpE* Heat Shock Gene. *J. Bacteriol*. **1994**, *176*, 6965–6973.

113 A. Buchberger, H. Schröder, M. Büttner, A. Valencia, and B. Bukau. A conserved loop in the ATPase domain of the DnaK chaperone is essential for stable binding of GrpE. *Nat Struct Biol*. **1994**, *1*, 95–101.

114 M. Zylicz, D. Ang, and C. Georgopoulos. The grpE protein of *Escherichia coli*. Purification and properties. *J. Biol. Chem*. **1987**, *262*, 17437–17442.

115 L. S. Chesnokova, S. V. Slepenkov, I. I. Protasevich, M. G. Sehorn, C. G. Brouillette, and S. N. Witt. Deletion of DnaK's lid strengthens

binding to the nucleotide exchange factor, GrpE: a kinetic and thermodynamic analysis. *Biochemistry* **2003**, *42*, 9028–9040.

116 K. M. Flaherty, C. Deluca-Flaherty, and D. B. McKay. Three-dimensional structure of the ATPase fragment of a 70K heat-shock cognate protein. *Nature* **1990**, *346*, 623–628.

117 A. Mally, and S. N. Witt. GrpE accelarates peptide binding and release from the high affinity state of DnaK. *Nat Struct Biol*. **2001**, *8*, 254–257.

118 W. Han, and P. Christen. Interdomain communication in the molecular chaperone DnaK. *Biochem J* **2003**, *369*, 627–634.

119 J. Höhfeld, and S. Jentsch. GrpE-like regulation of the Hsc70 chaperone by the anti-apoptotic protein BAG-1. *EMBO J*. **1997**, *16*, 6209–6216.

120 H. Sondermann, C. Scheufler, C. Scheider, J. Höhfeld, F.-U. Hartl, and I. Moarefi. Structure of a Bag/Hsc70 Complex: Convergent functional evolution of Hsp70 nucleotide exchange factors. *Science* **2001**, *291*, 1553–1557.

121 K. Briknarova, S. Takayama, L. Brive, et al. Structural analysis of BAG1 cochaperone and its interactions with Hsc70 heat shock protein. *Nat Struct Biol* **2001**, *8*, 349–352.

122 S. Takayama, T. Sato, S. Krajewski, K. Kochel, S. Irie, J. A. Millan, and J. C. Reed. Cloning and Functional Analysis of BAG-1: A Novel Bcl-2-Binding Protein with Anti-Cell Death Activity. *Cell* **1995**, *80*, 279–284.

123 H.-G. Wang, S. Takayam, U. R. Rapp, and J. C. Reed. Bcl-2 interacting protein, BAG-1, binds to and activates the kinase Raf-1. *Proc. Natl. Acad. Sci. USA* **1996**, *93*, 7063–7068.

124 M. Zeiner, and U. Gehring. A protein that interacts with members of the nuclear hormone receptor family: Identification and cDNA cloning. *Proc. Natl. Acad. Sci. USA* **1995**, *92*, 11465–11469.

125 A. Bardelli, P. Longati, D. Alberto, S. Goruppi, C. Schneider, C. Ponzetto, and P. M. Comoglio. HGF receptor associates with the anti-apoptotic protein BAG-1 and prevents cell death. *EMBO J*. **1996**, *15*, 6205–6212.

126 C. V. Clevenger, K. Thickman, W. Ngo, W. P. Chang, S. Takayama, and J. C. Reed. Role of Bag-1 in the survival and proliferation of the cytokine-dependent lymphocyte lines, Ba/F3 ad Nb2. *Mol Endocrinol* **1997**, *11*, 608–618.

127 M. Zeiner, M. Gebauer, and U. Gehring. Mammalian protein RAP46: an interaction partner and modulator of 70 kDa heat shock proteins. *EMBO J*. **1997**, *16*, 5483–5490.

128 J. Schneikert, S. Hubner, E. Martin, and A. C. Cato. A nuclear action of the eukaryotic cochaperone RAP46 in downregulation of glucocorticoid receptor activity. *J Cell Biol* **1999**, *146*, 929–940.

129 J. Lüders, J. Demand, and J. Höhfeld. The ubiquitin-related BAG-1 provides a link between the molecular chaperones Hsc70/Hsp70 and the proteasome. *J. Biol. Chem.* **2000**, *275*, 4613–4617.

130 S. Takayama, and J. C. Reed. Molecular chaperone targeting and regulation by BAG family proteins. *Nat Cell Biol* **2001**, *3*, E237–241.

131 S. Takayama, Z. Xie, and J. C. Reed. An evolutionarily conserved family of Hsp70/Hsc70 molecular chaperone regulators. *J Biol Chem* **1999**, *274*, 781–786.

132 K. Thress, J. Song, R. I. Morimoto, and S. Kornbluth. Reversible inhibition of Hsp70 chaperone function by Scythe and Reaper. *EMBO J*. **2001**, *20*, 1033–1041.

133 X. Yang, G. Chernenko, Y. Hao, Z. Ding, M. M. Pater, A. Pater, and S. C. Tang. Human BAG-1/RAP46 protein is generated as four isoforms by alternative translation initiation and overexpressed in cancer cells. *Oncogene* **1998**, *17*, 981–989.

134 S. Takayama, S. Krajewski, M. Krajewski, et al. Expression and

location of Hsp70/Hsc-binding anti-apoptotic protein BAG-1 and its variants in normal tissues and tumor cell lines. *Cancer Res.* **1998**, *58*, 3116–3131.

135 U. Schmidt, G. M. Wochnik, M. C. Rosenhagen, J. C. Young, F. U. Hartl, F. Holsboer, and T. Rein. Essential Role of the Unusual DNA-binding Motif of BAG-1 for Inhibition of the Glucocorticoid Receptor. *J Biol Chem* **2003**, *278*, 4926–4931.

136 M. Zeiner, Y. Niyaz, and U. Gehring. The hsp70-associating protein Hap46 binds to DNA and stimulates transcription. *Proc Natl Acad Sci USA* **1999**, *96*, 10194–10199.

137 A. Crocoll, J. Schneikert, S. Hubner, E. Martin, and A. C. Cato. BAG-1M: a potential specificity determinant of corticosteroid receptor action. *Kidney Int* **2000**, *57*, 1265–1269.

138 D. Bimston, J. Song, D. Winchester, S. Takayama, J. C. Reed, and R. I. Morimoto. BAG-1, a negative regulator of Hsp70 chaperone activity, uncouples nucleotide hydrolysis from substrate release. *EMBO J.* **1998**, *17*, 6871–6878.

139 J. Lüders, J. Demand, S. Schönfelder, M. Frien, R. Zimmermann, and J. Höhfeld. Cofactor-Induced Modulation of the Functional Specificity of the Molecular Chaperone Hsc70. *Biol. Chem.* **1998**, *379*, 1217–1226.

140 E. A. A. Nollen, J. F. Brunsting, J. Song, H. H. Kampinga, and R. I. Morimoto. Bag1 functions in vivo as a negative regulator of Hsp70 chaperone activity. *Mol Cell Biol.* **2000**, *20*, 1083–1088.

141 S. Takayama, D. N. Bimston, S.-i. Matsuzawa, B. C. Freeman, C. Aime-Sempe, Z. Xie, R. I. Morimoto, and J. C. Reed. BAG-1 modulates the chaperone activity of Hsp70/Hsc70. *EMBO J.* **1997**, *16*, 4887–4896.

142 K. C. Kanelakis, Y. Morishima, K. D. Dittmar, M. d. Galigniana, S. Takayama, J. C. Reed, and W. B. Pratt. Differential effects of the hsp70-binding protein BAG-1 on glucocorticoid receptor folding by the hsp90-based chaperone machinery. *J. Biol. Chem.* **1999**, *274*, 34134–34140.

143 M. Kabani, J. M. Beckerich, and C. Gaillardin. Sls1p stimulates Sec63p-mediated activation of Kar2p in a conformation-dependent manner in the yeast endoplasmic reticulum. *Mol Cell Biol* **2000**, *20*, 6923–6934.

144 K. T. Chung, Y. Shen, and L. M. Hendershot. BAP, a mammalian BiP-associated protein, is a nucleotide exchange factor that regulates the ATPase activity of BiP. *J Biol Chem* **2002**, *277*, 47557–47563.

145 M. Kabani, J. M. Beckerich, and J. L. Brodsky. Nucleotide exchange factor for the yeast Hsp70 molecular chaperone Ssa1p. *Mol Cell Biol* **2002**, *22*, 4677–4689.

146 M. Kabani, C. McLellan, D. A. Raynes, V. Guerriero, and J. L. Brodsky. HspBP1, a homologue of the yeast Fes1 and Sls1 proteins, is an Hsc70 nucleotide exchange factor. *FEBS Lett* **2002**, *531*, 339–342.

147 J. P. Grimshaw, I. Jelesarov, H. J. Schönfeld, and P. Christen. Reversible thermal transition in GrpE, the nucleotide exchange factor of the DnaK heat-shock system. *J. Biol. Chem.* **2001**, *276*, 6098–6104.

148 J. P. Grimshaw, I. Jelesarov, R. K. Siegenthaler, and P. Christen. Thermosensor Action of GrpE: The DnaK chaperone system at heat shock temperatures. *J Biol Chem* **2003**, *278*, 19048–19053.

149 Y. Groemping, and J. Reinstein. Folding properties of the nucleotide exchange factor GrpE from Thermus thermophilus: GrpE is a thermosensor that mediates heat shock response. *J Mol Biol* **2001**, *314*, 167–178.

150 A. D. Gelinas, K. Langsetmo, J. Toth, K. A. Bethoney, W. F. Stafford, and C. J. Harrison. A structure-based interpretation of E. coli GrpE thermodynamic properties. *J Mol Biol* **2002**, *323*, 131–142.

151 A. D. Gelinas, J. Toth, K. A. Bethoney, K. Langsetmo, W. F. Stafford, and C. J. Harrison. Thermodynamic linkage in the GrpE

nucleotide exchange factor, a molecular thermosensor. *Biochemistry* **2003**, *42*, 9050–9059.

152 L. D. D'Andrea, and L. Regan. TPR proteins: the versatile helix. *Trends Biochem Sci* **2003**, *28*, 655–662.

153 S. Chen, and D. F. Smith. Hop as an Adaptor in the Heat Shock Protein 70 (Hsp70) and Hsp90 Chaperone Machinery. *J. Biol. Chem.* **1998**, *273*, 35194–35200.

154 S. Tobaben, P. Thakur, R. Fernandez-Chacon, T. C. Sudhof, J. Rettig, and B. Stahl. A trimeric protein complex functions as a synaptic chaperone machine. *Neuron* **2001**, *31*, 987–999.

155 J. C. Young, N. J. Hoogenraad, and F. U. Hartl. Molecular chaperones Hsp90 and Hsp70 deliver preproteins to the mitochondrial import receptor Tom70. *Cell* **2003**, *112*, 41–50.

156 J. C. Young, J. M. Barral, and F. Ulrich Hartl. More than folding: localized functions of cytosolic chaperones. *Trends Biochem Sci* **2003**, *28*, 541–547.

157 J. Höhfeld, Y. Minami, and F. U. Hartl. Hip, a novel cochaperone involved in the eukaryotic Hsc70/Hsp40 reaction cycle. *Cell* **1995**, *83*, 589–598.

158 J. Frydman, and J. Hohfeld. Chaperones get in touch: the Hip-Hop connection. *Trends Biochem Sci* **1997**, *22*, 87–92.

159 V. Prapapanich, S. Chen, S. Nair, R. Rimerman, and D. Smith. Molecular cloning of human p48, a transient component of progesterone receptor complexes and an Hsp70-binding protein. *Mol Endocrinol.* **1996**, *10*, 420–431.

160 H. Irmer, and J. Höhfeld. Characterization of Functional Domains of the Eukaryotic Co-chaperone Hip. *J. Biol. Chem.* **1997**, *272*, 2230–2235.

161 F. Vignols, N. Mouaheb, D. Thomas, and Y. Meyer. Redox control of Hsp70-Co-chaperone interaction revealed by expression of a thioredoxin-like Arabidopsis protein. *J Biol Chem* **2003**, *278*, 4516–4523.

162 M. A. Webb, J. M. Cavaletto, P. Klanrit, and G. A. Thompson. Orthologs in Arabidopsis thaliana of the Hsp70 interacting protein Hip. *Cell Stress Chaperones* **2001**, *6*, 247–255.

163 M. Velten, B. O. Villoutreix, and M. M. Ladjimi. Quaternary structure of HSC70 cochaperone HIP. *Biochemistry* **2000**, *39*, 307–315.

164 B. D. Bruce, and J. Churchich. Characterization of the molecular-chaperone function of the heat-shock-cognate-70-interacting protein. *Eur. J. Biochem.* **1997**, *245*, 738–744.

165 K. C. Kanelakis, P. J. Murphy, M. D. Galigniana, Y. Morishima, S. Takayama, J. C. Reed, D. O. Toft, and W. B. Pratt. hsp70 interacting protein Hip does not affect glucocorticoid receptor folding by the hsp90-based chaperone machinery except to oppose the effect of BAG-1. *Biochemistry* **2000**, *39*, 14314–14321.

166 E. A. Nollen, A. E. Kabakov, J. F. Brunsting, B. Kanon, J. Hohfeld, and H. H. Kampinga. Modulation of in vivo HSP70 chaperone activity by Hip and Bag-1. *J Biol Chem* **2001**, *276*, 4677–4682.

167 F. A. Agarraberes, and J. F. Dice. A molecular chaperone complex at the lysosomal membrane is required for protein translocation. *J Cell Sci* **2001**, *114*, 2491–2499.

168 G. H. Fan, W. Yang, J. Sai, and A. Richmond. Hsc/Hsp70 interacting protein (hip) associates with CXCR2 and regulates the receptor signaling and trafficking. *J Biol Chem* **2002**, *277*, 6590–6597.

169 C. Nicolet, and E. Craig. Isolation and characterization of STI1, a stress-inducible gene from *Saccharomyces cerevisiae*. *Mol Cell Biol.* **1989**, *9*, 3638–3646.

170 D. F. Smith, W. P. Sullivan, T. N. Marion, K. Zaitsu, B. Madden, D. J. McCormick, and D. O. Toft. Identification of a 60-Kilodalton Stress-Related Protein, p60, which interacts with hsp90 and hsp70. *Mol Cell Biol.* **1993**, *13*, 869–876.

171 C. Scheufler, A. Brinker, G.

Bourenkov, S. Pegoraro, L. Moroder, H. Bartunik, F. U. Hartl, and I. Moarefi. Struture of TPR domain-peptide complexes: critical elements in the assembly of the Hsp70-Hsp90 multichaperone machine. *Cell* **2000**, *101*, 199–210.

172 A. Brinker, C. Scheufler, F. Von Der Mulbe, B. Fleckenstein, C. Herrmann, G. Jung, I. Moarefi, and F. U. Hartl. Ligand discrimination by TPR domains. Relevance and selectivity of EEVD-recognition in Hsp70 × Hop × Hsp90 complexes. *J Biol Chem* **2002**, *277*, 19265–19275.

173 O. O. Odunuga, J. A. Hornby, C. Bies, R. Zimmermann, D. J. Pugh, and G. L. Blatch. Tetratricopeptide repeat motif-mediated Hsc70-mSTI1 interaction. Molecular characterization of the critical contacts for successful binding and specificity. *J Biol Chem* **2003**, *278*, 6896–6904.

174 M. Gross, and S. Hessefort. Purification and Characterization of a 66-kDa Protein from Rabbit Reticulocyte Lysate which Promotes the Recycling of Hsp70. *J. Biol. Chem.* **1996**, *271*, 16833–16841.

175 H. Wegele, M. Haslbeck, J. Reinstein, and J. Buchner. Sti1 is a novel activator of the Ssa proteins. *J Biol Chem* **2003**, *278*, 25970–25976.

176 A. Brychzy, T. Rein, K. F. Winklhofer, F. U. Hartl, J. C. Young, and W. M. Obermann. Cofactor Tpr2 combines two TPR domains and a J domain to regulate the Hsp70/Hsp90 chaperone system. *Embo J* **2003**, *22*, 3613–3623.

177 Y. Morishima, K. C. Kanelakis, A. M. Silverstein, K. D. Dittmar, L. Estrada, and W. B. Pratt. The Hsp organizer protein Hop enhances the rate of but is not essential for glucocorticoid receptor folding by the multiprotein Hsp90-based chaperone system. *J. Biol. Chem.* **2000**, *275*, 6894–6900.

178 P. J. Murphy, K. C. Kanelakis, M. D. Galigniana, Y. Morishima, and W. B. Pratt. Stoichiometry, abundance, and functional significance of the hsp90/hsp70-based multiprotein chaperone machinery in reticulocyte lysate. *J Biol Chem* **2001**, *276*, 30092–30098.

179 K. Richter, and J. Buchner. Hsp90: chaperoning signal transduction. *J Cell Physiol* **2001**, *188*, 281–290.

180 J. C. Young, I. Moarefi, and F. U. Hartl. Hsp90: a specialized but essential protein-folding tool. *J Cell Biol* **2001**, *154*, 267–273.

181 K. Richter, P. Muschler, O. Hainzl, J. Reinstein, and J. Buchner. Sti1 is a non-competitive inhibitor of the Hsp90 ATPase. Binding prevents the N-terminal dimerization reaction during the atpase cycle. *J Biol Chem* **2003**, *278*, 10328–10333.

182 C. Prodromou, G. Siligardi, R. O'Brien, D. N. Woolfson, L. Regan, B. Panaretou, J. E. Ladbury, P. W. Piper, and L. H. Pearl. Regulation of Hsp90 ATPase activity by tetratricopeptide repeat (TPR)-domain co-chaperones. *EMBO J.* **1999**, *18*, 754–762.

183 L. Aravind, and E. V. Koonin. The U box is a modified RING finger – a common domain in ubiquitination. *Curr Biol* **2000**, *10*, R132–134.

184 C. A. Ballinger, P. Connell, Y. Wu, Z. Hu, L. J. Thompson, L. Y. Yin, and C. Patterson. Identification of CHIP, a novel tetratricopeptide repeat-containing protein that interacts with heat shock proteins and negatively regulates chaperone functions. *Mol Cell Biol* **1999**, *19*, 4535–4545.

185 J. Yan, J. Wang, Q. Li, J. R. Hwang, C. Patterson, and H. Zhang. AtCHIP, a U-box-containing E3 ubiquitin ligase, plays a critical role in temperature stress tolerance in Arabidopsis. *Plant Physiol* **2003**, *132*, 861–869.

186 R. Nikolay, T. Wiederkehr, W. Rist, G. Kramer, M. P. Mayer, and B. Bukau. Dimerization of the human E3 ligase, CHIP, via a coiled-coil domain is essential for its activity. *J Biol Chem* **2004**, *279*, 2673–2678.

187 J. Demand, S. Alberti, C. Patterson, and J. Hohfeld. Cooperation of a ubiquitin domain protein and an E3 ubiquitin ligase during chaperone/

proteasome coupling. *Curr Biol* **2001**, *11*, 1569–1577.

188 S. Hatakeyama, M. Yada, M. Matsumoto, N. Ishida, and K. I. Nakayama. U box proteins as a new family of ubiquitin-protein ligases. *J Biol Chem* **2001**, *276*, 33111–33120.

189 J. Jiang, C. A. Ballinger, Y. Wu, Q. Dai, D. M. Cyr, J. Hohfeld, and C. Patterson. CHIP is a U-box-dependent E3 ubiquitin ligase: Identification of Hsc70 as a target for ubiquitylation. *J Biol Chem* **2001**, *13*, 13.

190 S. Murata, Y. Minami, M. Minami, T. Chiba, and K. Tanaka. CHIP is a chaperone-dependent E3 ligase that ubiquitylates unfolded protein. *EMBO Rep* **2001**, *2*, 1133–1138.

191 D. M. Cyr, J. Hohfeld, and C. Patterson. Protein quality control: U-box-containing E3 ubiquitin ligases join the fold. *Trends Biochem Sci* **2002**, *27*, 368–375.

192 T. Wiederkehr, B. Bukau, and A. Buchberger. Protein turnover: a CHIP programmed for proteolysis. *Curr Biol* **2002**, *12*, R26–28.

193 P. Connell, C. A. Ballinger, J. Jiang, Y. Wu, L. J. Thompson, J. Hohfeld, and C. Patterson. The co-chaperone CHIP regulates protein triage decisions mediated by heat-shock proteins. *Nat Cell Biol* **2001**, *3*, 93–96.

194 G. C. Meacham, C. Patterson, W. Zhang, J. M. Younger, and D. M. Cyr. The Hsc70 co-chaperone CHIP targets immature CFTR for proteasomal degradation. *Nat Cell Biol.* **2001**, *3*, 100–105.

195 W. Xu, M. Marcu, X. Yuan, E. Mimnaugh, C. Patterson, and L. Neckers. Chaperone-dependent E3 ubiquitin ligase CHIP mediates a degradative pathway for c-ErbB2/Neu. *Proc Natl Acad Sci USA* **2002**, *99*, 12847–12852.

196 P. Zhou, N. Fernandes, I. L. Dodge, et al. ErbB2 degradation mediated by the co-chaperone protein CHIP. *J Biol Chem* **2003**, *278*, 13829–13837.

197 M. J. Lees, D. J. Peet, and M. L. Whitelaw. Defining the role for XAP2 in stabilization of the dioxin receptor. *J Biol Chem* **2003**, *278*, 35878–35888.

198 A. T. Chavez Zobel, A. Loranger, N. Marceau, J. R. Theriault, H. Lambert, and J. Landry. Distinct chaperone mechanisms can delay the formation of aggresomes by the myopathy-causing R120G alphaB-crystallin mutant. *Hum Mol Genet* **2003**, *12*, 1609–1620.

199 S. Alberti, J. Demand, C. Esser, N. Emmerich, H. Schild, and J. Hohfeld. Ubiquitylation of BAG-1 suggests a novel regulatory mechanism during the sorting of chaperone substrates to the proteasome. *J Biol Chem* **2002**, *277*, 45920–45927.

200 J. Jiang, D. Cyr, R. W. Babbitt, W. C. Sessa, and C. Patterson. Chaperone-dependent regulation of endothelial nitric-oxide synthase intracellular trafficking by the co-chaperone/ubiquitin ligase CHIP. *J Biol Chem* **2003**, *278*, 49332–49341.

201 Q. Dai, C. Zhang, Y. Wu, et al. CHIP activates HSF1 and confers protection against apoptosis and cellular stress. *EMBO J* **2003**, *22*, 5446–5458.

202 M. P. Deutscher (ed) *Guide to protein purification* Vol. 182. Methods in Enzymology. Edited by J. N. Abelson, and M. I. Simon, Academic Press. Inc., San Diego, **1990**.

203 W. J. Welch, and J. R. Feramisco. Rapid Purification of Mammalian 70,000-Dalton Stress Proteins: Affinity of the Proteins for Nucleotides. *Mol. Cell. Biol.* **1985**, *5*, 1229–1237.

204 D. M. Schlossman, S. L. Schmid, W. A. Braell, and J. E. Rothman. An Enzyme that Removes Clathrin Coats: Purification of an Uncoating ATPase. *J. Cell Biol.* **1984**, *99*, 723–733.

205 J. V. Anderson, D. W. Haskell, and C. L. Guy. Differential influence of ATP on native spinach 70-kilodalton heat-shock cognates. *Plant Physiol* **1994**, *104*, 1371–1380.

206 L. E. S. Vickery, Jonathan J. and Ta, Dennis T. Hsc66 and Hsc20, a new

heat shock cognate molecular chaperone system from *Escherichia coli*. *Protein Sci*. **1997**, *6*, 1047–1056.

207 M. Zylicz, D. Ang, K. Liberek, and C. Georgopoulos. Initiation of λ DNA replication with purified host- and bacteriophage-encoded proteins: the role of the DnaK, DnaJ and GrpE heat shock proteins. *EMBO J*. **1989**, *8*, 1601–1608.

208 J. Spence, A. Cegielska, and C. Georgopoulos. Role of *Escherichia coli* heat shock proteins DnaK and HtpG (C62.5) in response to nutritional deprivation. *J. Bacteriol* **1990**, *172*, 7157–7166.

209 B. Bukau, and G. Walker. Mutations altering heat shock specific subunit of RNA polymerase suppress major cellular defects of *E. coli* mutants lacking the DnaK chaperone. *EMBO J*. **1990**, *9*, 4027–4036.

210 J. Buchner, T. Weikl, H. Bugl, F. Pirkl, and S. Bose. Purification of Hsp90 partner proteins Hop/p60, p23, and FKBP52. *Methods Enzymol* **1998**, *290*, 418–429.

211 B. Miao, J. E. Davis, and E. A. Craig. Mge1 functions as a nucleotide release factor for Ssc1, a mitochondrial Hsp70 of *Saccharomyces cerevisiae*. *J. Mol. Biol*. **1997**, *265*, 541–552.

212 H. C. Schneider, B. Westermann, W. Neupert, and M. Brunner. The nucleotide exchange factor MGE exerts a key function in the ATP-dependent cycle of mt-Hsp70-Tim44 interaction driving mitochondrial protein import. *Embo J* **1996**, *15*, 5796–5803.

213 S. Schmidt, A. Strub, K. Rottgers, N. Zufall, and W. Voos. The two mitochondrial heat shock proteins 70, Ssc1 and Ssq1, compete for the cochaperone Mge1. *J Mol Biol* **2001**, *313*, 13–26.

214 D. A. Raynes, and V. Guerriero, Jr. Inhibition of Hsp70 ATPase Activity and Protein Renaturation by a Novel Hsp70-binding Protein. *J. Biol. Chem*. **1998**, *273*, 32883–32888.

215 A. Boisramé, M. Kabani, J. M. Beckerich, E. Hartmann, and C. Gaillardin. Interaction of Kar2p and Sls1p is required for efficient co-translational translocation of secreted proteins in the yeast Yarrowia lipolytica. *J Biol Chem* **1998**, *273*, 30903–30908.

216 N. Guex, and M. C. Peitsch. SWISS-MODEL and the Swiss-PdbViewer: An environment for comparative protein modelling. *Electrophoresis* **1997**, *18*, 2714–2723.

217 M. C. Peitsch. Protein modeling by E-mail. *Bio/Technology* **1995**, *13*, 658–660.

218 M. C. Peitsch. ProMod and Swiss-Model: Internet-based tools for automated comparative protein modelling. *Biochem. Soc. Trans*. **1996**, *24*, 274–279.

219 D. Brehmer, C. Gässler, W. Rist, M. P. Mayer, and B. Bukau. Influence of GrpE on DnaK-substrate interactions. *J Biol Chem* **2004**, *279*, 27957–27964.

16
Protein Folding in the Endoplasmic Reticulum Via the Hsp70 Family

Ying Shen, Kyung Tae Chung, and Linda M. Hendershot

16.1
Introduction

The endoplasmic reticulum (ER) is a membrane-enclosed organelle that is found in all eukaryotic organisms and that represents the entry site or origin of the secretory pathway. As such, the ER is a major site of protein folding and assembly. In some highly specialized secretory cells – such as immunoglobulin-producing plasma cells, serum-protein-producing liver cells, or insulin-producing pancreatic cells – the ER is highly developed and becomes the major site of protein biosynthesis for the cell. Proteins that are destined for the secretory pathway are synthesized in the cytosol on ER-associated ribosomes. A hydrophobic signal sequence present on the nascent polypeptide chain directs it to the translocon, which is a proteinaceous channel that traverses the ER membrane [108], allowing the protein to be translocated into the lumen of the ER, in many cases as it is being synthesized. The elongating nascent chain first passes through a channel in the ribosome and then through the translocon. This requires that ~70 amino acids of the nascent chain be translated before the N-terminus can enter the ER lumen [51]. It appears that the growing polypeptide chain remains unfolded during its transit through the ribosome and translocon [123, 216]. After it enters the ER, N-terminal signal sequences are often removed by a signal peptidase that is positioned at the lumenal side of the translocon. Once the site is ~14 amino acids into the lumen, *N*-linked glycans are added co-translationally by oligosaccharyl transferase (OST) to asparagine residues that are followed by a second amino acid, which can be anything but a proline, and then a serine or a threonine (N-X-S/T) [216]. The OST complex is also associated with the translocon. Inside the ER, the polypeptide chain begins folding co-translationally [7, 38], and in some cases, subunit assembly can occur before the individual chains are completely translated and inside the ER [8].

The modification of secretory pathway proteins with *N*-linked glycans serves in part to limit the ways the nascent protein can fold. In addition, the ER environment itself causes further constraints on and benefits to protein folding and assembly. The calcium required for many signal transduction pathways is stored here. Thus, proteins that are synthesized in this organelle have evolved to fold

Protein Folding Handbook. Part II. Edited by J. Buchner and T. Kiefhaber

ISBN: 3-527-30784-2

and assemble in a high calcium environment, and changes in the ER calcium levels can dramatically affect their folding [128]. Like the extracellular space that it is contiguous with, the ER also possesses an oxidizing environment [104]. This allows disulfide bonds to form between juxtaposed cysteine residues, which can serve to stabilize folded regions of the nascent chain. However, in the crowded environment of the ER lumen, where large numbers of unfolded polypeptide chains are being synthesized, the formation of disulfide bonds between the wrong regions of a protein or even between unrelated proteins could lead to the formation of large, insoluble aggregates. Surprisingly, this rarely occurs under normal conditions.

The high fidelity of protein folding in the ER is due to a stringent quality-control apparatus [58, 85]. Newly synthesized proteins are carefully scrutinized by two major families of molecular chaperones: the Hsp70 cognate BiP and the resident lectin-like proteins calnexin and calreticulin. Only when all aspects of an unfolded state have disappeared do the chaperones cease binding, and the newly synthesized protein is allowed to exit the ER for transport to the Golgi for further routing along the secretory pathway. Proteins that do not meet the stringent requirements of this quality-control system are retained in the ER, where molecular chaperones prevent them from aggregating and provide them with additional opportunities to achieve their correct conformation. Proteins that ultimately fail to mature properly are targeted for intracellular degradation by the 26S proteasome [86, 105, 214]. The regulated and carefully controlled assembly of subunit proteins into larger complexes also occurs in the ER and is monitored by the same quality-control apparatus.

16.2
BiP Interactions with Unfolded Proteins

Immunoglobulin heavy-chain-binding protein (BiP), the first component of the ER quality-control apparatus to be identified, was found by virtue of its association with the unassembled, non-transported heavy chains produced in pre-B cell lines [80]. BiP was subsequently shown to interact transiently with Ig assembly intermediates in mouse plasmacytoma lines, but not with completely assembled H_2L_2 molecules [17], and later was shown to interact with numerous other unfolded, unassembled, and misfolded proteins [74]. The presence of a tetrapeptide sequence (KDEL) at the extreme C-terminus of BiP prevents it from being transported further along the secretory pathway [156]. A receptor for the KDEL sequence exists in the intermediate compartment and *cis* Golgi and serves to redirect any KDEL-containing proteins, along with the unfolded proteins they carry with them, back to the ER [134, 135]. Like all Hsp70 proteins, BiP possesses an N-terminal ATPase domain that is crucial to its chaperoning activity [73, 96, 115, 207] and a C-terminal protein-binding domain that recognizes unfolded polypeptides [32, 97]. BiP homologues have now been identified in the ER of all eukaryotic organisms that have been examined, and the yeast protein Kar2p is an essential gene [180]. In addition to playing a role in protein folding in the yeast ER, Kar2p is also required for trans-

location of proteins into the ER lumen [23, 24, 208] and for degradation [25, 161] as described below.

Clues as to how BiP might recognize so many different proteins first came from studies showing that peptides of at least seven amino acids in length and composed of predominantly aliphatic residues were more likely to bind BiP and stimulate its ATPase activity than were those containing mostly hydrophilic or charged residues [65, 66]. By scanning known proteins for seven amino acid sequences that were enriched in hydrophobic residues, the authors were able to conclude that a ''potential'' BiP-binding site might occur about every 16 amino acids on most globular proteins! The makeup of the ''BiP-binding sequence'' was confirmed and extended when a peptide display library was used to elucidate the peptide sequences that could bind to BiP. A composite heptameric sequence, Hy-X-Hy-X-Hy-X-Hy, was derived from this data, where Hy is a bulky aromatic or hydrophobic residue and X is any amino acid [14]. The alternating pattern of Hy residues in the binding motif is compatible with BiP binding to proteins when they are in an extended conformation, causing the bulky aromatic/hydrophobic side chains to lie on one side of the protein and to presumably point into the protein-binding site on BiP. The results of these two studies further suggested that BiP would bind to hydrophobic stretches on nascent or unassembled polypeptides, which would become inaccessible after folding and assembly were complete. Studies that monitored the oxidation state of the vesicular stomatitis virus G-protein [140] or of Ig light chains [96, 119] as an indication of their folding status demonstrated that BiP bound to regions of the protein that were not yet oxidized and that loss of BiP binding corresponded to the protein achieving a completely oxidized state.

BiP's ability to bind and release substrate proteins is nucleotide-dependent, a feature that is conserved with all Hsp70 family members. The ATPase cycle has been described in great detail for bacterial and cytosolic family members and works as follows. Hsp70 associates best with client proteins when it is in the ATP-bound state. DnaJ proteins bind and catalyze the rapid hydrolysis of ATP to ADP [136], ''locking'' the Hsp70 protein onto the unfolded substrate. The next step involves the exchange of ATP back into the nucleotide binding cleft, which ''reopens'' the Hsp70 protein, thereby releasing the substrate protein and giving it an opportunity to fold. In bacteria and mitochondria, GrpE proteins regulate nucleotide exchange [136]. Mammalian GrpE homologues have not been identified in other organelles, but several other cytosolic proteins have been identified that play various roles in controlling nucleotide exchange [37, 78, 100, 101, 199]. Very recently, ER-localized nucleotide-releasing factors were identified in yeast [16, 206] and mammals [43].

BiP binds both to normal proteins that have not completely folded or assembled [17, 80] and to mutant proteins that are unable to fold [74]. BiP release is dependent on its ability to bind ATP and undergo a conformational change, thus altering the protein-binding domain so that the unfolded protein can be released and given the opportunity to fold. The premature release of T cell receptor subunits from BiP can be achieved in vivo by depleting calcium from the ER, which results in BiP release and the inappropriate secretion of individual subunits [194]. Alternatively, depletion of ATP from the ER with the drug CCCP results in prolonged association

of proteins with BiP and a block in their secretion [55]. However, it does not appear that BiP release is the only requirement for all proteins to fold properly. While the in vitro release of BiP from Ig light chains with ATP can lead to folding and disulfide bond formation [119], a similar release of BiP from Ig heavy chains results in the formation of large aggregates [207]. Thus, individual properties of proteins dictate whether they will be able to fold upon BiP release. Given estimates on molecular crowding inside the cell and the subsequent effects crowding can have on protein folding [142], it is reasonable to assume that BiP release might be a tightly regulated process in vivo. Data to support this idea came from studies to measure the rate of BiP cycling on and off unassembled Ig heavy chains. Both wild-type and ATPase-defective hamster BiP were co-expressed with Ig heavy chains under conditions where heavy chains bound equally to both wild-type and mutant BiP during a short pulse [207]. The mutant BiP was expected to act as a kinetic trap by binding to nascent heavy chains but not leasing them, whereas the wild-type BiP should release during its normal course of cycling. Each time the wild-type BiP releases, it should be replaced half the time by another wild-type BiP and the other half by a mutant. Eventually, and under steady-state conditions, all the heavy chains should be bound to mutant BiP. Instead, the study revealed that heavy chains remained bound to both wild-type and mutant BiP and that the ratio of the two types of BiP did not change over a long chase period [207]. However, introduction of light chains rapidly displaced wild-type but not mutant BiP, suggesting that the ATPase cycle of BiP is ''stalled'' when heavy chains are expressed alone and that assembly with light chains either releases a repressive factor or allows access of a stimulatory factor. This further suggests that the substrate itself can play a role in contributing to the release of BiP or the rate at which the ATPase cycle turns.

Although peptide-binding preferences for BiP have been determined, relatively little is known about actual BiP-binding sites on proteins. Early studies to identify the BiP-binding site on unassembled Ig heavy chains revealed that for all isotypes, the C_H1 domain, which pairs with Ig light chains, possesses the ''stable'' BiP-binding site [95]. A more recent study revealed that, unlike other domains on the heavy chain, the C_H1 domain remains unfolded until it assembles with light chains [131], thus providing a long-term BiP-binding site. An algorithm based on the binding of BiP to peptides displayed on bacterial phages [14] was applied to Ig domains, where it was found that each Ig domain possessed multiple potential BiP-binding sites [118]. Peptides corresponding to these sequences did indeed stimulate the ATPase activity of BiP, demonstrating that they were capable of binding to the chaperone. The more rapid folding of other domains probably accounts for the fact that BiP associates only transiently with them [112] or, in some cases, that BiP fails to bind altogether [94]. The fact that multiple potential BiP-binding sites were identified on the C_H1 domain [118], even though BiP binds in a 1:1 stoichiometry to this domain in vivo [149], suggests either that the binding of BiP to one site precludes its binding to others or that the algorithm does not accurately identify BiP-binding sites that are used on proteins in vivo. Further studies are needed to determine which is correct.

In addition to BiP, both yeast and mammals possess a second ER-localized

Hsp70 family member, Lhs1p [48] and GRP170 [57], respectively, that is less well characterized than BiP. Lhs1p (also known as Cer1p and Ssi1p) is an Hsp70-related protein that appears to be important for the translocation of a subset of proteins into the ER of *S. cerevisiae* [81, 206]. Lhs1p/Cer1p possesses an ATP-binding site like Kar2p and other members of the Hsp70 family [82]. The *CER1* RNA levels increase during UPR activation [48] and at lower temperatures, which is in keeping with the more severe defects in folding and translocation that are observed in the Δ*cer* strain at low temperatures [82]. These results suggest that Lhs1p/Cer1p provides an additional chaperoning activity in processes known to require Kar2p. In mammalian cells, GRP170 has been identified as an ATP-binding Hsp70 homologue [57] that is induced by ER stress [138] and hypoxia, which has led to its alternative designation as oxygen-regulated protein ORP150 [114, 166]. GRP170 can be co-precipitated with unassembled Ig heavy chains [138], although it is not clear whether it binds to them directly or as a component of the multi-chaperone complex that was recently identified in the ER [149]. GRP170 shows sequence similarity to Lhs1p and may also play a role in the translocation of nascent polypeptides into the ER lumen [53].

16.3 ER-localized DnaJ Homologues

The ATPase activity of Hsp70 proteins is stimulated by interactions with DnaJ proteins. The first DnaJ was discovered in *Escherichia coli*, where it cooperates with DnaK to aid in lambda phage replication [222]. It is a 43-kDa protein containing four domains, beginning with the N-terminal, ~73-amino-acid J-domain, which is present in all DnaJ family members and contains the hallmark tripeptide HPD motif (His-Pro-Asp) [36, 116]. A flexible Gly/Phe-rich domain links the J-domain to a cysteine-rich Zn^{2+}-binding domain [4, 195]. Distal to the Cys-rich domain is a poorly conserved region that accounts for nearly half of the DnaJ molecule and that may contain the substrate-binding domain [98]. Presently, more than 100 DnaJ family members have been identified, which can be found in all species and organelles. They can be divided into three subgroups based upon the degree of domain conservation with *E. coli* DnaJ [98]. Type I DnaJ-like proteins have the highest domain homology with *E. coli* DnaJ and possess all four domains. Type II DnaJ proteins have an N-terminal J-domain and the Gly/Phe-rich linker but lack the Zn^{2+}-binding domain. Type III proteins possess only a J-domain, which can occur anywhere in the protein.

Organelle-specific DnaJs work as cofactors to cooperate with their specific Hsp70 partners, and, unlike Hsp70s, when multiple DnaJs are present in an organelle, each one often regulates a different function. The yeast ER contains three DnaJ-like proteins: Sec63p [182, 183], Jem1p [160], and Scj1p [186]. Sec63p and Jem1p are both type III DnaJ proteins [59, 160], whereas Scj1p is a type I protein [186]. Sec63p is an integral membrane protein possessing three transmembrane domains, with its J-domain in the ER lumen and a large C-terminal domain exposed

to the cytosol [59]. As one subunit of the ER translocon, Sec63p interacts with Sec61p, Sec62p, Sec71p, and Sec72p and recruits yeast BiP, Kar2p, to the lumenal side of the translocation apparatus [45]. Sec63p assists Kar2p in pulling nascent proteins into the ER lumen during both co-translational and posttranslational translocation [23, 145, 225]. Sec63p also appears to be a component of the retrograde translocon, which plays a role in removing terminally misfolded proteins from the ER for degradation by the 26S proteasome [171]. Unlike Sec63p, which is a membrane protein required for growth, Jem1p and Scj1p are both soluble ER lumenal proteins that are not essential for cell viability under normal growth conditions. However, a double disruption of the *JEM1* and *SCJ1* genes causes growth arrest at elevated temperatures. Jem1p interacts with Kar2p to mediate nuclear membrane fusion or karyogamy during mating [160], while Scj1p cooperates with Kar2p to fold and assemble proteins in the ER lumen [186]. Recent studies show that both Scj1p and Jem1p may also assist Kar2p in maintaining lumenal ERAD substrates in a retrotranslocation-competent state [161].

Recently, five mammalian ER DnaJ homologues have been identified. They appear to include two Sec63 homologues, one Scj1 homologue, and two novel eukaryotic family members (Table 16.1). However, no JEM homologues have been identified at this time. According to their order of discovery, we propose they be named ERdj1–5 for ER-associated DnaJ proteins. They are ERdj1/Mtj1 [22, 41], ERdj2/hSec63 [191, 205], ERdj3/HEDJ [127, 149, 226], ERdj4/Mdg1 [176, 188], and ERdj5/JPDI [52, 102]. All of the ERdjs contain a J-domain, which interacts with

Tab. 16.1. Identification and characterization of mammalian ER DnaJ proteins

ERdj protein	*M.W.*	*Yeast homol.*	*Topology*	*UPR induction*
ERdj1/Mtj1	63 kD	Sec63	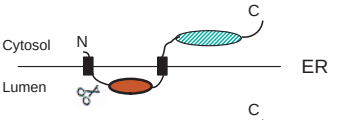	No
ERdj2/hSec63	85 kD	Sec63	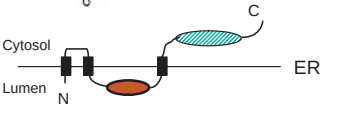	No
ERdj3/HEDJ	43 kD	Scj1	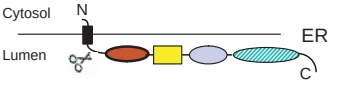	Yes
ERdj4/Mdg1	25 kD	none	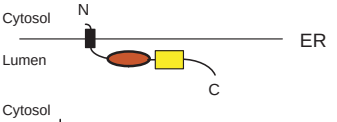	Yes
ERdj5/JPOI	96 kD	none	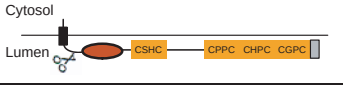	Yes

Signal peptide or TM
Cys-rich domain
J domain
Gly/Phe domain
CXXC thioredoxin, PDI-like domain
KDEL
C-term domain

BiP and stimulates its ATPase activity in vitro. Since mammalian BiP has multiple functions in the ER, it is possible that these ERdjs each regulate different BiP functions in vivo.

Like yeast Sec63p, ERdj1/Mtj1 (66 kDa) and ERdj2/hSec63 (97 kDa) are type III DnaJ proteins associated with the mammalian Sec61p complex in the ER membrane [56, 150, 205]. The N-terminal 190 amino acids of ERdj1/Mtj1 are oriented in the ER lumen and contain the J-domain, which could serve to recruit BiP to the translocon. A large C-terminal cytosolic domain is in close contact with SRP in the cytosol and appears to modulate translation [56]. Inspection of gene databases reveals that ERdj1/Mtj1 is highly conserved in mammals, with homologues present in *Drosophila melanogaster*, *Ciona intestinalis*, and *Anopheles gambiae*. ERdj2/hSec63 displays similar membrane topology and shares ~ 44% amino acid sequence similarity (~26% identity) with yeast Sec63p [191]. Like ERdj1/Mtj1, ERdj2/hSec63 is associated with Sec61 and Sec62, where it may act with BiP to translocate nascent polypeptides into the ER [150, 205]. ERdj2/hSec63 is expressed at relatively higher levels (1.98 μM) in pancreatic microsomes than is ERdj1/Mtj1 (0.36 μM) [56]. ERdj2/hSec63 homologues can also be found in organisms as diverse as *Arabidopsis thaliana*, *Caenorhabditis elegans*, *Neurospora crassa*, and *A. gambiae*.

ERdj3/HEDJ is a 43-kDa type I DnaJ protein that shows ~46% sequence similarity (~35% identity) to yeast Scj1p. Despite the absence of a KDEL retention signal, it appears to be a resident ER protein, although there is some controversy as to its intracellular localization [12, 127, 149, 226] and whether it is a membrane-anchored or soluble protein [127, 149, 226]. ERdj3/HEDJ was identified in association with Shiga toxin [226], which is taken up by the cell at the plasma membrane and passes through the ER before being retrotranslocated to the cytosol, where it performs its pathogenic function [107, 185]. The fact that ERdj3/HEDJ interacts with long-lived, BiP-bound, unassembled Ig heavy chains in vivo [149] suggests that it is likely to play a role in keeping nascent proteins from aggregating and in aiding protein folding and assembly. Alternatively, ERdj3 could act to target ERAD substrates to the retrotranslocon for degradation. Either function would be compatible with its association with Shiga toxin [226]. ERdj3 appears to be widely expressed, with highly homologous orthologs present in *D. melanogaster*, *C. elegans*, *Danio rerio*, *A. gambiae*, *A. thaliana*, and *Zea mays* in addition to yeast.

ERdj4/Mdg1 (26 kDa) is the first type II DnaJ homologue to be found in the ER of any organism [188]. It appears to be largely restricted to vertebrates, since no potential ERdj4 homologues could be found in the *D. melanogaster*, *C. elegans*, or *S. cerevisiae* genomic databases. ERdj4/Mdj1 is anchored in the ER membrane through its uncleaved signal peptide, thus orienting its J-domain and the rest of the protein inside the ER where it interacts with BiP [188]. However, another study using an N-terminal-tagged version of ERdj4/Mdg2 reported nuclear localization after heat shock and cytosolic expression before heat shock [176]. ERdj4 is expressed at the highest levels in secretory tissues and is highly induced by ER stress, suggesting that ERdj4/Mdj1 may play a role in either protein folding or ERAD [188]. Overexpression of ERdj4/Mdg1 inhibited cell death induced by ER stress [125], suggesting that it plays some protective role during the UPR.

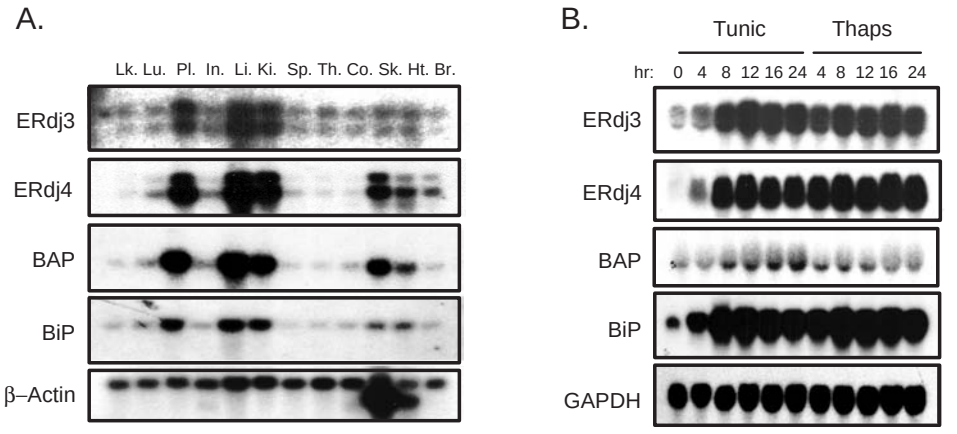

Fig. 16.1. Tissue distribution and ER stress inducibility of BiP and its cofactors. (A) A human multi-tissue Northern blot was hybridized with probes corresponding to the coding regions of human ERdj3, mouse ERdj4, human BAP, hamster BiP, and human β-actin genes. Lane 1: peripheral blood leukocytes; lane 2: lung; lane 3: placenta; lane 4: small intestine; lane 5: liver; lane 6: kidney; lane 7: spleen; lane 8: thymus; lane 9: colon; lane 10: skeletal muscle; lane 11: heart; lane 12: brain. (B) NIH3T3 fibroblasts were incubated with the ER stress-inducing agents tunicamycin or thapsigargin. RNA was isolated at the indicated times and subjected to Northern blot analyses using the indicated probes.

The last mammalian DnaJ homologue to be discovered, ERdj5/JPDI (87 kDa), contains a J-domain at its N-terminus, a PDI-like domain, a thioredoxin domain, and a KDEL sequence at its C-terminus [102]. This latter feature suggests that it is likely to be a soluble ER lumenal protein, although this has not been formally demonstrated. The presence of a thioredoxin-like domain suggests that ERdj5 may be involved in assisting protein folding and disulfide bond formation in the ER. Homologues of ERdj5/JPDI can also be found in *C. elegans*, *D. melanogaster*, *Ciona intestinalis*, and *A. gambiae*, but not in yeast or plants.

Like BiP and other ER chaperones, some of the ERdjs are also upregulated in response to ER stress. ERdj3 and ERdj4 transcripts are dramatically upregulated in response to UPR activation [188]. Combined with the fact that both are expressed at the highest levels in secretory tissues (Figure 16.1), it is likely that they play roles in either the refolding of unfolded proteins or the retrotranslocation of misfolded proteins, both of which diminish the accumulation of unfolded proteins that occurs in the ER during stress conditions. Inspection of genomic sequences upstream of these two genes reveals that *ERdj3/HEDJ* contains a putative ERSE element in its promoter, which could serve to regulate ERdj3 expression, but no potential ERSE can be found in the ERdj4 promoter. ERdj5/JPDI has been reported to contain one ERSE in its promoter and to respond to ER stress, albeit less dramatically than either ERdj3 or ERdj4 [52]. Unlike yeast Sec63, ERdj2/hSec63 is

not upregulated during ER stress [188]. This is compatible with the fact that translation and translocation of newly synthesized peptides slow down when mammalian cells encounter ER stress and that, unlike yeast, mammalian cells do not respond to ER stress by dramatically expanding the ER membranes [46, 203].

Because BiP has multiple functions in vivo and because a second Hsp70 homologue, GRP170/ORP150 [138], also exists in the mammalian ER, we anticipate that various ER DnaJ homologues will be specific to the different functions of the mammalian ER Hsp70s and that more ERdjs are therefore likely to be discovered. At present, little functional data are available for most of the mammalian ER DnaJs, and it is not known whether any of them interact with GRP170 in vivo.

16.4 ER-localized Nucleotide-exchange/releasing Factors

In order for Hsp70 proteins to be efficiently released from unfolded substrate proteins, ATP must replace ADP in the nucleotide-binding cleft. In bacteria, this feat is accomplished by the nucleotide-exchange factor GrpE, which binds to the ATPase domain of DnaK (the bacterial Hsp70 ortholog) and promotes the exchange of ADP to ATP, consequently releasing the unfolded substrate [136, 196]. In the mammalian cytosol, a number of both positive and negative regulators of nucleotide exchange have been identified. Hip is an Hsc70-interacting protein that binds to the ATPase domain of Hsc70 and stabilizes it in the ADP-bound state [101, 175]. The Bcl-2-binding anti-apoptotic factor BAG-1 was found to enhance nucleotide exchange from Hsp70 [13, 100, 193], but interestingly this does not always lead to enhanced folding activity. The third cofactor for Hsp70, HspBP1, promotes nucleotide exchange from Hsp70 in vitro, which actually inhibits its chaperoning activity for some proteins [178]. A homologue of HspBP1, Fes1p, was recently identified in *S. cerevisiae*, where it appears to be a much less efficient nucleotide-exchange factor than HspBP1 [110]. Interestingly, none of these Hsp70 cofactors share any homology with GrpE.

The first potential nuclear-exchange factor for BiP came from a genetic screen in the yeast *Yarrowia lipolytica* to identify genes that interacted with the signal recognition particle in co-translational translocation. This screen identified *SLS1*, a resident ER protein [15]. A homologue of Sls1p, ScSls1p, was identified in *S. cerevisiae*, which was independently identified as Per100p [203] and Sil1p [206]. Further studies revealed that Sls1p binds directly to the ATPase domain of Kar2p and, in the presence of the J-domain of Sec63p, enhances ATP hydrolysis [110, 206]. Binding studies revealed that Sls1p prefers Kar2p when it is in the ADP-bound form, suggesting that it could act as a nucleotide-exchange factor [16]. *SLS1/SIL1* is a nonessential gene, but its overexpression can suppress the lethal phenotype observed in yeasts that lack both Ire1p, the kinase that signals the unfolded protein response in yeast, and Lhs1p, a second resident ER Hsp70 family

member [206]. Recently, a mammalian nucleotide-releasing factor for BiP was identified in a yeast two-hybrid screen that used the ATPase domain of a BiP mutant as bait [43]. BAP (BiP-associated protein) shares low sequence homology with both Sls1p and HspBP1. BAP is an ER-localized glycoprotein that is ubiquitously expressed but which shows the highest levels of expression in tissues with a well-developed secretory pathway. BAP stimulates the ATPase activity of BiP by accelerating nucleotide release from BiP. Surprisingly, both ATP and ADP can be released by BAP in vitro, but, like Sls1p [16], BAP appears to bind better or more stably to the ADP-bound state of BiP [43]. This property may be critical in allowing BAP to drive the ATPase cycle of BiP forward. In contrast to Sls1p, whose expression level is increased by ER stress [206], BAP transcripts are not induced. In fact, BAP protein levels actually appear to decline [43], suggesting that mammalian cells might be able to regulate BiP release from substrates by controlling the ratio of BiP and BAP. It is not known whether BAP can also serve as a nucleotide-releasing factor for GRP170 or if another specific release factor exists. It has been suggested that nucleotide-exchange/releasing factors are not necessary for some Hsp70s including BiP, since nucleotide hydrolysis, not exchange, appears to be the rate-limiting step in the reaction [69, 143]. However, it is important to point out that these assays are done in the presence of only ATP and not with a combination of ATP and ADP as would be expected to occur in vivo, although currently there are no measurements of the relative ratio of the two nucleotides. The rate-limiting step in the ATPase cycle of DnaK is also ATP hydrolysis [144, 201], but it is clear that the nucleotide-exchange factor GrpE plays an important role in the DnaK cycle in vivo [173].

16.5 Organization and Relative Levels of Chaperones in the ER

Data obtained from a number of studies have demonstrated that multiple ER chaperones can associate with a given nascent protein. Sitia and coworkers demonstrated that unoxidized Ig light chains form disulfide bonds transiently with both PDI and ERp72 and suggested that these proteins may form a kind of affinity matrix in the ER that impedes the transport of unoxidized nascent proteins [179]. Similarly, both thyroglobulin [126] and HCGβ [60] can be cross-linked to BiP, GRP94, and ERp72 during their maturation, and the influenza hemagglutinin protein binds to a number of ER proteins including BiP, GRP94, calreticulin, and calnexin when cross-linking agents are added to the cells [200]. However, it was not clear from these studies whether the chaperones were binding as a complex or whether the individual chaperones were binding to distinct unfolded regions on these proteins. Recently, membrane-permeable cross-linking studies demonstrated the existence of a large ER-localized multi-protein complex bound to unassembled Ig heavy chains that is comprised of the molecular chaperones BiP, GRP94, CaBP1, PDI, ERdj3, cyclophilin B, ERp72, GRP170, UDP-glucosyltransferase (UDP-GT), and SDF2-L1 [149]. Except for ERdj3, and to a lesser extent PDI, this

complex also forms in the absence of nascent protein synthesis and is found in a variety of cell types, suggesting that this subset of ER chaperones forms an ER network that can bind to unfolded protein substrates instead of existing as free pools that assemble onto substrate proteins. It is notable that most of the components of the calnexin/calreticulin system, which include some of the most abundant chaperones inside the ER, either are not detected in this complex or are only very poorly represented [149]. Further support for this type of sub-organellar organization of chaperones comes from a study in which fluorescence microscopy was used. The precursor of the human asialoglycoprotein receptor, H2a, and the free heavy chains of MHC class I molecules accumulated in a compartment containing calnexin and calreticulin, but not BiP, PDI, or UDP-GT, when proteasomal degradation was inhibited [113]. Together these studies suggest a spatial separation of the two chaperone systems that may account for the temporal interactions observed in other studies [84, 117].

16.6 Regulation of ER Chaperone Levels

Changes in the normal physical environment of the cell (e.g., decreases in pH, energy, oxygen, glucose, or other nutrients) can dramatically affect the normal biosynthesis of proteins in the ER and can result in the accumulation of unfolded proteins. Under these conditions, a signal transduction pathway, termed the unfolded protein response (UPR), is activated to protect the cell by preventing the formation of insoluble protein aggregates. The hallmark of the ER stress response, and perhaps the only component of the response that is truly ER-specific, is the coordinate transcriptional upregulation of most ER chaperones and folding enzymes [128]. A second characteristic of the UPR, and one unique to metazoans, is the inhibition of protein synthesis, which serves to limit the accumulation of unfolded proteins in the ER. This occurs via phosphorylation of the α-subunit of eukaryotic translation initiation factor 2 (eIF2α) at Ser^{51}, which reduces the frequency of translation initiation and thereby inhibits new protein synthesis [169].

The UPR pathway was first delineated in yeast. The identification of an unfolded protein response element (UPRE) in the yeast Kar2 (BiP) promoter [120] allowed investigators to use genetic approaches to characterize the signaling pathway. Ire1/Ern1, the first component to be identified, is a transmembrane, ER-localized kinase that possesses an N-terminal stress-sensing domain in the lumen of the ER and cytoplasmic kinase domain [46, 154]. In response to ER stress, Ire1 dimerizes and is phosphorylated, which serves to activate a unique endonuclease activity at its C-terminus [190]. The target of this activity is a precursor mRNA that encodes the Hac1 transcription factor. After cleavage by Ire1p and religation by Rlg1, Hac1p is synthesized and regulates the expression of UPR target genes by binding to the UPRE in their promoter [47]. This single signaling cascade is responsible for activating the UPR in yeast.

In higher eukaryotes, the elements of this signaling pathway are conserved but

greatly expanded. Two Ire1 homologues exist in mammalian cells; Ire1α, which is ubiquitously expressed [202], and Ire1β, whose expression is restricted to gut epithelium [209]. Both proteins possess a lumen stress-sensing domain, a cytosolic kinase domain, and the unique endonuclease domain found in yeast Ire1p. The target of Ire1's endonuclease activity is XBP1 mRNA, which alters the C-terminus of this transcription factor so that it encodes a protein with both a DNA-binding domain and a strong transactivation domain [31, 224]. Although XBP1 was first identified in a screen to identify proteins that bind to ER stress-regulated elements in mammalian chaperone promoters [223], it does not appear that either Ire1 or XBP1 [9, 130] is required for chaperone upregulation during ER stress, since mouse embryonic fibroblasts that do not express these proteins are still capable of inducing the chaperones. Instead, it is possible that the ATF6 transcription factor, which is synthesized as an ER-localized transmembrane protein [91] is responsible for their induction [130]. Activation of the UPR in mammalian cells leads to transport of ATF6 to the Golgi, where it is cleaved by the S1P and S2P proteases [221], thus liberating the cytosolic transcription factor domain from the membranes. Cleaved ATF6 can then enter the nucleus, bind to conserved ER stress elements (ERSE) that are found in multiple copies in the promoters of most ER chaperones and folding enzymes, and presumably upregulate their transcription during ER stress [223]. The latter point remains to be formally demonstrated either by examining chaperone induction in cells that are null for ATF6 or by showing that endogenous ATF6 binds to the chaperone promoters in a stress-inducible manner. A third arm of the mammalian UPR is represented by PERK/PEK, an eIF-2α kinase that is responsible for the transient inhibition of protein synthesis that occurs during ER stress [89, 189]. Although PERK null cells can still upregulate ER chaperones and folding enzymes during ER stress, the magnitude of the response is not as high as in wild-type cells [88], suggesting that something downstream of PERK contributes to their transcriptional upregulation.

The mechanism by which the ER stress signal is transduced has been recently determined. Earlier studies revealed that the initial signal for activating the UPR was the accumulation of unfolded proteins in the ER [124] and that all the agents that induced the UPR would be expected to dramatically affect protein folding in this organelle [129]. However, not all unfolded proteins are able to activate the response. Apparently, those that bind to BiP do [124, 133], whereas those that bind to other chaperones do not [77]. Since only BiP-binding proteins appeared to activate the response, these studies suggested that levels of free BiP might be monitored by the cell to judge changes in the folding environment of the ER. Identification of the UPR transducer proteins allowed this to be examined directly. Studies revealed that both Ire1 and PERK were associated with BiP during normal physiological conditions, which kept them in a monomeric, non-activated state. Activation of the UPR with thapsigargin or DTT led to the rapid loss of BiP from the lumenal domain of these proteins and a concomitant oligomerization and activation of the two signal transducers [10]. Similar results have been obtained with yeast Ire1p [165]. Another study showed that the lumenal domain of ATF6 was also associated

with BiP prior to stress, which in this case served to retain ATF6 in the ER [187]. Activation of the stress response leads to BiP release and transport of ATF6 to the Golgi, where the cytosolic transcription factor domain is liberated by the S1P and S2P proteases that reside there [221]. Thus, BiP directly regulates the UPR by controlling the activation status of the three transducers. It is likely that as stress conditions are alleviated and the pool of free BiP increases, BiP also plays a role in shutting down the response. In keeping with a central role of BiP in regulating the response, a recent study found that BiP is not readily translated early in the stress response even though BiP transcripts begin to increase very early [139].

16.7 Disposal of BiP-associated Proteins That Fail to Fold or Assemble

Proteins that have ultimately failed ER quality control are degraded to prevent their accumulation in the ER, which might either titrate out the components of the chaperone systems or form large insoluble aggregates that would be toxic to the cell. This turnover mechanism is termed ER-associated protein degradation (ERAD), which is conserved from yeast to mammals [87, 214]. The final steps of this ERAD process have been best characterized in yeast. Both malfolded proteins and excess subunits of multimeric proteins are retrotranslocated or dislocated back into the cytosol through a structure, which appears to be similar to the translocon used by nascent polypeptide chains to enter the ER lumen [25]. This retrotranslocation process is usually coupled with ubiquitination, which occurs at the cytosolic surface of the ER membrane. Ubiquitin (Ub) is a highly conserved small protein that is universally expressed in eukaryotic cells. Ubiquitination of substrates is a multi-step process that is dependent on a Ub-activating enzyme (E1), a Ub-conjugating enzyme (E2), and a Ub ligase (E3) enzyme [67, 99]. E1 binds to Ub, adenylates its C-terminus, and then binds to an E2 to transfer Ub to its catalytic subunit. E3, which is usually substrate-specific, will bring the substrate to an E2 and mediate the polyubiquitination process. E2 enzymes, such as Ubc6p and Ubc7p in yeast, are recruited by Cue1p or E3 enzymes such as Hrd1p/Der3p to the ER membrane and positioned near the translocon to directly facilitate the ERAD process [11, 75, 218]. The ubiquitinated ERAD substrates are then degraded by the cytosolic 26S proteasome [162]. This appears to be an important process in maintaining ER homeostasis during normal physiological conditions, since interfering with this process by either expressing mutants of the ERAD pathway [68, 158, 203] or using proteasomal inhibitors [29] results in activation of the ER stress pathway.

However, the upstream ERAD signals that help cells select malfolded proteins and feed them into the downstream degradation mechanism remain fairly elusive. One mechanism for identifying malfolded glycoproteins for ERAD involves the ER chaperones calnexin, calreticulin, and calmegin, which constitute a machinery called the "CNX cycle" [30, 92]. Glycoproteins with nine mannoses are allowed to

bind to and are then released from calnexin by alternating actions of glucosidase II and UDP-GT. The incorrectly folded proteins are allowed multiple rounds of association and dissociation to acquire the correct conformation until the outermost unit of mannose from the middle branch of the sugar is cleaved by ER mannosidase I. Glycoproteins tagged with Man8-glycans now have a lower affinity for UDP-GT [168] but a higher affinity for EDEM [103]. Unlike CNX, EDEM is a UPR-inducible ER membrane protein with homology to α-mannosidase but lacks mannosidase activity. EDEM will then extract malfolded ERAD substrates from the CNX cycle and feed them into the downstream ERAD machinery via mechanisms that are still unclear [152, 163]. Calnexin is required for degradation of ERAD substrates in an in vitro system in which ER membranes from yeast are used [25]. Kar2p was shown to be important in keeping the ERAD substrates in a soluble and retrotranslocation-competent state in the yeast system [161]. Recent data on ERAD in mammalian cells have suggested that calnexin and BiP play sequential roles in identifying and targeting ERAD substrates for degradation [153].

16.8
Other Roles of BiP in the ER

In addition to their role in folding nascent proteins, both calnexin and BiP appear to aid the translocation of nascent polypeptide chains into the ER. BiP has been shown to "plug" the translocon during early stages of protein translocation to maintain the permeability barrier between the ER and cytosol [83]. This puts BiP in an ideal place to bind nascent chains as they enter the ER, and indeed a number of studies have shown that Kar2p together with Sec63p is required for the translocation of nascent proteins into the yeast ER [24, 184, 208]. However, there are currently no data to show a similar role for mammalian BiP. The recent identification of two mammalian homologues of Sec63 [22, 191] is certainly compatible with such a role. A final function of the ER is to house the calcium stores that are essential for many intracellular signaling pathways. Along with a number of other ER chaperones, BiP is a calcium-binding protein that contributes significantly to the calcium stores of the ER [137].

16.9
Concluding Comments

In conclusion, the ER is the site of most secretory protein synthesis, where aqueous channels must be opened to allow the nascent polypeptide chains to enter the ER lumen. Care must be taken to ensure that the permeability barrier between the ER and cytosol are preserved in order to maintain the unique environment of the ER. Once inside the ER lumen, the protein must fold and assemble into its mature tertiary and quaternary form. Proteins that fail to do so must be identified and

targeted for retrotranslocation into the cytosol, where they become substrates for the 26S proteasome. Changes in the physiological environment of the ER that could affect protein maturation must be monitored and responded to by increasing ER chaperones and presumably proteins involved in maintaining and restoring the ER environment. BiP has been shown to be involved in all of these functions and to directly regulate activation of the UPR that maintains ER homeostasis. As such BiP can be considered a master sensor and regulator of ER function. All of the ER functions, with the exception of calcium storage, require BiP's ATPase activity and as a result are likely to involve BiP regulators including the ERdjs and BAP. Thus, we believe that functions for the regulators in these processes will be revealed in the future and that additional family members are likely to be discovered.

16.10 Experimental Protocols

16.10.1 Production of Recombinant ER Proteins

16.10.1.1 General Concerns

Production of large amounts of biologically active recombinant ER proteins suffers from the same difficulties as encountered with any other protein as well as a number of unique ones. The common ones like codon usage, size limitations, internal start sites, and inefficient translation are dealt with in other chapters, and thus there is no need to repeat them here. Instead we will focus on those problems unique to ER proteins and systems for dealing with them. Due to the oxidizing and calcium-rich environment of the ER and to the presence of an apparatus for assembling and adding *N*-linked glycans to nascent chains, many ER-localized proteins have evolved to fold properly in the presence of calcium and only when they have been glycosylated and have formed disulfide bonds. Thus, the expression of recombinant proteins in the bacterial cytosol can have deleterious effects on the folding of ER proteins. This said, large quantities of enzymatically active BiP protein (which has no internal disulfide bonds and is not glycosylated) have been produced by this method [213]. The targeting of ER proteins to the periplasmic space of bacteria can support the formation of disulfide bonds in proteins, which in some cases is sufficient to allow their proper folding [54, 197]. However, as bacteria do not possess the enzymes for *N*-linked glycosylation, proteins that require this modification for solubility or function must be produced in a eukaryotic system. In the end, the choice of expression systems often relies on empirical trials. The second problem encountered is where and how to tag an ER protein for purification purposes. The presence of an N-terminal-targeting sequence, which will be present in all cases except bacterial cytosolic expression, makes the choice and placement of a tag more difficult. If it is clear where cleavage of the signal sequence will occur and if any downstream sequence is required, then it is possible to add the tag sequence

just C-terminal of the downstream sequence. Otherwise, tags need to be added to the C-terminus of the recombinant protein, which can interfere with ER retention mechanisms [156]. Tags of choice include both N- and C-terminal hexahistidine (His_6) and glutathione S-transferase (GST), which allows the recombinant protein to be purified on Ni-agarose or glutathione beads, respectively. The insertion of a cleavage sequence (i.e., Factor Xa, thrombin, TEV, or enterokinase) makes it possible to remove the tag after purification, although in the case of recombinant BiP protein, an N-terminal His_6 did not interfere with enzyme activity [213].

16.10.1.2 **Bacterial Expression**

In spite of the limitations for ER proteins, bacterial expression systems remain very popular due to their simplicity, speed, and the high production levels that can be obtained. Two sites of production are possible: cytosolic and periplasmic. If aggregation is a major problem with either expression site, it is possible to minimize this by using shorter times of IPTG induction, lower IPTG concentrations, or lower temperatures for induction. In all cases, lower expression levels occur, but higher yields of soluble, biologically active protein can be obtained [19, 43].

A: Cytosolic expression Secretory pathway proteins are targeted to the ER membrane by a stretch of 11–20 hydrophobic amino acids, which is often present at their N-termini and which may be removed after they are translocated into the ER lumen. Removal of this sequence from the cDNA ensures cytosolic expression, produces a protein more similar to the mature protein, and in some cases may increase the solubility of the recombinant protein. Algorithms are available for predicting the site of signal sequence cleavage [44]. This type of expression has been used successfully to produce recombinant wild-type and mutant BiP proteins [212, 213], the J-domains of ERdj proteins [41, 127, 188, 205], and BAP [43].

Materials and solutions for producing His-tagged proteins:

LB broth: 10 g L^{-1} tryptone, 5 g L^{-1} yeast extract, 10 g L^{-1} NaCl

IPTG (1 M): filter-sterilized and stored in aliquots at −20 °C

Ampicillin stock solution: 100 mg mL^{-1} in H_2O, filter-sterilized and stored in aliquots at −20 °C

Kanamycin stock solution: 25 mg mL^{-1} in H_2O, filter-sterilized and stored in aliquots at −20 °C

Lysis buffer: 50 mM NaH_2PO_4, 300 mM NaCl, pH 8.0, containing 10 mM imidazole

Wash buffer: 50 mM NaH_2PO_4, 300 mM NaCl, pH 8.0, containing 20 mM imidazole

Elution buffers: 50 mM NaH_2PO_4, 300 mM NaCl, containing 20 mM imidazole (at pH 7.0, 6.0, and 5.0).

Procedure:

1. Inoculate LB broth with M15 *E. coli* that have been transformed with the appropriate construct and incubate until OD_{600} reaches 0.7–0.9, then add 1 mM IPTG to induce protein expression.
2. After 1–3 h, pellet cells and resuspend in 8 mL lysis buffer containing 1 mg mL^{-1} lysozyme (add lysozyme fresh each time).
3. Transfer to a 30-mL Corex tube and incubate on ice for 5 min.
4. Sonicate on ice for total of 3 min and centrifuge the lysate at 8000 *g* for 30 min at 4 °C.
5. Apply the supernatant to a 1-mL bed-size Ni-NTA column that is equilibrated with lysis buffer and allow the sample to run through the column by gravity. Wash the column with 15 mL of wash buffer.
6. Elute the histidine-tagged protein by using a stepwise decrease in the pH of the elution buffer: pH 7.0 (3 mL), pH 6.0 (3 mL), and pH 5.0 (5 mL). Collect 1-mL fractions.
7. Run each fraction on an SDS-PAGE gel to find the histidine-tagged protein.
8. Pool the protein fractions. Keep the protein at 4 °C for immediate use; otherwise, concentrate the protein by a Centricon filter device, add glycerol to 50% (v/v), and store at −20 °C.

Alternative purification strategies:

1. Instead of eluting the Ni-agarose–bound protein with low pH, it is possible to use imidazole. In this case, 250 mM imidazole is added to the lysing buffer solution (50 mM NaH_2PO_4, 300 mM NaCl, pH 8.0). Binding and washing are done as above. Imidazole absorbs at 280 nm and therefore must be considered when monitoring elution and determining protein concentration.
2. Denaturants (either 6 M GuHCl or 8 M urea) can be added to aid in the solubilization of proteins. In this case the denaturant is added to a lysis buffer (100 mM NaH_2PO_4, 10 mM Tris, pH 8.0), which is used to bind the proteins to the column. After washing with the same buffer at pH 6.3, samples are eluted with the same buffer at pH 5.9 or pH 4.5. Solutions containing urea cannot be autoclaved and the pH must be adjusted just prior to their use. Solutions containing GuHCl precipitate in the presence of SDS, so samples must be TCA-precipitated before they can be analyzed on SDS gels. Refolding assays are the same as for other proteins that are obtained under denaturing conditions.
3. A GST-fusion system is widely used for purification of recombinant proteins because of its simplicity. The basic steps of this method are similar to those of the His_6-tagged system. The glutathione S-transferase sequence is added in frame to the target protein. Often, a cleavage site (i.e., Xa, thrombin, etc.) is added between the GST and the target protein in order to remove the GST moiety after purification. This method requires only PBS as the buffer to resuspend cells and to equilibrate and/or wash glutathione Sepharose beads. Bacteria are lysed by sonication followed by adding Triton X-100 to a final concentration of 1%. The recombinant protein can be eluted with glutathione-eluting solution

(100 mM reduced glutathione in sterile distilled water, aliquoted and stored at −20 °C).

B: Periplasmic expression The expression of an ER protein in the periplasmic space of bacteria, which supports the formation of disulfide bonds, can remedy the problems of insolubility or inactivity that are often encountered when secretory pathway proteins are expressed in cytosol. This targeting is achieved by fusing a bacterial signal sequence from ompT [40], ompA [19], pelB [174], or alkaline phosphatase [164] to the N-terminus of the protein. Although periplasmic expression allows a more simplified purification by osmotic shock [157], the yield of the desired protein is often lower than that achieved with cytoplasmic expression. Tags for purification can be engineered on the expressed protein either at the C-terminus or following the signal sequence cleavage site [197]. It is important to note that targeting secretory pathway proteins to the periplasmic space is not always sufficient to remedy insolubility problems, as the overexpressed recombinant proteins can still form inclusion bodies in this organelle [19]. This method was used to produce mouse BiP, which is free from contamination by DnaK [40].

Merits:

- The *Escherichia coli* host system provides a rapid and easily manipulable method for protein production.
- Very high expression rates can be obtained.
- A variety of expression systems are available.
- It is economical and easy to maintain the bacterial system compared to other expression systems

Limitations:

- Most ER-specific posttranslational modifications of the recombinant protein are not achieved.
- Eukaryotic proteins expressed intracellularly in *E. coli* often form inclusion bodies, which require denaturation, renaturation, and refolding processes that are not always successful.
- Codon usage for eukaryotic genes is different, which can result in lower protein expression.

16.10.1.3 Yeast Expression

Yeast systems for recombinant protein expression have proven attractive for the following reasons: (1) they allow production of soluble proteins from many different eukaryotes including mammalian species, (2) they support the production of proteins with the appropriate posttranslational modifications including *N*-linked and *O*-linked glycosylation, and (3) secretion of the protein to the extracellular medium can occur, making purification easier. Two different species of yeast are generally used to produce foreign proteins: *Saccharomyces cerevisiae* and *Pichia pastoris*. *S. cerevisiae* provides well-developed expression vectors and host strains, and many

genetically modified strains are available. The advantages encountered in using *P. pastoris* are the fact that (1) 10- to 100-fold higher expression levels of recombinant proteins can be achieved compared to those in *S. cerevisiae* and (2) *N*-linked glycosylation occurs with a shorter oligosaccharide chain that lacks the terminal α1–3 glycan linkage found in *S. cerevisiae* but which is not found in mammalian proteins [34, 50]. Protein expression vectors for *S. cerevisiae* contain yeast signal sequences derived from various secreted proteins including invertase, α-factor, and acid phosphatase, which are fused in-frame to the desired protein. At present it is necessary to engineer a yeast signal sequence in front of the protein of interest when using *P. pastoris*, and studies have shown that codon usage and yeast poly A sequences can be important for synthesis of mammalian proteins in this system [177]. Protocols for using either organism can be found in *Current Protocols in Molecular Biology* and *Protein Science* and in the Invitrogen manual.

16.10.1.4 **Baculovirus**

The baculovirus-based system utilizes an insect virus to transfer genes to insect cell lines, such as Sf9, Sf21, and High Five cells. This eukaryotic expression method supports processing events and posttranslational modifications, such as phosphorylation, myristoylation, and palmitoylation, similar to those found in higher eukaryotes, and the majority of the overexpressed protein often remains soluble in insect cells, in contrast to the inclusion bodies that often form in bacteria. In addition, the machinery for targeting proteins to the ER is highly conserved between insect and vertebrate cells, so it is not necessary to replace the native ER-targeting sequence. However, there are data to indicate that some posttranslational processing events appear to be different from those found in vertebrate cells [170]. In addition, cleavage of signal sequences, removal of hormonal prosequences, and cleavage of polyproteins do not always occur properly in the expressed proteins [93]. Glycosylation is generally similar between insect and vertebrate cells, except that the *N*-linked oligosaccharides in insect cells remain in the high-mannose form and are not processed to the complex form containing fucose, galactose, and sialic acid. *O*-linked glycosylation has been reported, but this is less well-characterized in insect cells [106]. Protocols of producing recombinant proteins are available in books [1] or on websites and manuals of several companies that provide the vectors and transfection reagents.

Procedure:

1. If protein must be tagged for detection or isolation, it is necessary to add the tag either at the C-terminus or just after the signal sequence cleavage site.
2. Clone cDNA of interest into pFASTBAC and transform MAX efficiency DH10 BAC-competent cells (both from Gibco BRL-Inuitrogen) to produce recombinant bacmid for transfection. Spread serial dilutions of bacteria (10^{-1}, 10^{-2}, and 10^{-3}) on agar plates and incubate for 24–48 h at 37 °C.
3. Pick white colonies that contain the recombinant bacmid and inoculate overnight at 37 °C (option: streak to fresh plates to confirm the color).

4. Isolate bacmid DNA with the CONCERT High Purity Plasmid Isolation System (GibcoBRL-Invitrogen) or other methods developed for isolating large plasmids (> 100 kb). For detailed steps, see the Bac-to-Bac Baculovirus Expression Systems instruction manual, GibcoBRL-Invitrogen.
5. Produce viruses by tranfecting insect cells with bacmid DNA and CELLFECTIN reagent according to instructions. A viral titer of 1×10^7 to 4×10^7 pfu mL^{-1} can be expected from the initial transfection. For the method to determine the viral titer, see Bac-to-Bac Baculovirus Expression Systems instruction manual, GibcoBRL-Invitrogen.
6. Amplify virus stock by infecting a log-phase suspension or monolayer Sf9 culture at a multiplicity of infection (MOI) of 0.01 to 0.1.
7. Harvest virus 48 h later by pelleting cells at 1000 *g* for 20 min, and store supernatant containing virus at 4 °C, protected from light.
8. Culture Sf9 cells in spinner flasks at 27 °C, and infect log-phase cells with virus at an MOI of 0.01 to 0.1.
9. After 48 h (or optional time for maximum protein expression), collect an aliquot ($0.5–1.0 \times 10^6$) of infected cells and control cells to monitor protein production. Lyse cells with lysing buffer (50 mM NaH_2PO_4 pH 8.0, 300 mM NaCl, 1% of NP-40, 1 mM PMSF, and 10 mM imidazole) and run cell extract on a SDS-PAGE gel. The protein expression levels obtained with the baculovirus system are usually not as high as those achieved through bacterial expression methods. Thus, a Western blot instead of coomassie staining is usually employed to detect the protein.
10. Harvest the remaining cells by centrifugation for 3 min at 500 *g* and wash twice with PBS (media residue may affect the purification efficiency).
11. Freeze and thaw cells twice to break the cell membrane and resuspend in lysing buffer (as described above).
12. Centrifuge the lysate at 10 000 *g* for 10 min at 4 °C.
13. Purify the recombinant protein as described above.

This method was developed by researchers at Monsanto. It is faster and more efficient than the traditional methods, which take weeks to pick a positive recombinant virus clone and achieve final high-titer stocks. However, the vector is not yet available with a C-terminal His_6 tag. Therefore, an additional step is required to tag the gene of interest with either a C-terminal tag or an N-terminal tag following the signal sequence.

Merits:

- It is a eukaryotic expression system using modification, processing, and transport systems similar to those found in vertebrate cells.
- Adaptation for growth in suspension cultures makes it possible to obtain moderate quantities of recombinant protein with relative ease.
- The majority of the proteins produced are soluble and possess the correct post-translational modifications.

- Adaptation to non-serum cultures cuts the costs and makes purification of the secreted proteins easier.
- It is safe and not hazardous to humans unlike viral expression systems.
- The virus can be preserved at 4 °C for long periods of time.

Limitations:

- Different modifications other than those observed in vertebrate species may occur.
- It is more time-consuming than bacterial expression methods.
- Insect cells recover slowly from frozen stocks.
- Cells grow fast but cannot be cultured at very low concentrations: frequent splitting at a 2:5 ratio every 2–3 days leads to high serum and medium costs.
- Additional tagging steps are required to isolate ER proteins.

16.10.1.5 Mammalian Cells

Mammalian cells are good hosts for expressing properly folded glycoproteins that possess all the correct posttranslational modifications that control their physiological functions as native proteins. There are a number of choices for expressing proteins in mammalian cells as described below, including both transient and stable methods.

A: Plasmid-based transfection When plasmid DNA is transferred into mammalian host cells, the majority of DNA remains extra-chromosomal and can support expression. The cells used for expression often express the SV40 large T antigen, which will replicate vectors containing the SV40 origin of replication (ori). Popular cell lines include COS and 293T cells. The vectors used for expression of the protein of interest often use strong viral promoters such as the cytomegalovirus (CMV) or adenovirus promoters, as well as the SV40 ori. DNA is introduced into the cells by Ca^{2+} precipitation, DEAE-dextran, or lipofection. These methods are quick and can provide a one-time production of from one to a few hundred micrograms of purified protein [1, 219]. On the other hand, a small percent of the DNA can integrate into a transcriptionally active chromosomal locus and express the protein on a permanent basis from generation to generation if an appropriate selectable marker is included in the transfection. This stable transfection allows the selection of clones that express high levels of the recombinant proteins. Popular host cell lines for stable expression include CHO (Chinese hamster ovary) cells, 293T (transformed human embryonic kidney) cells, myeloma cells, and BHK-21 (baby hamster kidney) cells. The DNA can be transfected into these host cells by using Ca^{2+} precipitation, DEAE-dextran, lipofection, or electroporation. Detailed protocols are described in Refs. [1, 2]. Finally, it is possible to obtain stable cell lines that can express toxic proteins by using regulated expression systems (i.e., tetracycline [76], heavy metal [215], or hormone-regulated systems [220, 227]).

Merits:

- The proteins produced are identical to the native proteins with good solubility and proper structures and functions.
- Transient expression is timesaving compared to the baculovirus system, if a single transient expression can produce enough protein.
- For stable lines, clones can be frozen and thawed for later repeat use.
- Regulated expression makes long-term production of toxic protein possible.
- There is no exposure to viruses and therefore no significant safety issue.

Limitations:

- It is time-consuming to screen a high-production, stable line.
- The product yield is often low compared to the baculovirus system; this may be improved by using suspension cultures that are grown in spinner flasks (1–50 mg L^{-1}).
- The types of host cells to choose from are limited.
- It is relatively expensive due to the high costs for medium and serum.

B: Viral infection Retrovirus infection is a useful technique for efficiently producing stable cell lines that express a heterologous protein. The non-viral gene is cloned into a retrovirus vector and transduced into a packaging cell line to produce viruses that carry the gene of interest. The virus can then be used to infect host cells as long as they are dividing and carry the appropriate retroviral receptors on their surface. After integration into the host chromosome, the retrovirus will stably produce a single copy of the viral genome including the gene of interest from the viral LTR. In order to lower the risk of this system, replication-incompetent retroviral vectors are derived from proviruses by deleting some or all of the genes encoding virion structural proteins. These vectors need to be transfected into a packaging cell line that provides these genes in *trans*. By using packaging lines that produce an ecotropic murine retrovirus instead of an amphotropic one, it is possible to further decrease the risk to humans. Although the efficiency of viral infection can be as high as 100%, retroviral infection is not commonly used to produce recombinant proteins because the LTR is not a strong promoter, and therefore the yield of recombinant protein is usually fairly low. However, retroviral infection is widely used to study the protein of interest in mammalian cells, due to the high efficiency and broad type of host cell lines that can be used.

Materials and reagents:

293T cells and NIH3T3 cells, transfection reagents (it is recommended to use Ca^{2+} precipitation or FuGENE6 (Boehringer-Mannheim))

0.45-μM filter bottle

Polybrene 2 mg mL^{-1} in water, aliquoted and stored at −20 °C

Procedures:

1. For virus production, seed 3×10^6 293T cells/100-mm dish and incubate overnight.
2. Transfect 20 μg total DNA including retrovirus vector containing the gene of interest along with helper vector, and incubate overnight.
3. In the morning, remove media, wash cells, and add 10 mL fresh media.
4. Incubate 4–5 h, aspirate media, and add 4 mL of fresh media to cells.
5. Begin harvesting the media containing retroviral particles by removing and adding fresh media every 4–6 h for 2 days. Combine all the media and filter through a 0.45-μM filter. Aliquot virus stock and save at −80 °C.
6. For recombinant protein expression, seed 2×10^5 NIH3T3 cells/100-mm dish and incubate overnight.
7. Aspirate all the media from the dishes, add enough virus stock containing 8–10 μg mL^{-1} polybrene to cover the cells, and then add additional virus every 3 h, at least 3 times.
8. Harvest cells ∼ 48 h after infection or treat cells with proper agent (i.e., G418) to select infected cells.

A second viral system that is commonly used for transient expression of a protein is the DNA-based adenovirus system [219]. Very high levels of expression can be obtained that can reach up to 10–20% of total protein. Adenovirus particles can target both dividing and non-dividing cells from a majority of human and many non-human cell types and produce multiple copies of the gene of interest [39, 71]. This wide variety of target cells combined with high-level gene expression levels makes the adenovirus system ideal for a number of research applications, including recombinant protein production, gene therapy, gene function analyses, antisense strategies, vaccine development, and transgenic animal studies. The disadvantages of adenoviral delivery include safety concerns due to the fact that they can infect human cells and the rather complex and time-consuming methods required to produce the virus. The lentivirus (an HIV-related retrovirus) represents another expression system that has been used to constitutively express proteins in a wide range of mammalian cells [192]. An advantage is that the host cell does not need to be replicating, but for recombinant protein production, this is rarely a concern. Again, their wide target range represents both an advantage and a disadvantage. Detailed protocols for using viral strategies for producing recombinant proteins can be found in the ViraPower manual under the section on adenoviral/lentiviral expression systems and in the Invitrogen manual. Methods for purifying recombinant proteins from mammalian cells infected with these viruses are similar to those for baculovirus-infected insect cells, as described above.

Merits:

- These viral delivery systems all use mammalian cells to produce proteins and should therefore be identical to the native proteins with good solubility and proper structures and functions.

- A broad range of host cells can be infected, including in some cases non-dividing cells.
- The high efficiency of infection makes it unnecessary to sort positive cells.
- Very high levels of expression can be obtained with adenovirus.

Limitations:

- Large fragments of DNA (> 8 kb) are difficult to transduce with this approach.
- The protein production levels achieved with retroviruses are relatively low.
- Adenovirus and retroviruses can infect human cells; therefore, extra caution must be used when handling them.
- Methods for producing and infecting with viruses are more cumbersome than simple transfection with other vectors.

16.10.2 Yeast Two-hybrid Screen for Identifying Interacting Partners of ER Proteins

The identification of interacting proteins can often provide insights into the regulation and function of a given protein. The yeast two-hybrid system has proven extremely useful for identifying interacting proteins, but it is best suited for cytosolic or nuclear proteins due to the underlying principles of the procedure. The bait and target proteins must both be expressed in the cytosol and transported to the nucleus to drive transcription of a reporter gene [141]. Thus, to find proteins that interact with an ER lumenal protein, the target cDNAs must have lost their ER-targeting sequence when the library is made, both the bait and target must fold properly in the cytosol in the absence of an oxidizing environment and *N*-linked glycosylation, and the interaction between the two proteins must be supported by the reducing, low-calcium environment of the cytosol and nucleus. In spite of these limitations, it has been possible to identify proteins that interact with secretory proteins by this method [43]. The problems encountered with finding interacting proteins for ER chaperones become even larger. Because chaperones interact with many unfolded proteins, it is reasonable to expect that by expressing the secretory pathway in the wrong environment, many "false positives" would be found. In fact, Hsps are often identified as false positives in screens with various bait proteins (http://www.fccc.edu/research/labs/golemis/main_false.html). However, a two-hybrid screen with cytosolic Hsc70 was successfully employed to identify HiP, a protein that interacts with the ATPase domain of Hsc70 and stabilizes its binding to ADP [101]. In order to minimize false positives, the peptide-binding domain of Hsc70 was removed. Similarly, a screen with the ATPase domain of human Hsp70 identified HspBP1, a protein that is abundant in heart and skeletal tissues and that regulates nucleotide release from Hsp70 [111, 178]. To identify BiP-interacting protein(s), the ATPase domain of a BiP mutant (T229G) that is unable to hydrolyze ATP [212] was used as bait in the screen. Since BiP is an ER-resident protein, the ER-targeting signal sequence was removed to prevent the Gal4-mutant ATPase domain fusion protein from being targeted to the ER [43]. In-

terestingly, none of the regulatory proteins that interact with cytosolic or nuclear Hsp70s were obtained in this screen.

There are several different commercially available yeast two-hybrid systems (BD Sciences, Invitrogen, and Stratagene) and a number of comprehensive descriptions of them [3, 61]. Briefly, the yeast transcription factor GAL4 contains an N-terminal DNA-binding domain (DNA-BD) and a C-terminal activation domain (AD). These two domains are functionally separable but must be brought together to initiate transcription. A known protein (the bait) is fused to the GAL4 DNA-BD. A cDNA library is expressed as fusions to GAL4 AD. When the bait and library fusion proteins interact, the DNA-BD and AD are brought into close proximity to allow the two components of GAL4 to come together and drive the transcription of a reporter gene (i.e., *lacZ*). Yeast colonies are then screened for β-galactosidase activity.

Materials and solutions:

Strain: HF7c transformed with the pAS (bait) vector. The transformed strain must be negative in an X-gal assay. In our case, a bait vector contained the ATPase domain of a BiP mutant without the signal sequence fused to Gal4 (pAS(T229G)44K) [43].

cDNA library: a human liver cDNA library (pACTII base) from Clontech (now BD Sciences). The cDNA library was amplified according to the manufacturer's instruction, and the amplified cDNA library was checked for its quality by a PCR reaction for known ER proteins and by restriction enzyme digestion of the library to detect the smear of inserted cDNAs.

SD synthetic minimal media: SD/dropout (DO) medium with DO supplements (Clontech): to prepare SD/–Leu/–Trp agar, you will need to combine SD minimal agar with –Leu/–Trp DO supplement (#8608-1).

1 M 3-AT (3-amino-1,2,4-triazole; Sigma #A-8056): prepared in deionized H_2O and filter-sterilized. Store at 4 °C. Plates containing 3-AT can be stored at 4 °C for up to 2 months.

X-gal (20 mg mL^{-1} in DMF): dissolve 5-bromo-4-chloro-3-indolyl-b-D-galactopyranoside in *N*,*N*-dimethylformamide. Store in the dark at −20 °C.

LiSORB: 100 mM lithium acetate, 10 mM Tris pH 8.0, 1 mM EDTA, 1 M sorbitol.

Procedure:

1. Incubate the recipient strain (HF7c) carrying pAS-bait vector in 2 mL of SD-Trp overnight at 30 °C.
2. Transfer the overnight culture to 100 mL of SD-Trp in a 500-mL flask and incubate overnight at 30 °C.
3. Dilute with YPD broth to obtain $OD_{600} = 0.3 \sim 0.4$.
4. Incubate the above culture in a 1000-mL flask for 3–4 h until $OD_{600} = 0.5 \sim 0.8$.

5. Collect cells in 50-mL conical tubes by centrifugation, wash with dH_2O once, and resuspend in 25 mL LiSORB in one tube. For 500 mL culture, make two tubes.
6. Incubate for 30 min at 30 °C with shaking. Meanwhile, boil 200 μL (4 mg) of sheared salmon sperm DNA for 10 min and mix with 600 μL LiSORB.
7. Centrifuge and resuspend the cell pellet with LiSORB to 1 mL final volume.
8. Keep on ice until library cDNA is added. This should be less than 1 min because at step 6, the boiled sperm DNA comes close to room temperature by mixing with 600 μL LiSORB.
9. Cool mixture to room temperature, and then add 100 μg library cDNA. Make the final volume to 1 mL.
10. Add 1 mL of the above DNA mix to 1 mL cell suspension in a 50-mL tube.
11. Add 18 mL 40% PEG/100 mM LiAc/10 mM TE and incubate for 30 min at 30 °C with gentle shaking.
12. Add 700 μL DMSO and mix gently.
13. Dispense 1 mL in 20 Eppendorf tubes and give heat shock for 15 min at 42 °C.
14. Cool on ice for 5 min and pool the cells in two 50-mL conical tubes.
15. Centrifuge and resuspend in 5 mL SC-Trp/-Leu/-His. Take 20 μL for transformation efficiency test.
16. Plate 100 μL per 150-mm plate (SD-Trp/-Leu/-His +25 mM 3-AT) using glass beads.
17. Colonies will appear after 3–5 days and can be tested for *β*-galactosidase activity using the X-gal colony filter assay. Blue colonies are saved for further study.

16.10.3 Methods for Determining Subcellular Localization, Topology, and Orientation of Proteins

16.10.3.1 Sequence Predictions

Inspection of the predicted amino acid sequence can provide information on the likely subcellular organization of a protein. Like other secretory pathway proteins, most ER lumenal resident proteins possess an N-terminal ER-targeting sequence, which is comprised of a relatively hydrophobic sequence of between 11 and 20 amino acids. Relative hydrophobicity can be determined by algorithms, which allow identification of both ER-targeting signal sequences and transmembrane domains. The presence of the C-terminal tetrapeptide KDEL, or a closely related sequence, serves as an ER retention sequence for soluble lumenal proteins [156], which is recognized by the KDEL receptor in cells ranging from yeast [135] to mammals [134]. The ExPASy (Expert Protein Analysis System) proteomics server of the Swiss Institute of Bioinfomatics is dedicated to the analysis of protein sequences and structures. Their website (http://us.expasy.org) provides links and tools to predict hydrophobicity or subcellular localization. PSORT is another commonly used program to identify structural motifs useful in localizing a protein, and it can be accessed at http://www.psort.org.

Tab. 16.2. Organelle-specific Markers

Organelle	*Antibodies*
Endoplasmic Reticulum, Lumen	ERp57, ERp72, GRP58, GRP78 (BiP), GRP94, KDEL, TAP1 UDP-GT
Endoplasmic Reticulum, Integral	Calnexin, HO-1, HO-2, Tapasin
Golgi, Cis	KDEL Receptor
Golgi, Medial	Membrin
Golgi, Trans	Syntaxin 6
Lysozome	Lamp1, Lamp2, *lysosomal storage enzymes*
Endosome, Early	Rab4, Rab5, Syntaxin 13
Endosome, Late	Rab9
Mitochondria, Matrix	Grp75 (mt Hsp70), mt Hsp60
Mitochondria, Outer Membrane	Bcl-2, Bcl-w
Nucleus	Estrogen Receptor, Histone H1, PARP
Plasma Membrane, Integral	Fas, TNF-R1, Transferrin Receptor
Plasma Membrane, Peripheral	FADD, Grb2, RAIDD, Ras
Cytosol	p38, Hsc70

16.10.3.2 **Immunofluorescence Staining**

If an antibody is available for the protein of interest, it is possible to obtain insights into its subcellular localization by staining fixed cells with the antibody and then co-staining with an antibody of a resident ER protein (or markers for other organelles), as long as they are of different species so that secondary antibodies conjugated to fluorochromes can be used for detection (Table 16.2). A standard fluorescence microscope can often give a relatively reliable indication of whether two proteins colocalize, particularly if they do not. However, a confocal microscope provides a more sensitive measure if they do. Epitope tagging has become a widely used method for analyzing proteins before an antiserum is available. While there are clear advantages to this technique, care must be taken to ensure that the tag does not change the intracellular targeting of a protein. For instance, the addition of an N-terminal tag to a protein can interfere with its targeting to the ER. Similarly, the addition of a C-terminal tag to an ER-resident protein can result in its secretion from the cell, since moving the KDEL sequence of BiP to a slightly more internal location inhibited its recognition by the KDEL receptor [156].

16.10.3.3 **Subcellular Fractionation**

Cell fractionation has been widely used among cell biologists for nearly half a century and continues to be the gold standard for determining where in the cell a given protein is expressed. This method is based on the different densities of the various membranous organelles, which can easily be separated from the nucleus and cytosol during centrifugation through glycerol or sucrose gradients [1, 64]. Isolated ER vesicles can then be used for membrane topography studies as described below.

The tissue or cells must first be made into single-cell suspensions and homogenized to break the cells into the various organelles as described in Refs. [207, 210].

From rat liver:

1. Remove liver from a freshly sacrificed rat that has fasted overnight. Keep the liver on ice as much as possible, weigh the liver, and then mince it coarsely with scissors or a razor blade.
2. Homogenize the minced liver at 20% (w/v) in homogenization medium (0.25–0.3 M sucrose) using five up-down strokes at 1700 rpm with a high-torque, motor-driven pestle.
3. Filter the homogenate through four layers of cheesecloth.

From cell lines:

1. Collect about 20–70 million cells, wash twice with PBS, and resuspend in 1 mL homogenization buffer (0.25 M sucrose, 10 mM HEPES pH 7.5).
2. Transfer to the Dounce homogenizer and homogenize 8–15 strokes, depending on the cells and the homogenizer.

Centrifugation to separate microsomes:

1. In both cases, spin the homogenate at 600 *g* in a microcentrifuge for 10 min at 4 °C to remove nuclei and unbroken cells.
2. Remove supernatant and centrifuge at 25 000 *g* using a SW50.1 rotor for 10 min at 4 °C to remove mitochondria.
3. Remove supernatant and either centrifuge at 124 000 *g* using a SW50.1 rotor for 1 h at 4 °C to pellet all remaining membranous organelles or layer over a stepwise sucrose gradient (0.6 M, 1.0 M, 1.3 M, and 2.0 M sucrose) to separate the rough ER, smooth ER, Golgi, and plasma membranes from the cytosol [17].
4. The purity of each fraction can be assayed by Western blotting an aliquot of each fraction for the various for organelle markers (Table 16.2).

A simplified method for isolating microsomes has been described [207, 210]. Briefly, cells are resuspended in homogenization buffer (25 mM HEPES-KOH, 125 mM KCl, pH 7.2) and broken by Dounce homogenization. The crude homogenates are centrifuged at 600 *g* to remove cell debris and nuclei. The supernatant containing ER microsomes and cytosol is centrifuged at 10 000 *g* to pellet the microsomes, which remain contaminated with mitochondria.

16.10.3.4 Determination of Topology

A: Protease protection assays Proteins or protein domains located inside the ER are protected by the impermeable membrane from digestion with proteases. Resistance to treatment with protease K can reveal whether the entire protein is located

inside the ER or if a portion of the protein is located inside the ER. When the membranes are treated with detergent and disrupted, the microsomes no longer protect the protein or domains unless they themselves are protease-resistant. Thus, detergent treatment of vesicles before protease should be included as a control. Either microsomes extracted from cell lines or tissues can be used if antibodies are available for multiple epitopes or at least for known epitopes. Alternatively, the full-length cDNA can be used in coupled in vitro transcription/translation assays that have dog pancreatic microsomes added to the reaction mixture. Because the cDNA is the primary protein translated, antibodies are not required to detect the protein. Known ER-resident proteins are recommended as controls (e.g., BiP and calnexin) to ensure that the membranes remain intact and the proteinase K behaves appropriately.

Procedure:

1. The microsomes are divided into three aliquots: one is left untreated, one is digested with 150 μg mL^{-1} proteinase K, and one is made 1% NP40 prior to treatment with protease and all are incubated for 1 h at 37 °C.
2. The samples are treated with 1 mM PMSF for 15 min to neutralize the protease.
3. SDS sample buffer is added to each reaction and the samples are analyzed by SDS-PAGE. If the samples are translated and labeled in vitro, they can be visualized by autoradiography; if not, the proteins must be detected by Western blotting.

B: Integral membrane vs. soluble protein Inspection of the primary sequence can often predict whether a protein is likely to be a membrane protein if it contains a second hydrophobic stretch of amino acids that can serve as a transmembrane domain. However, a single transmembrane domain can also act to anchor a protein in the membrane, if it remains uncleaved. Additionally, hydrophobic sequences that are a bit short or that contain charged amino acids can make it hard to predict whether or not they are transmembrane domains. Three methods are used to determine whether a protein is anchored to the membranes or soluble in the ER. The first relies on the ability of low concentrations of mild detergents to allow soluble proteins to leak out of ER membrane vesicles without completely destroying the membrane or solubilizing integral proteins.

Procedure:

1. Microsomes are pelleted and resuspended in 100 μL of cold PBS buffer alone or PBS containing either 0.1–0.2% digitonin or 1% in deoxycholic acid (DOC).
2. After rocking at 4 °C for 1 h, samples are centrifuged at 10 000 *g* for 5 min to sediment residual membranes [226].
3. The supernatant and pellet are separated and prepared for SDS-PAGE and Western blotting. To avoid cross-contamination, the pellet should be rinsed once with cold PBS.

Transmembrane proteins remain in the pellet fraction, whereas soluble lumenal proteins are released into the supernatant in the presence of low concentrations of digitonin. However, both protein types are found in the supernatant fraction when the microsomes are treated with 1% DOC. A good control for membrane-associated proteins is calnexin, and BiP can be used for soluble lumenal proteins.

The second method utilizes the fact that treatment of ER vesicles with high-pH buffers transforms the vesicles into open sheets, which release soluble lumenal contents but retain integral membrane proteins. The membrane sheets can be pelleted by centrifugation to separate membrane and soluble proteins [159], which can be analyzed as above. The third method takes advantage of preferential detergent binding to hydrophobic regions of proteins and of the fact that at a given temperature, detergents reach a ''cloud point'' that allows them to be precipitated from solutions. The detergent TritonX-114 is particularly useful for this application, since it precipitates at 20 °C and goes back into solution at 0 °C [18]. Unlike the characteristics of many detergents, these temperatures are not denaturing to proteins. Briefly, labeled cells or ER vesicles are resuspended in 200 µL separation buffer (10 mM Tris-HCl, pH 7.4, 150 mM NaCl), containing 0.5–1.0% Triton X-114 at 0 °C, and then overlaid on a sucrose cushion (the same buffer containing 6% sucrose, 0.06% Triton X-114). The sample is incubated at 30 °C for 3 min, and the clouded sample is centrifuged for 3 min at 300 *g* at 30 °C. The membrane proteins pellet to the bottom with the detergent phase, and soluble proteins remain in the upper aqueous phase. After separating the phases, detergent should be re-added to the aqueous fraction, and the detergent fraction should be resuspended in separation buffer. Both fractions should be cooled to 0 °C and re-fractionated. This can be repeated several times to increase the purity of the fractions [18].

16.10.3.5 *N*-linked Glycosylation

The covalent addition of oligosaccharides to translocating proteins is one of the major biosynthetic functions of the ER. Most secretory proteins that are made in the ER are glycoproteins. Conversely, very few proteins in the cytosol or nucleus are glycosylated, and those that are receive only a single trisaccharide addition that is not *N*-linked [90]. Oligosaccharides are specifically added co-translationally to asparagine residues in the sequence Asn-X-Ser/Thr, where X is any amino acid except proline. In addition, a simpler sugar modification can be added to the –OH group of serine, threonine, or hydroxylysine residues in the Golgi. Asparagine-linked or *N*-linked glycosylation is a stepwise procedure of oligosaccharide addition and removal that begins with the addition of a high-mannose dolichol intermediate. Glucose and mannose residues are trimmed while the protein is still in the ER, and these events serve as recognition structures for calnexin and calreticulin. The presence of *N*-linked glycosylation on a protein is a clear indication that it was synthesized in the ER. Tunicamycin, a fungal metabolite that inhibits the addition of the dolichol intermediate to nascent chains [132], is widely used to determine whether a protein is glycosylated. However, this approach is useful only in examining newly synthesized proteins and works best in biosynthetic assays. The *N*-linked glycans are further processed as the protein is transported through the *cis*, medial,

and *trans* Golgi. A number of glycosidases that have specificity for different glycan processing intermediates have been purified from bacteria and fungus and can be used to distinguish the various forms. Endoglycosidase H (Endo H) recognizes only the immature *N*-glycans found on proteins that are still in the ER [204], not those on proteins that have been transported to the Golgi [122]. These Endo H–resistant glycoproteins can be digested with either Endo D, which specifically recognizes and cleaves the processed complex *N*-linked sugars [121], or *N*-glycosidase F (PNGase F), which removes the *N*-linked oligosaccharides from both high-mannose ER forms and processed post-ER forms of glycoproteins [172, 198]. Thus, sensitivity of a protein to these various endoglycosidases can provide information on the subcellular localization of a glycoprotein. Because these treatments are done on cell lysates or immunoprecipitated proteins, they can be used in both biosynthetic and Western blotting assays.

A: Tunicamycin treatment

1. Pretreat cells with 1 μg mL^{-1} (effective concentration varies from 0.15–10 μg mL^{-1}) tunicamycin for ~1 h before labeling the cells with ^{35}S methionine. If Western blotting will be used to detect the protein of interest, longer treatment is required, depending on the synthetic and turnover rate of the protein. This treatment induces an unfolded protein response in cells, which can lead to lower protein synthetic rates and more rapid protein turnover.
2. Lyse cells and immunoprecipitate protein with the appropriate antibody.
3. Subject protein samples to SDS-PAGE analyses and autoradiography. Glycosylation slows down the protein mobility on the gel; thus, a tunicamycin-treated, non-glycosylated protein runs faster than the non-treated protein on SDS gels. One oligosaccharide adds ~2 kDa to the apparent molecular weight of the protein.

B: Endo H digestion

1. Obtain proteins either from in vitro translation reactions performed in the presence of microsomes or from immunoprecipitates of cell lysates. If in vitro–translated proteins are used, it is highly recommended to pellet the membrane fraction and discard the reticulocyte lysate before lysing to eliminate contamination with untranslocated, non-glycosylated forms of the protein.
2. After washing immunoprecipitated material three times, wash one additional time with reaction buffer (0.1 M sodium citrate, pH 5.5).
3. Resuspend in 49 μL of reaction buffer containing PMSF and add 3 mU of Endo H.
4. Incubate at 30–37 °C overnight.
2. Stop reaction by adding SDS sample buffer and heat to 95 °C for 5 min.
3. Subject to SDS-PAGE gel to detect the mobility changes by autoradiography or Western blotting.

In general, 50–250 mU of Endo H is sufficient to deglycosylate up to 1 mg high-mannose glycoprotein when incubated overnight. The pH optimum of Endo H is ~5–6. For glycans that are not readily removed, it is sometimes possible to increase their accessibility to the enzyme by denaturing the protein [1]. This is accomplished by adding SDS to 0.25% and mercaptoethanol (2-ME) to 0.5% and heating the sample to 95 °C for 5 min. The denatured sample should then be diluted ~1:3, and PMSF (1 mM) should be added to protect the protein and to prevent the inactivation of Endo H.

C: PNGase F digestion Obtain protein samples from in vitro translation reactions done in the presence of microsomes or from material immunoprecipitated from cell lysates. If in vitro–translated proteins are used, it is highly recommended to pellet the membrane fraction and discard the reticulocyte lysate to eliminate the untranslocated, non-glycosylated proteins.

1. Denature proteins (75–100 μg in ≤25 μL) by adding 25 μL freshly made denaturing buffer (0.5% SDS, 1% 2-ME) and heat to 95 °C for 5–15 min.
2. Add the following in order (50 μL total): 25 μL 0.5 M TrisCl, pH 8.0; 10 μL 0.1 M 1,10-phenanthroline; 10 μL 10% nonionic detergent; 5 μL 200 to 250 mU mL^{-1} PNGase F.
3. Incubate overnight at 30 °C.

The optimum working pH for PNGase F is from 7 to 9, although enzyme has some activity between pH 5 and 7.

D: Manipulation of glycosylation sites Not all ER proteins are glycosylated. The localization and topology of non-glycosylated ER protein can be determined by the protease-protection and detergent-release experiments described above. In addition, chimera proteins can be made in which the protein of interest is fused in-frame to a known ER glycoprotein that has had its signal sequence removed. This strategy was recently used to demonstrate that ERdj4 is a type II protein with an uncleaved signal sequence serving as the membrane anchor and with its J-domain oriented inside the ER lumen [188]. This method can also be used to confirm orientation of transmembrane proteins. Alternatively, *N*-linked glycosylation sites (NXS/T) can often be introduced into the protein of interest by replacing a single amino acid. In most cases the introduced site will be glycosylated, which can be monitored with tunicamycin treatment or Endo H digestion.

16.10.4 Nucleotide Binding, Hydrolysis, and Exchange Assays

16.10.4.1 Nucleotide-binding Assays

All Hsp70 family members bind and hydrolyze ATP, which regulates the ability of their C-terminal domain to bind and release unfolded protein substrates [26, 74].

The amino-terminal ~44-kDa domain of Hsp70 proteins encodes the nucleotide-binding site [35], and crystal structures for the ATP- and ADP-bound forms of bovine and rat Hsc70 have been determined [62, 63, 146]. The ATPase domain is comprised of two lobes with a deep cleft between them with nucleotide binding occurring at the base of the cleft. Due to the high degree of sequence similarly among family members, all are likely to form a similar structure. The differences between the ATP-bound and ADP-bound states of this isolated domain are limited to minor rearrangements of solvent-assessable side chains and those present near the scissile bond. Conversely, the two nucleotides dramatically alter the conformation of the full-length molecule as detected by protease-sensitivity assays [35, 115, 145, 212] and changes in far-UV CD spectra [42]. Currently there are no structures available for any full-length Hsp70s to determine how nucleotide binding alters the overall structure the Hsp70s. The ability to bind nucleotide can be altered by mutations [145, 212], and the nucleotide-bound state of an Hsp70 can be regulated by proteins that prevent exchange [101] or proteins that promote exchange [5, 19, 78, 110, 111]. When a potential cofactor for an Hsp70 protein is identified, an initial step is to assay its effects on the binding of nucleotide to the client Hsp70. Also, it is important to check whether the cofactor itself binds nucleotides. There is a critical difference between cofactors that bind and transfer nucleotides to target proteins and those that interact with the target protein and alter its ability to bind nucleotides. To date all of the known Hsp70 cofactors that have been identified are of the second class: non-nucleotide-binding. Following are two simple techniques to obtain qualitative data as to whether a protein binds nucleotides [43, 109] and one quantitative technique [69, 70]. The two simpler techniques worked equally well when characterizing BAP, which serves as a nucleotide-releasing factor for BiP.

A: Nitrocellulose membrane method

Procedure:

1. Mix 6 μg of each purified protein, such as BSA (negative control), recombinant BiP (positive control), or recombinant BAP, with 50 μCi [α-^{32}P]-ATP, add 2× buffer A (40 mM HEPES pH 7.2, 100 mM KCl and 10 mM $MgCl_2$, and 20 mM DTT) to make final reaction mix 1× at a total volume of 50 μL, and incubate for 10 min at 30 °C.
2. During the incubation, wet a piece of nitrocellulose membrane with chromatography buffer (20 mM Tris-HCl, pH 7.5, 20 mM NaCl, and 1 mM DTT). Remove extra buffer B, but avoid drying the nitrocellulose membrane.
3. Spot 2 μL of protein samples onto the wet nitrocellulose membrane and let it dry until spot marks disappear.
4. Rinse the nitrocellulose membrane with 10 mL buffer B twice for 10 s each to remove free ATP, which does not bind to the filter.
5. Air-dry the nitrocellulose membrane and expose to X-ray film.

B: Micro spin-column chromatography

Materials and solutions:

MicroSpin G-50 columns (Amersham Bioscience): In our experience, approximately 2/3 of the applied protein was recovered from a column. Do not apply more than 10 μL on a column; otherwise, free [α-^{32}P]ATP will appear in flow-through.

Thin-layer chromatography plate: polyethyleneimine cellulose sheets (Sigma)

Developing solution: 0.5 M formic acid and 0.5 M LiCl

Developing chamber

A desktop centrifuge with refrigerating function

Procedure:

1. Mix 3 μg of each protein with 50 μCi [α-^{32}P]-ATP with 2× buffer A to a final volume of 10 μL and incubate for 10 min at 30 °C.
2. During the incubation period, prepare MicroSpin G-50 columns at 4 °C according to manufacture's instruction and keep columns at 4 °C.
3. After incubation, transfer 10 μL of each protein sample onto a MicroSpin G-50 column and centrifuge for 2 min at 3000 rpm, 4 °C.
4. Analyze 2 μL of the flow-through solution (which contains the protein and bound nucleotide but not the free nucleotide) by thin-layer chromatography on a polyethyleneimine cellulose sheet using 0.5 M formic acid and 0.5 M LiCl.
   (Option: If separation of hydrolyzed products is not required, a nitrocellulose membrane can be substituted for the polyethyleneimine cellulose sheet and analyzed as above.)
5. Air-dry the TLC plate and expose to X-ray film.

C: Equilibrium dialysis More lengthy equilibrium dialysis assays are useful for determining actual binding constants for nucleotides and have been described previously [69, 70].

16.10.4.2 ATP Hydrolysis Assays

In addition to binding nucleotide, all Hsp70 proteins have a very weak intrinsic ATPase activity [79, 213, 228], and both potassium and magnesium are required for full activity [115, 167, 217]. This intrinsic ATPase activity can be regulated by positive and negative cofactors [13, 43, 72, 100, 111, 151]. The procedure introduced here employs use of a radioactive isotope of ATP, which can be either [γ-^{32}P]ATP or [α-^{32}P]ATP. In terms of separation, free [γ-^{32}P] gives slightly better resolution from unhydrolyzed ATP than does [α-^{32}P]ADP.

Materials and solutions:

Purified proteins should be dialyzed against the ATPase assay buffer.

[γ-^{32}P]ATP (3000 Ci mmol^{-1}, Amersham Bioscience)

Unlabeled ATP stock: 100 mM ATP in H_2O, pH 7.0. Store in small aliquots at −80 °C

Mixture of [γ-^{32}P]ATP and unlabeled ATP: 2 µL [γ-^{32}P]ATP (3000 Ci mmol^{-1}), 5 µL of unlabeled ATP (10 mM), and 43 µL of ATPase assay buffer. Final concentrations: 20 µCi and 1 mM ATP

ATPase assay buffer (freshly made): 20 mM HEPES, pH 7.2, 50 mM KCl, 5 mM $MgCl_2$, and 10 mM DTT

TLC plate: polyethyleneimine cellulose sheets (Sigma)

Developing solution: 0.5 M formic acid and 0.5 M LiCl

Procedure:

1. Pre-incubate the reaction mixture (0.5 µM BiP with and without the desired concentration of a cofactor (or combinations of cofactors) in ATPase assay buffer at a total volume of 45 µL) for 5 min at room temperature. Also, set up a negative control omitting BiP and adding bovine serum albumin.
2. Start the reaction by adding 5 µL of the mixture of [γ-^{32}P]ATP and unlabeled ATP to the pre-incubated reaction mixture.
3. Incubate at 30 °C.
4. At desired time points, remove a 2-µL aliquot of the reaction mixture and spot on a TLC plate immediately.
5. Once all time points have been spotted and dried, transfer plate to a developing chamber that has been saturated with the developing solution.
6. Allow the solvent front to migrate to approximately 15 cm from the spotted line, dry immediately, and expose the TLC plate to X-ray film.
7. Quantify ATP hydrolysis by a PhosphoImager (Molecular Dynamics).

16.10.4.3 **Nucleotide Exchange Assays**

In contrast to GTP exchange factors, all of the Hsp70 nucleotide-exchange or nucleotide-releasing factors that have been identified thus far do not bind to nucleotides themselves. Instead, the binding of these cofactors causes a conformational change in the Hsp70 protein, which decreases its affinity for ADP and/or ATP. The technique currently employed for nucleotide-exchange assays utilizes size-exclusive mini spin-column chromatography performed on a desktop centrifuge [43, 100, 151]. Spin-column chromatography is very rapid and convenient, allowing the immediate separation of protein-associated nucleotides from free nucleotides [136]. The assay consists of two parts. The first part is to prepare and isolate a complex of [α-^{32}P]ATP-bound Hsc70 (here, BiP). The second part is to exchange

the bound hot nucleotides with cold ones and then to recover the Hsp70. Therefore, the radioactive signal decreases more quickly if a nucleotide-exchange cofactor is present.

Materials and solutions:

Purified proteins should be dialyzed against ATPase assay buffer prior to assaying.

MicroSpin G-50 columns (Amersham Bioscience)

[α-^{32}P]ATP (3000 Ci mmol^{-1}, Amersham Bioscience)

Unlabeled ATP stock: 100 mM ATP in H_2O, pH 7.0. Store in small aliquots at $-80\,^{\circ}C$

Mixture of 100 μCi [α-^{32}P]ATP and 250 μM unlabeled ATP in ATPase assay buffer

ATPase assay buffer (freshly made): 20 mM HEPES, pH 7.2, 50 mM KCl, 5 mM $MgCl_2$, and 10 mM DTT

TLC plate: polyethyleneimine cellulose sheets (Sigma)

Developing solution: 0.5 M formic acid and 0.5 M LiCl

Procedure:

1. Incubate 2.5 μM BiP with 50 μM [α-^{32}P]ATP in 50 μL ATPase assay buffer for 5 min at room temperature and for 5 min on ice.
2. Apply 10 μL of reaction mixture per a cold MicroSpin G-50 column to separate the [α-^{32}P]ATP-BiP complex from free nucleotide, which is retained on the column.
3. Transfer approximately 0.5 μM [α-^{32}P]ATP-BiP complex to ATPase assay buffer containing 100 μM cold ATP and any regulator (e.g., 1 μM ERdj4 or 1 μM ERdj4 plus 1 μM BAP). Keep the final volume at 50 μL.
4. Incubate the reaction mixture at room temperature and remove 12-μL aliquots at 1, 3, 5, and 10 min. Freeze the removed aliquots immediately in an ethanol–dry ice bath.
5. Thaw aliquots one at a time at room temperature, and as soon as ice particles disappear, put 10 μL onto a cold MicroSpin G-50 column and spin.
6. Keep the flow-through on ice and repeat 5–6 steps for all other aliquots.
7. Remove 2 μL of the flow-through and spot on TLC plate.
8. Dry immediately and transfer to a developing chamber that has been saturated with developing solution.
9. Allow samples to migrate ~15 cm from the origin, dry immediately, and analyze the bound nucleotide by autoradiography.
10. Quantify signal by a PhosphoImager (Molecular Dynamics) if necessary.

Note: Unlike with Hsc70, we experienced difficulty in maintaining BiP in the ATP-bound form after the second micro-spin column. A significant portion of the

nucleotide was consistently hydrolyzed to ADP. This might be due to biochemical differences between BiP and Hsc70; for example, the k_{cat} value of BiP ($k_{cat} = 0.40$ min^{-1}) is three times higher than that of Hsp70 ($k_{ca} = 0.14$ min^{-1}) [13, 213]. Therefore, it is strongly recommended to do the assay as rapidly at possible and to keep everything at 4 °C to maintain as much [α-^{32}P]ATP-BiP as possible.

16.10.5
Assays for Protein–Protein Interactions in Vitro/in Vivo

ER chaperones form complexes with unfolded proteins that are essential to their functions of aiding and monitoring protein folding. These complexes can be detected using both in vitro and in vivo assays. Commonly used methods include in vitro GST pull-down assays, co-immunoprecipitation, covalent cross-linking agents, and yeast two-hybrid interactions. It is highly recommended to use a combination of several methods to avoid false positives or false negatives that can result from limitations in the experimental assays.

16.10.5.1 In Vitro GST Pull-down Assay

The in vitro GST pull-down assay is a convenient way to detect protein-protein interactions. One of the proteins of interest can be produced as a recombinant protein by the methods described above or can be in vitro translated. The other protein is produced as a GST fusion protein. The two are allowed to interact, and the GST-fusion protein is isolated by binding to glutathione-conjugated beads. Samples are separated by SDS-PAGE. Detection of the second interacting protein can be done by autoradiography, Western blotting, or simple Coomassie blue staining of the gel. This procedure allows the investigator to alter binding conditions, such as pH, divalent cations, or nucleotides. Some chaperone–co-chaperone interactions (i.e., Hsp70-DnaJ or BiP-BAP) are nucleotide-dependent [16, 43, 211].

Methods:

1. Produce one of the proteins of interest with a GST tag as described [226]. The other protein of interest should not be GST-tagged but can possess another tag for purification purposes (i.e., His_6, HA, or myc tag). The concerns about tagging ER proteins described above may have less of an effect in this type of in vitro assay.
2. Wash the glutathione beads with the appropriate assay buffer three times at 4 °C.
3. Gently rock the GST-fusion protein with the glutathione beads for 20 min at 4 °C.
4. Pellet beads and remove unbound GST-fusion proteins by washing with assay buffer.
5. Add the second protein to the GST-fusion protein–bound beads in a 100-µL reaction mix. Generally, for detecting BiP's interaction with its cofactors, use 1 mM ATP or ADP in standard ATPase buffer.
6. Rock the reaction system gently for 1 h at 4 °C.

7. Wash the beads with assay buffer in the absence or presence of nucleotide as indicated.
8. Separate bound proteins on SDS gels and stain with Coomassie blue or transfer for Western blotting.

16.10.5.2 Co-immunoprecipitation

The in vivo association between two proteins can be detected by immunoprecipitating one protein and examining the proteins that co-precipitate. It can be carried out under a variety of conditions, including the use of covalent cross-linking agents or mild detergents to stabilize complexes. In a typical experiment, cells are disrupted and a whole-cell extract is prepared under non-denaturing conditions. The protein of interest is precipitated from the lysate by using an appropriate antibody together with protein A/G beads to isolate the target protein along with any interacting proteins. The precipitate can be analyzed for the presence of other proteins directly by autoradiography or after ionic detergent disruption of the complex followed by re-precipitation with specific antisera, if the proteins are labeled, or by Western blotting or peptide sequencing, if the proteins are not labeled. This approach can be used for both native and epitope-tagged exogenous proteins. Negative controls to test the specificity of the interactions are crucial.

Methods:

1. Prepare whole-cell lysates by lysing with a nonionic detergent like DOC or NP40 (i.e., 50 mM Tris, pH 7.5, 150 mM NaCl, 0.5% DOC, and 0.5% NP40).
2. Clear the cell lysates of nuclei and other cellular debris by centrifugation at full speed in a microcentrifuge for 10 min at 4 °C.
3. Remove supernatant to at least two Eppendorf tubes and add corresponding antibody to one tube to a final concentration of ~10 μg mL^{-1} and leave second tube as is.
4. Rock the tubes gently for 1.5 h at 4 °C.
5. Add 50 μL protein A (for most antibody isotypes) or protein G (for IgM antibodies) beads (resuspended at a 1:1 volume of beads to lysing buffer).
6. Rock gently for 0.5 h at 4 °C.
7. Wash samples three times with lysing buffer containing 400 mM NaCl to reduce nonspecific binding.
8. Perform SDS-PAGE gel followed by autoradiography or Western blotting analysis.

This method can also be modified for using recombinant proteins or proteins translated in vitro.

16.10.5.3 Chemical Cross-linking

The detergents used to solubilize cellular membranes can often disrupt protein-protein interactions. Membrane-permeable, thiol-cleavable, covalent cross-linkers, such as dithiobis (succinimidyl propionate) (DSP) [33], have been widely used to stabilize ER chaperone–client protein complexes for investigation [147–149, 181,

188]. After cross-linking, cell extracts can be immunoprecipitated and complexes can be analyzed by one- or two-dimensional gel electrophoresis that combines non-reducing and reducing electrophoretic separation in perpendicular directions.

Protocol:

1. Wash cells three times in PBS to remove serum protein.
2. Resuspend cells in cross-linking buffer (25 mM HEPES-KOH, 125 mM KCl, pH 8.3).
3. Prepare a fresh 5-mg mL^{-1} solution of DSP in dimethyl sulfoxide and add to the cells to achieve a final concentration of 150 μg mL^{-1}; control sample is treated with DMSO containing no cross-linker.
4. Incubate on ice for 1 h with occasional shaking, and then quench with glycine (100 mM) for an additional 15 min on ice.
5. Lyse the cells and immunoprecipitate with appropriate antibody (see co-immunoprecipitation section for the detailed procedure).
6. For one-dimensional gel separation, load samples under reducing conditions to separate components of the complex.
7. For two-dimensional gel separation, electrophorese the sample under non-reducing conditions to separate different cross-linked complexes that may be present. Cut the gel strip corresponding to a single sample lane from the first gel and equilibrate in 5 mL of reducing SDS sample buffer for 40 min at room temperature on a rocker to reduce DSP and to liberate the various proteins in the complex. Then place the gel strip on the top of a second gel and run at a 90° angle to the first.
8. After electrophoresis, either stain the gel with Coomassie blue or silver nitrate or transfer for Western blotting.

Other membrane-permeable and -reversible cross-linkers include ethyleneglycolbis (succinimidylsuccinate) (EGS) [6], m-maleimidobenzoyl-*N*-hydroxysuccinimide ester (MBS) [27], dimethyl adipimidate (DMA) [28], and dimethyl suberimidate (DMS) [28].

16.10.5.4 Yeast Two-hybrid System

The interaction of proteins can also be assayed in vivo through the use of a modified yeast two-hybrid system. Briefly, one protein is fused to the GAL4 DNA-binding domain and the other to the GAL4 transactivation domain. The vectors encoding them are used to transform yeast cells, and the resulting colonies are screened for interaction by plating on selective media as described above.

16.10.6 In Vivo Folding, Assembly, and Chaperone-binding Assays

16.10.6.1 Monitoring Oxidation of Intrachain Disulfide Bonds

The folding of proteins in the ER is often stabilized by the formation of disulfide bonds between cysteine residues that are juxtaposed in the folded protein. These

bonds can restrain the conformation of a denatured protein, which can result in an increased mobility of the protein on SDS gels as compared to the same protein with the disulfide bonds broken by a reducing agent such as DTT or 2-ME. This property has been used to monitor the oxidation status of ER proteins, as an indication of their folded state [20, 21, 96, 131]. Because most ER proteins fold co-translationally [7, 38], a method was developed to maintain a pool of unoxidized protein in the cell with the reversible reducing agent DTT [20]. These proteins appear to be incompletely or unstably folded, as they are bound to ER chaperones during this time [20, 96, 131]. Removal of DTT from the culture allows the ER to reestablish an oxidizing environment and allows the pool of unfolded proteins to fold and form disulfide bonds, all of which is followed by monitoring their migration on non-reducing SDS gels. NEM, an alkylating agent, is added at the time of lysis to prevent post-lysis oxidation of free cysteine residues. Assembly of multimeric proteins that are stabilized by disulfide bonds can be monitored similarly on non-reducing gels, a technique that was originally used to demonstrate that BiP binds to incompletely assembled Ig intermediates but not to completely assembled H_2L_2 molecules [17].

16.10.6.2 **Detection of Chaperone Binding**

In many cases the binding of chaperones to nascent proteins is rapid and can even occur on proteins before they have reached their full length, making it very difficult or often impossible to catch these transient associations. For mutant proteins, or proteins that require subunit assembly to complete their folding, this can be easier. In most cases, pulse-chase experiments are preferable, as they allow the investigator to specifically monitor newly synthesized proteins that are more likely to be the targets of chaperone binding. Cells are disrupted with gentle nonionic detergents (e.g., NP40, DOC, digitonin, 3-[(3-cholamidopropyl)dimethylammonio]propanesulfonate (CHAPS), dodecylmaltoside (DDM), and Triton X-100) to aid in the preservation of protein-protein interactions. The chaperone-protein complexes are detected by co-immunoprecipitation assays, which can often be done in both directions [96]. Antibodies to the chaperone co-precipitate the client protein, which can be analyzed under non-reducing conditions to monitor its oxidation status, and antibodies to the client protein can be used to identify the chaperone(s) that co-precipitate. When the interaction of BiP with proteins is being monitored, it is often important to add apyrase to the lysing buffer. This hydrolyzes ATP to AMP and ensures that the cytosolic pools of ATP do not induce post-lysis release of BiP. A second method that has proven useful is to co-express BiP ATPase mutants with the protein of interest using a transient transfection method. The ATPase mutants still interact with most client proteins but are not released either in vivo or in vitro, so the associations are easier to detect [49, 96, 155]. These types of co-immunoprecipitation experiments have been used to demonstrate that BiP binds to those regions of proteins that remain unoxidized [96, 131, 140].

For other ER chaperones (e.g., PDI, GRP94, ERdj3, and ERdj4) that do not bind ATP, the use of apyrase is not useful in stabilizing complexes, and mutants have not been identified that bind more stably to client proteins in vivo. In addition,

the binding of some of these chaperones to client proteins is sensitive to the detergents that are used to disrupt membranes and gain access to ER proteins [149]. In these cases, membrane-permeable chemical cross-linking agents, such as DSP, have been very useful in stabilizing complexes for co-precipitation experiments, allowing investigators to monitor the binding of these chaperones to unfolded proteins [147–149, 181, 188]. After immunoprecipitating the client protein or the individual chaperone, the complex is dissociated with SDS sample buffer containing reducing agents. This liberates the various components, which can then be separated by electrophoresis on SDS gels. However, because client proteins and chaperone complexes are disrupted with 2-ME or DTT, it is not possible to examine the oxidation status of the associated protein.

Acknowledgements

We wish to thank Ms. Melissa Mann for help in preparing and editing the manuscript.

References

1 (1995). *Current Protocols in Protein Science* John Wiley & Sons, Inc.

2 Ausubel, F. M., Brent, R., Kingston, R. E., Moore, D. D., Seidman, J. G., Smith, J. A., & Struhl, K. (1989). *Current Protocols in Molecular Biology* John Wiley and sons, New York, NY.

3 Bai, C. & Elledge, S. J. (1996). Gene identification using the yeast two-hybrid system. *Methods Enzymol.* **273**, 331–347.

4 Banecki, B., Liberek, K., Wall, D., Wawrzynow, A., Georgopoulos, C., Bertoli, E., Tanfani, F., & Zylicz, M. (1996). Structure-function analysis of the zinc finger region of the DnaJ molecular chaperone. *J. Biol. Chem.* **271**, 14840–14848.

5 Banecki, B. & Zylicz, M. (1996). Real time kinetics of the DnaK/DnaJ/GrpE molecular chaperone machine action. *J. Biol. Chem.* **271**, 6137–6143.

6 Baskin, L. S. & Yang, C. S. (1980). Cross-linking studies of cytochrome P-450 and reduced nicotinamide adenine dinucleotide phosphate-cytochrome P-450 reductase. *Biochem.* **19**, 2260–2264.

7 Bergman, L. W. & Kuehl, W. M. (1979). Formation of an intrachain disulfide bond on nascent immunoglobulin light chains. *J. Biol. Chem.* **254**, 8869–8876.

8 Bergman, L. W. & Kuehl, W. M. (1979). Formation of intermolecular disulfide bonds on nascent immunoglobulin polypeptides. *J. Biol. Chem.* **254**, 5690–5694.

9 Bertolotti, A., Wang, X., Novoa, I., Jungreis, R., Schlessinger, K., Cho, J. H., West, A. B., & Ron, D. (2001). Increased sensitivity to dextran sodium sulfate colitis in IRE1beta-deficient mice. *J. Clin. Invest* **107**, 585–593.

10 Bertolotti, A., Zhang, Y., Hendershot, L. M., Harding, H. P., & Ron, D. (2000). Dynamic interaction of BiP and ER stress transducers in the unfolded-protein response. *Nat. Cell Biol.* **2**, 326–332.

11 Biederer, T., Volkwein, C., & Sommer, T. (1997). Role of Cue1p in ubiquitination and degradation at the ER surface. *Science* **278**, 1806–1809.

12 Bies, C., Guth, S., Janoschek, K.,

Nastainczyk, W., Volkmer, J., & Zimmermann, R. (1999). A Scj1p homolog and folding catalysts present in dog pancreas microsomes. *Biol. Chem.* **380**, 1175–1182.

13 Bimston, D., Song, J., Winchester, D., Takayama, S., Reed, J. C., & Morimoto, R. I. (1998). BAG-1, a negative regulator of Hsp70 chaperone activity, uncouples nucleotide hydrolysis from substrate release. *EMBO Journal* **17**, 6871–6878.

14 Blond-Elguindi, S., Cwirla, S. E., Dower, W. J., Lipshutz, R. J., Sprang, S. R., Sambrook, J. F., & Gething, M. J. (1993). Affinity panning of a library of peptides displayed on bacteriophages reveals the binding specificity of BiP. *Cell* **75**, 717–728.

15 Boisrame, A., Beckerich, J. M., & Gaillardin, C. (1996). Sls1p, an endoplasmic reticulum component, is involved in the protein translocation process in the yeast Yarrowia lipolytica. *J. Biol. Chem.* **271**, 11668–11675.

16 Boisrame, A., Kabani, M., Beckerich, J. M., Hartmann, E., & Gaillardin, C. (1998). Interaction of Kar2p and Sls1p is required for efficient co-translational translocation of secreted proteins in the yeast Yarrowia lipolytica. *J. Biol. Chem.* **273**, 30903–30908.

17 Bole, D. G., Hendershot, L. M., & Kearney, J. F. (1986). Posttranslational association of immunoglobulin heavy chain binding protein with nascent heavy chains in nonsecreting and secreting hybridomas. *J. Cell. Biol.* **102**, 1558–1566.

18 Bordier, C. (1981). Phase separation of integral membrane proteins in Triton X-114 solution. *J. Biol. Chem.* **256**, 1604–1607.

19 Bowden, G. A. & Georgiou, G. (1990). Folding and aggregation of beta-lactamase in the periplasmic space of Escherichia coli. *J. Biol. Chem.* **265**, 16760–16766.

20 Braakman, I., Helenius, J., & Helenius, A. (1992). Manipulating disulfide bond formation and protein folding in the endoplasmic reticulum. *EMBO. J.* **11**, 1717–1722.

21 Braakman, I., Hoover Litty, H., Wagner, K. R., & Helenius, A. (1991). Folding of influenza hemagglutinin in the endoplasmic reticulum. *J. Cell. Biol.* **114**, 401–411.

22 Brightman, S. E., Blatch, G. L., & Zetter, B. R. (1995). Isolation of a mouse cDNA encoding MTJ1, a new murine member of the DnaJ family of proteins. *Gene* **153**, 249–254.

23 Brodsky, J. L., Goeckeler, J., & Schekman, R. (1995). BiP and Sec63p are required for both co- and posttranslational protein translocation into the yeast endoplasmic reticulum. *Proc. Natl. Acad. Sci. U.S.A.* **92**, 9643–9646.

24 Brodsky, J. L. & Schekman, R. (1993). A Sec63p-BiP complex from yeast is required for protein translocation in a reconstituted proteoliposome. *J. Cell Biol.* **123**, 1355–1363.

25 Brodsky, J. L., Werner, E. D., Dubas, M. E., Goeckeler, J. L., Kruse, K. B., & McCracken, A. A. (1999). The requirement for molecular chaperones during endoplasmic reticulum-associated protein degradation demonstrates that protein export and import are mechanistically distinct. *J. Biol. Chem.* **274**, 3453–3460.

26 Bukau, B. & Horwich, A. L. (1998). The Hsp70 and Hsp60 chaperone machines. *Cell* **92**, 351–366.

27 Burgess, A. J., Matthews, I., Grimes, E. A., Mata, A. M., Munkonge, F. M., Lee, A. G., & East, J. M. (1991). Chemical cross-linking and enzyme kinetics provide no evidence for a regulatory role for the 53 kDa glycoprotein of sarcoplasmic reticulum in calcium transport. *Biochim. Biophys. Acta* **1064**, 139–147.

28 Burt, H. M. & Jackson, J. K. (1990). Role of membrane proteins in monosodium urate crystal-membrane interactions. II. Effect of pretreatments of erythrocyte membranes with membrane permeable and impermeable protein cross-linking agents. *J. Rheumatol.* **17**, 1359–1363.

29 Bush, K. T., Goldberg, A. L., & Nigam, S. K. (1997). Proteasome inhibition leads to a heat-shock response, induction of endoplasmic reticulum chaperones, and thermotolerance. *J. Biol. Chem.* **272**, 9086–9092.

30 Cabral, C. M., Liu, Y., & Sifers, R. N. (2001). Dissecting glycoprotein quality control in the secretory pathway. *Trends Biochem. Sci.* **26**, 619–624.

31 Calfon, M., Zeng, H., Urano, F., Till, J. H., Hubbard, S. R., Harding, H. P., Clask, S. G., & Ron, D. (2002). IRE1 couples endoplasmic reticulum load to secretory capacity by processing the *XBP-1* mRNA. *Nature* **415**, 92–96.

32 Cao, X., Zhou, Y., & Lee, A. S. (1995). Requirement of tyrosine- and serine/threonine kinases in the transcriptional activation of the mammalian grp78/BiP promoter by thapsigargin. *J. Biol. Chem.* **270**, 494–502.

33 Carlsson, J., Drevin, H., & Axen, R. (1978). Protein thiolation and reversible protein-protein conjugation. N-Succinimidyl 3-(2-pyridyldithio)propionate, a new heterobifunctional reagent. *Biochem. J.* **173**, 723–737.

34 Cereghino, G. P., Cereghino, J. L., Ilgen, C., & Cregg, J. M. (2002). Production of recombinant proteins in fermenter cultures of the yeast Pichia pastoris. *Curr. Opin. Biotechnol.* **13**, 329–332.

35 Chappell, T. G., Konforti, B. B., Schmid, S. L., & Rothman, J. E. (1987). The ATPase core of a clathrin uncoating protein. *J. Biol. Chem.* **262**, 746–751.

36 Cheetham, M. E. & Caplan, A. J. (1998). Structure, function and evolution of DnaJ: conservation and adaptation of chaperone function. *Cell Stress & Chaperones* **3**, 28–36.

37 Chen, S. & Smith, D. F. (1998). Hop as an adaptor in the heat shock protein 70 (Hsp70) and hsp90 chaperone machinery. *J. Biol. Chem.* **273**, 35194–35200.

38 Chen, W., Helenius, J., Braakman, I., & Helenius, A. (1995). Cotranslational folding and calnexin binding during glycoprotein synthesis. *Proc. Natl. Acad. Sci. U.S.A* **92**, 6229–6233.

39 Chengalvala, M. V., Lubeck, M. D., Selling, B. J., Natuk, R. J., Hsu, K. H., Mason, B. B., Chanda, P. K., Bhat, R. A., Bhat, B. M., Mizutani, S., et al. (1991). Adenovirus vectors for gene expression. *Curr. Opin. Biotechnol.* **2**, 718–722.

40 Chevalier, M., King, L., & Blond, S. (1998). Purification and properties of BiP. *Methods Enzymol.* **290**, 384–409.

41 Chevalier, M., Rhee, H., Elguindi, E. C., & Blond, S. Y. (2000). Interaction of murine BiP/GRP78 with the DnaJ homologue MTJ1. *J. Biol. Chem.* **275**, 19620–19627.

42 Chirico, W. J., Markey, M. L., & Fink, A. L. (1998). Conformational changes of an Hsp70 molecular chaperone induced by nucleotides, polypeptides, and N-ethylmaleimide. *Biochem.* **37**, 13862–13870.

43 Chung, K. T., Shen, Y., & Hendershot, L. M. (2002). BAP, a mammalian BiP associated protein, is a nucleotide exchange factor that regulates the ATPase activity of BiP. *J. Biol. Chem.* **277**, 47557–47563.

44 Claros, M. G., Brunak, S., & von Heijne, G. (1997). Prediction of N-terminal protein sorting signals. *Curr. Opin. Struct. Biol.* **7**, 394–398.

45 Corsi, A. K. & Schekman, R. (1997). The lumenal domain of Sec63p stimulates the ATPase activity of BiP and mediates BiP recruitment to the translocon in Saccharomyces cerevisiae. *J. Cell Biol.* **137**, 1483–1493.

46 Cox, J. S., Shamu, C. E., & Walter, P. (1993). Transcriptional induction of genes encoding endoplasmic reticulum resident proteins requires a transmembrane protein kinase. *Cell* **73**, 1197–1206.

47 Cox, J. S. & Walter, P. (1996). A novel mechanism for regulating activity of a transcription factor that controls the unfolded protein response [see comments]. *Cell* **87**, 391–404.

48 Craven, R. A., Egerton, M., & Stirling, C. J. (1996). A novel Hsp70

of the yeast ER lumen is required for the efficient translocation of a number of protein precursors. *EMBO J.* **15**, 2640–2650.

49 Creemers, J. W., van de Loo, J. W., Plets, E., Hendershot, L. M., & Van De Ven, W. J. (2000). Binding of BiP to the processing enzyme lymphoma proprotein convertase prevents aggregation, but slows down maturation. *J. Biol. Chem.* **275**, 38842–38847.

50 Cregg, J. M., Vedvick, T. S., & Raschke, W. C. (1993). Recent advances in the expression of foreign genes in Pichia pastoris. *Biotechnology (N. Y.)* **11**, 905–910.

51 Crowley, K. S., Liao, S., Worrell, V. E., Reinhart, G. D., & Johnson, A. E. (1994). Secretory proteins move through the endoplasmic reticulum membrane via an aqueous, gated pore. *Cell* **78**, 461–471.

52 Cunnea, P. M., Miranda-Vizuete, A., Bertoli, G., Simmen, T., Damdimopoulos, A. E., Hermann, S., Leinonen, S., Huikko, M. P., Gustafsson, J. A., Sitia, R., & Spyrou, G. (2003). ERdj5, an endoplasmic reticulum (ER)-resident protein containing DnaJ and thioredoxin domains, is expressed in secretory cells or following ER stress. *J. Biol. Chem.* **278**, 1059–1066.

53 Dierks, T., Volkmer, J., Schlenstedt, G., Jung, C., Sandholzer, U., Zachmann, K., Schlotterhose, P., Neifer, K., Schmidt, B., & Zimmermann, R. (1996). A microsomal ATP-binding protein involved in efficient protein transport into the mammalian endoplasmic reticulum. *EMBO J.* **15**, 6931–6942.

54 Digilio, F. A., Morra, R., Pedone, E., Bartolucci, S., & Rossi, M. (2003). High-level expression of Alicyclobacillus acidocaldarius thioredoxin in Pichia pastoris and Bacillus subtilis. *Protein Expr. Purif.* **30**, 179–184.

55 Dorner, A. J., Wasley, L. C., & Kaufman, R. J. (1990). Protein dissociation from GRP78 and secretion are blocked by depletion of cellular ATP levels. *Proc. Natl. Acad. Sci. U.S.A.* **87**, 7429–7432.

56 Dudek, J., Volkmer, J., Bies, C., Guth, S., Muller, A., Lerner, M., Feick, P., Schafer, K. H., Morgenstern, E., Hennessy, F., Blatch, G. L., Janoscheck, K., Heim, N., Scholtes, P., Frien, M., Nastainczyk, W., & Zimmermann, R. (2002). A novel type of co-chaperone mediates transmembrane recruitment of DnaK-like chaperones to ribosomes. *EMBO J.* **21**, 2958–2967.

57 Easton, D. P., Kaneko, Y., & Subjeck, J. R. (2000). The hsp110 and Grp170 stress proteins: newly recognized relatives of the Hsp70s. *Cell Stress. Chaperones.* **5**, 276–290.

58 Ellgaard, L., Molinari, M., & Helenius, A. (1999). Setting the standards: quality control in the secretory pathway. *Science* **286**, 1882–1888.

59 Feldheim, D., Rothblatt, J., & Schekman, R. (1992). Topology and functional domains of Sec63p, an endoplasmic reticulum membrane protein required for secretory protein translocation. *Mol. Cell. Biol.* **12**, 3288–3296.

60 Feng, W., Matzuk, M. M., Mountjoy, K., Bedows, E., Ruddon, R. W., & Boime, I. (1995). The asparagine-linked oligosaccharides of the human chorionic gonadotropin beta subunit facilitate correct disulfide bond pairing. *J. Biol. Chem.* **270**, 11851–11859.

61 Fields, S. & Song, O. (1989). A novel genetic system to detect protein-protein interactions. *Nature* **340**, 245–246.

62 Flaherty, K. M., DeLuca Flaherty, C., & McKay, D. B. (1990). Three-dimensional structure of the ATPase fragment of a 70K heat-shock cognate protein. *Nature* **346**, 623–628.

63 Flaherty, K. M., Wilbanks, S. M., DeLuca Flaherty, C., & McKay, D. B. (1994). Structural basis of the 70-kilodalton heat shock cognate protein ATP hydrolytic activity. II. Structure of the active site with ADP or ATP bound to wild type and mutant ATPase

fragment. *J. Biol. Chem.* **269**, 12899–12907.

64 Fleischer, S. & Kervina, M. (1974). Subcellular fractionation of rat liver. *Methods Enzymol.* **31**, 6–41.

65 Flynn, G. C., Chappell, T. G., & Rothman, J. E. (1989). Peptide binding and release by proteins implicated as catalysts of protein assembly. *Science* **245**, 385–390.

66 Flynn, G. C., Pohl, J., Flocco, M. T., & Rothman, J. E. (1991). Peptide-binding specificity of the molecular chaperone BiP. *Nature* **353**, 726–730.

67 Freiman, R. N. & Tjian, R. (2003). Regulating the regulators: lysine modifications make their mark. *Cell* **112**, 11–17.

68 Friedlander, R., Jarosch, E., Urban, J., Volkwein, C., & Sommer, T. (2000). A regulatory link between ER-associated protein degradation and the unfolded-protein response. *Nat. Cell Biol.* **2**, 379–384.

69 Gao, B., Emoto, Y., Greene, L., & Eisenberg, E. (1993). Nucleotide binding properties of bovine brain uncoating ATPase. *J. Biol. Chem.* **268**, 8507–8513.

70 Gao, B., Greene, L., & Eisenberg, E. (1994). Characterization of nucleotide-free uncoating ATPase and its binding to ATP, ADP, and ATP analogues. *Biochem.* **33**, 2048–2054.

71 Garnier, A., Cote, J., Nadeau, I., Kamen, A., & Massie, B. (1994). Scale-up of the adenovirus expression system for the production of recombinant protein in human 293S cells. *Cytotechnology* **15**, 145–155.

72 Gassler, C. S., Wiederkehr, T., Brehmer, D., Bukau, B., & Mayer, M. P. (2001). Bag-1M accelerates nucleotide release for human Hsc70 and Hsp70 and can act concentration-dependent as positive and negative cofactor. *J. Biol. Chem.* **276**, 32538–32544.

73 Gaut, J. R. & Hendershot, L. M. (1993). Mutations within the nucleotide binding site of immunoglobulin-binding protein inhibit ATPase activity and interfere with release of immunoglobulin heavy chain. *J. Biol. Chem.* **268**, 7248–7255.

74 Gething, M. J. & Sambrook, J. (1992). Protein folding in the cell. *Nature* **355**, 33–45.

75 Gilon, T., Chomsky, O., & Kulka, R. G. (2000). Degradation signals recognized by the Ubc6p–Ubc7p ubiquitin-conjugating enzyme pair. *Mol. Cell Biol.* **20**, 7214–7219.

76 Gossen, M. & Bujard, H. (1992). Tight control of gene expression in mammalian cells by tetracycline-responsive promoters. *Proc. Natl. Acad. Sci. U.S.A.* **89**, 5547–5551.

77 Graham, K. S., Le, A., & Sifers, R. N. (1990). Accumulation of the insoluble PiZ variant of human alpha 1-antitrypsin within the hepatic endoplasmic reticulum does not elevate the steady-state level of grp78/BiP. *J. Biol. Chem.* **265**, 20463–20468.

78 Gross, M. & Hessefort, S. (1996). Purification and characterization of a 66-kDa protein from rabbit reticulocyte lysate which promotes the recycling of hsp 70. *J. Biol. Chem.* **271**, 16833–16841.

79 Ha, J. H. & McKay, D. B. (1994). ATPase kinetics of recombinant bovine 70 kDa heat shock cognate protein and its amino-terminal ATPase domain. *Biochemistry.* **33**, 14625–14635.

80 Haas, I. G. & Wabl, M. (1983). Immunoglobulin heavy chain binding protein. *Nature* **306**, 387–389.

81 Hamilton, T. G. & Flynn, G. C. (1996). Cer1p, a novel Hsp70-related protein required for posttranslational endoplasmic reticulum translocation in yeast. *J. Biol. Chem.* **271**, 30610–30613.

82 Hamilton, T. G., Norris, T. B., Tsuruda, P. R., & Flynn, G. C. (1999). Cer1p functions as a molecular chaperone in the endoplasmic reticulum of Saccharomyces cerevisiae. *Mol. Cell Biol.* **19**, 5298–5307.

83 Hamman, B. D., Hendershot, L. M., & Johnson, A. E. (1998). BiP maintains the permeability barrier of the ER membrane by sealing the lumenal end of the translocon pore

before and early in translocation. *Cell* **92**, 747–758.

84 Hammond, C. & Helenius, A. (1994). Folding of VSV G protein: sequential interaction with BiP and calnexin. *Science* **266**, 456–458.

85 Hammond, C. & Helenius, A. (1995). Quality control in the secretory pathway. *Curr. Opin. Cell Biol.* **7**, 523–529.

86 Hampton, R. Y. (2002). ER-associated degradation in protein quality control and cellular regulation. *Curr. Opin. Cell Biol. 2002. Aug. ;14(4):476. -82.* **14**, 476–482.

87 Hampton, R. Y. (2002). ER-associated degradation in protein quality control and cellular regulation. *Curr. Opin. Cell Biol.* **14**, 476–482.

88 Harding, H. P., Novoa, I., Zhang, Y., Zeng, H., Wek, R., Schapira, M., & Ron, D. (2000). Regulated translation initiation controls stress-induced gene expression in mammalian cells. *Mol. Cell* **6**, 1099–1108.

89 Harding, H. P., Zhang, Y., & Ron, D. (1999). Protein translation and folding are coupled by an endoplasmic-reticulum-resident kinase. *Nature* **397**, 271–274.

90 Hart, G. W. (1997). Dynamic O-linked glycosylation of nuclear and cytoskeletal proteins. *Annu. Rev. Biochem.* **66**, 315–335.

91 Haze, K., Yoshida, H., Yanagi, H., Yura, T., & Mori, K. (1999). Mammalian transcription factor ATF6 is synthesized as a transmembrane protein and activated by proteolysis in response to endoplasmic reticulum stress. *Mol. Biol. Cell* **10**, 3787–3799.

92 Helenius, A. & Aebi, M. (2001). Intracellular functions of N-linked glycans. *Science* **291**, 2364–2369.

93 Hellers, M., Gunne, H., & Steiner, H. (1991). Expression of posttranslational processing of preprocecropin A using a baculovirus vector. *Eur. J. Biochem.* **199**, 435–439.

94 Hellman, R., Vanhove, M., Lejeune, A., Stevens, F. J., & Hendershot, L. M. (1999). The in vivo association of BiP with newly synthesized proteins is dependent on their rate and stability of folding and simply on the presence of sequences that can bind to BiP. *J. Cell. Biol.* **144**, 21–30.

95 Hendershot, L., Bole, D., Kohler, G., & Kearney, J. F. (1987). Assembly and secretion of heavy chains that do not associate posttranslationally with immunoglobulin heavy chain-binding protein. *J. Cell. Biol.* **104**, 761–767.

96 Hendershot, L., Wei, J., Gaut, J., Melnick, J., Aviel, S., & Argon, Y. (1996). Inhibition of immunoglobulin folding and secretion by dominant negative BiP ATPase mutants. *Proc. Natl. Acad. Sci. U.S.A.* **93**, 5269–5274.

97 Hendershot, L. M., Wei, J.-Y., Gaut, J. R., Lawson, B., Freiden, P. J., & Murti, K. G. (1995). In vivo expression of mammalian BiP ATPase mutants causes disruption of the endoplasmic reticulum. *Mol. Biol. Cell.* **6**, 283–296.

98 Hennessy, F., Cheetham, M. E., Dirr, H. W., & Blatch, G. L. (2000). Analysis of the levels of conservation of the J-domain among the various types of DnaJ-like proteins. *Cell Stress. Chaperones.* **5**, 347–358.

99 Hershko, A. & Ciechanover, A. (1998). The ubiquitin system. *Annu. Rev. Biochem.* **67**, 425–479.

100 Hohfeld, J. & Jentsch, S. (1997). GrpE-like regulation of the hsc70 chaperone by the anti-apoptotic protein BAG-1. *EMBO J.* **16**, 6209–6216.

101 Hohfeld, J., Minami, Y., & Hartl, F. U. (1995). Hip, a novel cochaperone involved in the eukaryotic Hsc70/Hsp40 reaction cycle. *Cell* **83**, 589–598.

102 Hosoda, A., Kimata, Y., Tsuru, A., & Kohno, K. (2003). JPDI, a novel endoplasmic reticulum-resident protein containing both a BiP-interacting J-domain and thioredoxin-like motifs. *J. Biol. Chem.* **278**, 2669–2676.

103 Hosokawa, N., Wada, I., Hasegawa, K., Yorihuzi, T., Tremblay, L. O., Herscovics, A., & Nagata, K. (2001). A novel ER alpha-mannosidase-like protein accelerates ER-associated degradation. *EMBO Rep.* **2**, 415–422.

104 Hwang, C., Sinskey, A. J., & Lodish, H. F. (1992). Oxidized redox state of glutathione in the endoplasmic reticulum. *Science* **257**, 1496–1502.

105 Jarosch, E., Lenk, U., & Sommer, T. (2003). Endoplasmic reticulum-associated protein degradation. *Int. Rev. Cytol. 2003. ;223. :39. -81.* **223**, 39–81.

106 Jarvis DL and Summers MD (1992). *Baculovirus expression vectors.* In Recombinant DNA vaccines: Rationale and Strategies, pp. 265–291, Marcel Dekker, New York.

107 Johannes, L. & Goud, B. (2000). Facing inward from compartment shores: how many pathways were we looking for? *Traffic.* **1**, 119–123.

108 Johnson, A. E. & van Waes, M. A. (1999). The translocon: a dynamic gateway at the ER membrane. *Annu. Rev. Cell Dev. Biol.* **15**, 799–842.

109 Jones, S., Litt, R. J., Richardson, C. J., & Segev, N. (1995). Requirement of nucleotide exchange factor for Ypt1 GTPase mediated protein transport. *J. Cell Biol.* **130**, 1051–1061.

110 Kabani, M., Beckerich, J. M., & Gaillardin, C. (2000). Sls1p stimulates Sec63p-mediated activation of Kar2p in a conformation-dependent manner in the yeast endoplasmic reticulum. *Mol. Cell Biol.* **20**, 6923–6934.

111 Kabani, M., McLellan, C., Raynes, D. A., Guerriero, V., & Brodsky, J. L. (2002). HspBP1, a homologue of the yeast Fes1 and Sls1 proteins, is an Hsc70 nucleotide exchange factor. *FEBS Lett.* **531**, 339–342.

112 Kaloff, C. R. & Haas, I. G. (1995). Coordination of immunoglobulin chain folding and immunoglobulin chain assembly is essential for the formation of functional IgG. *Immunity* **2**, 629–637.

113 Kamhi-Nesher, S., Shenkman, M., Tolchinsky, S., Fromm, S. V., Ehrlich, R., & Lederkremer, G. Z. (2001). A novel quality control compartment derived from the endoplasmic reticulum. *Mol. Biol. Cell* **12**, 1711–1723.

114 Kaneda, S., Yura, T., & Yanagi, H. (2000). Production of three distinct mRNAs of 150 kDa oxygen-regulated protein (ORP150) by alternative promoters: preferential induction of one species under stress conditions. *J. Biochem. (Tokyo)* **128**, 529–538.

115 Kassenbrock, C. K. & Kelly, R. B. (1989). Interaction of heavy chain binding protein (BiP/GRP78) with adenine nucleotides. *EMBO. J.* **8**, 1461–1467.

116 Kelley, W. L. (1998). The J-domain family and the recruitment of chaperone power. *Trends Biochem. Sci.* **23**, 222–227.

117 Kim, P. S. & Arvan, P. (1995). Calnexin and BiP act as sequential molecular chaperones during thyroglobulin folding in the endoplasmic reticulum. *J. Cell Biol.* **128**, 29–38.

118 Knarr, G., Gething, M. J., Modrow, S., & Buchner, J. (1995). BiP binding sequences in antibodies. *J. Biol. Chem.* **270**, 27589–27594.

119 Knittler, M. R., Dirks, S., & Haas, I. G. (1995). Molecular chaperones involved in protein degradation in the endoplasmic reticulum: Quantitative interaction of the heat shock cognate protein BiP with partially folded immunoglobulin light chains that are degraded in the endoplasmic reticulum. *Proc. Natl. Acad. Sci. U.S.A.* **92**, 1764–1768.

120 Kohno, K., Normington, K., Sambrook, J., Gething, M. J., & Mori, K. (1993). The promoter region of the yeast KAR2 (BiP) gene contains a regulatory domain that responds to the presence of unfolded proteins in the endoplasmic reticulum. *Mol. Cell. Biol.* **13**, 877–890.

121 Koide, N. & Muramatsu, T. (1975). Specific inhibition of endo-beta-N-acetylglucosaminidase D by mannose and simple mannosides. *Biochem. Biophys. Res. Commun.* **66**, 411–416.

122 Kornfeld, R. & Kornfeld, S. (1985). Assembly of asparagine-linked oligosaccharides. *Annu. Rev. Biochem* **54**, 631–664.

123 Kowarik, M., Kung, S., Martoglio, B., & Helenius, A. (2002). Protein

folding during cotranslational translocation in the endoplasmic reticulum. *Mol. Cell* **10**, 769–778.

124 Kozutsumi, Y., Segal, M., Normington, K., Gething, M. J., & Sambrook, J. (1988). The presence of malfolded proteins in the endoplasmic reticulum signals the induction of glucose-regulated proteins. *Nature* **332**, 462–464.

125 Kurisu, J., Honma, A., Miyajima, H., Kondo, S., Okumura, M., & Imaizumi, K. (2003). MDG1/ERdj4, an ER-resident DnaJ family member, suppresses cell death induced by ER stress. *Genes Cells* **8**, 189–202.

126 Kuznetsov, G., Chen, L. B., & Nigam, S. K. (1997). Multiple molecular chaperones complex with misfolded large oligomeric glycoproteins in the endoplasmic reticulum. *J. Biol. Chem.* **272**, 3057–3063.

127 Lau, P. P., Villanueva, H., Kobayashi, K., Nakamuta, M., Chang, B. H., & Chan, L. (2001). A DnaJ protein, apobec-1-binding protein-2, modulates apolipoprotein B mRNA editing. *J. Biol. Chem.* **276**, 46445–46452.

128 Lee, A. S. (1987). Coordinated regulation of a set of genes by glucose and calcium ionophores in mammalian cells. *Trends. Biochem Sci.* **12**, 20–23.

129 Lee, A. S. (1992). Mammalian stress response: induction of the glucose-regulated protein family. *Curr. Opin. Cell Biol.* **4**, 267–273.

130 Lee, K., Tirasophon, W., Shen, X., Michalak, M., Prywes, R., Okada, T., Yoshida, H., Mori, K., & Kaufman, R. J. (2002). IRE1-mediated unconventional mRNA splicing and S2P-mediated ATF6 cleavage merge to regulate XBP1 in signaling the unfolded protein response. *Genes Dev.* **16**, 452–466.

131 Lee, Y.-K., Brewer, J. W., Hellman, R., & Hendershot, L. M. (1999). BiP and Ig light chain cooperate to control the folding of heavy chain and ensure the fidelity of immunoglobulin assembly. *Mol. Biol. Cell.* **10**, 2209–2219.

132 Lehle, L. & Tanner, W. (1976). The specific site of tunicamycin inhibition in the formation of dolichol-bound N-acetylglucosamine derivatives. *FEBS Lett.* **72**, 167–170.

133 Lenny, N. & Green, M. (1991). Regulation of endoplasmic reticulum stress proteins in COS cells transfected with immunoglobulin mu heavy chain cDNA. *J. Biol. Chem.* **266**, 20532–20537.

134 Lewis, M. J. & Pelham, H. R. (1992). Sequence of a second human KDEL receptor. *J. Mol. Biol.* **226**, 913–916.

135 Lewis, M. J., Sweet, D. J., & Pelham, H. R. (1990). The ERD2 gene determines the specificity of the luminal ER protein retention system. *Cell* **61**, 1359–1363.

136 Liberek, K., Marszalek, J., Ang, D., Georgopoulos, C., & Zylicz, M. (1991). Escherichia coli DnaJ and GrpE heat shock proteins jointly stimulate ATPase activity of DnaK. *Proc. Natl. Acad. Sci. U.S.A.* **88**, 2874–2878.

137 Lievremont, J. P., Rizzuto, R., Hendershot, L., & Meldolesi, J. (1997). BiP, a major chaperone protein of the endoplasmic reticulum lumen, plays a direct and important role in the storage of the rapidly exchanging pool of Ca2+. *J. Biol. Chem.* **272**, 30873–30879.

138 Lin, H. Y., Masso-Welch, P., Di, Y. P., Cai, J. W., Shen, J. W., & Subjeck, J. R. (1993). The 170-kDa glucose-regulated stress protein is an endoplasmic reticulum protein that binds immunoglobulin. *Mol. Biol. Cell.* **4**, 1109–1119.

139 Ma, Y. & Hendershot, L. M. (2003). Delineation of the negative feedback regulatory loop that controls protein translation during ER stress. *J. Biol. Chem.* **278**, 34864–34873.

140 Machamer, C. E., Doms, R. W., Bole, D. G., Helenius, A., & Rose, J. K. (1990). Heavy chain binding protein recognizes incompletely disulfide-bonded forms of vesicular stomatitis virus G protein. *J. Biol. Chem.* **265**, 6879–6883.

141 Malby, R. L., Caldwell, J. B., Gruen,

L. C., Harley, V. R., Ivancic, N., Kortt, A. A., Lilley, G. G., Power, B. E., Webster, R. G., Colman, P. M., et al. (1993). Recombinant antineuraminidase single chain antibody: expression, characterization, and crystallization in complex with antigen. *Proteins* **16**, 57–63.

142 Martin, J. & Hartl, F. U. (1997). The effect of macromolecular crowding on chaperonin-mediated protein folding. *Proc. Natl. Acad. Sci. U.S.A* **94**, 1107–1112.

143 Mayer, M., Reinstein, J., & Buchner, J. (2003). Modulation of the ATPase cycle of BiP by peptides and proteins. *J. Mol. Biol.* **330**, 137–144.

144 McCarty, J. S., Buchberger, A., Reinstein, J., & Bukau, B. (1995). The role of ATP in the functional cycle of the DnaK chaperone system. *J. Mol. Biol.* **249**, 126–137.

145 McClellan, A. J., Endres, J. B., Vogel, J. P., Palazzi, D., Rose, M. D., & Brodsky, J. L. (1998). Specific molecular chaperone interactions and an ATP-dependent conformational change are required during post-translational protein translocation into the yeast ER. *Mol. Biol. Cell* **9**, 3533–3545.

146 McKay, D. B. (1993). Structure and mechanism of 70-kDa heat-shock-related proteins. *Adv. Protein. Chem.* **44**, 67–98.

147 Melnick, J., Aviel, S., & Argon, Y. (1992). The endoplasmic reticulum stress protein GRP94, in addition to BiP, associates with unassembled immunoglobulin chains. *J. Biol. Chem.* **267**, 21303–21306.

148 Melnick, J., Dul, J. L., & Argon, Y. (1994). Sequential interaction of the chaperones BiP and Grp94 with immunoglobulin chains in the endoplasmic reticulum. *Nature* **370**, 373–375.

149 Meunier, L., Usherwood, Y. K., Chung, K. T., & Hendershot, L. M. (2002). A subset of chaperones and folding enzymes form multiprotein complexes in endoplasmic reticulum to bind nascent proteins. *Mol. Biol. Cell* **13**, 4456–4469.

150 Meyer, H. A., Grau, H., Kraft, R., Kostka, S., Prehn, S., Kalies, K. U., & Hartmann, E. (2000). Mammalian Sec61 is associated with Sec62 and Sec63. *J. Biol. Chem.* **275**, 14550–14557.

151 Minami, Y., Hohfeld, J., Ohtsuka, K., & Hartl, F. U. (1996). Regulation of the heat-shock protein 70 reaction cycle by the mammalian DnaJ homolog, Hsp40. *J. Biol. Chem.* **271**, 19617–19624.

152 Molinari, M., Calanca, V., Galli, C., Lucca, P., & Paganetti, P. (2003). Role of EDEM in the release of misfolded glycoproteins from the calnexin cycle. *Science* **299**, 1397–1400.

153 Molinari, M., Galli, C., Piccaluga, V., Pieren, M., & Paganetti, P. (2002). Sequential assistance of molecular chaperones and transient formation of covalent complexes during protein degradation from the ER. *J. Cell Biol. 2002. Jul. 22. ;158. (2):247. -57.* **158**, 247–257.

154 Mori, K., Ma, W., Gething, M. J., & Sambrook, J. (1993). A transmembrane protein with a cdc2+/CDC28-related kinase activity is required for signalling from the ER to the nucleus. *Cell* **74**, 743–756.

155 Morris, J. A., Dorner, A. J., Edwards, C. A., Hendershot, L. M., & Kaufman, R. J. (1997). Immunoglobulin binding protein (BiP) function is required to protect cells from endoplasmic reticulum stress but is not required for the secretion of selective proteins. *J. Biol. Chem.* **272**, 4327–4334.

156 Munro, S. & Pelham, H. R. (1987). A C-terminal signal prevents secretion of luminal ER proteins. *Cell* **48**, 899–907.

157 Neu, H. C. & Heppel, L. A. (1965). The release of enzymes from Escherichia coli by osmotic shock and during the formation of spheroplasts. *J. Biol. Chem.* **240**, 3685–3692.

158 Ng, D. T., Spear, E. D., & Walter, P. (2000). The unfolded protein response regulates multiple aspects of secretory and membrane protein biogenesis and endoplasmic reticulum quality control. *J. Cell Biol.* **150**, 77–88.

159 Nicchitta, C. V. & Blobel, G. (1993). Lumenal proteins of the mammalian endoplasmic reticulum are required to complete protein translocation. *Cell* **73**, 989–998.

160 Nishikawa, S. & Endo, T. (1997). The yeast JEM1p is a DnaJ-like protein of the endoplasmic reticulum membrane required for nuclear fusion. *J. Biol. Chem.* **272**, 12889–12892.

161 Nishikawa, S. I., Fewell, S. W., Kato, Y., Brodsky, J. L., & Endo, T. (2001). Molecular chaperones in the yeast endoplasmic reticulum maintain the solubility of proteins for retrotranslocation and degradation. *J. Cell Biol.* **153**, 1061–1070.

162 Oberdorf, J., Carlson, E. J., & Skach, W. R. (2001). Redundancy of mammalian proteasome beta subunit function during endoplasmic reticulum associated degradation. *Biochem.* **40**, 13397–13405.

163 Oda, Y., Hosokawa, N., Wada, I., & Nagata, K. (2003). EDEM as an acceptor of terminally misfolded glycoproteins released from calnexin. *Science* **299**, 1394–1397.

164 Oka, T., Sakamoto, S., Miyoshi, K., Fuwa, T., Yoda, K., Yamasaki, M., Tamura, G., & Miyake, T. (1985). Synthesis and secretion of human epidermal growth factor by Escherichia coli. *Proc. Natl. Acad. Sci. U.S.A* **82**, 7212–7216.

165 Okamura, K., Kimata, Y., Higashio, H., Tsuru, A., & Kohno, K. (2000). Dissociation of Kar2p/BiP from an ER sensory molecule, Ire1p, triggers the unfolded protein response in yeast. *Biochem. Biophys. Res. Commun.* **279**, 445–450.

166 Ozawa, K., Tsukamoto, Y., Hori, O., Kitao, Y., Yanagi, H., Stern, D. M., & Ogawa, S. (2001). Regulation of tumor angiogenesis by oxygen-regulated protein 150, an inducible endoplasmic reticulum chaperone. *Cancer Res.* **61**, 4206–4213.

167 Palleros, D. R., Reid, K. L., Shi, L., Welch, W. J., & Fink, A. L. (1993). ATP-induced protein-Hsp70 complex dissociation requires K+ but not ATP hydrolysis. *Nature* **365**, 664–666.

168 Parodi, A. J. (2000). Role of N-oligosaccharide endoplasmic reticulum processing reactions in glycoprotein folding and degradation. *Biochem. J.* **348 Pt 1**, 1–13.

169 Pathak, V. K., Schindler, D., & Hershey, J. W. (1988). Generation of a mutant form of protein synthesis initiation factor eIF-2 lacking the site of phosphorylation by eIF-2 kinases. *Mol. Cell. Biol.* **8**, 993–995.

170 Piwnica-Worms, H., Williams, N. G., Cheng, S. H., & Roberts, T. M. (1990). Regulation of pp60c-src and its interaction with polyomavirus middle T antigen in insect cells. *J. Virol.* **64**, 61–68.

171 Plemper, R. K., Bohmler, S., Bordallo, J., Sommer, T., & Wolf, D. H. (1997). Mutant analysis links the translocon and BiP to retrograde protein transport for ER degradation. *Nature* **388**, 891–895.

172 Plummer, T. H., Jr., Elder, J. H., Alexander, S., Phelan, A. W., & Tarentino, A. L. (1984). Demonstration of peptide: N-glycosidase F activity in endo-beta-N-acetylglucosaminidase F preparations. *J. Biol. Chem.* **259**, 10700–10704.

173 Polissi, A., Goffin, L., & Georgopoulos, C. (1995). The Escherichia coli heat shock response and bacteriophage lambda development. *FEMS Microbiol. Rev.* **17**, 159–169.

174 Power, B. E., Ivancic, N., Harley, V. R., Webster, R. G., Kortt, A. A., Irving, R. A., & Hudson, P. J. (1992). High-level temperature-induced synthesis of an antibody VH-domain in Escherichia coli using the PelB secretion signal. *Gene* **113**, 95–99.

175 Prapapanich, V., Chen, S., Toran, E. J., Rimerman, R. A., & Smith, D. F. (1996). Mutational analysis of the hsp70-interacting protein Hip. *Mol. Cell Biol.* **16**, 6200–6207.

176 Prols, F., Mayer, M. P., Renner, O., Czarnecki, P. G., Ast, M., Gassler, C., Wilting, J., Kurz, H., & Christ, B. (2001). Upregulation of the cochaperone Mdg1 in endothelial cells is induced by stress and during in

vitro angiogenesis. *Exp. Cell Res.* **269**, 42–53.

177 Qian, P., Li, X., Tong, G., & Chen, H. (2003). High-level Expression of the ORF6 Gene of Porcine Reproductive and Respiratory Syndrome Virus (PRRSV) in Pichia pastoris. *Virus Genes* **27**, 189–196.

178 Raynes, D. A. & Guerriero, V., Jr. (1998). Inhibition of Hsp70 ATPase activity and protein renaturation by a novel Hsp70-binding protein. *J. Biol. Chem.* **273**, 32883–32888.

179 Reddy, P., Sparvoli, A., Fagioli, C., Fassina, G., & Sitia, R. (1996). Formation of reversible disulfide bonds with the protein matrix of the endoplasmic reticulum correlates with the retention of unassembled Ig light chains. *EMBO. J.* **15**, 2077–2085.

180 Rose, M. D., Misra, L. M., & Vogel, J. P. (1989). KAR2, a karyogamy gene, is the yeast homolog of the mammalian BiP/GRP78 gene [published erratum appears in Cell 1989 Aug 25; 58(4): following 801]. *Cell* **57**, 1211–1221.

181 Roth, R. A. & Pierce, S. B. (1987). In vivo cross-linking of protein disulfide isomerase to immunoglobulins. *Biochem.* **26**, 4179–4182.

182 Rothblatt, J. A., Deshaies, R. J., Sanders, S. L., Daum, G., & Schekman, R. (1989). Multiple genes are required for proper insertion of secretory proteins into the endoplasmic reticulum in yeast. *J. Cell Biol.* **109**, 2641–2652.

183 Sadler, I., Chiang, A., Kurihara, T., Rothblatt, J., Way, J., & Silver, P. (1989). A yeast gene important for protein assembly into the endoplasmic reticulum and the nucleus has homology to DnaJ, an Escherichia coli heat shock protein. *J. Cell Biol.* **109**, 2665–2675.

184 Sanders, S. L., Whitfield, K. M., Vogel, J. P., Rose, M. D., & Schekman, R. W. (1992). Sec61p and BiP directly facilitate polypeptide translocation into the ER. *Cell* **69**, 353–365.

185 Sandvig, K., Garred, O., Prydz, K., Kozlov, J. V., Hansen, S. H., & van Deurs, B. (1992). Retrograde transport of endocytosed Shiga toxin to the endoplasmic reticulum. *Nature* **358**, 510–512.

186 Schlenstedt, G., Harris, S., Risse, B., Lill, R., & Silver, P. A. (1995). A yeast DnaJ homologue, Scj1p, can function in the endoplasmic reticulum with BiP/Kar2p via a conserved domain that specifies interactions with Hsp70s. *J. Cell Biol.* **129**, 979–988.

187 Shen, J., Chen, X., Hendershot, L., & Prywes, R. (2002). ER stress regulation of ATF6 localization by dissociation of BiP/GRP78 binding and unmasking of Golgi localization signals. *Dev. Cell 2002. Jul. ;3(1):99. -111.* **3**, 99–111.

188 Shen, Y., Meunier, L., & Hendershot, L. M. (2002). Identification and characterization of a novel endoplasmic reticulum (ER) DnaJ homologue, which stimulates ATPase activity of BiP in vitro and is induced by ER stress. *J. Biol. Chem. 2002. May. 3;277. (18.):15947. -56.* **277**, 15947–15956.

189 Shi, Y., Vattem, K. M., Sood, R., An, J., Liang, J., Stramm, L., & Wek, R. C. (1998). Identification and characterization of pancreatic eukaryotic initiation factor 2 alpha-subunit kinase, PEK, involved in translational control. *Mol. Cell Biol.* **18**, 7499–7509.

190 Sidrauski, C. & Walter, P. (1997). The transmembrane kinase Ire1p is a site-specific endonuclease that initiates mRNA splicing in the unfolded protein response. *Cell* **90**, 1031–1039.

191 Skowronek, M. H., Rotter, M., & Haas, I. G. (1999). Molecular characterization of a novel mammalian DnaJ-like Sec63p homolog. *Biol. Chem.* **380**, 1133–1138.

192 Stebbins, J. & Debouck, C. (1994). Expression systems for retroviral proteases. *Methods Enzymol.* **241**, 3–16.

193 Stuart, J. K., Myszka, D. G., Joss, L., Mitchell, R. S., McDonald, S. M., Xie, Z., Takayama, S., Reed, J. C., & Ely, K. R. (1998). Characterization of interactions between the anti-apoptotic

protein BAG-1 and Hsc70 molecular chaperones. *J. Biol. Chem.* **273**, 22506–22514.

194 Suzuki, C. K., Bonifacino, J. S., Lin, A. Y., Davis, M. M., & Klausner, R. D. (1991). Regulating the retention of T-cell receptor alpha chain variants within the endoplasmic reticulum: Ca(2+)-dependent association with BiP. *J. Cell. Biol.* **114**, 189–205.

195 Szabo, A., Korszun, R., Hartl, F. U., & Flanagan, J. (1996). A zinc finger-like domain of the molecular chaperone DnaJ is involved in binding to denatured protein substrates. *EMBO J.* **15**, 408–417.

196 Szabo, A., Langer, T., Schroder, H., Flanagan, J., Bukau, B., & Hartl, F. U. (1994). The ATP hydrolysis-dependent reaction cycle of the Escherichia coli Hsp70 system DnaK, DnaJ, and GrpE. *Proc. Natl. Acad. Sci. U.S.A.* **91**, 10345–10349.

197 Tachibana, H., Takekoshi, M., Cheng, X. J., Maeda, F., Aotsuka, S., & Ihara, S. (1999). Bacterial expression of a neutralizing mouse monoclonal antibody Fab fragment to a 150-kilodalton surface antigen of Entamoeba histolytica. *Am. J. Trop. Med. Hyg.* **60**, 35–40.

198 Takahashi, N. (1977). Demonstration of a new amidase acting on glycopeptides. *Biochem. Biophys. Res. Commun.* **76**, 1194–1201.

199 Takayama, S., Bimston, D. N., Matsuzawa, S., Freeman, B. C., Aime-Sempe, C., Xie, Z., Morimoto, R. I., & Reed, J. C. (1997). BAG-1 modulates the chaperone activity of Hsp70/Hsc70. *EMBO Journal.* **16**, 4887–4896.

200 Tatu, U. & Helenius, A. (1997). Interactions between newly synthesized glycoproteins, calnexin and a network of resident chaperones in the endoplasmic reticulum. *J. Cell Biol.* **136**, 555–565.

201 Theyssen, H., Schuster, H. P., Packschies, L., Bukau, B., & Reinstein, J. (1996). The second step of ATP binding to DnaK induces peptide release. *J. Mol. Biol.* **263**, 657–670.

202 Tirasophon, W., Welihinda, A. A., & Kaufman, R. J. (1998). A stress response pathway from the endoplasmic reticulum to the nucleus requires a novel bifunctional protein kinase/endoribonuclease (Ire1p) in mammalian cells. *Genes. Dev.* **12**, 1812–1824.

203 Travers, K. J., Patil, C. K., Wodicka, L., Lockhart, D. J., Weissman, J. S., & Walter, P. (2000). Functional and genomic analyses reveal an essential coordination between the unfolded protein response and ER-associated degradation. *Cell* **101**, 249–258.

204 Trimble, R. B., Tarentino, A. L., Plummer, T. H., Jr., & Maley, F. (1978). Asparaginyl glycopeptides with a low mannose content are hydrolyzed by endo-beta-N-acetylglucosaminidase H. *J. Biol. Chem.* **253**, 4508–4511.

205 Tyedmers, J., Lerner, M., Bies, C., Dudek, J., Skowronek, M. H., Haas, I. G., Heim, N., Nastainczyk, W., Volkmer, J., & Zimmermann, R. (2000). Homologs of the yeast Sec complex subunits Sec62p and Sec63p are abundant proteins in dog pancreas microsomes. *Proc. Natl. Acad. Sci. U.S.A* **97**, 7214–7219.

206 Tyson, J. R. & Stirling, C. J. (2000). LHS1 and SIL1 provide a lumenal function that is essential for protein translocation into the endoplasmic reticulum. *EMBO J.* **19**, 6440–6452.

207 Vanhove, M., Usherwood, Y.-K., & Hendershot, L. M. (2001). Unassembled Ig heavy chains do not cycle from BiP in vivo, but require light chains to trigger their release. *Immunity* **15**, 105–114.

208 Vogel, J. P., Misra, L. M., & Rose, M. D. (1990). Loss of BiP/GRP78 function blocks translocation of secretory proteins in yeast. *J. Cell. Biol.* **110**, 1885–1895.

209 Wang, X.-Z., Harding, H. P., Zhang, Y., Jolicoeur, E. M., Kuroda, M., & Ron, D. (1998). Cloning of mammalian Ire1 reveals diversity in the ER stress responses. *EMBO. J.* **17**, 5708–5717.

210 Watkins, J. D., Hermanowski, A. L., & Balch, W. E. (1993). Oligomeriza-

tion of immunoglobulin G heavy and light chains in vitro. A cell-free assay to study the assembly of the endoplasmic reticulum. *J. Biol. Chem.* **268**, 5182–5192.

211 Wawrzynow, A. & Zylicz, M. (1995). Divergent effects of ATP on the binding of the DnaK and DnaJ chaperones to each other, or to their various native and denatured protein substrates. *Journal. of. Biological. Chemistry.* **270**, 19300–19306.

212 Wei, J.-Y., Gaut, J. R., & Hendershot, L. M. (1995). In vitro dissociation of BiP: peptide complexes requires a conformational change in BiP after ATP binding but does not require ATP hydrolysis. *J. Biol. Chem.* **270**, 26677–26682.

213 Wei, J.-Y. & Hendershot, L. M. (1995). Characterization of the nucleotide binding properties and ATPase activity of recombinant hamster BiP purified from bacteria. *J. Biol. Chem.* **270**, 26670–26677.

214 Werner, E. D., Brodsky, J. L., & McCracken, A. A. (1996). Proteasome-dependent endoplasmic reticulum-associated protein degradation: an unconventional route to a familiar fate. *Proc. Natl. Acad. Sci. U.S.A.* **93**, 13797–13801.

215 Westin, G., Gerster, T., Muller, M. M., Schaffner, G., & Schaffner, W. (1987). OVEC, a versatile system to study transcription in mammalian cells and cell-free extracts. *Nucleic. Acids. Res.* **15**, 6787–6798.

216 Whitley, P., Nilsson, I. M., & von Heijne, G. (1996). A nascent secretory protein may traverse the ribosome/endoplasmic reticulum translocase complex as an extended chain. *J. Biol. Chem.* **271**, 6241–6244.

217 Wilbanks, S. M., DeLuca Flaherty, C., & McKay, D. B. (1994). Structural basis of the 70-kilodalton heat shock cognate protein ATP hydrolytic activity. I. Kinetic analyses of active site mutants. *J. Biol. Chem.* **269**, 12893–12898.

218 Wilhovsky, S., Gardner, R., & Hampton, R. (2000). HRD gene dependence of endoplasmic reticulum-associated degradation. *Mol. Biol. Cell* **11**, 1697–1708.

219 Wurm, F. & Bernard, A. (1999). Large-scale transient expression in mammalian cells for recombinant protein production. *Curr. Opin. Biotechnol.* **10**, 156–159.

220 Xu, R., Kume, A., Matsuda, K. M., Ueda, Y., Kodaira, H., Ogasawara, Y., Urabe, M., Kato, I., Hasegawa, M., & Ozawa, K. (1999). A selective amplifier gene for tamoxifen-inducible expansion of hematopoietic cells. *J. Gene Med.* **1**, 236–244.

221 Ye, J., Rawson, R. B., Komuro, R., Chen, X., Dave, U. P., Prywes, R., Brown, M. S., & Goldstein, J. L. (2000). ER stress induces cleavage of membrane-bound ATF6 by the same proteases that process SREBPs. *Mol. Cell* **6**, 1355–1364.

222 Yochem, J., Uchida, H., Sunshine, M., Saito, H., Georgopoulos, C. P., & Feiss, M. (1978). Genetic analysis of two genes, dnaJ and dnaK, necessary for Escherichia coli and bacteriophage lambda DNA replication. *Mol. Gen. Genet.* **164**, 9–14.

223 Yoshida, H., Haze, K., Yanagi, H., Yura, T., & Mori, K. (1998). Identification of the cis-acting endoplasmic reticulum stress response element responsible for transcriptional induction of mammalian glucose-regulated proteins. Involvement of basic leucine zipper transcription factors. *J. Biol. Chem.* **273**, 33741–33749.

224 Yoshida, H., Matsui, T., Yamamoto, A., Okada, T., & Mori, K. (2001). XBP1 mRNA is induced by ATF6 and spliced by IRE1 in response to ER stress to produce a highly active transcription factor. *Cell* **107**, 881–891.

225 Young, B. P., Craven, R. A., Reid, P. J., Willer, M., & Stirling, C. J. (2001). Sec63p and Kar2p are required for the translocation of SRP-dependent precursors into the yeast endoplasmic reticulum in vivo. *EMBO J.* **20**, 262–271.

226 Yu, M., Haslam, R. H., & Haslam, D. B. (2000). HEDJ, an Hsp40 co-

chaperone localized to the endoplasmic reticulum of human cells. *J. Biol. Chem.* **275**, 24984–24992.

227 Zerby, D., Sakhuja, K., Reddy, P. S., Zimmerman, H., Kayda, D., Ganesh, S., Pattison, S., Brann, T., Kadan, M. J., Kaleko, M., & Connelly, S. (2003). In vivo ligand-inducible regulation of gene expression in a gutless adenoviral vector system. *Hum. Gene Ther.* **14**, 749–761.

228 Zylicz, M., LeBowitz, J. H., McMacken, R., & Georgopoulos, C. (1983). The dnaK protein of Escherichia coli possesses an ATPase and autophosphorylating activity and is essential in an in vitro DNA replication system. *Proc. Natl. Acad. Sci. U.S.A.* **80**, 6431–6435.

17
Quality Control In Glycoprotein Folding

E. Sergio Trombetta and Armando J. Parodi

17.1
Introduction

The concept of quality control of protein folding in the secretory pathway emerged in the late 1970s and early 1980s when it was noticed that not in all cases did insertion of proteins in the endoplasmic reticulum (ER) result in their appearance at the expected final destination, intra- or extracellular. Several experimental results showed that cells displayed mechanisms that ensured that only proteins in their native conformations could be produced by the secretory pathway. Those mechanisms received the collective denomination of ''quality control'' [1].

Protein folding in living cells is a complex, error-prone process. Numerous mechanisms are in place to ensure that newly synthesized proteins reach their folded functional form. One such mechanism is the addition of glycans occurring in the ER lumen. Covalently linked *N*-glycans affect protein folding in cell-free assays, as they provide bulky, highly hydrophilic substituents that maintain molecules in solution while protein moieties successively adopt a variety of different conformations before reaching their final structures. In addition, the highly hydrophilic nature of *N*-glycans forces the asparagine units to which they are linked and neighboring amino acids to be in or close to the water-protein interphase. This chapter will not deal with those effects, which certainly also occur in vivo, but with folding-efficiency enhancement and ER retention of folding intermediates and irreparably misfolded species mediated by the interaction of a specific glycan structure (monoglucosylated polymannose-type compounds) with the ER lectins calnexin (CNX) and calreticulin (CRT). Recent evidence suggesting a role for a specific putative lectin (EDEM/Htm1p/Man1p) on the disposal of irreparably misfolded glycoproteins will be discussed also.

17.2
ER *N*-glycan Processing Reactions

Glycosylation of asparagine units in eukaryotic cells (*N*-glycosylation) involves the transfer of a glycan ($Glc_3Man_9GlcNAc_2$ in most cells; Figure 17.1) from dolichol-P-

Protein Folding Handbook. Part II. Edited by J. Buchner and T. Kiefhaber

ISBN: 3-527-30784-2

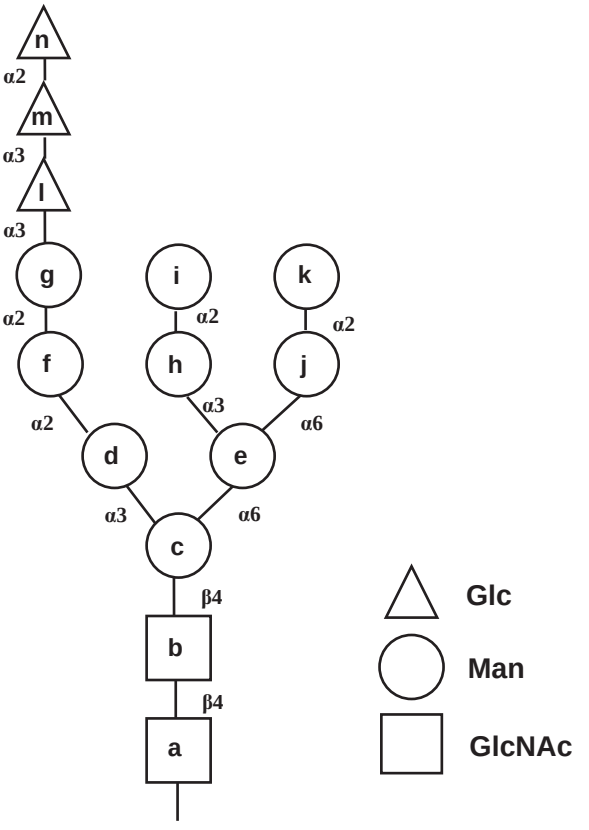

Fig. 17.1. *N*-glycan structures. Lettering (*a*–*n*) follows the order of addition of monosaccharides in the synthesis of $Glc_3Man_9GlcNAc_2$-P-P-Dol. Squares, circles, and triangles represent GlcNAc, Man, and Glc residues, respectively. GI removes residue *n* and GII removes residues *l* and *m*. GT adds residue *l* to residue *g*. The $Man_8GlcNAc_2$ isomer formed by mammalian cell or *S. cerevisiae* ER α-mannosidase I (M8B) lacks residues *i* and *l*–*n*, and the isomer formed by mammalian cell ER α-mannosidase II (M8C) is devoid of residues *k* and *l*–*n*. $Man_8GlcNAc_2$ isomer A (M8A) lacks residues *l*–*n* and *g*.

P (Dol-P-P) derivatives to consensus sequences (Asn-X-Ser/Thr, where X may be any amino acid except for Pro) in nascent polypeptide chains on the lumen of the ER [2]. Except for trypanosomatid protozoa (see below), the presence of the three glucose (Glc) units is required for efficient transfer of the glycan [3]. On the other hand, the consensus sequence is a necessary but insufficient condition for *N*-glycosylation. Processing of glycans (removal and addition of monosaccharide units) starts immediately after their transfer to proteins with the co-translational removal of the α(1,2)-linked external Glc unit (residue *n*; Figure 17.1) by glucosidase I (GI) (Figures 17.1 and 17.2). Further removal of the two remaining α(1,3)-linked Glc units is catalyzed by glucosidase II (GII). Additional *N*-glycan processing reactions such as removal of mannose (Man) units (residue *i* by mammalian or

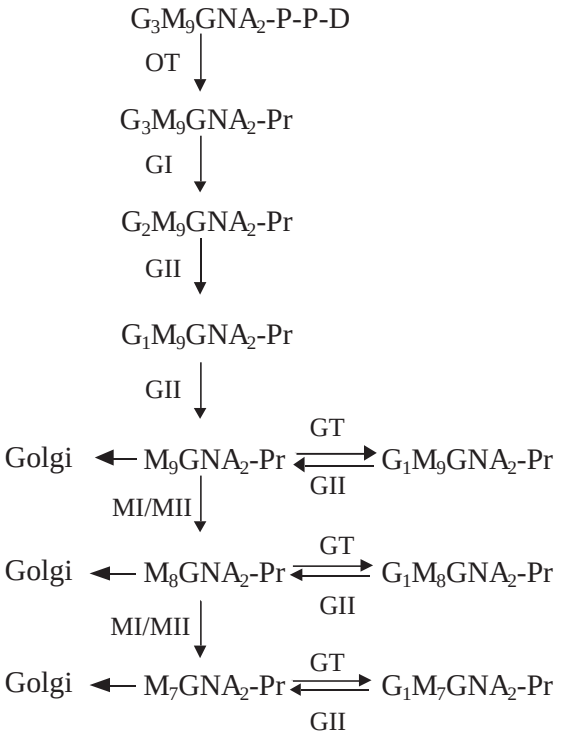

Fig. 17.2. Glycan processing in the mammalian cell ER. G, M, GNA, D, and Pr stand for Glc, Man, GlcNAc, Dol, and protein, respectively. OT, GI, GII, GT, MI and MII stand for oligosaccharyltransferase, glucosidase I, glucosidase II, UDP-Glc:glycoprotein glucosyltransferase, mannosidase I, and mannosidase II, respectively.

Saccharomyces cerevisiae ER α-mannosidase I and/or residue *k* by mammalian ER α-mannosidase II) do not necessarily occur for all glycoproteins [4]. Both the structure of the glycan transferred and the processing reactions occurring in the ER present only slight variations among protozoan, fungal, plant, and mammalian cells.

17.3 The UDP-Glc:Glycoprotein Glucosyltransferase

Beyond Glc and Man trimming, an additional processing reaction occurring in the ER is the transient reglucosylation of Glc-free protein-linked glycans ($Man_{7-9}GlcNAc_2$) (Figure 17.2) catalyzed by the UDP-Glc:glycoprotein glucosyltransferase (GT) [5–7]. The reaction products are the respective monoglucosylated derivatives that were previously deglucosylated by GII [8]. The single Glc unit is always added to Man *g* (Figure 17.1) in an α(1,3) linkage. That is, the compound

formed by partial deglucosylation of the protein-bound glycan (removal of residues *m* and *n*; Figure 17.1) is re-created by GT. The monoglucosylated species have a transient existence in vivo, as GII readily removes the re-added Glc residue. As will be further described below, a continuous interconversion between monoglucosylated and unglucosylated structures, catalyzed by the opposing activities of GT and GII, is then established. This energy-consuming, apparently futile cycle lasts until glycoproteins acquire their final native tertiary structure or, alternatively, until irreparably misfolded species are diverted to proteasomal degradation in the cytosol. GT, which is the only soluble glycosyltransferase occurring in the secretory pathway, has been detected in the ER and in the ER-Golgi intermediate compartment (ERGIC) [8, 9]. Except for that described in the protozoon *Trypanosoma cruzi*, all known GTs display KDEL-related sequences at their C-termini [6, 10]. GTs are large proteins (about 1500 amino acids) that require millimolar Ca^{2+} concentrations for activity. The relatively high Ca^{2+} requirement agrees with their subcellular location. GTs specifically use UDP-Glc as a sugar donor and an antiport transport system by which entrance of UDP-Glc into the mammalian cell ER lumen is coupled to exit of UMP [11]. Moreover, two UDPase/GDPase activities have been described in the same subcellular location [12, 13]. Except for glucuronosyltransferases that occur in the liver of higher organisms, the ubiquitous GT is the only other nucleotide sugar-dependent glycosyltransferase described to date in the ER lumen. The budding yeast *S. cerevisiae* is the only eukaryote known so far to lack an enzymatically active GT [14]. Removal of Man units by ER mannosidases I and/or II in the acceptor glycoprotein decreases glucosylation rates. Man removal from monoglucosylated glycans also decreases GII-mediated Glc excision [15, 16].

The most remarkable GT property is that it does not glucosylate properly folded or completely unfolded glycoproteins [8, 15]. Apparently, the enzyme has to somehow detect exposure of hydrophobic amino acid patches in collapsed, molten globule-like conformers to catalyze transfer of Glc units [17]. Glycans linked to peptide moieties displaying random coil conformations, such as ribonuclease B molecules in which disulfide bonds had been reduced and further alkylated, were only poorly glucosylated in spite of having hydrophobic amino acid-rich stretches [17, 18]. Similarly, addition of dithiothreitol to live *Schizosaccharomyces pombe* cells did not enhance GT-mediated protein glucosylation [19]. This result probably reflects the inability of most glycoproteins, which normally have disulfide bonds, to reach a compact, molten globule-like conformation when formation of those bonds is prevented. Further, GT only glucosylated *N*-glycans present in the vicinity of protein structural perturbations that result in the exposure of the above-mentioned patches [20].

GT is composed of at least two domains [6]. The N-terminal domain comprises 80% of the molecule, has no homology to other known proteins, and is probably involved in nonnative conformer recognition. The C-terminal or catalytic domain binds [β-^{32}P]5N$_3$UDP-Glc and displays a similar size and significant similarity to glycosyltransferase family 8 members [21]. All GT C-terminal domains from different species share a significant similarity (65–70%), but no such similarity occurs

between N-terminal domains [6]. For instance, *Rattus norvegicus* and *Drosophila melanogaster* GT N-terminal domains share a 32.6% similarity between them, but they show only a respective 15.5% and 16.3% similarity with the same portion of *S. pombe* GT. Nevertheless, the N-terminal domains of the fly and yeast enzymes were found to be mutually interchangeable, thus showing that they probably share common structural and functional features [22]. The notion that the N-terminal domain is responsible for recognition of nonnative conformers is supported by the enzymatic activities of chimeras constructed with N- and C-terminal domains of human cell GT homologues [23]. These cells express two GT homologues, only one of which is able to glucosylate misfolded glycoproteins. A chimera containing the catalytic domain of the inactive enzyme plus the N-terminal portion of the active one was found to glucosylate misfolded conformers. The notion of the N-terminal domain being the conformation sensor region agrees with the poor similarity found between those domains in different GTs. It should not be expected that the wide variety of hydrophobic amino acid patches exposed by different glycoproteins during their folding processes would require the corresponding sensor to display a stringently defined structure. Although the junction between both N- and C-terminal domains is extremely sensitive to proteolysis, both domains in the cleaved molecules could not be separated by a number of analytical procedures without losing enzymatic activity [22]. Further, the presence of the N-terminal domain appeared to be required for proper folding of the C-terminal one [22].

17.4
Protein Folding in the ER

The ER lumen has certain features that differentiate this subcellular compartment from others that also support protein folding, such as the cytosol or the mitochondria. The ER lumen is particularly rich in Ca^{2+}, which is required by several chaperones and folding-facilitating enzymes for activity, and it displays an oxidizing redox potential. Proteins following the secretory pathway are rich in cysteine residues, and several enzymes belonging to the protein disulfide isomerase family that facilitate proper formation of disulfide bridges have been described in the ER. Enzymes that catalyze *cis-trans* proline isomerization and several classical chaperones (Grp78/BiP, Grp94, Grp170) are also present in the ER lumen. Further, addition of *N*-glycans, an ER-exclusive process, is required for proper folding of most glycoproteins [5, 24].

17.5
Unconventional Chaperones (Lectins) Are Present in the ER Lumen

Two unconventional chaperones, CNX and CRT, are also present in the ER lumen [25–28]. As will be further described below, they do not directly interact

with protein moieties of folding intermediates, as classical chaperones do, but, as lectins, they specifically recognize monoglucosylated glycans either generated by GT-mediated reglucosylation or formed by partial deglucosylation of $Glc_3Man_9GlcNAc_2$ (Figure 17.1).

Mammalian CNX is a type I, approximately 572-amino-acid long transmembrane protein. The cytosolic portion has an ER-retrieval sequence at its C-terminus (RKPRRE). The single transmembrane stretch is followed by the lumenal domain. The middle region of the latter, called the P or proline-rich domain, contains two motifs, each of which is tandemly repeated four times. The lumenal portion is composed of a globular lectin domain and a long hairpin loop composed by an antiparallel arrangement of the repeated motifs. CRT is an approximately 400-amino-acid long soluble protein that has a consensus KDEL-related ER retrieval signal at its C-terminus. The middle or P-domain is highly similar to the respective CNX portion, but its two motifs are repeated only three times instead of four as in CNX. The lectin domains in CNX and CRT are structurally similar. In the ER lumen, both CNX and CRT P-domains are associated with ERp57, a protein belonging to the protein disulfide isomerase family that promotes correct disulfide bonding in monoglucosylated glycoproteins [29, 30]. Chemical cross-linking studies conducted on intact cells showed that CNX and CRT form part of a large, weakly associated, heterogeneous protein network including Grp78/BiP, Grp94, and other ER resident proteins [31].

In vitro studies have confirmed results previously obtained in vivo (see below) showing that both CNX and CRT behave as monovalent lectins specific for monoglucosylated *N*-glycans. These were the sole compounds retained by CNX- or CRT-immobilized columns when a mixture of labeled polymannose-type compounds was applied to them. Optimal binding was observed with $Glc_1Man_9GlcNAc_2$. Compounds having a lower Man content showed a diminished binding capacity, but $Glc_1Man_5GlcNAc_2$ (residues *a–g* and *l*; Figure 17.1) still had about 65% of the binding capacity of $Glc_1Man_9GlcNAc_2$ [32, 33]. On the other hand, $Glc_1Man_4GlcNAc_2$ (residues *a–d*, *f*, *g*, and *l*; Figure 17.1) was not retained by CNX or CRT. This indicated that the $\alpha(1,6)$ branch (Figure 17.1) is essential for recognition. It is worth mentioning that both Glc$\alpha(1,3)$Man and Glc$\alpha(1,3)$Glc inhibited binding of $Glc_1Man_9GlcNAc_2$ to the lectins to a similar degree. The former disaccharide is present at the non-reducing end of the glycan probe, whereas the latter one is that present in $Glc_2Man_9GlcNAc_2$, which is not retained by the lectins. This result emphasizes the importance of the polymannose core in glycan-CNX/CRT interaction, as non-relevance of the core would have probably resulted in exclusive inhibition by the former disaccharide. Isothermal titration calorimetry studies confirmed that CRT recognizes the entire Glc$\alpha(1,3)$Man$\alpha(1,2)$Man$\alpha(1,2)$Man branch in the *N*-glycan (Figure 17.1) and that the lectin has a single carbohydrate-binding site per molecule [34]. Moreover, no differences between the glycan-binding properties of CNX and CRT were found. Glycan-CNX/CRT binding required Ca^{2+}, and the presence of adenosine nucleotides or peptides linked to the glycan moiety had little or no effect on it. Monoglucosylated chicken IgG-CRT interaction, studied by surface plasmon resonance, yielded a micromolar association constant. Whereas free

$Glc_1Man_9GlcNAc_2$ inhibited the interaction, no effect of $Man_9GlcNAc_2$ was observed, attesting to its exquisite specificity [35].

17.6 In Vivo Glycoprotein-CNX/CRT Interaction

Numerous in vivo experiments involving pulse-chase labeling with [^{35}S]Met+Cys followed by cell lysis and co-immunoprecipitation with CNX/CRT antisera showed that many newly synthesized glycoproteins transiently interacted with CNX and/or CRT, irrespective of their soluble or membrane-bound status or of their final destination. Interaction was dependent on the presence of monoglucosylated *N*-glycans for the following reasons. (1) No glycoprotein-CNX/CRT interaction was detected in mammalian cell mutants lacking GI or GII activities in which either tri- or diglucosylated *N*-glycans accumulated, respectively, as a result of blocking the formation of protein-bound monoglucosylated glycans (Figure 17.2) [5, 6, 36, 37]. (2) The same effect was observed upon addition of cell-permeable GI/GII inhibitors (deoxynojirimycin or its *N*-methyl or *N*-butyl derivatives, castanospermine). (3) Addition of those same inhibitors actually significantly enhanced glycoprotein-CRT interaction in the human pathogen *T. cruzi* (trypanosomatids lack CNX) [38]. These parasitic protozoa are the only wild-type cells known so far to transfer unglucosylated glycans from Dol-P-P derivatives to nascent proteins ($Man_6GlcNAc_2$, $Man_7GlcNAc_2$, or $Man_9GlcNAc_2$, dependent on the species; the last compound is transferred in *T. cruzi*), and monoglucosylated *N*-glycans are exclusively formed in them by GT-mediated glucosylation. As expected, addition of GII inhibitors in these microorganisms leads to the accumulation of monoglucosylated species (Figure 17.2).

Although the above-mentioned in vitro studies showed no differences between CNX and CRT specificities for *N*-glycans, the pattern of glycoproteins interacting in vivo with both lectins only partially overlapped [5, 6]. This is apparently due to the CNX and CRT respective status of membrane-bound and soluble proteins, since a truncated version of CNX, displaying only its lumenal portion, and CRT recognized the same glycoproteins. The same recognition pattern was also observed in cells expressing an artificially membrane-anchored CRT and CNX. A detailed study using membrane-bound influenza virus hemagglutinin (HA) as a model glycoprotein substrate showed that CRT preferentially interacted with *N*-glycans in the top/hinge domain of the molecule, i.e., those more lumenally oriented, whereas CNX, although being more promiscuous, mainly recognized *N*-glycans in the proximity of the ER inner membrane [39]. An interesting case is that of the assembly of the human class I major histocompatibility complex (MHC). The heavy chain (a membrane glycoprotein) interacted first with CNX, but this interaction ceased upon association of the former protein with β_2 microglobulin (β_2m). CRT then associated with the heavy chain, and this interaction persisted during the rest of the assembly process, which involves transient interaction with the transporter associated with antigen processing (TAP, a trimeric complex

formed by TAP1, TAP2, and tapasin or TAP-A) and permanent association with a short, 8–10-amino-acid, peptide [40, 41]. The association first with CNX and then with CRT implies that the heavy-chain single *N*-glycan is first located close to the ER membrane but that a change in the heavy-chain conformation resulting from β_2m binding would make it more accessible to soluble ER proteins such as CRT.

17.7 Effect of CNX/CRT Binding on Glycoprotein Folding and ER Retention

One consequence of glycoprotein-CNX/CRT interaction is the ER retention of folding intermediates or of irreparably misfolded glycoproteins. Thus, the half-times of secretion of different glycoproteins synthesized in human hepatome cells, as well as those of different isotypic class I MHC molecules, correlated with their half-times of interaction with CNX [42, 43]. In addition, whereas thermosensitive G-protein of vesicular stomatitis virus ts045 mutants interacted with CNX at the non-permissive temperature, the interaction was lost and the glycoprotein correctly folded and secreted upon lowering the temperature [44]. Similarly, although both the wild-type and ΔF508 mutants of the chloride channel or transmembrane conductance regulator interacted with CNX, only the former protein was able to escape this interaction and migrate to the plasma membrane [45]. The indicated mutation is present in most cystic fibrosis patients. Furthermore, retention of GT-added Glc units in cruzipain caused by addition of GII inhibitors delayed arrival of this *T. cruzi* cysteine proteinase to lysosomes due to its prolonged interaction with CRT [46].

A model for the CNX-CRT-mediated quality control of glycoprotein folding, as initially proposed by A. Helenius and coworkers, is depicted in Figure 17.3 [47]. According to this model, a monoglucosylated glycoprotein molecule generated either by partial deglucosylation of the transferred glycan or by GT-mediated glucosylation would first interact with CNX/CRT. This interaction would be followed by a shuttle between glucosylated (CNX/CRT-bound) and deglucosylated (CNX/CRT-free) forms of the glycoprotein catalyzed by the opposing activities of GT and GII. Upon acquiring its proper tertiary structure, the glycoprotein would be deglucosylated by GII but not reglucosylated by GT and thus liberated from the CNX/CRT anchor. It follows that irreparably misfolded molecules would continue to interact with the lectins. The element sensing the conformational status of glycoproteins in this retaining mechanism is GT, an enzyme that tags folding intermediates and irreparably misfolded conformers with a Glc unit, not the unconventional chaperones (CNX/CRT). On the other hand, both the low affinity of CNX/CRT for glycoproteins and the CNX 3-D structure suggest that GII-mediated removal of Glc units occurs not on lectin-bound but on lectin-free species [35, 48].

This is not the only ER retention mechanism of incompletely folded glycoproteins. For instance, it was observed that less than 2% of truncated misfolded HA molecules were secreted by CHO cells infected with influenza virus in the presence of suboptimal puromycin concentrations that resulted in the synthesis of

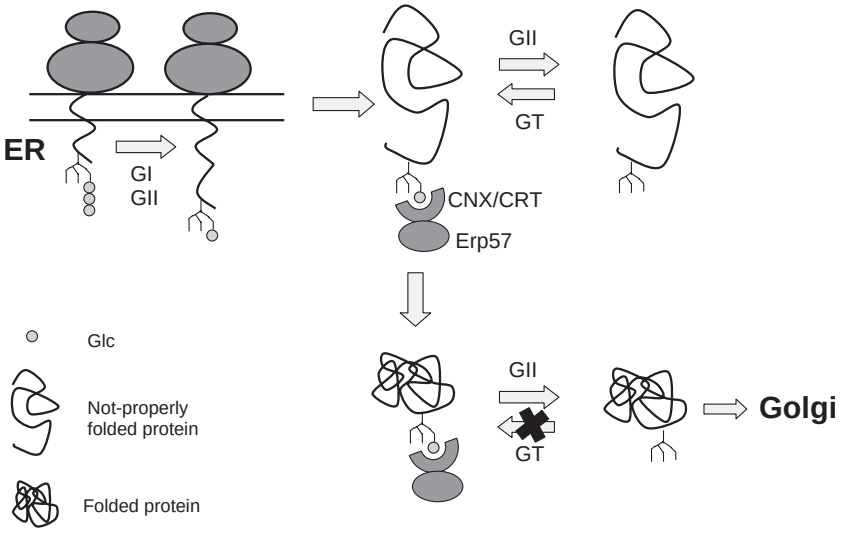

Fig. 17.3. Model proposed for the quality control of glycoprotein folding. Protein-linked $Glc_3Man_9GlcNAc_2$ is partially deglucosylated to the monoglucosylated derivative by GI and GII, and this structure is recognized by CNX/CRT. $Man_9GlcNAc_2$ is glucosylated by GT if complete deglucosylation occurs before lectin binding. The glycoprotein is liberated from the CNX/CRT anchor by GII and reglucosylated by GT only if it is not properly folded. On adoption of the native structure, the glycoprotein is released from CNX/CRT by GII and is not reglucosylated by GT. For further explanation, see text. ERp57 is a CNX/CRT-associated protein of the protein disulfide isomerase family that promotes formation of native disulfide bonds in monoglucosylated glycoproteins.

mostly C-terminal-truncated polypeptides [49]. The bulk of the molecules were found intracellularly in association with CNX/CRT but not with Grp78/BiP. Addition of GI/GII inhibitors increased the percentage of secreted species to 10%, and, as expected, no retained CNX/CRT-associated species were found. Instead and rather surprisingly, part of them was now bound to Grp78/BiP. As mentioned above, a lengthened glycoprotein-CRT interaction caused by the addition of a GII inhibitor to *T. cruzi* cells delayed arrival of a proteinase to lysosomes. Kinetics of arrival of the same glycoprotein in *T. cruzi* GT minus mutant cells was not affected by the inhibitor but was similar to that observed in wild-type cells in the presence of the drug due to a prolonged interaction with Grp78/BiP [10]. Further, synthesis of this last chaperone was upregulated in mutants. It follows that cells have alternative mechanisms applicable to both non-glycosylated proteins and glycoproteins for ER retention of folding intermediates and irreparably misfolded conformers such as binding to classical chaperones or formation of reversible disulfide bonds with ER matrix proteins.

Glycoprotein-CNX/CRT interaction not only prevents ER exit of misfolded conformers but also decreases the folding rate while increasing the folding efficiency of glycoproteins by preventing their premature oligomerization and degradation

and by facilitating formation of native disulfide bonds [5, 6, 36, 37]. The role of GT in glycoprotein-folding facilitation is highlighted by the fact that in both *S. pombe* and human cells its synthesis is induced as a consequence of the cell unfolded protein response (see Section 17.8), i.e., under conditions that promote ER accumulation of misfolded conformers (heat shock, inhibition of glycosylation, prevention of disulfide bond formation) [50, 51]. It was reported that simultaneous expression of CNX increased assembly of class I MHC heavy-chain molecules with β_2m in *D. melanogaster* cells [52]. A reduction in the level of aggregates and the use of conformational monoclonal antibodies revealed that this was due to a higher efficiency of heavy-chain folding. Similarly, addition of GI/GII inhibitors increased the folding rate of HA expressed in a rabbit reticulocyte–dog pancreas microsome system, although the overall efficiency decreased due to aggregation, premature trimerization and degradation, and formation of nonnative disulfide bridges [53]. Moreover, the same inhibitors produced similar effects on folding, disulfide bond formation, and productive homodimerization of the human insulin receptor expressed in CHO cells [54]. The effects observed upon glycoprotein-CNX/CRT interaction are not restricted to mammalian cells, as carboxypeptidase Y arrived at a higher rate, but in decreased amounts, at the vacuole (the yeast equivalent of the lysosome) of *S. pombe* GII minus mutants than at those of wild-type cells [55].

Why does glycoprotein-CNX/CRT interaction have such effects on glycoprotein folding? One of the main obstacles for productive folding is aggregation. It may be speculated that upon binding *N*-glycans, CNX/CRT maintain glycoproteins in solution, while the protein moieties acquire their proper tertiary structures helped by the sequential or simultaneous action of classical chaperones and other folding-assisting proteins. Although interaction with CNX/CRT and Grp78/BiP has been reported for several glycoproteins (coagulation factor FVIII, thyroglobulin, VSV-G, Semliki Forest virus [SFV] glycoprotein E1), other glycoproteins such as HA and SFV glycoprotein p62 exclusively interact with CNX/CRT [5, 6]. Analysis of interactions occurring between a number of glycoproteins and CNX/CRT or Grp78/BiP and mutational removal of *N*-glycosylation consensus sequences in HA revealed that *N*-glycans located approximately within the first 50 amino acids of the N-terminus determine the exclusive interaction with CNX/CRT [56]. As Grp78/BiP preferentially recognizes the presence of heptapeptides displaying aliphatic hydrophobic amino acids in alternating positions in extended conformers, steric hindrance caused by *N*-glycan proximity would probably prevent binding of the classical chaperone. It may be speculated that the length of approximately 50 amino acids within which an *N*-glycan apparently impairs Grp78/BiP binding could be related to the primary sequence information required by a polypeptide chain to adopt collapsed molten globule-like conformations that are known to display low or null Grp78/BiP-binding capacity and are suitable substrates for GT-mediated glucosylation [17]. That is, the absence of an *N*-glycan before the polypeptide collapses would allow Grp78/BiP binding, whereas its presence would prevent it. According to its specificity, GT exerts its action during the last steps of protein folding, when a newly synthesized protein accumulates enough sequence information to form long-range hydrophobic clusters characteristic of molten-globule conformations. It

may be expected that in previous folding steps other chaperones that have evolved to preferentially recognize extended hydrophobic structures, such as Grp78/BiP, could be more effective. There is evidence in several systems for a sequential intervention of Grp78/BiP and CNX/CRT to assist the entire protein-folding process. The different conformation recognition patterns between Grp78/BiP and GT provide a molecular rationale for such sequential intervention. The action of other chaperones also occurring in the ER (see Section 17.4) in conjunction of CNX/CRT has not been analyzed yet.

ERp57 is an enzyme belonging to the protein disulfide isomerase, intimately interacting with CNX/CRT in vivo as revealed by specific cross-linking with suitable reagents [29, 57–59]. It was found that ERp57 acted exclusively on monoglucosylated glycoproteins; moreover, a direct interaction between the enzyme and monoglucosylated glycoproteins (SFV glycoproteins E1 and p62) could be demonstrated by the isolation of mixed disulfide species [30]. Interaction of the classical protein disulfide isomerase (PDI) with the viral glycoproteins did not occur in ternary complexes with CNX/CRT. The participation of ERp57 in folding facilitation of class I MHC heavy-chain molecules in conjunction with CNX/CRT has also been reported. On the other hand, the effect of ERp57 addition in the proper folding of isolated bovine pancreas monoglucosylated RNase B was enhanced if CNX or CRT was added to the cell-free system [60]. The action of CNX/CRT could be simply to bring together ERp57 and a glycoprotein in order to facilitate formation of native disulfide bonds. Alternatively, the lectins may also facilitate glycoprotein folding by an additional mechanism, as ERp57 perhaps also displays a chaperone activity similar to that ascribed to PDI, a protein with which it shows 29% identity and 56% similarity. It is worth mentioning that ERp57 also interacts with glycoproteins lacking cysteine units through its association with CNX/CRT.

The already-mentioned shuttle between monoglucosylated (CNX/CRT-bound) and deglucosylated (CNX/CRT-free) forms of folding glycoproteins (Figure 17.3) is not necessarily required for increasing folding efficiency. As mentioned above, VSVts045 G-protein associated with CNX/CRT at the non-permissive temperature. Although a higher folding rate was observed upon lowering the temperature in the absence of GI/GII inhibitors (a condition that allowed the shuttle to occur), the overall folding efficiency was the same whether the inhibitors were added or not [44]. Similarly, in a *S. pombe alg6* mutant that synthesizes under-glycosylated glycoproteins, a glycoprotein essential for cell viability required GT-mediated glucosylation but not GII-mediated deglucosylation for proper folding at high temperature (see Section 17.8) [61].

17.8
Glycoprotein-CNX/CRT Interaction Is Not Essential for Unicellular Organisms and Cells in Culture

Folding facilitation and ER retention of folding intermediates and irreparably misfolded species mediated by glycoprotein-CNX/CRT interaction are not required for

single-cell viability under normal growth conditions. Mammalian or *S. pombe* cells deficient in GI or GII activities, in which monoglucosylated glycans cannot be formed by partial deglucosylation of $Glc_3Man_9GlcNAc_2$ or by GT-mediated glucosylation, do not present any discernable phenotype [50, 55, 62, 63]. Cells have alternative systems involving different chaperones for helping proteins to acquire their native structures. A deficient system is replaced by an alternative one, and, consequently, a substantial proportion of many glycoproteins may fold correctly in the absence of interaction with CNX/CRT. For instance, as mentioned above, the amount of carboxypeptidase Y that reached the vacuole in GII-deficient *S. pombe* cells after a short pulse with [^{35}S]Met decreased by only 50% with respect to wild-type cells, and about half of HA molecules folded properly when translated in a rabbit reticulocyte–dog pancreas microsome system in the presence of GI/GII inhibitors [53, 55]. Furthermore, accumulation of misfolded glycoproteins in the ER caused by a total or reduced ability of glycoproteins to interact with CNX/CRT triggers an upregulation of chaperones and other folding-assisting proteins (unfolded protein response). This has been observed in mammalian and *S. pombe* cells lacking GI/GII activities as well as in *S. pombe* and *T. cruzi* mutants lacking GT [10, 55, 64]. Further, even though several *T. cruzi* glycoproteins have been identified as essential components of differentiation and mammalian cell invasion processes, total hindering of monoglucosylated *N*-glycan formation caused by disruption of both GT-encoding alleles did not affect cell growth rate of epimastigote-form parasites and only partially affected differentiation and mammalian cell invasion [10].

The dispensable character of glycoprotein-CNX/CRT interaction for single-cell viability may be highlighted by the fact that this folding-facilitating mechanism is probably not operative in *S. cerevisiae* since this yeast lacks GT [14]. Also, contrary to what happens in *S. pombe*, *T. cruzi*, and mammalian cells, no induction of ER chaperones was observed under conditions that prevent formation of monoglucosylated *N*-glycans, thus indicating that the absence of glycoprotein-CNX interaction does not lead to an accumulation of misfolded species in the ER (both *S. cerevisiae* and *S. pombe* lack CRT) [65].

Nonetheless, glycoprotein-CNX/CRT interaction is essential for viability under conditions of excessive ER stress such as those caused by under-glycosylation of glycoproteins and high temperature: *alg6*/*gpt1 S. pombe* double mutants in which $Man_9GlcNAc_2$ is transferred (inefficiently, see Section 17.2) from lipid derivatives and that are devoid of GT activity grew at 28 °C but not at 37 °C. Growth at high temperature was rescued not only upon transfection with a GT-encoding expression vector but also by 1 M sorbitol addition, thus suggesting that the affected glycoprotein(s) might be involved in cell wall formation [61]. On the other hand, it was reported that GI/GII inhibitors prevented VSV maturation by interfering with G-protein folding, as well as with formation of infectious human immunodeficiency virus (HIV) type I particles, probably due to misfolding of loop V1–V2 in gp120 [66, 67]. In addition, the same inhibitors prevented folding of tyrosinase in melanoma cells and assembly of hepatitis B virus particles by blocking the correct folding of M glycoprotein [68, 69].

The results described above indicate that although not required for cell growth

under normal conditions, glycoprotein folding facilitation and irreparably misfolded glycoprotein ER retention mediated by glycoprotein-CNX/CRT interaction are indeed required under special conditions or for proper folding of particular proteins. Whether glycoprotein-CNX/CRT interaction is required for viability of multicellular organisms is presently unknown.

17.9
Diversion of Misfolded Glycoproteins to Proteasomal Degradation

Cells continuously monitor whether newly synthesized glycoproteins are in the process of proper folding or if, alternatively, they are irreparably misfolded. Both folding intermediates and misfolded species may be associated with CNX and CRT and thus retained in the ER. However, as permanent residence of the latter species in the ER is expected to have deleterious effects on cell viability, a mechanism for their recognition and subsequent diversion to degradation has been postulated to be necessarily required [70, 71]. It has been recently proposed that a particular glycan structure ($Man_8GlcNAc_2$ isomer B or M8B; Figure 17.1) could be the signal by which cells recognize that a glycoprotein molecule is unable to reach its native three-dimensional structure. As generation of M8B by ER α-mannosidase I is a slow process when compared to Glc removal by GI or GII, it has been speculated that if a protein folds extremely slowly or if it is irreparably misfolded, it would display the particular M8B structure that in turn would be recognized by an ER lectin and thus diverted to proteasomal degradation, a process known as ERAD (endoplasmic reticulum-associated degradation).

It was initially observed that in both *S. cerevisiae* and mammalian cells, degradation of glycoproteins unable to fold properly was delayed upon addition of ER α-mannosidase I inhibitors (deoxymannojirimycin, DMJ; kifunensin, KFN) to intact cells [72–77]. Furthermore, genetic manipulations that prevented M8B formation led to similar results. On the other hand, neither inhibitor addition nor genetic manipulation affected non-glycosylated protein degradation. Further research indicated the presence in the *S. cerevisiae* ER of an α-mannosidase I homologue (Man1p or Htm1p) that lacked mannosidase activity but for which a role of a lectin that recognized M8B was postulated [78–82]. Biochemical studies in mammalian cells showed that the mouse protein EDEM was a Man1p/Htm1p homologue, that it had no α-mannosidase activity, and that it localized to the ER and was upregulated upon an ER stress that triggered accumulation of misfolded proteins. Overexpression of this protein resulted in the accelerated ERAD of glycoproteins by promoting the release from CNX of irreparably misfolded glycoproteins but not of glycoproteins undergoing productive folding. On the contrary, downregulation of EDEM expression by the RNAi technique decreased misfolded glycoprotein disposal. Addition of KFN prevented the increased degradation that resulted from EDEM overexpression, thus suggesting that M8B was required for EDEM's role in misfolded glycoprotein degradation. EDEM co-immunoprecipitated with the misfolded glycoprotein, but it was not determined whether this represented a protein-

protein or a glycan-protein interaction. Further, EDEM interacted with CNX, but not with CRT, through their transmembrane regions. Both binding of substrates to CNX and their release from CNX were required for ERAD to occur. It was proposed that EDEM somehow prevented GT from reglucosylating irreparably misfolded molecules, thus facilitating their liberation from CNX anchors. Experiments performed with *S. cerevisiae* showed that the yeast EDEM homologue (Man1p/Htm1p) shared many of the mammalian cell protein properties.

It is evident that M8B cannot be per se a signal for degradation in *S. cerevisiae*. Although it is practically the only isomer produced in this yeast, all glycans transferred to nascent polypeptide chains are eventually converted to M8B in the ER in all glycoproteins, even in those that fold properly [83]. It may be speculated, nevertheless, that the putative lectin EDEM/Htm1p/Man1p would have to recognize both the *N*-glycan (M8B) and the misfolded status of the protein moiety to divert glycoproteins to ERAD. Even this model, however, does not explain how the putative lectin would discriminate between irreparably folded glycoproteins from folding intermediates.

Contrary to what happens in *S. cerevisiae*, where a single $Man_8GlcNAc_2$ isomer (M8B) is produced, in mammalian cells at least two isomers are formed (M8B and M8C; Figure 17.1). Whereas mammalian ER α-mannosidase I produces the first of such compounds, ER α-mannosidase II yields the second one [84–87]. ER α-mannosidase I is inhibited by both KFN and DMJ, whereas only the first compound affects ER α-mannosidase II activity. Because present evidence indicates that at least part of the proteins bound for ERAD are first transported to the *cis* Golgi cisternae and then retrieved to the ER, the products yielded by four other α-mannosidases present in the early mammalian cell secretory pathway are worth being described when considering the possible effects of glycan structures on driving misfolded glycoproteins to ERAD [71]. An endomannosidase occurs in the *cis* Golgi and in the ERGIC of high eukaryotes [88]. This enzyme liberates $Glc_{1-3}Man$ from the corresponding $Man_9GlcNAc_2$ derivatives, yielding $Man_8GlcNAc_2$ isomer A (M8A; Figure 17.1), and is not inhibited by either DMJ or KFN. As GT has also been reported to occur in the ERGIC, it is not inconceivable to assume that part of the glycoproteins degraded by proteasomes might display the M8A structure. Endomannosidase degradation of *N*-glycans would stop glucosylation-deglucosylation cycles, as M8A lacks the Man unit to which the Glc is added by GT (residue *g*; Figure 17.1). Three different *cis* Golgi α-mannosidases (IA, IB, and IC) have been described in mammalian cells. All of them are inhibited by DMJ and KFN and are able to degrade $Man_9GlcNAc_2$ to $Man_5GlcNAc_2$ [89, 90].

Although mammalian cell ER α-mannosidases I and II produce M8B and M8C, respectively, as first degradation products, both isomers may be further degraded to smaller compounds within the same subcellular location: the single *N*-glycan present in 3-hydroxy-3-methylglutaryl-CoA reductase (HMGR), an ER-resident membrane glycoprotein, was found to present the so-called microheterogeneity, as $Man_8GlcNAc_2$, $Man_7GlcNAc_2$, $Man_6GlcNAc_2$, and $Man_5GlcNAc_2$ glycans were detected on the enzyme [91]. M8B and a single $Man_6GlcNAc_2$ isomer were the main species. These results confirm that glycoproteins residing in the mammalian cell

ER for long periods of time, as irreparably misfolded species do, may have substantial amounts of glycans different from M8B and that glycoproteins displaying Man-trimmed glycans are not necessarily bound for degradation. In concurrence with these results, it was recently reported that both *S. cerevisiae* and mammalian ER α-mannosidase I is not as specific as initially thought, as the recombinant species were able to further degrade M8B to smaller glycans in vitro [92].

It was reported that addition of KFN and/or DMJ also delayed degradation of misfolded glycoproteins synthesized in the presence of GI and GII inhibitors [77, 93]. As those compounds prevent removal of Glc units from transferred glycans, this implies that the putative lectin(s) also recognizes $Glc_{1-3}Man_8GlcNAc_2$ in addition to M8B. These results, together with the variety of polymannose glycans present in glycoproteins after an extended ER residence, point not to a restricted but rather to a broad specificity of the putative ER lectin(s) involved in glycoprotein degradation. Further, it was reported that DMJ and KFN delayed ERAD in mutant mammalian cells in which neither M8B nor M8C could be formed, as in them, $Man_5GlcNAc_2$ rather than $Glc_3Man_9GlcNAc_2$ was transferred in protein *N*-glycosylation (residues *a–g*; Figure 17.1) [94]. More recent results would suggest that, at least in mammalian cells, *N*-glycans in glycoproteins bound to ERAD are degraded in the ER to $Man_{4-6}GlcNAc_2$ structures lacking Man residue *g*, i.e., the residue to which the Glc is added by GT [95]. Excision of the Man unit would remove irreparably misfolded glycoproteins from the CNX/CRT cycle, thus allowing their transport to the cytosol. This interpretation is at odds with the effect on ERAD of the addition of both mannosidase and glucosidase inhibitors: if the effect of the former on ERAD were caused by preventing disruption of CNX/CRT-glycoprotein interaction, then no effect of those same inhibitors would have been observed under conditions in which the interaction had been already prevented by retention of 2–3 Glc units in *N*-glycans.

It is clear from the results mentioned above that further studies are required to clarify the role of M8B and other Man-trimmed glycans in diversion of irreparably misfolded glycoproteins to ERAD. Regardless of the specific mechanism involved, the observed effects of KFN and DMJ might not be due to inhibition of α-mannosidase activity; being Man analogues, they could just as well affect lectin–*N*-glycan interactions.

Ubiquitination of misfolded proteins precedes their proteasomal degradation, but it is unclear whether the ubiquitination machinery somehow participates in recognition of irreparably misfolded species because the same *S. cerevisiae* ubiquitination components participate in the regulated degradation of a properly folded membrane glycoprotein such as Hmg2p (the yeast HMGR; see below) and of a soluble lumenal misfolded molecule such as a carboxypeptidase Y mutant [96]. An ubiquitin-ligase complex that specifically recognizes *N*-glycoproteins has been described in neuronal cells. Evidence was presented indicating that the complex was involved in the ERAD of ER glycoproteins, but neither the structure of the glycan moieties nor the folding status of substrate glycoproteins recognized by the complex was characterized [97]. A role of the ligase complex in driving irreparably misfolded species to proteasomal degradation is doubtful, as the interaction of the

ubiquitin-ligase complex with substrate glycoproteins occurred on the cytosolic side of the ER.

The possibility that there is no specific signal for diversion of irreparably misfolded glycoproteins to ERAD has not been ruled out. The intimate association between CNX and EDEM transmembrane regions suggests that perhaps EDEM/Htm1p/Man1p could be an unspecific polymannose lectin that could systematically trap and divert CNX-bound glycoproteins to ERAD. Species displaying robust folding would have less chance of being trapped, whereas poor folders or permanently misfolded glycoproteins would have increased chances of being diverted to ERAD due to a lengthened interaction with CNX. In this way, diversion to ERAD could simply be related to the time spent by folding intermediates and misfolded species in the proximity of EDEM/Htm1p/Man1p.

On the other hand, it is worth mentioning that factors different from the conformation of protein moieties or particular glycan structures may drive ER proteins to ERAD. For instance, the levels of HMGR, which catalyzes the major regulatory step in the mevalonate pathway that leads to the synthesis of cholesterol and a variety of essential non-sterol isoprenoids, are regulated not only by the rate of gene transcription, altered stability, and translational efficiency of its mRNA but also by accelerated proteasomal degradation of the enzyme when these requirements have been satisfied. As in the case with the *S. cerevisiae* HMGR homologue (Hmg2p), mevalonate-derived metabolic products are involved in triggering ERAD of the mammalian enzyme. It is believed that this might be due to metabolite-induced conformational changes in HMGR, resulting in its conversion to a quality-control substrate.

17.10
Unfolding Irreparably Misfolded Glycoproteins to Facilitate Proteasomal Degradation

As discussed in the previous section, the mechanism of recognition of irreparably misfolded glycoproteins by the ERAD machinery is presently not thoroughly understood. Glycoproteins that are in advanced folding stages, with several disulfide bonds formed correctly or incorrectly and that have been submitted to several rounds of CNX/CRT binding, have to be transformed into species able to traverse a channel connecting the ER lumen to the cytosol. This is probably the same translocon channel (Sec61) through which nascent polypeptides enter into the ER lumen, although a definitive identification of the protein exit channel is lacking. Once in the cytosol, proteins have to be ubiquitinated and degraded by the 26 S proteasome. The radius of the translocon channel was estimated to be 40–60 Å using fluorescent, actively translocating preproteins, but data obtained by electron microscopy suggest that the radius might be even narrower [99–101]. Moreover, it has been shown that the channel cannot allow folding of polypeptides into 35-Å diameter structures, thus indicating that if proteins bound to degradation do indeed traverse the Sec61 channel, they have to display narrower structures [102]. How are irreparably misfolded glycoproteins disentangled from aggregates, reduced, and unfolded to be able to be translocated through the channel? There are

firm indications that Grp78/BiP, PDI and probably also ERp57 are involved in that process.

A report in which an inefficiently folded membrane glycoprotein (a pancreatic isoform of human β-secretase) and its soluble variant were transiently expressed in human kidney cells illustrates events occurring during folding, unfolding, and degradation of glycoproteins [103]. A lag period after synthesis, during which both β-secretase variants were extensively oxidized and associated with CNX, Grp78/BiP, and PDI, preceded degradation. The degradative process was initiated by the release from the CNX anchor, followed by the transient formation of aggregates composed by the same secretases, Grp78/BiP and PDI, and the subsequent reduction of secretases and disulfide bridges in the aggregates. Apparently, ERp57 and another ER oxidoreductase (ERp72) were not involved in secretase degradation, but Grp78/BiP and PDI were paradoxically involved in both folding and unfolding processes. Addition of KFN delayed but did not abolish the onset of degradation. On the other hand, involvement of ERp57 in unfolding of other irreparably misfolded glycoproteins has been reported.

It is not easy to envisage a mechanism by which the same elements (Grp78/BiP, PDI, ERp57) responsible for attaining incompletely folded stages as molten globule-like structures in the ER oxidizing environment could also be responsible for the reverse process that allows passage of unfolded polypeptides through the translocon channel. In principle, the formation of the molten globule or related structures is a thermodynamically favored process, whereas polypeptide unfolding is not. Whether unfolding takes place in an ER subcompartment with a redox potential different from the rest of the ER, or if specific channels drive the reducing power and energy required to unfold irreparably misfolded species is presently unknown.

As we are dealing mainly with glycoproteins, it is pertinent to mention here the fate of the glycan moieties upon glycoprotein proteasomal degradation. A cytosolic peptide:*N*-glycanase (PNGase) that has been described in several organisms, from yeast to mammalian cells, is most probably responsible for *N*-glycan removal from glycoproteins destined for proteasomal degradation [104]. A cytosolic chitobiase-like enzyme then removes the *N*-acetylglucosamine residue at the reducing end, and a cytosolic α-mannosidase further degrades the *N*-glycan to the same $Man_5GlcNAc$ isomer that functions as an intermediate in the biosynthesis of Dol-P-P-derivatives (residues *a*–*g*; Figure 17.1) [105, 106]. *N*-glycans are then transported into the lysosomes in an ATP-dependent process for complete degradation by lysosomal glycosidases [107].

17.11 Summary and Future Directions

Proteins following the secretory pathway acquire their proper tertiary, and in certain cases also quarternary, structures in the ER. Incompletely folded species are prevented from transit to the Golgi apparatus and, if irreparably misfolded, are degraded in the proteasomes. This chapter deals with a mechanism, applicable to

ER *N*-glycosylated proteins, by which folding quality control is performed. Monoglucosylated glycans formed by glucosidase I- and glucosidase II (GII)-dependent partial deglucosylation of glycans transferred from lipid pyrophosphate derivatives to proteins ($Glc_3Man_9GlcNAc_2$) mediate glycoprotein recognition by two ER-resident chaperone lectins: calnexin (CNX), a transmembrane protein, and its soluble homologue, calreticulin (CRT). Further deglucosylation of glycans by GII liberates glycoproteins from their CNX/CRT anchors. Glycans may then be reglucosylated by the UDP-Glc:glycoprotein glucosyltransferase (GT), and thus recognized again by CNX/CRT, only when linked to protein moieties that are not yet properly folded. This enzyme behaves, therefore, as a sensor of glycoprotein conformations. Deglucosylation-reglucosylation cycles catalyzed by the opposing activities of GII and GT stop when proper folding is achieved, as glycoproteins then become substrates for GII but not for GT. Permanent liberation from CNX/CRT allows further glycoprotein transit through the secretory pathway. The CNX/CRT-monoglucosylated glycan interaction is one of the alternative mechanisms by which cells retain folding intermediates and irreparably misfolded glycoproteins in the ER; in addition, it enhances folding efficiency by preventing protein aggregation and allowing intervention of additional ER chaperones and folding-facilitating proteins. There is evidence suggesting that Man removal by resident ER mannosidases might be involved in recognition of irreparably misfolded glycoproteins bound for proteasomal degradation.

The mechanism described above constitutes a novel system, different from those of classical molecular chaperones, for retaining incompletely folded conformers and facilitating protein folding and oligomerization. CNX and CRT are unconventional chaperones that apparently do not directly sense the folding status of the substrate proteins as classical chaperones do. This task is reserved for an enzyme, GT, that introduces a covalent modification in glycoproteins not displaying their native conformations. It is this covalent modification that the element recognized by this new kind of chaperone. Although the main features of this system are already well defined, there are particular points that remain obscure and that will undoubtedly be the object of future studies, e.g., the mechanism by which GT recognizes nonnative structures, the precise way by which cells differentiate between folding intermediates from irreparably misfolded species, and the disentangling process of the latter, a process required for their transport through the translocon channel.

17.12
Characterization of *N*-glycans from Glycoproteins

17.12.1
Characterization of *N*-glycans Present in Immunoprecipitated Samples

It is possible to evaluate *N*-glycan structures on immunoprecipitated [^{35}S]-labeled proteins using glycosidases and SDS-PAGE analysis. These methods do not pro-

vide detailed carbohydrate structures but do take advantage of the immunoprecipitation technique: multiple samples can be studied simultaneously, the detection limit is very low, few cells are needed, and selected glycoproteins can be studied without the need for purification. When the protein under study is synthesized in large quantities, very short pulses are sufficient to produce an intense signal, and very early events (even co-translational) can be detected. The glycan structures are evaluated by their susceptibility to endo- and exoglycosidases, evidenced as small increases in mobility on SDS-PAGE. Each glycan removed by endo-*β*-*N*-acetylglucosaminidase H (Endo H) results in an increase in mobility of about 2 kDa, but exoglycosidases produce smaller shifts. For large proteins, the shifts are usually very small unless the glycosidases cleave *N*-glycans on several glycosylation sites.

The most common analysis is the evaluation of whether glycoproteins contain Endo H-sensitive glycans. This enzyme does not remove complex-type glycans generated in the Golgi but removes all *N*-glycoforms present in the ER. Therefore, when glycoproteins are sensitive to cleavage by Endo H, they are considered to have *N*-glycan structures similar to those acquired in the ER. Some exceptions to this rule are glycoproteins that traverse the Golgi but carry *N*-glycans that are not modified and thus remain partially or completely sensitive to Endo H. Also, certain yeasts elongate *N*-glycans in the Golgi but generate structures that remain sensitive to Endo H. In these cases, Golgi modifications can be identified by mobility shifts (the Golgi-modified forms run much slower and often diffuse) or with antibodies to *N*-glycans structures produced in the Golgi. To verify that the lack of Endo H cleavage is due to acquisition of complex-type *N*-glycans, parallel samples should be digested with Endo F or with *N*-glycosidase F. These enzymes cleave *N*-glycans irrespective of their structure and thus are insensitive to *N*-glycan modifications acquired in the Golgi.

For those glycoproteins that remain Endo H-sensitive due to their residence in the ER, the presence of glucosylated *N*-glycans can be evaluated by partial resistance to digestion with α-mannosidases displaying only exoglycosidase activity. Eight of the nine Man residues in ER-glycoforms are linked in the α-configuration and can be removed by α-mannosidases. *N*-glycans that carry a terminal Glc residue contain three Man residues protected from α-mannosidases. Therefore, glucosylated *N*-glycans are partially resistant to α-mannosidases, and a mobility difference between completely demannosylated and partially demannosylated proteins can often be detected by high-resolution SDS-PAGE (the magnitude of the shift observed with α-mannosidase digestion is smaller than with Endo H). It is difficult to distinguish between mono-, di-, and triglucosylated *N*-glycans by partial resistance to α-mannosidase. Pretreatment with GII renders di- and monoglucosylated *N*-glycans fully sensitive to α-mannosidases.

Except for GII, the other glycosidases are commercially available (Roche, Sigma, New England Biolabs, US Biologicals, Calbiochem). When α-mannosidase is obtained as an ammonium sulfate precipitate, it should be dialyzed against 50 mM sodium acetate buffer pH 5.0, and 0.1 mM zinc acetate prior to use. The washed immunoprecipitates are resuspended in 10–50 μL of 10-mM HEPES buffer pH 7.4, 0.5% SDS, 2 mM dithiothreitol and heated at 95 °C for 10 min. After a short cen-

trifugation, 1–5 μL of 10% Nonident-P40 is added to quench the SDS, and sufficient GII, Endo H, Endo F, *N*-glycanase, or α-mannosidase is added in (usually 1 μL). For α-mannosidase digestion, about 2–10 μL of 500-mM sodium acetate buffer pH 5.0, and 0.1 mM zinc acetate should be added. When appropriate, GII digestion can be performed before α-mannosidase to evaluate further the presence of glucosylated *N*-glycans. The samples are resuspended and incubated for 60–120 min at 37 °C. Reactions are stopped by addition of SDS-PAGE sample buffer and analyzed by electrophoresis and autoradiography.

17.12.2
Analysis of Radio-labeled *N*-glycans

The most common way of radio-labeling *N*-glycans is by incubating cells in growth media containing radioactive Glc or Man [108]. To achieve the most efficient labeling, cells need to be depleted from unlabeled intermediates as nucleotide sugars and Dol-P derivatives. This can be done by incubating them in media devoid of those sugars for 15–30 min. If glucosidase and/or mannosidase activities need to be inhibited, suitable compounds may be added at the onset of the starving period at 1–2.5 mM concentration, as those inhibitors penetrate rather slowly into cells. Labeling has to be performed in media containing 2–5 mM Glc, as lower concentrations may result in synthesis of truncated Dol-P-P derivatives and thence to formation of non-physiological protein-linked glycans. When sufficient radioactivity is used ([U-^{14}C]-Glc or [2-^{3}H]-Man), pulses can be kept short (5 min or less), and, conesquently, *N*-glycan processing can be followed during the early stages of glycoprotein biosynthesis. [U-^{14}C]-Glc can be converted into Man and GlcNAc, leading to Glc-, Man-, and GlcNAc-labeled *N*-glycans. Cells also convert Glc rapidly into labeled lipids and amino acids. As a consequence, glycans have to be purified extensively to avoid detection of radioactivity in other molecules. When *N*-glycans are labeled with [2-^{3}H]-Man, radioactivity is confined to Man and fucose residues only, since interconversion of Man into other sugars requires oxidation of the –OH group at position 2; therefore, radio-labeled glycans retain the label exclusively in the Man or fucose. Both Glc and Man internalized by cells can be incorporated into glycoproteins following incorporation into UDP-Glc or GDP-Man and further transferred to Dol-P-Glc or Dol-P-Man [109–111].

17.12.3
Extraction and Analysis of Protein-bound *N*-glycans

After the pulse/chase, cells are extracted by suspension in chloroform/methanol/water (3:2:1) (this is best done in a glass tube, 12 × 75 mm). After vigorous mixing, the sample is centrifuged at 3000 *g* for 5 min. A proteinaceous interphase that forms between two liquid phases is carefully recovered, discarding both the upper and lower liquid phases. The pellet is further washed twice with chloroform/methanol/water (3:2:1), followed by further washes with chloroform/methanol/water (10:10:3) to extract Dol-P-P-glycans (which can be saved for further analysis).

The washed proteinaceous pellet is then digested exhaustively with Pronase (2 mg mL^{-1}, Sigma) for 24 h in 1 mM $CaCl_2$ and 200 mM Tris-HCl buffer, pH 8.0. The digestion converts most of the insoluble pellet into amino acids, short peptides, and glycopeptides. The digest is cleared by centrifugation (10 000 *g* for 5 min), and the supernatant is desalted on a Sephadex G-10 column (2 × 60 cm), equilibrated, and run in 7% 2-propanol, in which the glycopeptides are excluded and separated from most amino acids and monosaccharides in the hydrolysate. The isolated glycopeptides are dried and resuspended in 50 mM sodium acetate buffer, pH 5.5, and digested with Endo H for 18 h. Tubes are boiled for 5 min and then passed over an Amberlite MB3 acetate column (0.5 × 5 cm) to retain amino acids and other charged contaminants. The neutral glycans (released by Endo H digestion) are recovered in the flow-through of the ion-exchange column and dried. They can be analyzed by a number of chromatographic techniques. The most simple technique, and arguably the one with highest resolving power, is descending paper chromatography in 1-propanol-nitromethane-water (5:2:4) [112]. Another simple alternative is thin-layer chromatography on silica plates [113]. *N*-glycans can also be analyzed by HPLC techniques, requiring dedicated equipment but providing good resolving power for free glycans without modification [114] or after derivatization with 2-aminopyridine [115] or perbenzoylation [116].

17.12.4 GII and GT Assays

17.12.4.1 Assay for GII

GII activity can be measured using two types of substrates: radioactive glycans or artificial substrate analogues. Radioactive [^{14}C]-Glc- or [^{3}H]-Glc-labeled $Glc_1Man_9GlcNAc$ is prepared in vitro by incubating rat liver microsomes (20 mg mL^{-1}) with 10–40 μM UDP-Glc (0.8–3.2 μCi of UDP-linked [^{14}C]-Glc or [^{3}H]-Glc should be added), 1 mM castanospermine or 1-deoxynojirimycin (Sigma, Roche, Calbiochem), 10 mg mL^{-1} denatured thyroglobulin (Sigma) (see Section 17.12.4.2, Assay for GT), 10 mM $CaCl_2$, 1% Triton-X100, 5 mM 2-mercaptoethanol, and 20 mM HEPES buffer, pH 7.4, in a final volume of 200 μL for 60 min at 37 °C. Under these conditions, the radio-labeled Glc is incorporated into *N*-glycans on glycoproteins directly via reglucosylation (mostly on the denatured thyroglobulin added as exogenous acceptor) or, additionally, via the dolichol pathway. At the end of the incubation, samples are extracted with chloroform/methanol/water as described above for isolation of radio-labeled *N*-glycans from cells (see Extraction and Analysis of Protein-bound *N*-glycans). $Glc_1Man_9GlcNAc$ has to be chromatographically purified from $Glc_3Man_9GlcNAc$ and $Glc_2Man_9GlcNAc$ that might have been formed via the Dol-P pathway.

To measure GII activity, radio-labeled glycans are incubated for 5–60 min at 37 °C, with test samples in a final volume of 50–100 μL containing 10 mM HEPES buffer, pH 7.4 (1% Triton-X100 has to be added when microsomal vesicles are used as enzyme source). At the end of the incubation, the released radioactive Glc ([^{14}C]-Glc or [^{3}H]-Glc) can be detected in a number of ways. One possibility is to

separate the released Glc from the intact oligosaccharide by paper chromatography [8, 117]. Another approach to separate the released Glc is to add 100 μL of concanavalin A (ConA) (1 mg mL^{-1}, Sigma) to 200 mM Tris-HCl buffer, pH 8.0, and 1 mM $CaCl_2$ to bind all the undegraded glycan, followed by polyethylene glycol addition to precipitate the glycan-lectin complex [118]. The Glc liberated by GII in the assay is not bound by ConA and therefore remains in the supernatant after centrifugation; it is then quantified by liquid scintillation counting.

GII activity can also be measured with the artificial substrate *p*-NO_2-phenyl-α-D-glucopiranoside (Sigma). GI does not cleave this substrate, and therefore GII is the main enzyme capable of cleaving this substrate at pH 8.0, since most lysosomal glycosidases are unstable and/or inactive at such pH. In this case, Glc removal is followed by Abs405 to detect the free *p*-NO_2-phenol released. Assays can be conducted in a final volume of 100 μL containing 1 mM *p*-NO_2-phenyl-α-D-glucopiranoside in 20 mM Tris-HCl buffer, pH 8.0, and 1 mM EDTA in a thermostated cuvette, monitored continuously at 405 nm.

17.12.4.2 **Assay for GT**

The assay for GT is based on the incorporation of radioactive Glc from the sugar donor (UDP-[^{14}C]-Glc or UDP-[^{3}H]-Glc) into polymannose glycans on unlabeled denatured acceptor glycoproteins. The radio-labeled reaction product (glucosylated glycoproteins) is separated from the radio-labeled substrate (UDP-Glc) by trichloroacetic acid (TCA) precipitation and is quantified by liquid scintillation counting. The acceptor glycoproteins (bovine thyroglobulin; soybean agglutinin, SBA; bovine pancreatic ribonuclease B, RNaseB; available from Sigma, Roche, Worthington) are prepared by chemical denaturation. Glycoproteins are dissolved at high concentrations (20–50 mg mL^{-1}) in 10 mM HEPES buffer, pH 7.4. One gram of solid urea is added per milliliter of protein solution, and the mixture is incubated at 60 °C for 4 h. The samples are then exhaustively dialyzed against 10 mM HEPES buffer, pH 7.4. The assay for GT is very specific, especially when solubilized extracts and subsequently purified fractions are used as source of enzyme. When microsomes are used, incorporation of radioactive Glc into proteins may potentially arise from the Dol-P pathway [119]. This involves the formation of Dol-P-Glc from UDP-Glc and endogenous Dol-P, leading to the formation of $Glc_3Man_9GlcNAc_2$-P-P-Dol followed by transfer of the entire glycans to Asn residues on vacant glycosylation sites on the denatured glycoproteins used as substrates [120]. The enzymes involved in this cascade of reactions are integral membrane proteins and are poorly extracted in the conditions utilized to solubilize GT [8]. As a consequence, radio-labeling of the acceptor glycoproteins via the Dol-P pathway occurs only when crude microsomal membranes are used and does not occur once GT is solubilized from microsomes. In some systems (such as those derived from yeasts or plants), incurporation of radioactive Glc into trichloroacetic acid (TCA)-insoluble polysaccharides may also be observed when crude extracts are used. Reactions are conducted in 50–100 μL final volume, containning 10 mM HEPES buffer, pH 7.4, 10 mM $CaCl_2$, 5 mM 2-mercaptoethanol, and 2.5 μM UDP-Glc (about 0.01–0.05 μCi of UDP-linked [^{14}C]-Glc or [^{3}H]-Glc should be added). Reactions are initiated by addition

of the test sample and incubated for 5–30 min at 37 °C and stopped by addition of 1 mL of 10% TCA. After boiling the stopped reactions for 5 min to allow complete protein insolubilization, the precipitated proteins are recovered by low-speed centrifugation (5 min at 2000 *g*) and washed three times with 1 mL of 10% TCA. The washed pellets are resuspended in 100 μL of 1-N KOH in methanol or other commercial solubilizers, diluted with 3 mL of scintillation cocktail, and quantified by liquid scintillation counting.

17.12.5 Purification of GII and GT from Rat Liver

Both GII and GT are soluble proteins of the lumen of the ER and therefore are soluble in the absence of detergents. Low concentrations of detergents may nevertheless be used to release the soluble content of the microsomes at the start of the purification, but detergents are not used in the subsequent purification steps. GT and GII are minor components of the ER, and typically less than 1 mg of GT or GII is obtained from 100–200 g of liver, with yields below 10%. Both enzymes are highly susceptible to proteases, and therefore it is critical to include protease inhibitors in the homogenization buffers, to maintain the pH above 7.0, and to process the microsomal extracts rapidly. Microsomes can be kept frozen for a few weeks, but it is important to go from the microsomes to the final step with minimal delays. Both enzymes are relatively stable after purification. GT is composed of a single polypeptide that runs at approximately 160 kDa in sodium dodecyl sulfate–polyacrylamide gel electrophoresis (SDS-PAGE) [121]. GII is composed of two different subunits: one running at approximately 110 kDa and a second subunit that runs as a slightly diffuse band at approximately 80 kDa [122].

Buffers and Chromatography Media

Buffer A: 0.25 M sucrose, 2 mM EDTA, 20 mM Tris-HCl pH 8.0, 5 mM 2-mercaptoethanol.

Buffer B: 150 mM NaCl, 20 mM Tris-HCl buffer, pH 8.0, 5 mM 2-mercaptoethanol.

Buffer C: 20 mM Tris-HCl buffer, pH 8.0, 5 mM 2-mercaptoethanol.

Buffer D: 1 M NaCl, 20 mM Tris-HCl buffer, pH 8.0, 5 mM 2-mercaptoethanol.

Buffer E: 1 M ammonium sulfate, 5 mM 2-mercaptoethanol.

Buffer F: 0.5 M sucrose, 10 mM imidazol buffer, pH 7.0, 5 mM 2-mercaptoethanol.

Chromatography media are from Pharmacia or Sigma.

Preparation of Rat Liver Microsomes

Rats (male or female, 4–12 weeks old) are starved overnight. They are euthanized and their livers are removed and rinsed in ice-cold buffer A. From this point, all procedures are carried out on ice or in a cold room, except for the elution step

from the ConA-Sepharose column. Livers are weighted and minced in a blender with two to four volumes of buffer A containing protease inhibitors (1 mM EDTA, 10 μM leupeptin, 10 μM pepstatin, 10 μM E-64, 10 μM TLCK, 10 μM TPCK, and 100 μM PMSF). The homogenate thus obtained is centrifuged at 10 000 *g* for 10 min. The supernatant is further centrifuged at 100 000 *g* for 60 min. The pellet containing the microsomal fraction is resuspended in buffer A and stored at −80 °C.

Extraction of GT and GII from Microsomes

Since both GT and GII are soluble proteins, they can be extracted in the absence of detergents by mechanical disruption of microsomes (10 mg mL^{-1}) in buffer C using sonication, French press, or equivalent method. After mechanical disruption, the soluble fraction is recovered from the supernatant after high-speed centrifugation (60 min at 100 000 *g*) and precipitated with ammonium sulfate at 50% saturation. The insoluble pellet is resuspended and dialyzed against buffer C. Alternatively, the microsomal fraction can be solubilized with detergents at low concentration. For this, microsomes are resuspended at 10 mg mL^{-1} in buffer C and extracted with 0.1% Triton-X-100 for 30 min on ice. The homogenate is then centrifuged at 100 000 *g* for 60 min, and the supernatant of the microsomal extraction containing most of the GT and GII activity is saved. Detergent extracts are not fractionated with ammonium sulfate.

DEAE-cellulose

The solubilized fractions obtained from either detergent extraction of microsomes or the ammonium sulfate cut are loaded onto a DEAE-cellulose column equilibrated in buffer C and washed in the same buffer until the Abs280 reaches background. Notice that no detergents are needed from this point on, since both GT and GII are soluble proteins. The column is then eluted with a gradient from 100% buffer C to 50% buffer D over 20 column volumes. The enzymatic activities for GT and GII are measured in the eluate of the DEAE-cellulose column (GT typically elutes before GII). From this point, the fractions containing GT activity are separated from GII activity and are pursued separately.

ConA-Sepharose

The fractions containing GT or GII activity from the DEAE-cellulose eluate are applied separately to ConA-Sepharose columns (5 mL) equilibrated in buffer B supplemented with 1 mM $CaCl_2$, 1 mM $MgCl_2$, and 1 mM $MnCl_2$. After washing in buffer B until the Abs280 reaches background, the column is filled with one volume (approximately 5 mL) of buffer B supplemented with 500 mM α-methyl-mannopyranoside (Sigma) prewarmed at 37 °C. The column is then stopped and kept at 37 °C for 15 min. The elution continues with more prewarmed buffer B supplemented with 500 mM α-methyl-mannopyranoside.

MonoQ

The fractions containing GT or GII activity eluted from their respective ConA-Sepharose columns are diluted fivefold and loaded (separately) onto a MonoQ 5/5 column equilibrated in buffer C. The column is then eluted with a gradient from 100% buffer C to 50% buffer D over 20 column volumes (20 mL), and 1-mL or 0.5-mL fractions are collected.

Gel Filtration

The fractions eluted from the MonoQ step containing GT or GII activity are further purified by gel-filtration chromatography on a Superdex S-200 column (or equivalent), equilibrated, and run in buffer B. At this stage, GII is usually homogenous. If necessary, the MonoQ or gel-filtration steps can be repeated to achieve a homogenous preparation. GII is stored in buffer B at −80 °C.

Phenyl Superose

After the gel-filtration step, GT usually requires further purification using hydrophobic interaction chromatography. The fractions eluted from the gel-filtration column containing GT activity are diluted 10-fold with buffer E, filtered, and loaded onto a Phenyl-Superose column (1 mL) equilibrated in buffer E. The column is eluted at 0.5 mL min^{-1} with a gradient from 100% buffer E to 100% buffer F over 20 mL and then further eluted with another 15 mL of buffer F. GT is strongly retained by the column and typically elutes during the beginning of the wash with buffer F. GT is usually homogenous at this step and can be stored in buffer F at −80 °C. If necessary, the MonoQ or gel-filtration steps can be repeated for further purification, but buffer exchange into buffer F is still recommended for storage of GT.

References

1 Hurtley, S. M. & Helenius, A. (1989). Protein oligomerization in the endoplasmic reticulum. *Annu. Rev. Cell Biol.* **5**, 277–308.

2 Kornfeld, R. & Kornfeld, S. (1985). Assembly of asparagine-linked oligosaccharides. *Annu. Rev. Biochem.* **54**, 631–664.

3 Parodi, A. J. (1993). *N*-glycosylation in trypanosomatid protozoa. *Glycobiology*, **3**, 193–199.

4 Herscovics, A. (2001). Structure and function of Class I α1,2-mannosidases involved in glycoprotein synthesis and endoplasmic reticulum quality control. *Biochimie*, **83**, 757–762.

5 Parodi, A. J. (2000). Protein glucosylation and its role in protein folding. *Annu. Rev. Biochem.* **69**, 69–95.

6 Trombetta. E. S. & Parodi, A. J. (2002). *N*-glycan processing and glycoprotein folding. *Adv. Prot. Chem.* **59**, 303–344.

7 Trombetta, E. S. (2003). The contribution of *N*-glycans and their processing in the endoplasmic reticulum to glycoprotein biosynthesis. *Glycobiology*, **13**, 77R–91R.

8 Trombetta, S., Bosch, M. & Parodi, A. J. (1989). Glucosylation of glycoproteins by mammalian, plant, fungal and trypanosomatid protozoa micro-

somal proteins. *Biochemistry*, **28**, 8108–8116.

9 Zuber, C., Fan, J., Guhl, B., Parodi, A. J., Fessler, J. H., Parker, C. et al. (2001). Immunolocalization of UDP-Glc:glycoprotein glucosyltransferase indicates involvement of pre-Golgi intermediates in protein quality control. *Proc. Natl. Acad. Sci. USA*. **98**, 10771–10715.

10 Conte, I., Labriola, C., Cazzulo, J. J., Docampo, R. & Parodi, A. J. (2003). The interplay between folding facilitating mechanisms in *Trypanosoma cruzi* endoplasmic reticulum. *Mol. Biol. Cell*, **14**, 3529–3540.

11 Pérez, M. & Hirschberg, C. (1986). Topography of glycosylation reactions in the rough endoplasmic reticulum membrane. *J. Biol. Chem.* **261**, 6822–6830.

12 Trombetta, E. S. & Helenius, A. (1999). Glycoprotein reglucosylation and nucleotide sugar utilization in the secretory pathway: identification of a nucleoside diphosphatase in the endoplasmic reticulum. *EMBO J*. **18**, 3282–3292.

13 Failer, B. U., Braun, N. & Zimmermann H. (2002). Cloning, expression, and functional characterization of a Ca^{2+}-dependent endoplasmic reticulum nucleoside diphosphatase. *J. Biol. Chem.* **277**, 36978–36986.

14 Parodi, A. J. (1999). Reglucosylation of glycoproteins and quality control of glycoprotein folding in the endoplasmic reticulum of yeast cells. *Biochim. Biophys. Acta*, **1426**, 287–295.

15 Sousa, M., Ferrero-García, M. & Parodi, A. J. (1992). Recognition of the oligosaccharide and protein moieties of glycoproteins by the UDP-Glc:glycoprotein glucosyltransferase. *Biochemistry*, **31**, 97–105.

16 Grinna, L. S. & Robbins, P. W. (1980). Substrate specificities of rat liver microsomal glucosidases which process glycoproteins. *J. Biol. Chem.* **255**, 2255–2258.

17 Caramelo, J. J., Castro, O., Alonso, L., de Prat-Gay, G. & Parodi, A. J. (2003). UDP-Glc:glycoprotein glucosyltransferase recognizes structured and solvent accessible hydrophobic patches in molten globule-like folding intermediates. *Proc. Natl. Acad. Sci. USA*. **100**, 86–91.

18 Trombetta, E. S. & Helenius, A. (2000). Conformational requirements for glycoprotein reglucosylation in the endoplasmic reticulum. *J. Cell Biol.* **148**, 1123–1129.

19 Fernández, F., D'Alessio, C., Fanchiotti, S. & Parodi, A. J. (1998). A misfolded protein conformation is not a sufficient condition for in vivo glucosylation by the UDP-Glc:glycoprotein glucosyltransferase. *EMBO J*. **17**, 5877–5886.

20 Ritter, C. & Helenius, A. (2000). Recognition of local glycoprotein misfolding by the ER folding sensor UDP-glucose:glycoprotein glucosyltransferase. *Nature Struct. Biol.* **7**, 278–280.

21 Tessier, D. C., Dignard, D., Zapun, A., Radominska-Pandya, A., Parodi, A. J., Begeron, J. J. M. et al. (2000). Cloning and characterization of mammalian UDP-glucose:glycoprotein glucosyltransferase and the development of a specific substrate for this enzyme. *Glycobiology*, **10**, 403–412.

22 Guerin, M. & Parodi, A. J. (2003). The UDP-Glc:glycoprotein glucosyltransferase is organized in at least two tightly bound domains from yeasts to mammals. *J. Biol. Chem.* **278**, 20540–20546.

23 Arnold, S. M. & Kaufman, R. J. (2003). The noncatalytic portion of human UDP-glucose:glycoprotein glucosyltransferase I confers UDP-glucose binding and transferase function to the catalytic domain. *J. Biol. Chem.* **278**, 43320–4328.

24 Helenius, A. (1994). How *N*-linked oligosccharides affect glycoprotein folding in the endoplasmic reticulum. *Mol. Biol. Cell*, **5**, 253–265.

25 Williams, D. B. (1995). Calnexin: a molecular chaperone with a taste for carbohydrate. *Biochem. Cell Biol.* **73**, 123–132.

26 Bergeron, J. J. M., Brenner, M. B., Thomas, D. Y. & Williams, D. B.

(1994). Calnexin: a membrane-bound chaperone of the endoplasmic reticulum. *Trends Biochem. Sci.* **19**, 124–128.

27 Michalak, M., Corbett, E. F., Mesaeli, N., Nakamura, K. & Opas, M. (1999). Calreticulin: one protein, one gene, many functions. *Biochem. J.* **344**, 281–292.

28 Schrag, J. D., Procopio, D. O., Cygler, M., Thomas, D. Y. & Bergeron, J. J. M. (2003). Lectin control of protein folding and sorting in the secretory pathway. *Trends Biochem. Sci.* **28**, 49–57.

29 Oliver, J. D., Llewelyn Roderick, H., Llewelyn, D. H. & High, S. (1999). ERp57 functions as a subunit of specific complexes formed with the ER lectins calreticulin and calnexin. *Mol. Biol. Cell*, **10**, 2573–2582.

30 Molinari, M. & Helenius, A. (1999). Glycoproteins form mixed disulphides with oxidoreductases during folding in living cells. *Nature*, **402**, 90–93.

31 Tatu, U. & Helenius, A. (1997). Interactions between newly synthesized glycoproteins, calnexin and a network of resident chaperones in the endoplasmic reticulum. *J. Cell Biol.* **136**, 555–565.

32 Spiro, R. G., Zhu, Q., Bhoyroo, V. & Söling, H.-D. (1996). Definition of the lectin-like properties of the molecular chaperone, calreticulin, and demonstration of its copurification with endomannosidase from rat liver Golgi. *J. Biol. Chem.* **271**, 11588–11594.

33 Vassilakos, A., Michalak, M., Lehrman, M. A. & Williams, D. B. (1998). Oligosaccharide binding characteristics of the molecular chaperones calnexin and calreticulin. *Biochemistry*, **37**, 3480–3490.

34 Kapoor, M., Srnivas, H., Kandiah, E., Gemma, E., Ellgaard, L., Oscarson, S. et al. (2003). Interactions of substrate with calreticulin, an endoplasmic reticulum chaperone. *J. Biol. Chem.* **278**, 6194–6200.

35 Patil, A. R., Thomas, C. J. & Surolia, A. (2000). Kinetics and the mechanism of interaction of the endoplasmic reticulum chaperone, calreticulin, with monoglucosylated ($Glc_1Man_9GlcNAc_2$) substrate. *J. Biol. Chem.* **275**, 24348–24356.

36 Hammond, C. & Helenius, A. (1997). Quality control in the secretory pathway. *Curr. Opin. Cell Biol.* **7**, 523–529.

37 Trombetta, E. S. & Helenius, A. (1998). Lectins as chaperones in glycoprotein folding. *Curr. Opin. Struct. Biol.* **8**, 587–592.

38 Labriola, C., Cazzulo, J. J. & Parodi, A. J. (1999). *Trypanosoma cruzi* calreticulin is a lectin that binds monoglucosylated oligosaccharides but not protein moieties of glycoproteins. *Mol. Biol. Cell*, **10**, 1381–1394.

39 Hebert, D. N., Zhang, J. X., Chen, W., Foellmer, B. & Helenius, A. (1997). The number and location of glycans on influenza hemagglutinin determine folding and association with calnexin and calreticulin. *J. Cell Biol.* **139**, 613–623.

40 Sadasivan, B., Lehner, P. J., Ortmann, B., Spies, T. & Cresswell, P. (1996). Roles for calreticulin and a novel glycoprotein, tapasin, in the interaction of MHC class I molecules with TAP. *Immunity*, **5**, 103–114.

41 Harris, M. R., Yu, Y. Y. L., Kindle, C. S., Hansen, T. H. & Solheim, J. C. (1998). Calreticulin and calnexin interact with different protein and glycan determinants during the assembly of MHC class I. *J. Immunol.* **160**, 5404–5409.

42 Ou, W.-J., Cameron, P. H., Thomas, D. Y. & Bergeron, J. J. M. (1993). Association of folding intermediates of glycoproteins with calnexin during protein maturation. *Nature*, **364**, 771–776.

43 Degen, E. & Williams, D. B. (1991). Participation of a novel 88-kDa protein in the biogenesis of murine class I histocompatibility molecules. *J. Cell Biol.* **112**, 1099–1115.

44 Cannon, K. & Helenius, A. (1999). Trimming and readdition of glucose to *N*-linked oligosaccharides determines calnexin association of a substrate glycoprotein in living cells. *J. Biol. Chem.* **274**, 7537–7544.

45 Pind, S., Riordan, J. R. & Williams, D. B. (1994). Participation of the endoplasmic reticulum chaperone calnexin (p88, IP90) in the biogenesis of the cystic fibrosis transmembrane conductance regulator. *J. Biol. Chem.* **269**, 12784–12789.

46 Labriola, C., Cazzulo, J. J. & Parodi, A. J. (1995). Retention of glucose residues added by the UDP-Glc:glycoprotein glucosyltransferase delays exit of glycoproteins from the endoplasmic reticulum. *J. Cell Biol.* **130**, 771–779.

47 Hammond, C., Braakman, I. & Helenius, A. (1994). Role of *N*-linked oligosaccharide recognition, glucose trimming, and calnexin in glycoprotein folding and quality control. *Proc. Natl. Acad. Sci. USA.* **91**, 913–917.

48 Schrag, J. D., Bergeron, J. J. M., Li, Y., Bonsova, S., Hahn, M., Thomas, D. Y. et al. (2001). The structure of calnexin, an ER chaperone involved in quality control of protein folding. *Mol Cell*, **8**, 633–644.

49 Zhang, J.-X., Braakman, I., Matlack, K. E. S. & Helenius, A. (1997). Quality control in the secretory pathway: the role of calreticulin, calnexin and BiP in the retention of glycoproteins with C-terminal truncations. *Mol. Biol. Cell*, **8**, 1943–1954.

50 Fernández, F., Jannatipour, M., Hellman, U., Rokeach, L. & Parodi, A. J. (1996). A new stress protein: synthesis of *Schizosaccharomyces pombe* UDP-Glc:glycoprotein glucosyltransferase mRNA is induced under stress conditions but the enzyme is not essential for cell viability. *EMBO J.* **15**, 705–713.

51 Arnold, S. M., Fessler, L. I., Fessler, J. H. & Kaufman, R. J. (2000). Two homologues encoding human UDP-glucose:glycoprotein glucosyltransferase differ in mRNA expression and enzymatic activity. *Biochemistry*, **39**, 2149–2163.

52 Vassilakos, A., Cohen-Doyle, M. F., Peterson, P. A., Jackson, M. R. & Williams, D. B. (1996). The molecular chaperone calnexin facilitates folding and assembly of class I histocompatibility molecules. *EMBO J.* **15**, 1495–1506.

53 Hebert, D. N., Foellmer, B. & Helenius, A. (1996). Calnexin and calreticulin promote folding, delay oligomerization and suppress degradation of influenza hemagglutinin in microsomes. *EMBO J.* **15**, 2961–2968.

54 Bass, J., Chiu, G., Argon, Y. & Steiner, D. F. (1998). Folding of insulin receptor monomers is facilitated by the molecular chaperones calnexin and calreticulin and impaired by rapid dimerization. *J. Cell Biol.* **141**, 637–646.

55 D'Alessio, C., Fernández, F., Trombetta, E. S. & Parodi, A. J. (1999). Genetic evidence for the heterodimeric structure of glucosidase II. The effect of disrupting the subunit-encoding genes on glycoprotein folding. *J. Biol. Chem.* **274**, 25899–25905.

56 Molinari, M. & Helenius, A. (2000). Chaperone selection during glycoprotein translocation into the endoplasmic reticulum. *Science*, **288**, 331–333.

57 Oliver, J. D., Van der Wal, F., Bulleid, N. J. & High, S. (1997). Interaction of the thiol-dependent reductase ERp57 with nascent glycoproteins. *Science*, **275**, 86–88.

58 Elliott, J. G., Oliver, J. D. & High, S. (1997). The thiol-dependent reductase ERp57 interacts specifically with *N*-glycosylated integral membrane proteins. *J. Biol. Chem.* **272**, 13849–13855.

59 Farmery, M. R., Allen, S., Allen, A. J. & Bulleid, N. J. (2000). The role of ERp57 in disulfide bond formation during the assembly of major histocompatibility complex class I in a synchronized semipermeabilized cell translation system. *J. Biol. Chem.* **275**, 14933–14938.

60 Zapun, A., Darby, N. J., Tessier, D. C., Michalak, M., Bergeron, J. J. M. & Thomas, D. Y. (1998). Enhanced catalysis of ribonuclease B folding by the interaction of calnexin or calreticu-

lin with ERp57. *J. Biol. Chem.* **273**, 6009–6012.

61 Fanchiotti, S., Fernández, F., D'Alessio, C. & Parodi, A. J. (1998). The UDP-Glc:glycoprotein glucosyltransferase is essential for *Schizosaccharomyces pombe* viability under conditions of extreme endoplasmic reticulum stress. *J. Cell Biol.* **143**, 625–635.

62 Ray, M. K., Young, J., Sundaram, S. & Stanley, P. (1991). A novel glycosylation phenotype expressed by Lec23, a Chinese hamster ovary mutant deficient in α-glucosidase I. *J. Biol. Chem.* **266**, 22818–22825.

63 Reitman, M. L., Trowbridge, L. S. & Kornfeld, S. (1982). A lectin-resistant mouse lymphoma cell line is deficient in glucosidase II, a glycoprotein processing enzyme. *J. Biol. Chem.* **257**, 10357–10363.

64 Balow, J. P., Weissman, J. D. & Kearse, K. P. (1995). Unique expression of major histocompatibility complex class I proteins in the absence of glucose trimming and calnexin association. *J. Biol. Chem.* **270**, 29025–29029.

65 Jakob, C. A., Burda, P., te Heesen, S., Aebi, M. & Roth, J. (1998). Genetic tayloring of *N*-linked oligosaccharides: the role of glucose residues in glycoprotein processing in *Saccharomyces cerevisiae* in vivo. *Glycobiology*, **8**, 155–164.

66 Hammond, C. & Helenius, A. (1994). Quality control in the secretory pathway: retention of a misfolded viral membrane glycoprotein involves cycling between the ER, intermediate compartment, and Golgi apparatus. *J. Cell Biol.* **126**, 41–52.

67 Fischer, P. B., Karlsson, G. B., Butters, T. D., Dwek, R. A. & Platt, F. M. (1996). N-butyldeoxynojirimycin-mediated inhibition of human immunodeficiency virus entry correlates with changes in antibody recognition of the V1–V2 region of gp120. *J. Virol.* **70**, 7143–7152.

68 Petrescu, S. M., Petrescu, A. J., Titu, H. N., Dwek, R. A. & Platt, F. M. (1997). Inhibition of *N*-glycan processing in B16 melanoma cells results in inactivation of tyrosinase but does not prevent its transport to the melanosome. *J. Biol. Chem.* **272**, 15796–15803.

69 Mehta, A., Lu, X., Block, T. M., Blumberg, B. S. & Dwek, R. A. (1997). Hepatitis B virus (HBV) envelope glycoproteins vary drastically in their sensitivity to glycan processing: evidence that alteration of a single *N*-linked glycosylation site can regulate HBV secretion. *Proc. Natl. Acad. Sci. USA* **94**, 1822–1827.

70 Elgaard, L. & Helenius, A. (2003). Quality control in the endoplasmic reticulum. *Nature Rev. Mol. Cell Biol.* **4**, 181–191.

71 Trombetta, E. S. & Parodi, A. J. (2003). Quality control and protein folding in the secretory pathway. *Annu. Rev. Cell Dev. Biol.* **19**, 649–676.

72 Jakob, C. A., Burda, P., Roth, J. & Aebi, M. (1998). Degradation of misfolded endoplasmic reticulum glycoproteins in *Saccharomyces cerevisiae* is determined by a specific oligosaccharide structure. *J. Cell Biol.* **142**, 1223–1233.

73 Marcus, N. Y. & Perlmutter, D. H. (2000). Glucosidase and mannosidase inhibitors mediate increased secretion of mutant α_1-antitrypsin Z. *J. Biol. Chem.* **275**, 1987–1992.

74 De Virgilio, M., Kitzmuller, C., Schwaiger, E., Klein, M., Kreibich, G. & Ivessa, N. E. (1999). Degradation of a short-lived glycoprotein from the lumen of the endoplasmic reticulum: the role of *N*-linked glycans and the unfolded protein response. *Mol. Biol. Cell*, **10**, 4059–4073.

75 Chung, D. H., Ohashi, K., Watanabe, M., Miyasaka, N. & Hirosawa, S. (2000). Mannose trimming targets mutant α_2-plasmin inhibitor for degradation by the proteasome. *J. Biol. Chem.* **275**, 4981–4987.

76 Fagioli, C. & Sitia, R. (2001). Glycoprotein quality control in the endoplasmic reticulum. Mannose trimming by endoplasmic reticulum mannosidase I times the proteasomal

degradation of unassembled immunoglobulin subunits. *J. Biol. Chem.* **276**, 12885–12892.

77 Wilson, C. M., Farmery, M. R. & Bulleid, N. J. (2000). Pivotal role of calnexin and mannose trimming in regulating the endoplasmic reticulum-associated degradation of major histocompatibility complex class I heavy chain. *J. Biol. Chem.* **275**, 21224–21232.

78 Nakatsukasa, K., Nishikawa, S., Hosokawa, N., Nagata, K. & Endo, T. (2001). Mnl1p, an α-mannosidase-like protein in yeast *Saccharomyces cerevisiae*, is required for endoplasmic reticulum-associated degradation of glycoproteins. *J. Biol. Chem.* **276**, 8635–8638.

79 Hosokawa, N., Wada, I., Hasegawa, K., Yorihuzi, T., Tremblay, L. O., Herscovics, A. and Nagata, A. (2001). A novel ER α-mannosidase-like protein accelerates ER-associated degradation. *EMBO Rep.* **2**, 415–422.

80 Jakob, C. A., Bodmer, D., Spirig, U., Batig, P., Marcil, A., Dignard, D. et al. (2001). Htm1p, a mannosidae-like protein, is involved in glycoprotein degradation in yeast. *EMBO Rep.* **2**, 423–430.

81 Oda, Y., Hosokawa, N., Wada, I. & Nagata, K. (2003). EDEM as an acceptor of terminally misfolded glycoproteins released from calnexin. *Science*, **299**, 1394–1397.

82 Molinari, M., Calanca, V., Galli, C., Lucca, P. & Paganetti, P. (2003). Role of EDEM in the release of misfolded glycoproteins from the calnexin cycle. *Science*, **299**, 1397–1400.

83 Byrd, J. C., Tarentino, A. L., Maley, F., Atkinson, P. H. & Trimble, R. B. (1982). Glycoprotein synthesis in yeast. Identification of $Man_8GlcNAc_2$ as an essential intermediate in oligosaccharide processing. *J. Biol. Chem.* **257**, 14657–14666.

84 Gonzalez, D. S., Karaveg, K., Vandersall-Nairn, A. S., Lal, A. & Moreman, K. W. (1999). Identification, expression, and characterization of a cDNA encoding human endoplasmic reticulum mannosidase I, the enzyme that catalyzes the first mannose trimming step in mammalian Asn-linked oligosaccharide biosynthesis. *J. Biol. Chem.* **274**, 21375–21386.

85 Tremblay, L. O. & Herscovics, A. (1999). Cloning and expression of a specific human α1,2-mannosidase that trims $Man_9GlcNAc_2$ to $Man_8GlcNAc_2$ isomer B during *N*-glycan biosynthesis. *Glycobiology*, **9**, 1073–1078.

86 Camirand, A., Heysen, A., Grondin, B. & Herscovics, A. (1991). Glycoprotein biosynthesis in *Saccharomyces cerevisiae*. Isolation and characterization of the gene encoding a specific processing alpha-mannosidase. *J. Biol. Chem.* **266**, 15120–15127.

87 Weng, S. & Spiro, R. G. (1993). Demonstration that a kifunensin-resistant α-mannosidase with a unique processing action on *N*-linked oligosaccharides occurs in rat liver endoplasmic reticulum and various cultured cells. *J. Biol. Chem.* **268**, 25656–25663.

88 Zuber, C., Spiro, M. J., Guhl, B., Spiro, R. & Roth, J. (2000). Golgi apparatus immunolocalization of endomannosidase suggests post-endoplasmic reticulum glucose trimming: implications for quality control. *Mol. Biol. Cell*, **11**, 4227–4240.

89 Lal, A., Pang, P., Kalelkar, S., Romero, P. A., Herscovics, A. & Moreman, K. W. (1998). Substrate specificity of recombinant murine Golgi α1,2-mannosidases IA and IB and comparison with endoplasmic reticulum and Golgi processing α1,2-mannosidases. *Glycobiology*, **8**, 981–995.

90 Tremblay, L. O. & Herscovics, A. (2000). Characterization of a cDNA encoding a novel human Golgi α1,2-mannosidase (IC) involved in *N*-glycan biosynthesis. *J. Biol. Chem.* **275**, 31655–31660.

91 Bischoff, J., Liscum, L. & Kornfeld, R. (1986). The use of 1-deoxymannojirimycin to evaluate the role of various α-mannosidases in oligosac-

charide processing in intact cells. *J. Biol. Chem.* **261**, 4766–4774.

92 Herscovics, A., Romero, P. A. & Tremblay, L. O. (2002). The specificity of the yeast and human class I α1,2-mannosidases involved in ER quality control is not as strict as previously reported. *Glycobiology*, **11**, 14G–15G.

93 Tokunaga, F., Brostrom, C., Koide, T. & Arvan, P. (2000). Endoplasmic reticulum (ER)-associated degradation of misfolded *N*-linked glycoproteins is suppressed upon inhibition of ER mannosidase I. *J. Biol. Chem.* **275**, 40757–40764.

94 Ermonval, M., Kitzmuller, C., Mir, A. M., Cacan, R. & Ivessa, N. E. (2001). *N*-glycan structure of a short-lived variant of ribophorin I expressed in the MadIA214 glycosylation-defective cell line reveals the role of a mannosidase that is not ER mannosidase I in the process of glycoprotein degradation. *Glycobiology*, **7**, 565–576.

95 Frenkel, Z., Gregory, W., Kornfeld, S. & Lederkremer, G. (2003). Endoplasmic reticulum-associated degradation of mammalian glycoproteins involves sugar trimming to $Man_{6-5}GlcNAc_2$. *J. Biol. Chem.* **278**, 34119–34124.

96 Hampton, R. Y. (2002). ER-associated degradation in protein quality control and cellular regulation. *Curr. Opin. Cell Biol.* **14**, 476–482.

97 Yoshida, Y., Chiba, T., Tokunaga, F., Kawasaki, H., Iwal, K., Suzuki, T. et al. (2002). E3 ubiquitin ligase that recognizes sugar chains. *Nature*, **418**, 438–442.

98 Hampton, R. Y. (2002). Proteolysis and sterol regulation. *Annu. Rev. Cell Dev. Biol.* **18**, 345–378.

99 Hamman, B. D., Chen, J. C., Johnson, E. E. & Johnson, A. E. (1997). The aqueous pore through the translocon has a diameter of 40–60 A during cotranslational protein translocation at the ER membrane. *Cell*, **89**, 535–544.

100 Menetret, J., Neuhof, A., Morgan, D. G., Plath, K., Rademacher, M., Rapoport, T. O. et al. (2000). The structure of ribosome-channel complexes engaged in protein translocation. *Mol. Cell*, **6**, 1219–1232.

101 Beckmann, R., Spahn, C. M. T., Eswar, N., Helmers, J., Penczek, P. A., Sali, A. et al. (2001). Architecture of the protein conducting channel associated with the translating 80S ribosome. *Cell*, **107**, 361–372.

102 Kowarik, M., Kung, S., Martoglio, B. & Helenius, A. (2002). Protein folding during cotranslational translocation in the endoplasmic reticulum. *Mol. Cell*, **10**, 769–778.

103 Molinari, M., Galli, C., Piccaluga, V., Pieren, M. & Paganetti, P. (2002). Sequential assistance of molecular chaperones and transient formation of covalent complexes during protein degradation from the ER. *J. Cell Biol.* **158**, 247–257.

104 Suzuki, T., Park, H., Hollingworth, N. M., Sternglanz, R. & Lennarz, W. J. (2000). *PNG1*, a yeast gene encoding a highly conserved peptide:*N*-glycanase. *J. Cell Biol.* **149**, 1039–1051.

105 Cacan, R., Dengremont, C., Labiau, O., Kmiécik, D., Mir, A. M. & Verbert, A. (1996). Occurrence of a cytosolic neutral chitobiase activity involved in oligomannoside degradation: a study with Mady-Darby bovine kidney (MDBK) cells. *Biochem. J.* **313**, 597–602.

106 Grard, T., Herman, V., Saint-Pol, A., Kmiécik, D., Labiau, O., Mir, A. M. et al. (1996). Oligomannosides or oligosaccharide-lipids as potential substrates for rat liver cytosolic α–D-mannosidase. *Biochem. J.* **316**, 787–792.

107 Saint-Pol, A., Codogno, P. & Moore, S. H. E. (1999). Cytosol to lysosome transport of free polymannose-type oligosaccharides. Kinetics and specificity studies using rat liver lysosomes. *J. Biol. Chem.* **274**, 13547–13555.

108 Varki, A. (1991). Radioactive tracer techniques in the sequencing of glycoprotein glycans. *FASEB J.* **5**, 226–235.

109 Panneerselvam, K. & Freeze, H. H. (1996). Mannose enters mammalian

cells using a specific transporter that is insensitive to glucose. *J. Biol. Chem.* **271**, 9417–9421.

110 Panneerselvam, K., Etchison, J. R. & Freeze, H. H. (1997). Human fibroblasts prefer mannose over glucose as a source of mannose for *N*-glycosylation. Evidence for the functional importance of transported mannose. *J. Biol. Chem.* **272**, 23123–23129.

111 Alton, G., Hasilik, M., Niehaus, R., Panneerselvam, K., Etchison, J. R., Fana, F. et al. (1998). Direct utilization of mannose for mammalian glycoprotein biosynthesis. *Glycobiology*, **8**, 285–295.

112 Staneloni, R. J. & Leloir, L. F. (1978). Glycans containing glucose and mannose in glycoproteins of the thyroid gland. *Proc. Natl. Acad. Sci. USA* **75**, 1162–1166.

113 Moore, S. E. H. & Spiro, R. G. (1990). Demonstration that Golgi endo-a-mannosidase provides a glucosidase independent pathway for the formation of complex *N*-linked oligosaccharides of glycoproteins. *J. Biol. Chem.* **265**, 13104–13112.

114 Mellis, S. J. & Baenziger, J. U. (1981). Separation of neutral oligosaccharides by high-performance liquid chromatography. *Anal. Biochem.* **114**, 276–280.

115 Hase, S. (1994). High-performance liquid chromatography of pyridylaminated saccharides. *Methods Enzymol.* **230**, 225–237.

116 Daniel, P. F. (1987). Separation of benzoylated oligosaccharides by reversed-phase high-pressure liquid chromatography: application to high-mannose type oligosaccharides. *Methods Enzymol.* **138**, 94–116.

117 Ugalde, R. A., Staneloni, R. J. & Leloir, L. F. (1979). Microsomal glucosidases acting on the saccharide moiety of the glucose-containing dolichyl diphosphate oligosaccharide. *Biochem. Biophys. Res. Commun.* **91**, 1174–1181.

118 Herscovics, A. & Jelinek-Kelly, S. (1987). A rapid method for assay of glycosidases involved in glycoprotein biosynthesis. *Anal. Biochem.* **166**, 85–89.

119 Pless, D. D. & Lennarz, W. J. (1977). Enzymatic conversion of proteins to glycoproteins. *Proc. Natl. Acad. Sci. U.S.A.* **74**, 134–138.

120 Hubbard, S. C. & Ivatt, R. I. (1981). Synthesis and processing of asparagine-linked oligosaccharides. *Annu. Rev. Biochem.* **50**, 555–583.

121 Trombetta, S. E. & Parodi, A. J. (1992). Purification to apparent homogeneity and partial characterization of rat liver UDP-glucose:glycoprotein glucosyltransferase. *J. Biol. Chem.* **267**, 9236–9240.

122 Trombetta, E. S., Simons, J. F. & Helenius, A. (1996). Endoplasmic reticulum glucosidase II is composed of a catalytic subunit, conserved from yeast to mammals, and a tightly bound non-catalytic HDEL-containing subunit. *J. Biol. Chem.* **271**, 27509–27516.

18
Procollagen Biosynthesis in Mammalian Cells

Mohammed Tasab and Neil J. Bulleid

18.1
Introduction

18.1.1
Variety and Complexity of Collagen Proteins

Collagen proteins are a very heterogeneous group of structural proteins with an array of different structure-function properties [1–3]. The biosynthesis of collagen within the cell is a complex process and cannot be considered to be typical of the biosynthesis of the "average" secretory protein. This is due to the special physicochemical properties of the large triple-helix-containing molecules that comprise the intracellular form of these proteins, known as procollagen. Furthermore, the variety and complexity of the different types of collagens that are expressed by animal tissues (currently in excess of 24) indicate that the biosynthetic characteristics of each type are different due to the multiple methods by which such types are assembled and modified within the cell. Each type must be assembled in such a way that it can fulfill its final function outside the cell. These functions include a variety of roles, from interactions with cells and cellular receptors, to roles such as attachment and signaling. Because of this diversity in structures and functions, it is difficult to generalize about mechanisms of molecular assembly and transport of collagen in vivo. However, some common themes do emerge.

In this chapter we have chosen to illustrate the concept of in vivo collagen bio-

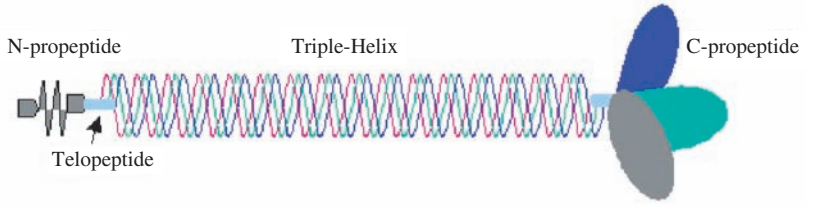

Fig. 18.1. Domain structure of a procollagen molecule.

Protein Folding Handbook. Part II. Edited by J. Buchner and T. Kiefhaber

ISBN: 3-527-30784-2

synthesis using the fibril-forming collagens. Fibril-forming collagens (also known as fibrillar collagens) are the most abundant of the collagen family, occurring commonly in most animal tissues. For this reason they are probably the best characterized among the collagen protein family. The main features of this group are their large molecule size and large uninterrupted triple helix. The fibrillar collagen molecule itself is a flexible ''rod-like'' structure that has the ability to associate laterally with similar molecules, giving rise to the well-known fibril structure outside the cell. Inside the cell the non-collagenous extremities known as the propeptide domains maintain the procollagen molecule in a soluble state.

18.1.2 Fibrillar Procollagen

The procollagens are the larger soluble intracellular precursors of the insoluble fibrillar collagen proteins [4, 5]. Members of the fibrillar collagen subgroup show significant homology to each other, and this is also true of their procollagen precursors [6]. This group consists of three major members including types I, II, and III and two smaller members, types V and XI. These collagens form essential constituents of vital structural tissues including bone, skin, blood vessels, and cartilage.

The triple-helical molecules of procollagen are formed from three constituent procollagen chains. The structure of the procollagen molecule is reflected in the amino acid sequence composition of the constituent chains. Complete cDNA and amino acid sequences for many types of procollagen chain are available and may be used in sequence homology analyses to compare and contrast sequences between chains [7–10]. In each procollagen chain, the domains responsible for the formation of the N-propeptide, the N-telopeptide, the triple helix, the C-telopeptide, and the C-propeptide have been identified [11]. The structure of the molecule is illustrated below in Figure 18.1, see p. 649. The characteristic repeating Gly-X-Y motif of the triple-helical domain is wound into the triple helix that is the core part of the trimeric procollagen molecule. While a great deal is known about the structure and properties of the triple helix, the globular propeptides are not so well characterized. The larger of the globular regions is the C-propeptide, which performs specialist functions that are discussed later. The N-propeptide domain is not as well characterized, but some specific roles have been identified. The propeptides are also involved in multiple interactions with various cellular factors that may be involved in the assembly and processing of procollagen molecules. The C-propeptides of the major procollagen types I, II, and III are cleaved by specific C-proteinases immediately upon exiting the cell, and this begins the process of fibrillogenesis.

18.1.3 Expression of Fibrillar Collagens

The complexity and diversity of collagen expression are essential to the developmental pathways that allow a higher organism to develop from its early embryonic

stages to the mature adult form. Furthermore, tissue renewal and repair processes that are necessary throughout the life of the organism indicate that some expression pathways operate constitutively while other pathways are induced to repair and replace damaged and worn tissues. Thus, expression of all collagens in terms of both development and maintenance is a tightly controlled operation regulated at both the genetic and biochemical levels. Collagen expression is linked to the expression of many other proteins. Some of these proteins are directly involved in processing procollagen in vivo, such as bone morphogenetic protein (BMP-1) and proteins that interact with immature procollagen such as protein disulfide isomerase (PDI), Hsp47, prolyl hydroxylase, lysyl hydroxylase, and other proteins that are co-expressed along with fibrillar collagens. This ensures that the intracellular procollagens are synthesized, correctly modified, and efficiently transported when required. Some regulatory factors such as TGF-β and IL-6 promote procollagen expression at the gene level. Other factors such as tumor necrosis factor TNF-α and IFN-γ appear to suppress procollagen expression. Thus, there is a whole spectrum of signals that appear to induce or suppress procollagen expression and constitute the physiological feedback mechanisms by which expression is regulated.

18.2 The Procollagen Biosynthetic Process: An Overview

Multi-exon genes such as COL1A1 and COL1A2 that encode the chains that make up type I procollagen reside on different chromosomes. Therefore, the production of fibrillar collagens from collagen genes must necessarily be a highly regulated and coordinated process so that the correct combinations of chains are produced at a given time in order to produce procollagen. Splicing of large mRNA precursors to produce specific mRNAs occurs within the nucleus. The mature mRNAs are transported out into the cytoplasm, where membrane-bound ribosomes can begin the biosynthesis of procollagen.

The biosynthesis of procollagen begins with the translation of specific mRNAs on ribosomal complexes [12–14]. The polypeptide chains are co-translationally inserted into the lumen of the endoplasmic reticulum (ER) [15–17]. An interaction between the translocon Sec61p protein and the lumenal chaperone BiP has been proposed to facilitate the completion of translocation into the ER [18, 19].

Enzymes involved in the biosynthetic process are located within the ER lumenal space [20–26]. Hydroxylation of some proline and lysine residues occurs as the triple-helical domain emerges into the lumen of the ER [27, 28]. Virtually all of the Y position proline residues, as well as some Y position lysine residues, are hydroxylated. This hydroxylation is important to the structural stability of the triple helix that is formed later. Some of the hydroxylysine residues in the triple-helical domains are further modified by *O*-linked glycosylation. This is distinct from the *N*-linked glycosylation that occurs in the C-propeptide domains, the function of which is not clear.

Once translocated, the C-propeptide domain is free to fold, forming its comple-

ment of intrachain disulfide bonds [29, 30]. The three polypeptide chains of procollagen must then associate at the C-propeptide domains, bringing the three chains into close proximity and thus allowing the formation of interchain disulfide bonds and nucleation of the triple-helix. The molecule is then able to form a triple-helix in a "zipper-like" fashion [31] starting at the C-terminal end and proceeding towards the N-terminal end of the chains [32]. This folding of the triple helix is rate limited by the conversion of *cis*-hydroxyproline residues to *trans*-hydroxyproline residues [33–36]. Current evidence suggests that only the non-triple-helical chains are substrates for the hydroxylase enzymes and that once the triple-helix is formed no further hydroxylation occurs. The hydroxylase enzymes lose affinity as the triple-helix is formed and this probably serves as the detachment mechanism that allows the triple-helical molecule to escape the clutches of these ER-resident proteins. The putative chaperone Hsp47 is believed to bind to the triple-helix as it is formed. Once helix formation is completed, the N-propeptides of the three constituent chains are able to associate, completing the assembly process. Assembled procollagen molecules are then transported through the secretory pathway via mechanisms that are not yet clear but that could involve vesicular transport or a process of cisternal maturation. A schematic of the biosynthetic process is shown in Figure 18.2.

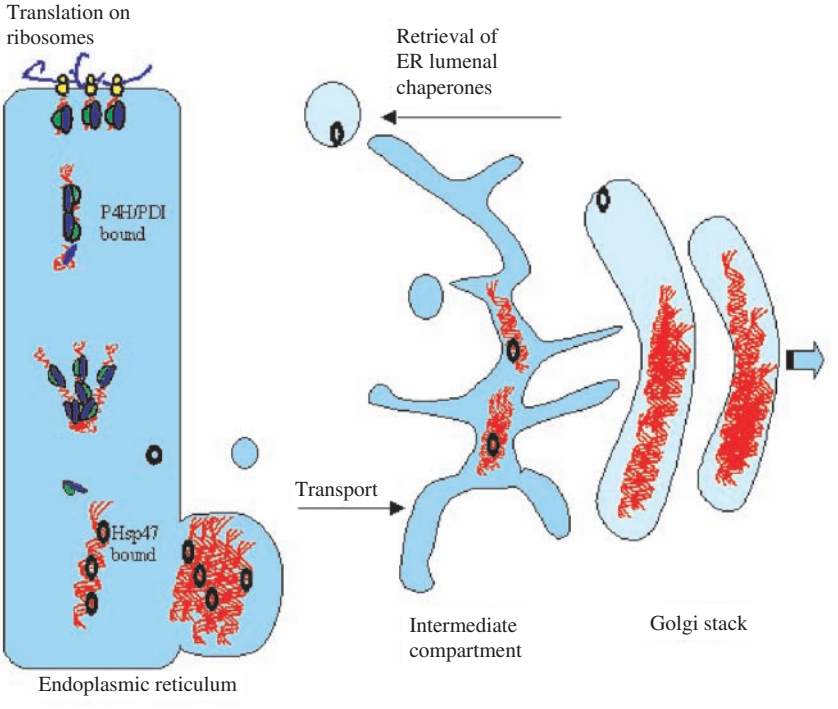

Fig. 18.2. Schematic of procollagen biosynthesis.

18.3
Disulfide Bonding in Procollagen Assembly

Cysteine residues, which form intrachain disulfide linkages, are more highly conserved than other residues in most cysteine-containing proteins [37]. This is unsurprising given that these bonds are extremely important for formation of the native structure of most cysteine-containing proteins. This rule is also applicable to the cysteines in procollagen chains, particularly those in the C-propeptide domain, where a number of intrachain disulfide linkages are thought to occur [6, 38, 39]. The strict conservation of these cysteines between different fibrillar collagen types and between species suggests that the same intrachain links are formed in all the C-propeptide domains and therefore that the tertiary structure of the C-propeptides is similar.

Most of the fibrillar procollagen C-propeptide domains contain eight cysteine residues in conserved positions relative to the C-proteinase cleavage site. These cysteines are numbered sequentially from the N-terminus of the C-propeptide domain. It is notable that both proα2(I) and proα2(V) C-propeptide domains possess only seven of these cysteine residues and that the second cysteine residue position that occurs in the other chains is occupied by a serine residue. Since both proα2(I) and proα2(V) are heterotrimer-forming chains, it was suggested that the lack of this cysteine could account for the inability of these chains to form homotrimers [40]. However, this theory is contradicted by work showing that restoration of a full complement of cysteines in the C-propeptide domain of proα2(I) does not enable them to form homotrimers [41].

Early models suggested that disulfide bonding did not occur while the procollagen chains were nascent and still attached to the polysomes [42]. Disulfide linkages were detected only when chains had been completed and apparently released from the ribosomal complexes. This observation is consistent with the prevailing view that synthesis of the whole C-propeptide domain must be completed before folding of these domains can begin. The last cysteine residue in the procollagen C-propeptide domain is located very close to the C-terminus of the chain; it is probable that this residue is essential to the structure of the C-propeptide and that correct folding cannot occur without it.

It is known that isolated C-propeptide domains can independently associate and form interchain disulfide linkages [30]. Subsequently, it was also shown that a construct with the C-telopeptide and C-propeptide domains from proα1(III) chains linked to a signal peptide folds and assembles into disulfide-linked trimers [43]. Thus, the C-propeptide can be considered as a domain that has a specific role in guiding the formation of the triple-helical procollagen molecule.

Interchain disulfide bonding between C-propeptide domains involves specific sets of cysteine residues on adjacent chains [38, 41, 44]. Early models suggested that only cysteines 5–8 form intrachain links [38] and that cysteines 1–4 were considered to be involved with interchain disulfide linkages [44]. More recent studies analyzing the effect of site-directed mutagenesis of the cysteines in the C-propeptide domain suggest that only cysteine 2 and cysteine 3 are involved in inter-

chain disulfide bond formation [41]. This model indicates that mutations of cysteines 1 and 4 affect the folding of the C-propeptide domain and therefore are probably involved in intrachain linkages. In contrast, the C-propeptide domains in mutants without cys2 or cys3 were folded correctly, suggesting that these residues would normally form interchain disulfide bonds.

18.4 The Influence of Primary Amino Acid Sequence on Intracellular Procollagen Folding

18.4.1 Chain Recognition and Type-specific Assembly

An interesting observation is that procollagen-expressing cells may express multiple types of fibrillar procollagen at a given time. For example, skin fibroblasts may co-express procollagen types I, III, and V [45–50]. Thus, up to six highly homologous chains may be co-expressed and assembled type-specifically into the correct combinations. This discrimination process is illustrated by the fact that proα2(I) chains will associate only with proα1(I) chains to form type I molecules [51] and that no homotrimeric proα2(I) molecules have been reported. This is in contrast to proα1(III) chains, which are solely homotrimer-forming and will not associate with any other type of chain [52, 53]. The formation of heterotypic molecules containing both type V and type XI chains is a known exception to the rule that assembly of fibrillar collagens is type-specific [54]. However, some workers consider types V and XI to be a single collagen type consisting of five polypeptide chains [55–57]. In addition, a highly glycosylated alternatively spliced version of the proα1(II) chain [58, 59] appears to be involved in heterotrimer formation with type XI chains [60, 61]. Despite these complications, it is clear that procollagen chains come together in only certain combinations despite the presence of highly homologous chains being expressed at the same time in the same ER lumenal space.

18.4.2 Assembly of Multi-subunit Proteins

Little is known about how the assembly of multi-subunit proteins, which may involve the interactions of folded and/or partially folded subunits, is achieved. Clearly, a recognition aspect must exist in order for the subunits to recognize each other. Regardless of whether this assembly/recognition is mediated by a catalyst or is an intrinsic property of subunits, the assembly will be unlikely to succeed in the absence of the correct primary information. Complex proteins are often made up of many subunits, which may or may not serve distinct functions. Some subunits can co-assemble with other types of subunits in particular combinations in different circumstances. One example of this versatility is the protein disulfide isomerase (PDI). PDI functions as a catalyst of disulfide bond formation but is also present as a constituent of prolyl-4-hydroxylase (P4H) [62, 63] and the microsomal lipid transfer complex [64–66]. There are important questions regarding how such

complex multi-subunit proteins are formed. Is the information for subunit association encoded within the constituent subunits? How are these constituent subunits able to recognize each other and associate together in the correct manner? How is the correct stoichiometric ratio determined? Is the recognition ability encoded within the primary amino acid sequence, or are other proteins in the biosynthetic machinery responsible for ''manufacturing'' the correct combinations of subunits?

18.4.3
Coordination of Type-specific Procollagen Assembly and Chain Selection

One theory of how chain selection can be achieved is to consider it as a problem of coordinated transcription and translation. These processes must be regulated spatially and temporally to bring about the correct combinations of procollagen chains within the same ER lumenal space [14, 67, 68]. While some studies have suggested that proα1(I) and proα2(I) genes are coordinately transcribed in a ratio close to 2:1 [69, 70], other studies show that the levels of mRNA for these chains deviate appreciably from this ratio [71]. Clearly, some degree of transcriptional coordination is necessary in order to produce heterotrimeric type I procollagen molecules, but this does not necessarily determine the ultimate chain selection or folding events.

Veis and coworkers [72] have shown that the ribosomes reading out mRNA transcripts appear in organized arrays along the ER. This model suggests that monocistronic mRNAs are brought together within the same ER compartment by a complex set of interactions that ensure coordinated synthesis [72]. This implies that some component of the ER membrane participates in the organization of the ribosomes and coordinates the synthesis of nascent chains. Further studies by Kirk [73] and Veis and Kirk [74] support a model of molecular assembly where chain selection and folding are determined by the attachment of the ribosomes to the ER membrane. Hu and coworkers [75] have also proposed that some component of the ER membrane participates in the chain selection process. This proposal is based on the observation that cell-free translations of proα1(I) and proα2(I) are coordinately altered in the presence of added membranes. It has long been postulated that C-propeptide anchoring of the nascent procollagen chains to the ER membrane could be important in chain assembly as this would restrict the freedom of the chains and decrease the concentration of chains required for association [76]. Observations of the behavior of procollagen chains on a monomolecular film suggest that procollagen chains could assemble while associated with the ER membrane [77]. However, this behavior is not a consequence of the interaction of the C-propeptide *N*-linked oligosaccharide chain with the membrane lectin calnexin, as mutagenesis of the site for oligosaccharide attachment does not prevent the resulting non-glycosylated C-propeptide from participating in assembly or secretion of procollagen [78]. It is possible that other membrane-associated proteins could interact with the procollagen C-propeptide and organize trimer assembly at the ER membrane. It is difficult to envisage how a C-propeptide domain can achieve its fully folded state if binding to the ER membrane restricts the C-terminal end. One explanation could be that completed procollagen chains

detach from the ER membrane to allow the C-propeptide domain to fold and are subsequently indirectly associated with the membrane via interaction with a membrane-bound chaperone. However, these models fail to explain how ribosomes or other membrane factors distinguish between proα2(I) and proα1(I) chains and bring them together in the correct combinations or why proα2(I) chains cannot form homotrimeric molecules.

18.4.4 Hypervariable Motifs: Components of a Recognition Mechanism That Distinguishes Between Procollagen Chains?

Multi-subunit proteins are crucial to the many complex cellular processes that take place in higher organisms. Clearly, mechanisms that determine the recognition and association of subunits are a vital element in generating multi-subunit proteins. Secondary structure predictions reveal striking similarities between predicted structures for the C-propeptide domains of proα2(I) and proα1(I) chains, despite sequence dissimilarities [38, 79]. Conversely, the same type of prediction suggests a different type of structure for the C-propeptide domain of proα1(II) chains. It has been argued that this could represent the structural basis for chain discrimination during procollagen biosynthesis [38]. Other workers have suggested that the diversity between C-propeptide sequences near the C-proteinase cleavage site might account for the differential chain selection between procollagen chains [80].

More recent studies exploiting advanced in vitro translation technology and genetic engineering have led to a new perspective on how selective association of procollagen chains is achieved. In this system recombinant procollagen chains are expressed in reticulocyte lysate in the presence of semi-permeabilized cells. The utility of this methodology for the analysis of procollagen assembly cannot be understated. Procollagen assembly can be analyzed under controlled experimental conditions while presserving the in vivo environment including the chaperones that are crucial for the assembly process. An experimental strategy based upon the specific exchange of variable sequences between the C-propeptide domains of the homotrimeric proα1(III) chain and the heterotrimer-forming proα2(I) chain has been used to investigate the mechanism of selective chain association [81, 82]. The analysis of procollagen assembly using the chimeric chains expressed in semi-permeabilized cells led to the identification of a specific short, discontinuous sequence of 15 amino acids (GNPELPEDVLDV.....SSR) within the proα1(III) C-propeptide, which directs procollagen self-association. This recognition sequence appears to be necessary and sufficient to drive homotrimer formation when placed in the correct context within the proα2(I) C-propeptide. This sequence is presumably responsible for the initial recognition event between chains and is therefore necessary to ensure selective chain association. The variable recognition sequence is interrupted by a central hydrophobic motif, Q(L/M)(T/A)F(L/M)(R/K)L(L/M), that is conserved between different fibrillar procollagen chains. This sequence possibly preserves some element of structural similarity in any recognition site that may be formed at the interface between the interacting C-propeptide domains.

18.4.5
Modeling the C-propeptide

It is known that sequence variations between subunit interfaces determine the specificity of subunit interactions in some proteins. Studies of protein folding and protein-protein interfaces also indicate that similar principles underlie both peptide folding and protein-protein association. In the absence of hard structural data, it is difficult to define the exact interactions that take place during procollagen chain recognition and association. An alternative strategy is to look at computer models based upon information from biophysical studies. Recent low-resolution models based on biophysical studies of the recombinant type III C-propeptide envisage the soluble trimer as ''cruciform-shaped'' structure with three large lobes and a minor lobe all in the same plane [83]. The larger lobes apparently correspond to each individual propeptide chain, and the minor lobe is proposed to correspond to the junction that links all three C-propeptide domains to the rest of the procollagen molecule. Interestingly, such models place the previously identified recognition sequences at the interface junctions between the individual C-propeptide domains, supporting the idea that such sequences are major determinants of chain selection.

18.4.6
Chain Association

The above models may suggest that recognition domains promote chain selection and association; however, these two events are not necessarily connected. Experimental data indicate that the recognition event is not necessarily followed by an association event. It is possible to envisage a situation where in vivo a certain sequence is responsible for recognition but another neighboring sequence is responsible for the association. Thus, the two events may be uncoupled. There is also sufficient evidence to indicate that trimer formation can be induced in the absence of the recognition sequences. Early sequence comparisons identified a group of aromatic residues within the C-propeptide domain that could be responsible for association among the three chains [84]. Experimental work has shown that the C-propeptide itself can be efficiently replaced by other sequences such as the transmembrane domain of hemagglutinin [43] and the 29-residue foldon domain from T4 bacteriophage fibritin, which are capable of bringing the three chains of procollagen into close proximity [85]. Thus, nonnative combinations of chains can be synthesized in the absence of selective regions. The alpha-helical coiled coil is a very common motif in oligomerizing proteins. These coils are believed to form oligomerization domains in fibrillar and non-fibrillar collagens and also in collagen-like proteins such as C1q. The widespread presence of these domains in collagens and other trimerizing proteins [86] suggests a general role in trimerization and perhaps a specific role in determining the association of procollagen chains in vivo.

18.5
Posttranslational Modifications That Affect Procollagen Folding

18.5.1
Hydroxylation and Triple-helix Stability

Hydroxylation of prolyl and lysyl residues in the triple-helical domain is critical for triple-helix formation and stability. Three types of enzyme are known to participate in hydroxylation of these residues: prolyl 4-hydroxylase (P4H), prolyl 3-hydroxylase (P3H), and lysyl hydroxylase (LH). These hydroxylating enzymes convert the peptidyl-lysine or peptidyl-proline to hydroxylysine or hydroxyproline. Only a small percentage of the peptidyl-prolines in the Y position of the Gly-X-Y triplet are hydroxylated by P3H, while the most important contribution to the stability of the triple-helical procollagen molecule is the hydroxylation of Y-position proline residues in the Gly-X-Y triplet by the P4H enzyme. Formation of the triple helix appears to prevent further hydroxylation [87–89], suggesting that triple-helical procollagen is not a substrate for P4H.

A detailed mechanism for the P4H reaction has been described by a number of workers [90–94]. The hydroxylation reaction requires a number of cofactors, including Fe^{2+}, 2-oxoglutarate, O_2, and ascorbate. The fact that the same cofactors are required for all three types of hydroxylases suggests that the mechanism of action is similar for all three hydroxylating enzymes.

The presence or absence of hydroxylation cofactors can be used experimentally as a tool for the analysis of procollagen production by cells. One example is the chelation of ferrous iron by inhibitors such as $\alpha\alpha'$-dipyridyl. This is a popular method for inhibiting the hydroxylation reaction experimentally. Treatment of procollagen-expressing fibroblasts with this agent leads to retention of unhydroxylated procollagen within the ER lumenal space. This ''block'' can be reversed by the addition of excess ferrous ions when required. Another method for achieving the same result is to deplete procollagen-producing cells of ascorbate. Ascorbate is an essential cofactor that is required for repeated cycles of enzyme activity. Readdition of ascorbate to depleted cells restores procollagen secretion. Such strategies are often used in experiments where it is necessary to build up a concentration of unfolded procollagen within the ER and to follow its maturation through the secretory pathway.

18.6
Procollagen Chaperones

18.6.1
Prolyl 4-Hydroxylase

Vertebrate P4H consists of tetramers composed of two α and two β subunits $\alpha 2\beta 2$ [95–99]. The α-subunit is the catalytic subunit for hydroxylation and is prone to

aggregation in the absence of the β-subunit [63, 100]. Thus, one function of the β-subunit in P4H appears to be keeping the α-subunit in the active soluble state [101, 102]. Isoforms of the α-subunit have been identified in human tissue [103], in mouse [104], and in *C. elegans* [105]. The β-subunit is identical to PDI and maintains its PDI activity even as part of the P4H complex [62, 63]. Another function of the β-subunit may be to retain the α-subunit within the ER lumen since the β-subunit has an ER retention motif, whereas the α-subunit does not.

Interestingly, P4H has been found in stable association with procollagen chains possessing a deletion in the triple-helical domain [106], suggesting a chaperone-type role for P4H. Since this result was obtained with antibodies directed against the β-subunit of P4H, this chaperone effect may be mediated by the PDI. However, current evidence suggests that P4H (both α and β subunits) can form stable associations with non-triple helical chains and that it is the major protein that interacts with procollagen chains during early biosynthesis [107]. This binding appears to be conformation-dependent so that P4H is able to distinguish between folded and unfolded procollagen molecules. Taken together with evidence that P4H has reduced affinity for hydroxylated chains [108], it appears that P4H may be a sophisticated hydroxylation- and conformation-sensitive chaperone that is able to mediate the retention of unfolded procollagen chains.

18.6.2 Protein Disulfide Isomerase

PDI is a key cellular folding enzyme that is important for the maturation of several secreted and membrane-associated proteins. This is particularly true for the folding and maturation of procollagen, where PDI is involved in a number of important steps. As well as functioning as part of the P4H complex, this chaperone has multiple other roles in procollagen biosynthesis as well as a general role in biogenesis of other disulfide-bonded proteins. The function of PDI as a component of enzymes such as P4H is independent of its disulfide isomerase activity [109]. PDI has been proposed to act as a general molecular chaperone by binding to unfolded proteins and thereby preventing aggregation [110–112]. This indicates that PDI assists in the refolding of certain denatured proteins in vitro. In other cases PDI appears to have no activity or even anti-chaperone activity with some substrates [113, 114]. PDI also has been shown to interact with newly synthesized proteins [115] and to catalyze the formation of both intrachain and interchain disulfide bonds [116, 117]. Studies using a cross-linking approach in a semi-permeabilized cell system have shown that PDI also appears to have a separate role in the chaperoning of monomeric chains and monomeric C-propeptide domains [118, 119]. The function of this binding appears to be to keep the monomeric chains in solution. These observations support a model where PDI plays a crucial role in binding to the C-propeptide, thereby coordinating heterotrimer assembly. Although the monomeric C-propeptide contains free thiol residues, no mixed disulfides have been detected between PDI and procollagen C-propeptides. Hence, the interaction is probably dependent on hydrophobic interactions.

18.6.3 Hsp47

Prolyl 4-hydroxylase is just one member of a group of chaperones that play a vital role in the biogenesis of procollagen within the cell. These chaperones carry out a number of functions in order to assist with procollagen biosynthesis, including folding, protection, retention, posttranslational modification, and degradation. This group of chaperones interacts with multiple proteins that require assistance with folding and assembly. However, it seems that the variety and complexity of proteins in the ER folding environment requires a second class of more specific protein chaperones that are limited to quality control of particular proteins. Heat shock protein 47 (Hsp47) falls into this second group and is specifically associated with procollagen biosynthesis. This stress-induced chaperone is linked with the production of procollagen in many types of cells. Hsp47 and type IV collagen have been found to decrease during the differentiation of mouse teratocarcinoma cells [120]. Upregulation of Hsp47 also occurs when expression of collagen types I and III is induced during fibrosis [121] and during mechanical and heat stress in embryonic chicken tendon cells [122].

Despite some 20 years of investigation, definitive roles for Hsp47 in procollagen biosynthesis have yet to be elucidated. This is in part due to conflicting evidence regarding the substrate preferences of Hsp47 and also to a lack of understanding of some aspects of procollagen biosynthesis such as how transport from the ER to the Golgi is achieved. The RDEL motif at the carboxy-terminus of Hps47 certainly limits the theater of its operations via the KDEL receptor retention mechanism. Any chaperone-type function must therefore necessarily occur prior to the *cis*-Golgi, where Hsp47 is believed to dissociate from procollagen probably as a result of a pH change that alters its conformation and its affinity for this substrate [123]. The importance of Hsp47 to the biosynthesis of procollagen is illustrated by the dramatic effect of disrupting the Hsp47 genes in a mouse model [124]. This mutation is lethal to the null mouse embryo within 11 days post coitus. The embryo itself is extremely fragile and displays defects in the basal lamina, which compromise basement membrane formation, and apparent defects in associated connective tissues. Most of these effects are likely to be due to the disruption of the extracellular matrix (ECM). Such observations indicate that any secreted collagens from cells lacking Hsp47 may have an abnormal conformation that causes the ECM disruption. The procollagens secreted by these cells were sensitive to proteolytic digestion, indicating that the triple helix may be malformed. Transient transfection of Hsp47 into the knockout cells appears to make the procollagen resistant to proteolysis, demonstrating a possible role in stabilization of the triple helix.

Studies looking at the interaction of Hsp47 with recombinant procollagen chains expressed in semi-permeabilized cells found that only triple-helical procollagen molecules were able to interact with Hsp47 with high affinity [125]. Procollagen chains that were engineered to remain monomeric or were prevented from forming a triple helix by inhibiting hydroxylation did not appear to interact with Hsp47.

This evidence together with evidence from work with collagen peptides [126] shows that Hsp47 has a much higher affinity for the triple-helical form of procollagen.

It has been established that the thermal stability of procollagen within the cell may be higher than that of the isolated protein [127], suggesting that the intracellular environment protects the collagen helix from heat denaturation. It is possible that the Hsp47-procollagen interaction leads to a stabilization of the procollagen triple helix, in particular stabilizing those regions of the helix with lower thermal stability [125]. However, work using triple helices designed to be highly stable without any regions of lower thermal stability shows that Hsp47 is still able to bind to these molecules [128]. Furthermore, this work and other evidence show that a minimum of one Gly-X-Arg triplet in the triple-helical domain is necessary for the binding of Hsp47 to procollagen [129].

An alternative explanation for the purpose of binding of Hsp47 to triple-helical procollagen could be to prevent the lateral association of the chains occurring within the ER. Once the procollagen molecule reaches the Golgi apparatus, it has been suggested to form higher-order aggregates, leading to distension of this organelle [130]. This ''aggregate form'' could be a necessary intermediate prior to propeptide processing and formation of collagen fibrils. The formation of aggregates within the ER would be an undesirable event, perhaps preventing the transport of procollagen to the Golgi apparatus; hence, the presence of Hsp47 could be required to ensure efficient procollagen transport.

18.6.4 PPI and BiP

Other proteins have been identified that have specific roles during procollagen biosynthesis. One example of this is during the formation of the triple helix. The unfolded procollagen chain contains peptide bonds statistically distributed between *cis* and *trans* configurations. Only the *trans* configuretion is compatible with the structure of the triple helix [131]. Conversion between the *cis* and *trans* configurations is limited by the pyrrolidine ring of the imino acids proline and hydroxyproline, which restricts rotation around the peptide bond. Since both proline and hydroxyproline occur frequently within the triple-helical domain of procollagen chains, the *cis-trans* isomerization reaction imposes a rate-limiting step on the propagation of the triple helix [35, 36]. This rate-limiting step is catalyzed by peptidyl-prolyl *cis-trans* isomerase (PPI), which is identical to the protein known as cyclophilin [132, 133]. This enzyme is inhibited by cyclosporin A (CsA), which has been shown to reduce the rate of triple-helix formation in vitro.

Immunoglobulin-binding protein (BiP), also known as GRP78, is a stress-induced protein implicated in the retention of misfolded proteins [134, 135]. However, it is not clear whether this protein plays a role during the normal biosynthesis of procollagen or whether its role is limited to quality control of misfolded procollagens in vivo. It is known that BiP is constitutively expressed during the produc-

tion of mutant chains produced in cases of osteogenesis imperfecta [136, 137]. The mutations where BiP is involved affect the C-propeptide and presumably interfere with chain association. The mechanism by which BiP recognizes misfolded C-propeptides is unknown but the binding is clearly one part of the quality-control mechanism that processes incorrectly folded procollagen in vivo.

18.7 Analysis of Procollagen Folding

As stated previously, the early stages of procollagen biosynthesis can be reconstituted in a semi-permeabilized cell system whereby conditions can be manipulated and specific aspects of the procollagen assembly process investigated. This methodology has been successfully employed to look at the assembly process itself as well as the role of chaperones such as Hsp47, PDI, and P4H. The volume of physiologically meaningful data resulting from this approach illustrates the power of this combination of in vivo and in vitro techniques. The technique is also very adaptable and may be used to look at assembly of virtually any protein entering the secretory pathway. Here we illustrate the methodology by describing the techniques as applied to procollagen assembly.

The procedure involves treating cells grown in culture with the detergent digitonin and isolating the cells free from their cytosolic component. The SP cell system allows protein assembly to be studied in an environment that more closely resembles that of the intact cell. As the ER remains morphologically intact, the interactions with endogenous chaperones and the spatial localization of folding are maintained. An in vitro translation system is combined in the presence of the SP cells so that individual components can be manipulated easily, providing a means by which cellular processes can be studied under a variety of conditions. Chemical cross-linking reagents can also be utilized posttranslationally in order to facilitate the study of interaction between proteins within the ER lumen [138, 139].

The basic protocol involves translation of mRNA transcripts encoding particular procollagen chains in a rabbit reticulocyte lysate supplemented with the semi-permeabilized HT1080 cells prepared as outlined below. This cell line is able to carry out the complex co- and posttranslational modifications required for the assembly of procollagen molecules into thermally stable triple helices [140]. The mRNA transcript encoding for the protein of interest is translated in the presence of a radio-labeled amino acid (^{35}S-methionine) such that the protein synthesized can be visualized by autoradiography. As the mRNA can be synthesized in vitro from cloned cDNA, the effect of manipulating the primary amino acid sequence upon folding and assembly can be examined. The procedures for preparing SP cells, transcribing cloned cDNAs, and translating the RNA transcripts are outlined below. In addition we describe some procedures for characterizing procollagen translation products.

18.8
Experimental Part

18.8.1
Materials Required

Transcription in vitro

1. 10 μg linearized plasmid DNA, containing the gene of interest downstream of the appropriate promoter, in RNase-free water
2. 5× Transcription buffer (400 mM HEPES buffer pH7.4, 60 mM $MgCl_2$, 10 mM spermidine)
3. Nucleotide triphosphates (ATP, UTP, CTP, and GTP) (25 mM each) (Roche)
4. 100 mM DTT (Sigma)
5. T3/T7 RNA polymerase (50 U μL^{-1}) (Promega)
6. RNase inhibitor (Promega)

Translation in vitro

1. Flexi rabbit reticulocyte lysate (Promega Corp.)
2. EasyTag ^{35}S-methionine (NEN Dupont)
3. 2.5 M KCl
4. Amino acid mix (minus methionine) (Promega Corp.)

Preparation of semi-permeabilized cells (all reagents are stored at −20 °C.)

1. Phosphate-buffered saline (Biowhittaker)
2. HT1080 cells (75-cm^2 flask of sub-confluent cells)
3. 1× Trypsin-EDTA solution (Biowhittaker)
4. KHM buffer: KOAc 110 mM, MgOAc 2 mM, HEPES 20 mM, pH 7.2
5. HEPES buffer: KOAc 50 mM, HEPES 50 mM, pH 7.2
6. Digitonin (40 mg mL^{-1} in DMSO, stored at −20 °C) (Calbiochem)
7. Soybean trypsin inhibitor (50 mg mL^{-1} in sterile water stored at −20 °C) (Sigma)
8. Trypan blue solution (0.4%)
9. $CaCl_2$ (100 mM, stored at −20 °C)
10. Micrococcal nuclease (1 mg mL^{-1} in sterile water, stored at −20 °C) (Sigma)
11. EGTA (0.4 M, stored at −20 °C).

Protease digestion assay

1. Chymotrypsin (Sigma): make up fresh in SOL buffer
2. Trypsin (Sigma): make up fresh in SOL buffer
3. Pepsin (Sigma): make up in H_2O

4. Triton X-100 (10% in H_2O, stored at 4 °C)
5. SOL buffer: 50 mM Tris-HCl, pH 7.4, 150 mM NaCl, 10 mM EDTA
6. Soybean trypsin inhibitor (50 mg mL^{-1} in sterile water stored at −20 °C) (Sigma)
7. 1 M HCl
8. 1 M Tris
9. 4× SDS-PAGE sample buffer

18.8.2 Experimental Protocols

Method 1: Preparation of SP Cells This procedure is a modification of the protocol used by Plutner and coworkers [141] adapted for the cell-free expression of proteins. Treatment of mammalian cells with the detergent digitonin renders the plasma membrane permeable to the components of the cell-free translation system while retaining the functionally intact ER membrane. This selective permeabilization is a consequence of the cholesterol-binding properties of digitonin. As cholesterol is a minor constituent of the internal membrane system of the cell, the ER and Golgi networks remain intact. Prior to beginning the protocol, refer to note 1.

1. Remove culture medium and rinse HT1080 cells in culture flask with 1 × 10 mL PBS. Drain and add 1 mL of trypsin solution (prewarmed to room temperature) and incubate for 3 min. All cells should now be detached by gently tapping the flask. Add 8 mL of KHM buffer and 20 µL soybean trypsin inhibitor (final concentration 100 µg mL^{-1}) to the tissue culture flask. Transfer cell suspension to a 15-mL Falcon tube on ice.
2. Pellet cells by centrifugation at 1200 rpm for 3 min at 4 °C. Aspirate the supernatant from the cell pellet.
3. Resuspend cells in 6 mL of ice-cold KHM. Add 6 µL digitonin (from 40 mg mL^{-1} stock, i.e., final concentration 40 µg mL^{-1}) and mix immediately by inversion. Incubate on ice for 5 min (see note 2).
4. Adjust the volume to 14 mL with ice-cold KHM and pellet cells by centrifugation as in step 2.
5. Aspirate the supernatant and resuspend cells in 14 mL ice-cold HEPES buffer. Incubate on ice for 10 min and pellet cells by centrifugation as in step 2.
6. Aspirate the supernatant and resuspend cells carefully in 1 mL ice-cold KHM (use a 1-mL Gilson and pipette gently up and down). Place on ice.
7. Transfer a 10-µL aliquot to a separate 1.5-mL microcentrifuge tube and add 10 µL of Trypan Blue.
8. Count cells in a hemocytometer and check for permeabilization.
9. Transfer cells to a 1.5-mL microcentrifuge tube and spin for 30 s at 13 000 *g*. Aspirate supernatant and resuspend the cells in 100 µL KHM using a pipette.
10. Add 1 µL of 0.1 M $CaCl_2$ and 1 µL of monococcal nuclease and incubate at room temperature for 12 min. This step removes the endogenous mRNA.

11. Add 1 μL of 0.4 M EGTA to chelate the calcium and inactivate the nuclease. Isolate the cells by centrifuging for 30 s in a microcentrifuge and resuspend in 100 μL of KHM.
12. Use approximately 1×10^5 cells per 25-μL translation reaction (approx. 4 μL of the 100 μL obtained).

Method 2: Transcription in Vitro The cDNA encoding the protein of interest must be placed in a suitable expression vector, such as pBluescript SK (Stratagene), upstream of a suitable promoter containing an RNA polymerase-binding site from which transcription is initiated. The cDNA clone must be linearized by an appropriate restriction enzyme to generate a template for mRNA synthesis. This method is a modification of a method described previously [142].

1. Prepare a 100-μL reaction mixture containing 44 μL H_2O, 10 μL linearized DNA (5–10 μg), 20 μL transcription buffer (5×), 10 μL 100 mM DTT, 1 μL RNasin (20 units), and 3 μL of each nucleotide.
2. Add 3 μL of the appropriate RNA polymerase (150 units) and incubate at 37 °C for 2 h (see note 3).
3. The RNA can be extracted with phenol/chloroform 1:1 and then twice with chloroform and precipitate by adding NaOAc, pH 5.2, to a final concentration of 300 mM and three volumes of ethanol. The RNA pellet is resuspended in 100 μL RNase-free H_2O containing 1 mM DTT and 1 μL RNasin.
4. To assess the yield of RNA, a 1-μL aliquot should be removed and analyzed on a 1% agarose gel (see note 4).

Method 3: Translation in Vitro The translation of proteins in vitro can be performed using either wheat germ extracts or rabbit reticulocyte lysates that contain ribosomes, tRNAs, and a creatine phosphate-based energy regeneration system.

1. Prepare a 25-μL reaction mixture containing 17.5 μL Flexi lysate, 0.5 μL amino acid, 0.5 μL KCl, 1.5 μL EasyTag ^{35}S-methionine, 1 μL mRNA, and 4 μL SP cells (see notes 5 and 6). Incubate the translation sample at 30 °C for 60 min and then place on ice.
2. Prepare the translation sample for SDS-PAGE by adding 2 μL of the product to 15 μL SDS-PAGE sample buffer (0.0625 M Tris/HCl pH 6.8, SDS [2% w/v], glycerol [10% v/v], and bromophenol blue) plus 2 μL DTT (1 M) and boiling the sample for 5 min.
3. The samples should be analyzed by SDS-PAGE. After running, the gel should be dried and exposed to autoradiography film (see note 7).

Method 4: Protease Digestion Assay A ''protease digestion'' assay is used to determine whether the translation products that have been formed within the SP cells contain triple-helical procollagen. A fully folded and correctly aligned triple helix is resistant to proteolysis by a combination of chymotrypsin, trypsin, and pepsin at temperatures below the characteristic melting temperature of a particular triple

helix. Misaligned helices or non-helical trimers of procollagen will be digested under the same conditions [143]. The characteristic melting temperature of the helix is a function of the hydroxyproline content and tends to vary between 35 °C and 42 °C for fibrillar collagen molecules.

1. Prepare a 25-μL translation reaction including freshly prepared SP cells as described above. After translation, place the sample on ice and gently disperse the SP cells using a pipette tip.
2. Remove 5 μL of the translation mix as a control to check for translation efficiency.
3. Isolate the SP cells from the remaining translation by centrifugation and wash with KHM twice to remove any remaining translation mixture.
4. Disrupt the cell pellet with a sterile pipette tip in SOL buffer containing 1% v/v Triton X-100. Leave on ice for 30 min to solubilize the SP cells.
5. Centrifuge the solubilized cells at 13 000 rpm for 20 min. Carefully remove the supernatant to a fresh microcentrifuge tube. Remove 5 μL of the supernatant as a non-treated control.
6. Digest the remaining supernatant with chymotrypsin (250 μg mL^{-1}) and trypsin (100 μg mL^{-1}) for 5 min at 30 °C. Add soybean trypsin inhibitor to 500 μg mL^{-1} and then acidify the digest by adding HCl to 100 mM.
7. Treat the sample with Pepsin (100 μg mL^{-1}) for 2 h at 30 °C or overnight at 4 °C.
8. Stop the reaction by neutralization with 100 mM Tris base and boiling 4× SDS-PAGE buffer. Add DTT to 50 mM for separation under reducing conditions.
9. Prepare the untreated samples for electrophoresis by adding SDS-PAGE buffer containing 50 mM DTT.
10. The samples should be separated by SDS-PAGE. After running, the gel should be dried and exposed to autoradiography film (see note 8).

Method 5: Analysis of Disulfide Bond Formation In the case of fibrillar procollagen chains, formation of the correct intrachain disulfide bonds in the carboxy-terminal domain (the C-propeptide) is necessary for the folding of these domains and is a prerequisite for trimer formation. The trimers in turn are stabilized by interchain disulfides. The formation of disulfide bonds during folding can be monitored by trapping folding intermediates using the alkylating reagent *N*-ethyl maleimide (NEM). The formation of intrachain disulfide bonds generally increases the electrophoretic mobility of proteins during SDS-PAGE analysis under non-reducing conditions as compared to reducing conditions. Procollagen molecules stabilized by interchain disulfide bonds have a markedly reduced migration under non-reducing conditions, as the linked chains form a much larger complex.

1. Prepare a 100-μL translation mix and divide this into four aliquots of 25 μL in separate microcentrifuge tubes.

2. At intervals of 15 min, remove one of the tubes, add NEM to a final concentration of 20 mM, and place on ice for the remainder of the time course.
3. Isolate and "wash" the SP cells as described in step 3 of method 4.
4. Solubilize each of the washed cell pellets in 50 μL SDS-PAGE buffer and then transfer 25 μL of each sample into fresh tubes containing 2 μL DTT. Boil the samples for 5 min prior to electrophoresis (see note 9).

Notes:

1. The procedure takes approximately one hour and should be carried out immediately prior to using the SP cells for translation in vitro, as SP cells do not efficiently reconstitute the translocation of proteins after storage. It is also advisable to use a minimum of one 75-cm^2 flask of cells (75–90% confluent) as it is difficult to work with a smaller quantity of cells. The size of the cell pellet will usually decrease during the procedure due to loss of the cell cytosol that is accompanied by a decrease in cell volume.
2. The digitonin concentration has been optimized for permeabilization of HT1080 cells (i.e., the lowest concentration of digitonin that results in 100% permeabilization). If a different cell line is used, the concentration of digitonin required for permeabilization should be assessed by titration. It is not essential to trypan blue-stain each batch of SP cells, although this is recommended if the procedure is not used routinely.
3. The yield of mRNA can be increased by a further addition of RNA polymerase (1 μL) after 1 h.
4. To minimize degradation of the mRNA, the use of sterile pipette tips and microcentrifuge tubes is recommended. If the yield is low or if the RNA is partially degraded, it is possible that apparatus or solutions have been contaminated with RNases.
5. The translation protocol should be optimized for each different mRNA transcript as the optimal salt concentrations (KCl and MgOAc) may vary.
6. Control translations in the absence of SP cells should also be carried out to test the translation efficiency of a new RNA preparation.
7. It may be necessary to denature any secondary structure in the mRNA by heating to 60 °C for 10 min prior to translation. Additional products with molecular weights smaller than the major translation product may be observed due to ribosome binding to "false" start sites downstream of the initiation codon. As natural procollagens are large molecules, a lower percentage gel is appropriate in order to visualize bands representing proteins in the range of 100–350 kDa.
8. Hydroxylation of proline and lysine residues in procollagen results in reduced electrophoretic mobility as compared to proteins predicted to be of the same size. An adaptation of this method can also be used to estimate the melting temperature of a triple-helical procollagen.
9. If reduced and non-reduced samples are to be run on the same gel, they should be separated by a gap of two lanes in order to prevent reduction of the non-reduced samples by DTT that may diffuse across the gel matrix during electrophoresis.

References

1 Kielty, C. M., Hopkinson, I. & Grant, M. E. (1993). The Collagen Family: Structure, Assembly and Organization in the Extracellular Matrix. In *Connective Tissue and its Heritable Disorders*, pp. 103–147. Wiley-Liss, Inc.

2 Kadler, K. (1994). *Protein profile*: Fibril forming collagens (Sheterline, P., ed.), Vol. 1. 2 vols. Academic Press, Oxford.

3 Prockop, D. J. & Kivirikko, K. I. (1995). Collagens – Molecular-Biology, Diseases, and Potentials For Therapy. *Ann Rev Biochem* 64, 403–434.

4 Schofield, J. D. & Prockop, D. J. (1973). Procollagen – a precursor form of collagen. *Clin Orthop* 97, 175–95.

5 Bornstein, P. (1974). The structure and assembly of procollagen – a review. *J Supramol Struct* 2, 108–20.

6 Dion, A. S. & Myers, J. C. (1987). COOH-terminal propeptides of the major human procollagens: structural, functional and genetic comparisons. *J Mol Biol* 193, 127–143.

7 Hofmann, H., Fietzek, P. P. & Kuhn, K. (1980). Comparative analysis of the sequences of the three collagen chains alpha 1(I), alpha 2 and alpha 1(III) Functional and genetic aspects. *J Mol Biol* 141, 293–314.

8 Bernard, M. P., Myers, J. C., Chu, M. L., Ramirez, F., Eikenberry, E. F. & Prockop, D. J. (1983). Structure of a cDNA for the pro alpha 2 chain of human type I procollagen. Comparison with chick cDNA for pro alpha 2(I) identifies structurally conserved features of the protein and the gene. *Biochemistry* 22, 1139–45.

9 Baldwin, C. T., Reginato, A. M., Smith, C., Jimenez, S. A. & Prockop, D. J. (1989). Structure of cDNA clones coding for human type II procollagen. The alpha 1(II) chain is more similar to the alpha 1(I) chain than two other alpha chains of fibrillar collagens. *Biochem J* 262, 521–8.

10 Greenspan, D. S., Cheng, W. & Hoffman, G. G. (1991). The Pro-Alpha-1(V) Collagen Chain – Complete Primary Structure, Distribution of Expression, and Comparison With the Pro-Alpha-1(XI) Collagen Chain. *J Biol Chem* 266, 24727–24733.

11 Kuhn, K. (1984). Structural and Functional Domains of Collagen – a Comparison of the Protein With Its Gene. *Collagen and Related Research* 4, 309–322.

12 Kerwar, S. S., Kohn, L. D., Lapiere, C. M. & Weissbach, H. (1972). In vitro synthesis of procollagen on polysomes. *Proc Natl Acad Sci USA* 69, 2727–31.

13 Kerwar, S. S. (1974). Studies on the nature of procollagen synthesized by chick embryo polysomes. *Arch Biochem Biophys* 163, 609–13.

14 Veis, A. & Brownell, A. G. (1977). Triple-helix formation on ribosome-bound nascent chains of procollagen: deuterium-hydrogen exchange studies. *Proc Natl Acad Sci USA* 74, 902–5.

15 Harwood, R., Grant, M. E. & Jackson, D. S. (1973). The sub-cellular location of inter-chain disulfide bond formation during procollagen biosynthesis by embryonic chick tendon cells. *Biochem Biophys Res Commun* 55, 1188–96.

16 Harwood, R., Bhalla, A. K., Grant, M. E. & Jackson, D. S. (1975). The synthesis and secretion of cartilage procollagen. *Biochem J* 148, 129–38.

17 Harwood, R., Grant, M. E. & Jackson, D. S. (1974). Secretion of procollagen: evidence for the transfer of nascent polypeptides across microsomal membranes of tendon cells. *Biochem Biophys Res Commun* 59, 947–54.

18 Nicchitta, C. V. & G, B. (1993). Lumenal proteins of the mammalian endoplasmic reticulum are required to complete protein translocation. *Cell* 73, 513–21.

19 Sanders, S. L., Whitfield, K. M., Vogel, J. P., Rose, M. D. & Schekman, R. W. (1992). Sec61p and BiP directly facilitate polypeptide translocation into the ER. *Cell* 69, 353–65.

20 Harwood, R., Grant, M. E. &

Jackson, D. S. (1974). Collagen biosynthesis. Characterization of subcellular fractions from embyonic chick fibroblasts and the intracellular localization of protocollagen prolyl and protocollagen lysyl hydroxylases. *Biochem J* 144, 123–30.

21 Harwood, R., Grant, M. E. & Jackson, D. S. (1975). Studies on the glycosylation of hydroxylysine residues during collagen biosynthesis and the subcellular localization of collagen galactosyltransferase and collagen glucosyltransferase in tendon and cartilage cells. *Biochem J* 152, 291–302.

22 Diegelmann, R. F., Bernstein, L. & Peterkofsky, B. (1973). Cell-free collagen synthesis on membrane-bound polysomes of chick embryo connective tissue and the localization of prolyl hydroxylase on the polysome-membrane complex. *J Biol Chem* 248, 6514–21.

23 Cutroneo, K. R., Guzman, N. A. & Sharawy, M. M. (1974). Evidence for a subcellular vesicular site of collagen prolyl hydroxylation. *J Biol Chem* 249, 5989–94.

24 Guzman, N. A., Rojas, F. J. & Cutroneo, K. R. (1976). Collagen lysyl hydroxylation occurs within the cisternae of the rough endoplasmic reticulum. *Arch Biochem Biophys* 172, 449–54.

25 Fessler, J. H. & Fessler, L. I. (1978). Biosynthesis of procollagen. *Annu Rev Biochem* 47, 129–62.

26 Prockop, D., Berg, R., Kivirikko, K. & Uitto, J. (1976). *Biochemistry of Collagen* (Ramachandran, G. & Reddi, H., Eds.), Plenum Press, New York.

27 Uitto, J. & Prockop, D. J. (1974). Hydroxylation of peptide-bound proline and lysine before and after chain completion of the polypeptide chains of procollagen. *Arch Biochem Biophys* 164, 210–7.

28 Vuust, J. & Piez, K. A. (1972). A kinetic study of collagen biosynthesis. *J Biol Chem* 247, 856–62.

29 Uitto, V. J., Uitto, J. & Prockop, D. J. (1981). Synthesis of Type-I Procollagen – Formation of Interchain Disulfide Bonds Before Complete Hydroxylation of the Protein. *Arch Biochem Biophys* 210, 445–454.

30 Doege, K. J. & Fessler, J. H. (1986). Folding of carboxyl domain and assembly of procollagen I. *J Biol Chem* 261, 8924–35.

31 Engel, J. & Prockop, D. J. (1991). The Zipper-Like Folding of Collagen Triple Helices and the Effects of Mutations That Disrupt the Zipper. *Ann Rev Biophysics and Biophysical Chem* 20, 137–152.

32 Bachinger, H. P., Fessler, L. I., Timpl, R. & Fessler, J. H. (1981). Chain assembly intermediate in the biosynthesis of type III procollagen in chick embryo blood vessels. *J Biol Chem* 256, 13193–9.

33 Bachinger, H. P., Bruckner, P., Timpl, R. & Engel, J. (1978). The role of *cis-trans* isomerization of peptide bonds in the coil leads to and comes from triple helix conversion of collagen. *Eur J Biochem* 90, 605–13.

34 Bachinger, H. P., Bruckner, P., Timpl, R., Prockop, D. J. & Engel, J. (1980). Folding mechanism of the triple-helix in type III collagen and type III pN-collagen: role of disulfide bridges and peptide bond isomerization. *Eur J Biochem* 106, 619–632.

35 Bruckner, P. & Eikenberry, E. F. (1984). Formation of the Triple Helix of Type-I Procollagen Incellulo – Temperature-Dependent Kinetics Support a Model Based On *Cis* Reversible *Trans* Isomerization of Peptide-Bonds. *Eur J Biochem* 140, 391–395.

36 Bruckner, P., Eikenberry, E. F. & Prockop, D. J. (1981). Formation of the triple helix of type I procollagen in cellulo. A kinetic model based on *cis-trans* isomerization of peptide bonds. *Eur J Biochem* 118, 607–13.

37 Thornton, J. M. (1981). Disulfide bridges in globular proteins. *J Mol Biol* 151, 261–87.

38 Olsen, B. R. (1982). The Carboxyl Propeptides of Procollagens: Structural and Functional Considerations. *New Trends Basement Memb Res*, 225–236.

39 Byers, P. H., Click, E. M., Harper, E. & Bornstein, P. (1975). Interchain disulfide bonds in procollagen are located in a large nontriple-helical COOH-terminal domain. *Proc Natl Acad Sci USA* 72, 3009–13.

40 Koivu, J. (1987). Disulfide bonding as a determinant of the molecular composition of types I, II and III procollagen. *FEBS Lett* 217, 216–20.

41 Lees, J. F. & Bulleid, N. J. (1994). The role of cysteine residues in the folding and association of the COOH-terminal propeptide of types I and III procollagen. *J Biol Chem* 269, 24354–60.

42 Lukens, L. N. (1976). Time of occurrence of disulfide linking between procollagen chains. *J Biol Chem* 251, 3530–8.

43 Bulleid, N. J., Dalley, J. A. & Lees, J. F. (1997). The C-propeptide domain of procollagen can be replaced with a transmembrane domain without affecting trimer formation or collagen triple helix folding during biosynthesis. *EMBO J* 16, 6694–6701.

44 Koivu, J. (1987). Identification of disulfide bonds in carboxy-terminal propeptides of human type I procollagen. *FEBS Lett* 212, 229–32.

45 Lenaers, A. & Lapiere, C. M. (1975). Type III procollagen and collagen in skin. *Biochim Biophys Acta* 400, 121–31.

46 Booth, B. A., Polak, K. L. & Uitto, J. (1980). Collagen biosynthesis by human skin fibroblasts. I. Optimization of the culture conditions for synthesis of type I and type III procollagens. *Biochim Biophys Acta* 607, 145–60.

47 Uitto, J., Booth, B. A. & Polak, K. L. (1980). Collagen biosynthesis by human skin fibroblasts. II. Isolation and further characterization of type I and type III procollagens synthesized in culture. *Biochim Biophys Acta* 624, 545–61.

48 Narayanan, A. S. & Page, R. C. (1983). Biosynthesis and regulation of type V collagen in diploid human fibroblasts. *J Biol Chem* 258, 11694–9.

49 Jimenez, S. A., Williams, C. J., Myers, J. C. & Bashey, R. I. (1986). Increased collagen biosynthesis and increased expression of type I and type III procollagen genes in tight skin (TSK) mouse fibroblasts. *J Biol Chem* 261, 657–62.

50 Kypreos, K. E. & Sonenshein, G. E. (1998). Basic fibroblast growth factor decreases type V/XI collagen expression in cultured bovine aortic smooth muscle cells. *J Cell Biochem* 68, 247–58.

51 Traub, W. & Piez, K. A. (1971). The chemistry and structure of collagen. *Adv Protein Chem* 25, 243–352.

52 Miller, E. J. & Gay, S. (1982). Collagen: an overview. *Methods Enzymol* 82 Pt A, 3–32.

53 Chung, E., Keele, E. M. & Miller, E. J. (1974). Isolation and characterization of the cyanogen bromide peptides from the alpha 1(3) chain of human collagen. *Biochemistry* 13, 3459–64.

54 Kleman, J. P., Hartmann, D. J., Ramirez, F. & Van der Rest, M. (1992). The human Rhabdomyosarcoma cell-line A204 lays down a highly insoluble matrix composed mainly of alpha-1 type XI and alpha-2 type V collagen chains. *Eur J Biochem* 210, 329–335.

55 Mayne, R., Brewton, R. G., Mayne, P. M. & Baker, J. R. (1993). Isolation and characterization of the chains of type-V and type-XI collagen present in bovine vitreous. *J Biol Chem* 268, 9381–9386.

56 Fichard, A., Kleman, J. P. & Ruggiero, F. (1995). Another Look At Collagen-V and Collagen-XI Molecules. *Matrix Biol* 14, 515–531.

57 Olsen, B. R., Winterhalter, K. H. & Gordon, M. K. (1995). FACIT collagens and their biological roles. *Trends Glycosci Glycotech* 7, 115–127.

58 Sandell, L. J., Morris, N., Robbins, J. R. & Goldring, M. B. (1991). Alternatively spliced type II procollagen mRNAs define distinct populations of cells during vertebral development: differential expression of the amino-propeptide. *J Cell Biol* 114, 1307–19.

59 Sandell, L. J., Nalin, A. M. & Reife, R. A. (1994). Alternative splice form of type II procollagen mRNA (IIA) is predominant in skeletal precursors and non-cartilaginous tissues during early mouse development. *Dev Dyn* 199, 129–40.

60 Cremer, M. A., Ye, X. J., Terato, K., Owens, S. W., Seyer, J. M. & Kang, A. H. (1994). Type-XI collagen-induced arthritis in the lewis rat – characterization of cellular and humoral immune-responses to native type-XI, type-V and type-II collagen and constituent alpha-chains. *Journal of Immunology* 153, 824–832.

61 Wu, J. J. & Eyre, D. R. (1995). Structural analysis of cross-linking domains in cartilage type-XI collagen – insights on polymeric assembly. *J Biol Chem* 270, 18865–18870.

62 Koivu, J., Myllyla, R., Helaakoski, T., Pihlajaniemi, T., Tasanen, K. & Kivirikko, K. I. (1987). A single polypeptide acts both as the beta subunit of prolyl 4-hydroxylase and as a protein disulfide-isomerase. *J Biol Chem* 262, 6447–9.

63 Pihlajaniemi, T., Helaakoski, T., Tasanen, K., Myllyla, R., Huhtala, M. L., Koivu, J. & Kivirikko, K. I. (1987). Molecular cloning of the beta-subunit of human prolyl 4-hydroxylase. This subunit and protein disulfide isomerase are products of the same gene. *EMBO J* 6, 643–9.

64 Lamberg, A., Jauhiainen, M., Metso, J., Ehnholm, C., Shoulders, C., Scott, J., Pihlajaniemi, T. & Kivirikko, K. I. (1996). The role of protein disulfide isomerase in the microsomal triacylglycerol transfer protein does not reside in its isomerase activity. *Biochem J* 315, 533–6.

65 Thompson, J., Sack, J., Jamil, H., Wetterau, J., Einspahr, H. & Banaszak, L. (1998). Structure of the microsomal triglyceride transfer protein in complex with protein disulfide isomerase. *Biophys J* 74, A138–A138.

66 Wetterau, J. R., Combs, K. A., Spinner, S. N. & Joiner, B. J. (1990). Protein disulfide isomerase is a component of the microsomal triglyceride transfer protein complex. *J Biol Chem* 265, 9801–7.

67 Brownell, A. G. & Veis, A. (1976). Intracellular location of triple helix formation of collagen. Enzyme probe studies. *J Biol Chem* 251, 7137–43.

68 de Wet, W. J., Chu, M. L. & Prockop, D. J. (1983). The mRNAs for the pro-alpha 1(I) and pro-alpha 2(I) chains of type I procollagen are translated at the same rate in normal human fibroblasts and in fibroblasts from two variants of osteogenesis imperfecta with altered steady state ratios of the two mRNAs. *J Biol Chem* 258, 14385–9.

69 Kosher, R. A., Kulyk, W. M. & Gay, S. W. (1986). Collagen gene expression during limb cartilage differentiation. *J Cell Biol* 102, 1151–6.

70 Vuust, J., Sobel, M. E. & Martin, G. R. (1985). Regulation of type I collagen synthesis. Total pro alpha 1(I) and pro alpha 2(I) mRNAs are maintained in a 2:1 ratio under varying rates of collagen synthesis. *Eur J Biochem* 151, 449–53.

71 Olsen, A. S. & Prockop, D. J. (1989). Transcription of Human Type-I Collagen Genes – Variation in the Relative Rates of Transcription of the Pro-Alpha-1 and Pro-Alpha-2 Genes. *Matrix* 9, 73–81.

72 Veis, A., Leibovich, S. J., Evans, J. & Kirk, T. Z. (1985). Supramolecular assemblies of mRNA direct the coordinated synthesis of type I procollagen chains. *Proc Natl Acad Sci USA* 82, 3693–7.

73 Kirk, T. Z., Evans, J. S. & Veis, A. (1987). Biosynthesis of type I procollagen. Characterization of the distribution of chain sizes and extent of hydroxylation of polysome-associated pro-alpha-chains. *J Biol Chem* 262, 5540–5.

74 Veis, A. & Kirk, T. Z. (1989). The Coordinate Synthesis and Cotranslational Assembly of Type-I Procollagen. *J Biol Chem* 264, 3884–3889.

75 Hu, G., Tylzanowski, P., Inoue, H. & Veis, A. (1995). Relationships

between translation of pro alpha1(I) and pro alpha2(I) mRNAs during synthesis of the type I procollagen heterotrimer. *J Cell Biochem* 59, 214–34.

76 Doege, K. J. & Fessler, J. H. (1986). Folding of Carboxyl Domain and Assembly of Procollagen-I. *J Biol Chem* 261, 8924–8935.

77 Beck, K., Boswell, B. A., Ridgway, C. C. & Bachinger, H. P. (1996). Triple helix formation of procollagen type I can occur at the rough endoplasmic reticulum membrane. *J Biol Chem* 271, 21566–73.

78 Lamande, S. R. & Bateman, J. F. (1995). The Type-I Collagen Pro-Alpha-1(I) COOH-Terminal Propeptide N-Linked Oligosaccharide – Functional-Analysis By Site-Directed Mutagenesis. *J Biol Chem* 270, 17858–17865.

79 Doering, T. E., Eikenberry, E. F., Olsen, B. R., Fietzek, P. P. & Brodsky, B. (1982). Secondary Structure of Collagen Propeptides and Telopeptides. *Biophys J* 37, A395–A395.

80 Ninomiya, Y. & Olsen, B. R. (1984). Molecular-Cloning of DNA Encoding a Chondrocyte-Specific Collagen of Novel and Unusual Structure. *Journal of the Tissue Culture Association* 20, 255–255.

81 Lees, J. F., Tasab, M. & Bulleid, N. J. (1996). Molecular Signals Within the C-Propeptide Which Determine Type-Specific Assembly of Procollagen Chains. *Matrix Biol* 15, 153–153.

82 Lees, J. F., Tasab, M. & Bulleid, N. J. (1997). Identification of the molecular recognition sequence which determines the type-specific assembly of procollagen. *EMBO J* 16, 908–916.

83 Bernocco, S., Finet, S., Ebel, C., Eichenberger, D., Mazzorana, M., Farjanel, J. & Hulmes, D. J. (2001). Biophysical characterization of the C-propeptide trimer from human procollagen III reveals a tri-lobed structure. *J Biol Chem* 276, 48930–6.

84 Brass, A., Kadler, K. E., Thomas, J. T., Grant, M. E. & Boot Handford, R. P. (1991). The aromatic zipper: a model for the initial trimerization event in collagen folding. *Biochem Soc Trans* 19, 365s.

85 Pakkanen, O., Hamalainen, E. R., Kivirikko, K. I. & Myllyharju, J. (2003). Assembly of stable human type I and III collagen molecules from hydroxylated recombinant chains in the yeast Pichia pastoris. Effect of an engineered C-terminal oligomerization domain foldon. *J Biol Chem* 278, 32478–83.

86 Engel, J. & Kammerer, R. A. (2000). What are oligomerization domains good for? *Matrix Biol* 19, 283–8.

87 Kivirikko, K. I. & Myllyla, R. (1985). Post-translational processing of procollagens. *Ann NY Acad Sci* 460, 187–201.

88 Kivirikko, K. I., Myllyla, R. & Pihlajaniemi, T. (1989). Protein hydroxylation: prolyl 4-hydroxylase, an enzyme with four cosubstrates and a multifunctional subunit. *FASEB J* 3, 1609–17.

89 Kivirikko, K. I., Helaakoski, T., Tasanen, K., Vuori, K., Myllyla, R., Parkkonen, T. & Pihlajaniemi, T. (1990). Molecular biology of prolyl 4-hydroxylase. *Ann NY Acad Sci* 580, 132–42.

90 Myllyla, R., Tuderman, L. & Kivirikko, K. I. (1977). Mechanism of the prolyl hydroxylase reaction. 2. Kinetic analysis of the reaction sequence. *Eur J Biochem* 80, 349–57.

91 Tuderman, L., Myllyla, R. & Kivirikko, K. I. (1977). Mechanism of the prolyl hydroxylase reaction. 1. Role of co-substrates. *Eur J Biochem* 80, 341–8.

92 Hanauske Abel, H. M. & Gunzler, V. (1982). A stereochemical concept for the catalytic mechanism of prolylhydroxylase: applicability to classification and design of inhibitors. *J Theor Biol* 94, 421–55.

93 Majamaa, K., Hanauske Abel, H. M., Gunzler, V. & Kivirikko, K. I. (1984). The 2-oxoglutarate binding site of prolyl 4-hydroxylase. Identification of distinct subsites and evidence for 2-oxoglutarate decarboxylation in a ligand reaction at the enzyme-bound

ferrous ion. *Eur J Biochem* 138, 239–45.

94 Majamaa, K., Turpeenniemi Hujanen, T. M., Latipaa, P., Gunzler, V., Hanauske Abel, H. M., Hassinen, I. E. & Kivirikko, K. I. (1985). Differences between collagen hydroxylases and 2-oxoglutarate dehydrogenase in their inhibition by structural analogues of 2-oxoglutarate. *Biochem J* 229, 127–33.

95 Pankalainen, M., Aro, H., Simons, K. & Kivirikko, K. I. (1970). Protocollagen proline hydroxyllase: molecular weight, subunits and isoelectric point. *Biochim Biophys Acta* 221, 559–65.

96 Berg, R. A. & Prockop, D. J. (1973). Affinity column purification of protocollagen proline hydroxylase from chick embryos and further characterization of the enzyme. *J Biol Chem* 248, 1175–82.

97 Tuderman, L., Kuutti, E. R. & Kivirikko, K. I. (1975). Radiommunoassay for human and chick prolyl hydroxylases. *Eur J Biochem* 60, 399–405.

98 Kuutti, E. R., Tuderman, L. & Kivirikko, K. I. (1975). Human prolyl hydroxylase. Purification, partial characterization and preparation of antiserum to the enzyme. *Eur J Biochem* 57, 181–8.

99 Berg, R. A., Kedersha, N. L. & Guzman, N. A. (1979). Purification and partial characterization of the two nonidentical subunits of prolyl hydroxylase. *J Biol Chem* 254, 3111–8.

100 Helaakoski, T., Vuori, K., Myllyla, R., Kivirikko, K. I. & Pihlajaniemi, T. (1989). Molecular cloning of the alpha-subunit of human prolyl 4-hydroxylase: the complete cDNA-derived amino acid sequence and evidence for alternative splicing of RNA transcripts. *Proc Natl Acad Sci USA* 86, 4392–6.

101 John, D. C. & Bulleid, N. J. (1994). Prolyl 4-hydroxylase: defective assembly of alpha-subunit mutants indicates that assembled alpha-subunits are intramolecularly disulfide bonded. *Biochemistry* 33, 14018–25.

102 Veijola, J., Pihlajaniemi, T. & Kivirikko, K. I. (1996). Coexpression of the Alpha-Subunit of Human Prolyl 4-Hydroxylase With BiP Polypeptide in Insect Cells Leads to the Formation of Soluble and Insoluble Complexes – Soluble Alpha-Subunit-BiP Complexes Have No Prolyl 4-Hydroxylase Activity. *Biochemical J* 315, 613–618.

103 Annunen, P., Helaakoski, T., Myllyharju, J., Veijola, J., Pihlajaniemi, T. & Kivirikko, K. I. (1997). Cloning of the human prolyl 4-hydroxylase alpha subunit isoform alpha(II) and characterization of the type II enzyme tetramer. The alpha(I) and alpha(II) subunits do not form a mixed alpha(I)alpha(II)beta2 tetramer. *J Biol Chem* 272, 17342–8.

104 Helaakoski, T., Annunen, P., Vuori, K., MacNeil, I. A., Pihlajaniemi, T. & Kivirikko, K. I. (1995). Cloning, baculovirus expression, and characterization of a second mouse prolyl 4-hydroxylase alpha-subunit isoform: formation of an alpha 2 beta 2 tetramer with the protein disulfide-isomerase/beta subunit. *Proc Natl Acad Sci USA* 92, 4427–31.

105 Veijola, J., Koivunen, P., Annunen, P., Pihlajaniemi, T. & Kivirikko, K. I. (1994). Cloning, baculovirus expression, and characterization of the alpha subunit of prolyl 4-hydroxylase from the nematode Caenorhabditis elegans. This alpha subunit forms an active alpha beta dimer with the human protein disulfide isomerase/beta subunit. *J Biol Chem* 269, 26746–53.

106 Chessler, S. D. & Byers, P. H. (1992). Defective Folding and Stable Association With Protein Disulfide Isomerase/Prolyl Hydroxylase of Type-I Procollagen With a Deletion in the Pro-Alpha-2(I) Chain That Preserves the Gly-X-Y Repeat Pattern. *J Biol Chem* 267, 7751–7757.

107 Walmsley, A. R., Batten, M. R., Lad, U. & Bulleid, N. J. (1999). Intracellular retention of procollagen within the endoplasmic reticulum is mediated by prolyl 4-hydroxylase. *J Biol Chem* 274, 14884–92.

108 Juva, K. & Prockop, D. J. (1969). Formation of enzyme-substrate complexes with protocollagen proline hydroxylase and large polypeptide substrates. *J Biol Chem* 244, 6486–92.

109 Vuori, K., Pihlajaniemi, T., Myllyla, R. & Kivirikko, K. I. (1992). Site-directed mutagenesis of human protein disulfide isomerase: effect on the assembly, activity and endoplasmic reticulum retention of human prolyl 4-hydroxylase in Spodoptera frugiperda insect cells. *EMBO J* 11, 4213–7.

110 Cai, H., Wang, C. C. & Tsou, C. L. (1994). Chaperone-like activity of protein disulfide isomerase in the refolding of a protein with no disulfide bonds. *J Biol Chem* 269, 24550–2.

111 Quan, H., Fan, G. & Wang, C. C. (1995). Independence of the chaperone activity of protein disulfide isomerase from its thioredoxin-like active site. *J Biol Chem* 270, 17078–80.

112 Yao, Y., Zhou, Y. & Wang, C. (1997). Both the isomerase and chaperone activities of protein disulfide isomerase are required for the reactivation of reduced and denatured acidic phospholipase A2. *EMBO J* 16, 651–8.

113 Puig, A., Lyles, M. M., Noiva, R. & Gilbert, H. F. (1994). The role of the thiol/disulfide centers and peptide binding site in the chaperone and anti-chaperone activities of protein disulfide isomerase. *J Biol Chem* 269, 19128–35.

114 Puig, A. & Gilbert, H. F. (1994). Protein disulfide isomerase exhibits chaperone and anti-chaperone activity in the oxidative refolding of lysozyme. *J Biol Chem* 269, 7764–71.

115 Klappa, P., Freedman, R. B. & Zimmermann, R. (1995). Protein Disulfide-Isomerase and a Lumenal Cyclophilin-Type Peptidyl-Prolyl *Cis-Trans* Isomerase Are in Transient Contact With Secretory Proteins During Late Stages of Translocation. *Eur J Biochem* 232, 755–764.

116 Bulleid, N. J. & Freedman, R. B. (1988). Defective Co-Translational Formation of Disulfide Bonds in Protein Disulfide-Isomerase-Deficient Microsomes. *Nature* 335, 649–651.

117 Koivu, J. & Myllyla, R. (1987). Interchain disulfide bond formation in types I and II procollagen. Evidence for a protein disulfide isomerase catalyzing bond formation. *J Biol Chem* 262, 6159–64.

118 Wilson, R., Lees, J. F. & Bulleid, N. J. (1998). Protein disulfide isomerase acts as a molecular chaperone during the assembly of procollagen. *J Biol Chem* 273, 9637–9643.

119 Bottomley, M. J., Batten, M. R., Lumb, R. A. & Bulleid, N. J. (2001). Quality control in the endoplasmic reticulum. PDI mediates the ER retention of unassembled procollagen C-propeptides. *Current Biol* 11, 1114–8.

120 Takechi, H., Hirayoshi, K., Nakai, A., Kudo, H., Saga, S. & Nagata, K. (1992). Molecular cloning of a mouse 47-kDa heat-shock protein (HSP47), a collagen-binding stress protein, and its expression during the differentiation of F9 teratocarcinoma cells. *Eur J Biochem* 206, 323–9.

121 Masuda, H., Fukumoto, M., Hirayoshi, K. & Nagata, K. (1994). Coexpression of the collagen-binding stress protein HSP47 gene and the alpha 1(I) and alpha 1(III) collagen genes in carbon tetrachloride-induced rat liver fibrosis. *J Clin Invest* 94, 2481–8.

122 Pan, H. & Halper, J. (2003). Regulation of heat shock protein 47 and type I procollagen expression in avian tendon cells. *Cell Tissue Res* 311, 373–82.

123 El-Thaher, T. S. H., Drake, A. F., Yokota, S., Nakai, A., Nagata, K. & Miller, A. D. (1996). The Ph-Dependent, Atp-Independent Interaction of Collagen Specific Serpin Stress Protein Hsp47. *Prot Pept Lett* 3, 1–8.

124 Nagai, N., Hosokawa, M., Itohara, S., Adachi, E., Matsushita, T., Hosokawa, N. & Nagata, K. (2000). Embryonic lethality of molecular

chaperone hsp47 knockout mice is associated with defects in collagen biosynthesis. *J Cell Biol* 150, 1499–506.

125 Tasab, M., Batten, M. R. & Bulleid, N. J. (2000). Hsp47: a molecular chaperone that interacts with and stabilizes correctly-folded procollagen. *EMBO J* 19, 2204–11.

126 Koide, T., Aso, A., Yorihuzi, T. & Nagata, K. (2000). Conformational requirements of collagenous peptides for recognition by the chaperone protein HSP47. *J Biol Chem* 275, 27957–63.

127 Bruckner, P. & Eikenberry, E. F. (1984). Procollagen is more stable in cellulo than in vitro. *Eur J Biochem* 140, 397–9.

128 Tasab, M., Jenkinson, L. & Bulleid, N. J. (2002). Sequence-specific recognition of collagen triple helices by the collagen-specific molecular chaperone HSP47. *J Biol Chem* 277, 35007–12.

129 Koide, T., Takahara, Y., Asada, S. & Nagata, K. (2002). Xaa-Arg-Gly Triplets in the Collagen Triple Helix Are Dominant Binding Sites for the Molecular Chaperone HSP47. *J Biol Chem* 277, 6178–6182.

130 Bonfanti, L., Mironov, A. A., Martinez-Menarguez, J. A., Martella, O., Fusella, A., Baldassarre, M., Buccione, R., Geuze, H. J. & Luini, A. (1998). Procollagen traverses the Golgi stack without leaving the lumen of cisternae: evidence for cisternal maturation. *Cell* 95, 993–1003.

131 Rich, A. & Crick, F. H. C. (1961). The molecular structure of collagen. *J Mol Biol* 3, 483–506.

132 Takahashi, N., Hayano, T. & Suzuki, M. (1989). Peptidyl-prolyl *cis-trans* isomerase is the cyclosporin A-binding protein cyclophilin. *Nature* 337, 473–5.

133 Fischer, G., Wittmann Liebold, B., Lang, K., Kiefhaber, T. & Schmid, F. X. (1989). Cyclophilin and peptidyl-prolyl *cis-trans* isomerase are probably identical proteins. *Nature* 337, 476–8.

134 Dorner, A. J., Bole, D. G. & Kaufman, R. J. (1987). The relationship of N-linked glycosylation and heavy chain-binding protein association with the secretion of glycoproteins. *J Cell Biol* 105, 2665–74.

135 Suzuki, C. K., Bonifacino, J. S., Lin, A. Y., Davis, M. M. & Klausner, R. D. (1991). Regulating the retention of T-cell receptor alpha chain variants within the endoplasmic reticulum: Ca(2+)-dependent association with BiP. *J Cell Biol* 114, 189–205.

136 Chessler, S. D. & Byers, P. H. (1993). BiP binds type I procollagen pro alpha chains with mutations in the carboxyl-terminal propeptide synthesized by cells from patients with osteogenesis imperfecta. *J Biol Chem* 268, 18226–33.

137 Lamande, S. R., Chessler, S. D., Golub, S. B., Byers, P. H., Chan, D., Cole, W. G., Sillence, D. O. & Bateman, J. F. (1995). Endoplasmic reticulum-mediated quality control of type I collagen production by cells from osteogenesis imperfecta patients with mutations in the pro alpha 1 (I) chain carboxyl-terminal propeptide which impair subunit assembly. *J Biol Chem* 270, 8642–9.

138 Wilson, R. R. & Bulleid, N. J. (2000). Semi-permeabilized cells to study procollagen assembly. *Methods Mol Biol* 139, 1–9.

139 Elliott, J. G., Oliver, J. D. & High, S. (1997). The thiol-dependent reductase ERp57 interacts specifically with N-glycosylated integral membrane proteins [published erratum appears in J Biol Chem 1997 Aug 8;272(32):20312]. *J Biol Chem* 272, 13849–55.

140 Pihlajaniemi, T., Myllyla, R., Alitalo, K., Vaheri, A. & Kivirikko, K. I. (1981). Posttranslational modifications in the biosynthesis of type IV collagen by a human tumor cell line. *Biochemistry* 20, 7409–15.

141 Plutner, H., Davidson, H. W., Saraste, J. & Balch, W. E. (1992). Morphological analysis of protein transport from the ER to Golgi mem-

branes in digitonin-permeabilized cells: role of the P58 containing compartment. *J Cell Biol* 119, 1097–116.

142 Gurevich, V. V., Pokrovskaya, I. D., Obukhova, T. A. & Zozulya, S. A. (1991). Preparative in vitro mRNA synthesis using SP6 and T7 polymerases. *Anal. Biochem*. 195, 207–213.

143 Bulleid, N. J., Wilson, R. R. & Lad, U. (1998). A cautionary note when using pepsin as a probe for the formation of a collagen triple helix. *Matrix Biol* 17, 233–236.

19
Redox Regulation of Chaperones

Jörg H. Hoffmann and Ursula Jakob

19.1
Introduction

The regulation of a chaperone's affinity to its substrate proteins is certainly one of the most crucial aspects in chaperone function. As a matter of fact, ''folding'' chaperones would never be able to function if it were not for their continuous cycling through high- and low-affinity binding states. The most prominent members of folding chaperones, the GroEL/ES (Hsp60/Hsp10) and DnaK (Hsp70) systems, for instance, utilize ATP binding and hydrolysis to allow cycling through distinct conformations [1]. This promotes refolding of the bound substrate proteins. Now, a small number of ''holdase'' chaperones have also been identified as existing in at least two different conformations: one that shows chaperone activity (''on''-conformation) and one that does not (''off''-conformation).

This chapter focuses on a recently discovered novel mechanism to regulate a chaperone's affinity to its substrate proteins. Changes in the redox state of the environment are sensed by highly reactive cysteines, which undergo reversible disulfide bond formation, thereby leading to changes in the protein conformation and chaperone activity. We will first discuss how disulfide bond formation functions as an elegant means to switch molecules between distinct conformational states, and then we will describe the two currently known redox-regulated chaperones, prokaryotic Hsp33 and eukaryotic PDI. We will discuss the physiological relevance of redox-regulated chaperones such as Hsp33 and present some of the standard techniques employed in this field of chaperone research.

19.2
Disulfide Bonds as Redox-Switches

19.2.1
Functionality of Disulfide Bonds

Disulfide bonds are important for protein stability and activity. They are introduced into proteins by the oxidative reaction of two thiols, which react to form a stable

Protein Folding Handbook. Part II. Edited by J. Buchner and T. Kiefhaber

ISBN: 3-527-30784-2

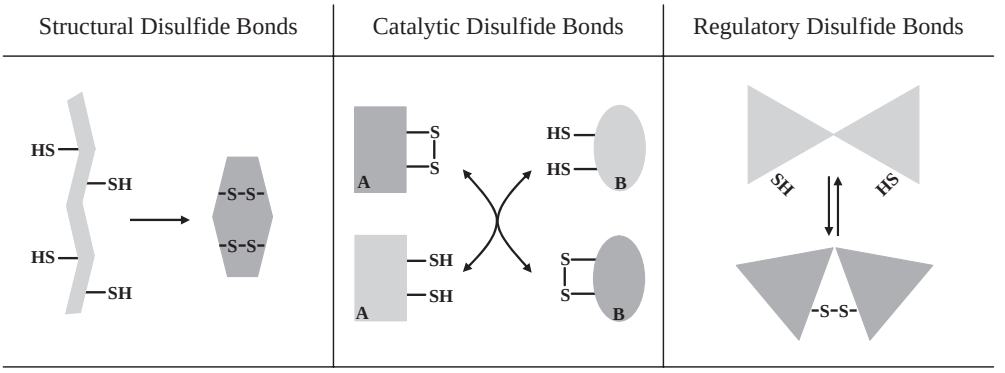

Fig. 19.1. The three types of disulfide bonds. Structural disulfide bonds are formed during the folding process of many proteins and contribute to the stability of the native protein. Catalytic disulfide bonds are crucial components of the active sites of thiol-disulfide oxidoreductases. Depending on their redox potential and that of the environment, oxidoreductases can catalyze disulfide bond formation (e.g., DsbA), disulfide bond reduction (e.g., TrxA), or isomerization (e.g., PDI). Regulatory disulfide bonds form and break during the mechanistic life cycle of redox-regulated proteins. A change in the thiol/disulfide status is accompanied by conformational changes, which lead to functional changes of the respective protein.

covalent sulfur-sulfur bond. Formation of disulfide bonds can occur spontaneously in vitro by air oxidation and the transfer of two electrons to molecular oxygen. In vivo, disulfide bond formation is very effectively catalyzed by sophisticated enzyme systems, as is reviewed elegantly in Chapter 9.

Based on the variety of functions that disulfide bonds can assume in proteins, they may be divided into three groups: structural disulfide bonds, active site disulfide bonds, and regulatory disulfide bonds (Figure 19.1).

Structural disulfide bonds are found in a large number of secreted proteins or extracellular domains of membrane proteins. In these proteins, disulfide bond formation is required for the proper folding of the respective proteins [2]. It is favored in oxidizing cellular compartments such as the periplasm in gram-negative bacteria or the endoplasmic reticulum in eukaryotes [3]. Here, disulfide bond formation is catalyzed by a distinct set of oxidizing enzymes that are present in these compartments (e.g., DsbA, PDI). In contrast, disulfide bonds are usually absent in proteins that reside within the reducing cytosol of cells.

Active-site disulfide bonds are mainly found in oxidative and reductive enzymes along with proteins that transport reducing equivalents across cellular barriers. This group of proteins includes thiol-disulfide oxidoreductases, enzymes that actively introduce, reduce, or isomerase disulfide bonds of other proteins. The active-site thiols are directly involved in the enzymatic reaction and reversibly change their redox status during the course of the reaction. Prominent members of this group of oxidoreductases are the cytosolic thioredoxins and glutaredoxins [4], the Dsb proteins in bacteria [5], as well as protein disulfide isomerase (PDI; [6]) and Ero1p in the ER ([7]). The third group of proteins uses disulfide bond for-

mation as a way to specifically regulate their activity. This group includes redox-regulated chaperones and will be discussed in more detail in the next section.

19.2.2 Regulatory Disulfide Bonds as Functional Switches

Regulatory disulfide bonds allow proteins to switch between at least two distinct protein conformations with significantly different functional features, depending on the redox state of the environment (reviewed in Ref. [8]). Similar to disulfide bonds in the active sites of thiol-disulfide oxidoreductases, regulatory disulfide switches are commonly found to involve specific cysteine motifs such as the CXXC motif [9] or a CXC motif, where X could be any other amino acid. Covalently linking two cysteines separated by only one or two amino acids can then induce significant structural rearrangements within the protein.

Whether the reduced state of the protein containing the free thiol groups or the oxidized state containing the disulfide bond(s) represents the functionally active conformation depends on the individual protein. In either case, ''the switch is flipped'' by the exposure of the protein to a sudden change in redox conditions. Because most redox-regulated proteins are found in the reducing environment of the cellular cytosol, in the majority of cases exposure to oxidizing conditions such as the accumulation of reactive oxygen species (ROS) triggers the switch.

In recent years, a growing number of proteins that use reversible disulfide bond formation as a redox switch have been identified. This group contains numerous kinases, phosphatases, eukaryotic and prokaryotic transcription factors, plant enzymes involved in photosynthesis [10, 11] and molecular chaperones. Prominent members of this group include Raf-kinase [12] and protein kinase C (PKC, [13]), PTEN phosphatase [14], the yeast oxidative stress transcription factor Yap1p [15, 16], the prokaryotic oxidative stress transcription factor OxyR of *E. coli* [17, 18] as well as the redox-regulated chaperones Hsp33 [19] and PDI [20].

A number of these redox-regulated proteins harbor metal cofactors in their reduced state that are coordinated by the redox-active thiol groups. For instance, four conserved cysteine residues in the redox-regulated chaperone Hsp33 stably coordinate one zinc (II) ion with very high affinity [21]. On the one hand, this metal coordination confers very high stability to the respective protein domain under reducing conditions. On the other hand, however, zinc-coordinating thiols appear to be particularly sensitive to oxidizing conditions. Upon exposure to H_2O_2, zinc is rapidly released as disulfide bonds form. The same principle appears to apply to the redox-sensitive zinc centers of RsrA [22, 23], PKC [13], Raf-kinase [12], and several zinc finger proteins such as replication protein A [24, 25]. This high sensitivity of zinc centers towards oxidation may be explained by the fact that zinc (II) primes the cysteine residues for rapid oxidation. Firstly, zinc (II) can act as a Lewis acid and lowers the pK_a values of the thiol groups involved. This stabilizes the thiolate anion status and, as a result, increases their reactivity. Secondly, zinc coordination brings cysteines in close proximity so that they can easily form disulfide bonds [21].

Interestingly, not all redox-regulated proteins use disulfide bond formation as a redox switch. FNR [26] and SoxR [27], two other important transcriptional regulators of *E. coli*, for instance, utilize redox-sensitive iron sulfur clusters as switches for protein activity (both reviewed in Ref. [28]). Other proteins such as the OhrR repressor or cAMP-dependent protein kinase (cAPK) are regulated by the oxidative modification of just a single cysteine residue [29, 30].

19.2.3
Redox Regulation of Chaperone Activity

In the case of molecular chaperones, redox switches appear to be used to reversibly change the chaperone from a conformation with high chaperone activity to one with very low chaperone activity. These two conformations may also be described as the high- and low-affinity binding state of the chaperone. Existence of two states with distinct affinities for substrate binding is reminiscent of chaperones such as GroEL and DnaK, which exist in two different affinity states based on the nucleotide-binding status of the protein.

To our knowledge, two molecular chaperones that use redox switches to regulate their chaperone activity have been reported in the literature so far: the prokaryotic heat shock protein Hsp33 [19, 31] and the eukaryotic oxidoreductase PDI [20]. Both proteins will be described in detail in the following two sections of this chapter.

19.3
Prokaryotic Hsp33: A Chaperone Activated by Oxidation

19.3.1
Identification of a Redox-regulated Chaperone

The heat shock protein 33 (Hsp33) of *E. coli* was the first reported redox-regulated molecular chaperone. The 32.9-kDa gene product of *hslO* (heat shock locus O [32]) is a member of a highly conserved family of heat shock proteins [19]. Hsp33 is present in more than 50 different prokaryotic organisms. Recently, Hsp33 has also been identified in the eukaryotic organisms *Chlamydomonas reinhardtii* [33] and *Dictyostelium discoideum*, where it is predicted to be localized to the mitochondria. Every prokaryotic family member is characterized by the presence of a C-X-C-X_{28-32}-C-X-X-C cysteine motif in the C-terminal regulatory domain of the protein.

Hsp33 was first discovered as a protein that efficiently prevents the aggregation of thermally unfolding proteins such as citrate synthase and luciferase in vitro. What made Hsp33 so unique as a chaperone, however, was the observation that its chaperone activity was dependent on the redox state of the environment. Under reducing conditions, the chaperone activity was greatly reduced. This effect was fully reversible by incubating Hsp33 in physiological oxidants such as H_2O_2. The investigation of this phenomenon revealed that Hsp33's four absolutely conserved

cysteines serve as redox sensors in the protein. This unique redox switch in Hsp33 allows the redox regulation of Hsp33's chaperone activity by the reversible formation of two intramolecular disulfide bonds [21]. The redox potential of Hsp33 was determined to be −170 mV [19]. This suggested that Hsp33 is inactive under normal conditions in the cell but can be quickly activated under conditions of cellular oxidative stress.

In addition to this posttranslational redox regulation, Hsp33 is also regulated as a typical heat shock protein on a transcriptional level. During heat shock, the transcription of Hsp33 is significantly upregulated, and the mRNA levels of Hsp33 increase by a factor of ∼30 [32]. This leads to about a twofold increase in the steady-state protein concentration and yields about 3 μM Hsp33 in *E. coli* at 43 °C [19]. This dual regulation positions Hsp33 at the crossroad between heat and oxidative stress.

19.3.2
Activation Mechanism of Hsp33

Under non-stress conditions, Hsp33 is present in the reducing *E. coli* cytosol and is inactive as a molecular chaperone. All four highly conserved cysteine residues, Cys_{232}, Cys_{234}, Cys_{265}, and Cys_{268}, are in the thiolate anion state and tightly coordinate one zinc (II) ion [21]. This zinc binding confers high stability to the reduced conformation of Hsp33 and guarantees that the chaperone function of Hsp33 stays downregulated unless oxidative stress is encountered.

Upon exposure of Hsp33 to reactive oxygen species (ROS) such as hydroxyl radicals (OH·), two disulfide bonds rapidly form between the two next-neighbor cysteines Cys_{232}/Cys_{234} and Cys_{265}/Cys_{268} and the zinc is concomitantly released [34]. The switch in Hsp33 is now in its "on" position and opens the road for the activation process of Hsp33's chaperone function. Interestingly, disulfide bond formation and zinc release account for only the first step in the activation process of Hsp33. To obtain fully active Hsp33, two oxidized Hsp33 monomers need to dimerize [35]. That the full activation of Hsp33 requires dimerization has been shown spectroscopically as well as by ultracentrifugation analysis. A K_D for dimerization of 0.6 μM at 20 °C was determined [35]. Significantly, in the presence of substrate proteins, the K_D is probably even lower. This was suggested by cross-linking experiments that revealed a shift to the dimeric conformation of Hsp33 when denatured substrate proteins are present [36].

In contrast to disulfide bond formation and zinc release, dimerization of Hsp33 is highly concentration- and temperature-dependent [35]. Thus, it is optimized for a protein that is overexpressed during heat shock and activated during oxidative stress. This finding confirms the hypothesis that Hsp33 is especially important under the self-propagating and most severe conditions of oxidative stress at elevated temperatures.

That the activation process of Hsp33 is accompanied by significant conformational changes was shown by Raman and coworkers, who used far-ultraviolet circular dichroism (far-UV CD) spectroscopy to monitor the secondary structure of

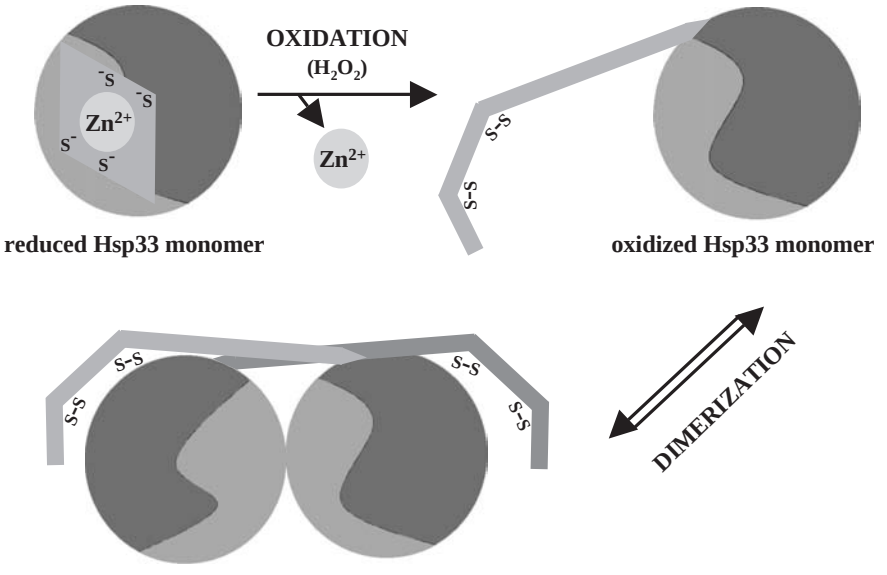

Fig. 19.2. Model for the activation mechanism of Hsp33. Under non-stress conditions, Hsp33 is reduced and inactive as a chaperone. Zinc coordination by four highly conserved cysteine residues in the carboxy-terminal domain of Hsp33 keeps the chaperone in this inactive, monomeric conformation. Upon exposure of Hsp33 to oxidative stress, two disulfide bonds form and zinc is quickly released. This leads to the concentration- and temperature-dependent association of two oxidized Hsp33 monomers and results in highly active Hsp33 dimers.

Hsp33. This analysis revealed that the activation of Hsp33 causes a dramatic loss of α-helical content in Hsp33 [37]. Importantly, these structural rearrangements are paralleled by a significant increase in Hsp33's hydrophobicity. Accessible hydrophobic patches are typical substrate-binding sites of molecular chaperones and are therefore a characteristic feature of active chaperones. Most likely these areas are either buried or simply absent in the reduced conformation of Hsp33 and are only exposed upon disulfide bond formation and dimerization of Hsp33 during oxidative activation. A model for the activation mechanism of Hsp33 is shown in Figure 19.2.

19.3.3 The Crystal Structure of Active Hsp33

The crystal structure of dimeric Hsp33 was independently solved by Vijayalakshmi et al. [38] and Kim et al. [36] at 2.2 Å and 2.7 Å, respectively. The core domain (amino acids 1–178) of each monomer shows a novel protein fold consisting of a single central α-helix sandwiched between a flattened barrel of two antiparallel β-sheets. After the absolutely conserved Pro_{178}, the polypeptide chain crosses over

(''domain swapping'') and folds into three helices, which interact with regions of the other protein subunit.

Both reported crystal structures lacked the C-terminal zinc-binding region. This was due to either the unintentional proteolysis of full-length Hsp33 during the crystallization process or the intentional crystallization of proteolytic Hsp33 fragments (1–255, [38] or 1–235, [36]). In the case of the 1–255 fragment, the electron densities of the region 236–255 could not be resolved, presumably because of its significant flexibility.

Structural analysis of dimeric Hsp33 revealed two putative substrate-binding sites in Hsp33 that extend over the surface of both Hsp33 molecules: an extended groove along the side of the Hsp33 dimer and an inter-subunit 10-stranded β-sheet ''saddle,'' which accounts for $\sim$2250 Å^2 of accessible surface in Hsp33 [38]. Both putative polypeptide-binding sites reveal a number of conserved hydrophobic patches capable of interacting with hydrophobic regions of unfolding proteins. Moreover, both sites harbor several conserved polar residues that might be involved in the interaction with the peptide backbone of substrates [38]. In contrast, the remaining surface of Hsp33 is highly acidic and presumably is not capable of interacting with unfolded substrate proteins.

19.3.4
The Active Hsp33-Dimer: An Efficient Chaperone Holdase

A number of different biochemical studies have revealed that activated Hsp33 functions as a chaperone ''holdase.'' Hsp33 recognizes and stably binds cellular proteins that unfold during stress. This interaction prevents stress-sensitive proteins from otherwise irreversible aggregation processes that would be fatal to the cell. In contrast to chaperone ''foldases,'' Hsp33 appears to be unable to actively (re)fold its substrate proteins.

Oxidized, dimeric Hsp33 has been shown to very efficiently prevent the aggregation of numerous thermally and chemically unfolded substrate proteins in vitro (e.g., citrate synthase, luciferase [19, 35], and ζ-crystallin [37]) and forms apparently very stable complexes with its substrate proteins. The stoichiometry of Hsp33:substrate complexes was determined with chemically denatured luciferase as model substrate protein and was found to be one Hsp33 dimer per molecule of luciferase [39]. Analysis of the stability of Hsp33–substrate protein complexes showed that stoichiometric amounts of active Hsp33 dimers prevent the aggregation of thermally unfolding proteins such as luciferase over more than 20 hours at heat shock temperatures in vitro [39]. Activated Hsp33 was also shown to directly protect other proteins from oxidative stress damage in vitro. Hsp33 successfully prevented the oxidative stress-induced aggregation of RrmJ (formerly FtsJ) [19], an rRNA methyltransferase of *E. coli* [40].

In summary, oxidized active Hsp33 dimers prevent the aggregation of numerous substrate proteins over extended periods of time by forming apparently very stable complexes. Reduced, zinc-bound Hsp33 monomers, on the other hand, are unable to function as molecular chaperones. A current model suggests that the C-terminal

zinc-binding domain masks or occupies the substrate-binding site and dimerization interface, thus downregulating the chaperone activity of reduced Hsp33 [33, 36, 38] (Figure 19.2).

19.3.5 Hsp33 is Part of a Sophisticated Multi-chaperone Network

In vivo, active Hsp33 accumulates in cells that are permanently oxidatively stressed [19]. In these cells, Hsp33 was shown to be an essential component for the survival of additional oxidative stress or elevated temperatures [19]. *E. coli* strains, which are permanently oxidatively stressed due to the absence of the cytosolic reductant thioredoxin (*trxA*$^-$), for example, show a 10 000-fold increase in H_2O_2 sensitivity upon additional deletion of *hslO*, the gene encoding Hsp33. Similarly, double mutants in thioredoxin reductase *trxB* and *hslO* are no longer able to grow on MacConkey agar at elevated temperatures unless functional Hsp33 is expressed (unpublished observations).

To investigate how Hsp33 fulfills this important protective task under severe oxidative stress conditions, we performed extensive in vitro and in vivo analysis of Hsp33's chaperone function. We found that Hsp33 plays the key role in a redox-regulated multi-chaperone network, which protects proteins during stress conditions and leads to their successful refolding after the stress. Active Hsp33 dimers, which are rapidly formed upon exposure of cells to oxidative stress, work as efficient chaperone holdases and bind tightly to unfolding proteins to protect them against irreversible aggregation. In vivo, oxidized Hsp33 dimer–substrate protein complexes are then quickly reduced by the cellular thioredoxin and glutaredoxin systems [39]. Importantly, this reduction of Hsp33 does not cause the dissociation of the bound substrate proteins. In contrast to reduced Hsp33 monomers, which show no significant chaperone activity, reduced Hsp33 dimers still actively bind their substrate protein [39]. The existence of reduced dimers as a third Hsp33 species adds a new dimension to Hsp33's regulation as a chaperone. While Hsp33 becomes activated by oxidation and dimerization, inactivation requires both reduction and monomerization. Thus, the activity of Hsp33 is tightly regulated by its redox state and by its oligomerization state.

The fact that Hsp33 dimers do not release their substrate proteins upon simple reduction guarantees that the chaperone is kept in its active conformation beyond the return of cells to normal redox conditions. This regulation successfully prevents substrate release under reducing yet non-permissive folding conditions, where any released substrate protein would immediately aggregate. We found that the reduction of Hsp33 dimers is the necessary prerequisite for the final step in the Hsp33 inactivation process, which involves the transfer of substrate proteins to the bacterial chaperone foldase system DnaK/DnaJ/GrpE. The substrate proteins are refolded by the DnaK/DnaJ/GrpE system [39], and the substrate-free reduced Hsp33 dimers dissociate into inactive monomers. Substrate transfer and Hsp33 inactivation appears to be dependent on both the reduction of Hsp33 and the availability of the DnaK/DnaJ/GrpE chaperone system. Under oxidizing conditions, the

DnaK/DnaJ/GrpE system is unable to take over the substrate proteins from Hsp33, and under reducing conditions, substrate release and refolding of the substrate proteins appear to be DnaK/DnaJ/GrpE system-specific. GroEL/ES as an alternate foldase system was unable to significantly release and reactivate substrate proteins bound to reduced Hsp33 dimers. It was, however, able to work in concert with the DnaK/DnaJ/GrpE system once the proteins were released from Hsp33 by the DnaK/DnaJ/GrpE system [39].

Interestingly, the DnaK/DnaJ/GrpE system is well known to function as the cellular thermosensor of *E. coli* [41, 42]. Thus, its availability is a good indicator that non-stress conditions have been reestablished and permissive folding conditions have been restored. Using the DnaK/DnaJ/GrpE system as a substrate-release factor enables this redox-regulated chaperone network to link substrate release from a chaperone holdase (Hsp33) to the presence of suitable folding conditions and sufficient amounts of a protein foldases (DnaK/DnaJ/GrpE) (Figure 19.3).

19.4
Eukaryotic Protein Disulfide Isomerase (PDI): Redox Shuffling in the ER

19.4.1
PDI, A Multifunctional Enzyme in Eukaryotes

Eukaryotic protein disulfide isomerase (PDI) has been the target of extensive research ever since its original discovery as a protein oxidase by Anfinsen and coworkers in 1963 [43]. In the last 40 years, a substantial amount of data has been collected describing PDI as a multifunctional enzyme in the endoplasmic reticulum (ER) and other compartments of eukaryotes. Protein disulfide isomerase has been shown to be a protein-thiol oxidoreductase capable of catalyzing the formation, reduction, and isomerization of disulfide bonds [6]. Moreover, it was accredited with ATP-independent chaperone function as well as foldase activity [44]. PDI was also found to be an obligatory subunit of the enzyme prolyl 4-hydroxylase P4H [45] as well as of the microsomal triglyceride transfer protein MTP [46].

Protein disulfide isomerase consists of four major domains: a, b, b′, and a′. All four domains contain a highly conserved thioredoxin fold with the characteristic secondary structure $\beta\alpha\beta\alpha\beta\beta\alpha$. In addition, PDI harbors an acidic extension at its C-terminus (c domain), which carries a KDEL (HDEL in yeast) ER-retention signal. Of the four thioredoxin-like domains, only the a and a′ domains harbor redox-active CXXC motifs. The b′ domain has been shown to be vital for substrate binding [47]. Interestingly, complex isomerization reactions require the presence of all PDI domains, including the b domain, while simple isomerizations reactions require only the b′ domain in linear combination with one of the a domains [48]. Simple redox reactions, on the other hand, require only one of the a domains [49] (reviewed in Ref. [50]).

PDI is highly abundant in the ER of yeast and mammalian cells, where its concentration can approach the millimolar range (reviewed in Ref. [51]). Here, PDI

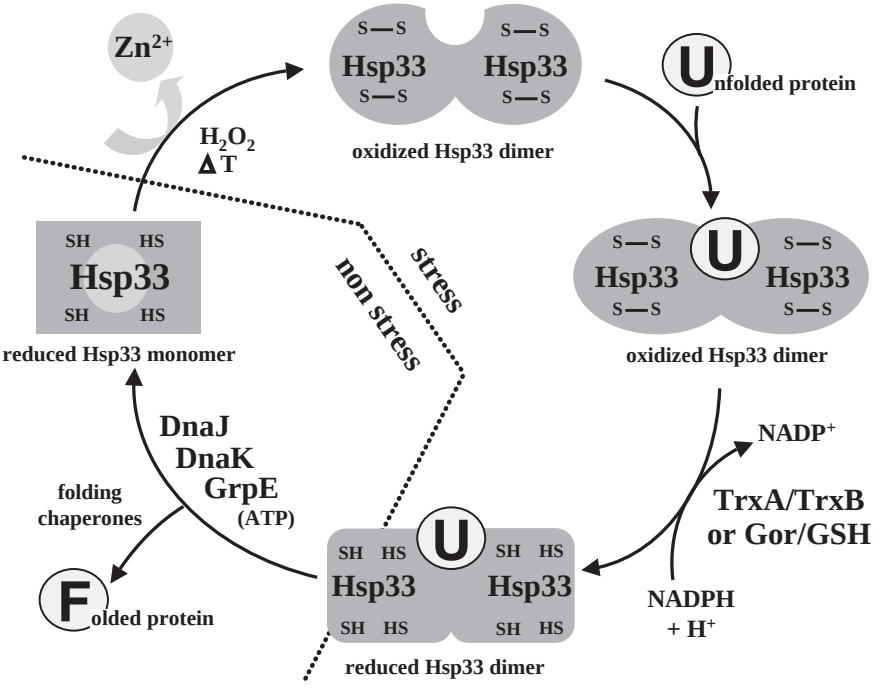

Fig. 19.3. Model for a redox-regulated chaperone network. Active, oxidized Hsp33 dimers act as a chaperone holdases and bind tightly to unfolding protein intermediates to protect them against irreversible aggregation. The thioredoxin or glutathione systems quickly reduce Hsp33–substrate protein complexes. This reduction primes Hsp33 for the interaction with the DnaK/DnaJ/GrpE chaperone system. Upon return to non-stress conditions, the DnaK/DnaJ/GrpE system becomes available again and causes the release of substrate proteins bound to Hsp33. This allows the DnaK/DnaJ/GrpE foldase system, either alone or in concert with the GroEL/GroES system, to refold the substrate proteins. Upon substrate transfer, reduced Hsp33 dimers dissociate into inactive Hsp33 monomers.

seems to be predominantly involved in disulfide bond formation and isomerization of disulfide bonds within secreted proteins. This latter activity is thought to make PDI essential in yeast [52].

To introduce disulfide bonds, PDI needs to be maintained in the oxidized state, which also appears to be the favored redox state of PDI under steady-state conditions in the yeast ER [53]. Re-oxidation of PDI is mediated by an essential protein relay involving the oxidase Ero1p [53], which uses the cofactor FAD to shuttle electrons ultimately onto molecular oxygen [7]. While PDI needs to be oxidized to promote disulfide bond formation, it is required to be in its reduced state to facilitate disulfide isomerization. Even though PDI is considered to be predominantly oxidized in the ER, its transient reduction is thought to be achieved by the presence of sufficient amounts of reduced glutathione (GSH).

PDI has also been discovered in various other cellular locations, such as the cytoplasm, endosomes, and plasma membrane of eukaryotic cells (reviewed in Ref. [54]). Here, the enzyme is less abundant than in the ER and is predominantly in its reduced form. It catalyzes the reduction of protein disulfides and is presumably regenerated by the thioredoxin system using reducing equivalents of NADPH [55].

In addition to being a powerful oxidoreductase, PDI has been shown to support the folding of denatured substrate proteins both in vitro and in vivo. As mentioned before, this polypeptide-binding activity appears to particularly involve the b′ domain. PDI has been found to chaperone the refolding of several proteins such as glyceraldehyde-3-phosphate dehydrogenase (GAPDH) [56], acidic phospholipase A_2, rhodanese [57], and proinsulin [58]. It is now widely accepted that it is this combination of oxidoreductase activity and chaperone activity that makes PDI such a capable and important enzyme [44, 50].

19.4.2
PDI and Redox Regulation

Recently, Rapoport and colleagues reported a novel feature of PDI. The authors found that PDI functions as a redox-dependent chaperone involved in the unfolding of cholera toxin in the ER [20]. Cholera toxin shows a sophisticated mechanism of action, which ultimately leads to a disastrous salt and water secretion from mammalian intestinal epithelial cells due to the uncontrolled opening of chloride channels. The toxin is originally assembled in the periplasm of the bacterium *Vibrio cholerae* and is secreted by the bacterium in an inactive form. In this stage, it consists of one A-subunit surrounded by five B-subunits. The pathogenic component A1 is a fragment of the A-chain. To set this fragment free and unleash its activity, several steps are required. First, the A-chain needs to be cleaved into its A1 and A2 fragments by a protease that is also secreted by *Vibrio cholerae*. Second, the cholera toxin needs to travel backwards through the secretory pathway of its target cell until it reaches the ER. Here, reduction of a crucial intramolecular disulfide bond, which still covalently links the A1 and A2 fragments, is required to release the A1 fragment. The A1 fragment is then unfolded and retro-translocated into the cytoplasm, where it finally takes up its enzymatic activity to ADP-ribosylate the heterotrimeric Gαs protein [59].

Rapoport and coworkers found that PDI plays the key role in the processing of the A1 fragment in the ER [20]. PDI appears to be responsible for the disassembly of the toxin and the unfolding of the A1 fragment, which finally triggers the reduction of the intramolecular disulfide bond and the retrograde translocation of A1 into the cytosol. Interestingly, it appeared that PDI was capable only of binding and subsequently unfolding the A1 fragment when reducing conditions were established and PDI's cysteines were reduced. This unfoldase activity of PDI, however, appeared to be independent of the oxidoreductase activity of PDI but seemed rather to be due to a redox-regulated change in the conformation and chaperone activity of PDI.

In conclusion, the authors proposed a model in which the chaperone activity of

PDI is regulated by the redox state of the protein. According to this model, reduced PDI binds to the A1-chain of cholera toxin and unfolds the polypeptide. Upon oxidation of PDI, conformational changes occur that decrease the substrate-binding affinity in PDI and cause the substrate protein to be released. This model appears to be particularly reasonable for the isomerase activity of PDI, where the chaperone activity of reduced PDI might be required to recognize proteins that are partly unfolded due to incorrect disulfide bonds. Upon binding, PDI would reshuffle these disulfide bonds, become oxidized, and, in turn, release the substrate proteins [20].

The authors also concluded that in analogy to ATP-dependent chaperones like DnaK, which drive protein folding by continuously cycling through high- and low-affinity states based on nucleotide binding, the chaperone activity of PDI could be driven by the continuous cycling through two different redox states [20]. In the case of DnaK, the cycle is further regulated by cofactors such as DnaJ and GrpE. Thus, one could envision respective cofactors for PDI that might affect its redox cycle [20].

In response to this model, Lumb and Bulleid set out to examine the potential redox regulation of PDI's chaperone activity using other known substrate proteins of PDI [60]. They examined the potential redox-dependent interaction of PDI with the C-propeptide of procollagen, a known transient substrate of PDI, as well as with the α-subunit of prolyl 4-hydroxylase (P4H), with which PDI is known to permanently associate to form an active $\alpha_2\beta_2$ tetramer. In both cases, the authors found that the binding of PDI to these proteins was independent of its redox state. The observation that high concentrations of GSSG caused the dissociation of PDI from its substrates was attributed to GSSG acting as a competitor for peptide binding rather than GSSG acting on the potential redox switch of PDI [60]. However, the fact that dissociation of the A1 fragment of cholera toxin from PDI was due to the oxidation-induced change in PDI's chaperone activity became evident when Tsai et al. showed that the natural PDI oxidant Ero1p worked as well as GSSG [61]. This finding supports the model that PDI acts as a redox-regulated chaperone for the A1-fragment of cholera toxin.

So far, cholera toxin is the only substrate in which binding of PDI was found to be redox-regulated. Several reports suggested that PDI's chaperone function is independent from its redox state, especially since redox-inactive variants of PDI still show chaperone activity [58, 62]. Until further investigations are conducted, however, it is impossible to evaluate the general relevance of PDI's redox regulation. Given the complexity of this enzyme, various alternatives seem possible. The future will show the outcome of this lively discussion concerning this attractive model.

19.5 Concluding Remarks and Outlook

This chapter focused on two distinct redox-regulated proteins, eukaryotic PDI and prokaryotic Hsp33. PDI is the first protein that oxidizes/reduces disulfide bonds

of substrate proteins and at the same time shows substrate-binding affinities that are regulated by its own redox state. This regulation of substrate-binding activity is thought to support the isomerase and oxidase function of PDI [20].

The redox-regulated chaperone Hsp33 appears to be a chaperone specifically designed to protect cells against severe oxidative stress conditions. Hsp33 is constitutively expressed and present in its inactive monomeric state during non-stress conditions. Once oxidative stress is encountered, however, Hsp33's chaperone activity is quickly turned on via disulfide bond formation. In addition to this posttranslational regulation of its chaperone activity, Hsp33 is also upregulated on transcriptional level. This makes Hsp33 particularly abundant and active under conditions of combined heat and oxidative stress. This dual regulation of Hsp33 reflects its unique, functional location at the interface of heat shock and oxidative stress. We have now found that Hsp33 is the key component of a highly sophisticated chaperone network that serves as a defense system to protect proteins against stress-induced unfolding.

Hsp33's unique regulation and its specific functional mechanism raise the question of why such specific chaperones as Hsp33 are designed for specific stress situations. Are other chaperone systems not capable of performing their regular tasks? Are they simply overwhelmed during severe stress conditions due to the increasing number of unfolded and damaged proteins? Do some of the housekeeping cellular chaperones themselves become victims of severe stress? All efforts to answer these questions seem to be highly valuable for the further understanding of cellular chaperones, cellular stresses, and beyond.

19.6 Appendix – Experimental Protocols

19.6.1 How to Work With Redox-regulated Chaperones in Vitro

19.6.1.1 Preparation of the Reduced Protein Species

One of the most important requirements for working with redox-regulated proteins is the use of homogeneous preparations of either fully reduced or fully oxidized protein. In the case of the reduced protein species, air oxidation needs to be avoided during the purification process and thereafter. Therefore, buffers should always be supplemented with at least 2 mM (fresh) DTT and the protein preparation should be kept on ice. In the case of metal-free proteins, air oxidation can be minimized by the addition of metal chelators such as EDTA (~1 mM). Often, it is also necessary to freshly reduce the samples before each experiment.

In the case of Hsp33, 100–400 μM of purified Hsp33 is reduced in the presence of 2–8 mM DTT in 40 mM HEPES-KOH (pH 7.5) for 60 min at 37 °C. When necessary, zinc ($ZnCl_2$ in ddH_2O) is added in stoichiometric amounts [21, 35]. It is not recommendable to use excess zinc, because of its nonspecific low-affinity bind-

ing (K_D in the micromolar range) to negative charges on protein surfaces, which could affect subsequent assays. In the case of PDI, reduction is achieved by the incubation of PDI in the presence of 1 mM GSH for 30 min at 30 °C [20] or in the presence of 10 mM DTT [60]. After the reduction, excess reductants (and metals) are removed by using a PD10 (Pharmacia) gel filtration column that has been equilibrated in 40 mM HEPES-KOH (pH 7.5). Then, the protein concentration is determined by using the specific extinction coefficient (http://ca.expasy.org/tools/protparam.html) of the respective protein.

To ascertain that the protein has been completely reduced, it is strongly recommended to monitor the redox state of the protein directly. This can be done by determining free thiols using Ellman's reagent [34, 63] or by performing thiol-trapping experiments (see Section 19.6.1.3). In the case of metal-binding proteins, the extent of metal association should also be determined. Zinc coordination, for instance, can be quantified using the PAR/PMPS assay (see Section 19.6.2.1). Other metal associations can be quantified with inductively coupled plasma atomic emission spectroscopy (ICP) analysis. After the complete reduction of the protein has been confirmed, the protein should be used immediately or shock frozen in aliquots and stored at −80 °C.

19.6.1.2 **Preparation of the Oxidized Protein Species**

Suitable agents for direct protein oxidation are oxidized glutathione (GSSG), hydrogen peroxide (H_2O_2), or dipyridyl sulfide (DPS). Oxidation of thiol groups with H_2O_2 is thought to first create sulfenic acid intermediates (R-SOH), which then react with nearby cysteines to form disulfide bonds ([64], reviewed in Ref. [8]). The oxidation process with H_2O_2 can be significantly accelerated in the presence of micromolar concentrations of Fenton reagents such as Fe (II) or Cu (I) [65]. The presence of these transition metals leads to the formation of hydroxyl radicals [65], which then react with thiol groups to create highly reactive thiyl radicals. These then rapidly form disulfide bonds. Because hydroxyl radicals are very reactive, nonspecific amino acid modifications and protein fragmentation can occur. This can be avoided by using the milder oxidant GSSG. After the oxidation process is complete, the oxidant needs to be removed and the extent of oxidation needs to be quantified.

In the case of Hsp33, it is important to start the oxidation with completely reduced, zinc-reconstituted protein, because correct disulfide bond formation requires the presence of the cofactor zinc. Reduced Hsp33 is concentrated using Centricon YM-30 concentrators; then 200 μM Hsp33 is oxidized in the presence of 2 mM H_2O_2 for 240 min at 43 °C. Alternatively, 50 μM of Cu(II) can be added to accelerate the oxidation process (for details see Ref. [35]). Next, H_2O_2 and released zinc are removed by gel filtration columns (PD10, Pharmacia). In the case of PDI, oxidation is usually performed in the presence of GSSG ($\geq$ 1 mM) [20] or in the presence of 1 mM or 5 mM dipyridyl sulfide [60]. To identify the location of the respective disulfide bonds in an oxidized protein species, disulfide mapping should be performed [34, 66].

19.6.1.3 In Vitro Thiol Trapping to Monitor the Redox State of Proteins

To monitor the redox status of proteins, one can make use of the distinct chemical features of reduced thiol groups. Whereas reduced thiols react quickly and quantitatively with so-called "thiol-specific probes", oxidized disulfide-linked thiol groups are not accessible to these reagents.

A commonly used thiol-specific probe, which selectively modifies reduced thiol groups in proteins, is 4-acetamido-4′-maleimidylstilbene-2,2′-disulfonic acid (AMS, Molecular Probes). This reagent is particularly suitable for distinguishing between the reduced and oxidized forms of proteins because the modification of each free thiol group with the AMS moiety adds an additional 500 Da of molecular mass to the respective protein. Thus, AMS-modified proteins migrate slower in SDS-PAGE, depending on the number of accessible, AMS-modified cysteine residues.

In vitro thiol trapping may be used either to confirm complete reduction or oxidation of a protein sample (see above) or to obtain kinetic information about the reduction or oxidation process of a redox-regulated protein. To perform thiol-trapping experiments with Hsp33, a protein solution of 5 μM oxidized or reduced Hsp33 (monomer concentration) is prepared in a suitable buffer such as 40 mM HEPES-KOH (pH 7.5). When the kinetics of the reduction or oxidation reactions are monitored, thiol-disulfide exchange reactions need to be stopped instantaneously. To achieve this, trichloroacetic acid (TCA) to a final concentration of 10% (w/v) is added. The low pH greatly slows all ongoing redox reactions (see review in Chapter 9) and denatures the proteins. This further disrupts any special thiol/disulfide interchange activities of the proteins. The protein samples are then stored on ice for at least 30 minutes and centrifuged (30 min, 16 100 *g*, 4 °C). The protein pellets are washed in 200 μL ice cold 10% (w/v) TCA followed by a wash in 200 μL 5% (w/v) TCA. The supernatant is quantitatively removed and the protein pellets are resuspended in 20 μL 15 mM AMS in a buffer containing 6 M urea, 200 mM Tris-HCl pH 8.5, 10 mM EDTA, and 0.5% w/v SDS. The trapping reaction is performed at 37 °C for 60 min in the dark under continuous shaking. Subsequently, the samples are analyzed on non-reducing SDS-PAGE.

19.6.2 Thiol Coordinating Zinc Centers as Redox Switches

19.6.2.1 PAR-PMPS Assay to Quantify Zinc

The amount of free zinc in a protein sample can easily be determined spectroscopically using the PAR assay [67]. This assay is based on the complex formation of free zinc with the zinc-chelating dye 4-(2-pyridylazo) resorcinol (PAR). $Zn(PAR)_2$ complexes have an intense red color with an absorption maximum λ_{max} at 500 nm. To account for slight differences in the extinction coefficient of $Zn(PAR)_2$ complexes caused by buffer composition, pH, and ionic strength, the exact ε_{500} should be determined for each buffer system using a zinc standard. PAR has sufficient affinity ($K_a = 10^{12}$ M^{-2} in 40 mM HEPES, pH 7.0) to complex free as well

as loosely associated, non-thiol-coordinated zinc. In order to determine the amount of thiol-coordinated zinc, which is often bound with $K_a > 10^{14}$ M^{-1}, however, zinc needs to be extracted. This can be achieved by covalently modifying the zinc-coordinating thiol residues with *p*-hydroxymercuriphenylsulfonic acid (PMPS). PMPS forms mercaptide bonds with thiols, which leads to the release of zinc into the solution. Zinc is then immediately complexed by PAR, thereby causing changes in A_{500} and allowing the quantitative analysis of the formerly thiol-coordinated zinc [67].

To analyze the amount of free or surface-bound zinc in Hsp33, the protein (final concentration 3 μM) is diluted into 100 μM PAR in 40 mM metal-free HEPES-KOH, pH 7.0, and the A_{500} is monitored. To determine the amount of thiol-bound zinc, 2-μL aliquots of PMPS (0.2 mM stock solution in 100 μM PAR, metal-free 40 mM HEPES-KOH, pH 7.0) is added and the signal at A_{500} is recorded until addition of PMPS does not lead to a further increase in A_{500}. A constant signal at A_{500} indicates that all thiol-bound zinc was released from the protein [21]. Changes in protein and PMPS concentrations due to the volume changes during the titrations have to be calculated accordingly.

19.6.2.2 Determination of Zinc-binding Constants

To determine the binding constant of zinc to a high-affinity cysteine-coordinating zinc center, metal chelators, which compete with the protein for zinc binding, can be used. Depending on the zinc affinity to the protein, a zinc chelator having zinc-binding properties similar to the protein has to be used. Various concentrations of the zinc chelator are incubated with a fixed protein concentration. After equilibrium has been reached, the chelator is removed by gel filtration and a PAR/PMPS assay is conducted to quantify the zinc that remained bound to the protein.

To determine the K_a of zinc binding for Hsp33, the metal-complexing agent *N*,*N*,*N*′,*N*′-tetrakis(2-pyridylmethyl)ethylenediamine (TPEN) was used. Reduced, zinc-coordinating, wild-type Hsp33 (40 μM) was incubated in metal-free 40 mM HEPES, pH 7.5, 0.2 mM DTT, and various concentrations of TPEN (20 μM to 5 mM) for 16 h at 23 °C. The effective TPEN concentration present at pH 7.5 was calculated according to the pK_a of 7.19 of TPEN [68]. After equilibrium was reached, the samples were applied onto PD10 columns to remove free and zinc-complexed TPEN. After determining the Hsp33 concentration in the eluate, the PAR/PMPS assay was used to determine the remaining amount of zinc bound to the cysteine center in Hsp33. The zinc-binding constant of Hsp33 can then be determined based on the binding constant of TPEN ($K_a = 10^{16}$ M^{-1}) according to Eq. (3). $[Hsp33 \cdot Zn]$ corresponds to the amount of zinc released from Hsp33 by the addition of PMPS, $[Hsp33_{free}]$ equals $[Hsp33_{total}] - [Hsp33 \cdot Zn]$, $[TPEN_{free}]$ equals $[TPEN_{total}] - [TPEN \cdot Zn]$, and $[TPEN \cdot Zn]$ corresponds to the amount of non-complexed Hsp33 $[Hsp33_{free}]$.

To determine zinc-binding affinities of proteins with weaker zinc affinities, PAR [69] can be used as a zinc chelator. The K_a for $Zn(PAR)_2$ complexes has been calculated to be 2×10^{12} M^{-2} at pH 7.0, when the PAR concentration is 100 μM and

the zinc concentration is below 12 μM [67, 69]. Here, the calculated amount of $Zn(PAR)_2$ corresponds directly to the fraction of zinc-free Hsp33 [$Hsp33_{free}$], and the thiol-bound zinc [$Hsp33 \cdot Zn$] corresponds to the amount of zinc that is released upon addition of PMPS. The zinc association constant can be calculated according to Eq. (4) [69].

$$K_a(TPEN) = \frac{[TPEN \cdot Zn]}{[TPEN_{free}] \times [Zn_{free}]} \quad (1)$$

$$K_a(Hsp33) = \frac{[Hsp33 \cdot Zn]}{[Hsp33_{free}] \times [Zn_{free}]} \quad (2)$$

$$K_a(Hsp33) = \frac{K_a(TPEN) \times [Hsp33 \cdot Zn] \times [TPEN_{free}]}{[TPEN \cdot Zn] \times [Hsp33_{free}]} \quad (3)$$

$$K_a(Hsp33) = \frac{K_a(PAR) \times [Hsp33 \cdot Zn] \times [PAR_{free}]^2}{[Zn(PAR)_2] \times [Hsp33_{free}]} \quad (4)$$

19.6.3 Functional Analysis of Redox-regulated Chaperones in Vitro/in Vivo

19.6.3.1 Chaperone Activity Assays

Activity assays for redox-regulated chaperones are performed similarly to those of many other chaperones. A very commonly used chaperone activity assay is to investigate the influence of the chaperone on the aggregation of either thermally or chemically unfolded substrate proteins (e.g., citrate synthase [70], luciferase [19]) following light scattering. This method makes use of the fact that insoluble particles such as protein aggregates scatter light. The extent of light scattering corresponds to the extent of protein aggregation and can easily be monitored using a fluorometer or spectrophotometer equipped with a thermostated cuvette holder.

Chaperone assays can be used to monitor the activity of the reduced and oxidized protein preparation and can be employed to analyze the activity of a redox-regulated chaperone during oxidation/reduction kinetics. When analyzing the influence of redox-regulated chaperones on thermally aggregating proteins at elevated temperatures using wavelengths in the UV range (e.g., 320 nm), re-oxidation of reduced protein preparations due to the production of reactive oxygen species in the cuvette is a potential hazard and should be avoided. If oxidation becomes a problem, the assay buffer can be degassed and supplemented with reducing agents such as DTT. Appropriate buffer controls need to be included to exclude any influence of the redox agent on the aggregation behavior of the substrate protein. In some cases it might be necessary to work with model substrate proteins that do not harbor any cysteine residues in order to fully exclude disulfide exchange reactions between the chaperone and the substrate. For both Hsp33 ([19, 21, 35]) and PDI (reviewed in Refs. [51, 71]), a number of different chaperone assays and substrate proteins have been described in the literature.

19.6.3.2 Manipulating and Analyzing Redox Conditions in Vivo

To analyze the redox state of the proteins in vivo, thiol-trapping experiments with AMS can be performed, given that an antibody against the protein of interest is available. To perform thiol trapping in vivo, cells are grown in minimal medium until the desired OD_{600} is reached. Then, the cells are exposed to the respective stress treatment (e.g., 4 mM H_2O_2 to induce oxidative stress, 1 mM diamide to induce disulfide stress [72]). Cells are then precipitated with ice-cold TCA (final concentration of 10% (w/v)) and incubated on ice for at least 30 min. The thiol trapping is then performed as described in Section 19.6.1.3. Western blot analysis is performed to visualize the protein of interest.

To analyze the thiol-disulfide status of redox-regulated proteins in vivo, it is often crucial to establish either reducing or oxidizing conditions in the cell. If the protein of interest is located in the cytosol, it is easy to analyze the protein under the normal reducing conditions, which are maintained by the thioredoxin and glutaredoxin systems. These potent reducing systems, along with other powerful cellular antioxidants (catalase, superoxide dismutase SOD, etc.) that battle oxidative stress, make it difficult, however, to maintain continuous oxidizing conditions in the cell. This is especially obvious for H_2O_2-induced oxidative stress, which leads only to a transient change in the redox environment [18, 39]. To circumvent this problem, mutant *E. coli* strains that lack components of the thioredoxin and/or glutaredoxin system, and are therefore intrinsically oxidatively stressed, can be used [4, 73]. The protein of interest should accumulate in its oxidized state as soon as its physiological redox system is absent from the cells. Detection of the protein in the reduced and oxidized states, depending on the strains and environmental conditions used, not only shows that the protein of interest is redox regulated in vivo but also reveals the physiological redox systems.

Acknowledgements

We thank Drs. James Bardwell, Paul Graf, and Jeannette Winter for critically reading this manuscript. The National Institutes of Health grant GM065318 and a Burroughs Wellcome Fund Career Award to U.J and a Ph.D. scholarship of the Boehringer Ingelheim Fonds to J.H.H supported this work.

References

1 Bukau, B., and Horwich, A. L. (1998). The Hsp70 and Hsp60 chaperone machines. *Cell* **92**, 351–366.

2 Wedemeyer, W. J., Welker, E., Narayan, M., and Scheraga, H. A. (2000). Disulfide bonds and protein folding. *Biochemistry* **39**, 4207–4216.

3 Frand, A. R., Cuozzo, J. W., and Kaiser, C. A. (2000). Pathways for protein disulphide bond formation. *Trends Cell Biol* **10**, 203–210.

4 Prinz, W. A., Aslund, F., Holmgren, A., and Beckwith, J. (1997). The role of the thioredoxin and glutaredoxin pathways in reducing protein disulfide bonds in the

Escherichia coli cytoplasm. *J Biol Chem* **272**, 15661–15667.

5 Collet, J. F., and Bardwell, J. C. (2002). Oxidative protein folding in bacteria. *Mol Microbiol* **44**, 1–8.

6 Noiva, R. (1999). Protein disulfide isomerase: the multifunctional redox chaperone of the endoplasmic reticulum. *Seminars in Cell & Developmental Biology* **10**, 481–493.

7 Tu, B. P., and Weissman, J. S. (2002). The FAD- and O(2)-dependent reaction cycle of Ero1-mediated oxidative protein folding in the endoplasmic reticulum. *Mol Cell* **10**, 983–994.

8 Linke, K., and Jakob, U. (2003). Not every disulfide lasts forever: disulfide bond formation as a redox switch. *Antioxid Redox Signal* **5**, 425–434.

9 Fomenko, D. E., and Gladyshev, V. N. (2003). Identity and functions of CxxC-derived motifs. *Biochemistry* **42**, 11214–11225.

10 Dai, S., Schwendtmayer, C., Schurmann, P., Ramaswamy, S., and Eklund, H. (2000). Redox signaling in chloroplasts: cleavage of disulfides by an iron-sulfur cluster. *Science* **287**, 655–658.

11 Dietz, K. J. (2003). Plant peroxiredoxins. *Annu Rev Plant Biol* **54**, 93–107.

12 Hoyos, B., Imam, A., Korichneva, I., Levi, E., Chua, R., and Hammerling, U. (2002). Activation of c-Raf kinase by ultraviolet light. Regulation by retinoids. *J Biol Chem* **277**, 23949–23957.

13 Knapp, L. T., and Klann, E. (2000). Superoxide-induced stimulation of protein kinase C via thiol modification and modulation of zinc content. *J Biol Chem* **275**, 24136–24145.

14 Leslie, N. R., Bennett, D., Lindsay, Y. E., Stewart, H., Gray, A., and Downes, C. P. (2003). Redox regulation of PI 3-kinase signalling via inactivation of PTEN. *EMBO J* **22**, 5501–5510.

15 Delaunay, A., Isnard, A. D., and Toledano, M. B. (2000). H2O2 sensing through oxidation of the Yap1 transcription factor. *EMBO J* **19**, 5157–5166.

16 Wood, M. J., Andrade, E. C., and Storz, G. (2003). The redox domain of the Yap1p transcription factor contains two disulfide bonds. *Biochemistry* **42**, 11982–11991.

17 Zheng, M., Aslund, F., and Storz, G. (1998). Activation of the OxyR transcription factor by reversible disulfide bond formation. *Science* **279**, 1718–1721.

18 Aslund, F., Zheng, M., Beckwith, J., and Storz, G. (1999). Regulation of the OxyR transcription factor by hydrogen peroxide and the cellular thiol-disulfide status. *Proc Natl Acad Sci USA* **96**, 6161–6165.

19 Jakob, U., Muse, W., Eser, M., and Bardwell, J. C. (1999). Chaperone activity with a redox switch. *Cell* **96**, 341–352.

20 Tsai, B., Rodighiero, C., Lencer, W. I., and Rapoport, T. A. (2001). Protein disulfide isomerase acts as a redox-dependent chaperone to unfold cholera toxin. *Cell* **104**, 937–948.

21 Jakob, U., Eser, M., and Bardwell, J. C. (2000). Redox switch of hsp33 has a novel zinc-binding motif. *J Biol Chem* **275**, 38302–38310.

22 Kang, J. G., Paget, M. S., Seok, Y. J., Hahn, M. Y., Bae, J. B., Hahn, J. S., Kleanthous, C., Buttner, M. J., and Roe, J. H. (1999). RsrA, an anti-sigma factor regulated by redox change. *EMBO J* **18**, 4292–4298.

23 Paget, M. S., Bae, J. B., Hahn, M. Y., Li, W., Kleanthous, C., Roe, J. H., and Buttner, M. J. (2001). Mutational analysis of RsrA, a zinc-binding anti-sigma factor with a thiol-disulphide redox switch. *Mol Microbiol* **39**, 1036–1047.

24 Park, J. S., Wang, M., Park, S. J., and Lee, S. H. (1999). Zinc finger of replication protein A, a non-DNA binding element, regulates its DNA binding activity through redox. *J Biol Chem* **274**, 29075–29080.

25 Wu, X., Bishopric, N. H., Discher, D. J., Murphy, B. J., and Webster, K. A. (1996). Physical and functional sensitivity of zinc finger transcription

factors to redox change. *Mol Cell Biol* **16**, 1035–1046.

26 Kiley, P. J., and Beinert, H. (1999). Oxygen sensing by the global regulator, FNR: the role of the iron-sulfur cluster. *FEMS Microbiol Rev* **22**, 341–352.

27 Pomposiello, P. J., and Demple, B. (2001). Redox-operated genetic switches: the SoxR and OxyR transcription factors. *Trends Biotechnol* **19**, 109–114.

28 Kiley, P. J., and Beinert, H. (2003). The role of Fe–S proteins in sensing and regulation in bacteria. *Current Opinion Microbio* **6**, 181–185.

29 Fuangthong, M., and Helmann, J. D. (2002). The OhrR repressor senses organic hydroperoxides by reversible formation of a cysteine-sulfenic acid derivative. *Proc Natl Acad Sci USA* **99**, 6690–6695.

30 Humphries, K. M., Juliano, C., and Taylor, S. S. (2002). Regulation of cAMP-dependent protein kinase activity by glutathionylation. *J Biol Chem* **277**, 43505–43511.

31 Aslund, F., and Beckwith, J. (1999). Bridge over troubled waters: sensing stress by disulfide bond formation. *Cell* **96**, 751–753.

32 Chuang, S. E., and Blattner, F. R. (1993). Characterization of twenty-six new heat shock genes of Escherichia coli. *J Bacteriol* **175**, 5242–5252.

33 Graf, P. C., and Jakob, U. (2002). Redox-regulated molecular chaperones. *Cell Mol Life Sci* **59**, 1624–1631.

34 Barbirz, S., Jakob, U., and Glocker, M. O. (2000). Mass spectrometry unravels disulfide bond formation as the mechanism that activates a molecular chaperone. *J Biol Chem* **275**, 18759–18766.

35 Graumann, J., Lilie, H., Tang, X., Tucker, K. A., Hoffmann, J. H., Vijayalakshmi, J., Saper, M., Bardwell, J. C., and Jakob, U. (2001). Activation of the redox-regulated molecular chaperone Hsp33 – a two-step mechanism. *Structure* **9**, 377–387.

36 Kim, S. J., Jeong, D. G., Chi, S. W., Lee, J. S., and Ryu, S. E. (2001). Crystal structure of proteolytic fragments of the redox-sensitive Hsp33 with constitutive chaperone activity. *Nat Struct Biol* **8**, 459–466.

37 Raman, B., Siva Kumar, L. V., Ramakrishna, T., and Mohan Rao, C. (2001). Redox-regulated chaperone function and conformational changes of Escherichia coli Hsp33. *FEBS Lett* **489**, 19–24.

38 Vijayalakshmi, J., Mukhergee, M. K., Graumann, J., Jakob, U., and Saper, M. A. (2001). The 2.2 A crystal structure of Hsp33: a heat shock protein with redox-regulated chaperone activity. *Structure* **9**, 367–375.

39 Hoffmann, J. H., Linke, K., Graf, P. C., Lilie, H., and Jakob, U. (2004). Identification of a redox-regulated chaperone network. *EMBO J* **23**, 160–168.

40 Bugl, H., Fauman, E. B., Staker, B. L., Zheng, F., Kushner, S. R., Saper, M. A., Bardwell, J. C., and Jakob, U. (2000). RNA methylation under heat shock control. *Mol Cell* **6**, 349–360.

41 Grimshaw, J. P., Jelesarov, I., Siegenthaler, R. K., and Christen, P. (2003). Thermosensor action of GrpE. The DnaK chaperone system at heat shock temperatures. *J Biol Chem* **278**, 19048–19053.

42 Diamant, S., and Goloubinoff, P. (1998). Temperature-controlled activity of DnaK-DnaJ-GrpE chaperones: protein-folding arrest and recovery during and after heat shock depends on the substrate protein and the GrpE concentration. *Biochemistry* **37**, 9688–9694.

43 Goldberger, R. F., Epstein, C. J., and Anfinsen, C. B. (1963). Acceleration of reactivation of reduced bovine pancreatic ribonuclease by a microsomal system from rat liver. *J Biol Chem* **238**, 628–635.

44 Wang, C. C. (1998). Isomerase and chaperone activities of protein disulfide isomerase are both required for its function as a foldase. *Biochemistry (Mosc)* **63**, 407–412.

45 Pihlajaniemi, T., Helaakoski, T., Tasanen, K., Myllyla, R., Huhtala,

M. L., Koivu, J., and Kivirikko, K. I. (1987). Molecular Cloning of the beta-subunit of human prolyl 4-hydroxylase. This subunit and protein disulphide isomerase are products of the same gene. *EMBO J* **6**, 643–649.

46 Wetterau, J. R., Combs, K. A., McLean, L. R., Spinner, S. N., and Aggerbeck, L. P. (1991). Protein disulfide isomerase appears necessary to maintain the catalytically active structure of the microsomal triglyceride transfer protein. *Biochemistry* **30**, 9728–9735.

47 Klappa, P., Ruddock, L. W., Darby, N. J., and Freedman, R. B. (1998). The b' domain provides the principal peptide-binding site of protein disulfide isomerase but all domains contribute to binding of misfolded proteins. *EMBO J* **17**, 927–935.

48 Darby, N. J., Penka, E., and Vincentelli, R. (1998). The multi-domain structure of protein disulfide isomerase is essential for high catalytic efficiency. *J Mol Biol* **276**, 239–247.

49 Darby, N. J., and Creighton, T. E. (1995). Functional properties of the individual thioredoxin-like domains of protein disulfide isomerase. *Biochemistry* **34**, 11725–11735.

50 Freedman, R. B., Klappa, P., and Ruddock, L. W. (2002). Protein disulfide isomerases exploit synergy between catalytic and specific binding domains. *EMBO Rep* **3**, 136–140.

51 Ferrari, D. M., and Soling, H. D. (1999). The protein disulphide-isomerase family: unravelling a string of folds. *Biochem J* **339**, 1–10.

52 Chivers, P. T., Laboissiere, M. C., and Raines, R. T. (1996). The CXXC motif: imperatives for the formation of native disulfide bonds in the cell. *EMBO J* **15**, 2659–2667.

53 Frand, A. R., and Kaiser, C. A. (1999). Ero1p oxidizes protein disulfide isomerase in a pathway for disulfide bond formation in the endoplasmic reticulum. *Mol Cell* **4**, 469–477.

54 Turano, C., Coppari, S., Altieri, F., and Ferraro, A. (2002). Proteins of the PDI family: unpredicted non-ER locations and functions. *J Cell Physiol* **193**, 154–163.

55 Lundstrom, J., and Holmgren, A. (1990). Protein disulfide-isomerase is a substrate for thioredoxin reductase and has thioredoxin-like activity. *J Biol Chem* **265**, 9114–9120.

56 Cai, H., Wang, C. C., and Tsou, C. L. (1994). Chaperone-like activity of protein disulfide isomerase in the refolding of a protein with no disulfide bonds. *J Biol Chem* **269**, 24550–24552.

57 Song, J. L., and Wang, C. C. (1995). Chaperone-like activity of protein disulfide-isomerase in the refolding of rhodanese. *Eur J Biochem* **231**, 312–316.

58 Winter, J., Klappa, P., Freedman, R. B., Lilie, H., and Rudolph, R. (2002). Catalytic activity and chaperone function of human protein-disulfide isomerase are required for the efficient refolding of proinsulin. *J Biol Chem* **277**, 310–317.

59 Shinoda, S. (1999). Protein toxins produced by pathogenic vibrios. *J Nat Toxins* **8**, 259–269.

60 Lumb, R. A., and Bulleid, N. J. (2002). Is protein disulfide isomerase a redox-dependent molecular chaperone? *EMBO J* **21**, 6763–6770.

61 Tsai, B., and Rapoport, T. A. (2002). Unfolded cholera toxin is transferred to the ER membrane and released from protein disulfide isomerase upon oxidation by Ero1. *J Cell Biol* **159**, 207–216.

62 Quan, H., Fan, G., and Wang, C. C. (1995). Independence of the chaperone activity of protein disulfide isomerase from its thioredoxin-like active site. *J Biol Chem* **270**, 17078–17080.

63 Creighton, T. E. (1993). *Protein Structure: A Practical Approach*, IRL Press, Oxford.

64 Wilcox, D. E., Schenk, A. D., Feldman, B. M., and Xu, Y. (2001). Oxidation of zinc-binding cysteine residues in transcription factor proteins. *Antioxid Redox Signal* **3**, 549–564.

65 Sutton, H. C., and Winterbourn, C. C. (1989). On the participation of higher oxidation states of iron and copper in Fenton reactions. *Free Radic Biol Med* **6**, 53–60.

66 Zhang, W., Marzilli, L. A., Rouse, J. C., and Czupryn, M. J. (2002). Complete disulfide bond assignment of a recombinant immunoglobulin G4 monoclonal antibody. *Anal Biochem* **311**, 1–9.

67 Hunt, J. B., Neece, S. H., and Ginsburg, A. (1985). The use of 4-(2-pyridylazo)resorcinol in studies of zinc release from Escherichia coli aspartate transcarbamoylase. *Anal Biochem* **146**, 150–157.

68 Anderegg, F. (1967). Pyridinderivate als Komplexbildner. VIII: Die Herstellung je eines neuen vier- und sechszaehnigen Liganden. *Helv. Chim. Acta* **50**, 2330–2332.

69 Zhou, Z. S., Peariso, K., Penner-Hahn, J. E., and Matthews, R. G. (1999). Identification of the zinc ligands in cobalamin-independent methionine synthase (MetE) from Eschericia coli. *Biochemistry* **38**, 15915–15926.

70 Buchner, J., Grallert, H., and Jakob, U. (1998). Analysis of chaperone function using citrate synthase as nonnative substrate protein. *Methods Enzymol* **290**, 323–338.

71 Wang, C. C. (1998). Protein disulfide isomerase assists protein folding as both an isomerase and a chaperone. *Ann N Y Acad Sci* **864**, 9–13.

72 Leichert, L. I., Scharf, C., and Hecker, M. (2003). Global characterization of disulfide stress in Bacillus subtilis. *J Bacteriol* **185**, 1967–1975.

73 Stewart, E. J., Aslund, F., and Beckwith, J. (1998). Disulfide bond formation in the Escherichia coli cytoplasm: an in vivo role reversal for the thioredoxins. *EMBO J* **17**, 5543–5550.

20
The *E. coli* GroE Chaperone

Steven G. Burston and Stefan Walter

20.1
Introduction

The Hsp60 chaperones, also known as chaperonins, are divided into two groups. Group I consists of the homologues found in eubacteria and their endosymbiotic counterparts in eukaryotes, while group II comprises the chaperone complexes from archaea and the eukaryotic cytosol. Of all Hsp60 proteins characterized so far, the GroE chaperone from *Escherichia coli*, a member of the first group, is the best understood on a molecular level.

GroE was first identified in the early 1970s by Costa Georgopoulos and coworkers, who observed that certain temperature-sensitive mutations in the *GroE* operon were unable to support the growth of bacteriophage λ [1]. It was subsequently demonstrated that both of the proteins encoded by the operon, GroEL and GroES, are essential for the viability of *E. coli* at all temperatures. Several years later, John Ellis and coworkers identified a protein component that was associated with chloroplast Rubisco prior to the formation of the holo-enzyme [2]. This was termed the Rubisco subunit-binding protein and was later identified as a homologue of GroEL. However, a molecular analysis of the GroE chaperones really began only in the late 1980s, when George Lorimer and colleagues showed that the efficiency of refolding of bacterial Rubisco could be drastically improved using purified GroEL and GroES with Mg-ATP [3]. At the same time another Hsp60 homologue was identified in the yeast mitochondrion as being essential for the folding of newly imported polypeptides [4]. Since then an enormous amount of data has been obtained describing structural and mechanistic aspects of the GroE chaperone.

20.2
The Structure of GroEL

GroEL is a large, cylindrical, oligomeric protein complex consisting of 14 identical 57-kDa subunits, which are arranged as two heptameric rings stacked back-to-back (Figure 20.1A, see p. 701). Each subunit is composed of three domains [5]: (1) an

Protein Folding Handbook. Part II. Edited by J. Buchner and T. Kiefhaber

ISBN: 3-527-30784-2

equatorial domain (residues 6–133 and 409–523), which contains the nucleotide-binding site as well as being responsible for the inter-ring and most of the intra-ring contacts; (2) an apical domain (residues 191–376) at the end of the cylinder; and (3) an intermediate domain (residues 134–190 and 377–408), which serves as a highly flexible linker between the two other domains. Upon nucleotide binding/hydrolysis and the binding of GroES, cooperative domain movements occur around two hinge regions on either end of the intermediate domain, leading to large changes in the GroEL structure.

Each heptameric ring contains a 45-Å wide cavity that is occluded from the other by the presence of the 14 N- and C-terminal extensions at the ring-ring interface. The opening to each cavity is lined with apical domain residues (Figure 20.1B), which are principally hydrophobic in character, and provides the binding site for unfolded polypeptide and GroES [5, 6]. Within the crystal structure of the R13G/A26V double mutant of GroEL, the two heptameric rings are related by twofold crystallographic symmetry [5]; however, more recent 10-Å image reconstructions from cryo-electron microscopy data (cryo-EM) of unliganded GroEL show a slight asymmetry between the two rings [7].

20.3 The Structure of GroEL-ATP

The X-ray structure of the R13G/A26V double mutant of GroEL complexed with ATPγS has also been determined, showing that the nucleotide-binding site is located at the top of the equatorial domain facing the central cavity. A highly conserved loop region composed of residues 87–91 (Asp-Gly-Thr-Thr-Thr) interacts with the β- and γ-phosphates [8]. However, rather puzzlingly, there appeared to be no significant conformational changes within the GroEL molecule, in contrast to what had been seen using low-resolution image reconstructions from cryo-EM [9] and which would provide a structural basis for the cooperativity observed in ATP binding [10]. Determining a structure of the GroEL-ATP$_7$ complex proved difficult because of the chaperone's intrinsic ATPase activity. Eventually, this problem was overcome by using the D398A-GroEL mutant, which was previously identified as having a drastically reduced rate of ATP hydrolysis [11]. This mutant GroEL complexed with ATP has been visualized using cryo-EM at a resolution of 10 Å [7]. The reconstructed images show that upon ATP binding the intermediate domains rotate downwards by $\sim 20^\circ$ while the apical domains extend and twist counterclockwise by $\sim 25^\circ$ in the ring occupied by ATP. As a result the salt bridge between Glu-386 and Arg-197 of the adjacent subunit, which was previously shown to be important for intra-ring allosteric communication [12–14], is broken. Glu-386 now makes contact with the top of helix C in the adjacent subunit in the region of Lys-80. The apical domain movement partially buries the hydrophobic subunit-subunit interface and radially expands the seven polypeptide-binding sites within the ring in the manner of increasing the aperture of an iris. These conformational changes and the switching of inter-subunit salt bridges provide a structural basis for the

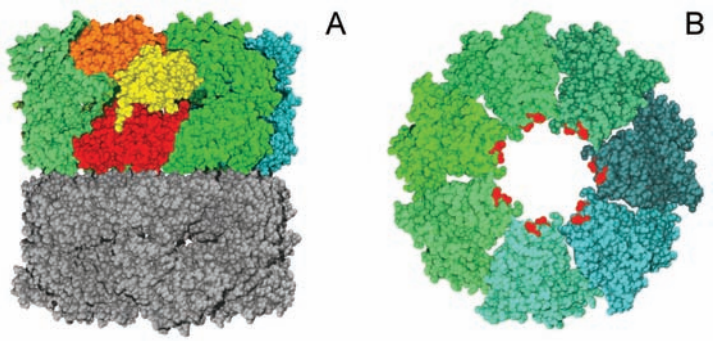

Fig. 20.1. Structure of the GroEL tetradecamer as determined by X-ray crystallography [5]. (A) In this side view, the seven subunits of the top ring are shown in color, while the bottom ring is shown in gray. Each subunit consists of three domains. The equatorial domains (red) provide the inter-ring contacts and most of the interactions between subunits of the same ring. Also, they contain the nucleotide-binding site. The apical domains (orange) are responsible for the binding of both the polypeptide substrate and the co-chaperone GroES. The intermediate domain (yellow) serves as a hinge and is important for the transmission of allosteric signals during the chaperonin cycle. (B) Top view of GroEL showing the sevenfold rotational symmetry of the chaperone. The central cavity has a diameter of 45 Å. The hydrophobic residues of the apical domains that comprise the binding site for GroES and the polypeptide substrate are colored in red.

propagation of the ATP-induced allosteric communication and are consistent with molecular dynamics simulations of the process [15].

20.4 The Structure of GroES and its Interaction with GroEL

GroEL functions with a smaller co-chaperone, GroES, which is encoded in the same *GroE* operon as GroEL [16]. The GroES polypeptide is 10 kDa in size and assembles into a single heptameric structure. The X-ray crystallographic structure of GroES has been determined [17], and when viewed from above, it has an axis of sevenfold rotational symmetry similar to that of GroEL (Figure 20.2A, see p. 704). Each subunit in the heptameric ring is an eight-stranded β-barrel with an extension directed upwards and towards the center of the sevenfold axis, giving GroES a dome-shaped structure. Protruding downwards from each subunit is the highly dynamic mobile loop region (Figure 20.2B, see p. 704, residues 17–34), which was originally identified as the site of interaction with GroEL by NMR studies on a peptide corresponding to the mobile loop [18]. GroES binds to one end, or in some conditions to both ends, of the GroEL cylinder in the presence of ATP or ADP [19–21] via interactions between the mobile loops of GroES and the apical domains of GroEL.

Low-resolution structures of the various GroEL-nucleotide-GroES complexes have been obtained using cryo-EM and single-particle analysis [9], and the X-ray crystallographic structure of the GroEL-$(ADP)_7$-GroES complex has been determined [21]. In contrast to the structure of the D398A-GroEL-ATP image reconstruction, which showed that the apical domains had extended and twisted $\sim 25^\circ$ *counterclockwise* [7], the binding of GroES apparently induces the apical domains to extend and twist $\sim 90^\circ$ *clockwise* relative to its position in the unliganded GroEL structure (Figure 20.2C, see p. 704). This means that the interaction of the seven GroES mobile loops with the apical domains of a GroEL-ATP complex induces the large rotation of the apical domains through a total of 115° (-25° through $+90^\circ$).

The opening and twisting of the apical domains upon GroES binding cause the hydrophobic residues of the GroEL peptide-binding surface to become buried within the wall of the central cavity. Thereby, the physicochemical nature of the central cavity is changed from largely hydrophobic to largely hydrophilic. At the same time, the volume of the GroEL central cavity beneath GroES is drastically increased from 85 000 $Å^3$ to 175 000 $Å^3$ (Figure 20.2C, see p. 704). It has been estimated that this is enough to accommodate folding intermediates of proteins up to $M_r \sim 60$ kDa [22]. The binding of GroES also effectively seals the top of the central cavity, trapping any polypeptide inside the cavity [23].

The GroEL-$(ADP)_7$-GroES complex alone is unable to promote efficient refolding of stringent GroE polypeptide substrates. However, the addition of either of the γ-phosphate analogues aluminum fluoride and beryllium fluoride to an SR1-rhodanese binary complex (SR1 is the single-ring version of GroEL) before mixing with GroES and ADP was found to promote efficient refolding [24]. The possibility that there may be a difference between the GroEL-$(ADP)_7$-GroES and GroEL-$(ATP)_7$-GroES structures to explain the ability of the γ-phosphate analogues to promote efficient refolding was investigated by solving the X-ray crystallographic structure of the GroEL-$(ADP \cdot AlF_3)_7$-GroES complex. Surprisingly, though, there were no significant differences between this structure and the GroEL-$(ATP)_7$-GroES structure [24].

20.5
The Interaction Between GroEL and Substrate Polypeptides

In vivo experiments with the yeast mitochondrial Hsp60 showed that a chaperone deficiency resulted in the aggregation of a large number of imported and newly synthesized proteins [4]. Like its endosymbiotic counterparts, GroEL can bind to a wide variety of unfolded or partially folded polypeptides. Approximately 40% of denatured proteins from *E. coli* cell extract are able to associate with GroEL in vitro [25]. Shifting an *E. coli* strain containing a temperature-sensitive mutation of GroEL to an elevated temperature resulted in a decrease in the rate of translation and strongly affected the folding of a number of cytoplasmic proteins [26]. More recently, a combination of pulse-chase radio-labeling in vivo, immunoprecipitation, and 2D PAGE was used to screen for *E. coli* polypeptide substrates of GroEL [27].

The identified proteins are involved in a diverse set of cellular roles including transcription, translation, metabolism, and other functions.

Unfolded proteins bind to the GroEL apical domains predominantly via hydrophobic interactions [6, 28]. Firstly, this mode of binding provides a means to distinguish unfolded or partially folded polypeptides from folded ones. Secondly, it shields the exposed, hydrophobic residues of these proteins from the environment and thus prevents their aggregation. Although GroEL appears to have the highest affinity for largely unfolded polypeptides exposing extended hydrophobic surfaces, it is also able to bind highly structured folding intermediates [29–33].

One controversial aspect of the interaction between GroEL and substrate polypeptide has been the question of whether GroEL recognizes any specific structural motifs [27]. An early NMR study on the interaction between a peptide and GroEL found that the peptide bound as an amphipathic α-helix [34]; however, GroEL was also shown to assist the refolding of an all β-sheet protein [35]. More recent data suggest that the most important factor is the spatial clustering of hydrophobic residues that can interact with the hydrophobic surface of the apical domains. As there is significant plasticity in the polypeptide, and perhaps in the GroEL apical domain, the binding affinity may be optimized by structural rearrangements [36–38].

20.6
GroEL is a Complex Allosteric Macromolecule

GroEL binds and hydrolyses ATP in a K^+-dependent manner and exhibits positive cooperativity, with a $K_{1/2}$ of 14 μM and a Hill constant of ~2 [10, 39, 40]. Subsequent analysis showed that while ATP binding within a heptameric ring is positively cooperative, negative cooperativity exists between the rings (Figure 20.3). Once the first ring of GroEL is fully saturated with ATP, binding of a further seven ATP molecules to the second ring occurs with a $K_{1/2}$ of 160 μM, corresponding to an inter-ring coupling energy of 31 kJ mol^{-1} [12, 41]. This behavior has been described using a nested model of cooperativity [41] in which the intra-ring allosteric changes from the T state (apo) to the R state (ATP-bound) are described by the MWC-type concerted model [42], whereas the conversion of each ring from T to R (Figure 20.3) occurs sequentially as described by the KNF model [43]. ATP hydrolysis is also asymmetric, and the optimal rate of hydrolysis (4 min^{-1} per subunit) is achieved when only one ring is occupied with ATP [41, 44]. However if both rings are saturated with ATP, then the rate of hydrolysis declines to half of its maximal rate (compare Figure 20.6) [41]. The rate-limiting step appears to be the cleavage of the anhydride bond between the β- and γ-phosphates [39].

The conformational transitions induced by ATP have also been investigated using fluorescence spectroscopy. A GroEL derivative in which on average one of the 14 subunits was covalently labeled with a pyrene fluorescent dye showed a large enhancement in fluorescence upon the addition of ATP [39]. When mixed with ATP in a stopped-flow apparatus, a single kinetic phase was observed whose hyper-

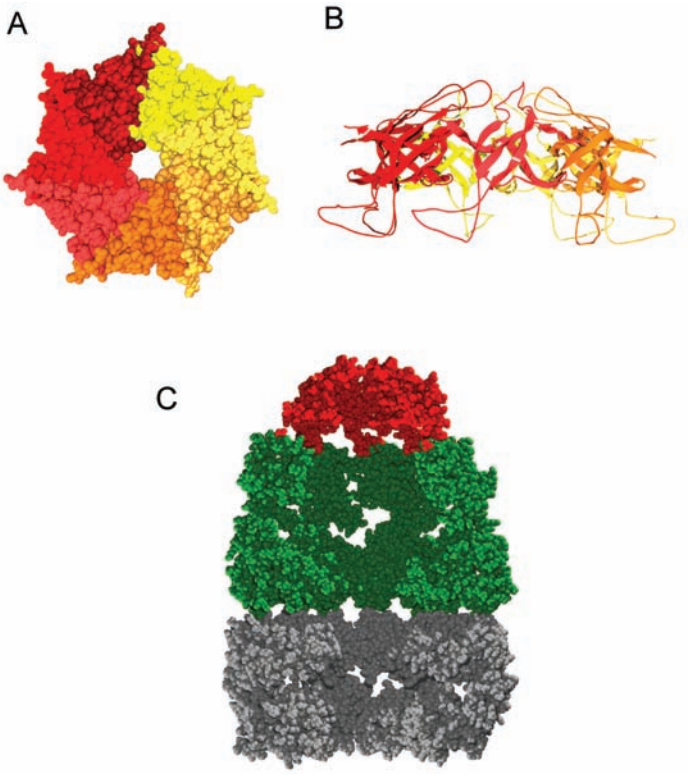

Fig. 20.2. Structures of the co-chaperone GroES (A, B) [17] and of a GroELS bullet complex (C) [21]. (A) GroES, here shown in a top view, consists of seven identical 10-kDa subunits and shares with GroEL the same sevenfold rotational symmetry. (B) Side view of GroES in a ribbon representation. A prominent feature of the GroES structure is the mobile loops, which protrude from the bottom of the heptamer and mediate the interaction with GroEL. (C) Side view of a GroELS complex (cross-section). Binding of GroES (red) to the top ring (green) of the GroEL tetradecamer converts the upper cavity into a large shielded compartment for protein folding. The cavity of the bottom ring (gray) is much smaller in volume.

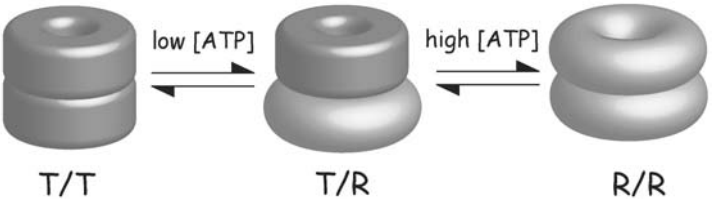

Fig. 20.3. Model for the allosteric transitions within GroEL. Owing to the positive intra-ring cooperativity, all seven subunits of one ring adopt the same conformation. In the absence of ligands (left), both rings are preferentially in the T (tense) state. This conformation displays a high affinity for unfolded polypeptides. Binding of ATP to the bottom ring causes this ring to adopt the R state (middle), in which the affinity for polypeptides is decreased. Because of the negative inter-ring cooperativity, binding of ATP to the second ring is disfavored, and the transition to the R/R state (right) occurs only at high concentrations of nucleotide.

bolic ATP dependence suggested a two-step binding process: ATP initially forms a weak complex with GroEL ($K_D = 4$ mM) before inducing a rapid conformational rearrangement ($t_{1/2} = 5$ ms). In contrast, a GroEL mutant in which a single Trp was inserted in the equatorial domain (F44W) reported three kinetic phases upon rapid mixing with ATP [45], while a similar mutant, Y485W GroEL, reported four distinct kinetic transients [46]. A very rapid (~1 ms) kinetic phase was observed with Y485W GroEL before the main fluorescence quench phase also reported by Y44W GroEL. This phase revealed a bi-sigmoid dependency on ATP concentration reminiscent of that seen in steady-state experiments and presumably represents conformational transitions occurring upon occupying first one heptameric ring with ATP and subsequently the second ring. However, the precise structural changes represented by these kinetic transitions are still under investigation.

In the presence of GroES, ATP binds to GroEL with a greater affinity ($K_{1/2} = 6$ μM) and displays an increased level of cooperativity. Under steady-state conditions, GroES inhibits the rate of ATP hydrolysis to ~35% of that seen with GroEL alone [10, 39, 40, 44]. During the hydrolytic cycle, the association of GroES with GroEL is highly dynamic [47]. GroES associates rapidly with the GroEL-ATP complex (5×10^7 M^{-1} s^{-1}) [44, 48] to form a highly stable complex. Hydrolysis of the *cis* ATP (i.e., that ATP bound to the same ring as GroES) weakens the interaction between GroEL and GroES before ATP binding to the *trans* GroEL ring forces the dissociation of GroES (and any encapsulated polypeptide) from the *cis* GroEL ring [11, 48–50].

20.7
The Reaction Cycle of the GroE Chaperone

The GroEL reaction cycle can be divided into the three distinct stages of polypeptide binding, encapsulation, and ejection [51]. In the first instance, a protein substrate that is unfolded, misfolded, or partially folded is able to interact with the hydrophobic surface on the apical domains of the *trans* ring, which adopts a conformation with a high affinity towards polypeptide substrate similar to the T-state rings found in unliganded GroEL (Figure 20.4). The binding of ATP to this ring induces the rapid dissociation of ligands from the opposite (previously *cis*) ring [48] and permits the binding of GroES to the same ring as the polypeptide. The binding of ATP and GroES results in a large increase in the volume of the central cavity and buries the hydrophobic polypeptide-binding surface within the intersubunit interface (Figure 20.4), thereby displacing the polypeptide substrate into the GroEL cavity where folding is initiated [7, 11]. There is evidence that the polypeptide may undergo some degree of forced mechanical unfolding upon the radial expansion of the protein-binding site [52]. Since the entrance to the cavity is sealed by GroES, the protein substrate may fold without interference by other aggregation-prone polypeptides. However, it is clear that at this stage the polypeptide is still able to interact with the walls of the cavity [53]. ATP hydrolysis in the *cis* ring ($t_{1/2} \sim 10$ s) dictates the lifetime of this enclosed folding compartment by weakening the interaction between GroEL and GroES [11] to prime the chaperone

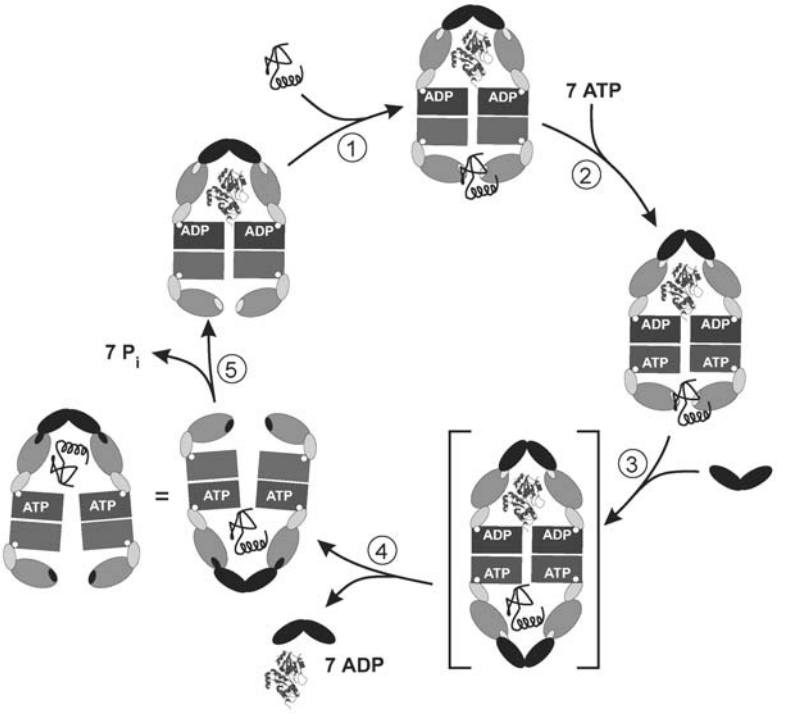

Fig. 20.4. Reaction cycle of the GroE chaperonin from *E. coli*. Although GroEL is composed of two rings, the functional cycle is best described on the level of individual rings, which represent the operational units of GroE. While both rings are active at the same time, they are in different phases of the cycle. Processing of an individual substrate polypeptide requires two revolutions of the GroE cycle, during which the polypeptide remains associated with the same GroEL ring. For graphical reasons, the orientation of the GroE complex is reversed after step 4.

The cycle of GroE-assisted folding can be dissected into three steps: capture, encapsulation/folding, and release. During capture (1), a hydrophobic polypeptide is prevented from aggregation by binding to GroEL. The acceptor ring (bottom ring) is nucleotide-free and therefore has a high affinity for the polypeptide. Binding of ATP (2) and GroES (3) to this ring induces a set of structural changes in GroEL. Most importantly, the affinity for the bound polypeptide is decreased, and it is released into the closed cavity where folding begins. Subsequent hydrolysis of ATP (5) induces a second conformational change in GroEL (top ring), which allows the bottom ring to bind polypeptide and initiate a new cycle. Upon binding of ATP and GroES in the next round, GroES is displaced from the top ring, and the substrate polypeptide is released (4). The formation of the symmetric complex shown in brackets is controversial.

complex for the ''ejection'' signal from the *trans* ring (Figure 20.4). ATP binding to the *trans* ring is sufficient to eject GroES and the polypeptide from the *cis* ring [11, 47, 49, 50], although this process is accelerated when polypeptide binds to the *trans* ring concomitantly. An intermediate complex with GroES bound to both ends of the GroEL tetradecamer has been observed during assisted protein-folding reac-

tions [54–56]. The role of these so-called ''football'' intermediates is not clear, as some results suggest that their formation is not required for efficient refolding [57]. One speculative possibility is that they may provide a means for the efficient trapping of a ''new'' polypeptide substrate to the *trans* ring just prior to ejection of the ''old'' polypeptide from the *cis* ring (Figure 20.4) [58].

The time in which the ejected polypeptide can fold in this protected environment is limited by the lifetime of the *cis* cavity. In the case of a monomeric protein, such as bovine mitochondrial rhodanese, it may be long enough to reach the fully functional native conformation. However, many substrate polypeptides are active as oligomers and therefore individual subunits must be released from GroEL sufficiently folded such that assembly into the active multimer can take place in bulk solution. The proportion of substrate polypeptide that has folded in the cavity depends upon the intrinsic rate of folding of that particular polypeptide. In most cases, the fraction of molecules that has not yet folded sufficiently to proceed rapidly and efficiently to its native conformation within the lifetime of the cavity will, upon ejection, still be competent to rebind to GroEL and proceed through another reaction cycle, where it will have another chance to refold. In this iterative manner, high yields of fully folded protein substrates can be obtained.

This kind of mechanism exploits several characteristics of the GroE complex:

1. The binding and hydrolysis of ATP serve to modulate the affinity of GroEL for unfolded polypeptide substrate. Systematic studies of the effect of the various GroEL-nucleotide complexes on the refolding rates and yields of a number of protein substrates have been performed [29, 59–62]. Unliganded GroEL has a low affinity for ATP and GroES but a high affinity for unfolded polypeptides, while the GroEL-ATP complex has precisely the reverse properties.
2. The binding of GroES and ATP to a GroEL-polypeptide binary complex ensures efficient displacement of the polypeptide substrate into the central cavity, where it starts to refold. The binding of GroES and ATP switches the chemical nature of the cavity from one lined at the entrance with hydrophobic side chains to one in which this hydrophobic surface is buried. The volume of the cavity is also significantly increased.
3. The positive intra-ring cooperativity with respect to ATP binding may ensure a concerted release of all parts of the polypeptide chain as it becomes displaced into the central cavity. This may be crucial for productive folding in cases where structure formation in one part of the polypeptide cannot proceed before other regions are released from the GroEL apical domains. An optimal level of intra-ring cooperativity appears to have evolved such that the T-to-R transition occurs at a rate that ensures a rapid release of the whole polypeptide chain into the cavity [63].
4. The inherent asymmetry in the GroEL macromolecule enables each heptameric ring to take part in coupled half-reactions. That is, when the central cavity of one ring contains a folding polypeptide encapsulated under GroES (i.e., *cis* ring), the opposite *trans* ring provides the signal for ejection of GroES and polypeptide. The roles of the two rings are then exchanged such that the *trans* ring

now binds GroES and becomes the *cis* ring. This communication between the two rings is essential for efficient protein folding, as indicated by the fact that the single-ring version of GroEL (SR1) cannot rescue a GroEL-depleted strain [64].

20.8 The Effect of GroE on Protein-folding Pathways

GroE is able to exert differing effects on the folding kinetics and efficiency of different protein substrates. In most cases GroE improves the final yield of fully folded protein substrates but does not affect the rate of refolding. There are a number of models have been proposed to account for this phenomenon.

In the first model GroE prevents aggregation by reducing the concentration of aggregation-prone intermediates in bulk solution [65]. This could be done passively by GroEL alone, but at the cost of a significant reduction in the rate of refolding [29, 39]. Dynamically cycling the polypeptide on and off the chaperone using ATP binding and hydrolysis to switch GroEL between conformations with alternately high and low affinity for protein substrate would allow faster rates of refolding to be achieved. An extension of this model is the so-called Anfinsen cage model in which encapsulating the folding protein within the central cavity of GroEL underneath GroES allows the polypeptide an opportunity to fold without the possibility of aggregation. In this instance the GroEL central cavity acts as an "infinite dilution" chamber. Multiple rounds of binding, encapsulation, and release ensure that the polypeptide is bound or encapsulated most of the time, thus preventing aggregation.

An alternative model suggests that the rate-limiting step during the refolding of many larger proteins involves the breaking of incorrect intramolecular interactions that arise during the rapid collapse of the unfolded protein chain. If this step is slow, then the protein chain is likely to aggregate before the isomerization to a productive conformation can occur. The chaperone can therefore improve the efficiency of protein folding by assisting in the unfolding of misfolded conformations [39, 47]. The chaperonin can assist this process in two possible ways. The first way is by annealing the polypeptide to the apical domain binding sites and then mechanically unfolding the polypeptide further upon binding ATP and GroES [52]. The application of this forced unfolding requires interaction with a number of apical domain polypeptide-binding sites on GroEL [66]. Multiple rounds of this forced unfolding as the protein binds and dissociates would ensure a high yield of folded protein. Alternatively, as long as the collapsed protein substrate can explore its available conformational space in rapid equilibrium, effective unfolding can be achieved by a thermodynamic coupling mechanism, since GroEL binds the most unfolded forms tightly [67, 68].

There are some notable instances in which an apparent enhancement in the rate of refolding is observed. Porcine mitochondrial malate dehydrogenase (mMDH) shows a 3.5-fold increase in its apparent rate of refolding with GroEL compared to

its spontaneous rate [69, 70], and the folding of bacterial Rubisco is increased four-fold over its spontaneous rate [71–73]. Two hypotheses to explain this have been suggested.

1. Ranson et al. [70] found that the misfolding of mMDH is the result of early steps in aggregation, presumably as small, low-order aggregates form, and that although the equilibrium normally heavily favors the formation of these smaller aggregates, this process is reversible. Remarkably, GroE was able to actively reverse these early aggregation steps even at sub-stoichiometric amounts, suggesting that it acts as a catalyst. Using cycles of binding and release, the chaperonin constantly recycles material from the unproductive aggregation pathway and resupplies the productive folding pathway. As a result the rate of refolding *apparently* increases although the *intrinsic* rate has not changed. A similar model has also been suggested to explain the apparent rate increase observed during the assisted refolding of bacterial Rubisco [72].
2. Alternatively, it has been proposed that confinement of the protein substrate within the narrow GroEL central cavity has the effect of smoothing the energy landscape in order to increase the flux of protein to its native conformation [73]. More recently, molecular simulations of the refolding process have been performed in systems with different accessible volumes, and it was noted that confinement was able to significantly stabilize the protein, leading to an enhancement in the rate of refolding [74].

Recently, the importance of the chemical properties of the central cavity has been strikingly demonstrated in an experiment in which directed evolution was used in an attempt to optimize the central cavity to maximize the efficiency of folding of the green fluorescent protein (GFP). This was achieved by altering the rate of ATP hydrolysis and the inherent allostery of the chaperonin complex and also by shifting the polarity of the central cavity in order to suit the folding pathway of GFP. However this enhanced specialization within GroEL was achieved at the expense of its ability to refold its natural protein substrates, demonstrating that GroE has had to evolve a balance of ATPase rate and central cavity properties in order to perform a very general role as a molecular chaperone [75].

Another important question concerns proteins that are too large to fit into the central cavity underneath GroES. Its volume was calculated to be in the range of 175 000 $Å^3$, which likely is large enough to accommodate folding intermediates of up to 60 kDa. Can GroEL also assist the folding of larger proteins? Yeast mitochondrial aconitase (82 kDa) was observed to aggregate in chaperonin-deficient mitochondria, indicating an in vivo role for the chaperonin [76]. In vitro mechanistic studies revealed that aconitase does not become encapsulated underneath GroES but interacts only with an open ring. GroES binding to the ring opposite to the protein substrate causes the release of the nonnative substrate into bulk solution, where it can refold. In this way aconitase passes through many cycles of binding and release without ever being encapsulated until it is in a conformation that can form the holo-enzyme [77, 78]. This demonstrates a mechanism that is quite dis-

tinct from that found when assisting the folding of proteins less than 60 kDa but that is also efficient at refolding to the native (or near-native) conformation.

20.9 Future Perspectives

Despite the enormous quantity of data now available describing the structure and mechanism of action of the chaperonins, there remain a number of secrets that GroE has yet to give up. For example, GroE is one of the most complex allosteric systems ever studied, and a great deal of work involving a combination of mutagenetic, kinetic, and thermodynamic studies needs to be done before the intricate macromolecular communication can be mapped onto the structure and the role of allostery in the assisted protein-folding reaction is really understood. Additionally, despite the large amount of structural data that has been collected, it is still not certain precisely what conformational ensemble of a polypeptide is recognized by GroEL and whether unfolding upon ATP and GroES binding is a general feature of the chaperonin reaction [33, 52]. Also unknown is the degree to which the nature of the central cavity can play a part in ensuring efficient folding. Does the cavity play an important role in helping the protein reach a folded conformation, or does it act merely as an "infinite dilution cage"? One new approach that may be able to unlock some of these puzzles is the extension of NMR techniques to the study of large macromolecular complexes such as the GroEL-GroES chaperonin [79]. This would permit structural and dynamic information about the chaperonin and any bound substrate. It is clear that an imaginative and multidisciplinary approach will likely be needed to understand the precise molecular details of this extraordinary protein complex.

20.10 Experimental Protocols

Protocol 1: Purification of GroEL and SR1 A large number of plasmids and constructs have been designed for the overexpression of GroEL in *E. coli* [5, 80–82]. They differ mainly in the resistance marker, promoter type, and expression level and in whether or not GroES is co-expressed. It is beyond the scope of this chapter to provide detailed protocols for the fermentation/protein production steps, as they will depend on the individual plasmid. Routinely, *E. coli* strains such as JM109, DH5α, or BL21 derivatives are used for overexpression. After harvesting the cells by centrifugation, the cell pellet may be stored at $-20\ ^{\circ}C$.

The single-ring mutant SR1 was first described by the group of Art Horwich [23]. SR1 cannot support cell viability [83], probably because it is defective in GroES release. Thus, it can be expressed only in *E. coli* strains that also express basal-level wild-type GroEL. Recently, a number of SR1 mutants have been generated that are functional as chaperones because they possess a decreased affinity to-

wards GroES [64]. SR1 can be separated from endogenous GroEL by size-exclusion chromatography, but a small fraction of SR1 heptamers may contain wild-type subunits.

Crude Extract Preparation

1. Thaw cells on ice.
2. Resuspend pellet in 25 mM Tris/HCl pH 7.5, 5 mM DTT, 2 mM EDTA (normally, no protease inhibitors are required).
3. Crack cells with a cell disruptor or a French press.
4. Add 10 mM $MgCl_2$ and 1 U mL^{-1} DNase I; stir at 4 °C for 1 h.
5. Centrifuge (45 000 *g*, 4 °C, 45 min) and discard pellet.
6. All subsequent steps should be carried out at 4 °C.

Anion-exchange Chromatography

1. Column: Q-Sepharose FF (Amersham Biotech), 150–200 mL of resin, linear flow: 12 cm h^{-1}.
2. Buffer A: 50 mM Tris/HCl pH 7.5, 2 mM DTT, 2 mM EDTA.
3. Buffer B: buffer A + 2 M NaCl.
4. Equilibrate column with at least three column volumes of buffer A.
5. Load crude extract on column.
6. Wash column with two column volumes of 7.5% buffer B.
7. Elute GroEL with a linear gradient of 7.5–30% buffer B in 10 column volumes.
8. Analyze elution profile with SDS-PAGE (12.5% gel), and pool GroEL-containing fractions.
9. Concentrate eluate with ultrafiltration (YM100) to ~30 mL.

Note: If it is additionally intended to purify GroES from a GroELS-overproducing strain, the salt concentration during washing should be lowered to 0% buffer B and the gradient run from 0–30% buffer B. GroES elutes earlier than GroEL, between 100 and 250 mM NaCl. To detect both GroEL and GroES in SDS-PAGE, gradient gels (5–20%) are recommended, but 12.5% gels will work as well.

Size-exclusion Chromatography

1. Column: Sephacryl S-300 HR (Amersham Biosciences), 300 mL of resin, linear flow: 20 cm h^{-1}.
2. Equilibrate with two column volumes of buffer A (see above).
3. Inject ~10 mL of concentrated protein per run, and collect fractions of 3 mL.
4. Analyze elution profile with SDS-PAGE (12.5% gel), and pool GroEL-containing fractions.
5. Concentrate eluate with ultrafiltration (YM100) to ~30 mL.

Note: If it is intended to obtain GroEL without Trp-containing contaminations, it is highly recommended to pool fractions based not only on SDS-PAGE but also on intrinsic fluorescence. The protocol provided below (Protocol 5) is rather time-consuming for screening a large number of samples. A simpler test uses an excita-

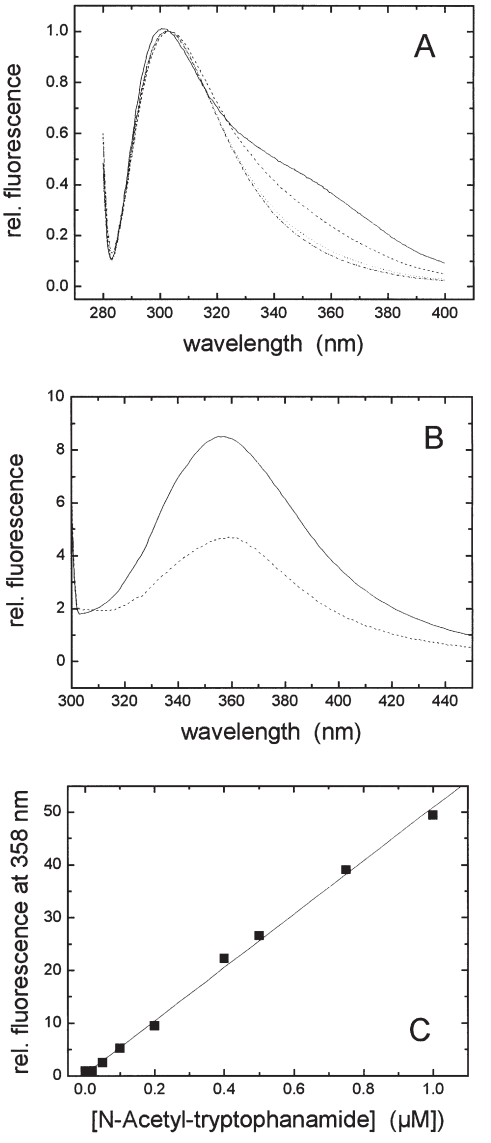

Fig. 20.5. Judging the purity of a GroEL preparation using fluorescence spectroscopy. (A) "Polishing" of GroEL by AffiGel Blue chromatography. Spectra of samples were recorded at 25 °C in 50 mM Tris/HCl pH 7.5, 2 mM DTT, and 2 mM EDTA using wavelengths of $\lambda_{ex} = 276$ nm and $\lambda_{em} = 280–400$ nm. The protein concentration in the samples was ~1 mg mL^{-1}. Spectra were normalized by setting the fluorescence intensity at 304 nm to 1. (–) GroEL pool before AffiGel Blue chromatography, (--) after one passage, (···) after two passages, (-·) and after three passages of AffiGel batch chromatography (see protocol 1). The pronounced shoulder at 350 nm is caused by Trp-containing impurities. (B) The tryptophan contents of a dirty (–) and a pure (--) GroEL sample of equal concentrations (20 μM monomer) were determined by protocol 5. The fluorescence intensity at 358 nm can be used to calculate the tryptophan concentration in the samples using the calibration curve shown in (C).

tion wavelength of 276 nm. Discard any fractions that have a pronounced Trp shoulder in their fluorescence spectrum (Figure 20.5A).

AffiGel Blue Batch Chromatography
This step will remove contaminations – mainly hydrophobic polypeptides – bound to GroEL. Besides the AffiGel Blue resin used in this protocol [84], a number of other dye-based resins have been successfully employed [85, 86]. Also, methods using organic solvents such as methanol or acetone have been developed for ''polishing'' GroEL [87, 88]. The AffiGel Blue procedure provides a good balance between yield and purity, but some of the alternative procedures may be considered when extremely pure GroEL (as judged by Trp fluorescence) is required.

1. Resin: AffiGel Blue (BioRad), 15 mL of dry resin.
2. Incubate resin in 30 mL 6-M GdmCl in buffer A and tumble gently overnight at 4 °C.
3. Sediment resin by centrifugation (3000 *g*) and resuspend it in 30 mL of buffer A; repeat five times to remove residual GdmCl.
4. Add GroEL solution to sedimented resin and tumble gently overnight at 4 °C.
5. Sediment resin and transfer the supernatant containing the purified GroEL to a new vial.
6. Record a fluorescence spectrum to determine the amount of Trp contamination; repeat the purification procedure if the purity is not satisfying.
7. Optional: Concentrate the GroEL solution up to 30 mg mL^{-1}.
8. Aliquot and freeze in liquid N_2; store at −80 °C.

Protocol 2: Purification of GroES GroES may be overexpressed alone or along with GroEL [89]. In the latter case, the first purification step should be the anion-exchange chromatography described above, which separates GroEL from GroES. After pooling GroES-containing fractions, the following protocol should be used. Depending on the level of overexpression and on the desired degree of purity, not all of the steps may be necessary.

pH Shift
GroES is quite soluble at low pH and retains its biological activity. Many other proteins, however, will precipitate during this step and can be removed by centrifugation.

1. Lower the pH of the GroES solution by adding one volume of 0.1-M sodium acetate/acetic acid pH 4.6.
2. Incubate for 1 h; spin down precipitated proteins (45 000 *g*, 45 min, 4 °C), and discard pellet.

Note: The buffering capacity of the GroES solution should be low. Otherwise, the resulting pH will be too high. Perfect for this purpose is 25 mM Tris/HCl buffer at pH 7.5.

Cation-exchange Chromatography

1. Column: SP-Sepharose FF (Amersham Biotech), ~50 mL of resin, linear flow: 12 cm h^{-1}.
2. Buffer A: 50 mM sodium acetate/acetic acid pH 4.6.
3. Buffer B = buffer A + 1 M NaCl.
4. Equilibrate column with at least three column volumes of buffer A.
5. Dilute the supernatant of the pH step 1:3 with H_2O.
6. Load the diluted protein solution on column.
7. Wash column with two column volumes of 0% buffer B.
8. Elute GroES with a linear gradient of 0–30% buffer B in 10 column volumes, fraction size 8 mL.
9. Analyze elution profile with SDS-PAGE (15% gel), and pool GroES-containing fractions.
10. Adjust the pH to 8 with a solution of 1 M Tris.
11. Concentrate eluate with ultrafiltration (YM10) to ~30 mL.

Temperature Shift

This step is quite efficient in removing contaminating proteins, although some GroES may be lost because of co-precipitation.

1. Gently stir the GroES solution in a water bath at 80 °C for 15 min.
2. Spin down precipitated proteins (45 000 *g*, 45 min, 4 °C) and discard pellet.

Size-exclusion Chromatography

1. Column: Superdex 200 (Amersham Biosciences), 300 mL of resin, linear flow: 20 cm h^{-1}.
2. Buffer C: 50 mM Tris/HCl pH 7.5, 2 mM DTT, 2 mM EDTA.
3. Equilibrate with two column volumes of buffer C.
4. Inject ~10 mL of concentrated protein per run, and collect fractions of 3 mL.
5. Analyze elution profile with SDS-PAGE (15% gel), and pool GroES-containing fractions.
6. Concentrate eluate with ultrafiltration (YM10) to ~30 mL.

Protocol 3: Preparation and Purification of Mixed-ring Complexes Mixed-ring complexes of GroEL have proven to be useful for studying the specific function of the two rings comprising the GroEL particle [11, 50]. In these complexes, one ring consists of wild-type subunits, while the second ring is made up of mutant GroEL subunits that are, e.g., defective in ATP hydrolysis or polypeptide binding.

Incubating a mixture of wild-type $GroEL_{14}$ and mutant $GroEL_{14}$ (G337S/I349E) at 42 °C for 45 min causes the double rings to dissociate and form mixed-ring complexes [83]. Apparently, the interactions between the subunits of the same ring are much stronger than interactions between rings, preventing the formation of complexes that have different types of subunits within the same ring. One important prerequisite is that wild-type and mutant GroEL have to differ sufficiently in their biophysical properties to allow the separation of mixed-ring GroEL from the starting material, i.e., the homotypic tetradecamers.

Protocol 4: Determining the Concentration of GroES and GroEL Both GroEL and GroES have a very low content of aromatic amino acids and do not contain any tryptophans. Thus, they show a relatively weak UV absorbance, and it is extremely important to ensure that their preparations are devoid of any contaminating proteins or peptides. Otherwise, these impurities will contribute over-proportionally to the UV absorbance, and thus the chaperone concentration will be overestimated.

The following protocol is based on the method introduced by Gill and von Hippel [90]. Denaturation of the sample is important because it (1) eliminates any perturbation of the UV absorbance by the protein structure and (2) reduces light scattering by the big GroEL particle.

1. Prepare a solution of 6 M GdmCl, 50 mM Tris/HCl pH 8, and 2 mM DTT (buffer P).
2. Pipet 950 µL of this solution in a 1-cm quartz cuvette.
3. Add 50 µL of protein solution and incubate for >5 min at room temperature.
4. Record a UV spectrum from 240 to 350 nm.
5. As a reference, mix 950 µL buffer P with 50 µL storage buffer and record a spectrum.
6. Subtract the reference from the sample.
7. The absorbance maximum of the resulting spectrum should be around 276 nm.
8. Calculate the protein concentration using the Lambert-Beer law with the following values: GroEL $A_{276\ nm}(0.1\%,\ 1\ cm) = 0.18$, GroES $A_{276\ nm}(0.1\%,\ 1\ cm) = 0.14$.

Protocol 5: Judging the Purity of GroEL Preparations by Determining the Tryptophan Content Although a GroEL preparation may look pure on Coomassie or silver-stained SDS gels, it is mandatory to further evaluate the purity using fluorescence spectroscopy [87]. GroEL has a high-affinity binding site for unfolded proteins, which may become contaminated with hydrophobic polypeptides during the purification process. These impurities must be removed since they may interfere with later experiments. The degree of contamination can be judged by measuring the Trp fluorescence of the GroEL sample (Figure 20.5B, C). GroEL itself does not contain Trp, whereas contaminations likely do due to the hydrophobic nature of this amino acid.

1. Prepare a solution of 6 M GdmCl (ultra-pure grade), 50 mM Tris/HCl pH 8, and 2 mM DTT (buffer P); pass it through a 0.2-µm filter and degas it.
2. Prepare five calibration solutions of 0.1, 0.25, 0.5, 0.75, and 1 µM *N*-acetyltryptophanamide in buffer P.
3. Prepare a solution of GroEL in buffer P ($\sim$1 mg mL^{-1}).
4. Record fluorescence spectra of buffer P, the protein sample, and the five calibration solutions; set the excitation to 295 nm and the emission to 310–400 nm.
5. Correct both the GroEL spectrum and the calibration spectra for buffer fluorescence; calculate the Trp content of the GroEL preparation using the calibration solutions.

Note: A good preparation of GroEL should have less than one Trp per $GroEL_{14}$. This protocol can also be used to evaluate the quality of your GroES preparation, although this is less crucial because GroES does not contain a binding site for unfolded proteins.

Protocol 6: ATP Hydrolysis by GroEL and Its Regulation by GroES There are several assay systems available to determine enzymatic ATP hydrolysis, all of which have certain merits and disadvantages. In general, continuous assays are to be preferred over discontinuous assays, because pipetting errors are less likely to occur. If a coupled assay is used, additional controls may be required to confirm that an observed effect, e.g., inhibition of ATP turnover by substance X, is really due to an effect of X on your ATPase and not on one of the helper enzymes. Also, an ATP-regenerating system may be of advantage in some cases. It can be added to most of the assay systems except the one based on the detection of α-[^{32}P]-ADP. The following protocol briefly describes a coupled regenerative assay.

Measuring ATP Hydrolysis by GroEL Using a Regenerative Assay
In this assay the ADP produced by the GroEL ATPase is converted back into ATP, as phosphoenol pyruvate (PEP) is converted to pyruvate by pyruvate kinase. The pyruvate is then reduced to lactate by lactate dehydrogenase, with the concomitant oxidation of NADH to NAD^+. The resulting decrease in absorbance at 340 nm provides a convenient optical signal with which to measure ATPase rates.

1. Assay buffer: 50 mM Tris/HCl pH 7.5, 10 mM KCl, and 10 mM $MgCl_2$.
2. Premix: 10 U mL^{-1} L-lactate dehydrogenase (rabbit muscle, Roche), 2 U mL^{-1} pyruvate kinase (rabbit muscle, Roche), 0.2 mM NADH, 2 mM PEP in assay buffer.
3. Equipment: UV-photometer with thermostated cell holder, 1 cm-quartz cuvettes.
4. Incubate 1 μM GroEL (0.8 mg mL^{-1}) in premix for 5 min at 25 °C.
5. Start reaction by adding 1 mM ATP from a 100-mM stock solution adjusted to pH 7–8.
6. Record decrease in absorbance at 340 nm.
7. The rate of turnover can be calculated using $\varepsilon_{340\,nm} = 6200\ M^{-1}\ cm^{-1}$ for NADH.

Owing to the two levels of cooperativity within the GroEL tetradecamer (see Section 20.6), the dependence of the turnover rate constant, k_{app}, on the ATP concentration is complex. At low ATP concentrations, a sigmoidal increase of k_{app} with increasing [ATP] is observed (Figure 20.6). Around 200 μM ATP, k_{app} reaches a maximum of ~4 min^{-1} at 25 °C [10, 40]. A further increase in [ATP] causes a drop in k_{app} by ~50% since the binding of ATP to the second ring inhibits ATP hydrolysis in the first ring [12]. In the case of SR1, this inhibition at high [ATP] is not observed due to the lack of a second ring. An additional complication arises from the fact that ATP hydrolysis by GroEL is highly dependent on K^+ concentration. In the presence of excess GroES, ATP hydrolysis is decreased to 40–50% of

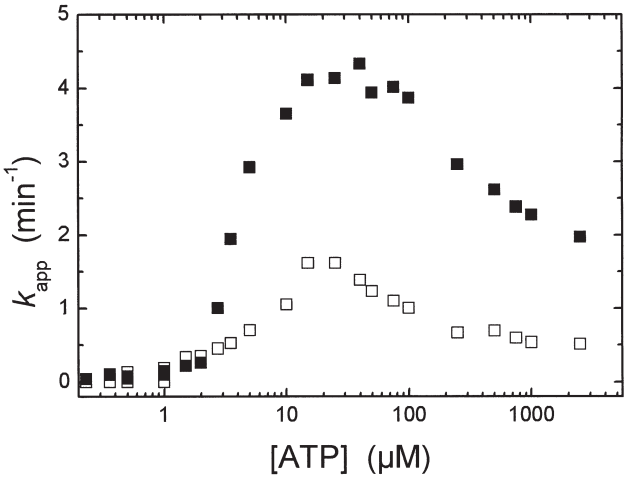

Fig. 20.6. ATP hydrolysis by GroEL and its regulation by GroES. The apparent rate constant of hydrolysis, $k_{app} = d[ATP]/(dt \cdot [GroEL])$ is plotted as a function of ATP concentration. The assay was carried out as described in protocol 6 using a GroEL concentration of 1 μM (monomer). The ATP dependence of k_{app} for GroEL alone (■) shows a bell-shaped behavior and reflects the two levels of cooperativity within the GroEL tetradecamer. When GroES is present at 2 μM (□), the rate of hydrolysis is decreased by ~2.5-fold.

the values measured in the absence of the co-chaperone (Figure 20.6). However, at low concentrations of K^+, inhibition was found to be almost complete [40].

Protocol 7: GroE-mediated Refolding of Malate Dehydrogenase (mMDH) A large number of enzymes have been used as substrates to evaluate the chaperone activity of GroE, including rhodanese (bovine liver), citric synthase (porcine mitochondria), Rubisco (*Rhodospirillum rubrum*), glutamine synthetase (*E. coli*), and DHFR (human). The advantages of malate dehydrogenase (porcine mitochondria) are that it is commercially available and that its assay is easy and cheap (Figure 20.7).

Unfolding of mMDH

Since GdmCl interferes with GroE function [71], urea is used in this protocol to denature mMDH. Depending on your mMDH stock, you may have to concentrate the enzyme prior to unfolding.

1. Remove stabilizing agents such as glycerol or $(NH_4)_2SO_4$ by dialysis or by using a desalting column (buffer: 50 mM Tris/HCl, 2 mM DTT); the concentration of mMDH monomers after this step should be at least 150 μM (5 mg mL^{-1}).
2. To 3 μL of mMDH (150 μM), add 6 μL of 9-M urea, 50 mM Tris/HCl pH 7.5, and 10 mM DTT; allow the protein to unfold for 30 min at 25 °C.

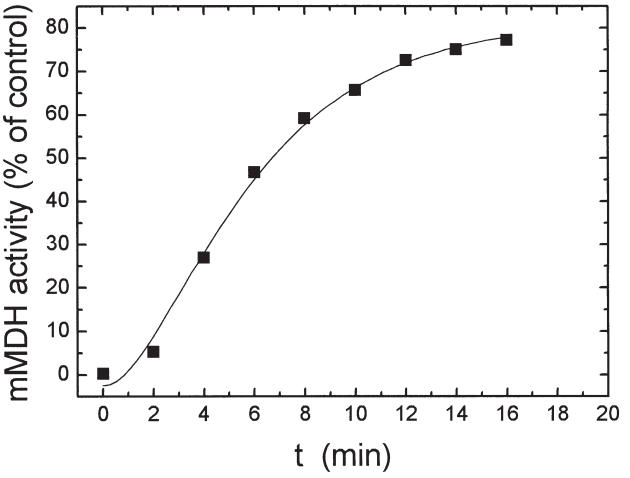

Fig. 20.7. GroE-mediated reactivation of malate dehydrogenase (mMDH). Refolding was carried out as described in protocol 7 using 0.5 μM mMDH, 1 μM $GroEL_{14}$, and 2 μM $GroES_7$ in the refolding assay. At the indicated time points, mMDH activity was monitored at 340 nm using the enzyme assay provided in the protocol. Refolding yields are normalized with respect to the mMDH activity before unfolding.

Refolding of mMDH by the GroE System

The concentration of mMDH in the refolding reaction is 0.5 μM. A twofold excess of GroEL and GroES is used.

1. Prepare a solution of 1 μM $GroEL_{14}$ in 198 μL 50 mM Tris/HCl pH 7.5, 10 mM DTT, 50 mM KCl, 10 mM $MgCl_2$ and incubate at 25 °C for 5 min.
2. Add 2 μL of unfolded mMDH and mix rapidly.
3. After 5 min, start reactivation by adding 2 μM $GroES_7$ and 1 mM ATP.
4. Withdraw aliquots of 20 μL every 2 min and determine the mMDH activity (see below).

To determine the extent of spontaneous refolding, conduct a control experiment without the chaperones. When using SR1 instead of wild-type GroEL, the reactivation protocol has to be modified since SR1 cannot release folded mMDH subunits from its cavity. In this case, incubate the withdrawn aliquots on ice for 5 min. This will release committed mMDH subunits, whereas the non-committed molecules will bind back to SR1. Next, incubate the samples for 15 min at 25 °C to allow dimerization of mMDH and then determine the enzyme activity.

Enzyme Assay for mMDH

mMDH catalyzes the reduction of ketomalonate or oxaloacetate by NADH, which can be followed by the decrease in absorbance at 340 nm using a standard UV spectrophotometer.

1. Assay buffer: 20 mM HEPES/KOH pH 7.3, 50 mM KCl.
2. Substrate: 10 mM ketomalonate; store at −20 °C.
3. Co-enzyme: 10 mM NADH; store at −20 °C.
4. Add 884 µL buffer + 80 µL ketomalonate + 16 µL NADH to a disposable cuvette and incubate at least 5 min at 25 °C.
5. Add 20 µL aliquot from the refolding reaction and mix rapidly.
6. Record $A_{340\,nm}$ for ∼1 min.

Acknowledgments

We thank K. Ruth for practical assistance concerning the described protocols. Support from the Deutsche Forschungsgemeinschaft, SFB594 (S.W.) and the Wellcome Trust (S.G.B.) is gratefully acknowledged.

References

1 Georgopoulos, C., Hendrix, R. W., Casjens, S. R., and Kaiser, A. D. (1973). Host participation in bacteriophage lambda head assembly. *J. Mol. Biol.* **76**, 45–60.

2 Barraclough, R. & Ellis, R. J. (1980). Protein synthesis in chloroplasts. IX. Assembly of newly-synthesized large subunits into ribulose bisphosphate carboxylase in isolated intact pea chloroplasts. *Biochim. Biophys. Acta* **607**, 19–31.

3 Goloubinoff, P., Christeller, J. T., Gatenby, A. A., and Lorimer, G. H. (1989). Reconstitution of active dimeric ribulose bisphosphate carboxylase from an unfolded state depends on two chaperonin proteins and Mg-ATP. *Nature* **342**, 884–889.

4 Cheng, M. Y., Hartl, F. U., Martin, J., Pollock, R. A., Kalousek, F., Neupert, W., Hallberg, R. L., and Horwich, A. L. (1989). Mitochondrial heat-shock protein hsp60 is essential for assembly of proteins imported into yeast mitochondria. *Nature* **337**, 620–625.

5 Braig, K., Otwinowski, Z., Hegde, R., Boisvert, D. C., Joachimiak, A., Horwich, A., and Sigler, P. B. (1994). The crystal structure of the bacterial chaperonin GroEL at 2.8 Å. *Nature* **371**, 578–586.

6 Fenton, W. A., Kashi, Y., Furtak, K., and Horwich, A. L. (1994). Residues in chaperonin GroEL required for polypeptide binding and release. *Nature* **371**, 614–619.

7 Ranson, N. A., Farr, G. W., Roseman, A. M., B., G., Fenton, W. A., Horwich, A. L., and Saibil, H. R. (2001). ATP-bound states of GroEL captured by cryo-electron microscopy. *Cell* **107**, 869–879.

8 Boisvert, D. C., Wang, J., Otwinowski, Z., Horwich, A. L., and Sigler, P. B. (1996). The 2.4 Å crystal structure of the bacterial chaperonin GroEL complexed with ATPγS. *Nat. Struct. Biol.* **3**, 170–177.

9 Roseman, A. M., Chen, S., White, H., Braig, K., and Saibil, H. R. (1996). The chaperonin ATPase cycle: Mechanism of allosteric switching and movements of substrate-binding domains in GroEL. *Cell* **87**, 241–251.

10 Gray, T. E. & Fersht, A. R. (1991). Cooperativity in ATP hydrolysis by GroEL is increased by GroES. *FEBS Lett.* **292**, 254–258.

11 Rye, H. S., Burston, S. G., Fenton, W. A., Beechem, J. M., Xu, Z., Sigler, P. B., and Horwich, A. L.

(1997). Distinct actions of cis and trans ATP within the double ring of the chaperonin GroEL. *Nature* **388**, 792–797.

12 Yifrach, O. & Horovitz, A. (1994). Two Lines of Allosteric Communication in the Oligomeric Chaperonin GroEL are Revealed by the Single Mutation Arg196 → Ala. *J. Mol. Biol.* **243**, 397–401.

13 White, H. E., Chen, S., Roseman, A. M., Yifrach, O., Horovitz, A., and Saibil, H. R. (1997). Structural basis of allosteric changes in the GroEL mutant Arg197 → Ala. *Nat. Struct. Biol.* **4**, 690–693.

14 Yifrach, O. & Horovitz, A. (1998). Mapping the Transition State of the Allosteric Pathway of GroEL by Protein Engineering. *Journal American Chemical Society* **120**, 13262–13263.

15 Ma, J., Sigler, P. B., and Karplus, M. (2000). A dynamic model for the allosteric mechanism of GroEL. *J. Mol. Biol.* **302**, 303–313.

16 Chandrasekhar, G. N., Tilly, K., Woolford, C., Hendrix, R., and Georgopoulos, C. (1986). Purification and properties of the groES morphogenetic protein of Escherichia coli. *J. Biol. Chem.* **261**, 12414–12419.

17 Hunt, J. F., Weaver, A. J., Landry, S. J., Gierasch, L., and Deisenhofer, J. (1996). The crystal structure of the GroES co-chaperonin at 2.8 Å resolution. *Nature* **379**, 37–45.

18 Landry, S. J., Zeilstra-Ryalls, J., Fayet, O., Georgopoulos, C., and Gierasch, L. (1993). Characterization of a functionally important mobile domain of GroES. *Nature* **364**, 255–258.

19 Saibil, H., Dong, Z., Wood, S., and auf der Mauer, A. (1991). Binding of chaperonins. *Nature* **353**, 25–26.

20 Langer, T., Pfeifer, G., Martin, J., Baumeister, W., and Hartl, F. U. (1992). Chaperonin-mediated protein folding: GroES binds to one end of the GroEL cylinder, which accomodates the protein substrate within its central cavity. *EMBO J.* **11**, 4757–4765.

21 Xu, Z., Horwich, A. L., and Sigler, P. B. (1997). The crystal structure of the asymmetric GroEL-GroES-(ADP) ∼ 7 chaperonin complex. *Nature* **388**, 741–750.

22 Sakihawa, C., Taguchi, H., Makino, Y., and Yoshida, M. (1999). On the maximum size of proteins to stay and fold in the cavity of GroEL underneath GroES. *J. Biol. Chem.* **274**, 21251–21256.

23 Weissman, J. S., Hohl, C. M., Kovalenko, O., Kashi, Y., Chen, S., Braig, K., Saibil, H. R., Fenton, W. A., and Horwich, A. L. (1995). Mechanism of GroEL action: Productive release of polypeptide from a sequestered position under GroES. *Cell* **83**, 577–587.

24 Chaudhry, C., Farr, G. W., Todd, M. J., Rye, H. S., Brunger, A. T., Adams, P. D., Horwich, A. L., and Sigler, P. B. (2003). Role of the γ-phosphate of ATP in triggering protein folding by GroEL-GroES: function, structure and energetics. *EMBO J.* **22**, 4877–4887.

25 Viitanen, P. V., Gatenby, A. A., and Lorimer, G. H. (1992). Purified chaperonin (GroEL) interacts with the nonnative states of a multitude of *Escherichia coli* proteins. *Protein Sci.* **1**, 363–369.

26 Horwich, A. L., Low, K. B., Fenton, W. A., and Hirshfield, I. N. (1993). Folding In Vivo of Bacterial Cytoplasmic Proteins: Role of GroEL. *Cell* **74**, 909–917.

27 Houry, W. A., Frishman, D., Eckerskorn, C., Lottspeich, F., and Hartl, F. U. (1999). Identification of in vivo substrates of the chaperonin GroEL. *Nature* **402**, 147–154.

28 Lin, Z., Schwarz, F. P., and Eisenstein, E. (1995). The hydrophobic nature of GroEL-substrate binding. *J. Biol. Chem.* **270**, 1011–1014.

29 Badcoe, I. G., Smith, C. J., Wood, S., Halsall, D. J., Holbrook, J. J., Lund, P., and Clarke, A. R. (1991). Binding of a chaperonin to the folding intermediates of lactate dehydrogenase. *Biochemistry* **30**, 9195–9200.

30 Robinson, C. V., Gross, M., Eyles, S. J., Ewbank, J. J., Mayhew, M., Hartl,

F. U., Dobson, C. M., and Radford, S. E. (1994). Conformation of GroEL-bound α-lactalbumin probed by mass spectrometry. *Nature* **372**, 646–651.

31 Zahn, R., Perrett, S., Stenberg, G., and Fersht, A. R. (1996). Catalysis of amide proton exchange by the molecular chaperones GroEL and SecB. *Science* **271**, 642–645.

32 Goldberg, M. S., Zhang, J., Sondek, S., Matthews, C. R., Fox, R. O., and Horwich, A. L. (1997). Native-like structure of a protein-folding intermediate bound to the chaperonin GroEL. *Proc. Natl. Acad. Sci. U.S.A.* **94**, 1080–1085.

33 Chen, J., Walter, S., Horwich, A. L., and Smith, D. L. (2001). Folding of malate dehydrogenase inside the GroEL-GroES cavity. *Nat. Struct. Biol.* **8**, 721–728.

34 Landry, S. J. & Gierasch, L. (1991). The chaperonin GroEL binds a polypeptide in an α-helical conformation. *Biochemistry* **30**, 7359–7362.

35 Schmidt, M. & Buchner, J. (1992). Interaction of GroE with an all β-protein. *J. Biol. Chem.* **267**, 16829–16833.

36 Chen, L. & Sigler, P. B. (1999). The crystal structure of a GroEL/peptide complex: plasticity as a basis for substrate diversity. *Cell* **99**, 757–768.

37 Wang, Z., Feng, H., Landry, S. J., Maxwell, J., and Gierasch, L. (1999). Basis of substrate binding by the chaperonin GroEL. *Biochemistry* **38**, 12537–12546.

38 Falke, S., Fisher, M. T., and Gogol, E. P. (2001). Structural changes in GroEL effected by binding of a denatured protein substrate. *J. Mol. Biol.* **308**, 569–577.

39 Jackson, G. S., Staniforth, R. A., Halsall, D. J., Atkinson, T., Holbrook, J. J., Clarke, A. R., and Burston, S. G. (1993). Binding and hydrolysis of nucleotides in the chaperonin catalytic cycle: implications for the mechanism of assisted protein folding. *Biochemistry* **32**, 2554–2563.

40 Todd, M. J., Viitanen, P. V., and Lorimer, G. H. (1993). Hydrolysis of Adenosine 5′-Triphosphate by Escherichia coli GroEL: Effects of GroES and Potassium Ion. *Biochemistry* **32**, 8560–8567.

41 Yifrach, O. & Horovitz, A. (1995). Nested cooperativity in the ATPase activity of the oligomeric chaperonin GroEL. *Biochemistry* **34**, 5303–5308.

42 Monod, J., Wyman, J., and Changeux, J.-P. (1965). On the nature of allosteric transitions: a plausible model. *J. Mol. Biol.* **12**, 88–118.

43 Koshland, D. E., Nemethy, G., and Filmer, D. (1966). Comparison of experimental binding data and theoretical models in proteins containing subunits. *Biochemistry* **5**, 365–385.

44 Burston, S. G., Ranson, N. A., and Clarke, A. R. (1995). The Origins and Consequences of Asymmetry in the Chaperonin Reaction Cycle. *J. Mol. Biol.* **249**, 138–152.

45 Yifrach, O. & Horovitz, A. (1998). Transient Kinetic Analysis of Adenosine 5′-Triphosphate Binding-Induced Conformational Changes in the Allosteric Chaperonin GroEL. *Biochemistry* **37**, 7083–7088.

46 Cliff, M. J., Kad, N. M., Hay, N., Lund, P. A., Webb, M. R., Burston, S. G., and Clarke, A. R. (1999). A Kinetic Analysis of the Nucleotide-induced Allosteric Transitions of GroEL. *J. Mol. Biol.* **293**, 667–684.

47 Todd, M. J., Viitanen, P. V., and Lorimer, G. H. (1994). Dynamics of the chaperonin ATPase cycle: implications for facilitated protein folding. *Science* **265**, 659–666.

48 Rye, H. S., Roseman, A. M., Chen, S., Furtak, K., Fenton, W. A., Saibil, H. R., and Horwich, A. L. (1999). GroEL-GroES Cycling: ATP and Nonnative Polypeptide Direct Alternation of Folding-Active Rings. *Cell* **97**, 325–338.

49 Weissman, J. S., Kashi, Y., Fenton, W. A., and Horwich, A. L. (1994). GroEL-Mediated Protein Folding Proceeds by Multiple Rounds of Binding and Release of Nonnative Forms. *Cell* **78**, 693–702.

50 Burston, S. G., Weissman, J. S., Farr, G. W., Fenton, W. A., and Horwich, A. L. (1996). Release of both native and non-native proteins from a cis-only GroEL ternary complex. *Nature* **383**, 96–98.

51 Ranson, N. A., Burston, S. G., and Clarke, A. R. (1997). Binding, Encapsulation and Ejection: Substrate Dynamics During a Chaperonin-assisted Folding Reaction. *J. Mol. Biol.* **266**, 656–664.

52 Shtilerman, M., Lorimer, G. H., and Englander, S. W. (1999). Chaperonin function: Folding by forced unfolding. *Science* **284**, 822–825.

53 Weissman, J. S., Rye, H. S., Fenton, W. A., Beechem, J. M., and Horwich, A. L. (1996). Characterization of the Active Intermediate of a GroEL-GroES-Mediated Protein Folding Reaction. *Cell* **84**, 481–490.

54 Schmidt, M., Rutkat, K., Rachel, R., Pfeifer, G., Jaenicke, R., Viitanen, P. V., Lorimer, G. H., and Buchner, J. (1994). Symmetric complexes of GroE chaperonins as part of the functional cycle. *Science* **265**, 656–659.

55 Azem, A., Kessel, M., and Goloubinoff, P. (1994). Characterization of a functional GroEL14(GroES7)2 chaperonin hetero-oligomer. *Science* **265**, 653–656.

56 Sparrer, H., Rutkat, K., and Buchner, J. (1997). Catalysis of protein folding by symmetric chaperone complexes. *Proc. Natl. Acad. Sci. U.S.A.* **94**, 1096–1100.

57 Hayer-Hartl, M. K., Ewalt, K. L., and Hartl, F. U. (1999). On the role of symmetrical and asymmetrical chaperonin complexes in assisted protein folding. *Biol. Chem.* **380**, 531–540.

58 Walter, S. (2002). Structure and function of the GroE chaperone. *Cellular and Molecular Life Sciences* **59**, 1589–1597.

59 Fisher, M. T. (1992). Promotion of the in vitro renaturation of dodecameric glutamine synthetase from Escherichia coli in the presence of GroEL (chaperonin-60) and ATP. *Biochemistry* **31**, 3955–3963.

60 Gray, T. E. & Fersht, A. R. (1993). Refolding of barnase in the presence of GroE. *J. Mol. Biol.* **232**, 1197–1207.

61 Staniforth, R. A., Burston, S. G., Atkinson, T., and Clarke, A. R. (1994). Affinity of chaperonin-60 for a protein substrate and its modulation by nucleotides and chaperonin-10. *Biochemical J.* **300**, 651–658.

62 Sparrer, H., Lilie, H., and Buchner, J. (1996). Dynamics of the GroEL-protein complex: effects of nucleotides and folding mutants. *J. Mol. Biol.* **258**, 74–87.

63 Yifrach, O. & Horovitz, A. (1999). Coupling between protein folding and allostery in the GroE chaperonin system. *Proc. Natl. Acad. Sci. U.S.A.* **97**, 1521–1524.

64 Sun, Z., Scott, D. J., and Lund, P. A. (2003). Isolation and characterisation of mutants of GroEL that are fully functional as single rings. *J. Mol. Biol.* **332**, 715–728.

65 Buchner, J., Schmidt, M., Fuchs, M., Jaenicke, R., Rudolph, R., Schmid, F. X., and Kiefhaber, T. (1991). GroE facilitates refolding of citrate synthase by suppressing aggregation. *Biochemistry* **30**, 1586–1591.

66 Farr, G. W., Furtak, K., Rowland, M. B., Ranson, N. A., Saibil, H. R., Kirchhausen, T., and Horwich, A. L. (2000). Multivalent Binding of Nonnative Substrate Proteins by the Chaperonin GroEL. *Cell* **100**, 561–574.

67 Zahn, R., Spitzfaden, C., Ottiger, M., Wüthrich, K., and Plückthun, A. (1994). Destabilization of the complete protein secondary structure on binding to the chaperone GroEL. *Nature* **368**, 261–265.

68 Walter, S., Lorimer, G. H., and Schmid, F. X. (1996). A thermodynamic coupling mechanism for GroEL-mediated unfolding. *Proc. Natl. Acad. Sci. U.S.A.* **93**, 9425–9430.

69 Staniforth, R. A., Cortes, A., Burston, S. G., Atkinson, T., Holbrook, J. J., and Clarke, A. R. (1994). The stability and hydrophobicity of cytosolic and mitochondrial

malate dehydrogenase and their relation to chaperonin-assisted folding. *FEBS Lett.* **344**, 129–135.

70 Ranson, N. A., Dunster, N. J., Burston, S. G., and Clarke, A. R. (1995). Chaperonins can Catalyse the Reversal of Early Aggregation Steps when a Protein Misfolds. *J. Mol. Biol.* **250**, 581–586.

71 Todd, M. J. & Lorimer, G. H. (1995). Stability of the asymmetric *Escherichia coli* chaperonin complex. Guanidine chloride causes rapid dissociation. *J. Biol. Chem.* **270**, 5388–5394.

72 Todd, M. J., Lorimer, G. H., and Thirumalai, D. (1996). Chaperonin-facilitated protein folding: optimization of rate and yield by an iterative annealing mechanism. *Proc. Natl. Acad. Sci. U.S.A.* **93**, 4030–4035.

73 Brinker, A., Pfeifer, G., Kerner, M. J., Naylor, D. J., Hartl, F. U., and Hayer-Hartl, M. K. (2001). Dual function of protein confinement in chaperonin-assisted protein folding. *Cell* **107**, 223–233.

74 Takagi, F., Koga, N., and Takada, S. (2003). How protein thermodynamics and folding mechanisms are altered by the chaperonin cage: molecular simulations. *Proc. Natl. Acad. Sci. U.S.A.* **100**, 11367–11372.

75 Wang, J. D., Herman, C., Tipton, K. A., Gross, C. A., and Weissman, J. S. (2002). Directed evolution of substrate-optimized GroEL/S chaperonins. *Cell* **111**, 1027–1039.

76 Dubaquie, Y., Looser, R., Fünfschilling, U., Jeno, P., and Rospert, S. (1998). Identification of in vivo substrates of the yeast mitochondrial chaperonins reveals overlapping but non-identical requirement for hsp60 and hsp10. *EMBO J.* **15**, 5868–5876.

77 Chaudhuri, T. K., Farr, G. W., Fenton, W. A., Rospert, S., and Horwich, A. L. (2001). GroEL/GroES-Mediated Folding of a Protein Too Large to Be Encapsulated. *Cell* **107**, 235–246.

78 Farr, G. W., Fenton, W. A., Chaudhuri, T. K., Clare, D. K., Saibil, H. R., and Horwich, A. L. (2003). Folding with and without encapsulation by *cis*- and *trans*-only GroEL-GroES complexes. *EMBO J.* **22**, 3220–3230.

79 Fiaux, J., Bertelson, E. B., Horwich, A. L., and Wüthrich, K. (2002). NMR analysis of a 900K GroEL-GroES complex. *Nature* **418**, 207–211.

80 Fayet, O., Louarn, J. M., and Georgopoulos, C. (1986). Suppression of the Escherichia coli dnaA46 mutation by amplification of the groES and groEL genes. *Mol. Gen. Genet.* **202**, 435–445.

81 Jenkins, A. J., March, J. B., Oliver, I. R., and Masters, M. (1986). A DNA fragment containing the groE genes can suppress mutations in the Escherichia coli dnaA gene. *Mol. Gen. Genet.* **202**, 446–454.

82 Ito, K. & Akiyama, Y. (1991). In vivo analysis of integration of membrane proteins in Escherichia coli. *Mol. Microbiol.* **5**, 2243–2253.

83 Horwich, A. L., Burston, S. G., Rye, H. S., Weissman, J. S., and Fenton, W. A. (1998). Construction of single-ring and two-ring hybrid versions of bacterial chaperonin GroEL. *Methods Enzymol.* **290**, 141–146.

84 Fisher, M. T. (1994). The effect of groES on the groEL-dependent assembly of dodecameric glutamine synthetase in the presence of ATP and ADP. *J. Biol. Chem.* **269**, 13629–13636.

85 Blennow, A., Surin, B. P., Ehring, H., McLennan, N. F., and Spangfort, M. D. (1995). Isolation and biochemical characterization of highly purified Escherichia coli molecular chaperone Cpn60 (GroEL) by affinity chromatography and urea-induced monomerization. *Biochim. Biophys. Acta* **1252**, 69–78.

86 Clarke, A. C., Ramanathan, R., and Frieden, C. (1998). Purification of GroEL with Low Fluorescence Background. *Methods Enzymol.* **290**, 100–118.

87 Todd, M. J. & Lorimer, G. H. (1998). Criteria for Assessing the Purity and Quality of GroEL. *Methods Enzymol.* **290**, 135–141.

88 Voziyan, P. A. & Fisher, M. T. (2000). Chaperonin-assisted folding of

glutamine synthetase under non-permissive conditions: off-pathway aggregation propensity does not determine the co-chaperonin requirement. *Protein Sci.* **9**, 2405–2412.

89 Eisenstein, E., Reddy, P., and Fisher, M. T. (1998). Overexpression, Purification, and Properties of GroES from *Escherichia coli*. *Methods Enzymol.* **290**, 119–134.

90 Gill, S. C. & von Hippel, P. H. (1989). Calculation of protein extinction coefficients from amino acid sequence data. *Anal. Biochem.* **182**, 319–326.

21
Structure and Function of the Cytosolic Chaperonin CCT

José M. Valpuesta, José L. Carrascosa, and Keith R. Willison

21.1
Introduction

A decade has passed since the discovery of the eukaryotic cytosolic chaperonin CCT (chaperonin-containing TCP-1; also termed TriC [TCP-1 ring complex] or c-cpn [cytosolic chaperonin]) [1–4]. However, characterization of the chaperonin occurred long after the discovery of one of its components, the t-complex polypeptide-1 (TCP-1), a protein that is abundantly expressed in the germ cells of the mouse testis [5] whose encoding gene was first molecularly cloned from mice [6] and then humans [7]. A history of the genetic analysis of the t-complex and its encoded genes, including TCP-1, was published recently [8]. TCP-1 is highly conserved in lower eukaryotes [9] and was found to be an essential protein involved in microtubule function in yeast [10]. Eventually, primary sequence comparison analyses revealed extensive sequence similarity between the TCP-1 protein and the Group I chaperonins [11, 12] and with thermophilic chaperonins [13], thus setting the scene for the rapid biochemical and functional characterization of the eukaryotic chaperonin. TCP-1, together with seven other homologous proteins, forms part of a chaperonin complex similar to GroEL and the chaperonin from archaea (thermosome or TF55) [1, 2, 4, 14]. All CCT preparations appear as toroidal structures constituted by two superimposed rings [1, 2, 4, 15]. Since then, the eight different subunits that constitute the oligomer have been sequenced from different organisms [16–21], and the biochemical, biophysical, and structural characterization of the cytosolic chaperonin has grown slowly but steadily. However, there is a still a paucity of information concerning the mechanism of action and functional cycle of CCT, especially when compared with the well-defined substrate-folding mechanism of GroEL from *E. coli*, but there is little doubt that CCT is unique when compared with other chaperonins. As will be discussed, its uniqueness lies not only in the fact that it is by far the most complex chaperonin, but also in its folding mechanism and in the range of proteins it assists in folding. The substrate proteins of CCT are critical components in various important cellular processes such as cytoskeletal formation of both microfilaments and microtubules, control of cell cycle progression, signal transduction, gene expression, and proteasome-

Protein Folding Handbook. Part II. Edited by J. Buchner and T. Kiefhaber

ISBN: 3-527-30784-2

associated degradation. This chapter discusses in detail what is known about this exciting molecular chaperone, in particular its structure and composition, functional cycle, and range of substrates and its interaction with other molecular chaperones.

21.2 Structure and Composition of CCT

Chaperonins are oligomeric structures composed of proteins with a ~60-kDa Mw and are divided into two groups according to their origin. Group I chaperonins are present in eubacteria and in eukaryotic organelles of endosymbiotic origin, whereas group II chaperonins are found in archaea and in the eukaryotic cytosol, the location of CCT. All chaperonins share a similar monomeric and oligomeric architecture, although the two groups of chaperonins show important differences. The atomic structure of the monomer is known for some group I and II chaperonins (GroEL from *E. coli* [22, 23] and the thermosome from *Thermoplasma acidophilum* [24], respectively), and they all share a three-domain topology (Figure 21.1, see p. 728): the equatorial domain that holds the nucleotide-binding site and most of the interactions between subunits of the same ring and the opposing one; the apical domain that contains the substrate recognition site; and the intermediate domain that transmits the signal originating in the equatorial domain upon nucleotide binding and hydrolysis to the apical domain, which results in large conformational changes in the latter. The main difference between the two groups of chaperonins resides in an extra helical region (helical protrusion) in group II chaperonins that is located at the tip of the apical domain [24–26] (Figure 21.1D) and that closes the chaperonin cavity during part of its functional cycle. The same role is fulfilled in group I chaperonins by a co-chaperonin called GroES, a small oligomer that is not present in group II chaperonins (Figure 21.1A, B).

The oligomeric structure is similar in both groups of chaperonins – a toroidal structure composed of two rings placed back to back – but major differences reside in their symmetry and composition. Whereas group I chaperonins are homo-oligomeric rings with sevenfold symmetry, the rings in the thermosomes can be composed of one to two different subunits with eightfold symmetry, three different subunits with ninefold symmetry [27], and, in the case of CCT, eight subunits with eightfold symmetry [28] (Figure 21.2B, see p. 728). A further important difference lies in the way the two rings interact (Figure 21.1A, C). Whereas in group II chaperonins each subunit interacts with one from the opposite ring, in group I chaperonins each subunit interacts with two from the opposite ring. This difference in inter-ring connectivity may cause important differences in the signaling between both rings and therefore in the functional cycle of both groups of chaperonins. In fact, inter-ring negative cooperativity in the ATP-induced allosteric transition of CCT is much stronger than that observed for GroEL [29].

No atomic structure has been obtained for the oligomeric CCT, and the structural information available has come mostly from electron microscopy studies. The first structural characterization obtained from image processing of negatively-stained specimens revealed the octameric nature of the CCT structure, a barrel-shaped cylinder with a diameter of ~150 Å and a height of ~160 Å, again different from the more rectangular shape of group I chaperonins [15] (Figure 21.2A–C and Figure 21.3A, see p. 729).

As has been clearly established for many different organisms, CCT is composed of eight different subunits [28]. This has been determined by different techniques such as protein sequencing [14, 16], characterization with different antibodies [30], and mass spectrometry [31]. The mammalian subunits are termed CCTα, CCTβ, CCTγ, CCTδ, CCTε, CCTζ, CCTη, and CCTθ, with CCT1–CCT8 corresponding to their respective counterparts in yeast. The eight CCT polypeptides share ~30% sequence identity in pairwise comparisons within a species, but homologous subunits across different eukaryotic species share a higher degree of similarity, which is indicative of a very early divergence time in the evolution of the CCT gene family (see Section 21.8). The subunits are arranged within each ring in a unique way (Figure 21.2B), and this was determined by characterizing the interaction of CCT microcomplexes of 2 to 3 subunits, which yielded a unique solution out of 5040 possibilities [32]. The ring order was deduced from the observation of the following CCT microcomplexes: (δ–η) (η–α) (α–ε) (ε–ζ) (ζ–β) (β–γ) (θ). Subsequent immunomicroscopy studies with monoclonal antibodies against specific CCT subunits have confirmed this arrangement [33, 34] (Table 21.1) and have shown that only one antibody molecule binds to each of the chaperonin rings [35], reinforcing the idea that a single copy of each subunit is present in each CCT ring and that both rings have the same composition. A ninth CCT subunit, CCTζ-2, has been discovered in vertebrates, which is specific for testis. CCTζ-2 is homologous to CCTζ, and seems to substitute for it in testis CCT, suggesting a specificity for this tissue-specific subunit and, indeed, as will be discussed for the whole chaperonin. An interesting but still obscure aspect regarding the interaction between CCT subunits has to do with the disassembly of the oligomeric structure. In one case, the double-ring has been shown to disassemble into the single-ring species, and this has been hypothesized to serve as a nucleation factor for the generation of new CCT particles [36]. Alternatively, CCT has been described to disassemble into individual subunits, and this has been hypothesized to have a role in the functional cycle of CCT [37].

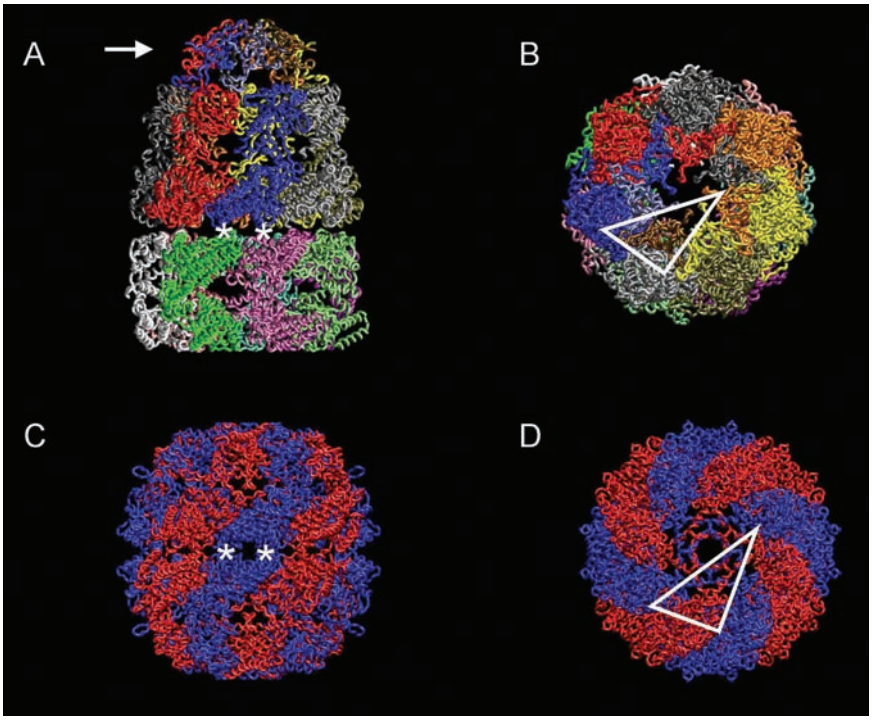

Fig. 21.1. Structural similarities and differences between type I and type II chaperonins. (A, B) Side and top view, respectively, of the atomic structure of the GroEL-GroES complex from *E. coli* [23] (pdb code 1aon). (C, D) Side and top view, respectively, of the atomic structure of the thermosome from *Thermoplasma acidophilum* [24] (pdb code 1a6d). In (A) the arrow points to the GroES oligomer. In (A) and (C) the asterisks highlight the interaction between the monomers of opposed rings, which is in phase in the case of the thermosome and staggered in the case of GroEL. In (B) and (D) the triangles limit the domains that in both types of chaperonins are involved in the closure of the cavity (the GroES oligomer in (B) and the apical protrusion in (D)).

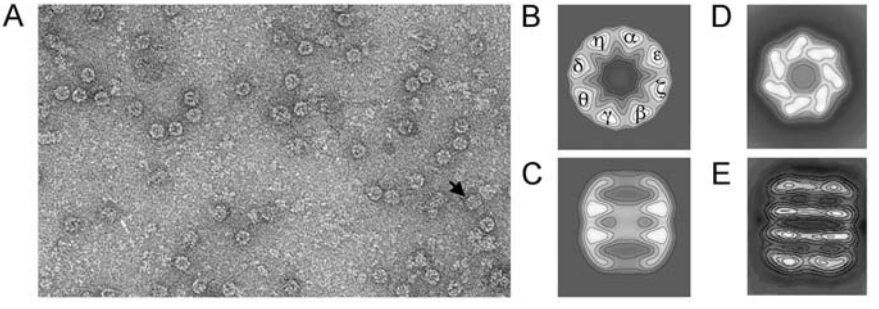

Fig. 21.2. The structure of CCT. (A) Electron micrograph of a field of CCT particles. Two views are observed: the most frequent top view, which shows its circular shape and the entrance of the chaperonin cavity, and the much less frequent side view (pointed with an arrow), which reveals the double toroidal structure typical of chaperonins. (B, C) Average images of the top and side views of CCT, respectively. (D, E) Average images of the top and side views of GroEL, respectively. The average images have been obtained in each case after averaging of several hundreds particles. The Greek letters in (B) indicate the arrangement of the CCT subunits.

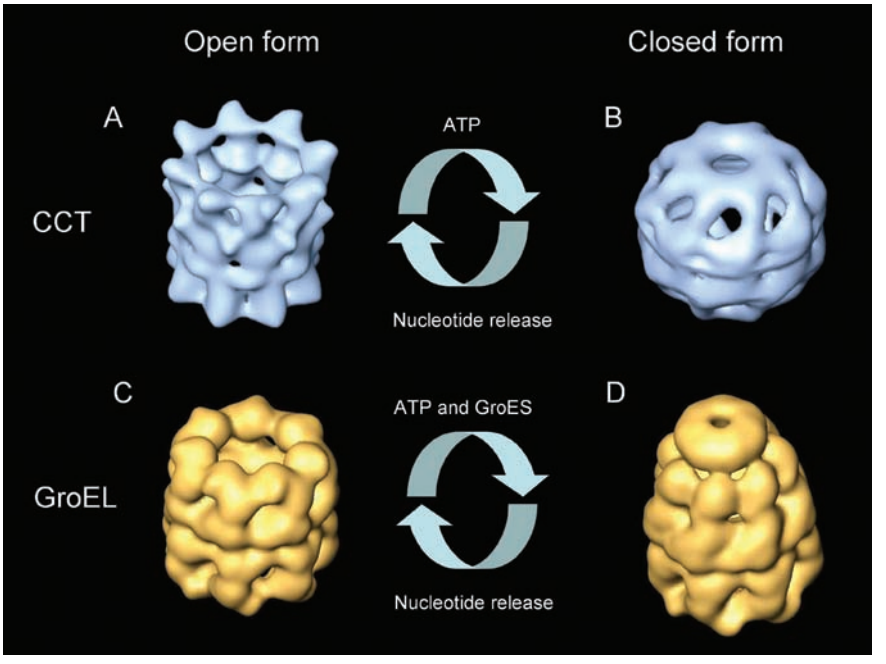

Fig. 21.3. The functional cycle of type I and type II chaperonins. (A, B) The open and closed forms of CCT, respectively. (C, D) The open and closed forms of GroEL, respectively. The two types of chaperonins have two main conformations: the open form, which is the substrate-receptive conformation, and the closed conformation, in which folding takes place. The closure of the chaperonin cavity is in both cases induced upon binding and hydrolysis of ATP, but in the case of CCT, it is physically performed by the movement of a helical protrusion and in the case of GroEL, upon binding of the co-chaperonin GroES. The three-dimensional structures of CCT have been obtained by cryo-electron microscopy; those of GroEL are a low-resolution (25 Å) representation of the nucleotide-free GroEL [22] (pdb code 1grl) and the GroEL-GroES complex [23] (pdb code 1aon).

21.3 Regulation of CCT Expression

In most mammalian cell types, CCT is not an abundant protein, although in testis germ cells there are approximately 3×10^5 oligomers per cell [1, 16] (less than 0.5% of soluble cytosolic protein). In the eukaryotic systems studied so far, all the CCT subunits seem to be expressed at similar levels [1, 18, 31], strengthening the idea of the predominance of the oligomeric form of the cytosolic chaperonin in vivo. CCT is not, like the rest of the chaperonins, a heat shock protein [1, 39, 40], although Tcp-1p/Cct1p has been suggested to be a cold shock protein in yeast [41]. CCT subunit levels in the cell can be increased by chemical stressors [42]. CCT abundance seems to correlate most strongly with growth rate [43], with CCT mRNA and protein levels being most abundant at the G1/S transition through early S-phase. Transcriptional regulation of mammalian CCT genes is mediated

Tab. 21.1. Summary of monoclonal antibody decoration experiments consistent with the CCT subunit arrangement model of Liou and Willison [32]. Monoclonal antibodies 91A, 23C, 8g, 81a, and PK-5h bind to CCTα subunits (91A and 23C), CCTδ subunits (8G), CCTη subunits (81a), and CCTθ (PK-5h) subunits, respectively.

CCT subunit	*MAb number*	*Substrate bound to CCT-Mab complexes*	*Figure**	*Reference*
CCTα	91A	α-actin	4A,B	33
CCTα	91A	β-actin.sub4	4C,D	33
CCTα	23C	None	1A–C	35
CCTδ	8g	α-actin	4E,F	33
CCTδ	8g	β-actin.sub4	4G,H	33
CCTδ	8g	α/β-tubulin	5A,B	34
CCTδ	8g	β-tubulin-f3	5E,F	34
CCTδ	8g	β-tubulin-f4	5G,H	34
CCTδ	8g	β-actinG150P	3B,C	77
CCTδ	8g	β-tubulin	6B	74
CCTη	81a	α/β-tubulin	Data not shown	34
CCTη	81a	β-tubulin-f5	Data not shown	34
CCTθ	PK-5h	α/β-tubulin	Data not shown	34
CCTθ	PK-5h	β-tubulin-f5	5C,D	34

* Figure number in respective reference.

through heat shock DNA elements and the factors HSF1 and HSF2 [44] as well as through the Ets domain transcription factors under the control of the Ras/MAPK pathway [45]. Further discussion of CCT gene and protein regulation can be found in Ref. [28].

21.4 Functional Cycle of CCT

Cryo-electron microscopy studies have characterized, albeit at low resolution, the two main conformers of CCT. The open conformation, generated in the absence of nucleotide [46] (Figure 21.3A), reveals structural features very similar to those obtained for group I (Figure 21.3C) and other group II chaperonins [47–49], with an open cavity ready to interact with the unfolded substrate. The helical protrusions are not visualized, probably due to the lack of high-resolution information in the reconstructions and to their closeness to the main body of the chaperonin structure in the open form, but they are visible in the closed conformation of CCT, generated in the presence of ATP, because they have undergone large movements (approx. 70° clockwise, viewed from the top) and have locked the chaperonin cavity [46] (Figure 21.3B), as also occurs in other group II chaperonins [47–49]. The structural rearrangements of the apical domains are therefore of a large magnitude [50] and have also been detected by biochemical techniques [51]. These changes are very similar to the ones that in GroEL are induced upon binding of its

co-chaperonin GroES and the subsequent closure of the chaperonin cavity (Figure 21.3D). The three-dimensional reconstruction of the CCT closed conformation fits very well with the atomic structure of the thermosome from *Thermoplasma acidophilum* [24]. This thermosome structure has been obtained in the absence of nucleotide, and small-angle neutron-scattering experiments have revealed that the closure of the cavity is induced by the crystallization conditions [52], thus mimicking the conditions generated by the presence of nucleotide. This suggests that the apical domains are very flexible, which is supported by experiments with complexes between CCT and a monoclonal antibody recognizing a C-terminal region of CCTα located in the interior of the cavity which folds actin and tubulin at normal rates in rabbit reticulocyte lysate [35].

Like all chaperonins, CCT is an ATPase that uses ATP binding and hydrolysis to maintain its functional cycle through movements that induce the closure and opening of the ring cavity. These movements are dictated by nested cooperativity that involves intra-ring positive and inter-ring negative cooperativity in ATP binding [53]. Small-angle X-ray scattering (SAXS) experiments suggest that ring closure of CCT requires not ATP binding but ATP hydrolysis to generate a trigonal-bipyramidal transition state of ATP hydrolysis [54]. This study challenges our EM studies, which showed that ATP- or AMPPNP binding closes the lids of CCT [46, 50] and the authors suggested that the AMPPNP we used must have been contaminated by ATP. However, we note that recent studies on *Thermococcus* thermosomes show that ATP- or AMPPNP binding closes the rings even under conditions whereby ATP hydrolysis is completely restricted [56] and that an X-ray structure of the same chaperonin with bound AMPPNP has been determined [57]. Further investigation of the allosteric changes in CCT induced by nucleotide is clearly required [55]. In the case of the cytosolic chaperonin, there are kinetic differences with respect to the better-studied GroEL that suggest that there may be differences in the intrinsic affinities for ATP among the subunits in a ring [29, 55]. Such differences in allosteric behavior would support a genetic model based on the analyses of mutants of the ATP site of several subunits of yeast CCT [58], which have shown that catalytic cooperativity of ATP binding and hydrolysis in CCT takes place in a sequential and hierarchical manner (CCT$\alpha \rightarrow$ CCT$\gamma \rightarrow$ CCT$\beta \rightarrow$ CCTζ; see arrows in Figure 21.4C, E), different from the concerted mechanism described for GroEL [53]. If this turns out to be the case, then closure of the CCT cavity would be sequential and the eight helical protrusions of the apical domains would act like an iris in this process.

21.5 Folding Mechanism of CCT

As in the case of the well-characterized GroEL, the conformational changes undergone by CCT upon ATP binding and hydrolysis are used by the chaperonin to facilitate the folding of substrate proteins. However, there are important differences between the two chaperonins that reside in the mechanism of assisted folding and in

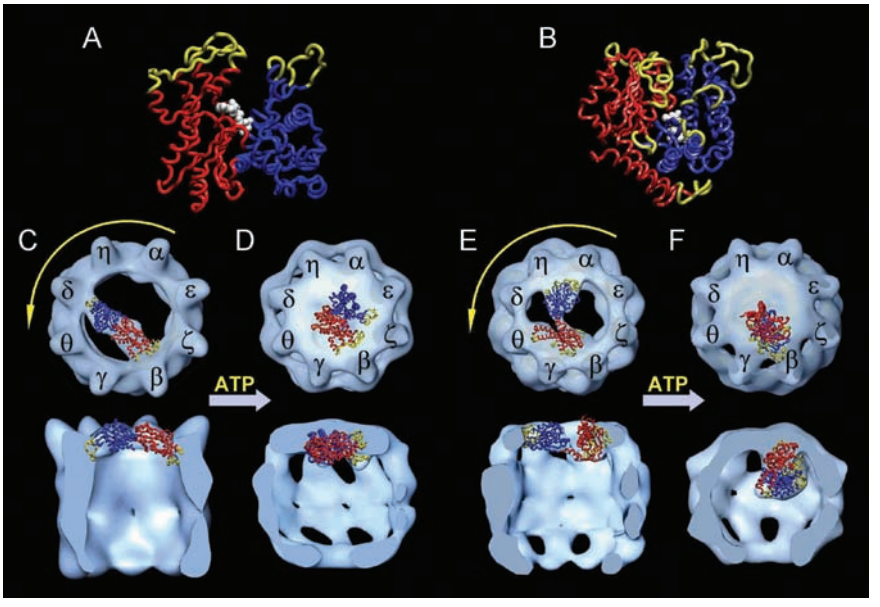

Fig. 21.4. The folding cycle of CCT. (A) The atomic structure of actin [82] (pdb code 1atn). The yellow domains correspond to the putative CCT-binding sites. The two topological domains of actin have been historically termed small and large domains and correspond respectively to the domains colored blue and red. The small domain is composed mainly of the N-terminal region, although a small stretch of residues of the C-terminal sequence (the last 35 residues) are also located in the small domain. (B) The atomic structure of tubulin [83] (pdb code 1tub). The color codes for the N-terminal domain, the C-terminal domain, and the putative CCT-binding sites are the same as used for actin in (A). (C, E) The three-dimensional reconstructions of the CCT-actin and CCT-tubulin complexes, respectively, in the nucleotide-free, open conformation, viewed from the top (top image) and from the side, cut view (bottom image). (D, F) The three-dimensional reconstructions of the CCT-actin and CCT-tubulin complexes, respectively, in the presence of nucleotide, which generates the closed conformation of CCT where folding takes place. The atomic structures of actin and tubulin have been docked in all four cases into the masses of the actin and tubulin components of the reconstructed complexes. In the nucleotide-free form, the atomic structures have been opened across their respective hinges to fit their reconstructed mass. In all the images, the actin and tubulin molecules have been colored respectively as in (A) and (B). Yellow arrows indicate the sequential conformational change in the CCT subunits induced by ATP binding, as proposed by Lin and Sherman [58]. This figure has been reproduced from Ref. [59] with permission from Wiley & Sons Limited.

the range of proteins they assist. Like GroEL, the open, nucleotide-free conformation of CCT is ready to recognize and interact with the unfolded substrate, and the interaction occurs through the apical domains. However, there are major differences between both chaperonins that are related to the substrate-chaperonin recognition mechanism and the conformational state of the interacting proteins [59]. In GroEL the interaction is nonspecific and occurs between the set of hydrophobic

residues located in any of the apical domains of the chaperonin ring and the exposed hydrophobic residues of any unfolded polypeptide [60–63]. In CCT, the interaction between the chaperonin and the unfolded polypeptide is of a different nature. Firstly, the CCT-interacting unfolded protein seems to posses a defined, quasi-native conformation as determined by structural [33, 34] and biochemical experiments [64]. The three-dimensional reconstructions of CCT complexed to denatured actin and tubulin show that both cytoskeletal proteins molecules adopt a defined conformation when bound to CCT because docking analysis between the reconstructed structures of the CCT-bound forms of both proteins and their corresponding atomic structures finds good fits (Figure 21.4A, B). Thus, the subdomains of these folding intermediates seem to contain an already high degree of folded structure, with the two proteins traversing the CCT cavity and interacting with two opposite regions (Figure 21.4C, E). Secondly, the substrate-binding region in CCT seems to be restricted not to the apical protrusions but to the base of the helical protrusions [34, 59]. Thirdly, both proteins interact with specific CCT subunits using defined regions of their sequence. Immunomicroscopy experiments with actin and tubulin have revealed that both proteins interact with CCT using two possible modes of interaction. In actin, its small domain can interact with CCTδ, and the large domain interacts with either CCTβ or CCTε [33]. In the case of tubulin, in one of the interactions the N-terminal region binds to CCTα and CCTη and its C-terminal domain binds to CCTβ, CCTγ, and CCTθ, while in the other possible interaction, the N-terminal region binds to CCTδ and CCTθ and its C-terminal domain to CCTε, CCTζ, and CCTβ (in Figure 21.4C and E, only one of the two possible modes of interaction for actin and tubulin is depicted in each). A docking analysis of the putative conformations of actin and tubulin bound to CCT has revealed four CCT-binding sites for actin and eight CCT-binding sites for tubulin [65], most of them previously suggested or subsequently confirmed by biochemical techniques in the case of both actin [66–68] and tubulin [66, 69–71]. Binding between CCT and the two cytoskeletal proteins therefore occurs through multiple sites that interact with the cytosolic chaperonin with weak affinity [70], although there are certain sites that interact more strongly with CCT (''hot spots'' [33, 34, 70, 71]). Finally, most of these CCT-binding sites in actin and tubulin are located in loops exposed on the surface of their native structure (Figure 21.4A, B) and contain a majority of charged and polar residues [59, 65, 67]. Likewise, the complementary substrate-binding region in CCT, located by cryo-electron microscopy studies in the apical domain and in part of the helical protrusion [33, 34] (Figure 21.4C, E), encompasses a region with the majority of residues in its surface being charged, and this is confirmed by the atomic structure of the apical domain of CCTγ [26]. All these results argue in favor of a specific interaction between the apical domains of specific CCT subunits and defined regions of actin and tubulin (and possibly of other CCT substrates), which, though unfolded, have acquired a substantial degree of native-like conformation before interaction with the cytosolic chaperonin is able to occur.

The next step in the folding cycle occurs upon the closure of the CCT cavity, induced, as in GroEL, by the binding and subsequent hydrolysis of ATP. In contrast

to the bacterial chaperonin, however, in CCT this closure is performed by the movement of the extra helical regions located at the tips of the apical domains. Another important difference resides in the state of the folding substrate after the closure of the ring, which in the case of GroEL is liberated in the cavity, where, free of any unwanted interactions with other proteins, it can fold using the information encoded in its own amino acid sequence. In the case of CCT, electron microscopy, kinetic, and genetic studies have shown that the cytosolic chaperonin follows a mechanism different from the "Anfinsen cage" described for GroEL [72, 73]. Cryo-electron microscopy studies carried out with CCT-actin and CCT-tubulin complexes in the presence of AMP-PNP, a non-hydrolyzable analogue of ATP, have revealed that the movements undergone by the apical domains induced upon nucleotide binding to seal the cavity are coupled to the folding movements of actin and tubulin, which remain bound to the apical domains of the cytosolic chaperonin and adopt a conformation very similar or possibly even identical to their native structure [74] (Figure 21.4D, F). Combining these results with the "sequential" model described above, a "sequential" folding mechanism of actin and tubulin mediated by CCT can be depicted, in which the N-terminal domains of actin and tubulin would be the first ones to undergo the structural rearrangements induced by the sequential movements of the CCT apical domains (see arrows in Figure 21.4C, E). The N-terminal domains of both cytoskeletal proteins bind to CCT with low affinity [34, 67, 71, 75], and as a consequence of the movements of the apical domains, the interaction with them is broken first. On the other hand, the C-terminal regions of actin and tubulin are the ones interacting with CCT with the highest affinity and are also the last ones to respond to the conformational change induced by ATP binding. As a result of these movements, actin and tubulin remain bound to the apical domains of CCT and adopt a conformation very similar or identical to their native structure [74]. In the case of tubulin, the conformational changes undergone by the protein have been found to be coupled to the binding of a GTP molecule to the protein nucleotide-binding site [64, 74, 76], which supports the notion that tubulin is folded on CCT to a state that is competent for GTP binding.

CCT therefore acts as a folding nanomachine that uses the conformational changes undergone by the apical domains upon ATP binding to force the folding of the two cytoskeletal proteins (and probably other substrates) by pushing together the two domains that were previously separated and interacting with two opposed regions of the chaperonin cavity. The movement of the two domains of actin has been corroborated by mutation of conserved residues in the putative hinge region of actin. These experiments have revealed that, upon reduction of the flexibility of this hinge by substituting conserved glycine residues for proline residues, such actin mutants cannot interact with both sides of the CCT cavity and remain bound to CCT [77]. The folding mechanism of CCT seems to be very efficient and sequential and in fact probably does not require multiple rounds of binding and release [76, 78]. This is very different from the more passive release mechanism of chaperonin GroEL (Figure 21.5). This specific mechanism explains why, although GroEL is able to bind actin and tubulin and undergo multiple cycles of release and rebind-

ing, only CCT is able to generate the native conformations of these two cytoskeletal proteins [79].

What is the role of CCT that makes it stringent for the folding of actin and tubulin? Although it is not yet proven, an interesting hypothesis points to the critical step being proper formation of the nucleotide-binding site of both cytoskeletal proteins [34]. CCT may have evolved from a thermosome-like ancestor to help overcome a specific kinetic barrier in the folding of actin and tubulin molecules, which have already reached a certain degree of conformational maturity before interacting with the cytosolic chaperonin [80]. CCT stabilizes an open conformation through the binding of their two topological domains with opposite sides of the chaperonin ring. In the case of actin, heat denaturation experiments have shown that its native conformation depends on the degree to which the nucleotide contributes to the connectivity between the two domains of the protein [81], and most of the bonds that connect the small and large domains occur through the ATP-binding site [82]. The situation is almost the same in tubulins, where GTP provides connectivity between domains [83], and some biochemical results indicate that GTP binding indeed stabilizes the molecule during the CCT-facilitated folding [64].

21.6 Substrates of CCT

Although it was originally believed that members of the actin and tubulin families were the only substrates of CCT, it has now become evident that the cytosolic chaperonin uses its structure to act on a large variety of proteins [84], perhaps as many as 9–15% of newly synthesized proteins [85]. However the folding mechanism described above suggests that the CCT-interacting proteins may have some shared structural or functional patterns and motifs. It is also becoming evident that the conformational changes undergone by CCT during its functional cycle are used not only for the generation of the native structure of certain proteins but also for other functions such as control of quaternary interactions and regulation of and protection from protein degradation (Figure 21.6). Nevertheless, a folding role for CCT has been shown, both in vivo and in vitro, for its major substrates actin and tubulin, since mutations in CCT subunits in yeast cause severe cytoskeletal defects [39, 86–88]. CCT also mediates the folding of other cytoskeletal proteins such as the actin-related proteins (ARPs) [89] and it has been shown to interact with myosin II heavy chain (HMM) [90], cofilin, and actin-depolymerizing factor (ADF1) [91].

Other proteins that are assisted in their folding by CCT are some viral proteins such as the hepatitis B virus capsid [92], the type D retrovirus Gag polyproteins [93], and the Epstein-Barr virus-encoded nuclear protein (EBNA-3) [94]. These are clear examples of opportunistic proteins that have parasitized the functional cycle of CCT to solve their specific folding problems. Other proteins involved in various cellular processes have been shown to be assisted by CCT in their folding, such as luciferase [95], the Gα subunit of the G-transducin complex involved in retinal

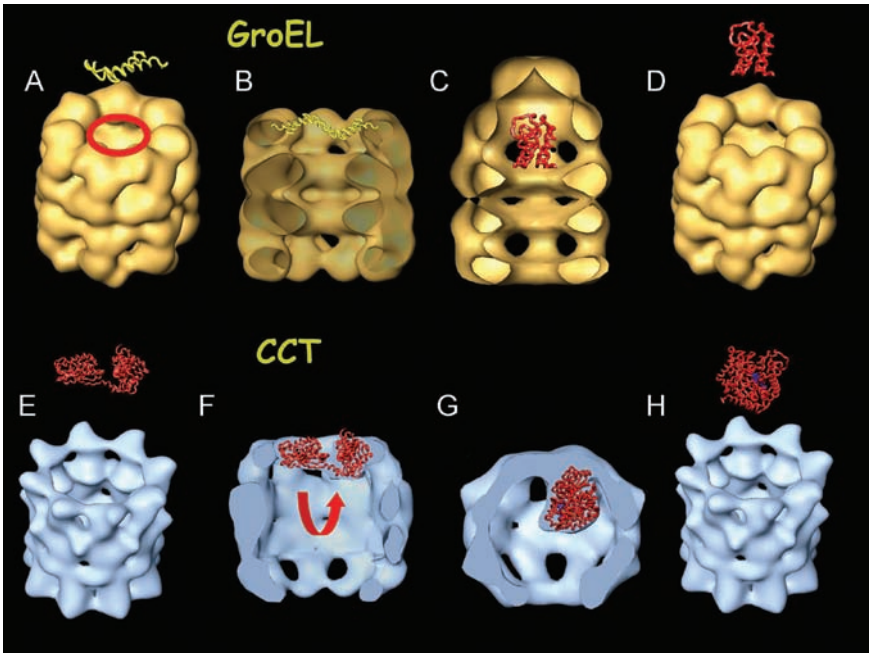

Fig. 21.5. Folding mechanism of GroEL (A–D) and CCT (E–H). In the case of GroEL, the hydrophobic residues located at the entrance of the cavity (circle in (A)) recognize any kind of unfolded polypeptide, provided that hydrophobic residues are exposed at its surface, and bind the polypeptide (B). The large conformational changes generated by ATP binding and the subsequent GroES binding, which occurs in the same region where the polypeptide is interacting with GroEL, liberate the polypeptide into a now much larger and locked cavity (C), where, free of any unwanted interactions, it can fold using the information encoded in the amino acid sequence. Hydrolysis of ATP and conformational changes occurring in the opposing ring liberate the GroES oligomer and the polypeptide, which may have attained its native conformation (D). If this is not the case, the polypeptide will be recognized by a GroEL molecule and would undergo the same again. The mechanism is not very efficient, but it serves a large number of different proteins. In contrast, CCT uses a different mechanism that seems to be very efficient and in which the substrate has already acquired a certain degree of conformation (E) before the interaction occurs between specific regions of the unfolded polypeptide and specific CCT subunits (F). The conformational changes undergone by the CCT apical domains upon ATP binding close the cavity and force the folding of the polypeptide (G). Subsequent hydrolysis and nucleotide release opens the chaperonin cavity and releases the folded protein (H).

phototransduction [76], and cyclin E, a protein implicated in the control of the cell cycle [96]. In the latter case, it has been proposed that interaction with CCT is necessary to generate a conformation that is apt to form a stable and functional complex with its partner protein, Cdk2. This also seems to be the situation with the interaction of CCT with other proteins involved in activation or repression of gene expression, such as the histone deacetylases Hos2 [97] and HDAC3 [98].

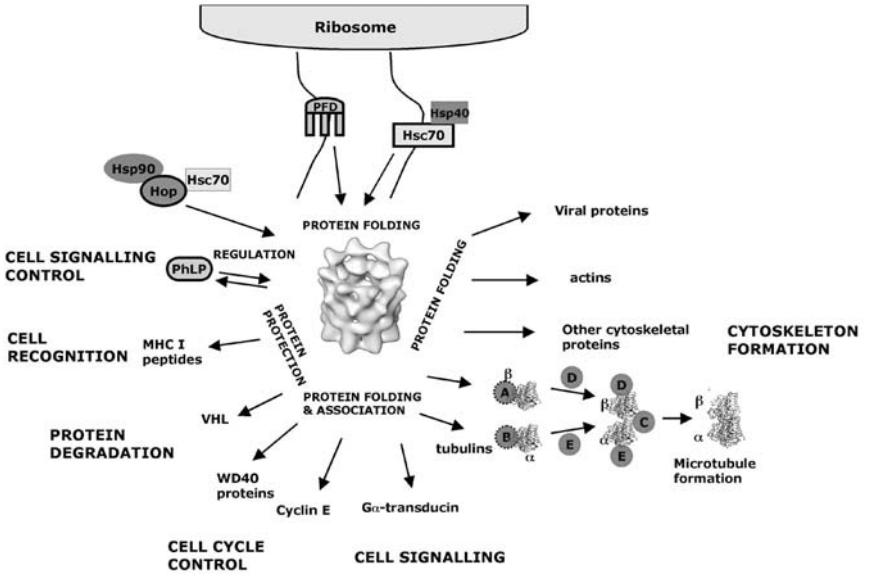

Fig. 21.6. Function of CCT and its interaction with its substrates and co-chaperones. The figure tries to convey the modes of interaction of CCT with different proteins to promote their folding, their quaternary association, their protection, or their presence in the cytosol. CCT seems to be at the core, through these interactions, of various important cellular processes.

The interaction of HDAC3 with CCT seems to be stringent for generating a stable and functional complex with a partner protein, the nuclear receptor co-repressor SMRT. Another example of this kind of interaction is the case of the von Hippel-Lindau tumor suppressor protein (VHL), a protein involved in several aspects of cell proliferation and tumor formation. The most well known role of VHL is as the substrate-recognition component of the VCB-Cul2 E3 ubiquitin protein–ligase complex, involved, like other E3 ubiquitin–ligase complexes, in protein degradation processes [99]. VHL forms a stable complex with the elongin BC complex, formed by the elongins B and C [100], but for this to occur, VHL must first interact with CCT, which helps this protein to adopt a conformation that can be recognized by the elongin BC complex [101]. This conformation is not stable, and in the absence of the elongin BC complex, the protein rebinds to the cytosolic chaperonin [101]. It is clear that in this case (and probably in the case of HDAC3), the conformational changes undergone by CCT during its functional cycle do not generate a native conformation but rather a specific transient one that is necessary for the interaction between and subsequent stabilization by other proteins. The fact that the VHL–elongin BC complex can be assembled in *E. coli* through co-expression of the three components and then crystallized supports the assembly model [100]. As often reiterated [102], the fact that native actins and tubulins cannot be obtained by expression in bacterial systems can be explained by their stringent requirement for CCT.

Other major CCT substrates are a large set of proteins containing WD40 repeats, a degenerate motif comprising 44–60 amino acid residues that typically contains a GH dipeptide at its N-terminal domain and the WD dipeptide at the C-terminus [103]. These WD40 repeats fold into four β-stranded domains, and together multiple repeats fold up into ring structures. The interaction between CCT and these proteins has been found by proteomic techniques using tagged open-reading frames to pull down multi-protein complexes [104], which has resulted in the identification of a group of at least 21 proteins that interact with the CCT oligomer (17% of the known WD40 proteins in yeast [84]). These proteins are implicated in various and important cellular processes, especially in cell cycle control and protein degradation. Most WD40 proteins possess in their polypeptide chains seven such WD40 repeats [103], and crystal structures of three such seven-bladed propellers have been determined so far. Curiously, a large number of the WD40 CCT-interacting proteins characterized so far have molecular masses larger than 60 kDa, the estimated mass that could be encapsulated into the CCT cavity, and therefore it is unlikely that these proteins are folded entirely inside the CCT cavity. It is therefore feasible with respect to these large proteins that the cytosolic chaperonin has other roles besides folding assistance and that it could be involved in regulating the proteins' activity by controlling their liberation or association with other proteins. Some recent studies show that some of these proteins indeed interact with CCT and that this interaction is necessary for their correct function. This is the case of the proteins Cdc20 and Cdh1, which are both implicated in the control of cell cycle through activation of the anaphase-promoting complex [105, 106], or Cdc55, a regulatory subunit of a PP2A protein phosphatase that acts in the cell cycle checkpoint inhibiting exit from mitosis in response to spindle or kinetochore damage [106, 107]. Other WD40 proteins shown in these studies to interact with CCT are TLE2 [106], Step4, Pex7, Prp46, and Sec7 [107], confirming that CCT interacts with several members of this structurally defined class of proteins. The interaction between the WD40 proteins and CCT is of a specific nature and, in the case of Cdc20, occurs through a region encompassed by specific WD40 repeats [105]. It is intriguing that certain WD40 proteins do not interact with CCT [106, 107], and this points towards a selective and specific CCT-binding mechanism as determined for actins and tubulins.

A role for CCT different from folding or regulation of protein association seems to be the reason behind the interaction between CCT and PhLP (phosducin-like protein). PhLP is involved, like its homologue phosducin, in regulation of cell signaling through binding to the G$\beta\gamma$-protein complex and blocking its interaction with the Gα-subunit [108]. PhLP has been shown to interact with CCT in its native form, and its overexpression in cells inhibits the actin-folding activity of the cytosolic chaperonin [109]. It is therefore likely that this interaction between PhLP and CCT may be a way to control CCT activity or, alternatively, to regulate the availability of PhLP to modulate G-protein signaling.

Finally, another role for CCT has been described recently, namely, protection against degradation of proteolytic intermediates of the MHC class I in the processing pathway until their delivery in the cell surface [110]. This is an exciting discov-

ery that further extends the already complex cellular functions of the cytosolic chaperonin.

21.7 Co-chaperones of CCT

It is increasingly evident that a host of molecular chaperones work in conjunction in protein-folding pathways. Numerous studies have revealed the intricacy in the function of chaperones such as Hsp90, Hsp70, Hsp60, Hsp40, and Hsp10 [111], and CCT is no exception to this rule, since CCT's interaction with several co-chaperones has been firmly established. These chaperones interact with the unfolded polypeptide either before or after the association with CCT. The best-characterized member of the former case, with the regard to its interaction with CCT, is the co-chaperone prefoldin [112, 113] (PFD; also termed GIM), a hetero-hexameric protein that exists in archaeabacterial and eukaryotic organisms and that in the latter has been shown to be involved in the folding of actins and tubulins [107, 112, 113] to the extent that its presence increases by at least fivefold the throughput of actin folded by CCT in vivo [78]. In this reaction, PFD transfers the substrate to CCT through a mechanism that involves a physical interaction between PFD and CCT [112]. This interaction, which has been observed by cryo-electron microscopy studies (Figure 21.7B), seems to occur through specific PFD and CCT subunits [114]. The three-dimensional reconstruction of the complex formed by eukaryotic PFD and unfolded actin also suggests that PFD delivers the unfolded actin to CCT in a quasi-folded conformation, ready to undergo the last step in its folding process in the chaperonin cavity [114] (Figure 21.7C).

CCT has also been shown to interact with members of the Hsp70/Hsc70 family (hereafter referred to as Hsc70); either directly or through association with the Hsp70/Hsp90 organizing protein (Hop, also termed p60), which links the cytosolic chaperonin with two of the major chaperone systems, the Hsp90 and Hsp70/Hsp40 systems (Figure 21.6). The interaction between CCT and Hsc70 has been known for a long time [1]. Proteomic analysis of CCT substrates has revealed that Hsc70 interacts with the cytosolic chaperonin [38], and several substrates are known to be transported by Hsc70 to CCT, including, among others, luciferase [95, 115], the tumor suppressor protein VHL [116], and several WD40 proteins [107]. Hop is a member of a structurally unrelated group of proteins including Bag-1, Hap46, and Hip, which associate with Hsc70 chaperones and regulate their activity [115, 117]. However, unlike the rest of the family members, Hop also binds to the chaperone Hsp90 [118, 119], and the complex formed by the three chaperones is involved in protein folding, especially in processes that have to do with the formation of mature progesterone and glucocorticoid receptors [118, 120]. Hop also interacts with CCT, and the interaction occurs through its C-terminal region [115], a domain that is different from the Hsc70-binding domain (N-terminus) and the Hsp90-binding domain (central part of the protein sequence). The interaction between CCT and Hop is dependent on the presence of nucleotide, and bind-

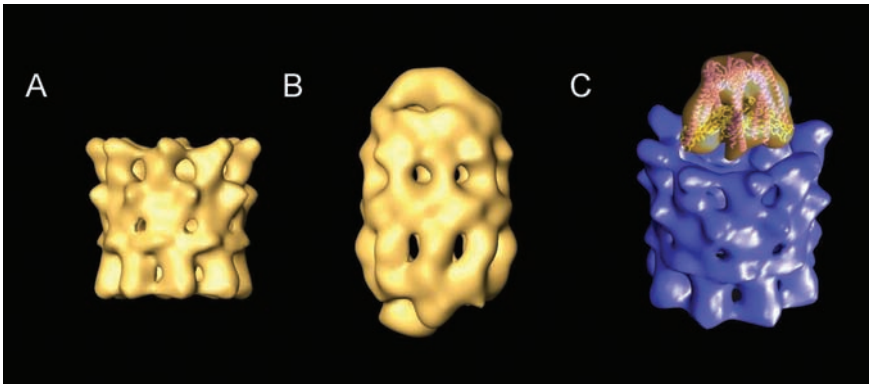

Fig. 21.7. Interaction between CCT and its co-chaperone PFD. (A, B) Three-dimensional reconstructions, obtained by cryo-electron microscopy and image processing, of the PFD-free CCT (A) and of the CCT-PFD symmetric complex (B) as described by Martín-Benito et al. [114]. (C) Model of the interaction between CCT and the complex formed by eukaryotic PFD and unfolded actin, obtained by electron microscopy and image processing. The atomic model docked into this three-dimensional reconstruction corresponds to the atomic structure of the homologous archaeal PFD from *Methanobacterium thermoautotrophicum* [154] (pdb code 1fxk) and the atomic model of CCT-bound actin, as suggested in Llorca et al. [34] and also depicted in Figure 21.4C. The model tries to describe the interaction between the complex formed by the co-chaperone PFD and its cargo, the unfolded actin, with the chaperonin CCT.

ing of this chaperone to CCT increases the chaperonin ADP/ATP exchange activity but decreases its substrate-binding affinity, thus suggesting for Hop a regulatory role of the cytosolic chaperonin [115].

While actin folded by CCT is readily incorporated into filaments, tubulin is folded by the cytosolic chaperonin to a unstable conformation that requires the assistance of several cofactors (A, B, C, D, and E) that facilitate the formation of the assembly-competent α/β tubulin dimers, necessary for the formation of the microtubules [121, 122] (Figure 21.6). According to the gathered biochemical information, after the sequential interaction of α-tubulin with cofactors B and E, and β-tubulin with cofactors A and D, a complex is formed that contains cofactors C, D, E, and α- and β-tubulin and that generates the formation and release of a stable α,β-tubulin heterodimer after the induced GTP hydrolysis of β-tubulin [102, 121, 123]. There is a paucity of structural information regarding these cofactors; only the atomic structure of cofactor A has been elucidated [124, 125], which reveals a rod-like structure, slightly convex in shape, formed by three α-helices. The central part of the structure contains the β-tubulin-binding domain, composed of a mixture of hydrophilic and hydrophobic residues [125]. Curiously, the structure of cofactor A strikingly resembles that of the BAG domain, and it has been hypothesized that both proteins could belong to the same family of chaperone cofactors [125]. Little is known about the interaction between CCT and cofactors A and B, and it is possible that the two cofactors only bind to the tubulin monomer after the chaper-

onin folding cycle. Although there is biochemical evidence for the interaction between cofactor A and CCT [126], some authors deny that such interaction occurs [127].

21.8 Evolution of CCT

It is clear that gene duplication is the main force behind the evolution of group II chaperonins [16, 128, 129]. In archaeal species complex patterns of gene duplication, gene loss, and gene conversion have allowed the appearance of one, two, or three homologous subunits in different thermosomes. Gene duplication has been hypothesized to occur as the result of the appearance of mutations in the intra-ring subunit domain of one subunit followed by compensatory changes in an evolved duplicate subunit, and this could have produced a tendency towards hetero-oligomerism, even in the absence of specialized roles for the duplicate subunits. This latter view is reinforced by the facts that duplicate chaperonin genes have occasionally been lost in evolution [130] and that gene conversions can homogenize the region encoding the thermosome putative substrate-binding domains [129].

It is clear that CCT has evolved from archaebacterial precursors because of the close sequence homology, but, in contrast to thermosomes, the eukaryotic chaperonin is the result of a series of duplications that occurred probably only once, at the very beginning of the evolution of the eukaryotic genome, approximately two billion years ago [16, 17, 131]. This is supported among other things by the fact that all eight CCT subunits are present not only in all the protists but also in amitochondriate protist lineages, which are believed to have diverged early in eukarya evolution [128]. Phylogenetic analysis of different eukaryotic organisms (animals, fungi, plants, and amitochondriate protists) reveals that the different CCT subunits group together with high statistical significance, which reinforces the notion that gene duplications took place in the ancestors of these organisms [131]. A recent comparison of synonymous versus non-synonymous nucleotide differences in CCT genes shows strong positive selection occurring after each duplication event to provide sub-functionalization of the new subunits [132].

What is the order of the duplication events? Although there is not yet a clear view of the original process that produced the eight subunits, due to the very long time since it happened, phylogenetic analyses reveal that there is more recent common ancestry between some CCT subunits, i.e., the CCTδ and CCTε groups and the CCTα, CCTη, and CCTβ groups [131, 132]. However, it is clear in the case of the two different vertebrate CCTζ subunits (1 and 2) that posses a high percentage of identity [19] (81%) that they are more related to each other than to CCTζ subunits from other organisms. The gene duplication that gave rise to these two genes occurred recently, around 200 million years ago, compared to the origin of CCT, which occurred two billion years ago [16]. As discussed above, CCTζ-2 is expressed only in testis, and it has been suggested that it originated to assist in

the folding of specific testis proteins [19]. This agrees with the hypothesis that CCT hetero-oligomerization occurred at the same time as the appearance of the cytoskeleton [17, 80, 133, 134]. The existence of a developed cytoskeleton in eukaryotes has given rise to functions that are unique to them, including, among others, chromosome segregation, locomotion, and phagocytosis, the latter undoubtedly involved in the endosymbiotic processes that generated and conserved mitochondria and chloroplasts in the eukaryotic cell. The evolution of CCT towards hetero-oligomerization and specialization has been paralleled by its co-chaperone PFD, which has evolved from a simple oligomer in archaea (composed of two differrent and homologous proteins, α and β) to a more complex assembly in eukarya (six different proteins, two α-like and four β-like). This co-evolution has likely served to generate a more efficient folding machinery for actins and tubulins through a mechanism involving specific interactions between defined regions of the cytoskeletal proteins with particular CCT and PFD subunits [17, 33, 34, 135]. In the case of CCT, several results point towards confirmation of this hypothesis, and the immunomicroscopy experiments with CCT-actin and CCT-tubulin complexes cited above reveal that CCT interacts with the two cytoskeletal proteins through specific subunits [33, 34]. The interaction between CCT and the two proteins occurs in the upper part of the apical domain, just below the helical protrusion in the case of actin and encompassing part of this protrusion in the case of tubulin [34], and it is in this region where sequence- and structure-based comparison analyses have revealed a region of highly conserved, subunit-specific residues, most of them charged [26, 131]. These findings strengthen the notion of a specialized function of the CCT subunits. In the case of actin and tubulin, sequence-comparison and structural analyses have shown that the domains of both cytoskeletal proteins putatively involved in CCT binding are absent or greatly modified in their corresponding prokaryote homologues FtsA/MreB and FtsZ, and most of these domains are also implicated in the formation of actin and tubulin polymers [65]. This further supports the coevolution of CCT with its two main substrates in the maintenance of the cytoskeletal structures that are the essence of all eukaryotic organisms.

What about the evolution of CCT interaction by the many CCT-binding proteins other than actins and tubulins? In the case of the large group from the family of WD40 proteins [84, 104–107], these proteins are found almost exclusively in eukaryotes and are involved generally in processes that are fundamental and unique to these organisms [103]. This CCT-binding subfamily of WD40 proteins probably also appeared at the beginning of the eukaryote evolution, similar to actins, tubulins, and CCT. Since WD40 repeats are not found in Archaea, it is likely that this fold entered the eukaryotic lineage by lateral transfer from a eubacterium, as is proposed for the actin/hexokinase/Hsp70 fold [28, 80]. It is likely that CCT, by virtue of its assistance in the folding of all these important proteins, sits at the heart of many processes that are at the core of eukaryotic cell function (Figure 21.6). Subsequent to the establishment of the CCT system at the very beginning of eukaryotic evolution, interactions between CCT and other proteins may have occurred as a result of selection of new functions and also from opportunistic processes such as the assistance of CCT in the folding of viral proteins.

21.9
Concluding Remarks

All the functional and structural results obtained so far point to CCT being a unique chaperonin, different from all the others in its functional mechanism and in the cellular roles in which it is involved. Besides its involvement in the folding of actin and tubulin, and therefore in the formation of the cytoskeleton, CCT is implicated in the folding or quaternary association of a host of proteins that are essential in a multitude of cellular processes such as cell cycle control, signal transduction, transcription, protection from degradation, etc. Many exciting issues remain to be uncovered, in particular, a more-detailed characterization of the functional cycle of CCT and its interaction with the new substrates that are now continuously being discovered.

21.10
Experimental Protocols

21.10.1
Purification

In the early phase of CCT discovery and characterization, various laboratories established protocols for purifying CCT from mammalian testis extracts [1, 2, 4]. CCT holo-complex is present at around 3×10^5 copies per cell in mouse testis germ cell preparations [1]. CCT has also been purified from rabbit reticulocyte lysate [2, 14, 136].

Bovine testis CCT is purified over Q-Sepharose HR (Pharmacia) followed by sucrose gradient size fractionation and affinity chromatography on an agarose-bound ATP column; a combination of the Gao et al. [1] and Frydman et al. [4] procedures led to the protocol of Melki and Cowan [137], and a detailed description is to be found in their paper. This protocol allows processing of up to 0.5 kg tissue. These bovine CCT preparations are active in actin and tubulin folding assays [1, 137]. Recently, bovine CCT was used to study steady-state ATP binding and hydrolysis [29], and this modified protocol involves sucrose gradient size fractionation, MonoQ HR 5/5 chromatography, HiTrap heparin chromatography, and final desalting using PD-10 Sephadex. This protocol was modified yet again, by replacing the MonoQ step with C-8 ATP-agarose to produce large amounts of CCT, for time-resolved fluorescence emission analysis of ATP-induced allosteric transitions, from 150-g aliquots of bovine testis and is described in useful detail in Kafri and Horovitz [55].

Mouse testis CCT has been used extensively in our laboratory for biochemical and structural studies. We always use sucrose gradient size fractionation as a first step, since this gives an immediate 900-fold enrichment [1] because of the large size of CCT (nearly 900 kDa). Presently, our general preferred protocol for purification of CCT from testis cells, tissue culture cell lines, or rabbit reticulocyte lysate consists of sucrose density gradient centrifugation, anion-exchange chromatogra-

phy (elution 0.1–0.3 M NaCl), heparin chromatography (elution 0.5–0.7 M NaCl), and buffer exchange by ultrafiltration [138]. The final material is 95% pure and particulate and is non-aggregated under the electron microscope [46, 50].

Antibody reagents recognizing a CCT subunit such as TCP-1 [1] (MAb 91A) or a pan-CCT reagent [30] (UM1) provide the most straightforward method to follow CCT during purification and have been used by many laboratories. However, once CCT is reasonably enriched it can be easily followed by its signature pattern of ~60-kDa polypeptides on SDS gels [1, 136].

We refer readers to protocols for purification of rabbit reticulocyte lysate CCT from Norcum [136] and Cowan [139]. The Norcum protocol was used by Szpikowska et al. [51] to examine MgATP-induced conformational changes in rabbit CCT.

21.10.2 ATP Hydrolysis Measurements

In early studies various steady-state ATP hydrolysis assays, measuring phosphate release from [γ-^{32}P]ATP, were established for CCT (reviewed in Ref. [17]). These gave values of between 14.3 and 19.3 nmol mg^{-1} min^{-1} at 37 °C (14–19 molecules of ATP hydrolyzed per CCT complex per minute). Recent studies from Horovitz and colleagues [29] measured initial rates of ATP hydrolysis by bovine testis CCT as a function of ATP concentration using a [γ-^{32}P]ATP and a ^{32}P-phosphate release quantitation assay first established for GroEL [140]. The value of k_{cat} for ATP hydrolysis by one ring and by both rings of CCT was 0.0119 sec^{-1} and 0.0183 sec^{-1}, respectively [29]. Kafri and Horovitz [55] have recently described stopped-flow analysis of ATP binding and hydrolysis by CCT using excitation at 280 nm and recording tryptophan emission beyond 320 nm using a cutoff filter.

21.10.3 CCT Substrate-binding and Folding Assays

CCT-mediated actin and tubulin folding assays have been established, in the main, by Cowan's laboratory [2, 137] and have been summarized by him in experimental detail [139]. They are analogous to the classic folding assays performed with GroEL and involve dilution of chemically denatured substrate proteins into buffer containing chaperonin. The appearance of native, folded proteins is monitored through native gel electrophoresis.

Several laboratories, including our own, have made use of rabbit reticulocyte lysate–based in vitro transcription/translation systems to monitor actin and tubulin folding [68, 71].

21.10.4 Electron Microscopy and Image Processing

Electron microscopy is widely used as a method for retrieving structural information of biological samples up to near-atomic resolution, and it is ideally suited for

the analysis of macromolecular complexes. To achieve maximal resolution, samples have to be imaged without any contrasting agent; the current method of attaining good structural preservation while allowing the operation under the conditions of electron microscopes is cryo-electron microscopy. In this method, samples are rapidly frozen at liquid nitrogen temperature with the use of cryogenic reagents and then transferred inside the microscope, where they can be imaged using limited electron dosage to prevent specimen destruction. Images obtained with this method preserve structural information but are extremely noisy. This, together with the fact that transmission electron images are two-dimensional projections of the objects under study (Figure 21.8A), implies that the data obtained by electron microscopy have to be treated in a mathematical way to retrieve the three-dimensional information.

CCT is a multimeric assembly that exhibits a certain degree of symmetry. Nevertheless, most of the procedures applied for extracting structural information from electron micrographs of CCT are essentially independent from those symmetry

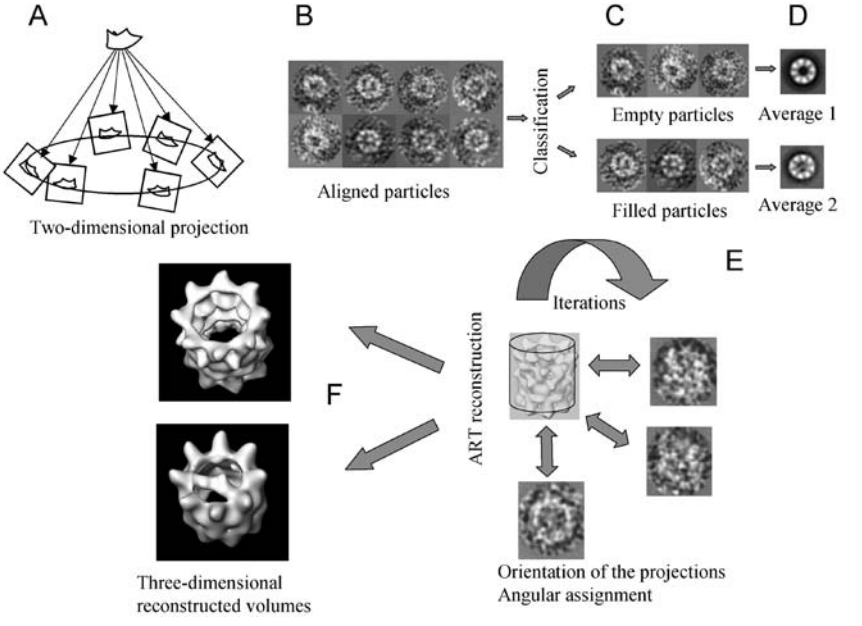

Fig. 21.8. Two- and three-dimensional image processing of single particles. (A) Generation of two-dimensional projections from a three-dimensional object following a conical geometry. (B) Gallery of images obtained after boxing and alignment of particles selected from electron micrographs. (C) Homogeneous subsets of views corresponding to different particle families obtained after classification of two mixed populations. (D) Average images obtained after averaging of the two different populations. (E) Three-dimensional reconstruction protocol including iterative angular assignment for the orientation of two-dimensional projections, volume reconstruction, and re-projection of the three-dimensional volume in projections using the determined orientations. (F) Three-dimensional volume representation including filtering at the calculated resolution.

constraints and hence are considered as "single-particle" processing procedures [141]. The first step in image processing is the digitization of the micrographs. Micrographs are converted in arrays of squared pixels with a size around 2–4 Å. The actual images corresponding to the chaperonin views are then selected in the computer and boxed (Figure 21.8B). Due to the fact that molecular aggregates are randomly distributed in solution, particles under study offer a complex set of projection views. The images selected are centered by subjecting them to translational and rotational alignment. This step is important and care has to be taken not to bias the alignment by using patterns; therefore, the use of free-pattern alignment algorithms is instrumental for this purpose [142, 143].

Once the images are aligned, a most critical analysis is the determination of variations among the different images. These differences can arise from biochemical differences, partial destruction of the particles under study, or, most relevant, different views of the object due to the out-of-plane orientation variations of the particles. Usually, there are a number of preferential views that produce different families of projections that must be sorted out [144]. The separation of the different populations can be carried out by a number of classification procedures (supervised, non-supervised, self-organizing, etc.). In our studies with CCT, we have used self-organizing maps based on neural networks [145] that provide a reduction in the number of vector images and a significant increment in the signal-to-noise ratio. This procedure facilitates the use of other subsequent classification methods, if required. Once the images are divided in homogeneous sets of views (Figure 21.8C), they can be averaged to render statistically significant data representing each two-dimensional projection of the objects under study (Figure 21.8D). Interpretation of the averaged views is fully dependent on the estimation of the resolution attained. This critical value depends upon the sample properties, the quality of the imaging method, and the number of averaged views, among other factors, and it is estimated using different criteria. We have used the spectral signal-to-noise ratio (SSNR), as proposed by Unser et al. [146]. Once the resolution is determined, the averages are filtered up to that value to remove those structural features inconsistent with the resolution level.

Reconstruction of the three-dimensional volume of the object is based on the use of the different two-dimensional projections obtained in the microscope. In principle, the random orientation of the particles in the thin ice layer used for cryo-electron microscopy is sufficient for rendering enough different views of the object so as to reconstruct the original volume. In other cases, different strategies for collecting data must be devised. One of the most popular is the random conical tilting method based on the collection of pairs of tilted and untilted micrographs [147]. Most of the reconstruction procedures are based on the projection theorem formulated by De Rosier and Klug [148]. The first problem in reconstruction is the definition of the orientation of the projections with respect to the three-dimensional original object (Figure 21.8E). We have used the angular refinement algorithms provided by the suite of programs called SPIDER [149], which determine the characteristic orientation parameters for each projection. Once these parame-

ters are assigned, there are different approaches to reconstruct the three-dimensional volume [141, 150]. We have used an algebraic reconstruction approximation [151] that renders a three-dimensional map that can be used as a reference to reproject two-dimensional views using the orientation data obtained during the first angular refinement. These projections can then be compared to the experimental ones, and, carrying out several iterations, a refinement of the structure can be approximated. Once the iterations converge to a stable solution, this volume is taken as final representation of the object (Figure 21.8F). In cases where the particles exhibit a certain degree of symmetry, it can be used in either the initial reference model production or the final stages of the processing (representation of the final volume).

The interpretation of the reconstructed volume is very dependent on the threshold chosen for representation, which must account for the expected mass of the object, as well as on the resolution attained. As in the case of the two-dimensional averaged images, the determination of the resolution is still an unsolved issue. Different methods have been proposed [152] and modified along the years. We actually use the Fourier shell correlation coefficient calculated from two independent reconstructions using the Bsoft program package [153]. Final volumes for interpretation must be filtered up to that resolution to remove those features corresponding to frequencies above the resolution threshold.

References

1 Lewis, V. A., Hynes, G. M., Zheng, D., Saibil, H. & Willison, K. R. (1992). T-complex polypeptide-1 is a subunit of a heteromeric particle in the eukaryotic cytosol. *Nature* **358**, 249–252.

2 Gao, Y., Thomas, J. O., Chow, R. L., Lee, G. H. & Cowan, N. J. (1992). A cytoplasmic chaperonin that catalyzes beta-actin folding. *Cell* **69**, 1043–1050.

3 Yaffe, M. B., Farr, G. W., Miklos, D., Horwich, A. L., Sternlicht, M. L. & Sternlicht, J. (1992). TCP1 complex is a molecular chaperone in tubulin biogenesis. *Nature* **358**, 245–248.

4 Frydman, J., Nimmesgern, E., Erdjument-Bromage, H., Wall, J. S., Tempst, P. & Hartl, F. U. (1992). Function in protein folding of TRiC, a cytosolic ring complex containing TCP-1 and structurally related subunits. *EMBO J.* **11**, 4767–4778.

5 Silver, L. M., Artz, K. & Bennett, D. (1979). A major testicular cell protein specified by a mouse T/t complex gene. *Cell* **17**, 275–284.

6 Willison, K. R., Dudley, K. & Potter, J. (1986). Molecular cloning and sequence analysis of a haploid expressed gene encoding *t*-complex polypeptide 1. *Cell* **44**, 727–738.

7 Willison, K. R., Kelly, A., Dudley, K., Goodfellow, P., Spurr, N., Groves, V., Gorman, P., Sheer, D. & Trowsdale, J. (1987). The human homologue of the mouse *t*-complex-gene *TCP1* is located on chromosome 6 but not near the HLA region. *EMBO J.* **6**, 1867–1874.

8 Willison, K. R. & Lyon, M. F. (2000). A UK-centric history of studies on the mouse *t*-complex. *Int. J. Dev. Biol.* **44**, 57–63.

9 Ursic, D. & Ganetzky, B. (1988). A

Drosophila melanogaster gene encodes a protein homologous to the mouse *t*-complex polypeptide 1. *Gene* **68**, 267–274.

10 Ursic, D. & Culbertson, M. R. (1991). The yeast homologue to mouse *Tcp-1* affects microtubule-mediated processes. *Mol. Cell. Biol.* **11**, 2629–2640.

11 Ellis, R. J. (1990). Molecular chaperones: the plant connection. *Science.* **250**, 954–959.

12 Gupta, R. S. (1990). Sequence and structural homology between a mouse t-complex protein TCP-1 and the "chaperonin" family of bacterial (GroEL, 60–65 kDa heat shock antigen) and eukaryotic proteins. *Biochem. Int.* **20**, 833–841.

13 Trent, J. D., Nimmersgeern, E., Wall, J. S., Hartl, F. U. & Horwich, A. L. (1991). A molecular chaperone from thermophilic archaebacterium is related to the eukaryotic protein t-complex polypeptide-1. *Nature* **354**, 490–493.

14 Rommelaere, H., van Troys, M., Gao, Y., Melki, R., Cowan, N. J., Vandekerckhove, J. & Ampe, C. (1993). Eukaryotic cytosolic chaperonin contains t-complex polypeptide 1 and seven related subunits. *Proc. Natl. Acad. Sci. USA* **90**, 11975–11979.

15 Marco, S., Carrascosa, J. L. & Valpuesta, J. M. (1994). Reversible interaction of *β*-actin along the channel of the TCP-1 cytoplasmic chaperonin. *Biophys. J.* **67**, 364–368.

16 Kubota, H., Hynes, G., Carne, A., Ashworth, A. & Willison, K. R. (1994). Identification of six *Tcp-1* related genes encoding divergent subunits of the TCP-1 containing chaperonin. *Curr. Biol.* **4**, 89–99.

17 Kubota, H., Hynes, G. & Willison, K. R. (1995). The chaperonin containing t-complex polypeptide 1(TCP-1): multisubunit machinery assisting in protein folding and assembly in the eukaryotic cytosol. *Eur. J. Biochem.* **230**, 3–16.

18 Kubota, H., Hynes, G. & Willison, K. R. (1995). The eighth *Cct* gene, *Cctq*, encoding the theta subunit of the cytosolic chaperonin that contains TCP-1. *Gene.* **154**, 231–236.

19 Kubota, H., Hynes, G., Kerr, S. M. & Willison, K. R. (1997). Tissue-specific subunit of the mouse cytosolic chaperonin–containing TCP-1. *FEBS Lett.* **402**, 53–56.

20 Kubota, H. & Willison, K. R. (1997). Introduction and 8 sections on CCT in Guidebook to molecular chaperones (M. J. Gething, Ed.) Sambrook/Tooze publications at Oxford University Press, Oxford.

21 Stoldt, V., Rademacher, F., Kehren, V., Ernst, J. F., Pearce, D. A. & Sherman, F. (1996). The Cct eukaryotic chaperonin subunits of *Saccharomyces cerevisiae* and other yeasts. *Yeast* **12**, 523–529.

22 Braig, K., Otwinowski, Z., Hegde, R., Boisvert, D. C., Joachimiak, A., Horwich, A. L. & Sigler, P. B. (1994). The crystal structure of the bacterial chaperonin GroEL at 2.8 Å. *Nature* **371**, 578–586.

23 Xu, Z., Horwich, A. L. & Sigler, P. B. (1997). The crystal structure of the asymmetric GroEL-GroES-$(ADP)_7$ chaperonin complex. *Nature* **388**, 741–750.

24 Ditzel, L., Löwe, J., Stock, D., Stetter, K. O., Huber, H., Huber, R. & Steinbacher, S. (1998). Crystal structure of the thermosome, the archaeal chaperonin and homologue of CCT. *Cell.* **93**, 125–138.

25 Klumpp, M., Baumeister, W. & Essen, L. O. (1997). Structure of the substrate binding domain of the thermosome, an archaeal group II chaperonin. *Cell* **91**, 263–70.

26 Pappenberger, G., Wilsher, J. A., Roe, S. M., Counsell, D. J., Willison, K. R., & Pearl, L. H. (2002). Crystal structure of the CCTγ apical domain: implications for substrate binding to the eukaryotic cytosolic chaperonin. *J. Mol. Biol.* **318**, 1367–1379.

27 Gutsche, I., Essen, L. O. & Baumeister, W. (1999). Group II chaperonins: new TRIC(k)s and turns of a protein folding machine. *J. Mol. Biol.* **293**, 295–312.

28 Willison, K. R. & Grantham, J. (2001). In *Molecular Chaperones: Frontiers in Molecular Biology* (P. Lund, Ed.) Oxford University Press, 90–118.

29 Kafri, G., Willison, K. R. & Horovitz, A. (2001). Nested allosteric interactions in the cytoplasmic chaperonin containing TCP-1 from bovine testis. *Protein Sci.* **10**, 445–449.

30 Hynes, G., Kubota, H. & Willison, K. R. (1995). Antibody characterization of two distinct conformations of the chaperonin containing TCP-1 from mouse testis. *FEBS lett.* **358**, 129–132.

31 Hynes, G., Celis, J. E., Lewis, V. A., Carne, A., U, S., Lauridsen, J. B. & Willison, K. R. (1996). Analysis of chaperonin-containing TCP-1 subunits in the human keratinocyte two-dimensional protein database: Further characterization of antibodies to individual subunits. *Electrophoresis.* **17**, 1720–1727.

32 Liou, A. K. & Willison, K. R. (1997). Elucidation of the subunit orientation in CCT (chaperonin containing TCP1) from the subunit composition of CCT micro-complexes. *EMBO J* **16**, 4311–4316.

33 Llorca, O., McCormack, E. A., Hynes, G., Grantham, J., Cordell, J., Carrascosa, J. L., Willison, K. R., Fernández, J. J. & Valpuesta, J. M. (1999). Eukaryotic type II chaperonin CCT interacts with actin through specific subunits. *Nature* **402**, 693–696.

34 Llorca, O., Martin-Benito, J., Ritco-Vonsovici, M., Grantham, J., Hynes, G. M., Willison, K. R., Carrascosa, J. L. & Valpuesta, J. M. (2000). Eukaryotic chaperonin CCT stabilizes actin and tubulin folding intermediates in open quasi-native conformations. *EMBO J.* **19**, 5971–5979.

35 Grantham, J., Llorca, O., Valpuesta, J. M. & Willison, K. R. (2000). Partial occlusion of both cavities of CCT with antibody has no effect upon the rates of β-actin or α-tubulin folding. *J. Biol. Chem.* **275**, 4587–4591.

36 Liou, A. K., McCormack, E. A. & Willison, K. R. (1998). The chaperonin containing TCP-1 (CCT) displays a single-ring mediated disassembly and reassembly cycle. *Biol Chem.* **379**, 311–319.

37 Roobol, A., Grantham, J., Whitaker, H. C. & Carden, M. J. (1999). Dissasembly of the cytosolic chaperonin in mammalian cell extracts at intracellular levels of K^+ and ATP. *J. Biol. Chem.* **274**, 19220–19227.

38 Hynes, G., Sutton, C. W. & Willison, K. R. (1996). Peptide mass fingerprinting of chaperonin-containing TCP-1 (CCT) and copurifying proteins. *FASEB J.* **10**, 137–147.

39 Ursic, D. & Culbertson, M. R. (1992). Is yeast TCP1 a chaperonin? *Nature.* **356**, 392.

40 Soares, H., Penaues, D., Mouta, C. & Rodrigues-Pousada, C. (1994). A tetrahymena orthologue of the mouse chaperonin subunit CCT gamma and its coexpression with tubulin during cilia recovery. *J. Biol. Chem.* **269**, 29299–29307.

41 Somer, L., Shmulman, O., Dror, T., Hashmueli, S. & Kashi, Y. (2002). The eukaryote chaperonin CCT is a cold shock protein in Saccharomyces cerevisiae. *Cell Stress & Chaperones* **7**, 47–54.

42 Yokota, S., Yanagi, H., Yura, T. & Kubota, H. (2000). Upregulation of cytosolic chaperonin CCT subunits during recovery from chemical stress that causes accumulation of unfolded proteins. *Eur. J. Biochem.* **267**, 1658–1664.

43 Yokota, S., Yanagi, H., Yura, T. & Kubota, H. (1999) Cytosolic chaperonin is upregulated during cell growth: preferential expressionand binding to tubulin at G1/S transition through early S phase. *J. Biol. Chem.* **270**, 37070–37078.

44 Kubota, H., Matsumoto, S., Yokata, S., Yanagi, H. & Yura, T. (1999). Transcriptional activation of mouse cytosolic chaperonin CCT subunit genes by heat shock factors HSF1 and HSF2. *FEBS Lett.* **461**, 125–129.

45 Yamazaki, Y., Kubota, H., Nozaki, M. & Nagata, K. (2003). Transcrip-

tional regulation of the cytosolic chaperonin theta subunit gene, Cctq, by Ets domain transcription factors Elk Sap-1a, and Net in the absence of serum response factor. *J. Biol. Chem.* **278**, 30642–30651.

46 Llorca, O., Smyth, M. G., Carrascosa, J. L., Willison, K. R., Radermacher, M., Steinbacher, S., Valpuesta, J. M. (1999). 3D reconstruction of the ATP-bound form of CCT reveals the asymmetric folding conformation of a type II chaperonin. *Nat. Struct. Biol.* **6**, 639–642.

47 Nitsch, M., Walz, J., Typke, D., Klumpp, M., Essen, L. O. & Baumeister, W. (1998). Group II chaperonin in an open conformation examined by electron tomography. *Nat. Struct. Biol.* **5**, 855–857.

48 Schoehn, G., Quaite-Randall, E., Jimenez, J. L., Joachimiak, A. & Saibil, H. R. (2000). Three conformations of an archaeal chaperonin, TF55 from *Sulfolobus shibatae*. *J. Mol. Biol.* **296**, 813–819.

49 Schoehn, G., Hayes, M., Cliff, M., Clarke, A. R. & Saibil, H. R. (2000). Domain rotations between open, closed and bullet-shaped forms of the Thermosome, an archael chaperonin. *J. Mol. Biol.* **301**, 323–332.

50 Llorca, O., Smyth, M. G., Marco, S., Carrascosa, J. L., Willison, K. R. & Valpuesta, J. M. (1998). ATP binding induces large conformational changes in the apical and equatorial domains of the eukaryotic cytoplasmic chaperonin (CCT). *J. Biol. Chem.* **273**, 10091–10094.

51 Szpikowska, B. K., Swiderek, K. M., Sherman, M. A. & Mas, M. T. (1998). MgATP binding to the nucleotide-binding domains of the eukaryotic cytoplasmic chaperonin induces conformational changes in the putative substrate-binding domains. *Prot. Sci.* **7**, 1524–1530.

52 Gutsche, I., Holzinger, J., Rauh, N., Baumeister, W. & May, R. P. (2001). ATP-induced structural change of the thermosome is temperature-dependent. *J. Struct. Biol.* **135**, 139–146.

53 Horovitz, A., Fridmann, Y., Kafri, G. & Yifrach, O. (2001). Allostery in chaperonins. *J. Struct. Biol.* **135**, 104–114.

54 Meyer, A. S., Gillespie, J. R., Walther, D., Millet, I. S., Doniach, S. & Frydman, J. (2003) Closing the folding chamber of the eukaryotic chaperonin requires the transition state of ATP hydrolysis. *Cell* **113**, 369–381.

55 Kafri, G. & Horovitz, A. (2003). Transient kinetic analysis of ATP-induced allosteric transitions in the eukaryotic chaperonin containing TCP-1. *J. Mol. Biol.* **326**, 981–988.

56 Iizuka, R., Yoshida, T., Shomura, Y., Miki, K., Maruyama, T., Odaka, M. & Yohda, M. (2003) ATP binding is critical for the conformational change from an open to closed state in archaeal group II chaperonin. *J. Biol. Chem.* **278**, 44959–44965.

57 Shomura, Y., Yoshida, T., Iizuka, R., Maruyama, M., Yohda, M. & Miki, K. (2004) Crystal structures of the group II chaperonin from *Thermococcus* strain KS-1: steric hindrance by the substituted amino acid, and inter-subunit rearrangement between two crystal forms. *J. Mol. Biol.* **335**, 1265–1278.

58 Lin, P. & Sherman, F. (1997). The unique hetero-oligomeric nature of the subunits in the catalytic cooperativity of the yeast Cct chaperonin complex. *Proc. Natl. Acad. Sci. USA* **94**, 10780–10785.

59 Gómez-Puertas, P., Martín-Benito, J., Carrascosa, J. L., Willison, K. R. & Valpuesta, J. M. (2004). The substrate recognition mechanisms in chaperonins. *J. Mol. Recog.* **17**, 85–94.

60 Fenton, W. A., Kashi, Y., Furtak, K. & Horwich, A. L. (1994). Residues in chaperonin GroEL required for polypeptide binding and release. *Nature.* **371**, 614–619.

61 Buckle, A. M., Zahn, R., Fersht, A. R. (1997). A structural model for GroEL-polypeptide recognition. *Proc. Natl. Acad. Sci. USA.* **94**, 3571–3575.

62 Chen, L. & Sigler, P. B. (1999). The crystal structure of a GroEL/peptide

complex: plasticity as a basis for substrate recognition. *Cell*. **99**, 757–768.

63 Farr, G. W., Furtak, K., Rowland, M. B., Ranson, N. A., Saibil, H. R., Kirchhausen, T. & Horwich, A. L. (2000). Multivalent binding of nonnative substrate proteins by the chaperonin GroEL. *Cell*. **100**, 561–573.

64 Tian, G., Vainberg, I. E., Tap, W. D., Lewis, S. A. & Cowan, N. J. (1995). Quasi-native chaperonin-bound intermediates in facilitated protein folding. *J. Biol. Chem.* **270**, 23910–23913.

65 Llorca, O., Martin-Benito, J., Gomez-Puertas, P., Ritco-Vonsovici, M., Willison, K. R., Carrascosa, J. L. & Valpuesta, J. M. (2001). Analysis of the interaction between the eukaryotic chaperonin CCT and its substrates actin and tubulin. *J Struct Biol*. **135**, 205–218.

66 Rommelaere, H., De Neve, M., Melki, R., Vandekerckhove, J. & Ampe, C. (1999). The cytosolic class II chaperonin CCT recognizes delineated hydrophobic sequences in its target proteins, *Biochemistry* **38**, 3246–3257.

67 Hynes, G. M. & Willison, K. R. (2000). Individual subunits of the chaperonin containing TCP-1 (CCT) mediate interactions with binding sites located on subdomains of β-actin, *J. Biol. Chem.* **275**, 18985–18994.

68 McCormack, E., Rohman, M. & Willison, K. R. (2001). Mutational screen identifies critical amino acid residues of β-actin mediating interaction between folding intermediates and cytosolic chaperonin TCP-1. *J. Struct. Biol*. **135**, 185–197.

69 Dobrzynski, J. K., Sternlicht, M. L., Farr, G. W. & Sternlicht, H. (1996). Newly-synthesized β-tubulin demonstrates domain-specific interactions with the cytosolic chaperonin. *Biochemistry*. **35**, 15870–15882.

70 Dobrzynski, J. K., Sternlicht, M. L., Peng, I., Farr, G. W. & Sternlicht, H. (2000). Evidence that β-tubulin induces a conformation change in the cytosolic chaperonin which stabilizes binding: implications for the mechanism of action. *Biochemistry*. **39**, 3988–4003.

71 Ritco-Vonsovici, M. & Willison, K. R. (2000). Defining the eukaryotic chaperonin-binding sites in human tubulins. *J. Mol. Biol*. **304**, 81–98.

72 Ellis, R. J. (1994). Opening and closing the Anfinsen cage. *Curr. Biol*. **4**, 633–635.

73 Weissmann, J. S., Rye, H. S., Fenton, W. A., Beechem, J. M. & Horwich, A. L. (1996). Characterization of the active intermediate of a GroEL-GroES mediated protein folding reaction, *Cell* **84**, 481–490.

74 Llorca, O., Martin-Benito, J., Grantham, J., Ritco-Vonsovici, M., Willison, K. R., Carrascosa, J. L. & Valpuesta, J. M. (2001). The 'sequential allosteric ring' mechanism in the eukaryotic chaperonin-assisted folding of actin and tubulin. *EMBO J*. **20**, 4065–4075.

75 McCallum, C. D., Do, H., Johnson, A. E. & Frydman, J. (2000). The interaction of the chaperonin tailless complex polypeptide 1 (TCP1) ring complex (TRiC) with ribosome-bound nascent chains examined using photo-cross-linking. *J. Cell Biol*. **149**, 591–601.

76 Farr, G. W., Scharl, E. C., Schumacher, R. J., Sondek, S., & Horwich, A. L. (1997). Chaperonin-mediated folding in the eukaryotic cytosol proceeds through rounds of release of native and nonnative forms. *Cell*. **89**, 927–937.

77 McCormack, E., Llorca, O., Carrascosa, J. L., Valpuesta, J. M. & Willison, K. R. (2001). Point mutations in a hinge linking the small and large domains of β-actin result in trapped folding intermediates bound to cytosolic chaperonin containing TCP-1. *J. Struct. Biol*. **135**, 198–204.

78 Siegers, K., Waldmann, T., Leroux, M. R., Grein, K., Shevchenko, A., Schiebel, E. & Hartl, F. U. (1999). Compartmentation of protein folding in vivo: sequestration of non-native polypeptide by the chaperonin-GimC system. *EMBO J*. **18**, 75–84.

79 Tian, G., Vainberg, I. E., Tap, W. D.,

Lewis, S. A., & Cowan, N. J. (1995). Specificity in chaperonin-mediated protein folding. *Nature* **375**, 250–253.

80 Willison, K. R. (1999). Composition and function of the eukaryotic cytosolic chaperonin-containing TCP1 in *Molecular Chaperones and Folding Catalysts* (Ed. Bernd Bukau) (Harwood Academic Publishers, Amsterdam), pp. 555–571.

81 Schüler, H., Lindberg, U., Schutt, C. E. & Karlsson, R. (2000). Thermal unfolding of G-actin monitored with the Dnase I-inhibition assay. *Eur. J. Biochem.*, **267**, 476–486.

82 Kabsch, W., Mannherz, H. G., Suck, D., Pai, E. F. & Holmes, K. C. (1990). Atomic structure of the actin: DNase I complex. *Nature*, **347**, 37–44.

83 Nogales, E., Wolf, S. G. & Downing, K. H. (1998). Structure of the $\alpha\beta$tubulin dimer by electron crystallography. *Nature*, **391**, 199–203.

84 Valpuesta, J. M., Martín-Benito, J., Gómez-Puertas, P., Carrascosa, J. L. & Willison, K. R. (2002). Structure and function of a protein folding machine: the eukaryotic cytosolic chaperonin CCT. *FEBS letters* **529**, 11–16.

85 Thulasariman, V., Yang, C. F. & Frydman, J. (1999). In vivo newly translated polypeptides are sequestered in a protective folding environment. *EMBO J.* **18**, 85–95.

86 Chen, X., Sullivan, D. S. & Huffaker, T. C. (1994). Two yeast genes with similarities to TCP-1 are required for microtubule and actin function in vivo. *Proc. Natl. Acad. Sci. USA* **91**, 9111–9115.

87 Vinh, D. B. & Drubin, D. G. (1994). A yeast TCP-1-like protein is required for actin function in vivo. *Proc. Natl. Acad. Sci. USA.* **91**, 9116–9120.

88 Miklos, D., Caplan, S., Martens, D., Hynes, G., Pitluk, Z., Barrell, B., Horwich, A. L. & Willison, K. R. (1994). Primary structure and function of a second essential member of heterooligomeric TCP1 chaperonin complex of yeast. *Proc. Natl. Acad. Sci. USA* **91**, 2743–2747.

89 Melki, R., Vainberg, I. E., Chow, R. L. & Cowan, N. J. (1993). Chaperonin-mediated folding of vertebrate actin-related protein and gamma-tubulin. *J. Cell Biol.* **122**, 1301–1310.

90 Srikakulam, R. & Winkelmann, D. A. (1999). Myosin II folding is mediated by a molecular chaperone. *J. Biol. Chem.* **274**, 27265–27273.

91 Melki, R., Batelier, G., Soulie, S. & Williams, R. C. Jr. (1997). Cytoplasmic chaperonin containing TCP-1: Structural and functional characterization. *Biochemistry* **36**, 5817–5826.

92 Lingappa, J. R., Martin, R. L., Wong, M. L., Ganem, D., Welch, W. J. & Lingappa, V. R. (1994). A eukaryotic cytosolic chaperonin is associated with a high molecular weight intermediate in the assembly of hepatitis B virus capsid, a multimeric particle. *J. Cell. Biol.* **125**, 99–111.

93 Hong, S., Choi, G., Park, S., Chung, A. S., Hunter, E. & Rhee, S. S. (2001). Type D retrovirus Gag polyprotein interacts with the cytosolic TriC. *J. Virol.* **75**, 2526–2534.

94 Kashuba, E., Pokrovskaja, K., Klein, G. & Szekely, L. (1999). Epstein-Barr virus-encoded nuclear protein EBNA-3 interacts with the ε-subunit of the T-complex protein 1 chaperonin complex. *J. Human. Virol.* **2**, 33–37.

95 Frydman, J., Nimmesgem, E., Ohtsuka, K. & Hartl, F. U. (1994). Folding of nascent polypeptide chains in a high molecular mass assembly with molecular chaperones. *Nature.* **370**, 111–117.

96 Won, K. A., Schumaker, R. J., Farr, G. W., Horwich, A. L. & Reed, S. I. (1998). Maturation of human cyclin E requires the function of eukaryotic chaperonin CCT. *Mol. Cell. Biol.* **18**, 7584–7589.

97 Pijnappel, W. W. M. P., Schaft, D., Rogue, V. A., Shevchenko, A., Tekotte, H., Wilm, M., Rigaut, G., Séraphin, B., Aasland, R. & Stewart, A. F. (2001). The *S. cerevisiae* SET3 complex includes two histone deacetylases, Hos2 and Hst1, and is a meiotic-specific repressor of the sporulation gene program. *Genes & Dev.* **15**, 2991–3004.

98 Guenther, M. G., Yu, J., Kao, G. D., Yen, T. J. & Lazar, M. A. (2002). Assembly of the SMRT-histone deacetylase 3 repression complex requires the TCP-1 ring complex. *Genes & Dev.* **16**, 3130–3135.

99 Kaelin, W. G. (1999). Cancer: many vessels, faulty genes. *Nature* **399**, 203–204.

100 Stebbins, C. E., Kaelin, W. G. & Pavletich, N. P. (1999). Structure of the VHL-elongingC-elonginB complex: implications for VHL tumor suppressor function. *Science* **284**, 455–461.

101 Feldman, D. E., Thulasariman, V., Ferreyra, R. G. & Frydman, J. (1999). Formation of the VHL-elongin BC tumor suppressor complex is mediated by the chaperonin TriC. *Mol. Cell.* **4**, 1051–1061.

102 Cowan, N. J. & Lewis, S. A. (2002) Type II chaperonins, prefoldin and the tubulin-specific chaperones. *Advances in Prot. Chem.* **59**, 73–104.

103 Smith, T. F., Gaitaztes, C., Saxena, K. & Neer, E. J. (1999). The WD40 repeat: a common architecture for diverse functions. *TIBS* **24**, 181–185.

104 Ho, Y. et al. (2002). Systematic identification of protein complexes in *Saccharomyces cerevisiae* by mass spectrometry. *Nature* **415**, 180–183.

105 Camasses, A., Bodganova, A., Shevchenko, A. & Zachariae, W. (2003). The CCT chaperonin promotes activation of the anaphase-promoting complex through the generation of functional Cdc20. *Mol. Cell.* **12**, 87–100.

106 Passmore, L. A., McCormack, E. A., Au, S. W. N., Paul, A., Willison, K. R., Harper, J. W. & Barford, D. (2003). Doc1 mediates the activity of the anaphase-promoting complex by contributing to substrate recognition. *EMBO J.* **22**, 786–796.

107 Siegers, K., Bölter, B., Schwarz, J. P., Böttcher, U. M. K., Guha, S. & Hartl, F. U. (2003). TRiC/CCT cooperates with different upstream chaperones in the folding of distinct protein classes. *EMBO J.* **22**, 5230–5240.

108 Gaudet, R., Bohm, A. & Sigler, P. B. (1996). Crystal Structure at 2.4 Å Resolution of the Complex of Transducin $\beta\gamma$ and Its Regulator, Phosducin. *Cell* **87**, 577–588.

109 McLaughlin, J. N., Thulin, C. D., Hart, S. D., Resing, K. A., Ahn, N. G. & Willardson, B. M. (2002). Regulatory interaction of phosducin-like protein with the cytosolic chaperonin complex. *Proc. Natl. Acad. Sci. USA* **99**, 7962–7967.

110 Kunisawa, J. & Shastri, N. (2003). The group II chaperonin TriC protects proteolytic intermediates from degradation in the MHC class I antigen processing pathway. *Mol. Cell* **12**, 565–576.

111 Mogk, A., Bukau, B. & Deuerling, E. (2001). Cellular functions of cytosolic *E. coli* chaperones. In *Molecular Chaperones in the cell* (Ed. Peter Lund) (Oxford University Press, Oxford), pp. 3–34.

112 Geissler, S., Siegers, K. & Schiebel, E. (1998). A novel protein complex promoting formation of functional alpha- and gamma-tubulin. *EMBO J.* **17**, 952–966.

113 Vainberg, I. E., Lewis, S. A., Rommelaere, H., Ampe, C., Vandekerckhove, J., Klein, H. L. & Cowan, N. J. (1998). Prefoldin, a chaperone that delivers unfolded proteins to cytosolic chaperonin. *Cell* **93**, 863–873.

114 Martín-Benito, J., Boskovic, J., Gómez-Puertas, P., Carrascosa, J. L., Simons, C., Lewis, S. A., Bartolini, F., Cowan, N. C. & Valpuesta, J. M. (2002). Structure of eukaryotic prefoldin and of its complexes with unfolded actin and the cytosolic chaperonin CCT. *EMBO J.* **21**, 6377–6386.

115 Gebauer, M., Melki, R. & Gehring, U. (1998). The chaperone cofactor Hop/p60 interacts with the cytosolic chaperonin-containing TCP-1 and affects its nucleotide exchange and protein folding activities. *J. Biol. Chem.* **273**, 29475–29480.

116 Melville, M. W., McClellan, A. J., Meyer, A. S., Darveau, A. & Frydman, J. (2003). The Hsp70 and TriC/CCT

chaperone systems cooperate in vivo to assemble the von Hippel-Lindau tumor suppressor complex. *Mol. Cell. Biol.* **23**, 3141–3151.

117 Song, J. & Morimoto, R. I. (2001) Hsp70 chaperones networks: the role of regulatory co-chaperones in coordinating stress responses with cell growth and death. In *Molecular Chaperones in the cell* (Ed. Peter Lund) (Oxford University Press, Oxford), pp. 142–163.

118 Chen, S., Prapapanich, V., Rimerman, R. A., Honoré, B. & Smith, D. F. (1996). Interactions of p60, a mediator of progesterone receptor assembly, with heat-shock proteins hsp90 and hsp70. *Mol. Endocrinol.* **10**, 682–693.

119 Johnson, B. D., Schumacher, R. J., Ross, E. D. & Toft, D. O. (1998). Hop modulates Hsp70/Hsp90 interactions in protein folding. *J. Biol. Chem.* **273**, 3679–3686.

120 Dittmar, K. D. & Pratt, W. B. (1997). Folding of the glucocorticoid receptor by the reconstituted Hsp90-based chaperone machinery. The initial Hsp90.p60. hsp70-dependent step is sufficient for creating the steroid binding conformation. *J. Biol. Chem.* **272**, 13047–13054.

121 Tian, G., Huang, Y., Rommelaere, H., Vandekerckhove, J., Ampe, C. & Cowan, N. J. (1996). Pathway leading to correctly-folded β-tubulin. *Cell* **86**, 287–296.

122 Tian, G., Lewis, S. A., Feierbach, B., Stearns, T., Rommelaere, H., Vandekerckhove, J., Ampe, C. & Cowan, N. J. (1997). Tubulin subunits exists in an activated conformational state generated and maintained by protein cofactors. *J. Cell. Biol.* **138**, 821–832.

123 López-Fanarraga, M., Avila, J., Guasch, A., Coll, M. & Zabala, J. C. (2001) Postchaperonin tubulin folding cofactors and their role in microtubule dynamics. *J. Struct. Biol.* **135**, 219–229.

124 Steinbacher, S. (1999). Crystal structure of the postchaperonin β-tubulin binding cofactor Rbl2p. *Nature Struct. Biol.* **6**, 1029–1032.

125 Guasch, A., Aloria, K., Pérez, R., Avila, J., Zabala, J. C. & Coll, M. (2002). Three dimensional structure of human tubulin chaperone cofactor A. *J. Mol. Biol.* **318**, 1139–1149.

126 Gao, Y., Melki, R., Walden, P. D., Lewis, S. A., Ampe, C., Rommelaere., Vandekerckhove, J. & Cowan, N. J. (1994). A novel co-chaperonin that modulates the ATPase activity of cytosplasmic chaperonin. *J. Cell. Biol.* **125**, 989–996.

127 Melki, R., Rommelaere, H., Leguy, R., Vandekerckhove, J. & Ampe, C. (1996). Cofactor A is a molecular chaperone required for β-tubulin folding: functional and structural characterization. *Biochem.* **32**, 10422–10435.

128 Archibald, J. M., Logsdon, J. M. Jr. & Ford Doolittle, W. (2000). Origin and evolution of eukarotic chaperonins: phylogenetic evidence for ancient duplications in CCT genes. *Mol. Biol. Evol.* **17**, 1456–1466.

129 Archibald, J. M. & Roger, A. J. (2002). Gene duplication and gene conversion shape the evolution of archaeal chaperonins. *J. Mol. Biol.* **316**, 1041–1050.

130 Archibald, J. M., Logsdon, J. M. Jr. & Ford Doolittle, W. (1999). Recurrent paralogy in the evolution of archaeal chaperonin. *Curr. Biol.* **9**, 1053–1056.

131 Archibald, J. M., Blouin, C. & Ford Doolittle, W. (2001). Gene duplication and the evolution of group II chaperonins: implications for structure and function. *J. Struct. Biol.* **135**, 157–169.

132 Fares, M. A. & Wolfe, K. H. (2003) Positive selection and subfunctionalization of duplicated CCT chaperonin subunits. *Mol. Biol. Evol.* **20**, 1588–1597.

133 Willison, K. R. and Horwich, A. L. (1996) Structure and function of chaperonins. In *The Chaperonins* (Ed. R. J. Ellis) 107–135 (Academic Press).

134 Leroux, M. R. & Hartl, F. U. (2000). Versatility of the cytosolic chaperonin TriC/CCT. *Curr. Biol.* **10**, R260–R264.

135 Rommelaere, H., De Neve, M.,

Neirynck, K., Peelaers, D., Waterschoot, D., Goethals, M., Fraeyman, N., Vandekerckhove, J. & Ampe, C. (2001). Prefoldin recognition motifs in the nonhomologous proteins of the actin and tubulin families. *J Biol Chem.* **276**, 41023–41028.

136 Norcum, M. T. (1996). Novel isolation method and structural stability of a eukaryotic chaperonin: the TCP-1 ring complex from rabbit reticulocyte. *Protein Sci*, **5**, 1366–1375.

137 Melki, R. & Cowan, N. J. (1994). Facilitated folding of actins and tubulins occurs via a nucleotide-dependent interaction between cytoplasmic chaperonin and distinctive folding intermediates. *Mol. Cell. Biol.* **14**, 2895–2904.

138 Rohman, M. (1999). Biochemical characterization of chaperonin containing TCP-1 (CCT) PhD Thesis, University of London, England.

139 Cowan, N. J. (1998) Mammalian cytosolic chaperonin. *Methods Enzymol.* **290**, 230–241.

140 Horovitz, A., Bochkareva, E. S., Kovalenko, O., and Girshovich, A. S. (1993). Mutation Ala2 → Ser destabilizes intersubunit interactions in the molecular chaperone GroEL. *J. Mol. Biol.* **231**, 58–64.

141 Frank, J. (1996). Three-dimensional Reconstruction. *Three-dimensional Electron Microscopy of Macromolecular Assemblies.* Academic Press, San Diego, pp. 182–246.

142 Penczek, P., Radermacher, M. & Frank, J. (1992). Three-dimensional reconstruction of single particles embedded in ice. *Ultramicroscopy* **40**, 33–53.

143 Marco, S., Chagoyen, M., de la Fraga, L. G., Carazo, J. M. & Carrascosa, J. L. (1996). A variant of the "random approximation" of the reference-free alignment algorithm. *Ultramicroscopy* **66**, 5–10.

144 van Heel, M. & Frank, J. (1981). Use of multivariate statistics in analysing the images of biological macromolecules. *Ultramicroscopy* **6**, 187–194.

145 Marabini, R. & Carazo, J. M. (1994). Pattern recognition and classification of images of biological macromolecules using artificial neural networks. *Biophys. J.* **66**, 1804–1814.

146 Unser, M., Trus, B. L. & Steven, A. C. (1987). A new resolution criterion based on spectral signal-to-noise ratios. *Ultramicroscopy* **23**, 39–51.

147 Radermacher, M. (1988). Three-dimensional reconstruction of single particles from random and non-random tilt series. *J. Electron Microsc. Tech.* **9**, 359–394.

148 De Rosier, D. & Klug, A. (1968). Reconstruction of three-dimensional structures from electron micrographs. *Nature.* **217**, 130–134.

149 Frank, J., Radermacher, M., Penczek, P., Zhu, J., Li, Y., Ladjadj, M. & Leith, A. (1996). SPIDER and WEB: processing and visualization of images in 3D electron microscopy and related fields. *J. Struct. Biol.* **116**, 190–199.

150 van Heel, M., Gowen, B., Matadeen, R., Orlova, E. V., Finn, R., Pape, T., Cohen, D., Stark, H., Schmidt, R., Schatz, M. & Patwardhan, A. (2000). Single-particle electron cryo-microscopy: towards atomic resolution. *Quart. Rev. Biophys.* **33**, 307–369.

151 Marabini, R., Herman, G. T. & Carazo, J. M. (1998). 3D reconstruction in electron microscopy using ART with smooth spherically symmetric volume elements (blobs). *Ultramicroscopy* **72**, 53–65.

152 Saxton, W. O. & Baumeister, W. (1982). The correlation averaging of a regularly arranged bacterial cell envelope protein. *J. Microsc.* **127**, 127–138.

153 Heymann, J. B. (2001). Bsoft: image and molecular processing in electron microscopy. *J. Struct. Biol.* **133**, 156–169.

154 Siegert, R., Leroux, M. R., Scheufler, C., Hartl, F. U. & Moarefi, I. (2000). Structure of the molecular chaperone prefoldin: unique interaction of multiple coiled coil tentacles with unfolded proteins. *Cell* **103**, 621–632.

22
Structure and Function of GimC/Prefoldin

Katja Siegers, Andreas Bracher, and F. Ulrich Hartl

22.1
Introduction

The hetero-oligomeric protein complex GimC/prefoldin, present in eukarya and archaea, is a critical co-factor of TRiC/CCT-assisted folding of actin and tubulins [1, 2]. The identification of homologues in mammals, plants, nematodes, and archaea and complementation studies in yeast revealed that GimC/prefoldin is a highly conserved component of the protein-folding machinery. While GimC/prefoldin in archaea is formed by only two types of distinct subunits, it is comprised of six distinct subunits in both yeast and mammalian cells. Unlike the GroES-like co-chaperones of group I chaperonins in bacteria, GimC/prefoldin plays a more active role in protein folding by interacting with unfolded proteins and stabilizing them against aggregation for subsequent folding by the eukaryotic chaperonin. GimC has been shown to assist in the transfer of nascent polypeptide chains to TRiC/CCT in vitro and in vivo and to prevent the premature release of nonnative chaperonin substrates into the cytosol [1, 3, 4]. GimC/prefoldin appears to have a special role in assisting TRiC in the folding of its major substrates, newly synthesized actin, and tubulins, and this function cannot be performed by other nascent chain-binding chaperones, such as Hsp70 [5]. A direct interaction of GimC/prefoldin with TRiC [1, 3, 6] may facilitate the delivery of actin and tubulins in a defined orientation relative to the subunit topology of the chaperonin ring [7]. It has been shown that eukaryotic and archaeal GimC/prefoldin has the general properties of a molecular chaperone, and, similar to the Hsp70 system, archaeal GimC/prefoldin complexes have been reported to prevent or retard the aggregation of a number of nonnative proteins and to stabilize them for subsequent folding [8, 9]. A combined deletion of genes encoding the nascent chain-binding chaperones GimC/prefoldin and Ssb-type Hsp70 in yeast results in a pronounced synthetic growth defect [5], resembling the drastic effect described for a combined trigger factor and DnaK deletion in the *E. coli* system [10, 11]. This points to the existence of a certain degree of functional redundancy among nascent chain-binding chaperones, in addition to the specialized function of eukaryotic GimC/prefoldin in TRiC/CCT-assisted folding of actin and tubulins. The simpler and more abundant archaeal version of

Protein Folding Handbook. Part II. Edited by J. Buchner and T. Kiefhaber

ISBN: 3-527-30784-2

GimC/prefoldin may have a more general function in stabilizing nascent polypeptides since archaea do not contain an extensive actin and tubulin cytoskeleton, and some archaea lack Hsp70 altogether [12].

22.2 Evolutionary Distribution of GimC/Prefoldin

Eukaryotic GimC/prefoldin complexes like bovine prefoldin and yeast GimC consist of six distinct protein subunits termed Pfd1–Pfd6 and Gim1–Gim6, respectively [1–3]. For each component, a closely related homologue has been found in the nematode *Caenorhabditis elegans*, suggesting that they are likely to be conserved in eukaryotes. Gim1 (Pfd6) and Gim5 (Pfd5) homologues have been identified in nearly all known archaeal genomes [1, 2].

A comprehensive phylogenetic analysis of Gim/prefoldin proteins from eukaryotes and archaea revealed that all sequences of Gim/prefoldin form two separate classes of proteins, represented by Gim2/5 (Pfd3/5) (denoted as the α class) and Gim1/3/4/6 (Pfd6/4/2/1) (β class). Unlike eukaryotes, however, archaeal genomes contain only one gene from each class. An exemplary sequence alignment of *Methanobacterium thermoautotrophicum* GimC/prefoldin subunits with one representative yeast homologue each is shown in Figure 22.1.

22.3 Structure of the Archaeal GimC/Prefoldin

In the crystal structure of the GimC/prefoldin from the archaeon *Methanobacterium thermoautotrophicum*, two α and four β subunits form a hexameric complex resembling the shape of a jellyfish (Figure 22.2) [13]. Its main body consists of two eight-stranded β barrels from which six long tentacle-like two-helical bundles protrude. As was correctly predicted [8], all subunits assume self-symmetric secondary structures with α-helical regions containing heptad repeats typical for coiled-coil structures at the chain termini and either two or four β-strands in the center. This arrangement folds into a hairpin-like structure with a 60–70 Å long two-helix bundle at its ends and either one or two β-hairpins at the tip, respectively. The core of the complex is composed of two α subunits, which contribute one β-hairpin to each β-barrel. The β-hairpins of two α chains complete each β-barrel.

The α-helical coiled coils forming the six long tentacles border a large central cavity (Figure 22.2). In the crystal structure, access to the cavity is not blocked by any structured elements. The individual coiled-coil rods expose mostly charged and polar side chains to the solvent, and there are virtually no interactions between the coiled coils from different subunits. In contrast to this, the distal regions of the coiled coils are partially unwound and therefore expose hydrophobic patches (Figure 22.2). These regions have been shown to be required for binding of nonnative proteins.

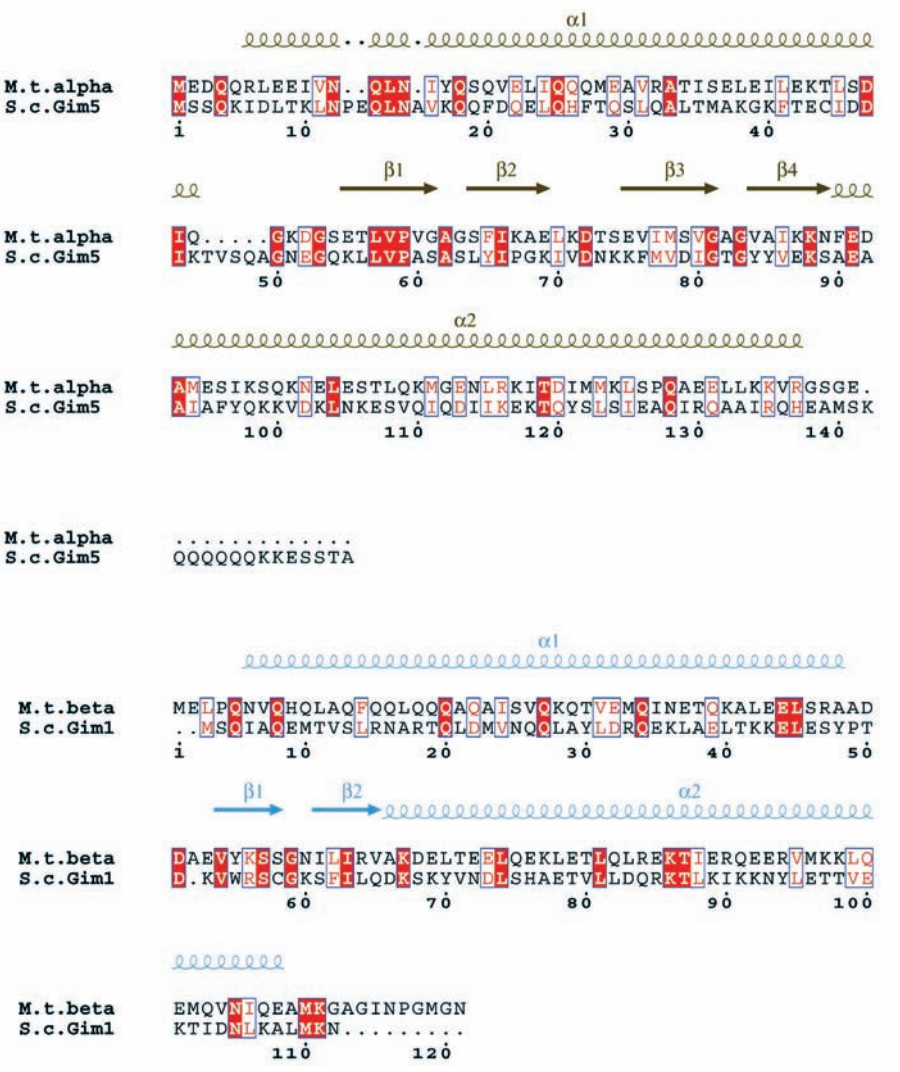

Fig. 22.1. Sequence alignment of GimC/prefoldin subunits from *M. thermoautotrophicum* and *S. cerevisiae*. *M. thermoautotrophicum* α and β subunits were aligned with yeast Gim5 and Gim1, respectively. Sequence conservation is indicated by red background for identical residues and blue boxes around homologous regions. The secondary structure elements of *M. thermoautotrophicum* GimC/prefoldin are shown on top of the alignment. Coils and arrows stand for α-helices and β-strands, respectively. The figure was created with ESPript [23].

The structure does not provide any evidence for the presence of a nucleotide-binding site, which is in accordance with the apparent lack of an ATP-regulated protein function for both archaeal and eukaryotic GimC/prefoldin [1, 8].

Electron microscopic studies indicated recently that eukaryotic GimC/prefoldin possesses an architecture similar to that of archaeal GimC, with six arms pro-

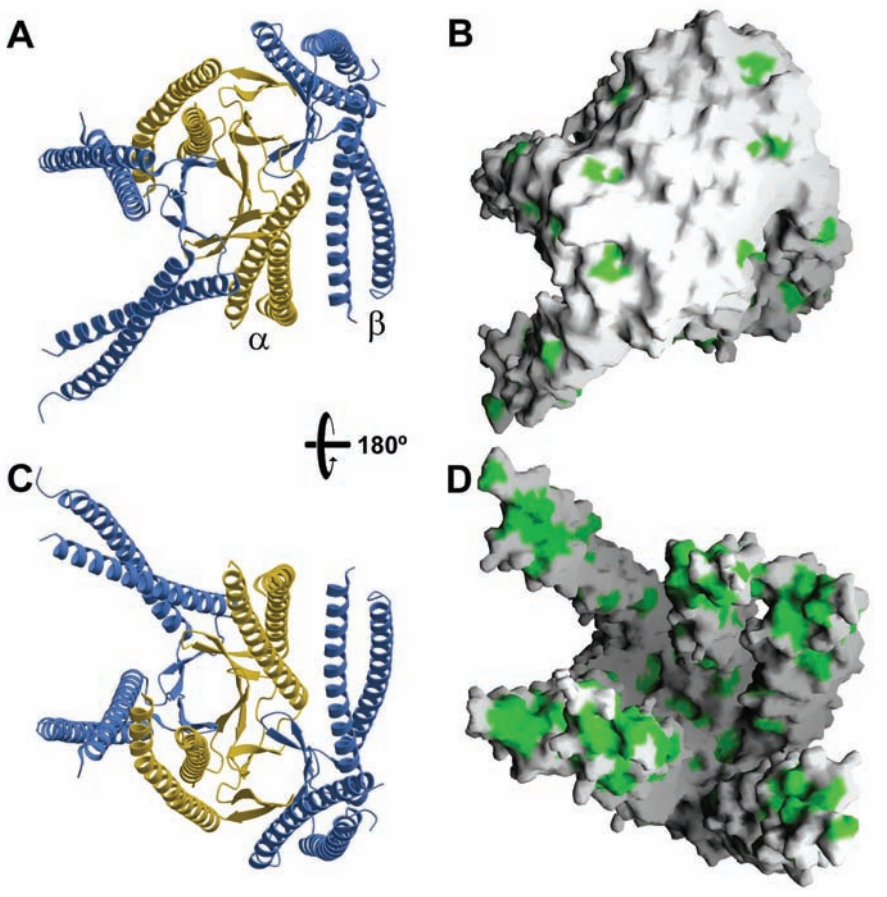

Fig. 22.2. Crystal structure of GimC/prefoldin from *M. thermoautotrophicum* [13]. In panels A and C, α and β subunits are depicted as yellow and blue ribbons, respectively. A molecular surface of GimC/prefoldin in the same orientation is shown on the right (panels B and D). Hydrophobic residues are highlighted in green. The bottom row shows the same representations of the GimC/prefoldin complex after 180° rotation. Ribbon diagrams were made using the programs Molscript and Raster-3D [24, 25]. The surface representations were generated with Grasp [26].

truding from the base of the oligomer [6]. Three-dimensional reconstruction of the same oligomer complexed with an unfolded actin molecule suggests that the prefoldin-bound target protein has a defined conformation that seems to interact with the tips of the chaperone's tentacles.

22.4 Complexity of the Eukaryotic/Archaeal GimC/Prefoldin

Biochemical and yeast complementation studies revealed that archaeal and eukaryotic GimC/prefoldin are likely to form a very similar hexameric arrangement [8].

The general architecture of archaeal and eukaryotic GimC/prefoldin is likely to be conserved, based on the finding that the archaeal α and β subunits are the founding members of the two classes of Gim subunits: the α class comprises subunits Gim2 (Pfd3) and Gim5 (Pfd5), and the β class comprises subunits Gim1 (Pfd6), Gim3 (Pfd4), Gim4 (Pfd2), and Gim6 (Pfd1) of GimC/prefoldin. Accordingly, the eukaryotic complex would consist of a heterodimer of Gim2 (Pfd3) and Gim5 (Pfd5), forming a core with which the Gim1 (Pfd6), Gim3 (Pfd4), Gim4 (Pfd2), and Gim6 (Pfd1) subunits associate.

That the archaeal and eukaryotic Gim/prefoldin complexes are structurally related is supported by the finding that both Gimα and Gimβ from *Methanobacterium thermoautotrophicum* can be co-immunoprecipitated with yeast Gim2 when expressed in strains lacking *GIM5* and *GIM1*, respectively, and that the archaeal Gimβ is able to partially complement defects in two yeast β class subunits, namely, Gim1 and Gim4 [8].

As reported [2], yeast Δ*gim1* and yeast Δ*gim5* strains are sensitive to the microtubule-depolymerizing drug benomyl. This phenotype in the Δ*gim1* yeast can be fully complemented by transforming the strain with plasmids expressing yeast or mouse *GIM1 (PFD6)*. Expression of archaeal *GIM*β (the *GIM1* homologue) in this strain was also shown to partially rescue the benomyl sensitivity of the yeast mutant (Figure 22.3) [8]. This effect is specific, as no visible changes in growth behavior can be observed upon expression of archaeal *GIM*α (the *GIM5* homologue) in the Δ*gim1* strain, and co-expression of both archaeal genes in the same strain is no more effective than expression of *GIM*β alone. Remarkably, archaeal *GIM*β was also found to be able to partially complement a yeast strain deleted for *GIM4*, encoding another member of the β class of GimC subunits, despite the low overall sequence homology between the two proteins.

Co-immunoprecipitation experiments with antibodies against yeast Gim2, an α

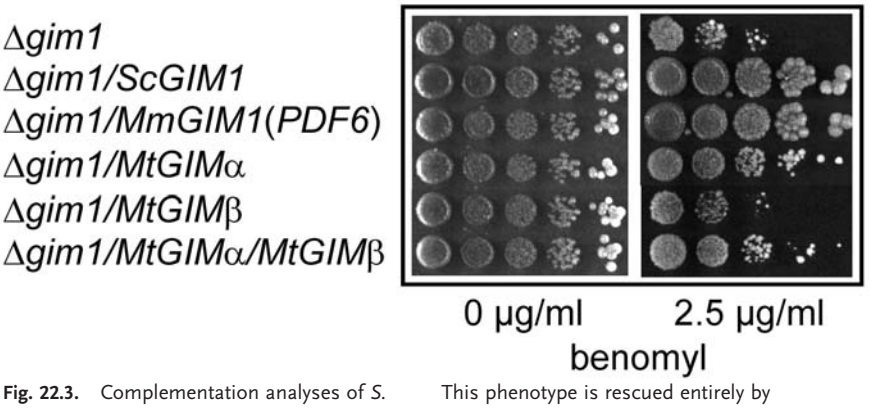

Fig. 22.3. Complementation analyses of *S. cerevisiae* Δ*gim1* [8]. Δ*gim1* mutants are highly sensitive to a 2.5-µg mL^{-1} concentration of the microtubule depolymerizing drug benomyl. This phenotype is rescued entirely by expression of yeast (Sc) and murine (Mm) *GIM1* and is partially complemented by expression of archaeal *MtGIM*β.

class subunit, revealed that the positive effect of archaeal *GIMβ* expression in the yeast Δ*gim1* strain can be directly attributed to the incorporation of Gimβ into the Gim1-deficient yeast GimC complex. In contrast, expression of Gimα was found to have no detectable rescuing effect in the Δ*gim5* strain, even though the archaeal protein can be co-immunoprecipitated with yeast Gim2 in Gim5-deficient yeast cells.

Together, these data confirmed that the archaeal Gimα and Gimβ are structural homologues of the yeast Gim5 and Gim1/Gim4 proteins, respectively, and that the function of archaeal Gimβ is similar to that of the yeast subunits Gim1 and Gim4. The reason for the inability of archaeal Gimα to partially complement the Δ*gim5* strain may be due to the fact that although Gimα can associate with Gim2 (of the α class), other yeast subunits of the β class may not assemble properly onto the archaeal Gimα protein due to possible structural differences in the yeast and archaeal subunits. It was also observed that co-expressing both archaeal *GIM* genes has no effect on the benomyl sensitivity of a yeast strain entirely lacking endogenous GimC. Since the archaeal protein complex appears to be functional at the growth temperature of yeast, these data suggest that eukaryotic GimC/prefoldin may have evolved specialized functions that cannot be performed by its archaeal counterpart.

22.5
Functional Cooperation of GimC/Prefoldin With the Eukaryotic Chaperonin TRiC/CCT

GimC/prefoldin has been reported to interact with TRiC in vivo as well as in vitro [1, 3]. Three-dimensional reconstruction from electron microscopic images of that complex suggests a symmetric arrangement with one GimC/prefoldin hexamer covering the axial pore of each ring in the chaperonin complex [6]. Consistent with the participation of GimC/prefoldin and TRiC in shared protein-folding pathways, deletion of *GIM* genes in yeast results in phenotypes related to defects in the actin and tubulin cytoskeleton. These phenotypes are essentially identical to those observed for various TRiC subunit mutants [1–3, 14]. In yeast strains deleted of one or more *GIM* genes, the folding of actin by TRiC is delayed approximately fivefold relative to wild-type cells (Figure 22.4). This reduced rate of folding correlates with a decreased rate of actin release from TRiC and an increased release of nonnative forms of actin into the cytosol [3]. Interestingly, GimC/prefoldin can bind denatured forms of actin and tubulin, suggesting that it plays a more active role during protein folding than does GroES, the co-chaperone of the group I chaperonin, which does not interact with nonnative polypeptides. However, the association of GimC/prefoldin with TRiC appears to be more transient than the interaction of GroES with GroEL, possibly reflecting the existence of dynamic ternary complexes during folding processes assisted by the eukaryotic chaperonin system. Both GimC and TRiC may bind to their substrates during translation [4, 15], and a role for GimC/prefoldin in targeting polypeptides to TRiC has been suggested [1, 4]. On the other hand, functional GimC is not essential for viability in budding yeast [2, 3], although the efficiency of the interaction of the chaperonin with its most abun-

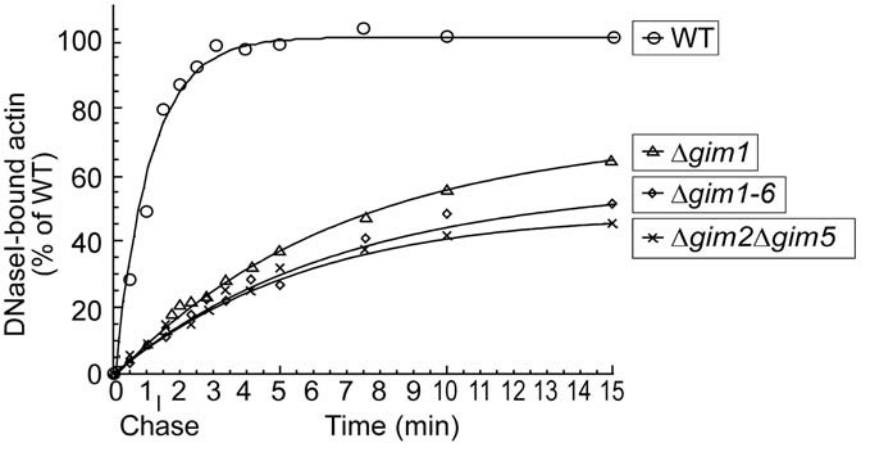

Fig. 22.4. Yields and rate of actin folding are reduced in GimC-deficient cells. Precipitation of newly synthesized, labeled actin from wild-type cells and various *gim*-mutants with DNase I-Sepharose. Native, DNaseI-bound actin was precipitated at the indicated time points and quantified.

dant substrate proteins, actin and tubulin, has been shown to be clearly reduced in the absence of functional GimC/prefoldin [5].

Removal of the hydrophobic patches at the distal parts of the coiled coils in archaeal GimC/prefoldin interferes with model substrate binding [13]. Studies on complexes reconstituted from partially truncated subunits indicate that the distal regions of the coiled coils in both classes of GimC/prefoldin subunits (α and β) are required for full chaperone activity. Substrate binding to GimC/prefoldin appears to require both classes of subunits at the same time, indicating multivalent substrate binding. The contribution of the four β subunits present in the complex was found to be greater than the contribution of the α dimer.

The eukaryotic chaperonin TRiC is thought to mediate protein folding by eventually forming an enclosed folding chamber around the nonnative substrate [16, 17], similar to the mechanism of GroEL/GroES. However, according to the current model, opening and closing of the TRiC cage is mediated by the ATP-dependent movement of helical extensions of the TRiC subunits, not by the binding and release of a separate GroES cofactor [16–19]. It was found that the capacity of TRiC to fold actin rapidly and efficiently in a sequestered environment depends on the activity of GimC/prefoldin [3, 5]. Thus, GimC/prefoldin may represent a general co-chaperone of group II chaperonins, necessary for efficient chaperonin-assisted folding. In contrast to GroES, GimC function is essential for cell growth only at low temperatures or when the function of TRiC is also compromised [2, 3].

Eukaryotic GimC/prefoldin binds to nascent chains of actin and tubulin in a cell-free translation extract and is thought to target these substrate proteins to TRiC [4]. Sucrose gradient fractionation of cell lysates revealed the association of substantial amounts of GimC and TRiC with translating ribosomes [5], extending the findings

from in vitro translation extracts [4, 15] to the in vivo situation. The association of the chaperones with translating ribosomes is abolished by treatment of the lysates with RNase A, which causes dissociation of polysome complexes and ribosome release of nascent chains.

The major known nascent chain-binding chaperone in the yeast cytosol is the ribosome-associated Ssb-type Hsp70, which interacts more or less unspecifically with newly synthesized polypeptide chains on translating ribosomes. However, the association of GimC and TRiC with translating ribosomes was found to be undiminished in a *SSB1/2* deletion strain [5], excluding the possibility that the Ssb-type Hsp70, Ssb1/2p, recruits GimC/TRiC to nascent chains.

Immunoprecipitation of actin and tubulin from ATP-depleted lysates of wild-type yeast cells results in the co-precipitation of Ssb1/2p, GimC, and TRiC [5]. It can be calculated from the amount of co-precipitated chaperonin that actin and α-tubulin each occupy approximately 15–20% of total TRiC, suggesting that about 50–60% of the chaperonin capacity is devoted to the folding of actin and α- and β-tubulin. The amount of TRiC and GimC associated with actin or tubulin was found to be independent of the presence of Ssb1/2p, consistent with the results of the polysome gradient analysis. In contrast, deletion of *GIM* genes results in a ∼60% reduction in the amount of TRiC-bound actin or tubulin, supporting the proposed role of GimC in actin/tubulin delivery to the chaperonin [4]. Thus, although both GimC/prefoldin and the nascent chain-binding yeast Hsp70, Ssb1/2p, interact with newly synthesized actin and tubulin, only GimC/prefoldin is required for the efficient recruitment of TRiC to these substrates.

Analysis of actin folding in wild-type and mutant yeast cells revealed that in vivo efficient actin folding on TRiC is critically dependent on the hetero-oligomeric co-chaperone GimC (Figure 22.4) [3, 5]. By interacting with folding intermediates and with TRiC, GimC was shown to accelerate actin folding at least fivefold and to prevent the premature release of nonnative folding intermediates from the chaperonin. In GimC-deficient yeast cells, the kinetics of actin folding and transit through TRiC is drastically slowed, suggesting that under these conditions folding involves multiple cycles of chaperonin action. This chaperonin cycling is inefficient and is accompanied by the loss of about 50% of actin chains into the cytosol in a nonnative state, where they fail to fold. Based on its ability to bind directly to nonnative substrate polypeptides and to TRiC, GimC may retain nonnative substrate proteins on TRiC and promote the formation of folding intermediates, resulting in acceleration of folding.

Removal of the nascent chain-binding Hsp70 Ssb in a yeast GimC/prefoldin mutant background does not further reduce the efficiency of actin folding or aggravate the impairment of the actin cytoskeleton. Likewise, loss of Ssb function does not increase the sensitivity of yeast GimC/prefoldin mutants towards the microtubule-destabilizing drug benomyl, suggesting that tubulin folding is also independent of the Ssb chaperones. Furthermore, overexpression of other cytosolic chaperones, such as yeast *SSB*, *SSA*, or *YDJ1*, does not alleviate the phenotypes observed for GimC/prefoldin mutants, demonstrating that the efficient folding of actin and tubulin requires the specific cooperation of TRiC with GimC/prefoldin [5].

However, it has been shown that TRiC also cooperates with other cytosolic chaperones, such as Hsp70, in the folding or assembly of other substrate proteins. In mammalian cells the constitutively expressed Hsc70 was found to cooperate with TRiC in the folding or assembly of the von Hippel-Lindau tumor-suppressor complex [20, 21]. Furthermore, a number of newly identified TRiC substrates, which belong to the family of WD-40 repeat proteins [5, 22], were found to require a specific posttranslational interaction with the Ssb-type Hsp70 of yeast. In the case of the WD-40 protein Cdc55p, it was observed that GimC/prefoldin can at least partially compensate for the loss of the Ssb-type Hsp70 in a deletion strain. In contrast to this, the Ssb chaperones were found to be unable to substitute for GimC in actin or tubulin folding, indicating the requirement of a specialized chaperone function for these highly abundant substrate proteins.

The ability of yeast GimC/prefoldin to at least partially replace Ssb1/2p in the folding of Cdc55p, and presumably other TRiC-dependent WD-40 substrates, demonstrates that although eukaryotic GimC/prefoldin has a specialized function in actin/tubulin folding, it can also fulfill a general chaperone function. GimC/prefoldin is present in all eukaryotic and archaeal genomes sequenced so far, but in contrast to eukaryotic cells, archaea do not contain an extensive actin and tubulin cytoskeleton and in certain cases lack the abundant nascent chain-binding Hsp70 system altogether [12]. Therefore, the simpler and more abundant archaeal version of GimC/prefoldin may have a more general function in stabilizing nascent polypeptides in these organisms.

22.6 Experimental Protocols

22.6.1 Actin-folding Kinetics

Measuring actin-folding kinetics in yeast cells involves the preparation of yeast spheroplasts and precipitation of folded actin from radio-labeled yeast lysates with DNase I beads.

Preparation of Spheroplasts Yeast cells are grown in 100-mL cultures to mid-log phase ($OD_{600} \sim 0.5$); harvested by centrifugation (3000 *g*, 5 min); resuspended in 5 mL of synthetic complete medium (0.67% yeast nitrogen base, 2% glucose), minus methionine and cysteine (SC-M-C), containing 1.2 M sorbitol and 30 mM DTT, pH 7.5; and incubated for 10 min at room temperature. Subsequently, cells are harvested as above and resuspended in the same medium without DTT containing 0.5 mg mL^{-1} Zymolyase 100T (ICN Biochemicals) and incubated for 30–60 min at 30 °C until conversion of the cells to spheroplasts is above 90%. The spheroplasts are harvested by centrifugation (1000 *g*, 15 min); washed twice in SC-M-C, 1.2 M sorbitol, pH 5.5; resuspended in 2–5 mL of the same buffer; and incubated at 30 °C for radio-labeling.

Radiolabeling of Yeast Cells and Actin Folding Pulse-chase radio-labeling of spheroplasts is performed with 100 μCi mL^{-1} [^{35}S]-methionine/cysteine ProMix (Amersham) followed by a chase with cycloheximide (0.36 mM). At various time points, aliquots of 250 μL of spheroplasts (100–200 μg of protein) are withdrawn, diluted 1:1 in cold 2× lysis buffer (2× PBS [20 mM Na_2HPO_4, 3.6 mM KH_2PO_4, 5.4 mM KCl, 280 mM NaCl] pH 7.4, 10 mM EDTA, 1% TWEEN-20, 2× complete protease inhibitors [Roche]), mixed, and immediately frozen in liquid nitrogen. At the end of the chase, all reactions are thawed on ice and cell extracts are cleared by centrifugation (20 000 *g*, 4 °C, 15 min).

To precipitate folded actin from the supernatant, 30 μL of DNase I-beads (1:1 suspension in 1× PBS, pH 7.4) (obtained by cross-linking purified DNase I [Sigma] to CNBr-activated Sepharose 4B-CL [Amersham] as described by the manufacturer) is added to the cleared lysates followed by incubation at 4 °C for 1 h. For the precipitation DNase I is in excess over the actin present. Beads are washed extensively once with 500 μL buffer W1 (1% Triton-X-100, 0.5% DOC, 150 mM NaCl, 50 mM Tris/HCl pH8, 5 mM EDTA) and twice with 500 μL buffer W2 (1% Triton-X-100, 500 mM NaCl, 50 mM Tris/HCl pH 8.0, 5 mM EDTA), followed by PBS, prior to SDS-PAGE and phosphorimager analysis.

22.6.2
Prevention of Aggregation (Light-scattering) Assay

Rabbit muscle actin (200 μM) (Sigma), lysozyme (160 μM) (Sigma), or bovine rhodanese (100 μM) (highly purified; Sigma), is prepared in denaturing buffer (6 M guanidine hydrochloride, 20 mM Tris pH 8.0, 100 mM NaCl, 1 mM $MgCl_2$, and 50 mM DTT in the case of lysozyme). The unfolded proteins are diluted 100-fold in buffer B (20 mM Tris pH 8.0, 100 mM NaCl, 1 mM $MgCl_2$) alone, as a reference for maximum aggregation or containing various amounts of GimC/prefoldin, or in IgG as negative control. Aggregation is measured at 25 °C over a period of 10 min by following the increase in light scattering at 320 nm. Alternatively, the effect of GimC/prefoldin on thermally induced aggregation of a 1 μM solution of native substrate proteins in buffer B can be monitored at 320 nm in a thermostated cuvette preheated to 43 °C.

22.6.3
Actin-binding Assay

To determine chaperone activity of purified chaperones, the separation of TRiC/CCT or GimC/prefoldin-bound radio-labeled actin is accomplished by native polyacrylamide electrophoresis.

Radio-labeled denatured actin is obtained by expressing cDNAs of yeast or mouse β-actin to high levels using the *E. coli* strain BL21 (DE3) pLysS in the presence of 1 mCi mL^{-1} [^{35}S]-methionine/cysteine, rifampicin (0.2 mg mL^{-1}), and IPTG (0.5 mM). The labeled actin is solubilized from isolated inclusion bodies using 8 M urea, 20 mM Tris-HCl pH 7.5, and 10 mM DTT.

GimC/prefoldin-actin complexes are formed by diluting denatured radio-labeled actin 100-fold to a final concentration of ~0.13 μM into 50 mM Tris-HCl pH 7.5, 50 mM NaCl, and 2 mM EDTA containing GimC/prefoldin (0.15 μM), followed by incubation for 30 min at 30 °C. Samples are separated on a non-denaturing 4.5% polyacrylamide, 80 mM MOPS-KOH pH 7.0 gel containing 1 mM Mg-ATP at 4 °C for 2.5 h.

Acknowledgements

We thank Dr. S. Grallath for critically reading the manuscript. Work in the authors' laboratory is supported by the Deutsche Forschungsgemeinschaft.

References

1 Vainberg, I. E., Lewis, S. A., Rommelaere, H., Ampe, C., Vandekerckhove, J., Klein, H. L., Cowan, N. J. (1998). Prefoldin, a chaperone that delivers unfolded proteins to cytosolic chaperonin. *Cell*, **93**, 863–873.

2 Geissler, S., Siegers, K., Schiebel, E. (1998). A novel protein complex promoting formation of functional α- and γ-tubulin. *EMBO J.*, **17**, 952–966.

3 Siegers, K., Waldmann, T., Leroux, M. R., Grein, K., Shevchenko, A., Schiebel, E., Hartl, F. U. (1999). Compartmentation of protein folding in vivo: sequestration of non-native polypeptide by the chaperonin-GimC system. *EMBO J.*, **18**, 75–84.

4 Hansen, W. J., Cowan, N. J., Welch, W. J. (1999). Prefoldin-nascent chain complexes in the folding of cytoskeletal proteins. *J. Cell Biol.*, **145**, 265–277.

5 Siegers, K., Boelter, B., Schwarz, J. P., Boettcher, U. M. K., Guha, S., Hartl, F. U. (2003). TRiC/CCT cooperates with different upstream chaperones in the folding of distinct protein classes. *EMBO J.*, **22**, 5230–5240.

6 Martin-Benito, J., Boskovic, J., Gomez-Puertas, P., Carrascosa, J. L., Simons, C. T., Lewis, S. A., Bartolini, F., Cowan, N. J., Valpuesta, J. M. (2002). Structure of eukaryotic prefoldin and of its complexes with unfolded actin and the cytosolic chaperonin CCT. *EMBO J.*, **21**, 6377–6386.

7 Llorca, O., McCormack, E. A., Hynes, G., Grantham, J., Cordell, J., Carrascosa, J. L., Willison, K. R., Fernandez, J. J., Valpuesta, J. M. (1999). Eukaryotic type II chaperonin CCT interacts with actin through specific subunits. *Nature*, **402**, 693–696.

8 Leroux, M., Fändrich, M., Klunker, D., Siegers, K., Lupas, A. N., Brown, J. R., Schiebel, E., Dobson, C., Hartl, F. U. (1999). MtGimC, a novel archaeal chaperone related to the eukaryotic chaperonin cofactor GimC/prefoldin. *EMBO J.*, **18**, 6730–6743.

9 Okochi, M., Yoshida, T., Maruyama, T., Kawarabayasi, Y., Kikuchi, H., Yohda, M. (2002). Pyrococcus prefoldin stabilizes protein-folding intermediates and transfers them to chaperonins for correct folding. *Biochem. Biophys. Res. Comm.* **4**, 769–774.

10 Deuerling, E., Schulze-Specking, A., Tomoyasu, T., Mogk, A., Bukau, B. (1999). Trigger factor and DnaK cooperate in folding of newly synthesised proteins. *Nature*, **400**, 693–696.

11 Teter, S. A., Houry, W. A., Ang, D.,

Tradler, T., Rockabrand, D., Fischer, G., Blum, P., Georgopoulos, C., Hartl, F. U. (1999). Polypeptide flux through bacterial Hsp70: DnaK cooperates with trigger factor in chaperoning nascent chains. *Cell*, **97**, 755–765.

12 Ruepp, A., Rockel, B., Gutsche, I., Baumeister, W., Lupas, A. N. (2001). The chaperones of the archaeon *Thermoplasma acidophilum*. *J. Struct. Biol.*, **135**, 126–138.

13 Siegert, R., Leroux, M. R., Scheufler, C., Hartl, F. U., Moarefi, I. (2000). Structure of the molecular chaperone prefoldin: Unique interaction of multiple coiled coil tentacles with unfolded proteins. *Cell*, **103**, 621–632.

14 Stoldt, V., Rademacher, F., Kehren, V., Ernst, J. F., Pearce, D. A., Sherman, F. (1996) Review: the Cct eukaryotic chaperonin subunits of *Saccharomyces cerevisiae* and other yeasts. *Yeast*, **12**, 523–529.

15 McCallum, C. D., Do, H., Johnson, A. E., Frydman, J. (2000). The interaction of the chaperonin tailless complex polypeptide 1 (*TCP1*) ring complex (TRiC) with ribosome-bound nascent chains examined using photo-cross-linking. *J. Cell Biol.*, **149**, 591–601.

16 Klumpp, M., Baumeister, W., Essen, L.-O. (1997). Structure of the substrate binding domain of the thermosome, an Archaeal Group II chaperonin. *Cell*, **91**, 263–270.

17 Ditzel, L., Lowe, J., Stock, D., Stetter, K. O., Huber, H., Huber, R., Steinbacher, S. (1998). Crystal structure of the thermosome, the archaeal chaperonin and homolog of CCT. *Cell*, **93**, 125–138.

18 Llorca, O., Smyth, M. G., Marco, S., Carrascosa, J. L., Willison, K. R., Valpuesta, J. M. (1998). ATP binding induces large conformational changes in the apical and equatorial domains of the eukaryotic chaperonin containing TCP-1 complex. *J. Biol. Chem.*, **273**, 10091–10094.

19 Meyer, A. S., Gillespie, J. R., Walther, D., Millet, I. S., Doniach, S., Frydman, J. (2003). Closing the folding chamber of the eukaryotic chaperonin requires the transition state of ATP hydrolysis. *Cell*, **113**, 369–381.

20 Feldman, D. E., Thulasiraman, V., Ferreyra, R. G., Frydman, J. (1999). Formation of the VHL-elongin BC tumor suppressor complex is mediated by the chaperonin TRiC. *Molecular Cell*, **4**, 1051–1061.

21 Melville, M. W., McClellan, A. J., Meyer, A. S., Darveau, A., Frydman, J. (2003). The Hsp70 and TRiC/CCT chaperone systems cooperate in vivo to assemble the von Hippel-Lindau tumor suppressor complex. *Mol. Cell. Biol.*, **23**, 3141–3151.

22 Camasses, A., Bogdanova, A., Shevchenko, A., Zachariae, W. (2003). The CCT chaperonin promotes activation of the anaphase-promoting complex through the generation of functional Cdc20. *Molecular Cell*, **12**, 87–100.

23 Gouet, P., Courcelle, E., Stuart, D. I., Metoz, F. (1999). ESPript: multiple sequence alignments in PostScript. *Bioinformatics*, **15**, 305–308.

24 Kraulis, P. (1991). MOLSCRIPT: a program to produce both detailed and schematic plots of protein structures. *J. Appl. Cryst.*, **24**, 946–950.

25 Merritt, E. A., Bacon, D. J. (1997). Raster3D photorealistic graphics. *Methods Enzymol.*, **277**, 505–524.

26 Nicholls, A., Sharp, K. A., Honig, B. (1991). Protein folding and association: insights from the interfacial and thermodynamic properties of hydrocarbons. *Proteins*, **11**, 281–296.

23
Hsp90: From Dispensable Heat Shock Protein to Global Player

Klaus Richter, Birgit Meinlschmidt, and Johannes Buchner

23.1
Introduction

Hsp90 is a cytosolic molecular chaperone that has been found in context with many signal transduction pathways in higher eukaryotes [1]. Its participation in these processes is still enigmatic but is thought to involve specific conformational changes in its substrate proteins, many of which are protein kinases and transcription factors. Because these conformational changes are required to confer activity to the substrates, Hsp90 has become a global player in the signal transduction network of eukaryotic cells. In contrast, the prokaryotic homologue of Hsp90 (HtpG) and the compartmentalized versions of Hsp90 from mitochondria, chloroplasts, and the endoplasmatic reticulum are thought to be predominantly folding helpers for the proteins that reside in or pass through these cellular structures. The evolution of Hsp90 function may be the result of the ever more complex set of cytosolic partner proteins that are known to associate in a substrate-specific way with Hsp90. In this chapter specific focus is put on the ATPase cycle of Hsp90, the interplay of Hsp90 with partner proteins or substrates, and the specific ways to investigate these complex macromolecular assemblies.

23.2
The Hsp90 Family in Vivo

23.2.1
Evolutionary Relationships within the Hsp90 Gene Family

About 130 genes have been unambiguously assigned to the Hsp90 gene family so far. Most of them account for cytosolic variants of Hsp90. Usually, one cytosolic Hsp90 gene is found in prokaryotes, but gene duplications have arisen in eukaryotes that have led to two Hsp90 genes in yeast [2], two Hsp90 genes in mammals [3], and four Hsp90 genes in *Arabidopsis thaliana* [4]. The functional differences between these proteins, and thus the reasons for duplications, are unknown, espe-

Protein Folding Handbook. Part II. Edited by J. Buchner and T. Kiefhaber

ISBN: 3-527-30784-2

cially as the degree of homology between them is very high (as much as 98% in yeast). However, differences in the regulation exist. Sequence alignments show that all the Hsp90 genes share a common organization consisting of conserved domains connected by flexible linkers [5, 6] (Figure 23.1B). Analysis of the individual domains has seen considerable progress in the past few years concerning both structure and function. The N-terminal domain is the nucleotide-binding site of the protein, whereas the C-terminal domain hosts the dimerization site of Hsp90. The middle domain seems to be involved in substrate binding and ATP hydrolysis (Figure 23.1B). Based on the many sequences available for Hsp90 and its homologous proteins, it is possible to trace the evolution of this protein family throughout the organismal kingdom.

The phylogenetic tree of the primary sequences of Hsp90 family members reveals interesting aspects of the evolutionary relationship (Figure 23.1A). First, eukaryotic (including chloroplast and ER members) differ from prokaryotic (including mitochondrial) Hsp90 proteins by a massive extension of the linker region between the N-terminal and the middle domain. This linker consists predominantly (about 90%) of charged amino acids and starts around amino acid 210. It has a maximal length of 92 amino acids in human Hsp90 genes, of about 40 amino acids in yeast Hsp90, and of seven amino acids in HtpG from *E. coli*. Its function is unknown and its presence is not required for yeast cell growth [7]. Second, cytosolic eukaryotic Hsp90 proteins differ from other eukaryotic Hsp90s by a C-terminal extension. This region, which includes the MEEVD motif at the C-terminal end of the protein, serves as the binding site for cytosolic partner proteins containing TPR motifs [8, 9]. This region is also not required for yeast cell growth [7]. Third, Grp94, the ER-resident species, shows an N-terminal extension of about 60 amino acids following the N-terminal signal sequence for ER import. The function and origin of this region are unknown, as it lacks any homology to known protein domains. Interestingly, the evolutionary tree indicates that the Hsp90s in chloroplasts [10] and ER are descendants of cytosolic variants and thus have evolved more recently, while the mitochondrial Hsp90 gene is of ancient, bacterial origin [6]. One feature that shows this origin is the presence of the linker between the N-terminal and the middle domain in the chloroplast and ER-resident Hsp90 isoforms, which is missing in the mitochondrial Hsp90 homologue [11]. The ER-resident Grp94 is found only in multicellular organisms, suggesting either a more recent development or a secondary loss of this gene by single-celled eukaryotes. Duplications of Hsp90 appear to have happened on multiple occasions during evolution, indicating a strong correlation of organismal evolution and Hsp90 evolution. Interestingly, in archaea Hsp90 genes have not been detected yet.

23.2.2 In Vivo Functions of Hsp90

Investigating the importance of a gene for an organism means in particular investigating phenotypes upon deletion of this gene. Knocking out HtpG, the bacterial Hsp90 homologue, produced a modest heat-sensitive phenotype in *E. coli* [12] but

A

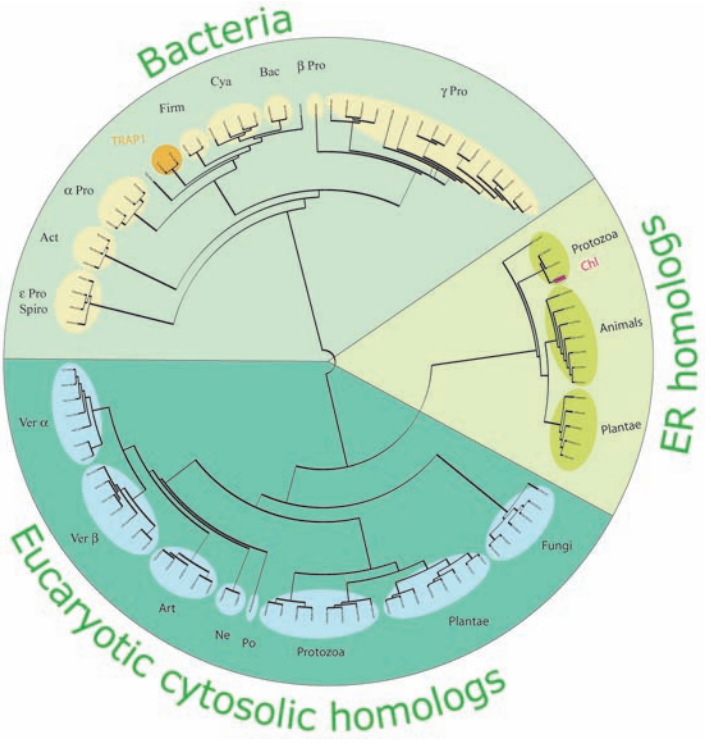
Bacteria
Cya
Bac
β Pro
γ Pro
Firm
TRAP1
α Pro
Act
ε Pro
Spiro
Protozoa
Chl
Animals
Plantae
ER homologs
Ver α
Ver β
Art
Ne
Po
Protozoa
Plantae
Fungi
Eucaryotic cytosolic homologs

B

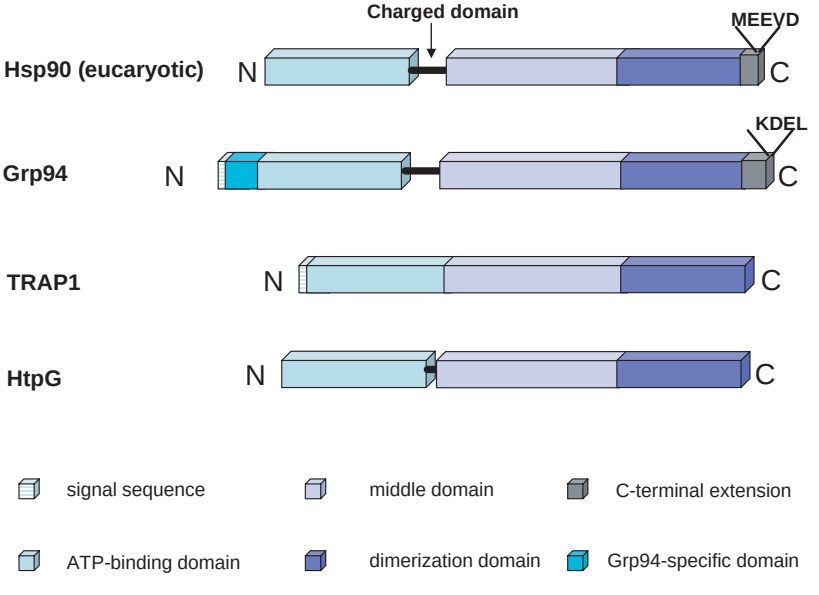
Charged domain
MEEVD
Hsp90 (eucaryotic)
N
C
KDEL
Grp94
N
C
TRAP1
N
C
HtpG
N
C
signal sequence
middle domain
C-terminal extension
ATP-binding domain
dimerization domain
Grp94-specific domain

a lack of thermoprotective functions in cyanobacteria [13]. As no substrate of HtpG is known to date, the role of HtpG in bacteria is largely enigmatic. A slight evolutionary advantage could be detected that leads to an outgrowth of HtpG-deficient bacteria by those that carry a functional HtpG gene [12]. In lower eukaryotes, like yeast, Hsp90 is essential, as knocking out both cytosolic Hsp90 genes results in the loss of viability [2]. The reasons for this are unknown, but it has been observed that the cell cycle of yeast is arrested at both the G_1/S and the G_2/M phases upon deletion of Hsp90s [14], which highlights the involvement of Hsp90 in cell cycle control [15, 16]. This view is further strengthened by the identification of Cdk4 as a substrate of Hsp90 in yeast [17]. Several other kinases, such as dsRNA-dependent protein kinase [18] and the cell cycle kinase Wee1 [19], were found to require functional Hsp90 in yeast. Hsp90 in higher eukaryotes was found to be involved in many different pathways, as best exemplified by the study of Rutherford and Lindquist [20]. Here, genotype-specific phenotypes could be generated by the reduction of Hsp90 levels in *Drosophila*. Hsp90 appeared to buffer the accumulation of mutations in target genes and thus allowed for the invisible accumulation of these events. Partial reduction of Hsp90 function resulted in the manifestation of the previously silent phenotypes and, consequently, led to a diverse set of developmentally defective flies [20]. Comparable effects were later found in *Arabidopsis*, suggesting a similar scenario in animals and plants [21].

In mammals, knockout studies indicated that at least Hsp90β is essential and that its knockout leads to defects in placental development [22]. Hsp90α is also required for embryonic development, as inhibition of the Hsp90 protein results in defects in muscle cell development in zebra fish [23]. For Grp94, on the other hand, studies with B-cell lines indicate an involvement in innate immunity [24]. Several other reports on Grp94 function suggest interactions of the major ER chaperones BiP and Grp94 in processing, folding, and quality control during protein production in the endoplasmic reticulum [25, 26]. In addition, there are reports of an active role of Grp94 in the loading of peptides onto MHCI complexes during the immune response [27].

Much less is known about the in vivo function of the recently discovered Hsp90 homologues of mitochondria and chloroplasts. Also, a shortened Hsp90 homologue, Hsp90N, lacking the N-terminal ATP-binding site, has recently been identified in human cell lines [28]. The function of this protein is still unknown.

Fig. 23.1. Overview of the Hsp90 family. (A) Evolutionary tree of the Hsp90 family. The evolutionary tree of the Hsp90 family has been calculated based on 120 Hsp90 sequences that are publicly accessible. The tree has been constructed as outlined in the Appendix. In principle, it is in agreement with previously constructed trees [5, 6]. ER: endoplasmic reticulum; Verα: vertebrata Hsp90α; Verβ: vertebrata Hsp90β; Art: Arthropoda; Ne: Nematoda; Po: Polifera; Chl: Chloroplast; Spiro: Spirochaetes; Pro: Proteobacteria; Firm: Firmicutes; Cya: Cyanobacteria; Bac: Bacteroides. (B) Schematic representation of the domain organization of the Hsp90 family. Functional equivalent domains are labeled with the same colors.

23.2.3 Regulation of Hsp90 Expression and Posttranscriptional Activation

To understand the function of proteins, it is helpful to investigate the specific requirements for their expression. Thus, the strongly enhanced expression of many Hsp90 isoforms as a response to heat stress hints at an involvement in the protective system of the cell. Conditions that lead to the expression of the Hsp90 gene in prokaryotes include exposure to ethanol, toxic substances, and radicicol as well as other harmful conditions [29, 30]. The regulation of HtpG expression is understood in detail only for heat shock. Here, the heat shock factor sigma 32 determines transcriptional control [31]. Upon heat-induced activation of sigma 32, the heat shock element upstream of the *htpG* gene is used as a docking site of the transcription factor, leading to strongly induced expression of the target protein [32]. To ensure coupling of transcriptional control of chaperones to the presence of unfolded proteins, sigma 32 is negatively regulated by DnaK/Hsp70 and other chaperones. This might add an additional level of control to the regulation, as it guarantees that expression is induced only if a lack of free chaperones is observed. Interestingly, the association of HtpG with sigma 32 is also described [33].

Very similar regulation patterns have been observed for the Hsp90 genes of eukaryotes. Regulation here is performed by the heat shock factor (HSF) [34]. This protein, while not sharing homology with sigma 32, behaves in a comparable way. Here, heat induces trimerization of the protein [35], leading to an active transcription factor, which binds to heat shock elements (HSEs) found in the promoters of all major heat shock proteins, sometimes in multiple redundant sequences [36–38].

If more than one cytosolic Hsp90 isoform exists, the expression is differentially regulated. In yeast, only Hsp82 is stress-regulated, while the 98% identical Hsc82 is constitutively expressed; its levels increase only modestly following stress [2]. Similar results were obtained for mammalian Hsp90. Here, Hsp90β is expressed constitutively and is only slightly upregulated following heat shock and interleukin-dependent signal transduction [39, 40]. The modest upregulation upon heat shock as well as the constitutive expression require a HSE sequence, which is found within the first intron of the gene [40]. Hsp90α instead is strongly heat-inducible, as it contains several HSEs in its 5′ upstream promoter sequence [41]. In addition, it is also under control of interleukin-induced signaling pathways [41, 42]. Other, less well-understood mechanisms – involving the signaling proteins PKCε [43] or STAT1 [44] – are involved in the regulation of Hsp90 expression and appear to couple the expression to an accurate control machinery. Interestingly, recent reports suggest that several chromosomal copies exist for each of the Hsp90 genes in humans [44].

The only other Hsp90 homologue for which the regulation of expression is understood in some detail is Grp94. Grp94 is controlled, among other pathways, by the unfolded protein response (UPR), which connects the appearance of unfolded proteins in the ER with the expression of the major chaperones in this compartment. The pathway starts with the recognition of unfolded proteins by the ER-

resident transmembrane kinase Ire1 and finally results in the activation of the transcription factor Xbp1 [45]. Here as well, molecular chaperones participate in the activation process as negative regulators of Ire1 [46, 47]. Similar pathways exist in lower eukaryotes as well [48].

Thus, throughout the whole animal kingdom, Hsp90 appears as a protein that, although highly expressed even under non-stress conditions, can be strongly induced following either heat stress or chemical stress. Especially the observed coupling of overexpression to the available chaperone activity, as is observed throughout the activation process of the required transcription factors, strongly hints to the origin of Hsp90 as a folding helper and participant in the homeostasis of protein stability in the cell. In yeast, for example, Hsp90 represents 1–2% of the cytosolic protein under permissive conditions and significantly more under stress conditions. Interestingly, only 1/20th of the amount of Hsp90 present under permissive conditions is required to ensure yeast cell growth, while significantly more Hsp90 is required under stress conditions [2].

23.2.4 Chemical Inhibition of Hsp90

In addition to knockout strategies, natural Hsp90 inhibitors were used to imitate the loss of Hsp90 functions in cell culture and some eukaryotic species [49]. Those mostly used are radicicol and geldanamycin (Figure 23.2). Radicicol (formerly monorden) is a product of the fungus *Neocosmospora tenuicristata* [50]. Geldanamycin, an ansamycin, is derived from *Streptomyces hygroscopicus* var. *geldanus* [51].

Several substances that are similar to geldanamycin were also found in streptomyces strains, including macbecin [52, 53] and herbimycin A/B [54, 55]. All these inhibitors appear similar in their efficiency to inhibit Hsp90 in vitro, and strong similarities exist in their in vivo effects [56, 57]. Geldanamycin originally was thought to be an inhibitor of tyrosine kinases, but this effect later was proved to be indirect via the inhibition of Hsp90 [58]. It was observed that incubation with Hsp90 inhibitors results in the rapid degradation of many substrate proteins [59, 60]. The potent inhibition of Hsp90 function is the result of a strong affinity for the N-terminal ATP-binding domain ($K_D = 19$ nM for radicicol, $K_D = 1.2$ μM for geldanamycin), which makes them competitive inhibitors of ATP. ATP binds at least 300-fold weaker to Hsp90 [61, 62]. Thus, the binding of these substances to Hsp90 inhibits the ATPase-dependent functions of Hsp90.

The strong effect of these substances on the tumorigenic growth of cell lines is probably the result of disruption of Hsp90-substrate complexes that are important for cell division. As many of these substrates are oncogenic or associated with pathways leading to cell growth and cell division, the antitumor potential of these substances has beem employed in clinical studies [63]. Especially one derivative of geldanamycin, 17-allylamino, 17-demethoxygeldanamycin (17AAG), shows promising results in the treatment of melanoma patients [64–66]. In particular, the ability of this inhibitor to simultaneously block multiple pathways required for tumor growth by disrupting the Hsp90 chaperone system holds great promise for cancer

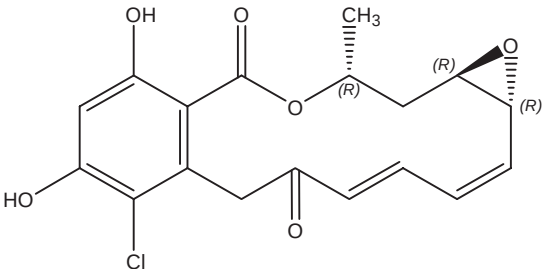

Radicicol

R1 $CH{=}CHCH_2NH$

R2 CH_3O

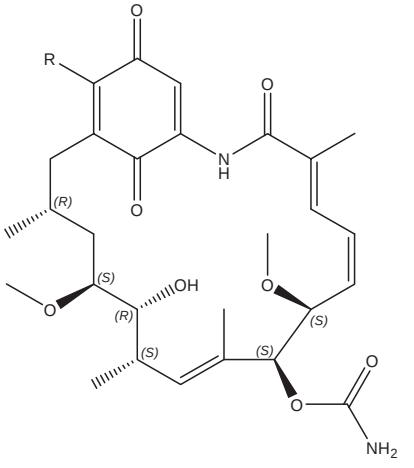

Geldanamycin

Fig. 23.2. Chemical structure of geldanamycin and radicicol. R2: Geldanamycin; R1: 17-allylamino, 17-demethoxygeldanamycin.

therapy [49]. Further, these substances appear to accumulate in cancer cells to concentrations far higher than in normal cells [67]. Considerable interest has arisen in identifying further artificial Hsp90 inhibitors, leading to structure-based strategies in the development of new compounds [68]. First progress in the form of potential lead structures based on purine-scaffolds has already been reported [69, 70].

23.2.5
Identification of Natural Hsp90 Substrates

The phenotypes observed after Hsp90 deletion in eukaryotes are likely the result of diminished activation of the Hsp90 substrate proteins. Many substrates were found

in specific, stable complexes with Hsp90 by co-purification or co-precipitation. This implies that, in sharp contrast to Hsp70, the interaction with this chaperone is long-lived. These substrates are derived from several different and seemingly unrelated protein families [1, 71]. Among them are protein kinases of the tyrosine and threonine/serine kinase family, such as Src, Raf, Mek, Cdk4. As these proteins are at the heart of signaling decisions in eukaryotes, Hsp90 is involved in many important cellular processes. Some other substrates can be grouped together into the large class of transcription factors, although no sequence homology exists between these proteins. Hsp90 targets are, e.g., p53 [72], steroid hormone receptors (SHR), and heat shock factor [73]. Several other unrelated proteins have also been found in complex with Hsp90. The known Hsp90 substrates are listed in Table 23.1.

Strikingly, regarding the strong response of Hsp90 expression to heat shock, none of the substrates identified to date gives any hint towards the chaperoning activity of Hsp90 at elevated temperatures. All of the known substrates require Hsp90 function even at permissive temperatures. Therefore, it may well be that the substrate range changes significantly at elevated temperatures.

23.3 In Vitro Investigation of the Chaperone Hsp90

23.3.1 Hsp90: A Special Kind of ATPase

The crystal structure of the N-terminal domain of Hsp90 was solved in 1997 [61, 74] (Figure 23.3A). These and subsequent studies revealed a new type of binding site for ATP and for the inhibitor geldanamycin [61, 75]. The only related fold known at that time was that of GyraseB [76].

As is evident from the structures with ADP and ATP, the nucleotide is bound in a cleft formed by α-helices on top of an eight-stranded β-sheet [75]. Four α-helices participate directly in the binding of the nucleotide, while three others surround them. Binding induces a special kinked conformation of the nucleotide. The adenine and ribose moieties are hidden inside the nucleotide-binding cleft, while the phosphate groups are oriented towards the surface of this domain. The γ-phosphate is highly unordered in the structure of the ATP-protein complex, leading to the assumption that it might be completely solvent-exposed [75]. This orientation of the nucleotide within the N-terminal domain is shared by other members of this ATPase family. The family of related proteins has grown and now includes, among others, the proteins GyraseB, MutL, and Pts and, with some restrictions, the histidine kinases EnvZ and CheA. Collectively they are called GHKL-ATPases [77]. These proteins share very similar 3D structures of their ATP-binding sites, although sequence homology is rather low. With the exception of the histidine kinases, the ATP-binding domains are located in the N-terminal part of the respective protein. They show a dimeric architecture, for which a C-terminal dimerization site is responsible. The surface exposure of the γ-phosphate [75] allows complex

Tab. 23.1. Hsp90 substrate proteins.[1]

	Protein	*References*
Transcription	Androgen receptor	212, 213
	Aryl hydrocarbon (Ah) receptor	214, 215
	CAR, transducer protein	216
	Ecdysone receptor	217
	Estrogen receptor	212, 218
	Glucocorticoid receptor	219
	Heme activator protein (Hap1)	220
	HSF-1	221
	Hypoxia-inducible factor-1α	222
	Mineralocorticoid receptor	223
	MTG8 myeloid leukemia protein	224
	p53	72
	PPARα (PPARβ); peroxisome proliferator-activated receptor	225, 226
	Progesterone receptor	227, 228
	Retinoid receptor	229
	Sim	230
	Stat3; Signal transducer and activator of transcription	231
	SV40 large T antigen	232
	Tumor promotor-specific binding protein	233
	v-erbA	234
	water mold Achlya steroid (antheridiol) receptor	235
Polymerases	Telomerase	236
	Hepatitis B virus reverse transcriptase	237
	DNA-polymerase α	191
Kinases	3-Phosphoinositide-dependent kinase-1; PDK1	238
	Akt	239
	Aurora B	240
	Bcr-Abl	59
	Calmodulin-regulated eEF-2 kinase	241
	Casein kinase II	103
	Cdc2	242
	Cdk4	17, 162
	Cdk6	243
	Cdk9	244
	Chk1	245
	c-Mos	246
	Epidermal growth factor receptor	247
	ErbB2	248
	Flt3	249
	Focal adhesion kinase	250
	GRK2	251
	Hck	252
	Heme-regulated eIF-2α kinase	253, 254
	IκB kinases $\alpha, \beta, \gamma, \varepsilon$	255
	Insulin receptor	256
	Insulin-like growth factor receptor	257

Tab. 23.1. *(continued)*

	Protein	*References*
	Ire1	258
	Kinase suppressor of ras (KSR)	165
	Lkb1	259, 260
	Lymphoid cell kinase $p56^{lck}$	261
	MAK-related kinase	262
	Male germ cell-associated kinase MAK	262
	MEK (MAP kinase kinase)	247
	MEKK1 and MEKK3	263
	Mik1	264
	Mitogen-activated protein kinase MOK	262
	MRK	240
	Nucleophosmin-Anaplastic Lymphoma Kinase	265
	Perk	258
	Phosphatidylinositol 4-kinase	266
	Pim-1	267
	PKR	18
	Platelet-derived growth factor receptor	268
	Polo mitotic kinase	269
	Raf family kinases: v-Raf, c-Raf, B-Raf, Gag-Mil, Ste11	7, 270, 271, 272, 273
	Receptor-interacting protein (RIP)	255
	Sevenless PTK	274
	Swe1	264
	Translation initiation factor kinase Gcn2	275
	Tropomyosin related kinase B (trkB)	276
	v-fes	277
	v-fps	277
	v-fgr, c-fgr	261, 278
	v-Src, c-Src	163, 279, 280
	v-yes	277
	VEGFR2	250
	Wee1	19
Others	Actin	281
	Apaf-1	282
	Apoprotein B	283
	Atrial natriuretic peptide receptor	284
	Bid	285
	calmodulin	286
	Calponin	287
	Centrin/centrosome	288
	Cna2 (catalytic subunit of calcineurin)	289
	CFTR	290
	Ctf13/Skp1 component of CBF3	291
	Endothelial NOS	292
	Ether-a-gogo-related cardiac potassium channel	293
	Fanconi anemia group C protein (FACC protein)	294
	G protein $\beta\gamma$	295

Tab. 23.1. *(continued)*

Protein	*References*
$G_{\alpha 0}$	296
$G_{\alpha 12}$	297
GERp95 (Golgi Endoplasmic Reticulum protein 95 kDa)	298
Glutathione S-transferase subunit 3 (KS type)	299
Guanylate cyclase (β-subunit)	300
HETE binding complex	301
Histones H1, H2A, H2B, H3 and H4	302
Inducible NOS	303
Lysosomal membrane	304
Macrophage scavenger receptor	305
Aminoacyl t-RNA synthetase	306
Mdm2	307
Myosin	308
NB-LRR proteins RPM1 and RPS2	182, 309
Neuronal NOS	310
Neuropeptide Y	311
$P2X_7$ purinergic receptor	312
PB2 subunit of influenza RNA pol.	313
Pancreatic bile salt-dependent lipase	314
Erythrocyte membrane protein (Plasmodium falciparum)	315
Protease-activated receptor 1 (PAR-1)	316
Proteasome	317
Rab-αGDI	318
Ral-binding protein 1	319
Reovirus protein σ1	320
Survivin	321
β-Galactosidase M15 truncation mutant	322
Thyroglobulin	323
Tubulin	324
Unassembled immunoglobulin chains	325
Vaccinia core protein 4a	326

[1] See also Picard [1] and (http://www.picard.ch/DP/downloads/Hsp90interactors.pdf), Wegele et al. [210], and Pratt and Toft [71].

formation with other parts of the protein. In several cases, the middle domain was found to serve this function, as is evident in the crystal structures of GyraseB (Figure 23.4, see p. 782) and MutL [78, 79]. The recent solution of the crystal structure of the middle domain of Hsp90 (Figure 23.3B) has given further evidence for the homology of Hsp90 with these proteins [80]. According to this structure, the ~150 amino acids immediately following the charged linker share marked similarity to the middle domain of GyraseB and MutL and thus indicate that it may be considered a part of the ATPase site [80]. The following 150 amino acids, in contrast, are unique in their structural organization. This might reflect the different substrate specificities of GyraseB, MutL, and Hsp90.

In the structures of GyraseB and MutL, in complex with the non-hydrolyzable

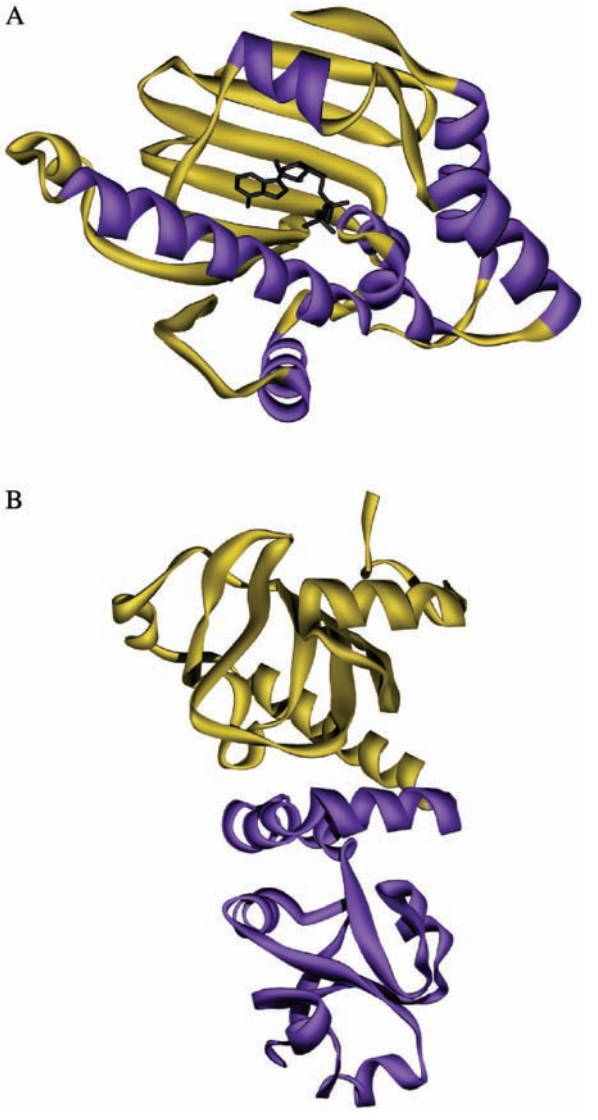

Fig. 23.3. Crystal structure of Hsp90 domains. (A) The crystal structure of the N-terminal domain of yeast Hsp90 as solved by Prodromou et al. [74]. The image is based on the PDB entry 1AM1. (B) The crystal structure of the middle domain of yeast Hsp90 was solved by Meyer et al. [188]. To construct the image, the coordinates of the PDB entry 1HK7 were used.

ATP analogue AMP-PNP, the N-terminal domains of both proteins form dimers. The way this dimerization is accomplished is noticeable. In both cases, GyraseB and MutL, the first strand of the β-sheet and the first α-helix of the protein are exchanged between the two N-terminal dimerized domains [78, 79]. To facilitate this

strand-swapping mechanism, apparently a loop consisting of two α-helices has to be moved within the N-terminal domain and claps over the ATP-binding site. This ''ATP lid'' then forms part of the receptor region for the N-terminal strand of the other domain. It directly interacts with the intruding strand of the other N-terminal domain and is therefore considered to be involved in the hydrolysis mechanism. In addition, complex formation between the γ-phosphate of AMP-PNP and the middle domain is evident in both crystal structures. In both cases, a specific lysine residue appears to serve the function of the γ-phosphate receptor. Concluding from these structures, the corresponding residue is expected to be in the region of amino acids 320–400 of Hsp90. Based on the crystal structure of the middle domain of Hsp90, residue Glu381 was suggested as the acceptor site of the γ-phosphate [80]. However, sequence alignments suggest other possible residues in that region. Further studies on the interaction between the N-terminal and the middle domain are needed for a conclusive understanding of participating segments and the order of conformational changes within this molecular machine.

23.3.2 The ATPase Cycle of Hsp90

Because the crystal structures present a rather static picture of one particular step during the ATPase reaction, much effort has been put into the dissection of the steps that lead to ATP hydrolysis by Hsp90. Yeast Hsp90 hydrolyzes ATP with a turnover of about one per minute [81, 82]. Early studies attempted to define the minimum requirements of Hsp90 to perform ATP hydrolysis. These studies, involving different fragments starting from the N-terminal ATP-binding site, showed the critical requirement of regions outside the ATP-binding pocket for ATP hydrolysis [83, 84]. Only 2% of the wild-type ATPase activity was obtained for the isolated N-terminal domain. A slight increase in ATPase activity (about 12% of wt activity) was observed if the middle domain was present in addition to the N-terminal domain [83, 84]. Higher concentrations of this fragment or its covalent dimerization by a C-terminal cysteine bridge lead to an increase in the ATPase activity [85, 86]. The latter approach led to wild-type ATPase activity, proving the necessity of dimer formation for hydrolysis [86]. Experiments involving heterodimeric variants of Hsp90 helped to identify the regions within Hsp90 that mediate the contacts in the dimer that are important for hydrolysis. These studies proved the transient N-terminal dimerization within the Hsp90 dimer during the ATPase reaction [85] that had been proposed by earlier studies [83, 87]. Further deletion studies imply that the critical region for formation of N-terminal dimers during the ATPase reaction of Hsp90 involves the first 24 amino acids of Hsp90 [88], matching the orientation observed in the crystal structure of the homologous ATPases.

Based on these studies, a cycle of coordinated conformational changes has been proposed for the ATP hydrolysis reaction of Hsp90 (Figure 23.5). This cycle starts with the binding of two ATP molecules to the N-terminal domains of Hsp90. Kinetic studies showed that ATP binding is a fast process, especially compared to

the turnover of Hsp90 [84]. A series of conformational changes results in the trapping of the ATP molecule as observed by Weikl et al. [84] for yeast Hsp90. Early investigations already had pointed to ATP-induced conformational changes within Hsp90 [89]. Several studies suggest that N-terminal dimerization and subsequent activation of the ATPase activity are critical steps during the ATPase reaction [83, 85, 87]. The activation is thought to be – in analogy to other GHKL-ATPases and based on biochemical data – the result of a strand-swapping reaction involving the very N-terminal amino acids [88]. Evidence is accumulating that the rate-limiting step of the hydrolysis reaction is the conformational change leading to the N-terminally dimerized state [88]. While it has not yet been possible to exactly map the order of conformational changes, mutagenesis studies allow defining of regions that help to facilitate this reaction [88]. A rational model for the N-terminal dimerization reaction can be envisioned. First, the swapping strand has to be released from its own domain, by breaking interactions of the α-helix and the accompanying ATP lid. Based on dynamics studies using NMR spectroscopy, it is assumed that ATP binding might facilitate the N-terminal dimerization reaction. The closure of the ATP lid after ATP binding might set this strand free [90]. One mutant – called Δ8-Hsp90 and which lacks the first eight amino acids – was found to form the N-terminal dimers much more efficiently and is thus especially useful for the investigation of the ATPase cycle. The rate-limiting step is shifted here from formation of the N-terminal dimer to the opening of the N-terminal dimer after hydrolysis [88]. These steps might facilitate the interaction with the middle domain to form the fully functional ATPase-active state. Unfortunately, it is not yet possible to determine whether the interaction with the middle domain precedes or follows the N-terminal dimerization reaction.

This cycle of conformational changes is based mostly on studies with yeast Hsp90, but, judging from the high degree of homology, it is assumed to be identical for the other Hsp90-like proteins. The ATPase activities determined for HtpG from *E. coli* (0.4 min^{-1}), yeast Hsp90 (0.5 min^{-1}), chicken TRAP1 (0.4 min^{-1}), and chicken Grp94 (0.4 min^{-1}) [11, 81, 91, 92] are quite similar, while human Hsp90 (0.04 min^{-1}) is significantly decelerated [91].

Interestingly, a second nucleotide-binding site has been suggested recently in the C-terminal domain of Hsp90 [93, 94]. The involvement of this site in the ATPase reaction and the specificity of this site have not yet been established. At present it is also possible that this site is the second part of the ATPase-active site that is thought to form contacts with the γ-phosphate.

23.3.3
Interaction of Hsp90 with Model Substrate Proteins

Compared to the ATPase reaction, the main functions of Hsp90 – the binding and processing of target proteins – are not understood sufficiently. Several studies attempted to identify the substrate-binding site using nonnative proteins such as thermally destabilized citrate synthase [82, 95–98], luciferase [97, 99], rhodanese [100], chemically destabilized insulin [82, 101], and thermally inactivated casein

Fig. 23.4. Crystal structure of a dimeric GyraseB fragment. The crystal structure of GyraseB in the AMP-PNP complexed N-terminal dimerized conformation was solved by Brino et al. [78]. The coloring of the structure highlights the mechanistic features of the N-terminal dimerization reaction. The swapped strand is colored purple, the N-terminal ATP-binding site is yellow, and the middle domain, including parts of the dimerization site, is red. The PDB accession number for this structure is 1EI1.

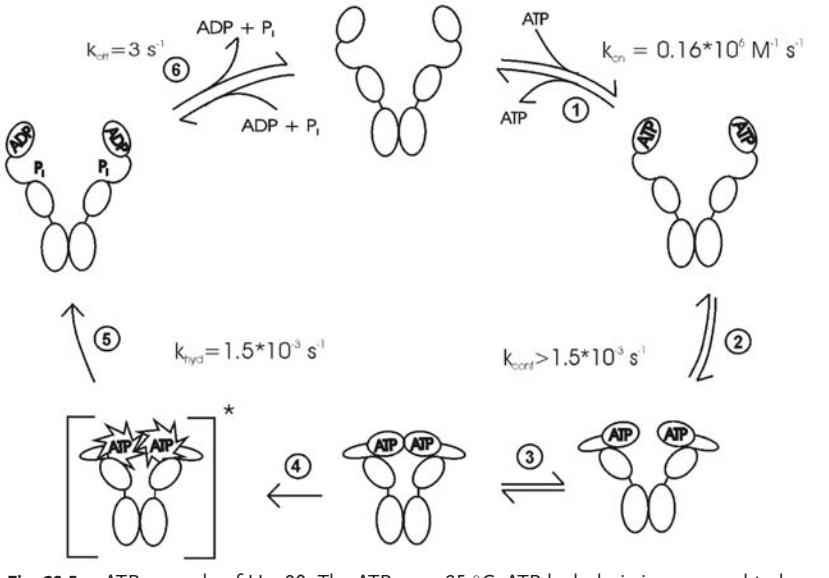

Fig. 23.5. ATPase cycle of Hsp90. The ATPase cycle of Hsp90 combines biochemical and structural evidence. The numbers are based on the work of Weikl et al. [84] and represent kinetic studies of yeast Hsp90 performed at 25 °C. ATP hydrolysis is supposed to happen within the N-terminal dimerized state as indicated by the asterisk. There is no evidence so far for the order of the conformational changes.

kinase [102–104]. These studies led to the identification of chaperone-active sites in all major domains of Hsp90 and thus show the difficulty in understanding Hsp90 interaction with substrate proteins. Many of these assays are based on the aggregation of proteins and thus represent rather complicated systems. This excludes complete understanding of the molecular interactions that influence these processes and thus does not allow obtaining of quantitative data. Based on these studies, the chaperone activity of Hsp90 originally was proposed to reside in the N-terminal domain and in a construct comprising the middle and the C-terminal domain [82, 100]. An N-terminal peptide-binding site has been described based on interactions with reduced insulin B-chain and several peptides including the viral VSV8 peptide [82]. The C-terminal construct instead was found to be more promiscuous with respect to interaction partners. Additionally, the interaction of Hsp90 with substrates in the C-terminal region was found to be independent of ATP binding or hydrolysis. One study addressed the specific state of the substrate during the interaction process. Here, using citrate synthase as a model target protein, it was observed that the Hsp90-interacting species is native-like and thus does not represent a fully unfolded or aggregated protein [95]. This is in agreement with in vivo studies, which suggest that Hsp90 is not involved in de novo protein folding [105]. Additionally, using the Hsp90 homologue from the ER, Grp94, attempts to identify substrate-binding sites were made [106–108]. This protein is thought to bind peptides tightly, which allows their co-purification [106, 109]. The interaction of Grp94 with peptides is still not understood completely, although recent data highlight the possibility of an N-terminal peptide-binding site that is controlled by nucleotide binding and radicicol [106, 109].

23.3.4
Investigating Hsp90 Substrate Interactions Using Native Substrates

Although more than 100 authentic Hsp90 substrates have been identified to date, the large-scale purification of these proteins presents great challenges. Therefore, unlike for GroE, it has not yet been possible to reconstitute a nucleotide-dependent processing of substrate proteins in the case of Hsp90. So far, in particular the protein kinases Lck and eIF2α kinase [110], the transcription factor MyoD [111, 112], the reverse transcriptase of the hepatitis B virus [113, 114], and the ligand-binding domain (LBD) of the steroid hormone receptor [91, 115, 116] have been used in interaction studies. The first three proteins were investigated in combination with truncated Hsp90 mutants. The resulting complex interaction patterns did not allow an unambiguous identification of a binding site. Studies by McLaughlin et al. regarding the effect of the LBD on the ATPase of Hsp90 showed a coupling of the ATPase cycle to substrate binding. Binding to Hsp90 appeared only weak; nevertheless, the LBD was found to stimulate the ATPase activity of human Hsp90 by a factor of 200 [91]. The mechanistic aspects of this stimulation remain unknown; however, studies like these will ultimately lead to a deeper understanding of the reactions involved in the processing of protein substrates.

It can be anticipated that the conformational changes that were observed as necessary for the hydrolysis of ATP might be translated into the change of substrate

conformation. This would require the movement of two substrate-binding sites against each other in an ATP-dependent reaction. The unambiguous identification of these sites remains to be achieved to further understand the chaperone function of Hsp90.

23.4 Partner Proteins: Does Complexity Lead to Specificity?

Several partner proteins of Hsp90 were consistently identified in Hsp90-substrate complexes of eukaryotes, and most of them were later found to bind directly to Hsp90. The investigation of these complexes, in the absence of substrates, led to important information about the assembly of the Hsp90 machinery. All partner proteins described to date are found only in eukaryotic cells and thus might present the evolutionary adaptation of the Hsp90 system to an increasing number of substrates. For some of the partner proteins, pronounced substrate specificity has been observed.

23.4.1 Hop, p23, and PPIases: The Chaperone Cycle of Hsp90

The first partner proteins were detected in complexes with SHRs. These macromolecular assemblies were described in 1966 as 9S receptor complexes [117], implying that several proteins in addition to the SHR were assembled into these structures. Subsequently, Hsp90 and some of its partner proteins were identified as the key components [118]. Attempts to reconstitute these complexes led to the observation that the capacity of SHRs to bind hormones is strictly connected to the assembly into Hsp90-containing protein structures. It additionally became evident that the assembly process appears to be a chronological progression through several distinct complexes [119, 120]. Dependent on the involvement of different partner proteins, these complexes were termed ''early complex,'' ''intermediate complex,'' and ''mature complex.'' The partner proteins were identified as Hop [121], p23 [122], Cyp40 [123], FKBP51, and FKBP52 [124, 125]. Yeast proteins with considerable homology were identified for Hop (Sti1), Cyp40 (Cpr6, Cpr7), and p23 (Sba1) [126]. Detailed studies by Smith and coworkers led to a chaperone cycle (Figure 23.6) that describes the chronological interaction of these partner proteins with Hsp90-SHR complexes [120]. Proteins of the ''early complex'' were identified to be Hsp70 [127] and Hsp40 [128, 129]. In the ''intermediate complex,'' the proteins Hsp70, Hop, and Hsp90 were found, while proteins of the ''late complex'' are Hsp90, p23, and FKBP51, FKBP52, or Cyp40 [130]. Similar heterocomplexes can be found in yeast and mammals [126]. The progression time through the cycle has been estimated to be about 5 min.

Recent biochemical experiments have shown that the ATP cycle is the potential driving force behind this sequence of interactions. Based on studies using the yeast system, a thermodynamically valid cycle for the exchange of partner proteins was

proposed [131]. The first biochemical evidence for the chaperone cycle in yeast came from investigations using the yeast proteins homologous to Hop and Cyp40 [132]. It was shown that the protein Sti1 is a high-affinity inhibitor of Hsp90 ATPase and that Cpr6 could replace Sti1 from Hsp90. The binding site for both proteins was identified to be in the C-terminal region [132]. Further information about the inhibitory mechanism of Sti1 was obtained by the identification of an additional weak binding site in the N-terminal domain of Hsp90 [9, 133]. The inhibitory mechanism was found to be noncompetitive concerning ATP. Interestingly, Sti1 inhibits the N-terminal dimerization reaction required for efficient ATP hydrolysis [133]. However, ATP can still bind to this inhibited conformation. This static complex can be resolved efficiently by the combined action of ATP, Sba1, and Cpr6 [130, 131]. Sba1 was found to bind only to an N-terminal dimerized conformation of Hsp90 that can be accumulated by using the non-hydrolyzable ATP analogue AMP-PNP [83, 134, 135] or by Hsp90 mutants in which the rate-limiting step is shifted from N-terminal dimerization to ATP hydrolysis [131]. The binding constant of Sba1 to this conformation is in the nanomolar range. Binding results in a decrease of the turnover by about 60% [131, 136].

Thus, it is possible to describe the chaperone cycle as an exchange of partner proteins that is driven by the conformational changes of the Hsp90 molecular chaperone. As these rearrangements are the result of the hydrolysis reaction, the exchange of partner proteins itself is driven by ATP turnover. It can be envisioned that substrate turnover, at least in the presence of these partner proteins, is achieved by conformational changes that are driven by ATP hydrolysis (Figure 23.7).

Of particular interest is how the progression of the substrate through the individual complexes affects the conformation of the substrate. For SHRs, the substrate enters the chaperone cycle probably by interaction with Hsp40 proteins [137]. These proteins recognize hydrophobic surfaces on nonnative proteins with relatively low specificity. The interaction of Hsp40 proteins with Hsp70 allows a transfer of the substrate to Hsp70. Hsp70, itself an ATPase, interacts with Hop. For the yeast system, it was shown that Sti1 activates the ATPase activity of yeast Hsp70 tremendously and thus might facilitate the processing of the substrate in this early complex [138]. Substrate transfer to Hsp90 occurs in the intermediate complex and might be accomplished by ATP hydrolysis of the Hsp70 component [139]. Whether the substrate is already active in this complex is not clear. The exchange of cofactors leading to the mature complex clearly results in an active SHR [71]. Hormone binding to this complex is allowed and results in the release of SHR from the chaperoning machinery [71]. Progression through the chaperone cycle may occur even in the absence of hormones, and it might be speculated that ATP is turned over in the p23-containing mature complex. This is followed by release of p23 and the release of SHR. If the SHR is hormone-free, it will again be a client for the reloading machinery of Hsp40/Hsp70. Thus, the low p23-inhibited ATPase activity of Hsp90 in the mature complex would function as a timer, controlling the active state of the SHR.

In addition to the partner proteins mentioned in the context of the SHRs, many

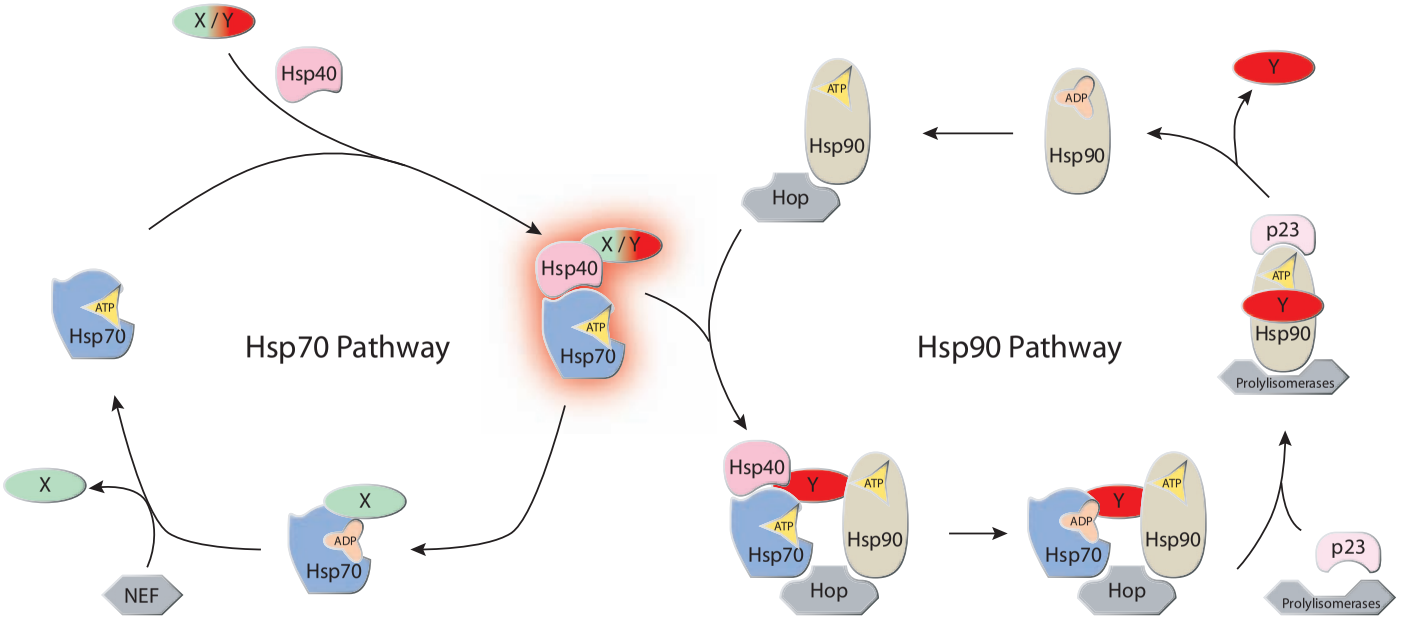

Fig. 23.6. The chaperone cycle of Hsp70/Hsp90. This cycle was established by Smith et al. [120] for the substrate protein glucocorticoid receptor. The substrate is transferred from Hsp70 to Hsp90 and further processed there to reach its activated state. This cycle may look different for other substrates as, especially in the case of kinases, different partner proteins can be found in Hsp90-containing chaperone complexes (see also Wegele et al. [210]).

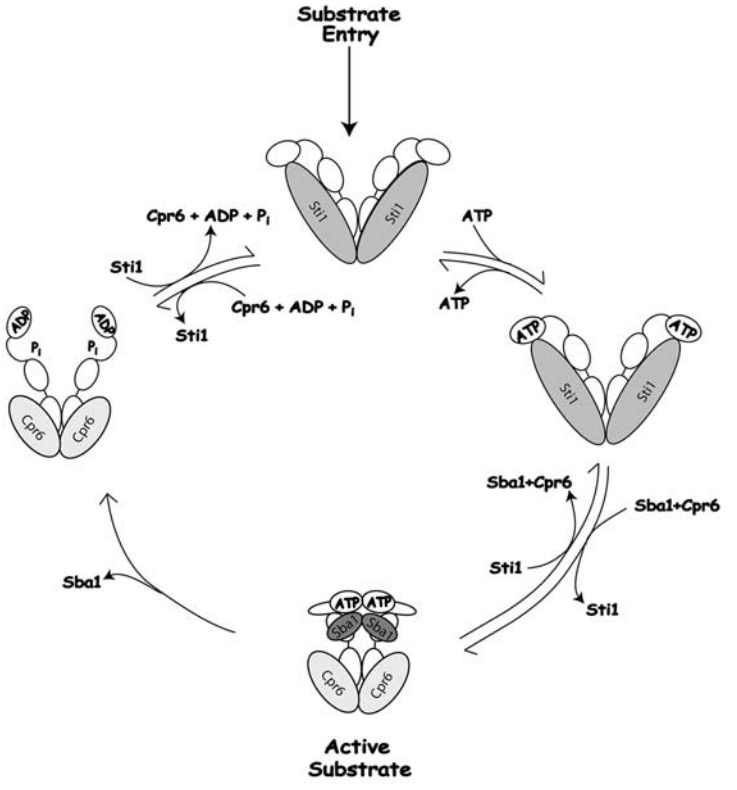

Fig. 23.7. ATPase and co-chaperone binding. Based on the conformational changes during the ATPase cycle, it is possible to integrate the co-chaperones into this cycle. Some of the co-chaperones, such as p23 and Sti1, clearly have different affinities for specific conformations of Hsp90. Therefore, the exchange of co-chaperones as observed in the chaperone cycle may be the result of ATP-induced conformational changes of Hsp90.

more are known in the yeast and mammalian systems. The individual functions of these proteins in the context of the Hsp90 chaperone activities are, with some exceptions, unknown. A striking feature is the presence of TPR domains in a number of partner proteins (Figure 23.8).

23.4.2
Hop/Sti1: Interactions Mediated by TPR Domains

The protein Hop has been identified as outlined above by the specific interaction with Hsp90-containing SHR complexes. Further experiments resulted in the observation that this protein greatly enhances the ability to assemble the SHR heterocomplexes from purified proteins [140]. This probably is due to its ability to work as an adaptor protein between Hsp90 and Hsp70. Three TPR domains have been identified in the protein Hop. Each of these domains is composed of three tandem

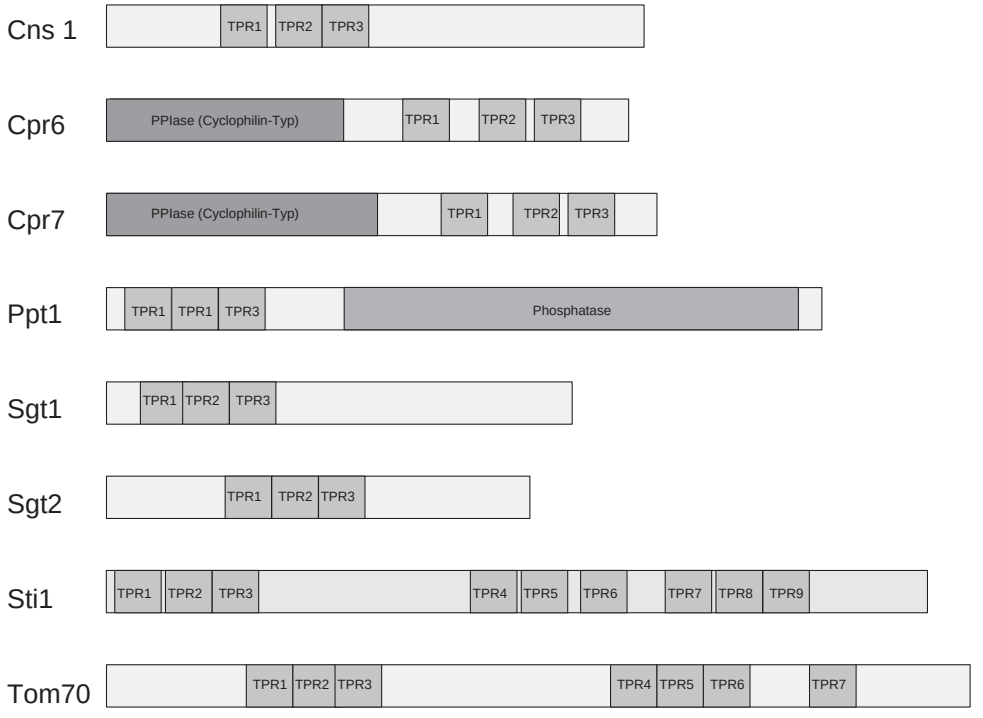

Fig. 23.8. Schematic representation of the TPR-containing Hsp90 partner proteins in yeast and the localization of the TPR domains within the protein.

TPR motifs. A TPR motif is formed structurally by two antiparallel α-helices connected by a turn (Figure 23.9). Therefore, a full TPR motif is built from six (in some cases seven) α-helices that form a binding site for a peptide [8, 141].

In the case of Hop, the specific interactors of the TPR motifs are known only partially. TPRI (the most N-terminal) binds Hsp70, and TPRIIa (the middle domain) binds Hsp90; the function of TPRIIb is not yet fully understood [8, 142, 143]. The same arrangement can be found in the yeast homologue of Hop, Sti1. In both cases, the main interacting peptide is the very C-terminal extension of the chaperones, which is formed by the amino acid sequence MEEVD. As described before, Hop/Sti1 function not only includes binding to Hsp90 and Hsp70. Sti1 is known to inhibit the ATPase activity of yeast Hsp90, and this inhibitory interaction has been found to be the result of two binding sites [132, 133]. Therefore, a more complex interaction pattern is found in this case. The same is true for the interaction of Sti1 with the yeast Hsp70 protein Ssa1. Sti1 strongly activates the ATPase activity of this protein by accelerating the hydrolysis reaction, indicating a more complex interaction as well [138]. None of these effects have been observed for

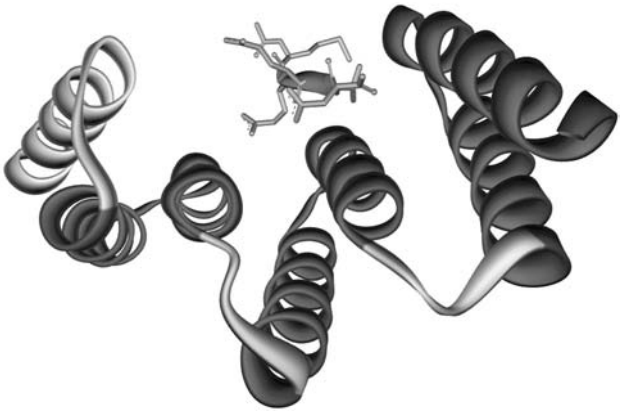

Fig. 23.9. TPR binding to the C-terminal peptide of Hsp90. The TPR domain found in many of the Hsp90 co-chaperones binds with considerable affinity to the C-terminal peptide of Hsp90. The crystal structure of the middle TPR domain of Hop in complex with the pentapeptide MEEVD was solved by Scheufler et al. [8]. Its PDB accession number is 1ELR.

the human Hsp90 system, which indicates that the regulation of the Hsp90 system has been subject to evolutionary changes.

23.4.3
p23/Sba1: Nucleotide-specific Interaction with Hsp90

The protein p23 was also identified in the context of the chaperone cycle of Hsp90 [122]. Its presence leads to a much higher yield of active SHRs [144]. The participation of p23 in the heterocomplexes remarkably stabilizes these assemblies and thus keeps SHRs in the active conformation much longer [134, 144]. This is achieved by specifically binding to a nucleotide-induced conformation of Hsp90 [130, 135]. This conformation has been shown to be N-terminal dimerized [87]. Truncation of the dimerization site resulted in a complete loss of p23-binding activity [9].

p23 is a small, acidic protein. It is composed of an antiparallel β-sandwich built from 10 strands (Figure 23.10). This domain has been shown to be responsible for the interaction with Hsp90 [145, 146]. The C-terminal of this domain is a flexible extension of about 70 amino acids. This is the chaperone-active site of p23, but it does not influence Hsp90 binding [145, 146]. Interestingly, the N-terminal structured part of p23 shares strong similarity with the structure of the small heat shock protein Hsp16 from *Methanococcus jannaschii*. The significance of this observation is unknown, but, based on the chaperone activity of p23, it may well be that they share a common origin.

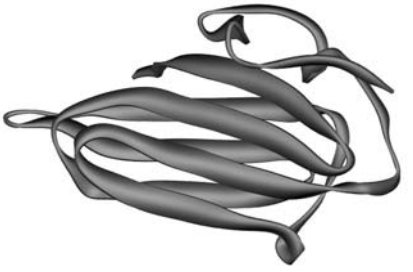

Fig. 23.10. Structure of p23. The crystal structure of p23 was solved by Weaver et al. [146]. Its PDB accession number is 1EJF.

23.4.4

Large PPIases: Conferring Specificity to Substrate Localization?

Analysis of SHR-containing heterocomplexes resulted in the identification of the proteins FKBP51, FKBP52, and Cyp40. These proteins have a domain structure that is composed of a PPIase domain of either the FKBP type (FKBP51, FKBP52) or the cyclophilin type (Cyp40). This peptidyl-prolyl *cis*/*trans* isomerase activity [147, 148] is known to accelerate the *cis*/*trans* isomerization of peptide bonds prior to proline residues. Due to the specific conformation of proline, these bonds have a remarkably slow rotation rate and thus need assistance to flip from the *cis* to the *trans* position and vice versa. The PPIase activity of the large PPIases is quite low compared to related enzymes. In addition to the PPIase domain, they contain a TPR domain that mediates the interaction with Hsp90 (Figure 23.11).

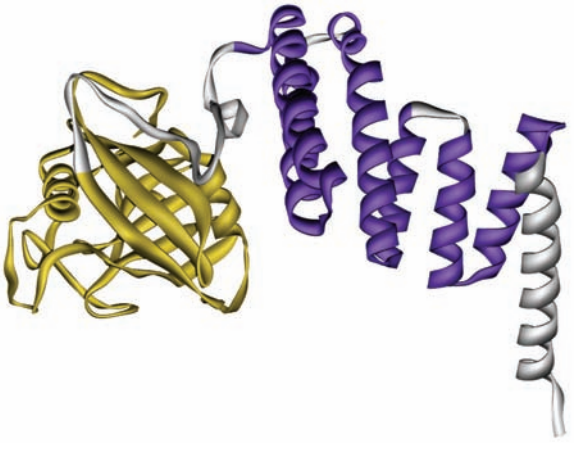

Fig. 23.11. Structure of FKBP51. The crystal structure of FKBP51 was solved by Taylor et al. [211]. Its PDB accession number is 1IHG. Highlighted in different colors is the domain organization of this protein. The N-terminal PPIase domain (yellow) is followed by a TPR-containing domain (purple) that serves as interaction site with Hsp90.

All these PPIases were found to bind to the C-terminal end of Hsp90 and the accompanying sequences [9, 133]. Hsp90 binding by the TPR-containing large PPIases is governed not only by the TPR domain but also by other C-terminal sequences outside this binding site [149, 150]. In addition, the appearance of the specific PPIase in substrate complexes seems to be determined by the substrate. Especially the duplication of these proteins in higher eukaryotes and the appearance of two classes of PPIases (the FKBPs and the cyclophilins) as TPR-containing Hsp90 co-chaperones raise important questions about the specific function of these proteins for specific substrates. Interestingly, the large PPIases come in different numbers in different organisms – two cyclophilins in yeast, one FKBP in *C. elegans*, and two FKBPs plus one cyclophilin in mammals. This may represent a further indication for the evolutionary adaptation of the Hsp90 system towards specific chaperone requirements. Analysis of the SHR-containing complexes showed the presence of all three PPIases in these complexes, although probably not simultaneously [151].

Differences regarding specific functions of the individual large PPIases have been reported. In yeast, Cpr6 is nonessential, whereas deletion of Cpr7 results in a slow-growth phenotype. The reasons for this are unknown [152]. In mammals, special focus has been set on differences between FKBP51 and FKBP52. Both proteins show chaperoning activity [153, 154] and both bind to the C-terminus of Hsp90 with comparable affinity [148]. One specific difference might be the appearance of a nuclear localization signal in the primary sequence of FBKP52. Indeed, FKBP52 appears to be localized to the nucleus, and specific interaction with the transcription factor and Hsp90 substrate HSF1 has been reported [155]. Another interesting feature is the complex formation between FKBP52 and dynein [156, 157]. This interaction may be required for the transport of Hsp90 substrates to the nucleus [158]. This has been demonstrated recently for the transport of transcription factor and the Hsp90 substrate p53 from the cytosol to the nucleus, which occurs in a complex containing Hsp90 and FKBP52 [159]. For SHRs, which also require a shuttling system from the cytosol to the nucleus, a similar dependency on FKBP52 has been observed [160]. Therefore, evidence is accumulating that the differential interaction of Hsp90 substrate complexes with PPIases also determines the cellular localization of the active substrate. Thus, they add specificity to the Hsp90 system.

23.4.5
Pp5: Facilitating Dephosphorylation

Pp5/PPT is a phosphatase that associates with Hsp90 based on TPR regions and their interaction with the C-terminus of Hsp90 [132]. The specific function of Pp5 in the context of Hsp90 substrate complexes is unknown, although several reports indicate that Pp5 as well might be involved in the activation process of SHRs [161]. Binding, at least in vitro, appears to occur in competition with FKBPs and other TPR-containing proteins [132]. The structure of the TPR-domain of Pp5 was solved before any other TPR structure was known [141].

The involvement of phosphorylation on the functionality of the Hsp90 system and on the activity of many Hsp90 substrate proteins has not been investigated in detail. Thus, it is unknown what specific function the phosphatase might serve. Interestingly, many of the known substrates of Hsp90, such as the heat shock factor and several kinases, are clearly regulated by phosphorylation and dephosphorylation, and thus there are ample possibilities to include phosphatases into the regulatory functions of Hsp90-containing protein complexes.

23.4.6
Cdc37: Building Complexes with Kinases

Of particular interest in the context of protein kinase substrates is the co-chaperone Cdc37. Cdc37 was identified as a part of Hsp90 complexes with Src kinase in eukaryotes [162, 163]. In these complexes, Cdc37 is thought to bind to Hsp90 with its C-terminal part and to the kinase with its N-terminal part [164]. This interaction seems to confer specificity to the otherwise promiscuous Hsp90-substrate interaction. Cdc37-containing complexes were sometimes found to be multi-protein complexes in the megadalton range, involving several other proteins [165]. In addition, the possibility exists that Cdc37 is also able to work independently in the activation process of kinase targets [166].

Besides the many kinases that are known to associate with Hsp90 and Cdc37, it is still not clear exactly what the function of these two proteins in the context of the activation of kinases is. Src kinase appears to be shuttled by the system from the nascent state to the cell membrane, where the kinase becomes activated upon myristoylation and insertion of the N-terminus into the plasma membrane [163, 167, 168]. Disruption of the Hsp90 system leaves these substrates inactive and prone to degradation. The same has been observed for most other tyrosine kinases of the Src family, many serine/threonine kinases, and several kinases involved in cell cycle control such as Cdk4 [169]. Experiments using heterologously expressed Src kinase in yeast showed that yeast Cdc37 can substitute for human Cdc37 in the activation of the kinase. This is remarkable, as significant homology between yeast and human Cdc37 is restricted to 25 amino acids in the N-terminal part of the protein [170].

The interaction of Cdc37 with Hsp90 results in low-affinity inhibition of the ATPase activity [171]. Recently, the crystal structure of human Cdc37 with the N-terminal domain of yeast Hsp90 was solved [172]. The observed interaction between the N-terminal domain of Hsp90 and the co-crystallized Cdc37 fragment is remarkable (Figure 23.12, see p. 794). Cdc37 binds as a dimeric protein to the two N-terminal domains of Hsp90. This orientation prevents the N-terminal dimerization reaction required for ATP hydrolysis by Hsp90 and explains the inhibitory effect of Cdc37 on the ATPase activity of Hsp90 [172]. Its direct interaction site is the ATP lid, which has been implicated in the ATP hydrolysis reaction. Thus, as with p23 and Hop/Sti1, a mechanism has been found to couple the binding of a co-chaperone to a distinct step in the ATPase cycle of Hsp90. According to genetic

experiments, Cdc37 shares overlapping functions with Sti1 in vivo and thus appears to function in the loading of substrates onto Hsp90 complexes [173].

This simplistic view of Cdc37 as a kinase-specific cofactor of Hsp90 is challenged by recent discoveries [174]. In addition to functions in the activation of Hsp90 substrates other than kinases, Cdc37 seems to have Hsp90-independent functions. Furthermore, it has been found to form complexes with the Hsp90 co-chaperone Sti1, even in the absence of Hsp90 [175]. In addition, Cdc37 is known to be a molecular chaperone on its own [176].

23.4.7
Tom70: Chaperoning Mitochondrial Import

Tom70 is an integral part of the mitochondrial import machinery. It serves as a receptor of preproteins in the outer mitochondrial membrane. The substrates to be imported into mitochondria are transferred from Tom70 to the mitochondrial import channel. Tom70 was found to associate with Hsp90 via its TPR domain [177]. The association allows delivering certain preproteins from the cytosol onto the Tom70 receptor as a first step of mitochondrial import. This interaction could be shown to be required for the transport of several targets into the mitochondrial matrix [177]. Further experiments showed that the ATPase activity of Hsp90 is involved. Interestingly, both Hsp70 and Hsp90 are able to interact with the single TPR domain of Tom70 in yeast and mammals [177]. The individual affinities of these chaperones for Tom70 vary in different organisms. In humans, Hsp90 appears to be the preferred cytosolic chaperone to deliver preproteins, whereas in yeast most preproteins are delivered by cytosolic Hsp70 [177]. Thus, this example indicates that besides the well-documented involvement of Hsp90 in the activation of signal transducers, some general folding functions remain to be discovered. The specific function and localization of Hsp90 in complex with its substrate protein may be governed to a large degree by its association with a specific co-chaperone [178].

23.4.8
CHIP and Sgt1: Multiple Connections to Protein Degradation

Hsp90 has long been speculated to be involved in protein degradation in addition to its role in protein folding [60]. In particular, the fast degradation observed for several substrates after Hsp90 inhibition hints towards this possibility [59, 60]. The recent identification of the co-chaperone CHIP in mammalian cells has intensified these considerations, as this protein apparently directs substrates towards degradation by the proteasome [179]. CHIP is composed of two domains: a TPR domain mediating the interaction with Hsp70 and Hsp90 and an ubiquitin-ligase domain [180]. The latter domain is involved in the attachment of ubiquitin chains to degradation-prone proteins [180]. Therefore, it can be envisioned that via this

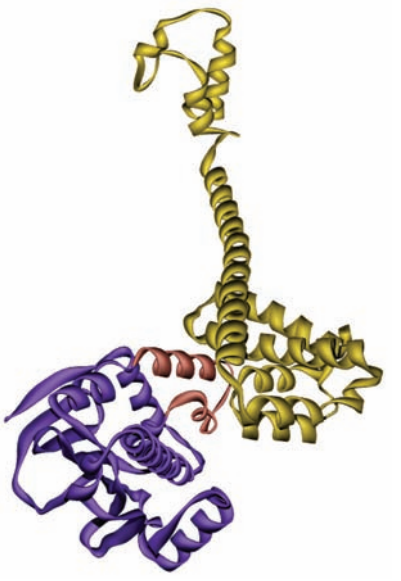

Fig. 23.12. Interaction between Cdc37 and Hsp90. The crystal structure of the complex between the N-terminal domain of Hsp90 and a fragment of the co-chaperone Cdc37 was reported by Roe et al. [172]. In this structure the C-terminal part of Cdc37 (yellow) interacts with the N-terminal domain of Hsp90 (purple). The primary interaction site is the ATP lid (red). The PDB accession number of this structure is 1US7.

partner protein, Hsp90 substrates are marked for degradation. How the decision between folding and degradation is made is the subject of intense research.

Sgt1, another Hsp90 co-chaperone that was identified recently, is also involved in protein degradation. Sgt1 is part of the SCF (Skp1-Cul1-F-box) ubiquitin-ligase complex [181] and was found to bind to Hsp90 [182]. Disturbance of its interaction with Hsp90 results in defects in genomic defense mechanisms of plants [183, 184]. The interaction of Sgt1 with Hsp90 is not fully understood. Recent results indicate that the domain of Sgt1, which binds to Hsp90, is similar to p23. Binding seems to be slightly ATP-dependent [185, 186]. Interestingly, the TPR domain also present in Sgt1 appears not to be involved in Hsp90 binding. This new co-chaperone seems to localize primarily to the kinetochore, and therefore a nuclear function of Hsp90 has to be envisioned in the context of this chaperone [181].

23.4.9
Aha1 and Hch1: Just Stimulating the ATPase?

In the late 1990s, two temperature-sensitive Hsp90 variants were used in yeast to identify cellular suppressors of the *ts*-associated defects [187]. Overexpression of three proteins was found to decrease the *ts* effects. These proteins were identified

as Cns1, Ssf1, and Hch1 [187]. Subsequent biochemical investigations led to the determination that Hch1 is a stimulator of the ATPase activity of Hsp90 [136]. Although binding was found to be weak (in the high micromolar range), the effect on the turnover number of Hsp90 is strong, leading to a 20-fold increase in ATP hydrolysis. Using bioinformatics approaches, a homologue of Hch1 (Aha1) was identified and shown to bind with greater affinity to Hsp90 [136]. It also stimulates the ATPase activity of Hsp90. Cellular roles for these proteins are unknown to date, although yeast experiments using heterologously expressed v-Src as an Hsp90 substrate indicate that the interaction between Hsp90 and Aha1 is important for the maturation of Hsp90 substrates [136]. While Hch1 is a fairly small protein composed of 140 amino acids, Aha1 consists of two domains. The N-terminal domain of Aha1 is homologous to Hch1, and the C-terminal domain is of unknown origin. The isolated N-terminal domain of Aha1 is sufficient to bind to and stimulate the ATPase activity of Hsp90. While Aha1 is present in all eukaryotes, Hch1 has so far been found only in yeast.

The crystal structure of the complex between Hsp90 and Aha1 suggests a mechanism for the stimulation of the ATPase activity of Hsp90 by Aha1 [188] (Figure 23.13). Aha1 binds to the middle domain of Hsp90 [80, 189]. This leads to the reorientation of a loop involved in ATP hydrolysis in other GHKL-ATPases as well. The loop is thought to interact with the γ-phosphate of the bound nucleotide, and this interaction appears to be facilitated by Aha1 [188].

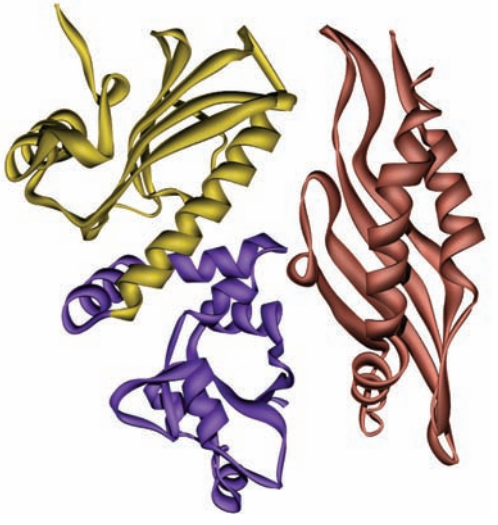

Fig. 23.13. Interaction of Aha1 with Hsp90. The crystal structure of this complex was solved by Meyer et al. [188]. Aha1 (red) interacts with the middle domain of Hsp90. The interaction sites within the middle domain reside in the ATPase-interacting part (yellow) as well as in the part supposed to interact with substrates (purple). The PDB accession number of this structure is 1USU.

23.4.10
Cns1, Sgt2, and Xap2: Is a TPR Enough to Become an Hsp90 Partner?

Several other proteins from *S. cerevisiae* contain TPR domains with homology to those of Cpr6, Hop, or Ppt1. In particular, for the TPR proteins Cns1, Sgt2, and mammalian Xap2, an interaction with either Hsp90 or Hsp70 or both has been described. Cns1, which was identified as a suppressor of temperature-sensitive Hsp90 phenotypes [187], has been detected as an Hsp90 co-chaperone in different contexts [190]. The interaction has been confirmed in *Drosophila* [191]. Recent biochemical investigations showed that Cns1, like the co-chaperone CHIP, is able to interact with both Hsp90 and Hsp70 with its single TPR domain [192]. In addition, it was found to strongly stimulate the ATPase activity of yeast Hsp70 [192]. In contrast to Sti1, the binding of Cns1 to Hsp90 does not influence its ATPase activity. Interestingly, Cns1 is one of the few essential co-chaperones in yeast [190, 193]. In this context, a close genetic relationship between Cns1 and Cp7 was reported [193] and a direct interaction between the two proteins was observed [194].

Xap2 contains a TPR domain and interacts with Hsp90 during the chaperoning of the substrate reverse transcriptase from hepatitis B virus [195, 196] and the dioxin receptor, a cytosolic receptor with some functional similarity to the steroid receptors [197]. In both cases, the function of Xap2 is unknown and the participation of further proteins in this process is very likely.

Using bioinformatics approaches, several other proteins with TPR domains have been identified. The characterization of their function in the Hsp90 chaperone cycle is just beginning. These include Sgt2, Cdc23, Cdc26, Tom34, Tpr2, and others [141, 198, 199]. Sequence homology studies so far have failed to predict a clear differentiation between Hsp90- and Hsp70-binding motifs within the TPR domains. Ultimately, an investigation of binding affinities between Hsp90/Hsp70 and these co-chaperones will have to be performed to fully establish the Hsp90 network within the cell.

23.5
Outlook

The evolution of the Hsp90 system from an obviously single, nonessential protein to an essential network of specific substrates, co-chaperones, and cellular functions highlights the importance of this protein system for the eukaryotic cells. In recent years, great progress has been achieved regarding the identification of new participants in the system, the biochemistry of the ATPase reaction, the interaction with partner proteins, and the identification of new substrates. Nevertheless, despite over 2000 publications on Hsp90, a clear understanding of its cellular function is still lacking.

Many of the studies performed with Hsp90 to date address the interaction of partner proteins in the absence of substrates. The functional aspects of the co-chaperone–Hsp90 interactions are beginning to emerge for the best-described

partner proteins. For the others, information is scarce. It thus is of utmost importance to integrate the partner proteins into the ATPase cycle and to determine which partner proteins associate to heterogenic complexes and which bind mutually exclusively to Hsp90. These investigations in combination with in vitro studies on substrates will ultimately result in the elucidation of critical functions of the Hsp90 chaperone machine.

23.6
Appendix – Experimental Protocols

For the investigation of the molecular chaperone Hsp90, a set of techniques, ranging from in vivo techniques to biophysics, has been established to address the specific functions of this protein.

23.6.1
Calculation of Phylogenetic Trees Based on Protein Sequences

Phylogenetic trees for the evolutionary investigation of the Hsp90 protein family can be calculated using a combination of freely available software packages. Sequences related to Hsp90 are obtained by BLAST searches (http://www.ncbi.nlm.nih.gov/BLAST/) using either full-length Hsp90 or partial sequences thereof as input. Preliminary sequence alignment is done using the ClustalW alignment algorithm (http://www.ebi.ac.uk/clustalw/). This alignment is then refined manually to include all the necessary structural and functional information that can be derived from the literature, such as mutational studies and structural and biochemical information.

The BioEdit software (http://www.mbio.ncsu.edu/BioEdit/bioedit.html) allows manual adjustment of a large number of sequences. Subsequently, the adjusted alignment is incorporated into the Phylip format.

Phylip (http://evolution.genetics.washington.edu/phylip.html) allows calculating of evolutionary trees based on several available algorithms. These include parsimony and bootstrap calculation of distances. Rooted or un-rooted trees can be calculated, depending on the selection of specific out-groups. The resulting tree can be imported into Adobe Illustrator or any other postscript-compatible program for further graphical rearrangements.

23.6.2
Investigating the in Vivo Effect of Hsp90 Mutations in *S. cerevisiae*

The yeast homologues of Hsp90, i.e., Hsp82 and Hsc82, are essential proteins, and the knockout of both of these proteins is lethal [2]. Therefore, the investigation of specific point mutations of Hsp90 fragments with respect to the essential function of Hsp90 is possible. For this experiment, a yeast strain lacking both genomic Hsp90 versions is used. As a knockout of both genomic Hsp90 copies is lethal, vi-

ability of the yeast strain before transformation with the plasmid-encoded Hsp90 variant has to be ensured. Therefore, wt Hsp82 is supplied on a plasmid containing the URA-selection marker. In the experiment, the plasmid-encoded wt Hsp90 is exchanged for a plasmid-encoded mutant Hsp90. Only in the case that the mutant Hsp90 is fully functional is growth of the yeast strain ensured.

The fragment or *hsp90* gene carrying the mutation is subcloned into a yeast shuttle vector, e.g., the vector p2HGal or any other yeast expression vector. This vector uses the gene HIS3 as a selection marker. The Hsp82 variant of interest is expressed under the control of the galactose promoter. Other combinations of selection marker (TRP, LEU, or ADE) and promoter (constitutive GPD promoter or Cu-inducible promoter) are available as well and might be equally useful. To start expression of the Hsp90 variant, cells are plated on medium with galactose as the only carbon source. Residual glucose will lead to the repression of the galactose promoter. Lack of galactose also leads to repressed expression. Because the reduction of intracellular glucose levels will require time after shifting to galactose-containing minimal medium, it is advised that yeasts be shifted to raffinose medium for several hours to allow complete depletion of intracellular glucose before they finally are transferred to the galactose medium. This will allow complete depletion of the intracellular glucose levels and thus will lead to the immediate expression of the galactose-controlled gene after exposure to galactose. Generally, it is good practice to prove the expression of the Hsp90 variant by Western blotting to avoid being misled by negative results due to low expression levels.

After transformation with the p2HGal-encoded Hsp90 variant, yeasts are grown on medium lacking HIS and URA and containing galactose as the carbon source. This selection ensures the maintenance of both plasmids. It is possible to counterselect against URA-containing plasmids by using 1% 5-fluororotic acid (5-FOA) in the medium [200]. This substance is converted into a toxic compound by the URA gene used as selection marker on the wt Hsp90 plasmid. Therefore, a strong selection pressure is applied for the loss of this plasmid, due to the accumulation of toxic compounds in the presence of the URA gene. With the loss of this plasmid, the wt Hsp90 gene is lost. As a consequence, cell proliferation is possible only if the supplied Hsp90 variant on the p2HGal plasmid is functional.

Additionally, in some cases, a dominant negative effect of truncated versions of Hsp90 has been observed in yeast, leading to slower growth, if these variants were overexpressed [201]. To investigate this, the same plasmid as for the complementation experiment can be used. Overexpression is started by using galactose-containing medium, and the growth of the yeast strain containing the truncated version is compared to a strain containing the wt version or an empty plasmid.

23.6.3 Well-characterized Hsp90 Mutants

A number of mutations in Hsp90 have been described that are particularly useful for the investigation of functional aspects. The specific amino acid numbers refer to yeast Hsp82. Conserved residues can be found in homologous Hsp90 proteins.

The first set of mutations affects the ATPase activity of Hsp90. This activity is essential in vivo, and amino acid residues involved in this reaction have been identified [81, 202]. Amino acid Asp79 participates in the binding of the nucleotide. It makes contacts at the base of the binding pocket [75]. Its mutation to Asn (D79N) leaves the structure of the mutant fully intact but strongly reduces the ability of the Hsp90 mutant to bind ATP [81, 202]. Thus, it is possible to use this mutant to investigate the importance of ATP binding for a specific reaction under investigation. Another particularly useful amino acid is Glu33. This residue participates in the hydrolysis reaction leading to ADP. The mutation of this residue to alanine (E33A) leads to an Hsp90 variant that binds ATP with mostly unchanged affinity but is unable to hydrolyze it [81, 202]. The conformational changes involved in ATP hydrolysis are blocked at the point of hydrolysis. Used in combination, the two mutants allow differentiation between the effects of nucleotide binding and hydrolysis.

A second set of mutations involves the regions implicated in the N-terminal dimerization reaction. As such mutants, deletions of the first 8, 16, and 24 amino acids were characterized [88]. These mutations can be used to investigate the N-terminal dimerization and the effects of this reaction on the binding of partner proteins. For several of the partner proteins, especially those that influence ATPase activity, N-terminal dimerization would affect their binding. The investigation of these differences relies on the known behavior of these mutants [133]. Full-length Hsp90 does not form N-terminal dimers stably unless the nucleotide AMP-PNP is used. Δ8-Hsp90 forms stable N-terminal dimers in the presence of ATP and AMP-PNP [88]. The rate-limiting step of hydrolysis is therefore shifted from the formation of N-terminal dimers to the dissociation of the N-terminal domains, allowing investigation of binding to this conformation specifically. The deletion of the first 24 amino acids results in the elimination of the ability to form N-terminal dimers.

Another set of mutations is particularly useful for in vivo studies. Several mutations were identified that show temperature-sensitive effects [105, 187]. These mutations can be used to investigate essential cellular functions of Hsp90, as the yeast strains are viable at permissive temperature and inhibit growth at elevated temperatures. One such mutation is G170D. This mutant is viable only below 34 °C [105]. Other temperature-sensitive mutants are T101I, E381K, and G313S [105]. These mutations also have been used to perform suppressor screens in order to identify new components of the Hsp90 system.

For the interaction of Hsp90 with the large number of TPR proteins, a mutant that lacks the C-terminal extension MEEVD has been used extensively. Exchanging this protein for the wt Hsp90 in yeast leads to no detectable phenotype [7]. Especially for the investigation of in vitro interactions, this mutant has proven to be a great control, as the deletion of these residues leads to complete inhibition of the binding of several partner proteins [9, 133].

Last but not least, it is worth mentioning that the addition of a His_6 tag at the N-terminus of Hsp90 has been used extensively to facilitate purification. This modification of the protein apparently does not influence the activity of Hsp90 in vivo

[126]. It allows co-purification of Hsp90 partner proteins. In vitro, the addition of the His_6 tag from the pET28 vector results in an ATPase activity about twice as high as the wt Hsp90 (unpublished data). This might be the result of changes in the N-terminal dimerization properties that are controlled to a large extent by the very N-terminal amino acids (see Section 23.3.1).

23.6.4
Investigating Activation of Heterologously Expressed Src Kinase in *S. cerevisiae*

It is widely accepted that the function of Hsp90 is the activation of a large number of substrate proteins. Yeast lacks many known Hsp90 target proteins found in higher eukaryotes. Therefore, well-known mammalian Hsp90 targets have been expressed in the cytosol of yeast. One of the best studied mammalian Hsp90 substrates is the tyrosine kinase c-Src and its oncogenic variant v-Src [163]. These proteins can be expressed in yeast from a plasmid [168]. Both proteins require Hsp90 to gain activity. Interestingly, the function of mammalian Hsp90 can be substituted by the endogenous yeast Hsp90 system [167, 168]. While overexpression of c-Src does not lead to a phenotype, v-Src overexpression is lethal, as the amount of uncontrolled tyrosine phosphorylation is obviously damaging in yeast [168]. This assay allows investigation of the functionality of non-lethal Hsp90 mutations and the influence of partner proteins on Src maturation in yeast. In addition, if non-functional Hsp90 mutants are concerned, sometimes the overexpression of these in a wt yeast background results in damaging effects on the activation of the substrate protein studied, for example, as partner proteins are depleted from the functional Hsp90 system of the cell [201]. Thus, this assay nicely complements the growth assays described before.

To determine the activity of the Src protein, global cellular tyrosine phosphorylation is measured by Western blotting [167, 168]. To ensure comparability between different yeast strains, equal amounts of cells are loaded onto the SDS-PAGE. Detection is performed using a commercially available anti-phosphotyrosine antibody.

23.6.5
Investigation of Heterologously Expressed Glucocorticoid Receptor in *S. cerevisiae*

Another known target of Hsp90 in mammals are SHRs, such as the glucocorticoid receptor (GR) or the progesterone receptor. These proteins require the function of Hsp90 and several of its partner proteins for their hormone binding activity. Like Src kinase, GR can be expressed in yeast [105, 160, 203]. Its activity can be detected using a GR-inducible reporter gene construct (β-galactosidase), which is on a second plasmid that has been co-transformed into the yeast strain. The activity of GR as a transcription factor after external addition of hormone is measured by the activity of GR-induced β-galactosidase in a reporter gene assay. This assay allows addressing of questions similar to those of the Src kinase assay. Due to the fact that Hsp90 substrates do not share obvious functional or structural homology, per-

forming of both assays is advised, as mutations or truncations in Hsp90 may affect the substrates in different ways.

To perform this assay, the GR is expressed from a yeast plasmid. The activity of the GR is switched on by the addition of deoxycorticosterone (DOC), which acts as a GR agonist. This substance represents a long-lived, membrane-permeable analogue of the glucocorticoid hormone. To allow quantitation, it has to be ensured that equal amounts of protein extract are used, and great care has to be employed to use standardized conditions for the preparation of the samples. The activity of the reporter gene is detected using X-gal as substrate in an OMPG test. The production of a blue color is quantified at 495 nm in a spectrometer. Investigation of the β-galactosidase activity at different optical densities (OD_{600}] greatly increases the resolving power of this assay. The result indicates whether the Hsp90 system in the specific yeast strain is sufficient to ensure activation of the GR receptor. Using this assay, it has been shown that some Hsp90 fragments, when overexpressed, do influence the activity of the GR in a negative way [201], matching the dominant negative effects also observed in some growth assays.

23.6.6 Investigation of Chaperone Activity

Most of the investigations regarding the chaperoning activity of Hsp90 have relied on traditional chaperone assays. The specific protocols to perform chaperone activity measurements are described elsewhere in this book (see Chapter 5). Several of these assays give positive results for Hsp90 as well. In particular, Hsp90 markedly slows down the thermal inactivation and aggregation of citrate synthase [98]. Also, the aggregation of insulin upon reduction of its disulfide bonds is inhibited by Hsp90 [82]. Assays employed to investigate the potential of Hsp90 to suppress aggregation of proteins also include the proteins rhodanese and luciferase [97, 100]. The quantitation of aggregation relies on either UV absorbance measurements at 360–600 nm in a spectrometer or the measurement of light scattering. To detect light scattering, a conventional fluorescence instrument can be used. The excitation and the emission wavelength are set to the same value (between 360 and 600 nm). Generally, lower protein concentrations can be used in light-scattering setups, as the sensitivity is much higher. For citrate synthase aggregation, 2 μM of citrate synthase gives sufficient signal in the UV/VIS measurement, while only 150 nM citrate synthase has to be used in the light-scattering measurement. Due to the very complex events leading to aggregation, it is impossible to perform a quantitative analysis of the aggregation curve.

The thermal inactivation of citrate synthase is a useful assay that allows a more quantitative description of the chaperoning activity of Hsp90. The assay can be analyzed using a single exponential function to determine the rate constant for the inactivation reaction [95]. This rate constant varies depending on the buffer conditions. In 40 mM HEPES/KOH, pH 7.5, its value is usually 0.4 min^{-1} at 43 °C. In the presence of Hsp90, this can be slowed down to 0.04 min^{-1}, indicating that

Hsp90 is able to stabilize citrate synthase in a native-like conformation [95]. Especially if this assay is performed to elucidate the chaperoning activity of Hsp90 fragments, it is advisable to investigate the thermal stability of these proteins first, as it is possible that truncations lead to a massive loss of intrinsic stability.

23.6.7 Analysis of the ATPase Activity of Hsp90

To investigate the ATPase activity of Hsp90, standard assays are used. The most commonly used assay is a coupled enzymatic detection system that regenerates hydrolyzed ATP from ADP and thus connects this reaction to the consumption of NADH [204]. There are commercially available assays for this format. Conversion of NADH to NAD^+ can be followed at a wavelength of 340 nm. The differential extinction coefficient ($\varepsilon_{NADH} - \varepsilon_{NAD^+}$) at this wavelength is 6200. The difference in absorbance observed during the time course of the experiment can be directly correlated to the amount of ATP hydrolyzed during this time. The regeneration system is based on phosphoenolpyruvate (PEP). The enzymes used are pyruvate kinase for the conversion of PEP and ADP to pyruvate and ATP and lactate dehydrogenase for the further conversion of pyruvate to lactate and the generation of NAD^+.

When performing the assays, it is advisable to use 150-μL cuvettes and a photometer that can handle several assays at a time. Buffer conditions can be varied according to specific needs. However, controls should be performed to test the influence of a specific change in the condition. For example, the ATPase activity of yeast Hsp90 is influenced by the concentration of KCl present in the assays. Increasing salt concentrations result in increased ATPase activities. Generally, as the ATPase activity of Hsp90 is rather weak, it is advisable to use sufficient amounts of Hsp90. Reasonable concentrations for yeast Hsp90 are in the range of 2–8 μM. The availability of specific Hsp90 inhibitors allows unambiguous determination of the Hsp90-specific ATPase activity. This is achieved by addition of sufficient concentrations of these compounds (about fivefold excess) and determination of the residual ATPase activity. Background that may arise from other ATP-hydrolyzing enzymes present in the protein purification can then be substracted.

Other assays that can be used to determine the turnover of Hsp90 are based on the detection of phosphate. This can be done either by using a phosphate detection system, such as the EnzCheck assay (Molecular Probes, Leiden, Netherlands), or by a malachite green–based assay [205]. Both assays have been used for Hsp90, but both assays lack the reproduction of ATP from the produced ADP. This can become a problem if longer assay times are desired, as ADP binds much stronger to the nucleotide-binding site and therefore product inhibition may take place [101].

In addition, radioactive assays can be performed. These assays rely on ATP molecules that are labeled with ^{32}P on their α-phosphate atom. Conversion of ATP to ADP results in differential running behavior in thin-layer chromatography plates, which allows simultaneous quantitation of the ATP and ADP levels at desired time points during the reaction [206]. Small aliquots are therefore removed from the re-

action mix and stopped by the addition of EDTA. Detection of ^{32}P levels is performed by autoradiography of the films or phosphoimaging after the exposure of specific screens. This assay setup is especially used to perform single-turnover investigations [84, 86]. These measurements allow determination of the exact turnover of the first ATP molecule to be encountered by the protein and thus allow investigation of whether the hydrolysis reaction is the rate-limiting step or whether the product release is rate-limiting. For these measurements, high protein concentrations and substoichiometric amounts of ATP are employed. This guarantees that every ATP molecule is bound to a protein from the beginning. Again, the reaction is stopped at different time points. This kinetics represents the hydrolysis reaction of the ATP molecule without the need to release it. If this value corresponds to the steady-state approaches described before, the rate-limiting step would be before the hydrolysis reaction. If the turnover instead is faster in the single-turnover experiment compared to the steady-state experiment, the rate-limiting step would be product release. In the case of Hsp90, the need for high protein concentrations leads to difficulties. These concentrations have to be well above the K_D value of ATP to guarantee complete saturation. For Hsp90, the K_D value of ATP is very high (about 400 μM).

23.6.8
Detecting Specific Influences on Hsp90 ATPase Activity

Several compounds and partner proteins are known to influence the ATPase activity of Hsp90 [62]. The affinity of these compounds (geldanamycin, radicicol) can be determined by measuring the ATPase activity of Hsp90 in the presence of different concentrations of these substances. The resulting plot can be analyzed to yield an I_{50} value that roughly correlates to the affinity value K_D. Using the same approach, the influence of partner proteins on the ATPase activity also can be described [91, 132, 133].

Of particular interest is the influence of dimer formation on the ATPase activity of Hsp90. To investigate this, one specific assay involves the formation of heterodimers of mutant Hsp90 with wt Hsp90. In the case that the mutant Hsp90 does not contain ATPase activity, it is possible to detect the influences of mixtures of the two proteins directly during the ATPase measurement. Formation of heterodimers is rather quick, with a half-time of less than a minute. To quantify the influence, different concentrations of the mutant Hsp90 are used in combination with constant concentrations of wt Hsp90, and the ATPase activity is determined. The analysis of the resulting curve can be performed according to the following equation (see also Figure 23.14):

$$v = v_{\mathrm{Hsp90}} \cdot \frac{n \cdot c_{\mathrm{Hsp90}}}{n \cdot c_{\mathrm{Hsp90}} + c_{\mathrm{Frag}}} + v_{\mathrm{Hetero}} \cdot \frac{c_{\mathrm{Frag}}}{n \cdot c_{\mathrm{Hsp90}} + c_{\mathrm{Frag}}} \qquad (1)$$

The equation contains the following parameters: v, the hydrolysis rate; v_{Hsp90}, the wt ATPase activity; v_{Hetero}, the ATPase activity of the heterodimer; c_{Hsp90} and c_{Frag},

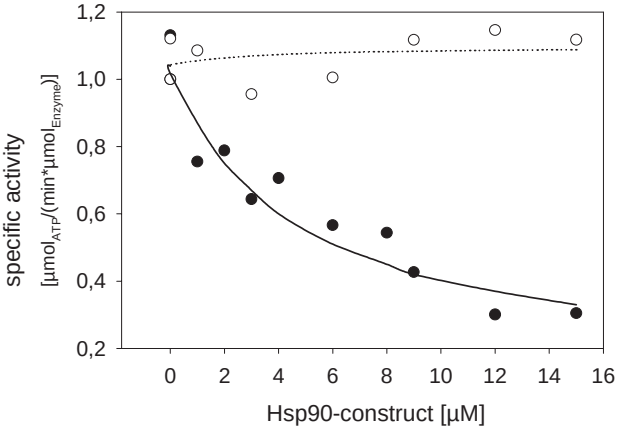

Fig. 23.14. Influence of dimer formation on the ATPase activity of Hsp90. By mixing wt Hsp90 with ATPase-deficient mutant Hsp90, it is possible to form heterodimers. Formation of these heterodimers can be directly visualized in ATPase assays if the heterodimer has a different ATPase activity from the homodimer. In this figure, Δ24-Hsp90 forms heterodimers with strongly reduced ATPase activity, while Δ16-Hsp90 forms heterodimers that still hydrolyze ATP efficiently.

the concentrations of Hsp90 and the fragment; and *n*, a coefficient that is related to the efficiency of heterodimer formation compared to homodimer.

23.6.9
Investigation of the Quaternary Structure by SEC-HPLC

Analytical ultracentrifugation is the method of choice if the quaternary structure of a protein should be explored. This method, which is applicable for addressing oligomerization issues, is explained elsewhere in this book (see Chapter 2).

Size-exclusion chromatography (SEC)-HPLC is able to resolve dimerization constants far below the concentrations normally used for analytical ultracentrifugation, if a sensitive fluorescence detection system is coupled to the HPLC instrument [85]. If homodimeric proteins, such as yeast Hsp90, are in constant subunit exchange on the timescale far below the elution time of the protein, it is possible to obtain one peak for all the concentration applied. This peak shifts from a monomeric position at low protein concentrations to a dimeric position at high protein concentrations. At intermediate concentrations, the protein shows an apparent molecular weight between these two positions. For Hsp90, the plot of protein concentration versus elution time results in a dissociation curve [85] (see Fig. 23.15). The only limitation of this technique is the dilution of the protein during the run, which results in ambiguity with respect to the protein concentration during the run. Assumptions for the dilution factor can be obtained from the peak shape, and back calculation of the actual concentration on the column can be performed using the injection volume and the width of the peak. In general, it is better to use

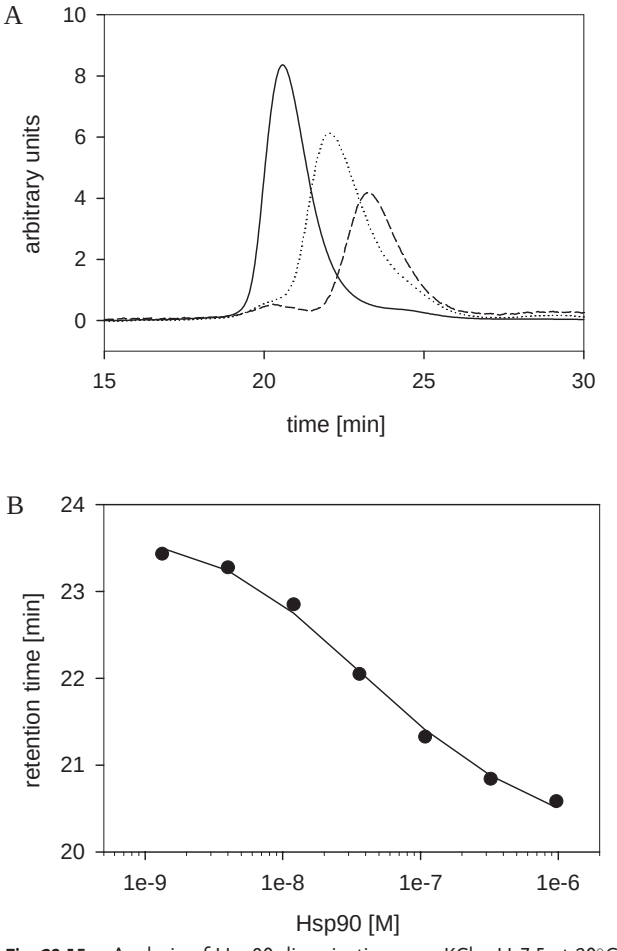

Fig. 23.15. Analysis of Hsp90 dimerization. (A) Size-exclusion chromatography of different concentrations of Hsp90. The elution time of Hsp90 is shifted depending on the protein concentration used, highlighting the possibility of obtaining a monomer-dimer transition. Running buffer was 40 mM HEPES, 150 mM KCl, pH 7.5 at 20°C. Solid line, 1 µM Hsp90; dotted line, 0.03 µM Hsp90; dashed line, 5 nM Hsp90. (B) Monomer/dimer transition of Hsp90. The plot of protein concentration versus elution time can be fitted according to the model described.

larger injection volumes, as dilution effects are less pronounced then. The dilution factor obtained by this method for a Superdex 200HR 10/30 column (Amersham Biosciences, Freiburg, Germany) is about seven, if 100 µL of injection volume is used at a flow rate of 500 µL min^{-1}. Calculation of the homodimerization constant can be then performed according to the following equation:

$$RT = \left(-\frac{K_D}{4 \cdot c_t} + \frac{K_D}{4 \cdot c_t} \cdot \sqrt{\frac{1}{{c_t}^2} + \frac{8}{K_D \cdot c_t}} \right) \cdot (RT_{Monomer} - RT_{Dimer}) + RT_{Dimer} \qquad (2)$$

where RT represents the retention time, K_D the dissociation constant, $RT_{Monomer}$ and RT_{Dimer} the retention times of the monomer and the dimer, and c_t the protein concentration in the injection solution.

23.6.10 Investigation of Binding Events Using Changes of the Intrinsic Fluorescence

The intrinsic fluorescence of the protein can be a very useful parameter where the binding of substrates to proteins is concerned. A variety of different ligands such as ADP, ATP, geldanamycin, and radicicol bind to the N-terminal domain of Hsp90. Some of these ligands, such as radicicol, induce a huge change in intrinsic fluorescence of yeast Hsp90 upon binding, especially if the isolated N-terminal domain is investigated [88]. The advantage of this method is the low amount of protein required for the investigation (about 1 μM). In addition, here the binding event is determined in an equilibrium setup of unmodified binding partners, as no labeling or coupling is required.

However, in the case of radicicol, binding constants cannot be derived from this titration, as binding is much too strong ($K_D = 19$ nM), with a dissociation constant far below the required protein concentration. As binding is stoichiometric under these conditions, this assay can be used to estimate the number of active sites that are present in the protein preparation. Therefore, the binding curve has to be evaluated according to the following functions:

$$F = F_{ML} + (F_M - F_{ML}) \cdot \frac{[L]}{K_D + [L]} \tag{3}$$

$$[L] = \frac{-(K_D + [M]_t - [L]_t) + \sqrt{(K_D + [M]_t - [L]_t)^2 + 4 \cdot [L]_t \cdot K_D}}{2} \tag{4}$$

where F represents the fluorescence, F_{ML} the fluorescence of the liganded macromolecule, F_M the fluorescence of the unliganded macromolecule, K_D the dissociation constant, [L] the concentration of the ligand, and [M] the concentration of the macromolecule.

Other ligands do not induce a strong change in the intrinsic fluorescence of yeast Hsp90, although binding of ADP to the N-terminal domain can be observed, especially if higher salt concentrations are used [88]. For the titration with nucleotides, it is very important to avoid inner-filter effects, as these compounds show strong absorbance, even at wavelengths of 280 nm. Therefore, use of the highest possible excitation wavelength (295 nm) is advised. Otherwise, the inner-filter effect has to be taken into account, which is possible, based on the knowledge of the extinction coefficient of the nucleotide at the excitation wavelength. The resulting titration curve can be analyzed using the standard Longmuir adsorption isotherm, as binding is rather weak, with a K_D value far above the protein concentration used. The equation used for this calculation is Eq. (3).

23.6.11
Investigation of Binding Events Using Isothermal Titration Calorimetry

To analyze protein-ligand interactions in the Hsp90 system, isothermal titration calorimetry (ITC) has proved to be extremely useful in the determination of both stoichiometries and thermodynamic parameters. In this setup, the heat change upon binding of the ligand or partner protein is detected by the ITC instrument for several injections of ligand to the protein solution (usually around 35 injections are automatically performed). The successive saturation of the protein leads to a binding curve that can be analyzed by using the appropriate equation, which in most cases will be the binding of one ligand to one binding site. All parameters can be derived from one ITC experiment with great confidence, if sufficient protein ligand (usually 15 μM in the cell and 150 μM in the injection device) is used to generate a sufficiently high signal. Great care should be taken to match the buffers of the two reaction solutions in order to avoid signals arising from dilution effects of buffer components.

Experiments have been performed for the binding of radicicol, geldanamycin, ADP, and AMP-PNP to the N-terminal domain of Hsp90 [62, 81, 101]. ITC has been used to determine the stoichiometries and the affinities of the binding sites. Especially in the case of small ligands, ITC may in addition provide very useful information regarding the nature of the binding event. The binding enthalpy can be correlated with the specific interactions within the binding pocket and thus yield some structural information. Therefore, it is useful to compare either the interactions of compounds with limited changes in their functional groups with wt Hsp90 or different point mutations of Hsp90 with one ligand to gain understanding about the interactions within the binding pocket that lead to the specificity and affinity of the interaction.

Regarding the binding of partner proteins, ITC was successfully used for the systems Sti1-Hsp90, Cpr6-Hsp90, Aha1-Hsp90, Cdc37-Hsp90, and Sba1-Hsp90-AMP-PNP [80, 131, 132, 172]. The stoichiometry of these complexes is 1:1 and binding constants have been determined to be between 100 nM and 10 μM. The only disadvantage of these measurements is the high protein concentrations required, which usually range from 10 μM to 100 μM in the 1.5-mL cell and far higher in the injection device. Therefore, methods that rely on smaller amounts of proteins and produce results with similar quality are interesting.

23.6.12
Investigation of Protein-Protein Interactions Using Cross-linking

Several of the interactions within the Hsp90 system can be observed by chemical cross-linking. Glutardialdehyde and the cleavable cross-linker DTSSP have been used as cross-linkers [145]. In both cases, it is possible to visualize the cross-linking success on SDS-PAGE. For better resolution, it may be advisable to use Western blotting subsequently to identify the composition of specific bands after cross-linking.

One example in which cross-linking in particular is useful is the interaction between Hsp90 and Sba1/p23. Here, extensive investigations revealed a nucleotide-dependent association of the proteins [207]. Cross-linking was used to monitor optimum binding conditions. For both cross-linkers, the buffer must not contain free amine groups, as these would react with the cross-linker. Therefore, this experiment usually is performed in HEPES buffer (e.g., 40 mM HEPES, pH 7.5, 150 mM KCl, 5 mM $MgCl_2$). The overall volume of the reaction can be as low as 20 µL. Next, 1.6 µL of 2.5% glutardialdehyde is added to the proteins (usually 5 µg of each) and cross-linking is performed for 5 min at room temperature. Then, 5 µL of 1 M Tris, pH 8.5, is added to stop the reaction. Separation of the cross-linking species is achieved on SDS-PAGE. Depending on the size of the protein components and the cross-linking products, gradient gels, ranging from 4% to 12% acrylamide, may be used. However, limitations exist for this technique, as cross-linking artificially selects for species that have lysine residues in the right positioning. Another limitation that has been observed frequently is artificial positive results if high concentrations of cross-linker and/or proteins are used or long reaction times are employed.

23.6.13 Investigation of Protein-Protein Interactions Using Surface Plasmon Resonance Spectroscopy

Surface plasmon resonance spectroscopy (SPR) has been used recently to investigate Hsp90 partner protein interactions in detail. The application of this relatively new technique requires only small amounts of protein, and the experiments are fast and reproducibility is high. The detected signal directly monitors a binding/dissociation event. The high sensitivity, on the other hand, imposes some difficulties as well, as artificial signals arise sometimes. This makes it necessary to carefully establish binding assays and to perform the appropriate controls.

SPR theory has been reviewed extensively by others [208, 209]. In short, a light beam is sent onto a gold slide, which is on top of a dextran matrix to which the protein is coupled. The light intruding into the gold slide is reflected without changing the angle. When the angle of the intruding light is varied, under one specific angle, a resonance phenomenon is observed that leads to the production of an evanescent wave within the gold slide and to the excitation of the plasmons within this slide. Under this angle, a reflection is no longer observed, as the light energy dissipates into the chip surface. This angle, on the other hand, is very sensitive to the weight of the gold slide and the refractive index of the solution within a short distance of the gold slide. As this refractive index changes upon binding of protein to the chip surface, a change in this angle is observed. This change is directly related to the ''resonance units'' representing the output signal. Thus, any binding/dissociation event can be quantified. Therefore, it is possible to couple one protein covalently to the sensor surface (most often via lysine residues) and apply another protein onto the chip surface to investigate binding of a potential interaction partner. The flow-through system allows defined association and dissociation kinetics

to be obtained. The combination of equilibrium approaches, where the signal height is plotted against the concentration of the applied protein, with kinetic approaches, where the observed kinetics is analyzed, offers unique approaches to study interactions.

Although theoretically very straightforward, the technique imposes some challenges. First, the protein has to be coupled to the sample cell. Several chips differing in their surfaces and coupling methods are available. As such, streptavidin-coated chips can be used to couple biotinylated macromolecules, Ni-NTA chips can be used to couple His_6-tagged proteins, and CM5 chips are available to couple covalently primary amines. While coupling in the first two cases requires only applying the protein onto the matrix, in the last case, the COOH groups of the CM5 matrix have to be activated first. This is done by EDC/NHS solution, which is part of the BiaCore coupling kit. The activated groups readily react with primary amines, e.g., lysine residues. To perform this reaction with satisfactory efficiency, the affinity of the protein towards the acidic matrix should be increased by lowering the pH of the coupling buffer below the isoelectric point of the protein. This sometimes imposes some uncertainty regarding the native state of the coupled protein. In the case of yeast Hsp90, 40 mM potassium acetate, pH 4.5, has been used successfully for coupling. Hsp90 coupled in this way has good affinity towards Sti1 and Cpr6 and several other TPR-containing proteins [147, 192]. Specific binding curves are obtained using different concentrations of partner proteins, until at sufficiently high concentrations no further increase in resonance units is observed due to complete saturation of the Hsp90 bound to the chip surface. This saturation behavior is a first indication of a specific binding event. As running buffer 40 mM HEPES, pH 7.5, 150 mM KCl, 1 mM EDTA, and 0.002% Tween20 is recommended, although other buffer composition can also be used. In some cases, it may be advantageous to couple the partner protein instead of Hsp90. One such example is Sba1. The binding of Sba1 requires specific conformations of Hsp90 that are induced by nucleotides, and it is apparently not possible to couple Hsp90 in a conformation to allow Sba1 binding. In addition, the coupling of Sba1 allows the use of different nucleotides to influence the Hsp90 conformations accordingly and investigation of the influence of nucleotides on the interaction between Sba1 and Hsp90.

Additional types of assays are competitive experiments. The coupled protein can be used as competitor. This allows investigation of an equilibrium between a soluble interaction partner and the chip-bound interaction partner. By further increasing the concentration of the soluble interaction partner, it should be possible to completely suppress the binding to the chip surface, as all the protein is already complexed in the injection solution [133, 147]. This is possible for all the interactions described, and generally this is a very powerful method to prove the specificity of the interaction. In addition, this method allows investigation of the binding affinities by an independent titration. Here, the direct and the indirect titration should lead to similar K_D values. It is not necessary that the competitor be the chip-bound protein itself. Another binding partner can be added, and if binding between the chip-bound protein (e.g., Sba1) and the third protein (e.g., Sti1) is

competitive, Sti1 will reduce the amount of Hsp90 binding to the coupled Sba1. If the third protein binds by forming a ternary complex (e.g., Cpr6), the binding signal will further increase above the value recorded for Hsp90 alone [131].

Acknowledgements

The authors would like to acknowledge Didier Picard for critically reading the manuscript. We thank Stefan Walter for help with the equations and Benjamin Bösl for drawing of chemical structures. In addition, we would like to thank Lin Mueller and Harald Wegele for providing graphic material. This work was supported by grants of the DFG and the Fonds der chemischen Industrie.

References

1 Picard, D. (2002). Heat-shock protein 90, a chaperone for folding and regulation. *Cell Mol. Life Sci.*, **59**, 1640–1648.

2 Borkovich, K. A., Farrelly, F. W., Finkelstein, D. B., Taulien, J., and Lindquist, S. (1989). hsp82 is an essential protein that is required in higher concentrations for growth of cells at higher temperatures. *Mol. Cell Biol.*, **9**, 3919–3930.

3 Hickey, E., Brandon, S. E., Smale, G., Lloyd, D., and Weber, L. A. (1989). Sequence and regulation of a gene encoding a human 89-kilodalton heat shock protein. *Mol. Cell Biol.*, **9**, 2615–2626.

4 Krishna, P. and Gloor, G. (2001). The Hsp90 family of proteins in Arabidopsis thaliana. *Cell Stress. Chaperones.*, **6**, 238–246.

5 Gupta, R. S. (1995). Phylogenetic analysis of the 90 kD heat shock family of protein sequences and an examination of the relationship among animals, plants, and fungi species. *Mol. Biol. Evol.*, **12**, 1063–1073.

6 Emelyanov, V. V. (2002). Phylogenetic relationships of organellar Hsp90 homologs reveal fundamental differences to organellar Hsp70 and Hsp60 evolution. *Gene*, **299**, 125–133.

7 Louvion, J. F., Warth, R., and Picard, D. (1996). Two eukaryote-specific regions of Hsp82 are dispensable for its viability and signal transduction functions in yeast. *Proc. Natl. Acad. Sci. U.S.A*, **93**, 13937–13942.

8 Scheufler, C., Brinker, A., Bourenkov, G., Pegoraro, S., Moroder, L., Bartunik, H., Hartl, F. U., and Moarefi, I. (2000). Structure of TPR domain-peptide complexes: critical elements in the assembly of the Hsp70-Hsp90 multichaperone machine. *Cell*, **101**, 199–210.

9 Chen, S., Sullivan, W. P., Toft, D. O., and Smith, D. F. (1998). Differential interactions of p23 and the TPR-containing proteins Hop, Cyp40, FKBP52 and FKBP51 with Hsp90 mutants. *Cell Stress. Chaperones.*, **3**, 118–129.

10 Schmitz, G., Schmidt, M., and Feierabend, J. (1996). Characterization of a plastid-specific HSP90 homologue: identification of a cDNA sequence, phylogenetic descendence and analysis of its mRNA and protein expression. *Plant Mol. Biol.*, **30**, 479–492.

11 Felts, S. J., Owen, B. A., Nguyen, P., Trepel, J., Donner, D. B., and Toft, D. O. (2000). The hsp90-related protein TRAP1 is a mitochondrial

protein with distinct functional properties. *J. Biol. Chem.*, **275**, 3305–3312.

12 Bardwell, J. C. and Craig, E. A. (1988). Ancient heat shock gene is dispensable. *J. Bacteriol.*, **170**, 2977–2983.

13 Tanaka, N. and Nakamoto, H. (1999). HtpG is essential for the thermal stress management in cyanobacteria. *FEBS Lett.*, **458**, 117–123.

14 Morano, K. A., Santoro, N., Koch, K. A., and Thiele, D. J. (1999). A *trans*-activation domain in yeast heat shock transcription factor is essential for cell cycle progression during stress. *Mol. Cell Biol.*, **19**, 402–411.

15 Endo, N., Tashiro, E., Umezawa, K., Kawada, M., Uehara, Y., Doki, Y., Weinstein, I. B., and Imoto, M. (2000). Herbimycin A induces G1 arrest through accumulation of p27(Kip1) in cyclin D1-overexpressing fibroblasts. *Biochem. Biophys. Res. Commun.*, **267**, 54–58.

16 Shiotsu, Y., Neckers, L. M., Wortman, I., An, W. G., Schulte, T. W., Soga, S., Murakata, C., Tamaoki, T., and Akinaga, S. (2000). Novel oxime derivatives of radicicol induce erythroid differentiation associated with preferential G(1) phase accumulation against chronic myelogenous leukemia cells through destabilization of Bcr-Abl with Hsp90 complex. *Blood*, **96**, 2284–2291.

17 Dai, K., Kobayashi, R., and Beach, D. (1996). Physical interaction of mammalian CDC37 with CDK4. *J. Biol. Chem.*, **271**, 22030–22034.

18 Donze, O., Abbas-Terki, T., and Picard, D. (2001). The Hsp90 chaperone complex is both a facilitator and a repressor of the dsRNA-dependent kinase PKR. *EMBO J.*, **20**, 3771–3780.

19 Aligue, R., Akhavan-Niak, H., and Russell, P. (1994). A role for Hsp90 in cell cycle control: Wee1 tyrosine kinase activity requires interaction with Hsp90. *EMBO J.*, **13**, 6099–6106.

20 Rutherford, S. L. and Lindquist, S. (1998). Hsp90 as a capacitor for morphological evolution. *Nature*, **396**, 336–342.

21 Queitsch, C., Sangster, T. A., and Lindquist, S. (2002). Hsp90 as a capacitor of phenotypic variation. *Nature*, **417**, 618–624.

22 Voss, A. K., Thomas, T., and Gruss, P. (2000). Mice lacking HSP90beta fail to develop a placental labyrinth. *Development*, **127**, 1–11.

23 Lele, Z., Hartson, S. D., Martin, C. C., Whitesell, L., Matts, R. L., and Krone, P. H. (1999). Disruption of zebrafish somite development by pharmacologic inhibition of Hsp90. *Dev. Biol.*, **210**, 56–70.

24 Randow, F. and Seed, B. (2001). Endoplasmic reticulum chaperone gp96 is required for innate immunity but not cell viability. *Nat. Cell Biol.*, **3**, 891–896.

25 Gass, J. N., Gifford, N. M., and Brewer, J. W. (2002). Activation of an Unfolded Protein Response during Differentiation of Antibody-secreting B Cells. *J. Biol. Chem.*, **277**, 49047–49054.

26 Meunier, L., Usherwood, Y. K., Chung, K. T., and Hendershot, L. M. (2002). A subset of chaperones and folding enzymes form multiprotein complexes in endoplasmic reticulum to bind nascent proteins. *Mol. Biol. Cell*, **13**, 4456–4469.

27 Binder, R. J. and Srivastava, P. K. (2004). Essential role of CD91 in representation of gp96-chaperoned peptides. *Proc. Natl. Acad. Sci. U.S.A.*

28 Grammatikakis, N., Vultur, A., Ramana, C. V., Siganou, A., Schweinfest, C. W., Watson, D. K., and Raptis, L. (2002). The role of Hsp90N, a new member of the Hsp90 family, in signal transduction and neoplastic transformation. *J. Biol. Chem.*, **277**, 8312–8320.

29 Heitzer, A., Mason, C. A., Snozzi, M., and Hamer, G. (1990). Some effects of growth conditions on steady state and heat shock induced htpG gene expression in continuous cultures of Escherichia coli. *Arch. Microbiol.*, **155**, 7–12.

30 Aranda, A., Querol, A., and del

Olmo, M. (2002). Correlation between acetaldehyde and ethanol resistance and expression of HSP genes in yeast strains isolated during the biological aging of sherry wines. *Arch. Microbiol.*, **177**, 304–312.

31 Zhou, Y. N., Kusukawa, N., Erickson, J. W., Gross, C. A., and Yura, T. (1988). Isolation and characterization of Escherichia coli mutants that lack the heat shock sigma factor sigma 32. *J. Bacteriol.*, **170**, 3640–3649.

32 Cowing, D. W., Bardwell, J. C., Craig, E. A., Woolford, C., Hendrix, R. W., and Gross, C. A. (1985). Consensus sequence for Escherichia coli heat shock gene promoters. *Proc. Natl. Acad. Sci. U.S.A*, **82**, 2679–2683.

33 Nadeau, K., Das, A., and Walsh, C. T. (1993). Hsp90 chaperonins possess ATPase activity and bind heat shock transcription factors and peptidyl prolyl isomerases. *J. Biol. Chem.*, **268**, 1479–1487.

34 Zarzov, P., Boucherie, H., and Mann, C. (1997). A yeast heat shock transcription factor (Hsf1) mutant is defective in both Hsc82/Hsp82 synthesis and spindle pole body duplication. *J. Cell Sci.*, **110 (Pt 16)**, 1879–1891.

35 Ahn, S. G., Liu, P. C., Klyachko, K., Morimoto, R. I., and Thiele, D. J. (2001). The loop domain of heat shock transcription factor 1 dictates DNA-binding specificity and responses to heat stress. *Genes Dev.*, **15**, 2134–2145.

36 Gross, D. S., Adams, C. C., English, K. E., Collins, K. W., and Lee, S. (1990). Promoter function and in situ protein/DNA interactions upstream of the yeast HSP90 heat shock genes. *Antonie Van Leeuwenhoek*, **58**, 175–186.

37 Gross, D. S., English, K. E., Collins, K. W., and Lee, S. W. (1990). Genomic footprinting of the yeast HSP82 promoter reveals marked distortion of the DNA helix and constitutive occupancy of heat shock and TATA elements. *J. Mol. Biol.*, **216**, 611–631.

38 Erkine, A. M., Adams, C. C., Gao, M., and Gross, D. S. (1995). Multiple protein-DNA interactions over the yeast HSC82 heat shock gene promoter. *Nucleic Acids Res.*, **23**, 1822–1829.

39 Ripley, B. J., Stephanou, A., Isenberg, D. A., and Latchman, D. S. (1999). Interleukin-10 activates heat-shock protein 90beta gene expression. *Immunology*, **97**, 226–231.

40 Shen, Y., Liu, J., Wang, X., Cheng, X., Wang, Y., and Wu, N. (1997). Essential role of the first intron in the transcription of hsp90beta gene. *FEBS Lett.*, **413**, 92–98.

41 Zhang, S. L., Yu, J., Cheng, X. K., Ding, L., Heng, F. Y., Wu, N. H., and Shen, Y. F. (1999). Regulation of human hsp90alpha gene expression. *FEBS Lett.*, **444**, 130–135.

42 Dugyala, R. R., Claggett, T. W., Kimmel, G. L., and Kimmel, C. A. (2002). HSP90alpha, HSP90beta, and p53 expression following in vitro hyperthermia exposure in gestation day 10 rat embryos. *Toxicol. Sci.*, **69**, 183–190.

43 Wu, J. M., Xiao, L., Cheng, X. K., Cui, L. X., Wu, N. H., and Shen, Y. F. (2003). PKC epsilon is a unique regulator for hsp90 beta gene in heat shock response. *J. Biol. Chem.*, **278**, 51143–51149.

44 Sreedhar, A. S., Kalmar, E., Csermely, P., and Shen, Y. F. (2004). Hsp90 isoforms: functions, expression and clinical importance. *FEBS Lett.*, **562**, 11–15.

45 Rutkowski, D. T. and Kaufman, R. J. (2004). A trip to the ER: coping with stress. *Trends Cell Biol.*, **14**, 20–28.

46 Okamura, K., Kimata, Y., Higashio, H., Tsuru, A., and Kohno, K. (2000). Dissociation of Kar2p/BiP from an ER sensory molecule, Ire1p, triggers the unfolded protein response in yeast. *Biochem. Biophys. Res. Commun.*, **279**, 445–450.

47 Kimata, Y., Kimata, Y. I., Shimizu, Y., Abe, H., Farcasanu, I. C., Takeuchi, M., Rose, M. D., and Kohno, K. (2003). Genetic evidence for a role of BiP/Kar2 that regulates Ire1 in response to accumulation of

unfolded proteins. *Mol. Biol. Cell*, **14**, 2559–2569.

48 Patil, C. and Walter, P. (2001). Intracellular signaling from the endoplasmic reticulum to the nucleus: the unfolded protein response in yeast and mammals. *Curr. Opin. Cell Biol.*, **13**, 349–355.

49 Neckers, L. and Ivy, S. P. (2003). Heat shock protein 90. *Curr. Opin. Oncol.*, **15**, 419–424.

50 Horakova, K. and Betina, V. (1977). Cytotoxic activity of macrocyclic metabolites from fungi. *Neoplasma*, **24**, 21–27.

51 Johnson, R. D., Haber, A., and Rinehart, K. L., Jr. (1974). Geldanamycin biosynthesis and carbon magnetic resonance. *J. Am. Chem. Soc.*, **96**, 3316–3317.

52 Muroi, M., Izawa, M., Kosai, Y., and Asai, M. (1980). Macbecins I and II, new antitumor antibiotics. II. Isolation and characterization. *J. Antibiot. (Tokyo)*, **33**, 205–212.

53 Tanida, S., Hasegawa, T., and Higashide, E. (1980). Macbecins I and II, new antitumor antibiotics. I. Producing organism, fermentation and antimicrobial activities. *J. Antibiot. (Tokyo)*, **33**, 199–204.

54 Omura, S., Miyano, K., Nakagawa, A., Sano, H., Komiyama, K., Umezawa, I., Shibata, K., and Satsumabayashi, S. (1984). Chemical modification and antitumor activity of herbimycin A. 8,9-Epoxide, 7,9-cyclic carbamate, and 17 or 19-amino derivatives. *J. Antibiot. (Tokyo)*, **37**, 1264–1267.

55 Omura, S., Iwai, Y., Takahashi, Y., Sadakane, N., Nakagawa, A., Oiwa, H., Hasegawa, Y., and Ikai, T. (1979). Herbimycin, a new antibiotic produced by a strain of Streptomyces. *J. Antibiot. (Tokyo)*, **32**, 255–261.

56 Uehara, Y., Hori, M., Takeuchi, T., and Umezawa, H. (1986). Phenotypic change from transformed to normal induced by benzoquinonoid ansamycins accompanies inactivation of p60src in rat kidney cells infected with Rous sarcoma virus. *Mol. Cell Biol.*, **6**, 2198–2206.

57 Uehara, Y. (2003). Natural product origins of Hsp90 inhibitors. *Curr. Cancer Drug Targets.*, **3**, 325–330.

58 Whitesell, L. and Cook, P. (1996). Stable and specific binding of heat shock protein 90 by geldanamycin disrupts glucocorticoid receptor function in intact cells. *Mol. Endocrinol.*, **10**, 705–712.

59 An, W. G., Schulte, T. W., and Neckers, L. M. (2000). The heat shock protein 90 antagonist geldanamycin alters chaperone association with p210bcr-abl and v-src proteins before their degradation by the proteasome. *Cell Growth Differ.*, **11**, 355–360.

60 Schneider, C., Sepp-Lorenzino, L., Nimmesgern, E., Ouerfelli, O., Danishefsky, S., Rosen, N., and Hartl, F. U. (1996). Pharmacologic shifting of a balance between protein refolding and degradation mediated by Hsp90. *Proc. Natl. Acad. Sci. U.S.A*, **93**, 14536–14541.

61 Stebbins, C. E., Russo, A. A., Schneider, C., Rosen, N., Hartl, F. U., and Pavletich, N. P. (1997). Crystal structure of an Hsp90-geldanamycin complex: targeting of a protein chaperone by an antitumor agent. *Cell*, **89**, 239–250.

62 Roe, S. M., Prodromou, C., O'Brien, R., Ladbury, J. E., Piper, P. W., and Pearl, L. H. (1999). Structural basis for inhibition of the Hsp90 molecular chaperone by the antitumor antibiotics radicicol and geldanamycin. *J. Med. Chem.*, **42**, 260–266.

63 Neckers, L. (2002). Hsp90 inhibitors as novel cancer chemotherapeutic agents. *Trends Mol. Med.*, **8**, S55–S61.

64 Workman, P. (2004). Combinatorial attack on multistep oncogenesis by inhibiting the Hsp90 molecular chaperone. *Cancer Lett.*, **206**, 149–157.

65 Kelland, L. R., Sharp, S. Y., Rogers, P. M., Myers, T. G., and Workman, P. (1999). DT-Diaphorase expression and tumor cell sensitivity to 17-allylamino, 17-demethoxygeldanamycin, an inhibitor of heat shock protein 90. *J. Natl. Cancer Inst.*, **91**, 1940–1949.

66 Sausville, E. A., Tomaszewski, J. E.,

and Ivy, P. (2003). Clinical development of 17-allylamino, 17-demethoxygeldanamycin. *Curr. Cancer Drug Targets.*, **3**, 377–383.

67 Kamal, A., Thao, L., Sensintaffar, J., Zhang, L., Boehm, M. F., Fritz, L. C., and Burrows, F. J. (2003). A high-affinity conformation of Hsp90 confers tumour selectivity on Hsp90 inhibitors. *Nature*, **425**, 407–410.

68 Rowlands, M. G., Newbatt, Y. M., Prodromou, C., Pearl, L. H., Workman, P., and Aherne, W. (2004). High-throughput screening assay for inhibitors of heat-shock protein 90 ATPase activity. *Anal. Biochem.*, **327**, 176–183.

69 Chiosis, G., Timaul, M. N., Lucas, B., Munster, P. N., Zheng, F. F., Sepp-Lorenzino, L., and Rosen, N. (2001). A small molecule designed to bind to the adenine nucleotide pocket of Hsp90 causes Her2 degradation and the growth arrest and differentiation of breast cancer cells. *Chem. Biol.*, **8**, 289–299.

70 Chiosis, G., Lucas, B., Huezo, H., Solit, D., Basso, A., and Rosen, N. (2003). Development of purine-scaffold small molecule inhibitors of Hsp90. *Curr. Cancer Drug Targets.*, **3**, 371–376.

71 Pratt, W. B. and Toft, D. O. (2003). Regulation of signaling protein function and trafficking by the hsp90/hsp70-based chaperone machinery. *Exp. Biol. Med. (Maywood.)*, **228**, 111–133.

72 Blagosklonny, M. V., Toretsky, J., Bohen, S., and Neckers, L. (1996). Mutant conformation of p53 translated in vitro or in vivo requires functional HSP90. *Proc. Natl. Acad. Sci. U.S.A*, **93**, 8379–8383.

73 Zou, J., Guo, Y., Guettouche, T., Smith, D. F., and Voellmy, R. (1998). Repression of heat shock transcription factor HSF1 activation by HSP90 (HSP90 complex) that forms a stress-sensitive complex with HSF1. *Cell*, **94**, 471–480.

74 Prodromou, C., Roe, S. M., Piper, P. W., and Pearl, L. H. (1997). A molecular clamp in the crystal structure of the N-terminal domain of the yeast Hsp90 chaperone. *Nat. Struct. Biol.*, **4**, 477–482.

75 Prodromou, C., Roe, S. M., O'Brien, R., Ladbury, J. E., Piper, P. W., and Pearl, L. H. (1997). Identification and structural characterization of the ATP/ADP-binding site in the Hsp90 molecular chaperone. *Cell*, **90**, 65–75.

76 Wigley, D. B., Davies, G. J., Dodson, E. J., Maxwell, A., and Dodson, G. (1991). Crystal structure of an N-terminal fragment of the DNA gyrase B protein. *Nature*, **351**, 624–629.

77 Dutta, R. and Inouye, M. (2000). GHKL, an emergent ATPase/kinase superfamily. *Trends Biochem. Sci.*, **25**, 24–28.

78 Brino, L., Urzhumtsev, A., Mousli, M., Bronner, C., Mitschler, A., Oudet, P., and Moras, D. (2000). Dimerization of Escherichia coli DNA-gyrase B provides a structural mechanism for activating the ATPase catalytic center. *J. Biol. Chem.*, **275**, 9468–9475.

79 Ban, C., Junop, M., and Yang, W. (1999). Transformation of MutL by ATP binding and hydrolysis: a switch in DNA mismatch repair. *Cell*, **97**, 85–97.

80 Meyer, P., Prodromou, C., Hu, B., Vaughan, C., Roe, S. M., Panaretou, B., Piper, P. W., and Pearl, L. H. (2003). Structural and functional analysis of the middle segment of hsp90: implications for ATP hydrolysis and client protein and cochaperone interactions. *Mol. Cell*, **11**, 647–658.

81 Panaretou, B., Prodromou, C., Roe, S. M., O'Brien, R., Ladbury, J. E., Piper, P. W., and Pearl, L. H. (1998). ATP binding and hydrolysis are essential to the function of the Hsp90 molecular chaperone in vivo. *EMBO J.*, **17**, 4829–4836.

82 Scheibel, T., Weikl, T., and Buchner, J. (1998). Two chaperone sites in Hsp90 differing in substrate specificity and ATP dependence. *Proc. Natl. Acad. Sci. U.S.A*, **95**, 1495–1499.

83 Prodromou, C., Panaretou, B., Chohan, S., Siligardi, G., O'Brien, R., Ladbury, J. E., Roe, S. M., Piper,

P. W., and Pearl, L. H. (2000). The ATPase cycle of Hsp90 drives a molecular 'clamp' via transient dimerization of the N-terminal domains. *EMBO J.*, **19**, 4383–4392.

84 Weikl, T., Muschler, P., Richter, K., Veit, T., Reinstein, J., and Buchner, J. (2000). C-terminal regions of Hsp90 are important for trapping the nucleotide during the ATPase cycle. *J. Mol. Biol.*, **303**, 583–592.

85 Richter, K., Muschler, P., Hainzl, O., and Buchner, J. (2001). Coordinated ATP hydrolysis by the Hsp90 dimer. *J. Biol. Chem.*, **276**, 33689–33696.

86 Wegele, H., Muschler, P., Bunck, M., Reinstein, J., and Buchner, J. (2003). Dissection of the contribution of individual domains to the ATPase mechanism of Hsp90. *J. Biol. Chem.*, **278**, 39303–39310.

87 Chadli, A., Bouhouche, I., Sullivan, W., Stensgard, B., McMahon, N., Catelli, M. G., and Toft, D. O. (2000). Dimerization and N-terminal domain proximity underlie the function of the molecular chaperone heat shock protein 90. *Proc. Natl. Acad. Sci. U.S.A*, **97**, 12524–12529.

88 Richter, K., Reinstein, J., and Buchner, J. (2002). N-terminal residues regulate the catalytic efficiency of the Hsp90 ATPase cycle. *J. Biol. Chem.*, **277**, 44905–44910.

89 Grenert, J. P., Sullivan, W. P., Fadden, P., Haystead, T. A., Clark, J., Mimnaugh, E., Krutzsch, H., Ochel, H. J., Schulte, T. W., Sausville, E., Neckers, L. M., and Toft, D. O. (1997). The amino-terminal domain of heat shock protein 90 (hsp90) that binds geldanamycin is an ATP/ADP switch domain that regulates hsp90 conformation. *J. Biol. Chem.*, **272**, 23843–23850.

90 Dehner, A., Furrer, J., Richter, K., Schuster, I., Buchner, J., and Kessler, H. (2003). NMR Chemical Shift Perturbation Study of the N-Terminal Domain of Hsp90 upon Binding of ADP, AMP-PNP, Geldanamycin, and Radicicol. *Chembiochem.*, **4**, 870–877.

91 McLaughlin, S. H., Smith, H. W., and Jackson, S. E. (2002). Stimulation of the weak ATPase activity of human hsp90 by a client protein. *J. Mol. Biol.*, **315**, 787–798.

92 Owen, B. A., Sullivan, W. P., Felts, S. J., and Toft, D. O. (2002). Regulation of heat shock protein 90 ATPase activity by sequences in the carboxyl terminus. *J. Biol. Chem.*, **277**, 7086–7091.

93 Soti, C., Racz, A., and Csermely, P. (2002). A Nucleotide-dependent molecular switch controls ATP binding at the C-terminal domain of Hsp90. N-terminal nucleotide binding unmasks a C-terminal binding pocket. *J. Biol. Chem.*, **277**, 7066–7075.

94 Garnier, C., Lafitte, D., Tsvetkov, P. O., Barbier, P., Leclerc-Devin, J., Millot, J. M., Briand, C., Makarov, A. A., Catelli, M. G., and Peyrot, V. (2002). Binding of ATP to heat shock protein 90: evidence for an ATP-binding site in the C-terminal domain. *J. Biol. Chem.*, **277**, 12208–12214.

95 Jakob, U., Lilie, H., Meyer, I., and Buchner, J. (1995). Transient interaction of Hsp90 with early unfolding intermediates of citrate synthase. Implications for heat shock in vivo. *J. Biol. Chem.*, **270**, 7288–7294.

96 Nemoto, T. K., Ono, T., and Tanaka, K. (2001). Substrate-binding characteristics of proteins in the 90 kDa heat shock protein family. *Biochem. J.*, **354**, 663–670.

97 Johnson, B. D., Chadli, A., Felts, S. J., Bouhouche, I., Catelli, M. G., and Toft, D. O. (2000). Hsp90 chaperone activity requires the full-length protein and interaction among its multiple domains. *J. Biol. Chem.*, **275**, 32499–32507.

98 Wiech, H., Buchner, J., Zimmermann, R., and Jakob, U. (1992). Hsp90 chaperones protein folding in vitro. *Nature*, **358**, 169–170.

99 Thulasiraman, V. and Matts, R. L. (1996). Effect of geldanamycin on the kinetics of chaperone-mediated renaturation of firefly luciferase in

rabbit reticulocyte lysate. *Biochemistry*, **35**, 13443–13450.

100 Young, J. C., Schneider, C., and Hartl, F. U. (1997). In vitro evidence that hsp90 contains two independent chaperone sites. *FEBS Lett.*, **418**, 139–143.

101 Scheibel, T., Siegmund, H. I., Jaenicke, R., Ganz, P., Lilie, H., and Buchner, J. (1999). The charged region of Hsp90 modulates the function of the N-terminal domain. *Proc. Natl. Acad. Sci. U.S.A*, **96**, 1297–1302.

102 Csermely, P., Miyata, Y., Soti, C., and Yahara, I. (1997). Binding affinity of proteins to hsp90 correlates with both hydrophobicity and positive charges. A surface plasmon resonance study. *Life Sci.*, **61**, 411–418.

103 Miyata, Y. and Yahara, I. (1992). The 90-kDa heat shock protein, HSP90, binds and protects casein kinase II from self-aggregation and enhances its kinase activity. *J. Biol. Chem.*, **267**, 7042–7047.

104 Miyata, Y. and Yahara, I. (1995). Interaction between casein kinase II and the 90-kDa stress protein, HSP90. *Biochemistry*, **34**, 8123–8129.

105 Nathan, D. F., Vos, M. H., and Lindquist, S. (1997). In vivo functions of the Saccharomyces cerevisiae Hsp90 chaperone. *Proc. Natl. Acad. Sci. U.S.A*, **94**, 12949–12956.

106 Vogen, S., Gidalevitz, T., Biswas, C., Simen, B. B., Stein, E., Gulmen, F., and Argon, Y. (2002). Radicicol-sensitive peptide binding to the N-terminal portion of GRP94. *J. Biol. Chem.*, **277**, 40742–40750.

107 Wearsch, P. A. and Nicchitta, C. V. (1997). Interaction of endoplasmic reticulum chaperone GRP94 with peptide substrates is adenine nucleotide-independent. *J. Biol. Chem.*, **272**, 5152–5156.

108 Wearsch, P. A., Voglino, L., and Nicchitta, C. V. (1998). Structural transitions accompanying the activation of peptide binding to the endoplasmic reticulum Hsp90 chaperone GRP94. *Biochemistry*, **37**, 5709–5719.

109 Gidalevitz, T., Biswas, C., Ding, H., Schneidman-Duhovny, D., Wolfson, H. J., Stevens, F., Radford, S., and Argon, Y. (2004). Identification of the N-terminal Peptide Binding Site of Glucose-regulated Protein 94. *J. Biol. Chem.*, **279**, 16543–16552.

110 Scroggins, B. T., Prince, T., Shao, J., Uma, S., Huang, W., Guo, Y., Yun, B. G., Hedman, K., Matts, R. L., and Hartson, S. D. (2003). High affinity binding of Hsp90 is triggered by multiple discrete segments of its kinase clients. *Biochemistry*, **42**, 12550–12561.

111 Shue, G. and Kohtz, D. S. (1994). Structural and functional aspects of basic helix-loop-helix protein folding by heat-shock protein 90. *J. Biol. Chem.*, **269**, 2707–2711.

112 Shaknovich, R., Shue, G., and Kohtz, D. S. (1992). Conformational activation of a basic helix-loop-helix protein (MyoD1) by the C-terminal region of murine HSP90 (HSP84). *Mol. Cell Biol.*, **12**, 5059–5068.

113 Hu, J., Toft, D., Anselmo, D., and Wang, X. (2002). In vitro reconstitution of functional hepadnavirus reverse transcriptase with cellular chaperone proteins. *J. Virol.*, **76**, 269–279.

114 Beck, J. and Nassal, M. (2003). Efficient Hsp90-independent in vitro activation by Hsc70 and Hsp40 of duck hepatits B virus reverse transcriptase, an assumed Hsp90 client protein. *J. Biol. Chem.*

115 Young, J. C. and Hartl, F. U. (2000). Polypeptide release by Hsp90 involves ATP hydrolysis and is enhanced by the co-chaperone p23. *EMBO J.*, **19**, 5930–5940.

116 Scherrer, L. C., Dalman, F. C., Massa, E., Meshinchi, S., and Pratt, W. B. (1990). Structural and functional reconstitution of the glucocorticoid receptor-hsp90 complex. *J. Biol. Chem.*, **265**, 21397–21400.

117 Toft, D. and Gorski, J. (1966). A receptor molecule for estrogens: isolation from the rat uterus and

preliminary characterization. *Proc. Natl. Acad. Sci. U.S.A*, **55**, 1574–1581.

118 Sanchez, E. R., Meshinchi, S., Schlesinger, M. J., and Pratt, W. B. (1987). Demonstration that the 90-kilodalton heat shock protein is bound to the glucocorticoid receptor in its 9S nondeoxynucleic acid binding form. *Mol. Endocrinol.*, **1**, 908–912.

119 Smith, D. F., Schowalter, D. B., Kost, S. L., and Toft, D. O. (1990). Reconstitution of progesterone receptor with heat shock proteins. *Mol. Endocrinol.*, **4**, 1704–1711.

120 Smith, D. F. (1993). Dynamics of heat shock protein 90-progesterone receptor binding and the disactivation loop model for steroid receptor complexes. *Mol. Endocrinol.*, **7**, 1418–1429.

121 Smith, D. F., Sullivan, W. P., Marion, T. N., Zaitsu, K., Madden, B., McCormick, D. J., and Toft, D. O. (1993). Identification of a 60-kilodalton stress-related protein, p60, which interacts with hsp90 and hsp70. *Mol. Cell Biol.*, **13**, 869–876.

122 Johnson, J. L., Beito, T. G., Krco, C. J., and Toft, D. O. (1994). Characterization of a novel 23-kilodalton protein of unactive progesterone receptor complexes. *Mol. Cell Biol.*, **14**, 1956–1963.

123 Owens-Grillo, J. K., Hoffmann, K., Hutchison, K. A., Yem, A. W., Deibel, M. R., Jr., Handschumacher, R. E., and Pratt, W. B. (1995). The cyclosporin A-binding immunophilin CyP-40 and the FK506-binding immunophilin hsp56 bind to a common site on hsp90 and exist in independent cytosolic heterocomplexes with the untransformed glucocorticoid receptor. *J. Biol. Chem.*, **270**, 20479–20484.

124 Renoir, J. M., Pahl, A., Keller, U., and Baulieu, E. E. (1993). Immunological identification of a 50 kDa Mr FK506-binding immunophilin as a component of the non-DNA binding, hsp90 and hsp70 containing, heterooligomeric form of the chick oviduct progesterone receptor. *C. R. Acad. Sci. III*, **316**, 1410–1416.

125 Smith, D. F., Baggenstoss, B. A., Marion, T. N., and Rimerman, R. A. (1993). Two FKBP-related proteins are associated with progesterone receptor complexes. *J. Biol. Chem.*, **268**, 18365–18371.

126 Chang, H. C. and Lindquist, S. (1994). Conservation of Hsp90 macromolecular complexes in Saccharomyces cerevisiae. *J. Biol. Chem.*, **269**, 24983–24988.

127 Perdew, G. H. and Whitelaw, M. L. (1991). Evidence that the 90-kDa heat shock protein (HSP90) exists in cytosol in heteromeric complexes containing HSP70 and three other proteins with Mr of 63,000, 56,000, and 50,000. *J. Biol. Chem.*, **266**, 6708–6713.

128 Johnson, J. L. and Craig, E. A. (2000). A role for the Hsp40 Ydj1 in repression of basal steroid receptor activity in yeast. *Mol. Cell Biol.*, **20**, 3027–3036.

129 Kimura, Y., Yahara, I., and Lindquist, S. (1995). Role of the protein chaperone YDJ1 in establishing Hsp90-mediated signal transduction pathways. *Science*, **268**, 1362–1365.

130 Johnson, J., Corbisier, R., Stensgard, B., and Toft, D. (1996). The involvement of p23, hsp90, and immunophilins in the assembly of progesterone receptor complexes. *J. Steroid Biochem. Mol. Biol.*, **56**, 31–37.

131 Richter, K., Walter, S., and Buchner, J. (2004). Sba1 connects the ATPase reaction of Hsp90 to the progression of the chaperone cycle. *manuscript submitted.*

132 Prodromou, C., Siligardi, G., O'Brien, R., Woolfson, D. N., Regan, L., Panaretou, B., Ladbury, J. E., Piper, P. W., and Pearl, L. H. (1999). Regulation of Hsp90 ATPase activity by tetratricopeptide repeat (TPR)-domain co-chaperones. *EMBO J.*, **18**, 754–762.

133 Richter, K., Muschler, P., Hainzl, O., Reinstein, J., and Buchner, J. (2003). Sti1 is a non-competitive inhibitor of the Hsp90 ATPase. Binding prevents the N-terminal

dimerization reaction during the atpase cycle. *J. Biol. Chem.*, **278**, 10328–10333.

134 Johnson, J. L. and Toft, D. O. (1995). Binding of p23 and hsp90 during assembly with the progesterone receptor. *Mol. Endocrinol.*, **9**, 670–678.

135 Sullivan, W. P., Owen, B. A., and Toft, D. O. (2002). The influence of ATP and p23 on the conformation of hsp90. *J. Biol. Chem.*

136 Panaretou, B., Siligardi, G., Meyer, P., Maloney, A., Sullivan, J. K., Singh, S., Millson, S. H., Clarke, P. A., Naaby-Hansen, S., Stein, R., Cramer, R., Mollapour, M., Workman, P., Piper, P. W., Pearl, L. H., and Prodromou, C. (2002). Activation of the ATPase activity of hsp90 by the stress-regulated cochaperone aha1. *Mol. Cell*, **10**, 1307–1318.

137 Hernandez, M. P., Chadli, A., and Toft, D. O. (2002). HSP40 binding is the first step in the HSP90 chaperoning pathway for the progesterone receptor. *J. Biol. Chem.*, **277**, 11873–11881.

138 Wegele, H., Haslbeck, M., Reinstein, J., and Buchner, J. (2003). Sti1 is a novel activator of the Ssa proteins. *J. Biol. Chem*, **278**, 25970–25976.

139 Morishima, Y., Kanelakis, K. C., Murphy, P. J., Shewach, D. S., and Pratt, W. B. (2001). Evidence for iterative ratcheting of receptor-bound hsp70 between its ATP and ADP conformations during assembly of glucocorticoid receptor.hsp90 heterocomplexes. *Biochemistry*, **40**, 1109–1116.

140 Morishima, Y., Kanelakis, K. C., Silverstein, A. M., Dittmar, K. D., Estrada, L., and Pratt, W. B. (2000). The Hsp organizer protein hop enhances the rate of but is not essential for glucocorticoid receptor folding by the multiprotein Hsp90-based chaperone system. *J. Biol. Chem.*, **275**, 6894–6900.

141 Das, A. K., Cohen, P. W., and Barford, D. (1998). The structure of the tetratricopeptide repeats of protein phosphatase 5: implications for TPR-mediated protein-protein interactions. *EMBO J.*, **17**, 1192–1199.

142 Brinker, A., Scheufler, C., Von Der, M. F., Fleckenstein, B., Herrmann, C., Jung, G., Moarefi, I., and Hartl, F. U. (2002). Ligand discrimination by TPR domains. Relevance and selectivity of EEVD-recognition in Hsp70 × Hop × Hsp90 complexes. *J. Biol. Chem.*, **277**, 19265–19275.

143 Odunuga, O. O., Hornby, J. A., Bies, C., Zimmermann, R., Pugh, D. J., and Blatch, G. L. (2003). Tetratricopeptide repeat motif-mediated Hsc70-mSTI1 interaction. Molecular characterization of the critical contacts for successful binding and specificity. *J. Biol. Chem.*, **278**, 6896–6904.

144 Johnson, J. L. and Toft, D. O. (1994). A novel chaperone complex for steroid receptors involving heat shock proteins, immunophilins, and p23. *J. Biol. Chem.*, **269**, 24989–24993.

145 Weiki, T., Abelmann, K., and Buchner, J. (1999). An unstructured C-terminal region of the Hsp90 co-chaperone p23 is important for its chaperone function. *J. Mol. Biol.*, **293**, 685–691.

146 Weaver, A. J., Sullivan, W. P., Felts, S. J., Owen, B. A., and Toft, D. O. (2000). Crystal structure and activity of human p23, a heat shock protein 90 co-chaperone. *J. Biol. Chem.*, **275**, 23045–23052.

147 Mayr, C., Richter, K., Lilie, H., and Buchner, J. (2000). Cpr6 and Cpr7, two closely related Hsp90-associated immunophilins from Saccharomyces cerevisiae, differ in their functional properties. *J. Biol. Chem.*, **275**, 34140–34146.

148 Pirkl, F. and Buchner, J. (2001). Functional analysis of the Hsp90-associated human peptidyl prolyl *cis*/*trans* isomerases FKBP51, FKBP52 and Cyp40. *J. Mol. Biol.*, **308**, 795–806.

149 Carrigan, P. E., Nelson, G. M., Roberts, P. J., Stoffer, J., Riggs, D. L., and Smith, D. F. (2004). Multiple Domains of the Co-chaperone Hop

Are Important for Hsp70 Binding. *J. Biol. Chem.*, **279**, 16185–16193.

150 Cheung-Flynn, J., Roberts, P. J., Riggs, D. L., and Smith, D. F. (2003). C-terminal sequences outside the tetratricopeptide repeat domain of FKBP51 and FKBP52 cause differential binding to Hsp90. *J. Biol. Chem.*, **278**, 17388–17394.

151 Nair, S. C., Rimerman, R. A., Toran, E. J., Chen, S., Prapapanich, V., Butts, R. N., and Smith, D. F. (1997). Molecular cloning of human FKBP51 and comparisons of immunophilin interactions with Hsp90 and progesterone receptor. *Mol. Cell Biol.*, **17**, 594–603.

152 Duina, A. A., Marsh, J. A., Kurtz, R. B., Chang, H. C., Lindquist, S., and Gaber, R. F. (1998). The peptidyl-prolyl isomerase domain of the CyP-40 cyclophilin homolog Cpr7 is not required to support growth or glucocorticoid receptor activity in Saccharomyces cerevisiae. *J. Biol. Chem.*, **273**, 10819–10822.

153 Bose, S., Weikl, T., Bugl, H., and Buchner, J. (1996). Chaperone function of Hsp90-associated proteins. *Science*, **274**, 1715–1717.

154 Pirkl, F., Fischer, E., Modrow, S., and Buchner, J. (2001). Localization of the chaperone domain of FKBP52. *J. Biol. Chem.*, **276**, 37034–37041.

155 Bharadwaj, S., Ali, A., and Ovsenek, N. (1999). Multiple components of the HSP90 chaperone complex function in regulation of heat shock factor 1 In vivo. *Mol. Cell Biol.*, **19**, 8033–8041.

156 Silverstein, A. M., Galigniana, M. D., Kanelakis, K. C., Radanyi, C., Renoir, J. M., and Pratt, W. B. (1999). Different regions of the immunophilin FKBP52 determine its association with the glucocorticoid receptor, hsp90, and cytoplasmic dynein. *J. Biol. Chem.*, **274**, 36980–36986.

157 Galigniana, M. D., Radanyi, C., Renoir, J. M., Housley, P. R., and Pratt, W. B. (2001). Evidence that the peptidylprolyl isomerase domain of the hsp90-binding immunophilin FKBP52 is involved in both dynein interaction and glucocorticoid receptor movement to the nucleus. *J. Biol. Chem.*, **276**, 14884–14889.

158 Davies, T. H., Ning, Y. M., and Sanchez, E. R. (2002). A new first step in activation of steroid receptors: hormone-induced switching of FKBP51 and FKBP52 immunophilins. *J. Biol. Chem.*, **277**, 4597–4600.

159 Galigniana, M. D., Harrell, J. M., O'Hagen, H. M., Ljungman, M., and Pratt, W. B. (2004). Hsp90-binding immunophilins link p53 to dynein during p53 transport to the nucleus. *J. Biol. Chem.*

160 Riggs, D. L., Roberts, P. J., Chirillo, S. C., Cheung-Flynn, J., Prapapanich, V., Ratajczak, T., Gaber, R., Picard, D., and Smith, D. F. (2003). The Hsp90-binding peptidylprolyl isomerase FKBP52 potentiates glucocorticoid signaling in vivo. *EMBO J.*, **22**, 1158–1167.

161 Silverstein, A. M., Galigniana, M. D., Chen, M. S., Owens-Grillo, J. K., Chinkers, M., and Pratt, W. B. (1997). Protein phosphatase 5 is a major component of glucocorticoid receptor.hsp90 complexes with properties of an FK506-binding immunophilin. *J. Biol. Chem.*, **272**, 16224–16230.

162 Stepanova, L., Leng, X., Parker, S. B., and Harper, J. W. (1996). Mammalian p50Cdc37 is a protein kinase-targeting subunit of Hsp90 that binds and stabilizes Cdk4. *Genes Dev.*, **10**, 1491–1502.

163 Brugge, J. S. (1986). Interaction of the Rous sarcoma virus protein pp60src with the cellular proteins pp50 and pp90. *Curr. Top. Microbiol. Immunol.*, **123**, 1–22.

164 Grammatikakis, N., Lin, J. H., Grammatikakis, A., Tsichlis, P. N., and Cochran, B. H. (1999). p50(cdc37) acting in concert with Hsp90 is required for Raf-1 function. *Mol. Cell Biol.*, **19**, 1661–1672.

165 Stewart, S., Sundaram, M., Zhang, Y., Lee, J., Han, M., and Guan, K. L. (1999). Kinase suppressor of Ras forms a multiprotein signaling complex and modulates MEK

localization. *Mol. Cell Biol.*, **19**, 5523–5534.

166 Tatebe, H. and Shiozaki, K. (2003). Identification of Cdc37 as a novel regulator of the stress-responsive mitogen-activated protein kinase. *Mol. Cell Biol.*, **23**, 5132–5142.

167 Xu, Y., Singer, M. A., and Lindquist, S. (1999). Maturation of the tyrosine kinase c-src as a kinase and as a substrate depends on the molecular chaperone Hsp90. *Proc. Natl. Acad. Sci. U.S.A*, **96**, 109–114.

168 Xu, Y. and Lindquist, S. (1993). Heat-shock protein hsp90 governs the activity of pp60v-src kinase. *Proc. Natl. Acad. Sci. U.S.A*, **90**, 7074–7078.

169 Lamphere, L., Fiore, F., Xu, X., Brizuela, L., Keezer, S., Sardet, C., Draetta, G. F., and Gyuris, J. (1997). Interaction between Cdc37 and Cdk4 in human cells. *Oncogene*, **14**, 1999–2004.

170 Perdew, G. H., Wiegand, H., Vanden Heuvel, J. P., Mitchell, C., and Singh, S. S. (1997). A 50 kilodalton protein associated with raf and pp60(v-src) protein kinases is a mammalian homolog of the cell cycle control protein cdc37. *Biochemistry*, **36**, 3600–3607.

171 Siligardi, G., Panaretou, B., Meyer, P., Singh, S., Woolfson, D. N., Piper, P. W., Pearl, L. H., and Prodromou, C. (2002). Regulation of Hsp90 ATPase activity by the co-chaperone Cdc37p/p50cdc37. *J. Biol. Chem*, **277**, 20151–20159.

172 Roe, S. M., Ali, M. M., Meyer, P., Vaughan, C. K., Panaretou, B., Piper, P. W., Prodromou, C., and Pearl, L. H. (2004). The Mechanism of Hsp90 regulation by the protein kinase-specific cochaperone p50(cdc37). *Cell*, **116**, 87–98.

173 Lee, P., Shabbir, A., Cardozo, C., and Caplan, A. J. (2004). Sti1 and Cdc37 can stabilize Hsp90 in chaperone complexes with a protein kinase. *Mol. Biol. Cell*, **15**, 1785–1792.

174 MacLean, M. and Picard, D. (2003). Cdc37 goes beyond Hsp90 and kinases. *Cell Stress. Chaperones.*, **8**, 114–119.

175 Abbas-Terki, T., Briand, P. A., Donze, O., and Picard, D. (2002). The Hsp90 co-chaperones Cdc37 and Sti1 interact physically and genetically. *Biol. Chem*, **383**, 1335–1342.

176 Kimura, Y., Rutherford, S. L., Miyata, Y., Yahara, I., Freeman, B. C., Yue, L., Morimoto, R. I., and Lindquist, S. (1997). Cdc37 is a molecular chaperone with specific functions in signal transduction. *Genes Dev.*, **11**, 1775–1785.

177 Young, J. C., Hoogenraad, N. J., and Hartl, F. U. (2003). Molecular chaperones Hsp90 and Hsp70 deliver preproteins to the mitochondrial import receptor Tom70. *Cell*, **112**, 41–50.

178 Young, J. C., Barral, J. M., and Ulrich, H. F. (2003). More than folding: localized functions of cytosolic chaperones. *Trends Biochem. Sci.*, **28**, 541–547.

179 Ballinger, C. A., Connell, P., Wu, Y., Hu, Z., Thompson, L. J., Yin, L. Y., and Patterson, C. (1999). Identification of CHIP, a novel tetratricopeptide repeat-containing protein that interacts with heat shock proteins and negatively regulates chaperone functions. *Mol. Cell Biol.*, **19**, 4535–4545.

180 Murata, S., Minami, Y., Minami, M., Chiba, T., and Tanaka, K. (2001). CHIP is a chaperone-dependent E3 ligase that ubiquitylates unfolded protein. *EMBO Rep.*, **2**, 1133–1138.

181 Kitagawa, K., Skowyra, D., Elledge, S. J., Harper, J. W., and Hieter, P. (1999). SGT1 encodes an essential component of the yeast kinetochore assembly pathway and a novel subunit of the SCF ubiquitin ligase complex. *Mol. Cell*, **4**, 21–33.

182 Takahashi, A., Casais, C., Ichimura, K., and Shirasu, K. (2003). HSP90 interacts with RAR1 and SGT1 and is essential for RPS2-mediated disease resistance in Arabidopsis. *Proc. Natl. Acad. Sci. U.S.A*, **100**, 11777–11782.

183 Liu, Y., Burch-Smith, T., Schiff, M., Feng, S., and Dinesh-Kumar, S. P. (2004). Molecular chaperone Hsp90 associates with resistance protein N

and its signaling proteins SGT1 and Rar1 to modulate an innate immune response in plants. *J. Biol. Chem.*, **279**, 2101–2108.

184 Austin, M. J., Muskett, P., Kahn, K., Feys, B. J., Jones, J. D., and Parker, J. E. (2002). Regulatory role of SGT1 in early R gene-mediated plant defenses. *Science*, **295**, 2077–2080.

185 Garcia-Ranea, J. A., Mirey, G., Camonis, J., and Valencia, A. (2002). p23 and HSP20/alpha-crystallin proteins define a conserved sequence domain present in other eukaryotic protein families. *FEBS Lett.*, **529**, 162–167.

186 Lee, Y. T., Jacob, J., Michowski, W., Nowotny, M., Kuznicki, J., and Chazin, W. J. (2004). Human Sgt1 Binds HSP90 through the CHORD-Sgt1 Domain and Not the Tetratricopeptide Repeat Domain. *J. Biol. Chem.*, **279**, 16511–16517.

187 Nathan, D. F., Vos, M. H., and Lindquist, S. (1999). Identification of SSF1, CNS1, and HCH1 as multicopy suppressors of a Saccharomyces cerevisiae Hsp90 loss-of-function mutation. *Proc. Natl. Acad. Sci. U.S.A*, **96**, 1409–1414.

188 Meyer, P., Prodromou, C., Liao, C., Hu, B., Mark, R. S., Vaughan, C. K., Vlasic, I., Panaretou, B., Piper, P. W., and Pearl, L. H. (2004). Structural basis for recruitment of the ATPase activator Aha1 to the Hsp90 chaperone machinery. *EMBO J.*, **23**, 511–519.

189 Lotz, G. P., Lin, H., Harst, A., and Obermann, W. M. (2003). Aha1 binds to the middle domain of Hsp90, contributes to client protein activation, and stimulates the ATPase activity of the molecular chaperone. *J. Biol. Chem.*, **278**, 17228–17235.

190 Dolinski, K. J., Cardenas, M. E., and Heitman, J. (1998). CNS1 encodes an essential p60/Sti1 homolog in Saccharomyces cerevisiae that suppresses cyclophilin 40 mutations and interacts with Hsp90. *Mol. Cell Biol.*, **18**, 7344–7352.

191 Crevel, G., Bates, H., Huikeshoven, H., and Cotterill, S. (2001). The Drosophila Dpit47 protein is a nuclear Hsp90 co-chaperone that interacts with DNA polymerase alpha. *J. Cell Sci.*, **114**, 2015–2025.

192 Hainzl, O., Wegele, H., Richter, K., and Buchner, J. (2004). Cns1 is an activator of the Ssa1 ATPase activity. *J. Biol. Chem.*

193 Marsh, J. A., Kalton, H. M., and Gaber, R. F. (1998). Cns1 is an essential protein associated with the hsp90 chaperone complex in Saccharomyces cerevisiae that can restore cyclophilin 40-dependent functions in cpr7Delta cells. *Mol. Cell Biol.*, **18**, 7353–7359.

194 Tesic, M., Marsh, J. A., Cullinan, S. B., and Gaber, R. F. (2003). Functional Interactions between Hsp90 and the Co-chaperones Cns1 and Cpr7 in Saccharomyces cerevisiae. *J. Biol. Chem*, **278**, 32692–32701.

195 Ramadoss, P., Petrulis, J. R., Hollingshead, B. D., Kusnadi, A., and Perdew, G. H. (2004). Divergent roles of hepatitis B virus X-associated protein 2 (XAP2) in human versus mouse Ah receptor complexes. *Biochemistry*, **43**, 700–709.

196 Meyer, B. K. and Perdew, G. H. (1999). Characterization of the AhR-hsp90-XAP2 core complex and the role of the immunophilin-related protein XAP2 in AhR stabilization. *Biochemistry*, **38**, 8907–8917.

197 Lees, M. J., Peet, D. J., and Whitelaw, M. L. (2003). Defining the role for XAP2 in stabilisation of the dioxin receptor. *J. Biol. Chem.*

198 Angeletti, P. C., Walker, D., and Panganiban, A. T. (2002). Small glutamine-rich protein/viral protein U-binding protein is a novel cochaperone that affects heat shock protein 70 activity. *Cell Stress. Chaperones.*, **7**, 258–268.

199 Brychzy, A., Rein, T., Winklhofer, K. F., Hartl, F. U., Young, J. C., and Obermann, W. M. (2003). Cofactor Tpr2 combines two TPR domains and a J domain to regulate the Hsp70/Hsp90 chaperone system. *EMBO J.*, **22**, 3613–3623.

200 Boeke, J. D., Trueheart, J.,

Natsoulis, G., and Fink, G. R. (1987). 5-Fluoroorotic acid as a selective agent in yeast molecular genetics. *Methods Enzymol.*, **154**, 164–175.

201 Scheibel, T., Weikl, T., Rimerman, R., Smith, D., Lindquist, S., and Buchner, J. (1999). Contribution of N- and C-terminal domains to the function of Hsp90 in Saccharomyces cerevisiae. *Mol. Microbiol.*, **34**, 701–713.

202 Obermann, W. M., Sondermann, H., Russo, A. A., Pavletich, N. P., and Hartl, F. U. (1998). In vivo function of Hsp90 is dependent on ATP binding and ATP hydrolysis. *J. Cell Biol.*, **143**, 901–910.

203 Picard, D., Khursheed, B., Garabedian, M. J., Fortin, M. G., Lindquist, S., and Yamamoto, K. R. (1990). Reduced levels of hsp90 compromise steroid receptor action in vivo. *Nature*, **348**, 166–168.

204 Ali, J. A., Jackson, A. P., Howells, A. J., and Maxwell, A. (1993). The 43-kilodalton N-terminal fragment of the DNA gyrase B protein hydrolyzes ATP and binds coumarin drugs. *Biochemistry*, **32**, 2717–2724.

205 Lanzetta, P. A., Alvarez, L. J., Reinach, P. S., and Candia, O. A. (1979). An improved assay for nanomole amounts of inorganic phosphate. *Anal. Biochem.*, **100**, 95–97.

206 Kornberg, A., Scott, J. F., and Bertsch, L. L. (1978). ATP utilization by rep protein in the catalytic separation of DNA strands at a replicating fork. *J. Biol. Chem.*, **253**, 3298–3304.

207 Freeman, B. C., Felts, S. J., Toft, D. O., and Yamamoto, K. R. (2000). The p23 molecular chaperones act at a late step in intracellular receptor action to differentially affect ligand efficacies. *Genes Dev.*, **14**, 422–434.

208 Malmqvist, M. (1993). Surface plasmon resonance for detection and measurement of antibody-antigen affinity and kinetics. *Curr. Opin. Immunol.*, **5**, 282–286.

209 Szabo, A., Stolz, L., and Granzow, R. (1995). Surface plasmon resonance and its use in biomolecular interaction analysis (BIA). *Curr. Opin. Struct. Biol.*, **5**, 699–705.

210 Wegele, H., Muller, L., and Buchner, J. (2004). Hsp70 and Hsp90-a relay team for protein folding. *Rev. Physiol Biochem. Pharmacol.*

211 Taylor, P., Dornan, J., Carrello, A., Minchin, R. F., Ratajczak, T., and Walkinshaw, M. D. (2001). Two structures of cyclophilin 40: folding and fidelity in the TPR domains. *Structure. (Camb.)*, **9**, 431–438.

212 Joab, I., Radanyi, C., Renoir, M., Buchou, T., Catelli, M. G., Binart, N., Mester, J., and Baulieu, E. E. (1984). Common non-hormone binding component in non-transformed chick oviduct receptors of four steroid hormones. *Nature*, **308**, 850–853.

213 Veldscholte, J., Berrevoets, C. A., Brinkmann, A. O., Grootegoed, J. A., and Mulder, E. (1992). Anti-androgens and the mutated androgen receptor of LNCaP cells: differential effects on binding affinity, heat-shock protein interaction, and transcription activation. *Biochemistry*, **31**, 2393–2399.

214 Denis, M., Cuthill, S., Wikstrom, A. C., Poellinger, L., and Gustafsson, J. A. (1988). Association of the dioxin receptor with the Mr 90,000 heat shock protein: a structural kinship with the glucocorticoid receptor. *Biochem. Biophys. Res. Commun.*, **155**, 801–807.

215 Perdew, G. H. (1988). Association of the Ah receptor with the 90-kDa heat shock protein. *J. Biol. Chem.*, **263**, 13802–13805.

216 Yoshinari, K., Kobayashi, K., Moore, R., Kawamoto, T., and Negishi, M. (2003). Identification of the nuclear receptor CAR:HSP90 complex in mouse liver and recruitment of protein phosphatase 2A in response to phenobarbital. *FEBS Lett.*, **548**, 17–20.

217 Arbeitman, M. N. and Hogness, D. S. (2000). Molecular chaperones activate the Drosophila ecdysone

receptor, an RXR heterodimer. *Cell*, **101**, 67–77.

218 Sabbah, M., Redeuilh, G., and Baulieu, E. E. (1989). Subunit composition of the estrogen receptor. Involvement of the hormone-binding domain in the dimeric state. *J. Biol. Chem.*, **264**, 2397–2400.

219 Ben Or, S. (1989). Evidence that 5 S intermediate state in glucocorticoid receptor transformation contains hsp90 in addition to the steroid-binding protein. *J. Steroid Biochem.*, **33**, 899–906.

220 Zhang, L., Hach, A., and Wang, C. (1998). Molecular mechanism governing heme signaling in yeast: a higher-order complex mediates heme regulation of the transcriptional activator HAP1. *Mol. Cell Biol.*, **18**, 3819–3828.

221 Ali, A., Bharadwaj, S., O'Carroll, R., and Ovsenek, N. (1998). HSP90 interacts with and regulates the activity of heat shock factor 1 in Xenopus oocytes. *Mol. Cell Biol.*, **18**, 4949–4960.

222 Minet, E., Mottet, D., Michel, G., Roland, I., Raes, M., Remacle, J., and Michiels, C. (1999). Hypoxia-induced activation of HIF-1: role of HIF-1alpha-Hsp90 interaction. *FEBS Lett.*, **460**, 251–256.

223 Rafestin-Oblin, M. E., Couette, B., Radanyi, C., Lombes, M., and Baulieu, E. E. (1989). Mineralocorticosteroid receptor of the chick intestine. Oligomeric structure and transformation. *J. Biol. Chem.*, **264**, 9304–9309.

224 Komori, A., Sueoka, E., Fujiki, H., Ishii, M., and Kozu, T. (1999). Association of MTG8 (ETO/CDR), a leukemia-related protein, with serine/threonine protein kinases and heat shock protein HSP90 in human hematopoietic cell lines. *Jpn. J. Cancer Res.*, **90**, 60–68.

225 Sumanasekera, W. K., Tien, E. S., Davis, J. W., Turpey, R., Perdew, G. H., and Vanden Heuvel, J. P. (2003). Heat shock protein-90 (Hsp90) acts as a repressor of peroxisome proliferator-activated receptor-alpha (PPARalpha) and PPARbeta activity. *Biochemistry*, **42**, 10726–10735.

226 Sumanasekera, W. K., Tien, E. S., Turpey, R., Vanden Heuvel, J. P., and Perdew, G. H. (2003). Evidence that peroxisome proliferator-activated receptor alpha is complexed with the 90-kDa heat shock protein and the hepatitis virus B X-associated protein 2. *J. Biol. Chem.*, **278**, 4467–4473.

227 Catelli, M. G., Binart, N., Jung-Testas, I., Renoir, J. M., Baulieu, E. E., Feramisco, J. R., and Welch, W. J. (1985). The common 90-kd protein component of non-transformed '8S' steroid receptors is a heat-shock protein. *EMBO J.*, **4**, 3131–3135.

228 Schuh, S., Yonemoto, W., Brugge, J., Bauer, V. J., Riehl, R. M., Sullivan, W. P., and Toft, D. O. (1985). A 90,000-dalton binding protein common to both steroid receptors and the Rous sarcoma virus transforming protein, pp60v-src. *J. Biol. Chem.*, **260**, 14292–14296.

229 Holley, S. J. and Yamamoto, K. R. (1995). A role for Hsp90 in retinoid receptor signal transduction. *Mol. Biol. Cell*, **6**, 1833–1842.

230 McGuire, J., Coumailleau, P., Whitelaw, M. L., Gustafsson, J. A., and Poellinger, L. (1995). The basic helix-loop-helix/PAS factor Sim is associated with hsp90. Implications for regulation by interaction with partner factors. *J. Biol. Chem.*, **270**, 31353–31357.

231 Shah, M., Patel, K., Fried, V. A., and Sehgal, P. B. (2002). Interactions of STAT3 with caveolin-1 and heat shock protein 90 in plasma membrane raft and cytosolic complexes: preservation of cytokine signaling during fever. *J. Biol. Chem.*

232 Miyata, Y. and Yahara, I. (2000). p53-independent association between SV40 large T antigen and the major cytosolic heat shock protein, HSP90. *Oncogene*, **19**, 1477–1484.

233 Hashimoto, Y. and Shudo, K. (1991). Cytosolic-nuclear tumor promoter-specific binding protein: association with the 90 kDa heat shock protein and translocation into nuclei by

treatment with 12-O-tetradecanoyl-phorbol 13-acetate. *Jpn. J. Cancer Res.*, **82**, 665–675.

234 Privalsky, M. L. (1991). A subpopulation of the v-erb A oncogene protein, a derivative of a thyroid hormone receptor, associates with heat shock protein 90. *J. Biol. Chem.*, **266**, 1456–1462.

235 Brunt, S. A., Perdew, G. H., Toft, D. O., and Silver, J. C. (1998). Hsp90-containing multiprotein complexes in the eukaryotic microbe Achlya. *Cell Stress. Chaperones.*, **3**, 44–56.

236 Holt, S. E., Aisner, D. L., Baur, J., Tesmer, V. M., Dy, M., Ouellette, M., Trager, J. B., Morin, G. B., Toft, D. O., Shay, J. W., Wright, W. E., and White, M. A. (1999). Functional requirement of p23 and Hsp90 in telomerase complexes. *Genes Dev.*, **13**, 817–826.

237 Hu, J. and Seeger, C. (1996). Hsp90 is required for the activity of a hepatitis B virus reverse transcriptase. *Proc. Natl. Acad. Sci. U.S.A*, **93**, 1060–1064.

238 Fujita, N., Sato, S., Ishida, A., and Tsuruo, T. (2002). Involvement of Hsp90 in signaling and stability of 3-phosphoinositide-dependent kinase-1. *J. Biol. Chem.*, **277**, 10346–10353.

239 Sato, S., Fujita, N., and Tsuruo, T. (2000). Modulation of Akt kinase activity by binding to Hsp90. *Proc. Natl. Acad. Sci. U.S.A*, **97**, 10832–10837.

240 Miyata, Y. and Nishida, E. (2004). CK2 controls multiple protein kinases by phosphorylating a kinase-targeting molecular chaperone, Cdc37. *Mol. Cell Biol.*, **24**, 4065–4074.

241 Palmquist, K., Riis, B., Nilsson, A., and Nygard, O. (1994). Interaction of the calcium and calmodulin regulated eEF-2 kinase with heat shock protein 90. *FEBS Lett.*, **349**, 239–242.

242 Munoz, M. J. and Jimenez, J. (1999). Genetic interactions between Hsp90 and the Cdc2 mitotic machinery in the fission yeast Schizosaccharomyces pombe. *Mol. Gen. Genet.*, **261**, 242–250.

243 Mahony, D., Parry, D. A., and Lees, E. (1998). Active cdk6 complexes are predominantly nuclear and represent only a minority of the cdk6 in T cells. *Oncogene*, **16**, 603–611.

244 O'Keeffe, B., Fong, Y., Chen, D., Zhou, S., and Zhou, Q. (2000). Requirement for a kinase-specific chaperone pathway in the production of a Cdk9/cyclin T1 heterodimer responsible for P-TEFb-mediated tat stimulation of HIV-1 transcription. *J. Biol. Chem.*, **275**, 279–287.

245 Arlander, S. J., Eapen, A. K., Vroman, B. T., McDonald, R. J., Toft, D. O., and Karnitz, L. M. (2003). Hsp90 inhibition depletes Chk1 and sensitizes tumor cells to replication stress. *J. Biol. Chem.*, **278**, 52572–52577.

246 Fisher, D. L., Mandart, E., and Doree, M. (2000). Hsp90 is required for c-Mos activation and biphasic MAP kinase activation in Xenopus oocytes. *EMBO J.*, **19**, 1516–1524.

247 Stancato, L. F., Silverstein, A. M., Owens-Grillo, J. K., Chow, Y. H., Jove, R., and Pratt, W. B. (1997). The hsp90-binding antibiotic geldanamycin decreases Raf levels and epidermal growth factor signaling without disrupting formation of signaling complexes or reducing the specific enzymatic activity of Raf kinase. *J. Biol. Chem.*, **272**, 4013–4020.

248 Xu, W., Mimnaugh, E., Rosser, M. F., Nicchitta, C., Marcu, M., Yarden, Y., and Neckers, L. (2001). Sensitivity of mature Erbb2 to geldanamycin is conferred by its kinase domain and is mediated by the chaperone protein Hsp90. *J. Biol. Chem.*, **276**, 3702–3708.

249 Minami, Y., Kiyoi, H., Yamamoto, Y., Yamamoto, K., Ueda, R., Saito, H., and Naoe, T. (2002). Selective apoptosis of tandemly duplicated FLT3-transformed leukemia cells by Hsp90 inhibitors. *Leukemia*, **16**, 1535–1540.

250 Masson-Gadais, B., Houle, F., Laferriere, J., and Huot, J. (2003). Integrin alphavbeta3, requirement for VEGFR2-mediated activation of SAPK2/p38 and for Hsp90-dependent

phosphorylation of focal adhesion kinase in endothelial cells activated by VEGF. *Cell Stress. Chaperones.*, **8**, 37–52.

251 Luo, J. and Benovic, J. L. (2003). G protein-coupled receptor kinase interaction with Hsp90 mediates kinase maturation. *J. Biol. Chem.*, **278**, 50908–50914.

252 Scholz, G., Hartson, S. D., Cartledge, K., Hall, N., Shao, J., Dunn, A. R., and Matts, R. L. (2000). p50(Cdc37) can buffer the temperature-sensitive properties of a mutant of Hck. *Mol. Cell Biol.*, **20**, 6984–6995.

253 Matts, R. L. and Hurst, R. (1989). Evidence for the association of the heme-regulated eIF-2 alpha kinase with the 90-kDa heat shock protein in rabbit reticulocyte lysate in situ. *J. Biol. Chem.*, **264**, 15542–15547.

254 Rose, D. W., Wettenhall, R. E., Kudlicki, W., Kramer, G., and Hardesty, B. (1987). The 90-kilodalton peptide of the heme-regulated eIF-2 alpha kinase has sequence similarity with the 90-kilodalton heat shock protein. *Biochemistry*, **26**, 6583–6587.

255 Lewis, J., Devin, A., Miller, A., Lin, Y., Rodriguez, Y., Neckers, L., and Liu, Z. G. (2000). Disruption of hsp90 function results in degradation of the death domain kinase, receptor-interacting protein (RIP), and blockage of tumor necrosis factor-induced nuclear factor-kappaB activation. *J. Biol. Chem.*, **275**, 10519–10526.

256 Takata, Y., Imamura, T., Iwata, M., Usui, I., Haruta, T., Nandachi, N., Ishiki, M., Sasaoka, T., and Kobayashi, M. (1997). Functional importance of heat shock protein 90 associated with insulin receptor on insulin-stimulated mitogenesis. *Biochem. Biophys. Res. Commun.*, **237**, 345–347.

257 Jerome, V., Leger, J., Devin, J., Baulieu, E. E., and Catelli, M. G. (1991). Growth factors acting via tyrosine kinase receptors induce HSP90 alpha gene expression. *Growth Factors*, **4**, 317–327.

258 Marcu, M. G., Doyle, M., Bertolotti, A., Ron, D., Hendershot, L., and Neckers, L. (2002). Heat shock protein 90 modulates the unfolded protein response by stabilizing IRE1alpha. *Mol. Cell Biol.*, **22**, 8506–8513.

259 Boudeau, J., Deak, M., Lawlor, M. A., Morrice, N. A., and Alessi, D. R. (2003). Heat-shock protein 90 and Cdc37 interact with LKB1 and regulate its stability. *Biochem. J.*, **370**, 849–857.

260 Nony, P., Gaude, H., Rossel, M., Fournier, L., Rouault, J. P., and Billaud, M. (2003). Stability of the Peutz-Jeghers syndrome kinase LKB1 requires its binding to the molecular chaperones Hsp90/Cdc37. *Oncogene*, **22**, 9165–9175.

261 Hartson, S. D. and Matts, R. L. (1994). Association of Hsp90 with cellular Src-family kinases in a cell-free system correlates with altered kinase structure and function. *Biochemistry*, **33**, 8912–8920.

262 Miyata, Y., Ikawa, Y., Shibuya, M., and Nishida, E. (2001). Specific association of a set of molecular chaperones including HSP90 and Cdc37 with MOK, a member of the mitogen-activated protein kinase superfamily. *J. Biol. Chem.*, **276**, 21841–21848.

263 Cissel, D. S. and Beaven, M. A. (2000). Disruption of Raf-1/heat shock protein 90 complex and Raf signaling by dexamethasone in mast cells. *J. Biol. Chem.*, **275**, 7066–7070.

264 Goes, F. S. and Martin, J. (2001). Hsp90 chaperone complexes are required for the activity and stability of yeast protein kinases Mik1, Wee1 and Swe1. *Eur. J. Biochem*, **268**, 2281–2289.

265 Bonvini, P., Gastaldi, T., Falini, B., and Rosolen, A. (2002). Nucleophosmin-anaplastic lymphoma kinase (NPM-ALK), a novel Hsp90-client tyrosine kinase: down-regulation of NPM-ALK expression and tyrosine phosphorylation in ALK(+) CD30(+) lymphoma cells by the Hsp90 antagonist 17-allylamino, 17-demethoxygeldanamycin. *Cancer Res.*, **62**, 1559–1566.

266 Flanagan, C. A. and Thorner, J. (1992). Purification and characterization of a soluble phosphatidylinositol 4-kinase from the yeast Saccharomyces cerevisiae. *J. Biol. Chem.*, **267**, 24117–24125.

267 Mizuno, K., Shirogane, T., Shinohara, A., Iwamatsu, A., Hibi, M., and Hirano, T. (2001). Regulation of Pim-1 by Hsp90. *Biochem. Biophys. Res. Commun.*, **281**, 663–669.

268 Sakagami, M., Morrison, P., and Welch, W. J. (1999). Benzoquinoid ansamycins (herbimycin A and geldanamycin) interfere with the maturation of growth factor receptor tyrosine kinases. *Cell Stress. Chaperones.*, **4**, 19–28.

269 de Carcer, G., do Carmo, A. M., Lallena, M. J., Glover, D. M., and Gonzalez, C. (2001). Requirement of Hsp90 for centrosomal function reflects its regulation of Polo kinase stability. *EMBO J.*, **20**, 2878–2884.

270 Jaiswal, R. K., Weissinger, E., Kolch, W., and Landreth, G. E. (1996). Nerve growth factor-mediated activation of the mitogen-activated protein (MAP) kinase cascade involves a signaling complex containing B-Raf and HSP90. *J. Biol. Chem.*, **271**, 23626–23629.

271 Lovric, J., Bischof, O., and Moelling, K. (1994). Cell cycle-dependent association of Gag-Mil and hsp90. *FEBS Lett.*, **343**, 15–21.

272 Stancato, L. F., Chow, Y. H., Hutchison, K. A., Perdew, G. H., Jove, R., and Pratt, W. B. (1993). Raf exists in a native heterocomplex with hsp90 and p50 that can be reconstituted in a cell-free system. *J. Biol. Chem.*, **268**, 21711–21716.

273 Wartmann, M. and Davis, R. J. (1994). The native structure of the activated Raf protein kinase is a membrane-bound multi-subunit complex. *J. Biol. Chem.*, **269**, 6695–6701.

274 Cutforth, T. and Rubin, G. M. (1994). Mutations in Hsp83 and cdc37 impair signaling by the sevenless receptor tyrosine kinase in Drosophila. *Cell*, **77**, 1027–1036.

275 Donze, O. and Picard, D. (1999). Hsp90 binds and regulates Gcn2, the ligand-inducible kinase of the alpha subunit of eukaryotic translation initiation factor 2 [corrected]. *Mol. Cell Biol.*, **19**, 8422–8432.

276 Bernstein, S. L., Russell, P., Wong, P., Fishelevich, R., and Smith, L. E. (2001). Heat shock protein 90 in retinal ganglion cells: association with axonally transported proteins. *Vis. Neurosci.*, **18**, 429–436.

277 Lipsich, L. A., Cutt, J. R., and Brugge, J. S. (1982). Association of the transforming proteins of Rous, Fujinami, and Y73 avian sarcoma viruses with the same two cellular proteins. *Mol. Cell Biol.*, **2**, 875–880.

278 Ziemiecki, A., Catelli, M. G., Joab, I., and Moncharmont, B. (1986). Association of the heat shock protein hsp90 with steroid hormone receptors and tyrosine kinase oncogene products. *Biochem. Biophys. Res. Commun.*, **138**, 1298–1307.

279 Hutchison, K. A., Brott, B. K., De Leon, J. H., Perdew, G. H., Jove, R., and Pratt, W. B. (1992). Reconstitution of the multiprotein complex of pp60src, hsp90, and p50 in a cell-free system. *J. Biol. Chem.*, **267**, 2902–2908.

280 Oppermann, H., Levinson, W., and Bishop, J. M. (1981). A cellular protein that associates with the transforming protein of Rous sarcoma virus is also a heat-shock protein. *Proc. Natl. Acad. Sci. U.S.A*, **78**, 1067–1071.

281 Koyasu, S., Nishida, E., Kadowaki, T., Matsuzaki, F., Iida, K., Harada, F., Kasuga, M., Sakai, H., and Yahara, I. (1986). Two mammalian heat shock proteins, HSP90 and HSP100, are actin-binding proteins. *Proc. Natl. Acad. Sci. U.S.A*, **83**, 8054–8058.

282 Saleh, A., Srinivasula, S. M., Balkir, L., Robbins, P. D., and Alnemri, E. S. (2000). Negative regulation of the Apaf-1 apoptosome by Hsp70. *Nat. Cell Biol.*, **2**, 476–483.

283 Gusarova, V., Caplan, A. J., Brodsky, J. L., and Fisher, E. A. (2001). Apoprotein B degradation is promoted

by the molecular chaperones hsp90 and hsp70. *J. Biol. Chem.*, **276**, 24891–24900.

284 Kumar, R., Grammatikakis, N., and Chinkers, M. (2001). Regulation of the atrial natriuretic peptide receptor by heat shock protein 90 complexes. *J. Biol. Chem.*, **276**, 11371–11375.

285 Zhao, C. and Wang, E. (2004). Heat shock protein 90 suppresses tumor necrosis factor alpha induced apoptosis by preventing the cleavage of Bid in NIH3T3 fibroblasts. *Cell Signal.*, **16**, 313–321.

286 Nishida, E., Koyasu, S., Sakai, H., and Yahara, I. (1986). Calmodulin-regulated binding of the 90-kDa heat shock protein to actin filaments. *J. Biol. Chem.*, **261**, 16033–16036.

287 Bogatcheva, N. V., Ma, Y., Urosev, D., and Gusev, N. B. (1999). Localization of calponin binding sites in the structure of 90 kDa heat shock protein (Hsp90). *FEBS Lett.*, **457**, 369–374.

288 Uzawa, M., Grams, J., Madden, B., Toft, D., and Salisbury, J. L. (1995). Identification of a complex between centrin and heat shock proteins in CSF-arrested Xenopus oocytes and dissociation of the complex following oocyte activation. *Dev. Biol.*, **171**, 51–59.

289 Imai, J. and Yahara, I. (2000). Role of HSP90 in salt stress tolerance via stabilization and regulation of calcineurin. *Mol. Cell Biol.*, **20**, 9262–9270.

290 Loo, M. A., Jensen, T. J., Cui, L., Hou, Y., Chang, X. B., and Riordan, J. R. (1998). Perturbation of Hsp90 interaction with nascent CFTR prevents its maturation and accelerates its degradation by the proteasome. *EMBO J.*, **17**, 6879–6887.

291 Stemmann, O., Neidig, A., Kocher, T., Wilm, M., and Lechner, J. (2002). Hsp90 enables Ctf13p/Skp1p to nucleate the budding yeast kinetochore. *Proc. Natl. Acad. Sci. U.S.A*, **99**, 8585–8590.

292 Garcia-Cardena, G., Fan, R., Shah, V., Sorrentino, R., Cirino, G., Papapetropoulos, A., and Sessa, W. C. (1998). Dynamic activation of endothelial nitric oxide synthase by Hsp90. *Nature*, **392**, 821–824.

293 Ficker, E., Dennis, A. T., Wang, L., and Brown, A. M. (2003). Role of the cytosolic chaperones Hsp70 and Hsp90 in maturation of the cardiac potassium channel HERG. *Circ. Res.*, **92**, e87–100.

294 Hoshino, T., Wang, J., Devetten, M. P., Iwata, N., Kajigaya, S., Wise, R. J., Liu, J. M., and Youssoufian, H. (1998). Molecular chaperone GRP94 binds to the Fanconi anemia group C protein and regulates its intracellular expression. *Blood*, **91**, 4379–4386.

295 Inanobe, A., Takahashi, K., and Katada, T. (1994). Association of the beta gamma subunits of trimeric GTP-binding proteins with 90-kDa heat shock protein, hsp90. *J. Biochem. (Tokyo)*, **115**, 486–492.

296 Busconi, L., Guan, J., and Denker, B. M. (2000). Degradation of heterotrimeric Galpha(o) subunits via the proteosome pathway is induced by the hsp90-specific compound geldanamycin. *J. Biol. Chem.*, **275**, 1565–1569.

297 Vaiskunaite, R., Kozasa, T., and Voyno-Yasenetskaya, T. A. (2001). Interaction between the G alpha subunit of heterotrimeric G(12) protein and Hsp90 is required for G alpha(12) signaling. *J. Biol. Chem.*, **276**, 46088–46093.

298 Tahbaz, N., Carmichael, J. B., and Hobman, T. C. (2001). GERp95 belongs to a family of signal-transducing proteins and requires Hsp90 activity for stability and Golgi localization. *J. Biol. Chem.*, **276**, 43294–43299.

299 Mayama, J., Kumano, T., Hayakari, M., Yamazaki, T., Aizawa, S., Kudo, T., and Tsuchida, S. (2003). Polymorphic glutathione S-transferase subunit 3 of rat liver exhibits different susceptibilities to carbon tetrachloride: differences in their interactions with heat-shock protein 90. *Biochem. J.*, **372**, 611–616.

300 Venema, R. C., Venema, V. J., Ju, H., Harris, M. B., Snead, C., Jilling, T.,

Dimitropoulou, C., Maragoudakis, M. E., and Catravas, J. D. (2003). Novel complexes of guanylate cyclase with heat shock protein 90 and nitric oxide synthase. *Am. J. Physiol Heart Circ. Physiol*, **285**, H669–H678.

301 Herbertsson, H., Kuhme, T., and Hammarstrom, S. (1999). The 650-kDa 12(S)-hydroxyeicosatetraenoic acid binding complex: occurrence in human platelets, identification of hsp90 as a constituent, and binding properties of its 50-kDa subunit. *Arch. Biochem. Biophys.*, **367**, 33–38.

302 Schnaider, T., Oikarinen, J., Ishiwatari-Hayasaka, H., Yahara, I., and Csermely, P. (1999). Interactions of Hsp90 with histones and related peptides. *Life Sci.*, **65**, 2417–2426.

303 Joly, G. A., Ayres, M., and Kilbourn, R. G. (1997). Potent inhibition of inducible nitric oxide synthase by geldanamycin, a tyrosine kinase inhibitor, in endothelial, smooth muscle cells, and in rat aorta. *FEBS Lett.*, **403**, 40–44.

304 Agarraberes, F. A. and Dice, J. F. (2001). A molecular chaperone complex at the lysosomal membrane is required for protein translocation. *J. Cell Sci.*, **114**, 2491–2499.

305 Nakamura, T., Hinagata, J., Tanaka, T., Imanishi, T., Wada, Y., Kodama, T., and Doi, T. (2002). HSP90, HSP70, and GAPDH directly interact with the cytoplasmic domain of macrophage scavenger receptors. *Biochem. Biophys. Res. Commun.*, **290**, 858–864.

306 Kang, J., Kim, T., Ko, Y. G., Rho, S. B., Park, S. G., Kim, M. J., Kwon, H. J., and Kim, S. (2000). Heat shock protein 90 mediates protein-protein interactions between human aminoacyl-tRNA synthetases. *J. Biol. Chem.*, **275**, 31682–31688.

307 Peng, Y., Chen, L., Li, C., Lu, W., and Chen, J. (2001). Inhibition of MDM2 by hsp90 contributes to mutant p53 stabilization. *J. Biol. Chem.*, **276**, 40583–40590.

308 Kellermayer, M. S. and Csermely, P. (1995). ATP induces dissociation of the 90 kDa heat shock protein (hsp90) from F-actin: interference with the binding of heavy meromyosin. *Biochem. Biophys. Res. Commun.*, **211**, 166–174.

309 Hubert, D. A., Tornero, P., Belkhadir, Y., Krishna, P., Takahashi, A., Shirasu, K., and Dangl, J. L. (2003). Cytosolic HSP90 associates with and modulates the Arabidopsis RPM1 disease resistance protein. *EMBO J.*, **22**, 5679–5689.

310 Bender, A. T., Silverstein, A. M., Demady, D. R., Kanelakis, K. C., Noguchi, S., Pratt, W. B., and Osawa, Y. (1999). Neuronal nitric-oxide synthase is regulated by the Hsp90-based chaperone system in vivo. *J. Biol. Chem.*, **274**, 1472–1478.

311 Ishiwatari-Hayasaka, H., Maruya, M., Sreedhar, A. S., Nemoto, T. K., Csermely, P., and Yahara, I. (2003). Interaction of neuropeptide Y and Hsp90 through a novel peptide binding region. *Biochemistry*, **42**, 12972–12980.

312 Adinolfi, E., Kim, M., Young, M. T., Di Virgilio, F., and Surprenant, A. (2003). Tyrosine phosphorylation of HSP90 within the P2X7 receptor complex negatively regulates P2X7 receptors. *J. Biol. Chem.*, **278**, 37344–37351.

313 Momose, F., Naito, T., Yano, K., Sugimoto, S., Morikawa, Y., and Nagata, K. (2002). Identification of Hsp90 as a stimulatory host factor involved in influenza virus RNA synthesis. *J. Biol. Chem.*, **277**, 45306–45314.

314 Bruneau, N., Lombardo, D., and Bendayan, M. (1998). Participation of GRP94-related protein in secretion of pancreatic bile salt-dependent lipase and in its internalization by the intestinal epithelium. *J. Cell Sci.*, **111 (Pt 17)**, 2665–2679.

315 Banumathy, G., Singh, V., and Tatu, U. (2002). Host chaperones are recruited in membrane-bound complexes by Plasmodium falciparum. *J. Biol. Chem.*, **277**, 3902–3912.

316 Pai, K. S., Mahajan, V. B., Lau, A., and Cunningham, D. D. (2001). Thrombin receptor signaling to

cytoskeleton requires Hsp90. *J. Biol. Chem.*, **276**, 32642–32647.

317 Tsubuki, S., Saito, Y., and Kawashima, S. (1994). Purification and characterization of an endogenous inhibitor specific to the Z-Leu-Leu-Leu-MCA degrading activity in proteasome and its identification as heat-shock protein 90. *FEBS Lett.*, **344**, 229–233.

318 Sakisaka, T., Meerlo, T., Matteson, J., Plutner, H., and Balch, W. E. (2002). Rab-alphaGDI activity is regulated by a Hsp90 chaperone complex. *EMBO J.*, **21**, 6125–6135.

319 Hu, Y. and Mivechi, N. F. (2003). HSF-1 interacts with Ral-binding protein 1 in a stress-responsive, multiprotein complex with HSP90 in vivo. *J. Biol. Chem.*, **278**, 17299–17306.

320 Gilmore, R., Coffey, M. C., and Lee, P. W. (1998). Active participation of Hsp90 in the biogenesis of the trimeric reovirus cell attachment protein sigma1. *J. Biol. Chem.*, **273**, 15227–15233.

321 Fortugno, P., Beltrami, E., Plescia, J., Fontana, J., Pradhan, D., Marchisio, P. C., Sessa, W. C., and Altieri, D. C. (2003). Regulation of survivin function by Hsp90. *Proc. Natl. Acad. Sci. U.S.A*, **100**, 13791–13796.

322 Abbas-Terki, T. and Picard, D. (1999). Alpha-complemented beta-galactosidase. An in vivo model substrate for the molecular chaperone heat-shock protein 90 in yeast. *Eur. J. Biochem.*, **266**, 517–523.

323 Muresan, Z. and Arvan, P. (1997). Thyroglobulin transport along the secretory pathway. Investigation of the role of molecular chaperone, GRP94, in protein export from the endoplasmic reticulum. *J. Biol. Chem.*, **272**, 26095–26102.

324 Sanchez, E. R., Redmond, T., Scherrer, L. C., Bresnick, E. H., Welsh, M. J., and Pratt, W. B. (1988). Evidence that the 90-kilodalton heat shock protein is associated with tubulin-containing complexes in L cell cytosol and in intact PtK cells. *Mol. Endocrinol.*, **2**, 756–760.

325 Melnick, J., Aviel, S., and Argon, Y. (1992). The endoplasmic reticulum stress protein GRP94, in addition to BiP, associates with unassembled immunoglobulin chains. *J. Biol. Chem.*, **267**, 21303–21306.

326 Hung, J. J., Chung, C. S., and Chang, W. (2002). Molecular chaperone Hsp90 is important for vaccinia virus growth in cells. *J. Virol.*, **76**, 1379–1390.

24
Small Heat Shock Proteins: Dynamic Players in the Folding Game

Franz Narberhaus and Martin Haslbeck

24.1
Introduction

The most poorly conserved molecular chaperone family comprises the vertebrate eye lens α-crystallins and numerous small heat shock proteins (sHsps). Although proteins belonging to this superfamily are diverse, most of them share six characteristic features: (1) a modestly conserved α-crystallin domain of about 90 amino acids, (2) a small molecular mass between 12 and 43 kDa, (3) induction by stress conditions, (4) chaperone-like activity in preventing other proteins from aggregation, (5) formation of large oligomers, and (6) a highly dynamic quaternary structure [1–9]. This chapter reports on the structural and functional properties of sHsps with an emphasis on their dynamic oligomeric nature.

24.2
α-Crystallins and the Small Heat Shock Protein Family: Diverse Yet Similar

The vertebrate eye lens α-crystallins are the founding members of a protein superfamily, the small heat shock proteins, sHsps or α-Hsps for short [2, 7, 8]. Two isoforms, αA- and αB-crystallin, which exhibit close to 60% amino acid sequence identity, usually occur in a molar ratio of three to one and makeup one-third of the eye lens [10]. As the name implies, functional α-crystallins are crucial for transparency of the eye lens, a crowded environment with an extremely high protein concentration. While αA-crystallin is mainly confined to the lenticular compartment, its close relative αB-crystallin was found to be a heat-inducible protein present in many other tissues [11–13]. Ignolia and Craig were the first to notice that four small heat shock proteins from *Drosophila* are related to mammalian α-crystallins [14]. Meanwhile, members of the sHsp family have been reported in all kingdoms from archaea and bacteria to plants and animals [2, 3, 7, 8]. A notable exception are at least 11 pathogenic bacteria, whose completed genome sequences do not provide any hint at the presence of α-Hsp genes [2, 15, 16]. On the other hand, many organisms encode multiple sHsps. Distinct sHsp classes residing in different cellular compartments can be distinguished in plants. For example, the *Arabidopsis* genome revealed a total of 13 sHsps belonging to six classes defined on the

Protein Folding Handbook. Part II. Edited by J. Buchner and T. Kiefhaber

ISBN: 3-527-30784-2

basis of their intracellular localization and sequence similarity. Six additional open reading frames potentially encode further family members [17]. A list of representative sHsps from prokaryotes and eukaryotes is presented in Table 24.1.

The molecular mass of the majority of sHsps is around 20 kDa giving rise to their designation small Hsp. However, the full range extends from 12 to 43 kDa. Unlike other molecular chaperones, sHsps are poorly conserved and often exhibit not more than 20% sequence identity in pairwise alignments. Common to all family members is a moderately conserved α-crystallin domain of about 90 amino acids flanked by a variable N-terminal region and a short C-terminal extension (Figure 24.1). Multiple sequence alignments including sHsps from all kingdoms revealed only very few consensus residues [2, 7, 8]. Not a single amino acid is invariant or shared by all family members. The most common denominators are two short motifs (FxRxxxL and AxxxxGVL) towards the end of the α-crystallin domain and an IxI sequence in the C-terminal extension (Figure 24.1). The N-terminal region varies substantially in both length and sequence. While Hsp12 proteins of *Caenorhabditis elegans* carry a short N-terminus of about 20 amino acids [18], Hsp42 from yeast owes its length to an extended N-terminal region [19]. Sequence similarities in the N-terminal domain are restricted to closely related proteins. Phylogenetic analyses suggest that sHsps diverged very early in evolution [7]. A complex history of repeated gene duplications and lateral gene transfer probably accounts for the presence of multiple sHsps in some organisms. Bacteria lacking these proteins might have lost the corresponding gene(s) during adaptation to specialized conditions. Since sHsps are generally less critical for survival than the major chaperones, weaker functional constraints might have allowed a much higher diversification as compared to Hsp60 and Hsp70.

Many sHsps are not expressed under normal physiological conditions but rapidly accumulate during heat stress by classical prokaryotic or eukaryotic heat shock control mechanisms [2, 20, 21]. Microarray-based gene expression profiling in *E. coli* revealed a 300-fold induction of *ibpAB*, which by far exceeds the induction of all other heat shock genes [22]. Massive heat induction of sHsps was also reported in animal and plant tissues [3, 23]. Interestingly, the presence of sHsps is not restricted to eye lenses and heat-stressed cells. In bacteria, plants, and animals, they have been discovered during development processes, metabolic transitions, environmental insults, and many other conditions [2, 3, 9, 23, 24]. The broad expression pattern of sHsps is consistent with both a general protective function on one hand and specialized tasks in certain cell types on the other.

24.3 Cellular Functions of α-Hsps

24.3.1 Chaperone Activity in Vitro

From in vitro studies in the early 1990s, it emerged that the primary function of sHsps might be to bind denatured proteins in order to prevent their aggregation.

Tab. 24.1. Representative members of the α-Hsp family.

Kingdom	*Organism*	*Protein*	*Complex*	*Chaperone*	*Comments*	*References*
Archaea	*M. jannaschii*	Hsp16.5	24mer	Yes	Crystal structure, hollow sphere	110, 156
	P. furiosus	Pfu-sHsp	Large	Yes		157, 158
Bacteria	*E. coli*	IbpA/B	Large	Yes	Associates with inclusion bodies	53, 159
	M. tuberculosis	Hsp16.3	9mer	Yes	Antigen, trimer of trimers	115, 160
	Synechocystis sp.	Hsp17 (16.6)	24mer	Yes	Stabilizes membranes	97, 122
Eukaryotes	Yeast	Hsp26	24mer	Yes	Temperature-regulated chaperone	114
		Hsp42	12mer	Yes		161
	C. elegans	Hsp12.6	Monomer	No		18
	Wheat	Hsp16.9	12mer	Yes	Crystal structure, two hexameric rings	113
	Pea	Hsp18.1	12mer	Yes		29
	Mouse	Hsp25	16mer	Yes	Concentration-dependent equilibrium among 16mer, tetramers, and dimers	46, 107, 162
	Vertebrates	αA/B-crystallin	Large	Yes	Variable quaternary structure, molar ratio of 3:1 in the eye lens	25, 163

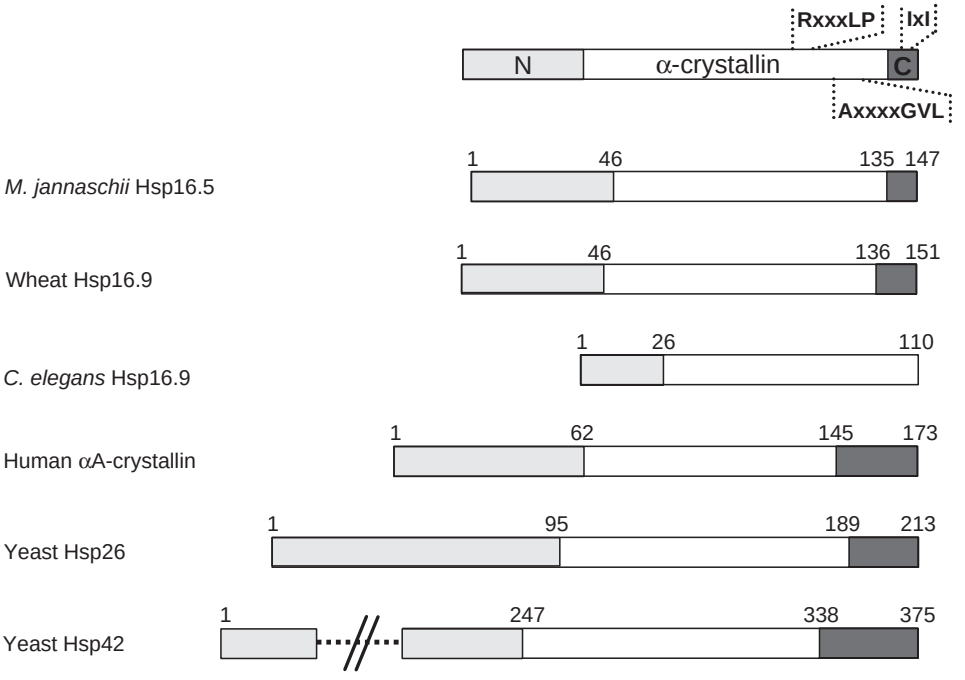

Fig. 24.1. Domain structure of sHsps. The overall domain structure is depicted on top of the figure. The N-terminal region, α-crystallin domain, C-terminal extension, and conserved motifs are indicated. Representative sHsps are shown below. Numbering is based on the assignment by Kim et al. [110].

Bovine α-crystallin was first reported to have chaperone-like activity [25]. It prevented thermal aggregation of various model substrates. Since then, it has been demonstrated that almost all sHsps are able to prevent the formation of thermally or chemically induced light-scattering aggregates (Table 24.1). Some additional examples are human Hsp27 [26], frog Hsp30C [27], shrimp p26 [28], pea Hsp17.7 [29], tobacco Hsp18 [30], two classes of sHsps from the soybean symbiont *Bradyrhizobium japonicum* [31], Lo18 from the lactic acid bacterium *Oenococcus oeni* [32], and Hsp16 and $sHsp_{Tm}$ from the thermophilic bacteria *Synechococcus vulcanus* and *Thermotoga maritima*, respectively [33, 34]. Only the smallest known representatives of the sHsp family, Hsp12.2, Hsp12.3, and Hsp12.6 of *C. elegans*, have failed to show chaperone-like properties [18, 35].

Since natural substrates are largely unknown, the model substrates chosen for in vitro studies usually are commercially available proteins, such as citrate synthase (CS) or malate dehydrogenase (MDH) from pig heart mitochondria, hog muscle lactate dehydrogenase, or bovine insulin. Some fairly robust chaperone assays will be described in the Appendix. The fact that such a wide spectrum of artificial substrates is protected from precipitation suggests that sHsps act as rather promis-

cuous chaperones, accepting a variety of client proteins. It is still unclear which regions in these substrate proteins are bound by sHsps and whether common recognition motifs exist. Only a single α-crystallin-binding site was identified in yeast alcohol dehydrogenase (ADH) by a cross-linking approach [36]. The side corresponds to amino acids 40–60 in the enzyme and is rich in beta-sheet-forming amino acids. The corresponding synthetic peptide formed a complex with α-crystallin at 48 °C. Since the same peptide exhibited chaperone-like activity and prevented aggregation of ADH and other proteins [37], it is possible that it has an inherent potential to interact with other β-sheets either in unfolded proteins or in sHsps. Target sites in other substrates need to be defined before a putative recognition motif can be established by the compilation of binding sequences.

Likewise, the residues in sHsps involved in substrate interaction are largely unknown. Circumstantial evidence by incorporation of hydrophobic dyes has suggested that substrates might bind to short segments in the N-terminal region or at the beginning of the α-crystallin domain [38, 39]. Results from cross-linking experiments supported this notion [40, 41]. An exchange of the highly conserved G in the AxxxGVL motif of HspH from *B. japonicum* specifically impaired chaperone activity without interfering with other properties of the protein [42]. This finding suggests that the C-terminal part of the α-crystallin domain might also be involved in substrate binding.

Light-scattering experiments demonstrated that precipitation of most substrates can be avoided by the addition of an equimolar amount of sHsps, suggesting that each chaperone particle is able to capture one substrate molecule. However, certain size limitations and steric restrictions seem to apply, as it was shown that α-crystallin is a more potent chaperone with small substrate proteins [43]. Large substrates probably tie up two or more Hsp molecules simultaneously [44]. At any rate, the binding capacity of sHsps is much higher than that of other multimeric chaperones such as GroEL, which accommodates only one or two substrates in its central cavity formed by 14 subunits [45]. With enzymatic substrates it could be shown that binding to sHsps did not prevent their inactivation [29, 46]. Bound proteins have already experienced some unfolding and are thought to be in a disordered and aggregation-prone molten-globule state, in which tertiary structure is lost but secondary structure remains [47–49]. The major chaperoning task of sHsps is to prevent irreversible inactivation and aggregation of such (un)folding intermediates by maintaining them in a soluble and folding-competent state [38, 46]. ATP does not play a direct role in this ''holding'' activity, but it might modulate the structural and functional properties of some sHsps [50–52].

Once formed, complexes between substrate and sHsp are very stable [46, 53]. Electron microscopic images have revealed large complexes of defined size and shape whose morphology is strictly dependent on the substrate protein but independent of the chaperone [54]. When several different nonnative proteins were incorporated into one complex, its overall shape was determined by the first substrate bound. Substrate proteins are not loosely attached to sHsps but are incorporated into mixed aggregates whose size and solubility correlate with the availability of the chaperone [55]. In plants, the formation of large heat shock granules consist-

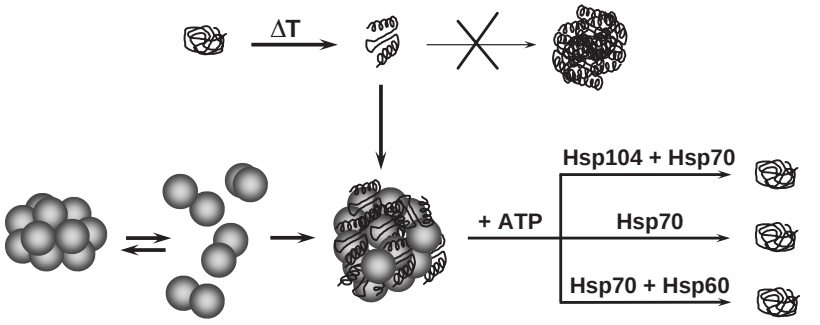

Fig. 24.2. Dynamic behavior and protein quality-control function of sHsps. Partially unfolded proteins that accumulate after temperature upshift (ΔT) are prevented from aggregation by binding to dissociated sHsp particles, resulting in large chaperone-substrate complexes. Refolding of the substrate proteins requires the action of ATP-dependent chaperones.

ing of sHsps, unfolded proteins, and mRNA has been reported during prolonged heat stress [56]. The association of heat shock granules is a specific and ordered process [57]. A consequence of the stable interaction between unfolded proteins and sHsps is that the substrates are neither transferred between different sHsp complexes nor spontaneously released. While trapping of aggregation-prone polypeptides might be sufficient in the static environment of the eye lens, the precious reservoir of folding-competent proteins is destined for reuse in other cell types. Some release of CS from Hsp25 could be achieved by the addition of oxaloacetate, a stabilizing ligand of CS [46]. However, productive release of substrate proteins requires additional cellular components in an ATP-dependent reaction [38, 58]. It has been demonstrated that substrate proteins are specifically transferred to the Hsp70/DnaK system for refolding [46, 59–61]. Disaggregation of sHsp/substrate complexes by DnaK is facilitated by ClpB, in particular when large insoluble particles have been formed [55]. The Hsp60/GroEL system does not directly participate in release of sHsp bound substrates, but it can accelerate the rate of refolding by operating downstream of Hsp70 in a cooperative multi-chaperone network [60] (Figure 24.2).

24.3.2
Chaperone Function in Vivo

Many cellular functions of sHsps can be reconciled in light of their reported chaperone activity. In the center of the human eye lens, the protein concentration reaches up to 450 mg mL^{-1} [62]. The structural lens proteins in this crowded environment unfold with age and are prevented from forming light-scattering aggregates by the combined action of αA- and αB-crystallin [58, 63, 64]. The most compelling documentation that α-crystallins are essential for lens transparency stems from αA-crystallin knockout mice that developed severe cataracts at an early age

[65]. An R116G exchange αA-crystallin is responsible for autosomal dominant congenital cataract in humans [66]. The mutated protein was shown to have reduced chaperone activity [67–69]. An equivalent mutation in αB-crystallin (R120G) causes cataract formation and desmin-related myopathy, an inherited neuromuscular disorder [70]. The aggregation of desmin filaments is thought to result from the reported defect in chaperone activity [67, 71, 72]. Somewhat surprisingly, a mouse deleted of the αB-crystallin gene carried normal eye lenses and developed normally except for a reduced life span [73].

Interestingly, αB-crystallin is overexpressed in many neurological disorders such as Alzheimer [74], Creutzfeld-Jakob [75], and other diseases [76, 77]. The clinical importance of sHsps is further underlined by an ever-growing number of other reported activities, among them, interaction with actin filaments and microtubules [78], protection against oxidative stress and modulation of the intracellular redox state [79], interference with apoptosis [80], translation inhibition [81], and neuroprotective effects [82]. The involvement of Hsps in disease and important cellular processes is potentially applicable to the development of diagnostic tests and novel drugs [83, 84].

Specific subsets of the multiple sHsps in plants are induced by an amazing array of conditions including germination, embryo and pollen development, and fruit maturation [3, 24]. How the complex developmental expression pattern is coordinated remains to be determined. Osmotic shock, oxidative stress, cold storage, and heavy metals also trigger the induction of certain sHsp species. Again, it is tempting to speculate that protein misfolding is a common theme in all of these events and that the sHsps carry out a principle protective function by preventing deleterious protein aggregation. In fact, it has been demonstrated by an in vivo reporter system that expression of various sHsps protects firefly luciferase in *Arabidopsis* cell suspension cultures [85, 86]. Interestingly, the expression of various plant sHsps has been reported to enhance thermotolerance of *E. coli*, again emphasizing a general rather than specific protective effect of these chaperones [87, 88]. Much to the same effect, overexpression of endogenous sHsps increased stress tolerance of *E. coli* and *A. thaliana* [89, 90], whereas disruption of the *hsp30* gene in *Neurospora crassa* resulted in reduced thermotolerance [91]. In contrast to the Hsp60 and Hsp70 chaperones, one of which is often essential for survival in many cell types, sHsps are dispensable. Apparently, their lack can be offset by the other constituents of the multi-chaperone network. Growth defects associated with accumulation of aggregated proteins were observed only in an *E. coli ibpAB* mutant during extreme heat shock [92, 93]. The defect was more pronounced in combination with a *dnaK* mutant allele, suggesting that a functional interaction between sHsps and the Hsp70 system also exists in vivo [92].

24.3.3 Other Functions

Inactivation of the *hsp17* gene of *Synechocystis* sp. PCC6803 coding for the single sHsp member in this cyanobacterium resulted not only in decreased thermotoler-

ance but also in reduced activity of the photosynthetic apparatus and disrupted integrity of thylakoid membranes [94, 95]. Hsp17 was found to be associated with thylakoid membranes, and transcription of *hsp17* responded to changes in membrane physical order, which led to its designation as "fluidity gene" [96]. Purified Hsp17 exhibited a dual function, acting either as chaperone by binding to denatured proteins or as stabilizer of hyperfluid lipid membranes by penetrating into the membrane hydrophobic core [97]. Preservation of membrane integrity by sHsps was postulated to be a general mechanism because α-crystallin stabilized synthetic and cyanobacterial membranes much like Hsp17 [98]. The observed membrane association of α-crystallin [99] and other sHsps [100–102] supports this hypothesis. Partitioning between soluble and membrane-bound states may be the key to whether chaperone function or membrane stabilization prevails.

Several reports have documented an interaction between sHsps and nucleic acids. Untranslated mRNAs have been detected in heat shock granules from plants and mammals [56, 103]. It is not clear, however, whether it is a fortuitous association mediated via other proteins that are integrated into the granules or whether the sHsps have a direct affinity towards nucleic acids. Some reports show that sHsps are indeed able to bind single-stranded or double-stranded DNA [104, 105], probably by helical structures [106]. Many interesting sHsp activities in maintaining the integrity of various cellular macromolecules may still remain to be explored.

24.4 The Oligomeric Structure of α-Hsps

Despite their sequence diversity, sHsps share secondary structure. Predictions that suggest a high β-sheet content in the α-crystallin domain are consistent with CD-spectra dominated by β-sheets in several sHsps [107, 108]. Calculation of the β-sheet content from far UV spectra of Hsp25, Hsp26, and α-crystallin revealed β-sheet contents between 20% and 30% [107, 109], correlating directly with the content of α-crystallin domain in the overall sequence and indicating high α-helical and unstructured parts in the N-terminal domain.

One of the most striking features of sHsps is their organization in large oligomeric structures, comprising nine to about 50 subunits. For three family members the structure of these complexes has been solved (Figure 24.3), revealing hollow, globule-like structures with outside diameters of 120 and 190 Å. While the quaternary structure of Hsp16.5 from *Methanococcus jannaschii* is well ordered [110], the oligomers formed by α-crystallin and Hsp27 show more structural variability and the ability to acquire and release subunits [111, 112]. Interestingly, wheat Hsp16.9 assembles into a dodecameric double disk. Each disk is organized as a trimer of dimers [113]. Hydrophobic patches become exposed upon disassembly of the complex into dimers. The structures of all sHsps solved so far support the idea that a dimer is the smallest exchangeable unit. This minimal dimeric building block seems to be conserved and may represent the functional unit concerning chaper-

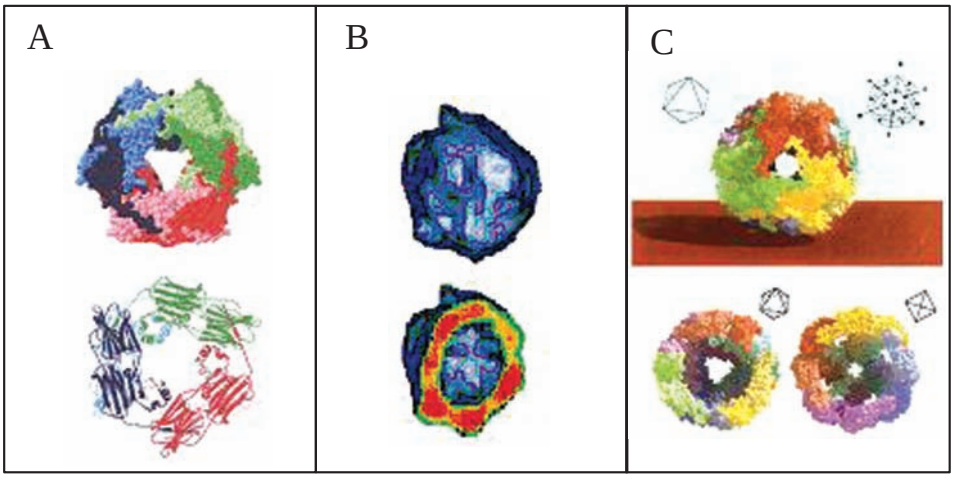

Fig. 24.3. Three-dimensional structure of sHsps. (A) Crystal structure of wheat Hsp16.9 [113]. The dodecamer arranged as two hexameric discs is 9.5 nm wide and 5.5 nm high. (B) Cryo-electron microscopic image of α-crystallin [111]. The outer diameter of the 32mer is 18 nm [111]. (C) Crystal structure of Hsp16.5 from *M. jannaschii*, which assembles into a 24mer with an outer diameter of 12 nm [110]. Reproduced with permission of the publisher and authors.

one properties [9, 109, 113, 114]. The necessary exception to this general picture might be Hsp16.3 from *Mycobacterium tuberculosis*, for which a trimeric substructure has been proposed. According to cryo-electron microscopy data, the triangular particle is composed of nine subunits organized as a trimer of trimers [115].

It is matter of controversy which parts of sHsps contribute to the association of the oligomeric structures and which are involved in the interaction with nonnative proteins [2, 4, 9]. A common property of all sHsp structures is the localization of the N-terminal regions in the interior of the oligomeric structures. In Hsp16.5 and α-crystallin, these disordered regions sequester inside the sphere; in the case of Hsp16.9, they are buried in the oligomeric structure. The liberated, hydrophobic N-terminal part might represent the substrate-binding site of disassembled sHsp particles [109, 113].

To asses the role of the N-terminal region, the four Hsp12 proteins from *C. elegans* have been investigated [18, 35]. They are the smallest naturally occurring representatives of the family and are reduced to the α-crystallin domain preceded by an exceptionally short N-terminal region of 25 or 26 residues. They form complexes from monomers to tetramers, but neither of them displays chaperone activity. Only 16.2 from *C. elegans*, a typical member with an N-terminal extension of 41 residues, builds a higher oligomer of 14 to 24 subunits and displays chaperone activity [116]. N-terminal deletions resulted in trimeric or tetrameric complexes lacking chaperone activity. In recent studies on yeast Hsp26, an N-terminally truncated construct turned out to be dimeric and inactive [109]. It was concluded that regions that are important for both the assembly of the 24mer and the interaction

with nonnative proteins reside in the N-terminal part of the protein. This view is supported by thermal unfolding experiments that show that full-length Hsp26 exhibits two transitions, one in the heat shock temperature range and one at much higher temperatures. Only the high-temperature transition was observed in the case of Hsp26ΔN. Furthermore, these results suggest that less energy is required for dissociation of the 24mer than for the dissociation and unfolding of the dimer. Quantitative data for the changes in energy involved in these processes were obtained by analyzing urea-induced unfolding transitions at 25 °C and 43 °C. These data are in good agreement with the unfolding transitions and support the hypothesis of a thermolabile Hsp26 assembly that dissociates to stable dimers at elevated temperatures [109, 114].

Many efforts to identify individual amino acid residues involved in subunit interaction or chaperone activity by point mutagenesis have had limited success [52, 117–120]. Although some point mutations resulted in significantly enlarged assemblies, chaperone activity was barely affected. Point mutations in bacterial sHsps have been more telling because they pinpointed a number of residues in the α-crystallin domain and C-terminal extension that are critical for oligomerization and chaperone activity [42, 121–123]. In summary, the emerging picture is that residues in all three domains of sHsp are required for oligomerization [2]. While the α-crystallin domain is necessary for dimer formation and thus assembles the basic building block, both flanking regions promote the formation of higher-order structures.

The oligomeric state of mammalian sHsps can be altered by various posttranslational modifications, in particular by serine-specific phosphorylation [124–126]. Human Hsp27, for example, possesses three phosphorylation sites, S15, S78, and S82, whose modification via a MAP kinase cascade leads to eight possible isoforms [127]. Thr143 comprises an alternative phosphorylation site in Hsp27 that is phosphorylated by a cGMP-dependent protein kinase [128]. The only reported example of a phosphorylated plant sHsp is Hsp22 from maize mitochondria. Covalent modification occurs at a serine residue by an unspecified kinase activity [129]. Phosphorylation of human Hsp27 and αB-crystallin decreased its oligomeric size and reduced chaperone activity [130–132]. With the exception of αA-crystallin, phosphorylation of mammalian sHsps is regulated in response to stress, cytokines, and growth factors [133–135]. Phosphatase-mediated dephosphorylation regulates the phosphorylation state [136–138]. Apart from the ambient physical and chemical conditions, controlled covalent modification of sHsp provides an additional mechanism to modulate the structural and functional properties of sHsps according to the cellular demands.

24.5
Dynamic Structures as Key to Chaperone Activity

While the crystal structures of Hsp16.5 and Hsp16.9 might appear rather rigid and stable, sHsp complexes in fact are very dynamic, enabling them to exchange

subunits and to form hetero-oligomeric assemblies. For example, *Triticum aestivum* Hsp16.9 has been shown to dissociate into sub-oligomeric species at higher temperatures. As a consequence, Hsp16.9 is able to interact and form complexes with its close homologue *Pisum sativum* Hsp18.1 [113]. Complex formation between both sHsps involves subunit exchange, as has been demonstrated elegantly by electrospray mass spectrometry [139].

The exchange of subunits between sHsps has also been demonstrated for other sHsps from plants and bacteria [31, 140]. Exchange occurred only if the proteins were from the same class of sHsps. In mammals, various sHsps frequently exchange subunits. In the vertebrate eye lens, for example, α-crystallin forms hetero-aggregates containing αA and αB subunits [141]. In addition, αA-crystallin exchanges subunits with Hsp27 [112]. Mixed polymers of αA-crystallin, αB-crystallin, and Hsp25 [107], and between HspB2 and HspB3, have been described [142]. It is not clear what the function of this intermolecular subunit exchange in sHsps might be. However, in the case of cells that express several sHsps in the same compartment, the formation of hetero-complexes most likely is relevant in vivo.

It is possible that mixed complexes are the result of a fortuitous interaction of closely related proteins maintaining them in an inactive storage form. Regardless of whether homo-oligomeric or hetero-oligomeric complexes have been formed, they need to dissociate in order to gain chaperone function (Figure 24.2). One interpretation of this dynamic behavior is that substrate-binding sites are buried in the complex but become exposed by dissociation. Major structural rearrangements upon substrate binding lead to the formation of even larger substrate-sHsp complexes that need to be taken apart with the help of other chaperones [54, 55]. The spontaneous dissociation-reassociation process might be some sort of sensing process monitoring the presence of nonnative proteins in the cellular environment.

24.6 Experimental Protocols

24.6.1 Purification of sHsps

Purification of Affinity-tagged sHsps

It is well documented that sHsps carrying a short tag that facilitates purification are functional chaperones. N-terminally histidine-tagged IbpA and IbpB of *E. coli* [143], C-terminally histidine-tagged class A and class B sHsps from *B. japonicum* [31], and C-terminally Strep-tagged pea Hsp18.1 and *Synechocystis* Hsp16.6 [144] were shown to suppress light-scattering of model substrates. Affinity-tagged sHsps can be purified according to standard protocols.

Purification of Hsp26 from *Saccharomyces cerevisiae*

The purification method described below allows the overexpression and purification of Hsp26 from *Saccharomyces cerevisiae* [114, 145]. A typical yield to be

achieved is about 3–5 mg of purified protein from one liter of cell culture. One liter of cell culture amounted to an average of 4 g wet cells. The purity of the protein was estimated to be >95% by densitometric scanning. After each purification step, fractions were pooled according to the appearance of the respective band on SDS-PAGE. If the band pattern was ambiguous, Western blot analysis using specific antibodies against the sHsp was performed.

Protein Expression

High-level expression of Hsp26 was achieved using the shuttle-vector pJV517, which is a derivative of the 2μ plasmid pRS464. The high copy number ensured good expression levels. The plasmid contained the Ura3 gene for selection of yeast cells and the *β*-lactamase gene that allowed selection in *E. coli*. For protein expression, the Ura-yeast strain JT(DIP) GPD26(A) was used. The yeast strain and the plasmid were a generous gift from S. Lindquist (University of Chicago). Cells were grown at 30 °C to late logarithmic phase to an optical density of about 0.8 at 595 nm and harvested by centrifugation (2500 *g*, 5 min, 4 °C).

Purification

Purification of Hsp26 was accomplished by two different anion exchanges and a gel filtration column. During the purification, all buffers and reaction vessels were pre-cooled on ice and the purification steps were always carried out at 4 °C.

1. The cell pellet was washed with ice-cold buffer A (40 mM HEPES-KOH pH 7.5, 1 mM DTE, 1 mM EDTA) + 50 mM NaCl. The buffer contained a protease-inhibitor mix (1 μM Leupeptin, 2.5 mM *p*-amino benzoic acid (PABA), 1 mM Pefabloc, 1 μM Pepstatin) to avoid protease degradation during the purification procedure.
2. The cell pellet was resuspended 1:2 in buffer A + 50 mM NaCl + protease-inhibitor mix, and cells were broken with a Basic Z cell disrupter (Constant Systems).
3. The cell lysate was centrifuged (20 200 *g*, 45 min, 4 °C), fresh protease inhibitors were added, and the soluble extract was applied to a 50-mL DEAE Sephacel (Amersham Biosciences) ion exchange chromatography column equilibrated in buffer A + 50 mM NaCl. Hsp26 was eluted with a 500-mL NaCl gradient in buffer A ranging from 50 to 500 mM NaCl. Hsp26 containing fractions that eluted at 200–300 mM NaCl were pooled and dialyzed against buffer A + 50 mM NaCl.
4. The protein solution was loaded onto a 6-mL Resource-Q ion exchange column (Amersham Bisciences), equilibrated in buffer A + 50 mM NaCl. A linear NaCl gradient (50–500 mM) was used for elution. Hsp26 eluted in the range of 200–250 mM NaCl.
5. The Hsp26-containing fractions were pooled and further purified on a 90-mL Superdex S200 pg column (Amersham Biosciences) equilibrated in buffer B (40 mM HEPES-KOH pH 7.5, 1 mM DTE, 1 mM EDTA) + 200 mM NaCl. The

column was operated at a flow rate of 0.5 mL min^{-1}. Hsp26 eluted at about 60-mL buffer volume, indicating a large oligomeric species. Fractions containing pure Hsp26 were pooled, dialyzed against buffer A + 50 mM NaCl, and concentrated to approximately 3 mg mL^{-1} by ultrafiltration using an Amicon cell with a YM30 membrane and Centricon Microconcentrators with 30-kDa cutoff. The protein solution was centrifuged at 20 000 *g* at 4 °C, aliquoted, frozen in liquid nitrogen, and stored at −80 °C.

Purification of Recombinant Murine Hsp25 and Human Hsp27

The method described below allows the purification of about 10 mg of recombinant mammalian sHsp (mouse Hsp25, human Hsp27) per liter of cell culture [26, 46, 145, 146]. One liter of cell culture amounted to a wet cell pellet of about 3 g. The protocol typically led to a purity of ≥90%.

Protein Expression

For recombinant expression of Hsp25 and Hsp27, we used the *E. coli* strain BL21 (DE3) and the plasmids pAK3038Hsp25 [26] and pAK3038Hsp27 [146], respectively. A 50-mL pre-culture in LB medium containing 200 μg mL^{-1} ampicillin was inoculated with single colonies of *E. coli* BL21 (DE3) harboring the plasmid pAK3038Hsp25/27 grown overnight on an LB agar plate containing 100 μg mL^{-1} ampicillin. The pre-culture was grown at 37 °C for 135 min.

To inoculate each of six 1-L cultures (LB medium containing 0.4% glucose, 200 μg mL^{-1} ampicillin), 5 mL of the pre-culture was used. After about 4 h shaking at 37 °C, the expression of Hsp25/27 was induced by addition of IPTG (final concentration: 0.4 mM). The cells were incubated for another 2 h at 37 °C and subsequently harvested and pooled by centrifugation at 2600 *g* and 4 °C. The wet cell pellet can be stored at −80 °C if necessary.

Purification

The purification of recombinant mammalian sHsps was achieved by ammonium sulfate precipitation and anion exchange chromatography.

1. The cell pellet was resuspended in 50 mL lysis buffer (50 mM Tris/HCl, pH 8.0, 100 mM NaCl, 1 mM EDTA) and centrifuged for 10 min at 4 °C and 4000 *g*.
2. For lysis, 60 mL lysis buffer, 160 μL 50 mM PMSF (freshly dissolved in methanol, final concentration: 0.13 mM), and 2 mL lysozyme (25 mg mL^{-1} in lysis buffer) were added to the pellet, and re-dissolved cells were incubated on ice for 20 min. Subsequently, 80 mg solid sodium desoxycholate was added and cells were transferred to 37 °C. After 15 min incubation under constant stirring with a glass rod, about 1–2 mg of lyophilized DNase I was added and this step was repeated every 5 min until the viscosity of the solution decreased significantly (about 15 min after first addition of DNase I). The solution was then centrifuged for 15 min at 4 °C at 20 000 *g*.
3. The supernatant was transferred to room temperature, and a saturated solution of ammonium sulfate (pH 7.0) was added drop-wise under constant stirring un-

til a final saturation of 40% was reached. The stirring was continued for a further 30 min, and the sample was then centrifuged for 10 min at 20 400 *g* and 20 °C. The supernatant was discarded and the Hsp25/27-containing pellet was re-dissolved in 20 mL of buffer 1 (20 mM Tris/HCl, pH 7.6, 10 mM $MgCl_2$, 30 mM ammonium chloride, 0.5 mM dithiothreitol, 0.05 mM NaN_3, 2 μM PMSF). The re-dissolved pellet was dialyzed three times for at least 6 h at 4 °C against 600 mL of buffer 1 and then centrifuged again as described above.

4. Ion exchange chromatography was carried out on a 135-mL DEAE-Sepharose CL-6B (Amersham Biosciences) column. After equilibration of the column with 300 mL of buffer 1, the dialyzed sample was applied and the column was washed with 100 mL of buffer 1 and developed with a 500-mL gradient from 0 to 200 mM NaCl in buffer 1. Hsp25 eluted as a single peak at about 100 mM NaCl, whereas Hsp27 eluted at about 120 mM NaCl.
5. Pooled peak fractions containing Hsp25/27 were precipitated overnight at 4 °C after adding solid ammonium sulfate to a final saturation of 50%. The precipitated protein was pelleted by centrifugation for 10 min at 20 000 *g* and 20 °C.
6. The pellet was re-dissolved in 2 mL of buffer 1 and dialyzed three times against 600 mL of buffer 1 at 4 °C. The dialyzed sample was again centrifuged as above. The supernatant contains Hsp25/27, which can be stored in aliquots at −80 °C.

24.6.2 Chaperone Assays

Analysis of Chaperone Function

Progress in understanding the mechanism of chaperone function has been achieved mainly by a reductionist biochemical approach using purified chaperones and "model substrate proteins." This term implies that the substrate proteins do not necessarily represent natural, in vivo substrates. In many cases, the underlying rationale was that proteins that are recalcitrant folders in vitro may also have problems folding in the cell and are therefore good representatives of the unknown natural targets.

A number of different substrate proteins have been used to study the function of chaperones including RuBisCO [147], rhodanese [148], malate dehydrogenase [149, 150], and citrate synthase [145, 151]. Those substrates differ in their quaternary structure, their rate of folding, and their tendency to undergo irreversible side reactions during folding and unfolding [152].

Citrate Synthase Assay

Description of Enzyme

Enzyme: Citrate synthase (CS), mitochondrial, from pig heart
E.C.: 4.1.3.7.
MW: 48.969 kDa
$E^{280\ nm}$ 1.56, d = 1 cm
Sp. activity: ∼150 U/mg at 25 °C, pH 8.0 using dithionitrobenzoic acid (DTNB)

Description of Assay

CS catalyzes the reaction of oxaloacetic acid (OAA) and acetyl-coenzymeA (Ac-CoA) to citrate and CoA. The enzyme activity is determined by a colorimetric test using DTNB. DTNB reacts with the free thiol groups of the reaction product CoA. This reaction can be easily followed in a spectrophotometer at 412 nm. CS can be used as a substrate for chaperones since it rapidly denatures and aggregates at heat shock temperatures >37 °C [145]. OAA stabilizes CS, shifting the midpoint of thermal transition from 43 °C to 66.5 °C.

Materials and Suppliers

Acetyl-CoA (Roche)
Oxaloacetic acid (OAA) (Sigma)
Dithionitrobenzoic acid (DTNB) (Sigma)
Disposable cuvettes, d = 1 cm
Spectrophotometer with thermostated cell holder

Solutions

CS stock solution: 15 μM in 50 mM TE buffer [153] or commercially available CS (Sigma), dialyzed against TE buffer.
TE buffer: 50 mM Tris/HCl, 2 mM EDTA, pH 8.0
OAA solution: 10 mM, dissolve in 50 mM Tris no pH ⇒ ~pH 8.0
DTNB solution: 10 mM, dissolve in TE buffer, pH 8.0, DTNB is poorly soluble, requires extended stirring to dissolve
Ac-CoA solution: 5 mM, dissolve in TE buffer, pH 8.0
Do not freeze and thaw the substrate solutions, store on ice

Assay

The reaction mixture for the activity assay consists of 930 μL TE, 10 μL OAA solution, 10 μL DTNB solution, and 30 μL Ac-CoA solution. The reaction is started by the addition of 20 μL of 0.15 μM CS (monomer), and the change in absorbance is followed for 1 min in a UV spectrophotometer at 412 nm. The specific activity can be calculated as follows:

$$\text{Specific activity (U mg}^{-1}) = \Delta E/\text{min} \times V/(\varepsilon dvc)$$

where V is the test volume (mL), ε is the molar extinction coefficient of DTNB (13 600 M^{-1} cm^{-1}), d is the path length of the cell (cm), v is the sample volume (mL), and c is the enzyme concentration (mg mL^{-1}). The specific activity of native CS from pig heart is 150 U mg^{-1}.

Thermal Inactivation and Reactivation

CS (15 μM) is diluted 100-fold with stirring into the corresponding buffer (usually 40 mM HEPES-KOH, pH 7.5 or 50 mM Tris-HCL, pH 8.0 (25 °C), which is pre-

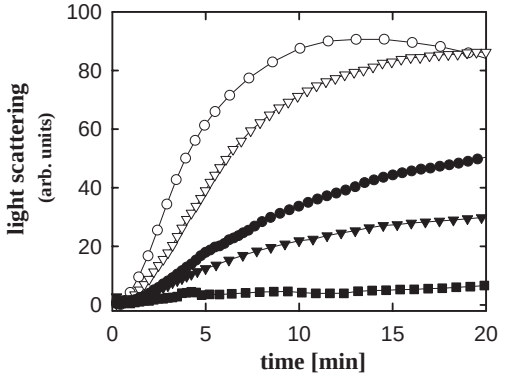

Fig. 24.4. Typical chaperone assay using CS as substrate. Influence of Hsp26 on the thermal aggregation of CS. CS (final concentration: 75 nM) was diluted into a thermostated solution of 37.5 nM (▽), 55 nM (●), 75 nM (τ), and 150 nM Hsp26 complex (■). Open circles represent the spontaneous aggregation of CS at 43 °C. The kinetics of aggregation was determined by measuring light scattering of the samples.

incubated at 25 °C in a 2-mL Eppendorf tube equipped with a small stirring bar. The activity is determined and set to 100%. The inactivation is started by placing the test tube in a 43 °C water bath. During the time course of inactivation, aliquots are withdrawn to determine activity.

Reactivation of CS can be initiated either by a temperature shift back to 25 °C or by addition of 1 mM OAA at 43 °C. During the time course of reactivation, aliquots are withdrawn to determine activity.

Thermal Aggregation of CS

Light scattering is used to examine the influence of sHsps on the thermal aggregation of CS (Figure 24.4). CS (15 μM) is diluted 1:50 in 40 mM HEPES/KOH, pH 7.5, and equilibrated at 43 °C in the presence and in the absence of sHsps. Aggregation kinetics is measured in a fluorescence spectrophotometer in a stirred and thermostated quartz cell at 400 nm. Alternatively, the aggregation of 2–4 μM (end concentration) of CS can be monitored in a VIS photometer at 400 nm.

Insulin Assay

Description of Enzyme

Insulin is a two-chain polypeptide hormone produced by the β-cells of pancreatic islets. The A (21 aa) and B (30 aa) chains are joined by two interchain disulfide bonds. The A chain contains an additional intrachain disulfide bond.
Insulin from bovine pancreas
MW: 5.8 kDa
$A_{280\ nm,0.1\%} = 1.06$
1.06 OD is 1 mg mL^{-1}

Assay Description

On reduction of the disulfide bonds of insulin with dithiothreitol (DTT), the insulin B chain will aggregate and precipitate, while the A chain remains in solution. This unfolding process can be monitored by measuring the apparent absorbance due to the increase in scattering.

This is a simple semi-quantitative assay to describe the ability of the protein under investigation to act as a chaperone [154]. The assay can be used at different temperatures and salt conditions but seems very sensitive to pH changes: the higher the pH, the weaker the aggregation reaction. The aggregation reaction is slightly faster at higher temperatures.

Materials and Suppliers

Insulin (Sigma)
UV cuvettes, d = 1 cm, 120 μL
Spectrophotometer with thermostated cell holder
240 mM stock solution of DTT

Separation of Stock Solution of Insulin

1. Resuspend 10 mg of insulin to a concentration of 7 mg mL^{-1} in buffer (10 mM $NaPO_4$, pH 7.0).
2. To dissolve the insulin, add concentrated HCl until the solution is clear, than increase the pH by adding concentrated NaOH until the solution gets slightly cloudy again.
3. Stock solution can be kept on ice or at −20 °C.

Assay

Conditions: 25–45 °C

Add different amounts of the potential chaperone to 50 μM insulin in a total volume of 115 μL and use the same amount of dialysis buffer as control. The reaction is started by adding this solution to a 120-μL cuvette already containing 10 μL of DTT solution. The aggregation is significantly slower when lower DTT concentrations are used. The cuvette is placed in the UV spectrophotometer and the kinetics of aggregation is followed at 400 nm.

24.6.3 Monitoring Dynamics of sHsps

Size-exclusion Chromatography

The dynamics of sHsps has been studied by various techniques, among them electron microscopy [111, 114], native PAGE [114], affinity co-purification [42], fluorescence resonance energy transfer [44], and mass spectrometry [139, 155]. The most frequently used method is size-exclusion HPLC (SEC). A critical aspect in such gel filtration experiments is to use columns that can be operated at varying temperatures or buffer conditions. Here, TosoHaas TSK 3000 PW (30 cm × 0.75 cm; sepa-

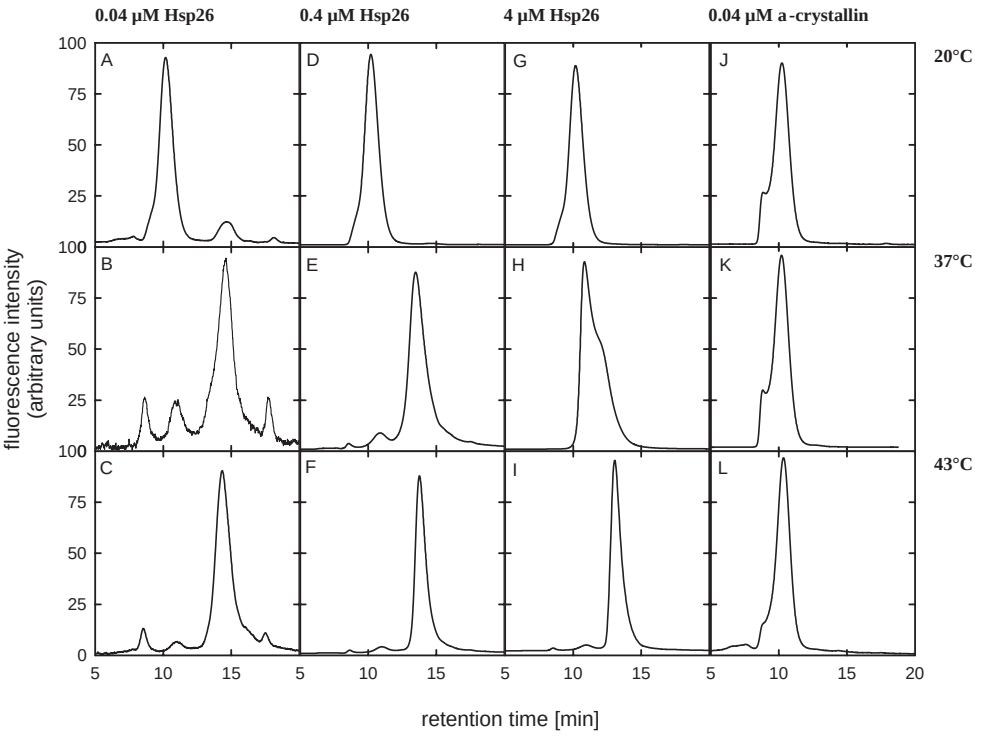

Fig. 24.5. Influence of elevated temperature and concentration on Hsp26 and α-crystallin quaternary structure. SEC was performed using a TosoHaas TSK 4000 PW column at different temperatures with a flow rate of 0.75 mL min^{-1} in 40 mM HEPES/KOH, 150 mM KCl, pH 7.4. Hsp26 and α-crystallin were incubated for 20 min at the indicated concentrations and temperatures and then applied to the column, which was kept at the same temperatures. The signal intensity was normalized.

ration range 0.5–800 kDa) or TSK 4000 PW columns (30 cm × 0.75 cm; separation range 0.5–1200 kDa) proved to be useful. Chromatography usually is carried out at 10–50 °C in buffers containing 150–300 mM salt at physiological pH conditions, with a flow rate of 0.5–0.75 mL min^{-1} (Figure 24.5). To analyze the dynamics of sHsps, it is important to perform the experiments at different concentrations of sHsps, since the concentration often has a high impact on the oligomeric state and stability of sHsp complexes.

Acknowledgements

We thank Hauke Hennecke and Johannes Buchner for generous support. Work in our laboratories was financed by grants from the Swiss National Foundation for Scientific Research and the Swiss Federal Institute of Technology to F.N. and by a grant from the Deutsche Forschungsgemeinschaft (SFB 594) to J.B. and M.H.

References

1 MacRae, T. H. (2000) Structure and function of small heat shock/α-crystallin proteins: established concepts and emerging ideas. *Cell. Mol. Life Sci.* **57**, 899–913.

2 Narberhaus, F. (2002) α-Crystallin-type heat shock proteins: Socializing minichaperones in the context of a multichaperone network. *Microbiol. Mol. Biol. Rev.* **66**, 64–93.

3 Waters, E. R., Lee, G. J., and Vierling, E. (1996) Evolution, structure and function of the small heat shock proteins in plants. *J. Exp. Bot.* **47**, 325–338.

4 Haslbeck, M., and Buchner, J. (2002) Chaperone function of sHsps. *Prog. Mol. Subcell. Biol.* **28**, 37–59.

5 Haslbeck, M. (2002) sHsps and their role in the chaperone network. *Cell. Mol. Life Sci.* **59**, 1649–1657.

6 Ehrnsperger, M., Buchner, J., and Gaestel, M. (1998) Structure and function of small heat-shock proteins. In *Molecular chaperones in the life cycle of proteins: Structure, function and mode of action* (Fink, A. L., and Goto, Y., eds), pp. 533–575, Marcel Dekker, Inc., New York.

7 De Jong, W. W., Caspers, G. J., and Leunissen, J. A. M. (1998) Genealogy of the α-crystallin – small heat-shock protein superfamily. *Int. J. Biol. Macromol.* **22**, 151–162.

8 Caspers, G. J., Leunissen, J. A. M., and de Jong, W. W. (1995) The expanding small heat-shock protein family, and structure predictions of the conserved 'α-crystallin domain'. *J. Mol. Evol.* **40**, 238–248.

9 Van Montfort, R., Slingsby, C., and Vierling, E. (2001) Structure and function of the small heat shock protein/α-crystallin family of molecular chaperones. *Adv. Protein Chem.* **59**, 105–156.

10 Horwitz, J. (2003) Alpha-crystallin. *Exp. Eye Res.* **76**, 145–153.

11 Klemenz, R., Fröhli, E., Steiger, R. H., Schäfer, R., and Aoyama, A. (1991) αB-crystallin is a small heat shock protein. *Proc. Natl. Acad. Sci. USA* **88**, 3652–3656.

12 Dubin, R. A., Wawrousek, E. F., and Piatigorsky, J. (1989) Expression of the murine αB-crystallin gene is not restricted to the lens. *Mol. Cell. Biol.* **9**, 1083–1091.

13 Bhat, S. P., and Nagineni, C. N. (1989) αB subunit of lens-specific protein α-crystallin is present in other ocular and non-ocular tissues. *Biochem. Biophys. Res. Commun.* **158**, 319–325.

14 Ingolia, T. D., and Craig, E. A. (1982) Four small *Drosophila* heat shock proteins are related to each other and to mammalian α-crystallin. *Proc. Natl. Acad. Sci. USA* **79**, 2360–2364.

15 Münchbach, M., Nocker, A., and Narberhaus, F. (1999) Multiple small heat shock proteins in rhizobia. *J. Bacteriol.* **181**, 83–90.

16 Kappé, G., Leunissen, J. A., and de Jong, W. W. (2002) Evolution and diversity of prokaryotic small heat shock proteins. *Prog. Mol. Subcell. Biol.* **28**, 1–17.

17 Scharf, K. D., Siddique, M., and Vierling, E. (2001) The expanding family of *Arabidopsis thaliana* small heat stress proteins and a new family of proteins containing α-crystallin domains (Acd proteins). *Cell Stress Chaperones* **6**, 225–237.

18 Leroux, M. R., Ma, B. J., Batelier, G., Melki, R., and Candido, E. P. M. (1997) Unique structural features of a novel class of small heat shock proteins. *J. Biol. Chem.* **272**, 12847–12853.

19 Wotton, D., Freeman, K., and Shore, D. (1996) Multimerization of Hsp42p, a novel heat shock protein of *Saccharomyces cerevisiae*, is dependent on a conserved carboxyl-terminal sequence. *J. Biol. Chem.* **271**, 2717–2723.

20 Nover, L., and Scharf, K. D. (1997) Heat Stress Proteins and Transcription Factors. *Cell. Mol. Life Sci.* **53**, 80–103.

21 Morimoto, R. I. (1998) Regulation of the heat shock transcriptional response: cross talk between a family of heat shock factors, molecular chaperones, and negative regulators. *Genes Dev.* **12**, 3788–3796.

22 Richmond, C. S., Glasner, J. D., Mau, R., Jin, H., and Blattner, F. R. (1999) Genome-wide expression profiling in *Escherichia coli* K-12. *Nucleic Acids Res.* **27**, 3821–3835.

23 Arrigo, A. P., and Landry, J. (1994) Expression and function of the low-molecular-weight heat shock proteins. In *The biology of heat shock proteins and molecular chaperones* (Morimoto, R. I., Tissiéres, A., and Georgopoulos, C., eds), pp. 335–373, Cold Spring Harbor Laboratory Press, Cold Spring Harbor, N.Y.

24 Sun, W., Van Montagu, M., and Verbruggen, N. (2002) Small heat shock proteins and stress tolerance in plants. *Biochim. Biophys. Acta* **1577**, 1–9.

25 Horwitz, J. (1992) α-crystallin can function as a molecular chaperone. *Proc. Natl. Acad. Sci. USA* **89**, 10449–10453.

26 Jakob, U., Gaestel, M., Engel, K., and Buchner, J. (1993) Small heat shock proteins are molecular chaperones. *J. Biol. Chem.* **268**, 1517–1520.

27 Fernando, P., and Heikkila, J. J. (2000) Functional characterization of *Xenopus* small heat shock protein, Hsp30C: the carboxyl end is required for stability and chaperone activity. *Cell Stress Chaperones* **5**, 148–159.

28 Liang, P., Amons, R., Macrae, T. H., and Clegg, J. S. (1997) Molecular characterization of a small heat shock/alpha-crystallin protein in encysted Artemia embryos. *Eur. J. Biochem.* **243**, 225–232.

29 Lee, G. J., Pokala, N., and Vierling, E. (1995) Structure and in vitro molecular chaperone activity of cytosolic small heat shock proteins from pea. *J. Biol. Chem.* **270**, 10432–10438.

30 Smýkal, P., Masin, J., Hrdý, I., Konopásek, I., and Zárský, V. (2000) Chaperone activity of tobacco HSP18, a small heat-shock protein, is inhibited by ATP. *Plant J.* **23**, 703–713.

31 Studer, S., and Narberhaus, F. (2000) Chaperone activity and homo- and hetero-oligomer formation of bacterial small heat shock proteins. *J. Biol. Chem.* **275**, 37212–37218.

32 Delmas, F., Pierre, F., Coucheney, F., Divies, C., and Guzzo, J. (2001) Biochemical and physiological studies of the small heat shock protein Lo18 from the lactic acid bacterium *Oenococcus oeni*. *J. Mol. Microbiol. Biotechnol.* **3**, 601–610.

33 Michelini, E. T., and Flynn, G. C. (1999) The unique chaperone operon of *Thermotoga maritima*: Cloning and initial characterization of a functional Hsp70 and small heat shock protein. *J. Bacteriol.* **181**, 4237–4244.

34 Roy, S. K., Hiyama, T., and Nakamoto, H. (1999) Purification and characterization of the 16-kDa heat-shock-responsive protein from the thermophilic cyanobacterium *Synechococcus vulcanus*, which is an α-crystallin-related, small heat shock protein. *Eur. J. Biochem.* **262**, 406–416.

35 Kokke, B. P. A., Leroux, M. R., Candido, E. P. M., Boelens, W. C., and deJong, W. W. (1998) *Caenorhabditis elegans* small heat-shock proteins Hsp12.2 and Hsp12.3 form tetramers and have no chaperone-like activity. *FEBS Lett.* **433**, 228–232.

36 Santhoshkumar, P., and Sharma, K. K. (2002) *Caenorhabditis elegans* small heat-shock proteins Hsp12.2 and Hsp12.3 form tetramers and have no chaperone-like activity. *Biochim. Biophys. Acta* **1598**, 115–121.

37 Bhattacharyya, J., Santhoshkumar, P., and Sharma, K. K. (2003) A peptide sequence-YSGVCHTDLHA-WHGDWPLPVK [40–60]-in yeast alcohol dehydrogenase prevents the aggregation of denatured substrate proteins. *Biochem. Biophys. Res. Commun.* **307**, 1–7.

38 Lee, G. J., Roseman, A. M., Saibil, H. R., and Vierling, E. (1997) A

small heat shock protein stably binds heat denatured model substrates and can maintain a substrate in a folding competent state. *EMBO J.* **16**, 659–671.

39 Sharma, K. K., Kumar, G. S., Murphy, A. S., and Kester, K. (1998) Identification of 1,1′-Bi(4-anilino)naphthalene-5,5′-disulfonic acid binding sequences in α-crystallin. *J. Biol. Chem.* **273**, 15474–15478.

40 Sharma, K. K., Kumar, R. S., Kumar, G. S., and Quinn, P. T. (2000) Synthesis and characterization of a peptide identified as a functional element in αA-crystallin. *J. Biol. Chem.* **275**, 3767–3771.

41 Sharma, K. K., Kaur, H., and Kester, K. (1997) Functional elements in molecular chaperone α-crystallin: identification of binding sites in αB-crystallin. *Biochem. Biophys. Res. Commun.* **239**, 217–222.

42 Lentze, N., Studer, S., and Narberhaus, F. (2003) Structural and functional defects caused by point mutations in the α-crystallin domain of a bacterail α-heat shock protein. *J. Mol. Biol.* **328**, 927–937.

43 Lindner, R. A., Kapur, A., Mariani, M., Titmuss, S. J., and Carver, J. A. (1998) Structural alterations of α-crystallin during its chaperone action. *Eur. J. Biochem.* **258**, 170–183.

44 Bova, M. P., Ding, L. L., Horwitz, J., and Fung, B. K. (1997) Subunit exchange of a α-crystallin. *J. Biol. Chem.* **272**, 29511–29517.

45 Hartl, F. U. (1996) Molecular chaperones in cellular protein folding. *Nature* **381**, 571–580.

46 Ehrnsperger, M., Gräber, S., Gaestel, M., and Buchner, J. (1997) Binding of non-native protein to Hsp25 during heat shock creates a reservoir of folding intermediates for reactivation. *EMBO J.* **16**, 221–229.

47 Rajaraman, K., Raman, B., and Rao, C. M. (1996) Molten-globule state of carbonic anhydrase binds to the chaperone-like α-crystallin. *J. Biol. Chem.* **271**, 27595–27600.

48 Rawat, U., and Rao, M. (1998) Interactions of chaperone alpha-crystallin with the molten globule state of xylose reductase. Implications for reconstitution of the active enzyme. *J. Biol. Chem.* **273**, 9415–9423.

49 Lindner, R. A., Kapur, A., and Carver, J. A. (1997) The interaction of the molecular chaperone, α-crystallin, with molten globule states of bovine α-lactalbumin. *J. Biol. Chem.* **272**, 27722–27729.

50 Wang, K., and Spector, A. (2001) ATP causes small heat shock proteins to release denatured protein. *Eur. J. Biochem.* **268**, 6335–6345.

51 Muchowski, P. J., and Clark, J. I. (1998) ATP-enhanced molecular chaperone functions of the small heat shock protein human αB crystallin. *Proc. Natl. Acad. Sci. USA* **95**, 1004–1009.

52 Muchowski, P. J., Hays, L. G., Yates, J. R., and Clark, J. I. (1999) ATP and the core "α-crystallin" domain of the small heat-shock protein αB-crystallin. *J. Biol. Chem.* **274**, 30190–30195.

53 Allen, S. P., Polazzi, J. O., Gierse, J. K., and Easton, A. M. (1992) Two novel heat shock genes encoding proteins produced in response to heterologous protein expression in *Escherichia coli*. *J. Bacteriol.* **174**, 6938–6947.

54 Stromer, T., Ehrnsperger, M., Gaestel, M., and Buchner, J. (2003) Analysis of the interaction of small heat shock proteins with unfolding proteins. *J. Biol. Chem.* **278**, 18015–18021.

55 Mogk, A., Schlieker, C., Friedrich, K. L., Schönfeld, H. J., Vierling, E., and Bukau, B. (2003) Refolding of substrates bound to small Hsps relies on a disaggregation reaction mediated most efficiently by ClpB/Dank. *J. Biol. Chem.* **278**, 31033–31042.

56 Nover, L., Scharf, K. D., and Neumann, D. (1989) Cytoplasmic heat shock granules are formed from precursor particles and are associated with a specific set of mRNAs. *Mol. Cell. Biol.* **9**, 1298–1308.

57 Kirschner, M., Winkelhaus, S., Thierfelder, J. M., and Nover, L.

(2000) Transient expression and heat-stress-induced co-aggregation of endogenous and heterologous small heat-stress proteins in tobacco protoplasts. *Plant J.* **24**, 397–411.

58 Wang, K., and Spector, A. (1994) The chaperone activity of bovine α-crystallin. Interaction with other lens crystallins in native and denatured states. *J. Biol. Chem.* **269**, 13601–13608.

59 Smýkal, P., Hrdý, I., and Pechan, P. M. (2000) High-molecular-mass complexes formed in vivo contain smHSPs and HSP70 and display chaperone-like activity. *Eur. J. Biochem.* **267**, 2195–2207.

60 Veinger, L., Diamant, S., Buchner, J., and Goloubinoff, P. (1998) The small heat-shock protein IbpB from *Escherichia coli* stabilizes stress-denatured proteins for subsequent refolding by a multichaperone network. *J. Biol. Chem.* **273**, 11032–11037.

61 Lee, G. J., and Vierling, E. (2000) A small heat shock protein cooperates with heat shock protein 70 systems to reactivate a heat-denatured protein. *Plant Physiol.* **122**, 189–197.

62 Fagerholm, P. P., Philipson, B. T., and Lindström, B. (1981) Normal human lens – the distribution of proteins. *Exp. Eye Res.* **33**, 615–620.

63 Rao, P. V., Huang, Q. L., Horwitz, J., and Zigler, J. S., Jr. (1995) Evidence that *a*-crystallin prevents non-specific protein aggregation in the intact eye lens. *Biochim. Biophys. Acta* **1245**, 439–447.

64 Carver, J. A., Nicholls, K. A., Aquilina, J. A., and Truscott, R. J. (1996) Age-related changes in bovine α-crystallin and high-molecular-weight protein. *Exp. Eye Res.* **63**, 639–647.

65 Brady, J. P., Garland, D., Duglas-Tabor, Y., Robison, W. G. J., Groome, A., and Wawrousek, E. F. (1997) Targeted disruption of the mouse αA-crystallin gene induces cataract and cytoplasmic inclusion bodies containing the small heat shock protein αB-crystallin. *Proc. Natl. Acad. Sci. USA* **94**, 884–889.

66 Litt, M., Kramer, P., LaMorticella, D. M., Murphey, W., Lovrien, E. W., and Weleber, R. G. (1998) Autosomal dominant congenital cataract associated with a missense mutation in the human alpha crystallin gene CRYAA. *Hum. Mol. Genet.* **7**, 471–474.

67 Kumar, L. V., Ramakrishna, T., and Rao, C. M. (1999) Structural and functional consequences of the mutation of a conserved arginine residue in αA and αB crystallins. *J. Biol. Chem.* **274**, 24137–24141.

68 Cobb, B. A., and Petrash, J. M. (2000) Characterization of α-crystallin-plasma membrane binding. *Biochemistry* **39**, 15791–15798.

69 Shroff, N. P., Cherian-Shaw, M., Bera, S., and Abraham, E. C. (2000) Mutation of R116C results in highly oligomerized αA-crystallin with modified structure and defective chaperone-like function. *Biochemistry* **39**, 1420–1426.

70 Vicart, P., Caron, A., Guicheney, P., Li, Z., Prevost, M. C., Faure, A., Chateau, D., Chapon, F., Tome, F., Dupret, J. M., Paulin, D., and Fardeau, M. (1998) A missense. mutation in the αB-crystallin chaperone gene causes a desmin-related myopathy. *Nat. Genet.* **20**, 92–95.

71 Perng, M. D., Muchowski, P. J., van den Ijssel, P., Wu, G. J., Hutcheson, A. M., Clark, J. I., and Quinlan, R. A. (1999) The cardiomyopathy and lens cataract mutation in αB-crystallin alters its protein structure, chaperone activity, and interaction with intermediate filaments in vitro. *J. Biol. Chem.* **274**, 33235–33243.

72 Bova, M. P., Yaron, O., Huang, Q. L., Ding, L. L., Haley, D. A., Stewart, P. L., and Horwitz, J. (1999) Mutation R120G in αB-crystallin, which is linked to a desmin-related myopathy, results in an irregular structure and defective chaperone-like function. *Proc. Natl. Acad. Sci. USA* **96**, 6137–6142.

73 Brady, J. P., Garland, D. L., Green, D. E., Tamm, E. R., Giblin, F. J., and Wawrousek, E. F. (2001) αB-crystallin

in lens development and muscle integrity: a gene knockout approach. *Invest. Ophthalmol. Vis. Sci.* **42**, 2924–2934.

74 Renkawek, K., Voorter, C. E., Bosman, G. J., van Workum, F. P., and de Jong, W. W. (1994) Expression of αB-crystallin in Alzheimer's disease. *Acta Neuropathol.* **87**, 155–160.

75 Renkawek, K., de Jong, W. W., Merck, K. B., Frenken, C. W., van Workum, F. P., and Bosman, G. J. (1992) αB-crystallin is present in reactive glia in Creutzfeldt-Jakob disease. *Acta Neuropathol.* **83**, 324–327.

76 Lowe, J., Landon, M., Pike, I., Spendlove, I., McDermott, H., and Mayer, R. J. (1990) Dementia with beta-amyloid deposition: involvement of alpha B-crystallin supports two main diseases. *Lancet* **336**, 515–516.

77 Head, M. W., Corbin, E., and Goldman, J. E. (1993) Overexpression and abnormal modification of the stress proteins αB-crystallin and HSP27 in Alexander disease. *Am. J. Pathol.* **143**, 1743–1153.

78 Mounier, N., and Arrigo, A. P. (2002) Actin cytoskeleton and small heat shock proteins: how do they interact? *Cell Stress Chaperones* **7**, 167–176.

79 Arrigo, A. P., Paul, C., Ducasse, C., Sauvageot, O., and Kretz-Remy, C. (2002) Small stress proteins: modulation of intracellular redox state and protection against oxidative stress. *Prog. Mol. Subcell. Biol.* **28**, 171–184.

80 Arrigo, A. P., Paul, C., Ducasse, C., Manero, F., Kretz-Remy, C., Virot, S., Javouhey, E., Mounier, N., and Diaz-Latoud, C. (2002) Small stress proteins: novel negative modulators of apoptosis induced independently of reactive oxygen species. *Prog. Mol. Subcell. Biol.* **28**, 185–204.

81 Cuesta, R., Laroia, G., and Schneider, R. J. (2000) Chaperone hsp27 inhibits translation during heat shock by binding eIF4G and facilitating dissociation of cap-initiation complexes. *Genes Dev.* **14**, 1460–1470.

82 Akbar, M. T., Lundberg, A. M., Liu, K., Vidyadaran, S., Wells, K. E., Dolatshad, H., Wynn, S., Wells, D. J., Latchman, D. S., and de Belleroche, J. (2003) The neuroprotective effects of heat shock protein 27 overexpression in transgenic animals against kainate-induced seizures and hippocampal cell death. *J. Biol. Chem.* **278**, 19956–19965.

83 Clark, J. I., and Muchowski, P. J. (2000) Small heat-shock proteins and their potential role in human disease. *Curr. Opin. Struct. Biol.* **10**, 52–59.

84 Crabbe, M. J. C., and Hepburne-Scott, H. W. (2001) Small heat shock proteins (sHsps) as potential drug targets. *Curr. Pharm. Biotech.* **2**, 77–111.

85 Löw, D., Brändle, K., Nover, L., and Forreiter, C. (2000) Cytosolic heat-stress proteins Hsp17.7 class I and Hsp17.3 class II of tomato act as molecular chaperones in vivo. *Planta* **211**, 575–582.

86 Forreiter, C., Kirschner, M., and Nover, L. (1997) Stable transformation of an Arabidopsis cell suspension culture with firefly luciferase providing a cellular system for analysis of chaperone activity in vivo. *Plant Cell* **9**, 2171–2181.

87 Yeh, C. H., Chang, P. F. L., Yeh, K. W., Lin, W. C., Chen, Y. M., and Lin, C. Y. (1997) Expression of a gene encoding a 16.9-kDa heat-shock protein, Oshsp16.9, in *Escherichia coli* enhances thermotolerance. *Proc. Natl. Acad. Sci. USA* **94**, 10967–10972.

88 Soto, A., Allona, I., Collada, C., Guevara, M. A., Casado, R., Rodriguez-Cerezo, E., Aragoncillo, C., and Gomez, L. (1999) Heterologous expression of a plant small heat-shock protein enhances *Escherichia coli* viability under heat and cold stress. *Plant Physiol.* **120**, 521–528.

89 Sun, W., Bernard, C., van de Cotte, B., Van Montagu, M., and Verbruggen, N. (2001) At-HSP17.6A, encoding a small heat-shock protein in *Arabidopsis*, can enhance

osmotolerance upon overexpression. *Plant J.* **27**, 407–415.

90 Kitagawa, M., Matsumura, Y., and Tsuchido, T. (2000) Small heat shock proteins, IbpA and IbpB, are involved in resistances to heat and superoxide stresses in *Escherichia coli*. *FEMS Microbiol. Lett.* **184**, 165–171.

91 Plesofsky-Vig, N., and Brambl, R. (1995) Disruption of the gene for *hsp30*, an α-crystallin-related heat shock protein of *Neurospora crassa*, causes defects in thermotolerance. *Proc. Natl. Acad. Sci. USA* **92**, 5032–5036.

92 Thomas, J. G., and Baneyx, F. (1998) Roles of the *Escherichia coli* small heat shock proteins IbpA and IbpB in thermal stress management: Comparison with ClpA, ClpB, and HtpG in vivo. *J. Bacteriol.* **180**, 5165–5172.

93 Kuczynska-Wisnik, D., Kedzierska, S., Matuszewska, E., Lund, P., Taylor, A., Lipinska, B., and Laskowska, E. (2002) The *Escherichia coli* small heat-shock proteins IbpA and IbpB prevent the aggregation of endogenous proteins denatured in vivo during extreme heat shock. *Microbiology* **148**, 1757–1765.

94 Lee, S., Owen, H. A., Prochaska, D. J., and Barnum, S. R. (2000) HSP16.6 is involved in the development of thermotolerance and thylakoid stability in the unicellular cyanobacterium, *Synechocystis* sp. PCC 6803. *Curr. Microbiol.* **40**, 283–287.

95 Lee, S. Y., Prochaska, D. J., Fang, F., and Barnum, S. R. (1998) A 16.6-kilodalton protein in the cyanobacterium *Synechocystis* sp. PCC 6803 plays a role in the heat shock response. *Curr. Microbiol.* **37**, 403–407.

96 Horváth, I., Glatz, A., Varvasovszki, V., Török, Z., Páli, T., Balogh, G., Kovács, E., Nádasdi, L., Benkö, S., Joó, F., and Vigh, L. (1998) Membrane physical state controls the signaling mechanism of the heat shock response in *Synechocystis* PCC 6803: identification of *hsp17* as a "fluidity gene". *Proc. Natl. Acad. Sci. USA* **95**, 3513–3518.

97 Török, Z., Goloubinoff, P., Horváth, I., Tsvetkova, N. M., Glatz, A., Balogh, G., Varvasovszki, V., Los, D. A., Vierling, E., Crowe, J. H., and Vigh, L. (2001) *Synechocystis* HSP17 is an amphitropic protein that stabilizes heat-stressed membranes and binds denatured proteins for subsequent chaperone-mediated refolding. *Proc. Natl. Acad. Sci. USA* **98**, 3098–3103.

98 Tsvetkova, N. M., Horvath, I., Török, Z., Wolkers, W. F., Balogi, Z., Shigapova, N., Crowe, L. M., Tablin, F., Vierling, E., Crowe, J. H., and Vigh, L. (2002) Small heat-shock proteins regulate membrane lipid polymorphism. *Proc. Natl. Acad. Sci. USA* **99**, 13504–13509.

99 Cobb, B. A., and Petrash, J. M. (2000) Characterization of α-crystallin-plasma membrane binding. *J. Biol. Chem.* **275**, 6664–6672.

100 Lee, B. Y., Hefta, S. A., and Brennan, P. J. (1992) Characterization of the major membrane protein of virulent *Mycobacterium tuberculosis*. *Infect. Immun.* **60**, 2066–2074.

101 Lünsdorf, H., Schairer, H. U., and Heidelbach, M. (1995) Localization of the stress protein SP21 in indole-induced spores, fruiting bodies, and heat-shocked cells of *Stigmatella aurantiaca*. *J. Bacteriol.* **177**, 7092–7099.

102 Jobin, M. P., Delmas, F., Garmyn, D., Diviès, C., and Guzzo, J. (1997) Molecular characterization of the gene encoding an 18-kilodalton small heat shock protein associated with the membrane of *Leuconostoc oenos*. *Appl. Environ. Microbiol.* **63**, 609–614.

103 Kedersha, N. L., Gupta, M., Li, W., Miller, I., and Anderson, P. (1999) RNA-binding proteins TIA-1 and TIAR link the phosphorylation of eIF-2α to the assembly of mammalian stress granules. *J. Cell. Biol.* **147**, 1431–1442.

104 Singh, K., GrothVasselli, B., and Farnsworth, P. N. (1998) Interaction of DNA with bovine lens α-crystallin: its functional implications. *Int. J. Biol. Macromol.* **22**, 315–320.

105 Pietrowski, D., Durante, M. J., Liebstein, A., Schmitt-John, T., Werner, T., and Graw, J. (1994) α-Crystallins are involved in specific interactions with the murine gamma D/E/F-crystallin-encoding gene. *Gene* **144**, 171–178.

106 Bloemendal, M., Toumadje, A., and Johnson, W. C. (1999) Bovine lens crystallins do contain helical structures: a circular dichroism study. *Biochim. Biophys. Acta* **1432**, 234–238.

107 Merck, K. B., Groenen, P. J. T. A., Voorter, C. E. M., de Haard-Hoekman, W. A., Horwitz, J., Bloemendal, H., and de Jong, W. W. (1993) Structural and functional similarities of bovine α-crystallin and mouse small heat-shock protein – A family of chaperones. *J. Biol. Chem.* **268**, 1046–1052.

108 Dudich, I. V., Zav'yalov, V. P., Pfeil, W., Gaestel, M., Zav'yalova, G. A., Denesyuk, A. I., and Korpela, T. (1995) Dimer structure as a minimum cooperative subunit of small heat-shock proteins. *Biochim. Biophys. Acta* **1253**, 163–168.

109 Stromer, T., Fischer, E., Richter, K., Haslbeck, M., and Buchner, J. (2004) Analysis of the regulation of the molecular chaperone Hsp26 by temperature-induced dissociation: the N-terminal domail is important for oligomer assembly and the binding of unfolding proteins. *J. Biol. Chem.* **278**, 25970–25976.

110 Kim, K. K., Kim, R., and Kim, S. H. (1998) Crystal structure of a small heat-shock protein. *Nature* **394**, 595–599.

111 Haley, D. A., Horwitz, J., and Stewart, P. L. (1998) The small heat-shock protein, α-B-crystallin, has a variable quaternary structure. *J. Mol. Biol.* **277**, 27–35.

112 Bova, M. P., McHaourab, H. S., Han, Y., and Fung, B. K. K. (2000) Subunit exchange of small heat shock proteins – Analysis of oligomer formation of αA-crystallin and Hsp27 by fluorescence resonance energy transfer and site-directed truncations. *J. Biol. Chem.* **275**, 1035–1042.

113 van Montfort, R. L., Basha, E., Friedrich, K. L., Slingsby, C., and Vierling, E. (2001) Crystal structure and assembly of a eukaryotic small heat shock protein. *Nat. Struct. Biol.* **8**, 1025–1030.

114 Haslbeck, M., Walke, S., Stromer, T., Ehrnsperger, M., White, H. E., Chen, S. X., Saibil, H. R., and Buchner, J. (1999) Hsp26: a temperature-regulated chaperone. *EMBO J.* **18**, 6744–6751.

115 Chang, Z. Y., Primm, T. P., Jakana, J., Lee, I. H., Serysheva, I., Chiu, W., Gilbert, H. F., and Quiocho, F. A. (1996) *Mycobacterium tuberculosis* 16-kDa antigen (Hsp16.3) functions as an oligomeric structure in vitro to suppress thermal aggregation. *J. Biol. Chem.* **271**, 7218–7223.

116 Leroux, M. R., Melki, R., Gordon, B., Batelier, G., and Candido, E. P. M. (1997) Structure-function studies on small heat shock protein oligomeric assembly and interaction with unfolded polypeptides. *J. Biol. Chem.* **272**, 24646–24656.

117 Derham, B. K., van Boekel, M. A., Muchowski, P. J., Clark, J. I., Horwitz, J., Hepburne-Scott, H. W., de Jong, W. W., Crabbe, M. J., and Harding, J. J. (2001) Chaperone function of mutant versions of αA- and αB-crystallin prepared to pinpoint chaperone binding sites. *Eur. J. Biochem.* **268**, 713–721.

118 Horwitz, J., Bova, M., Huang, Q. L., Ding, L., Yaron, O., and Lowman, S. (1998) Mutation of αB-crystallin: effects on chaperone-like activity. *Int. J. Biol. Macromol.* **22**, 263–269.

119 Koteiche, H. A., and Mchaourab, H. S. (1999) Folding pattern of the α-crystallin domain in αA-crystallin determined by site-directed spin labeling. *J. Mol. Biol.* **294**, 561–577.

120 Smulders, R. H. P. H., Carver, J. A., Lindner, R. A., van Boekel, M. A. M., Bloemendal, H., and de Jong, W. W. (1996) Immobilization of the C-terminal extension of bovine αA-crystallin reduces chaperone-like activity. *J. Biol. Chem.* **271**, 29060–29066.

121 Studer, S., Obrist, M., Lentze, N., and Narberhaus, F. (2002) A critical motif for oligomerization and chaperone activity of bacterial α-heat shock proteins. *Eur. J. Biochem.* **269**, 3578–3586.

122 Giese, K. C., and Vierling, E. (2002) Changes in oligomerization are essential for the chaperone activity of a small heat shock protein in vivo and in vitro. *J. Biol. Chem.* **277**, 46310–46318.

123 Berengian, A. R., Parfenova, M., and Mchaourab, H. S. (1999) Site-directed spin labeling study of subunit interactions in the α-crystallin domain of small heat-shock proteins: Comparison of the oligomer symmetry in αA-crystallin, Hsp27 and Hsp16.3. *J. Biol. Chem.* **274**, 6305–6314.

124 Kantorow, M., and Piatigorsky, J. (1998) Phosphorylations of alpha A- and alpha B-crystallin. *Int. J. Biol. Macromol.* **22**, 307–314.

125 Gaestel, M. (2002) sHsp-phosphorylation: enzymes, signaling pathways and functional implications. *Prog. Mol. Subcell. Biol.* **28**, 151–169.

126 Derham, B. K., and Harding, J. J. (1999) α-crystallin as a molecular chaperone. *Prog. Retin. Eye Res.* **18**, 463–509.

127 Kemp, B. E., and Pearson, R. B. (1990) Protein kinase recognition sequence motifs. *Trends Biochem. Sci.* **15**, 342–346.

128 Butt, E., Immler, D., Meyer, H. E., Kotlyarov, A., Laass, K., and Gaestel, M. (2001) Heat shock protein 27 is a substrate of cGMP-dependent protein kinase in intact human platelets: phosphorylation-induced actin polymerization caused by HSP27 mutants. *J. Biol. Chem.* **276**, 7108–7113.

129 Lund, A. A., Rhoads, D. M., Lund, A. L., Cerny, R. L., and Elthon, T. E. (2001) In vivo modifications of the maize mitochondrial small heat stress protein, HSP22. *J. Biol. Chem.* **276**, 29924–29929.

130 Ito, H., Kamei, K., Iwamoto, I., Inaguma, Y., Nohara, D., and Kato, K. (2001) Phosphorylation-induced Change of the Oligomerization State of αB-crystallin. *J. Biol. Chem.* **276**, 5346–5352.

131 Kato, K., Hasegawa, K., Goto, S., and Inaguma, Y. (1994) Dissociation as a result of phosphorylation of an aggregated form of the small stress protein, hsp27. *J. Biol. Chem.* **269**, 11274–11278.

132 Rogalla, T., Ehrnsperger, M., Preville, X., Kotlyarov, A., Lutsch, G., Ducasse, C., Paul, C., Wieske, M., Arrigo, A. P., Buchner, J., and Gaestel, M. (1999) Regulation of Hsp27 oligomerization, chaperone function, and protective activity against oxidative stress/tumor necrosis factor alpha by phosphorylation. *J. Biol. Chem.* **274**, 18947–18956.

133 Ito, H., Okamoto, K., Nakayama, H., Isobe, T., and Kato, K. (1997) Phosphorylation of αB-crystallin in response to various types of stress. *J. Biol. Chem.* **272**, 29934–29941.

134 van den IJssel, P. R., Overkamp, P., Bloemendal, H., and de Jong, W. W. (1998) Phosphorylation of αB-crystallin and HSP27 is induced by similar stressors in HeLa cells. *Biochem. Biophys. Res. Commun.* **247**, 518–523.

135 Voorter, C. E., de Haard-Hoekman, W. A., Roersma, E. S., Meyer, H. E., Bloemendal, H., and de Jong, W. W. (1989) The in vivo phosphorylation sites of bovine αB-crystallin. *FEBS Lett.* **259**, 50–52.

136 Gaestel, M., Benndorf, R., Hayess, K., Priemer, E., and Engel, K. (1992) Dephosphorylation of the small heat shock protein hsp25 by calcium/calmodulin-dependent (type 2B) protein phosphatase. *J. Biol. Chem.* **267**, 21607–21611.

137 Cairns, J., Qin, S., Philp, R., Tan, Y. H., and Guy, G. R. (1994) Dephosphorylation of the small heat shock protein Hsp27 in vivo by protein phosphatase 2A. *J. Biol. Chem.* **269**, 9176–9183.

138 Moroni, M., and Garland, D. (2001) In vitro dephosphorylation of α-crystallin is dependent on the state of

oligomerization. *Biochim. Biophys. Acta* **1546**, 282–290.

139 Sobott, F., Benesch, J. L., Vierling, E., and Robinson, C. V. (2002) Subunit exchange of multimeric protein complexes. Real-time monitoring of subunit exchange between small heat shock proteins by using electrospray mass spectrometry. *J. Biol. Chem.* **277**, 38921–38929.

140 Helm, K. W., Lee, G. J., and Vierling, E. (1997) Expression and native structure of cytosolic class II small heat shock proteins. *Plant Physiol.* **114**, 1477–1485.

141 van den Oetelaar, P. J., van Someren, P. F., Thomson, J. A., Siezen, R. J., and Hoenders, H. J. (1990) A dynamic quaternary structure of bovine alpha-crystallin as indicated from intermolecular exchange of subunits. *Biochemistry* **10**, 3488–3493.

142 Sugiyama, Y., Suzuki, A., Kishikawa, M., Akutsu, R., Hirose, T., Waye, M. M., Tsui, S. K., Yoshida, S., and Ohno, S. (2000) Muscle develops a specific form of small heat shock protein complex composed of MKBP/HSPB2 and HSPB3 during myogenic differentiation. *J. Biol. Chem.* **275**, 1095–1104.

143 Kitagawa, M., Miyakawa, M., Matsumura, Y., and Tsuchido, T. (2002) *Escherichia coli* small heat shock proteins, IbpA and IbpB, protect enzymes from inactivation by heat and oxidants. *Eur. J. Biochem.* **269**, 2907–2917.

144 Friedrich, K. L., Giese, K. C., Buan, N. R., and Vierling, E. (2004) Interactions between small heat shock protein subunits and substrate in small heat shock protein/substrate complexes. *J. Biol. Chem.* **279**, 1080–1089.

145 Buchner, J., Grallert, H., and Jakob, U. (1998) Analysis of chaperone function using citrate synthase as nonnative substrate protein. *Methods Enzymol.* **290**, 323–338.

146 Gaestel, M., Gross, B., Benndorf, R., Strauss, M., Schunk, W. H., Kraft, R., Otto, A., Bohm, H., Stahl, J., Drabsch, H., and et al. (1989) Molecular cloning, sequencing and expression in *Escherichia coli* of the 25-kDa growth-related protein of Ehrlich ascites tumor and its homology to mammalian stress proteins. *Eur. J. Biochem.* **179**, 209–213.

147 Goloubinoff, P., Christeller, J. T., Gatenby, A. A., and Lorimer, G. H. (1989) Reconstitution of active dimeric ribulose bisphosphate carboxylase from an unfoleded state depends on two chaperonin proteins and Mg-ATP. *Nature* **342**, 884–889.

148 Mendoza, J. A., Rogers, E., Lorimer, G. H., and Horowitz, P. M. (1991) Chaperonins facilitate the in vitro folding of monomeric mitochondrial rhodanese. *J. Biol. Chem.* **266**, 13044–13049.

149 Ranson, N. A., Burston, S. G., and Clarke, A. R. (1997) Binding, encapsulation and ejection: substrate dynamics during a chaperonin-assisted folding reaction. *J. Mol. Biol.* **266**, 656–664.

150 Chen, S., Roseman, A. M., Hunter, A. S., Wood, S. P., Burston, S. G., Ranson, N. A., Clarke, A. R., and Saibil, H. R. (1994) Location of a folding protein and shape changes in GroEL-GroES complexes imaged by cryo-electron microscopy. *Nature* **371**, 261–264.

151 Buchner, J., Schmidt, M., Fuchs, M., Jaenicke, R., Rudolph, R., Schmid, F. X., and Kiefhaber, T. (1991) GroE facilitates refolding of citrate synthase by suppressing aggregation. *Biochemistry* **30**, 1586–1591.

152 Jaenicke, R. (1993) What does protein refolding in vitro tell us about protein folding in the cell? *Philos. Trans. R. Soc. Lond. B Biol. Sci.* **339**, 287–294.

153 Haslbeck, M., Schuster, I., and Grallert, H. (2003) GroE-dependent expression and purification of pig heart mitochondrial citrate synthase in Escherichia coli. *J. Chromatogr. B Analyt. Technol. Biomed. Life Sci.* **786**, 127–136.

154 Farahbakhsh, Z. T., Huang, Q. L.,

Ding, L. L., Altenbach, C., Steinhoff, H. J., Horwitz, J., and Hubbell, W. L. (1995) Interaction of α-crystallin with spin-labeled peptides. *Biochemistry* **34**, 509–516.

155 Aquilina, J. A., Benesch, J. L., Bateman, O. A., Slingsby, C., and Robinson, C. V. (2003) Polydispersity of a mammalian chaperone: mass spectrometry reveals the population of oligomers in αB-crystallin. *Proc. Natl. Acad. Sci. USA* **100**, 10611–10616.

156 Kim, R., Kim, K. K., Yokota, H., and Kim, S. H. (1998) Small heat shock protein of *Methanococcus jannaschii*, a hyperthermophile. *Proc. Natl. Acad. Sci. USA* **95**, 9129–9133.

157 Laksanalamai, P., Jiemjit, A., Bu, Z., Maeder, L., and Robb, T. (2003) Multi-subunit assembly of the *Pyrococcus furiosus* small heat shock protein is essential for cellular protection at high temperature. *Extremophiles* **7**, 79–83.

158 Laksanalamai, P., Maeder, D. L., and Robb, F. T. (2001) Regulation and mechanism of action of the small heat shock protein from the hyperthermophilic archaeon *Pyrococcus furiosus*. *J. Bacteriol.* **183**, 5198–5202.

159 Shearstone, J. R., and Baneyx, F. (1999) Biochemical characterization of the small heat shock protein IbpB from *Escherichia coli*. *J. Biol. Chem.* **274**, 9937–9945.

160 Young, D., Lathriga, R., Hendrix, R., Sweetser, D., and Young, R. A. (1988) Stress proteins are immune targets in leprosy and tuberculosis. *Proc. Natl. Acad. Sci. USA* **85**, 4267–4270.

161 Haslbeck, M., Braun, N., Stromer, T., Richter, B., Model, N., Weinkauf, S., and Buchner, J. (2004) Hsp42 is the general small heat shock protein in the cytosol of Saccharomyces cerevisiae. *EMBO J.* **23**, 638–649.

162 Ehrnsperger, M., Lilie, H., Gaestel, M., and Buchner, J. (1999) The dynamics of Hsp25 quaternary structure – Structure and function of different oligomeric species. *J. Biol. Chem.* **274**, 14867–14874.

163 Haley, D. A., Bova, M. P., Huang, Q. L., McHaourab, H. S., and Stewart, P. L. (2000) Small heat-shock protein structures reveal a continuum from symmetric to variable assemblies. *J. Mol. Biol.* **298**, 261–272.

25
Alpha-crystallin: Its Involvement in Suppression of Protein Aggregation and Protein Folding

Joseph Horwitz

25.1
Introduction

Alpha-crystallins are one of the major protein components of the mammalian eye lens. There are two alpha-crystallin genes, alpha A and alpha B. In humans, the alpha A gene is found on chromosome 21 and encodes for a polypeptide containing 173 amino acid residues. The alpha B gene is on chromosome 11 and encodes for a polypeptide containing 175 amino acid residues. The amino acid sequence homology between alpha A and alpha B is about 57%. Alpha-crystallins are members of the small heat shock protein family [1]. All of the small heat shock proteins contain an ''alpha-crystallin domain,'' which is a stretch of about 90 amino acids in the C-terminal domain that shares some degree of homology among the various members [1]. The properties of alpha-crystallins as well as of other small heat shock protein have been reviewed extensively [2–9]. A key property of the small heat shock proteins is their ability to interact with unfolded proteins [10–11].

25.2
Distribution of Alpha-crystallin in the Various Tissues

By far the organ with the highest concentration of alpha-crystallin is the eye lens. The concentration of alpha-crystallin in many mammalian lenses is estimated to be between 25% and 40% of the total soluble lens proteins. In fish lenses, the amount of alpha-crystallin is generally less than 10%. In the eye lens, the alpha A species is dominant. In most mammalian lenses, the weight ratio of alpha A to alpha B is about 3 to 1. Alpha-crystallin is not found in any of the invertebrate lenses that have been examined thus far. In 1989 it was first reported that alpha B crystallin exists in many organs and cells outside the lens [5, 12–14]. Shortly thereafter, it was shown to be a bona fide small heat shock protein [15]. In the heart, for example, alpha B accounts for about 2% of the total protein mass. In some of the neurological diseases in which alpha B is known to be overexpressed, the concentration of alpha B can be extremely high [16].

Protein Folding Handbook. Part II. Edited by J. Buchner and T. Kiefhaber

ISBN: 3-527-30784-2

25.3 Structure

When isolated from organs or cells, alpha-crystallin is always found as a heterogeneous multimeric assembly with a molecular weight distribution ranging from approximately 300,000 to over one million. The quaternary structure of the small heat shock proteins has been the subject of many studies (reviewed in Refs. [5, 6, 9]). At present, the crystal structures of only two members of the small heat shock protein family are known: MjHsp16.5 from *Methanococcus jannaschii* [17] and Hsp16.9 from wheat [18]. It is important to note that MjHsp16.5 and Hsp16.9 are both homogeneous in nature and possess a discrete number of subunits, whereas alpha-crystallin Hsp27 and many other small heat shock proteins are innately polydispersed. This can be seen in Figure 25.1, where the gel filtration elution profile and molecular weight distribution of a preparation of recombinant alpha B, Hsp27, and MjHsp16.5 are shown. This data was obtained with a system that utilizes size-exclusion chromatography with online laser light-scattering, absorbance, and refractive index detectors [19–21]. As seen in Figure 25.1, the molecular weight distribution of MjHsp16.5 does not change much across the elution profile. This profile is what one would expect from a homogeneous sample. In contrast, the heterogeneity of alpha B crystallin and Hsp27 is evident (Figure 25.1).

For Hsp27 the molecular weight obtained at the peak is 460 000. At the half-bandwidth point of the leading elution profile (~12.3 mL), the molecular weight is about 550 000, whereas the molecular weight at the trailing edge (~14 mL) is 360 000. The molecular weight of the monomeric Hsp27 is ~22 800, meaning that at the peak the complex is made up of 20 subunits, whereas at the half-bandwidth point, the complexes are made up of ~16–24 subunits. Similarly, for alpha B, the native oligomeric structure shown covers a range of 26–34 subunits. This may explain in part its inability to crystallize native alpha-crystallin or Hsp27.

The oligomeric structure of alpha-crystallin is not rigid. In 1990, Van Der Oetelaar et al. were the first to observe that there is an intermolecular exchange of subunits in alpha-crystallins, pointing to a dynamic quaternary structure [22]. More recently, Bova et al. [23] reexamined the subunit exchange properties of alpha A crystallin using fluorescence resonance energy transfer (FRET). These measurements proved that the subunit exchange strongly depends on temperature. Subunit exchange is a property that occurs in many if not all members of the small heat shock protein family [6]. Even the extremely stable 24mer small heat shock protein Hsp16.5 isolated from the hyperthermophilic Archaea *Methanococcus jannaschii* exhibits subunit exchange at temperatures that are physiologically relevant [24]. The dynamic structure of alpha-crystallin and other small heat shock proteins is believed to be a key property for its chaperone activity (reviewed in Ref. [6]).

In recent years, major advances into the secondary and tertiary structure of alpha-crystallin were achieved especially by using site-directed spin labeling [25, 26]. However, in the absence of x-ray crystal structure, we are forced to rely mostly on modeling [5]. The recent models rely mostly on the x-ray structure of Hsp16.9 and MjHsp16.5, which both possess the "alpha-crystallin domain" [5,

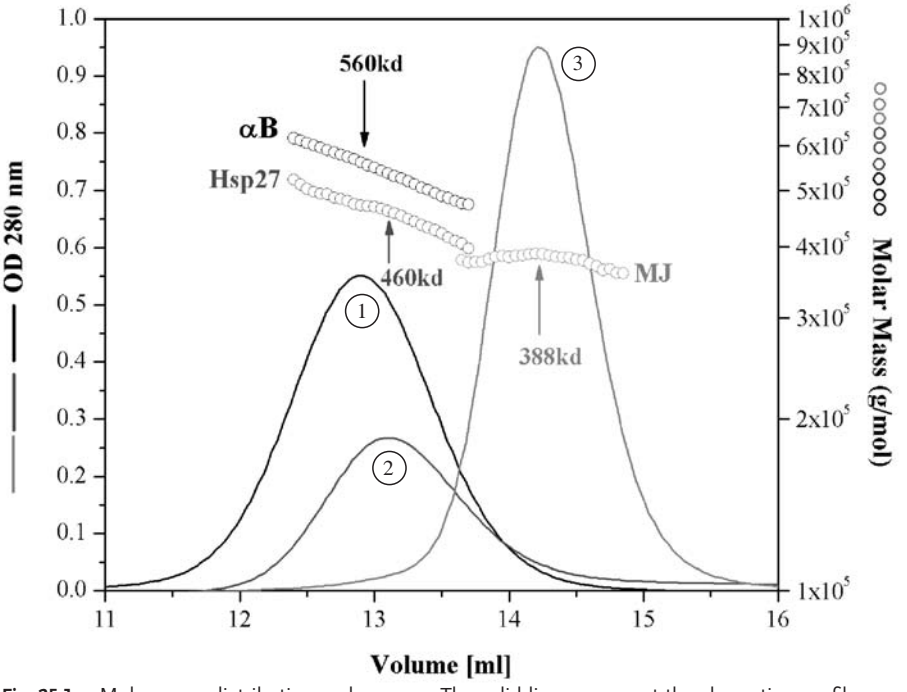

Fig. 25.1. Molar mass distribution and absorption spectra of recombinant alpha B crystallin, recombinant Hsp27, and recombinant Hsp16.5 from *Methanococcus jannaschii*. Size-exclusion chromatography was carried out on a Pharmacia Superose HR 6 column (1 × 30 cm) driven by a Pharmacia AKTA Basic system with a UV 900 monitor connected in line with an 18-angle laser light-scattering detector and a refractive index detector (DAWN EOS, Optilab DSP; Wyatt-Technology Corp. Santa Barbara, CA, USA). The solid lines represent the absorption profile of the eluted protein. The circles represent the molecular weight obtained as a function of the elution volume. The molecular weight is determined continuously every 20 microliters. Line spectra (1) obtained from 0.12 mg of alpha B. Line spectra (2) obtained from 0.1 mg of Hsp27. Line spectra (3) obtained from 0.15 mg of MjHsp16.5. All samples were dissolved in 50 mM phosphate buffer and 0.1 M NaCl, pH 7. Elution was performed at a rate of 0.5 mL min^{-1} and a temperature of 25 °C.

27]. Advances in cryo-electron microscopy provide a low-resolution picture of alpha-crystallin. These studies suggest that alpha-crystallin possesses a variable quaternary structure and a central cavity [28, 29]. The crystal structure of wheat Hsp16.9 as well as a cryo-electron microscopic image of alpha-crystallin and the crystal structure of Hsp16.5 from *M. jannaschii* are shown in Figure 24.3.

25.4
Phosphorylation and Other Posttranslation Modification

Alpha-crystallin is known to undergo many posttranslational modifications such as age-dependent truncation, glycation, deamidation, racemization, etc. [3, 30]. Of

particular interest are the effects of phosphorylation on the function and structure of alpha-crystallin. The effects of phosphorylation on alpha-crystallin and other small heat shock proteins have been reviewed previously [5, 31, 32]. The effects of phosphorylation on the function of alpha-crystallin are controversial at present [9]. Recently, using site-directed mutagenesis to mimic phosphorylation, Ito et al. [33] reported a reduction in the size of the alpha B crystallin oligomer from 500 000 for native protein to 300 000 for the mimic-phosphorylated protein. Using lactate dehydrogenase at 50 °C as a target protein, the authors concluded that the phosphorylated mimic has a significantly reduced chaperone activity. Koteiche and Mchaourab [34], using T4 lysozyme as a target protein, showed that phosphorylation enhances the chaperone activity. In our laboratory we observed that phosphorylation of alpha B did not significantly affect its chaperone properties when lysozyme or lactalbumin were unfolded at 37 °C by reducing the disulfide bonds (unpublished data). These results underscore the importance of choosing an appropriate target protein as well as the unfolding conditions when assaying for the chaperone properties of alpha-crystallin.

25.5 Binding of Target Proteins to Alpha-crystallin

A common property of all the small heat shock proteins is to interact with unfolded or denatured target proteins and to prevent their nonspecific aggregation and precipitation (reviewed in Refs. [2, 6] and in Chapter 24). Alpha-crystallin will not interact with native protein but will recognize and interact with unfolded structures that are in a molten-globule-like state [35–38]. It will react more efficiently with slowly aggregating target proteins. This point was clearly demonstrated by Carver et al., who showed that alpha-crystallin was more efficient in arresting the aggregation of apo-α-lactalbumin as compared to holo-α-lactalbumin, which tends to aggregate much faster when the disulfide bonds are reduced [39]. Another example is comparing the interaction of alpha-crystallin with reduced lysozyme and apo-α-lactalbumin. Figure 25.2 shows the unfolding and aggregation of lysozyme and α-lactalbumin when the disulfide bonds are reduced with TCEP. To achieve complete suppression of the aggregation at 37 °C, the weight ratio of native bovine alpha-crystallin to lactalbumin is about 1:1, whereas for lysozyme the ratio of alpha-crystallin to lysozyme has to be 5:1. Alpha-lactalbumin and lysozyme are structurally closely related. However, they differ greatly in their unfolding behavior: lysozyme unfolds in a classic two-state model for protein denaturation, while alpha-lactalbumin unfolds through an intermediate molten-globule state [40, 41]. As can be seen in Figure 25.2, the kinetics of aggregation of lysozyme is significantly faster than that of alpha-lactalbumin. The lag time typically observed in this kind of experiment occurs because time is needed for nucleation and growth of the aggregate before scattering can be observed. Note that the lag-time for lysozyme is significantly shorter. The fact that kinetic considerations are extremely important in studying the interaction of alpha-crystallin with a target protein can also be exemplified with insulin. Insulin is another common target protein used to study

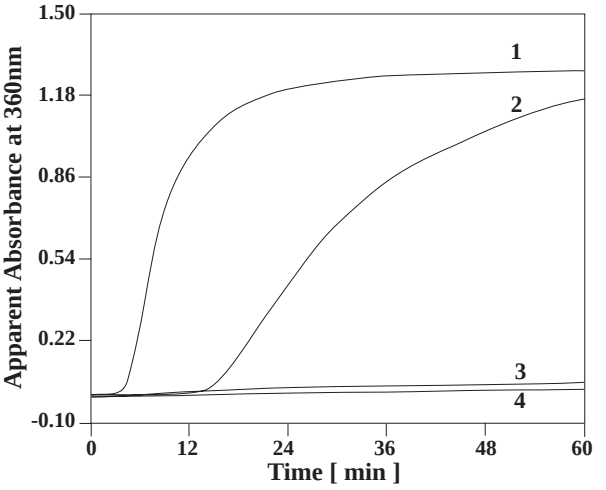

Fig. 25.2. Kinetics of the aggregation of lysozyme and bovine α-lactalbumin upon reduction of the disulfide bonds with Tris (2-carboxyethyl) phosphine (TCEP). Curve 1, 0.1 mg of lysozyme in 0.4 mL of buffer, pH 7.0, with 1 mM TCEP; Curve 2, 0.25 mg of α-lactalbumin in 0.4 mL of buffer, pH 6.7, with 5 mM of TCEP; Curve 3, same as curve 1, but with 0.5 mg of native bovine alpha-crystallin; Curve 4, same as curve 2, but with 0.25 mg of native bovine alpha-crystallin. Measurements were performed at 37 °C in a Shimadzu UV-2401PC absorption spectrophotometer. The temperature of the samples was controlled with a Peltier system; the path length was 1.0 cm.

the properties of small heat shock proteins [42, 43]. Upon reduction of the disulfide bonds, the B-chain of insulin will aggregate. The aggregation can be monitored by simple turbidometric measurements [42–44]. Holmgren found that thioredoxin catalyzes the reduction of insulin by DTT. He showed that thioredoxin at 5 μM concentration accelerated the reaction of 0.130 mM insulin with 1.0 mM DTT at pH 7 and 23 °C by about 20-fold [44]. The amount of native bovine alpha-crystallin needed to completely suppress the aggregation of 0.1 mg insulin dissolved in 0.4 mL of buffer is about 0.5 mg. In the presence of 5 μM of thioredoxin, 2 mg of native alpha-crystallin was needed to completely suppress the aggregation (data not shown).

Relatively little is known about the binding site and the mechanisms of the chaperone function of alpha-crystallin. Sharma and his coworkers have identified a region in the alpha A crystallin domain (residues 70–88) that binds to the target protein that they were using [45]. Interestingly, a synthetic peptide corresponding to this region can bind and suppress the aggregation of denatured protein, albeit with a much reduced efficiency [45, 46]. Other works suggest that the N-terminus of alpha-crystallin may also be involved in the binding of the target protein [47]. Recently, using site-directed spin labeling and electron paramagnetic resonance spectroscopy on a well-defined target protein (T4 lysozyme), Mchaourab et al. were able to show through careful thermodynamic analysis that alpha-crystallin

possesses two modes of binding. One mode is a low-capacity mode that binds compact, native-like states. A second mode is a high-capacity mode that binds globally unfolded states. These two modes have different affinities and different numbers of binding sites [34, 48].

25.6 The Function of Alpha-crystallin

The various functions of the small heat shock proteins have been reviewed extensively ([5–7]; see also Chapter 24). One of the functions of the small heat shock proteins is to trap aggregation-prone denatured proteins and keep them in a refoldable conformation [49, 50]. The complex of the sHsp target protein can then interact with another chaperone system, such as Hsp70, in an ATP-dependent process to refold the target protein (see Figure 24.2). In the eye lens, however, the functions of alpha-crystallin are different. The first function of alpha-crystallin is, by virtue of its relatively high concentration, to contribute the necessary refractive index that the lens needs. The chaperone properties of alpha-crystallin are needed to control the unavoidable protein denaturation that takes place in the lens as a result of normal aging (reviewed in Refs. [8] and [9]). Because of the unique growth pattern of the lens, there is no protein turnover in the center of the lens. Thus, the center of a 60-year-old lens, for example, contains proteins that were synthesized during embryogenesis. These proteins undergo major posttranslational modification that result in aggregation and scattering, thereby compromising lens transparency. The data to date suggest that alpha-crystallin complexes with the old, denatured proteins and controls the unavoidable age-dependent aggregation processes [51–56].

While alpha-crystallin by itself is not a very efficient chaperone for refolding denatured proteins, there are many examples in the literature showing that it can protect in vivo other proteins and enzymes from various insults [3, 57–62].

25.7 Experimental Protocols

25.7.1 Preparation of Alpha-crystallin

A: Native Lens Alpha-crystallin

The preparation and purification of native eye lens alpha-crystallin have been described in detail previously [43]. Most investigators in the field use calf or cow lenses, as these are readily available from local slaughterhouses. The molar ratio of alpha A to alpha B in this preparation is about 3 to 1. As was mentioned previously, native lens crystallins undergo major posttranslational modification [30]. Thus, the age of the lens used may affect the quality and the properties of the alpha-crystallin obtained [43].

To separate the alpha A and alpha B isoforms from native alpha-crystallin, ion-exchange chromatography in the presence of a high concentration of urea (≥ 6 M) is generally used [63]. It should be emphasized, however, that after treatment of alpha-crystallin with urea the quaternary structure obtained following the removal of urea is different from the native state [64]. Thus, treatment with urea is not completely reversible. Whenever a high concentration of urea is used, care should be taken that the cyanate being generated does not carbamylate the alpha-crystallin. The native alpha A and alpha B subunits that are isolated from the native alpha-crystallin are also phosphorylated to various degrees [63].

B: Recombinant Alpha B and Alpha A-crystallin

Recombinant alpha-crystallin can be easily obtained according to standard procedures. A detailed procedure for the preparation of recombinant alpha B crystallin is described elsewhere [43]. The recombinant alpha-crystallin can be produced at relatively high yields and without the need to use urea or other chaotropic salts for solubilization. The purity of the preparation can be assessed by standard SDS-polyacrylamide gel electrophoresis. However, bacterial nucleotides that commonly bind the recombinant alpha-crystallin could be a major source of contamination. This contamination will not be visible on the SDS gels. Therefore, it is important to record the near-UV absorption spectra of the recombinant alpha-crystallin preparations. For highly purified preparations, a ratio of A280/A260 ≥ 1.5 should be obtained [43].

While native alpha-crystallin from eye lens as well as recombinant alpha A and alpha B possess many common properties, there are also major differences in some of their critical properties, such as conformational stability, quaternary structure, and ability to interact and suppress the aggregation of various target proteins [65–69]. Thus, it is important to choose the relevant species of alpha-crystallin for the specific question that is being studied.

C: Molecular Weight Determination

As stated previously, alpha-crystallin preparations in their native state are always heterogeneous. Mutations of some key residues in alpha-crystallin have a significant effect on the weight average and the heterogeneity of the alpha-crystallin complex. In addition, there is sometimes the need to know the molecular weight of the complex of alpha-crystallin with its target protein. The most frequently used method for determining the average molecular weight is size-exclusion chromatography (see Chapter 24). Other standard methods such as analytical ultracentrifugation and various light-scattering techniques are also being used. It is well established that standard size-exclusion chromatography may sometimes yield erroneous results because of the shape of the protein in question, possible interactions of the protein with the column, and the dependence on standard proteins for calibration of the column. As was mentioned earlier in Section 25.3 and shown in Figure 25.1, size-exclusion chromatography with an online multi-angle laser light-scattering detector and a refractive index detector can greatly improve the accuracy of molecular weight determination [19–21].

One of the major advantages of such a system is the ability to obtain reliable data at elevated temperatures. In general, the absorbance detectors that are used in most commercial liquid chromatography systems cannot operate at temperatures above 50 °C. The same problem exists with the commercially available analytical ultracentrifuges, where it is impossible to obtain data at high temperatures. The chromatographic and detection systems used in Figure 25.1 can be used at temperatures even higher than 100 °C. Thus, we were able to show that the small heat shock protein 16.5 from *Methanococcus jannaschii* retains its multimeric structure and subunit organization at 70 °C (see Figure 2 in Ref. [24]).

Another example of the advantage of the multi-angle laser light-scattering system is shown below in Figure 25.3, where the effects of phosphorylation mimics on the quaternary structure of alpha B crystallin are shown. Figure 25.3 compares the molecular weight distribution of recombinant alpha B crystallin with alpha B crystallin in which all three of the phosphorylation sites were mutated to aspartate to mimic phosphorylation. Ito et al. [33] were the first to study the effects of these mutations on the quaternary structure of alpha B crystallin. They fractionated wild-type alpha B and the mutated alpha B using sucrose density-gradient

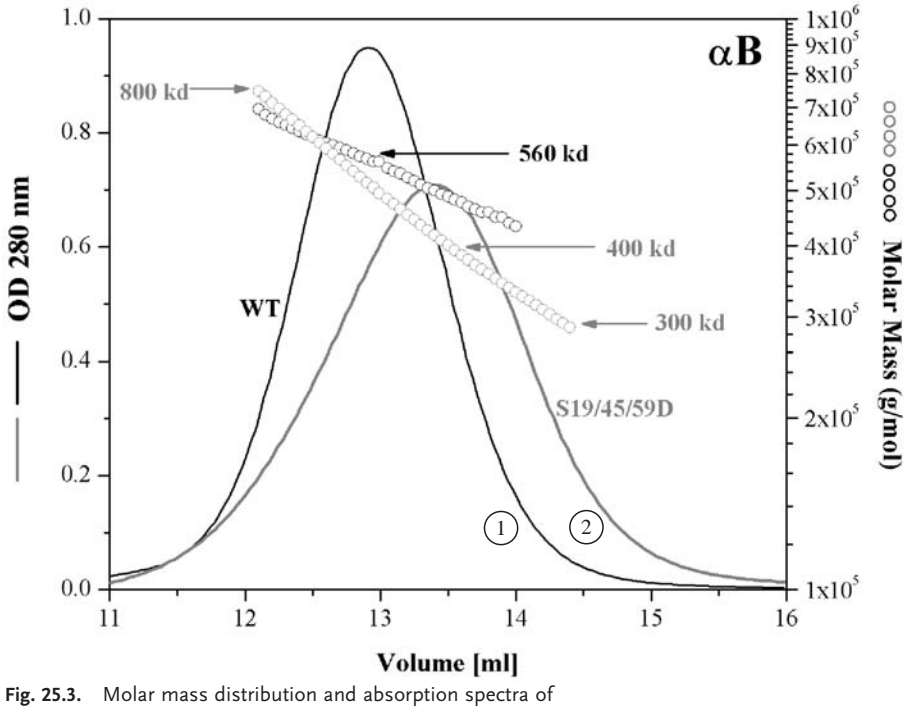

Fig. 25.3. Molar mass distribution and absorption spectra of recombinant alpha B and alpha B, where serine 19, 45, and 59 were mutated to aspartate. Curve (1), recombinant alpha B crystallin. Curve (2), S19/45/59 alpha B crystallin. All other conditions are the same as in Figure 25.1.

centrifugation. The fractions were than subjected to SDS-PAGE analysis followed by immunostaining with antibodies against the C-terminal of alpha B crystallin. Quantitation of these Western blot analyses suggested that the main peak of wild-type alpha B corresponds to a molecular weight of 500 000, whereas the molecular weight of the tripled phosphorylated mimics corresponds to 300 000. Using gel filtration analysis, they reported a molecular weight of 550 000 for wild-type alpha B and of 390 000 for the S19/45/59D mimics [33]. The data shown in Figure 25.3 is in excellent agreement with their gel filtration data. It should be noted, however, that in one single run a complete picture of the polydisperse nature of alpha-crystallin is observed with an accurate molecular weight of the whole elution profile. As can be noted from the slope of the line representing the molecular weight, the phosphorylation mimics not only decreased the weight average of alpha B but also significantly increased its polydispersity in agreement with the observation of Ito et al. [33]. The data presented in Figure 25.3 take less than an hour to obtain.

The Use of Mass Spectrometry for the Determination of the Quaternary Structure of Alpha-crystallin and Other Small Heat Shock Proteins

Recent advances in mass spectrometry make it possible to analyze high-molecular-weight protein complexes [70]. This powerful technology was recently utilized for real-time monitoring of subunit exchange between small heat shock proteins [71]. It was also used successfully to study the polydisperse nature of alpha B crystallin [73]. It can be expected that this approach will yield valuable information on the function and structure of alpha-crystallin as well as of other small heat shock proteins.

D: Chaperone Assays for Alpha-crystallin

The most commonly used method for assaying the chaperone properties of alpha-crystallin is monitoring its ability to suppress the aggregation of nonnative forms of proteins during the unfolding processes. Aggregation can be easily monitored by measuring the increase in light scattering [73–75]. Standard spectrophotometers or fluorometers are generally used [43, 76]. Typical data obtained is shown in Figure 25.2. Because the aggregation process is highly temperature-dependent, it is important that the temperature of the cell be controlled. Many proteins can serve as a target for the aggregation assay. Some of the more common target proteins, which cover a wide range of molecular weights, are given in Table 25.1.

E: Comments on Specific Proteins

Unfolding of Proteins by Breaking Disulfide Bonds Using Dithiothreitol or Tris (2-carboxyethyl) Phosphine

For target proteins such as insulin, lysozyme, α-lactalbumin, ovotransferrin [77], or abrin [79], in which unfolding is achieved by reducing the disulfide bonds, dithiothreitol (DTT) is generally used. In recent years, a new reagent for the specific reduction of disulfide bonds has become more popular, namely, Tris (2-carboxyethyl) phosphine (TCEP). This compound has major advantages over DTT [80, 81]. TCEP

Tab. 25.1. Target proteins commonly used for chaperone assay of alpha-crystallin.

Protein (MW)	*Unfolded by:*	*Assay temperature*	*References*
Insulin (6000)	Reduction with DTT, TCEP	25–37 °C	42, 43, Chapter 24
Lysozyme (14 400)	Reduction with DTT, TCEP	25–37 °C	77, 78
α-lactalbumin (14 400)	Reduction with DTT, TCEP	25–37 °C	43
Alcohol dehydrogenase (yeast) (4 × 35 000)	Heat to 37 °C	37 °C	43
Malate dehydrogenase (2 × 35 000)	Heat to 45 °C	45 °C	
Citrate synthase (mitochondrial pig heart) (49 000)	Heat to 43 °C 6 M guanidinium chloride at 25 °C	43 °C 25 °C	Chapter 24, 76

is more stable than DTT at a pH above 7.5 and in general is a faster and stronger reductant than DTT [81]. For example, instead of using 20 mM DTT for reducing insulin in a chaperone assay, we can use only 4 mM or less TCEP for a typical aggregation assay. Another advantage is that TCEP does not have any absorbance at 280 nm, whereas the molar absorptivity of oxidized DTT or DTE is $\varepsilon_{283} = 273\ M^{-1}\ cm^{-1}$. Thus, in many cases oxidized DTT interferes with protein measurements at 280 nm. TCEP is commercially available from Pierce Chemical Company or Molecular Probes.

Insulin Assay

Details for the assay are given in Refs. [42] and [43] and in Chapter 24. Insulin from bovine pancreas or human recombinant insulin can be obtained from Sigma and Roche.

Alpha-lactalbumin Assay

Details are given in Ref. [43]. The aggregation assay is very sensitive to pH [82]. For α-lactalbumin at concentration of 0.5 mg mL^{-1} or lower, the pH should be below 7.0. The assay works well in the pH range of 6.5–6.8. Calcium-depleted α-lactalbumin is used.

Assay conditions:

Bovine α-lactalbumin (calcium-depleted) obtained from Sigma Chemical Co. is dissolved in a buffer containing 50 mM sodium phosphate, 0.1 M NaCl, and 2 mM ethylenediaminetetraacetic acid (EDTA). The final pH should be 6.7. Stock solutions should be kept over ice, and fresh solutions should be made daily.

For an aggregation assay using a standard absorption spectrophotometer with a 1.0-cm path length cell, a concentration of ~0.5 mg mL^{-1} lactalbumin will produce a good signal. Aggregation is initiated by adding DTT or TCEP to the sample.

Assay temperature: 25–50 °C.

For bovine α-lactalbumin: $E_{280}^{0.1\%} = 2$

Lysozyme Assay

Lysozyme assay is performed under conditions similar to those described for α-lactalbumin. Lysozyme is not as sensitive to pH as α-lactalbumin, and the assay works well at neutral pH.

Assay conditions:

Lysozyme obtained from Roche or Sigma is dissolved in a buffer containing 50 mM sodium phosphate and 0.1 M NaCl, pH 7.

For an aggregation assay using a standard absorption spectrophotometer with a 1.0-cm path length cell, a concentration of ~0.2 mg mL^{-1} will produce a good signal. Aggregation is initiated by adding 20 mM DTT or 2–5 mM TCEP.

Assay temperature: 25–50 °C.

For lysozyme: $E_{280}^{0.1\%} = 2.6$

Assays Involving Aggregation of Proteins by Heat Denaturation

Heat denaturation is commonly used for studying the chaperone properties of small heat shock proteins. Some of the commonly used target proteins include alcohol dehydrogenase, malate dehydrogenase, citrate synthase, luciferase, rhodanese, and α-glucosidase. The advantage of using these proteins as a target protein for alpha-crystallin is that all of them aggregate at temperatures below 50 °C, where alpha-crystallin still retains its native structure [83–85].

Alcohol Dehydrogenase

Yeast alcohol dehydrogenase will unfold and aggregate at 37 °C under the conditions described in Ref. [43].

Assay conditions:

Alcohol dehydrogenase (yeast) obtained from Roche or Sigma is dissolved in a buffer containing 50 mM sodium phosphate containing 0.1 M NaCl and 1 mM 1,10-phenanthroline. Stock solutions should be kept over ice, and fresh solutions should made daily.

For a standard aggregation assay as described above, a concentration of ~0.5 mg mL^{-1} is used. Aggregation is initiated by increasing the cell temperature to 37 °C.

Assay temperature: 37–40 °C.

For yeast alcohol dehydrogenase: $E_{280}^{0.1\%} = 1.3$

Note: For a fluorometer-based scattering analysis, a concentration as low as 15 μg mL^{-1} alcohol dehydrogenase can be used.

Malate Dehydrogenase

Malate dehydrogenase (pig heart, mitochondrial) is suitable for aggregation studies at temperatures around 45 °C.

Assay conditions:

Malate dehydrogenase (pig heart, mitochondrial) obtained from Roche is dissolved in a buffer containing 50 mM sodium phosphate and 0.1 M NaCl, pH 7. Stock solutions should be kept over ice.

For a standard aggregation assay as described above, a concentration of ~0.5 mg mL^{-1} is generally used. Aggregation is initiated by heating the enzyme to 45 °C.

Assay temperature: 45–48 °C.

For malate dehydrogenase: $E_{280}^{0.1\%} = 0.29$

Citrate Synthase

Citrate synthase is widely used for many chaperone studies. Details are given in Ref. [76] and in Chapter 24. Citrate synthase is available from Roche.

F: Interpretation of Light-scattering and Turbidometric Data Obtained During Protein Aggregation and During Suppression of the Aggregation with Alpha-crystallin

As was mentioned previously, the most common technique used to monitor protein aggregation and the effects of chaperones on the aggregation is light-scattering or turbidometric measurements in an absorption spectrophotometer or a fluorometer. The kinetics of aggregation, such as those shown in Figure 25.2 or Figure 24.4, is widely found in the published literature. However, to get meaningful kinetic parameters from such data is not a trivial matter. It should be emphasized that all of these aggregation-based assays are done under non-equilibrium conditions. The aggregation in most cases is an irreversible process. Thus, it is not simple to obtain kinetic parameters [48, 70, 86]. In addition to being strongly dependent on protein concentration and temperature, other conditions may have a significant effect on the kinetic parameters obtained from the light-scattering data, e.g., mixing the reaction solution during the aggregation measurements. It is obvious from the published data that most investigators who use turbidometric techniques do not mix the reactant during the measurements. In many cases, the published data show that there is a sudden drop in the intensity of the apparent absorbance or the light-scattering signal. This happens simply because the protein aggregates become so large that they sink to the bottom of the cell, thereby decreasing the apparent absorbance or the intensity of the light scattering. Thus, the distribution of aggregates in the cell may not be homogenous. Mixing during the reaction may have its own problems. For example, we have observed that with lysozyme, visibly large aggregates of various sizes occupy the entire cuvette during the unfolding with TCEP (Figure 25.2). If the solution is mixed during the reaction with a small magnetic stirrer, the aggregates observed are very fine. However, they tend to adsorb with time to the quartz cuvette wall, causing a slow decrease in the

apparent absorbance measured as a function of time. The kinetics of aggregation observed under these two conditions is not the same. Similar results were obtained with malate dehydrogenase that was denatured by heating to 45 °C (data not shown).

Recently Kurganov [87, 88] studied the kinetics of irreversible protein aggregation in a system that utilizes measuring the increase in apparent absorbance as a function of time. This study shows that if the aggregation of the protein substrate follows first-order kinetics, then useful parameters may be obtained. This approach may be useful for characterizing the chaperone activity of alpha-crystallin and other small heat shock proteins.

G: Chaperone Assays Involving Protection of Enzyme Activities by Alpha-crystallin

It has been shown by several investigators that alpha-crystallin could protect in vitro some enzymes from inactivation when they are subjected to various stresses such as heat, ultraviolet light, or glycation [3, 57–62]. Enzyme activity assays can be more informative then the commonly used aggregation-based assays because protection from aggregation does not necessarily mean protection of enzyme activity. Some of the enzymes that were used included sorbitol dehydrogenase [58], several restriction enzymes [57, 59], Na/K-ATPase [62], catalase, glutathione reductase, superoxidase dismutase, and various enzymes from the glycolytic pathway [3, 61]. A commonly used enzyme is citrate synthase. Details about using citrate synthase for chaperone assays are given in Ref. [76] and in Chapter 24.

Acknowledgements

I thank Linlin Ding and Qingling Huang for continuous support of my research program. This work was supported by the National Eye Institute Merit R-37 EY3897 and by the National Eye Institute core grant EY 000331.

References

1 W. W. de Jong, G. J. Caspers and J. A. M. Leunissen, Genealogy of the alpha-crystallin-small heat-shock protein superfamily. *Int. J. Biol. Macromol.* **1998**, *22*, 151–162.

2 M. Ehrnsperger, M. Gaestel and J. Buchner, Molecular Chaperones in the Life Cycle of Proteins, **1998**, 553–577.

3 B. K. Derham and J. J. Harding, *Progress in Retinal and Eye Research* Vol. 18, Pergamon: Elsevier EB, **1999**, pp. 431–462.

4 R. Jaenicke and C. Slingsby, Lens crystallins and their microbial homologs: structure, stability, and function. *Crit. Rev. Biochem. Molec. Biol.* **2001**, *36*, 435–499.

5 R. van Montfort, C. Slingsby and E. Vierling, *Adv. Protein Chem. 5a*, Academic Press, **2002**, 105–156.

6 F. Narberhaus, Alpha-crystallin-type heat shock proteins: socializing minichaperones in the context of a multichaperone network. *Microbiol. Mol. Biol. Rev.* **2002**, *66*, 64–93.

7 A. P. Arrigo and W. E. G. Müller, *Small Stress Proteins*, **2002**, Springer-Verlag, Berlin.

8 J. Horwitz, The function of alpha-crystallin in vision. *Sem. Cell and Devel. Biol.* **2000**, *11*, 53–60.

9 J. Horwitz, Alpha-crystallin. *Exp. Eye Research*, **2003**, *76*, 145–153.

10 J. Horwitz, Alpha-crystallin can function as a molecular chaperone. *Proc. Natl. Acad. Sci. USA*, **1992**, *89*, 10449–10453.

11 U. Jakob, M. Gaestel, K. Engel and J. Buchner, Small heat shock proteins are molecular chaperones. *J. Biol. Chem.* **1993**, *268*, 1517–1520.

12 S. P. Bhat and C. N. Nagineni, Alpha B subunit of lens-specific protein alpha-crystallin is present in other ocular and non-ocular tissues. *Biochem. Biophys. Res. Commun.* **1989**, *158*, 319–325.

13 R. A. Dubin, E. F. Wawrousek, J. Piatigorsky, Expression of the murine alpha B-crystallin gene is not restricted to the lens. *Mol Cell Biol.* **1989**, *3*, 1083–1091.

14 T. Iwaki, A. Kume-Iwaki, R. K. Liem and J. E. Goldman, Alpha B-crystallin is expressed in non-lenticular tissues and accumulates in Alexander's disease brain. *Cell*, **1989**, *57*, 71–78.

15 R. Klemenz, E. Frohli, R. H. Steiger, R. Schafer and A. Aoyama, Alpha B-crystallin is a small heat shock protein. *Proc. Nat. Acad. Sci. USA*, **1991**, *88*, 3652–3656.

16 M. W. Head, G. E. Goldman, Small heat shock proteins, the cytoskeleton, and inclusion body formation. *Neuropathol Appl Neurobiol.* **2000**, *26*, 304–312.

17 K. K. Kim, R. Kim and S. H. Kim, Crystal structure of a small heat-shock protein. *Nature*, **1998**, *394*, 595–599.

18 R. L. M. van Montfort, E. Basha, K. L. Friedrich, C. Slingsby and E. Vierling, Crystal structure and assembly of a eukaryotic small heat shock protein. *Nature Struct. Biol.* **2001**, *8*, 1025–1030.

19 P. J. Wyatt, Light scattering and the absolute characterization of macromolecules. *Anal. Chim. Acta.* **1993**, *272*, 1–40.

20 J. Wen, T. Arakawa and J. S. Philo, Size-exclusion chromatography with on-line light-scattering, absorbance, and refractive index detectors for studying proteins and their interactions. *Anal. Biochem.* **1996**, *240*, 155–166.

21 E. Folta-Stogniew and K. R. Williams, Determination of molecular masses of proteins in solution: implementation of an HPLC size exclusion chromatography and laser light scattering service in a core laboratory. *J Biomolec. Tech.* **1999**, *10*, 51–63.

22 P. J. van den Oetelaar, P. F. van Someren, J. A. Thomson, R. J. Siezen, H. J. Hoenders, A dynamic quaternary structure of bovine alpha-crystallin as indicated from intermolecular exchange of subunits. *Biochemistry*, **1990**, *14*, 3488–3493.

23 M. P. Bova, L. L. Ding, J. Horwitz, B. K. Fung, Subunit exchange of αA-crystallin. *J Biol Chem.* **1997**, *272*, 29511–29517.

24 M. P. Bova, O. Huang, L. Ding, J. Horwitz, Subunit exchange, conformational stability, and chaperone-like function of the small heat shock protein 16.5 from *Methanococcus jannaschii*. *J Biol Chem.* **2002**, *277*, 38468–38475.

25 H. A. Koteiche and H. S. Mchaourab, Folding pattern of the alpha-crystallin domain in alphaA-crystallin determined by site-directed spin labeling. *J. Mol. Biol.* **1999**, *294*, 561–577.

26 H. A. Koteiche and H. S. Mchaourab, The determinants of the oligomeric structure in Hsp16.5 are encoded in the alpha-crystallin domain. *FEBS Lett.* **2002**, *519*, 16–22.

27 K. Guruprasad and K. Kumari, Three-dimensional models corresponding to the C-terminal domain of human αA and αB-crystallins based on the crystal structure pf the small heat-shock protein HSP16.9 from wheat. *Int. J. Biol. Macromol.* **2003**, *33*, 107–112.

28 D. A. Haley, J. Horwitz and P. L. Stewart, The small heat-shock protein, alphaB-crystallin, has a variable quaternary structure. *J. Mol. Biol.* **1998**, *277*, 27–35.

29 D. A. Haley, M. P. Bova, Q. L. Huang, H. S. Mchaourab and P. L. Stewart, Small heat-shock protein structures reveal a continuum from symmetric to variable assemblies. *J. Mol. Biol.* **2000**, *298*, 261–272.

30 P. J. Groenen, K. B. Merck, W. W. de Jong and H. Bloemendal, Structure and modifications of the junior chaperone alpha-crystallin. From lens transparency to molecular pathology. *Eur J Biochem.* **1994**, *225*, 1–19.

31 M. Gaestel, sHsp-phosphorylation: enzymes, signaling pathways and functional implications. In: A. P. Arrigo and W. E. G. Müller, Editors, *Small Stress Proteins* **2002**, *28*, 151–184.

32 K. Kato, H. Ito and Y. Inaguma, Expression and phosphorylation of mammalian small heat shock proteins. In: A. P. Arrigo and W. E. G. Müller, Editors, *Small Stress Proteins* **2002**, *28*, 129–150.

33 K. Kamei, I. Iwamoto, Y. Inaguma, D. Nohara and K. Kato, H. Ito, Phosphorylation-induced change of the oligomerization state of αB-crystallin. *J. Biol. Chem.* **2001**, *276*, 5346–5352.

34 H. A. Koteiche and H. S. Mchaourab, Mechanism of chaperone function in small heat-shock proteins. *J Biol Chem.* **2003**, *278*, 10361–10367.

35 K. P. Das, J. M. Petrash and W. K. Surewicz, Conformational properties of substrate proteins bound to a molecular chaperone α-crystallin. *J Biol Chem.* **1996**, *271*, 10449–10452.

36 K. P. Das, L. P. Choo-sith, J. M. Petrash and W. K. Surewicz, Insight into the secondary structure of non-native proteins bound to a molecular chaperone α-crystallin. *J Biol Chem.* **1999**, *274*, 33209–33212.

37 R. A. Lindner, A. Kapur and J. A. Carver, The interaction of the molecular chaperone, α-crystallin, with molten globule states of bovine α-lactalbumin. *J Biol Chem.* **1997**, *272*, 27722–27729.

38 K. Rajaraman, B. Raman, T. Ramakrishna and C. M. Rao, The chaperone-like alpha-crystallin forms a complex only with the aggregation-prone molten globule state of alpha-lactalbumin. *Biochem. Biophys. Res. Commun.* **1998**, *249*, 917–921.

39 J. A. Carver, R. A. Lindner, C. Lyon, D. Canet, H. Hernandez, C. M. Dobson and C. Redfield, The interaction of the molecular chaperone alpha-crystallin with unfolding alpha-lactalbumin: a structural and kinetic spectroscopic study. *J Mol Biol.* **2002**, *318*, 815–827.

40 C. M. Dobson, P. A. Evans, S. E. Radford, Understanding how proteins fold: the lysozyme story so far. *Trends Biochem Sci.* **1994**, *19*, 31–37.

41 S. E. Radford and C. M. Dobson, Insights into protein folding using physical techniques: studies of lysozyme and alpha-lactalbumin. *Philos Trans R Soc Lond B Biol Sci.* **1995**, *348*, 17–25.

42 Z. T. Farahbakhsh, Q. L. Huang, L. Ding, C. Altenbach, H. J. Steinhoff, J. Horwitz and W. L. Hubbell, Interaction of α-crystallin with spin-labeled peptides. *Biochemistry*, **1995**, *34*, 509–516.

43 J. Horwitz, Q. L. Huang, L. Ding and M. P. Bova, Lens alpha-crystallin: chaperone-like properties. *Methods in Enzymology*, **1998**, *290*, 365–383.

44 A. Holmgren, Thioredoxin catalyzes the reduction of insulin disulfides by dithiothreitol and dihydrolipoamide. *J Biol Chem.* **1979**, *254*, 9627–9632.

45 K. K. Sharma, R. S. Kumar, G. S. Kumar, and P. T. Quinn, Synthesis and characterization of a peptide identified as a functional element in αA-crystallin. *J Biol Chem*, **2000**, *275*, 3767–3771.

46 J. Bhattacharyya and K. K. Sharma, Conformational specificity of mini-alphaA-crystallin as a molecular

chaperone. *J Pept Res*. **2001**, *57*, 428–434.

47 J. B. Smith, Y. Lin and D. L. Smith, Identification of possible regions of chaperone activity in lens alpha-crystallin. *Exp. Eye Res*. **1996**, *63*, 125–128.

48 H. S. Mchaourab, E. K. Dodson, and H. A. Koteiche, Mechanism of chaperone function in small heat shock proteins. Two-mode binding of the excited states of T4 lysozyme mutants by αA-crystallin. *J Biol Chem*, **2002**, *277*, 40557–40566.

49 M. Ehrnsperger, S. Graber, M. Gaestel and J. Buchner, Binding of non-native protein to Hsp25 during heat shock creates a reservoir of folding intermediates for reactivation. *EMBO J*. **1997**, *16*, 221–229.

50 G. J. Lee, A. M. Roseman, H. R. Saibil and E. Vierling, A small heat shock protein stably binds heat-denatured model substrates and can maintain a substrate in a folding-competent state. *EMBO J*. **1997**, *16*, 659–671.

51 K. Wang and A. Spector, The chaperone activity of bovine alpha crystallin. Interaction with other lens crystallins in native and denatured states. *J. Biol. Chem*. **1994**, *269*, 13601–13608.

52 D. Boyle and L. Takemoto, Characterization of the alpha-gamma and alpha-beta complex: evidence for an in vivo functional role of alpha-crystallin as a molecular chaperone. *Exp. Eye Res*. **1994**, *58*, 9–16.

53 P. V. Rao, Q. L. Huang, J. Horwitz and S. J. Zigler, Evidence that alpha-crystallin prevents non-specific protein aggregation in the intact eye lens. *Biochem. Biophys. Acta*. **1995**, *1245*, 439–447.

54 J. A. Carver, K. A. Nicholls, J. A. Aquilina and R. J. W. Truscott, Age-related changes in bovine alpha-crystallin and high-molecular-weight protein. *Exp. Eye Res*. **1996**, *63*, 639–647.

55 Y. C. Chen, G. E. Reid, R. J. Simpson and R. J. W. Truscott, Molecular evidence for the involvement of alpha crystallin in th colouration/ crosslinking of crystallins in age-related nuclear cataract. *Exp. Eye Res*. **1997**, *65*, 835–840.

56 R. J. W. Truscott, Y. C. Chen and D. C. Shaw, Evidence for the participation of alpha B-crystallin in human age-related nuclear cataract. *Int. J. Biol. Macromol*. **1998**, *22*, 321–330.

57 J. F. Hess and P. G. FitzGerald, Protection of a restriction enzyme from heat inactivation by [alpha]-crystallin. *Mol. Vision*. **1998**, *4*, 29–32.

58 I. Marini, R. Moschini, A. Del Corso and U. Mura, Complete protection by alpha-crystallin of lens sorbitol dehydrogenase undergoing thermal stress. *J. Biol. Chem*. **2000**, *275*, 32559–32565.

59 P. Santhoshkumar and K. K. Sharma, Analysis of alpha-crystallin chaperone function using restriction enzymes and citrate synthase. *Mol. Vision*. **2001**, *7*, 172–177.

60 G. B. Reddy, P. Y. Reddy and P. Suryanarayana, AlphaA- and alphaB-crystallins protect glucose-6-phosphate dehydrogenase against UVB irradiation-induced inactivation. *Biochem Biophys Res Commun*. **2001**, *282*, 712–716.

61 B. K. Derham and J. J. Harding, Enzyme activity after resealing within ghost erythrocyte cells, and protection by alpha-crystallin against fructose-induced inactivation. *Biochem J*. **2002**, *368*, 865–874.

62 B. K. Derham, J. C. Ellory, A. J. Bron and J. J. Harding, The molecular chaperone alpha-crystallin incorporated into red cell ghosts protects membrane Na/K-ATPase against glycation and oxidative stress. *Eur J Biochem*. **2003**, *270*, 2605–2611.

63 H. Bloemendal and G. Groenewoud, One-step separation of the subunits of alpha-crystallin by chromatofocusing in 6 M urea. *Anal Biochem*. **1981**, *117*, 327–329.

64 E. W. Doss-Pepe, E. L. Carew and J. F. Koretz, Studies of the denaturation patterns of bovine alpha-crystallin using an ionic denaturant, guanidine

hydrochloride and a non-ionic denaturant, urea. *Exp Eye Res*. **1998**, *67*, 657–679.

65 M. A. van Boekel, F. de Lange, W. J. de Grip, W. W. de Jong, Eye lens alphaA- and alphaB-crystallin: complex stability versus chaperone-like activity. Biochim Biophys Acta. **1999**, *1434*, 114–123.

66 J. Horwitz, M. P. Bova, L. L. Ding, D. A. Haley, P. L. Stewart, Lens alpha-crystallin: function and structure. Eye. **1999**, *13*, 403–408.

67 T. X. Sun, N. J. Akhtar, J. J. Liang, Thermodynamic stability of human lens recombinant alphaA- and alphaB-crystallins. *J Biol Chem*. **1999**, *274*, 34067–34071.

68 S. Abgar, J. Backmann, T. Aerts, J. Vanhoudt, J. Clauwaert, The structural differences between bovine lens alphaA- and alphaB-crystallin. *Eur J Biochem*. **2000**, *267*, 5916–5925.

69 J. J. Liang, T. X. Sun, N. J. Akhtar, Heat-induced conformational change of human lens recombinant alphaA- and alphaB-crystallins. *Mol Vis*. **2000**, *6*, 10–14.

70 F. Sobott, C. V. Robinson, Protein complexes gain momentum. *Curr Opin Struct Biol*. **2002**, *12*, 729–734.

71 F. Sobott, J. L. Benesch, E. Vierling, C. V. Robinson, Subunit exchange of multimeric protein complexes. Real-time monitoring of subunit exchange between small heat shock proteins by using electrospray mass spectrometry. *J Biol Chem*. **2002**, *277*, 38921–38929.

72 J. A. Aquilina, J. L. Benesch, O. A. Bateman, C. Slingsby, C. V. Robinson, Polydispersity of a mammalian chaperone: mass spectrometry reveals the population of oligomers in alphaB-crystallin. *Proc Natl Acad Sci USA*. **2003**, *100*, 10611–10616.

73 G. Zettlmeissl, R. Rudolph, R. Jaenicke, Reconstitution of lactic dehydrogenase. Noncovalent aggregation vs. reactivation. 1. Physical properties and kinetics of aggregation. *Biochemistry*. **1979**, *18*, 5567–5571.

74 J. Buchner, M. Schmidt, M. Fuchs, R. Jaenicke, R. Rudolph, F. X. Schmid, T. Kiefhaber, GroE facilitates refolding of citrate synthase by suppressing aggregation. *Biochemistry*. **1991**, *30*, 1586–1591.

75 J. Buchner, Supervising the fold: functional principles of molecular chaperones. *FASEB J*. **1996**, *10*, 10–19.

76 J. Buchner, H. Grallert, U. Jakob, Analysis of chaperone function using citrate synthase as nonnative substrate protein. *Methods Enzymol*. **1998**, *290*, 323–338.

77 S. Abgar, N. Yevlampieva, T. Aerts, J. Vanhoudt, J. Clauwaert, Chaperone-like activity of bovine lens alpha-crystallin in the presence of dithiothreitol-destabilized proteins: characterization of the formed complexes. *Biochem Biophys Res Commun*. **2000**, *276*, 619–625.

78 S. Abgar, J. Vanhoudt, T. Aerts, J. Clauwaert, Study of the chaperoning mechanism of bovine lens alpha-crystallin, a member of the alpha-small heat shock superfamily. *Biophys J*. **2001**, *80*, 1986–1995.

79 G. B. Reddy, S. Narayanan, P. Y. Reddy, I. Surolia, Suppression of DTT-induced aggregation of abrin by alphaA- and alphaB-crystallins: a model aggregation assay for alpha-crystallin chaperone activity in vitro. *FEBS Lett*. **2002**, *522*, 59–64.

80 E. B. Getz, M. Xiao, T. Chakrabarty, R. Cooke, P. R. Selvin, A comparison between the sulfhydryl reductants tris(2-carboxyethyl)phosphine and dithiothreitol for use in protein biochemistry. *Anal Biochem*. **1999**, *273*, 73–80.

81 J. C. Han, G. Y. Han, A procedure for quantitative determination of tris(2-carboxyethyl)phosphine, an odorless reducing agent more stable and effective than dithiothreitol. *Anal Biochem*. **1994**, *220*, 5–10.

82 K. Rajaraman, B. Raman, T. Ramakrishna, C. M. Rao, The chaperone-like alpha-crystallin forms a complex only with the aggregation-

prone molten globule state of alpha-lactalbumin. *Biochem Biophys Res Commun*. **1998**, *249*, 917–921.

83 A. Tardieu, D. Laporte, P. Licinio, B. Krop, M. Delaye, Calf lens alpha-crystallin quaternary structure. A three-layer tetrahedral model. *J Mol Biol*. **1986**, *192*, 711–724.

84 W. K. Surewicz, P. R. Olesen, On the thermal stability of alpha-crystallin: a new insight from infrared spectroscopy. *Biochemistry*. **1995**, *34*, 9655–9660.

85 K. P. Das, W. K. Surewicz, Temperature-induced exposure of hydrophobic surfaces and its effect on the chaperone activity of alpha-crystallin. *FEBS Lett*. **1995**, *369*, 321–325.

86 M. A. Speed, J. King, D. I. C. Wang, Polymerization mechanism of polypeptide chain aggregation. *Biotechnology and Bioengineering*. **1997**, *54*, 333–343.

87 B. I. Kurganov, Kinetics of protein aggregation. Quantitative estimation of the chaperone-like activity in test-systems based on suppression of protein aggregation. *Biochemistry (Moscow)*. **2002**, *67*, 409–422.

88 K. Wang, B. I. Kurganov, Kinetics of heat- and acidification-induced aggregation of firefly luciferase. *Biophys Chem*. **2003**, *106*, 97–109.

26
Transmembrane Domains in Membrane Protein Folding, Oligomerization, and Function

Anja Ridder and Dieter Langosch

26.1
Introduction

26.1.1
Structure of Transmembrane Domains

Integral membrane proteins traverse the membrane with one or more transmembrane segments (TMSs). The basic architecture of a membrane consists of a hydrophobic region of about 30 Å, formed by the lipid acyl chains, and two more polar interface regions that are both about 15 Å thick [1]. In order to fulfill the hydrogen bond–forming capacity of the polypeptide, proteins generally span the membrane either with α-helices or β-strands (Figure 26.1).

Since in β-strands hydrogen bonds are formed between residues in adjacent segments, proteins have to form cylindrical β-barrels to satisfy all their hydrogen bonds. In α-helices, hydrogen bonds are formed between residues within the same segment. Therefore, proteins can either span the membrane with a single hydrophobic α-helical transmembrane segment (bitopic proteins) or form a bundle of helices (polytopic proteins).

As an increasing number of polytopic membrane proteins are structurally characterized with high-resolution methods, and as oligomerization of more and more bitopic membrane proteins is studied with biochemical, biophysical, and genetic techniques, it is becoming increasingly clear that folding of membrane-integral domains and biological function is strongly dependent on interactions between α-helical TMSs. A number of excellent reviews have been published recently covering membrane protein folding and TMS-TMS interactions from different perspectives [1–12], and a related chapter on membrane protein folding by Tamm is available in Volume 1 of this handbook. Naturally, the structure of the membrane-spanning domains of the β-barrel type, as observed with many bacterial outer-membrane proteins, is also dependent on interactions between their TMSs [13, 14]. Because these interactions are less well understood than those between α-helical TMSs, they will be excluded from the present review.

Protein Folding Handbook. Part II. Edited by J. Buchner and T. Kiefhaber

ISBN: 3-527-30784-2

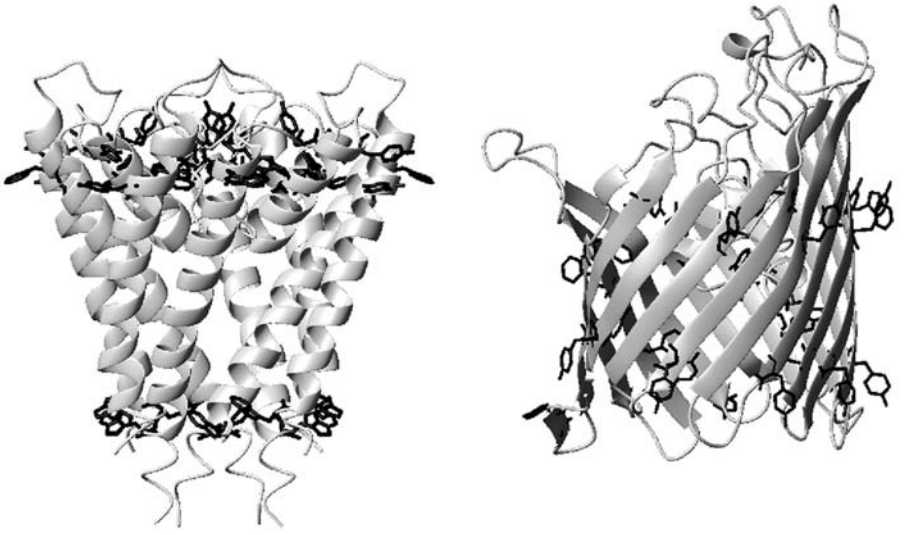

Fig. 26.1. Structures of two membrane proteins. On the left is the α-helical potassium channel from *Streptomyces lividans* [272] (PDB access code 1BL8). On the right, the β-barrel protein PhoE from *Escherichia coli* is shown [273] (PDB access code 1PHO). The side chains of tryptophan and tyrosine residues in the proteins are shown in black.

26.1.2
The Biosynthetic Route towards Folded and Oligomeric Integral Membrane Proteins

It appears that some proteins or peptides have the ability to insert into membranes spontaneously, i.e., without the use of proteinaceous factors. In the thylakoid membrane of chloroplasts, several proteins seem to insert as helical hairpins, depending on the hydrophobicity of the TMSs [15–17]. Small proteins with a single hydrophobic segment and small, if any, flanking regions also seem to be able to insert spontaneously into lipid bilayers [18], a situation that may also apply to some toxins or antimicrobial peptides.

However, most proteins become integrated into biological membranes via proteinaceous machineries. Co-translational membrane integration is a process that is similar in the eukaryotic endoplasmic reticulum (ER) membrane and bacterial inner membranes [19–22]. In the first step, a signal recognition particle (SRP) binds to the N-terminal signal sequence or to the first TMS of the protein when it emerges from the ribosome. These ribosome–nascent chain complexes are targeted to the SRP receptor in the membrane (performed by FtsY in bacteria) and subsequently transferred to the translocon. In eukaryotic ER membranes, this is the Sec61p complex, consisting of α-, β-, and γ-subunits, while in *E. coli* the homologous proteins are called SecYEG. The protein is then further translated and TMSs exit the translocation channel laterally into the lipid bilayer. For some proteins this occurs during translation, while other membrane proteins are transferred into the

lipids only after the complete protein is synthesized. In the latter case, interactions between TMSs can occur within the translocon. It is commonly thought that TMSs are initially oriented and integrated into the membrane as independent units. However, recent results show that intraprotein interactions, stop-transfer effector proteins, and co-translational modifications can also play a role in determining the final topology of proteins within the membrane [21].

The membrane insertion of individual helices is the first stage in the widely accepted two-stage model of membrane protein folding, while in the second stage the helices come together through helix-helix interactions to produce the final folded conformation of the protein [7, 23]. It has been shown early on for a number of cases that membrane protein fragments produced by proteolytic cleavage of the loops or by co-expression of separate domains can be reconstituted to functional proteins. The most prominent example is bacteriorhodopsin, where a large number of different TMS fragments were produced and reassembled and where none of the connecting loops appears to be absolutely required for function [24–26]. Other examples are reviewed elsewhere [10, 12]. These results demonstrate that the information directing folding of functional membrane proteins is at least partly contained within the structure and sequence of the TMSs.

26.1.3 Structure and Stability of TMSs

26.1.3.1 Amino Acid Composition of TMSs and Flanking Regions

In contrast to the wealth of structural information obtained for soluble proteins, very few detailed structures of membrane proteins have been obtained. Nevertheless, much can be deduced about the structure of membrane proteins by examining their primary amino acid sequences.

The average length of a transmembrane (TM) helix is 20–25 amino acids, which is enough to span the hydrophobic part of a lipid bilayer [27–29]. Due to the need to be accommodated in the hydrophobic part of a lipid bilayer, TMSs are enriched in the hydrophobic amino acids Phe, Ile, Leu, Met, and Val [28, 30–33]. Single-spanning membrane protein TMSs tend to be more hydrophobic than TMSs from multi-spanning proteins and contain fewer polar amino acids [27, 32, 33]. The nucleotide bias of a particular organism affects the amino acid composition of TMSs such that organisms with a higher GC content in their genomes have more Val and Ala in their TMSs, whereas organisms with a lower GC content contain more Ile and Phe residues [34]. It is presently unknown whether the resulting difference in hydrophobicity is compensated for by the length of the TMSs.

In the membrane-flanking regions of TMSs, positively charged residues are more abundant at the cytoplasmic side of the membrane than at the periplasmic side, while there is no such bias for negatively charged residues [31–33]. Positive charges are more difficult to translocate across the membrane and thus control the topology of membrane proteins; this is called the ''positive-inside rule'' [35].

In most of the structures of membrane proteins that have been determined, a remarkable distribution of aromatic amino acids is observed. In β-barrel as well as

α-helical proteins, these residues form aromatic belts at the membrane-water interface (see Figure 26.1). This interfacial enrichment of aromatic residues has been confirmed by statistical analysis of membrane proteins [18, 27, 31, 36]. The role of these belts is not completely clear, but it is probably related to the strong affinity of Trp and Tyr residues for the interfacial region of lipid bilayers [37–40]. This may anchor proteins within the membrane and influence their precise positioning [40–42].

Using the information described above, it can be quite reliably predicted which proteins are membrane proteins and where TMSs are located in the sequence. Most of these prediction programs are based on hydrophobicity plots and scan an amino acid sequence for hydrophobic stretches of about 20 residues. Very often used are the Kyte and Doolittle [43] or GES [44] hydrophobicity scales. If the hydrophobicity of a segment is higher than a certain threshold value, it is considered to be a TMS. Other methods are based on comparisons with TMSs of well-characterized membrane proteins [45, 46] or use evolutionary information [47] to determine which amino acids are likely to be in the membrane [48]. When the TMSs have been determined, the transmembrane topology of a protein can subsequently be predicted by considering the preference of certain amino acids for the *cis* or *trans* side of the membrane [49–51]. Until now, the nucleotide bias of a particular organism usually has not been taken into account in these predictions [34].

26.1.3.2 **Stability of Transmembrane Helices**

In general, the stability of an α-helix depends both on intrahelical N–H···O=C hydrogen bonds between backbone atoms of successive helical turns and on intrahelical interactions between adjacent amino acid side chains [52]. As all of these interactions are essentially electrostatic in nature (see Section 26.2.1.1), it follows that their strength increases when a polypeptide chain is transferred from polar aqueous solution (dielectricity constant $\varepsilon = 80$) into the apolar part of a lipid bilayer. The magnitude of this increase depends on amino acid sequence and on the dielectric constant of the bilayer. That TM helices in apolar environments are indeed more stable than soluble helices is experimentally supported by the finding that denaturation of membrane proteins in detergent solution by heat or denaturants often causes only minimal loss of helical structure [3].

In soluble proteins, Leu and Ala residues rank among the best helix promoters, while Ile and Val destabilize α-helices and are over-represented in β-sheets; Gly strongly destabilizes soluble helices, and Pro is known to be a helix breaker [53–57]. Using a host-guest approach, different residue types were placed into the invariant framework of a model peptide and the latter's structure in media of different polarity was determined. It was found that the helix-destabilizing effect of Gly, Val, and Ile was much smaller upon insertion of the peptide into the apolar membrane-mimetic environment of detergent or lipid micelles than in aqueous buffer [58]. In a later study, the same authors showed that Ile, Leu, and Val were the residue types with the highest propensity of α-helices in apolar media, whereas Gly and Pro had the most destabilizing effects [59, 60]. That residues with β-branched

side chains are effective helix formers in membranes is supported by the observation that Ile and/or Val make up about half of the α-helical TMSs of the bacteriophage M13 major coat protein [61] and of the pulmonary surfactant–associated polypeptide SP-C [62].

As in soluble helices, Pro residues have a destabilizing effect on TM-helices for two reasons: (1) the imide within its cyclic side chain cannot hydrogen bond to the carbonyl oxygen of the peptide bond at the i-3 or i-4 position, and (2) a steric clash between the Pro ring and the backbone carbonyl group at the i-4 position is produced [63]. Despite these destabilizing effects, Pro is well tolerated in TM helices due to their greater overall stability; in addition, the missing hydrogen bond may partially be replaced by a weak hydrogen bond involving the proton linked to the δ carbon of the Pro ring and the carbonyl group at i-4 [64]. Nevertheless, Pro residues in TMSs are frequently, but not always, associated with local bends or distortions of helical structure that may be relevant for protein function [63, 65]. A similar situation may apply to Gly residues that occur with high frequency in TMSs. Gly is thought to locally disrupt intrahelical side chain packing and appears to have a greater destabilizing effect on helices in a polar environment than in apolar media [58]. Interestingly, bends in TM helices are frequently seen when Pro and Gly residues are spaced four residues apart [66].

26.2 The Nature of Transmembrane Helix-Helix Interactions

26.2.1 General Considerations

A complete thermodynamic description of TMS-TMS interactions is a complex task since partitioning of the helices into the lipid bilayer, stability of and attractive forces between the helices, entropic factors, competition between protein-protein, protein-lipid, and lipid-lipid interactions, and environmental constraints have to be taken into account. At present, the degrees by which these factors define a given interaction are not understood at a quantitative level and we therefore limit the discussion to qualitative descriptions. We will summarize first how TMS-TMS interactions result from different attractive forces and entropic factors. Second, we will discuss how these concepts evolved from the study of polytopic and bitopic membrane proteins. Finally, we discuss how TMS-TMS interactions may be influenced by protein-lipid interactions.

26.2.1.1 Attractive Forces within Lipid Bilayers

Of the four basic attractive forces – i.e., weak and strong nuclear forces, gravitation, and electrostatic interactions – the latter account for folding of and interactions between proteins. Electrostatic interactions are commonly classified into three main categories. Ionic, or coulomb, interactions attract stable point charges such as ionized amino acid side chains. These are strong and decrease proportionally with the

distance between them. Hydrogen bonds are based on protons that are shared by appropriately positioned electronegative atoms and are of primarily electrostatic nature. Dipole-dipole, or van der Waals, forces develop between permanent dipoles, between permanent and induced dipoles, or between induced and thus fluctuating dipoles (dispersion forces). In general, van der Waals forces are weaker than ionic interactions or hydrogen bonds; their strength depends on the polarity and polarizability of the binding partners and decreases with the sixth power of distance [52]. It has frequently been noted that the strength of ionic interactions and hydrogen bonds strongly increases when the polarity of the environment decreases, since electrostatic forces are inversely related to the dielectric constant ε. It is often overlooked, however, that the same applies to van der Waals interactions [67, 68]. These considerations imply that all attractive forces mediating protein-protein interaction are generally stronger in the low dielectric environment of the lipid bilayer acyl chain region than in aqueous solution.

26.2.1.2 **Forces between Transmembrane Helices**

All of the forces discussed in Section 26.2.1.1 – that is, ionic interactions, hydrogen bonds, and van der Waals interactions – can contribute to TMS-TMS interactions. Their relative contributions to the total enthalpy of interaction largely depend on amino acid composition and sequence. Since TMSs are built mostly from apolar amino acids, van der Waals interactions between their side chains appear to be a major and universal driving force in TMS assembly. Albeit weak, unidirectional, and strongly dependent on distance, van der Waals interactions apply to any type of side chain atom and may accumulate over entire interfacial regions. This is of particular relevance where an interface forms between helix surfaces that are complementary in shape and therefore form extensive interfacial areas. Interhelical hydrogen bonds appear to come in a variety of flavors, distinguished by the electronegativity and proximity of donors and acceptors that determine their strength. Hydrogen bonds can form (1) between the side chains of polar, yet non-ionizable, residues; (2) between the hydrogens connected to C_α carbon atoms and main-chain carbonyl groups or polar side chains; (3) between N–H groups of the main chain and polar side chains; and (4) between isolated ionizable residues that are likely to be uncharged, yet polar, in the membrane. There is experimental evidence for all of these alternatives, as is described in Section 26.2.2. Since hydrogen bonds exhibit a greater degree of directionality than van der Waals interactions, they are likely to complement the latter and to enhance specificity and stability of membrane protein folding and interaction [5]. Whether interactions between ionized side chains occur between TMSs is an unsettled question. The considerable enthalpic cost of transferring a point charge into an apolar environment makes the existence of isolated ionized side chains in membranes quite unlikely [69]. On the other hand, this cost would drop substantially provided that two charges of opposite sign interact and thus neutralize each other. Formation of strong ionic bonds between TMSs is therefore a realistic scenario.

As outlined in Section 26.2.1.1, electrostatic forces are strengthened in apolar environments. Whereas standard textbooks frequently depict the acyl chain region of

a lipid bilayer as a slab of uniformly low polarity with dielectric constants $\varepsilon \sim 2$, the situation is more complex in reality. Nitroxide radicals, whose spin density depends on the polarity of the surrounding medium, were coupled to different positions of phospholipids, fatty acids, or cholesterol in order to report the polarity of model bilayers at different depths of penetration by electron paramagnetic resonance spectroscopy. The results revealed steep polarity gradients within the acyl chain region. Specifically, the apolar character of membranes composed of monounsaturated phospholipids increased from the headgroup region towards the middle of the acyl chain region. Inclusion of cholesterol reduced polarity in the central regions of saturated membranes and broadened the apolar central region in unsaturated membranes [70]. A similar picture emerged from neutron diffraction studies, where it was found that the concentration of the strongly hydrophobic molecule hexane dissolved in a bilayer peaked at its center and decreased towards its boundaries [71]. Accordingly, TMSs may experience the lowest polarity, and therefore strongest interactions, at their central regions. The same argument would apply to TMSs in detergent micelles, since their terminal regions would be close to the charged surface of the micelle, whereas the central regions would be embedded in its strongly hydrophobic core.

26.2.1.3 Entropic Factors Influencing Transmembrane Helix-Helix Interactions

Apart from enthalpic contributions, the free energy of TMS-TMS interactions is likely to be influenced by entropic factors in ways that are significantly different from the situation encountered with soluble proteins. First, TMSs are pre-oriented in the membrane upon biosynthetic insertion, with their long axes roughly perpendicular to the plane of the bilayer. Therefore, the loss of backbone entropy that is associated with any protein-protein interaction is expected to be smaller upon assembly of TMSs than of soluble helices tumbling freely in isotropic solution [72]. Second, helix-helix interactions are also influenced by the loss of side chain entropy upon association, provided that residues buried within interfaces exhibit only one out of several alternative rotameric states. On first approximation, this phenomenon would be of equal importance for soluble and membrane-embedded helices. On the other hand, the number of accessible rotameric states available to many side chains drops when a helix folds from the denatured state. Therefore, association of soluble helices that are usually in equilibrium with denatured states would be accompanied with a greater entropic penalty than assembly of preformed TM helices. Loss of side chain entropy is absent for Gly and minimal for those residues that adopt only one (Val) or three (Leu and Ile) rotamers in helices [10]; this would favor these amino acids in TMS-TMS interfaces. Furthermore, the hydrophobic effect is considered to be a major driving force in soluble protein folding. This effect is thought to evolve when apolar protein surfaces interact and thereby release ordered networks of water molecules associated with them [52]. It may be more important for inducing hydrophobic collapse than for stabilization of the folded structure, since many enzymes remain functional in apolar organic solvents [73]. Due to the scarcity of water molecules in the hydrophobic part of the membrane, the hydrophobic effect is thought to be of little or no importance for TMS-

TMS interactions [2, 10]. It has been argued, however, that other solvophobic factors based on lipids play a role in the membrane. Accordingly, the entropy of a membrane may increase as soon as lipids are removed from interacting protein surfaces [9].

26.2.2 Lessons from Sequence Analyses and High-resolution Structures

Careful analyses of the amino acid sequences and crystal structures of membrane proteins can provide insight into how TMSs pack together. Transmembrane helices of polytopic proteins that are adjacent in sequence always pack against each other in an antiparallel mode in the folded structure due to the topological constraints of the connecting loops. TMSs farther apart in sequence or TMSs from interacting subunits may pack in either parallel or antiparallel mode [74–76]. Thus, loops are at least partially responsible for the sequential order and relative orientation of the TMSs in a folded structure. An antiparallel arrangement of helices seems to allow for tighter packing than a parallel one [77]. A role for the helix dipole moment in antiparallel packing of TMSs does not seem likely [78].

Similar to the situation with soluble globular proteins [79], interacting TM helices within polytopic membrane proteins rarely display exactly parallel long axes but rather adopt either positive or negative crossing angles Ω, i.e., they form left- or right-handed pairs, respectively [74, 80] (Figure 26.1). The sign of the crossing angles depends on the geometry of side chain packing in the common interface. Packing of TM helices is predominantly left-handed [76, 77, 80], with crossing angles at around $+20^\circ$ [74], although this result may be biased by the limited number of available high-resolution structures. Pairs of helices with positive crossing angles have a larger average interaction surface than those with negative crossing angles [77].

TMS-TMS interfaces adopting positive crossing angles follow a repeated heptad [*abcdefg*] pattern of amino acids whose side chains interact via a ''knobs-into-holes'' packing reminiscent of soluble leucine zipper interaction domains [80]. There, residues located at the *a* or *d* positions protrude into cavities formed by *a*-, *d*-, *e*-, and *g*-type residues of the partner helix. An analysis of three membrane protein structures showed that the positions in such heptad repeat patterns are predominantly occupied by hydrophobic amino acids. Their composition is thus similar to the general composition of TMSs, although Trp seems to be over-represented. In that study, no positional specificity of particular amino acids was found [80].

The other general mode of TMS-TMS packing, generating negative crossing angles, is described more appropriately by ''ridges-into-grooves'' packing, where ridges are formed from protruding side chains and grooves correspond to the valleys between them [2, 79].

Sequence analyses showed that amino acid substitutions in general are more likely to occur at residues facing the lipid bilayer than at helix-helix interfaces, due to the need to conserve specific packing [81]. In support of this, single-spanning transmembrane proteins are more tolerant to mutation than multi-spanning pro-

teins, indicating that they experience less sequence constraints [32, 33]. Surprisingly, the oligomerizing surfaces of polytopic transmembrane proteins are not well conserved [81]. However, this observation is probably caused by the fact that only membrane proteins with large, extended contacting surfaces located on different helices were analyzed.

In contrast to soluble helices, Gly and Pro are relatively common in TMSs and by themselves do not necessarily disrupt α-helical structure [66, 75], although disruption of helices is frequently observed when two Pro or a Pro and a Gly together are present within the same helix [66]. Conserved motifs in TMSs of membrane protein families often contain Gly or Pro residues [82]. This points to special roles for these potentially helix-breaking residues in transmembrane helices. Pro residues are enriched in the middle of TM helices compared to soluble ones [32, 33] and are usually oriented towards the protein interior where they contribute to tight packing [65, 75, 77, 83, 84]. A likely reason for this is that it would be unfavorable to direct the unsatisfied hydrogen bond of the carbonyl group of the residue at i-4 towards the lipids, whereas in the protein interior it could hydrogen bond to another helix or to prosthetic groups. Another function for Pro residues in TMSs was recently proposed [85]. In the cystic fibrosis transmembrane conductance regulator, a Pro prevents aggregation of the protein in the aqueous phase or in the translocation pore by hindering the formation of β-sheet structure. By counteracting the β-sheet propensities of surrounding amino acids in the TMS, Pro may thus destabilize misfolded states of the protein [85].

Gly residues in TMSs frequently occur in pairs that are spaced four amino acids apart [27] and thus localize to the same face of the helix. Indeed, the GxxxG motif is the single most enriched pairwise motif found in membrane-spanning segments, where it frequently occurs with β-branched residues at neighboring positions [28]. In addition, pairs of small residues with spacings of four or seven amino acids are conspicuous in light of their high degree of conservation within homologous TMSs in membrane protein families [85] and are therefore thought to play essential roles in the packing of transmembrane helices. In support of this, the small residues Gly, Ala, Ser, and Thr show a large preference for being oriented towards the interior of membrane proteins, where they do not create voids or pockets but pack tightly with other residues [66, 75, 84–86].

In contrast, large hydrophobic amino acids seem to be more loosely packed in membrane proteins than these small residues and are more often oriented to the lipids [75, 86]. Nevertheless, they are important for TMS packing, since in crystallized membrane protein structures 15 of the most frequent 20 pairs of neighboring residues in TM regions contain at least one L, I, or V residue [84]. Hydrophobic residues appear to be highly mutable in TMSs, indicating that they are relatively interchangeable. However, Leu was found to be only half as mutable as the other hydrophobic residues, which could indicate a special role for Leu in the packing of TMSs as leucine zippers [32, 33].

The more polar faces of transmembrane helices are enriched in aromatic amino acids, indicating that these residues are generally buried within the protein interior [83, 87]. Phe appears to be very versatile, since it can pack with a large variety of

other residues [77, 84]. Trp and Tyr residues show a tendency to cluster together, which is probably due to their enrichment in the membrane-water interface, where they can interact with the lipid headgroups [27] (see Section 26.1.3.1).

Polar residues tend to be fairly conserved in membrane proteins, suggesting special roles in packing and/or function [77], e.g., in the formation of hydrogen bonds, ionic interactions, and/or cofactor binding.

Comparison of transmembrane sequences of mesophilic and thermophilic organisms can provide insight into the importance of certain sequence motifs in the packing and stability of membrane proteins [29]. Thermophilic organisms contain more Asp and Glu residues in their TMSs, which can form stronger hydrogen bonds than the Asn and Gln residues more often found in mesophilic organisms. A striking reduction in the occurrence of Cys residues was found in thermophiles, most likely because their reactivity could be harmful, especially at higher temperatures [29]. The fact that it can readily be replaced by other residues indicates that Cys in most cases has no specific function. Indeed, Cys residues rarely contact each other in TMSs [84], suggesting that S–S bridges almost never occur within the membrane. In thermophilic organisms, more of the small residues Gly, Ala, and Ser are found in pair motifs, which could allow for tighter packing between helices and thus for higher thermal stability than in mesophilic organisms [29].

Almost all transmembrane helices form hydrogen bonds with other helices, and the corresponding interfaces are packed more closely than those without [88]. The modes of interhelical hydrogen bonding appear to be more diverse in the membrane than between α-helices from soluble proteins [84] (see Section 26.2.1.2).

Asn and Gln show a high propensity to form strong hydrogen bonds in TMSs [84]. Consequently, these polar residues are often conserved in transmembrane helices, where they interact with other polar amino acids [75]. When located in the middle of TMSs, they tend to be buried within the TMS-TMS interfaces, while they do not show this preferential orientation in the lipid headgroup region [86].

Ser and Thr residues can form hydrogen bonds with the carbonyl atoms at positions i-4 or i-3 on the same helix [76] or can form interhelical hydrogen bonds, e.g., with backbone nitrogens [75].

Interhelical hydrogen bonds and backbone contacts occur more frequently between helix pairs crossing each other at positive packing angles [76]. Indeed, such interactions are often found where helices cross each other via GxxxG motifs, since Gly allows the helices to come into close contact [76, 84]. In addition, Gly has not one but two H atoms that can participate in C_α–H $\cdots$ O hydrogen bonds.

Multiple interhelical hydrogen bonds appear to be arranged in two kinds of spatial motifs [84]. In the ''serine zipper,'' the side chains of two amino acids located on opposing helices form hydrogen bonds with the peptide backbone at the opposite residue. This is mostly seen for Ser-Ser pairs, and the seven-residue spacing is reminiscent of the leucine-zipper motif [84]. Indeed, such a serine zipper can often be found in combination with a leucine zipper, forming a mixed serine–leucine-zipper interface [89]. The second spatial arrangement of hydrogen bonds, the ''polar clamp,'' is formed by three amino acids on two different helices, with two hydrogen bonds between them, so that a polar residue (Glu, Lys, Asn, Gln,

Arg, Ser, Thr) is clamped by hydrogen bonds to either backbone atoms or other side chains [84].

26.2.3 Lessons from Bitopic Membrane Proteins

Although the atomic structure of only one bitopic dimeric membrane protein TMS is currently known [90, 91], residue patterns of a number of TMS-TMS interfaces have been mapped by mutational analysis (see protocols, Section 26.4). Accordingly and in analogy to polytopic proteins (see Section 26.2.2), bitopic membrane proteins may be grouped into two broad categories. One exhibits interfacial $[abcd]_n$ repeats, where *a* and *b* correspond to interfacial residues and the TMSs appear to form right-handed pairs, i.e., they cross each other at negative angles. The other one is based on the $[abcdefg]_n$ heptad repeat motif of left-handed pairs characterized by positive crossing angles.

26.2.3.1 Transmembrane Segments Forming Right-handed Pairs

The homodimeric glycophorin A, an erythrocyte protein of unknown function, has long served as the paradigm for TMSs interacting at a negative angle, thus forming a right-handed pair. The interface between its TMSs corresponds to the pattern LI. .GV. .GV. .T, as originally shown by Engelman and coworkers and others by mutational analysis (see Section 26.4) in detergent solution [92–94] and in membranes [95–97]. The structure of this interface gives rise to a negative crossing angle as implied by molecular modeling [98, 99] and confirmed by nuclear magnetic resonance studies in detergent [90] and membranes [91]. This interaction is dominated by a GxxxG motif that is central to the TMS-TMS interface, as mutation of these Gly residues to Ala destabilizes the interaction much more than mutation of the other interfacial residues [93, 95, 100, 101]. The glycophorin A TMS-TMS interaction is apparently driven by a complex mixture of attractive forces and entropic factors. The GxxxG motif may drive assembly by formation of a flat helix surface that allows multiple van der Waals interactions to form. In addition, the entropy loss upon association is considered minimal for Gly and the neighboring Val residues [102]. Moreover, the Gly residues reduce the distance between the helix axes and thus may facilitate hydrogen bond formation between their C_α-hydrogens and the backbone of the partner helix [76]. That the GxxxG motif is of prime importance is supported by the observation that changing the residue spacing between both Gly residues affects dimerization [103, 104] and that a GxxxG pair induces self-interaction of oligo-methionine or oligo-valine helices in membranes [103]. Interestingly, GxxxG motifs appear also to drive homophilic interactions of TMSs that are otherwise unrelated in sequence and are derived from membrane proteins of diverse function, including M13 major coat protein [105] and syndecan 3 [106]. Further, degenerate versions of this motif have been proposed to mediate TMS-TMS interactions of erbB receptors [107]. Apart from their occurrence in TMSs, GxxxG motifs seem to be prevalent in helix-helix interfaces of soluble proteins where they are also supported by $C_\alpha H \cdots O$ hydrogen bonds [108].

A traditional interhelical hydrogen bond between the Thr residues of the glycophorin TMS is not seen in detergent [90] but is suggested by the structure determined in membranes [91]. It should also be noted that the distance between the dimerization motif and the C-terminal flanking charged residues influences glycophorin TMS-TMS packing for reasons that are not entirely clear [109].

A residue pattern similar to that of glycophorin A accounts for interactions between the TMSs of SNARE (soluble NSF-attachment protein receptor) proteins. SNAREs form an evolutionarily conserved family of proteins that are essential for all types of intracellular membrane fusion events [110]. These proteins form a stable ternary complex that appears to bridge apposed membranes prior to their actual fusion [111]. While crystallographic analysis [112] has shown that a soluble version of the complex corresponds to a coiled-coil structure, the crystal structure of the complete SNARE complex including the TMSs is not known. In vivo, a fraction of the SNARE synaptobrevin II not participating in SNARE complex formation appears to exist in association with the synaptic vesicle protein synaptophysin or as a homodimer, as revealed by cross-linking experiments performed on brain fractions [113–115] or visualization of fluorescently tagged molecules in live cells [116]. A homodimeric form also develops from recombinant full-length synaptobrevin II in detergent solution [117], liposomes [118], or bacterial membranes [119]. Alanine-scanning mutagenesis indicated that synaptobrevin homodimerization depends on a specific residue pattern within its TMS: LxxICxxxLxxII. Grafting these six residues onto an inert oligo-alanine host sequence restored homodimerization in detergent solution; two additional residues were required to complete the motif when assayed in membranes: ILxxICxxILxxII [119]. These amino acids form a contiguous patch on the synaptobrevin TM helix and are thus supposed to constitute the TMS-TMS interface (Figure 26.2). The spacing of these interfacial residues suggests that the self-interacting TMSs adopt a negative crossing angle [117, 119]. These experimental results are supported by a computational study revealing that the critical residues form a tightly packed interface between α-helices that approach each other most closely at Cys103 and cross each other at a packing angle of -38° [120]. In the model, the synaptobrevin TMS-TMS interface comprises a much smaller molecular surface area (3.96 nm^2) than that of glycophorin A (5.50 nm^2), is based mainly on van der Waals interactions, and is not stabilized by intermolecular hydrogen bonds. Although the loss of side chain rotamer entropy upon burying Leu and Ile side chains within interfaces is considered to be small (see Section 26.2.1.3), it appears to exceed that of glycophorin TMS-TMS dimerization [120]. These differences are most likely due to the fact that the synaptobrevin TMS does not harbor a GxxxG motif. Interestingly, the interfacial residues of the synaptobrevin II TMS are almost completely conserved within the TMS of syntaxin 1A, the natural binding partner of synaptobrevin II [119]. This suggested that the TMS also mediates self-assembly of syntaxin or its heterophilic association with synaptobrevin, and this prediction was experimentally confirmed [118, 119]. A number of hypotheses concerning the functional relevance of synaptobrevin TMS-TMS interaction have been forwarded, including stabilization [117] or multimerization [119, 121] of the SNARE complex and/or propagating the "zippering up" of the

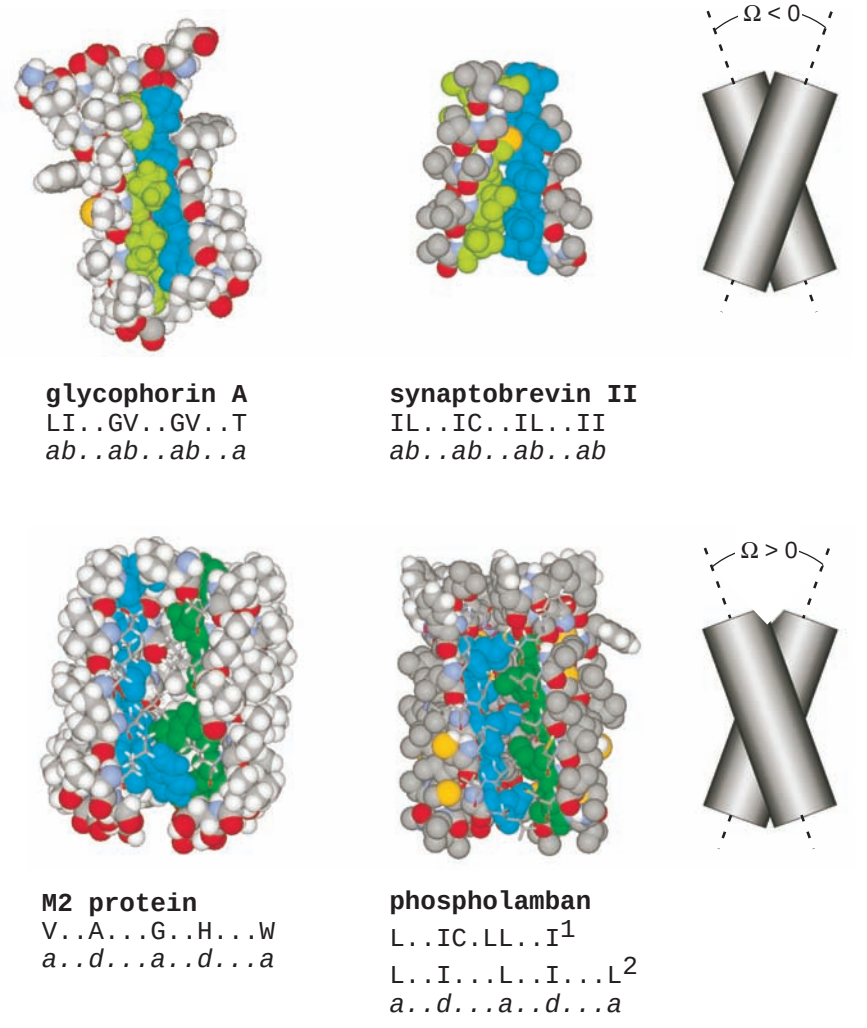

Fig. 26.2. Models of self-assembling TMSs from bitopic membrane proteins. The TMSs of glycophorin A (PDB code 1afo; only residues 70–90 are shown) and synaptobrevin II (PDB coordinates kindly provided by Dr. Karen Fleming) form right-handed homodimers with crossing angles $\Omega < 0°$, whereas the TMSs from the tetrameric influenza M2 protein (PDB coordinates kindly provided by Dr. William DeGrado) or from the pentameric phospholamban (PDB coordinates kindly provided by Dr. Isaiah Arkin) form left-handed pairs with $\Omega > 0°$. For easier visualization of TMS-TMS packing, the interfacial residues from neighboring helices are colored green and blue, respectively (the sulfur atom of synaptobrevin Cys 103 is in yellow). In the M2 protein and phospholamban, part of the residues is shown not in CPK but in stick representation to allow for better visual access to the interface. The patterns of the dominant interfacial residues as given below the models were determined by NMR (glycophorin A [90]) and/or mutational or functional analyses (glycophorin A [93]; synaptobrevin II [117]; M2 protein [123]; phospholamban [127][1] and [128][2]). Lowercase letters underneath the interfacial residues denote the interfacial residue positions according to the consensus patterns for negative ($[ab..]_n$) or positive ($[a..d..]_n$) helix-helix crossing angels.

cytoplasmic coiled-coil domains into the membrane at the onset of membrane fusion [118, 119]. In addition, the ability of SNARE proteins to enter the SNARE complex may be influenced by TMS-mediated homodimerization.

26.2.3.2 Transmembrane Segments Forming Left-handed Assemblies

The M2 proton channel from influenza A virus is one example of a TMS that is likely to adopt positive crossing angles. M2 forms a tetramer that is stabilized by intermolecular disulfide bonds. Since these are not essential for tetramerization, the protein can assemble by way of noncovalent TMS-TMS interactions. Its function is to form a proton channel in the envelope of the virus that is blocked by the antiviral drug amantadine [122]. Channel function can be reconstituted in mRNA-injected *Xenopus laevis* oocytes and proton translocation can be determined electrophysiologically. DeGrado, Pinto, and coworkers have determined the degree of amantadine blockage for a range of point mutants generated by cysteine-scanning mutagenesis in comparison with the wild-type protein. A pattern of sensitive residues (V. .A. . .G. .H. . .W) emerged with the periodicity of *a* and *d* positions in a left-handed helix-helix pair, suggesting a positive interhelical crossing angle [123]. This model was supported by direct analysis of oligomeric states upon disulfide oxidation [124] and refined by molecular modeling [125] and spectroscopic analysis ([10] and references cited therein).

Phospholamban TMSs also appear to cross each other at a positive packing angle upon homophilic assembly. This protein is part of the sarcoplasmatic reticulum membrane, where it functions as a regulator of Ca^{2+}-ATPase function [126]. Recombinant phospholamban forms a mixture of different oligomeric species in detergent solution up to a predominant pentamer, and the relevance of the individual TMS residues for assembly has been determined by saturation [127] and scanning [128] mutagenesis. Although the patterns of sensitive residues slightly deviated in both studies (L. .IC.LL. .I [127]; L. .I. . .L. .I. . .L [128]), it became apparent that the interfacial residues follow a heptad periodicity indicative of a positive crossing angle. Molecular modeling supported this view [129–131]. The exclusive participation of Leu, Ile, and Cys residues in interface formation is reminiscent of the situation of SNARE proteins as described in the previous section. It suggests that the interaction is driven mainly by van der Waals interactions and may be supported by minimal entropy loss upon association.

A leucine-zipper type of TMS-TMS interaction was also proposed by us to contribute to homodimerization of erythropoietin receptors. Whereas these cytokine receptors were originally thought to be activated by ligand-mediated dimerization, more recent evidence has revealed the existence of preformed dimers whose active conformation is stabilized by ligand binding [132, 133]. That the TMS may participate in receptor assembly was suggested by its ability to self-interact in membranes [134] and was confirmed by showing that the wild-type TMS sequence is important for receptor assembly [135] and function [136]. Thus, TMS-TMS assembly may support formation of a ligand-independent receptor dimer. The relevant interface was mapped by asparagine-scanning mutagenesis (see Section 26.4.3), which confirmed that it corresponds to a heptad repeat pattern [274]. Interestingly, the same face of the mEpoR TM helix may alternatively mediate homophilic interaction or

heterophilic binding to the TMS of the viral membrane protein gp55-P in cells infected with polycythemic Friend spleen focus-forming virus. The disulfide-linked, single-span, homodimeric gp55-P binds to the erythropoietin receptor in a way that depends on the TMS sequences of both proteins and thereby induces constitutive activation [137]. Computational searching of low-energy structures and model building provided a 3-D model of this TMS-TMS interface and predicted that it corresponds to a left-handed leucine zipper stabilized by van der Waals interactions [137]. Since the residues that account for homophilic assembly of the erythropoietin receptor TMS correspond precisely to the residues contacting the gp55-P TMS in the model, homophilic interaction may compete with heterophilic interaction in the membrane of an infected erythroid cell.

A TMS-TMS interaction of the leucine zipper type was also proposed for cadherins that are calcium-dependent, cell-cell adhesion molecules whose function requires lateral clustering within the cell's plasma membrane [134]. Lateral cadherin clustering involves interactions between extracellular and cytoplasmic domains [138]. In addition, their TMSs appear to contribute to lateral assembly, since mutations reducing TMS-TMS interactions also reduced adhesiveness of E-cadherin in transfected cells [139].

Apart from these natural sequences, model systems have been developed in order to study the forces driving TMS-TMS assembly. For example, an oligo-Leu sequence that functions as an artificial TMS has been shown to self-interact in membranes and in detergent solution, where it forms oligomeric structures of mixed stoichiometry ([134, 275]). As self-interaction was preserved with a heptad-repeat pattern of Leu residues, the oligo-Leu sequence is regarded as a prototypical membrane-spanning leucine-zipper interaction domain [134] whose assembly is presumably driven by van der Waals interactions. Interestingly, the affinity of the oligo-Leu sequence was dramatically enhanced when Engelman and coworkers placed an Asn residue within the oligo-Leu TMS. A nuclear magnetic resonance study revealed that an intermolecular hydrogen bond had formed between the carboxamide side chains of Asn [140]. In a different study, DeGrado and coworkers investigated the effect of Asn on self-assembly of the GCN4 leucine-zipper domain that was reengineered to a membrane-soluble molecule (termed MS1) by exchanging most hydrophilic residues to apolar ones [141]. In the original GCN4 molecule, the leucine-zipper domain mediates high-affinity homodimerization and its structural features are known in great detail [142–145]. The *a* and *d* positions of this domain are occupied by Leu and Val residues, respectively, except for one *d* position that corresponds to an Asn. In the water-soluble form, this Asn residue is destabilizing relative to a hydrophobic interaction but specifies the dimeric state in favor of other oligomeric forms [144, 146]. In the membrane-soluble MS1 peptide, however, Asn strongly increased thermodynamic stability [141], whereas the Leu and Val residues at the other *a* and *d* positions contributed little to the free energy of association [10]. Thus, hydrogen bond formation between Asn side chains appears to provide a much stronger attractive force within the apolar milieu of detergent micelles or membranes than in aqueous solution. Later, it was shown that other polar amino acids such as Asp, Gln, Glu, and His also strongly enhanced

self-assembly of the membrane-spanning leucine-zipper models [147, 148]. We recently used the effect exerted by Asn to probe the interface of the original oligo-Leu model. When all positions of the oligo-Leu sequence were systematically mutated in asparagine-scanning mutagenesis, the most sensitive positions correspond to a heptad repeat pattern of residues, confirming a leucine-zipper type of side chain packing. Further, asparagines had a much stronger impact on self-assembly when located at the center of the oligo-leucine sequence than at the termini, and a similar phenomenon was observed upon asparagine mutagenesis of the erythropoietin receptor TMS [274]. We believe that the dependence of the strength of the hydrogen bond between Asn residues on their depth of bilayer penetration is related to polarity gradients in lipid bilayers (see Section 26.2.1.2). This conclusion is supported by a recent study addressing the effect of asparagine on self-assembly of the MS1 peptide [86]. By analytical ultracentrifugation of corresponding synthetic peptides in detergent micelles, these authors showed that asparagine residues located within the apolar region of the peptide provide a significantly larger driving force on helix-helix interaction than an asparagine at a position near the apolar/polar interface of the micelle.

It has been argued that the existence of polar residues forming hydrogen bonds between TMSs could actually be dangerous since they might induce unspecific assembly in the membrane [140]. That this danger is real is highlighted by a number of growth factor receptors that are constitutively activeted by TMS mutations in different hereditary diseases. For example, the *neu* tyrosine kinase receptor is activated by a substitution of V664 within its TMS for a glutamic acid residue [149] that appears to induce permanent receptor dimerization by interhelical hydrogen bond formation [69]. The tyrosine kinase activity of fibroblast growth factor receptor 3 is activated by a glycine-to-arginine exchange within its TMS in patients suffering from achondroplasia [150]. Further, mutating S498 of the thrombopoietin receptor TMS to asparagine rendered this receptor constitutively active [151], and mutation of T617 to asparagine within the granulocyte colony-stimulating factor receptor TMS as found in patients with acute myeloid leukemia conferred growth-factor independence in expressing cells [152].

In addition to hydrogen bonds, it is quite likely that ionic interactions between charged residues take place in the apolar environment. Conceptually, charge-charge interactions between TMSs are difficult to envision since ionizable residues are likely to be integrated into membranes in an uncharged state. The T cell receptor is a model where this issue has been examined in considerable detail. This receptor is composed of six different chains that form the $\alpha\beta$ heterodimer responsible for ligand recognition plus the CD3$\gamma\varepsilon$, CD3$\delta\varepsilon$, and $\zeta\zeta$ signaling modules [153]. Three basic residues are found in the TM domains of the T cell receptor $\alpha\beta$ heterodimer, while a pair of acidic residues is present in each of the three associated signaling dimers. It was shown earlier that interactions between TMS residues of opposite charge contribute to association of certain receptor subunits [154–156], while a recent study addressed the role of charged residues in formation of the complete receptor complex [153]. According to this model, each of the nine ionizable residues is essential for receptor assembly. Each assembly step is promoted by

interaction between the basic residues of the $\alpha\beta$ heterodimer and the acidic residues of the different signaling modules. Whether these residues are truly ionized prior to interaction is not clear. It was shown previously that unassembled α and β chains have a short half-life in cell membranes due to the basic residues [157], and model proteins with basic residues remain associated with the Sec61p channel of the endoplasmic reticulum rather than diffusing into the lipid [158]. Therefore, it was argued that newly synthesized subunits might stay at the vicinity of the translocon where their ionizable residues could be in the charged state before associating with cognate subunits [153]. This model of T cell receptor assembly is an interesting case, as it provides evidence that certain types of TMS-TMS interactions may depend on chaperoning by accessory proteins.

The issue of ionic interactions between TMSs was also addressed recently by an in vitro study based on synthetic hydrophobic peptides with non-natural sequences. Upon reconstitution into liposomal membranes, self-interaction of these oligo-Leu-based peptides was not enhanced by the presence of ionizable residues that were of opposite signs. It was thus proposed that ionic interactions would not contribute to TM helix-helix interactions [159]. The reason for the obvious discrepancy in the results obtained with the T cell receptor [153] is not known. Clearly, no chaperoning factors were present in the liposome system, and it is not certain that these peptides were inserted correctly into the plane of the bilayer.

26.2.4 Selection of Self-interacting TMSs from Combinatorial Libraries

Another tool for exploring the mechanisms underlying TMS-TMS interactions is the selection of transmembrane sequences capable of self-interaction from combinatorial libraries [102, 160, 161]. These libraries are created by randomization of amino acid motifs characteristic for TMS-TMS interfaces. In these systems, TMS-TMS interaction results in a phenotype that can be selected for. For this purpose, the ToxR transcription activator system is used, which exists in two versions: TOXCAT [96] and POSSYCCAT [160] (see Section 26.4).

Randomization of the LIxxGVxxGVxxT pattern that mediates the high-affinity dimerization of glycophorin A followed by selection of self-interacting sequences using TOXCAT yielded GxxxG motifs in over 80% of all isolates [102]. As discussed previously, Gly residues reduce the distance between the helix axes and thus may facilitate hydrogen bond formation between C_α-hydrogens and the backbone of the partner helix [76]. In addition, β-branched residues (Ile, Val) were apparently preferred at positions adjacent to the glycines. Such motifs might drive TMS-TMS packing by formation of a flat helix surface. Moreover, the side chains of Ile and Val prefer a single rotameric state in an α-helix; this limits the entropy loss that is normally associated with the freezing of side chain conformations upon protein-protein interaction [102]. When the glycophorin motif was randomized with a set of hydrophobic residues from which Gly was excluded, clusters of Ser and Thr residues were enriched in the selected self-interacting TMSs [161]. Although single Ser or Thr residues did not support TMS-TMS interactions in previous studies

[147, 148], multiples of them apparently do. This suggests that multiple weak interhelical hydrogen bonds – formed either between hydroxylated side chains or between them and main-chain atoms – may act cooperatively to drive TMS-TMS assembly.

The heptad repeat motif *ga..de.ga..de.ga* characteristic of TMS-TMS interfaces adopting positive crossing angles was randomized with three different sets of mostly hydrophobic residues, and self-interacting sequences were selected with the POSSYCCAT system [160]. A set of only five hydrophobic residues (Leu, Ile, Val, Met, and Phe) yielded heptad patterns that were capable of self-interaction in a rather sequence-independent way, although Val was over-represented in those TMSs with the highest affinities. Randomizing with more complex amino acid mixtures drastically decreased the fraction of self-interacting TMSs and resulted in an enrichment of Ile and Leu in high-affinity sequences.

It is likely that these aliphatic side chains contribute to TMS-TMS interaction by virtue of their relatively large contribution to van der Waal's interactions in a well-packed interface. In addition, loss of side chain entropy may be minimal for Leu, Ile, and Val. In contrast to the results obtained upon randomizing the motif associated with negative crossing angles [102, 161], no enrichment of GxxxG motifs or hydroxylated amino acids was seen, and the content of Pro residues was negatively correlated to self-interaction of the heptad pattern [160]. On the other hand, Pro was abundant in high-affinity sequences assumed to adopt negative crossing angles, where the free i-4 carbonyl was proposed to engage in interhelical hydrogen bonding to a Ser or Thr residue of the partner helix [161]. These differences suggest that weak interhelical hydrogen bonding may be more relevant for right-handed TMS pairs than for left-handed ones. This is in agreement with the observation that interhelical hydrogen bonds involving C_α-hydrogens were primarily associated with TM helix pairs crossing each other at negative packing angles [76].

26.2.5
Role of Lipids in Packing/Assembly of Membrane Proteins

The packing of transmembrane helices is likely to be influenced by the surrounding lipids. Excellent reviews of lipid-protein interactions in biological membranes have recently appeared, with an extensive treatment of high-resolution structures of membrane proteins that contain tightly bound lipid molecules even after detergent solubilization [162–164]. In a number of cases, these lipids are found at or between protein interaction surfaces and thus might directly support oligomerization by stabilizing TMS-TMS interactions. In the crystal structure of bacteriorhodopsin, which normally occurs as a trimer in its native purple membrane, six glycolipids were found in the central compartment of the trimer. Mutations in the binding sites for these lipids disrupted the trimeric organization of the protein [165]. For a review about lipid-protein interactions in the purple membrane, see Ref. [166]. When tightly bound cardiolipin molecules were removed from bovine cytochrome *c* oxidase by digestion with phospholipase, two subunits dissociated from the complex [167]. The structure of cytochrome *bc*1 also contains several

phospholipids, which are suggested to play a role in stabilization of the multisubunit complex [168]. Moreover, a phosphatidylcholine (PC) molecule has been found at the interface between the L and M subunits of the photosynthetic reaction center [169], and three cardiolipin molecules are present at the trimer interface of formate dehydrogenase [170].

Apart from this direct role, lipids may influence TMS-TMS interactions in more indirect ways. First, interactions between proteins and lipids in a membrane are thermodynamically coupled. Thus, the free energy of helix-helix association in lipid bilayers can be described as:

$$\Delta G_a = \Delta G_{HH} + n/2\Delta G_{LL} - n\Delta G_{HL} \quad (1)$$

where $\Delta G_{HH}, \Delta G_{LL}$, and ΔG_{HL} are the free energies of helix-helix, lipid-lipid, and helix-lipid interactions, respectively, and it is assumed that n lipid molecules are displaced from the helices upon interaction [1]. Therefore, oligomerization of transmembrane helices will be facilitated when helix-helix or lipid-lipid interactions are more favorable than helix-lipid interactions. Molecular dynamics simulations of glycophorin A in lipid bilayers suggest that these helix-helix and helix-lipid interactions can be quite similar [171]. Studies with transmembrane model peptides indicate that the free energy of helix-helix interaction increases with increasing lipid acyl chain length [172], presumably because the lipid-lipid interactions become more favorable. Other theoretical descriptions of how lipid properties can influence transmembrane helix-helix interactions have recently been reviewed [173–175]. Also, entropic factors play a role, since upon helix-helix association within the lipid bilayer, the displacement of protein-bound lipids to the bulk lipid increases overall entropy. In other words, reduction of the solvent-exposed surface would be associated with an increase in overall entropy. This is analogous to the hydrophobic effect, which is one force driving the folding of soluble proteins in water [9].

Second, oligomerization or aggregation of membrane proteins has been proposed to be one of the possible consequences of hydrophobic mismatch with the membrane. Hydrophobic mismatch occurs when the length of a hydrophobic TMS is not equal to the thickness of the apolar part of the lipid bilayer. The resulting exposure of hydrophobic surfaces to a hydrophilic environment is unfavorable, and a number of possible ways of relieving potential mismatch have been proposed [176, 177]. The area of the protein that is exposed to the lipid bilayer can be reduced by adaptation of the lipids, tilting of transmembrane helices, or oligomerization of the protein. This indeed occurs with bacteriorhodopsin, which was monomeric when reconstituted into phosphatidylcholines with chain lengths from 12 to 22 carbon atoms but aggregated in thinner or thicker bilayers [178]. This effect of hydrophobic mismatch seems to occur especially with α-helices that are too long to span the lipid bilayer, and therefore the resulting tilted conformation has been suggested to assist in helix packing [179].

Third, oligomerization of membrane proteins naturally depends on their concentration within the membrane, as exemplified by bacteriorhodopsin, which is monomeric at low molar ratios but trimerizes when the concentration is increased [180,

181]. In lipid bilayers containing separate domains of lipids in the fluid (liquid crystalline) and in the gel phase, transmembrane helices tend to be excluded from the gel-phase regions [41, 182]. This increases the local concentration of these proteins in the liquid-crystalline part of the bilayer and thus can lead to increased oligomer formation [41, 182, 183]. In lipid bilayers composed entirely of gel-state lipids, this can even lead to the formation of large, highly ordered peptide-containing domains [184]. The same local enrichment phenomenon might also apply to membranes containing liquid-ordered domains, also called rafts. The lipid acyl chains in such domains are tightly packed like gel-state lipids, but the lateral diffusion of lipids is nearly the same as in the fluid phase. Increasing concentrations of the raft lipids sphingomyelin and/or cholesterol lead to an increase in dimerization of transmembrane peptides [159, 172, 185]. This could be due to exclusion of the transmembrane peptides from liquid-ordered domains [186], although other membrane proteins are believed to be anchored within rafts via their TMSs [187–189]. Other effects of cholesterol, such as the ordering of the lipid acyl chains and the resulting increase in membrane thickness, could also play a role.

Not only the lipids but also the choice of detergents used to study transmembrane peptides can severely influence the extent of interaction that is observed. The negatively charged SDS is much more disruptive for transmembrane helix-helix interactions than are zwitterionic detergents [97, 101, 190]. In addition, the acyl chain length of the detergent is very important, since optimal packing of transmembrane peptides of cystic fibrosis transmembrane conductance regulator was observed with detergents with acyl chain of eight or nine carbon atoms. This may be related to the hydrophobic diameter of the detergent micelles [190].

Taken together, lipids may influence TMS-TMS interactions at various levels, although the extent to which this is relevant is currently not clear due to the paucity of experimental data. On the other hand, those few examples where TMS-TMS interactions have been compared in lipids and detergents [90, 91, 101] suggest that the environment may influence the fine structure and/or the association equilibrium [97, 100, 101], but not the identity of the interface [93, 95, 119, 134].

26.3 Conformational Flexibility of Transmembrane Segments

TM helices are often described as rather rigid structures, a notion that is reinforced by the stabilizing influence of the apolar environment of a lipid membrane (see Section 26.1.3.2). There is mounting evidence, however, that TMSs can exhibit considerable conformational flexibility and that this can be of significant functional relevance. Consistent with the fact that the network of intrachain hydrogen bonding is incomplete at helix termini, the internal flexibility of model helices was found to be greater at terminal positions than at the centers [191, 192]. Further, helix-destabilizing Pro and Gly residues appear to locally increase flexibilities of TM helices. Early indications for this were obtained by Deber and coworkers, who found that Pro residues are significantly over-represented in the TMSs of transport-

ers and channels [193]. It was concluded that Pro residues facilitate the conformational changes during solute transport mediated by these proteins. As noted above (see Section 26.1.3.2), Pro residues in TM helices are frequently associated with local kinks, especially when a Gly residue is present in the vicinity, and it has been argued that these kinks may function as "molecular hinges," i.e., sites of increased local flexibility [63]. Indeed, a number of experimental and computational studies support these arguments. For example, Pro hinges have been reported to be important for gating of voltage-gated potassium channels [194] and for activation of G-protein-coupled receptors [195] or solute transporters [196]. Pro and Gly are frequently found in natural peptides, such as alamethicin and mellitin, that exhibit channel function and/or disrupt lipid bilayer structure. Replacing a Pro at a central location of the alamethicin sequence with alanine or shifting it to a different position influences conductance states and channel lifetimes [197, 198]. Alamethicin forms a helix that exhibits conformational flexibility around the Gly residue at the i-3 position of the central Pro residue in organic solvent as well in lipid bilayers [199, 200]. Mutational analysis of this GxxP pair suggested that the Pro residue by itself had little influence on bending of the helix, while concurrent mutation of Gly significantly reduced its flexibility [201].

Heck and coworkers studied the conformational flexibility of analogues of a non-natural model peptide reconstituted into liposomal membranes by hydrogen-deuterium exchange. They demonstrated that insertion of a Pro residue at the center of the TMS strongly enhanced the accessibility to deuterium of the amide groups of the entire central hydrophobic region that was largely inaccessible in the parental structure. This is likely to reflect an effect of Pro on helix flexibility that was, however, not seen upon insertion of Gly [202].

Conformational flexibility of TM helices has recently been proposed to play a role at the terminal stages of lipid membrane fusion [203–205]. Membrane fusion involves a restructuring of lipid bilayers brought into close proximity by single-span, membrane-anchored fusion proteins [110, 206, 207]. During the initial stages of the fusion process, these proteins mediate membrane apposition and undergo global conformational changes [208]. Late stages require the TMSs, as their replacement by lipid anchors or mutation abrogated the ability of various viral fusion proteins [110, 206, 207, 209–213] or SNAREs [214, 215] to mediate complete bilayer mixing. We and others showed that synthetic peptides corresponding to the TMSs of vesicular stomatitis virus (VSV) G-protein [204, 205] or of presynaptic SNAREs [203] induce unregulated sequence-specific membrane fusion upon reconstitution into liposomal membranes. In the case of the VSV G-protein, the peptide mimics partly reproduced the effects of point mutations affecting full-length VSV G-protein function in HeLa cells [204, 205]. Interestingly, these TMS mutations correspond to exchanges of Gly or of mostly β-branched residues for helix promoters. At the same time, these mutations increased the stability of the helical structures in isotropic solution [203, 205]. Gly and/or β-branched residues are generally over-represented in TMSs of viral fusion proteins [213] and SNAREs [203]. It was proposed, therefore, that the fusogenic activities of the TMSs at the final stage of lipid merger might require their conformational flexibility [203–205]. There are

a few other cases known where TMS mutations suppressed the fusogenicity of full-length viral proteins. This is exemplified by influenza hemagglutinin, whose function was compromised by a Gly-to-Leu exchange [209], and by a murine leukemia virus glycoprotein where mutations of Pro and Phe residues had the strongest effects [211]. That fusogenic TMSs may be characterized by high internal flexibility is also consistent with hydrogen/deuterium exchange experiments conducted on the membrane-embedded TM helix of influenza hemagglutinin [216]. While the conformational effects of Gly and Pro residues are likely to result from local packing defects as discussed above, the situation is more complex with β-branched amino acids. The conformation of the latter has been extensively analyzed in the case of the TMS of lung surfactant protein C, which includes two segments of seven and four consecutive valyls. This TMS exists as a stable and very well-defined α-helix in phosphocholine micelles but refolds to β-sheet aggregates in organic solvent [217]. Its amide protons were virtually non-exchangeable in the helical state but accessible upon spontaneous unfolding. Thus, consecutive valyl side chains appear to protect a helical peptide backbone by tight interlocking [217]. Similarly, the amide protons of oligo-Leu helices were virtually non-exchangeable in bilayers and exchanged very slowly in organic solvent [218]. These and other data [59, 60] show that both Leu and Val residues form stable α-helices in membranes. One may wonder, therefore, whether the observed over-representation of β-branched residues in TMSs of fusogenic proteins [203, 213] is primarily related to their ability to self-interact or to fusogenicity. It will be interesting to determine the conformational and functional properties of β-branched residues in mixed sequences.

26.4 Experimental Protocols

In the following sections, we give an overview on the most widely used techniques for the characterization of TMS-TMS interactions. Whereas most of these techniques monitor protein-protein interaction upon solubilization with a suitable detergent that prevents unspecific aggregation [219], others are suited for analysis of membrane proteins reconstituted into lipid membranes. Experimental approaches not covered here include the use of electron paramagnetic resonance, Fourier transform infrared spectroscopy, small angle X-ray scattering, and nuclear magnetic resonance spectroscopy [220].

26.4.1 Biochemical and Biophysical Techniques

Most standard techniques developed for the characterization of interactions between soluble proteins can be adopted for the purpose of studying TMS-TMS interactions in the context of native or recombinant membrane proteins or of synthetic peptides. Recombinant membrane proteins are frequently produced by *E. coli*,

which can be a difficult task due to toxic effects exerted by hydrophobic protein domains on the host cells. For high-level expression, therefore, it is often of considerable advantage to drive the recombinant protein into insoluble, and hence harmless, inclusion bodies that can later be detergent-solubilized upon cell lysis. Full-length membrane proteins or TMS sequences are frequently genetically fused to any of a variety of soluble proteins, such as glutathione-S-transferase or *Staphylococcus aureus* nuclease A, or to short epitope tags in order to facilitate expression and/or later detection as reviewed recently [221]. Expression in eukaryotic host systems, based on Sf9 insect cells, yeast, or mammalian cell lines, has the advantage of proper integration into eukaryotic membranes and proper posttranslational modifications but involves more cumbersome experimental procedures and frequently results in low protein yields [222, 223]. Alternatively, in vitro translation in the presence [153, 224–228] or absence [128] of microsomal membranes (derived from endoplasmatic reticulum) has been used to produce membrane protein subunits in sufficient quantity for investigation of their oligomeric structures. Translocation into microsomal membranes has the advantage that chaperoning factors and enzymes adding posttranslational modifications are present and active.

Short sequences representing TMSs from a variety of membrane proteins have also been synthesized by solid-phase chemical methods. Generally, synthesis of TMS peptides is a difficult task, as the sequences tend to aggregate nonspecifically on the resin, resulting in premature termination of the growing chains. Depending on the actual sequences, the standard 9-fluorenylmethoxycarbonyl (F-moc) methodology has been used successfully [147, 229, 230]. In certain instances, using the *tert*-butyloxycarbonyl (Boc) strategy appears to be better suited for production of pure peptides in satisfactory yields ([231] and our unpublished results).

26.4.1.1 Visualization of Oligomeric States by Electrophoretic Techniques

Denaturing Electrophoresis Sodium dodecyl sulfate polyacrylamide gel electrophoresis (SDS-PAGE) is generally used to determine the molecular weights of proteins based on comparison of their electrophoretic mobilities with a set of reference proteins [232]. Provided that the domains responsible for protein-protein interaction, e.g., TMSs, are not denatured by SDS, this technique is a simple and reliable tool for monitoring formation of oligomers. Stoichiometries and even subunit compositions of digomers can be investigated based on their molecular weights, and subsequent Western blotting reveals their identities. The preservation of noncovalent protein adducts in the presence of SDS is generally facilitated under mild conditions, i.e., using low SDS concentrations in sample buffer, omission of sample heating, and running of the gels in the cold room. Depending on the affinity of the TMS-TMS interaction under study and its competition by SDS binding, it is generally helpful to use protein concentrations in the micromolar range. Nevertheless, sample dilution during electrophoresis frequently results in partial dissociation of the protein complexes, thus producing smears on the gels. A major concern with this technique – as with any other method that monitors protein-protein interaction in detergent solution – is the issue of potential unspecific adduct formation.

Several criteria have been applied to exclude unspecific protein-protein interaction. First, inclusion of urea in sample buffer and gel significantly reduces unspecific interactions [233]. A critical aspect here is that the structure of the interaction domain must not be destroyed by urea, as seems to be the case with at least some TMSs [117, 119]. Second, the disruptive effect of certain point mutations within a TMS on adduct formation is a good indication of its specific nature and can reveal the identity of interfacial residues. By the same token, systematic point mutagenesis has been used to identify amino acid patterns of entire TMS-TMS interfaces (see Section 26.4.3). Third, competition of protein-protein interaction by added synthetic TMS peptides has been used to demonstrate the role of the TMSs in interaction and specificity [92, 147].

Natural TMSs whose interaction was previously studied by SDS-PAGE include those of glycophorin A [92, 93], Mas70p [234], phospholamban [127, 128], the major coat protein of M13 phage [235], and presynaptic SNAREs [117–119].

In cases where noncovalent protein-protein interaction cannot be detected in the presence of SDS, it has been proposed to substitute SDS with a novel detergent, perfluorooctanoic acid, which protects assembly of some membrane protein oligomers and allows their molecular weight determination [236]. Further, it is frequently helpful to stabilize weak interactions before SDS-PAGE analysis with homo- or heterobifunctional chemical cross-linking agents that are available in great variety with respect to chemical specificities, spacer lengths, and cleavability [237, 238].

Non-denaturing Electrophoresis The problem of denatured or masked TMSs upon SDS binding as encountered with SDS-PAGE is alleviated with non-denaturing or native PAGE. The membrane protein is solubilized with mild nonionic detergents and ε-aminocaproic acid. In the original version (''colorless native PAGE''), membrane protein migration in the electric field depended on the isoelectric point. Electrophoretic separation was greatly improved upon addition of the negatively charged dye Coomassie brilliant blue, which binds to membrane proteins, resulting in negatively charged dye-protein complexes at neutral pH. These complexes display reduced unspecific aggregation and travel towards the anode [239–242]. A problematic point with this technique, termed ''blue native PAGE,'' is that precise determination of molecular weights is difficult since the ratio of negative charge to molecular weight is far less uniform than with SDS-PAGE. Further, its success depends on the nature of the respective protein and requires careful control of the ratio of detergent, dye, and protein concentrations.

26.4.1.2 Hydrodynamic Methods

Hydrodynamic methods such as gel-filtration chromatography and ultracentrifugation on density gradients have traditionally been used to study oligomeric complexes of soluble proteins and to calculate their molecular weights with reference to marker proteins. For membrane proteins, these techniques are carried out in the presence of non-denaturing detergents that may allow detection of TMS-TMS interactions that could be destroyed under the harsher conditions of SDS-PAGE

[134]. To make the molecular weight increment of the detergent molecules that are bound to the protein invisible, D_2O is added to the solution such as to adjust its density to the density of the detergent [243]. In analytical ultracentrifugation, the free-energy change of an interaction as well as the stoichiometry of a complex can be determined [10]. The method has been applied to the TMSs of glycophorin A [100] and of the influenza M2 protein [10] and to TMS peptide models engineered to self-interact [141, 147].

26.4.1.3 Fluorescence Resonance Transfer

Techniques based on fluorescence resonance energy transfer (FRET) between suitable chromophores enjoy widespread use in protein-protein interaction research. Their advantage for membrane proteins is that they are capable of monitoring interactions in detergent micelles, upon reconstitution into synthetic bilayers, or even in membranes of live cells depending on the experimental approach taken. The principle of FRET is that two interacting proteins must carry different fluorescent chromophores, termed ''donor'' and ''acceptor,'' with complementary spectral characteristics. Fluorescent energy emitted by the donor can transfer to the acceptor in a radiation-less process, which is also called ''Förster transfer,'' provided that both are sufficiently close to each other. Since the efficiency of radiation-less transfer, as determined by measuring the decreasing intensity of donor fluorescence, decreases with the sixth power of the distance, FRET is used to measure intermolecular distances and is also dubbed as ''molecular ruler'' [10, 244–246]. The molecular distances between interaction partners that are amenable to FRET analysis are typically in the tens of angstroms and depend on the type of FRET pair used. A variety of donor/acceptor pairs have been successfully employed for analyzing TMS-TMS interactions using recombinant proteins or synthetic peptides. Many chromophores that are commercially available are conjugated to *N*-hydroxysuccinimide esters or maleimides that react with free primary amine groups or sulfhydryl groups, respectively. Synthetic peptides are labeled either after or during synthesis. Some examples include the pairs carboxyfluorescein/tetramethylrhodamine [247], dansyl/dabcyl [230], pyrene acetic acid/7-dimethylcoumarin-4-acetic acid [97], and 7-nitro-2-1,3-benzoxadiazol-4-yl/5(6) carboxy tetramethylrhodamine [248]. In an alternative to synthetic chromophores, FRET was measured between synthetic peptides containing the pair tryptophan/pyrenylalanine [159]. Natural TMSs whose interaction was studied by the FRET technique include those of the pore-forming domain of *Bacillus thuringiensis* delta-endotoxin [249], phospholamban [250], the major coat protein of Ff bacteriophage [230], and glycophorin A [97, 251]. The latter case is particularly interesting since FRET measurements in detergent micelles have revealed a strong dependence of the TMS-TMS affinity, but not of helicity, on the type and concentration of detergent used [97].

Apart from small molecule chromophores, derivatives of the green fluorescent protein have been developed that are suitable as donor/acceptor pairs and can be genetically fused to the protein under study. While the first-generation derivatives suffered from low absorbances and spectral overlap [252], cyan and yellow fluores-

cent proteins [253–255] offer great hope for analysis of protein-protein interaction within the membranes of live cells [116, 256].

A technique based on bioluminescence resonance energy transfer (BRET) was recently described [257]. In that method, luciferase is genetically fused to the protein of interest; its luminescence is induced by addition of the membrane-permeable coelenterazine and excites yellow fluorescent protein fused to an interaction partner [258–260]. BRET has also been used to monitor membrane protein interactions in live cells and may have a number of advantages over FRET in that direct excitation of the acceptor and photobleaching of the donor are excluded; further, autofluorescence of endogenous cellular components does not interfere with the measurement [257].

26.4.2 Genetic Assays

A number of genetic assay systems have been developed for the analysis of isolated TMS sequences or full-length membrane proteins in natural membranes. Their unifying hallmark is that protein-protein interaction elicits expression of reporter genes whose products can be quantitated and qualitatively represent the efficiency of the underlying interaction.

26.4.2.1 The ToxR System

The single-span membrane protein ToxR transcription activator protein is the central regulator of virulence gene expression in *Vibrio cholerae*. Upon self-assembly in the inner membrane, the ToxR molecule activates the *ctx* promoter, thereby initiating transcription of downstream genes [261]. For a system that is suitable for studying TMS-TMS self-association, a tripartite protein consisting of the cytoplasmic ToxR domain, a TMS, and a periplasmatically located maltose-binding protein (MalE) has been engineered. Variants of this protein with TMSs of choice are expressed in *Escherichia coli* reporter strains, where reporter genes are under transcriptional control of the *ctx* promoter. While the original version of the ToxR system utilizes the *lacZ* gene as reporter [95, 262], the TOXCAT system is based on plasmid-borne chloramphenicol acetyltransferase [96]. Specific activities of the reporter enzymes in cell lysates reflect the degree of self-assembly of the ToxR proteins in the inner bacterial membrane. Since TMS-TMS interactions are concentration-dependent like any other protein-protein interaction, it is desirable to regulate the concentration of the ToxR proteins in the membrane. While ToxR expression in the first-generation vector is constitutive [95, 262], later versions make use of the regulatable *lac* [96] or arabinose [160] promoters, respectively. One advantage of regulatable promoters is that expression can be driven to levels that are high enough for protein solubilization, purification, and biochemical analysis (W. Ruan and D. L. Langosch, submitted).

It should be borne in mind that the orientation of the interacting face of a TMS relative to the DNA-binding ToxR domain is a critical factor since it influences

the coupling of TMS-TMS interaction to transcription activation ([95, 274]). Therefore, the effect of inserting a TMS at different phases into ToxR chimeric proteins should initially be determined. Assuming α-helicity of the TMS, stepwise insertion of at least four additional residues at its N-terminus concurrent with stepwise deletion of four residues at its C-terminus rotates the potential TMS-TMS interface by up to $4 \times 100 = 400^{\circ}$, i.e., more than a full helical turn, relative to the ToxR domain and thus reveals one construct whose orientation within the construct is suitable for further analysis.

Control experiments are advisable to ascertain similar levels of ToxR expression and correct membrane integration. Concentrations of ToxR proteins in inner bacterial membranes can be compared by determining their ability to complement the deficiency in maltose-binding protein (MalE) of an *E. coli* deletion strain (PD28) [103]. This strain cannot grow in minimal medium with maltose as the only carbon source unless the C-terminal MalE domain of expressed ToxR chimeric proteins is successfully translocated to the periplasmic space [263]. Further, correct vectoriality of membrane integration can be confirmed by proteolytic digestion of the MalE domain in spheroplast preparations [96, 107].

The ToxR system has been used to study self-assembly of TMSs derived from glycophorin A [95, 96, 103], E-cadherin [139], erythropoietin receptors [136], SNARE proteins [119], receptor epidermal growth factor receptors [107], etc. [134, 140]. A variation of the ToxR system has been described where synthetic TMS peptides added to the culture medium inhibit homodimerization of endogenously expressed ToxR proteins by heterophilic association [231].

Apart from investigating defined TMS-TMS interactions, ToxR-based systems, i.e., TOXCAT [96, 102, 161] and POSSYCCAT [160], have been most useful for the construction and selection of self-assembling TMSs from combinatorial libraries, since the interacting proteins and the corresponding genetic information are part of one particle, the bacterial cell. In other words, the physical coupling of phenotype to genotype allows for selection of functional properties (see Section 26.2.4).

Disadvantages of these systems in their present form are that heterophilic interactions cannot be determined and that no information on the stoichiometries of the ToxR complexes can be obtained.

26.4.2.2 **Other Genetic Assays**

Another in vivo genetic assay system for detecting homophilic TMS-TMS interactions is based on the bacteriophage lambda cI repressor C-terminal dimerization domain. There, the native C-terminal dimerization domain of the lambda repressor is replaced by candidate TMSs. The ability of the TMSs to drive dimerization of the lambda repressor headpiece is tested by measuring the effectiveness of the hybrid proteins in preventing infection by a lambda phage missing its repressor [264]. This system has been used to identify new self-interacting TMSs in a library of natural membrane proteins from *E. coli* [276, 277].

In an attempt to make heterophilic TMS-TMS interactions accessible to investigation, a system, termed GALLEX, was recently developed wherein the TMSs are fused to two LexA DNA-binding domains with different DNA-binding specificities.

Heterodimeric association of the TMSs in *E. coli* inner membranes induces repression of a β-galactosidase reporter gene [265]. As discussed by these authors, the potential disadvantage of this system is that homophilic TMS-TMS interactions that exist in parallel may indirectly influence reporter gene expression, since the equilibria of homo- and heterophilic interactions in the membrane are coupled.

To assess homo- and heterophilic membrane protein interactions in yeast membranes, a modification of the split-ubiquitin system [266] was presented. There, two potential interaction partners *x* and *y* are genetically fused to an altered N-terminal half ($N_{ub}G$) or the C-terminal half (C_{ub}) of ubiquitin, respectively. In addition, an epitope-tagged reporter protein *R* is linked to the C-terminus of C_{ub}. Upon *xy* interaction, $N_{ub}G$ and C_{ub}-*R* re-associate and thus allow for proteolytic release of *R* by ubiquitin-specific proteases in the cell [266]. For membrane protein interactions, the reporter consists of an artificial transcription factor consisting of LexA and the herpes simplex VP16. Assembly of *x* and *y* then releases the transcription factor, thus inducing activation of a reporter gene [267]. Alternatively, the reporter consists of the yeast Ura3 protein that converts added 5-fluoroorotic acid to a toxic substrate, thus killing the cells. Once $N_{ub}G$ and C_{ub}-*ura3* re-associate due to *xy* interaction, Ura3 is proteolytically released and quickly degraded in the cell. Interaction of *x* and *y* thus prevents substrate conversion and allows for the cell's survival [268].

Other methods for membrane interactions have been described that depend on genetic assays or complementation of enzyme function [269].

26.4.3
Identification of TMS-TMS Interfaces by Mutational Analysis

In principle, any of the above methods can be used to assess the effect of individual point mutations on the degree of interaction. Thereby, the critical residues constituting TMS-TMS interfaces can be mapped. Point mutations have been introduced by random mutagenesis using degenerate codons [93] or by successive replacement of the residues in different types of scanning mutagenesis. Alanine-scanning mutagenesis is frequently used for this purpose [95, 117], as exchange of most residue types to alanine creates voids and/or replaces side chains involved in hydrogen bonding, etc., thus resulting in incremental reductions of protein-protein affinity. Alternatively, asparagine-scanning mutagenesis has been developed, which is based on the observation that asparagine residues located within TMSs drive their self-interaction by hydrogen bond formation in apolar environments such as a lipid membrane [140, 141]. Systematic replacement of TMS residues by asparagine therefore results in different enhancements of TMS-TMS affinity depending on whether the mutated position is closely juxtaposed to its counterpart within the helix-helix interface or not [274]. Covalent linkages between TMSs have been introduced upon systematically replacing the residues by cysteine. If oxidation of the cysteine leads to formation of a disulfide cross-link, the respective residue is regarded as interfacial [124, 270, 271].

References

1 White, S. H. & Wimley, W. C. (1999). Membrane protein folding and stability: physical principles. *Annu. Rev. Biophys. Biomol. Struct.* 28, 319–365.

2 Lemmon, M. A. & Engelman, D. M. (1994). Specificity and promiscuity in membrane helix interactions. *Q. Rev. Biophys.* 27, 157–218.

3 Haltia, T. & Freire, E. (1995). Forces and factors that contribute to the structural stability of membrane proteins. *Biochim. Biophys. Acta* 1228, 1–27.

4 Fleming, K. G. (2000). Riding the wave: structural and energetic principles of helical membrane proteins. *Curr. Opin. Biotechnol.* 11, 67–71.

5 Ubarretxena-Belandia, I. & Engelman, D. M. (2001). Helical membrane proteins: diversity of functions in the context of simple architecture. *Curr. Opin. Struct. Biol.* 11, 370–376.

6 Arkin, I. T. (2002). Structural aspects of oligomerization taking place between the transmembrane alpha-helices of bitopic membrane proteins. *Biochim. Biophys. Acta* 1565, 347–363.

7 Popot, J.-L. & Engelman, D. M. (2000). Helical membrane protein folding, stability and evolution. *Annu. Rev. Biochem.* 69, 881–922.

8 Langosch, D., Lindner, E. & Gurezka, R. (2002). In vitro selection of self-interacting transmembrane segments – membrane proteins approached from a different perspective. *IUBMB Life* 54, 1–5.

9 Helms, V. (2002). Attraction within the membrane – Forces behind transmembrane protein folding and supramolecular complex assembly. *EMBO Rep.* 3(12), 1133–1138.

10 DeGrado, W. F., Gratkowski, H. & Lear, J. D. (2003). How do helix-helix interactions help determine the folds of membrane proteins? Perspectives from the study of homo-oligomeric helical bundles. *Prot. Sci.* 12(4), 647–65.

11 Chamberlain, A. K., Faham, S., Yohannan, S. & Bowie, J. U. (2003). Construction of helix-bundle membrane proteins. *Adv. Protein Chem.* 63, 19–46.

12 Shai, Y. (2001). Molecular recognition within the membrane milieu: Implications for the structure and function of membrane proteins. *J. Membr. Biol.* 182(2), 91–104.

13 Koebnik, R. (1999). Membrane assembly of the Escherichia coli outer membrane protein OmpA: exploring sequence constraints on transmembrane β-strands. *J. Mol. Biol.* 285, 1805–1810.

14 Koebnik, R. (1996). In vivo membrane assembly of split variants of the E. coli outer membrane protein OmpA. *EMBO J.* 15, 3529–3537.

15 Thompson, S. J., Kim, S. J. & Robinson, C. (1998). Sec-independent insertion of thylakoid membrane proteins – Analysis of insertion forces and identification of a loop intermediate involving the signal peptide. *J. Biol. Chem.* 273(30), 18979–18983.

16 Thompson, S. J., Robinson, C. & Mant, A. (1999). Dual signal peptides mediate the signal recognition particle Sec-independent insertion of a thylakoid membrane polyprotein, psbY. *J. Biol. Chem.* 274(7), 4059–4066.

17 Mant, A., Woolhead, C. A., Moore, M., Henry, R. & Robinson, C. (2001). Insertion of PsaK into the thylakoid membrane in a 'horse-shoe' conformation occurs in the absence of signal recognition particle, nucleoside triphosphates, or functional Albino3. *J. Biol. Chem.* 276(39), 36200–36206.

18 Ridder, A., Morein, S., Stam, J. G., Kuhn, A., de Kruijff, B. & Killian, J. A. (2000). Analysis of the role of interfacial tryptophan residues in controlling the topology of membrane proteins. *Biochemistry* 39(21), 6521–6528.

19 Muller, M., Koch, H. G., Beck, K. &

Schaefer, U. (2001). Protein traffic in bacteria: Multiple routes from the ribosome to and across the membrane. *Prog. Nucl. Acid Res. Mol. Biol.* 66(107), 107–157.

20 Chin, C. N., von Heijne, G. & de Gier, J. W. L. (2002). Membrane proteins: shaping up. *Trends Biochem. Sci.* 27(5), 231–234.

21 Ott, C. M. & Lingappa, V. R. (2002). Integral membrane protein biosynthesis: why topology is hard to predict. *J. Cell Sci.* 115(10), 2003–2009.

22 Drew, D., Froderberg, L., Baars, L. & de Gier, J. W. L. (2003). Assembly and overexpression of membrane proteins in Escherichia coli. *Biochim. Biophys. Acta* 1610(1), 3–10.

23 Popot, J.-L. & Engelman, D. M. (1990). Membrane Protein Folding and Oligomerization: the two-stage model. *Biochemistry* 29, 4031–4037.

24 Popot, J. L., Trewhella, J. & Engelman, D. M. (1986). Reformation of crystalline purple membrane from purified bacteriorhodopsin fragments. *Embo* 5, 3039–3044.

25 Ozawa, S., Hayashi, R., Masuda, A., Iio, T. & Takahashi, S. (1997). Reconstitution of bacteriorhodopsin from a mixture of a proteinase V_8 fragment and two synthetic peptides. *Biochim. Biophys. Acta* 1323, 145–153.

26 Marti, T. (1998). Refolding of bacteriorhodopsin from expressed polypeptide fragments. *J. Biol. Chem.* 273, 9312–9322.

27 Arkin, I. T. & Brünger, A. T. (1998). Statistical analysis of predicted transmembrane alpha-helices. *Biochim. Biophys. Acta* 1429, 113–128.

28 Senes, A., Gerstein, M. & Engelman, D. M. (2000). Statistical analysis of amino acid patterns in transmembrane helices: the GxxxG motif occurs frequently and in association with β-branched residues at neighboring positions. *J. Mol. Biol.* 296, 921–936.

29 Schneider, D., Liu, Y., Gerstein, M. & Engelman, D. M. (2002). Thermostability of membrane protein helix-helix interaction elucidated by statistical analysis. *FEBS Lett.* 532(1–2), 231–236.

30 von Heijne, G. (1986). The distribution of positively charged residues in bacterial inner membrane proteins correlates with the *trans*-membrane topology. *EMBO J.* 5, 3021–3027.

31 Landolt-Marticorena, C., Williams, K. A., Deber, C. M. & Reithmeier, R. A. F. (1993). Non-random distribution of amino acids in the transmembrane segments of human type I single span membrane proteins. *J. Mol. Biol.* 229, 602–608.

32 Jones, D. T., Taylor, W. R. & Thornton, J. M. (1994). A mutation data matrix for transmembrane proteins. *FEBS Lett.* 339(3), 269–275.

33 Jones, D. T., Taylor, W. R. & Thornton, J. M. (1994). A model recognition approach to the prediction of all-helical membrane protein structure and topology. *Biochemistry* 33(10), 3038–3049.

34 Stevens, T. J. & Arkin, I. T. (2000). The effect of nucleotide bias upon the composition and prediction of transmembrane helices. *Prot. Sci.* 9, 505–511.

35 von Heijne, G. (1989). Control of topology and mode of assembly of a polytopic membrane protein by positively charged residues. *Nature* 341(6241), 456–458.

36 Wallin, E., Tsukihara, T., Yoshikawa, S., von Heijne, G. & Elofsson, A. (1997). Architecture of helix bundle membrane proteins: an analysis of cytochrome c oxidase from bovine mitochondria. *Prot. Sci.* 6, 808–815.

37 Wimley, W. C. & White, S. H. (1996). Experimentally determined hydrophobicity scale for proteins at membrane interfaces. *Nat. Struct. Biol.* 3(10), 842–848.

38 Yau, W. M., Wimley, W. C., Gawrisch, K. & White, S. H. (1998). The preference of tryptophan for membrane interfaces. *Biochemistry* 37(42), 14713–14718.

39 Persson, S., Killian, J. A. & Lindblom, G. (1998). Molecular ordering of interfacially localized

tryptophan analogs in ester- and ether-lipid bilayers studied by 2H-NMR. *Biophys. J.* 75(3), 1365–1371.

40 Killian, J. A. & von Heijne, G. (2000). How proteins adapt to a membrane-water interface. *Trends Biochem. Sci.* 25, 429–434.

41 Mall, S., Broadbridge, R., Sharma, R. P., Lee, A. G. & East, J. M. (2000). Effects of aromatic residues at the ends of transmembrane alpha-helices on helix interactions with lipid bilayers. *Biochemistry* 39(8), 2071–2078.

42 de Planque, M. R., Bonev, B. B., Demmers, J. A., Greathouse, D. V., Koeppe, R. E., 2nd, Separovic, F., Watts, A. & Killian, J. A. (2003). Interfacial anchor properties of tryptophan residues in transmembrane peptides can dominate over hydrophobic matching effects in peptide-lipid interactions. *Biochemistry* 42(18), 5341–5348.

43 Kyte, J. & Doolittle, R. F. (1982). A simple method for displaying the hydropathic character of a protein. *J. Mol. Biol* 157, 105–132.

44 Engelman, D. M., Steitz, T. A. & Goldman, A. (1986). Identifying nonpolar transbilayer helices in amino acid sequences of membrane proteins. *Annu. Rev. Biophys. Biophys. Chem.* 15, 321–353.

45 Cserzo, M., Wallin, E., Simon, I., von Heijne, G. & Elofsson, A. (1997). Prediction of transmembrane alpha-helices in prokaryotic membrane proteins: the dense alignment surface method. *Protein Eng.* 10(6), 673–676.

46 Pasquier, C., Promponas, V. J., Palaios, G. A., Hamodrakas, J. S. & Hamodrakas, S. J. (1999). A novel method for predicting transmembrane segments in proteins based on a statistical analysis of the SwissProt database: the PRED-TMR algorithm. *Protein Eng.* 12(5), 381–385.

47 Rost, B., Casadio, R., Fariselli, P. & Sander, C. (1995). Prediction of helical transmembrane segments at 95% accuracy. *Prot. Sci.* 4, 521–533.

48 Chen, C. P., Kernytsky, A. & Rost, B. (2002). Transmembrane helix predictions revisited. *Protein Sci.* 11(12), 2774–2791.

49 von Heijne, G. (1992). Membrane protein structure prediction. Hydrophobicity analysis and the positive-inside rule. *J. Mol. Biol.* 225, 487–494.

50 Persson, B. & Argos, P. (1996). Topology prediction of membrane proteins. *Protein Sci.* 5(2), 363–371.

51 Persson, B. & Argos, P. (1997). Prediction Of Membrane Protein Topology Utilizing Multiple Sequence Alignments. *Journal Of Protein Chemistry* 16(5), 453–457.

52 Creighton, T. E. (1993). *Proteins: Structures and Molecular Properties*, Freeman, New York.

53 Padmanabhan, S., Marqusee, S., Ridgeway, T., Laue, T. M. & Baldwin, R. L. (1990). Relative helix-forming tendencies of nonpolar amino acids. *Nature* 344, 268–270.

54 O'Neil, K. T. & DeGrado, W. F. (1990). A thermodynamic scale for the helix-forming tendencies of the commonly occuring amino acids. *Science* 250, 646–651.

55 Blaber, M., Zhang, X. & Matthews, B. W. (1993). Structural basis for amino acid alpha helix propensity. *Science* 260, 1637–1640.

56 Smith, C. K., Withka, J. M. & Regan, L. (1994). A thermodynamic scale for the β-sheet forming tendencies of the amino acids. *Biochemistry* 33, 5510–5517.

57 Street, A. G. & Mayo, S. L. (1999). Intrinsic β-sheet propensities result from van der Waals interactions between side chains and the local backbone. *Proc. Natl. Acad. Sci. USA* 96, 9074–9076.

58 Li, S. C. & Deber, C. M. (1992). Glycine and beta-branched residues support and modulate peptide helicity in membrane environments. *FEBS Lett.* 311, 217–220.

59 Li, S. C. & Deber, C. M. (1994). A measure of helical propensity for amino acids in membrane environments. *Nature Struct. Biol.* 1, 368–373.

60 Liu, L.-P. & Deber, C. M. (1998). Uncoupling hydrophobicity and helicity in transmembrane segments. *J. Biol. Chem.* 273, 23645–23648.

61 Deber, C. M., Li, Z. M., Joensson, C., Glibowicka, M. & Xu, G. Y. (1992). Transmembrane Region of Wild-Type and Mutant M13 Coat Proteins – Conformational Role of Beta-Branched Residues. *J. Biol. Chem.* 267(8), 5296–5300.

62 Johansson, J., Szyperski, T., Curstedt, T. & Wüthrich, K. (1994). The NMR structure of pulmonary surfactant-associated polypeptide SP-C in a apolar solvent contains a valyl-rich α-helix. *Biochemistry* 33, 6015.

63 Cordes, F. S., Bright, J. N. & Sansom, M. S. P. (2002). Proline-induced Distortions of Transmembrane Helices. *J. Mol. Biol.* 323, 951–960.

64 Chakrabarti, P. & Chakrabarti, S. (1998). C–H–O hydrogen bond involving proline residues in alpha-helices. *J. Mol. Biol.* 284(4), 867–873.

65 von Heijne, G. (1991). Proline kinks in transmembrane alpha-helices. *J. Mol. Biol.* 218, 499–503.

66 Javadpour, M. M., Eilers, M., Groesbeek, M. & Smith, S. O. (1999). Helix packing in polytopic membrane proteins: Role of glycine in transmembrane helix association. *Biophys. J.* 77(3), 1609–1618.

67 Daniel, J. M., Friess, S. D., Rajagopalan, S., Wendt, S. & Zenobi, R. (2002). Quantitative determination of noncovalent binding interactions using soft ionization mass spectrometry. *Int. J. Mass. Spec.* 216, 1–27.

68 Israelachvili, J. N. (1991). *Intermolecular and surface forces*, Academic Press, London.

69 Smith, S. O., Smith, C. S. & Bormann, B. J. (1996). Strong hydrogen bonding interactions involving a buried glutamic acid in the transmembrane sequence of the neu/erbB-2 receptor. *Nature Structural Biology* 3, 252–258.

70 Subczynski, W. K., Wisniewska, A., Yin, J.-J., Hyde, J. S. & Kusumi, A. (1994). Hydrophobic Barriers of Lipid Bilayer Membranes Formed by Reduction of Water Penetration by Alkyl Chain Unsaturation and Cholesterol. *Biochemistry* 33, 7670–7681.

71 White, S. H., King, G. I. & Cain, J. E. (1981). Location of hexane in lipid bilayers determined by neutron diffraction. *Nature* 290, 161–163.

72 Grasberger, B., Minton, A. P., DeLisi, C. & Metzger, H. (1986). Interaction between proteins localized in membranes. *Proc. Natl. Acad. Sci. USA* 83, 6258–6262.

73 Klibanov, A. M. (2001). Improving enzymes by using them in organic solvents. *Nature* 409, 241–246.

74 Bowie, J. U. (1997). Helix packing in membrane proteins. *J. Mol. Biol.* 272, 780–789.

75 Eilers, M., Shekar, S. C., Shieh, T., Smith, S. O. & Fleming, P. J. (2000). Internal packing of helical membrane proteins. *Proc. Natl. Acad. Sci.* 97, 5796–5801.

76 Senes, A., Ubarretxena-Belandia, I. & Engelman, D. M. (2001). The Ca–H···O hydrogen bond: A determinant of stability and specifity in transmembrane helix interactions. *Proc. Natl. Acad. Sci.* 98, 9056–9061.

77 Eilers, M., Patel, A. B., Liu, W. & Smith, S. O. (2002). Comparison of helix interactions in membrane and soluble alpha-bundle proteins. *Biophys. J.* 82(5), 2720–2736.

78 Ben-Tal, N. & Honig, B. (1996). Helix-helix interactions in lipid bilayers. *Biophys. J.* 71(6), 3046–3050.

79 Chothia, C., Levitt, M. & Richardson, D. (1981). Helix to helix packing in proteins. *J. Mol. Biol.* 145, 215–250.

80 Langosch, D. & Heringa, J. (1998). Interaction of transmembrane helices by a knobs-into-holes geometry characteristic of soluble coiled coils. *Proteins Struct. Funct. Genet.* 31, 150–160.

81 Stevens, T. J. & Arkin, I. T. (2001). Substitution rates in alpha-helical transmembrane proteins. *Protein Science* 10(12), 2507–2517.

82 Liu, Y., Engelman, D. M. &

Gerstein, M. (2002). Genomic analysis of membrane protein families: abundance and conserved motifs. *Genome Biol.* 3(10), RESEARCH0054.1–0054.12.

83 Pilpel, Y., Ben-Tal, N. & Lancet, D. (1999). kPROT: a knowledge-based scale for the propensity of residue orientation in transmembrane segments. Application to membrane protein structure prediction. *J. Mol. Biol.* 294, 921–935.

84 Adamian, L. & Liang, J. (2001). Helix-Helix Packing and Interfacial Pairwise Interactions of Residues in Membrane Proteins. *J. Mol. Biol.* 311, 891–907.

85 Wigley, W. C., Corboy, M. J., Cutler, T. D., Thibodeau, P. H., Oldan, J., Lee, M. G., Rizo, J., Hunt, J. F. & Thomas, P. J. (2002). A protein sequence that can encode native structure by disfavoring alternate conformations. *Nat. Struct. Biol.* 9(5), 381–388.

86 Lear, J. D., Gratkowski, H., Adamian, L., Liang, J. & DeGrado, W. F. (2003). Position-dependence of stabilizing polar interactions of asparagine in transmembrane helical bundles. *Biochemistry* 42(21), 6400–6407.

87 Samatey, F. A., Xu, C. & Popot, J.-L. (1995). On the distribution of amino acid residues in transmembrane α-helix bundles. *Proc. Natl. Acad. Sci.* 92, 4577–4581.

88 Adamian, L. & Liang, J. (2002). Interhelical hydrogen bonds and spatial motifs in membrane proteins: polar clamps and serine zippers. *Proteins-Structure Function and Genetics* 47, 209–218.

89 Adamian, L., Jackups, R., Jr., Binkowski, T. A. & Liang, J. (2003). Higher-order interhelical spatial interactions in membrane proteins. *J. Mol. Biol.* 327(1), 251–272.

90 MacKenzie, K. R., Prestegard, J. H. & Engelman, D. M. (1997). A transmembrane helix dimer: structure and implications. *Science* 276, 131–133.

91 Smith, S. O., Song, D., Shekar, S., Groesbeek, M., Ziliox, M. & Aimoto, S. (2001). Structure of the Transmembrane Dimer Interface of Glycophorin A in Membrane Bilayers. *Biochemistry* 40(22), 6553–6558.

92 Lemmon, M. A., Flanagan, J. M., Hunt, J. F., Adair, B. D., Bormann, B.-J., Dempsey, C. E. & Engelman, D. M. (1992). Glycophorin A dimerization is driven by specific interactions between transmembrane alpha-helices. *J. Biol. Chem.* 267, 7683–7689.

93 Lemmon, M. A., Flanagan, J. M., Treutlein, H. R., Zhang, J. & Engelman, D. M. (1992). Sequence specificity in the dimerization of transmembrane alpha-helices. *Biochemistry* 31, 12719–12725.

94 Lemmon, M. A., Treutlein, H. R., Adams, P. D., Brünger, A. T. & Engelman, D. (1994). A dimerization motif for transmembrane alpha-helices. *Nature Struct. Biol.* 1, 157–163.

95 Langosch, D. L., Brosig, B., Kolmar, H. & Fritz, H.-J. (1996). Dimerisation of the glycophorin A transmembrane segment in membranes probed with the ToxR transcription activator. *J. Mol. Biol.* 263, 525–530.

96 Russ, W. P. & Engelman, D. M. (1999). TOXCAT: A measure of transmembrane helix association in a biological membrane. *Proc. Natl. Acad. Sci. USA* 96, 863–868.

97 Fisher, L. E., Engelman, D. M. & Sturgis, J. N. (1999). Detergents modulate dimerization but not helicity, of the glycophorin A transmembrane domain. *J. Mol. Biol.* 293(3), 639–651.

98 Treutlein, H. R., Lemmon, M. A., Engelman, D. M. & Brünger, A. T. (1992). The glycophorin A transmembrane domain dimer: sequence-specific propensity for a right-handed supercoil of helices. *Biochemistry* 31, 12726–12733.

99 Adams, P. D., Engelman, D. M. & Brünger, A. T. (1996). Improved prediction for the structure of the dimeric transmembrane domain of glycophorin A obtained through global searching. *Proteins* 26, 257–261.

100 Fleming, K. G., Ackerman, A. L. & Engelman, D. M. (1997). The Effect Of Point Mutations On the Free Energy Of Transmembrane Alpha Helix Dimerization. *J. Mol. Biol.* 272, 266–275.

101 Fleming, K. G. & Engelman, D. M. (2001). Specificity in transmembrane helix-helix interactions can define a hierarchy of stability for sequence variants. *Proceedings of the National Academy of Sciences of the United States of America* 98(25), 14340–14344.

102 Russ, W. P. & Engelman, D. M. (2000). The GxxxG motif: a framework for transmembrane helix-helix association. *J. Mol. Biol.* 296, 911–919.

103 Brosig, B. & Langosch, D. (1998). The dimerization motif of the glycophorin A transmembrane segment in membranes: importance of glycine residues. *Protein Sci.* 7, 1052–1056.

104 Mingarro, I., Whitley, P., Lemmon, M. A. & von Heijne, G. (1996). Ala-insertion scanning mutagenesis of the glycophorin A transmembrane helix: a rapid way to map helix-helix interactions in integral membrane proteins. *Protein Sci.* 5, 1339–1341.

105 Williams, K. A., Glibowicka, M., Li, Z., Li, H., Khan, A. R., Chen, Y. M. Y., Wang, J., Marvin, D. A. & Deber, C. M. (1995). Packing of coat protein amphipathic and transmembrane helices in filamentous bacteriophage M13: role of small residues in protein oligomerization. *J. Mol. Biol.* 252, 6–14.

106 Asundi, V. K. & Carey, D. J. (1995). Self-association of N-syndecan (syndecan-3) core protein is mediated by a novel structural motif in the transmembrane domain and ecto-domain flanking region. *J. Biol. Chem.* 270, 26404–26410.

107 Mendrola, J. M., Berger, M. B., King, M. C. & Lemmon, M. A. (2002). The single transmembrane domains of ErbB receptors self-associate in cell membranes. *J. Biol. Chem.* 277(7), 4704–4712.

108 Kleiger, G., Grothe, R., Mallick, P. & Eisenberg, D. (2002). GXXXG and AXXXA: Common alpha-helical interaction motifs in proteins, particularly in extremophiles. *Biochemistry* 41(19), 5990–5997.

109 Orzaez, M., Perez-Paya, E. & Mingarro, I. (2000). Influence of the C-terminus of the glycophorin A transmembrane fragment on the dimerization process. *Prot. Sci.* 9, 1246–1253.

110 Jahn, R., Lang, T. & Südhof, T. C. (2003). Membrane Fusion. *Cell* 112, 519–533.

111 Söllner, T., Bennett, M. K., Whiteheard, S. W., Scheller, R. H. & Rothman, J. E. (1993). A protein assembly-disassembly pathway in vitro that may correspond to sequential steps of synaptic vesicle docking, activation, and fusion. *Cell* 75, 409–418.

112 Sutton, R. B., Fasshauer, D., Jahn, R. & Brünger, A. T. (1998). Crystal structure of a SNARE complex involved in synaptic exocytosis at 2.4 A resolution. *Nature* 395, 347–353.

113 Calakos, N. & Scheller, R. H. (1994). Vesicle-associated membrane protein and synaptophysin are associated on the synaptic vesicle. *J. Biol. Chem.* 269, 24534–24537.

114 Washbourne, P., Schiavo, G. & Montecucco, C. (1995). Vesicle-associated membrane protein-2 (synaptobrevin-2) forms a complex with synaptophysin. *Biochem. J.* 305, 721–724.

115 Edelman, L., Hanson, P. I., Chapman, E. R. & Jahn, R. (1995). Synaptobrevin binding to synaptophysin: a potential mechanism for controlling the exocytotic fusion machine. *EMBO J.* 14, 224–231.

116 Pennuto, M., Dunlap, D., Contestabile, A., F., B. & Valtorta, F. (2002). Fluorescence Resonance Energy Transfer Detection of Synaptophysin I and Vesicle-associated Membrane Protein 2 Interactions during Exocytosis from Single Live Synapses. *Mol. Biol. Cell* 13, 2706–2717.

117 Laage, R. & Langosch, D. (1997). Dimerization of the synaptic vesicle

protein synaptobrevin/VAMP II depends on specific residues within the transmembrane segment. *Eur. J. Biochem.* 249, 540–546.

118 Margittai, M., Otto, H. & Jahn, R. (1999). A stable interaction between syntaxin 1a and synaptobrevin 2 mediated by their transmembrane domains. *FEBS Lett.* 446, 40–44.

119 Laage, R., Rohde, J., Brosig, B. & Langosch, D. (2000). A conserved membrane-spanning amino acid motif drives homomeric and supports heteromeric assembly of presynaptic SNARE proteins. *J. Biol. Chem.* 275, 17481–17487.

120 Fleming, K. G. & Engelman, D. M. (2001). Computation and mutagenesis suggest a right-handed structure for the synaptobrevin transmembrane dimer. *Proteins* 45(4), 313–317.

121 Poirier, M. A., Hao, J. C., Malkus, P. N., Chan, C., Moore, M. F., King, D. S. & Bennett, M. K. (1998). Protease resistance of syntaxin – SNAP-25 – VAMP complexes – Implications for assembly and structure. *J. Biol. Chem.* 273, 11370–11377.

122 Holsinger, L. J., Nichani, D., Pinto, L. H. & Lamb, R. A. (1994). Influenza – a Virus M(2) Ion-Channel Protein – a Structure-Function Analysis. *J. Virol.* 68(3), 1551–1563.

123 Pinto, L. H., Dieckmann, G. R., Gandhi, C. S., Papworth, C. G., Braman, J., Shaugnessy, M. A., Lear, J. D., Lamb, R. A. & DeGrado, W. F. (1997). A functionally defined model for the M2 proton channel of influenza A virus suggests a mechanism for its ion selectivity. *Proc. Natl. Acad. Sci. USA* 94, 11301–11306.

124 Bauer, C. M., Pinto, L. H., Cross, T. A. & Lamb, R. A. (1999). The Influenza Virus M2 Ion Channel Protein: Probing the Structure of the Transmembrane Domain in Intact Cells by Using Engineered Disulfide Cross-Linking. *Virology* 254, 196–209.

125 Dieckmann, G. R. & DeGrado, W. F. (1997). Modeling transmembrane helical oligomers. *Curr. Opin. Struct. Biol.* 7, 486–494.

126 Arkin, I. T., Adams, P. D., Brünger, A. T., Smith, S. & Engelman, D. M. (1997). Structural perspectives of phospolamban, a helical transmembrane pentamer. *Annu. Rev. Biophys. Biomol. Struct.* 26, 157–179.

127 Arkin, I. T., Adams, P. D., MacKenzie, K. R., Lemmon, M. A., Brünger, A. T. & Engelman, D. M. (1994). Structural organization of the pentameric transmembrane alpha-helices of phospholamban, a cardiac ion channel. *EMBO J.* 13, 4757–4764.

128 Simmerman, H. K. B., Kobayashi, Y. M., Autry, J. M. & Jones, L. R. (1996). A leucine zipper stabilizes the pentameric membrane domain of phospholamban and forms a coiled-coil pore structure. *J. Biol. Chem.* 271, 5941–5946.

129 Arkin, I. T., Rothman, M., Ludlam, C. F. C., Aimoto, S., Engelman, D., Rothschild, K. J. & Smith, S. O. (1995). Structural Model of the phospholamban ion channel complex in phospholipid membranes. *J. Mol. Biol.* 248, 824–834.

130 Karim, C. B., Stamm, J. D., Karim, J., Jones, L. R. & Thomas, D. D. (1998). Cysteine reactivity and oligomeric structures of phospholamban and its mutants. *Biochemistry* 37(35), 12074–12081.

131 Torres, J., Kukol, A. & Arkin, I. T. (2001). Mapping the energy surface of transmembrane helix-helix interactions. *Biophysical Journal* 81(5), 2681–2692.

132 Livnah, O., Stura, E. A., Middleton, S. A., Johnson, D. L., Jolliffe, L. K. & Wilson, I. A. (1999). Crystallographic evidence for preformed dimers of eryhtropoietin receptor before ligand activation. *Science* 283, 987–990.

133 Remy, I., Wilson, I. A. & Michnick, S. W. (1999). Erythropoietin receptor activation by a ligand-induced conformation change. *Science* 283, 990–993.

134 Gurezka, R., Laage, R., Brosig, B. & Langosch, D. (1999). A Heptad Motif of Leucine Residues Found in Membrane Proteins Can Drive Self-

Assembly of Artificial Transmembrane Segments. *J. Biol. Chem.* 274, 9265–9270.

135 Constantinescu, S. N., Keren, T., Socolovsky, M., Nam, H. S., Henis, Y. I. & Lodish, H. F. (2001). Ligand-independent oligomerization of cell-surface erythropoietin receptor is mediated by the transmembrane domain. *Proc. Natl. Acad. Sci. U.S.A.* 98, 4379–4384.

136 Kubatzky, K. F., Ruan, W., Gurezka, R., Cohen, J., Ketteler, R., Watowich, S. S., Neumann, D., Langosch, D. & Klingmüller, U. (2001). Self-assembly of the transmembrane domain is a crucial mediator for signalling through the erythropoietin receptor. *Current Biology* 11, 110–115.

137 Constantinescu, S. N., Liu, X., Beyer, W., Fallon, A., Shekar, S., Henis, Y. I., Smith, S. O. & Lodish, J. F. (1999). Activation of the erythropoietin receptor by the gp55-P viral envelope protein is determined by a single amino acid in its transmembrane domain. *EMBO J.* 18, 3334–3347.

138 Shapiro, L. & Colman, D. R. (1998). Structural biology of cadherins in the nervous system. *Curr. Opin. Neurobiol.* 8, 593–599.

139 Huber, O., Kemmler, R. & Langosch, D. (1999). Mutations affecting transmembrane segment interaction impair adhesiveness of E-cadherin. *J. Cell Sci.* 112, 4415–4423.

140 Zhou, F. X., Cocco, M. J., Russ, W. P., Brunger, A. T. & Engelman, D. M. (2000). Interhelical hydrogen bonding drives strong interactions in membrane proteins. *Nature Struct. Biol.* 7, 154–160.

141 Choma, C., Gratkowski, H., Lear, J. D. & DeGrado, W. F. (2000). Asparagine-mediated self-association of a model transmembrane helix. *Nature Struct. Biol.* 7, 161–166.

142 O'Shea, E. K., Klemm, J. D., Kim, P. S. & Alber, T. (1991). X-ray structure of the GCN4 leucine zipper, a two-stranded, parallel coiled coil. *Science* 243, 539–544.

143 Alber, T. (1992). Structure of the leucine zipper. *Corr. Op. Genet. and Developm.* 2, 205–210.

144 Harbury, P. B., Zhang, T., Kim, P. S. & Alber, T. (1993). A switch between two-, three-, and four-stranded coiled coils in GCN4 leucine zipper mutants. *Science* 262, 1401–1406.

145 Gonzalez, L., Plecs, J. J. & Alber, T. (1996). An engineered allosteric switch in leucine-zipper oligomerization. *Nature Struct. Biol.* 3, 510–515.

146 Harbury, P. B., Kim, P. S. & Alber, T. (1994). Crystal structure of an isoleucine-zipper trimer. *Nature* 371, 80–83.

147 Gratkowski, H., Lear, J. D. & DeGrado, W. F. (2001). Polar side chains drive the association of model transmembrane peptides. *Proc. Natl. Acad. Sci. USA* 98, 880–885.

148 Zhou, F. X., Merianos, H. J., Brünger, A. T. & Engelman, D. M. (2001). Polar residues drive association of polyleucine transmembrane helices. *Proc. Natl. Acad. Sci. USA.*

149 Weiner, D. B., Liu, J., Cohen, J. A., Williams, W. V. & Greene, M. I. (1989). A point mutation in the neu oncogene mimics ligand induction of receptor aggregation. *Nature* 339, 230–231.

150 Webster, M. & Donoghue, J. (1996). Constitutive activation of fibroblast growth factor receptor 3 by the transmembrane domain point mutation found in achondroplasia. *EMBO J.* 15, 520–527.

151 Onishi, M., Mui, A. L. F., Morikawa, Y., Cho, L., Kinoshita, S., Nolan, G. P., Gorman, D. M., Miyajima, A. & Kitamura, T. (1996). Identification of an oncogenic form of the thrombopoietin receptor MPL using retrovirus-mediated gene transfer. *Blood* 88(4), 1399–1406.

152 Forbes, L. V., Gale, R. E., Pizzey, A., Pouwels, K., Nathwani, A. & Linch, D. C. (2002). An activating mutation in the transmembrane domain of the granulocyte colony-stimulating factor receptor in patients with acute myeloid leukemia. *Oncogene* 21(39), 5981–5989.

153 Call, M. E., Pyrdol, J., Wiedmann, M. & Wucherpfennig, K. W. (2002). The Organizing Principle in the Formation of the T Cell Receptor-CD3 Complex. *Cell* 111, 967–979.

154 Alcover, A., Mariuzza, R. A., Ermonval, M. & Acuto, O. (1990). Lysine 271 in the Transmembrane Domain of the T-Cell Antigen Receptor Beta-Chain Is Necessary for Its Assembly with the Cd3 Complex but Not for Alpha Beta-Dimerization. *J. Biol. Chem.* 265(7), 4131–4135.

155 Blumberg, R. S., Alarcon, B., Sancho, J., McDermott, F. V., Lopez, P., Breitmeyer, J. & Terhorst, C. (1990). Assembly and Function of the T-Cell Antigen Receptor – Requirement of Either the Lysine or Arginine Residues in the Transmembrane Region of the Alpha-Chain. *J. Biol. Chem.* 265(23), 14036–14043.

156 Cosson, P., Lankford, S., Bonifacino, J. S. & Klausner, R. D. (1991). Membrane protein association by potential intramembrane charge pairs. *Nature* 351, 414–416.

157 Bonifacino, J. S., Suzuki, C. K. & Klausner, R. D. (1990). A peptide sequence confers retention and rapid degradation in the endoplasmic reticulum. *Science* 247, 79–82.

158 Heinrich, S. U., Mothes, W., Brunner, J. & Rapoport, T. A. (2000). The Sec61p complex mediates the integration of a membrane protein by allowing lipid partitioning of the transmembrane domain. *Cell* 102(2), 233–244.

159 Shigematsu, D., Matsutani, M., Furuya, T., Kiyota, T., Lee, S., Sugihara, G. & Yamashita, S. (2002). Roles of peptide-peptide charge interaction and lipid phase separation in helix-helix association in lipid bilayer. *Biochim. Biophys. Acta* 1564, 271–280.

160 Gurezka, R. & Langosch, D. (2001). In vitro selection of membrane-spanning leucine zipper protein-protein interaction motifs using POSSYCCAT. *J. Biol. Chem.* 276, 45580–45587.

161 Dawson, J. P., Weinger, J. S. & Engelman, D. M. (2002). Motifs of serine and threonine can drive association of transmembrane helices. *J. Mol. Biol.* 316(3), 799–805.

162 Pebay-Peyroula, E. & Rosenbusch, J. P. (2001). High-resolution structures and dynamics of membrane protein–lipid complexes: a critique. *Curr. Opin. Struct. Biol.* 11(4), 427–432.

163 Fyfe, P. K., McAuley, K. E., Roszak, A. W., Isaacs, N. W., Cogdell, R. J. & Jones, M. R. (2001). Probing the interface between membrane proteins and membrane lipids by X-ray crystallography. *Trends Biochem. Sci.* 26(2), 106–112.

164 Lee, A. G. (2003). Lipid-protein interactions in biological membranes: a structural perspective. *Biochim. Biophys. Acta* 1612(1), 1–40.

165 Essen, L., Siegert, R., Lehmann, W. D. & Oesterhelt, D. (1998). Lipid patches in membrane protein oligomers: crystal structure of the bacteriorhodopsin-lipid complex. *Proc. Natl. Acad. Sci. USA* 95(20), 11673–11678.

166 Cartailler, J. P. & Luecke, H. (2003). X-ray crystallographic analysis of lipid-protein interactions in the bacteriorhodopsin purple membrane. *Annu. Rev. Biophys. Biomol. Struct.* 32, 285–310.

167 Sedlak, E. & Robinson, N. C. (1999). Phospholipase A(2) digestion of cardiolipin bound to bovine cytochrome c oxidase alters both activity and quaternary structure. *Biochemistry* 38(45), 14966–14972.

168 Lange, C., Nett, J. H., Trumpower, B. L. & Hunte, C. (2001). Specific roles of protein-phospholipid interactions in the yeast cytochrome bc(1) complex structure. *EMBO J.* 20(23), 6591–6600.

169 Camara-Artigas, A., Brune, D. & Allen, J. P. (2002). Interactions between lipids and bacterial reaction centers determined by protein crystallography. *Proc. Natl. Acad. Sci. USA* 99(17), 11055–11060.

170 Jormakka, M., Tornroth, S., Byrne, B. & Iwata, S. (2002). Molecular basis

of proton motive force generation: structure of formate dehydrogenase-N. *Science* 295(5561), 1863–1868.

171 Petrache, H. I., Grossfield, A., MacKenzie, K. R., Engelman, D. M. & Woolf, T. B. (2000). Modulation of glycophorin A transmembrane helix interactions by lipid bilayers: molecular dynamics calculations. *J. Mol. Biol.* 302(3), 727–746.

172 Mall, S., Broadbridge, R., Sharma, R. P., East, J. M. & Lee, A. G. (2001). Self-association of model transmembrane alpha-helices is modulated by lipid structure. *Biochemistry* 40(41), 12379–12386.

173 Gil, T., Ipsen, J. H., Mouritsen, O. G., Sabra, M. C., Sperotto, M. M. & Zuckermann, M. J. (1998). Theoretical analysis of protein organization in lipid membranes. *Biochim. Biophys. Acta* 1376(3), 245–266.

174 Cantor, R. S. (1999). Lipid composition and the lateral pressure profile in bilayers. *Biophys. J.* 76(5), 2625–2639.

175 Cantor, R. S. (2002). Size distribution of barrel-stave aggregates of membrane peptides: influence of the bilayer lateral pressure profile. *Biophys. J.* 82(5), 2520–2525.

176 Killian, J. A. (1998). Hydrophobic mismatch between proteins and lipids in membranes. *Biochim. Biophys. Acta* 1376(3), 401–415.

177 Dumas, F., Lebrun, M. C. & Tocanne, J. F. (1999). Is the protein/lipid hydrophobic matching principle relevant to membrane organization and functions? *FEBS Lett.* 458(3), 271–277.

178 Lewis, B. A. & Engelman, D. M. (1983). Bacteriorhodopsin remains dispersed in fluid phospholipid bilayers over a wide range of bilayer thicknesses. *J. Mol. Biol.* 166(2), 203–210.

179 Ren, J., Lew, S., Wang, J. & London, E. (1999). Control of the transmembrane orientation and interhelical interactions within membranes by hydrophobic helix length. *Biochemistry* 38, 5905–5912.

180 Dencher, N. A., Kohl, K. D. & Heyn, M. P. (1983). Photochemical cycle and light-dark adaptation of monomeric and aggregated bacteriorhodopsin in various lipid environments. *Biochemistry* 22(6), 1323–1334.

181 Piknova, B., Perochon, E. & Tocanne, J. F. (1993). Hydrophobic mismatch and long-range protein/lipid interactions in bacteriorhodopsin/phosphatidylcholine vesicles. *Eur. J. Biochem.* 218(2), 385–396.

182 Horowitz, A. D. (1995). Exclusion of SP-C, but not SP-B, by gel phase palmitoyl lipids. *Chem. Phys. Lipids* 76(1), 27–39.

183 Zhang, Y. P., Lewis, R. N., Hodges, R. S. & McElhaney, R. N. (2001). Peptide models of the helical hydrophobic transmembrane segments of membrane proteins: interactions of acetyl-K2-(LA)12-K2-amide with phosphatidylethanolamine bilayer membranes. *Biochemistry* 40(2), 474–482.

184 Rinia, H. A., Kik, R. A., Demel, R. A., Snel, M. M., Killian, J. A., van Der Eerden, J. P. & de Kruijff, B. (2000). Visualization of highly ordered striated domains induced by transmembrane peptides in supported phosphatidylcholine bilayers. *Biochemistry* 39(19), 5852–5858.

185 Jones, D. H., Rigby, A. C., Barber, K. R. & Grant, C. W. M. (1997). Oligomerization Of the EGF Receptor Transmembrane Domain: a H^2 NMR Study In Lipid Bilayers. *Biochemistry* 36, 12616–12624.

186 Van Duyl, B. Y., Rijkers, D. T. S., Kruijff, B. d. & Killian, J. A. (2002). Influence of hydrophobic mismatch and palmitoylation on the association of transmembrane a-helical peptides with detergent-resistant membranes. *FEBS Lett.*, 79–84.

187 Scheiffele, P., Roth, M. G. & Simons, K. (1997). Interaction Of Influenza Virus Haemagglutinin With Sphingolipid Cholesterol Membrane Domains Via Its Transmembrane Domain. *EMBO J.* 16, 5501–5508.

188 Perschl, A., Lesley, J., English, N., Hyman, R. & Trowbridge, I. S.

(1995). Transmembrane domain of CD44 is required for its detergent insolubility in fibroblasts. *J. Cell Sci.* 108(Pt 3), 1033–1041.

189 Field, K. A., Holowka, D. & Baird, B. (1999). Structural aspects of the association of FcepsilonRI with detergent-resistant membranes. *J. Biol. Chem.* 274(3), 1753–1758.

190 Therien, A. G. & Deber, C. M. (2002). Interhelical packing in detergent micelles – Folding of a cystic fibrosis transmembrane conductance regulator construct. *J. Biol. Chem.* 277, 6067–6072.

191 Vogel, H. (1992). Structure and dynamics of polypeptides and proteins in lipid membranes. *Q. Rev. Biophys.* 25, 433–457.

192 Belohorcova, K., Davis, J. H., Woolf, T. B. & Roux, B. (1997). Structure and Dynamics of an Amphiphilic Peptide in a Lipid Bilayer: A Molecular Dynamics Study. *Biophys. J.* 73, 3039–3055.

193 Brandl, C. J. & Deber, C. M. (1986). Hypothesis About the Function of Membrane-Buried Proline Residues in Transport Proteins. *Proc. Natl. Acad. Sci. U.S.A.* 83(4), 917–921.

194 Labro, A. J., Raes, A. L., Ottschytsch, N. & Snyders, D. J. (2001). Role of the S6 tandem proline motif in gating of Kv channels. *Biophys. J.* 80(1), 441A–441A.

195 Sansom, M. S. P. & Weinstein, H. (2000). Hinges, swivels and switches: the role of prolines in signalling via transmembrane a-helices. *Trends. Pharmacol. Sci.* 21, 445–451.

196 Shelden, M. C., Loughlin, P., Tierney, M. L. & Howitt, S. M. (2001). Proline residues in two tightly coupled helices of the sulphate transporter, SHST1, are important for sulphate transport. *Biochem. J.* 356, 589–594.

197 Duclohier, H., Molle, G., Dugast, J. Y. & Spach, G. (1992). Prolines Are Not Essential Residues in the Barrel-Stave Model for Ion Channels Induced by Alamethicin Analogs. *Biophys. J.* 63(3), 868–873.

198 Kaduk, C., Duclohier, H., Dathe, M., Wenschuh, H., Beyermann, M., Molle, G. & Bienert, M. (1997). Influence of proline position upon the ion channel activity of alamethicin. *Biophys. J.* 72(5), 2151–2159.

199 Gibbs, N., Sessions, R. B., Williams, P. B. & Dempsey, C. E. (1997). Helix bending in alamethicin: molecular dynamics simulations and amide hydrogen exchange in methanol. *Biophys. J.* 72, 2490–2495.

200 Tieleman, D. P., Sansom, M. S. P. & Berendsen, H. J. C. (1999). Alamethicin Helices in a Bilayer and in Solution: Molecular Dynamics Simulations. *Biophys. J.* 76, 40–49.

201 Jacob, J., Duclohier, H. & Cafiso, D. S. (1999). The Role of Proline and Glycine in Determining the Backbone Flexibility of a Channel-Forming Peptide. *Biophys. J.* 76, 1367–1376.

202 Demmers, J. A. A., Duijn, E. v., Haverkamp, J., Greathouse, D. V., II. R. E., K., Heck, A. J. R. & Kilian, J. A. (2001). Interfacial Positioning and Stability of Transmembrane Peptides in Lipid Bilayers Studied by Combining Hydrogen/Deuterium Exchange and Mass Spectrometry. *J. Biol. Chem.* 276, 34501–34508.

203 Langosch, D., Crane, J. M., Brosig, B., Hellwig, A., Tamm, L. K. & Reed, J. (2001). Peptide mimics of SNARE transmembrane segments drive membrane fusion depending on their conformational plasticity. *J. Mol. Biol.* 311, 709–721.

204 Langosch, D., Brosig, B. & Pipkorn, R. (2001). Peptide mimics of the vesicular stomatitis virus G-protein transmembrane segment drive membrane fusion in vitro. *J. Biol. Chem.* 276, 32016–32021.

205 Dennison, S. M., Greenfield, N., Lenard, J. & Lentz, B. R. (2002). VSV transmembrane domain (TMD) peptide promotes PEG-mediated fusion of liposomes in a conformationally sensitive fashion. *Biochemistry* 41(50), 14925–14934.

206 Li, L. & Chin, L. S. (2003). The molecular machinery of synaptic vesicle exocytosis. *Cell. Mol. Life Sci.* 60(5), 942–960.

207 Scales, S. J., Bock, J. B. & Scheller, R. H. (2000). Cell biology – The specifics of membrane fusion. *Nature* 407, 144–146.

208 Blumenthal, R., Clague, M. J., Durell, S. T. & Epand, R. M. (2003). Membrane Fusion. *Chem. Rev.* 103, 53–69.

209 Melikyan, G. B., Lin, S. S., Roth, M. G. & Cohen, F. S. (1999). Amino acid sequence requirements of the transmembrane and cytoplasmic domains of influenza virus hemagglutinin for viable membrane fusion. *Mol. Biol. Cell* 6, 1821–1836.

210 Owens, R. J., Burke, C. & Rose, J. K. (1994). Mutations in the membrane-spanning domain of the human immunodeficiency virus envelope glycoprotein that affect fusion activity. *J. Virol.* 68, 570–574.

211 Taylor, G. M. & Sanders, D. A. (1999). The role of the membrane-spanning domain sequence in glycoprotein-mediated membrane fusion. *Mol. Biol. Cell* 10, 2803–2815.

212 Odell, D., Wanas, E., Yan, J. & Ghosh, H. P. (1997). Influence of membrane anchoring and cytoplasmic domains on the fusogenic activity of vesicular stomatitis virus glycoprotein G. *J. Virol.* 71, 7996–8000.

213 Cleverley, D. Z. & Lenard, J. (1998). The transmembrane domain in viral fusion: essential role for a conserved glycine residue in vesicular stomatitis virus G protein. *Proc. Natl. Acad. Sci. USA* 95, 3425–3430.

214 Grote, E., Baba, M., Ohsumi, Y. & Novick, P. J. (2000). Geranylgeranylated SNAREs are dominant inhibitors of membrane fusion. *J. Cell Biol.* 151, 453–465.

215 Rohde, J., Dietrich, L., Langosch, D. & Ungermann, C. (2003). The transmembrane domain of Vam3 affects the composition of *cis*- and *trans*-SNARE complexes to promote homotypic vacuole fusion. *J. Biol. Chem.* 278(3), 1656–1662.

216 Tatulian, S. A. & Tamm, L. K. (2000). Secondary structure, orientation, oligomerization, and lipid interactions of the transmembrane domain of influenza hemagglutinin. *Biochemistry* 39, 496–507.

217 Szyperski, T., Vandenbussche, G., Curstedt, T., Ruysschaert, J. M., Wüthrich, K. & Johansson, J. (1998). Pulmonary surfactant-associated polypeptide C in a mixed organic solvent transforms from a monomeric alpha-helical state into insoluble beta-sheet aggregates. *Protein Sci.* (12), 2533–40.

218 Zhang, Y.-P., Lewis, R. N. A. H., Hodges, R. S. & McElhaney, R. N. (1992). FTIR Spectroscopic studies of the conformation and amide hydrogen exchange of a peptide model of the hydrophobic transmembrane α-helices of membrane proteins. *Biochemistry* 31, 11572–11578.

219 Helenius, A., McCaslin, D. R., Fries, E. & Tanford, C. (1979). Properties of Detergents. *Meth. Enzymol.* 56, 734–749.

220 Torres, J., Stevens, T. J. & Samso, M. (2003). Membrane proteins: the 'Wild West' of structural biology. *Trends Biochem. Sci.* 28(3), 137–144.

221 Laage, R. & Langosch, D. (2001). Strategies for prokaryotic expression of eukaryotic membrane proteins. *Traffic* 2, 99–104.

222 Grisshammer, R. & Tate, C. G. (1995). Overexpression of integral membrane proteins for structural studies. *Q. Rev. Biophys.* 28, 315–422.

223 Tate, C. G. & Grisshammer, R. (1996). Heterologous expression of G-protein-coupled receptors. *TIBTECH* 14, 426–430.

224 Hackam, A. S., Wang, T.-L., Guggino, W. B. & Cutting, G. R. (1997). The N-terminal domain of human GABA receptor ρ1 subunits contains signals for homooligomeric and heterooligomeric interaction. *J. Biol. Chem.* 272, 13750–13757.

225 Szczesna Skorupa, E. & Kemper, B. (1991). Cell-free analysis of targeting of cytochrome P450 to microsomal membranes. *Methods Enzymol.* 206, 64–75.

226 Rosenberg, R. L. & East, J. E. (1992). Cell-free expression of functional

Shaker potassium channels. *Nature* 360, 166–169.

227 Rusinol, A. E., Jamil, H. & Vance, J. E. (1997). In vitro reconstitution of assembly of apolipoprotein B48-containing lipoproteins. *J. Biol. Chem.* 272, 8019–8025.

228 Huppa, J. B. & Ploegh, H. L. (1997). In vitro translation and assembly of a complete T cell receptor-CD3 complex. *J. Exp. Med.* 186, 393–403.

229 Fisher, L. E. & Engelman, D. M. (2001). High-yield synthesis and purification of an alpha-helical transmembrane domain. *Analytical Biochemistry* 293(1), 102–108.

230 Melnyk, R. A., Partridge, A. W. & Deber, C. M. (2002). Transmembrane domain mediated self-assembly of major coat protein subunits from Ff bacteriophage. *J. Mol. Biol.* 315(1), 63–72.

231 Gerber, D. & Shai, Y. (2001). In vivo detection of hetero-association of glycophorin-A and its mutants within the membrane. *J. Biol. Chem.* 276(33), 31229–31232.

232 Laemmli, U. K. (1970). Cleavage of structural proteins during the assembly of the head of bacteriophage T4. *Nature* 227, 680–685.

233 Soulié, S., Moller, J. V., Falson, P. & Maire, l. M. (1996). Urea Reduces the Aggregation of Membrane Proteins on Sodium Dodecyl Sulfate-Polyacrylamide Gel Electrophoresis. *Anal. Biochem.* 236, 363–364.

234 Millar, D. G. & Shore, G. C. (1993). The signal anchor sequence of mitochondrial Mas70p contains an oligomerization domain. *J. Biol. Chem.* 268, 18403–18406.

235 Deber, C. M., Khan, A. R., Zuomei, L., Joensson, C., Glibowicka, M. & Wang, J. (1993). Val-Ala mutations selectively alter helix-helix packing in the transmembrane segment of phage M13 coat protein. *Proc. Natl. Acad. Sci. USA* 90, 11648–11652.

236 Ramjeesingh, M., Huan, L., Garami, E. & Bear, C. E. (1999). Novel method for evaluation of the oligomeric structure of membrane proteins. *Biochem. J.* 342, 119–123.

237 Peters, K. & Richards, M. (1977). Chemical Cross-linking: Reagents and Problems in Studies of Membrane Structure. *Annu. Rev. Biochem.* 46, 523–551.

238 Gaffney, B. J. (1985). Chemical and biochemical crosslinking of membrane components. *Biochim. Biophys. Acta* 822, 289–317.

239 Schägger, H., Cramer, W. A. & von Jagow, G. (1994). Analysis of molecular masses and oligomeric states of protein complexes by blue native electrophoresis and isolation of membrane protein complexes by two-dimensional native electrophoresis. *Anal. Biochem.* 217, 220–230.

240 Schägger, H. & von Jagow, G. (1991). Blue native electrophoresis for isolation of membrane protein complexes in enzymatically active form. *Anal. Biochem.* 199, 223–231.

241 Poetsch, A., Neff, D., Seelert, H., Schägger, H. & Dencher, N. A. (2000). Dye removal, catalytic activity and 2D crystallization of chloroplast H^+-ATP synthase purified by blue native electrophoresis. *Biochim. Biophys. Acta* 1466, 339–349.

242 Rexroth, S., Meyer zu Tittingdorf, J. M. W., Krause, F., Dencher, N. A. & Seelert, H. (2003). Thylakoid membrane at altered metabolic state: Challenging the forgotten realms of the proteome. *Electrophoresis* 24, 2814–2823.

243 Clarke, S. (1975). Size and Detergent Binding of Membrane Proteins. *J. Biol. Chem.* 250(14), 5459–5469.

244 Selvin, P. R. (1995). Fluorescence resonance energy transfer. *Meth. Enzymol.* 246, 300–334.

245 Clegg, R. M. (1995). Fluorescence resonance energy transfer. *Curr. Op. Biotech.* 6, 103–110.

246 Wu, P. a. B., L. (1994). Resonance energy transfer: methods and applications. *Anal. Biochem.* 218, 1–13.

247 Peled, H. & Shai, Y. (1993). Membrane interaction and self-assembly within phospholipid membranes of synthetic segments corresponding to the H-5 region of the

shaker K+ channel. *Biochemistry* 32, 7879–7885.

248 Yano, Y., Takemoto, T., Kobayashi, S., Yasui, H., Sakurai, H., Ohashi, W., Niwa, M., Futaki, S., Sugiura, Y. & Matsuzaki, K. (2001). Topological Stability and Self-Association of a Completely Hydrophobic Model Transmembrane Helix in Lipid Bilayers. *Biochemistry* 41, 3073–3080.

249 Gazit, E. & Shai, Y. (1995). The assembly and organization of the alpha5 and alpha7 helices from the pore-forming domain of Bacillus thuringiensis delta-endotoxin. *J. Biol. Chem.* 270, 2571–2578.

250 Li, M., Reddy, L. G., Bennett, R., Silva, N. D., Jones, L. R. & Thomas, D. D. (1999). A fluorescence energy transfer method for analyzing protein oligomeric structure: application to phospholamban. *Biophys. J.* 76, 2587–2599.

251 Adair, B. D. & Engelman, D. M. (1994). Glycophorin A helical transmembrane domains dimerize in phospholipid bilayers: a resonance energy transfer study. *Biochemistry* 33, 5539–5544.

252 Mitra, R. D., Silva, C. M. & Youvan, D. C. (1996). Fluorescence resonance energy transfer between blue-emitting and red-shifted excitation derivatives of the green fluorescent protein. *Gene* 173, 13–17.

253 Heim, R. & Tsien, R. Y. (1996). Engineering green fluorescent protein for improved brightness, longer wavelenghts and fluorescence resonance energy transfer. *Curr. Biol.* 6, 178–182.

254 Ellenberg, J., Lippincott-Schwartz, J. & Presley, J. F. (1999). Dual-color imaging with GFP variants. *Trends. Cell Biol.* 9, 52–56.

255 Lippincott-Schwartz, J. & Patterson, G. H. (2003). Development and Use of Fluorescent Protein Markers in Living Cells. *Science* 300, 87–91.

256 Majoul, I., Straub, M., Duden, R., Hell, S. W. & Söling, H.-D. (2002). Fluorescence resonance energy transfer analysis of protein-protein interactions in single living cells by multifocal multiphoton microscopy. *Rev. Mol. Biotech.* 82, 267–277.

257 Couturier, C., Ayoub, M. A. & Jockers, R. (2002). BRET ermöglicht die Messung von Protein-Interaktionen in lebenden Zellen. *Biospektrum* 5, 612–615.

258 Ayoub, M. A., Couturier, C., Lucas-Meunier, E., Angers, S., Fossier, P., Bouvier, M. & Jockers, R. (2002). Monitoring of ligand-independent dimerization and ligand-induced conformational changes of melatonin receptors in living cells by bioluminescence resonance energy transfer. *J. Biol. Chem.* 277(24), 21522–21528.

259 Kroeger, K. M., Hanyaloglu, A. C. & Eidne, K. A. (2001). Applications of BRET to study dynamic G-protein coupled receptor interactions in living cells. *Letters Pep. Sci.* 8(3–5), 155–162.

260 Eidne, K. A., Kroeger, K. M. & Hanyaloglu, A. C. (2002). Applications of novel resonance energy transfer techniques to study dynamic hormone receptor interactions in living cells. *Trends Endocrin. Metabol.* 13(10), 415–421.

261 DiRita, V. (1992). Co-ordinate expression of virulence genes by ToxR in *Vibrio cholerae*. *Mol. Microbiol.* 6, 451–458.

262 Kolmar, H., Fritsch, C., Kleeman, G., Götze, K., Stevens, F. J. & Fritz, H. J. (1994). Dimerization of bence jones proteins: linking the rate of transcription from an Escherichia coli promoter to the association constant of REIv. *Biol. Chem. Hoppe-Seyler* 375, 61–69.

263 Bedouelle, H. & Duplay, P. (1988). Production in Escherichia coli and one-step purification of bifunctional hybrid proteins which bind maltose – export of the Klenow polymerase into the periplasmic space. *Eur. J. Biochem.* 171, 541–549.

264 Leeds, J. A. & Beckwith, J. (1998). Lambda repressor n-terminal DNA-binding domain as an assay for protein transmembrane segment interactions in vivo. *J. Mol. Biol.* 280(5), 799–810.

265 Schneider, D. & Engelman, D. M. (2003). GALLEX: a measurement of heterologous association of transmembrane helices in a biological membrane. *J. Biol. Chem.* 278, 3105–3111.

266 Johnsson, N. & Varshavsky, A. (1994). Split ubiquitin as a sensor of protein interactions in vivo. *Proc. Natl. Acad. Sci. USA* 91, 10340–10344.

267 Stagljar, I., Korostensky, C., Johnsson, N. & TeHeesen, S. (1998). A genetic system based on split-ubiquitin for the analysis of interactions between membrane proteins in vivo. *Proc. Natl. Acad. Sci. USA* 95, 5187–5192.

268 Wittke, S., Lewke, N., Muller, S. & Johnsson, N. (1999). Probing the molecular environment of membrane proteins in vivo. *Mol. Biol. Cell* 10(8), 2519–2530.

269 Stagljar, I. & Fields, S. (2002). Analysis of membrane protein interactions using yeast-based technologies. *Trends. Biochem. Sci.* 27, 559–563.

270 Lee, G. F. & et al. (1994). Deducing the organization of a transmembrane domain by disulfide crosslinking. *J. Biol. Chem.* 269, 29920–29927.

271 Pakula, A. A. & Simon, M. I. (1992). Determination of transmembrane protein structure by disulfide cross-linking: the *Escherichia coli* Tar receptor. *Proc. Natl. Acad. Sci. USA* 89, 4144–4148.

272 Doyle, D. A., Cabral, J. M., Pfuetzner, R. A., Kuo, A., Gulbis, J. M., Cohen, S. L., Chait, B. T. & MacKinnon, R. (1998). The structure of the potassium channel: molecular basis of K^+ conduction and selectivity. *Science* 280, 69–77.

273 Cowan, S. W., Schirmer, T., Rummel, G., Steiert, M., Ghosh, R., Pauptit, R. A., Jansonius, J. N. & Rosenbusch, J. P. (1992). Crystal structures explain functional properties of two E. coli porins. *Nature* 358, 727–733.

274 Ruan, W., Becker, V., Klingmuller, U., Langosch, D. The interface between self-assembling erythropoietin receptor transmembrane segments corresponds to a membrane-spanning leucine zipper. *J. Biol. Chem.* 279(5), 3273–3279.

275 Ruan, W., Lindner, E., and Langosch, D. (2004). The interface of a membrane-spanning leucine zipper mapped by asparagine-scanning mutagenesis. *Prot. Sci.* 13, 555–559.

276 Toutain, C. M., Clarke, D. J., Leeds, J. A., Kuhn, J., Beckwith, J., Holland, I. B., Jacq, A. (2003). The transmembrane domain of the DnaJ-like protein DjlA is a dimerisation domain. *Mol. Genet. Genom.* 268(6), 761–770.

277 Leeds, J. A., Boyd, D., Huber, D. R., Sonoda, G. K., Luu, H. T., Engelman, D. M., Beckwith, J. (2001). Genetic selection for and molecular dynamic modeling of a protein transmembrane domain multimerization motif from a random Escherichia coli genomic library. *J. Mol. Biol.* 313(1), 181–195.

27
SecB

Arnold J. M. Driessen, Janny de Wit, and Nico Nouwen

27.1
Introduction

Most components of the protein export apparatus of *Escherichia coli* have been identified by genetic approaches that were conducted in the late 1980s. Since many of these components are essential for viability, genetic screens were aimed at the isolation of conditional lethal mutants with pleiotropic secretion defects. In 1983, Kumamoto and Beckwith [1] reported a gene that appeared nonessential for *E. coli* viability but that when mutated or even completely eliminated adversely affected the export of a subset of envelope proteins, including the periplasmic maltose-binding protein (MBP). This gene, termed *secB*, was found to map near min 81 on the *E. coli* chromosome [1]. Strains carrying SecB mutations, although unable to grow on Luria Bertani broth plates, were still viable on minimal media [2]. To define its function, it was necessary to biochemically analyze the SecB protein. Using a pulse-labeling approach, Gannon and Kumamoto [3] demonstrated that *secB* mutations caused a defect in co-translational processing of MBP. The preMBP that accumulated in cells of the *secB* mutant had folded into a protease-resistant conformation, and it was suggested that SecB stabilized the unfolded state of preproteins prior to their translocation. Direct evidence for an anti-folding activity of SecB was provided by in vitro experiments by the group of Phil Bassford [4]. In the absence of SecB, the rate of folding of in vitro synthesized wild-type preMBP was accelerated and was greatly retarded when excess SecB was present. This defined a biochemical function for SecB that complemented early work by Randall and Hardy, who correlated the folding of preMBP into a stable tertiary structure in the cytoplasm with a loss of export competence [5]. A further understanding of the function of the *secB* gene was obtained after overproduction and purification of the SecB protein in 1988 [6]. SecB was shown to be needed for the efficient in vitro translocation of preMBP into inverted inner-membrane vesicles. Moreover, SecB was found to associate and to retard the folding of preMBP and several other preproteins. In 1990, Hartl and Wickner [7] provided evidence for a targeting function of SecB. By means of biochemical assays, SecB and the binary SecB-preprotein complex were found to bind with high affinity to the membrane-

Protein Folding Handbook. Part II. Edited by J. Buchner and T. Kiefhaber

ISBN: 3-527-30784-2

Tab. 27.1. Chronology of some important findings in the SecB function.

Year	*Finding*	*References*
1983	Isolation of *secB* mutants	1
1988	Demonstration of an anti-folding activity of SecB	4
1988	Purification of SecB Demonstration that SecB stimulates preprotein translocation in vitro	6, 95, 96
1990	Demonstration of a preprotein-targeting activity of SecB and evidence for a specific SecB-SecA interaction at the membrane	7
1994	Definition of the SecB-binding frame in the mature region of preproteins excluding the signal sequence	47
1995	Identification of the C-terminus of SecA as the SecB-binding domain	79
1997	Definition of the SecB-targeting cycle and preprotein transfer mechanism to SecA	8
1999	Identification of a critical zinc ion in the SecB-binding domain of SecA	80
2000	Elucidation of the crystal structure of SecB	9
2003	Elucidation of the structure of SecB in complex with the SecA C-terminal-binding domain	81

bound motor of the preprotein translocase, the SecA protein. This led to the understanding that SecB has a dual function in the cell, i.e., stabilizing the preprotein prior to translocation and transferring it to the membrane-bound SecA [8], a protein that catalyzes the next step in the translocation reaction. In 2000, the three-dimensional structure of the *Haemophilus influenzae* SecB protein was solved [9], which now provides a handle to correlate function to structure. A historical timeline is shown in Table 27.1.

27.2 Selective Binding of Preproteins by SecB

Folding of newly synthesized proteins inside the cell depends on a set of conserved proteins known as molecular chaperones. These molecular chaperones essentially prevent nonproductive interactions between nonnative polypeptides and typically increase the yield of a folding reaction. In *Escherichia coli* and other bacteria, export of newly synthesized proteins from the cytoplasm to the exterior involves at least one transport step across the inner membrane [10]. In order to pass the inner membrane, proteins need to be in an unfolded state [5]. Therefore, newly synthesized precursor proteins (preproteins) need to bypass the cellular folding apparatus and funnel into a pathway that directs them in an unfolded state to the preprotein translocase at the inner membrane. In *E. coli*, we can discriminate two in-

dependent targeting pathways for preproteins. One pathway involves a bacterial homologue of the eukaryotic signal recognition particle (SRP) and its membrane-associated receptor (FtsY), which will not be further discussed here. The other pathway involves the SecB protein. Both pathways converge at the translocase [11]. Translocase is a membrane-bound complex that consists of the SecA protein, a preprotein receptor and ATP-driven molecular motor device, and the SecYEG complex, a preprotein-conducting channel in the membrane [12].

SecB is a tetrameric chaperone in *E. coli* with a cellular function that is dedicated to preprotein translocation [13, 14]. It is important to note that SecB is found only in the subgroup of α-, β-, and γ-proteobacteria that includes the majority of known gram-negative bacteria of medical, industrial, and agricultural significance such as *Vibrio*, *Pseudomonas*, *Rickettsia*, *Neisseria*, and *Haemophilus* [15]. The *secB* gene is, however, not essential in Gram-negative bacteria [1] and is even absent in Gram-positive bacteria and archaea [16, 17]. Although *E. coli secB* null and mutant strains show pleiotropic defects in protein secretion, this growth defect is specific for rich media and has been attributed to a reduced expression of *gpsA* located downstream from the *secB* gene [18]. GpsA encodes an sn-glycerol-3-phosphate dehydrogenase that is involved in phospholipids biosynthesis. Its reduced expression affects the membrane lipid composition that indirectly influences the preprotein translocase, therefore leading to a secretion defect. One of the reasons that SecB is not essential relates to backup functions in the cell that ensure the proper translocation of essential proteins. In this respect, protein translocation in a *secB* null or mutant strain is supported by more general chaperones, in particular DnaK [19–21].

In vivo, SecB binds to a subset of nascent preproteins [22–24], while in vitro, it interacts with many unrelated proteins provided that they are in a nonnative state [25]. Studies with model protein substrates such as barstar revealed that SecB does not bind the folded or unfolded state but traps a near-native-like molten-globule state [26–28]. SecB has also been shown to bind partially folded states of α-lactalbumin, bovine pancreas trypsin inhibitor (BPTI), and ribonuclease A (RNase A) [29]. These model substrates are rather small, and in all cases, binding occurs with a stoichiometry of one polypeptide chain per SecB monomer [28, 30–32]. Calorimetric studies suggest that between 7 and 29 amino acid residues are buried upon substrate binding to SecB [30, 33]. Unfolded preprotein substrates, however, bind with a stoichiometry of one preprotein per SecB tetramer and a K_d that is in the nanomolar range [31, 34–36]. Short peptide substrates bind to SecB with a K_d value in the micromolar range [37]. SecB's key activity is to maintain preproteins in a so-called translocation-competent state [5, 38–40]. The exact nature of this state is unknown, but based on the studies with model substrates, it is generally assumed that this is a molten-globule state. Partially folded species such as molten globules have exposed hydrophobic surfaces, and hence nonproductive interactions readily lead to aggregation, a state that is not compatible with translocation. Indeed, with an authentic preprotein substrate such as the precursor of outer membrane protein A (proOmpA), SecB stabilizes a partially folded state with native-like secondary structure but incomplete tertiary structure [38]. The stoichiometric binding reaction prevents proOmpA, which is rich in β-sheet structure, from aggre-

gation. With the precursor of maltose-binding protein (preMBP), the anti-folding activity of SecB seems to be of major importance. Unlike refolded preMBP, SecB-bound preMBP is particularly protease-sensitive, which is indicative of an unfolded conformation [5]. Moreover, various slowly folding mutants of preMBP exhibit a reduced SecB dependence for translocation [41]. Although SecB readily interacts with mature, unfolded MBP [42], it has been shown that the presence of a signal sequence retards the folding of the mature domain [43, 44], thereby allowing a greater time window for SecB interaction.

A range of biochemical methods has been used to understand the nature of the SecB-binding frame in preproteins [45–48]. An extensive screen of a peptide library for SecB binding indicates that a typical peptide substrate (SecB-binding motif) is approximately nine residues long and enriched in aromatic and basic residues; acidic residues are strongly disfavored. The majority of the binding energy for these peptides results from hydrophobic interactions [33]. The structures of *H. influenzae* (See Figure 27.1) [9] and *E. coli* SecB [49] have been solved, leading to some major insights as to the mode of polypeptide interaction. These highly homologous proteins show an identical structure. The SecB monomer has a simple $\alpha + \beta$ fold, but the overall rectangular-shaped structure is a tetramer organized as a dimer of dimers (Figure 27.1). This quaternary organization agrees well with the observed dynamic dimer-tetramer equilibrium of SecB in solution [36, 50] and with thermodynamic studies [51] that indicate that SecB is a stable, well-folded, and tightly packed tetramer. Although SecB has been crystallized without a peptide substrate, the structure suggests that substrate binding occurs at a surface site rather than at an interior cavity (Figure 27.2). A long surface-exposed channel is present on each side of the tetramer that has all the characteristics of a peptide-binding site. Each channel is proposed to contain two peptide-binding subsites

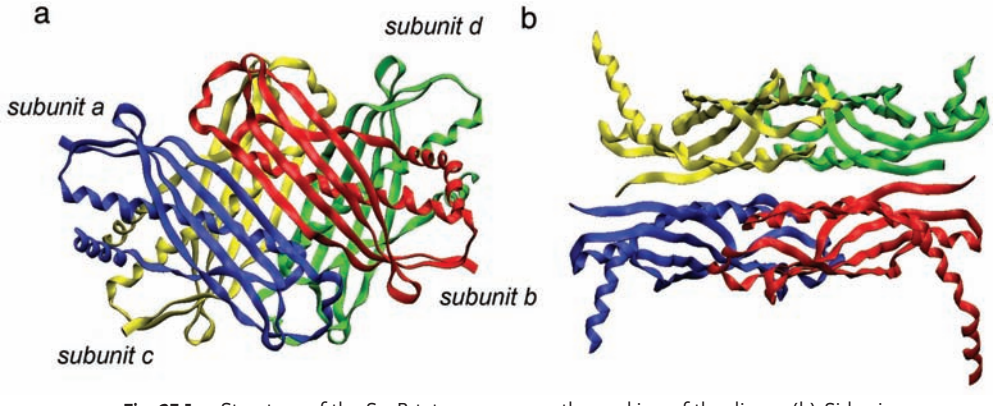

Fig. 27.1. Structure of the SecB tetramer. Ribbon drawing of the *H. influenzae* SecB tetramer (based on the coordinates deposited in the Protein Data Bank as 1FX3) [9] in two orthogonal views. (a) Front view, showing the four-stranded β-sheet of each monomer and the packing of the dimer. (b) Side view, showing the dimer-dimer interface formed by the α-helices. Each subunit in the tetramer is shown in a different color and is numbered from a to d.

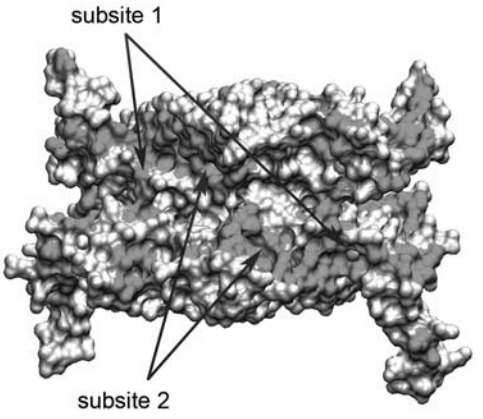

Fig. 27.2. The peptide-binding groove on SecB. Solvent-accessible surface of the proposed peptide-binding groove on one face of the *H. influenzae* SecB tetramer [9], shown in the same orientation as in Figure 27.1b. The hydrophobic residues are indicated in dark gray, and the positions of subsite 1 and the shallow subsite 2 are indicated by the arrows.

that might recognize distinct features of the preprotein [9]. Subsite 1 is a deep cleft located in a narrow constriction in the middle of the surface-exposed channel (Figure 27.2). It might recognize hydrophobic and aromatic regions of polypeptides, as most of the amino acids that line the surface are aromatic and conserved. The length of this cleft is sufficient to accommodate peptides of the size of the SecB-binding motif. Subsite 2 is a shallow, open groove with a hydrophobic surface (Figure 27.2). It lacks aromatic residues and might bind extended regions of polypeptides by forming regular main-chain hydrogen bonds. Negatively charged residues are positioned around the groove, and this could explain the selectivity for basic residues, which was particularly evident in studies with modified peptide substrates. Introduction of stretches of basic residues in preproteins that translocate in a SecB-independent manner renders these proteins SecB-dependent [52, 53]. Those studies, however, did not define a consensus SecB-binding motif. Moreover, since SecB is a highly acidic protein (see also Figure 27.4b) [9], it may more or less nonspecifically interact with basic protein stretches. The entry of subsite 1 contains a conserved tryptophan residue of SecB, and this residue has been used to monitor the binding of model substrates such as BPTI, which further support the notion that the structurally distinct grooves are indeed involved in substrate binding.

In vitro studies [25, 54, 55] have suggested that SecB discriminates between secretory and cytosolic proteins by the rate of folding. Cytosolic proteins would fold too fast and thereby escape the SecB binding. It is difficult to understand this "kinetic partitioning model" when it concerns the association of SecB with ribosome-bound nascent chains. Moreover, other studies indicate that SecB associates with unfolded proteins at a rate that is diffusion-limited [28, 31] and thus exceeds the rate of folding of most proteins. The kinetic partition model also does not explain how SecB differentiates between proteins in vivo [56], where binding seems to be dictated by a high affinity interaction [22, 23]. Although it has been suggested that SecB functions as a kind of cytosolic signal sequence recognition factor [57, 58],

the signal sequence is not considered to be the prime target for SecB binding, as unfolded mature preprotein domains readily interact with SecB [42, 59, 60]. With some preproteins such as preLamB, the signal sequence showed some affinity for SecB, but it did not correspond to the major binding sites in preLamB [61]. SecB binds to long nascent chains of a subset of preproteins [23]. These ribosome-bound nascent proteins likely encounter a variety of chaperones before they are recognized by SecB. Stage- and site-specific cross-linking approaches suggest that the signal sequence of preproteins such as proOmpA, immediately after emerging from the ribosome, associates with Ffh, a subunit of the bacterial SRP, and with SecA, while remaining attached to the surface of the ribosome via protein L23 [62]. Hydrophobic signal sequences or transmembrane segments of nascent membrane proteins remain SRP-bound, and the ternary ribosome–nascent chain–SRP complex is subsequently targeted to the translocation sites at the membrane [11, 63]. With most preproteins, however, such proposed contacts with SRP will be only transient and lost upon further growth of the nascent chain. Experimental data indicate that the signal sequence then interacts with the chaperone trigger factor, a protein with peptidyl-prolyl *cis*/*trans* isomerase activity [63–65]. While the preprotein further emerges from the ribosome, trigger factor will scan the nascent chain, but, eventually, domains will become exposed that interact with SecB. It should be stressed that some of the cross-linking experiments [62] rely on cellular lysates that are supplemented with cross-linking partners. This may lead to a false bias of possible interactions. Nevertheless, in the cell, SecB is known to associate with ribosome-bound nascent chains after they have reached a length of ~150 residues [23, 24]. These chain lengths correspond with the location of SecB-binding sites mapped by proteolysis [45–47]. Because SecB recognizes peptide sequences that typically occur within core regions of folded proteins [48], it binds preferentially to the unfolded conformation of the mature part of preproteins. The long binding regions have been proposed to occupy multiple binding sites on SecB simultaneously [66], thereby allowing the high binding affinity of nonnative preproteins (K_d = 5–50 nM). To occupy the peptide-binding grooves on both sites, long, unstructured polypeptide segments presumably are wrapped around the rectangular tetrameric shape of SecB.

The SecB structure provides only a first glimpse of how preproteins might bind, but to reveal the molecular details of this interaction [9], a structure of SecB with bound polypeptide substrate is required. Specific mutations in *E. coli* SecB (C76Y, V78F, and Q80R) disrupt the interaction between SecB and preproteins [67]. In these mutants, which show only mild translocation defects, the tetramer-dimer equilibrium in solution is shifted towards the dimer [68]. In the SecB structure, these residues are located on a surface-exposed β-strand that on one face points towards the core of the molecule [9, 49]. The mutated residues are not part of the peptide-binding groove, nor do they directly contribute to the dimer-dimer interface. However, these residues appear crucial for tight packing that involves interactions between the β-sheet and long α-helices that are at the dimer-dimer interface (Figure 27.1b) [9, 49]. It is conceivable that the mutations destabilize this interface and thereby impair preprotein binding while leaving the SecB dimer intact. Although this process is induced by mutations, it may also have some functional sig-

nificance for the SecB-mediated preprotein transfer reaction towards SecA, as will be discussed in the following section.

As to the physiological role of SecB in preventing aggregation of nonnative proteins, it is unclear to what extent the cell takes advantage of this general chaperone activity. During protein binding, there is a rapid equilibrium between bound and free states that allows partitioning of the polypeptide between folding and rebinding to SecB. As the signal sequence retards folding of the mature region of proteins, it will favor re-association with SecB and thus indirectly contribute to the specificity. However, the dedicated role of SecB in protein translocation more likely results from events downstream of the SecB-preprotein interaction, in particular the association of SecA with SecB and the exposed signal sequence [8]. In the past, suppressor mutants have been selected that restore the translocation of preproteins with a defective or even missing signal sequence. Such mutations reside in the core components of the preprotein translocase, in particular SecY (PrlA) and SecA (PrlD) [69]. Strikingly, translocation of such preprotein substrates in PrlA mutants is remarkably dependent on SecB, even though the original preprotein substrate may not have been SecB-dependent for translocation [70–73]. This phenomenon has been attributed to the targeting function of SecB rather than the unfolding activity [74]. The supportive targeting function may be more prominently required when the intrinsic targeting information in the signal sequence of preproteins is defective.

Although SecB fulfils its function as a secretion-specific chaperone that tightly interlinks with the Sec system, it is also involved in the secretion of HasA, a hemophore of the heme acquisition system in *Serratia marcescens* [75]. This protein is secreted by a specific ABC transporter. Inactivation of SecB abolishes HasA secretion, and this relates to the ability of SecB to maintain the translocation competence of HasA [76]. Point mutations in SecB that affect the interaction with SecA (see Section 27.3) are without effect, but mutations that disrupt the SecB-preprotein interaction also block HasA secretion [77]. HasA is a rapidly folding protein, and binding to SecB results in a nearly complete inhibition of folding. Slowly folding mutants of HasA are secreted essentially independently from SecB. This demonstrates that the anti-folding function of SecB is required for the HasA ABC secretion pathway. It is not known whether SecB also fulfils a function in the targeting of HasA, but so far, this appears as a unique requirement that is not observed with other polypeptide substrates of ABC transporters.

27.3 SecA-SecB Interaction

An essential aspect of the SecB function is its affinity for SecA, the ATPase motor domain of the preprotein translocase. SecB and SecA interact with low affinity in solution ($K_d = \sim 1.6\ \mu M$) [78], but when SecA is bound to the protein-conducting SecYEG channel, it is primed for the high-affinity interaction with SecB ($K_d = 10–30$ nM) [7, 8]. This high-affinity interaction directs the binary SecB-preprotein complex to the translocation site at the membrane, which is instrumental for the tar-

geting function of SecB. A study with SecA deletion mutants and fusion proteins revealed that the site on SecA that binds SecB comprises only the highly conserved carboxyl-terminal 22-amino-acyl residues of SecA [8, 79]. This region is conserved in the SecA proteins of most bacteria, even though they lack a SecB protein. In bacteria such as *Streptomyces*, *Mycobacteria*, and *Mycoplasma*, the carboxyl-terminus consists of a non-conserved polypeptide stretch with a high abundance of positively charged amino acyl residues [16]. Strikingly, the conserved carboxyl-terminal domain of SecA is essential for viability [79] even though SecB is not! This apparent discrepancy likely relates to the reduced ability of SecB to transfer preproteins to SecA when the SecB-binding frame in the carboxyl-terminus is missing, whereas in the absence of SecB, proteins can rely on the signal sequence for targeting. The SecB-binding region of SecA is rich in arginyl and lysyl residues, resulting in a net positive charge. The carboxyl-terminus therefore also shows a high tendency to electrostatically associate with the lipid surface [79], although the functional significance of this phenomenon is not clear. In addition, the carboxyl-terminus of SecA contains conserved cysteine and histidine residues that coordinate a divalent zinc ion required for the functional interaction between SecB and SecA [80]. The crystal structure of SecB has been solved in complex with the carboxyl-terminal 27-amino-acyl residues from *H. influenzae* SecA (Figure 27.3) [81]. This SecA peptide is highly structured as a CCCH zinc-binding motif (Figure 27.3c). Mutagenesis of the cysteine residues, and thus likely the loss of zinc binding, results in defective SecB-mediated preprotein translocation [82], which has been attributed to the deficient interaction between SecA and SecB [8]. The high content of proline and glycine residues in this conserved stretch provides the conformational flexibility needed to coordinate the zinc ion. Importantly, the structure shows one SecB tetramer that is bound by two SecA peptides (Figure 27.3a) [81]. The positively charged SecA peptide interacts with an acidic surface on SecB that consists of the eight-stranded β-sheet formed by two monomers (Figure 27.3b). The interactions at the interface are predominantly electrostatic and involve extensive intermolecular salt bridges and hydrogen-bonding interactions. Four residues from the SecA peptide contribute to the high-affinity interaction: one neutral polar residue (Asn882) and three positively charged residues (Arg881, Lys891, and Lys893) (residue numbering according to the *E. coli* SecA) (Figure 27.3c). Site-directed mutagenesis of these residues into Ala disrupts the high affinity SecB-SecA peptide interaction but does not interfere with the ability of the SecA peptide to bind zinc [81]. On the other hand, the well-conserved amino acid residues Asp20, Glu24, Leu75, and Glu77 of the *E. coli* SecB are important for the high-affinity SecB-SecA interaction [3, 67]. Mutations of these residues cause disruption of the high-affinity binding of SecB to the membrane-bound SecA, but they do not interfere with preprotein binding [74]. The corresponding residues in *H. influenzae* SecB are spatially clustered on the flat solvent-exposed surface on both sides of the SecB tetramer [9]. The structural analysis confirms that this surface is negatively charged and that it electrostatically interacts with the SecA peptide that corresponds to the SecB-binding frame on SecA. The high degree of conservation of the interacting residues on both SecA and SecB supports the notion that the interaction between SecA and SecB is highly specific. In general, disruption of this high-

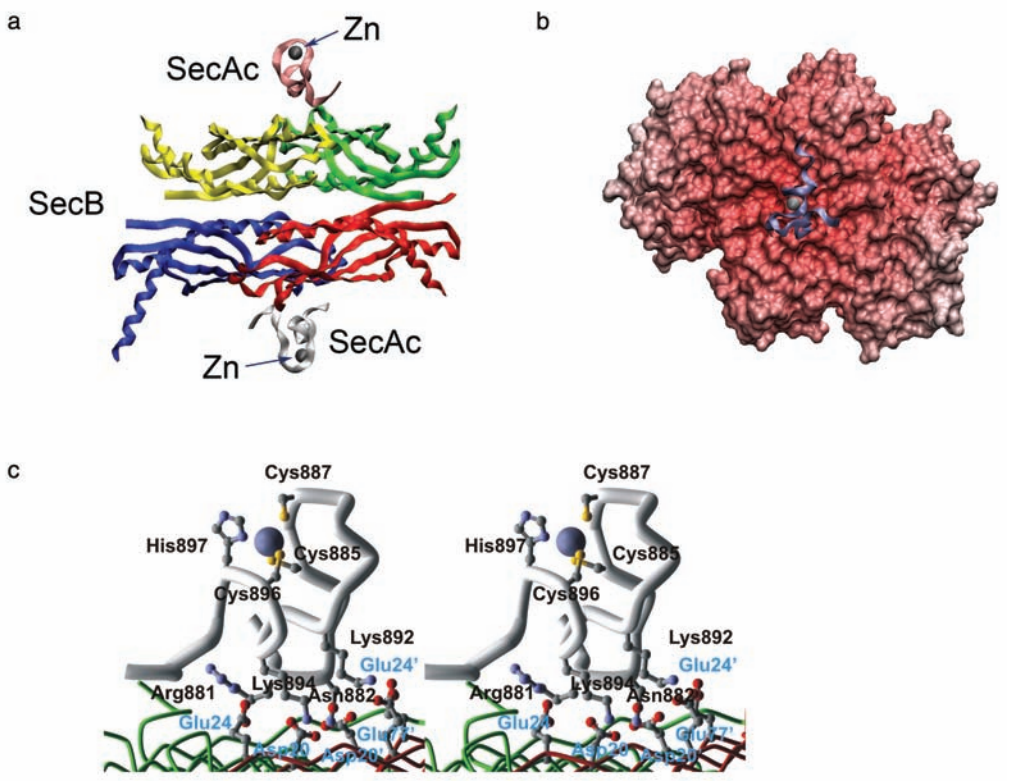

Fig. 27.3. Structural basis for the high-affinity SecB-SecA interaction. (a) Structure of *H. influenzae* SecB in complex with peptides that correspond to the carboxyl-terminal SecB-binding domain of SecA. SecB is shown in the same orientation as in Figure 27.1b, using identical coloring. The two SecA carboxyl-terminal peptides (residues 876–899, in white and pink) both contain a zinc ion, which is shown as a silver sphere. The figure was generated using the VMD software package [94] and is based on the coordinates deposited to the Protein Data Bank as 1OZB [81]. (b) Electrostatic interaction between SecB and the SecB-binding peptide of SecA. The solvent-accessible surface of the tetrameric SecB, shown as a front view that constitutes the SecA-binding site, is drawn and colored according to the surface potential (ranging from −30 to +30 kT); red: negative electrostatic potential; blue: positive electrostatic potential). The SecA peptide is show as a ribbon diagram with the central zinc ion. (c) A magnified stereo view of the coordination of the zinc ion by the SecA peptide and the specific interactions between SecB and the SecA carboxyl-terminal peptide. Residues of SecB and SecA involved in the interaction and zinc coordination are shown as ball and stick models. Residues of SecA are indicated in black, and residues of SecB are indicated in blue. Numbering is according to the *E. coli* SecA and SecB proteins.

affinity interaction leads to a loss of the targeting function of SecB and, consequently, a defect in preprotein translocation [74]. While wild-type SecB promotes preprotein translocation through its dual function, i.e., maintenance of the preprotein translocation-competent state and targeting to SecA, SecB mutants defective in

SecA interaction are inhibitory to translocation [74]. Although these mutants still maintain the preprotein in a translocatio-competent state, they are unable to release the preprotein to SecA (see Section 27.4).

The low-affinity SecB-SecA interaction in solution [78] requires neither the carboxyl terminus of SecA nor the negatively charged binding cluster on SecB [83]. At present, the functional significance of this low-affinity interaction for protein translocation is unclear. This will first require the selection of mutants specifically impaired in low-affinity binding. The 13-amino-acid carboxyl terminus of SecB has also been implicated in SecA binding [84]. Unfortunately, this solvent-exposed acidic region is barely resolved in the SecB structure, consistent with its being highly mobile. Interestingly, the (incomplete) α-helical carboxyl termini protrude out of the core structure as long arms, as if they embrace the carboxyl-terminal SecB-binding site on SecA. The crystals of the SecB-SecA peptide complex showed two SecB tetramers in the asymmetric unit, one with bound SecA peptide and one without [81]. This allowed comparison of two states; however, the structures revealed no significant conformational changes except for conformational variations in the amino- and carboxyl-terminal tails of SecB that extend away from the main SecB core and that are not in contact with the SecA peptide.

27.4 Preprotein Transfer from SecB to SecA

Another critical feature of the SecB function is that it mediates the transfer of the preprotein to SecA. In the presence of a preprotein, SecB more tightly interacts with the SecYEG-bound SecA [8]. This reaction can be mimicked with synthetic signal sequences, and it is believed that the increased SecA-SecB-binding affinity is triggered by the binding of the exposed signal sequence region of the SecB-bound preprotein to SecA. Due to the tighter interaction, the preprotein is dislocated from SecB and transferred to SecA [8]. The structural basis for this transfer reaction is unknown. Although the quaternary structure of SecB with and without the SecA peptide provides a nice solution to the dilemma of how the SecB tetramer binds the homodimeric SecA, it shows only a glimpse of how the preprotein may be transferred from SecB to SecA. Each SecA subunit within the dimer interacts with the negatively charged surface formed by one dimer of SecB [8, 81]. The stoichiometry of the SecA-SecB-preprotein ternary complex is 2:4:1. A docking model has been proposed based on the *H. influenzae* SecB [9] and *B. subtilis* SecA [85] structure, although with the latter the carboxyl-terminal residues are missing, including a region that is believed to function as a conformational flexible linker that connects the conserved SecB-binding domain with the SecA core. In the docking structure [81], the two conserved SecA zinc-binding carboxyl-termini clamp the SecB molecule such that the preprotein-binding channels are sandwiched between SecA and SecB. These channels are in juxtaposition close to the putative preprotein-binding domain on SecA. This spatial organization may facilitate the binding of the exposed preprotein signal sequence to SecA. Once this is achieved,

the preprotein will be released from SecB, whereupon it is transferred to SecA. How this tighter SecB-SecA interaction is accomplished upon signal sequence binding by SecA is not known, but it may require additional interactions between SecA and SecB. Also, it is not known how the tighter binding elicits a reduced binding affinity of SecB for preproteins. It is of interest to note that some of the mutations that interfere with preprotein binding and the tetramer-dimer equilibrium [67, 68] map at different faces of a β-strand that contacts the long α-helices constituting the dimer-dimer interface of SecB [9, 49]. Hypothetically, the high-affinity binding of SecA to SecB could cause a reduction in the preprotein binding affinity, as may influencing the SecB dimer-dimer interfacial contact much akin to the mutations that shift the tetramer-dimer equilibrium. Loosing of the dimer-dimer interaction will result in a destabilization of the peptide-binding groove and thus cause the release the preprotein. In this respect, when bound with high affinity to SecA, SecB exhibits no affinity for the mature preprotein domain [8], which suggests that the peptide-binding groove indeed has an altered conformation in this interacting state. This mechanism also ensures that as long as SecB remains engaged with the carboxyl terminus of SecA, re-occupancy of the peptide-binding groove of SecB will not be possible. Release of SecB from SecA is directly coupled to translocation. Upon the binding of ATP to SecA, preprotein translocation is initiated and concomitantly results in the release of SecB from the membrane [8]. The structural basis of this event is also unknown, but it may simply reflect a reversal of the tightened SecA-SecB interaction that occurs when SecA releases the preprotein signal sequence domain to the SecYEG channel. It is noteworthy that the formation of SecA-SecB complexes results in a small stimulation of the SecA ATPase activity [86, 87], which may facilitate the SecB release and preprotein translocation initiation reaction. Figure 27.4 summarizes the ordered reactions that result in the targeting and transfer of preprotein from SecB to the SecYEG-bound SecA protein.

27.5 Concluding Remarks

SecB is a rather peculiar chaperone. It uses its entire molecular surface for its two key functions, i.e., the binding of unfolded preproteins and of SecA. However, for preprotein release and its own membrane release, SecB relies on the catalytic activity of SecA. This defines SecB as a translocation-specific molecular chaperone, and maybe even as a co-chaperone, as it has been suggested that SecA bears chaperone activity on its own [88]. The recent insights into the structure-function relationship of the SecB-preprotein and the SecB-SecA interaction have greatly increased our knowledge about the mechanism of chaperone-mediated protein targeting in bacteria. However, the exact mechanisms of preprotein recognition and selectivity have remained elusive, while the structural basis for the preprotein transfer reaction to SecA remains to be solved. These will be challenges for the future.

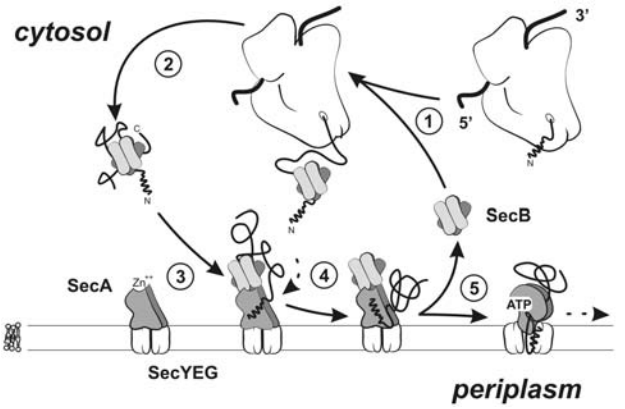

Fig. 27.4. Catalytic model SecB preprotein targeting cycle. Cytosolic SecB binds to the mature domain of a nascent preprotein (step 1) and stabilizes its unfolded state (step 2). The binary SecB-preprotein complex is targeted to the SecYEG-bound SecA (step 3) or, alternatively, first associates with cytosolic SecA through a low-affinity interaction (not shown) before it is targeted to the membrane to replace the SecYEG-bound SecA. Targeting requires the high-affinity binding of SecB to the carboxyl terminus of SecA (step 3). Binding of the signal sequence to SecA tightens the SecB-SecA interaction and elicits the release of the preprotein from the SecB-bound state with the concomitant transfer to SecA (step 4). Upon binding of ATP by SecA, preprotein translocation is initiated and SecB is released from the ternary complex (step 5) and can rebind a newly synthesized preprotein in the cytosol.

27.6 Experimental Protocols

27.6.1 How to Analyze SecB-Preprotein Interactions

The SecB-preprotein interaction is most conveniently assayed by utilizing a radiolabeled preprotein unfolded in urea or guanidine buffer, whereupon it is added to a suspension containing His-tagged SecB. The binary SecB-preprotein complex can than be collected by a batch-type of Ni-NTA affinity chromatography. Alternatively, SecB-preprotein complexes can be recovered by sucrose gradient centrifugation [39].

Materials

^{35}S-proOmpA is synthesized by an in vitro transcription/translation reaction using plasmid pET149 [89], affinity purified with OmpA antibodies [90], and solubilized in an unfolded state in 6 M urea and 50 mM TrisHCl, pH 7.8. His-tagged SecB is purified from *E. coli* MM152 (MC4100 *secB::Tn5 zhe::Tn10 mal Tcon*; [2]) transformed with plasmid pHKSB366 that contains the His-tagged *secB* gene under control of the *trc* promoter [74]. Cells are grown on Luria broth at 37 °C to an optical density of 1.0, induced with 1 mM IPTG, and grown for another 2 h. Next, the cells are harvested by centrifugation (10 min, 10 000 *g*) and passed twice through a French pressure cell (18 000 psi) in 50 mM NaP_i, pH 8.0. After removal of cell de-

bris by another centrifugation step (15 min, 30 000 *g*), the supernatant is supplemented with 60 mM imidazole, pH 8.0, and applied onto a Ni-NTA column that was pretreated according to the manufacturer's instructions (Pharmacia, Biotech). The column is washed with several column volumes of 50 mM NaP_i and 60 mM imidazole, pH 8.0. Next, His-tagged SecB protein is eluted with a buffer containing 50 mM NaP_i, 500 mM imidazole, and 300 mM NaCl, pH 6.0. After overnight dialysis against 50 mM TrisHCl, pH 7.6, at 4 °C, the His-tagged SecB can be further purified by MonoQ FPLC anion-exchange chromatography [8].

Methods

^{35}S-proOmpA (20 nM) is 50-fold diluted into 50 µL of buffer A (50 mM HEPES-KOH, pH 7.5, 0.5 mg mL^{-1} BSA) containing His-tagged SecB (100 nM). The suspension is incubated on ice, and after 30 min 50 µL of prewashed Ni-NTA agarose slurry in buffer A is added. Incubation is continued on ice for 25 min with regular vortexing. Subsequently, the bead suspension is centrifuged (5 min, 3000 rpm) through a 200 µL sucrose cushion (0.2 M sucrose in buffer A) to separate the SecB-bound from free preprotein fraction. The pellet is washed once with 150 µL buffer A, and the pellet and combined supernatant fractions are collected and quantitated by liquid scintillation counting.

26.6.2
How to Analyze SecB-SecA Interaction

High-affinity interaction between SecB and SecA is observed only when SecA is bound to the SecYEG complex. Therefore, inner-membrane vesicles (IMVs) need to be used, preferentially containing overexpressed levels of SecYEG complex because of the greater number of binding sites that provide an increased sensitivity of the assay. These IMVs are prepared by French pressure treatment, which results in closed membranes vesicles with an inside-out orientation, i.e., the SecA-binding site of the SecYEG complex faces the outer surface of the vesicles. To these membranes, saturating amounts of SecA are added. Next, radio-labeled SecB is added and the membrane-bound and free SecB fractions are separated by centrifugation of the membranes through a sucrose cushion. Binding of SecB to the membranes is strictly SecA-dependent, and when an appropriate SecB concentration range is chosen, the binding reaction can be quantitated and analyzed by Scatchard analysis.

Materials

His-tagged SecB and SecA [91] are purified as described. Untagged SecB is purified from *E. coli* BL21 transformed with plasmid pJW25, which contains *secB* gene under control of the T7 promoter [6]. Cells are grown on Luria broth at 30 °C to an optical density of 1.0, induced with 1 mM IPTG, and grown for another 2 h. Next, the cells are harvested by centrifugation (10 min, 10 000 *g*), resuspended in 20 mM TrisHCl, pH 7.4, and passed twice through a French pressure cell (18 000 psi). After removal of cell debris by a centrifugation step (15 min, 30 000 *g*), membranes are removed by ultracentrifugation (1 h, 135 000 *g*). The cell-free extract is applied onto a Hi-Trap Q-Sepharose column equilibrated with 20 mM TrisHCl and 150 mM NaCl. The column is washed with seven volumes of 20 mM TrisHCl, pH 7.4,

and 180 mM NaCl, and the bound SecB is eluted with 20 column volumes of a linear salt gradient (180–500 mM NaCl, 20 mM TrisHCl, pH 7.4). Fractions are analyzed on SDS-PAGE, pooled, and diluted with one volume of 20 mM TrisHCl, pH 7.4. To concentrate the sample, protein is applied onto a Hi-Trap Q-Sepharose column and step-eluted with 20 mM TrisHCl, pH 7.4, and 500 mM NaCl. Fractions containing concentrated SecB are pooled and applied onto a Sephacryl S300 gel filtration column (XK16/100) equilibrated with 20 mM TrisHCl, pH 7.4, and 150 mM NaCl. Fractions containing pure SecB are pooled and stored at −80 °C or concentrated by an additional anion-exchange step on a MonoQ 5/5 column.

IMVs are prepared from SF100 cells transformed with plasmid pET340, which allows for overproducing the SecYEG complex [92] by means of French pressure lysis and differential centrifugation, and treated with 6 M urea and 50 mM TrisHCl, pH 7.8 [93]. Purified SecB is labeled with carrier-free ^{125}I (Radiochemical Centre, Amersham, U.K.) to a specific activity of about 5×10^4 cpm pmol^{-1} according to the following procedure: SecB (100 μg) in buffer A (50 mM TrisHCl, pH 8.0, 50 mM KCl, 5 mM $MgCl_2$, and 10% glycerol) is transferred to a reaction vial coated with IODO-GEN Iodination Reagent (Pierce, Rockford, IL). The reaction is started by adding 2 μL of K^{125}I (200 μCi), incubated for 15 min at room temperature, and terminated by transferring the mixture into a new reaction vial containing dithiothreitol (DTT) at a final concentration of 10 mM. Free iodine is removed by chromatography on a PD-10 Sephadex column (Amersham Biotech AB, Uppsala, Sweden) which is prewashed with buffer A containing 1 mM DTT.

Methods

Binding of ^{125}I SecB to IMVs can be assayed essentially as described previously [7]. Urea-treated IMVs (10 μg of membrane protein) are suspended in 100 μL of buffer B (50 mM HEPES-KOH, pH 7.6, 30 mM KCl, 0.5 mg mL^{-1} BSA, 10 mM DDT, 2 mM Mg-acetate) and incubated for 20 min at room temperature with 0–50 nM ^{125}I-SecB in the presence or absence of 100 nM SecA. After 20 min, the solution containing the IMVs is layered on top of a 100-μL 0.2-M sucrose cushion in buffer B and spun with a Beckman Airfuge (30 psi, 10 min, 4 °C). The amount of ^{125}I-SecB in the supernatant and pellet is quantitated by liquid scintillation counting, and the data are analyzed by nonlinear regression assuming biphasic-binding kinetics. The biphasic kinetics results from a major high-affinity binding reaction that is SecA- and SecYEG-dependent and from a low, nonspecific component that is due to the non-saturable and SecA- and SecYEG-independent association of SecB with the membrane surface.

Acknowledgements

This work was supported by the Council for Chemical Sciences of the Netherlands Organization for Scientific Research and the Earth and Life Sciences Foundation, which are subsidized by the Dutch Organization for the Advancement of Scientific Research, the Royal Dutch Academy of Sciences (to N.N.) and by EC RTN contract HPRN-2000-00075. The authors wish to thank members of the protein secretion group for valuable discussion.

References

1 C. A. Kumamoto, J. Beckwith (1983). Mutations in a new gene, *secB*, cause defective protein localization in *Escherichia coli*. *J. Bacteriol.* **154**, 253–260.

2 C. A. Kumamoto, J. Beckwith (1985). Evidence for specificity at an early step in protein export in *Escherichia coli*. *J. Bacteriol.* **163**, 267–274.

3 P. M. Gannon, C. A. Kumamoto (1993). Mutations of the molecular chaperone protein SecB which alter the interaction between SecB and maltose-binding protein. *J. Biol. Chem.* **268**, 1590–1595.

4 D. N. Collier, V. A. Bankaitis, J. B. Weiss, P. J. Bassford, Jr. (1988). The antifolding activity of SecB promotes the export of the *E. coli* maltose-binding protein. *Cell* **53**, 273–283.

5 L. L. Randall, S. J. Hardy (1986). Correlation of competence for export with lack of tertiary structure of the mature species: a study *in vivo* of maltose-binding protein in *E. coli*. *Cell* **46**, 921–928.

6 J. B. Weiss, P. H. Ray, P. J. Bassford, Jr. (1988). Purified *secB* protein of *Escherichia coli* retards folding and promotes membrane translocation of the maltose-binding protein *in vitro*. *Proc. Natl. Acad. Sci. U.S.A.* **85**, 8978–8982.

7 F. U. Hartl, S. Lecker, E. Schiebel, J. P. Hendrick, W. Wickner (1990). The binding cascade of SecB to SecA to SecY/E mediates preprotein targeting to the *E. coli* plasma membrane. *Cell* **63**, 269–279.

8 P. Fekkes, C. van der Does, A. J. M. Driessen (1997). The molecular chaperone SecB is released from the carboxy-terminus of SecA during initiation of precursor protein translocation. *EMBO J.* **16**, 6105–6113.

9 Z. Xu, J. D. Knafels, K. Yoshino (2000). Crystal structure of the bacterial protein export chaperone secB. *Nat. Struct. Biol.* **7**, 1172–1177.

10 W. Wickner, A. J. M. Driessen, F. U. Hartl (1991). The enzymology of protein translocation across the *Escherichia coli* plasma membrane. *Annu. Rev. Biochem.* **60**, 101–124.

11 Q. A. Valent, P. A. Scotti, S. High, J. W. de Gier, G. von Heijne, G. Lentzen, W. Wintermeyer, B. Oudega, J. Luirink (1998). The *Escherichia coli* SRP and SecB targeting pathways converge at the translocon. *EMBO J.* **17**, 2504–2512.

12 L. Brundage, J. P. Hendrick, E. Schiebel, A. J. M. Driessen, W. Wickner (1990). The purified *E. coli* integral membrane protein SecY/E is sufficient for reconstitution of SecA-dependent precursor protein translocation. *Cell* **62**, 649–657.

13 A. J. M. Driessen (2001). SecB, a molecular chaperone with two faces. *Trends Microbiol.* **9**, 193–196.

14 L. L. Randall, S. J. Hardy (2002). SecB, one small chaperone in the complex milieu of the cell. *Cell Mol. Life Sci.* **59**, 1617–1623.

15 P. Fekkes, A. J. M. Driessen (1999). Protein targeting to the bacterial cytoplasmic membrane. *Microbiol. Mol. Biol. Rev.* **63**, 161–173.

16 K. H. M. van Wely, J. Swaving, M. Klein, R. Freudl, A. J. M. Driessen (2000). The carboxyl terminus of the Bacillus subtilis SecA is dispensable for protein secretion and viability. *Microbiology* **146**, 2573–2581.

17 K. H. M. van Wely, J. Swaving, R. Freudl, A. J. M. Driessen (2001). Translocation of proteins across the cell envelope of Gram-positive bacteria. *FEMS Microbiol. Rev.* **25**, 437–454.

18 H. Shimizu, K. Nishiyama, H. Tokuda (1997). Expression of *gpsA* encoding biosynthetic sn-glycerol 3-phosphate dehydrogenase suppresses both the LB-phenotype of a *secB* null mutant and the cold-sensitive phenotype of a *secG* null mutant. *Mol. Microbiol.* **26**, 1013–1021.

19 E. Altman, C. A. Kumamoto, S. D. Emr (1991). Heat-shock proteins can substitute for SecB function during protein export in *Escherichia coli*. *EMBO J.* **10**, 239–245.

20 J. Wild, E. Altman, T. Yura, C. A. Gross (1992). DnaK and DnaJ heat shock proteins participate in protein export in *Escherichia coli*. *Genes Dev.* **6**, 1165–1172.

21 J. Wild, P. Rossmeissl, W. A. Walter, C. A. Gross (1996). Involvement of the DnaK-DnaJ-GrpE chaperone team in protein secretion in *Escherichia coli*. *J. Bacteriol.* **178**, 3608–3613.

22 C. A. Kumamoto (1989). *Escherichia coli* SecB protein associates with exported protein precursors *in vivo*. *Proc. Natl. Acad. Sci. U.S.A.* **86**, 5320–5324.

23 C. A. Kumamoto, O. Francetic (1993). Highly selective binding of nascent polypeptides by an *Escherichia coli* chaperone protein *in vivo*. *J. Bacteriol.* **175**, 2184–2188.

24 L. L. Randall, T. B. Topping, S. J. Hardy, M. Y. Pavlov, D. V. Freistroffer, M. Ehrenberg (1997). Binding of SecB to ribosome-bound polypeptides has the same characteristics as binding to full-length, denatured proteins. *Proc. Natl. Acad. Sci. U.S.A.* **94**, 802–807.

25 S. J. Hardy, L. L. Randall (1991). A kinetic partitioning model of selective binding of nonnative proteins by the bacterial chaperone SecB. *Science* **251**, 439–443.

26 V. G. Panse, J. B. Udgaonkar, R. Varadarajan (1998). SecB binds only to a late native-like intermediate in the folding pathway of barstar and not to the unfolded state. *Biochemistry* **37**, 14477–14483.

27 R. Zahn, S. Perrett, A. R. Fersht (1996). Conformational states bound by the molecular chaperones GroEL and secB: a hidden unfolding (annealing) activity. *J. Mol. Biol.* **261**, *261*, 43–61.

28 G. Stenberg, A. R. Fersht (1997). Folding of barnase in the presence of the molecular chaperone SecB. *J. Mol. Biol.* **274**, *274*, 268–275.

29 R. Zahn, S. Perrett, G. Stenberg, A. R. Fersht (1996). Catalysis of amide proton exchange by the molecular chaperones GroEL and SecB. *Science* **271**, *271*, 642–645.

30 V. G. Panse, C. P. Swaminathan, A. Surolia, R. Varadarajan (2000). Thermodynamics of substrate binding to the chaperone SecB. *Biochemistry* **39**, 2420–2427.

31 P. Fekkes, T. den Blaauwen, A. J. M. Driessen (1995). Diffusion-limited interaction between unfolded polypeptides and the *Escherichia coli* chaperone SecB. *Biochemistry* **34**, 10078–10085.

32 N. L. Vekshin (1998). Protein sizes and stoichiometry in the chaperone SecB-RBPTI complex estimated by ANS fluorescence. *Biochemistry (Mosc)*. **63**, 485–488.

33 L. L. Randall, T. B. Topping, D. Suciu, S. J. Hardy (1998). Calorimetric analyses of the interaction between SecB and its ligands. *Protein Sci.* **7**, 1195–1200.

34 S. Lecker, D. Meyer, W. Wickner (1989). Export of prepro-alpha-factor from *Escherichia coli*. *J. Biol. Chem.* **264**, 1882–1886.

35 E. L. Powers, L. L. Randall (1995). Export of periplasmic galactose-binding protein in *Escherichia coli* depends on the chaperone SecB. *J. Bacteriol.* **177**, 1906–1907.

36 J. E. Bruce, V. F. Smith, C. Liu, L. L. Randall, R. D. Smith (1998). The observation of chaperone-ligand noncovalent complexes with electrospray ionization mass spectrometry. *Protein Sci.* **7**, 1180–1185.

37 L. L. Randall (1992). Peptide binding by chaperone SecB: implications for recognition of nonnative structure. *Science* **257**, 241–245.

38 S. H. Lecker, A. J. M. Driessen, W. Wickner (1990). ProOmpA contains secondary and tertiary structure prior to translocation and is shielded from aggregation by association with SecB protein. *EMBO J.* **9**, 2309–2314.

39 S. Lecker, R. Lill, T. Ziegelhoffer, C. Georgopoulos, P. J. Bassford, Jr., C. A. Kumamoto, W. Wickner (1989). Three pure chaperone proteins of *Escherichia coli*-SecB, trigger factor and GroEL-form soluble complexes with precursor proteins *in vitro*. *EMBO J.* **8**, 2703–2709.

40 R. Kusters, T. de Vrije, E.

Breukink, B. de Kruijff (1989). SecB protein stabilizes a translocation-competent state of purified prePhoE protein. *J. Biol. Chem.* **264**, 20827–20830.

41 D. L. Diamond, S. Strobel, S. Y. Chun, L. L. Randall (1995). Interaction of SecB with intermediates along the folding pathway of maltose-binding protein. *Protein Sci.* **4**, 1118–1123.

42 P. M. Gannon, P. Li, C. A. Kumamoto (1989). The mature portion of *Escherichia coli* maltose-binding protein (MBP) determines the dependence of MBP on SecB for export. *J. Bacteriol.* **171**, 813–818.

43 G. Liu, T. B. Topping, L. L. Randall (1989). Physiological role during export for the retardation of folding by the leader peptide of maltose-binding protein. *Proc. Natl. Acad. Sci. U.S.A.* **86**, 9213–9217.

44 G. P. Liu, T. B. Topping, W. H. Cover, L. L. Randall (1988). Retardation of folding as a possible means of suppression of a mutation in the leader sequence of an exported protein. *J. Biol. Chem.* **263**, 14790–14793.

45 V. F. Smith, S. J. Hardy, L. L. Randall (1997). Determination of the binding frame of the chaperone SecB within the physiological ligand oligopeptide-binding protein. *Protein Sci.* **6**, 1746–1755.

46 V. J. Khisty, G. R. Munske, L. L. Randall (1995). Mapping of the binding frame for the chaperone SecB within a natural ligand, galactose-binding protein. *J. Biol. Chem.* **270**, 25920–25927.

47 T. B. Topping, L. L. Randall (1994). Determination of the binding frame within a physiological ligand for the chaperone SecB. *Protein Sci.* **3**, 730–736.

48 N. T. Knoblauch, S. Rüdiger, H.-J. Schönfeld, A. J. M. Driessen, J. Schneider-Mergener, B. Bukau (1999). Substrate specificity of the SecB chaperone. *J. Biol. Chem.* **274**, 34219–34225.

49 C. Dekker, B. de Kruijff, P. Gros (2003). Crystal structure of SecB from *Escherichia coli*. *J. Struct. Biol.* **144**, 313–319.

50 T. B. Topping, R. L. Woodbury, D. L. Diamond, S. J. Hardy, L. L. Randall (2001). Direct demonstration that homotetrameric chaperone SecB undergoes a dynamic dimer-tetramer equilibrium. *J. Biol. Chem.* **276**, 7437–7441.

51 V. G. Panse, C. P. Swaminathan, J. J. Aloor, A. Surolia, R. Varadarajan (2000). Unfolding thermodynamics of the tetrameric chaperone, SecB. *Biochemistry* **39**, 2362–2369.

52 J. Kim, D. A. Kendall (1998). Identification of a sequence motif that confers SecB dependence on a SecB-independent secretory protein *in vivo*. *J. Bacteriol.* **180**, 1396–1401.

53 J. Kim, J. Luirink, D. A. Kendall (2000). SecB dependence of an exported protein is a continuum influenced by the characteristics of the signal peptide or early mature region. *J. Bacteriol.* **182**, 4108–4112.

54 D. L. Diamond, L. L. Randall (1997). Kinetic partitioning. Poising SecB to favor association with a rapidly folding ligand. *J. Biol. Chem.* **272**, 28994–28998.

55 T. B. Topping, L. L. Randall (1997). Chaperone SecB from *Escherichia coli* mediates kinetic partitioning via a dynamic equilibrium with its ligands. *J. Biol. Chem.* **272**, 19314–19318.

56 V. J. Khisty, L. L. Randall (1995). Mapping of the binding frame for the chaperone SecB within a natural ligand, galactose-binding protein. *J. Bacteriol.* **177**, 3277–3282.

57 M. Watanabe, G. Blobel (1995). High-affinity binding of *Escherichia coli* SecB to the signal sequence region of a presecretory protein. *Proc. Natl. Acad. Sci. U.S.A.* **92**, 10133–10136.

58 M. Watanabe, G. Blobel (1989). SecB functions as a cytosolic signal recognition factor for protein export in *E. coli*. *Cell* **58**, 695–705.

59 L. L. Randall, T. B. Topping, S. J. Hardy (1990). No specific recognition of leader peptide by SecB, a chaperone involved in protein export. *Science* **248**, 860–863.

60 S. Park, G. Liu, T. B. Topping, W. H.

Cover, L. L. Randall (1988). Modulation of folding pathways of exported proteins by the leader sequence. *Science* **239**, 1033–1035.

61 E. Altman, S. D. Emr, C. A. Kumamoto (1990). The presence of both the signal sequence and a region of mature LamB protein is required for the interaction of LamB with the export factor SecB. *J. Biol. Chem.* **265**, 18154–18160.

62 G. Eisner, H. G. Koch, K. Beck, J. Brunner, M. Muller (2003). Ligand crowding at a nascent signal sequence. *J. Cell Biol.* **163**, 35–44.

63 K. Beck, L. F. Wu, J. Brunner, M. Muller (2000). Discrimination between SRP- and SecA/SecB-dependent substrates involves selective recognition of nascent chains by SRP and trigger factor. *EMBO J.* **19**, 134–143.

64 Q. A. Valent, D. A. Kendall, S. High, R. Kusters, B. Oudega, J. Luirink (1995). Early events in preprotein recognition in *E. coli*: interaction of SRP and trigger factor with nascent polypeptides. *EMBO J.* **14**, 5494–5505.

65 T. Hesterkamp, S. Hauser, H. Lutcke, B. Bukau (1996). *Escherichia coli* trigger factor is a prolyl isomerase that associates with nascent polypeptide chains. *Proc. Natl. Acad. Sci. U.S.A.* **93**, 4437–4441.

66 L. L. Randall, S. J. Hardy, T. B. Topping, V. F. Smith, J. E. Bruce, R. D. Smith (1998). The interaction between the chaperone SecB and its ligands: evidence for multiple subsites for binding. *Protein Sci.* **7**, 2384–2390.

67 H. H. Kimsey, M. D. Dagarag, C. A. Kumamoto (1995). Diverse effects of mutation on the activity of the *Escherichia coli* export chaperone SecB. *J. Biol. Chem.* **270**, 22831–22835.

68 E. M. Muren, D. Suciu, T. B. Topping, C. A. Kumamoto, L. L. Randall (1999). Mutational alterations in the homotetrameric chaperone SecB that implicate the structure as dimer of dimers. *J. Biol. Chem.* **274**, 19397–19402.

69 P. N. Danese, T. J. Silhavy (1998). Targeting and assembly of periplasmic and outer-membrane proteins in *Escherichia coli*. *Annu. Rev. Genet.* **32**, 59–94.

70 O. Francetic, M. P. Hanson, C. A. Kumamoto (1993). *prlA* suppression of defective export of maltose-binding protein in *secB* mutants of *Escherichia coli*. *J. Bacteriol.* **175**, 4036–4044.

71 O. Francetic, C. A. Kumamoto (1996). *Escherichia coli* SecB stimulates export without maintaining export competence of ribose-binding protein signal sequence mutants. *J. Bacteriol.* **178**, 5954–5959.

72 N. J. Trun, J. Stader, A. Lupas, C. Kumamoto, T. J. Silhavy (1988). *prlA* suppression of defective export of maltose-binding protein in *secB* mutants of *Escherichia coli*. *J. Bacteriol.* **170**, 5928–5930.

73 A. I. Derman, J. W. Puziss, P. J. Bassford, Jr., J. Beckwith (1993). A signal sequence is not required for protein export in *prlA* mutants of *Escherichia coli*. *EMBO J.* **12**, 879–888.

74 P. Fekkes, J. G. de Wit, J. P. van der Wolk, H. H. Kimsey, C. A. Kumamoto, A. J. M. Driessen (1998). Preprotein transfer to the *Escherichia coli* translocase requires the co-operative binding of SecB and the signal sequence to SecA. *Mol. Microbiol.* **29**, 1179–1190.

75 P. Delepelaire, C. Wandersman (1998). The SecB chaperone is involved in the secretion of the *Serratia marcescens* HasA protein through an ABC transporter. *EMBO J.* **17**, 936–944.

76 L. Debarbieux, C. Wandersman (2001). Folded HasA inhibits its own secretion through its ABC exporter. *EMBO J.* **20**, 4657–4663.

77 G. Sapriel, C. Wandersman, P. Delepelaire (2002). The N terminus of the HasA protein and the SecB chaperone cooperate in the efficient targeting and secretion of HasA via the ATP-binding cassette transporter. *J. Biol. Chem.* **277**, 6726–6732.

78 T. den Blaauwen, E. Terpetschnig, J. R. Lakowicz, A. J. M. Driessen (1997). Interaction of SecB with soluble SecA. *FEBS Lett.* **416**, 35–38.

79 E. Breukink, N. Nouwen, A. van

Raalte, S. Mizushima, J. Tommassen, B. de Kruijff (1995). The C terminus of SecA is involved in both lipid binding and SecB binding. *J. Biol. Chem.* **270**, 7902–7907.

80 P. Fekkes, J. G. de Wit, A. Boorsma, R. H. Friesen, A. J. M. Driessen (1999). Zinc stabilizes the SecB binding site of SecA. *Biochemistry* **38**, 5111–5116.

81 J. Zhou, Z. Xu (2003). Structural determinants of SecB recognition by SecA in bacterial protein translocation. *Nat. Struct. Biol.* **10**, 942–947.

82 T. Rajapandi, D. Oliver (1994). Carboxy-terminal region of *Escherichia coli* SecA ATPase is important to promote its protein translocation activity *in vivo*. *Biochem. Biophys. Res. Commun.* **200**, 1477–1483.

83 R. L. Woodbury, T. B. Topping, D. L. Diamond, D. Suciu, C. A. Kumamoto, S. J. Hardy, L. L. Randall (2000). Complexes between protein export chaperone SecB and SecA. Evidence for separate sites on SecA providing binding energy and regulatory interactions. *J. Biol. Chem.* **275**, 24191–24198.

84 T. L. Volkert, J. D. Baleja, C. A. Kumamoto (1999). A highly mobile C-terminal tail of the *Escherichia coli* protein export chaperone SecB. *Biochem. Biophys. Res. Commun.* **264**, 949–954.

85 J. F. Hunt, S. Weinkauf, L. Henry, J. J. Fak, P. McNicholas, D. B. Oliver, J. Deisenhofer (2002). Nucleotide control of interdomain interactions in the conformational reaction cycle of SecA. *Science* **297**, 2018–2026.

86 J. Kim, A. Miller, L. Wang, J. P. Muller, D. A. Kendall (2001). Evidence that SecB enhances the activity of SecA. *Biochemistry* **40**, 3674–3680.

87 A. Miller, L. Wang, D. A. Kendall (2002). SecB modulates the nucleotide-bound state of SecA and stimulates ATPase activity. *Biochemistry* **41**, 5325–5332.

88 M. Eser, M. Ehrmann (2003). SecA-dependent quality control of intracellular protein localization. *Proc. Natl. Acad. Sci. U.S.A.* **100**, 13231–13234.

89 J. P. van der Wolk, P. Fekkes, A. Boorsma, J. L. Huie, T. J. Silhavy, A. J. M. Driessen (1998). PrlA4 prevents the rejection of signal sequence defective preproteins by stabilizing the SecA-SecY interaction during the initiation of translocation. *EMBO J.* **17**, 3631–3639.

90 E. Crooke, W. Wickner (1987). Trigger factor: a soluble protein that folds pro-OmpA into a membrane-assembly-competent form. *Proc. Natl. Acad. Sci. U.S.A.* **84**, 5216–5220.

91 R. J. Cabelli, L. Chen, P. C. Tai, D. B. Oliver (1988). SecA protein is required for secretory protein translocation into *E. coli* membrane vesicles. *Cell* **55**, 683–692.

92 C. van der Does, E. H. Manting, A. Kaufmann, M. Lutz, A. J. M. Driessen (1998). Interaction between SecA and SecYEG in micellar solution and formation of the membrane-inserted state. *Biochemistry* **37**, 201–210.

93 K. Cunningham, R. Lill, E. Crooke, M. Rice, K. Moore, W. Wickner, D. Oliver (1989). SecA protein, a peripheral protein of the *Escherichia coli* plasma membrane, is essential for the functional binding and translocation of proOmpA. *EMBO J.* **8**, 955–959.

94 W. Humphrey, A. Dalke, K. Schulten (1996). VMD: visual molecular dynamics. *J. Mol. Graph.* **14**, 33–38.

95 J. B. Weiss, P. J. Bassford, Jr. (1990). The folding properties of the *Escherichia coli* maltose-binding protein influence its interaction with SecB *in vitro*. *J. Bacteriol.* **172**, 3023–3029.

96 C. A. Kumamoto, L. Chen, J. Fandl, P. C. Tai (1989). Purification of the *Escherichia coli secB* gene product and demonstration of its activity in an *in vitro* protein translocation system. *J. Biol. Chem.* **264**, 2242–2249.

28
Protein Folding in the Periplasm and Outer Membrane of *E. coli*

Michael Ehrmann

28.1
Introduction

The cell envelope of Gram-negative bacteria such as *E. coli* is comprised of the periplasm and the outer membrane. The periplasm contains the proteoglycan layer providing cell shape and rigidity against osmotic stresses that often occur in the natural habitat of these organisms. The periplasm is thought to occupy about 30% of the cell volume and to have a width of around 50 nm [1]. However, these values can change according to the osmolarity of the growth medium. In addition, the periplasm is believed to be rather viscous and it is thought to have a higher concentration of protein than does the cytoplasm [2]. The outer membrane is, in contrast to the cytoplasmic membrane, asymmetric. It is composed of an inner leaflet of phospholipids and an outer leaflet containing the glycolipid lipopolysaccharide. Lipopolysaccharide comprises three components: a lipid A moiety containing sugar and multiple fatty acyl chains, a core oligosaccharide, and the O-antigen. The O-antigen is a complex polysaccharide consisting of repeats of oligosaccharide units. The cell envelope is responsible for communication with the environment, including, for example, nutrient uptake; exclusion of toxic compounds; interaction with host cells, other bacteria, or bacteriophages; and cell division. These functions are mediated by proteins whose folding, functionality, and abundance must be continuously monitored for optimal performance of the entire organism. Given the vast number of proteins and their different properties and abundance, protein quality control, repair, and degradation are challenging tasks. These issues have been elegantly solved by nature and are the focus of intensive research. This chapter describes the known cellular factors involved, the most commonly studied substrates, and the regulation of the unfolded protein response that coordinates important elements involved in the regulation of protein composition. The cell envelope of the gram-negative bacterium *E. coli* represents an experimental system that is well suited to address the important question of mechanism of protein quality control. The fact that most cellular factors involved in this process are nonessential and ATP independent is a major advantage, as both features simplify experimental approaches. Nonessential factors allow us to work with rather healthy

Protein Folding Handbook. Part II. Edited by J. Buchner and T. Kiefhaber

ISBN: 3-527-30784-2

mutants and stable genetic backgrounds. The absence of ATPase domains reduces the number of issues to consider and thus simplifies mutant construction and the interpretation of data. Another important property of the cell envelope is that it is oxidizing. Therefore, many proteins contain disulfide (S–S) bonds, providing additional structural stability.

Protein composition in *E. coli* can be derived from its genome sequence [3], indicating that about two-thirds of all proteins are localized in the cytoplasm, that 20% of all proteins are in the cytoplasmic membrane, and that roughly 10% of all proteins are sorted to the cell envelope. We estimate that about 150 different proteins are localized in the periplasm and about 320 in outer membrane. A comprehensive list of periplasmic and outer membrane proteins can be accessed via the ECCE database (http://www.cf.ac.uk/biosi/staff/ehrmann/tools/ecce/ecce.htm). The largest class of proteins in the periplasm is the substrate-binding proteins of ABC transporters. There are also enzymes that are involved in metabolism and murein biogenesis, proteins that are involved in regulation, and those that are part of large protein complexes involved in, for example, motility, cell division, and virulence. In addition there are quite a number of proteases, chaperones, and folding catalysts, such as proline isomerases and proteins involved in disulfide bond formation. The outer membrane has proteins that are involved in transport (the porins); enzymes such as proteases, lipases, and glucosidases; and components of export machines involved in detoxification and protein secretion. A common structural feature of outer membrane proteins is that their membrane-spanning segments are β-sheets, which is in contrast to cytoplasmic membrane proteins whose transmembrane segments adopt an α-helical secondary structure. Most outer membrane proteins contain a β-barrel domain that is integral to the membrane, and some proteins have additional domains either in the periplasm or on the cell surface, which can be quite extensive in size (for review, see Refs. [4–6]).

A common feature of periplasmic and outer membrane proteins is that they have to be initially translocated across the cytoplasmic membrane. There are two main routes for this purpose: via the classical secretion machinery (Sec) or via the twin arginine pathway (TAT) (For review, see Refs. [7–9]). About 420 proteins probably use the Sec route, while it is believed that the TAT pathway has about 30 substrates. These estimates were derived from inspection of the 452 signal sequences found in *E. coli* proteins for TAT motifs (see ECCE database). While substrates of the Sec system need to be unfolded during translocation, TAT substrates fold in the cytoplasm and are believed to be fully functional after translocation is completed. In fact, folding is a prerequisite for TAT-dependent translocation [10]. The post-translocational folding of proteins that are delivered by the Sec pathway may be considered as reminiscent of folding of nascent polypeptide chains in the cytoplasm after or during emergence from the ribosome. Thus, we should expect that similar principles would apply for the folding of polypeptide chains emerging from the translocon or the ribosome. After proteins have folded, each has its lifespan, which can be affected by certain types of environmental conditions that interfere with the folded and functional state. These conditions include osmo, redox, heat,

radiation, pH, and chemical stresses. Because the outer membrane is ''leaky'' for compounds smaller than 600 Da, the periplasm is less protected than the cytoplasm, which is surrounded by the semipermeable cytoplasmic membrane. The fate of damaged proteins is determined by three pathways: repair, degradation, and, if the latter fail, aggregation. Aggregated proteins can impose a severe threat to cells because they can cause lethal damage, e.g., when an aggregated protein has an essential function or when the aggregates physically interfere with the function of other important proteins or the integrity of cells.

It is of interest to study these processes on the mechanistic level to understand the basic physiology of the cell and its regulatory principles, but also for practical aspects including recombinant protein production and vaccine or drug development. Initially, and as has been often the case with general scientific insights obtained from studying bacteria, knowledge was gained from genetic evidence. Because genetic evidence can be considered as indirect, in vitro biochemical evidence using purified components has helped to verify genetic data. So far we have learned that there are four proline isomerases, several proteins dealing with formation and isomerization of disulfide bonds, one general chaperone, several specific chaperones, and a large number of proteases. Another important aspect that has become apparent is that several proteins involved in quality control can be bifunctional. For example, some proline isomerases can have chaperone function that is independent of their enzymatic activity, which is also true for at least one protease (see Section 28.2.3.3).

28.2
Individual Cellular Factors

Molecular chaperones recognize and selectively bind proteins that are present in a nonnative state, which may occur during translocation across membranes, folding, assembly of oligomeric complexes, and various environmental stresses. Chaperones recognize surface-exposed hydrophobicity, thereby discriminating against native proteins. In contrast to the cytoplasm, where the major chaperone systems have been identified and are well understood [11], not much is known about general chaperones in the cell envelope. The only protein that is believed to function exclusively as a general chaperone is Skp, which has so far been attributed to the folding and assembly of outer membrane proteins and to improvement of the folding of recombinant antibody fragments (see below).

Protein folding catalysts carry out similar functions, but, in contrast to chaperones, they improve slow steps in protein folding by catalyzing covalent modifications such as S–S bonds or the *cis-trans* isomerization of proline residues. The redox machinery is genetically and biochemically well studied. The main players belong to the Dsb family, which are involved in the formation, reduction, and isomerization of S–S bonds (see Chapter 9). Native substrates of the Dsb system include dozens of proteins containing S–S bonds, such as alkaline phosphatase,

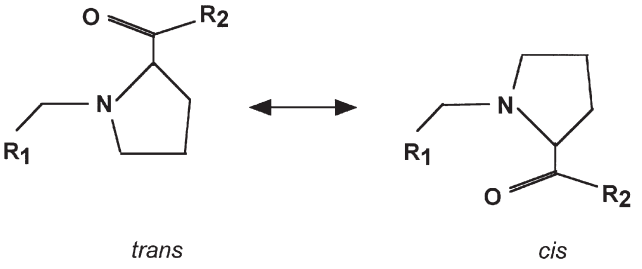

Fig. 28.1. Proline isomerization. The *trans* and *cis* conformations of a proline residue are shown.

OmpA, heat-stable enterotoxins, the maltoporin LamB, periplasmic binding proteins, pilin proteins, and components of various secretion apparatuses involved in virulence. There are also four proline isomerases in the cell envelope. Even though knockout mutations are available, proline isomerase activity could be demonstrated in vitro, and involvement in outer membrane biogenesis was suggested, their entire physiological implications remain to be determined [12].

28.2.1
The Proline Isomerases FkpA, PpiA, SurA, and PpiD

One major rate-limiting step in protein folding is the *cis-trans* isomerization of peptidyl bonds occurring N-terminally to each proline residue (Figure 28.1). In general, the *trans* peptide bond is energetically most favorable, and this configuration is represented in almost all peptide bonds. However, *cis* and *trans* peptide bonds involving proline have similar stabilities and both are found in native proteins [13]. Peptidyl-proline bonds are mostly present in *trans* conformation, while about 10% are present in *cis* conformation [14], and the isomeric state of each proline is characteristic of a specific protein. Because the *cis-trans* isomerization is a slow process with high activation energies of about 20 kcal mol^{-1} [15], this step is catalyzed by peptidyl prolyl isomerases that are widely conserved in nature. The *E. coli* cell envelope has four enzymes that can be classified into three families, i.e., the cyclophilin PpiA, the FK506-binding protein (FKBP) FkpA, and the parvulins SurA and PpiD. Proline isomerases have been initially characterized by in vitro methods. These tests use the fact that proteases exclusively cleave a peptide bond that is present in a *trans* conformation, thus having the potential to change the *cis-trans* equilibrium of peptidyl-prolyl isomers. A classical setup uses a tetrameric peptide containing one Pro residue as well as a chromogenic group at the C-terminus and, e.g., α-chymotrypsin as a protease. After mixing these components, a rapid cleavage of the *trans* isomers is observed, which is followed by a slow cleavage after *cis-trans* isomerization. Since these tests were established, a number of more sensitive assays have been developed, including dynamic NMR, direct spectroscopic meth-

ods that are independent of an added protease, and refolding reactions using chemically denatured protein such as Rnase T1 (for review, see Ref. [14]). The latter provides direct evidence that proline isomerases are indeed involved in protein-folding reactions.

28.2.1.1 FkpA

FkpA was identified as a member of the FKBP family because its carboxyl domain contains the consensus FK506-binding motif, including those amino acids at the active site that form hydrogen bonds with the drug [16]. In addition, high-affinity binding to such drugs has been verified experimentally [17]. FkpA has two domains that can be expressed separately. In addition to its C-terminal PPIase domain, FkpA has a second domain, located between residues 1 and 122, that has been implicated in dimerization but not in chaperone activity. When both domains were expressed separately, and when using RNAse T1 and citrate synthase as substrates, it was found that the FKPA domain had full chaperone but reduced PPIase activity [17]. Chaperone activity of FkpA was also detected for single chain Fv (scFv) antibody fragments in vivo and in vitro [18, 19]. As FkpA-dependent refolding was observed in scFv fragments that do not contain *cis*-prolines, it was concluded that chaperone function of FkpA could be independent of its proline isomerase activity. Also, co-expression of the periplasmic PPIases PpiA and SurA did not increase the level of functional scFv fragments, indicating at least some specificity of the PPIases tested [20]. Similar results were obtained when the aggregation of MBP mutant 31 was analyzed [21]. It was shown that FkpA, but not PpiA or SurA, was able to suppress aggregation of MBP31. Again, after disrupting active site residues, the chaperone activity of FkpA remained functional. These data suggest that the capacity of binding denatured polypeptides might be sufficient to stimulate refolding of chemically denatured proteins and to prevent aggregation. It is also interesting to note that only small changes to the overall structure are sufficient to cause aggregation and inclusion body formation of MBP31. This was recognized when the protein, containing the two point mutations $Gly_{32}Asp$ and $Ile_{33}Pro$, was crystallized. The structure of MBP31 closely resembled the wild type. Only a small dislocation of the changed residues that are part of the loop connecting the first α-helix to the first β-strand of MBP was observed [22].

28.2.1.2 PpiA

In *E. coli*, PpiA (also called Rotamase A or CypA) was the first proline isomerase that was cloned, purified, and crystallized [23–25]. It belongs to the cyclophilin family that is inhibited by the immunosuppressant cyclosporin A. The apparent Ki is in the micromolar range, which is about several orders of magnitude higher than for the eukaryotic enzymes [26, 27]. Compton et al. have also shown catalyzed refolding of denatured type III collagen, but there are currently no native substrates of PpiA known. The only indirect evidence available that PpiA is important for general protein-folding reactions can be derived from the fact that its gene is regulated by the Cpx stress pathway ([28]; see also Section 28.4.2).

28.2.1.3 SurA

The *surA* gene has been identified to be essential for survival in the stationary phase [29], and it was shown later that the elevated pH of the growth medium and the absence of the stationary-phase sigma factor S were responsible for this phenotype [30]. Another striking phenotype of *surA* mutants is the marked sensitivity to toxic compounds such as detergents, dyes, chelators, and antibiotics [31] that may be attributed to a defective outer membrane. Consistent with this idea, it was found that in vivo, SurA is required for folding of the three outer membrane proteins OmpA, OmpF, and LamB [31–33]. Co-immunoprecipitation experiments suggested a preference for binding of outer membrane proteins such as PhoE, LamB, and OmpF versus periplasmic or cytoplasmic proteins such as MBP, beta-lactamase, or chloramphenicol transacetylase [33]. Studies with LamB revealed that SurA could convert unfolded monomers into assembly-competent folded monomers [33]. Therefore, these studies support existing models for the assembly of porins, which can be divided into at least three stages: release from the translocon, folding of monomers in the periplasm, followed by the final assembly into functional trimers (for review, see Ref. [8]).

SurA can be divided into four domains: an N-terminal domain, two PPIase domains, and a C-terminal domain of about 40 residues. A functional analysis of each of these domains indicated that the C-terminal PPIase domain is catalytically active, while the N-terminal domain PPIase domain is not [34]. The chaperone function is localized in the non-catalytic parts of SurA [34], and the crystal structure (Figure 28.2) showed that the chaperone and the PPIase domains indeed are distinct structural units, the catalytic domain being tethered via linkers to the rest of the molecule comprised of the N-terminus, the inactive PPIase domain, and the C-terminal domain [35]. The fortunes of crystal packing allowed identification of a possible substrate-binding site because nine residues of an adjacent SurA monomer bound to a 50 Å long channel formed by the non-catalytic domain. One part of the N-terminal domain forms a nonpolar flap facing the interior of a crevice that also has a hydrophobic binding pocket. This part actually binds to a Leu residue of the peptide. This finding is in agreement with earlier results showing that most binding sites of molecular chaperones have hydrophobic patches that are ideally suited to bind exposed hydrophobicity of unfolded substrates. The crystal structure, however, provides little information about the catalysis of peptidyl-prolyl isomerization, and the question of whether a peptide bound to the chaperone domain can undergo proline isomerization is not yet clear.

28.2.1.4 PpiD

Like SurA, PpiD belongs to the parvulin family. It has one N-terminal transmembrane segment, and residues 37–623 are localized in the periplasm. In the middle of this rather large protein, a PPIase domain can be recognized comprising residues 266–355. This domain has PPIase activity, and several mutations in this region have been shown to lead to a loss of catalytic activity. *ppiD* knockouts have phenotypes that are comparable to *surA* mutants, i.e., reduced levels of outer mem-

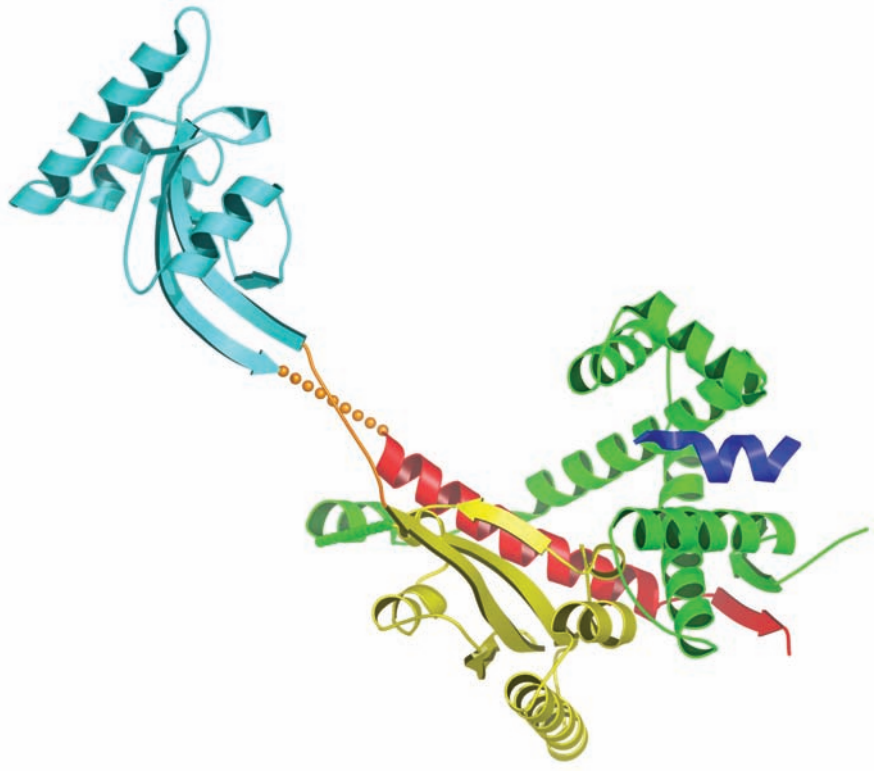

Fig. 28.2. Structure of SurA. Ribbon diagram of the SurA monomer with bound peptide from an adjacent molecule. The N-terminal domain is green, the PPIase domain 1 is gold, the PPIase domain 2 is light blue, the C-terminus is red, and the bound peptide is dark blue [35].

brane proteins OmpA, OmpF, OmpC, and LamB as well as increased sensitivity to SDS and antibiotics. Because *ppiD* was isolated as a high-copy suppressor of *surA* mutants, it can be speculated that SurA and PpiD are functionally redundant [36].

28.2.2 Skp

Skp is a small periplasmic protein of 17 kDa that exists as a homotetramer, and several lines of evidence suggest a general chaperone function. (1) Skp was shown to bind to an affinity column with Sepharose-bound outer membrane porin OmpF. It also binds to outer membrane proteins such as OmpA, OmpC, and LamB [37]. (2) Skp was found to interact in vitro with nascent chains of OmpA precursor and in spheroplasts with trapped translocation intermediates of PhoE. These data indicate that Skp can interact with folding intermediates of outer membrane proteins

[38, 39]. While *skp* knockout mutants are viable [37, 38], *skp degP* double mutants are lethal at 37 °C and accumulate protein aggregates in the periplasm [38]. (3) *skp surA* double mutants also exhibit a synthetic lethal phenotype, and a dramatic decrease in levels of LamB, MBP, and OmpA proteins was detected as early as after 6 h of depletion of SurA [40]. (4) Direct evidence for the participation of Skp in the folding of OmpA was obtained from in vitro refolding experiments. However, folding of OmpA required the additional presence of lipopolysaccharide. Also, it appeared that OmpA bound to Skp and lipopolysaccharide was kept in an unfolded state in solution. The fact that unfolded OmpA in complex with Skp and lipopolysaccharide folded faster into phospholipid bilayers than did urea-unfolded OmpA provides evidence that Skp assists in folding of outer membrane proteins [41].

From these data it could be speculated that Skp mainly functions in outer membrane protein biogenesis. However, several publications report beneficial effects of Skp in the production of functional antibody fragments [42–46]. These data support the model that Skp might have general molecular chaperone function. In fact, Skp is the only protein known to date that could exclusively function as a general chaperone in the cell envelope. All other proteins that were shown to have chaperone function normally either are involved in protein degradation, redox reactions, and proline isomerization or are specific chaperones. The large family of specific chaperones includes some that are well studied and that are involved in pilus assembly (for review, see Refs. [47, 48] and Chapter 29) and the periplasmic chaperone LolA, which is essential for viability and, together with other Lol proteins, is involved in transfer, insertion, and assembly of outer membrane lipoproteins [49–51].

The genomic localization of the *skp* gene is conserved in many gram-negative bacteria. Skp is part of a large gene cluster whose members mediate lipopolysaccharide-, phospholipid-, and fatty-acid synthesis. Directly upstream of *skp*, two other genes that have been shown to be essential for viability and important for cell envelope protein biogenesis, *yaeL* and *yaeT* (o810 or Omp85), are localized. The YaeL protease is involved in the unfolded protein response (Section 28.4.1), and, from work carried out in *Neisseria meningitidis*, YaeT has been postulated to be involved in lipid export [52]. After prolonged depletion, *yaeT* mutants were found to be defective in outer membrane protein assembly [53]. However, direct evidence from biochemical in vitro experiments using purified components is required to identify the precise function of this important gene.

28.2.3
Proteases and Protease/Chaperone Machines

Proteases are in charge of protein turnover by catalyzing the cleavage of peptide bonds. They serve essential housecleaning functions by degrading damaged proteins and signal peptides. Other important functions include regulation via, e.g., activation or inactivation of signaling proteins. There are at least 24 different peptidases and proteases in the cell envelope of *E. coli*. While a few are well studied, many have been identified only via bioinformatics (see the EPD database

at www.cf.ac.uk/biosi/staff/ehrmann/tools/proteases.index.html). Among these, several genes are, at least in prokaryotes, widely conserved (*degP*, *degQ*, *degS*, *nlpC*, *ptrA*, *tsp*, *ydcP*, *ydgD*, *ydhO*, *yebA*, *yhbU*, *yhjJ*, *nlpD*, *ompT*, *sohB*, and *yfbL*), indicating an important physiological function.

28.2.3.1 The HtrA Family of Serine Proteases

The defining feature of the over 180 family members is the combination of a catalytic serine protease domain with one or more C-terminal PDZ domains. PDZ domains are protein modules that mediate specific protein-protein interactions and bind preferentially to the C-terminal 3–4 residues of the target protein. Some, but not all, family members are classic heat shock proteins. They are typically localized in extracytoplasmic compartments such as the periplasm of gram-negative bacteria, the ER or mitochondria of eukaryotes, the chloroplast of plants, or in the extracellular space. Prokaryotic HtrA has been attributed to the tolerance against various folding stresses as well as to pathogenicity. Human homologues are believed to be involved in arthritis, cell growth, unfolded stress response, apoptosis, muscular dystrophy, cancer, and aging. One family member, DegP of *E. coli*, has both chaperone and protease functions. These functions switch in a temperature-dependent manner, the protease activity being most apparent at elevated temperatures (for review, see Ref. [54]). There are other factors in the cell envelope that are believed to have more than one function. For example, chaperone activity has been demonstrated for the proline isomerases FkpA and SurA (Sections 28.2.1.1 and 28.2.1.3) and the redox proteins DsbC and DsbG [55, 56].

28.2.3.2 *E. coli* HtrAs

Three HtrA proteins, DegP, DegQ, and DegS, have been identified in *E. coli*. Originally, DegP was purified from cell extracts and was called protease Do. It was shown to be inhibited by the serine protease inhibitor diisopropyl fluorophosphate (DFP) and to be oligomeric [57]. Subsequently, the *degP* gene was identified as a heat shock gene [58] and *degP* mutants were shown to stabilize membrane protein-PhoA fusions [59].

degQ and *degS* (also termed *hhoA* and *hhoB*) were identified as multicopy suppressors of conditional lethal *prc* (tail specific protease) null mutants [60] and as genes located downstream of the *mdh* gene [61]. Both *degQ* and *degS* are located directly next to each other, but are not co-regulated, and neither are induced by heat shock.

28.2.3.3 DegP and DegQ

DegP has two functions in the regulation of protein composition in the cell envelope. As a rather unspecific protease, it is a key player in the turnover of damaged and nonnative cell envelope proteins, including misfolded periplasmic *E. coli* proteins such as MBP [62], PhoA [63], or MalS [64]; the misfolded outer membrane protein LamB [65]; mislocalized cytoplasmic proteins such as TreF [66] and β-Gal [67]; proteins that have failed to assemble into hetero-oligomeric complexes, such as HflKC of *E. coli* [68] and HMW1 adhesin of *Haemophilus influenzae* [69]; and

hybrid proteins [59, 70] and recombinant proteins [71, 72]. In addition, DegP is required for maturation of colicin A [73]. It is interesting that the proteolytic function dominates at elevated temperatures, where protein repair is less effective compared with low temperatures [64].

At low temperature, DegP has a protein repair function that was first recognized by its complementation of a *dsbA* mutant in the folding process of the periplasmic amylase MalS. Additional evidence for the chaperone function of DegP was obtained from in vitro refolding assays [64] and from genetic studies [40, 74, 75].

Not much is known about DegQ, but because it can complement the temperature sensitivity of *degP* null mutants, it is thought to have functions similar to those of DegP [61].

28.2.3.4 DegS

DegS is homologous to DegP and DegQ but differs in substrate specificity, oligomeric state, and function. DegS has an N-terminal transmembrane segment, is a trimer, and has a regulatory function [76, 77]. It is highly specific [61] and is required for viability because it is essential for the sigma E pathway ([78]; see also Section 28.4.1). It is also required for virulence, although the precise function of DegS in pathogenesis is not understood [79]. The proteolytic activity of DegS seems to be modulated by its PDZ domains. Activation of DegS function is mediated by binding of peptides corresponding to the C-terminus of outer membrane proteins [80]. These peptides are thought to be related to the identified YQF or YYF motifs. These sequences must provide an appropriate fit to the specific substrate-binding pocket in the PDZ domain. It has been speculated that in the absence of activating peptide, the PDZ domain sterically blocks entry of substrates to the active site of the protease domain. Upon binding of peptide, the PDZ domain would then rotate away from the active site to make it accessible for substrates [80, 81]. However, other models are equally likely; for example, activating peptide could simply induce a conformational change in the catalytic triad of the protease without rotation of the PDZ domain. This model is based on the fact that the active sites of DegP and human HtrA2 were found in an inactive conformation in the recently determined crystal structures [54].

28.2.3.5 The Structure of HtrA

The functional unit of HtrA appears to be a trimer that is stabilized exclusively by residues of the protease domains [82–84]. The basic trimer has a funnel-like shape, with the protease domains located at its top and the PDZ domains protruding to the outside. While the protease domains form the rigid part of the funnel, the PDZ domains are highly mobile elements. This construction is reminiscent of a ''molecular anemone,'' with the PDZ domains swinging around to capture substrates. After binding, substrates have to be delivered into the interior of the funnel and to the proteolytic sites.

The recently solved crystal structure of *E. coli* DegP indicates that it exists as a hexamer of stacked trimers and that the protease domains are localized in an inner cavity. Access to this cavity is controlled by 12 PDZ domains, which form the mo-

bile sidewalls of the particle [82] (Figure 28.3). Therefore, DegP represents a novel type of self-compartmentalizing protease. Self-compartmentalization is an ingenious architectural feature by which the accessibility of active sites becomes exclusive, in this case for proteins that are at least partially unfolded. This strategy prevents folded proteins from being substrates. This mechanism is widely used in nature and is also found in other proteases such as ClpP (Hsp100) [85], in the proteasome [86] and the tricorn [87], and in the Hsp60 (GroEL) chaperone [88].

Compared to other proteases of known structure, the DegP particle has no rigid sidewalls. The PDZ domains that could fulfill this function are highly flexible and are able to adopt different conformations within the hexamer. The PDZ domains represent side doors, which may either swing open or close the complex. In addition, because short peptides binding to PDZ domains have been found to activate the proteolytic activity of DegP and DegS [80, 89], it is likely that the conformation or position of the PDZ domains could be involved in regulation of protease activity. It should be noted in this context that the protease activity can be reversibly switched on and off. This remarkable reversibility is mediated by the geometric arrangement of the active site. Perhaps binding of substrate to the PDZ domains could have knock-on effects leading to conformational changes in the active site i.e., the proper positioning of the catalytic triad and the formation of the oxyanion hole.

28.2.3.6 **Other Proteases**

Prc or tsp (tail specific protease) is a conserved periplasmic serine protease that has one PDZ domain that precedes the active site. It is a member of the S41 family according to the MEROPS classification and is therefore related to the tricorn protease. Prc is a rather large protein of 660 residues that recognizes preferentially hydrophobic C-termini [90]. The specificity of Prc seems to be mediated by its PDZ domain, which is capable of binding a nonpolar peptide with a dissociation constant of 1.9 μM [91]. It was also found that Prc has a preference for at least partially unfolded substrates [92] or substrates that are only partially synthesized [93]. Given this preference for nonnative conformations, it might be speculated that Prc could be involved in protection against protein folding stresses.

Protease III is a large periplasmic metalloprotease, and its sequence and size are highly conserved in evolution. Homologues can be found in most organisms, including higher plants and humans. In *E. coli* it was shown to be involved in the degradation of the misfolded MBP31 mutant [62], but it also cleaves insulin [94] and levels of beta-lactamase were found to be increased in protease III mutants [71]. Like Prc, protease III is expected to play a role in degradation of damaged proteins, but its precise contributions remain to be determined.

OmpT is an integral outer membrane protein that functions as a protease. The *ompT* gene is often deleted in strains that are used for the production of recombinant proteins. Among the several genes that are upregulated upon induction of overexpression of recombinant proteins are *degP* and *ompT* [95, 96]; OmpT was found to be associated with aggregates of yeast alpha-glucosidases when produced in *E. coli* [97] and it was also implicated in virulence [98]. Taken together, these

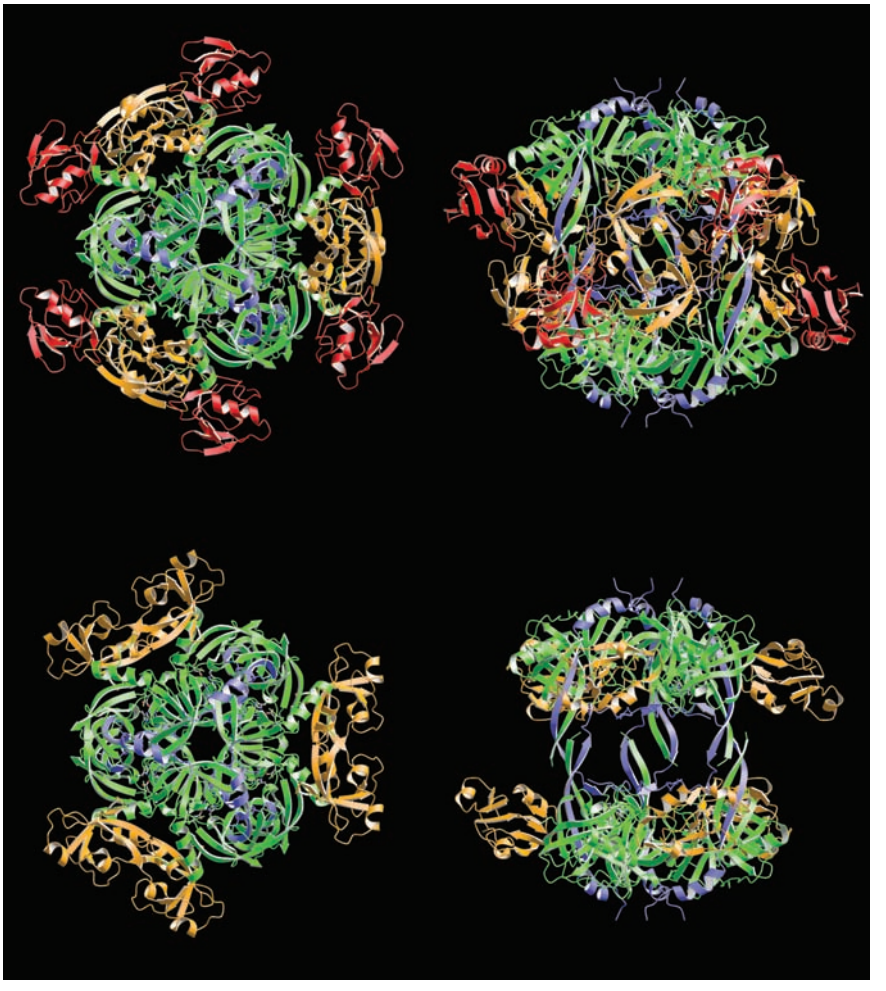

Fig. 28.3. Structure of DegP. DegP is shown in its hexameric conformation where two trimers are stacked upon each other. In the crystals, DegP was present in the closed (upper part) as well as in the open (lower part) conformation. While the structures in the top view (left-hand side) are similar, the side views show that in the open conformation the PDZ domains are rotated away from the protease domains and allow access to the inner cavity. On the top and bottom of the cavity, the active sites of the protease domains are localized. The pillars of the particle are formed by N-terminal extensions that reach from one monomer into the active site of another monomer in the opposite trimer (for review, see Refs. [82] and [54]). It should be noted that in the open conformation, the structure of only one of the two PDZ domains was solved. However, the density of the second PDZ domain is found directly adjacent to the first PDZ domain. The protease domains are shown in green, the N-terminal extensions in blue, and the PDZ domains in brown and red.

data suggest that OmpT is involved in protein quality control in the cell envelope and, given its cellular localization, perhaps particularly in the outer membrane.

28.3 Organization of Folding Factors into Pathways and Networks

Although direct evidence has been obtained for several individual folding catalysts and proteases that they are involved in protein folding and degradation, it is obvious that these factors do not work in isolation. Based on evidence from other biological systems, we can expect that several pathways dealing with protein quality control and protein metabolism exist. We can also expect that these pathways are connected and organized into networks. However, the knowledge of these pathways and networks is very limited. Because they are critical for the basic physiology of bacterial cells, as well as for commercial exploitation, they are well worth being studied experimentally.

28.3.1 Synthetic Lethality and Extragenic High-copy Suppressors

To distinguish the various pathways involved in protein folding, quality control, and protein turnover and to recognize functional redundancies, bacterial genetics is a useful tool for initial analysis. An experimentally simple and straightforward approach is to look for synthetic lethal phenotypes of combinations of individual knockout mutations of nonessential genes. Synthetic lethality occurs when the combination of two mutations that alone are not lethal makes the double mutant inviable. Such synthetic lethal mutations can indicate that the two mutations affect (1) a single function or (2) a pathway. Also, the complementation of essential genes or of synthetic lethality by extragenic multicopy suppressors can indicate functional redundancy.

As an example of (1) above, both Skp and DegP have chaperone activity, and the absence of both chaperone activities in an *skp degP* double null mutant is lethal. Also, expression of a catalytically inactive *degP* mutant that still has chaperone activity but no longer has protease activity complements the *skp degP* double mutant [38, 40]. These phenotypes indicate a functional redundancy of Skp and DegP in vivo.

As an example of (2) above, it was found that combining *degP* with other null mutations could cause a lethal phenotype in more than one case. For example, *degP* and *surA* as well as *degP* and *skp* double mutants are synthetic lethals. Because the protease activity of DegP is required to complement the *degP surA* double mutant but the chaperone activity of DegP complements the *degP skp* double mutant, it can be postulated that two pathways exist, one involving Skp and another involving SurA [40].

There is one potential problem that should not be ignored when carrying out such analyses: not every lethal combination represents a true synthetic lethal phe-

notype. It is possible that an observed lethality is due to two ''unhealthy'' single mutations, the combination of which is just too much. Even in light of such limitations, initial studies clearly indicate that the construction and careful analysis of synthetic lethal double mutants are very useful approaches to identifying and studying protein-folding and degradation pathways.

28.3.2
Reconstituted in Vitro Systems

To further verify and explain the observed phenotypes, in vitro refolding and proteolysis experiments can be informative. Such in vitro systems can provide direct quantitative evidence for the quality-control pathways identified. For this purpose, refolding and, if applicable, degradation of model substrates are studied in the presence and absence of folding factors and proteases that are thought to be part of a specific pathway. Interesting questions to address include: is folding or quality control different (faster or more efficient) if the entire network of cellular factors is present in the reconstituted system?

For example, a mini-chaperone derived from GroEL, together with DsbA and a prolyl isomerase, exhibited synergistic assistance during refolding of a scorpion toxin [99]. Also, the combination of a chaperone and protein disulfide isomerase increased the production of functional antibody in a cell-free system [100]. Although these experiments did not completely mimic the in vivo situation (because factors originally residing in different cellular compartments were used), they do provide initial evidence that such approaches could yield important information.

28.4
Regulation

E. coli has developed compartment-specific responses to react to the presence of misfolded proteins. In the cell envelope, three systems have been identified: sigma E, Cpx, and Bae. Because stress occurs in the cell envelope while the regulation of gene expression is carried out in the cytoplasm, these systems must detect misfolded cell envelope proteins, transmit signals across the cytoplasmic membrane, and stimulate transcription of protein folding and degradation factors in the cytoplasm. It is generally accepted that misfolded proteins, protein fragments, and mislocalized outer membrane proteins are activators of these stress response pathways. Such activation occurs under any kind of stress situation that causes protein-folding problems, including heat shock, pH, and osmo-stress, and also when proteins are overproduced from nonnative expression systems.

28.4.1
The Sigma E Pathway

The key component of the essential sigma E pathway is the alternative sigma factor RpoE. Sigma factors interact with RNA polymerase and stimulate binding to and

transcription of promoters that contain specific binding sites for these sigma factors. Because sigma E is a cytoplasmic protein, there are additional factors in the cell envelope that regulate its activity. Three proteins are known to regulate sigma E function: the anti-sigma factor RseA, the RseB protein that modulates the stability of the sigma E–RseA complex, and RseC, whose function remains to be determined. RseA is a membrane protein comprised of a cytoplasmic domain, one transmembrane segment, and a periplasmic domain. Sigma E binds to the cytoplasmic segment of RseA and is inactive in this conformation. The anti-sigma activity of RseA is regulated on the level of protein stability. After proteolytic inactivation of RseA, sigma E is free to activate certain promoters (for review, see Ref. [12]). Recent evidence suggests that two proteases, DegS and YaeL, are involved in the proteolytic inactivation of RseA [77, 101]. YaeL is a metalloprotease and an integral cytoplasmic membrane protein that belongs to the RIP family (regulated intramembrane proteolysis) [102]. DegS is a member of the HtrA family of serine proteases (Section 28.2.3.4), and it was shown that peptides corresponding to the C-terminus of outer membrane proteins activate protease activity of DegS by binding to its PDZ domains [80]. Activated DegS initiates cleavage of RseA and the sigma E cascade. It is therefore believed that when outer membrane proteins accumulate in the periplasm, they serve as signals for folding stress and thus activate the sigma E pathway. Substrates of the sigma E pathway include the *degP* and *fkpA* promoters; *rpoH*, which encodes the cytoplasmic heat shock sigma factor; and *rpoE* and *rseABC* themselves (for review, see Ref. [12]).

28.4.2 The Cpx Pathway

Cpx belongs to the family of two-component signal transduction systems [103]. Two proteins, CpxR and CpxA, carry out signal transduction, and CpxP is also involved in regulation of Cpx function. The cytoplasmic membrane protein CpxA is the sensor kinase, and cytoplasmic CpxR is the response regulator and a DNA-binding protein. CpxA modulates the phosphorylation state of CpxR. The signal transduction cascade is initiated by a conformational change in CpxA that triggers autophosphorylation of a conserved His residue. Subsequently, the phosphorylation is transferred to a conserved Asp residue in CpxR. Phosphorylated CpxR then acts as a transcription factor. In the absence of signals, CpxA dephosphorylates CpxR, providing a tight regulation of CpxR activity.

CpxP is a periplasmic protein that inhibits CpxA. Because overproduction of CpxP increases inhibition of CpxA, it is the current hypothesis that CpxP interacts with CpxA. Release of CpxP induces conformational change and activates the Cpx cascade (for review, see Ref. [12]). A recent analysis indicates, however, that the mode of regulation is more sophisticated. This might be the case, because a rather large number of stresses induce the Cpx pathway. For example, typical envelope stress conditions induce Cpx via CpxA but not via NlpE, while the mechanisms of induction via adhesion and growth phase appear to be distinct from envelope stress. The response to adhesion requires the outer membrane lipoprotein NlpE

but not CpxP, and the induction by growth phase seems to be independent of CpxA, indicating that induction by growth phase is distinct from adhesion and envelope stress [104].

Besides its role in the unfolded protein response, the Cpx pathway is also involved in regulation of chemotaxis [105], biofilms [106], and pili biogenesis [107] as well as in attachment of bacteria to surfaces [108]. However, these implications might represent only the tip of the iceberg, as a recent study suggests that Cpx may be directly involved in regulation of about 100 operons. Via its interaction with other signal transduction pathways, its effects can even be greater [109]. Among the known protein quality-control factors that are regulated by Cpx are the promoters of the *degP*, *dsbA*, *ppiD*, and *ppiA* genes [12] and also *htpX*, which encodes a heat shock protease that is an integral cytoplasmic membrane protein with a cytoplasmic active site [110]. Perhaps surprisingly, it was also shown that phosphorylated CpxR protein directly interacts with one promoter of the *rpoErseABC* operon, indicating that the sigma E pathway may be negatively controlled by the Cpx pathway [109].

28.4.3 The Bae Pathway

Spy (spheroplast protein Y), a protein of unknown function that has been identified to be induced by spheroplast formation [111], is also induced by the Cpx pathway, and its deletion leads to upregulation of the sigma E pathway [112]. However, since induction via spheroplast formation is only partially Cpx-dependent, a novel two-component signal transduction system, Bae, has been identified that regulates *spy* expression [113]. BaeS is the sensor kinase, while BaeR is the response regulator. It was also shown that, in analogy to Cpx, the Bae system responds to cell envelope stress, and because Spy is homologous to CpxP, it was suggested that the Bae system represents a third system that senses and responds to protein-folding stress in the cell envelope.

28.5 Future Perspectives

The study of protein folding in the cell envelope not only is adding to the increasing perception of basic cellular functions but also is leading to new methods for protein production as well as for diagnosis, therapy, and prevention of infectious diseases caused by pathogenic bacteria. Although several key cellular factors have been identified and studied in detail, much work remains to be done to complete our understanding and to eventually allow us to model a virtual cell and to simulate the cellular response to various important environmental factors such as heat, drought, antimicrobial drugs, and the immune system among many others.

It is now important to study the action of individual cellular factors not only in isolation but also in conjunction with each other. Perhaps only then it will be rec-

ognized that, for example, Skp promotes folding and not only holding (preventing aggregation), as is seen in some in vitro systems. Also, it may well be that the activity of individual factors is modulated by other factors, either directly via protein-protein interaction or indirectly when, for example, one factor acting at an early stage of folding produces a folding intermediate that is required so that a second factor can catalyze the folding process to completion. Therefore, future studies will address (1) the identification and characterization of pathways involved in protein folding, repair, and degradation; (2) their organization into networks of pathways; and (3) the identification of key players in this network that, for example, function as bottlenecks by catalyzing rate-limiting reactions or by connecting individual pathways.

Much remains to be learned about outer membrane proteins. For example, because in vitro the refolding and membrane insertion reactions are very slow (on the order of one generation time of the whole organism), it is obvious that cellular factors must exist that catalyze these processes (for review, see Ref. [114]). In this respect, it is surprising that despite intense efforts no cellular machine has been identified that catalyzes membrane insertion. In addition, a quality-control system for properly inserted, native outer membrane proteins has not yet been described or systematically studied. In the same context, the cell envelope has many hetero-oligomeric protein complexes such as pili, flagella, and multi-drug resistance pumps that can be very large and their architecture complex. The functional assembly and quality control of these complexes are not well understood and provide a challenge for future studies. The cell envelope hosts a great number of proteins of unknown function, many of which are conserved and several of which will turn out to be important for protein biogenesis and quality control.

Finally, additional regulatory systems and mechanisms remain to be discovered. For example, a recent study identified that ribonuclease E is involved in regulation of *dsbC* expression, and here a new protein, RraA (regulator of ribonuclease activity A), was shown to inhibit RNase E endonuclease by binding [115]. Clearly, posttranscriptional regulatory events must play an important role in cell envelope protein biogenesis, and exciting developments can be expected in the near future.

28.6 Experimental Protocols

28.6.1 Pulse Chase Immunoprecipitation

Rationale

Pulse-chase immunoprecipitation allows determination of the stability of proteins and thus provides in vivo evidence on the folded state of proteins and, if applicable, the rates of its degradation. In principle, all proteins are labeled with ^{35}S-methionine for a short period of time. After labeling, excess of unlabelled methionine is added to stop the labeling reaction. At various time points, further samples

are taken. A specific antibody is used to isolate one target protein, the level and stability of which is investigated. This experiment allows us to follow the fate of a particular protein because it is labeled during synthesis and its stability is monitored over time.

Such an approach is useful if, for example, the effects of a mutation in a folding factor or of protease on a particular substrate are to be examined. Comparing the levels and thus stability of the target protein in wild-type and mutant background provides evidence for the involvement of a chosen cellular factor in the folding and stability of a substrate.

Protocol

1. Grow cells overnight in minimal medium M9, 0.2% glycerol supplemented with 18 amino acids and 0.01% thiamine.
2. Dilute cells 1/25 in the same medium.
3. Grow to $OD_{600} = 0.3–0.5$ (if required, induce the promoter at OD $\approx$ 0.2).

Pulse

1. Place 4.5 mL of cells in a prewarmed plastic vial (do all steps at 37 °C with vigorous aeration).
2. Add 10–50 µCi ^{35}S-methionine.
3. Label for 1–2 min.
4. Transfer 1 mL of cells into Eppendorf tube containing ice (time point 1).

Chase

1. To the remaining 3.5 mL of cells, add 0.05% cold methionine (or 20 mM final) −640 µL (0.2 M methionine stock solution).
2. After 1, 5, and 15 min, transfer 1 mL of cells into Eppendorf tubes containing ice (time points 2–4).

Immunoprecipitation

1. Spin all samples for 1 min in an Eppendorf centrifuge.
2. Resuspend pellet in 1% SDS, 1 mM EDTA, 50 mM Tris HCl pH 7.5.
3. Heat 10 min at 65 °C (or 3 min at 95 °C).
4. Add 1 mL of HS buffer.
5. Spin 10 min.
6. Take 970 µL supernatant.
7. Add 10 µL Sephacryl protein A.
8. Incubate on ice for 30 min.
9. Spin 1 min.
10. Take 900 µL supernatant.
11. Add antibody (2–10 µL) directed against the target protein.

12. Keep on ice for 4 h or overnight.
13. Add 10 µL Sephacryl protein A.
14. Keep 30 min on ice.
15. Invert tubes occasionally.
16. Wash 1× in 1 mL HS buffer.
17. Wash 1× in 1 mL Li-buffer.
18. Wash 1× in 1 mL 50 mM Tris HCl pH 7.5
19. Resuspend in 50 µL sample buffer
20. Heat 10 min 65 °C (or 3–5 min 95 °C).
21. Spin 5 min to remove Sephacryl protein A.
22. Take supernatant.
23. Load half on SDS-PAGE.
24. Dry gel and place into phosphorimager.

Notes

Various proteins have different requirements for heating. Soluble proteins are easy: just boil for 2 min. Cytoplasmic membrane proteins: incubate 10 min at RT or 42 °C. Boiling can cause aggregation in some cases. Outer membrane proteins tend to form stable trimers, and monomers do not easily denature: 10–30 min of boiling is required.

Solutions and Buffers

HS buffer: 50 mM Tris HCl pH = 8
1 M NaCl
1% Triton × 100
1 mM EDTA

Li-buffer: 50 mM Tris HCl pH = 7.5
0.1% SDS
0.5 M LiCl

Minimal Medium 9 (10×):

$Na_2HPO_4 \cdot 2H_2O$: 76.54 g
KH_2PO_4: 30 g
NaCl: 5 g
NH_4Cl: 10 g
Autoclave, let cool and add:
MgSO4: 1 mM
$CaCl_2$: 0.1 mM (use 100 mM stock, 1 M precipitates immediately)

Liquid Culture (5 mL)

4.5 mL H_2O
0.5 mL M9 10×

0.2–0.4% carbon source
1× 18 amino acid mix
0.01% thiamine

Hydrophobic Amino Acids (50×)

1. Add 250 mg of each Ile, Phe, Trp, and Tyr to 100 mL H_2O.
2. Boil and adjust pH to 8.0 using $NaCO_2$.
3. Filter sterilize while hot.
4. Make aliquots and store at −70 °C.

Hydrophilic Amino Acids (100×)

1. Add 250 mg of each Gly, Ala, Val, Leu, Ser, Thr, Asp, Asn, Glu, Gln, Lys, Arg, His, and Pro to 50 mL H_2O.
2. Filter sterilize.
3. Make aliquots and store at −70 °C.

Note

Bacteria grown in minimal media tolerate a lower concentration of antibiotics compared to growth in rich media. Concentrations for minimal media (μg mL^{-1}):

Ampicillin: 100
Kanamycin: 50
Tetracycline: 5
Chloramphenicol: 12

Acknowledgements

I would like to thank Dave McKay for a picture of the SurA structure, Tim Clausen for a picture of the DegP structure, and Tracy Raivio, George Georgiou, and Susan Marqusee for communicating unpublished results.

References

1 Wülfing, C. & Plückthun, A. (1994). Protein folding in the periplasm of *E. coli*. *Mol. Microbiol.* 12, 685–692.
2 Brass, J. M., Higgins, C. F., Foley, M., Rugman, P. A., Birmingham, J. & Garland, P. B. (1986). Lateral diffusion of proteins in the periplasm of *Escherichia coli*. *J. Bacteriol.* 165, 787–795.
3 Blattner, F. R., Plunkett, G., 3rd, Bloch, C. A., Perna, N. T., Burland, V., Riley, M., Collado-Vides, J., Glasner, J. D., Rode, C. K., Mayhew, G. F., Gregor, J., Davis, N. W., Kirkpatrick, H. A., Goeden, M. A.,

Rose, D. J., Mau, B. & Shao, Y. (1997). The complete genome sequence of *Escherichia coli K-12*. *Science* 277, 1453–1474.

4 Schulz, G. E. (2002). The structure of bacterial outer membrane proteins. *Biochim. Biophys. Acta* 1565, 308–317.

5 Koronakis, V., Andersen, C. & Hughes, C. (2001). Channel-tunnels. *Curr. Opin. Struct. Biol.* 11, 403–407.

6 Andersen, C., Hughes, C. & Koronakis, V. (2001). Protein export and drug efflux through bacterial channel-tunnels. *Curr. Opin. Cell Biol.* 13, 412–416.

7 van Wely, K. H., Swaving, J., Freudl, R. & Driessen, A. J. (2001). Translocation of proteins across the cell envelope of Gram-positive bacteria. *FEMS Microbiol Rev.* 25, 437–454.

8 Danese, P. N. & Silhavy, T. J. (1998). Targeting and assembly of periplasmic and outer-membrane proteins in *Escherichia coli*. *Annu. Rev. Genet.* 32, 59–94.

9 Palmer, T. & Berks, B. C. (2003). Moving folded proteins across the bacterial cell membrane. *Microbiology* 149, 547–556.

10 DeLisa, M. P., Tullman, D. & Georgiou, G. (2003). Folding quality control in the export of proteins by the bacterial twin-arginine translocation pathway. *Proc. Natl. Acad. Sci. USA* 100, 6115–6120.

11 Bukau, B. & Horwich, A. (1998). The Hsp70 and Hsp60 chaperone machines. *Cell* 92, 351–366.

12 Raivio, T. L. & Silhavy, T. J. (2001). Periplasmic stress and ECF sigma factors. *Annu. Rev. Microbiol.* 55, 591–624.

13 Ramachandran, G. N. & Mitra, A. K. (1976). An explanation for the rare occurrence of cis peptide units in proteins and polypeptides. *J. Mol. Biol.* 107, 85–92.

14 Gothel, S. F. & Marahiel, M. A. (1999). Peptidyl-prolyl cis-trans isomerases, a superfamily of ubiquitous folding catalysts. *Cell. Mol. Life Sci.* 55, 423–436.

15 Schmid, F. X. & Baldwin, R. L. (1978). Acid catalysis of the formation of the slow-folding species of RNase A: evidence that the reaction is proline isomerization. *Proc. Natl. Acad. Sci. USA* 75, 4764–4768.

16 Horne, S. & Young, K. (1995). *Escherichia coli* and other species of the Enterobacteriaceae encode a protein similar to the family of Mip-like FK506-binding proteins. *Arch. Microbiol.* 163, 357–365.

17 Ramm, K. & Pluckthun, A. (2001). High enzymatic activity and chaperone function are mechanistically related features of the dimeric *E. coli* peptidyl-prolyl-isomerase FkpA. *J. Mol. Biol.* 310, 485–498.

18 Bothmann, H. & Pluckthun, A. (2000). The periplasmic *Escherichia coli* peptidylprolyl cis,trans-isomerase FkpA. I. Increased functional expression of antibody fragments with and without cis-prolines. *J. Biol. Chem.* 275, 17100–17105.

19 Ramm, K. & Pluckthun, A. (2000). The periplasmic *Escherichia coli* peptidylprolyl cis,trans-isomerase FkpA. II. Isomerase-independent chaperone activity in vitro. *J. Biol. Chem.* 275, 17106–17113.

20 Balbach, J., Steegborn, C., Schindler, T. & Schmid, F. X. (1999). A protein folding intermediate of ribonuclease T1 characterized at high resolution by 1D and 2D real-time NMR spectroscopy. *J. Mol. Biol.* 285, 829–842.

21 Arie, J. P., Sassoon, N. & Betton, J. M. (2001). Chaperone function of FkpA, a heat shock prolyl isomerase, in the periplasm of *Escherichia coli*. *Mol. Microbiol.* 39, 199–210.

22 Saul, F. A., Mourez, M., Vulliez-Le Normand, B., Sassoon, N., Bentley, G. A. & Betton, J. M. (2003). Crystal structure of a defective folding protein. *Protein Sci.* 12, 577–585.

23 Liu, J. & Walsh, C. T. (1990). Peptidyl-prolyl *cis-trans*-isomerase from *Escherichia coli*: a periplasmic homolog of cyclophilin that is not inhibited by cyclosporin A. *Proc. Natl. Acad. Sci. USA* 87, 4028–4032.

24 Hayano, T., Takahashi, N., Kato, S., Maki, N. & Suzuki, M. (1991). Two distinct forms of peptidylprolyl-*cis-trans*-isomerase are expressed separately in periplasmic and cytoplasmic compartments of *Escherichia coli* cells. *Biochemistry* 30, 3041–3048.

25 Clubb, R. T., Ferguson, S. B., Walsh, C. T. & Wagner, G. (1994). Three-dimensional solution structure of *Escherichia coli* periplasmic cyclophilin. *Biochemistry* 33, 2761–2772.

26 Liu, J., Chen, C. M. & Walsh, C. T. (1991). Human and *Escherichia coli* cyclophilins: sensitivity to inhibition by the immunosuppressant cyclosporin A correlates with a specific tryptophan residue. *Biochemistry* 30, 2306–23010.

27 Compton, L. A., Davis, J. M., Macdonald, J. R. & Bachinger, H. P. (1992). Structural and functional characterization of *Escherichia coli* peptidyl-prolyl *cis-trans* isomerases. *Eur. J. Biochem.* 206, 927–934.

28 Pogliano, J., Lynch, A., Belin, D., Lin, E. & Beckwith, J. (1997). Regulation of *Escherichia coli* cell envelope proteins involved in protein folding and degradation by the Cpx two-component system. *Genes and Dev.* 11, 1169–1182.

29 Tormo, A., Almiron, M. & Kolter, R. (1990). *surA*, an *Escherichia coli* gene essential for survival in stationary phase. *J. Bacteriol.* 172, 4339–4347.

30 Lazar, S. W., Almiron, M., Tormo, A. & Kolter, R. (1998). Role of the *Escherichia coli* SurA protein in stationary-phase survival. *J. Bacteriol.* 180, 5704–5711.

31 Missiakas, D., Betton, J. M. & Raina, S. (1996). New components of protein folding in extracytoplasmic compartments of *Escherichia coli* SurA, FkpA and Skp/OmpH. *Mol. Microbiol.* 21, 871–884.

32 Lazar, S. W. & Kolter, R. (1996). SurA assists the folding of *Escherichia coli* outer membrane proteins. *J. Bacteriol.* 178, 1770–1773.

33 Rouviere, P. E. & Gross, C. A. (1996). SurA, a periplasmic protein with peptidyl-prolyl isomerase activity, participates in the assembly of outer membrane porins. *Genes Dev.* 10, 3170–3182.

34 Behrens, S., Maier, R., de Cock, H., Schmid, F. X. & Gross, C. A. (2001). The SurA periplasmic PPIase lacking its parvulin domains functions in vivo and has chaperone activity. *EMBO J.* 20, 285–294.

35 Bitto, E. & McKay, D. B. (2002). Crystallographic structure of SurA, a molecular chaperone that facilitates folding of outer membrane porins. *Structure* 10, 1489–1498.

36 Dartigalongue, C. & Raina, S. (1998). A new heat-shock gene, *ppiD*, encodes a peptidyl-prolyl isomerase required for folding of outer membrane proteins in *Escherichia coli*. *Embo J.* 17, 3968–3980.

37 Chen, R. & Henning, U. (1996). A periplasmic protein (Skp) of *Escherichia coli* selectively binds a class of outer membrane proteins. *Mol. Microbiol.* 19, 1287–1294.

38 Schafer, U., Beck, K. & Muller, M. (1999). Skp, a molecular chaperone of gram-negative bacteria, is required for the formation of soluble periplasmic intermediates of outer membrane proteins. *J. Biol. Chem.* 274, 24567–24574.

39 Harms, N., Koningstein, G., Dontje, W., Muller, M., Oudega, B., Luirink, J. & de Cock, H. (2001). The early interaction of the outer membrane protein PhoE with the periplasmic chaperone Skp occurs at the cytoplasmic membrane. *J. Biol. Chem.* 276, 18804–18811.

40 Rizzitello, A. E., Harper, J. R. & Silhavy, T. J. (2001). Genetic evidence for parallel pathways of chaperone activity in the periplasm of *Escherichia coli*. *J. Bacteriol.* 183, 6794–6800.

41 Bulieris, P. V., Behrens, S., Holst, O. & Kleinschmidt, J. H. (2003). Folding and insertion of the outer membrane protein OmpA is assisted by the chaperone Skp and by

lipopolysaccharide. *J. Biol. Chem.* 278, 9092–9099.

42 Bothmann, H. & Pluckthun, A. (1998). Selection for a periplasmic factor improving phage display and functional periplasmic expression. *Nat. Biotechnol.* 16, 376–380.

43 Hayhurst, A. & Harris, W. J. (1999). *Escherichia coli skp* chaperone coexpression improves solubility and phage display of single-chain antibody fragments. *Protein Expr. Purif.* 15, 336–343.

44 Strachan, G., Williams, S., Moyle, S. P., Harris, W. J. & Porter, A. J. (1999). Reduced toxicity of expression, in *Escherichia coli*, of antipollutant antibody fragments and their use as sensitive diagnostic molecules. *J. Appl. Microbiol.* 87, 410–417.

45 Mavrangelos, C., Thiel, M., Adamson, P. J., Millard, D. J., Nobbs, S., Zola, H. & Nicholson, I. C. (2001). Increased yield and activity of soluble single-chain antibody fragments by combining high-level expression and the Skp periplasmic chaperonin. *Protein Expr. Purif.* 23, 289–295.

46 Levy, R., Weiss, R., Chen, G., Iverson, B. L. & Georgiou, G. (2001). Production of correctly folded Fab antibody fragment in the cytoplasm of *Escherichia coli trxB gor* mutants via the coexpression of molecular chaperones. *Protein Expr. Purif.* 23, 338–347.

47 Sauer, F. G., Barnhart, M., Choudhury, D., Knight, S. D., Waksman, G. & Hultgren, S. J. (2000). Chaperone-assisted pilus assembly and bacterial attachment. *Curr. Opin. Struct. Biol.* 10, 548–556.

48 Knight, S. D., Berglund, J. & Choudhury, D. (2000). Bacterial adhesins: structural studies reveal chaperone function and pilus biogenesis. *Curr. Opin. Chem. Biol.* 4, 653–660.

49 Takeda, K., Miyatake, H., Yokota, N., Matsuyama, S., Tokuda, H. & Miki, K. (2003). Crystal structures of bacterial lipoprotein localization factors, LolA and LolB. *Embo J.* 22, 3199–3209.

50 Yokota, N., Kuroda, T., Matsuyama, S. & Tokuda, H. (1999). Characterization of the LolA-LolB system as the general lipoprotein localization mechanism of *Escherichia coli*. *J. Biol. Chem.* 274, 30995–30999.

51 Matsuyama, S., Yokota, N. & Tokuda, H. (1997). A novel outer membrane lipoprotein, LolB (HemM), involved in the LolA (p20)-dependent localization of lipoproteins to the outer membrane of *Escherichia coli*. *Embo J.* 16, 6947–6955.

52 Genevrois, S., Steeghs, L., Roholl, P., Letesson, J. J. & van der Ley, P. (2003). The Omp85 protein of Neisseria meningitidis is required for lipid export to the outer membrane. *Embo J.* 22, 1780–1789.

53 Voulhoux, R., Bos, M. P., Geurtsen, J., Mols, M. & Tommassen, J. (2003). Role of a highly conserved bacterial protein in outer membrane protein assembly. *Science* 299, 262–265.

54 Clausen, T., Southan, C. & Ehrmann, M. (2002). The HtrA Family of Proteases. Implications for Protein Composition and Cell Fate. *Mol. Cell* 10, 443–455.

55 Chen, J., Song, J. L., Zhang, S., Wang, Y., Cui, D. F. & Wang, C. C. (1999). Chaperone activity of DsbC. *J. Biol. Chem.* 274, 19601–19605.

56 Shao, F., Bader, M. W., Jakob, U. & Bardwell, J. C. (2000). DsbG, a protein disulfide isomerase with chaperone activity. *J. Biol. Chem.* 275, 13349–13352.

57 Swamy, K. H., Chung, C. H. & Goldberg, A. L. (1983). Isolation and characterization of protease do from *Escherichia coli*, a large serine protease containing multiple subunits. *Arch. Biochem. Biophys.* 224, 543–554.

58 Lipinska, B., Sharma, S. & Georgopoulos, C. (1988). Sequence analysis and regulation of the *htrA* gene of *Escherichia coli*: a sigma 32-independent mechanism of heat-inducible transcription. *Nucleic Acids Res.* 16, 10053–10067.

59 Strauch, K. L. & Beckwith, J. (1988).

An *Escherichia coli* mutation preventing degradation of abnormal periplasmic proteins. *Proc. Natl. Acad. Sci. USA* 85, 1576–1580.

60 Bass, S., Gu, Q. & Christen, A. (1996). Multicopy suppressors of *prc* mutant *Escherichia coli* include two HtrA (DegP) protease homologs (HhoAB), DksA, and a truncated R1pA. *J. Bacteriol.* 178, 1154–1161.

61 Waller, P. & Sauer, R. (1996). Characterization of *degQ* and *degS*, *Escherichia coli* genes encoding homologs of the DegP protease. *J. Bacteriol.* 178, 1146–1153.

62 Betton, J.-M., Sassoon, N., Hofnung, M. & Laurent, M. (1998). Degradation versus aggregation of misfolded maltose-binding protein in the periplasm of *Escherichia coli*. *J. Biol. Chem.* 273, 8897–8902.

63 Sone, M., Kishigami, S., Yoshihisa, T. & Ito, K. (1997). Roles of disulfide bonds in bacterial alkaline phosphatase. *J. Biol. Chem.* 272, 6174–6178.

64 Spiess, C., Beil, A. & Ehrmann, M. (1999). A temperature-dependent switch from chaperone to protease in a widely conserved heat shock protein. *Cell* 97, 339–347.

65 Misra, R., Peterson, A., Ferenci, T. & Silhavy, T. J. (1991). A genetic approach for analyzing the pathway of LamB assembly into the outer membrane of *Escherichia coli*. *J. Biol. Chem.* 266, 13592–13597.

66 Uhland, K., Mondigler, M., Spiess, C., Prinz, W. & Ehrmann, M. (2000). Determinants of translocation and folding of TreF, a trehalase of *Escherichia coli*. *J. Biol. Chem.* 275, 23439–23445.

67 Snyder, W. & Silhavy, T. (1995). Beta-galactosidase is inactivated by intermolecular disulfide bonds and is toxic when secreted to the periplasm of *Escherichia coli*. *J. Bacteriol.* 177, 953–963.

68 Kihara, A. & Ito, K. (1998). Translocation, folding, and stability of the HflKC complex with signal anchor topogenic sequences. *J. Biol. Chem.* 273, 29770–29775.

69 St Geme, J. & Grass, S. (1998). Secretion of the *Haemophilus influenzae* HMW1 and HMW2 adhesins involves a periplasmic intermediate and requires the HMWB and HMWC proteins. *Mol. Microbiol.* 27, 617–630.

70 Guigueno, A., Belin, P. & Boquet, P. (1997). Defective export in *Escherichia coli* caused by DsbA′-PhoA hybrid proteins whose DsbA′ domain cannot fold into a conformation resistant to periplasmic proteases. *J. Bacteriol.* 179, 3260–3269.

71 Baneyx, F. & Georgiou, G. (1991). Construction and characterization of *Escherichia coli* strains deficient in multiple secreted proteases: protease III degrades high-molecular-weight substrates in vivo. *J. Bacteriol.* 173, 2696–2703.

72 Arslan, E., Schulz, H., Zufferey, R., Kunzler, P. & Thony-Meyer, L. (1998). Overproduction of the *Bradyrhizobium japonicum* c-type cytochrome subunits of the cbb3 oxidase in *Escherichia coli*. *Biochem. Biophys. Res. Commun.* 251, 744–777.

73 Cavard, D. (1995). Role of DegP protease on levels of various forms of colicin A lysis protein. *FEMS Microbiol. Lett.* 125, 173–178.

74 Misra, R., CastilloKeller, M. & Deng, M. (2000). Overexpression of protease-deficient DegP(S210A) rescues the lethal phenotype of *Escherichia coli* OmpF assembly mutants in a *degP* background. *J. Bacteriol.* 182, 4882–4888.

75 CastilloKeller, M. & Misra, R. (2003). Protease-deficient DegP suppresses lethal effects of a mutant OmpC protein by its capture. *J. Bacteriol.* 185, 148–154.

76 Ades, S. E., Connolly, L. E., Alba, B. M. & Gross, C. A. (1999). The *Escherichia coli* sigma(E)-dependent extracytoplasmic stress response is controlled by the regulated proteolysis of an anti-sigma factor. *Genes Dev.* 13, 2449–2461.

77 Alba, B. M., Leeds, J. A., Onufryk, C., Lu, C. Z. & Gross, C. A. (2002).

DegS and YaeL participate sequentially in the cleavage of RseA to activate the sigma(E)-dependent extracytoplasmic stress response. *Genes Dev.* 16, 2156–2168.

78 Alba, B. M., Zhong, H. J., Pelayo, J. C. & Gross, C. A. (2001). *degS* (*hhoB*) is an essential *Escherichia coli* gene whose indispensable function is to provide sigma activity. *Mol. Microbiol.* 40, 1323–1333.

79 Redford, P., Roesch, P. L. & Welch, R. A. (2003). DegS is necessary for virulence and is among extraintestinal *Escherichia coli* genes induced in murine peritonitis. *Infect. Immun.* 71, 3088–3096.

80 Walsh, N. P., Alba, B. M., Bose, B., Gross, C. A. & Sauer, R. T. (2003). OMP peptide signals initiate the envelope-stress response by activating DegS protease via relief of inhibition mediated by its PDZ domain. *Cell* 113, 61–71.

81 Young, J. C. & Hartl, F. U. (2003). A stress sensor for the bacterial periplasm. *Cell* 113, 1–2.

82 Krojer, T., Garrido-Franco, M., Huber, R., Ehrmann, M. & Clausen, T. (2002). Crystal structure of DegP (HtrA) reveals a new protease-chaperone machine. *Nature* 416, 455–459.

83 Li, W., Srinivasula, S. M., Chai, J., Li, P., Wu, J. W., Zhang, Z., Alnemri, E. S. & Shi, Y. (2002). Structural insights into the pro-apoptotic function of mitochondrial serine protease HtrA2/Omi. *Nat. Struct. Biol.* 9, 436–441.

84 Kim, D. Y., Kim, D. R., Ha, S. C., Lokanath, N. K., Lee, C. J., Hwang, H. Y. & Kim, K. K. (2003). Crystal structure of the protease domain of a heat-shock protein HtrA from *Thermotoga maritima*. *J. Biol. Chem.* 278, 6543–6551.

85 Wang, J., Hartling, J. A. & Flanagan, J. M. (1997). The structure of ClpP at 2.3 A resolution suggests a model for ATP-dependent proteolysis. *Cell* 91, 447–456.

86 Groll, M., Ditzel, L., Lowe, J., Stock, D., Bochtler, M., Bartunik, H. D. & Huber, R. (1997). Structure of 20S proteasome from yeast at 2.4 A resolution. *Nature* 386, 463–471.

87 Brandstetter, H., Kim, J. S., Groll, M. & Huber, R. (2001). Crystal structure of the tricorn protease reveals a protein disassembly line. *Nature* 414, 466–470.

88 Braig, K., Otwinowski, Z., Hegde, R., Boisvert, D., Joachimiak, A., Horwich, A. & Sigler, P. (1994). The crystal structure of the bacterial chaperonin GroEL at 2.8 A. *Nature* 371, 578–586.

89 Jones, C. H., Dexter, P., Evans, A. K., Liu, C., Hultgren, S. J. & Hruby, D. E. (2002). *Escherichia coli* DegP protease cleaves between paired hydrophobic residues in a natural substrate: the PapA pilin. *J. Bacteriol.* 184, 5762–5771.

90 Silber, K. R., Keiler, K. C. & Sauer, R. T. (1992). Tsp: a tail-specific protease that selectively degrades proteins with nonpolar C termini. *Proc. Natl. Acad. Sci. USA* 89, 295–299.

91 Beebe, K. D., Shin, J., Peng, J., Chaudhury, C., Khera, J. & Pei, D. (2000). Substrate recognition through a PDZ domain in tail-specific protease. *Biochemistry* 39, 3149–3155.

92 Keiler, K. C., Silber, K. R., Downard, K. M., Papayannopoulos, I. A., Biemann, K. & Sauer, R. T. (1995). C-terminal specific protein degradation: activity and substrate specificity of the Tsp protease. *Protein Sci.* 4, 1507–1515.

93 Keiler, K. C., Waller, P. R. & Sauer, R. T. (1996). Role of a peptide tagging system in degradation of proteins synthesized from damaged messenger RNA. *Science* 271, 990–993.

94 Ding, L., Becker, A. B., Suzuki, A. & Roth, R. A. (1992). Comparison of the enzymatic and biochemical properties of human insulin-degrading enzyme and *Escherichia coli* protease III. *J. Biol. Chem.* 267, 2414–2420.

95 Gill, R. T., Valdes, J. J. & Bentley, W. E. (2000). A comparative study of global stress gene regulation in response to overexpression of

recombinant proteins in *Escherichia coli*. *Metab. Eng.* 2, 178–189.

96 Gill, R. T., DeLisa, M. P., Shiloach, M., Holoman, T. R. & Bentley, W. E. (2000). OmpT expression and activity increase in response to recombinant chloramphenicol acetyltransferase overexpression and heat shock in *E. coli*. *J Mol Microbiol Biotechnol* 2, 283–289.

97 Jurgen, B., Lin, H. Y., Riemschneider, S., Scharf, C., Neubauer, P., Schmid, R., Hecker, M. & Schweder, T. (2000). Monitoring of genes that respond to overproduction of an insoluble recombinant protein in *Escherichia coli* glucose-limited fed-batch fermentations. *Biotechnol. Bioeng.* 70, 217–224.

98 Stathopoulos, C. (1998). Structural features, physiological roles, and biotechnological applications of the membrane proteases of the OmpT bacterial endopeptidase family: a micro-review. *Membr. Cell. Biol.* 12, 1–8.

99 Altamirano, M. M., Garcia, C., Possani, L. D. & Fersht, A. R. (1999). Oxidative refolding chromatography: folding of the scorpion toxin Cn5. *Nat. Biotechnol.* 17, 187–191.

100 Ryabova, L. A., Desplancq, D., Spirin, A. S. & Pluckthun, A. (1997). Functional antibody production using cell-free translation: effects of protein disulfide isomerase and chaperones. *Nat. Biotechnol.* 15, 79–84.

101 Kanehara, K., Ito, K. & Akiyama, Y. (2002). YaeL (EcfE) activates the sigma(E) pathway of stress response through a site-2 cleavage of anti-sigma(E), RseA. *Genes Dev.* 16, 2147–2155.

102 Brown, M. S., Ye, J., Rawson, R. B. & Goldstein, J. L. (2000). Regulated intramembrane proteolysis: a control mechanism conserved from bacteria to humans. *Cell* 100, 391–398.

103 Hellingwerf, K. J., Postma, P. W., Tommassen, J. & Westerhoff, H. V. (1995). Signal transduction in bacteria: phospho-neural network(s) in *Escherichia coli*? *FEMS Microbiol. Rev.* 16, 309–321.

104 DiGiuseppe, P. A. & Silhavy, T. J. (2003). Signal detection and target gene induction by the CpxRA two-component system. *J. Bacteriol.* 185, 2432–2440.

105 De Wulf, P., Kwon, O. & Lin, E. C. (1999). The CpxRA signal transduction system of *Escherichia coli*: growth-related autoactivation and control of unanticipated target operons. *J. Bacteriol.* 181, 6772–6778.

106 Dorel, C., Vidal, O., Prigent-Combaret, C., Vallet, I. & Lejeune, P. (1999). Involvement of the Cpx signal transduction pathway of *E. coli* in biofilm formation. *FEMS Microbiol. Lett.* 178, 169–175.

107 Hung, D. L., Raivio, T. L., Jones, C. H., Silhavy, T. J. & Hultgren, S. J. (2001). Cpx signaling pathway monitors biogenesis and affects assembly and expression of P pili. *Embo J.* 20, 1508–1518.

108 Otto, K. & Silhavy, T. J. (2002). Surface sensing and adhesion of *Escherichia coli* controlled by the Cpx-signaling pathway. *Proc Natl Acad Sci USA* 99, 2287–2292.

109 De Wulf, P., McGuire, A. M., Liu, X. & Lin, E. C. (2002). Genome-wide profiling of promoter recognition by the two-component response regulator CpxR-P in *Escherichia coli*. *J. Biol. Chem.* 277, 26652–26661.

110 Shimohata, N., Chiba, S., Saikawa, N., Ito, K. & Akiyama, Y. (2002). The Cpx stress response system of *Escherichia coli* senses plasma membrane proteins and controls HtpX, a membrane protease with a cytosolic active site. *Genes Cells* 7, 653–662.

111 Hagenmaier, S., Stierhof, Y. D. & Henning, U. (1997). A new periplasmic protein of *Escherichia coli* which is synthesized in spheroplasts but not in intact cells. *J. Bacteriol.* 179, 2073–2076.

112 Raivio, T. L., Laird, M. W., Joly, J. C. & Silhavy, T. J. (2000). Tethering of CpxP to the inner membrane prevents spheroplast induction of the cpx envelope stress response. *Mol. Microbiol.* 37, 1186–1197.

113 Raffa, R. G. & Raivio, T. L. (2002). A third envelope stress signal transduc-

tion pathway in *Escherichia coli*. *Mol. Microbiol.* 45, 1599–1611.

114 Tamm, L. K., Arora, A. & Kleinschmidt, J. H. (2001). Structure and assembly of beta-barrel membrane proteins. *J. Biol. Chem.* 276, 32399–32402.

115 Lee, K., Zhan, X., Gao, J., Qiu, J., Feng, Y., Meganathan, R., Cohen, S. & Georgiou, G. (2003). RraA: a Protein Inhibitor of RNase E Activity that Globally Modulates RNA Abundance in *E. coli*. *Cell* 114, 623–634.

29
Formation of Adhesive Pili by the Chaperone-Usher Pathway

Michael Vetsch and Rudi Glockshuber

29.1
Basic Properties of Bacterial, Adhesive Surface Organelles

Adhesive surface organelles of gram-negative bacteria are classified into four distinct categories based on their assembly pathway. A first pathway, found in a wide variety of bacteria, requires a specialized pair of a periplasmic chaperone and an outer-membrane assembly platform, termed usher [1]. This pathway is the main topic of this article. A second pathway is employed for the assembly of type 4 or bundle-forming pili. Type 4 pilus formation requires a minimum of 14 assembly components that are homologous to many accessory proteins of the type II secretion pathway in gram-negative bacteria and to the flagellum biogenesis machinery of archaea [2]. A third pathway is used for the formation of curli, which form amorphous matrices surrounding certain bacteria. The subunits of curli are thought to be secreted as monomers to the cell surface, where accessory proteins promote their polymerization into fibers [3]. A fourth pathway is proposed for the biogenesis of CS1, CS2, and CFA/I fimbriae from enterotoxic *Escherichia coli*. Like the chaperone-usher pathway, this mechanism appears to involve a dedicated periplasmic assembly factor and a specialized outer-membrane assembly platform, but these proteins share no sequence similarity with the components of the chaperone-usher pathway [4].

The chaperone-usher pathway is the common assembly mechanism of at least 37 different bacterial surface filaments found in pathogenic bacterial strains. Moreover, there are at least an additional 23 pairs of chaperones and ushers in protein databases that are thought to promote the assembly of yet unknown fibers (Table 29.1). Organelles assembled by the chaperone-usher pathway are divided into pilus and non-pilus fibers [5]. Nevertheless, the fiber subunits from both classes have the same fold, and the same principles underlie subunit-subunit interactions and interactions of subunits with chaperones and ushers. The best-studied member of non-pilus fibers is the capsular F1 antigen from the plague pathogen *Yersinia pestis* [6–8].

In contrast to the non-pilus fibers, pili have a complex architecture. They are composite structures made of a rigid helical rod and a thin, flexible tip fibrillum

Protein Folding Handbook. Part II. Edited by J. Buchner and T. Kiefhaber

ISBN: 3-527-30784-2

Tab. 29.1. Overview of adhesive organelles assembled by the chaperone-usher pathway

Organelle	*Organism*	*Chaperone*	*Usher*	*Disease*	*References*
FGS class					
AF/R1 pilus	*Escherichia coli*	AfrC	AfrB	Diarrhea in rabbits	61
Atf pilus	*Proteus mirabilis*	AtfB	AtfC	UTI	62
CS18	*E. coli*	FotB	FotD	Diarrhea	63
CS31A pilus	*E. coli*	ClpE	ClpD	Diarrhea	64, 65
F1C pilus	*E. coli*	FocC	FocD	Cystitis?	66, 67
F17 pilus	*E. coli*	F17D	F17papC	Diarrhea in piglets	68, 69
F18	*E. coli*	FedB	FedC	Diarrhea in piglets	70
Haf pilus	*Haemophilus influenzae* biogroup *aegyptus*	HafB	HafC	Brazilian purpuric fever	71
Hif pilus	*H. influenzae*	HifB	HifC	Otitis media, meningitis	72
K88 pilus	*E. coli*	FaeE	FaeD	Neonatal diarrhea in piglets	73–75
K99 pilus	*E. coli*	FanE	FanD	Diarrhea in lambs, calves, piglets	76, 75
Lpf pilus	*Salmonella typhimurium*, *E. coli*	LpfB	LpfC	Gastroenteritis, salmonellosis?	77
MRF	*Photorhabdus temperata*	MrfD	MrfC	Entomopathogenicity	78
MR/K (type3) pilus	*Klebsiella pneumoniae*	MrkB	MrkC	Pneumonia	79
MR/P pilus	*P. mirabilis*	MrpD	MrpC	Nosocomial UTI	80, 81
P pilus	*E. coli*	PapD	PapC	Pyelonephritis, cystitis	33, 82
Pef pilus	*S. typhimurium*	PefD	PefC	Gastroenteritis, salmonellosis	83
Pix pilus	*E. coli*	PixD	PixC	UTI	84
PMF pilus	*P. mirabilis*	PmfD	PmfC	Nosocomial UTI	85, 86
S pilus	*E. coli*	SfaE	SfaF	UTI, NBM	87
Sef	*S. typhi*	SefB	SefC	Gastroenteritis, salmonellosis	88, 89
Sef	*Serratia entomophila*	SefD	SefC	Amber disease	90
Sfp	*E. coli*	SfpD	SfpC	Diarrhea, hemolytic-uremic syndrome	91
Type 1 pilus	*E. coli*, *S. typhi*, *Pseudomonas putida*, *K. pneumoniae*	FimC	FimD	Cystitis	34
Type 2 and 3 pili	*Bordetella pertussis*	FimB (FhaD)	FimC (FhaA)	Whooping cough	92, 93
987P pilus	*E. coli*	FasB	FasD	Diarrhea in piglets	94, 95
	E. coli	CshC	CshB		*
	E. coli	EcpD	HtrE		96
	E. coli	RalE	RalD	Diarrhea in rabbits	97
	E. coli	SfmC	SfmD		*
	E. coli, *Shigella flexineri*	YbgP	YbgQ		*
	E. coli	YcbR	YcbS		*
	E. coli	YehC	YehB		*
	E. coli	YqiH	YqiG		*
	E. coli	YraI	YraJ		*
	Edwardsiella tarda	EtfB	EtfC		98, *
	Haemophilus spp	GhfB	GhfC	Neonatal genital tract infections	99

Tab. 29.1. *(continued)*

Organelle	*Organism*	*Chaperone*	*Usher*	*Disease*	*References*
	Photorhabdus luminescens	PhfC	PhfD		*
	S. typhimurium	BcfB,G?	BcfC	Gastroenteritis?	100
	S. typhi	StaB	StaC	Gastroenteritis?	100
	S. typhi, S. typhimurium	StbB	StbC	Gastroenteritis?	100
	S. typhi	StcB	StcC	Gastroenteritis?	100
	S. typhi	StdC	StdB	Gastroenteritis?	100
	S. typhi	SteC	SteB	Gastroenteritis?	100
	S. typhimurium	StfD	StfC	Gastroenteritis	101
	S. typhimurium	SthA	SthB	Gastroenteritis?	100
	S. typhi	StiB	StiC	Gastroenteritis?	102
	S. flexineri	YcbF	YcbS		*
FGL class					
AAF/I	*E. coli*	AggD	AggC	Diarrhea	103
AAF/II	*E. coli*	AafD	AafC	Infantile diarrhea	104
Afa-1	*E. coli*	AfaB	AfaC	UTI, diarrhea	105, 106
CS3	*E. coli*	Cs3-1	Cs3-2	Traveler's diarrhea	107, 108
CS6 pilus	*E. coli*	CssC	CssD	Diarrhea	109, 110
Dr/Afa-111	*E. coli*	DraB	DraC	UTI, diarrhea	111, *
F1 antigen	*Yersinia pestis*	Caf1M	Caf1A	Plague	112, 113
MFA1-6 family	*E. coli*	NfaE	NfaC	UTI, NBM	114, 115
Myf	*Y. enteritidis*	MyfB	MyfC	Enterocolitis	116
PH6 antigen	*Y. pestis, Y. pseudotuberculosis*	PsaB	PsaC	Plague	117
Saf	*S. typhimurium*	SafB	SafC	Gastroenteritis, enteric fever	118

* Entry in SwissProt or TrEMBL.

joined to the distal end of the rod. Type 1 pili and P pili from enteropathogenic *E. coli* are two prominent and well-characterized members of this class. The rod of type 1 pili consists of 500–3000 FimA subunits, has a diameter of 6.9 nm, and is up to 2 μm long. The tip fibrillum is approximately 15 nm long and is formed by a linear array of the adaptor subunits FimF and FimG and the adhesive subunit FimH at the end of the pilus (Figures 29.1 and 29.2) [9–11]. The role of another potential subunit, FimI, presently remains unclear [12, 13].

Compared to type 1 pili, P pili have a longer tip fibrillum but otherwise similar dimensions. The rod of P pili is formed by the main structural subunit PapA, and the tip fibrillum consists mainly of the subunit PapE. The minor subunit PapK links the tip fibrillum to the rod, while PapF serves as an adaptor between the tip fibrillum and the adhesin PapG [14, 15]. Whereas non-pilus fibers generally do not contain a specialized adhesin, binding of pili to specific target molecules is accomplished by dedicated adhesin subunits. The adhesins, in contrast to all other subunits, which are single-domain proteins, usually contain two domains with different functions. The N-terminal lectin domains mediate binding to sugar moieties in glycoprotein receptors, whereas the C-terminal pilin domains are required for incorporation of the adhesins into the pilus structure [16–18].

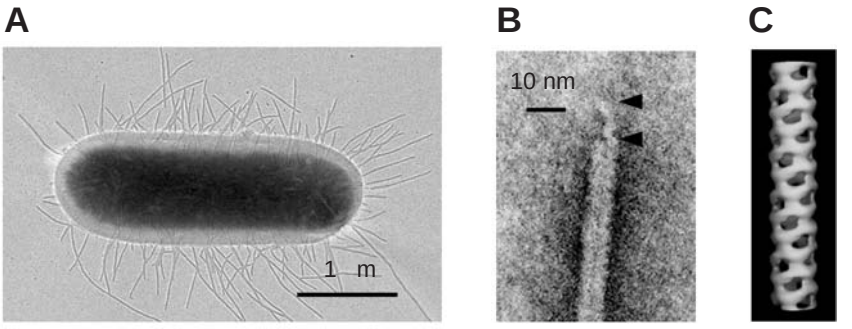

Fig. 29.1. Morphology of type 1 pili, which mediate binding of bacteria to the bladder epithelium. (A) Electron micrograph of an *Escherichia coli* cell bearing type 1 pili. A single *E. coli* cell may bear several hundred type 1 pili. (B) At the distal end of the rigid pilus rod, a thin, flexible tip fibrillum (between the arrowheads) is observed that contains the mannose-binding adhesin. (C) 3D reconstruction from electron microscopy data showing a type 1 pilus rod segment comprising 40 FimA subunits.

Pili are often associated with the capability of bacterial strains to cause infections (cf. Table 29.1). For example, the vast majority of urinary tract infections are caused by uropathogenic *E. coli* strains expressing a number of virulence factors that enable them to colonize the urinary tract and to persist despite robust host defense mechanisms [19]. The interplay between uropathogenic bacteria and the defense mechanisms in the bladder is reviewed thoroughly in Ref. [20]. Importantly, the initial step in establishing pathogenesis critically relies on the ability of the bacteria to attach to host tissue through specific adhesins. Among uropathogenic *E. coli* strains, type 1 pili are the most widely distributed adhesive organelles [21]. The adhesin of type 1 pili, FimH, mediates mannose-sensitive binding to the glycoprotein uroplakin Ia, an abundant integral membrane protein of the bladder epithelium [22]. Moreover, FimH triggers the internalization of bacteria into bladder cells [23]. Within the host cell, bacteria are protected from a variety of host defense mechanisms as well as antibiotics. Internalized bacteria not only persist but in some cases even replicate [24] and thus constitute a reservoir of pathogenic bacteria, which may cause the recurrent infections that are seen in a large portion of women with urinary tract infections [25]. P pili from uropathogenic *E. coli* strains enable the bacteria to bind to galα1-4gal units from glycolipids in the human kidney and thus to gain an initial foothold in the kidney [26], where they cause pyelonephritis [27].

Figure 29.2 illustrates important principles in the formation of fibers by the chaperone-usher pathway, using type 1 pili from *E. coli* as example. The formation of each type of fiber involves two dedicated proteins: a periplasmic chaperone (FimC in Figure 29.2) and an assembly platform, termed usher, in the outer membrane (FimD in Figure 29.2). Both components are essential for the assembly of fibers [28, 29]. The subunit polypeptides that eventually assemble into the fiber (FimA, FimF, FimG, and FimH in Figure 29.2) have N-terminal signal sequences and enter the periplasm through the SecYEG translocon. During translocation of the subunits or shortly thereafter, signal peptidase cleaves off the signal sequence

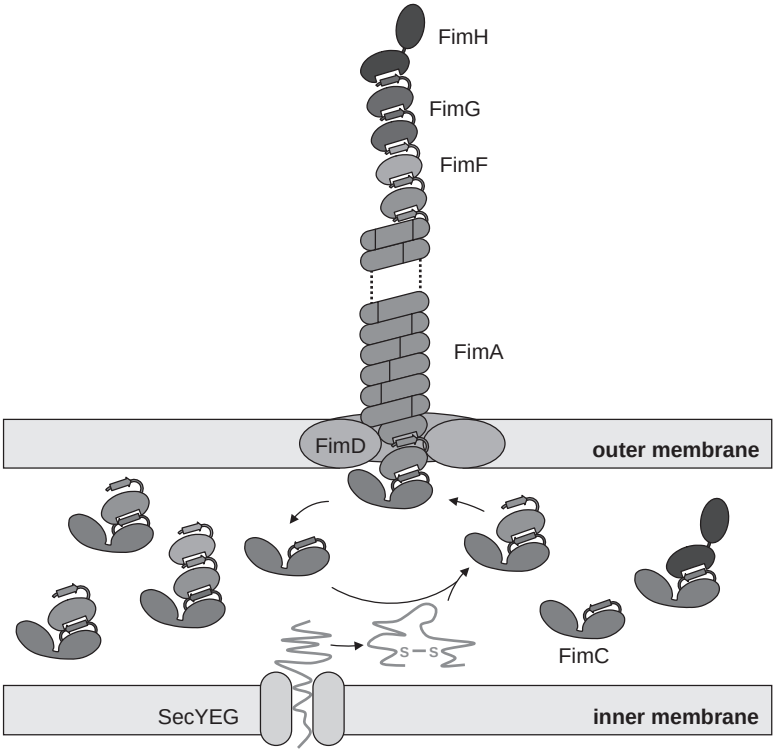

Fig. 29.2. Schematic presentation of the current view of type 1 pilus assembly via the chaperone-usher pathway. When newly synthesized structural pilus subunits (FimA, FimF, FimG, and FimH) enter the periplasm, their signal sequence is cleaved off and a single disulfide bridge is introduced into each pilin polypeptide. The subunits then fold and form heterodimers with the type 1 pilus chaperone FimC. These complexes bind to the usher FimD in the outer membrane, which triggers dissociation of the chaperone-subunit complexes. While the chaperone is released to the periplasm, the subunit is incorporated into the growing pilus. Translocation of subunits occurs via FimD, which is a ring-shaped oligomer with a central pore that allows translocation of folded subunits to the cell surface. In the quaternary structure of the pilus, every subunit donates an N-terminal extension, termed donor strand, to the preceding subunit, thereby complementing the fold of the preceding subunit.

and DsbA, the periplasmic dithiol oxidase of *E. coli* [30], introduces a single disulfide bond, which is invariant in all subunits. This disulfide bond most likely enhances the stability of the subunits but appears to be dispensable for the assembly process in the case of type 1 pili, as *E. coli* strains lacking DsbA retain the ability to produce functional type 1 fibers [31]. The fact that DsbA is not required for type 1 pilus assembly could be due to the extraordinary stability of the quaternary structure of type 1 pili against dissociation and denaturation, which may compensate for a lower intrinsic stability of non-oxidized subunits. In the case of P pili, however, DsbA is required [32], possibly because the single disulfide bond in the P pilus chaperone PapD is required for PapD's structural integrity.

After signal sequence cleavage and disulfide bond formation, the subunits fold

and form soluble complexes with the periplasmic pilus chaperones [33, 34]. The chaperone-subunit complexes diffuse to the outer membrane, where they dissociate upon contact with the usher. The free pilus chaperone is released to the periplasm for another round of subunit binding and subunit transport to the usher. Thus, the chaperone is a true assembly factor and not part of the final pilus structure [33]. The usher itself is a ring-shaped oligomer with a central pore, which most likely allows translocation of subunits in their folded state [12, 35]. The thermodynamic drive for pilus assembly might come from quaternary structure formation in the extracellular space. Pilus formation after subunit secretion to the periplasm would thus be a spontaneous process that does not require ATP or other energy sources [36].

29.2 Structure and Function of Pilus Chaperones

To date, the structures of four bacterial pilus chaperones are known. The structures of PapD (P pilus system of *E. coli*), FimC (type 1 pilus system of *E. coli*), SfaE (S pilus system of *E. coli*), and Caf1M (capsular F1 antigen of *Y. pestis*) were solved by X-ray crystallography or NMR [7, 16, 37–41]. The tertiary structures of all these chaperones are very similar. Each pilus chaperone comprises two immunoglobulin (Ig)-like domains joined at approximately right angles. The two last strands of the N-terminal domain (the F1- and G1-strands) are connected by a long loop (F1-G1 loop) protruding away from the domain (Figure 29.3). Structure-based sequence alignments of all known pilus chaperones showed that the length of the F1-G1 loop is a criterion to distinguish between two closely related but different classes of pilus chaperones. FGS chaperones (e.g., PapD, FimC, or SfaE) have a short F1-G1 loop and are required for the assembly of rigid pili. In contrast, FGL chaperones (e.g., Caf1M) have a long F1-G1 loop and assist in the formation of non-pilus fibers [5]. The F1-G1 loop comprises a motif of alternating hydrophobic and hydrophilic residues, which play a critical role in subunit binding (see Section 29.3). The motif contains three hydrophobic residues in FGS chaperones and four to five hydrophobic residues in most FGL chaperones [6]. A comparison of monomeric chaperones and chaperones with bound pilus subunit shows that upon binding of subunits, the conformation of the F1-G1 loop alters significantly while the overall structure of the chaperone structure is not affected [16, 38]. In addition to the variable loop length, a second difference between the two classes is observed. FGL chaperones contain a conserved disulfide bond connecting the F- and the G-strand of the N-terminal domain [8], while FGS chaperones lack this disulfide bond. The disulfide bond that is found in some FGS chaperones (e.g., PapD) is close to the C-terminus and connects the two C-terminal β-strands. Formation of this disulfide is critical for the in vivo function of PapD [32].

Periplasmic pilus chaperones are multifunctional proteins. They prevent both premature assembly of pilus subunits [42, 43] and nonspecific aggregation of subunits in the periplasm [42, 44, 45]. But unlike classical chaperones, the pilus chaperones form stable complexes with folded substrate proteins. The kinetic stability

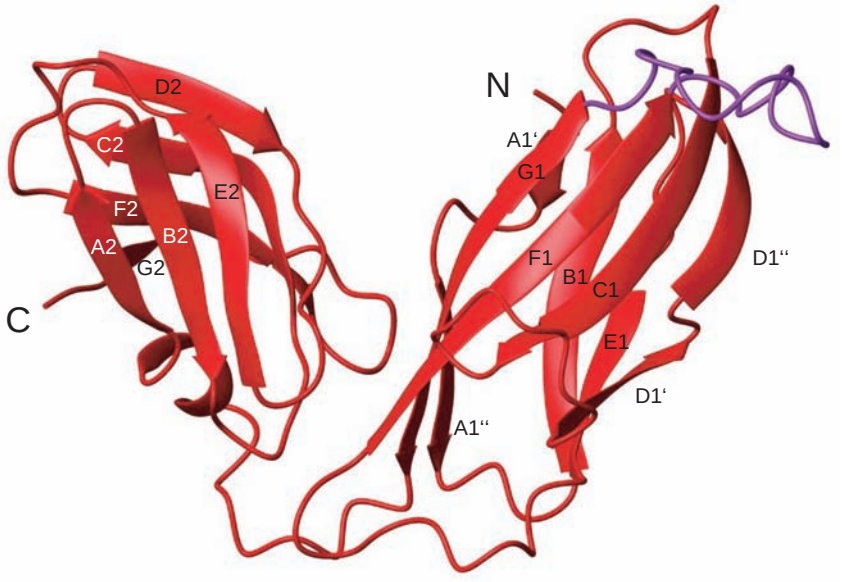

Fig. 29.3. Ribbon diagram of the type 1 pilus chaperone FimC [40]. The loop connecting the F1- and G1-strands is colored purple. Based on the length of the F1-G1 loop, pilus chaperones are classified into FGL chaperones (long loops) and FGS chaperones (short loops), of which FimC is a member. FimC (23 kDa) is a β-sheet protein composed of two domains (residues 1–115 and 131–205), connected by a 15-amino-acid linker.

of such complexes against dissociation most likely prevents formation of subunit-subunit complexes in the periplasm. This model is supported by the finding that pilus chaperones cap a region of the subunits that is required for the interaction with a neighboring subunit in the pilus [8, 39], as originally proposed by Soto et al. [43]. Despite the relatively strong interactions between pilus chaperones and their target subunits, bacterial pili assemble within a few minutes in vivo [36]. This suggests that chaperone-subunit complexes dissociate rapidly only when they are in contact with the outer-membrane usher. In addition, pilus chaperones bind to peptides corresponding to the C-terminal β-strand of target subunits, suggesting that pilus chaperones may recognize unfolded subunits and assist subunit folding [43, 46]. Another function of pilus chaperones, discussed in more detail below, is targeting of chaperone-subunit complexes to the ushers, which have a periplasmically oriented binding domain that exclusively recognizes chaperone-subunit complexes [47].

29.3
Structure and Folding of Pilus Subunits

Three recently determined crystal structures of chaperone-subunit complexes have contributed enormously to our understanding of the pilus assembly process [8, 16, 38]. The common, most striking finding was that the subunits have an atypical Ig-like fold that lacks the C-terminal G-strand. This creates a large hydrophobic

groove on the subunit surface. In the chaperone-subunit complex, this groove is occupied by an extrinsic β-strand, provided by the chaperone [8, 16, 38]. This remarkably tight interaction is referred to as ''donor strand complementation'', and the extrinsic β-strand is called ''donor strand''. Specifically, a part of the G1-strand of the chaperone that includes the motif with alternating hydrophobic residues in the F1-G1 loop is inserted between the A″- and the F-strand of the subunit (Figures 29.4B and 29.5B, see p. 974/975). The conserved hydrophobic residues in the F1-G1 loop of the chaperone, which are solvent-exposed in the free chaperone, reach deep into the hydrophobic core of the bound subunit. The complemented structure of the subunit has an atypical Ig-like fold because the donated strand runs parallel to the F-strand of the subunit rather than antiparallel (Figures 29.4B and 29.5B).

The second important result from the structures of chaperone-subunit complexes, modeling studies, and biochemical experiments is that donor strand complementation also might govern subunit-subunit interactions in the quaternary structure of pili [16, 38]. Sequence alignment of structural pilus subunits shows that they are structurally homologous, single-domain β proteins in which the N-terminal ~14 amino acids are not part of the tertiary structure of the subunits. These N-terminal segments serve as donor strands for a preceding subunit in the pilus and replace the donor strand of the chaperone in this subunit. In contrast to the donor strand of the chaperone, however, the donor strand provided by a neighboring pilus subunit is assumed to insert antiparallel to the F-strand of the acceptor subunit (Figure 29.5C), creating a canonical Ig-like fold [16, 38]. The concept proposing that pilus subunits are both β-strand donors and β-strand acceptors also nicely explains why pilus adhesins are located only at the tip of the pilus [11]. Unlike other subunits, the adhesins lack the N-terminal donor strand, which is replaced by a lectin domain (e.g., PapG in the case of P pili and FimH in the case of type 1 pili). Thus, adhesins are only donor stand acceptors and act as pilus caps: they are either incorporated as the first subunit at the tip of a pilus or not at all (cf. also Figure 29.2).

The structural proof of donor strand complementation between pilus subunits came from the X-ray structure of the ternary complex between the chaperone Caf1M and two subunits of Caf1, which forms the homo-oligomeric fiber of the *Yersinia pestis* F1 capsular antigen [8]. In this structure, the first Caf1 subunit is bound to the chaperone via parallel donor strand complementation, while the second Caf1 subunit interacts with the first subunit via antiparallel donor strand complementation. Comparison of the structures of both Caf1 subunits revealed that the two β-sheets of the Ig-like fold in the chaperone-bound subunit have low shape correlation statistics [48], reflecting a loosely packed hydrophobic core. Meanwhile, the second Caf1 subunit that is complexed with the first Caf1 has a tightly packed hydrophobic core, as is typically observed for β-barrels consisting of two β-sheets. This, in more general terms, suggests a collapse of the hydrophobic core of a subunit upon release from the chaperone and assembly into the fiber oligomer. This conformational change could result in a gain in free folding energy. Zavaliov et al. [8] propose that this potential difference in free energy might constitute a driving force for fiber assembly, in addition to stabilizing intermolecular con-

tacts in the quaternary structure. It remains to be tested whether subunit-subunit interactions are indeed thermodynamically more stable than chaperone-subunit interactions and, if this proves true, how periplasmic pilus chaperones prevent spontaneous formation of more stable subunit-subunit interactions in the periplasm.

Removal of an extrinsic donor strand from a pilus subunit causes a significant exposure of the subunit's hydrophobic core to the solvent. This led to the hypothesis that pilus subunits lack essential steric information to fold autonomously to a defined tertiary structure and that they strictly require assistance of the chaperone to fold [16, 38]. Support for this model came from the observation that high-level expression of pilus subunits is possible only when the corresponding chaperone is co-expressed [44] and from unsuccessful attempts to refold chemically denatured subunits in the absence of chaperone in vitro [49]. More recent experiments, however, challenge this hypothesis. It was found that the pilin domain of FimH folds autonomously and with a cooperativity that is characteristic for a protein of the size of the pilin domain [45]. However, the thermodynamic stability of the pilin domain is very low ($\Delta G^{\circ}_{fold} = -10$ kJ mol^{-1}), such that a small but significant fraction of molecules is unfolded even under native conditions. This explains the high tendency of the pilin domain to aggregate nonspecifically in the absence of stoichiometric amounts of the chaperone FimC. The simplest conclusion from these data is that pilin domains can fold autonomously but are intrinsically very unstable without the donor strand. Thermodynamic stabilization by donor strand complementation through the chaperone thus most likely prevents nonspecific aggregation of pilus subunits. The role of pilus chaperones in the subunit folding reactions is presently unknown. On the one hand, there is evidence that subunits can fold autonomously prior to binding to the chaperone in vitro [50, 51]. On the other hand, refolding of pilus subunits in the presence of the chaperone increases the yield of chaperone-subunit complexes compared to refolding of the subunit alone and subsequent addition of the chaperone. This may indicate a more ''active'' role of pilus chaperones in pilus subunit folding [49]. This view is supported by the observation that spontaneous folding of the FimH pilin domain is very slow [45], especially compared to the fast incorporation of subunits into pili in vivo [36].

29.4 Structure and Function of Pilus Ushers

The only specialized membrane protein involved in pilus assembly is the pilus usher, which is located in the outer bacterial membrane. In the absence of the usher, chaperone-subunit complexes accumulate in the periplasm and no fibers are assembled [7, 29, 33]. PapC (86 kDa per subunit) and FimD (91 kDa per subunit) are the ushers required for formation of P pili and type 1 pili, respectively. Electron microscopy revealed that they comprise 6–12 subunits forming ring-shaped oligomers with an outer diameter of 15 nm and a pore that is about 2 nm wide [12, 35]. Proteoliposome swelling assays with PapC and FimD showed that the ushers indeed form pores [35]. A pore with a diameter of 2 nm is too small to accommodate pilus rods, which are about 7 nm wide [11, 52]. It has therefore been

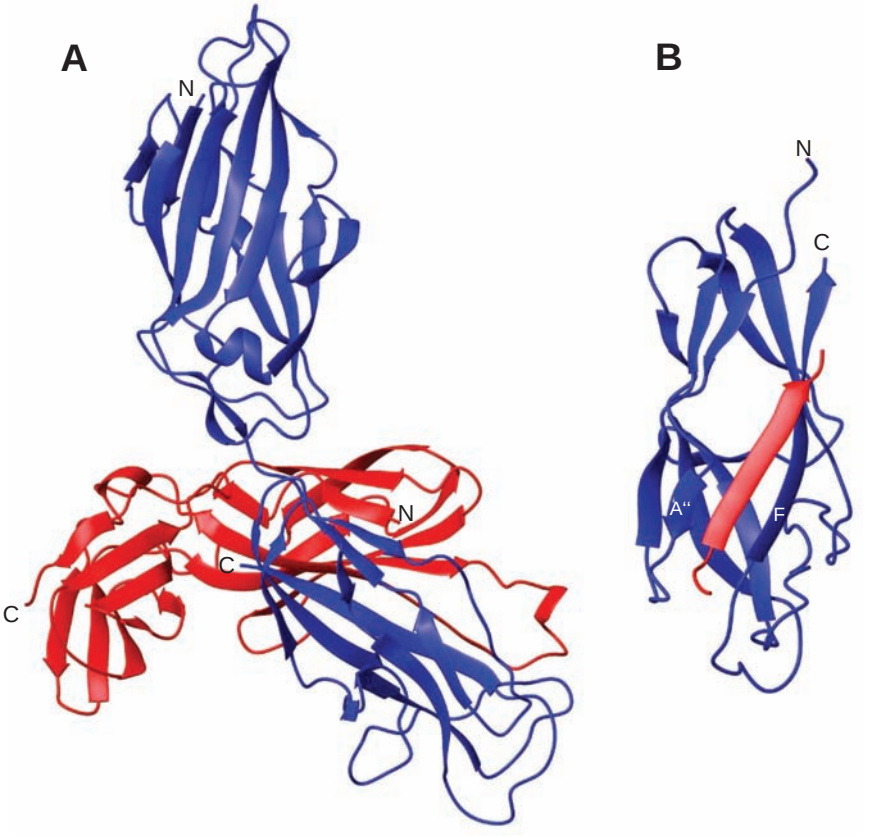

Fig. 29.4. Donor strand complementation in chaperone-subunit complexes [16]. (A) Ribbon diagram of the X-ray structure of the FimC-FimH complex. The type 1 pilus adhesin FimH (blue) has two domains with different roles. The N-terminal lectin domain binds to mannosylated uroplakin Ia on the bladder epithelium, while the C-terminal pilin domain mediates the association with the subunit FimG in the intact pilus. FimC (red) almost exclusively interacts with the pilin domain of FimH via its N-terminal domain. There is no interaction between the lectin domain of FimH and FimC. (B) View of the pilin domain of FimH in the context of the FimC-FimH complex. The pilin domain (blue) has an incomplete Ig-like β-fold lacking one β-strand and is structurally homologous to the other pilus subunits FimA, FimF, and FimG. In the chaperone-subunit complex, the missing strand, termed donor strand, is provided by the chaperone and inserted between the N-terminal A″-strand and the C-terminal F-strand of the pilin domain. Because the orientation of the donor strand of FimC (red) is parallel relative to the F-strand of the pilin domain, an atypical Ig-like fold is created.

proposed that assembled subunits leave the periplasm as a linear array of subunits and that formation of the helical rod occurs on the bacterial surface [35]. This model is supported by the observation that subunits interact head-to-tail with each other [8, 39]. Hence, it is conceivable that subunits are translocated through the central pore of the ushers as an extended, linear oligomer, including subunits like PapA and FimA, which eventually form helical pilus rods.

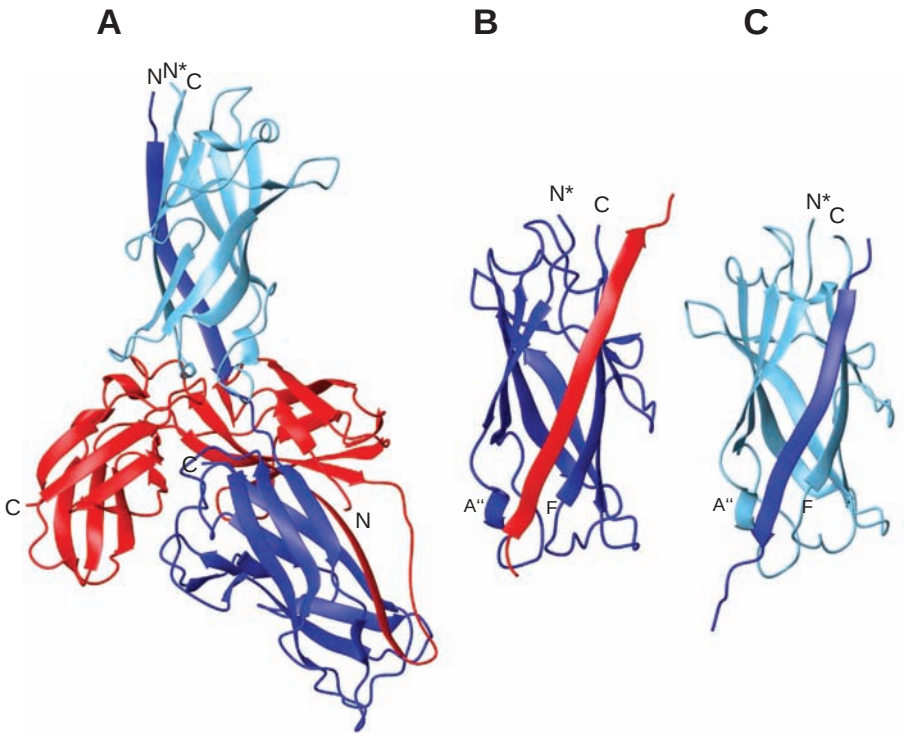

Fig. 29.5. Structural basis of donor strand complementation in subunit-subunit interactions. The F1 capsular antigen of *Yersinia pestis* is a linear, homo-oligomeric fiber of Caf1 subunits. The structure of the ternary complex between two Caf1 subunits and the assembly chaperone Caf1M was solved by X-ray crystallography [8]. (A) Ribbon diagram of the Caf1M-Caf1-Caf1 complex. The chaperone Caf1M (red) interacts with the first Caf1 subunit (dark blue), to which the second Caf1 subunit (light blue) is bound. (B) A close-up of the chaperone-bound Caf1 subunit reveals that the Ig-like fold of the subunit is complemented by a donor strand from the chaperone (red) running parallel to the C-terminal F-strand of the subunit. Exactly the same observation was made for the pilin domain of FimH in the FimC-FimH complex [16] (cf. Figure 4B) and for PapK in the PapD-PapK complex [38]. The asterisk indicates that the N-terminal 15-residue donor strand was omitted for clarity. (C) Inspection of the second Caf1 subunit shows that the donor strand provided by the first subunit also inserts between the A″- and F-strands of the acceptor subunit, but in the opposite, antiparallel orientation. Due to the antiparallel insertion of the extrinsic donor strand relative to the F-strand of the subunit, a canonical Ig-like fold is obtained.

The ushers of type 1 and P pili (FimD and PapC, respectively) were reported to bind their target chaperone-subunit complexes with affinities in the nanomolar to micromolar range [53]. In both pilus systems, the affinities of the ushers for the different chaperone-subunit complexes differ by several orders of magnitude. Strikingly, the chaperone-subunit complexes containing the adhesin (FimH and PapG, respectively) have the highest affinity for their cognate usher [53]. Because the adhesins are thought to be the first subunits to become incorporated into the pilus, this observation has led to the hypothesis that the relative affinities of the usher

for the various chaperone-subunit complexes determine the order of the subunits within the pilus [53, 54]. At the least, this mechanism would ensure that a substantial fraction of pili bear an adhesin at their tip. Besides the specific affinities of the ushers for the various chaperone-subunit complexes, the relative affinities of the subunits towards each other are most likely another critical factor determining the final quaternary structure of pili.

Little is known about the molecular details of the binding of chaperone-subunit complexes to the ushers. It is established that isolated pilus chaperones are not bound by ushers [53]. This could mean that pilus subunits contain sufficient structural information for being recognized by the ushers. The finding that different chaperone-subunit complexes containing the same chaperone have different affinities for the target usher supports this view, together with the report that the pilin domain of the type 1 pilus subunit FimH has the capability to bind to the usher FimD even in the absence of the chaperone FimC [55].

Primary structure analysis of pilus ushers indicates that these proteins share a common topology. Computational sequence analysis and biochemical topology analysis of the usher FaeD from K88 fimbriae suggest a central transmembrane domain flanked by N- and C-terminal periplasmically oriented domains [56, 57]. Recent experiments with the P pilus usher PapC indicate that the ability of ushers to bind chaperone-subunit complexes resides in their N-terminal regions, while central and C-terminal parts appear to be required for subunit assembly or translocation [58]. Progress towards a more detailed understanding of the interactions between chaperone-subunit complexes and ushers has been made by Nishiyama et al. [47], who discovered that the N-terminal, periplasmic domain of the usher FimD ($FimD_N$), comprising the N-terminal 139 FimD residues, can be expressed as a soluble, monomeric protein that folds autonomously. In addition, $FimD_N$ specifically binds chaperone-subunit complexes and, like full-length FimD, does not bind the isolated chaperone FimC. Unilke FimD, however, $FimD_N$ fails to recognize isolated subunits [47, 55]. In addition, the affinity of $FimD_N$ for chaperone-subunit complexes is lower compared to that reported for full-length FimD. A possible reason for these lower affinities may be the monomeric state of $FimD_N$. Ring-shaped FimD oligomers are supposed to have multiple $FimD_N$ binding sites in close proximity, which may increase the apparent affinity of the oligomer for pilus subunits. Moreover, important segments of FimD involved in recognition of chaperone-subunit complexes may not be contained in $FimD_N$. Despite these uncertainties, the availability of $FimD_N$ opens the possibility of structure determination of ternary complexes among $FimD_N$, FimC, and different type 1 pilus subunits. These ternary complexes are predicted intermediates in pilus assembly.

29.5 Conclusions and Outlook

In the past few years, our understanding of the assembly of bacterial pili has tremendously improved through the determination of the three-dimensional structures of chaperone-subunit complexes from different pilus systems. These struc-

tures have revealed the mechanism of donor strand complementation as the common principle underlying pilus subunit stabilization and subunit binding by pilus chaperones, as well as subunit-subunit interactions in the context of the quaternary structure of pili. Despite these important fundamental insights, there are still many intriguing questions to be answered to gain a complete mechanistic understanding of bacterial pilus assembly: Do pilus chaperones influence or even catalyze folding of pilus subunits? Why are pili extremely stable macromolecular assemblies that resist unfolding by acid or high concentrations of denaturants, while individual pilus subunits are comparably unstable? Which factors determine the average pilus length distribution and average number of pili per cell? What are the three-dimensional structures and detailed mechanisms of the ushers? Ushers are predicted not only to bind specifically to chaperone-subunit complexes but also to catalyze pilus assembly by accelerating the dissociation of chaperone-subunit complexes and promoting subunit-subunit interactions. No functional in vitro assay for a purified, intact assembly platform complex could be established so far. In principle, catalytic amounts of a functional usher should immediately trigger pilus formation in vitro when added to a mixture of purified chaperone-subunit complexes. The latter experiment is most likely the key towards the complete in vitro reconstitution of macromolecular pilus assembly.

29.6 Experimental Protocols

29.6.1 Test for the Presence of Type 1 Piliated *E. coli* Cells

The presence of adhesive pili on the bacterial surface can often be tested easily by agglutination with other cells bearing the target molecule of the pilus adhesin. In the case of type 1 pili from *E. coli*, agglutination with yeast cells is used (Figure 29.6). Bacteria are grown in LB medium without shaking for two days, harvested by centrifugation, and resuspended in PBS buffer, pH 7.5, to a final optical density at 600 nm of 1. A 500-µl aliquot is mixed with 20 µl of a 10% (w/v) suspension of dry baker's yeast in PBS. The extent of agglutination is examined 5 min after mixing. Baker's yeast cells bear multiple mannose units on their surface and therefore agglutinate with bacterial strains expressing functional type 1 pili to three-dimensional networks. This leads to the formation of large, visible clots. In the absence of type 1 pili, no agglutination is observed.

29.6.2 Functional Expression of Pilus Subunits in the *E. coli* Periplasm

Both functional expression of pilus subunits in the periplasm of *E. coli* and purification of pilus subunits critically depend on the presence of stoichiometric amounts of chaperone. High expression yields are achieved with dicistronic operons ensuring a 1:1 ratio of both genes at the mRNA level. To minimize degradation of pilus

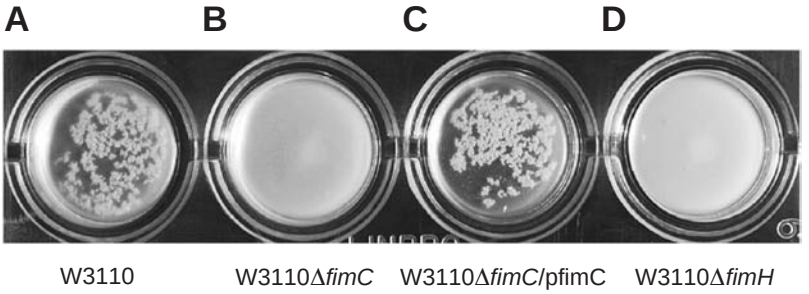

Fig. 29.6. Agglutination of yeast cells by *E. coli* cells bearing type 1 pili. The presence of functionnal type 1 pili can be tested by agglutination of the bacteria with bakers yeast. (A) The adhesin FimH at the tip of type 1 pili of *E. coli* strain W3110 binds to mannose units on the surface of yeast cells. As a consequence, visible clots are formed consisting of bacteria and yeast cells. (B) An isogenic W3110 strain lacking the gene encoding the pilus chaperone FimC (W3110Δ*fimC*) is unable to assemble pili. No agglutination is observed. (C) The ability of W3110Δ*fimC* to agglutinate with yeast cells is restored when the strain carries the plasmid pfimC for expression of FimC. (D) The strain W3110Δ*fimH* expresses type 1 pili, but these lack the adhesin FimH at their tip. Thus, no agglutination occurs.

subunits, *E. coli* strains lacking periplasmic proteases, e.g., strain HM 125 [59], can be employed. Expression yields strongly depend on the individual subunit. For example, comparison of the expression yields of the complexes FimC-FimH and FimC-FimA using analogous, dicistronic operons shows that the chaperone FimC is expressed at identical levels in both cases, while the subunit FimH is expressed in much higher amounts than the subunit FimA (M. Vetsch, unpublished results). Similar amounts of FimH and FimA are probably produced, but FimH possibly has a higher affinity for FimC than does FimA. Subunits that dissociate from the chaperone are subject to kinetic competition between rebinding to the chaperone on the one hand and nonspecific aggregation or self-polymerization on the other hand. The latter side reactions are most likely responsible for the difficulty in expressing soluble, monomeric subunits in the periplasm. In addition, isolated subunits are certainly also prone to proteolytic degradation, due to their low thermodynamic stability.

29.6.3
Purification of Pilus Subunits from the *E. coli* Periplasm

Chaperone-subunit complexes can be purified from periplasmic extracts by ion-exchange and hydrophobic chromatography. Alternatively, a hexahistidine tag may be fused to the C-terminus of the chaperone. This extension does not affect the interaction with subunits, which essentially interact with the N-terminal domain of the chaperone. When the chaperone is tagged, immobilized metal-affinity chroma-

tography (IMAC) can be used to isolate the chaperone with the bound subunit from periplasmic extracts. Because co-expression of the chaperone and a subunit generally results in accumulation of both chaperone-subunit complexes and an excess of monomeric chaperone, an additional purification step is necessary to obtain a homogenous preparation of chaperone-subunit complex. Usually, ion-exchange chromatography is used for this purpose. Chaperone-subunit complexes are in most cases very stable and can therefore be stored for prolonged periods of time. To isolate the subunits, chaperone-subunit complexes are unfolded and dissociated with chemical denaturants such as 5 M urea or 2.5 M guanidinium chloride (GdmCl). The subunits can then be separated from the chaperone by ion-exchange chromatography in the presence of urea or by IMAC in the presence of GdmCl or urea (if the chaperone has a hexahistidine tag). Due to the high tendency of subunits to aggregate in the absence of chaperone, subunits should always be freshly prepared directly before further biochemical experiments [45, 47, 51].

29.6.4
Preparation of Ushers

Preparation of pure and functional oligomeric ushers is a prerequisite for biochemical studies aimed at a detailed understanding of usher function. So far, only the ushers PapC and FimD, both containing a hexahistidine tag at the C-terminus, have been purified successfully [35, 53]. The C-terminal tag does not interfere with the biological activity of the ushers, as the tagged usher variants complement usher deficiency in strains with chromosomal usher deletions. On the other hand, high-level expression of ushers is often detrimental for cell growth. Consequently, tightly regulated promoters such as the arabinose-inducible P_{BAD} promoter [60] and short-term induction of protein expression are used for high-level expression of ushers. After disruption of the cells, differential centrifugation is used to enrich the membranes. Subsequently, proteins of the inner membrane are selectively solubilized with the detergent sarcosyl (1%) to enrich outer-membrane proteins. Finally, the detergents Zwittergent 3–14 (1%) or Elugent (1%) are used to solubilize the outer-membrane ushers, which are then purified by IMAC [35, 53]. Ushers isolated according to this procedure were shown to retain the ability to bind chaperone-subunit complexes in the presence of Zwittergent 3–14 (0.1%) or Elugent (0.1%) [35, 53]. As this function lies in the N-terminal chaperone-subunit–binding domain of the ushers, however, this is not proof for an entirely functional usher molecule with an intact transmembrane region. Further functional assays for purified ushers have not been reported so far.

Acknowledgements

We would like to thank Chasper Pourger for preparing Table 29.1 and Ulla Grauschopf for critically reading the manuscript.

References

1 Sauer, F. G., Barnhart, M., Choudhury, D., Knight, S. D., Waksman, G. & Hultgren, S. J. (2000). Chaperone-assisted pilus assembly and bacterial attachment. *Curr Opin Struct Biol* **10**, 548–56.

2 Peabody, C. R., Chung, Y. J., Yen, M. R., Vidal-Ingigliardi, D., Pugsley, A. P. & Saier, M. H., Jr. (2003). Type II protein secretion and its relationship to bacterial type IV pili and archaeal flagella. *Microbiology* **149**, 3051–72.

3 Chapman, M. R., Robinson, L. S., Pinkner, J. S., Roth, R., Heuser, J., Hammar, M., Normark, S. & Hultgren, S. J. (2002). Role of Escherichia coli curli operons in directing amyloid fiber formation. *Science* **295**, 851–5.

4 Smyth, C. J., Marron, M. B., Twohig, J. M. & Smith, S. G. (1996). Fimbrial adhesins: similarities and variations in structure and biogenesis. *FEMS Immunol Med Microbiol* **16**, 127–39.

5 Hung, D. L., Knight, S. D., Woods, R. M., Pinkner, J. S. & Hultgren, S. J. (1996). Molecular basis of two subfamilies of immunoglobulin-like chaperones. *Embo J* **15**, 3792–805.

6 MacIntyre, S., Zyrianova, I. M., Chernovskaya, T. V., Leonard, M., Rudenko, E. G., Zav'Yalov, V. P. & Chapman, D. A. (2001). An extended hydrophobic interactive surface of Yersinia pestis Caf1M chaperone is essential for subunit binding and F1 capsule assembly. *Mol Microbiol* **39**, 12–25.

7 Zavialov, A. V., Kersley, J., Korpela, T., Zav'yalov, V. P., MacIntyre, S. & Knight, S. D. (2002). Donor strand complementation mechanism in the biogenesis of non-pilus systems. *Mol Microbiol* **45**, 983–95.

8 Zavialov, A. V., Berglund, J., Pudney, A. F., Fooks, L. J., Ibrahim, T. M., MacIntyre, S. & Knight, S. D. (2003). Structure and biogenesis of the capsular F1 antigen from Yersinia pestis: preserved folding energy drives fiber formation. *Cell* **113**, 587–96.

9 Klemm, P. & Christiansen, G. (1987). Three fim genes required for the regulation of length and mediation of adhesion of Escherichia coli type 1 fimbriae. *Mol Gen Genet* **208**, 439–45.

10 Jones, C. H., Pinkner, J. S., Roth, R., Heuser, J., Nicholes, A. V., Abraham, S. N. & Hultgren, S. J. (1995). FimH adhesin of type 1 pili is assembled into a fibrillar tip structure in the Enterobacteriaceae. *Proc Natl Acad Sci USA* **92**, 2081–5.

11 Hahn, E., Wild, P., Hermanns, U., Sebbel, P., Glockshuber, R., Haner, M., Taschner, N., Burkhard, P., Aebi, U. & Muller, S. A. (2002). Exploring the 3D molecular architecture of Escherichia coli type 1 pili. *J Mol Biol* **323**, 845–57.

12 Saulino, E. T., Bullitt, E. & Hultgren, S. J. (2000). Snapshots of usher-mediated protein secretion and ordered pilus assembly. *Proc Natl Acad Sci USA* **97**, 9240–5.

13 Valenski, M. L., Harris, S. L., Spears, P. A., Horton, J. R. & Orndorff, P. E. (2003). The Product of the fimI gene is necessary for Escherichia coli type 1 pilus biosynthesis. *J Bacteriol* **185**, 5007–11.

14 Lindberg, F., Lund, B., Johansson, L. & Normark, S. (1987). Localization of the receptor-binding protein adhesin at the tip of the bacterial pilus. *Nature* **328**, 84–7.

15 Jacob-Dubuisson, F., Heuser, J., Dodson, K., Normark, S. & Hultgren, S. (1993). Initiation of assembly and association of the structural elements of a bacterial pilus depend on two specialized tip proteins. *Embo J* **12**, 837–47.

16 Choudhury, D., Thompson, A., Stojanoff, V., Langermann, S., Pinkner, J., Hultgren, S. J. & Knight, S. D. (1999). X-ray structure of the FimC-FimH chaperone-adhesin complex from uropathogenic Escherichia coli. *Science* **285**, 1061–6.

17 Dodson, K. W., Pinkner, J. S., Rose, T., Magnusson, G., Hultgren, S. J. & Waksman, G. (2001). Structural basis of the interaction of the pyelone-

phritic E. coli adhesin to its human kidney receptor. *Cell* **105**, 733–43.

18 Merckel, M. C., Tanskanen, J., Edelman, S., Westerlund-Wikstrom, B., Korhonen, T. K. & Goldman, A. (2003). The structural basis of receptor-binding by Escherichia coli associated with diarrhea and septicemia. *J Mol Biol* **331**, 897–905.

19 Hooton, T. M. & Stamm, W. E. (1997). Diagnosis and treatment of uncomplicated urinary tract infection. *Infect Dis Clin North Am* **11**, 551–81.

20 Mulvey, M. A., Schilling, J. D., Martinez, J. J. & Hultgren, S. J. (2000). Bad bugs and beleaguered bladders: interplay between uropathogenic Escherichia coli and innate host defenses. *Proc Natl Acad Sci USA* **97**, 8829–35.

21 Langermann, S., Palaszynski, S., Barnhart, M., Auguste, G., Pinkner, J. S., Burlein, J., Barren, P., Koenig, S., Leath, S., Jones, C. H. & Hultgren, S. J. (1997). Prevention of mucosal Escherichia coli infection by FimH-adhesin-based systemic vaccination. *Science* **276**, 607–11.

22 Zhou, G., Mo, W. J., Sebbel, P., Min, G., Neubert, T. A., Glockshuber, R., Wu, X. R., Sun, T. T. & Kong, X. P. (2001). Uroplakin Ia is the urothelial receptor for uropathogenic Escherichia coli: evidence from in vitro FimH binding. *J Cell Sci* **114**, 4095–103.

23 Martinez, J. J., Mulvey, M. A., Schilling, J. D., Pinkner, J. S. & Hultgren, S. J. (2000). Type 1 pilus-mediated bacterial invasion of bladder epithelial cells. *Embo J* **19**, 2803–12.

24 Mulvey, M. A., Schilling, J. D. & Hultgren, S. J. (2001). Establishment of a persistent Escherichia coli reservoir during the acute phase of a bladder infection. *Infect Immun* **69**, 4572–9.

25 Schilling, J. D., Lorenz, R. G. & Hultgren, S. J. (2002). Effect of trimethoprim-sulfamethoxazole on recurrent bacteriuria and bacterial persistence in mice infected with uropathogenic Escherichia coli. *Infect Immun* **70**, 7042–9.

26 Lund, B., Lindberg, F., Marklund, B. I. & Normark, S. (1987). The PapG protein is the alpha-D-galactopyranosyl-(1–4)-beta-D-galactopyranose-binding adhesin of uropathogenic Escherichia coli. *Proc Natl Acad Sci USA* **84**, 5898–902.

27 Roberts, J. A., Marklund, B. I., Ilver, D., Haslam, D., Kaack, M. B., Baskin, G., Louis, M., Mollby, R., Winberg, J. & Normark, S. (1994). The Gal(alpha 1–4)Gal-specific tip adhesin of Escherichia coli P-fimbriae is needed for pyelonephritis to occur in the normal urinary tract. *Proc Natl Acad Sci USA* **91**, 11889–93.

28 Norgren, M., Baga, M., Tennent, J. M. & Normark, S. (1987). Nucleotide sequence, regulation and functional analysis of the papC gene required for cell surface localization of Pap pili of uropathogenic Escherichia coli. *Mol Microbiol* **1**, 169–78.

29 Klemm, P. & Christiansen, G. (1990). The fimD gene required for cell surface localization of Escherichia coli type 1 fimbriae. *Mol Gen Genet* **220**, 334–8.

30 Bardwell, J. C., McGovern, K. & Beckwith, J. (1991). Identification of a protein required for disulfide bond formation in vivo. *Cell* **67**, 581–9.

31 Hultgren, S. J., Jones, C. H. & Normark, S. (1996). Bacterial adhesins and their assebly. In *Escherichia coli and Salmonella* (Neidhardt, F. C., ed.), Vol. 2, pp. 2730–2756. 2 vols. ASM Press, Washington, DC.

32 Jacob-Dubuisson, F., Pinkner, J. S., Xu, Z., Striker, R. T., Padmanhban, A. & Hultgren, S. J. (1994a). PapD chaperone function in pilus biogenesis depends on oxidant and chaperone-like activities of DsbA. *Proc Natl Acad Sci USA* **91**, 11552–11556.

33 Lindberg, F., Tennent, J. M., Hultgren, S. J., Lund, B. & Normark, S. (1989). PapD, a periplasmic transport protein in P-pilus biogenesis. *J Bacteriol* **171**, 6052–8.

34 Jones, C. H., Pinkner, J. S., Nicholes, A. V., Slonim, L. N., Abraham, S. N. & Hultgren, S. J. (1993). FimC is a periplasmic PapD-like chaperone that directs assembly of

type 1 pili in bacteria. *Proc Natl Acad Sci USA* **90**, 8397–401.

35 Thanassi, D. G., Saulino, E. T., Lombardo, M. J., Roth, R., Heuser, J. & Hultgren, S. J. (1998). The PapC usher forms an oligomeric channel: implications for pilus biogenesis across the outer membrane. *Proc Natl Acad Sci USA* **95**, 3146–51.

36 Jacob-Dubuisson, F., Striker, R. T. & Hultgren, S. J. (1994b). Chaperone-assisted self-assembly of pili independent of cellular energy. *J. Biol. Chem.* **269**, 12447–12455.

37 Holmgren, A. & Branden, C. I. (1989). Crystal structure of chaperone protein PapD reveals an immunoglobulin fold. *Nature* **342**, 248–51.

38 Sauer, F. G., Futterer, K., Pinkner, J. S., Dodson, K. W., Hultgren, S. J. & Waksman, G. (1999). Structural basis of chaperone function and pilus biogenesis. *Science* **285**, 1058–61.

39 Sauer, F. G., Pinkner, J. S., Waksman, G. & Hultgren, S. J. (2002). Chaperone priming of pilus subunits facilitates a topological transition that drives fiber formation. *Cell* **111**, 543–51.

40 Pellecchia, M., Guntert, P., Glockshuber, R. & Wuthrich, K. (1998). NMR solution structure of the periplasmic chaperone FimC. *Nat Struct Biol* **5**, 885–90.

41 Knight, S. D., Choudhury, D., Hultgren, S., Pinkner, J., Stojanoff, V. & Thompson, A. (2002). Structure of the S pilus periplasmic chaperone SfaE at 2.2 A resolution. *Acta Crystallogr D Biol Crystallogr* **58**, 1016–22.

42 Kuehn, M. J., Normark, S. & Hultgren, S. J. (1991). Immunoglobulin-like PapD chaperone caps and uncaps interactive surfaces of nascently translocated pilus subunits. *Proc Natl Acad Sci USA* **88**, 10586–90.

43 Soto, G. E., Dodson, K. W., Ogg, D., Liu, C., Heuser, J., Knight, S., Kihlberg, J., Jones, C. H. & Hultgren, S. J. (1998). Periplasmic chaperone recognition motif of subunits mediates quaternary interactions in the pilus. *Embo J* **17**, 6155–67.

44 Jones, C. H., Danese, P. N., Pinkner, J. S., Silhavy, T. J. & Hultgren, S. J. (1997). The chaperone-assisted membrane release and folding pathway is sensed by two signal transduction systems. *Embo J* **16**, 6394–406.

45 Vetsch, M., Sebbel, P. & Glockshuber, R. (2002). Chaperone-independent folding of type 1 pilus domains. *J Mol Biol* **322**, 827–40.

46 Kuehn, M. J., Ogg, D. J., Kihlberg, J., Slonim, L. N., Flemmer, K., Bergfors, T. & Hultgren, S. J. (1993). Structural basis of pilus subunit recognition by the PapD chaperone. *Science* **262**, 1234–41.

47 Nishiyama, M., Vetsch, M., Puorger, C., Jelesarov, I. & Glockshuber, R. (2003). Identification and Characterization of the Chaperone-Subunit Complex-binding Domain from the Type 1 Pilus Assembly Platform FimD. *J Mol Biol* **330**, 513–25.

48 Lawrence, M. C. & Colman, P. M. (1993). Shape complementarity at protein/protein interfaces. *J Mol Biol* **234**, 946–50.

49 Barnhart, M. M., Pinkner, J. S., Soto, G. E., Sauer, F. G., Langermann, S., Waksman, G., Frieden, C. & Hultgren, S. J. (2000). From the cover: PapD-like chaperones provide the missing information for folding of pilin proteins [see comments]. *Proc Natl Acad Sci USA* **97**, 7709–14.

50 Hermanns, U., Sebbel, P., Eggli, V. & Glockshuber, R. (2000). Characterization of FimC, a Periplasmic Assembly Factor for Biogenesis of Type 1 Pili in Escherichia coli. *Biochemistry* **39**, 11564–11570.

51 Pellecchia, M., Sebbel, P., Hermanns, U., Wuthrich, K. & Glockshuber, R. (1999). Pilus chaperone FimC-adhesin FimH interactions mapped by TROSY-NMR. *Nat Struct Biol* **6**, 336–9.

52 Bullitt, E. & Makowski, L. (1995). Structural polymorphism of bacterial adhesion pili. *Nature* **373**, 164–7.

53 Saulino, E. T., Thanassi, D. G., Pinkner, J. S. & Hultgren, S. J. (1998). Ramifications of kinetic

partitioning on usher-mediated pilus biogenesis. *Embo J* **17**, 2177–85.

54 Dodson, K. W., Jacob-Dubuisson, F., Striker, R. T. & Hultgren, S. J. (1993). Outer-membrane PapC molecular usher discriminately recognizes periplasmic chaperone-pilus subunit complexes. *Proc Natl Acad Sci USA* **90**, 3670–4.

55 Barnhart, M. M., Sauer, F. G., Pinkner, J. S. & Hultgren, S. J. (2003). Chaperone-subunit-usher interactions required for donor strand exchange during bacterial pilus assembly. *J Bacteriol* **185**, 2723–30.

56 Valent, Q. A., Zaal, J., de Graaf, F. K. & Oudega, B. (1995). Subcellular localization and topology of the K88 usher FaeD in Escherichia coli. *Mol Microbiol* **16**, 1243–57.

57 Harms, N., Oudhuis, W. C., Eppens, E. A., Valent, Q. A., Koster, M., Luirink, J. & Oudega, B. (1999). Epitope tagging analysis of the outer membrane folding of the molecular usher FaeD involved in K88 fimbriae biosynthesis in Escherichia coli. *J Mol Microbiol Biotechnol* **1**, 319–25.

58 Thanassi, D. G., Stathopoulos, C., Dodson, K., Geiger, D. & Hultgren, S. J. (2002). Bacterial outer membrane ushers contain distinct targeting and assembly domains for pilus biogenesis. *J Bacteriol* **184**, 6260–9.

59 Meerman, H. J. & Georgiou, G. (1994). Construction and characterization of a set of E. coli strains deficient in all known loci affecting the proteolytic stability of secreted recombinant proteins. *Biotechnology (NY)* **12**, 1107–10.

60 Guzman, L. M., Belin, D., Carson, M. J. & Beckwith, J. (1995). Tight regulation, modulation, and high-level expression by vectors containing the arabinose PBAD promoter. *J Bacteriol* **177**, 4121–30.

61 Cantey, J. R., Blake, R. K., Williford, J. R. & Moseley, S. L. (1999). Characterization of the Escherichia coli AF/R1 pilus operon: novel genes necessary for transcriptional regulation and for pilus-mediated adherence. *Infect Immun* **67**, 2292–8.

62 Massad, G., Fulkerson, J. F., Jr., Watson, D. C. & Mobley, H. L. (1996). Proteus mirabilis ambient-temperature fimbriae: cloning and nucleotide sequence of the aft gene cluster. *Infect Immun* **64**, 4390–5.

63 Honarvar, S., Choi, B. K. & Schifferli, D. M. (2003). Phase variation of the 987P-like CS18 fimbriae of human enterotoxigenic Escherichia coli is regulated by site-specific recombinases. *Mol Microbiol* **48**, 157–71.

64 Girardeau, J. P., Der Vartanian, M., Ollier, J. L. & Contrepois, M. (1988). CS31A, a new K88-related fimbrial antigen on bovine enterotoxigenic and septicemic Escherichia coli strains. *Infect Immun* **56**, 2180–8.

65 Bertin, Y., Girardeau, J. P., Der Vartanian, M. & Martin, C. (1993). The ClpE protein involved in biogenesis of the CS31A capsule-like antigen is a member of a periplasmic chaperone family in gram-negative bacteria. *FEMS Microbiol Lett* **108**, 59–67.

66 Klemm, P., Christiansen, G., Kreft, B., Marre, R. & Bergmans, H. (1994). Reciprocal exchange of minor components of type 1 and F1C fimbriae results in hybrid organelles with changed receptor specificities. *J Bacteriol* **176**, 2227–34.

67 Klemm, P., Jorgensen, B. J., Kreft, B. & Christiansen, G. (1995). The export systems of type 1 and F1C fimbriae are interchangeable but work in parental pairs. *J Bacteriol* **177**, 621–7.

68 Lintermans, P. F., Pohl, P., Bertels, A., Charlier, G., Vandekerckhove, J., Van Damme, J., Schoup, J., Schlicker, C., Korhonen, T., De Greve, H. & et al. (1988). Characterization and purification of the F17 adhesin on the surface of bovine enteropathogenic and septicemic Escherichia coli. *Am J Vet Res* **49**, 1794–9.

69 Holmgren, A., Kuehn, M. J., Branden, C. I. & Hultgren, S. J. (1992). Conserved immunoglobulin-like features in a family of periplasmic pilus chaperones in bacteria. *Embo J* **11**, 1617–22.

70 Smeds, A., Hemmann, K., Jakava-Viljanen, M., Pelkonen, S., Imberechts, H. & Palva, A. (2001). Characterization of the adhesin of Escherichia coli F18 fimbriae. *Infect Immun* **69**, 7941–5.

71 Read, T. D., Dowdell, M., Satola, S. W. & Farley, M. M. (1996). Duplication of pilus gene complexes of Haemophilus influenzae biogroup aegyptius. *J Bacteriol* **178**, 6564–70.

72 Stull, T. L., Mendelman, P. M., Haas, J. E., Schoenborn, M. A., Mack, K. D. & Smith, A. L. (1984). Characterization of Haemophilus influenzae type b fimbriae. *Infect Immun* **46**, 787–96.

73 Stirm, S., Orskov, F., Orskov, I. & Birch-Andersen, A. (1967). Episome-carried surface antigen K88 of Escherichia coli. 3. Morphology. *J Bacteriol* **93**, 740–8.

74 Foged, N. T., Klemm, P., Elling, F., Jorsal, S. E. & Zeuthen, J. (1986). Monoclonal antibodies to K88ab, K88ac and K88ad fimbriae from enterotoxigenic Escherichia coli. *Microb Pathog* **1**, 57–69.

75 Bakker, D., Vader, C. E., Roosendaal, B., Mooi, F. R., Oudega, B. & de Graaf, F. K. (1991). Structure and function of periplasmic chaperone-like proteins involved in the biosynthesis of K88 and K99 fimbriae in enterotoxigenic Escherichia coli. *Mol Microbiol* **5**, 875–86.

76 Duchet-Suchaux, M., Bertin, A. & Dubray, G. (1988). Morphological description of surface structures on strain B41 of bovine enterotoxigenic Escherichia coli bearing both K99 and F41 antigens. *J Gen Microbiol* **134 (Pt 4)**, 983–95.

77 Baumler, A. J. & Heffron, F. (1995). Identification and sequence analysis of lpfABCDE, a putative fimbrial operon of Salmonella typhimurium. *J Bacteriol* **177**, 2087–97.

78 Meslet-Cladiere, L. M., Pimenta, A., Duchaud, E., Holland, I. B. & Blight, M. A. (2004). In vivo expression of the mannose-resistant fimbriae of Photorhabdus temperata K122 during insect infection. *J Bacteriol* **186**, 611–22.

79 Allen, B. L., Gerlach, G. F. & Clegg, S. (1991). Nucleotide sequence and functions of mrk determinants necessary for expression of type 3 fimbriae in Klebsiella pneumoniae. *J Bacteriol* **173**, 916–20.

80 Bahrani, F. K., Johnson, D. E., Robbins, D. & Mobley, H. L. (1991). Proteus mirabilis flagella and MR/P fimbriae: isolation, purification, N-terminal analysis, and serum antibody response following experimental urinary tract infection. *Infect Immun* **59**, 3574–80.

81 Bahrani, F. K. & Mobley, H. L. (1994). Proteus mirabilis MR/P fimbrial operon: genetic organization, nucleotide sequence, and conditions for expression. *J Bacteriol* **176**, 3412–9.

82 Kuehn, M. J., Heuser, J., Normark, S. & Hultgren, S. J. (1992). P pili in uropathogenic E. coli are composite fibres with distinct fibrillar adhesive tips. *Nature* **356**, 252–5.

83 Friedrich, M. J., Kinsey, N. E., Vila, J. & Kadner, R. J. (1993). Nucleotide sequence of a 13.9 kb segment of the 90 kb virulence plasmid of Salmonella typhimurium: the presence of fimbrial biosynthetic genes. *Mol Microbiol* **8**, 543–58.

84 Lugering, A., Benz, I., Knochenhauer, S., Ruffing, M. & Schmidt, M. A. (2003). The Pix pilus adhesin of the uropathogenic Escherichia coli strain X2194 (O2:K(-): H6) is related to Pap pili but exhibits a truncated regulatory region. *Microbiology* **149**, 1387–97.

85 Bahrani, F. K., Cook, S., Hull, R. A., Massad, G. & Mobley, H. L. (1993). Proteus mirabilis fimbriae: N-terminal amino acid sequence of a major fimbrial subunit and nucleotide sequences of the genes from two strains. *Infect Immun* **61**, 884–91.

86 Massad, G. & Mobley, H. L. (1994). Genetic organization and complete sequence of the Proteus mirabilis pmf fimbrial operon. *Gene* **150**, 101–4.

87 Schmoll, T., Morschhauser, J., Ott, M., Ludwig, B., van Die, I. & Hacker, J. (1990). Complete genetic organization and functional aspects of the Escherichia coli S fimbrial

adhesion determinant: nucleotide sequence of the genes sfa B, C, D, E, F. *Microb Pathog* **9**, 331–43.

88 Muller, K. H., Collinson, S. K., Trust, T. J. & Kay, W. W. (1991). Type 1 fimbriae of Salmonella enteritidis. *J Bacteriol* **173**, 4765–72.

89 Clouthier, S. C., Muller, K. H., Doran, J. L., Collinson, S. K. & Kay, W. W. (1993). Characterization of three fimbrial genes, sefABC, of Salmonella enteritidis. *J Bacteriol* **175**, 2523–33.

90 Hurst, M. R., O'Callaghan, M. & Glare, T. R. (2003). Peripheral sequences of the Serratia entomophila pADAP virulence-associated region. *Plasmid* **50**, 213–29.

91 Brunder, W., Khan, A. S., Hacker, J. & Karch, H. (2001). Novel type of fimbriae encoded by the large plasmid of sorbitol-fermenting enterohemorrhagic Escherichia coli O157:H(-). *Infect Immun* **69**, 4447–57.

92 Steven, A. C., Bisher, M. E., Trus, B. L., Thomas, D., Zhang, J. M. & Cowell, J. L. (1986). Helical structure of Bordetella pertussis fimbriae. *J Bacteriol* **167**, 968–74.

93 Willems, R. J., van der Heide, H. G. & Mooi, F. R. (1992). Characterization of a Bordetella pertussis fimbrial gene cluster which is located directly downstream of the filamentous haemagglutinin gene. *Mol Microbiol* **6**, 2661–71.

94 Schifferli, D. M. & Alrutz, M. A. (1994). Permissive linker insertion sites in the outer membrane protein of 987P fimbriae of Escherichia coli. *J Bacteriol* **176**, 1099–110.

95 Khan, A. S. & Schifferli, D. M. (1994). A minor 987P protein different from the structural fimbrial subunit is the adhesin. *Infect Immun* **62**, 4233–43.

96 Raina, S., Missiakas, D., Baird, L., Kumar, S. & Georgopoulos, C. (1993). Identification and transcriptional analysis of the Escherichia coli htrE operon which is homologous to pap and related pilin operons. *J Bacteriol* **175**, 5009–21.

97 Adams, L. M., Simmons, C. P., Rezmann, L., Strugnell, R. A. & Robins-Browne, R. M. (1997). Identification and characterization of a K88- and CS31A-like operon of a rabbit enteropathogenic Escherichia coli strain which encodes fimbriae involved in the colonization of rabbit intestine. *Infect Immun* **65**, 5222–30.

98 Sakai, T., Kanai, K., Osatomi, K. & Yoshikoshi, K. (2003). Identification of a 19.3-kDa protein in MRHA-positive Edwardsiella tarda: putative fimbrial major subunit. *FEMS Microbiol Lett* **226**, 127–33.

99 Bruant, G., Gousset, N., Quentin, R. & Rosenau, A. (2002). Fimbrial ghf gene cluster of genital strains of Haemophilus spp. *Infect Immun* **70**, 5438–45.

100 Townsend, S. M., Kramer, N. E., Edwards, R., Baker, S., Hamlin, N., Simmonds, M., Stevens, K., Maloy, S., Parkhill, J., Dougan, G. & Baumler, A. J. (2001). Salmonella enterica serovar Typhi possesses a unique repertoire of fimbrial gene sequences. *Infect Immun* **69**, 2894–901.

101 Emmerth, M., Goebel, W., Miller, S. I. & Hueck, C. J. (1999). Genomic subtraction identifies Salmonella typhimurium prophages, F-related plasmid sequences, and a novel fimbrial operon, stf, which are absent in Salmonella typhi. *J Bacteriol* **181**, 5652–61.

102 Humphries, A. D., Raffatellu, M., Winter, S., Weening, E. H., Kingsley, R. A., Droleskey, R., Zhang, S., Figueiredo, J., Khare, S., Nunes, J., Adams, L. G., Tsolis, R. M. & Baumler, A. J. (2003). The use of flow cytometry to detect expression of subunits encoded by 11 Salmonella enterica serotype Typhimurium fimbrial operons. *Mol Microbiol* **48**, 1357–76.

103 Savarino, S. J., Fox, P., Deng, Y. & Nataro, J. P. (1994). Identification and characterization of a gene cluster mediating enteroaggregative Escherichia coli aggregative adherence fimbria I biogenesis. *J Bacteriol* **176**, 4949–57.

104 Elias, W. P., Jr., Czeczulin, J. R., Henderson, I. R., Trabulsi, L. R. & Nataro, J. P. (1999). Organization of biogenesis genes for aggregative

adherence fimbria II defines a virulence gene cluster in enteroaggregative Escherichia coli. *J Bacteriol* **181**, 1779–85.

105 Le Bouguenec, C., Garcia, M. I., Ouin, V., Desperrier, J. M., Gounon, P. & Labigne, A. (1993). Characterization of plasmid-borne afa-3 gene clusters encoding afimbrial adhesins expressed by Escherichia coli strains associated with intestinal or urinary tract infections. *Infect Immun* **61**, 5106–14.

106 Garcia, M. I., Labigne, A. & Le Bouguenec, C. (1994). Nucleotide sequence of the afimbrial-adhesin-encoding afa-3 gene cluster and its translocation via flanking IS1 insertion sequences. *J Bacteriol* **176**, 7601–13.

107 Levine, M. M., Ristaino, P., Marley, G., Smyth, C., Knutton, S., Boedeker, E., Black, R., Young, C., Clements, M. L., Cheney, C. & et al. (1984). Coli surface antigens 1 and 3 of colonization factor antigen II-positive enterotoxigenic Escherichia coli: morphology, purification, and immune responses in humans. *Infect Immun* **44**, 409–20.

108 Jalajakumari, M. B., Thomas, C. J., Halter, R. & Manning, P. A. (1989). Genes for biosynthesis and assembly of CS3 pili of CFA/II enterotoxigenic Escherichia coli: novel regulation of pilus production by bypassing an amber codon. *Mol Microbiol* **3**, 1685–95.

109 Knutton, S., McConnell, M. M., Rowe, B. & McNeish, A. S. (1989). Adhesion and ultrastructural properties of human enterotoxigenic Escherichia coli producing colonization factor antigens III and IV. *Infect Immun* **57**, 3364–71.

110 Wolf, M. K., Andrews, G. P., Tall, B. D., McConnell, M. M., Levine, M. M. & Boedeker, E. C. (1989). Characterization of CS4 and CS6 antigenic components of PCF8775, a putative colonization factor complex from enterotoxigenic Escherichia coli E8775. *Infect Immun* **57**, 164–73.

111 Nowicki, B., Svanborg-Eden, C., Hull, R. & Hull, S. (1989). Molecular analysis and epidemiology of the Dr hemagglutinin of uropathogenic Escherichia coli. *Infect Immun* **57**, 446–51.

112 Galyov, E. E., Karlishev, A. V., Chernovskaya, T. V., Dolgikh, D. A., Smirnov, O., Volkovoy, K. I., Abramov, V. M. & Zav'yalov, V. P. (1991). Expression of the envelope antigen F1 of Yersinia pestis is mediated by the product of caf1M gene having homology with the chaperone protein PapD of Escherichia coli. *FEBS Lett* **286**, 79–82.

113 Karlyshev, A. V., Galyov, E. E., Smirnov, O., Guzayev, A. P., Abramov, V. M. & Zav'yalov, V. P. (1992). A new gene of the f1 operon of Y. pestis involved in the capsule biogenesis. *FEBS Lett* **297**, 77–80.

114 Goldhar, J., Perry, R., Golecki, J. R., Hoschutzky, H., Jann, B. & Jann, K. (1987). Nonfimbrial, mannose-resistant adhesins from uropathogenic Escherichia coli O83:K1:H4 and O14:K?:H11. *Infect Immun* **55**, 1837–42.

115 Ahrens, R., Ott, M., Ritter, A., Hoschutzky, H., Buhler, T., Lottspeich, F., Boulnois, G. J., Jann, K. & Hacker, J. (1993). Genetic analysis of the gene cluster encoding nonfimbrial adhesin I from an Escherichia coli uropathogen. *Infect Immun* **61**, 2505–12.

116 Iriarte, M., Vanooteghem, J. C., Delor, I., Diaz, R., Knutton, S. & Cornelis, G. R. (1993). The Myf fibrillae of Yersinia enterocolitica. *Mol Microbiol* **9**, 507–20.

117 Lindler, L. E. & Tall, B. D. (1993). Yersinia pestis pH 6 antigen forms fimbriae and is induced by intracellular association with macrophages. *Mol Microbiol* **8**, 311–24.

118 Folkesson, A., Advani, A., Sukupolvi, S., Pfeifer, J. D., Normark, S. & Lofdahl, S. (1999). Multiple insertions of fimbrial operons correlate with the evolution of Salmonella serovars responsible for human disease. *Mol Microbiol* **33**, 612–22.

30
Unfolding of Proteins During Import into Mitochondria

Walter Neupert, Michael Brunner, and Kai Hell

30.1
Introduction

The eukaryotic cell is divided into a number of subcellular compartments, the cell organelles. Mitochondria represent one of them. In contrast to most other organelles, mitochondria are delineated by two membranes: the outer membrane, which forms a kind of envelope, and the inner membrane, which usually forms numerous invaginations, the cristae. The membranes enclose two compartments: the matrix space surrounded by the inner membrane and the intermembrane space between the inner and outer membranes.

Mitochondria fulfill a variety of important functions. They are often called powerhouses of the cell, as they generate ATP by the process of oxidative phosphorylation. The free energy in the hydrolysis of ATP to ADP is used to drive a plethora of cellular reactions. In addition, many other metabolic processes take place within mitochondria, such as fatty acid oxidation, the Krebs cycle, parts of the urea cycle, and the biosynthesis of cofactors and amino acids. The biogenesis of Fe/S clusters is an essential process for cell viability that is also located within mitochondria. In order to perform these functions, the mitochondria have a specific set of proteins.

Mitochondria harbor their own genome; this, however, codes for only a small subset of mitochondrial proteins: eight in *Saccharomyces cerevisiae* and 13 in human. Most mitochondrial proteins are encoded by nuclear DNA and synthesized in the cytoplasm as precursor proteins. They contain specific targeting sequences, which are recognized by receptor proteins on the surface of the mitochondrial outer membrane. Proteinaceous machineries, termed protein translocases, mediate the transport of the precursor proteins into and across mitochondrial membranes [3, 29, 52, 90, 121, 136].

The translocation processes across membranes require a driving force. In the case of import of proteins into the mitochondrial matrix, energy is provided by two sources. The electrochemical potential across the inner membrane drives the transfer of the targeting signals of preproteins across the inner membrane. ATP in the matrix fuels a proteinaceous machinery, the import motor. The import mo-

Protein Folding Handbook. Part II. Edited by J. Buchner and T. Kiefhaber

ISBN: 3-527-30784-2

tor is associated with the translocase at the *trans* side of the inner membrane and completes the translocation of the precursor proteins across the mitochondrial membranes.

Proteins are translocated into mitochondria in a largely unfolded state. In this respect, their import into mitochondria differs from their translocation into peroxisomes or their transport by the TAT translocase in bacteria and chloroplasts [46, 114], but it is similar to most translocation pathways in the endoplasmatic reticulum (ER) and chloroplasts and to the Sec translocase in bacteria [23, 51, 54, 56, 75]. Unfolding of proteins during translocation across the mitochondrial outer membrane (OM) and inner membrane (IM) is mediated by the mitochondrial import machinery [76, 91]. Protein unfolding by the mitochondrial import motor has become a paradigm for protein unfolding, a physiological process occurring in virtually every cell. Unfolding of proteins is also essential for other cellular processes, in particular protein degradation. Here, we discuss the import of proteins into mitochondria and the unfolding of proteins by the mitochondrial import motor during the translocation process.

30.2
Translocation Machineries and Pathways of the Mitochondrial Protein Import System

Three translocation machineries that mediate the import of precursor proteins into mitochondria are known (see Figure 30.1). The translocase of the outer membrane (TOM complex) functions in the recognition of precursor proteins, their insertion into the outer membrane, and in translocation across the outer membrane (for details, see [98, 101, 104]). Chaperones have been reported to interact with the precursor proteins in the cytosol to keep them in a translocation-competent state and to support their transport to the TOM complex [21, 41, 88, 158].

The process of translocation across the TOM complex is followed by sorting proteins either directly to the intermembrane space or to two translocases of the inner membrane (TIM): the TIM23 complex and the TIM22 complex [3, 52, 58, 113]. The TIM23 complex transports proteins with typical mitochondrial targeting sequences across or into the mitochondrial inner membrane, while the TIM22 complex inserts a subclass of inner-membrane proteins with internal targeting signals into the membrane. This subclass includes the proteins of the carrier family and components of the inner-membrane translocases such as Tim22 and Tim23.

An interesting case is the sorting of β-barrel proteins of the outer membrane. They first use the TOM complex and are then inserted and assembled in the membrane with the help of the recently discovered TOB/SAM complex [36, 60, 99, 152].

We later focus on the translocation pathway of proteins destined for the mitochondrial matrix. These proteins are translocated across the inner membrane by the TIM23 complex.

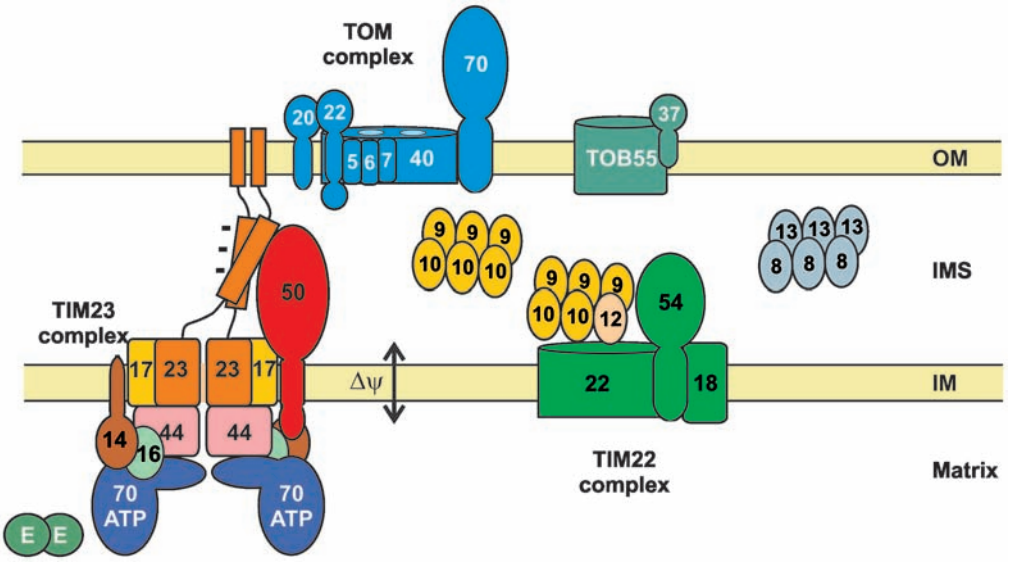

Fig. 30.1. Translocation machineries of the mitochondrial protein import system. The translocase of the outer membrane (TOM complex) mediates the translocation of proteins across and into the outer membrane. All proteins analyzed so far enter mitochondria via the TOM complex. The TOM complex consists of the receptor subunits Tom20, Tom70, and Tom22 and the general import pore. The general import pore is made up of the core subunit Tom40, the integral part of the Tom22 receptor and of the small TOM proteins Tom5, Tom6, and Tom7. There are two translocases of the inner membrane, the TIM23 and TIM22 complexes. The TIM22 complex inserts polytopic proteins with internal targeting signals into the inner membrane. It is composed of two subcomplexes. The peripherally attached Tim9/10/12 subcomplex is associated with the membrane-integrated components Tim22, Tim54, and Tim18. The soluble Tim9/10 complex and the Tim8/13 complex in the intermembrane space cooperate with the Tim22 complex in the transport of carrier proteins and of Tim23, respectively. The TIM23 complex mediates the translocation of proteins with N-terminal targeting sequences across or into the inner membrane. Tim50 and the N-terminal domains of Tim23 guide the precursor proteins to the translocation channel in the inner membrane, which is formed by the integral C-terminal segments of Tim23 and Tim17. Translocation is completed by the import motor of the TIM23 translocase. Tim44 recruits the Tim14/Tim16 (Pam18/Pam16) subcomplex and mtHsp70 to the translocation channel. The co-chaperone Mge1 interacts with the mtHsp70 chaperone. The TOB complex (topogenesis of outer-membrane β-barrel proteins) inserts and assembles β-barrel proteins into the outer membrane. Two subunits have been identified: the main pore-forming component Tob55 (Sam50) and Mas37.

30.2.1 Import of Proteins Destined for the Mitochondrial Matrix

Matrix-targeted proteins in most cases have amino-terminal presequences that have the potential to form an amphipathic α-helix [66, 146]. These targeting signals direct the proteins to mitochondria by binding to the surface-exposed receptor proteins of the TOM complex on the cytoplasmic side of the outer membrane, the *cis* side [28]. The receptor protein Tom20 preferentially recognizes presequence proteins, whereas the Tom70 receptor protein binds mostly proteins with internal targeting signals [28]. From the initial receptor proteins, the preproteins are transferred to the general import pore (GIP) via the receptor domain of Tom22 [47, 57]. GIP is made up of five other membrane-embedded components of the TOM complex: Tom40, Tom22, and the three small subunits Tom7, Tom6, and Tom5 [2, 20]. The only essential component of the TOM complex in *Saccharomyces cerevisiae*, Tom40, is able to form a conducting pore in the membrane and is the main constituent of the protein-conducting channel [1, 45].

Following translocation through this channel, the preprotein binds to the "*trans*-binding site" on the inner face of the outer membrane [79, 106]. It has been suggested that the *trans*-binding site has a higher affinity for preproteins than do the preprotein-binding sites of the TOM complex at the surface of the outer membrane. This would drive translocation of the presequence across the outer membrane [8, 79, 105, 120].

Next, the presequences interact with the TIM23 complex of the inner membrane. The TIM23 complex translocates the presequences across the inner membrane in a membrane potential–dependent ($\Delta\Psi$) and ATP-dependent manner. Three functions have been assigned to the $\Delta\Psi$. First, it triggers dimerization of the Tim23 presequence receptor [4]. Second, it exerts an electrophoretic effect and drives the translocation of the presequence across the inner membrane [73]. Third, it can support unfolding of protein domains on the surface of the mitochondria [48]. Once the presequence has reached the matrix side of the inner membrane, complete translocation of proteins into the matrix is driven by ATP hydrolysis [44, 78, 90, 102]. Inner-membrane proteins containing a matrix-targeting signal followed by one hydrophobic transmembrane segment are also imported via the TIM23 pathway. They are not completely translocated across the inner membrane but instead are laterally inserted into the inner membrane [82, 115]. If the hydrophobic segment of these proteins is located directly after the matrix-targeting signal, their import is independent of matrix ATP [34, 115].

The TIM23 complex can be structurally and functionally divided into three parts: the hydrophilic domains in the intermembrane space, the membrane-embedded part, and the mitochondrial import motor on the matrix side of the inner membrane. The amino-terminal domain of Tim23 spans the mitochondrial outer membrane and links the outer membrane with the inner membrane [22]. The conserved intermembrane space domain of the single transmembrane protein Tim50 facilitates the transfer of the preprotein from the TOM complex to the TIM23 complex, probably to the receptor domain of Tim23 in the intermembrane space [37, 84,

157]. The integral part of the complex is made up by the two proteins with four transmembrane domains, Tim17 and Tim23, which most likely form the protein-conducting channel [5, 18, 19, 27, 71, 81, 118, 119, 137].

The mitochondrial import motor consists of at least five components: Tim44, mtHsp70, Tim14/Pam18, Tim16/Pam16, and Mge1 (see Figure 30.1) [24, 32, 59, 85, 90, 138]. Tim44 is crucial for recruiting mtHsp70 to the outlet of the protein-conducting channel [62, 85, 109, 123]. The chaperone mtHsp70 is the central component of the import motor. Like all DnaK-type chaperones, it consists of an N-terminal adenine nucleotide-binding domain, a peptide-binding domain, and a C-terminal ''lid'' domain [11, 61, 86, 134]. When ATP is bound to mtHsp70, the peptide-binding domain is in an open conformation [11, 40]. MtHsp70 in the ATP form binds to the incoming polypeptide chain emerging from the channel [69, 85, 123]. Conversion to the ADP form of mtHsp70 results in the closure of the peptide-binding domain and high-affinity binding of the polypeptide chain [11, 116]. This efficient trapping at the outlet of the channel inhibits backsliding of the polypeptide chain and drives its translocation across the mitochondrial membranes. Tim14 is a membrane-bound DnaJ homologue that is associated with the TIM23 translocase [24, 85, 138]. It interacts with Tim44 and mtHsp70 in an ATP-dependent manner and stimulates the ATPase activity of mtHsp70, thereby promoting the efficient binding of the polypeptide. Then the mtHsp70 bound to the polypeptide chain dissociates from Tim44 [123, 124, 139, 140]. Tim44 is present in the TIM23 translocase as a dimer, and therefore a second mtHsp70 is already present at the translocation pore [87]. Dissociation of the first mtHsp70 and further translocation allow the second one to bind to the next incoming segment of the polypeptide chain. Such ''hand-over-hand'' action results in efficient translocation. Tim44 can be viewed as an organizer that integrates the import motor with the components of the translocation channel. It recruits mtHsp70, Tim14, and Tim16 to the Tim17-Tim23 subcomplex [85] and interacts with the incoming precursor protein and transfers it to mtHsp70 [123]. Tim16 is a J-domain-related protein that has similarity to Tim14 and forms a stable subcomplex with Tim14 [32, 59]. It is structurally important, as it mediates the interaction of Tim14 with the TIM23 complex. The nucleotide-exchange factor Mge1 mediates the release of ADP from mtHsp70 [8, 65, 89, 151], which allows binding of an ATP and thereby release of mtHsp70 from the polypeptide chain. Thus, the mtHsp70 can be reused for a next cycle of binding and release. Mge1 seems to regulate the binding of mtHsp70 to Tim44 [69, 124]. MtHsp70 also binds in the ADP form to Tim44. Mge1 dissociates such an unproductive interaction, as ADP-bound mtHsp70 cannot bind incoming polypeptides. Indeed, cross-linking experiments showed that mtHsp70 binds to Tim44 in the presence of ATP in intact mitochondria [85].

Following translocation of the precursor protein into the mitochondrial matrix, the targeting signal is cleaved by the matrix-processing peptidase and, in some cases, the mitochondrial intermediate peptidase [90]. Then the extended polypeptide chain folds into its native form, which in many cases is supported by the mitochondrial chaperones mtHsp70, Hsp60, and peptidyl-prolyl *cis*/*trans* isomerase [14, 55, 95, 110].

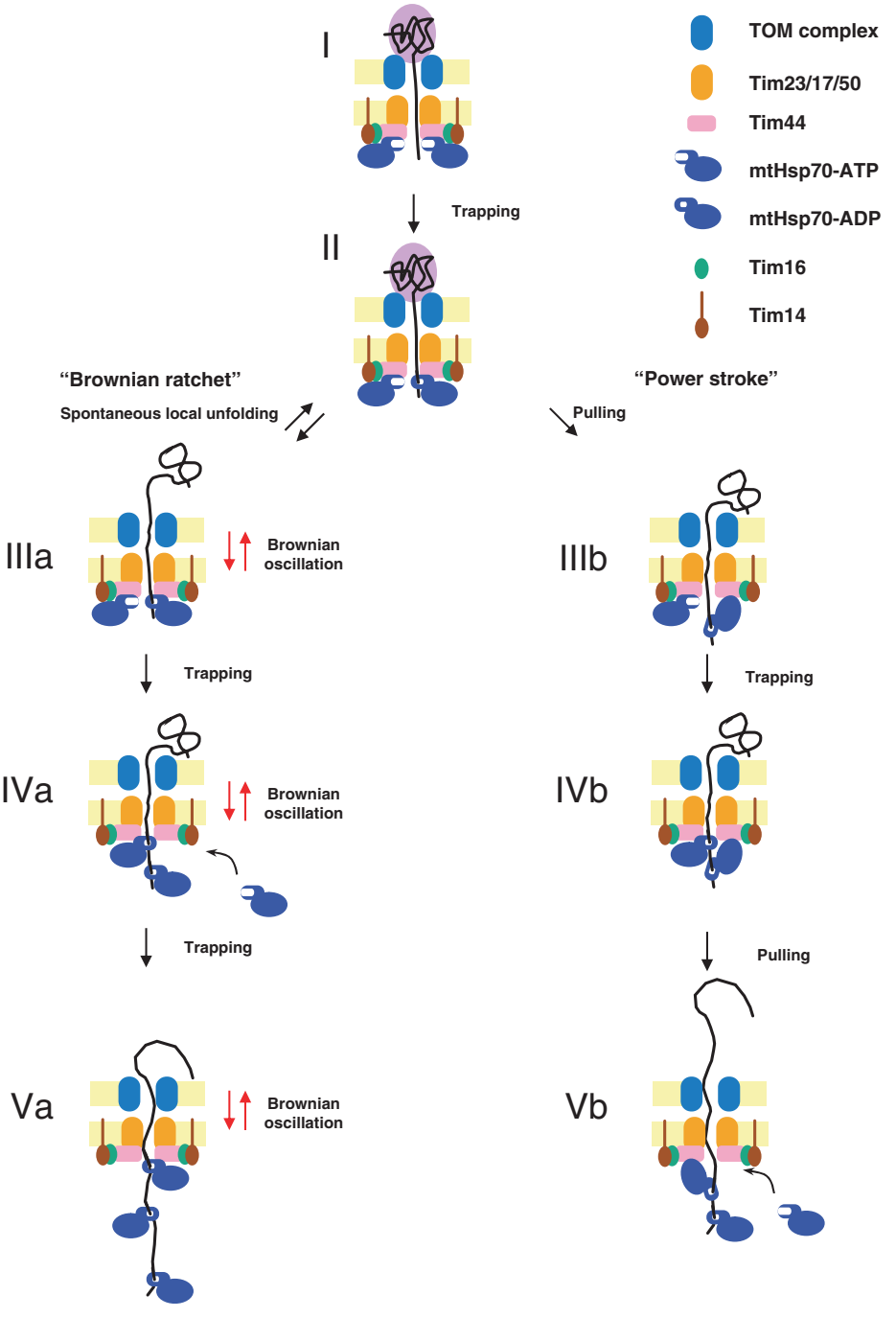
I
Trapping
II
TOM complex
Tim23/17/50
Tim44
mtHsp70-ATP
mtHsp70-ADP
Tim16
Tim14
"Brownian ratchet"
Spontaneous local unfolding
"Power stroke"
Pulling
IIIa
Brownian oscillation
IIIb
Trapping
Trapping
IVa
Brownian oscillation
IVb
Trapping
Pulling
Va
Brownian oscillation
Vb

30.3
Import into Mitochondria Requires Protein Unfolding

The structures of the isolated native TOM complex or the TOM core complex of the mitochondrial outer membrane and the TIM22 complex were analyzed by single-particle electron microscopy. The observed structures suggested pores with an internal diameter of about 20–25 Å for the TOM complex and stain-filled pits with a diameter of 16 Å for the TIM22 complex [2, 63, 83, 112]. The integral membrane core component Tom40 appears to be the subunit forming the pore of the TOM complex, with a diameter of about 22–25 Å [1, 45].

Such a pore diameter is consistent with observations that precursors containing bulky elements can be transported into mitochondria. Examples are precursors containing branched polypeptides or oligonucleotides linked to the C-terminus of a precursor or precursors containing neighboring β-strands that were covalently altered by chemical cross-linking prior to import [125, 142, 144]. It was also reported that the AAC precursor protein and Tim23 cross the TOM complex in a loop con-

Fig. 30.2. The ''Brownian ratchet'' and the ''power-stroke'' models for unfolding and translocation of precursor proteins into mitochondria. Stage I: Membrane potential–dependent translocation of the N-terminal targeting signal of a precursor protein into the matrix and its cleavage by the mitochondrial processing peptidase generate a preprotein spanning the mitochondrial outer and inner membranes. The folded domain of this early translocation intermediate is on the surface of mitochondria. Stage II: When the preprotein emerges from the translocation channel, it is bound by the mitochondrial heat shock protein 70 (mtHsp70), which is recruited by Tim44 to the translocation channel. ATP hydrolysis by mtHsp70 is stimulated by Tim14. The conversion of the ATP-bound form of mtHsp70 to the ADP-bound form leads to a conformational change of the peptide-binding domain and the tight binding of the preprotein. ''Brownian ratchet'' model: Stage IIIa: Thermal fluctuations lead to fast local unfolding and refolding of the preprotein, termed ''thermal breathing.'' Stage IVa: The mtHsp70 bound to the preprotein dissociates from Tim44. Unfolded segments of the preprotein can slide back and forth in the translocation channel due to random thermal fluctuations (Brownian oscillations). This exposes a new segment of the incoming polypeptide chain at the exit of the import channel, which is trapped by a second mtHsp70 bound to the second Tim44 in the TIM23 complex. Tim14 stimulates ATP hydrolysis of this mtHsp70 and allows efficient trapping. Thus, backsliding of the preprotein is prevented, and therefore the preprotein cannot refold outside of mitochondria. Stage Va: Another mtHsp70 is recruited by Tim44 and traps the next segment of the oscillating preprotein at the exit of the channel. ''Power-stroke'' model: Stage IIIb: MtHsp70 exerts a pulling force perpendicular to the inner membrane, which leads to unfolding of the preprotein on the surface of mitochondria and transport of a segment of the preprotein into the matrix space. The force is generated by a conformational change of mtHsp70. Stage IVb: Tim14 stimulates ATP hydrolysis of the second recruited mtHsp70. The ADP-bound form of mtHsp70 binds tightly to a newly exposed segment of the preprotein. Stage Vb: The first mtHsp70 dissociates from Tim44 and the second mtHsp70 undergoes a conformational change, generating a pulling force.

formation [15, 30, 153]. In other studies experimental evidence suggests that the BCS1 precursor protein is imported across the outer and inner membrane as a loop structure, formed by hydrophobic interactions between its transmembrane domain and the subsequent amphipathic α-helical targeting signal [31, 133]. However, it seems impossible that translocation pores with the observed diameters import fully folded proteins. Indeed, experiments have clearly demonstrated that tightly folded domains cannot be imported. The first evidence was obtained using a fusion protein consisting of the first 22 amino acid residues of the cytochrome oxidase subunit IV presequence fused to mouse dihydrofolate reductase (DHFR). This protein was imported into isolated mitochondria like an authentic mitochondrial precursor protein [50]. Binding of methotrexate, a specific ligand of DHFR, leading to a stably folded DHFR domain inhibited translocation of the precursor protein into mitochondria [26]. Further studies demonstrated that mitochondrial precursor proteins containing the tightly folded heme-binding domain of (HBD) of cytochrome b_2 or the bacterial ribonuclease barnase as folded passenger proteins are transported into mitochondria only in an unfolded state [35, 39, 49, 77]. In an elegant study by Schwartz et al. [125], rigid gold clusters of specific dimensions were cross-linked to the C-terminus of a precursor protein and their import was studied. Above a certain size, these clusters were not imported, confirming that the translocases cannot transport large structures. Clusters of specific dimensions allowed estimating the internal diameter of the TOM complex to be between 20 Å and 26 Å. Comparison with the diameter observed in the electron microscopy studies suggests that the pore diameter of the TOM complex does not alter significantly during translocation. The TIM23 translocase in the inner membrane might behave differently. Calculations based on channel conductance and size exclusion suggest that renatured recombinant Tim23 forms a channel with an even smaller inner diameter of 13 Å [137]. The pore of the TIM23 complex is narrower than the TOM complex. However, the TIM23 complex appears not to have a well-defined rigid pore, as preproteins cross-linked to 20-Å gold clusters were still imported by the TIM23 complex, albeit with strongly reduced efficiency [126].

Most precursor proteins are imported posttranslationally into mitochondria. Therefore, they may fold in the cytoplasm prior to import. The requirement of unfolding of preproteins prior to their import has been observed not only in vitro but also in vivo. When a hybrid protein of the amino-terminal portion of the mitochondrial precursor protein cytochrome b_2 and of DHFR was expressed in intact yeast cells and the specific ligand methotrexate was added to the cells, the precursor protein was arrested in mitochondrial contact sites, demonstrating the importance of protein unfolding for translocation in vivo [154]. It has also been shown that the heme-binding domain, an authentic mitochondrial domain, folds in the cytosol [10]. Further research is needed to determine which endogenous mitochondrial proteins are held in a translocation-competent unfolded state by cytosolic chaperones and which ones fold and have to be unfolded prior to their translocation into mitochondria. However, it is obvious that some precursor proteins have to be unfolded by the mitochondrial import machinery.

30.4 Mechanisms of Unfolding by the Mitochondrial Import Motor

The mitochondrial import motor drives the unfolding of protein domains and the translocation of polypeptides across the mitochondrial membranes. Two models have been proposed to explain how the mitochondrial import motor exerts its function (see Figure 30.2). In the ''targeted Brownian ratchet model,'' the import motor acts as a molecular ratchet that traps the incoming polypeptide chain directly at the outlet of the protein-conducting channel of the inner membrane [92, 123, 127]. In the ''power-stroke model'' or ''pulling model,'' the mitochondrial import motor exerts a power stroke perpendicular to the membrane and generates a pulling force on the polypeptide chain [38, 39].

30.4.1 Targeted Brownian Ratchet

Proteins partially unfold and fold in the range of milliseconds, a process also termed ''thermal breathing''. If an unfolded segment is exposed due to ''thermal breathing'' during protein import, the unfolded segment of the polypeptide chain can move into the translocation channel due to Brownian motion [140]. Within the translocation channel it can oscillate in both directions [140]. MtHsp70 of the import motor binds to segments of the polypeptide chain as they are emerging from the translocation channel at the matrix side. According to this model, the import motor acts as a ratchet that permits forward movement but not backsliding of the polypeptide chain [81, 86, 87, 94, 123, 124]. Thereby it transduces spontaneous Brownian movement into vectorial transport. The polypeptide chain is trapped and refolding of the polypeptide on the outside of mitochondria is impossible. Such a mechanism requires a very efficient trapping process. The attachment of mtHsp70 to the TIM23 complex by Tim44 targets the trapping device to the site of the emerging polypeptide and assures immediate binding and trapping. In summary, the targeted molecular ratchet unfolds proteins, because it inhibits the refolding of spontaneously unfolded segments of the protein at the outside of mitochondria [35, 54].

30.4.2 Power-stroke Model

In the power-stroke model, the action of the mitochondrial import motor generates a force on the polypeptide chain spanning the mitochondrial membranes. This force is transmitted by the polypeptide chain and is required for unfolding of protein domains on the outside of mitochondria [38, 53, 78, 103, 148]. An ATP-induced conformational change of mtHsp70 exerts the pulling force, which is transferred by a lever arm to the polypeptide chain. Following the power stroke, mtHsp70 has to be released from Tim44 so that the next mtHsp70 can bind and

exert another power stroke. Backsliding of the polypeptide chain before binding of the next mtHsp70 must be prevented. It was proposed that the protein-conducting channel fulfills such a function [13, 19]. Multiple cycles of a power stroke would result in a regular stepwise translocation.

30.5 Studies to Discriminate between the Models

Studies to discriminate between the two models have addressed the mode of unfolding of preproteins on the outside of mitochondria during the protein translocation as well as mechanistic aspects of the mitochondrial import motor.

30.5.1 Studies on the Unfolding of Preproteins

Before discussing protein unfolding in the context of mitochondrial protein import, two modes of unfolding will be distinguished: global and local unfolding of proteins. Global unfolding results in a completely unfolded polypeptide chain without any structured elements. The equilibrium between the folded and unfolded states is described by the thermodynamic stability of a protein. The thermodynamic stability of folded proteins seems to correlate with their resistance against protease digestion, which requires extensive unfolding of domains [35].

In contrast, local unfolding, also termed "breathing," is characterized by perpetual thermal fluctuations within a protein [159]. These fluctuations occur in the time range of nanoseconds to seconds and result in local unfolding events. Binding of denaturants such as urea [159], chemical modification of side chains of amino acid residues [35], or interaction with other proteins such as chaperones leads to the trapping of such local unfolded segments with varying efficiencies [49, 68]. These segments cannot refold once they are trapped. Further unfolding occurs and eventually a completely unfolded state results within milliseconds to minutes.

30.5.1.1 Comparison of the Import of Folded and Unfolded Proteins

In order to understand the unfolding of precursor proteins during import, proteins containing folded domains were analyzed in comparison with the same proteins harboring the domains in an unfolded state. In most cases mouse cytosolic dihydrofolate reductase (DHFR) was used as passenger protein and was fused to a mitochondrial presequence [50]. The unfolded state was acquired by addition of urea prior to the import reaction [25, 96] or by using a mutant form, which does not stably fold [143]. The import process was started by allowing the presequence to translocate across the TIM23 complex with the help of $\Delta\tilde{\Psi}$. In this way the precursor chain was threaded into the translocation pores of the TOM and TIM23 complexes.

Import of the unfolded form of the protein was always faster than import of the folded counterpart [33, 35, 68, 81, 143, 145, 149]. According to the Brownian ratchet model, movement of the polypeptide chain in the import channels is stopped when a folded domain reaches the TOM complex. Only when local spontaneous unfolding events occur will unfolded segments be exposed and then be able to enter the translocation channels. The kinetics of this breathing determines the average time period for which the forward movement of a folded domain is halted. Experimental observations support this. Folded, but not unfolded, DHFR-containing precursor proteins do pause upon import [35]. The import kinetics of preproteins with folded DHFR show a notable lag phase. After unfolding by urea, no lag phase in the import was observed [68]. Furthermore, passenger proteins such as HBD and titin (see below and Section 30.5.1.3) showed lag phases with different time periods [35, 94]. It should be noted that most significant lag phases were observed for proteins with short amino-terminal presequences in front of the folded domain, such as cyt b_2(47)-DHFR [68]. In these cases the presequences in front of the folded domain are not long enough to interact with the import motor, and therefore local spontaneous unfolding events of the folded domain cannot be trapped or promoted by the import motor in the initial stage of the translocation process. Preproteins with longer presequences interact with the import motor, spontaneous local unfolding events are trapped, and backsliding of the polypeptide chain is inhibited. In the case of pSu9(1-69)DHFR, a fusion protein consisting of the presequence of the subunit 9 of *Neurospora* F_1F_0-ATPase and mouse DHFR, the rate of import was determined for different forms of the DHFR passenger. When wild-type DHFR was present, import was much slower than when an unfolded mutant form of DHFR was present [35]. A sequence of 69 amino acid residues was shown to be sufficient to reach the mitochondrial import motor; about 50 residues were reported to be required to span both the outer and inner membranes [108, 140]. Therefore, the faster import of the mutant form must have been due to the unfolded state of the passenger DHFR.

One would expect that the kinetics of import of folded proteins after the lag phase is similar to those of urea-unfolded proteins. Indeed, this was observed, demonstrating that a preprotein following the initial unfolding events reflects the behavior of an unfolded protein [68].

According to the power-stroke model, a folded domain will be unfolded by a power stroke of the import motor. One power stroke should be sufficient to cause a nearly complete collapse of the folded structure. The power stroke is supposed to be exerted by a fast conformational change. Assuming one fast power stroke, it is difficult to explain that the lag phases of import are in the range of minutes.

In addition, unfolding and import of preproteins were compared with regard to their temperature dependence [35]. Import of folded and unfolded DHFR at 30 °C occurred with similar rates. The permanently unfolded mutant variant of DHFR has a twofold lower import rate into mitochondria at 10 °C than at 30 °C. This result indicates that the import motor has a moderate temperature dependence. On

the other hand, the import rates of folded DHFR were 30-fold faster at 30 °C than at 10 °C, and there was very little import at 4 °C. In the case of a power-stroke mechanism, the temperature dependence of the import would be determined by that of the import motor and is expected to be similar for the import of folded and unfolded proteins. This was not observed.

According to the Brownian ratchet model, import of folded DHFR depends on its spontaneous unfolding at the N-terminus. The kinetics of N-terminal breathing was analyzed by measuring the modification by N-ethylmaleimide (NEM) of the cysteine residue in position 7 of DHFR [35]. This cysteine is buried and therefore inaccessible to NEM in the folded protein. Upon breathing of the DHFR, the N-terminal segment moves out and can be modified by NEM. The modified protein cannot refold and is sensitive to added protease, in contrast to the folded protein. The measured rates of amino-terminal unfolding confirmed, for all temperatures analyzed, that unfolding is faster than import. Furthermore, the amino-terminal breathing is strongly reduced at low temperature. At 30 °C the unfolding at the N-terminus was observed to be ca. 14-fold faster than at 10 °C. The temperature dependence of the import rates can be explained by the temperature dependence of spontaneous unfolding, but not by the temperature dependence of the import motor.

The heme-binding domain of cytochrome b_2 (HBD) was another passenger domain studied in this respect. The domain was fused to mitochondrial presequences and its import characteristics were investigated [35]. The behavior of the HBD differed from that of DHFR. The import rates of HBD passenger proteins were only twofold higher at 30 °C than at 10 °C, and import was still quite efficient at 0–4 °C. Thus, import of the HBD displayed a very weak temperature dependence. This correlates with a faster local unfolding of HBD than of DHFR [35]. The rate of local unfolding of HBD was measured by chemical modification of residues buried in the folded domain. Interestingly, local unfolding of HBD was less temperature-dependent than that of DHFR. This is consistent with the finding that pausing of preproteins containing HBD, as described for DHFR-containing constructs, was not observed. When the global thermodynamic stability of the proteins was assessed by their protease resistance, HBD was found to be much more stable than DHFR [35]. In conclusion, the kinetics of spontaneous local unfolding and not the thermodynamic stability of a folded domain is the crucial parameter for the efficiency of import.

The observed results with DHFR and HBD are in agreement with those from experiments using bacterial RNase barnase as a passenger protein [49]. When the import of barnase fused to mitochondrial presequences was analyzed, it was observed that its import kinetics were faster than that of fusion proteins consisting of DHFR and presequences, although the thermodynamic stability of barnase is higher than that of DHFR. In addition, it was observed that import of barnase into mitochondria results in an unfolding pathway that differs from the one of global unfolding in solution [49]. During import the barnase was unfolded from its N-terminus. The amino-terminal structure of barnase consists of an

α-helix on the surface of the folded barnase structure and can therefore unfold with a relatively high probability [78]. Such an arrangement is also found in the HBD. In contrast, the amino-terminal β-strand of DHFR is buried in a central β-stranded core and therefore does not unfold easily. The amino-terminal structures of DHFR on the one hand and HBD and barnase on the other hand appear to be the reason for their different import and unfolding behavior.

In conclusion, spontaneous unfolding together with a targeted ratchet mechanism is sufficient to explain the temperature dependence of import, the pausing of import at folded domains, and the amino-terminal unfolding behavior of the protein domains analyzed.

30.5.1.2 Import of Preproteins With Different Presequence Lengths

Precursor proteins that have segments of different length in front of a folded DHFR domain were imported with very different rates [35, 77]. Rather slow import was observed for precursors with 60 residues in front of DHFR, whereas precursors with segments of 90 or more residues had 10- to 40-fold higher import rates. The import rate increased dramatically at lengths between 60–70 residues due to accessibility of the presequence to the molecular import motor. To span both mitochondrial membranes and to reach the matrix space, a preprotein needs a minimal length of ca. 50–60 residues in front of folded DHFR. This allows binding of mtHsp70, which, together with the other motor proteins, promotes forward movement and unfolding of the DHFR domain. In contrast, precursors containing less than 50–60 residues in front of DHFR (referred to as shorter precursors) are not able to reach the matrix without unfolding of a sufficiently long segment [35, 77]. Without unfolding, mtHsp70 cannot bind and support import.

In the Brownian ratchet model, spontaneous unfolding and forward movement by Brownian motion occur with longer as well as with shorter precursors. However, with a longer precursor mtHsp70 can trap a segment of the precursor at the outlet of the import channel. Therefore, backward sliding is inhibited and refolding of the DHFR is strongly impaired. In contrast, shorter precursors can slide back and refold because mtHsp70 does not reach the precursor. Backsliding and refolding compete with forward movement and import, so that overall import is much slower [35].

According to the power-stroke model, longer precursors have faster import kinetics because an amino-terminal segment of the polypeptide chain reaches into the mitochondrial matrix and mtHsp70 can exert a pulling force and cause a collapse of the folded domain on the mitochondrial surface [77, 78]. Thus, both models explain the higher import rates of precursors having longer presequences in front of a folded domain compared to the rates of those with short presequences. The Brownian ratchet model, in contrast to the power-stroke model, predicts that the dependence of import rates on the length of the N-terminal stretch varies among folded domains, which have a different rate of spontaneous unfolding. This was indeed observed with DHFR and HBD as passenger proteins [35].

30.5.1.3 Import of Titin Domains

Strong evidence in favor of the targeted Brownian ratchet mechanism was obtained using the immunoglobulin (Ig)-like domains of muscle titin as a passenger protein. The Ig-like domains are tightly folded. Experiments with atomic force microscopy indicated that mechanical pulling with forces of 200–300 pN is needed to unfold these domains [12, 67, 72, 128]. However, import of these domains into isolated mitochondria occurs efficiently when they are combined with a mitochondrial targeting sequence [94]. This raises the question of what kind of force a hypothetical power stroke of mtHsp70 could generate. The well-known motor proteins myosin or kinesin generate forces of about 5 pN [129, 130]. Thus, a reasonable assumption would estimate similar forces for mtHsp70. Furthermore, one single stroke and therefore hydrolysis of one ATP should lead to the complete collapse and hence unfolding of a folded domain. Estimating a stroke length of 3.5 nm, the equivalent of ca. 10 extended amino acid residues, the energy in one ATP can exert a force of about 14 pN [94]. Although the force measurements were performed under in vitro conditions and the values may be slightly different in the biological system, it appears impossible that the required force in the range of 200–300 pN could be generated by a power stroke of mtHsp70. It also has to be kept in mind that rapid cycles of mtHsp70 binding and release of the incoming polypeptide chain take place at the import site, when a folded domain on the outside of the mitochondria blocks forward movement [35, 94]. This excludes titin unfolding with low force by a slow power stroke in the minute range.

30.5.1.4 Unfolding by the Mitochondrial Membrane Potential $\Delta\Psi$

Some precursor proteins have a targeting sequence of such length in front of a folded domain that they do not reach into the matrix to interact with mtHsp70. However, if they are of sufficient length that their positively charged presequences are exposed in the import channel of the inner membrane, then the membrane potential across the inner membrane can act on them. Since the electrical potential is negative at the inner surface of the membrane, the positively charged presequence is driven towards the matrix. It has been reported that such an action of $\Delta\Psi$ on the presequence can result in unfolding of a protein on the surface of mitochondria [48]. According to this view, spontaneous local unfolding events at the N-terminus of the folded domain can be trapped by the membrane potential. The activation barrier for spontaneous local unfolding events at the N-terminus of the folded domain may be lowered by the force generated by the action of the membrane potential on the presequence [48, 76]. However, this intriguing possibility has yet to be verified.

30.5.2 Mechanistic Studies of the Import Motor

30.5.2.1 Brownian Movement of the Polypeptide Within the Import Channel

The polypeptide chain can move within the translocation channels of the TOM and TIM23 complexes in forward and reverse direction. Studies using intact mitochon-

dria, isolated outer-membrane vesicles, and purified TOM complex demonstrate that the presequence of a precursor protein can translocate across the TOM complex and bind to the *trans* side of the complex independent of an energy source [79, 132]. In the absence of a membrane potential, the preprotein interacts with a component of the inner-membrane translocase, Tim50, as demonstrated by a cross-linking approach [84, 157]. However, the membrane potential is needed for further translocation across the inner membrane because it appears to be involved in the gating of the TIM23 complex [4, 137]. Subsequently, the polypeptide chain traverses the outer and inner membranes at the same time [26, 107]. Intermediates that span both membranes were used to demonstrate retrograde movement of the polypeptide chain within the translocation channels [35, 124, 139, 140]. When mitochondria were depleted of ATP, mtHsp70 was unable to arrest the intermediates in the matrix, and these intermediates slid back and fell out of the import channels. Forward movement of the polypeptide chain without the function of mtHsp70 was supported by experiments with specific precursor proteins. A certain group of precursor proteins is sorted into the inner membrane by arrest of their single-transmembrane segment in the translocase and subsequent lateral release into the lipid bilayer, a process termed stop-transfer pathway [82, 115]. In these precursors the transmembrane segment follows the amino-terminal presequence in a short distance of about 20 amino acid residues. The enzyme D-lactate dehydrogenase (D-LD) [115] and a mutant form of subunit 5A of cytochrome oxidase [34] are such preproteins. Neither matrix ATP nor a functional mtHsp70 is needed for import of these preproteins. It appears that the polypeptide chain moves in the forward direction until the hydrophobic transmembrane segment is trapped in the translocation channel of the TIM23 complex. These proteins apparently do not require the mtHsp70 motor.

Another group of precursor proteins was genetically engineered. A presequence was fused to a segment of 25 or 50 residues of glutamate or glycine residues followed by the coding sequence of mouse DHFR [94]. Stretches of these amino acid residues could not be bound by mtHsp70, which is consistent with the substrate specificity of the binding pocket of its bacterial homologue DnaK [40, 116]. Although mtHsp70 was not able to bind and therefore to "pull" on the preprotein, import of these fusion proteins into mitochondria occurred efficiently.

These experiments support the view that movement of polypeptide chains within the import channels in a forward and reverse direction can occur without the mtHsp70 and a power stroke being involved.

30.5.2.2 **Recruitment of mtHsp70 by Tim44**

Tim44 anchors the mtHsp70 chaperone to the TIM23 complex at the matrix side of the inner membrane [62, 109, 123]. An analysis of the interaction of Tim44 with mtHsp70 may help to discriminate between the two models. MtHsp70 consists of an ATPase domain, a peptide-binding domain (PBD), and a carboxy-terminal domain or "lid" [11, 42]. According to the Brownian ratchet model, any of these domains could interact with Tim44 to allow mtHsp70 to act as a targeted trapping device. In the power-stroke model, Tim44 is expected to bind the ATPase domain

of mtHsp70, so that an ATP hydrolysis–dependent conformational change could generate a vectorial movement. In this case the PBD could move relative to the membrane anchor and function as a lever arm. Such a pulling of the polypeptide chain would be impossible if the PBD were bound to Tim44.

In two studies, the interaction between Tim44 and mtHsp70 was analyzed by co-immunoprecipitation experiments following the import of domains of mtHsp70 and hybrids between mtHsp70 and mitochondrial homologues of mtHsp70 into isolated mitochondria [61, 134]. The PBD of mtHsp70 in combination with the various ATPase domains were co-precipitated with Tim44 with an efficiency of about 50%, whereas the ATPase domains without the PBD were not precipitated or only minor quantities of about 10% precipitated. When a construct consisting of the peptide-binding and lid domain was imported, no interaction was observed; the functionality of the construct, however, was not shown [61, 134].

Another study was performed with hybrids between mtHsp70 and the closely related DnaK from *E. coli*, which were expressed in mitochondria [86]. In addition, truncated versions of mtHsp70 were imported into mitochondria. Co-immunoprecipitation analysis revealed that the PBD alone binds to Tim44. Together with the lid domain, the PBD was essential to transmit information on the nucleotide state of the ATPase domain to the rest of the chaperone. In addition, a mutant form of mtHsp70, the *ssc1-2* mutant, was isolated [55]. The *ssc1-2* mutation is present within the PBD. The interaction of mtHsp70 with Tim44, and therefore mitochondrial import, is compromised in the *ssc1-2* mutant [33, 55, 123, 147]. Intragenic suppressors were isolated that restore binding of the mutant form of mtHsp70 to Tim44 [145]. The suppressor mutations also reside within the PBD. The position of the mutations in the *ssc1-2* mutant is consistent with an interaction between the PBD and Tim44. In summary, it appears that the PBD of mtHsp70 cannot function as a lever arm, as it seems to bind to Tim44.

30.5.2.3 **Import Without Recruitment of mtHsp70 by Tim44**

According to the targeted Brownian ratchet model, the polypeptide chain will be trapped directly at the outlet of the import channel. Therefore, mtHsp70 has to be recruited to this site.

It was suggested that mtHsp70 can act as a ratchet in the mitochondrial matrix and import unfolded, but not folded, proteins without anchoring of mtHsp70 to Tim44 [68, 80, 145]. A trapping mechanism was proposed to be sufficient for import of unfolded proteins, but import of folded domains would require a Tim44-mtHsp70 interaction supporting the power-stroke model [78, 111, 145]. However, it has to be kept in mind that a Tim44-mtHsp70 interaction is equally essential for a targeted ratchet. The argumentation was based on experiments with two conditional mutant strains. One strain carries a mutant form of Tim44 and the other strain, *ssc1-2*, carries a mutation in the gene encoding mtHsp70. At non-permissive temperature these strains are unable to grow. When isolated mitochondria of the Tim44 mutant were incubated at non-permissive temperature, unfolded preproteins were imported, but import of folded preproteins was strongly reduced [9].

The same was found with *ssc1-2* mutant mitochondria after incubation at non-permissive temperature. At non-permissive temperature a prolonged binding of mtHsp70 to unfolded polypeptide chains was detected, but mtHsp70 did not interact with Tim44 anymore [145]. However, the prolonged binding does not reflect a stronger trapping capacity of the mutant Hsp70, Ssc1-2p, because its association and dissociation rates towards the polypeptide are not strongly altered [70]. Rather, folding of the polypeptide is affected, and therefore more unfolded precursor is present, which then interacts with mtHsp70. Binding to Tim44 and import of folded precursors could be restored by intragenic suppressors of *ssc1*-2 [145].

Two explanations for this behavior were discussed. First, binding to the polypeptide chain by mtHsp70 without recruitment to the import channel could be sufficient for import of unfolded, but not folded, proteins. Second, there might be residual activities in the mutant forms that are sufficient for import of unfolded precursors.

The *ssc1-2* strain and a strain with reduced levels of functional Tim44 were used in another study that demonstrated that the activity of import of high amounts of recombinant unfolded precursor (picomoles) was drastically reduced in these mitochondria [81]. The level of reduction in import activity in mitochondria of the *ssc1-2* strain might depend on the precursor protein studied and on subtle experimental differences, as a modest reduction was observed in another report [68]. Still, these mitochondria imported radio labeled, unfolded precursors that were produced in a cell-free translation system (femtomoles) [81]. Residual activities of the conditional mutants were able to promote import of unfolded, but not folded, preproteins in small quantities. These experiments indicate that Tim44 and mtHsp70 are essential for efficient import [81].

In conclusion, both proposed models, the targeted molecular ratchet and the power-stroke mechanism, require the Tim44-mtHsp70 interaction to mediate efficient import of unfolded proteins. Therefore, these studies [68, 80, 81, 145] are not suited to discriminate between these models.

30.5.2.4 **MtHsp70 Function in the Import Motor**

MtHsp70 in the ATP-bound form is recruited by Tim44 to the import sites and efficiently binds to the incoming polypeptide chains. Tim14 then stimulates ATP hydrolysis, which leads to a conformational change in mtHsp70 so that the PBD of the ADP-bound form closes. Repeated cycles lead to inward movement of the polypeptide chain. Two classes of interactions of the unfolded polypeptide chain with mtHsp70s can be distinguished. The first class is mediated by Tim44 together with Tim14 at the outlet of the import channel. Even low-affinity complexes, which lead to short-lived interactions of substrate with mtHsp70 and which do not contribute to efficient trapping of the chain, may be formed. The on-rate of mtHsp70 to the substrate is high due to the presence of the J-domain protein Tim14 in the import motor, but the off-rate is also high due to the low binding affinity. Thus, there is a high rate of binding and release. Only a few binding sites of very high

affinity are present in proteins [117, 122]. High-affinity binding can contribute to efficient trapping of segments exposed in the matrix space. This explains why high ATP levels in the matrix are necessary to find a pool of complexes of mtHsp70 in the import motor associated with the translocating precursor [84, 123, 139]. High ADP levels lead to a loss of this pool, as the ADP form of this mtHsp70 is rapidly released and Tim44-mediated cycling of the ATP form cannot occur.

The second class comprises high-affinity interactions. MtHsp70 entering the precursor at the import motor will remain tightly bound to a few segments of an unfolded polypeptide chain. These longer-lived complexes remain stable even after movement into the mitochondrial matrix. Moreover, dissociation of these complexes is dependent on the action of the nucleotide-exchange factor Mge1 and subsequent ATP uptake. Once mtHsp70 is released, but the protein still does not reach a folded state, mtHsp70 will rebind to the high-affinity binding sites with the help of the mitochondrial matrix co-chaperone Mdj1. High ATP in the matrix favors the open ATP-bound form of mtHsp70, and therefore steady-state levels of high-affinity complexes mediated by Mdj1 are low.

In conclusion, the mode of interaction of mtHsp70 with preproteins apparently depends on its location and its partner proteins. When ATP levels are high, Tim44-mediated interactions with preproteins at the import sites are observed, whereas at low ATP levels, interactions with preproteins in the matrix mediated by Mdj1 are observed [139, 140]. This demonstrates the specialized nature of the mitochondrial import motor, which allows efficient trapping of incoming precursor proteins. The recruitment of mtHsp70 and the J-protein Tim14 by Tim44 directly to the translocation channel allows efficient trapping, and even precursor segments with lower affinity and short-lived interactions can contribute. On the other hand, Mdj1-supported interactions of mtHsp70 with a few high-affinity sites of the polypeptide generate long-lived complexes in the matrix. These latter complexes may be able to prevent large-scale retrograde movements of the preprotein, but not the small-scale oscillations in the import channel that have to be ratcheted, in particular to promote unfolding at the mitochondrial surface.

30.6 Discussion and Perspectives

Mitochondrial precursor proteins are imported in a largely unfolded state. The translocases of the mitochondrial membranes are not able to transport proteins in a folded state across the membranes. There are at least three mechanisms that result in an unfolded polypeptide chain. First, co-translational import makes protein folding prior to translocation impossible. Second, molecular chaperones can interact with newly synthesized proteins. They protect the proteins against aggregation and keep them in an unfolded, translocation-competent state. Third, unfolding of proteins is mediated by the molecular import motor. It remains to be investigated

which substrates have to be unfolded by the mitochondrial import motor in vivo and which substrates are kept in a translocation-competent state by cytosolic chaperones. It will be interesting to see how it is determined whether a protein folds or interacts with chaperones prior to the import into mitochondria.

The Brownian ratchet mechanism is widely accepted as a mechanism to drive protein translocation across membranes. This is the case not only for the mitochondrial system but also for translocation into the endoplasmic reticulum [53, 74, 145]. In mitochondria, protein translocation and protein unfolding on the surface of mitochondria are driven by the mitochondrial import motor. The targeted Brownian ratchet mechanism is sufficient to explain all experimental observations on the function and structure of the mitochondrial protein import motor. One of these functions is the unfolding of proteins during mitochondrial import. Folded proteins do not have requirements for their import that are different from or additional to those of folded proteins. It is still debated whether the import motor can exert a power stroke or whether it can switch to a power-stroke mode, in particular for the import of folded proteins. So far direct evidence for a power stroke has not been presented. It cannot be excluded that there is a weak pulling force generated by the import motor that assists in protein translocation. However, such a form does not seem to be either helpful or necessary. In the case of a power stroke, it should be possible to measure directly the force generated by the import motor. In order to support the power-stroke model, experimental proof for a lever-arm function of mtHsp70 would be required. In addition, experimental proof for an import in regular steps that correlates with the lever-arm dimensions would be required. As it was suggested that the import motor could switch from the trapping to the pulling mode to achieve unfolding by one power stroke, such a switching mechanism must be supported by experimental evidence as well.

A promising approach to address the mechanism of the import motor will be to reconstitute the import motor with purified components. Initial experiments have already been performed [69]. The observations made in this study are consistent with a Brownian ratchet, but not with a power-stroke mode. However, this study did not include the complete set of import motor components. The discovery of two new essential components of the import motor indicates that the motor is more complex than previously thought [24, 32, 59, 85, 138]. The search for further possible components of the motor will be a major task in the future, as it might provide us with new insights into the action of the import motor during the translocation process. For example, the membrane integration of the J-protein Tim14, one of the new components, clearly demonstrates that the ATP hydrolysis occurs at the membrane and not in the matrix space. After having identified the complete set of components, it will be necessary to reconstitute the mitochondrial import motor. This will allow us to analyze the system under experimentally defined conditions. One characteristic feature of the import motor is its association with the membrane-integrated translocation channel. Therefore, in the long run the import motor will have to be reconstituted into proteoliposomes together with the components of the translocation channel.

30.7 Experimental Protocols

30.7.1 Protein Import Into Mitochondria in Vitro

Import into isolated mitochondria of *Saccharomyces cerevisiae* is an important tool for analyzing whether a protein has a mitochondrial location. In addition, it is a powerful assay to study the mechanisms of the mitochondrial import machinery and its energetic and structural requirements.

In an in vitro import assay, precursor proteins are incubated together with isolated mitochondria and the uptake of precursor proteins by the mitochondria is analyzed. Precursor proteins are synthesized either in vitro in radiochemical amounts or in vivo in chemical amounts. For in vitro synthesis of radio labeled precursor proteins, purified plasmid DNA encoding the gene of interest under control of the SP6 promoter is first transcribed with SP6 RNA polymerase. The mRNA obtained is used in an in vitro translation reaction in the presence of [^{35}S]methionine (specific activity 1000 Ci/mM) using rabbit reticulocyte lysate (Promega) [16, 100]. Chemical amounts of precursor proteins are produced by expression of the precursor protein in *E. coli* and subsequent purification of the protein from the bacterial lysate (e.g., [19, 81]). Mitochondria are isolated from yeast cells according to published procedures [17, 43]. They are resuspended to a protein concentration of 10 mg mL^{-1} in SEM buffer (250 mM sucrose, 1 mM EDTA, 10 mM MOPS, pH 7.2), aliquoted, quick-frozen in liquid nitrogen, and stored at −80 °C. Mitochondria are thawed directly before use. For import into mitochondria from *N. crassa* and mammalian cells, mitochondria have to be prepared directly before use in the import assay [97, 150, 155]. Freezing them will drastically decrease their import efficiency.

In the in vitro import assay, mitochondria are added to import buffer (0.5 M sorbitol, 80 mM KCl, 10 mM magnesium acetate, 2 mM KH_2PO_4, 2.5 mM EDTA, 5 mM $MnCl_2$, 2 mM ATP, 2 mM NADH, 0–3% [w/v] bovine serum albumin [BSA, fatty acid-free], 50 mM HEPES, adjusted to pH 7.2 with KOH) in a 1.5-mL microcentrifuge tube. In general, 50–200 μg mitochondrial protein is used per 200 μL of buffer. The import efficiency of some precursor proteins is increased by the addition of BSA. The BSA has to be free of fatty acids, as these damage the mitochondrial membranes. Normally, ATP and NADH are added to energize the mitochondria and to maintain a high mitochondrial membrane potential.

The samples are mixed and then adjusted to the temperature of the import reaction for 3 min. The reaction is started by the addition of reticulocyte lysate containing the precursor protein (1–4% [v/v]) or the purified precursor protein (about 800 pmol mg^{-1} mitochondria). Following the import reaction, samples are placed on ice and 1 μM valinomycin, which destroys the membrane potential across the inner membrane, is added (stock: 100 μM in EtOH, store at −20 °C) to stop the reaction. The sample is divided into two aliquots and diluted with 400 μL ice-cold SHKCl (0.6 M sorbitol, 80 mM KCl 20 mM HEPES, adjusted to pH 7.2 with

KOH). One aliquot is treated with 50–100 μg mL^{-1}proteinase K (PK, stock solution: 10 mg mL^{-1}, stored in aliquots at −20 °C) for 30 min on ice. PK action is stopped by addition of 1 mM phenylmethylsulfonyl fluoride (PMSF 200 mM stock in EtOH, prepare fresh) and incubated for 5 min on ice. Then mitochondria are reisolated by centrifugation at 15 000 *g* for 15 min at 4 °C. The pellet is washed, but not resuspended, with 300 μL SHKCl containing 0.3 mM PMSF and centrifuged as before. Pelleted mitochondria are resuspended in SDS-polyacrylamide gel electrophoresis (SDS-PAGE) buffer and heated immediately to 95 °C for 5 min to inhibit the protease completely. Samples are analyzed by SDS-PAGE followed by autoradiography and quantification using a phosphoimaging system or by immunodecoration and quantification by densitometry. One lane of the SDS-PAGE is loaded with 5–20% of the solution containing the precursor protein used per import sample to provide a standard that allows determination of the amount of imported radio labeled precursor protein. In order to determine the amount of imported recombinant precursor protein, several amounts (1–20%) of recombinant protein are loaded onto the SDS-PAGE gel and the values obtained by immunodecoration and quantification are used as standards. However, analysis by immunodecoration is not possible if a mitochondrial protein is imported, as the signal of the endogenous protein would interfere with the imported protein in the immunodecoration. In this case the protein has to be radio labeled.

Each precursor protein has a linear time range of import. To analyze and compare different import parameters, the import of the precursor protein should be performed in this linear range of import. To obtain import kinetics for a precursor protein, one larger sample is prepared in a 1.5-mL microcentrifuge tube as above and started by the addition of precursor protein. At certain time points (normally about five points in the range of the first 30 min), aliquots are removed and then processed and analyzed as described above.

In the case of precursor proteins with a cleavable presequence, import can be monitored by their processing. The precursor protein (p-form) is converted and catalyzed by the matrix-processing peptidase (MPP) to a lower-molecular-weight mature protein (m-form). Protection against added protease indicates that the mature form or a non-processed precursor protein with internal targeting signal is translocated into mitochondria. As a control for specific translocation of the precursor protein, the import reaction should be performed in the absence of a membrane potential, $\Delta\Psi$ across the inner membrane. Without $\Delta\Psi$ import of presequence-containing proteins and inner-membrane proteins into mitochondria does not take place. $\Delta\Psi$ can be depleted by the addition of uncouplers, such as 1 μM valinomycin.

In order to analyze whether a protein is imported into the mitochondrial matrix or is located completely or partly in the intermembrane space, the outer membrane is selectively opened by hypotonic treatment of mitochondria in the presence of protease. To this end one aliquot of the import reaction is diluted with nine volumes of 20-mM HEPES, pH 7.2, and treated with 50–100 μg mL^{-1} PK (see above). The resulting mitoplasts are isolated and analyzed as described for the mitochondria. If the protein or parts of it are located in the IMS, the protein will be digested

completely or to smaller fragments. For control, mitochondria are lysed with 0.2% (w/v) of Triton X-100 and treated with the protease. Then total protein is precipitated with trichloroacetic acid. This confirms that no protease-resistant fragment is generated due to a stably folded structure but rather due to protection by a mitochondrial membrane.

30.7.2 Stabilization of the DHFR Domain by Methotrexate

The enzyme DHFR catalyzes the reduction of dihydrofolate to tetrahydrofolate using NADPH as co-substrate [6]. Methotrexate (MTX) is a substrate analogue of dihydrofolate that binds to DHFR, stabilizes its folded structure, and inhibits the enzyme activity [26, 135]. DHFR is not a mitochondrial protein. However, a fusion protein of DHFR and a mitochondrial targeting signal can be efficiently translocated into mitochondria. The fused targeting signal usually does not interfere with the folding of the DHFR [26]. MTX blocks the unfolding of the DHFR and thus inhibits translocation across the mitochondrial membranes [26]. The DHFR-containing precursor protein is incubated in the presence of 1 mM NADPH (stock solution: 100 mM in H_2O, make fresh each time) and 1 μM MTX (10 mM in SEM buffer stock solution; store at −20 °C and dilute further before use) in import buffer for 10 min on ice. Then isolated mitochondria are added and the samples are further treated as in a normal in vitro import assay.

If the N-terminal segment of a DHFR-containing precursor protein starting with the targeting signal is long enough to reach the mitochondrial matrix, a translocation intermediate spanning both mitochondrial membranes can be generated in the presence of MTX. Such translocation intermediates have proved to be a very useful tool for analyzing the characteristics of mitochondrial import. It has been demonstrated that precursor proteins with N-terminal targeting sequences traverse the mitochondrial membrane as an extended chain in an unfolded conformation and that ca. 50 amino acid residues are needed to span both membranes [26, 108]. In addition to the conformational state of the translocation intermediate, the energetic requirements, the sequential steps, and the mechanistic aspects of the translocation process also have been defined with the help of translocation intermediates [139, 140]. To this end, MTX-arrested translocation intermediates were generated in a first reaction [16]. They can be completely imported into mitochondria in a second reaction, if the MTX is removed from the reaction. If it is planned to remove MTX in the second reaction, the import of the DHFR-containing precursor protein is blocked with lower concentrations of MTX (5 nM MTX) in the first reaction. Then mitochondria are re-isolated, washed to remove the MTX, and incubated for the second import reaction [16].

Translocation intermediates were also used to define the import pathway of preproteins and to identify components of the translocation machinery by chemical cross-linking to and co-immunoprecipitation of the arrested intermediate [64, 84, 141, 157].

Studies with MTX-arrested translocation intermediates are not restricted to proteins with N-terminal presequences. Experiments performed with MTX-arrested

DHFR fusion proteins containing internal targeting signals have demonstrated that they enter mitochondria in a loop conformation [15, 30, 133, 153].

30.7.3 Import of Precursor Proteins Unfolded With Urea

Unfolding of precursor proteins with urea allows comparing the import characteristics of proteins in the unfolded state and the folded state. In order to unfold precursor proteins, they are first precipitated by the addition of a saturated ammonium sulfate solution [95]. Two volumes of saturated ammonium sulfate solution are added to the reticulocyte lysate containing the precursor protein in three steps with vigorous mixing following each step. The sample is incubated for 30 min on ice and centrifuged at 20 000 *g* for 15 min at 4 °C, and the pellet is resuspended in the original volume of urea-containing buffer (8 M urea 20 mM HEPES/KOH, pH 7.4, and freshly added 100 mM DTT). The precursor protein–containing sample is diluted into the import reaction so that the final urea concentration is below 300 mM. Then the import reaction is performed as described above.

30.7.4 Kinetic Analysis of the Unfolding Reaction by Trapping of Intermediates

Thermal breathing results in transient partial unfolding events of a protein. Partial unfolding leads to the exposure of amino acid side chains to the solvent, which are normally buried and inaccessible in the folded state of the protein. In the unfolded state chemical reagents have access to these amino acid side chains and can chemically modify them [35]. Determination of the kinetics of the chemical modification allows estimating the rates of the transient unfolding events. The minimal rate of transient unfolding is obtained, as reversible unfolding events that are faster than the chemical modification reaction cannot be trapped. The chemical modification prevents refolding of the protein domain, and therefore the partial unfolded intermediate is trapped. In the unfolded state, in contrast to the folded state, the protein is accessible to added protease, and the ratio of protease-sensitive to protease-resistant protein reflects the percentage of chemically modified protein and hence the amount of the transiently unfolded protein domain. The modification is performed for increasing time periods, and the data obtained will give the kinetics of the transient unfolding process.

Transient local unfolding events might occur throughout the protein. However, only the local unfolding of the protein domain in which the modified amino acid residue is located will be analyzed. Preproteins carrying an N-terminal presequence are imported in an N-to-C-terminal direction. Therefore, the unfolding of the N-terminal segment of the protein domain is the limiting step for the import. Unfolding kinetics of this segment has to be compared with the kinetics of import.

Transient Unfolding of DHFR

The sequence of mouse DHFR has one unique cysteine residue close to the N-terminus at position 7 (Cys7). Normally, Cys7 is buried inside the folded protein

[93, 131]. We analyzed the accessibility of this cysteine to the water-soluble, alkylating reagent *N*-ethylmaleimide (NEM). In the folded state of DHFR, Cys7 is not modified by NEM, whereas it is modified by NEM in the unfolded state [35]. Therefore, NEM modification of Cys7 can be used to monitor the thermal unfolding of DHFR. This could be shown by the concentration-dependent aggregation of DHFR after NEM treatment following unfolding at higher temperature [35]. Alkylation of Cys7 interferes with refolding of the DHFR and destabilizes its structure, resulting in increased protease sensitivity of the modified DHFR.

To estimate the rates of transient unfolding, reticulocyte lysate containing the in vitro–synthesized radio labeled precursor protein pSu9(1-69)-DHFR [35] is diluted 10-fold with import buffer containing 0.1% (w/v) BSA and preincubated for 4 min at the reaction temperature. Then 3 mM NEM is added to the sample, and after 0, 1, 3, 9, and 30 min aliquots are taken, put on ice, and immediately treated with 45 mM DTT to quench the NEM. Samples are incubated with 50 μg mL^{-1} PK for 25 min on ice. The protease treatment is stopped by the addition of 2 mM PMSF and samples are analyzed by SDS-PAGE, autoradiography, and quantification using a phosphoimaging system. Protease treatment results in generation of a fragment if the DHFR domain was folded and not modified by NEM. The amount of this PK-resistant fragment was quantified for all time points, corrected for the loss of radio labeled methionine, and compared to the signal of the DHFR in the untreated sample. The percentage of protease-resistant fragment was plotted versus the time, and the unfolding rate (percentage of degraded protein per minute) was determined by fitting the data to a first-order equation.

Transient Unfolding of the Heme-binding Domain (HBD)

Yeast cytochrome b_2 contains a tightly folded domain of about 99 amino acid residues, i.e., the heme-binding domain (HBD). The HBD containing bound heme is degraded by PK to a core fragment (amino acid residues 9 to approximately 90) under native conditions, whereas it is totally degraded in the heme-free form [35]. This indicates that the HBD is not tightly folded in the absence of its ligand. The HBD contains three histidine residues at positions 19, 43, and 66. His43 and His66 are located in the heme-binding pocket and are involved in ligand binding [156]. Modification of the imidazole group of these histidine residues by treatment with diethylpyrocarbonate (DEPC) results in protease sensitivity of the HBD. This indicates that the modified HBD is not folded [35]. The rate of the DEPC modification of the HBD monitors the amount of transient unfolding of the HBD. In order to estimate the rate of transient unfolding of the HBD, the kinetics of the DEPC modification of the histidine residues in the HBD is analyzed by protease resistance. The analysis is performed with a construct, pSu9(1-69)HBD, containing a mitochondrial targeting signal fused to the full-sized HBD (residues 1–99 of mature cytochrome b_2) [35]. Reticulocyte lysate containing this radio labeled precursor protein (10 μL) is diluted 50-fold in 100 mM KH_2PO_4, pH 7.4. Samples are pretreated for 5 min and then incubated with 6.9 mM DEPC at the temperature chosen. After 0, 1, 3, 9, and 30 min, an aliquot (50 μL) is withdrawn and the DEPC is quenched with an excess of imidazole (final concentration 200 mM). The samples (40% of

the total volume) are treated with PK (1 mg mL^{-1}) for 25 min at 37 °C and 2 mM PMSF is added to stop PK. Local protein unfolding rates are determined by quantification of the protease-resistant fragment as described above for the kinetic determination of the NEM modification of DHFR.

DEPC is a clear, colorless liquid with a molarity of 6.9 M. It is very sensitive to moisture. Once opened, the DEPC should be stored under a nitrogen layer and the closed bottle should be stored at 0–4 °C to avoid hydrolysis of the DEPC. DEPC should be used carefully, as it is suspected to be carcinogenic.

References

1 Ahting, U., Thieffry, M., Engelhardt, H., Hegerl, R., Neupert, W. and Nussberger, S. (2001) Tom40, the pore-forming component of the protein-conducting TOM channel in the outer membrane of mitochondria. *J. Cell Biol.*, **153**, 1151–1160.

2 Ahting, U., Thun, C., Hegerl, R., Typke, D., Nargang, F. E., Neupert, W. and Nussberger, S. (1999) The TOM core complex: the general protein import pore of the outer membrane of mitochondria. *J. Cell Biol.*, **147**, 959–968.

3 Bauer, M. F., Hofmann, S., Neupert, W. and Brunner, M. (2000) Protein translocation into mitochondria: the role of TIM complexes. *Trends Cell Biol.*, **10**, 25–31.

4 Bauer, M. F., Sirrenberg, C., Neupert, W. and Brunner, M. (1996) Role of Tim23 as voltage sensor and presequence receptor in protein import into mitochondria. *Cell*, **87**, 33–41.

5 Berthold, J., Bauer, M. F., Schneider, H. C., Klaus, C., Dietmeier, K., Neupert, W. and Brunner, M. (1995) The MIM complex mediates preprotein translocation across the mitochondrial inner membrane and couples it to the mt-Hsp70/ATP driving system. *Cell*, **81**, 1085–1093.

6 Blakley, R. L. (1995) Eukaryotic dihydrofolate reductase. *Adv. Enzymol. Relat. Areas Mol. Biol.*, **70**, 23–102.

7 Bolliger, L., Deloche, O., Glick, B. S., Georgopoulos, C., Jeno, P., Kronidou, N., Horst, M., Morishima, N. and Schatz, G. (1994) A mitochondrial homolog of bacterial GrpE interacts with mitochondrial hsp70 and is essential for viability. *EMBO J.*, **13**, 1998–2006.

8 Bolliger, L., Junne, T., Schatz, G. and Lithgow, T. (1995) Acidic receptor domains on both sides of the outer membrane mediate translocation of precursor proteins into yeast mitochondria. *EMBO J.*, **14**, 6318–6326.

9 Bomer, U., Maarse, A. C., Martin, F., Geissler, A., Merlin, A., Schonfisch, B., Meijer, M., Pfanner, N. and Rassow, J. (1998) Separation of structural and dynamic functions of the mitochondrial translocase: Tim44 is crucial for the inner membrane import sites in translocation of tightly folded domains, but not of loosely folded preproteins. *EMBO J.*, **17**, 4226–4237.

10 Bomer, U., Meijer, M., Guiard, B., Dietmeier, K., Pfanner, N. and Rassow, J. (1997) The sorting route of cytochrome b2 branches from the general mitochondrial import pathway at the preprotein translocase of the inner membrane. *J. Biol. Chem.*, **272**, 30439–30446.

11 Bukau, B. and Horwich, A. L. (1998) The Hsp70 and Hsp60 chaperone machines. *Cell*, **92**, 351–366.

12 Carrion-Vazquez, M., Oberhauser, A. F., Fowler, S. B., Marszalek, P. E., Broedel, S. E., Clarke, J. and Fernandez, J. M. (1999) Mechanical

and chemical unfolding of a single protein: a comparison. *Proc. Natl. Acad. Sci. USA*, **96**, 3694–3699.

13 Chauwin, J. F., Oster, G. and Glick, B. S. (1998) Strong precursor-pore interactions constrain models for mitochondrial protein import. *Biophys. J*, **74**, 1732–1743.

14 Cheng, M. Y., Hartl, F. U., Martin, J., Pollock, R. A., Kalousek, F., Neupert, W., Hallberg, E. M., Hallberg, R. L. and Horwich, A. L. (1989) Mitochondrial heat-shock protein hsp60 is essential for assembly of proteins imported into yeast mitochondria. *Nature*, **337**, 620–625.

15 Curran, S. P., Leuenberger, D., Schmidt, E. and Koehler, C. M. (2002) The role of the Tim8p-Tim13p complex in a conserved import pathway for mitochondrial polytopic inner membrane proteins. *J. Cell Biol.*, **158**, 1017–1027.

16 Cyr, D. M., Ungermann, C. and Neupert, W. (1995) Analysis of mitochondrial protein import pathway in Saccharomyces cerevisiae with translocation intermediates. *Methods Enzymol.*, **260**, 241–252.

17 Daum, G., Bohni, P. C. and Schatz, G. (1982) Import of proteins into mitochondria. Cytochrome b2 and cytochrome c peroxidase are located in the intermembrane space of yeast mitochondria. *J. Biol. Chem.*, **257**, 13028–13033.

18 Dekker, P. J., Keil, P., Rassow, J., Maarse, A. C., Pfanner, N. and Meijer, M. (1993) Identification of MIM23, a putative component of the protein import machinery of the mitochondrial inner membrane. *FEBS Lett.*, **330**, 66–70.

19 Dekker, P. J., Martin, F., Maarse, A. C., Bomer, U., Muller, H., Guiard, B., Meijer, M., Rassow, J. and Pfanner, N. (1997) The Tim core complex defines the number of mitochondrial translocation contact sites and can hold arrested preproteins in the absence of matrix Hsp70-Tim44. *EMBO J.*, **16**, 5408–5419.

20 Dekker, P. J., Ryan, M. T., Brix, J., Muller, H., Honlinger, A. and Pfanner, N. (1998) Preprotein translocase of the outer mitochondrial membrane: molecular dissection and assembly of the general import pore complex. *Mol. Cell. Biol.*, **18**, 6515–6524.

21 Deshaies, R. J., Koch, B. D., Werner-Washburne, M., Craig, E. A. and Schekman, R. (1988) A subfamily of stress proteins facilitates translocation of secretory and mitochondrial precursor polypeptides. *Nature*, **332**, 800–805.

22 Donzeau, M., Kaldi, K., Adam, A., Paschen, S., Wanner, G., Guiard, B., Bauer, M. F., Neupert, W. and Brunner, M. (2000) Tim23 links the inner and outer mitochondrial membranes. *Cell*, **101**, 401–412.

23 Driessen, A. J., Manting, E. H. and van der Does, C. (2001) The structural basis of protein targeting and translocation in bacteria. *Nat. Struct. Biol.*, **8**, 492–498.

24 D'Silva, P. D., Schilke, B., Walter, W., Andrew, A. and Craig, E. A. (2003) J protein cochaperone of the mitochondrial inner membrane required for protein import into the mitochondrial matrix. *Proc. Natl. Acad. Sci. USA*, **100**, 13839–13844.

25 Eilers, M., Hwang, S. and Schatz, G. (1988) Unfolding and refolding of a purified precursor protein during import into isolated mitochondria. *EMBO J.*, **7**, 1139–1145.

26 Eilers, M. and Schatz, G. (1986) Binding of a specific ligand inhibits import of a purified precursor protein into mitochondria. *Nature*, **322**, 228–232.

27 Emtage, J. L. and Jensen, R. E. (1993) MAS6 encodes an essential inner membrane component of the yeast mitochondrial protein import pathway. *J. Cell Biol.*, **122**, 1003–1012.

28 Endo, T. and Kohda, D. (2002) Functions of outer membrane receptors in mitochondrial protein import. *Biochim. Biophys. Acta*, **1592**, 3.

29 Endo, T., Yamamoto, H. and Esaki, M. (2003) Functional cooperation and separation of translocators in protein

import into mitochondria, the double-membrane bounded organelles. *J. Cell Sci.*, **116**, 3259–3267.

30 Endres, M., Neupert, W. and Brunner, M. (1999) Transport of the ADP/ATP carrier of mitochondria from the TOM complex to the TIM22.54 complex. *EMBO J.*, **18**, 3214–3221.

31 Foelsch, H., Guiard, B., Neupert, W. and Stuart, R. A. (1996) Internal targeting signal of the BCS1 protein: a novel mechanism of import into mitochondria. *EMBO J.*, **15**, 479–487.

32 Frazier, A., Dudek, J., Guiard, B., Voos, W., Li, Y., Lind, M., Meisinger, C., Geissler, A., Sickmann, A., Meyer, H. E., Bilanchone, V., Cumsky, M. G., Truscott, K. N., Pfanner, N. and Rehling, P. (2004) Pam16 plays an essential role in the mitochondrial protein import motor. *Nature Struct. Mol. Biol.*, **11**, 226–233.

33 Gambill, B. D., Voos, W., Kang, P. J., Miao, B., Langer, T., Craig, E. A. and Pfanner, N. (1993) A dual role for mitochondrial heat shock protein 70 in membrane translocation of preproteins. *J. Cell Biol.*, **123**, 109–117.

34 Gärtner, F., Voos, W., Querol, A., Miller, B. R., Craig, E. A., Cumsky, M. G. and Pfanner, N. (1995) Mitochondrial import of subunit Va of cytochrome c oxidase characterized with yeast mutants – Independence from receptors, but requirement for matrix hsp70 translocase function. *J. Biol. Chem.*, **270**, 3788–3795.

35 Gaume, B., Klaus, C., Ungermann, C., Guiard, B., Neupert, W. and Brunner, M. (1998) Unfolding of preproteins upon import into mitochondria. *EMBO J.*, **17**, 6497–6507.

36 Gentle, I., Gabriel, K., Beech, P., Waller, R. and Lithgow, T. (2004) The Omp85 family of proteins is essential for outer membrane biogenesis in mitochondria and bacteria. *J. Cell Biol.*, **164**, 19–24.

37 Geissler, A., Chacinska, A., Truscott, K. N., Wiedemann, N., Brandner, K., Sickmann, A., Meyer, H. E., Meisinger, C., Pfanner, N. and Rehling, P. (2002) The mitochondrial presequence translocase: an essential role of Tim50 in directing preproteins to the import channel. *Cell*, **111**, 507–518.

38 Glick, B. S. (1995) Can Hsp70 proteins act as force-generating motors? *Cell*, **80**, 11–14.

39 Glick, B. S., Wachter, C., Reid, G. A. and Schatz, G. (1993) Import of cytochrome b2 to the mitochondrial intermembrane space: the tightly folded heme-binding domain makes import dependent upon matrix ATP. *Protein Sci.*, **2**, 1901–1917.

40 Gragerov, A., Zeng, L., Zhao, X., Burkholder, W. and Gottesman, M. E. (1994) Specificity of DnaK-peptide binding. *J. Mol. Biol.*, **235**, 848–854.

41 Hachiya, N., Komiya, T., Alam, R., Iwahashi, J., Sakaguchi, M., Omura, T. and Mihara, K. (1994) MSF, a novel cytoplasmic chaperone which functions in precursor targeting to mitochondria. *EMBO J.*, **13**, 5146–5154.

42 Hartl, F. U. and Hayer-Hartl, M. (2002) Molecular chaperones in the cytosol: from nascent chain to folded protein. *Science*, **295**, 1852–1858.

43 Herrmann, J. M., Foelsch, H., Neupert, W. and Stuart, R. A. (1994) Isolation of yeast mitochondria and study of mitochondrial protein translation. In Celis, J. E. (ed.), *Cell Biology: A Laboratory Handbook*. Academic Press, San Diego, Vol. 1, pp. 538–544.

44 Herrmann, J. M. and Neupert, W. (2000) What fuels polypeptide translocation? An energetical view on mitochondrial protein sorting. *Biochim. Biophys. Acta*, **1459**, 331–338.

45 Hill, K., Model, K., Ryan, M. T., Dietmeier, K., Martin, F., Wagner, R. and Pfanner, N. (1998) Tom40 forms the hydrophilic channel of the mitochondrial import pore for preproteins. *Nature*, **395**, 516–521.

46 Holroyd, C. and Erdmann, R. (2001) Protein translocation machineries of peroxisomes. *FEBS Lett.*, **501**, 6–10.

47 Hönlinger, A., Kübrich, M., Moczko, M., Gärtner, F., Mallet, L., Bussereau, F., Eckerskorn, C., Lottspeich, F., Dietmeier, K., Jacquet, M. and Pfanner, N. (1995) The mitochondrial receptor complex: Mom22 is essential for cell viability and directly interacts with preproteins. *Mol. Cell. Biol.*, **15**, 3382–3389.

48 Huang, S., Ratliff, K. S. and Matouschek, A. (2002) Protein unfolding by the mitochondrial membrane potential. *Nat. Struct. Biol.*, **9**, 301–307.

49 Huang, S., Ratliff, K. S., Schwartz, M. P., Spenner, J. M. and Matouschek, A. (1999) Mitochondria unfold precursor proteins by unraveling them from their N-termini. *Nat. Struct. Biol.*, **6**, 1132–1138.

50 Hurt, E. C., Pesold-Hurt, B. and Schatz, G. (1984) The cleavable prepiece of an imported mitochondrial protein is sufficient to direct cytosolic dihydrofolate reductase into the mitochondrial matrix. *FEBS Lett.*, **178**, 306–310.

51 Jarvis, P. and Soll, J. (2002) Toc, tic, and chloroplast protein import. *Biochim. Biophys. Acta*, **1590**, 177–189.

52 Jensen, R. and Dunn, C. (2002) Protein import into and across the mitochondrial inner membrane: role of the TIM23 and TIM22 translocons. *Biochim. Biophys. Acta*, **1592**, 25.

53 Jensen, R. E. and Johnson, A. E. (1999) Protein translocation: is Hsp70 pulling my chain? *Curr. Biol.*, **9**, R779–782.

54 Johnson, A. E. and Haigh, N. G. (2000) The ER translocon and retrotranslocation: is the shift into reverse manual or automatic? *Cell*, **102**, 709–712.

55 Kang, P. J., Ostermann, J., Shilling, J., Neupert, W., Craig, E. A. and Pfanner, N. (1990) Requirement for hsp70 in the mitochondrial matrix for translocation and folding of precursor proteins. *Nature*, **348**, 137–143.

56 Keegstra, K. and Froehlich, J. E. (1999) Protein import into chloroplasts. *Curr. Opin. Plant Biol.*, **2**, 471–476.

57 Kiebler, M., Keil, P., Schneider, H., van der Klei, I. J., Pfanner, N. and Neupert, W. (1993) The mitochondrial receptor complex: a central role of MOM22 in mediating preprotein transfer from receptors to the general insertion pore. *Cell*, **74**, 483–492.

58 Koehler, C. M. (2000) Protein translocation pathways of the mitochondrion. *FEBS Lett.*, **476**, 27–31.

59 Kozany, C., Mokranjac, D., Sichting, M., Neupert, W., and Hell, K. (2004) The J-domain related co-chaperone Tim16 is a constituent of the mitochondrial TIM23 preprotein translocase. *Nature Struct. Mol. Biol.*, **11**, 234–241.

60 Kozjak, V., Wiedemann, N., Milenkovic, D., Lohaus, C., Meyer, H. E., Guiard, B., Meisinger, C. and Pfanner, N. (2003) An essential role of Sam50 in the protein sorting and assembly machinery of the mitochondrial outer membrane. *J. Biol. Chem.*, **278**, 48520–48523.

61 Krimmer, T., Rassow, J., Kunau, W. H., Voos, W. and Pfanner, N. (2000) Mitochondrial protein import motor: the ATPase domain of matrix Hsp70 is crucial for binding to Tim44, while the peptide binding domain and the carboxy-terminal segment play a stimulatory role. *Mol. Cell. Biol.* **20**, 5879–5887.

62 Kronidou, N. G., Oppliger, W., Bolliger, L., Hannavy, K., Glick, B. S., Schatz, G. and Horst, M. (1994) Dynamic interaction between Isp45 and mitochondrial hsp70 in the protein import system of the yeast mitochondrial inner membrane. *Proc. Natl. Acad. Sci. U.S.A.*, **91**, 12818–12822.

63 Kunkele, K. P., Heins, S., Dembowski, M., Nargang, F. E., Benz, R., Thieffry, M., Walz, J., Lill, R., Nussberger, S. and Neupert, W. (1998) The preprotein translocation channel of the outer membrane of mitochondria. *Cell*, **93**, 1009–1019.

64 Kurz, M., Martin, H., Rassow, J.,

Pfanner, N. and Ryan, M. T. (1999) Biogenesis of Tim proteins of the mitochondrial carrier import pathway: differential targeting mechanisms and crossing over with the main import pathway. *Mol. Biol. Cell*, **10**, 2461–2474.

65 Laloraya, S., Gambill, B. D. and Craig, E. A. (1994) A role for a eukaryotic GrpE-related protein, Mge1p, in protein translocation. *Proc. Natl. Acad. Sci. U.S.A.*, **91**, 6481–6485.

66 Lee, C. M., Neupert, W. and Stuart, R. A. (2000) Mitochondrial targeting signals. In J. A. F. op den Kamp, e. (ed.), *Protein, Lipid and Membrane Traffic: Pathways and Targeting*. IOS Press, Amsterdam, pp. 151–159.

67 Li, H., Oberhauser, A. F., Fowler, S. B., Clarke, J. and Fernandez, J. M. (2000) Atomic force microscopy reveals the mechanical design of a modular protein. *Proc. Natl. Acad. Sci. USA*, **97**, 6527–6531.

68 Lim, J. H., Martin, F., Guiard, B., Pfanner, N. and Voos, W. (2001) The mitochondrial Hsp70-dependent import system actively unfolds preproteins and shortens the lag phase of translocation. *EMBO J.*, **20**, 941–950.

69 Liu, Q., D'Silva, P., Walter, W., Marszalek, J. and Craig, E. A. (2003) Regulated cycling of mitochondrial Hsp70 at the protein import channel. *Science*, **300**, 139–141.

70 Liu, Q., Krzewska, J., Liberek, K. and Craig, E. A. (2001) Mitochondrial Hsp70 Ssc1: role in protein folding. *J. Biol. Chem.*, **276**, 6112–6118.

71 Maarse, A. C., Blom, J., Keil, P., Pfanner, N. and Meijer, M. (1994) Identification of the essential yeast protein MIM17, an integral mitochondrial inner membrane protein involved in protein import. *FEBS Lett.*, **349**, 215–221.

72 Marszalek, P. E., Lu, H., Li, H., Carrion-Vazquez, M., Oberhauser, A. F., Schulten, K. and Fernandez, J. M. (1999) Mechanical unfolding intermediates in titin modules. *Nature*, **402**, 100–103.

73 Martin, J., Mahlke, K. and Pfanner, N. (1991) Role of an energized inner membrane in mitochondrial protein import. Delta psi drives the movement of presequences. *J. Biol. Chem.*, **266**, 18051–18057.

74 Matlack, K. E., Misselwitz, B., Plath, K. and Rapoport, T. A. (1999) BiP acts as a molecular ratchet during posttranslational transport of prepro-alpha factor across the ER membrane. *Cell*, **97**, 553–564.

75 Matlack, K. E., Mothes, W. and Rapoport, T. A. (1998) Protein translocation: tunnel vision. *Cell*, **92**, 381–390.

76 Matouschek, A. (2003) Protein unfolding – an important process in vivo? *Curr. Opin. Struct. Biol.*, **13**, 98–109.

77 Matouschek, A., Azem, A., Ratliff, K., Glick, B. S., Schmid, K. and Schatz, G. (1997) Active unfolding of precursor proteins during mitochondrial protein import. *EMBO J.*, **16**, 6727–6736.

78 Matouschek, A., Pfanner, N. and Voos, W. (2000) Protein unfolding by mitochondria. The Hsp70 import motor. *EMBO Rep.*, **1**, 404–410.

79 Mayer, A., Neupert, W. and Lill, R. (1995) Mitochondrial protein import: Reversible binding of the presequence at the trans side of the outer membrane drives partial translocation and unfolding. *Cell*, **80**, 127–137.

80 Merlin, A., Voos, W., Maarse, A. C., Meijer, M., Pfanner, N. and Rassow, J. (1999) The J-related segment of tim44 is essential for cell viability: a mutant Tim44 remains in the mitochondrial import site, but inefficiently recruits mtHsp70 and impairs protein translocation. *J. Cell Biol.*, **145**, 961–972.

81 Milisav, I., Moro, F., Neupert, W. and Brunner, M. (2001) Modular structure of the TIM23 preprotein translocase of mitochondria. *J. Biol. Chem.*, **276**, 25856–25861.

82 Miller, B. R. and Cumsky, M. G. (1993) Intramitochondrial sorting of the precursor to yeast cytochrome c oxidase subunit Va. *J. Cell Biol.*, **121**, 1021–1029.

83 Model, K., Prinz, T., Ruiz, T.,

Radermacher, M., Krimmer, T., Kuhlbrandt, W., Pfanner, N. and Meisinger, C. (2002) Protein Translocase of the Outer Mitochondrial Membrane: Role of Import Receptors in the Structural Organization of the TOM Complex. *J. Mol. Biol.*, **316**, 657–666.

84 Mokranjac, D., Paschen, S. A., Kozany, C., Prokisch, H., Hoppins, S. C., Nargang, F. E., Neupert, W. and Hell, K. (2003a) Tim50, a novel component of the TIM23 preprotein translocase of mitochondria. *EMBO J.*, **22**, 816–825.

85 Mokranjac, D., Sichting, M., Neupert, W. and Hell, K. (2003b) Tim14, a novel key component of the import motor of the TIM23 protein translocase of mitochondria. *EMBO J.*, **22**, 4945–4956.

86 Moro, F., Okamoto, K., Donzeau, M., Neupert, W. and Brunner, M. (2002) Mitochondrial protein import: molecular basis of the ATP-dependent interaction of MtHsp70 with Tim44. *J. Biol. Chem.*, **277**, 6874–6880.

87 Moro, F., Sirrenberg, C., Schneider, H. C., Neupert, W. and Brunner, M. (1999) The TIM17.23 preprotein translocase of mitochondria: composition and function in protein transport into the matrix. *EMBO J.*, **18**, 3667–3675.

88 Murakami, H., Pain, D. and Blobel, G. (1988) 70-kD heat shock-related protein is one of at least two distinct cytosolic factors stimulating protein import into mitochondria. *J. Cell. Biol.*, **107**, 2051–2057.

89 Nakai, M., Kato, Y., Ikeda, E., Toh-e, A. and Endo, T. (1994) Yge1p, a eukaryotic Grp-E homolog, is localized in the mitochondrial matrix and interacts with mitochondrial Hsp70. *Biochem. Biophys. Res. Commun.* **200**, 435–442.

90 Neupert, W. (1997) Protein import into mitochondria. *Annu. Rev. Biochem.*, **66**, 863–917.

91 Neupert, W. and Brunner, M. (2002) The protein import motor of mitochondria. *Nat. Rev. Mol. Cell Biol.*, **3**, 555–565.

92 Neupert, W., Hartl, F. U., Craig, E. A. and Pfanner, N. (1990) How do polypeptides cross the mitochondrial membranes? *Cell*, **63**, 447–450.

93 Oefner, C., D'Arcy, A. and Winkler, F. K. (1988) Crystal structure of human dihydrofolate reductase complexed with folate. *Eur. J. Biochem.*, **174**, 377–385.

94 Okamoto, K., Brinker, A., Paschen, S. A., Moarefi, I., Hayer-Hartl, M., Neupert, W. and Brunner, M. (2002) The protein import motor of mitochondria: a targeted molecular ratchet driving unfolding and translocation. *EMBO J.*, **21**, 3659–3671.

95 Ostermann, J., Horwich, A. L., Neupert, W. and Hartl, F. U. (1989) Protein folding in mitochondria requires complex formation with hsp60 and ATP hydrolysis. *Nature*, **341**, 125–130.

96 Ostermann, J., Voos, W., Kang, P. J., Craig, E. A., Neupert, W. and Pfanner, N. (1990) Precursor proteins in transit through mitochondrial contact sites interact with hsp70 in the matrix. *FEBS Lett.*, **277**, 281–284.

97 Pallotti, F. and Lenaz, G. (2001) Isolation and subfractionation of mitochondria from animal cells and tissue culture lines. *Methods Cell Biol.*, **65**, 1–35.

98 Paschen, S. A. and Neupert, W. (2001) Protein import into mitochondria. *IUBMB Life*, **52**, 101–112.

99 Paschen, S. A., Waizenegger, T., Stan, T., Preuss, M., Cyrklaff, M., Hell, K., Rapaport, D. and Neupert, W. (2003) Evolutionary conservation of biogenesis of beta-barrel membrane proteins. *Nature*, **426**, 862–866.

100 Pelham, H. R. B. and Jackson, R. J. (1976) An efficient mRNA-dependent translation system from reticulocyte lysates. *Eur. J. Biochem.*, **67**, 247–256.

101 Pfanner, N. and Chacinska, A. (2002) The mitochondrial import machinery: preprotein-conducting channels with binding sites for presequences. *Biochim. Biophys. Acta*, **1592**, 15.

102 Pfanner, N. and Geissler, A. (2001) Versatility of the mitochondrial protein import machinery. *Nat. Rev. Mol. Cell. Biol.*, **2**, 339–349.

103 Pfanner, N. and Meijer, M. (1995) Protein sorting. Pulling in the proteins. *Curr. Biol.*, **5**, 132–135.

104 Rapaport, D. (2002) Biogenesis of the mitochondrial TOM complex. *Trends Biochem. Sci.*, **27**, 191–197.

105 Rapaport, D., Kunkele, K. P., Dembowski, M., Ahting, U., Nargang, F. E., Neupert, W. and Lill, R. (1998) Dynamics of the TOM complex of mitochondria during binding and translocation of preproteins. *Mol. Cell. Biol.*, **18**, 5256–5262.

106 Rapaport, D., Neupert, W. and Lill, R. (1997) Mitochondrial protein import. Tom40 plays a major role in targeting and translocation of preproteins by forming a specific binding site for the presequence. *J. Biol. Chem.*, **272**, 18725–18731.

107 Rassow, J., Guiard, B., Wienhues, U., Herzog, V., Hartl, F. U. and Neupert, W. (1989) Translocation arrest by reversible folding of a precursor protein imported into mitochondria. A means to quantitate translocation contact sites. *J. Cell Biol.*, **109**, 1421–1428.

108 Rassow, J., Hartl, F. U., Guiard, B., Pfanner, N. and Neupert, W. (1990) Polypeptides traverse the mitochondrial envelope in an extended state. *FEBS Lett.*, **275**, 190–194.

109 Rassow, J., Maarse, A. C., Krainer, E., Kubrich, M., Muller, H., Meijer, M., Craig, E. A. and Pfanner, N. (1994) Mitochondrial protein import: biochemical and genetic evidence for interaction of matrix hsp70 and the inner membrane protein MIM44. *J. Cell Biol.*, **127**, 1547–1556.

110 Rassow, J., Mohrs, K., Koidl, S., Barthelmess, I. B., Pfanner, N. and Tropschug, M. (1995) Cyclophilin 20 is involved in mitochondrial protein folding in cooperation with molecular chaperones Hsp70 and Hsp60. *Mol. Cell. Biol.*, **15**, 2654–2662.

111 Rassow, J. and Pfanner, N. (2000) The protein import machinery of the mitochondrial membranes. *Traffic*, **1**, 457–464.

112 Rehling, P., Model, K., Brandner, K., Kovermann, P., Sickmann, A., Meyer, H. E., Kuhlbrandt, W., Wagner, R., Truscott, K. N. and Pfanner, N. (2003a) Protein insertion into the mitochondrial inner membrane by a twin-pore translocase. *Science*, **299**, 1747–1751.

113 Rehling, P., Pfanner, N. and Meisinger, C. (2003b) Insertion of hydrophobic membrane proteins into the inner mitochondrial membrane – a guided tour. *J. Mol. Biol.*, **326**, 639–657.

114 Robinson, C. and Bolhuis, A. (2001) Protein targeting by the twin-arginine translocation pathway. *Nat. Rev. Mol. Cell Biol.*, **2**, 350–356.

115 Rojo, E. E., Guiard, B., Neupert, W. and Stuart, R. A. (1998) Sorting of D-lactate dehydrogenase to the inner membrane of mitochondria. Analysis of topogenic signal and energetic requirements. *J. Biol. Chem.*, **273**, 8040–8047.

116 Rudiger, S., Buchberger, A. and Bukau, B. (1997a) Interaction of Hsp70 chaperones with substrates. *Nat. Struct. Biol.*, **4**, 342–349.

117 Rudiger, S., Germeroth, L., Schneider-Mergener, J. and Bukau, B. (1997b) Substrate specificity of the DnaK chaperone determined by screening cellulose-bound peptide libraries. *EMBO J.*, **16**, 1501–1507.

118 Ryan, K. R. and Jensen, R. E. (1993) Mas6p can be cross-linked to an arrested precursor and interacts with other proteins during mitochondrial protein import. *J. Biol. Chem.*, **268**, 23743–23746.

119 Ryan, K. R., Menold, M. M., Garrett, S. and Jensen, R. E. (1994) SMS1, a high-copy suppressor of the yeast mas6 mutant, encodes an essential inner membrane protein required for mitochondrial protein import. *Mol. Biol. Cell*, **5**, 529–538.

120 Schatz, G. (1997) Just follow the acid chain. *Nature*, **388**, 121–122.

121 Schatz, G. and Dobberstein, B. (1996) Common principles of protein

translocation across membranes. *Science*, **271**, 1519–1526.

122 Schmid, D., Baici, A., Gehring, H. and Christen, P. (1994) Kinetics of molecular chaperone action. *Science*, **263**, 971–973.

123 Schneider, H. C., Berthold, J., Bauer, M. F., Dietmeier, K., Guiard, B., Brunner, M. and Neupert, W. (1994) Mitochondrial Hsp70/MIM44 complex facilitates protein import. *Nature*, **371**, 768–774.

124 Schneider, H. C., Westermann, B., Neupert, W. and Brunner, M. (1996) The nucleotide exchange factor MGE exerts a key function in the ATP-dependent cycle of mt-Hsp70-Tim44 interaction driving mitochondrial protein import. *EMBO J.*, **15**, 5796–5803.

125 Schwartz, M. P., Huang, S. and Matouschek, A. (1999) The structure of precursor proteins during import into mitochondria. *J. Biol. Chem.*, **274**, 12759–12764.

126 Schwartz, M. P. and Matouschek, A. (1999) The dimensions of the protein import channels in the outer and inner mitochondrial membranes. *Proc. Natl. Acad. Sci. U.S.A.*, **96**, 13086–13090.

127 Simon, S. M., Peskin, C. S. and Oster, G. F. (1992) What drives the translocation of proteins? *Proc. Natl. Acad. Sci. USA*, **89**, 3770–3774.

128 Smith, D. A. and Radford, S. E. (2000) Protein folding: pulling back the frontiers. *Curr. Biol.*, **10**, R662–664.

129 Spudich, J. A. (1994) How molecular motors work. *Nature*, **372**, 515–518.

130 Spudich, J. A. (2001) The myosin swinging cross-bridge model. *Nat. Rev. Mol. Cell Biol.*, **2**, 387–392.

131 Stammers, D. K., Champness, J. N., Beddell, C. R., Dann, J. G., Eliopoulos, E., Geddes, A. J., Ogg, D. and North, A. C. (1987) The structure of mouse L1210 dihydrofolate reductase-drug complexes and the construction of a model of human enzyme. *FEBS Lett.*, **218**, 178–184.

132 Stan, T., Ahting, U., Dembowski, M., Kunkele, K. P., Nussberger, S., Neupert, W. and Rapaport, D. (2000) Recognition of preproteins by the isolated TOM complex of mitochondria. *EMBO J.*, **19**, 4895–4902.

133 Stan, T., Brix, J., Schneider-Mergener, J., Pfanner, N., Neupert, W. and Rapaport, D. (2003) Mitochondrial protein import: recognition of internal import signals of BCS1 by the TOM complex. *Mol. Cell. Biol.*, **23**, 2239–2250.

134 Strub, A., Rottgers, K. and Voos, W. (2002) The Hsp70 peptide-binding domain determines the interaction of the ATPase domain with Tim44 in mitochondria. *EMBO J.*, **21**, 2626–2635.

135 Touchette, N. A., Perry, K. M. and Matthews, C. R. (1986) Folding of dihydrofolate reductase from Escherichia coli. *Biochemistry*, **25**, 5445–5452.

136 Truscott, K. N., Brandner, K. and Pfanner, N. (2003a) Mechanisms of protein import into mitochondria. *Curr. Biol.*, **13**, R326–337.

137 Truscott, K. N., Kovermann, P., Geissler, A., Merlin, A., Meijer, M., Driessen, A. J., Rassow, J., Pfanner, N. and Wagner, R. (2001) A presequence- and voltage-sensitive channel of the mitochondrial preprotein translocase formed by Tim23. *Nat. Struct. Biol.*, **8**, 1074–1082.

138 Truscott, K. N., Voos, W., Frazier, A. E., Lind, M., Li, Y., Geissler, A., Dudek, J., Muller, H., Sickmann, A., Meyer, H. E., Meisinger, C., Guiard, B., Rehling, P. and Pfanner, N. (2003b) A J-protein is an essential subunit of the presequence translocase-associated protein import motor of mitochondria. *J. Cell Biol.*, **163**, 707–713.

139 Ungermann, C., Guiard, B., Neupert, W. and Cyr, D. M. (1996) The delta psi- and Hsp70/MIM44-dependent reaction cycle driving early steps of protein import into mitochondria. *EMBO J.*, **15**, 735–744.

140 Ungermann, C., Neupert, W. and Cyr, D. M. (1994) The role of Hsp70 in conferring unidirectionality on protein translocation into mitochondria. *Science*, **266**, 1250–1253.

141 Vestweber, D., Brunner, J., Baker, A. and Schatz, G. (1989) A 42K outer-membrane protein is a component of the yeast mitochondrial protein import site. *Nature*, **341**, 205–209.

142 Vestweber, D. and Schatz, G. (1988a) Mitochondria can import artificial precursor proteins containing a branched polypeptide chain or a carboxy-terminal stilbene disulfonate. *J. Cell Biol.*, **107**, 2045–2049.

143 Vestweber, D. and Schatz, G. (1988b) Point mutations destabilizing a precursor protein enhance its post-translational import into mitochondria. *EMBO J.*, **7**, 1147–1151.

144 Vestweber, D. and Schatz, G. (1989) DNA-protein conjugates can enter mitochondria via the protein import pathway. *Nature*, **338**, 170–172.

145 Voisine, C., Craig, E. A., Zufall, N., von Ahsen, O., Pfanner, N. and Voos, W. (1999) The protein import motor of mitochondria: Unfolding and trapping of preproteins are distinct and separable functions of matrix Hsp70. *Cell*, **97**, 565–574.

146 Von Heijne, G. (1986) Mitochondrial targeting sequences may form amphiphilic helices. *EMBO J.*, **5**, 1335–1342.

147 Voos, W., Gambill, B. D., Guiard, B., Pfanner, N. and Craig, E. A. (1993) Presequence and mature part of preproteins strongly influence the dependence of mitochondrial protein import on heat shock protein 70 in the matrix. *J. Cell Biol.*, **123**, 119–126.

148 Voos, W. and Rottgers, K. (2002) Molecular chaperones as essential mediators of mitochondrial biogenesis. *Biochim. Biophys. Acta*, **1592**, 51.

149 Voos, W., von Ahsen, O., Muller, H., Guiard, B., Rassow, J. and Pfanner, N. (1996) Differential requirement for the mitochondrial Hsp70-Tim44 complex in unfolding and translocation of preproteins. *EMBO J.*, **15**, 2668–2677.

150 Werner, S. and Neupert, W. (1972) Functional and biogenetical heterogeneity of the inner membrane of rat-liver mitochondria. *Eur. J. Biochem.*, **25**, 379–396.

151 Westermann, B., Prip-Buus, C., Neupert, W. and Schwarz, E. (1995) The role of the GrpE homologue, Mge1p, in mediating protein import and protein folding in mitochondria. *EMBO J.*, **14**, 3452–3460.

152 Wiedemann, N., Kozjak, V., Chacinska, A., Schonfisch, B., Rospert, S., Ryan, M. T., Pfanner, N. and Meisinger, C. (2003) Machinery for protein sorting and assembly in the mitochondrial outer membrane. *Nature*, **424**, 565–571.

153 Wiedemann, N., Pfanner, N. and Ryan, M. T. (2001) The three modules of ADP/ATP carrier cooperate in receptor recruitment and translocation into mitochondria. *EMBO J.*, **20**, 951–960.

154 Wienhues, U., Becker, K., Schleyer, M., Guiard, B., Tropschug, M., Horwich, A. L., Pfanner, N. and Neupert, W. (1991) Protein folding causes an arrest of preprotein translocation into mitochondria in vivo. *J. Cell Biol.*, **115**, 1601–1609.

155 Wienhues, U., Koll, H., Becker, K., Guiard, B. and Hartl, F.-U. (1992) Protein targeting to mitochondria. In *A Practical Approach to Protein Targeting*. IRL (Oxford University Press), pp. 135–159.

156 Xia, Z. X. and Mathews, F. S. (1990) Molecular structure of flavocytochrome b2 at 2.4 A resolution. *J. Mol. Biol.*, **212**, 837–863.

157 Yamamoto, H., Esaki, M., Kanamori, T., Tamura, Y., Nishikawa, S. and Endo, T. (2002) Tim50 is a subunit of the TIM23 complex that links protein translocation across the outer and inner mitochondrial membranes. *Cell*, **111**, 519–528.

158 Young, J. C., Hoogenraad, N. J. and Hartl, F. U. (2003) Molecular chaperones Hsp90 and Hsp70 deliver preproteins to the mitochondrial import receptor Tom70. *Cell*, **112**, 41–50.

159 Zhuang, X., Ha, T., Kim, H. D., Centner, T., Labeit, S. and Chu, S. (2000) Fluorescence quenching: A tool for single-molecule protein-folding study. *Proc. Natl. Acad. Sci. USA*, **97**, 14241–14244.

31
The Chaperone System of Mitochondria

Wolfgang Voos and Nikolaus Pfanner

31.1
Introduction

Mitochondrial protein biogenesis comprises a complex set of reactions starting with the import of cytosolically synthesized preproteins, followed by folding and assembly processes to acquire a functional conformation, and ending with proteolysis to remove unwanted proteins and to reutilize their amino acids. All steps require specific proteinaceous machineries that assist the progress of the respective substrate proteins along this pathway and prevent irregular side reactions. Based on the endosymbiotic origin of the organelle, mitochondria utilize in part mechanisms that are similar to bacterial organisms. However, their intracellular localization requires the evolution of organelle-specific processes that are distinct from their bacterial ancestors and also different from the reaction pathways in the eukaryotic cytosol. Due to the limited capacity to produce endogenous proteins, mitochondria face specific problems in importing proteins that were synthesized in the cytosol and in the coordination of mitochondrial and cytosolic protein expression. For these reasons, mitochondria contain a complex system of chaperone proteins that are involved in practically all steps of protein biogenesis. During many processes a closely coordinated function of chaperone proteins from different subclasses and with different functional specificities has been observed, resulting in the description of the chaperone system as an essential functional network [1]. Most chaperone proteins also require interaction with specific partner proteins that have no genuine chaperone function on their own but are required for the regulation of activity and functional specificity of their corresponding chaperone partners (Table 31.1). The specific roles of the mitochondrial chaperone proteins and their co-chaperones are discussed in this chapter.

31.2
Membrane Translocation and the Hsp70 Import Motor

Most mitochondrial polypeptides are synthesized by cytosolic ribosomes as precursor proteins and transported posttranslationally to their final location. Correct pro-

Protein Folding Handbook. Part II. Edited by J. Buchner and T. Kiefhaber

ISBN: 3-527-30784-2

Tab. 31.1. Mitochondrial chaperones and partner proteins in *S. cerevisiae*.

Chaperone	*Protein*	*Function*	*Partner proteins*
Hsp70	mtHsp70/Ssc1	Preprotein import, protein folding, stress protection	Tim44, Mdj1, Pam18, Mge1
	Ssq1	Protein complex assembly, Fe/S cluster biogenesis	Jac1, Mge1
	Ssc3 (Ecm10)	Unknown	Mge1
Co-chaperone (DnaJ type)	Mdj1	Protein folding, regulation of mtHsp70 activity, mitochondrial DNA replication	Ssc1
	Mdj2	Unknown	
	Jac1	Protein assembly, Fe/S cluster biogenesis	Ssq1
	Pam16	Preprotein import, Ssc1-Tim44 interaction	Ssc1
	Pam18	Preprotein import, stimulation of mtHsp70 activity	Ssc1
Co-chaperone	Tim44	Preprotein import, membrane anchor for mtHsp70	Ssc1, Tim23, Tim17
Co-chaperone (GrpE type)	Mge1	Nucleotide-exchange factor for mtHsp70	Ssc1, Ssq1, Ssc3
Hsp60	Hsp60	Protein folding	Hsp10
	Hsp10	Regulation of Hsp60 activity	Hsp60
Cyclophilin	Cpr3	Protein folding, peptidyl-prolyl isomerization	
Hsp100/Clp	Hsp78	Protection against aggregation, protein degradation	Ssc1, Pim1
	Mcx1	Unknown	
Proteases with putative chaperone activity	Pim1	ATP-dependent proteolysis of soluble proteins in the matrix	Hsp78
	Yme1	Proteolysis of inner-membrane proteins, assembly of respiratory chain complexes	
	Yta12/Yta10	Proteolysis of inner-membrane proteins	

tein localization is ensured by specific targeting sequences contained within the proteins that are recognized by dedicated receptor proteins in the outer mitochondrial membrane. Two general types of targeting sequences have been identified. Proteins destined for the mitochondrial matrix as well as some inner-membrane proteins contain amino-terminal extensions (presequences) that are removed after import by specific processing peptidases [2]. Polytopic membrane proteins of the

inner membrane contain non-cleavable internal targeting sequences that enable an insertion into the inner membrane. The transport of the polypeptide chain is in both cases initiated by the insertion of the precursor protein into the outer and inner membranes. These steps are performed with the help of specialized membrane-integrated translocase complexes, which form pore structures in the membrane [3, 4]. In addition, many accessory proteins of the translocase complexes have significant roles in enhancing translocation activity. Interestingly, the dimensions of the pore structures with a diameter of 1.2–2 nm limit the possible conformations a precursor protein can adopt during the translocation process, as only unfolded or at most α-helical structures can be accommodated [5, 6]. Derived from these structural prerequisites, two aspects of the import process require the input of exogenous energy for efficient polypeptide transport. First, energy is required for the vectorial movement of the polypeptide chain through the translocation channels. Second, the unfolding of the preprotein polypeptide required for the passage through the pore structures in the membranes has to be coupled to energy consumption. The strong correlation between precursor folding state and energy consumption in preprotein translocation suggests that chaperone proteins are involved in several steps of the import reaction.

While chaperone proteins may interact with newly synthesized preproteins early in the targeting process, the initial insertion of preproteins into the outer membrane does not require an involvement of mitochondrial chaperone proteins. The participation of cytosolic chaperones in the translocation process is described in chapter 30. The insertion of the amino-terminal presequences into the inner membrane is driven via an electrophoretic mechanism by the membrane potential ($\Delta\psi$) generated by the respiratory chain, as amino-terminal targeting signals have an overall net positive charge [7]. Full translocation of the polypeptide chain into the mitochondrial matrix, however, does require an additional energy source. The mitochondrial Hsp70 (mtHsp70), in *Saccharomyces cerevisiae* encoded by the gene *SSC1*, is localized in the matrix compartment and utilizes the hydrolysis of ATP to drive completion of preprotein transport [8]. As mtHsp70 is the only ATPase implicated in the protein import process to date, it is a key component of the import pathway. The energy generated by ATP hydrolysis is utilized in two separate processes: the vectorial movement of the polypeptide chain through the translocation pores and unfolding of carboxy-terminal domains of preproteins on the outer side of the mitochondrial membranes [9–11]. After mtHsp70-driven translocation, preproteins are processed to their mature forms by the matrix-processing peptidase and are folded and assembled. All matrix proteins analyzed so far are dependent on mtHsp70 for translocation through the membranes. Membrane proteins can usually insert into the inner membrane independent of matrix ATP and mtHsp70 [12], but some inner-membrane proteins, primarily those that expose bulky domains on the matrix face of the inner membrane, do require involvement of mtHsp70 [13].

During the import process, mtHsp70 cooperates with two additional proteins, Mge1 and Tim44 (Figure 31.1). These proteins have been shown to form a stable protein complex that is sensitive to the presence of ATP [14]. Since the complex is

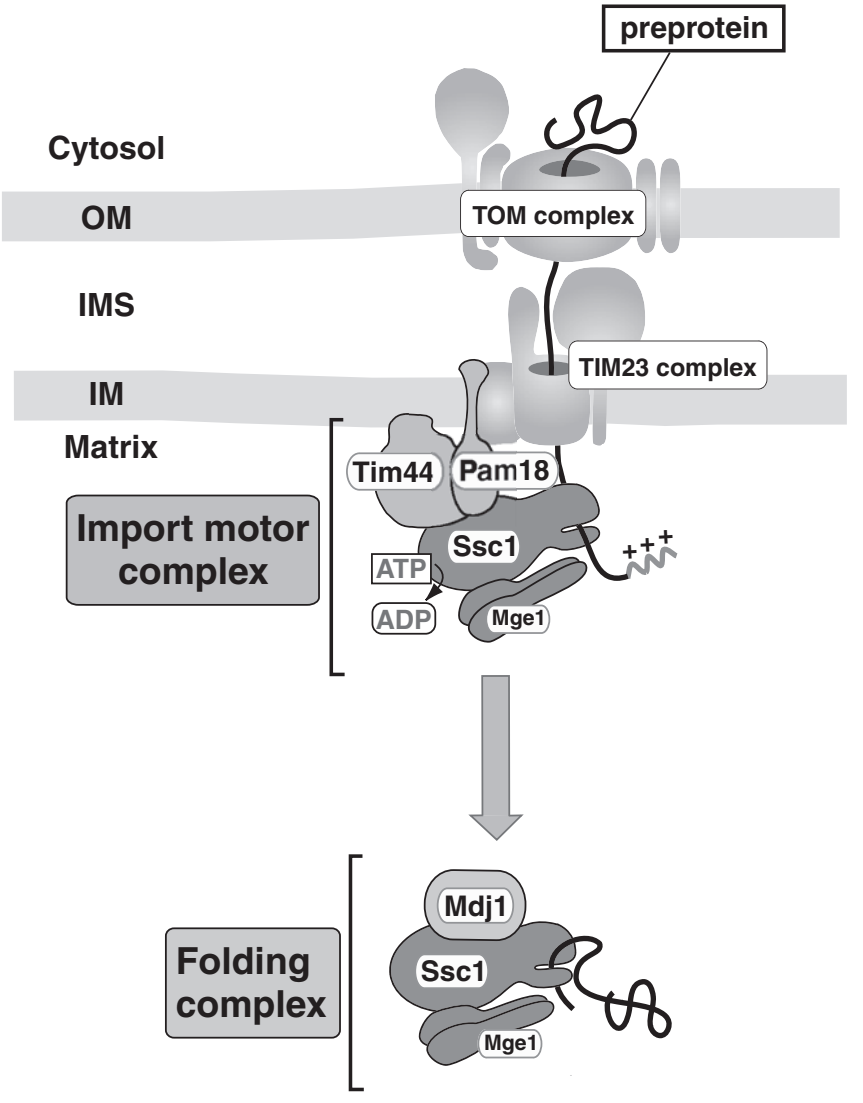

Fig. 31.1. The role of mtHsp70 (Ssc1) and its specific partner proteins during protein import and folding in the mitochondrial matrix. ATP-dependent translocation of the incoming polypeptide chain through the mitochondrial membranes (OM, outer membrane; IMS, intermembrane space; IM, inner membrane) into the matrix is driven by the import motor complex composed of mtHsp70 (Ssc1) as the core component, the nucleotide-exchange factor Mge1, the membrane anchor Tim44, and the DnaJ-type protein Pam18. The pore structures for preprotein import are provided by the TOM (translocase of the outer membrane) and TIM23 (presequence translocase of the inner membrane) complexes. After completion of polypeptide transport, the amino-terminal presequence is cleaved off and folding reactions are carried out with the assistance of the folding complex composed of mtHsp70 (Ssc1), Mge1, and the mitochondrial DnaJ homologue Mdj1.

in a close local and functional proximity to the inner-membrane translocase complex, the functional unit of mtHsp70, Mge1, and Tim44 has been dubbed import motor complex [15]. MtHsp70, Mge1, and Tim44 are essential proteins in yeast, with null mutations leading to lethal phenotypes. This observation enhances the significance of the import motor components for the overall import process, as the only other proteins of the matrix translocation pathway encoded by essential genes are the core components of the membrane translocase complexes, Tom40 and Tim23/17. The protein Mge1, a member of the bacterial GrpE protein family, acts as a nucleotide-exchange factor for mitochondrial Hsp70s [16, 17]. Mge1 favors the release of hydrolyzed ADP at the end of the Hsp70 reaction cycle and facilitates binding of a new ATP molecule, enhancing the ATPase activity of mtHsp70 significantly. Thus, Mge1 is a key regulator of the ATP-dependent import reaction cycle of mtHsp70. It not only enhances the activity of mtHsp70 but also regulates the interaction with protein substrates and the membrane anchor Tim44 [18]. To further illustrate the importance of Mge1, it has been shown that the protein, via its interaction with mtHsp70, associates with preproteins in transit but not with preproteins that have been completely translocated [19]. The essential role of Mge1 is certainly represented by its assistance in preprotein translocation; however, Mge1 is also involved in protein-folding reactions that occur subsequent to the transport into the matrix [20].

For efficient import of matrix-targeted proteins, the soluble chaperone machinery has to coordinate its activity closely with the inner-membrane translocase. MtHsp70 and the membrane protein Tim44 tightly interact in a nucleotide-regulated manner, essentially tethering a portion of the soluble mtHsp70 pool to the inner membrane [21–23]. Tim44 is also peripherally associated with the inner-membrane translocase, and via the interaction with Tim44, mtHsp70 is brought into the direct vicinity of the import pore. Several studies have established the importance of the Tim44/mtHsp70 interaction for the overall translocation process. It has been shown that mtHsp70 is found bound to imported polypeptides in the absence of functional Tim44 but that efficient translocation requires the reversible binding of mtHsp70 to Tim44 [11, 24]. MtHsp70 must interact with Tim44 for efficient preprotein translocation since a deletion of a potential mtHsp70 interaction site in Tim44 resulted in a strong translocation defect in vitro and a lethal phenotype in vivo [25].

Several models have been proposed to explain the function of mtHsp70 during the preprotein import. One model is based on the tight interaction of mtHsp70 with translocating unfolded preprotein polypeptide chains [26]. The interaction of mtHsp70 with the preprotein would trap the membrane-spanning preprotein in the translocation pore and prevent backward movement of the polypeptide chain. Any forward movement, generated by random Brownian motion, would expose further binding sites for additional mtHsp70s. Several repetitions of this binding cycle would result in the complete translocation of the preprotein. By influencing the affinity of mtHsp70 to the preprotein, the hydrolysis of ATP would lock the preprotein bound to the peptide-binding domain of mtHsp70, while the release of ADP and rebinding of ATP would destabilize the substrate interaction, resulting

in the dissociation of the bound preprotein. This model describes the action of mtHsp70 essentially as a passive "ratchet" that traps preprotein segments in the matrix [24, 27, 28]. The interaction of mtHsp70 with Tim44 serves in this model essentially to increase the local concentration of mtHsp70 at the import site. A passive mechanism of mtHsp70 as a "Brownian ratchet" for the translocation of preprotein chains has been supported by several studies. However, a significant translocation activity in an mtHsp70 mutant that is restricted to a ratchet mechanism could be observed only with preproteins that either were completely unfolded, e.g., after denaturation by urea, or that had a low overall thermodynamic stability [8, 11]. Another study has shown that mitochondria were able to import preprotein constructs containing Hsp70 binding sites separated by large patches of nonbinding residues. Again, the import efficiencies of stably folded C-terminal domains were significantly reduced [29].

Several experimental observations indicate that mtHsp70 may perform a more active role during the translocation of precursor proteins. For preproteins with stably folded domains, binding to mtHsp70 alone was not sufficient to effectively drive preprotein import into the matrix [30, 31]. By detailed analysis of preprotein import kinetics, it was determined that the rates of preprotein translocation are faster than the rate of spontaneous unfolding of preproteins [32, 33]. A prerequisite for active unfolding by the translocation machinery is an efficient interaction with the mtHsp70 motor complex. Especially the import of preproteins with short N-terminal extensions that do not expose sufficient Hsp70 binding sites in the matrix becomes susceptible to mutations in the motor complex components [33, 34]. It was also observed that the import process, proceeding in an N-to-C-terminal direction, can significantly alter the unfolding pathway of a preprotein [35]. These experiments led to the conclusion that mtHsp70 performs an active role in preprotein transport. It was suggested that the unfolding of preproteins was achieved by mtHsp70 by generating an inward-directed translocation force on the polypeptide chain. The force exerted on the preprotein in transit might be small but may be sufficient to lower the activation energy necessary to unfold preprotein domains on the outer face of the outer membrane [36]. Interestingly, by this "pulling" on the polypeptide chain, the energy of ATP hydrolysis in the matrix can be utilized to catalyze the required unfolding of protein domains on the outer face of the mitochondrial membrane system. In this model, termed the "active motor" mechanism, interaction of mtHsp70 with Tim44 would serve as an anchor point to produce the necessary leverage for a force generation [37–39]. In support of this model analysis of mitochondria carrying a conditional mutant of Tim44 showed defects mainly in the import of preproteins containing stably folded domains [40]. Taken together, these results suggest that the ATP hydrolysis cycle induces a conformational change in mtHsp70, resulting in the "pulling" of preproteins into the matrix. As there is evidence in support of both models, it is likely that protein translocation in vivo is driven by a combination of the pulling and trapping mechanisms.

However, direct evidence for a force generation by an mtHsp70 power stroke is still lacking. Recent experiments to reconstitute the import motor with purified

components consisting of mtHsp70, Tim44, and Mge1 in vitro failed to reproduce a crucial prerequisite for the "active motor" mechanism, the formation of a ternary complex among mtHsp70, substrate proteins, and Tim44 [41]. However, it is possible that the mitochondrial import motor might be more complex than previously noted, as recently two new essential components of the translocation machinery have been identified. The small, membrane-embedded protein Pam18 (presequence translocase associated motor subunit of 18 kDa) was found in association with the inner-membrane translocase TIM23 [42, 43]. Pam18 (also named Tim14) contains a so-called J-domain that is found in Hsp70 co-chaperones of the DnaJ-family. The J-domain is exposed to the matrix, indicating a functional relationship with mtHsp70 during the import reaction. Indeed, Pam18 was shown to activate the ATPase activity of mtHsp70 substantially and is required for the mtHsp70-dependent import of preproteins into the matrix [42, 44]. Interestingly, Pam18 forms a complex with the second new essential translocation component, Pam16 [45, 46]. Similar to Pam18, Pam16 (or Tim16) is a small, membrane-bound protein with some similarity to J-domain-containing proteins. Pam16 is required for the preprotein translocation into the matrix, although it cannot activate the ATPase activity of mtHsp70. It becomes evident that both proteins potentially form a functional interface between the polypeptide pore in the inner membrane and the mtHsp70-dependent translocation motor complex. Despite the progress made in the biochemical characterization of the mitochondrial translocation reaction, the molecular mechanism of mtHsp70 during import is still only partially understood. Future studies need to integrate the novel components into the mtHsp70 translocation-specific reaction cycle.

31.3
Folding of Newly Imported Proteins Catalyzed by the Hsp70 and Hsp60 Systems

Mitochondrial preproteins must cross the membranes as an unfolded polypeptide chain. As a result, the acquisition of the native protein conformation must occur in the matrix of mitochondria following completion of the translocation reaction. Since the matrix chaperone mtHsp70 is crucial to the preprotein translocation reaction, the interaction of preproteins with the mtHsp70 system represents the first step of the protein-folding pathway in the matrix [47]. Folding of imported proteins therefore follows the "classical" order of chaperone-catalyzed folding reactions [48]. First, interaction of preproteins with the Hsp70 system stabilizes and protects unfolded substrate proteins, while the acquisition of the native conformation is mainly assisted by the Hsp60 chaperonin system (Figure 31.2). In that respect, the folding process in the mitochondrial matrix shares similar features with other organellar systems [49], including folding of newly synthesized proteins at the ribosome [50] and protein folding in the bacterial cytosol [51].

Interestingly, the dual function of mtHsp70 in protein translocation and folding in mitochondria is reflected in its differential interaction with specific partner proteins (Figure 31.1). As stated above, interaction of mtHsp70 with the inner-

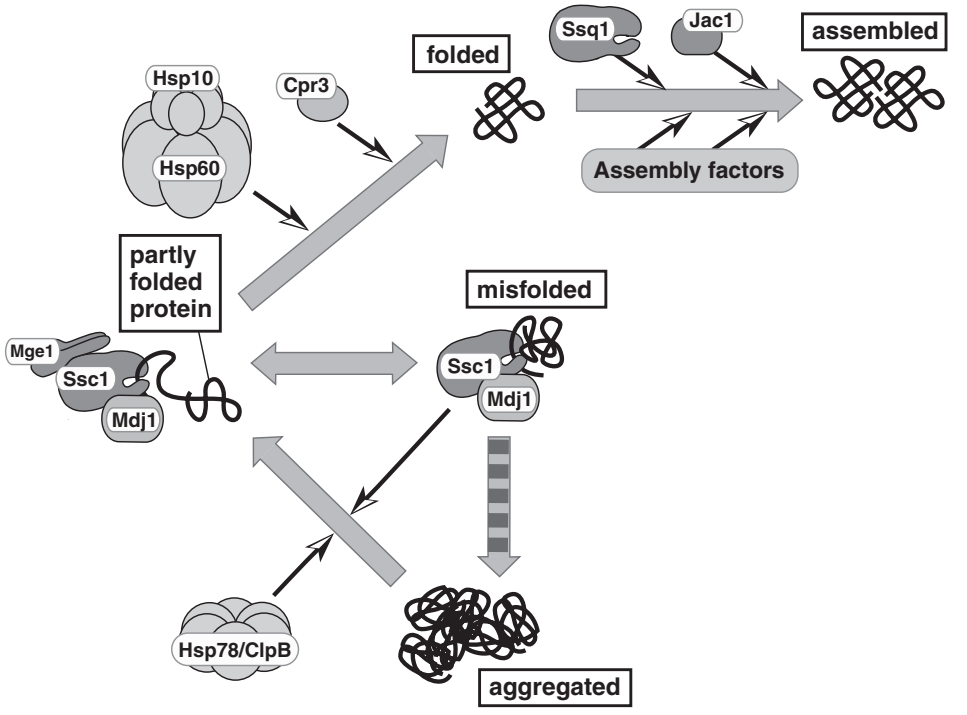

Fig. 31.2. The mitochondrial chaperone network employed for protein folding and complex assembly. Protein folding in the mitochondrial matrix is assisted by the mtHsp70 system and the Hsp60/Hsp10 chaperonin complex in the matrix. Cpr3 is a peptidyl-prolyl isomerase that accelerates folding by the *cis/trans* isomerization of prolyl bonds. Further maturation reactions and the assembly of macromolecular protein complexes are catalyzed by the Hsp70 family member Ssq1 with its DnaJ-type co-chaperone Jac1 and other numerous assembly factors (see text). Denatured and/or misfolded proteins are stabilized mainly by the mtHsp70 system. Aggregated proteins can be resolubilized and renatured by a concerted action of the mitochondrial ClpB homologue Hsp78 and the mtHsp70 system.

membrane protein Tim44 is required for the translocation function, but during protein folding mtHsp70 forms a complex with the co-chaperone Mdj1 [47]. Mdj1 is the mitochondrial homologue of the bacterial DnaJ protein [52]. Members of this diverse protein family are generally involved in protein-folding reactions by assisting substrate binding by the corresponding Hsp70s and activation of their ATPase activity [53]. Mutations in Mdj1 do not result in defects in protein translocation but reduce or abolish folding of newly imported proteins [54]. The role of Mdj1 and mtHsp70 in protein folding reactions could be demonstrated directly in in vitro experiments [55]. It is assumed that the mechanism of Mdj1 during protein-folding reactions closely resembles the action of its bacterial relative DnaJ [56]. A dysfunction of Mdj1 has direct or indirect deleterious consequences on

many mitochondrial functions that result in a respiratory defect of the respective mutations [57].

In recent years, other mitochondrial members of the mitochondrial DnaJ protein family have been identified, although information about their functional role is still scarce. Of all mitochondrial proteins containing homology to the bacterial DnaJ, only the above-mentioned Pam18 is essential for cellular viability. Its essential role is most probably related to the translocation function in the import motor during preprotein import. Another integral membrane protein of the inner membrane, termed Mdj2, exposes a J-homology domain to the matrix compartment. However, a deletion mutant in yeast did not show any phenotype. As a result, no specific function could be attributed to Mdj2 [58]. A small soluble protein, Jac1, also contains a J-homology domain. A mutation of *JAC1* has strong negative effects on growth on both fermentable and non-fermentable carbon sources, indicating an involvement in a prominent metabolic function of mitochondria. Recent data showed that Jac1 is involved in the formation of Fe/S clusters, required for the function of several mitochondrial and cytosolic enzymes [59–61]. In this role, Jac1 cooperates with a second member of the mitochondrial Hsp70 family, termed Ssq1 in yeast [62, 63]. Under normal conditions, Ssq1 is far less abundant than the major mitochondrial Hsp70 Ssc1. In contrast to Ssc1 null mutations, a deletion mutant of *SSQ1* is viable but shows a cold-sensitive phenotype. Ssq1 seems to be able to perform standard chaperone functions and is also regulated in its activity by the nucleotide-exchange factor Mge1 [64]. Despite many similarities between the two mitochondrial Hsp70 systems, Ssq1 with its co-chaperone Jac1 cannot substitute for the functions of Ssc1 in protein translocation and folding reactions even upon overexpression of the protein. The main reason for this inability seems to be the lack of interaction of Ssq1 with the typical co-chaperones of Ssc1: Tim44 for preprotein translocation reaction or Mdj1 for protein-folding events in the matrix. Ssq1 seems to play a more specialized role during the assembly reaction of Fe/S clusters, but its mechanistic role in that process remains to be clarified.

While the mtHsp70 system is the first to interact with imported preproteins, the main chaperone involved in protein folding in the matrix is certainly the mitochondrial Hsp60. Preproteins have been shown to follow a well-defined pathway of chaperone interactions in the mitochondrial matrix [65, 66]. Hsp70 is generally regarded as a stabilizing component, preventing irregular interactions of unfolded preproteins while the actual folding is catalyzed by the oligomeric Hsp60 protein complex. The important role of Hsp60 in mitochondrial protein biogenesis was identified before that of Hsp70 by the analysis of mutant Hsp60 yeast strains. Mutants in Hsp60 showed strong defects in the mitochondrial metabolism due to the importance of Hsp60 for protein biogenesis [67, 68]. A deletion of Hsp60 in yeast is lethal, also emphasizing the importance of this component for mitochondrial and, indirectly, cellular metabolism. It has been shown that proteins imported in vivo physically interact with Hsp60 after their import is completed [69]. Mitochondria with defective Hsp60 are able to import preproteins, but imported proteins do not fold to their native conformation and likely end up as insoluble aggregates. The molecular mechanism of the mitochondrial Hsp60 is similar to the well-studied

bacterial homologue, GroEL [70]. Hsp60 forms a homo-oligomeric protein complex with a large central cavity. Nonnative proteins up to a certain size threshold are able to enter this cavity and to interact with hydrophobic residues at the inner face of the cavity wall. As in the bacterial system, the cavity can be closed by an interaction with a second essential component, the mitochondrial Hsp10 [71]. Hsp10 is a homologue of the bacterial GroES and forms as a homoheptameric complex, which serves as a lid to block the entrance of the Hsp60 ring complex. Since Hsp60 and Hsp10 form a functional unit, deletion of Hsp10 in yeast is also lethal [72]. Its involvement in protein folding has been primarily analyzed through the use of temperature-sensitive mutants. Hsp10 has been shown to be involved not only in the folding of many soluble imported proteins but also in the sorting of precursor proteins destined for the inner mitochondrial membrane [73]. The Hsp60-Hsp10 complex thereby provides a protected environment where the spontaneous folding processes of the substrate protein can occur without the ability to interact with other proteins. Activity of Hsp60 is strictly regulated by an ATP-dependent reaction cycle. Binding of ATP induces a conformational change in the Hsp60 complex, which results in substrate release from the cavity wall, allowing the substrate to undergo folding reactions. After a certain time, determined by the velocity of ATP hydrolysis, the substrate protein is discharged from the Hsp60 cavity. It has been shown that apart from Hsp10's structural role in the interaction with Hsp60, it also has a regulatory effect on the ATPase activity of the Hsp60 complex [74].

Despite general similarities between the bacterial GroEL system and the mitochondrial Hsp60, there is one major structural difference between the two chaperones. The mitochondrial Hsp60 functions as a single heptameric ring complex, while GroEL forms a double-ring system where both rings are functionally interconnected. The single-ring system of mitochondrial Hsp60 seems to be fully competent in protein folding [75] and can substitute for the function of GroEL in bacteria [76]. Similar to the bacterial homologue, Hsp60 is not absolutely required for the folding of all imported proteins, as the analysis of the folding process of several substrate proteins with different biochemical properties revealed [77]. Dependence on Hsp60 during the folding process is largely determined by the specific folding characteristics of the individual proteins. An elegant assay using the complete set of mitochondrial precursor proteins generated by in vitro translation of isolated cellular mRNA revealed the general substrate specificity range of Hsp60 [78]. It is interesting to note that even substrate proteins that interact with the Hsp60 complex may vary in the requirement for the co-chaperone Hsp10 for folding. This indicates that the interaction of Hsp10 with Hsp60 is not strictly required for catalyzing successful protein folding. Although not every imported preprotein depends on Hsp60 for folding, the lethal phenotype of the *hsp60* null mutation indicates that at least some important mitochondrial proteins are strictly dependent on Hsp60. An alternate hypothesis would be that a deactivation of folding catalysis in general would generate significant damage to the mitochondrial functions to be incompatible with cellular survival.

The prevention of unproductive side reactions through the stabilization of non-

native folding intermediates is the typical function of molecular chaperones such as Hsp70 and Hsp60. In mitochondria, however, protein folding in the matrix is facilitated by a second mechanism. The peptidyl-prolyl isomerase cyclophilin accelerates a rate-limiting step of protein folding and has been shown to increase the folding rate of imported preproteins [79, 80]. In mitochondria lacking cyclophilin, encoded by the gene *CPR3* in yeast, the folding of a DHFR fusion protein was delayed although not completely abolished. Similar observations were made with wild-type mitochondria that were treated with a specific inhibitor of cyclophilin, cyclosporin A. The fact that cyclophilin is not absolutely required for protein folding correlates well with its proposed rate-enhancing role. As a result of the complementary role of cyclophilin in enhancing the rate of protein folding with the stabilizing role of chaperone machineries in the mitochondrial matrix, it is no surprise that a close functional cooperation has been observed between the two machineries. Chaperones can partially substitute for the function of cyclophilin by binding and stabilizing the incompletely folded substrate protein, while cyclophilin enhances the acquisition of a native conformation and as a result decreases the amount of chaperone-bound substrate proteins.

31.4
Mitochondrial Protein Synthesis and the Assembly Problem

Mitochondria synthesize a small subset of about a dozen proteins by their endogenous protein-synthesis machinery. Most of the mitochondrially encoded proteins are very hydrophobic in nature and are integral membrane proteins of the inner membrane. These proteins are subunits either of respiratory chain complexes or of the membrane-integrated F_o-ATPase complex. The hydrophobicity of these components is the likely reason for the evolutionary retention of a mitochondrial protein-synthesis capability. Despite the synthesis in the mitochondrial matrix, mechanisms have to be employed to prevent aggregation of the nascent hydrophobic polypeptides and to ensure their functional assembly into the inner-membrane complexes. As the primary role of chaperone proteins is the prevention of protein aggregation, it is not surprising that the mtHsp70 chaperone system is involved in the stabilization of the mitochondrially encoded proteins [81]. As with the folding catalysis of soluble proteins, mtHsp70 closely cooperates with its partner protein Mdj1 in the assembly reaction of mitochondrially encoded proteins [82]. Similar to its counterpart in the cytosol, it is thought that the mtHsp70 system can interact with nascent polypeptide chains as they emerge from mitochondrial ribosomes. This interaction stabilizes the polypeptide chain during synthesis until they fold to their native conformation or assemble into the respective protein complexes.

The large size and complex protein composition of the respiratory chain enzymes in the inner mitochondrial membrane not only require coordinated protein synthesis of nuclear and mitochondrially encoded subunits but also pose significant challenges for the assembly of these complexes. As a result, it is not surprising that several proteins have been identified that are required for the enzymatic

function of the inner-membrane complexes but are not components of the functional oligomers. Based on this observation they have been described as assembly factors, but to date their functional role in the assembly reaction is unclear. For example, the assembly factors Atp11 and Atp12 are required for the function of the F_1F_o-ATPase [83, 84], while the cytochrome bc_1 complex requires the factor Bcs1 for assembly. The cytochrome *c*–oxidase (COX) complex is formed with the help of a different set of specific factors [85–87]. Interestingly, Tcm62, a mitochondrial membrane protein with a small but significant homology to Hsp60, has been identified and has been shown to be required for the functional assembly of the succinate dehydrogenase (SDH) complex [88]. It is uncertain whether these assembly factors can be designated as genuine ''molecular chaperones'' since their function seems to be restricted to a single function and seems to be specific for the assembly of a defined set of inner membrane components.

Biogenesis of the mitochondrial respiratory chain complexes requires a close coordination of mitochondrial and cytosolic protein synthesis since components encoded in both cellular compartments must be assembled into the same oligomeric structures. The presence of excess subunits from either source would present the danger of irregular aggregation reactions and eventual mitochondrial damage. A set of proteins has been described in mitochondria that combines both chaperone and protease functions in one polypeptide to prevent damage by the accumulation of unassembled subunits. Two of these proteins, Rca1 (Yta12) and Afg3 (Yta10), were found by the analysis of mutants that show defects in mitochondrial respiration [89, 90]. Mutations of Rca1 or Afg3 cause defects in the assembly of functional inner-membrane protein complexes such as the F_1F_o-ATPase [91]. A third protein, Yme1, was initially shown to be required for maintenance of mitochondrial DNA [92] and was later shown to have protease properties [93].

All three proteins have ATPase activity and belong to the widespread family of AAA proteins (ATPases associated with various cellular activities) that are involved in diverse cellular processes such as vesicular transport, organelle biogenesis, microtubule rearrangement, and protein degradation. The AAA proteases have a metal-dependent peptidase activity and mediate the degradation of non-assembled membrane proteins. Rca1 and Afg3 form a hetero-oligomeric protein complex, named the m-AAA protease, that is located in the inner mitochondrial membrane with its proteolytic sites exposed to the matrix [94]. In contrast, the active site of the homo-oligomeric complex formed by Yme1 faces the intermembrane space but is also inserted into the inner membrane. The Yme1 complex has therefore been termed i-AAA protease [95]. It has been shown that Yme1 is able to sense the folding state of protein domains exposed to the intermembrane space and to specifically degrade unfolded membrane proteins [96]. The affinity of Yme1 for unfolded polypeptides closely resembles the activity of molecular chaperones. The purified AAA domain of Yme1 was shown to bind unfolded polypeptides and to suppress their aggregation, which are features typical for chaperone proteins. Yme1 displays a modular structure with a separate proteolytic domain and a chaperone-like ATPase domain. Although the molecular mechanism of Yme1 function has not been determined in detail, it is hypothesized that the ATPase domain

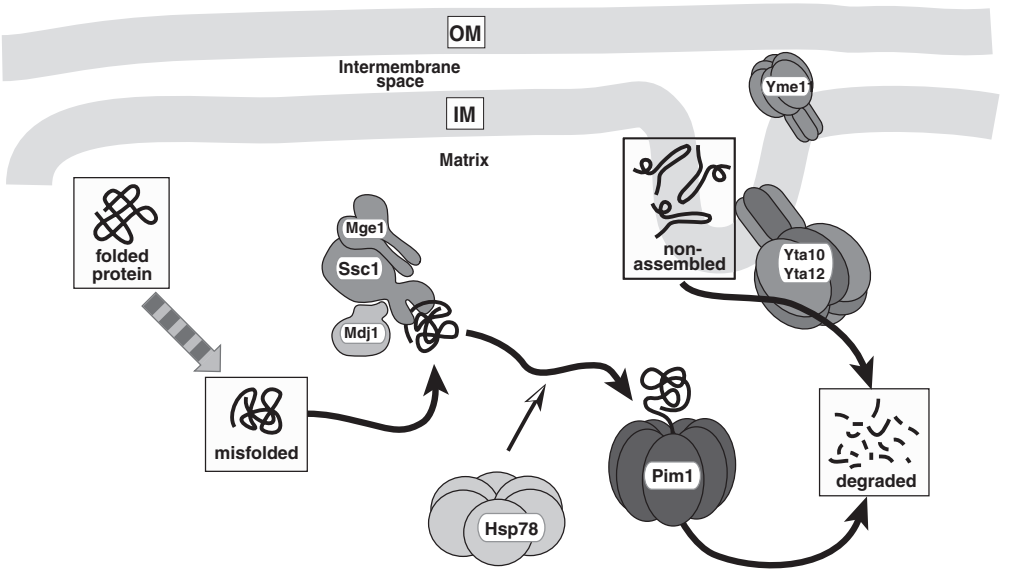

Fig. 31.3. Through the cooperation of chaperones and proteases, a mitochondrial protein quality-control system is formed. Proteins of the mitochondrial matrix that are damaged and/or misfolded are recognized by the mtHsp70 (Ssc1) system and are targeted for degradation by the soluble protease Pim1/LON. The degradation efficiency is enhanced by the mitochondrial ClpB homologue Hsp78. Membrane proteins of the inner membrane (IM) that are misfolded or fail to assemble are degraded by two protease complexes located in the inner membrane. The i-AAA protease (Yme1) degrades proteins exposed to the intermembrane space, while the m-AAA protease (Yta10/Yta12) acts on proteins with domains facing the matrix. Both complexes are also involved in the biogenesis of inner-membrane protein complexes.

of the protein might extract substrate proteins from the membrane and stabilize the polypeptide chain until proteolysis is complete.

A different proteolytic system exists in the mitochondrial matrix (Figure 31.3). A high-molecular-weight complex of the Pim1 protein forms an ATP-dependent protease that is highly homologous to the bacterial LON protease and also belongs to the AAA protein family [97, 98]. Pim1 is primarily involved in the degradation of soluble unfolded proteins in the matrix and shows a close functional coordination with the mtHsp70 system, especially under stress conditions [99]. It is thought that the chaperone proteins mtHsp70 and Mdj1 stabilize substrate proteins against aggregation, but if the attempts to refold the proteins fail, the damaged proteins are removed by the Pim1 protease. Similar to membrane-bound AAA proteases, Pim1 may exhibit chaperone properties, as it was found that a proteolytically inactive Pim1 could partially substitute for Rca1 and Afg3 in assembly of the inner-membrane respiratory complexes [100]. However, the mechanistic details of the possible chaperone function still have to be clarified. In their unique combination

of protease and chaperone functions, the AAA proteases serve as a dedicated protein quality-control system of mitochondria, responsible for both the coordinated assembly of protein complexes and the removal of surplus polypeptides.

31.5 Aggregation versus Degradation: Chaperone Functions Under Stress Conditions

The functional network of chaperone proteins and proteases in mitochondria plays an even more important role under stress conditions such as elevated temperature and high concentrations of reactive oxygen species or other toxic chemicals. These conditions lead to damage and/or denaturation of endogenous proteins. Apart from the loss of the enzymatic activities, high amounts of these damaged proteins favor aggregation reactions that have indirect but significant deleterious effects on mitochondrial function. In a process similar to other cellular systems, mitochondria employ a two-pronged approach to tackle the problem of protein aggregation. First, interaction of damaged proteins with chaperones will keep them in solution and increase the probability of refolding them to the native conformation under more benign conditions (Figure 31.2). Chaperone systems are even capable of resolubilizing aggregated protein material and reactivating them for refolding. Second, terminally damaged proteins will have to be removed from the mitochondrial protein pool by proteolytic reactions coordinating chaperone and protease functions (Figure 31.3). The ultimate fate of the substrate proteins is likely determined by kinetic partitioning. A short interaction of folding-competent substrate proteins leads to refolding, while an extended binding of misfolded proteins, which fail to refold, favors degradation.

The main chaperone family involved in protection from protein aggregation is the Hsp100/Clp family. Initial characterization in bacteria identified these chaperones as components of a proteolytic system, the Clp protease (caseinolytic protease). In this system the protease subunit, ClpP, forms a ring-shaped oligomeric complex that interacts with a chaperone component, either the ClpA or ClpX proteins. The chaperone component recognizes and unfolds potential substrate proteins in an ATP-dependent reaction. The unfolded polypeptide chain is then translocated to the interior of the ClpP protease subunit, where it is degraded [101, 102]. In bacteria, ClpA and ClpX have been shown to act as chaperones independently of an association with the ClpP complex. In mitochondria the only homologue of this system identified to date is Mcx1, a homologue of the bacterial ClpX. A deletion of this gene in yeast did not result in a discernible phenotype; therefore, its cellular function is unclear.

In bacteria an additional member of the Hsp100/Clp family has been identified that has no direct role in proteolysis. This protein, ClpB, forms a ring-shaped oligomeric complex and seems to be involved in protective reactions under stress conditions. In eukaryotes, both a cytosolic homologue, Hsp104, and a mitochondrial homologue, Hsp78, have been identified [103, 104]. Both ClpB and Hsp104 have been shown to reduce protein aggregation in vitro and in vivo [105, 106]. ClpB's

main activity seems to be the resolubilization of aggregated proteins, not the prevention of aggregation per se. Although ClpB and homologues can bring aggregated proteins back into solution, refolding of proteins to their native conformation requires the Hsp70 chaperone system [107, 108]. ClpB may act to resolubilize proteins by actively exposing new Hsp70 binding sites in the aggregated proteins in an ATP-driven process [109]. However, the details of the molecular mechanism of the disaggregation reaction remain to be determined.

In yeast mitochondria, an Hsp78 deletion mutant shows no phenotype at normal growth conditions, but Hsp78 plays a role in thermotolerance and in the protection of mitochondrial functions under stress conditions [110, 111]. Again, a functional cooperation of Hsp78 and the mitochondrial Hsp70 system in the maintenance of respiratory competence and genome integrity was observed. The bi-chaperone system of Hsp78 and mtHsp70 is able to efficiently refold heat-inactivated substrate proteins in vitro [112]. It is interesting to note that mtHsp70 could not be replaced by the bacterial homologue DnaK in these experiments, indicating a specific functional cooperation between mtHsp70 and Hsp78. The role of Hsp78 in genome maintenance is probably indirect and is a result of its function in protein stabilization, as it has a direct effect on the restoration of DNA polymerase activity after heat shock [113]. In addition, Hsp78 is also involved in the degradation of proteins in the matrix by the protease Pim1 [114]. A deletion mutant of Hsp78 showed a significant reduction in Pim1-dependent proteolysis of imported reporter proteins. This effect was already obvious at normal growth conditions and was not correlated with the function of Hsp78 in the protection from protein aggregation. The involvement of Hsp78 in proteolytic reactions represents a novel level of cooperation among different protein families, expanding the concept of a closely coordinated functional network composed of chaperone proteins and proteases in mitochondria.

31.6 Experimental Protocols

31.6.1 Chaperone Functions Characterized With Yeast Mutants

Selection of Temperature-sensitive Mutants

The major mitochondrial chaperones Hsp60 and Hsp70 are encoded by essential genes. Since null mutations of these genes result in a lethal phenotype, a functional analysis of these proteins requires the use of conditional mutants. Usually temperature-sensitive alleles are generated for the biochemical analysis. The procedure follows standard yeast genetic procedures and will be described only briefly. Temperature-sensitive mutations in yeast are generated by a random mutagenesis (usually error-prone PCR) of the respective gene cloned into a single-copy yeast vector. The mutated plasmids are transformed into a strain that has a deletion of the original gene on the chromosome but carries the wild-type gene on another

plasmid. By a plasmid-shuffling procedure, the plasmid with the wild-type gene is removed and the appropriate mutant is selected [115].

Purification of Mitochondria and Preproteins

The effects of chaperone mutations on the import and folding of mitochondrial proteins are best analyzed by an in vitro assay system utilizing isolated intact mitochondria. This approach allows the use of specifically designed preproteins that are imported in the in vitro system and act as reporter molecules for the translocation and folding reaction. In addition, the in vitro assay permits the manipulation of experimental conditions and the import activity of mitochondria to a high extent while leaving the biochemical environment inside the mitochondria largely intact.

Purification of yeast mitochondria and preprotein import reactions is performed by standard procedures [116]. The precursor proteins can be used in radio-labeled form after in vitro transcription-translation or in purified form as recombinant proteins. In most cases, fusion proteins with an amino-terminal part derived from an authentic mitochondrial protein and a carboxy-terminal dihydrofolate reductase (DHFR) domain are used. While the targeting information is supplied by the mitochondrial protein, the import and folding of the heterologous DHFR domain can be followed directly.

Protein Import Reaction, Non-Permissive Conditions

Import reactions are performed in a volume of 100 μL import buffer (3% bovine serum albumin, 250 mM sucrose, 80 mM KCl, 5 mM $MgCl_2$, 2 mM KH_2PO_4, 5 mM methionine, 10 mM MOPS-KOH, pH 7.2) containing mitochondria (25 μg mitochondrial protein) that were isolated under permissive growth conditions. To induce the temperature-sensitive phenotype, the reaction mix is heated to 37 °C for 15 min. After cooling to 25 °C, 2 mM ATP and 2 mM NADH are added. The import reaction is started by the addition of up to 10 μL of reticulocyte lysate from the in vitro translation reaction containing the radio-labeled preprotein. Import reactions are typically performed at 25 °C for 2–30 min, depending on the translocation efficiency of the preprotein used.

Precursor proteins imported into the matrix are processed by the matrix-processing peptidase (MPP) to their mature form, indicated by a characteristic increase in electrophoretic mobility. In addition, complete import of the polypeptide chain is indicated by the resistance of the imported protein against external proteases. Non-imported proteins are digested by a treatment of the mitochondria with 20–150 μg mL^{-1} proteinase K for 10 min at 0 °C. The protease is inactivated by 2 mM phenylmethylsulfonyl fluoride (PMSF) for 5 min at 0 °C. Mitochondria are then pelleted by centrifugation C at 13 000 *g* for 10 min at 2°. The supernatant is discarded and the mitochondria are solubilized by electrophoresis sample buffer (2% [w/v] SDS, 5% [w/v] 2-mercaptoethanol, 10% [v/v] glycerol, 60 mM TRIS/HCl, pH 6.8, 0.02% [w/v] bromophenol blue). Imported proteins are analyzed by standard SDS-PAGE. A useful control reaction is to perform the import reaction in the presence of a mixture of inhibitors of the mitochondrial respiratory chain. In the absence of an inner-membrane potential, insertion of the preprotein into

the inner membrane is blocked and no processing or protease resistance is observed. The following concentrations are used: 8 μM antimycin A, 1 mM valinomycin, and 20 μM oligomycin. The three inhibitors can be mixed together in a 100× stock solution in ethanol and stored at −20 °C.

Temperature-sensitive mutants of the mtHsp70, Ssc1, show two types of translocation defects [9]. A complete inactivation of Ssc1, e.g., using a mutation in the ATPase domain (mutant strain *ssc1-3*), results in a block of translocation of matrix proteins. Under these conditions, preproteins remain bound to the surface of the outer membrane. Although insertion of preproteins into the inner membrane driven by the membrane potential is possible, typically no processing or protease resistance is observed for matrix proteins due to the lack of import motor activity in the matrix. A second type of mutant is affected in its binding to protein substrates. An example is the mutant *ssc1-2*, which contains an alteration in the peptide-binding domain. This mutation locks the mtHsp70 in its high-affinity state. In principle, mutant *ssc1-2* mitochondria are import-competent as a result of a high binding efficiency to imported proteins, but significant translocation efficiency was observed only with preproteins unfolded prior to import by treatment with 7 M urea.

31.6.2 Interaction of Imported Proteins With Matrix Chaperones

Co-immunoprecipitation

Physical interactions of imported preproteins with mitochondrial chaperones can be detected by co-immunoprecipitation with specific antibodies. The binding conditions described here have been optimized for the mtHsp70. The binding conditions with other chaperones or other substrate proteins might be significantly different; therefore, the binding conditions need to be closely monitored and changed if appropriate.

First, the respective antibodies need to be pre-bound to protein A Sepharose (PAS). Per import reaction, 10 μL wet volume of PAS is incubated with 5–20 μL of antiserum for 1 h in a volume of 500 μL TBS (0.9% NaCl, 10 mM TRIS/HCl, pH 7.4). The amount of antiserum needed depends on the avidity of the individual antibody and has to be established by test experiments. Two washing steps with TBS result in the removal of unbound material, and the wet PAS pellet can be stored for several hours at 4 °C. Second, an import reaction with radio-labeled precursor proteins is performed as described above. The import reaction is stopped by the addition of 1 μM valinomycin after a short incubation time of 1–5 min. In order to analyze the kinetics of the preprotein-chaperone association, a further incubation at 25 °C can be included. After completion of the import reaction, the mitochondrial pellet is solubilized in 200 μL IP buffer (0.1% Triton X-100, 10 mM TRIS/HCl, pH 7.4, 100 mM NaCl, 5 mM EDTA, proteinase inhibitors) under native conditions. After 5 min vigorous shaking at 4 °C, the mitochondrial lysate is centrifuged at 13 000 *g* for 5 min at 2 °C to remove insoluble material. The super-

natants are incubated with the PAS material containing the pre-bound antibodies for 30 min at 4 °C with gentle agitation. The PAS is washed three times with lysis buffer and once with 10 mM TRIS/HCl (pH 7.4). Bound proteins are eluted by electrophoresis sample buffer and separated by SDS-PAGE.

Gel Filtration

Physical interactions of substrate proteins with the mitochondrial Hsp60 system can also be analyzed by gel filtration [69]. Due to the large size of the oligomeric Hsp60 complex, bound and unbound substrate proteins can be easily separated by a simple one-step gel filtration procedure. In principle, the method can be employed for any substrate or chaperone provided that the molecular weight difference between unbound and bound substrate is large enough. For each reaction, a small column of about 10 cm in length and 0.5 cm in diameter is filled with S-200 Sepharose (Amersham Biosciences) and buffered in column buffer (10 mM TRIS/HCl, pH 7.4, 100 mM NaCl, 5 mM EDTA). Radio-labeled substrate proteins are imported into isolated mitochondria as described above, and after solubilization under native conditions and removal of insoluble material, the supernatant is passed over the gel-filtration column. The column is run with column buffer, and fractions of about 1 mL are collected. The fractions are then analyzed for the presence of Hsp60 and substrate proteins by SDS-PAGE and Western blot.

31.6.3 Folding of Imported Model Proteins

Folding reactions of imported preproteins can be followed if a specific assay for the conformational state is available. In most experiments to date, the folding state of an imported DHFR domain has been monitored [30, 69, 80]. In its native conformation, DHFR is resistant to proteolysis by proteinase K and can be easily distinguished as a protein with a molecular weight of about 20 kDa on SDS-PAGE. In principle any other protein domain with a behavior similar to DHFR can be used in the assay.

Since DHFR lacks the proper targeting information for mitochondria, an in vitro import reaction is performed with DHFR fusion proteins containing an amino-terminal segment containing a mitochondrial presequence that directs the resulting preprotein into the matrix. After a standard import reaction, the mitochondrial pellet is lysed in 200 μL lysis buffer (0.3% Triton X-100, 30 mM TRIS/HCl, pH 7.4, 80 mM KCl, 5% glycerol) in the presence of 50 μg mL^{-1} proteinase K and incubated for 2–10 min at 0 °C. After inactivation of the protease with PMSF, insoluble material is removed, and the supernatant is treated with trichloroacetic (TCA) acid to precipitate the proteins and then is analyzed by SDS-PAGE and autoradiography.

In the case of the DHFR-based assay, it is absolutely essential to perform a control import reaction where the membrane potential of the inner membrane has been dissipated, because excess preprotein in the assay reaction results in a back-

ground of folded DHFR in the absence of an import reaction. The folding assays are usually performed at low temperatures (4–15 °C), as the folding reactions in wild-type mitochondria proceed at a high rate.

31.6.4 Assaying Mitochondrial Degradation of Imported Proteins

Similar to the assays described above, mitochondrial degradation reactions can be analyzed by reduction of the amount of imported radio-labeled preprotein over time. The mitochondria are preloaded with suitable substrate proteins by an import reaction in vitro. In this assay, fusion proteins between the mitochondrial cytochrome b_2 and the DHFR domain from mouse have been used extensively. For this precursor, translocation into the matrix is ensured by a deletion of 19 amino acids from the intermembrane space sorting signal of cytochrome b_2 [117]. The fusion proteins are recognized as foreign proteins and are degraded by the Pim1 protease in the matrix. The influence of certain protein components such as chaperones can be assessed by using mutant mitochondria [99, 114]. Authentic mitochondrial proteins usually show a very slow rate of degradation at normal growth conditions, which may not be detected over the time this assay is performed. However, damage inflicted on mitochondrial proteins, which leads to protein denaturation or unfolding, is recognized by the proteolytic system by an unknown mechanism, and these proteins are degraded [118, 119]. Per time point, 25 μg mitochondria (protein amount) is used for the import reaction. Following an incubation of 15 min at 25 °C, the translocation is stopped and unimported preprotein is removed by a short treatment with proteinase K. The mitochondria are then pelleted and resuspended in 100 μL import buffer per sample. To maintain a maximum level of activity, an ATP-regenerating system (3 mM ATP, 20 mM creatine phosphate, 200 μg mL^{-1} creatine kinase) should be included in the degradation reaction. Proteolysis of the imported protein is assessed by removing aliquots of mitochondria (25 μg of mitochondrial protein each) at several time points over the course of about 2 h. The collected aliquots are centrifuged at 13 000 *g* for 10 min at 2 °C, and the mitochondria are lysed in electrophoresis sample buffer and analyzed by SDS-PAGE and autoradiography.

31.6.5 Aggregation of Proteins in the Mitochondrial Matrix

If the proteolytic system is overwhelmed by high amounts of destabilized or unfolded proteins, aggregation of substrate proteins in the matrix compartment can occur. The aggregation of imported reporter substrates can be tested based on the in vitro import assay. Depending on the particular properties of the reporter protein used, only a low level of aggregation is observed. As a result, proteins containing mutations that affect conformational instability should be used in this assay. This can be achieved by the import of either mutant preproteins or aggregation-prone reporter domains that are targeted to mitochondria. For exam-

ple, a destabilized mutant of DHFR, containing the mutations Cys7Ser, Ser42Cys, and Asn49Cys [120], can be used for the assay because it shows significant aggregation at elevated temperature (37 °C or higher). After the import reaction, mitochondria are re-isolated and subjected to different experimental conditions. Protein aggregation is tested by differential centrifugation. Per sample, 25 μg mitochondria (protein amount) is lysed in 200 μL lysis buffer (see above) containing a proteinase inhibitor cocktail and subjected to a high-spin centrifugation (100 000 *g* for 15 min). Soluble proteins stay in the supernatant, while protein aggregates are sedimented and can be recovered in the pellet. The pellet is extracted once with fresh lysis buffer to remove contaminating membrane proteins, and the aggregated material is resolubilized in electrophoresis sample buffer and analyzed by SDS-PAGE and autoradiography.

References

1 Voos, W. & Röttgers, K. (2002). Molecular chaperones as essential mediators of mitochondrial biogenesis. *Biochim. Biophys. Acta* **1592**, 51–62.

2 Gakh, O., Cavadini, P. & Isaya, G. (2002). Mitochondrial processing peptidases. *Biochim. Biophys. Acta* **1592**, 63–77.

3 Pfanner, N. & Wiedemann, N. (2002). Mitochondrial protein import: two membranes, three translocases. *Curr. Opin. Cell Biol.* **14**, 400–411.

4 Jensen, R. & Dunn, C. (2002). Protein import into and across the mitochondrial inner membrane: role of the TIM23 and TIM22 translocons. *Biochim. Biophys. Acta* **1592**, 25–34.

5 Hill, K., Model, K., Ryan, M. T., Dietmeier, K., Martin, F., Wagner, R. & Pfanner, N. (1998). Tom40 forms the hydrophilic channel of the mitochondrial import pore for preproteins. *Nature* **395**, 516–521.

6 Truscott, K. N., Kovermann, P., Geissler, A., Merlin, A., Meijer, M., Driessen, A. J. M., Rassow, J., Pfanner, N. & Wagner, R. (2001). A presequence- and voltage-sensitive channel of the mitochondrial preprotein translocase formed by Tim23. *Nat. Struct. Biol.* **8**, 1074–1082.

7 Voos, W., Martin, H., Krimmer, T. & Pfanner, N. (1999). Mechanisms of protein translocation into mitochondria. *Biochim. Biophys. Acta* **1422**, 235–254.

8 Kang, P. J., Ostermann, J., Shilling, J., Neupert, W., Craig, E. A. & Pfanner, N. (1990). Requirement for hsp70 in the mitochondrial matrix for translocation and folding of precursor proteins. *Nature* **348**, 137–143.

9 Gambill, B. D., Voos, W., Kang, P. J., Miao, B., Langer, T., Craig, E. A. & Pfanner, N. (1993). A dual role for mitochondrial heat shock protein 70 in membrane translocation of preproteins. *J. Cell Biol.* **123**, 109–117.

10 Ungermann, C., Neupert, W. & Cyr, D. M. (1994). The role of hsp70 in conferring unidirectionality on protein translocation. *Science* **266**, 1250–1253.

11 Voos, W., von Ahsen, O., Müller, H., Guiard, B., Rassow, J. & Pfanner, N. (1996). Differential requirement for the mitochondrial Hsp70-Tim44 complex in unfolding and translocation of preproteins. *EMBO J.* **15**, 2668–2677.

12 Wachter, C., Schatz, G. & Glick, B. S. (1992). Role of ATP in the intramitochondrial sorting of cytochrome c_1 and the adenine nucleotide transporter. *EMBO J.* **11**, 4787–4794.

13 Herrmann, J. M., Neupert, W. & Stuart, R. A. (1997). Insertion into

the mitochondrial inner membrane of a polytopic protein, the nuclear-encoded Oxa1p. *EMBO J.* **16**, 2217–2226.

14 von Ahsen, O., Voos, W., Henninger, H. & Pfanner, N. (1995). The mitochondrial protein import machinery. Role of ATP in dissociation of the Hsp70.Mim44 complex. *J. Biol. Chem.* **270**, 29848–29853.

15 Strub, A., Lim, J. H., Pfanner, N. & Voos, W. (2000). The mitochondrial protein import motor. *Biol. Chem.* **381**, 943–949.

16 Miao, B., Davis, J. E. & Craig, E. A. (1997). Mge1 functions as a nucleotide release factor for Ssc1, a mitochondrial Hsp70 of *Saccharomyces cerevisiae*. *J. Mol. Biol.* **265**, 541–552.

17 Dekker, P. J. T. & Pfanner, N. (1997). Role of mitochondrial GrpE and phosphate in the ATPase cycle of matrix Hsp70. *J. Mol. Biol.* **270**, 321–327.

18 Schneider, H. C., Westermann, B., Neupert, W. & Brunner, M. (1996). The nucleotide exchange factor MGE exerts a key function in the ATP-dependent cycle of mt-Hsp70-Tim44 interaction driving mitochondrial protein import. *EMBO J.* **15**, 5796–5803.

19 Voos, W., Gambill, B. D., Laloraya, S., Ang, D., Craig, E. A. & Pfanner, N. (1994). Mitochondrial GrpE is present in a complex with hsp70 and preproteins in transit across membranes. *Mol. Cell. Biol.* **14**, 6627–6634.

20 Westermann, B., Prip-Buus, C., Neupert, W. & Schwarz, E. (1995). The role of the GrpE homologue, Mge1p, in mediating protein import and protein folding in mitochondria. *EMBO J.* **14**, 3452–3460.

21 Kronidou, N. G., Oppliger, W., Bolliger, L., Hannavy, K., Glick, B. S., Schatz, G. & Horst, M. (1994). Dynamic interaction between Isp45 and mitochondrial hsp70 in the protein import system of the yeast mitochondrial inner membrane. *Proc. Natl. Acad. Sci. USA* **91**, 12818–12822.

22 Schneider, H.-C., Berthold, J., Bauer, M. F., Dietmeier, K., Guiard, B., Brunner, M. & Neupert, W. (1994). Mitochondrial Hsp70/MIM44 complex facilitates protein import. *Nature* **371**, 768–774.

23 Rassow, J., Maarse, A. C., Krainer, E., Kübrich, M., Müller, H., Meijer, M., Craig, E. A. & Pfanner, N. (1994). Mitochondrial protein import: biochemical and genetic evidence for interaction of matrix hsp70 and the inner membrane protein MIM44. *J. Cell Biol.* **127**, 1547–1556.

24 Ungermann, C., Guiard, B., Neupert, W. & Cyr, D. M. (1996). The delta psi- and Hsp70/MIM44-dependent reaction cycle driving early steps of protein import into mitochondria. *EMBO J.* **15**, 735–744.

25 Merlin, A., Voos, W., Maarse, A. C., Meijer, M., Pfanner, N. & Rassow, J. (1999). The J-related segment of Tim44 is essential for cell viability: a mutant Tim44 remains in the mitochondrial import site, but inefficiently recruits mtHsp70 and impairs protein translocation. *J. Cell Biol.* **145**, 961–972.

26 Simon, M. S., Peskin, C. S. & Oster, G. F. (1992). What drives the translocation of proteins? *Proc. Natl. Acad. Sci. USA* **89**, 3770–3774.

27 Bauer, M. F., Hofmann, S., Neupert, W. & Brunner, M. (2000). Protein translocation into mitochondria: the role of TIM complexes. *Trends Cell Biol.* **10**, 25–31.

28 Neupert, W. & Brunner, M. (2002). The protein import motor of mitochondria. *Nat. Rev. Mol. Cell Biol.* **3**, 555–565.

29 Okamoto, K., Brinker, A., Paschen, S. A., Moarefi, I., Hayer-Hartl, M., Neupert, W. & Brunner, M. (2002). The protein import motor of mitochondria: a targeted molecular ratchet driving unfolding and translocation. *EMBO J.* **21**, 3659–3671.

30 Voisine, C., Craig, E. A., Zufall, N., von Ahsen, O., Pfanner, N. & Voos, W. (1999). The protein import motor of mitochondria: unfolding and

trapping of preproteins are distinct and separable functions of matrix Hsp70. *Cell* **97**, 565–574.

31 Geissler, A., Rassow, J., Pfanner, N. & Voos, W. (2001). Mitochondrial import driving forces: enhanced trapping by matrix hsp70 stimulates translocation and reduces the membrane potential dependence of loosely folded preproteins. *Mol. Cell. Biol.* **21**, 7097–7104.

32 Matouschek, A., Azem, A., Ratliff, K., Glick, B. S., Schmid, K. & Schatz, G. (1997). Active unfolding of precursor proteins during mitochondrial protein import. *EMBO J.* **16**, 6727–6736.

33 Lim, J. H., Martin, F., Guiard, B., Pfanner, N. & Voos, W. (2001). The mitochondrial Hsp70-dependent import system actively unfolds preproteins and shortens the lag phase of translocation. *EMBO J.* **20**, 941–950.

34 Milisav, I., Moro, F., Neupert, W. & Brunner, M. (2001). Modular structure of the TIM23 preprotein translocase of mitochondria. *J. Biol. Chem.* **276**, 25856–25861.

35 Huang, S., Ratliff, K. S., Schwartz, M. P., Spenner, J. M. & Matouschek, A. (1999). Mitochondria unfold precursor proteins by unraveling them from their N-termini. *Nat. Struct. Biol.* **6**, 1132–1138.

36 Matouschek, A., Pfanner, N. & Voos, W. (2000). Protein unfolding by mitochondria. The Hsp70 import motor. *EMBO Rep.* **1**, 404–410.

37 Pfanner, N. & Meijer, M. (1995). Protein sorting: Pulling in the proteins. *Curr. Biol.* **5**, 132–135.

38 Glick, B. S. (1995). Can Hsp70 proteins act as force-generating motors? *Cell* **80**, 11–14.

39 Jensen, R. E. & Johnson, A. E. (1999). Protein translocation: Is hsp70 pulling my chain? *Curr. Biol.* **9**, R779–782.

40 Bömer, U., Maarse, A. C., Martin, F., Geissler, A., Merlin, A., Schönfisch, B., Meijer, M., Pfanner, N. & Rassow, J. (1998). Separation of structural and dynamic functions of the mitochondrial translocase: Tim44 is crucial for the inner membrane import sites in translocation of tightly folded domains, but not of loosely folded preproteins. *EMBO J.* **17**, 4226–4237.

41 Liu, Q., D'Silva, P., Walter, W., Marszalek, J. & Craig, E. A. (2003). Regulated cycling of mitochondrial Hsp70 at the protein import channel. *Science* **300**, 139–141.

42 Truscott, K. N., Voos, W., Frazier, A. E., Lind, M., Li, Y., Geissler, A., Dudek, J., Müller, H., Sickmann, A., Meyer, H. E., Meisinger, C., Guiard, B., Rehling, P. & Pfanner, N. (2003). A J-protein is an essential subunit of the presequence translocase associated protein import motor of mitochondria. *J. Cell Biol.* **163**, 707–713.

43 Mokranjac, D., Sichting, M., Neupert, W. & Hell, K. (2003). Tim14, a novel key component of the import motor of the TIM23 protein translocase of mitochondria. *EMBO J.* **22**, 4945–4956.

44 D'Silva, P., Schilke, B., Walter, W., Andrew, A. & Craig, E. (2003). J-protein co-chaperone of the mitochodrial inner membrane required for protein import into the mitochondrial matrix. *Proc. Natl. Acad. Sci. USA* **100**, 13839–13844.

45 Frazier, A. E., Dudek, J., Guiard, B., Voos, W., Li, Y., Lind, M., Meisinger, C., Geissler, A., Sickmann, A., Meyer, H. E., Bilanchone, V., Cumsky, M. G., Truscott, K. N., Pfanner, N. & Rehling, P. (2004). Pam16 has an essential role in the mitochondrial protein import motor. *Nat. Struct. Mol. Biol.* **11**, 226–233.

46 Kozany, C., Mokranjac, D., Sichting, M., Neupert, W. & Hell, K. (2004). The J domain-related cochaperone Tim16 is a constituent of the mitochondrial TIM23 preprotein translocase. *Nat. Struct. Mol. Biol.* **11**, 234–241.

47 Horst, M., Oppliger, W., Rospert, S., Schönfeld, H. J., Schatz, G. & Azem, A. (1997). Sequential action of

two hsp70 complexes during protein import into mitochondria. *EMBO J.* **16**, 1842–1849.

48 Langer, T., Lu, C., Echols, H., Flanagan, J., Hayer-Hartl, M. K. & Hartl, F.-U. (1992). Successive action of DnaK (Hsp70), DnaJ, and GroEL (Hsp60) along the pathway of chaperone-assisted protein folding. *Nature* **356**, 683–689.

49 Rapoport, T. A., Jungnickel, B. & Kutay, U. (1996). Protein transport across the eukaryotic endoplasmic reticulum and bacterial inner membranes. *Annu. Rev. Biochem.* **65**, 271–303.

50 Hartl, F. U. & Hayer-Hartl, M. (2002). Molecular chaperones in the cytosol: from nascent chain to folded protein. *Science* **295**, 1852–1858.

51 Bukau, B. & Horwich, A. L. (1998). The Hsp70 and Hsp60 chaperone machines. *Cell* **92**, 351–366.

52 Deloche, O., Kelley, W. L. & Georgopoulos, C. (1997). Structure-function analyses of the Ssc1p, Mdj1p, and Mge1p *Saccharomyces cerevisiae* mitochondrial proteins in *Escherichia coli*. *J. Bacteriol.* **179**, 6066–6075.

53 Cyr, D. M., Langer, T. & Douglas, M. G. (1994). DnaJ-like proteins: molecular chaperones and specific regulators of Hsp70. *Trends Biochem. Sci.* **19**, 176–181.

54 Rowley, N., Prip-Buus, C., Westermann, B., Brown, C., Schwarz, E., Barrell, B. & Neupert, W. (1994). Mdj1p, a novel chaperone of the DnaJ family, is involved in mitochondrial biogenesis and protein folding. *Cell* **77**, 249–259.

55 Kubo, Y., Tsunehiro, T., Nishikawa, S., Nakai, M., Ikeda, E., Toh-e, A., Morishima, N., Shibata, T. & Endo, T. (1999). Two distinct mechanisms operate in the reactivation of heat-denatured proteins by the mitochondrial Hsp70/Mdj1p/Yge1p chaperone system. *J. Mol. Biol.* **286**, 447–464.

56 Deloche, O., Liberek, K., Zylicz, M. & Georgopoulos, C. (1997). Purification and biochemical properties of *Saccharomyces cerevisiae* Mdj1p, the mitochondrial DnaJ homologue. *J. Biol. Chem.* **272**, 28539–28544.

57 Duchniewicz, M., Germaniuk, A., Westermann, B., Neupert, W., Schwarz, E. & Marszalek, J. (1999). Dual Role of the Mitochondrial Chaperone Mdj1p in Inheritance of Mitochondrial DNA in Yeast. *Mol. Cell. Biol.* **19**, 8201–8210.

58 Westermann, B. & Neupert, W. (1997). Mdj2p, a novel DnaJ homolog in the mitochondrial inner membrane of the yeast *Saccharomyces cerevisiae*. *J. Mol. Biol.* **272**, 477–483.

59 Voisine, C., Cheng, Y. C., Ohlson, M., Schilke, B., Hoff, K., Beinert, H., Marszalek, J. & Craig, E. A. (2001). Jac1, a mitochondrial J-type chaperone, is involved in the biogenesis of Fe/S clusters in *Saccharomyces cerevisiae*. *Proc. Natl. Acad. Sci. USA* **98**, 1483–1488.

60 Lutz, T., Westermann, B., Neupert, W. & Herrmann, J. M. (2001). The mitochondrial proteins Ssq1 and Jac1 are required for the assembly of iron sulfur clusters in mitochondria. *J. Mol. Biol.* **307**, 815–825.

61 Kim, R., Saxena, S., Gordon, D. M., Pain, D. & Dancis, A. (2001). J-domain protein, Jac1p, of yeast mitochondria required for iron homeostasis and activity of Fe-S cluster proteins. *J. Biol. Chem.* **276**, 17524–17532.

62 Schilke, B., Forster, J., Davis, J., James, P., Walter, W., Laloraya, S., Johnson, J., Miao, B. & Craig, E. A. (1996). The cold sensitivity of a mutant of *Saccharomyces cerevisiae* lacking a mitochondrial heat shock protein 70 is suppressed by loss of mitochondrial DNA. *J. Cell Biol.* **134**, 603–613.

63 Knight, S. A. B., Sepuri, N. B. V., Pain, D. & Dancis, A. (1998). Mt-Hsp70 homolog, Ssc2p, required for maturation of yeast frataxin and mitochondrial iron homeostasis. *J. Biol. Chem.* **273**, 18389–18393.

64 Schmidt, S., Strub, A., Röttgers, K., Zufall, N. & Voos, W. (2001). The two mitochondrial heat shock proteins

70, Ssc1 and Ssq1, compete for the cochaperone Mge1. *J. Mol. Biol.* **313**, 13–26.

65 Manning-Krieg, U. C., Scherer, P. E. & Schatz, G. (1991). Sequential action of mitochondrial chaperones in protein import into mitochondria. *EMBO J.* **10**, 3273–3280.

66 Heyrovska, N., Frydman, J., Höhfeld, J. & Hartl, F. U. (1998). Directionality of polypeptide transfer in the mitochondrial pathway of chaperone-mediated protein folding. *Biol. Chem.* **379**, 301–309.

67 Cheng, M. Y., Hartl, F. U., Martin, J., Pollock, R. A., Kalusek, F., Neupert, W., Hallberg, E. M., Hallberg, R. L. & Horwich, A. L. (1989). Mitochondrial heat-shock protein hsp60 is essential for assembly of proteins imported into yeast mitochondria. *Nature* **337**, 620–625.

68 Reading, D. S., Hallberg, R. L. & Myers, A. M. (1989). Characterization of the yeast HSP60 gene coding for a mitochondrial assembly factor. *Nature* **337**, 655–659.

69 Ostermann, J., Horwich, A. L., Neupert, W. & Hartl, F. U. (1989). Protein folding in mitochondria requires complex formation with hsp60 and ATP hydrolysis. *Nature* **341**, 125–130.

70 Walter, S. (2002). Structure and function of the GroE chaperone. *Cell. Mol. Life Sci.* **59**, 1589–1597.

71 Lubben, T., Gatenby, A., Donaldson, G., Lorimer, G. & Viitanen, P. (1990). Identification of a groES-like chaperonin in mitochondria that facilitates protein folding. *Proc. Natl. Acad. Sci. USA* **87**, 7683–7687.

72 Rospert, S., Junne, T., Glick, B. S. & Schatz, G. (1993). Cloning and disruption of the gene encoding yeast mitochondrial chaperonin 10, the homolog of *E. coli* groES. *FEBS Lett.* **335**, 358–360.

73 Höhfeld, J. & Hartl, F. U. (1994). Role of the chaperonin cofactor Hsp10 in protein folding and sorting in yeast mitochondria. *J. Cell Biol.* **126**, 305–315.

74 Dubaquie, Y., Looser, R. & Rospert, S. (1997). Significance of chaperonin 10-mediated inhibition of ATP hydrolysis by chaperonin 60. *Proc. Natl. Acad. Sci. USA* **94**, 9011–9016.

75 Nielsen, K. L. & Cowan, N. J. (1998). A single ring is sufficient for productive chaperonin-mediated folding *in vivo*. *Mol. Cell* **2**, 93–99.

76 Nielsen, K. L., McLennan, N., Masters, M. & Cowan, N. J. (1999). A single-ring mitochondrial chaperonin (Hsp60-Hsp10) can substitute for GroEL-GroES *in vivo*. *J. Bacteriol.* **181**, 5871–5875.

77 Rospert, S., Looser, R., Dubaquié, Y., Matouschek, A., Glick, B. S. & Schatz, G. (1996). Hsp60-independent protein folding in the matrix of yeast mitochondria. *EMBO J.* **15**, 764–774.

78 Dubaquie, Y., Looser, R., Fünfschilling, U., Jenö, P. & Rospert, S. (1998). Identification of *in vivo* substrates of the yeast mitochondrial chaperonins reveals overlapping but non-identical requirement for hsp60 and hsp10. *EMBO J.* **17**, 5868–5876.

79 Matouschek, A., Rospert, S., Schmid, K., Glick, B. S. & Schatz, G. (1995). Cyclophilin catalyzes protein folding in yeast mitochondria. *Prc. Natl. Acad. Sci. USA* **92**, 6319–6323.

80 Rassow, J., Mohrs, K., Koidl, S., Barthelmess, I. B., Pfanner, N. & Tropschug, M. (1995). Cyclophilin 20, is involved in mitochondrial protein folding in cooperation with molecular chaperones Hsp70 and Hsp60. *Mol. Cell. Biol.* **15**, 2654–2662.

81 Herrmann, J. M., Stuart, R. A., Craig, E. A. & Neupert, W. (1994). Mitochondrial heat shock protein 70, a molecular chaperone for proteins encoded by mitochondrial DNA. *J. Cell Biol.* **127**, 893–902.

82 Westermann, B., Gaume, B., Herrmann, J. M., Neupert, W. & Schwarz, E. (1996). Role of the mitochondrial DnaJ homolog Mdj1p as a chaperone for mitochondrially synthesized and imported proteins. *Mol. Cell. Biol.* **16**, 7063–7071.

83 Bowman, S., Ackerman, S. H., Griffiths, D. E. & Tzagoloff, A. (1991). Characterization of *ATP12*, a yeast nuclear gene required for the assembly of the mitochondrial F_1-ATPase. *J. Biol. Chem.* **266**, 7517–7523.

84 Ackerman, S. H., Martin, J. & Tzagoloff, A. (1992). Characterization of *ATP11* and detection of the encoded protein in mitochondria of *Saccharomyces cerevisiae*. *J. Biol. Chem.* **267**, 7386–7394.

85 Glerum, D. M., Koerner, T. J. & Tzagoloff, A. (1995). Cloning and characterization of *COX14*, whose product is required for assembly of yeast cytochrome oxidase. *J. Biol. Chem.* **270**, 15585–15590.

86 Glerum, D. M., Muroff, I., Jin, C. & Tzagoloff, A. (1997). *COX15* codes for a mitochondrial protein essential for the assembly of yeast cytochrome oxidase. *J. Biol. Chem.* **272**, 19088–19094.

87 Souza, R. L., Green-Willms, N. S., Fox, T. D., Tzagoloff, A. & Nobrega, F. G. (2000). Cloning and characterization of *COX18*, a *Saccharomyces cerevisiae* PET gene required for the assembly of cytochrome oxidase. *J. Biol. Chem.* **275**, 14898–14902.

88 Dibrov, E., Fu, S. & Lemire, B. D. (1998). The Saccharomyces cerevisiae *TCM62* gene encodes a chaperone necessary for the assembly of the mitochondrial succinate dehydrogenase (complex II). *J. Biol. Chem.* **273**, 32042–32048.

89 Guélin, E., Rep, M. & Grivell, L. A. (1994). Sequence of the AFG3 gene encoding a new member of the FtsH/Yme1/Tma subfamily of the AAA-protein family. *Yeast* **10**, 1389–1394.

90 Tzagoloff, A., Yue, J., Jang, J. & Paul, M. F. (1994). A new member of a family of ATPases is essential for assembly of mitochondrial respiratory chain and ATP synthetase complexes in Saccharomyces cerevisiae. *J. Biol. Chem.* **269**, 26144–26151.

91 Paul, M. F. & Tzagoloff, A. (1995). Mutations in RCA1 and AFG3 inhibit F1-ATPase assembly in Saccharomyces cerevisiae. *FEBS Lett.* **373**, 66–70.

92 Thorsness, P. E., White, K. H. & Fox, T. D. (1993). Inactivation of YME1, a member of the ftsH-SEC18-PAS1-CDC48 family of putative ATPase-encoding genes, causes increased escape of DNA from mitochondria in Saccharomyces cerevisiae. *Mol. Cell Biol.* **13**, 5418–5426.

93 Weber, E. R., Hanekamp, T. & Thorsness, P. E. (1996). Biochemical and functional analysis of the YME1 gene product, an ATP and zinc-dependent mitochondrial protease from S. cerevisiae. *Mol. Biol. Cell* **7**, 307–317.

94 Arlt, H., Tauer, R., Feldmann, H., Neupert, W. & Langer, T. (1996). The YTA10-12 complex, an AAA protease with chaperone-like activity in the inner membrane of mitochondria. *Cell* **85**, 875–885.

95 Leonhard, K., Herrmann, J. M., Stuart, R. A., Mannhaupt, G., Neupert, W. & Langer, T. (1996). AAA proteases with catalytic sites on opposite membrane surfaces comprise a proteolytic system for the ATP-dependent degradation of inner membrane proteins in mitochondria. *EMBO J.* **15**, 4218–4229.

96 Leonhard, K., Stiegler, A., Neupert, W. & Langer, T. (1999). Chaperone-like activity of the AAA domain of the yeast Yme1 AAA protease. *Nature* **398**, 348–351.

97 Van Dyck, L., Pearce, D. A. & Sherman, F. (1994). PIM1 encodes a mitochondrial ATP-dependent protease that is required for mitochondrial function in the yeast *Saccharomyces cerevisiae*. *J. Biol. Chem.* **269**, 238–242.

98 Suzuki, C. K., Suda, K., Wang, N. & Schatz, G. (1994). Requirement for the yeast gene *LON* in intramitochondrial proteolysis and maintenance of respiration. *Science* **264**, 273–276.

99 Wagner, I., Arlt, H., van Dyck, L., Langer, T. & Neupert, W. (1994).

Molecular chaperones cooperate with PIM1 protease in the degradation of misfolded proteins in mitochondria. *EMBO J.* **13**, 5135–5145.

100 Rep, M., van Dijl, J. M., Suda, K., Schatz, G., Grivell, L. A. & Suzuki, C. K. (1996). Promotion of mitochondrial membrane complex assembly by a proteolytically inactive yeast Lon. *Science* **274**, 103–106.

101 Wawrzynow, A., Banecki, B. & Zylicz, M. (1996). The Clp ATPases define a novel class of molecular chaperones. *Mol. Microbiol.* **21**, 895–859.

102 Porankiewicz, J., Wang, J. & Clarke, A. K. (1999). New insights into the ATP-dependent Clp protease: *Escherichia coli* and beyond. *Mol. Microbiol.* **32**, 449–458.

103 Parsell, D. A., Sanchez, Y., Stitzel, J. D. & Lindquist, S. (1991). Hsp104 is a highly conserved protein with two essential nucleotide- binding sites. *Nature* **353**, 270–273.

104 Leonhardt, S. A., Fearon, K., Danese, P. N. & Mason, T. L. (1993). *HSP78* encodes a yeast mitochondrial heat shock protein in the Clp family of ATP-dependent proteases. *Mol. Cell. Biol.* **13**, 6304–6313.

105 Mogk, A., Tomoyasu, T., Goloubinoff, P., Rüdiger, S., Röder, D., Langen, H. & Bukau, B. (1999). Identification of thermolabile Escherichia coli proteins: prevention and reversion of aggregation by DnaK and ClpB. *EMBO J.* **18**, 6934–6949.

106 Parsell, D. A., Kowal, A. S., Singer, M. A. & Lindquist, S. (1994). Protein disaggregation mediated by heat-shock protein Hsp104. *Nature* **372**, 475–478.

107 Goloubinoff, P., Mogk, A., Zvi, A. P., Tomoyasu, T. & Bukau, B. (1999). Sequential mechanism of solubilization and refolding of stable protein aggregates by a bichaperone network. *Proc. Natl. Acad. Sci. USA* **96**, 13732–13737.

108 Zolkiewski, M. (1999). ClpB cooperates with DnaK, DnaJ, and GrpE in suppressing protein aggregation. A novel multi-chaperone system from *Escherichia coli*. *J. Biol. Chem.* **274**, 28083–28086.

109 Ben-Zvi, A. P. & Goloubinoff, P. (2001). Mechanisms of disaggregation and refolding of stable protein aggregates by molecular chaperones. *J. Struct. Biol.* **135**, 84–93.

110 Moczko, M., Schönfisch, B., Voos, W., Pfanner, N. & Rassow, J. (1995). The mitochondrial ClpB homolog Hsp78 cooperates with matrix Hsp70 in maintenance of mitochondrial function. *J. Mol. Biol.* **254**, 538–543.

111 Schmitt, M., Neupert, W. & Langer, T. (1996). The molecular chaperone Hsp78 confers compartment-specific thermotolerance to mitochondria. *J. Cell Biol.* **134**, 1375–1386.

112 Krzewska, J., Langer, T. & Liberek, K. (2001). Mitochondrial Hsp78, a member of the Clp/Hsp100 family in *Saccharomyces cerevisiae*, cooperates with Hsp70 in protein refolding. *FEBS Lett.* **489**, 92–96.

113 Germaniuk, A., Liberek, K. & Marszalek, J. (2002). A bi-chaperone (Hsp70-Hsp78) system restores mitochondrial DNA synthesis following thermal inactivation of Mip1p polymerase. *J. Biol. Chem.* **277**, 27801–27808.

114 Röttgers, K., Zufall, N., Guiard, B. & Voos, W. (2002). The ClpB homolog Hsp78 is required for the efficient degradation of proteins in the mitochondrial matrix. *J. Biol. Chem.* **277**, 45829–45837.

115 Strub, A., Röttgers, K. & Voos, W. (2002). The Hsp70 peptide-binding domain determines the interaction of the ATPase domain with Tim44 in mitochondria. *EMBO J.* **21**, 2626–2635.

116 Ryan, M. T., Voos, W. & Pfanner, N. (2001). Assaying protein import into mitochondria. *Methods Cell Biol.* **65**, 189–215.

117 Koll, H., Guiard, B., Rassow, J., Ostermann, J., Horwich, A. L., Neupert, W. & Hartl, F.-U. (1992). Antifolding activity of hsp60 couples protein import into the mitochondrial matrix with export to the intermembrane space. *Cell* **68**, 1163–1175.

118 Langer, T. & Neupert, W. (1996). Regulated protein degradation in mitochondria. *Experientia* **52**, 1069–1076.

119 Rep, M. & Grivell, L. A. (1996). The role of protein degradation in mitochondrial function and biogenesis. *Curr. Genet.* **30**, 367–380.

120 Vestweber, D. & Schatz, G. (1988). Point mutations destabilizing a precursor protein enhance its post-translational import into mitochondria. *EMBO J.* **7**, 1147–1151.

32
Chaperone Systems in Chloroplasts

Thomas Becker, Jürgen Soll, and Enrico Schleiff

32.1
Introduction

More than 25 years ago the terminology of molecular chaperones was invented by Laskey [1] to describe nucleoplasmin required for the assembly of nucleosomes from DNA and histones. Ten years later Pelham [2] offered a refined definition. Molecular chaperones prevent the formation of incorrect structures and disassemble aggregated structures, but they do not form part of the final structure, nor do they possess steric information–specifying assembly. At this time, several proteins of the 70-kDa heat shock protein (Hsp70) class were identified in mammal systems [3, 4], and the first homologue of the chaperonin of the 60-kDa (Cpn60) family was discovered in plants in the form of the Rubisco large subunit-binding protein in chloroplasts [5–7]. Since then, much effort has been made to understand the molecular composition and action of the chaperone machineries. It became clear that the chaperone activity was not limited to the cytoplasm but was also found in organelles, for example, in plastids, which are endosymbiotically derived organelles [8]. Plastids evolved from prokaryotic cyanobacteria, which were captured by a mitochondria-containing host cell. During evolution most but not all of the genes of the endosymbiont were transferred to the nucleus [9]. In turn, some of the gene products are now targeted back toward plastids and others are replaced by gene products of the host cell [10]. Therefore, present-day molecular machines in plastids are often composed of plastid and nuclear gene products of prokaryotic and eukaryotic origin. The molecular chaperones essential for plastid biogenesis in higher plants are generally nuclear-encoded but assemble proteins of both prokaryotic and eukaryotic origin.

Whereas many components of the chaperone family were identified in plastids, not much is known about their specific function in this organelle. In most cases the function was proposed to be similar to the prokaryotic or eukaryotic homologues of these proteins. In plastids these machineries are involved in many essential processes such as protein translocation, intra-organellar transport, protein folding and storage, complex assembly, and stress adaptation (Figure 32.1). In the past the research was focused on the regulation of the chaperone family and their developmental expression profiles. In this chapter we describe the identified proteins

Protein Folding Handbook. Part II. Edited by J. Buchner and T. Kiefhaber

ISBN: 3-527-30784-2

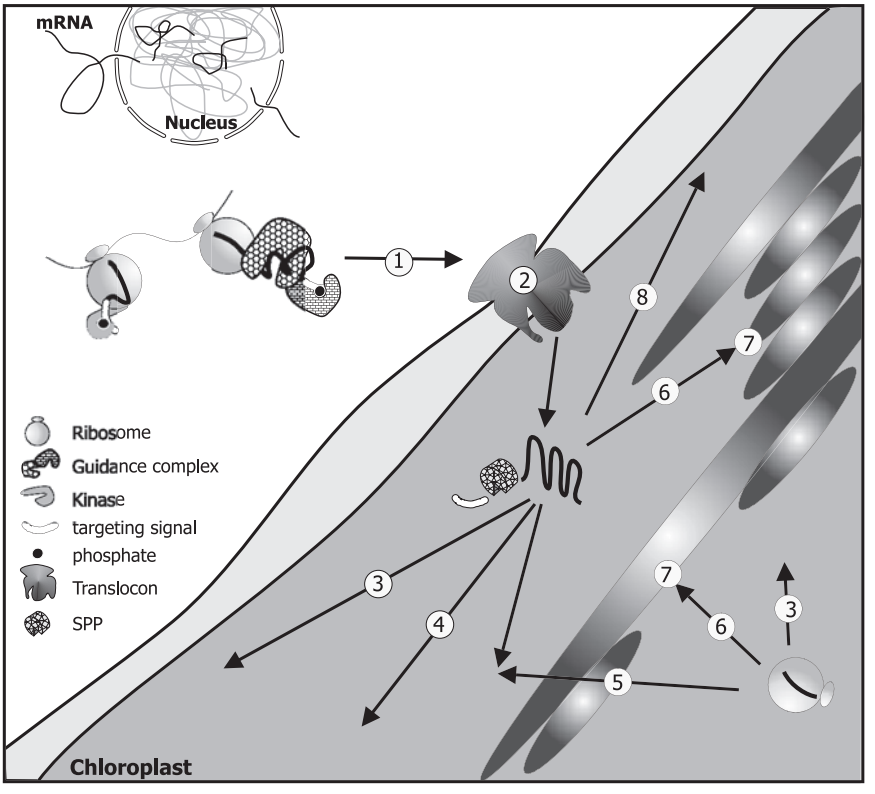

Fig. 32.1. Chaperones are involved in many processes essential for the function of plastids. Chaperones are found to be involved in protein targeting of preproteins toward plastids (1) and in their translocation across the two envelope membranes (2). Molecular chaperones facilitate folding (3) of imported and plastidial-synthesized proteins in the stroma. Furthermore, chaperones are found to be necessary for the storage of proteins (4) and for the assembly of proteinaceous complexes (5). They are also needed for intra-organellar transport of proteins toward the thylakoid membranes (6) and for protein insertion into the thylakoid membrane and lumen (7). Last but not least, molecular chaperones are involved in protein degradation (8) and in stress tolerance.

and their expression regulation and discuss the functional pathways where molecular chaperones are involved.

32.2 Chaperone Systems within Chloroplasts

32.2.1 The Hsp70 System of Chloroplasts

Hsp70 proteins fulfill a set of different functions in prokaryotes and eukaryotes. They are involved in folding of newly synthesized proteins, in protein transloca-

tion into cell organelles, in protein degradation, and in protection of cells against aggregation of proteins with nonnative conformations caused, for example, by heat. Hsp70s are characterized by an N-terminal ATP-binding and a C-terminal substrate-binding domain. Thus, the chaperone activity comprises substrate binding and release, which is coupled to the ATPase activity of the Hsp70 protein [11]. Cell organelles such as the endoplasmatic reticulum, mitochondria, and chloroplasts harbor their own Hsp70 isoforms. In higher plants, several Hsp70 homologues are expressed. For example, in *A. thaliana*, 17 Hsp70 proteins and in spinach, 12 Hsp70 proteins are annotated [12, 13]. The number of Hsps in higher plants often exceeds that of other eukaryotes such as *Saccharomyces cerevisiae*, with 14 annotated Hsp70 homologues, or *Homo sapiens*, with 12.

The difference can be explained by the existence of plastids as an additional cell organelle with various biochemical functions. Consequently, several Hsp70 proteins have been identified in chloroplasts of higher plants. The majority of the plastid-localized Hsp70s are nuclear-encoded and posttranslationally imported into the organelle. Only one chloroplast-encoded Hsp70 has so far been identified in the chromophytic algae *Pavlova lutherii* [14]. Two stromal and two outer envelope –localized Hsp70s are present in *Pisum sativum* [15, 16]. By screening the *A. thaliana* genome, three Hsp70s were predicted with chloroplast localization (Table 32.1) [13]. Furthermore, at least one Hsp70 was identified in spinach chloroplasts, and the existence of further homologues remains likely [12]. In the green algae *Chlamydomonas reinhardtii*, one Hsp70 is localized in chloroplasts [17]. Sequence analysis revealed that stromal Hsp70s are more related to the DnaK of *Synechocystis* than to Hsp70 proteins of mitochondria, the cytosol, or the endoplasmatic reticulum, suggesting an endosymbiotic origin of the plastid Hsp70 proteins [18].

32.2.1.1 The Chloroplast Hsp70s

One major stromal Hsp70 is identified in pea (Css1), in spinach (Hsp70-9), and in *Chlamydomonas reinhardtii* (Hsp70B) [15, 17, 19]. They are constitutively expressed but can be further induced upon heat stress. After heat treatment, pea Css1 transcripts were increased ninefold [20]. Likewise, the transcript level of Hsp70-9 of spinach was increased upon heat stress [17, 19]. For Hsp70B from *Chlamydomonas reinhardtii*, a 16-fold increase of the transcript level was reported upon heat treatment [21]. Interestingly, a heat-independent induction of Hsp70 expression by light was described for Hsp70B [22–24]. Further studies revealed that an intermediate of chlorophyll biosynthesis is involved in a signal transduction chain for induction of Hsp70B expression [22, 23]. In a *Chlamydomonas reinhardtii* mutant defective in MgPROTO synthesis, Hsp70B expression remained heat- but not light-inducible [25]. Exogenous application of MgPROTO or $MgPROTOMe_2$ to *Chlamydomonas reinhardtii* cells induced expression of Hsp70B, whereas the application of other intermediates of the chlorophyll biosynthesis pathway showed no effect. Furthermore, mutant cells defective in a later stage of chlorophyll biosynthesis, namely, in the formation of chlorophyllide from protochlorohyllide, show light-inducible Hsp70 expression [25]. Therefore, it is concluded that MgPROTO or $MgPROTOMe_2$ is a part of a signaling chain leading to increased Hsp70B expression in *Chlamydomonas reinhardtii* upon illumination.

Tab. 32.1. Chloroplast chaperones in the *A. thaliana* genome. In the following the chloroplast and putative chloroplast chaperones, chaperonins, and chaperone-like proteins are listed. The localization of the proteins was predicted by using the TargetP prediction program, which is available on the Internet (*www.cbs.dtu.dk/services/TargetP/*). Name, AtG code classification, size of the protein in number of amino acids, and the presence of EST clones are listed for each predicted chloroplast chaperone.

Class	*Atg number*	*Name*	*EST clones*	*Length*
FKBP proteins	At5g45680	FKBP-1	+	208
	At4g39710	Unknown protein	+	217
	At1g73655	PPIase-like protein	+	234
	At4g26555	Unknown protein	–	191
Cyclophilins	At3g62030	Roc4	+	260
	At5g13120	Roc8 (TLP 20)	+	259
	At1g74070	Putative cyclophilin	+	317
	At3g01480	AtCyp38	+	437
	At3g15520	AtCyp37	+	406
Hsp70	At4g24280	AtHsp70-7	+	718
	At5g49910	AtHsp70-7	+	718
	At2g32120	AtHsp70-8	+	563
GrpE	At1g36390	Putative Hsp	+	279
	At5g17710	Chloroplast GrpE	+	326
DnaJ	At1g80920	Putative J8	+	163
	At4g36040	AtJ11	+	161
	At5g23240	Unknown protein	+	465
	At2g42750	Unknown protein	+	344
	At2g17880	Putative DnaJ	–	160
	At3g17830	Putative DnaJ	–	493
	At1g77930	DnaJ-like protein	+	271
	At1g80030	Unknown protein	+	500
	At5g05750	DnaJ-like protein	+	294
GroEL	At3g13470	Cpn60β like	+	596
	At1g55490	Cpn60β	+	600
	At5g56500	Cpn60β precursor	+	596
	At2g28000	Cpn60α	+	586
	At1g26230	Putative chaperonin	+	611
	At5g18820	Cpn60α-like protein	–	575
GroES	At5g20720	Cpn20	+	253
	At3g60210	Unknown protein	+	138
	At2g44650	Cpn10	+	139
Hsp90	At2g04030	Hsp-like	+	780
Hsp21	At4g27670	Hsp21	+	227
ClpA	At5g50920	ATP-binding Clp Subunit	+	929
	At3g48870	AtClpC	+	952
	At5g51070	Erd1	+	945
	At5g15450	ClpB-like	+	968

Tab. 32.1. *(continued)*

Class	*Atg number*	*Name*	*EST clones*	*Length*
	At4g12060	Unknown protein	+	267
	At4g25370	Unknown protein	+	238
	At5g49840	ClpX-like	+	608
	At4g30350	Hsp101-like	+	924

Pea Css1 and spinach Hsp70-9 are constitutively expressed in both photosynthetic and non-photosynthetic tissues [12, 20]. The expression level in leaves is higher than in roots, suggesting a role in photosynthesis [12, 20]. Furthermore, a diurnally regulated expression of spinach Hsp70-9 is reported. From this observation, the authors suggested a light-controlled expression of the gene [26]. Although for the pea CSS1 such investigations are still missing, the light induction of the major stromal Hsp70 is probably a common feature among plants.

Using polyclonal Hsp70 antibodies, a second 75-kDa stromal Hsp70 homologue beside the 78-kDa Css1 was detected in the stroma of pea chloroplasts. The expression level of this Hsp70 is not affected by heat treatment [20]. In line with the presence of multiple stromal Hsp70 proteins, three open reading frames of Hsp70 homologues with a predicted chloroplast-targeting signal were found in the *A. thaliana* genome (Table 32.1) [13]. The implications of the presence of multiple stromal Hsp70 remain to be clarified.

In addition to the stromal Hsp70s, two outer-envelope membrane–localized Hsp70 proteins are also described in pea chloroplasts [15, 16]. The one localized on the cytosolic site of the outer membrane of chloroplasts, Com70, was not induced upon heat stress [16]. Com70 is thought to be involved in protein translocation [27], which might explain the missing heat sensitivity. Similarly, the expression of another Hsp70 involved in protein translation across the outer envelope of pea chloroplasts is also not induced upon heat treatment. This chaperone is localized in the outer-envelope membrane and faces the intermembrane space [15].

32.2.1.2 The Co-chaperones of Chloroplastic Hsp70s

The ATP-dependent cycle of substrate binding and releasing by Hsp70 proteins is regulated by co-chaperones. The best-known Hsp70 homologue, DnaK of *E. coli*, requires DnaJ, a so-called J-protein, and GrpE as co-chaperones. DnaJ stimulates ATPase activity of Hsp70, which leads to a strong binding of Hsp70 to its substrate. The stimulating activity is mediated by the interaction of the characteristic J-domain of DnaJ proteins with the ATP-binding pocket of Hsp70 homologues. For substrate release, ADP is exchanged for ATP, which is catalyzed by GrpE proteins [11]. Since stromal Hsp70s show high homology to prokaryotic Hsp70 such as the DnaK of *Synechocystis*, co-chaperones from prokaryotic types are expected in the stroma. Indeed, use of polyclonal DnaJ antibody led to detection of a stromal-localized J-protein in isolated pea chloroplasts [28], which was subsequently termed PCJ1. The nuclear-encoded 431-amino-acid PCJ1 consists of an N-terminal

J-domain as well as a glycine- and cysteine-rich region in the C-terminal region [28]. The glycine- and cysteine-rich region is proposed to be involved in substrate binding. The identity of the interacting Hsp70 is not yet known. Another J-protein, called Toc12, was identified in the outer envelope of chloroplasts [29]. The 103 amino acids of Toc12 comprise an N-terminal membrane anchor and a C-terminal J-domain facing the intermembrane space [29]. The J-domain of Toc12 is capable of stimulating DnaK ATPase activity. Furthermore, computer-supported structural analysis predicts the formation of a disulfide bridge in order to provide a functional J-domain [29]. The outer-envelope membrane–localized intermembrane space-facing Hsp70 was identified as the interaction partner of Toc12.

Despite the identification of nine DnaJ proteins in the *A. thaliana* genome with predicted chloroplast localization (Table 32.1), only one stromal J-protein is characterized in chloroplasts [30]. The nuclear-encoded 125-amino-acid AtJ11 comprises only a J-domain. AtJ11 can stimulate the ATPase activity of DnaK twofold. However, AtJ11 does not stimulate the refolding activity of DnaK [30]. The protein is strongly expressed in roots, stems, flowers and siliques, whereas the expression level in leaves is rather low compared to the other tissues [30]. However, the function and interaction partner remain to be investigated. Remarkably, DnaJ co-chaperones of the major stromal Hsp70s in pea, spinach, and *Chlamydomonas reinhardtii* are not identified.

The second class of co-chaperones of Hsp70 proteins is the family of GrpE homologues. Two open reading frames of GrpE homologues with predicted chloroplast localization were identified in the *A. thaliana* genome (Table 32.1). Using antiserum against *E. coli* GrpE, a GrpE homologue of 19 kDa was detected in a stromal fraction of pea [28]. Further analyses are still missing. In *Chlamydomonas reinhardtii* a 26-kDa GrpE homologue named CGE1 was co-immunoprecipitated by Hsp70B antibodies [21]. Hsp70B and CGE1 form complexes of 120 kDa and 230 kDa. It is assumed that one Hsp70B together with two CGE1 build up the 120-kDa complex, since CGE1 was found to form dimers and tetramers. Therefore, it was further suggested that two Hsp70 and four CGE1 proteins form the 230-kDa complex [21]. The nuclear-encoded CGE1 is localized in the stroma, with a minor fraction associated with membranes [21]. Further sequence analysis revealed that this protein exists in two isoforms, CGE1a and CGE1b, which is longer by two amino acids. The isoforms emerged from differential RNA splicing. Interestingly, CGE1a is predominantly transcribed in response to light stress and under non-stress conditions, whereas under heat stress the transcript level of CGE1b is higher than that of CGE1a [21]. The transcript level of both isoforms together is enhanced 16 times during heat stress and twofold upon light stress. The functionality of both CGE1 isoforms was further demonstrated by complementation of a GrpE-deficient mutation in *E. coli* [21].

32.2.2 The Chaperonins

Chaperonins are divided into two classes. The eubacterial, mitochondrial, and chloroplastic chaperonins form the first class. They require GroES homologues

for proper function. The second class includes eukaryotic cytosolic and archaebacterial chaperonins, which act independently of GroES proteins [31]. The best-characterized chaperonin is the GroEL/GroES machinery of eubacteria. It is involved in the folding of approximately 10–15% of the newly synthesized proteins after the folding reaction by the Hsp70 system [31]. GroEL forms two heptameric rings that enclose a central cavity. This barrel-like structure can enclose proteins up to 60 kDa to provide an appropriate environment for folding. The ATP-dependent folding reaction is regulated by the transient association of a homoheptameric ring of GroES proteins [31].

Chloroplastic Cpn60 was the first identified chaperonin. It was found binding to newly synthesized large subunits of Rubisco in isolated pea chloroplasts before holo-enzyme assembly of Rubisco occurred [32]. Cpn60 proteins share high homology to cyanobacterial Cpn60s, which further supports the notion of the endosymbiotic origin of chloroplasts [33–35]. Sequence analysis showed that Cpn60s are highly conserved among plants [7]. Cpn60s of higher plants are nuclear-encoded and are translated in the cytosol with an N-terminal transit peptide for posttranslational import [7]. So far only one plastome-encoded Cpn60 was identified, namely, a Cpn60 in the cryptomonad *Pyrenomonas salino* [33].

Cpn60s were found at a concentration of 90 μM in the chloroplast stroma of pea chloroplasts [36]. Surprisingly, there are two Cpn60 isoforms present in a 1:1 ratio [36], which is unique in comparison to non-plastid chaperonin systems. These isoforms, the 61-kDa αCpn60 and the 60-kDa βCpn60, form mixed tetradecameric complexes in vitro and in situ [37, 38]. The amino acid sequences are 50% identical [39]. In the *A. thaliana* genome, six open reading frames with predicted chloroplast localization were found (Table 32.1), indicating the presence of further Cpn60 isoforms. Furthermore, αCpn60 has 46% and βCpn60 has 50% sequence identity to the bacterial homologues [7]. Cpn60 was found to be heat-inducible in barley [40] but not in pea [35]. A crucial function of βCpn60 is further indicated by observed pleiotropic effects in transgenic plants with low βCpn60 expression level [41].

Since plastid Cpn60 requires co-chaperones for proper refolding of Rubisco, size-exclusion fractions of stromal extract from *Rhodospirillum rubrum* were incubated with GroEL, ATP, and bacterial Rubisco. Refolding of the bacterial Rubisco was attributed to a 55-kDa fraction, which contained a 24-kDa protein interacting with GroEL in the presence of ADP, subsequently identified as Cpn20 [42]. Cpn20 is widely distributed among mono- and dicots, mosses and liverworts [43]. The spinach Cpn20 is localized in the stroma and forms tetramers in vitro and in situ. These tetramers stimulate refolding of citrate synthase by GroEL in vitro [44]. This observation suggests that the tetramer is the functional form of Cpn20. In line with this proposal is the observation that from multiple oligomers of recombinantly expressed Cpn20, only one oligomer is competent to form a complex in an ATP-dependent manner with the *E. coli* GroEL [45]. The protein comprises two GroES domains organized in tandem. The N-terminal GroES-like domain shows prokaryotic origin, whereas the C-terminal GroES-like domain is more similar to eukaryotic chaperonins [42]. Each of the domains alone is able to replace GroES in order to support phage assembly, but each failed to stimulate Rubisco refolding by GroEL in vitro [43]. Whether the double-sized GroES homologue Cpn20 refers

to a specific requirement of Cpn60 complexes composed of two different subunits remains to be investigated.

In addition, a normal-sized GroES-like protein, Cpn10, was detected in the thylakoid lumen of pea [46]. A later report describes a Cpn10 with putative plastid localization in the EST database of *A. thaliana*, tomato, and soybean [47]. Performing immuno-gold labeling of chloroplasts of leaves from a transgenic *A. thaliana* plant reveals a stromal localization of Cpn10 with a thylakoid-associated population. Whether this protein is homologous to the previously described thylakoid lumen Cpn10 of pea chloroplasts is still not known. In *A. thaliana* two open reading frames encode for Cpn10 proteins with predicted plastid localization (Table 32.1). Sequence analysis reveals that Cpn10 is largely different from other GroES homologues, including Cpn20 [47]. The stromal Cpn10 forms heptameric structures, which can stimulate the refolding activity of *E. coli* GroEL in vitro [45, 47]. Cpn10 seems to be expressed in later stages of plant development than is Cpn20, and its expression is less stimulated by light in comparison to Cpn20. Northern blot analysis revealed that Cpn10 is present in leaves and stems but not in roots [47]. The expression pattern of the chloroplastic GroES-like proteins indicates a differential requirement of the two GroES homologues in plastids.

The requirement of different Cpn10 homologues within chloroplasts is not yet understood. It might be connected to the expression of various Cpn60s in chloroplasts. In the *A. thaliana* genome, two open reading frames coding for αCpn60 and four open reading frames coding for βCpn60 are reported. EST clones are available for only one αCpn60 and three βCpn60s (Table 32.1) [47]. Furthermore, there is also a report about a thylakoid lumen–localized Cpn60 with an isoelectric point different from that of the stromal isoforms [46]. However, apart from the expression of different Cpn60s, different arrangements of the Cpn60 subunits in the tetradecameric complex remain possible, which is implicated by the results of various studies of complex formation and function (Figure 32.2) [38, 48]. Cloney and coworkers [48] demonstrated tetradecameric complex formation of chloroplast Cpn60s of *Brassica napus*, which were overexpressed in *E. coli*. Whereas expression of αCpn60 alone failed to form such complexes, expression of βCpn60 alone, as well as of both Cpn60 isoforms together, leads to complex formation (Figure 32.2). These results implicate that αCpn60 requires βCpn60 for complex formation but not vice versa. Functional analysis of Rubisco folding of these complexes revealed different requirements for GroES [49]. Thus, *E. coli* strains expressing βCpn60 are capable of Rubisco refolding independent of enhanced expression of GroES, whereas expression of both Cpn60s requires increased GroES expression for efficient Rubisco refolding. Due to missing complex formation, expression of αCpn60 did not lead to a refolding of Rubisco [49]. Similar observations were made for in vitro reconstitution of purified Cpn60s of pea chloroplasts [38]. αCpn60 failed to reconstitute in tetradecameric complexes, whereas βCpn60 and a mixture of both Cpn60 proteins lead to a successful reconstitution. It was found that the complex formation of a mixture of both Cpn60s is more enhanced by GroES proteins such as the bacterial GroES, mitochondrial Cpn10, or plastid Cpn20 in an ATP-dependent manner than is the complex formation by βCpn60 alone [38]. That the mixed Cpn60 complexes are approximately two times more

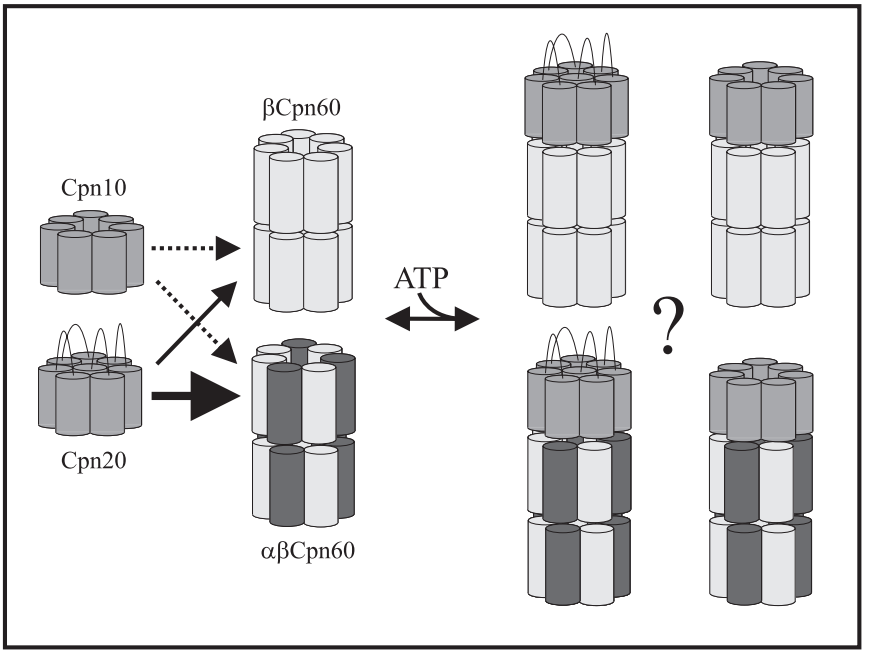

Fig. 32.2. The chaperonin system in chloroplasts. In line with the prokaryotic chaperonin structure of GroEL/GroES, the chaperonin of chloroplasts has to be assembled by a small and a large subunit. Within the chloroplasts, two homologues of the GroES, namely, cpn10 and cpn20, as well as two homologues to GroEL, namely, αCpn60 and βCpn60, exist. Whereas βcpn60 can assemble a homoheptameric complex, αCpn60 requires βCpn60 for complex formation. A heptameric formation of Cpn10 and a tetrameric structure of Cpn20 are assumed (left side). Therefore, there exist several possibilities for the ATP-dependent assembly of the chaperonin complex. However, assembly with Cpn60 homo- or heteroheptamers was observed only for the Cpn20 tetramer. For Cpn10, similar investigations are still missing.

dependent on the presence of GroES explains the observed complex formation in *E. coli* with overexpressed GroES [49]. Complex formation requires ATP hydrolysis, since the addition of the non-hydrolysable ATP analogue AMP-PNP inhibits complex formation in vitro [38]. In contrast, for βCpn60 the presence of endogenous GroES was sufficient for complex formation [49]. In electron micrographs no difference between the architecture of the two complexes was determined, suggesting that the refolding activity of both complex types is based on similar structures [38]. For refolding analysis the dimeric Rubisco from *Rhodospirillum rubrum* was used, since the refolding of the hexadecameric Rubisco of higher plants by chaperonins was not accomplished in vitro. The refolding of acid-denatured Rubisco of both complexes was dependent on the presence of diverse GroES homologues and ATP. The refolding activity was three to ten times more efficient when using the mixed complexes compared to the complexes composed only of βCpn60. The latter refolds Rubisco only in the presence of the mitochondrial Cpn10, but not in the presence of the chloroplast Cpn20 or the bacterial GroES [38]. Whether the assem-

bly of a tetrameric complex by βCpn60 subunits alone reflects an in vitro artifact or is also present in the stroma remains to be clarified. The latter possibility provides an explanation for the presence of two different GroES homologues in chloroplasts and points to Cpn10 as a potential co-chaperone (Figure 32.2).

The molecular basics for the folding activity are well documented for the bacterial GroEL/ES machinery [31]. Much less is known about the plastid Cpn60. Electron micrographs and the tetrameric structure of Cpn60 complexes [35, 38, 48] suggest a mechanism similar to that described for GroEL/ES. This is further supported by the exchangeability of the GroES homologues within the bacterial, plastid, and mitochondrial chaperonin systems [38, 43]. The complex containing Cpn60s and Cpn20 is formed in the presence of ADP and forms asymmetric, bullet-shaped particles [35] that are remarkably similar to the structure of the bacterial GroEL/GroES system [5, 50]. It is proposed that such a complex consists of two rings of seven Cpn60 subunits and two rings formed by Cpn20 [35]. Due to the tandem organization of Cpn20, there has to be a difference from GroEL/ES complexes, which are composed of seven GroES subunits [11]. Accordingly, the stoichiometry of a complex composed of GroEL and Cpn20 was determined to be 14:3.6 [44]. Therefore, it seems likely that four Cpn20s form one ring. In the absence of nucleotides and co-chaperones, the Cpn60 complex reveals a symmetrical structure and is most likely composed of two heptameric rings (Figure 32.2) [35]. The folding activity of the bacterial homologues is dependent on the dynamic association and dissociation of the heptameric GroES ring to the barrel-like GroEL tetradecamer [11]. For refolding of acid-denatured Rubisco by purified chloroplast Cpn60 complexed with Cpn20, a half-time of 3 min was determined [35]. This rate is comparable to that of GroEL and GroES under similar conditions [51]. It was further observed that the assembly of Rubisco holo-enzyme proceeds through intermediates of different sizes in an ATP-dependent manner [6]. There were two particles of 7S and 29S described that contain both Cpn60 and the large subunit of Rubisco. The 29S particle is stabilized by ATP depletion and dissociates upon ATP addition, which leads to the 7S particles. At low ATP levels the 7S particles are competent for Rubisco assembly, which ends in the holo-enzyme formation of Rubisco [6]. It remains to be investigated whether the 7S particles present a building block of the 29S particles when substrate proteins are bound. Interestingly, the ATP-dependent refolding activity of Cpn60 complexes was potassium-independent [35]. This would be in contrast to other described chaperonin systems. However, the authors could not rule out that the purified proteins had already-bound potassium cations [35]. Further structural analysis of the chaperonin complexes and their structure might help to explain the specific features of chloroplast chaperonins.

32.2.3 The HSP100/Clp Protein Family in Chloroplasts

Hsp100 proteins fulfill multiple functions in the cell. In different prokaryotic and eukaryotic organisms [52], their expression is induced under extreme stress conditions such as starvation, heat shock, salt, oxidative stress, glucose/oxygen depriva-

tion, and ethanol or puromycin treatment. Furthermore, Hsp100 homologues have been found to regulate gene expression and are involved in the virulence of *Leishmania* [53]. The functions of these proteins are based on their ATPase activity and formation of ring-structured hexamers, which are both mediated by the nucleotide-binding regions [53]. In this competent complex stage, Hsp100/Clp proteins resolubilize protein aggregates for proteolysis, reactivation, or regulation. The first biochemically characterized member was ClpA of *E. coli*, a component of an ATP-dependent protease complex, which was able to digest casein in vitro [54, 55]. The Hsp100/Clp family is divided into two classes: the feature of the proteins of the first class – ClpA, ClpB, ClpC, and ClpD – is the presence of two ATP-binding domains. ClpM, ClpN, ClpX, and ClpY of the second class comprise only one ATP-binding domain [53]. Structural organization and consensus features distinguish the subfamilies. Class 1 proteins are further characterized by the size of the region between the two nucleotide-binding regions [53].

In chloroplasts two Hsp100/Clp homologues were identified, namely, ClpC and ClpD, also named Erd1 [56, 57]. ClpD is unique for plants, whereas ClpC is also described for gram-positive bacteria and cyanobacteria [52]. In *A. thaliana* eight open reading frames for ClpA proteins with predicted plastid localization (Table 32.1) have been found. Two genes encode for ClpC, one for ClpD, and one for a ClpC-like protein (ClpS) [58, 59]. The presence of several Hsp100/Clp proteins in one organelle is concomitant with the expression of multiple chloroplast-localized ClpP proteins [60, 61]. Since ClpC and ClpD most likely form the regulatory subunit of a ClpP-protease complex, the presence of multiple hetero-complexes with distinct functions in the chloroplast stroma remains possible. ClpC was first identified as an inner-envelope membrane–associated stromal protein in pea. The 92-kDa protein is nuclear-encoded with an N-terminal transit sequence and imported into chloroplasts posttranslationally [56]. However, more detailed studies of the *A. thaliana* homologue revealed an exclusive stromal localization [62].

Although ClpC and ClpD are constitutively expressed [62, 63], the expression pattern of both chloroplastic Hsp100/Clp proteins reveals some differences. Thus, high mRNA and protein levels of ClpC were found in leaves, whereas rather low levels were described for roots, and for etiolated as well as senescing tissues [64–66]. Therefore, ClpC seems to be involved in protection of the plastid against stress conditions caused by the photosynthesis activity. Furthermore, the *Synechocystis* homologue is highly light- and CO_2-induced, but is not heat-induced [67]. The growth rate of *Synechocystis* correlates positively with the ClpC protein content, indicating an essential role of ClpC for photosynthetic growth [67]. The essential role of ClpC in cell survival is further documented by a nonviable knockout of the gene in *Synechocystis* [67]. In addition, it was not possible to generate a viable antisense plant of ClpC in *A. thaliana* [62].

For ClpD a higher transcript level was found in roots and in etiolated and senescing tissues of *A. thaliana* when compared to photosynthetic tissues [65]. Remarkably, the protein level of ClpD in leaves and stems is higher than in roots [61]. Therefore, the authors suggest a posttranslational regulation of ClpD expression. In agreement with this notion, the ClpD transcript level increased during se-

nescence concomitant with a decrease in protein level [63]. The transcript level of ClpD is strongly enhanced under several stress conditions, including cold, light, or oxidative stress. To date, biochemical studies of ClpD, which could explain the altered protein requirements as suggested by the alteration of the expression levels, are still missing. Moreover, further work is required in order to underline the different requirement of the two Hsp100/Clp proteins in chloroplasts.

Only little is known about the biochemical features of the chloroplast Hsp100/Clp proteins. However, several studies on ClpC implicate their involvement in proteolysis. The *A. thaliana* ClpC together with ClpP in the presence of ATP is able to promote degradation of ^{3}H-methylcasein [62]. Furthermore, atClpC is able to functionally replace ClpA in *E. coli*, indicating a similar function of both proteins [62]. ClpC from spinach was found in several high-molecular-weight complexes when stromal extracts were fractionated by size-exclusion chromatography [68]. Fractions of higher molecular weight contain both ClpC and ClpP, indicating a complex formation of both proteins [68] that is ATP-dependent in the stroma [69–71]. In addition, in the presence of ATP, the ClpC-like ClpS1 is present in a 350-kDa complex together with different ClpP proteins [60]. The structure of the ClpP/ClpC complex reveals two heptameric rings similar to that described for the Clp protease of *E. coli* [72–74]. Therefore, for chloroplast Hsp100 proteins, an involvement in the Clp-protease complex is documented. However, evidence of a chaperone activity of these proteins is still missing.

32.2.4 The Small Heat Shock Proteins

The 15- to 42-kDa sHsps are produced in prokaryotic and eukaryotic cells upon heat stress [75]. In plants, sHsps are the most dominant proteins expressed during heat shock [76]. The important role of the small chaperones in plants is underlined by the presence of a larger variety of sHsps when compared to other eukaryotic organisms. Thus, in the *A. thaliana* genome 19 ORFs coding for sHsp-related proteins were identified [77]. The nuclear-encoded sHsps are divided into six classes. The proteins of the first three classes are distributed in the cytosol and nucleus. Furthermore, the small Hsps of the endoplasmatic reticulum, mitochondria, and plastids form individual classes [76]. Common for all sHsps is the C-terminal alpha-crystallin domain [77]. It consists of two consensus sequences separated by a hydrophilic domain of variable length and forms a beta-sandwich structure of two antiparallel β-sheets [77–79]. This domain distinguishes sHsps from other small heat-inducible proteins [80]. Furthermore, the proposed chaperone activity of sHsps is not ATP-dependent.

Plastid-localized sHsps can be identified by a third consensus motif in the N-terminus. It comprises an amphipathic helix with a 100% conserved hydrophilic site and conserved methionine residues on the hydrophobic site. This feature is characteristic for plastid sHsps of mono- and dicotyledons, whereas two Hsp21s of *Funaria hygrometria* do not share the conserved methionine bristle [81]. Therefore, the authors suggest a phylogenetic division of Hsp21 of monocotyledons and

dicotyledons and then branching to mosses [81]. Comparison of the amino acid sequence of *Chlamydomonas reinhardtii* Hsp22 with sHsps of higher plants reveals even lower similarity in this region. Therefore, it is proposed that the methionine bristle evolved during land plant development. Since the amino acid sequences of plastid sHsps are distantly related to *Synechocystis* Hsp16, it is assumed that these proteins originated by gene duplication of a nuclear gene [81].

Pea Hsp21 mRNA is almost not detectable under non-stress conditions, whereas upon heat-stress treatment, the mRNA of Hsp21 increases up to 0.75% of total poly(A)RNA content [82]. Under non-stress conditions only a low protein level of pea Hsp21 was observed [83], whereas it accumulates upon heat stress to >200-fold in leaves and roots, with a half-life of 52 h [84]. Furthermore, overproduction of AtHsp25.3-P in *A. thaliana* provides an increased tolerance against heat and light stress [85]. The detailed mode of sHsps during stress conditions is not sufficiently clarified. Several studies indicate that the PSII complex is one target of sHsps activity. Hsp21 prevents heat-induced damage of PSII in tomato [86].

Pea and *A. thaliana* Hsp21 are localized in the stromal fraction [84], whereas for *Chlamydomonas reinhardtii* a thylakoid grana association and for *Chenopedium allum* a thylakoid lumen localization was reported [87, 88]. Upon posttranslational import into chloroplasts and subsequent processing to the mature size, pea and *A. thaliana* Hsp21 forms homo-oligomers of 200–230 kDa and 300 kDa in native polyacrylamide gels, respectively [89, 90]. The size of the complexes is consistent with complexes formed by recombinant-expressed Hsp21 [90]. After heat shock treatment, the 300-kDa oligomer of atHsp21 undergoes a conformational change, which results in a lower mobility in a native PAGE [85]. Not much is known about the structure and function of plastid-localized sHsp complexes. A chaperone activity of recombinant-expressed *A. thaliana* Hsp21 oligomers was documented by the prevention of thermal-induced aggregation of citrate synthase in vitro [91]. Therefore, the chaperone activity is attributed to the complex structure, which is in line with proposed dissociation and reassembly of the complex during substrate protein interaction and binding (Figure 32.3a) [77]. The current knowledge about structure and function of the oligomers derives from the crystal structure of wheat cytosolic Hsp16.9 [92]. The building blocks of a homo-oligomer are dimers assembled in a dodecameric double disk, which is conserved in sHsps (Figure 32.3a) [77, 92]. Such dimers were also found for the chloroplast Hsp21 of pea directly after import [89]. In heat-treated chloroplasts such dimers were immediately used for complex formation, whereas in non-heat-treated chloroplasts, only the dimer form of Hsp21 was detected [89]. These results implicate a requirement of a specific concentration of Hsp21 dimers or Hsp21 substrates in chloroplasts in order to form oligomeric structures (Figure 32.3a). Therefore, the C-terminal heat shock domain is crucial for contact of other subunits and structural maintenance in the oligomer [93, 94]. Additional heat treatment of already heat-stressed tissues leads to the formation of large insoluble granules of MDa size [95]. To the same extent as heat stress granules (HSG) are formed, a decrement of the 230-kDa complexes was observed, suggesting the aggregation of the oligomers to the insoluble HSG (Figure 32.3a). The HSGs are insensitive to detergent, salt, and nucleotide treatment [95]. Such HSGs

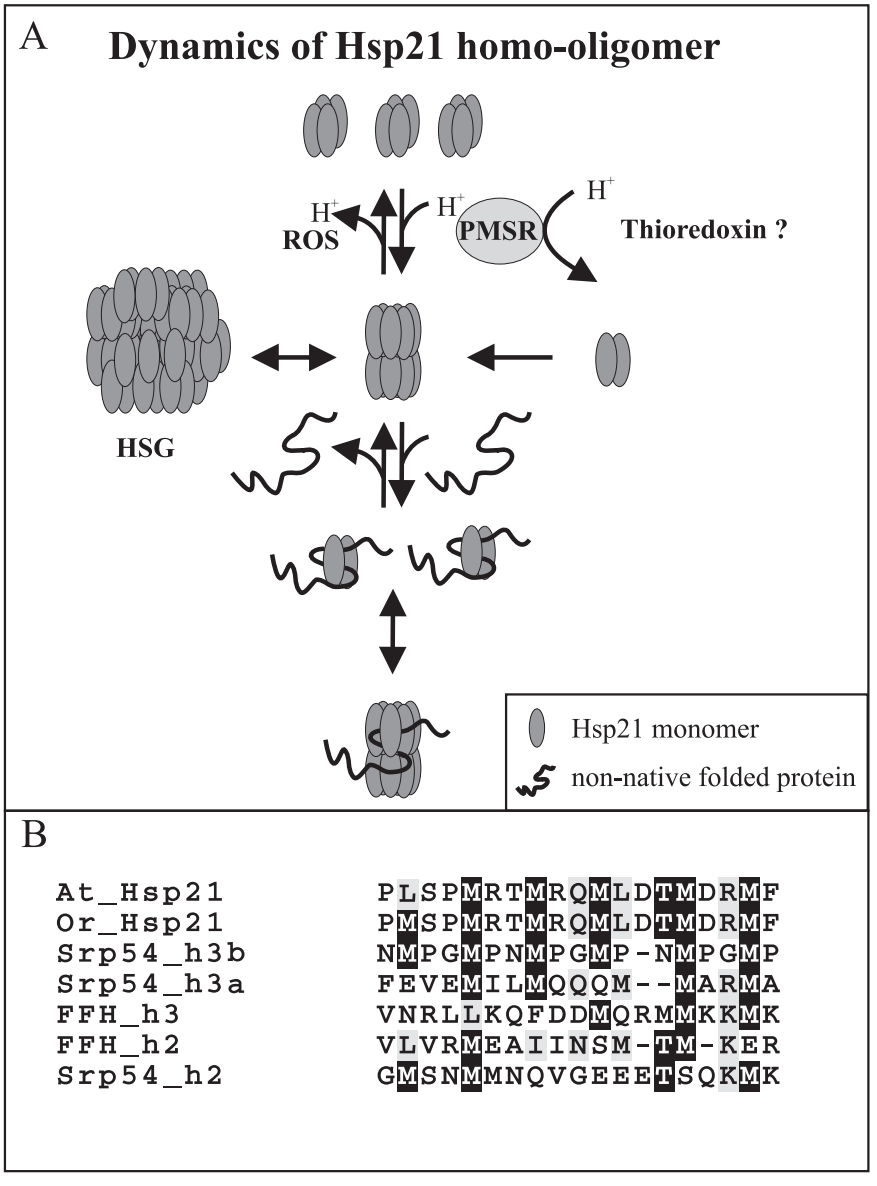

Fig. 32.3. The small heat shock proteins. (A) sHsps form several distinct complex structures in vitro and in situ. The dimeric building blocks assemble in a complex structure, which exhibits chaperone activity by binding of substrate proteins via a cycle of disassembly and assembly (left and lower part). Prolonged stress exposure leads to the formation of nonfunctional high-molecular-weight heat shock granules (HSG). The aggregation is reversible by subsequent cooling (right part). Finally, the active sHsp complex dissociates upon sulfo-oxidation by radical oxygen species (ROS) into tetramers, which lack chaperone activity. The functional complexes can be reformed upon reduction by a stromal thioredoxin-regulated peptide methionine sulfo reductase (PMSR). (B) The methionine-rich

are thought to be formed as long as the refolding capacity of the Hsp70 system is exceeded [96]. According to the documented presence of Hsp70 chaperones in HSG of cytoplasmic sHsps [96, 97], a presence of high-molecular-weight chaperones in chloroplastic HSG remains elusive. Finally, the oligomeric stage of plastid atHsp21 is also affected by sulfo-oxidation of the N-terminal methionine bristle. Sulfo-oxidation leads to a dissociation of the complex in 100-kDa oligomers, which do not exhibit chaperone activity (Figure 32.3a) [91]. Upon reduction of the inactive 100-kDa oligomers by a redox-regulated peptide methionine sulfo-oxide reductase (PMSR), the active complex structures are reassembled (Figure 32.3a) [98].

The chaperone activity is attributed to the N-terminal methionine-rich region [99]. Consistent with this conclusion is the homology of the methionine bristle to methionine-rich regions in Srp54 of yeast and its *E. coli* homologue Ffh (Figure 32.3b) [100], which forms the substrate-binding pocket [101].

32.2.5
Hsp90 Proteins of Chloroplasts

Hsp90 proteins have been described for some eubacteria, cyanobacteria, and eukaryotes. In eukaryotes Hsp90s were found in the cytosol, endoplasmatic reticulum, mitochondria, and chloroplasts [102]. Hsp90s participate in signal transduction, gene expression, and protein degradation [103]. Hsp90s generally are not involved in protein folding but exhibit a preferred recognition of proteins of signal transduction chains as substrate. In the cytosol the ATP-dependent chaperones Hsp70 and Hsp90 cooperate in the folding of nuclear receptors such as the glucocorticoid receptor. Thereby, Hsp90 is thought to receive substrate proteins with almost native conformation from Hsp70 [103]. In contrast, bacterial and endoplasmatic reticulum–localized Hsp90s function independently of co-chaperones [103]. For mitochondrial and chloroplast Hsp90s, analysis of the requirement of co-chaperones is still missing.

The first chloroplast Hsp90 was found in rye and was named, according to its molecular weight, cpHsp82 [104]. It was identified in a cDNA library made of ribosome-deficient plastids isolated from leaves of rye grown at 32 °C. The rye cpHsp82 is nuclear-encoded and synthesized with an N-terminal transit peptide to ensure targeting to chloroplasts. In *A. thaliana* one open reading frame coding for Hsp90 is described (Table 32.1), which contains an N-terminal transit peptide [102]. This protein can be imported in isolated chloroplasts in vitro [105]. Interestingly, for the Hsp90 of rye a higher protein content was found in etiolated and

region of the small heat shock proteins of *A. thaliana* (atHsp21) and *Oryza sativa* (orHsp21) are aligned to the predicted α-helix-forming regions of the M-domain of SRP from *Saccharomyces cerevisae* and its homologue from *E. coli* (FFH). Depicted is an alignment of the methionine-rich domain of *A. thaliana* Hsp21 (88–106); *Oryza sativa* Hsp21 (92–110); helix 2 (363–381), helix 3a (421–437), and helix 3b (459–476) of Srp54 from yeast; and helix 2 (372–388) and helix 3 (413–431) from ffh of *E. coli*. Conserved residues are marked by a black box and homologue residues by a gray box.

chlorotic 70S ribosome-deficient leaves than in photosynthetic active leaves. Furthermore, high Hsp90 protein content was observed in tomato pericarp and in all tomato fruits [104]. In contrast, the plastid-localized Hsp90 of *A. thaliana* reveals a more pronounced expression in leaves and flowers than in roots or stems [105]. High Hsp90 expression levels in reproductive organs and in early post-germination stages indicate a role of the chaperones in plant development. The Hsp90 mutant cr88 harbors a point mutation in a conserved motif, which is probably involved in dimerization and substrate recognition [106–108]. The chlorate-resistant mutant plants grow slower than wild-type plants and exhibit long hypocotyls in red light [105]. Micrograph images revealed less developed chloroplasts in cotyledons and young leaves. Furthermore, light-induced genes such as the gene encoding for the chlorophyll-binding protein show reduced expression. Interestingly, the expression of Hsp90 is light-induced. Based on these observations, the authors proposed an involvement of the plastid Hsp90 in photomorphogenesis [105]. The expression of rye and *A. thaliana* Hsp90 is heat-inducible [104]. However, the function of Hsp90 during heat stress and the role of Hsp90 during plant development or in cell survival against heat shock still are not understood.

The evolutionary origin of chloroplast-localized Hsp90 is still under debate. Based on sequence homology, Schmitz and coworkers [104] suggested a eubacterial origin of cpHsp82. Support comes from the identification of an Hsp90 in *Synechocystis* since it is assumed that chloroplasts derive from a cyanobacterial ancestor. In contrast, when performing signature search, traditional phylogenetic analysis, and statistical tests, Emelyanov [102] postulated that the chloroplast Hsp90 from rye and *A. thaliana* derives from endoplasmatic reticulum homologues.

32.2.6 Chaperone-like Proteins

32.2.6.1 The Protein Disulfide Isomerase (PDI)

PDIs are predominantly found in the ER lumen, where the proteins catalyze the formation, reduction, and isomerization of disulfide bonds during protein folding [109]. At high concentrations, the endoplasmatic reticulum PDI was reported to fulfill a chaperone-like function, distinct from its disulfide bond interaction, such as the inhibition of aggregation of hydrophobic proteins [110, 111]. The only known chloroplast-localized PDI, RB60, was identified in *Chlamydomonas reinhardtii* [112]. It exhibits high homology to endoplasmic reticulum–localized PDIs and contains a C-terminal ER retention signal, KDEL [112]. RB60 is translated as a precursor form and can be imported in isolated pea and *Chlamydomonas reinhardtii* chloroplasts [113]. RB60 partitions between stroma and thylakoids in chloroplasts [113]. The protein is part of a complex that regulates the expression of the psbA gene by binding to the 5′ untranslated region [114]. The complex is composed of four components: RB38, RB47, RB55, and RB60. The complex regulates the association of polysomes to psbA mRNA and thus translation of the gene [114–117]. Binding of the complex is regulated by two distinct mechanisms. ADP-dependent

phosphorylation of RB60 inhibits complex binding at ATP levels attained in chloroplasts only in the dark [118]. Furthermore, the activity of the complex is regulated by dithiol reduction; in vivo, it is probably mediated by thioredoxin [114]. As a target site for redox regulation, vicinal dithiol groups of RB60 are assumed [119]. Thus, reduction of RB60 in the light – most likely by the ferredoxin-thioredoxin system – results in the binding of the complex to the 5′ untranslated region of psbA mRNA and leads to its translation [120]. In line with this proposal, RB60 was found to catalyze the binding of RB47, a protein with high homology to poly (A)-binding proteins [116, 117], to the 5′ untranslated region of psbA mRNA [121]. Thus, the known PDI of chloroplasts participates in the regulation of the expression of a central component of the PSII in response to light and dark conditions. Despite the presence of Rb60, a protein-folding function for PDIs in chloroplasts has not yet been identified.

32.2.6.2 The Peptidyl-prolyl *cis* Isomerase (PPIase)

PPIase catalyzes the interconversion of *cis*- and *trans*-rotamers of peptidyl-prolyl amide bonds [122, 123]. This rotamase activity accelerates the folding of proline-containing proteins in vitro and apparently in vivo [124]. The *cis-trans* isomerization is the rate-limiting step in the folding pathway of proteins. Protein-folding studies with carbonic anhydrase further indicate a function of PPIase as chaperone [125]. PPIases are also referred to as immunophilins in regard to their binding to immunosuppressive drugs. Immunophilins are divided into two classes corresponding to their interacting drug: cyclophilins bind to cyclosporin A (CsA), while FKBPs (FK506-binding protein) bind to FK506 and rapamycin. The cyclophilin A-CsA and FKPB-FK506 complexes interact and thus inhibit the activity of calcineurin and thereby block the Ca^{2+}-dependent signal transduction pathway in a variety of cells, including human T-lymphocytes [126–128]. PPIase are widely distributed from bacteria to mammals and have been found in all subcellular compartments [129, 130]. Although in the *A. thaliana* genome 51 open reading frames coding for immunophilins have been found [131], only little is known about the function of these proteins.

In chloroplasts of several higher plants including spinach (*Spinacea oleracea*), fava bean (*Vicia faba*), pea (*Pisum sativum*), and *A. thaliana*, PPIase activity has been described [131–135]. Low-molecular-weight immunophilins have been reported for chloroplasts, and cyclophilins have been found in the stroma and the thylakoid lumen. For the latter, FKBPs and cyclophilins are described [132]. In line with the diversity in the *A. thaliana* genome, four open reading frames for FKBPs and five for cyclophilins with predicted plastid localization have been found (Table 32.1). It was demonstrated that the stromal-localized PPIase of pea or fava bean chloroplasts can be blocked by CsA and therefore belongs to the cyclophilins. Subsequently, the protein of *Vicia faba* was named cyclophilin B [133, 134]. The rotamase activity of cyclophilin B exhibits a low substrate activity. The combination of CsA and cyclophilin B inhibits phosphatase activity of bovine calcineurin, confirming cyclophilin B as a member of the immunophilins [134]. The cDNA clone coding for cyclophilin B of 248 amino acids was isolated and exhibits an

N-terminal putative transit peptide of 65 amino acids [133, 134]. In *A. thaliana* a stromal-localized cyclophilin named Roc4 was reported [136]. A cDNA clone of Roc4 has 248 amino acid lengths with an N-terminal transit peptide predicted to be 82 amino acids in length [136]. Roc4 is synthesized in the cytosol and after import into chloroplasts is processed to the mature size. The presence of a CsA-sensitive PPIase in a stroma extract of *A. thaliana* chloroplasts has been documented. Whether this activity is based on Roc4 remains to be investigated [136]. Furthermore, Roc4 reveals only 66% sequence identity to human cytosolic cyclophilin, which is lower than for most plant cyclophilins. These features lead to the proposal that Roc4 belongs to a new class of cyclophilins [136]. Therefore, it can be assumed that at least one immunophilin is present in the stroma of chloroplasts of higher plants.

The expression of cyclophilin B and Roc4 is light-induced [133, 134, 136]. Cyclophilin B is also heat-inducible [133, 134]. Northern blot analysis revealed that Roc4 is expressed in leaves and stems but not in roots [136]. In line with this finding, the cyclophilin B protein content was significantly higher in leaves than in roots [133]. These data suggest a pronounced requirement of chloroplasts for PPIase in the stroma in photosynthetically active tissues. However, additional biochemical characterizations are required to identify the substrate proteins and therefore the function of stromal cyclophilins.

CsA-sensitive PPIase activity has been reported for a thylakoid fraction of isolated pea chloroplasts [132]. Since chlorophyll interferes with the PPIase assays, the PPIase activity of the thylakoid fraction was determined after removal of chlorophyll by solubilization and subsequent purification using anion-exchange chromatography [132]. Later studies identified two more cyclophilins in the thylakoid lumen of spinach chloroplasts, TLP40 and TLP20 (thylakoid lumen protein). Both were CsA-sensitive and therefore belong to the family of cyclophilins [135, 137]. Luan and coworkers [133] identified an immunophilin from the rapamycin-binding type in the thylakoid lumen of isolated chloroplasts of *Vicia faba*, which was subsequently named FKBP13. Investigation of its homologue in *A. thaliana* revealed the existence of a bipartite signal present in the cytosolic-synthesized precursor form. The protein was further identified to facilitate the ΔpH pathway [131].

In contrast to stromal cyclophilins, some functional details have been explored about thylakoid lumen–localized immunophilins [131, 135, 137]. The expression of FKBP13 in *Vicia faba* is strongly light-induced, and the expression pattern indicates a restriction to photosynthetic tissues since no FKBP13 was found in roots or in etiolated plants [133]. This observation argues for a requirement of FKBP13 in chloroplasts connected to photosynthesis. Indeed, when using a two-hybrid screen and in vitro protein-protein interaction assays, the cytosolic and intermediate stromal precursor forms of FKBP13 of *A. thaliana* were found to interact with both the precursor and mature form of the Rieske subunit of the cytochrome *b* complex [131]. However, further examinations are required to verify this notion. Furthermore, the function of the mature FKBP13 in the thylakoid lumen remains elusive.

For thylakoid fractions of spinach chloroplasts, the CsA-sensitive PPIase activity has been attributed to TLP20. The authors suggest that TLP20 is the major PPIase

and that it catalyzes protein folding in the thylakoid lumen [137]. However, experimental data are missing to support this proposal. The spinach TLP40 was copurified with a strong phosphatase activity out of isolated thylakoids [135]. Tlp40 comprises a C-terminal cyclophilin domain and an N-terminal leucine zipper as well as a phosphatase-binding region. The cyclophilin domain shows only 25% sequence identity to the human cytosolic cyclophilin and exhibits a CyA-insensitive PPIase activity. The 40-kDa protein is nuclear-encoded, with an N-terminal bipartite transit peptide. TLP40 is more abundant in stroma than in grana of thylakoids [135]. The mRNA level is only moderately stimulated by illumination, which is in line with the detection of TLP40 in etiolated plant tissues [135]. According to the phosphatase-binding region of TLP40, an interaction with phosphatase activity was demonstrated by co-immunoprecipitation [135]. This interaction with the thylakoid membrane phosphatase is salt-sensitive [138]. On one site the activity of the phosphatase is inhibited by the interaction of TLP40 in the presence of a substrate peptide for the cyclophilin. On the other site binding of the PPIase inhibitor CyA leads to an activation of the phosphatase activity [138]. Therefore, the thylakoid lumen binding of TLP40 regulates the phosphatase on the stromal site of the thylakoids. Furthermore, high temperature induces a dissociation of TLP40 from the membrane to the thylakoid lumen, which is coincident with the activation of phosphatase [139]. The dephosphorylation of central components of PSII is thought to trigger repair of photodamaged PSII [139]. Thus, TLP40 might be involved in regulation of the turnover of central photosynthetic protein in the thylakoid membrane.

32.3 The Functional Chaperone Pathways in Chloroplasts

32.3.1 Chaperones Involved in Protein Translocation

The great majority of chloroplast proteins are nuclear-encoded, synthesized in the cytosol, and posttranslationally imported into the target organelle. The protein import comprises two major steps, which are also characterized by their specific chaperone requirements. The first part is the cytosolic synthesis of preproteins with an N-terminal transit peptide as well as the transport through the cytosol to the chloroplast surface, which involves cytosolic Hsp70s and a 14-3-3 protein. Subsequently, the second process of the translocation across the outer- and inner-envelope membrane of chloroplasts takes place. The ATP requirement of the translocation process can be divided into three major steps (Figure 32.4). First, the preproteins bind in an energy-independent manner to the chloroplast outer-envelope translocon, which asks for the unfolding activity of molecular chaperones to ensure translocation through the channel. Cytosolic Hsp70s and the outer-envelope-associated Hsp70, Com70, are likely candidates to fulfill this function (Figure 32.4, step 1). Subsequently, translocation across the outer envelope takes place. The low energy

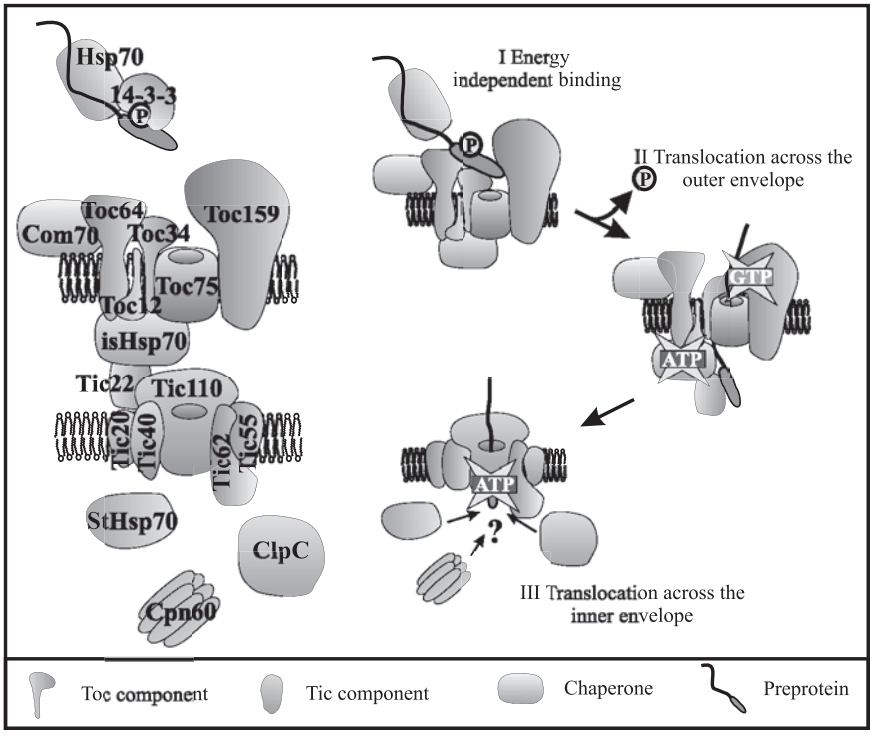

Fig. 32.4. Protein translocation across the envelope membranes. On the left side the molecular architecture of the translocon of the chloroplast envelope membranes is shown. Toc components are marked in blue, whereas Tic components are depicted in red. Chaperones involved in protein translocation are colored yellow. On the right side the translocation process is shown in a three-step model. First the preprotein is bound in an energy-independent way by the Toc receptors Toc34, Toc64, and Toc159 (step1). Upon dephosphorylation of the targeting signal and upon GTP hydrolysis by the GTPases Toc159 and Toc34, the preprotein is translocated across the outer-envelope membrane via the pore-forming Toc75. The translocation event is probably accompanied by the action of the intermembrane space facing Hsp70 via ATP hydrolysis (step 2). For the import in the stroma across the inner-envelope membrane via the Tic translocon, higher ATP levels are required. There are three chaperones suggested to be involved in this translocation process: Cpn60, Hsp70, and ClpC. Their specific role remains to be elucidated (step 3).

consumption for stable association with the Toc machinery is most likely based on the activity of two GTPases, Toc159 and Toc34, as well as of the intermembrane space facing Hsp70 (Figure 32.4, step 2). Finally, the translocation across the inner envelope into the stroma requires higher levels of ATP for the activity of stromal chaperones (Figure 32.4, step 3). However, their identity and docking site on the translocon remains to be clarified.

The involvement of chaperones of the Hsp70 type is most likely mediated by the nature of the transit peptide. Sequence analysis of a set of transit peptides with two

different algorithms revealed the presence of at least one binding site for DnaK, the *E. coli* Hsp70 homologue. This feature is shared by >75% of the analyzed transit peptides [140–142]. There is still a debate about the location of the binding site within the transit peptide. Whereas Rial and coworkers [142] predicted binding sites within the central part, Ivey and coworkers [141] suggest a binding site at the N-terminus of the transit peptide. The presence of this predicted binding site is further supported by in vitro binding assays of Dnak and Css1, the major stromal Hsp70 in pea chloroplasts, to the two precursor proteins pSSU (precursor of the small subunit of the Rubisco) and pFNR (precursor of ferredoxin NADP oxidoreductase) in a transit peptide–dependent manner [140–142]. In vitro ATP application causes a dissociation of the Hsp70 homologues from pFNR, revealing characteristics of a substrate interaction of the chaperone [140, 141]. Rial and coworkers introduce mutations into the transit peptide of pFNR, which results in lower binding of Css1 [143]. However, such mutants are efficiently translocated into isolated chloroplasts in vitro. Based on this observation, the authors suggest only a minor role of Hsp70 homologues during protein translocation [143]. But it remains unknown whether Hsp70 binding is limited to the transit sequence or comprises further targets in the mature domain. When using different fusion proteins, Rial and coworkers [142] could not detect any binding of DnaK to the mature part of FNR unless an artificial binding site was introduced. However, studies using preproteins other than pFNR are still missing, and it remains elusive whether this observation can be generalized. On one hand, Pilon and coworkers [144] have demonstrated that an N-terminal deletion within the presequence of ferredoxin results in loss of import, whereas mutations in this region seemed not to affect protein translocation into the organelle. On the other hand, the studies of Rial were performed with a stromal-targeted preprotein, and therefore the binding of Hsp70 proteins to transmembrane regions of integral membrane proteins in order to prevent unspecific aggregation cannot be excluded. Finally, Rial and coworkers focused their investigation on the stromal Hsp70 Css1 and did not address the impact of the outer envelope Hsp70s of chloroplasts (see below).

Cytosolic targeting of precursor proteins to the chloroplast surface fulfils three major challenges. It prevents preprotein accumulation in the cytosol, it holds the precursors in an unfolded, import-competent state, and it warrants that the enzymatic activity of those proteins does not take place in a wrong cellular compartment. Since these demands are similar to chaperone function, the involvement of Hsp70 proteins is reasonable. Currently, three different pathways are proposed. These are (1) the direction of outer-envelope proteins to the chloroplast surface for membrane insertion, (2) the targeting pathway of non-phosphorylated precursor with the aid of unidentified proteins to the translocation machinery, and (3) the guiding to the chloroplast surface by the interaction to a hetero-oligomeric protein complex called guidance complex [145]. In all cases selective protein targeting through the cytosol most likely starts directly at the ribosome during the synthesis of preproteins. A probable common feature is Hsp70 binding during or after translation. Support for this idea comes from import studies of heterologously expressed and urea-denatured pLCHP (precursor of the light-harvesting protein).

The translocation across the envelope membranes is stimulated by leaf extract and by addition of purified Hsp70 and an additional unknown ATP-dependent factor [146]. However, the import of denatured pSSU and pFd was not stimulated by the addition of Hsp70 [147, 148], even though association of pSSU with HSP70 could be identified [149].

A subset of the precursor proteins contains a phosphorylation motif within the N-terminal transit peptide, which is specifically phosphorylated on serine or threonine by a cytosolic kinase [150]. The phosphorylation motif shares similarities to 14-3-3 binding sites. In line with this observation, size exclusion of the post-ribosomal supernatant of freshly wheat germ lysate–translated pSSU resulted in the identification of a so-called guidance complex [149]. This hetero-oligomeric complex consists of 14-3-3, Hsp70, and maybe other so far unknown components. Furthermore, May and Soll [149] demonstrated that the 14-3-3 of the cytosolic guidance complex is different from the mitochondrial import stimulating factor (MSF), another 14-3-3 protein postulated to promote import of a subset of mitochondrial precursor proteins [151, 152]. Without phosphorylation of the transit sequence, pSSU is found only in association with Hsp70 and imports with an efficiency about fourfold less compared to the guidance complex–bound precursor. Moreover, the guidance complex is not essential for pSSU import in vitro but provides a strong stimulating effect [149]. Whether the guidance complex is responsible for targeting of the preprotein to the receptor or whether the increase of the efficiency of the import process results from bypassing early steps in translocation is still unclear. Furthermore, the docking site of this hetero-oligomeric complex and the stage and mode of guidance complex dissociation remain to be investigated. In summary, the cytosolic targeting involves a 14-3-3 protein and Hsp70 homologues. Both proteins are thought to stimulate trafficking to the chloroplast surface. The Hsp70 system keeps preproteins in an unfolded state to ensure their transfer through the translocation channel. The binding of chaperones to integral membrane proteins is most likely based on the prevention of aggregation by the association of hydrophobic stretches.

The protein translocation process across the two envelope membranes comprises different steps, which are distinguished by their energy requirement. The guided preprotein is recognized by the chloroplast outer-envelope translocon in an energy-independent manner. Toc64, a dynamic associated receptor component, is suggested as a docking site for the guidance complex [153]. The consumption of low ATP levels results in a stable association of the preprotein with the translocon. The two outer-envelope membrane Hsp70 proteins are discussed as a possible source of ATP requirement. However, due to the presence of nucleotide kinases, a conversion of ATP to other nucleotide triphosphates remains possible. Therefore, the energy consumption for stable preprotein association might also reflect the activity of the two GTPases of the Toc translocon.

The translocation apparatus of the outer-envelope membrane is accompanied by two molecular chaperones, namely, Com70 on the cytosolic side [27] and another Hsp70 facing the intermembrane space [15, 154, 155]. Com70 is exposed to the cytosolic site of the outer envelope since it is degraded upon thermolysin treatment

[27]. Hints for its involvement in protein import come from its cross-links to preproteins at the early stage of import [27, 156]. The function of Com70 is still not understood. It might prevent back diffusion of preproteins into the cytosol or it might be involved in protein unfolding prior to translocation. Furthermore, Com70 could keep preproteins in an unfolded state to facilitate precursor passage through the translocation channel.

The second outer-envelope Hsp70 persists in the membrane upon high salt and alkali treatment, indicating an integral membrane character [15]. Thermolysin treatment of intact outer-envelope vesicles did not result in degradation of the chaperone. However, after solubilization of the membranes by Triton X-100 treatment, the protein became susceptible to thermolysin, indicating an orientation to the intermembrane space [15]. The similarity to other eukaryotic Hsp70 homologues shown by partial sequencing and the detection by Hsp70 antiserum against Hsp70 of human HeLa cells underline the identity of the protein as a molecular chaperone [155]. The association of Hsp70 with trapped precursor proteins and the binding to purified pSSU indicate an involvement in protein translocation [29, 155]. Furthermore, co-immunoprecipitation of Toc159 with antiserum against Hsp70 in the presence of a bound preprotein shows an interaction with the translocon of the outer-envelope membrane [154]. Interestingly, the intermembrane space Hsp70 was found as part of an intermembrane space complex. This complex is composed of Toc64, the inner-membrane-associated Tic22, and a J-domain-containing Toc12 [29]. However, a direct interaction with pSSU was demonstrated for Toc64 and Tic22 in vitro. Therefore, Toc12 probably recruits the Hsp70 protein to the complex, since no interaction between Toc12 and pSSU was observed in vitro [29]. The function of this complex remains elusive. However, it seems likely that the complex keeps preproteins in an unfolded state to facilitate translocation across the inner membrane and to prevent protein aggregation in the intermembrane space. It is argued that this pathway is specialized for a certain subset of preproteins, since the components of the intermembrane space complex are less abundant than the components of the core complex.

The translocation process across the inner-envelope membrane of chloroplasts is assisted by chaperones as well. Several chaperones are discussed for association of the inner-envelope translocon, such as ClpC, Cpn60, and a stromal Hsp70, named S78 [157–159]. Cpn60 was co-immunoprecipitated by antibodies against the major component of the inner-membrane translocon, Tic110, in the presence of preproteins [157]. Therefore, a transient interaction of Cpn60 to the translocon for folding of the incoming preprotein is proposed [157]. However, Cpn60 was identified as a Rubisco assembly factor (Section 32.3.3), which raises the question of whether the identified association of the chaperonin might be specific to the bait used in this experiment. In contrast, ClpC (Hsp 100) was also found in a cross-linked complex in the presence of a preprotein [158, 159]. This observation leads the authors to the proposal of ClpC being associated with the Toc-Tic super complex [159]. However, both Cpn60 and the Hsp100 molecule were identified after isolation of the translocon joint by a translocation intermediate of the small subunit of Rubisco, and in vitro analysis of interaction with recombinant proteins is still miss-

ing. Furthermore, one has to keep in mind that for the plastid ClpC no chaperone activity has been demonstrated so far. It is only known as a regulatory component of the Clp protease of the chloroplast stroma. Interestingly, the small subunit of Rubisco is rapidly degraded if it is not integrated into a functional complex, a process involving ClpC (Section 32.3.4). This raises the question of whether the association was specific or resulted from the prolonged experimental procedure. Therefore, the functional significance of these data remains to be clarified. In a high-molecular-weight complex after cross-linking and during translocation, the stromal Hsp70, termed S78, was also found. Furthermore, Tic40, a component of the translocon facing the stroma, comprises a C-terminal TPR domain, which is 32% identical to the Hop protein Sti1p. Hop proteins are involved in the formation of chaperone complexes by mediating the interaction between Hsp70 and Hsp90, and deletion of these proteins results in a drastic reduction of growth [160]. Tic40 was found by screening for a homologue of the Cim/Com44 of *Brassica napus* [161] in *Pisum sativum* [162]. Since a stromal exposition of the soluble C-terminal domain is proposed, Tic40 might act as a co-chaperone. However, evidence for such a role of Tic40 is still missing. Surprisingly, a null mutant of Tic40 is not lethal [160], which would have been expected in the case of such a crucial function in protein translocation.

32.3.2
Protein Transport Inside of Plastids

Proteins imported into chloroplasts (see Section 32.4.1) or synthesized in the organelle [163] have to be transported toward their place of function (Figure 32.1, pathway 6). This process is coupled either to the import of the preproteins or to their translation.

For the first case it is still under debate, which chaperone might be involved in the translocation event at the stromal side (Section 32.3.1). The ATP dependence of the translocation of proteins across the inner membrane [164–168] strongly suggests the action of a chaperone. Indeed, one stromal Hsp70, namely S78, was identified in high molecular Toc/Tic complexes [13, 169, 170]. Strikingly, this would assemble the current picture on the final translocation across membranes, since the mitochondrial import or bacterial export system also requires the action of an Hsp70 homologue. However, Hsp100 or Cpn60 were also found to be associated with the translocon (Section 32.3.1). Therefore, it remains under debate, which chaperone is generally involved in protein translocation across the inner envelope.

So far, not much is known about the transport systems within chloroplasts, since only few examples were studied. For the Rieske FeS protein inserted into the thylakoids by the TAT pathway [171] it was observed, that shortly after translocation into the stroma the protein is associated with the Cpn60. During further transport toward the TAT translocon the protein becomes associated with one of the stromal Hsp70 [172]. This would lead to the assumption that Cpn60 mediates the transport from the membrane into the stroma and Hsp70 is involved in the translocation into the thylakoids. However, knowing that Cpn60 and Hsp70 are also involved in

folding (Section 32.3.3) and that TAT substrates are only translocated in a folded state it cannot be clearly distinguished between folding and targeting. Investigation of the translocation of a second protein, namely the precursor of the stromal ferredoxin-NADP reductase (FNR) revealed a different mode. pFNR first associates with Hsp70 and only subsequently with Cpn60 upon import into the stroma [173]. Furthermore, in vitro studies suggested that the association with Hsp70 is necessary for processing, whereas association with the Cpn60 homologue GroEL cannot restore processing [174]. These results indicate that Hsp70 might even be involved in the late translocation events of protein import. Even though more studies have to confirm this result, it can be suggested that one Hsp70 is involved in late steps of protein import or early steps of protein transport preceding the processing. Cpn60 might then be required for quality control and or folding and a second Hsp70 in further transport of thylakoid proteins toward the membrane or their storage in the stromal compartment (Section 32.3.5).

However, not only Hsp70 proteins are involved in transport of proteins toward thylakoids. One routing systems was found for the LHCP proteins, which require a signal recognition particle for their transport [175], which is essential and sufficient to target LHCP. However, the influence of an Hsp70 on this process was discussed controversially. On one hand it was suggested that Hsp70 is needed for the insertion process [176]. In contrast, it was demonstrated that addition of Hsp70 to unfolded protein could not restore translocation [177]. It might therefore be that Hsp70 is required for partly unfolding of the incoming protein to keep it competent for recognition by SRP. However, this again would suggest that an Hsp70 isoform is involved in the late translocation/early folding events.

32.3.3
Protein Folding and Complex Assembly Within Chloroplasts

Assembly of the functional form of Rubisco was found to be dependent on the Rubisco binding protein, which subsequently was identified as Cpn60. The first direct evidence for its function in assembly derived from the observation that antibodies against Cpn60 block the Rubisco holo-enzyme assembly [6]. The later identified chaperonin complex is not only essential but also sufficient to drive the formation of the active form of Rubisco in vitro [178]. However, investigations on the dimeric form of Rubisco of *Rhodospirillum rubrum* suggested that Cpn60 is actually involved in the folding of the subunits of the complex rather than in its assembly [178, 179]. In contrast to its bacterial homologue, Cpn60 does not require potassium for its action. An interaction of Cpn60 with a set of proteins after their translocation into the chloroplasts was demonstrated by non-denaturing gel electrophoresis. These proteins also include the monomeric β-lactamase, which does not form any functional oligomers [180]. Later studies further revealed that Cpn60 is involved in folding of ferredoxin and Rieske iron-sulfur protein [172, 173]. Therefore, Cpn60 is involved not only in the folding and assembly of components of multimeric complexes but also in the folding of monomeric proteins.

In addition, urea-denatured CF_1 subunits of the chloroplast F-type ATP synthe-

tase require Cpn60 and Hsp70 for reconstitution in a functional CF_1 complex in vitro [181]. It is thought that first the trimeric complex of the α- and β-subunit is formed and then the γ-subunit is assembled [181]. However, the specific requirement of the chaperone systems in the specific steps remains unknown.

The integration of proteins into the thylakoids (for review see Ref. [182]) and the assembly of protein complexes require the action of chaperones or proteins with chaperone-like function. For example, the assembly of the photosystem II (PSII) requires HCF136. Even though it remains unknown how this protein influences the assembly of this complex, the deletion of HCF136 results in an inhibition of the assembly of the reaction center of PSII [183]. Similarly, the assembly of PSI is mediated by factors including the investigated Ycf3. Ycf3 contains a TPR motif at the amino terminus, which is essential for the assembly of the components of PSI. However, it remains elusive whether the TPR-containing region itself acts as assembly factor or if this region recruits other components of a larger assembly machinery.

32.3.4
Chloroplast Chaperones Involved in Proteolysis

Chloroplast development and biogenesis are strongly related to the adaptation of the proteome on the developmental condition and on removal of misfolded or unassembled proteins. Therefore, it is not surprising that a complex system for protein degradation was identified in the stroma of chloroplasts and that the expression of the components of the system is light- and developmental-dependent (see Section 32.2.3). It could be demonstrated that proteins of the stroma become degraded in an ATP-dependent manner [69, 184, 185]. Investigation of this degradation suggested that ClpP is involved in this process. When ClpP is downregulated, the adaptation to a high concentration of CO_2 is reduced, leading to the conclusion that these proteins are also involved in degradation of fully or partly assembled cytochrome b_6f complexes [185]. However, the proteolytic activity of ClpP is controlled by a variety of cofactors, and several distinct complexes have been identified (Section 32.2.3). The functional complementation of the ClpP from *E. coli* by ClpC cofactors of tobacco [62] suggests that the ClpP/ClpC system in plants has similar functional properties when compared to the *E. coli* system [52]. However, the extra amino acids on the N-terminus of ClpP suggest a more complex system than that found in the prokaryotic ancestor [65]. This is also supported by the observation that ClpP isolated from plastids can degrade the same peptide as its homologue from *E. coli*. One of the best-investigated co-factors for ClpP within chloroplasts is the nuclear-coded ClpC (Section 32.2.3). This protein is involved in the degradation of newly synthesized proteins within isolated chloroplasts [186]. ClpC is also involved in the ATP-dependent degradation of mistargeted and therefore unassembled proteins such as the 33-kDa subunit of the oxygen-evolving complex [69]. Furthermore, the data suggest that this protein is involved in the regulation of the Rubisco stoichiometry [52]. This is in line with the observation that the nuclear-encoded and subsequently translocated small subunit of Rubisco becomes rapidly

degraded if not integrated in a Rubisco holo-complex [187]. Therefore, it becomes clear that the identified Clp system is involved in the housekeeping of the proteome. The Clp system could also be involved in protection against cellular damage caused by photo-inhibition by degradation of affected proteins. However, despite the stated observations, not much is known about protein degradation within chloroplasts and its regulation.

32.3.5 Protein Storage Within Plastids

Plastids undergo drastic changes during their transitions from one type to the other. This kind of transition requires a large change of the proteome. Not only the transition of plastids but also developmental or environmental changes require changes in the proteome. One way of adaptation is the increase of protein import for new proteins (Section 32.3.1) and protein degradation of proteins no longer required (Section 32.3.4). However, a further backup system might be the storage of proteins for further use. It could be demonstrated that the typically membrane-associated phytoene desaturase exists in a soluble form in forming chromoplasts. These ''stored'' proteins are complexed with Hsp70 [188, 189]. After association of the phytoene desaturase with FAD, the complex between the enzyme and the chaperone disassembles and the enzyme is targeted to the membrane surface. The authors discuss that this association prevents the degradation of the phytoene desaturase. Since chromoplasts derive from chloroplasts, massive changes of the ultrastructure are required [190], leading to the formation of up to 50 concentrically stacked membranes [188, 189]. This might require the preceding translocation of nuclear-encoded preproteins and their storage for further use. Even though the phytoene desaturase is the only studied example, it seems likely that chaperones, especially of the Hsp70 class, are involved in the storage of a subset of proteins during plastid transitions in order to prevent those pre-imported proteins from degradation. However, subsequent investigations will have to reveal whether this process is limited to a small subset of proteins with low expression levels, such as the studied phytoene desaturase [188], or whether this is a general mechanism within plastids.

It could also be demonstrated that immunophilins (Section 32.2.6.2) serve as molecular anchors for proteins. For example, the lumenal domain of the Rieske subunit of the cytochrome *b* complex was found to interact with the intermedial, stromal-localized form of FKBP13 [131]. In this way FKBP13 might regulate the content of the Rieske subunit in the thylakoid membrane and further serve as a reservoir of the Rieske subunit for conditions with pronounced requirements of proteins of the photosynthetic electron chain. This is further supported by the observation that gene silencing of FKBP13 by RNAi leads to a 70% increment of the Rieske subunit proteins in the thylakoid membranes [131]. Again, this demonstrates that stromal protein storage is essential for the adaptation to drastic developmental or environmental changes and that chaperones or chaperone-like proteins are involved in this storage.

32.3.6 Protein Protection and Repair

Photodamage of the photosystems can occur under high light conditions. The protection and/or repair of the photosystems are essential for the functionality of chloroplasts. A function of the proteins of the Hsp70 family could already be expected, since the expression of some isoforms was found to be light-inducible. Thus, studies with mutant strains exhibiting a lower expression of Hsp70-B render the photosystem II more sensitive to light-induced damage than the wild type. In contrast, overexpression leads to a higher protection of the PSII [191]. The higher expression leads especially to the stabilization of two proteins of the PSII, namely, D1 and CP43, two proteins highly sensitive to photodamage [192]. Further support comes from the observation that high light treatment induces the formation of a 320-kDa complex containing Hsp70 and the photodamaged but non-degraded D1, D2, and CP47 [193]. This complex was discussed to represent a photosystem II repair intermediate. In line with these observations, 5–25% of the total chloroplast content of Hsp70-B is membrane-associated [194]. Small Hsps were also proposed to be involved in protection from photodamage. It is proposed that small plastidial chaperones can act as scavengers for radical oxygen species (ROS) induced by heat or light stress or might be involved in prevention of protein aggregation. It was suggested that the surface-exposed amphipathic helix of the methionine bristle in the N-terminus can be sulfo-oxidized and might function as scavenger for ROS [91]. This conclusion is supported by the proposed function of methionine residues as antioxidant defense mechanism [195]. The sulfo-oxidation of methionine residues in the N-terminus results in drastic conformational changes of the *A. thaliana* Hsp21 in vitro. Therefore, sulfo-oxidation reduces the amount of surface-exposed amphipathic helices [91]. Sulfo-oxidation under cold stress leads to a formation of a 450-kDa oligomer. In contrast, under heat stress the functional oligomer dissociates upon sulfo-oxidation into nonfunctional 100-kDa complexes, which probably resemble tetramers [91]. These 100-kDa complexes do not possess chaperone activity. Similarly, phosphorylation of cytosolic Hsp27 of mammals leads to tetramer formation, which abolishes chaperone activity [196]. For plastid atHsp21, in vitro reduction of methionines of 100-kDa complexes by the peptide methionine sulfo-oxide reductase (PMSR) leads to the reassembly of functional oligomeric complexes [98]. The chloroplast-localized PMSR is highly expressed in photosynthetic tissues in *A. thaliana* [197]. Its activity is redox-regulated, which is shown by inactivation through sulfo-oxidation and reactivation through DTT treatment [98]. The authors suggest thioredoxin as a reductant of PMSR in vivo [98]. Thus, Hsp21 might play an essential role in protection of the photosynthetic apparatus as an ROS scavenger. However, data providing a direct connection between the in vitro data of sulfo-oxidation and the in vivo observed stabilization of PSII are still missing.

The second parameter that drastically influences the biogenesis of plastids is temperature. Temperature adaptation is largely achieved by alteration of the expression levels of the needed proteins. However, heat stress also induces oxidative

stress, and the functionality of the complexes has to be warranted under high temperatures. In line with the observation that small Hsps are involved in protection of the photosystem II, heat stress leads to an association with the grana thylakoids as well [88]. As before, a function in protection of the photosystem II was suggested [87, 198]. Moreover, it could be demonstrated that small Hsps are involved in restoring electron transport in pre-heat-stressed plants [86]. Furthermore, biochemical evidence for chaperone activity of sHsps is provided by the prevention of thermal-induced aggregation of citrate synthase by Hsp21 in vitro [91]. Therefore, Hsp21 is thought to prevent substrate proteins from aggregation in order to keep them competent for the plastid refolding machinery [97]. Plastid sHsps seems to function not only under heat stress but also under cold stress. Thus, in tomato (*Lycopersicon esculentum*) plastid induction of Hsp21 provides cold-stress tolerance [199]. In addition, Cpn60 also seems to be involved in heat-stress adaptation, since a tDNA insertion in the gene of βCpn60 results in accelerated cell death in response to heat stress [200]. The molecular mechanism of this observation, however, remains to be investigated.

32.4 Experimental Protocols

32.4.1 Characterization of Cpn60 Binding to the Large Subunit of Rubisco via Native PAGE (adopted from Ref. [6])

1. Isolation of chloroplasts: Harvest leaves of 9- to 11-day-old peas. Disrupt the tissues with a blender in homogenization medium (20 mM Mops, 13 mM Tris, 0.1 mM $MgCl_2$, 330 mM sorbit, 0.02% BSA). Filtrate the homogenate through four layers mull and one layer gauze. Pellet chloroplasts (1500 *g*, 4 °C, 5 min) and apply the resuspended pellet on a Percoll (Amersham Bioscience, Upsalla, Sweden) gradient (10 min, 4°C, 7000 rpm). The Percoll gradient consists of a 40% and an 80% layer in 330 mM sorbit, 50 mM MOPS/KOH pH 7.9. Collect the intact chloroplasts on the 40% Percoll layer with a Pasteur pipette and transfer them in 12–14 mL of ice-cold resuspension buffer (50 μM EDTA, 0.2 mM $MgCl_2$, 375 mM sorbit, 35 mM HEPES/KOH pH 8.3, 0.96 mM DTT, 200 μM isoleucine, 200 μM threonine). Centrifuge the mixture (4000 *g* and brake immediately) and resuspend the pellet in a minimal volume of resuspension buffer. Determine the chlorophyll content according to Arnon [201].
2. *In Organello* protein synthesis: Illuminate isolated chloroplasts for 24 min in the presence of 400 mCi [^{35}S]methionine (> 1000 Ci mmol^{-1}). Resuspend the chloroplasts in a 10-fold excess of resuspension buffer and pellet the chloroplasts (4000 *g* and brake immediately).
3. Lyse the chloroplasts in 10 mM Tris/HCl pH 7.6, 1 mM benzamidine, 1 mM ε-aminocaproic acid, 7 mM β-mercaptoethanol, and 1 mM PMSF.

4. Remove the membranes by centrifugation (100 000 *g*, 30 min, 4 °C).
5. Divide the cleared lysate into 90 µL aliquots.
6. Bring the aliquot to 50 mM HEPES/KOH pH 7.6, 220 mM KCl, 6 mM $MgCl_2$, 20 mM DTT.
7. Incubate for 30 min at 0°C.
8. Incubate the sample for 60 min at 24°C.
9. Apply the sample on a non-denaturating polyacrylamide gel and run the gel overnight at 4°C.
10. Native PAGE: Prepare all buffers and gel solutions as described [202], but omit SDS. Pour a slab gel of 7.5% (w/v) polyacrylamide and a stacking gel of 4% (w/v) polyacrylamide concentration without the addition of an SDS cocktail. Add glycerol to the sample to a final concentration of 10% and apply it on the gel. Run the gel at a constant voltage of 2.5 mA until the voltage reaches 150–200 V. At this time switch the gel to a constant voltage of 150–200 V and run it for 18–24 h at 4 °C.
11. Soak the gel in EN^{3}HANCE, dry it, and expose it to X-ray film. Develop the film for analysis.

32.4.2

Purification of Chloroplast Cpn60 From Young Pea Plants (adopted from Ref. [203])

1. Plant material: Plant peas as a dense monolayer in trays with compost. The trays are subsequently incubated at low light (20–40 $\mu Em^2\ s^{-1}$) at 18–22 °C with a 12-h illumination cycle and rich watering. Cut leaves from 10-day-old plants (usually from four standard trays) for protein isolation.
2. Protein extract preparation: Perform all steps on ice or in the cold room. Grind the plants using Polytron homogenizer (usually in 10 portions) with 200 mL of ice-cold buffer (20 mM Tris/HCl pH 7.5, 10 mM $MgCl_2$, 10 mM EDTA, 50 mM β-mercaptoethanol, 50 g L^{-1} PVPP, 1 mM PMSF) per portion. Typical grinding conditions: four bursts of 10 s at the maximal speed. Add immediately prior grinding 50 mM β-mercaptoethanol, 50 g L^{-1} PVPP, and 1 mM PMSF (0.4 mL of 0.5 M solution in methanol per 200 mL). Centrifuge the homogenate in a high-volume rotor and filter the supernatant through eight layers of muslin.
3. Ammonium sulfate precipitation: Add solid $(NH_4)_2SO_4$ to the extract (2×1 L) to make 40% saturation. Allow the precipitate to form for 30 min in the cold room on a magnetic stirrer and subsequently centrifuge at 10 000 *g* for 30 min (Beckman JA10 rotor). Discard the pellets, add solid $(NH_4)_2SO_4$ to the supernatant to 60% saturation, and allow the precipitate to form for an hour. Collect the protein precipitate by centrifugation as described above (supernatant discarded) and dissolve in 1 L of cold column buffer (20 mM Tris/HCl pH 8, 0.1 mM EDTA, 10 β-mercaptoethanol, 0.5 mM PMSF [add before use]). Precipitate proteins by adding $(NH_4)_2SO_4$ to 60% saturation (usually left overnight).
4. Desalting on Sephadex G25: Centrifuge protein precipitate as above (supernatant discarded). Dissolve the pellets in a small volume of the column buffer ($<$ 130 mL resulting solution) and centrifuge at 18 000 *g* for 60 min (Sorvall

SS34 rotor). Discard green pellets, and pass the supernatant through a column filled with 400 mL Sephadex G-25 (medium). Combine all protein-containing fractions (eluted after the void volume of the column) and centrifuge as above; discard green pellets.

5. Q-Sepharose chromatography: Load the desalted material onto a column containing 300 mL of Q-Sepharose Fast Flow (Amersham Biosciences) equilibrated with the column buffer. Elute proteins in a gradient of 0–0.8 M NaCl (1-L gradient volume). Analyze the fractions by SDS-PAGE (using a gel composed of 15% acrylamide and 0.15% *bis*-acrylamide). Chloroplast Cpn60 elutes after Rubisco (the protein of the highest abundance) and is easily distinguished, as it exhibits characteristic dual bands due to the presence of two polypeptides of very similar size around 60 kDa (which could be resolved only on low cross-linked gels).
6. Fractogel TSK butyl 650 (S) chromatography: Combine fractions containing chloroplast Cpn60 and load onto a column (1.6 × 15 cm) with Fractogel TSK butyl 650(S) (Merck) equilibrated with buffer containing 20 mM Tric/HCl pH 8, 0.2 mM EDTA, 5 mM β-mercaptoethanol, and 20% of saturation of $(NH_4)_2SO_4$. Apply a decreasing (20% to 0%) $(NH_4)_2SO_4$ gradient followed by isocratic elution (no ammonium sulfate). Chloroplast Cpn60 elutes as a sharp peak soon after the end of the gradient.
7. MonoQ HR5/5 chromatography: Combine the Cpn60-containing fractions and apply the pooled sample onto a MonoQ HR5/5 column. Run a gradient of 0–0.5 M NaCl in 20 mM Tris/HCl pH 8, 5 mM β-mercaptoethanol. Collect the fractions containing Cpn60.
8. Superdex 200 HR10/30 chromatography: Combine the Cpn60-containing fractions from the MonoQ HR5/5 column and apply the sample on a Superdex 200 HR10/30 size-exclusion column. Use 40 mM triethanolamine acetate pH 7.5, 0.1 M potassium acetate, 0.1 mM EDTA, and 1 mM DTT for gel filtration. Concentrate the Cpn60-containing fractions and store them at −20 °C.

32.4.3 Purification of Chloroplast Hsp21 From Pea (*Pisum sativum*) (adopted from [90])

1. Plant material: Peas (*Pisum sativum* L. cv. Little Marvel) are planted on vermiculite and grown for 9 days at 22 °C using a 16-h photoperiod. Before harvest on the ninth day, the growth temperature has to be shifted from 22°C to 38 °C at a rate of 4°C per hour. The plants will then be kept for 4 h at 38°C before the temperature has to be decreased to 22°C at a rate of 4°C per hour.
2. Chloroplast isolation and stroma purification: Leaf tissues from 1 kg plant material (step I) are homogenized in a blender in isolation medium (330 mM sorbit, 20 mM Mops, 13 mM Tris, 0.1 mM $MgCl_2$, 0.02% BSA). The slurry is filtrated through four layers of mull and one layer of gauze. Chloroplasts are recovered by centrifugation at 1500 *g* for 5 min at 4 °C. The obtained pellet is resuspended in isolation media before loading on a Percoll step gradient composed of 13 mL 40% and 10 mL 80% Percoll in 50 mM HEPES/KOH pH 7.9; 330 mM sorbit. Intact chloroplasts on the interface between the 40% and 80%

Percoll layer are collected, resuspended in wash medium (330 mM sorbit, 50 mM HEPES/KOH pH 7.6, 3 mM $MgCl_2$) and pelleted by centrifugation at 1500 *g* for 5 min at 4°C. The washing step is then repeated. Washed chloroplasts have to be diluted in 10 mM HEPES/KOH pH 8, 10 mM *ε*-amino-*n*-caproic acid and 1 mM benzamidine to a final chlorophyll concentration of 5 mg mL^{-1}. Removal of sorbit results in lyses of chloroplasts. After incubation for 10 min at 4°C, chloroplast membranes are removed by centrifugation (100 000 *g*, 1 h). Subsequently the supernatant is collected and stored at −20°C for further use.

3. Ammonium sulfate precipitation: Add 0.1 M citrate buffer (one and half volume of the stromal extract) and ammonium sulfate to 40% final concentration to the stromal extract. After incubation for 1.5 h at 4°C protein precipitate is removed by centrifugation at 12 000 *g* for 45 min at 4°C. The supernatant contains Hsp21, which can be controlled by SDS-PAGE and immunoblotting.
4. Hydrophobic interaction column: In order to purify Hsp21, the supernatant will be filtered through a 0.2-μm filter and applied on a hydrophobic interaction column (21.4 × 100 mm, 300-Å pore size; model 83-B23-E, Dynamax Hydropore, Rainin, Woburn, MA). Hsp21 will be eluted by a gradient from 2 M to 0 M ammonium sulfate in 100 mM sodium phosphate, pH 7.0. A 50-mL gradient has to be applied with a flow rate of 5 mL min^{-1}. Five-milliliter fractions were collected and dialyzed against 10 mM Tris/HCL pH 8. The Hsp21-containing fractions are then identified by SDS-PAGE and immunoblotting.

32.4.4
Light-scattering Assays for Determination of the Chaperone Activity Using Citrate Synthase as Substrate (adopted from [196])

The oxidation of Hsp21 influences the functionality of the chaperone. First, oxidation induces the formation of larger oligomers of Hsp21, which can be assayed by native PAGE electrophoresis (see Section 32.1.1). Second, oxidation reduces the chaperone activity, which can be assayed as follows:

1. Oxidized Hsp21 is prepared by incubation of 0.4 mg mL^{-1} Hsp21 with 5 mM H_2O_2, 0.1 M ammonium bicarbonate buffer, pH 7.8 at 37 °C for 2 h.
2. For control, the oxidation of Hsp21 can be reverted by addition of 12 mM $MgCl_2$ (final), 34 mM KCl (final), 15 mM DTT, and 5 mM peptide methionine sulfoxide reductase (EC 1.8.4.6) to a final ratio of 1:50 (PMSR:Hsp21). This mixture has to be incubated for 30 min at 25 °C prior to use.
3. To assay the activity of Hsp21, the thermal aggregation/denaturation of citrate synthase can be determined. For this, 37.5 nM citrate synthase in 40 mM HEPES/KOH, pH 7, in the absence or presence of a 30-fold molar excess of Hsp21, Hsp21 oxidized, or Hsp21 oxidized and reduced is placed in a cuvette to determine the aggregation by light scattering. The sample will then be shifted to 43°C and the time-dependent light scattering will be recorded, for example, facilitating a RF-5301PC Shimadzu spectrofluorometer. The rate of aggregation

of citrate synthase can be monitored by a simple time scan where both the excitation and emission wavelengths are set to 500 nm with a spectral bandwidth of 2 nm.

32.4.5

The Use Of *Bis*-ANS to Assess Surface Exposure of Hydrophobic Domains of Hsp17 of *Synechocystis* (adopted from [202])

Bis-ANS (1,1′-*bis*(4-anilino)naphtalene-5,5′-disulfonic acid) is widely used for monitoring the surface exposure of hydrophobic domains to the protein surface. *Bis*-ANS is excited at 390 nm and shows a maximum fluorescence emission at 520 nm in aqueous buffer. *Bis*-ANS binds to accessible hydrophobic domains, which results in a shift of the maximum of the spectra to 495 nm. Therefore, by addition of a protein the hydrophobic exposure can be determined. Such assays can be used to determine the thermal-induced exposure of such regions as well as the interaction-induced exposure of hydrophobic surfaces induced by small heat shock proteins.

1. In order to monitor the thermal-induced exposure of hydrophobic surfaces in Hsp17 from *Synechocystis* and in malate dehydrogenase, 10 μM *bis*-ANS (final) is incubated with 1 μM Hsp17 or 0.8 μM malate dehydrogenase in 100 mM Tris/HCl pH 7.5; 150 mM KCl, and 20 mM Mg acetate at 25 °C. The increase of fluorescence at 495 nm in comparison to 10 μM *bis*-ANS can be determined. The protein-fluorophor mixture is then shifted to 47°C to determine the heat-induced fluorescence increase. The temperature can be controlled by a circulating water bath and directly measured in the cuvettes by a platinum probe.
2. To monitor the protein-induced exposure of hydrophobic surfaces, the increase of the fluorescence in the presence of 10 μM *bis*-ANS (final), 1 μM Hsp17, and 0.8 μM malate dehydrogenase in 100 mM Tris/HCl pH 7.5; 150 mM KCl, and 20 mM Mg acetate at 47°C is determined. The observed increase is then compared to the sum of the increase of the individual proteins. In this particular case, measurements were performed in a Quanta Master QM-1 fluorescence spectrometer (Photon Technology International, Princeton) [202].

32.4.6

Determination of Hsp17 Binding to Lipids (adopted from Refs. [204, 205])

Interaction with Lipids Determined by Steady-state Anisotropy Fluorescence

1. Lipid mixtures mimicking the membrane surface have to be created. In the cited manuscripts, DOPC (1,2-dioleolyl-sn-glycero-3-phosphochoiline), DOPG (1,2-dioleolyl-sn-glycero-3-phosphoglycerol), or total polar lipid extract of *Synechocystis* was used. Lipids are solubilized in chloroform.
2. Before preparation of large unilamellar vesicles (LUVs), 1,6-diphenyl-1,3,5-hexatriene (DPH) or 1-(4-trimethylammoniumphenyl)-6-phenyl-1,3,5-hexatridiene (TMA-DPH) is added to the lipid mixture in organic solvent before drying

of the lipid film by a constant nitrogen flow. The lipid-to-probe ratio should be between 1:1000 and 1:500 molar ratio (label to lipids total).

3. LUVs are created by resuspension of the lipid film in degassed appropriate buffer to the desired lipid concentration. Here, lipids were dissolved in 100 mM Tris pH 7.5, 150 mM KCl, and 20 mM Mg acetate to a final lipid concentration of 50 μM. The lipid film is then destroyed by five freeze/thaw cycles (using liquid N_2) to create multilamellar vesicles. The multilamellar vesicles have to be extruded 25 times through a 100-nm pore polycarbonate filter mounted in the mini-extruder (Liposofast, Avestin, Inc) to give unilamellar liposomes.
4. The effect of protein addition on the membrane physical state of the LUVs can now be determined. After determination of the fluorescence anisotropy of the label in LUVs without protein at 20 °C in 100 mM Tris/HCl pH 7.5; 150 mM KCl, and 20 mM Mg acetate for 300 s, purified Hsp17 is added to a final concentration of 1.5 μM. The measurement should be continued with constant stirring for the same time range after addition of the protein. In the cited manuscript, a T-format fluorescence spectrometer (Quanta Master QM-1, Photon Technology International, Princeton) was used. Excitation and emission wavelengths were set to 360 nm and 430 nm, respectively (5-nm slits). The temperature was measured directly in the cuvettes by a platinum probe and was controlled by a circulating water bath.

Interaction with Lipids Determined by Monolayer Experiments

The association of proteins with a lipid surface can also be determined using the monolayer technology as described below.

1. Monolayer experiments are carried out with a KSV3000 Langmuir Blodget instrument (KSV Instruments, Helsinki) in the work cited. A Teflon dish was used with a volume of 6.5 mL and a surface area of 9 cm^2 at 23 °C in buffer A (50 mM TEA·HCl, pH 7.5, 10 mM MgCl2, 100 mM KCl). Surface pressure is measured by the Wilhelmy method, using a platinum plate. Monomolecular lipid layers of 75% DOPE, 20% DOPG, and 5% ECCL (wt%) are spread from $CHCl_3$ lipid solution to give the desired initial surface pressure on a subphase of buffer A at the air-buffer interface. The subphase is continuously stirred with a magnetic bar. The subphase has to be washed in between the experiments by injecting and ejecting buffer solution at opposite sides of the dish, typically with a rate of about 10 mL min^{-1}.
2. Purified Hsp17 (0.5 μM final) is injected through a 0.5-cm^2 hole at an extended corner of the dish underneath a monolayer spread on 6.5 mL of 100 mM Tris/HCl pH 7.5; 150 mM KCl, 20 mM Mg acetate. The injected volume has to be kept below 1% of the total subphase volume. The increase of surface pressure by addition of the protein is a measure for insertion of hydrophobic protein segments into the lipid monolayer. With such a method the treatment-specific exposure of hydrophobic regions of proteins can be determined. The associated protein can be further analyzed by collecting the monolayer followed by Western blot analysis.

References

1 Laskey, R. A., Honda, B. M., Mills, A. D. & Finch, J. T. (1978). Nucleosomes are assembled by an acidic protein which binds histones and transfers them to DNA. *Nature* **275**, 416–420.

2 Pelham, H. R. (1986). Speculations on the functions of the major heat shock and glucose-regulated proteins. *Cell* **46**, 959–961.

3 Munro, S. & Pelham, H. R. (1986). An Hsp70-like protein in the ER: identity with the 78 kd glucose-regulated protein and immunoglobulin heavy chain binding protein. *Cell* **46**, 291–300.

4 Lewis, M. J. & Pelham, H. R. (1985). Involvement of ATP in the nuclear and nucleolar functions of the 70 kd heat shock protein. *EMBO J.* **4**, 3137–3143.

5 Pushkin, A. V., Tsuprun, V. L., Solovjeva, N. A., Shubin, V. V., Evstigneeva, Z. G. & Kretovich, W. L. (1982). High molcular weight pea leaf protein similar to the groE protein of escherichia coli. *Biochim. Biophys. Acta* **704**, 379–384.

6 Cannon, S., Wang, P. & Roy, H. (1986). Inhibition of ribulose bisphosphate carboxylase assembly by antibody to a binding protein. *J. Cell Biol.* **103**, 1327–1335.

7 Hemmingsen, S. M., Woolford, C., van der Vies, S. M., Tilly, K., Dennis, D. T., Georgopoulos, C. P., Hendrix, R. W. & Ellis, R. J. (1988). Homologous plant and bacterial proteins chaperone oligomeric protein assembly. *Nature* **333**, 330–334.

8 Cavalier-Smith, T. (1987). The simultaneous symbiotic origin of mitochondria, chloroplasts, and microbodies. *Ann. NY. Acad. Sci.* **503**, 55–71.

9 Martin, W. & Herrmann, R. G. (1998). Gene transfer from organelles to the nucleus: how much, what happens, and Why? *Plant Physiol.* **118**, 9–17.

10 Leister, D. (2003). Chloroplast research in the genomic age. *Trends Genet.* **19**, 47–56.

11 Bukau, B. & Horwich, A. L. (1998). The Hsp70 and Hsp60 chaperone machines. *Cell* **92**, 351–366.

12 Guy, C. L. & Li, Q. B. (1998). The organization and evolution of the spinach stress 70 molecular chaperone gene family. *Plant Cell* **10**, 539–556.

13 Lin, B. L., Wang, J. S., Liu, H. C., Chen, R. W., Meyer, Y., Barakat, A. & Delseny, M. (2001). Genomic analysis of the Hsp70 superfamily in Arabidopsis thaliana. *Cell Stress Chaperones* **6**, 201–208.

14 Scaramuzzi, C. D., Stokes, H. W. & Hiller, R. G. (1992). Heat shock Hsp70 protein is chloroplast-encoded in the chromophytic alga Pavlova lutherii. *Plant Mol. Biol.* **18**, 467–476.

15 Marshall, J. S., DeRocher, A. E., Keegstra, K. & Vierling, E. (1990). Identification of heat shock protein hsp70 homologues in chloroplasts. *Proc. Natl. Acad. Sci. USA.* **87**, 374–378.

16 Ko, K., Bornemisza, O., Kourtz, L., Ko, Z. W., Plaxton, W. C. & Cashmore, A. R. (1992). Isolation and characterization of a cDNA clone encoding a cognate 70-kDa heat shock protein of the chloroplast envelope. *J. Biol. Chem.* **267**, 2986–2993.

17 Drzymalla, C., Schroda, M. & Beck, C. F. (1996). Light-inducible gene HSP70B encodes a chloroplast-localized heat shock protein in Chlamydomonas reinhardtii. *Plant Mol. Biol.* **31**, 1185–1194.

18 Karlin, S. & Brocchieri, L. (1998). Heat shock protein 70 family: multiple sequence comparisons, function, and evolution. *J. Mol. Evol.* **47**, 565–577.

19 Li, Q. B., Haskell, D. W. & Guy, C. L. (1999). Coordinate and non-coordinate expression of the stress 70 family and other molecular chaperones at high and low temperature in spinach and tomato. *Plant Mol. Biol.* **39**, 21–34.

20 Marshall, J. S. & Keegstra, K.

(1992). Isolation and Characterization of a cDNA clone encoding the major Hsp70 of the peachloroplastic stroma. *Plant Physiol.* **100**, 1048–1054.

21 Schroda, M., Vallon, O., Whitelegge, J. P., Beck, C. F. & Wollman, F. A. (2001). The chloroplastic GrpE homolog of Chlamydomonas: two isoforms generated by differential splicing. *Plant Cell* **13**, 2823–2839.

22 von Gromoff, E. D., Treier, U. & Beck, C. F. (1989). Three light-inducible heat shock genes of Chlamydomonas reinhardtii. *Mol. Cell Biol.* **9**, 3911–3918.

23 Muller, F. W., Igloi, G. L. & Beck, C. F. (1992). Structure of a gene encoding heat-shock protein HSP70 from the unicellular alga Chlamydomonas reinhardtii. *Gene* **111**, 165–173.

24 Kropat, J., von Gromoff, E. D., Muller, F. W. & Beck, C. F. (1995). Heat shock and light activation of a Chlamydomonas HSP70 gene are mediated by independent regulatory pathways. *Mol. Gen. Genet.* **248**, 727–734.

25 Kropat, J., Oster, U., Rudiger, W. & Beck, C. F. (1997). Chlorophyll precursors are signals of chloroplast origin involved in light induction of nuclear heat-shock genes. *Proc. Natl. Acad. Sci. USA.* **94**, 14168–14172.

26 Li, Q. B., Haskell, D., Zhang, C., Sung, D. Y. & Guy, C. (2000). Diurnal regulation of Hsp70s in leaf tissue. *Plant J.* **21**, 373–378.

27 Kourtz, L. & Ko, K. (1997). The early stage of chloroplast protein import involves Com70. *J. Biol. Chem.* **272**, 2808–2813.

28 Schlicher, T. & Soll, J. (1997). Chloroplastic isoforms of DnaJ and GrpE in pea. *Plant Mol. Biol.* **33**, 181–185.

29 Becker, T., Hritz, J., Vogel, M., Caliebe, A., Bukau, B., Soll, J. & Schleiff, E. (2004). Toc 12, A Novel Subunit of the Intermembrane Space Preprotein Translocon of Chloroplasts. *Mol. Biol. Cell.* in press.

30 Orme, W., Walker, A. R., Gupta, R. & Gray, J. C. (2001). A novel plastid-targeted J-domain protein in Arabidopsis thaliana. *Plant Mol. Biol.* **46**, 615–626.

31 Hartl, F. U. & Hayer-Hartl, M. (2002). Molecular chaperones in the cytosol: from nascent chain to folded protein. *Science* **295**, 1852–1858.

32 Barraclough, R. & Ellis, R. J. (1980). Protein synthesis in chloroplasts. IX. Assembly of newly-synthesized large subunits into ribulose bisphosphate carboxylase in isolated intact pea chloroplasts. *Biochim. Biophys. Acta* **608**, 19–31.

33 Maier, U. G., Rensing, S. A., Igloi, G. L. & Maerz, M. (1995). Twintrons are not unique to the Euglena chloroplast genome: structure and evolution of a plastome cpn60 gene from a cryptomonad. *Mol. Gen. Genet.* **246**, 128–311.

34 Viale, A. (1995). GroEL (Hsp60)-based eubacterial and organellar phylogenies. *Mol. Microbiol.* **17**, 1013.

35 Viitanen, P. V., Schmidt, M., Buchner, J., Suzuki, T., Vierling, E., Dickson, R., Lorimer, G. H., Gatenby, A. & Soll, J. (1995). Functional characterization of the higher plant chloroplast chaperonins. *J Biol Chem* **270**, 18158–64.

36 Musgrove, J. E., Johnson, R. A. & Ellis, R. J. (1987). Dissociation of the ribulosebisphosphate-carboxylase large-subunit binding protein into dissimilar subunits. *Eur. J. Biochem.* **163**, 529–534.

37 Nishio, K., Hirohashi, T. & Nakai, M. (1999). Chloroplast chaperonins: evidence for heterogeneous assembly of alpha and beta Cpn60 polypeptides into a chaperonin oligomer. *Biochem. Biophys. Res. Commun.* **266**, 584–587.

38 Dickson, R., Weiss, C., Howard, R. J., Alldrick, S. P., Ellis, R. J., Lorimer, G., Azem, A. & Viitanen, P. V. (2000). Reconstitution of higher plant chloroplast chaperonin 60 tetradecamers active in protein folding. *J. Biol. Chem.* **275**, 11829–11835.

39 Martel, R., Cloney, L. P., Pelcher, L. E. & Hemmingsen, S. M. (1990). Unique composition of plastid

chaperonin-60: alpha and beta polypeptide-encoding genes are highly divergent. *Gene* **94**, 181–187.

40 Hartman, D. J., Dougan, D., Hoogenraad, N. J. & Høj, P. B. (1992). Heat shock proteins of barley mitochondria and chloroplasts Identification of organellar hsp 10 and 12: putative chaperonin 10 homologues. *FEBS-Let.* **305**, 147–150.

41 Zabaleta, E., Assad, N., Oropeza, A., Salerno, G. & Herrera-Estrella, L. (1994). Expression of one of the members of the Arabidopsis chaperonin 60 beta gene family is developmentally regulated and wound-repressible. *Plant Mol. Biol.* **24**, 195–202.

42 Bertsch, U., Soll, J., Seetharam, R. & Viitanen, P. V. (1992). Identification, characterization, and DNA sequence of a functional "double" groES-like chaperonin from chloroplasts of higher plants. *Proc. Natl. Acad. Sci. USA.* **89**, 8696–8700.

43 Baneyx, F., Bertsch, U., Kalbach, C. E., van der Vies, S. M., Soll, J. & Gatenby, A. A. (1995). Spinach chloroplast cpn21 co-chaperonin possesses two functional domains fused together in a toroidal structure and exhibits nucleotide-dependent binding to plastid chaperonin 60. *J. Biol. Chem.* **270**, 10695–10702.

44 Koumoto, Y., Shimada, T., Kondo, M., Takao, T., Shimonishi, Y., Hara-Nishimura, I. & Nishimura, M. (1999). Chloroplast Cpn20 forms a tetrameric structure in Arabidopsis thaliana. *Plant J.* **17**, 467–477.

45 Sharkia, R., Bonshtien, A. L., Mizrahi, I., Weiss, C., Niv, A., Lustig, A., Viitanen, P. V. & Azem, A. (2003). On the oligomeric state of chloroplast chaperonin 10 and chaperonin 20. *Biochim. Biophys. Acta* **1651**, 76–84.

46 Schlicher, T. & Soll, J. (1996). Molecular chaperones are present in the thylakoid lumen of pea chloroplasts. *FEBS Lett.* **379**, 302–304.

47 Koumoto, Y., Shimada, T., Kondo, M., Hara-Nishimura, I. & Nishimura, M. (2001). Chloroplasts have a novel Cpn10 in addition to Cpn20 as co-chaperonins in Arabidopsis thaliana. *J. Biol. Chem.* **276**, 29688–29694.

48 Cloney, L. P., Wu, H. B. & Hemmingsen, S. M. (1992). Expression of plant chaperonin-60 genes in Escherichia coli. *J. Biol. Chem.* **267**, 23327–23332.

49 Cloney, L. P., Bekkaoui, D. R., Wood, M. G. & Hemmingsen, S. M. (1992). Assessment of plant chaperonin-60 gene function in Escherichia coli. *J. Biol. Chem.* **267**, 23333–23336.

50 Saibil, H. R., Zheng, D., Roseman, A. M., Hunter, A. S., Watson, G. M. F., Chen, S., Auf der Mauer, A., O'Hara, B. P., Wood, S. P., Mann, N. H., Barnett, L. K. & Ellis, R. J. (1993). ATP induces large quaternary rearrngemants in a cage-like chaperonin structure. *Curr. Biol.* **3**, 265–273.

51 Dickson, R., Larsen, B., Viitanen, P. V., Tormey, M. B., Geske, J., Strange, R. & Bemis, L. T. (1994). Cloning, expression, and purification of a functional nonacetylated mammalian mitochondrial chaperonin 10. *J. Biol. Chem.* **269**, 26858–26864.

52 Porankiewicz, J., Wang, J. & Clarke, A. K. (1999). New insights into the ATP-dependent Clp protease: Escherichia coli and beyond. *Mol. Microbiol.* **32**, 449–458.

53 Schirmer, E. C., Glover, J. R., Singer, M. A. & Lindquist, S. (1996). HSP100/Clp proteins: a common mechanism explains diverse functions. *Trends. Biochem. Sci.* **21**, 289–296.

54 Hwang, B. J., Park, W. J., Chung, C. H. & Goldberg, A. L. (1987). Escherichia coli contains a soluble ATP-dependent protease (Ti) distinct from protease La. *Proc. Natl. Acad. Sci. USA.* **84**, 5550–5554.

55 Katayama, Y., Gottesman, S., Pumphrey, J., Rudikoff, S., Clark, W. P. & Maurizi, M. R. (1988). The two-component, ATP-dependent Clp protease of Escherichia coli. Purification, cloning, and mutational analysis of the ATP-binding

component. *J. Biol. Chem.* **263**, 15226–15236.

56 Moore, T. & Keegstra, K. (1993). Characterization of a cDNA clone encoding a chloroplast-targeted Clp homologue. *Plant Mol. Biol.* **21**, 525–537.

57 Kiyosue, T., Yamaguchi-Shinozaki, K. & Shinozaki, K. (1993). Characterization of cDNA for a dehydration-inducible gene that encodes a ClpA, B-like protein in Arabidopsis thaliana L. *Biochem. Biophys. Res. Commun.* **196**, 1214–1220.

58 Peltier, J. B., Friso, G., Kalume, D. E., Roepstorff, P., Nilsson, F., Adamska, I. & van Wijk, K. J. (2000). Proteomics of the chloroplast: systematic identification and targeting analysis of lumenal and peripheral thylakoid proteins. *Plant Cell* **12**, 319–341.

59 Adam, Z., Adamska, I., Nakabayashi, K., Ostersetzer, O., Haussuhl, K., Manuell, A., Zheng, B., Vallon, O., Rodermel, S. R., Shinozaki, K. & Clarke, A. K. (2001). Chloroplast and mitochondrial proteases in Arabidopsis. A proposed nomenclature. *Plant Physiol.* **125**, 1912–1918.

60 Peltier, J. B., Ytterberg, J., Liberles, D. A., Roepstorff, P. & van Wijk, K. J. (2001). Identification of a 350-kDa ClpP protease complex with 10 different Clp isoforms in chloroplasts of Arabidopsis thaliana. *J. Biol. Chem.* **276**, 16318–16327.

61 Zheng, B., Halperin, T., Hruskova-Heidingsfeldova, O., Adam, Z. & Clarke, A. K. (2002). Characterization of Chloroplast Clp proteins in Arabidopsis: Localization, tissue specificity and stress responses. *Physiol. Plant* **114**, 92–101.

62 Shanklin, J., DeWitt, N. D. & Flanagan, J. M. (1995). The stroma of higher plant plastids contain ClpP and ClpC, functional homologs of Escherichia coli ClpP and ClpA: an archetypal two-component ATP-dependent protease. *Plant Cell* **7**, 1713–1722.

63 Weaver, L. M., Froehlich, J. E. & Amasino, R. M. (1999). Chloroplast-targeted ERD1 protein declines but its mRNA increases during senescence in Arabidopsis. *Plant Physiol.* **119**, 1209–1216.

64 Ostersetzer, O. & Adam, Z. (1996). Effects of light and temperature on expression of ClpC, the regulatory subunit of chloroplastic Clp protease, in pea seedlings. *Plant Mol. Biol.* **31**, 673–676.

65 Nakabayashi, K., Ito, M., Kiyosue, T., Shinozaki, K. & Watanabe, A. (1999). Identification of clp genes expressed in senescing Arabidopsis leaves. *Plant Cell Physiol.* **40**, 504–514.

66 Nakashima, K., Kiyosue, T., Yamaguchi-Shinozaki, K. & Shinozaki, K. (1997). A nuclear gene, erd1, encoding a chloroplast-targeted Clp protease regulatory subunit homolog is not only induced by water stress but also developmentally up-regulated during senescence in Arabidopsis thaliana. *Plant J.* **12**, 851–861.

67 Clarke, A. K. & Eriksson, M. J. (1996). The cyanobacterium Synechococcus sp. PCC 7942 possesses a close homologue to the chloroplast ClpC protein of higher plants. *Plant Mol. Biol.* **31**, 721–730.

68 Sokolenko, A., Lerbs-Mache, S., Altschmied, L. & Herrmann, R. G. (1998). Clp protease complexes and their diversity in chloroplasts. *Planta* **207**, 286–295.

69 Halperin, T. & Adam, Z. (1996). Degradation of mistargeted OEE33 in the chloroplast stroma. *Plant Mol. Biol.* **30**, 925–933.

70 Desimone, M., Weiss-Wichert, W., Wagner, E., Altenfeld, U. & Johanningmeier, U. (1997). Immunochemical studies on the Clp-protease in chloroplasts: evidence for the formation of a ClpC/P complex. *Bot. Acta* **110**, 234–239.

71 Halperin, T., Ostersetzer, O. & Adam, Z. (2001). ATP-dependent association between subunits of Clp protease in pea chloroplasts. *Planta* **213**, 614–619.

72 Flanagan, J. M., Wall, J. S., Capel, M. S., Schneider, D. K. & Shanklin, J. (1995). Scanning transmission electron microscopy and small-angle scattering provide evidence that native Escherichia coli ClpP is a tetradecamer with an axial pore. *Biochem.* **34**, 10910–10917.

73 Shin, D. H., Lee, C. S., Chung, C. H. & Suh, S. W. (1996). Molecular symmetry of the ClpP component of the ATP-dependent Clp protease, an Escherichia coli homolog of 20 S proteasome. *J. Mol. Biol.* **262**, 71–76.

74 Wang, S. & Liu, X. Q. (1997). Identification of an unusual intein in chloroplast ClpP protease of Chlamydomonas eugametos. *J. Biol. Chem.* **272**, 11869–11873.

75 Vierling, E. (1997). The small heat shock protein in plants are members of an ancient family of heat induced proteins. *Acta Physiol. Plant.* **19**, 539–547.

76 Sun, W., Van Montagu, M. & Verbruggen, N. (2002). Small heat shock proteins and stress tolerance in plants. *Biochim. Biophys. Acta* **1577**, 1–9.

77 Scharf, K.-D., Siddique, M. & Vierling, E. (2001). The expanding family of Arabidopsis thaliana small heat stress proteins and a new family of proteins containing-crystallin domains (Acd proteins). *Cell Stress Chaperones* **6**, 225–237.

78 Vierling, E. (1991). The roles of heat shock proteinsin plants. *Rev. Plant Physiol. Plant Mol. Biol.* **42**, 579–620.

79 Waters, E. R., Lee, G. J. & Vierling, E. (1996). Evolution, structure and function of the small heat shock proteins in plants. *J. Exp. Bot.* **47**, 325–338.

80 Boston, R. S., Viitanen, P. V. & Vierling, E. (1996). Molecular chaperones and protein folding in plants. *Plant Mol. Biol.* **32**, 191–222.

81 Waters, E. R. & Vierling, E. (1999). Chloroplast small heat shock proteins: evidence for atypical evolution of an organelle-localized protein. *Proc. Natl. Acad. Sci. USA.* **96**, 14394–14399.

82 Vierling, E., Mishkind, M. L., Schmidt, G. W. & Key, J. L. (1986). Specific heat shock proteins are transported into chloroplasts. *Proc. Natl. Acad. Sci. USA.* **83**, 361–365.

83 Vierling, E., Harris, L. M. & Chen, Q. (1989). The major low-molecular-weight heat shock protein in chloroplasts shows antigenic conservation among diverse higher plant species. *Mol. Cell Biol.* **9**, 461–468.

84 Chen, Q., Lauzon, L. M., DeRocher, A. E. & Vierling, E. (1990). Accumulation, stability, and localization of a major chloroplast heat-shock protein. *J. Cell Biol.* **110**, 1873–1883.

85 Harndahl, U., Hall, R. B., Osteryoung, K. W., Vierling, E., Bornman, J. F. & Sundby, C. (1999). The chloroplast small heat shock protein undergoes oxidation-dependent conformational changes and may protect plants from oxidative stress. *Cell Stress Chaperones* **4**, 129–138.

86 Heckathorn, S. A., Downs, C. A., Sharkey, T. D. & Coleman, J. S. (1998). The small, methionine-rich chloroplast heat-shock protein protects photosystem II electron transport during heat stress. *Plant Physiol.* **116**, 439–444.

87 Adamska, I. & Kloppstech, K. (1991). Evidence for the localization of the nuclear-coded 22-kDa heat-shock protein in a subfraction of thylakoid membranes. *Eur. J. Biochem.* **198**, 375–381.

88 Downs, C. A., Coleman, J. S. & Heckathorn, S. A. (1999). The chloroplast 22-Ku heat-shock protein: a lumenal protein that associates with the oxygen evolving complex and protects photosystem II during heat stress. *J. Plant Physiol.* **155**, 477–487.

89 Chen, Q., Osteryoung, K. & Vierling, E. (1994). A 21-kDa chloroplast heat shock protein assembles into high molecular weight complexes in vivo and in Organelle. *J. Biol. Chem.* **269**, 13216–13223.

90 Suzuki, T. C., Krawitz, D. C. & Vierling, E. (1998). The chloroplast small heat-shock protein oligomer is

not phosphorylated and does not dissociate during heat stress in vivo. *Plant Physiol.* **116**, 1151–1161.

91 Harndahl, U., Kokke, B. P., Gustavsson, N., Linse, S., Berggren, K., Tjerneld, F., Boelens, W. C. & Sundby, C. (2001). The chaperone-like activity of a small heat shock protein is lost after sulfoxidation of conserved methionines in a surface-exposed amphipathic alpha-helix. *Biochim. Biophys. Acta* **1545**, 227–237.

92 van Montfort, R. L., Basha, E., Friedrich, K. L., Slingsby, C. & Vierling, E. (2001). Crystal structure and assembly of a eukaryotic small heat shock protein. *Nat. Struct. Biol.* **8**, 1025–1030.

93 Kim, K. K., Kim, R. & Kim, S.-H. (1998). Crystal structure of a small heat-shock protein. *Nature* **394**, 595–599.

94 Kirschner, M., Winkelhaus, S., Thierfelder, J. M. & Nover, L. (2000). Transient expression and heat-stress-induced co-aggregation of endogenous and heterologous small heat-stress proteins in tobacco protoplasts. *Plant J.* **24**, 397–411.

95 Osteryoung, K. W. & Vierling, E. (1994). Dynamics of small heat shock protein distribution within the chloroplasts of higher plants. *J. Biol. Chem.* **269**, 28676–28682.

96 Löw, D., Brändle, K., Nover, L. & Forreiter, C. (2000). Cytosolic heat-stress proteins Hsp17.7 class I and Hsp17.3 class II of tomato act as molecular chaperones in vivo. *Planta* **211**, 575–582.

97 Lee, G. J. & Vierling, E. (2000). A small heat shock protein cooperates with heat shock protein 70 systems to reactivate a heat-denatured protein. *Plant Physiol.* **122**, 189–198.

98 Gustavsson, N., Kokke, B. P., Harndahl, U., Silow, M., Bechtold, U., Poghosyan, Z., Murphy, D., Boelens, W. C. & Sundby, C. (2002). A peptide methionine sulfoxide reductase highly expressed in photosynthetic tissue in Arabidopsis thaliana can protect the chaperone-like activity of a chloroplast-localized small heat shock protein. *Plant J.* **29**, 545–553.

99 Plater, M. L., Goode, D. & Crabbe, M. J. (1996). Effects of site-directed mutations on the chaperone-like activity of alphaB-crystallin. *J. Biol. Chem.* **271**, 28558–28566.

100 Chen, Q. & Vierling, E. (1991). Analysis of conserved domains identifies a unique structural feature of a chloroplast heat shock protein. *Mol. Gen. Genet.* **226**, 425–431.

101 Keenan, R. J., Freymann, D. M., Stroud, R. M. & Walter, P. (2001). The signal recognition particle. *Annu. Rev. Biochem.* **70**, 755–775.

102 Emelyanov, V. V. (2002). Phylogenetic relationships of organellar Hsp90 homologs reveal fundamental differences to organellar Hsp70 and Hsp60 evolution. *Gene* **299**, 125–133.

103 Young, J. C., Moarefi, I. & Hartl, F. U. (2001). Hsp90: a specialized but essential protein-folding tool. *J. Cell Biol.* **154**, 267–273.

104 Schmitz, G., Schmidt, M. & Feierabend, J. (1996). Characterization of a plastid-specific HSP90 homologue: identification of a cDNA sequence, phylogenetic descendence and analysis of its mRNA and protein expression. *Plant Mol. Biol.* **30**, 479–492.

105 Cao, D., Froehlich, J. E., Zhang, H. & Cheng, C. L. (2003). The chlorate-resistant and photomorphogenesis-defective mutant cr88 encodes a chloroplast-targeted HSP90. *Plant J.* **33**, 107–118.

106 Nemoto, T., Ohara-Nemoto, Y., Ota, M., Takagi, T. & Yokoyama, K. (1995). Mechanism of dimer formation of the 90-kDa heat-shock protein. *Eur. J. Biochem.* **233**, 1–8.

107 Young, J. C., Schneider, C. & Hartl, F. U. (1997). In vitro evidence that hsp90 contains two independent chaperone sites. *FEBS Lett.* **418**, 139–143.

108 Scheibel, T., Weikl, T. & Buchner, J. (1998). Two chaperone sites in Hsp90 differing in substrate specificity and ATP dependence. *Proc. Natl. Acad. Sci. USA.* **95**, 1495–1499.

109 Freedman, R. B. (1989). Protein disulfide isomerase: multiple roles in the modification of nascent secretory proteins. *Cell* **57**, 1069–1072.

110 Cai, H., Wang, C. C. & Tsou, C. L. (1994). Chaperone-like activity of protein disulfide isomerase in the refolding of a protein with no disulfide bonds. *J. Biol. Chem.* **269**, 24550–24552.

111 Song, J. L. & Wang, C. C. (1995). Chaperone-like activity of protein disulfide-isomerase in the refolding of rhodanese. *Eur. J. Biochem.* **231**, 312–316.

112 Kim, J. & Mayfield, S. P. (1997). Protein disulfide isomerase as a regulator of chloroplast translational activation. *Science* **278**, 1954–1957.

113 Trebitsh, T., Meiri, E., Ostersetzer, O., Adam, Z. & Danon, A. (2001). The protein disulfide isomerase-like RB60 is partitioned between stroma and thylakoids in Chlamydomonas reinhardtii chloroplasts. *J. Biol. Chem.* **276**, 4564–4569.

114 Danon, A. & Mayfield, S. P. (1991). Light regulated translational activators: identification of chloroplast gene specific mRNA binding proteins. *EMBO J.* **10**, 3993–4001.

115 Yohn, C. B., Cohen, A., Danon, A. & Mayfield, S. P. (1996). Altered mRNA binding activity and decreased translational initiation in a nuclear mutant lacking translation of the chloroplast psbA mRNA. *Mol. Cell Biol.* **16**, 3560–3566.

116 Yohn, C. B., Cohen, A., Danon, A. & Mayfield, S. P. (1998). A poly(A) binding protein functions in the chloroplast as a message-specific translation factor. *Proc. Natl. Acad. Sci. USA.* **95**, 2238–2243.

117 Yohn, C. B., Cohen, A., Rosch, C., Kuchka, M. R. & Mayfield, S. P. (1998). Translation of the chloroplast psbA mRNA requires the nuclear-encoded poly(A)-binding protein, RB47. *J. Cell Biol.* **142**, 435–442.

118 Danon, A. & Mayfield, S. P. (1994). ADP-dependent phosphorylation regulates RNA-binding in vitro: implications in light-modulated translation. *EMBO J.* **13**, 2227–2235.

119 Trebitsh, T., Levitan, A., Sofer, A. & Danon, A. (2000). Translation of chloroplast psbA mRNA is modulated in the light by counteracting oxidizing and reducing activities. *Mol. Cell Biol.* **20**, 1116–1123.

120 Trebitsh, T. & Danon, A. (2001). Translation of chloroplast psbA mRNA is regulated by signals initiated by both photosystems II and I. *Proc. Natl. Acad. Sci. USA.* **98**, 12289–12294.

121 Kim, J. & Mayfield, S. P. (2002). The active site of the thioredoxin-like domain of chloroplast protein disulfide isomerase, RB60, catalyzes the redox-regulated binding of chloroplast poly(A)-binding protein, RB47, to the 5′ untranslated region of psbA mRNA. *Plant Cell Physiol.* **43**, 1238–1243.

122 Fischer, G., Wittmann-Liebold, B., Lang, K., Kiefhaber, T. & Schmid, F. X. (1989). Cyclophilin and peptidyl-prolyl *cis-trans* isomerase are probably identical proteins. *Nature* **337**, 476–478.

123 Harding, M. W., Galat, A., Uehling, D. E. & Schreiber, S. L. (1989). A receptor for the immuno-suppressant FK506 is a *cis-trans* peptidyl-prolyl isomerase. *Nature* **341**, 758–760.

124 Gething, M. J. (1991). Molecular chaperones: individualists or groupies? *Curr. Opin. Cell Biol.* **3**, 610–614.

125 Freskgard, P. O., Bergenhem, N., Jonsson, B. H., Svensson, M. & Carlsson, U. (1992). Isomerase and chaperone activity of prolyl isomerase in the folding of carbonic anhydrase. *Science* **258**, 466–468.

126 Liu, J., Farmer, J. D. Jr, Lane, W. S., Friedman, J., Weissman, I. & Schreiber, S. L. (1991). Calcineurin is a common target of cyclophilin-cyclosporin A and FKBP-FK506 complexes. *Cell* **66**, 807–815.

127 Clipstone, N. A. & Crabtree, G. R. (1992). Identification of calcineurin as a key signalling enzyme in T-lymphocyte activation. *Nature* **357**, 695–697.

128 O'Keefe, S. J., Tamura, J., Kincaid, R. L., Tocci, M. J. & O'Neill, E. A. (1992). FK-506- and CsA-sensitive activation of the interleukin-2 promoter by calcineurin. *Nature* **357**, 692–694.

129 Schreiber, S. L. (1991). Chemistry and Biology of the Immunophilins and Their Immunosuppressive Ligands. *Science* **251**, 283–287.

130 Fink, A. L. (1999). Chaperone-mediated protein folding. *Physiol. Rev.* **79**, 425–449.

131 Gupta, R., Mould, R. M., He, Z. & Luan, S. (2002). A chloroplast FKBP interacts with and affects the accumulation of Rieske subunit of cytochrome bf complex. *Proc. Natl. Acad. Sci. USA.* **99**, 15806–15811.

132 Breiman, A., Fawcett, T. W., Ghirardi, M. L. & Mattoo, A. K. (1992). Plant organelles contain distinct peptidylprolyl *cis*,*trans*-isomerases. *J. Biol. Chem.* **267**, 21293–21296.

133 Luan, S., Albers, M. W. & Schreiber, S. L. (1994). Light-regulated, tissue-specific immunophilins in a higher plant. *Proc. Natl. Acad. Sci. USA.* **91**, 984–988.

134 Luan, S., Lane, W. S. & Schreiber, S. L. (1994). pCyP B: a chloroplast-localized, heat shock-responsive cyclophilin from fava bean. *Plant Cell* **6**, 885–892.

135 Fulgosi, H., Vener, A. V., Altschmied, L., Herrmann, R. G. & Andersson, B. (1998). A novel multi-functional chloroplast protein: identification of a 40 kDa immunophilin-like protein located in the thylakoid lumen. *EMBO J.* **17**, 1577–1587.

136 Lippuner, V., Chou, I. T., Scott, S. V., Ettinger, W. F., Theg, S. M. & Gasser, C. S. (1994). Cloning and characterization of chloroplast and cytosolic forms of cyclophilin from Arabidopsis thaliana. *J. Biol. Chem.* **269**, 7863–7868.

137 Edvardsson, A., Eshaghi, S., Vener, A. V. & Andersson, B. (2003). The major peptidyl-prolyl isomerase activity in thylakoid lumen of plant chloroplasts belongs to a novel cyclophilin TLP20. *FEBS Lett.* **542**, 137–141.

138 Vener, A. V., Rokka, A., Fulgosi, H., Andersson, B. & Herrmann, R. G. (1999). A cyclophilin-regulated PP2A-like protein phosphatase in thylakoid membranes of plant chloroplasts. *Biochem.* **38**, 14955–14965.

139 Rokka, A., Aro, E. M., Herrmann, R. G., Andersson, B. & Vener, A. V. (2000). Dephosphorylation of photosystem II reaction center proteins in plant photosynthetic membranes as an immediate response to abrupt elevation of temperature. *Plant Physiol.* **123**, 1525–1536.

140 Ivey, R. A. 3rd & Bruce, B. D. (2000). In vivo and in vitro interaction of DnaK and a chloroplast transit peptide. *Cell Stress Chaperones* **5**, 62–71.

141 Ivey, R. A. 3rd, Subramanian, C. & Bruce, B. D. (2000). Identification of a Hsp70 recognition domain within the rubisco small subunit transit peptide. *Plant Physiol.* **122**, 1289–1299.

142 Rial, D. V., Arakaki, A. K. & Ceccarelli, E. A. (2000). Interaction of the targeting sequence of chloroplast precursors with Hsp70 molecular chaperones. *Eur. J. Biochem.* **267**, 6239–6248.

143 Rial, D. V., Ottado, J. & Ceccarelli, E. A. (2003). Precursors with altered affinity for Hsp70 in their transit peptides are efficiently imported into chloroplasts. *J. Biol. Chem.* [Epub ahead of print].

144 Pilon, M., Wienk, H., Sips, W., de Swaaf, M., Talboom, I., van't Hof, R., de Korte-Kool, G., Demel, R., Weisbeek, P. & de Kruijff, B. (1995). Functional domains of the ferredoxin transit sequence involved in chloroplast import. *J. Biol. Chem.* **270**, 3882–3893.

145 Schleiff, E. & Soll, J. (2000). Travelling of proteins through membranes: translocation into chloroplasts. *Planta* **211**, 449–456.

146 Waegemann, K., Paulsen, H., Soll, J. (1990) Translocation of proteins into chloroplasts requires cytosolic factors

to obtain import competence. *FEBS-Lett.* **161**, 89–92.

147 Pilon, M., de Boer, A. D., Knols, S. L., Koppelman, M. H., van der Graaf, R. M., de Kruijff, B. & Weisbeek, P. J. (1990). Expression in Escherichia coli and purification of a translocation-competent precursor of the chloroplast protein ferredoxin. *J. Biol. Chem.* **265**, 3358–3361.

148 Pilon, M., de Kruijff, B. & Weisbeek, P. J. (1992). New insights into the import mechanism of the ferredoxin precursor into chloroplasts. *J. Biol. Chem.* **267**, 2548–2556.

149 May, T. & Soll, J. (2000). 14-3-3 proteins form a guidance complex with chloroplast precursor proteins in plants. *Plant Cell* **12**, 53–64.

150 Waegemann, K. & Soll, J. (1996). Phosphorylation of the transit sequence of chloroplast precursor proteins. *J. Biol. Chem.* **271**, 6545–6554.

151 Hachiya, N., Mihara, K., Suda, K., Horst, M., Schatz, G. & Lithgow, T. (1995). Reconstitution of the initial steps of mitochondrial protein import. *Nature* **376**, 705–709.

152 Pfanner, N. & Geissler, A. (2001). Versatility of the mitochondrial protein import machinery. *Nat. Rev. Mol. Cell. Biol.* **2**, 339–349.

153 Sohrt, K. & Soll, J. (2000). Toc64, a new component of the protein translocon of chloroplasts. *J. Cell Biol.* **148**, 1213–1221.

154 Waegemann, K., Soll, J. (1991) Characterization of the protein import apparatus in isolated outer enevlopes of chloroplasts. *Plant Journal* **1**, 149–158.

155 Schnell, D. J., Kessler, F. & Blobel, G. (1994). Isolation of components of the chloroplast protein import machinery. *Science* **266**, 1007–1012.

156 Wu, C., Seibert, F. S. & Ko, K. (1994). Identification of chloroplast envelope proteins in close physical proximity to a partially translocated chimeric precursor protein. *J. Biol. Chem.* **269**, 32264–32271.

157 Kessler, F., Blobel, G. (1996) Interaction of the protein import and folding machineries of the chloroplast. *Proc. Natl. Acad. Sci. USA.* **93**, 7684–7689.

158 Akita, M., Nielsen, E. & Keegstra, K. (1997). Identification of protein transport complexes in the chloroplastic envelope membranes via chemical cross-linking. *J. Cell Biol.* **136**, 983–994.

159 Nielsen, E., Akita, M., Davila-Aponte, J. & Keegstra, K. (1997). Stable association of chloroplastic precursors with protein translocation complexes that contain proteins from both envelope membranes and a stromal Hsp100 molecular chaperone. *EMBO J.* **16**, 935–946.

160 Chou, M. L., Fitzpatrick, L. M., Tu, S. L., Budziszewski, G., Potter-Lewis, S., Akita, M., Levin, J. Z., Keegstra, K. & Li, H. M. (2003). Tic40, a membrane-anchored co-chaperone homolog in the chloroplast protein translocon. *EMBO J.* **22**, 2970–2980.

161 Ko, K., Budd, D., Wu, C., Seibert, F., Kourtz, L. & Ko, Z. W. (1995). Isolation and characterization of a cDNA clone encoding a member of the Com44/Cim44 envelope components of the chloroplast protein import apparatus. *J. Biol. Chem.* **270**, 28601–28608.

162 Stahl, T., Glockmann, C., Soll, J. & Heins, L. (1999). Tic40, a new "old" subunit of the chloroplast protein import translocon. *J. Biol. Chem.* **274**, 37467–37472.

163 Choquet, Y. & Wollman, F. A. (2002). Translational regulations as specific traits of chloroplast gene expression. *FEBS Lett.* **529**, 39–42.

164 Flügge, U. I. & Hinz, G. (1986). Energy dependence of protein translocation into chloroplasts. *Eur. J. Biochem.* **160**, 563–570.

165 Schindler, C., Hracky, R., Soll, J. (1987) Protein transport in chloroplasts: ATP is prerequisit. *Zeitschr. Naturfrosch.* **42c**, 103–108.

166 Pain, D. & Blobel, G. (1987). Protein import into chloroplasts requires a chloroplast ATPase. *Proc. Natl. Acad. Sci. USA.* **84**, 3288–3292.

167 Olsen, L. J., Theg, S. M., Selman, B. R. & Keegstra, K. (1989). ATP is required for the binding of precursor proteins to chloroplasts. *J. Biol. Chem.* **264**, 6724–6729.

168 Olsen, L. J. & Keegstra, K. (1992). The binding of precursor proteins to chloroplasts requires nucleoside triphosphates in the intermembrane space. *J. Biol. Chem.* **267**, 433–439.

169 Breton, G., Danyluk, J., Charron, J. B. & Sarhan, F. (2003). Expression profiling and bioinformatic analyses of a novel stress-regulated multispanning transmembrane protein family from cereals and Arabidopsis. *Plant Physiol.* **132**, 64–74.

170 Leszczynski, D., Pitsillides, C. M., Pastila, R. K., Rox Anderson, R. & Lin, C. P. (2001). Laser-beam-triggered microcavitation: a novel method for selective cell destruction. *Radiat. Res.* **156**, 399–407.

171 Molik, S., Karnauchov, I., Weidlich, C., Herrmann, R. G. & Klosgen, R. B. (2001). The Rieske Fe/S protein of the cytochrome b6/f complex in chloroplasts: missing link in the evolution of protein transport pathways in chloroplasts? *J. Biol. Chem.* **276**, 42761–42766.

172 Madueno, F., Napier, J. A. & Gray, J. C. (1993). Newly Imported Rieske Iron-Sulfur Protein Associates with Both Cpn60 and Hsp70 in the Chloroplast Stroma. *Plant Cell* **5**, 1865–1876.

173 Tsugeki, R. & Nishimura, M. (1993). Interaction of homologues of Hsp70 and Cpn60 with ferredoxin-NADP+ reductase upon its import into chloroplasts. *FEBS Lett.* **320**, 198–202.

174 Dionisi, H. M., Checa, S. K., Krapp, A. R., Arakaki, A. K., Ceccarelli, E. A., Carrillo, N. & Viale, A. M. (1998). Cooperation of the DnaK and GroE chaperone systems in the folding pathway of plant ferredoxin-NADP+ reductase expressed in Escherichia coli. *Eur. J. Biochem.* **251**, 724–728.

175 Li, X., Henry, R., Yuan, J., Cline, K. & Hoffman, N. E. (1995). A chloroplast homologue of the signal recognition particle subunit SRP54 is involved in the posttranslational integration of a protein into thylakoid membranes. *Proc Natl Acad Sci USA.* **92**, 3789–93.

176 Yalovsky, S., Paulsen, H., Michaeli, D., Chitnis, P. R. & Nechushtai, R. (1992). Involvement of a chloroplast HSP70 heat shock protein in the integration of a protein (light-harvesting complex protein precursor) into the thylakoid membrane. *Proc. Natl. Acad. Sci. USA.* **89**, 5616–5619.

177 Yuan, J., Henry, R. & Cline, K. (1993). Stromal factor plays an essential role in protein integration into thylakoids that cannot be replaced by unfolding or by heat shock protein Hsp70. *Proc. Natl. Acad. Sci. USA.* **90**, 8552–8556.

178 Goloubinoff, P., Christeller, J. T., Gatenby, A. A. & Lorimer, G. H. (1989). Reconstitution of active dimeric ribulose bisphosphate carboxylase from an unfoleded state depends on two chaperonin proteins and Mg-ATP. *Nature* **342**, 884–889.

179 Viitanen, P. V., Lubben, T. H., Reed, J., Goloubinoff, P., O'Keefe, D. P. & Lorimer, G. H. (1990). Chaperonin-facilitated refolding of ribulosebis-phosphate carboxylase and ATP hydrolysis by chaperonin 60 (groEL) are K+ dependent. *Biochem.* **29**, 5665–5671.

180 Lubben, T. H., Donaldson, G. K., Viitanen, P. V. & Gatenby, A. A. (1989). Several proteins imported into chloroplasts form stable complexes with the GroEL-related chloroplast molecular chaperone. *Plant Cell* **1**, 1223–1230.

181 Chen, G. G. & Jagendorf, A. T. (1994). Chloroplast molecular chaperone-assisted refolding and reconstitution of an active multisubunit coupling factor CF1 core. *Proc. Natl. Acad. Sci. USA.* **91**, 11497–11501.

182 Choquet, Y. & Vallon, O. (2000). Synthesis, assembly and degradation of thylakoid membrane proteins. *Biochimie* **82**, 615–634.

183 Plucken, H., Muller, B.,

Grohmann, D., Westhoff, P. & Eichacker, L. A. (2002). The HCF136 protein is essential for assembly of the photosystem II reaction center in Arabidopsis thaliana. *FEBS Lett.* **532**, 85–90.

184 Liu, X.-Q. & Jagendorf, A. T. (1984). ATP-dependent proteolysis in pea chloroplasts. *FEBS Lett.* **166**, 248–252.

185 Majeran, W., Wollman, F. A. & Vallon, O. (2000). Evidence for a role of ClpP in the degradation of the chloroplast cytochrome b(6)f complex. *Plant Cell* **12**, 137–150.

186 Malek, L., Bogorad, L., Ayers, A. R. & Goldberg, A. L. (1984). Newly synthesized proteins are degraded by an ATP-stimulated proteolytic process in isolated pea chloroplasts. *FEBS Lett.* **166**, 253–257.

187 Schmidt, G. W. & Mishkind, M. L. (1983). Rapid degradation of unassembled ribulose-1,5-bisphosphate carboxylase small subunit in chloroplasts. *Proc. Natl. Acad. Sci. USA.* **80**, 2632–2636.

188 Al-Babili, S., von Lintig, J., Haubruck, H. & Beyer, P. (1996). A novel, soluble form of phytoene desaturase from Narcissus pseudonarcissus chromoplasts is Hsp70-complexed and competent for flavinylation, membrane association and enzymatic activation. *Plant J.* **9**, 601–612.

189 Bonk, M., Tadros, M., Vandekerckhove, J., Al-Babili, S. & Beyer, P. (1996). Purification and characterization of chaperonin 60 and heat-shock protein 70 from chromoplasts of Narcissus pseudonarcissus. *Plant Physiol.* **111**, 931–939.

190 Liedvogel, B., Sitte, P. & Falk, H. (1976). Chromoplasts in the daffodil: fine structure and chemistry. *Cytobiology* **12**, 155–174.

191 Schroda, M., Vallon, O., Wollman, F. A. & Beck, C. F. (1999). A chloroplast-targeted heat shock protein 70 (HSP70) contributes to the photoprotection and repair of photosystem II during and after photoinhibition. *Plant Cell* **11**, 1165–1178.

192 Schuster, G., Timberg, R. & Ohad, I. (1988). Turnover of thylakoid photosystem II proteins during photoinhibition of Chlamydomonas reinhardtii. *Eur. J. Biochem.* **177**, 403–410.

193 Yokthongwattana, K., Chrost, B., Behrman, S., Casper-Lindley, C. & Melis, A. (2001). Photosystem II damage and repair cycle in the green alga Dunaliella salina: involvement of a chloroplast-localized HSP70. *Plant Cell Physiol.* **42**, 1389–1397.

194 Schroda, M., Kropat, J., Oster, U., Rudiger, W., Vallon, O., Wollman, F. A. & Beck, C. F. (2001). Possible role for molecular chaperones in assembly and repair of photosystem II. *Biochem. Soc. Trans.* **29**, 413–418.

195 Levine, R. L., Mosoni, L., Berlett, B. S. & Stadtman, E. R. (1996). Methionine residues as endogenous antioxidants in proteins. *Proc. Natl. Acad. Sci. USA.* **93**, 15036–15040.

196 Rogalla, T., Ehrnsperger, M., Preville, X., Kotlyarov, A., Lutsch, G., Ducasse, C., Paul, C., Wieske, M., Arrigo, A. P., Buchner, J. & Gaestel, M. (1999). Regulation of Hsp27 oligomerization, chaperone function, and protective activity against oxidative stress/tumor necrosis factor alpha by phosphorylation. *J. Biol. Chem.* **274**, 18947–18956.

197 Sadanandom, A., Poghosyan, Z., Fairbairn, D. J. & Murphy, D. J. (2000). Differential regulation of plastidial and cytosolic isoforms of peptide methionine sulfoxide reductase in Arabidopsis. *Plant Physiol.* **123**, 255–264.

198 Glaczinski, H. & Kloppstech, K. (1988). Temperature-dependent binding to the thylakoid membranes of nuclear-coded chloroplast heat-shock proteins. *Eur. J. Biochem.* **173**, 579–583.

199 Sabehat, A., Lurie, S. & Weiss, D. (1998). Expression of small heat-shock proteins at low temperatures. A possible role in protecting against chilling injuries. *Plant Physiol.* **117**, 651–658.

200 Ishikawa, A., Tanaka, H., Nakai, M. & Asahi, T. (2003). Deletion of a

chaperonin 60 beta gene leads to cell death in the Arabidopsis lesion initiation 1 mutant. *Plant Cell Physiol.* **44**, 255–261.

201 Arnon, D. (1949). Copper enzyme in isolated chloroplasts. Polyphend oxidase in Beta vulgaris. *Plant. Physiol.* **24**, 1–15.

202 Laemmli, U. K. (1970). Cleavage of structural proteins during assembly of phage T4 head. *Nature* **227**, 680–685.

203 Lissin, N. M. (1995). In vitro dissociation of self-assembly of three chaperonin 60s: the role of ATP. *FEBS Lett.* **361**, 55–60.

204 Török, Z., Goloubinoff, P., Horváth, I., Tsvetkova, N. M., Glatz, A., Balogh, G., Varvasovski, V., Los, D. A., Vierling, E., Crowe, J. h., and Vigh, L. (2001) Synechocystis Hsp17 is an amphitropic protein that stabililizes heat-stressed membranes and binds denaturated proteins for subsequent chaperone-mediated refolding. *Proc. Natl. Acad. Sci. USA.* **98**, 3098–3103.

205 Török, Z., Horváth, I., Goloubinoff, P., Kovács, E., Glatz, A., Balogh, G., and Vigh, L. (1997) Evidence for a lipochaperonin: association of active protein-folding GroESL oligomers with lipids can stabilize membranes under heat shock conditions. *Proc. Natl. Acad. Sci. USA.* **94**, 2192–2197.

33
An Overview of Protein Misfolding Diseases

Christopher M. Dobson

33.1
Introduction

The ability of even the most complex protein molecules to fold to their biologically functional states is perhaps the most fundamental example of biological self-assembly, one of the defining characteristics of living systems [1]. In recent years, considerable progress has been made in understanding both the general principles of protein folding and the specific structural transitions that are involved in the folding of individual proteins [2, 3]. In addition to the detailed mechanistic studies that have largely been carried out in vitro, considerable efforts have been directed at understanding the manner in which folding occurs in vivo. Although the fundamental principles underlying the mechanism of folding are unlikely to differ in any significant manner from those elucidated from in vitro studies, many details of the way in which individual proteins fold undoubtedly depend on the environment in which they are located. In particular, given the complexity and stochastic nature of the folding process, it is inevitable that misfolding events will occur under some circumstances [4]. As misfolded or even incompletely folded chains inevitably expose to the outside world many regions of the polypeptide molecule that are buried in the native state, such species are prone to aberrant interactions with other molecules within the complex and crowded cellular environment [5]. Such interactions can result both in the disruption of normal cellular processes and in self-association or aggregation. In order to cope with the inevitable issues of misfolding and aggregation, therefore, living systems have evolved a range of elaborate strategies, including molecular chaperones, folding catalysts, and quality-control and degradation mechanisms [6, 7].

The fact that proteins can misfold and interact inappropriately with one another is well established. For example, one of the major problems in generating recombinant protein for research purposes or for use in biotechnology is recovering significant quantities of soluble and fully active protein from in vitro refolding procedures carried out in the laboratory [8]. The fact that misfolding, and its consequences such as aggregation, can be an important feature of the behavior of proteins in vivo is clearly evident from observations that the levels of certain pro-

Protein Folding Handbook. Part II. Edited by J. Buchner and T. Kiefhaber

ISBN: 3-527-30784-2

teins known to be able to deal with such problems are increased substantially during cellular stress [9]. Indeed, many molecular chaperones were first recognized in prokaryotic (bacterial) systems that had been subjected to stress generated by exposure to elevated temperatures, as their nomenclature as heat shock proteins (Hsps) indicates. As well as assisting folding and preventing incompletely folded chains from forming misfolded species, it is clear that some molecular chaperones are able to rescue proteins that have misfolded and allow them a second chance to fold correctly. There are also examples of molecular chaperones that are known to be able to solubilize misfolded aggregates under at least some circumstances. Such active intervention requires energy, and, not surprisingly, ATP is required for many of the molecular chaperones to function correctly [5]. Despite the fact that molecular chaperones are often expressed at high levels only in stressed systems, it is clear that they have a critical role to play in all organisms even when present at lower levels under normal physiological conditions.

In eukaryotic systems, many of the proteins that are synthesized in a cell are destined for secretion to the extracellular environment. These proteins are translocated into the ER, where folding takes place prior to secretion through the Golgi apparatus. The ER contains a wide range of molecular chaperones and folding catalysts to promote efficient folding; in addition, the proteins involved are subject to stringent quality control [6]. The quality-control mechanism in the ER can involve a complex series of glycosylation and deglycosylation processes and acts to prevent misfolded proteins from being secreted from the cell. Once recognized, unfolded and misfolded proteins are targeted for degradation through the ubiquitin-proteasome pathway [7]. The details of how these regulatory systems operate provide remarkable evidence of the stringent mechanisms that biology has established to ensure that misfolding and its consequences are minimized. The importance of such a process is underlined by the fact that recent experiments suggest that up to half of all polypeptide chains fail to satisfy the quality-control mechanism in the ER, and for some proteins the success rate is even lower [10]. Like the ''heat shock response'' in the cytoplasm, the ''unfolded protein response'' in the ER is upregulated during stress and, as we shall see below, is strongly linked to the avoidance of misfolding diseases.

33.2
Protein Misfolding and Its Consequences for Disease

Folding and unfolding are the ultimate ways of generating and abolishing specific cellular activities, and unfolding is also the precursor to the ready degradation of a protein [11]. Moreover, it is increasingly apparent that some events in the cell, such as translocation across membranes, can require proteins to be in unfolded or partially folded states. Processes as apparently diverse as trafficking, secretion, the immune response, and the regulation of the cell cycle are in fact now recognized to be directly dependent on folding and unfolding [12]. It is not surprising, therefore, that failure to fold correctly, or to remain correctly folded, gives rise to the malfunc-

Tab. 33.1. Representative protein-folding diseases (adapted from Ref. [14]).

Disease	*Protein*	*Site of folding*
Hypercholesterolemia	Low-density lipoprotein receptor	ER
Cystic fibrosis	Cystic fibrosis transmembrane regulator	ER
Phenylketonuria	Phenylalanine hydroxylase	Cytosol
Huntington's disease	Huntingtin	Cytosol
Marfan syndrome	Fibrillin	ER
Osteogenesis imperfecta	Procollagen	ER
α1-Antitrypsin deficiency	α1-Antitrypsin	ER
Tay-Sachs disease	β-Hexosaminidase	ER
Scurvy	Collagen	ER
Alzheimer's disease	Amyloid β-peptide/tau	ER
Parkinson's disease	α-Synuclein	Cytosol
Scrapie/Creutzfeldt-Jakob disease	Prion protein	ER
Familial amyloidoses	Transthyretin/lysozyme	ER
Retinitis pigmentosa	Rhodopsin	ER
Cataract	Crystallins	Cytosol
Cancer	p53	Cytosol

tioning of living systems and therefore to disease. Indeed, it is becoming increasingly evident that a wide range of human diseases is associated with aberrations in the folding process (Table 33.1) [13, 14]. Some of these diseases (e.g., cystic fibrosis) can be attributed to the simple fact that if proteins do not fold correctly, they will not able to exercise their proper function; such misfolded species are often degraded rapidly within the cell. Others (e.g., disorders associated with α1-antitrypsin) result at least in part from the failure of proteins to be trafficked to the appropriate organs in the body [15, 16]. In other cases, misfolded proteins escape all the protective mechanisms discussed above and form intractable aggregates within cells or in extracellular space. An increasing number of pathologies – including Alzheimer's and Parkinson's diseases, the spongiform encephalopathies, and late-onset diabetes – are known to be directly associated with the deposition of such aggregates in tissue (Table 33.2) [13, 14, 17–19]. Diseases of this type are among the most debilitating, socially disruptive, and costly in the modern world, and they are becoming increasingly prevalent as our societies age and as new agricultural, dietary, and medical practices are adopted [20].

One of the most characteristic features of many of the aggregation diseases is that they give rise to the deposition of proteins in the form of amyloid fibrils and plaques [17, 18]. Such deposits can form in the brain, in vital organs such as the liver and spleen, or in skeletal tissue, depending on the disease involved. In the case of neurodegenerative diseases, the quantity of such aggregates can be almost undetectable in some cases, while in systemic diseases, kilograms of protein can be found in such deposits. Each amyloid disease primarily involves the aggregation of a specific peptide or protein, although a range of additional components, including other proteins and carbohydrates, are also incorporated into the deposits when they

Tab. 33.2. Examples of diseases associated with amyloid deposition (adapted from Refs. [14] and [18]).

Clinical syndrome	*Fibril component*	*Type*
Alzheimer's disease	Aβ peptide, 1-42, 1-43	Organ limited
Spongiform encephalopathies	Full-length prion or fragments	Organ limited
Primary systemic amyloidosis	Intact light chain or fragments	Systemic
Secondary systemic amyloidosis	76-residue fragment of amyloid A protein	Systemic
Familial amyloidotic polyneuropathy I	Transthyretin variants and fragments	Systemic
Senile systemic amyloidosis	Wild-type transthyretin and fragments	Systemic
Hereditary cerebral amyloid angiopathy	Fragment of cystatin-C	Organ limited
Hemodialysis-related amyloidosis	β2-microglobulin	Systemic
Familial amyloidotic polyneuropathy II	Fragments of apolipoprotein A-I	Systemic
Finnish hereditary amyloidosis	71-residue fragment of gelsolin	Systemic
Type II diabetes	Islet-associated polypeptide	Organ limited
Medullary carcinoma of the thyroid	Fragments of calcitonin	Organ limited
Atrial amyloidosis	Atrial natriuretic factor	Organ limited
Lysozyme amyloidosis	Full-length lysozyme variants	Systemic
Insulin-related amyloidosis	Full-length insulin	Systemic
Fibrinogen α-chain amyloidosis	Fibrinogen α-chain variants	Systemic

form in vivo. The characteristics of the soluble forms of the 20 or so proteins involved in the well-defined amyloidoses vary greatly, ranging from intact globular proteins to largely unstructured peptide molecules, but the aggregated forms have many common characteristics [21]. Thus, amyloid deposits all show specific optical properties (such as birefringence) on binding certain dye molecules, notably Congo red; these properties have been used in diagnosis for over a century. The fibrillar structures that are characteristic of many of these types of aggregates have very similar morphologies (long, unbranched, and often twisted structures a few nanometers in diameter) and a characteristic "cross-beta" X-ray fiber diffraction pattern [21]. The latter reveals that the organized core structure is composed of β-sheets with the strands running perpendicular to the fibril axis (Figure 33.1, see p. 1100) [22]. Fibrils having the essential characteristics of those found in ex vivo deposits can be reproduced in vitro from the component proteins under appropriate conditions, showing that they can self-assemble without the need for other components.

For many years it was generally assumed that the ability to form amyloid fibrils with the characteristics described above was limited to a relatively small number of proteins, largely those seen in disease states, and that these proteins must possess specific sequence motifs encoding the amyloid core structure. However, recent studies have suggested that the ability of polypeptide chains to form such structures is common and indeed can be considered a generic feature of polypeptide

chains [4, 23–25]. The most direct evidence for the latter statement is that fibrils can be formed under appropriate conditions by many different proteins that are not associated with disease, including such well-known proteins as myoglobin [26], as well as by homopolymers such as polythreonine or polylysine [27]. Remarkably, fibrils of similar appearance to those containing large proteins can be formed by peptides with just a handful of residues [28]. One can consider that amyloid fibrils are highly organized structures (effectively one-dimensional crystals) adopted by an unfolded polypeptide chain when it behaves as a typical polymer molecule; similar types of structures can be formed, for example, by synthetic polymers. The essential features of such structures are therefore determined by the physicochemical properties of the polymer chain. As with other highly organized materials (including crystals) whose structures are based on repetitive long-range interactions, the most stable structures are usually those consisting of a single type of molecular species (e.g., a specific peptide sequence) where such interactions can be optimized [25].

33.3 The Structure and Mechanism of Amyloid Formation

Studies of amyloid fibrils formed by both disease-associated and other peptides and proteins have enabled many of the features of these structures to be defined [21, 29–33], although no complete structure has yet been determined in atomic detail. It is clear that the core structure of the fibrils is stabilized primarily by interactions, particularly hydrogen bonds, involving the atoms of the extended polypeptide main chain. As the main chain is common to all polypeptides, this observation explains why fibrils formed from polypeptides of very different amino acid sequences are similar in appearance. The side chains are likely to be incorporated in whatever manner is most favorable for a given sequence within the amyloid structures; they appear to affect the details of the fibrillar assembly but not the fundamental structure of the fibril [34]. In addition, the proportion of a polypeptide chain that is incorporated in the core structure can vary substantially; in some cases only a handful of residues may be involved in such structure, with the remainder of the chain associated in some other manner with the fibrillar assembly. This generic type of structure contrasts strongly with the globular structures of most natural proteins that result from the uniquely favorable packing of a given set of side chains into a particular fold. On the conceptual model outlined here, structures such as amyloid fibrils occur because interactions associated with the highly specific packing of the side chains can sometimes override the conformational preferences of the main chain [24–27]. The strands and helices so familiar in the structures of native proteins are then the most stable structures that the main chain can adopt in the folds that are primarily defined by the side chain interactions. However, if the solution environment (pH, temperature, concentration, etc.) in which the molecules are found is such that these side chain interactions are insufficiently

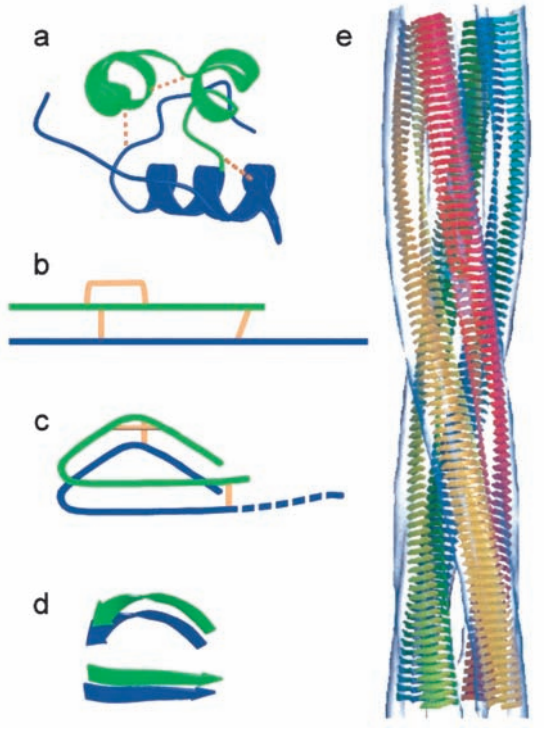

Fig. 33.1. Molecular model of an amyloid fibril. This model is derived from cryo-EM analysis of fibrils grown from bovine insulin whose native topology is indicated in (a). The two chains (A, green, and B, blue) are connected by three disulfide bridges (b). A possible topology for insulin in the fibrils is illustrated in (c), while (d) indicates how strands could be assembled in a complete fibril, a model of which is shown in (e). The fibril consists of four ''protofilaments'' that twist around one another to form a regular pattern with a diameter of approximately 10 nm (from Ref. [31]).

stable, the structures can unfold and may then, at least under some circumstances, reassemble in the form of amyloid fibrils.

In order to understand the occurrence and significance of amyloid formation in biological systems, it is essential to establish the mechanism by which such structures are assembled from the soluble precursor species. In globular proteins the polypeptide main chain is largely buried within the folded structure. Conditions that favor formation of any form of aggregate by such species are therefore ones in which the molecules involved are at least partially unfolded, as occurs, for example, at low pH or elevated temperature [23, 35]. Because of the importance of the globular fold in preventing aggregation, the fragmentation of proteins, through proteolysis or other means, is another ready mechanism to stimulate amyloid formation. Indeed, many amyloid disorders, including Alzheimer's disease, involve aggregation of fragments of larger precursor proteins that are unable to fold in the absence of the remainder of the protein structure (see Table 33.2). Experiments

in vitro indicate that the formation of fibrils, by appropriately destabilized or fragmented proteins, is then generally characterized by a lag phase followed by a period of relatively rapid growth [36]. Behavior of this type is typical of nucleated processes such as crystallization; as with crystallization, the lag phase in amyloid formation can generally be eliminated by addition of preformed fibrils to fresh solutions, a process known as seeding [36]. Although the specific events taking place during fibril growth are not yet elucidated in any detail, it is becoming possible to simulate the overall kinetic profiles using relatively simple models that incorporate well-established principles of nucleated processes [37].

One of the key findings of studies of the formation of amyloid fibrils is that there are many common features in the behavior of the different systems that have been examined [19, 36, 38, 39]. The first phase of the aggregation process generally appears to involve the formation of more or less disordered oligomeric species as a result of relatively nonspecific interactions, although in some cases specific structural transitions, such as domain swapping [40], may be involved if such processes increase the rate of aggregation. The earliest species visible by electron or atomic force microscopy often resemble small bead-like structures, sometimes described as amorphous aggregates or as micelles. These early ''pre-fibrillar aggregates'' then appear to transform into species with more distinctive morphologies, sometimes described as ''protofibrils'' or ''protofilaments'' [39, 41]. These structures are commonly short, thin, sometimes curly, fibrillar species that are thought to be able to assemble into mature fibrils, perhaps by lateral association accompanied by some degree of structural reorganization [42] (Figure 33.2). The extent to which aggregates dissolve and reassemble into more regular structures involved at the different stages of fibril assembly is not clear, but it could well be important under the slow growth conditions in which the most highly structured fibrils are formed. The earliest aggregates are likely in most situations to be relatively disorganized structures that expose to the outside world a variety of segments of the protein that are normally buried in the globular state. In other cases, however, such species appear to adopt distinctive structures, including the well-defined ''doughnut-shaped'' species that have been seen for a number of systems (Figure 33.2) [39, 44].

Although the ability of polypeptides to form amyloid fibrils appears generic, the propensity to do so varies dramatically with amino acid composition and sequence. At the most fundamental level, some types of amino acids are much more soluble than others, such that the concentration required for aggregation to occur will be much greater for some polypeptides than for others. In addition, the aggregation process, like crystallization, needs to be nucleated and the rates at which this process takes place can be highly dependent on many different factors. It is clear that even single changes of amino acids in protein sequences can change the rates at which the unfolded polypeptide chains aggregate by an order of magnitude or more [45]. Moreover, it has recently proved possible to correlate changes in aggregation rates caused by mutations with changes in simple properties that result from substitutions, such as charge, secondary structure propensities, and hydrophobicity [45]. As this correlation has been found to hold for a wide range of different sequences (see Figure 33.3), it strongly endorses the concept of a common

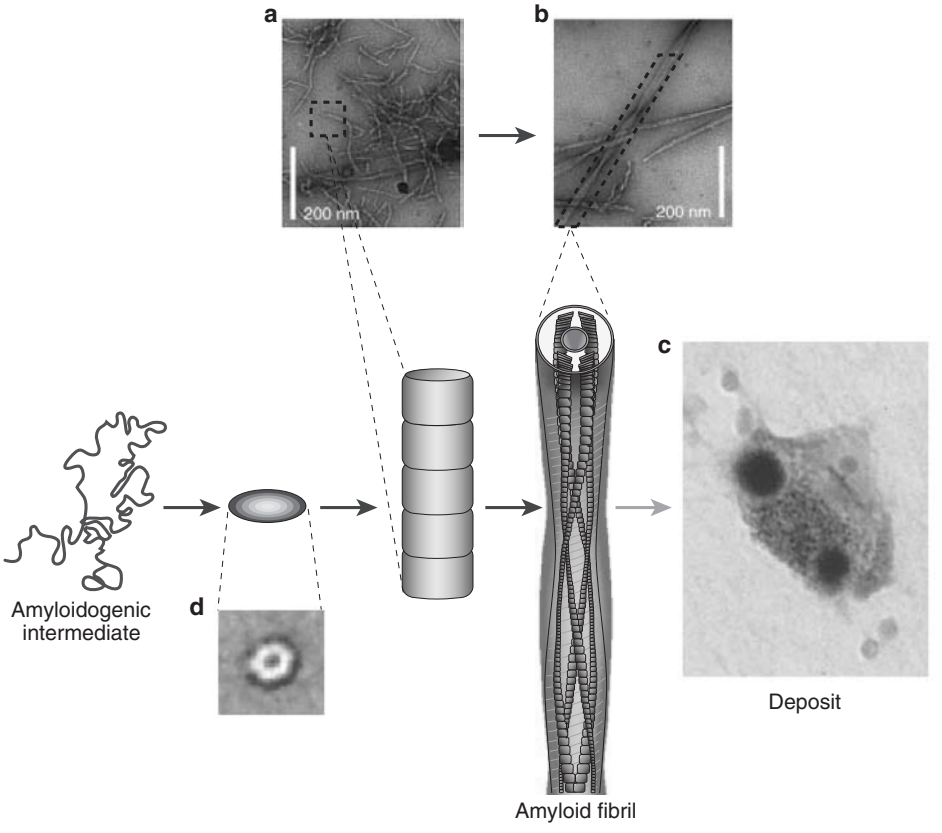

Fig. 33.2. Schematic representation of the formation of amyloid fibrils and pathological deposits. An unfolded or partially unfolded peptide or protein initially forms small soluble aggregates that then assemble to form a variety of ''pre-fibrillar'' species, some or all of which appear to be toxic to living cells. These species undergo a series of additional assembly and reorganizational steps to give ordered amyloid fibrils of the type illustrated in Figure 33.3. Pathological deposits such as the Lewy bodies associated with Parkinson's disease [43] frequently contain large assemblies of fibrillar aggregates, along with other components including molecular chaperones (from Ref. [4]).

mechanism of amyloid formation. In accordance with such ideas, those proteins that are completely or partially unfolded under normal conditions in the cell have sequences that are likely to have very low propensities to aggregate. An interesting and potentially important additional observation is that specific regions of the polypeptide chain appear to be responsible for nucleating the aggregation process [46]. Interestingly, the residues that nucleate the folding of a globular protein seem to be distinct from those that nucleate its aggregation into amyloid fibrils. Such a characteristic, which may reflect the different nature of the partially folded species that initiate the assembly processes, offers the opportunity for evolutionary pressure to select sequences that favor folding over aggregation [46, 47].

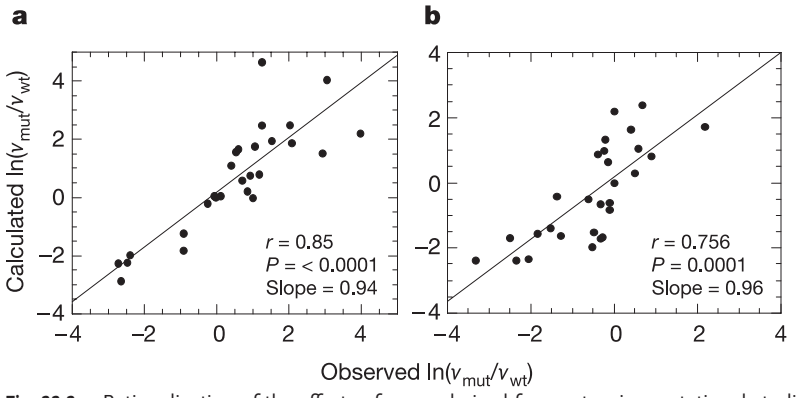

Fig. 33.3. Rationalization of the effects of mutations on the aggregation rates of peptides and proteins. The experimental aggregation rates of a variety of short peptides or natively unfolded proteins, including amylin, amyloid β-peptide, tau, and α-synuclein (see Tables 33.1 and 33.2 for a summary of the diseases with which these are associated), are shown plotted against rates calculated from an algorithm derived from extensive mutational studies of the protein acylphosphatase; the analogous plot of the data for acylphosphatase is shown in (b). The correlation shown in (a) argues strongly for a common mechanism for amyloid formation and provides a platform for both predicting the effects of natural mutations and designing polypeptides with altered aggregation properties (from Ref. [45]).

33.4
A Generic Description of Amyloid Formation

It is clear that proteins can adopt different conformational states under different conditions and that there can be considerable similarities in this regard between different proteins. This situation can be summarized by using a schematic representation of the different states that are in principle accessible to a polypeptide chain (see Figure 33.4) [4, 25, 48]. In such a situation, the state that a given system populates under specific conditions will depend on the relative thermodynamic stabilities of the different states (in the case of oligomers and aggregates, the concentration will be a critical parameter) and on the kinetics of the various interconversion processes. In this diagram, amyloid fibrils are included as just one of the types of aggregates that can be formed by proteins, although they have particular significance in that their highly organized, hydrogen-bonded structure gives them unique kinetic stability. This type of representation emphasizes that complex biological systems have become robust by controlling and regulating the various states accessible to a given polypeptide chain at given times and under given conditions, just as they regulate and control the various chemical transformations that take place in the cell [4, 24]. The latter is achieved primarily through enzymes and the former by means of the molecular chaperones and degradation mechanisms mentioned above. And just as the aberrant behavior of enzymes can cause metabolic disease, the aberrant behavior of the chaperone and other machinery regulating polypeptide conformations can contribute to misfolding and aggregation diseases [49].

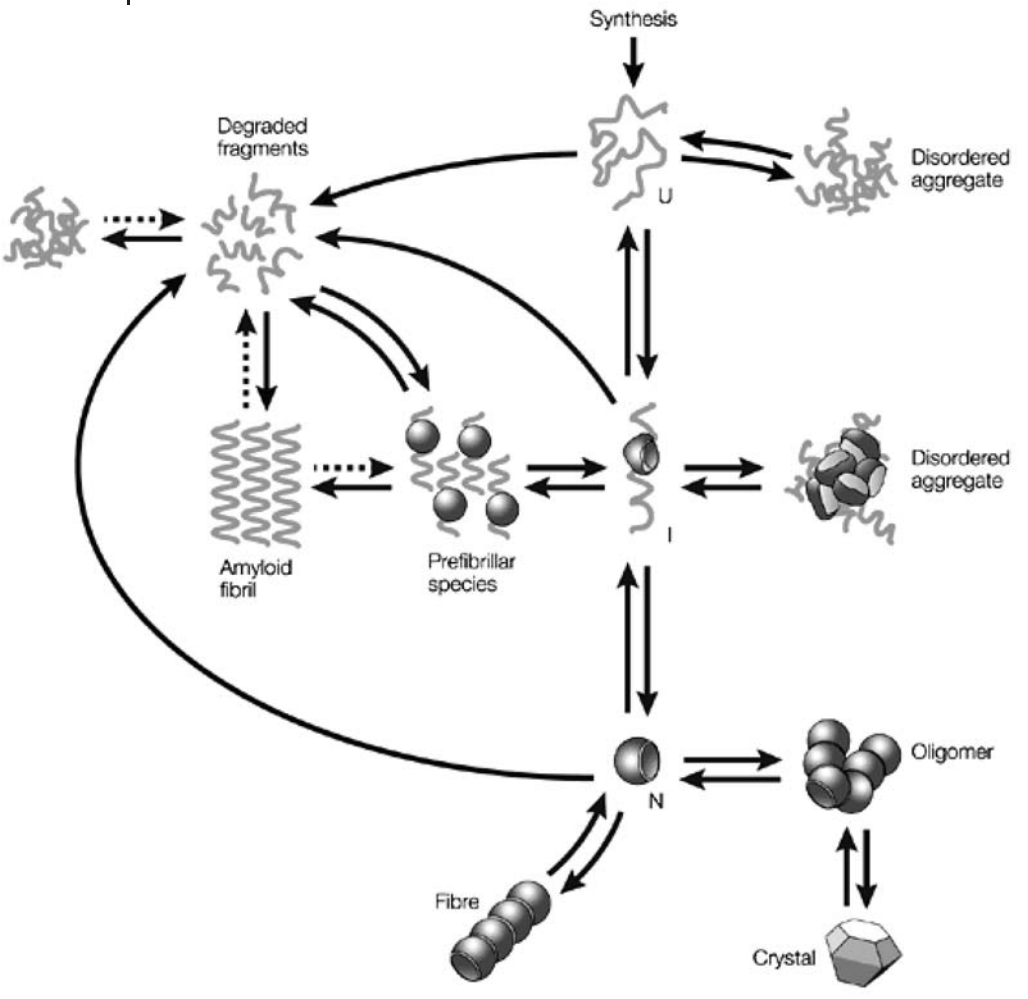

Fig. 33.4. Schematic representation of some of the states accessible to a polypeptide chain following its synthesis on a ribosome. The relative populations of the different states depend on the kinetics and thermodynamics of the various equilibria shown in the diagram. In living systems the fate of a given molecule is closely regulated, using mechanisms such as those illustrated in Figures 33.1 and 33.2, rather like metabolic pathways in cells are controlled by enzymes and associated molecules such as cofactors (from Ref. [25]).

The type of diagram shown in Figure 33.4 serves as a framework for understanding the fundamental molecular events that underlie the regulatory and quality-control mechanisms and the origins of the amyloid diseases that can result when these fail or are overwhelmed. As we have discussed above, partially or completely unfolded polypeptides are highly aggregation-prone and represent the species that trigger amyloid formation. Such species are, however, inherent in the folding process, and for this reason a variety of molecular chaperones is present in abundance in the cellular compartments wherever such processes occur. It is possible, however, that chaperones also exist in environments where *ab initio* folding does not take place. Indeed, an extracellular chaperone (clusterin) has been identified recently [50]. Nevertheless, it is undoubtedly important in the context of avoiding aggregation that proteins are correctly folded prior to their secretion from the cell, hence the need for a highly effective system of quality control in the ER. In this context it is interesting that the majority of the diseases associated with amyloid formation involve deposits that are extracellular in nature, although it is not yet clear exactly where their formation in fact takes place [19]. As biology is a dynamic process, there is a continuous need to degrade as well as synthesize proteins, and the degradative mechanisms target misfolded as well as redundant proteins. It is during such processes, which require unfolding and proteolysis of polypeptide chains, that aggregation may be particularly likely. Degradation pathways, such as those of the ubiquitin-proteasome system, are therefore highly regulated in order to avoid the occurrence of such events [7, 51].

In order to understand misfolding and aggregation diseases, we need to know not only how such systems function efficiently but also why they fail to do so under some circumstances [51–53]. The effects of many pathogenic mutations can be particularly well understood from the schematic representation given in Figure 33.4. Many of the mutations associated with the familial deposition diseases increase the population of partially unfolded states either within or outside the cell by decreasing the stability or cooperativity of the native state [54–56]. Cooperativity is in fact a crucial factor in enabling proteins to remain soluble, as it ensures that, even for a protein that is marginally stable, the equilibrium population of unfolded molecules or of unfolded regions of the polypeptide chain is minimal [24]. Other familial diseases are associated with the accumulation of fragments of native proteins, which are often produced by aberrant processing or incomplete degradation; such species are usually unable to fold into aggregation-resistant states. Other pathogenic mutations act by enhancing the propensities of such species to aggregate, for example, by increasing their hydrophobicity or decreasing their charge [45]. In the case of the transmissible encephalopathies, it is likely that ingestion of pre-aggregated states of an identical protein (e.g., by cannibalistic means or by contamination of surgical instruments) dramatically increases the rate of aggregation within the individual concerned and hence underlies the mechanism of transmission [36, 57, 58]. Such seeding phenomena may also at least partly explain why some deposition conditions such as Alzheimer's disease progress so rapidly once the initial symptoms are evident [36, 59].

33.5 The Fundamental Origins of Amyloid Disease

Despite our increasing knowledge of the general principles that underlie protein misfolding diseases, the manner in which improperly folded proteins and aggregated proteins can generate pathological behavior is not yet understood in detail. In the case of systemic disease, the sheer mass of protein that can be deposited may physically disrupt the functioning of specific organs [17]. In other cases it may be that the loss of functional protein results in the failure of some crucial cellular process [39]. For neurodegenerative disorders such as Alzheimer's disease, however, it appears that the primary symptoms arise from the destruction of cells such as neurons by a "toxic gain of function" that results from the misfolding and aggregation process [19, 39]. It has recently become apparent that the early pre-fibrillar aggregates of proteins associated with neurological disorders can be highly damaging to cells; by contrast, the mature fibrils are relatively benign [39, 60]. There is evidence, however, that the toxic nature of protein aggregates is not restricted to species formed from the peptides and proteins associated with pathological conditions. Experiments have recently indicated that pre-fibrillar aggregates of several proteins that are not connected with any known diseases have a degree of toxicity comparable to that of similar species formed from the Aβ-peptide [61]. The concept that the effects of such aggregates on cells are more strongly related to their generic nature than to their specific sequence has recently been reinforced through experiments with polyclonal antibodies that cross-react with early aggregates of different peptides and proteins and, moreover, inhibit their toxicity in cellular assays [62]. It is possible that there are specific mechanisms for such toxicity, for example, through the doughnut-shaped aggregates that resemble the toxins produced by bacteria that form pores in membranes and disrupt the ion balance in cells [44]. It is also possible that disorganized early aggregates, or even misfolded monomers, are toxic through a less specific mechanism, e.g., because exposed, nonnative hydrophobic surfaces may stimulate aberrant interactions with cell membranes or other cellular components [53, 63, 64].

Such findings raise the question as to how cellular systems are able to tolerate the intrinsic tendency of incompletely folded proteins to aggregate. The answer is almost certainly that under normal circumstances the molecular chaperones and other "housekeeping" mechanisms are remarkably efficient in ensuring that such potentially toxic species are neutralized [5, 61]. Molecular chaperones of various types are able to shield hydrophobic regions, to unfold some forms of aggregates, or to alter the partitioning between different forms of aggregates. The latter mechanism, for example, could convert the precursors of amyloid fibrils into less intractable species, allowing them to be refolded or disposed of by the cellular degradation systems. Indeed, evidence has been obtained that such a situation occurs with polyglutamine sequences associated with disorders such as Huntington's disease [65]. In this case the precursors of amyloid fibrils appear to be diverted into amorphous, and hence more readily degradable, species by the action of molecular chaperones. If such protective processes fail, it may be possible for potentially

harmful species to be sequestered in relatively harmless forms such as inclusion bodies in bacteria or aggresomes in eukaryotic systems. Indeed, it has been suggested that the formation of mature amyloid fibrils, whose toxicity appears to be much lower than that of their precursors (as we have discussed above), may itself represent a protective mechanism in some cases [19, 36].

Most of the aggregation diseases, however, do not result from genetic mutations or infectious agents but rather are sporadic or associated with old age. The ideas summarized in this chapter offer a qualitative explanation of why such a situation arises. We have seen that all proteins have an inherent tendency to aggregate unless they are maintained in a highly regulated environment. Selective pressure during evolution has therefore resulted in protein molecules that are normally able to resist aggregation during our normal lifespan, enabling us to develop, to pass on genes, and to give appropriate protection to our offspring. Evolution, however, can only generate sequences and cellular environments that are adequate for those conditions under which selective pressure exists [20]. There is no reason to suppose that random mutations will in general further reduce the propensity to aggregate; indeed they will generally increase it – just as random mutations generally reduce the stability of native proteins. We can see, therefore, that our recent ability to prolong life [66] is leading to the proliferation of these diseases as the limitations in their ability to resist reversion to aggregates, including the intractable and damaging amyloid structures, become evident. However, it is intriguing to speculate that favorable mutations in aggregation-prone proteins might be the reason that some in the population do not readily succumb to diseases such as Alzheimer's even in extreme old age [45].

The link with aging is likely to involve more than just a greater probability of aggregation taking place as we get older. It is likely to be linked more fundamentally to the failure of the ''housekeeping'' mechanisms in our bodies under such circumstances [20, 67]. This failure may in part be a result of the need for greater protective capacity in old age as aggregation becomes more prevalent, perhaps as a consequence of the increasing accumulation of misfolded and damaged proteins, leading to chaperone overload [68]. But as we age, it is likely that the activity of our chaperone response and degradative mechanisms declines, resulting in the increasing probability that the protective mechanisms are overwhelmed. One reason for this decline, although there may be many, is that cells become less efficient in producing the ATP that is needed for the effective functioning of many chaperones. Similarly, the rapidity with which we have introduced practices that have not been experienced previously in history – including new agricultural practices (associated with the emergence of BSE and variant CJD [57]), a changing diet and lifestyle (associated with the prevalence of type II diabetes [69]), and new medical procedures (e.g., resulting in iatrogenic diseases such as CJD [57] and amyloid deposition in hemodialysis, during which the concentration of β-2 microglobulin in serum increases [70]) – means that we have not had time to evolve effective protective mechanisms [20]. Thus, we are now increasingly observing the limitations of our proteins and their environments to resist aggregation under conditions that differ from those under which natural selection has taken place.

33.6 Approaches to Therapeutic Intervention in Amyloid Disease

The progress made in understanding the underlying causes of the amyloid diseases is also leading to new approaches to their prevention and treatment [71, 72]. For proteins whose functional state is a tightly packed globular fold, we have seen that an essential first step in fibril formation is undoubtedly the partial or complete unfolding of the native structure that otherwise protects the aggregation-prone polypeptide backbone. Thus, many of the familial forms of amyloid disease are associated with genetic mutations that decrease protein stability and thereby promote unfolding. In such cases, one approach to therapy is to find ways of stabilizing the native states of amyloidogenic protein variants. In accordance with this proposal, a recent study has reported a series of small-molecule analogues of the hormone thyroxine, the natural ligand of transthyretin, that act in this manner. Transthyretin is the protein associated with the most common type of systemic amyloidosis, and these potential drugs have been found to dramatically inhibit the rate at which the disease-associated variants aggregate, at least in vitro [73]. In a similar approach, specific antibodies raised against lysozyme have been found to prevent amyloid fibril formation by pathogenic forms of this well-know antibacterial protein whose aggregation is linked to another systemic amyloidosis [74]. Moreover, quinacrine, a drug previously used to combat malaria, has been found to limit dramatically the replication in cell cultures of the pathogenic form of the prion protein associated with CJD [75]. The finding that this molecule interacts with the soluble form of the protein [76] suggests that a similar mechanism could be operating here. Quinacrine is already entering clinical trials, and determined efforts are now underway to find more potent forms of this compound [75].

A possible therapeutic strategy for those amyloid diseases that result from the aggregation of proteolytic fragments rather than intact proteins would be to reduce the levels of the aggregation-prone peptides by inhibiting the enzymes through whose action the fragments are generated. An extremely important example of this approach involves the 40- or 42-residue Aβ-peptide derived from the amyloid precursor protein (APP), as the aggregation of this species is linked to Alzheimer's disease. Much is now known about the complex secretase enzymes whose role in processing APP gives rise to the Aβ-peptide, and a number of potent inhibitors have already been developed as potential therapeutics for this debilitating neurodegenerative disease [77, 78]. Another way of reducing the levels of aggregation-prone species in an organism is to enhance their clearance from the body. A number of strategies based on this general idea have emerged recently, some of the most exciting of which involve the action of antibodies raised against specific amyloid-forming polypeptides. Of particular interest is the finding that active immunization with Aβ-peptides can result in the extensive clearance of amyloid deposits in transgenic mice that overexpress the Aβ-peptide. Although the first set of clinical trials with human Alzheimer victims was terminated as a result of an inflammatory response in a significant number of patients, the potential of this type of

approach has been clearly demonstrated [79]. One possible variation on the original procedure is to use passive immunotherapy, in which antibodies are infused into, rather than generated within, the patient. Additionally, there are means of stimulating clearance other than by the direct action of antibodies. In a study of the effects of a ligand designed to bind to serum amyloid P (SAP), a protein that is associated with amyloid deposits in vivo and is known to inhibit natural clearance mechanisms, the levels of SAP in serum were reduced dramatically [80]. It remains to be established how such molecules fare in ongoing clinical trials, but the general principle of using small molecules to target specific proteins for degradation is an extremely interesting development.

Enhancing the clearance of the amyloidogenic species may well be of particular importance in other forms of amyloid disorders that involve the deposition of peptides and proteins that, although intact, appear not to fold to globular structures even under normal physiological conditions. Examples of such cases include α-synuclein, whose aggregation is associated with Parkinson's disease, and IAPP (amylin), which is involved in type II diabetes [14, 18]. Another strategy that has been proposed is to intervene in the aggregation process directly by means of small peptides or peptide analogues designed to bind tightly to fibrils as they form, hence blocking their further growth. A variety of such species is being explored, particularly in the context of Alzheimer's disease [81]. A potential problem with this approach is that inhibition of the formation of amyloid fibrils might occur at the expense of the small aggregates that are their precursors. Such an effect could be highly counterproductive, as the latter appear to be the primary pathogenic agents, at least in the neurodegenerative forms of amyloid disease, as we discuss above. But provided that problems of this type can be avoided, this approach could potentially be rather generally applicable.

It is a particularly satisfying aspect of research directed at understanding the origins of the amyloid disorders to find that so many different therapeutic approaches can be rationalized using the relatively simple framework illustrated in Figure 33.4 [72]. Particularly, as there are a number of different stages in the aggregation process where intervention is potentially possible, one can be optimistic that novel and efficacious forms of treatment will emerge in the not-too-distant future. Moreover, with the increasing evidence for the generic nature of the amyloid conditions, it is interesting to speculate that there might be generic approaches to inhibiting a variety, perhaps even all, of the amyloid diseases with a single drug [25, 72]. That such an idea could in principle be realized is suggested by the observation that antibodies raised against small aggregates of the Aβ-peptide not only recognize but also suppress the toxicity of similar aggregates formed from other proteins [62]. An approach of this type would be particularly dramatic in light of the number of different types of amyloid disorders that increasingly place the aging populations of the world at risk. Alternatively, one might even speculate that a means could be found to extend the period of time that our natural defenses are able to combat aggregation, and hence defer the onset of these disorders. And looking perhaps even further into the future, our ability to design peptides and proteins whose tenden-

cies to aggregate are reduced, often substantially, provides the basis for a range of exciting approaches involving gene therapy and stem cell techniques [45].

33.7 Concluding Remarks

This chapter has discussed the state of our developing knowledge of the origin of amyloid disease from the perspective of our increasing understanding of the fundamental properties of proteins. We have stressed the fact that the structure and biological effects of amyloid deposition can be considered to be generic and that this fact can be rationalized, at least in outline, through the ideas of polymer science. The propensities of different sequences to aggregate under specific conditions, however, can vary significantly, and it is becoming possible to explain the origins of pathogenic behavior in terms of the factors that affect such propensities. The amyloid diseases can be thought of as fundamentally resulting from the reversion of normally soluble proteins to the generic amyloid structure as a result of the failures of the mechanisms that have evolved to prevent such behavior. A range of novel approaches is now being developed to combat the various amyloid diseases and can to a large extent be rationalized in terms of intervention at different steps in the process of aggregation as represented in Figure 33.4. Many of these approaches show considerable promise for the treatment of specific diseases, and the generic nature of amyloid formation raises the exciting possibility that there could be generic approaches to preventing some or indeed all of the various members of the family of diseases. We can therefore be optimistic that the better understanding of protein misfolding and aggregation that is developing from recent research of the type discussed in this article will enable us to devise increasingly effective strategies for drug discovery based on rational arguments.

Acknowledgements

The ideas in this article have emerged from extensive discussions with outstanding students, research fellows, and colleagues over many years. I am most grateful to all of them; they are too numerous to mention here, but the names of many appear in the list of references. The content of this chapter is derived in part from a review article published in *Nature* in 2003 [4] and a perspective published in *Science* in 2004 [72]. The research of C.M.D. is supported by Programme Grants from the Wellcome Trust and the Leverhulme Trust, as well as by the BBSRC, EPSRC, and MRC.

References

1 M. Vendruscolo, J. Zurdo, C. E. MacPhee and C. M. Dobson, ''Protein Folding and Misfolding: A Paradigm of Self-Assembly and Regulation in Complex Biological Systems'', *Phil. Trans. R. Soc. Lond.*, **A 361**, 1205–1222 (2003).

2 A. R. Fersht, *Structure and Mechanism in Protein Science; A Guide to Enzyme Catalysis and Protein Folding*, W.H. Freeman, New York, 1999.

3 R. H. Pain (Ed.), *Protein Folding* (2nd ed.) Oxford University Press, Oxford, 2000.

4 C. M. Dobson, ''Protein Folding and Misfolding'', *Nature*, **426**, 884–890 (2003).

5 F. U. Hartl and M. Hayer-Hartl, ''Molecular Chaperones in the Cytosol: From Nascent Chain to Folded Protein'', *Science*, **295**, 1852–1858 (2002).

6 R. Sitia and I. Braakman, ''Quality Control in the Endoplasmic Reticulum Protein Factory'', *Nature*, **426**, 891–894 (2003).

7 A. L. Goldberg, ''Protein Degradation and Protection against Misfolded or Damaged Proteins'', *Nature*, **426**, 895–899 (2003).

8 R. R. Kopito, ''Aggresomes, Inclusion Bodies and Protein Aggregates'', *Trends Cell Biol.*, **10**, 524–530 (2000).

9 H. R. Pelham, ''Speculations on the Functions of the Major Heat Shock and Glucose-Regulated Proteins'', *Cell*, **46**, 959–961 (1968).

10 U. Schubert, L. C. Anton, J. Gibbs, C. C. Orbyry, J. W. Yewdell and J. R. Bennink, ''Rapid Degradation of a Large Fraction of Newly Synthesized Proteins by Proteasomes, *Nature*, **404**, 770–774 (2000).

11 A. Matouschek, ''Protein Unfolding – an Important Process in Vivo?'', *Curr. Opin. Struct. Biol.*, **13**, 98–109 (2001).

12 S. E. Radford and C. M. Dobson, ''From Computer Simulations to Human Disease: Emerging Themes in Protein Folding'', *Cell*, **97**, 291–298 (1999).

13 P. J. Thomas, B. H. Qu and P. L. Pedersen, ''Defective Protein Folding as a Basis of Human Disease'', *Trends Biochem. Sci.*, **20**, 456–459 (1995).

14 C. M. Dobson, ''The Structural Basis of Protein Folding and its Links with Human Disease'', *Phil. Trans. R. Soc. Lond.*, **B 356**, 133–145 (2001).

15 K. Powell and P. L. Zeitlin, ''Therapeutic Approaches to Repair Defects in ΔF508 CFTR Folding and Cellular Targeting'', *Adv. Drug Deliv. Rev.*, **54**, 1395–1408 (2002).

16 R. W. Carrell and D. A. Lomas, ''Mechanisms of Disease. α1-Antitrypsin Deficiency – A Model for Conformational Diseases'', *N. Engl. J. Med*, **346**, 45–53 (2002).

17 M. B. Pepys, ''Amyloidoses'' in The Oxford Textbook of Medicine (eds D. J. Weatherall, J. G. Ledingham and D. A. Warrel), 3rd Edition Oxford University Press, Oxford, 1512–1524 (1995).

18 D. J. Selkoe, ''Folding Proteins in Fatal Ways'', *Nature*, **426**, 900–904 (2003).

19 E. H. Koo, P. T. Lansbury Jr., and J. W. Kelly, ''Amyloid Diseases: Abnormal Protein Aggregation in Neurodegeneration'', *Proc. Natl. Acad. Sci. USA*, **96**, 9989–9990 (1999).

20 C. M. Dobson, ''Getting Out of Shape – Protein Misfolding Diseases'', *Nature*, **418**, 729–730 (2002).

21 M. Sunde and C. C. F. Blake, ''The Structure of Amyloid Fibrils by Electron Microscopy and X-ray Diffraction'', *Adv. Protein Chem.*, **50**, 123–159 (1997).

22 J. L. Jiménez, J. I. Guijarro, E. Orlova, J. Zurdo, C. M. Dobson, M. Sunde and H. R. Saibil, ''Cryo-electron Microscopy Structure of an SH3 Amyloid Fibril and Model of the Molecular Packing'', *EMBO J.*, **18**, 815–821 (1999).

23 F. Chiti, P. Webster, N. Taddei, A.

Clark, M. Stefani, G. Ramponi and C. M. Dobson, "Designing Conditions for in vitro Formation of Amyloid Protofilaments and Fibrils", *Proc. Natl. Acad. Sci. USA*, **96**, 3590–3594 (1999).

24 C. M. Dobson, "Protein Misfolding, Evolution and Disease", *Trends Biochem. Sci.*, **24**, 329–332 (1999).

25 C. M. Dobson, "Protein Folding and Disease: A View from the First Horizon Symposium", *Nature Rev. Drug Disc.*, **2**, 154–160 (2003).

26 M. Fändrich, M. A. Fletcher and C. M. Dobson, "Amyloid Fibrils from Muscle Myoglobin", *Nature*, **410**, 165–166 (2001).

27 M. Fändrich and C. M. Dobson, "The Behavior of Polyamino Acids Reveals an Inverse Side-chain Effect in Amyloid Structure Formation", *EMBO J.*, **21**, 5682–5690 (2002).

28 M. Lopez de la Paz, K. Goldie, J. Zurdo, E. Lacrois, C. M. Dobson, A. Hoenger and L. Serrano, "De Novo Designed Peptide-based Amyloid Fibrils", *Proc. Natl. Acad. Sci. USA*, **99**, 16052–16057 (2002).

29 L. C. Serpell, C. C. F. Blake and P. E. Fraser, "Molecular Structure of a Fibrillar Alzheimer's Aβ Fragment", *Biochemistry*, **39**, 13269–13275 (2000).

30 H. Wille, M. D. Michelitsch, V. Guenebaut, S. Supattapone, A. Serban, F. E. Cohen, D. A. Agard and S. B. Prusiner, "Structural Studies of the Scrapie Prion Protein by Electron Crystallography", *Proc. Natl. Acad. Sci, USA*, **99**, 3563–3568 (1999).

31 J. L. Jiménez, E. J. Nettleton, M. Bouchard, C. V. Robinson, C. M. Dobson and H. R. Saibil, "The Protofilament Structure of Insulin Amyloid Fibrils", *Proc. Natl. Acad. Sci. USA*, **99**, 9196–9201 (2002).

32 A. T. Petkova, Y. Ishii, J. J. Balbach, O. N. Antzutkin, R. D. Leapman, F. Delaglio and R. Tycko, "A Structural Model for Alzheimer's β-amyloid Fibrils Based on Experimental Constraints from Solid State NMR", *Proc. Natl. Acad. Sci. USA*, **99**, 16742–16747 (2002).

33 C. P. Jaroniec, C. E. MacPhee, V. S. Bajaj, M. T. McMahon, C. M. Dobson and R. G. Griffin, "High Resolution Molecular Structure of a Peptide in an Amyloid Fibril Determined by Magic Angle Spinning NMR Spectroscopy", *Proc. Natl. Acad. Sci. USA*, **101**, 711–716 (2004).

34 A. Chamberlain, C. E. MacPhee, J. Zurdo, L. A. Morozova-Roche, H. A. O. Hill, C. M. Dobson and J. Davis, "Ultrastructural Organisation of Amyloid Fibrils by Atomic Force Microscopy", *Biophys. J.*, **79**, 3282–3293 (2000).

35 J. Kelly, "Alternative Conformation of Amyloidogenic Proteins and their Multi-step Assembly Pathways", *Curr. Opin. Struct. Biol.*, **8**, 101–106 (1998).

36 J. D. Harper and P. T. Lansbury Jr., "Models of Amyloid Seeding in Alzheimer's Disease and Scrapie: Mechanistic Truths and Physiological Consequences of the Time-dependent Solubility of Amyloid Proteins", *Annu. Rev. Biochem.*, **66**, 385–407 (1997).

37 S. B. Padrick and A. D. Miranker, "Islet Amyloid" Phase Partitioning and Secondary Nucleation are Central to the Mechanism of Fibrillogenesis", *Biochemistry*, **41**, 4694–4703 (2002).

38 E. J. Nettleton, P. Tito, M. Sunde, M. Bouchard, C. M. Dobson and C. V. Robinson, "Characterization of the Oligomeric States of Insulin in Self-assembly and Amyloid Fibril Formation by Mass Spectrometry", *Biophys. J.*, **79**, 1053–1065 (2000).

39 B. Caughey and P. T. Lansbury Jr., "Protofibrils, Pores, Fibrils, and Neurodegeneration: Separating the Responsible Protein Aggregates from the Innocent Bystanders", *Annu. Rev. Neurosci.*, **26**, 267–298 (2003).

40 M. P. Schlunegger, M. J. Bennett and D. Eisenberg, "Oligomer Formation by 3D Domain Swapping: A Model for Protein Assembly and Misassembly", *Adv. Protein Chem.*, **50**, 61–122 (1997).

41 G. Bitan, M. D. Kirkitadze, A. Lomakin, S. S. Vollers, G. B. Benedek and D. B. Teplow. "Amyloid β-protein assembly: Aβ40 and Aβ42

oligomerize through distinct pathways,'' *Proc. Natl. Acad. Sci. USA*, **100**, 330–335 (2003).

42 M. Bouchard, J. Zurdo, E. J. Nettleton, C. M. Dobson and C. V. Robinson, ''Formation of Insulin Amyloid Fibrils Followed by FTIR Simultaneously with CD and Electron Microscopy'', *Protein Sci.*, **9**, 1960–1967 (2000).

43 M. G. Spillantini, M. L. Schmidt, V. M.-Y. Lee, J. Q. Trojanowski, R. Jakes and M. Goedert, ''α-Synuclein in Lewy Bodies'', *Nature*, **388**, 839–840 (1997).

44 H. A. Lashuel, D. Hartley, B. M. Petre, T. Walz, P. T. Lansbury Jr., ''Neurodegenerative Disease: Amyloid Pores from Pathogenic Mutations'', *Nature*, **418**, 291 (2002).

45 F. Chiti, M. Stefani, N. Taddei, G. Ramponi and C. M. Dobson, ''Rationalisation of Mutational Effects on Peptide and Protein Aggregation Rates'', *Nature*, **424**, 805–808 (2003).

46 F. Chiti, N. Taddei, F. Baroni, C. Capanni, M. Stefani, G. Ramponi and C. M. Dobson, ''Kinetic Partitioning of Protein Folding and Aggregation'', *Nature Struct. Biol.*, **9**, 137–143 (2002).

47 S. W. Raso and J. King, ''Protein Folding and Human Disease'', in **Protein Folding**, R. H. Pain (Ed.), (2nd ed) Oxford University Press, Oxford, 2000, pp 406–428.

48 C. M. Dobson, ''How Do We Explore the Energy Landscape for Folding?'', *Simplicity and Complexity in Proteins and Nucleic Acids* (eds. H. Fraunfelder, J. Deisenhofer and P. G. Wolynes), Dahlem University Press, Berlin, pp. 15–37 (1999).

49 A. J. L. Macario and E. C. de Macario, ''Sick Chaperones and Ageing: A Perspective'', *Ageing Res. Rev.*, **1**, 295–311 (2002).

50 M. R. Wilson and S. B. Easterbrook-Smith, ''Clusterin is a Secreted Mammalian Chaperone'', *Trends Biochem Sci.*, **25**, 95–98 (2000).

51 N. F. Bence, R. M. Sampat and R. R. Kopito, ''Impairment of the Ubiquitin-proteosome System by Protein Aggregation'', *Science*, **292**, 1552–1555 (2001).

52 A. Horwich, ''Protein Aggregation in Disease: A Role for Folding Intermediates Forming Specific Multimeric Interactions'', *J. Clin Invest.*, **110**, 1221–1232 (2002).

53 M. Stefani and C. M. Dobson, ''Protein Aggregation and Aggregate Toxicity: New Insights into Protein Folding, Misfolding Diseases and Biological Evolution'', *J. Mol. Med.*, **81**, 678–699 (2003).

54 D. R. Booth, M. Sunde, V. Bellotti, C. V. Robinson, W. L. Hutchinson, P. E. Fraser, P. N. Hawkins, C. M. Dobson, S. E. Radford, C. C. F. Blake and M. B. Pepys, ''Instability, Unfolding and Aggregation of Human Lysozyme Variants Underlying Amyloid Fibrillogenesis'', *Nature*, **385**, 787–793 (1997).

55 M. Ramirez-Alvarado, J. S. Merkel and L. Regan, ''A Systematic Exploration of the Influence of Protein Stability on Amyloid Fibril Formation in vitro'', *Proc. Natl. Acad. Sci. USA*, **97**, 8979–8984 (2000).

56 M. Dumoulin, A. M. Last, A. Desmyter, K. Decanniere, D. Canet, A. Spencer, D. B. Archer, S. Muyldermans, L. Wyns, A. Matagne, C. Redfield, C. V. Robinson and C. M. Dobson, ''A Camelid Antibody Fragment Inhibits Amyloid Fibril Formation by Human Lysozyme'', *Nature*, **424**, 783–788 (2003).

57 S. Prusiner, ''Prion Diseases and the BSE Crisis'', *Science*, **278**, 245–251 (1997).

58 P. Chien, A. H. DePace, S. R. Collins and J. S. Weissman, ''Generation of Prion Transmission Barriers by Mutational Control of Amyloid Conformations'', *Nature*, **424**, 948–951 (2003).

59 M. F. Perutz and A. H. Windle, ''Cause of Neuronal Death in Neurodegenerative Diseases Attributable to Expansion of Glutamine Repeats'', *Nature*, **412**, 143–144 (2001).

60 D. M. Walsh, I. Klyubin, J. V. Fadeeva, W. K. Cullen, R. Anwyl, M. S. Wolfe, M. J. Rowan and D. J.

Selkoe, "Naturally Secreted Oligomers of Amyloid Beta Protein Potently Inhibit Hippocampal Long-term Potentiation in vivo", *Nature*, **416**, 535–539 (2002).

61 M. Bucciantini, E. Giannoni, F. Chiti, F. Baroni, L. Formigli, J. Zurdo, N. Taddei, G. Ramponi, C. M. Dobson and M. Stefani, "Inherent Cytotoxicity of Aggregates Implies a Common Origin for Protein Misfolding Diseases", *Nature*, **416**, 507–511 (2002).

62 R. Kayed, E. Head, J. L. Thompson, T. M. McIntire, S. C. Milton, C. W. Cotman and C. G. Glabe, "Common Structure of Soluble Amyloid Oligomers Implies Common Mechanisms of Pathogenesis", *Science*, **300**, 486–489 (2003).

63 M. Svensson, H. Sabharwal, A. Hakansson, A. K. Mossberg, P. Lipniunas, H. Leffler, C. Svanborg, S. Linset, "Molecular Characterization of α-Lactalbumin Folding Variants that Induce Apoptosis in Tumor Cells", *J. Biol. Chem.*, **274**, 6388–6396 (1999).

64 P. Polverino de Laureto, N. Taddei, E. Frare, C. Capanni, S. Constantini, J. Zurdo, F. Chiti, C. M. Dobson and A. Fontana, "Protein Aggregation and Amyloid Fibril Formation by an SH3 Domain Probed by Limited Proteolysis", *J. Mol. Biol.*, **334**, 129–141 (2003).

65 P. J. Muchowski, G. Schaffar, A. Sittler, E. E. Wanker, M. K. Hayer-Hartl and F. U. Hartl, "Hsp70 and Hsp40 Chaperones Can Inhibit Self-assembly of Polyglutamine Proteins into Amyloid-like Fibrils", *Proc. Natl. Acad. Sci. USA*, **97**, 7841–7846 (2000).

66 J. Oeppen and J. W. Vaupel, "Broken Limits to Life Expectancy", *Science*, **296**, 1029–31 (2002).

67 P. Csermely, "Chaperone Overload is a Possible Contributor to 'Civilization Diseases'", *Trends Gen.*, **17**, 701–704 (2001).

68 A. J. L. Macario and E. C. Macario, "Sick Chaperones and Ageing: A Perspective", *Ageing Res.*, **Rev. 1**, 295–311 (2002).

69 J. W. M. Höppener, M. G. Nieuwenhuis, T. M. Vroom, B. Ahrén and C. J. M. Lips, "Role of Islet Amyloid in Type 2 Diabetes Mellitus: Consequence or Cause?", *Mol. Cell. Endocrin.*, **197**, 205–212 (2002).

70 F. Gejyo, N. Homma, Y. Suzuki and M. Arakawa, "Serum Levels of β2-microglobulin as a New Form of Amyloid Protein in Patients Undergoing Long-term Hemodialysis", *N. Engl. J. Med.*, **314**, 585–586 (1986).

71 F. E. Cohen and J. W. Kelly, "Therapeutic Approaches to Protein-misfolding Diseases", *Nature*, **426**, 905–909 (2003).

72 C. M. Dobson, "In the Footsteps of Alchemists", *Science*, **304**, 1259–1262 (2004).

73 P. Hammarstrom, R. L. Wiseman, E. T. Powers and J. W. Kelly, "Prevention of Transthyretin Amyloid Disease by Changing Protein Misfolding Energetics", *Science*, **299**, 713–716 (2003).

74 M. Dumoulin, A. M. Last, A. Desmyter, K. Decanniere, D. Canet, G. Larsson, A. Spencer, D. B. Archer, J. Sasse, S. Muyldermans, L. Wyns, C. Redfield, A. Matagne, C. V. Robinson and C. M. Dobson, "A Camelid Antibody Fragment Inhibits the Formation of Amyloid Fibrils by Human Lysozyme", *Nature*, **424**, 783–788 (2003).

75 B. C. May, A. T. Fafarman, S. B. Hong, M. Rogers, L. W. Deady, S. B. Prusiner, F. E. Cohen, "Potent Inhibition of Scrapie Prion Replication in Cultured Cells by Bis-acridines", *Proc. Natl. Acad. Sci. USA*, **100**, 3416–3421 (2003).

76 M. Vogtherr, S. Grimme, B. Elshorst, D. M. Jacobs, K. Fiebig, C. Griesinger and R. Zahn, "Antimalarial Drug Quinacrine Binds to C-terminal Helix of Cellular Prion Protein", *J. Med. Chem.*, **46**, 3563–3564 (2003).

77 M. S. Wolfe, "γ-Secretase as a Target for Alzheimer's Disease", *Curr. Top. Med. Chem.*, **2**, 371–383 (2002).

78 R. Vassar, "Beta-secretase (BACE) as a Drug Target for Alzheimer's

Disease'', *Adv. Drug Deliv. Rev.*, **54**, 1589–1602 (2002).

79 J. A. R. Nicoll, D. Wilkinson, C. Holmes, P. Steart, H. Markham and R. O. Weller, ''Neuropathology of Human Alzheimer Disease after Immunization with Amyloid-beta Peptide: A Case Report'', *Nature Med.*, **9**, 448–452 (2003).

80 M. B. Pepys, J. Herbert, W. L. Hutchinson, G. A. Tennent, H. J. Lachmann, J. R. Gallimore, L. B. Lovat, T. Bartfai, A. Alanine, C. Hertel, T. Hoffmann, R. Jakob-Roetner, R. D. Norcross, J. A. Kemp, K. Yamamura, M. Suzuki, G. W. Taylor, S. Murray, D. Thompson, A. Purvis, S. Kolstoe, S. P. Wood, P. N. Hawkins, ''Targeted Pharmacological Depletion of Serum Amyloid P Component for Treatment of Human Amyloidosis'', *Nature*, **417**, 254–259 (2002).

81 C. Soto, ''Unfolding the Role of Protein Misfolding in Neurodegenerative Diseases'', *Nature Rev. Neurosci*, **4**, 49–60 (2003).

34
Biochemistry and Structural Biology of Mammalian Prion Disease

Rudi Glockshuber

34.1
Introduction

34.1.1
Prions and the "Protein-Only" Hypothesis

Transmissible spongiform encephalopathies (TSEs) or prion diseases in humans and mammalians have been the subject of intensive research during the last decade, and there are excellent reviews available dealing with all aspects of TSEs [1–8]. This chapter focuses on biophysical and structural studies on the recombinant prion protein (PrP) and their implications for understanding the mechanism of prion propagation in mammals.

In contrast to infectious diseases caused by microorganisms or viruses, mammalian transmissible spongiform encephalopathies (TSEs) are caused by an infectious agent, the prion (for prion terminology, see Table 34.2), which appears to be devoid of informational nucleic acid [9, 10]. According to the "protein-only" hypothesis [11–13], the prion consists mainly, if not entirely, of the insoluble, oligomeric scrapie isoform (PrP^{Sc}) of the monomeric, cellular prion protein (PrP^{C}) that is produced by the infected host [14]. The protein-only hypothesis further assumes that the subunits in PrP^{Sc} oligomers have the same covalent structure as PrP^{C} [15–17], but a different tertiary structure [18], and that PrP^{Sc} oligomers propagate by triggering the conversion of PrP^{C} (e.g., from a non-infected cell) into new PrP^{Sc} molecules. These basic assumptions are supported by the fact that highly enriched prions isolated from the brain of infected animals essentially consist of PrP^{Sc} oligomers [9, 10, 19] and, unlike nucleic acid–containing infectious agents, are resistant to strong UV irradiation [11, 20]. The strongest evidence in favor of the protein-only hypothesis comes from the fact that knockout mice devoid of the gene encoding the murine prion protein are resistant to prion infections, and transgenic mice overexpressing PrP^{C} are particularly susceptible to prions [21]. This proves that PrP is indeed an indispensable component in prion propagation. In addition, all inherited prion diseases in humans described to date are associated with mutations in the gene encoding human PrP [1, 22], arguing that these mutations favor

Protein Folding Handbook. Part II. Edited by J. Buchner and T. Kiefhaber

ISBN: 3-527-30784-2

spontaneous formation of PrP^{Sc} in the corresponding individuals. Despite these facts, the protein-only hypothesis on the nature of TSE prions still cannot be considered proven [23].

At first view, it appears that the prion phenomenon is not in accordance with one of the basic principles in protein biochemistry, namely, the dogma that polypeptide chains adopt only one specific conformation, which is the thermodynamically most stable state in aqueous solution [24]. The prion hypothesis now suggests that there are at least two conformational states of the prion protein (PrP^{C} and PrP^{Sc}) and implies that PrP^{Sc} is more stable than the functional, cellular form of the prion protein. A simple way to resolve this apparent contradiction is to restrict the central dogma of protein folding to the physiologically relevant association state of proteins in vivo. Under these prerequisites, monomeric PrP^{C} would be more stable than monomeric PrP^{Sc}, which agrees well with the fact that monomeric PrP^{Sc} has indeed never been observed. Moreover, it is practically impossible to assess the thermodynamic stability of PrP^{Sc} because it cannot be reversibly dissociated and reassembled in vitro [25]. The tertiary structure of PrP^{Sc} thus appears to be stable only in the context of the quaternary structure of the PrP^{Sc} oligomer. Overall, the thermodynamic stability of the PrP^{Sc} oligomer is not accessible experimentally, and there is no principle theoretical difficulty in combining the protein-only hypothesis with Anfinsen's central dogmas of protein folding [24]. Table 34.1 summarizes the known forms of human and mammalian TSEs.

34.1.2 Models of PrP^{Sc} Propagation

A key feature of any infectious agent is its ability to replicate. In contrast to amyloids associated with amyloid diseases in humans, including Alzheimer's and Parkinson diseases, PrP^{Sc} aggregates are the only known protein aggregates in mammalians that can be *transmitted* and cause disease by propagation in the newly infected host. Within the framework of the protein-only hypothesis, there are mainly two potential mechanisms that are discussed for replication of PrP^{Sc} aggregates, i.e., formation of new PrP^{Sc} oligomers from PrP^{C} of the host. These models also account for the de novo formation of prions in inherited or sporadic prion diseases. The template assistance or heterodimer model [26] proposes that the rate-limiting step in the de novo generation of PrP^{Sc} is formation of a PrP^{Sc} monomer from PrP^{C}. A PrP^{Sc} monomer would then form a heterodimer with a benign PrP^{C} molecule and convert this PrP^{C} into PrP^{Sc}. This requires direct or indirect specific recognition of PrP^{C} by PrP^{Sc}. Newly converted PrP^{Sc} molecules would then further convert PrP^{C} molecules into PrP^{Sc} (Figure 34.1A). The nucleation-polymerization model [27] (Figure 34.1B) assumes that PrP^{C} and PrP^{Sc} are always in a dynamic equilibrium, but PrP^{C} monomers are by far more stable than PrP^{Sc} monomers, such that the small fraction of PrP^{Sc} monomers is not observed experimentally. Here, the rate-limiting step in spontaneous PrP^{Sc} formation is the oligomerization of the small fraction of PrP^{Sc} monomers to an oligomer of critical size, which is

Tab. 34.1. Transmissible spongiform encephalopathies in humans and mammals.

Disease	*Origin/Mechanism*
Human prion diseases	
Sporadic Creutzfeld-Jakob disease (CJD)	Spontaneous formation of prions from PrP^C Most common human prion disease; nevertheless extremely rare (1 case per one million per year) Affected individuals are almost exclusively homozygous with respect to the polymorphism at residue 129 (Met/Met or Val/Val) Average age of onset: >60 years
Variant CJD	Infection from bovine prions Infected individuals are generally Met/Met homozygous with respect to the polymorphism at residue 129, which is also Met in bovine PrP
Familial CJD	Germ-line mutations in the PrP gene
Gerstmann-Sträussler-Scheinker disease	Germ-line mutations in the PrP gene
Fatal familial insomnia	Germ-line mutations in the PrP gene
Iatrogenic CJD	Infection from prion-contaminated human growth hormone, dura mater grafts, etc.
Kuru	Infection through ritual cannibalism (Fore people)
Prion diseases in mammals	
Bovine spongiform encephalopathy	BSE-contaminated food
Scrapie (sheep and goats)	Genetic susceptibility to spontaneous formation of scrapie prions. Transmission among sheep?
Transmissible mink encephalopathy	Infection with prions from cattle or sheep
Chronic wasting disease (elk, deer)	Origin and transmission unknown
Feline spongiform encephalopathy (cats)	Infection with prion-contaminated beef

sufficiently stabilized by quaternary structure contacts such that it can no longer dissociate. This nucleus is capable of growing further, by pulling additional PrP^{Sc} monomers from the equilibrium into the PrP^{Sc} oligomer. An important difference between the models is that the nucleation-polymerization model does not necessarily require a direct contact and specific recognition between PrP^C and PrP^{Sc}. Moreover, it much better accounts for the prion strain phenomenon, as will be discussed below (see Section 34.5).

In addition to these models for the generation of PrP^{Sc}, another mechanism of amyloid formation has been postulated for the aggregation of human lysozyme variants in hereditary systemic amyloidosis. Here, single amino acid replacements in lysozyme destabilize the native state relative to partially structured intermedi-

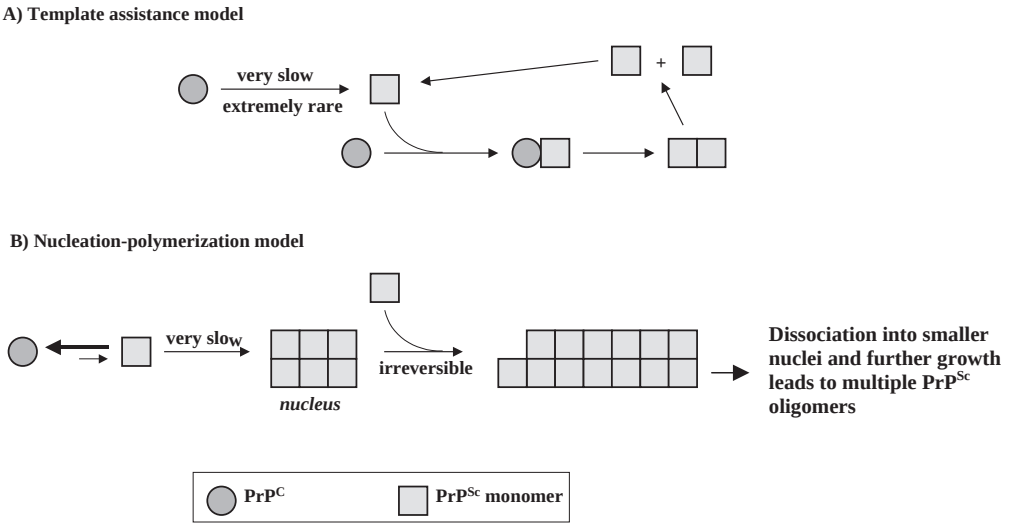

Fig. 34.1. Schematic representation of the template-assistance model (A) and nucleation-polymerization model (B) of PrP^{Sc} propagation.

ates. This leads to an increase of the fraction of partially folded intermediates that act as amyloid precursors and are pulled from the normal folding equilibrium during amyloid propagation [28]. A further mechanism is observed in the formation of amyloid fibrils of transthyretin (TTR), which are the putative cause of senile systemic amyloidosis (SSA) and familial amyloidotic polyneuropathy (FAP). Here, dissociation of the native TTR homotetramer into monomers is the rate-limiting step in amyloid formation, which is followed by partial monomer denaturation and misassembly into fibrils [29].

34.2 Properties of PrP^C and PrP^{Sc}

Mammalian PrP^C is a cell surface glycoprotein of about 210 amino acids that is strongly expressed in neurons but is also present in most other tissues. PrP^C belongs to the most conserved proteins known, and pairwise alignment of PrPs from different species generally reveals more than 90% sequence identity [30, 31]. In addition, there are three types of invariant posttranslational modifications found in mature PrP^C: two *N*-glycosylation sites at Asn181 and Asn197 [34], a single disulfide bond between Cys179 and Cys214 [33], and a C-terminal glycosylphosphatidyl-inositol (GPI) anchor at residue 231 (amino acid numbering according to human PrP) [16, 17, 32]. Another typical feature of mammalian PrP sequences is a segment of five octapeptide repeats in the N-terminal region (Figure

34.3A). Although the strong conservation of PrP in mammals suggests an important cellular role of the protein, the biological function of PrP^C remains unknown to date. This is mainly due to the fact that PrP knockout mice are essentially healthy [35] and show only subtle phenotypes that are not completely preserved in different knockout strains. Proposed functions for PrP include roles in signal transduction [36], copper storage [37], circadian rhythm regulation [38], and maintenance of synaptic function [39] and Purkinje cell survival [40] (also reviewed in Ref. [8]). PrP^C is monomeric, is soluble in non-denaturing detergents, and contains a high fraction of α-helical secondary structure [18]. In vivo, PrP^C is enriched in cholesterol and sphingolipid-rich membrane rafts, subject to caveolae-mediated endocytosis [41], and has a half-life of about 3–6 h [42]. There is evidence that raft localization of PrP^C and co-localization with PrP^{Sc} in the same membrane are required for its conversion into PrP^{Sc} [43]. Most PrP molecules synthesized in the cell reach the cell surface and are anchored to the cell membrane via their GPI anchor, but two intracellular transmembrane forms of PrP have been identified that span the ER membrane in different orientations, of which the form with the C-terminus towards the ER lumen (^{Ctm}PrP) may be associated with neurodegeneration in prion-infected individuals [44]. Whether aberrant membrane topology of PrP at the ER has general functional implications still has to be determined. Moreover, retrograde transport of misfolded PrP from the ER to the cytosol normally leads to PrP degradation by the proteasome, but if this degradation is compromised, the accumulation of cytosolic PrP has severe toxic effects on neurons and has been proposed to be the general mechanism underlying the death of neurons during prion pathogenesis [45].

The insoluble, oligomeric scrapie form PrP^{Sc} has so far been isolated only from the brain of prion-infected individuals or prion-infected cell cultures. Although the subunits in PrP^{Sc} have the same covalent structure and posttranslational modifications as PrP^C, it differs from PrP^C with respect to all its biochemical properties: it is insoluble in non-denaturing detergents and shows an increased β-sheet content and a decreased α-helix content compared to PrP^C [18]. Another important property of PrP^{Sc} is its partial resistance to proteinase K (PK). While PrP^C is readily degraded by PK, the polypeptide chains in PrP^{Sc} exhibit a protease-resistant core ranging from approximately residue 90 to the C-terminal residue 231. In contrast, the N-terminal PrP^{Sc} segment from residue 23 to approximately residue 90 is degraded (Figure 34.2) [46, 47]. As will be discussed in Section 34.5, this observation has important implications, as it shows that PrP^{Sc} is an *ordered* oligomer in which all subunits appear to have a very similar structural environment that protects residues 90–231 in *every* subunit from access by PK. This is a strong hint that PrP^{Sc} does not represent a nonspecific, inclusion body–like protein aggregate but rather a regular array of subunits with identical tertiary structures in which both the fold of the subunits and their quaternary structure contacts confer protease resistance. This is in good agreement with the nucleation-polymerization model of PrP^{Sc} propagation [27], which assumes specific subunit-subunit contacts in the nucleation and further growth of the PrP^{Sc} oligomer. The importance of the protease-resistant core of PrP^{Sc}, termed PrP27–30, is further underlined by the

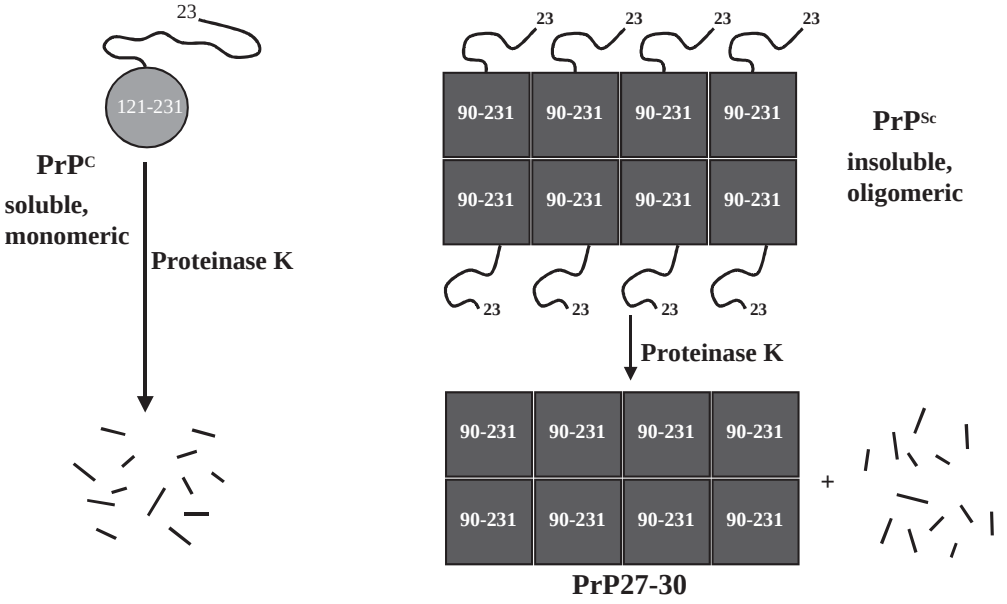

Fig. 34.2. Protease resistance of PrP^{Sc}. While PrP^C is readily degraded by proteinase K into peptide fragments, the subunits of PrP^{Sc} contain a protease-resistant core (PrP27–30) from about residue 90 to the C-terminal residue 231 (amino acid numbering according to human PrP). Thus, only the N-terminal segment 23–90 in PrP^{Sc} subunits is accessible to proteinase K degradation. The structure of PrP^C, comprised of the flexibly disordered N-terminal tail 23–120, and the structured C-terminal domain PrP(121–231) (cf. Figure 34.3) are also indicated.

fact that it retains prion infectivity and forms amyloid-like fibers [19]. In addition, transgenic mice exclusively expressing N-terminally truncated forms of PrP that still contain segment 90–231 are susceptible to prions and able to replicate prions [48]. This shows that the octapeptide repeats in the N-terminal segment of PrP^C are not required for prion propagation. The identification of PrP27–30 after proteinase K treatment of brain extracts, protein separation by SDS-PAGE, and immunospecific detection in Western blots represents the basis for both post-mortem and pre-clinical detection of prions, e.g., in BSE-infected cattle, and, as outlined in Section 34.5, biochemical characterization of prion strains [6, 47]. Interestingly, a high-molecular-weight polysaccharide consisting of 1,4-, 1,6-, and 1,4,6-linked glucose units was found to be associated with infectious preparations of PrP27–30, and it was postulated that this polysaccharide is a scaffold that promotes formation of PrP^{Sc} and contributes to its extraordinary physical and chemical stability [49]. Additional structural information on PrP^{Sc} has become available from fiber diffraction studies and atomic force microscopy studies indicating that PrP^{Sc} contains β-sheets that are arranged perpendicular to the fiber axis [50] and may form parallel β-helices [51].

34.3 Three-dimensional Structure and Folding of Recombinant PrP

34.3.1 Expression of the Recombinant Prion Protein for Structural and Biophysical Studies

The protein-only hypothesis and all theoretical models of PrP^C to PrP^{Sc} conversion imply that knowledge of the three-dimensional structures of PrP^C and PrP^{Sc} is the prerequisite for understanding prion propagation at a molecular level. As PrP^{Sc} is insoluble, and because no soluble, low-molecular-weight oligomers with defined stoichiometry have been isolated so far, PrP^{Sc} has not been accessible to atomic structure determination by X-ray crystallography or nuclear magnetic resonance (NMR) spectroscopy.

Because it is extremely difficult to purify milligram quantities of PrP^C from mammalian brain, production of recombinant PrP in *Escherichia coli* has proved to be necessary to determine the three-dimensional structure of the monomeric protein. Since there is neither *N*-linked glycosylation nor GPI anchor biogenesis in *E. coli*, bacterially produced PrP lacks these modifications. Nevertheless, there is no evidence at present that these modifications significantly influence the tertiary structure of the prion protein. To allow formation of the invariant disulfide bond between Cys179 and 214 in the recombinant prion protein, two strategies have been pursued. As disulfide bonds cannot form in the reducing environment of the bacterial cytoplasm, the prion protein and N-terminally truncated fragments were secreted into periplasm with the *E. coli* OmpA signal sequence [52]. The disulfide bond was formed, but the protein was N-terminally degraded by periplasmic proteases such that only the fragment from residues 121–231 stayed stable in the periplasm. The fragment was termed PrP(121–231) [52]. This was the first evidence that the entire N-terminal segment 23–120 of recombinant PrP does not adopt a defined structure in solution (see below). Because any attempt to produce full-length PrP in the bacterial periplasm has failed so far, the full-length protein was expressed in the cytoplasm where the protein accumulates in the reduced form and nonspecifically aggregates into inclusion bodies. Oxidative refolding from the inclusion body fraction in vitro and further purification yielded large quantities of homogeneous, recombinant PrP for structure analysis and biochemical characterrization [53, 54]. Details on different refolding protocols are given in the Experimental Section.

34.3.2 Three-dimensional Structures of Recombinant Prion Proteins from Different Species and Their Implications for the Species Barrier of Prion Transmission

34.3.2.1 Solution Structure of Murine PrP

The first three-dimensional structure of a recombinant prion protein was reported in 1996 for the fragment PrP(121–231) of the murine prion protein, which was determined by nuclear magnetic resonance spectroscopy (NMR) [56, 57] (Figure

34.3B). PrP(121–231) adopts a unique fold that has so far not been found in other proteins. The fold consists of a short, two-stranded, antiparallel β-sheet (residues 128–131 and 161–164) and three α-helices (residues 144–154, 175–194, and 200–226). The fold is additionally characterized by a tightly packed hydrophobic core of 20 amino acids (residues 134, 137, 139, 141, 158, 161, 175, 176, 179, 180, 184, 198, 203, 205, 206, 209, 210, 213, 214, and 215). The invariant disulfide bond between Cys179 and Cys214 is part of this hydrophobic core and connects the second with the third α-helix. The hydrophobic core is surrounded by a shell of hydrogen-bonded residues that further stabilize the fold [58]. Overall, the structure of PrP(121–231) resembles a flat ellipsoid that is characterized by an uneven distribution of surface charges between the two flat surfaces. The two glycosylation sites at Asn181 and Asn189 are located on the negatively charged side of the molecule, while the opposite surface is positively charged. It has been proposed that the uneven charge distribution may contribute to the orientation of PrP^C relative to the cell membrane. One would expect that the protein associates via its positively charged surface with the membrane, such that the two glycosylation sites would be oriented towards the extracellular space [56].

The NMR structure of full-length murine PrP, which was reported in 1997, revealed that residues 23–120 (including the octapeptide repeats), in contrast to the compact domain PrP(121–231), are flexibly disordered in solution (Figure 34.3B), with all residues in this segment being flexible on a sub-nanosecond timescale [59]. The structure of residues 121–231 in the context of the full-length protein proved to be indistinguishable from that in isolated PrP(121–231). The functional role of the flexible tail is presently unclear. However, a plausible model has been proposed for structure formation within the octapeptide repeat regions upon cooperative binding of Cu^{2+} ions [60]. As there is increasing evidence that a substantial fraction of cellular proteins are ''natively unfolded'' in isolation and adopt a defined tertiary structure only in complex with target molecules [61], it appears likely that the flexible tail of PrP is required for the interaction of PrP^C with its natural ligands.

Overall, the structure of recombinant, non-glycosylated, full-length PrP produced in *E. coli* is in full agreement with the known properties of PrP^C isolated from mammalian cells. As natural PrP^C, it predominantly contains α-helical secondary structure and is soluble and monomeric. It is therefore generally accepted that the structure of recombinant PrP corresponds to that of the benign cellular prion protein. As will be discussed in Section 34.3.2.2, the NMR structure of murine PrP is also very similar to the structures of other mammalian prion proteins. Because the segment 90–231 is protease-resistant in PrP^{Sc}, an important conclusion from the structure of full-length PrP(23–231) is that residues 90–120, which are required for prion propagation [36], must adopt a defined three-dimensional structure in PrP^{Sc}. This corresponds to the minimal structural change that has to be postulated for a PrP polypeptide when it is converted from PrP^C to a subunit of PrP^{Sc} (Figure 34.3B).

As one might expect from the flexibly disordered N-terminal tail, attempts to crystallize recombinant prion proteins have failed so far. The only exception is the X-ray structure of human PrP(90–231), which crystallized as a covalently linked

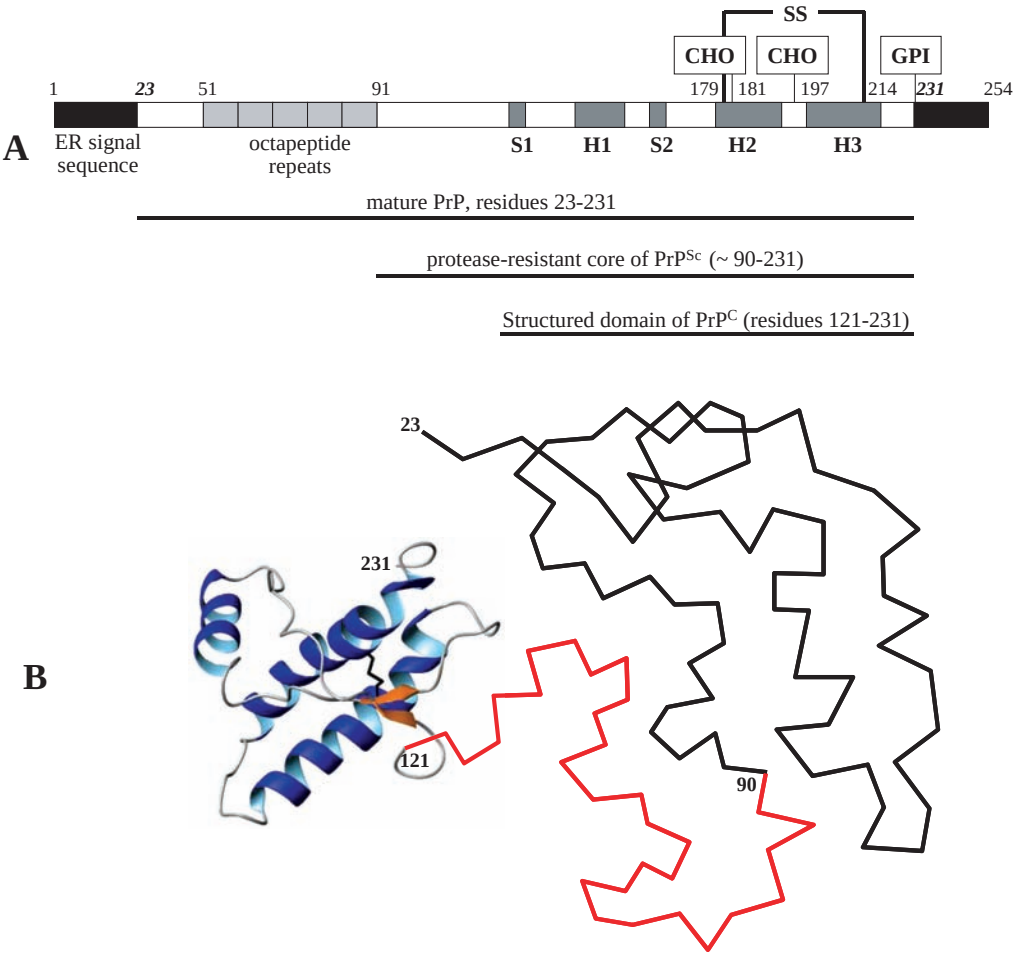

Fig. 34.3. Posttranslational modifications of PrP^C and three-dimensional structure of recombinant PrP. (A) Mammalian prion proteins contain an N-terminal signal sequence (residues 1–22) that directs the protein to the endoplasmic reticulum, where glycans (CHO) at Asn181 and Asn197 are attached, the C-terminal peptide 232–254 is replaced by a GPI anchor at the carboxylate of residue 231, and the single disulfide bridge between Cys179 and Cys214 is formed (amino acid numbering according to human PrP). Positions of β-strands (S1, S2) and α-helices (H1–H3) in the NMR structure of the recombinant PrP are indicated, as well the length of the protease-resistant core of PrP^{Sc} and the structured C-terminal domain PrP(121–231). (B) Ribbon diagram of the NMR structure of recombinant murine PrP. The protein is composed of a flexibly disordered N-terminal tail (residues 23–120, represented as random coil C^{α} trace) and a structured domain (residues 121–231), which consists of a two-stranded, antiparallel β-sheet and three α-helices. The single disulfide bond (black lines) connects the second and third α-helix and is completely shielded from the solvent. The solvent-accessible residues 90–120, which become protease-resistant in PrP^{Sc}, are indicated as red lines.

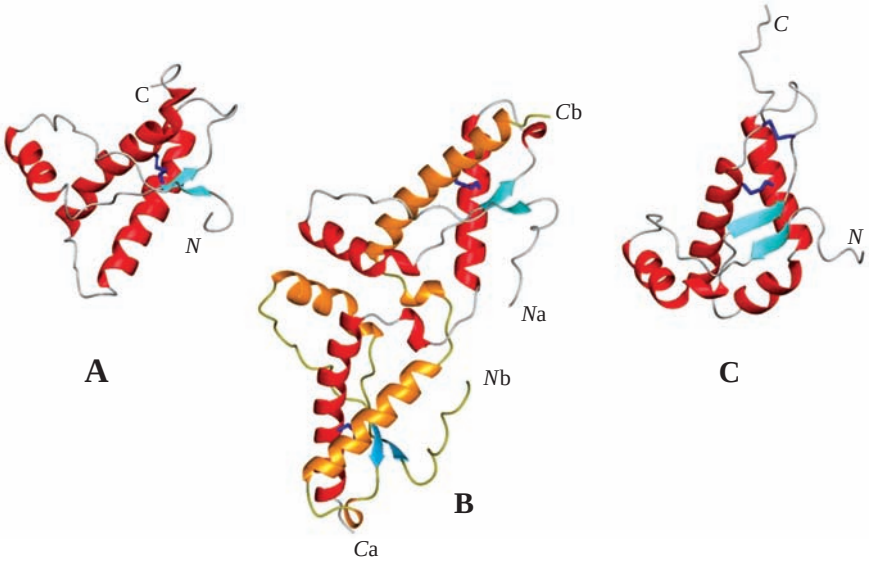

Fig. 34.4. Comparison of the NMR structure of recombinant murine PrP(121–231) (pdb code: 1AG2) (A) with the X-ray structure of a dimer of recombinant human PrP(90–231) (B) (code1I4M) and the NMR structure of the murine Doppel protein (C) (code 1I17). (B) In the dimer of human PrP(90–231), the C-terminal α-helices are swapped and disulfide is cross-linked with the second α-helix of the other subunit. The molecule may be an artifact resulting from oxidative refolding of the recombinant protein from *E. coli* inclusion bodies under nonnative conditions. (C) Note that the Doppel protein is stabilized by two intramolecular disulfide bonds (dark blue lines).

homodimer in which α-helices 3 are swapped between the subunits such that α-helix 2 in each subunit is now disulfide-bonded to α-helix 3 from the other subunit (Figure 34.4B) [62]. This structure may be an experimental artifact that was produced during oxidative in vitro refolding of the recombinant protein under conditions that favored intermolecular disulfide bond formation. Disulfide-bonded homodimers have not been observed for PrP^{C}, nor have intermolecular disulfide bonds been reported for PrP^{Sc} oligomers [33].

As mentioned above, the structure of the C-terminal domain of the mammalian prion protein represents a new fold that has not been observed in other proteins. In this context, it is interesting to discuss the recently solved NMR structure of the mammalian protein with closest homology to the prion protein, termed Doppel (Dpl) [63] (Figure 34.4C). Dpl lacks the N-terminal octapeptide repeats found in PrP and is most likely not linked with prion diseases, as it is normally not expressed in the central nervous system. In contrast, it was shown to be required for male fertility in mice by controlling male gametogenesis and sperm-egg interaction [64]. Figure 34.4C shows the NMR structure of murine Dpl [65], which shares 21% amino acid sequence identity with murine PrP and is very similar to

the structure of human Dpl [66]. The Dpl fold is similar to that of PrP(121–231) in that the secondary structures fall in the same positions in the two proteins. Differences are observed mainly in the lengths of the α-helices and the positions of the β-strands (in Dpl, the strands are displaced by one to two residues relative to those in the PrP structure). Moreover, Dpl contains two intramolecular disulfide bonds. The disulfide bond 109–143 corresponds to that of PrP(121–231), and the second disulfide 95–148 connects the segment after β-strand 1 with the C-terminal segment following α-helix 3. The strongest structural difference between the proteins is that the plane of the β-sheet is parallel to the axis of α-helix 2 in Dpl, while it is perpendicular to this axis in the structure of PrP(121–231). Moreover, there is a marked kink in α-helix 2 of Dpl, which is not observed in PrP(121–231). In summary, the structured domains of Dpl and PrP appear to have evolved from the same ancestor by gene duplication but now fulfill different functions.

34.3.2.2 Comparison of Mammalian Prion Protein Structures and the Species Barrier of Prion Transmission

In addition to the structure of murine PrP, the NMR structures of the recombinant prion proteins from hamster [67, 68], human [69], and cattle [70] have been determined. All proteins consist of very similar global architectures, i.e., the flexible N-terminal tail of about 100 residues, followed by the folded C-terminal domain. The folds of C-terminal domains are again very similar but exhibit interesting local differences [57]. For example, α-helix 3 is kinked in the structure of murine PrP but straight in the structures of hamster, bovine, and human PrP. Comparison of the structures of mouse and hamster PrP revealed a better-defined loop segment between β-strand 1 and α-helix 2 and slight local differences between the structures in the segment between α-helix 1 and β-strand 2. In the structure of human PrP, α-helix 3 is also straight and well defined and extends to residue 228. Interestingly, the C-terminal turns of α-helices 2 and 4 appear to be in a local unfolding equilibrium. In addition, short, transient contacts between the flexible tail and the folded C-terminal domain were detected for human PrP, which may slightly contribute to a stabilization of the C-terminal residues of α-helices 2 and 3 against unfolding [57]. The structure of bovine PrP is most closely related to that of human PrP but shows the differences in local backbone conformation from murine and hamster PrP described above (Figure 34.5).

Comparison of the structure of bovine PrP(121–231) with that from humans, mice, and hamsters revealed RMSD values of 0.98 Å, 1.66 Å, and 1.68 Å, respectively [57, 70]. The striking structural similarity between bovine and human PrP^C, in conjunction with the fact that BSE prions can be transmitted to humans and cause new variant Creutzfeld-Jakob disease (CJD) (Table 34.1), suggests that the structural relationship at the level of PrP^C inversely correlates with the species barrier of prion transmission. The species-barrier phenomenon has so far been discussed mainly at the level of sequence similarity between PrPs from different species with the view that the transmission barrier decreases with increasing sequence identity [30, 31]. A detailed structural comparison of all available PrP solu-

tion structures suggests that the most relevant structural feature with regard to the species-barrier phenomenon, besides the conformational differences described above, are differences in local surface charges, even though the uneven surface charge distribution on both flat surfaces of the C-terminal PrP domain is preserved in all structures [57].

In the context of the nucleation-polymerization mechanism of prion propagation, an inverse correlation between structural similarity of PrP^Cs from different species and species barrier could mean that those parts of the PrP^C structure that are similar between a pair of species but different in other PrP^C structures are preserved in the structure of the PrP^{Sc} subunits and possibly are involved in subunit-subunit contacts. This could mean that substantial parts of the structure of the PrP^C segment 121–231 are still contained in the tertiary structure of PrP^{Sc} subunits. In addition, a host-specific factor, called "protein X," may be responsible for the species-barrier phenomenon. "Protein X" is believed to be contained in every mammalian species and to be required for prion propagation [71].

34.3.3 Biophysical Characterization of the Recombinant Prion Protein

34.3.3.1 Folding and Stability of Recombinant PrP

Studies on the folding and thermodynamic stability of murine PrP(121–231) at neutral pH and 25 °C revealed that the C-terminal PrP domain behaves perfectly according to the two-state model as one would expect for a one-domain domain protein. It shows entirely reversible unfolding and refolding transitions in denaturant-induced equilibrium experiments, with a free energy of folding of -30 kJ mol^{-1} and a cooperativity expected for a 111-residue protein ($m = 4.8$ kJ mol^{-1}/M urea) [52]. In the context of full-length PrP(23–231), the stability of the domain is slightly decreased (–26 kJ mol^{-1}), which is due to a somewhat lower cooperativity, while the transition midpoint is the same as that of PrP(121–231) (6.3 M urea). The lower folding cooperativity observed for full-length PrP may be due to formation of residual structure in the unfolded state in which residues 23–120 interact with the parts of segment 121–231 [55]. Reversible unfolding transitions at neutral pH were also confirmed for human PrP(90–231) [72–75]. Hydrogen-exchange experiments on human PrP(90–231) revealed that only a small segment of about 10 residues around the disulfide bond retains residual structure in the unfolded state [74]. Further studies revealed that the stability of recombinant PrP decreases with decreasing pH [87, 96] and shows an unusual salt dependence in that salts destabilize the protein at concentrations below 50 mM increase the stability at high concentrations according to the Hofmeister series [96].

Assuming that folding of recombinant PrP corresponds to that of PrP^C, the complete reversibility of PrP^C folding nicely explains within the framework of the protein-only hypothesis why treatment of prions with denaturants such as urea or guanidinium chloride (GdmCl) completely abolishes infectivity, even after subsequent removal of the denaturant [76]: high denaturant concentrations dissociate

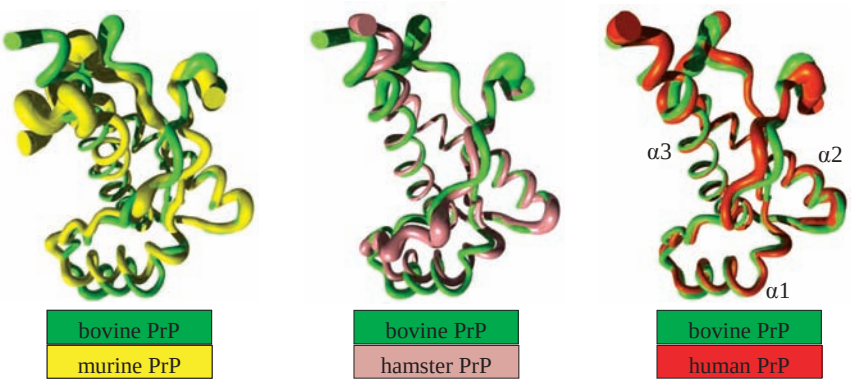

Fig. 34.5. Comparison of the NMR structure of bovine PrP(121–231) (green, pdb code 1DX0) with that of recombinant PrP(121–231) from mice (yellow, code 1AG2), hamsters (pink, code 1B10), and humans (red, code 1E1J). The C^{α} traces are represented as spline functions, and the thickness of the cylindrical rods represents the mean global displacement per residue after superposition of the backbone atoms in the set of energy-minimized conformers that represents each NMR structure (picture from Dr. R. Riek, ETH Zurich).

PrP^{Sc} into monomers and denature its subunits, so that a solution of dissociated and unfolded PrP^{Sc} is identical to a solution of unfolded PrP^{C}. Consequently, unfolded PrP^{Sc} subunits will always refold to PrP^{C}.

Analysis of the kinetics of folding of murine PrP(121–231) showed that the C-terminal domain belongs to the fastest folding proteins described so far. It folds with a half-time of about 200 μs at neutral pH and 4 °C and unfolds with a half-time of 4.6 min under these conditions [77]. Rapid folding of PrP(121–231) is consistent with the absence of *cis*-proline peptide bonds in the three-dimensional structure [57, 67–70]. Analysis of the dependence of the rate constants of unfolding and refolding on denaturant concentration showed that the compactness of the transition state of folding is closer to the unfolded state than to the native state. No transient folding intermediates have been detected so far in the kinetics of folding of PrP(121–231). However, a kinetic folding intermediate has been identified in the folding of recombinant human PrP(90–231), which nevertheless also folds extremely rapidly [78, 79]. Whether this difference is due to the additional segment 90–120 in human PrP(90–231) or reflects intrinsic differences in the folding of human and murine PrP(121–231) still has to be established. Overall, the very rapid folding of PrP seems to exclude that kinetic folding intermediates can serve as a source of PrP^{Sc} at neutral pH. However, the population of kinetic intermediates is uniformly higher in all recombinant human PrP(90–231) variants that bear mutations linked with inherited human TSEs [79].

PrP^{Sc} has been shown to accumulate in lysosomes of prion-infected cells [80–82] where the pH varies between 4 and 6 [83]. This opens the possibility that conver-

sion of PrP^C into PrP^{Sc} does not occur at the cell surface but rather in the acidic environment of lysosomes. For this reason, folding of recombinant PrP has also been analyzed in detail under acidic conditions, where the properties of the protein indeed change dramatically. At pH 4, the folding mechanism ($U \leftrightarrow N$) of murine PrP(121–231) changes from a two-state to a three-state equilibrium in which an acid-induced unfolding intermediate is observed by a pronounced plateau phase in the circular dichroism signal at 222 nm [72, 84–86]. At pH 4, the intermediate is maximally populated at 3 M urea and still significantly populated in the absence of urea [85]. In contrast to the α-helical CD spectrum of native PrP(121–231) at pH 4, the intermediate shows far-UV CD spectra of a β-sheet protein with a single minimum at 215 nm that are reminiscent of PrP^{Sc}. The transition from two-state to three-state equilibrium transitions has an apparent pK_a of 4.5, which indicates that protonation of acidic side chains is required for stabilization of the intermediate [85]. Very similar results were obtained for the folding of the full-length murine PrP(23–231) and human PrP(90–231). Consequently, formation of the acid-induced unfolding intermediate is an intrinsic property of the domain PrP(121–231). Further investigations demonstrated that formation of the intermediate is dependent on protein concentration and that the intermediate is most likely is a homodimer. In addition, ionic strengths above 50 mM are required for the intermediate to be observed. Equilibrium folding of recombinant PrP at neutral and acidic pH can thus by described by the following scheme [87]:

pH 4–8, low ionic strength at pH 4–5: $U \leftrightarrow N$
pH 4, ionic strength $> 50\ \mu M$, $[PrP] > 20$ mM: $2\ U \leftrightarrow I_2 \leftrightarrow 2\ N$

An attractive hypothesis resulting from these data is that the intermediate represents an early dimeric intermediate in the formation of oligomeric PrP^{Sc}. Indeed, starting with conditions that favor the population of the intermediate, fibrillar aggregates of recombinant PrP(90–231) could be obtained that showed a somewhat increased resistance to proteinase K [88]. Nevertheless, as in all attempts to generate prions de novo from recombinant PrP performed so far, it could not be demonstrated that these aggregates are infectious and relevant for understanding prion propagation. The same holds true for a β-sheet-rich conformation of human PrP(91–231), which is observed after thermal unfolding and cooling of the protein [86].

34.3.3.2 Role of the Disulfide Bond in PrP

The disulfide bond between the only cysteine residues of PrP, Cys179, and Cys214 is invariant in all mammalian prion protein sequences [31]. It is formed quantitatively in PrP^C, and it has been shown unequivocally that free thiol groups are also absent in PrP^{Sc} [33]. Thus, there is primarily no indication that reduced PrP is involved in the mechanism of prion propagation. Nevertheless, a series of interesting recent observations argue in favor of a transient reduction of the disulfide bond during PrP^{Sc} formation. For example, it could be that the disulfide bond of

PrP^C, after caveolin-dependent endocytosis into lysosomes, becomes reduced and oligomerizes into reduced PrP^{Sc} in which the subunits again become re-oxidized when PrP^{Sc} is released into the extracellular space after death of the infected cell. Alternatively, it could be that reduced PrP is required for formation of PrP^{Sc} nuclei but that further incorporation of oxidized PrP into these nuclei eventually leads to a PrP^{Sc} oligomer in which the vast majority of subunits are oxidized, such that the small fraction of reduced PrP that was initially present is no longer detectable.

The characterization of reduced, recombinant prion proteins has indeed revealed that the prion protein has the property of adopting two entirely different tertiary structures, depending on whether or not the Cys179-Cys214 disulfide is formed. This was first observed for recombinant PrP(91–231) [89, 90]. Reduction of the disulfide bond in human PrP(90–231) at pH 4 and low ionic strength leads to transition of the predominantly α-helical protein to a monomeric polypeptide that shows β-sheet-like CD spectra [90]. Loss of chemical shift dispersion in $^1H-^{15}N$ heteronuclear NMR spectra, however, indicates that the tertiary structure content in this conformational state is significantly lower compared to that of the oxidized protein. Increase in ionic strength at acidic pH then leads to formation of amyloid-like fibers of reduced PrP(91–231), which show increased protease resistance [90]. In addition to these in vitro experiments, several studies on the expression of full-length PrP in the reducing environment of the yeast cytoplasm have revealed that self-replicating amyloid-like fibers of reduced PrP are formed in vivo and show a protease-resistance pattern similar to that of the non-glycosylated PrP from PrP^{Sc} [91, 92]. In this context, it is very interesting that an in vitro protocol for transformation of recombinant hamster PrP(90–231) into amyloids could be developed that requires reduction and re-oxidation of the recombinant protein. The subunits in the resulting oligomers were connected by intermolecular disulfide bonds, which can be explained by a sub-domain swapping mechanism according to which each PrP molecule is covalently connected to two other PrPs via its cysteine residues and each oligomer has two non-satisfied ends with a free thiol group [93]. Here, the domain contacts and the structures of the monomers must be different compared to the X-ray structure of homodimeric human PrP(90–231), which lacks free thiols, as each Cys179 is disulfide-bonded with Cys214 of the other subunit of the dimer [62].

In summary, amyloid-like oligomers can be formed with both oxidized and reduced recombinant PrP in vitro. In none of these cases, however, could it be shown that infectious prions were generated. In this context, it should be emphasized that strong evidence has been accumulated during the past few years that nearly any protein, including purely α-helical proteins such as myoglobin that are not related to known amyloid diseases, can be converted into β-sheet-rich amyloid fibrils in vitro [94, 95]. This suggests that protein amyloids are primarily stabilized by β-sheet hydrogen bonds between main chain atoms. Thus, amyloid formation appears to be an intrinsic property of any polypeptide chain, independent of the amino acid sequence [95]. Therefore, it could well be that none of the aggregates of recombinant PrP reported so far are related to infectious PrP^{Sc}.

34.3.3.3 Influence of Point Mutations Linked With Inherited TSEs on the Stability of Recombinant PrP

All known inherited prion diseases in humans are associated with mutations in the gene encoding human PrP. There are three different familial human TSEs, all of which are autosomal dominant: the familial Creutzfeld-Jakob diseases (CJD), Gerstmann-Sträussler-Scheinker syndrome (GSS), and fatal familial insomnia (FFI) (Table 34.1) [1]. Figure 34.6A summarizes the location of amino acid replacements in human PrP linked with the three different disease phenotypes. Interestingly, the mutation D178N causes either CJD or FFI, depending on the polymorphism at position 129 (Val or a Met, respectively). Figure 34.6B shows that disease-related mutations are mainly located in the folded C-terminal domain of PrP. There is, however, no structural clustering of amino acid replacements related to a specific disease phenotype. As the affected individuals with a point mutation in one of the two PrP alleles spontaneously develop prions without having had contact with external prions, an obvious mechanism underlying this phenomenon could be a destabilization of PrP^C due to the mutation and, consequently, a facilitated conversion to PrP^{Sc}. Inspection of the NMR structure of recombinant PrP indeed predicts a destabilization in the case of the replacements D178N (loss of a salt bridge to Arg164), T183A (loss of two hydrogen bonds from the hydroxyl group of Thr183 to the H^N of Tyr163 and the carbonyl oxygen of Cys179), F198S (generation of a cavity), and Q2017R (loss of a hydrogen bond to the carbonyl atom of Ala133) [57, 58]. However, there are no clear-cut predictions for the other amino acid replacements, and the GSS mutations P102L, P105L, and A117V are located in the flexible tail and should not affect the stability of PrP^C at all.

Therefore, all disease-related point mutations were introduced into recombinant PrP(121–231), and the thermodynamic stabilities of the variants were analyzed. All variants showed far-UV CD spectra that were indistinguishable from that of the wild-type protein, demonstrating that none of these mutations a priori induces a PrP^{Sc}-like, β-sheet-rich conformation [55]. The thermodynamic stabilities of the PrP(121–231) variants with single disease-related amino acid replacements are summarized in Figure 34.6C and reveal that some but not all mutations destabilize PrP^C. A significant destabilization was indeed observed only for the above replacements that were predicted to be destabilizing from analysis of the three-dimensional structure. The most destabilizing mutation proved to be T183A, which decreases the free energy of folding relative to the wild-type protein from -30 to -10 kJ mol^{-1} [55]. Other mutations such as E220K or V210I were completely neutral with respect to PrP^C stability. Analogous results were obtained for variants of recombinant PrP(90–231) [62]. Consequently, destabilization of PrP^C cannot be the only mechanism underlying the spontaneous formation of prions in inherited human TSEs, and destabilization may trigger disease only in the case of mutations D178N, T183A, F198S, R208H, and Q217R (Figure 34.6C). Another result from this analysis is that there is no correlation between the thermodynamic stability of a TSE-related PrP^C variant and the disease phenotype. For example, both the most destabilizing mutation T183A and the ''neutral'' mutation E200K are linked with inherited CJD (Figure 34.6). It follows that there are most likely

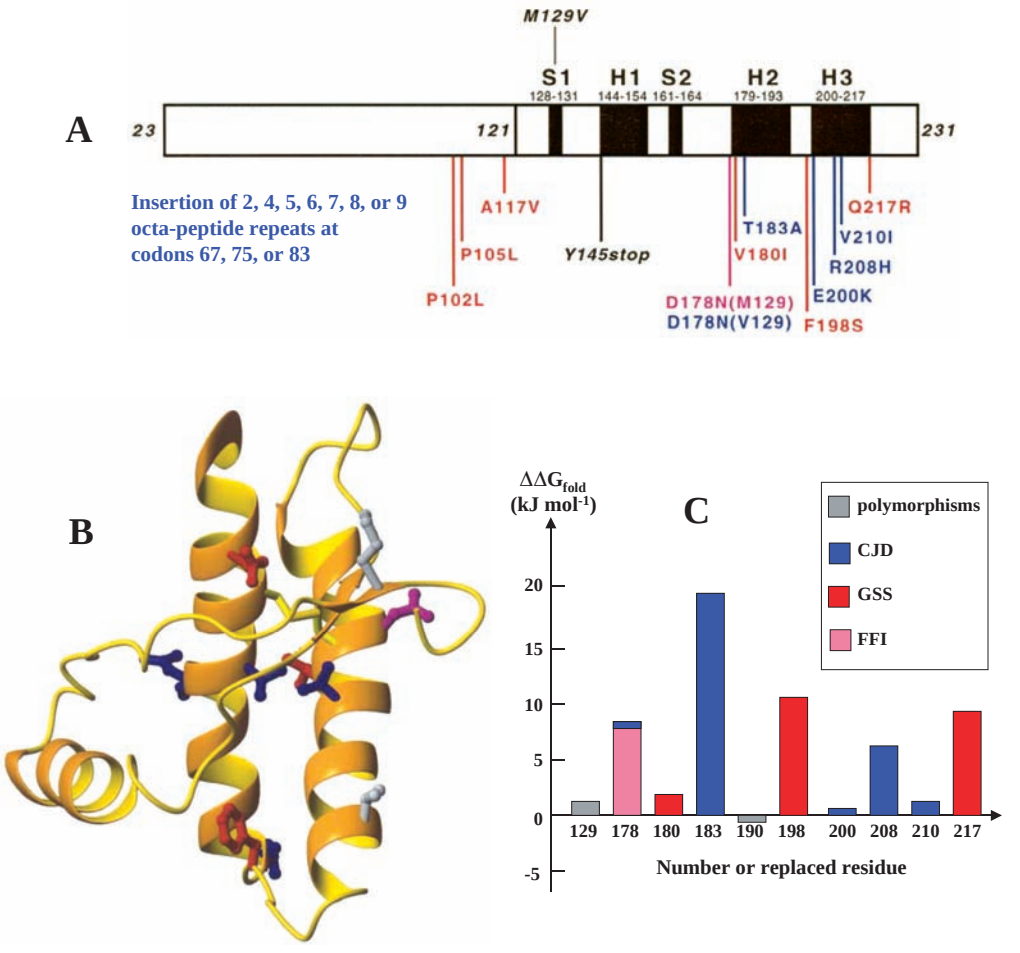

Fig. 34.6. Point mutations in human PrP that are associated with inherited prion diseases and their effect on the intrinsic stability of recombinant PrP(121–231). (A) Scheme of the primary structure of mature human PrP^C, with the amino acid replacements that are linked with the three inherited human TSEs: CJD (blue), GSS (red), and FFI (pink). The Met/Val polymorphism at residue 129 (gray) determines the phenotype of the disease related to the replacement D178N (FFI or CJD, respectively). (B) Location of residues that are replaced in inherited TSE in the structure of PrP(121–231). The polymorphism in murine PrP at residue 190 is also shown (same color code as in (A)). (C) Thermodynamic stabilities of recombinant variants of PrP(121–231), with disease-related, single amino acid replacements, relative to PrP(121–231) wild type. Positive $\Delta\Delta G^\circ$ values indicate that the variant is less stable than wild-type PrP(121–231) (same color code as in (A)). Wild-type PrP(121–231) has a free energy of folding of -30 kJ mol^{-1}. The least stable variant T183A is thus destabilized threefold relative to the wild-type protein.

multiple and independent mechanisms that can lead to spontaneous generation of prions as a consequence of a mutation in PrP. Such mechanisms may, e.g., be an increased stability of PrP^{Sc} (“wild-type” PrP^{Sc} has a half-life of about two days in vivo) or faster nucleation kinetics of PrP^{Sc}. The latter may be caused by the above-mentioned higher fraction of kinetic folding intermediates that has been reported for variants of human PrP(90–231) bearing amino acid replacements associated with inherited TSEs [78, 79].

34.4 Generation of Infectious Prions in Vitro: Principal Difficulties in Proving the Protein-Only Hypothesis

Most scientists would consider the in vitro generation of prions from purified PrP^{C} the final proof of the protein-only hypothesis [8]. In principle, there are several ways to perform such an experiment. One approach is the propagation of prions by inoculation of purified PrP^{C} (or recombinant PrP) with catalytic amounts of PrP^{Sc} isolated from the brain of prion-infected animals. Another (and possibly even more convincing) experiment is the de novo generation of prions from purified PrP^{C} or recombinant PrP by applying in vitro conditions that favor both spontaneous formation and propagation of PrP^{Sc}. The only way to monitor the success of these experiments is to test newly converted PrP^{Sc} molecules for infectivity. This is done by injection of prions into the brain of transgenic mice that overexpress PrP^{C}, and are therefore particularly susceptible to prions, and determination of the incubation time until the onset of the disease. Unfortunately, there is only a very rough, inverse linear correlation between the logarithm of the concentration of infectious units and incubation time [48, 97]. In practice, this means that differences in prion concentration between two samples (e.g., before and after an in vitro conversion experiment) can be detected reliably only when the concentrations differ by two to three orders of magnitude. If we assume that a difference in concentration of infectious units by a factor of 100 is minimally required to distinguish two prion preparations, a conversion experiment in which an infectious PrP^{Sc} preparation is used as an inoculum has to be designed such that PrP^{C} is used at 100-fold excess over PrP^{Sc} and that the conversion would be 100%. It is, however, obvious that the conditions for an in vitro conversion experiment will not be optimal. Thus, if the conversion efficiency was, e.g., only 1%, PrP^{C} would have to be used at an excess of at least 10 000-fold over PrP^{Sc}. In summary, the low sensitivity of the only available assay for infectious prions requires very high in vitro conversion efficiencies for detection of newly generated prions.

The most promising attempts to convert PrP^{C} to the protease-resistant, oligomeric form (which is also termed PrP^{res}) are experiments in which ^{35}S-labeled PrP^{C} isolated from mammalian cells is incubated with PrP^{Sc} in vitro [47, 98]. Numerous experiments performed according to the following reaction scheme revealed that ^{35}S-labeled PrP^{C} can indeed be converted in vitro into a protease-resistant form, PrP^{res}, which has the same biochemical properties as proteinase K–treated PrP^{Sc} [47].

^{35}S-labeled PrP^{C} from mammalian cells + PrP^{Sc} from prion-infected individuals

↓ Incubation

↓ Proteinase K treatment

↓ Detection of protease-resistant ^{35}S-PrP (PrP^{res})

Further mechanistic studies demonstrated that this in vitro conversion of PrP^{C} to PrP^{res} is characterized by a rapid and specific binding step of PrP^{C} to PrP^{Sc} oligomers, followed by a slow conformational transition to PrP^{res} in the PrP^{Sc}-bound state [47]. Strikingly, this assay reproduces experimentally determined species barriers of prion diseases, in that PrP^{Sc} preparations from one species convert PrP^{C} from another species with similar efficiency, as the disease can be transmitted between the two species [99]. Unfortunately, the seeded in vitro conversion of PrP^{C} to PrP^{sen} generally does not generate more than stoichiometric amounts of PrP^{res} relative to the PrP^{Sc} molecules used as seeds [47], which prevents detection of newly generated infectivity. However, the seeded in vitro conversion has been significantly improved recently by a protocol in which growing PrP^{Sc}/PrP^{res} oligomers were subjected to repeated rounds of sonification and re-incubation with PrP^{C}, with the idea of breaking growing oligomers into smaller nuclei by the sonification step and thereby increasing the concentration of "growing ends" [100]. Indeed, this PCR-like approach strongly increased the efficiency of the in vitro conversion process, such that a 50-fold molar excess of converted PrP^{sen} over the initial PrP^{Sc} seeds was achieved. Despite this significant improvement, it could still not be shown that the concentration of infectivity increased and new prions were generated. In any case, this new method is predicted to improve the sensitivity of prion assays based on the detection of protease-resistant PrP by almost two orders of magnitude. Regarding the above described principle difficulties in proving generation of prions from PrP^{C} when PrP^{Sc} is used as an inoculum, the de novo generation of prions from recombinant PrP, which requires only a qualitative proof of existence of infectivity, may be the more promising approach towards the final proof of the protein-only hypothesis. However, the seeded in vitro conversion method has the potential of being further improved through the finding that mammalian RNA preparations stimulate the in vitro amplification of PrP^{res} [101]. This hints at a role for host-encoded stimulatory RNA molecules in prion pathogenesis, which is, e.g., principally possible after retrograde transport of PrP into the cytosol.

34.5 Understanding the Strain Phenomenon in the Context of the Protein-Only Hypothesis: Are Prions Crystals?

The most frequently raised argument against the protein-only hypothesis is the occurrence of prion strains. This relates to the fact that different prions can be isolated from a single species that differ in incubation time, clinical signs, vacuolar

Tab. 34.2. Glossary of prion terminology.

Prion	Infectious agent of transmissible spongiform encephalopathies. According to the protein-only hypothesis, the prion is identical with PrP^{Sc}.
PrP^{C}	Benign, cellular form of the prion protein.
PrP^{Sc}	Insoluble, oligomeric form of the prion protein that can so far be isolated only from the brains of prion-infected individuals or from prion-infected cell cultures.
PrP27–30	Oligomeric, protease-resistant core of the prion protein comprised of PrP subunits containing residues 90–231.
PrP^{res}	Protease-resistant form of the prion protein. PrP^{res} can be generated in vitro from PrP^{c} by incubation of PrP^{C} with PrP^{Sc} and is biochemically indistinguishable from PrP27–30.
Recombinant PrP	Prion protein produced in bacteria, composed of amino acids 23–231 but lacking the C-terminal GPI anchor at residue 231 and the two glycans at Asn181 and Asn197.
PrP(121–231)	Structured C-terminal fragment of the recombinant prion protein, comprising residues 121–231.
"Protein X"	Host-encoded factor that has been postulated to be required for prion replication and to regulate in the species barrier of prion transmission.

brain pathology, and PrP^{Sc} deposition in the brain [8, 23]. These specific phenotypic properties of a given prion strain are reproducibly preserved during consecutive rounds of experimental infection and re-isolation of the strain from the brain of the infected individual. Strain phenomena are typically observed for viruses, which are subject to high mutation rates of the viral genome. The prion strain phenomenon can, however, be explained in the context of the protein-only hypothesis on the basis of the nucleation-polymerization model of prion propagation [47]. This is because there is very convincing evidence that prion strains differ not only with respect to the above phenotypic criteria but also in the biochemical properties of their PrP^{Sc} deposits [6, 47, 102]. Figure 34.7A schematically depicts a Western blot analysis of human PrP^{Sc} from the brain of different patients after proteinase K digestion and SDS-PAGE separation [102]. It shows that the proteinase K–resistant core of the PrP^{Sc} oligomers that are associated with a given strain differs both in the fractions of the incorporated PrP glycoforms (in mammalian cells, there is always a mixture of non-glycosylated, mono-glycosylated, and di-glycosylated PrP^{C}) and in the exact length of the proteinase K–resistant polypeptide fragments. Like the phenotypic properties described above, the characteristic strain-specific banding patterns are always preserved, even after crossing the species barrier, and thus are diagnostic for each prion strain. For example, a characteristic feature of BSE prions from cattle is the high fraction of di-glycosylated PrP contained in the PrP^{Sc} oligomers, which is also observed in PrP^{Sc} isolated from patients with variant CJD [102] (Figure 34.7A, Table 34.1). The simplest model that explains these similarities is that PrP^{Sc} is a crystal-like oligomer. Similar to the fact that proteins frequently form different crystal forms, even under identical crystallization conditions, PrP^{Sc} appears to be capable of forming multiple macromolecular assemblies

that differ in subunit composition and arrangement in their quaternary structures and possibly also in the tertiary structures of their subunits (Figure 34.7B). Each prion strain thus would correspond to a different PrP^{Sc} "crystal form," and this single crystal form then acts as a seed for formation of new PrP^{Sc} oligomers that grow further in the same crystal form. This model can also explain why humans who are heterozygous with respect to the polymorphism at amino acid 129 (Met or Val in humans) are essentially protected from sporadic CJD: although about 51% of the European population is Met/Met or Val/Val homozygous and 49% is Met/Val heterozygous, 95% of all sporadic CJD patients are homozygous [103, 104]. If we assume that residue 129 is solvent-exposed in PrP^{Sc} subunits (as it is in PrP^{C}; Figure 34.6B) and involved in subunit-subunit contacts in PrP^{Sc}, it is

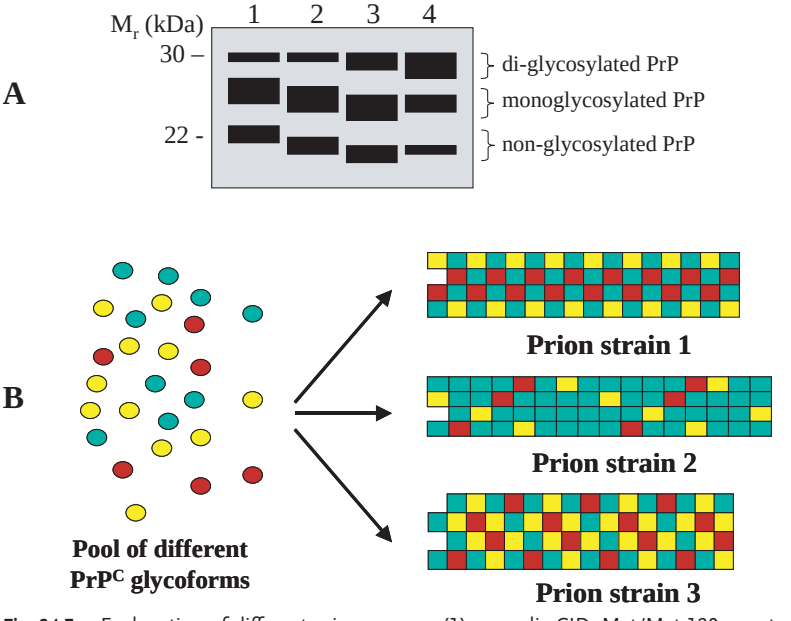

Fig. 34.7. Explanation of different prion strains within the framework of the protein-only hypothesis: (A) Besides disease symptoms and incubation time, prion strains isolated from mammalians and humans can be distinguished on the basis of the biochemical properties of PrP^{Sc} subunits after proteinase K treatment and separation by SDS-PAGE and Western blotting. Specifically, prion strains differ in the fractions of non-glycosylated, mono-glycosylated, and doubly glycosylated PrP contained in PrP^{Sc} oligomers, as well as the N-terminus of the protease-resistant core of the individual subunits. The figure schematically shows the Western blot band patterns of four different human prion strains after proteinase K treatment of PrP^{Sc}: (1) sporadic CJD, Met/Met 129 genotype; (2) sporadic CJD, Val/Val 129 genotype; (3) iatrogenic CJD, Val/Val129 genotype; (4) variant CJD, Met/Met129 genotype. (B) The simplest explanation for the occurrence of different prion strains are crystal-like PrP^{Sc} oligomers that differ in the fractions of the incorporated PrP glycoforms, the arrangement of subunits in the quaternary structure, and/or slightly different tertiary structures of incorporated subunits. In this model, each prion strain corresponds to a specific crystal form. Only one crystal form of PrP^{Sc} would then occur in a prion-infected individual, and only this crystal form would be further propagated when the disease is transmitted to another individual.

easy to imagine that a PrP^{Sc} oligomer composed of identical polypeptide chains could more easily assemble spontaneously into a quaternary structure with a regular array of subunits, compared to a 1:1 mixture of different polypeptides that are incorporated statistically into the oligomer. Another remarkable finding in this context is that residue 129 is exclusively Met in cattle PrP, and variant CJD patients are exclusively Met/Met homozygous [105].

34.6 Conclusions and Outlook

Although essentially all available experimental data on TSE prions and their propagation are either in agreement with or can be explained within the framework of the protein-only hypothesis, the most convincing proof of the prion hypothesis, i.e., the experimental replication of TSE prions in vitro, has not been reported to date. Some of the principal difficulties in proving the generation of infectious prions in vitro by seeding experiments have already been addressed in Section 34.4. In addition, if the "crystal model" of PrP^{Sc} that explains the strain-specific fractions of the different PrP glycoforms in PrP^{Sc} is correct, it follows that the PrP glycans are critically involved in subunit-subunit contacts that determine the quaternary structure of PrP^{Sc}. In the worst case, this means that it will not be possible to produce a PrP^{Sc} oligomer that is infectious and identical to PrP^{Sc} isolated from prion-infected brains from non-glycosylated, recombinant PrP. Moreover, experiments on the de novo formation of prions from recombinant PrP have so far essentially been performed in solution, while the conversion process in vivo most likely occurs at the surface of membranes. The covalent linkage to the GPI anchor and a membrane localization of PrP may therefore be additional prerequisites for generation of prions in vitro. A new protocol for the preparation of recombinant PrP covalently attached to liposomes has recently been established [106] that will allow in vitro conversion experiments with membrane-bound, recombinant PrP. In addition, like cellular RNAs [101], the glucose-based polyglycans found to be associated with PrP^{Sc} [49] may be another critical cofactor of prion replication.

A more general question is which experimental strategies should be pursued to gain mechanistic insights into prion propagation at the molecular level. Because there appears to be an inverse correlation between structural similarity at the level of recombinant PrP and species barrier, the determination of additional structures of recombinant PrPs is certainly a promising approach towards a further understanding of the species barrier. Even more important, however, appears to be the investigation of the oligomeric structure of PrP^{Sc}. For example, PrP^{Sc} oligomers that are spontaneously formed in inherited human prion diseases can either be homo-oligomers of the mutated prion protein or hetero-oligomers of mutated and non-mutated PrP. Both cases have been reported (see references in [55]), but no comprehensive mechanistic investigation on these phenomena is available. As PrP^{Sc} is insoluble and not accessible to structure determination by NMR spectroscopy and X-ray crystallography, the combination of electron microscopy, electron crystallography, and biochemical and genetic studies will be required to obtain further insights into the molecular details of the PrP^{Sc} quaternary structure.

In contrast to mammalian TSEs, the protein-only hypothesis can be considered proven in the case of the yeast prions Ure2p and Sup35p, which are responsible for the non-genetically transmissible phenotypes [*URE3*] and [*PSI*], respectively [107–109]. Specifically, infectious aggregates of Sup35p have been generated from recombinant, bacterial protein in vitro and then successfully transmitted to yeast cells that further propagated the [*PSI*] phenotype [110]. In addition, the species-barrier phenomenon was unequivocally shown to be caused by *specific* aggregates of Sup35p from different yeasts that replicate independently in the same test tube [111]. Thus, there are no principle reasons that the protein-only hypothesis should not be valid for mammalian TSEs.

34.7 Experimental Protocols

As outlined in Section 34.3.1, milligram quantities of correctly folded, disulfide-bonded recombinant prion proteins for biochemical and structural studies can be obtained from *E. coli* by either refolding cytoplasmically expressed proteins from inclusion bodies [53–55] or, in the case of PrP(121–231), by purification from the bacterial periplasm after secretory expression [52]. The more efficient method is the production of recombinant full-length PrP(23–231) and the N-terminally truncated forms PrP(90–231) and PrP(121–231) as cytoplasmic inclusion bodies under control of the T7 promoter, followed by oxidative refolding and purification to homogeneity. For this purpose, essentially two protocols are available, which are briefly described below.

34.7.1 Protocol 1 [53, 55]

Reduced, recombinant PrP is solubilized by treatment of the inclusion bodies with 8 M urea and purification of PrP under denaturing conditions by cation-exchange chromatography and gel filtration in 8 M deionized urea. Disulfide bond formation at pH 8.5 is then initiated by addition of 1 mM $CuSO_4$ as a catalyst of air oxidation for 2 h. The oxidation reaction is then stopped by addition of EDTA and a shift to pH 6, oxidized, and unfolded prion protein is concentrated to 10 mg mL^{-1} and refolded by 1:50 dilution at pH 6. After a final cation-exchange chromatography step at pH 6 under native conditions, homogeneous, recombinant PrP is obtained with yields of about 20 mg per liter of bacterial culture.

34.7.2 Protocol 2 [54]

The full-length prion protein or fragments thereof are expressed with the N-terminal oligo-histidine tag NH_3^+-MRGSHHHHHHGLVPR$^{\downarrow}$GS ..., which can be cleaved specifically by trypsin (cleavage site indicated by the arrow). Cytoplasmic inclusion bodies of the tagged prion proteins are solubilized by 6 M guanidinium chloride (GdmCl) and applied to a Ni^{2+}-NTA column at pH 8. The prion proteins

are then re-oxidized by air and refolded by using a gradient from 6 M to 0 M GdmCl while bound to the column. On-column refolding prevents nonspecific aggregation and intermolecular disulfide bond formation. After cleavage of the histidine tag with thrombin and removal of thrombin by an anion-exchange resin, pure recombinant prion proteins are obtained after a last cation-exchange chromatography step with yields of 10–50 mg per liter of bacterial culture.

For periplasmic production of PrP(121–231) in *E. coli*, the protein is secreted through fusion of the bacterial OmpA signal sequence to its N-terminus under control of the *lac* promoter [52]. The signal sequence is correctly cleaved by *E. coli* signal peptidase. Expression is performed at 25 °C in order to obtain maximum yields of soluble PrP(121–231) in the periplasmic fraction. PrP(121–231) can then be purified to homogeneity from the periplasmic extract by anion-exchange chromatography at pH 7, hydrophobic chromatography at pH 6, and gel filtration at pH 6, with yields of about 3 mg pure PrP(121–231) per liter of bacterial culture.

Purified recombinant prion proteins can be stored at −20 °C after dialysis against distilled water. If recombinant PrP(23–231) or PrP(90–231) is stored at 4 °C, addition of protease inhibitor tablets (''COMPLETE,'' Roche) is recommended. Very detailed protocols for cytoplasmic expression of recombinant PrP(23–231), PrP(90–231), and PrP(121–231) as inclusion bodies, on-column refolding, and isolation of periplasmically expressed PrP(121–231), including information on expression vectors and bacterial growth conditions, are given in Refs. [52–55].

Finally, a protocol for covalent attachment of recombinant, full-length PrP to liposomes has been established. For this purpose, murine PrP(23–231), elongated by the hexapeptide $(Gly)_5$-Cys-CO_2^- at its C-terminus, is cytoplasmically expressed in *E. coli*, refolded, and purified from inclusion bodies essentially as described under Protocol 2. The recombinant PrP(23–231) variant with its free C-terminal thiol is then covalently coupled to the thiol-reactive lipid *N*-((2-pyridyldithio)-propionyl)-1,2-dihexdecanoyl-sn-glycero-3-phosphoethanolamine (PDP-DHPE; Molecular Probes) that has previously been incorporated into liposomes (100-nm diameter) composed of phosphatidylcholine, cholesterol (molar ratio 1:1), and 1% (w/w) PDP-DHPE. Liposome-bound PrP can then be separated from soluble PrP and nonspecific aggregates of PrP by ultracentrifugation. Typically, liposomes bearing 200 molecules of PrP(23–231) at their surface are obtained. Circular dichroism spectra and limited proteolysis experiments revealed that liposome-bound PrP has the same structure and stability as recombinant PrP(23–231) in solution. A very detailed protocol is given in Ref. [106].

Note added in the proof:

While this article was in press, the group of Stanley B. Prusiner reported the first generation of synthetic prions from recombinant PrP (Lagname G. et al., *Science* **305**, 673–676). Recombinant murine PrP(89-231) was polymerized into amyloid fibrils with high β-sheet content in vitro. When these fibrils were used for intracerebral inoculation of transgenic mice exclusively overexpressing murine PrP(89-231), all infected animals developed neurologic disease between 380 and 660 days after inoculation, while control animals inoculated with phosphate-buffered saline did

not show signs of disease after 660 days. Prions isolated from brains of mice inoculated with synthetic PrP(89-231) fibrils could be successfully transmitted to wild type mice and mice overexpressing full-length PrP(23-231) with incubation times of 150 and 90 days, respectively, and analysis of brain extracts revealed accumulation of protease K resistant PrP^{Sc}. The authors state that their findings provide compelling evidence that TSE prions are infectious proteins.

References

1 Prusiner, S. B. (1997). Prion diseases and the BSE crisis. *Science* **278**, 245–51.
2 Cohen, F. E. (1999). Protein misfolding and prion diseases. *Journal of Molecular Biology* **293**, 313–320.
3 Weissmann, C. (1999). Molecular Genetics of Transmissible Spongiform Encephalopathies. *J. Biol. Chem.* **274**, 3–6.
4 Aguzzi, A., Montrasio, F. & Kaeser, P. S. (2001). Prions: health scare and biological challenge. *Nat Rev Mol Cell Biol* **2**, 118–26.
5 Weissmann, C., Enari, M., Klohn, P. C., Rossi, D. & Flechsig, E. (2002). Transmission of prions. *J Infect Dis* **186 Suppl 2**, S157–65.
6 Wadsworth, J. D., Hill, A. F., Beck, J. A. & Collinge, J. (2003). Molecular and clinical classification of human prion disease. *Br Med Bull* **66**, 241–54.
7 Osherovich, L. Z. & Weissman, J. S. (2002). The utility of prions. *Dev Cell* **2**, 143–51.
8 Aguzzi, A. & Polymenidou, M. (2004). Mammalian prion biology: one century of evolving concepts. *Cell* **116**, 313–27.
9 Bolton, D. C., McKinley, M. P. & Prusiner, S. B. (1982). Identification of a protein that purifies with the scrapie prion. *Science* **218**, 1309–11.
10 Riesner, D., Kellings, K., Wiese, U., Wulfert, M., Mirenda, C. & Prusiner, S. B. (1993). Prions and nucleic acids: search for "residual" nucleic acids and screening for mutations in the PrP-gene. *Dev Biol Stand* **80**, 173–81.
11 Alper, T., Cramp, W. A., Haig, D. A. & Clarke, M. C. (1967). Does the agent of scrapie replicate without nucleic acid? *Nature* **214**, 764–6.
12 Griffith, J. S. (1967). Self-replication and scrapie. *Nature* **215**, 1043–4.
13 Prusiner, S. B. (1982). Novel proteinaceous infectious particles cause scrapie. *Science* **216**, 136–44.
14 Basler, K., Oesch, B., Scott, M., Westaway, D., Walchli, M., Groth, D. F., McKinley, M. P., Prusiner, S. B. & Weissmann, C. (1986). Scrapie and cellular PrP isoforms are encoded by the same chromosomal gene. *Cell* **46**, 417–28.
15 Hope, J., Morton, L. J., Farquhar, C. F., Multhaup, G., Beyreuther, K. & Kimberlin, R. H. (1986). The major polypeptide of scrapie-associated fibrils (SAF) has the same size, charge distribution and N-terminal protein sequence as predicted for the normal brain protein (PrP). *Embo J* **5**, 2591–7.
16 Stahl, N. & Prusiner, S. B. (1991). Prions and prion proteins. *Faseb J* **5**, 2799–807.
17 Stahl, N., Baldwin, M. A., Teplow, D. B., Hood, L., Gibson, B. W., Burlingame, A. L. & Prusiner, S. B. (1993). Structural studies of the scrapie prion protein using mass spectrometry and amino acid sequencing. *Biochemistry* **32**, 1991–2002.
18 Pan, K. M., Baldwin, M., Nguyen, J., Gasset, M., Serban, A., Groth, D., Mehlhorn, I., Huang, Z., Fletterick, R. J., Cohen, F. E. & et al. (1993). Conversion of alpha-helices into beta-sheets features in the formation of the scrapie prion proteins. *Proc Natl Acad Sci USA* **90**, 10962–6.
19 Prusiner, S. B., McKinley, M. P., Bowman, K. A., Bolton, D. C., Bendheim, P. E., Groth, D. F. & Glenner, G. G. (1983). Scrapie prions aggregate to form amyloid-like birefringent rods. *Cell* **35**, 349–58.
20 Alper, T. (1985). Scrapie agent unlike

viruses in size and susceptibility to inactivation by ionizing or ultraviolet radiation. *Nature* **317**, 750.

21 Bueler, H., Aguzzi, A., Sailer, A., Greiner, R. A., Autenried, P., Aguet, M. & Weissmann, C. (1993). Mice devoid of PrP are resistant to scrapie. *Cell* **73**, 1339–47.

22 Hsiao, K., Baker, H. F., Crow, T. J., Poulter, M., Owen, F., Terwilliger, J. D., Westaway, D., Ott, J. & Prusiner, S. B. (1989). Linkage of a prion protein missense variant to Gerstmann-Straussler syndrome. *Nature* **338**, 342–5.

23 Chesebro, B. (1998). BSE and prions: uncertainties about the agent. *Science* **279**, 42–3.

24 Anfinsen, C. B. (1973). Principles that govern the folding of protein chains. *Science* **181**, 223–30.

25 Prusiner, S. B., Groth, D., Serban, A., Stahl, N. & Gabizon, R. (1993). Attempts to restore scrapie prion infectivity after exposure to protein denaturants. *Proc Natl Acad Sci USA* **90**, 2793–7.

26 Prusiner, S. B. (1991). Molecular biology of prion diseases. *Science* **252**, 1515–22.

27 Jarrett, J. T. & Lansbury, P. T., Jr. (1993). Seeding "one-dimensional crystallization" of amyloid: a pathogenic mechanism in Alzheimer's disease and scrapie? *Cell* **73**, 1055–8.

28 Booth, D. R., Sunde, M., Bellotti, V., Robinson, C. V., Hutchinson, W. L., Fraser, P. E., Hawkins, P. N., Dobson, C. M., Radford, S. E., Blake, C. C. & Pepys, M. B. (1997). Instability, unfolding and aggregation of human lysozyme variants underlying amyloid fibrillogenesis. *Nature* **385**, 787–93.

29 Hammarstrom, P., Wiseman, R. L., Powers, E. T. & Kelly, J. W. (2003). Prevention of transthyretin amyloid disease by changing protein misfolding energetics. *Science* **299**, 713–6.

30 Schatzl, H. M., Da Costa, M., Taylor, L., Cohen, F. E. & Prusiner, S. B. (1995). Prion protein gene variation among primates. *J Mol Biol* **245**, 362–74.

31 Wopfner, F., Weidenhofer, G., Schneider, R., von Brunn, A., Gilch, S., Schwarz, T. F., Werner, T. & Schatzl, H. M. (1999). Analysis of 27 mammalian and 9 avian PrPs reveals high conservation of flexible regions of the prion protein. *J Mol Biol* **289**, 1163–78.

32 Hope, J., Morton, L. J., Farquhar, C. F., Multhaup, G., Beyreuther, K. & Kimberlin, R. H. (1986). The major polypeptide of scrapie-associated fibrils (SAF) has the same size, charge distribution and N-terminal protein sequence as predicted for the normal brain protein (PrP). *Embo J* **5**, 2591–7.

33 Turk, E., Teplow, D. B., Hood, L. E. & Prusiner, S. B. (1988). Purification and properties of the cellular and scrapie hamster prion proteins. *Eur J Biochem* **176**, 21–30.

34 Caughey, B., Race, R. E., Ernst, D., Buchmeier, M. J. & Chesebro, B. (1989). Prion protein biosynthesis in scrapie-infected and uninfected neuroblastoma cells. *J Virol* **63**, 175–81.

35 Bueler, H., Fischer, M., Lang, Y., Bluethmann, H., Lipp, H. P., DeArmond, S. J., Prusiner, S. B., Aguet, M. & Weissmann, C. (1992). Normal development and behaviour of mice lacking the neuronal cell-surface PrP protein. *Nature* **356**, 577–82.

36 Shmerling, D., Hegyi, I., Fischer, M., Blattler, T., Brandner, S., Gotz, J., Rulicke, T., Flechsig, E., Cozzio, A., von Mering, C., Hangartner, C., Aguzzi, A. & Weissmann, C. (1998). Expression of amino-terminally truncated PrP in the mouse leading to ataxia and specific cerebellar lesions. *Cell* **93**, 203–14.

37 Brown, D. R., Qin, K., Herms, J. W., Madlung, A., Manson, J., Strome, R., Fraser, P. E., Kruck, T., von Bohlen, A., Schulz-Schaeffer, W., Giese, A., Westaway, D. & Kretzschmar, H. (1997). The cellular prion protein binds copper in vivo. *Nature* **390**, 684–7.

38 Tobler, I., Gaus, S. E., Deboer, T., Achermann, P., Fischer, M., Rulicke, T., Moser, M., Oesch, B., McBride, P. A. & Manson, J. C. (1996). Altered circadian activity rhythms and sleep in mice devoid of prion protein. *Nature* **380**, 639–42.

39 Collinge, J., Whittington, M. A., Sidle, K. C., Smith, C. J., Palmer, M. S., Clarke, A. R. & Jefferys, J. G. (1994). Prion protein is necessary for normal synaptic function. *Nature* **370**, 295–7.

40 Sakaguchi, S., Katamine, S., Nishida, N., Moriuchi, R., Shigematsu, K., Sugimoto, T., Nakatani, A., Kataoka, Y., Houtani, T., Shirabe, S., Okada, H., Hasegawa, S., Miyamoto, T. & Noda, T. (1996). Loss of cerebellar Purkinje cells in aged mice homozygous for a disrupted PrP gene. *Nature* **380**, 528–31.

41 Baron, G. S., Wehrly, K., Dorward, D. W., Chesebro, B. & Caughey, B. (2002). Conversion of raft associated prion protein to the protease-resistant state requires insertion of PrP-res (PrP(Sc)) into contiguous membranes. *Embo J* **21**, 1031–40.

42 Peters, P. J., Mironov, A., Jr., Peretz, D., van Donselaar, E., Leclerc, E., Erpel, S., DeArmond, S. J., Burton, D. R., Williamson, R. A., Vey, M. & Prusiner, S. B. (2003). Trafficking of prion proteins through a caveolae-mediated endosomal pathway. *J Cell Biol* **162**, 703–17.

43 Caughey, B. & Raymond, G. J. (1991). The scrapie-associated form of PrP is made from a cell surface precursor that is both protease- and phospholipase-sensitive. *J Biol Chem* **266**, 18217–23.

44 Hegde, R. S., Mastrianni, J. A., Scott, M. R., DeFea, K. A., Tremblay, P., Torchia, M., DeArmond, S. J., Prusiner, S. B. & Lingappa, V. R. (1998). A transmembrane form of the prion protein in neurodegenerative disease. *Science* **279**, 827–34.

45 Ma, J., Wollmann, R. & Lindquist, S. (2002). Neurotoxicity and neurodegeneration when PrP accumulates in the cytosol. *Science* **298**, 1781–5.

46 McKinley, M. P., Bolton, D. C. & Prusiner, S. B. (1983). A protease-resistant protein is a structural component of the scrapie prion. *Cell* **35**, 57–62.

47 Caughey, B., Raymond, G. J., Callahan, M. A., Wong, C., Baron, G. S. & Xiong, L. W. (2001). Interactions and conversions of prion protein isoforms. *Adv Protein Chem* **57**, 139–69.

48 Fischer, M., Rulicke, T., Raeber, A., Sailer, A., Moser, M., Oesch, B., Brandner, S., Aguzzi, A. & Weissmann, C. (1996). Prion protein (PrP) with amino-proximal deletions restoring susceptibility of PrP knockout mice to scrapie. *Embo J* **15**, 1255–64.

49 Appel, T. R., Dumpitak, C., Matthiesen, U. & Riesner, D. (1999). Prion rods contain an inert polysaccharide scaffold. *Biol Chem* **380**, 1295–306.

50 Nguyen, J. T., Inouye, H., Baldwin, M. A., Fletterick, R. J., Cohen, F. E., Prusiner, S. B. & Kirschner, D. A. (1995). X-ray diffraction of scrapie prion rods and PrP peptides. *J Mol Biol* **252**, 412–22.

51 Wille, H., Michelitsch, M. D., Guenebaut, V., Supattapone, S., Serban, A., Cohen, F. E., Agard, D. A. & Prusiner, S. B. (2002). Structural studies of the scrapie prion protein by electron crystallography. *Proc Natl Acad Sci USA* **99**, 3563–8.

52 Hornemann, S. & Glockshuber, R. (1996). Autonomous and reversible folding of a soluble amino-terminally truncated segment of the mouse prion protein. *J Mol Biol* **261**, 614–9.

53 Hornemann, S., Korth, C., Oesch, B., Riek, R., Wider, G., Wuthrich, K. & Glockshuber, R. (1997). Recombinant full-length murine prion protein, mPrP(23–231): purification and spectroscopic characterization. *FEBS Lett* **413**, 277–81.

54 Zahn, R., von Schroetter, C. & Wuthrich, K. (1997). Human prion proteins expressed in Escherichia coli and purified by high-affinity column refolding. *FEBS Lett* **417**, 400–4.

55 Liemann, S. & Glockshuber, R. (1999). Influence of amino acid substitutions related to inherited human prion diseases on the thermodynamic stability of the cellular prion protein. *Biochemistry* **38**, 3258–67.

56 Riek, R., Hornemann, S., Wider, G., Billeter, M., Glockshuber, R. &

Wuthrich, K. (1996). NMR structure of the mouse prion protein domain PrP(121–321). *Nature* **382**, 180–2.

57 Wuthrich, K. & Riek, R. (2001). Three-dimensional structures of prion proteins. *Adv Protein Chem* **57**, 55–82.

58 Riek, R., Wider, G., Billeter, M., Hornemann, S., Glockshuber, R. & Wuthrich, K. (1998). Prion protein NMR structure and familial human spongiform encephalopathies. *Proc Natl Acad Sci USA* **95**, 11667–72.

59 Riek, R., Hornemann, S., Wider, G., Glockshuber, R. & Wuthrich, K. (1997). NMR characterization of the full-length recombinant murine prion protein, mPrP(23–231). *FEBS Lett* **413**, 282–8.

60 Viles, J. H., Cohen, F. E., Prusiner, S. B., Goodin, D. B., Wright, P. E. & Dyson, H. J. (1999). Copper binding to the prion protein: structural implications of four identical cooperative binding sites. *Proc Natl Acad Sci USA* **96**, 2042–7.

61 Dyson, H. J. & Wright, P. E. (2002). Coupling of folding and binding for unstructured proteins. *Curr Opin Struct Biol* **12**, 54–60.

62 Knaus, K. J., Morillas, M., Swietnicki, W., Malone, M., Surewicz, W. K. & Yee, V. C. (2001). Crystal structure of the human prion protein reveals a mechanism for oligomerization. *Nat Struct Biol* **8**, 770–4.

63 Moore, R. C., Lee, I. Y., Silverman, G. L., Harrison, P. M., Strome, R., Heinrich, C., Karunaratne, A., Pasternak, S. H., Chishti, M. A., Liang, Y., Mastrangelo, P., Wang, K., Smit, A. F., Katamine, S., Carlson, G. A., Cohen, F. E., Prusiner, S. B., Melton, D. W., Tremblay, P., Hood, L. E. & Westaway, D. (1999). Ataxia in prion protein (PrP)-deficient mice is associated with upregulation of the novel PrP-like protein doppel. *J Mol Biol* **292**, 797–817.

64 Behrens, A., Genoud, N., Naumann, H., Rulicke, T., Janett, F., Heppner, F. L., Ledermann, B. & Aguzzi, A. (2002). Absence of the prion protein homologue Doppel causes male sterility. *Embo J* **21**, 3652–8.

65 Mo, H., Moore, R. C., Cohen, F. E., Westaway, D., Prusiner, S. B., Wright, P. E. & Dyson, H. J. (2001). Two different neurodegenerative diseases caused by proteins with similar structures. *Proc Natl Acad Sci USA* **98**, 2352–7.

66 Luhrs, T., Riek, R., Guntert, P. & Wuthrich, K. (2003). NMR structure of the human doppel protein. *J Mol Biol* **326**, 1549–57.

67 James, T. L., Liu, H., Ulyanov, N. B., Farr-Jones, S., Zhang, H., Donne, D. G., Kaneko, K., Groth, D., Mehlhorn, I., Prusiner, S. B. & Cohen, F. E. (1997). Solution structure of a 142-residue recombinant prion protein corresponding to the infectious fragment of the scrapie isoform. *Proc Natl Acad Sci USA* **94**, 10086–91.

68 Donne, D. G., Viles, J. H., Groth, D., Mehlhorn, I., James, T. L., Cohen, F. E., Prusiner, S. B., Wright, P. E. & Dyson, H. J. (1997). Structure of the recombinant full-length hamster prion protein PrP(29–231): the N terminus is highly flexible. *Proc Natl Acad Sci USA* **94**, 13452–7.

69 Zahn, R., Liu, A., Luhrs, T., Riek, R., von Schroetter, C., Lopez Garcia, F., Billeter, M., Calzolai, L., Wider, G. & Wuthrich, K. (2000). NMR solution structure of the human prion protein. *Proc Natl Acad Sci USA* **97**, 145–50.

70 Lopez Garcia, F., Zahn, R., Riek, R. & Wuthrich, K. (2000). NMR structure of the bovine prion protein. *Proc Natl Acad Sci USA* **97**, 8334–9.

71 Telling, G. C., Scott, M., Mastrianni, J., Gabizon, R., Torchia, M., Cohen, F. E., DeArmond, S. J. & Prusiner, S. B. (1995). Prion propagation in mice expressing human and chimeric PrP transgenes implicates the interaction of cellular PrP with another protein. *Cell* **83**, 79–90.

72 Swietnicki, W., Petersen, R., Gambetti, P. & Surewicz, W. K. (1997). pH-dependent stability and conformation of the recombinant human prion protein PrP(90–231). *J Biol Chem* **272**, 27517–20.

73 Swietnicki, W., Petersen, R. B., Gambetti, P. & Surewicz, W. K. (1998). Familial mutations and the thermodynamic stability of the recombinant human prion protein. *J Biol Chem* **273**, 31048–52.

74 Hosszu, L. L., Baxter, N. J., Jackson, G. S., Power, A., Clarke, A. R., Waltho, J. P., Craven, C. J. & Collinge, J. (1999). Structural mobility of the human prion protein probed by backbone hydrogen exchange. *Nat Struct Biol* **6**, 740–3.

75 Jackson, G. S., Hosszu, L. L., Power, A., Hill, A. F., Kenney, J., Saibil, H., Craven, C. J., Waltho, J. P., Clarke, A. R. & Collinge, J. (1999a). Reversible conversion of monomeric human prion protein between native and fibrilogenic conformations. *Science* **283**, 1935–7.

76 Prusiner, S. B., Groth, D., Serban, A., Stahl, N. & Gabizon, R. (1993). Attempts to restore scrapie prion infectivity after exposure to protein denaturants. *Proc Natl Acad Sci USA* **90**, 2793–7.

77 Wildegger, G., Liemann, S. & Glockshuber, R. (1999). Extremely rapid folding of the C-terminal domain of the prion protein without kinetic intermediates. *Nat Struct Biol* **6**, 550–3.

78 Apetri, A. C. & Surewicz, W. K. (2002). Kinetic intermediate in the folding of human prion protein. *J Biol Chem* **277**, 44589–92.

79 Apetri, A. C., Surewicz, K. & Surewicz, W. K. (2004). The effect of disease-associated mutations on the folding pathway of human prion protein. *J Biol Chem* **279**, 18008–14.

80 Vey, M., Pilkuhn, S., Wille, H., Nixon, R., DeArmond, S. J., Smart, E. J., Anderson, R. G., Taraboulos, A. & Prusiner, S. B. (1996). Subcellular colocalization of the cellular and scrapie prion proteins in caveolae-like membranous domains. *Proc Natl Acad Sci USA* **93**, 14945–9.

81 Arnold, J. E., Tipler, C., Laszlo, L., Hope, J., Landon, M. & Mayer, R. J. (1995). The abnormal isoform of the prion protein accumulates in late-endosome-like organelles in scrapie-infected mouse brain. *J Pathol* **176**, 403–11.

82 Borchelt, D. R., Taraboulos, A. & Prusiner, S. B. (1992). Evidence for synthesis of scrapie prion proteins in the endocytic pathway. *J Biol Chem* **267**, 16188–99.

83 Lee, R. J., Wang, S. & Low, P. S. (1996). Measurement of endosome pH following folate receptor-mediated endocytosis. *Biochim Biophys Acta* **1312**, 237–42.

84 Zhang, H., Stockel, J., Mehlhorn, I., Groth, D., Baldwin, M. A., Prusiner, S. B., James, T. L. & Cohen, F. E. (1997). Physical studies of conformational plasticity in a recombinant prion protein. *Biochemistry* **36**, 3543–53.

85 Hornemann, S. & Glockshuber, R. (1998). A scrapie-like unfolding intermediate of the prion protein domain PrP(121–231) induced by acidic pH. *Proc Natl Acad Sci USA* **95**, 6010–4.

86 Jackson, G. S., Hill, A. F., Joseph, C., Hosszu, L., Power, A., Waltho, J. P., Clarke, A. R. & Collinge, J. (1999b). Multiple folding pathways for heterologously expressed human prion protein. *Biochim Biophys Acta* **1431**, 1–13.

87 Glockshuber, R. (2001). Folding dynamics and energetics of recombinant prion proteins. *Adv Protein Chem* **57**, 83–105.

88 Swietnicki, W., Morillas, M., Chen, S. G., Gambetti, P. & Surewicz, W. K. (2000). Aggregation and fibrillization of the recombinant human prion protein huPrP90-231. *Biochemistry* **39**, 424–31.

89 Mehlhorn, I., Groth, D., Stockel, J., Moffat, B., Reilly, D., Yansura, D., Willett, W. S., Baldwin, M., Fletterick, R., Cohen, F. E., Vandlen, R., Henner, D. & Prusiner, S. B. (1996). High-level expression and characterization of a purified 142-residue polypeptide of the prion protein. *Biochemistry* **35**, 5528–37.

90 Jackson, G. S., Hosszu, L. L., Power, A., Hill, A. F., Kenney, J., Saibil, H., Craven, C. J., Waltho, J. P., Clarke, A. R. & Collinge, J. (1999a).

Reversible conversion of monomeric human prion protein between native and fibrilogenic conformations. *Science* **283**, 1935–7.

91 Ma, J. & Lindquist, S. (1999). De novo generation of a PrPSc-like conformation in living cells. *Nat Cell Biol* **1**, 358–61.

92 Ma, J., Wollmann, R. & Lindquist, S. (2002). Neurotoxicity and neurodegeneration when PrP accumulates in the cytosol. *Science* **298**, 1781–5.

93 Lee, S. & Eisenberg, D. (2003). Seeded conversion of recombinant prion protein to a disulfide-bonded oligomer by a reduction-oxidation process. *Nat Struct Biol* **10**, 725–30.

94 Fandrich, M., Fletcher, M. A. & Dobson, C. M. (2001). Amyloid fibrils from muscle myoglobin. *Nature* **410**, 165–6.

95 Dobson, C. M. (2003). Protein folding and misfolding. *Nature* **426**, 884–90.

96 Apetri, A. C. & Surewicz, W. K. (2003). Atypical effect of salts on the thermodynamic stability of human prion protein. *J Biol Chem* **278**, 22187–92.

97 Brandner, S., Isenmann, S., Raeber, A., Fischer, M., Sailer, A., Kobayashi, Y., Marino, S., Weissmann, C. & Aguzzi, A. (1996). Normal host prion protein necessary for scrapie-induced neurotoxicity. *Nature* **379**, 339–43.

98 Kocisko, D. A., Come, J. H., Priola, S. A., Chesebro, B., Raymond, G. J., Lansbury, P. T. & Caughey, B. (1994). Cell-free formation of protease-resistant prion protein. *Nature* **370**, 471–4.

99 Raymond, G. J., Hope, J., Kocisko, D. A., Priola, S. A., Raymond, L. D., Bossers, A., Ironside, J., Will, R. G., Chen, S. G., Petersen, R. B., Gambetti, P., Rubenstein, R., Smits, M. A., Lansbury, P. T., Jr. & Caughey, B. (1997). Molecular assessment of the potential transmissibilities of BSE and scrapie to humans. *Nature* **388**, 285–8.

100 Saborio, G. P., Permanne, B. & Soto, C. (2001). Sensitive detection of pathological prion protein by cyclic amplification of protein misfolding. *Nature* **411**, 810–3.

101 Deleault, N. R., Lucassen, R. W. & Supattapone, S. (2003). RNA molecules stimulate prion protein conversion. *Nature* **425**, 717–20.

102 Collinge, J., Sidle, K. C., Meads, J., Ironside, J. & Hill, A. F. (1996a). Molecular analysis of prion strain variation and the aetiology of 'new variant' CJD. *Nature* **383**, 685–90.

103 Palmer, M. S., Dryden, A. J., Hughes, J. T. & Collinge, J. (1991). Homozygous prion protein genotype predisposes to sporadic Creutzfeldt-Jakob disease. *Nature* **352**, 340–2.

104 Collinge, J., Palmer, M. S. & Dryden, A. J. (1991). Genetic predisposition to iatrogenic Creutzfeldt-Jakob disease. *Lancet* **337**, 1441–2.

105 Collinge, J., Beck, J., Campbell, T., Estibeiro, K. & Will, R. G. (1996b). Prion protein gene analysis in new variant cases of Creutzfeldt-Jakob disease. *Lancet* **348**, 56.

106 Eberl, H., Tittmann, P. & Glockshuber, R. (2004). Characterization of recombinant, membrane-attached full-length prion protein. *J Biol Chem* **279**, 25058–65.

107 Uptain, S. M. & Lindquist, S. (2002). Prions as protein-based genetic elements. *Annu Rev Microbiol* **56**, 703–41.

108 Osherovich, L. Z. & Weissman, J. S. (2002). The utility of prions. *Dev Cell* **2**, 143–51.

109 Wickner, R. B., Edskes, H. K., Roberts, B. T., Pierce, M. & Baxa, U. (2002). Prions of yeast as epigenetic phenomena: high protein ''copy number'' inducing protein ''silencing''. *Adv Genet* **46**, 485–525.

110 Sparrer, H. E., Santoso, A., Szoka, F. C., Jr. & Weissman, J. S. (2000). Evidence for the prion hypothesis: induction of the yeast [PSI+] factor by in vitro – converted Sup35 protein. *Science* **289**, 595–9.

111 Santoso, A., Chien, P., Osherovich, L. Z. & Weissman, J. S. (2000). Molecular basis of a yeast prion species barrier. *Cell* **100**, 277–88.

35
Insights into the Nature of Yeast Prions

Lev Z. Osherovich and Jonathan S. Weissman

35.1
Introduction

The concept of an infectious protein (prion) was first put forth to explain the properties of a set of related transmissible spongiform encephalopathies (TSEs) including scrapie in sheep and Cruetzfeld-Jakob disease (CJD) in man (for reviews, see Prusiner 1998; Weissmann 1999). Purification of the infectious agent revealed that it was composed largely (if not entirely) of a single endogenous protein called PrP. Remarkably, PrP can interconvert between two states: the normal form (termed PrP^{c}) and its infectious variant (PrP^{Sc}). PrP^{c} has high α-helical content, whereas PrP^{Sc} adopts a β-sheet-rich conformation and in some cases aggregates to form long polymers termed amyloid fibers. These findings led to the "protein only" hypothesis in which replication of the infectious agent results from the ability of aggregated PrP^{Sc} to bind and catalyze conversion of PrP^{c} to PrP^{Sc}.

TSEs such as mad cow disease continue to imperil domesticated mammals and potentially threaten human health. Since the advent of the prion concept, a great deal of effort has been put into understanding the mechanisms for the appearance and transmission of protein-based infectious diseases, with considerable success. However, the inability to reconstitute critical aspects of mammalian prion diseases in vitro, as well as the difficulty of working with animal models, has greatly slowed efforts to investigate many key aspects of prion biology. In particular, the origin and limits of the barriers that inhibit the transmission of prion diseases between different species as well as the molecular basis of the strain phenomenon, wherein prions composed of the same infectious protein can cause distinct disease states, have remained largely mysterious.

Wickner (1994) extended the prion concept to explain the inheritance of two enigmatic non-Mendelian elements in the yeast *Saccharomyces cerevisiae*, called [*URE3*] and [PSI^{+}] (for review, see Uptain and Lindquist 2002). In contrast to the mammalian case, yeast prions do not cause cell death but rather act as epigenetic modulators of protein function. The phenotypes associated with [*URE3*] or [PSI^{+}] elements are not particularly remarkable: [*URE3*] alters nitrogen catabolite uptake (Lacroute 1971), while [PSI^{+}] allows for the suppression of some nonsense

Protein Folding Handbook. Part II. Edited by J. Buchner and T. Kiefhaber

ISBN: 3-527-30784-2

mutations (Cox 1965). Indeed, traditional loss-of-function mutations in the chromosomally encoded nitrogen catabolism repressor Ure2p and the essential translation termination factor Sup35p mimic the [*URE3*] and [*PSI*$^+$] states, respectively. What makes [*URE3*] and [*PSI*$^+$] remarkable are their epigenetic properties; for example, they are inherited by all of the meiotic progeny of ''heterozygous'' diploid cells and can be transmitted by transfer of cytoplasm from one cell to another without the exchange of genetic material.

To explain the unusual inheritance of [*URE3*] and [*PSI*$^+$], Wickner (1994) proposed that these states result from the presence of self-propagating (prion) forms of the Ure2p and Sup35p proteins, respectively (see Figure 35.1). This model provides a mechanism for the non-nuclear inheritance and faithful propagation of the [*URE3*] and [*PSI*$^+$] states; the prion forms can convert free molecules of the affected protein and are themselves distributed along with the cytoplasm to all of the cell's progeny. The prion model also explains why the phenotypes of [*URE3*] and [*PSI*$^+$] mimic the loss of function of Ure2p and Sup35p, as conversion inactivates the affected protein. Since this time, new fungal prions and prion-like states have been identified, including the naturally occurring yeast prion [*RNQ*$^+$] (Sondheimer and Lindquist 2000) (also known as [*PIN*$^+$]) (Derkatch et al. 2001), the artificial prion [*NU*$^+$] (Santoso et al. 2000), and the *Podospora anserina* prion [*Het-s*] (Coustou et al. 1997). These have been comprehensively reviewed elsewhere (Uptain and Lindquist 2002; Osherovich and Weissman 2002). Importantly, formal proof of the prion hypothesis has come from studies with [*PSI*$^+$] and [Het-s]. When introduced into cells, prion seeds generated in vitro from purified recombinant Sup35p (Sparrer et al. 2000; Tanaka et al. 2004; King and Diaz-Avalos 2004) or HET-s protein (Maddelein et al. 2002) are able to cause de novo formation of the [*PSI*$^+$] and [Het-s] states, respectively. The powerful genetic tools of the yeast *S. cerevisae* together with the ability to create infectious material from recombinant protein have greatly facilitated efforts to understand the requirements and properties of prion inheritance. Drawing on our detailed understanding of the yeast prions, we examine the general principles of prion formation, replication, and transmission. In addition we discuss the possibility that, by allowing for stable self-organizing structures, prion-like conformations may play a broader role in normal biology (for reviews of the mammalian prion literature, see Prusiner 1998; Weissmann 1999).

35.2
Prions as Heritable Amyloidoses

Prion-based inheritance requires that a protein be capable of adopting at least one alternate, infectious protein state that is able to bind and convert the normal cellular form of the protein. A range of studies indicate that both mammalian and yeast prions accomplish this by directing the conformational change of a normal cellular – or, in the case of PrP, cell surface – host protein into an alternate prion conformation. These alternate conformations are β-sheet-rich multimers and re-

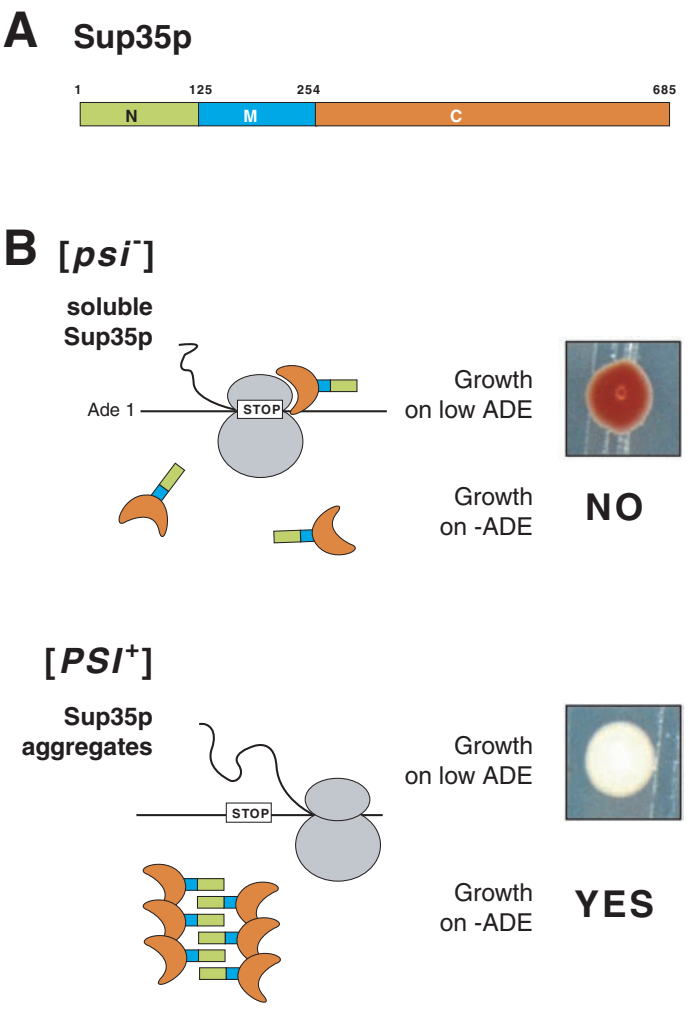

Fig. 35.1. The yeast prions [*PSI*$^+$] and [*URE3*] are due to self-propagating protein conformations. Adapted from (Chien et al. 2004). (A) Sup35p is an essential modular protein involved in translation termination whose self-propagating aggregation is responsible for the [*PSI*$^+$] phenotype. The N-terminus, (N), residues 1–125 (green), is glutamine- and asparagine-rich and mediates prion behavior. The middle domain (M), residues 126–254 (blue), is rich in charged residues. Commonly, purified NM fusions are used in vitro. The C-terminal domain (C), residues 254–685 (orange), is the essential part of the protein and is responsible for faithful translation termination at stop codons. (B) In [*psi*$^-$] yeast, Sup35p is soluble and able to interact with the ribosome to facilitate translation termination. In [*PSI*$^+$] yeast, Sup35p is aggregated, sequestering it from the ribosome and therefore allowing nonsense suppression. Typically, the [*PSI*$^+$] nonsense-suppression phenotype is monitored by measuring read-through of a reporter gene carrying a premature stop, such as the *ade*-1 gene, which leads to a convenient color change on low-adenine media and to a differential growth phenotype on media lacking adenine.

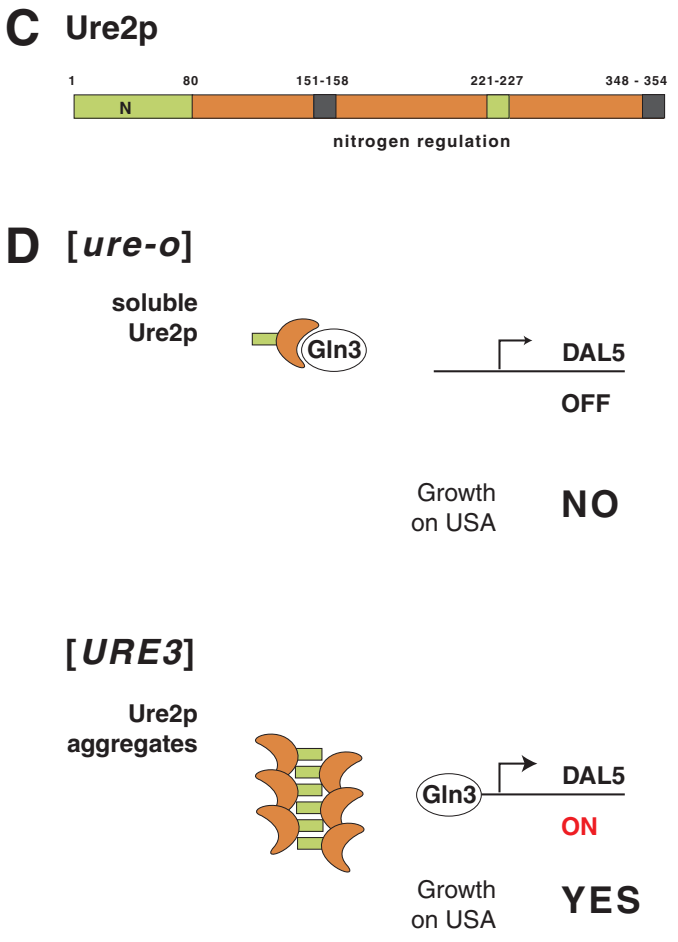

Fig. 35.1. (C) Ure2p is a modular protein involved in regulation of nitrogen catabolism whose self-propagating aggregation is responsible for the [*URE3*] phenotype. In addition to the glutamine/asparagine-rich amino terminus (green), Ure2p also contains another region that facilitates prion behavior (green) and portions that antagonize prion formation (black). The C-terminus (C), residues 81–354 (orange), resembles glutathione-S-transferase, and signals the presence of high-quality nitrogen sources through Gln3. (D) Normally, Ure2p binds the transcription factor Gln3p in the cytoplasm, keeping Gln3p from turning on a host of genes required for uptake of poor nitrogen sources, such as *DAL5*, a plasma membrane import protein. Serendipitously, Dal5p imports not only the poor nitrogen source allantoate but also USA (*N*-carbamyl-aspartate), an intermediate in uracil biosynthesis. This allows selection for [URE3] on USA medium in a uracil auxotroph. In a [ure-o] yeast, Ure2p is complexed with Gln3, and DAL5 is turned off, prohibiting growth on USA medium. In a [URE3] yeast, Ure2p is aggregated, releasing Gln3 to the nucleus, where it activates transcription of *DAL5* and allows USA uptake and growth on USA medium.

semble a broader class of ordered protein aggregates often referred to as amyloids (Dobson 2001). In the past few years, amyloids have received a great deal of attention due to their involvement in a wide variety of protein-misfolding disorders, including neuropathies such as Alzheimer's, Parkinson's, and Huntington's diseases (Taylor et al. 2002) as well as a number of systemic amyloidoses. A number of non-disease-associated proteins, such as acylphosphatase and the SH3 domain from PIP_3 kinase, have been shown to form amyloid under mildly denaturing conditions (Chiti et al. 1999; Guijarro et al. 1998). The ability of so many unrelated proteins to form amyloids argues that this fold is generally accessible to polymers of amino acids, perhaps because it is stabilized by main-chain rather than side-chain interactions (Dobson 1999). Polyglutamine amyloids of the kind implicated in trinucleotide expansion diseases may gain additional stability due to hydrogen bonding between main-chain and side-chain amide moieties (Perutz et al. 1994).

Like mammalian prions, fungal prions appear to be amyloid conformational variants of normal cellular proteins. All fungal prion proteins identified have been shown to form high-molecular-weight complexes in prion-containing cells (Coustou et al. 1997; Masison and Wickner 1995; Patino et al. 1996; Paushkin et al. 1996; Santoso et al. 2000; Sondheimer and Lindquist 2000), although the extent of aggregation can vary from strain to strain (Ripaud et al. 2003). These prion aggregates can in some conditions be visualized in cells by expressing GFP fusions of the prion protein. These reporter fusions are soluble and are distributed evenly throughout the cytoplasm in prion-free cells but coalesce into punctate foci in prion-containing cells (Osherovich and Weissman 2001; Patino et al. 1996; Sondheimer and Lindquist 2000; Zhou et al. 2001). Ure2p has also been visualized by thin-section EM followed by immunogold staining and has been shown to form short cytoplasmic fibrils specifically in [*URE3*] yeast (Speransky et al. 2001). These prion aggregates are typically stable and have altered resistance to protease digestion (Coustou et al. 1997; Masison and Wickner 1995; Patino et al. 1996; Paushkin et al. 1996). Finally, de novo formation of these aggregates is slow, but once formed they are stably inherited by daughter cells during mitosis.

Self-propagating amyloid aggregation is only one of a number of possible mechanisms of protein-based epigenetic inheritance (Griffith 1967). Indeed, Roberts and Wickner (2003) have used a zymogen, or self-activating enzyme, to create a heritable positive feedback loop that resembles a prion in its inheritance and transmissibility but does not involve protein aggregation. However, all hitherto described naturally occurring prions are based on self-propagating amyloid aggregates.

The fungal prions have proven to be far more amenable to reconstitution in vitro than the mammalian prion system. Extracts from [PSI^+] yeast can induce conversion of soluble Sup35p in extracts from [*psi*$^-$] yeast (Paushkin et al. 1997). Moreover, Sup35p, Ure2p, HET-s, and Rnq1p, the prion proteins responsible for [PSI^+], [*URE3*], [Het-s], and [RNQ^+]/[PIN^+], respectively, have all been shown to form self-seeding amyloids in vitro (Baxa et al. 2003; Dos Reis et al. 2002; Glover et al. 1997; Jiang et al. 2004; King et al. 1997; Taylor et al. 1999). Non-amyloid fibrillar forms of Ure2p have also been suggested to underlie [*URE3*] (Bousset et al. 2002; Fay et al. 2003). Several lines of evidence argue that self-seeded aggregation drives

prion inheritance in vivo. For example, mutations in Sup35 that affect aggregation in vivo have parallel effects on in vitro polymerization (DePace et al. 1998; Liu and Lindquist 1999; Patino et al. 1996). More directly for Sup35p and HET-s, it has been possible to create amyloids in vitro from recombinant protein and to use these to convert wild-type cells to the prion state when introduced into the cytoplasm of prion-free cells (Maddelein et al. 2002; Sparrer et al. 2000; Tanaka et al. 2004; King and Diaz-Avalos 2004). These experiments have provided the first direct demonstration that a pure protein can indeed act as a conformationally based infectious agent. Although the self-seeding nature of amyloid aggregates constitutes the basis of prion-based inheritance, not all self-seeding amyloids can support prion inheritance (see below).

35.3 Prion Strains and Species Barriers: Universal Features of Amyloid-based Prion Elements

Studies of the yeast prion [*PSI*$^+$] have shed light on two of the most perplexing features of prion biology. One of these is the existence of transmission barriers that inhibit the passage of prions between related species (Chien et al. 2004). The primary structure of the prion protein is a critical determinant of the specificity of propagation, as susceptibility to cross-species infection is intimately related to the degree of similarity between the sequences of the two prion proteins (Collinge 2001; Prusiner et al. 1990; Scott et al. 1989). Indeed, even point mutations or allelic variants can have dramatic effects on the specificity of prion propagation (Bossers et al. 1997; Bruce et al. 1994; Manson et al. 1999, 2000; Mastrianni et al. 2001).

The second remarkable feature is the existence of multiple prion strains, wherein infectious particles composed of the same protein give rise to a range of prion states that vary in incubation time, pathology, and other phenotypic aspects (Chien et al. 2004). Strain variability had been observed long before the prion hypothesis; in fact, it was originally interpreted as evidence for the existence of a nucleic acid genome in the infectious particle, with strain variation arising from mutations in this genome. To reconcile the presence of prion strain with the protein-only hypothesis, it has been proposed that a single polypeptide can misfold into multiple infectious conformations, at least one for each phenotypic variant (Aguzzi and Haass 2003; Weissmann 1991). Rather than being peculiarities of mammalian prions, it is now clear that both transmission barriers and strain variation are common features of amyloid-based prion elements and that both arise from the general ability of prion proteins to adopt multiple amyloid conformations.

Barriers inhibiting yeast prion transmission have been extensively studied using the yeast prion [*PSI*$^+$]. The cloning of *SUP35* genes from a broad range of budding yeast revealed that although the sequence of the amino-terminal domain varies, these domains can support prion states when expressed in a heterologous *S. cerevisiae* system (Chernoff et al. 2000; Kushnirov et al. 2000a; Santoso et al. 2000) and, in one case, in the original yeast species (*Kluyveromyces lactis*) from which it was

derived (Nakayashiki et al. 2001). As with mammalian prions, the induction and transmission of [*PSI*$^+$] prions are typically confined to proteins from the same species (Chernoff et al. 2000; Crist et al. 2003; Kushnirov et al. 2000a; Nakayashiki et al. 2001; Santoso et al. 2000). An example of a particularly robust barrier is that between prions of *S. cerevisiae*- and *Candida albicans*-derived SUP35 prion domains. Although these organisms would not naturally interact, specificity can be studied using genetically manipulated yeast. Overexpression of *S. cerevisiae* Sup35p induces [*PSI*$^+$] in wild-type *S. cerevisiae* but not in yeast where the *SUP35* gene encodes the *C. albicans* prion domain and vice versa (Santoso et al. 2000). Even a single point mutation within the *S. cerevisiae SUP35* sequence is sufficient to alter specificity (DePace et al. 1998). However, in some cases, cross-transmission of a prion state between different *SUP35* proteins is possible, albeit with reduced efficiency compared to homotypic transmission (Chernoff et al. 2000; Chien et al. 2003).

Although cellular factors such as chaperones are needed for the inheritance of prions (see below), they do not determine specificity of prion propagation, as the species barrier can be reconstituted solely from recombinant prion proteins (Chien et al. 2003; Glover et al. 1997; Santoso et al. 2000). For example, both *S. cerevisiae*- and *C. albicans*-derived prion domains form amyloid fibers in vitro after characteristic lag times; addition of preformed fibers of *S. cerevisiae* Sup35p prion domains efficiently seeds polymerization of *S. cerevisiae* Sup35p prion domains but not of domains derived from *C. albicans* and vice versa. Even when present together in the same reaction, these two species of prion domains form homopolymeric fibers (Santoso et al. 2000). Specificity seems to be a common feature of amyloids (including those of noninfectious proteins) and can be explained by a requirement for conformational compatibility between amyloid fibril ends and soluble monomers during growth (Chien et al. 2004; O'Nuallain et al. 2004). Nevertheless, this does not preclude a role for host factors in modulating the host specificity of certain prions.

Like mammalian prions (Prusiner 1998) and other yeast prions (Bradley et al. 2002; Schlumpberger et al. 2001), [*PSI*$^+$] exhibits a range of heritable phenotypic strain variants (Derkatch et al. 1996), which are linked to differences in the conformation of the infectious prion protein. [*PSI*$^+$] strain variants differ in mitotic stability (Derkatch et al. 1996), in their interaction with cellular chaperone machinery (Kushnirov et al. 2000b), and in the solubility and activity of Sup35p protein (Derkatch et al. 1996; Zhou et al. 1999). Sup35p aggregates purified from different [*PSI*$^+$] strains also differ in their ability to seed polymerization of purified Sup35 in vitro (Uptain et al. 2001). In addition, strains can play a major role in determining specificity of prion transmission: [*PSI*$^+$] prion strains differ greatly in their ability to recruit various mutant forms of Sup35p (Chien et al. 2003; Chien and Weissman 2001).

The strain phenomenon is in fact intimately related to the alternative conformational states available to prion aggregates. For example, a chimeric prion domain containing the first 40 amino acids of *S. cerevisiae* SUP35 fused to the remainder of the *C. albicans* SUP35 prion domain can adopt at least two amyloid conforma-

tions, one that seeds *S. cerevisiae* protein and another that seeds *C. albicans* protein (Chien and Weissman 2001). Each conformation results in a phenotypically distinctive prion state that recapitulates the variation observed between naturally occurring prion strains (Chien et al. 2003). Moreover, the infection of yeast with recombinant Sup35p in distinct amyloid conformations generated in vitro leads to heritable differences in [*PSI*$^+$] prion strains (Tanaka et al. 2004; King and Diaz-Avalos 2004). These studies provide the first proof that prion strain difference can be "encoded" within the conformation of the infectious protein.

A synthesis of a wide range of experimental observations points to the following findings linking prion strains, species barriers, and the physical principles that govern protein misfolding to form amyloid aggregates (Chien et al. 2004).

1. Self-propagation of amyloid-like protein aggregates underlies prion growth and specificity.
2. A single protein can often misfold into multiple different amyloid conformations (Figure 35.2).
3. The phenotypic consequences resulting from an aggregated protein are highly dependent on the specific amyloid conformation.
4. The particular amyloid conformation that a protein adopts determines the specificity of growth.
5. Changes in protein sequence can modulate the spectrum of favored amyloid conformations.

Based on these observations, a model emerges in which prion strains and transmission barriers are in large part two different manifestations of the same phenomenon: the ability of a protein to misfold into multiple amyloid conformations (Figure 35.2). These conformations determine both the specificity of growth and the phenotypic consequences of harboring a prion. Changes in sequence in turn alter the range of preferred amyloid conformations, thereby modulating transmission barriers and strain phenotypes. The ability of mutations to alter the conformation and thus the specificity of the prion forms preferred by a given protein helps to explain the ubiquitous presence of species barriers.

35.4 Prediction and Identification of Novel Prion Elements

[*URE3*] and [*PSI*$^+$] (but not [Het-s] or the mammalian prions) are examples of a broader phenomenon of glutamine- and asparagine-rich (Gln/Asn-rich) protein aggregation of the kind implicated in human polyGln expansion disorders such as Huntington's disease (Cummings and Zoghbi 2000). Ure2p and the various Sup35 homologues from budding yeast all contain prion domains with a very high glutamine and asparagine (Q/N) content. High Q/N content is also a conserved feature in Ure2p, but whether Ure2p proteins from yeasts other than *S. cerevisiae* can support prion inheritance remains an open question (Baudin-Baillieu

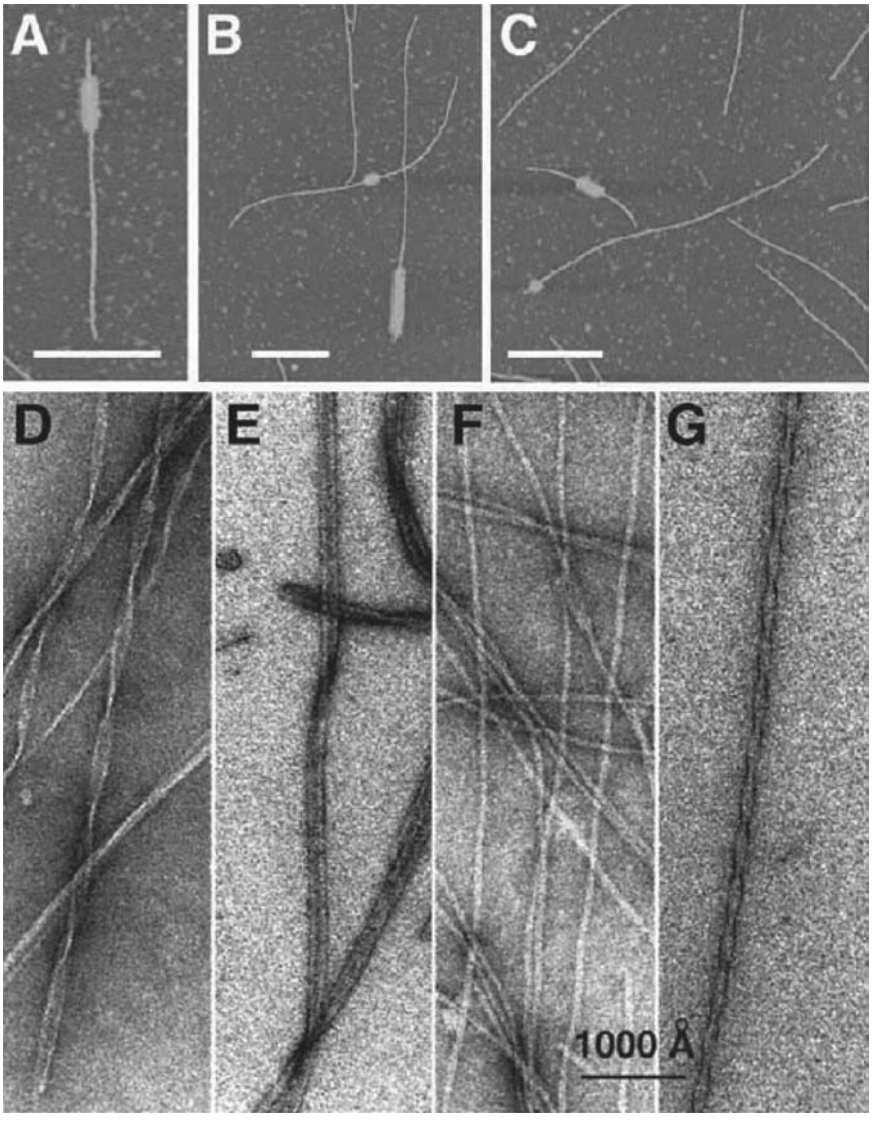

Fig. 35.2. Amyloid fibers adopt multiple distinguishable structures (adapted from Chien et al. 2004). (A–C). Amyloid fibers formed spontaneously by Sup35p vary in their growth patterns, including overall rate and polarity of growth (from DePace and Weissman 2002). Four kinetic fiber types visualized by an AFM single-fiber growth assay are shown. The original seed is labeled with antibody and therefore is wider than the new growth extending from its ends. Note the presence of long and short symmetric and asymmetric fibers. Scale bar is 500 nm. Polarity in growth has also been seen by EM (Inoue et al. 2001) and fluorescence-based assays (Scheibel et al. 2001). (D–G) Negative stain EM of amyloid fibers formed spontaneously by the SH3 domain from PIP_3 kinase illustrates that they vary in the number of protofilaments and helical pitch. Scale bar is 100 nm.

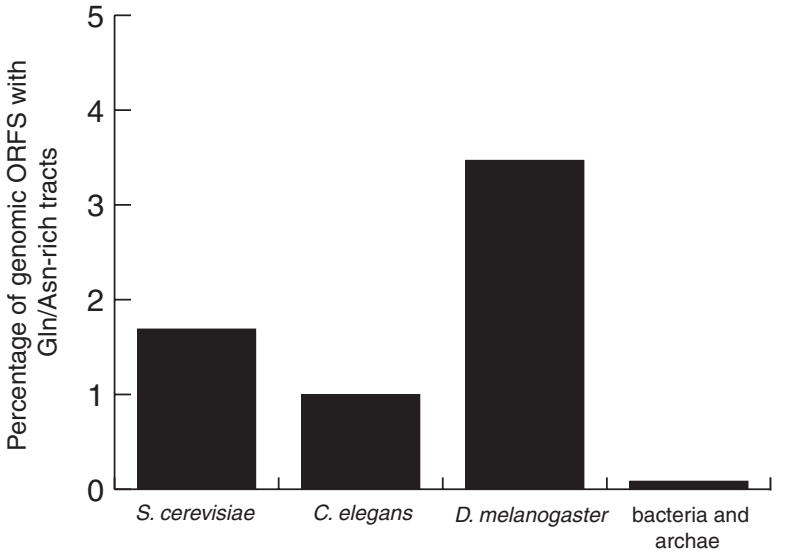

Fig. 35.3. Gln/Asn-rich tracts are abundant in certain eukaryotic proteomes (adapted from Michelitsch and Weissman 2000). The complete genomic sequences of three eukaryotes as well as of 20 bacteria and archaea were searched for Gln/Asn-rich tracts, defined as regions of open reading frames (ORFs) with 30 or more Gln and Asn residues per 80-residue window. The frequency of such sequences in the eukaryotes is much greater than expected if amino acid composition were due to chance. Interestingly, the recently sequenced human genome has a lower abundance (~0.3%) of predicted Gln/Asn-rich tracts than do other metazoans.

et al. 2003; Edskes and Wickner 2002). Moreover, mutational studies on Sup35 have established that this high glutamine/asparagine content plays a critical role in mediating the formation of amyloid aggregates (DePace et al. 1998). The structural basis of Q/N-rich aggregation has been suggested to involve formation of "polar zippers" in which the β-sheets are stabilized by a network of hydrogen bonds involving the glutamine and asparagine side chains (Perutz et al. 1994).

A surprisingly large number of Q/N-rich sequences reminiscent of the prion domains of Ure2p and Sup35p are found in many eukaryotic genomes, including those of *S. cerevisiae*, *C. elegans*, and *D. melanogaster* (Figure 35.3) (Harrison and Gerstein 2003; Michelitsch and Weissman 2000). Efforts to test prion formation by these proteins have largely focused on yeast because of the ease of manipulating this organism (Santoso et al. 2000; Si et al. 2003b; Sondheimer and Lindquist 2000). As it is difficult to anticipate the prion-associated phenotypes for a given protein, such studies have typically started by fusing putative prion domains to reporter proteins whose activity can be readily monitored.

Using this "artificial prion" method, two previously uncharacterized proteins (New1p and Rnq1p) were found to contain prion domains. A fusion of the first 153 residues of New1p and the translation domain of Sup35p could interconvert between two states, termed [nu^-] and [NU^+], which respectively resulted from sol-

uble and aggregated forms of the reporter protein (Santoso et al. 2000). Similarly, a Sup35p fusion with the carboxy-terminal portion of Rnq1p could reversibly form an aggregated state (Sondheimer and Lindquist 2000). The full-length Rnq1p also formed a genuine endogenous prion in a number of wild-type yeast strains.

Another prion phenomenon was described in yeast some years earlier, although initial evidence was strictly genetic. Derkatch et al. (1997) uncovered a cryptic epigenetic state called [*PIN*$^+$] (PSI inducibility) that influenced the cell's susceptibility to the de novo induction of [*PSI*$^+$]; only strains that possessed the [*PIN*$^+$] trait could readily convert to [*PSI*$^+$] upon overexpression of Sup35p. [*PIN*$^+$] had all the hallmarks of a prion, including cytoplasmic inheritance, reversible curing, and dependence on cellular chaperones (Derkatch et al. 1997, 2000). Fortuitously, the protein responsible for the naturally occurring [*PIN*$^+$] state turned out to be Rnq1p (Derkatch et al. 2001; Osherovich and Weissman 2001). However, several other proteins containing Q/N-rich domains were also found to confer a PIN phenotype when overexpressed in a manner that correlated with the aggregation of the overexpressed protein (Derkatch et al. 2001; Osherovich and Weissman 2001). Whereas heterologous Q/N-rich aggregates have a stimulatory effect on de novo prion induction and the aggregation of polyglutamine proteins, in another context such aggregates can interfere with prion inheritance (Bradley and Liebman 2003). The mechanism of this cross-interaction between different prions remains a mystery.

A recent study (Si et al. 2003b) suggests that prion-like aggregation may play an important role in the normal (non-pathological) biology of metazoans including man. Si et al. identified a neuronal member of the cytoplasmic polyadenylation element-binding protein (CPEB) family that has an amino-terminal extension that resembles yeast prion proteins in its Q/N content. When fused to a reporter protein in yeast, this Gln-rich region displayed certain features of an epigenetically heritable state, including interconversion between soluble and aggregated forms. The full-length protein underwent similar interconversion, but it was the prion-like form that was most active in stimulating translation of CPEB-regulated mRNA. These authors suggest that conversion of CPEB to a prion-like state in stimulated synapses helps to maintain long-term synaptic changes associated with memory storage (Si et al. 2003a). It will thus be important to explore the prion-like properties of CPEB in its natural context.

35.5 Requirements for Prion Inheritance beyond Amyloid-mediated Growth

Although a broad range of unrelated proteins can form amyloid fibrils (Dobson 2001), very few such aggregates are infectious and/or heritable prions. The distinction between prions and more common amyloids appears to lie in the way in which they interact with cellular factors. These interactions involve features of the prion distinct from those required for amyloid formation. The complete prion replication cycle requires the periodic alternation of growth, division, and transmission (Tuite and Cox 2003) (Figure 35.4a). While the self-seeding nature of amyloids

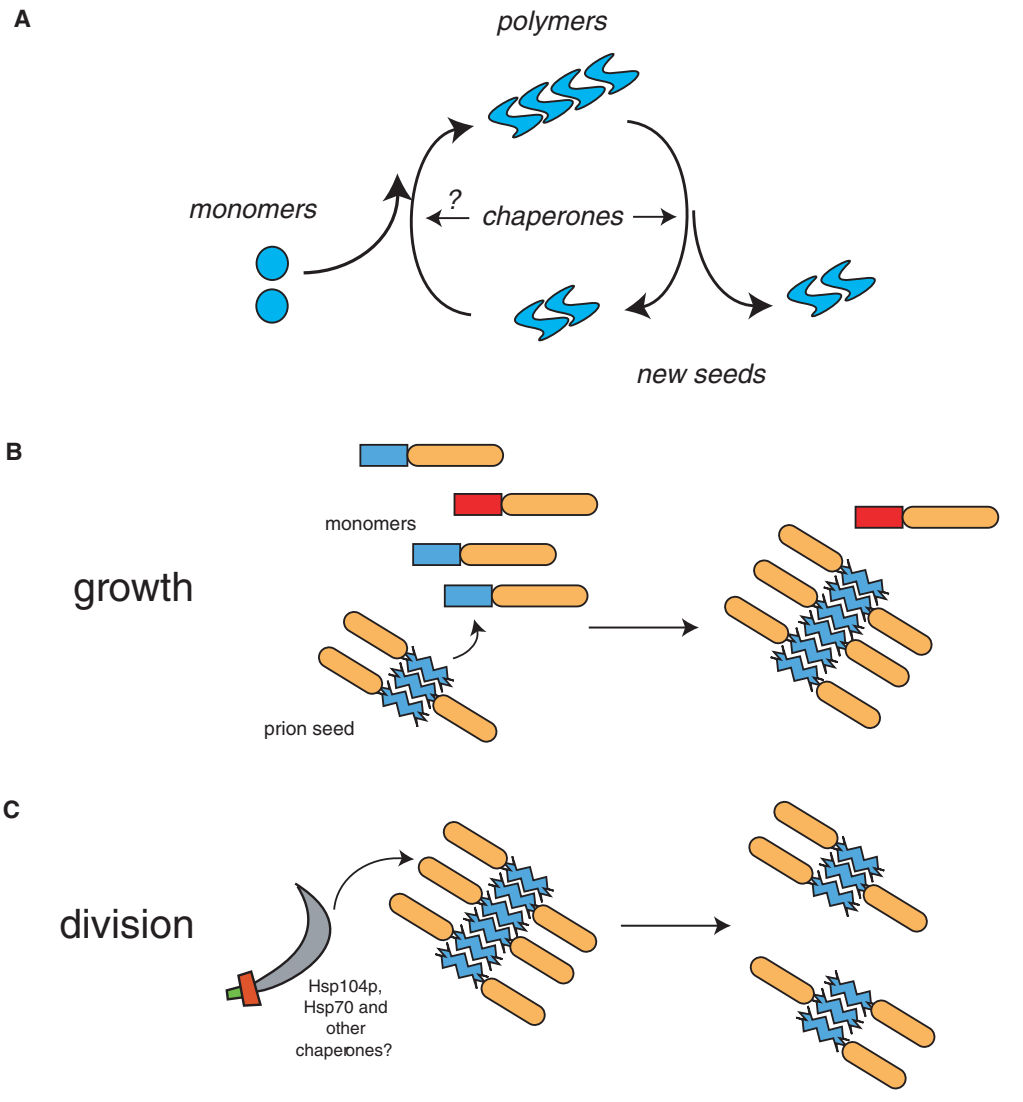

Fig. 35.4. Model for yeast prion replication (adapted from Osherovich et al. 2004). (A) A general schematic of the prion replication cycle. Monomer addition to polymer ends occurs spontaneously in vitro but may involve the action of chaperones in vivo. New seeds, consisting of small polymers, are generated by the chaperone-mediated severing of large polymers (see Kushnirov and Ter-Avanesyan 1998). (B) During prion growth, polymers seed the incorporation of monomers through interactions between Q/N-rich aggregation sequences (blue). Proteins with non-cognate aggregation sequences (red) are excluded. (C) The division phase of prion replication requires replication elements (orange), such as the oligopeptide repeats of Sup35p and New1p. These may serve as binding sites for chaperones such as the Hsp104p/Hsp70/Hsp40 complex (scimitar) or may alter the structure of the polymer in a way that facilitates chaperone action. New seeds are then partitioned between mother and daughter cells.

accounts for the growth phase of the prion replication cycle, in yeast prion division, and perhaps transmission, is dependent on the cell's chaperone machinery (Osherovich and Weissman 2002). A range of studies has now begun to define the sequence elements within the prion protein and the chaperone requirements for the replication and transmission steps.

Mutational and functional analyses argue that the Sup35p and New1p prion domains have a largely modular structure (Osherovich et al. 2004). In both proteins, a Q/N-rich tract mediates sequence-specific aggregation (Balbirnie et al. 2001; Hara et al. 2003; Osherovich et al. 2004). These Q/N-rich tracts may form the core of the amyloid structure, thereby allowing the self-specific growth of the prion state (Figure 35.4B). In contrast, the replication and transmission (Figure 35.4C) of both Sup35p and New1p prions are mediated by a stretch of oligopeptide repeats with the consensus sequence (P/Q)QGGYQ(Q/S)YN (Osherovich et al. 2004), which loosely resembles a repeating sequence (PHGGGWGQ) in mammalian PrP (Liu and Lindquist 1999; Parham et al. 2001).

The sequence features required for prion replication and transmission in other prion-forming proteins remain poorly understood. For example, Ure2p and Rnq1p lack obvious oligopeptide repeats, although a region (residues 218–405) of the Rnq1p prion domain has an amino acid content reminiscent of the oligopeptide repeat sequence (i.e., numerous Q, N, S, Y, and G residues) (Resende et al. 2003). Although mammalian PrP contains a sequence resembling the oligopeptide repeat that can functionally replace one of the Sup35p repeats (Parham et al. 2001), it is unclear what role this sequence plays in the replication of the PrP^{Sc} state. A better understanding of the sequence requirements for prion replication and transmission could greatly aid in the identification of novel prion elements. Of the 100 or so Q/N-rich domains encoded in the *S. cerevisiae* genome, only two other proteins (YDR210W and YBR016W) have clearly recognizable oligopeptide repeats as well as Q/N-rich regions. YBR016W forms aggregates when overexpressed (Sondheimer et al. 2001), but it is not known whether either protein can maintain a heritable aggregated state.

Based on this modular model for prion domains, we have designed two novel artificial prions by fusing the replication element of Sup35p to aggregation sequences from other proteins, including pathogenically expanded polyglutamine (Osherovich et al. 2004). The first such artificial prion, termed $[F^+]$, consists of the aggregation sequence of New1p and the oligopeptide repeat of Sup35p. Despite a sequence derived primarily from Sup35p, the F chimera showed induction and growth properties similar to those of New1p, consistent with the notion that the Q/N-rich region forms the amyloid core of the prion and dictates self-specificity. A second prion, termed $[Q^+]$, consists of an aggregation-prone sequence derived from pathogenically expanded glutamine fused to the Sup35 oligopeptide repeat sequence. The $[Q^+]$ prion demonstrates that it is possible to turn a generic aggregating sequence into a heritable prion element. Such artificial prions could potentially serve as models for aggregate-chaperone interactions in metazoans as well as a genetic system for the high-throughput screening of modulators of human aggregation diseases (Li and Lindquist 2000; Meriin et al. 2003; Muchowski et al. 2000).

35.6
Chaperones and Prion Replication

The division of prion seeds into heritable units depends on *trans*-acting cellular chaperones, among which HSP104 plays a central role (Chernoff et al. 1995). Genetic and pharmacological analysis places Hsp104p in the division phase of prion replication (Eaglestone et al. 2000; Jung and Masison 2001), consistent with its biochemical activity as a general disaggregase capable of untangling large complexes of misfolded proteins (Glover and Lindquist 1998). Hsp104p is not required for the de novo formation of prion seeds in vivo or of amyloid fibrils in vitro (Glover et al. 1997), although it may contribute to prion growth in vitro (Shorter and Lindquist, 2004). However, diminished HSP104 activity through mutation, deletion, or pharmacological inhibition by guanidinium chloride (GdmCl) results in the arrest of prion replication, evident through the appearance of [*psi*$^-$] colonies as [*PSI*$^+$] cells continue to divide without replenishing their prion titer (Eaglestone et al. 2000; Tuite et al. 1981). Consistent with this model, HSP104 activity is needed to maintain [*PSI*$^+$] only so long as the cells are dividing (Eaglestone et al. 2000). A mutation within the oligopeptide repeats of Sup35p mimics the effect of Hsp104p inhibition (Osherovich et al. 2004), suggesting that Sup35p and Hsp104p may interact through this region, although perhaps indirectly.

A mechanistic understanding of how Hsp104p interacts with amyloid aggregates to promote prion inheritance is now the major challenge to workers in this field. A recent report (Shorter and Lindquist, 2004) demonstrates that purified recombinant Hsp104p can act on Sup35p amyloids to facilitate prion replication. However, evidence suggests that Hsp104p does not act alone in the disaggregation of misfolded proteins and the replication of prion aggregates. Rather, it is likely that Hsp104p works together with Hsp70 and Hsp40 cofactors to recognize prion proteins as substrates and remodel them in a way that generates new prion seeds and/or promotes prion transmission (Chernoff et al. 1999; Jones and Masison 2003; Jung et al. 2000; Moriyama et al. 2000a; Newnam et al. 1999; Sondheimer et al. 2001).

Hsp70s are ubiquitous ATPases involved in the folding and localization of proteins during translation and after protein folding stresses such as heat shock (Bukau and Horwich 1998; Hartl and Hayer-Hartl 2002). In yeast, two cytosolic Hsp70s (SSB1 and SSB2) facilitate co-translational protein folding, while four highly homologous Hsp70s (SSA1–SSA4) act independently of the ribosome to maintain protein solubility under stressful conditions (Craig et al. 1995). All Hsp70s require the action of co-chaperones, which modulate the cycle of ATP binding and hydrolysis needed for substrate recognition and release. These include the DnaJ/Hsp40 proteins, marked by the presence of a J-domain, as well as other structurally distinct co-chaperone families, such the tetratricopeptide repeat (TPR) ''clamp'' proteins and so-called Bag domain proteins. The yeast genome encodes a large number of known and putative co-chaperones, many of which are involved in the subcellular localization of Hsp70 for specific tasks (Young et al. 2003).

Biochemical and genetic evidence points to a concerted role for Hsp104p and

the Hsp70/co-chaperone system in prion replication. In vitro refolding of model substrates such as heat-denatured luciferase requires the joint action of Hsp104p with Ssa1p and Ydj1p, a cytoplasmic Hsp40 protein (Glover et al. 1997). In vivo, Hsp104p is needed for the inheritance of all naturally occurring yeast prions (Chernoff et al. 1999; Moriyama et al. 2000b; Sondheimer and Lindquist 2000), suggesting that it performs a common biochemical activity needed for prion maintenance. Whereas Hsp70s and Hsp40 co-chaperones have also been implicated in prion maintenance, their effects are highly specific to each prion protein (summarized in Osherovich and Weissman 2002). At least one Hsp70 or Hsp40 is required for the stable inheritance of each type of prion, and many prions (both natural and artificial) are sensitive to the dosage of various Hsp70 and Hsp40 genes. For example, the inheritance of [RNQ^+] depends on the interaction of Rnq1p with a region of the Hsp40 protein Sis1p (Lopez et al. 2003; Sondheimer et al. 2001; Yang Fan et al. 2003), while two Hsp70s (Ssa1p and Ssa2p) are involved in the maintenance of [PSI^+] and [*URE3*], respectively (Jung et al. 2000; Roberts et al. 2004).

The general role of Hsp104p in prion maintenance compared with the highly specific genetic interaction of Hsp70 and co-chaperones with prions suggests that cytoplasmic Hsp70 and its co-chaperones act as coupling factors to recruit Hsp104p to prion aggregates. Electron microscopy of Sup35p yeast prion amyloids has shown that fibrils are laterally decorated with non-amyloidogenic portions of the protein, which protrude at regular intervals from the amyloid core like bristles from a bottle brush (Glover et al. 1997). The specific features of these potentially nonnative protein surfaces could attract Hsp70 and co-chaperones, which recognize and attempt to refold these proteins by working together with the more general disaggregation activity of Hsp104p. An appealing model for the chaperone-dependent replication of prion particles involves the liberation of partially solubilized but still amyloidogenic "seeds" from large prion aggregates by the combined action of Hsp104p, Hsp70, and Hsp40 co-chaperones.

35.7 The Structure of Prion Particles

Two recent studies have helped to better define the genetic and physical characteristics of yeast prions in vivo. Through the clever manipulation of chaperone activity, Cox and coworkers have devised a means of counting the number of heritable prion units or propagons in [PSI^+] cells and have used this method to probe the temporal and spatial regulation of prion replication (Cox et al. 2003). Two observations from this study point to unexpected interplay between the prion replication cycle and the broader cell division cycle. First, propagons are replicated discontinuously, with a sharp increase during the G2 phase, perhaps because of variation in chaperone activity during the cell cycle. Second, the partitioning of propagons displays a strong maternal bias, suggesting that the physical segregation of propagons that is proposed to take place after seed division may require an active transport process, perhaps involving interactions with cytoskeletal components.

What are propagons physically? From the number of genetically defined propagons and the number of Sup35p molecules present in typical cells, it can been estimated that propagons consist of 10–200 molecules of Sup35p (Cox et al. 2003). The minimum number of molecules needed to form a physically stable amyloid seed is unknown. However, it is unlikely that large amyloid fibrils of the kind observed in vitro in the absence of shearing activity can be acted upon by cellular chaperones; indeed, a mutant of Sup35p lacking much of the oligopeptide repeat region forms large, linear aggregates in vivo that can be visualized with GFP staining and that correlate with the loss of [*PSI*$^+$] (Osherovich, unpublished observations). A hint at the macromolecular nature of the propagon comes from a recent study in which Sup35p from [*psi*$^-$] and [*PSI*$^+$] strains could be distinguished using non-denaturing gel electrophoresis (Kryndushkin et al. 2003). Whereas Sup35p from [*psi*$^-$] migrates as a monomer, the material from [*PSI*$^+$] cells migrates as a broad smear between 700 and 4000 kDa. This large complex, termed a prion polymer by the authors, corresponds to 9–50 Sup35p monomers by molecular mass. As a number of proteins other than Sup35p have previously been found in association with prion aggregates, an estimate based solely on non-dentaturing gel migration may in fact overestimate the number of Sup35p molecules needed to make a minimal amyloid ''seed.'' Nonetheless, it is possible that heritable prion units (propagons) consist of bundles of coalesced amyloid polymers.

35.8
Prion-like Structures as Protein Interaction Modules

The sequence requirements for prion inheritance are now understood to be more stringent than simply high Q/N content. For this reason, despite the general propensity of Q/N-rich proteins to misfold into amyloid aggregates, very few of these are likely to adopt heritable prion states. Why, then, are there so many Q/N-rich sequences (Michelitsch and Weissman 2000)? One possibility is that Q/N-rich domains act as protein-protein interaction modules that organize stable multicomponent complexes in a manner that may be structurally similar to amyloid aggregates (Perutz et al. 2002). Two examples of amyloid formation in the context of normal biological processes have been reported recently (Berson et al. 2003; Chapman et al. 2002). Non-prion ''pseudo-amyloid'' complexes may feature discrete structures held together by the same cross-pleated β-sheet interactions found in prions, but with limited opportunities for growth.

Although this model is speculative in general, studies in yeast hint at a role for Q/N-rich proteins in organizing multicomponent complexes. Perhaps the best-studied example occurs at the interface of the actin cytoskeleton and the endocytic apparatus (Jeng and Welch 2001). Pan1p is an essential EH domain protein that, together with Sla1p and End3p, recruits and activates the Arp2/3 complex to the surface of nascent endocytic vesicles, generating the cortical actin structures needed for endocytosis (Duncan et al. 2001; Tang et al. 2000). The amino terminal

portion of Pan1p is extremely Q/N-rich and interacts with the comparably Q/N-rich carboxy-terminal region of Sla1p; this interaction is needed for the recruitment of the Arp2/3-activating C-terminus of Pan1p to clathrin-coated endocytic vesicles. Interestingly, the C-terminus of Sla1p can itself interact with the prion domain of Sup35p in a yeast two-hybrid assay (Bailleul et al. 1999), suggesting that this Q/N-rich domain can bind promiscuously to other Q/N-rich proteins. When overexpressed as a GFP fusion, the Q/N-rich portion of Pan1p forms visible aggregates similar to those of Sup35p (Osherovich and Weissman 2001). Unlike proper prions, these aggregates are not heritable and vanish after overexpression is stopped.

Another possible example comes from the study of the nonsense-mediated mRNA decay pathway (Gonzalez et al. 2001). Here, a complex of proteins coalesces into punctate structures termed P bodies that are the site of mRNA decapping and degradation (Sheth and Parker 2003). Several P body components, including Lsm4p and Dhh1p, have Q/N-rich regions, although whether these prion-like sequences are needed for P body formation or activity is unknown. However, Lsm4p had been identified as a PIN factor (Derkatch et al. 2001), forming [PSI^+]-promoting aggregates when overexpressed. Likewise, several Q/N-rich members of the SWI/SNF complex, which is involved in heterochromatin remodeling in yeast (Martens and Winston 2003), also came out of the screen for PIN factors.

The potential for Q/N-rich sequences to act as modular interaction domains may well explain their abundance in eukaryotic genomes. In turn, these relatively common Q/N-rich domains may have provided the raw material from which the true prions (those of Sup35p, Ure2p, and Rnq1p) arose. In this view, prions may be an accidental elaboration of a broader class of "pseudo-amyloid" protein complexes.

35.9 Experimental Protocols

35.9.1 Generation of Sup35 Amyloid Fibers in Vitro

Production of Sup35 Prion Domain (NM)

The prion domain of Sup35 is produced by overexpression in *E. coli* using a plasmid in which the T7 promoter drives expression of a gene encoding the NM domains (residues 1–254) or NM tagged with either three repeats of the intact hemagglutinin (HA) epitope (NM-HA_3) or a derivative (NM-$HA^*{}_3$) containing three conservative point mutations that prevent antibody recognition (the plasmids are termed, pAED4-NM, pAED4-NM-HA_3, and pAED4-NM-$HA_3{}^*$, respectively). In all cases the NM domains also contain a histidine tag (six to seven histidines long) at the C-terminus to facilitate purification. *E. coli* BL21(DE3) freshly transformed with the appropriate plasmid is grown to $OD_{650} = 0.5$ in LB broth supplemented with 100 μg mL^{-1} carbenicillin. Following 3 h induction, cell pellets from 1–2 L of growth are lysed in 30 mL of buffer A (25 mM Tris pH 7.8, 300 mM NaCl, 8 M urea). Subsequent to centrifugation at 25 000 *g* (20 min), the supernatant is filtered

by a 0.22-μm filter (Millipore) and applied to a 20-mL Ni-NTA agarose (Qiagen) column. The column is washed with five column volumes of buffer A and eluted with a pH gradient (pH 7.8 to pH 4.5) in the same buffer without NaCl. Pooled fractions are applied to a 6-mL Resource S column (Pharmacia) equilibrated in 50 mM MES pH 6.0, 8 M urea, and eluted with 0–1 M NaCl gradient in the same buffer. Pure NM is concentrated using a microcon-10 (Amicon), filtered by microcon-100 (Amicon), yielding a final concentration of at least 500 μM, aliquoted, and stored at −80 °C. Protein concentration is determined by UV absorption at 275 nm using an extinction coefficient of 24.2 mM^{-1} cm^{-1}.

Preparation of NM Fibers

To initiate amyloid formation, concentrated NM is diluted at least 100-fold into buffer B (5 mM potassium phosphate, 150 mM NaCl) in 2-mL microcentrifuge tubes at room temperature to a final concentration of 2.5 μM. The solution is subjected to constant rotation (7.5 rpm) using a RKVS Rotamix (ATR, Inc.) for at least 2 h. The extent of amyloid formation can be monitored by thioflavin T, a dye that specifically binds amyloid fibers, leading to a large increase in fluorescence. This is accomplished by removing an aliquot of the polymerization reaction, adding an equal volume of 25 μM thioflavin T (pH 8.5 in 50 mM glycine), and monitoring fluorescence using an excitation wavelength of 442 nm and an emission wavelength of 483 nm. In order to obtain consistent size distributions easily visualized by AFM, it is important to generate new NM amyloid seeds for each AFM elongation reaction. To generate short fibers convenient for AFM measurements, prior to use, fibers are sheared by pulling through a 25-gauge needle 10 times, resulting in seeds that vary in length between 50 and 500 nm.

35.9.2

Thioflavin T–based Amyloid Seeding Efficacy Assay (Adapted from Chien et al. 2003)

Conversion of a soluble protein to an amyloid form is typically a multi-step process involving de novo amyloid seed formation, breakage of preexisting seed to generate new seed, and growth of soluble monomers onto the ends of existing seeds. Here we describe an assay that makes it possible to specifically measure the ability of a given preparation of preformed amyloid seeds to polymerize soluble protein. This is accomplished by measuring the initial rate of amyloid growth upon addition of preformed amyloid seeds to soluble protein. By examining initial rates of polymerization, complications due to the breakage of preexisting fibers or to the de novo formation of amyloid seeds can be minimized. Differences in seeding efficacy measured in this assay reflect differences in elongation rates of fibers and/or differences in the number of fiber ends. This assay is performed in a 96-well microplate using a microplate spectrofluorometer, so that many samples can be analyzed in parallel. It is a continuous assay and thus samples need be prepared only once and then monitored over time by the instrument. To control for the possible effects of thioflavin T on amyloid formation, it is important to confirm the results by an alternative means (e.g., a discontinuous assay in which thioflavin T is added after polymerization).

Preparation of Samples

In a microplate well, mix 100 μL of 25-μM thioflavin T (pH 8.5 in 50 mM glycine) and 90 μL of the soluble protein whose polymerization you wish to monitor at 2.22 times the desired final concentration (we usually use 2.5 μM final soluble NM). Seed should be added immediately before reading in the microplate fluorometer because polymerization will begin as soon as the seed is added. To each well add 10 μL of the desired seed preparation. Insert the plate into the microplate spectrophotometer and read every 30 s for 2 h. Fluorescence of thioflavin T is measured by excitation at 442 nm and emission at 483 nm.

Analysis of Seeding Efficacy

The initial rate of amyloid formation is determined by measuring the rate of increase in thioflavin T fluorescence at early time points (thioflavin T binds amyloid fibers, leading to a large increase in fluorescence). The initial rate is determined by taking the slope of the initial linear phase of the reaction (often the first 10 or 20 min), before the rate starts to decline as soluble protein starts to be depleted. Care should be taken in comparing rates from experiments performed on different days since the age or degree of exposure to light can affect the fluorescence of a thioflavin T solution. Additionally, care should be taken in comparing rates of polymerization from seeds made from different proteins, since fibers of different proteins may stimulate fluorescence of thioflavin T to varying degrees.

35.9.3 AFM-based Single-fiber Growth Assay

The following protocols describe a nanometer-resolution single-fiber growth assay (DePace and Weissman 2002) based on two variants of the Sup35 prion domain (NM) that can be differentially labeled with antibodies and distinguished by atomic force microscopy (AFM). The two Sup35 variants used in our assay consist of the N and M domains (residues 1–254) tagged with either three repeats of the intact hemagglutinin (HA) epitope (NM-HA_3) or a derivative (NM-HA^*_3) containing three conservative point mutations that prevent antibody recognition. Because C-terminal fusions do not interfere with prion activity, these epitope tags were introduced at the C-terminus, followed by a six-histidine tag to facilitate purification. The strategy of this assay is to produce short fibers of one variant and to use these to seed polymerization of the other variant in solution for a defined period of time. The elongation reactions are then rapidly quenched (10–20 s) by deposition onto freshly cleaved mica, and unpolymerized monomer is removed by washing. Fibers are subsequently labeled by incubation with an HA antibody directly on the mica. The fibers are then visualized by AFM, which can readily distinguish regions of the fibers that are bound by antibody from those that are not, allowing measurement of the growth of new NM monomers onto preformed amyloid seed (Figure 35.5). While the assay described below has been optimized for the analysis of Sup35 fibers, in principle it should be straightforward to use a similar method to monitor the growth of any amyloid fiber the can be epitope-labeled.

The assay has the following desirable properties. First, because the antibody la-

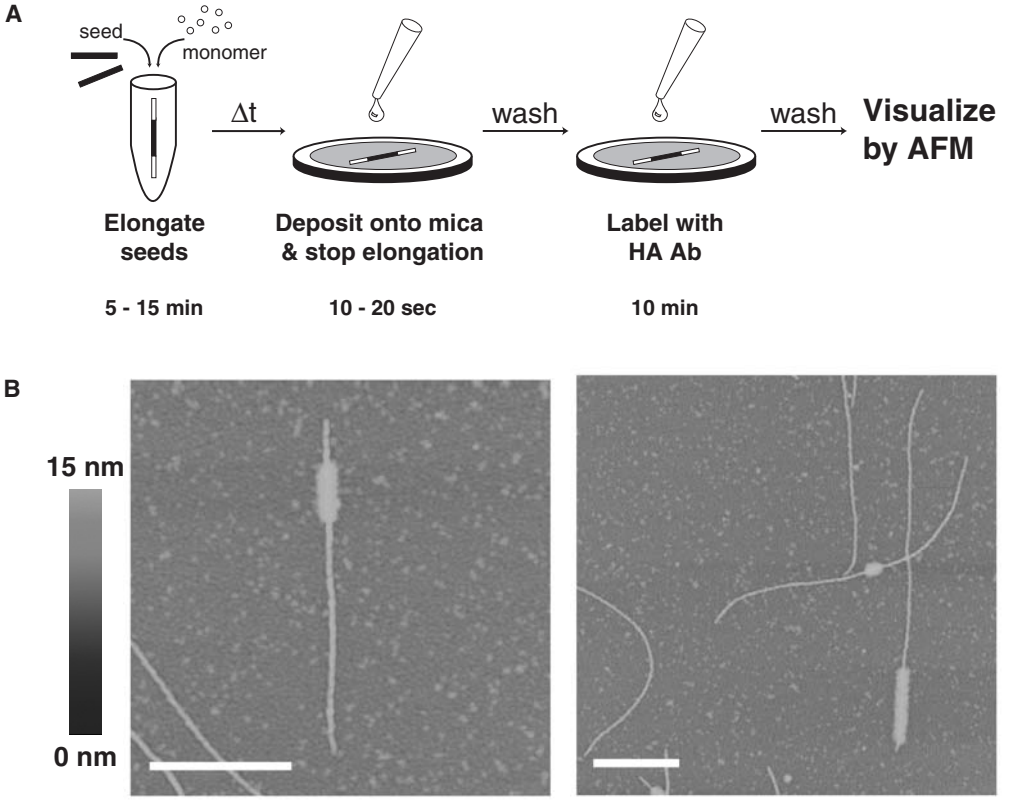

Fig. 35.5. Visualization of growth from single Sup35-NM fibers. (A) Schematic representation of the single-fiber elongation assay protocol. (B) Representative images of NM-HA_3 seeds elongated with NM-HA^*_3 monomer. Note the presence of both long and short symmetric and asymmetric fibers.

beling is dense and compact and provides a well-defined boundary between the seeds, new growth is unambiguously distinguishable from the seed. Second, elongation is measured in solution, avoiding complications arising from assembling fibers directly on a substrate, which can strongly alter the spectrum of fibrillar species observed. Third, the elongation reaction is rapidly quenched to allow precise time measurements. Fourth, the labeling step takes place after the reaction has been quenched, which avoids possible complications due to steric interference from the label. Finally, the assay is simple and rapid. Multiple samples can prepared in parallel and then can be stored indefinitely prior to analysis by AFM, and hundreds of fibers can be measured in a day.

Preparing Samples for Single-round Growth Assays

For visualization of growth from single fibers composed of NM-HA_3, seeds are elongated by incubation with 2.5 μM monomeric NM-HA_3^* in buffer B; these re-

actions are not rotated to avoid shearing forces. At the appropriate time point 20 μL of the elongation reaction is removed and deposited onto freshly cleaved mica. The reaction is allowed to incubate on the mica for 30 s, and then 200 μL of water is added to the disc and immediately aspirated away. This wash step is repeated once. Twenty microliters of FAB-fragmented 16B12 (Babco) diluted to 20 ng μL^{-1} in buffer B is added directly to the mica surface. Antibody is incubated on the mica for 10 min and then washed twice with 200 μL of water as above. Samples are allowed to air dry for at least 1 h before imaging. To avoid shearing during all manipulations, wide-bore pipette tips are used; 200-μL yellow tips are clipped, removing 2 cm from the end to create an opening 3 mm in diameter.

Preparing Fibers for Two-round Growth Assays

In the first reaction, NM-HA^*_3 seeds, generated as described above, are used at 25% (v/v) to seed 2.5 μM NM-HA_3 monomer. This reaction is allowed to proceed for 7.5 min and then is diluted 1:10 into a new polymerization reaction containing 2.5 μM monomeric NM-HA^*_3. The second reaction is allowed to proceed for 7.5 min before it is deposited directly onto mica (in some cases it is helpful to dilute the reactions 1:2 or 1:5 in polymerization buffer before deposition). The remainder of the sample preparation proceeds as described above. High seed concentration (25% v/v) is used in the initial polymerization reaction to allow for a convenient fiber concentration following dilution into the second elongation reaction. Additionally, higher seed concentrations help to deplete NM-HA_3 monomer, which would otherwise interfere with visualization of growth in the second round.

Imaging Fiber Growth by Atomic Force Microscopy

We collect our images using a Digital Instruments MultiMode AFM, equipped with a Nanoscope IIIa controller. Tapping mode is employed with all samples; either Digital Instrument's TESP or Micromasch's non-contact NSC15 tips are used. To measure growth from individual seeds, 25-μm^2 scans are taken. To measure fiber height, 1.0-μm^2 scans of representative fibers are taken using the same TESP tip.

Image Analysis/Measurement of Fiber Dimensions

Fiber lengths are determined using the point-and-click measurement tool available in the Nanoscope software. When fibers are curved, a series of lines is used to trace the fiber axis, and all individual line segments are added. Height is determined using the section tool of the Nanoscope software.

35.9.4

Prion Infection Protocol (Adapted from Tanaka et al. 2004)

Preparation of Infectious Material From Pure Protein or Yeast Extracts

Amyloid fibers of NM are formed as described above. Fibers are collected by centrifugation at 20 000 *g* for 20 min, resuspended with buffer B, and sonicated (10 s 20% power on a Sonic Dismembrator Model 500 [Fisher Scientific] equipped with

a micro-tip probe). The final concentration of amyloid fiber in infection experiments is typically 2.5 μM calculated in terms of Sup35 monomers. For preparation of yeast extracts containing prions, [*PSI*$^+$] yeast cells were spheroplasted with lyticase and sonicated. Concentration of total protein in the yeast extracts was measured by Bradford assay (Pierce). For infections involving extracts, the final concentration of total protein of the crude yeast extract is 200 μg mL^{-1}.

Prion Infection

[*psi*$^-$] yeast strains (W303 [*ade1-14*, *his3-11,15*, *leu2-3*, *trp1-1*, *ura3-1*] or 74D-694 [MATa *ade1-14 his3 leu2 trp1 ura3* [*PIN*$^+$] [Chernoff et al. 1995]) are grown in YEPD media to an OD_{600} of 0.5 and successively washed with sterile H_2O, 1 M sorbitol, and SCE-buffer (1 M sorbitol, 10 mM EDTA, 10 mM DTT, 100 mM citrate, pH 5.8). Cells are spheroplasted with lyticase (∼250 μg for yeast cells of 50 mL YEPD) in SCE buffer at 30 °C for 30 min (see below for description of lyticase preparation). Spheroplasts are washed with 1 M sorbitol and STC buffer (1 M sorbitol, 10 mM $CaCl_2$, 10 mM Tris, pH 7.5). Pelleted cells are resuspended in STC buffer and mixed with sonicated amyloid fibers, *URA3* marked plasmid (pRS316) (20 μg mL^{-1}), and salmon sperm DNA (100 μg mL^{-1}). Fusion is induced by addition of nine volumes of PEG buffer (20% [w/v] PEG 8000, 10 mM $CaCl_2$, 10 mM Tris, pH 7.5) for 30 min. Cells are centrifuged, resuspended in SOS buffer (1 M sorbitol, 7 mM $CaCl_2$, 0.25% yeast extract, 0.5% bacto-peptone), incubated at 30 °C for 30 min, and plated on synthetic media lacking uracil overlaid with top agar (2.5% agar).

Identification of [*PSI*$^+$]-infected Yeast

Individual Ura+ colonies are re-streaked on 1/4 YEPD (2.5 g yeast extract, 5 g bacto-peptone, 20 g agar, 1 L H_2O plus 40 mL 50% filter-sterilized glucose added after autoclaving above solution). Strong [*PSI*$^+$] and [*psi*$^-$] strains are included as controls on all plates to aid in judging color phenotype. Plates are examined after 3–5 days of incubation at 30 °C. [*PSI*$^+$] colonies are confirmed by GdmCl curing: colonies are streaked onto YEPD plates supplemented with 3 mM GdmCl and re-streaked on 1/4YEPD to look for loss of [*PSI*$^+$].

35.9.5

Preparation of Lyticase

An *E coli*. bacterial plasmid that express periplasmically localized lyticase under control of T7 promoter (pUV5-lyticase; Scott and Schekman 1980) was transformed into *E coli*. BL21(DE3). A single colony was inoculated into 100 mL of LB media including 100 μg mL^{-1} ampicillin and cultured at 37 °C until OD_{600} reached ∼0.5. Twenty milliliters of the culture media was transferred to 1 L of LB media and cultured again at 37 °C at 200 rpm (Innova 4400, New Brunswick Scientific). Isopropyl-*β*-thiogalactoside (final concentration of 0.5 mM) was added when OD_{600} reached ∼0.5 to initiate protein expression. After 3 h, the culture media was centrifuged (5000 rpm) and the pellet was washed with distilled H_2O. Cells were resus-

pended in 20 mL of 25-mM Tris-HCl (pH 7.4), incubated at room temperature with gentle agitation for 30 min using a nutator, and centrifuged at 7500 rpm (Sorvall SS-34 Rotor, Du Pont Instruments) for 10 min. The pellet was resuspended in 20 mL of 5-mM $MgCl_2$, incubated at 4 °C for 30 min, and centrifuged at 15 000 rpm for 30 min (Sorvall SS-34 Rotor, Du Pont Instruments) to separate periplasmic components. This supernatant was dialyzed against 2 L of 50-mM sodium citrate buffer (pH 5.8) overnight and was stored at −80 °C. Concentration of lyticase was determined by the Bradford method, and ∼250 μg of lyticase was used to spheroplast pelleted yeast cells obtained from 50 mL of YEPD media ($OD_{600} = \sim 0.5$).

35.9.6

Protocol for Counting Heritable Prion Units (Adapted from Cox et al. 2003)

Principle

The replication of prion particles depends on the action of Hsp104p, a chaperone that can be inhibited by the small molecule GdmCl. To count the number of heritable prion particles (propagons) in [*PSI*$^+$] cells, we perform a pulsed shutoff of Hsp104p activity using GdmCl. The transient arrest of prion replication while cells continue to divide eventually dilutes the prion particles to one or fewer per cell. At this point, the prion replication arrest is lifted by the removal of GdmCl, and the cells are recovered in a medium that selects for [*PSI*$^+$] (SD-ade with a dash of YEPD to aid initial growth). Thus, the total number of [*PSI*$^+$] progeny of a single cell that has undergone this transient prion replication arrest reports on the number of propagons the cell harbored at the start of the experiment.

Materials

- YEPD + GdmCl agar plates (1% yeast extract, 1% peptone, 2% dextrose supplemented to 3 mM guanidine hydrochloride from a sterile 3-M stock)
- SD-ade + 5% YEPD agar plates (synthetic defined medium lacking adenine to which a 5% volume of YEPD liquid medium has been added prior to pouring)
- Yeast micromanipulator microscope such as Singer MSM system or Zeiss Axioskop 40 Tetrad system
- Low-powered stereo dissection microscope with a 10× objective and illuminated stage
- 1000 microliter micropipette tips, with ∼5 mm of tip trimmed away with a sterile razor blade

Procedure

Day 1: Inoculate a [*PSI*$^+$] culture into YEPD or appropriate selective medium and grow overnight until mid-logarithmic phase. It is important to use actively dividing cells.

Day 2: Spot 30 μL of the overnight culture onto a YEPD + GdmCl plate. Using

the micromanipulator, move >40 individual cells away from the spot onto a widely spaced grid. Be consistent in choosing the cell cycle stage of cells; propagon numbers can vary throughout the cell cycle. We prefer cells that are showing a hint of a bud (G1 phase). Incubate overnight at 30 °C.

Day 3: In the morning, check for colony formation by individual picked cells. It is vital to allow the cells to have doubled at least 10 times but not to have grown to such a size as to make picking the entire colony difficult. Ideally, proceed to the next step when microcolonies are ~0.5 mM in diameter, consisting of 2000–4000 cells. Note that not all cells with have grown and that there will be some heterogeneity in the colony size. Allow colonies to grow to an appropriate size by incubating for longer if necessary.

Pick the Colonies

1. When microcolonies are ready, aliquot 500 μL of sterile water into microcentrifuge tubes for each colony that you intend to pick.
2. Using the dissection microscope for magnification, punch out an entire colony using a trimmed micropipette tip. It is critical to encapsulate the entire colony in the pipette tip; practice until you get it down.
3. Resuspend the colony and the agar plug in a water aliquot and plate the entire volume onto an SD-Ade + 5% YEPD plate.
4. Repeat as necessary using fresh tips and tubes.
5. Incubate at 30 °C for 5–7 days, depending on the yeast strain used. W303-derived [PSI^+] strains grow more quickly (5 days) than 74D694 and other [PSI^+] strains.

Count [PSI^+] Colonies

After 5–7 days, you should see several thousand tiny red microcolonies that will be [psi^-] due to the effect of GdmCl. Interspersed among them will be [PSI^+] colonies that have grown past the microcolony stage as a result of their adenine prototrophy. Genuine [PSI^+] colonies will be pink and will turn red when re-streaked onto YEPD + GdmCl. There will also be a small number of Ade+ revertants that typically form larger colonies than [PSI^+] cells and do not turn red upon YEPD + GdmCl re-streaking. Wild-type [PSI^+] strains typically yield 50–200 [PSI^+] colonies, with a small number of "jackpot" cells yielding > 500 propagons (see Cox et al. 2003).

Acknowledgements

L.Z.O was supported by a Howard Hughes Medical Institute Predoctoral Fellowship and the Jane Coffin Childs Foundation. J.S.W. is funded through the Howard Hughes Medical Institute, the Packard Foundation, and the NIH. We thank Angela DePace, Sean Collins, Peter Chien and Motomasa Tanaka for contributing protocols. J.S.W. thanks Strai-Kin Lee for critical insights.

References

1 Aguzzi, A., and Haass, C. (2003). Games played by rogue proteins in prion disorders and Alzheimer's disease. *Science 302*, 814–818.

2 Bailleul, P. A., Newnam, G. P., Steenbergen, J. N., and Chernoff, Y. O. (1999). Genetic study of interactions between the cytoskeletal assembly protein sla1 and prion-forming domain of the release factor Sup35 (eRF3) in Saccharomyces cerevisiae. *Genetics 153*, 81–94.

3 Balbirnie, M., Grothe, R., and Eisenberg, D. S. (2001). An amyloid-forming peptide from the yeast prion Sup35 reveals a dehydrated beta-sheet structure for amyloid. *Proc Natl Acad Sci USA 98*, 2375–2380.

4 Baudin-Baillieu, A., Fernandez-Bellot, E., Reine, F., Coissac, E., and Cullin, C. (2003). Conservation of the prion properties of Ure2p through evolution. *Mol Biol Cell 14*, 3449–3458.

5 Baxa, U., Taylor, K. L., Wall, J. S., Simon, M. N., Cheng, N., Wickner, R. B., and Steven, A. C. (2003). Architecture of Ure2p prion filaments: the N-terminal domains form a central core fiber. *J Biol Chem 278*, 43717–43727.

6 Berson, J. F., Theos, A. C., Harper, D. C., Tenza, D., Raposo, G., and Marks, M. S. (2003). Proprotein convertase cleavage liberates a fibrillogenic fragment of a resident glycoprotein to initiate melanosome biogenesis. *J Cell Biol 161*, 521–533.

7 Bossers, A., Belt, P., Raymond, G. J., Caughey, B., de Vries, R., and Smits, M. A. (1997). Scrapie susceptibility-linked polymorphisms modulate the in vitro conversion of sheep prion protein to protease-resistant forms. *Proc Natl Acad Sci USA 94*, 4931–4936.

8 Bousset, L., Thomson, N. H., Radford, S. E., and Melki, R. (2002). The yeast prion Ure2p retains its native alpha-helical conformation upon assembly into protein fibrils in vitro. *EMBO J 21*, 2903–2911.

9 Bradley, M. E., Edskes, H. K., Hong, J. Y., Wickner, R. B., and Liebman, S. W. (2002). Interactions among prions and prion "strains" in yeast. *Proc Natl Acad Sci USA 99 Suppl 4*, 16392–16399.

10 Bradley, M. E., and Liebman, S. W. (2003). Destabilizing interactions among [PSI(+)] and [PIN(+)] yeast prion variants. *Genetics 165*, 1675–1685.

11 Bruce, M., Chree, A., McConnell, I., Foster, J., Pearson, G., and Fraser, H. (1994). Transmission of bovine spongiform encephalopathy and scrapie to mice: strain variation and the species barrier. *Philos Trans R Soc Lond B Biol Sci 343*, 405–411.

12 Bukau, B., and Horwich, A. L. (1998). The Hsp70 and Hsp60 chaperone machines. *Cell 92*, 351–366.

13 Chapman, M. R., Robinson, L. S., Pinkner, J. S., Roth, R., Heuser, J., Hammar, M., Normark, S., and Hultgren, S. J. (2002). Role of Escherichia coli curli operons in directing amyloid fiber formation. *Science 295*, 851–855.

14 Chernoff, Y. O., Galkin, A. P., Lewitin, E., Chernova, T. A., Newnam, G. P., and Belenkiy, S. M. (2000). Evolutionary conservation of prion-forming abilities of the yeast Sup35 protein. *Molecular Microbiology 35*, 865–876.

15 Chernoff, Y. O., Lindquist, S. L., Ono, B., Inge-Vechtomov, S. G., and Liebman, S. W. (1995). Role of the chaperone protein Hsp104 in propagation of the yeast prion-like factor [psi+]. *Science 268*, 880–884.

16 Chernoff, Y. O., Newnam, G. P., Kumar, J., Allen, K., and Zink, A. D. (1999). Evidence for a protein mutator in yeast: role of the Hsp70-related chaperone ssb in formation, stability, and toxicity of the [PSI] prion. *Molecular and Cellular Biology 19*, 8103–8112.

17 Chien, P., DePace, A. H., Collins, S. R., and Weissman, J. S. (2003).

Generation of prion transmission barriers by mutational control of amyloid conformations. *Nature 424*, 948–951.

18 Chien, P., and Weissman, J. S. (2001). Conformational diversity in a yeast prion dictates its seeding specificity. *Nature 410*, 223–227.

19 Chien, P., Weissman, J. S., and DePace, A. H. (2004). Emerging Principles of Conformation-based Prion Inheritance. *Annu Rev Biochem in press*.

20 Chiti, F., Webster, P., Taddei, N., Clark, A., Stefani, M., Ramponi, G., and Dobson, C. M. (1999). Designing conditions for in vitro formation of amyloid protofilaments and fibrils. *Proc Natl Acad Sci USA 96*, 3590–3594.

21 Collinge, J. (2001). Prion diseases of humans and animals: their causes and molecular basis. *Annu Rev Neurosci 24*, 519–550.

22 Coustou, V., Deleu, C., Saupe, S., and Begueret, J. (1997). The protein product of the het-s heterokaryon incompatibility gene of the fungus Podospora anserina behaves as a prion analog. *Proc Natl Acad Sci USA 94*, 9773–9778.

23 Cox, B. S. (1965). y, a cytoplasmic suppressor of super-suppressor in yeast. *Heredity 20*, 505–521.

24 Cox, B. S., Ness, F., and Tuite, M. F. (2003). Analysis of the Generation and Segregation of Propagons: Entities That Propagate the [PSI+] Prion in Yeast. *Genetics 165*, 23–33.

25 Craig, E., Ziegelhoffer, T., Nelson, J., Laloraya, S., and Halladay, J. (1995). Complex multigene family of functionally distinct Hsp70s of yeast. *Cold Spring Harb Symp Quant Biol 60*, 441–449.

26 Crist, C. G., Nakayashiki, T., Kurahashi, H., and Nakamura, Y. (2003). [PHI+], a novel Sup35-prion variant propagated with non-Gln/Asn oligopeptide repeats in the absence of the chaperone protein Hsp104. *Genes Cells 8*, 603–618.

27 Cummings, C. J., and Zoghbi, H. Y. (2000). Trinucleotide repeats: mechanisms and pathophysiology. *Annu Rev Genomics Hum Genet 1*, 281–328.

28 DePace, A. H., Santoso, A., Hillner, P., and Weissman, J. S. (1998). A critical role for amino-terminal glutamine/asparagine repeats in the formation and propagation of a yeast prion. *Cell 93*, 1241–1252.

29 DePace, A. H., and Weissman, J. S. (2002). Origins and kinetic consequences of diversity in Sup35 yeast prion fibers. *Nat Struct Biol 9*, 389–396.

30 Derkatch, I. L., Bradley, M. E., Hong, J. Y., and Liebman, S. W. (2001). Prions affect the appearance of other prions: the story of [PIN(+)]. *Cell 106*, 171–182.

31 Derkatch, I. L., Bradley, M. E., Masse, S. V., Zadorsky, S. P., Polozkov, G. V., Inge-Vechtomov, S. G., and Liebman, S. W. (2000). Dependence and independence of [PSI(+)] and [PIN(+)]: a two-prion system in yeast? *EMBO J 19* 1942–1952.

32 Derkatch, I. L., Bradley, M. E., Zhou, P., Chernoff, Y. O., and Liebman, S. W. (1997). Genetic and environmental factors affecting the de novo appearance of the [PSI+] prion in Saccharomyces cerevisiae. *Genetics 147*, 507–519.

33 Derkatch, I. L., Chernoff, Y. O., Kushnirov, V. V., Inge-Vechtomov, S. G., and Liebman, S. W. (1996). Genesis and variability of [PSI] prion factors in Saccharomyces cerevisiae. *Genetics 144*, 1375–1386.

34 Dobson, C. M. (1999). Protein misfolding, evolution and disease. *Trends Biochem Sci 24*, 329–332.

35 Dobson, C. M. (2001). The structural basis of protein folding and its links with human disease. *Philos Trans R Soc Lond B Biol Sci 356*, 133–145.

36 Dos Reis, S., Coulary-Salin, B., Forge, V., Lascu, I., Begueret, J., and Saupe, S. J. (2002). The HET-s prion protein of the filamentous fungus Podospora anserina aggregates in vitro into amyloid-like fibrils. *J Biol Chem 277*, 5703–5706.

37 Duncan, M. C., Cope, M. J., Goode, B. L., Wendland, B., and Drubin, D. G. (2001). Yeast Eps15-like endocytic protein, Pan1p, activates the Arp2/3 complex. *Nat Cell Biol 3*, 687–690.

38 Eaglestone, S. S., Ruddock, L. W., Cox, B. S., and Tuite, M. F. (2000). Guanidine hydrochloride blocks a critical step in the propagation of the prion-like determinant [PSI(+)] of Saccharomyces cerevisiae. *Proc Natl Acad Sci USA 97*, 240–244.

39 Edskes, H. K., and Wickner, R. B. (2002). Conservation of a portion of the S. cerevisiae Ure2p prion domain that interacts with the full-length protein. *Proc Natl Acad Sci USA 99 Suppl 4*, 16384–16391.

40 Fay, N., Inoue, Y., Bousset, L., Taguchi, H., and Melki, R. (2003). Assembly of the yeast prion Ure2p into protein fibrils. Thermodynamic and kinetic characterization. *J Biol Chem 278*, 30199–30205.

41 Glover, J. R., Kowal, A. S., Schirmer, E. C., Patino, M. M., Liu, J. J., and Lindquist, S. (1997). Self-seeded fibers formed by Sup35, the protein determinant of [PSI+], a heritable prion-like factor of S. cerevisiae. *Cell 89*, 811–819.

42 Glover, J. R., and Lindquist, S. (1998). Hsp104, Hsp70, and Hsp40: a novel chaperone system that rescues previously aggregated proteins. *Cell 94*, 73–82.

43 Gonzalez, C. I., Wang, W., and Peltz, S. W. (2001). Nonsense-mediated mRNA decay in Saccharomyces cerevisiae: a quality control mechanism that degrades transcripts harboring premature termination codons. *Cold Spring Harb Symp Quant Biol 66*, 321–328.

44 Griffith, J. S. (1967). Self-replication and scrapie. *Nature 215*, 1043–1044.

45 Guijarro, J. I., Sunde, M., Jones, J. A., Campbell, I. D., and Dobson, C. M. (1998). Amyloid fibril formation by an SH3 domain. *Proc Natl Acad Sci USA 95*, 4224–4228.

46 Hara, H., Nakayashiki, T., Crist, C. G., and Nakamura, Y. (2003). Prion domain interaction responsible for species discrimination in yeast [PSI+] transmission. *Genes Cells 8*, 925–939.

47 Harrison, P. M., and Gerstein, M. (2003). A method to assess compositional bias in biological sequences and its application to prion-like glutamine/asparagine-rich domains in eukaryotic proteomes. *Genome Biol 4*, R40.

48 Hartl, F. U., and Hayer-Hartl, M. (2002). Molecular chaperones in the cytosol: from nascent chain to folded protein. *Science 295*, 1852–1858.

49 Inoue, Y., Kishimoto, A., Hirao, J., Yoshida, M. & Taguchi, H. (2001). Strong growth polarity of yeast prion fiber revealed by single fiber imaging. *J. Biol. Chem. 276*, 35227–35230.

50 Jeng, R. L., and Welch, M. D. (2001). Cytoskeleton: actin and endocytosis – no longer the weakest link. *Curr Biol 11*, R691–694.

51 Jiang, Y., Li, H., Zhu, L., Zhou, J. M., and Perrett, S. (2004). Amyloid nucleation and hierarchical assembly of Ure2p fibrils. Role of asparagine/glutamine repeat and nonrepeat regions of the prion domains. *J Biol Chem 279*, 3361–3369.

52 Jones, G. W., and Masison, D. C. (2003). Saccharomyces cerevisiae Hsp70 mutations affect [PSI+] prion propagation and cell growth differently and implicate Hsp40 and tetratricopeptide repeat cochaperones in impairment of [PSI+]. *Genetics 163*, 495–506.

53 Jung, G., Jones, G., Wegrzyn, R. D., and Masison, D. C. (2000). A role for cytosolic hsp70 in yeast [PSI(+)] prion propagation and [PSI(+)] as a cellular stress. *Genetics 156*, 559–570.

54 Jung, G., and Masison, D. C. (2001). Guanidine Hydrochloride Inhibits Hsp104 Activity In Vivo: A Possible Explanation for Its Effect in Curing Yeast Prions. *Current Microbiology 43*, 7–10.

55 King, C. Y., Tittmann, P., Gross, H., Gebert, R., Aebi, M., and Wüthrich, K. (1997). Prion-inducing domain 2-114 of yeast Sup35 protein transforms in vitro into amyloid-like filaments.

Proc Natl Acad Sci USA 94, 6618–6622.

56 King, C. Y. and Diaz-Avalos, R. (2004) Protein only transmission of three prion strains: Sup35 amyloid causes [*PSI*$^{+}$]. *Nature 428*, 319–323.

57 Kryndushkin, D. S., Alexandrov, I. M., Ter-Avanesyan, M. D., and Kushnirov, V. V. (2003). Yeast [PSI+] prion aggregates are formed by small Sup35 polymers fragmented by Hsp104. *J Biol Chem 278*, 49636–43.

58 Kushnirov, V. V., Kochneva-Pervukhova, N. V., Chechenova, M. B., Frolova, N. S., and Ter-Avanesyan, M. D. (2000a). Prion properties of the Sup35 protein of yeast Pichia methanolica. *EMBO J 19*, 324–331.

59 Kushnirov, V. V., Kryndushkin, D. S., Boguta, M., Smirnov, V. N., and Ter-Avanesyan, M. D. (2000b). Chaperones that cure yeast artificial [PSI+] and their prion-specific effects. *Current Biology 10*, 1443–1446.

60 Kushnirov, V. V., and Ter-Avanesyan, M. D. (1998). Structure and replication of yeast prions. *Cell 94*, 13–16.

61 Lacroute, F. (1971). Non-Mendelian mutation allowing ureidosuccinic acid uptake in yeast. *J Bacter 106*, 519–522.

62 Li, L., and Lindquist, S. (2000). Creating a protein-based element of inheritance. *Science 287*, 661–664.

63 Lindquist, S. (1997). Mad cows meet psi-chotic yeast: the expansion of the prion hypothesis. *Cell 89*, 495–498.

64 Liu, J. J., and Lindquist, S. (1999). Oligopeptide-repeat expansions modulate 'protein-only' inheritance in yeast. *Nature 400*, 573–576.

65 Lopez, N., Aron, R., and Craig, E. A. (2003). Specificity of class II Hsp40 Sis1 in maintenance of yeast prion [RNQ+]. *Mol Biol Cell 14*, 1172–1181.

66 Maddelein, M. L., Dos Reis, S., Duvezin-Caubet, S., Coulary-Salin, B., and Saupe, S. J. (2002). Amyloid aggregates of the HET-s prion protein are infectious. *Proc Natl Acad Sci USA 99*, 7402–7407.

67 Manson, J. C., Barron, R., Jamieson, E., Baybutt, H., Tuzi, N., McConnell, I., Melton, D., Hope, J., and Bostock, C. (2000). A single amino acid alteration in murine PrP dramatically alters TSE incubation time. *Arch Virol Suppl*, 95–102.

68 Manson, J. C., Jamieson, E., Baybutt, H., Tuzi, N. L., Barron, R., McConnell, I., Somerville, R., Ironside, J., Will, R., Sy, M. S., et al. (1999). A single amino acid alteration (101L) introduced into murine PrP dramatically alters incubation time of transmissible spongiform encephalopathy. *EMBO J 18*, 6855–6864.

69 Martens, J. A., and Winston, F. (2003). Recent advances in understanding chromatin remodeling by Swi/Snf complexes. *Curr Opin Genet Dev 13*, 136–142.

70 Masison, D. C., and Wickner, R. B. (1995). Prion-inducing domain of yeast Ure2p and protease resistan of Ure2p in prion-containing cells. *Science 270*, 93–95.

71 Mastrianni, J. A., Capellari, S., Telling, G. C., Han, D., Bosque, P., Prusiner, S. B., and DeArmond, S. J. (2001). Inherited prion disease caused by the V210I mutation: transmission to transgenic mice. *Neurology 57*, 2198–2205.

72 Meriin, A. B., Zhang, X., Miliaras, N. B., Kazantsev, A., Chernoff, Y. O., McCaffery, J. M., Wendland, B., and Sherman, M. Y. (2003). Aggregation of expanded polyglutamine domain in yeast leads to defects in endocytosis. *Mol Cell Biol 23*, 7554–7565.

73 Michelitsch, M. D., and Weissman, J. S. (2000). A census of glutamine/asparagine-rich regions: implications for their conserved function and the prediction of novel prions. *Proc Natl Acad Sci USA 97*, 11910–11915.

74 Moriyama, H., Edskes, H. K., and Wickner, R. B. (2000a). [URE3] prion propagation in Saccharomyces cerevisiae: requirement for chaperone Hsp104 and curing by overexpressed chaperone Ydj1p. *Mol Cell Biol 20*, 8916–8922.

75 Moriyama, H., Edskes, H. K., and

Wickner, R. B. (2000b). [URE3] prion propagation in Saccharomyces cerevisiae: requirement for chaperone Hsp104 and curing by overexpressed chaperone Ydj1p. *Mol Cell Biol 20*, 8916–8922.

76 Muchowski, P. J., Schaffar, G., Sittler, A., Wanker, E. E., Hayer-Hartl, M. K., and Hartl, F. U. (2000). Hsp70 and hsp40 chaperones can inhibit self-assembly of polyglutamine proteins into amyloid-like fibrils. *Proc Natl Acad Sci USA 97*, 7841–7846.

77 Nakayashiki, T., Ebihara, K., Bannai, H., and Nakamura, Y. (2001). Yeast [PSI+] ''prions'' that are crosstransmissible and susceptible beyond a species barrier through a quasi-prion state. *Mol Cell 7*, 1121–1130.

78 Newnam, G. P., Wegrzyn, R. D., Lindquist, S. L., and Chernoff, Y. O. (1999). Antagonistic interacttions between yeast chaperones Hsp104 and Hsp70 in prion curing. *Mol Cell Biology 19*, 1325–1333.

79 O'Nuallain, B., Williams, A. D., Westermark, P., and Wetzel, R. (2004). Seeding specificity in amyloid growth induced by heterologous fibrils. *J Biol Chem*.

80 Osherovich, L. Z., Cox, B. S., Tuite, M. F., and Weissman, J. S. (2004). Dissection and Design of Yeast Prions. *PLoS Biology 2*.

81 Osherovich, L. Z., and Weissman, J. S. (2001). Multiple Gln/Asn-rich prion domains confer susceptibility to induction of the yeast [PSI(+)] prion. *Cell 106*, 183–194.

82 Osherovich, L. Z., and Weissman, J. S. (2002). The utility of prions. *Dev Cell 2*, 143–151.

83 Parham, S. N., Resende, C. G., and Tuite, M. F. (2001). Oligopeptide repeats in the yeast protein Sup35p stabilize intermolecular prion interactions. *EMBO J 20*, 2111–2119.

84 Patino, M. M., Liu, J. J., Glover, J. R., and Lindquist, S. (1996). Support for the prion hypothesis for inheritance of a phenotypic trait in yeast. *Science 273*, 622–626.

85 Paushkin, S. V., Kushnirov, V. V., Smirnov, V. N., and Ter-Avanesyan, M. D. (1996). Propagation of the yeast prion-like [psi+] determinant is mediated by oligomerization of the SUP35-encoded polypeptide chain release factor. *EMBO J 15*, 3127–3134.

86 Paushkin, S. V., Kushnirov, V. V., Smirnov, V. N., and Ter-Avanesyan, M. D. (1997). In vitro propagation of the prion-like state of yeast Sup35 protein. *Science 277*, 381–383.

87 Perutz, M. F., Johnson, T., Suzuki, M., and Finch, J. T. (1994). Glutamine repeats as polar zippers: their possible role in inherited neurodegenerative diseases. *Proc Natl Acad Sci USA 91*, 5355–5358.

88 Perutz, M. F., Pope, B. J., Owen, D., Wanker, E. E., and Scherzinger, E. (2002). Aggregation of proteins with expanded glutamine and alanine repeats of the glutamine-rich and asparagine-rich domains of Sup35 and of the amyloid beta-peptide of amyloid plaques. *Proc Natl Acad Sci USA 99*, 5596–5600.

89 Prusiner, S. B. (1998). Prions. *Proc Natl Acad Sci USA 95*, 13363–13383.

90 Prusiner, S. B., Scott, M., Foster, D., Pan, K. M., Groth, D., Mirenda, C., Torchia, M., Yang, S. L., Serban, D., Carlson, G. A., and et al. (1990). Transgenetic studies implicate interactions between homologous PrP isoforms in scrapie prion replication. *Cell 63*, 673–686.

91 Resende, C. G., Outeiro, T. F., Sands, L., Lindquist, S., and Tuite, M. F. (2003). Prion protein gene polymorphisms in Saccharomyces cerevisiae. *Mol Microbiol 49*, 1005–1017.

92 Ripaud, L., Maillet, L., and Cullin, C. (2003). The mechanisms of [URE3] prion elimination demonstrate that large aggregates of Ure2p are dead-end products. *EMBO J 22*, 5251–5259.

93 Roberts, B. T., Moriyama, H., and Wickner, R. B. (2004). [URE3] prion propagation is abolished by a mutation of the primary cytosolic Hsp70 of budding yeast. *Yeast 21*, 107–117.

94 Roberts, B. T., and Wickner, R. B. (2003). Heritable activity: a prion that propagates by covalent autoactivation. *Genes Dev 17*, 2083–2087.

95 Santoso, A., Chien, P., Osherovich, L. Z., and Weissman, J. S. (2000). Molecular basis of a yeast prion species barrier. *Cell 100*, 277–288.

96 Scheibel, T., Kowal, A. S., Bloom, J. D., and Lindquist, S. L. (2001). Bidirectional amyloid fiber growth for a yeast prion determinant. *Curr Biol 11*, 366–369.

97 Schlumpberger, M., Prusiner, S. B., and Herskowitz, I. (2001). Induction of distinct [URE3] yeast prion strains. *Mol Cell Biol 21*, 7035–7046.

98 Scott, J. H., and R. Schekman. (1980). Lyticase: endoglucanase and protease activities that act together in yeast cell lysis. *J Bacteriol 142*, 414–423.

99 Scott, M., Foster, D., Mirenda, C., Serban, D., Coufal, F., Walchli, M., Torchia, M., Groth, D., Carlson, G., DeArmond, S. J., and et al. (1989). Transgenic mice expressing hamster prion protein produce species-specific scrapie infectivity and amyloid plaques. *Cell 59*, 847–857.

100 Sheth, U., and Parker, R. (2003). Decapping and decay of messenger RNA occur in cytoplasmic processing bodies. *Science 300*, 805–808.

100a Shorter, J. and Lindquist, S. (2004). Hsp104 catalyzes formation and elimination of self-replicating Sup35 prion conformers. *Science 304*, 1793–1797.

101 Si, K., Giustetto, M., Etkin, A., Hsu, R., Janisiewicz, A. M., Miniaci, M. C., Kim, J. H., Zhu, H., and Kandel, E. R. (2003a). A neuronal isoform of CPEB regulates local protein synthesis and stabilizes synapse-specific long-term facilitation in aplysia. *Cell 115*, 893–904.

102 Si, K., Lindquist, S., and Kandel, E. R. (2003b). A neuronal isoform of the aplysia CPEB has prion-like properties. *Cell 115*, 879–891.

103 Sondheimer, N., and Lindquist, S. (2000). Rnq1: an epigenetic modifier of protein function in yeast. *Mol Cell 5*, 163–172.

104 Sondheimer, N., Lopez, N., Craig, E. A., and Lindquist, S. (2001). The role of Sis1 in the maintenance of the [RNQ+] prion. *EMBO J 20*, 2435–2442.

105 Sparrer, H. E., Santoso, A., Szoka, F. C., Jr., and Weissman, J. S. (2000). Evidence for the prion hypothesis: induction of the yeast [PSI+] factor by in vitro-converted Sup35 protein. *Science 289*, 595–599.

106 Speransky, V. V., Taylor, K. L., Edskes, H. K., Wickner, R. B., and Steven, A. C. (2001). Prion filament networks in [URE3] cells of Saccharomyces cerevisiae. *J Cell Biol 153*, 1327–1336.

107 Tanaka, M., Chien, P., Naber, N., Cooke, R. and Weissman, J. S. (2004). Conformation Variations in Infectious Particles Determine Prion Differences. *Nature 428*, 323–328.

108 Tang, H. Y., Xu, J., and Cai, M. (2000). Pan1p, End3p, and S1a1p, three yeast proteins required for normal cortical actin cytoskeleton organization, associate with each other and play essential roles in cell wall morphogenesis. *Mol Cell Biol 20*, 12–25.

109 Taylor, J. P., Hardy, J., and Fischbeck, K. H. (2002). Toxic proteins in neurodegenerative disease. *Science 296*, 1991–1995.

110 Taylor, K. L., Cheng, N., Williams, R. W., Steven, A. C., and Wickner, R. B. (1999). Prion domain initiation of amyloid formation in vitro from native Ure2p. *Science 283*, 1339–1343.

111 Tuite, M. F., and Cox, B. S. (2003). Propagation of yeast prions. *Nat Rev Mol Cell Biol 4*, 878–890.

112 Tuite, M. F., Mundy, C. R., and Cox, B. S. (1981). Agents that cause a high frequency of genetic change from [psi+] to [psi−] in Saccharomyces cerevisiae. *Genetics 98*, 691–711.

113 Uptain, S. M., and Lindquist, S. (2002). Prions as protein-based genetic elements. *Annu Rev Microbiol 56*, 703–741.

114 Uptain, S. M., Sawicki, G. J., Caughey, B., and Lindquist, S. (2001). Strains of [PSI(+)] are

distinguished by their efficiencies of prion-mediated conformational conversion. *EMBO J 20*, 6236–6245.

115 Weissmann, C. (1991). Spongiform encephalopathies. The prion's progress. *Nature 349*, 569–571.

116 Weissmann, C. (1999). Molecular genetics of transmissible spongiform encephalopathies. *J Biol Chem 274*, 3–6.

117 Wickner, R. B. (1994). [URE3] as an altered URE2 protein: evidence for a prion analog in Saccharomyces cerevisiae. *Science 264*, 566–569.

118 Yang Fan, C., Lee, S., Ren, H. Y., and Cyr, D. M. (2003). Exchangeable chaperone modules contribute to specification of Type I and Type II Hsp40 cellular function. *Mol Biol Cell*.

119 Young, J. C., Barral, J. M., and Ulrich Hartl, F. (2003). More than folding: localized functions of cytosolic chaperones. *Trends Biochem Sci 28*, 541–547.

120 Zhou, P., Derkatch, I. L., and Liebman, S. W. (2001). The relationship between visible intracellular aggregates that appear after overexpression of Sup35 and the yeast prion-like elements [PSI(+)] and [PIN(+)]. *Mol Microbiol 39*, 37–46.

121 Zhou, P., Derkatch, I. L., Uptain, S. M., Patino, M. M., Lindquist, S., and Liebman, S. W. (1999). The yeast non-Mendelian factor [ETA+] is a variant of [PSI+], a prion-like form of release factor eRF3. *EMBO J 18*, 1182–1191.

36
Polyglutamine Aggregates as a Model for Protein-misfolding Diseases

Soojin Kim, James F. Morley, Anat Ben-Zvi, and Richard I. Morimoto

36.1
Introduction

Protein aggregation is common to a number of human neurodegenerative diseases including Alzheimer's disease, Parkinson's disease, prion disorders, amyotrophic lateral sclerosis, and polyglutamine diseases (see Chapters 33–35). The correlation between the appearance of inclusion bodies and neuropathology has led to a widely held hypothesis that aggregates are toxic. Recent studies, however, suggest that toxicity of misfolded proteins correlates imperfectly with aggregates, leading to the proposal that other intermediate species, distinct from the monomers and fibrils, may also contribute to neurotoxicity. While the identity of the "toxic species" remains an issue of debate, the common underlying features in these diseases are the self-association and accumulation of the misfolded proteins as visible subcellular aggregates.

In this chapter, we discuss various approaches to studying misfolded and aggregation-prone proteins using polyglutamine-containing proteins as a model system, and address the role of misfolded proteins in toxicity. Finally, we discuss various modulators of protein aggregation.

36.2
Polyglutamine Diseases

36.2.1
Genetics

Polyglutamine disorders refer to a group of nine neurodegenerative diseases including Huntington's disease (HD); spinal and bulbar muscular atrophy (SBMA); dentatorubral-pallidoluysian atrophy (DRPLA); and spinocerebellar ataxia (SCA)-1, -2, -3, -6, -7, and -17, in which expansion of glutamine repeats in the affected protein is directly linked to neuropathology [1–4]. For each of these disorders, the dis-

Protein Folding Handbook. Part II. Edited by J. Buchner and T. Kiefhaber

ISBN: 3-527-30784-2

ease is dominantly inherited, with the exception of SBMA. Genetic analysis of HD patient populations has revealed that the huntingtin gene contains more than 35–40 CAG repeats (encoding the amino acid glutamine, Q), whereas the huntingtin gene from normal individuals contains fewer than 30–34 CAG repeats [5–7]. Similar genetic features exist for the other polyglutamine diseases with regard to the relationship between normal and pathogenic repeat lengths and neurotoxicity, with the exception of SCA6, which contains 21–33 CAG repeats in the disease state and 4–18 CAG repeats in normal alleles [1]. These observations support the hypothesis of a polyglutamine-length threshold beyond which pathogenic mechanisms are triggered [2]. In addition, genotype-phenotype studies have established a strong inverse correlation between repeat length and the age of onset such that an increase in the number of CAG repeat leads to an earlier manifestation of the disease with more severe symptoms, indicating a direct involvement of polyglutamine length in the disease progression.

36.2.2
Polyglutamine Diseases Involve a Toxic Gain of Function

Polyglutamine diseases exhibit genetic dominance such that neuropathologies of heterozygous and homozygous individuals are nearly identical for Huntington's disease [8]. Huntingtin or ataxin-1 knockout mice or deletion in humans exhibited phenotypes that are distinct from the respective neuropathologies, suggesting that polyglutamine diseases are not the result of downregulation of the respective affected proteins but rather due to a gain-of-function toxicity associated with the polyglutamine expansion [9–14]. A gain-of-function hypothesis is further supported by observations that expression of either full-length or truncated mutant genes containing the expanded glutamine repeat or the expanded polyglutamine alone expressed in mice, *Drosophila*, and *C. elegans* is sufficient to cause neurological dysfunctions [15–19]. Taken together, these observations support the hypothesis that polyglutamine expansion is the principal cause of the toxic gain of function associated with expression of these mutant proteins.

36.3
Polyglutamine Aggregates

36.3.1
Presence of the Expanded Polyglutamine Is Sufficient to Induce Aggregation in Vivo

The presence of protein aggregates is a pathological hallmark of polyglutamine diseases. Nuclear inclusion bodies have been identified in postmortem brains from HD, SCA-1, SCA-3, SCA-7, DRPLA, and SBMA patients [2, 20–26]. In all cases, these inclusion bodies contain the mutant proteins with the expanded polyglutamines. For huntingtin, only the N-terminal fragment containing the polyglutamine tract was detected in the inclusions, suggesting a role for proteolytic cleav-

age in huntingtin aggregation [20]. These inclusion bodies also stained positive, by immunohistochemistry, for a common cohort of proteins including ubiquitin, molecular chaperones, and components of proteasomes [20, 21, 23, 27–31]. As these factors are typically associated with the cellular response to misfolded proteins, it has been proposed that the polyglutamine expansion leads to misfolding and altered conformational states and, subsequently, to aggregation of the affected protein.

Evidence that the expanded glutamine stretch is the source of protein aggregation comes from observations that expression of expanded glutamine repeats alone or in the context of the truncated mutant proteins induces formation of protein aggregates in a number of model systems. In all model organisms studied, including *E. coli*, *S. cerevisiae*, *Drosophila*, *C. elegans*, mice, and mammalian cell culture, expression of polyglutamine lengths above 40Q led to the formation of large visible aggregates [15–19, 21, 27, 28, 32–38]. Moreover, transgenic mice expressing expanded glutamine repeats within the context of a heterologous gene, hypoxanthine phosphoribosyltransferase (HPRT), exhibited multiple features of polyglutamine diseases, including formation of nuclear inclusion bodies and death of motor neurons, demonstrating that expanded polyglutamine sequence alone is sufficient to induce aggregation and toxicity [39].

36.3.2 Length of the Polyglutamine Dictates the Rate of Aggregate Formation

The rate of aggregate formation and the degree of toxicity are directly correlated to polyglutamine length. Expression of various lengths of glutamine repeats in model organisms, such as *E. coli*, *S. cerevisiae*, *Drosophila*, *C. elegans*, or cell culture, demonstrated that expression of sub-threshold glutamine length (< 40Q) did not affect the viability of the host cells and that the polyglutamine proteins expressed showed a diffused localization [17–19, 21, 29–33, 36–38]. In contrast, cells expressing polyglutamine lengths above this threshold induced toxicity and readily formed punctate aggregated structures that were detergent-insoluble. Toxicity and aggregation frequency increased with polyglutamine length. In *C. elegans* expressing YFP-fused polyglutamines in muscle cells, diffuse fluorescence was detected in young adult *C. elegans* expressing 0Q, 19Q, 29Q, and 33Q, whereas animals expressing 44Q, 64Q, or 82Q exhibited only punctate fluorescent structures corresponding to protein aggregates. 35Q- and 40Q-expressing animals, however, displayed polymorphic distribution of the polyglutamine-YFP with diffuse fluorescence in some cells and punctate fluorescence in others (Figure 36.1A). A direct correlation was observed between toxicity and aggregation. Animals expressing 40Q or 82Q exhibited a rapid loss in motility in contrast to 19Q-, 29Q-expressing or wild-type animals, which were unaffected (Figure 36.1B, C). Similar toxic effects of increasing polyglutamine length have also been demonstrated in *E. coli*, in *Drosophila* eye development, and in cell culture models [19, 21, 29–32, 36–38, 40, 41]. These observations that aggregate formation and toxicity are polyglutamine length-dependent and that model organisms are also sensitive to similar polyglutamine-length thresholds

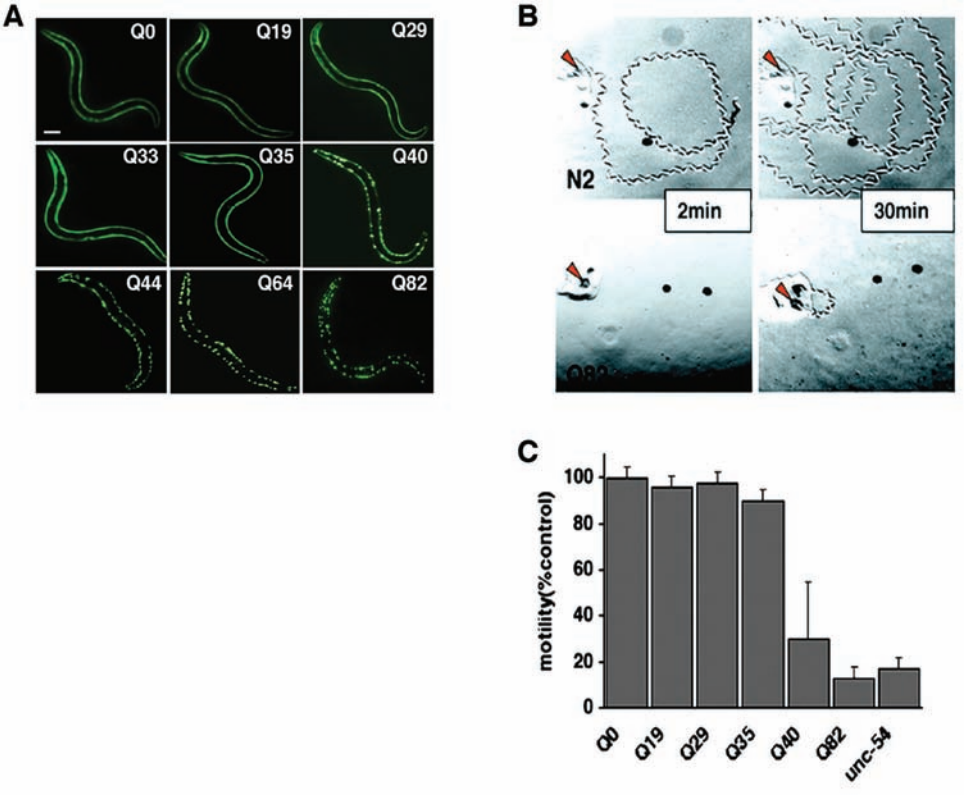

Fig. 36.1. Polyglutamine length-dependent aggregation and motility defect in *C. elegans*. (A) Epifluoresence micrographs of 3- to 4-day-old *C. elegans* expressing different lengths of polyQ-YFP (0Q, 19Q, 29Q, 33Q, 35Q, 40Q, 44Q, 64Q, 82Q). Bar = 0.1 mm. (B) Time lapse micrographs illustrating tracks left by 5-day-old wild-type (N2) and 82Q animals 2 min and 30 min after being placed at the position marked by the red arrow. (C) Quantitation of motility index for 4- to 5-day-old 0Q, 19Q, 29Q, 35Q, 40Q, 82Q, and motility defective *unc-54*(r293) animals. Data are mean ± SD for at least 50 animals of each type as a percentage of N2 (wild-type) motility.

(40Qs) as detected in human diseases indicate a common underlying biochemical principle for polyglutamine aggregation and toxicity.

The kinetics of polyglutamine aggregation has been studied intensively in vitro using synthetic polyglutamine peptides and recombinant proteins (see Chapters 6 and 37). Studies using purified polyglutamines were initially hampered by the strong propensity for even short polyglutamine peptides to precipitate in aqueous solution [42]. These difficulties have been overcome, to some extent, by flanking the polyglutamine peptides with basic residues to improve their solubility, by employing mixtures of aqueous and organic solvents (such as trifluoroacetic acid and hexafluoroisopropanol), or by generating chimeric proteins in which the polyglut-

amine is fused to a soluble protein such as GST and aggregate formation is initiated by proteolytic cleavage, liberating the polyglutamine fragment [43–45].

One striking observation from biochemical studies on polyglutamine aggregation was that the correlation between the repeat length and aggregation kinetics in vitro paralleled closely with that observed in vivo. An Htt exon 1-GST protein containing an expansion of 51Q formed insoluble aggregates as detected by filter-trap assay upon protease cleavage of the GST moiety, whereas peptides of 20Q or 30Q remained soluble [44]. The aggregation kinetics of peptides released from cleaved Htt exon 1-GST fusion proteins or synthetic polyglutamine peptides was positively correlated to the increasing glutamine repeat length, whereas the lag time for aggregation was inversely correlated with polyglutamine length [45–47]. These data suggest that the intrinsic biophysical parameters governing polyglutamine aggregation in vitro is analogous to the relationship between repeat length and aggregation observed in vivo.

36.3.3
Polyglutamine Aggregates Exhibit Features Characteristic of Amyloids

The structural determinant for polyglutamine aggregation is hypothesized to be the formation of stable β-sheet interactions. Perutz and co-workers proposed that repetitive sequences of polar residues are capable of linking β-strands together through hydrogen bonds between their main-chain amides and their polar side charges [43]. Consequently, formation of intramolecular hydrogen bonds of amide groups in an expanded glutamine stretch may provide the biochemical basis for polyglutamine self-association. Studies on a short polyglutamine peptide (D_2-Q_{15}-K_2) demonstrated that glutamine repeats form oligomers consisting of β-pleated sheets [43]. Additionally, circular dichroism (CD) analysis of recombinant or synthetic polyglutamine peptides demonstrated that while a monomeric polyglutamine exists as a random coil, oligomers of the expanded glutamines have substantial β-structures, suggesting that a conformational switch to a β-sheet-rich state is key to polyglutamine aggregation [42, 43, 45, 47, 48]. An in vitro analysis using two stretches of 9Qs linked together by Gly-Pro pairs (predicted to induce β-turns) revealed that the minimal unit required for stable β-hairpin structures is 40Qs [49]. These results are intriguing since 40Q is the threshold polyglutamine length for the aggregation phenotype in human disease. These observations have contributed to the hypothesis that stabilization of expanded polyglutamines in β-sheet conformation promotes self-association of the mutant proteins.

Electron microscopic (EM) studies on purified proteins have revealed that polyglutamine expansions above the threshold length form fibrous, ribbon-like amyloid structures, whereas sub-threshold-length glutamine repeats form oligomeric globular or amorphous structures [44, 46, 50–52]. Staining of these purified aggregates with amyloidophilic dyes, such as Thioflavin T or Congo red, has established that polyglutamine aggregates have structural features common to other amyloid-forming proteins [44, 45, 53]. Formation of fibrous amyloid structures consisting of β-sheets has also been observed for other amyloidogenic proteins includ-

ing Aβ-peptide, prions, α-synuclein, and superoxide dismutase [54–57]. As the folding of β-sheets is driven predominantly by backbone interactions, it has been proposed that formation of amyloid structures is independent of side chain interactions [58]. If so, protein aggregation may be primary sequence–independent, as stabilization of β-sheet structures is the common mechanism behind aggregate formation.

36.3.4 Characterization of Protein Aggregates in Vivo Using Dynamic Imaging Methods

In vivo studies on polyglutamine aggregates using the live-cell imaging technique fluorescent recovery after photobleaching (FRAP) provided insights as to the organization, composition, and properties of self-associated polyglutamine structures without disrupting the cell [59–62]. Monitoring fluorescence recovery following photobleaching of fluorescent proteins containing polyglutamine expansions has revealed that the mobility of proteins within aggregates is very slow and essentially undetectable whether in cultured cells or in *C. elegans* (Figure 36.2). The nature of the molecular interactions of aggregate-associated proteins can be examined in cells by using fluorescence resonance energy transfer (FRET) analysis using pairs of differently fluorescently labeled proteins [62, 63] (see Chapter 17 in Part I). For example, co-expression of polyglutamine-expansion proteins fused to either YFP or CFP exhibited energy transfer within polyglutamine aggregates, indicating 40- to 100-Å distances between polyglutamine molecules in the aggregate. These results demonstrate that polyglutamine-expansion proteins form immobile aggregates comprised of self-associated interactions that are highly compacted and ordered. Taken together, the complement of in vitro and in vivo studies supports the hy-

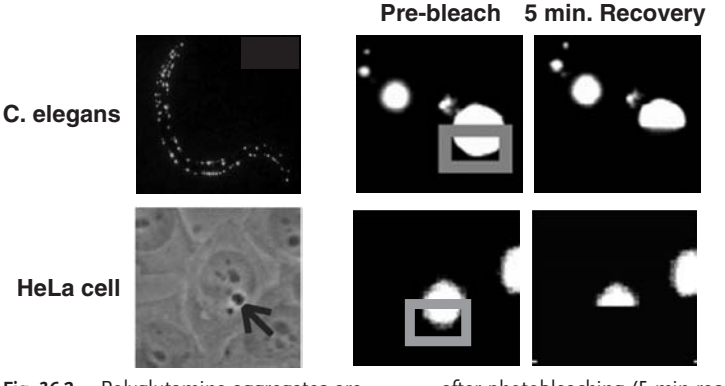

Fig. 36.2. Polyglutamine aggregates are immobile. FRAP analysis of *C. elegans* (top) and Hela cells (bottom). Light-colored foci in *C. elegans* and dark-colored foci in aHeLa cell (arrow) are Q82-GFP aggregates (left panels). Higher magnification fluorescence images of the aggregates before (pre-bleach) and 5 min after photobleaching (5-min recovery). Boxes indicate the area that was subjected to photobleaching. Fluorescence in the aggregate did not recover fully even after two hours of monitoring, indicating a stable structure of polyglutamine aggregate.

pothesis that misfolded proteins are stabilized by adopting β-sheet structures, which serve as the basis for the formation of ordered and immobile aggregates.

36.4
A Role for Oligomeric Intermediates in Toxicity

Despite the prevalence of observations that pathology is associated with the appearance of protein aggregates, a question that remains unresolved is the identity of the "toxic species" or whether there are multiple "toxic species." Demonstrations that the localization of mutant ataxin-1 to the nucleus or that the blocking of ubiquination of huntingtin accelerates toxicity in the absence of visible aggregates have led to the proposal that aggregates could be protective or that toxicity may be induced by microscopically undetectable species [42, 64–67]. These visually undetectable species have become of particular interest since non-fibrous oligomeric intermediates have been detected at the earlier phases of misfolding and aggregation as well as at a very low temperature during aggregation of the purified huntingtin fragments in vitro [45, 51, 52]. The observation that the formation of mature fibers, but not early globular or protofibrillar species, was inhibited by the amyloid-binding dye Congo red suggests that these intermediates may be structurally distinct from β-hairpin-containing structures [52]. Although the role of oligomeric intermediates as toxic species in polyglutamine diseases is not established, cell death caused by addition of protofilaments (Aβ-peptide) to the media of cultured neurons suggests that polyglutamine toxicity may be induced in a similar fashion [68–71]. A common conformational state shared among intermediates species, rather than the presence of a specific sequence, is responsible for toxicity, since addition of other non-disease-related, small globular proteins such as PI3-SH3 (SH3 domain from bovine phosphatidyl-inositol-3′-kinase) or HypF-N (the N-terminal "acylphosphatase-like" domain of the *E. coli* HypF protein) to neuronal cultures also induces cell death [72]. Additional support that aggregation-prone proteins can adopt a common conformational state comes from immunological studies in which an antibody, derived against a small soluble oligomeric state of Aβ-peptide, detects protofilament structures but not soluble monomers or visible aggregates [73]. A striking property of this antibody is the ability to detect not only the protofilaments of Aβ but also intermediate species generated by α-synuclein, prion, and polyglutamine-expansion proteins. Taken together, these studies support the presence of a common conformational state associated with intermediate species in otherwise distinct proteins with divergent sequences.

36.5
Consequences of Misfolded Proteins and Aggregates on Protein Homeostasis

Immunolocalization studies of polyglutamine protein aggregates have established that a number of cellular proteins, including molecular chaperones (Hsp70, Hdj1,

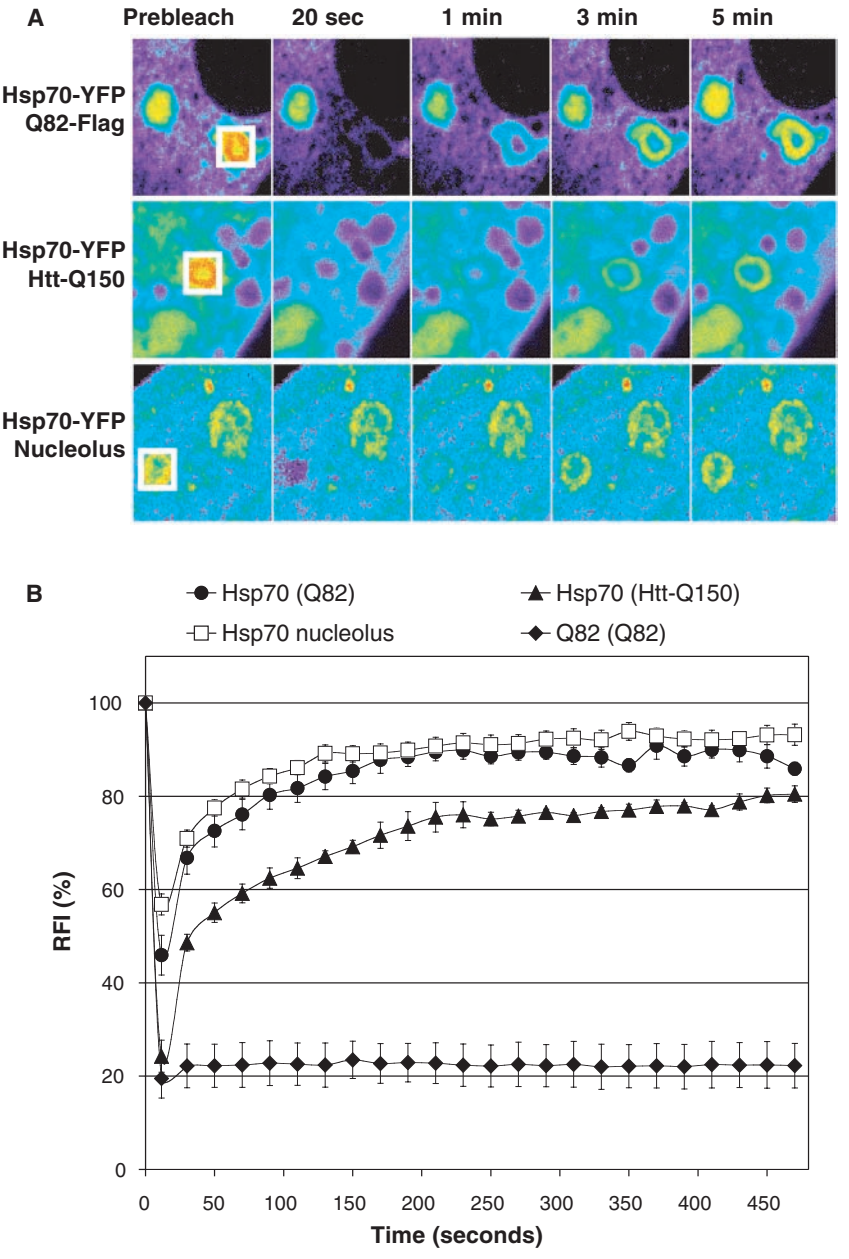

Fig. 36.3. Hsp70 associates transiently with polyglutamine aggregates via chaperon-substrate interactions. (A) FRAP analysis of Hsp70-YFP associated with polyglutamine aggregates. Pseudo-color images represent fluorescence intensity. Hsp70-YFP associated with Q82-Flag aggregate (top panels), Hsp70-YFP associated with Htt-Q150 aggregate (middle panels), and Hsp70-YFP in nucleolus following heat shock at 45 °C for 30 min and recovery at 37 °C for 1–2 h (bottom panels) were photobleached in the boxed area. Single

and Hdj2), proteasome subunits (20S), structural proteins (neurofilaments), and short glutamine repeat–containing transcription factors (TBP and CBP), colocalize with polyglutamine aggregates [27, 28, 74–77]. A question that follows from studies on fixed cells or biochemical analyses of isolated aggregates is whether these aggregate-associated proteins are stably or transiently bound in vivo. To address this question, FRAP analysis was used to show that the basal transcription factors TBP (TATA-binding protein) and CBP (CREB-binding protein) bind stably and do not diffuse away from huntingtin or ataxin-3 aggregates at a detectable rate [59, 62]. These results suggest that polyglutamine toxicity stems from irreversible sequestration of essential transcription factors.

Whereas transient association of molecular chaperones (Figure 36.3A, B) with polyglutamine aggregates likely represents a protective cellular response to a disruption of protein homeostasis, irreversible sequestration of transcription factors into polyglutamine aggregates could lead to the loss of their normal cellular functions. RT-PCR, differential display, and DNA microarray approaches have demonstrated altered expression of numerous genes in transgenic models of polyglutamine diseases [78–80]. Many of these changes can be observed before the onset of symptoms, arguing for a causal role of transcriptional dysregulation in toxicity.

CBP has been studied as a sequestration model of toxicity; CBP contains 19 glutamine repeats at its C-terminus, and deletion of this region abolishes the interaction with polyglutamine aggregates [81]. Expression of expanded polyglutamine downregulates soluble CBP and CBP-dependent gene expressions, whereas overexpression of CBP rescues transcriptional dysregulation and cellular toxicity caused by expanded polyglutamines. Depletion of CBP activity has a role in toxicity, as brain-specific chromosomal deletion of CREB in mice leads to neurodegeneration, suggesting that normal regulation of CBP target genes is required for neuronal function and survival [82]. Taken together, these observations suggest that sequestration of essential cellular factors by polyglutamine aggregates may contribute to cellular toxicity.

The range of cellular proteins that polyglutamine aggregates recruit may be large given that short glutamine repeats or polar-rich motifs can interact with polyglutamine-expansion proteins. Recruitment of normally soluble polyglutamine lengths (~19Q) into aggregates composed of long stretches (~82Q) has been observed both in vitro and in vivo [35, 45]. In addition, the interaction between yeast prion determinants consisting of polar (glutamine/asparagine)-rich motifs and

scanned images were taken before photobleaching (pre-bleach) and at the indicated time points following photobleaching. Hsp70 association with polyglutamine or huntingtin aggregates and heat-shocked nucleolus exhibited fast recovery indicative of transient interactions. (B) Quantitative FRAP analysis of the Hsp70-YFP associated with polyglutamine aggregates or localized to the nucleolus of a heat-shocked cell as in (A). Q82-Flag or Htt-Q150 was used to seed aggregates as indicated. The relative fluorescence intensity (RFI) was determined for each time point and was represented as the average of analysis of five cells. Error bars indicate the standard error of the mean (SEM). Data from Q82-GFP analysis was included as a reference for an immobile protein.

polyglutamine stretches has also been detected [83]. These results together with bioinformatics studies on eukaryotic genomes, which propose that 1–5% of proteins have polar-rich motifs, suggest that a substantial complement of proteins could be sequestered into polyglutamine aggregates [84].

However, it is also clear that some of the proteins that associate with aggregates do not have glutamine- or polar-rich motifs. For these proteins, it has been hypothesized that localization to aggregates occurs by virtue of their interactions with sequences other than the polyglutamine repeats or indirectly by association with other recruited proteins [85, 86]. Yeast two-hybrid screens and biochemical methods have identified a number of cellular factors that associate with huntingtin or ataxia-1, but the role of these interacting cellular proteins in polyglutamine toxicity remains to be elucidated [85, 87–89].

Recruitment of cellular proteins by polyglutamine aggregates reveals that an underlying mechanism for polyglutamine toxicity may be due to sequestration of essential cellular factors. It may be that expansion of polyglutamine in the affected proteins causes misfolding, which abolishes or enhances interactions with its normal associating partners or creates new interactions. Whether such interactions require the presence of large aggregates is uncertain, since smaller oligomeric species should be as effective in associating with other cellular proteins. A study using purified polyglutamine peptides demonstrated that oligomers are more efficient in propagating aggregation than are large aggregates, which supports the hypothesis that oligomers are more toxic than large aggregates [45, 72]. It may be that large aggregates are not as toxic, since most of the interactive surfaces are occupied, ordered amyloidal structures, although this hypothesis remains untested.

36.6 Modulators of Polyglutamine Aggregation and Toxicity

Whereas it can take decades for aggregates to form in human disease, the same process can occur in vitro in a matter of hours. This reveals the importance of in vivo genetic modifiers that regulate protein-folding homeostasis even when challenged by expression of highly aggregation-prone proteins. Identification of the factors that modulate the aggregation process and toxicity will be important in understanding disease pathology and invaluable for the development of therapeutic strategies.

36.6.1 Protein Context

The influence of the protein context in aggregation was first demonstrated in studies on ataxin-1 where deletion of the self-association domain, distinct from the polyglutamine-expansion region, prevented the formation of visible aggregates [64]. Similarly, mutation of an Akt phosphorylation site (S776A) decreased aggregation and neuropathology induced by ataxin-1 despite the presence of 82Qs [89].

Phosphorylation of serine 776 has been suggested to stabilize ataxin-1 through interactions with 14-3-3 (a multifunctional regulatory protein), thus exacerbating aggregate formation and neurodegeneration [88]. These results offer the insight that aggregation and neurotoxicity, even in the presence of the polyglutamine expansion, can be modulated by other sequences within the disease-causing protein.

36.6.2 Molecular Chaperones

The role of molecular chaperones as modifiers of polyglutamine-induced toxicity and aggregation has been well established; however, there is no mechanistic understanding of how chaperones suppress or modulate such phenotypes [90, 91]. In *Drosophila*, p-element insertion into the dHdj1 gene or knocking down HSPA1L expression enhanced polyglutamine-mediated toxicity [40, 41, 92]. Moreover, overexpression of Hsp70, Hdj1, and/or Hdj2 in *Drosophila*, mice, and cell culture models reduced polyglutamine aggregate toxicity (Table 36.1). Similar modulatory effects on polyglutamine proteins were also observed with elevated expression of Hsp104 in *S. cerevisiae*, *C. elegans*, and cell culture [34, 35, 93]. In contrast, overexpression of Hsp70 alone had inconsistent results on suppression of aggregate formation, whereas overexpression of co-chaperones, Hdj1 and Hdj2, yielded more-consistent results on reduction of both aggregation and toxicity (Table 36.1). Co-expression of Hsp70 and co-chaperones consistently exhibited synergistic effects on aggregation and toxicity [31, 94]. Taken together, these observations strongly support the ability of molecular chaperones to have potent effects on protein aggregation and toxicity while leaving unanswered questions on the mechanism and chaperone specificity.

There are several possible mechanisms by which molecular chaperones can modulate protein aggregation. The property of molecular chaperones to prevent aggregate formation is well established from a large number of in vitro studies in which the addition of molecular chaperones to heat- or chemically denatured substrates reduced aggregation and subsequently enhanced the refolding to the native state in an ATP-dependent manner [95, 96]. Similarly, in vitro studies using purified huntingtin exon-1 demonstrated that Hsc70 with Hdj1 prevented polyglutamine aggregate formation, thus supporting the ability of chaperones to prevent amyloidogenesis [94]. From these studies, it seems self-evident that the major effect of chaperone overexpression is to prevent aggregation. However, aggregation and toxicity were reversed by preventing further huntingtin expression, suggesting that chaperones can act on preformed aggregates to dissociate and presumably degrade them [97]. Are molecular chaperones responsible for dissociating preformed aggregates? A number of in vitro studies demonstrated that DnaK, the Hsp70 bacterial homologue, promotes disaggregation and reactivation of stable preformed protein aggregates both in vitro and in vivo [95, 98–100]. In addition, yeast Hsp104 and Hsp70 have also been shown to have similar effects on preformed aggregates [101, 102]. Whether mammalian molecular chaperones also have this capacity to dissociate preformed amyloids, however, remains to be demonstrated. There are

Tab. 36.1. Effects of molecular chaperones on polyglutamine-mediated aggregation and toxicity. Summary of the overexpressed molecular chaperones (as indicated) and their effects on different types of polyglutamine aggregates as determined by reduction of aggregation and/or toxicity. The list does not include studies from *S. cerevisiae* or *E. coli* models (n.a.: information was not available).

Family	*Overexpressed chaperones*	*Polyglutamine protein*	*Model system*	*Reduced aggregates*	*Reduced cell death*	*Reference*
Hsp60	apoGroEL	EGFP-HDQ74	COS7	+	+	93
	apoGroEL	EGFP-HDQ74	PC12	+	+	93
Hsp40	hdj1	HA-Q78	COS7	+	n.a.	29
	hdj1	NLS-ataxin3 (Q78)	COS7	+	n.a.	29
	hdj1	httEx1-Q74 (GFP)	Sk-N-SH	+	+	113
	hdj1	GFP-Q80	PC12	+	+	29
	hdj1	NLS-ataxin3 (Q78)	PC12	+	n.a.	29
	Hsp40 (hdj1)	120Q (HD exon1)	HEK293	+	+	111
	hdj1	tNhtt-150Q (GFP)	Neuro2a-ecdy	+	+	30
	dhdj1	127Q	*Drosophila* eye	–	+	92
	dhdj1	MJDtr-Q78	*Drosophila* eye	–	+	112
	hdj2	ataxin-1-GFP (Q92)	HeLa	+	n.a.	27
	hdj2	ARQ48 (GFP)	HeLa	+	n.a.	28
	hdj2	HA-Q78	COS7	+	n.a.	29
	hdj2	NLS-ataxin3 (Q78)	COS7	+	n.a.	29
	hdj2	GFP-Q80	PC12	–	n.a.	29
	hdj2	NLS-ataxin3 (Q78)	PC12	–	n.a.	29
	hdj2	tAR97-GFP	Neuro2a	–	–	31
Hsp70	Hsp70	HA-Q78	COS7	–	n.a.	29
	Hsp70	NLS-ataxin3 (Q78)	COS7	–	n.a.	29
	Hsp70	httEx1-Q74 (GFP)	COS7	–	–	113
	Hsp70	120Q (HD exon1)	HEK293	–	+	111
	Hsp70	tAR97-GFP	Neuro2a	+	+	31
	Hsp70	tNhtt-150Q (GFP)	Neuro2a-ecdy	–	n.a.	30
	Hsc70	tNhtt-150Q (GFP)	Neuro2a-ecdy	+	–	30
	Hsp70	httEx1-Q103 (GFP)	SK-N-SH	+	+	113
	HSPA1L (Hsp70)	MJDtr-Q78	*Drosophila* eye	–	+	40
	Hsp70	MJDtr-Q78	*Drosophila* eye	–	–	112
	Hsp70	SCA1	SCA1 mouse	–	+	114
Hsp70 & Hsp40	Hsp70 + Hsp40	tAR97-GFP	Neuro2a	+	+	31
	Hsc70 + hdj1	tNhtt-150Q (GFP)	Neuro2a-ecdy	–	+	30
	Hsp70 + hdj2	tAR97-GFP	Neuro2a	–	–	31
	Hsp70 + dhdj1	MJDtr-Q78	*Drosophila* eye	–	+	112
Hsp104	Hsp104	EGFP-HDQ74	COS7	+	+	93
	Hsp104	EGFP-HDQ74	PC12	+	+	93
	Hsp104	Q82-GFP	*C. elegans*	+	n.a.	35

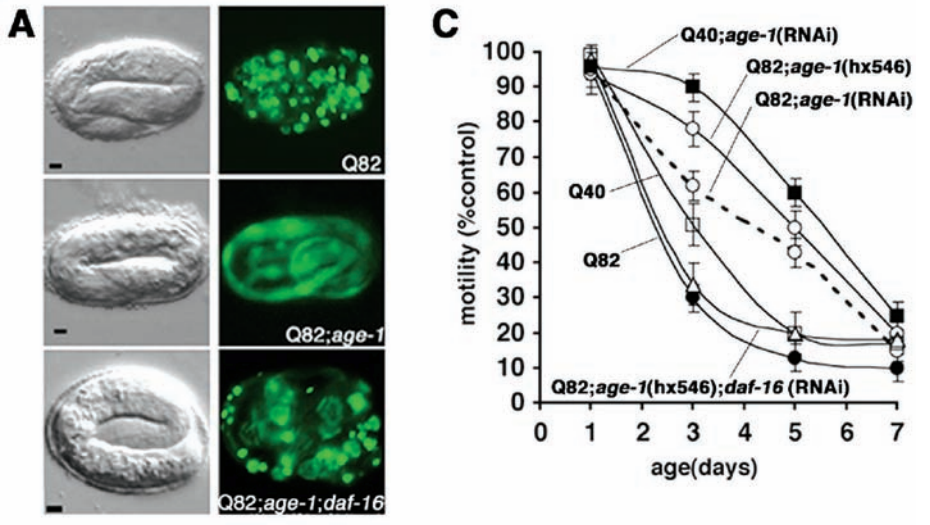

B

		% of aggregates versus wild type background		
	background	day 1	day 2	N
Q82 line 1	*age-1* (hx546)	55 ± 5	57 ± 4	45
	age-1 (RNAi)	69 ± 5	71 ± 3	60
Q82 line 2	*age-1* (hx546)	52 ± 3	48 ± 4	108
	daf-16 (RNAi)	95 ± 6	98 ± 8	90
	age-1 (hx546); *daf-16* (RNAi)	98 ± 4	98 ± 6	90
Q40	*age-1* (RNAi)	47 ± 7	38 ± 6	60

Fig. 36.4. An extended lifespan mutation delays polyglutamine aggregate accumulation and onset of toxicity. (A) DIC (left panels) and epifluorescence (right panels) micrographs showing embryos expressing Q82 in wild-type (top), *age-1* (hx546) (middle), or *age-1* (hx546); *daf-16* (RNAi) (bottom) genetic backgrounds. (B) Aggregate accumulation in larval animals expressing Q40 or Q82 in the indicated genetic backgrounds relative to aggregate accumulation in wild-type background (data are mean ± SEM). Aggregate formation in Q82-expressing embryo was inhibited in *age-1* background. The suppression of aggregation by *age-1* was dependent on *daf-16*. (C) Motility index for animals expressing Q40 or Q82 in the indicated genetic backgrounds (data are mean ± SEM for 30 animals of each type). Motility of non-transgenic wild-type and *age-1* animals was similar to that of wild-type animals (N2). The motility defects observed paralleled the degree of aggregate formation.

indications from an in vivo study on the association of human Hsp70 with polyglutamine aggregate that the chaperone may associate with nonnative proteins in the aggregate [62]. FRAP analysis of YFP-tagged Hsp70 showed transient interactions with aggregates and exhibited association kinetics identical to the interactions with unfolded substrates localized to the nucleolus during heat shock (Figure 36.3A, B). Furthermore, the association of Hsp70 with aggregates was dependent on chaperone activity, as mutations in Hsp70 that rendered the chaperone inactive

prevented association with polyglutamine aggregates. This suggests that Hsp70 binding to misfolded polyglutamine proteins or other cellular proteins trapped in the polyglutamine aggregates reflects a productive intent to dislodge, refold, and/or target aggregate for degradation. Taken together, these observations suggest that aggregate formation reflects an imbalance in the kinetics among association, prevention, and dissociation by molecular chaperones.

36.6.3 Proteasomes

The proteasome is another central component in protein quality control that is essential for the clearance of damaged proteins and aggregates. Observations that proteasomes associate with polyglutamine aggregates suggest that proteasome activity could be involved in aggregate dissociation [27, 28, 103, 104]. In support of this hypothesis, inhibition of proteasome activity delayed aggregate clearance in tet-regulated huntingtin mice and in 293 tet-off cells [105, 106]. Conversely, the presence of aggregates results in the inhibition of proteasome activity [107, 108]. It is unclear whether there are distinct populations of soluble or aggregate-associated proteasomes and whether this would correspond to different proteasome activities. It seems likely that aggregate formation is a consequence of a competition between proteasome-dependent degradation of the misfolded proteins and the inhibitory effect of aggregates on proteasome activity.

36.6.4 The Protein-folding "Buffer" and Aging

The late age of onset observed in patients with neurodegenerative diseases seems to indicate a decline in the ability of a cell's "protein-folding buffer" to cope with persistent misfolded proteins. The observation of age-dependent aggregation is not limited to humans but can be recapitulated in a *C. elegans* polyglutamine model. The ability to visualize fluorescently tagged polyglutamine proteins in living, transparent animals has allowed monitoring of the age-dependent formation of polyglutamine aggregates in animals expressing a range of glutamines from 0Q to 82Q (Figure 36.1A) [61]. In this model, an age-dependent intensification of aggregate formation that paralleled a decline in motility was observed for all animals expressing polyglutamine above 29Qs.

What is the link between aging and the cell's protein-folding buffer? The relationship between the rate of aging and the progressive nature of polyglutamine-mediated phenotypes was observed in *C. elegans* expressing 82Q in the *age-1* (hx546) background, a mutation in the insulin-like signaling pathway that extends lifespan [61]. These mutant animals lived longer and exhibited delayed aggregate formation and motility defects relative to an 82Q-expressing animal in the wild-type background (Figure 36.4, see p. 1191). Both the delay in aggregate formation and the loss of motility in the *age-1* background were dependent on the activity of Daf-16 (a forkhead transcription factor known to act downstream of Age-1). These

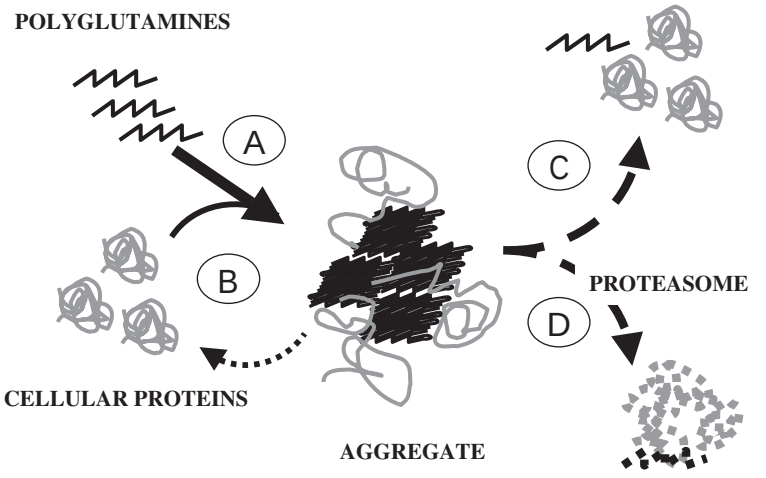

Fig. 36.5. Role of protein aggregation modifiers in reducing aggregate formation. Molecular modifiers can regulate different processes during protein aggregate formation and dissociation. Aggregate modifiers can prevent or delay oligomerization (A), prevent or delay interaction between the misfolded and aggregated proteins with other cellular proteins (B), alter the stability of the aggregate to facilitate dissociation by removing and refolding aggregating proteins along with the associated cellular proteins (C), or facilitate degradation of the components of aggregates (D).

observations indicate that the modulators of aging may also regulate factors involved in protein-folding homeostasis. Indeed, downregulation of Daf-16 leads to decreased expression of molecular chaperones [109]. Downregulation of Hsf-1, a master transcriptional regulator for protein-folding quality control, also causes premature aging and affects many of the same molecular chaperones that are involved in aging [110]. These findings suggest that the ability of cells to sense and respond adequately to the appearance of misfolded and aggregate-prone proteins diminishes with aging as a consequence of altered molecular chaperone levels [61].

36.6.5 Summary

A common denominator among the modulators of protein aggregation discussed in this review appears to be the ability to shield the interactive surfaces of the misfolding proteins from the rest of the cellular environment (Figure 36.5). Whether it is the protein context or protein homeostasis machinery, the prevention of intra- and inter-molecular interactions is a major requirement in the molecular events regulating protein aggregation. Molecular modifiers may also have the capacity to dissociate large aggregates. It may be that the same set of modulators is involved in both processes, as Hsp70 appears to function in both aggregate formation and dissolution. Almost certainly, there are other, still unidentified protein-folding modulators that can prevent aggregation by facilitating the refolding or degradation of

misfolded proteins. In all cases, the ability to clear the cell of these noxious proteins may be the first line of defense against the appearance and persistence of such toxic entities. As we decipher how cells combat protein aggregates, the identification of other novel regulators of protein misfolding and aggregation that can be manipulated will be invaluable in understanding the course of protein-misfolding diseases.

36.7 Experimental Protocols

36.7.1 FRAP Analysis

Background

The ability to attach a fluorescent tag to a protein of interest, such as green fluorescent protein (GFP), allows researchers to study the protein in living cells without disrupting the cellular environment. A fluorescently tagged protein is useful in following the protein localization but is not limited to this, as mobility of the fluorescently tagged protein is also informative of its microenvironments. Protein mobility is affected by its size and shape, the viscosity of the environment, and interactions with organelles in the cell or with other proteins. Therefore, delay in mobility, compared to the predicted mobility, is a reflection of its biophysical state. For example, if a protein is bound to a cellular structure, its mobility is expected to be significantly slower than the soluble, unattached form.

One method that has become useful in deciphering the protein's mobility is fluorescence recovery after photobleaching (FRAP). In FRAP, a short pulse of intense laser light irreversibly destroys fluorescence of the molecules (photobleaching). The recovery of fluorescence in the photobleached area, therefore, is a result of diffusional exchange between the bleached and unbleached fluorescent molecules. By monitoring the time required for fluorescence recovery in the photobleached region, one can determine the speed at which the protein of interest travels from point A to point B. Therefore, we have used FRAP methodology to study mobility of the proteins associated with the polyglutamine aggregates to further understand the microenvironment of the co-associated protein as well as the polyglutamine aggregates themselves.

Microscope

FRAP analysis is usually done using a confocal microscope equipped with the ability to define a region of interest (ROI) for photobleaching and to acquire time series images at defined time intervals (preferably in milliseconds).

Software

Most commercially available confocal microscope operating software allows programming of the FRAP routines as macros, but some training is required. FRAP protocols using a specific operating software are usually available through the individual companies. Average fluorescent intensity can be determined using dif-

ferent imaging software, such as Metamorph (Universal Imaging Corp., Downingtown, PA) or Image J, which can be downloaded at no cost from http://rsb.info.nih.gov/ij/.

Sample Preparations

FRAP analysis was done with tissue cultured cells grown in a glass-bottom chamber (MatTreK Corp., Ashland, MA) or *C. elegans* mounted on a 2% agar pad glass slide and immobilized in 1 mM levamisole.

Controls for General Photobleaching

An important aspect in generating useful FRAP images is to include a control for general photobleaching. Although the general photobleaching is minimal with current confocal microscopes, especially since minimal laser power is used to scan the images, it is generally a good idea to have a non-photobleached sample. This control not only would determine the level of general photobleaching but also could be used to monitor lateral movements of the target cell during image acquisition. For this, the best control would be an adjacent cell expressing the fluorescent protein. However, depending on the transfection efficiency, it may be difficult to find an adjacent fluorescent cell. As a control, we tried an un-photobleached area of the aggregates as well as an adjacent cell (when possible) and found no significant differences. Therefore, we used the un-photobleached area next to the aggregates as control for our experiments.

Image Acquisition

The following protocol is outlined for FRAP analysis using a GFP-tagged sample; only a general description of the bleaching routine is outlined.

1. Scan a single image using a low laser power (at 488 nm) and save the image.
   The level of the laser power should be sufficiently low not to photobleach the sample and yet generate a good image. This condition will vary depending on the microscope. Scan the image near saturation but do not exceed it. (Pre-bleach)
2. Define the region of interest (ROI) for the photobleaching.
3. Set the laser power to maximum (100%) power. GFP (488 nm) and YFP (514 nm) lasers are better in photobleaching.
4. Scan the ROI (bleaching area) at maximum laser power until the fluorescence is no longer detectable.
   Optimal time for photobleaching can be determined using a fixed fluorescent sample and photobleaching at different durations ($\sim$3–10 s) until the fluorescence (only at ROI) is undetectable. Choose the minimal time for complete photobleaching since prolonged exposure to high-intensity laser can be harmful to the cell and also cause photobleaching outside of the ROI. (Bleach)
5. Reset the laser and the scan setting to the same condition as the pre-bleach condition.
6. Scan the image at desired intervals. This interval can range from microseconds to minutes depending on the mobility of the protein that is being observed.

Data Analysis

Determine the average fluorescence intensity of the area that was (1) subjected to photobleaching and (2) the adjacent control for each time point. Relative fluorescence intensity (RFI) is calculated using the following equation:

$$RFI = (Net/N1t)/(Ne0/N10)$$

where *Net* = average fluorescence intensity of the ROI (photobleached) area at time *x*;
N1t = average fluorescence intensity of the control (non-photobleached) area at time *x*;
Ne0 = average fluorescence intensity of the ROI at time zero (pre-bleaching);
N10 = average fluorescence intensity of the control area at time zero.

FRAP References

The following are excellent references for FRAP analysis:

Spector, D. L., Goldman, R. D., Leinwand, L. A. (1998) *Cells: a laboratory manual; Volume 2: Light Microscopy and Cell Structure*. pp. 79.1–79.23. Cold Spring Harbor Laboratory press.

Lippincott-Schwartz, J., Snapp, E., Kenworthy, A. (2001) Studying protein dynamics in living cells. *Nat. Rev. Mol. Cell. Biol*, 2,444–456.

References

1 Zoghbi, H. Y. & Orr, H. T. (2000). Glutamine repeats and neurodegeneration. *Annu Rev Neurosci* 23, 217–47.

2 Gusella, J. F. & MacDonald, M. E. (2000). Molecular genetics: unmasking polyglutamine triggers in neurodegenerative disease. *Nat Rev Neurosci* 1, 109–15.

3 Orr, H. T. (2001). Beyond the Qs in the polyglutamine diseases. *Genes Dev* 15, 925–32.

4 Nakamura, K., Jeong, S. Y., Uchihara, T., Anno, M., Nagashima, K., Nagashima, T., Ikeda, S., Tsuji, S. & Kanazawa, I. (2001). SCA17, a novel autosomal dominant cerebellar ataxia caused by an expanded polyglutamine in TATA-binding protein. *Hum Mol Genet* 10, 1441–8.

5 Andrew, S. E., Goldberg, Y. P., Kremer, B., Telenius, H., Theilmann, J., Adam, S., Starr, E., Squitieri, F., Lin, B. & Kalchman, M. A. (1993). The relationship between trinucleotide (CAG) repeat length and clinical features of Huntington's disease. *Nature genetics*. 4(4), 398–403.

6 Snell, R. G., MacMillan, J. C., Cheadle, J. P., Fenton, I., Lazarou, L. P., Davies, P., MacDonald, M. E., Gusella, J. F., Harper, P. S. & Shaw, D. J. (1993). Relationship between trinucleotide repeat expansion and phenotypic variation in Huntington's disease. *Nat Genet* 4, 393–7.

7 Duyao, M., Ambrose, C., Myers, R., Novelletto, A., Persichetti, F., Frontali, M., Folstein, S., Ross, C., Franz, M., Abbott, M. & et al. (1993). Trinucleotide repeat length instability and age of onset in Huntington's disease. *Nat Genet* 4, 387–92.

8 Wexler, N. S., Young, A. B., Tanzi, R. E., Travers, H., Starosta-

Rubinstein, S., Penney, J. B., Snodgrass, S. R., Shoulson, I., Gomez, F., Ramos Arroyo, M. A. & et al. (1987). Homozygotes for Huntington's disease. *Nature* 326, 194–7.

9 Duyao, M. P., Auerbach, A. B., Ryan, A., Persichetti, F., Barnes, G. T., McNeil, S. M., Ge, P., Vonsattel, J. P., Gusella, J. F., Joyner, A. L. & et al. (1995). Inactivation of the mouse Huntington's disease gene homolog Hdh. *Science* 269, 407–10.

10 Nasir, J., Floresco, S. B., O'Kusky, J. R., Diewert, V. M., Richman, J. M., Zeisler, J., Borowski, A., Marth, J. D., Phillips, A. G. & Hayden, M. R. (1995). Targeted disruption of the Huntington's disease gene results in embryonic lethality and behavioral and morphological changes in heterozygotes. *Cell* 81, 811–23.

11 Zeitlin, S., Liu, J. P., Chapman, D. L., Papaioannou, V. E. & Efstratiadis, A. (1995). Increased apoptosis and early embryonic lethality in mice nullizygous for the Huntington's disease gene homologue. *Nat Genet* 11, 155–63.

12 Matilla, A., Roberson, E. D., Banfi, S., Morales, J., Armstrong, D. L., Burright, E. N., Orr, H. T., Sweatt, J. D., Zoghbi, H. Y. & Matzuk, M. M. (1998). Mice lacking ataxin-1 display learning deficits and decreased hippocampal paired-pulse facilitation. *J Neurosci* 18, 5508–16.

13 Ambrose, H. J., Byrd, P. J., McConville, C. M., Cooper, P. R., Stankovic, T., Riley, J. H., Shiloh, Y., McNamara, J. O., Fukao, T. & Taylor, A. M. (1994). A physical map across chromosome 11q22-q23 containing the major locus for ataxia telangiectasia. *Genomics* 21, 612–9.

14 Davies, A. F., Mirza, G., Sekhon, G., Turnpenny, P., Leroy, F., Speleman, F., Law, C., van Regemorter, N., Vamos, E., Flinter, F. & Ragoussis, J. (1999). Delineation of two distinct 6p deletion syndromes. *Hum Genet* 104, 64–72.

15 Bates, G. P., Mangiarini, L., Mahal, A. & Davies, S. W. (1997). Transgenic models of Huntington's disease. *Hum Mol Genet* 6, 1633–7.

16 Rubinsztein, D. C. (2002). Lessons from animal models of Huntington's disease. *Trends Genet* 18, 202–9.

17 Marsh, J. L., Pallos, J. & Thompson, L. M. (2003). Fly models of Huntington's disease. *Hum Mol Genet* 12 Spec No 2, R187–93.

18 Faber, P. W., Alter, J. R., MacDonald, M. E. & Hart, A. C. (1999). Polyglutamine-mediated dysfunction and apoptotic death of a Caenorhabditis elegans sensory neuron. *Proc Natl Acad Sci USA* 96, 179–84.

19 Parker, J. A., Connolly, J. B., Wellington, C., Hayden, M., Dausset, J. & Neri, C. (2001). Expanded polyglutamines in Caenorhabditis elegans cause axonal abnormalities and severe dysfunction of PLM mechanosensory neurons without cell death. *Proc Natl Acad Sci USA* 98, 13318–23.

20 DiFiglia, M., Sapp, E., Chase, K. O., Davies, S. W., Bates, G. P., Vonsattel, J. P. & Aronin, N. (1997). Aggregation of huntingtin in neuronal intranuclear inclusions and dystrophic neurites in brain. *Science* 277, 1990–3.

21 Paulson, H. L., Perez, M. K., Trottier, Y., Trojanowski, J. Q., Subramony, S. H., Das, S. S., Vig, P., Mandel, J. L., Fischbeck, K. H. & Pittman, R. N. (1997). Intranuclear inclusions of expanded polyglutamine protein in spinocerebellar ataxia type 3. *Neuron* 19, 333–44.

22 Skinner, P. J., Koshy, B. T., Cummings, C. J., Klement, I. A., Helin, K., Servadio, A., Zoghbi, H. Y. & Orr, H. T. (1997). Ataxin-1 with an expanded glutamine tract alters nuclear matrix-associated structures. *Nature* 389, 971–4.

23 Holmberg, M., Duyckaerts, C., Durr, A., Cancel, G., Gourfinkel-An, I., Damier, P., Faucheux, B., Trottier, Y., Hirsch, E. C., Agid, Y. & Brice, A. (1998). Spinocerebellar ataxia type 7 (SCA7): a neurodegenerative disorder with neuronal intra-

nuclear inclusions. *Hum Mol Genet* 7, 913–8.

24 Hayashi, Y., Kakita, A., Yamada, M., Egawa, S., Oyanagi, S., Naito, H., Tsuji, S. & Takahashi, H. (1998). Hereditary dentatorubral-pallidoluysian atrophy: ubiquitinated filamentous inclusions in the cerebellar dentate nucleus neurons. *Acta Neuropathol (Berl)* 95, 479–82.

25 Li, M., Miwa, S., Kobayashi, Y., Merry, D. E., Yamamoto, M., Tanaka, F., Doyu, M., Hashizume, Y., Fischbeck, K. H. & Sobue, G. (1998). Nuclear inclusions of the androgen receptor protein in spinal and bulbar muscular atrophy. *Ann Neurol* 44, 249–54.

26 Ross, C. A. (1997). Intranuclear neuronal inclusions: a common pathogenic mechanism for glutamine-repeat neurodegenerative diseases? *Neuron* 19, 1147–50.

27 Cummings, C. J., Mancini, M. A., Antalffy, B., DeFranco, D. B., Orr, H. T. & Zoghbi, H. Y. (1998). Chaperone suppression of aggregation and altered subcellular proteasome localization imply protein misfolding in SCA1. *Nat Genet* 19, 148–54.

28 Stenoien, D. L., Cummings, C. J., Adams, H. P., Mancini, M. G., Patel, K., DeMartino, G. N., Marcelli, M., Weigel, N. L. & Mancini, M. A. (1999). Polyglutamine-expanded androgen receptors form aggregates that sequester heat shock proteins, proteasome components and SRC-1, and are suppressed by the HDJ-2 chaperone. *Hum Mol Genet* 8, 731–41.

29 Chai, Y., Koppenhafer, S. L., Bonini, N. M. & Paulson, H. L. (1999). Analysis of the role of heat shock protein (Hsp) molecular chaperones in polyglutamine disease. *J Neurosci* 19, 10338–47.

30 Jana, N. R., Tanaka, M., Wang, G. & Nukina, N. (2000). Polyglutamine length-dependent interaction of Hsp40 and Hsp70 family chaperones with truncated N-terminal huntingtin: their role in suppression of aggregation and cellular toxicity. *Hum Mol Genet* 9, 2009–18.

31 Kobayashi, Y., Kume, A., Li, M., Doyu, M., Hata, M., Ohtsuka, K. & Sobue, G. (2000). Chaperones Hsp70 and Hsp40 suppress aggregate formation and apoptosis in cultured neuronal cells expressing truncated androgen receptor protein with expanded polyglutamine tract. *J Biol Chem* 275, 8772–8.

32 Onodera, O., Roses, A. D., Tsuji, S., Vance, J. M., Strittmatter, W. J. & Burke, J. R. (1996). Toxicity of expanded polyglutamine-domain proteins in Escherichia coli. *FEBS Lett* 399, 135–9.

33 Meriin, A. B., Zhang, X., He, X., Newnam, G. P., Chernoff, Y. O. & Sherman, M. Y. (2002). Huntington toxicity in yeast model depends on polyglutamine aggregation mediated by a prion-like protein Rnq1. *J Cell Biol* 157, 997–1004.

34 Krobitsch, S. & Lindquist, S. (2000). Aggregation of huntingtin in yeast varies with the length of the polyglutamine expansion and the expression of chaperone proteins. *Proc Natl Acad Sci USA* 97, 1589–94.

35 Satyal, S. H., Schmidt, E., Kitagawa, K., Sondheimer, N., Lindquist, S., Kramer, J. M. & Morimoto, R. I. (2000). Polyglutamine aggregates alter protein folding homeostasis in Caenorhabditis elegans. *Proc Natl Acad Sci USA* 97, 5750–5755.

36 Cooper, J. K., Schilling, G., Peters, M. F., Herring, W. J., Sharp, A. H., Kaminsky, Z., Masone, J., Khan, F. A., Delanoy, M., Borchelt, D. R., Dawson, V. L., Dawson, T. M. & Ross, C. A. (1998). Truncated N-terminal fragments of huntingtin with expanded glutamine repeats form nuclear and cytoplasmic aggregates in cell culture. *Hum Mol Genet* 7, 783–90.

37 Moulder, K. L., Onodera, O., Burke, J. R., Strittmatter, W. J. & Johnson, E. M., Jr. (1999). Generation of neuronal intranuclear inclusions by polyglutamine-GFP: analysis of inclusion clearance and toxicity as a function of polyglutamine length. *J Neurosci* 19, 705–15.

38 Sato, A., Shimohata, T., Koide, R., Takano, H., Sato, T., Oyake, M., Igarashi, S., Tanaka, K., Inuzuka, T., Nawa, H. & Tsuji, S. (1999). Adenovirus-mediated expression of mutant DRPLA proteins with expanded polyglutamine stretches in neuronally differentiated PC12 cells. Preferential intranuclear aggregate formation and apoptosis. *Hum Mol Genet* 8, 997–1006.

39 Ordway, J. M., Tallaksen-Greene, S., Gutekunst, C. A., Bernstein, E. M., Cearley, J. A., Wiener, H. W., Dure, L. S. t., Lindsey, R., Hersch, S. M., Jope, R. S., Albin, R. L. & Detloff, P. J. (1997). Ectopically expressed CAG repeats cause intranuclear inclusions and a progressive late onset neurological phenotype in the mouse. *Cell* 91, 753–63.

40 Warrick, J. M., Chan, H. Y., Gray-Board, G. L., Chai, Y., Paulson, H. L. & Bonini, N. M. (1999). Suppression of polyglutamine-mediated neurodegeneration in Drosophila by the molecular chaperone HSP70. *Nat Genet* 23, 425–8.

41 Fernandez-Funez, P., Nino-Rosales, M. L., de Gouyon, B., She, W. C., Luchak, J. M., Martinez, P., Turiegano, E., Benito, J., Capovilla, M., Skinner, P. J., McCall, A., Canal, I., Orr, H. T., Zoghbi, H. Y. & Botas, J. (2000). Identification of genes that modify ataxin-1-induced neurodegeneration. *Nature* 408, 101–6.

42 Perutz, M. F. (1999). Glutamine repeats and neurodegenerative diseases: molecular aspects. *Trends Biochem Sci* 24, 58–63.

43 Perutz, M. F., Johnson, T., Suzuki, M. & Finch, J. T. (1994). Glutamine repeats as polar zippers: their possible role in inherited neurodegenerative diseases. *Proc Natl Acad Sci USA* 91, 5355–8.

44 Scherzinger, E., Lurz, R., Turmaine, M., Mangiarini, L., Hollenbach, B., Hasenbank, R., Bates, G. P., Davies, S. W., Lehrach, H. & Wanker, E. E. (1997). Huntingtin-encoded polyglutamine expansions form amyloid-like protein aggregates in vitro and in vivo. *Cell* 90, 549–58.

45 Chen, S., Berthelier, V., Yang, W. & Wetzel, R. (2001). Polyglutamine aggregation behavior in vitro supports a recruitment mechanism of cytotoxicity. *J Mol Biol* 311, 173–82.

46 Scherzinger, E., Sittler, A., Schweiger, K., Heiser, V., Lurz, R., Hasenbank, R., Bates, G. P., Lehrach, H. & Wanker, E. E. (1999). Self-assembly of polyglutamine-containing huntingtin fragments into amyloid-like fibrils: implications for Huntington's disease pathology. *Proc Natl Acad Sci USA* 96, 4604–9.

47 Chen, S., Berthelier, V., Hamilton, J. B., O'Nuallain, B. & Wetzel, R. (2002). Amyloid-like features of polyglutamine aggregates and their assembly kinetics. *Biochemistry* 41, 7391–9.

48 Tanaka, M., Machida, Y., Nishikawa, Y., Akagi, T., Hashikawa, T., Fujisawa, T. & Nukina, N. (2003). Expansion of polyglutamine induces the formation of quasi-aggregate in the early stage of protein fibrillization. *J Biol Chem* 278, 34717–24.

49 Thakur, A. K. & Wetzel, R. (2002). Mutational analysis of the structural organization of polyglutamine aggregates. *Proc Natl Acad Sci USA* 99, 17014–9.

50 Georgalis, Y., Starikov, E. B., Hollenbach, B., Lurz, R., Scherzinger, E., Saenger, W., Lehrach, H. & Wanker, E. E. (1998). Huntingtin aggregation monitored by dynamic light scattering. *Proc Natl Acad Sci USA* 95, 6118–21.

51 Tanaka, M., Morishima, I., Akagi, T., Hashikawa, T. & Nukina, N. (2001). Intra- and intermolecular beta-pleated sheet formation in glutamine-repeat inserted myoglobin as a model for polyglutamine diseases. *J Biol Chem* 276, 45470–5.

52 Poirier, M. A., Li, H., Macosko, J., Cai, S., Amzel, M. & Ross, C. A. (2002). Huntingtin spheroids and protofibrils as precursors in polyglutamine fibrilization. *J Biol Chem* 277, 41032–7.

53 Sanchez, I., Mahlke, C. & Yuan, J. (2003). Pivotal role of oligomerization in expanded polyglutamine neurodegenerative disorders. *Nature* 421, 373–9.

54 Sipe, J. D. & Cohen, A. S. (2000). Review: history of the amyloid fibril. *J Struct Biol* 130, 88–98.

55 Rochet, J. C. & Lansbury, P. T., Jr. (2000). Amyloid fibrillogenesis: themes and variations. *Curr Opin Struct Biol* 10, 60–8.

56 Taylor, J. P., Hardy, J. & Fischbeck, K. H. (2002). Toxic proteins in neurodegenerative disease. *Science* 296, 1991–5.

57 Temussi, P. A., Masino, L. & Pastore, A. (2003). From Alzheimer to Huntington: why is a structural understanding so difficult? *EMBO J* 22, 355–61.

58 Fandrich, M. & Dobson, C. M. (2002). The behaviour of polyamino acids reveals an inverse side chain effect in amyloid structure formation. *EMBO J* 21, 5682–90.

59 Chai, Y., Shao, J., Miller, V. M., Williams, A. & Paulson, H. L. (2002). Live-cell imaging reveals divergent intracellular dynamics of polyglutamine disease proteins and supports a sequestration model of pathogenesis. *Proc Natl Acad Sci USA*.

60 Stenoien, D. L., Mielke, M. & Mancini, M. A. (2002). Intranuclear ataxin1 inclusions contain both fast- and slow-exchanging components. *Nat Cell Biol* 4, 806–10.

61 Morley, J. F., Brignull, H. R., Weyers, J. J. & Morimoto, R. I. (2002). The threshold for polyglutamine-expansion protein aggregation and cellular toxicity is dynamic and influenced by aging in Caenorhabditis elegans. *Proc Natl Acad Sci USA* 99, 10417–22.

62 Kim, S., Nollen, E. A., Kitagawa, K., Bindokas, V. P. & Morimoto, R. I. (2002). Polyglutamine protein aggregates are dynamic. *Nat Cell Biol* 4, 826–31.

63 Rajan, R. S., Illing, M. E., Bence, N. F. & Kopito, R. R. (2001). Specificity in intracellular protein aggregation and inclusion body formation. *Proc Natl Acad Sci USA* 98, 13060–5.

64 Klement, I. A., Skinner, P. J., Kaytor, M. D., Yi, H., Hersch, S. M., Clark, H. B., Zoghbi, H. Y. & Orr, H. T. (1998). Ataxin-1 nuclear localization and aggregation: role in polyglutamine-induced disease in SCA1 transgenic mice. *Cell* 95, 41–53.

65 Saudou, F., Finkbeiner, S., Devys, D. & Greenberg, M. E. (1998). Huntingtin acts in the nucleus to induce apoptosis but death does not correlate with the formation of intranuclear inclusions. *Cell* 95, 55–66.

66 Sisodia, S. S. (1998). Nuclear inclusions in glutamine repeat disorders: are they pernicious, coincidental, or beneficial? *Cell* 95, 1–4.

67 Soto, C. (2003). Unfolding the role of protein misfolding in neurodegenerative diseases. *Nat Rev Neurosci* 4, 49–60.

68 Lambert, M. P., Barlow, A. K., Chromy, B. A., Edwards, C., Freed, R., Liosatos, M., Morgan, T. E., Rozovsky, I., Trommer, B., Viola, K. L., Wals, P., Zhang, C., Finch, C. E., Krafft, G. A. & Klein, W. L. (1998). Diffusible, nonfibrillar ligands derived from Abeta1-42 are potent central nervous system neurotoxins. *Proc Natl Acad Sci USA* 95, 6448–53.

69 Hartley, D. M., Walsh, D. M., Ye, C. P., Diehl, T., Vasquez, S., Vassilev, P. M., Teplow, D. B. & Selkoe, D. J. (1999). Protofibrillar intermediates of amyloid beta-protein induce acute electrophysiological changes and progressive neurotoxicity in cortical neurons. *J Neurosci* 19, 8876–84.

70 Pillot, T., Drouet, B., Queille, S., Labeur, C., Vandekerchkhove, J., Rosseneu, M., Pincon-Raymond, M. & Chambaz, J. (1999). The nonfibrillar amyloid beta-peptide induces apoptotic neuronal cell death: involvement of its C-terminal fusogenic domain. *J Neurochem* 73, 1626–34.

71 Zhu, Y. J., Lin, H. & Lal, R. (2000). Fresh and nonfibrillar amyloid beta protein(1-40) induces rapid cellular degeneration in aged human

fibroblasts: evidence for AbetaP-channel-mediated cellular toxicity. *Faseb J* 14, 1244–54.

72 Bucciantini, M., Giannoni, E., Chiti, F., Baroni, F., Formigli, L., Zurdo, J., Taddei, N., Ramponi, G., Dobson, C. M. & Stefani, M. (2002). Inherent toxicity of aggregates implies a common mechanism for protein misfolding diseases. *Nature* 416, 507–11.

73 Kayed, R., Head, E., Thompson, J. L., McIntire, T. M., Milton, S. C., Cotman, C. W. & Glabe, C. G. (2003). Common structure of soluble amyloid oligomers implies common mechanism of pathogenesis. *Science* 300, 486–9.

74 Perez, M. K., Paulson, H. L., Pendse, S. J., Saionz, S. J., Bonini, N. M. & Pittman, R. N. (1998). Recruitment and the role of nuclear localization in polyglutamine-mediated aggregation. *J Cell Biol* 143, 1457–70.

75 Kazantsev, A., Preisinger, E., Dranovsky, A., Goldgaber, D. & Housman, D. (1999). Insoluble detergent-resistant aggregates form between pathological and nonpathological lengths of polyglutamine in mammalian cells. *Proc Natl Acad Sci USA* 96, 11404–9.

76 Nagai, Y., Onodera, O., Chun, J., Strittmatter, W. J. & Burke, J. R. (1999). Expanded polyglutamine domain proteins bind neurofilament and alter the neurofilament network. *Exp Neurol* 155, 195–203.

77 Schmidt, T., Lindenberg, K. S., Krebs, A., Schols, L., Laccone, F., Herms, J., Rechsteiner, M., Riess, O. & Landwehrmeyer, G. B. (2002). Protein surveillance machinery in brains with spinocerebellar ataxia type 3: redistribution and differential recruitment of 26S proteasome subunits and chaperones to neuronal intranuclear inclusions. *Ann Neurol* 51, 302–10.

78 Li, S. H., Cheng, A. L., Li, H. & Li, X. J. (1999). Cellular defects and altered gene expression in PC12 cells stably expressing mutant huntingtin. *J Neurosci* 19, 5159–72.

79 Lin, X., Antalffy, B., Kang, D., Orr, H. T. & Zoghbi, H. Y. (2000). Polyglutamine expansion down-regulates specific neuronal genes before pathologic changes in SCA1 [see comments]. *Nat Neurosci* 3, 157–63.

80 Sugars, K. L. & Rubinsztein, D. C. (2003). Transcriptional abnormalities in Huntington disease. *Trends Genet* 19, 233–8.

81 Nucifora, F. C., Jr., Sasaki, M., Peters, M. F., Huang, H., Cooper, J. K., Yamada, M., Takahashi, H., Tsuji, S., Troncoso, J., Dawson, V. L., Dawson, T. M. & Ross, C. A. (2001). Interference by huntingtin and atrophin-1 with cbp-mediated transcription leading to cellular toxicity. *Science* 291, 2423–8.

82 Mantamadiotis, T., Lemberger, T., Bleckmann, S. C., Kern, H., Kretz, O., Martin Villalba, A., Tronche, F., Kellendonk, C., Gau, D., Kapfhammer, J., Otto, C., Schmid, W. & Schutz, G. (2002). Disruption of CREB function in brain leads to neurodegeneration. *Nat Genet* 31, 47–54.

83 DePace, A. H., Santoso, A., Hillner, P. & Weissman, J. S. (1998). A critical role for amino-terminal glutamine/asparagine repeats in the formation and propagation of a yeast prion. *Cell* 93, 1241–52.

84 Michelitsch, M. D. & Weissman, J. S. (2000). A census of glutamine/asparagine-rich regions: implications for their conserved function and the prediction of novel prions. *Proc Natl Acad Sci USA* 97, 11910–5.

85 Suhr, S. T., Senut, M. C., Whitelegge, J. P., Faull, K. F., Cuizon, D. B. & Gage, F. H. (2001). Identities of sequestered proteins in aggregates from cells with induced polyglutamine expression. *J Cell Biol* 153, 283–94.

86 Harjes, P. & Wanker, E. E. (2003). The hunt for huntingtin function: interaction partners tell many different stories. *Trends Biochem Sci* 28, 425–33.

87 Koshy, B., Matilla, T., Burright,

E. N., Merry, D. E., Fischbeck, K. H., Orr, H. T. & Zoghbi, H. Y. (1996). Spinocerebellar ataxia type-1 and spinobulbar muscular atrophy gene products interact with glyceraldehyde-3-phosphate dehydrogenase. *Hum Mol Genet* 5, 1311–8.

88 Chen, H. K., Fernandez-Funez, P., Acevedo, S. F., Lam, Y. C., Kaytor, M. D., Fernandez, M. H., Aitken, A., Skoulakis, E. M., Orr, H. T., Botas, J. & Zoghbi, H. Y. (2003). Interaction of Akt-phosphorylated ataxin-1 with 14-3-3 mediates neurodegeneration in spinocerebellar ataxia type 1. *Cell* 113, 457–68.

89 Emamian, E. S., Kaytor, M. D., Duvick, L. A., Zu, T., Tousey, S. K., Zoghbi, H. Y., Clark, H. B. & Orr, H. T. (2003). Serine 776 of ataxin-1 is critical for polyglutamine-induced disease in SCA1 transgenic mice. *Neuron* 38, 375–87.

90 Opal, P. & Zoghbi, H. Y. (2002). The role of chaperones in polyglutamine disease. *Trends Mol Med* 8, 232–6.

91 Muchowski, P. J. (2002). Protein misfolding, amyloid formation, and neurodegeneration: a critical role for molecular chaperones? *Neuron* 35, 9–12.

92 Kazemi-Esfarjani, P. & Benzer, S. (2000). Genetic suppression of polyglutamine toxicity in Drosophila. *Science* 287, 1837–40.

93 Carmichael, J., Chatellier, J., Woolfson, A., Milstein, C., Fersht, A. R. & Rubinsztein, D. C. (2000). Bacterial and yeast chaperones reduce both aggregate formation and cell death in mammalian cell models of Huntington's disease. *Proc Natl Acad Sci USA* 97, 9701–5.

94 Muchowski, P. J., Schaffar, G., Sittler, A., Wanker, E. E., Hayer-Hartl, M. K. & Hartl, F. U. (2000). Hsp70 and hsp40 chaperones can inhibit self-assembly of polyglutamine proteins into amyloid-like fibrils. *Proc Natl Acad Sci USA* 97, 7841–6.

95 Ben-Zvi, A. P. & Goloubinoff, P. (2001). Review: mechanisms of disaggregation and refolding of stable protein aggregates by molecular chaperones. *J Struct Biol* 135, 84–93.

96 Hartl, F. U. & Hayer-Hartl, M. (2002). Molecular chaperones in the cytosol: from nascent chain to folded protein. *Science* 295, 1852–8.

97 Yamamoto, A., Lucas, J. J. & Hen, R. (2000). Reversal of neuropathology and motor dysfunction in a conditional model of Huntington's disease. *Cell* 101, 57–66.

98 Skowyra, D., Georgopoulos, C. & Zylicz, M. (1990). The E. coli dnaK gene product, the hsp70 homolog, can reactivate heat-inactivated RNA polymerase in an ATP hydrolysis-dependent manner. *Cell* 62, 939–44.

99 Diamant, S., Ben-Zvi, A. P., Bukau, B. & Goloubinoff, P. (2000). Size-dependent disaggregation of stable protein aggregates by the DnaK chaperone machinery. *J Biol Chem* 275, 21107–13.

100 Mogk, A., Tomoyasu, T., Goloubinoff, P., Rudiger, S., Roder, D., Langen, H. & Bukau, B. (1999). Identification of thermolabile *Escherichia coli* proteins: prevention and reversion of aggregation by DnaK and ClpB. *EMBO J* 18, 6934–49.

101 Parsell, D. A., Kowal, A. S., Singer, M. A. & Lindquist, S. (1994). Protein disaggregation mediated by heat-shock protein Hsp104. *Nature* 372, 475–8.

102 Glover, J. R. & Lindquist, S. (1998). Hsp104, Hsp70, and Hsp40: a novel chaperone system that rescues previously aggregated proteins. *Cell* 94, 73–82.

103 Chai, Y., Koppenhafer, S. L., Shoesmith, S. J., Perez, M. K. & Paulson, H. L. (1999). Evidence for proteasome involvement in polyglutamine disease: localization to nuclear inclusions in SCA3/MJD and suppression of polyglutamine aggregation in vitro. *Hum Mol Genet* 8, 673–82.

104 Wyttenbach, A., Carmichael, J., Swartz, J., Furlong, R. A., Narain, Y., Rankin, J. & Rubinsztein, D. C. (2000). Effects of heat shock, heat shock protein 40 (HDJ-2), and proteasome inhibition on protein

aggregation in cellular models of Huntington's disease. *Proc Natl Acad Sci USA* 97, 2898–903.

105 Martin-Aparicio, E., Yamamoto, A., Hernandez, F., Hen, R., Avila, J. & Lucas, J. J. (2001). Proteasomal-dependent aggregate reversal and absence of cell death in a conditional mouse model of Huntington's disease. *J Neurosci* 21, 8772–81.

106 Waelter, S., Boeddrich, A., Lurz, R., Scherzinger, E., Lueder, G., Lehrach, H. & Wanker, E. E. (2001). Accumulation of mutant huntingtin fragments in aggresome-like inclusion bodies as a result of insufficient protein degradation. *Mol Biol Cell* 12, 1393–407.

107 Bence, N. F., Sampat, R. M. & Kopito, R. R. (2001). Impairment of the ubiquitin-proteasome system by protein aggregation. *Science* 292, 1552–5.

108 Verhoef, L. G., Lindsten, K., Masucci, M. G. & Dantuma, N. P. (2002). Aggregate formation inhibits proteasomal degradation of polyglutamine proteins. *Hum Mol Genet* 11, 2689–700.

109 Hsu, A. L., Murphy, C. T. & Kenyon, C. (2003). Regulation of aging and age-related disease by DAF-16 and heat-shock factor. *Science* 300, 1142–5.

110 Morley, J. F. & Morimoto, R. I. (2004). Regulation of longevity in Caenorhabditis elegans by heat shock factor and molecular chaperones. *Mol Biol Cell* 15, 657–64.

111 Zhou, H., Li, S. H. & Li, X. J. (2001). Chaperone suppression of cellular toxicity of huntingtin is independent of polyglutamine aggregation. *J Biol Chem* 276, 48417–24.

112 Chan, H. Y., Warrick, J. M., Gray-Board, G. L., Paulson, H. L. & Bonini, N. M. (2000). Mechanisms of chaperone suppression of polyglutamine disease: selectivity, synergy and modulation of protein solubility in Drosophila. *Hum Mol Genet* 9, 2811–20.

113 Wyttenbach, A., Sauvageot, O., Carmichael, J., Diaz-Latoud, C., Arrigo, A. P. & Rubinsztein, D. C. (2002). Heat shock protein 27 prevents cellular polyglutamine toxicity and suppresses the increase of reactive oxygen species caused by huntingtin. *Hum Mol Genet* 11, 1137–51.

114 Cummings, C. J., Sun, Y., Opal, P., Antalffy, B., Mestril, R., Orr, H. T., Dillmann, W. H. & Zoghbi, H. Y. (2001). Over-expression of inducible HSP70 chaperone suppresses neuropathology and improves motor function in SCA1 mice. *Hum Mol Genet* 10, 1511–8.

37
Protein Folding and Aggregation in the Expanded Polyglutamine Repeat Diseases

Ronald Wetzel

37.1
Introduction

There are at least 15 human diseases associated with the genetic expansion of a chromosomal trinucleotide repeat sequence [1–3]. Some of these occur in noncoding regions, while others are located in open reading frames coding for a variety of proteins. Most of the diseases associated with expressed protein repeats involve CAG repeats coding for polyglutamine (polyGln). The common feature of DNA that underlies the genetic nature of these diseases is the genetic instability of triplet repeats of some of the 64 possible DNA nucleotide triplets [1].

Currently there are nine known diseases involving expansion of a polyGln sequence [3]. While these diseases on average vary one from the other in details of brain pathology and symptoms [3], there are also significant similarities. The polyGln repeat length threshold separating the normal population from at-risk individuals is strikingly similar for eight of the nine diseases [3]. All nine diseases are progressive and uniformly lethal and tend to present in midlife [3]. Of particular significance to this chapter, polyGln aggregates have been demonstrated in each of these diseases [3].

The demonstration of polyGln-containing inclusions in patient material [4] and in animal and cellular models [5–7] also suggested their resemblance to other neurodegenerative diseases [8] involving protein deposition into amyloid or other aggregated deposits. As a subject for studying protein aggregation diseases at the molecular level, however, the polyGln diseases have pluses and minuses. On the one hand, the uniform monotony of glutamine that constitutes the pathogenic core of the disease proteins does not inspire immediate insights into disease mechanisms or protein-folding mechanisms. Indeed, standard site-directed mutagenesis approaches are technically difficult at the DNA level, due to the lack of unique internal restriction sites [9], and in any case may be of questionable value at the protein level, due to the likely ability of the sequence to shift and slide while aggregating so as to accommodate, and negate the effect of, potential modifying mutations [10]. On the other hand, there is something attractive about the simplicity of a homopolymer as a subject for addressing fundamental problems in protein folding and

Protein Folding Handbook. Part II. Edited by J. Buchner and T. Kiefhaber

ISBN: 3-527-30784-2

aggregation; for example, studying a real-world homopolymer should provide data more easily related to theoretical protein-folding studies that are often based on highly simplified model structures. A significant additional attraction to studying these diseases is the prospect of contributing to the development of therapies. As summarized below, protein-folding and aggregation studies of these sequences in vitro are making significant contributions to a better understanding of the molecular basis of these diseases and along the way are providing unique systems for better characterizing the role of protein structure in ordered aggregation processes.

37.2 Key Features of the Polyglutamine Diseases

The literature on the clinical, genetic, cellular, and biochemical aspects of the expanded polyGln diseases has grown enormously since the discovery of the disease genes over the past decade. There are excellent books reviewing the various aspects of each disease [11, 12], and a steady stream of review articles and essays discuss possible disease mechanisms from various points of view [2, 13–31]. These reviews reflect the lively, ongoing debate on the importance of polyGln oligomers and aggregates in the disease mechanism. The discussion here is very brief and necessarily centered on the toxicity of polyGln peptides, especially the possibility that polyGln aggregates play a toxic role.

37.2.1 The Variety of Expanded PolyGln Diseases

There are currently nine human diseases linked to a genetic expansion in an in-frame, translated CAG repeat [3], of which the most recently identified is spinocerebellar ataxia 17, involving expansions in the transcription factor TBP, or TATA-binding protein [32]. Table 37.1 lists the known diseases, the disease protein involved, its molecular weight and subcellular localization, and the CAG repeat lengths for the normal and pathological ranges. The most well known and most common of these diseases is Huntington's disease (HD). There are a number of genetic ataxias whose disease gene has not yet been identified [33, 34], and at least some of these may eventually be found to also involve CAG repeat expansion.

37.2.2 Clinical Features

Except for the X-linked spinal and bulbar muscular atrophy (SBMA), involving CAG repeat expansions in the gene for the androgen receptor, the other eight known polyGln diseases exhibit autosomal dominant genetics [3]. Huntington's disease normally presents as a motor disorder, although a significant minority of patients present with psychiatric symptoms [12]. The expanded CAG repeat ataxias involve a wide range of symptoms and significant variability [3]. Early-onset forms

Tab. 37.1. Overview of expanded CAG repeat diseases.[a]

Disease	*Gene product*	*Cellular localization*	*MW (kDa)*	*Normal CAG repeat range*	*Mutant CAG repeat range*
Huntington's	huntingtin	Cytoplasm/nucleus	348	6–39	36–>200
DRPLA[b]	atrophin-1	Cytoplasm/nucleus	190	3–35	49–88
SBMA[c]	androgen rec.	Cytoplasm/nucleus	104	9–33	38–65
SCA1[d]	ataxin-1	Cytoplasm/nucleus	87	6–44	39–83
SCA2[d]	ataxin-2	Cytoplasm	145	13–33	32–>200
SCA3[d]/MJD[e]	ataxin-3	Cytoplasm/nucleus	46	3–40	54–89
SCA6[d]	CACNA1A[f]	Cytoplasm	280	4–19	20–33
SCA7[d]	ataxin-7	Cytoplasm/nucleus	95	4–35	37–306
SCA17[d]	TBP[g]	Nucleus	38	24–44	46–63

[a] Data from Ref. [12].
[b] Dentatorubral-pallidoluysian atrophy
[c] Spinal and bulbar muscular atrophy
[d] Spinocerebellar ataxia
[e] Machado-Joseph Disease
[f] α_{1A} voltage-dependent calcium channel
[g] TATA box-binding protein

tend to present with distinct, more-aggressive symptoms that set them apart from the later-onset forms. The large variations in the course of disease for patients with the same CAG repeat length suggest important roles for secondary factors, including environment and modifying genes, and these are currently under investigation in those diseases with statistically significant amounts of patient data.

37.2.2.1 Repeat Expansions and Repeat Length

DNA triplet expansions leading to genetic disease can occur in expressed open reading frames or in non-coding regions [1]. Of the possible triplet repeat sequences, only a few are known to be involved in triplet expansion genetic disorders [1]. Although it is presumed that there are unique structural aspects to the DNA of those triplets whose instability during one or more enzymatic process in the cell leads to expansion-based diseases, the structural basis of repeat instability is unclear and continues to be evaluated [35]. The stability of the CAG repeat, in particular, appears to depend on a number of factors, including the length of the repeat before expansion, its sequence context, and whether the donor of that gene is the mother or the father [3, 36]. The normal role of benign repeat lengths of the polyGln sequence in the various proteins in which it is found remains a mystery. In fact, since homologues of the same protein often vary considerably in their polyGln repeat length, while other parts of the protein may show very little variation, it is possible that polyGln in most cases is not functionally important. The hypothesis that normal-length polyGln sequences serve no important function that might be compromised upon sequence expansion is consistent with the widely accepted view that expanded CAG repeat diseases are predominantly gain-of-function disorders [3].

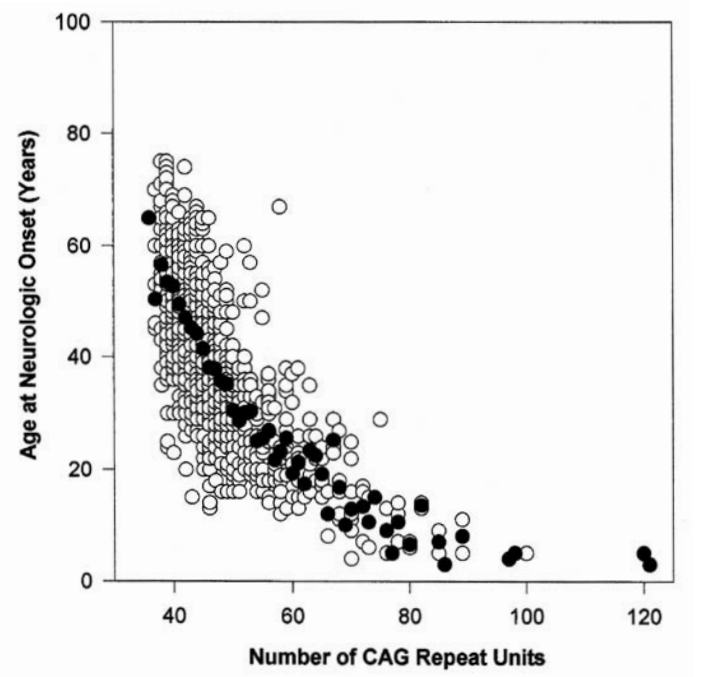

Fig. 37.1. *HD* CAG repeat length is correlated with the age at onset of neurologic symptoms. The relationship between the expanded *HD* CAG repeat length ("Number of CAG Repeat Units") and the age at neurologic onset is given for 1070 HD patients reported in the literature. The mean age at onset for any given *HD* CAG repeat length is depicted by filled symbol. Power regression analysis reveals a significant inverse correlation between expanded CAG repeat size and age at onset ($r = -0.87$, $P < 0.0001$), although individuals with the same expanded repeat exhibit widely different ages at onset, suggesting the existence of modifiers of the disease process. Figure and analysis courtesy of Marcy MacDonald.

Table 37.1 shows the clear separation of benign repeat lengths from pathological repeat lengths in the expanded CAG repeat diseases. In all cases but one (SCA 6, which uniquely involves a resident transmembrane channel protein), the pathological cutoff lies in the mid- to upper-30s. In HD, within this critical region, repeat length also influences penetrance, the percentage of individuals with the mutation that eventually develop disease symptoms [37]. Within the pathological repeat length range, age of onset correlates strongly with repeat length, as shown for HD in Figure 37.1. One of the clinical characteristics of the disease, recognized prior to the discovery of the disease genes, is that of anticipation, in which a parent presents with a disease only after it is already recognized in a child. With the discovery of the dynamic genetic nature of the triplet repeat diseases, anticipation is now understood by the fact that repeat expansions, especially when passed on by the father, can be large, and large repeat expansions tend to dramatically decrease age of onset (Figure 37.1) [1].

37.2.3
The Role of PolyGln and PolyGln Aggregates

Although a few genetic ataxias involve CAG expansions in non-coding regions [33, 34], the bulk of the characterized disorders are associated with expression of the polyGln sequence at the protein level. Loss of function may play a role in some mutations in the gene associated with SCA 6 [3]. Further, a decline in normal levels of active protein, perhaps mediated by aggregation, may also contribute to symptoms in some expanded CAG repeat diseases [38, 39]. On the whole, however, the dominant effect of polyGln expansion appears to be a gain of toxic function. It seems very unlikely that the expanded polyGln disorders, with their often overlapping clinical features and very similar genetics, do not share intimate details of their molecular mechanisms, and it is further unlikely that the molecular mechanisms involving these otherwise unrelated protein sequences are not centered in the behavior of the polyGln sequence. This is further supported by the generation of animal models based on expression of artificial proteins containing in-frame CAG repeats spliced to proteins not known to be associated with disease [5, 40].

Opinion in the field has been divided as to whether expanded polyGln is cytotoxic due to the induction, within the soluble monomer, of a toxic conformation or, alternatively, to the accelerated aggregation of the monomer into a toxic, oligomeric state. Although the ability of a series of antibodies to bind preferentially to expanded polyGln has been interpreted as evidence for the existence of a novel conformation within the monomer, recent studies suggest that the increased avidity observed for such antibodies can be explained by the multiplicity of independent, oligoGln-binding sites in the expanded sequence (a linear lattice effect) [41]. Most other data (reviewed in Chapter 3) is consistent with no significant change in the conformation of bulk-phase polyGln upon its sequence expansion.

In contrast, substantial evidence points to a central role for polyGln aggregation in the disease process [25, 27–29], beginning with the observation of intraneuronal, nuclear inclusions (NII) in cell and animal models of polyGln disease [5–7]. Similar aggregates are found in brain tissue from HD and other diseases listed in Table 37.1, but not in normal, aged control brain [3, 4]. Genetically identified suppressers of polyGln toxicity, such as PQE1 [42] and dHDJ1 [40], have been shown to be aggregation suppressors in vitro (see Section 37.8). Further, designed polypeptide-based inhibitors of polyGln aggregation also protect cells from the toxic effects of expanded polyGln sequences [43] and polyGln aggregates [44] (see Section 37.8.1). As discussed in detail below, the repeat length–dependent aggregation properties of polyGln closely mirror the repeat-length dependence of disease risk shown in Table 37.1. Also as discussed below, polyGln aggregates made in vitro and delivered to the nuclei of cells in culture are very cytotoxic [45]. Although the appearance of visible aggregates does not always closely correlate with cytotoxicity in cell and animal models [2, 17, 21], there are reasonable explanations for how such observations might still be consistent with cytotoxic aggregates. Some of these rationales will be alluded to in this chapter.

37.3 PolyGln Peptides in Studies of the Molecular Basis of Expanded Polyglutamine Diseases

If the effect of sequence expansion on the physicochemical properties of the polyGln sequence plays a central role in the expanded CAG repeat diseases, then it is of particular importance to study polyGln behavior with respect to repeat length in well-defined biophysical experiments. Chapter 3 consists of an overview of studies using either chemically synthesized peptides or recombinant proteins to conduct studies on the conformational preferences of soluble polyGln and on the aggregation efficiency of these sequences. Later chapters expand into details of certain aspects of their biophysical behavior, concentrating on aggregation. The poor solution behavior of the polyGln sequence has provided substantial barriers to conducting such studies, and much has been learned simply in the effort to produce molecules amenable to analysis.

37.3.1 Conformational Studies

Initial studies on the favored conformation of the polyGln sequence gave conflicting results. Working with chemically synthesized polyGln sequences well below the pathological threshold repeat length, Altschuler et al. found the sequence to exist in random coil [46], while Sharma et al. found peptides of similar length to be dominated by β-sheet [47]. This discrepancy was resolved with the later realization, as discussed in Chapter 4, of the importance of applying rigorous methods of peptide disaggregation as part of the solubilization protocol [48]. Using such protocols, Chen et al. showed that polyGln sequences in solution in PBS exhibit the signature CD spectrum of a statistical coil [49]. More importantly, they also showed that the CD spectra of polyGln peptides both below and above the pathological threshold repeat length give essentially identical CD spectra [49], providing the first experimental indication that a pure conformational change within a monomeric polyGln protein is not likely to underlie the repeat-length dependence of clinical features. Similar results were later obtained with various polyGln repeat lengths within the context of *E. coli*-expressed fusion proteins containing either naked polyGln sequences [50] or polyGln sequences embedded in a fragment of *huntingtin* [41]. Importantly, these studies also show that results obtained with synthetic peptides, such as those described here, are not compromised by the disaggregation protocol.

The above discussion notwithstanding, the CD spectrum generally assigned to the random coil state is not unambiguous. In fact, a recent study has confirmed earlier suggestions that polypeptides exhibiting the random coil CD spectrum might actually exist in the ordered conformation known as polyproline type II helix [51]. Indeed, recent studies suggest that the amino acid glutamine is particularly comfortable in this form of secondary structure [52]. While the exact nature of the conformation of monomeric polyGln may ultimately be of significant importance

to understanding disease mechanisms, the main important lesson to date from solution studies is that there appears to be no difference between the solution structures of polyGln sequences below and above the pathological repeat length range. Absent some more subtle conformational difference between short and long polyGln, some other aspect of the polyGln sequence must underlie the repeat-length dependence of disease risk.

37.3.2 Preliminary in Vitro Aggregation Studies

With the revelation that expanded polyGln sequences are responsible for the diseases listed in Table 37.1, and in light of the importance of protein aggregation in other neurodegenerative diseases such as Alzheimer's disease, Perutz speculated that polyGln expansion might lead to an increased propensity of proteins containing these sequences to aggregate and thereby cause disease [53]. Working with a Q_{15} sequence flanked by pairs of charged residues, the Perutz lab reported facile aggregation of the peptide in aqueous solution to yield aggregates exhibiting the cross-β structure characteristic of amyloid [53]. In analogy to the leucine zippers designed by nature to promiscuously self-associate in the creation of dimeric transcription factors, Perutz coined the term ''polar zipper'' for the tendency of polyGln sequences to aggregate, presenting a model in which hydrogen bonding by side chain amide groups contributes to the stability of the aggregate [53].

Scherzinger et al. were able to overcome many of the limitations encountered in the above preliminary studies by using a recombinantly expressed form of glutathione S-transferase (GST) fused with the exon 1 fragment of *huntingtin* containing the polyGln sequence [54, 55]. Fusion of GST with *htt* exon 1 renders the protein reasonably well behaved so that it can be extracted and partially purified while maintaining it in a soluble form. By the ingenious use of an installed protease site, Scherzinger et al. were able to cleave this soluble protein between its GST and *htt* components in a controlled reaction, releasing the polyGln portion in situ so that its aggregation could be monitored in a synchronized reaction [54]. By doing so, and by following the generation of aggregate using a filter trap assay, they were able to observe a clear increase in the aggressiveness of spontaneous aggregation as polyGln repeat length increased, with a significant increase in aggregation rate as repeat length increased through the pathological cutoff range [54, 55]. This correspondence between the repeat length threshold for disease risk and the threshold for rapid aggregation continues to be one of the most striking features of polyGln behavior in solution, and it has been invoked as supporting evidence for hypotheses involving aggregation in the disease mechanism.

37.3.3 In Vivo Aggregation Studies

In addition to contributing to our understanding of the disease mechanism, cell and animal models involving recombinant expression of polyGln-containing dis-

ease proteins have contributed greatly to our knowledge of the aggregation process itself. The dependence of aggregation efficiency on polyGln repeat length was characterized qualitatively in a number of in vivo experiments comparing a limited variety of repeat length constructs [6, 7, 54, 56]. At the same time, it is also possible for non-pathological repeat length polyGlns to form aggregates under certain conditions in the cell [57], emphasizing that even sequences below the pathological threshold have some potential to aggregate. Transgene experiments have implicated a modulating role for flanking sequences and/or flanking domains in the aggregation of expanded polyGln, consistent with the possibility that proteolytic processing may play an important role in controlling aggregation and toxicity in the cell. For example, mice expressing exon 1–like fragments of *htt* tend to develop aggregates (and pathology) more rapidly and aggressively than do mice expressing full-length *htt* [26]. Besides the mammalian systems mentioned here, a number of other organisms, such as yeast [58], *D. melanogaster* and *C. elegans* [59], have been used to learn details about how polyglutamine aggregates in the cellular environment.

The promiscuity of polyGln aggregation was noted early on in the observation that an aggregate initiated by an expanded polyGln sequence is capable of recruiting the normal-length polyGln protein into the deposit [57]. More recently, recruitment of the normal allele of *htt* by expanded polyGln htt aggregates has also been observed, suggesting that expanded CAG repeat diseases may include an overlay of loss of function in the disease mechanism [39]. The possible role of generalized polyGln aggregation in the cell was also suggested by the observation that expression of expanded polyGln containing a nuclear localization signal (NLS) could mediate nuclear localization of green fluorescent protein (GFP) linked to a normal-length polyGln [60]. One of the intriguing possible mechanisms of polyGln cytotoxicity is that cellular polyGln aggregates might deplete the soluble cellular pools of other polyGln-containing factors by recruiting them into the aggregate in an ongoing elongation reaction [57, 61, 62]. Such mechanisms are supported by the observation of co-localization of TBP [57, 61] and CBP (CREB-binding protein) [60, 63] to cellular aggregates in tissue from patients and/or from cell and animal models.

37.4
Analyzing Polyglutamine Behavior With Synthetic Peptides: Practical Aspects

Given the limited success of previous studies of polyGln behavior using synthetic peptides and the comparative success of studies using recombinant proteins in vitro and in vivo (see Chapter 3), one might legitimately question the value of putting further efforts into the chemical approach. There are a number of reasons for doing so, however.

While polypeptides, even unnatural fusions, expressed in a cellular environment might be considered to be ''more native'' than chemically synthesized peptides ex-

posed, even transiently, to organic solvents, the situation is complicated by the central role of the prior aggregation state of a protein in biasing its aggregation behavior in vitro. This is illustrated by early experiments in the Alzheimer's disease field, in which studies of the amyloid peptide Aβ were confused by investigators' ignorance of the aggregation state of the peptide and the importance it plays in cytotoxicity and aggregation. This led to an odd lore concerning certain manufacturers' batches of synthetic peptide as being "good" (cytotoxic right out of the vial) or "bad" (nontoxic) batches. Eventually, both cytotoxicity [64] and aggressive aggregation ability [65] were clearly shown to be attributable to traces of aggregates resident in the vialed material. As shown below, methods now exist for rigorously removing preexisting aggregates from synthetic peptides. Such methods are chemically benign, allow complete removal of the organic solvent, and are compatible with peptides whose natural state as a soluble monomer in native buffer is relatively unstructured. In contrast, recombinant proteins are potentially much more complex and, once nonnative assembly occurs, the unnatural oligomeric state may be much more difficult to recognize and reverse. For example, expression of a GST-AT-3 fusion containing a Q_{27} sequence led to an enriched, soluble protein that, however, migrated as an oligomer on native gel filtration [66]; similar soluble oligomers can be observed in isolation of *htt* exon-1 fusion proteins (G. Thiagaragan and R. Wetzel, unpublished). Clearly, it is possible, at least with relatively short polyGln repeats, to prepare monomeric, folded proteins by recombinant expression [41], but a great level of care and analytical scrutiny is required to insure that the preparation is aggregate-free, and the challenges increase dramatically with increasing repeat length. Thus, there may be situations in which chemically synthesized peptides, exposed transiently to non-aqueous solvents to effect efficient disaggregation, are "more native" than a recombinant protein prepared and maintained in aqueous buffers.

An additional attractive feature of focusing on chemically synthesized polyGln peptides is that optical studies are not complicated by the presence of other segments of polypeptide. For example, this allows relatively clean interpretation of the CD spectra of subject polypeptides without having to be concerned about the contributions of other domains and how those other domains may or may not also be changing during the experiment. Work with synthetic peptides also allows facile use of chemical tags such as biotin [67] and fluorescein [45], as well as nonnatural amino acids such as D-amino acids [10]. Synthetic peptides often make it more possible to conduct studies requiring relatively large amounts of material and to accomplish the studies in a shorter time.

Finally, while it is clear that the most appropriate studies, if they can be done on pristine protein samples, are those that are chemically and physically most similar to the toxic fragments generated in vivo, it is also true that studies on simple polyGln peptides will allow baselines to be established for their biophysical behavior, so that further studies on the sequence in the natural settings of the disease proteins can be placed into context and the specific effects of sequence context be cleanly appreciated.

37.4.1 Disaggregation of Synthetic Polyglutamine Peptides

In the review of the aggregation literature in Section 37.3.2, one troubling inconsistency stands out. Work with recombinant protein fragments yields results on the repeat-length dependence of aggregation that mirror the repeat-length dependence of disease risk in HD and other expanded CAG diseases, with sequences up to about Q_{35} being relatively resistant to aggregation. In contrast, however, previous work with chemically synthesized peptides established an apparent solubility ceiling of Q_{15}–Q_{22}, above which it appeared that peptides could not be studied in solution [46, 47, 53]. This appeared to be so even when charged flanking residues were included in an attempt to improve peptide solubility. However, we now understand that this apparent discrepancy between the transient solubilities of recombinant and chemically synthesized peptides is due to the presence, in the latter, of residual polyGln aggregates, leading to a situation not unlike that described above for Aβ peptides.

This is dramatically demonstrated by two examples. Although attempts to directly dissolve a $K_2Q_{44}K_2$ sequence in aqueous buffer failed to give significant soluble peptide [48], pretreatment of a $K_2Q_{44}K_2$ peptide (or a $K_2Q_{20}K_2$ peptide) with a trifluoroacetic acid/hexafluoroisopropanol disaggregation protocol adapted from the Aβ literature [68] yields peptides that display excellent initial solubility in aqueous buffers [48]. Even more dramatic is the effect this protocol has on the peptide $K_2Q_{15}K_2$. This peptide readily dissolves directly from the synthetic lyophilized powder in low salt, pH 3 buffer to yield a transparent, low light-scattering solution. When this solution is adjusted to phosphate-buffered saline conditions, however, aggregation occurs very rapidly to form a protofibril-like product [48]. In contrast, when this same peptide is exposed to the TFA/HFIP disaggregation protocol prior to solubilization in water and then is adjusted to PBS conditions, the peptide remains in solution for months at 37 °C, finally reaching an equilibrium position of aggregation after about six months [48]. Although the composition of $K_2Q_{15}K_2$ directly dissolved in water has not been further investigated, it is most likely that the suspended peptide exists as a mixture of dissolved monomer and microaggregates, the latter of which seed aggregation by the former when the solution is adjusted to PBS conditions. This tediously slow aggregation kinetics of the $K_2Q_{15}K_2$ peptide after disaggregation now qualitatively matches the behavior of short polyGln sequences in recombinant proteins and is also consistent with the lack of disease risk in humans with short polyGln sequences in *htt* and other disease proteins.

This change in the character of the $K_2Q_{15}K_2$ peptide is not a consequence of any covalent chemical change in the peptide [48], and no significant amounts of organic solvent remain after the treatment. To ensure that all traces of aggregates are removed, a preparative ultracentrifuge step is included. The sequential treatment of the lyophilized, synthetic peptide with TFA, followed by HFIP, as described for treatment of Aβ peptides [68], is adequate for disaggregating polyGln

peptides up to repeat length 40. Above this, the synthetic peptides do not dissolve well in TFA. However, it was found that peptides of higher repeat length dissolve well in a 1:1 mixture of TFA and HFIP and that, with sufficient incubation time and care, they can be completely disaggregated in this solvent mixture [48]. This treatment also appears to dissolve other aggregation-prone peptides that are resistant to the sequential method. The method is described in detail in the experimental Section 37.10.

37.4.2 Growing and Manipulating Aggregates

Although many studies on disease mechanism in HD and other protein aggregation diseases involve analysis of aggregation behavior, the study of the aggregation products is also important, since it is likely that it is the aggregates themselves, or a continuing aggregation process supported by these aggregates, that are responsible for cytotoxicity. In analogy to the above discussion on working with the peptides, therefore, a few words must also be said about the growth and handling of aggregates. Simple polyGln peptides incubated at 37 °C grow into a variety of morphologically related structures, as reviewed in Section 37.6.1. In general, these aggregates appear to be variations on the assembly of narrow protofilaments, in analogy to the substructures of amyloid fibrils. The aggregate formation reaction is quite reproducible, so long as the peptides are processed as described above and growth conditions are held constant. The aggregates are quite stable, with critical concentrations well below micromolar for polyGln peptides of repeat length 30 or more [49]. Aggregate suspensions in PBS can be snap-frozen in liquid nitrogen and stored at −80 °C for extended periods without noticeable change in properties.

37.4.2.1 Polyglutamine Aggregation by Freeze Concentration

Simple polyGln peptides dissolved in PBS, when incubated for one day or more in the frozen state at −5 to −20 °C, are highly aggregated upon thawing [66]. This is true even for Q_{15} peptides, which, when incubated at 37 °C in the completely disaggregated state, require months to achieve significant levels of aggregation. Studies on the mechanism of this effect showed that aggregate formation under these conditions is due to the process of freeze-concentration [69, 70]. Peptide solutions in buffer stored frozen at temperatures above the eutectic points of the buffer components consist of a solid ice phase and fissures of liquid phase containing most of the solutes, including the peptide [69, 70]. Since the liquid phase is only a small volume of the total, the solute concentrations in the liquid phase are enormous, with, for example, NaCl concentrations of several molar resulting from the freezing of a simple PBS ([NaCl] ∼ 0.15 M) solution. These conditions often result in the formation of protein aggregates, which is why it is often advisable to store protein solutions either above 0 °C or below 0 °C with freezing-point depression agents such as glycerol. Interestingly, because ice structure at modest freezing temperatures is rather unstable, solutions of polyGln peptides may be snap-frozen in liquid nitrogen, but if they are then stored at −20 °C, they will still develop ag-

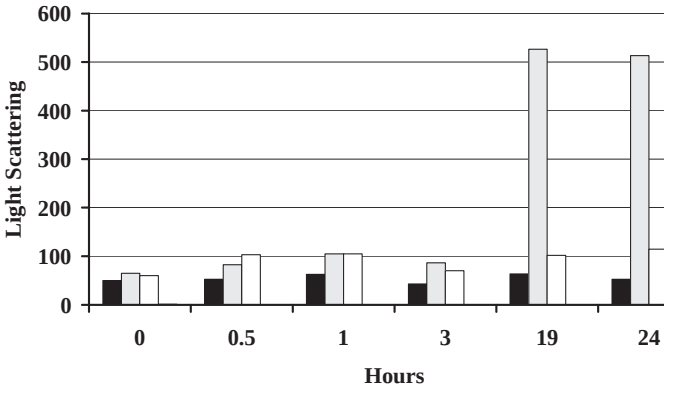

Fig. 37.2. Time course of freeze-concentration aggregation monitored by light scattering. Samples of 10 μM disaggregated $K_2Q_{37}K_2$ in PBS were incubated at 37 °C (solid black bars), at −10 °C in the liquid state (open bars), or at −10 °C in the frozen state (gray bars). The latter sample was snap-frozen in liquid nitrogen then transferred to the −10 °C bath. From Ref. [66] with permission from the American Chemical Society.

gregates as the ice structure equilibrates to that normally formed at the −20 °C storage temperature. Figure 37.2 shows the time course of aggregate formation in the ice state versus liquid state in the −5 to −10 °C range [66].

The freeze-concentration-induced aggregation of polyGln has several implications. First, there is no reason to suspect that any polyGln sequence, even in the context of other protein sequences, will not be susceptible to this effect. We have found that polyGly peptides can be stored for months at −80 °C if they are first disaggregated, adjusted to low concentrations, and snap-frozen in liquid nitrogen before storage. It is recommended that all polyGln-containing proteins be stored with similar care or not frozen at all. Interestingly, we found that the Aβ(1-40) peptide does not form amyloid by freeze-concentration. Thus, the same level of care required for working with polyGln sequences may not be required when working with other amyloid systems. It is important to be aware, however, of the potential for the seemingly benign freezing process to wreck havoc with samples of any protein, especially aggregation-prone proteins.

37.4.2.2 **Preparing Small Aggregates**

In addition to this potential for undesired aggregation, the freeze-concentration-induced aggregation of polyGln sequences is important because it generates aggregates with somewhat different properties compared to those grown from the same peptide at 37 °C [66]. As discussed in Section 37.6, these aggregates appear to be more like the protofibril assembly intermediates of other amyloid growth reactions than like the mature aggregates grown at 37 °C. These aggregates, once formed, are stable and do not assemble further on incubation at 37 °C. On a weight basis, aggregates prepared by freeze-concentration are much better seeds for fibril elongation than are aggregates grown at 37 °C [49]. At the same time,

37 °C aggregation reactions seeded (and hence greatly accelerated) with aggregates prepared by freeze-concentration produce aggregates indistinguishable from those grown by spontaneous aggregation at 37 °C, indicating that the substructures of these aggregates must be quite similar.

We have used freeze-concentration to produce aggregates of small sizes to facilitate their uptake into mammalian cells [45]. After aggregates are grown in frozen buffer, reactions are thawed and the aggregates collected by centrifugation. Aggregates are sonicated with a probe sonicator and then pushed through a series of molecular weight cutoff membrane filters to produce the finest possible aggregate size. This procedure is critical for the ability of mammalian cells to take up naked polyGln aggregates [45] (see Section 37.7.1.1).

37.5 In vitro Studies of PolyGln Aggregation

The central importance of the expansion of the polyGln repeat in this family of neurodegenerative diseases logically leads to the study of the biophysical properties of various repeat lengths of polyGln in search of clues to molecular mechanisms. Coincidentally, focusing on the polyGln sequence in isolation also makes accessible certain experimental approaches not possible with more complex proteins. For example, circular dichroism (CD) spectra can be cleanly interpreted in terms of what the polyGln sequence is doing, without being concerned about sequences and other elements of secondary structure. Solution concentrations of non-aggregated peptide can be quantified with great precision and accuracy using reverse-phase HPLC, as described in the experimental Section. Insolubility can be cleanly interpreted in terms of polyGln aggregation, without worrying about the aggregation tendency of other protein sequences in unnatural fusion proteins or truncated native proteins. The data from studies on isolated polyGln sequences establish a baseline for the fundamental behavioral trends of the polyGln sequence, so that further studies with sequences more closely resembling the complex structures of disease proteins can be put into context.

37.5.1 The Universe of Protein Aggregation Mechanisms

The broad phenomenon of particulate aggregation is systematized in the field of colloidal assembly and coagulation. The aggregation of proteins, especially in response to heat and as a side reaction in protein folding, has been viewed historically as a problem in colloidal assembly [71]. Early generalized models of the kinetics of coagulation involved models of particles undergoing hierarchical assembly into larger and larger clusters. Cluster formation in these models was considered to be controlled either by simple diffusion limits or by an energy barrier that determined the productiveness of each collision, but the assumption in either case was that each productive collision was irreversible [72]. However, since many protein

aggregation reactions such as crystallization and amyloid fibril formation reach equilibrium positions in which both aggregates and monomers are populated, the possibility of productive collisions being reversible must be considered, which complicates the modeling [72]. Protein crystallization and amyloid formation may differ from classical colloidal assembly in another respect; rather than a hierarchical assembly mechanism involving the interactions of intermediates of ever-increasing size, protein crystals and amyloids, once formed, might be capable of growing by the addition of monomeric or oligomeric protein units [72]. This could occur, for example, if the protein in the aggregated state projects a docking surface that is capable of recruiting bulk-phase monomer very efficiently, compared to the relatively inefficient process of nucleation.

Such a nucleation-dependent polymerization model has been developed [73, 74] and successfully applied to hemoglobin aggregation [75]. The model also takes into account the potential reversibility of steps in the aggregation process and thus treats the nucleation process as an unfavorable pre-equilibrium before a series of increasingly favorable elongation steps; that is, the kinetic nucleus is viewed as the least stable species on the aggregation pathway. The unfavorability of the nucleation step gives rise to a ''lag phase,'' during which no mature aggregates are formed and negligible amounts of monomer are consumed, followed by a rapid growth phase. Since this is a relatively simple model that has been successfully applied to protein systems, and since there is no evidence from in vitro studies of a more coagulation-based assembly mechanism for polyGln aggregation, this model has been applied to polyGln aggregation data, as described in the following section.

37.5.2
Basic Studies on Spontaneous Aggregation

Rigorously disaggregated polyglutamine peptides (Section 37.4.1) incubated in PBS at 37 °C undergo a spontaneous aggregation process that generally exhibits a lag phase typical of nucleated growth polymerization. These lag times become shorter as the repeat length gets longer, with aggregation becoming much more aggressive at repeat lengths about 35 [49]. These results agree with previous observations based on studies of exon I fragments of *huntingtin* [55]. Following the kinetics by a number of different windows on the aggregation process – light scattering, ThT fluorescence, CD, and solubility – reveals overlapping growth curves (Figure 37.3), suggesting that there are no major hidden species in the process [76]. The fact that the CD transition, from a spectrum consistent with random coil to one consistent with β-sheet, coincident with the reaction as monitored by aggregate formation and peptide solubility suggests that there is no pre-assembly in the bulk-phase monomer to a β-sheet containing monomeric species before aggregation occurs [76]. This interpretation is reinforced by an experiment in which the aggregation reaction is stopped midway and centrifuged [76]. The resuspended centrifugation pellet gives a typical β-sheet CD spectrum, while the supernatant gives the same random coil signature spectrum as seen in the starting reaction mixture (Figure 37.4). The implication is that the mechanism by which

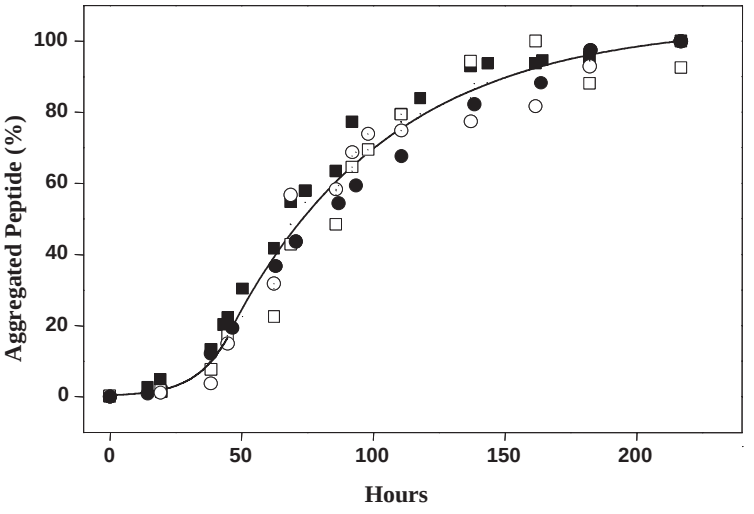

Fig. 37.3. Spontaneous aggregation of a polyGln peptide monitored by four independent measures. A sample of 66 μM freshly disaggregated $K_2Q_{42}K_2$ in 10 mM Tris-TFA, pH 7.0, was incubated at 37 °C and aggregation was monitored by circular dichroism signal at 200 nm (■), determining remaining soluble monomer by HPLC (●), light scattering (□), and thioflavin T fluorescence (○). From Ref. [76] with permission from the National Academy of Sciences (USA).

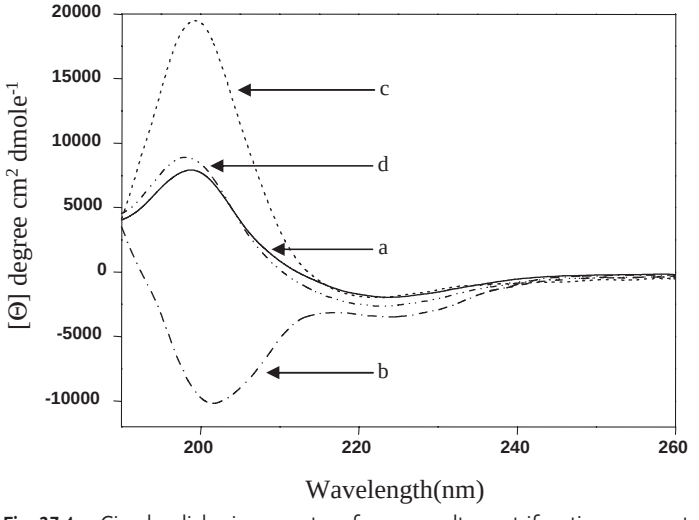

Fig. 37.4. Circular dichroism spectra of various fractions of a polyGln aggregation reaction midpoint. The reaction described in the legend of Figure 37.3 was sampled after 90-h incubation and CD spectra were collected after various treatments: no treatment (a); ultracentrifugation supernatant (b); resuspended ultracentrifugation pellet (c); sum of the supernatant and pellet spectra (d). Adapted from Ref. [76] with permission from the National Academy of Sciences (USA).

the bulk-phase polyGln peptides take on β-sheet characteristics occurs either through a concerted mechanism, in which molecules take on β-structure as they become ensconced onto the end of the growing aggregate, or through a mechanism in which isolated monomers rapidly add to aggregates as soon as they acquire β-structure.

37.5.3 Nucleation Kinetics of PolyGln

The increasing efficiency with which peptides undergo spontaneous aggregation (see previous section) suggests that it may be this property of the polyGln sequence that is responsible for the critical importance of repeat length in the expanded CAG repeat diseases. The source of the repeat-length dependence of aggregation is not immediately obvious, however. To investigate whether the repeat-length effect is played out at the level of nucleation and to learn more about the nucleation process, we applied a successful model for the nucleation-dependent aggregation of sickle hemoglobin [74] to the polyGln aggregation process [76]. In this model, the formation of an oligomeric kinetic nucleus from a bulk phase of monomeric proteins is treated as a pre-equilibrium, the favorability of which is dependent on the equilibrium constant and the number of monomers that cluster together to form the nucleus. This latter number, which is of particular importance because it becomes an exponential factor in the equation describing nucleation kinetics, is called the "critical nucleus," n^*. Whether any particular nucleus collapses back to n^* monomers, or progresses on to committed aggregate growth, depends on the efficiency with which it is stabilized through the elongation of the nucleus into a growing aggregate, as determined by the rate constant describing this elongation step. Since the number of kinetic nuclei formed during a nucleation-dependent polymerization reaction is vanishingly small and cannot be directly observed, the concentration of nuclei present at any one time is inferred by the kinetics with which observable aggregates develop, as described by the rate constant for elongation of aggregates. The overall nucleation kinetics equation (Eq. (1)) emerging from this model describes Δ, the increase in the concentration of monomers that have been converted into aggregates at time t, as it depends on the concentration of monomers in the bulk phase, c, the nucleation (pre-)equilibrium constant K_{n^*}, and the rate constants for elongation of the nucleus and aggregate, k_+, which, for simplicity, are assumed to be identical.

$$\Delta = 1/2{k_+}^2 K_{n^*} c^{(n^*+2)} t^2 \tag{1}$$

Eq. (1) accounts for the time lag observed for nucleation-dependent growth kinetics and for the concentration dependence of the lag phase and the underlying nucleation kinetics. It also predicts two other features of nucleation kinetics: (1) that the kinetics should be dependent on $time^2$, and (2) that a log-log plot of the term emerging from the t^2 plot, with respect to monomer concentration, will yield a line of slope $n^* + 2$, from which n^*, the number of monomers in the kinetic

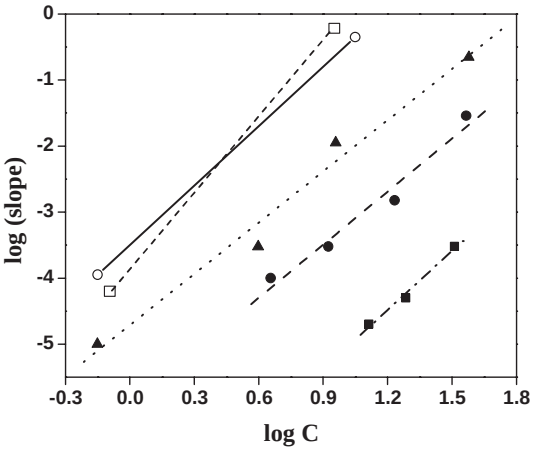

Fig. 37.5. Critical nucleus analysis for polyGln peptides of various lengths. Nucleation kinetics for each peptide at several concentrations was determined as described in the text and analyzed by t^2 plots. The log of the slope of the t^2 plot is plotted against the log of peptide concentration. The slope of the straight line fitting this data is $n^* + 2$, where n^* is the critical nucleus. Shown are data for $K_2Q_{28}K_2$ (■), $K_2Q_{36}K_2$ (●), and $K_2Q_{47}K_2$ (▲). Also shown are theoretical lines showing slopes of 3 (○) and 4 (□). From Ref. [76] with permission from the National Academy of Sciences (USA).

nucleus, can be derived. In fact, analysis of polyGln peptides with repeat lengths below and above the pathological threshold region shows linear t^2 plots at all peptide concentrations examined [76]. Figure 37.5 shows that plotting the log of the slopes of the t^2 plots at each concentration, against the log of the concentration, gives a straight line for each repeat length. The equivalence of the slopes for peptides above, at, and below the pathological threshold, as shown in Figure 37.5, shows that, within this range, repeat length does not alter the size of the critical nucleus. Table 37.2 shows the surprising result that the kinetics analyses for these peptides yield slopes of 3, reducing, therefore, to $n^* = 1$ in each case. Table 37.2 also shows that the source of the more aggressive nucleation kinetics, as polyGln repeat length increases, is therefore the larger value of the $k_+{}^2K_{n^*}$ term, rather than a change in the value of n^*. Since it was previously shown that elongation rates do not change dramatically as polyGln repeat lengths change [49], it can

Tab. 37.2. Kinetic parameters for polyGln nucleation of aggregation.[a]

	Q_{28}	Q_{36}	Q_{47}
Slope of the log-log plot	2.98	2.68	2.59
Calculated critical nucleus (n^*) from slope	0.98	0.68	0.59
$k_+{}^2K_{n^*}$ ($M^{-2}s^{-2}$)	0.001128	0.09193	1.8304

[a] Data from Ref. [76].

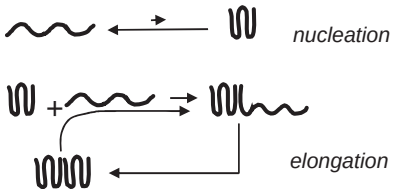

Fig. 37.6. A model for the nucleation-dependent polymerization of polyGln peptides. Reversible formation of the monomeric nucleus, the least stable species on the aggregation pathway, is visualized as an unfavorable folding reaction. Elongation is visualized as a cyclic two-step process involving addition of bulk-phase polyGln monomer to the nucleus or growing aggregate, followed by consolidation of the structure of the newly added monomer to extend the structure of the aggregate. From Ref. [76] with permission from the National Academy of Sciences (USA).

be concluded that the major source of the increased aggressiveness of polyGln aggregation above the pathological threshold is an increase in the nucleation (pre-)equilibrium constant K_{n^*}.

The result of this analysis, i.e., that the kinetic nucleus for nucleation-dependent polymerization of polyGln sequences contains a single molecule of polyGln, is a surprising, if not shocking, result. The whole theoretical basis for nucleation in nucleation-dependent polymerization and colloidal assembly theories is a model in which the nucleus is itself an oligomer on the assembly pathway. Based on general colloidal assembly models [72] and on water condensation analysis [77], the stability derived from the growth of the nucleus is basically attributed to an improved surface-to-volume quotient for this particulate cluster [78]. The recognition, however, that monomeric polyGln peptides, even long ones, assume a non-β-sheet conformation in solution makes conceptually possible a model in which the nucleation event is an unfavorable folding reaction within the monomer population. Figure 37.6 illustrates this model schematically, showing bulk-phase monomer as random coil and the nucleus as a monomer collapsed into an antiparallel β-sheet conformation. Interestingly, despite the fact that the model for the nucleation process was developed based on the assumption of an oligomeric critical nucleus, the mathematical analysis growing out of this model is sufficiently robust that it also describes quite well the situation in which $n^* = 1$. The reason for this is that the most fundamental definition of the critical nucleus is more mathematical than physical, stating only that the nucleus is the least stable species on the assembly pathway. The critical nucleus for polyGln assembly into amyloid-like aggregates achieves this distinction by being the product of a highly unfavorable folding reaction. How unfavorable these reactions are in the polyGln series is presently unknown, since the $k_+{}^2 K_{n^*}$ term cannot be deconvoluted due to (1) a present inability to independently determine the value of k_+ and (2) the inability to independently observe the nucleation equilibrium without its leading to aggregation. Direct observation of the nucleation process, determination of K_{n^*}, and derivation of molar elongation rate constants remain challenges for future research.

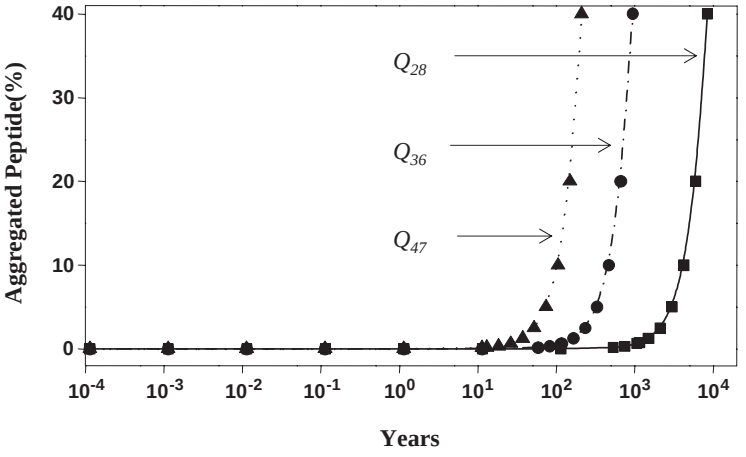

Fig. 37.7. Calculated nucleation kinetics curves for 100-pM polyGln peptides in PBS at 37 °C, based on kinetic parameters derived from in vitro studies at higher concentrations. From Ref. [76] with permission from the National Academy of Sciences (USA).

The ability of the nucleation kinetics model to accommodate polyGln aggregation made possible the calculated estimation of the expected kinetics curves for nucleation-dependent polymerization of polyGln at relatively low steady-state concentrations, i.e., of magnitudes similar to those expected in vivo. Figure 37.7 shows the resulting curves for assumed polyGln concentrations of 100 pM, which show predicted ages of onset for the three polyGln repeat lengths studied that differ by orders of magnitude and in a way that is consistent with disease statistics (Figure 37.1). The actual steady-state concentrations of the aggregation-prone proteolytic fragments of *huntingtin* or other expanded CAG repeat disease proteins are not known, and it is clear that the molecular complexity of cells and organisms is likely to foil attempts at adequately describing disease through test tube experiments in simple buffers alone. However, the simulation in Figure 37.7 illustrates how nucleation propensity, as controlled simply by repeat-length variation, is capable of contributing significantly to disease risk and age of onset. Ongoing studies of simple peptides in defined buffers are also providing quantitative descriptions of the roles of molecular crowding, molecular chaperones, downstream amino acid sequences, and other polyGln-containing molecules on impacting aggregation nucleation (A. Thakur, A. Bhattacharyya, G. Thiagaragan, and R. Wetzel, unpublished results).

37.5.4 Elongation Kinetics

The model for polyGln aggregate growth shown in Figure 37.6 shows that the nucleus elongates by successive productive encounters with bulk-phase monomer.

Although other models have been proposed for fibril elongation that may be followed by some proteins under some solution conditions [79], growth by monomer additions is likely to be the major pathway by which amyloid fibrils grow in vivo, especially in most systems where precursor protein concentrations are quite low. The kinetics of this process have been successfully modeled [80] as a simple bimolecular reaction between aggregate and monomer, such that the observed rate depends on monomer concentration, aggregate (molar) concentration, and the second-order rate constant. However, since in a heavily seeded reaction, aggregation mass builds primarily by the lengthening of the seeds, the molar concentration of aggregate (or the molar concentration of growth sites) does not change appreciably over the course of a simple elongation reaction, and the rate expression reduces to a pseudo-first-order kinetics equation involving monomer concentration and the first-order rate constant. (This rate constant is not a universal constant for this peptide, however, since it incorporates the molar concentration of fibrils used as seeds, which is not trivial to determine.)

Understanding more about the polyGln aggregate elongation process is important not only because of how this process contributes to the deposition of the disease protein in neurons but also because of the possible importance of the recruitment of other polyGln-containing proteins in the disease mechanism (Section 37.3.3). If the polyGln aggregate, or the aggregation process itself, is responsible for the neurotoxicity observed in these diseases, it is also important to learn how we might interfere with this process therapeutically. The need to discover and characterize aggregation inhibitors adds to the importance of having available one or more ways of quantifying elongation in vitro.

37.5.4.1 Microtiter Plate Assay for Elongation Kinetics

One convenient way of studying the elongation reaction is by immobilizing preformed aggregate on a surface, incubating the surface in a solution of monomer, and monitoring the growth of the aggregate seed. Aβ elongation has been studied by this approach in two ways, by using either fibrils fixed to microtiter plate wells and following elongation with radio-labeled monomer [81] or fibrils fixed to a dextran surface and following elongation by an increase in fibril mass as detected by surface plasmon resonance [82]. A modification of the microplate approach has been used to develop a polyGln elongation assay, which has been described in detail [67, 83]. In this assay, very small masses (typically 20–100 ng per well) of polyGln aggregates are immobilized onto microtiter plate wells. An aqueous solution of a disaggregated polyGln, with a biotin covalently attached to the N-terminus, is supplied at low concentration (typically 10 nM) and incubated. After incubation, excess biotinylated peptide is washed out and the amount of biotin remaining on the solid phase by virtue of a continuation of the polyGln aggregation process is measured with a streptavidin-linked reagent. High sensitivity is achieved through using streptavidin complexed with europium, which in turn can be measured with great sensitivity using time-resolved fluorescence. Since the microplate must be processed intact, kinetics are accomplished by phasing the start times of multiple reactions so that their common termination will deliver a time course. A

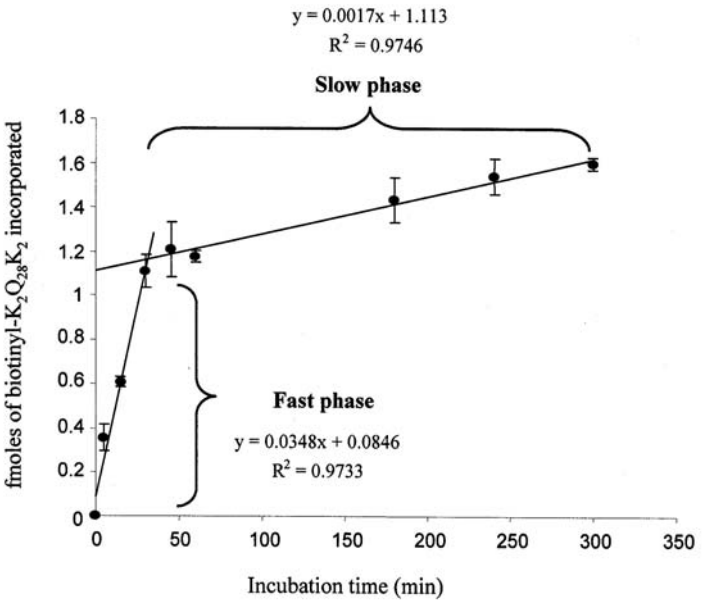

Fig. 37.8. Kinetics of polyGln aggregate elongation monitored by a microtiter plate–based assay. Twenty nanograms of $K_2Q_{28}K_2$ aggregates were immobilized by adsorption to each microtiter plate well, and the wells were incubated for various times with 10 nM biotinyl-$K_2Q_{28}K_2$. Signal was developed using europium-tagged streptavidin and time-resolved fluorescence. From Ref. [67] with permission from Elsevier.

typical kinetics progress curve for this polyGln elongation reaction is pictured in Figure 37.8. The division of the kinetics into fast and slow phases, as seen in Figure 37.8, has also been observed in the Aβ microplate assay [84]. As predicted by the kinetic model described above, the magnitude of the kinetic phases increases both with the increase of the amount of deposited polyGln aggregate and with an increase in monomer concentration. This assay is proving useful in working out some fundamental aspects of the polyGln elongation reaction [49], in screening for inhibitors of polyGln aggregate elongation (see following section), and in characterizing HD brain material.

37.5.4.2 Repeat-length and Aggregate-size Dependence of Elongation Rates

The repeat-length dependence of spontaneous polyGln aggregation is grounded in the repeat-length dependence of the unfavorable folding of the monomeric kinetic nucleus (Section 37.5.3) and is the simplest available explanation for how the gross features of the repeat-length effect on disease risk and age of onset are established. The repeat-length effect of the elongation phase of aggregate growth is also important, however. If the ability of polyGln aggregates to cause cell death and/or dysfunction is due to their ability to recruit other polyGln-containing proteins into

inactivating aggregates, then the dependence of the efficiency of recruitment on polyGln repeat length will determine the range of polyGln-containing proteins that are at risk of being recruited. Experiments using the microtiter plate elongation assay show that there is, indeed, a length dependence of recruitment kinetics, but it is not nearly as dramatic as that for nucleation-dependent aggregation [49]. PolyGln peptides in the 5–10 repeat length range are not strongly recruited into preexisting aggregates. At repeat lengths in the Q_{15} to Q_{20} range, however, elongation rates become more substantial and continue to increase with increasing repeat length up to about Q_{40}, above which there appears to be little effect on rate of increasing repeat length. This suggests that polyGln proteins with repeat lengths in the 5–10 range are not likely to impact polyGln aggregation processes very much. However, at repeats of Q_{15} and above, the existence of polyGln proteins, and their relative concentrations and functions in the cell, may well impact expanded CAG repeat diseases. These results are consistent with observations that neuronal polyGln aggregates often contain CREB-binding protein (which has a repeat length of 18 Gln residues), but that the homologous protein P300, which has a polyGln repeat of only 6, is not recruited into cellular aggregates [85]. The rate of aggregate elongation, as determined by polyGln repeat length and concentration, may also significantly contribute to other aspects of polyGln aggregation and pathology (A. M. Bhattacharyya and R. Wetzel, manuscript in preparation).

Size also matters in considering the mass-normalized recruitment activity of polyGln aggregates. Microtiter plate experiments show that, on an equal mass basis, the ability of a preformed aggregate to serve as a template for polyGln elongation improves as the average particle size of the aggregate decreases [49]. The data support the idea that not all polyGln aggregates are functionally equivalent and that small aggregates are substantially better than the larger ones at supporting elongation. If polyGln aggregates are, in fact, toxic by virtue of their ability to recruit polyGln-containing proteins and thus remove them from their normal sites of action, it stands to reason that more recruitment-active aggregates would be more toxic. That is, aggregates too small to be easily detected by light/fluorescence microscopy may be far more cytotoxic than the relatively recruitment-inert aggregates that can be so visualized. These conclusions are further supported by staining cellular aggregates for recruitment activity, which will be discussed in Section 37.6.2.

37.6
The Structure of PolyGln Aggregates

Like other amyloid-like fibrils, the interior, atomic-level structure of the polyGln aggregate remains opaque, due to its inaccessibility to standard high-resolution methods and the limited resolution of the available methods. The following sections catalog what we do know about polyGln aggregate structure, with an emphasis on the extent to which these aggregates resemble other amyloids.

37.6.1 Electron Microscopy Analysis

Perutz and coworkers first showed that the polyGln aggregate has a fibrillar construction. The aggregates obtained from a Q_{15} peptide immediately upon adjusting a pH 3 solution of the synthetic product to pH 7 [53] resemble in the electron microscope the protofibrils observed as assembly intermediates in amyloid formation by other peptides, such as Aβ [86]. Similar structures are observed from Q_{15} or Q_{20} peptides after they are rigorously disaggregated and then incubated in PBS (Figure 37.9). In addition, aggregates of longer polyGln sequences take on this same protofibril-like appearance when they are grown in PBS at -20 °C by freeze-concentration (Section 37.4.4.1) (Figure 37.9). It is possible that aggregation stops at this stage at -20 °C because the diffusion of the protofibrils is limited by the ice lattice. The generation of protofibril-like structures from simple polyGln peptides in vitro has also been accomplished through the use of nonnative buffer conditions [87]; the relationship of these aggregates to those formed, for example, by freeze-concentration has not been explored.

When simple polyGln peptides longer than Q_{20} are incubated at 37 °C in PBS, they grow into more complex aggregated structures that appear in the EM as ribbons of about 20 nm in diameter and with substructures suggesting assembly from parallel-aligned protofibrils or protofilaments (Figure 37.9). Attempts to detect protofibril intermediates in these assembly reactions have not been successful, however (unpublished results), suggesting that under native conditions in simple PBS buffers protofibrils either do not exist, or have a very short lifetime. The observation of polyGln-associated protofibril-like structures in cells [88] may be due to the presence of flanking protein sequences and/or other molecules in the milieu altering the assembly pathway.

When longer polyGln peptides (Q_{45} or higher) are incubated in PBS at 37 °C, especially in low salt buffer, they grow into long filamentous aggregates that match the structures of typical amyloid fibrils (Figure 37.9). Incubation in vitro of fusion proteins containing *huntingtin* exon 1 fragments with expanded polyGln repeats also generates amyloid fibrils [54], and some EM studies suggest a fibrillar appearance of the substructures of polyGln inclusions in cells [4]. Thus, there appears to be a hierarchy of form in the world of polyGln aggregates, all of which exhibit a similar protofilament substructure that is capable of assembling in higher-ordered structures depending on polyGln repeat length, protein and cellular context, and growth conditions.

37.6.2 Analysis with Amyloid Dyes Thioflavin T and Congo Red

The early history of amyloids is associated with the discovery of the ability of certain heteroaromatic dyes to bind selectively to fibrils and, through binding, take on altered spectroscopic properties that can be monitored. In 1927, Divry reported that amyloid deposits in tissue, previously detected by a starch-like reaction to iodide

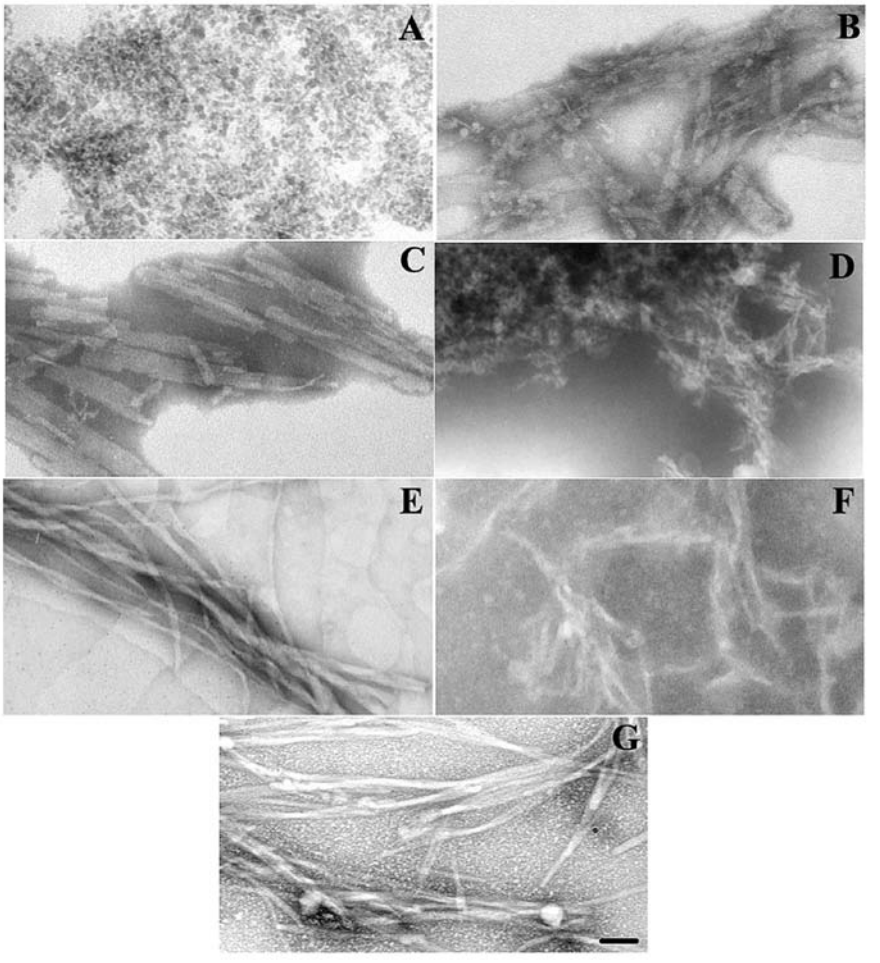

Fig. 37.9. Electron micrographs of various protein aggregates. (A) $D_2Q_{15}K_2$ aggregates grown in PBS at 37 °C. (B) $K_2Q_{20}K_2$ aggregates grown in PBS at 37 °C. (C) $K_2Q_{37}K_2$ aggregates grown in PBS at 37 °C. (D) $K_2Q_{37}K_2$ aggregates grown in PBS in the frozen state at −20 °C. (E) Fluorescein-tagged $K_2Q_{42}K_2$ aggregates grown in PBS at 37 °C. (F) $K_2Q_{42}K_2$ aggregates grown in Tris-HCl, pH 7.2 at 37 °C. (G) Aβ(1-40) fibrils grown in PBS at 37 °C. The bar represents 50 nm. From Ref. [66] with permission from the American Chemical Society.

staining, could be easily detected by staining the tissue with the dye Congo red (CR) followed by polarized light microscopy [89]. The success of the method, which remains the primary pathological stain for amyloid [90], depends not only on the ability of CR to bind to amyloid fibrils but also on the ability of the fibrils to confer onto the bound CR a macroscopic order that can be detected as birefringence in light microscopy. Since the resolution of light microscopy is limited by the wavelength range of visible light, birefringence is observed only if the ordered

array of CR molecules that produces it extends into that size range. Since amyloid fibril diameters are in the 10 nm range, it is clear that for fibrils to be detected by CR birefringence, the fibrils have to be arranged in a higher level of order, that is, oriented non-randomly in the field. In fact, EM of fibrils often shows them to be loosely bundled together in an approximate parallel arrangement. This type of order is required in tissue for amyloid to be detected by CR birefringence. Perhaps this explains the lack of success in detecting polyGln aggregates in tissue by amyloid reagents. CR staining of polyGln aggregates grown in vitro produces a red cast, suggesting that the aggregates bind CR, but does not yield significant birefringence [66], suggesting that a lack of macroscopic order, rather than an absence of the fundamental amyloid fold, may be the explanation for the lack of signal. CR binding to amyloid in vitro can be detected by virtue of a spectral shift conferred onto CR upon binding [91], but there appear to be no data on whether polyGln aggregates produce this effect.

Another important dye for amyloid analysis is thioflavin T (ThT). ThT has the ability to bind to many different amyloid fibrils [92, 93], and when it does, the binding produces a characteristic change in ThT's fluorescent properties. The fluorescence yield upon ThT binding is linear with the number of ThT molecules bound, and therefore (under saturating conditions) also with the mass of amyloid, which allows the dye to be used to quantify amyloid in vitro [93]. PolyGln aggregates produce a typical amyloid-like ThT response [49]. PolyGln aggregation kinetics monitored by ThT track exactly, within experimental error, with other measures of aggregate formation (Figure 37.3).

The molecular mechanisms by which CR and ThT bind to polyGln and other amyloids are not known. CR, as a sulfonate, carries a strong negative charge, while ThT carries a positive charge, at neutral pH. The charged nature of these dyes has led to speculation that electrostatics play an important role in their binding to amyloids, most of which are derived from sequences possessing charged amino acids. PolyGln sequences carry only the neutral glutamine side chain, however, casting doubt on any overriding role for electrostatics in the binding of ThT. Although the synthetic polyGln molecules summarized here contain flanking Lys residues for peptide solubility, their aggregates, displaying only positively charged Lys side chains, are still capable of binding the positively charged ThT.

37.6.3
Circular Dichroism Analysis

As discussed in Section 37.5.2, the CD spectra of aggregated polyGln peptides are consistent with high levels of β-sheet (Figure 37.4), and the progress of the CD signal change at 200 nm that marks the progress of the two-state transition from soluble peptide to aggregate overlaps the aggregation kinetic curves determined by other means (Figure 37.3). The ease of obtaining an interpretable CD spectrum of the polyGln aggregate is somewhat unusual in the amyloid field, where attempts to collect CD spectra of amyloid fibrils in suspension are marred by high levels of light scattering. That polyGln aggregates are better behaved in

CD must be due to lower light scattering, presumably due to smaller average particle sizes. In fact, while Rayleigh light scattering in a fluorometer is a very sensitive means of following amyloid fibril formation by Aβ (B. O'Nuallain and R. Wetzel, unpublished observations), equivalent weight concentrations of polyGln aggregates scatter light much less well, although still to a useful extent [48, 76]. When polyGln aggregation reactions are carried beyond the point when the ThT reaction has reached plateau and the solution-phase peptide is essentially depleted, further, relatively small, changes occur in the CD spectra (S. Chen and R. Wetzel, unpublished). Similar changes have been seen in other β-sheet proteins, where they have been interpreted as reflecting increasing degrees of twist in the sheet [94].

37.6.4
Presence of a Generic Amyloid Epitope in PolyGln Aggregates

Recently, a class of antibody has been described that has the unusual, unanticipated ability to recognize a conformational epitope that seems to be present to some extent on all amyloid fibrils while not being present in the native state of the monomer [95, 96]. For example, the mouse MAb WO1 was generated by challenging mice with an Aβ(1-40) amyloid fibril immunogen, but the resulting antibody binds not only to Aβ fibrils but also to amyloid fibrils derived from IAPP, β2-microglobulin, transthyretin, immunoglobulin light chain, etc. [96]. This antibody also binds to the amyloid-like aggregates of synthetic polyGln peptides [96], offering another indication of the relatedness of the polyGln aggregate to the generic amyloid motif [66]. Conversely, some MAbs generated from mice immunized with polyGln aggregates are able to bind well to other amyloid fibrils such as Aβ fibrils (B. O'Nuallain, R. Wetzel, S. Ou, J. Ko, P. Patterson, unpublished), further indicating the presence of an amyloid epitope on the polyGln aggregate. Such pan-amyloid antibodies tend to be IgMs, limiting their use as tissue-staining reagents. These antibodies have a number of other uses, however, as diagnostics for the amyloid motif and as a means of quantifying certain features of fibrils [10].

37.6.5
Proline Mutagenesis to Dissect the Polyglutamine Fold Within the Aggregate

One of the central questions in amyloid research is how the constituent polypeptide folds upon itself to engage the amyloid structural motif. Amyloid fibrils clearly possess a cross-β structure, in which the peptide chains are perpendicular to the fibril axis, while the H-bonds between strands in the β-sheets are parallel to the axis [97]. The details of how the peptide chains are arranged is space within these simple, minimal restraints have not, however, been established for any amyloid. Mutagenesis, especially with proline residues [98], has been used in other amyloid systems to garner details about how the sequence of the amyloidogenic peptide folds within the fibril. In Aβ, for example, it is clear from a variety of techniques that the N-terminal 10–15 amino acids, as well as the C-terminal 3–4 amino acids, are not involved in tight β-sheet H-bonding [99]. Proline analysis, which is based

on the observation that loops, floppy ends, and some turn positions can comfortably accept Pro residues, while β-sheets are destabilized by them, also suggests the location of turns in the Aβ fibril [99].

A major problem confronts the use of mutagenesis to dissect polyGln structure in the aggregate, however. The problem is the prospect that the polyGln sequence will be promiscuous in how it adopts its fold within the aggregate. This means that any particular sequence position of a Q_{40} sequence, let's say position 10, might be found in a number of environments when a series of Q_{40} molecules folds into the aggregate. Further, should position 10 be favored in a certain kind of structure in the aggregate, a mutation at position 10 that is unfavorable in that type of structure will likely simply lead to adjustments in the polyGln chain as it engages the aggregate structure, to place residue 10 in the least damaging – that is, least destabilizing – place in the aggregate.

A modified mutagenesis strategy, taking the above complication into account, has led to some insights into polyGln structure within the aggregate. It is based on the hypothesis that polyGln folds in the aggregate in a series of extended chain segments, of some unknown optimal length, alternating with turn segments [10]. This hypothesis was then tested by analysis of the aggregation kinetics of a series of mutant polyGln peptides composed of alternating segments of oligoGln and Pro-Gly sequences, the latter being especially comfortable in turn elements. It was found that the peptide PGQ_9, consisting of four Q_9 segments interspersed with three PG pairs, undergoes spontaneous aggregation essentially as fast as a Q_{42} peptide of the same length. Since peptides with shorter Q_N elements aggregate less rapidly, while a PGQ_{10} peptide aggregates only marginally more rapidly, it was concluded that the best model for how an unbroken polyGln sequence aggregates is PGQ_9. Since each turn may involve one or two Gln residues bordering the PG pair, this corresponds to extended chain segments of 7–8 residues interspersed with turns of 3–4 residues.

Two further mutagenesis tests on PGQ_9 support such models. To test the interpretation that the PG pairs are located in turns in the aggregate, a PGQ_9 peptide was synthesized containing D-prolines in place of L-prolines; this peptide aggregates more rapidly than the L-Pro form, consistent with data showing D-Pro-Gly to be more compatible in β-turns than L-Pro-Gly [100]. To test the interpretation that the oligoGln sequences between the PG pairs are in extended chain in the aggregate, mutant peptides were synthesized in which additional proline residues were inserted in the middle of one or more of these oligoGln sequences. When a single Pro residue is placed in the middle of either the second (PGQ_9P^2) or third (PGQ_9P^3) of the four Q_9 segments, these peptides are completely incapable of forming aggregates under conditions where PGQ_9 aggregates readily. This replicates the strong inhibition of amyloid formation when a single Pro residue is placed in the middle of a β-sheet region in Aβ peptides [98, 99] and strongly supports the model for the aggregate structure of PGQ_9. That the structure of the PGQ_9 aggregate is very similar to that of a Q_{42} aggregate was shown by a number of studies, including EM, WO1 binding (Section 37.6.4) and the abilities of each aggregate to seed elongation of the other peptide [10].

Interestingly, the aggregation of another Q_{42} analogue, containing only a single proline residue at the same residue position as the additional proline in PGQ_9P^2, is nearly as rapid as that of an unbroken Q_{42} peptide. This confirms the concerns about folding promiscuity in polyGln aggregation that guided the design of the PGQ_9 series. That is, simple mutagenesis experiments on unbroken polyGln will generally be very difficult to interpret with confidence, because of the ability of the polyGln sequence to accommodate to the mutation by slightly altering its fold in the aggregate.

The model of a repeat structure consisting of alternating extended chains and turns is compatible with either an antiparallel β-sheet motif or an irregular parallel β-helix motif of the kind seen in certain globular proteins [101]. Previously, Starikov et al. proposed an antiparallel β-sheet model, noting that the number of residues required to make a four-stranded version of such a model is very close to the pathological threshold for most expanded CAG repeat diseases [102]. Perutz and coworkers proposed a "water-filled nanotube" model for the polyGln aggregate [103], which is related to parallel β-helix models previously proposed for the amyloid structure [101, 104]. It is not clear whether the central core of water would be energetically favorable or whether a more stable variation might be to exclude the water to generate an irregular helix more like those seen in parallel β-helical proteins [101, 105]. However, the "ideal" water-filled nanotube model [103] might be expected to be destabilized by Pro or Pro-Gly insertions, given the uniform extended chain and continuous twisted β-sheet in the model. The ability of polyGln aggregates to tolerate certain periodicities of Pro-Gly insertion is also incompatible with aggregates consisting of very long strands of polyGln extended chain [27].

Interestingly, the mechanism of nucleation of polyGln aggregation does not seem to be altered in these Pro-Gly mutants. Thus, analysis of the concentration dependence of the early phases of spontaneous aggregation for the peptide PGQ_9 yields a value of $n^* = 1$ for the critical nucleus [10], the same number obtained for unbroken polyGln sequences.

37.7 Polyglutamine Aggregates and Cytotoxicity

There is little disagreement that the expansion of the polyGln sequence plays a major role in expanded CAG repeat diseases, but opinions differ considerably as to the mechanisms by which this effect plays out. Many reviews are available that summarize the data and argue for and against an active involvement of polyGln aggregates [2, 13–31]. One of the central barriers to reaching a consensus on the nature of the polyGln effect is the difficulty in characterizing and/or controlling the aggregation state of polyGln in cells. This problem has an impact in various ways. For example, in order to produce *htt* aggregates in a reasonable time frame in a cell or animal model, it is necessary to express unnaturally high concentrations of monomeric protein in the cell; if toxicity is observed, is it then due to the aggregates or to the high concentration of monomer required to make the aggregate? At the

same time, genetic analyses for binding partners of expanded polyGln proteins may in some cases be mediated by an aggregated form of the bait molecule rather than the assumed monomeric form.

Semantics and sensitivity of detection may also play roles in the controversy over the toxic species in polyGln diseases. To a protein chemist, an aggregate is any oligomeric protein state held together by noncovalent interactions, even including native oligomers; thus, a nonnative dimer of huntingtin, for example, would be considered an aggregate. Some workers, however, interpret an absence of large, macroscopic cellular inclusions as definitively ruling out the involvement of aggregates in toxicity.

If the neuronal dysfunction and death characteristics of expanded CAG repeat diseases can in fact be attributed to polyGln aggregates, it remains to be determined how aggregates produce their effects at the molecular and cellular level. A number of theories have been put forward to explain the toxicity of protein aggregates in neurodegeneration. Aggregates might saturate and/or otherwise inactivate the cellular machinery, such as molecular chaperones, the ubiquitin-proteasome system [106], and the aggresome system [107], responsible for dealing with protein misfolding. Aggregates might insert into membranes and alter their properties [108]. One mechanism that is uniquely feasible for polyGln aggregation and that has received significant attention and confirmatory data is the recruitment-sequestration model [24, 57, 61, 62, 85]. Since it is well established that amyloid-like aggregates of one polyGln sequence are capable of being elongated by the addition of other polyGln sequences, it is possible that polyGln aggregates in the cell might recruit other polyGln-containing proteins. Many such proteins exist in the human genome [109–111], in particular among proteins involved in nucleic acid binding, such as transcription factors. In a pivotal paper, Ross and coworkers showed that expanded polyGln cytotoxicity in a cell model appears to be mediated by the recruitment of the transcription factor CREB-binding protein (CBP), which contains a Q_{18} repeat, into the polyGln aggregates [85]. Expression of high levels of a functional, polyGln-minus version of CBP protects cells from expanded polyGln toxicity [85].

As discussed below, synthetic polyGln peptides have contributed to the debate about the toxicity of expanded polyGln sequences by addressing some of these technical barriers.

37.7.1 Direct Cytotoxicity of PolyGln Aggregates

One way to more directly test the toxicity of aggregates would be to deliver polyGln aggregates produced in vitro into cells. This would eliminate the need for producing unnaturally high levels of monomeric polyGln, the toxicity of which then becomes an important question if the experimental result is to be properly interpreted. The ability to produce a variety of well-characterized polyGln aggregates in relative bulk, as described above, makes possible experiments involving delivery of aggregates to cells. In addition, the ability to deliver aggregates essentially com-

posed of only the polyGln sequence addresses the question of the role of other sequence elements in cytotoxicity of expanded CAG repeat proteins.

37.7.1.1 Delivery of Aggregates into Cells and Cellular Compartments

The challenge in analyzing the cytotoxicity of exogenous aggregates is their delivery into the cell. In fact, liposome encapsulation does allow polyGln peptide aggregates to be taken up by cells in a relatively short time [45]. Interestingly, however, a control experiment of polyGln aggregate mixed directly with cells in culture also resulted in very good cellular uptake of the aggregate [45]. Sonication and membrane filtration (Section 37.4.2.2) to generate smaller average sizes of aggregates improves cellular uptake [45]. Uptake through the cellular membrane was confirmed by confocal microscopy on fluorescently tagged aggregates. The mechanism by which cells take up these aggregates is not clear, but it may be related to an electrostatic attraction between the negatively charged phospholipid membrane and the highly positively charged aggregates, which are composed of peptides consisting of polyGln flanked by pairs of Lys residues. The process does not require polyGln, since a control amyloid fibril is also readily taken up [45].

Since nuclear polyGln inclusions are often observed in cell and animal models, it is also of interest to deliver aggregates into the nucleus. In an attempt to do this, polyGln peptides were prepared that contain an N-terminal nuclear localization signal (NLS) peptide sequence as well as a fluorescein tag. In fact, aggregates of such peptides are not only taken up by the cell but also are transported into the nucleus, as confirmed by confocal microscopy of isolated nuclei [45]. A control amyloid fibril from a peptide containing a NLS is also readily taken up into the nucleus. The ability of the nuclear transporter to manage such aggregates is somewhat surprising, since the aggregates appear to exceed 100 nm in diameter (based on their ability to resist filtration through a 100-nm filter membrane), while the diameter of the nuclear pore is on the order of 26 nm [112]. It is possible that the multiple display of NLS signal peptides along the surface of the aggregate provides a repeat that allows it to "ratchet" through the pore [112]. It is also possible that the large aggregates mixed with and taken up by cells may transiently break apart to individual protofibrillar aggregates, as seen in EMs of these aggregates; these have diameters in the range of 5 nm.

It is very unlikely that aggregates get into cells or nuclei by way of full dissociation to monomers followed by reassembly on the other side of the membrane. These polyGln aggregates are very stable in vitro in physiological conditions [45]. Further, such a mechanism could not explain the ability of Q_{20} aggregates to invade the cell and nucleus, since the very slow aggregation kinetics of the monomer, especially at the concentrations likely to obtain in this scenario, rules out any efficient aggregation after dissociation.

37.7.1.2 Cell Killing by Nuclear-targeted PolyGln Aggregates

The ability to deliver various protein aggregates into cells and their nuclei makes it possible to study the toxicity of these aggregates. PolyGln, as well as control, aggregates delivered to the cytoplasm of either PC12 or Cos-7 cells in culture exhibit

little or no toxicity to these cells when examined by a number of standard methods for determining cell death: propidium iodide exclusion, lactate dehydrogenase release, and MTT reduction [45]. In contrast, polyGln aggregates delivered to cell nuclei rapidly kill cells, with very similar results from all three measures of cell killing. Although amyloid fibrils of cold shock protein peptide B-1 (CspB1) are efficiently delivered to cell nuclei, they do not kill cells, indicating the importance of the polyGln sequence. Interestingly, nuclear-targeted aggregates of Q_{20} and Q_{42} peptides are equally effective at killing cells. This strongly suggests that any aggregated polyGln peptide can be toxic when delivered to the nucleus and reinforces the conclusion derived from the aggregation kinetics (Section 37.5.2) that the distinction between a toxic (Q_{42}) and benign (Q_{20}) repeat-length sequence is made at the level of aggregation efficiency (Section 37.5).

Although the ability of nuclear-localized polyGln aggregates to rapidly kill cells may thus be responsible for the neuronal loss observed in end-stage expanded CAG repeat brain stem, it remains possible that cytoplasmic polyGln aggregates might also have harmful effects that may be less dramatic and difficult to detect in a one-day cell culture. The cell death induced in cultured cells by nuclear uptake of polyGln aggregates appears to be related to an apoptotic process (W. Yang and R. Wetzel, manuscript in preparation).

37.7.2
Visualization of Functional, Recruitment-positive Aggregation Foci

One possible explanation for why easily detected polyGln aggregates do not correlate with cytotoxicity in all cases is that the wrong aggregates are being monitored. If the cell killing by expanded polyGln sequences is due to recruitment of cellular polyGln proteins by aggregates of the polyGln disease protein, then the ability of these aggregates to efficiently recruit other polyGln sequences – their ''recruitment activity'' – is of paramount importance to their cytotoxicity. Recruitment activity can be defined as a measure of the number of monomeric polyGln peptides that can be recruited into a polyGln aggregate of a certain mass in a certain time. Interestingly, even in vitro aggregates of simple polyGln peptides can exhibit different recruitment activities depending on the way they are prepared and on their sizes [49]. Larger aggregates exhibit lower recruitment activity than smaller aggregates, presumably because of the greater surface area of the latter [49] (Section 37.5.4).

Thus, if the recruitment hypothesis is valid, then the best way to gauge the polyGln aggregate burden of a cell or tissue would be to assess the recruitment activity in the tissue, either as a tissue stain or as an activity measurement akin to an enzymatic assay. Both of these approaches are feasible, because of the robustness and specificity of the polyGln elongation reaction, and both have been shown to work when using human brain material. Aggregates in an enriched fraction isolated from HD brain tissue, when fixed to microplate wells, exhibit the same ability to recruit biotinylated polyGln peptides as synthetic aggregates exhibit (V. Berthelier and R. Wetzel, unpublished). HD brain slices incubated with biotinylated polyGln pick up the peptide in small, punctate, intracellular centers called aggrega-

tion foci [113]. The ability to characterize cells and tissue for levels of functional polyGln aggregates should provide sharper tools for addressing the question of the role of polyGln aggregates in cell dystrophy and death in expanded CAG repeat diseases.

37.8 Inhibitors of polyGln Aggregation

If polyGln aggregates are toxic to cells, a viable therapeutic approach for expanded CAG repeat diseases would be the use of specific inhibitors of spontaneous polyGln aggregation and/or elongation. Such inhibitors clearly exist in nature. For example, several genetic screens in HD disease models reveal that increased expression of DnaJ class chaperones can protect cells and animals from polyGln toxicity. Investigations of the molecular basis of this effect reveal that recombinant HDJ1, a human DnaJ homologue, is very effective at inhibiting both spontaneous polyGln aggregation and seeded elongation, presumably by binding to nuclei or small aggregates and inhibiting their elongation with additional polyGln monomers (A. Bhattacharyya and R. Wetzel, unpublished). This suggests that inhibitors of polyGln aggregation can have a protective effect.

37.8.1 Designed Peptide Inhibitors

A similar result has been obtained with a structure-based elongation inhibitor. Not only is the peptide $PGQ_9\text{-}P^2$ incapable of spontaneously aggregating (see Section 37.6.5), it can also inhibit the aggregation of other polyGln peptides. In the microplate assay described earlier, $PGQ_9\text{-}P^2$ inhibits Q_{42} elongation with an IC_{50} in the low micromolar range (Figure 37.10) [44]. Furthermore, cells pre-incubated with $PGQ_9\text{-}P^2$ are protected, in a dose-dependent manner, from the cytotoxicity of polyGln aggregates in the cell model described in Section 37.7.1.2 [44]. This implies not only that aggregates are toxic but also that the basis of their toxicity is their ability to recruit other polyGln peptides in the cell. This in turn suggests that even cells that have already entered the aggregation pathway might be protected from aggregate toxicity by appropriate inhibitors.

37.8.2 Screening for Inhibitors of PolyGln Elongation

As discussed above, polypeptide-based inhibitors of polyGln aggregation exist. However, small molecules with comparable activities would presumably be better drug candidates. In order to discover and refine such inhibitors, viable assays are needed. A filter blot assay that allows screening of small compound libraries for inhibitors of the aggregation of the polyGln-containing *htt* exon 1 domain has iden-

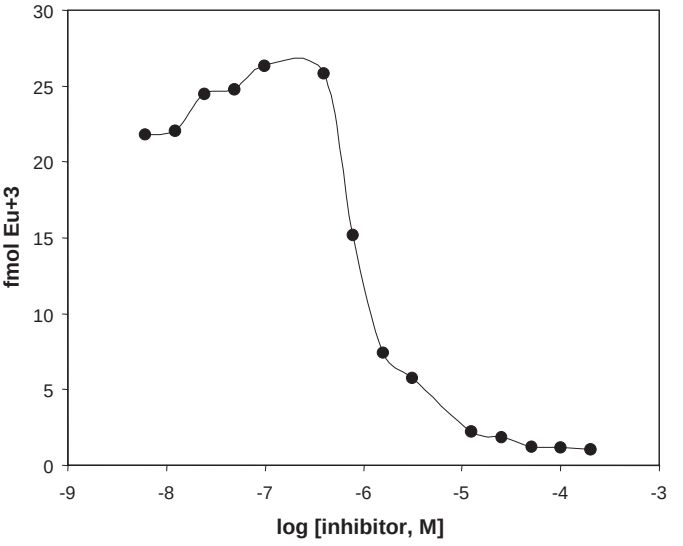

Fig. 37.10. Concentration-dependent inhibition of polyGln aggregate elongation by PGQ_9-based peptide inhibitors. Microtiter plate wells containing adsorbed Q_{45} polyGln aggregates (100 ng per well) were incubated with 10 nM biotinyl-Q_{28} and various concentrations of PGQ_9P^2 (●) for 45 min at 37 °C. The derived EC_{50} value is 1.1 μM.

tified a number of small molecule inhibitors [114]. The microtiter plate elongation assay described in Section 37.5.4.1 was initially designed for the same purpose [67, 83]. The assay has several important features, including reproducibility, insensitivity to small concentrations of DMSO and small pH changes, good throughput, and the ability to operate at low polyGln concentrations approaching physiological. This assay has been used to screen a number of small libraries of drug-like compounds as well as to determine dose-response curves for hits and analogues (V. Berthelier and R. Wetzel, unpublished). A typical screening result is shown in Figure 37.11.

37.9 Concluding Remarks

Historically, protein aggregation has been viewed as a nonspecific, amorphous process that is very difficult to study and unlikely to be relevant to events in the cell. Recent studies of amyloid-like phenomena, however, are showing that at least some aggregation processes are highly specific, more closely resembling crystallization phenomena. As described in this article, a logical approach that assumes such crystal-like packing and growth as a starting point for focused analytical experiments can make great progress in understanding the aggregation process both in vitro and in vivo. Far from being alien to the cell environment, it is now

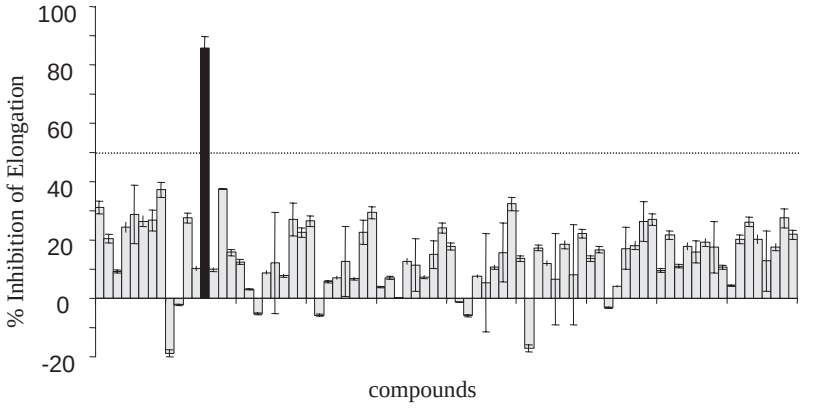

Fig. 37.11. Microtiter plate screen of a small compound library for inhibitors of biotinyl-polyGln elongation on adsorbed polyGln aggregates. Amount of elongation for each compound was compared to elongation without added compound, and the percent inhibition was calculated. In this plate, 1 out of 80 compounds tested gave >50% inhibition. Error bars from triplicate analysis.

known that aggregation is a continuing background problem in the life of the cell. Although cells can normally manage the process pretty well, in some cases, as in the amyloid-related neurodegenerative diseases, the normal cellular safeguards break down, are overwhelmed, or are isolated by cellular compartmentalization, and protein aggregation proceeds unabated, with devastating consequences. Protein aggregation, long swept under the rug in the protein-folding field, is now very much a viable subject for biophysical studies. While there has long been a perception that protein misfolding and aggregation are shadowy events occurring behind a veil impenetrable to the experimentalist, a variety of analytical methods exist [115], and improved methods are being developed [99, 116–120], that are capable of revealing these processes with analytical clarity.

Many techniques have been discussed or alluded to in this article. The protocols described in detail below represent central technologies necessary to getting started in polyGln studies, and they may be transportable, with modification, to studies of other protein aggregation phenomena as well.

37.10
Experimental Protocols

37.10.1
Disaggregation of Synthetic PolyGln Peptides

The procedures described for working with synthetic polyGln peptides have been developed through the almost exclusive use of polyGln peptides flanked by pairs

of Lys residues, for better solution behavior of the peptides prior to their aggregation. Other flanking-charged residues work to varying extents. Peptides without flanking-charged residues are quite poorly behaved and aggregate very rapidly after being adjusted to PBS conditions [66].

Purification

Lyophilized, crude synthetic product is purified by reverse-phase HPLC as follows. Working in a chemical fume hood, 2 mg of the dry product is dissolved in 4 mL of a 1:1 mixture of trifluoroacetic acid (TFA) and hexafluoroisopropanol (HFIP) in a 20-mL Erlenmeyer flask and allowed to stand for up to 5 h at RT. Normally this should completely dissolve the sample; if there is any visible undissolved material after 5 h, the supernatant should be removed to a fresh flask. The volatile solvents are removed, in the fume hood, under a stream of argon gas, being careful to avoid splashing of the solution. The residue is dissolved in 5 mL of distilled water adjusted to pH 3 with TFA and filtered through a 0.45-μm membrane filter. The filtrate is loaded onto a 9.4 × 250-mm C3 HPLC column equilibrated to 0.05% TFA, 1% acetonitrile in water. The column is developed with a linear gradient of 1–21% acetonitrile in 0.05 % TFA at 4 mL min^{-1}. Column fractions are checked for purity by analytical HPLC under similar conditions and by mass spectrometry, and the fractions are pooled. Synthetic polyGln peptides longer than Q_{20} may have significant amounts of truncated side products, and these become more significant as repeat length increases; these truncated products are difficult to fully separate from the desired repeat length. Thus, most synthetic peptides longer than Q_{25} after purification will be mixtures of two to four different repeat lengths. A weighted average is calculated based on MS analysis of the purified pool, and this is the quoted repeat length. There is no indication that such mixtures behave substantially differently than homogeneous repeat length peptides. The pooled fractions are lyophilized and the powder is stored at −80 °C.

Disaggregation

Lyophilized purified peptide is dissolved in 1:1 TFA:HFIP to 0.5 mg mL^{-1} and incubated at RT as described above. For peptides of repeat length Q_{50} or above (and perhaps for shorter repeat lengths with alternative flanking sequences), it may be important to continue incubation in TFA/HFIP until completion is confirmed by a light-scattering test, as described in Ref. [48]. In this test, a small aliquot of the TFA/HFIP solution is removed and dried under argon, then further dried under vacuum, resuspended in pH 3 (TFA) distilled water, and brought to PBS conditions by addition of a one-ninth volume of 10× PBS buffer concentrate with stirring. The Rayleigh light scattering of this sample (in a fluorometer with both excitation and emission set to 450 nm, and with slit widths set such that aggregated versions of similar weight concentrations of polyGln give significant signals) should be essentially identical to that of buffer alone. If that is not the case, the incubation in TFA/HFIP should be continued, at least until the light scattering of the test reaches a low plateau.

When this point is reached, the bulk of the reaction is dried under an argon stream and then under vacuum. The residue is dissolved in pH 3 (TFA) distilled water to a concentration in the range of 100 μM or less, as required (higher concentrations may be possible, but such experiments should be carefully conducted and monitored to ensure that no continuing undesired aggregation process is initiated. This solution is centrifuged at 386 000 *g* for at least 3 h (or overnight) in a tabletop ultracentrifuge to remove any residual aggregates. The top two-thirds of the supernatant is carefully decanted and checked for concentration by HPLC as described in the next protocol. Appropriate buffer concentrate is then added to adjust the solution conditions, and additional buffer is added, as required, to bring the solution to the desired polyGln concentration. Ideally, this final solution should again be checked for polyGln concentration.

In general, it is advisable to carry out this entire procedure each time a new study is initiated, especially in the case of more aggregation-prone samples. As discussed in this chapter, freezing of polyGln solutions is generally not a good way to preserve their integrity, due to freeze-concentration-induced aggregation. Aggregates tend to build up slowly even in solutions stored at −80 °C. However, very low (low nanomolar) concentrations of polyGln peptides can be stored in PBS at −80 °C for one month, if 10% DMSO is included.

37.10.2
Determining the Concentration of Low-molecular-weight PolyGln Peptides by HPLC

As discussed in this chapter, monitoring the concentration of solution-phase, low-molecular-weight polyGln is probably the best way to conduct detailed aggregation kinetics studies. Obviously, while this technique leads to highly reproducible solubility values, other methods must be used for any given peptide and reaction conditions to confirm the nature of the aggregated product. The fundamental assumption of the approach described here is that the A_{220} weight-concentration extinction coefficient, based primarily on the absorbance of the amide bonds in the peptide, will be essentially identical for all polyGln peptides. While the same assumption is not valid for other peptides, since some amino acids in peptides make different contributions to the A_{220}, it is a reasonable assumption for polyGln peptides. By making this assumption, we can use the standard curve generated from a standard of a given repeat length to analyze the unknown concentrations of solutions of other repeat length polyGln peptides. This HPLC method works equally well for other peptides, such as the Alzheimer's disease amyloid plaque peptide Aβ [117], so long as a standard curve appropriate for that peptide is generated.

Preparation of the Standard

A synthetic polyGln peptide in the length range Q_{25} is purified and disaggregated as described above. A stock solution of an approximate concentration appropriate for use as a standard (∼65 μM) is prepared in pH 3 water containing 20% formic acid and the solution is aliquoted into convenient volumes, snap-frozen in liquid

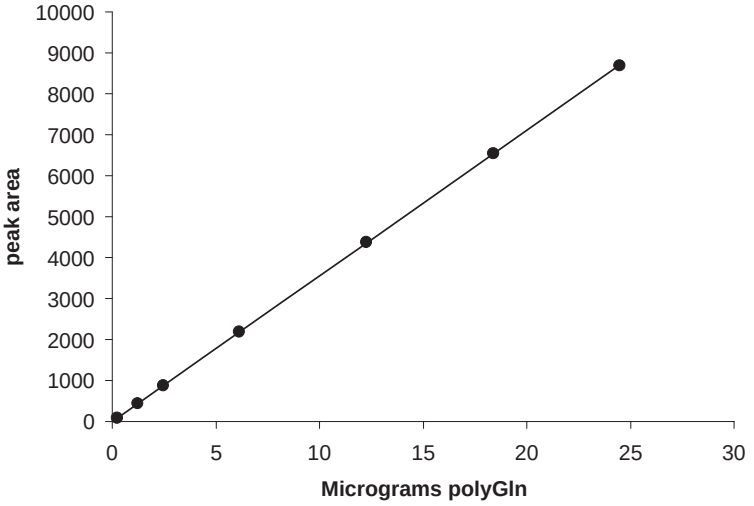

Fig. 37.12. HPLC standard curve relating peak area to mass of $K_2Q_{25}K_2$ injected into the system, as described in the experimental Section.

nitrogen, and stored at −80 °C. An aliquot of the stock is removed prior to freezing and diluted into pH 3 (TFA) water, the dilution factor is recorded, and the diluted solution is subjected to amino acid composition analysis to obtain a highly accurate concentration. The dilution factor is then applied to the concentration value obtained to generate a highly accurate concentration for the frozen standard. Peptides shorter than Q_{20}–Q_{25} may present problems when injected under certain solution conditions, such as eluting at somewhat earlier positions. Data from shorter peptides also are more dominated by the contribution of the Lys flanking residues and therefore may be less ideal standards for longer polyGln peptides. Peptides longer than Q_{25} may present problems because of a tendency to aggregate on long-term storage of the standard.

Generation of a Standard Curve

An HPLC system with a digital, computer-controlled variable wavelength detector is required. Aliquots of the polyGln standard generated above are injected onto an analytical reverse-phase HPLC column and developed with a 1–21% acetonitrile gradient in 0.05% TFA. The eluate is monitored at A_{220}. The polyGln peak is integrated and the area units from the integration are plotted with respect to peptide load. A typical standard curve for the standard $K_2Q_{25}K_2$ is shown in Figure 37.12. It must be emphasized that the standard curve is valid only for the HPLC system on which the data was collected. Different detectors will give substantially different curves. Standard curves from the same detector can also degrade over time, due, for example, to fouling of the detector cell windows altering the absorbance

characteristics of the detector. Therefore, standard curves should be rerun every few months.

Use of the Standard Curve to Generate Solubility Data

Analysis of an aliquot of a centrifugation supernatant will yield a peak whose integrated area units will correspond to a certain weight of standard polyGln peptide. It is assumed that this value also corresponds to the same weight concentration of the test polyGln peptide, even though its repeat length is different. The molar concentration can then be calculated from the molecular weight of the test peptide. Extrapolation of the curve to very low, nonzero weight concentrations of polyGln should not be assumed to be linear, since a certain amount of low background irreversible absorption of peptide may occur. That is, the standard curve should be extended into the required analysis range. The standard curve shown in Figure 37.12 is linear to 0.25 μg of $K_2Q_{25}K_2$.

Detailed kinetics experiments involve many time points and multiple replicates and are most conveniently analyzed using an autosampler. Care must be taken, however, to ensure that there is no loss of signal, due to aggregation, in samples left standing in the autosampler for many hours. This is especially of concern for pathological length polyGln peptides. We have found that doping centrifugation supernatants with formic acid to a final concentration of 20% stabilizes polyGln peptide solutions for at least 20 h at RT in an autosampler tray. (It is important to emphasize that this method of stabilizing samples against aggregation while awaiting analysis may be effective only for centrifugation supernatants – i.e., for largely aggregate-free samples of polyGln; it appears not to be effective if there are significant aggregation seeds in the sample.) Whatever conditions are used for preserving sample integrity, it is a good idea to confirm that they are working by analyzing one or more samples at two times, spanning the range of times that samples are required to sit awaiting analysis. If the concentration of polyGln differs substantially in the repeated analyses, there may be a problem with time-dependent aggregation in the autosampler.

Acknowledgements

The author would like to thank Geetha Thiagarajan for help with the experimental Section of this chapter and Angela Williams, Valerie Berthelier, and Ashwani Thakur for permission to include unpublished data. I am also very grateful to Marcy MacDonald for providing Figure 37.1. I would like to acknowledge past and present members of my laboratory, in particular, Songming Chen, Valerie Berthelier, J. Bradley Hamilton, Wen Yang, Ashwani Thakur, Anusri Bhattacharyya, Brian O'Nuallain, Alex Osmand, Angela Williams, and Tina Richey, for their work and ideas in developing the body of work summarized here. I gratefully acknowledge the Hereditary Disease Foundation and the NIH (R01 AG19322) for sustained funding and Ethan Signer, Carl Johnson, and Nancy Wexler for their enthusiastic support.

References

1 Wilmot, G. R. & Warren, S. T. (1998). A new mutational basis for disease. In *Genetic Instabilities and Hereditary Neurological Diseases* (Wells, R. D. & Warren, S. T., eds.), pp. 3–12. Academic Press, San Diego.

2 Cummings, C. J. & Zoghbi, H. Y. (2000). Fourteen and counting: unraveling trinucleotide repeat diseases. *Hum Mol Genet* 9, 909–916.

3 Bates, G. P. & Benn, C. (2002). The polyglutamine diseases. In *Huntington's Disease* (Bates, G. P., Harper, P. S. & Jones, L., eds.), pp. 429–472. Oxford University Press, Oxford, U.K.

4 DiFiglia, M., Sapp, E., Chase, K. O., Davies, S. W., Bates, G. P., Vonsattel, J. P. & Aronin, N. (1997). Aggregation of huntingtin in neuronal intranuclear inclusions and dystrophic neurites in brain. *Science* 277, 1990–3.

5 Ordway, J. M., Tallaksen-Greene, S., Gutekunst, C. A., Bernstein, E. M., Cearley, J. A., Wiener, H. W., Dure, L. S. t., Lindsey, R., Hersch, S. M., Jope, R. S., Albin, R. L. & Detloff, P. J. (1997). Ectopically expressed CAG repeats cause intranuclear inclusions and a progressive late onset neurological phenotype in the mouse [In Process Citation]. *Cell* 91, 753–63.

6 Davies, S. W., Turmaine, M., Cozens, B. A., DiFiglia, M., Sharp, A. H., Ross, C. A., Scherzinger, E., Wanker, E. E., Mangiarini, L. & Bates, G. P. (1997). Formation of neuronal intranuclear inclusions underlies the neurological dysfunction in mice transgenic for the HD mutation. *Cell* 90, 537–48.

7 Paulson, H. L., Perez, M. K., Trottier, Y., Trojanowski, J. Q., Subramony, S. H., Das, S. S., Vig, P., Mandel, J. L., Fischbeck, K. H. & Pittman, R. N. (1997). Intranuclear inclusions of expanded polyglutamine protein in spinocerebellar ataxia type 3. *Neuron* 19, 333–44.

8 Martin, J. B. (1999). Molecular basis of the neurodegenerative disorders [published erratum appears in N Engl J Med 1999 Oct 28;341(18):1407]. *N Engl J Med* 340, 1970–80.

9 Chen, Y. W. (2003). Site-specific mutagenesis in a homogeneous polyglutamine tract: application to spinocerebellar ataxin-3. *Protein Eng* 16, 1–4.

10 Thakur, A. & Wetzel, R. (2002). Mutational analysis of the structural organization of polyglutamine aggregates. *Proc Natl Acad Sci USA* 99, 17014–17019.

11 Wells, R. D. & Warren, S. T. (1998). *Genetic Instabilities and Hereditary Neurological Diseases*, Academic Press, San Diego.

12 Bates, G. P., Harper, P. S. & Jones, L., Eds. (2002). Huntington's Disease. Oxford, U.K.: Oxford University Press.

13 Reddy, P. S. & Housman, D. E. (1997). The complex pathology of trinucleotide repeats. *Curr Opin Cell Biol* 9, 364–72.

14 Gusella, J. F. & MacDonald, M. E. (1998). Huntingtin: a single bait hooks many species. *Curr Opin Neurobiol* 8, 425–30.

15 Reddy, P. H., Williams, M. & Tagle, D. A. (1999). Recent advances in understanding the pathogenesis of Huntington's disease. *Trends Neurosci* 22, 248–55.

16 Lin, X., Cummings, C. J. & Zoghbi, H. Y. (1999). Expanding our understanding of polyglutamine diseases through mouse models. *Neuron* 24, 499–502.

17 Zoghbi, H. Y. & Orr, H. T. (1999). Polyglutamine diseases: protein cleavage and aggregation. *Curr Opin Neurobiol* 9, 566–70.

18 Paulson, H. L. (1999). Protein fate in neurodegenerative proteinopathies: polyglutamine diseases join the (mis)fold. *Am J Hum Genet* 64, 339–45.

19 Ferrigno, P. & Silver, P. A. (2000). Polyglutamine expansions: proteolysis, chaperones, and the dangers of promiscuity. *Neuron* 26, 9–12.

20 Tobin, A. J. & Signer, E. R. (2000). Huntington's disease: the challenge for cell biologists. *Trends Cell Biol* 10, 531–536.

21 Zoghbi, H. Y. & Orr, H. T. (2000). Glutamine repeats and neurodegeneration. *Annu Rev Neurosci* 23, 217–47.

22 Bates, G. (2000). Huntington's disease. In reverse gear. *Nature* 404, 944–5.

23 Cha, J. H. (2000). Transcriptional dysregulation in Huntington's disease. *Trends Neurosci* 23, 387–92.

24 McCampbell, A. & Fischbeck, K. H. (2001). Polyglutamine and CBP: fatal attraction? *Nat Med* 7, 528–30.

25 Ross, C. A. (2002). Polyglutamine pathogenesis: emergence of unifying mechanisms for Huntington's disease and related disorders. *Neuron* 35, 819–22.

26 Rubinsztein, D. C. (2002). Lessons from animal models of Huntington's disease. *Trends Genet* 18, 202–9.

27 Ross, C. A., Poirier, M. A., Wanker, E. E. & Amzel, M. (2003). Polyglutamine fibrillogenesis: the pathway unfolds. *Proc Natl Acad Sci USA* 100, 1–3.

28 Bates, G. (2003). Huntingtin aggregation and toxicity in Huntington's disease. *Lancet* 361, 1642–4.

29 Michalik, A. & Van Broeckhoven, C. (2003). Pathogenesis of polyglutamine disorders: aggregation revisited. *Hum Mol Genet* 12 Suppl 2, R173–86.

30 Paulson, H. (2003). Polyglutamine neurodegeneration: minding your Ps and Qs. *Nat Med* 9, 825–826.

31 Rudnicki, D. D. & Margolis, R. L. (2003). Repeat expansion and autosomal dominant neurodegenerative disorders: consensus and controversy. *Exp. Rev. Mol. Med.* 5, 1–24.

32 Koide, R., Kobayashi, S., Shimohata, T., Ikeuchi, T., Maruyama, M., Saito, M., Yamada, M., Takahashi, H. & Tsuji, S. (1999). A neurological disease caused by an expanded CAG trinucleotide repeat in the TATA-binding protein gene: a new polyglutamine disease? *Hum Mol Genet* 8, 2047–53.

33 Margolis, R. L. (2002). The spinocerebellar ataxias: order emerges from chaos. *Curr Neurol Neurosci Rep* 2, 447–56.

34 Albin, R. L. (2003). Dominant ataxias and Friedreich ataxia: an update. *Curr Opin Neurol* 16, 507–14.

35 Bowater, R. P. & Wells, R. D. (2001). The intrinsically unstable life of DNA triplet repeats associated with human hereditary disorders. *Prog Nucleic Acid Res Mol Biol* 66, 159–202.

36 Harper, P. S. & Jones, L. (2002). Huntington's disease: genetic and molecular studies. In *Huntington's Disease* (Bates, G. P., Harper, P. S. & Jones, L., eds.), pp. 113–158. Oxford University Press, Oxford, U.K.

37 Myers, R. H., Marans, K. S. & MacDonald, M. E. (1998). Huntington's Disease. In *Genetic Instabilities and Hereditary Neurological Diseases* (Wells, R. D. & Warren, S. T., eds.), pp. 301–323. Academic Press, San Diego.

38 Zajac, J. D. & MacLean, H. E. (1998). Kennedy's disease: clinical aspects. In *Genetic Instabilities and Hereditary Neurological Diseases* (Wells, R. D. & Warren, S. T., eds.), pp. 87–111. Academic Press, San Diego.

39 Cattaneo, E., Rigamonti, D., Goffredo, D., Zuccato, C., Squitieri, F. & Sipione, S. (2001). Loss of normal huntingtin function: new developments in Huntington's disease research. *Trends Neurosci* 24, 182–8.

40 Kazemi-Esfarjani, P. & Benzer, S. (2000). Genetic suppression of polyglutamine toxicity in Drosophila. *Science* 287, 1837–40.

41 Bennett, M. J., Huey-Tubman, K. E., Herr, A. B., West, A. P., Ross, S. A. & Bjorkman, P. J. (2002). A linear lattice model for polyglutamine in CAG expansion diseases. *Proc Natl Acad Sci USA* 99, 11634–11639.

42 Faber, P. W., Voisine, C., King, D. C., Bates, E. A. & Hart, A. C. (2002). Glutamine/proline-rich PQE-1 proteins protect Caenorhabditis elegans neurons from huntingtin

polyglutamine neurotoxicity. *Proc Natl Acad Sci USA* 99, 17131–6.

43 Kazantsev, A., Walker, H. A., Slepko, N., Bear, J. E., Preisinger, E., Steffan, J. S., Zhu, Y. Z., Gertler, F. B., Housman, D. E., Marsh, J. L. & Thompson, L. M. (2002). A bivalent Huntingtin binding peptide suppresses polyglutamine aggregation and pathogenesis in Drosophila. *Nat Genet* 25, 25.

44 Thakur, A. K., Yang, W., & Wetzel, R. (2004). Inhibition of polyglutamine aggregate cytotoxicity by a structure-based elongation inhibitor. *FASEB J.* 18, 923–925.

45 Yang, W., Dunlap, J. R., Andrews, R. B. & Wetzel, R. (2002). Aggregated polyglutamine peptides delivered to nuclei are toxic to mammalian cells. *Hum Mol Genet* 11, 2905–2917.

46 Altschuler, E. L., Hud, N. V., Mazrimas, J. A. & Rupp, B. (1997). Random coil conformation for extended polyglutamine stretches in aqueous soluble monomeric peptides. *J Pept Res* 50, 73–5.

47 Sharma, D., Sharma, S., Pasha, S. & Brahmachari, S. K. (1999). Peptide models for inherited neurodegenerative disorders: conformation and aggregation properties of long polyglutamine peptides with and without interruptions. *FEBS Lett* 456, 181–5.

48 Chen, S. & Wetzel, R. (2001). Solubilization and disaggregation of polyglutamine peptides. *Protein Science* 10, 887–891.

49 Chen, S., Berthelier, V., Yang, W. & Wetzel, R. (2001). Polyglutamine aggregation behavior in vitro supports a recruitment mechanism of cytotoxicity. *J. Mol. Biol.* 311, 173–182.

50 Masino, L., Kelly, G., Leonard, K., Trottier, Y. & Pastore, A. (2002). Solution structure of polyglutamine tracts in GST-polyglutamine fusion proteins. *FEBS Lett* 513, 267–72.

51 Shi, Z., Olson, C. A., Rose, G. D., Baldwin, R. L. & Kallenbach, N. R. (2002). Polyproline II structure in a sequence of seven alanine residues. *Proc Natl Acad Sci USA* 99, 9190–5.

52 Rucker, A. L., Pager, C. T., Campbell, M. N., Qualls, J. E. & Creamer, T. P. (2003). Host-guest scale of left-handed polyproline II helix formation. *Proteins* 53, 68–75.

53 Perutz, M. F., Johnson, T., Suzuki, M. & Finch, J. T. (1994). Glutamine repeats as polar zippers: their possible role in inherited neurodegenerative diseases. *Proc Natl Acad Sci USA* 91, 5355–8.

54 Scherzinger, E., Lurz, R., Turmaine, M., Mangiarini, L., Hollenbach, B., Hasenbank, R., Bates, G. P., Davies, S. W., Lehrach, H. & Wanker, E. E. (1997). Huntingtin-encoded polyglutamine expansions form amyloid-like protein aggregates in vitro and in vivo. *Cell* 90, 549–58.

55 Scherzinger, E., Sittler, A., Schweiger, K., Heiser, V., Lurz, R., Hasenbank, R., Bates, G. P., Lehrach, H. & Wanker, E. E. (1999). Self-assembly of polyglutamine-containing huntingtin fragments into amyloid-like fibrils: implications for Huntington's disease pathology. *Proc Natl Acad Sci USA* 96, 4604–9.

56 Onodera, O., Burke, J. R., Miller, S. E., Hester, S., Tsuji, S., Roses, A. D. & Strittmatter, W. J. (1997). Oligomerization of expanded-polyglutamine domain fluorescent fusion proteins in cultured mammalian cells. *Biochem Biophys Res Commun* 238, 599–605.

57 Perez, M. K., Paulson, H. L., Pendse, S. J., Saionz, S. J., Bonini, N. M. & Pittman, R. N. (1998). Recruitment and the role of nuclear localization in polyglutamine-mediated aggregation. *J Cell Biol* 143, 1457–70.

58 Sherman, M. Y. & Muchowski, P. J. (2003). Making yeast tremble: yeast models as tools to study neurodegenerative disorders. *Neuromolecular Med* 4, 133–46.

59 Driscoll, M. & Gerstbrein, B. (2003). Dying for a cause: invertebrate genetics takes on human neurodegeneration. *Nat Rev Genet* 4, 181–94.

60 Kazantsev, A., Preisinger, E.,

Dranovsky, A., Goldgaber, D. & Housman, D. (1999). Insoluble detergent-resistant aggregates form between pathological and nonpathological lengths of polyglutamine in mammalian cells. *Proc Natl Acad Sci USA* 96, 11404–9.

61 Huang, C. C., Faber, P. W., Persichetti, F., Mittal, V., Vonsattel, J. P., MacDonald, M. E. & Gusella, J. F. (1998). Amyloid formation by mutant huntingtin: threshold, progressivity and recruitment of normal polyglutamine proteins. *Somat Cell Mol Genet* 24, 217–33.

62 Preisinger, E., Jordan, B. M., Kazantsev, A. & Housman, D. (1999). Evidence for a recruitment and sequestration mechanism in Huntington's disease. *Philos Trans R Soc Lond B Biol Sci* 354, 1029–34.

63 McCampbell, A., Taylor, J. P., Taye, A. A., Robitschek, J., Li, M., Walcott, J., Merry, D., Chai, Y., Paulson, H., Sobue, G. & Fischbeck, K. H. (2000). CREB-binding protein sequestration by expanded polyglutamine. *Hum Mol Genet* 9, 2197–202.

64 Howlett, D. R., Jennings, K. H., Lee, D. C., Clark, M. S., Brown, F., Wetzel, R., Wood, S. J., Camilleri, P. & Roberts, G. W. (1995). Aggregation state and neurotoxic properties of Alzheimer beta-amyloid peptide. *Neurodegeneration* 4, 23–32.

65 Wood, S. J., Chan, W. & Wetzel, R. (1996). Seeding of Aβ fibril formation is inhibited by all three isotypes of apolipoprotein E. *Biochem.* 35, 12623–12628.

66 Chen, S., Berthelier, V., Hamilton, J. B., O'Nuallain, B. & Wetzel, R. (2002). Amyloid-like features of polyglutamine aggregates and their assembly kinetics. *Biochemistry* 41, 7391–7399.

67 Berthelier, V., Hamilton, J. B., Chen, S. & Wetzel, R. (2001). A microtiter plate assay for polyglutamine aggregate extension. *Anal Biochem* 295, 227–36.

68 Zagorski, M. G., Yang, J., Shao, H., Ma, K., Zeng, H. & Hong, A. (1999). Methodological and chemical factors affecting amyloid-β amyloidogenicity. *Meth Enzymol* 309, 189–204.

69 Franks, F. (1985). *Biophysics and biochemistry at low temperatures*, Cambridge University Press, Cambridge.

70 Franks, F. (1993). Storage stabilization of proteins. In *Protein Biotechnology: Isolation, Characterization and Stabilization* (Franks, F., ed.), pp. 489–531. Humana Press, New York.

71 Jaenicke, R. & Seckler, R. (1997). Protein Assembly In Vitro. In *Protein Misassembly* (Wetzel, R., ed.), Vol. 50, pp. 1–59. Academic Press, San Diego.

72 Anderson, V. J. & Lekkerkerker, H. N. (2002). Insights into phase transition kinetics from colloid science. *Nature* 416, 811–5.

73 Bishop, M. F. & Ferrone, F. A. (1984). Kinetics of nucleation-controlled polymerization. A perturbation treatment for use with a secondary pathway. *Biophys J* 46, 631–44.

74 Ferrone, F. (1999). Analysis of protein aggregation kinetics. *Meths. Enzymol.* 309, 256–274.

75 Cao, Z. & Ferrone, F. A. (1996). A 50th order reaction predicted and observed for sickle hemoglobin nucleation. *J Mol Biol* 256, 219–22.

76 Chen, S., Ferrone, F. & Wetzel, R. (2002). Huntington's Disease age-of-onset linked to polyglutamine aggregation nucleation. *Proc. Natl. Acad. Sci. USA* 99, 11884–11889.

77 Abraham, F. F. (1974). *Homogeneous Nucleation Theory*, Academic Press, New York.

78 Perutz, M. F. & Windle, A. H. (2001). Cause of neural death in neurodegenerative diseases attributable to expansion of glutamine repeats. *Nature* 412, 143–4.

79 Serio, T. R., Cashikar, A. G., Kowal, A. S., Sawicki, G. J., Moslehi, J. J., Serpell, L., Arnsdorf, M. F. & Lindquist, S. L. (2000). Nucleated conformational conversion and the replication of conformational information by a prion determinant. *Science* 289, 1317–21.

80 Naiki, H. & Gejyo, F. (1999). Kinetic analysis of amyloid fibril formation. *Meths Enzymol* 309, 305–318.

81 Esler, W. P., Stimson, E. R., Ghilardi, J. R., Felix, A. M., Lu, Y. A., Vinters, H. V., Mantyh, P. W. & Maggio, J. E. (1997). A beta deposition inhibitor screen using synthetic amyloid. *Nat Biotechnol* 15, 258–63.

82 Myszka, D. G., Wood, S. J. & Biere, A. L. (1999). Analysis of fibril elongation using surface plasmon resonance biosensors. In *Amyloid, Prions and other Protein Aggregates* (Wetzel, R., ed.), Vol. 309, pp. 386–402. Academic Press, San Diego.

83 Berthelier, V. & Wetzel, R. (2003). An assay for characterizing the in vitro kinetics of polyglutamine aggregation. In *Methods in Molecular Medicine: Neurogenetics* (N. T. Potter, e., ed.), pp. 295–303. Humana Press, New York.

84 Esler, W. P., Stimson, E. R., Jennings, J. M., Vinters, H. V., Ghilardi, J. R., Lee, J. P., Mantyh, P. W. & Maggio, J. E. (2000). Alzheimer's disease amyloid propagation by a template-dependent dock-lock mechanism. *Biochemistry* 39, 6288–95.

85 Nucifora, F. C., Jr., Sasaki, M., Peters, M. F., Huang, H., Cooper, J. K., Yamada, M., Takahashi, H., Tsuji, S., Troncoso, J., Dawson, V. L., Dawson, T. M. & Ross, C. A. (2001). Interference by huntingtin and atrophin-1 with cbp-mediated transcription leading to cellular toxicity. *Science* 291, 2423–8.

86 Harper, J. D., Wong, S. S., Lieber, C. M. & Lansbury, P. T. (1997). Observation of metastable Abeta amyloid protofibrils by atomic force microscopy. *Chem Biol* 4, 119–25.

87 Kayed, R., Head, E., Thompson, J. L., McIntire, T. M., Milton, S. C., Cotman, C. W. & Glabe, C. G. (2003). Common structure of soluble amyloid oligomers implies common mechanism of pathogenesis. *Science* 300, 486–9.

88 Poirier, M. A., Li, H., Macosko, J., Cai, S., Amzel, M. & Ross, C. A. (2002). Huntingtin spheroids and protofibrils as precursors in polyglutamine fibrilization. *J Biol Chem* 277, 41032–7.

89 Divry, P. & Florkin, M. (1927). Sur les proprietes optiques de l'amyloide. *C. R. Seances Soc Biol* 97, 1808–10.

90 Westermark, G. T., Johnson, K. H. & Westermark, P. (1999). Staining methods for identification of amyloid in tissue. *Methods Enzymol* 309, 3–25.

91 Klunk, W. E., Jacob, R. F. & Mason, R. P. (1999). Quantifying amyloid beta-peptide (Abeta) aggregation using the congo red-abeta (CR-abeta) spectrophotometric assay [In Process Citation]. *Anal Biochem* 266, 66–76.

92 Naiki, H., Higuchi, K., Hosokawa, M. & Takeda, T. (1989). Fluorometric determination of amyloid fibrils in vitro using the fluorscent dye, thioflavine T. *Anal. Biochem.* 177, 244–249.

93 LeVine, H. (1999). Quantification of β-sheet amyloid fibril structures with thioflavin T. *Meth Enzymol* 309, 274–84.

94 Woody, R. W. (1996). Theory of circular dichroism of proteins. In *Circular Dichroism and Conformational Analysis of Biomolecules* (Fasman, G. D., ed.), pp. 25–67. Plenum, New York.

95 Hrncic, R., Wall, J., Wolfenbarger, D. A., Murphy, C. L., Schell, M., Weiss, D. T. & Solomon, A. (2000). Antibody-Mediated Resolution of Light Chain-Associated Amyloid Deposits. *Am J Pathol* 157, 1239–1246.

96 O'Nuallain, B. & Wetzel, R. (2002). Conformational antibodies recognizing a generic amyloid fibril epitope. *Proc Natl Acad Sci USA* 99, 1485–1490.

97 Sunde, M. & Blake, C. (1997). The structure of amyloid fibrils by electron microscopy and X-ray diffraction. *Adv Protein Chem* 50, 123–159.

98 Wood, S. J., Wetzel, R., Martin, J. D. & Hurle, M. R. (1995). Prolines and amyloidogenicity in fragments of the Alzheimer's peptide β/A4. *Biochem.* 34, 724–730.

99 Williams, A., Portelius, E.,

Kheterpal, I., Guo, J., Cook, K., Xu, Y. & Wetzel, R. (2004). Mapping Aβ amyloid fibril secondary structure using scanning proline mutagenesis. *J. Mol. Biol.*, 335, 833–42.

100 Venkatraman, J., Shankaramma, S. C. & Balaram, P. (2001). Design of folded peptides. *Chem Rev* 101, 3131–52.

101 Wetzel, R. (2002). Ideas of order for amyloid fibril structure. *Structure* 10, 1031–1036.

102 Starikov, E. B., Lehrach, H. & Wanker, E. E. (1999). Folding of oligoglutamines: a theoretical approach based upon thermodynamics and molecular mechanics. *J Biomol Struct Dyn* 17, 409–27.

103 Perutz, M. F., Finch, J. T., Berriman, J. & Lesk, A. (2002). Amyloid fibers are water-filled nanotubes. *Proc Natl Acad Sci USA* 99, 5591–5.

104 Jenkins, J. & Pickersgill, R. (2001). The architecture of parallel beta-helices and related folds. *Prog Biophys Mol Biol* 77, 111–75.

105 Pickersgill, R. W. (2003). A primordial structure underlying amyloid. *Structure (Camb)* 11, 137–8.

106 Bence, N. F., Sampat, R. M. & Kopito, R. R. (2001). Impairment of the ubiquitin-proteasome system by protein aggregation. *Science* 292, 1552–5.

107 Kopito, R. R. (2000). Aggresomes, inclusion bodies and protein aggregation. *Trends Cell Biol* 10, 524–30.

108 Lashuel, H. A., Hartley, D., Petre, B. M., Walz, T. & Lansbury, P. T., Jr. (2002). Neurodegenerative disease: amyloid pores from pathogenic mutations. *Nature* 418, 291.

109 Margolis, R. L., Abraham, M. R., Gatchell, S. B., Li, S. H., Kidwai, A. S., Breschel, T. S., Stine, O. C., Callahan, C., McInnis, M. G. & Ross, C. A. (1997). cDNAs with long CAG trinucleotide repeats from human brain. *Hum Genet* 100, 114–22.

110 Hancock, J. M., Worthey, E. A. & Santibanez-Koref, M. F. (2001). A role for selection in regulating the evolutionary emergence of disease-causing and other coding CAG repeats in humans and mice. *Mol Biol Evol* 18, 1014–23.

111 Collins, J. R., Stephens, R. M., Gold, B., Long, B., Dean, M. & Burt, S. K. (2003). An exhaustive DNA micro-satellite map of the human genome using high performance computing. *Genomics* 82, 10–9.

112 Talcott, B. & Moore, M. S. (1999). Getting across the nuclear pore complex. *Trends Cell Biol* 9, 312–8.

113 Osmand, A. P., Berthelier, V. & Wetzel, R. (2002). Identification of aggregation foci, intracellular neuronal structures in the neocortex in Huntington's disease capable of recruiting polyglutamine. *Program 293.6, 2002 Abstract Viewer/Itinerary Planner.* Washington, DC: Society for Neuroscience, 2002. Online.

114 Heiser, V., Scherzinger, E., Boeddrich, A., Nordhoff, E., Lurz, R., Schugardt, N., Lehrach, H. & Wanker, E. E. (2000). Inhibition of huntingtin fibrillogenesis by specific antibodies and small molecules: Implications for Huntington's disease therapy. *Proc. Natl. Acad. Sci. (USA)* 97, 6739–6744.

115 Wetzel, R., Ed. (1999). Amyloid, Prions, and other Protein Aggregates. Methods in Enzymology. Edited by Abelson, J. N. & Simon, M. I. San Diego, CA: Academic Press.

116 Kheterpal, I., Zhou, S., Cook, K. D. & Wetzel, R. (2000). Abeta amyloid fibrils possess a core structure highly resistant to hydrogen exchange. *Proc Natl Acad Sci USA* 97, 13597–601.

117 Kheterpal, I., Williams, A., Murphy, C., Bledsoe, B. & Wetzel, R. (2001). Structural features of the Aβ amyloid fibril elucidated by limited proteolysis. *Biochem.* 40, 11757–11767.

118 Torok, M., Milton, S., Kayed, R., Wu, P., McIntire, T., Glabe, C. G. & Langen, R. (2002). Structural and Dynamic Features of Alzheimer's Abeta Peptide in Amyloid Fibrils Studied by Site-directed Spin Labeling. *J Biol Chem* 277, 40810–40815.

119 Petkova, A. T., Ishii, Y., Balbach, J. J., Antzutkin, O. N., Leapman, R. D., Delaglio, F. & Tycko, R. (2002). A structural model for Alzheimer's beta-amyloid fibrils based on experimental constraints from solid state NMR. *Proc Natl Acad Sci USA* 99, 16742–7.

120 Foguel, D., Suarez, M. C., Ferrao-Gonzales, A. D., Porto, T. C., Palmieri, L., Einsiedler, C. M., Andrade, L. R., Lashuel, H. A., Lansbury, P. T., Kelly, J. W. & Silva, J. L. (2003). Dissociation of amyloid fibrils of alpha-synuclein and transthyretin by pressure reveals their reversible nature and the formation of water-excluded cavities. *Proc Natl Acad Sci USA* 100, 9831–6.

38
Production of Recombinant Proteins for Therapy, Diagnostics, and Industrial Research by in Vitro Folding

Christian Lange and Rainer Rudolph

38.1
Introduction

Twenty years ago protein folding was regarded as a highly fascinating topic of pure basic research. Although tremendous progress has been made in our understanding of this enigmatic process, protein folding is still a very attractive field for academic research, as is documented in this handbook. However, at that time nobody would have anticipated that protein folding would today be a well-established downstream process in industrial production. Researchers in industry working on recombinant protein production are frequently confronted with misfolded, inactive material. They either can try to find a way to produce correctly folded native protein by using alternative expression systems or they can take up the challenge of in vitro protein folding. Since efficient processes are now available that allow medium- to large-scale production of recombinant proteins by in vitro folding, many recombinant proteins for therapy, diagnostics, and industrial applications are successfully and profitably produced via this process.

38.1.1
The Inclusion Body Problem

Before the advent of recombinant DNA technology, proteins for medical, diagnostic, or industrial applications were difficult to obtain from human body fluids, from animal or plant tissue, or from microorganisms. Potentially low availability and the risk of viral contamination or high antigenicity put severe limitations on the use of natural proteins in therapy. The extraction of proteins from natural sources was often very cost-intensive, requiring large amounts of raw material, water, and energy. Recombinant DNA technology has dramatically changed this situation. It has opened the way for the large-scale, low-cost production of almost any imaginable protein [1, 2]. Proteins that are available in only minute amounts from natural sources can now be produced in huge quantities in host cells such as *E. coli*. Expression levels up to 50% of the total cell protein can be obtained with standard expression systems (reviewed, e.g., in Ref. [3]). Using high-density fermentation

Protein Folding Handbook. Part II. Edited by J. Buchner and T. Kiefhaber

ISBN: 3-527-30784-2

Fig. 38.1. *E. coli* cell filled with inclusion bodies (lower third of cell volume).

techniques, gram amounts of the desired proteins can be obtained per liter of fermentation broth [4–6].

There is, however, one major problem associated with overexpression in *E. coli*. Often the desired polypeptide is synthesized in these host cells, but not in the correctly folded, native form. Instead of the biologically active product, aggregates – inclusion bodies – are formed [7]. These dense particles, which may span the whole diameter of the host cell, are mostly biologically inactive and generally are insoluble in non-denaturing buffer systems (Figure 38.1). Inclusion bodies predominantly contain the overexpressed recombinant protein and only small amounts of host cell material such as inclusion body binding proteins (IBPs) [8], outer-membrane proteins, RNA polymerase, and ribosome components including ribosomal RNA as well as circular and nicked forms of plasmid DNA [9]. Some of these impurities may originate from co-precipitation of these cellular components together with the recombinant protein during inclusion body formation. However, most of the impurities found in inclusion body preparations may originate from incomplete removal of particulate host cell material during their isolation [10].

Inclusion body formation is not restricted to the overexpression of heterologous gene products in bacteria. Overexpression of autologous *E. coli* proteins in the cytosol of this organism has been observed to lead to inclusion body formation. For example, the overexpression of endogenous β-galactosidase in *E. coli* led to the formation of inclusion bodies that showed only partial enzymatic activity [11]. Inclusion body formation may also occur upon overexpression of proteins in eukaryotic host cells [12]. Apparently, high-level expression of any gene product beyond certain limits is sufficient to drive the recombinant protein into aggregation and inclusion body formation. Based on this observation, a simple kinetic model for inclusion body formation was proposed [13]. This model, which takes only the zero-order rate of protein synthesis and a subsequent competition between first-order folding and second-order aggregation into account, provides a fairly accurate description of inclusion body formation. In agreement with this model, inclusion body formation can be reduced or even prevented by decreasing the rate of protein synthesis. This can be achieved, for example, by cultivation at low temperature or by limited induction [14, 15].

Except for the presence of disulfide bonds, other molecular characteristics of proteins such as size, hydrophobicity, secondary structure content, etc., do not correlate well with the observed propensity for inclusion body formation. Small proteins containing few disulfide bonds are often expressed in soluble form, while inclusion body formation predominates upon cytosolic production of large proteins containing multiple disulfide bonds. Correct oxidative folding of more complex proteins is apparently not possible in the reducing cytosolic environment, in line with the finding that naturally secreted proteins mostly contain disulfide bonds, while the cysteine residues of intracellular proteins usually stay reduced [16]. The oxidative folding of secreted proteins occurs in the periplasm and the endoplasmic reticulum of prokaryotes and eukaryotes, respectively. These compartments offer optimum oxidizing conditions as well as thiol-disulfide isomerases for the formation of correct disulfide bonds [17–20]. Upon overexpression of disulfide-bonded proteins in the reducing bacterial cytosol, oxidative folding is massively impaired, and, as a consequence, inclusion body formation predominates even upon low-level expression.

By selecting for mutations in *E. coli*, which allow for disulfide bond formation in the cytoplasm, Beckwith and coworkers could isolate mutant strains with reduced or eliminated thioredoxin reductase activity [21–23]. These and other, further-improved, mutant strains showed increased cytosolic oxidative folding of disulfide-bonded proteins as compared to wild-type strains [24]. However, in spite of this recent progress in the soluble overexpression of heterologous proteins in *E. coli*, in many cases the formation of inclusion bodies still prevails.

The exact mechanism by which inclusion body formation is induced and the reason that the recombinant protein is deposited predominantly in the inclusion bodies are still unclear. Apart from the changes in the kinetic competition between folding and aggregation caused by changing the rate of protein synthesis, essential components of the chaperone machinery may be simply oversaturated upon massive overproduction of recombinant proteins. It is, however, not yet clear which

chaperones are involved in this process. In some cases, inclusion body formation can be suppressed by co-overexpression of molecular chaperones such as GroE or DnaK and its cohort chaperones [25, 26]. Although this approach was quite efficient upon overexpression of some proteins, co-expression of chaperones had no effect whatsoever in other cases.

Because of the frequent, and sometimes frustrating, observation of inclusion bodies upon overexpression of recombinant proteins in *E. coli*, other host cell systems have been studied in detail for industrial protein production. Although very efficient in some cases, none of these expression systems offers the ultimate solution for recombinant protein production. Incorrect glycosylation in yeast and insect cells as well as long development times and high production costs in mammalian cell culture systems limit the general applicability of these alternatives. Therefore, enormous efforts have been made to develop efficient procedures for the reactivation of inactive bacterial inclusion body material by in vitro folding. These efforts relied heavily on the body of information available on in vitro protein folding that had been gathered over the years by basic research. Many protein folders from academia were approached by industry to help in setting up industrial folding processes. Since the main goal of academic research on protein folding was the identification of folding intermediates in order to understand the folding pathway of proteins in minute detail, the final goal of the industrial effort, which was to develop an efficient, reproducible, and cost-effective production process, sometimes came out of focus. In most previous academic in vitro folding studies, model proteins that showed more or less quantitative refolding under standard buffer conditions had been chosen. Many proteins of industrial relevance, on the other hand, form inactive aggregates under these conditions. In order to develop efficient processes, the "dark side" of in vitro folding, namely misfolding and aggregation, had to be taken into consideration. These unproductive side reactions had to be analyzed in detail in order to be overcome in maximizing the yield of the desired, correctly folded, native protein [10, 27–30].

Although subject to its specific problems and limitations, the industrial production of recombinant proteins for therapy, diagnostics, and research by overexpression into inclusion bodies and subsequent refolding has by now turned out to be an attractive and viable option. For example, Ernst et al. carefully compared the production cost for soluble expression of the recombinant heparinase in *E. coli* and for its production via inclusion bodies [31]. Mainly due to the low level of soluble expression, the isolation of the soluble protein was estimated to be 50% more expensive than the production of the enzyme by refolding of inclusion body material.

38.1.2 Cost and Scale Limitations in Industrial Protein Folding

Protein refolding is a relatively new unit operation in industrial processes for recombinant protein production. To date, there are no generally applicable protocols available for the optimization of a refolding process. There are, however, some

guidelines. Protein-dependent variables make it difficult to estimate the final production cost before an extensive optimization of a given process has been carried out. It is impossible to predict the yield of refolding without analysis of a large number of parameters such as the maximum concentration at which refolding of a particular protein can be successfully carried out, optimum pH, temperature, time, and ionic strength, and the effect of one or more of many possible additives. While some proteins, like most of those described in this volume, refold quantitatively in simple buffer solutions, others may need sophisticated process design and cost-intensive additives to achieve the successful refolding of at least some of the starting material.

The protein concentration at which refolding can be performed best is a specific property of any particular protein. Because of the kinetic competition between first-order folding and higher-order unproductive aggregation, the yield of correct refolding decreases upon increasing the initial concentration of unfolded protein [10, 32]. While some proteins can be refolded to a high yield at high protein concentrations in the milligram per milliliter range, other proteins refold effectively only at concentrations on the order of micrograms per milliliter. For industrial processes, where comparatively huge amounts of proteins must be produced, the cost is extremely high if both the yield and the concentration of refolding are low. In an interesting case study, the process economics for the production of human tissue-type plasminogen activator (t-PA) by *E. coli* fermentation and in vitro folding were analyzed in detail. Human t-PA is a relatively complex protein, consisting of 527 amino acid residues that are organized in five structural domains. The native protein contains 17 disulfide bonds and one additional free cysteine and has a rather low solubility even in its native state. Because of the astronomical number of statistically possible disulfide bond pairings (2.2×10^{20}) and the low solubility of folding intermediates, t-PA poses an enormous problem for in vitro folding. This therapeutic protein activates plasmin at the surface of blood clots and is therefore ideally suited for treating patients suffering from acute myocardial infarction by inducing fibrinolysis. Its market potential justified the enormous efforts that were directed towards the optimization of its in vitro folding. Based on a low yield of refolding, to be obtained only at an extremely low protein concentration, Datar et al. calculated the process economics for the production of recombinant human t-PA from *E. coli* inclusion bodies [33]. The authors estimated that enormous refolding reactors (1500 m^3) would be necessary for production of the required amounts of protein. These reactors would account for 75% of the total equipment costs [34]. A simple comparison of the economics of the process involving the refolding of inclusion body protein from *E. coli* with an alternative process involving protein expression in Chinese hamster ovary cells led to the conclusion that the latter, despite the considerable costs of mammalian cell culture systems, was economically far more advantageous.

These studies seemed to demonstrate that it was clearly not feasible to set up an economic process for the production of recombinant human t-PA by bacterial overexpression and in vitro folding. However, a deletion variant of the plasminogen activator, Rapilysin, which was approved by the authorities in 1996 and has by now

attained a considerable market share, is in fact produced by in vitro folding. A process was developed in which the protein is refolded in high yield at relatively high concentrations [35–37]. The clue to this success lay in careful process design and the inclusion of the low-molecular-weight additive L-arginine (L-Arg), which has proved effective for t-PA and many other proteins (cf. Section 38.3.4), in the refolding buffer. The presence of this additive led to a tremendous increase in the yield of refolding.

38.2 Treatment of Inclusion Bodies

38.2.1 Isolation of Inclusion Bodies

After cell lysis, inclusion bodies are usually harvested by solid-liquid separation. With this simple isolation procedure, the recombinant protein can be obtained in a relatively pure form, provided that all particulate matter of the *E. coli* host cells is disintegrated by a rigorous lysis procedure. Rather homogenous inclusion body isolates can be obtained by lysozyme treatment, subsequent high-pressure dispersion, and incubation with detergent at high salt concentrations [10]. This combination of cell disruption techniques provides for a nearly complete removal of cell wall debris and membrane fragments. As a consequence, highly enriched inclusion body material should be present in the pellet fraction of the subsequent sedimentation step.

After sedimentation, inclusion bodies form a very dense pellet. Impurities are difficult to extract from this glutinous material by later washing steps. Therefore, sedimentation should be performed after cell lysis and removal of membrane proteins by detergent and high salt concentrations (cf. Protocol 1). After the inclusion bodies have been collected by centrifugation, detergents and other buffer components that might interfere with the following solubilization and renaturation steps can be removed by repeated resuspension and sedimentation. This inclusion body isolation procedure, which combines different methods for cell lysis and disintegration, is rather robust and yields relatively pure inclusion body isolates (Figure 38.2), even in those cases where the lysis of *E. coli* is difficult due to changes in the cell wall morphology, which may occur as a response to the physiological stress caused by protein overexpression [38, 39].

38.2.2 Solubilization of Inclusion Bodies

Inclusion bodies are usually solubilized in high concentrations of denaturing agents such as 6 M guanidinium chloride (GdmCl) or 8 M urea. Guanidinium chloride, which is the stronger denaturant, may allow solubilization of inclusion body isolates that are resistant to urea. Since urea rapidly decomposes into cyanate

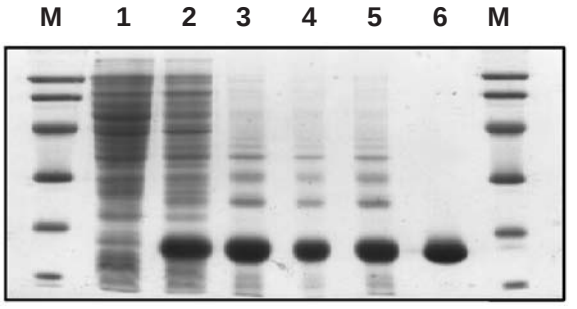

M: Marker proteins
lane 1: *E. coli* lysate from non-induced cells
lane 2: *E. coli* lysate from induced cells
lane 3: inclusion bodies
lane 4: insoluble fraction after refolding
lane 5: soluble fraction after refolding
lane 6: purified nGLP1-R

Fig. 38.2. Expression in *E. coli*, inclusion body preparation, and purification of the N-terminal domain of human glucagon-like peptide 1 receptor. Reproduced from Ref. [54].

under certain solvent conditions (e.g., high pH values), care must be taken to avoid side chain modification of lysine and cysteine residues if this denaturant is used [40–42].

Although disulfide bonds are hardly formed in the reducing environment of the cytosol in vivo, random formation of these bonds, either within the same protein molecule or between different polypeptide chains, may occur by air oxidation during cell lysis and inclusion body isolation. This is of special importance in an industrial setting, where the incubation times may change upon scaling up the process. In order to guarantee the complete reduction of any accidentally formed disulfide bonds, reducing agents such as dithiothreitol (DTT), dithioerythritol (DTE), or β-mercaptoethanol should be present during solubilization. (cf. Protocol 2).

Provided that the level of overexpression is sufficiently high, the recombinant protein is usually found highly enriched in the inclusion body isolate (Figure 38.2). In this case, further purification of the recombinant protein in the denatured state prior to renaturation is not necessary. Contaminating proteins and other components of the host cells found in inclusion body isolates have no significant effect on protein refolding in most cases. Since the chromatographic resolution during the purification of unfolded proteins is sometimes poor and chromatographic purification represents a relatively cost-intensive unit operation, it should be avoided at this stage in industrial processes. In certain cases, however, contaminating proteins may co-precipitate during refolding of a given protein [43, 44]. The solubilized protein then has to be purified by, e.g., reversed-phase HPLC [45] or immobilized metal-affinity chromatography [46]. During research and process de-

velopment, purification of the solubilized recombinant protein is essential if spectroscopic techniques such as fluorescence, circular dichroism, or light scattering are used to optimize refolding conditions.

38.3 Refolding in Solution

The following section aims to give an overview of the factors that have to be taken into account when dealing with the in vitro folding of a recombinant protein from inclusion bodies. Aggregation of unfolded protein and misfolded intermediates is in most cases the major complication during protein refolding. The ideas and methods that have been explored and used in order to overcome the problem posed by this unproductive side reaction will be discussed in some detail.

38.3.1 Protein Design Considerations

As already mentioned, the behavior of a protein upon refolding is a specific property of its given amino acid sequence. This property may be influenced by protein engineering, e.g., with respect to the pI value and the hydrophobicity. The refolding yield of a number of proteins could indeed be improved by protein design. The in vitro folding of human insulin-like growth factor was greatly enhanced by expressing it as a fusion protein with two Z domains derived from staphylococcal protein A [47]. This effect was mainly due to a more than 100-fold increase in the solubility of the reduced denatured polypeptide. In a similar fashion, the renaturation yield of granulocyte colony-stimulating factor could be systematically improved by fusion to various hydrophilic peptide sequences between 2 and 20 amino acids long [48].

Many important proteins naturally contain pro-sequences, which are later removed by specific proteolytic processing. These pro-sequences may also affect in vitro structure formation and act as natural folding helpers. The potentially beneficial "intramolecular chaperone" effect of pro-sequences was analyzed in detail for the folding of subtilisin [49] as well as for α-lytic protease [50]. Interestingly, the pro-region of α-lytic protease also promoted the correct folding of the enzyme when co-expressed in *trans*. In the case of human nerve growth factor, the pro-sequence was found to have a tremendously beneficial effect on both the rate and the yield of correct refolding and disulfide bond formation [51, 52].

Upon in vitro folding of proteins whose pro-sequences have been truncated or, more generally, of isolated protein domains, the refolding pathway may be corrupted by the absence of those parts of the protein that are essential for guiding structure formation towards the native state. This is especially true if any of the deleted parts strongly interact with the isolated domain in the native state. The energetic contribution of such an interaction may be essential for correct folding. In spite of these considerations, isolated domains have been successfully produced by

in vitro folding. For example, the N-terminal extracellular domains of class B G protein-coupled receptors could be refolded in functional form [53, 54].

Finally, folding of polypeptides that naturally form part of a hetero-oligomeric protein may require the presence of all subunits of the complex for the formation of a thermodynamically stable, native state. The expression of fully functional tetrameric human hemoglobin in *E. coli*, for example, required the co-expression of the α and β globin genes [55]. Separate expression of the individual subunits resulted in a marked decrease in protein production as well as in inclusion body formation. In agreement with this observation, in vitro folding of β globin could proceed well only in the presence of α globin and the heme cofactor required for the formation of a functional tetramer [56].

38.3.2
Oxidative Refolding With Disulfide Bond Formation

Before designing a refolding strategy, it is essential to establish whether the target protein contains disulfide bonds in its native structure. While most cytosolic proteins contain only free cysteine residues, secreted proteins or those localized in cell organelles often form intramolecular cystine bridges [16]. Highly conserved cysteines in homologous sequences as well as the presence of export signals usually indicate the presence of disulfide bonds. In such a case, folding conditions must be chosen that facilitate their fast, efficient, and, above all, correct formation during oxidative refolding, since otherwise inactive, incorrectly disulfide-bonded products may accumulate, with potentially dramatic negative effects on the renaturation yield.

The number of possible combinations of disulfide bonds increases exponentially with the number of cysteines that are available for pairing (see Table 38.1). However, the problem is not as ill-behaved as it may look at first glance since pure statistics are usually overcome by effects that energetically favor the correct refolding pathway. Disulfide bond formation is directed towards the correct pairings by the conformational energy gained upon formation of the native structure [57–60]. Furthermore, during the in vivo folding of proteins, disulfide isomerases promote the reshuffling of disulfide bonds, avoiding kinetic trapping of misfolded conformations with incorrectly formed disulfide bridges (for recent reviews, see, e.g., Refs. [20, 61–63]).

The first experiments on in vitro folding with concomitant disulfide bond formation were performed using air as the oxidizing agent [64]. The rate and yield of reactivation that may be obtained by air oxidation have been found to be quite low. The reproducibility is usually low due to variations in surface-to-volume ratio, additional oxidation processes (e.g., methionine oxidation), and the presence of trace amounts of transition metal ions (especially Cu^{2+}) in variable concentrations in the buffer solutions. These metal ions act as efficient catalysts for air oxidation in a concentration range (low micromolar) that is experimentally difficult to control [65]. Because of these inherent drawbacks of air oxidation, more defined and efficient methods for disulfide bond formation in vitro have been developed.

Tab. 38.1. Number of possible combinations of $2n$ cysteines to form n disulfide bonds.

n	*Number of combinations*[1]
1	1
2	3
3	15
4	105
5	945
6	10 395
7	135 135
8	2 027 025
9	34 459 425
10	654 729 075
11	$1\,374\,931\,058 \times 10^{10}$
12	$3\,162\,341\,432 \times 10^{11}$
13	$7\,905\,853\,581 \times 10^{12}$
14	$2\,134\,580\,467 \times 10^{14}$
15	$6\,190\,283\,354 \times 10^{15}$
16	$1\,918\,987\,840 \times 10^{17}$
17	$6\,332\,659\,871 \times 10^{18}$
18	$2\,216\,430\,955 \times 10^{20}$
...	...

[1] $(2n-1)\cdot(2n-3)\cdot(2n-5)\cdot\ldots\cdot 3\cdot 1$

As mentioned above, the reshuffling of incorrectly formed disulfide bridges is an essential step on the pathway towards the formation of native structure. In some cases, catalytic amounts of disulfide isomerase enzymes have been used for the efficient refolding of proteins (e.g., proinsulin) [66]. In general, however, thiol-disulfide exchange reactions between reduced polypeptide and low-molecular-weight thiols are used to facilitate disulfide bond shuffling [67, 68]. Reduced/oxidized glutathione (GSH/GSSG) are most commonly used as oxido-shuffling reagents, although other low-molecular-weight thiols such as cystine/cysteine, cystamine/cysteamine, or bis-β-hydroxyethyl disulfide/2-mercaptoethanol have been found to be equally effective in most cases. Since the thiolate anion is the active species in thiol-disulfide exchange, the pH of the refolding buffer must lie in the range of the pK_a of the thiol group (i.e., between pH 8.5 and pH 9.5).

Over the past few years, several low-molecular-weight thiol compounds have been designed with the aim of improving thiol-disulfide exchange during the oxidative refolding of proteins. For example, the synthetic dithiol ($\pm$)-*trans*-1,2-bis(2-mercaptoacetamido)cyclohexane (Vectrase P), which has a pK_a value of 8.3 and an $E^{0'}$ value of -0.24 V, was designed to mimic the properties of the active site of protein disulfide isomerases [69]. This compound improved the activation of scrambled RNAse A more efficiently than comparable monothiols. The synthetic dithiol compound also improved the refolding yield of human proinsulin [70]. Recently, various aromatic monothiols, characterized by low thiol pK_a values, were

tested for their effect on rate and yield of the oxidative refolding of scrambled RNAse A [71, 72]. At slightly acidic pH values (pH 6.0), the aromatic thiols increased the refolding rate by a factor of 10 to 23 over that observed with glutathione. Since the nucleophilicity of the redox buffer thiolate determines the rate of thiol-disulfide exchange, the rate of RNAse A refolding was increased with decreasing thiol pK_a value.

Oxidative refolding is sometimes complicated by the low solubility of the aggregation-prone reduced-denatured polypeptide chains. This problem may be circumvented by the reversible redox modification of cysteine residues of a protein in its solubilized state prior to refolding. The formation of the mixed disulfide with glutathione introduces additional negatively charged residues on the polypeptide chain and may thereby reduce precipitation of unfolded protein during the initial states of oxidative refolding [73]. This idea has been demonstrated for the in vitro folding of human tissue-type plasminogen activator [37].

As an alternative to the complete removal of the reducing agent (DTT or DTE), which is present during solubilization (cf. Section 38.2.2), before oxidative refolding is carried out in a defined redox buffer, the solubilized protein solution (still containing DTT or DTE) may be directly diluted into a refolding buffer containing an oxidized monothiol (e.g., oxidized glutathione) [74]. Redox equilibration between the reduced dithiol and the oxidized monothiol will then result in predominantly oxidized dithiol and a redox buffer consisting of the reduced and oxidized monothiol. An elegant and simple approach towards oxidative refolding was demonstrated by Honda et al. [75]. They succeeded in refolding recombinant human growth/differentiation factor 5 (rhGDF-5) with a yield of 63% at high protein concentrations (2.4 mg mL^{-1}). The inclusion bodies were first solubilized in the presence of 32 mM cysteine/HCl for disulfide bond reduction. The solubilized protein solution was then diluted into a refolding buffer without any additional thiol reagent. Apparently, the reducing potential of the residual cysteine gradually decreased with time due to air oxidation, thus providing an oxidative redox-shuffling system composed of reduced and oxidized cysteine that was appropriate for rhGDF-5 refolding. It remains to be tested whether this simple and cost-effective protocol can be used for the refolding of other recombinant proteins at high concentrations.

38.3.3
Transfer of the Unfolded Proteins Into Refolding Buffer

The question of whether the buffer exchange from unfolding to folding conditions should be performed by dialysis or dilution is still controversial. On some occasions, higher folding yields might be obtained by dialysis as compared to rapid dilution of the denaturant. For a number of proteins, protocols comprising gradual removal of the denaturant have been reported. For example, mouse interleukin 4 [76], a recombinant fragment of bovine conglutinin [77], the fungal protease rhizopuspepsin [78], recombinant bovine guanylate cyclase-activating protein 1 [79], and human interleukin-21 [80] were obtained using stepwise dialysis for the removal of the denaturant. Recently, Umetsu et al. performed a detailed analysis of the refold-

ing pathway of a single-chain antibody fragment during a complex dialysis protocol for the stepwise reduction of the GdmCl concentration [81].

For industrial processes, however, buffer exchange by dialysis presents considerable disadvantages with respect to reproducibility, handling, and ease of scale-up. Furthermore, many proteins form highly aggregation-prone folding intermediates at intermediate denaturant concentrations. Slow removal of the denaturant by dialysis then inevitably leads to quantitative and irreversible precipitation of these intermediates. In these cases, rapid removal of the denaturant by dilution reduces protein losses by aggregate formation, especially if carried out under properly controlled process conditions and in the presence of low-molecular-weight folding enhancers (cf. Section 38.3.4). Diluting the solubilized protein into refolding buffer is in most cases much more convenient and efficient than the removal of the denaturing agent by dialysis.

The rate of aggregation processes, which are of second or higher order, increases dramatically upon increasing the initial concentration of unfolded protein, while the first-order rate of productive folding processes does not change. Therefore, at high concentrations of denatured protein, aggregation processes predominate in the refolding reaction mixture, and this may represent a major difficulty for the design of an efficient refolding process. This problem can be at least partially overcome by process engineering (cf. Protocol 3). Since correctly folded protein does not participate in aggregation side reactions, high concentrations of native protein can be obtained by stepwise addition of the denatured protein to the refolding vessel [35]. By stepwise addition of the solubilized denatured protein at time intervals that are sufficiently large for the polypeptides to fold past the aggregation-prone early stages on the folding pathway, the concentration of unfolded protein and folding intermediates is kept sufficiently low at any given time during the refolding process (Figure 38.3). For example, this method has made possible the development of an economically feasible refolding process for Rapilysin, a variant of

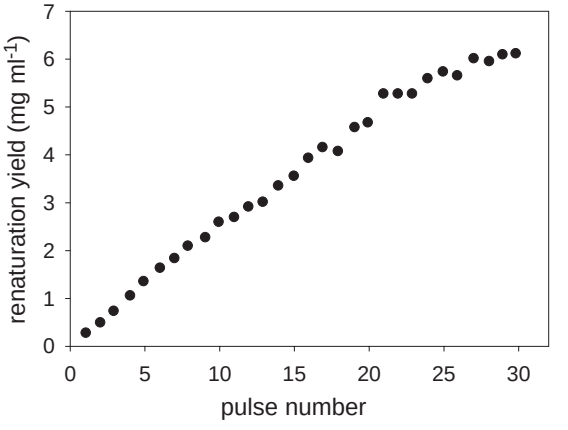

Fig. 38.3. Renaturation yield of proinsulin upon stepwise dilution of denatured protein into the refolding buffer. Reproduced from Ref. [82].

tissue-type plasminogen activator in refolding reactors that are about three orders of magnitude smaller than the huge and prohibitively expensive 1500-m^3 tanks that were considered necessary in the initial analysis [34].

38.3.4 Refolding Additives

One would be hard-pressed to give an exhaustive account of all low-molecular-weight compounds that have been found to improve in vitro folding of one or another model protein under some conditions. This section aims at giving a, necessarily incomplete, overview of additives that show no, in a biochemical sense, specific interaction with the refolded proteins but rather act as co-solvents that modify the solvation properties of the buffer for dissolved polypeptides and thereby influence the pathways of refolding and of its unproductive side reactions, potentially to great effect. Systematic studies by Timasheff and coworkers (see, e.g., Refs. [83, 84]) have greatly contributed to our understanding of the interplay among polypeptides, water, and co-solvents. Generally speaking, when using low-molecular-weight compounds as co-solvents in refolding reactions, the task is to strike a balance between, on the one hand, preserving the relative stability of the native state and, on the other hand, stabilizing denatured polypeptides and intermediates in solution in order to prevent them from following the path down to aggregation.

The earliest and most simple substances used to enhance refolding were the denaturing agents GdmCl and urea themselves, at non-denaturing concentrations [85]. Among other denaturing substances, alkyl ureas, carbonic acid amides [37], and alcohols [86] have been used to improve in vitro folding. The positive effect of theses substances on refolding is most probably caused by their very properties as denaturing agents, as they thermodynamically stabilize unfolded and misfolded forms of polypeptides in solution. As a consequence, the solubility of denatured protein and folding intermediates is increased and aggregation is reduced.

For a number of proteins, improved refolding has been observed upon addition of polyethylene glycol to the refolding buffer [87, 88]. Although polyethylene glycols do not act as denaturants, they have been found to decrease the thermostability of proteins with increasing average hydrophobicity of the amino acid sequence. An analysis of solvent-protein interactions indicated that the polyethylene glycols interact favorably with the hydrophobic side chains exposed upon unfolding at elevated temperatures [89]. Again, these hydrophobic interactions contribute to the stability of denatured polypeptides, folding intermediates, and misfolded forms in solution.

Detergents represent another class of substances that may be assumed to stabilize aggregation-prone states of polypeptides in solution by hydrophobic interactions. Indeed, detergents or phospholipid-detergent mixed micelles have been found to promote the correct refolding of various proteins [86, 90, 91]. Interestingly, the nonionic detergent Brij 58P was recently reported to be highly effective in preventing aggregation and promoting folding at very low, near-stoichiometric concentrations [92].

In other cases, osmolytes that generally stabilize the native states of proteins, such as sugars, polyalcohols, and trimethylamine oxide (TMAO), were found to be beneficial for the in vitro folding of various proteins [93, 94]. For example, a destabilized variant of hen egg white lysozyme, containing only three disulfide bonds, could be efficiently refolded in the presence of 20% glycerol [95]. In the case of human placental alkaline phosphatase, refolding could be achieved only in the presence of stabilizing sugars or Hofmeister salts [96]. In these cases efficient folding apparently depends on the relative stabilization of the native state and productive intermediates with respect to nonnative conformational states. However, the balance between the beneficial effect of stabilizing the desired native state of a protein and destabilizing the intermediates it has to pass on its folding pathway is apparently delicate. TMAO, for example, was recently found to hinder the productive refolding of lactate dehydrogenase [97]. Stabilizing osmolytes are therefore generally not the first choice as co-solvents for in vitro folding, unless the stability of the native state is an issue.

Several amino acids have been found to have a beneficial effect on the in vitro folding of certain proteins. For example, the presence of 5 M proline could prevent aggregation and, consequently, improve the refolding yield of bovine carbonic anhydrase II [98]. The refolding of lactate dehydrogenase, however, was negatively influenced by the presence of proline [97]. Recently, all naturally occurring amino acids (with the exception of cysteine, histidine, and the aromatic amino acids) were screened for their efficiency in suppressing the aggregation of lysozyme during thermal denaturation and during dilution of the reduced-carboxymethylated denatured protein from a urea solution into buffer [99]. In this study, the most basic amino acid, L-Arg, was found to be the most effective suppressor of aggregation. This is in line with the fact that L-Arg has probably been the most widely used low-molecular-weight refolding enhancer since it was first described in a patent application almost 20 years ago (cf. Ref. [35]). The presence of L-Arg as a co-solvent in concentrations above 0.4 M (up to 1.2 M) was found to promote the refolding of many different proteins. It was successfully used in the refolding of human tissue-type plasminogen activator [35], recombinant Fab antibody fragments [74], single-chain antibody fragments [100], engineered recombinant immunotoxins [101], human gamma interferon [102], human matrix metalloproteinase-7 [103], human interleukin-21 [80], and many others (Figure 38.4A).

Like GdmCl, L-Arg increases the solubility of unfolded polypeptides and of folding intermediates and prevents their aggregation. Although it contains a guanidino group, however, L-Arg, in contrast to GdmCl, was found to have no effect or only a minor effect on the thermodynamic stability of natively folded proteins [104, 105] (Figure 38.4B). Exactly how L-Arg exerts its effect as a suppressor of aggregation is still subject to discussion. As already mentioned, no dramatic relative stabilization of denatured polypeptides with respect to the native state by L-Arg could be observed. At molal concentrations above 0.1 mol kg^{-1}, L-Arg is preferentially excluded from the surface hydration sphere of proteins, which means it is expected to act as a weakly stabilizing osmolyte, while at lower concentrations it is preferentially bound and therefore should exert a slightly destabilizing effect [83, 106]. Be-

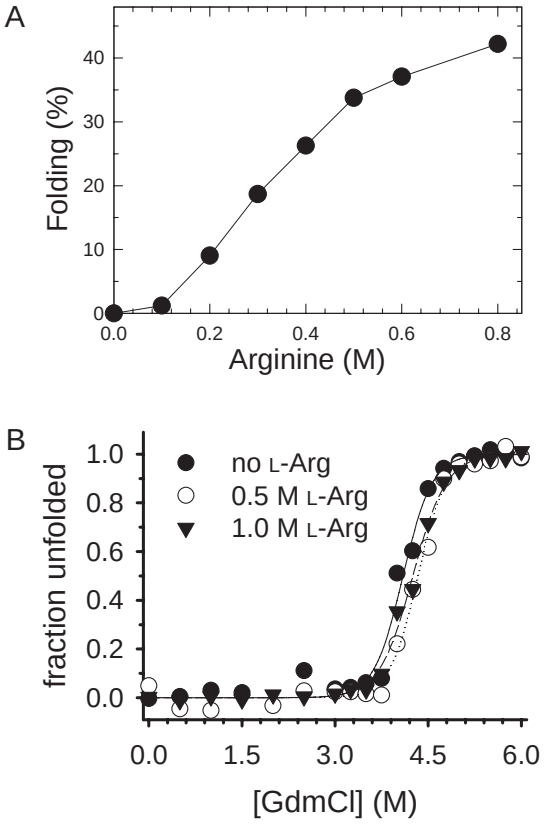

Fig. 38.4. (A) Refolding yield of human tissue-type plasminogen activator as a function of the concentration of L-Arg. Reproduced from Ref. [30]. (B) Influence of L-Arg on the GdmCl-induced folding/unfolding of hen egg white lysozyme. A final concentration of 20 μg mL^{-1} hen egg white lysozyme was incubated for 12 h at 20 °C in 50 mM HEPES/NaOH, pH 7, in the presence of increasing concentrations of GdmCl and 0 M, 0.5 M, and 1.0 M L-Arg, respectively, as indicated. The folding/unfolding transition was monitored by tryptophan fluorescence. Data are courtesy of Mr. Ravi Charan Reddy.

cause no straightforward classification as either a stabilizing or a destabilizing co-solvent is possible, more or less specific direct interactions of its functional groups with the functional groups of dissolved polypeptides will have to be involved to explain the effects of L-Arg as a refolding enhancer.

Recently, organic solvent systems with low water contents have received some attention as potential media for the in vitro folding of proteins. Rariy and Klibanov were able to show that it is possible to refold hen egg white lysozyme to its native state in 99.8% dry glycerol, albeit at low yields [107]. The same group later reported that in buffered organic media (1,ω-alkanediols, oligoethylene glycols, and *N*-methyl formamide), the presence of high concentrations of a stabilizing salt,

namely, LiCl up to 2 M, resulted in markedly enhanced refolding yields as compared to the organic buffer system alone [108]. However, at water contents below 30% (w/w), the observed refolding yields for lysozyme were still extremely low. The renaturation of lysozyme was also reported in buffer systems containing the liquid organic salts ethyl ammonium nitrate and butyl ammonium nitrate [109]. These salts were found to have an effect similar to other denaturing agents (see above) by suppressing aggregation during refolding in concentrations up to approx. 0.5 M, while dissolving lysozyme in the pure liquid salts resulted in unfolded protein. With different liquid organic salts, however, efficient refolding of lysozyme and of human tissue-type plasminogen activator was observed up to salt concentrations above 90% (w/w) (Hauke Lilie, personal communication). Liquid organic salts represent a rather novel, and very versatile, class of polar organic solvents (for recent reviews, see, e.g., Refs. [110–112]). As the organic ions that form these salts may be easily derivatized, they can potentially be optimized as solvents for any given biochemical reaction. The potential of these ''tailor-made'' media for in vitro folding should be kept in view.

38.3.5 Cofactors in Protein Folding

It is a straightforward assumption that for proteins, whose structural integrity depends on the presence of strongly bound prosthetic groups or metal ions, these factors must be present during refolding in order to guide structure formation towards the stable native state. Cofactors that only weakly interact with the native state may also have a beneficial effect on in vitro folding by guiding folding intermediates towards native structure formation. Price et al. found that Ca^{2+}, although not strongly bound to bovine pancreatic DNAse, was necessary for correct disulfide bond formation [113]. Upon refolding of recombinant horseradish peroxidase C from *E. coli* inclusion bodies, the presence of Ca^{2+} and heme during the refolding process was essential for the formation of native, active enzyme [114]. In this case, protein folding was performed at a concentration of 220 μg mL^{-1} in redox buffer containing an additional 5 mM of $CaCl_2$ and 5 μM hemin. The refolding procedure was later successfully applied to other heme-containing proteins [115, 116]. Horse liver alcohol dehydrogenase requires Zn^{2+} for both enzymatic activity and stability. Upon refolding of this dimeric enzyme in the absence of Zn^{2+}, an inactive intermediate is formed. Addition of the metal ion initiates dimerization and recovery of native enzymatic activity [117]. Reactivation was observed only at moderate concentrations of Zn^{2+}, while higher concentrations of the metal ion seemed to sequestrate inactive intermediates in an inactive conformation.

Other cofactors such as NAD(P)H, ATP, or FADH can be essential for structure formation. Upon refolding of tetrameric yeast glyceraldehyde phosphate dehydrogenase, NAD^+ led to a significant increase in the final yield of reactivation [118]. In the case of proteins interacting with NAD(P)H, ATP, or DNA, the effect of these molecules during in vitro folding can be mimicked to a certain extent by including

pyrophosphate in the refolding buffer. For example, human p53 tumor suppressor protein could be successfully refolded in the presence of 50 mM pyrophosphate [119].

38.3.6
Chaperones and Folding-helper Proteins

An elegant method to prevent aggregation during protein folding is to make use of the machinery designed by nature to promote correct folding in living cells, i.e., molecular chaperones and other folding-helper proteins such as protein disulfide isomerases and peptidyl-prolyl *cis*/*trans* isomerases (for recent reviews, see, e.g., Refs. [120, 121]). Both the yield and the rate of in vitro folding processes can be increased tremendously by chaperones and foldases [122]. Both classes of proteins are, however, not yet used in large-scale industrial production processes. The reason lies once again in cost considerations. Using molecular chaperones or foldases for in vitro protein folding would require the prior, cost-intensive production of these proteins. Since some chaperones and folding catalysts must be present in stoichiometric amounts to improve in vitro folding, large amounts of these compounds would be needed in production processes. ATP, which is essential for the function of many chaperones, would also add to the production costs.

Buchner et al. first reported the successful use of the chaperones GroEL/ES and DnaK, together with protein disulfide isomerase, as folding enhancers in the renaturation of a single-chain, antibody-based immunotoxin [123]. In this work, DnaK was found to retain its folding-helper activity when immobilized on a matrix. Immobilization of foldases allows for repeated use, thus reducing the necessary amount of chaperone and improving the process economy. This methodology was taken up by Fersht and coworkers, who co-immobilized a functional fragment of the *E. coli* chaperone GroEL, which was no longer ATP-dependent, together with DsbA, a bacterial disulfide isomerase, and peptidyl-prolyl isomerase [124, 125]. The disulfide-containing scorpion protein toxin Cn5 could be successfully refolded on the obtained multifunctionalized matrix. The use of chaperones and foldases will, however, need considerable further optimization before it can be implemented in industrial production processes.

38.3.7
An Artificial Chaperone System

It has been known for some time that cyclodextrins have a destabilizing effect on the native state of proteins [126]. This can be explained by a shift in the equilibrium in favor of the unfolded state, which is caused by the direct interaction of the cyclodextrins with buried hydrophobic side chains of the protein. During protein folding, this interaction may be exploited for transient shielding of hydrophobic regions of the unfolded polypeptide chain and thereby reducing unproductive aggregation [127].

This use of cyclodextrins in protein-folding processes was further improved in the artificial chaperone-assisted refolding process described by Gellman and coworkers [128, 129]. In this refolding protocol, chemically denatured protein (e.g., inclusion bodies solubilized by GdmCl) is first diluted in a "capture step" into a detergent solution. During this step, the denaturant is diluted to a non-denaturing concentration. However, protein folding, as well as aggregation, is still prevented by the formation of a protein-detergent complex. In a second step, a cyclodextrin is added to the solution to strip the protein of detergent, thereby inducing refolding. This procedure has by now been optimized with respect to the choice of detergent and the respective cyclodextrin. Efficient stripping of the detergent is achieved by its intercalation into the cyclodextrin ring [130, 131]. The artificial chaperone system was further improved by using β-cyclodextrin coupled to epichlorohydrin copolymers. This eliminated the unit operation of removal of the cyclodextrin-detergent complex in the liquid-phase artificial chaperone system [132]. Using the β-cyclodextrin beads in an expanded-bed mode allows in vitro folding on a large process scale. The only drawback of this elegant technique is the limited commercial availability of cyclodextrins coupled to hydrophilic resins.

38.3.8 Pressure-induced Folding

High hydrostatic pressure leads to reversible dissociation of oligomeric proteins [133], while pressures above 4 kbar lead to protein unfolding. Although folded proteins are highly incompressible, high hydrostatic pressures force conformational changes that lead to a reduction in the overall volume of the system. This effect can be described by taking into account the decrease in volume resulting from the exposure of hydrophobic groups from the interior of a protein, as well as the effect of pressure on the dynamic structure of water [134].

Lately, various attempts have been made to make use of high pressure for applied protein refolding processes. The basic idea is to shift the competition between correct folding and aggregate formation to the direction of the productive pathway. Since oligomeric proteins can be reversibly dissociated using high hydrostatic pressure, it could be assumed that the propensity for aggregate formation during in vitro folding should also be reduced upon increasing pressure. This hypothesis was confirmed by Gorovits and Horowitz [135]. They were able to show that at 2 kbar pressure the refolding yield of urea-denatured rhodanese increased to approx. 25% in contrast to a recovery of approx. 5% observed at ambient pressure. Upon further addition of 4 M glycerol during pressure treatment, the yield of refolding could be further increased up to 56%. Using P22 tail-spike protein as a model system, Foguel et al. showed that aggregates could be dissociated when subjected to hydrostatic pressures of 2.4 kbar [136]. Finally, St. John et al. demonstrated that native β-lactamase could be obtained by simply subjecting inclusion bodies to high pressure [137]. The effect of high pressure on the refolding of covalently cross-linked aggregates of lysozyme was analyzed concerning the effect of

non-denaturing concentrations of GdmCl and the ratio of oxidized to reduced glutathione [138]. Under optimal conditions, refolding yields of up to 80% could be obtained.

The general applicability of high-pressure techniques for inclusion body solubilization and refolding remains to be demonstrated. Amorphous aggregates are formed upon decompression of RNAse A and of bovine pancreatic trypsin inhibitor after high-pressure treatment in the presence of reducing agents [139], indicating that, at least for some proteins, misfolded, nonnative states may be favored by high hydrostatic pressures.

38.3.9 Temperature-leap Techniques

The optimum temperature for in vitro folding is often significantly lower than the temperature at which a given protein functions under physiological conditions. For example, the optimum temperature for refolding of several mammalian proteins lies in the range of 5–15 °C. During in vivo folding, molecular chaperones that promote correct structure formation by preventing aggregation processes allow folding at higher temperatures than under in vitro conditions. Increasing temperatures during in vitro folding may lead to a stabilization of unproductive hydrophobic interactions and thus accelerate the rate of aggregate formation. Xie and Wetlaufer made use of the temperature dependency of the yield of refolding in designing an elegant and efficient folding protocol: the "temperature-leap tactic" [140]. Using bovine carbonic anhydrase II as a model system, refolding was optimal when first induced at 4 °C for 120 min, followed by a final folding phase after warming the solution to 36 °C. During the refolding of carbonic anhydrase II, an early intermediate is formed that is still susceptible to aggregation. If refolding is performed at elevated temperatures, this intermediate is largely converted to aggregates. If, however, the initial stage of refolding is allowed to proceed at lower temperatures, the early intermediate rearranges to a late intermediate that is more resistant to aggregation and can then be refolded at a higher rate at higher temperatures. The efficacy of this method, however, depends on the reaction pathway-dependent presence or absence of aggregation-prone refolding intermediates. Therefore, its applicability has to be checked and folding temperatures have to be optimized on a case-by-case basis. In another case, a short hydrophobic protein could be refolded after extensive purification of the solubilized inclusion bodies using a temperature-leap protocol [141]. In yet another example, oxidative renaturation of ovotransferrin from the fully reduced form was achieved by raising the temperature during folding [142]. Here the reduced protein was first diluted into refolding buffer containing 1 mM GSH and pre-incubated at 0 °C for varying times. To initiate the final oxidative folding of the preformed, still reduced, intermediates, 1 mM GSSG was added and the temperature was increased to 22 °C. The pre-incubation at 0 °C significantly decreased the aggregation, as measured by turbidity, during refolding.

38.3.10
Recycling of Aggregates

Upon in vitro folding, the complete conversion of the unfolded protein into its native biologically active form is rarely achieved. Instead, a significant amount of material is sequestered into inactive aggregates. These aggregates may comprise more than 90% of the initial solubilized protein material, depending on the particular protein and the refolding conditions. It should be possible to recover this material by recycling through a second round of solubilization and refolding. This was demonstrated in principle quite some time ago, using porcine lactate dehydrogenase as a model protein [143]. However, mistranslated forms or protein molecules containing nonnative covalent modifications may accumulate in the aggregated material and corrupt the correct refolding pathway during recycling. By using electron spray mass spectroscopy (ES-MS) for the analysis of the recycled aggregates after in vitro folding of the N-terminal domain of tissue inhibitor of metalloproteinase-2, it could be shown that even after partial purification the material was extremely heterogeneous in mass [144]. Thus, the need for the elaborate purification of the recycled protein, together with the relative ease of obtaining fresh inclusion bodies from the overexpression of a given target protein as starting material for in vitro folding, renders the recycling of aggregates unattractive.

38.4
Alternative Refolding Techniques

38.4.1
Matrix-assisted Refolding

The basic idea in matrix-assisted protein refolding is to make use of the specific interaction of the protein that is to be refolded with a solid support in order to prevent unspecific aggregation. To achieve this goal, three prerequisites must be fulfilled. First, protein binding to the matrix must be possible under denaturing conditions; second, the interaction between the protein and the matrix during the refolding step must allow for the flexibility of the polypeptide chain that is required for proper structure formation; and third, the interaction must be tight enough to prevent interchain interaction, which might result in aggregate formation.

The technology of matrix-assisted protein refolding was pioneered by Creighton [145, 146], using the transient interaction of the unfolded protein with an ion-exchange resin and the gradual removal of the denaturing agent to allow refolding. As an alternative, hydrophobic matrices were tested for the same purpose [147]. In another, slightly exotic, example, the MalK subunit of the *Salmonella typhimurium* maltoside transport complex was recovered in native form after solubilizing *E. coli* inclusion bodies in urea and subsequent binding of the material to a red agarose column, followed by refolding through buffer exchange [148].

Specific binding of solubilized protein to matrices can be achieved by using se-

quence tags, which must be chosen to allow for binding under denaturing conditions. For example, N- or C-terminal hexa-arginine tags were used to bind urea-unfolded α-glucosidase from *Saccharomyces cerevisiae* to polyanionic supports [149]. Careful optimization of the renaturation conditions was necessary, as ionic interactions of the refolding polypeptide with the matrix caused a drastic decrease in renaturation yields at low salt concentrations, while at high salt concentrations, renaturation was prevented by hydrophobic interactions with the matrix. Under optimum conditions, however, immobilized α-glucosidase could be renatured with a high yield at protein concentrations up to 5 mg mL^{-1}. Folding of the enzyme in solution had previously been feasible only at concentrations below 15 μg mL^{-1}.

Recently, binding of His-tagged proteins to Ni-chelate affinity material has been increasingly used for matrix-assisted refolding. In the case of cysteine-rich proteins or proteins containing multiple disulfide bonds, incorrect disulfide bond formation due to metal-catalyzed air oxidation may hamper proper renaturation. Bassuk et al. described a method for isolation and partial refolding of a reduced His-tagged protein on a Ni-nitrilotriacetic acid (NTA) column, followed by disulfide shuffling using a redox buffer system composed of reduced and oxidized glutathione [150]. In another case, an overnight linear gradient, starting with 8 M urea, 100 mM NaH_2PO_4, 10 mM Tris/HCl, pH 8.0, and 13 mM β-mercaptoethanol and finishing with refolding buffer (100 mM NaH_2PO_4, 10 mM Tris/HCl, pH 8.0, 2 mM GSH, and 0.2 mM GSSG), was successfully used for the refolding of the His-tagged recombinant human and mouse myelin oligodendrocyte glycoproteins on a Ni-NTA column [151]. Franken et al. recently reported a protocol for the refolding of matrix-bound His-tagged proteins, which includes a washing step with a buffer containing 60% isopropanol prior to refolding for the efficient removal of contaminants, namely detergents and bacterial endotoxins [152].

Apart from soluble proteins, membrane proteins also could be refolded after immobilizing the solubilized inclusion body material on a Ni-chelating matrix [153]. Here, the inclusion bodies were solubilized by urea in the presence of sodium *N*-lauryl sarcosinate and glycerol. After the binding to a Ni-chelate affinity matrix, folding was initiated by omitting urea from the elution buffer. With the protein still bound to the column, *N*-lauryl sarcosinate was exchanged against Triton X-100, and the refolded protein was finally eluted with imidazole.

Another interesting approach to matrix-assisted protein refolding was described by Berdichevsky et al. [154]. In this case, the folding of a single-chain Fv antibody fragment fused to a cellulose-binding domain from *Clostridium thermocellum* (CBD) was analyzed in the matrix-bound form and compared to standard refolding in solution. Interestingly, the CBD was found to retain its specific cellulose-binding capacity even in the presence of up to 6 M urea. Following solubilization of the inclusion bodies of the fusion protein in urea, the CBD recovered its native structure, while the Fv part was still unfolded. After binding to crystalline cellulose, the antibody fragment could then be refolded while bound to the matrix via its fusion partner, the already native CBD.

Protein refolding by transient interaction of folding intermediates with solid supports can also be achieved by using disulfide-carrying polymeric microspheres

during oxidative refolding of disulfide bond-containing proteins [155]. Here, cystamine-functionalized microspheres were present during the oxidative refolding of reduced lysozyme. Due to transient binding of folding intermediates to the matrix by thiol-disulfide exchange, an increase in the yield of productive refolding could be achieved.

38.4.2 Folding by Gel Filtration

Surprisingly, unfolded proteins can in some cases be refolded simply by passing the solubilized, unfolded protein solution through a size-exclusion column equilibrated with refolding buffer [156–158]. Even more surprisingly, this refolding procedure often functions at relatively high protein concentrations. Several reasons may contribute to the feasibility of protein refolding by gel filtration. First, the unfolded polypeptide, characterized by a higher hydrodynamic radius than the chemical denaturant (GdmCl or urea) will run ahead of the denaturant and thus gradually move into conditions that promote correct refolding. Now either the protein can complete correct refolding and outrun the denaturant front, or higher aggregates may form, which then precipitate within the gel. The following denaturant front will re-dissolve these aggregates, giving them a renewed chance for correct folding. Furthermore, limited diffusion as well as physical separation of the refolding polypeptide chains within the pores of the gel may reduce the propensity for aggregate formation. Finally, transient interaction of the intermediates with the gel matrix may also contribute to a reduction in aggregate formation.

The use of size-exclusion chromatography for refolding was further improved by Gu et al., who used urea gradients to guarantee the gradual transfer of the unfolded protein to refolding conditions [159]. In a very thorough analysis, chromatographic refolding methods were compared to more traditional refolding techniques using *E. coli* inclusion bodies of recombinant single-chain antibody fragments [160]. Refolding by dilution and dialysis was compared to protein refolding using an immobilized metal affinity matrix and gel filtration. The highest yield was obtained using gel filtration with decreasing urea and, in parallel, increasing pH gradient. In the presence of the appropriate redox buffer, composed of reduced and oxidized glutathione, decreasing urea concentrations allowed structure formation, while increasing pH values promoted formation of disulfide bonds by thiol-disulfide exchange. This method allowed high-yield recovery of correctly refolded protein. Since the oxidative refolding of antibody fragments is a relatively slow process, low flow rates had to be used during gel filtration. In another study Gu et al. compared the efficacy of different gel-filtration media for size-exclusion chromatographic refolding of denatured bovine carbonic anhydrase B [161].

Although folding by gel filtration seems to be an elegant and promising approach to the renaturation of inclusion body material, several inherent difficulties may limit its practical applicability. Clogging of the gel-filtration column by aggregates can be a severe problem for many proteins, and the refolding conditions have to be carefully optimized with respect to buffer conditions, flow rate, and gradient vol-

ume in each case. Low maximum flow rates and the cost of large size-exclusion columns represent barriers to the scale-up of a process for industrial production.

38.4.3 Direct Refolding of Inclusion Body Material

As the properties of proteins vary so widely depending on their individual amino acid sequence, it is obviously to be expected that the inclusion bodies formed by different recombinant proteins also differ in their morphology. Using the same procedure for isolation may in one case yield inclusion body preparations that are extremely resistant to solubilization, while isolates of other proteins may be redissolved even under non-denaturing conditions. In general, inclusion body preparations of secreted proteins containing multiple disulfide bonds are quite stable, so that strong denaturants are a prerequisite for solubilization. Inclusion body isolates of intracellular proteins, on the other hand, are often found to be quite labile, so that the folded or partially folded protein contained in these inclusion bodies can be solubilized by a simple incubation in physiological buffer systems. For example, native protein could be extracted from inclusion body isolates obtained after massive overexpression of the endogenous *E. coli* β-galactosidase (R. Rudolph, unpublished observation). In another study, Tsumoto et al. reported the extraction of active green fluorescent protein (GFP) from inclusion bodies using non-denaturing solvent conditions [162]. In this case, the inclusion bodies already contained some native GFP, as indicated by their fluorescence. This native material, together with partially folded intermediates, could be solubilized using non-denaturing concentrations of GdmCl or, even more effectively, using L-Arg in concentrations ranging from 0.5 M to 2 M. In other cases, the mild detergent *N*-lauryl sarcosine was used to extract active protein from inclusion body material. Native *E. coli* RNA polymerase σ factor could be recovered by dissolving the inclusion bodies in buffer containing 0.4% (w/v) sarcosyl, followed by 10-fold dilution at 4 °C [163]. Actin could be recovered from inclusion body material by using 1.5% (w/v) sarcosyl in the presence of 1 mM ethylenediamine tetraacetic acid (EDTA) [164]. In the absence of divalent cations, only actin was extracted from the inclusion body material, while contaminating *E. coli* outer-membrane proteins were not solubilized.

Recombinant proteins that form more resistant inclusion bodies may still be directly solubilized and refolded by applying strongly alkaline buffer conditions. Although this procedure may appear relatively harsh, it has indeed been used in industrial processes. For example, prochymosin was extracted by suspending the inclusion body material in 0.05 M K_2HPO_4/K_2NaPO_4, 1 mM EDTA, 0.1 M NaCl, pH 10.7. After incubation for a least 1 h at 4 °C, the pH of the supernatant was adjusted to pH 8.0 by addition of concentrated HCl to induce final refolding [165]. In another case, bovine somatotropin was recovered by incubating inclusion bodies in dilute NaOH, pH 12.5. After 20 min at 25 °C, the inclusion bodies were completely dissolved. After adjusting the pH to 11.5, oxidative refolding proceeded, presumably by air oxidation, during a further incubation for 8 h [166].

38.5 Conclusions

Although almost all chapters in this handbook deal with fundamental aspects of both the in vivo and the in vitro structure formation of proteins, protein folding has lost its virgin status and become the subject of industrial exploitation for many years. By now a large number of proteins of industrial relevance are produced by processes involving refolding. Among the most prominent examples are recombinant human proteins of high market potential produced by in vitro folding from *E. coli* inclusion body material. These examples include human insulin, human granulocyte colony-stimulating factor, human growth hormone, and Rapilysin, an engineered variant of human tissue-type plasminogen activator. Other proteins used for drug discovery by screening or rational, structure-based design are also produced by in vitro folding.

In this chapter only a selection of the techniques that have been used for protein refolding could be mentioned. Unfortunately, many of the refolding protocols described in the literature work well for only one particular target protein. Folding protocols have to be optimized with respect to protein concentration, temperature, pH, redox conditions, additives, and specific methodology on a case-by-case basis. However, "standard procedures" have been developed over the last couple of years, which may serve as fairly general guidelines (cf. Protocol 3). Chances are high that native, biologically active protein can be obtained from inclusion body material by following these protocols. These procedures, however, may not straightforwardly lead to the most cost-efficient process for the large-scale production of a given protein. In designing an industrial process, other alternatives that are mentioned in this chapter should be kept in view as possibilities for the optimization of process economics.

38.6 Experimental Protocols

38.6.1 Protocol 1: Isolation of Inclusion Bodies

Equipment and Reagents

- Ultraturrax
- French press
- Centrifuge
- 0.1 M Tris/HCl pH 7, 1 mM EDTA
- Lysozyme
- $MgCl_2$
- DNAse

- 60 mM EDTA, 6% Triton X-100, 1.5 M NaCl, pH 7
- 0.1 M Tris/HCl pH 7, 20 mM EDTA

Method

1. Homogenize cells (5 g wet weight) in 25 mL 0.1 M Tris/HCl pH 7, 1 mM EDTA, at 4 °C, using an Ultraturrax (10 000 rpm).
2. Add 1.5 mg lysozyme per gram cells, mix briefly with the Ultraturrax, and incubate at 4 °C for 30 min.
3. Use sonication or high-pressure homogenization (French press) to disrupt the cells.
4. In order to digest DNA, add $MgCl_2$ to a final concentration of 3 mM and DNAse to a final concentration of 10 μg mL^{-1}, and incubate for 30 min at 4 °C.
5. Add 0.5 volume of 60 mM EDTA, 6% Triton X-100, 1.5 M NaCl, pH 7, and incubate for 30 min at 4 °C.
6. Pellet inclusion bodies (IB) by centrifugation at 31 000 *g* for 10 min at 4 °C.
7. Resuspend the pellet in 40 mL 0.1 M Tris/HCl pH 7, 20 mM EDTA, using the Ultraturrax.
8. Repeat centrifugation.
9. The IB pellet may be stored frozen at −20 °C for at least two weeks.

38.6.2
Protocol 2: Solubilization of Inclusion Bodies

Reagents

- 6 M GdmCl (or 8 M urea), 0.1 M Tris/HCl pH 8, 100 mM DTE (or DTT), 1 mM EDTA
- 1 M HCl
- 4 M GdmCl (or 6 M urea), 10 mM HCl

Method

1. Resuspend 50 mg IB pellet from Protocol 1 in 5 mL 6 M GdmCl (or 8 M urea), 0.1 M Tris/HCl pH 8, 100 mM DTE (or DTT), 1 mM EDTA, and incubate for 2 h at 25 °C.
2. Lower the pH of the solution to a value between pH 3 and pH 4 by drop-wise addition of HCl.
3. Remove debris by centrifugation at 10 000 g.
4. Completely remove the DTE (or DTT) by exhaustive dialysis (twice) against 500 mL of 4 M GdmCl (or 6 M urea), 10 mM HCl, for 2 h at 25 °C. Dialyze again at 4 °C overnight against 1 L of 4 M GdmCl (or 6 M urea). (In the case of proteins that do not contain disulfide bonds, the dialysis step may be omitted.)
5. Determine the protein concentration by a Bradford assay [167] using bovine serum albumin (BSA) in 4 M GdmCl (or 6 M urea), 10 mM HCl as standard protein.

Tab. 38.2. Buffer conditions for initial refolding screening.

Buffer	*pH*[1]	*Additive*	*GSH/GSSG*[2]	*EDTA*[3]
0.1 M Tris/HCl	8.5	–	5 mM/0.5 mM	1 mM
"	"	0.5 M L-Arg/HCl	"/"	"
"	"	1.0 M L-Arg/HCl	"/"	"
"	7.5	0.5 M L-Arg/HCl	"/"	"
"	9.5	"	"/"	"
"	8.5	"	0.5 mM/5 mM	"
"	"	"	−/−	"
"	"	0.5 M Na_2SO_4	5 mM/0.5 mM	"
"	"	20% (w/v) Sorbitol	"/"	"

[1] Care should be taken to adjust the pH value only after addition of all buffer components.
[2] Presence of the redox buffer system composed of oxidized and reduced glutathione is necessary only if the protein contains disulfide bonds; if the protein does **not** contain disulfide bonds, GSH/GSSG may be replaced by 5 mM DTT (or DTE). Stock solutions of GSH, DTT, and DTE should not be stored for longer than 24 h at 4 °C.
[3] EDTA should be added only if the native protein does not contain bound metal ions; if the protein **does** contain bound metal ions, low concentrations of the respective metal should be included (e.g., in fivefold molar excess over the protein).

6. Aliquots of the protein solution may be stored at −70 °C for at least two weeks.

38.6.3
Protocol 3: Refolding of Proteins

Refolding by Rapid Dilution of Denatured Protein

1. The optimal choice of the refolding buffer depends on the particular protein. Table 38.2 represents a series of buffer conditions that should be tested in an initial screening and may serve as starting points for further optimization.
2. Dilute the solubilized proteins obtained according to Protocol 2 into the precooled refolding buffer (10 °C) under rapid mixing. The final protein concentration should be within the range of 10–30 μg mL^{-1}. This concentration should be obtained by diluting the solubilized inclusion bodies in a ratio of approx. 1:100 (v/v).
3. After 12 h refolding at 10 °C, the sample should be dialyzed against a dilute buffer system appropriate for the given protein, which must not contain L-Arg. Apart from improving refolding, L-Arg may also keep misfolded forms of the protein in solution and should therefore be removed. A precipitate may form during this dialysis step.
4. After removal of the precipitate by centrifugation, the biological activity of the refolded protein should be assessed using an appropriate assay. If no activity as-

say is available, solubility may be taken as a first indication for correct refolding. Upon quantification of the refolding yield, take into account volume changes that may have occurred during dialysis due to osmosis.

Refolding by Stepwise Addition of Denatured Protein

To achieve refolding at higher final concentrations of renatured protein, the dilution of the solubilized inclusion body material may be carried out in a stepwise manner, according to the following rules:

1. Determine the upper limit of the concentration of denatured protein (Δc) that can be refolded at high yield upon a single dilution into renaturation buffer.
2. Determine the time Δt that is required for renaturation to 90% of the final value.
3. Determine the maximum residual denaturant concentration that is compatible with native structure formation.
4. Refolding is performed by stepwise addition of concentration increments Δc of the denatured protein to the refolding buffer at time intervals Δt. The addition of denatured protein solution can be repeated until the maximum residual denaturant concentration is reached.
5. After refolding is complete, proceed with dialysis according to step 3 of the standard protocol (see above).

Acknowledgements

The group's ongoing work on the in vitro folding of proteins is supported by the German Federal Ministry of Education and Research (BMBF grant no. 03WKB01 A) and the Federal State (Land) of Saxony-Anhalt (grant no. 3537 A/0903 L).

References

1 Itakura, K., Hirose, T., Crea, R., Riggs, A. D., Heynecker, H. L., Bolivar, F., and Boyer, H. W. (1977). Expression in *Escherichia coli* of a chemically synthesized gene for the hormone somatostatin. *Science* **198**, 1056–1063.

2 Goeddel, D. V., Kleid, D. G., Bolivar, F., Heyneker, H. L., Yansura, D. G., Crea, R., Hirose, T., Kraszewski, A., Itakura, K., and Riggs, A. D. (1979). Expression in *Escherichia coli* of chemically synthesized genes for human insulin. *Proc. Natl. Acad. Sci. USA* **76**, 106–110.

3 Makrides, S. C. (1996). Strategies for Achieving High-Level Expression of Genes in *Escherichia coli*. *Microbiol. Rev.* **60**, 512–538.

4 Yee, L., and Blanch, H. W. (1992). Recombinant protein expression in high cell density fed-batch cultures of *Escherichia coli*. *Bio/Technology* **10**, 1550–1556.

5 Kleman, G. L., and Strohl, W. R.

(1994). Developments in high cell density and high productivity microbial fermentation. *Curr. Opin. Biotechnol.* **5**, 180–186.

6 Lee, S. Y. (1996). High cell-density culture of Escherichia coli. *Trends Biotechnol.* **14**, 98–105.

7 Marston, F. A. O. (1986). The purification of eukaryotic polypeptides synthesized in *Escherichia coli*. *Biochem. J.* **240**, 1–12.

8 Allen, S. P., Polazzi, J. O., Gierse, J. K., and Easton, A. M. (1992). Two Novel Heat Shock Genes Encoding Proteins Produced in Response to Heterologous Protein Expression in *Escherichia coli*. *J. Bacteriol.* **174**, 6938–6947.

9 Hartley, D. L., and Kane, J. F. (1988). Properties of inclusion bodies from recombinant *Escherichia coli*. *Biochem. Soc. Trans.* **16**, 101–102.

10 De Bernardez Clark, E., Schwarz, E., and Rudolph, R. (1999). Inhibition of Aggregation Side Reactions during in vitro Protein Folding. *Meth. Enzymol.* **309**, 217–236.

11 Worrall, D. M., and Goss, N. H. (1989). The Formation of Biologically Active *β*-Galactosidase Inclusion Bodies in *Escherichia coli*. Austral. *J. Biotechnol.* **3**, 28–32.

12 Flamand, M., Chevalier, M., Henchal, E., Girard, M., and Deubel, V. (1995). Purification and Renaturation of Japanese Encephalitis Virus Nonstructural Glycoprotein NS1 Overproduced by Insect Cells. *Protein Expr. Purif.* **6**, 519–527.

13 Kiefhaber, T., Rudolph, R., Kohler, H.-H., and Buchner, J. (1991). Protein aggregation in vitro and in vivo: A quantitative Model of the kinetic competition between folding and aggregation. *Bio/Technology* **9**, 825–829.

14 Schein, C. H., and Noteborn, M. H. M. (1988). Formation of soluble recombinant proteins in *Escherichia coli* is favored by lower growth temperature. *Bio/Technology* **6**, 291–294.

15 Kopetzki, E., Schumacher, G., and Buckel, P. (1989). Control of formation of active soluble or inactive insoluble baker's yeast *α*-glucosidase PI in *Escherichia coli* by induction and growth conditions. *Mol. Gen. Genet.* **216**, 149–155.

16 Fahey, R. C., Hunt, J. S., and Windham, G. C. (1977). On the cysteine and cystine content of proteins. Differences between intracellular and extracellular proteins. *J. Mol. Evol.* **10**, 155–163.

17 Freedman, R. B. (1995). The formation of protein disulphide bonds. *Curr. Opin. Struct. Biol.* **5**, 85–91.

18 Raina, S., and Missiakas, D. (1997). Making and Breaking of Disulfide Bonds. *Annu. Rev. Microbiol.* **51**, 179–202.

19 Fabianek, R. A., Hennecke, H., and Thöny-Meyer, L. (2000). Periplasmic protein thiol:disulfide oxidoreductases of *Escherichia coli*. *FEMS Microbiol. Rev.* **24**, 303–316.

20 Kadokura, H., Katzen, F., and Beckwith, J. (2003). Protein Disulfide Bond Formation in Prokaryotes. *Annu. Rev. Biochem.* **72**, 111–135.

21 Derman, A. I., Prinz, W. A., Belin, D., and Beckwith, J. (1993). Mutations That Allow Disulfide Bond Formation in the Cytoplasm of *Escherichia coli*. *Science* **262**, 1744–1747.

22 Prinz, W. A., Aslund, F., Holmgren, A., and Beckwith, J. (1997). The role of the thioredoxin and glutaredoxin pathways in reducing protein disulfide bonds in the *Escherichia coli* cytoplasm. *J. Biol. Chem.* **272**, 15661–15667.

23 Stewart, E. J., Aslund, F., and Beckwith, J. (1998). Disulfide bond formation in the *Escherichia coli* cytoplasm: an in vivo role reversal for the thioredoxins. *EMBO J.* **17**, 5543–5550.

24 Bessette, P. H., Åslund, F., Beckwith, J., and Georgiou, G. (1999). Efficient folding of proteins with multiple disulfide bonds in the *Escherichia coli* cytoplasm. *Proc. Natl. Acad. Sci. USA* **96**, 13703–13708.

25 Georgiou, G., and Valax, P. (1996). Expression of correctly folded proteins in *Escherichia coli*. *Curr. Opin. Biotechnol.* **7**, 190–197.

26 Vonrhein, C., Schmidt, U., Ziegler, G. A., Schweiger, S., Hanukoglu, I., and Schulz, G. E. (1999). Chaperone-assisted expression of authentic bovine adrenodoxin reductase in *Escherichia coli*. *FEBS Lett.* **443**, 167–69.

27 Rudolph, R. (1996). Successful Protein Folding on an Industrial Scale. in: Protein Engineering: Principles and Practice. Cleland, J. L., and Craik, C. S. (eds.). Wiley-Liss Inc., New York, USA. pp. 283–298.

28 Rudolph, R., and Lilie, H. (1996). In vitro folding of inclusion body proteins. *FASEB J.* **10**, 49–56.

29 Rudolph, R., Böhm, G., Lilie, H., and Jaenicke, R. (1997). Folding proteins. in: Protein Function: A Practical Approach. Creighton, T. E. (ed.). IRL Press, Oxford, UK. pp. 57–99.

30 Rudolph, R., Lilie, H., and Schwarz, E. (1999). In vitro Folding of Inclusion Body Proteins on an Industrial Scale. in: Biotechnology (2nd ed.), Vol. 5a: Recombinant Proteins, Monoclonal Antibodies and Therapeutic Genes. Mountain, A., Ney, U., and Schomburg, D. (eds.). Wiley-VCH, Weinheim, Germany. pp. 112–123.

31 Ernst, S., Garro, O. A., Winkler, S., Venkataraman, G., Langer, R., Cooney, C. L., and Sasisekharan, R. (1997). *Biotechnol. Bioeng.* **53**, 575–582.

32 Zettlmeissl, G., Rudolph, R., and Jaenicke, R. (1979). Reconstitution of Lactic Dehydrogenase. Noncovalent Aggregation vs. Reactivation. 1. Physical Properties and Kinetics of Aggregation. *Biochemistry* **18**, 5567–5571.

33 Datar, R. V., Cartwright, T., and Rosen, C.-G. (1993). Process Economics of Animal Call and Bacterial Fermentations: A Case Study Analysis of Tissue Plasminogen Activator. *Bio/Technology* **11**, 349–357.

34 Middelberg, A. P. J. (1996). The influence of protein refolding strategy on cost for competing reactions. *Chem. Eng. J.* **61**, 41–52.

35 Rudolph, R., and Fischer, S. (1990). Process for obtaining renatured proteins. *U.S. Patent* 4,933,434.

36 Kohnert, U., Rudolph, R., Verheijen, J. H., Jacoline, E., Weening-Verhoeff, D., Stern, A., Opitz, U., Martin, U., Lill, H., Prinz, H., Lechner, M., Kresse, G.-B., Buckel, P., and Fischer, S. (1992). *Protein Eng.* **5**, 93–100.

37 Rudolph, R., Fischer, S., and Mattes, R. (1995). Process for the activation of t-PA or Ing after genetic expression in prokaryotes. *U.S. Patent* 5,453,363.

38 Jürgen, B., Lin, H. Y., Riemschneider, S., Scharf, C., Neubauer, P., Schmid, R., Hecker, M., and Schweder, T. (2000). Monitoring of Genes that Respond to Overproduction of an Insoluble Recombinant Protein in *Escherichia coli* Glucose-Limited Fed-Batch Fermentations. *Biotechnol. Bioeng.* **70**, 217–224.

39 Hunke, S., and Betton, J.-M. (2003). Temperature effect on inclusion body formation and stress response in the periplasm of *Escherichia coli*. *Mol. Microbiol.* **50**, 1579–1589.

40 Stark, G. R., Stein, W. H., and Moore, S. (1960). Reactions of the Cyanate Present in Aqueous Urea with Amino Acids and Proteins. *J. Biol. Chem.* **235**, 3177–3181.

41 Stark, G. R. (1965). Reactions of Cyanate with Functional Groups of Proteins. III. Reactions with Amino Carboxyl Groups. *Biochemistry* **4**, 1030–1036.

42 Hagel, P., Gerding, J. J. T., Fieggen, W., and Bloemendal, H. (1971). Cyanate Formation in Solutions of Urea. I. Calculation of Cyanate Concentrations at Different Temperature and pH. *Biochim. Biophys. Acta* **243**, 366–373.

43 Goldberg, M. E., Rudolph, R., and Jaenicke, R. (1991). A Kinetic Study of the Competition between Renaturation and Aggregation during the Refolding of Denatured-Reduced Egg White Lysozyme. *Biochemistry* **30**, 2790–2797.

44 Trivedi, V. D., Raman, B., Mohan

Rao, Ch., and Ramakrishna, T. (1997). Co-refolding denatured-reduced hen egg white lysozyme with acidic and basic proteins. *FEBS Lett.* **418**, 363–366.

45 Ramage, P., Cheneval, D., Chvei, M., Graff, P., Hemmig, R., Heng, R., Kocher, H. P., Mackenzie, A., Memmert, K., Revesz, L., and Wishart, W. (1995). Expression, Refolding, and Autocatalytic Proteolytic Processing of the Interleukin-1β-converting Enzyme Precursor. *J. Biol. Chem.* **270**, 9378–9383.

46 Hochuli, E., Bannwarth, W., Döbeli, H., Gentz, R., and Stüber, D. (1988). Genetic Approach to Facilitate Purification of Recombinant Proteins with a Novel Metal Chelate Adsorbent. *Bio/Technology* **6**, 1321–1325.

47 Samuelsson, E., and Uhlen, M. (1996). Chaperone-like effect during in vitro refolding of insulin-like growth factor I using a solubilizing fusion partner. *Ann. N.Y. Acad. Sci.* **782**, 486–494.

48 Ambrosius, D., Dony, C., and Rudolph, R. (1996). Activation of recombinant proteins. *U.S. Patent* 5,578,710.

49 Zhu, X. L., Ohta, Y., Jordan, F., and Inouye, M. (1989). Pro-sequence of subtilisin can guide the refolding of denatured subtilisin in an intramolecular process. *Nature* **339**, 483–484.

50 Silen, J. L., and Agard, D. A. (1989). The α-lytic protease pro-region does not require a physical linkage to activate the protease domain in vivo. *Nature* **341**, 462–464.

51 Rattenholl, A., Ruoppolo, M., Flagiello, A., Monti, M., Vinci, F., Marino, G., Lilie, H., Schwarz, E., and Rudolph, R. (2001a). Pro-Sequence Assisted Folding and Disulfide Bond Formation of Human Nerve Growth Factor. *J. Mol. Biol.* **305**, 523–533.

52 Rattenholl, A., Lilie, H., Grossmann, A., Stern, A., Schwarz, E., and Rudolph, R. (2001b). The pro-sequence facilitates folding of human nerve growth factor from *Escherichia coli* inclusion bodies. *Eur. J. Biochem.* **268**, 3296–3303.

53 Grauschopf, U., Lilie, H., Honold, K., Wozny, M., Reusch, D., Esswein, A., Schaefer, W., Rücknagel, K. P., and Rudolph, R. (2000). The N-Terminal Fragment of Human Parathyroid Hormone Receptor 1 Constitutes a Hormone Binding Domain and Reveals a Distinct Disulfide Pattern. *Biochemistry* **30**, 8878–8887.

54 Bazarsuren, A., Grauschopf, U., Wozny, M., Reusch, D., Hoffmann, E., Schaefer, W., Panzner, S., and Rudolph, R. (2002). In vitro folding, functional characterization, and disulfide pattern of the extracellular domain of human GLP-1 receptor. *Biophys. Chem.* **96**, 305–318.

55 Hoffman, S. J., Looker, D. L., Roehrich, J. M., Cozart, P. E., Durfee, S. L., Tedesco, J. L., and Stetler, G. L. (1990). Expression of fully functional tetrameric human hemoglobin in *Escherichia coli*. *Proc. Natl. Acad. Sci. USA* **87**, 8521–8525.

56 Nagai, K., Perutz, M., and Poyart, C. (1985). Oxygen binding properties of human mutant hemoglobins synthesized in *Escherichia coli*. *Proc. Natl. Acad. Sci. USA* **82**, 7252–7255.

57 Creighton, T. E. (1978). Experimental Studies of Protein Folding and Unfolding. *Prog. Biophys. Molec. Biol.* **33**, 231–297.

58 Pace, C. N., and Creighton, T. E. (1986). The Disulphide Folding Pathway of Ribonuclease T_1. *J. Mol. Biol.* **188**, 477–486.

59 Weissman, J. S., and Kim, P. S. (1991). Reexamination of the folding of BPTI: predominance of native intermediates. *Science* **253**, 1386–1393.

60 Weissman, J. S., and Kim, P. S. (1992). Kinetic role of nonnative species in the folding of bovine pancreatic trypsin inhibitor. *Proc. Natl. Acad. Sci. USA* **89**, 9900–9904.

61 Frand, A. R., Cuozzo, J. W., and Kaiser, C. A. (2000). Pathways for protein disulphide bond formation. *Trends Cell Biol.* **10**, 203–210.

62 Woycechowsky, K. J., and Raines, R. T. (2000). Native disulfide bond formation in proteins. *Curr. Opin. Chem. Biol.* **4**, 533–539.

63 Hiniker, A., and Bardwell, J. C. A. (2003). Disulfide Bond Isomerization in Prokaryotes. *Biochemistry* **42**, 1179–1185.

64 Sela, M., White, F. H., and Anfinsen, C. B. (1957) Reductive cleavage of disulfide bridges in ribonuclease. *Science* **125**, 691–692.

65 Ahmed, A. K., Schaffer, S. W., and Wetlaufer, D. B. (1975). Nonenzymatic reactivation of reduced bovine pancreatic ribonuclease by air oxidation and by glutathione oxidoreduction buffers. *J. Biol. Chem.* **250**, 8477–8482.

66 Winter, J., Klappa, P., Freedman, R., Lilie, H., and Rudolph, R. (2002a). Catalytic Activity and Chaperone Function of Human Protein-disulfide Isomerase are Required for the Efficient Refolding of Proinsulin. *J. Biol. Chem.* **277**, 310–317.

67 Saxena, V. P., and Wetlaufer, D. B. (1970). Formation of three-dimensional structure in proteins. I. Rapid nonenzymic reactivation of reduced lysozyme. *Biochemistry* **9**, 5015–5023.

68 Wetlaufer, D. B. (1984). Nonenzymatic formation and isomerization of protein disulfides. *Meth. Enzymol.* **107**, 301–304.

69 Woycechowsky, K. J., Wittrup, K. D., and Raines, R. T. (1999). A small-molecule catalyst of protein folding in vitro and in vivo. *Chem. Biol.* **6**, 871–879.

70 Winter, J., Lilie, H., and Rudolph, R. (2002b). Recombinant expression and in vitro folding of proinsulin are stimulated by the synthetic dithiol Vectrase-P. *FEMS Microbiol. Lett.* **213**, 225–230.

71 Gough, J. D., Williams, R. H. Jr., Donofrio, A. E., and Lees, W. J. (2002). Folding Disulfide-Containing Proteins Faster with an Aromatic Thiol. *J. Am. Chem. Soc.* **124**, 3885–3892.

72 Gough, J. D., Gargano, J. M., Donofrio, A. E., and Lees, W. J. (2003) Aromatic Thiol pK_a Effects on the Folding Rate of a Disulfide Containing Protein. *Biochemistry* **42**, 11787–11797.

73 Light, A., and Higaki, J. N. (1987). Detection of Intermediate Species in the Refolding of Bovine Trypsinogen. *Biochemistry* **26**, 5556–5564.

74 Buchner, J., and Rudolph, R. (1991). Renaturation, Purification, and Characterization of Recombinant F_{ab}-Fragments Produced in *Escherichia coli*. *Bio/Technology* **9**, 157–162.

75 Honda, J., Andou, H., Mannen, T., and Sugimoto, S. (2000). Direct Refolding of Recombinant Human Growth Differentiation Factor 5 for Large-Scale Production Process. *J. Biosci. Bioeng.* **89**, 582–589.

76 Levine, A. D., Rangwala, S. H., Horn, N. A., Peel, M. A., Matthews, B. K., Leimgruber, R. M., Manning, J. A., Bishop, B. F., and Olins, P. O. (1995). High Level Expression and Refolding of Mouse Interleukin 4 Synthesized in *Escherichia coli*. *J. Biol. Chem.* **270**, 7445–7452.

77 Wang, J.-Y., Kishore, U., and Reid, K. B. M. (1995). A recombinant polypeptide, composed of the α-helical neck region and the carbohydrate recognition domain of conglutinin, self-associates to give a functionally intact homotrimer. *FEBS Lett.* **376**, 6–10.

78 Lowther, W. T., Majer, P., and Dunn, B. M. (1995). Engineering the substrate specificity of rhizopuspepsin: The role of Asp 77 of fungal aspartic proteinases in facilitating the cleavage of oligopeptide substrates with lysine in P_1. *Protein Sci.* **4**, 689–702.

79 Schrem, A., Lange, C., and Koch, K.-W. (1999). Identification of a Domain in Guanylyl Cyclase-activating Protein 1 that Interacts with a Complex of Guanylyl Cyclase and Tubulin in Photoreceptors. *J. Biol. Chem.* **274**, 6244–6249.

80 Asano, R., Kudo, T., Makabe, K., Tsumoto, K., and Kumagai, I. (2002). Antitumor activity of interleukin-21 prepared by novel refolding procedure

from inclusion bodies expressed in *Escherichia coli*. *FEBS Lett.* **528**, 70–76.

81 Umetsu, M., Tsumoto, K., Hara, M., Ashish, K., Goda, S., Adschiri, T., and Kumagai, I. (2003). How Additives Influence the Refolding of Immunoglobulin-folded Proteins in a Stepwise Dialysis System. *J. Biol. Chem.* **278**, 8979–8978.

82 Winter, J., Lilie, H., and Rudolph, R. (2002c). Renaturation of human proinsulin – a study on refolding and conversion to insulin. *Anal. Biochem.* **310**, 148–155.

83 Timasheff, S. N., and Arakawa, T. (1989). Stabilization of protein structure by solvents. in: Protein structure. A practical approach. Creighton, T. E. (ed.). IRL Press, Oxford, UK. pp. 331ff.

84 Timasheff, S. N. (2002). Protein Hydration, Thermodynamic Binding, and Preferential Hydration. *Biochemistry* **41**, 13473–13482.

85 Orsini, G., and Goldberg, M. E. (1978). The Renaturation of Reduced Chymotrypsinogen A in Guanidine HCl. Refolding versus Aggregation. *J. Biol. Chem.* 253, 3453–3458.

86 Wetlaufer, D. B., and Xie, Y. (1995) Control of aggregation in protein refolding: A variety of surfactants promote renaturation of carbonic anhydrase II. *Protein Sci.* **4**, 1536–1543.

87 Cleland, J. L., Hedgepeth, C., and Wang, D. I. C. (1992a). Polyethylene Glycol Enhanced Refolding of Bovine Carbonic Anhydrase B. *J. Biol. Chem.* **267**, 13327–13334.

88 Cleland, J. L., Builder, S. E., Swartz, J. R., Winkler, M., Chang, J. Y., and Wang, D. I. C. (1992b). Polyethylene Glycol Enhanced Protein Refolding. *Bio/Technology* **10**, 1013–1019.

89 Lee, L. L.-Y., and Lee, J. C. (1987). Thermal Stability of Proteins in the Presence of Poly(ethylene glycols). *Biochemistry* **26**, 7813–7819.

90 Tandon, S., and Horowitz, P. (1988). The effects of lauryl maltoside on the reactivation of several enzymes after treatment with guanidinium chloride. *Biochim. Biophys. Acta* **955**, 19–25.

91 Zardenata, G., Horowitz, P. M. (1994). Protein Refolding at High Concentrations Using Detergent/Phospholipid Mixtures. *Anal. Biochem.* **218**, 392–398.

92 Krause, M., Rudolph, R., and Schwarz, E. (2002). The non-ionic detergent Brij 58P mimics chaperone effects. *FEBS Lett.* **532**, 253–255.

93 Yancey, P. H., Clark, M. E., Hand, S. C., Bowlus, R. D., and Somero, G. N. (1982). Living with water stress: evolution of osmolyte systems. *Science* **24**, 1214–1222.

94 Bolen, D. W., and Baskakov, I. V. (2001). The osmophobic effect: natural selection of a thermodynamic force in protein folding. *J. Mol. Biol.* **310**, 955–963.

95 Sawano, H., Koumoto, Y., Ohta, K., Sasaki, Y., Segawa, S., and Tachibana, H. (1992). Efficient in vitro folding of the three-disulfide derivatives of hen lysozyme in the presence of glycerol. *FEBS Lett.* **303**, 11–14.

96 Michaelis, U., Rudolph, R., Jarsch, M., Kopetzki, E., Burtscher, H., and Schumacher, G. (1995). Process for the production and renaturation of recombinant, biologically active, eukaryotic alkaline phosphatase. *U.S. Patent* 5,434,067.

97 Chilson, O. P., and Chilson, A. E. (2003). Perturbation of folding and reassociation of lactate dehydrogenase by proline and trimethylamine oxide. *Eur. J. Biochem.* **270**, 4823–4834.

98 Kumar, T. K. S., Samuel, D., Jayaraman, G., Srimathi, T., and Yu, C. (1998). The role of proline in the prevention of aggregation during protein folding in vitro. *Biochem. Mol. Biol. Int.* **46**, 509–517.

99 Shiraki, K., Kudou, M., Fujiwara, S., Imanaka, T., and Takagi, M. (2002). Biophysical Effect of Amino Acids on the Prevention of Protein Aggregation. *J. Biochem. (Tokyo)* **132**, 591–595.

100 Buchner, J., Pastan, I., and Brinkmann, U. (1992a). A Method

for Increasing the Yield of Properly Folded Recombinant Fusion Proteins: Single-Chain Immunotoxins from Renaturation of Bacterial Inclusion Bodies. *Anal. Biochem.* **205**, 263–270.

101 Brinkmann, U., Buchner, J., Pastan, I. (1992). Independent domain folding of Pseudomonas exotoxin and single-chain immunotoxins: influence of interdomain connections. *Proc. Natl. Acad. Sci. USA* **89**, 3075–3079.

102 Arora, D., and Khanna, N. (1996). Method for increasing the yield of properly folded recombinant human gamma interferon from inclusion bodies. *J. Biotechnol.* **52**, 127–133.

103 Oneda, H., and Inouye, K. (1999). Refolding and recovery of recombinant human matrix metalloproteinase 7 (matrilysin) from inclusion bodies expressed by *Escherichia coli*. *J. Biochem.* **126**, 905–911.

104 Taneja, S., and Ahmad, F. (1994). Increased thermal stability of proteins in the presence of amino acids. *Biochem. J.* **303**, 147–153.

105 Arakawa, T., and Tsumoto, K. (2003). The effects of arginine on refolding of aggregated proteins: not facilitate refolding, but suppress aggregation. *Biochem. Biophys. Res. Comm.* **304**, 148–152.

106 Kita, Y., Arakawa, T., Lin, T.-Y., and Timasheff, S. N. (1994). Contribution of the Surface Free Energy Perturbation to Protein–Solvent Interactions. *Biochemistry* **33**, 15178–15189.

107 Rariy, R. V., and Klibanov, A. M. (1997). Correct protein folding in glycerol. *Proc. Natl. Acad. Sci. USA* **94**, 13520–13523.

108 Rariy, R. V., and Klibanov, A. M. (1999). Protein Refolding in Predominantly Organic Media Markedly Enhanced by Common Salts. *Biotechnol. Bioeng.* **62**, 704–710.

109 Summers, C. A., and Flowers, R. A. II (2000). Protein renaturation by the liquid organic salt ethylammonium nitrate. *Protein Sci.* **9**, 2001–2008.

110 Welton, T. (1999). Room-temperature ionic liquids. Solvents for synthesis and catalysis. *Chem. Rev.* **99**, 2071–2083.

111 Kragl, U., Eckstein, M., and Kaftzik, N. (2002). Enzyme catalysis in ionic liquids. *Curr. Opin. Biotechnol.* **13**, 565–571.

112 van Rantwijk, F., Madeira Lau, R., and Sheldon, R. A. (2003). Biocatalytic transformations in ionic liquids. *Trends Biotechnol.* **21**, 131–138.

113 Price, P. A., Stein, W. H., and Moore, S. (1969). Effect of Divalent Cations on the Reduction and Reformation of the Disulfide Bonds of Deoxyribonuclease. *J. Biol. Chem.* **244**, 929–932.

114 Smith, A. T., Santama, N., Dacey, S., Edwards, M., Bray, R. C., Thorneley, R. N. F., and Burke, J. F. (1990). Expression of a Synthetic Gene for Horseradish Peroxidase C in *Escherichia coli* and Folding and Activation of the Recombinant Enzyme with Ca^{2+} and Heme. *J. Biol. Chem.* **265**, 13335–13343.

115 Whitwam, R. E., Gazarian, I. G., and Tien, M. (1995). Expression of Fungal Mn Peroxidase in *E. coli* and Refolding to Yield Active Enzyme. *Biochem. Biophys. Res. Comm.* **216**, 1013–1017.

116 Doyle, W. A., and Smith, A. T. (1996). Expression of lignin peroxidase H8 in *Escherichia coli*: folding and activation of the recombinant enzyme with Ca^{2+} and Haem. *Biochem. J.* **315**, 15–19.

117 Rudolph, R., Gerschitz, J., and Jaenicke, R. (1978). Effect of Zinc(II) on the Refolding and Reactivation of Liver Alcohol Dehydrogenase. *Eur. J. Biochem.* **87**, 601–606.

118 Rudolph, R., Heider, I., and Jaenicke, R. (1977). Mechanism of Reactivation and Refolding of Glyceraldehyde-3-Phosphate Dehydrogenase form Yeast after Denaturation and Dissociation. *Eur. J. Biochem.* **81**, 563–570.

119 Bell, S., Hansen, S., and Buchner, J. (2002). Refolding and structural characterization of the human p53 tumor suppressor protein. *Biophys. Chem.* **96**, 243–257.

120 Wang, C.-C., and Tsou, C.-L. (1998).

Enzymes as chaperones and chaperones as enzymes. *FEBS Lett.* **425**, 382–384.

121 Schiene, C., and Fischer, G. (2000). Enzymes that catalyse the restructuring of proteins. *Curr. Opin. Struct. Biol.* **10**, 40–45.

122 Walter, S., and Buchner, J. (2002). Molecular Chaperones – Cellular Machines for Protein Folding. *Angew. Chem. Int. Ed.* **41**, 1098–1113.

123 Buchner, J., Brinkmann, U., and Pastan, I. (1992b). Renaturation of a Single-Chain Immunotoxin Facilitated by Chaperones and Protein Disulfide Isomerase. *Bio/Technology* **10**, 682–685.

124 Altamirano, M. M., Golbik, R., Zahn, R., Buckle, A. M., and Fersht, A. R. (1997) Refolding chromatography with immobilized mini-chaperones. *Proc. Natl. Acad. Sci. USA* **94**, 3576–3578.

125 Altamirano, M. M., García, C., Possani, L. D., and Fersht, A. R. (1999). Oxidative refolding chromatography: folding of the scorpion toxin Cn5. *Nature Biotechnol.* **17**, 187–191.

126 Cooper, A. (1992). Effect of Cyclodextrins on the Thermal Stability of Globular Proteins. *J. Am. Chem. Soc.* **114**, 9208–9209.

127 Sharma, L., and Sharma, A. (2001). Influence of cyclodextrin ring substituents on folding-related aggregation of bovine carbonic anhydrase. *Eur. J. Biochem.* **268**, 2456–2463.

128 Rozema, D., and Gellman, S. H. (1996a). Artificial Chaperone-assisted Refolding of Carbonic Anhydrase B. *J. Biol. Chem.* **271**, 3478–3487.

129 Rozema, D., and Gellman, S. H. (1996b). Artificial Chaperone-Assisted Refolding of Lysozyme: Competition between Renaturation and Aggregation. *Biochemistry* **35**, 15760–15771.

130 Daugherty, D. L., Rozema, D., Hanson, P. E., and Gellman, S. H. (1998) Artificial Chaperone-assisted Refolding of Citrate Synthase. *J. Biol. Chem.* **273**, 33961–33971.

131 Hanson, P. E., and Gellman, S. E. (1998). Mechanistic comparison of artificial-chaperone-assisted and unassisted refolding of urea-denatured carbonic anhydrase B. *Folding & Design* **3**, 457–468.

132 Mannen, T., Yamaguchi, S., Honda, J., Sugimoto, S., and Nagamune, T. (2001). Expanded-Bed Protein Refolding Using a Solid-Phase Artificial Chaperone. *J. Biosci. Bioeng.* **91**, 403–408.

133 Schade, B. C., Rudolph, R., Lüdemann, H.-D., and Jaenicke, R. (1980). Reversible High-Pressure Dissociation of Lactic Dehydrogenase from Pig Muscle. *Biochemistry* **19**, 1121–1126.

134 Hillson, N., Onuchic, J. N., and García, A. E. (1999). Pressure-induced protein-folding/unfolding kinetics. *Proc. Natl. Acad. Sci. USA* **96**, 14848–14853.

135 Gorovits, B. M., and Horowitz, P. M. (1998). High Hydrostatic Pressure Can Reverse Aggregation of Protein Folding Intermediates and Facilitate Acquisition of Native Structure. *Biochemistry* **37**, 6132–6135.

136 Foguel, D., Robinson, C. R., Caetano de Sousa, P. Jr., Silva, J. L., and Robinson, A. S. (1999). Hydrostatic Pressure Rescues Native Protein from Aggregates. *Biotechnol. Bioeng.* **63**, 552–558.

137 St. John, R. J., Carpenter, J. F., and Randolph, T. W. (1998) High pressure fosters protein refolding from aggregates at high concentrations. *Proc. Natl. Acad. Sci. USA* **23**, 13029–13033.

138 St. John, R. J., Carpenter, J. F., and Randolph, T. W. (2002) High-Pressure Refolding of Disulfide-Cross-Linked Lysozyme Aggregates: Thermodynamics and Optimization. *Biotechnol. Prog.* **18**, 565–571.

139 Meersman, F., and Heremans, K. (2003). High pressure induces the formation of aggregation-prone states of proteins under reducing conditions. *Biophys. Chem.* **104**, 297–304.

140 Xie, Y., and Wetlaufer, D. B. (1996) Control of aggregation in protein refolding: The temperature-leap tactic. *Protein Sci.* **5**, 517–523.

141 Lajmi, A. R., Wallace, T. R., and Shin, J. A. (2000). Short, Hydrophobic, Alanine-Based Proteins Based on the Basic Region/Leucine Zipper Protein Motif: Overcoming Inclusion Body Formation and Protein Aggregation during Overexpression, Purification, and Renaturation. *Protein Expr. Purif.* **18**, 394–403.

142 Hirose, M., Akuta, T., and Takahashi, N. (1989). Renaturation of Ovotransferrin Under Two-step Conditions Allowing Primary Folding of the Fully Reduced Form and the Subsequent Regeneration of the Intramolecular Disulfides. *J. Biol. Chem.* **264**, 16867–16872.

143 Rudolph, R., Zettlmeissl, G., and Jaenicke, R. (1979). Reconstitution of Lactic Dehydrogenase. Noncovalent Aggregation vs. Reactivation. 2. Reactivation of Irreversibly Denatured Aggregates. *Biochemistry* **18**, 5572–5575.

144 Williamson, R. A., Natalia, D., Gee, C. K., Murphy, G., Carr, M. D., and Freedman, R. B. (1996). Chemically and conformationally authentic active domain of human tissue inhibitor of metalloproteinases-2 refolded from bacterial inclusion bodies. *Eur. J. Biochem.* **241**, 476–483.

145 Creighton, T. E. (1985). Folding of proteins adsorbed reversibly to ion-exchange resins. *UCLA Symp. Mol. Cell. Biol.* 39, 249–258.

146 Creighton, T. E. (1990). Process for the production of a protein. *U.S. Patent* 4,977,248.

147 Geng, X., and Chang, X. (1992). High-performance hydrophobic interaction chromatography as a tool for protein refolding. *J. Chromatogr.* **599**, 185–194.

148 Walter, C., Höner zu Bentrup, K., and Schneider, E. (1992). Large Scale Purification, Nucleotide Binding Properties, and ATPase Activity of the MalK Subunit of *Salmonella typhimurium* Maltose Transport Complex. *J. Biol. Chem.* **267**, 8863–8869.

149 Stempfer, G., Höll-Neugebauer, B., and Rudolph, R. (1996). Improved Refolding of an Immobilized Fusion Protein. *Nature Biotechnol.* **14**, 329–334.

150 Bassuk, J. A., Braun, L. P., Motamed, K., Baneyx, F., and Sage, H. E. (1996). Renaturation of SPARC Expressed in *Escherichia coli* Requires Isomerization of Disulfide Bonds for Recovery of Biological Activity. *Int. J. Cell Biol.* **28**, 1031–1043.

151 Liñares, D., Echevarria, I., and Mañá, P. (2004). Single-step purification and refolding of recombinant mouse and human myelin oligodendrocyte glycoprotein and induction of EAE in mice. *Protein Expr. Purif.* **34**, 249–256.

152 Franken, K. L. M. C., Hiemstra, H. S., van Meijgaarden, K. E., Subronto, Y., den Hartigh, J., Ottenhoff, T. H. M., and Drijfhout, J. W. (2000). Purification of His-Tagged Proteins by Immobilized Chelate Affinity Chromatography: The Benefits from the Use of Organic Solvents. *Protein Expr. Purif.* **18**, 95–99.

153 Rogl, H., Kosemund, K., Kühlbrandt, W., and Collinson, I. (1998) Refolding of *Escherichia coli* produced membrane protein inclusion bodies immobilised by nickel chelating chromatography. *FEBS Lett.* **432**, 21–26.

154 Berdichevsky, Y., Lamed, R., Frenkel, D., Gophna, U., Bayer, E. A., Yaron, S., Shoham, Y., and Benhar, I. (1999). Matrix-Assisted Refolding of Single-Chain Fv-Cellulose Binding Domain Fusion Proteins. *Protein Expr. Purif.* **17**, 249–259.

155 Shimizu, H., Fujimoto, K., and Kawaguchi, H. (2000). Improved refolding of denatured/reduced lysozyme using disulfide-carrying polymeric microspheres. *Colloids Surfaces B: Biointerfaces* **18**, 137–144.

156 Shalongo, W., Ledger, R., Jagannadham, M. V., and Stellwagen, E. (1987). Refolding of denatured thioredoxin observed by size-exclusion chromatography. *Biochemistry* **26**, 3135–3141.

157 Shalongo, W., Jagannadham, M. V.,

Flynn, C., and Stellwagen, E. (1989). Refolding of denatured ribonuclease observed by size-exclusion chromatography. *Biochemistry* **28**, 4820–4825.

158 Werner, M. H., Clore, G. M., Gronenborn, A. M., Kondoh, A., and Fisher, R. J. (1994). Refolding proteins by gel filtration chromatography. *FEBS Lett.* **345**, 125–130.

159 Gu, Z., Su, Z., and Janson, J.-C. (2001). Urea gradient size-exclusion chromatography enhanced the yield of lysozyme refolding. *J. Chromatogr.* A **918**, 311–318.

160 Gu, Z., Weidenhaupt, M., Ivanova, N., Pavlov, M., Xu, B., Su, Z.-G., and Janson, J.-C. (2002). Chromatographic Methods for the Isolation of, and Refolding of Proteins from, *Escherichia coli* inclusion Bodies. *Protein Expr. Purif.* **25**, 174–179.

161 Gu, Z., Zhu, X., Zhou, H., and Su, Z. (2003) Inhibition of aggregation by media selection, sample loading and elution in size exclusion chromatographic refolding of denatured bovine carbonic anhydrase B. *J. Biochem. Biophys. Methods* **56**, 165–175.

162 Tsumoto, K., Umetsu, M., Kumagai, I., Ejima, D., and Arakawa, T. (2003). Solubilization of active green fluorescent protein from insoluble particles by guanidine and arginine. *Biochem. Biophys. Res. Comm.* **312**, 1381–1386.

163 Burgess, R. R. (1996). Purification of Overproduced *Escherichia coli* RNA Polymerase σ Factors by Solubilizing Inclusion Bodies and Refolding from Sarkosyl. *Methods Enzymol.* **273**, 145–149.

164 Frankel, S., Sohn, R., and Leinwand, L. (1991). The use of sarkosyl in generating soluble protein after bacterial expression. *Proc. Natl. Acad. Sci. USA* **88**, 1192–1196.

165 Lowe, P. A., Marston, F. A. O., Sarojani, A., and Schoemaker, J. A. (1994). Process for the recovery of recombinantly produced protein from insoluble aggregate. *U.S. Patent* 5,340,926.

166 McCoy, K. M., and Frost, R. A. (1991). Method for solubilization and naturation of somatotropin. *U.S. Patent* 5,064,943.

167 Bradford, M. M. (1976). A rapid and sensitive method for the quantitation of microgram quantities of protein utilizing the principle of protein-dye binding. *Anal. Biochem.* **72**, 248–254.

39
Engineering Proteins for Stability and Efficient Folding

Bernhard Schimmele and Andreas Plückthun

39.1
Introduction

The industrial, biotechnological, and medical applications of proteins are often limited by an insufficient protein stability or related problems. Such applications commonly require that proteins be produced on a large scale and remain stable enough to fulfill their functions for a reasonable length of time, often under harsh conditions. However, natural proteins are typically only marginally stable, and it is thus a major challenge for protein engineers to optimize stability and folding efficiency. The approaches that have been successfully employed to achieve this goal are rational design, semi-rational strategies based on sequence comparisons, and the methods of directed protein evolution. Of course, these methods are not mutually exclusive and can be combined to solve practical problems. All studies employing these methods have revealed important rules for protein engineering and at the same time shed light on the principles and mechanisms responsible for the folding and stability of proteins. Recent advances in stability engineering have demonstrated that merely small changes in a given protein sequence can have profound effects on its biophysical properties. The major challenge is therefore to correctly identify and remedy these shortcomings. It is the goal of this chapter to summarize the biophysical principles and technological approaches useful in improving the biophysical properties of proteins through sequence modification.

Considering the enormous array of technologies involved in this endeavor, ranging from computer algorithms to selection technologies, it is not possible to give detailed experimental protocols in this chapter; instead, we will guide the reader to the cited literature.

39.2
Kinetic and Thermodynamic Aspects of Natural Proteins

39.2.1
The Stability of Natural Proteins

Evolution does not per se provide proteins with high stability. In fact, stability is just one of many evolutionary constraints on proteins. Proteins have to fold to a

Protein Folding Handbook. Part II. Edited by J. Buchner and T. Kiefhaber

ISBN: 3-527-30784-2

defined structure with adequate yield in a reasonable time and then have to be just stable enough to perform their function over a certain period. There is no evolutionary incentive to make a protein any ''better'' than what is needed to fulfill its cellular functions. In contrast, the use of a protein in a formulation at high concentration, its prolonged activity at 37 °C, and its large-scale expression and crystallization, just to name a few conditions, may put far higher demands on the protein than its natural environment. Thus, the natural sequence may not be able to provide these properties, but a mutant sequence may.

Proteins exist and have evolved in order to fulfill a given function, and evolution drives the structural properties of a protein mainly towards increased functionality [1]. In fact, most proteins are only marginally stable, with $\Delta G_{folding}$ in the range of -20 to -60 kJ mol^{-1}. It is still a matter of debate whether this marginal stability is actually a ''design feature,'' e.g., to allow degradation at a certain rate, whether it is caused by the selection pressure towards higher functionality that may not be compatible with high stability, or whether it is just a side effect of the lack of selection for high stability. Function is often linked to higher structural flexibility in certain regions of a protein. Lower stability as a result of this higher local structural flexibility might therefore simply represent an adaptation to increased functionality [2]. If this were generally true, however, stability engineering would fail in most cases, as it would not be able to reconcile stability with preserved protein function. An alternative, more optimistic view for the protein engineer is that marginal stability can be interpreted as a result of genetic drift [3]. In other words, lower stability is not intended; but it simply does not matter, provided that function is maintained. Random mutations occurring during evolution are more likely to destabilize the structure of a given parental protein sequence than to stabilize it or be neutral. However, as long as this stability decrease is not sufficient to render the protein nonfunctional, these destabilizing mutations are likely to accumulate in the sequence. This tendency has also been referred to as ''sequence entropy'' [4]. As a consequence, stability engineering could be interpreted as the art of identifying these unfavorable mutations in order to reestablish a more stable sequence.

The concept discussed above also sets the basis for the consensus approach to stability engineering, which is discussed in Section 39.3.1 Based on the physical principles of protein folding and a structure-based analysis of the interactions between amino acid residues, rational design can give hints as to which residues need to be altered to achieve a desired effect, and this is discussed in Section 39.3.2. The third focus will be set on the methods of directed evolution, which mimic the mechanisms of Darwinian evolution to evolve proteins with enhanced folding and stability properties (see Section 39.4).

39.2.2
Different Kinds of ''Stability''

Before discussing in detail different strategies for rendering a protein more stable, it is worth taking a closer look at some basic features associated with protein stability and folding properties. The term ''stability'' itself is rather vague, and its precise

meaning has often been adapted depending on the problem being addressed. This leads to different definitions of "stability." We will now briefly analyze the definitions and differences between thermodynamic, kinetic, and thermal stability, as well as folding efficiency, which is also sometimes discussed in this context. Even though these properties are interconnected, they are not equivalent. This has important implications for protein engineering, as it is difficult to predict in advance how a given mutation will influence each of these properties. These influences will in fact be different for any protein under investigation according to the free energies of the native and unfolded states and the folding intermediates, as well as the folding pathway and the respective rate constants.

39.2.2.1 Thermodynamic Stability

Thermodynamics describes the global unfolding behavior of a protein. The corresponding *thermodynamic stability* ΔG describes the differences between the free energies of the native (N) and the unfolded (U) states. Importantly, ΔG is an equilibrium property for a reaction involving two or more states. The simplest model of an unfolding reaction is the equilibrium of a two-state unfolding reaction:

$$\mathrm{N} \underset{k_{\mathrm{folding}}}{\overset{k_{\mathrm{unfolding}}}{\rightleftharpoons}} \mathrm{U}$$

where $k_{\mathrm{unfolding}}$ and k_{folding} are the rate constants of the respective unfolding and folding reactions. As a consequence, values for ΔG can be deduced only if the described process is fully reversible and no intermediate states are populated to a significant extent, unless they are explicitly known and measured. ΔG describes to what degree the two states are populated at a given temperature according to

$$\Delta G_{\mathrm{unfolding}} = -RT \ln K \tag{1}$$

where K is the equilibrium constant of the unfolding process. The treatment of experimental data is much simplified in such a model, as stability is affected only by the free energies of the folded and unfolded states. Because ΔG also provides an overall measure of all energetic contributions of interactions occurring upon protein folding, it is a convenient quantity for comparing the energetic effects of single amino acid replacements in a given folded structure. Because of the great scientific interest in deducing the principles of protein folding on a quantitative basis, many studies have been carried out with carefully selected model systems in which these strict requirements that allow the determination of ΔG are fulfilled. Moreover, ΔG represents an intrinsic quantity, at a given temperature in a given buffer, that is independent of the experimental setup and therefore reproducible in any case. The major problem in such studies, however, is confirmation that the observed transition can in fact be described as a fully reversible process, and denaturant-induced transition data alone are often not sufficient to allow reliable judgment. Only if data derived from measurements on the basis of different spectral probes (or better yet, additionally by differential scanning calorimetry, yielding the model-independent enthalpy change of unfolding) agree with each other are

the deduced ΔG values likely to be correct. Nevertheless, many useful conclusions can be drawn about the effects of mutations even if these strict requirements cannot be completely fulfilled in all cases.

Another fact complicates the use of ΔG as a measure for protein stability. Mostly as a result of the fact that the hydrophobic effect is the major driving force of protein folding [5], ΔG itself is a characteristic, curved function of temperature. It is defined as

$$\Delta G(T) = G^U - G^N = \Delta H(T) - T\Delta S(T) = -RT \ln K \tag{2}$$

emphasizing especially that the enthalpy change ΔH is itself a function of temperature. This change of ΔH with T can be described by the heat capacity change

$$\Delta C_p = \left(\frac{\partial \Delta H(T)}{\partial T}\right)_p \tag{3}$$

Although often ignored, the temperature dependence of ΔG should thus not be left out of the account if one is dealing with the stability engineering of proteins. The large heat capacity change upon the transfer of nonpolar solutes to water, which is the basis of the hydrophobic effect, results in a curved function of ΔG versus temperature. By using the definition of ΔC_p, ΔG can be approximated as a function of T, the melting temperature T_m, the enthalpy change at T_m $\Delta H(T_m)$, and ΔC_p.

$$\Delta G(T) = \left(1 - \frac{T}{T_m}\right)\Delta H(T_m) + (T - T_m)\Delta C_p - T\Delta C_p \ln \frac{T}{T_m} \tag{4}$$

If $\Delta G(T)$ is plotted as a function of T, the curve increases at low temperatures and decreases at high temperatures (Figure 39.1). The temperature at which folded and unfolded states are equally populated, and thus $\Delta G = 0$, is called the melting temperature T_m.

The respective curvature of ΔG versus temperature is strongly dependent on the change of heat capacity ΔC_p upon unfolding. A mutation may change ΔC_p, $\Delta H(T_m)$, and T_m in any combination, thereby altering the shape and the position of this curve. Higher thermodynamic stability at a given temperature ($\Delta G(T)$) can thus be achieved, e.g., by an upshift of this curve with constant maximum. Right-shifting of the curve will decrease ΔG at lower temperatures but increase it at higher temperatures, which goes along with an increase of T_m. Flattening of the curve due to a lower change of heat capacity upon unfolding may cause lower thermodynamic stability at most temperatures, even though T_m is increased.

These considerations contain important implications for the analysis of engineered mutants. First, a measured decrease of ΔG at a certain temperature does not necessarily mean that at higher temperatures the thermodynamic stability might not have been increased. Second, by determining the change of ΔG, no conclusions can be drawn about a potential change of the melting temperature T_m. While they are typically related, a low ΔG at a given temperature does not necessar-

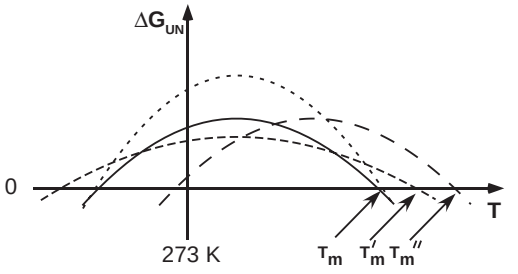

Fig. 39.1. The complex relationship between the melting temperature and the free energy of folding. Schematic representations of the free energy difference between the folded and unfolded states of a protein, ΔG_N, as a function of temperature, T. A typical protein is shown in curve 1 (————). The shape of this curve changes if a mutation affects ΔC_p, $\Delta H(T_m)$, and/or T_m of the protein. In the examples shown, not just one but several of these parameters are changed. Higher thermodynamic stability at a given temperature can phenomenologically be the result of a curve upshift (·-·-·-·-·). Right-shifting the curved function (— — — —) results in a right-shift of the maximum of the ΔG_N function as well as in a shift of the melting temperature T_m towards higher temperatures (T_m'). If the ΔG_N function is flattened because of a small ΔC_p (– – – –), a higher melting temperature (T_m'') can result, even though the thermodynamic stability is actually decreased over a broad temperature range. All depicted curves represent extreme cases, and typically a combination of the described alterations will occur upon mutating a protein.

ily mean that T_m will be decreased. T_m and ΔG must therefore be regarded as different properties. It should also be recalled that thermodynamic parameters, while easily reproduced, give no information about how long it will take until equilibrium is reached or, in the case of a nonreversible reaction, until a certain fraction of proteins is inactivated. Thus, thermodynamic stability does not necessarily provide information about whether a protein will meet the stability requirements for an intended application.

T_m itself often serves as a measure of protein stability, more precisely of *thermal stability*. In the literature, the expression "thermal stability" is again used with different meanings. In the described case, it represents the melting temperature for a reversible process. However, a complete thermodynamic analysis of the vast majority of proteins is not possible, because either intermediate folding states are populated or folding in the absence of denaturants that solubilize the unfolded state is not a fully reversible process. As will be discussed in the following section, thermal stability can nevertheless serve as a very practical means of describing protein stability, defined either as the transition temperature of an irreversible process or as the half-life of a protein under a given set of conditions.

39.2.2.2 **Kinetic Stability**

In most cases, outside the biophysical research lab, protein unfolding is an irreversible reaction. Initially, the aggregation of unfolded molecules or of folding intermediates prevent the back-reaction of folding, and this is followed, after pro-

longed times at high temperature, by chemical inactivation or, in impure samples, proteolysis. In a simple model, kinetic inactivation can be described as

$$N \underset{k_{folding}}{\overset{k_{unfolding}}{\rightleftharpoons}} U \xrightarrow{k_{agg}} X$$

As discussed in the Introduction, one evolutionary constraint on proteins is that their three-dimensional structure remains viable for a certain period of time. In the case of non-equilibrium conditions and irreversible reactions, reaction kinetics becomes the important parameter. The folded state can resist high temperatures for a considerably long time if either the rate constant of inactivation or the rate constant of unfolding is sufficiently low. The rate constants are determined by the free energy of activation, e.g., the difference in energy between the folded state and the transition state of unfolding. Proteins can thus be kinetically stabilized by increasing this activation barrier.

This kinetic stability is different in some crucial aspects from the thermodynamic stability mentioned above. Engineering of proteins for enhanced stability has to deal with both aspects. The best mutations for enhancing kinetic stability will not necessarily be the best mutations for enhancing thermodynamic stability, and not every mutation that increases thermodynamic stability will automatically have a positive effect on protein half-life.

Kinetic stabilization is a common theme in nature, and there are several indications that many proteins from thermophilic organisms are indeed stabilized kinetically rather than thermodynamically [6, 7]. Another important example is that of proteins from the coats of viruses and phages that have to protect their genetic material under very adverse conditions [8]. In extreme cases the native state of a protein can even be less stable than its denatured state, but the native fold can still be kinetically trapped, and large kinetic unfolding barriers can provide the protein with an extremely long half-life [9].

There are different ways of describing and determining kinetic stability. Even if the reaction proceeds in an irreversible way, a practical ''melting curve'' can still be determined, and the observed transition is cooperative. The midpoint of this transition can serve as a practical means to compare the thermal resistance of different protein variants. Alternatively, one can use the half-life of the protein at a given temperature as an empirical means of stability. However, one has to be aware that this will not reflect equilibrium conditions. The observed values are actually kinetic values and thus are not independent of the exact experimental conditions, such as the protein concentration, the heating rate, etc. A more thorough analysis of kinetic stabilization must include kinetic measurements to determine the respective unfolding rates at different temperatures [10, 11].

For medical applications, engineered proteins usually have to fulfill defined stability requirements such as the absence of aggregation in the formulation used, long-term stability, and prolonged activity at 37 °C. The mere analysis of thermodynamic and kinetic parameters under defined reaction conditions in vitro is not always a reliable indicator of protein behavior under in vivo conditions. Mechanisms other than the intrinsic properties of the protein, such as proteolysis or ag-

gregation with other proteins, can affect half-life. For practical utility, the half-life can therefore also be determined by measuring the percentage of molecules that retain their function after incubation under the respective conditions, e.g., in human serum at 37 °C for several days [12].

39.2.2.3 Folding Efficiency

A different issue of kinetics is related not to unfolding but to the folding of the protein in vivo. More precisely, the question is, which percentage of a protein will actually fold to the native state, as opposed to going to misfolded states, soluble aggregates, or inclusion bodies? Even though the folding efficiency in vivo is not directly related to stability, correlations can often be observed [13]. Additionally, the efficiency of protein folding in vivo is usually the predominant factor influencing the expression yield and is therefore also crucial for large-scale production of functionally intact proteins. Importantly, many mammalian proteins with a high potential for medical applications, especially those secreted or expressed on the cell surface, can rely on the complex folding machinery of the eukaryotic cell to reach their final native state, and the secretory quality-control system of eukaryotic cells allows discrimination of proteins by their folding behavior [14]. Moreover, they usually do not need to be expressed in high amounts in their native physiological context. The resulting lack of selection pressure on their efficiency of folding during evolution is likely to be one of the causes for the difficulties often observed when attempting their overexpression. Unfortunately, these tend to be the proteins of greatest pharmacological utility.

Despite the fact that thermodynamic stability underlies folding efficiency, the kinetic partitioning into productive folding or aggregation is influenced by many different factors. For illustrative purposes, we can again describe this by a very simple scheme:

$$\mathrm{U} \xrightarrow{k_{\mathrm{int}}} \mathrm{I} \begin{cases} \xrightarrow{k_{\mathrm{folding}}} \mathrm{N} \\ \xrightarrow{k_{\mathrm{agg}}} \mathrm{Agg} \end{cases}$$

Folding intermediates are often the source of aggregation, and the overall folding efficiency will therefore depend mainly on the nature of these intermediates. This includes the free energy of the folding intermediates themselves, as well as their half-lives and any efficient pathways to aggregation. In vivo, the situation becomes much more complex, as additional parameters such as interactions with cellular components and chaperones or degradation by host cell proteases come into play. The final output of a properly folded protein will therefore depend on all of these kinetic competitions [15]. Protein expression in the bacterial cytoplasm in many cases shows correlations between soluble expression yield and thermodynamic stability of the protein [16, 17]. Additional complications can arise from transport steps. For example, the expression of proteins in the periplasm of *E. coli* is dependent on the prior transport of the polypeptide chain through the inner membrane, and the folding yield is subsequently influenced by the folding and aggregation

reaction in the periplasmic space as well as by interactions with periplasmic factors such as chaperones and proteases. In some cases, mutations that show positive effects on in vivo folding yield have no influence on the overall stability of the protein [18]. Conversely, mutations that strongly increase thermodynamic stability sometimes result in lower folding yields [19]. Nevertheless, many mutations act synergistically on both properties, because they are likely to reduce the free energy of the folded state as well as the free energy of folding intermediates and thereby lower the energetic activation barrier to folding [13].

39.3 The Engineering Approach

39.3.1 Consensus Strategies

39.3.1.1 Principles

As discussed in the preceding sections, marginal protein stability is likely to be a side effect of ''sequence entropy'' occurring during natural evolution, because the major driving force of evolution is positive selection towards an enhanced functional property, while stability has to be maintained at only a minimum level to secure function. Mutations are likely to occur in a random fashion during this process; the probability that a mutation will have a stabilizing effect on the protein is very low, whereas the probability that the mutation will have destabilizing effects is very high. However, as long as the remaining amino acid sequence is still able to fold into a given structure and the overall domain stability does not fall below a certain threshold, the resulting protein sequences will not be eliminated during the course of evolution [20]. Destabilizing mutations are therefore often selectively neutral and thus accumulate in a given parental sequence. The same should also be true for folding efficiencies. Most proteins are not needed at high concentrations or may even become harmful to the organism in such a case. Similar to stability, folding yield is selectively neutral, provided that the minimum level for cellular function is maintained.

This sets the basis for a semi-rational approach to protein stabilization, which is called the consensus approach [21] and is based on sequence statistics. Because mutations occur randomly, the distribution of amino acids at a given position in a set of homologous proteins can be described, in a very crude approximation, by Boltzmann's law. The consensus approach assumes that at a specific position in a sequence alignment of homologous proteins, the contribution of the respective consensus amino acid to the stability of the protein is on average higher than the contribution of any non-consensus amino acid. Replacement of all non-consensus amino acids in a sequence by the respective consensus amino acid should therefore increase the overall stability of the protein. Obvious advantages of the consensus approach are that it is comparatively simple and is not strictly dependent on structural information at high resolution.

The prerequisite for building a non-biased consensus is the availability of sequences homologous to the protein under investigation. The number of sequences should be large enough to make the sequence statistics reliable and to exclude bias in the resulting consensus sequences. Figure 39.2 shows an alignment of homologous sequences of single repeat modules, the smallest structural entity of a class of proteins known as leucine-rich repeat (LRR) proteins. Because the length of these modules varies among the different classes of LRR proteins – influencing their topology – only repeat modules of a length of 24 amino acid residues have been used for this alignment. The probability of each amino acid occurring at a given position is calculated to derive a consensus sequence, representing the most frequently occurring amino acid residue at each position. The distribution of residues at each position can provide information on structurally forbidden residues and allows weighing the consensus with respect to variability. In most cases, the consensus will contain the residues important for defining the structure of the proteins. In the case of an enzyme family, it will also include the ''functional'' residues, i.e., those of the active site. In the case of binding proteins, such as antibodies or repeat proteins, the ''functional'' residues (those involved in binding) are not conserved but are different for each individual molecule, which has to adapt to its target.

Although at first sight no sophisticated structural analysis seems to be required, this is true in only the simplest of cases, where a single family of related sequences can be represented by a single consensus. Frequently, multiple families have emerged that use mutually incompatible solutions of packing. A good example is that of antibodies for which subgroup-specific consensus building has been very fruitful [22]. Averaging over all families would simply yield the consensus of the most-represented family and, if they are equally represented, may result in mutually incompatible residues. Thus, structural analysis can be very helpful in deciding whether an ''averaging'' of different sequence families is permissible or not. Because of this problem of interacting residues, a simple averaging may lead to incompatible pairs; therefore, these residues should be changed only as groups. The danger of disrupting these interactions by substitutions with consensus residues is especially high in cases where a very broad set of sequences is used for the alignment. To minimize this risk, the sequence statistics can be extended by analysis of covariance in order to derive probabilities that describe the joint occurrence of amino acid residues at two defined positions [23]. As explained above, before deriving a consensus, the aligned sequences can be divided into subclasses, which are likely to contain interacting pairs or groups of residues. Certain variations of residues involved in salt bridges, distinct hydrogen-bonding patterns, or packing of the hydrophobic core are characterized by complementary changes between these subclasses, with mutations to a certain residue at one position being compensated by a mutation to a complementary residue at another position. The subclasses can be built either by being based on sequence homology alone or by including structural information if available. Even though the definition of these subclasses is always dependent on the homology cutoff set by the investigator, a simple dendrogram analysis can be used to group the complete set of sequences into distinct families. Additionally, by building the consensus sequence of each family separately, fol-

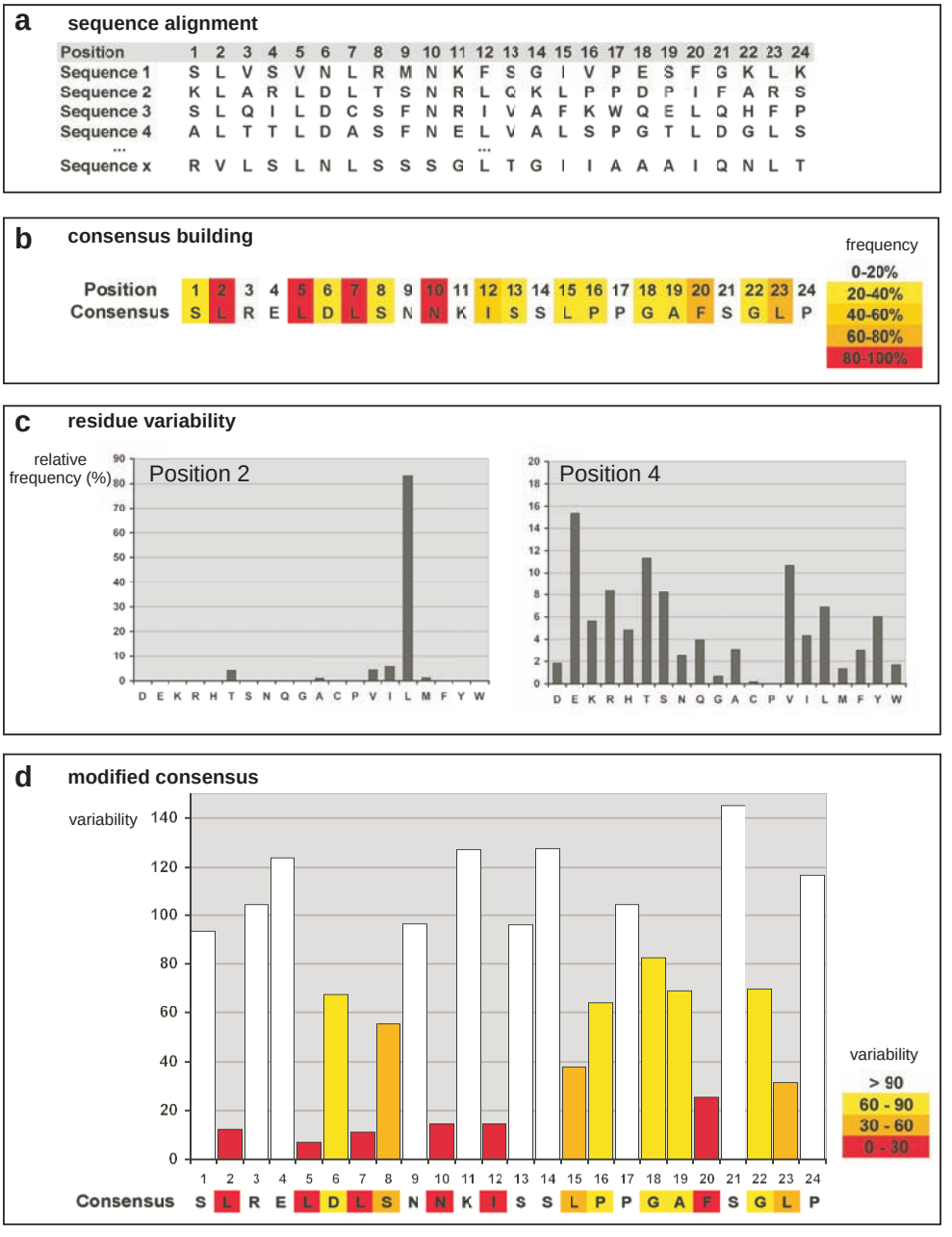

Fig. 39.2. Example of the analysis for deriving and analyzing a consensus sequence. (a) From a sequence alignment of 3077 sequences of 24 amino acid LRR motifs of the Pfam database (http://www.sanger.ac.uk/Software/Pfam/), the relative frequencies of amino acid residues at each position are calculated. (b) Based on the relative frequencies calculated from the alignment, a consensus sequence can be derived representing the most frequently

lowed by a comparison of these consensus sequences, distinct structural features of each group can be recognized in some cases.

The consensus concept has been applied successfully to a large variety of proteins and structural motifs to date. Important lessons for an effective application of the consensus approach can be learned from these studies, and we will therefore give a few examples to briefly discuss some of the advantages and limitations of the method.

39.3.1.2 **Examples**

There is always the concern that the stabilizing and destabilizing effects of introduced mutations will counterbalance each other and that the overall change in protein stability will be small. Steipe et al. [20] applied the method for the first time on immunoglobulin V_L domains and predicted 10 potentially stabilizing mutations. Six mutations were indeed stabilizing, three had no effect, and one was destabilizing. When applied to GroEL mini-chaperones, 34 predicted amino acid replacements were individually checked, out of which 13 were stabilizing, five showed no effect, and 16 were destabilizing [24]. Lehmann et al. [25] extended the approach to an entire protein. In a first set of experiments, 13 homologous sequences of a fungal phytase were used to build the consensus, and the resulting consensus enzyme showed an increase of 15–22 degrees in unfolding temperature and an increase of the temperature optimum for catalysis of 16–26 degrees compared with each of its parents. In a second set of experiments, additional mutations were predicted by simply adding more sequences to the alignment. By checking the effects of the individual mutations on thermal stability and combining mutations with positive effects, the unfolding temperature could be increased by an additional 21 degrees to 90 °C. No loss of catalytic activity of the enzyme was observed in any case. This work showed that the number of sequences used for the alignment is indeed an

occurring residue at each position. The color code is given on the right hand side of the panel. Residues occurring in more than 80% of all sequences at the respective position are colored in red. Based on these values, consensus sequences with a given homology threshold can be derived (not shown), i.e., with a higher threshold, more positions will be ''undefined.'' (c) Preferences at a given position are reflected not only by the absolute frequency but also by the total number of different amino acid types occurring at each position (residue variability). As an example, the relative frequencies of each amino acid are shown for the highly conserved position 2 and the highly variable position 4. By plotting the relative frequencies of amino acids at a particular position, preferences for certain amino acid types as well as ''forbidden'' residues can be identified. At position 2, a strong preference for leucine can be observed, and the occurrence of other residues is restricted mostly to hydrophobic side chains. At position 4, all residues are ''allowed'' except for proline, which is ''disallowed'' due to secondary structure propensity reasons. (d) By normalizing the relative frequency of the consensus amino acid with the number of ''allowed'' residues at a given position, a modified consensus sequence can be deduced. The variability V is calculated according to $V = 100 \times N/F$, where N is the total number of different residue types occurring at each position and F is the frequency of the most frequent residue in percentage.

important factor because it might help to optimize ambiguous positions. In addition, the observed large increase in thermal stability could not be attributed to the effect of one single amino acid substitution but rather to the synergistic effects of many replacements.

Even though these and other studies show clearly that the consensus approach allows one to predict stabilizing mutations with a rather high success rate in a rapid way, the effect of each predicted mutation carries some uncertainty, and it is possible that some may contribute destabilizing effects that can counterbalance the stabilizing ones. However, the effects of stabilizing mutations were often found to be additive. Therefore, instead of examining each mutation individually, it is often useful to combine groups of ''rather certain'' mutations and others that are more speculative.

The application of the consensus concept to families of repeat proteins [23, 26–28] represents, in some respects, a special case due to a number of favorable features. It can nevertheless illustrate the importance of some principles of the approach. The non-globular fold of repeat proteins consists of repeated motifs of 20–40 amino acids. Several results indicate that consensus repeat proteins are indeed much more stable than natural repeat proteins [29, 30]. Repeat proteins might represent an extreme case in which the principles of the consensus approach become very apparent. The structural entities (the repeat modules) are small and thus each protein contributes several repeats to the databases; the number of available sequences consequently becomes very large compared with other proteins. Therefore, a consensus sequence for a single repeat module can easily be assigned and ambiguous positions will occur with lower frequency in the statistical output (Figure 39.2). In addition, interactions that are present within or between several repeats will add to the free energy of folding multiple times, while problem spots would equally be potentiated. Therefore, effects on stability are likely to be consecutively added by introducing additional modules to the array. Even though more-detailed analyses are still needed, initial results pinpoint some of the structural reasons for the stability gains observed upon building a consensus in each of these studies. The regular arrangement of structural motifs gives rise to a more regular H-bonding pattern with a higher number of inter- and intra-repeat H bonds [30]. Loop insertions in natural repeat proteins that are likely to result in more flexible local regions are removed, thereby eliminating local centers of unfolding. In the left-handed helical and disallowed regions of the Ramachandran plot, glycine residues are always present in the consensus proteins, while they are avoided in other places by this design, where their flexibility is not needed and may be harmful to stability.

39.3.2 Structure-based Engineering

Structure-based engineering relies on a detailed analysis of 3D structures, followed by site-directed mutagenesis. We avoid the term ''rational'' engineering, as it would elicit expectations of perfect predictability and implicitly suggest that all other ap-

proaches are free of logical reasoning. In structure-based engineering, positions have to be identified at which suboptimal amino acids in the original sequences lead to a loss of stability. Subsequently it needs to be specified which amino acids should be introduced as a replacement. The *ab initio* prediction of protein structure, however, is still not a feasible task due to the multitude of potential interactions within the protein and between protein and solvent, which leads to an extremely high number of possible conformations and intermediates of similar energy [31]. Hence, a prerequisite for structure-based engineering is, next to experimentally determined structures, usually the existence of a large experimental dataset within a group of structural homologues that can be used as a basis for predictions. High-resolution structures are necessary to allow the estimation of possible conformational, energetic, and steric influences upon replacement of particular amino acid side chains and can thus help to avoid unfavorable strain in the resulting mutants. Because of the present efforts in the field of structural genomics, these structure-based approaches are likely to become even more important in the future. With this structural information in hand, the goal of designing more stable variants is then to pinpoint particular regions and positions associated with possible stability defects and to subsequently find a better solution to the problem. In contrast, semi-rational approaches like the previously discussed consensus concept are rather crude methods for introducing stabilizing features. Structural and energetic analysis can be used to reexamine the changes proposed by the consensus approach and to fine-tune the system to reintroduce structural features that might have been lost in the averaging process.

Proteins of hyperthermophilic organisms have been of special interest for examining the structural mechanisms of thermostabilization and have been contemplated as guides for the engineering of "problem" proteins for better properties. From a phenomenological point of view, the basis of increased thermostability is frequently set by a flattened ΔG-versus-T curve that is due to a smaller change of heat capacity upon unfolding (Figure 39.1) or by a kinetic stabilization that is due to a strong decrease in the rate of unfolding. The crucial question is, however, what the molecular differences are that give these proteins their favorable properties. Genome-wide comparisons between hyperthermophilic and mesophilic organisms with respect to amino acid composition did not yield any obvious common rules of how these effects are achieved [32]. Therefore, hope was placed on the increasing number of pairwise high-resolution structure comparisons of thermophilic proteins with their mesophilic counterparts. While they provided a more differentiated picture, a "global" rule still could not be derived. A few highly specific mutations are often enough to provide considerably stabilizing effects, but the additive effect of many small contributions, none of them dramatic by itself, may be the usual case. Moreover, rather than relying on one universal strategy, nature utilizes a variety of strategies for the thermal adaptation of proteins [33]. In fact, the list of stabilizing structural features in hyperthermophilic proteins reflects the diverse principles of protein stability and folding that protein engineers try to exploit and that will be discussed in this section. High-resolution structures of thermophilic proteins can thus provide a detailed view of how nature implements these principles

to create proteins of higher stability [34]. However, the lack of a unifying ''rule'' and the multitude of strategies nature uses provide an important lesson for protein engineers. Depending on the protein under investigation, the strategy of choice can be different, and even for a given protein there may be more than one optimal solution to the problem. Before choosing from the available set of strategies, the focus should therefore be on identifying potential ''weak points'' responsible for stability defects in a given protein structure.

We will now discuss some structural features associated with protein stability as well as strategies for altering these features towards more favorable biophysical properties. The given list of course lays no claim to completeness but should point out some important principles. Any replacement in a given sequence may have multiple effects on protein stability, and destabilizing effects can often outweigh the stabilizing ones. An assessment of potential destabilizing effects is therefore crucial. Wherever possible, references are made to the different forms of ''stability'' discussed in the Introduction. In the case study provided at the end of this section, an example will be given to demonstrate how consensus approaches and structural analysis can be combined to yield useful results.

39.3.2.1 Entropic Stabilization

An obvious strategy for increasing the free-energy difference between the folded and unfolded states, and thus the thermodynamic stability, is to decrease the entropy of the unfolded state. The underlying concept is to decrease the flexibility of the polypeptide chain, usually by introducing an additional intrachain linkage. Such entropic stabilization has become a common strategy for protein engineers. The prerequisite for success is that the mutations rendering the unfolded protein less flexible do not introduce unfavorable strain in the folded three-dimensional structure or result in any steric incompatibilities [35]. We now discuss several ways to achieve an entropic stabilization.

Introduction of Disulfide Bridges The introduction of additional disulfide bridges is a straightforward way of establishing an intrachain linkage to reduce the entropy of the unfolded state [36, 37]. The magnitude of the entropic effect is thought, as a crude approximation, to be proportional to the logarithm of the number of residues between the two bridged cysteines [38]. The spatial distance between the residues to be replaced with cysteines has to be evaluated with care in the model of the folded protein in order to prevent perturbations of the native structure upon formation of the disulfide bridge. It should be noted, however, that the energetic effect of additional disulfide bridges is not only entropic but also of a far more complex nature, giving rise to entropic as well as enthalpic contributions to the change in the free energy of folding [39, 40]. For example, an additional decrease in the free energy of folding can result from the reduced solvation energy of the unfolded state [40]. In contrast, a reduced solvation energy of the folded state would have the opposite effect, while residual structure in the denatured state would again push the equilibrium to the side of the folded protein. Because the disulfide bond itself is hydrophobic in nature, it is often engineered into the inte-

rior of the protein. This is not an easy task, as it can negatively affect core packing. Even though there are several examples of successful protein stabilization by introducing artificial disulfide bridges [41, 42], the complex energetic effects can also cause a destabilization of the protein [43]. Furthermore, the introduction of additional cysteines often results in a rather drastic decrease in folding efficiency, because incorrect and intermolecular disulfide formation can remove large portions of expressed protein by aggregation. Since disulfide formation does not occur in the cytoplasm, secretion to the bacterial periplasm or to the eukaryotic ER is required for functional expression, usually associated with lower yields than for the production of cytoplasmic proteins. Alternatively, if the protein is produced by refolding, redox conditions have to be adjusted, which can be difficult if the native protein also contains free cysteines.

Circularization An alternative approach with the same underlying concept is the circularization of proteins by fixing the loose N- and C-termini via a peptide bond. In addition to the entropic effect, the fixing of the loose ends can prevent local unfolding events occurring at the termini and thereby kinetically stabilize the native structure. With the discovery of inteins, which mediate protein-splicing reactions, a tool that allows the directed formation of peptide bonds between ends fused to different parts of the intein became available. Intein-mediated protein ligation has been used to covalently link the termini of β-lactamase, a protein that is especially amenable to this strategy due to the close proximity of its N- and C-termini [44]. In accordance with polymer theory, the thermal stability of the protein was enhanced by about 6 degrees, from 45 °C to 51 °C. For circularized DHFR [45] an increased half-life at elevated temperature was observed. The close proximity of the termini is of course a prerequisite for this procedure, and the stabilizing effect is likely to become marginal if the loose ends are linked via long unstructured loops. Similar to the situation upon introduction of artificial disulfide bridges, destabilizing enthalpic effects may negate the favorable entropic contribution [46]. In addition, low protein ligation efficiencies and difficulties in separating circular from linear forms of the protein often cause additional technical challenges. It remains to be seen whether this technology is robust enough for biotechnological or biomedical applications.

Shortening Solvent-exposed Loops Short, solvent-exposed loops are rather fixed in the native state, but a comparably large number of additional conformations become accessible in the unfolded state, while long loops have a large number of conformations also available in the native state. Thus, the shortening of loops should in principle lead to a relative decrease in the loss of conformational entropy upon folding. Conversely, increasing the loop lengths by insertion of glycine residues into the loops of the four-helix bundle protein Rop has indeed resulted in a strong and continuous decrease in thermodynamic stability [47]. In addition, loop shortening can have the effect of abolishing hot spots of local unfolding events and may result in kinetic stabilization. Even though it has become obvious that loop shortening or tying down of loops by external interactions is a common theme in

thermostable proteins of thermophilic organisms [48, 49], the strategy is often hard to realize for a given protein target, as the danger of introducing additional strain in the native state is high, and solvent-exposed loops are often important with respect to function.

Reduction of Chain Entropies By considering the conformational entropies of amino acid side chains, another strategy for decreasing the entropy of the unfolded state becomes apparent. Because of the five-membered-ring nature of the proline side chain, it not only restricts the possible conformations of the preceding residue but also can adopt only a few conformations itself. It therefore has the lowest conformational entropy of all amino acids [50]. In contrast, glycine, which has no side chain, has the highest conformational entropy. Substitutions of non-glycine residues with proline or the replacement of glycines by other residues should therefore reduce the entropy of the unfolded state.

Positions that allow substitutions with proline are, however, very rare. Because proline is poorly compatible with α-helices and incompatible with β-strands, the position of a new proline must not be part of these secondary structure elements. At most positions in the native structure, the respective torsion angles will be incompatible, and the mutations are thus very much restricted to loop and turn regions. Again, care should be taken not to remove any favorable interactions of the replaced amino acid side chain [51]. In order to examine in advance whether the respective site is permissive for a substitution with proline, the dihedral angles of the site can be checked and should lie in the range of ϕ/ψ -50 to $-80/120$ to 180 or, alternatively, -50 to $-70/-10$ to -50.

Similar restrictions apply for the replacement of glycines with any other residue. In many cases this will create steric overlaps, and such negative structural crowding effects can outweigh the positive energetic benefits.

39.3.2.2 Hydrophobic Core Packing

Exposed residues are often directly involved in ligand or substrate binding and therefore often play a functional role. In contrast, the residues of a protein's interior usually play mostly a structural role, and the associated hydrophobic effect is thought to be the main driving force of protein folding and thermodynamic stability.

In known structures the core residues fill almost the entire interior space, provide many favorable van der Waals interactions, and maximize hydrophobic stabilization by exclusion of the solvent. In principle, an increase in thermodynamic stability of 4–8 kJ mol^{-1} can be achieved for each additional methylene group buried [52]. Paradoxically, the importance of the hydrophobic effect for folding and stability of proteins simultaneously limits its applicability for protein engineering. Because the hydrophobic core is already densely packed in almost all native proteins, most changes here will create over-packing or packing defects, causing an overall destabilization rather than an improvement in stability. In addition, even subtle changes of core residues can lead to a rearrangement of external residues and thereby alter the functional properties of the protein [53]. Care should also be taken to avoid the introduction of conformational strain by the mutation of core

residues, as destabilizing effects from a strained conformation can sometimes compensate the energetic gain of an increase in buried hydrophobic volume [54]. Improvement of core packing must therefore be based on analyses made from high-resolution structural information in combination with sequence comparisons. This allows one to specifically look for cavities in the core that indicate imperfect packing. If the hydrophobic surface area around the cavity is large, additional van der Waals interactions can be provided by the introduction of sterically fitting alkyl or aryl groups from hydrophobic side chains, thereby decreasing the size of the cavity [55, 56].

39.3.2.3 **Charge Interactions**

Oppositely charged amino acid residues, if appropriately positioned, have the potential to form salt bridges, whereas like-charged residues lead to repulsions. The magnitude of the effect of charge-charge interactions on overall protein stability is still a matter of discussion [57]. In the case of ionic interactions between side chains buried in the hydrophobic core, the high energetic cost of transferring charged ions from aqueous solution to the low-dielectric interior of the protein also has to be taken into account. If a single charge were buried in a protein, which would be extremely rare in a natural protein, the design of an ion pair would be very attractive. However, if a hydrophobic pair were to be replaced by an ion pair, the resulting energy would have to be higher than the loss of the previous pair plus the cost of burying the charge. Nevertheless, the high contribution of buried salt bridges to the overall stability of the native protein structure underlines their potential for introducing additional stability [58]. The optimal spatial arrangement of the interacting side chains and their respective charges is, however, crucial. Moreover, buried charged side chains are often not only part of interacting charge pairs but also part of complex charge clusters built from many side chains, which are able to magnify the effect.

Similar rules apply for the interactions of charged residues on the protein surface. Only the perfect arrangement of charges seems to be able to make up for the desolvation penalty that has to be paid upon formation of a salt bridge. The effect on thermal stability, however, can be drastic. Increasing the free energy of unfolding by the changing of charges includes maximizing the number of salt bridges and, equally important, the removal of repulsive interactions [59], which are not uncommon in natural proteins. Predictions on a structural basis can be difficult due to the often higher flexibility of side chains on the protein surface, but simple models that allow predictions about potential stabilizing and destabilizing surface charges can be used [60]. The key is to consider not only nearest neighbors but also a whole network of charges that have to optimally interact and avoid repulsions. Because the surface charge distribution can have a huge impact on stability, but is defined by many residues at different positions, these residues are also a valuable target to be combined with selection techniques as discussed in Section 39.4.

A special case of electrostatic interaction is the ''helix dipole.'' By reducing the net partial charges at the helical ends through placement of side-chains, which pro-

ductively interact with the helix dipole, the helical structure is stabilized [61]. Introduction of negatively charged residues at the N-terminal end and positively charged residues at the C-terminal end leads to this stabilizing effect. The provided stability gain is, however, marginal (less than 4 kJ mol^{-1}).

39.3.2.4 Hydrogen Bonding

There was no initial reason to believe that intrachain hydrogen bonds in the native state would be more energetic than those of the unfolded chain to water [5]. By including terms of entropy change of the solvent and additional van der Waals interactions upon polar group burial, however, the positive contribution of hydrogen bonding to protein stability has become generally accepted [58, 62]. Despite this ongoing discussion, hydrogen-bonding patterns are a highly valuable target for the stability engineering of proteins. Because engineering deals with improving folded proteins, the major concern has to be how to satisfy the existing hydrogen-bonding network in a structural context. The basis for this endeavor is structural information of high resolution, and the most lucrative goal is to identify potential residues that represent buried but unsatisfied donors of hydrogen bonds. Site-directed mutagenesis of a nearby residue to provide a hydrogen-bonding acceptor can cause a stability gain in the range of 2–10 kJ mol^{-1}, depending on the geometry and other compensating effects [63, 64].

A special structural context that can provide significant additional stabilization by either hydrogen bonds or ionic interactions is the anchoring of relatively loose structural elements like loop structures or the N- and C-termini, thereby tightening ''hot spots'' of local unfolding [49, 65].

39.3.2.5 Disallowed Phi-Psi Angles

The stereochemistry of the polypeptide backbone can be defined by the dihedral angles ϕ and ψ, and any individual residue in a structure is defined by a single set of ϕ, ψ values. For conformational analysis of protein structures, the Ramachandran plot representing the dihedral angle space is an excellent starting point [66]. The ϕ, ψ values of amino acid residues in protein structures usually reside in three preferred or ''allowed'' regions of the Ramachandran plot, called right-handed helical, extended, and left-handed helical. The right-handed and extended conformations correspond to α-helix and β-strand secondary structures, respectively, and the vast majority of non-glycine residues lie within these two regions. The left-handed region corresponds to structural features at the termini of secondary structure elements and describes regions involved in the reversal of the polypeptide chain. There is a high preference in this region for glycine residues, as the β-carbons of non-glycine residues can sterically interact with the polypeptide backbone, resulting in unfavorable energies. In some cases, the substitution of non-glycine residues by glycines in the left-handed helical region increases thermodynamic stability (up to 8 kJ mol^{-1} in RNase H) [67]. Although the strict introduction of glycines in such positions is an important point to consider for de novo protein design, it does not represent a general rule for stabilizing the native states of proteins. In

some cases, the energy penalty for the accommodation of unfavorable strain can be offset by lost unfavorable or new favorable local interactions, such as hydrogen bonding or hydrophobic interactions. Some replacements of this kind can therefore even lead to destabilization rather than stabilization [68].

The same rules apply in principle to the disallowed regions of the Ramachandran plot. Steric clashes result in a high energetic cost in the folded structure, especially for non-glycine residues in all disallowed regions. Stabilizing mutations to glycine have been introduced with energy gains of up to 18 kJ mol^{-1} [69]. It has been noted, however, that certain non-glycine residues also have propensities to occur in the disallowed regions – such as Asn and Ala in the type II′ turn region – and the energetic cost of their occurrences is often low [70]. Other residues found in the disallowed regions are small polar residues [71] that compensate for the energy cost by making additional hydrogen bonds. Unfavorable conformations often occur in very short loops [72], where the rest of the structure may constrain the loop efficiently, and interactions with the solvent may also offset the energy costs.

Conformational analysis by the Ramachandran plot therefore provides a convenient and fast way to assess possible conformational strain in the tertiary structure associated with particular target residues. However, a close inspection of possible side chain interactions is required, and the analysis should be extended to identify potential compensating features of the residues to be replaced.

39.3.2.6 **Local Secondary Structure Propensities**

Effects on the overall stability of a protein can also be influenced by the respective secondary structure propensities of amino acid residues for the α-helical and β-sheet conformations. However, these effects are usually marginal. Nevertheless, even at the expense of other favorable trends, such as avoiding the exposure of hydrophobic side chains to the solvent, a given residue is often favored at a certain position due to its secondary structure propensity [73]. If a particular secondary structure element does not form efficiently, many interactions between this element and other parts of the protein can be lost. The energetic consequences and the influences on folding efficiency are, however, hard to predict at this point.

39.3.2.7 **Exposed Hydrophobic Side Chains**

The removal of exposed hydrophobic side chains increases the polar surface of a protein. Such mutations are not likely to affect thermodynamic stability but presumably do affect the folding efficiency by influencing the rate of aggregation of intermediates. Interestingly, they also do not affect the solubility per se (the amount of native protein that can be dissolved in buffer) and seem to act mostly on folding intermediates [74]. Because of lateral interactions, e.g., between neighboring loops, partially exposed hydrophobic amino acids can even increase stability. It must be kept in mind however, that not only the aggregation pathway, but also the stabilities of folding intermediates are an important parameter for kinetic stability, which can possibly be influenced by the existence of exposed hydrophobic side chains. Moreover, hydrophobic cavities at the protein surface are often in-

volved in specific binding functions of the protein, and the removal of these "functional hot spots" has to be avoided. Therefore, the hydrophobicity of the protein surface must be carefully balanced.

39.3.2.8 Inter-domain Interactions

In proteins consisting of more than one domain, additional principles come into play. The overall stability not only reflects the intrinsic stabilities of the single domains but is also influenced by the stability of the interface of the domains in cases where they are interacting with each other. Stabilization of this interface can be achieved mainly by increasing and optimizing the hydrophobic surface area of the interface. Because hydrophobic side chains at the interface are usually exposed during folding and transient opening of the domain interface, a tradeoff between interface stability and folding efficiency is often observed. Additional dramatic effects on stability can be observed in cases where the two domains exhibit very different intrinsic stabilities [75]. In such a scenario, the unfolding of the protein and the loss of function are strongly related to the unfolding of the less stable domain [76]. An important aspect of kinetic stabilization can be observed in two-domain proteins, where one domain can slow down the unfolding, and therefore the aggregation, of the other. Thus, the native state becomes kinetically stabilized in the assembly and a stable domain interface reduces the extent of its transient openings and, thereby, the resulting exposure of hydrophobic patches that would favor aggregation. Alternatively, covalent cross-links (e.g., disulfide bonds) between the interfaces of multimeric proteins can be introduced. For example, the introduction of disulfide bonds between the interfaces of *Lactobacillus* thymidylate synthase not only increases their thermal stability but also leads to reversible thermal unfolding [77].

39.3.3 Case Study: Combining Consensus Design and Rational Engineering to Yield Antibodies with Favorable Biophysical Properties

The following example illustrates how consensus approaches, rational design, and experimental data can be combined in a synergistic fashion to iteratively optimize biophysical properties.

The smallest form of an antibody able to bind the antigen in the same manner as the whole IgG consists of two domains, the variable domain of the heavy chain (V_H) and the variable domain of the light chain (V_L). Both domains interact with each other via an interfacial region of highly hydrophobic character. In single-chain Fv (scFv) antibody fragments, the two domains are covalently linked by a flexible linker region of typically 15–20 amino acids (Figure 39.3a). The binding site for the antigen usually involves three loop regions in each of the domains, named complementarity-determining regions (CDRs). Antibodies that are based on human antibody sequences possess great potential for many medical applications, either directly as an antibody fragment or after reconstructing an IgG [78]. Antibody fragments can be expressed in a convenient manner in *E. coli*, thereby providing

rapid access to these proteins [79]. Nevertheless, there are often drastic differences between individual antibodies concerning their expression yield and their stabilities. Ideally, the recombinant antibodies would all provide favorable biophysical properties.

The starting point for such recombinant antibodies is a library. One fully synthetic library of this kind, the human combinatorial antibody library (HuCAL), was designed based on the consensus concept [22]. Based on human antibody germ-line sequences, several sequence families were created. Importantly, instead of averaging over all possible human antibody sequences, the consensus sequences were built for each family separately, resulting in seven consensus frameworks for V_H (V_H1a, V_H1b, V_H2, V_H3, V_H4, V_H5, and V_H6) and seven frameworks for V_L ($V_\kappa1$, $V_\kappa2$, $V_\kappa3$, $V_\kappa4$, $V_\lambda1$, $V_\lambda2$, and $V_\lambda3$). This diversity is important, as the use of different frameworks allows a variety of non-CDR contacts to the target, thereby greatly increasing the range of targets being recognized. By using this strategy, each human V_H and V_L subfamily that is frequently used during an immune response is represented by one consensus framework, and thus the immune response is closely mimicked. The consensus building was further restricted to the framework regions, while the CDRs were diversified in a manner guided by structure. Thereby, functional diversity is maintained in optimized sets of frameworks.

Instead of fully relying on the statistical output of the consensus building, structural modeling was employed in order to decrease the risk of disrupting interactions between certain amino acid residues that might be in contact with each other in the three-dimensional structure. Because many structures of antibody domains are available, the modeled structures of each framework family could be compared with the respective natural template structures. The models were checked according to several principles, which have been outlined in the preceding section. At this point the models were mostly checked for whether the interactions in natural antibody domains were correctly recreated. The consensus sequence models were inspected for any unfavorable strain in the structures, represented by unfavorable regions of the Ramachandran plot or any obvious cavities in the hydrophobic core. Moreover, the sequences were checked for the existence of residues already known to be involved in conserved intra-domain interaction patterns – such as conserved charge clusters and hydrogen-bonding patterns – as well as for exposed hydrophobic side chains known to decrease expression levels. Nevertheless, differences between the natural subclasses became apparent in the models.

Empirical results had suggested that certain natural framework types display more favorable stabilities and expression levels than others. These differences are already existing in the original natural human germ-line sequences. The intrinsic differences in terms of biophysical properties for each subtype were then experimentally explored in a systematic fashion, first on single domains, then on scFv fragments [13]. The experiments confirmed the observed trends, showing that V_H3 displays the highest thermodynamic stability and soluble expression level, when expressed as an individual domain, among all V_H subtypes. In contrast, V_H2, V_H4, and V_H6 display the least favorable properties in terms of stability, folding yield, and the tendency to aggregate. For the V_L domains, members of the V_κ

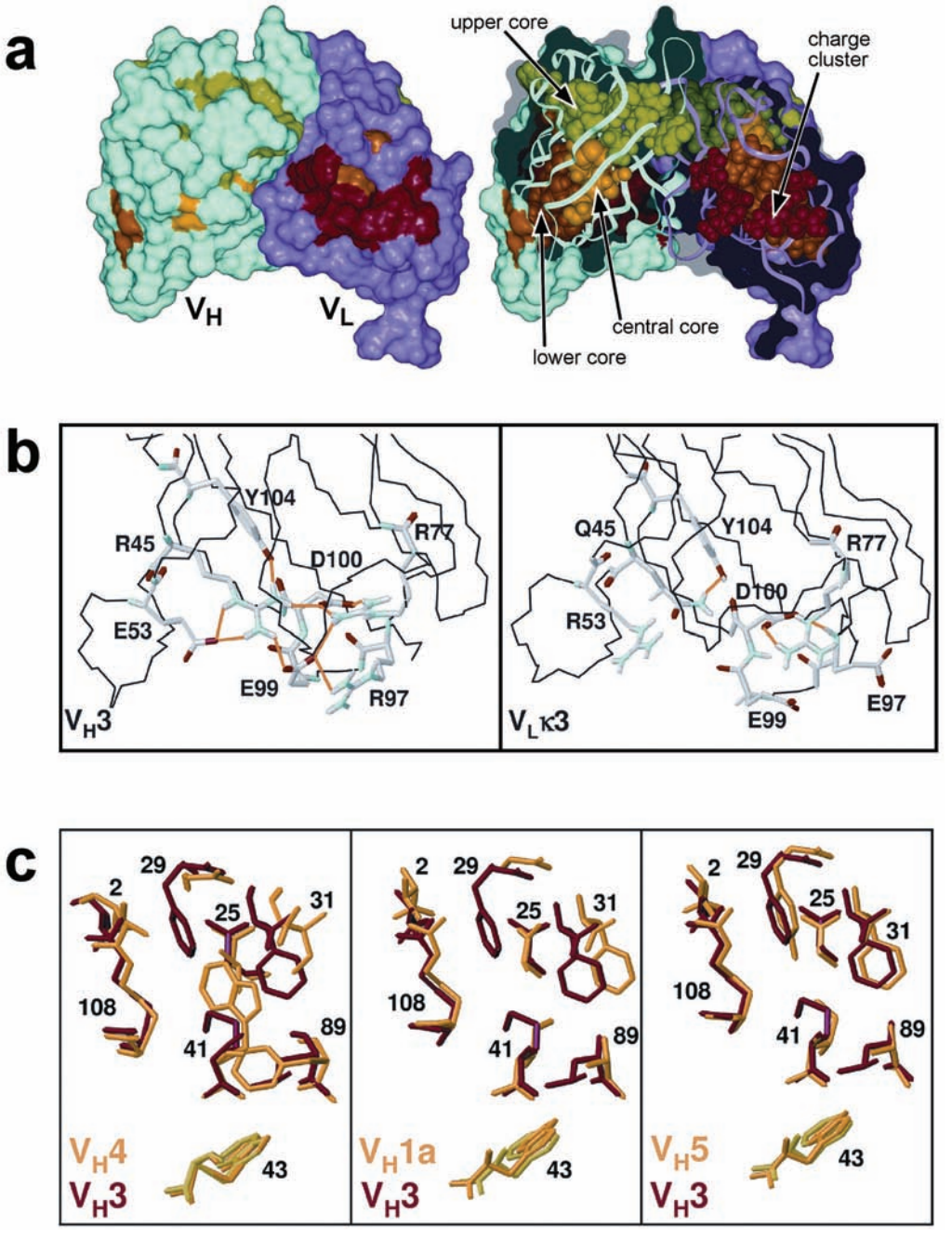

Fig. 39.3. (a) Structure of an antibody Fv fragment consisting of the variable heavy chain (V_H) and the variable light chain (V_L). Each domain V_H and V_L is characterized by three hydrophobic core regions (upper [green], central [yellow], and lower [orange] core) and a charge cluster at the base of each domain (red). Even though the residues defining these

subtypes showed slightly higher stabilities and expression yields than the V_λ subtypes, but the behavior was much more homogenous overall. In order to trace back these differences to the structural level, the model structures of the different subtypes were compared with each other. Several structural features can be invoked to explain the extraordinary stability of V_H3 domains in comparison with the even-numbered V_H subtypes.

First, differences in the hydrogen-bonding networks have an influence on the thermodynamic stabilities. Long-range interactions involving several residues are concentrated in a charge cluster at the base of V_H domains to establish a complex interaction network. In V_H3 domains the ionic and hydrogen-bonding interactions within this charge cluster are very well satisfied, whereas fewer interactions are observed at the analogous positions in other subtypes (Figure 39.3b). Corresponding to the subclass, different hydrogen-bonding networks are formed in the charge cluster of V_H domains. Some of these networks are less extended and contain a smaller number of interactions than in V_H3.

Additionally, based on the residues at three different positions in the first β-strand of the V_H domains, the domains can be classified into four different structural subtypes with respect to their conformations in the first framework region [80]. Mutations bringing together incompatible residues and thus "mixing" subtypes have previously been shown to have a large unfavorable effect on the stability of the whole scFv [81].

Also, clear differences can be observed for hydrophobic core packing of the family subtypes. The upper core region of V_H3 is densely packed, whereas cavities can be identified in V_H4, V_H1a, and V_H5 on the basis of structural alignments (Figure 39.3c). In the lower core, two of the stable domains have an aromatic residue, while the others do not.

Finally, a comparison of the Ramachandran plots showed additional non-glycine residues with positive ϕ-angles and residues with higher secondary structure pro-

regions are conserved within the same germline family, these sequence motifs differ between different germ-line families. (b) Arrangement of the residues defining the charge cluster of V_H3 and $V_\kappa3$ domains [13]. Importantly, the charge cluster consists of a network of buried charges and hydrogen bonds rather than pairwise interactions between individual residues. (c) Furthermore, subtype-dependent packing differences occur. As an example, the residues defining the upper hydrophobic core region of different human V_H subtypes are shown as structural superpositions. Structural alignments are shown of V_H4 (PDB entry 1DHV), V_H1a (1DHA), and V_H5 (1DHW) [22], with the most stable framework, V_H3 (1DHU) (left panel). While the upper core residues of V_H3 are densely packed, cavities occur for the other subtypes. In the least stable subtypes, V_H4 and V_H6, the bulky aromatic residues Phe29 and Phe31 are replaced by smaller residues, and the created space is only partly filled up by compensating residues Trp41 and Val25. The loss of the phenyl ring by replacement with Gly in V_H1a (middle panel) as well as the substitution of Leu89 by Ala are not compensated for by larger side chains at other positions, thereby creating hydrophobic cavities. The same is true for position 89 in V_H5 (right panel). Adapted from Ewert et al. [13].

pensity at certain positions for the even-numbered subtypes compared with the odd-numbered ones.

The immediate question was, therefore, whether the results of this structural trouble-shooting could be used to project favorable properties of V_H3 domains onto the less stable subtypes and thereby add another step to the optimization of antibody sequences while maintaining the structural diversity of the immune system. Instead of using the stable V_H3 framework exclusively, resulting in a loss of diversity, some point mutations might be enough to correct some of the shortcomings of the less stable domains.

Based on these comparisons, the mutation of six residues in a scFv containing a V_H6 framework led to an overall increase in thermodynamic stability of 20 kJ mol^{-1} and a fourfold increase in soluble expression yield [73], indeed bringing this framework to the level of V_H3. The effects of the single mutations on stability were almost fully additive, while the effects of folding efficiency (soluble expression yield) were only qualitatively additive. The most dramatic effects on thermodynamic stability were obtained by mutations removing an unsatisfied H-bond donor in the hydrophobic core and introducing glycines at positions with positive ϕ-angles. Individually, all mutations, except the one in the hydrophobic core, led to slight increases in soluble expression yield. Interestingly, one mutation that removed a hydrophilic, solvent-exposed glutamine residue by a replacement with hydrophobic valine on the basis of higher secondary structure propensity also significantly increased the expression yield, possibly since valine secures this stretch to be in β-sheet structure.

In antibodies, disulfide bond engineering has also been investigated. Optimized disulfide bonds engineered between V_H and V_L indeed significantly increased the half-life of an Fv fragment at 37 °C [82]. This strategy was subsequently extended to interchain disulfides in generic framework positions [83]. Even more stable proteins can be obtained by combining the single-chain Fv approach with the engineered disulfide [84, 85]. It should be pointed out, however, that the additional inter-domain disulfide significantly reduces the yield of folded protein when produced in the bacterial periplasm, and such proteins have to be prepared by in vitro refolding. Therefore, the additional disulfides are not ideal for antibody libraries; instead, optimized frameworks have shown the greatest promise for combining diversity with stability.

In summary, the consensus concept provides a convenient tool for proceeding with large steps in sequence space and a high probability of accumulating features that are favorable for higher stability. In many cases, structural analysis can serve as a trouble-shooting tool to identify shortcomings that might have been created by the consensus-building process or, as in the case of the antibodies described here, that are inherent to the natural sequence. In addition, it serves to rank the potential mutations identified by the consensus approach, keeping the mutational load on the target molecule to a minimum. Experimental data are important not only to validate these results but also to give important hints for future design approaches. Many entries in the table of experimental antibody stability data linked to mutations have come from directed evolution experiments. By combining

semi-rational and rational approaches with experimental data, optimization of biophysical properties can be achieved in an iterative fashion. This interplay of experiment and structural analysis can therefore be an effective way to probe the vast sequence space in a systematic manner in order to find the valleys of free energy.

39.4 The Selection and Evolution Approach

39.4.1 Principles

The previous section may have led to the impression that mutations enhancing the biophysical properties of proteins can rapidly be identified. In the highlighted case of antibody domains, only the wealth of structural data and empirical measurements available allowed predictions with a high probability of success. Some of the empirical data used successfully for structure-based engineering have come, paradoxically, from directed evolution experiments (see Section 39.3.3). Despite the rapidly increasing amount of structural data and the better understanding of folding mechanisms of proteins, the effects of introduced mutations still cannot be predicted with a high degree of accuracy in most cases. The main reason is that even slight alterations in the primary sequence can lead to profound conformational changes in tertiary or quaternary structure; consequently, structural predictions have to be very accurate and usually must be backed up by empirical data.

Because rational engineering uses site-directed mutagenesis followed by biophysical investigation to probe the effects of specific amino acid substitutions, it becomes very labor-intensive if many mutants have to be checked individually and if no additional hints are available. Additionally, as soon as small synergistic effects of several mutations need to be checked, the combinatorial explosion rapidly exceeds the sample number that can be handled efficiently. More importantly, the restriction to certain target residues automatically excludes alternative solutions to a given problem that may not have been obvious by the initial analysis. For example, affinity improvement of a protein to its binding partner is often achieved more efficiently by slight spatial adjustments of residues directly involved in binding, rather than by substitution of these residues. This kind of spatial adjustment can be caused by mutation of residues whose location in the native structure is further away from the actual binding site (so-called ''second-sphere mutations'') [86]. Today, it is almost impossible to predict this kind of mutation by rational means.

When it comes to stability engineering of proteins, the problems associated with rational design procedures are even intensified. First, because the energetic contributions of single-site mutations are usually small, the need to sample multiple mutants – in which synergistic effects of several mutations are combined – is more acute. Second, the factors and principles responsible for the overall stability of a native protein are still far from being completely understood, and a multitude of different forces and interactions contribute to it. A complete analysis will have to

consider not only the interaction network of the native protein but also the effects on the denatured state. Additionally, potential aggregation pathways will have to be considered. Even simple substitutions like the ones discussed in the previous sections often make contributions to the entropy as well as the enthalpy of the folded and unfolded states, including the solvent in either state. Third, because rational approaches always rely on the current theoretical knowledge, new principles underlying protein stability will rarely be uncovered. In any case, rational engineering requires a clear definition of the problem by the investigator in order to find a solution. Ironically, in the field of protein engineering, the exact definition of the problem is often the problem itself.

Thus, to overcome these limitations, an experimental setup is needed that allows the creation of a vast number of variants of a given protein and that subsequently can identify ''superior'' molecules that best fulfill a desired property. Nature samples the vast sequence space by the strategy of Darwinian evolution, a cyclic iteration of randomization and selection. Nature thereby adapts proteins to fulfill a function under the given environmental conditions. Recent developments in molecular biology have made it possible to mimic Darwinian evolution in a reasonable time in vitro. Not only has this ''evolutionary approach'' become the most powerful method to date for engineering proteins towards a desired property, but it also provides new insights into the mechanisms and principles that are responsible for this property. However, as has been illustrated in the case study on antibodies, such experiments can be used not only to solve a particular problem but also to gather information about which residues tend to become enriched in particular positions. This again provides a database for rational engineering.

Many different selection and evolution strategies have been developed in recent years, but all of them have several features in common that reflect the principles of Darwinian evolution. The starting point is the generation of a genetic library of mutants derived from the wild-type sequence of the protein under examination. Several methods exist to create sequence diversity. In error-prone PCR, the error rate of polymerases is increased by performing the PCR reaction in the presence of deoxynucleotide analogues or in the presence of other metal ions. By using bacterial mutator strains, which are characterized by deficient DNA repair systems, random mutations are introduced during DNA amplification in the bacterial cell, albeit usually at a lower frequency [87]. In DNA shuffling, which mimics the natural process of sexual recombination, genes are randomly fragmented by nuclease digestion and reassembled by a PCR reaction in which homologous fragments act as primers for each other [88] (Figure 39.4). The staggered extension process [89] is another possibility to obtain recombined genes in vitro. Here, the polymerase-catalyzed extension of template sequences is extremely abbreviated, and repeated cycles of denaturation and extension lead to several template switches – thereby recombining elements from different genes – before the extension finally yields full-length products. Additionally, techniques are available to focus the diversity to certain regions on the whole gene, such as the use of degenerate primers in PCR or the ''doping'' of a shuffling reaction with degenerate primers. Depending on the problem and the sequence under investigation, each of these methods has its

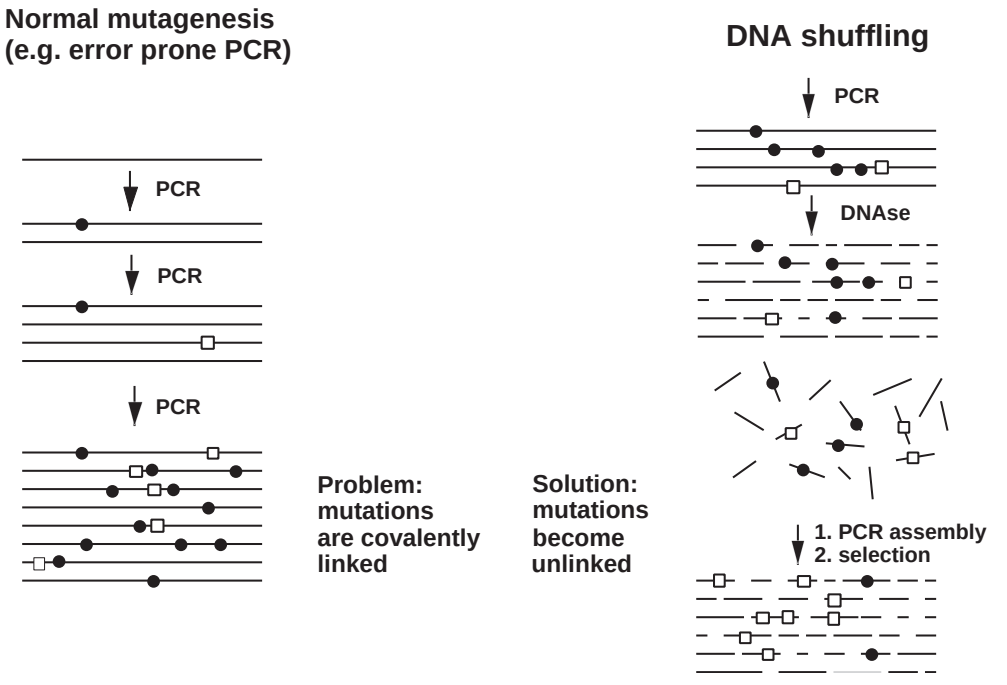

Fig. 39.4. Methods to create genetic diversity by biochemical means. On the left, error-prone PCR (see text) is depicted schematically. Two types of mutations are shown: favorable ones (open squares) and unfavorable ones (closed circles). In successive cycles of PCR, more mutations of each are introduced, and usually molecules will contain some of either type. Thus, the beneficial effect of the favorable mutations can be completely obscured by the presence of unfavorable ones, if the error rate is too high. Therefore, this method is most successful if it is not used at too high an error rate. On the right, DNA shuffling according to Stemmer [88] is shown. A short DNAse digestion breaks up the DNA into small pieces, and PCR is used to reassemble the gene. Thereby, mutations are ''crossed'' and genes with largely favorable mutations can be obtained that can be enriched by selection. Nevertheless, successful evolution experiments have been carried out with either method.

advantages and disadvantages. In any case, the generated library should obey two major criteria: it must be diverse enough to contain individual sequences with beneficial mutations, and it should be of high enough quality to reduce the experimental ''noise'' (such as sequences with stop codons or frameshifts) in the subsequent selection experiment [90].

A primary prerequisite of any selection system is the coupling of the genotype (the gene sequence) and phenotype (the respective protein displaying the properties) of any individual library member. Briefly, this can be done by two strategies. Either the gene and the protein need to be compartmentalized in cells or artificial compartments, such that the ''improved'' phenotype stays connected to the altered gene, or the protein has to be physically coupled to the gene, such that they can be isolated as a particle containing both gene and protein (Figure 39.5). By selecting

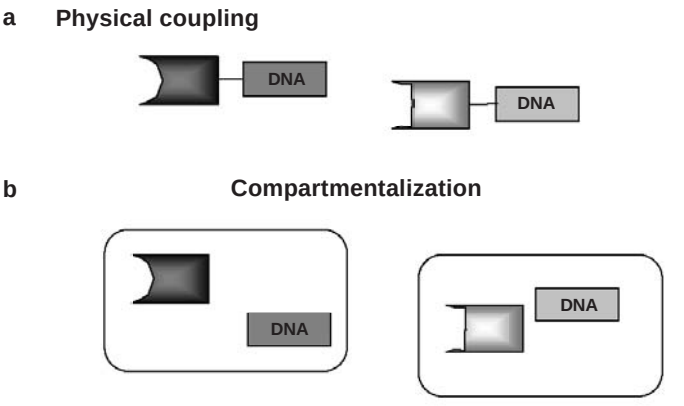

Fig. 39.5. Two principal strategies to link phenotype and genotype are depicted. The genetic material must be connected in a unique way to the protein, which defines the phenotype, such that the gene encoding the valuable mutation can be selectively amplified. A collection of two mutant proteins and mutant genes is shown (light gray and dark gray). (a) This connection can be realized through a direct link (e.g., in phage display or ribosome display), as shown on the top. In this case, all assemblies can freely diffuse in the same volume and the selection must filter out those proteins with the desired function, e.g., by binding to a ligand. (b) Alternatively, gene and protein must be in the same compartment. In nature, this is realized in cells, and microbial cells can be manipulated so that each takes up one variant of a mutant collection. The key is to identify the improved phenotype. This can be done by screening (individual assays on cells) or selection (giving cells with the desired property of the protein a growth advantage). Rather than natural cells, water-in-oil emulsions can be used to create artificial compartments of small water droplets in an oil phase. Usually, the emulsion must be broken and the proteins must be selected by binding to identify the one with the desired phenotype. For details, see text.

the proteins displaying the desired properties, the linked gene sequence can be inherited and amplified subsequently. The various selection technologies differ mainly in the way this physical linkage or compartmentalization is achieved. This will be discussed in more detail in the following section. The library must then be screened or subjected to selection for a certain function, and a defined selection pressure can be applied to direct the selection towards a molecular quantity of interest.

It is necessary at this point to discriminate between ''screening'' and ''selection.'' Screening methods examine individual members of a library for a given property (e.g., catalytic activity or solubility). For certain properties, screening is often the only way to go. The number of mutants to be screened in a reasonable time depends on the versatility of the screening method. Despite constant progress in automation and miniaturization, even the best screens to date usually do not allow assessment of more than 10^6 variants in a reasonable time. In contrast, selection methods force the single library members to compete with each other, and members that best fulfill the specified criteria are enriched. Often, the selection is based

on the binding of particular variants to an immobilized ligand. Note that the binding is only a ''surrogate quantity'' of the real property to be improved. The basis for a successful enrichment is an efficient counter-selection of variants that do not possess properties fulfilling these criteria. Especially during the selection of proteins for higher stability, an efficient counter-selection, in addition to the correct choice of the applied selection pressure, is one of the major experimental challenges [91].

The basic rule of screening and selection technology describes the importance of assigning the correct selection pressure. This has been succinctly phrased: ''You only get what you screen for!'' [92]. An analogous statement can be made for selection. Even though the rule sounds plausible, it is often difficult to translate this statement into an experimental setup, because an additional complication is introduced by the fact that an explicit selection pressure towards just one property is impossible to realize. Depending on the selection procedure used, more than one molecular property will have an influence on the enrichment process, including, for example, affinity or catalytic activity, thermodynamic stability, folding efficiency, and toxicity of the respective molecule. The outcome of the selection experiment will therefore always be a ''compromise solution'' with respect to the weighting of many properties in a given experimental setup. Assigning the right selection pressure therefore means biasing the selection towards a certain property, rather than exclusively altering this property. For these reasons we will discuss the application of the various selection technologies with an emphasis on the available selection pressures for stability engineering. Some of the described methods and examples will be based on mere screening of library members, but the main focus will be on the selection for favorable protein variants.

Choosing the appropriate selection pressure is just one side of the coin. The proper adjustment of its strength is another important factor. If the selection pressure on the system is too low, molecules with the desired properties will be lost in the background noise of the experiment – i.e., they are not enriched. On the other hand, if the selection pressure is too stringent, even the best variants might not pass the ''survival threshold.''

The genes of variants that survive the applied selection pressures are subsequently amplified and subjected to another so-called ''round of selection.'' This either can be performed in the absence of further mutagenesis to simply enrich the best members of the initial library (which is constant) or, to completely mimic the Darwinian principle, the selected members can be subjected to alternating rounds of randomization or recombination before subsequent selection, leading to an adaptation of the library from round to round. However, as most of the mutations will be non-beneficial, care has to be taken that the mutation rate is low enough to allow successful enrichment of improved members and not to extinguish the whole population. We use the terms ''combinatorial selection'' for a process in the absence of such mutations and ''evolutionary selection'' for a process that includes such mutations.

It has been pointed out that the method of DNA family shuffling is in some respects similar to the consensus approach because it combines gene fragments

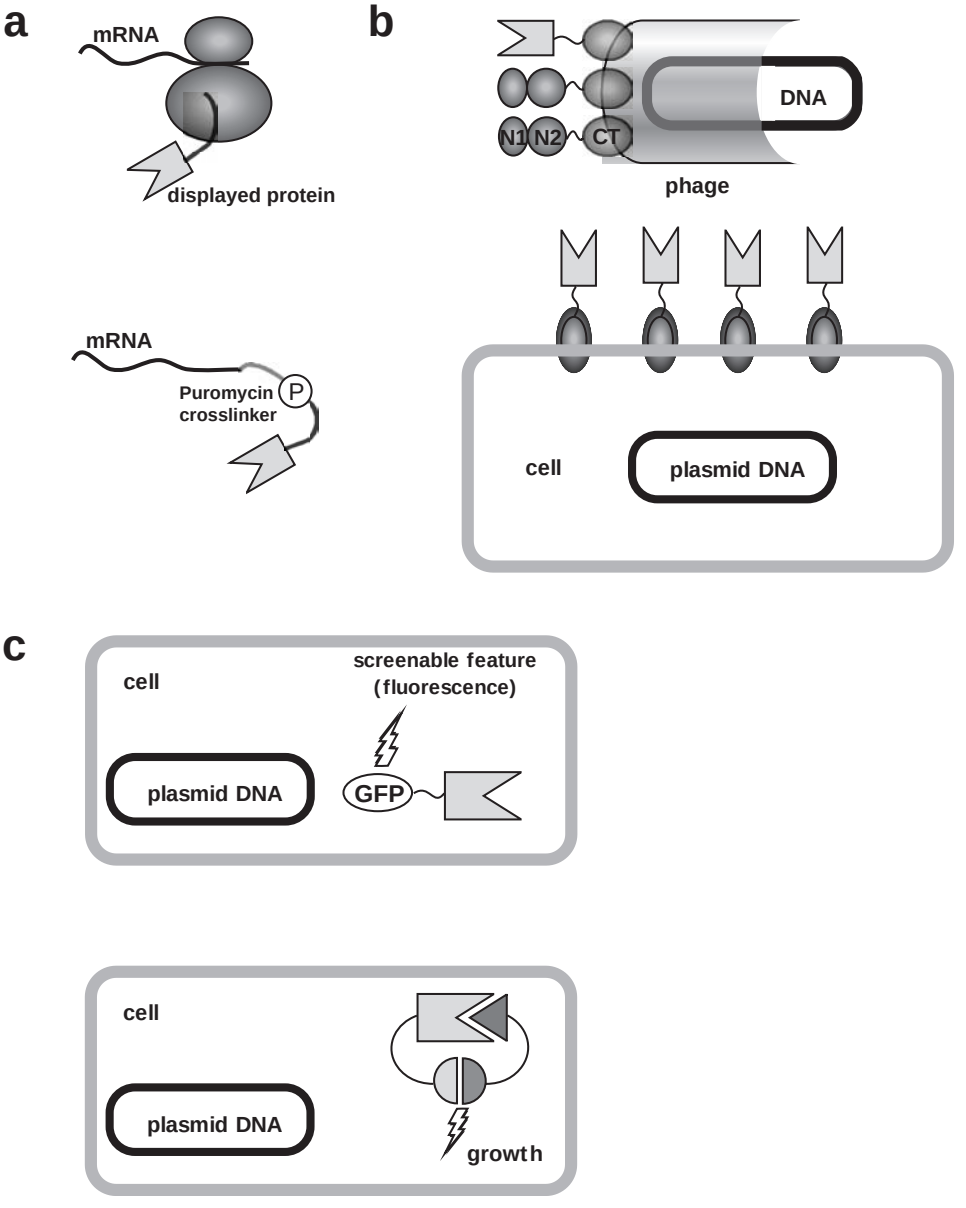

Fig. 39.6. Common display systems used for selection for enhanced biophysical properties. In in vitro display technologies (a), the proteins are produced by in vitro translation, and protein production does not rely on a host organism. The displayed proteins are linked to RNA either by stabilized ternary complexes (ribosome display, upper panel) or by a covalent puromycin cross-linker (mRNA display, lower panel), thereby establishing the genotype-phenotype linkage. (b) In contrast, partial in vitro display systems rely on cells to produce the displayed protein, but selections can be performed in vitro. In phage display (upper panel), the protein is displayed on the surface of filamentous phages, usually fused to

from homologous sources in a random fashion. For mere statistical reasons, the probability of replacing a residue with a consensus residue by gene shuffling is also higher than replacing it with a non-consensus residue [93]. There is, however, a crucial difference: when recombining genes in a random fashion, a selection or screening step is needed subsequently to identify the "fittest" members of the resulting collection. Rather than being based on theoretical assumptions, gene-shuffling methods mimic the natural process of evolution by identifying the members exhibiting a desired property by explicitly subjecting them to selective pressure for this desired property. In practice, however, even with the largest of libraries, a full "re-equilibration" of residues will not take place. In contrast, the consensus approach is based on the explicit assumption that the statistical preferences in a given (often limited or biased) set of sequences indeed reflect the energetic preferences. However, there may be other reasons that certain sequences are prominent.

39.4.2
Screening and Selection Technologies Available for Improving Biophysical Properties

As described above, any selection technology relies on four major steps: (1) generation of a genetic library, (2) establishment of the link between genotype and phenotype upon translation into protein, (3) subsequent screening or selection under defined conditions, and (4) re-amplification of selected members. Depending on how these steps are performed, selection technologies can be subdivided into in vitro methods, partial in vitro methods, and in vivo methods.

While in vivo systems rely on a host organism to express the protein and to carry the respective genetic information, all in vitro display technologies have in common that the protein production and the selection process are performed entirely in vitro, i.e., that the protein is obtained by cell-free translation. In the partial in vitro methods, the genetic information is introduced in cells, where protein production occurs, while the selection process is performed in vitro. All techniques differ in the way the physical linkage between the protein and its genetic information is established. The principles of linking genotype and phenotype are shown in Figure 39.6.

◀

the CT domain of the minor coat protein g3p. The three domains (N1, N2, and CT) of the minor coat protein g3p are depicted. The phage particle also carries the gene encoding the displayed protein. In other partial in vitro technologies, the proteins are displayed on the surface of the expressing host cell itself, which are either bacterial cells (bacterial surface display) or yeast cells (yeast surface display) (lower panel) that also harbor the respective plasmid DNA. (c) In vivo screening or selection systems use the properties of fused reporter proteins for screening (upper panel) or split proteins for intracellular selection (lower panel) in which cellular growth and therefore amplification of the genetic material occurs only if the two protein halves are reconstituted upon interaction of the fused library protein with its target.

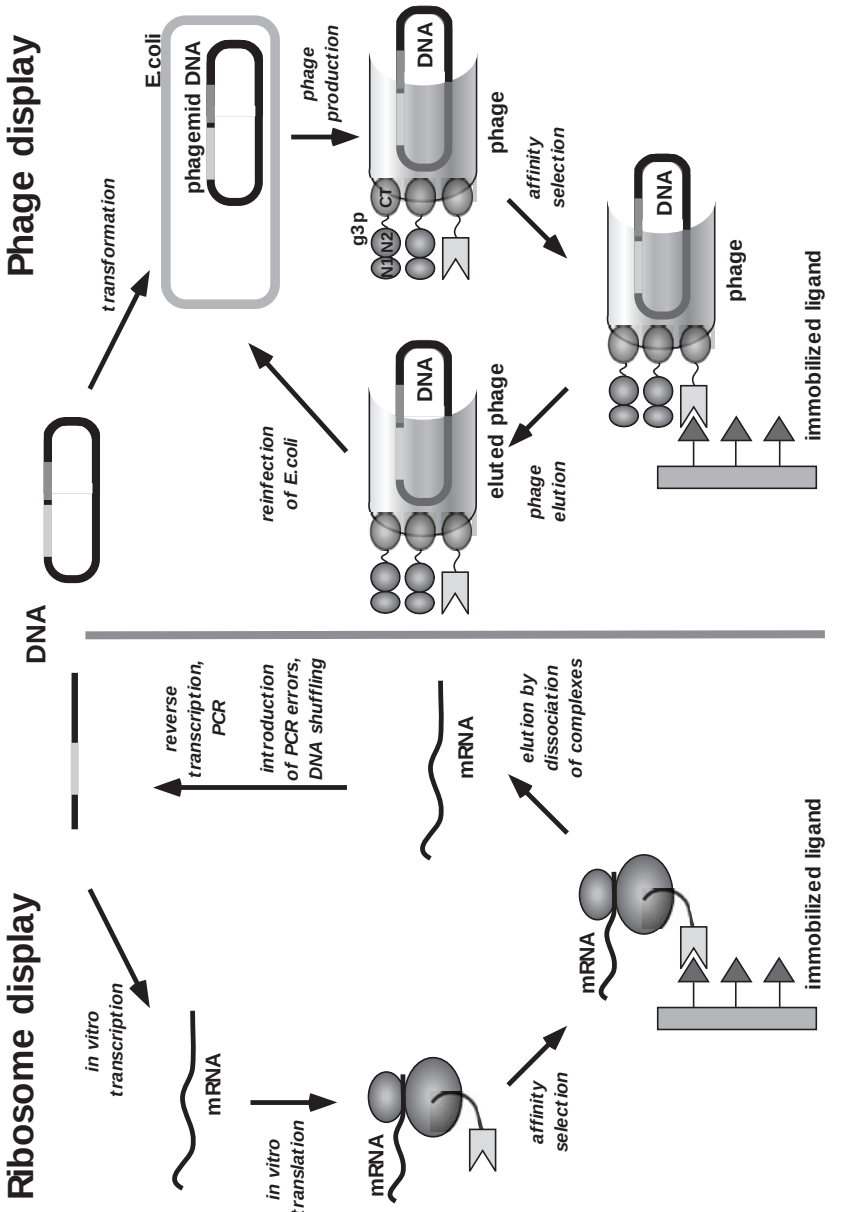
Phage display
transformation
E.coli
phagemid DNA
phage production
DNA
g3p
N1
N2
CT
DNA
phage
affinity selection
reinfection of E.coli
DNA
eluted phage
phage elution
DNA
phage
immobilized ligand
DNA
reverse transcription, PCR
introduction of PCR errors, DNA shuffling
mRNA
elution by dissociation of complexes
Ribosome display
in vitro transcription
mRNA
in vitro translation
mRNA
affinity selection
mRNA
immobilized ligand

Fig. 39.7

39.4.2.1 In Vitro Display Technologies

In vitro display technologies started off with the selection of peptides [94] and were then made efficient enough to select for functional proteins [95]. A number of technologies have been developed, which will be described briefly: ribosome display [95, 96], RNA-peptide fusions [97, 98], and water-in-oil emulsions [99, 100]. Water-in-oil emulsions constitute artificial compartments, rather than a physical link, and thereby create a phenotype-genotype coupling and can also use a selection step for interaction with a target.

In ribosome display, the genetic library, usually in the form of a PCR product, is directly used to produce mRNA by in vitro transcription. This mRNA contains a ribosome-binding site for the subsequent translation of the protein and several features that stabilize it against degradation. The encoded protein variants are expressed in a cell-free translation reaction by a stoichiometric number of ribosomes. The essential linkage of the translated proteins to their respective mRNA molecule is achieved by eliminating the stop codon and stabilizing the ribosomal complexes, which prevents the release of the translated protein from the ribosome. In the related method of mRNA-peptide fusions, additional steps are used after this stoichiometric translation to covalently couple a linker between the end of the mRNA and the protein. The ribosome is then removed and the complexes are purified. These complexes are then used to bind to an immobilized target. In all these methods, after the selection process the re-amplification of genetic material can be performed solely by biochemical means, using reverse transcriptase to first synthesize RNA-DNA hybrids, which are then subsequently amplified in a PCR reaction. The resulting DNA then serves as a template for the production of mRNA used for the next round of selection (Figure 39.7).

In vitro display technologies offer several advantages over in vivo selection systems. First, much larger library sizes are accessible because the creation of large molecular diversity on the genetic level does not pose a great challenge, and diversities up to 10^{13} are easily achieved. For in vivo systems, the critical step that limits the size of the displayed library is the transformation efficiency of the respective host organism. Only a small fraction of the initially generated pool will actually enter the cells, and, depending on the host organism, library sizes of about 10^7 variants in yeast or up to 10^{11} variants in bacteria can be achieved. In contrast, for

Fig. 39.7. Selection cycle of ribosome display (left panel) and phage display (right panel). For ribosome display, all necessary steps are performed in vitro, whereas for phage display protein translation, folding, and phage assembly take place in the bacterial host cell. Other selection criteria can be applied to the protein of interest (see Figure 39.8) before selecting for binding to a target, thereby introducing selection pressures for higher stability. It has to be guaranteed, however, that the selection conditions are not too harsh to destroy the linkage of genotype and phenotype. Importantly, the genetic pool of library members in phage display remains constant in the course of several selection rounds, whereas in ribosome display, the genetic pool undergoes continuous modifications during the in vitro amplification steps by the limited accuracy of the polymerases, resulting in a true Darwinian evolution. In addition, this pool can deliberately and conveniently be altered by introducing additional mutations or recombination events such as DNA shuffling.

in vitro selection systems such a transformation step is not necessary and the diversity of the library is defined by the number of different RNA molecules added to the cell-free translation reaction or by the number of functional ribosomes, whichever number is smaller. For a library of 10^{14}, a 10-mL translation reaction is required. A second advantage is that, because translation and protein folding take place in vitro, reagents can be added during protein synthesis, which can either promote protein folding or minimize aggregation of the displayed proteins (e.g., chaperones), or substances that exert certain selection pressures can be added. In vitro translation encompasses an additional advantage: many proteins are not compatible with in vivo selection systems because the wild type or at least some of the mutants are toxic to the host organism, undergo severe degradation, or cannot be expressed functionally in the respective cellular environment. Last but not least, a major advantage results from the amplification process after the selection has been performed. Because all enzymes used to convert and amplify the genetic material possess an intrinsic error rate, the genetic pool is never constant and is continuously modified from round to round. Therefore, even without special measures to increase the error rate, usually some "evolution" is observed. The error rates can be additionally increased by performing error-prone PCR or by recombining favorable mutations by means of DNA shuffling as explained in the previous section.

39.4.2.2 **Partial in Vitro Display Technologies**

We define partial in vitro display technologies as those methods in which host organisms are employed to carry and amplify the genetic information and to produce the proteins from this genetic library, usually encoded on plasmids. The selection step, however, is performed in vitro. Therefore, selection pressures similar to those in the in vitro methods can be applied. The array of available techniques includes phage display [101], bacterial surface display [102], and surface display on yeast [103].

Phage display is still the most popular selection technique, and due to its robustness, most of the studies that aim for enhanced biophysical properties of proteins have utilized this technique. Originally, phage display was applied as a method for the identification and selection of peptides or proteins binding to a specific target [101]. More recently, several developments paved the way for its application as a tool for studying protein folding, and as a result, it is now used for the selection of proteins with improved biophysical properties.

We will briefly review the main principles of phage display in its most common format. Variants of the protein of interest are fused to the minor coat protein g3p of the filamentous bacteriophage, which consists of three domains (namely, N1, N2, and CT) that are connected by glycine-rich linkers. The fusion protein is usually encoded on a phagemid vector, expressed in the E. coli host and assembled. Typically, the other proteins necessary to produce an intact phage particle are provided by the helper phage. The assembled phages are secreted by the cell, which does not lyse, and the phages can be collected. While the protein is displayed on the exterior of the phage (typically as an N-terminal fusion to either N1 or CT), the gene of interest encoding a library member is packed into the phage particle

upon its assembly in the bacterial host. The phages can then be subjected to the selection process. Phages compete with each other for binding to an immobilized target, using the displayed library members for interaction, and can thereby be captured. Optionally, before capturing, the phages can be subjected to harsh environmental conditions. The captured phages are subsequently amplified by re-infecting bacteria, which then produce phages for a new round of selection (Figure 39.7). In the ideal case, only phages that specifically recognize the target would be amplified. Due to reasons such as nonspecific ''sticking'' of phages to the surface, the efficiency of selection is in practice at most a 1000- to 10 000-fold enrichment over nonspecific molecules and can even be very much lower.

Several aspects are important when phage display is used as a means of evolving proteins with improved biophysical properties. The correct folding of the fusion protein during phage morphogenesis is an important parameter determining the frequency of incorporation of correctly folded proteins displayed on the phage. Folding intermediates that have a strong aggregation tendency lead to aggregation of a particular library member during the assembly process, and rather than the g3p fusion, the g3p wild-type protein from the helper phage will be incorporated. Despite this inherent selection pressure for the folding efficiency of displayed proteins, the enrichment of improved variants is slow [104], and the utility of phage display to study and improve folding of a given protein was initially not obvious [105]. Combined with a selection for protein functionality, it nevertheless sets the basis for selecting proteins according to their folding properties, as will be discussed in Section 39.4.3.2.

Since the selection procedure is performed in vitro, a large variety of external selection pressures can be applied to the phage particles and be combined with functional selection. If function is omitted as a direct indicator for the native state, other criteria that directly correlate with the native state have to be translated into a selectable feature. This opens the door to select for proteins, which do not bind a ligand, albeit with the caveat that it is not assured that the native state is being selected. Such general selection approaches for physical properties take advantage of the fact that unfolded proteins are more susceptible to proteolytic cleavage than are compactly folded ones [106]. One variation on this theme makes use of the modular nature of the g3p protein, thereby linking phage infectivity directly to the proteolytic susceptibility of the target protein. This system has been called ''Proside'' (protein stability increase by directed evolution) [107] and will be discussed in Section 39.4.4.4.

39.4.2.3 **In Vivo Selection Technologies**

In vivo selection technologies such as the yeast two-hybrid system [108, 109] or other split protein complementation assays [110, 111] are valuable tools for studying protein-protein interactions in living cells. They commonly employ reporter systems, in which a covalent link between the protein of interest and another so-called reporter protein is established. Cell growth or a colorimetric reaction is dependent on either a specific protein-protein interaction or the solubility of a critical component. The reporter protein transduces certain properties of the host protein,

most importantly its native fold and its ability to interact and/or its solubility or its resistance to cellular proteases, to a screenable or selectable feature of the fused reporter protein itself [112]. Examples of reporter proteins are transcription factors [108], critical metabolic enzymes [111], or proteins that can easily be assayed [113].

Several facts, however, limit the applicability of in vivo systems for stability engineering. First, as the viability of the host organism has to be guaranteed, external selection pressures cannot easily be applied. Thermophilic organisms represent in some cases an interesting alternative, but conditions allowing selections are hard to establish. Additionally, the host environment as well as the fused reporter proteins possibly perturb the characteristics of the target protein. Furthermore, control experiments must ensure that growth is really dependent on the interaction of interest and that mutations in the host have not "short-circuited" the selection strategy.

39.4.3 Selection for Enhanced Biophysical Properties

As has been explained in the Introduction, desirable biophysical parameters include solubility, stability, and folding efficiency. Even though the various selection methods and conditions usually do not improve one of these properties exclusively, they are often biased towards one of them. We will therefore discuss different ways to exert selection pressure on the system with respect to the property that is likely to be changed.

39.4.3.1 Selection for Solubility

Solubility, correctly defined as the maximal concentration of the native protein that can be kept in solution, is usually not a property to be selected, as most proteins – with the exception of membrane proteins – are sufficiently soluble. The word "solubility" in the context of screening is often inaccurately used to refer to "soluble expression yield," and thus it usually mirrors the efficiency of folding in the cell. Even though soluble expression yield is not necessarily equivalent to the folding properties and even less to the stability of a protein, a correlation can often be observed, and soluble expression yield is comparatively easy to screen for. In some cases, a function for a given protein cannot be assigned, or it is difficult and laborious to screen for, and then this property becomes especially important.

The fluorescence yield of bacterial colonies expressing proteins or protein domains fused to the green fluorescent protein (GFP) correlates over a wide range with the soluble expression yield of the fused domain [114]. Screening for fluorescence intensity is a versatile method, and, combined with directed evolution, has the potential to select variants of proteins that are less aggregation-prone than their progenitors [115, 116]. In a similar setup, reporter proteins can be used as selection markers instead, such as by fusing the protein of interest to chloramphenicol acetyltransferase [117]. Assays exploiting protein-protein interactions can also be used for this purpose and they have the additional advantage that the fused reporter sequence can be much smaller and thereby minimize the risk of a perturb-

ing influence of the reporter itself on the domain of interest [113]. To completely exclude such perturbing influences, reporter systems might possibly be established that do not need any fusion at all and exploit instead the stress response of the expression host cell. As the overexpression of proteins often activates particular stress response genes by the accumulation of insoluble aggregates, the respective gene promoters can be employed to activate reporter genes instead [118].

In special cases, reporter systems can also be combined with other selection methods to select for folding properties. Many intrinsically stable proteins contain permissive sites in loops, into which polypeptide chains of variable length can be inserted without loss of function of the host protein. The higher the number of residues inserted, the larger the entropic cost of ordering these residues will be. Consequently, the overall stability of the host protein should decrease. However, the entropic cost of inserting a folded sequence will be lower than that of an unfolded sequence of the same length. The probability of the host protein reaching the native (functional) state should thus correlate directly with the ability of the inserted sequence to fold into a compact structure. If host proteins with various inserted sequences are displayed on phages and if the host protein allows a selection for "foldedness" by means of binding to a target, folded sequence insertions are enriched. This system has been termed "loop entropy reduction phage display selection" [119]. While attractive in theory, it was found experimentally that mostly sequences that keep the hybrid protein soluble are enriched.

Protein solubility, as used here, can also be interpreted as a lower degree of exposed hydrophobic residues, and folded proteins usually display fewer hydrophobic residues on their surface than do unfolded proteins. Conversely, the exposure of hydrophobic residues is usually a sign of non-native states. Display technologies can thus, for example, use the interaction with hydrophobic surfaces to select against more hydrophobic, i.e., less "folded," proteins [120].

In summary, protein solubility can reflect in many cases the folding properties of proteins and thus be used as a selection criterion. Moreover, soluble expression in vivo is often a major requirement for the large-scale production and the convenient in vitro handling of proteins. In any case, solubility should never be confused with protein stability. Even though both properties might correlate in some cases, the governing principles are often of a different nature.

39.4.3.2 **Selection for Protein Display Rates**

The in vivo folding efficiency of proteins represents an intrinsic selection pressure when using phage display. Because correct folding is a prerequisite for both incorporation into the phage coat and binding to the target, the subsequent selection of phages that are able to bind to the target is partly influenced by the folding properties of the displayed molecule.

However, this does not automatically imply that the selection is driven towards superior folding properties. As mentioned above, the enrichment factors of proteins with superb folding behavior over the poorly folding members are low [104]. Moreover, even though the binding of a given protein to its target is a very direct way to monitor and screen for its proper folding, the selection criterion "folding"

is not decoupled from the selection criterion "binding affinity." If the enrichment factor for one property (folding) is low, the selection is more likely to be driven towards the other (affinity). As a result, selected members will represent a compromise between folding properties, which only have to be sufficient under the given experimental conditions, and the binding affinity to their target.

By randomizing exclusively the residues that build the hydrophobic core of the IgG binding domain of peptostreptococcal protein L, which are not involved in ligand binding but determine the stability and folding kinetics of this small protein, Gu et al. [121] could unambiguously demonstrate the utility of phage display for studying the stability and folding efficiency of proteins. A more extensive randomization effort with subsequent characterization of the selected variants pointed out some important aspects of selection for folding [122]. First, it showed that folding kinetics is not the critical parameter for the selection but rather the overall stability of the mutants, a tendency which could be confirmed by more advanced selection approaches (see Section 39.4.4.2). Second, the authors demonstrated the utility of selection methods to identify certain residues that are important for the folding mechanism. Third, the selected pools were highly diverse and the thermodynamic stabilities of all variants were lower compared to the wild type. In fact, most of the selected proteins denatured just above room temperature.

These results illustrate the principle that any selection – be it natural or in the test tube – simply continues until the minimum requirements are met, in this case, functionality at the selection temperature. Consequently, this suggests that additional, more stringent selection pressures are necessary to really accomplish a directed evolution for improved properties.

39.4.3.3 Selection on the Basis of Cellular Quality Control

Additional selection pressure can be provided by the host organism itself. For example, the secretory quality-control system of eukaryotic cells discriminates proteins according to their folding behavior in an efficient way. This is based on mechanisms that lead to retention of misfolded proteins in the endoplasmic reticulum (ER), followed by degradation of these proteins. In yeast, the Golgi complex can reroute misfolded proteins, which have escaped ER retention, to the vacuole for degradation, thereby constituting an additional important quality-control pathway [14]. In combination with yeast surface display, these mechanisms can be employed to bias functional selections towards enhanced folding efficiency. Several studies have shown that the surface display rate of proteins strongly correlates with their thermostability and their soluble secretion efficiency [123, 124]. As an example, by making use of elevated temperatures during expression as an additional selection pressure, improved T-cell receptor fragments, whose thermostability exceeded by far the expression temperatures, could be obtained [125]. Even though the low transformation efficiency of yeast restricts the accessible library size, one obvious advantage of the method is the applicability to glycosylated eukaryotic proteins, which generally are not amenable to yeast two-hybrid or phage display methodologies [126].

39.4.4 Selection for Increased Stability

39.4.4.1 General Strategies

The key to all selections for stability is to introduce a threshold that separates the molecule with desired properties from the starting molecules. If the population initially lacks functionality, while only a few members are above the selection threshold, the selection system can distinguish between these slight energetic differences. This is the starting situation if the target protein is initially of very low stability and should be brought to ''average'' properties.

If, however, the starting protein is already of considerable stability, but should be brought to even higher stability, it can be advantageous to intentionally destabilize it prior to selection in order to find stabilizing mutations that reconstitute its functionality. This principle can be applied to very different kinds of proteins, provided that mutations are known that destabilize the protein to an extent that will subsequently allow the selection for alternative stabilizing mutations (Figure 39.8a). Because the effects of independent stabilizing mutations are often additive, the deliberately introduced destabilizing mutations can be reverted in the context of the additional newly selected ones, thereby rendering the molecule far more stable than the original one (Figure 39.8b).

In principle, all reagents and conditions known to destabilize proteins can decrease the number of library members populating the folded state and can therefore be used to exert increasing selection pressure on the system. Increased temperature and denaturing agents are obvious methods that are useful for selecting proteins of higher thermodynamic stability. The major problem is presented by the compatibility of the conditions with the selection method used.

39.4.4.2 Protein Destabilization

An example of the stabilization of a naturally unstable domain by using phage display was a selection performed with the prodomain of the protease subtilisin BPN′ [127]. At room temperature the prodomain folds into a stable conformation only upon binding to subtilisin. By randomizing positions that are not directly in contact with subtilisin and subsequent selection on subtilisin, a mutant was selected that showed an increase of $\Delta G_{\text{unfolding}}$ by 25 kJ mol^{-1}, from -8 kJ mol^{-1} to 17 kJ mol^{-1}, despite the fact that the library size was comparatively small. Intriguingly, the predominant energetic contribution was mediated by a selected disulfide bond. Previously, a similar strategy had been used to select for thermodynamically favored β-turns of the B1 domain of protein G [128]. Based on considerations described above and on the fact that the replacement of amino acids on the surface of proteins would be predicted to have only moderate effects on stability, the authors reasoned that such a selection could be successful only for proteins of marginal stability. Most of the substitutions would then lead to a positive free energy of folding, and thus the molecule would fail to fold into a functional form at all. In fact, selected turn sequences showed clear sequence preferences only if less stable

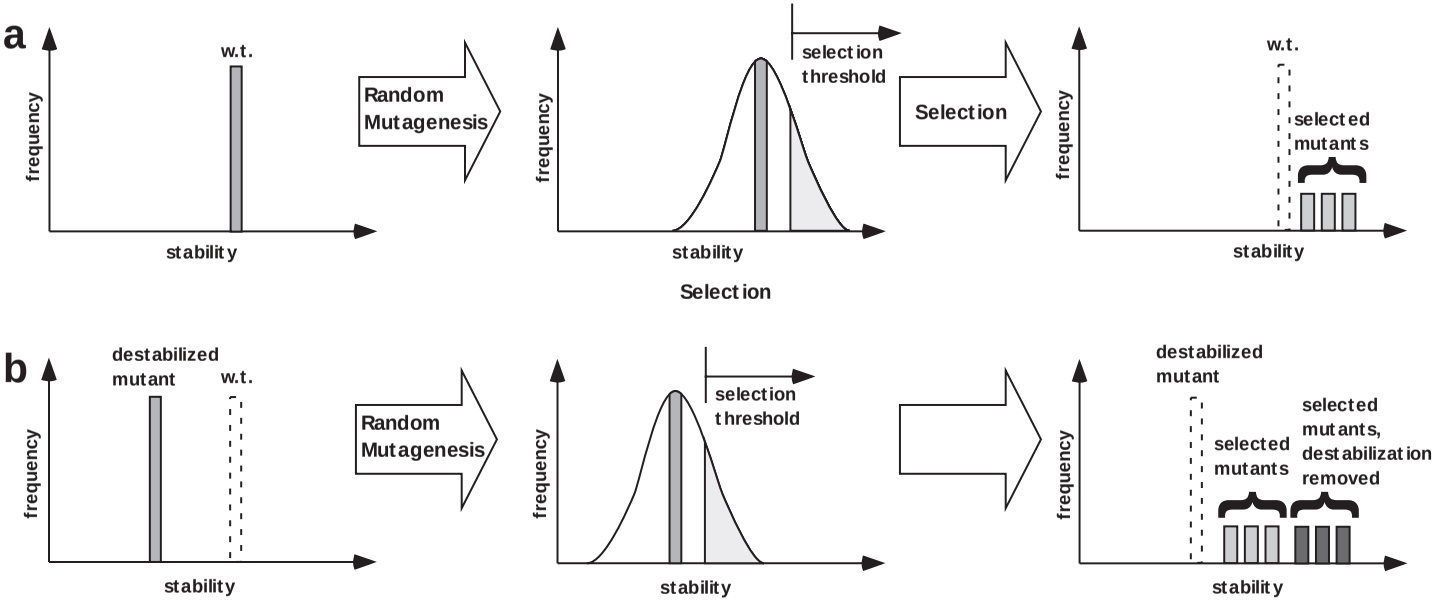

Fig. 39.8. Principle of selection for proteins with improved stability. (a) By random mutagenesis of a given sequence, many mutations are obtained. Some of these mutations are favorable for the stability of the native protein and others are unfavorable. As a result, a diverse pool of proteins with a distribution of different energies is created. Upon exposure of the pool to an external selection pressure, only mutants with stabilities exceeding the selection threshold can be recovered and amplified. However, the selection threshold has to be set high enough to allow an efficient selection of "improved" members. (b) Destabilization of the wild-type sequence prior to selection allows reducing the necessary selection threshold. Thereby, alternative mutations that stabilize the native fold of the protein can be identified and the selection process becomes more efficient. Moreover, additional stability gains can be achieved by removing the deliberately introduced destabilizing mutations after the selection. The initially lost energy is therefore regained, resulting in mutants of higher stability than the wild-type protein. Adapted from Wörn et al. [76].

host proteins were used to accept the turn. In this case, the selected sequences either resembled the wild-type turn or reflected the statistical preferences of turn sequences in the databases and stabilized the protein by 12–20 kJ mol^{-1}, compared to random sequences. Moreover, increased temperature was used as an additional selection pressure during the phage selection.

As discussed in the previous section, the inability of the wild-type target protein to fold is the prerequisite for performing an efficient positive selection for functionality by additional mutations. The internal disulfide bond of immunoglobulin domains significantly contributes to the stability of antibodies [129]. The dramatic loss of free energy of folding upon their removal usually renders antibodies nonfunctional. By first destabilizing a scFv antibody fragment through replacement of cysteines with other residues in both variable domains separately, a completely disulfide-free antibody was identified after several cycles of functional selection and recombination by DNA shuffling [17]. One globally stabilizing mutation was found to compensate for the initial stability loss. This study illustrates some important features of how several parameters exert influence on different stages of the selection process. Interestingly, the stabilizing mutation was already selected during the first rounds, showing that the loss of thermodynamic stability was the primary problem that had to be overcome. Because the stability gain of this mutation was large enough to shift the free energy of folding above the required threshold, all successive rounds did not affect protein stability but led to a fine-tuning with respect to the improvement of folding yield [17]. To illustrate the principle of additivity, reintroduction of the disulfide bridge into the selected variant yielded a scFv antibody of very high stability and superior expression yields [84].

39.4.4.3 **Selections Based on Elevated Temperature**

In vivo selection systems using thermophilic expression hosts have been employed for the stabilization of enzymes [130]. However, a rather large set of requirements must be met to apply such a selection system. In order to use stability of the enzyme at elevated temperatures as the selection criterion, its enzymatic activity must be vital to the thermophilic organism, and the corresponding gene of the thermophilic host has to be deleted. Randomized versions of a mesophilic enzyme can then be screened by means of metabolic selection. Although the approach is very powerful, the utility of these systems is restricted to special cases.

To evolve enzymes with altered thermal stability, conventional screening for enzymatic activity in vitro after randomization or recombination of the respective gene and subsequent expression of the enzyme is still the most widely used method. An activity screen rapid and sensitive enough to identify slightly improved members from a vast pool of mutants is the key feature of this directed evolution approach [131]. However, individual screens have to be developed for each specific class of enzymes. Even though screening limits the explorable sequence space considerably compared to selection, mesophilic enzymes such as subtilisin E [132] and *p*-nitrobenzyl esterase [133] could be converted into mutants functionally equivalent to thermophilic enzymes by only a few rounds of directed evolution. Similar to observations discussed before, only very few mutations were necessary to in-

crease the melting temperatures by more than 14 degrees. An important feature of screening compared to selection is that the much smaller library size is partially compensated for by directly measuring the quantity of interest: enzymatic activity at elevated temperature. In contrast, most selection systems use a surrogate measure where ''false positives'' can lead to the phenotype by mechanisms different from the ones desired.

Elevated temperatures not only can be used in screening but also can be combined with selection technologies. While ribosome display is not an option – because low temperatures are essential to keep the ternary complexes of RNA, ribosome, and nascent polypeptide intact and thus ensure the coupling of genotype and phenotype – phage display has proved to be a very suitable method for harsh conditions due to the robustness of the phage particles. Nevertheless, future improvements of in vitro technologies may allow their application under more stringent conditions. As of today, in the case of in vitro technologies, it is vital to destabilize the protein first (see Section 39.4.4.2); then, very significant stability improvements can be selected [134].

The upper temperature limit for selections using filamentous M13 phages is approximately 60 °C [135]. Above this temperature, re-infection titers of the phages are severely decreased, presumably due to the irreversible heat denaturation of phage coat proteins. Phages displaying the protein of interest can be incubated up to this temperature, and proteins still able to function can be selected. It should be noted that the exposure of phages to higher temperature after phage assembly exerts a somewhat different stress on the proteins than in the methods described before. While in the previous examples the functionality of the proteins was influenced mainly by in vivo folding efficiency and the protein stability during the panning procedure, it is the irreversible unfolding reaction at a given temperature that now becomes an additional parameter. The fraction of unfolded molecules will therefore reflect the rate of unfolding and thus kinetic stability.

39.4.4.4 Selections Based on Destabilizing Agents

The use of protein destabilizing agents for biasing the selection pressure towards stability is limited to in vitro and partial in vitro display methods. Like temperature, the concentrations of denaturing agents can be controlled precisely and can be varied from round to round, allowing a gradual increase of stringency.

Even though phages are quite resistant to denaturing agents [136], one should be aware of possible general problems when selections are based on the chemical denaturation properties of the displayed proteins. However, if chemical denaturation is combined with a selection for binding, high concentrations of denaturant can prevent binding to the target, even if the protein is not yet unfolded: as the forces governing ligand binding are very similar to those responsible for protein stability, both are disturbed by chemical denaturants. Conversely, because chemical denaturation is in fact often reversible, removal or dilution of the denaturant prior to ligand binding will often result in refolding on the phage and thus release of selection pressure. Moreover, ionic denaturants such as guanidinium chloride weaken electrostatic interactions and strengthen hydrophobic ones. This might im-

pair the selection of mutations that introduce additional ionic interactions on the protein surface [59] and may favor additional hydrophobic interactions, which is not necessarily desired.

If the protein is known to be stabilized by disulfide bridges, a strategy similar to the one used by Proba et al. [17] described above may be applicable. To identify globally stabilizing mutations, which compensate for the stability loss upon removal of disulfide bridges, selection can be performed in the presence of reducing agents such as DTT. Thus, the disulfide-forming cysteines do not have to be removed in advance. However, one should be aware of the fact that some disulfide bridges in proteins, once formed, are often hard to reduce, especially if they are buried within the protein core. Thus, it is advantageous to add the reducing agent at a time when the protein is not yet folded. Jermutus et al. [134] stabilized a scFv antibody fragment by using ribosome display. In contrast to the phage display method, the synthesis of the targeted protein occurs in vitro, which makes the polypeptide chain accessible to reagents during its synthesis on the ribosome and before folding has taken place. DTT was added during translation of the scFv, and its concentration was continuously increased from round to round. When using ribosome display, the population undergoes slight changes due to mutations occurring during PCR, resulting in an iterative adjustment of the selected variants towards tolerating the increasingly stringent conditions.

39.4.4.5 Selection for Proteolytic Stability

In each of the examples cited above, selection for stability was based on a functional selection. Therefore, only those proteins for which a specific function can be assigned could be targeted; in addition, this function has to be screenable or, better yet, selectable. It would be highly advantageous to completely uncouple function from stability in the selection process to extend the range of problems to which this can be applied. A more general approach would thus be an invaluable tool for engineering any given protein and for selecting stable folds from a pool of de novo designed proteins. For functional selections, an additional problem arises from the fact that after a certain stability threshold is reached, allowing enough proteins to populate the folded state, the selection is likely to run towards improved binding properties instead. On the other hand, certain mutations might be stabilizing but might result in slight structural rearrangements that affect functionality in a negative way. Thus, it will not be possible to recover these mutations [106].

A general approach that has proved to be powerful for stability engineering is based on the concept that compactly folded proteins are much more resistant to proteolysis than are partly folded or unfolded proteins [137]. Several variations on this theme have been applied to phage display selections. In principle, it is only necessary that the phages displaying proteins, which can be cleaved by the protease, can be efficiently separated from the phages displaying protease-resistant proteins. This can be achieved in a physical way by providing the displayed protein with an N-terminal tag sequence allowing capture of only phages with non-cleaved proteins [106]. Alternatively, the ability of phages to re-infect bacteria can be directly linked to the protease resistance of the protein of interest [107, 136]. This

second alternative takes advantage of the modular structure of the protein domains responsible for phage infection. If the displayed domains are inserted between the carboxy-terminal domain of gp3 and the amino-terminal domains N1 and N2, which are required for phage infectivity, proteolytic cleavage of the displayed domain renders the phage noninfectious. This was inspired by the so-called selectively infective phage method (SIP), where it was shown that the g3p domains could be interrupted by additional domains and even an interacting pair [138]. By employing a phage system derived from the SIP technique, which lacks any wild-type g3p, it is assured that infectivity is completely abolished upon proteolytic cleavage [107] (Figure 39.9). Alternatively, phages can be engineered to make the remaining wild-type g3p itself susceptible to the proteolytic attack [136]. The principle of protease selection can also be applied to in vitro selection techniques in which the displayed protein is freely accessible [120].

Even though proteolysis seems at first glance to be less correlated to the stability of proteins than temperature, it is suitable for optimizing packing of the hydrophobic core [139] as well as for optimizing electrostatic interactions on the protein surface [59]. One reason for the strength of this approach is based on the fact that proteolytic cleavage is an irreversible reaction, which is not necessarily the case for denaturation by temperature or denaturing agents. Furthermore, protease resistance monitors the flexibility of the polypeptide chain rather than complete denaturation. It is therefore capable not only of selecting against completely unfolded variants but also of detecting local unfolding events. Because sites of local unfolding often initiate the global unfolding process, it can be advantageous to remove such sites. Nevertheless, the effective cleavage of flexible parts of the protein restricts the method to proteins that do not have extended flexible regions in the native state. Furthermore, a selection against the primary recognition sequence of the protease is clearly a possible outcome of such experiments.

None of the described methods can stand completely on its own. Many methods can easily be combined to increase the stringency of a selection. A combination of temperature stress and increasing amounts of denaturing agents may, for example, lead to higher flexibility in certain regions of the protein, thereby increasing the sensitivity of the subsequent proteolytic attack. Additionally, temperature and the concentration of denaturing agents allow a much tighter control of the selection pressure than do increasing concentrations of protease and thus open the possibility of a well-controlled gradual increase of selection stringency.

39.5 Conclusions and Perspectives

Several different approaches are now available for engineering proteins for enhanced biophysical properties. In many cases, few and specific mutations are sufficient to provide proteins of marginal stability with considerably stabilizing features. Thus, the challenge for protein engineering is to identify these positions in a given sequence among the vast number of possible changes and to correctly alter them. Each of the applied techniques has its own merits and bottlenecks. Instead

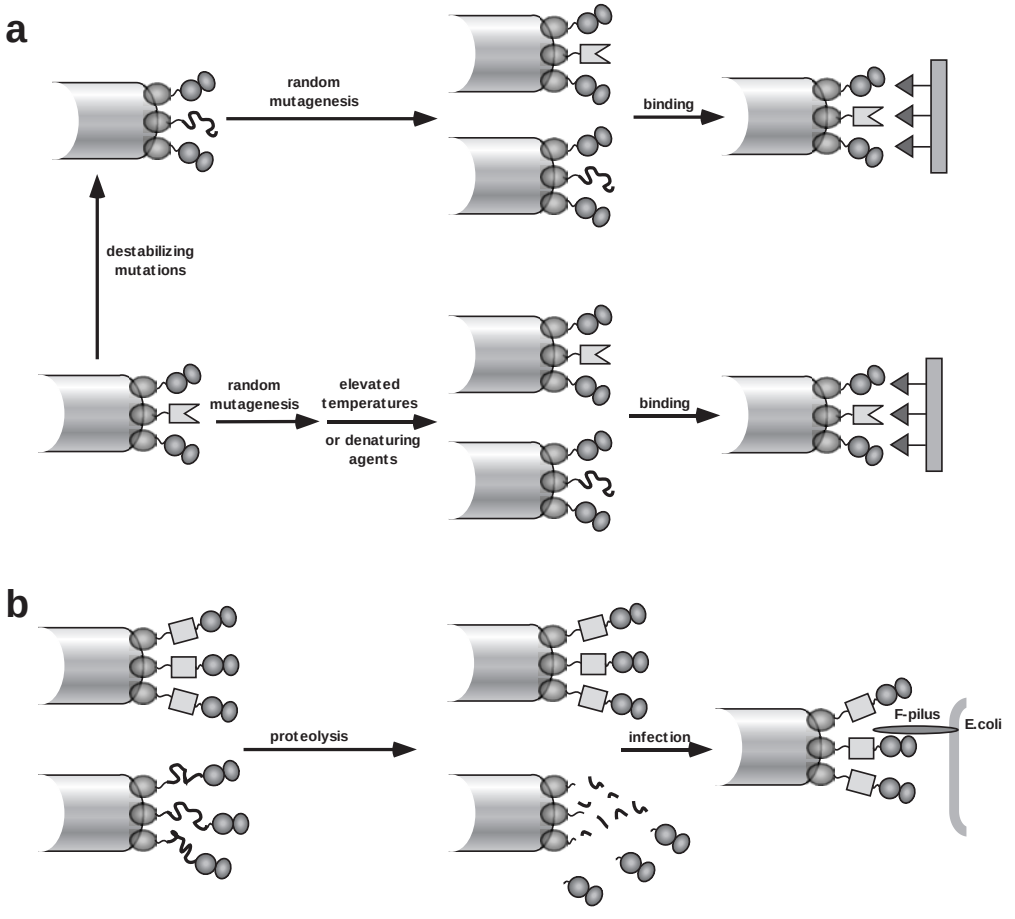

Fig. 39.9. Strategies for selecting for improved protein stability and folding by phage display. (a) Methods utilizing the binding to a given target (affinity selection) as a means for selecting members with improved folding behavior and higher stability from a protein library. Several types of selection pressure can be applied in order to recover mutants with enhanced stability. Destabilizing mutations are deliberately introduced (top) to render the protein "nonfunctional," and alternative stabilizing mutations are identified by selecting variants whose functionality is regained. Alternatively (bottom), elevated temperatures or denaturing agents can be used to render most of the protein variants "nonfunctional," allowing the selection of simply the "fittest" members. (b) The resistance of the target protein to a protease can be combined with the ability of phages to re-infect bacteria. The protein library is inserted between the C-terminal domain and the N-terminal domain in all copies of the g3p protein (cloned into the phage genome), which are needed for re-infection of bacterial cells. By proteolytic cleavage of the inserted protein, these domains are cut off and phage infectivity is lost. In alternative approaches, an N-terminal tag sequence is fused to the protein of interest instead of the N-terminal g3p domains. Upon proteolytic cleavage, the tag is lost. In contrast, phages presenting proteins that are resistant to proteolytic cleavage can subsequently be captured on an affinity matrix binding to the tag sequence. In order to further increase the selection threshold, the shown selection strategies can also be combined.

of playing them off against each other, the future challenge will be to find ways to synergistically use them to improve a given molecular property.

Evolutionary methods have the advantage of being much less biased by theoretical assumptions or working hypotheses. Additionally, proteins stable in new environments may be evolved, e.g., proteins that fulfill a given function in non-aqueous solutions or high concentrations of detergents. Because the biophysical principles in such environments are of a different nature, rational design has to rely on a much smaller empirical dataset. While rational approaches are likely to become more important as more structural and experimental data become available, notably also those from selection experiments, the large number of variations that are potentially able to improve the biophysical properties of a protein often still exceeds the experimentally accessible number. Moreover, because rational engineering has to rely on the available dataset, mutations that lie off the beaten track will rarely be identified. Nevertheless, selection experiments often identify the same "key" mutations in proteins. It is then useful to exploit this information and directly introduce such mutations. A "rational" analysis can also help to recombine important "key" mutations in selected clones and to reduce the effects of a selection-neutral genetic drift. Another combination of rational and combinatorial methods is the creation of "smart" libraries of variants. Library design that is based on such structural considerations and principles will therefore allow more accurate focusing of the selection on specific regions of interest and thereby increase the chances for success.

Acknowledgements

The authors thank Drs. Daniela Röthlisberger, Casim Sarkar and Annemarie Honegger for critical reading of the manuscript. B. S. was the recipient of a Kekulé fellowship from the Fonds der Chemischen Industrie.

References

1 Taverna, D. M. & Goldstein, R. A. (2002). Why are proteins marginally stable? *Proteins* 46, 105–9.

2 Zavodszky, P., Kardos, J., Svingor & Petsko, G. A. (1998). Adjustment of conformational flexibility is a key event in the thermal adaptation of proteins. *Proc. Natl. Acad. Sci. U.S.A.* 95, 7406–11.

3 Arnold, F. H., Giver, L., Gershenson, A., Zhao, H. & Miyazaki, K. (1999). Directed evolution of mesophilic enzymes into their thermophilic counterparts. *Ann. N.Y. Acad. Sci.* 870, 400–3.

4 Govindarajan, S. & Goldstein, R. A. (1995). Searching for Foldable Protein Structures Using Optimized Energy Functions. *Biopolymers* 36, 43–51.

5 Dill, K. A. (1990). Dominant forces in protein folding. *Biochemistry* 29, 7133–55.

6 Pappenberger, G., Schurig, H. & Jaenicke, R. (1997). Disruption of an ionic network leads to accelerated thermal denaturation of D-glyceraldehyde-3-phosphate dehydrogenase from the hyperthermophilic bacterium Thermotoga maritima. *J. Mol. Biol.* 274, 676–83.

7 Sterner, R. & Liebl, W. (2001).

Thermophilic adaptation of proteins. *Crit. Rev. Biochem. Mol. Biol.* 36, 39–106.

8 Zlotnick, A. & Stray, S. J. (2003). How does your virus grow? Understanding and interfering with virus assembly. *Trends Biotechnol.* 21, 536–42.

9 Jaswal, S. S., Sohl, J. L., Davis, J. H. & Agard, D. A. (2002). Energetic landscape of alpha-lytic protease optimizes longevity through kinetic stability. *Nature* 415, 343–6.

10 Fersht, A. R., Bycroft, M., Horovitz, A., Kellis, J. T., Jr., Matouschek, A. & Serrano, L. (1991). Pathway and stability of protein folding. *Philos. Trans. R. Soc. Lond. B. Biol. Sci.* 332, 171–6.

11 Jäger, M. & Plückthun, A. (1999). Domain interactions in antibody Fv and scFv fragments: effects on unfolding kinetics and equilibria. *FEBS Lett.* 462, 307–12.

12 Willuda, J., Honegger, A., Waibel, R., Schubiger, P. A., Stahel, R., Zangemeister-Wittke, U. & Plückthun, A. (1999). High thermal stability is essential for tumor targeting of antibody fragments: engineering of a humanized anti-epithelial glycoprotein-2 (epithelial cell adhesion molecule) single-chain Fv fragment. *Cancer Res.* 59, 5758–67.

13 Ewert, S., Huber, T., Honegger, A. & Plückthun, A. (2003). Biophysical properties of human antibody variable domains. *J. Mol. Biol.* 325, 531–53.

14 Ellgaard, L., Molinari, M. & Helenius, A. (1999). Setting the standards: quality control in the secretory pathway. *Science* 286, 1882–8.

15 Martineau, P. & Betton, J. M. (1999). In vitro folding and thermodynamic stability of an antibody fragment selected in vivo for high expression levels in Escherichia coli cytoplasm. *J. Mol. Biol.* 292, 921–9.

16 Schuler, B. & Seckler, R. (1998). P22 tailspike folding mutants revisited: effects on the thermodynamic stability of the isolated beta-helix domain. *J. Mol. Biol.* 281, 227–34.

17 Proba, K., Wörn, A., Honegger, A. & Plückthun, A. (1998). Antibody scFv fragments without disulfide bonds made by molecular evolution. *J. Mol. Biol.* 275, 245–53.

18 Knappik, A. & Plückthun, A. (1995). Engineered turns of a recombinant antibody improve its in vivo folding. *Protein Eng.* 8, 81–9.

19 Wörn, A. & Plückthun, A. (1999). Different equilibrium stability behavior of ScFv fragments: identification, classification, and improvement by protein engineering. *Biochemistry* 38, 8739–50.

20 Steipe, B., Schiller, B., Plückthun, A. & Steinbacher, S. (1994). Sequence statistics reliably predict stabilizing mutations in a protein domain. *J. Mol. Biol.* 240, 188–92.

21 Lehmann, M. & Wyss, M. (2001). Engineering proteins for thermostability: the use of sequence alignments versus rational design and directed evolution. *Curr. Opin. Biotechnol.* 12, 371–5.

22 Knappik, A., Ge, L., Honegger, A., Pack, P., Fischer, M., Wellnhofer, G., Hoess, A., Wolle, J., Plückthun, A. & Virnekäs, B. (2000). Fully synthetic human combinatorial antibody libraries (HuCAL) based on modular consensus frameworks and CDRs randomized with trinucleotides. *J. Mol. Biol.* 296, 57–86.

23 Mosavi, L. K., Minor, D. L., Jr. & Peng, Z. Y. (2002). Consensus-derived structural determinants of the ankyrin repeat motif. *Proc. Natl. Acad. Sci. U.S.A.* 99, 16029–34.

24 Wang, Q., Buckle, A. M., Foster, N. W., Johnson, C. M. & Fersht, A. R. (1999). Design of highly stable functional GroEL minichaperones. *Protein Sci.* 8, 2186–93.

25 Lehmann, M., Loch, C., Middendorf, A., Studer, D., Lassen, S. F., Pasamontes, L., van Loon, A. P. & Wyss, M. (2002). The consensus concept for thermostability engineering of proteins: further proof of concept. *Protein Eng.* 15, 403–11.

26 Binz, H. K., Stumpp, M. T., Forrer, P., Amstutz, P. & Plückthun, A.

(2003). Designing repeat proteins: well-expressed, soluble and stable proteins from combinatorial libraries of consensus ankyrin repeat proteins. *J. Mol. Biol.* 332, 489–503.

27 Main, E. R., Xiong, Y., Cocco, M. J., D'Andrea, L. & Regan, L. (2003). Design of stable alpha-helical arrays from an idealized TPR motif. *Structure (Camb)* 11, 497–508.

28 Stumpp, M. T., Forrer, P., Binz, H. K. & Plückthun, A. (2003). Designing repeat proteins: modular leucine-rich repeat protein libraries based on the mammalian ribonuclease inhibitor family. *J. Mol. Biol.* 332, 471–87.

29 Forrer, P., Binz, H. K., Stumpp, M. T. & Plückthun, A. (2004). Consensus design of repeat proteins. *Chembiochem* 5, 183–9.

30 Kohl, A., Binz, H. K., Forrer, P., Stumpp, M. T., Plückthun, A. & Grütter, M. G. (2003). Designed to be stable: crystal structure of a consensus ankyrin repeat protein. *Proc. Natl. Acad. Sci. U.S.A.* 100, 1700–5.

31 Levitt, M., Gerstein, M., Huang, E., Subbiah, S. & Tsai, J. (1997). Protein folding: the endgame. *Annu. Rev. Biochem.* 66, 549–79.

32 Bohm, G. & Jaenicke, R. (1994). Relevance of sequence statistics for the properties of extremophilic proteins. *Int. J. Pept. Protein Res.* 43, 97–106.

33 Jaenicke, R. & Bohm, G. (1998). The stability of proteins in extreme environments. *Curr. Opin. Struct. Biol.* 8, 738–48.

34 Vieille, C. & Zeikus, G. J. (2001). Hyperthermophilic enzymes: sources, uses, and molecular mechanisms for thermostability. *Microbiol. Mol. Biol. Rev.* 65, 1–43.

35 van den Burg, B. & Eijsink, V. G. (2002). Selection of mutations for increased protein stability. *Curr. Opin. Biotechnol.* 13, 333–7.

36 Matsumura, M., Signor, G. & Matthews, B. W. (1989). Substantial increase of protein stability by multiple disulphide bonds. *Nature* 342, 291–3.

37 Perry, L. J. & Wetzel, R. (1984). Disulfide bond engineered into T4 lysozyme: stabilization of the protein toward thermal inactivation. *Science* 226, 555–7.

38 Pace, C. N., Grimsley, G. R., Thomson, J. A. & Barnett, B. J. (1988). Conformational stability and activity of ribonuclease T1 with zero, one, and two intact disulfide bonds. *J. Biol. Chem.* 263, 11820–5.

39 Zhang, T., Bertelsen, E. & Alber, T. (1994). Entropic effects of disulphide bonds on protein stability. *Nat. Struct. Biol.* 1, 434–8.

40 Doig, A. J. & Williams, D. H. (1991). Is the hydrophobic effect stabilizing or destabilizing in proteins? The contribution of disulphide bonds to protein stability. *J. Mol. Biol.* 217, 389–98.

41 Martensson, L. G., Karlsson, M. & Carlsson, U. (2002). Dramatic stabilization of the native state of human carbonic anhydrase II by an engineered disulfide bond. *Biochemistry* 41, 15867–75.

42 Ivens, A., Mayans, O., Szadkowski, H., Jurgens, C., Wilmanns, M. & Kirschner, K. (2002). Stabilization of a $(\beta\alpha)_8$-barrel protein by an engineered disulfide bridge. *Eur. J. Biochem.* 269, 1145–53.

43 Betz, S. F. & Pielak, G. J. (1992). Introduction of a disulfide bond into cytochrome c stabilizes a compact denatured state. *Biochemistry* 31, 12337–44.

44 Iwai, H. & Plückthun, A. (1999). Circular beta-lactamase: stability enhancement by cyclizing the backbone. *FEBS Lett.* 459, 166–72.

45 Scott, C. P., Abel-Santos, E., Wall, M., Wahnon, D. C. & Benkovic, S. J. (1999). Production of cyclic peptides and proteins in vivo. *Proc. Natl. Acad. Sci. U.S.A.* 96, 13638–43.

46 Camarero, J. A., Fushman, D., Sato, S., Giriat, I., Cowburn, D., Raleigh, D. P. & Muir, T. W. (2001). Rescuing a destabilized protein fold through backbone cyclization. *J. Mol. Biol.* 308, 1045–62.

47 Nagi, A. D. & Regan, L. (1997). An inverse correlation between loop

length and stability in a four-helix-bundle protein. *Fold. Des.* 2, 67–75.

48 Russell, R. J., Ferguson, J. M., Hough, D. W., Danson, M. J. & Taylor, G. L. (1997). The crystal structure of citrate synthase from the hyperthermophilic archaeon pyrococcus furiosus at 1.9 Å resolution. *Biochemistry* 36, 9983–94.

49 Macedo-Ribeiro, S., Darimont, B., Sterner, R. & Huber, R. (1996). Small structural changes account for the high thermostability of 1[4Fe-4S] ferredoxin from the hyperthermophilic bacterium Thermotoga maritima. *Structure* 4, 1291–301.

50 Matthews, B. W., Nicholson, H. & Becktel, W. J. (1987). Enhanced protein thermostability from site-directed mutations that decrease the entropy of unfolding. *Proc. Natl. Acad. Sci. U.S.A.* 84, 6663–7.

51 Sriprapundh, D., Vieille, C. & Zeikus, J. G. (2000). Molecular determinants of xylose isomerase thermal stability and activity: analysis of thermozymes by site-directed mutagenesis. *Protein Eng.* 13, 259–65.

52 Pace, C. N. (1992). Contribution of the hydrophobic effect to globular protein stability. *J. Mol. Biol.* 226, 29–35.

53 Lim, W. A., Hodel, A., Sauer, R. T. & Richards, F. M. (1994). The crystal structure of a mutant protein with altered but improved hydrophobic core packing. *Proc. Natl. Acad. Sci. U.S.A.* 91, 423–7.

54 Ventura, S., Vega, M. C., Lacroix, E., Angrand, I., Spagnolo, L. & Serrano, L. (2002). Conformational strain in the hydrophobic core and its implications for protein folding and design. *Nat. Struct. Biol.* 9, 485–93.

55 Ohmura, T., Ueda, T., Ootsuka, K., Saito, M. & Imoto, T. (2001). Stabilization of hen egg white lysozyme by a cavity-filling mutation. *Protein Sci.* 10, 313–20.

56 Chen, J. & Stites, W. E. (2001). Higher-order packing interactions in triple and quadruple mutants of staphylococcal nuclease. *Biochemistry* 40, 14012–9.

57 Hendsch, Z. S. & Tidor, B. (1994). Do salt bridges stabilize proteins? A continuum electrostatic analysis. *Protein Sci.* 3, 211–26.

58 Pace, C. N. (2001). Polar group burial contributes more to protein stability than nonpolar group burial. *Biochemistry* 40, 310–3.

59 Martin, A., Sieber, V. & Schmid, F. X. (2001). In-vitro selection of highly stabilized protein variants with optimized surface. *J. Mol. Biol.* 309, 717–26.

60 Loladze, V. V., Ibarra-Molero, B., Sanchez-Ruiz, J. M. & Makhatadze, G. I. (1999). Engineering a thermostable protein via optimization of charge-charge interactions on the protein surface. *Biochemistry* 38, 16419–23.

61 Shoemaker, K. R., Kim, P. S., York, E. J., Stewart, J. M. & Baldwin, R. L. (1987). Tests of the helix dipole model for stabilization of alpha-helices. *Nature* 326, 563–7.

62 Pace, C. N., Shirley, B. A., McNutt, M. & Gajiwala, K. (1996). Forces contributing to the conformational stability of proteins. *FASEB J.* 10, 75–83.

63 Loladze, V. V., Ermolenko, D. N. & Makhatadze, G. I. (2002). Thermodynamic consequences of burial of polar and non-polar amino acid residues in the protein interior. *J. Mol. Biol.* 320, 343–57.

64 McDonald, I. K. & Thornton, J. M. (1994). Satisfying hydrogen bonding potential in proteins. *J. Mol. Biol.* 238, 777–93.

65 Hennig, M., Darimont, B., Sterner, R., Kirschner, K. & Jansonius, J. N. (1995). 2.0 Å structure of indole-3-glycerol phosphate synthase from the hyperthermophile Sulfolobus solfataricus: possible determinants of protein stability. *Structure* 3, 1295–306.

66 Ramachandran, G. N., Ramakrishnan, C. & Sasisekharan, V. (1963). Stereochemistry of polypeptide chain configurations. *J. Mol. Biol.* 7, 95–9.

67 Kimura, S., Kanaya, S. & Nakamura, H. (1992). Thermostabilization of

Escherichia coli ribonuclease HI by replacing left-handed helical Lys95 with Gly or Asn. *J. Biol. Chem.* 267, 22014–7.

68 Takano, K., Yamagata, Y. & Yutani, K. (2001). Role of amino acid residues in left-handed helical conformation for the conformational stability of a protein. *Proteins* 45, 274–80.

69 Stites, W. E., Meeker, A. K. & Shortle, D. (1994). Evidence for strained interactions between side-chains and the polypeptide backbone. *J. Mol. Biol.* 235, 27–32.

70 Vega, M. C., Martinez, J. C. & Serrano, L. (2000). Thermodynamic and structural characterization of Asn and Ala residues in the disallowed II′ region of the Ramachandran plot. *Protein Sci.* 9, 2322–8.

71 Gunasekaran, K., Ramakrishnan, C. & Balaram, P. (1996). Disallowed Ramachandran conformations of amino acid residues in protein structures. *J. Mol. Biol.* 264, 191–8.

72 Pal, D. & Chakrabarti, P. (2002). On residues in the disallowed region of the Ramachandran map. *Biopolymers* 63, 195–206.

73 Ewert, S., Honegger, A. & Plückthun, A. (2003). Structure-based improvement of the biophysical properties of immunoglobulin V_H domains with a generalizable approach. *Biochemistry* 42, 1517–28.

74 Nieba, L., Honegger, A., Krebber, C. & Plückthun, A. (1997). Disrupting the hydrophobic patches at the antibody variable/constant domain interface: improved in vivo folding and physical characterization of an engineered scFv fragment. *Protein Eng.* 10, 435–44.

75 Brandts, J. F., Hu, C. Q., Lin, L. N. & Mos, M. T. (1989). A simple model for proteins with interacting domains. Applications to scanning calorimetry data. *Biochemistry* 28, 8588–96.

76 Wörn, A. & Plückthun, A. (2001). Stability engineering of antibody single-chain Fv fragments. *J. Mol. Biol.* 305, 989–1010.

77 Gokhale, R. S., Agarwalla, S., Francis, V. S., Santi, D. V. & Balaram, P. (1994). Thermal stabilization of thymidylate synthase by engineering two disulfide bridges across the dimer interface. *J. Mol. Biol.* 235, 89–94.

78 Hudson, P. J. (1999). Recombinant antibody constructs in cancer therapy. *Curr. Opin. Immunol.* 11, 548–57.

79 Plückthun, A., Krebber, A., Krebber, C., Horn, U., Knüpfer, U., Wenderoth, R., Nieba, L., Proba, K. & Riesenberg, D. (1996). Producing antibodies in *Escherichia coli*: From PCR to fermentation. In *Antibody Engineering* (McCafferty, J., Hoogenboom, H. R. & Chiswell, D. J., eds.), pp. 203–252. IRL Press, Oxford.

80 Honegger, A. & Plückthun, A. (2001). The influence of the buried glutamine or glutamate residue in position 6 on the structure of immunoglobulin variable domains. *J. Mol. Biol.* 309, 687–99.

81 Jung, S., Spinelli, S., Schimmele, B., Honegger, A., Pugliese, L., Cambillau, C. & Plückthun, A. (2001). The importance of framework residues H6, H7 and H10 in antibody heavy chains: experimental evidence for a new structural subclassification of antibody V_H domains. *J. Mol. Biol.* 309, 701–16.

82 Glockshuber, R., Malia, M., Pfitzinger, I. & Plückthun, A. (1990). A comparison of strategies to stabilize immunoglobulin Fv-fragments. *Biochemistry* 29, 1362–7.

83 Jung, S. H., Pastan, I. & Lee, B. (1994). Design of interchain disulfide bonds in the framework region of the Fv fragment of the monoclonal antibody B3. *Proteins* 19, 35–47.

84 Wörn, A. & Plückthun, A. (1998). Mutual stabilization of V_L and V_H in single-chain antibody fragments, investigated with mutants engineered for stability. *Biochemistry* 37, 13120–7.

85 Young, N. M., MacKenzie, C. R., Narang, S. A., Oomen, R. P. & Baenziger, J. E. (1995). Thermal stabilization of a single-chain Fv antibody fragment by introduction of a disulphide bond. *FEBS Lett.* 377, 135–9.

86 Arkin, M. R. & Wells, J. A. (1998). Probing the importance of second sphere residues in an esterolytic antibody by phage display. *J. Mol. Biol.* 284, 1083–94.

87 Low, N. M., Holliger, P. H. & Winter, G. (1996). Mimicking somatic hypermutation: affinity maturation of antibodies displayed on bacteriophage using a bacterial mutator strain. *J. Mol. Biol.* 260, 359–68.

88 Stemmer, W. P. (1994). Rapid evolution of a protein in vitro by DNA shuffling. *Nature* 370, 389–91.

89 Zhao, H., Giver, L., Shao, Z., Affholter, J. A. & Arnold, F. H. (1998). Molecular evolution by staggered extension process (StEP) in vitro recombination. *Nat. Biotechnol.* 16, 258–61.

90 Amstutz, P., Forrer, P., Zahnd, C. & Plückthun, A. (2001). In vitro display technologies: novel developments and applications. *Curr. Opin. Biotechnol.* 12, 400–5.

91 Forrer, P., Jung, S. & Plückthun, A. (1999). Beyond binding: using phage display to select for structure, folding and enzymatic activity in proteins. *Curr. Opin. Struct. Biol.* 9, 514–20.

92 Zhao, H. & Arnold, F. H. (1997). Combinatorial protein design: strategies for screening protein libraries. *Curr. Opin. Struct. Biol.* 7, 480–5.

93 Lehmann, M., Pasamontes, L., Lassen, S. F. & Wyss, M. (2000). The consensus concept for thermostability engineering of proteins. *Biochim. Biophys. Acta* 1543, 408–415.

94 Mattheakis, L. C., Bhatt, R. R. & Dower, W. J. (1994). An in vitro polysome display system for identifying ligands from very large peptide libraries. *Proc. Natl. Acad. Sci. U.S.A.* 91, 9022–6.

95 Hanes, J. & Plückthun, A. (1997). In vitro selection and evolution of functional proteins by using ribosome display. *Proc. Natl. Acad. Sci. U.S.A.* 94, 4937–4942.

96 He, M. & Taussig, M. J. (1997). Antibody-ribosome-mRNA (ARM) complexes as efficient selection particles for in vitro display and evolution of antibody combining sites. *Nucleic Acids Res* 25, 5132–4.

97 Roberts, R. W. & Szostak, J. W. (1997). RNA-peptide fusions for the in vitro selection of peptides and proteins. *Proc. Natl. Acad. Sci. U.S.A.* 94, 12297–302.

98 Kurz, M., Gu, K., Al-Gawari, A. & Lohse, P. A. (2001). cDNA – protein fusions: covalent protein–gene conjugates for the in vitro selection of peptides and proteins. *ChemBioChem* 2, 666–72.

99 Tawfik, D. S. & Griffiths, A. D. (1998). Man-made cell-like compartments for molecular evolution. *Nat. Biotechnol.* 16, 652–6.

100 Doi, N. & Yanagawa, H. (1999). STABLE: protein-DNA fusion system for screening of combinatorial protein libraries in vitro. *FEBS Lett.* 457, 227–30.

101 Smith, G. P. (1985). Filamentous fusion phage: novel expression vectors that display cloned antigens on the virion surface. *Science* 228, 1315–7.

102 Georgiou, G., Stathopoulos, C., Daugherty, P. S., Nayak, A. R., Iverson, B. L. & Curtiss, R., 3rd. (1997). Display of heterologous proteins on the surface of microorganisms: from the screening of combinatorial libraries to live recombinant vaccines. *Nat. Biotechnol.* 15, 29–34.

103 Boder, E. T. & Wittrup, K. D. (1997). Yeast surface display for screening combinatorial polypeptide libraries. *Nat. Biotechnol.* 15, 553–7.

104 Jung, S. & Plückthun, A. (1997). Improving in vivo folding and stability of a single-chain Fv antibody fragment by loop grafting. *Protein Eng.* 10, 959–66.

105 Hoess, R. H. (2001). Protein design and phage display. *Chem. Rev.* 101, 3205–18.

106 Finucane, M. D., Tuna, M., Lees, J. H. & Woolfson, D. N. (1999). Core-directed protein design. I. An experimental method for selecting

stable proteins from combinatorial libraries. *Biochemistry* 38, 11604–12.

107 Sieber, V., Plückthun, A. & Schmid, F. X. (1998). Selecting proteins with improved stability by a phage-based method. *Nat. Biotechnol.* 16, 955–60.

108 Fields, S. & Song, O. (1989). A novel genetic system to detect protein-protein interactions. *Nature* 340, 245–6.

109 Bai, C. & Elledge, S. J. (1996). Gene identification using the yeast two-hybrid system. *Methods Enzymol.* 273, 331–47.

110 Johnsson, N. & Varshavsky, A. (1994). Split ubiquitin as a sensor of protein interactions in vivo. *Proc. Natl. Acad. Sci. U.S.A.* 91, 10340–4.

111 Michnick, S. W. (2001). Exploring protein interactions by interaction-induced folding of proteins from complementary peptide fragments. *Curr. Opin. Struct. Biol.* 11, 472–7.

112 Waldo, G. S. (2003). Genetic screens and directed evolution for protein solubility. *Curr. Opin. Chem. Biol.* 7, 33–8.

113 Wigley, W. C., Stidham, R. D., Smith, N. M., Hunt, J. F. & Thomas, P. J. (2001). Protein solubility and folding monitored in vivo by structural complementation of a genetic marker protein. *Nat. Biotechnol.* 19, 131–6.

114 Waldo, G. S., Standish, B. M., Berendzen, J. & Terwilliger, T. C. (1999). Rapid protein-folding assay using green fluorescent protein. *Nat. Biotechnol.* 17, 691–5.

115 Pedelacq, J. D., Piltch, E., Liong, E. C., Berendzen, J., Kim, C. Y., Rho, B. S., Park, M. S., Terwilliger, T. C. & Waldo, G. S. (2002). Engineering soluble proteins for structural genomics. *Nat. Biotechnol.* 20, 927–32.

116 Wurth, C., Guimard, N. K. & Hecht, M. H. (2002). Mutations that reduce aggregation of the Alzheimer's Aβ42 peptide: an unbiased search for the sequence determinants of Aβ amyloidogenesis. *J. Mol. Biol.* 319, 1279–90.

117 Maxwell, K. L., Mittermaier, A. K., Forman-Kay, J. D. & Davidson, A. R. (1999). A simple in vivo assay for increased protein solubility. *Protein Sci.* 8, 1908–11.

118 Lesley, S. A., Graziano, J., Cho, C. Y., Knuth, M. W. & Klock, H. E. (2002). Gene expression response to misfolded protein as a screen for soluble recombinant protein. *Protein Eng.* 15, 153–60.

119 Minard, P., Scalley-Kim, M., Watters, A. & Baker, D. (2001). A "loop entropy reduction" phage-display selection for folded amino acid sequences. *Protein Sci.* 10, 129–34.

120 Matsuura, T. & Plückthun, A. (2003). Selection based on the folding properties of proteins with ribosome display. *FEBS Lett.* 539, 24–8.

121 Gu, H., Yi, Q., Bray, S. T., Riddle, D. S., Shiau, A. K. & Baker, D. (1995). A phage display system for studying the sequence determinants of protein folding. *Protein Sci.* 4, 1108–17.

122 Kim, D. E., Gu, H. & Baker, D. (1998). The sequences of small proteins are not extensively optimized for rapid folding by natural selection. *Proc. Natl. Acad. Sci. U.S.A.* 95, 4982–6.

123 Kowalski, J. M., Parekh, R. N., Mao, J. & Wittrup, K. D. (1998). Protein folding stability can determine the efficiency of escape from endoplasmic reticulum quality control. *J. Biol. Chem.* 273, 19453–8.

124 Shusta, E. V., Kieke, M. C., Parke, E., Kranz, D. M. & Wittrup, K. D. (1999). Yeast polypeptide fusion surface display levels predict thermal stability and soluble secretion efficiency. *J. Mol. Biol.* 292, 949–56.

125 Shusta, E. V., Holler, P. D., Kieke, M. C., Kranz, D. M. & Wittrup, K. D. (2000). Directed evolution of a stable scaffold for T-cell receptor engineering. *Nat. Biotechnol.* 18, 754–9.

126 Boder, E. T. & Wittrup, K. D. (2000). Yeast surface display for directed evolution of protein expression, affinity, and stability. *Methods Enzymol.* 328, 430–44.

127 Ruan, B., Hoskins, J., Wang, L. & Bryan, P. N. (1998). Stabilizing the subtilisin BPN′ pro-domain by phage display selection: how restrictive is the amino acid code for maximum protein stability? *Protein Sci.* 7, 2345–53.

128 Zhou, H. X., Hoess, R. H. & DeGrado, W. F. (1996). In vitro evolution of thermodynamically stable turns. *Nat. Struct. Biol.* 3, 446–51.

129 Goto, Y. & Hamaguchi, K. (1979). The role of the intrachain disulfide bond in the conformation and stability of the constant fragment of the immunoglobulin light chain. *J. Biochem. (Tokyo)*. 86, 1433–41.

130 Akanuma, S., Yamagishi, A., Tanaka, N. & Oshima, T. (1999). Further improvement of the thermal stability of a partially stabilized Bacillus subtilis 3-isopropylmalate dehydrogenase variant by random and site-directed mutagenesis. *Eur. J. Biochem.* 260, 499–504.

131 Farinas, E. T., Bulter, T. & Arnold, F. H. (2001). Directed enzyme evolution. *Curr. Opin. Biotechnol.* 12, 545–51.

132 Zhao, H. & Arnold, F. H. (1999). Directed evolution converts subtilisin E into a functional equivalent of thermitase. *Protein Eng.* 12, 47–53.

133 Giver, L., Gershenson, A., Freskgard, P. O. & Arnold, F. H. (1998). Directed evolution of a thermostable esterase. *Proc. Natl. Acad. Sci. U.S.A.* 95, 12809–13.

134 Jermutus, L., Honegger, A., Schwesinger, F., Hanes, J. & Plückthun, A. (2001). Tailoring in vitro evolution for protein affinity or stability. *Proc. Natl. Acad. Sci. U.S.A.* 98, 75–80.

135 Jung, S., Honegger, A. & Plückthun, A. (1999). Selection for improved protein stability by phage display. *J. Mol. Biol.* 294, 163–80.

136 Kristensen, P. & Winter, G. (1998). Proteolytic selection for protein folding using filamentous bacteriophages. *Fold. Des.* 3, 321–8.

137 Fontana, A., Polverino de Laureto, P., De Filippis, V., Scaramella, E. & Zambonin, M. (1997). Probing the partly folded states of proteins by limited proteolysis. *Fold. Des.* 2, R17–26.

138 Krebber, C., Spada, S., Desplancq, D. & Plückthun, A. (1995). Co-selection of cognate antibody-antigen pairs by selectively-infective phages. *FEBS Lett.* 377, 227–31.

139 Finucane, M. D. & Woolfson, D. N. (1999). Core-directed protein design. II. Rescue of a multiply mutated and destabilized variant of ubiquitin. *Biochemistry* 38, 11613–23.